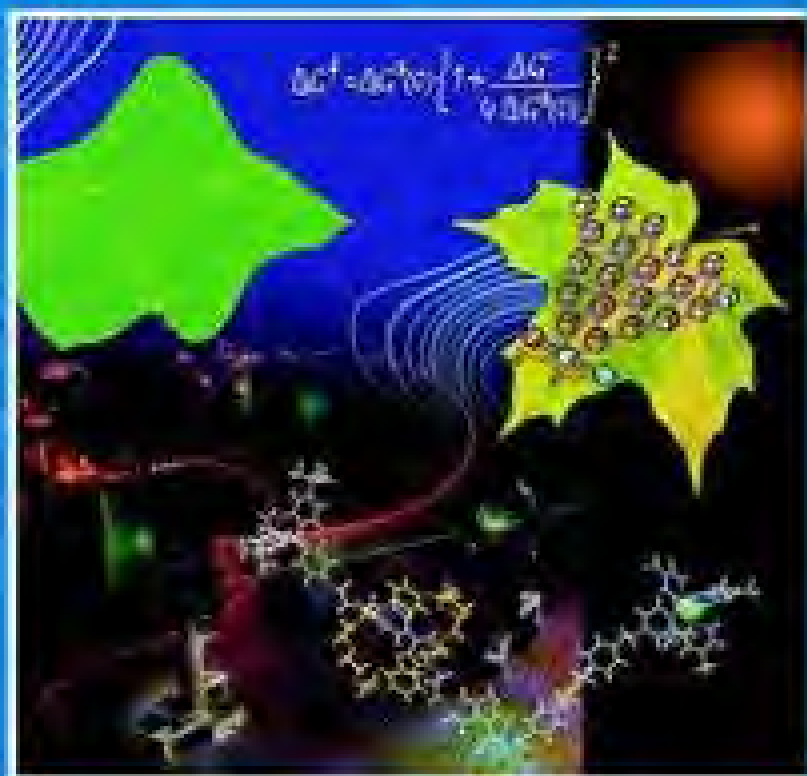


Vincenzo Balzani (Ed.)

Electron Transfer in Chemistry

Volume 1:
Principles, Theories, Methods,
and Techniques



Vincenzo Balzani (Ed.)

Electron Transfer in Chemistry

 **WILEY-VCH**

Vincenzo Balzani (Ed.)

Electron Transfer in Chemistry

 **WILEY-VCH**

Weinheim · New York · Chichester
Brisbane · Singapore · Toronto

Prof. Vincenzo Balzani
Dipartimento de Chimica „G. Ciamician“
Università di Bologna
via Selmi 2
40126 Bologna
Italy

This book was carefully produced. Nevertheless, editors, authors and publisher do not warrant the information contained therein to be free of errors. Readers are advised to keep in mind that statements, data, illustrations, procedural details or other items may inadvertently be inaccurate.

Library of Congress Card No.: applied for

A catalogue record for this book is available from the British Library.

Die Deutsche Bibliothek – CIP Cataloguing-in-Publication-Data

A catalogue record for this publication is available from Die Deutsche Bibliothek

ISBN 3-527-29912-2

© WILEY-VCH Verlag GmbH, D-69469 Weinheim (Federal Republic of Germany). 2001

Printed on acid-free paper.

All rights reserved (including those of translation in other languages). No part of this book may be reproduced in any form – by photoprinting, microfilm, or any other means – nor transmitted or translated into machine language without written permission from the publishers. Registered names, trademarks, etc. used in this book, even when not specifically marked as such, are not to be considered unprotected by law.

Composition: Asco Typesetters, Hongkong.

Printing: betz-druck gmbh, 64291 Darmstadt.

Bookbinding: Wilhelm Osswald & Co., D-67433 Neustadt.

Printed in the Federal Republic of Germany.

Foreword

During the past half-century, the field of electron transfer reactions has undergone a remarkable expansion. This development began in the middle to late 1940s, with studies of what proved to be the simplest class of reactions in all of Chemistry— isotopic exchange electron transfers in solution. At the same time, new electronic techniques were developed for studying electron transfers at metal electrodes. Before that time, the electrochemical reactions studied involved instead a breaking (typically slow) of chemical bonds and the formation of new ones. Later, isotope exchange reactions were also studied in favorable cases by methods other than those using isotopic labels—for example, by the use of various spin resonance techniques—and became more generally known as self-exchange reactions.

For simple electron transfers no chemical bond is either broken or formed. Instead, only readjustments of bond geometry (distances and sometimes angles) in each reactant, and rearrangements of the likely configurations of the environment, such as solvent molecules, around the reactants are needed. This situation permitted the development of a relatively simple detailed analytic theory for these processes. The resulting equations and their consequences were especially convenient for comparison by experiment, as well as for predicting new results and new relations.

The various experimental studies in these two different fields had stimulated the development of theory, which in turn stimulated new experiments. The further introduction of new technology—lasers for example—expanded the variety of systems which could be studied, ultimately extending to ultra-fast reactions in the pico-second (e.g., photosynthesis) or even the femtosecond regime. Indeed, some of these reactions occur so rapidly that the sluggishness of the solvent (e.g., solvent dielectric relaxation) becomes a rate-controlling or partially rate-controlling factor.

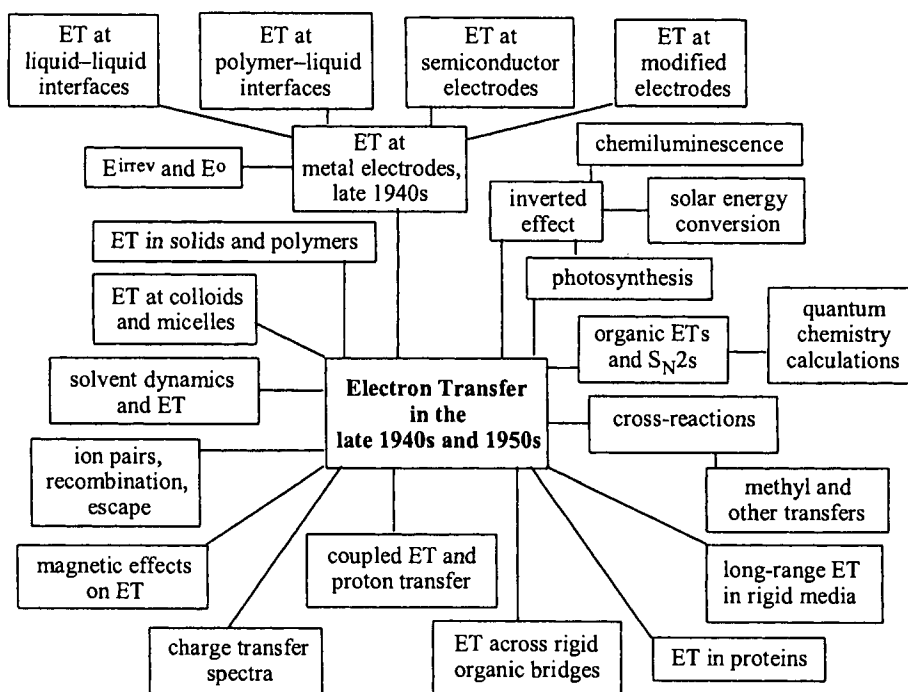
One of the more striking effects to be identified in the field was the “inverted effect,” in which the reaction rate constant k decreased, rather than increased, with increasing “driving force”, namely, increasingly negative standard free energy of reaction, $-\Delta G^\circ$, when ΔG° is very negative. The normal effect is for k to increase with increasingly negative ΔG° , but in the inverted region the opposite is true. As is

well known, some twenty-five years elapsed before this prediction was confirmed experimentally. In the interim, there had been indirect confirmation in the form of the observation of chemiluminescent electron transfer reactions.

There has been much discussion in the literature of electronically adiabatic versus nonadiabatic electron transfers. In the inverted region the electron transfer is electronically nonadiabatic, since it involves a “jumping” from one potential energy surface to another, rather than remaining on a single surface. In the “normal” region the transfer may be adiabatic or, when the electronic coupling of the reactants is weak, nonadiabatic. The parallelism of the maximum in the bell-shaped charge transfer absorption spectrum to the maximum in the k versus $-\Delta G^\circ$ curve is noteworthy. The spectrum to the red of the maximum corresponds to the “normal” region, and that to the blue to the “inverted” region. This parallelism was not realized in the early days (in fact, it may still not be fully appreciated today), but both phenomena have the same origin.

Some of the new theoretical relations, the cross-relation between the rates of a “cross-reaction” of two different redox species with those of the two relevant self-exchange reactions, were later adapted to non-electron transfer reactions involving simultaneous bond rupture and formation of a new bond (atom, ion, or group transfer reactions). The theory had to be modified, but relations such as the cross-relation or the effect of driving force ($-\Delta G^\circ$) on the reaction rate constant were again obtained in the theory, in a somewhat modified form. For example, apart from some proton or hydride transfers under special circumstances, there is no predicted “inverted” effect. Experimental confirmation of the cross-relation followed, and an inverted effect has only been reported for an H^+ transfer in some nonpolar solvents. The various results provide an interesting example of how ideas obtained for a simple, but analyzable, process can prompt related, yet different, ideas for a formalism for more complicated processes.

Eventually, the field grew in many different directions, some of which are shown in the figure below, and many of which were quite unanticipated. This growth is, in retrospect, no longer surprising, since electron transfers have been shown to occur in a wide array of phenomena. The figure is also not comprehensive, and new examples may well occur in the present series of volumes. The understanding and insight gained in the fundamental studies of electron transfers has had a variety of important or potentially important applications, whether in the field of solar energy conversion, nanosized devices at interfaces, batteries, corrosion, respiration, or even the light emission by fireflies.



Professor Balzani and his section editors have made an impressive contribution in bringing together a broad array of interesting topics which now contribute to this dynamic electron transfer field.

Rudolph A. Marcus
Pasadena, California
July 21, 2000

Preface

Today, there is barely an aspect of our lives that is not touched fundamentally by Chemistry. We know that Chemistry is *in* us, because our body is composed of atoms and molecules, and functions through the extremely intricate patterns of their interactions. However, Chemistry is also *around* us, in natural phenomena such as photosynthesis, and in the artificial products and materials that sustain the development of our civilization: medicines, fertilizers, plastics, semiconductors, etc. Moreover, the most important global problems—those relating to food, human health, energy and the environment—cannot be solved without the aid of Chemistry.

Chemistry occupies a central position among scientific disciplines, and provides the main links between Biology and Physics. In addition, Materials Science, Chemical Engineering, Earth Sciences, Ecology, and related areas are largely based on Chemistry. And, in the near future our medical problems—and perhaps also our feelings, thoughts, and emotions—will be described and discussed on a molecular (i.e., a chemical) basis. Chemistry, in fact, is far more than a discrete scientific discipline, since its methods, concepts, and practitioners are penetrating virtually all fields of science and technology. Chemistry can, therefore, also be regarded as a trans-disciplinary science that provides an essential means and a fundamental language to understand fully these other scientific disciplines.

A key feature of chemistry is chemical reactivity, and of all the chemical reactions *electron transfer* is undoubtedly the most important. First, electron transfer is the key step in a number of biological processes that have enormous relevance to life, such as photosynthesis and respiration. Second, it is a fundamental feature of many processes of vast technological impact, such as information storage (photography) and energy conversion (batteries). Third, electron transfer is a type of reaction that is amenable to detailed experimental investigation and accurate theoretical descriptions. But perhaps most importantly, the ubiquity of electron transfer in Chemistry and related fields has helped to demolish—and is still demolishing—the arbitrarily created barriers that until now have subdivided Chemistry into its separate organic, inorganic, physical, and analytical branches. In this respect, electron

transfer encourages research at the cross-roads of different disciplines where scientific and technological progress is more likely to occur.

During the past decade, our knowledge of electron transfer has grown at an astonishing rate, and it was for this reason that a need was recognised for a unified view of the field. This Handbook, with its five volumes, 12 parts, and 78 chapters, emphasizes the central role of electron transfer in Chemistry, and reflects the enormously wide range of electron transfer aspects that are currently of interest, from both fundamental and practical viewpoints. The authors of the various chapters have been chosen from among those carrying out the most interesting and forward-looking research in their respective fields. Some chapters, by their own nature, are introductory, others are advanced, and others are focussed on specific theoretical or applicative aspects of electron transfer. Each chapter is enriched by figures and tables that illustrate the topic dealt with in the most convenient way. In addition, since interest in electron transfer processes is moving rapidly towards complexity (artificial supramolecular species, dendrimers, heterogeneous systems, biological systems), several chapters have a large number of structures and schemes.

Volume 1 contains two Parts—the first relating to Principles and Theories, and the second to Methods and Techniques. The first Part (1.1) introduces the reader to the fundamental theories and to the various types of electron transfer processes: adiabatic and non-adiabatic, homogeneous and heterogeneous, one-electron and multi-electron, ground-state and excited-state. The relationship between electron and electronic excitation transfer is also discussed. Part 1.2 includes chapters dealing with the most important methods by which electron transfer processes can be induced and their rates measured: classical methods, electrochemistry, radiation chemistry, and photochemistry. Since many natural and artificial electron transfer processes are induced by light, particular care has been devoted to the description of laser flash photolysis, which is not only the most powerful but also the only technique capable of elucidating the intimate reaction mechanisms of photoinduced processes. Needless to say, knowledge of the theoretical basis of electron transfer processes and of the techniques used most to reveal the presence, to monitor the occurrence, and to measure the rate of electron transfer reactions is a clear requisite for people working in the fields of Chemistry, Biology and Materials Science.

Volume 2 is dedicated to a detailed description of the most important classes of electron transfer reactions involving organic molecules (Part 2.1) and organometallic and inorganic compounds (Part 2.2). In several cases the reactions described are important not only from the viewpoint of fundamental research on reaction mechanisms, but also for their catalytic and synthetic applications. The emerging fields of electron transfer reactions of fullerenes, electron-reservoir complexes, and biomimetic electron transfer chemistry of porphyrins are discussed in depth.

Volume 3 deals with electron transfer in supramolecular systems. Part 3.1 is dedicated to the most important processes that take place in biological systems, from photoinduced charge-separation processes occurring in photosynthesis to electron transfer reactions involving nucleic acids and enzymes. This Part clearly shows that the useful functions performed by biological systems (e.g., solar energy conversion) result from an extremely high degree of organization not only in the space dimension (i.e., in the relative positions of the molecular components partic-

ipating in the process), but also in the dimensions of energy and time. The nine chapters of Part 3.2 discuss electron transfer processes in a variety of artificial supramolecular (multicomponents) systems. Some of these systems (dyads, triads, etc.) have been designed to investigate (and then, to optimize) photoinduced charge separation, which is a fundamental step along the route towards artificial solar energy conversion. Other supramolecular systems, based on hydrogen-bonded self-assembly, have been investigated to elucidate the interplay between electron and proton transfer. Species such as host–guest systems, rotaxanes, catenanes, and dendrimers have revealed new potentialities of electron transfer processes in the emerging fields of fluorescence sensors, molecular-level information processing, and molecular-level machines.

Volume 4 is dedicated to three important topics: Catalysis (Part 4.1), Heterogeneous Systems (Part 4.2), and Gas Phase Systems (Part 4.3). The six chapters of Part 4.1 cover the most important aspects of electron transfer catalysis, from fundamental concepts to organic synthesis, from carbon dioxide fixation to protein catalysis, from redox modulation to biomimetic catalysis. Part 4.2 deals with the basic aspects and the latest developments in electron transfer on semiconductors, dye-sensitized electrodes, mono- and multilayers, intercalated compounds, zeolites, micelles and related systems. Part 4.3 covers gas phase systems, from atoms to small molecules, exciplexes, and supermolecules.

Volume 5 deals more directly with applications of electron transfer, including those already in use, and those at the near horizon. Part 5.1, which is dedicated to the emerging field of molecular-level electronics, reports on the latest developments in the area of nonlinear optics and in the design, construction, and properties of molecular-level wires, switches, rectifiers, logic gates, antennas, and memories. Part 5.2 describes very important applications in the field of imaging and information: photography, electrophotography, photorefractive materials, and photopolymers for imaging. Finally, Part 5.3 deals with applications in the fields of environment and energy, with chapters on solar energy conversion, batteries, and waste remediation.

In general, whilst the chapters of this Handbook focus attention on the developments of recent years, they also place earlier studies in their proper perspective. Therefore the Handbook is intended to serve a joint purpose, both as a reference resource and as an introductory overview, covering practically all kinds of electron transfer processes that occur in Chemistry, from biological systems to materials science. Although the Handbook is not aimed at being a specific lecture course, several sections or chapters can profitably be used as the basis for both advanced graduate and postgraduate courses.

A major feature that emerges from this Handbook is the wide range of perspectives offered by the cross-fertilization of electron transfer research due to its being located at the intersection of Chemistry, Biology, and Physics. Thus, it might be appropriate to ask: in which direction is research in the field of electron transfer heading? In his Foreword, Rudy Marcus suggests that very few of the present-day developments of electron transfer were anticipated when the era of modern electron transfer research began about fifty years ago. He also points out that those developments which did occur were in large part consequences of newly available technologies, such as lasers for pulsed excitation and computers for resolution of X-ray

structures. Whilst new technologies (in particular, nanotechnologies) will certainly orient electron transfer research towards now unpredictable basic aspects and applications, it is clear that three very important fields are likely to benefit from the progress being made currently in electron transfer research, namely the life sciences, artificial solar energy conversion, and molecular-level information processing.

Vincenzo Balzani
Bologna, Italy
August 2000

Contents

Volume I

	Foreword	v
	Preface	ix
	About the Editors	lv
	List of Authors	lxvii
Part 1	Principles and Theories	1
	Piotr Piotrowiak (Ed.)	
1	Electron Transfer: Theoretical Models and Computational Implementation	3
	<i>Marshall D. Newton</i>	
1.1	Introduction	3
1.2	Kinetic Schemes	7
1.3	Rate-Constant Models	10
1.3.1	System Hamiltonian and Electronic States	10
1.3.2	Diabatic Energy Surfaces	13
1.3.3	TST Models	16
1.3.4	Role of Solvent Dynamics	23
1.4	Coupling Elements	26
1.4.1	Basic Properties	26
1.4.2	Comparison of Thermal and Optical Processes	30
1.4.3	Pathway Analysis of T_{if}	34
1.5	Applications of Theory	38
1.5.1	Comparisons Based on Experimental Data	38
1.5.2	Computational Studies	44

1.6	Concluding Remarks	57
	Acknowledgments	58
	References.....	58
2	Adiabatic versus Non-Adiabatic Electron Transfer	64
	<i>Hitoshi Sumi</i>	
2.1	Adiabatic- versus Static-Coupling Scheme.....	64
2.2	Non-Adiabatic Limit	69
2.2.1	Single-Mode Model.....	69
2.2.2	Atom-Tunneling Regime	72
2.2.3	Semiclassical and Classical Regimes	74
2.2.4	Multimode Model	77
2.3	Adiabatic Limit	78
2.3.1	Semiclassical Regime	78
2.3.2	Attempt Frequency	80
2.4	From the Adiabatic to the Non-Adiabatic Limit	83
2.4.1	Adiabaticity Parameter	83
2.4.2	Between the Adiabatic and the Non-Adiabatic Limit	86
2.5	Further Development.....	91
2.5.1	Large-Energy-Quantum Intramolecular Modes	91
2.5.2	Electron Transfer to or from a Continuum of Free States	95
2.5.3	Solvent-Fluctuation-Controlled Regime	97
	Appendices.....	104
	Appendix A: Direct Derivation of Equation 23	104
	Appendix B: Wigner Distribution Function	104
	References.....	107
3	Single- and Multi-electron Transfer Processes.....	109
	<i>Spiros S. Skourtis and David N. Beratan</i>	
3.1	Introduction.....	109
3.2	Single-Electron Transfer Reactions	109
3.3	Multi-Electron Transfer Reactions.....	120
3.4	Conclusions	123
	Acknowledgments	123
	References.....	124
4	Electron Transfer at Electrodes and Interfaces	126
	<i>Daniël Vanmaekelbergh</i>	
4.1	Scope	126
4.2	Open Electron Systems	127
4.2.1	The Electrochemical Potential.....	127
4.2.2	Electronic Equilibrium between Two Phases	129
4.2.3	Deviations from Equilibrium.....	131
4.3	The Electronic Structure of Solids	132
4.3.1	Free and Independent Electrons.....	133
4.3.2	The Sommerfeld Model for Free Electrons in a Metallic Phase	134

4.3.3	Occupation of the Electron-Energy Levels	137
4.3.4	The Origin of Energy Bands.....	137
4.3.5	Metals, Semiconductors and Insulators	140
4.3.6	Extrinsic Semiconductors	141
4.4	Electron-Energy Levels Corresponding to a Redox System	142
4.4.1	The Electrochemical Potential of a Dissolved Redox System	143
4.4.2	The Fluctuating-Energy-Level Model Proposed by Gerischer.....	144
4.5	Interfacial Structure.....	149
4.5.1	Metal Surfaces	150
4.5.2	Physisorption and Chemisorption	154
4.5.3	The Metal/Solution Interface	155
4.5.4	The Semiconductor/Solution Interface	158
4.6	Electron Tunneling.....	161
4.6.1	The Probability of Electron Tunneling.....	161
4.6.2	Interfacial Electron Tunneling Between Two Metals	163
4.6.3	Experimental Tunneling Spectroscopy	165
4.7	Electrochemical Reactions: Kinetics and Mechanism	167
4.7.1	The Diversity of Electrochemical Processes.....	167
4.7.2	Electrochemical Ion Transfer and Electrochemical Electron Transfer (ECIT and ECET)	169
4.7.3	Current Density vs Overpotential: Experimental Results.....	170
4.7.4	A Heuristic Treatment of Electrochemical Kinetics	171
4.8	Electron Transfer between a Metal and a Simple Redox System.....	176
4.8.1	Comparison between Electrochemical Electron Tunneling and Tunneling between Two Metals	176
4.8.2	Current Density as a Function of Overpotential.....	177
4.8.3	Marcus, Gerischer and the Phenomenological Rate Equations	181
4.9	Comparison of Electron Transfer at a Semiconductor With Electron Transfer at a Metal Electrode	182
	References	187
5	Proton-Coupled Electron Transfer	189
	<i>Sharon Hammes-Schiffer</i>	
5.1	Introduction	189
5.2	Continuum Theory for Single-Charge Transfer.....	191
5.2.1	Single-Electron Transfer	192
5.2.2	Single-Proton Transfer.....	195
5.3	Multistate Continuum Theory for Proton-Coupled Electron Transfer	198
5.3.1	Four-State Formulation	198
5.3.2	Two-State Formulation	201
5.3.3	Incorporation of Inner-Sphere Reorganization	207
5.3.4	Extension to More than Two Charge-Transfer Reactions.....	208
5.4	Applications of Proton-Coupled Electron Transfer in Solution	209
5.4.1	Calculation of Input Quantities.....	209
5.4.2	Proton-Coupled Electron Transfer through Asymmetric Salt Bridges	209

5.5	Fundamental Principles of Proton-Coupled Electron Transfer.....	212
5.6	Future Directions	213
	Acknowledgments	213
	References.....	213
6	Relationship between Electron and Electronic Excitation Transfer.....	215
	<i>Piotr Piotrowiak</i>	
6.1	Introduction.....	215
6.2	Singlet Energy Transfer.....	217
6.3	Triplet Energy Transfer.....	223
6.4	Summary.....	232
	Acknowledgments	233
	References.....	234
7	Charge-Transfer Excited States of Transition Metal Complexes.....	238
	<i>John F. Endicott</i>	
7.1	Definitions and General Concepts	238
7.1.1	Basic Concepts.....	238
7.1.2	The Idealized Limit of Weak D/A Electronic Coupling (LWEC)	239
7.2	Charge-Transfer Absorption Spectroscopy	241
7.2.1	The Energies of Charge-Transfer Absorptions.....	241
7.2.2	Charge-Transfer Excited-State Terms and Assignments.....	244
7.2.3	The Analysis of Spectroscopic Absorption Bands	245
7.3	Charge-Transfer Emission Spectroscopy.....	247
7.3.1	The Interpretation of Charge-Transfer Emission Spectra	248
7.4	The Classification of Charge-Transfer Absorption Bands.....	248
7.5	The Electronic States Generated by Charge-Transfer Absorptions ...	248
7.5.1	The Franck–Condon State in Transition Metal Complexes.....	249
7.5.2	The Vibrationally Equilibrated Excited States (VEqES)	249
7.6	Excited-State Relaxation Processes.....	249
7.6.1	Vibrationally Equilibrated Excited States Relaxation Processes	250
7.6.2	Upper-Excited-State Electronic-State Relaxation.....	251
7.7	Observations on the Weak Electronic Coupling Limit: Ion-Pair Charge-Transfer Absorption Bands	252
7.7.1	The Correlation of Observed Ion-Pair Charge-Transfer Energies with Experimental Electron-Transfer Parameters.....	252
7.7.2	Electronic Coupling in Ion-Pair Charge-Transfer Systems	253
7.7.3	Ion-Pair Charge-Transfer Absorption Band Widths.....	256
7.8	Ligand-to-Metal Charge-Transfer (LMCT) Absorption Bands.....	257
7.8.1	Energy Correlations for Simple Systems: $M^{III}(NH_3)_5(X^-)$ Complexes	257
7.8.2	More Complex Ligand-to-Metal Charge-Transfer (LMCT) Systems.	259
7.8.3	Ligand-to-Metal Charge-Transfer (LMCT) Band Shapes and Intensities	261
7.9	Metal-to-Ligand Charge-Transfer (MLCT) Absorption Band Energies	261

7.9.1	General Comments	261
7.9.2	Metal-to-Ligand Charge-Transfer (MLCT) Excited-State Energies..	262
7.9.3	Band Shapes and Intensities	265
7.10	Excited-State Lifetimes and Luminescence Properties	265
7.11	Perspectives and Conclusions	266
	Acknowledgements.....	267
	References.....	267
8	Synthetic Applications of Photocatalytic Oxidation and Reduction Reactions of Organic Reactants on Irradiated Semiconductor Surfaces	271
	<i>Marye Anne Fox</i>	
8.1	Introduction	271
8.2	Principles Governing Photoelectrochemistry	273
8.2.1	Redox Reactions on Irradiated Semiconductor Surfaces	273
8.2.2	Comparison of a Photoelectrochemically Generated Electron-Hole Pair and a Molecular Excited State	277
8.2.3	Energy Considerations.....	278
8.2.4	Solvent Effects	280
8.2.5	Semiconductor Stability toward Catalytic Cycling.....	281
8.2.6	Photosensitization	281
8.3	Mechanism	282
8.4	Chemical Selectivity through Photoelectrochemical Activation	286
8.4.1	Adsorption and Surface Effects.....	286
8.4.2	Potential Control.....	290
8.4.3	Current Control.....	292
8.5	Selective Photoelectrochemical Transformations.....	293
8.5.1	Oxidations.....	294
8.5.2	Reductions	301
8.5.3	Cycloadditions and Retrocycloadditions	303
8.5.4	Geometric Isomerizations.....	304
8.5.5	Miscellaneous Reactions.....	305
8.6	Conclusions	305
	Acknowledgments.....	306
	References.....	307
9	Radiative Charge Recombination and Electrochemiluminescence.....	312
	<i>Ann-Margret Andersson and Russell H. Schmehl</i>	
9.1	Introduction	312
9.2	Processes Leading to Radiative Charge Recombination.....	313
9.2.1	Annihilation of Anion and Cation Radicals	313
9.2.2	Excimer and Exciplex Emission	314
9.2.3	Reactions of Radical Ions with Other Reagents	316
9.2.4	Chemically Induced Electron-Exchange Luminescence	317
9.3	Kinetic Aspects.....	319
9.4	Experimental Considerations: Techniques and Molecular Systems ..	323

9.4.1	Generation and Characterization of Reactive Species.....	323
9.4.2	Molecular Systems.....	328
9.5	Applications.....	331
9.5.1	Sensors for Organic Substrates Employing [Ru(bpy) ₃] ²⁺ and Derivatives.....	331
9.5.2	Sensors Employing Other ECL Chromophores.....	335
9.5.3	Device Applications.....	337
9.6	Summary.....	338
	Acknowledgments.....	338
	References.....	338
10	Electron Transfer Reactions in Organic Chemistry.....	342
	<i>Stephen F. Nelsen</i>	
10.1	Introduction.....	342
10.2	Inner- and Outer-Sphere Electron Transfer Reactions.....	343
10.3	Bond Cleavage.....	347
10.3.1	Reductive Cleavage of Single Bonds.....	347
10.3.2	Heterolytic versus Homolytic Bond-Cleavage Reactions.....	352
10.4	Rearrangements Initiated by Bond Cleavage in Radical Cations.....	354
10.5	Additions to Single Bonds of Radical Cations.....	357
10.6	Additions to π Systems of Radical Cations.....	362
10.7	Trisubstituted Nitrogen Oxidations and Aminium Radical Cation Deprotonations.....	370
10.8	Studies Focusing on Electron Transfer Kinetics of Organic Systems.....	373
10.8.1	Intermolecular Reactions.....	373
10.8.2	Intramolecular Reactions: Donor–Bridge–Acceptor Systems.....	376
10.8.3	Intramolecular Reactions: Intervalence Compounds.....	379
	References.....	386
Part 2	Methods and Techniques.....	393
	Michael A. J. Rodgers (Ed.)	
1	Classical Methods.....	395
	<i>Andreja Bakac</i>	
1.1	Introduction.....	395
1.2	Mixing Methods.....	395
1.2.1	Manual Mixing.....	395
1.2.2	Rapid Mixing.....	397
1.3	Relaxation Methods.....	403
1.3.1	Temperature Jump.....	404
1.3.2	Pressure Jump.....	406
1.3.3	Spin-Relaxation Methods.....	407
1.4	High-Pressure Techniques.....	412
1.5	Indirect Methods and Special Cases.....	414

1.5.1	Competition Kinetics	414
1.5.2	Exchange Reactions.....	418
	Acknowledgments.....	419
	Abbreviations	419
	References	420
2	Electrochemical Techniques	422
	<i>Steen Uttrup Pedersen and Kim Daasbjerg</i>	
2.1	Electrochemical Techniques	422
2.1.1	Introduction	422
2.1.2	Heterogeneous Kinetics.....	425
2.1.3	Mass Transport	427
2.1.4	Homogeneous Kinetics	429
2.2	Potential-Step Experiments	431
2.2.1	Chronoamperometry.....	431
2.2.2	Sampled-Current Voltammetry.....	437
2.2.3	Double-Potential-Step Chronoamperometry.....	437
2.3	Linear Sweep Voltammetry and Cyclic Voltammetry	440
2.3.1	Charge-Transfer Reactions	443
2.3.2	Nernstian Charge Transfer	444
2.3.3	Quasi-Reversible and Irreversible Charge Transfer	444
2.3.4	Ohmic Drop.....	446
2.3.5	Coupled Chemical Reactions.....	446
2.3.6	Mixed Charge Transfer and Kinetic Control	449
2.4	Ultra-microelectrodes	451
2.4.1	Fast-Transient Techniques.....	455
2.4.2	Applications of UME in Resistive Media and under Industrial Conditions.....	458
2.4.3	Steady-State Measurements at UMEs for Monitoring Slow Homogeneous Reactions.....	462
2.4.4	Sensors	465
2.5	Hydrodynamic Electrochemical Techniques	468
2.5.1	Preparative Electrolysis.....	470
2.5.2	Rotating Disc Electrode	472
2.6	Combination of Electrochemistry and Spectroscopy.....	477
2.6.1	Type 1	477
2.6.2	Type 2	483
2.6.3	Type 3	491
2.7	Indirect Electrolysis	491
	References	499
3	Radiation-Chemical Techniques.....	503
	<i>George V. Buxton and Quinto G. Mulazzani</i>	
3.1	Introduction	503
3.2	Interaction of Ionizing Radiation with Condensed Matter	504

3.3	The Radiation Chemistry of Water	505
3.3.1	Properties of the Primary Radicals	507
3.3.2	Generation of Secondary Radicals	510
3.4	The Radiation Chemistry of Organic Liquids	514
3.5	One-Electron Reduction and Oxidation in Nonaqueous Solvents	515
3.5.1	Alcohols.....	515
3.5.2	Acetone	518
3.5.3	Acetonitrile.....	518
3.5.4	Chlorinated Hydrocarbons	519
3.5.5	2-Methyltetrahydrofuran and 2,2,4-Trimethylpentane	520
3.5.6	Cyclohexane	521
3.5.7	Dimethyl Sulfoxide	522
3.5.8	Ammonia	522
3.5.9	Solvent Mixtures.....	523
3.6	Pulse Radiolysis.....	523
3.6.1	Historical Perspective.....	523
3.7	Pulse Radiolysis Facilities	529
3.7.1	A Typical Modern Pulse Radiolysis Facility.....	530
3.8	Other Methods of Detection	543
3.8.1	Polarography.....	543
3.8.2	Microwave Detection.....	544
3.8.3	Magnetic Resonance.....	545
3.9	Picosecond Pulse Radiolysis.....	546
3.10	Data Capture and Analysis.....	548
3.11	Purification of Materials and Preparation of Solutions.....	549
3.11.1	Purification of Solvents.....	551
3.12	Concluding Remarks	552
	References.....	552
	Further Reading	557
4	Photochemical Techniques	558
	<i>Kevin Henbest and Michael A. J. Rodgers</i>	
4.1	Introduction.....	558
4.2	The Significance of Photoexcitation for Electron Transfer	559
4.2.1	Advantages of Photoexcitation.....	560
4.3	The Methodology of Photokinetics	563
4.3.1	Instrumentation Considerations	564
4.3.2	Excitation Sources	564
4.4	Detection and Measurement Techniques	569
4.4.1	Optical Absorption Spectrometry	569
4.4.2	Light-Scattering Spectrometry.....	580
4.4.3	Fluorescence Instrumentation	582
4.4.4	Frequency-Domain (Phase-Shift) Measurements	586
4.5	Concluding Remarks	588
	Acknowledgments	588
	References.....	588

Volume II

Part 1	Organic Molecules	1
	Jochen Mattay (Ed.)	
1	Reactivity Patterns of Radical Ions—A Unifying Picture of Radical-anion and Radical-cation Transformations	5
	<i>Michael Schmittel and Manas K. Ghorai</i>	
1.1	Introduction	5
1.2	A Unifying Picture of Radical-anion and Radical-cation Chemistry	5
1.3	A Construction Set of Electrophores and its Relevance for Devising Selective Reactions via Radical Ions	7
1.4	Reductive and Oxidative Bond-cleavage Reactions	14
1.4.1	General Principles of Bond Cleavage	14
1.4.2	Synthetic, Kinetic and Thermodynamic Aspects of Reductive Bond Cleavage	17
1.4.3	Synthetic, Kinetic and Thermodynamic Aspects of Oxidative Bond Cleavage	23
1.5	Reductive and Oxidative Bond-formation Reactions	29
1.5.1	General Principles of Bond Formation	29
1.5.2	Synthetic, Kinetic and Thermodynamic Aspects of Reductive Bond-formation	29
1.5.3	Synthetic, Kinetic, and Thermodynamic Aspects of Oxidative Bond-formation	33
1.6	Pericyclic Reactions	37
1.6.1	General Principles of Pericyclic Reactions	37
1.6.2	Synthetic, Kinetic and Thermodynamic Aspects	38
1.7	Conclusion	40
	Acknowledgments	40
	References	40
2	Electron Transfer from Aliphatic and Alicyclic Compounds	55
	<i>Heinz D. Roth</i>	
2.1	Introduction	55
2.2	Electron-transfer Reactions of Aliphatic Compounds	56
2.2.1	High-energy Irradiation of Matrices	56
2.2.2	Electron Spin Resonance	57
2.2.3	Electron-transfer Reactions of Methane	59
2.2.4	Electron-transfer Reactions of <i>n</i> -Alkanes	61
2.2.5	Deprotonation of <i>n</i> -Alkane Radical Cations	66
2.2.6	Electron-transfer Reactions of Branched Alkanes	68
2.2.7	Electron Transfer from Alkanes to Zeolites	69
2.3	Electron-transfer Reactions of Cycloalkanes	71
2.3.1	Electron Transfer from C ₃ –C ₈ Prototype Cycloalkanes	72
2.3.2	Cyclopropane Radical Cations	77

2.3.3	Electron-transfer Reactions of Substituted Cyclobutane Systems	97
2.3.4	Electron-transfer Reactions of Cycloalkanes in Zeolites	99
2.4	Electron-transfer Reactions of Bicyclic Systems	100
2.4.1	Electron Transfer of Strained Bicyclic Systems	101
2.4.2	Electron Transfer of Unstrained Bicyclic Systems	116
2.4.3	Electron-transfer Chemistry of Bicyclic and Higher Ring Systems....	118
2.4.4	Triplet Recombination of Radical Ion Pairs.....	124
2.4.5	Concluding Remarks	126
	References.....	127
3	The Electron-transfer Chemistry of Carbon–Carbon Multiple Bonds..	133
	<i>Nathan L. Bauld and Daxin Gao</i>	
3.1	Introduction.....	133
3.2	Electron Transfer Chemistry Involving C–C Multiple Bonds as Single-electron Donors	134
3.2.1	Discovery of Cation Radicals	134
3.2.2	A Molecular-orbital Picture of Cation Radical Formation	135
3.2.3	Cation Radical Structures	136
3.2.4	The Generation of Cation Radicals in Solution	138
3.2.5	Cation Radical Cyclobutanation	141
3.2.6	Formation of 1,2-Dioxetanes by Cation Radical Additions to Triplet Dioxygen.....	147
3.2.7	Cation Radical Diels–Alder Cycloadditions.....	147
3.2.8	Cation Radical Diels–Alder Cycloadditions to Dioxygen.....	160
3.2.9	Mechanisms of Formation of Substrate Cation Radicals from the Aminium Salt	160
3.2.10	Neutralization of the Product Cation Radical	163
3.2.11	Mechanistic Diagnosis of Cation Radical Cycloadditions.....	165
3.2.12	Absolute Reaction Rates and Cation Radical Probes	167
3.2.13	General Theoretical Considerations in Cation Radical Cycloadditions	169
3.2.14	Computational Results	170
3.2.15	Natural Product Synthesis and Synthetic Methodology using Cation Radical Cycloaddition Reactions	171
3.2.16	Cation Radical Polymerization.....	172
3.2.17	The Cation Radical Vinylcyclobutane (VCB) Rearrangement.....	173
3.2.18	The Cation Radical ‘Phenylcyclobutane’ Rearrangement.....	175
3.2.19	The Cation Radical Vinylcyclopropane Rearrangement	176
3.2.20	Cation Radical Chain Cyclopropanation	177
3.2.21	Cation Radical Cycloadditions Forming Five-membered Rings	179
3.2.22	The Cation Radical Cope Reaction	180
3.2.23	A [1,16] Sigmatropic Shift.....	182
3.2.24	Electrocyclic Reactions of Cation Radicals.....	182
3.2.25	Cation Radical Cyclizations.....	184
3.2.26	Other Reactions of Cation Radicals	186

3.3	Electron Transfer Chemistry Involving C–C Multiple Bonds as Single Electron Acceptors.....	188
3.3.1	The Three-electron Bond of the Ethene Anion Radical	188
3.3.2	The Shape of the SOMO of a Pi Anion Radical.....	189
3.3.3	The Butadiene Anion Radical	190
3.3.4	Disproportionation of Anion Radicals to Dianions and Neutrals....	190
3.3.5	Dianion Radicals, Trianion Radicals, and Multianion Radicals	191
3.3.6	Methods for Generating Anion Radicals.....	192
3.3.7	The Birch Reduction of Non-Terminal Alkynes.....	193
3.3.8	Birch Reduction of Conjugated Dienes	194
3.3.9	Coupling of Anion Radicals.....	195
3.3.10	Intramolecular Cyclizations Involving Anion Radicals.....	196
3.3.11	Pericyclic Reactions of Anion Radicals	199
3.4	Electron Transfer Reactions of C–C Multiple Bonds Which Involve Both Single Electron Donation and Acceptance.....	202
3.4.1	Reactions Involving both Anion Radicals and Cation Radicals	202
	Acknowledgment.....	202
	References.....	202
4	Electron-transfer Reactions of Aromatic Compounds.....	206
	<i>Georg Gescheidt and Md. Nadeem Khan</i>	
4.1	Introduction.....	206
4.2	Computational Methods for Organic Radicals	207
4.3	Ion Pairing	209
4.4	Radical Cations	211
4.4.1	π Systems.....	211
4.4.2	Olefins	226
4.4.3	Heteronuclear Radical Cations.....	230
4.5	Radical Anions.....	235
4.5.1	π Systems.....	235
4.5.2	Alkenes.....	248
4.5.3	Heteronuclear Radical Anions	250
4.6	So what?—Conclusions and Outlook	254
	References.....	254
5	Electron-transfer Chemistry of Fullerenes.....	270
	<i>Shunichi Fukuzumi and Dirk M. Guldi</i>	
5.1	Introduction.....	270
5.2	Fundamental Electron-transfer Properties of Fullerenes.....	272
5.3	Thermal Electron Transfer	275
5.3.1	Radiolytically Generated Radical Species.....	275
5.3.2	Electron-transfer Reactions of Fullerene Anions	282
5.4	Intermolecular Photoinduced Electron Transfer	290
5.4.1	Formation of Fullerene Radical Anions	291
5.4.2	Selective Two-electron Reduction	294

5.4.3	C–C Bond Formation via Photoinduced Electron Transfer.....	296
5.5	Intramolecular Photoinduced Electron Transfer.....	305
5.5.1	Fullerene Electron-donor Systems.....	305
5.5.2	Fullerene Electron-acceptor Systems.....	309
5.5.3	Fullerene Chromophore Systems.....	310
5.6	Oxidation of Fullerenes.....	323
5.6.1	Gas-phase Oxidation	323
5.6.2	Oxidation of Fullerenes in Solution.....	323
5.7	Summary.....	325
	Acknowledgment	326
	References.....	326
6	Electron-transfer Reactions of Heteroaromatic Compounds.....	338
	<i>Angelo Albini and Maurizio Fagnoni</i>	
6.1	Introduction.....	338
6.2	Structure of the Radical Ions of Heteroaromatic Compounds.....	339
6.2.1	Radical Cations	339
6.2.2	Radical Anions	341
6.2.3	Stable Radical Ions	342
6.3	Chemical Reactions via Electron Transfer—The Heteroaromatic Compound is the Donor.....	342
6.3.1	General Scheme.....	342
6.3.2	Electron and Proton Transfer	344
6.3.3	Ring Opening and Rearrangement.....	345
6.3.4	Coupling, Dimerization, and Polymerization.....	346
6.3.5	Functionalization of the Ring	350
6.3.6	Cycloadditions	360
6.3.7	Oxygenation	360
6.4	Chemical Reactions via Electron Transfer—The Heteroaromatic is the Acceptor	361
6.4.1	General Scheme.....	361
6.4.2	Ring Opening and Rearrangement.....	362
6.4.3	Coupling, Dimerization and Polymerization.....	363
6.4.4	Direct Ring Functionalization	364
6.4.5	Cleavage of a Group	367
6.4.6	Substitution of a Group	369
6.4.7	Cycloaddition	371
6.4.8	Ring Reduction	372
6.5	Conclusions and Outlook.....	373
	Acknowledgment	373
	References.....	373
7	Electron-transfer Reactions of Amines.....	379
	<i>Suresh Das and Velate Suresh</i>	
7.1	Introduction.....	379
7.2	Mechanistic Studies.....	379

7.2.1	Thermal Oxidation.....	380
7.2.2	Electrochemical Oxidation.....	381
7.2.3	Radiation Chemical Studies of Amines	383
7.2.4	Photoinduced Electron Transfer.....	389
7.2.5	Electron-transfer Reactions of Amines in Biochemical Systems.....	402
7.3	Synthetic Applications.....	411
7.3.1	Thermal Methods.....	411
7.3.2	Electrochemical Methods.....	418
7.3.3	Photoinduced Electron-transfer Reactions	427
	Acknowledgment.....	448
	References.....	448
8	Electron-transfer Reactions of Carbonyl Compounds.....	457
	<i>Axel G. Griesbeck and Stefan Schieffer</i>	
8.1	Generation of Carbonyl Radical Ions by Electron Transfer.....	457
8.1.1	Electrochemical Generation of Carbonyl Radical Anions.....	457
8.1.2	Chemical Generation of Carbonyl Radical Anions.....	462
8.1.3	Photochemical Generation of Carbonyl Radical Anions	472
8.1.4	Generation of Carbonyl Radical Cations	485
8.2	Reactivity Pattern of Carbonyl Radical Ions	487
	References.....	489
9	Electron Transfer in Radicals.....	494
	<i>Massimo Bietti and Steen Steenken</i>	
9.1	Introduction.....	494
9.2	Oxidation of S by X [•] (ET by Addition–Elimination (The ‘ad–el’ Mechanism)	495
9.2.1	S = alkene.....	495
9.2.2	S = X–C–C–H (activation by H-abstraction)	501
9.2.3	S = Aromatic (Ar).....	511
9.3	Intramolecular Electron Transfer with Bond Formation	517
9.4	Reduction of S by X [•] , X = E–C [•] < (E = Hetero Atom).....	519
9.5	Intramolecular Electron Transfer Accompanied by Bond Cleavage in Radical Ions.....	519
9.5.1	Oxidative Bond-cleavage Processes.....	520
9.5.2	Reductive Bond-Cleavage Processes.....	558
	References.....	571
Part 2	Organometallic and Inorganic Molecules.....	581
	Didier Astruc (Ed.)	
1	Reflections on the Two-state Electron-transfer Model.....	583
	<i>Bruce S. Brunschwig and Norman Sutin</i>	
1.1	Introduction.....	583
1.2	Zero-order Energy Surfaces.....	584
1.3	Semiclassical Treatment	587

1.3.1	First-order Energy Surfaces	587
1.3.2	Rate Constant Expressions	593
1.3.3	Reorganization Parameters.....	594
1.3.4	Optical Charge Transfer.....	600
1.4	Quantum Mechanical Treatment.....	606
1.4.1	The Electronic Coupling Element.....	607
1.4.2	The Thermally Averaged Franck–Condon Factor	609
1.5	Conclusions	615
	Acknowledgments	616
	References.....	616
2	Charge-transfer Interactions and Electron-transfer-activated Reactions of Organometallic Complexes.....	618
	<i>Stephan M. Hubig and Jay K. Kochi</i>	
2.1	Introduction.....	618
2.2	Organometallic Complexes as Electron Donors or Acceptors.....	620
2.2.1	Organometallic Donors.....	621
2.2.2	Organometallic Acceptors	625
2.3	Electron Donor–Acceptor Interactions	625
2.3.1	Formation of Organometallic EDA Complexes	626
2.3.2	UV–Vis Spectroscopic Evidence for Charge-transfer Interactions in Organometallic EDA Complexes.....	628
2.3.3	Structural Changes due to Charge Transfer and/or Ion Pairing in Organometallic EDA Complexes.....	632
2.4	Electron-transfer Intermediates in Organometallic Reactions.....	636
2.4.1	Charge-Transfer Excitation of Organometallic EDA Complexes Followed by Efficient Back Electron Transfer	637
2.4.2	Charge-Transfer Activated Reactions of Organometallic EDA Complexes	640
2.5	Inner-sphere and Outer-sphere Mechanisms for Electron Transfer ...	662
2.5.1	Electron-transfer Reactions of Alkylmetals.....	664
2.5.2	Steric Control of Inner-sphere or Outer-sphere Electron Transfers ...	668
2.6	Concluding Remarks	670
	Acknowledgment	671
	References.....	671
3	The Thermodynamics of Organometallic Systems Involving Electron-transfer Paths.....	677
	<i>Mats Tilset</i>	
3.1	Introduction.....	677
3.2	Introduction to Electrochemical Cycles in the Study of Bond-cleavage Reactions of Molecules and Ions	678
3.3	Absolute Bond-dissociation Energies for M–H, Coordinated Ligand C–H, and M–M Bonds.....	680
3.3.1	Thermochemical Cycle for Determination of Absolute M–H Bond-dissociation Energies	680

3.3.2	M–H Bond-dissociation Energies Determined in Acetonitrile.....	682
3.3.3	M–H Bond-dissociation Energies Determined in Solvents other than Acetonitrile.....	684
3.3.4	Discussion of Ligand Effects on M–H BDE Data.....	690
3.3.5	C–H Bond-dissociation Energies of Coordinated Ligands	693
3.3.6	Metal–Metal BDEs from Redox Equilibrium and Electrode Potential Measurements	695
3.4	Metal–Hydride Cation Radical Acidities	696
3.5	Metal–Hydride Bond-dissociation Energies in Cation Radicals.....	698
3.6	Metal–Halide Bond Energies.....	701
3.7	Bonding of 2-Electron Donor Ligands in 18- and 19-Electron Complexes.....	703
3.8	Changes in Ligand C–H Bond Strengths Induced by Electron Transfer	705
3.8.1	Benzylic C–H Bonds of π -Coordinated Arenes.....	705
3.8.2	α - and β -C–H Bonds in Metal Alkyls	707
3.8.3	Bridging Alkylidyne Ligands in Dinuclear Complexes	709
3.9	Concluding Remarks.....	710
	Abbreviations	711
	References.....	711
4	Electron-transfer Reactions of Electron-reservoir Complexes and other Monoelectronic Redox Reagents in Transition-metal Chemistry	714
	<i>Didier Astruc</i>	
4.1	Introduction.....	714
4.2	Standard Redox Potentials and Complementary References	715
4.3	Reductants	717
4.3.1	Alkali- and other Metals; Amalgams and Alloys	717
4.3.2	Aromatic Radical Anions and Anions	723
4.3.3	Hydrides, Grignard Reagents, Metal-alkyls and Metal-aryls, and Other Reductants	727
4.3.4	Miscellaneous Reductants	731
4.3.5	Metallocenes and bis-Arene Metal Sandwiches.....	732
4.4	Oxidants.....	745
4.4.1	Fe ^{III} Sandwich Complexes: Ferrocenium Salts [FeCp ₂][X] and [FeCp*(η^6 -C ₆ Me ₆)] [SbX ₆] ₂	746
4.4.2	Silver(I) Salts.....	747
4.4.3	Copper(II) Salts.....	748
4.4.4	Iron(III) Chloride.....	749
4.4.5	Cerium(IV) Ammonium Nitrate (CAN).....	749
4.4.6	Miscellaneous High-oxidation-state Inorganic Complexes	749
4.4.7	Nitrosonium Salts, [NO]X.....	750
4.4.8	Phosphorus, Arsenic, and Antimony Pentahalides and Aluminum Trichloride	751
4.4.9	Dioxygenyl cation, O ₂ ^{•+} , dioxygen O ₂ , and superoxide anion O ₂ ^{•-} ..	752
4.4.10	Halogens: Cl ₂ , Br ₂ , and I ₂	753

4.4.11	Arenediazonium, $[\text{N}_2\text{aryl}]^{++}$	753
4.4.12	Acids	754
4.4.13	Triarylaminium Cations, $[\text{N}(\text{aryl})_3]^{++}$	755
4.4.14	Thianthrene Radical Cation	757
4.4.15	Carbocations: Trityl, $[\text{C}(\text{aryl})_3]^+$, Salts and Salts of other Carbocations	757
4.4.16	TCNE, TCNQ, and other Cyanocarbons	759
4.4.17	Miscellaneous Organic Oxidants	760
4.5	Electron-transfer-chain (ETC) Catalysis	761
4.5.1	Historical Background, Main Types of Reaction, and Principle	761
4.5.2	The Electron-reservoir Complexes $[\text{Fe}^{\text{I}}\text{Cp}(\eta^6\text{-arene})]$ as ETC Catalysts	763
4.5.3	The Ferrocenium Salts as ETC Catalysts	775
4.6	Redox Catalysis	782
4.6.1	Principle of Redox Catalysis of Electrochemical Reactions	782
4.6.2	Catalysis of Cathodic Reduction of Nitrates and Nitrites by the Electron-reservoir Complexes $[\text{Fe}^{\text{I}}(\eta^5\text{-C}_5\text{H}_4\text{R})(\eta^6\text{-arene})]$	784
4.6.3	Mediation by Ferrocenium Cation: Derivatized Electrodes	786
4.7	Sensors	788
4.8	Conclusion	789
4.9	Experimental: Syntheses of the Electron-reservoir Complexes $[\text{Fe}^{\text{II}}(\eta^5\text{-C}_5\text{R}_5)(\eta^6\text{-C}_6\text{Me}_6)]\text{PF}_6$, $[\text{Fe}^{\text{I}}(\eta^5\text{-C}_5\text{R}_5)(\eta^6\text{-C}_6\text{Me}_6)]$, and $[\text{Fe}^{\text{III}}(\eta^5\text{-C}_5\text{R}_5)(\eta^6\text{-C}_6\text{Me}_6)]\text{[SbCl}_6\text{]}_2$ ($\text{R} = \text{H}$ or Me)	792
4.9.1	$[\text{Fe}^{\text{II}}\text{Cp}(\eta^6\text{-C}_6\text{Me}_6)]\text{PF}_6$	792
4.9.2	$[\text{Fe}^{\text{I}}\text{Cp}(\eta^6\text{-C}_6\text{Me}_6)]$	792
4.9.3	$[\text{Fe}^{\text{I}}(\eta^5\text{-C}_5\text{Me}_5)(\eta^6\text{-C}_6\text{Me}_6)]$	793
4.9.4	$[\text{Fe}^{\text{III}}(\eta^5\text{-C}_5\text{Me}_5)(\eta^6\text{-C}_6\text{Me}_6)]\text{[SbCl}_6\text{]}_2$	793
	References	793
5	Electron-transfer Processes in Mononuclear Polypyridine-type Metal Complexes*	804
	<i>Antonín Vlček, Jr, and J. Heyrovský</i>	
5.1	Introduction	804
5.2	Electron-transfer Properties of Ground-state Polypyridine Complexes: A Survey	807
5.2.1	The 2,2'-Bipyridine and other Polypyridine Ligands	807
5.2.2	Polypyridine Complexes	809
5.3	Electron-transfer Properties of Ground-state Polypyridine Complexes: Phenomena	820
5.3.1	Localization of Redox Steps	820
5.3.2	Redox Patterns	823
5.3.3	Control of Redox Potentials by the Polypyridine Ligand Structure	828
5.3.4	Electron-transfer Kinetics	830
5.3.5	Ligand Labilization	833
5.3.6	Redox Properties of Supramolecules Containing Metal–Polypyridine Units	834

5.3.7	Applications of Ground-state Electron Transfer	836
5.4	Electron-transfer Properties of Electronically Excited Polypyridine Complexes.....	837
5.4.1	Basic Thermodynamic and Kinetic Aspects of Excited-state Electron Transfer	838
5.4.2	Excited States of Polypyridine Complexes	840
5.4.3	Control of the Electron-transfer Properties of MLCT Excited States of Polypyridine Complexes	842
5.4.4	Properties of Some Common Photo-redox-active Metal– Polypyridine Chromophores.....	846
5.4.5	Bimolecular Electron-transfer Reactions	850
5.4.6	Ultra-fast Electron Injection to Semiconductor Electrodes.....	851
5.4.7	Excited-state Electron-transfer in Supramolecules Containing Metal–polypyridine Chromophores	853
5.4.8	Chemiluminescence	857
5.4.9	Applications of Photochemical Electron Transfer	858
5.5	Conclusions	862
	Appendix	864
	References	868
6	Electron Transfer in Catalytic Dinitrogen Reduction	878
	<i>Alexander E. Shilov</i>	
6.1	Introduction	878
6.2	Peculiarities of the N ₂ Molecule.....	879
6.3	Dinitrogen Complexes with Transition Metals: Possible Catalysts for N ₂ Reduction	882
6.4	Mononuclear Complexes M–N≡N.....	883
6.5	Linear Dinuclear Complexes M–N≡N–M	883
6.6	Polynuclear Dinitrogen Complexes.....	884
6.7	Polynuclear Complex as Optimum Catalyst for N ₂ Reduction.....	885
6.8	Electron Transfer in Biological Nitrogen Fixation.....	886
6.9	N ₂ Reduction in Aprotic Media.....	891
6.10	Dinitrogen Reduction in Protic Media	892
6.11	Soluble Complexes of Vanadium (II)	894
6.12	Catalytic Dinitrogen Reduction	897
6.13	Catalytic Dinitrogen Reduction by Amalgams	899
6.14	FeMoco as Catalyst for the Reduction of Nitrogenase Substrates at Amalgam Surfaces	901
	References	903
7	Transition-metal Complexes as Models of the Active Sites of Hydrogenases*	905
	<i>Cameron E. Forde and Robert H. Morris</i>	
7.1	Hydrogen Chemistry.....	905
7.1.1	Introduction	905
7.1.2	Metal Hydride Chemistry.....	906

7.1.3	Metal Dihydrogen Chemistry	906
7.2	Hydrogenase Enzymes.....	909
7.2.1	Introduction to Hydrogenase Enzymes	909
7.2.2	Spectroscopic Characterization of Hydrogenase Enzymes	910
7.2.3	Hydrogenase Function	915
7.2.4	Structural Characterization of Hydrogenase Enzymes	915
7.3	Modeling with Transition-metal Complexes	916
7.3.1	Introduction.....	916
7.3.2	Spectroscopic Modeling	917
7.3.3	Functional Modeling	918
7.3.4	Structural Modeling	920
7.3.5	Theoretical Modeling.....	921
7.4	Conclusions	923
	References.....	924
8	Biomimetic Electron-transfer Chemistry of Porphyrins and Metalloporphyrins.....	927
	<i>Shunichi Fukuzumi and Hiroshi Imahori</i>	
8.1	Introduction.....	927
8.2	High-valent Intermediates of Heme Enzymes	928
8.2.1	P-450 Catalytic Mechanisms	928
8.2.2	Reaction Pathways of $[(P)Fe^{IV}=O]^{+}$	930
8.2.3	Reorganization Energies for Electron-transfer Reactions of High-valent Iron Porphyrins	933
8.2.4	Electron-transfer Pathway of $[(P)Fe^{IV}=O]^{+}$	934
8.2.5	Electron Transfer Compared with Direct Oxygen Transfer	938
8.2.6	'Agostic' Interaction	941
8.2.7	Site of Electron Transfer in Compound I	943
8.2.8	Photoinduced Electron-transfer Oxidation.....	944
8.2.9	Oxygen-evolving Complex.....	947
8.3	Catalytic Reduction of Oxygen	949
8.3.1	Two-electron Reduction	950
8.3.2	Four-electron Reduction	952
8.4	Electron Transfer in Organized Media.....	954
8.4.1	Electrocatalysis of Self-assembled Monolayers of Porphyrins.....	955
8.4.3	Photoinduced Electron Transfer of Metalloporphyrins in Self-assembled Monolayers.....	957
8.4.4	Self-assembled Monolayers of Porphyrin-containing Dyads	960
8.4.5	Self-assembled Monolayers of Porphyrin-containing Triads	963
8.5	Summary.....	965
	Acknowledgment	966
	References.....	966
9	ESR Spectroscopy of Inorganic and Organometallic Radicals	976
	<i>Wolfgang Kaim</i>	
9.1	Introduction: The Information Accessible from ESR	976

9.2	Inorganic and Organometallic Radicals: Definition, Generation and Peculiarities.....	976
9.3	Selected ESR Parameters	979
9.3.1	Concentration and Lifetime of Radicals	979
9.3.2	Line-width and Temperature	980
9.3.3	The g Factor	981
9.3.4	Electron–Nuclear Hyperfine Coupling	985
9.3.5	Zero-field Splitting and Exchange Coupling	991
9.3.6	Dynamic Effects.....	991
9.3.7	ESR Information and Chemical Reactivity	996
9.3.8	Concluding Remarks.....	998
	Acknowledgments.....	998
	References.....	998

Volume III

Part 1	Biological Systems	1
	Harry B. Gray and Jay R. Winkler (Eds.)	
1	Electron Transfer in Metalloproteins	3
	<i>Harry B. Gray and Jay R. Winkler</i>	
1.1	Introduction.....	3
1.2	The Semiclassical Model of Electron Transfer.....	3
1.3	Ru-Modified Proteins.....	5
1.4	Reorganization Energy	6
1.4.1	Cytochrome <i>c</i>	6
1.4.2	Azurin.....	9
1.5	Electronic Coupling.....	10
1.5.1	Theoretical Models	10
1.5.2	Blue Copper Proteins	13
1.5.3	Heme Proteins	15
1.5.4	High-Potential Iron-Sulfur Protein (HiPIP)	17
1.6	Electron Tunneling through Water.....	17
1.7	Tunneling Timetables.....	19
	Acknowledgment	20
	References.....	20
2	Photosynthesis: Bacterial Reaction Center	24
	<i>Christopher C. Moser, Christopher C. Page, and P. Leslie Dutton</i>	
2.1	The Bioenergetic Context of Bacterial Reaction Centers.....	24
2.2	Tunneling Revealed in Photosynthesis	26
2.3	Basic Electron Tunneling Theory	27
2.3.1	The V_R^2 Term	28
2.3.2	The FC Term	28
2.3.3	An Empirical Tunneling Expression with Quantized FC.....	30
2.4	Devault and Chance's Prediction.....	31
2.5	The Design of Natural Electron Transfer Chains.....	33
2.5.1	The High Potential Redox Cofactor Chain in <i>Rp. viridis</i>	33
2.5.2	The Low-Potential Chain in <i>Rp. viridis</i> and <i>Rb. sphaeroides</i>	36
	References.....	38
3	Respiration: Cytochrome Oxidase	39
	<i>Bo G. Malmström</i>	
3.1	Introduction.....	39
3.2	Structure of Cytochrome Oxidase.....	40
3.3	Methods for Studying Electron Transfer in Cytochrome Oxidase	41
3.3.1	Electron Injection into Cytochrome Oxidase	42
3.3.2	Flash Photolysis of Mixed-Valence Carboxycytochrome Oxidase	42
3.3.3	The Flow-Flash Technique: The Reduced Cytochrome Oxidase– Dioxygen Reaction	43

3.4	Electron Transfer Reactions in Cytochrome Oxidase.....	44
3.4.1	Reduction of the Initial Electron Acceptor	44
3.4.2	Internal Electron Transfer Reactions.....	48
3.4.3	The Reduction of Dioxygen	48
3.4.4	Coupling between Electron and Proton Transfer	50
3.5	Concluding Remarks.....	51
	Acknowledgments.....	52
	References.....	52
4	Redox Enzymes: Correlation of Three-Dimensional Structure and Mechanism for Heme-Containing Oxygenases and Peroxidases.....	56
	<i>Alycen E. Pond, Amy P. Ledbetter, Masanori Sono, David B. Goodin, and John H. Dawson</i>	
4.1	Introduction	56
4.2	Cytochrome P450	58
4.2.1	Introduction	58
4.2.2	Reaction Cycle of P450	60
4.2.3	Molecular Structure of P450.....	64
4.2.4	Mechanism of Oxygen Activation.....	66
4.3	Nitric Oxide Synthase.....	71
4.3.1	Introduction	71
4.3.2	The Isoforms	72
4.3.3	The Molecular Structure of NOS.....	75
4.3.4	The Mechanism of NOS.....	78
4.4	Heme-Containing Plant Peroxidases	83
4.4.1	Introduction	83
4.4.2	The Molecular Structure of Heme Peroxidases	84
4.4.3	The Catalytic Mechanism of Heme Peroxidases	88
4.4.4	Can Peroxidases Catalyze Peroxygenase Chemistry?	93
4.4.5	Development of CCP as a Protein Model System for Heme-Containing Enzymes	94
4.5	Conclusions	97
	Acknowledgments.....	97
	Abbreviations	98
	References.....	99
5	Electron Transfer and Charge Transport Process in DNA	105
	<i>Frederick D. Lewis</i>	
5.1	Introduction	105
5.1.1	Background	105
5.1.2	Structure and Properties of DNA	106
5.1.3	Direct Ionization of DNA	116
5.2	Collisional and Static Contact Electron Transfer in DNA	120
5.2.1	Energetics and Dynamics of Direct Electron Transfer Processes.....	120
5.2.2	Bimolecular Electron Transfer Processes of Nucleosides, Nucleotides, and Oligonucleotides.....	123

5.2.3	Electron Transfer Process Involving Covalently Attached Nearest-Neighbor Nucleobases.....	130
5.2.4	Electron Transfer Quenching of Intercalated Acceptors by Nearest-Neighbor Nucleobases.....	138
5.3	Single-Step Electron Transfer Process in Acceptor–DNA–Donor Systems.....	139
5.3.1	Background	139
5.3.2	Electron Transfer in Donor–DNA–Acceptor Systems	141
5.3.3	DNA-Mediated Oxidation of Nucleobases	147
5.3.4	Summary of Results for Single-Step Electron Transfer	153
5.4	Photoinitiated Charge Transport in DNA	154
5.4.1	Background	154
5.4.2	DNA Cleavage and Thymine Dimer Repair over Long Distances ...	156
5.4.3	Distance-Dependent Hole Migration in DNA.....	160
5.5	Conductivity of Ionized DNA Assemblies	164
5.5.1	Background	164
5.5.2	DNA Fibers and Single Molecules.....	165
5.5.3	Thin Films and Monolayer Assemblies	166
5.6	Conclusions and Prospects	167
	Acknowledgments	169
	References.....	169
Part 2	Artificial Supramolecular Systems	177
	Vincenzo Balzani (Ed.)	
1	Covalently Linked Systems Based on Organic Components.....	179
	<i>Michael N. Paddon-Row</i>	
1.1	Introduction.....	179
1.2	The Superexchange Mechanism	183
1.3	Experimental Investigations of the Superexchange Mechanism for ET Processes	188
1.4	Examples of TS- and TB-Mediated Photoinduced ET Reactions.....	197
1.5	Distance Dependence of TB-Mediated ET in Saturated Hydrocarbon Bridges	201
1.6	A Simple Model for Dissecting TB Coupling in Bridges	216
1.7	Interference Effects in TB Coupling.....	217
1.8	Porphyrin and C ₆₀ Chromophores	225
1.9	Superexchange versus Molecular Wire Behavior	230
1.10	Superexchange through Aromatic Bridges.....	235
1.11	Electron Transfer Mediated by π -Stacks in DNA	238
1.12	Electron Transfer Mediated through Hydrogen Bonds.....	243
1.13	The Effect of Orbital Symmetry on ET Dynamics	243
1.14	Effect of Donor–Acceptor Orientation on ET Rates	246
1.15	Modulation of Electron Transfer Dynamics by Electric Fields	249
1.16	Design of Dyads with Rapid Solvent-Independent Charge Separation.....	252

1.17	Verification of the Marcus Inverted Region.....	253
1.17.1	Through-Bond-Mediated Electronic Energy Transfer	254
1.18	Electron Transfer Mediated by Solvent Molecules	258
1.19	Epilogue.....	265
	Acknowledgments.....	266
	References.....	266
2	Covalently Linked Systems Containing Porphyrin Units	272
	<i>Devens Gust, Thomas A. Moore and Ana L. Moore</i>	
2.1	Introduction	272
2.2	Basic Principles Underlying Photoinduced Electron Transfer	273
2.2.1	Electronic Coupling.....	275
2.2.2	Solvent Effects	275
2.3	Intramolecular Photoinduced Electron Transfer in Porphyrin-Based Systems: Dyads	276
2.3.1	Porphyrins Covalently Linked to Other Porphyrins	278
2.3.2	Porphyrins Covalently Linked to Quinones.....	284
2.3.3	Porphyrins Covalently Linked to Fullerenes.....	295
2.3.4	Porphyrins Covalently Linked to Carotenoid Polyenes.....	300
2.3.5	Porphyrins Covalently Linked to Aromatic Imides.....	301
2.3.6	Porphyrins Covalently Linked to Viologens	303
2.4	Intramolecular Photoinduced Electron Transfer in Porphyrin-Based Systems: Triads.....	304
2.4.1	Triads with Porphyrin–Quinone Components	305
2.4.2	Triads with Diporphyrin Components	311
2.4.3	Triads with Fullerene Components.....	312
2.4.4	Triads with Aromatic Imide Components.....	314
2.4.5	Triad with a Viologen Component	317
2.5	Intramolecular Photoinduced Electron Transfer in Complex Porphyrin-Based Systems: Tetrads, Pentads, and Hexads	318
2.5.1	Sequential Multistep Electron Transfer Process: Tetrads.....	318
2.5.2	Sequential and Parallel Multistep Electron Transfer Process: Pentads	322
2.5.3	An Artificial Photosynthetic Antenna–Reaction Center System	324
2.6	Conclusions	328
	References.....	329
3	Covalently Linked Systems Containing Metal Complexes.....	337
	<i>Franco Scandola, Claudio Chiorboli, Maria Teresa Indelli, and Maria Anita Rampi</i>	
3.1	Introduction.....	337
3.1.1	Scope and Limitations	337
3.1.2	Covalently Linked Systems as Supramolecular Species.....	340
3.1.3	Intercomponent Processes: A Short Summary	341
3.1.4	Coordination Compounds as Molecular Components.....	350
3.2	Bimetallic and Polymetallic Systems	351

3.3	Chromophore–Quencher Systems.....	372
3.3.1	Ferrocenes	372
3.3.2	Fullerenes	373
3.3.3	Amines	374
3.3.4	Pyridinium Ions.....	375
3.3.5	Other Systems.....	376
3.4	Selected Topics.....	377
3.4.1	Electronic Energy Transfer in Bimetallic Systems: Ru(II)–Os(II) Dyads	377
3.4.2	Photoinduced Electron Transfer in Bimetallic Systems: Ru(II)– Rh(III) dyads	383
3.4.3	Reversible Energy Transfer in Systems with Aromatic Hydrocarbon Units	390
3.4.4	Photoinduced Charge Shift in Chromophore–Quencher Systems.....	393
3.4.5	Multi-Step Charge Separation in Triads	395
3.5	Concluding Remarks	396
	Appendix.....	401
	References.....	403
4	Electron Transfer in Hydrogen-Bonded Donor–Acceptor Supramolecules.....	409
	<i>Christopher J. Chang, Joshua D. K. Brown, Michelle C. Y. Chang, Erin A. Baker and Daniel G. Nocera</i>	
4.1	Introduction.....	409
4.2	Background	410
4.3	Scope of the Chapter	412
4.4	Electron Transfer Reactivity of D—[H]—A Supramolecule Systems.....	413
4.4.1	Carboxylic Acid Dimers.....	414
4.4.2	Cofacial Porphyrin–Quinone Systems	417
4.4.3	Quinone Recognition by Cyclophanes	421
4.4.4	Peptide-Based Motifs	424
4.4.5	Watson–Crick Base-Pairing	427
4.4.6	Diimide-Based Assemblies.....	433
4.4.7	Mixed-Valence Metal Complexes	438
4.4.8	Barbituric Acid-Containing Complementary Pairs	440
4.4.9	Miscellaneous Hydrogen-Bonded Ensembles	440
4.4.10	Salt Bridge Systems.....	443
4.5	Concluding Remarks	452
	Acknowledgments	457
	References.....	457
5	Host–Guest and Cage-Type Systems	462
	<i>Luigi Fabbrizzi, Maurizio Licchelli and Angelo Taglietti</i>	
5.1	Metal Ions Inside Aza-Crowns.....	462
5.2	Anions Inside Aza-Crowns	469

5.3	Metals Inside Aza-Cages.....	471
5.4	Metals Inside Thia-Crowns.....	477
5.5	Anions Inside Zn ^{II} -Polyamine-Based Systems.....	482
5.6	Cyclodextrins.....	487
5.7	Calixarenes and Related Compounds.....	490
5.8	Carcerands and Hemicarcerands.....	495
	References.....	498
6	Electron Transfer Processes in Pseudorotaxanes.....	501
	<i>Margherita Venturi, Alberto Credi, and Vincenzo Balzani</i>	
6.1	Introduction.....	501
6.2	Main Types of Pseudorotaxanes.....	501
6.3	Some General and Particular Aspects of Pseudorotaxane Chemistry.....	504
6.4	Spectroscopic and Electrochemical Consequences of Charge- Transfer Interactions.....	508
6.4.1	Absorption and Emission Spectra.....	508
6.4.2	Electrochemical Properties.....	510
6.5	Electron Transfer Controlling Dethreading/Rethreading Processes..	511
6.5.1	Pseudorotaxanes as Simple Molecular Machines.....	511
6.5.2	Photochemically Induced Processes.....	512
6.5.3	Electrochemically Induced Processes.....	516
6.5.4	Chemically Induced Processes.....	521
6.6	Electron Transfer Controlled by Dethreading/Rethreading Processes.....	525
6.6.1	Pseudorotaxanes and Information Processing.....	525
6.6.2	Plug-socket Systems.....	525
6.6.3	Extensions.....	526
6.6.4	Logic Gates and Switches.....	527
6.6.5	Sensors.....	529
6.6.6	Other Systems.....	530
6.7	Heterogeneous Systems.....	531
6.8	Conclusions.....	531
	Acknowledgments.....	534
	References.....	534
7	Electron Transfer Processes in Rotaxanes and Catenanes.....	539
	<i>Roberto Ballardini, Maria Teresa Gandolfi, and Vincenzo Balzani</i>	
7.1	Introduction.....	539
7.2	Synthesis.....	539
7.3	Spectroscopic and Electrochemical Consequences of Charge- Transfer Interactions.....	546
7.3.1	Absorption and Emission Spectra.....	547
7.3.2	Electrochemical Behavior.....	548
7.4	Rotaxanes.....	550
7.4.1	Rotaxane Chemistry.....	550

7.4.2	Shuttling Processes.....	552
7.4.3	Electrochemically Controlled Shuttling Processes	553
7.4.4	Photochemically Controlled Shuttling Processes.....	556
7.4.5	Chemically Controlled Shuttling Processes	561
7.5	Catenanes	561
7.5.1	Functional Catenanes.....	561
7.5.2	Ring Motions	566
7.5.3	Electrochemically Controlled Ring Motions.....	570
7.5.4	Photochemically Controlled Ring Motions	573
7.5.5	Chemically Controlled Ring Motions.....	573
7.6	Molecular-Level Machines	574
7.7	Modified Electrodes and Heterosupramolecular Systems	575
7.8	Conclusions	577
	Acknowledgments	577
	References.....	577
8	Metal-Assembled Catenanes, Rotaxanes, and Knots	582
	<i>Nicola Armaroli, Jean-Claude Chambron, Jean-Paul Collin,</i> <i>Christiane Dietrich-Buchecker, Lucia Flamigni, Jean-Marc Kern, and</i> <i>Jean-Pierre Sauvage</i>	
8.1	Introduction.....	582
8.2	Electrochemical Properties of Metallocatenates and Knots	583
8.2.1	Introduction.....	583
8.2.2	Metallo[2]catenates in which the Metal is in a Tetrahedral Environment: Stabilization of Low Oxidation States.....	584
8.2.3	Copper [2]catenates	587
8.2.4	Electrochemical Study of Various Monometallated Catenanes in which the Metal is Tetracoordinated.....	591
8.2.5	Dimetallic [3]Catenates	596
8.2.6	Dimetallic Molecular Trefoil Knots.....	601
8.2.7	A Mononuclear Hexacoordinated Ruthenium Bis-Terpyridine [2]Catenate	603
8.3	Photophysical Properties of Catenates and Knots	605
8.3.1	Introduction.....	605
8.3.2	Metallo-[2]catenates	605
8.3.3	Multicomponent Metallo-[3]catenates.....	608
8.3.4	Proton [2]- and [3]Catenates.....	610
8.3.5	Multicomponent Metallo-[2]catenates.....	612
8.3.6	Homo- and Heterodinuclear Knots	614
8.3.7	Quenching by Dioxxygen	617
8.4	Porphyritic Rotaxanes: Control of the Photoinduced Electron Transfer Rate between PZn and PAu ⁺ by the Assembler Metal.....	618
8.4.1	Introduction.....	618
8.4.2	Properties of the Reference Compounds	620
8.4.3	Photochemistry of the Zinc/Gold Bisporphyrin	621

8.4.4	Photochemistry of the Copper(I)-complexed Zinc/Gold Bisporphyrin-Stoppered [2]Rotaxane.....	622
8.4.5	Comparison of the Electron Transfer Rates for both Systems	627
8.4.6	Conclusion	629
8.5	Catenanes in Motion: Electrochemically and Photochemically Driven Machine-Like Molecules	629
8.5.1	Introduction	629
8.5.2	A Nonsymmetrical Copper [2]Catenate	632
8.5.3	A Symmetrical Copper [2]Catenate	636
8.6	Rotaxanes: Gliding of the Ring on its Axle under the Action of an Electrochemical or Photochemical Signal	640
8.6.1	Introduction	640
8.6.2	Electrochemically Driven Motion	641
8.6.3	Photochemically Driven Motion [99].....	644
8.7	Conclusions	649
	Acknowledgments.....	650
	References.....	650
9	Dendrimers	655
	<i>Alberto Juris</i>	
9.1	Introduction	655
9.2	Electroactive Units.....	656
9.3	Types of Electron Transfer Reactions	658
9.3.1	Electrochemical Reactions.....	658
9.3.2	Photoinduced Electron Transfer Reactions	658
9.4	Dendrimers Containing Electroactive Units	659
9.4.1	Ferrocene and other Sandwich Compounds	659
9.4.2	Metal–Polypyridine Complexes	668
9.4.3	Porphyrins and Phthalocyanins.....	679
9.4.4	Tetrathiafulvalene.....	686
9.4.5	Fullerene	688
9.4.6	Naphthalene Diimide	692
9.4.7	Triaryl Amines	695
9.4.8	Other Electroactive Units.....	697
9.5	Electroinactive Dendrimers.....	706
9.6	Concluding Remarks.....	709
	References.....	710

Volume IV

Part 1	Catalysis of Electron Transfer	1
	Shunichi Fukuzumi (Ed.)	
1	Fundamental Concepts of Catalysis in Electron Transfer.....	3
	<i>Shunichi Fukuzumi</i>	
1.1	Introduction.....	3
1.2	Factors to Accelerate Rates of Electron Transfer	5
1.3	Acid Catalysis in Electron Transfer.....	8
1.3.1	Catalysis of Brønsted Acid	8
1.3.2	Deceleration and Acceleration Effects of Brønsted Acid	14
1.3.3	Catalysis of Metal Ions	15
1.3.4	Acid Catalysis in Overall Reactions.....	27
1.3.5	Lewis Acid Catalysis in C–C bond Formation via Electron Transfer	43
1.3.6	Acid Catalysis in Photoinduced Electron Transfer	44
1.4	Base Catalysis in Electron Transfer	47
1.4.1	Base Catalysis by Deprotonation of Electron Donors.....	48
1.4.2	Base Catalysis via Formation of Base Adducts.....	51
1.4.3	Control of Reorganization Energy by Base Catalysis	54
1.5	Conclusions and Future Prospects	58
	Acknowledgments	59
	References.....	59
2	Redox Modulation by Molecular Recognition	68
	<i>Vincent M. Rotello</i>	
2.1	Introduction.....	68
2.2	Modulation of Redox Potentials by Noncovalent Interactions	69
2.2.1	Hydrogen Bonding	71
2.2.2	Aromatic Stacking	74
2.2.3	Other Electrostatic Interactions	77
2.3	Recognition-mediated Control of Molecular Orbital Geometries.....	79
2.4	Proton-coupled Electron Transfer.....	82
2.5	Summary and Outlook	85
	References.....	86
3	Homogeneous Redox Catalysis in CO₂ Fixation	88
	<i>Etsuko Fujita and Bruce S. Brunschwig</i>	
3.1	Introduction.....	88
3.2	Macrocyclic Complexes of Cobalt and Nickel.....	89
3.2.1	Overview of CO ₂ Reduction Systems Mediated by Cobalt and Nickel Macrocycles.....	89
3.2.2	Properties of the Cobalt and Nickel Macrocycles	92
3.2.3	Electrocatalytic Systems	97

3.2.4	Photocatalytic Systems.....	98
3.3	Re(α -diimine)(CO) ₃ X, Re(α -diimine)(CO) ₂ XX' and Similar Complexes.....	104
3.3.1	Overview of CO ₂ Reduction System-mediated Rhenium Complexes.....	104
3.3.2	Properties of Re(α -diimine)(CO) ₃ X and Re(α -diimine)(CO) ₂ XX'	104
3.3.3	Electrochemical Systems: One- and Two-electron Pathways	116
3.3.4	Photochemical Systems	118
3.4	Conclusions	121
	Acknowledgments.....	122
	Abbreviations	122
	References.....	123
4	The Electrochemical and Photochemical Activation of Redox Enzymes	127
	<i>Eugenii Katz, Andrew N. Shipway and Itamar Willner</i>	
4.1	Introduction	127
4.2	The Electrochemical Activation of Enzymes.....	128
4.2.1	Direct, Nonmediated Electron Transfer Between Enzymes and Electrodes	128
4.2.2	Electron Transfer Between Enzymes and Electrodes Provided by Diffusional Mediators.....	131
4.2.3	Electrochemistry of Enzymes at Electrodes Functionalized with Monolayers of Redox Relays.....	133
4.2.4	Electrochemical Activation of Enzymes by the Attachment of Redox Relays to the Protein Backbone	135
4.2.5	Electrical 'Wiring' of Enzymes Entrapped in Polymeric Matrices on Electrode Supports.....	140
4.2.6	Electrical 'Wiring' of Enzymes Incorporated into Inorganic Matrices	146
4.2.7	Electrical 'Wiring' of Nano-engineered Enzymes	151
4.2.8	Biosensor, Bioelectronic and Biotechnological Applications of Electrically 'Wired' Enzymes	159
4.3	The Photochemical Activation of Enzymes	170
4.3.1	Biological Transformations Driven by the Photochemical Regeneration of NAD(P) ⁺ /NAD(P)H Cofactors.....	172
4.3.2	Enzymatic Reactions Driven by the Photochemical Regeneration of Synthetic Electron Relays.....	179
4.3.3	Photochemical Activation of Enzymes Using Dyes Covalently Tethered to the Protein Backbone.....	181
4.3.4	Photochemical Activation of Semi-synthetic Enzymes Reconstituted with Non-natural Photosensitive Cofactors	185
4.3.5	Applications of Photoactivated Redox Enzymes.....	190
4.4	Conclusion and Perspectives.....	191
	Acknowledgments.....	193
	References.....	193

5	Interprotein and Intraprotein Electron Transfer Mechanisms	202
	<i>Gordon Tollin</i>	
5.1	Introduction.....	202
5.2	Experimental Methods for Investigating Protein ET Reactions.....	205
5.2.1	Time-resolved Spectrophotometry	205
5.2.2	Use of Ionic Strength to Probe Electrostatic Interactions	208
5.3	Interprotein Electron Transfer Reactions	210
5.3.1	Ferredoxin (Fd)–Ferredoxin:NADP ⁺ Reductase (FNR)	210
5.3.2	Cytochrome <i>f</i> (Cyt <i>f</i>)–Plastocyanin (Pc)	218
5.3.3	Cytochrome <i>c</i> (cyt <i>c</i>)–Cytochrome <i>c</i> Peroxidase (ccp)	221
5.4	Intraprotein Electron Transfer Reactions.....	222
5.4.1	Flavocytochrome <i>b</i> ₂ (Fcyt <i>b</i>).....	222
5.4.2	Sulfite Oxidase (SO)	224
5.4.3	Cytochrome P450BM-3.....	225
5.5	Conclusions	227
	Acknowledgments	228
	References.....	228
6	Novel Organic Syntheses Through Semiconductor Photocatalysis	232
	<i>Horst Kisch and Matthias Hopfner</i>	
6.1	Scope and Introduction.....	232
6.2	Heterogeneous Photocatalysis with Semiconductor Powders.....	234
6.2.1	Fundamentals.....	234
6.2.2	Thermodynamic Aspects	235
6.2.3	Kinetic Aspects	237
6.2.4	Surface Area and Particle Size	239
6.2.5	Photocorrosion.....	240
6.2.6	Characterization of ZnS and CdS	242
6.3	Semiconductor Photocatalysis Type A.....	245
6.3.1	Dealkylation, Cyclization and Hydroalkylation	245
6.3.2	Dehydromerization of Cyclic Enol/Allyl Ethers and Olefins.....	248
6.4	Semiconductor Photocatalysis Type B	256
6.4.1	Linear Addition of Cyclic Enol/Allyl Ethers and Olefins to 1,2-Diazenes	256
6.4.2	Linear Addition of Cyclic Enol/Allyl Ethers and Olefins to Imines...	264
6.5	Summary and Outlook	270
	References.....	270
Part 2	Heterogeneous Systems	277
	Thomas E. Mallouk (Ed.)	
1	Electron Transfer at Semiconductor–Electrolyte Interfaces	279
	<i>Krishnan Rajeshwar</i>	
1.1	Introduction and Scope.....	279
1.2	Electron Energy Levels in Semiconductors and Energy Band Model	280
1.3	The Semiconductor–Electrolyte Interface at Equilibrium	285

1.3.1	The Equilibration Process	285
1.3.2	The Depletion Layer	287
1.3.3	Mapping of the Semiconductor Band-edge Positions Relative to Solution Redox Levels	289
1.3.4	Surface States and Other Complications	293
1.4	Experimental Methods for Studying Charge Transfer at Semiconductor–Electrolyte Interfaces	294
1.5	Charge-transfer Processes in the Dark	296
1.5.1	Current–Potential Behavior	296
1.5.2	Dark Processes Mediated by Surface States or by Space Charge Layer Recombination	301
1.5.3	Rate-limiting Steps in Charge-transfer Processes in the Dark	304
1.6	Light Absorption by the Semiconductor Electrode and Carrier Collection	306
1.6.1	Light Absorption and Carrier Generation	306
1.6.2	Carrier Collection	307
1.6.3	Photocurrent–Potential Behavior	312
1.6.4	Dynamics of Photoinduced Charge Transfer	315
1.6.5	Hot Carrier Transfer	320
1.7	Multi-electron Photoprocesses	322
1.8	Nanocrystalline Semiconductor Films and Size Quantization	327
1.8.1	Introductory Remarks	327
1.8.2	Preparation of Nanocrystalline Electrode Films	328
1.8.3	The Nanocrystalline Film–Electrolyte Interface and Charge Storage Behavior in the Dark	329
1.8.4	Photoexcitation and Carrier Collection: Steady-state Behavior	330
1.8.5	Photoexcitation and Carrier Collection: Dynamic Behavior	333
1.8.6	Size Quantization	335
1.9	Charge Transfer Across Chemically Modified Semiconductor– Electrolyte Interfaces	336
1.9.1	Single Crystals	336
1.9.2	Nanocrystalline Semiconductor Films and Composites	338
1.10	Concluding Remarks	342
	Acknowledgments	342
	References	343
2	Dye Sensitization of Electrodes	353
	<i>Ping Qu and Gerald J. Meyer</i>	
2.1	Dye Sensitization of Planar Electrodes	353
2.1.1	Thermodynamics and Sensitization Mechanisms	354
2.1.2	Examples of Sensitization Studies at Planar Electrodes	366
2.2	Dye Sensitization of Colloidal Semiconductor Electrodes	377
2.2.1	Materials, Spectroscopic and Electrochemical Properties of Nanocrystalline TiO ₂	379
2.2.2	Examples of Interfacial Electron Transfer at Colloidal Semiconductor Electrodes	392

2.3	Conclusions	405
	Acknowledgments	406
	References.....	406
3	Electron-transfer Processes in Zeolites and Related Microheterogeneous Media	412
	<i>Anand S. Vaidyalingam, Michael A. Coutant and Prabir K. Dutta</i>	
3.1	Introduction.....	412
3.2	Description of Porous Media.....	413
3.2.1	Microporous Materials and Zeolites	413
3.2.2	Mesoporous Materials.....	423
3.2.3	Sol–Gel Materials	427
3.3	Electron-transfer Reactions.....	429
3.3.1	Microporous Materials and Zeolites	429
3.3.2	Mesoporous Materials.....	465
3.3.3	Sol–Gel Materials	469
3.4	Conclusions	478
	Acknowledgments	479
	References.....	479
4	Electron Transfer in Layered and Intercalated Compounds	487
	<i>Vasudeva Bhat and Kazunari Domen</i>	
4.1	Introduction.....	487
4.2	Layered Oxides of Transition Metals	487
4.2.1	$K_4Nb_6O_{17}$	489
4.2.2	$KTiNbO_5$ -type Oxides.....	505
4.2.3	Perovskite-related Layered Oxides	511
4.3	Clays	519
4.3.1	TiO_2 in Montmorillonite	520
4.3.2	Fe_2O_3 in Montmorillonite	521
4.3.3	CdS and ZnS Mixtures in Colloidal Montmorillonite.....	521
4.3.4	Photoactive Species Intercalated into Lamellar Oxides.....	522
4.4	Layered Double Hydroxides (LDHs) [171–174].....	526
4.4.1	Photocatalysis in LDHs Intercalated with CdS and CdS/ZnS	527
4.4.2	Photocatalysis in LDHs Pillared with Polyoxometallates	527
4.4.3	LDHs Intercalated with Photoresponsive Species	528
4.5	Artificially Built Multilayer Systems	528
4.5.1	Towards Photoinduced Charge Separation	529
4.6	Conclusion	535
	References.....	536
5	Fundamental Aspects of Electron Transfer in Substrate-supported Organized Molecular Assemblies	541
	<i>Robert S. Clegg and James E. Hutchison</i>	
5.1	Introduction.....	541
5.2	Background	543
5.2.1	Monolayer and Multilayer Systems	543

5.2.2	Characterization of Molecular Assemblies	546
5.3	Fundamental Studies of Electron Transfer in Organized Assemblies.....	550
5.3.1	Electron Transfer in Langmuir–Blodgett Systems	550
5.3.2	Electron Transfer in Self-assembled Systems.....	552
5.4	Summary and Outlook.....	572
	References.....	574
6	Electron Transfer in Self-organizing Systems of Amphiphiles	578
	<i>James K. Hurst and Rafail F. Khairutdinov</i>	
6.1	Introduction	578
6.2	General Attributes of Surfactant Assemblies.....	578
6.2.1	Micelles and Reversed Micelles.....	579
6.2.2	Vesicles and Membranes.....	581
6.3	Surfactant Assembly Microenvironments	584
6.3.1	Partitioning of Dopants in Micelles	585
6.3.2	Partitioning of Dopants in Vesicles.....	586
6.3.3	Microviscosities of Surfactant Assemblies.....	586
6.3.4	Local Polarity and Electric Field Gradients.....	589
6.4	Electron-transfer Reactions in Micelles	592
6.4.1	Stabilization of Charge-separated States	592
6.4.2	Kinetic Analysis of Electron-transfer Reactions in Micelles.....	597
6.5	Electron-transfer Reactions in Vesicles and Membranes	601
6.5.1	Biological Electron Transport and ‘Artificial Photosynthesis’.....	601
6.5.2	Primary Charge Separation Events.....	602
6.5.3	Kinetic Analyses	607
6.5.4	Transmembrane Oxidation–Reduction Reactions	609
	Acknowledgments.....	617
	References	618
Part 3	Gas-phase Systems	625
	Yehuda Haas (Ed.)	
1	Introduction and Theoretical Background.....	627
	<i>Yehuda Haas</i>	
1.1	Some Novel Experimental Advances.....	629
1.2	Theoretical Background	630
2	Electron-transfer Reactions Involving Atoms, Molecules and Clusters	632
	<i>Benoit Soep and Jean Michel Mestdagh</i>	
2.1	Introduction.....	632
2.2	Experimental Methods.....	635
2.3	The Harpoon Model and Beyond: a Historical Review	637
2.3.1	The Early Age: the Harpoon, a Model to Describe Reactions of Ground-state Alkali Metal Atoms.....	637
2.3.2	A First Multi-dimensional Reaction Model: the DIPR-DIP Model	640

2.3.3	The Double Harpoon: a Mechanism Adapted to Alkaline Earth Metal Atom Reactions	642
2.3.4	Beyond the Harpoon Model: the HOMO/LUMO Matching to Describe Transition Metal Reactivity	647
2.3.5	Multicenter Harpoon Reactions.....	649
2.3.6	Harpoon Reactions with Surfaces.....	650
2.4	Effect of Changing the Internal State of the Reactants.....	651
2.4.1	Changing the Vibrational State of the Molecular Reactant	651
2.4.2	Electronic Excitation to Overcome an Endoergicity Barrier	652
2.4.3	Effect of Electronic Excitation on the Reaction Dynamics.....	654
2.5	Stereodynamics of the Electron Transfer	660
2.6	Van der Waals Complexes: a Tool to Explore the Potential Energy Surface in the Electron-transfer Region.....	662
2.6.1	Local Excitation and Subsequent Electron Transfer.....	663
2.6.2	Time-resolved Observation of Electron Transfer in Excited-state Reactions: the Ba-FCH ₃ case.....	675
2.6.3	Direct Excitation of an Electron-transfer Complex.....	675
2.7	Prereactive Behavior in Ground States.....	677
2.7.1	Stabilizing an Electron-transfer Complex	677
2.7.2	Observing Partial Electron Transfers in the Gas Phase.....	678
2.8	Towards Electron-transfer Reactions in Condensed Phases.....	680
2.8.1	Solvent-induced Electron Transfer in Clusters	680
2.8.2	Dynamics of Electron Solvation in Finite Water Clusters.....	681
2.8.3	Cluster Isolated Chemical Reactions.....	681
2.9	Summary and Conclusions	687
	References.....	688
3	TICT Molecules.....	697
	<i>Jerzy Herbich and Bernhard Brutschy</i>	
3.1	Photoinduced Electron Transfer in Donor–Acceptor (D–A) Molecules in Solutions.....	697
3.1.1	Introduction.....	697
3.1.2	Solvent-dependent Dual Luminescence	698
3.1.3	Electronic and Molecular Structure of Large D–A π -Systems	701
3.1.4	TICT Molecules	706
3.2	Supersonic Jet Spectroscopy of Selected D–A Molecules	707
3.2.1	Introduction.....	707
3.2.2	Bare Molecules	711
3.2.3	Microsolvation Effects.....	716
3.2.4	Concluding Remarks	731
3.3	Summary and Perspectives	732
	Acknowledgments	733
	References.....	734
4	Exciplexes of Large Molecules	742
	<i>Yehuda Haas</i>	
4.1	Introduction.....	742

4.1.1	Evidence for Electron Transfer in Isolated Systems.....	745
4.2	Structure–Reactivity Relationships.....	747
4.2.1	The Co-existence of Several Isomers	748
4.2.2	Hole-burning Spectroscopy	748
4.2.3	Two-color Photoionization	757
4.3	Distance Dependence of Charge Separation; Mechanisms	758
4.4	Rate of Electron Transfer.....	761
4.5	Exciplexes in Reactive Systems.....	763
4.6	Modeling	769
4.7	Conclusions	772
	Acknowledgments.....	773
	References	773
5	Isolated Supermolecules	775
	<i>Yasuhiro Ohshima, Okitsugu Kajimoto and Kiyokazu Fuke</i>	
5.1	Introduction	775
5.2	Stepwise Charge Separation in Alkali Metal Atom-containing Clusters.....	776
5.2.1	Alkali Metal Atom Clusters Solvated with Ammonia Molecules	777
5.2.2	Hydrated Clusters of Alkali Metal Atoms	781
5.3	Charge Transfer in Solvated Anion Clusters.....	786
5.3.1	Dipole-bound Excited States in I^- Clusters Solvated with Small Organic Molecules	787
5.3.2	CTTS Precursor States in $I^-(\text{water})_n$ Clusters	789
5.3.3	Dipole-bound Excited State in $I^-(\text{Xe})_n$ Clusters	793
5.4	Electron-transfer Reactions in Large Donor–Acceptor Molecules Studied Under Jet-cooled Conditions	795
5.4.1	Directly Connected EDA Molecules	796
5.4.2	Bridged EDA Molecules.....	800
5.5	Conclusion and Outlook	801
	References	802

Volume V

Part 1	Molecular-Level Electronics	1
	A. Prasanna de Silva (Ed.)	
1	Wires Based on Metal Complexes	3
	<i>Jean-Pierre Launay and Christophe Coudret</i>	
1.1	Introduction.....	3
1.2	Bimetallic Metal Complexes as Models of Molecular Wires	4
1.3	Synthetic Strategies	6
1.3.1	Redox Centers	7
1.3.2	Conjugated Bridges	12
1.4	Theory	20
1.4.1	Outline of the Theoretical Treatment of Mixed-valence Compounds.....	20
1.4.2	Processes Related to the V_{ab} Coupling	22
1.5	Review of the Different Studies	26
1.5.1	Intervallence Electron Transfer	26
1.5.2	Electron Transfer through a Monolayer at an Electrode.....	33
1.5.3	Excited-state Electron Transfer.....	34
1.5.4	Dexter-type Energy Transfer	35
1.5.5	Other Effects	36
1.6	Conclusions	38
1.6.1	The Decay Law	38
1.6.2	Cyclometallated Compounds.....	42
1.6.3	Puzzling Compounds	43
1.6.4	Mixed-valence Complexes and Metal/Molecule/Metal Nanjunctions	43
	References.....	44
2	Approaches to an Optically Controlled Molecular Switch.....	48
	<i>Aaron S. Lukas and Michael R. Wasielewski</i>	
2.1	Introduction.....	48
2.2	Systems Consisting of Single Molecules.....	50
2.2.1	Two-level Systems	50
2.3	Photochromic Systems.....	51
2.3.1	Photoisomerizations	52
2.3.2	Open–Closed Ring Systems	55
2.3.3	Photorearrangements	59
2.4	Electron Transfer Based Systems.....	59
2.4.1	Intermolecular Electron Transfer.....	60
2.4.2	Intramolecular Electron Transfer	61
2.5	Energy Transfer Based Systems	73
2.6	Conclusions and Future Prospects	88
	Acknowledgment	89
	References.....	89

3	Photonic Wires Containing Metal Complexes	97
	<i>Luisa De Cola and Peter Belser</i>	
3.1	Introduction	97
3.2	Choice and Assembly of the Components for Photoactive Systems	98
3.3	Intercomponent Photoinduced Processes	100
3.4	What is a Molecular Wire?	103
3.5	Systems Containing Saturated Spacers	104
3.6	Systems Containing Conjugated Spacers	109
3.6.1	Polyene-bridged Bimetallic Compounds	109
3.6.2	Oligoyne-bridged Bimetallic Compounds	111
3.6.3	Phenylene-bridged Bimetallic Compounds	114
3.6.4	Other Conjugated Systems	119
3.7	Modulation of the Electronic Interactions in Dinuclear Complexes	123
3.8	Conclusions	130
	Abbreviations	132
	References	132
4	Rectifiers	137
	<i>Alan C. Brady and J. Roy Sambles</i>	
4.1	Introduction	137
4.2	Molecular Conduction	138
4.3	Molecular Rectifier	139
4.4	Practical Investigation of a Molecular Rectifier	145
4.5	The Langmuir–Blodgett Technique	146
4.6	Junction Design	148
4.7	Electrical Characterizations of LB Films	150
4.8	Other Techniques	154
4.9	Conclusions	154
	References	154
5	Logic Gates	156
	<i>A. Prasanna de Silva, Nathan D. McClenaghan, and Colin P. McCoy</i>	
5.1	Introduction	156
5.2	Photochemical Approaches to Molecular-scale Logic	157
5.2.1	Chemical/Optical Input/Output	157
5.2.2	All-optical Input/Output	168
5.3	Other Approaches to Molecular-scale Information Processing	172
5.3.1	Mechanochemical Approach	172
5.3.2	Oligonucleotide Approach	175
5.3.3	Quantum Approach	177
5.3.4	Electronic Approach	180
5.4	Conclusion	182

	Acknowledgements	182
	References.....	182
6	Antennas	186
	<i>Sebastiano Campagna, Scolastica Serroni, Fausto Puntoriero,</i> <i>Cinzia Di Pietro, and Vittorio Ricevuto</i>	
6.1	Introduction.....	186
6.2	Natural Antennas.....	188
6.3	Artificial Antennas.....	190
6.3.1	Principles of Design.....	190
6.3.2	Examples.....	193
6.4	Concluding Remarks	211
	References.....	211
7	Memories	215
	<i>Masahiro Irie and Kenji Matsuda</i>	
7.1	Introduction.....	215
7.2	Irreversible Memory Media	216
7.3	Reversible Memory Media	218
7.3.1	Diarylethenes	220
7.3.2	Furyl Fulgide Derivatives	229
7.3.3	Phenoxynaphthacene Quinones	235
7.3.4	Stilbene Derivatives.....	236
7.4	Nondestructive Readout.....	237
7.5	Near-field Memory	239
7.6	Conclusions	240
	References.....	240
8	Nonlinear Optics	243
	<i>Stephan Houbrechts, Eric Hendrickx, Thierry Verbiest, Koen Clays,</i> <i>and André Persoons</i>	
8.1	Introduction to Nonlinear Optics	243
8.1.1	The Basics of Nonlinear Optics	243
8.1.2	Symmetry Restrictions.....	245
8.1.3	Systems of Units.....	246
8.2	Measurement Techniques.....	247
8.2.1	Electric-field-induced Second-harmonic Generation (EFISHG)	247
8.2.2	Hyper-Rayleigh Scattering (HRS)	250
8.3	Second-order Nonlinear Optical Molecules.....	252
8.3.1	Dipolar Molecular Structures	252
8.3.2	Rigid Multichromophoric Molecules	255
8.3.3	Octopolar Molecules.....	264
8.3.4	Metallo-organic Compounds.....	268
8.4	Macroscopic Nonlinearities	273

Acknowledgments.....	276
References.....	276
Part 2 Imaging and Information	283
Ian R. Gould (Ed.)	
1 Electron Transfer Processes in Silver Halide Photography	285
<i>John R. Fyson, Peter J. Twist, and Ian R. Gould</i>	
1.1 Introduction.....	285
1.2 Developers	286
1.2.1 Introduction.....	286
1.2.2 Chemical Development	287
1.2.3 Coupling.....	335
1.3 Bleaching/Bleach-Fixing	336
1.3.1 Introduction—General Mechanisms	336
1.3.2 Solvent Bleaches	338
1.3.3 Bleach-Fixes	344
1.3.4 Diffusion	346
1.3.5 Specific Bleaching Agents.....	347
1.3.6 Dye-Bleaches	354
1.3.7 Fixing and Washing	355
1.4 Spectral Sensitization	355
1.4.1 Introduction	355
1.4.2 Electronic Properties of Silver Halides	356
1.4.3 Sensitizing Dyes.....	357
1.4.4 Sensitization Mechanisms.....	363
1.4.5 Kinetic Measurements of Electron Injection	370
1.4.6 Supersensitization	372
References	373
2 Electrophotography.....	379
<i>David S. Weiss, J. Robin Cowdery, and Ralph H. Young</i>	
2.1 Introduction.....	379
2.2 Electrophotographic Developers.....	381
2.3 Organic Photoreceptor Fabrication and Characterization.....	383
2.4 Corona Charging.....	388
2.5 Charge Carrier Generation	390
2.5.1 Background and Methodologies.....	390
2.5.2 Models	393
2.5.3 Organic Photoreceptors.....	398
2.5.4 Summary of Carrier Generation Mechanisms	428
2.6 Charge Transport	429
2.6.1 Typical Materials	429
2.6.2 Charge Carrier Mobility	431
2.6.3 Chemical Desiderata for Charge-transporting Molecules.....	460

2.7	Concluding Remarks	462
	References.....	463
3	Photorefractive Materials	472
	<i>David P. West and Mark D. Rahn</i>	
3.1	The Photorefractive Effect in Crystals and Amorphous Organic Media	472
3.1.1	Scenarios of Potential Applications	472
3.1.2	An Overview of the Sequence of Processes Leading to Photorefractivity	473
3.1.3	A Historical Perspective	479
3.2	Electron Transfer in Amorphous Organic Photorefractive Media	481
3.2.1	Optical Generation of Bound Pairs	482
3.2.2	Dissociation of Bound Pairs into Free Charges.....	484
3.2.3	Choice of Photosensitizer.....	484
3.2.4	Specific Material Systems.....	488
3.2.5	Fully Functional and Permanently Poled Materials	494
3.3	Charge Transport Processes in Amorphous Organic Media	494
3.3.1	Transport in Disordered Media	495
3.3.2	Specific Examples of Hole Transport Materials for Organic Photorefractives.....	499
3.3.3	Pulsed Excitation and Charge Trapping	501
3.4	An Overview of Amorphous Organic Photorefractives and Their Applications.....	503
3.4.1	The Electro-optic Response	503
3.4.2	Holographic Optical Data Storage and Other Applications.....	508
	Acknowledgements	513
	References.....	513
4	Photoinduced Electron Transfer Initiating Systems for Free-radical Polymerization	516
	<i>Jerzy Paczkowski and Douglas C. Neckers</i>	
4.1	Introduction.....	516
4.2	General Scheme.....	517
4.3	Dye Photoinitiators–mechanisms	519
4.3.1	Photoinitiating Donor–Acceptor Pairs with Electrostatic Interaction in the Ground State (Ground-state Ion Pair) and Neutral after Photoinduced Electron Transfer Process.....	519
4.3.2	Photoinitiating Donor–Acceptor Pair without Electrostatic Interaction in Ground State and after an Electron Transfer	538
4.3.3	Photoinitiating Donor–Acceptor Pair Neutral in a Ground State and Charged after an Electron Transfer (Radical-ion Pair).	545
4.4	Kinetics	568
	Acknowledgments	580
	References.....	580

Part 3	Energy and the Environment	587
	Ian R. Gould (Ed.)	
1	Solar Energy Conversion	589
	<i>Michael Grätzel and Jacques-E. Moser</i>	
1.1	Introduction and Scope	589
1.2	Efficiency Restrictions in Photochemical Conversion	589
1.2.1	Maximum Power Extraction	590
1.2.2	Limitations due to the Entropy of Light	591
1.2.3	Further Increase of Entropy on Absorption or Scattering	592
1.2.4	Efficiency of Energy Conversion under Polychromatic Radiation....	594
1.3	Status of Photochemical Energy Conversion Systems	595
1.4	Molecular Photovoltaics	596
1.4.1	Mimicking Natural Photosynthesis	597
1.4.2	Mesoscopic Oxide Semiconductor Films	600
1.4.3	Photoinduced Charge Separation at the Solid/Electrolyte Interface..	603
1.4.4	Charge Separation in Molecular Photovoltaic Devices	623
1.4.5	Charge Separation in Nanocrystalline Heterotriads	628
1.4.6	Photovoltaic Performances of Dye-sensitized Nanocrystalline Solar Cells	634
1.5	Water Cleavage by Visible Light	636
1.5.1	Analogues of Photosystem II of Green Plants	637
1.5.2	Colloidal Semiconductor Systems	637
1.5.3	Tandem Systems for Water Cleavage by Visible Light	638
1.6	Future Outlook and Concluding Remarks	639
	Acknowledgments.....	641
	References.....	641
2	Batteries	645
	<i>Catia Arbizzani, Marina Mastragostino, and Francesca Soavi</i>	
2.1	Introduction	645
2.2	Basic Aspects	647
2.2.1	Thermodynamics and Electrochemical Kinetics	650
2.2.2	Battery Performance	656
2.3	Energy Conversion Systems	657
2.3.1	Primary Cells.....	657
2.3.2	Secondary Cells	661
2.3.3	Supercapacitors	668
2.3.4	Fuel Cells.....	673
2.4	Lithium Rechargeable Batteries	676
2.4.1	Lithium-Metal Batteries	677
2.4.2	Lithium-ion Batteries	681
2.4.3	Insertion Electrode Materials.....	682
2.5	Present Status and Future Prospects	690
	References.....	691

3	Principles of Semiconductor-assisted Photocatalysis for Waste Remediation	695
	<i>Marion C. Thurnauer, Tijana Rajh, and Nada M. Dimitrijevic</i>	
3.1	Introduction.....	695
3.2	Colloidal Semiconductors	696
3.2.1	Optical Properties of Semiconductors.....	696
3.2.2	Quantization Effect	698
3.2.3	Space Charge Layer and Band Banding	699
3.2.4	Energy Band Structure of TiO ₂	701
3.3	Basic Mechanisms of Semiconductor-assisted Photocatalysis	703
3.3.1	Photogeneration of Charge Pairs and Intrinsic Properties of Semiconductors	703
3.3.2	Charge Pair Separation and Charge Carrier Trapping	706
3.3.3	Charge Carrier Recombination and Interfacial Electron Transfer	707
3.3.4	Nature of Trapping Sites	709
3.3.5	Adsorption.....	709
3.4	Enhanced Charge Separation: Route for Efficient Photodegradation.....	712
3.4.1	Metallization of Semiconductor Particles.....	712
3.4.2	Surface Modification	713
3.4.3	Dye Sensitization	714
3.5	Radiation-induced Catalysis on Semiconductor Surfaces	714
3.6	Summary.....	716
	Acknowledgment	716
	References.....	716
	Index	719

About the Editors

Editor in Chief and editor of Volume III, Part 2



Vincenzo Balzani received his "laurea" in Chemistry at the University of Bologna, Italy, in 1960 and has been Professor of Chemistry at the same university since 1972. He has obtained several awards, including the Canizzarro Gold Medal of the Italian Chemical Society, the Doctorate Honoris Causa from the University of Fribourg, Switzerland, the Ziegler-Natta Lectureship of the Gesellschaft Deutscher Chemiker, the Italgas European Prize for Research and Innovation, the Centenary Lecture of the Royal Society of Chemistry, as well as the Porter Medal on Photochemistry. He is a fellow of the Royal Society of Chemistry, the American Association for the Advancement of Science, and the Italian Accademia Nazionale dei Lincei. He has served or is now serving as a member of the Editorial Boards of several scientific journals, including *Chemistry – A European Journal*, *Chemical Society Review*, *Inorganic Chemistry*, *Nanotechnology*, *ChemPhysChem*, *RSC Dalton Transactions*, and *Accounts of Chemical Research*. He is the author of more than 400 scientific papers, two edited books, and two monographs. His research interests include electron-transfer processes, photochemistry, photophysics, supramolecular chemistry, and artificial molecular machines.

Editor of Volume I, Part 1



Piotr Piotrowiak was born in Wrocław, Poland, and grew up in a small town in the foothills of the Sudety Mountains. He graduated from the University of Wrocław in 1982 (Magisterium with H. Ratajczak). After a brief stay at Stony Brook, he joined the group of G. L. Closs at the University of Chicago, where he received his Ph.D. in 1988. In 1991, after a postdoctoral appointment with J. R. Miller at the Argonne National Laboratory, he took a faculty position at the University of New Orleans in Louisiana, where he became Associate Professor in 1996. Since 1997 he has been an Associate Professor at Rutgers University in Newark, New Jersey. His current research interests include vibronically mediated electron and excitation transfer in compounds with symmetry-forbidden interactions, properties of non-aqueous electrolyte solutions, solvation in mixed media, donor-acceptor systems with heteroatom bridges, and the propagation of electronic interactions across the walls of molecular cages. The work of his group involves the synthesis of model compounds and a variety of time-resolved laser spectroscopy measurements.

Editor of Volume I, Part 2



Michael A. J. Rodgers graduated from the Royal Institute of Chemistry in 1963. In 1964 he received his M.Sc., and two years later his Ph.D., from the University of Manchester. In 1966 he became a postdoctoral fellow at the Lawrence Berkeley Laboratory, later he became a Senior Associate and finally a Lecturer in Chemistry at the University of Manchester. In 1976 he went to the University of Texas at Austin to become Deputy Director and Scientific Coordinator of the Center for Fast Kinetics Research and later Director of that institution. Since 1988 he has been Ohio Board of Regents Eminent Scholar in Photochemical Science and Professor of Chemistry at Bowling Green State University. He held the chair of the department of chemistry from 1996 to 1999. Rodgers has received several awards including the Olscamp (BGSU) Research Award (1996), the American Society of Photobiology Research Award (1997), and he is the 2001 research award winner of the Inter-American Photochemical Society. He has been a visiting professor at the University of Bologna, the University of Puerto Rico (Mayaguez), and at EHICS, Strasbourg. His research interests include excited state dynamics of tetrapyrrole macrocycles, photodynamic and photothermal damage in biological systems, energy transfer involving oxygen, electron transfer in proteins and peptides as well as the design, assembly and use of high-technology instrumentation for transient spectroscopy.

Editor of Volume II, Part 1



Before graduating from high school (Abitur), Jochen Mattay was trained as a laboratory technician (Chemielaborant) at Asta-Werke (Bielefeld). He obtained his diploma (M.Sc.) and later his Dr. rer. nat. (Ph.D.) from the College of Technology at Aachen for his work on synthetic and mechanistic studies of various photoreactions (enones, arenes) under the supervision of H.-D. Scharf. He then spent more than a year as a NATO fellow at Columbia University, New York, where he worked on micellar and magnetic field effects of photocleavage reactions in the group of N. J. Turro. Returning to Aachen in 1980, he started his own projects and finished his habilitation in 1983. In the following year, he was appointed lecturer (Privatdozent). Before joining the chemistry faculty at the University of Bielefeld in 1998, Jochen Mattay held various positions from that of Associate Professor to full Professor at the universities of Aachen (1985–89), Münster (1989–95), and Kiel (1995–98). He also spent some time as Visiting Professor at Osaka University (1995) and at the University of Berne (1996). His research interests include photochemistry, the chemistry of calixarenes and resorcarenes (supramolecular chemistry), fullerene chemistry, as well as stereoselective cycloadditions and radical additions.

Editor of Volume II, Part 2



Didier Astruc is Professor of Chemistry at the Université de Bordeaux I and a Member of the Institut Universitaire de France where he holds the Chair of Supramolecular Organometallic Chemistry. He was born in Versailles and did all his studies in Rennes including his thesis on ferrocene cages under the supervision of Professor René Dabard. He was a NATO post-doctoral fellow at MIT, Cambridge (USA), where he worked with Professor Richard R. Schrock, then took a CNRS position in Rennes and became Maître de Recherche before moving to the Université de Bordeaux I as a full Professor in 1984. He has developed the concept of "Electron-Reservoirs" and its applications, and synthesized with his research group the first organometallic dendrimers. He is interested in supramolecular nanomolecules and nanoscopic materials, and their applications in catalysis, molecular recognition, sensors, and devices.

Editors of Volume III, Part I



Harry B. Gray (on the left-hand side) studied inorganic chemistry at Northwestern University in Evanston, Illinois (1957–60) and at the University of Copenhagen (1960–61) before joining the chemistry faculty of Columbia University, New York. In 1966 he moved to Caltech where he is the Arnold O. Beckman Professor of Chemistry and Director of the Beckman Institute. His research interests include inorganic spectroscopy and photochemistry, bio-inorganic chemistry, and electron transfer in proteins. Jay R. Winkler (on the right-hand side) received his Ph.D. from Caltech in 1984. After a stay at the Brookhaven National Laboratory he moved back to Caltech in 1990 where he is now Director of the Laser Resource Center and a Member of the Beckman Institute.

Editor of Volume IV, Part 1

Shunichi Fukuzumi was born in 1950. He graduated from the Tokyo Institute of Technology in 1973, where he also received his Ph.D. in 1978. After a postdoctoral fellowship with Prof. J. K. Kochi at the Indiana University, he became Assistant Professor at the Department of Applied Chemistry, Faculty of Engineering, Osaka University in 1981. After a stay as Invited Professor at the Department of Chemistry, Marseilles University, he became Associate Professor in 1993 and Professor as Head of the Laboratory of Industrial Physical Chemistry in 1994. Since 1995 he has been Professor at the Department of Material and Life Science, Graduate School of Engineering, Osaka University. Fields of interest include electron-transfer chemistry of biologically important compounds, organometallic compounds, and metal complexes.

Editor of Volume IV, Part 2



Thomas E. Mallouk was born in New York and received an Sc.B. degree from Brown University. He was a graduate student at the University of California, Berkeley, and a postdoctoral fellow at MIT, Cambridge (USA). In 1985, he joined the Chemistry faculty at the University of Texas at Austin. He moved to Penn State in 1993, where he is now DuPont Professor of Materials Chemistry. He is best known for his work on inorganic self-assembly and on the chemistry of layered and zeolitic materials. His research has focused on the application of inorganic materials to different chemical problems, including chiral separations, chemical sensing, photochemical energy conversion, microelectronics, fuel cell electrochemistry, and environmental chemistry. He is author or co-author of approximately 160 scientific publications, including a few good ones, and has also edited three books on chemical sensing and solid state chemistry. He is currently Associate Editor of the *Journal of the American Chemical Society* and serves on the editorial advisory boards of several other journals.

Editor of Volume IV, Part 3



Yehuda Haas was born in Israel in 1939. In 1971 he received his Ph.D. from the Hebrew University of Jerusalem and has been on the staff of the Physical Chemistry Department since 1975, becoming a Professor in 1984. Between 1989 and 1992 he was Vice President for Research and Development of the University. Professor Haas has held several visiting positions at the Max-Planck-Institute in Göttingen (1980), at the University of Southern California in Los Angeles (1981), at the Université de Paris Sud in Orsay (1986), at the Institute of Molecular Science in Okazaki (1992), and at the University of Oxford (1996). His main scientific interests are photochemistry and photophysics, laser-induced chemistry, photo-induced electron transfer, and matrix isolation. His publication list includes more than 120 papers and one book.

Editor of Volume V, Part 1



A. P. de Silva's learning, teaching, and research experiences are a tale of two cities and their universities. The University of Colombo, Sri Lanka, and the Queen's University of Belfast, Northern Ireland, have played host to him alternately. He received his early education in chemistry at Colombo in 1970–75. This was followed by Ph.D. and postdoctoral research in organic photochemistry at Belfast during the period 1976–80. After spending six years lecturing in chemistry at Colombo, he returned to Belfast where he has been lecturer (1986–91), reader (1991–97), and professor since 1997.

Editor of Volume V, Part 2 and Part 3

Ian R. Gould was born in Cleveleys, England, in 1957. He received his M.Sc. in 1978 and, two years later his Ph.D., both with A. A. Gorman at the University of Manchester. After postdoctoral training with N. J. Turro at Columbia University, he became Research Associate there. In 1986 he moved to the Eastman Kodak Company. He has been an Assistant Professor at Arizona State University since 1998. Ian R. Gould has obtained several awards, including the Organic Chemistry Prize (Manchester University), the Gramatacakis Neumann Award (European Photochemical Association), and the C. E. K. Mees Award (Eastman Kodak Company). He is a member of the American Chemical Society, the Inter-American Photochemical Society, and the European Photochemical Association. His research interests include organic photochemistry and photophysics, fundamental mechanisms of electron- and proton-transfer reactions, photonic materials, biopolymers, reactions of organic radical ions, spectral sensitization of semiconductors, fast reaction kinetics, and pulsed laser techniques.

List of Authors

Authors for Volume I

Ann-Margret Andersson
Department of Chemistry
Tulane University
New Orleans
Louisiana 70118
USA

Andreja Bakac
Ames Laboratory
Iowa State University
Ames
Iowa 50011
USA

David N. Beratan
Department of Chemistry
University of Pittsburgh
Pittsburgh
Pennsylvania 15260
USA

George V. Buxton
Centre for Joint Honours in Science
University of Leeds
Leeds LS2 9JT
UK

Kim Daasbjerg
Department of Chemistry
University of Aarhus
Langelandsgade 140
8000 Aarhus C
Denmark

John F. Endicott
Department of Chemistry
Wayne State University
Detroit
Michigan 48202
USA

Marye Ann Fox
Department of Chemistry
North Carolina State University
Raleigh
North Carolina 27695
USA

Sharon Hammes-Schiffer
Department of Chemistry and
Biochemistry
University of Notre Dame
Notre Dame
Indiana 46556-5670
USA

Kevin Henbest
Department of Chemistry
Howard L. Hunter Chemistry
Laboratory
Clemson University
Clemson
South Carolina 29634-1905
USA

Quinto G. Mulazzani
Istituto di Fotochimica e Radiazioni
d'Alta Energia del C.N.R.
Via P. Gobetti 101
40129 Bologna
Italy

Stephen F. Nelsen
Department of Chemistry
University of Wisconsin
1101 University Avenue
Madison
Wisconsin 53706-1396
USA

Marshall D. Newton
Department of Chemistry
Brookhaven National Laboratory
Box 5000
Upton
New York 11973
USA

Steen Uttrup Pedersen
Department of Chemistry
University of Aarhus
Langelandsgade 140
8000 Aarhus C
Denmark

Piotr Piotrowiak
Department of Chemistry
Rutgers University
University Heights
Newark
New Jersey 07102
USA

Michael A. J. Rodgers
Center for Photochemical Sciences
Department of Chemistry
Bowling Green State University
Bowling Green
Ohio 43403
USA

Russell H. Schmehl
Department of Chemistry
Tulane University
New Orleans
Louisiana 70118
USA

Spiros S. Skourtis
Department of Natural Sciences
University of Cyprus
Box 20537
Nicosia 1678
Cyprus

Hitoshi Sumi
Institute of Materials Science
University of Tsukuba
Tsukuba
305-8573
Japan

Daniel Vanmaekelbergh
Condensed Matter, Debye Institute
University of Utrecht
P.O. Box 80000
3508 TA Utrecht
The Netherlands

Authors of Volume II

Angelo Albini
Department of Organic Chemistry
University of Pavia
Via Taramelli 10
27100 Pavia
Italy

Didier Astruc
Groupe de Chimie Supramoléculaire
des Métaux de Transition
LCOO
UMR CNRS No. 5802
Université Bordeaux I
33405 Talence Cédex
France

Nathan L. Bauld
Department of Chemistry and
Biochemistry
The University of Texas
Austin
Texas 78712
USA

Massimo Bietti
Dipartimento di Scienze e Tecnologie
Chimiche
Università di Roma 'Tor Vergata'
00133 Roma
Italy

Bruce S. Brunschwig
Chemistry Department
Brookhaven National Laboratory
Upton
New York 11973-5000
USA

Suresh Das
Photochemistry Research Unit
Regional Research Laboratory
(Council of Scientific and Industrial
Research)
Trivandrum-695019
India

Maurizio Fagnoni
Department of Organic Chemistry
University of Pavia
Via Taramelli 10
27100 Pavia
Italy

Cameron E. Forde
Department of Chemistry
University of Toronto
80 St. George Street
Toronto
Ontario M5S 3H6
Canada

Shunichi Fukuzumi
Department of Material and Life
Science
Graduate School of Engineering
Osaka University
CREST, Japan Science and Technology
Corporation
Suita
Osaka 565-0871
Japan

Daxin Gao
Department of Chemistry and
Biochemistry
The University of Texas
Austin
Texas 78712
USA

Georg Gescheidt
Institut für Physikalische Chemie
Universität Basel
Klingenbergstrasse 80
4056 Basel
Switzerland

Manas K. Ghorai
Fachbereich 8-OC1 (Chemie und
Biologie)
Universität Siegen
Adolf-Reichwein-Strasse
57068 Siegen
Germany

Axel G. Griesbeck
Institut für Organische Chemie der
Universität zu Köln
Greinstrasse 4
50939 Köln
Germany

Dirk M. Guldi
Radiation Laboratory
University of Notre Dame
Notre Dame
Indiana 46556
USA

J. Heyrovský
Institute of Physical Chemistry
Academy of Sciences of the
Czech Republic
Dolejšková 3
182 23 Prague
Czech Republic

Stephan M. Hubig
Department of Chemistry
University of Houston
Houston
Texas 77204-5641
USA

Hiroshi Imahori
Department of Material and Life
Science
Graduate School of Engineering
Osaka University
CREST, Japan Science and Technology
Corporation
Suita
Osaka 565-0871
Japan

Wolfgang Kaim
Institut für Anorganische Chemie
Universität Stuttgart
Pfaffenwaldring 55
70550 Stuttgart
Germany

Nadeem Khan
Institut für Physikalische Chemie
Universität Basel
Klingenbergstrasse 80
4056 Basel
Switzerland

Jay K. Kochi
Department of Chemistry
University of Houston
Houston
Texas 77204-5641
USA

Robert H. Morris
Department of Chemistry
University of Toronto
80 St. George Street
Toronto
Ontario M5S 3H6
Canada

Heinz D. Roth
Rutgers University
Wright–Rieman Laboratories
New Brunswick
New Jersey 08854-8087
USA

Stefan Schieffer
Institut für Organische Chemie der
Universität zu Köln
Greinstrasse 4
50939 Köln
Germany

Michael Schmittl
Fachbereich 8–OC1 (Chemie und
Biologie)
Universität Siegen
Adolf-Reichwein-Strasse
57068 Siegen
Germany

Alexander E. Shilov
Institute of Chemical Physics Problems
142432 Chergolovka
Russia

Steen Steenken
Max-Planck-Institut für Strahlenchemie
45470 Mülheim
Germany

Velate Suresh
Photochemistry Research Unit
Regional Research Laboratory
(Council of Scientific and Industrial
Research)
Trivandrum-695019
India

Norman Sutin
Chemistry Department
Brookhaven National Laboratory
Upton
New York 11973-5000
USA

Mats Tilset
Department of Chemistry
University of Oslo
P.O. Box 1033 Blindern
0315 Oslo
Norway

Antonín Vlček, Jr.
Department of Chemistry
Queen Mary and Westfield College
(University of London)
London E1 4NS
UK

Authors of Volume III

Nicola Armaroli
Istituto FRAE-CNR
Via P. Gobetti 101
40129 Bologna
Italy

Erin A. Baker
Department of Chemistry, 6-335
Massachusetts Institute of Technology
77 Massachusetts Avenue
Cambridge
Massachusetts 022130-4307
USA

Roberto Ballardini
Istituto FRAE-CNR
Via P. Gobetti 101
40129 Bologna
Italy

Vincenzo Balzani
Dipartimento di Chimica
“G. Ciamician”
Università di Bologna
Via Selmi 2
40126 Bologna
Italy

Joshua D. K. Brown
Department of Chemistry, 6-335
Massachusetts Institute of Technology
77 Massachusetts Avenue
Cambridge
Massachusetts 022130-4307
USA

Jean-Claude Chambron
Université Louis Pasteur
Institut Le Bel
4 rue Blaise Pascal
67000 Strasbourg
France

Christopher J. Chang
Department of Chemistry, 6-335
Massachusetts Institute of Technology
77 Massachusetts Avenue
Cambridge
Massachusetts 022130-4307
USA

Michelle C.Y. Chang
Department of Chemistry, 6-335
Massachusetts Institute of Technology
77 Massachusetts Avenue
Cambridge
Massachusetts 022130-4307
USA

Claudio Chiorboli
Dipartimento di Chimica
Università di Ferrara
Centro di Fotoreattività e Catalisi
CNR
44100 Ferrara
Italy

Jean-Paul Collin
Université Louis Pasteur
Institut Le Bel
4 rue Blaise Pascal
67000 Strasbourg
France

Alberto Credi
Dipartimento di Chimica "G.
Ciamician"
Università di Bologna
Via Selmi 2
40126 Bologna
Italy

John H. Dawson
Department of Chemistry and
Biochemistry and School of Medicine
University of South Carolina
Columbia
South Carolina 29208
USA

Christiane Dietrich-Buchecker
Université Louis Pasteur
Institut Le Bel
4 rue Blaise Pascal
67000 Strasbourg
France

P. Leslie Dutton
Department of Biochemistry and
Biophysics
University of Pennsylvania
1005 Stellar-Chance Building
Philadelphia
Pennsylvania 19104
USA

Luigi Fabbrizzi
Dipartimento di Chimica Generale
Università di Pavia
Via Taramelli 12
27100 Pavia
Italy

Lucia Flamigni
Istituto FRAE-CNR
Via P. Gobetti 101
40129 Bologna
Italy

Maria Teresa Gandolfi
Dipartimento di Chimica "G.
Ciamician"
Università di Bologna
Via Selmi 2
40162 Bologna
Italy

David B. Goodin
Department of Molecular Biology
The Scripps Research Institute
La Jolla
California 92037
USA

Harry B. Gray
Beckman Institute, MC 139-74,
California Institute of Technology
Pasadena
California 91125
USA

Devens Gust
Center for the Study of Early Events in
Photosynthesis
Department of Chemistry and
Biochemistry
Arizona State University
Tempe
Arizona 85287-1604
USA

Maria Teresa Indelli
Dipartimento di Chimica
Università di Ferrara
Centro di Fotoreattività e Catalisi CNR
44100 Ferrara
Italy

Alberto Juris
Dipartimento di Chimica "G.
Ciamician"
Università di Bologna
Via Selmi 2
40126 Bologna
Italy

Jean-Marc Kern
Université Louis Pasteur
Institut Le Bel
4 rue Blaise Pascal
67000 Strasbourg
France

Amy P. Ledbetter
Department of Chemistry and
Biochemistry
University of South Carolina
Columbia
South Carolina 29208
USA

Frederick D. Lewis
Department of Chemistry
Northwestern University
Evanston
Illinois 60208
USA

Maurizio Licchelli
Dipartimento di Chimica Generale
Università di Pavia
Via Taramelli 12
27100 Pavia
Italy

Bo G. Malmström
Department of Chemistry
(Biochemistry and Biophysics)
Göteborg University
P.O. Box 462
405 30 Göteborg
Sweden

Ana L. Moore
Center for the Study of Early Events in
Photosynthesis
Department of Chemistry and
Biochemistry
Arizona State University
Tempe
Arizona 85287-1604
USA

Thomas A. Moore
Center for the Study of Early Events in
Photosynthesis
Department of Chemistry and
Biochemistry
Arizona State University
Tempe
Arizona 85287-1604
USA

Christopher C. Moser
Johnson Research Foundation
University of Pennsylvania
Philadelphia
Pennsylvania 19104
USA

Daniel G. Nocera
Department of Chemistry, 6-335
Massachusetts Institute of Technology
77 Massachusetts Avenue
Cambridge
Massachusetts 022130-4307
USA

Michael N. Paddon-Row
School of Chemistry
University of New South Wales
Sydney
NSW 2052
Australia

Christopher C. Page
Johnson Research Foundation
University of Pennsylvania
Philadelphia
Pennsylvania 19104
USA

Alycen E. Pond
Department of Molecular Biology
The Scripps Research Institute
La Jolla
California 92037
USA

Maria Anita Rampi
Dipartimento di Chimica
Università di Ferrara
Centro di Fotoreattività e Catalisi
CNR
44100 Ferrara
Italy

Jean-Pierre Sauvage
Université Louis Pasteur
Institut Le Bel
4 rue Blaise Pascal
67000 Strasbourg
France

Franco Scandola
Dipartimento di Chimica
Università di Ferrara
Centro di Fotoreattività e Catalisi
CNR
44100 Ferrara
Italy

Masanori Sono
Department of Chemistry and
Biochemistry
University of South Carolina
Columbia
South Carolina 29208
USA

Angelo Taglietti
Dipartimento di Chimica Generale
Università di Pavia
Via Taramelli 12
27100 Pavia
Italy

Margherita Venturi
Dipartimento di Chimica "G.
Ciamician"
Università di Bologna
Via Selmi 2
40126 Bologna
Italy

Jay R. Winkler
Beckman Institute, MC 139-74
California Institute of Technology
Pasadena
California 91125
USA

Authors of Volume IV

Vasudeva Bhat
Research Laboratory of Resources
Utilization
Tokyo Institute of Technology
CREST Japan Science and Technology
Corporation
4259 Nagatsuta-cho
Midori-ku
Yokohama 226-8503
Japan

Bernhard Brutschy
Johann Wolfgang Goethe-Universität
Marie-Curie Strasse
60439 Frankfurt am Main
Germany

Bruce S. Brunschwig
Chemistry Department
Brookhaven National Laboratory
Upton
New York 11973
USA

Robert S. Clegg
Department of Chemistry
University of Oregon
Eugene
Oregon 97403-1253
USA

Michael A. Coutant
Department of Chemistry
The Ohio State University
Columbus
Ohio 43210
USA

Kazunari Domen
Research Laboratory of Resources
Utilization
Tokyo Institute of Technology
CREST
Japan Science and Technology
Corporation
4259 Nagatsuta-cho
Midori-ku
Yokohama 226-8503
Japan

Prabir K. Dutta
Department of Chemistry
The Ohio State University
Columbus
Ohio 43210
USA

Etsuko Fujita
Chemistry Department
Brookhaven National Laboratory
Upton
New York 11973
USA

Kiyokazu Fuke
Department of Chemistry
Faculty of Science
Kobe University
Kobe
Japan

Shunichi Fukuzumi
Department of Materials and Life
Science
Graduate School of Engineering
CREST
Japan Science and Technology
Corporation
Suita
Osaka 565-0871
Japan

Yehuda Haas
Department of Physical Chemistry
and the Farkas Center for Light
Induced Processes
The Hebrew University of Jerusalem
Jerusalem 91904
Israel

Jerzy Herbich
Institute of Physical Chemistry
Polish Academy of Sciences
Kasprzaka 44
01-224 Warsaw
Poland

Matthias Hopfner
Institut für Anorganische Chemie
Egerlandstrasse 1
91058 Erlangen
Germany

James K. Hurst
Department of Chemistry
Washington State University
Pullman
Washington 99164-463
USA

James E. Hutchison
Department of Chemistry
University of Oregon
Eugene
Oregon 97403-1253
USA

Okitsugu Kajimoto
Department of Chemistry
Kyoto University
Kitashirakava-Oiwakecho
Kyoto
Japan

Eugenii Katz
Institute of Chemistry
The Hebrew University of Jerusalem
Jerusalem 91904
Israel

Rafail F. Khairutdinov
Department of Chemistry
Washington State University
Pullman
Washington 99164-463
USA

Horst Kisch
Institut für Anorganische Chemie
Egerlandstrasse 1
91058 Erlangen
Germany

Jean Michel Mestdagh
CEA/DRECAM/Service des Photons
Atomes et Molécules
CEN Saclay
91191 Gif-sur-Yvette cedex
France

Gerald J. Meyer
Department of Chemistry
Johns Hopkins University
Baltimore
Maryland 21211
USA

Yasuhiro Ohshima
Department of Chemistry
Graduate School of Science
Kyoto University
Kyoto
Japan

Ping Qu
Department of Chemistry
Johns Hopkins University
Baltimore
Maryland 21211
USA

Krishnan Rajeshwar
Department of Chemistry and
Biochemistry
The University of Texas at Arlington
Arlington
Texas 76019-0065
USA

Vincent M. Rotello
Department of Chemistry
University of Massachusetts
Amherst
Maryland 01003
USA

Andrew N. Shipway
Institute of Chemistry
The Hebrew University of Jerusalem
Jerusalem 91904
Israel

Benoit Soep
CNRS/Laboratoire de Photophysique
Moléculaire
Université Paris-Sud
91405 Orsay
France

Gordon Tollin
Department of Biochemistry
University of Arizona
Tucson
Arizona 85721
USA

Anand S. Vaidyalingam
Department of Chemistry
The Ohio State University
Columbus
Ohio 43210
USA

Itamar Willner
Institute of Chemistry
The Hebrew University of Jerusalem
Jerusalem 91904
Israel

Authors of Volume V

Catia Arbizzani
Dipartimento di Chimica "G.
Ciamician"
Universita' di Bologna
Via Selmi 2
40126 Bologna
Italy

Peter Belser
Institute of Inorganic Chemistry
University of Fribourg
Pérolles
1700 Fribourg
Switzerland

Alan C. Brady
Thin Film Photonics Group
School of Physics
Stocker Road
Exeter EX4 4QL
UK

Sebastiano Campagna
Dipartimento di Chimica Inorganica,
Chimica Analitica e Chimica Fisica
Università di Messina
Via Sperone 31
98166 Messina
Italy

Koen Clays
Laboratory of Chemical and Biological
Dynamics
Center for Research on Molecular
Electronics and Photonics
University of Leuven
Celestijnenlaan 200D
3001 Leuven
Belgium

Christophe Coudret
Molecular Electronics Group
CEMES, CNRS
29 Rue Jeanne Marvig
31055 Toulouse Cedex 04
France

J. Robin Cowdery
Heidelberg Digital L.L.C.
1999 Lake Avenue
Rochester, New York 14650-2108
USA

Luisa De Cola
Molecular Photonics Group, IMC
Universiteit van Amsterdam
Nieuwe Achtergracht 166
1018 WV Amsterdam
The Netherlands

A. Prasanna de Silva
School of Chemistry
Queen's University of Belfast
Belfast BT9 5AG
Northern Ireland

Nada M. Dimitrijevic
Chemistry Division
Argonne National Laboratory
Argonne
Illinois 60439
USA

Cinzia Di Pietro
Dipartimento di Chimica Inorganica,
Chimica Analitica e Chimica Fisica
Università di Messina
Via Sperone 31
98166 Messina
Italy

John R. Fyson
Kodak European R&D
Kodak Limited
Headstone Drive
Harrow HA1 4TY
UK

Ian R. Gould
Department of Chemistry and
Biochemistry
Arizona State University
Tempe
Arizona 85287-1604
USA

Michael Grätzel
Laboratory for Photonics and
Interfaces
Institute of Physical Chemistry
Swiss Federal Institute of Technology
1015 Lausanne
Switzerland

Eric Hendrickx
Laboratory of Chemical and Biological
Dynamics
Center for Research on Molecular
Electronics and Photonics
University of Leuven
Celestijnenlaan 200D
3001 Leuven
Belgium

Stephan Houbrechts
Laboratory of Chemical and Biological
Dynamics
Center for Research on Molecular
Electronics and Photonics
University of Leuven
Celestijnenlaan 200D
3001 Leuven
Belgium

Masahiro Irie
Department of Chemistry and
Biochemistry
Graduate School of Engineering
Kyushu University
Fukuoka 812-8581
Japan

Jean-Pierre Launay
Molecular Electronics Group
CEMES, CNRS
29 Rue Jeanne Marvig
31055 Toulouse Cedex 04
France

Aaron S. Lukas
Department of Chemistry
Northwestern University
Evanston
Illinois 60208-3113
USA

Nathan D. McClenaghan
School of Chemistry
Queen's University of Belfast
Belfast BT9 5AG
Northern Ireland

Colin P. McCoy
School of Pharmacy
Queen's University of Belfast
Belfast BT9 7BL
Northern Ireland

Maria Mastragostino
Istituto di Scienze Chimiche
Universita' di Bologna
Via San Donato 15
40127 Bologna
Italy

Kenji Matsuda
Department of Chemistry and
Biochemistry
Graduate School of Engineering
Kyushu University
Fukuoka 812-8581
Japan

Jacques-E. Moser
Laboratory for Photonics and
Interfaces
Institute of Physical Chemistry
Swiss Federal Institute of Technology
1015 Lausanne
Switzerland

Douglas C. Neckers
Center for Photochemical Sciences
Bowling Green State University
Bowling Green, Ohio 43403
USA

Jerzy Paczkowski
Faculty of Technology and Chemical
Engineering
University of Technology and
Agriculture
Seminaryjna 3
85-326 Bydgoszcz
Poland

André Persoons
Laboratory of Chemical and Biological
Dynamics
Center for Research on Molecular
Electronics and Photonics
University of Leuven
Celestijnenlaan 200D
3001 Leuven
Belgium

Fausto Punzorio
Dipartimento di Chimica Inorganica,
Chimica Analitica e Chimica Fisica
Università di Messina
Via Sperone 31
98166 Messina
Italy

Mark D. Rahn
Department of Physics and Astronomy
Hicks Building
University of Sheffield
Sheffield S3 7RH
UK

Tijana Rajh
Chemistry Division
Argonne National Laboratory
Argonne
Illinois 60439
USA

Vittorio Ricevuto
Dipartimento di Chimica Inorganica,
Chimica Analitica e Chimica Fisica
Università di Messina
Via Sperone 31
98166 Messina
Italy

J. Roy Sambles
Thin Film Photonics Group
School of Physics
Stocker Road
Exeter EX4 4QL
UK

Scolastica Serroni
Dipartimento di Chimica Inorganica,
Chimica Analitica e Chimica Fisica
Università di Messina
Via Sperone 31
98166 Messina
Italy

Francesca Soavi
Dipartimento di Chimica "G.
Ciamician"
Università di Bologna
Via Selmi 2
40126 Bologna
Italy

Marion C. Thurnauer
Chemistry Division
Argonne National Laboratory
Argonne
Illinois 60439
USA

Peter J. Twist
Kodak European R&D
Kodak Limited
Headstone Drive
Harrow HA1 4TY
UK

Thierry Verbiest
Laboratory of Chemical and Biological
Dynamics
Center for Research on Molecular
Electronics and Photonics
University of Leuven
Celestijnenlaan 200D
3001 Leuven
Belgium

Michael R. Wasielewski
Department of Chemistry
Northwestern University
Evanston
Illinois 60208-3113
USA

David S. Weiss
Heidelberg Digital L.L.C.
1999 Lake Avenue
Rochester
New York 14650-2108
USA

David P. West
Schuster Laboratory
University of Manchester
Brunswick Street
Manchester M13 9PL
UK

Ralph H. Young
Department of Chemistry
University of Rochester
Rochester
New York 14627-0201
USA

Volume I

Part 1

Principles and Theories

1 Electron Transfer: Theoretical Models and Computational Implementation

Marshall D. Newton

1.1 Introduction

Electron transfer (ET) plays a central role in a broad array of processes in the physical, chemical, and biological sciences [1–10]. These processes are of interest in a rich variety of environments, ranging from the gas phase to homogeneous and inhomogeneous condensed-phase media (e.g., at surfaces modified by self-assembled films), and their description involves a number of fundamental issues in chemical energetics, dynamics, and geometric and electronic structure. In spite of the complexity of these issues, it should be noted that the seminal theoretical contributions of Marcus and the Russian school nearly half a century ago [11] have successfully passed the test of ever-increasing experimental scrutiny and remain a vital force in guiding current research, as made clear in a number of recent reviews [1–10]. Complementing the models for thermal ET, the approach of Hush for treating optical electron transfer [12] has led to an extended framework, often referred to as the Marcus–Hush theory.

Present-day mechanistic understanding of electron transfer is reflected in theoretical models of rapidly expanding sophistication [13–21]. A major driving force in the evolution of these theories has been the need to respond to the challenges posed by the spectacular advances in experimental capabilities in recent times [1–5, 10, 22–29] (e.g., ultrafast laser probes and techniques in synthesis and assembly). The theoretical models play two important complementary roles: (1) leading (in conjunction with modern computational techniques and computing power) to realistic computational implementation; and (2) allowing analysis of the results of such calculations (as well as those from experiment) in terms of compact predictive models grounded in simple concepts of chemical structure and bonding. The power of the current array of theoretical tools for elucidating the details of ET dynamics is underscored by their typically generic applicability: for example, to ground-state or photoinitiated processes [30], both homogeneous and interfacial [31–33]. The continuing goal, of course, is to convert the rapidly accumulating mechanistic infor-

mation about ET processes (often representable in terms of simple rate constants) into precise tools for fine-tuned control of the kinetics and for design of molecular-based systems which meet specified ET characteristics. In the remainder of this paper, unless specified otherwise, the label “ET” is used generically to refer to electron-, hole-, or hybrid one-particle transfer [34].

Current theoretical techniques permit detailed treatment of the various electronic and heavy-particle modes of complex ET systems (including both discrete solute species and surrounding medium) at quantum mechanical, semiclassical or classical levels, as dictated by the nature of the relevant competing timescales [13, 14, 16, 19, 20, 35]. Typically (e.g., see [1]), one identifies and quantum mechanically treats the electronic manifolds of the local molecular donor (D) and acceptor (A) sites, and then formulates the manner in which the effective coupling facilitating the ET process is mediated by the energetic and electronic features of the intervening medium (the “bridge” B) as well as the surrounding environment. The energetics and dynamics associated with activation are treated with either classical or quantum mechanical models. Large-scale molecular dynamics (MD) or Monte Carlo (MC) computer simulation studies are playing an increasingly valuable role in probing mechanistic details at the molecular level (e.g., [15, 33, 36, 37]).

A generic DBA system is schematically depicted in Figure 1, showing examples of coupling of the intramolecular (e.g., where D and A are covalently linked by a molecular bridge B) and intermolecular (e.g., where the “bridge” B could be solvent)

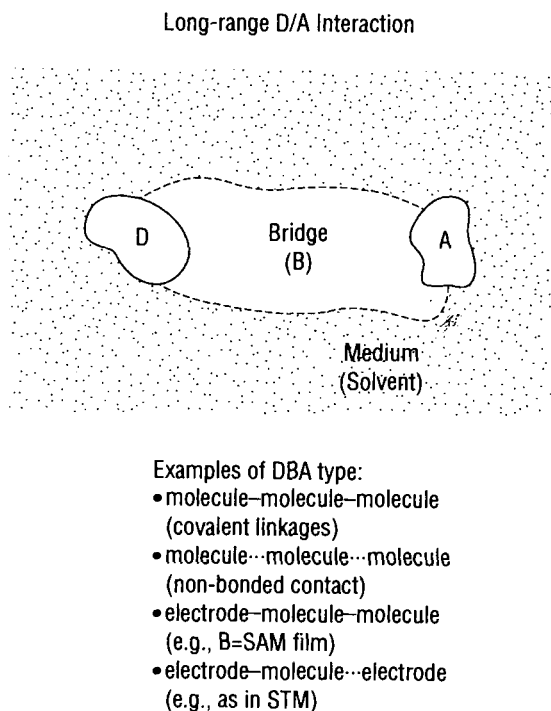


Figure 1. Schematic depiction of a generic DBA system, comprised of local donor (D) and acceptor (A) sites, the intervening bridge (B), and the surrounding medium (e.g., solvent). In the two-state approximation (TSA), ET kinetics for the $\text{DBA} \rightarrow \text{D}^+\text{BA}^-$ process may be modeled in terms of initial- (Ψ_i) and final-state (Ψ_f) wavefunctions, in which the transferring charge is localized primarily on the D and A sites, respectively. In the case of electrodes (e.g., metal or semiconductor), where multiple electronic states are involved, the D and A sites may still be taken to be localized and to involve atomic sites of the electrode near the site/or sites of attachment or contact with the bridge); SAM \equiv self assembled monolayer; STM \equiv scanning tunneling microscopy.

types. Figure 1 also provides examples in which the localized molecular D and A sites are replaced by electrodes. In these situations, one may still be able to identify effective local D and A sites near the points of attachment or contact between the electrodes and the bridge, but one must take due account of the special features of the electrodes (e.g., density of states and spatial delocalization of metallic orbitals) [38]. As noted below, electron transfer ($\text{DBA} \rightarrow \text{D}^+\text{BA}^-$) is one of several related processes of interest involving bridge-mediated D/A coupling.

The flavor of the diversity in current ET research can be appreciated by noting a number of recent advances which serve to broaden perspectives about underlying electron-transfer mechanisms. These developments have benefited especially from ultrafast laser pump/probe experiments [1, 2, 23, 24, 39–42], which have opened up a broader and better-controlled dynamic range, thus forcing the community to address a number of new issues related to the nature of the interacting states and the dynamics of their evolution.

Photoinitiated and optical electron-transfer processes and their relationship to corresponding ground-state thermal processes provide important new tests of theory, especially when comparisons are made: for a given DBA system, of charge separation (CS) and charge recombination (CR), or of thermal and optical electron transfer (e.g., [27]). Photoinitiated processes have also been valuable in providing access to the dynamics of electron transfer in the “activationless” and “inverted” kinetic regimes (e.g., [43, 44]).

Relative to the simple classical kinetic model based on a single-solvent reaction coordinate [11a] (still useful in many situations, e.g., [27]), ET dynamics is now generally recognized [1, 10, 13, 14, 16, 24, 43, 44] to involve a wide range of time-scales (both high- and low-frequency modes, and relaxation processes spanning the limits of fast inertial and diffusive, strongly overdamped response), governing a number of solvent and molecular coordinates. Despite the complexity of ET dynamics (often nonexponential), rate constants and associated rate-determining steps may be identified in limiting cases (e.g., under steady-state conditions [8] or as discussed in [13a]). The transition-state kinetic model for electronically adiabatic ET (i.e., strong D/A electronic coupling), once thought to be superseded in most cases by overdamped solvent dynamics, is now recognized to be a much more subtle and complex issue [35].

Long-range ET between a given D and A site may involve a direct coherent (e.g., superexchange) process or an incoherent (or possibly coherent [45]) stepwise process, depending on the trade-offs governed by the electronic coupling and energy gaps of the DBA system and by electronic relaxation due to the medium [19, 46].

Theoretical formulations of reorganization in the course of electron-transfer processes have undergone a number of advances in recent years. The relative importance of various solvent contributions (including translational as well as orientational response, and inductive and dispersion as well as electrostatic interactions) can depend strongly on the polarity (i.e., dipolar, higher multipolar, or nonpolar) as well as other molecular features of the solvent [21, 47–49]. Molecular-level perspectives on solvent response are of great utility in helping to parameterize effective cavity models (e.g., in conjunction with conventional [50] or spatially nonlocal [47] dielectric models). Additivity relationships traditionally assumed to pertain to sol-

vent and molecular (“inner sphere”) reorganization energy [8] are coming under new scrutiny, as the role of solvent-driven cavity fluctuations begins to receive attention [51]. (These are distinct from the traditional “inner-sphere” fluctuations governed by the coordinates of the DBA solute [8, 9]). The possibility of the effective cavity sizes being appreciably frequency-dependent, corresponding to different frequency domains of the medium response has also been considered in recent studies [52]. A particularly interesting consequence of the new, molecular-level understanding of medium reorganization is the prediction [21] and recent experimental confirmation [53, 54] of sizable entropic components of solvent reorganization free energies, with sign (positive) opposite to that predicted by standard continuum models for solvents of moderate or high polarity. Other molecular-level features of reorganization involve specific solvation effects (inferred from solvent-dependent “inner-sphere” energetics [24, 55]). The possible influence of ion-pairing or other aspects of finite ionic strength on solvent reorganization energy has also been considered [56, 57], but with indications that the effect is likely to be small. Analysis of resonance Raman data has recently become a rich source of mode-specific molecular as well as solvent contributions to reorganization energy [55, 58, 59].

Traditional models of D/A coupling in ET processes have generally been cast in terms of a two-state framework based on charge-localized diabatic states. A recent generalization [30] of the Mulliken-Hush model [12] has provided a complete prescription of the diabatic basis and associated D/A coupling entirely in terms of adiabatic state information (e.g., experimental spectroscopic data or data based on calculated eigenstates). This approach yields a natural definition of effective D/A separation distance and can be easily extended to accommodate an expanded electronic framework in situations where the two-state level is inadequate. Calculation and superexchange analysis of D/A coupling has yielded correlations of coupling element signs and magnitudes within families of DBA systems, and numerous instances of interference among multiple superexchange pathways (both constructive and destructive) have been identified [4, 6, 10, 27, 34, 60–64].

In spite of the utility of formulations based on diabatic states, especially for ground-state thermal processes, it has recently been argued [65] that for some cases of initial states prepared by photoexcitation, an adiabatic basis and associated non-Born–Oppenheimer (BO) coupling must be adopted in accounting for electron-transfer dynamics. Other manifestations of departures from the simple BO framework and the Condon approximation [66] are the appreciable sensitivity of D/A coupling magnitudes to fluctuations in various intra- and intermolecular coordinates [60, 67–70], and the frequent need to supplant a model cast in a purely electronic framework (with its convenient symmetry-based selection rules) with a more general vibronic model in which “intensity borrowing” becomes increasingly likely as the density of vibronic states increases [71].

Looking at the broader context of long-range D/A interactions (see Figure 1), we emphasize that aside from the already rich and complex domain of electron- and hole-transfer kinetics, there is rapidly accelerating interest in related phenomena such as electronic conductivity (especially in nano- and subnano-scale systems) [3, 38, 72], STM [3, 72b], and electron transmission through thin films [73], all quasi-one-particle processes, and excitation-energy transfer [26, 62, 74–76] and magnetic-

[28, 77, 78] and double [6, 79] exchange, quasi-two-particle processes. When both D and A sites have paramagnetic “cores”, the D/A coupling elements become spin-state dependent [77].

Another area of increasing emphasis is the elucidation of chemical bonding rearrangements either initiated by or accompanying ET; for example, coupled proton– (or other ion–) electron transfer (*cpet*) [20, 22] and dissociative ET [80]. Such a focus, of course, lies at the heart of much current research in solar-energy conversion. An especially exciting recent development is the construction of a functioning biomimetic photon-driven proton pump [81].

Against the above background, the primary objective of this chapter is the illustration of some of the current techniques exploited in the theoretical formulation and computational implementation and analysis of ET in complex molecular aggregates; it will be shown how the control of the kinetics (e.g., enhancing desired processes, while inhibiting others) is established by the interplay between system dynamics, energetics, and coupling magnitudes. In the following sections we deal, in succession, with phenomenological kinetic schemes and microscopic formulation of rate-constant expressions, associated aspects of energetics (activation parameters and reaction coordinates), and effective D/A coupling. We then consider a number of tests of theoretical models based on direct comparison of experimental data or detailed computational studies, and offer examples of the extent to which meaningful contact can be established between theory and experiment. Complementary in-depth treatments of many of the topics touched on here are offered elsewhere in this series.

1.2 Kinetic Schemes

As a prelude to a detailed consideration of microscopic rate constants, we discuss a number of ET processes of current interest in terms of simple kinetic schemes; the insights gained by invoking a steady-state model are emphasized [8]. The following equation represents a simple picture of activated ET:



where the reactants (DBA) in their equilibrium (R) and activated (R^\ddagger , the transition state) states are connected by rate constants a and b , and passage (assumed irreversible) to products ($P \equiv D^+BA^-$) is governed by rate constant c . At the level of steady state for the intermediate R^\ddagger (valid for sufficiently long times if the condition $a/(b+c) \ll 1$ is also satisfied) [82], k_{et} is given by the so-called mean-first-passage (*mfp*) rate constant, k_{mfp} [83], where:

$$\dot{P} = k_{mfp}R \quad (2)$$

and

$$k_{\text{mfp}} = ac/(b + c) \quad (3)$$

For sufficiently fast consumption of R^\ddagger to form product ($b \ll c$), the rate-determining step is the activation process governed by $k^{\text{act}} \equiv a$. On the other hand, in the opposite limit ($b \gg c$), the ratio of R and R^\ddagger is maintained at the equilibrium value and transition state theory (TST) may be employed. Now the $R^\ddagger \rightarrow P$ process is the rate-determining step:

$$k_{\text{et}} = k^{\text{TST}} \equiv (a/b)c \quad (4)$$

We note that k_{mfp} (Eq. 3) has the form expected for two kinetic processes in series:

$$1/k_{\text{mfp}} = 1/k^{\text{TST}} + 1/k^{\text{act}} \quad (5)$$

To place the mfp approach in a broader context, we now extend Eq. 1 to deal more explicitly with the ultimate formation of equilibrated product P [83]. In the case of weak D/A coupling, where a diabatic basis comprised of charge-localized valence-bond structures may be employed to represent the relevant states of the reacting system, the “first-passage process” can be viewed as the conversion of the activated reactants (R^\ddagger) to the resonant state of activated products (P^\ddagger); subsequently P^\ddagger may “recross” to R^\ddagger (i.e., pass back through the hypersurface in configuration space defining the transition state) or proceed irreversibly to P :



The overall steady-state rate constant k_{et} (cf. Eq. 3) is given by [83],

$$k_{\text{et}} = k_{\text{mfp}}/[(b/b')(k_{\text{mfp}}/a) + 1] \quad (7)$$

where we assume $c = c'$. Among interesting limiting cases, we note that for “slow passage” ($c \ll b, b'$),

$$k_{\text{et}} = k^{\text{TST}} \quad (8)$$

as given by Eq. 4. In the limit of slow activation (where $k_{\text{mfp}} = a$),

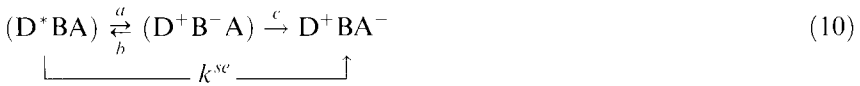
$$k_{\text{et}} = k_{\text{mfp}}/2 = a/2 \quad (9)$$

In Eqs. 8 and 9 we take, for simplicity’s sake, the limiting case, $b = b'$. The factor of $\frac{1}{2}$ underscores the importance of successful deactivation as well as activation. In the case of appreciable D/A coupling, where diffusion occurs across an activation barrier of appreciable extent, diffusive or TST limits may also be obtained [84].

Steady-state models analogous to those introduced above may also be applied to more complex situations involving sequential activation processes, for example, activation with respect to inertial or diffusive medium modes, followed by activa-

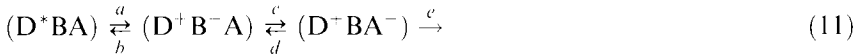
tion involving inertial molecular modes [8, 85]. For example, a scheme following Eq. 1 corresponds to a special limiting case of the kinetic model of Sumi and Marcus (SM) [13a], in which a and b govern diffusion in a solvent reaction coordinate, and c denotes a TST rate constant (for a fixed transition state value, a point “sink,” of the solvent coordinate) involving an inertial low-frequency molecular coordinate. In general, the SM kinetic model includes contributions from a finite distribution of values of the solvent coordinate.

A scheme following Eq. 1 is also of value for dealing with sequential (incoherent) ET processes (k^{seq}) in DBA systems, for comparison with competing direct (coherent superexchange) processes (k^{se}). Recasting Eq. 1 gives, for example,



where (D^*BA) is a photoexcited state (e.g., as in the initial ET event in bacterial-photosynthesis (BPS) [78]) and the second sequential step c is assumed irreversible. In the limit of $b \ll a, c$ (which may be justified in terms of arguments based on relative density-of-states and reaction exothermicities [19b, 78]), the steady-state result for the overall sequential process is simply $k^{\text{seq}} = a$ (which may be compared with k^{se} [78]), and the steady-state ratio of $(\text{D}^+\text{B}^-\text{A})$ and D^*BA is a/c , a result similar to that obtained for BPS by Marcus using a more detailed treatment [78a] (Marcus has also discussed a related sequential process which is coherent [45]).

As part of a general study of electron transfer through molecular bridges, Bixon and Jortner examined sequential electron transfer in terms of a somewhat extended kinetic scheme [19b]:



They neglected the reverse rate governed by b (assuming an exothermic initial step) and assumed rapid nonradiative relaxation of nascent D^+BA^- (governed by rate constant e). The steady-state result once again identifies the charge injection process as the rate-determining step (i.e., $k_{\text{et}} = a$) under the conditions $d \ll e$.

A similar picture has emerged from analysis of experimental data by Davis et al [86]. Charge injection (first step in Eq. 10), may be rate-determining in an overall incoherent sequential process when the charge-injection step is quasi-thermoneutral, whereas for appreciably endothermic injection (large positive gap), coherent superexchange dominates (governed by d in Eq. 10). For sequential ET in sufficiently extended bridges (with many intermediate sites), the weakly distance-dependent diffusive hopping within the bridge is eventually expected to become the rate-determining step [19a, 19c].

In related model studies [19a], the competition of parallel sequential and superexchange processes was studied in terms of the dependence of the steady-state rate constant on magnitudes of nearest-neighbor D/A coupling, gap-separating D/A

and bridge levels, and dephasing (represented by a Bloch-type phenomenological model):

$$k_{\text{et}} = k^{\text{seq}} + k^{\text{se}} \quad (12)$$

The occurrence of sequential and superexchange ET processes in parallel has also been discussed in detail in [19b]. In this formulation, the intermediate species ($\text{D}^+\text{B}^-\text{A}$ in Eq. 10 is not required to be thermally relaxed.

1.3 Rate-Constant Models

As illustrated in the previous section, the kinetics associated with an ET process may be complex when diffusion or relaxation processes create dynamic bottlenecks. In limiting cases, however, a simple model based on transition state theory (TST) suffices. According to TST, the system maintains thermal equilibrium between different positions along the reaction coordinate [87]. We consider the TST rate constant for electron transfer after some preliminary comments about state manifolds and energetics.

1.3.1 System Hamiltonian and Electronic States

The rate-constant models considered below depend ultimately on the Hamiltonian adopted for the DBA system of interest:

$$H = H^n + H^{\text{el}} \quad (13)$$

where H^{el} is the electronic Hamiltonian (including electronic–nuclear interactions) and H^n is the nuclear kinetic energy operator. In the spirit of the Born–Oppenheimer approximation (BOA), system wavefunctions may be taken as simple “vibronic” products of electronic (ψ_{el}) and nuclear (χ_n) wavefunctions (vibrations, rotations, etc). Under the BOA, an ET process may be viewed as *adiabatic*—that is, occurring on a potential energy surface associated with a *single* electronic state, ψ_{el} . On the other hand, breakdown of the timescale separation underlying the BOA leads to a *non-adiabatic* process, involving two or more electronic states and their associated energy surfaces [8].

An adequate account of many ET processes of interest is provided by the so-called two-state approximation (TSA), according to which the dynamics of ET is assumed to be adequately accounted for by the two-component space (denoted as the D/A space) spanned by states in which the transferring electron is primarily confined to the D and A sites [6, 60]. (When one or both of the two states are degenerate or near-degenerate, a somewhat more elaborate “two-level” model must be adopted [60].) In general, the two-state approximation is only valid if the gap

between the intermediate electron-transfer states involving the bridge from those of the D/A space is large relative to the strength of the coupling of D and A to the bridge [88]. While the basis set for representing the D/A space is to a large extent arbitrary, convenience generally dictates the choice of either the appropriate adiabatic states (i.e., those which diagonalize the electronic Hamiltonian of the system, H^{el}), denoted ψ_1 and ψ_2 , or the “diabatic” states ψ_i and ψ_f , related to ψ_1 and ψ_2 by a unitary transformation,

$$\psi_1 = \cos \theta \psi_i + \sin \theta \psi_f \quad (14a)$$

$$\psi_2 = -\sin \theta \psi_i + \cos \theta \psi_f, \quad (14b)$$

defined operationally so as to correspond optimally to the actual (nonstationary) states presumed to be involved in the dynamic process underlying the electron-transfer kinetics [6, 60].

For ET initiated in ground-state systems, ψ_1 and ψ_2 will generally be the two lowest-energy adiabatic states, whereas higher-energy states will be involved in photoinitiated ET [89]. We emphasize that the definition of ψ_i and ψ_f is never unique [30b], and the utility of a given prescription must ultimately rest on the results of detailed applications. In typical situations, ψ_i and ψ_f correspond to charge-localized valence-bond structures (e.g., DBA and D^+BA^-). Such structures, aside from their chemically intuitive appeal, also have the advantage that their coupling is dominated by the electronic Hamiltonian, with only minor non-Born–Oppenheimer coupling (i.e., from the nuclear momentum operator) expected [8]. In some situations, however, especially those involving photoinitiated ET in cases of strong D/A coupling, the initially prepared states may involve significant mixing of charge-localized states (e.g., [39]). A criterion for defining maximally charge-localized diabatic states in terms of dipole-moment matrix elements will be presented in Section 1.4 of this chapter.

In thermally activated ET we are interested in the electronic states at the transition state (TS). When the system is at equilibrium in either the initial or final state (where D and A are well out of resonance), the diabatic states, ψ_i and ψ_f , can be taken to be essentially the same as their adiabatic counterparts, ψ_1 and ψ_2 . When the system with weakly coupled D and A is suddenly carried into the TS by a fluctuation, we adopt the picture that the system remains in the (now nonstationary) ψ_i state until (with some finite probability) it dynamically “tunnels” (see below) to ψ_f and irreversibly relaxes to the equilibrium product. The required resonance of D and A is a statement of the Franck–Condon control of thermally activated electron transfer [6, 8, 60]; that is, at the TS,

$$\langle \psi_i | H^{\text{el}} | \psi_i \rangle = \langle \psi_f | H^{\text{el}} | \psi_f \rangle \quad (15)$$

and that this electronic energy matches will be central to some of the models for D/A coupling given below (i.e., those pertinent to thermal ET). Of course, vibronic effects allow some departure from strict electronic energy matching in thermal processes.

In optical electron transfer, the photon energy helps to balance the electronic mismatch associated with vertical excitation from equilibrium, where, as noted

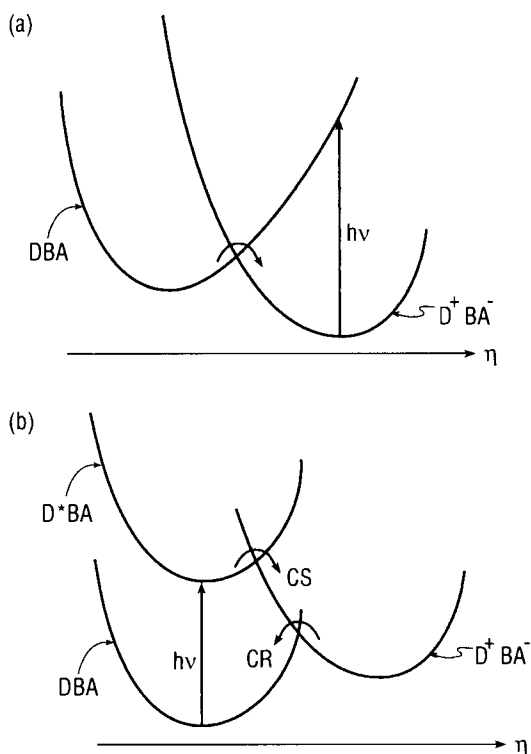


Figure 2(a). Schematic representation of optical- and thermal ET, corresponding, respectively, to the vertical transition with excitation energy $h\nu$ and passage through the transition-state (or crossing) region. In experimental studies, the thermodynamically stable state, which is the *final* state in the *thermal* ET process, generally serves as the *initial* state in the corresponding *optical* process. **(b)** Sequence of photoinitiated electron transfer: charge separation (CS) from a locally excited state, followed by charge recombination (CR) back to the ground state. The CS, CR notation is generally limited to cases where the D and A sites are initially charge neutral (as drawn).

above, the distinction between adiabatic and diabatic states is typically minor for weakly coupled D/A sites (for exceptions in the case of strong D/A coupling, see, e.g., [39]). The formulation of effective D/A coupling for the nonresonant optical electron-transfer process is generally different from that employed for thermal (resonant) electron transfer [6, 89], as discussed in Section 1.4 of this chapter.

Examples of ground-state and photoinitiated ET and optical ET are illustrated schematically in Figure 2 in terms of energy profiles along a reaction coordinate (η), according to the TSA, in which each process involves a pair of electronic states. The nature of the energy profiles and reaction coordinates will be discussed below. The cases displayed include:

- 1) Ground-state thermally activated ET proceeding through the transition state (TS) in the crossing region (Figure 2a); the designation “ground-state” indicates that the TSA involves the two lowest-lying states of the system.
- 2) Optical electron transfer (often designated “intervalence transfer,” IT, in the case of binuclear mixed-valence transition metal complexes [6, 12]), occurring vertically from the equilibrium configuration of the initial state (Figure 2a).
- 3) Photoinitiated ET (following initial photoexcitation, typically to a locally excited non-charge-transfer state), involving charge separation (CS), followed perhaps

by subsequent photochemistry (not shown) occurring in competition with charge-recombination (CR) back to the ground state (Figure 2b). The photo-initiated ET will be a thermal process, provided the vibrational relaxation of the initially excited states is sufficiently rapid. The notation CS and CR is generally applied to situations in which D^* and A (or D and A^*) are charge-neutral groups (e.g., [90]). When, for example, the species D^* has a negative charge, the $D^*BA \rightarrow D^+BA^-$ process is frequently referred to as a charge-shift (CSH) reaction.

1.3.2 Diabatic Energy Surfaces

The energetics needed to characterize ET between weakly coupled diabatic states, ψ_i and ψ_f , can be expressed in terms of free energy quantities based on the Hamiltonians for nuclear motion (H_i and H_f) at the level of the BOA [47],

$$H_y = H^n + V_y; y = i, f \quad (16)$$

where the effective potential energy, V_y , is given by the expectation value of H^{el} (already introduced in Eq. 15),

$$V_y \equiv \langle \psi_y | H^{\text{el}} | \psi_y \rangle; y = i, f \quad (17)$$

The equilibrium free energies G_i and G_f are then expressed in terms of partition functions, Z ,

$$Z_y \equiv \exp(-G_y/k_B T) = A \int d\{Q\} \exp(-H_y/k_B T); y = i, f \quad (18)$$

where $\{Q\}$ denotes the set of nuclear coordinates, k_B is the Boltzmann constant, and A is a proportionality constant. The net free energy of the ET process is given by the following equation:

$$\Delta G^\circ = G_f - G_i \quad (19)$$

To formulate non-equilibrium free energies such as the activation (G^\ddagger) and reorganization (λ) free energy, we consider *constrained* free energies, $G_y(\eta)$, based on imposed configuration space relations of the type represented below:

$$f\{Q\} = \eta \quad (20)$$

where η is an arbitrary constant. A single collective ET reaction coordinate is often defined in terms of the vertical potential energy difference,

$$f(\{Q\}) = \Delta V_{if} \equiv V_f - V_i \quad (21)$$

The probability of ΔV_{if} having a value η is proportional to:

$$\exp[-G_r(\eta)/k_B T] = B \int d\{Q\} [\exp(-H_r/k_B T)] [\delta(\Delta V_{if} - \eta)];$$

$$r = i, f \quad (22)$$

where B is a constant common to states i and f and δ is a Dirac delta function. The $G_r(\eta)$ quantities are denoted as potentials of mean force and serve as the effective potential-energy functions governing the electron-transfer process. From Eq. 22, Eq. 23 can be derived [91]:

$$G_f(\eta) = G_i(\eta) + \eta \quad (23)$$

and hence $G_i(\eta)$ and $G_f(\eta)$ have identical curvatures with respect to η at a given η value. The reaction coordinate can be identified with the continuous variable η , or some linear function of η [13, 47, 83, 84, 91]. In general, such a coordinate will define a reaction path quite distinct from alternatives such as a steepest-descent path on an adiabatic energy surface (e.g. [9c]).

Some important free-energy relationships are presented in terms of the diabatic energy profiles G_i and G_f in Figure 3. The vertical and horizontal shifts of the G_f profile relative to that for G_i correspond, respectively, to the driving force of the ET process ($-\Delta G_{if}^\circ$) and the reorganization energy (λ) of nuclear modes (shifts of equilibrium coordinate values).

As drawn, Figure 3 corresponds to the “normal” regime, $-\Delta G_{if}^\circ < \lambda$, where the diabatic crossing (the transition state) occurs between the reactant and product minima along the η coordinate. This is in contrast to the “inverted” regime, where $-\Delta G_{if}^\circ > \lambda$. Practical details concerning the evaluation of $G_i(\eta)$ and $G_f(\eta)$ have been discussed, for example, in [92]. The vertical gaps at the initial (η_i) and final (η_f) state minima are, respectively, η_i and $-\eta_f$ (defined in this manner, both gaps are positive for the normal regime depicted in Figure 3), and the corresponding reorganization free energies for the initial and final states are given by Eqs. 24a and 24b [47]:

$$\lambda_i = G_i(\eta_f) - G_i(\eta_i) \quad (24a)$$

$$\lambda_f = G_f(\eta_i) - G_f(\eta_f) \quad (24b)$$

Thus, for a given diabatic state, λ is the free energy difference between the minimum energy point and the point corresponding to the minimum energy of the other state. The effective λ value for the two-state system can be taken as the arithmetic mean of λ_i and λ_f [47] (i.e., one-half of the Stokes shift for the optical ET process).

The diabatic crossing occurs at $\eta = \eta^\ddagger = 0$ (i.e., $G_i(0) = G_f(0)$), yielding the diabatic activation free energy,

$$G_i^\ddagger = G_i(0) - G_i(\eta_i) \quad (25)$$

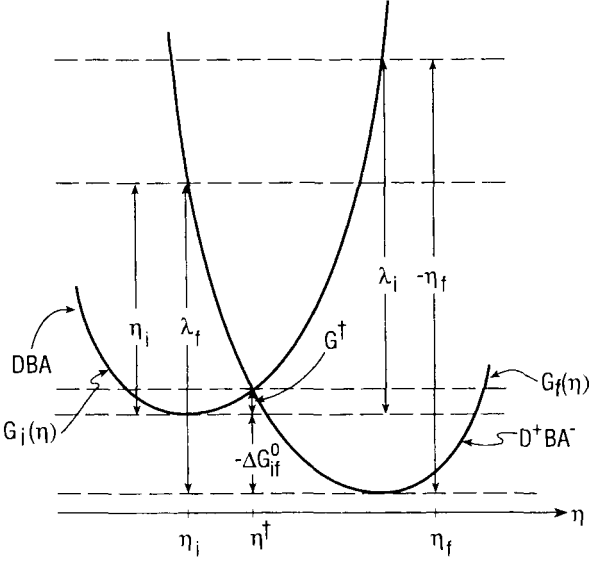


Figure 3. Effective energy profiles along the reaction coordinate (η) for the initial and final diabatic states, indicating the reorganization energy (λ), activation-free energy (G^\ddagger), and reaction driving force ($-\Delta G^\circ$). In a linear system, with parabolic profiles of equal curvature and $\lambda_i = \lambda_f = \lambda$ (as implied by the figure), the free energy change ΔG° can be equated to the gap, ΔG_{if}° , between the minima of the two (constrained) free energy profiles [47] (a near equality is expected in general); the vertical energy gap (η_i) at the equilibrium configuration for the initial state (DBA) is equal to $\lambda + \Delta G^\circ$ [9]. Correspondingly, the final-state (D^+BA^-), gap, $-\eta_f$, is given by $\lambda - \Delta G^\circ$.

We note that the net diabatic free energy change,

$$G_{if}^\circ = G_f(\eta_f) - G_i(\eta_i) \quad (26)$$

is not in general identical to the quantity ΔG° based on the unconstrained free energies (Eq. 19), although the difference is expected to be minor (e.g., [36, 47]).

When $G_i(\eta)$ and $G_f(\eta)$ are taken to be parabolic, corresponding to linear coupling of the transferring electron to the rest of system with respect to progress along the reaction coordinate, considerable simplification is possible, leading in the classical (high temperature) limit to the familiar relationships of the Marcus theory [9], notably, the quadratic dependence of G_i^\ddagger on ΔG° (in the remainder of this chapter we ignore the distinction between ΔG° and ΔG_{if}°):

$$G_i^\ddagger = (\lambda + \Delta G^\circ)^2 / 4\lambda \quad (27)$$

where

$$\lambda = \lambda_i = \lambda_f \quad (28)$$

Enthalpic and entropic analogs of Eq. 27 are dealt with in [93], neglecting any temperature variation of λ (cf., [21]).

To be consistent with the condition noted following Eq. 23, the two parabolic profiles must have the same curvature, which can be represented by a harmonic force constant, k_η . Thus, we may write:

$$\lambda = k_\eta(\eta_i - \eta_f)^2/2 \quad (29)$$

When the reaction coordinate η corresponds to the solvent polarization mode, the dielectric continuum theory analog of Eq. 29 is:

$$\lambda = (1/\epsilon_{op} - 1/\epsilon_s) \int [D(\rho_f) - D(\rho_i)]^2 \quad (30)$$

where ϵ_{op} and ϵ_s are, respectively, the optical and static dielectric constants, and the displacement field D is a linear functional of the initial- (ρ_i) and final-state (ρ_f) charge density [9, 11a, 11b, 83, 89]. More detailed formulation and evaluation of λ is discussed in [94], with attention drawn to the indirect screening role of high-frequency (optical) modes in modifying the direct contributions of the lower-frequency (nuclear) modes.

While the use of effective energy surfaces defined in terms of free energies is commonplace in the electron transfer literature, we note an equivalent, alternative viewpoint, in which k_{et} is expressed in terms of probability distributions of the fluctuating potential-energy gap specified by η (as in Eqs. 20 and 21) [95].

1.3.3 TST Models

We now consider specific TST rate-constant models, taking explicit account of nuclear coordinates, Q , and wavefunctions, χ_n (see Section 1.3.1 of this chapter), so as to be able to include nuclear tunneling when necessary.

Golden rule

A convenient point of departure is provided by the golden-rule non-adiabatic rate-constant expression [8, 60] appropriate under the usual two-state approximation (TSA),

$$k_{et}^{TST} = (2\pi/\hbar)(T_{if})^2(FCWD), \quad (31)$$

where the “transfer integral” T_{if} is the *effective* electronic Hamiltonian matrix element coupling the initial (ψ_i) and final (ψ_f) states [17, 60], which differ, respectively, by having an electron localized primarily at D and A sites (see Figure 1). Comparative comments about different notations used to denote “D/A coupling elements” are deferred until Section 1.4.3 of this chapter.

The Franck–Condon-weighted density of states (FCWD) reflects the influence of all of the nuclear modes of the system, often represented in terms of effective normal

coordinates (Q_{r_i} and Q_{w_f} for the initial and final states, respectively) and associated quantum-mechanical Franck–Condon factors.

High-temperature classical limit

For sufficiently high temperature (where all nuclear frequencies ω obey the relation $\hbar\omega \ll k_B T$), FCWD takes on a limiting classical form,

$$\text{FCWD} = \exp(-G^\ddagger/k_B T)/(4\pi k_B T \lambda)^{1/2} \quad (32)$$

where G^\ddagger for the case of linear (harmonic) coupling to the medium is given by Eq. 27. It is important to distinguish G^\ddagger (Eq. 27), which may have appreciable entropic content, from the Arrhenius activation *energy* (or enthalpy) [36, 93]. Equation 32 may be reexpressed as

$$\text{FCWD} = \rho(0), \quad (33)$$

where $\rho(\eta)$ is the normalized classical density of initial states with respect to the gap η (i.e., $\rho(\eta) d\eta$ is the probability of finding the initial state in a configuration corresponding to a vertical gap in the range η to $\eta + d\eta$; see Figure 3); for linear coupling we have:

$$\rho(\eta) = \exp(-\{(\lambda + \Delta G^\circ - \eta)^2/4\lambda k_B T\})/(4\pi\lambda k_B T)^{1/2} \quad (34)$$

Thus, in the classical limit, the consequence of the energy-conserving golden-rule expression (Eq. 31) is simply to invoke the classical density of states at the transition state (i.e., the crossing, where $\eta = \eta^\ddagger = 0$, the point to which a radiationless electronic transition is confined due to the constraints of the Franck–Condon principle).

It has been noted [95] that λ in Eq. 34 plays two rather distinct roles: λ in the quadratic expression is a solvation energy which defines (with ΔG°) the vertical gap at equilibrium, whereas the other λ 's control the width of the Gaussian distribution characteristic of the linear coupling model.

The FCWD expressions for thermal ET (e.g., Eq. 32 or its low-temperature quantal counterpart) may be adjusted to accommodate optical electron transfer if ΔG° is replaced with $\Delta G^\circ + \hbar\nu$ (emission) or $\Delta G^\circ - \hbar\nu$ (absorption), where $\hbar\nu$ is the optical transition energy [96]. The relationship between thermal and optical coupling elements is discussed in Section 1.4.2 of this chapter.

Quantal effects

At lower temperatures, where quantal effects become appreciable for the high-frequency modes, Eq. 31 may be recast as a superposition of vibronic state-to-state processes [14],

$$k_{\text{et}}^{\text{TST}} = (2\pi/\hbar) \sum_{r_i w_f} (P_{r_i})(T_{r_i w_f})^2 (\text{FCWD}')_{r_i w_f} \quad (35)$$

where P_{r_i} is the normalized distribution of initial vibronic states (typically in terms

of Boltzmann factors), where the vibronic coupling factor $(T_{v,w_f})^2$ is given by

$$(T_{v,w_f})^2 = (T_{if})^2 (S_{v,w_f})^2, \quad (36)$$

and $(S_{v,w_f})^2$ is a vibrational Franck–Condon factor (i.e., the square of the corresponding vibrational overlap integral). The implicit relationship between the quantities $(\text{FCWD}')_{v,w_f}$ and FCWD, as obtained from comparison of Eqs. 31, 35, and 36, is given by

$$\text{FCWD} = \sum_{v,w_f} P_{v_i} (S_{v,w_f})^2 (\text{FCWD}')_{v,w_f} \quad (37)$$

The nuclear tunneling implicit in the Franck–Condon factors is of particular importance in the inverted region ($-\Delta G^\circ > \lambda$). In such cases, the effective barrier is greatly reduced as a result of nuclear tunneling [14], in comparison with the classical barrier, which according to Eq. 27 would rise monotonically with increasing exothermicity in the inverted region.

Condon approximation

In Eqs. 31, 36, and 37 we have employed the Condon approximation [66], factoring T_{if} out of the full vibronic matrix element, with the understanding that T_{if} is to be evaluated for values of the nuclear coordinates pertinent to the configuration or range of configurations of the system in which the ET process occurs. The validity of the Condon factorization depends on the extent to which T_{if} varies with the coordinates Q , a topic to which we return below. The coordinates of interest in this connection include the reaction coordinate (η in Figure 3), as well as others such as conformational modes of the DBA system. The influence of fluctuations in these coordinates (and hence in the magnitude of T_{if}) on the overall kinetics depends in detail on the relationship between the timescale for such fluctuations and the timescales of the other dynamic processes [97].

The use of the Condon approximation [66] leads to electronic symmetry control, dictating vanishing rate constants when ψ_i and ψ_f belong to different irreducible representations of a given point group. In such cases, vibronic coupling (e.g., involving $\partial T_{if}/\partial Q_{v_i}$, etc.) may actually lead to rate constants of substantial magnitude [71]. On the other hand, in other related cases, symmetry control appears to be operative, as expected on a purely electronic basis [90].

Techniques for treating quantized nuclear motion

It is desirable to bridge the gap between the general quantal expression for k_{et} given by Eqs. 35–37 with its explicit summation of vibronic contributions and the simplicity of the classical, harmonic model displayed in Eqs. 33 and 34. As one device for achieving this goal, we switch perspectives from the constrained diabatic free energies, $G_i(\eta)$ and $G_f(\eta)$, as in Eq. 22, to an auxiliary (unconstrained) free-energy function, $G(\tau)$, based on the “hybrid” partition function $Z(\tau)$ [36, 98] (cf., Eq. 18):

$$Z(\tau) = \int d\{Q\} \exp[-(1-\tau)H_i/k_B T] \exp(-\tau H_f/k_B T) \quad (38)$$

$$G(\tau) = -(k_B T) \ln Z(\tau) \quad (39)$$

where, in general, H_i and H_f are quantum-mechanical Hamiltonians.

The continuous variable τ , which may be thought of as a “charging parameter” spanning the reactant ($\tau = 0$) and product ($\tau = 1$) limits, corresponds closely to the parameter m introduced originally by Marcus [11a] and may be employed as the reaction coordinate [36, 98] (an alternative to η). Strictly speaking, τ is a dimensionless quantity referring to a point on the imaginary time axis (t), arising in conjunction with analytic continuation of the Fourier representation of the Dirac delta function in the fundamental statement of the golden rule [36, 99]:

$$\tau = it/(\hbar/k_B T) \quad (40)$$

Solution of the golden-rule expression for the non-adiabatic ET rate constant by applying the saddle-point (or stationary phase) approximation yields [36],

$$k_{\text{ct}} = (2\pi/\hbar)(T_{if})^2 \exp(-G^\ddagger/k_B T) / \{4\pi k_B T [-(1/2)d^2 G(\tau)/d\tau^2|_{\tau^\ddagger}]\}^{1/2} \quad (41)$$

where τ^\ddagger is defined by the condition

$$dG/d\tau|_{\tau^\ddagger} = 0 \quad (42)$$

and where the activation free energy G^\ddagger is given by

$$G^\ddagger = G(\tau^\ddagger) - G(0) \quad (43)$$

In contrast to the delta-function constraint of Eq. 22, where the transition state corresponds to $\eta = \eta^\ddagger = 0$, the transition state represented by Eqs. 42 and 43 occurs at the τ value for which the mean value of ΔV_{if} (Eq. 21) is zero [36]:

$$\left(\int d\{Q\} \rho(\tau^\ddagger) \Delta V_{if} \right) / Z(\tau^\ddagger) = 0 \quad (44)$$

where the hybrid density operator $\rho(\tau^\ddagger)$ is the integrand of Eq. 38 when $\tau = \tau^\ddagger$.

In the case of a two-state system linearly coupled to a harmonic oscillator bath (the spin-boson model), Eq. 41 for a thermoneutral process ($\Delta G^\circ = 0$), where $\tau^\ddagger = 1/2$ [99], may be reexpressed compactly in the following semiclassical form [18, 94, 99a]:

$$k_{\text{ct}} = (2\pi/\hbar)(T_{if})^2 \left(\exp \left\{ - \sum_j (\lambda_j/4k_B T) [\tanh(u_j/4)/(u_j/4)] \right\} \right) / \left((4\pi k_B T) \sum_j \{ \lambda_j (u_j/2) [\text{csch}(u_j/2)] \} \right)^{1/2} \quad (45)$$

where $u_j \equiv \hbar\omega_j/k_B T$, ω_j is the frequency of the j -th harmonic mode, and λ_j is the additive contribution of the j -th mode to λ (for arbitrary ΔG° , τ^\ddagger must be determined numerically, except in the case of a single mode [99a]). In the high-temperature classical limit ($\hbar\omega_j \ll k_B T$), Eqs. 31–34 are recovered. In this case, one may identify the quantity $-(1/2)d^2G|d\tau^2|_{\tau^\ddagger}$ with λ , and $G(\tau)$ is given by [36, 98],

$$G(\tau) = (\Delta G^\circ + \lambda)\tau - \lambda\tau^2 \quad (46)$$

From Eq. 46 it is easily seen that $\tau^\ddagger = (\Delta G^\circ + \lambda)/2\lambda$, yielding the classical result for G^\ddagger (Eq. 27). In general, the argument of the exponential in Eq. 45 gives an explicit expression for reduction of the activation barrier due to nuclear tunnelling [36, 94, 99]. The influence of nuclear tunneling at finite temperatures on the magnitude of the prefactor (second line of Eq. 45) is typically minor [26, 160].

The techniques of discretized Feynman path integrals make the use of Eq. 41 practical for the more general case of quantized nuclear motion which is not restricted to harmonic behavior [36, 94, 99b]. Applications of this approach are discussed in Section 1.5 of this chapter.

Mixed quantal–classical treatment

At temperatures where quantal effects may be significant only for a well-defined subset of nuclear modes, a hybrid quantal–classical variant of Eqs. 35–37 may be employed, if separable quantal and classical modes are assumed, in which the summation in Eq. 35 is restricted to the quantized manifold of nuclear states. If the classical modes are assumed to be harmonic, then the modified (FCWD) $_{v_i w_f}$ is given by [14, 100]:

$$(\text{FCWD})_{v_i w_f} = \exp(-G_{v_i w_f}^\ddagger/k_B T)/(4\pi\lambda_{\text{cl}}k_B T)^{1/2} \quad (47)$$

where

$$G_{v_i w_f}^\ddagger = (\Delta G^\circ + \Delta E_{v_i w_f} + \lambda_{\text{cl}})^2/4\lambda_{\text{cl}} \quad (48)$$

and where $\Delta E_{v_i w_f}$ is the energy change in the quantal manifold. In this approach, the single collective reaction coordinate η for *all* nuclear modes (as in Section 1.3.2) is replaced by a collective *classical* reaction coordinate, and the total rate constant is based on a superposition of quantal state-to-state processes, each governed by the *classical* reorganization free energy (λ_{cl}) and the appropriate effective net free-energy charge (see Eq. 48),

$$\Delta G_{v_i w_f}^\circ = \Delta G^\circ + \Delta E_{v_i w_f} \quad (49)$$

If the quantized nuclear motion is represented by a set of (harmonic) normal coordinates common to both initial and final diabatic states, then $\Delta E_{v_i w_f}$ is given by:

$$\Delta E_{v_i w_f} = \sum_j (\Delta n_j)_{v_i w_f} (\hbar\omega_j) \quad (50)$$

where $(\Delta n_j)_{v_i w_j}$ is the change in quantum number of mode j in the $v_i \rightarrow w_j$ transition and ω_j is the frequency. For harmonic modes, explicit expressions for the Franck-Condon factors $[(S_{v_i w_j})^2]$ are available [100]. For the often-used model based on a single mode initially in its ground-state, FCWD (Eq. 37) is given by [14, 100]:

$$\begin{aligned} \text{FCWD} = & (4\pi\lambda_{\text{cl}}k_{\text{B}}T)^{-1/2} \sum_{w=0}^{\infty} [\exp(-S)](S^w/w!) \\ & \times \exp[-(\lambda_{\text{cl}} + \Delta G^\circ + w\hbar\omega)^2/4\lambda_{\text{cl}}k_{\text{B}}T] \end{aligned} \quad (51)$$

where $S = \lambda_r/\hbar\omega$ and λ_r and ω are, respectively, the reorganization energy and the harmonic frequency associated with the quantized mode. Equation 51 may be straightforwardly generalized to include more than one quantized harmonic mode [100].

The partitioning of the nuclear manifolds outlined above may be formally treated in terms of a convolution integral of a product of “lineshape” functions for the quantal and classical manifolds, allowing energy interchange between the manifolds, subject to overall energy conservation [101]. Analogous convolution-based treatments have been applied to energy-transfer kinetics [102], where the partitioning is between manifolds of the donor and acceptor sites. Such a partitioning in the case of ET has been shown to be invalid in cases where λ involves coherent coupling of D and A sites [101b].

Departure from the non-adiabatic limit

The non-adiabatic expressions for $k_{\text{et}}^{\text{TST}}$ (Eqs. 31 and 35) will be valid provided that the rate-determining step is resonant “electron tunnelling” [89] (whose probability is controlled by T_{if}), in contrast to possible alternative dynamic bottlenecks associated with the various nuclear degrees of freedom [13, 14, 35, 84]. (Examples of adiabatic electron transfer in organic mixed-valence systems are discussed in [161].) Within the TST regime at high temperature, the Landau–Zener (LZ) model [103] in the case of a harmonic system shows that the non-adiabatic (golden rule) limit is valid when the following inequality is obeyed [8, 9]:

$$\kappa_{\text{cl}} = (T_{if})^2(\pi^{3/2})/(\hbar\omega_{\text{eff}})(k_{\text{B}}T\lambda)^{1/2} \ll 1 \quad (52)$$

where κ_{cl} is the electronic transmission factor (independent of ΔG° , at the level adopted here), and ω_{eff} is the effective frequency associated with vibrational motion along the reaction coordinate. The expression for κ_{cl} in Eq. 52 is based on the assumption of inertial (ballistic) motion of the system through the crossing region (cf. [104]). Equation 52, which in effect implies that the effective frequency of the transferring electron is small compared with that associated with the reaction coordinate η in Figure 3, is a statement of the breakdown of the validity of the BOA (hence the designation “non-adiabatic”) [8, 9b]. However, as noted in Section 1.3.1, the use of a diabatic basis (which varies slowly with Q_{v_i} and Q_{w_j}) usually permits the

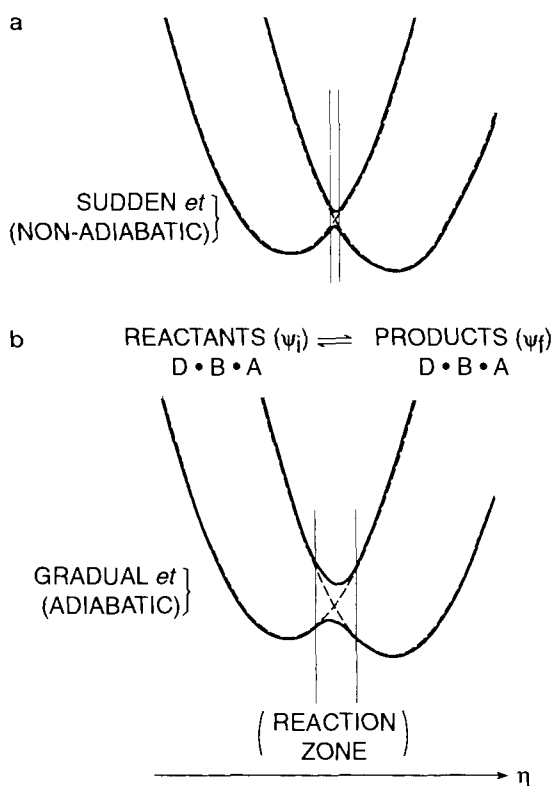


Figure 4. Schematic depiction of the limits of (a) weak (non-adiabatic) and (b) strong (adiabatic) coupling. The dashed and solid lines refer to diabatic and adiabatic surfaces, respectively. The vertical bars denote the “reaction zone” in which D and A sites are close to resonance [105].

neglect of non-Born–Oppenheimer coupling elements [8], thus yielding a model cast in terms of purely electronic (T_{if}) and vibrational [$(S_{r,w_i})^2$] matrix elements.

As the strength of D/A coupling increases, governed by T_{if} , a number of adjustments to the TST rate constant formulation may be required. If nuclear quantum effects are minor, the LZ model may be applied to cases of arbitrary T_{if} magnitude, expressed either in terms of a diabatic or adiabatic basis [8]. The relative merits of the two bases (as well as limitations in the applicability of the LZ model) have been discussed recently in conjunction with the analysis of electron transfer from strongly-coupled D/A initial states prepared optically [39, 65].

The coupling strength also affects the activation free energy. The simple expression for G^\ddagger in Eq. 27 based on the harmonic weak-coupling (small T_{if}) limit must be modified to reflect the consequences of avoided crossing on the height and shape of the barrier [9, 84c]. This effect is depicted schematically in Figure 4, showing as examples the non-adiabatic (weak D/A coupling) limit ($\kappa_{el} \ll 1$) with a cusp-like adiabatic barrier (Figure 4a), and the situation of stronger D/A coupling ($\kappa_{el} \lesssim 1$), which results in a rounded adiabatic barrier (Figure 4b). The “width” of the region along the reaction coordinate for which quasi-resonant ET is appreciable (in the sense of the half-width at half-height of the function $\langle \psi_2 | d/d\eta | \psi_1 \rangle$) is given [105] by $|\eta| \sim 2|T_{if}|$. At a more fundamental level, the magnitude of T_{if} influences G^\ddagger

indirectly by defining the effective timescale of the transferring electron compared with the timescale of the electronic response of the medium [16].

The double-well form of the lower-energy adiabatic energy profile at the level of the TSA (as in Figure 4), pertains to systems in the normal regime and with $2|T_{if}| \leq \lambda$.

Beyond the TSA

While the two-state approximation (TSA) introduced in Section 1.3.1 accounts well for many classes of electron-transfer kinetics, there are, of course, situations in which a high density of electronic states in the initial- and final-state manifolds makes it necessary to generalize the TSA expressions given, for example, by Eqs. 31–37. A paramount example is the case of metal or semiconductor electrodes, where one must deal essentially with an electronic continuum [25, 31, 32, 106]. In spite of this complication, one may still obtain k_{et} expressions with similar form to those shown above when reaction “exothermicity” is small (i.e., the difference between the electrode Fermi level and the standard potential of the redox species is small compared to λ) [25b]. Nevertheless, in the “inverted region”, k_{et} at electrodes is generally observed to approach a constant maximum value with increasing driving force (for an exception, see [107]), in contrast to the fall-off predicted in the case of the TSA (see Eq. 27).

A number of other situations may require a modest extension of the TSA; for example, 1) Multiple initial and final diabatic states involved in coupled electron/proton transfer [20]; 2) Cases of D/A systems undergoing photoinitiated charge-separation (CS) and charge-recombination (CR) processes (Figure 2b), where state mixing makes a combined three-state treatment preferable [71b,c] to separate two-state treatments; and 3) Cases involving the presence of low-lying intermediate states, such as those associated with the intervening bridge (e.g., [86]). When dealing with electronic coupling in the context of extended state manifolds of this type, one must also consider the possible importance of vibronic features [71b].

1.3.4 Role of Solvent Dynamics

It is of considerable interest to examine the extent to which solvent (or other medium) modes may lead to dynamical bottlenecks requiring a departure from the TST framework [35]. This effect can be represented by a transmission factor, κ [84, 87], where

$$k_{\text{et}} = \kappa k_{\text{et}}^{\text{TST}} \quad (53)$$

where $k_{\text{et}}^{\text{TST}}$, in turn, may be expressed as

$$k_{\text{et}}^{\text{TST}} = \kappa_{\text{cl}} k_{\text{et}}^{\text{AD}} \quad (54)$$

with κ_{cl} (Eq. 52) spanning the range from non-adiabatic ($\ll 1$) to weakly adiabatic (≤ 1) and strongly adiabatic ($\kappa_{\text{cl}} = 1$), denoted below, respectively, as NA, WA, and

SA (see Figure 4). In Eq. 54, $k_{\text{ct}}^{\text{AD}}$ is the TST expression $(\omega_{\text{eff}}/2\pi) \exp(-G^\ddagger/k_{\text{B}}T)$, where ω_{eff} was introduced in Eq. 52.

Classical solvent models

Early treatments focused on a classical overdamped solvent model (zero-frequency friction) [13b, 14]. In the NA and WA cases, where initial- and final-state wells are sharply defined, separated by a narrow cusp-like barrier, one may adopt a steady-state model of the type displayed in Eq. 7,

$$k_{\text{ct}} = (ac_f)/(b + 2c_f) \quad (55)$$

where, for simplicity, we treat the case of a symmetric ET process, where $b = b'$.

Taking k^{TST} as given by Eq. 4, we thus have:

$$\kappa = (c_f/c)/(1 + 2c_f/b) \quad (56)$$

Here we allow for the possibility of diffusion control in the barrier-crossing process (c_f) in contrast to the inertial rate constant (c) generally assumed for passage from activated reactants to products in the TST model [84, 87]. The activation (a) or deactivation (b) rate constants may also be diffusive. The occurrence of $\kappa < 1$ reflects diffusive recrossings of the system in the TS region. In the absence of diffusional bottlenecks ($c_f = c \ll b$), κ becomes unity (i.e., the TST limit).

The activation rate constant a controlling diffusion within the wells is expressed by the following equation [84]:

$$a = k_D = (1/\tau_L^{\text{eff}})(\Delta G^\ddagger/\pi k_{\text{B}}T)^{1/2} \phi \exp(-G^\ddagger/k_{\text{B}}T), \quad (57)$$

where τ_L^{eff} is an effective longitudinal relaxation time, the correction factor ϕ may be taken as unity for $\Delta G^\ddagger/k_{\text{B}}T \geq 5$, and $a/b = \exp(-G^\ddagger/k_{\text{B}}T)$. Solvent dielectric relaxation also controls the barrier-crossing dynamics (c_f) and may be modeled using Grote–Hynes theory [108], which is not limited to overdamped solvent response.

While significant departures of κ from unity might be expected in the WA or SA case if τ_L^{eff} is taken as the conventional longitudinal relaxation time, τ_L (or some suitable mean value for non-Debye solvents), corresponding to zero-frequency friction, it has been shown from formal analysis and computer simulation [84] that taking proper account of the relevant higher-frequency components of the friction leads to substantially smaller departures of κ from unity (i.e., a reduced importance of barrier recrossing). Furthermore, even when the barrier is quite cusp-like, the most important manifestation of solvent dynamics is found in the barrier region (c_f), as opposed to within the wells (k_D). In the SA limit, when the diabatic cusp becomes sufficiently rounded (as characterized by imaginary frequency ω_b associated with the barrier curvature at the TS), one reaches the situation where the zero-frequency friction, ζ_L , is dominant, and we obtain the Smoluchowski result [84]:

$$\kappa = \omega_b/\zeta_L \quad (58)$$

where ζ_L is related to τ_L by the inertial solvent frequency (ω_L),

$$\zeta_L = \omega_L^2 \tau_L \quad (59)$$

In the limit of Eq. 58, we have $c_f = (\omega_b/\omega_L)/\tau_L$, where the rate constant c in k^{TST} (Eq. 4) is equated to ω_L .

Inclusion of molecular modes

Current views of solvent dynamics recognize the importance of a complex interplay among solvent and molecular modes, which involves a variety of timescales [35]. In contrast to the simple solvent-only models, which implicitly confine the reactive transition to a “pinhole sink” at the TS, where $\eta = 0$, some recent models “dilute” the influence of solvent dynamics by introducing a classical (and rapidly relaxing) low-frequency molecular mode, which serves to provide a reactive sink of finite width with respect to a diffusive solvent mode [13a, 24]. Inclusion of quantal, high-frequency modes is, of course, necessary for proper account of nuclear tunneling [14, 24] (see Section 1.3.3), although these modes by themselves do not relax the pinhole constraint [35]. Some essential features of the new models are represented by the following generic form for the effective activation free energy,

$$G_{\text{eff}}^\ddagger = (\Delta G_{\text{eff}}^\circ + \lambda_{\text{cl}}')^2 / 4\lambda_{\text{cl}}' \quad (60)$$

where λ_{cl}' is a classical reorganization energy. It should be noted that Eq. 60 neglects any contribution to G^\ddagger arising from temperature-dependence of medium relaxation times (e.g., τ_L^{eff} in Eq. 57).

In the Bixon–Jortner (BJ) model [14a], a steady-state form of the type given in Eq. 3 is employed for k_{ct} , where $k_{\text{ct}}^{\text{TST}} = (a/b)c$ is the single-mode quantal non-adiabatic TST expression given by Eqs. 31 and 51, with $\lambda_{\text{cl}}' = \lambda_s$ (the solvent reorganization energy) and $\Delta G_{\text{eff}}^\circ$ given by Eq. 49, and where a is given by the zero-frequency diffusion expression, Eq. 57, with $a/b = \exp(-\Delta G^\circ/k_B T)$.

In the Sumi–Marcus (SM) model [13a], the perspective is changed, with a TST rate constant k_m^{TST} based on a low-frequency molecular mode (m) as the reaction coordinate, and with G^\ddagger dependent on a diffusive solvent coordinate X . For ease of comparison with other models, we transform X (relative to its definition in [13a]) so as to correspond to a continuous charging parameter ($X = 0$ for the bottom of the reactant well, and $X = 1$ for the bottom of the product well; for the case of parabolic free energy profiles the transformation is linear; the more general situation is dealt with in [98]). Also, $\lambda_{\text{cl}} = \lambda_s + \lambda_m$ and $\lambda_{\text{cl}}' = \lambda_m$, where λ_m is the reorganization energy associated with the low-frequency mode m . These definitions lead to the following equation:

$$\Delta G_{\text{eff}}^\circ(X) = \Delta G^\circ + (1 - 2X)\lambda_s \quad (61)$$

and $G_{\text{eff}}^\ddagger(X)$ in Eq. 60 is defined accordingly. The larger $\lambda_m/\lambda_{\text{cl}}'$ is, the broader the distribution available in the solvent coordinate for reaction $[(k_B T \lambda_m / 2\lambda_s^2)^{1/2}]$ is, as

governed by the X -dependent k_m^{TST} [13a]. In the BJ model, which does not include low-frequency molecular modes, one effectively has $\lambda_m = 0$ (i.e., the pinhole sink limit). It should be noted that the width of the “reactive sink” with respect to the solvent coordinate discussed here is quite distinct from the effective “width” for resonant ET introduced at the end of Section 1.3.3 (see also Figure 4).

Barbara and coworkers [24] combined the flexibility of the finite-sink SM approach with the quantal features of the BJ model; this yielded a hybrid model defined once again by $\lambda_{\text{cl}}' = \lambda_m$, but with $\Delta G_{\text{eff}}^\circ$ given by

$$\Delta G_{\text{eff}}^\circ(X) = \Delta G^\circ + \Delta E_{\text{icfr}} + (1 - 2X)\lambda_s \quad (62)$$

(cf., Eqs. 49 and 50).

In addition to the crucial role of molecular modes, both low and high frequency, Bagchi has also emphasized the further need to consider the role of ultrafast (underdamped) solvent response [35] (see also Section 1.3.4 and [84]).

Aside from the energetics and dynamics of solvent reorganization, the roles of dissolved electrolyte on ET processes carried out in solution with finite ionic strengths have been the subject of recent experimental [56] and theoretical [57] study. The various analyses suggest that continuum-based treatments or Debye–Hückel descriptions of ionic atmospheres are inadequate and point to the importance of specific ion-pairing effects, including dynamic as well as energetic factors.

1.4 Coupling Elements

1.4.1 Basic Properties

Theoretical and computational electronic structure techniques have led to major progress in the elucidation of the detailed basis of long-range coupling between D and A sites. There now is a theoretical framework [6, 17, 30, 34, 38, 61–64, 70, 89] which permits the calculation of coupling elements (T_{if}) for complex ET systems in generally good accord with available estimates based on experimental data (e.g., see reviews in [1] and [3]). The calculated coupling elements may be analyzed in terms of local chemical units, which allow the overall magnitude to be represented as a superposition of a number of competing “pathways” (e.g., [34, 60–64, 109–114]), thus making possible an assessment of the relative importance of the various pathways in achieving the overall coupling, although due account must be taken of cancellation due to destructive interference [27, 60, 63]. The information obtained from such analyses helps to provide a rational basis for synthesizing coupling elements for families of DBA systems, where transferable quantities defined in terms of the chosen local units are used (e.g., see [63], [70], and [111]).

The ideas so fruitful in dealing with the coupling that controls ET are increasingly finding useful application where related energy transfer [26, 76] and magnetic exchange [77–79] phenomena are analyzed; the power of superexchange models (dealt with in detail in Section 1.4.3) is, in particular, exploited for providing a

unified account of diverse D/A interactions. In this section, we highlight a number of theoretical features of importance in formulating expressions for T_{if} .

In the case of thermal ET, which applies either to ground state ET or photo-initiated ET from a vibrationally relaxed excited state (cf., [15d]), we now define the effective coupling T_{if} by employing the two-state approximation (TSA) introduced in Eqs. 14–15:

$$T_{if} = (E_1 - E_2)/2 = (\langle \psi_1 | H^{\text{el}} | \psi_1 \rangle - \langle \psi_2 | H^{\text{el}} | \psi_2 \rangle)/2 \quad (63)$$

where $E_1(E_2)$ is the eigenvalue associated with $\psi_1(\psi_2)$ in the transition state (TS). The diabatic energy matching at the TS (Eq. 15) then implies (via Eq. 14, where we have 50:50 mixing or $\cos \theta = \sin \theta = 1/\sqrt{2}$):

$$T_{if} = \langle \psi_i | H^{\text{el}} | \psi_f \rangle, \quad (64)$$

thus demonstrating that T_{if} may be expressed either in terms of adiabatic or diabatic quantities. The sign of T_{if} is a physical observable, but is contingent on the phase conventions entailed in the definitions of ψ_i and ψ_f (and hence via Eq. 14, also ψ_1 and ψ_2) [6, 34, 60].

Many-particle framework

In a process of the type (see Figure 1) described below:



a single electron is nominally transferred from D to A (analogous processes involving multiple-electron transfer are also possible; see the chapter by Skourtis and Beratan). Does this mean that T_{if} can be viewed as a simple one-electron matrix element or resonance integral? Analysis of D/A coupling, based on a detailed examination of the electronic manifolds of B, however, suggests that, in general, the process described by Eq. 65 is more properly viewed as a superposition of a number of one-particle charge-transfer processes (“pathways”) occurring in parallel, including transfer of an electron in one direction and transfer of a “hole” in the opposite direction, as well as more complex processes involving both electrons and holes [6, 34, 60, 109, 111, 113–115]. While the issue of electron *vs* hole transfer in this context constitutes a physical (not semantic) distinction, one must be careful, because the precise details depend on the basis employed for the analysis of the electronic manifolds of the DBA system. Superimposed on the net transfer of charge between D and A, one may also expect local response (i.e., polarization relaxation) of the system to the oxidation and reduction occurring, respectively, at D and A [6, 60, 114]. We note that “system” in this connection may be broadly understood to include the “solvent” as well as the DBA “solute”.

With the foregoing multiparticle perspective in mind, it is of interest to combine analysis and calculation to determine the extent to which T_{if} , strictly speaking a many-electron quantity, may be cast as an effective one-particle (i.e., orbital) matrix element, T_{DA} , where DA in this context denotes the “donor” and “acceptor” orbi-

tals, confined primarily to the D and A sites, respectively. In particular, it has been found in a number of cases [6, 60, 114] that the many-electron (relaxation) effects may be captured by electronic Franck–Condon-type overlap integrals, S_{if}^{el} , with magnitude ≥ 0.9 :

$$T_{if} = S_{if}^{\text{el}} T_{\text{DA}} \quad (66)$$

where T_{DA} may be viewed as the matrix element of an effective one-particle Hamiltonian (e.g., [114]), and S_{if}^{el} represents the influence of an effective background many-electron core (in addition to “solute,” i.e., DBA, contributions to S_{if}^{el} , similar effects due to solvent have been reported [16b]). The *electronic* S_{if}^{el} factor is of course quite distinct from the *vibrational* overlap integrals ($S_{v_i v_f}$, as in Eq. 36) which may be used to “dress” the electronic factor (T_{if}) [14].

The estimates for S_{if}^{el} cited above were all for thermal ground-state systems, based on self-consistent field (SCF) wavefunctions. Studies with more elaborate wavefunction models have provided examples where electron-correlation effects (relative to the mean-field SCF level) make appreciable contributions to T_{if} magnitudes (e.g., [110, 116]). Furthermore, for the important case of excited state ET processes, where the SCF approach is not generally applicable, the viability of a one-particle model for T_{if} becomes less clear.

Multistate framework and spin-state dependence of T_{if}

While a single-matrix element, T_{if} , suffices for the simple TSA, an extended treatment may be required in cases of degenerate or quasi-degenerate initial and final states associated with open-shell reactants and/or products, since the ET process may then involve a distribution of thermally populated initial states and several possible final states. Even in such a multistate framework, it may be possible to cast the overall rate constants as a superposition of individual processes, each treated at the level of the TSA.

Cases of near-degeneracy due to both space and spin have been dealt with in the literature (e.g., see [117]). Here we consider specifically the case of spin [77]. In the simplest case, an ET process involves a single electron transferring between D and A cores, each of which has a singlet spin state ($S_{\text{D}} = S_{\text{A}} = 0$). In the general case where each core has a non-zero spin, the system involves both electron transfer and magnetic exchange (“double exchange”) and T_{if} becomes spin-state dependent [77, 79]. For example, when each core has spin S_{c} and the transferring electron is high-spin coupled to S_{c} at the site where it is resident (D or A), the dependence of T_{if} on the overall spin of the system, S , may be expressed by the following equation [77a]:

$$T_{if}(S_{\text{c}}, S) = T_{if} f(S_{\text{c}}, S) \quad (67a)$$

where

$$f(S_{\text{c}}, S) \propto [(2S + 1)^2 / 2(2S_{\text{c}} + 1)(2S_{\text{c}} + 2)]^{1/2} \quad (67b)$$

Thus, the electronic transmission factor κ_{el} (Eq. 52) will increase monotonically

with the overall spin (S) for a given S_c , creating the possibility that one may pass from the non-adiabatic to the adiabatic regime in the course of spanning the range of S values ($1/2$ to $2S_c + 1/2$). In weighting the contribution of spin state S to k_{et} for a thermal process (proportional to $[T_{if}(S_c, S)]^2$ in the non-adiabatic limit), one must also include the spin degeneracy factor, $2S + 1$, as well as a Boltzmann factor (based, for example, on a Heisenberg magnetic exchange model for relative spin-state energies, or a more elaborate model if electronic delocalization is appreciable) [77a]. If there are spatially degenerate (or quasi-degenerate) D or A orbitals, then one must also consider orientation-dependence of the spatial factor (T_{if} in Eq. 67a) with respect to different members of the degenerate set. As a practical device, one may employ an orientationally averaged T_{if} value (in the root-mean-square sense) [117]. Spin-orbit coupling provides another mechanism for spin-control of T_{if} magnitude. In its absence, a finite T_{if} value requires overall spin conservation. Even when such conservation is maintained, spin-orbit coupling may be crucial, as in the case of $[\text{Co}(\text{NH}_3)_6]^{2+/3+}$ self-exchange, involving primarily low-spin (singlet) Co^{3+} and high-spin quartet Co^{2+} [117]. Despite the fact that this process is formally spin-allowed, without a modest spin-orbit mixing of the low-spin (doublet) with the high-spin Co^{2+} state, the coupling would be very weak, corresponding to a “three-electron” process (involving intra-site electronic reorganization as well as inter-site electron exchange) [117]. See also Ref. [36].

A final comment pertains to the continuous electronic manifolds in the case of electron transfer at electrodes. Here one may formulate T_{if} to depend explicitly on the states within the accessible portion of the electrode band structure [31]. Alternatively, one may employ a mean value (e.g., based on the Fermi level) [25b, 32b, 106].

Nonorthogonality

The preceding discussion has been based on the assumption of orthonormal electronic states (see Eq. 14). In some cases it is advantageous to employ a non-orthogonal diabatic basis, especially when T_{if} is evaluated directly in terms of variationally determined charge-localized SCF [34] (or, in some cases, correlated [116a]) wavefunctions, which are generally nonorthogonal:

$$S_{if} = \int \psi_f \psi_i \neq 0 \quad (68)$$

where S_{if} is the total electronic overlap integral, in contrast to the electronic Franck-Condon factor S_{if}^{el} (Eq. 66), which pertains only to the “core” of spectator electrons. We now have the following equation:

$$T_{if} = (H_{if} - S_{if}\bar{H})/(1 - S_{if}^2) \quad (69)$$

where, for thermal electron transfer (resonant D and A sites) [6, 60],

$$\bar{H} = H_{ii} = H_{ff} \quad (70)$$

$$H_{if} = \langle \psi_i | H^{\text{el}} | \psi_f \rangle \quad (71)$$

(Eq. 64 corresponds to the special case where $S_{if} = 0$).

We also note that Eq. 69 may be generalized to accommodate the nonresonant situation ($H_{ii} \neq H_{jj}$) [6, 60]:

$$T_{if} = (H_{if} - S_{if} H_{jj}) / (1 - S_{if}^2) \quad (72)$$

$$T_{ji} = (H_{ji} - S_{ji} H_{ii}) / (1 - S_{ji}^2) \quad (73)$$

The apparent non-Hermitian relationship (i.e., $T_{if} \neq T_{ji}$, even though $H_{if} = H_{ji}$ and $S_{if} = S_{ji}$), is an artifact of the Condon factorization of the full vibronic matrix element, and, in a complete vibronic model, the vibrational manifold would compensate the mismatch in H_{ii} and H_{jj} [6, 60]. In using the Condon-factorized form (Eqs. 72 and 73), one may simply bypass the problem by using a mean value (\bar{H}) for H_{ii} and H_{jj} , thereby reverting to the Hermitian form of Eq. 69.

Influence of medium on T_{if}

There are a number of ways in which the medium might be expected to influence T_{if} magnitudes (over and above the modest many-electron Franck–Condon effect noted above). By medium we refer to the environment of the DBA complex (Figure 1). Typically, it will be a polar solvent. Solvent molecules may, of course, constitute part of the “bridge” (e.g., in the case of solvent-separated ion pairs [118]), which does not necessarily consist of a complete sequence of covalent linkages between D and A [34, 60, 89, 110, 111].

A polar medium may affect T_{if} as a result of its electrostatic field, either long-range (as representable by a continuum or molecular-level model) or short-range (e.g., by specific hydrogen-bonding). The field (which varies with fluctuations of the medium) can modulate the tails of the D and A orbitals, either directly by controlling the degree of radial localization of the orbitals, or indirectly by modifying the energy gaps which control superexchange coupling (Section 1.4.3). In practice, such effects may be quite small [119]. In addition to these electrostatic effects, the electronic manifold of the medium in the immediate vicinity of the primary bridge may provide superexchange pathways, which substantially affect the overall magnitude of T_{if} , thus, in effect, serving to expand the size of the bridge. The operational choice of the “bridge” is guided by the objective of including all sites for which direct orbital participation has an appreciable effect on T_{if} [89, 90]. In some cases, of course, local D and A groups may be defined as being in contact (as in contact ion pairs), thus eliminating the need for a “bridge” altogether.

1.4.2 Comparison of Thermal and Optical Processes

The Mulliken–Hush model

Important connections between optical and thermal ET may be established if the matrix elements of the dipole moment operator (μ) as well as the Hamiltonian are used [12, 30]. In particular, we note two expressions defined within the above TSA; the first of these is given by Eq. 74:

$$T_{if} = |\bar{\mu}_{12}| \Delta E_{12} / |\Delta \mu_{if}| \quad (74)$$

where

$$\mu_{k\ell} = \langle k | \hat{\mu} | \ell \rangle \equiv \int \psi_k \hat{\mu} \psi_\ell \quad (75)$$

$$\Delta \mu_{k\ell} \equiv \mu_{\ell\ell} - \mu_{kk} \quad (76)$$

$$\Delta E_{12} \equiv E_2 - E_1 \quad (77)$$

The second expression is given by Eq. 78:

$$\Delta \mu_{12} = \Delta q \Delta \mu_{if} \quad (78)$$

where

$$\Delta q = 1 - 2(\sin \theta)^2 \quad (79)$$

Here, Δq is the fraction of an electronic charge transferred within the TSA (see Eq. 14). In Eqs. 74–79, we have adopted the common assumption [12] that the inter-site diabatic dipole matrix element μ_{if} is negligibly small. With this assumption, it also follows that $\Delta \mu_{12}$, μ_{12} , and $\Delta \mu_{if}$ are collinear. Of course, if $\mu_{if} \neq 0$ in actual practice, this collinear situation will not be maintained. In such a case, one may adopt a reference direction (e.g., as defined by $\Delta \mu_{12}$), and then use the projections of the other dipole matrix elements along this direction [30]. We note that practical use of Eq. 74 requires some estimate of $\Delta \mu_{if}$, a measure of the effective separation of the D and A sites. We also note that the preceding equations are exact within the stated assumptions and do not depend on the use of perturbation theory [120]. A final caveat about the charge-transfer direction: in the limiting case of symmetry-equivalent D/A sites corresponding to a C_n point group (as might pertain to a TS structure), there is no charge transfer between *adiabatic* states (i.e., the component of $\Delta \mu_{12}$ perpendicular to the symmetry axis vanishes), but there may be a finite, extraneous component of $\Delta \mu_{12}$ along the symmetry axis.

Defining the effective D/A separation as

$$r_{DA} = |\Delta \mu_{if} / e| \quad (80)$$

we may reexpress Eq. 74 in the familiar Mulliken–Hush (MH) form:

$$|T_{if}| = |\mu_{12} \Delta E_{12}| / (e r_{DA}) \quad (81)$$

where r_{DA} in the past has typically been estimated on the basis of molecular structural data (e.g., [120]). We emphasize that r_{DA} is an effective D/A separation, since it includes not only the distance between centroids of the D and A orbitals, but also reflects the consequence of the polarization of the spectator electrons in response to the primary electron transfer between D and A orbitals [121].

A frequently used expression equivalent to Eq. 81, but based on directly obtained spectral quantities (peak absorption frequency, $\nu_{\max}/\text{cm}^{-1}$, band width, $\Delta\nu_{1/2}/\text{cm}^{-1}$, and molar absorptivity, $\epsilon_{\max}/\text{cm}^{-1} \text{ mol}^{-1}$), with T_{if} in cm^{-1} and r_{DA} in Å, is given by [12, 120],

$$T_{if} = 2.06 \times 10^{-2} (\nu_{\max} \epsilon_{\max} \Delta\nu_{1/2})^{1/2} / r_{\text{DA}} \quad (82)$$

The spectral transition energy $h\nu$ corresponds to ΔE_{12} in Eq. 74. A refinement of Eq. 82, for which a scaled (“reduced”) lineshape $[e(v) \cdot v]$ and a refractive index correction are used is discussed in [27] and [96a]. The first-order perturbation theory embodied in Eq. 82 is an excellent approximation for field strengths used in conventional spectroscopy.

A recent analysis [30a] has shown that the exact solution of the two-state problem (subject only to the MH assumption, $\mu_{if} = 0$ as introduced in connection with Eqs. (74, 81, and 82) yields an expression for $\Delta\mu_{if}$ entirely in terms of the matrix elements of the dipole moment in the adiabatic basis (see also Eq. 78):

$$|\Delta\mu_{if}| = [(\Delta\mu_{12})^2 + 4(\mu_{12})^2]^{1/2} \quad (83)$$

Thus, Eq. 74, with $|\Delta\mu_{if}|$ replaced by the right-hand side of Eq. 83, allows T_{if} to be specified exclusively in terms of adiabatic observables [30a], that is, ΔE_{12} and μ_{12} (obtainable from spectral energy and intensity) and $\Delta\mu_{12}$ (obtainable from Stark spectroscopy [122, 123]). Of course, these quantities may also be obtained from quantum calculations [30]. In typical applications, Eq. 74 or 83 pertains to a vertical transition for a value of the reaction coordinate (Figure 2a) at the equilibrium position of the initial state (where, in general, $\psi_1 \approx \psi_i$). It is worth noting, however, that in the limit of resonant transfer (i.e., $H_{ii} = H_{ff}$, the TS for thermal electron transfer), we obtain the expected result (Eq. 63):

$$T_{if} = \Delta E_{12}/2. \quad (84)$$

since in this case (where $\cos\theta = \sin\theta = 1/\sqrt{2}$ in Eq. 14), $\mu_{12} = \Delta\mu_{if}/2$.

The generalized Mulliken–Hush model and formulation of diabatic states

The use of Eq. 83 in conjunction with the MH expression, Eqs. 80 and 81, is an important example of the so-called Generalized Mulliken Hush (GMH) model [30], implemented at the level of the TSA. The core idea of the GMH model [30] is to exploit the fact that diagonalization of the dipole moment matrix (selecting the vector components in the charge-transfer direction, as discussed above) yields the maximally charge-localized state functions (at the TSA level, this yields the maximum value of $\Delta\mu$), and we adopt the resulting eigenfunctions as physically appropriate definitions of diabatic states in the case of ET processes (earlier approaches of this type, implemented in a pairwise fashion, have been reported in [124]; see also related approaches in [143]). From this perspective, Eq. 74 follows directly at the TSA level and need no longer be viewed as being dependent on the “neglect” of the

transition moment in the diabatic basis (rather, the diagonal nature of the dipole moment matrix is entailed in the very definition of the diabatic basis). Furthermore, the GMH approach may be employed in a multi-state framework (e.g., when treating both CS and CR processes, as in Figure 2b). Typically, one starts with H^{el} and $\bar{\mu}$ in an n -state adiabatic basis (the one directly pertinent to spectroscopic observables, where H^{el} is diagonal), defines the diabatic basis in terms of the unitary transformation which diagonalizes $\bar{\mu}$, and then generates H^{el} in the diabatic basis by applying the same unitary transformation to the adiabatic H^{el} matrix.

When the multistate GMH transformation as defined here yields more than one diabatic state localized on the same site, we impose the additional condition that a block of the diabatic Hamiltonian associated with a single site be diagonal, thus yielding states diabatic in the GMH sense with respect to inter-site coupling, but “locally adiabatic” within each site or local region [30]. Clearly, this approach rests on a distance scale separation: D and A sites of small spatial extent relative to r_{DA} . In a multistate situation, the GMH analysis employs the component of each dipole vector in the mean direction defined by the adiabatic dipole shifts for the various electron transfer processes of interest.

As already noted above in connection with the two-state MH model (now recognized as a special case of GMH), we emphasize that the GMH method can be implemented solely in terms of experimental quantities. Observed excitation energies, transition dipoles from intensity measurements, and adiabatic dipole moment differences from Stark measurements yield direct experimental estimates of diabatic coupling elements according to the above procedure. At the multistate level, the relative sign relations among the transition moments must be known, and may be taken from calculations if not available from analyses of the experimental data. (These phase relations are “observables,” as distinct from phase “conventions;” e.g., for a three-state system two distinct cases arise: an even or odd number of positive transition dipole moments.) Finally, we mention that as in the two-state case (see Eq. 83), the GMH diabatic dipole-moment matrix in the general multistate framework directly yields estimates of the centroids of the different states of the system of interest and the associated r_{DA} values (i.e., effective separation distances of D and A sites), quantities of great utility in interpreting charge-transfer data obtained from Stark spectroscopy or quantum calculations [27, 30, 90b, 122, 123].

In computational applications, the formulation of the GMH approach in terms of adiabatic (H^{el} eigenvectors) quantities is very convenient, since it can be implemented in terms of eigenfunctions obtained from configuration interaction (CI) calculations [27, 30, 36, 69, 90b]. Such wavefunctions may be necessary for proper characterization of excited states, in contrast to the SCF wavefunctions, which are generally limited to use in ground-state thermal processes. Another advantage is the applicability for arbitrary values of the reaction coordinate or other coordinates of the system, thus offering a means of testing the Condon approximation [66].

One of the central physical characteristics of the GMH model, the block diagonal form of the diabatic dipole-moment matrix, where a block includes all states charge-localized at a given site, may be compared with the picture emerging from alternative formulations of diabatic states, which (unlike the GMH model) do not involve any assumptions about dipole matrix elements, being based instead on the details of

the eigenvectors of the Hamiltonian obtained from multistate quantum-chemical calculations [30b]. One such technique, in the spirit of the so-called “least-motion block diagonal” formulations, has been shown to give generally close adherence to results based on the GMH approach [30b].

1.4.3 Pathway Analysis of T_{if}

To shed light on the detailed electronic factors controlling overall D/A coupling as represented by $T_{if} \approx T_{DA}$ (see Eq. 66), we turn to the concept of the “electronic pathway”, a sequence of intermediate states of the bridge by which the transferring electron proceeds from the D to the A site. The pathway concept is generally used in the context of coherent D/A coupling involving *virtual* intermediate states (with vanishing lifetimes), as treated by superexchange (perturbation) theory in cases where the gap separating the D/A and the bridge levels are large, and this will be the focus of the present section [17, 60, 88]. In contrast, small gaps tend to favor incoherent hopping processes involving a finite residence time of the transferring charge on the bridge sites [19].

States and orbitals

While the most fundamental formulation of D/A coupling is in terms of many-electron states [6, 60], it is often possible to recast the formulation in terms of an orbital picture [34, 60] (see Section 1.4.1). For simplicity, we use the state language here. In the TSA, the initial and final diabatic states have the transferring charge largely confined to the D and A sites, respectively, and yet the coupling is crucially dependent on the D and A tails which extend onto the bridge. Superexchange (*se*) theory [6, 17, 60, 64, 125] provides a detailed account of these tails in terms of an auxiliary basis of zeroth-order states, $\psi_D^\circ, \psi_A^\circ, \psi_{B_1}^\circ, \dots, \psi_{B_n}^\circ$, which can be taken as essentially fully-localized on their respective sites (subject to maintenance of orthogonality), where the bridge is represented by n distinct units, B_j ($\psi_D^\circ, \psi_A^\circ$, and $\psi_{B_j}^\circ$ for the case of *electron* transfer correspond, respectively, to valence bond structures DBA, D^+BA^- , and $D^+B_j^-A$). These states may be taken as eigenfunctions of some zeroth-order Hamiltonian, $(H^{\text{el}})^0$, where

$$H^{\text{el}} = (H^{\text{el}})^0 + V \quad (85)$$

Here the perturbation V generates the D and A tails through mixing of the $\{\psi^\circ\}$. Note that first-order terms ($\langle \psi^\circ | V | \psi^\circ \rangle$) are generally assumed to vanish. In the following discussion of *se* models, it is understood that all D-, A-, and B-state labels refer to the zeroth-order states, and we won’t use zero as the superscript.

Superexchange models

The perturbative McConnell model for coupling by a single pathway is based on a bridge consisting of a homologous linear sequence of units, B_j , each with a single charge-localized state, ψ_{B_j} , lying above the resonant D/A energy level by a common

gap Δ [125]:

$$|T_{if}| = |T(t/\Delta)^{n-1}(T/\Delta)| \quad (86)$$

where it is assumed that $|T/\Delta|, |t/\Delta| \ll 1$. In this model, only nearest-neighbor (NN) pairs of sites are coupled:

$$T \equiv T_{DB_1} = T_{B_n A} \quad (87)$$

where, for example, $T_{DB_1} \equiv \int \psi_D V \psi_{B_1}$ and

$$t \equiv t_{B_i B_{i+1}} = \int \psi_{B_i} V \psi_{B_{i+1}} \quad (88)$$

This compact expression (Eq. 86), which is second-order with respect to linkage of D and A to the bridge and $(n-1)$ th order with respect to coupling within B, clearly predicts exponential fall-off. The decay coefficient with respect to n ($-\ln|t/\Delta|$) can be converted to the conventional measure of distance dependence, β ,

$$\beta = -2 \ln|t/\Delta|/\Delta r \quad (89)$$

where Δr is the effective length of a bridge unit. The factor of two is included to correspond to the distance-dependence of the factor $(T_{if})^2$ in the non-adiabatic expression for k_{et} (Eq. 31):

$$(T_{if})^2 \propto \exp(-\beta \Delta r) \quad (90)$$

The distance-dependence of the overall k_{et} may depart from that given by Eq. 90 due to additional distance-dependence arising from λ or ΔG° [9, 119], or in cases of incoherent sequential electron hopping [19]. The role of the gap Δ , particularly in the quantity t/Δ , is seen to be crucial in controlling both the magnitude and distance dependence of T_{if} .

It is of course a matter of choice as to how finely the total bridge is divided into subunits. The optimal choice involves various trade-offs, including chemical transferability (favoring small subunits), compactness of representation when it comes to synthesizing the overall coupling T_{if} (favoring larger subunits), and theoretical considerations such as the applicability of perturbation theory (here the trade-off is complex, but often favors larger subunits [34, 126]). Furthermore, the number of states, ψ_{B_i} , required in each unit to give adequate account of the coupling would tend to increase with the size of the unit, thus requiring an extension of the single-pathway McConnell model.

The sign of T_{if} for a given pathway is of interest, especially when the overall T_{if} involves the superposition of several pathways. Determination of sign requires careful consideration of all phase conventions used in defining the states involved in coupling elements T and t . In many cases of interest, the sign of t/Δ in Eq. 86 can be taken to be negative, thus yielding the prediction that the sign of T_{if} alternates

with n while its magnitude fall off exponentially [6]. This is the basis of the so-called parity rule [127]. Of course, in more complex situations (beyond the simple NN homologous case), the sign patterns are expected to be more complicated [34, 63, 70b].

Through its dependence on the NN transfer integrals T and t , and a measure of distance scale, Δr , Eq. 86 represents, at least in a minimal fashion, the inhomogeneous nature of the electronic structure of the bridge. This is to be contrasted with the Gamow model for electronic tunneling through a homogeneous barrier of height Δ^G [128], where β is given by the following equation:

$$\beta^G = 2(2m_e\Delta^G)^{1/2}/\hbar \quad (91)$$

and where m_e is the mass (actual or effective) of the tunneling electron. An important distinction is made between the roles of the gaps Δ in Eqs. 89 and 91. In the former case, Δ (for a particular bridge subunit) is, in principle (and in some cases in practice), a spectroscopic observable, whereas the phenomenological Δ^G , which represents the full bridge in Eq. 91, is not in general directly accessible as an observable. Effective Δ^G values may, of course, be inferred from Eq. 91 on the basis of experimental β values, but attempts to use experimentally determined energy gaps (e.g., from redox potentials or spectroscopy) frequently lead to exaggerated β magnitudes [129]. Eq. 91 is more usefully applied to the direct or “through-space” (ts) D/A coupling when no bridge is present. In this case, Δ^G may be identified with the relevant ionization potential of D [130]. Equation 86 may be generalized in a number of ways including the following [6, 60]:

a) Distinct bridging units:

$$T_{if} = (T_{DB_1}) \left[\prod_{j=1}^{n-1} t_{B_j B_{j+1}} / \Delta_j \right] (T_{B_n A} / \Delta_n) \quad (92)$$

where the subscripts on T and t denote NN coupling, and Δ_j denotes the gap between the D/A level and the energy of bridge unit j .

- b) Summation over multiple pathways of the generic type exemplified by Eq. 92, where advantage is taken of the additive contributions of the various perturbative terms and non-NN pathways are also included. Such non-NN contributions are expected to enhance the sensitivity of T_{if} to conformational variations of the bridge and will also tend to reduce the distinction between covalently linked bridges and those which involve nonbonded contact [60].
- c) Involvement of more than one charge-localized state on each site, including, for example, those based on both occupied and unoccupied bridge bands, thereby leading to competitive (either constructive or destructive) interference among “hole”, “electron”, and “hybrid” pathways [34, 60, 109]. The case for hole- and electron transfer involving two bridge sites is illustrated in Figure 5. Alternatively, one may have competition between different components of a given occupied or unoccupied manifold—for example, σ - vs π -types [70].

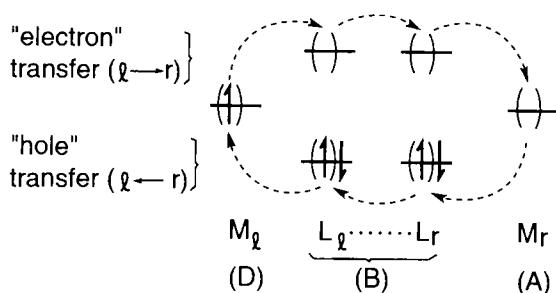


Figure 5. Schematic representation of bridge-mediated superexchange of the “electron” (top, left to right) and “hole” (bottom, right to left) type, illustrated for the case of intermolecular electron transfer between two metal/ligand (M/L) complexes, where $D \equiv M_l$, $B \equiv L_l \cdots L_r$, and $A \equiv M_r$. The virtual intermediate states for the hole and electron processes involve, respectively, charge localization based on the filled (“valence”) and empty (“conduction”) bands of the bridge.

Equations 86 and 92 may be derived in terms of effective Hamiltonians based on partitioning schemes [131], or when Green-function techniques are used [17]. A number of detailed computational studies have been carried out in which T_{if} was additively decomposed into contributions from competing pathways defined in terms of states based on localized bonding, antibonding, and lone-pair orbitals [34, 109–111]. The general conclusion is that the McConnell NN pathway, if interpreted in terms of localized bonding or antibonding orbitals, often has a very minor role, and that in most cases no single pathway plays a dominant role. Nevertheless, the form of the simple McConnell expression (Eq. 86), or limited extensions thereof (e.g., Eq. 92 or a NN model with two states per site [70]) may be very useful for representing the results of detailed calculations of T_{if} (see also [63] and [111]) Examples are considered in Section 1.5, together with a discussion on interference effects.

When the gaps Δ_j are large, their variation with nuclear coordinates (e.g., bridge modes or the reaction coordinate) may be neglected. More detailed approaches are discussed in [9, 32a, 132]. Relative to the perturbative result given in Eqs. 89 and 90, a more general expression displaying exponential decay is also found when the constraints of perturbation theory are relaxed, provided that $|T/\Delta|$ remains small and the D/A level remains outside the band of bridge levels ($|\Delta| > |2t|$ for the linear NN case) [88]. Special care must be exercised when the D/A level begins to overlap the electronic bands of the bridge [133]. In such a situation the distance-dependence of T_{if} will, in general, not be exponential, and thus fitting of experimental or calculated T_{if} data to an expression of the form given by Eq. 90 is no longer appropriate.

An aside on notation

We comment briefly on the notation employed here and in [17, 34, 60 and 89] for the D/A coupling element (T_{if} or T_{DA}). The symbol “ T ” denotes the “transfer integral”, which may be viewed as the matrix element of a “transfer operator”, which couples the *zeroth-order* basis functions ψ_j^0 defined above; T_{if} is equivalent to H_{if}^{el} , if

the latter is understood to be the matrix element of H^{el} (see Eq. 13) with respect to the *full* diabatic functions ψ_i and ψ_f (i.e., including tails) in the TSA. The “ H ” notation in this sense was employed in [6] (H_{if}) and [8] (H_{ps}). The symbol “ T ” was used in a different manner in [8] (nuclear kinetic energy operator) and [125] (NN coupling elements in the zeroth-order basis).

1.5 Applications of Theory

The models and concepts presented in Sections 1.1–1.4 have been extensively tested in recent years. Some of these tests involved comparison of quantitative relationships between experimental observables with predictions of simple models. In other tests, the theoretical predictions and experimental data were compared with the results of detailed numerical calculations. We offer several examples of each type of comparison.

1.5.1 Comparisons Based on Experimental Data

A number of interesting consistency tests of models for ET kinetics and D/A coupling are provided by available thermal and optical data.

Tests of superexchange models

Mixed-valence complexes

The optical ET data for the class of mixed-valence systems of the type shown in Eq. 93 has provided a rich test bed of experimental data [120–123, 134, 135].



We consider charge-localized systems (Robin–Day class II [136]) in which the bridging ligand L provides one coordination site for each ruthenium atom. The other five coordination sites at each ruthenium are provided by ammine or other nitrogen-based ligands. The effective Ru–Ru coupling elements for these processes may be estimated directly if the MH expression (Eq. 82) is used to analyze the intervalence transition (IT). Alternatively, one may employ a superexchange model, where Eq. 82 is used in conjunction with data for optical ET between L and the Ru sites [120]. For the specific system under consideration (Eq. 93), we employ the subscripts M and M' for the two Ru sites and L for the bridging ligand,

$$T_{if} = T_{MM'}^{\text{op}} = \frac{T_{ML}^{\text{op}} T_{M'L}^{\text{op}}}{2\Delta E_{ML}^{\text{eff}}} + \frac{T_{LM'}^{\text{op}} T_{LM}^{\text{op}}}{\Delta_{LM}^{\text{eff}}}, \quad (94)$$

where T_{jk}^{op} denotes the coupling for the relevant optical ET process ($jk \equiv MM', ML, LM$, etc). The two terms correspond, respectively, to electron- and hole-transfer mechanisms, facilitated by virtual intermediate states, respectively, of the metal-to-ligand (MLCT) and ligand-to-metal (LMCT) charge-transfer type. Each of these terms can be recognized to have the simple McConnell form (the factor of two in the first term is discussed in [120]), although the formal derivation for the present case of nonresonant D/A sites is distinct from that for the resonant sites entailed in the McConnell derivation [6]. The effective energy gap for optical electron transfer is given by the following equation [6, 120]:

$$\Delta E_{ML}^{\text{eff}} = [0.5(1/E_{MLCT} + 1/(E_{MLCT} - E_{IT}))]^{-1} \quad (95)$$

(and analogously for $\Delta E_{LM}^{\text{eff}}$ in the hole-transfer term). Here E_{MLCT} and E_{IT} are the vertical excitation energies for the MLCT and MM'CT (IT) processes. The T_{ML}^{op} and T_{LM}^{op} quantities may be obtained from the relevant spectral data in conjunction with the MH expression [120]. For simplicity, the assumption is made that $T_{ML}^{\text{op}} = T_{M'L}^{\text{op}}$ and $T_{LM}^{\text{op}} = T_{LM'}^{\text{op}}$, even though the coordination geometries at the 2+ and 3+ sites are not identical [120, 135]. In the following, we leave out the superscript “op” and distinguish $T_{MM'}$ obtained directly from the MH model for the IT process and the *se* model (Eq. 94) as $T_{MM'}^{MH}$ and $T_{MM'}^{se}$, respectively.

An important feature of Eqs. 82 and 94 is that they can in principle be implemented entirely in terms of experimental spectral data. One point requiring special comment is the determination of r_{DA} in Eq. 82. While this may be obtained by Eq. 83 if the results of Stark spectroscopy are available, such data are still relatively scarce, thus making it common to use structural data (e.g., $r_{MM'}$ or r_{ML} based on the metal site and the ligand midpoint [120, 135]), as estimated upper limits. In cases where Stark data are at hand, r_{DA} is often found to be appreciably smaller than $r_{MM'}$ (or r_{ML}), especially in cases of strong ML coupling [89, 121–123] (examples are given in Section 1.5.1). Nevertheless, recent analyses based on $r_{MM'}$ and r_{ML} have given numerous examples of reasonable correspondence between $T_{MM'}^{MH}$ and $T_{MM'}^{se}$. One study of relatively weak MM' coupling ($T_{MM'}^{se} \leq 1000 \text{ cm}^{-1}$) involving pyridyl-based ligands (L), where the electron-transfer mechanism (first term in Eq. 94) was thought to be dominant, systematically yielded $T_{MM'}^{se} \geq T_{MM'}^{MH}$ and within a factor of two or better [120]. Similar results were also found for cases of relatively weak coupling (i.e., $T_{MM'}^{se} \leq 2000 \text{ cm}^{-1}$) in a more recent study [135] employing the ligand dicyd²⁻ \equiv 1,4-dicyanoamido benzene ($[\text{NCN}-\text{C}_6\text{H}_4-\text{NCN}]^{2-}$), where the hole mechanism (second term in Eq. 94) was taken as dominant. For cases from the same study in which the coupling was stronger ($T_{MM'}^{se} \geq 3000$), values of 3–5 for $T_{MM'}^{se}/T_{MM'}^{MH}$ were found, suggesting (inter alia) greater uncertainty in the appropriate r_{DA} values. Nevertheless, these results offer encouraging support for the use of simple superexchange models like Eq. 94, and also offer an incentive for further Stark measurements so as to provide better r_{DA} estimates (in conjunction with Eq. 83) and thereby allow more quantitative testing of the superexchange model. Finally, we note, as a caveat, a recent study of a family of MLM' systems in which the trends implied by Eq. 94 were not observed; this suggests that specific vibronic effects may be required to account for the relevant MM' coupling [137].

Electron-transfer coupling vs magnetic exchange

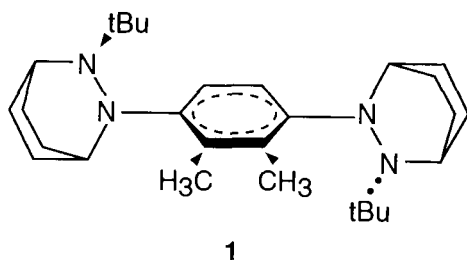
It is well known that superexchange theory provides useful relationships between one- and two-electron coupling elements (e.g., [28, 78, 138]). We consider the simple case of a monocation electron transfer system,



and the corresponding dication, D^+BA^+ , in which the coupling of the localized doublet spins at the D and A sites is triplet (ferromagnetic) or singlet (antiferromagnetic) [28]. We also assume for simplicity that D and A are symmetry-equivalent sites. Defining $E_{\text{singlet}} - E_{\text{triplet}} = 2J$, where J is the Heisenberg exchange integral, and assuming that only the singlet state is stabilized by D/A coupling, we obtain:

$$J = (\alpha T_{if})^2 / \Delta E_{CT} \quad (97)$$

where α is a numerical coefficient, T_{if} is the one-electron transfer integral and ΔE_{CT} is the energy of the vertical charge-transfer process from the diabatic ground-state singlet diradical, D^+BA^+ , to the diabatic excited state, a symmetric mixture of $D^{2+}BA$ and DBA^{2+} resonance structures. Nelson and coworkers [28] have tested Eq. 97 for DBA system **1** by obtaining independent estimates of the four parameters in the equation. The spectral data yielded $T_{if} = 3.3$ kcal/mol and $\Delta E_{CT} = 64.1$ kcal/mol for the monocation ($\mathbf{1}^+$) and $J = 0.18$ – 0.21 kcal/mol for the dication ($\mathbf{1}^{2+}$). Comparison of the optical spectra for ($\mathbf{1}^+$) and ($\mathbf{1}^{2+}$) yielded $\alpha \approx 1.2$, to be compared to the zeroth-order theoretical prediction, $\alpha = \sqrt{2}$. In either case, the right-hand side of Eq. 97 is found to be in good accord with the experimental J value: 0.23 kcal/mol ($\alpha = 1.2$) or 0.34 ($\alpha = \sqrt{2}$), thus providing impressive support for the superexchange model.

 *β Values for One- and two-electron processes*

T_{if} for electron (or hole) transfer may essentially be thought of as a one-electron integral (T_{DA} , as in Eq. 66) involving the exchange density, $\phi_D\phi_A$, where the tails of ϕ_D and ϕ_A involve mixing of zeroth-order D and A orbitals with the unfilled (electron) or filled (hole) manifolds of the bridge. In triplet energy transfer by the Dexter mechanism [139], the corresponding two-electron (2e) coupling element involves two exchange densities, $\phi_D\phi_A$ and $\phi_D^*\phi_A^*$:

$$T_{if}^{2c} = \int d\tau d\tau' \phi_D(r) \phi_A(r) (1/r_{12}) \phi_D^*(r') \phi_A^*(r') \quad (98)$$

where ϕ_D , ϕ_D^* and ϕ_A , ϕ_A^* are the orbital pairs involved in the local triplet excitation being transferred between D and A sites. If the tails of D and A (D^* and A^*) are assumed to be dominated by mixing with the filled (unfilled) bridge manifolds, we conclude that a good estimate of the exponential decay coefficient of $(T_{if}^{2c})^2$ with bridge length, β^{2c} , might be given by the sum of the electron (β^e) and hole (β^h) decay coefficients for the corresponding one-particle processes. In fact, just such a relationship was demonstrated on the basis of experimental data for a series of $(DBA)^+$ systems where D = 4-biphenyl (electron or hole transfer) or 4-benzophenonyl (triplet transfer), A = 2-naphthyl, and B was based on cyclohexyl or decalin moieties, that is, the observed rate constants for triplet energy transfer were found to agree well with predictions based on $\beta^{2c} = \beta^e + \beta^h$ [76]. This result was also supported by ab initio calculations for related model systems [62].

Thermal vs optical electron transfer

Given the wide use of the MH analysis of optical data (Eq. 82), it is of considerable interest to ascertain the quantitative validity of transferring T_{if} values obtained from optical electron transfer at equilibrium for use in analyzing thermal electron transfer occurring at the TS.

Mixed-valence $Fe^{2+/3+}$ complexes

A convincing demonstration of such transferability was recently obtained by Elliott et al [27], using a mixed-valence Fe^{2+}/Fe^{3+} system involving tethered tris-bipyridyl Fe complexes, **2** ($M = 4$). The analysis in this case was greatly simplified since no high-frequency inner-sphere modes were appreciably coupled to the ET process, thereby permitting a classical treatment of the energetics. The salient results are summarized in Table 1. In the analysis of the optical ET data, r_{DA} was estimated to be very close to r_{MM} , a consequence of the rather symmetric nature of the Fe coordination shells, in contrast to the more asymmetric coordination shells of most of the systems investigated by Stark spectroscopy [122, 123]. The optical T_{if} estimates are seen to depend modestly on the specific form of refractive index correction employed. When T_{if} was estimated from the thermal data, the result was found

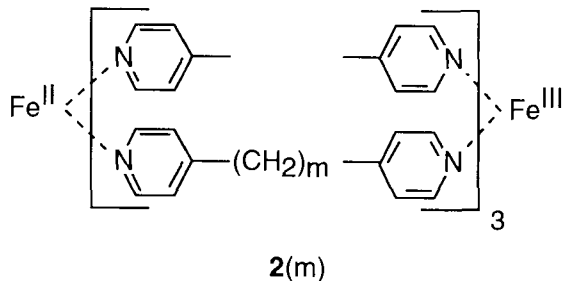


Table 1. Comparison of optical and thermal T_{if} and λ values for $2(m = 4)$.

Refractive index correction factor ^b		Optical ^a T_{if} (cm ⁻¹) ^c	λ (cm ⁻¹)
Birks ^d	$1/n$	5.4 ± 0.7	
Chako ^e	$n/\{(n^2 + 2)/9\}$	5.8 ± 0.7	7900 ± 200
None	1	6.3 ± 0.8	

Model for $(\partial\lambda/\partial T)_p$ (cm ⁻¹ K ⁻¹)		Thermal ^f T_{if} (cm ⁻¹) ^g	λ (cm ⁻¹)
None	0	15 ± 3	
Continuum ^h	5.5	40 ± 7	7500 ± 300
Molecular ⁱ	-6.6	4.7 ± 0.9	

^aObtained from the reduced extinction coefficient, $\varepsilon'(v) = \varepsilon(v)v$, for the IT band of $2(m = 4)$ in acetonitrile [27] (Table 2 of [27], adapted with kind permission. Copyright 1998, American Chemical Society).

^bAdditional factor included within the square root in Eq. 82, where a value of 1.342 was used for the refractive index (n) of acetonitrile [27].

^cBased on Eq. 82.

^d[147].

^e[148].

^fBased on NMR kinetic data [27].

^gBased on fits of the kinetic data to Eqs. 31 and 32, with $G^\ddagger = \lambda/4$.

^hBased on the two-sphere Marcus continuum model (see [27]).

ⁱ[21, 27].

to be rather sensitive to the manner in which the temperature-dependence of λ was treated. It is now recognized that such dependence is often quantitatively significant and that estimates of this dependence based on a continuum model have an incorrect (positive) sign for polar solvents [21, 27, 53, 54, 140]. The preferred estimate, based on a molecular-level model [21], yields a result ($T_{if} = 4.7 \pm 0.9$ cm⁻¹) in quite good agreement with the preferred optical value (5.4 ± 0.7 cm⁻¹). As a final test of consistency, the values of λ inferred from the optical (7900 ± 200 cm⁻¹) and thermal (7500 ± 300 cm⁻¹) data are in good accord.

Analysis of a series of Ru^{2+/3+} mixed-valence systems

The same series of Ru²⁺/Ru³⁺ systems that were used to compare T_{if} values obtained from direct use of the MH model (Eq. 82) with the T_{if} values obtained from a superexchange model (Eq. 94), as discussed in Section 1.5.1, were also employed for a comparison of optical and thermal T_{if} values [135]. In this case the thermal T_{if} values were inferred indirectly from the estimated “resonance-exchange component” ($\Delta G_r'$) of the free energy change (ΔG_c) associated with the measured disproportionation equilibrium between the 3+/3+, 2+/2+, and 2+/3+ oxidation states. According to the perturbative model adopted for the Robin/Day class-II system [136], one obtains

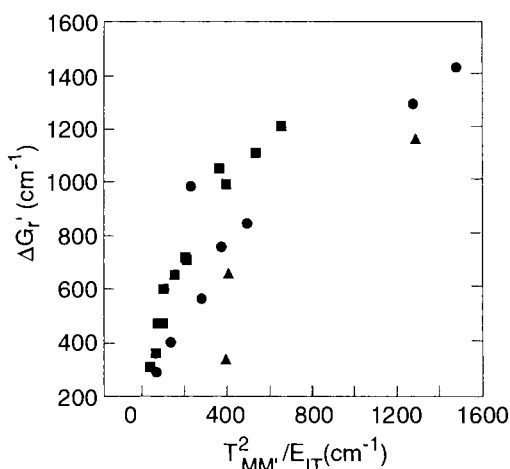


Figure 6. Estimates from thermal and optical ET data for the resonance stabilization ($\Delta G'_r$) [135] of mixed-valence systems of the type $\text{Ru}^{2+}\text{BRu}^{3+}$ due to metal-metal coupling ($T_{MM'}$), where B is based on the "dicyd²" bidentate ligand (1,4-dicyanoamido-benzene), and the D and A moieties are Ru pentaammine (■), tetraammine (●), or triammine (▲) complexes [135]. The thermal estimates of $\Delta G'_r$ are obtained from measured comproportionation constants, while the optical estimates are based on use of the second-order perturbation theory expression, Eq. 99, evaluated in terms of spectral data in conjunction with the MH model (Section 1.4.2), where the r_{DA} that is used is based on the Ru-Ru' separation. (Figure 6 of [135], reprinted with permission. Copyright 1998, American Chemical Society).

$$\Delta G'_r = (T_{MM'})^2 / \Delta E_{IT}. \quad (99)$$

where $T_{MM'}$ is the quantity introduced in Section 1.5.1. While Eq. 99 resembles a second-order perturbation-theory result, it is in fact exact within the two-state harmonic approximation for diabatic states [9c]. As indicated in Figure 6, Eq. 99 based on $T_{MM'}^{\text{sc}}$ (see Section 1.5.1) gives a reasonably good account of the trend relating the thermal (left-hand side) and optical (right-hand side) measures of $M-M'$ coupling, thus once again offering encouraging support for the transferability of thermal and optical T_{if} values (the use of $T_{MM'}^{\text{MH}}$ as an estimate of the optical $T_{MM'}$ value, see Section 1.5.1, did not yield a good correlation with $\Delta G'_r$). For achieving more quantitative correlations, the choice of r_{DA} values entailed in the MH model must be scrutinized and, in the case of strongest coupling, efforts should be made to relax the constraints of the model underlying Eq. 99 [135].

Other work

A number of other comparisons of thermal and optical data have been reported; these provide additional support for the transferability of T_{if} quantities, a manifestation of the reliability of the Condon approximation. We note, for example, the recent work of Nelsen et al. [141], and the earlier work of Penfield et al. [142].

Table 2. Effective separation of D/A sites (r_{DA} , Å).

Electron transfer system	From molecular geometry ^a	From two-State analysis of spectral data ^b	
		Diabatic	Adiabatic
(NH ₃) ₅ (Ru ²⁺ L) ^c :			
MLCT $\left\{ \begin{array}{l} \text{L} = \text{pz} \\ \text{L} = \text{pzH}^+ \\ \text{L} = \text{bpy} \\ \text{L} = \text{bpyH}^+ \end{array} \right.$	3.5	2.2	1.0
	3.5	2.1	<0.1
	5.6	3.4	2.9
	5.6	4.3	3.6
(NH ₃) ₅ (Ru ²⁺ L Ru ³⁺) (NH ₃) ₅ ^c			
IT $\left\{ \begin{array}{l} \text{L} = \text{pz} \\ \text{L} = \text{bpy} \end{array} \right.$	6.8	1.4	<0.1
	11.3	5.2	5.1

^aBased on separation of M and ligand midpoint (for MLCT cases) or $r_{MM'}$ (for IT cases), where M and M' denote Ru atom sites.

^bBased on spectral data analyzed in terms of the two-state GMH model (Eq. 83). In the analysis, a value of $f = 1.3$ was used to relate the local to the applied external electric field in the Stark measurements ($E_{\text{loc}} = fE_{\text{ext}}$).

^cFrom Refs. [121–123]; pz \equiv pyrazine; bpy \equiv 4,4-bipyridine.

Estimates of r_{DA}

In cases where optical electron-transfer data include Stark spectral results, one may compare r_{DA} estimates based on molecular structure r_{DA}^{geom} with those obtained from diabatic r_{DA}^{diabat} and adiabatic r_{DA}^{adiabat} dipole-moment shifts associated with the ET process. Some examples from IT and MLCT spectra are summarized in Table 2; a uniform trend is obvious, namely,

$$r_{DA}^{\text{geom}} > r_{DA}^{\text{diabat}} > r_{DA}^{\text{adiabat}} \quad (100)$$

where r_{DA}^{geom} is based on the MM' distance or the distance between M and the L midpoint, and r_{DA}^{diabat} and r_{DA}^{adiabat} are defined by the GMH model (Eq. 83). Clearly, the ratio of r_{DA}^{diabat} to r_{DA}^{geom} departs significantly from unity (0.5–0.8 for the ML and class-II MM' complexes and 0.2 for the class-III MM' complex, where L = pz; this underscores the importance of careful choice of r_{DA} values when the MH model is implemented (Eq. 82). Significant quantitative differences between r_{DA}^{diabat} and r_{DA}^{adiabat} are revealed as well.

1.5.2 Computational Studies

A number of computational approaches have been exploited for evaluating the crucial coupling (T_{if}) and energetic quantities (especially, G^\ddagger and λ) controlling

electron transfer kinetics. As illustrated in the following examples, these studies play several important complementary roles in helping to elucidate ET mechanisms, as has been extensively documented and reviewed in the recent literature [1, 3, 4, 10]). These roles include tests of simple theoretical models (thereby helping the formulation of compact predictive models), comparisons with experimental results (helping to guide the design of new experiments), and illuminating interpretive analyses.

Calculations of coupling elements involve the basic electronic structure model, the procedure for extracting T_{if} estimates from the calculated wavefunctions, and schemes for inferring detailed molecular contributions to overall T_{if} values. Ab initio and semi-empirical orbital models, and also density functional theory (DFT) [143] have been employed. The orbital models have been implemented at the mean-field level (e.g., Hartree–Fock, HF, or self-consistent field, SCF) or in an extended framework (e.g., configuration interaction, CI), which permits treatment of excited states and account of electron correlation. In evaluating T_{if} , one may use a simple energy splitting model as given by Eq. 63, based on an effective Hamiltonian or Green function defined in terms of the calculated electronic structure [60] if the D and A sites are resonant (in general this may be achieved if some “external” perturbation is imposed, such as an electric field). Alternatively, the GMH model (Eqs. 81 and 83) may be employed for nonresonant situations. A promising DFT-based approach has recently been reported [143], whereby T_{if} is inferred from the response of the ground-state charge density to a variable external field which causes a continuous switch of the charge-transfer character (e.g., from DBA to D^+BA^-). Contributions to T_{if} have been analyzed in terms of additive pathway schemes based on localized orbitals (at both SCF [34, 109–111] and CI [112e,f] levels) and other decomposition schemes [112a–d], in an attempt to spatially identify the most important pathways or bridging units (e.g., amino acid residues).

Procedures for evaluating activation parameters range from simple continuum models to full-blown molecular-level simulations (molecular dynamics, MD, or Monte Carlo, MC) at either a classical or quantal level [15, 21, 33, 36, 47, 49, 52a, 84b, 94, 119]. In such treatments, the DBA system may be represented by a simple point-charge model or one based on a detailed electronic structure calculation, which can, if desired, be self-consistently adjusted to the response of the medium [119].

Response of T_{if} to structural change in a DBA system

Since no DBA system is fully rigid, it is important to know the consequence of structural fluctuations on kinetic parameters (e.g., those fluctuations corresponding to distinct conformational isomers, or those of smaller amplitude within a given local minimum). We consider some examples (see also [71c]) of structural coordinates of the bridge (B), which modulate T_{if} values, but are not strongly coupled to the fluctuating energy gap (i.e., reaction coordinate η in Eqs. 20–23). These coordinates thus provide useful controlled probes of non-Condon behavior [66], since they have a small effect on activation energetics (some sensitivity of λ may arise for fluctuations which affect the magnitude of r_{DA} , as has been noted in [89] and [119]).

Table 3. Conformational Dependence of T_{if} for $(\text{CH}_2)_6^\pm$ Radical Ions^a.

Conformation of D and A orbitals relative to bridge	Conformation of C ₄ bridge	T_{if} ^c	
		Radical cation	Radical anion
In plane	<i>trans</i> (C _{2h})	−11.0	−8.4
	<i>gauche</i> (C ₂)	−2.4	−4.5
	<i>cis</i> (C _{2v})	−0.3	−4.3
Perpendicular to plane	<i>trans</i> (C _{2h})	−1.1	+0.3
	<i>gauche</i> (C ₂)	+3.6	+2.0
	<i>cis</i> (C _{2v})	+7.9	+9.9

^aIn these model (DBA)⁺ systems, the terminal CH_2^\pm and CH_2 groups serve as D and A sites, while the internal $(\text{CH}_2)_4$ moiety is the bridge (B). (Table 2 of [149], reprinted with kind permission. Copyright 1996, Elsevier Press).

^bAngle of the D(A) π orbital relative to plane formed by the carbon atom of the terminal D(A) methylene group and the closest two carbon atoms of the bridge.

^cCalculated results based on ab initio SCF calculations; T_{if} in units of mhartree (1 mhartree = 0.027 eV $\approx k_B T$ at room temperature). The sign conventions are defined in [149].

Alkane-chain conformation

A simple but important example of conformational sensitivity of T_{if} is illustrated in Table 3, in which results for *trans* staggered (*t*), *gauche* (*g*), and *cis* (*c*) conformations of some C₄ alkane bridges are compared and in which sign changes as well as significant changes of magnitude are seen [144]. A similar pattern in more complex bridge moieties has been observed in both computational and experimental data [62, 110]. This situation offers a caveat regarding distance-dependence of T_{if} in families of DBA systems. Although a $(\text{CH}_2)_n$ sequence may be considered to be homologous, one would not necessarily expect a simple exponential fall-off with n if the different members of the series have different conformational structures. Nevertheless, it has been noted that compensating factors (e.g., a variable number of equivalent “pathways” of the $(\text{CH}_2)_n$ type) may lead to overall exponential fall-off [34, 62, 110].

Oligophenylene ethynylene (OPE) bridges

Recent kinetic studies have yielded β values for electron transfer through bridges comprised of phenylene–ethynylene (OP) moieties (i.e., alternating benzene and acetylene units) [70a, 145]. The range of β values ($\sim 0.4\text{--}0.6 \text{ \AA}^{-1}$) is intermediate between typical values for conjugated unsaturated ($\geq 0.3 \text{ \AA}^{-1}$) and fully saturated ($\geq 0.8 \text{ \AA}^{-1}$) bridges [6]. Since the intrinsic barrier to rotation of a phenylene group in OPE is thought to be quite small [70] ($\leq k_B T$ at room temperature; this favors the planar conformation of a pair of adjacent phenylene groups), the likelihood of wide-amplitude conformational fluctuations, and the attendant modulation of D/A coupling through the bridge, must be addressed. A rather simple model for T_{if} as a function of an arbitrary set of phenylene conformational angles, θ_j , $j = 1 - m$

Table 4. Variation of exponential decay coefficient (β) with bridge type^a.

Bridge repeat unit	β (\AA^{-1})		Experimental
	Cation	Anion	
<i>trans</i> ($\text{CH}=\text{CH}-$)	0.31	0.32	0.2–0.3 ^c
($-\text{C}=\text{C}-p\text{C}_6\text{H}_4-$)			
planar ($\theta_j = 0$)	0.39	0.43	
random θ_j ^d	0.51	0.54	0.36 ^{e,f} , 0.57 ^{f,g}
perpendicular ($\theta_j = \pi/2$)	0.97	1.00	
staggered ($-\text{CH}_2-\text{CH}_2-$)	0.83	1.00	0.9 ± 0.1 ^h

^aThe OPE bridge is displayed as $3(m)$. (Table II of [70b], reprinted with kind permission. Copyright 2000, John Wiley & Sons, Inc.)

^bBased on the slopes of linear least-squares fits of calculated $\ln(T_{if}^2)$ vs r_{DA} values (in all cases, the regression coefficient $r > 0.99$), with r_{DA} taken as the distance between the C atoms of the terminal D and A groups (r_{DA} values obtained by Eq. 83 are somewhat smaller).

^c[150].

^d β values are based on root-mean square values of T_{if} , averaged over a uniform $\{\Theta_j\}$ distribution.

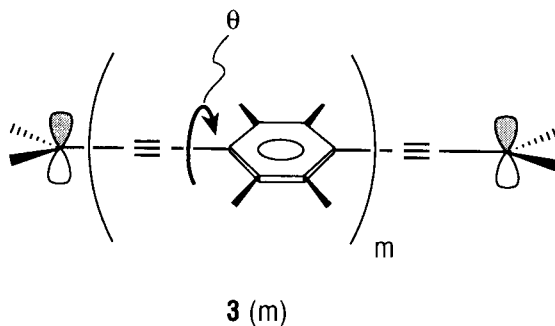
^eBased on OPE bridges with some of the phenylene groups substituted with alkyl or alkoxy groups [145].

^fThe Θ_j distribution is unknown.

^g[70a].

^h[25b].

(where $\text{OPE} \equiv (\text{PE})_m$) was formulated [70] by use of the compact form of the McConnell pathway (Eq. 92), and by effective parameters of the type T , t , and A being defined in terms of detailed CI calculations used in conjunction with the GMH model (Eqs. 81 and 83). Before outlining this model, which shows the utility of a suitably extended and parameterized version of the basic McConnell concept, we first summarize the calculated results for β in comparison with experimental estimates (Table 4). The OPE calculations were based on the radical ions represented by $3(m)$, $m = 1-4$ (the radical cations and radical anions yielded similar β



values), with terminal CH_2^+ and CH_2 moieties, respectively, as model D and A groups (other details of the calculations are given in [70]). The most notable result is the strong dependence of β on the distribution of Θ_j values, as shown for three limiting cases: 1) D, A, and all phenylenes conjugated (i.e., coplanar); 2) random Θ_j ; and 3) all phenylenes perpendicular to the D/A plane and thus fully out of conjugation with D and A; this yields, not surprisingly, a β value similar to that for a saturated, (σ -bonded) alkane bridge. The initial experimental OPE study [70a], based on *unsubstituted* phenylenes, yielded a β value (0.57 \AA^{-1}) suggesting (in comparison with the calculated results) significant dispersion of Θ_j values. In a more recent study [145], in which some of the phenylenes were substituted with methyl or propyloxy groups, an appreciably smaller β value was observed (0.36 \AA^{-1}). Since the substituents are not expected to cause this shift in β exclusively as a result of a direct electronic effect, it is thought likely that they affect the coupling indirectly through alteration of the intermolecular interactions of a given OPE with its neighbors in the self-assembled monolayers employed in the experimental studies.

The theoretical model underlying the OPE calculations is based on the idea that for arbitrary Θ_j , each PE unit may facilitate the coupling both through its π -manifold and (in a hyperconjugative sense) through orbitals of the appropriate “ π -type” nodal structure contained in its σ -manifold. This leads to a superposition (with phase) of 2^m pathways of the type given in Eq. 92,

$$|T_{if}| = \left| \sum_{\{x\}} (T_{DB_1}^{x_1}) \left[\prod_{j=1}^{m-1} (t_{B_j B_{j+1}}^{x_j, x_{j+1}} / \Delta_{B_j}^{x_j}) \right] (T_{B_m A}^{x_m} / \Delta_{B_m A}^{x_m}) \right| \quad (101)$$

where each superscript x_j denotes a π - or σ -manifold.

Since the most important orbitals in the model system **3** (the D and A π -orbitals and the relevant highest occupied and lowest unoccupied molecular orbitals (MO's) of each PE moiety) have the same qualitative nodal structure with respect to rotation about the OPE axis (i.e., a single node), we approximate the transformation behavior under such rotations (Θ_j) in terms of $\sin \Theta_j$ and $\cos \Theta_j$. Accordingly, the hopping integrals (T, t) in Eq. 101 may be elaborated as follows:

$$T_{DB_1}^\pi = (T_{DB_1}^\pi)_0 \cos \Theta_1 \quad (102a)$$

$$T_{DB_1}^\sigma = (T_{DB_1}^\sigma)_0 \sin \Theta_1, \text{ etc.}, \quad (102b)$$

and analogously for $T_{B_m A}^\pi$ and $T_{B_m A}^\sigma$,

$$t_{B_j B_{j+1}}^{\pi\pi} = (t_{B_j B_{j+1}}^{\pi\pi})_0 \begin{pmatrix} \cos \Theta_j \cos \Theta_{j+1} \\ + \sin \Theta_j \sin \Theta_{j+1} \end{pmatrix} \quad (103a)$$

$$t_{B_j B_{j+1}}^{\sigma\sigma} = (t_{B_j B_{j+1}}^{\sigma\sigma})_0 \begin{pmatrix} \cos \Theta_j \cos \Theta_{j+1} \\ + \sin \Theta_j \sin \Theta_{j+1} \end{pmatrix}, \text{ etc} \quad (103b)$$

The parameters with “0” subscripts, denoting limiting Θ_j values (0 or $\pi/2$), were

fitted [70] with the results of detailed CI/GMH calculations based on the INDO/s semi-empirical Hamiltonian [146]. For the range $m = 1$ to 4, the results of the model (Eq. 101) and full calculations agreed to better than 10 % [70].

An interesting feature of Eq. 101 is a degree of destructive interference arising from the pure π -pathway (the exclusive one when all $\Theta_j = 0$) being governed by a parity rule. As a result, when the σ contributions are suppressed (in the $2^m - 1$ pathways in which they would normally participate), the T_{if} magnitude and the β value actually *increase* [70b].

Presumably, other efforts to exploit the concept of the McConnell-type pathway (analogous to the approach just outlined) can be successful, provided a suitable method for defining the associated parameters can be found. Another approach is to extend the NN form of the McConnell pathway by introducing a limited set of longer-range (non-NN) interactions, once again using an independent set of calculations to determine the parameters of the extended model (e.g., see [111]).

Fluctuations in protein bridges and liquid water

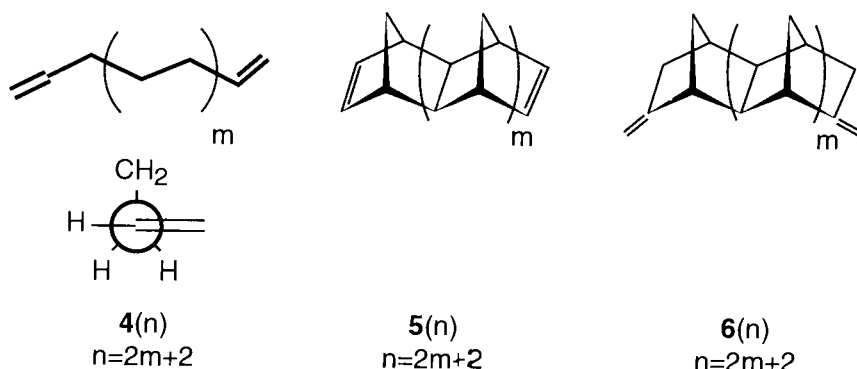
Several recent studies have used MD simulations to assess the role of fluctuations on T_{if} , either dynamically [67] or in terms of thermally-equilibrated systems [69]. The electronic-structure models were based on semi-empirical Hamiltonians, with some tests based on ab initio results also carried out [69]. For protein systems [67], the calculations yielded significant dynamic modulation of T_{if} , although the extent of this effect was sensitive to details of the gap between the D/A and bridge levels (the “tunneling energy” parameter employed in the Green-function-based treatments). In addition to elastic modulation, a model for fluctuation-induced inelastic tunneling was proposed [67a,b], and it will be interesting to ascertain from detailed computational studies the magnitude of such contributions. In studies of what was presumed to be primarily hole transfer through liquid water [69], thermal averaging was found to lead to a pronounced increase in β magnitudes ($\beta \approx 1.5\text{--}1.8 \text{ \AA}^{-1}$) relative to those based on idealized hydrogen-bonded water bridges. In experimental studies of aqueous electron transfer with the hydrated electron as the donor species [151], a value of $\beta = 0.75 \text{ \AA}^{-1}$ was estimated, suggesting (from comparison of [69] and [151]) the possibility of significantly different distance-dependence for electron and hole transfer through water.

Pathway interference

Patterns of constructive and destructive interference were obtained from comparisons of T_{if} values obtained from detailed orbital calculations [60, 63, 70b, 110] and were analyzed in some cases in terms of the simple parity rule (the sign alternation with m of a pathway of the type given in Eq. 86) or suitable generalizations [6, 63].

Norbornane-based bridges

Relative to T_{if} for hole transfer through a single staggered alkane chain, norbornane-based bridges, characterized by two parallel alkane chains (relays linked by single



bonds or CH_2 cross-bridges) yield strong interference effects [63]. For example, considering olefinic D and A groups, we compare the reference single-chain system **4(n)** with **5(n)** and **6(n)**. Relative to the through-bond (*tb*) coupling in **4(n)**, the decay of T_{ij} with $n(\beta)$ is greater for **5(n)**, primarily as a result of through-space (*ts*) “cross-talk” between the two relays [63], which interferes destructively with the coupling through each relay. On the other hand, when the olefinic groups are in *exo* configurations, unsymmetrical with respect to the two relays, as in **6(n)**, the pathways involving cross-talk are all found (from analysis of NBO-based ab initio calculations) to be in phase with the intra-relay pathways, thus yielding substantial constructive reinforcement; this result which can be rationalized in terms of an extended parity rule taking account of the phases of the individual local orbitals as well as the number of orbital units in each competing pathway [63a]. These results are illustrated for $n = 14$ in Table 5. Even more dramatic effects were observed in some variants of **6(n)**, thus leading to the designation “superbridges” for this class of DBA systems.

Table 5. Inter-relay interference effects^a.

	T_{ij} (eV)	β (\AA^{-1})
Single relay ^b [4(n)]	0.018	0.25
Two relays ^c		
matched ^d [5(n)]	0.010	0.34
offset ^e [6(n)]	0.035	0.15

^aBased on ab initio calculations reported in [63].

^b*Trans* staggered alkane bridge.

^cNorbornane-based bridge (two cross-linked alkane chain relays).

^dEach olefinic D and A group symmetric with respect to the two relays.

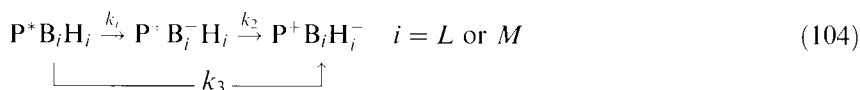
^eEach *exo* olefinic D or A group disposed asymmetrically with respect to the long axis of the bridge.

Tethered Fe complexes

For the series $\mathbf{2}(m)$, $m = 2-4$, T_{if} values were obtained from optical electron-transfer data and r_{DA} values were estimated as well [27]. For these systems, diabatic r_{DA} values based on Eq. 83 are within $\sim 0.01 \text{ \AA}$ of r_{FcFc} values. Results are summarized in Table 5. In spite of the homologous character of the series, the sequence of T_{if} and r_{DA} values does not yield a simple trend with m or r_{DA} . Detailed orbital calculations did not give a good quantitative account of T_{if} (values of 60 cm^{-1} , 46 cm^{-1} , and 0.4 cm^{-1} were obtained for $m = 2, 3$, and 4 , respectively), but the analysis of the calculations did yield some useful qualitative insights [27]. Specifically, comparison of T_{if} values for the full $m = 2$ and $m = 4$ systems and those in which the $(\text{CH}_2)_m$ tethers were excised revealed significant destructive interference between pathways involving ts coupling of adjacent pyridyl groups (pairs which are tethered in the full ligand) and th pathways involving the tethers. In contrast, for $m = 3$, removal of the tether left T_{if} unchanged, suggesting no th coupling. The results for $m = 2$ and 4 are qualitatively consistent with the simple parity rule, for which the ts pathway and the th pathways involving an odd number of CC bonds would be expected to have opposite phases [27]. This pattern has been found in calculations for cases of both *gauche* (the present case) and *trans* staggered tether conformations. The fact that th coupling is almost entirely “quenched” in the $m = 3$ case (in contrast to expectations of constructive interference) has been attributed to the highly constricted conformation of the $m = 3$ tethers (intermediate between *gauche* and *cis* limits) [27].

Coupling of monomer units in the bacterial photosynthetic reaction center

The availability of X-ray crystal-structure data for the bacterial photosynthetic reaction center (RC) has stimulated a wide variety of theoretical and computational studies with the goal of helping to resolve the mechanistic details of the fast (3 ps) initial electron-transfer event from the photoexcited special pair (bacteriochlorophyll dimer P) to the bacteriopheophyll (H) residing 17 Å away (based on center-to-center separation). Convenient recent summaries of much of the relevant research are given in [152] and [153]. Among the major issues of interest are the intermediate role of the accessory bacteriochlorophyll (B) lying close to both P and H, and to understand the kinetic preference for one pathway, the so-called L-side branch involving the P–B_L–H_L triad, over another, the M-side branch involving the P–B_M–H_M triad, which superficially appears quasi-symmetry-equivalent to the L-branch. The relevant kinetics can be represented schematically as (see also Eq. 10),



where the dimer **P** is common to both branches. Early debates about the relative importance of a direct superexchange process governed by rate constant k_3 (in which $\text{P}^+\text{B}^-\text{H}$ plays the role of a virtual state) as opposed to a sequential process (with rate constants k_1 and k_2) involving a bona fide intermediate $\text{P}^+\text{B}^-\text{H}$ species, have

recently approached a consensus favoring the latter model, with the first step being the slower one (i.e., $k_2 > k_1 \gg k_3$) [78, 152, 153]. The daunting task of obtaining, from molecular-level computations, reliable estimates of the energy gaps for modeling the rate constants continues to be a major challenge, especially when it comes to consistently balancing the energetics of the P,B, and H chromophores and of the protein medium [112e, 154, 155].

While the accurate evaluation of electronic coupling (T_{if}) among the different chromophores is also very difficult, and is undoubtedly sensitive to uncertainties in the experimental atomic coordinates, several studies (based either on *ab initio* electronic structure calculations [112e, 154] or a quantum dynamical simulation with parameters adjusted to reproduce experimental kinetic data [156]) have yielded results in general accord with each other and also with earlier estimates inferred from experimental kinetic data based on a non-adiabatic model [152, 153]. The results are summarized in Table 6, and show two clear trends in coupling magnitudes:

$$T_{if}(L) > T_{if}(M) \quad (105)$$

$$T_{if}(B^-H \rightarrow BH^-) > T_{if}(P^*B \rightarrow P^+B^-) \quad (106)$$

Table 6. Calculated T_{if} values linking the bacterial photosynthetic chromophores.

Branch ^a	Chromophore Pair in electron transfer process ^b	$ T_{if} $ (cm ⁻¹)		Experiment ^d
		Ab initio electronic structure calculation SCF ^d	Quantum dynamics calculation ^c CI ^e	
L-side	P*B → P ⁺ B ⁻	17	35	22
	B ⁻ H → BH	122	71	135
M-side	P*B → P ⁺ B	(~1) ^h	9	—
	B ⁻ H → BH ⁻	95	28	—

^aActive and inactive branches are denoted, respectively, L-side and M-side.

^bThe bacteriochlorophyll dimer (special pair), accessory bacteriochlorophyll, and bacteriopheophytin are denoted, respectively, as P,B, and H.

^c T_{if} values obtained from phenomenological analysis of experimental kinetic data based on quantum dynamics simulation [156].

^d T_{if} based on SCF calculations for appropriate states (neutral, excited singlet, or radical ion) of individual chromophores. The P^* state was represented as the 50:50 mixture of locally excited P states (P_L^* and P_M^*), constructed as two-configuration wavefunctions based on filled and virtual SCF orbitals of the separate P_L and P_M moieties [154].

^e T_{if} based on SAC-CI wavefunctions for the appropriate states (neutral, excited singlet, or radical ion) of the P,B, and H moieties [112c].

^f[153]. Similar values (26 and 51) were inferred [153] from the results presented in [152].

^gEstimated value for the $PB^*H \rightarrow PB^+H^-$ process, which involves the same lowest unoccupied orbitals (lumo) of the neutral B and H moieties as in the $P^+B^-H \rightarrow P^+BH^-$ process [157].

^hMagnitude uncertain because of near-cancellation of P_L^* and P_M^* contributions.

Thus, as far as electron coupling is concerned, the L-side is preferred to the M-side, and the first step in the sequence (Eq. 104) is the slower one; the trend is the same one exhibited by the overall rate-constant estimates [152, 153].

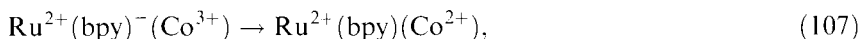
In the *ab initio* electronic-structure calculations, some attempt was made to assess the sensitivity of T_{if} magnitudes, by comparing results based on *in vacuo* chromophore pairs with those including nearby amino acid residues or crude representations of the extended environment, with point-charge or dielectric-continuum models. The results were found to be rather insensitive to such variations. Insensitivity of this type has been observed in previous model calculations. For example, in the case of the $\phi\text{H}/\text{Cl}$ charge-transfer system, *in vacuo* T_{if} values were found to change by $\leq 10\%$ when an aqueous medium was represented by a dielectric-continuum model, even though the solvation in this case caused a 50 % red shift in the vertical ET gap [30b]. In long-range superexchange coupling, solvent-dependent energy gaps (e.g., Δ in the McConnell model (Eq. 86) might be expected to cause appreciable variation in T_{if} for a given DBA system. In cases where a number of different types of pathways are superposed, however, such solvent sensitivity may be attenuated.

Calculation of activation parameters

As a final example, we summarize some results of a recent ambitious attempt to provide a comprehensive mechanistic account of long-range ET in a complex molecular solute in aqueous solution by exploiting molecular dynamics and electronic-structure techniques [36].

Reactive system

The DBA system, displayed in Figure 7, consists of a derivatized $[\text{Ru}(\text{bpy})_3]^{1+}$ donor group (where $\text{bpy} = 2,2$ -bipyridine), a $(\text{pro})_4$ bridge (where $\text{pro} = \text{proline}$ and the tetrapeptide is in a polyproline II helical conformation), and a $[\text{OC}(\text{NH}_3)_5]^{2+}$ acceptor group. The nominal redox process corresponds schematically to



where the excess electron localized on the bpy linked (by a carbonyl group) to the $(\text{pro})_4$ bridge reduces the Co^{3+} site. This system is of interest for detailed theoretical study because it is a member of a homologous series for which a large body of kinetic data exists [158].

Mechanistic issues

Of the mechanistic issues dealt with in the full study (including kinetic trade-offs between different Co^{2+} spin states in the reaction product and the role of solvent and conformational fluctuations of the DBA system), we focus here on the activation parameters and related nuclear tunneling and entropy effects which are crucial for establishing meaningful contact with the Arrhenius parameters obtained from the experimental rate data [158]. The theoretical analysis also led to new insights

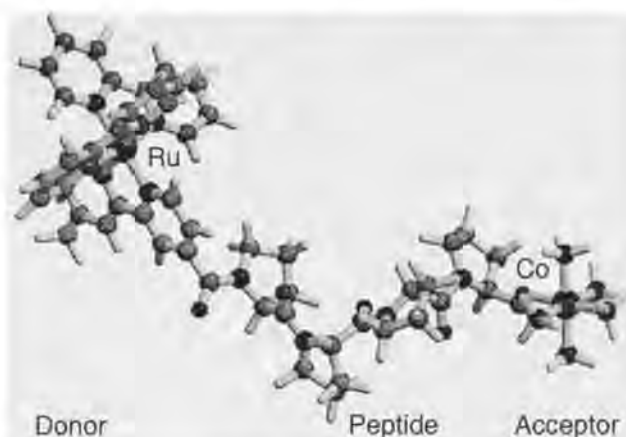


Figure 7. Diagram of the electron-transfer system modeled by MD simulation in [36]. The peptide bridge contains four proline residues, the donor is a $\text{Ru}(\text{bpy})_3$ derivative (where bpy = 2,2-bipyridine, with the transferring electron in the initial state largely localized on the bpy ligand linked to the bridge), and the acceptor is $-\text{OCO}(\text{NH}_3)_5$. (Figure 1 of [36], reprinted with permission, Copyright 1999, American Chemical Society).

regarding the extent to which different thermodynamic quantities are harmonic with respect to the electron transfer reaction coordinate [36].

Computational model

The structure and energetics of the nuclear coordinates were modeled with a Charmm-type force field for the DBA system (Figure 7) and a TIP3P potential for the approximately 1000 water molecules representing the solvent [36, 159]. Free-energy and enthalpic and entropic contributions were obtained from molecular dynamics (MD) simulations. Nuclear tunneling (Section 1.3.3) was included by discretized path-integral techniques (for the acceptor group, a major site of tunneling) and semiclassical techniques (for the remainder of the DBA system and for the solvent) [18, 94, 99]. T_{if} values were obtained from GMH (Eqs. 81 and 83) analysis of the results of INDO/s CI calculations [146] for the DBA system. A final crucial aspect of the model arises from the fact that the reaction has a finite driving force ($-\Delta G^\circ \neq 0$). Thus, in contrast to previous simulations, which dealt with symmetric exchange reactions ($\Delta G^\circ = 0$), the model Hamiltonian for the final state of the ET process (Eq. 107) was adjusted with a constant offset, which, by construction, constrained the overall calculated ΔG° at room temperature to match experimental estimates based on redox reduction potentials and spectral data (a value of $\Delta G^\circ = -13.84$ kcal/mol was adopted, based on low-spin Co^{2+} [36]). The offset does not, of course, constrain the individual enthalpy (ΔH°) and entropy (ΔS°) terms; they are left to be determined by the detailed simulations. It is important to emphasize that, in spite of the large number of empirical parameters used to define the initial and final state Hamiltonians, they are all derived from basic structural and energetic data and in no sense are fitted to kinetic data.

Matching of phenomenological and theoretical rate constant models

The rate constant (k_{et}) was expressed in terms of the results of the computer simulations, for which a non-adiabatic transition-state theory (TST) model was used. Since the experimental results were analyzed in terms of a phenomenological Arrhenius model [158], we relate experiment (left-hand side) and theory (right-hand side) in terms of the following two equations. For the weakly temperature-dependent prefactor we have:

$$(k_B T/h) \exp(S^\ddagger/k_B) = (2\pi T_{if}^2/\hbar)(4\pi k_B T\lambda)^{-1/2} \exp(S^\ddagger/k_B) \quad (108)$$

and for the Boltzmann factor:

$$\exp(-E_a/k_B T) = \exp(-H^\ddagger/k_B T) \quad (109)$$

In Eq. 108, S^\ddagger is the “true” activation entropy, being defined as

$$S^\ddagger = -dG^\ddagger/dT, \quad (110)$$

where G^\ddagger is defined in Eq. 43. By contrast, $S^{\ddagger'}$ is a “pseudo” entropy of activation, which includes the contribution from the non-adiabatic prefactor of Eq. 108 in addition to the quantity S^\ddagger defined in Eq. 110. Thus, in order to infer the value of T_{if} from the experimental data ($S^{\ddagger'}$), one must know the value of S^\ddagger , (not directly available from the data of [158]). In Eq. 109, E_a is the Arrhenius activation energy and H^\ddagger is given by

$$H^\ddagger = G^\ddagger + TS^\ddagger \quad (111)$$

Relationship between activation and net thermodynamic quantities

It is well known from Marcus theory that for diabatic free energies that are harmonic with respect to the reaction coordinate, G^\ddagger is a quadratic function of ΔG° (Eq. 27) [8, 9]. This result may be extended to H and S and is represented as follows [36, 93]:

$$X^\ddagger = (1 + \alpha)(\Delta X^0/2) + (1 - \alpha^2)(\lambda_X/4) \quad (112)$$

where $X \equiv G, H$, or S ,

$$\begin{aligned} \lambda_G &\equiv \lambda \\ \lambda_S &= -d\lambda/dT \\ \lambda_H &= \lambda + T\lambda_S \end{aligned} \quad (113)$$

and where

$$\alpha \equiv \Delta G^\circ/\lambda \quad (114)$$

is a relative measure of the driving force (the reorganizational entropy, λ_S , should not be confused with the solvent reorganization free energy, λ_s , introduced in Section 1.3.4 and also included in Table 7). Thus, in the harmonic regime, a knowledge of ΔX° (and also λ_X) directly yields an estimate of X^\ddagger . In the case of reaction 107, ΔS° is not known experimentally.

Results of calculations

Room temperature simulations at the classical level yielded values of all ΔX° and X^\ddagger quantities. Quantal results for G^\ddagger were also obtained from path integral simulations (in conjunction with Eq. 41) or semiclassical results based on spectral densities from the classical simulations [36]. The calculated classical G^\ddagger and λ values and the ΔG° value were found to conform well to Eq. 112, and $G_i(\eta)$ and $G_f(\eta)$ functions were close to parabolic in form. Due to systematic deficiencies in the aqueous solvent model (a nonpolarizable force field and finite Coulombic cut-off, ca. 10 Å), corrections to λ were made on the basis of reference dielectric continuum models, and then G^\ddagger was corrected accordingly on the basis of Eq. 112.

The calculations yield S^\ddagger and ΔS° values of appreciable magnitude, +18 eu: (cal mol⁻¹ K⁻¹) and +10 eu, respectively, and in contrast to the free energies, calculated S and H quantities depart substantially from the quadratic relationship given by Eq. 112. In the case of small α and also small λ_S , one expects, from Eq. 112, the value of $S^\ddagger/\Delta S^\circ$ to be approximately 0.5, whereas the calculations yield a ratio of approximately 2 (the distinction is pronounced even when the sizable estimated statistical uncertainties (± 5 eu) in the calculated entropies is taken account of). For this result to be compatible with Eq. 112, it would require a sizable positive value of λ_S , but in fact the simulation results indicated $\lambda_S \approx 0$. Thus, for reaction 107, as represented by the simulation and model molecular Hamiltonian [36], we infer that near room temperature the separate entropy and enthalpy quantities are not well accounted for by a harmonic model, whereas, due to compensating effects, harmonic behavior is recovered when they are combined in the free-energy quantities.

The final results, including the corrections noted above and the quantal tunneling suppression of the activation barrier (~ 2 kcal/mol, of which more than 50 % comes from solvent modes), are summarized in Table 7. (We note that nuclear tunneling is expected to make only a minor, negative, contribution to S^\ddagger [160]).

Comparison with experiment

With the data of Table 7 in hand, one may now make quantitative contact with experiment in terms of Eqs. 108 and 109. The experimental $S^{\ddagger'}$ value together with the calculated S^\ddagger value and Eq. 108 yields an estimate of T_{if} (0.1–2 cm⁻¹) that is close to the calculated range (0.5–5 cm⁻¹). Given the estimated uncertainties, the experimental (E_a) and calculated (H^\ddagger) activation energies are seen to be in reasonable accord as well. The primary results are summarized in Table 8.

The preceding analysis indicates the great importance of knowing S^\ddagger when it comes to unraveling the contributions to $S^{\ddagger'}$ from an Arrhenius analysis (failure to distinguish between the $S^{\ddagger'}$ and S^\ddagger values in Table 8 amounts to an error of a factor of approximately 20 in the T_{if} magnitude), and also offers an example in which

Table 7. Calculated thermodynamic quantities for the $\{\text{Ru}(\text{bpy})_2(\text{bpy}')(\text{pro})_4[\text{OCO}(\text{NH}_3)_5]\}^{3+}$ electron-transfer system^{a,b}.

G^\ddagger (kcal/mol)	5.7 ± 0.1
H^\ddagger (kcal/mol)	11.2 ± 1.5
S^\ddagger (eu) ^c	18.3 ± 5
ΔG° (kcal/mol)	$(-13.8)^d$
ΔS° (eu) ^c	10 ± 5
ΔH° (kcal/mol)	-10.8 ± 1.5
λ (kcal/mol)	
total	55 ± 0.1
solvent (λ_s)	39 ± 0.1
α^e	-0.25

^aThe full DBA structure is displayed in Figure 7. The electron transfer process corresponds nominally to the reduction of Co^{3+} by an electron localized on the bpy' ligand attached (by a carbonyl substituent) to the $(\text{pro})_4$ bridge; this leads to the low-spin (doublet) Co^{2+} final state. The G^\ddagger , H^\ddagger , and λ values were corrected for systematic limitations of the solvent model (as described in detail in [36]), and G^\ddagger and H^\ddagger include contributions from quantal tunneling.

^bAll results are taken from [36].

^ceu = cal mol⁻¹ K⁻¹.

^dConstrained by a constant offset in the final-state Hamiltonian (Section 1.5.2).

^e $\alpha \equiv \Delta G^\circ / \lambda$.

Table 8. Experimental vs calculated activation parameters^a.

Experiment ^b	Calculation ^c
$S^\ddagger = 5.5 \pm 0.8$ eu	$S^\ddagger = 18.3 \pm 5$ eu
$E_a = 9.4 \pm 0.2$ kcal/mol	$H^\ddagger = 11.2 \pm 1.5$ kcal/mol
$ T_{if} = 0.1 \text{--} 2$ cm ⁻¹	$ T_{if} = 0.5 \text{--} 5$ cm ⁻¹

^aSee Eqs. 108 and 109.

^b[158].

^c[36].

even if ΔS° was available from experiment, it would not be a useful guide for estimating S^\ddagger (i.e., by Eq. 112).

1.6 Concluding Remarks

As a result of rapidly evolving and mutually reinforcing advances in theoretical, experimental, and computational techniques, enormous recent progress has been achieved in the quantitative mechanistic understanding of electron transfer (ET)

processes at the molecular level. A number of detailed examples of this progress were offered in Section 1.5, and showed two distinct ways in which theory may be tested by experiment: first, by appropriate comparisons of independent sets of experimental data for distinct, but interrelated properties, and, second, by comparison of experimental data with the results of theory obtained on the basis of detailed computational implementation.

The exploitation of a number of powerful quantal, semiclassical, and classical approaches (many of which are surveyed in the present chapter), makes it possible to give a satisfactory quantitative account of the crucial energetic and dynamic features controlling ET kinetics and to assemble them into overall ET rate constants for DBA aggregates of increasingly rich chemical complexity.

While progress abounds, key challenges remain for the future. At the technical level, aside from the need for across-the-board refinements and extensions of techniques for dealing with the individual mechanistic components (e.g., practical schemes for treating polarizable molecular-level response of the medium), it is essential to combine these components in a balanced, self-consistent manner when rate constants are formulated. This latter issue is especially important when it comes to interfacing detailed quantal and/or molecular-level treatments of crucial portions of "reactive sites" with "coarser-grained" treatments of peripheral regions of a reactive system. Another challenge, at the quantal level, is to ascertain the limitations of purely electronic models (e.g., of the superexchange type) more systematically and to identify situations where vibronic factors are essential.

A key focus for the future is to broaden the chemical context of electron-transfer processes by addressing the full range of coherent and incoherent electron transport phenomena occurring in condensed phases, by extending kinetic models to accommodate electron transfer occurring together with chemical bonding rearrangements, and by exploiting the many interrelationships between ET and other manifestations of donor/acceptor interactions.

Acknowledgments

This work was carried out at Brookhaven National Laboratory under contract DE-AC02-98CH10886 with the U.S. Department of Energy and supported by its Division of Chemical Sciences, Office of Basic Energy Sciences. Thanks are also due to Norman Sutin for a number of helpful comments.

References

1. (a) *Adv. Chem. Phys.* **106**, J. Jortner and M. Bixon, Eds., (1999) (entire volume). (b) *Adv. Chem. Phys.* **107**, J. Jortner and M. Bixon, Eds., (1999) (entire volume).
2. P. F. Barbara, T. J. Meyer, and M. A. Ratner, *J. Phys. Chem.* **100**, 13148 (1996).
3. *Molecular Electronics*, J. Jortner and M. A. Ratner, Eds., Blackwell Science Ltd., Oxford, 1997.
4. *Chem. Rev.* 92, issue no. 3 (1992) (entire issue).

5. A. Aviram, *Molecular Electronics—Science and Technology*, Am. Inst. Phys., New York, 1992.
6. M. D. Newton, *Chem. Rev.* **91**, 767 (1991).
7. N. S. Hush, *J. Electroanal. Chem.* **460**, 5 (1999).
8. M. D. Newton and N. Sutin, *Ann. Rev. Phys. Chem.* **35**, 437 (1984).
9. (a) R. A. Marcus and N. Sutin, *Biochim. Biophys. Acta* **811**, 265 (1985). (b) N. Sutin, *Prog. Inorg. Chem.* **30**, 441 (1983). (c) B. S. Brunschwig, N. Sutin, *Coord. Chem. Rev.* **187**, 233 (1999).
10. *Chem. Phys.* **176**, issues no. 2,3 (1993) (entire issues).
11. (a) R. A. Marcus, *J. Chem. Phys.* **24**, 966 (1956). (b) R. A. Marcus, *J. Chem. Phys.* **24**, 979 (1956). (c) S. Pekar, *Investigations of the Electronic Theory of Crystals*, Moscow, 1951; English translation: US AEC document AEC-tr-5575. (d) V. G. Levich, *Adv. Electrochem. Electrochem. Eng.* **4**, 249 (1966).
12. N. S. Hush, *Electrochim. Acta* **13**, 1005 (1968).
13. (a) H. Sumi and R. A. Marcus, *J. Chem. Phys.* **84**, 4894 (1984). (b) L. D. Zusman, *Chem. Phys.* **49**, 295 (1980).
14. (a) J. Jortner and M. Bixon, *J. Chem. Phys.* **88**, 167 (1988). (b) J. Ulstrup and J. Jortner, *J. Chem. Phys.* **63**, 4358 (1975).
15. (a) J. S. Bader and D. Chandler, *Chem. Phys. Lett.* **157**, 501 (1989). (b) J. S. Bader, R. A. Kuharski, and D. Chandler, *J. Chem. Phys.* **93**, 230 (1990). (c) J. N. Gehlen, M. Marchi, and D. Chandler, *Science* **263**, 499 (1994). (d) R. D. Coalson, D. G. Evans, and A. Nitzan, *J. Chem. Phys.* **101**, 436 (1994).
16. (a) J. N. Gehlen, D. Chandler, H. J. Kim, and J. T. Hynes, *J. Phys. Chem.* **96**, 1748 (1992). (b) J. N. Gehlen and D. Chandler, *J. Chem. Phys.* **97**, 4958 (1992). (c) H. J. Kim and J. T. Hynes, *J. Chem. Phys.* **96**, 5088 (1992). (d) H. J. Kim, R. Bianco, B. J. Gertner, and J. T. Hynes, *J. Phys. Chem.* **97**, 1723 (1993).
17. M. A. Ratner, *J. Phys. Chem.* **94**, 4877 (1990).
18. J. Cao and G. A. Voth, *J. Chem. Phys.* **106**, 1769 (1997).
19. (a) W. B. Davis, M. R. Wasielewski, M. A. Ratner, V. Mujica, and A. Nitzan, *J. Phys. Chem. A* **101**, 6158 (1997). (b) M. Bixon and J. Jortner, *J. Chem. Phys.* **107**, 5154 (1997). (c) J. Jortner, M. Bixon, T. Langenbacher, and M. E. Michel-Beyerle, *Proc. Natl. Acad. Sci. USA* **95**, 12759 (1998).
20. (a) A. Soudackov and S. Hammes-Schiffer, *J. Am. Chem. Soc.* **121**, 10598 (1999). (b) R. I. Cukier, D. G. Nocera, *Annu. Rev. Phys. Chem.* **49**, 337 (1998).
21. (a) D. V. Matyushov, *Chem. Phys.* **174**, 199 (1993). (b) D. V. Matyushov and R. Schmid, *J. Phys. Chem.* **98**, 5152 (1994). (c) D. V. Matyushov, *Chem. Phys.* **211**, 47 (1996). (d) D. V. Matyushov and R. Schmid, *Chem. Phys. Lett.* **220**, 359 (1994). (e) D. Matyushov, *J. Phys. Chem. A* **102**, 5027 (1998).
22. A. Roberts, J. P. Kirby and D. G. Nocera, *J. Am. Chem. Soc.* **117**, 8051 (1995).
23. C. Wang, B. Akhremichev, and G. C. Walker, *J. Phys. Chem. A* **101**, 2735 (1997).
24. G. C. Walker, E. Åkesson, A. E. Johnson, N. E. Levinger, and P. F. Barbara, *J. Phys. Chem.* **96**, 3728 (1992).
25. (a) C. E. D. Chidsey, *Science* **251**, 919 (1991). (b) J. F. Smalley, S. W. Feldberg, C. E. D. Chidsey, M. R. Linford, M. D. Newton, and Y.-P. Liu, *J. Phys. Chem.* **99**, 13141 (1995).
26. E. K. L. Yeow, D. J. Haines, and K. P. Ghiggino, *J. Phys. Chem. A* **103**, 6517 (1999).
27. (a) C. M. Elliott, D. L. Derr, D. V. Matyushov, and M. D. Newton, *J. Am. Chem. Soc.* **120**, 11714 (1998). (b) C. M. Elliott, D. L. Derr, S. Ferrere, M. D. Newton, and Y.-P. Liu, *J. Am. Chem. Soc.* **118**, 5221 (1996).
28. S. F. Nelsen, R. F. Ismagilov, and Y. Teki, *J. Am. Chem. Soc.* **120**, 2200 (1998).
29. P. Piotrowiak, *Chem. Soc. Rev.* **28**, 143 (1999).
30. (a) R. J. Cave and M. D. Newton, *Chem. Phys. Lett.* **249**, 15 (1996). (b) R. J. Cave and M. D. Newton, *J. Chem. Phys.* **106**, 9213 (1997); R. J. Cave, Y.-P. Liu, and M. D. Newton, unpublished.
31. (a) C.-P. Hsu and R. A. Marcus, *J. Chem. Phys.* **106**, 584 (1997). (b) C.-P. Hsu, *J. Electroanal. Chem.* **438**, 27 (1997). (c) W. Schmickler and J. Ulstrup, *Chem. Phys.* **19**, 217 (1977). (d) A. A. Kornyshev, A. M. Kuznetsov, and J. Ulstrup, *J. Phys. Chem.* **98**, 3832 (1994).

32. (a) R. A. Marcus, *J. Chem. Soc., Faraday Trans* **92**, 3905 (1996). (b) W. J. Royea, A. M. Fajardo, N. S. Lewis, *J. Phys. Chem.* **101**, 11152 (1997). (c) W. J. Royea, A. M. Fajardo, N. S. Lewis, *J. Phys. Chem.* **102**, 3653 (1998).
33. J. B. Straus, A. Calhoun, and G. A. Voth, *J. Chem. Phys.* **102**, 1 (1995).
34. C. Liang and M. D. Newton, *J. Phys. Chem.* **97**, 3199 (1993).
35. B. Bagchi and N. Gayathri, *Adv. Chem. Phys.* **107**, 1 (1999).
36. L. W. Ungar, M. D. Newton, and G. A. Voth, *J. Phys. Chem. B* **103**, 7367 (1999).
37. M. Marchi and D. Chandler, *J. Chem. Phys.* **95**, 889 (1991).
38. V. Mujica, A. Nitzan, Y. Mao, W. Davis, M. Kempt, A. Roitberg, and M. A. Ratner, *Adv. Chem. Phys.* **107**, 403 (1999).
39. K. Wynne, C. Galli, and R. M. Hochstrasser, *J. Chem. Phys.* **100**, 4797 (1994).
40. M. L. Horng, J. Gardecki, A. Papazyan, and M. Maroncelli, *J. Phys. Chem.* **99**, 17311 (1995).
41. G. P. Wiederrecht, W. A. Svec, M. P. Niemczyk, and M. R. Wasielewski, *J. Phys. Chem.* **99**, 8918 (1995).
42. (a) F. Pöllinger, C. Musewald, H. Heitele, and M. E. Michel-Beyerle, *Ber. Bunsenges. Phys. Chem.* **100**, 2076 (1996). (b) T. Häberle, J. Hirsch, F. Pöllinger, H. Heitele, and M. E. Michel-Beyerle, *J. Phys. Chem.* **100**, 18269 (1996).
43. A. E. Johnson, N. E. Levinger, W. Jarzeba, R. E. Schlieff, D. A. V. Kliner, and P. F. Barbara, *Chem. Phys.* **176**, 555 (1993).
44. (a) J. M. Zaleski, W. Wu, C. K. Chang, G. E. Leroy, R. I. Cukier, and D. G. Nocera, *Chem. Phys.* **176**, 483 (1993). (b) J. M. Zaleski, C. K. Chang, and D. G. Nocera, *J. Phys. Chem.* **97**, 13206 (1993).
45. (a) R. A. Marcus and R. Almeida, *J. Phys. Chem.* **94**, 2973 (1990). (b) R. A. Marcus and R. Almeida, *J. Phys. Chem.* **94**, 2978 (1990).
46. A. K. Felts, W. T. Pollard, and R. A. Friesner, *J. Phys. Chem.* **99**, 2929 (1995); W. T. Pollard, A. K. Felts and R. A. Friesner, *Adv. Chem. Phys.* **93**, 77 (1996) and references therein.
47. (a) B.-C. Perng, M. D. Newton, F. O. Raineri, and H. L. Friedman, *J. Chem. Phys.* **104**, 7153 (1996). (b) B.-C. Perng, M. D. Newton, F. O. Raineri, and H. L. Friedman, *J. Chem. Phys.* **104**, 7177 (1996).
48. (a) L. Reynolds, J. A. Gardecki, S. J. V. Frankland, M. L. Horng, and M. Maroncelli, *J. Phys. Chem.* **100**, 10337 (1996). (b) D. V. Matyushov and G. A. Voth, *J. Chem. Phys.* **111**, 3630 (1999).
49. S.-H. Chong, S.-I. Miura, G. Basu, F. Hirata, *J. Phys. Chem.* **99**, 10526 (1995).
50. (a) G. J. Tawa and L. R. Pratt, *J. Am. Chem. Soc.* **117**, 1625 (1995). (b) R. M. Levy, M. Belhadj, and D. B. Kitchen, *J. Chem. Phys.* **95**, 3627 (1991).
51. J. Jeon and H. J. Kim, *J. Chem. Phys.* **106**, 5979 (1997).
52. (a) M. V. Basilevsky, I. V. Rostov, and M. D. Newton, *Chem. Phys.* **232**, 189 (1998); M. D. Newton, I. V. Rostov, and M. V. Basilevsky, *Chem. Phys.* **232**, 201 (1998). (b) P. G. Wolynes, *J. Chem. Phys.* **86**, 5133 (1987).
53. (a) D. L. Derr and C. M. Elliott, *J. Phys. Chem. A* **103**, 7888 (1999). (b) P. Finckh, H. Heitele, M. Volk, and M. E. Michael-Beyerle, *J. Phys. Chem.* **92**, 6584 (1988).
54. P. Vath, M. B. Zimmt, D. V. Matyushov and G. A. Voth, *J. Phys. Chem. B* **103**, 9130 (1999).
55. C. Wang, B. K. Mohny, R. Williams, J. T. Hupp, and G. C. Walker, *J. Am. Chem. Soc.* **120**, 5848 (1998).
56. P. Piotrowiak, *Inorg. Chim. Acta* **225**, 269 (1994).
57. R. A. Marcus, *J. Phys. Chem. B* **102**, 10071 (1998).
58. R. D. Williams, V. I. Petrov, H. P. Lu, and J. T. Hupp, *J. Phys. Chem. B* **101**, 8070 (1997).
59. A. M. Kelley, *J. Phys. Chem. A* **103**, 6891 (1999).
60. M. D. Newton and R. J. Cave, "Molecular Control of Electron and Hole Transfer Processes: Electronic Structure Theory and Application", p. 73 of [3].
61. L. A. Curtiss, C. A. Naleway, and J. R. Miller, *J. Phys. Chem.* **99**, 1182 (1995).
62. N. Koga, K. Sameshima, and K. Morokuma, *J. Phys. Chem.* **97**, 13117 (1993).
63. (a) M. N. Paddon-Row and M. J. Shephard, *J. Am. Chem. Soc.* **119**, 5355 (1997). (b) M. J. Shephard, M. N. Paddon-Row and K. D. Jordan, *J. Am. Chem. Soc.* **116**, 5328 (1994).
64. S. S. Skourtis and N. Beratan, *Adv. Chem. Phys.* **106**, 377 (1999).
65. K. Wynne and M. Hochstrasser, *Adv. Chem. Phys.* **107**, 263 (1999).

66. J. N. Onuchic, D. N. Beratan, and J. J. Hopfield, *J. Phys. Chem.* **90**, 3707 (1986).
67. (a) I. Daizadeh, E. S. Medvedev and A. A. Stuchebrukhov, *Proc. Natl. Acad. Sci. USA* **94**, 3703 (1997). (b) E. S. Medvedev and A. A. Stuchebrukhov, *J. Chem. Phys.* **107**, 3821 (1997). (c) Q. Xie, G. Archontis, and S. S. Skourtis, *Chem. Phys. Lett.* **312**, 237 (1999).
68. G. Iverson, Y. I. Kharkats, A. M. Kuznetsov, and J. Ulstrup, *Adv. Chem. Phys.* **107**, 453 (1999).
69. N. E. Miller, M. C. Wander, and R. J. Cave, *J. Phys. Chem. A* **103**, 1084 (1999).
70. (a) S. B. Sachs, S. P. Dudek, R. P. Hsung, L. R. Sita, J. F. Smalley, M. D. Newton, S. W. Feldberg, and C. E. D. Chidsey, *J. Am. Chem. Soc.* **119**, 10563 (1997). (b) M. D. Newton, *Int. J. Quant. Chem.* in press (2000).
71. (a) J. R. Reimers and N. S. Hush, *Chem. Phys.* **146**, 105 (1990). (b) M. Bixon, J. Jortner, and J. W. Verhoeven, *J. Am. Chem. Soc.* **116**, 7349 (1994). (c) G. A. Jones, B. K. Carpenter, and M. N. Paddon-Row, *J. Am. Chem. Soc.* **121**, 11171 (1999). (d) K. G. Spears, X. Wen, and R. Zhang, *J. Phys. Chem.* **100**, 10206 (1996). (e) N. A. Van Dantzig, D. H. Levy, C. Vigo, and P. Piotrowiak, *J. Chem. Phys.* **103**, 4894 (1995).
72. (a) M. A. Reed, C. Zhou, C. J. Muller, T. P. Burgin, and J. M. Tour, *Science* **278**, 252 (1997). (b) W. Han, E. N. Durantini, T. A. Moore, A. L. Moore, D. Gust, P. Rez, G. Leatherman, G. R. Seely, N. Tao, and S. M. Lindsay, *J. Phys. Chem. B* **101**, 10719 (1997).
73. (a) R. Naaman, R. Haran, A. Nitzan, D. Evans, and M. Galperin, *J. Phys. Chem. B* **102**, 3658 (1998). (b) A. Nitzan and I. Benjamin, *Acc. Chem. Res.* **32**, 854 (1999).
74. H. Sternlicht, G. C. Nieman, and G. W. Robinson, *J. Chem. Phys.* **38**, 1326 (1963).
75. N. A. van Dantzig, D. H. Levy, C. Vigo, and P. Piotrowiak, *J. Chem. Phys.* **103**, 4894 (1995).
76. (a) G. L. Closs, M. D. Johnson, J. R. Miller, and P. Piotrowiak, *J. Am. Chem. Soc.* **111**, 3751 (1989). (b) I. Place, A. Farran, K. Deshayes, and P. Piotrowiak, *J. Am. Chem. Soc.* **120**, 12626 (1998).
77. (a) P. A. Cox, *Chem. Phys. Lett.* **69**, 340 (1980). (b) J.-J. Girerd, *J. Chem. Phys.* **79**, 1766 (1983). (c) E. L. Bominaar, C. Achim, S. A. Borshch, J.-J. Girerd, and E. Münck, *Inorg. Chem.* **36**, 3689 (1997).
78. (a) R. A. Marcus, *Chem. Phys. Lett.* **133**, 471 (1987). (b) R. A. Marcus, *Chem. Phys. Lett.* **146**, 13 (1988).
79. (a) C. Zener, *Phys. Rev.* **82**, 403 (1951). (b) P.-G. De Gennes, *Phys. Rev.* **118**, 141 (1960).
80. J.-M. Saveant, *J. Am. Chem. Soc.* **109**, 6788 (1987).
81. G. Steinberg-Yfrach, P. A. Liddell, S.-C. Hung, A. L. Moore, D. Gust, and T. A. Moore, *Nature* **385**, 239 (1997).
82. H. S. Johnston, *Gas Phase Reaction Rate Theory*, The Ronald Press Company, New York (1966).
83. M. D. Newton and H. L. Friedman, *J. Phys. Chem.* **88**, 4460 (1988).
84. (a) J. T. Hynes, *J. Phys. Chem.* **90**, 3701 (1986). (b) B. B. Smith, A. Staib, and J. T. Hynes, *Chem. Phys.* **176**, 521 (1993). (c) D. A. Zichi, G. Ciccotti, J. T. Hynes, and M. Ferrario, *J. Phys. Chem.* **93**, 6261 (1989).
85. B. L. Tembe, H. L. Friedman, and M. D. Newton, *J. Chem. Phys.* **76**, 1490 (1982).
86. W. B. Davis, W. A. Svec, M. A. Ratner, and M. R. Wasielewski, *Nature* **396**, 60 (1998).
87. (a) B. J. Gertner, J. P. Bergsma, K. R. Wilson, S. Lee, and J. T. Hynes, *J. Chem. Phys.* **86**, 1377 (1987). (b) B. J. Gertner, K. R. Wilson, and J. T. Hynes, *J. Chem. Phys.* **90**, 3537 (1989).
88. (a) J. W. Evenson and M. Karplus, *J. Chem. Phys.* **96**, 5272 (1992). (b) J. W. Evenson and M. Karplus, *Science* **262**, 1247 (1993).
89. M. D. Newton, *Adv. Chem. Phys.* **106**, 303 (1999). Erratum: the factor of $\frac{1}{4}$ in Eq. (3.27a) should be replaced by the factor 4.
90. (a) K. Kumar, Z. Lin, D. H. Waldeck, and M. B. Zimmt, *J. Am. Chem. Soc.* **118**, 243 (1996). (b) R. J. Cave, M. D. Newton, K. Kumar, and M. B. Zimmt, *J. Phys. Chem.* **99**, 17501 (1995). (c) I. Read, A. Napper, R. Kaplan, M. B. Zimmt, and D. H. Waldeck, *J. Am. Chem. Soc.* **121**, 10976 (1999).
91. M. Tachiya, *J. Phys. Chem.* **93**, 7050 (1989).
92. G. King and A. Warshel, *J. Chem. Phys.* **93**, 8682 (1990).
93. (a) R. A. Marcus and N. Sutin, *Comments Inorg. Chem.* **5**, 119 (1986). (b) *Inorg. Chem.* **14**, 213 (1975).

94. X. Song and R. A. Marcus, *J. Chem. Phys.* **99**, 7768 (1993).
95. M. Tachiya, *J. Chem. Phys.* **97**, 5911 (1993).
96. (a) I. R. Gould, D. Noukakis, L. Gomez-Jahn, R. H. Young, J. L. Goodman, and S. Farid, *Chem. Phys.* **176**, 439 (1993). (b) R. A. Marcus, *J. Phys. Chem.* **93**, 3078 (1989).
97. (a) J. Tang, *J. Chem. Phys.* **98**, 6263 (1993). (b) I. A. Goychuk, E. G. Petrov, and V. May, *J. Chem. Phys.* **103**, 4937 (1995).
98. H.-X. Zhou and A. Szabo, *J. Chem. Phys.* **103**, 3481 (1995).
99. (a) R. P. van Duyne and S. F. Fischer, *Chem. Phys.* **5**, 183 (1974). (b) P. G. Wolynes, *J. Chem. Phys.* **87**, 6559 (1987).
100. (a) M. Bixon, J. Jortner, J. Cortes, H. Heitele, and M. E. Michel-Beyerle, *J. Phys. Chem.* **98**, 7289 (1994). (b) J. Cortes, H. Heitele, and J. Jortner, *J. Phys. Chem.* **98**, 2527 (1994). (c) A. M. Kjaer and J. Ulstrup, *J. Am. Chem. Soc.* **109**, 1934 (1987).
101. (a) N. R. Kestner, J. Logan, and J. Jortner, *J. Phys. Chem.* **78**, 2148 (1974). (b) J. Jortner, *J. Chem. Phys.* **64**, 4860 (1976).
102. (a) J. J. Hopfield, *Proc. Natl. Acad. Sci. USA* **71**, 36 (1974). (b) T. F. Soules and C. B. Duke, *Phys. Rev.* **B3**, 262 (1970).
103. L. Landau, *Phys. Z. Sowjet.* **2**, 46 (1932); C. Zener, *Proc. Roy. Soc. London Ser. A* **137**, 696 (1932).
104. P. A. Frantsuzov, S. F. Fischer, and A. A. Zharikov, *Chem. Phys.* **241**, 95 (1999).
105. S. Larsson, *Theoret. Chim. Acta (Berl.)* **60**, 111 (1981).
106. M. D. Newton, S. W. Feldberg, and J. F. Smalley, "Theory and Computational Modeling: Medium Reorganization and Donor-Acceptor Coupling in Electron Transfer Processes," in *Interfacial Electrochemistry Theory, Experiment, and Applications*, A. Wieckowski, Ed., Marcel Dekker, New York, p. 97 (1999).
107. X. Dang and J. T. Hupp, *J. Am. Chem. Soc.* **121**, 8399 (1999).
108. R. F. Grote and J. T. Hynes, *J. Chem. Phys.* **73**, 2715 (1980).
109. L. A. Curtiss, C. A. Naleway, and J. R. Miller, *Chem. Phys.* **176**, 387 (1993).
110. B. P. Paulson, L. A. Curtiss, B. Bal, G. L. Closs, and J. R. Miller, *J. Am. Chem. Soc.* **118**, 378 (1996).
111. M. J. Shepard, M. N. Paddon-Row, and K. D. Jordan, *Chem. Phys.* **176**, 289 (1993).
112. (a) S. S. Skourtis and D. N. Beratan, *J. Phys. Chem. B* **101**, 1215 (1997). (b) S. S. Skourtis, J. N. Onuchic, and D. N. Beratan, *Inorg. Chim. Acta* **243**, 167 (1996). (c) A. Okada, T. Kakitani, and J. Inoue, *J. Phys. Chem.* **99**, 2946 (1995). (d) A. A. Stuchebrukhov, *J. Chem. Phys.* **104**, 8424 (1996). (e) J. Hasegawa and H. Nakatsuji, *J. Phys. Chem. B* **102**, 10420 (1998). (f) S. Hayashi and S. Kato, *J. Phys. Chem. A* **102**, 2878 (1998).
113. J. N. Onuchic and D. N. Beratan, *J. Chem. Phys.* **92**, 722 (1990).
114. M. D. Newton, K. Ohta, and E. Zhong, *J. Phys. Chem.* **95**, 2317 (1991).
115. A. A. Stuchebrukhov, *Chem. Phys. Lett.* **225**, 55 (1994).
116. (a) M. Braga and S. Larsson, *Chem. Phys. Lett.* **200**, 573 (1992). (b) M. Braga and S. Larsson, *Chem. Phys. Lett.* **213**, 217 (1993). (c) K. Kim, K. D. Jordan, and M. N. Paddon-Row, *J. Phys. Chem.* **98**, 11053 (1994). (d) L. A. Curtiss and J. R. Miller, *J. Phys. Chem. A* **102**, 160 (1998).
117. M. D. Newton, *J. Phys. Chem.* **95**, 30 (1991).
118. B. R. Arnold, D. Noukakis, S. Farid, J. L. Goodman, and I. R. Gould, *J. Am. Chem. Soc.* **117**, 4399 (1995).
119. Y.-P. Liu and M. D. Newton, *J. Phys. Chem.* **99**, 12382 (1995).
120. C. Creutz, M. D. Newton, and N. Sutin, *J. Photochem. Photobiol. A: Chem.* **82**, 47 (1994).
121. J. R. Reimers and N. S. Hush, *J. Phys. Chem.* **95**, 9773 (1991).
122. D. H. Oh, M. Sano, and S. G. Boxer, *J. Am. Chem. Soc.* **113**, 6880 (1991).
123. Y.-G. Shin, B. S. Brunschwig, C. Creutz, and N. Sutin, *J. Phys. Chem.* **100**, 8157 (1996). (b) B. S. Brunschwig, C. Creutz, and N. Sutin, *Coordination Chem. Rev.* **177**, 61 (1998).
124. (a) H.-J. Werner and W. Meyer, *J. Chem. Phys.* **74**, 5802 (1981). (b) A. Macias and A. Riera, *J. Phys.* **B11**, L489 (1989). (c) S. Kato and Y. Amatatsu, *J. Chem. Phys.* **92**, 7241 (1990).
125. H. M. McConnell, *J. Chem. Phys.* **74**, 6746 (1981).
126. P. Siddarth and R. A. Marcus, *J. Phys. Chem.* **96**, 3213 (1992).
127. (a) J. W. Verhoeven and P. Pasman, *Tetrahedron* **37**, 943 (1984). (b) M. N. Paddon-Row, *Acc. Chem. Res.* **15**, 245 (1982).

128. G. Gamow, *Z. Phys.* **51**, 204 (1961).
129. J. R. Miller and J. V. Beitz, *J. Chem. Phys.* **74**, 6746 (1981).
130. R. J. Cave, D. V. Baxter, W. A. Goddard III, and J. D. Baldeschwieler, *J. Chem. Phys.* **87**, 926 (1987).
131. S. Larsson, *J. Am. Chem. Soc.* **103**, 4034 (1981).
132. (a) A. M. Kuznetsov and J. Ulstrup, *J. Chem. Phys.* **75**, 2047 (1981). (b) D. N. Beratan, J. N. Onuchic, and J. J. Hopfield, *J. Chem. Phys.* **86**, 4488 (1987).
133. V. Mujica, M. Kemp, and M. A. Ratner, *J. Chem. Phys.* **101**, 6856 (1994).
134. C. Creutz, *Prog. Inorg. Chem.* **30**, 1 (1983).
135. C. E. B. Evans, M. L. Naklicki, A. R. Rezvani, C. A. White, V. V. Kondratiev, and R. J. Crutchley, *J. Am. Chem. Soc.* **120**, 13096 (1998).
136. M. B. Robin and P. Day, *Adv. Inorg. Chem. Radiochem.* **10**, 247 (1967).
137. A. V. Macatangay, J. F. Endicott, and X. Song, *J. Phys. Chem. A* **102**, 7537 (1998).
138. Y. J. Wang, M. D. Newton, and J. W. Davenport, *Phys. Rev. B* **46**, 935 (1992).
139. D. L. Dexter, *J. Chem. Phys.* **21**, 836 (1953).
140. K. Kumar, I. V. Kurnikov, D. N. Beratan, D. H. Waldeck, and M. B. Zimmt, *J. Phys. Chem. A* **102**, 5529 (1998).
141. S. F. Nelsen, R. F. Ismagilov, K. E. Gentile, and D. R. Powell, *J. Am. Chem. Soc.* **121**, 7108 (1999).
142. K. W. Penfield, J. R. Miller, M. N. Paddon-Row, E. Cotsaris, A. M. Oliver, and N. S. Hush, *J. Amer. Chem. Soc.* **109**, 5061 (1987).
143. O. V. Prezhdo, J. T. Kindt, and J. C. Tully, *J. Chem. Phys.* **111**, 7818 (1999).
144. C. Liang and M. D. Newton, *J. Phys. Chem.* **96**, 2855 (1992).
145. S. Creager, C. J. Yu, C. Bamdad, S. O'Connor, T. MacLean, E. Lam, Y. Chong, G. T. Olsen, J. Luo, M. Gozin, and J. F. Kayyem, *J. Am. Chem. Soc.* **121**, 1059 (1999).
146. M. C. Zerner, G. H. Loew, R. F. Kirchner, and U. T. Mueller-Westerhoff, *J. Am. Chem. Soc.* **102**, 589 (1980).
147. J. B. Birks, *Photophysics of Aromatic Molecules*, Wiley-Interscience, New York, (1970).
148. N. Chako, *Q. J. Chem. Phys.* **2**, 644 (1934).
149. M. D. Newton, *J. Electroanal. Chem.* **438**, 3 (1997).
150. (a) S. Woitellier, J. P. Launay, and C. W. Spangler, *Inorg. Chem.* **28**, 273 (1989). (b) J. R. Reimers and N. S. Hush, *Inorg. Chem.* **29**, 3686 (1990). (c) J. R. Reimers and N. S. Hush, *Inorg. Chem.* **29**, 4510 (1990).
151. K. H. Schmidt, P. Han and D. M. Bartels, *J. Phys. Chem.* **99**, 10530 (1995).
152. M. Bixon, J. Jornter and M. E. Michel-Beyerle, *Chem. Phys.* **197**, 389 (1995).
153. S. Tanaka and R. A. Marcus, *J. Phys. Chem. B* **101**, 5031 (1997).
154. L. Y. Zhang and R. A. Friesner, *Proc. Natl. Acad. Sci. USA* **95**, 13603 (1998).
155. J. Hasegawa, K. Ohkawa, and H. Nakatsuji, *J. Phys. Chem. B* **102**, 10410 (1998).
156. N. Makri, E. Sim, D. E. Makarov, and M. Topaler, *Proc. Natl. Acad. Sci. USA* **93**, 3926 (1996).
157. H. Zhou and S. G. Boxer, *J. Phys. Chem. B* **102**, 9148 (1998).
158. M. Y. Ogawa, J. F. Wishart, Z. Young, J. R. Miller and S. S. Isied, *J. Phys. Chem.* **97**, 11456 (1993).
159. B. R. Brooks, R. E. Brucoleri, B. D. Olafson, D. J. States, S. Swaminathan and M. Karplus, *J. Comput. Chem.* **4**, 187 (1983).
160. B. S. Brunschwig, J. Logan, M. D. Newton, and N. Sutin, *J. Am. Chem. Soc.* **102**, 5798 (1980).
161. S. F. Nelsen, R. F. Ismagilov, and D. A. Trieber II, *Science* **278**, 846 (1997).

2 Adiabatic versus Non-Adiabatic Electron Transfer

Hitoshi Sumi

2.1 Adiabatic versus Static Coupling Scheme

It is assumed throughout this chapter that the relative positions of the donor and acceptor molecules between which an electron is transferred are fixed either within a large molecule or by a molecular bridge in solvents. In this situation, electron-transfer (ET) reactions are governed by first-order kinetics. In second-order reactions [1], the donor and acceptor first diffuse to mutually appropriate positions where the reaction takes place with a position-dependent rate constant. In that case, this is the rate constant discussed in the present article.

Integration signs without integration limits will often be used in this article. They are understood to be performed from $-\infty$ to ∞ unless it is explicitly stated to be otherwise.

Electrons with mass m and atoms with mass M that can move freely have average velocities $(3k_{\text{B}}T/m)^{1/2}$ and $(3k_{\text{B}}T/M)^{1/2}$, respectively, at temperature T , where k_{B} is the Boltzmann constant. Therefore, electrons move much faster than atoms, since the ratio of the electron speed to the atom speed, ca. $(M/m)^{1/2}$, is much larger than unity. In this situation, an approximation is justified that, an electron can be regarded to move in a potential of, atoms stopping at certain positions. This is called the adiabatic approximation, because the energy recoil of the atoms that is caused by the interaction with the electron is neglected. The eigenenergy of the electron given as a function of coordinates of the atoms, supplemented by the distortion energy for atomic displacement, is called the adiabatic potential. Since this approximation was first devised by Born and Oppenheimer [2], it is named after them.

In electron-transfer reactions occurring in condensed matter, this approximation is not always justified, since the electrons and atoms participating in the transfer are not free. Electron motion is confined only to that occurring between a donor and an acceptor molecule, and atoms can vibrate only around their equilibrium positions. In the transition state of an electron transfer reaction, an electron stays at either the donor or the acceptor for a time of about \hbar/J where J represents the interaction

energy for electron transfer between them, called the transfer integral hereafter, and \hbar represents the Planck constant divided by 2π . When the average energy quantum of vibrations of the atoms around their equilibrium positions is written as $\hbar\bar{\omega}$, the average period of their vibrations is given by $2\pi/\bar{\omega}$. In order for the adiabatic approximation to be justified in this situation, \hbar/J must be much smaller than $\hbar/(\hbar\bar{\omega})$, that is, J must be much larger than $\hbar\bar{\omega}$. The value of J is typically of the order of 100 cm^{-1} or less, while $\hbar\bar{\omega}$ varies from several tens cm^{-1} for protein-matrix vibrations [3] to about 3500 cm^{-1} for proton vibrations [4]. The adiabatic approximation is therefore not always applicable to ET reactions in condensed matter.

Let us consider, for simplicity, that an electron (with mass m) to be transferred interacts with atoms through a single reaction coordinate Q . To be more concrete, Q is a coordinate which passes through the atomic configuration relaxed at the reactant state and that at the product state in the multi-dimensional configuration-coordinate space for atomic displacement. Let us consider that atoms with mass M move along this reaction coordinate, and also that atoms at position Q on this reaction coordinate exert a potential $V(\mathbf{r}; Q)$ on the electron at position vector \mathbf{r} . The Hamiltonian for this system is given by

$$H = -\frac{\hbar^2}{2m}\Delta_{\mathbf{r}} - \frac{\hbar^2}{2M}\frac{\partial^2}{\partial Q^2} + V(\mathbf{r}; Q) + U(Q) \quad (1)$$

where $\Delta_{\mathbf{r}}$ represents the Laplacian operator with respect to \mathbf{r} , and $U(Q)$ represents the distortion energy for atomic displacement along the coordinate Q .

In the adiabatic approximation, the electron motion is diagonalized under the condition that the atoms are fixed at a value Q of the reaction coordinate, as a solution to a Schrödinger equation

$$\left[-\frac{\hbar^2}{2m}\Delta_{\mathbf{r}} + V(\mathbf{r}; Q) \right] \varphi(\mathbf{r}; Q) = E(Q)\varphi(\mathbf{r}; Q) \quad (2)$$

with an eigenfunction $\varphi(\mathbf{r}; Q)$ and an eigenenergy $E(Q)$, both of which depend on Q as a parameter. In the next step, the atoms are allowed to move on a potential $U(Q) + E(Q)$ supplemented by $E(Q)$, as a solution to a Schrödinger equation

$$\left[-\frac{\hbar^2}{2M}\frac{\partial^2}{\partial Q^2} + U(Q) + E(Q) \right] \chi(Q) = E\chi(Q) \quad (3)$$

with an eigenfunction $\chi(Q)$ and an eigenenergy E . Accordingly, the eigenfunction of H in Eq. 1 is approximated by a product of $\varphi(\mathbf{r}; Q)\chi(Q)$, and its eigenenergy by E .

$U(Q) + E(Q)$ is the adiabatic potential. It describes the total energy of the reaction system (composed of the electron and atoms) under the adiabatic condition that the atoms are fixed at a value Q of the reaction coordinate. In the typical example shown in Figure 1, it consists of a lower and an upper branch, arising from a pair of $E(Q)$ curves. The lower branch is a double well; the electron to be trans-

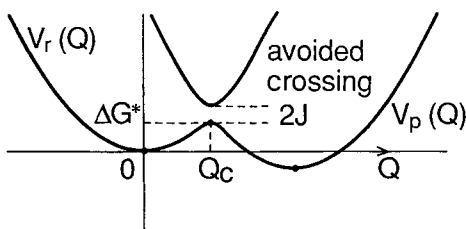


Figure 1. An example of a pair of adiabatic potentials with an avoided crossing at $Q = Q_c$ where the energy separation is $2J$. As the energy difference between them becomes much larger than J , each of them approaches one of the diabatic potentials $V_r(Q)$ and $V_p(Q)$ of Figure 2.

ferred is at the donor in the reactant-state well on the left-hand side, whose minimum is taken as the zero of the reaction coordinate Q . The electron is at the acceptor in the product-state well on the right-hand side, with a minimum at $Q \neq 0$, and the reaction system is in the transition state at the top of the barrier at $Q = Q_c$. The upper branch reaches a minimum at $Q = Q_c$, and crossing with the lower one is avoided. The energy separation between them at $Q = Q_c$ is $2J$.

This adiabatic eigenfunction $\phi(r; Q)\chi(Q)$ is not a rigorous eigenfunction of H , since

$$H\phi(r; Q)\chi(Q) = (E + H')\phi(r; Q)\chi(Q) \quad (4)$$

with

$$H'\phi(r; Q)\chi(Q) = -\frac{\hbar^2}{2M} \left[2\frac{\partial\phi(r; Q)}{\partial Q} \frac{d\chi(Q)}{dQ} + \frac{\partial^2\phi(r; Q)}{\partial Q^2} \chi(Q) \right] \quad (5)$$

In the adiabatic approximation, H' in Eq. 4 is neglected. H' is called the non-adiabaticity operator, and causes phenomena deviating from the adiabatic approximation such as nonradiative transitions between adiabatic states. The adiabatic-coupling scheme is a procedure for investigating such phenomena on the basis of H' .

This scheme is, however, not easy to pursue because H' of Eq. 5 is a differential operator with respect to Q . Moreover, the Q -dependence of H' is related to the highly anharmonic form of the adiabatic potential around the avoided-crossing point $Q = Q_c$ in Figure 1, since $\phi(r; Q)$ in Eq. 5 is an eigenfunction whose eigenenergy is given by the adiabatic potential at Q . They must be treated consistently with one another. Nevertheless, because of these difficulties, H' has often been approximated into simplified forms, not taking due account of its consistency with the highly anharmonic adiabatic potential. This can result in unpleasant situations [5], so that calculations based on H' , for example, those of nonradiative transition rates deviate very much from experimental observations.

To avoid such difficulties with H' , another scheme has been devised, where calculation of such quantities as nonradiative transition rates is approached from the

non-adiabatic limit. In this scheme, the static-coupling scheme [5], electronic states are defined by the diagonalization of a Hamiltonian for an electron which moves in a potential $V(\mathbf{r}; Q_0)$ produced by atoms at a value Q_0 of the reaction coordinate Q . It is convenient to choose Q_0 to be the Q value of zero at the bottom of the reactant well in Figure 1. Eigenstates $[\varphi_b(\mathbf{r})]$ in this scheme are solutions to a Schrödinger equation

$$\left[-\frac{\hbar^2}{2m} \Delta_r + V(\mathbf{r}; 0) \right] \varphi_b(\mathbf{r}) = E_b \varphi_b(\mathbf{r}) \quad (6)$$

with eigenenergy E_b , where $b = r$ for the reactant state with the electron localized at the donor and $b = p$ for the product state with the electron localized at the acceptor. Since both $\varphi_r(\mathbf{r})$ and $\varphi_p(\mathbf{r})$ are assumed to be nondegenerate, it can be taken as a real function. Since a part of $V(\mathbf{r}; 0)$ in $V(\mathbf{r}; Q)$ was incorporated in defining the electronic states, interaction between the electron and vibrational motions of atoms is caused by $V(\mathbf{r}; Q) - V(\mathbf{r}; 0)$. Here, two sets of phonon representations are introduced in association with the reactant and the product state $\varphi_r(\mathbf{r})$ and $\varphi_p(\mathbf{r})$ of the electron, as diagonalizing different Hamiltonians

$$H_b \equiv -\frac{\hbar^2}{2M} \frac{\partial^2}{\partial Q^2} + V_b(Q) \quad (7)$$

with

$$V_b(Q) \equiv U(Q) + \langle \varphi_b | [V(\mathbf{r}; Q) - V(\mathbf{r}; 0)] | \varphi_b \rangle + E_b \quad (8)$$

for $b = r$ or p , where $\langle \varphi_b | f(\mathbf{r}) | \varphi_b \rangle \equiv \int \varphi_b(\mathbf{r})^2 f(\mathbf{r}) d\mathbf{r}$. Let us confine ourselves to a subspace spanned by $\varphi_r(\mathbf{r})$ and $\varphi_p(\mathbf{r})$, assuming that their energy is well separated from other electronic states. Under this simplification, the Hamiltonian, H , of Eq. 1 can be rewritten, with the representation of Dirac's bra and ket vectors [6], into

$$H = H_r |\varphi_r\rangle \langle \varphi_r| + H_p |\varphi_p\rangle \langle \varphi_p| + J(Q) (|\varphi_p\rangle \langle \varphi_r| + |\varphi_r\rangle \langle \varphi_p|) \quad (9)$$

with

$$J(Q) \equiv \langle \varphi_p | [V(\mathbf{r}; Q) - V(\mathbf{r}; 0)] | \varphi_r \rangle \quad (10)$$

where $\langle \varphi_p | f(\mathbf{r}) | \varphi_r \rangle \equiv \int \varphi_p(\mathbf{r}) f(\mathbf{r}) \varphi_r(\mathbf{r}) d\mathbf{r}$ and $J(Q)$ is real, since both $\varphi_r(\mathbf{r})$ and $\varphi_p(\mathbf{r})$ are taken as real functions. The Hamiltonian, H , of Eq. 9 is the basis of the static coupling scheme, where we should note that $J(Q)$ which causes coupling between the electron states in Eq. 9 is not a differential operator but a simple real number, unlike in H' of Eq. 5 in the adiabatic coupling scheme. Both $V_r(Q)$ and $V_p(Q)$ are diabatic potentials, in contrast to the adiabatic potentials in the adiabatic approximation.

Figure 2 shows the diabatic potentials which give rise to the adiabatic potentials of Figure 1.

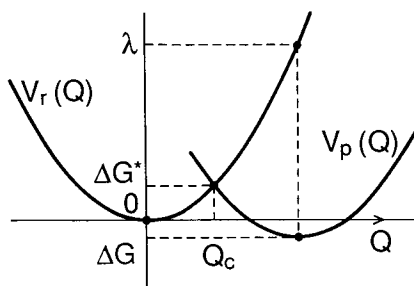


Figure 2. Diabatic potentials which give rise to the adiabatic potentials of Figure 1 in the adiabatic approximation.

The adiabatic potential $U(Q) + E(Q)$ in the adiabatic approximation is an eigenvalue of

$$V_r(Q)|\varphi_r\rangle\langle\varphi_r| + V_p(Q)|\varphi_p\rangle\langle\varphi_p| + J(Q)(|\varphi_p\rangle\langle\varphi_r| + |\varphi_r\rangle\langle\varphi_p|), \quad (11)$$

and $\varphi(r; Q)$ in Eq. 2 is an eigenstate of it. Of the two eigenenergies of the Hamiltonian of Eq. 11, the lower one represents the lower adiabatic potential in Figure 1 as a function of Q , and the upper one represents the upper adiabatic potential. At the avoided-crossing point between the two adiabatic potentials, $Q = Q_c$,

$$V_p(Q) = V_r(Q) \quad (12)$$

At this point, therefore, the upper and the lower adiabatic potentials are separated by

$$V_r(Q_c) \pm J, \quad \text{where } J \equiv |J(Q_c)| \quad (13)$$

with the eigenstates given by $\varphi(r) = [\varphi_r(r) \pm \varphi_p(r)]/\sqrt{2}$, where the reactant and the product state are equally mixed. Note that J in Figure 1 can be obtained from Eq. 13.

In the region of Q where the separation between $V_r(Q)$ and $V_p(Q)$ is much larger than $|J(Q)|$, the upper and the lower adiabatic potential, obtained by diagonalization of Eq. 11, merge into either $V_r(Q)$ or $V_p(Q)$, as indicated in Figure 1. At $Q = 0$ in Figure 1, $V_r(Q)$ and $V_p(Q)$ coincide exactly with the lower and the upper adiabatic potential, respectively, since $J(Q) = 0$ in Eq. 11. We assume hereafter that this region also covers the bottom of the product well in Figure 1. In this case, around the bottom of the reactant and the product well they are nearly equal to $V_r(Q)$ and $V_p(Q)$, respectively. The energy at the bottom of the reactant well was taken as the origin of the energy in Figure 1. Since the bottom was taken to be located also at the origin of coordinate Q , we should have

$$V_r(Q) \propto Q^2 \quad \text{in the vicinity of } Q = 0. \quad (14)$$

Around $Q = Q_c$, on the other hand, the adiabatic potentials given by Eq. 13 deviate markedly from both $V_r(Q)$ and $V_p(Q)$, which cross each other there as shown by Eq. 12. Adiabatic potentials approach either $V_r(Q)$ or $V_p(Q)$ in the limit of small J . This is a reason why both $V_r(Q)$ and $V_p(Q)$ are called diabatic potentials.

We have seen that the Hamiltonian in Eq. 4 for the adiabatic coupling scheme as well as that of Eq. 9 for the static coupling scheme are different representations of the same initial Hamiltonian of Eq. 1. Moreover, since the lower adiabatic potential was assumed to be nearly equal to $V_p(Q)$ at the bottom of the product well, both the initial and the final states of electron transfer are the same for the adiabatic and the static coupling scheme. These two features ensure that the two schemes are equivalent, as long as they are treated correctly. In fact, it has been shown, by explicit manipulation, that the adiabatic and the static coupling schemes give the same rate constant for electron transfer between donor and acceptor in the calculation of the lowest (i.e., second) order in the coupling strength J of Eq. 13 [5]. In this case, it is important to take due account of the consistency between the Q dependence of H' and the highly anharmonic form of the adiabatic potential around the avoided-crossing point in the adiabatic coupling scheme.

This condition for the adiabatic coupling scheme makes itself much more difficult to pursue than the static coupling scheme. In fact, reliable theories have been developed only on the basis of the static coupling scheme. Since the two approaches are equivalent, from this point on we consider only those based on static coupling. The rate constant for electron transfer between donor and acceptor becomes proportional to J^2 in the limit of small J , where the diabatic potentials in Figure 2 are most appropriate for describing the reaction. This limit is the non-adiabatic limit. The condition justifying this limit will be dealt with later. In the limit of large J , where the adiabatic potentials in Figure 1 are most appropriate for describing the reaction, the rate constant becomes independent of J , as will also be shown later. This limit is called the adiabatic limit.

The rate constant k_{FW} for forward electron transfer, that is, from donor to acceptor, is related to k_{BW} for reverse electron transfer, that is, from acceptor to donor, by the principle of chemical equilibrium. Specifically, they should satisfy

$$k_{FW}/k_{BW} = e^{-\beta\Delta G} \text{ (= Equilibrium constant).} \quad (15)$$

where ΔG represents the free energy of reaction, that is, the free energy at the product state (with an electron transferred to the acceptor), with the reactant state (with the electron staying at the donor) as the reference point. For the sake of simplicity, we will hereafter assume that the forward reaction is exothermic, with a negative ΔG . The rate constant for an endothermic reaction, with a positive ΔG , can be derived by Eq. 15 from k_{FW} for an exothermic reaction whose free energy of reaction is $-|\Delta G|$.

2.2 Non-Adiabatic Limit

2.2.1 Single-Mode Model

In the static coupling scheme, $J(Q)$ of Eq. 10 causes transitions of an electron from the donor to the acceptor. It works most effectively around $Q = Q_c$, where diabatic

potentials $V_r(Q)$ and $V_p(Q)$ cross each other, as shown in Figure 2. For the sake of simplicity, therefore, let us assume $J(Q) = J$ with J defined by Eq. 13, neglecting the Q dependence of $J(Q)$; this is called the Condon approximation. It is reasonable in the static coupling scheme, although risky in the adiabatic coupling scheme [5]. Thus, Eq. 9 can be approximated by

$$H = H_r|\varphi_r\rangle\langle\varphi_r| + H_p|\varphi_p\rangle\langle\varphi_p| + J(|\varphi_p\rangle\langle\varphi_r| + |\varphi_r\rangle\langle\varphi_p|) \quad (16)$$

Let us assume, moreover, that $V_r(Q)$ defined by Eq. 8 for $b = r$ is quadratic in the entire Q region, not only in Eq. 14, and also that $V_p(Q)$ for $b = p$ deviates from $V_r(Q)$ only by a linear function of Q . In this situation, it is convenient to express H_r in Eq. 7 for $b = r$ as

$$H_r = \frac{1}{2}\hbar\bar{\omega}P^2 + V_r(Q), \quad \text{with } V_r(Q) = \frac{1}{2}\hbar\bar{\omega}Q^2 \quad (17)$$

where $P \propto \hat{c}/\hat{c}Q$. In this model, the single-mode model, P and Q are a pair of conjugate operators of a single phonon mode, and they satisfy a commutation relation $[Q, P] = i$ with $[A, B] \equiv AB - BA$. In this case, $\hbar\bar{\omega}$ gives the energy quantum of this phonon mode. In reality, the reaction coordinate Q is a linear combination of various coordinates of phonons with various energy quanta, as explicitly shown later. Therefore, $\hbar\bar{\omega}$ should be regarded as an average energy quantum of all phonons contributing to Q . Even in this case, if all these phonons correspond to a single energy quantum, Q can still be regarded as a normal mode, since any linear combination of these still result in a normal mode.

Parallel to Eq. 17 for H_r , we express H_p in Eq. 7 for $b = p$ as

$$H_p = \frac{1}{2}\hbar\bar{\omega}P^2 + V_p(Q), \quad \text{with } V_p(Q) = \frac{1}{2}\hbar\bar{\omega}(Q - \sqrt{2\lambda/\hbar\bar{\omega}})^2 + \Delta G \quad (18)$$

where ΔG is the free energy of reaction in Eq. 15, and gives the energy at the bottom of $V_r(Q)$. According to Eq. 18, after reaction, atoms relax to a configuration described by $Q = \sqrt{2\lambda/\hbar\bar{\omega}}$ from that described by $Q = 0$. Since $V_p(0) - V_p(\sqrt{2\lambda/\hbar\bar{\omega}}) = \lambda$, this λ represents the energy of atomic reorganization after reaction, called the reorganization energy.

Diabatic potentials $V_r(Q)$ and $V_p(Q)$ cross each other at $Q = (\lambda + \Delta G)/(2\hbar\bar{\omega}\lambda)^{1/2}$, which gives Q_c in Figure 2. The energy of the crossing point measured from the bottom of $V_r(Q)$ is given by $V_r(Q_c) = (\lambda + \Delta G)^2/(4\lambda)$. This expression is called the Marcus relation, which gives the thermal activation energy ΔG^* for electron transfer in the non-adiabatic limit [7]. In the adiabatic limit, the thermal activation energy is reduced by J because of energy splitting by $2J$ at the crossing point, as shown in Figure 1. Since $(\lambda + \Delta G)^2/(4\lambda)$ in the non-adiabatic limit is a value of the lowest (i.e., zeroth) order in J , it seems reasonable to approximate the thermal activation energy for electron transfer by

$$\Delta G^* = (\lambda + \Delta G)^2/(4\lambda) - J \quad (19)$$

as long as the second term is a small correction of the right-hand side.

In the non-adiabatic limit, the rate constant for ET is determined in the lowest (i.e., the second) order in J . Therefore, the rate constant is given by Fermi's Golden Rule,

$$k = \frac{2\pi}{\hbar} J^2 \int \text{Tr} \delta(E - H_p) \delta(E - H_r) \rho_r dE \quad (20)$$

with

$$\rho_r \equiv \exp(-H_r/k_B T) / \text{Tr}[\exp(-H_r/k_B T)] \quad (21)$$

where Tr indicates that a trace is taken over all coupled phonons, and ρ_r is the density matrix for phonons in the reactant state. Since the phonon Hamiltonians H_r and H_p do not commute with each other, the two delta functions on the right-hand side of Eq. 20 cannot be united by integration over E .

In 1950, Huang and Rhys [8] were the first to obtain from Eq. 20 an analytic expression for the rate constant for electron transfer. They diagonalized H_r and H_p , respectively, by eigenstates $|m; r\rangle$ with eigenenergies $(m + \frac{1}{2})\hbar\bar{\omega}$ for $m = 0, 1, 2, \dots$ and eigenstates $|n; p\rangle$ with eigenenergies $(n + \frac{1}{2})\hbar\bar{\omega} + \Delta G$ for $n = 0, 1, 2, \dots$. Thus, Eq. 20 reduces to

$$k = \frac{2\pi}{\hbar} J^2 (1 - e^{-\beta\hbar\bar{\omega}}) \sum_{m,n} |\langle n; p | m; r \rangle|^2 \delta[-\Delta G - (n - m)\hbar\bar{\omega}] e^{-\beta m \hbar \bar{\omega}} \quad (22)$$

with $\beta \equiv 1/(k_B T)$. Here, $|\langle n; p | m; r \rangle|^2$ does not vanish for $m \neq n$ since $|m; r\rangle$ and $|n; p\rangle$ diagonalize the different Hamiltonians H_r and H_p , before and after the reorganization of atoms, respectively. When $n - m$ is written as ℓ , Eq. 22 can be rewritten as

$$k = (2\pi/\hbar) J^2 \sum_{\ell=-\infty}^{\infty} F_{\ell} \delta(-\Delta G - \ell \hbar \bar{\omega}) \quad (23)$$

with

$$F_{\ell} = \exp \left[\frac{\beta \ell \hbar \bar{\omega}}{2} - s \coth \left(\frac{\beta \hbar \bar{\omega}}{2} \right) \right] I_{\ell} \left(\frac{s}{\sinh(\beta \hbar \bar{\omega}/2)} \right) \quad (24)$$

for $s \equiv \lambda/(\hbar\bar{\omega})$, where $I_{\ell}(z)$ is a modified Bessel's function of the first kind of the ℓ -th order of argument z [9], and s represents a coupling constant called the Huang–Rhys factor. As shown in Appendix A, Eq. 23 with Eq. 24 can also be derived directly [10].

The right-hand side of Eq. 23 vanishes unless $\Delta G/(\hbar\bar{\omega})$ is an integer. This inconvenience arises from our initial assumption that the reaction coordinate Q constitutes a single normal mode with the energy quantum $\hbar\bar{\omega}$. In reality, Q should be composed of various normal modes of phonons with various energy quanta.

Keeping this in mind, we utilize the fact that $I_\ell(z) [= I_{-\ell}(z)]$ for an integer ℓ can be extended smoothly to $I_\nu(z)$ for a non-integral number ν , and we are led to the Huang–Rhys formula [8]

$$k = \frac{2\pi J^2}{\hbar^2 \bar{\omega}} \exp \left[-\frac{\beta \Delta G}{2} - s \coth \left(\frac{\beta \hbar \bar{\omega}}{2} \right) \right] I_{|\Delta G / \hbar \bar{\omega}|} \left(\frac{s}{\sinh(\beta \hbar \bar{\omega} / 2)} \right) \quad (25)$$

This formula is applicable to both exothermic reactions, with $\Delta G < 0$, and endothermic ones, with $\Delta G > 0$. In fact, the rate constant for reverse electron transfer, from acceptor to donor, k_{BW} , can be obtained by simply replacing ΔG with $-\Delta G$ in Eq. 25. It can easily be checked that they obey the principle of chemical equilibrium in Eq. 15. A special case of Eq. 25, for $\Delta G = 0$, was obtained in conjunction with hopping rates of small polarons on a deformable lattice [11].

2.2.2 Atom-Tunneling Regime

$I_\nu(z)$ can be approximated by $(z/2)^{|\nu|} / \Gamma(|\nu| + 1)$ when $z/2 \ll (|\nu| + 1)^{1/2}$, where $\Gamma(x)$ represents the gamma function of argument x [9]. Accordingly, Eq. 25 reduces to

$$k \approx (2\pi/\hbar) J_{\text{eff}}^2 / \hbar \bar{\omega} \quad (26)$$

with

$$J_{\text{eff}}^2 = J^2 \exp \left[-s \coth \left(\frac{\beta \hbar \bar{\omega}}{2} \right) \right] \frac{[s(\bar{n} + 1)]^{|\Delta G| / \hbar \bar{\omega}}}{\Gamma(1 + |\Delta G| / \hbar \bar{\omega})} \quad (27)$$

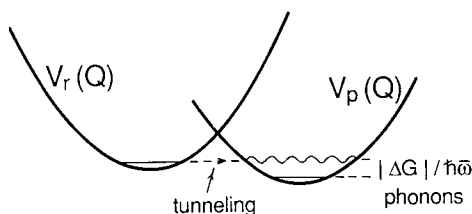
when

$$\frac{1}{2} s / \sinh(\beta \hbar \bar{\omega} / 2) \ll (1 + |\Delta G| / \hbar \bar{\omega})^{1/2}, \quad (28)$$

where $\bar{n} \equiv 1/(e^{\beta \hbar \bar{\omega}} - 1)$ represents the Planck distribution function of phonons. Eq. 27 is applicable only to exothermic reactions with $\Delta G < 0$.

The rate constant for ET can mathematically be regarded as the optical spectrum of a localized electron in the limit where the photon energy to be absorbed or emitted approaches zero. From the theory of radiative transitions [10, 12] and $\Gamma(\ell + 1) = \ell!$ for a positive integer ℓ , we see that the factor multiplied to J^2 on the right-hand side of Eq. 27 represents the thermally renormalized value of the Franck–Condon factor [i.e., the squared overlap integral between the lowest phonon state in $V_r(Q)$ and the $(|\Delta G|/\hbar \bar{\omega})$ -th one in $V_p(Q)$] for ET. The renormalization manifests itself in the Debye–Waller factor $\exp[-s \coth(\beta \hbar \bar{\omega} / 2)]$, smaller than e^{-s} , which appears also in neutron or X-ray scattering [12a]. Therefore, J_{eff} in Eq. 27 represents the effective matrix element for electron tunneling from the lowest phonon state in the reactant well with simultaneous emission of $(|\Delta G|/\hbar \bar{\omega})$ phonons,

Figure 3. Tunneling of atoms from the reactant-state potential $V_r(Q)$ to the product-state potential $V_p(Q)$ accompanied by emission of $(|\Delta G|/\hbar\bar{\omega})$ phonons.



shown in Fig. 3. In the rate constant for reverse electron transfer, in contrast, $(\bar{n} + 1)^{|\Delta G|/\hbar\bar{\omega}}$ in J_{eff}^2 is changed to $\bar{n}^{|\Delta G|/\hbar\bar{\omega}}$, since electron tunneling accompanies absorption of $(|\Delta G|/\hbar\bar{\omega})$ phonons. The last factor, $1/\hbar\bar{\omega}$, on the right-hand side of Eq. 26 represents the average density of final phonon states in ET. These features indicate that in this regime, ET (i.e., electron tunneling) from the donor to the acceptor is accompanied by simultaneous tunneling of atoms from the lowest phonon state in the reactant well around $Q = 0$ [Eq. 17] to the product well around $Q = \sqrt{2}s$ [Eq. 18], as shown schematically in Figure 3.

The condition of Eq. 28 for this atom-tunneling regime is definitely satisfied at low temperatures of $k_B T \ll \hbar\bar{\omega}$, irrespective of the magnitude of s and $|\Delta G|/\hbar\bar{\omega}$. Then the rate constant k of Eq. 26 becomes nearly independent of temperature, approaching $(2\pi/\hbar^2\bar{\omega})J^2 e^{-s|\Delta G|/\hbar\bar{\omega}}/\Gamma(1 + |\Delta G|/\hbar\bar{\omega})$. A typical example of this behavior is the electron transfer from cytochrome c to the oxidized special pair in the reaction center for photosynthesis at temperatures below ca. 60 K [13] (Figure 4).

The condition Eq. 28 is also satisfied for large $|\Delta G|/\hbar\bar{\omega} \gg 1$ where $\Delta G < 0$, as long as s is not much larger than unity in a temperature region of $k_B T \lesssim \hbar\bar{\omega}$. In this case, Stirling's formula $\Gamma(A + 1) \approx (A/e)^A$ for $A = |\Delta G|/\bar{\omega}$ enables us to rewrite Eq. 26 as

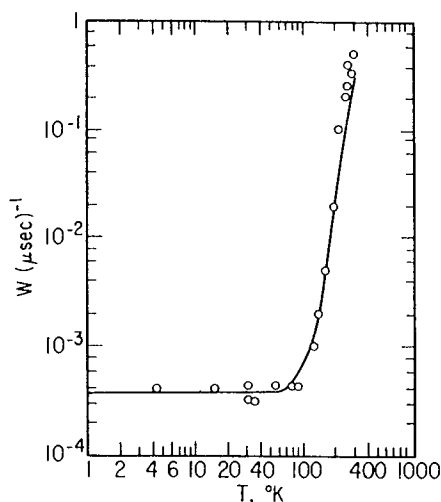


Figure 4. Temperature dependence of the rate constant for electron transfer from cytochrome c to the oxidized special pair in the reaction center of photosynthesis [13, 14].

$$k \propto \exp[-\alpha|\Delta G|/(\hbar\bar{\omega})], \quad (29)$$

with

$$\alpha = \log \left[\frac{|\Delta G|}{e s \hbar \bar{\omega}} (1 - e^{-\beta \hbar \bar{\omega}}) \right], \quad (30)$$

where α has a magnitude of the order of unity. According to Eq. 29, $\log k$ is an approximately linear function of $|\Delta G|/(\hbar\bar{\omega})$, with a slope of order unity, nearly independent of temperature. This relation is called the energy-gap law for a large gap of $|\Delta G|$. A typical example is nonradiative transitions of an electron between multiplet levels in rare-earth and alkaline-earth elements [15], where the electron is so shielded in an inner shell of an atom that it interacts only weakly with vibrations of surrounding atoms as $s \lesssim 1$.

2.2.3 Semiclassical and Classical Regimes

Rewriting $\delta(-\Delta G - \hbar\bar{\omega})$ into $(2\pi\hbar)^{-1} \int \exp[i(\Delta G + \hbar\bar{\omega})t/\hbar] dt$ and utilizing the relation $\sum_{\lambda} I_{\lambda}(z) a^{\lambda} = \exp[z(a + a^{-1})/2]$ for $a = \exp(i\bar{\omega}t + \beta\hbar\bar{\omega}/2)$ [9], we can recast Eq. 23 as

$$k = \left(\frac{J}{\hbar}\right)^2 \int \exp \left[i \frac{\Delta G}{\hbar} t - s \coth \left(\frac{\beta \hbar \bar{\omega}}{2} \right) + s \frac{e^{i\bar{\omega}t + \beta \hbar \bar{\omega}/2} + e^{-i\bar{\omega}t - \beta \hbar \bar{\omega}/2}}{2 \sinh(\beta \hbar \bar{\omega}/2)} \right] dt \quad (31)$$

This expression can also be obtained directly from Eq. 20 by the method of generating functions (Ref. [12] and Appendix B), as first done independently by Kubo and Lax [16].

Let us expand in t the exponent in the integrand on the right-hand side of Eq. 31, assuming that t satisfying $|\bar{\omega}t| \ll 1$ is most important in the integration over t . The reason for this assumption is explained below. Under this assumption, Eq. 31 reduces to

$$k \approx \left(\frac{J}{\hbar}\right)^2 \int \exp \left[i \frac{\lambda + \Delta G}{\hbar} t - \frac{s \bar{\omega}^2 t^2}{2} \coth \left(\frac{\beta \hbar \bar{\omega}}{2} \right) \right] dt \quad (32)$$

where λ represents the reorganization energy. Accordingly, the condition justifying this expansion turns out to be

$$s k_{\text{B}} T' \gg \hbar \bar{\omega}, \quad (33)$$

with

$$k_{\text{B}} T' \equiv \frac{\hbar \bar{\omega}}{2} \coth \left(\frac{\beta \hbar \bar{\omega}}{2} \right) = \begin{cases} k_{\text{B}} T, & \text{for } k_{\text{B}} T \gg \hbar \bar{\omega} \\ \frac{1}{2} \hbar \bar{\omega}, & \text{for } k_{\text{B}} T \ll \hbar \bar{\omega} \end{cases} \quad (34)$$

Here, the first equation in Eq. 34 can be expressed also as $k_{\text{B}}T' \equiv \hbar\bar{\omega}(\bar{n} + \frac{1}{2})$, with the use of the Planck distribution function \bar{n} in Eq. 27. Since $\hbar\bar{\omega}(\bar{n} + \frac{1}{2})$ is equal to the thermal average of the phonon Hamiltonian H_{r} in Eq. 17, the first equation in Eq. 34 represents

$$\langle V_{\text{r}}(Q) \rangle = k_{\text{B}}T'/2 \quad (34')$$

where $\langle f(Q) \rangle$ represents the thermal average of $f(Q)$ with respect to Q . Since $V_{\text{r}}(Q) \propto Q^2$, we see that T' represents an effective temperature measured by the average amplitude of fluctuations of the reaction coordinate Q . As noted in the last equation of Eq. 34, it approaches real temperature T at high temperatures of $k_{\text{B}}T \gg \hbar\bar{\omega}$, where Eq. 34' reduces to the equipartition law of energy in classical statistical mechanics. At low temperatures of $k_{\text{B}}T \ll \hbar\bar{\omega}$, on the other hand, T' approaches a nonvanishing value reflecting the zero-point vibration of Q , given by the last equation of Eq. 34.

Integration over t of the right-hand side of Eq. 32 is easy, and gives

$$k \approx \frac{J^2}{\hbar} \left(\frac{\pi}{\lambda k_{\text{B}}T'} \right)^{1/2} \exp\left(-\frac{\Delta G^*}{k_{\text{B}}T'}\right) \quad (35)$$

with ΔG^* of Eq. 19, where J on the right-hand side can be neglected in the present calculation which is lowest (i.e., second) order in J in the non-adiabatic limit. The regime giving the rate constant of Eq. 35 is called the semiclassical regime, realized under the condition of Eq. 33. As long as the Huang–Rhys factor s is much larger than unity, this condition is satisfied at any temperature. At low temperatures of $k_{\text{B}}T \ll \hbar\bar{\omega}$, the rate constant k of Eq. 35 becomes nearly independent of temperature. This behavior reflects that of the atom-tunneling regime, since its condition of Eq. 28 is satisfied at low temperatures irrespective of whether the condition of Eq. 33 for the semiclassical regime is satisfied or not, as pointed out in the previous subsection. At high temperatures of $k_{\text{B}}T \gg \hbar\bar{\omega}$, where T' approaches T , on the other hand, the condition of Eq. 33 is always satisfied, as long as s is not much smaller than unity. In this case, k of Eq. 35 shows thermally activated temperature dependence with activation energy ΔG^* , and the semiclassical regime reduces to the classical one. In the classical regime, atoms move classically without tunneling, although the transferred electron always moves quantum-mechanically.

In Eq. 35, the exponential factor on the right-hand side plays a dominant role in determining the magnitude of k . Two of the cases shown in Figure 5 give the same ΔG^* . In the semiclassical regime, therefore, the magnitude of the rate constant k should be similar for these two cases. The case where $-\Delta G < \lambda$ is the normal region, where k increases with an increase in the driving potential ($-\Delta G$) for chemical reaction due to a decrease in ΔG^* . This behavior follows common chemical intuition. However, for the inverted region, that is, where $-\Delta G > \lambda$, k decreases inversely with an increase in the driving potential ($-\Delta G$) because of an accompanying increase in ΔG^* . Accordingly, k reaches a maximum at the boundary between the two regions, at $-\Delta G \approx \lambda$. The existence of these two regions was first predicted by

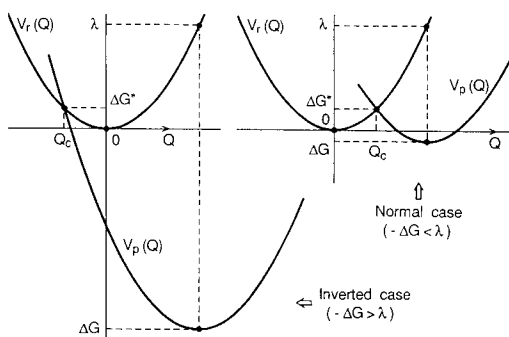


Figure 5. Relative arrangement of diabatic potentials $V_r(Q)$ and $V_p(Q)$ for the reactant and product states, respectively, in the normal case for $-\Delta G < \lambda$, and the inverted case for $-\Delta G > \lambda$.

Marcus [17], and was confirmed experimentally by Miller and his collaborators [18], but only 24 years after its prediction. Additional aspects of the inverted region will be discussed in Section 2.5.1 which focuses on the different roles played by solvent and intrasolute modes of phonons.

The atom-tunneling regime under the condition of Eq. 28 always appears at low temperatures, $k_B T \ll \hbar\bar{\omega}$, irrespective of the magnitude of s . Accordingly, the rate constant k for electron transfer becomes nearly temperature-independent at low temperatures, whereas thermal activation occurs at high temperatures, $k_B T \gg \hbar\bar{\omega}$, as long as s is not much smaller than unity. A typical example of such a change in the temperature dependence of the rate constant can be found in the electron transfer from cytochrome c to the oxidized special pair in the reaction center for photosynthesis at ca. 90 K [13], as shown in Figure 4.

Integration variable t in Eq. 31 gives a measure of the time needed for an electron to make a transition from the donor to the acceptor in the phonon field. In the semiclassical approximation under the condition of Eq. 33, the time region of $|\bar{\omega}t| \ll 1$, that is, $|t| \ll 1/\bar{\omega}$, is most important in the integration in Eq. 31. Since $1/\bar{\omega}$ gives a measure of the vibration period of atoms, this means that the electron transition takes place in a time period much shorter than the vibration period, that is, it takes place while the atomic positions can be regarded as fixed during vibration. In this situation, it is said that the transition obeys the Franck–Condon principle, which was found empirically during the study of optical spectra of molecules in condensed matter [19]. We have seen that this principle can be justified by the condition of Eq. 33 for the semiclassical approximation [12, 16b, 20].

According to the Franck–Condon principle, electron transition from donor to acceptor takes place while the atomic positions can be regarded as fixed on the reaction coordinate Q . This means that it takes place at the crossing point between the diabatic potentials $V_r(Q)$ and $V_p(Q)$ for the reactant and product states, respectively, because energy conservation is satisfied only at that point under this principle. This situation can be formulated by

$$k \approx \frac{2\pi}{\hbar} J^2 \frac{\int \delta[V_p(Q) - V_r(Q)] \exp[-V_r(Q)/k_B T'] dQ}{\int \exp[-V_r(Q)/k_B T'] dQ} \quad (36)$$

where the weighting factor, $\exp[-V_r(Q)/k_B T']$, for the thermal average in Q , is justified by Eq. 34' since $V_r(Q) \propto Q^2$. Inserting $V_r(Q)$ and $V_p(Q)$ of Eqs. 17 and 18, we can see that k of Eq. 36 reproduces k of Eq. 35. However, Eq. 36 is considered to be more general than Eq. 35 in the semiclassical regime, since it allows that both $V_r(Q)$ and $V_p(Q)$ can have more general forms than those of Eqs. 17 and 18.

2.2.4 Multimode Model

Since the phonon energy quantum $\hbar\bar{\omega}$ does not explicitly appear in both Eqs. 35 and 36, these formulas for the rate constant in the semiclassical regime should be derived without the single-mode model being relied on. That is, we should not neglect that various phonon modes contributing to the reaction coordinate Q have, in reality, various energy quanta. In this case, the phonon Hamiltonian in the reactant state (where the electron to be transferred is at the donor) consists of various normal modes,

$$H_r = \frac{1}{2} \sum_j \hbar\omega_j (p_j^2 + q_j^2) \quad (37)$$

where p_j and q_j respectively represent the momentum and the coordinate operator of the j th normal mode with the energy quantum $\hbar\omega_j$, satisfying the commutation relation $[q_j, p_{j'}] = i\delta_{j,j'}$. Similarly, the phonon Hamiltonian in the product state (where the electron has been transferred to the acceptor) is written in a form generalizing Eq. 18, as

$$H_p = \frac{1}{2} \sum_j \hbar\omega_j [p_j^2 + (q_j - \sqrt{2s_j})^2] + \Delta G \quad (38)$$

with the Huang–Rhys factor s_j for the j th mode. The contribution to the reorganization energy from the j th mode and the total reorganization energy are given respectively by

$$\lambda_j = s_j \hbar\omega_j \quad \text{and} \quad \lambda = \sum_j \lambda_j \quad (39)$$

The reaction coordinate Q is defined as describing the difference between H_r and H_p , as

$$H_r - H_p = Q - (\lambda + \Delta G) \quad (40)$$

In this definition, Q has energy dimensions, giving the energy difference between the diabatic potentials for the reactant and the product states, while Q in Eqs. 17 and 18 was defined to be dimensionless. Inserting Eqs. 38 and 39 into Eq. 40, we get

$$Q = \sum_j (2\hbar\omega_j \lambda_j)^{1/2} q_j \quad (41)$$

The diabatic potential for the reactant state is given by the smallest value of $\sum_j \hbar \omega_j q_j^2 / 2$ under the condition of Eq. 41, as a function $V_r(Q)$ of the reaction coordinate Q . Since the potential for the product state differs from $V_r(Q)$ by only $(-Q + \lambda + \Delta G)$ from Eq. 40, it can also be given by a function $V_p(Q)$ of Q . Their explicit expressions are

$$V_r(Q) = \frac{Q^2}{4\lambda} \quad \text{and} \quad V_p(Q) = \frac{(Q - 2\lambda)^2}{4\lambda} + \Delta G \quad (42)$$

They cross each other at $Q = \lambda + \Delta G (= Q_c)$. We can also show that $V_r(Q_c)$ equal to $(\lambda + \Delta G)^2 / (4\lambda)$ agrees exactly with the smallest energy of $\sum_j \hbar \omega_j q_j^2 / 2$ under the condition of $Q = Q_c$, in agreement also with the right-hand side of Eq. 19 where J can be neglected in the present non-adiabatic limit. This means that the crossing point $Q = Q_c$ located on the reaction coordinate Q is really a saddle point on the crossing surface $Q = Q_c$ between the diabatic potentials for the reactant and the product states in the multidimensional coordinate space spanned by a number of q_j . Since Q is defined by Eq. 41, it in general does not correspond to a normal mode of the phonons, but is very convenient for describing the reaction, that is, as the reaction coordinate. In spectroscopy, the same coordinate is called in terms of the interaction mode [12b].

When Eq. 36 is extended to multimodes, the rate constant in the semiclassical approximation is given by

$$k \approx \frac{2\pi}{\hbar} J^2 \frac{\prod_j (\int dq_j \exp[-q_j^2 / \coth(\beta \hbar \omega_j / 2)]) \delta(Q - Q_c)}{\prod_j [\pi \coth(\beta \hbar \omega_j / 2)]^{1/2}} \quad (43)$$

The numerator on the right-hand side can be integrated with the use of $\delta(Q - Q_c) = (2\pi\hbar)^{-1} \int \exp[i(Q_c - Q)t/\hbar] dt$ for Q of Eq. 41. Finally, integrating over t , we can, as expected, reach the same expression for k as in Eq. 35, when we redefine T' there by

$$k_B T' = (2\lambda)^{-1} \sum_j \lambda_j \hbar \omega_j \coth(\beta \hbar \omega_j / 2) \quad (44)$$

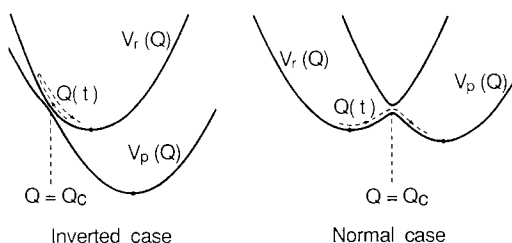
This is a straightforward generalization of Eq. 34 in the multimode model, being an average of $\hbar \omega_j \coth(\beta \hbar \omega_j / 2) / 2$, with weight λ_j , whose sum equals λ by Eq. 39.

2.3 Adiabatic Limit

2.3.1 Semiclassical Regime

The non-adiabatic limit is justified when the transfer integral J for electron transfer is sufficiently small. On the other hand, when J is large enough, we approach the

Figure 6. Relative arrangement of the upper and lower branches of adiabatic potentials in the normal and the inverted case, arising from the diabatic potentials in Figure 5.



adiabatic limit. The following two sections are devoted to discussing the change in the rate constant with an increase in J , that is, the change from the non-adiabatic to the adiabatic limit. It is, however, only in the semiclassical regime under the condition of Eq. 33 with Eqs. 44 or 34 that this change has been clarified fully. Therefore, we confine ourselves to this regime in these sections.

In the semiclassical regime, ET can take place only at fixed atomic positions. Therefore, electron transfer takes place only in the vicinity of $Q \approx Q_c$.

In the adiabatic limit, the reaction can be described by the adiabatic potentials which are composed of the upper and the lower branch and whose energy separation is given by $2J$ at $Q = Q_c$, as shown in Figure 1. The relative positions of the branches are quite different for the normal and the inverted cases: the positions of the diabatic potentials appropriate for the non-adiabatic limit, shown in Figure 5, change to those shown in Figure 6 in the adiabatic limit for both the normal and the inverted case. In the normal case, the reactant-state potential corresponds to the left-hand well in the lower branch of the adiabatic potential. In the inverted case, on the other hand, it corresponds to the upper branch, which consists of a single well.

Reflecting the thermal atomic vibrations, the reaction system fluctuates along the reaction coordinate Q in the reactant-state potential. This motion is described as $Q(t)$ as a function of time t . In the reactive trajectory, $Q(t)$ approaches $Q \approx Q_c$ from the bottom of the reactant-state potential. In the normal case, after $Q(t)$ reaches $Q \approx Q_c$ on the lower-branch adiabatic potential, it passes $Q \approx Q_c$, tracing this branch as it extends, and enters the product-state potential, as shown in Figure 6. Therefore, the rate constant for ET is given by the frequency per unit time with which $Q \approx Q_c$ is reached as a result of thermal fluctuations of the system in the reactant-state potential, that is, in the normal case, by

$$k = \nu \exp(-\Delta G^*/k_B T') \quad (45)$$

with the height ΔG^* of the barrier at $Q \approx Q_c$ in the double-well adiabatic potential in Eq. 19 and the effective temperature T' determined by Eqs. 44 or 34. Here, ν represents an average frequency of phonons contributing to the reaction coordinate, and is called the attempt frequency. Its concrete value will be derived in the next subsection.

In the transition state theory for rates of chemical reactions [21], the value of ν was chosen a priori at the thermal frequency $k_B T/h$ with Planck's constant h , on the

assumption that $h\nu$ may be estimated by the average thermal energy $k_B T$ per phonon mode in the equipartition law of energy of classical statistical mechanics. This assumption was adopted without a theoretical formulation for the ν value. Its applicability seems questionable. In fact, classical statistical mechanics is justified only when $k_B T$ is much larger than the average energy quantum of phonons contributing to the reaction coordinate. Therefore, to be selfconsistent, $k_B T/h$ must be much larger than the average frequency ν of these phonons.

In the inverted case, on the other hand, after $Q(t)$ reaches $Q \approx Q_c$ from the bottom of the reactant-state potential, which is now the upper-branch of the adiabatic potential, $Q(t)$ returns back to the bottom of the initial reactant-state potential along the upper branch, as shown in Figure 6. Accordingly, in the inverted case, the

$$(\text{preexponential factor of } k) \Rightarrow 0 \quad (46)$$

2.3.2 Attempt Frequency

In the single-mode model, where all the modes contributing to the reaction coordinate are regarded as having the same energy quantum $\hbar\bar{\omega}$, the attempt frequency ν in Eq. 45 should be given by $\bar{\omega}/(2\pi)$. In the multimode model which is more realistic than the single-mode model, the expression of ν is not self-evident, since various modes contribute to the reaction coordinate with different energy quanta. The attempt frequency ν represents the frequency per unit time with which the reaction coordinate $Q(t)$ passes through $Q = Q_c$ in the course of its thermal fluctuations from the bottom of the reactant-state potential. To obtain ν , potentials around $Q = Q_c$ can be approximated by those of the diabatic potentials $V_r(Q)$ and $V_p(Q)$ crossing at that point, as schematically shown in Figure 7.

The Hamiltonian for the reactant-state potential in the multimode model is given by Eq. 37. In the semiclassical regime, both the coordinate q_j and its conjugate momentum p_j of the j th mode for $j = 1, 2, 3, \dots$ in the Hamiltonian can be regarded not as operators but as c -numbers. In this situation, Q of Eq. 41, given by a linear combination of q_j values, is regarded as the initial value of $Q(t)$ at $t = 0$. The distribution of these q_j values is given by $C_j^{-1} \exp[-q_j^2/\coth(\beta\hbar\omega_j/2)]$ in the semiclassical regime, as shown in Section 2.2, where $\hbar\omega_j$ is the energy quantum of the j th

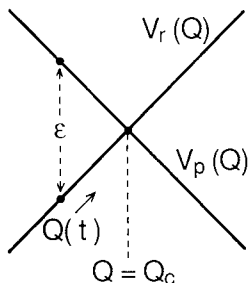


Figure 7. Crossing between the diabatic potentials $V_r(Q)$ and $V_p(Q)$ at $Q = Q_c$ in the normal case, and the time evolution of the reaction coordinate $Q(t)$ approaching the crossing point $Q = Q_c$ in the course of its thermal fluctuations in the reactant-state potential.

mode, and C_j is a normalization constant explicitly written in the denominator on the right-hand side of Eq. 43. The momentum p_j values should also contribute to the determination of the time evolution of $Q(t)$. Because of the symmetry between q_j and p_j in the Hamiltonian of Eq. 37, the distribution of the p_j values should have the same form as that of the q_j values. If the distribution of the latter is extended, the distribution function for a set of $\{p_j, q_j\}$ should be given by

$$\rho_r(\mathbf{p}, \mathbf{q}) = \prod_j \frac{\exp[-(p_j^2 + q_j^2)/\coth(\beta\hbar\omega_j/2)]}{\pi \coth(\beta\hbar\omega_j/2)} \quad (47)$$

where \mathbf{p} and \mathbf{q} are vectors whose j th components are given by p_j and q_j , respectively.

Equation 47 is the same as the Wigner distribution function [22] which is the semiclassical expression of the density matrix ρ_r of Eq. 21, as shown in Appendix B. In fact, adopting Eq. 47 for ρ_r in Eq. 20 for the rate constant k in the non-adiabatic limit, we can obtain Eq. 43 for k in the semiclassical regime directly from Eq. 20, as shown below. Hamiltonians H_r and H_p are approximated as commutable with one another in the semiclassical regime. In this situation, two delta functions in Eq. 20 can be united into a single delta function $\delta(Q - \lambda - \Delta G) [= \delta(Q - Q_c)]$ by integration over E with the use of Eq. 40. Then, with the trace operation in Eq. 20 regarded as integrations in q_j and p_j values, Eq. 43 is obtained, where p_j integrations have been performed, being canceled out by their normalization constants in the denominator, since Q does not depend on the p_j values.

Time evolution of q_j and p_j is regulated by the Hamiltonian H_r of Eq. 37. When they are written as $q_j(t)$ and $p_j(t)$, respectively, they satisfy a set of equations of motion

$$dq_j(t)/dt = \omega_j p_j(t) \quad \text{and} \quad dp_j(t)/dt = -\omega_j q_j(t) \quad (48)$$

This set of equations is the same for quantum and classical mechanics. Under the initial condition of $q_j(0) = q_j$ and $p_j(0) = p_j$, the solution to Eq. 48 is given by a set of

$$q_j(t) = q_j \cos(\omega_j t) + p_j \sin(\omega_j t) \quad (49)$$

and $p_j(t)$ which can be determined by the first equation in Eq. 48. Inserting this $q_j(t)$ for q_j on the right-hand side of Eq. 41, we obtain the expression of $Q(t)$ as

$$Q(t) = \sum_j \sqrt{2\hbar\omega_j\lambda_j} [q_j \cos(\omega_j t) + p_j \sin(\omega_j t)] \quad (50)$$

where q_j and p_j can take various values under the Wigner distribution function (Eq. 47). When a set of $\{p_j, q_j\}$ is adopted, it determines a time evolution of $Q(t)$ by Eq. 50. We denote by t_c the time at which $Q(t)$ thus determined crosses $Q = Q_c$ with a positive velocity from the left to the right in Figure 7. Then, since $Q(t)$ has an oscillatory-damping time dependence, we should obtain a series of t_c values. The

frequency (until t) with which $Q = Q_c$ is passed by $Q(t)$ with a positive velocity is given by the τ integration of $\delta(\tau - t_c)$ from zero to t . Since $Q(t)$ is a specific trajectory determined by a specific set of $\{p_j, q_j\}$, what we want to obtain is only the average value of the times, given by

$$N(t) = \int_0^t \langle \delta(\tau - t_c) \rangle_r d\tau \quad (51)$$

where $\langle \cdots \rangle_r$ represents the average in $\{p_j, q_j\}$ over the Wigner distribution function (Eq. 47).

In the adiabatic limit, the rate constant k in the normal case is given by the average frequency per unit time with which $Q = Q_c$ is passed with $\dot{Q}(t) > 0$, that is, by $dN(t)/dt$ of

$$k = \langle \delta(t - t_c) \rangle_r. \quad (52)$$

Although this expression of k seems to be time-dependent, it is not, because of ergodicity which is satisfied after the averaging of $\langle \cdots \rangle_r$ in thermal equilibrium. Although $t = t_c$ is satisfied by $Q(t) = Q_c$ with $\dot{Q}(t) > 0$, the condition of only $Q(t) = Q_c$ is realized twice as often as $t = t_c$, since both signs of $\dot{Q}(t)$ are counted. Therefore, Eq. 52 can be rewritten as

$$k = \frac{1}{2} \langle |\dot{Q}(t)| \delta[Q(t) - Q_c] \rangle_r = \frac{1}{2} \langle |\dot{Q}(t)| \rangle_r \langle \delta[Q(t) - Q_c] \rangle_r, \quad (53)$$

where the second equality is ensured since $Q(t)$ and $\dot{Q}(t)$ are statistically independent.

Here, it is convenient to introduce the distribution function of the reaction coordinate $\langle \delta(Q - x) \rangle_r$ and that of its velocity $\langle \delta(\dot{Q} - v) \rangle_r$ with $Q = Q(0)$ and $\dot{Q} = \dot{Q}(0)$. We can calculate them by rewriting, for example, $\delta(\dot{Q} - v)$ into $(2\pi)^{-1} \int \exp[i(\dot{Q} - v)t] dt$, and by integrating in q_j and p_j for $\langle \cdots \rangle_r$ and finally by that in t . The result is

$$F(x) = \langle \delta(Q - x) \rangle_r = \frac{1}{\sqrt{4\pi\lambda k_B T'}} \exp\left(-\frac{x^2}{4\lambda k_B T'}\right) \quad (54)$$

and

$$G(v) = \langle \delta(\dot{Q} - v) \rangle_r = \frac{1}{\sqrt{4\pi\bar{\omega}^2 \lambda k_B T'}} \exp\left(-\frac{v^2}{4\bar{\omega}^2 \lambda k_B T'}\right) \quad (55)$$

with

$$\bar{\omega}^2 \equiv \sum_j \omega_j^3 \lambda_j \coth\left(\frac{\beta \hbar \omega_j}{2}\right) / \sum_j \omega_j \lambda_j \coth\left(\frac{\beta \hbar \omega_j}{2}\right) \quad (56)$$

where T' represents the effective temperature determined by Eq. 44.

Both the $\langle \cdots \rangle_r$ entities on the right-hand side of Eq. 53 can be calculated at $t = 0$, without a change in the result, because of ergodicity. Especially, $\langle \delta[Q(t) - Q_c] \rangle_r$ equals $F(Q_c)$ and $\langle |\dot{Q}(t)| \rangle_r$ equals $\int |v| G(v) dv$. Performing this integration in v , we obtain k of Eq. 53 as

$$k = (\bar{\omega}/2\pi) \exp(-\Delta G^*/k_B T') \quad (57)$$

where $Q_c = \lambda + \Delta G$ was used for the crossing point Q_c in Figure 7. Thus, we see that the attempt frequency ν in Eq. 45 is given by $\bar{\omega}/(2\pi)$ where $\bar{\omega}$ is determined by Eq. 56. In fact, ν represents an average frequency of phonons contributing to the reaction coordinate Q of Eq. 41. Since the temperature dependence of the quantity on the right-hand side of Eq. 56 is weak, it can be estimated at high temperatures. Therefore, we get

$$\nu = \bar{\omega}/(2\pi) \approx (2\pi)^{-1} \left(\sum_j \omega_j^2 \lambda_j / \lambda \right)^{1/2} \quad (58)$$

with the reorganization energy λ in Eq. 39. Equation 58 was first derived by Rice [23]. The full semiclassical expression of $\bar{\omega}$ in Eq. 56 was given by the present author [24].

2.4 From the Adiabatic to the Non-Adiabatic Limit

2.4.1 Adiabaticity Parameter

Discrimination between the adiabatic and the non-adiabatic limit is deeply related to the uncertainty of quantum-mechanical observation of the product state by an electron at the reactant state (and vice versa) through the interaction J between them [24]. Let us consider that the reaction system is about to approach the crossing point $Q = Q_c$ in Figure 7 in the course of its time evolution $Q(t)$ on the reactant-state potential $V_r(Q)$ in the semiclassical regime. Let us denote by ε the energy difference between the reactant and the product state at the position $Q(t)$ of the reaction coordinate. Although atomic motions are treated semiclassically, an electron to be transferred always behaves quantum-mechanically. The quantum-mechanical energy modification brought about by the interaction J is given by J^2/ε in the second-order perturbation in J . The uncertainty principle of Heisenberg [6] predicts that the time required for this energy modification is at least of the order of $\hbar/(J^2/\varepsilon) (= \hbar\varepsilon/J^2)$. This means that it takes an amount of time of at least this order for the electron in the reactant state to fully recognize the product state through the interaction J between them. This time increases with an increase in the energy difference ε between the two states, or with a decrease in the interaction J . However, the reaction system moves along the reaction coordinate with an average velocity,

say, v , and it stays only for a time of $\sim 2\varepsilon/v$ in a region where the energy difference is smaller than ε . In this situation, we can consider the following two limits.

(a) $2J^2/(\hbar v) \gg 1$: In this limit, $\hbar\varepsilon/J^2 \ll 2\varepsilon/v$ is realized. Therefore, the passage of the reaction system through the crossing point $Q = Q_c$ in Figure 7 is so slow (or, the interaction J is so strong) that an electron in the reactant state has a sufficiently long time to observe the product state. Accordingly, the passage is accomplished with the reactant and the product states fully mixed quantum-mechanically. Therefore, transfer of the electron from the reactant to the product state has certainly taken place after a single passage. This situation can be described appropriately by the adiabatic potentials in Figures 1 and 6. We see, therefore, that the adiabatic limit is realized under inequality (a).

(b) $2J^2/(\hbar v) \ll 1$: In this limit, $\hbar\varepsilon/J^2 \gg 2\varepsilon/v$ is satisfied. Therefore, the passage of the reaction system through the crossing point $Q = Q_c$ is so fast (or, the interaction J is so weak) that an electron in the reactant state does not have a sufficient time to recognize the product state. Accordingly, the reactant and the product states are scarcely mixed quantum-mechanically in the course of the passage. Therefore, the transition of the electron from the reactant to the product state rarely takes place after a single passage. This situation can be described appropriately by the diabatic potentials in Figures 2 and 5. We see thus that the non-adiabatic limit is realized under inequality (b).

It is important that inequalities (a) and (b) do not depend on the magnitude of the energy difference ε between the reactant and the product state in the course of the passage. Therefore, they can be applied throughout the passage. (It is interesting to notice that such situations (a) and (b) arising from the uncertainty of observation can also be found in human relations, although we do not behave quantum-mechanically.)

Intermediate cases between (a) and (b) can be described by the Landau–Zener formula [25]. It was obtained in conjunction with a different problem of atomic collision of the second kind, where a collision of two atoms, say, A and B gives rise to ionized atoms, for example, A^+ and B^- . Since the energy of the product state ($A^+ + B^-$) decreases with a decrease in the interatomic distance because of Coulombic attraction, it crosses the energy of the reactant state ($A + B$) in this collision. A transition from the reactant to the product state takes place as a result of a transfer of an electron from A to B by the transfer interaction, say, J in the vicinity of the crossing point. This situation is schematically illustrated in Figure 8. When the speed with which the energy difference between the two state changes with variation of the interatomic distance is written as v , the formula tells us that the probability with which the ionized pair is found after the collision is given by

$$P(v) = 1 - \exp[-2\pi J^2/(\hbar v)] \quad (59)$$

Accordingly, $1 - P(v)$ gives the probability with which the ionized pair is not formed.

Here, $P(v)$ approaches unity when $2\pi J^2/(\hbar v) \gg 1$, describing situation (a) in the adiabatic limit. When $2\pi J^2/(\hbar v) \ll 1$, on the other hand, it approaches $2\pi J^2/(\hbar v)$,

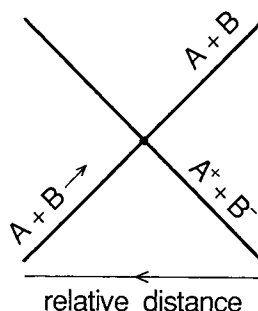


Figure 8. Energies of the initial ($A + B$) and the final ($A^+ + B^-$) state in a collision of the second kind between atoms A and B, crossing one another with a change in interatomic distance.

which is much smaller than unity, thus corresponding to situation (b) mentioned above. In this non-adiabatic limit, $P(v) (\ll 1)$ can also be obtained by the perturbation calculation second-order in J , since it is proportional to J^2 . The perturbation calculation can be used only when $P(v) \ll 1$. In the opposite limit, $P(v)$ becomes saturated at a value of one, independent of J .

In the atomic collision, the v value has been determined extrinsically by the initial relative velocity of the two atoms. In the present problem of electron transfer between donor and acceptor, v takes various values, arising from the thermal fluctuations of atoms along the reaction coordinate. On a trajectory $Q(t)$ along the reaction coordinate in the semiclassical picture, the value of v is given by the time derivative $\dot{Q}(t)$ since Q was defined as the energy difference between the diabatic potentials for the reactant and the product state (Eq. 40). Since fluctuations in $\dot{Q}(t)$ are statistically independent of those in $Q(t)$, the average value of v is the same at any value of $Q(t)$.

The distribution function of $v [= \dot{Q}(t)]$ values has already been determined as $G(v)$ of Eq. 55. Since v itself, not v^2 , appears in the Landau-Zener formula (Eq. 59), and is regarded as a positive quantity, it is appropriate to estimate the average value of v by

$$\bar{v} \equiv \int |v| G(v) dv = 2\bar{\omega}(\lambda k_B T' / \pi)^{1/2} \quad (60)$$

where $\bar{\omega}$, determined by Eq. 56, represents the average angular frequency of phonons contributing to the reaction coordinate, λ represents the reorganization energy of Eq. 39, and T' represents the effective temperature of Eq. 44.

On the basis of the Landau-Zener formula (Eq. 59), the parameter for discriminating between the adiabatic and the non-adiabatic limits of ET should be given by

$$\gamma \equiv 2\pi J^2 / (\hbar \bar{v}) = \pi^{3/2} J^2 / [\hbar \bar{\omega} (\lambda k_B T')^{1/2}] \quad (61)$$

This dimensionless parameter has been called the adiabaticity parameter. When $\gamma \gg 1$, the adiabatic limit is realized, while the non-adiabatic limit is realized in the limit of $\gamma \ll 1$. As the average energy quantum $\hbar \bar{\omega}$ of phonons approaches zero, γ of Eq. 61 diverges, and only the adiabatic limit becomes justifiable. Born and Oppen-

heimer's idea of the adiabatic approximation [2] comes from this situation, as mentioned in Section 2.1.

In the non-adiabatic limit, the rate constant k can be calculated by Eq. 43 and is given by Eq. 35 with the effective temperature T' defined by Eq. 44, as mentioned before. Although k of Eq. 35 does not explicitly include the average angular frequency $\bar{\omega}$ of phonons, it is instructive to see that the preexponential factor of k is equal to $2\gamma(\bar{\omega}/2\pi)$: With the attempt frequency $\bar{\omega}/(2\pi)$ in Eq. 58, $(\bar{\omega}/2\pi)\exp(-\Delta G^*/k_B T')$ represents a rate per unit time with which the reaction system reaches the crossing point $Q = Q_c$ along the reaction coordinate Q as a result of thermal fluctuations of atoms in the reactant state. Each time the reaction system reaches the crossing point, it passes through the crossing point twice, that is, upward and downward, in a round trip from the bottom of the diabatic potential for the reactant state. Therefore, in the preexponential factor $2\gamma(\bar{\omega}/2\pi)$ of the rate constant, γ represents the average probability with which the transition of an electron from the reactant to the product state takes place per single passage in the non-adiabatic limit. This interpretation of γ is in accordance with its definition of Eq. 61 on the basis of the Landau-Zener formula (Eq. 59). We see, simultaneously, that the preexponential factor of the rate constant must be much smaller than the average frequency $\bar{\omega}/(2\pi)$ of phonons in the non-adiabatic limit for $\gamma \ll 1$.

2.4.2 Between the Adiabatic and the Non-Adiabatic Limit

The rate constant in cases intermediate to the adiabatic and the non-adiabatic limits can be obtained when the Landau-Zener formula (Eq. 59) is applied for each trajectory $Q(t)$ of the reaction system in the course of thermal fluctuations of atoms in the reactant state in the semiclassical regime [24]. We confine ourselves to a case where the barrier height ΔG^* for reaction is much larger than $k_B T$. In this case, $Q(t)$ can be regarded as starting from the bottom of the diabatic potential for the reactant state. Although the rate constant in the non-adiabatic limit is given by the same expression (Eq. 35) for the normal and the inverted cases (Figure 5), this situation cannot be obtained when we step beyond this limit.

Let us first investigate the inverted case in Figure 5, since it turns out that it is simpler than the normal case. In the inverted case, only two channels exist for a reactive trajectory $Q(t)$ along the reaction coordinate Q . As shown in part (a) of Figure 9, an electron makes a transition from the reactant state (state 1) to the product state (state 2) at time t_1 , when $Q(t)$ first passes the crossing point, in one channel. Just after the transition, both $Q(t)$ and its velocity $\dot{Q}(t)$ are conserved to those just before the transition in the semiclassical regime, as verified in Ref. [24], but $Q(t)$ begins to climb up the diabatic potential for state 2. Shortly after, $Q(t)$ returns to the crossing point at time t_{11} . As shown in part (b) of Figure 9, the electron does not make a return transition to state 1, and $Q(t)$ begins to descend down from the crossing point toward the bottom of the diabatic potential for state 2, the reaction in this channel being accomplished. In the other channel, shown in part (c) of Figure 9, the electron does not make a transition from state 1 to state 2 at time t_1 ; climbing up the diabatic potential for state 1, $Q(t)$ returns back to the crossing point

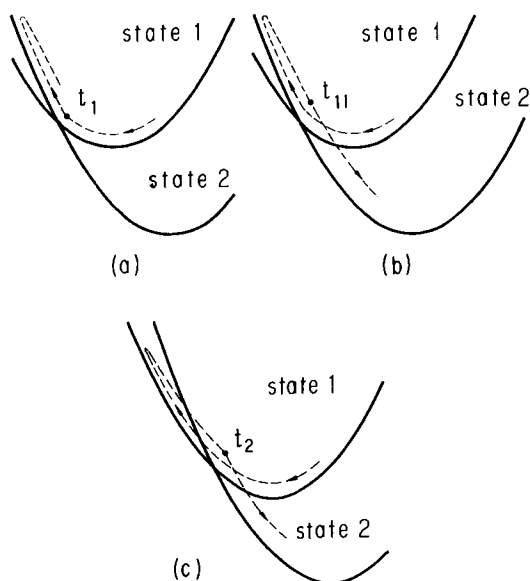


Figure 9. Two channels for a reactive trajectory $Q(t)$ of the reaction coordinate in the inverted case; one, (a) followed by (b), and the other, (c).

at time t_2 . Now the electron makes a transition from state 1 to state 2 without a change in its velocity, and the reaction in this channel is accomplished.

When the Landau-Zener probability, $1 - \exp[-2\pi J^2/(\hbar|v(t_i)|)]$ with $v(t_i) = \dot{Q}(t_i)$, is written as P_i , this trajectory $Q(t)$ has a reaction yield given by $P_1(1 - P_{11})$ in the first channel and $(1 - P_1)P_2$ in the second channel. How this result can be derived directly from the Hamiltonians in Eqs. 37 and 38 is shown in Ref. [24]. Since velocities $v(t_1)$, $v(t_{11})$, and $v(t_2)$ have approximately the same absolute value, they can be replaced by velocity $v(t_c)$ at the first crossing time $t_c = t_1$. Therefore, the reaction takes place with a yield given by

$$Y[\dot{Q}(t_c)] = 2P_c(1 - P_c), \quad \text{with } P_c = 1 - \exp\left(-\frac{2\pi J^2}{\hbar|\dot{Q}(t_c)|}\right) \quad (62)$$

in the inverted case in Figure 5, where a trajectory $Q(t)$ reaches the crossing point $Q = Q_c$ at time t_c from the bottom of the diabatic potential for the reactant state.

In the normal case, there is a series of channels for reactive trajectory $Q(t)$ where it starts from the bottom of the diabatic potential for the reactant state. In the first channel, described in part (a) of Figure 10, the electron makes a transition from the reactant state (state 1) to the product state (state 2) at time t_1 when $Q(t)$ first passes through the crossing point. After that, with the same velocity as before the transition, $Q(t)$ begins to descend down from the crossing point toward the bottom of the diabatic potential for state 2, and the reaction in this channel is accomplished. In the second channel, the electron does not make a transition to state 2 at time t_1 . $Q(t)$ continues to climb up the diabatic potential for state 1, and shortly after, at

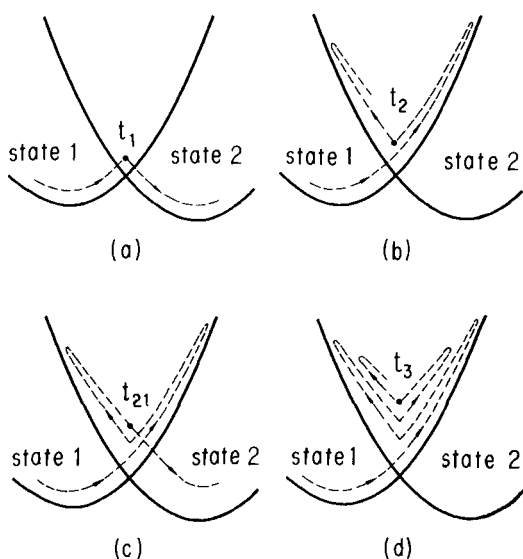


Figure 10. First three channels for a reactive trajectory $Q(t)$ of the reaction coordinate in the normal case; the first one is shown in (a), the second one in (b) followed by (c), and the third one is shown in (d), followed by an event duplicating (c).

time t_2 , it returns back to the crossing point. As shown in part (b) of Figure 10, the electron makes a transition to state 2 without a change in its velocity, and $Q(t)$ begins to climb up the diabatic potential for state 2. Shortly after, it returns back to the crossing point at time t_{21} , as shown in part (c) of Figure 10. This motion of $Q(t)$ from t_1 to t_{21} has been called a swing [24]. After this swing, the electron does not make a return transition to state 1 at time t_{21} , and $Q(t)$ begins to descend down toward the bottom of the diabatic potential for state 2, the reaction in the second channel being accomplished. In the third channel, the electron makes a transition at time t_{21} again, and $Q(t)$ makes a swing once more, as shown in part (d) of Figure 10. After time t_3 in the course of the swing, $Q(t)$ returns back to the crossing point at time t_{31} (not shown in Figure 10), and the electron does not make a return transition to state 1, for accomplishment of the reaction in the third channel.

With the Landau-Zener probability P_i at time t_i , this trajectory $Q(t)$ has a reaction yield given by P_1 in the first channel, given by $(1 - P_1)P_2(1 - P_{21})$ in the second channel, given by $(1 - P_1)P_2P_{21}P_3(1 - P_{31})$ in the third channel, and so forth. The absolute value of the velocity $\dot{Q}(t)$ can be approximated to have the same magnitude at a series of the crossing times, as before. We have $P + (1 - P)^2P + (1 - P)^2P^3 + \dots = 2P/(1 + P)$ since $P^2 < 1$. Therefore,

$$Y[\dot{Q}(t_c)] = 2 \frac{P_c}{1 + P_c} \quad \text{with } P_c = 1 - \exp\left(-\frac{2\pi J^2}{\hbar |\dot{Q}(t_c)|}\right) \quad (63)$$

gives the yield in the normal case of Figure 5 at time t_c when a trajectory $Q(t)$ reaches the crossing point $Q = Q_c$ from the bottom of the diabatic potential for the reactant state.

The right-hand side of Eq. 52 gives the average frequency per unit time with which $Q(t)$ passes through the crossing point $Q = Q_c$ with a positive velocity $\dot{Q}(t)$ in the normal case or with a negative velocity in the inverted case. Therefore, for the rate constant k in a situation outside the adiabatic limit to be obtained, the thermal average over the trajectory $Q(t)$ on the right-hand side of Eq. 52 must be supplemented by the yield $Y[\dot{Q}(t_c)]$ obtained above, so that

$$k = \langle Y[\dot{Q}(t_c)] \delta(t - t_c) \rangle_r \quad (64)$$

Similar to the situation in Eq. 52, this expression for k appears to be time-dependent, but is not because of ergodicity satisfied after the averaging of $\langle \dots \rangle_r$ in thermal equilibrium. Just as Eq. 52 could be rewritten as Eq. 53, the rate constant k of Eq. 64 can be recast as

$$k = \frac{1}{2} \langle |\dot{Q}(t)| Y[\dot{Q}(t)] \rangle_r \langle \delta[Q(t) - Q_c] \rangle_r \quad (65)$$

Equation 54 gives $\langle \delta[Q(t) - Q_c] \rangle_r = (4\pi\lambda k_B T')^{-1/2} \exp(-\Delta G^*/k_B T')$ where ΔG^* is given by $Q_c^2/(4\lambda) = (\lambda + \Delta G)^2/(4\lambda)$ as the energy of the crossing point $Q = Q_c$ between the diabatic potentials. Therefore, k of Eq. 65 can be expressed as

$$k = \kappa (\bar{\omega}/2\pi) \exp(-\Delta G^*/k_B T') \quad (66)$$

when a factor κ is introduced. Here, κ supplements the average frequency per unit time, $(\bar{\omega}/2\pi) \exp(-\Delta G^*/k_B T')$, with which $Q(t)$ passes through the crossing point $Q = Q_c$ with a positive velocity $\dot{Q}(t)$ in the normal case or with a negative velocity in the inverted case. Therefore, κ represents the average probability with which reaction really takes place when the reaction system reaches the transition state as a result of thermal fluctuations in the reactant state. This κ (< 1) has been called the transmission coefficient in the transition-state theory [21]. From Eqs. 65 and 66, κ is given by $\langle |\dot{Q}(t)| Y[\dot{Q}(t)] \rangle_r (4\bar{\omega}^2 \lambda k_B T'/\pi)^{-1/2}$, where $\langle \dots \rangle_r$ is given by an average over the distribution function $G(v)$ [of Eq. 55] of the velocity $[v = \dot{Q}(t)]$ fluctuating in the reactant state. Thus, we obtain

$$\kappa = \frac{1}{4\bar{\omega}^2 \lambda k_B T'} \int |v| Y(v) \exp\left(-\frac{v^2}{4\bar{\omega}^2 \lambda k_B T'}\right) dv \quad (67)$$

In Eq. 67, $Y(v)$ is represented by Eqs. 62 or 63 in the inverted or normal case, respectively, with $v = \dot{Q}(t_c)$. We see, especially, that κ of Eq. 67 is a function only of the adiabaticity parameter γ of Eq. 61. When $\gamma \ll 1$, moreover, the two cases have the same κ , since both Eqs. 62 and 63 give $Y(v) \approx 4\pi J^2/(\hbar|v|)$. Therefore, we get, for both cases,

$$\kappa \approx 2\gamma \quad \text{for } \gamma \ll 1 \quad (68)$$

in the non-adiabatic limit. Shown in Figure 11 is the γ -dependence of κ , obtained

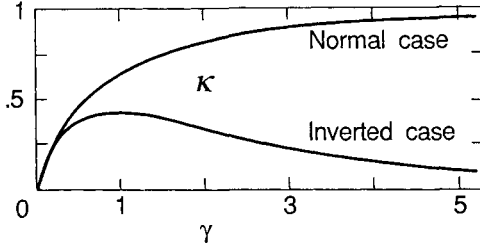


Figure 11. Transmission coefficient κ of the reaction as a function of the adiabaticity parameter γ in the normal and inverted cases.

by numerical calculation of Eq. 67 in Ref. [24]. When $\gamma \gtrsim 1$, κ deviates from the linear dependence on γ . In the adiabatic limit of $\gamma \gg 1$, κ approaches the saturation value of one in the normal case, since $Y(v) \approx 1$ in this limit in Eq. 67. In the inverted case, on the other hand, $Y(v)$ approaches zero in Eq. 67 and, hence, so does κ in this limit. The γ -dependence of κ in the both limits mentioned above is in agreement with that pointed out in Sections 2.3 and 2.4.1.

Estimating the integration in Eq. 67 by the method of steepest descent for $\gamma \gg 1$, we can obtain the asymptotic behavior in the γ -dependence of κ . In the normal case, inserting $Y(v) \approx 1 - \frac{1}{2} \exp[-2\pi J^2/(\hbar|v|)]$, obtained from Eq. 63, into Eq. 67, we obtain

$$\kappa \approx 1 - \frac{(\pi\gamma)^{1/3}}{2^{1/3}3^{1/2}} \exp\left(-\frac{3\gamma^{2/3}}{(4\pi)^{1/3}}\right) \quad \text{for } \gamma \gg 1 \quad (69)$$

In the inverted case, $Y(v) \approx 2 \exp[-2\pi J^2/(\hbar|v|)]$, obtained from Eq. 62, enables us to obtain

$$\kappa \approx \frac{2^{5/3}(\pi\gamma)^{1/3}}{3^{1/2}} \exp\left(-\frac{3\gamma^{2/3}}{(4\pi)^{1/3}}\right) \quad \text{for } \gamma \gg 1 \quad (70)$$

Therefore, in the adiabatic limit of the inverted case, the rate constant approaches

$$k \approx \frac{2\bar{\omega}}{3\sqrt{\pi}} \left(\frac{E_J}{k_B T'}\right)^{1/6} \exp\left[-\frac{\Delta G^*}{k_B T'} - \left(\frac{E_J}{k_B T'}\right)^{1/3}\right] \quad (71)$$

with

$$E_J \equiv 27\pi^2 J^4 / [4(\hbar\bar{\omega})^2 \lambda] \quad (72)$$

where $E_J \gg k_B T'$ under the condition of $\gamma \gg 1$. This asymptotic behavior with an additional thermal-activation factor was first pointed out by Christov [26].

2.5 Further Development

2.5.1 Large-Energy-Quantum Intramolecular Modes

When the donor–acceptor assembly is immersed in a solvent, the transferred electron interacts with both the atomic motions of the donor–acceptor super-molecule as well as the molecular motions in the solvent. In this situation, electron transfer gives rise to two types of reorganization, namely, atomic rearrangement within the solute molecules and molecular rearrangement in the solvent. The former has been called inner-sphere reorganization, and the latter outer-sphere reorganization [27]. The reorganization energy is written as λ_i for the former and λ_o for the latter. Energy quanta of molecular motions contributing to the latter are small, with magnitudes of at most ca. 100 cm^{-1} , while λ_o is usually larger than ca. 1000 cm^{-1} . Writing the average energy quantum of these molecular motions as $\hbar\bar{\omega}_o$, we see that the average Huang-Rhys factor $s_o = \lambda_o/(\hbar\bar{\omega}_o)$ is usually much larger than unity. Therefore, for outer-sphere reorganization the condition Eq. 33 for the semiclassical approximation is usually satisfied at all temperatures, where the effective temperature T' is given by Eq. 44 as an average over the various modes contributing to outer-sphere reorganization. This is the situation for which Marcus first constructed his theory on electron transfer in solution [7], taking into account only λ_o .

If intramolecular vibrations contributing to inner-sphere reorganization are also in the semiclassical regime, it is not necessary to separate the inner- and the outer-sphere reorganization as was done in the formulation in the previous sections. However, intramolecular vibrations with large energy quanta of ca. 1000 cm^{-1} and with appreciable reorganization energies of ca. 1000 cm^{-1} often contribute to inner-sphere reorganization. The average Huang-Rhys factor of these vibrations is not much larger than unity, and hence these vibrations cannot be treated within the semiclassical approximation.

In this situation, it is convenient to treat the large-energy-quantum modes by the single-mode approximation, where they are regarded as having a single energy quantum $\hbar\bar{\omega}_a$, contributing by an amount of λ_a to the inner-sphere-reorganization energy. In reality, $\hbar\bar{\omega}_a$ is determined as an average of various energy quanta of such modes. The remaining modes contributing to inner-sphere reorganization, as well as the outer-sphere-reorganization modes, are treated as in the semiclassical regime, and can be treated with the multimode model. We denote the contribution to the reorganization energy of these two kinds of modes in the semiclassical regime by λ , and the reaction coordinate given by a linear combination of their coordinates as in Eq. 41 by Q . Then, the diabatic potentials are given by the same $V_r(Q)$ and $V_p(Q)$ as in Eq. 42 for the reactant and product states, respectively. These semiclassical modes also determine the effective temperature T' (Eq. 44) as an average. Additionally, we take into account the large-energy-quantum modes at individual distortions described by coordinate Q . In this situation, the diabatic potential of the reactant state is composed of multiple parabolas of $V_r(Q) + m\hbar\bar{\omega}_a$ for $m = 0, 1, 2, \dots$, while that of the product state is composed of those $V_p(Q) + n\hbar\bar{\omega}_a$ for $n = 0, 1, 2, \dots$, as shown in Figure 12.

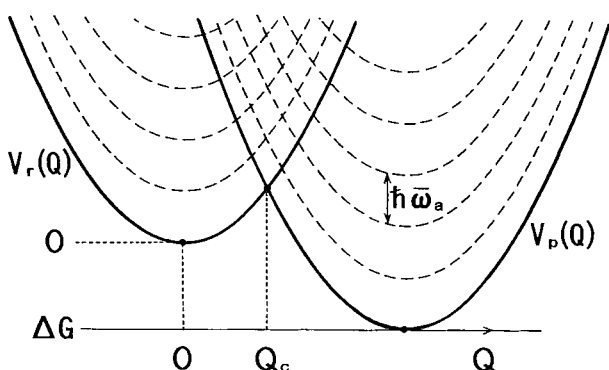


Figure 12. Diabatic potential for the reactant state composed of multiple parabolas of $V_r(Q) + m\hbar\omega_a$ for $m = 0, 1, 2, \dots$, and for the product state composed of $V_p(Q) + n\hbar\omega_a$ for $n = 0, 1, 2, \dots$, in a mutual arrangement of the normal case.

In the semiclassical regime, the value of coordinate Q must be conserved on transition of an electron from the reactant and the product state under the Franck–Condon principle. Since the diabatic potentials for these states are composed of multiple parabolas due to participation of large-energy-quantum intramolecular vibrations, the transition is specified by a simultaneous change in the quantum state of these vibrations, for example, from the m th state $|m; r\rangle$ in the reactant state to the n th state $|n; p\rangle$ in the product state for both m and $n = 0, 1, 2, \dots$. Therefore, in this case, the squared matrix element J^2 for the electronic part of the transition must be accompanied by $|\langle n; p|m; r\rangle|^2$, which is nonvanishing irrespective of $n \neq m$, since $|m; r\rangle$ and $|n; p\rangle$ are eigenstates of the intramolecular vibrations before and after their reorganization by energy λ_a .

At each crossing point between $V_r(Q) + m\hbar\omega_a$ and $V_p(Q) + n\hbar\omega_a$, we can define a reaction yield $\Upsilon_{n,m}(\dot{Q})$ per single forward passage with velocity \dot{Q} . It is obtained when J^2 is replaced with $|\langle n; p|m; r\rangle|^2 J^2$ in $\Upsilon(\dot{Q})$ of Eqs. 62 and 63 in the inverted and the normal case, respectively. Except in the non-adiabatic limit, $\Upsilon_{n,m}(\dot{Q})$ is in general not much smaller than unity, and the counter yield $1 - \Upsilon_{n,m}(\dot{Q})$ of no reaction after a single forward passage through the crossing point decreases from unity appreciably. In this situation, successive crossings in the course of time evolution of the reaction coordinate influence in each other's contribution to the rate constant. Such complexities do not occur in the non-adiabatic limit where J^2 is so small that $\Upsilon_{n,m}(\dot{Q})$ is much smaller than unity, and the rate constant is obtained simply as the sum of the yields at all possible crossing points. In this limit, $\Upsilon_{n,m}(\dot{Q}) \propto J^2$ has the same form for the normal and the inverted case. In the non-adiabatic limit, therefore, the rate constant is given by the thermal average over m and the sum over n on the right-hand side of Eq. 43 with $|\langle n; p|m; r\rangle|^2 J^2$ inserted for J^2 , as

$$k = \frac{2\pi}{\hbar} J^2 (1 - e^{-\beta\hbar\omega_a}) \sum_{m,n} |\langle n; p|m; r\rangle|^2 \langle \delta[Q - Q_c - (n - m)\hbar\omega_a] \rangle_r e^{-\beta m\hbar\omega_a}, \quad (73)$$

where we used $V_r(Q) + m\hbar\omega_a - [V_p(Q) + n\hbar\omega_a] = Q - Q_c - (n - m)\hbar\omega_a$ from Eq.

42, and $\langle \cdots \rangle_r$ represents the thermal average in q_j values on the right-hand side of Eq. 43.

Since Eq. 73 has the same structure as Eq. 22, it can be cast into a form similar to Eq. 23 with $n - m = \ell$. Since $\langle \delta(Q - Q_c - \ell \hbar \bar{\omega}_a) \rangle_r = F(Q_c + \ell \hbar \bar{\omega}_a)$ (from Eq. 54), Eq. 73 which gives the rate constant in the non-adiabatic limit can be expressed as

$$k = \frac{J^2}{\hbar} \left(\frac{\pi}{\lambda k_B T'} \right)^{1/2} \sum_{\ell=-\infty}^{\infty} F_{\ell} \exp \left(- \frac{(\lambda + \Delta G + \ell \hbar \bar{\omega}_a)^2}{4 \lambda k_B T'} \right) \quad (74)$$

with

$$F_{\ell} \equiv \exp \left[\frac{\beta \ell \hbar \bar{\omega}_a}{2} - s_a \coth \left(\frac{\beta \hbar \bar{\omega}_a}{2} \right) \right] I_{\ell} \left(\frac{s_a}{\sinh(\beta \hbar \bar{\omega}_a / 2)} \right) \quad (75)$$

where $s_a = \lambda_a / (\hbar \bar{\omega}_a)$ represents the Huang–Rhys factor for the large-energy-quantum intramolecular vibrations. This formula was first derived by Jortner [14].

In the limit of $s_a \rightarrow 0$, Eq. 74 reduces to Eq. 35, since $I_{\ell}(x) \rightarrow \delta_{\ell,0}$ for $x \rightarrow 0$. $\hbar \bar{\omega}_a$ ($\gtrsim 1000 \text{ cm}^{-1}$) is usually much larger than $k_B T$ ($\lesssim 200 \text{ cm}^{-1}$) below room temperature. Therefore, the interaction with the large-energy-quantum modes is usually in the atom-tunneling regime for any value of ℓ in Eq. 74, satisfying the condition (Eq. 28) where $\Delta G / (\hbar \bar{\omega})$, s , and $\bar{\omega}$ are replaced by ℓ , s_a , and $\bar{\omega}_a$, respectively. Hence, Eq. 74 reduces to

$$F_{\ell} \approx \begin{cases} e^{-s_a} s_a^{\ell} / \ell!, & \text{for } \ell \geq 0 \\ 0, & \text{otherwise} \end{cases} \quad (76)$$

since $\hbar \bar{\omega}_a \gg k_B T$ in the usual cases. When Eq. 76 is applicable, Eq. 74 means that transition of an electron from the reactant to the product state takes place at each crossing point between $V_r(Q)$ and $V_p(Q) + \ell \hbar \bar{\omega}_a$ for $\ell = 0, 1, 2, \dots$ in Figure 12, that is, at $Q = Q_c + \ell \hbar \bar{\omega}_a$ ($= \lambda + \Delta G + \ell \hbar \bar{\omega}_a$) from Eq. 42. In Figure 12, where diabatic potentials for the reactant and the product states are arranged in the normal case for $\lambda + \Delta G > 0$ of Figure 5, all the crossing points for $\ell \geq 1$ are located on the energy side which is higher along the reactant-state potential $V_r(Q)$ than that for $\ell = 0$. Therefore, Jortner's modification of Eq. 74 with Eqs. 75 or 76 is not very important in the normal region. His modification becomes crucial in the inverted region, that is, for $\lambda + \Delta G < 0$ of Figure 5, where the multiple parabolas above $V_r(Q)$ and those above $V_p(Q)$ are arranged as shown in Figure 13. In this case, the crossing point for $\ell = 0$ is located at $Q = Q_c$ ($= \lambda + \Delta G$) in the negative Q region along $V_r(Q)$, and in general, lower-energy crossing points with $|Q| < |\lambda + \Delta G|$ exist for certain values of $\ell \geq 1$, as seen also in Figure 13. Electron transfer takes place more rapidly through these lower-energy crossing points for $\ell \geq 1$ than through that for $\ell = 0$. In the inverted region, therefore, the rate constant becomes much larger than that given by Eq. 35, when large-energy-quantum intramolecular vibrations contribute to the inner-sphere reorganization with an appreciable reorganization energy $\lambda_a = s_a \hbar \bar{\omega}_a$.

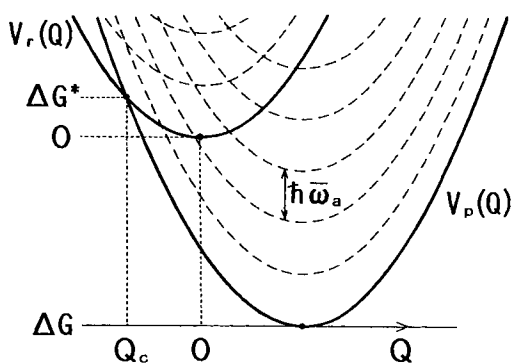


Figure 13. Diabatic potentials for the reactant and the product state composed of the multiple parabolas as in Figure 12, but here shown for the inverted case.

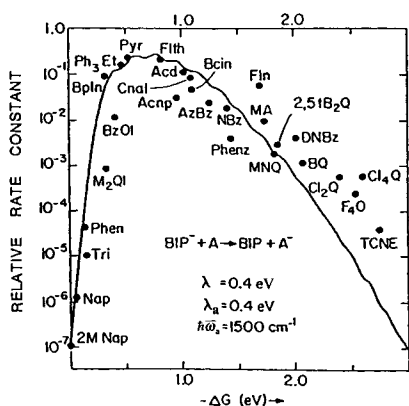


Figure 14. $(-\Delta G)$ -dependence of the relative magnitude of the observed rate constant for electron transfer from biphenyl to various acceptor molecules where they are bridged by a spacer molecule at a distance ca. 17 Å in a glass at 77 K [18].

Such enhancement of the rate constant in the inverted region has, indeed, been observed by Miller and his collaborators [18]. They used biphenyl as a donor in a glass at 77 K. Various molecules were used as the acceptor for realizing various values of the free energy of reaction ΔG . Figure 14 shows the relative magnitudes of the observed rate constants of ET (scaled by the prefactor before the summation in Eq. 74) as a function of $-\Delta G$ which represents the free-energy drop of the reaction. When $-\Delta G \lesssim 0.8$ eV, the rate constant increases with an increase in $-\Delta G$, indicating that the reaction is in the normal region. When $-\Delta G \gtrsim 0.8$ eV, the rate constant decreases with an increase in $-\Delta G$, the reaction entering the inverted region. Since the average donor-acceptor distance is large (~ 17 Å), giving a small transfer integral J , the reaction is considered to be in the non-adiabatic limit. If the reaction is in the semiclassical regime as a whole, the rate constant k should be given by Eq. 35, and $\log k$ should change in proportion to ΔG^* equal to $(\lambda + \Delta G)^2/(4\lambda)$. When it is plotted as a function of $-\Delta G$, one obtains the so-called Marcus parabola peaking at $-\Delta G = \lambda$ and symmetric on the both sides. Figure 14 shows that the rate constant is much larger in the inverted region than expected from the Marcus parabola. This arises from participation of large-energy-quantum intramolecular vibrations in the

inner-sphere reorganization. The solid line in Figure 14 represents the theoretical fit to Eq. 74 with Eq. 75 for $\lambda = \lambda_a = 0.4$ eV and for $\hbar\bar{\omega}_a = 1500$ cm⁻¹ [18].

2.5.2 Electron Transfer to or from a Continuum of Free States

One of the central problems in semiconductor devices is the nonradiative capture of an electron of the conduction band into a localized defect level with energy deep in the forbidden gap [28]. Free electrons in the conduction band interact only weakly with phonons, but in such a localized state an electron interacts strongly with them [29]. This enables the localized state to capture a free electron with simultaneous emission of many phonons [30]. This type of electron transfer and the corresponding inverse process are slightly different from the electron transfer between localized states discussed before. In this case, either the donor or the acceptor is a collection of delocalized free states with a continuum of energy levels, while the other is a localized state with only a single energy level. Let us consider the case where the former is the donor and the latter is the acceptor. An example of diabatic potentials for describing these electron transfer processes is given by Figure 15, where $V_d(Q)$ represents that for the lowest free state above which a continuum of free states exists, as shown by thin solid lines, at each value Q of the reaction coordinate. The diabatic potential $V_p(Q)$ for the localized acceptor state in Figure 15 has a minimum shifted from that of $V_r(Q)$ due to strong interaction with the phonons. Capture and emission of free electrons by the deep level are also illustrated in Figure 15.

Let us denote by R_c the rate with which an unoccupied acceptor captures a free electron from the conduction band in a unit time, and by k_e the rate constant for emission of a captured electron from an occupied acceptor into the conduction band. Similarly to Eq. 15, the principle of microscopic equilibrium relating these is given by

$$(g_f n_T R_c / n) \exp(-\beta E_t) = g_i k_e \quad (77)$$

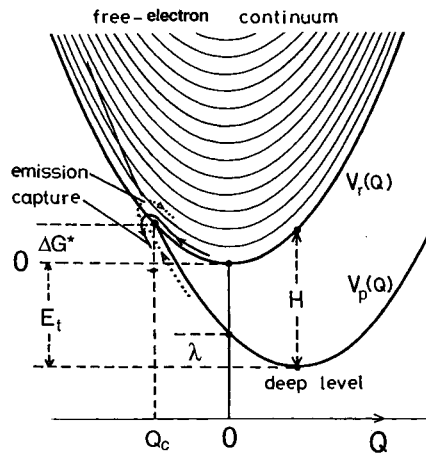


Figure 15. Diabatic potential $V_r(Q)$ for the lowest free state above which a continuum of free states exists, as shown by thin solid lines, at each Q value of the reaction coordinate. $V_p(Q)$ for the localized deep state has a minimum shifted from the minimum of $V_r(Q)$ due to a strong interaction with phonons.

where n , g_f , and g_t respectively represent the free-electron density, the number of equivalent valleys in the conduction band, and the degeneracy of the acceptor level whose energy is lower than the bottom of the conduction band by E_t (>0); n_T represents the effective density of conduction-band states available at temperature T in a single valley. For an effective mass m^* of free electrons in the conduction band, n_T is given by

$$n_T = [m^* k_B T / (2\pi\hbar^2)]^{3/2} \quad (78)$$

Since $R_c \propto n$, as an n -independent quantity, the capture cross-section σ_c is introduced by

$$R_c = n v_T \sigma_c \quad (79)$$

where $v_T \equiv (3k_B T / m^*)^{1/2}$ represents the average velocity of a free electron at temperature T .

Since each of the delocalized free states in the conduction band has only an infinitesimal amplitude at the site of the acceptor, electron transfer from each free state to the acceptor is always in the non-adiabatic limit. It was shown in Ref. [30] that the average magnitude \bar{J} of the transfer integral between them is of the order of B/\sqrt{N} , where B and N respectively represent the half-width of the conduction band and the total number of unit cells in the crystal. Therefore, a distinction between the normal and the inverted case similar to that given in Section 2.4 does not arise in the present problem [30]. To be more precise, both σ_c and k_e are saturated at a single value independent of B in the adiabatic limit for large B , irrespective of differences in the arrangement of the diabatic potentials similar to those shown in Figure 5.

The adiabaticity of ET in the present problem is determined by taking into account all the infinitesimal interactions between the individual conduction-band states and the localized acceptor state. For simplicity, we will hereafter confine ourselves to the classical regime for $k_B T \gg \hbar\bar{\omega}$, where $\bar{\omega}$, the average angular frequency of phonons contributing to the reaction coordinate Q , written as Eq. 41, is determined by Eq. 58. In this regime, the adiabaticity parameter is given by the following equation [30]:

$$\gamma = 4\sqrt{B}\lambda k_B T / [3\hbar\bar{\omega}(E_t + \lambda)^{3/2}] \quad (80)$$

where λ represents the reorganization energy of the reaction, as before. The parameter γ has a magnitude of the order of $Na^3 n_T \bar{J}^2 / [\hbar\bar{\omega}(\lambda k_B T)^{1/2}]$, with a^3 representing the unit-cell volume, since $(\hbar/a)^2 / m^*$ in $n_T a^3$ has a magnitude of the order of B . Therefore, γ has the same structure as the adiabaticity parameter γ of Eq. 61 for electron transfer between two localized states: The latter is of the order of $J^2 / [\hbar\bar{\omega}(\lambda k_B T)^{1/2}]$, while $Na^3 n_T$ in the former represents the total number of conduction-band states available in the whole crystal with volume Na^3 .

The adiabatic limit in this case corresponds to the situation where an electron is emitted from the localized acceptor state into the conduction band whenever large-amplitude fluctuations of atoms push the acceptor level up to the conduction-band

states. Therefore, k_e should approach the same form as Eq. 57 for ET between two localized states in the adiabatic limit. Accordingly, it is convenient to express k_e as

$$k_e = \kappa(\bar{\omega}/2\pi) \exp[-(\Delta G^* + E_t)/k_B T] \quad (81)$$

with the transmission coefficient κ as in Eq. 66, where $\Delta G^* = (\lambda - E_t)^2/(4\lambda)$ represents the thermal activation energy for the capture of free electrons by the acceptor. It was shown in Ref. [30] that κ is a function of only γ of Eq. 80, approaching

$$\kappa = \begin{cases} (3\pi/2)\gamma & \text{for } \gamma \ll 1 \\ 1 - (5\pi/9\sqrt{3})\gamma^{-2/3} & \text{for } \gamma \gg 1 \end{cases} \quad (82)$$

in the non-adiabatic and the adiabatic limit, respectively. The capture cross-section of the acceptor, σ_c , can be obtained from Eq. 81 for k_e , since they are related by Eqs. 77 and 79.

Usually, B is of the order of several eV, while both λ and E_t are at most several tenths of eV, and $\hbar\bar{\omega}$ is ca. 10 meV, determined by lattice vibrations. Therefore, the adiabaticity parameter γ of Eq. 80 is appreciably larger than unity, and hence the capture process is near the adiabatic limit of $\kappa \approx 1$. This feature was confirmed experimentally [30, 31].

2.5.3 Solvent-Fluctuation-Controlled Regime

A characteristic feature of the adiabatic limit is that the rate constant becomes independent of the transfer integral J or \bar{J} . This occurs because the electron to be transferred adjusts itself so rapidly to the motion of the atoms that the reaction is controlled only by the fluctuations of atoms which give rise to the transition state at $Q = Q_c$. It is important to note that this does not necessarily specify the same adiabatic limit mentioned so far. This behavior is, in fact, also possible in viscous solvents where molecular motions contributing to the outer-sphere reorganization are so slow that their speed controls the whole reaction. This situation is independent of whether the system is at the non-adiabatic or the adiabatic limit, while is characterized by the rate constant becoming only weakly dependent or completely independent of the magnitude of J or \bar{J} . This situation has been called the solvent-fluctuation-controlled (adiabatic) regime. There are, accordingly, two regimes for adiabaticity.

The traditional theory for the rate of chemical reactions is the transition-state theory [21] (abbreviated as TST). In fact, all the rate constants given so far in previous sections were formulated, in general terms, within the framework of the TST. It is tacitly assumed in this theory that fluctuations in the reactant state are so rapid that all the substates comprising the reactant state are always thermally equilibrated in the course of reaction. According to this assumption, the reactant population in the transition state is always maintained in thermal equilibrium with the population in the reactant state since both states are located on the reactant-state adiabatic (or diabatic) potential. Therefore, calculation of the rate constant is greatly simplified

in the TST, since we do not need to worry about how much of the population of the reactants is found in the transition state in the course of reaction. We only need to calculate the transmission coefficient κ in Eqs. 66 and 81, which gives the probability with which these reactants at the transition state proceed towards the product state. The assumption of thermal equilibration in the reactant state is reflected in the density matrix ρ_r of Eq. 21 used for calculation of the rate constant by Eq. 20, or in the Wigner distribution function of Eq. 47 for calculation of the thermally averaged $\langle \cdots \rangle_r$ in Eqs. 64 and 65.

When τ expresses the relaxation time of the molecular-arrangement fluctuations in a solvent, then, in the solvent-fluctuation-controlled regime, τ is so large (e.g., in viscous solvents) that reactions taking place in solute molecules are controlled by τ , with the rate constants decreasing with an increase in τ . In the TST, in contrast, the rate constant does, in principle, not depend on τ , since it has been assumed from the beginning that the substates of the reactant state corresponding to different arrangements of solvent molecules are always thermally equilibrated during reaction. This means that the solvent-fluctuation-controlled regime is located outside the framework of the TST.

Usually, τ is proportional to the viscosity of the solvent, η . In many kinds of solution reactions, the rate constant decreases with an increase in η [32]. These reactions cover not only elementary reactions such as electron-, excitation-, atom-group-transfer reactions, and isomerization reactions, but also composite reactions such as biological ones, including enzymatic reactions. The general formula for rates of solution reactions has not been clarified fully yet, in spite of solution reactions being one of the most central subjects in chemistry.

Outside the framework of the TST, we must determine the distribution of reactants among substates during the course of reaction. They differ in the arrangement of the solvent molecules around the reactive site. Already in 1940, when the TST was still in the process of being established [21], Kramers [33] treated such a regime theoretically. Molecular-arrangement fluctuations in solvents can be regarded as diffusive (i.e., Brownian) motions at least close to room temperature. Kramers modeled chemical reactions as surmounting a potential barrier from the reactant to the product well caused by diffusive motions of reactants along the one-dimensional reaction coordinate, as shown by the zigzag trajectory in Figure 16. In his reaction scheme, not only the surmount over the potential barrier but also the relaxation in the reactant well are simultaneously determined by the diffusive motions of reactants, without a priori assumption of their rapid thermalization in the reactant well. His theory, however, had not attracted much attention for a long time. It can be said that his theory was presented too early [34]. It is a natural order in the development of theories in science that an event (such as a reaction) causing a deviation from thermal equilibrium is first treated as a small perturbation on a thermalized system (as in the TST, but also more generally), as in the linear-response theory for kinetic coefficients [35]. His theory started to gain in popularity only in the 1980s, when dynamic effects in solution reactions, as non-TST behaviors, began to attract the attention of many people [36].

When we treat only diffusive motions in coordinate of reactants after rapid thermalization of their momentum, they can be described by the Smoluchowski equa-

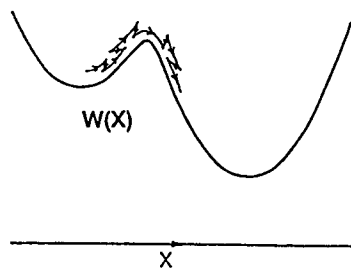


Figure 16. A double-well potential for reaction $W(X)$ along a one-dimensional reaction coordinate X in the Kramers model, and a reactive diffusive trajectory represented by a zigzag line surmounting a reaction barrier from the reactant to the product well.

tion [37]:

$$\frac{\partial}{\partial t} P(X; t) = \frac{1}{\omega_o^2 \tau} \frac{\partial}{\partial X} \left[k_B T \frac{\partial}{\partial X} + \frac{dW(X)}{dX} \right] P(X; t) \quad (83)$$

where $P(X; t)$ represents the population of reactants at reaction coordinate X at time t in the double-well potential $W(X)$ in Figure 16. The curvature around the bottom of the reactant well in $W(X)$ is represented by ω_o^2 ; $W(X)$ can be expanded to

$$W(X) \approx \frac{1}{2} \omega_o^2 X^2 \quad \text{around } X = 0. \quad (84)$$

We can easily check that τ in Eq. 83 gives the relaxation time of diffusive motions of X in the reactant well: The temporal evolution of the average value of X is described by $\bar{X}(t) \equiv \int X P(X; t) dX$. Around the bottom of the reactant well, where Eq. 84 is applicable, Eq. 83 enables us to get the desired equation $d\bar{X}(t)/dt = -\bar{X}(t)/\tau$, by use of $\int X(\partial^2 P/\partial X^2) dX = 0$ and $\int X[\partial(XP)/\partial X] dX = -\bar{X}(t)$, obtained by partial integration.

Since the total number of reactants $\int P(X; t) dX$ is conserved in Eq. 83, its solution is, in equilibrium, described by the thermal equilibrium distribution $\exp[-\beta W(X)]$ in the double-well potential $W(X)$. The distribution relaxes toward this thermal-equilibrium one.

$W(X)$ in the vicinity of the top of its potential barrier, say, at $X = X_b$, is written as

$$W(X) \approx W(X_b) - \frac{1}{2} \omega_b^2 (X - X_b)^2, \quad \text{around } X = X_b \quad (85)$$

with a negative curvature $-\omega_b^2$. In the large- τ region of $\tau \omega_o^2/\omega_b \gg 1$, the forward rate constant given by the Kramers model of Eq. 83 approaches

$$k_{KR} \approx \frac{1}{\tau} \frac{\omega_b}{2\pi\omega_o} \exp\left(-\frac{W(X_b)}{k_B T}\right) \quad (86)$$

The characteristics of $k_{KR} \propto \tau^{-1}$ can easily be understood [38]: When $\tau = \infty$, friction retarding the motion of X becomes infinite in proportion to τ , and X cannot help stopping at a certain position. When τ is not infinite, although very large, X manages to move, but very slowly, as an accumulation of small movements back

and forth induced by collisions with solvent molecules with frequency proportional to τ . In this situation, it takes time proportional to τ for the X value to move over a definite length toward the product well. This is the reason why the reaction time given by Eq. 86 is proportional to τ .

Usually, τ is proportional to the viscosity, η , of solvents. Therefore, the Kramers model predicts that the rate constant becomes proportional to η^{-1} in viscous solvents. Indeed, in solution reactions, including electron transfer reactions, rate constants are known to decrease with an increase in η , as mentioned before. However, the observed dependence is not η^{-1} , but

$$k_{\text{obs}} \propto \eta^{-\alpha} \quad \text{with } 0 < \alpha \leq 1. \quad (87)$$

The reason for this discrepancy is that Kramers' model is inappropriate in describing ET reactions as the surmount over a potential barrier by diffusive motions of reactants, as shown in Figure 16. In ET reactions, the diffusive fluctuations occur as molecular rearrangement motions in a solvent, which give rise to outer-sphere reorganization. The reaction coordinate for ET reactions also contains intrasolute vibrational motions that give rise to inner-sphere reorganization. They are much faster than slow molecular-arrangement fluctuations in viscous solvents, with speeds characterized by vibration periods that are not influenced by the solvent viscosity. In this situation, ET reactions can be regarded as taking place at each arrangement of solvent molecules with the aid of intrasolute vibrational fluctuations. Such a model was proposed by Sumi and Marcus [39].

In this model, rearrangement motions of solvent molecules are described by a one-dimensional coordinate X , with energy described as $V(X)$. At each X value reaction takes place with an intrinsic rate constant $k(X)$ induced by the much faster intrasolute vibrational fluctuations. Then, the probability $P(X; t)$ with which the reaction system is found at X is regarded as being governed not by the diffusion equation of Eq. 83, but by a diffusion-reaction equation:

$$\frac{\partial}{\partial t} P(X; t) = \frac{1}{\omega_o^2 \tau} \frac{\partial}{\partial X} \left[k_B T \frac{\partial}{\partial X} + \frac{dV(X)}{dX} \right] P(X; t) - k(X) P(X; t) \quad (88)$$

Here, the potential $V(X)$ for diffusive fluctuations of X can be a single well potential with curvature ω_o^2 in the vicinity of its minimum of $X = 0$, because the reaction takes place due to the sink (i.e., the second term on the right-hand side). Let us describe the intrasolute vibrational motions, giving rise to the inner-sphere reorganization, by a coordinate q . This model is characterized by two components of reaction coordinate X and q . An example of the potential surface spanned by them is given in Figure 17, where the bottom O' of the product surface is distorted along the abscissa X by the outer-sphere reorganization energy λ_o , and along the ordinate q by the inner-sphere reorganization energy λ_i . The reactant and the product surfaces cross one another along line C, and electron tunneling takes place when the reaction system reaches this line in the course of thermal fluctuations along both coordinates on the reactant surface. Energy is lowest at point S on this line. Therefore, this point gives the location of the transition state. Three points O, S, and O'

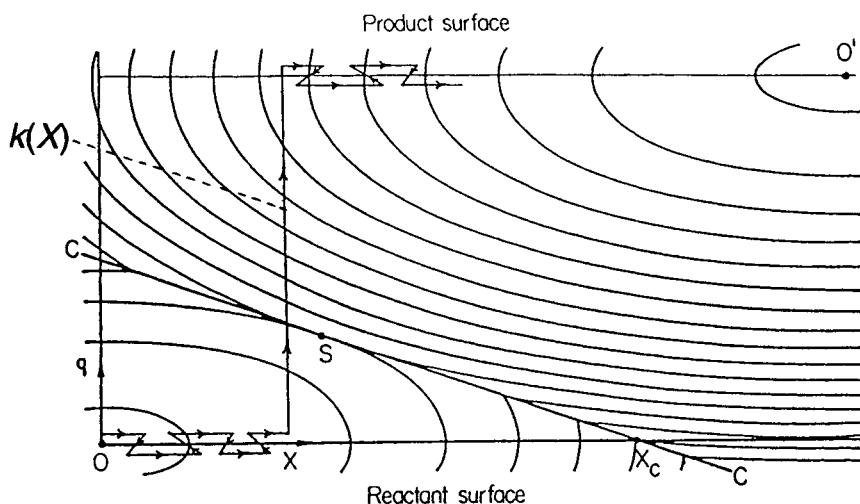


Figure 17. Two-dimensional double-well potential for reaction in the Sumi–Marcus model spanned by slow (diffusive) molecular-arrangement fluctuations in solvents on the abscissa for the coordinate X and fast (ballistic) intrasolute vibrational fluctuations on the ordinate. Also shown is a reactive trajectory surmounting the transition-state barrier on the line C with an X -dependent rate constant $k(X)$.

are on a straight line, since both the reactant and the product surface are quadratic with the same curvature, by assumption (Figure 17). The reaction coordinate Q of Eq. 41 is nothing but a coordinate along this line. In the TST, trajectories on the reactant surface are not important since populations at each point are assumed to be always thermally equilibrated. Under this assumption, it is convenient to discuss the reaction along this reaction-coordinate line since the reaction can be related only to the fraction of the population that reaches the product surface through the transition-state point S .

In the Sumi–Marcus model of Figure 17, trajectories on the reactant surface are also important. Since molecular-arrangement fluctuations in solvents (the abscissa X) are assumed to be much slower than intrasolute-vibrational fluctuations (the ordinate q), a reactive trajectory should be the one shown in Figure 17: The reaction system is first taken to an X value by slow diffusive motions along the abscissa X , as represented by a zigzag line. Subsequently, when the reaction system is taken to line C by rapid vibrational motions on the ordinate q at this X value, electron tunneling takes place with an X -dependent intrinsic rate constant $k(X)$, as represented by a vertical straight line. For TST to be justified in this model, the most probable X value should be around that of the saddle point S .

At X on the abscissa in Figure 17, energy on the reactant surface is given by $\frac{1}{2}\omega_o^2 X^2$, while that on the product surface is given by $\frac{1}{2}\omega_o^2 (X - \sqrt{2\lambda_o}/\omega_o)^2 + \Delta G$. Therefore, the height of the line C from this X value on the abscissa is given by

$$\Delta G(X)^* = (\lambda + \Delta G - \omega_o \sqrt{2\lambda_o} X)^2 / (4\lambda_i) \quad (89)$$

where $\lambda \equiv \lambda_i + \lambda_o$ represents the total reorganization energy. This $\Delta G(X)^*$ gives the thermal activation energy of $k(X)$. Therefore, $k(X)$ can be expressed as

$$k(X) = \kappa \frac{\bar{\omega}}{2\pi} \exp[-\Delta G(X)^*/k_B T] \quad (90)$$

in the form of Eq. 66 in the classical regime, with the use of the transmission coefficient κ determined in Section 2.4.2, and the average angular frequency $\bar{\omega}$ of phonons contributing to the inner-sphere reorganization energy λ_i , determined by Eq. 58. When the reactant and the product surfaces are in the relative arrangement of the normal case, as in Figure 17, $k(X)$ of Eq. 90 is sufficient, as mentioned in Section 2.5.1. When they are in the relative arrangement of the inverted case, however, participation of large-energy-quantum intramolecular vibrations becomes important as pointed out in Section 2.5.1. An extension of the model, Eq. 90, along this line in the inverted case was pursued by Barbara and coworkers [40].

The rate constant derived from Eq. 88 was verified [41] to have the form

$$k = 1/(k_{\text{TST}}^{-1} + k_f^{-1}) \quad (91)$$

where k_{TST} represents the rate constant expected from the TST and is independent of the relaxation time τ of molecular-arrangement fluctuations in solvents, while the k_f term carries the τ dependence of k . Here, k_{TST} is given by the thermal average of $k(X)$ as

$$k_{\text{TST}} = \int k(X) e^{-\beta V(X)} dX / \int e^{-\beta V(X)} dX \quad (92)$$

Although an analytical expression of k_f has not been obtained yet, a systematic method for its calculation has been given [32, 41]. The k_f is proportional to τ^{-1} in its perturbational calculation of the lowest-order in $k(X)$, but it becomes proportional to $\tau^{-\alpha}$, with $0 < \alpha < 1$, when the perturbational calculation diverges [42]. To be more exact, k_f has a dependence as

$$k_f \propto \kappa^{1-\alpha} \tau^{-\alpha}, \quad \text{with } 0 < \alpha \leq 1 \quad (93)$$

where κ represents the strength of $k(X)$ in Eq. 90. When the thermal activation energy $\Delta G(X)^*$ of $k(X)$ is given by Eq. 89, it can be shown [32, 43] that α is given by

$$\alpha = \begin{cases} |1 - \lambda_i/\lambda_o|, & \text{for } 0 \leq \lambda_i/\lambda_o \leq 2 \\ 1, & \text{otherwise} \end{cases} \quad (94)$$

where the discontinuous derivatives of α at $\lambda_i/\lambda_o = 1$ and 2 should be rounded off, because the procedure for obtaining α becomes approximate at these points.

The component k_f decreases with an increase in the solvent viscosity, $\eta \propto \tau$. In low-viscosity solvents for $k_{\text{TST}} \ll k_f$, Eq. 91 reduces to $k \approx k_{\text{TST}}$, supporting TST. In high-viscosity solvents for $k_f \ll k_{\text{TST}}$, it reduces to $k \approx k_f \propto \tau^{-\alpha}$, invalidating TST. In this solvent-fluctuation-controlled regime, therefore, k becomes proportional to $\eta^{-\alpha}$, reproducing the observations of Eq. 87. When $\alpha < 1$, the control of the reaction by solvent fluctuations is only partial, since the rate constant still increases as $\kappa^{1-\alpha}$ with an increase in κ , which represents the strength of reaction in $k(X)$ of Eq. 90. The thermal-activation energy of the slow X motions is given by $\frac{1}{2}\omega_0^2 X^2$, which is appreciably smaller than that of k_{TST} given by the height of the transition state S in Figure 17. The reaction described by $k(X)$ contributes to k_f in proportion to $\kappa^{1-\alpha}$ in Eq. 93, but its thermal activation energy, $\Delta G(X)^*$, is also smaller than that of k_{TST} . Therefore, the thermal activation energy of k is smaller in the solvent-fluctuation-controlled regime ($k \approx k_f$) than in the TST regime ($k \approx k_{\text{TST}}$). This behavior can be detected if the solvent viscosity is kept constant to suppress a change in $\tau^{-1}(\propto \eta^{-1})$ which has a large activation energy in itself.

The η dependence of Eq. 87 has often been observed in isomerization reactions of organic molecules [32]. In such a case, it has been considered [43] that molecular-arrangement fluctuations in solvents give rise to cavities (i.e., free volumes) around a solute molecule, corresponding to slow diffusive motions along the abscissa in Figure 17. When the cavities are large enough, isomerization can take place by twisting motions which correspond to the rapid intrasolute vibrational motions along the ordinate in Figure 17.

The rate-constant formula of Eq. 91 is a general one, covering the whole range from TST to the non-TST regime in solution reactions. It can be applied not only to elementary reactions such as electron-, proton-, atom-group-transfer, and isomerization reactions in solvents, but also to biomolecular reactions such as enzymatic ones accomplished through a series of intermediate products. In fact, it has often been observed [32] that rate constants of biomolecular reactions decrease with an increase in the solvent viscosity, obeying Eq. 87. This means that such reactions are in the non-TST regime. In this case, slow diffusive fluctuations of solvent molecules drive those of the solvated conformation of a protein in which the reaction takes place. Observations of Eq. 87 indicate that biomolecular reactions are controlled by the slow speed of these fluctuations. This situation has often been referred to as *conformational gating* (or *control*). In the non-TST regime, the rate constants become smaller than k_{TST} .

Evolution over a long period has resulted in living organisms adapting beautifully their functions to their living conditions. It is interesting, then, to ask why they have “chosen” the non-TST regime with rate constants smaller than k_{TST} . It seems reasonable enough to answer [32] that they utilize solvent fluctuations (to be more exact, solvent-fluctuation-driven conformational fluctuations in the solvated structure of proteins) to accomplish their functions, positively utilizing the situation of *conformational gating*. Enzymes must execute at least three reaction steps (i.e., complex formation with a substrate, its transformation into the product, and its release). Each step requires a different conformation. To execute all of them by a single molecule, an enzyme must have a large flexible body, which can easily change its conformation diffusively in water each time a reaction step is accomplished.

Appendices

Appendix A: Direct Derivation of Equation 23

A term specified by m and n in the summation on the right-hand side of Eq. 22 describes an electron tunneling from donor to acceptor which is accompanied by the absorption of m phonons at the donor site and the emission of n phonons at the acceptor site. This process results from interaction between the electron and phonons with a coupling constant given by the Huang–Rhys factor s . The average number of thermal phonons, $\bar{n} = 1/(e^{\beta\hbar\bar{\omega}} - 1)$, is given by the Planck distribution for their energy quantum $\hbar\bar{\omega}$; the square of the electronic matrix element J is accompanied by $\exp(-s\bar{n})(s\bar{n})^m/m!$ for the absorption of m phonons and by $\exp[-s(\bar{n}+1)][s(\bar{n}+1)]^n/n!$ for the emission of n phonons [10]. The exponential terms arise from normalization which requires that the total sum of these factors in each category must be unity. Therefore, Eq. 22 should reduce to

$$k = \frac{2\pi}{\hbar} J^2 e^{-s(2\bar{n}+1)} \sum_{m,n} \frac{(s\bar{n})^m [s(\bar{n}+1)]^n}{m!n!} \delta[-\Delta G - (n-m)\hbar\bar{\omega}] \quad (\text{A1})$$

If $\Delta G \leq 0$ in Eq. (A1), $\ell \equiv n - m$ is positive, and we get F_ℓ in Eq. 23 by

$$\begin{aligned} F_\ell &= e^{-s(2\bar{n}+1)} \sum_{m=0}^{\infty} s^{(2m+\ell)} \bar{n}^m (\bar{n}+1)^{m+\ell} / [m!(m+\ell)!] \\ &= e^{-s(2\bar{n}+1)} \left(\frac{\bar{n}+1}{\bar{n}} \right)^{\ell/2} \sum_{m=0}^{\infty} \frac{(s\sqrt{\bar{n}(\bar{n}+1)})^{2m+\ell}}{m!(m+\ell)!}. \end{aligned} \quad (\text{A2})$$

This expression is equivalent to that of Eq. 24, since the summation in Eq. (A2) is equal to $I_\ell(2s\sqrt{\bar{n}(\bar{n}+1)})$ for $\ell \geq 0$, and $2\bar{n}+1$, $(\bar{n}+1)/\bar{n}$, and $\bar{n}(\bar{n}+1)$ can be expressed by $\coth(\beta\hbar\bar{\omega}/2)$, $\exp(\beta\hbar\bar{\omega})$, and $[2\sinh(\beta\hbar\bar{\omega}/2)]^{-2}$, respectively, in terms of Section 2.2.1.

Equation 24 for F_ℓ in Eq. 23 was derived above under the condition of $\Delta G \leq 0$. When $\Delta G > 0$, the backward rate constant, k_{BW} , can be obtained, since the reverse of the forward reaction for this free energy of reaction satisfies this condition. The value k_{FW} can be determined from k_{BW} by the relation of microscopic equilibrium, $k_{\text{FW}}/k_{\text{BW}} = \exp(-\beta|\Delta G|)$ in Eq. 15. The rate constant k given by Eq. 23 satisfies this relation without any modification, since $I_{-\ell}(x) = I_\ell(x)$. Therefore, Eq. 23 turns out to be applicable irrespective of the sign of ΔG .

Appendix B: Wigner Distribution Function

The rate-constant formula (Eq. 20) in the non-adiabatic limit is applicable irrespective of whether the phonon Hamiltonians H_r and H_p for the reactant and the

product state, respectively, consist of a single mode or of multimodes. Let us take the multimode model, where H_r and H_p are given by Eqs. 37 and 38, respectively.

Delta functions appearing on the right-hand side of Eq. 20 can be converted into exponential functions, as $\delta(E - H_p) = (2\pi\hbar)^{-1} \int \exp[-i(E - H_p)t/\hbar] dt$ and $\delta(E - H_r) = (2\pi\hbar)^{-1} \int \exp[i(E - H_r)t'/\hbar] dt'$. Substituting them into Eq. 20, we can integrate over E , to obtain $2\pi\hbar\delta(t - t')$. Consequently, we have converted the energy-integrated expression of Eq. 20 for the rate constant k into the time-integrated one

$$k = \frac{J^2}{\hbar^2 \text{Tr}[U_r(\beta)]} \int \text{Tr} \left[U_p \left(-i \frac{t}{\hbar} \right) U_r \left(\beta + i \frac{t}{\hbar} \right) \right] dt \quad (\text{A3})$$

with

$$U_b(x) = \exp(-xH_b) \quad \text{for } b = r \quad \text{or} \quad p \quad (\text{A4})$$

Here, x can be a complex variable under the condition that its real part is non-negative.

Quantum mechanics has various representations [6], for example, by eigenfunctions of observables in Schrödinger's picture, or by matrices in Heisenberg's picture. They can be treated equivalently in Dirac's picture by state vectors. The coordinate of a particle is an observable which can take continuous values. Eigenfunctions in Schrödinger's picture are the coordinate representation of state vectors in Dirac's picture. Equations 37 and 38 are the coordinate representation of phonon Hamiltonians H_r and H_p , where p_j is represented by $-i\partial/\partial q_j$ under the commutation relation $[q_j, p_{j'}] = i\delta_{j,j'}$. Both H_r and H_p are diagonal in this representation. Let us write eigenfunctions of H_r as $\Psi_M(\mathbf{q})$ with eigenenergy E_M for $M = 1, 2, 3, \dots$, where \mathbf{q} represents a multidimensional vector whose j th component q_j represents the coordinate of the j th phonon mode for $j = 1, 2, 3, \dots$. $\Psi_M(\mathbf{q})$ and E_M are composed of the $j(M)$ -th eigenfunction $\psi_{j(M)}(q_j)$ with eigenenergy $\varepsilon_{j(M)}$ of the j th mode, by

$$\Psi_M(\mathbf{q}) = \prod_j \psi_{j(M)}(q_j) \quad \text{and} \quad E_M = \sum_j \varepsilon_{j(M)} \quad (\text{A5})$$

The coordinate representation of $U_r(x)$ of Eq. A4 is expressed by $\Psi_M(\mathbf{q})$ and E_M as

$$\langle \mathbf{q}' | U_r(x) | \mathbf{q} \rangle = \sum_M \Psi_M(\mathbf{q}') \exp(-xE_M) \Psi_M(\mathbf{q})^* \quad (\text{A6})$$

The M summation on the right-hand side of Eq. A6 can be performed [44], giving

$$\langle \mathbf{q}' | U_r(x) | \mathbf{q} \rangle = \prod_j \frac{1}{\sqrt{2\pi \sinh(x\hbar\omega_j)}} \exp \left(-\frac{(q_j^2 + q_j'^2) \cosh(x\hbar\omega_j) - 2q_j q_j'}{2 \sinh(x\hbar\omega_j)} \right), \quad (\text{A6}')$$

with $\hbar\omega_j$ in Eq. 37. The validity of Eq. A6' can be checked by ascertaining that it satisfies $(\partial/\partial x + H_r)(\mathbf{q}'|U_r(x)|\mathbf{q}) = 0$ under the initial condition that $(\mathbf{q}'|U_r(x)|\mathbf{q})$ approaches $\prod_j \delta(q_j - q'_j)$ as $x \rightarrow +0$. The expression of $(\mathbf{q}'|U_p(x)|\mathbf{q})$ can be obtained if $q_j - \sqrt{2s_j}$ and $q'_j - \sqrt{2s_j}$ are substituted for q_j and q'_j on the right-hand side of Eq. A6' and the whole expression is simultaneously multiplied by $\exp(-x\Delta G)$. When $\int d\mathbf{q}$ represents the multidimensional integration with respect to q_j for $j = 1, 2, 3, \dots$, we can express $\text{Tr}[U_r(\beta)]$ and the t -integration part on the right-hand side of Eq. A3 by the \mathbf{q} integration, respectively, as

$$\text{Tr}[U_r(\beta)] = \int (\mathbf{q}|U_r(\beta)|\mathbf{q}) d\mathbf{q} = \prod_j \frac{1}{2 \sinh(\beta \hbar \omega_j / 2)} \quad (\text{A7})$$

and

$$\int dt \int d\mathbf{q} \int d\mathbf{q}' \left(\mathbf{q} \left| U_p \left(-i \frac{t}{\hbar} \right) \right| \mathbf{q}' \right) \left(\mathbf{q}' \left| U_r \left(\beta + i \frac{t}{\hbar} \right) \right| \mathbf{q} \right) \quad (\text{A8})$$

Substituting $(\mathbf{q}'|U_r(\beta + it/\hbar)|\mathbf{q})$ and $(\mathbf{q}|U_p(-it/\hbar)|\mathbf{q}')$ into Eq. A8, we can perform Gaussian integrations over \mathbf{q} and \mathbf{q}' , and see that Eq. A3 for the rate constant k can be cast into Eq. 31, where only the t integration remains to be executed for the calculation of k .

Wigner [22] introduced a new vector \mathbf{p} (composed of p_1, p_2, p_3, \dots) besides \mathbf{q} , so that

$$U_r(\mathbf{p}, \mathbf{q}) \equiv \int \left(\mathbf{q} + \frac{1}{2} \mathbf{b} \left| U_r(\beta) \right| \mathbf{q} - \frac{1}{2} \mathbf{b} \right) \exp(-i\mathbf{p} \cdot \mathbf{b}) d\mathbf{b} \quad (\text{A9})$$

This \mathbf{p} corresponds to the momentum conjugate to \mathbf{q} when \mathbf{q} corresponds to a coordinate vector of phonons. This can be checked by the mediation of an eigenfunction $\exp(i\mathbf{p} \cdot \mathbf{q})$ of the momentum operator $-i\partial/\partial \mathbf{q}$ for an eigenvalue \mathbf{p} . It has an amplitude projected onto the state of $\Psi_M(\mathbf{q})$, equal to $\Phi_M(\mathbf{p}) = \int \exp(-i\mathbf{p} \cdot \mathbf{q}) \Psi_M(\mathbf{q}) d\mathbf{q}$. The \mathbf{q} integration of $U_r(\mathbf{p}, \mathbf{q})$ of Eq. A9 can be shown to reduce to the thermal average of $|\Phi_M(\mathbf{p})|^2$, which gives the probability with which phonons of the state $\Psi_M(\mathbf{q})$ have a momentum \mathbf{p} :

$$\int U_r(\mathbf{p}, \mathbf{q}) d\mathbf{q} = \sum_M |\Phi_M(\mathbf{p})|^2 \exp(-\beta E_M) \quad (\text{A10})$$

The right-hand side represents the distribution function of the momentum vector \mathbf{p} . The \mathbf{p} integration of $U_r(\mathbf{p}, \mathbf{q})$ reduces to the thermal average of $|\Psi_M(\mathbf{q})|^2$, which gives the probability with which phonons of the state $\Psi_M(\mathbf{q})$ are found at coordinate \mathbf{q} ,

$$\int U_r(\mathbf{p}, \mathbf{q}) d\mathbf{p} \propto (\mathbf{q}|U_r(\beta)|\mathbf{q}) = \sum_M |\Psi_M(\mathbf{q})|^2 \exp(-\beta E_M) \quad (\text{A11})$$

The right-hand side represents the distribution function of the coordinate vector \mathbf{q} .

Equations A10 and A11 allow us to regard $U_r(\mathbf{p}, \mathbf{q})$ of Eq. A9 as the probability with which phonons can be found at coordinate vector \mathbf{q} with momentum vector \mathbf{p} (although it is not normalized yet). Since the coordinate and its conjugate momentum cannot be determined simultaneously at definite values in quantum mechanics [6], this probability must be approximate. In fact, it happens to have (nonphysical) negative values in some systems [22]. In phonon systems, fortunately, it is always positive, and it can be used as a semiclassical simultaneous distribution function for the coordinate \mathbf{q} and the momentum \mathbf{p} . After normalization, the Wigner distribution function thus obtained is given by

$$\rho_r(\mathbf{p}, \mathbf{q}) \equiv U_r(\mathbf{p}, \mathbf{q}) / \iint U_r(\mathbf{p}', \mathbf{q}') d\mathbf{q}' d\mathbf{p}' \quad (\text{A12})$$

Inserting Eq. A6' into Eq. A9 and performing Gaussian integrations over \mathbf{b} , we obtain an explicit expression of $U_r(\mathbf{p}, \mathbf{q})$, and of $\rho_r(\mathbf{p}, \mathbf{q})$ of Eq. A12. The $\rho_r(\mathbf{p}, \mathbf{q})$ thus obtained turns out to be given by Eq. 47, which is normalized as $\iint \rho_r(\mathbf{p}, \mathbf{q}) d\mathbf{q} d\mathbf{p} = 1$.

References

1. For reviews, see (a) U. M. Gösele, *Prog. React. Kinet.* **1984**, 13, 63; (b) S. A. Rice, *Diffusion-Limited Reactions*, **1985**, Comprehensive Chemical Kinetics, Vol. 25, Elsevier, Amsterdam.
2. M. Born and R. Oppenheimer, *Ann. Phys. (Leipzig)* **1927**, 84, 457.
3. (a) P. A. Lyle, S. V. Kolaczowski and G. J. Small, *J. Phys. Chem.* **1993**, 97, 6924; (b) J. S. Ahn, Y. Kanematsu, M. Enomoto and T. Kushida, *Chem. Phys. Lett.* **1995**, 215, 336.
4. For example, L. G. Bellamy, *The Infra-red Spectra of Complex Molecules*, 2nd ed., Methuen & Co., London, **1958**.
5. (a) K. Huang, *Scientia Sinica*, **1981**, 24, 27; E. Gutsche, *Phys. Status Solidi B* **1982**, 109, 583; (b) K. Peuker, R. Enderline, A. Schenk and E. Gutsche, *Phys. Status Solidi B* **1982**, 109, 599; (c) M. G. Burt, *J. Phys. C* **1983**, 16, 4137; (d) V. Denner and M. Wagner, *J. Phys. C* **1984**, 17, 153; (e) R. Pässler, *Czech. J. Phys. B* **1989**, 39, 155.
6. For example, A. Messiah, *Mécanique Quantique*, Dunod, Paris, **1959**.
7. R. A. Marcus, *J. Chem. Phys.* **1956**, 24, 966 and 979.
8. K. Huang and A. Rhys, *Proc. R. Soc. A* **1950**, 204, 406.
9. M. Abramowitz and I. A. Stegun, *Handbook of Mathematical Functions*, Dover Publications, New York, **1965**.
10. (a) D. Curie, in *Optical Properties of Ions in Solids* (Ed.: B. Di Bartolo), Plenum, New York, **1975**, p. 71; (b) B. Di Bartolo, in *Radiationless Processes* (Ed.: B. Di Bartolo), Plenum, New York, **1980**, p. 39.
11. (a) J. Yamashita and T. Kurosawa, *J. Phys. Chem. Solids* **1958**, 5, 34; (b) T. Holstein, *Ann. Phys. (New York)* **1959**, 8, 343.
12. (a) A. A. Maradudin, in *Solid State Phys.*, Vol. 18 (Eds.: F. Seitz, D. Turnbull), Academic, New York, **1966**, p. 392; (b) Y. Toyozawa, in *Dynamical Processes in Solid State Optics* (Eds.: R. Kubo, H. Kamimura), Syokabo, Tokyo, and Benjamin, New York, **1967**, p. 90.
13. D. De Vault and B. Chance, *Biophys. J.* **1966**, 6, 825; *Nature* **1967**, 215, 642.
14. J. Jortner, *J. Chem. Phys.* **1976**, 64, 4860.
15. L. A. Riseberg, in *Radiationless Processes* (Ed.: B. Di Bartolo), Plenum, New York, **1980**, p. 369.
16. (a) R. Kubo, *Phys. Rev.* **1952**, 86, 929; (b) M. Lax, *J. Chem. Phys.* **1952**, 20, 1752.
17. R. A. Marcus, *Discuss. Faraday Soc.* **1960**, 29, 21.

18. J. R. Miller, J. V. Beitz and R. K. Huddleston, *J. Am. Chem. Soc.* **1984**, *106*, 5057.
19. G. Herzberg, *Molecular Spectra*, Prentice-Hall Inc., New York, **1939**.
20. R. Kubo and Y. Toyozawa, *Prog. Theor. Phys.* **1955**, *13*, 160.
21. S. Glasstone, K. J. Laidler and H. Eyring, *The Theory of Rate Processes*, McGraw Hill, New York, **1941**.
22. (a) E. Wigner, *Phys. Rev.* **1932**, *40*, 749; see also, (b) R. P. Feynman, *Statistical Mechanics*, Benjamin, Reading, **1972**.
23. (a) S. A. Rice, *Phys. Rev.* **1958**, *112*, 804; see also (b) M. D. Feit, *Phys. Rev.* **1971**, *B3*, 1223.
24. H. Sumi, *J. Phys. Soc. Jpn.* **1980**, *49*, 1701.
25. (a) L. D. Landau, *Phys. Z. Sowjetunion* **1932**, *1*, 88 and 2, 46 (see also, L. D. Landau and E. M. Lifshitz, *Quantum Mechanics*, Pergamon, Oxford, **1958**); (b) C. Zener, *Proc. R. Soc.* **1932**, *A137*, 696 and **1933**, *A140*, 660.
26. S. G. Christov, *Collision Theory and Statistical Theory of Chemical Reactions*, Springer, Berlin, **1980**.
27. (a) H. Taube, H. Myers and R. L. Rich, *J. Am. Chem. Soc.* **1953**, *75*, 4118; see also, (b) H. Taube, *Electron Transfer Reactions in Solution*, Academic, New York, **1971**.
28. As a review, G. F. Neumark and K. Kosai, in *Semiconductors and Semimetals* (Eds.: R. K. Willardson and A. C. Beer), Academic, New York, **1983**, Vol. 19, p. 1.
29. Y. Toyozawa, *Physica*, **1980**, *116 B&C*, 7.
30. H. Sumi, *Phys. Rev.* **1983**, *27*, 2374.
31. M. Ogura, M. Mizuta and H. Kukimoto, *Jpn. J. Appl. Phys.* **1984**, *23*, 44.
32. As a review, H. Sumi, in *Electron Transfer: From Isolated Molecules to Biomolecules, Part Two* (Ed.: J. Jortner and M. Bixon), Wiley, New York, **1999**, (*Adv. Chem. Phys.* 107) p. 601.
33. H. A. Kramers, *Physica* (Leipzig) **1940**, *7*, 284.
34. M. Dresden, *Phys. Today* **1988**, Sept. p. 28.
35. R. Kubo, *J. Phys. Soc. Jpn.* **1957**, *12*, 570.
36. G. R. Fleming and P. Hänggi, *Activated Barrier Crossing: Applications in Physics, Chemistry and Biology*, World Scientific, Singapore, **1995**.
37. For example, H. Risken, *The Fokker-Planck equations*, Springer, Berlin, **1984**.
38. See also, H. Frauenfelder and P. G. Wolynes, *Science* **1985**, *229*, 337.
39. (a) H. Sumi and R. A. Marcus, *J. Chem. Phys.* **1986**, *84*, 4894; (b) W. Nadler and R. A. Marcus, *J. Chem. Phys.* **1987**, *86*, 3906.
40. (a) G. C. Walker, E. Akesson, A. E. Johnson, N. E. Levinger and P. F. Barbara, *J. Phys. Chem.* **1992**, *96*, 3728; (b) A. E. Johnson, N. E. Levinger, W. Jarzeba, R. E. Schlieff, D. A. V. Klinier and P. F. Barbara, *Chem. Phys.* **1993**, *176*, 555; (c) K. Tominaga, D. A. V. Klinier, A. E. Johnson, N. E. Levinger and P. F. Barbara, *J. Chem. Phys.* **1993**, *98*, 1228.
41. H. Sumi, *J. Phys. Chem.* **1991**, *95*, 3334.
42. H. Sumi, *Chem. Phys.* **1996**, *212*, 9.
43. H. Sumi, *J. Mol. Liq.* **2000**, in press.
44. K. Husimi, *Proc. Phys.-Math. Soc. Jpn.* **1940**, *22*, 406.

3 Single- and Multi-Electron Transfer Processes

Spiros S. Skourtis and David N. Beratan

3.1 Introduction

Many of the models for electron-transfer (ET) reactions discussed in this work assume the following: 1) just one electron is transferred, 2) the transfer occurs from donor to acceptor in a single step, and 3) the bridge is “rigid” during the process. Recent experimental and theoretical advances indicate that these assumptions are insufficient in many circumstances. Indeed, multi-electron, multistate, and dynamic bridge effects enrich the subject substantially. In this chapter we shall examine the influence of these effects on chemical and biological ET reactions.

We begin with a summary of the standard single-electron rigid-bridge model for electron transport [1, 2], and then describe effects that arise from bridge dynamics. We next examine issues in multistep multi-center electron transfer. The closely related problem of two-electron transfer is then discussed. Multi-center and multi-electron processes are of great relevance for ET in DNA, proteins, and catalytic reactions.

3.2 Single-Electron Transfer Reactions

The non-adiabatic ET rate is given by [1]

$$k_{\text{ET}} = \frac{2\pi}{\hbar} |T_{\text{DA}}|^2 (\text{FC}) \quad (1)$$

Here, T_{DA} is the tunneling matrix element between the donor (D) and acceptor (A) wave functions and (FC) is the Franck–Condon-weighted density of states. This is a description appropriate for an effective two-level system [3, 4, 5] with weak coupling

between donor- and acceptor-localized states. In the high-temperature regime, the continuum-solvent Gaussian model of Marcus predicts that the Franck–Condon factor is of the form

$$(\text{FC}) = \frac{1}{\sqrt{4\pi\lambda k_B T}} \exp[-(\Delta G^\circ + \lambda)^2 / 4\lambda k_B T] \quad (2)$$

where ΔG° is the standard free energy of the reaction, and λ is the solvent-reorganization energy (the sum of inner- and outer-sphere components), k_B is the Boltzmann factor, and T is the temperature. The tunneling matrix element, T_{DA} , reflects the electronic structure of the donor, acceptor, and bridging groups [6]. The two-level reduction of the ET problem results in the coupling [7, 8]

$$T_{\text{DA}} = \sum_{ij} (\mathbf{V} - E_{\text{tun}} \mathbf{S})_{\text{Di}} G_{ij}(E_{\text{tun}}) (\mathbf{V} - E_{\text{tun}} \mathbf{S})_{\text{jA}} \quad (3)$$

where \mathbf{V} is the electronic coupling matrix between the D(A) wavefunctions and bridge localized orbitals $i(j)$, \mathbf{S} is the overlap matrix, and E_{tun} is the tunneling energy of the electron. $G_{ij}(E_{\text{tun}})$ is the matrix element of the bridge Green's function between bridge orbitals i and j [8].

$$G_{ij}(E_{\text{tun}}) = [(E_{\text{tun}} \mathbf{S} - \mathbf{H})^{-1}]_{ij} \quad (4)$$

where \mathbf{H} is the Hamiltonian of the bridge. Here, the bridge is defined as the medium between D and A. T_{DA} grows as the energetics of the D and A species (E_{tun}) approach the bridge states. The rate formulation assumes that E_{tun} does not come close enough to the bridge state energies to destroy the validity of the two-level approximation [4, 5].

Numerical strategies for computing both the electronic and nuclear components of the ET rate are now rather advanced (see the chapter by Newton). For example, in both proteins and small molecules, finite-difference Poisson–Boltzmann methods are widely used for computing the outer-sphere component of the solvent reorganization energy λ_o [9, 10, 11, 12]:

$$\lambda_o = \left(\frac{1}{2}\right) \sum_i \Delta q_i^{\text{DA}} (\phi_i^{\epsilon_0} - \phi_i^{\epsilon_\infty}) \quad (5)$$

where \sum_i sums over points on a three-dimensional grid, Δq_i^{DA} is the change in electron density at grid point i when the electron is transferred, ϕ are the potentials at the grid points with the charge distribution given by Δq_i^{DA} , and the solvent dielectric is fixed at the static (ϵ_0) or optical values (ϵ_∞), respectively [1, 9]. These numerical calculations of λ_o reduce to the Marcus equation [1, 13] when a two-sphere description of the donor and acceptor is used. Methodologies for computing the electronic interaction rely upon direct applications of Eq. 3, or upon varying the

structure of donor and acceptor and searching for the “minimum energy splitting” (associated with $2T_{\text{DA}}$) between the initial- and the charge-transfer states. [8, 14].

In protein systems, where direct computation of T_{DA} proves challenging because of system size and structure, semi-empirical [15, 16, 17, 18, 19, 20], “divide-and-conquer” [21], and “pruned-protein” [22, 23, 24] approaches are frequently employed. The simplest empirical method is pathway analysis, which simply distinguishes the much more rapid decay of tunneling propagation through space compared to the decay through bond. For a given protein, empirical decay factors for tunneling propagation are assigned to all interatomic interactions on the basis of atom type and separation distances as established from X-ray crystallography. As such, the pathway strategy approximation is:

$$T_{\text{DA}} = A \times \text{Max} \left\{ \prod_i \varepsilon_i^{\text{C}} \prod_j \varepsilon_j^{\text{H}} \prod_k \varepsilon_k^{\text{S}} \right\} \quad (6)$$

where $\text{Max}\{\}$ represents the sequence of decay factors (between 0 and 1) associated with the strongest coupling pathway from D to A (i.e., resulting in the largest possible product of these factors). For a given protein structure, values of ε are assigned according to a simple recipe, depending on whether the contacts are covalent, hydrogen-bonded, or through-space [25]. The prefactor A depends on the donor and acceptor structure, and is approximately 0.1 eV for some proteins. T_{DA} is often compared for families of proteins with similar prefactors [26].

This simple view predicts that protein connectivity in a relatively compact region between donor and acceptor determines the strength of the coupling. Extensive analysis beyond the pathways level has supported the generic predictions of the model [21]: secondary structure influences the average decay of the coupling with distance; decay of rate with distance is not purely exponential but rather depends upon the tunneling medium; and hydrogen-bond connections [25, 27, 28] provide critical “short cuts” for tunneling propagation [29].

The pathway methodology has been used extensively to understand substantial rate differences that arise in the near activationless regime at equivalent distances [30, 31] (see chapter by Gray and Winkler). The connectivity of the medium in the zone between donor and acceptor can cause order-of-magnitude changes in rate. Moreover, secondary structure is found to cause differences in average decay exponents [31], as predicted by pathway analysis [25]. Creative pathway “engineering” was recently demonstrated by the building, binding, and characterizing of a cytochrome P-450 binding substrate tethered to an electron-transfer active species by a long methylene chain. Upon assembly, an approximately 20-Å covalent pathway was created between the surface ET active species and the heme.

Dutton and coworkers (see Dutton chapter) advocated analyzing T_{DA} in the context of the density of atoms in a zone between donor and acceptor. This is equivalent to the pathway analysis, because the density-dependent factor proposed by Dutton and coworkers [33] is:

$$T_{\text{DA}} \propto \exp\{-(R - 3.6)[f_{\text{atom}}\beta_{\text{atom}} + (1 - f_{\text{atom}})\beta_{\text{vac}}]\}. \quad (7)$$

Here f_{atom} is the fraction of the intervening medium filled by atoms and the two distinct β values characterize the through-bond and through-space propagation. This equation is easily rewritten in pathway language as [34]

$$T_{\text{DA}} \propto \varepsilon_{\text{c}}^{2N_{\text{c}}} \varepsilon_{\text{S}}^{2N_{\text{S}}} \quad (8)$$

where

$$\varepsilon_{\text{c}}^{2N_{\text{c}}} = \exp\{-f_{\text{atom}}\beta_{\text{atom}}(R - 3.6)\} \quad (9a)$$

and

$$\varepsilon_{\text{S}}^{2N_{\text{S}}} = \exp\{-(1 - f_{\text{atom}})\beta_{\text{vac}}(R - 3.6)\} \quad (9b)$$

As such, the pathway and density methods are the same, except for modest differences between the parameter sets employed. Both methods derive their protein-medium dependence from the decay (β) parameters for through-bond and through-space propagation. They both neglect to include explicitly multiple-pathway and quantum-interference effects, except through adopting parameters that might take these effects into account in an average sense. Analysis of T_{DA} in a multiple-pathway framework, including the effects of interfering paths, is now routine [21, 24, 35, 36]. For developing structure–function relationships from these more complex multi-orbital approaches, information-reduction schemes are needed. Examples of such schemes include importance-value [37] and electron-transfer contact-map analysis [38, 39]. A comprehensive review of structure–function analysis in electron transfer is given in Ref. [8].

Fluctuating bridge effects on electron transfer

Important to the structural interpretation of electron-tunneling mediation in proteins is an understanding of how a protein’s internal motion influences the tunneling from donor to acceptor. The structure–function analyses of tunneling described above are based on a “frozen” X-ray crystallographic (or energy-minimized) structure of the protein. A Hamiltonian is derived from a static protein structure—describing the atomic orbital energies and the interorbital interactions that give rise to through-bond and through-space couplings—and either a pathway or a higher-level analysis is carried out based on this Hamiltonian. However, in the case of long-distance electron transfer, the intervening protein bridge between donor and acceptor has enough time to undergo internal motions during the electron-tunneling reaction. The atomic-orbital energies and interorbital interactions thus change with time, limiting the validity of any frozen-structure description of tunneling.

Mikkelsen, Ulstrup, and Zakaraya [40], suggested a time-independent variational formulation for the treatment of the fluctuating-bridge problem. The starting point of their approach is the construction of free-energy functionals for the electron-transfer system when the electron occupies D or A. Each free-energy functional incorporates the electron’s kinetic energy, its potential energy of interaction with the

effective nuclear charges of the D and A atoms, and its interaction with the solvent inertial polarization. Each functional (F) is expressed in terms of the transition-state (nonequilibrium) inertial solvent polarization (\bar{P}_{in}^*), and the electron's wave function $\Psi_{\text{D}}(r)$ or $\Psi_{\text{A}}(r)$, that is, $F_{\text{D}} = F_{\text{D}}[\Psi_{\text{D}}, \bar{P}_{\text{in}}^*]$, $F_{\text{A}} = F_{\text{A}}[\Psi_{\text{A}}, \bar{P}_{\text{in}}^*]$. By relating \bar{P}_{in}^* in $F_{\text{D}}(F_{\text{A}})$ to the free energy of the reaction, ΔG° , the temperature, and the initial and final (equilibrium) inertial polarizations of the ET reaction, the authors obtained free-energy functionals that are functions of these variables and of $\Psi_{\text{D}}(r)$ and $\Psi_{\text{A}}(r)$. Minimization of these functionals with respect to $\Psi_{\text{D}}(r)$ and $\Psi_{\text{A}}(r)$ gives $\Psi_{\text{D}}(r)$ and $\Psi_{\text{A}}(r)$ "wave functions" whose tails depend on the above variables. Therefore, the corresponding matrix element between $\Psi_{\text{D}}(r)$ and $\Psi_{\text{A}}(r)$, T_{DA} , depends on the temperature and the free energy of the reaction. Although the approach is not explicitly time-dependent, it does allow for the interaction of the D and A "wave-function" tails with the solvent polarization at the transition state. The "wave functions" and T_{DA} obtained from this method are statistical (ensemble-averaged) quantities. The authors suggested that experiments on Ru-modified proteins that measure the free-energy dependence of the ET rate at different distances could illuminate the free-energy dependence of the rate that arises from T_{DA} "polarization." A more complete self-consistent approach based on this idea was later provided by Kuznetsov, Vigdorovich, and Ulstrup [41].

A different approach to this problem avoids the use of a statistical variational treatment. Rather, a two-state D–A Hamiltonian is assumed with an off-diagonal element T_{DA} that depends on some nuclear (bridge) coordinates and is thus time-dependent as these positions change. The two-state Hamiltonian is then used to compute a thermally averaged rate in the golden-rule non-adiabatic limit. An early example of this method is provided by Beratan, da Gama, Onuchic, and Hopfield [42, 43]. The authors assume that bridge vibrations y_i are coupled to T_{DA} through exponential decay factors of the form $\exp[-\beta(y_i - y_i^0)]$. This exponential dependence models the decay of T_{DA} across a through-bond or through-space contact (of length y_i) that oscillates harmonically around an equilibrium separation y_i^0 . The authors demonstrate that, in the golden-rule rate expression, this dependence introduces thermally averaged prefactors similar to the thermally averaged Franck–Condon factors arising from coupling of local modes to the electron's location at D or A. The averaging involves the probability of having different numbers of vibrational quanta in the bridge mode prior to electron transfer. As such, bridge fluctuations give rise to additional temperature-dependence of the rate that is solely due to the influence of bridge fluctuations on T_{DA} .

Alternative models for medium fluctuations explicitly incorporate the time-dependence of T_{DA} . Tang [44] analyzed the non-adiabatic rate behavior for a time-dependent T_{DA} with an exponentially decaying correlation function $\langle T_{\text{DA}}(t)T_{\text{DA}}(t + \tau) \rangle = T_{\text{DA}}^2 \exp(-\tau/\tau_c)$, and a vanishing average $\langle T_{\text{DA}} \rangle = 0$. For high temperatures and a long correlation time, τ_c , he was able to recover the static Marcus-rate expression. For intermediate τ_c , he found that T_{DA} fluctuations reduce the electron-transfer rate for small activation energies and increase the rate for systems with large activation energies. In the limit of very short τ_c , the rate becomes independent of the free-energy gap and reorganization energy, and is controlled solely by the T_{DA} fluctuations. These effects are most significant for systems with

large activation energies and are relevant to situations where there is, on average, zero or very weak coupling between donor and acceptor.

In an attempt to describe regimes with nonvanishing average T_{DA} values, Goychuk, Petrov, and May [45] adopted a different two-state model with $T_{\text{DA}}(t) = \langle T_{\text{DA}} \rangle + [(V_1 - V_2)/2]\alpha(t)$, where $\langle T_{\text{DA}} \rangle = (V_1 + V_2)/2 \neq 0$, $\alpha(t) = \pm 1$, $\langle \alpha(t) \rangle = 0$ and $\langle \alpha(t)\alpha(t+\tau) \rangle = \exp(-\tau/\tau_c)$. This model describes gated time dependence, where T_{DA} fluctuates stochastically between two different values (V_1 and V_2). The authors observed that the rate changes from adiabatic ($k \propto \tau_c^{-1}$) to non-adiabatic as τ_c decreases. For intermediate and short τ_c , the rate resembles a Marcus-like expression. For intermediate τ_c , the electronic coupling enters the rate as $\langle T_{\text{DA}}^2 \rangle$, whereas for short τ_c it appears as $\langle T_{\text{DA}} \rangle^2$. This analysis implies that interpretation of the ET rate should be based on such time-averages of T_{DA} .

Daizadeh, Medvedev, and Stuchebrukhov [46, 47] arrived at an expression for the non-adiabatic rate that does not assume a specific functional form for the time-dependence of T_{DA} . The overall ET rate for a reaction with free energy gap ΔG° and reorganization energy λ is expressed in their analysis as a weighted sum of Marcus-like rate functions (Eqs. 1 and 2). Each rate-expression element in the sum describes an inelastic tunneling process during which the electron exchanges energy ε_n with bridge vibrations. The weight of the process is the probability of energy exchange $P(\varepsilon_n)$, and the sum is over all possible ε_n (as in [43]). In each rate-expression element, T_{DA}^2 is replaced by $\langle T_{\text{DA}}^2 \rangle$ and the standard free energy of the reaction ΔG° is replaced by an “effective” free energy $\Delta G^\circ + \varepsilon_n$. The contribution of no energy exchange ($\varepsilon_n = 0$) corresponds to elastic tunneling and is described by the standard nonadiabatic rate expression (ΔG°). If the electron absorbs energy from the bridge vibrations as it tunnels ($\varepsilon_n < 0$), it feels a reduced “effective” free energy in comparison to the case of no energy exchange (i.e., $\Delta G^\circ + \varepsilon_n < \Delta G^\circ$). If it loses energy ($\varepsilon_n > 0$), it feels an increased “effective” free energy ($\Delta G^\circ + \varepsilon_n > \Delta G^\circ$). The authors offer an expression for the probability of energy exchange $P(\varepsilon_n)$ in terms of the bridge eigenstates and their Boltzmann populations. This probability is generally D–A distance dependent (the longer the bridge the higher the probability of energy exchange), giving rise to regimes where the rate is enhanced as the D–A distance increases, in analogy to the earlier non-Born–Oppenheimer results of Beratan and Hopfield [48].

The functional form of the ET rate formulated in Refs. [46, 47] suggests that its free-energy dependence can be very different from the free-energy dependence of the classical (elastic) Marcus rate expression. The rate is a sum of Gaussians of identical widths, centered at different free-energy values ($-\lambda - \varepsilon_n$). Therefore, the rate as a function of free energy is described by an envelope of Gaussian functions with a much larger composite width than each individual component. Since the weight of each Gaussian, $P(\varepsilon_n)$, is both D–A-distance and temperature-dependent, the envelope is also distance- and temperature-dependent. These observations led the authors to suggest that experiments measuring distance and temperature effects on the free-energy dependence of ET rates will shed light on the inelastic tunneling contributions to the rate. In particular, they find that their rate expression is consistent with the free-energy-dependent measurements of Winkler, Gray, and

coworkers on Ru-modified myoglobins [49], that indicated the lack of an inverted region. It is not possible to experimentally deconvolute the inelastic-tunneling contributions to the free-energy dependence from other effects, as similar effects could arise from local modes coupled to donor and acceptor or from electron transfer to an excited state of the acceptor [49].

Wolfgang, Risser, Priyadarshy, and Beratan [50] analyzed the dependence of T_{DA} on the geometry of peptides. They computed the bridge Green function that enters T_{DA} for different geometries of fluctuating α -helical and β -strand polypeptides by using CNDO/S methods at different fixed tunneling energies. They observed that the Green function (and hence T_{DA}) changes sign and magnitude with structural variation. Similar observations were later made by Daizadeh et al. [46] in extended-Hückel calculations of T_{DA} for different geometries of a segment of azurin at two tunneling energies. Both studies demonstrate large fluctuations in T_{DA} on short timescales (tens of fs). In a similar study, Kurnikov, Zusman, Kurnikova, Farid, and Beratan showed that geometrical fluctuations cause significant changes in both T_{DA} and λ for covalently linked iridium-pyridinium D–A systems [9]. An understanding of these geometry-dependent parameters is essential for understanding the observed electron-transfer rates.

The validity of the two-state description for a fluctuating D–bridge–A system was examined by Xie, Archontis, and Skourtis [51]. Rather than assuming a two-state Hamiltonian from the start and using it in an expression for the rate, they solved the time-dependent Schrödinger equation for a fluctuating β -sheet bridge using a time-dependent Hamiltonian for the entire system (obtained from CNDO calculations performed every fs of classical molecular dynamics). With the electron initially in a D state, they computed the probability of electron transfer to an A state as a function of time. They then constructed time-dependent two-state Hamiltonians that, when introduced to the time-dependent Schrödinger equation, reproduced the main features of the electron-transfer probability accurately. Their analysis shows that such effective D–A Hamiltonians must necessarily contain $T_{\text{DA}}(t)$ with a time-dependent tunneling energy. Fixed tunnelling-energy effective Hamiltonians (and hence fixed-tunneling energy $T_{\text{DA}}(t)$ values) may lose their validity on short timescales. This effect should be taken into account when studying T_{DA} as a function of structural fluctuations (Figure 1). In Ref. [51], the ET probability for the fluctuating β -sheet bridge and the static bridge were compared by using identical sets of D–A pairs. The timescale of deviation of the two probabilities was studied as a function of increasing D–A distance.

Ungar, Newton, and Voth [52] have simulated an electron-transfer system consisting of a solvated proline tetramer with transition-metal D and A. Their starting point was the non-adiabatic (golden-rule) expression for the rate, with a time-dependent T_{DA} (as in [44, 45, 46, 47]). A detailed study of the free-energy dependence of the rate was performed with the use of molecular-dynamics simulations, for which enthalpic and entropic effects were separated. The time-dependence of T_{DA} was also analyzed at the INDO/S level, and significant T_{DA} fluctuations were observed at fixed D–A distances, as in Refs. [46, 47, 49, 50]. The computational methods employed in [52] are promising for simulating conformationally fluctuat-

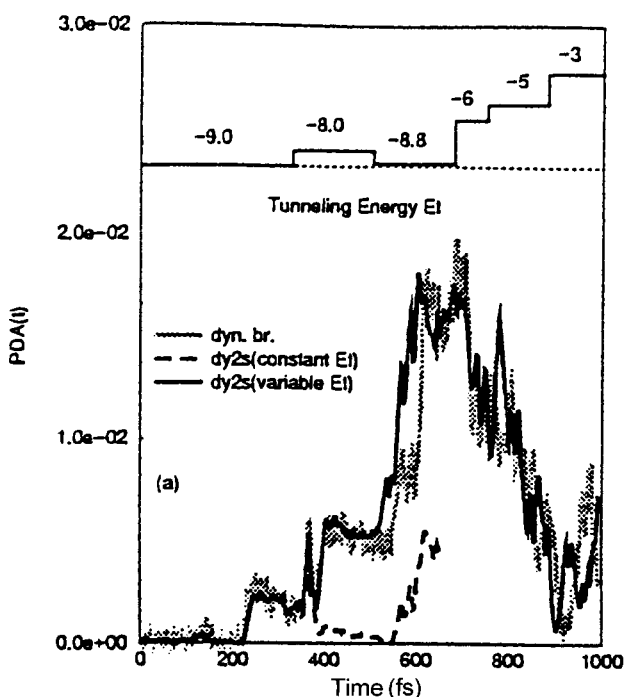


Figure 1. ET dynamics characteristics of a fluctuating β -sheet. (a) dyn. br. The electron-transfer probability between the α -carbons of Met 121 and Gly 123 (D–A pair) of the β -sheet of azurin. The “dynamic bridge” probability is computed by solving the time-dependent Schrödinger equation with a time-dependent Hamiltonian for the entire β -sheet system. The Hamiltonian is constructed at the CNDO level from classical molecular dynamics trajectories of the solvated azurin molecule. (b) dy2s with constant E_{tun} . The ET probability is computed using the time-dependent Schrödinger equation with an effective time-dependent two-state (D–A) Hamiltonian obtained from the full Hamiltonian in (a) via projection (the “dynamic two-state approximation” [51]). E_{tun} is kept constant at -9 eV. The probability deviates from its exact counterpart in (a) (dyn. br.) within 400 fs. (c) dy2s with variable E_{tun} . The ET probability computed using a “dynamic two-state approximation” with time-dependent E_{tun} . For a good approximation of the exact electron-transfer probability (dyn. br.) for $t > 400$ fs, the tunneling energy (E_{tun}) used in the projection of the “dynamic two-state” approximation must be varied as a function of time. The time dependence of E_{tun} in (c) is shown at the top of the figure, where it is compared to the E_{tun} value of -9 eV used in (b).

ing ET systems. As pointed out by the authors, a central goal in this area is to compute the probability of accessing conformations with large T_{DA} values, and hence to understand their contributions to the rate.

Fluctuations in geometry may cause ET mechanism changes as well as introduce T_{DA} modulation and inelastic tunneling. Long-range ET processes may proceed in a single coherent step from donor to acceptor, or may be incoherent (involving many short-range hops) with localization and trapping at intervening sites. What

determines the propensity for one mechanism or another is the Boltzmann penalty factor for populating sites that may be “uphill” ($\exp[-\Delta E/k_B T]$) compared to the tunneling penalty factor ($\exp[-\beta R_{DA}]$). For transport distances of 40 Å with β values of 1 Å⁻¹, the two exponents are about equal at room temperature. As such, the mechanisms should compete with one another at very long distances. In instances of competition, the relaxation dynamics of the intermediate states is critical for determining the ET dynamics.

In a pure two-level system in which an electron is launched from the donor at time, $t = 0$, its probability of being found on A rises as $\sin^2[(T_{DA}/\hbar)t]$ and leads to ET rates proportional to $|T_{DA}|^2$. Even at zero temperature, the two-level approach for describing the ET rate processes may fail. This may be the case because interatomic interactions lead to substantial electronic population of the bridge-centered orbitals. That is, when mixing between donor and bridge states becomes comparable to the energy gap between donor/acceptor and bridge states, the electronic dynamics is no longer well described by the two-level description. As bridge states approach D and A in energy, the simple $\sin^2[(T_{DA}/\hbar)t]$ envelope is destroyed, and substantial amplitude arises on sites other than donor and acceptor. An illustration of such behavior appears in Ref. [53], where a two-state approximation could not be readily used for the prediction of a rate.

Three-state electron transfer

A critical issue in ET concerns the crossover from pure superexchange mediation via bridge orbitals to a mechanism involving substantial population of the bridging orbitals. Considerable electronic amplitude can move through the bridge coherently, or—alternatively—relaxation processes may further trap amplitude on the bridge. Recent studies have formulated the problem in such a way that one may interpolate between these two limiting regimes [1, 2].

The three-state (three-potential-energy surface) problem is of interest for redox chains, chemical triad model systems, DNA electron transfer, and the primary charge separation in photosynthesis. As there are two energy-gap fluctuations in these reactions, and the fluctuations are not simply related to each other (in contrast to the case of two-electron transfer in two-center systems, *vide infra*), the problem is intrinsically two-dimensional. Marchi et al. [54], Zusman and Beratan [55], and Okada and Bandyopadhyay [56] have analyzed the nature of these potential energy surfaces and the electron-transfer kinetics. In the steady-state approximation for species 2,

$$k_{13} = \frac{k_{12}k_{23}}{k_{21} + k_{23}} + k_{13}^S \quad (10)$$

the rates k_{12} , k_{21} , and k_{23} describe electron transfer between neighboring sites, while k_{13}^S describes superexchange-mediated transfer from site 1 to 3. A new geometry-dependent parameter b arises to describe these reaction rates. This parameter, associated with the size and position of the three ET species, can be estimated from

simulation [54] and in a three-sphere model [55]

$$b = \frac{(1/R_1) - (1/|\mathbf{r}_2 - \mathbf{r}_1|) - (1/|\mathbf{r}_3 - \mathbf{r}_1|) + (1/|\mathbf{r}_3 - \mathbf{r}_2|)}{(1/R_1) + (1/R_3) - (2/|\mathbf{r}_3 - \mathbf{r}_1|)} \quad (11)$$

where R_1 is the radius of the donor, R_3 is the radius of the acceptor, \mathbf{r}_1 is the vector position of the donor, \mathbf{r}_2 the vector position of the bridge, and \mathbf{r}_3 the vector position of the acceptor. An approximate perturbation-theory estimate for the superexchange coupling averaged over fluctuation of the intermediate state coordinates is the following equation [55]

$$\bar{T}_{DA} \approx \frac{V_{12}V_{23}}{\Delta G_{12} + \lambda_{12} - b(\Delta G_{13} + \lambda_{13})} \quad (12)$$

which generalizes the two-sphere model expression [13]. The interplay between the superexchange matrix element and the free-energy dependence of the stepwise vs. superexchange rate channels leads to nonparabolic dependencies of k_{13} on the overall reaction free energy. Several groups [57, 58] have employed rate analysis along these lines in an attempt to ascertain the reaction mechanism for the primary charge separation event(s) in photosynthesis, which involve the special pair (electron donor), a bridging chlorophyll (supporting a real or virtual intermediate state), and a pheophytin (electron acceptor) species (see Figure 2a). This mechanistic issue in the reaction center remains somewhat open, and is complicated by questions of whether the initial or the intermediate species (if it exists) equilibrates thermally during the transport process [59].

Multistate electron transfer

DNA is an electron-transfer bridge that can access multistep hopping under some circumstances. Although of interest for some time [60], DNA ET has received focused interest recently through a series of innovative studies with well-defined donor and acceptor groups (see chapter by F.D. Lewis). In Barton's group, studies with intercalated donor and acceptor transition-metal species and with tethered and intercalated species suggested soft distance dependence for excited-state quenching in DNA [61, 62, 63, 64]. A body of recent experiments, utilizing DNA base oxidation, indicate a range of distance dependencies and a role for both short-distance superexchange-mediated transport as well as long-distance multistep hopping transport [65, 66, 67, 68, 69, 70]. Although the long-range superexchange coupling between distant bases is predicted by theoretical studies to decay rapidly with distance [71, 72], much softer apparent distance decays may be observed if multistep short-range hopping is energetically accessible [1]. In the multistep scenario, superexchange plays a role, mediating each hop between bases at relatively small distances. There is evidence, as well, for single-step long-range superexchange transfer in DNA with substantial distance decay [65, 66, 68]. Ongoing theoretical and experimental studies of sequence, geometry, and donor/acceptor dependence are revealing a great richness and diversity of mechanisms [70].

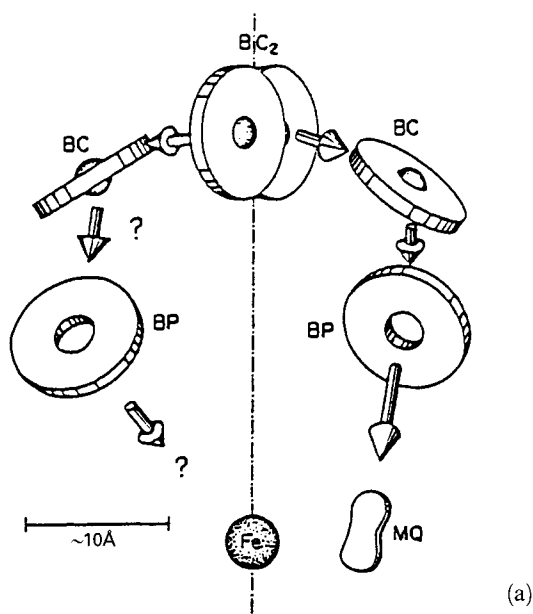
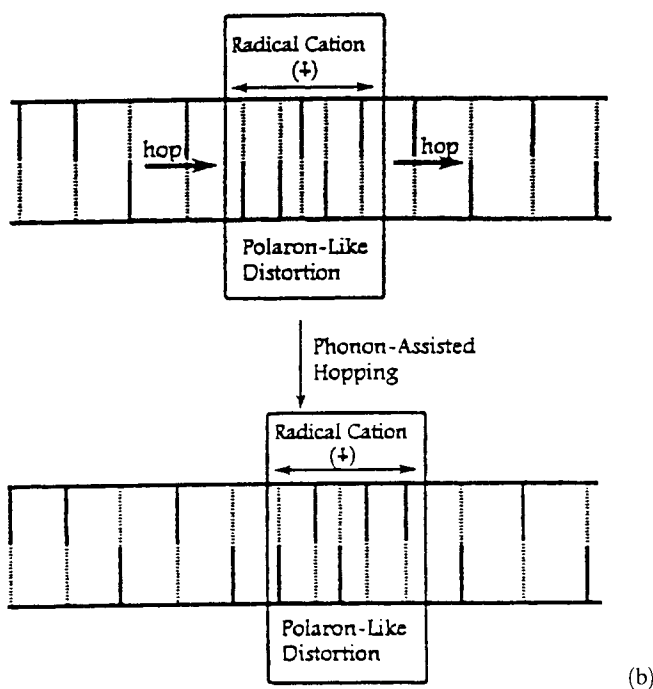


Figure 2. (a) The ET pathways in the bacterial photosynthetic reaction are shown proceeding from the special pair (B) via the bridging bacteriochlorophyll (BC) to the bacteriopheophytin (BP) (the right-hand branch is active). Arrows represent the nearest-neighbor interactions between chromophores. The B-BC and BC-BP interactions may produce either a real or a virtual intermediate localized on BC during the reaction [88]. (b) A proposed vibronically-coupled hole-hopping mechanism for ET in DNA is shown [69]. This mechanism emphasizes the delocalization of the hole.



3.3 Multi-Electron Transfer Reactions

Multi-electron transport is particularly important in catalytic biological systems. For example, biological nitrogen fixation involves the delivery of eight electrons to nitrogenase [73]. A great challenge is to understand the choreography of electron delivery and of coupled electron proton transfer in catalytic systems. In many biochemical instances, the ET reactions occur one by one and are well described by the ET theories discussed above. Many redox couples ($\text{Pt}^{2+}/\text{Pt}^{4+}$ for example) also involve stable species whose charge differs by two. We now consider the issue of single vs two-electron transport (outer sphere, without coupled proton transfer). This serves as an example of another three-state and “three-parabola” problem. We are particularly interested in the rates of competing single-step and concerted two-(or multi)-electron events. Closely related mechanistic issues arise when the competing superexchange and hopping pathways discussed earlier are considered.

In a unimolecular ET system (or a fixed contact ion pair), the kinetic equations



lead, in the steady-state approximation for D^-A^- , to the overall rate for the two-electron transfer being given by the following equation [74, 75, 76]:

$$k_{13} = \frac{k_{12}k_{23}}{k_{21} + k_{23}} + k_{13}^C \quad (14)$$

where k_{13}^C is the rate of concerted two-electron transfer from donor to acceptor. Formulation of the three-parabola framework for the two-electron problem is relatively straightforward. Assuming a simple charge distribution on the two centers (such as two charged spheres) and that the shape of the charge distributions does not change upon ET (allowing only the amount of charge on D and A to vary), the energy gap fluctuations associated with single electron ET and those associated with concerted two-electron ET are proportional to one another [74]. Moreover, the reorganization energies differ by a factor of four, since the reorganization energy scales with the amount of charge transferred squared. As such, two-electron transfer is described by three parabolas along a (one-dimensional) reaction coordinate, with the minima of the free-energy parabolas spaced equally along the reaction coordinate in the order $D^{\bullet}=A$, $D^{\bullet}A^{\bullet-}$, DA^{\bullet} . The steady-state approximation is that the single-electron transfer species is of fixed concentration, valid in the regime where the ET reaction proceeds via an unstable $D^{\bullet}A^{\bullet-}$ intermediate. The electronic coupling interaction for two-particle tunneling is anticipated to be smaller (the virtual intermediate energy will be approximately twice as large) than in the case of single-electron tunneling.

The mechanistic regimes involving unstable D^-A^- intermediates are summarized in Figure 3. In (a), the activation barrier for stepwise transfer (crossing points of

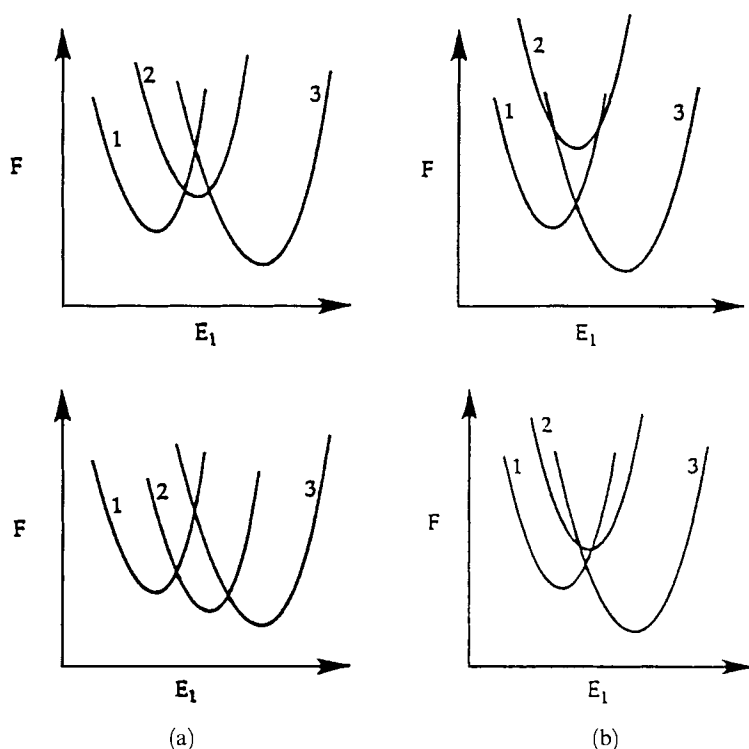


Figure 3. The potential energy surfaces for two-electron transfer involves the states $D^{\bullet}A$ (1), $D^{\bullet-}A^{\bullet-}$ (2), and DA^{\bullet} (3) [75]. Assuming that only the amount of charge on D and A changes upon ET (but that the shape of its distribution does not change), the problem maps onto a one-dimensional reaction coordinate with equally spaced wells. The competition between sequential and concerted (two-electron) mechanisms is determined by the positions of the crossing points between wells and the magnitude of the one- and two-electron coupling matrix elements. In (a), the activation energy associated with the stepwise mechanism is lower than that for the concerted process. In (b), the reverse ordering of activation energies is shown.

curves 1 and 2, and 2 and 3) is lower than the barrier for concerted transfer (crossing point of curves 1 and 3). In (b), the activation energy for the concerted channel dominates.

The activation free energies for the stepwise (two-step) transport process may fall into two regimes. For an unstable intermediate species (species 2, $D^{\bullet-}A^{\bullet-}$) with free-energy minimum below the crossing point of curves 1 ($D^{\bullet}A$) and 3 (DA^{\bullet}) [75]

$$\Delta F^{\ddagger} = \frac{[\Delta G_{21} + (\lambda_{31}/4)]^2}{\lambda_{31}} \quad (15a)$$

λ_{13} is the reorganization energy associated with concerted two-electron transfer from $D^{\bullet}A$ to DA^{\bullet} ; the reorganization energy for the single-electron steps is $\frac{1}{4}$ of

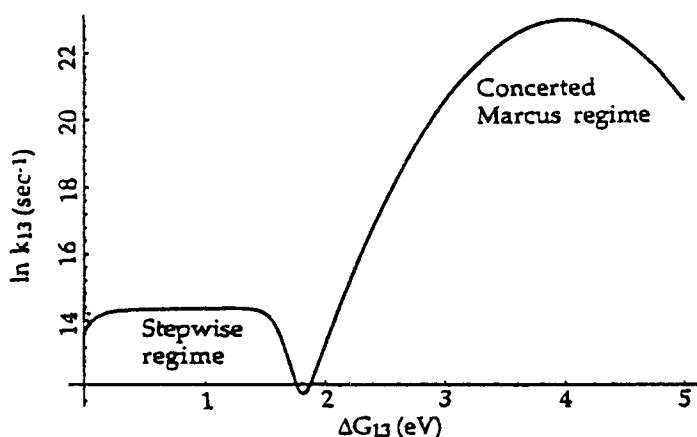


Figure 4. Plots of (log) rate vs ΔG_{13} for fixed ΔG_{12} in a two-electron transfer system. Note the weak dependence on driving force for small driving forces and the parabolic Marcus-like regime at higher driving forces [75].

λ_{13} . For an unstable intermediate with free-energy minimum above the crossing point of curves 1 and 3

$$\Delta F^\ddagger = \frac{[\Delta G_{32} + (\lambda_{31}/4)]^2}{\lambda_{31}} \quad (15b)$$

Finally, for the concerted two-electron transport (the curve 1–curve 3 crossing process)

$$\Delta F^\ddagger = \frac{(\Delta G_{31} + \lambda_{31})}{4\lambda_{31}} \quad (15c)$$

Figure 4 shows the rate dependence on overall free energy (ΔG_{13}), with ΔG_{12} held fixed for two-electron ET. In the pure concerted regime (right-hand side of diagram), the Marcus parabolic dependence with a reorganization energy four times that of the one-electron value is obtained. In the stepwise regime, the activation energy is controlled by the fixed value of ΔG_{12} , and the reaction rate is weakly dependent on the overall reaction free energy (ΔG_{13}). The multi-electron mechanisms seem most plausible at very large driving forces, where free energy-reorganization energy matching can occur, and where the larger single-electron-transfer matrix element is offset by a large single-electron activation energy. Tests of these predictions may be accessible in cyclooctatetraene/cyclooctatetraene dianion “mixed-valence” species (Figure 5) in which intramolecular electron exchange has been observed recently [77]. These two-electron processes are known to be sensitive to the counterions present, so construction of species where the dianion charge is compensated in the bridging unit itself is desirable.

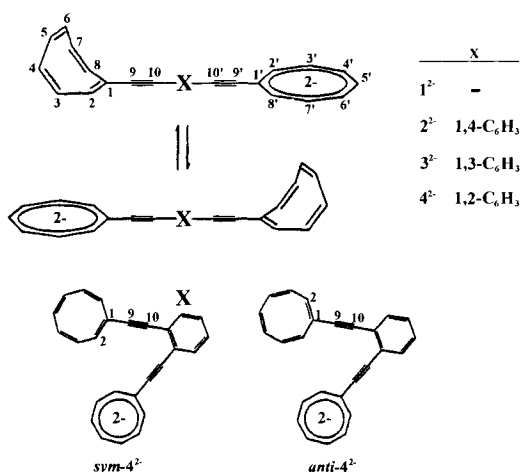


Figure 5. Structure of “mixed valence” cyclooctatetraene/cyclooctatetraene dianion species studied by Staley and coworkers [77].

3.4 Conclusions

Many of the issues of current interest in electron-transfer chemistry are associated with complexity that arises from multiple-site hopping (see chapter by Gust, Moore, and Moore), relaxation and dephasing, competing pathways, bridge dynamics, hopping-superexchange transitions, proton-coupled processes (see chapters by Hammes-Schiffer and Nocera), and multi-electron catalysis [78, 79, 80, 81, 82, 83, 84]. The borders between chemical electron transfer and mesoscopic physics are becoming fuzzy, as issues of conductivity quantization, pathway dephasing, single-molecule/single-electron electronic devices come to the fore as well [85]. On the biological side, imaging of redox proteins via STM is becoming possible, and issues of dynamic fluctuations, hopping vs superexchange transport, and transport mechanisms are arising in new contexts [86, 87].

Acknowledgments

The authors thank the fellows of All Souls College, Oxford, for their generous hospitality and for sharing their outstanding wine cellar with us during our visits. DNB thanks the JS Guggenheim Foundation and the Burroughs–Wellcome Fund for additional support. The research at the University of Cyprus is supported by the Cyprus government through the research program “From Strong Interactions to Molecular Recognition: Theoretical and Computational Studies.” In Pittsburgh, the research is supported by grants from the National Science Foundation and the National Institutes of Health. We thank our colleagues and collaborators for their contributions to the research described in this chapter.

References

1. M. Bixon and J. Jortner (eds.) *Adv Chem Phys* 106 vols. 1 and 2 (1999).
2. J. Jortner and M. Ratner, *Molecular Electronics*, Blackwell Scientific, Oxford (1997).
3. S. Larsson, *J Am Chem Soc* 103, 4034 (1981).
4. S. S. Skourtis and J. N. Onuchic, *Chem Phys Lett* 209, 171 (1993).
5. S. S. Skourtis, D. N. Beratan, and J. N. Onuchic, *Chem Phys* 176, 501 (1993).
6. D. N. Beratan and S. S. Skourtis, *Curr Opin Chem Biol* 2, 235 (1998).
7. S. Priyadarshy, S. S. Skourtis, S. M. Risser and D. N. Beratan, *J Chem Phys* 104, 9473 (1996).
8. S. S. Skourtis and D. N. Beratan, *Adv Chem Phys* 107, 377 (1999).
9. I. V. Kurnikov, L. D. Zusman, M. G. Kurnikova, R. S. Farid, and D. N. Beratan, *J Am Chem Soc* 119, 5690 (1997).
10. K. Kumar, I. V. Kurnikov, D. N. Beratan, D. H. Waldeck, M. B. Zimmt, *J Phys Chem A* 102, 5529 (1998).
11. K. Sharp, *Biophys J*, 74, 1241 (1998).
12. M. D. Newton, *Adv Chem Phys*, 106, 303 (1999).
13. R. A. Marcus and N. Sutin, *Biochim Biophys Acta* 811, 265 (1985).
14. R. J. Cave, M. D. Newton, *J Chem Phys* 106, 9213 (1997).
15. S. Larsson, A. Broo, L. Sjölin, *J Phys Chem* 99, 4860 (1995).
16. S. Larsson, M. Braga, *J Photochem Photobiol A* 82, 61 (1994).
17. P. Siddarth and R. A. Marcus *J Phys Chem* 97, 6112 (1993).
18. P. Siddarth and R. A. Marcus *J Phys Chem* 99, 7581 (1995).
19. J. N. Gruschus and A. Kuki, *J Phys Chem* 97, 5581 (1993).
20. W. B. Curry, M. D. Grabe, I. V. Kurnikov, S. S. Skourtis, D. N. Beratan, J. J. Regan, A. J. A. Aquino, P. Beroza, J. N. Onuchic, *J Bioenerg Biomemb* 27, 285 (1995).
21. I. V. Kurnikov and D. N. Beratan, *J Chem Phys* 105, 9561 (1996).
22. H. E. M. Christensen, L. S. Conrad, K. V. Mikkelsen, and J. Ulstrup, *J Phys Chem* 96, 4451 (1992).
23. A. Okada, T. Kakitani, and J. Inoue, *J Phys Chem* 99, 2946 (1995).
24. J. N. Gehlen, I. Daizadeh, A. A. Stuchebrukhov, and R. A. Marcus, *Inorg Chim Acta* 243, 271 (1996).
25. D. N. Beratan, J. N. Betts, J. N. Onuchic, *Science* 252, 1285 (1991).
26. J. N. Onuchic, D. N. Beratan, J. R. Winkler, and H. B. Gray, *Ann Rev Biophys Biomol Struct*, 21, 349 (1992).
27. J. N. Onuchic and D. N. Beratan, *J Chem Phys* 92, 722 (1990).
28. P. J. F. DeRege, S. A. Williams, M. J. Therien, *Science* 269, 1409 (1995).
29. D. N. Beratan, J. N. Onuchic, J. R. Winkler and H. B. Gray, *Science* 258, 1740 (1992).
30. D. N. Beratan, J. N. Betts, J. N. Onuchic, *J Phys Chem* 96, 2852 (1992).
31. H. B. Gray and J. R. Winkler, *Annu Rev Biochem* 65, 537 (1996).
32. I. J. Dmochowski, B. R. Crane, J. J. Wilker, J. R. Winkler, and H. B. Gray, *Proc Natl Acad Sci (USA)* 96, 12987 (1999).
33. C. C. Page, C. C. Moser, X. Chen, and P. L. Dutton, *Nature*, 402, 47 (1999).
34. S. S. Skourtis and D. N. Beratan in *Biological Electron Transfer Chains: Genetics, Composition, and Mode of Operation*, GW Canters and E. Vliegenhart (eds) Kluwer Academic Publishers, The Netherlands (1998).
35. J. J. Regan, S. M. Risser, D. N. Beratan, and J. N. Onuchic, *J Phys Chem* 97, 13083 (1993).
36. J. J. Regan and J. N. Onuchic *Adv Chem Phys* 107, 497 (1999).
37. S. S. Skourtis, J. J. Regan, and J. N. Onuchic, *J Phys Chem* 98, 3379 (1994).
38. S. S. Skourtis and D. N. Beratan, *J Phys Chem B* 101, 1215 (1997).
39. S. S. Skourtis and D. N. Beratan, *J Biol Inorg Chem* 2, 378 (1997).
40. K. V. Mikkelsen, J. Ulstrup, and M. G. Zakaraya, *J Am Chem Soc* 111, 1315 (1989).
41. A. M. Kuznetsov, M. D. Vigdorovich, and J. Ulstrup, *Chem Phys* 176, 539 (1993).
42. J. N. Onuchic and A. A. S. da Gama, *Theor Chim Acta* 69, 89 (1986).
43. D. N. Beratan, J. N. Onuchic, and J. J. Hopfield, *J Chem Phys* 86, 4488 (1987).
44. J. Tang, *J Chem Phys* 98 6263 (1993).
45. I. A. Goychuk, E. G. Petrov, and V. May, *J Chem Phys* 103, 4937 (1995).

46. I. Daizadeh, E. S. Medvedev, and A. Stuchebrukhov, *Proc Natl Acad USA* 94 3703 (1997).
47. E. S. Medvedev and A. Stuchebrukhov *J Chem Phys* 107, 3821 (1997).
48. D. N. Beratan and J. J. Hopfield, *J Chem Phys* 81, 5753 (1984).
49. G. A. Mines, M. J. Bjerrum, M. G. Hill, D. R. Casimiro, I.-J. Chang, J. R. Winkler, and H. B. Gray, *J Am Chem Soc* 118, 1961 (1996).
50. J. Wolfgang, S. M. Risser, S. Priyadarshy, and D. N. Beratan, *J Phys Chem B* 101, 2986 (1997).
51. Q. Xie, G. Archontis and S. S. Skourtis, *Chem Phys Lett* 312, 237 (1999).
52. L. W. Ungar, M. D. Newton, and G. A. Voth, *J Phys Chem B* 103, 7367 (1999).
53. S. S. Skourtis and S. Mukamel, *Chem Phys* 197, 367 (1995).
54. M. Marchi, G. N. Gehlen, D. Chandler, M. Newton, *J Am Chem Soc* 115, 4178 (1993).
55. L. D. Zusman and D. N. Beratan, *J Chem Phys* 110, 10468 (1999).
56. A. Okada and T. Bandyopadhyay, *J Chem Phys* 111, 1137 (1999).
57. M. Bixon, J. Jortner, and M. E. Michel-Beyerle, *Chem Phys* 197, 389 (1995).
58. L. D. Zusman and D. N. Beratan, *Spectrochim Acta A* 54 1211 (1998).
59. S. S. Skourtis, A. J. R. da Silva, W. Bialek, J. N. Onuchic, *J Phys Chem* 96, 8034 (1992).
60. D. D. Eley and D. I. Spivey, *Trans Faraday Soc* 58, 411 (1962).
61. C. J. Murphy, M. R. Arkin, N. D. Ghattia, S. H. Bossmann, N. J. Turro, and J. K. Barton, *Science* 262, 1025 (1993).
62. M. R. Arkin, E. D. A. Stemp, R. E. Holmlin, J. K. Barton, A. Hormann, E. J. C. Olson, and P. F. Barbara *Science*, 273, 475 (1996).
63. E. J. C. Olson and P. Barbara, *Adv Chem Phys* 107, 647 (1999).
64. P. Lincoln, E. Tuite, B. Norden, *J Am Chem Soc* 119 1454 (1997).
65. S. O. Kelley and J. K. Barton *Science* 283, 375 (1999).
66. F. D. Lewis, T. Wu, Y. Zhang, R. L. Letsinger, S. R. Greenfield, and M. R. Wasielewski, *Science* 277, 673 (1997).
67. M. Bixon, B. Giese, S. Wessely, T. Langenbacher, M. E. Michel-Beyerle, and J. Jortner *Proc Natl. Acad Sci (USA)* 96, 11713 (1999).
68. K. Fukui and K. Tanaka *Angew Chem Int Ed Engl* 37, 158 (1998).
69. P. T. Henderson, D. Jones, G. Hampikian, Y. Kan, and G. B. Schuster, *Proc Natl. Acad Sci (USA)* 96, 8353 (1999).
70. J. Jortner, M. Bixon, T. Langenbacher, and M. E. Michel-Beyerle, *Proc Natl. Acad Sci (USA)* 95, 12759 (1998).
71. D. N. Beratan, S. Priyadarshy, and S. M. Risser *Chem Biol* 4, 3 (1997).
72. S. Priyadarshy, S. M. Risser, and D. N. Beratan, *J Phys Chem* 100, 17678 (1996).
73. S. J. Lippard and J. M. Berg, *Principles of Bioinorganic Chemistry*, University Science Books, Mill Valley, California (1994).
74. L. D. Zusman and D. N. Beratan, *J Chem Phys* 105, 165 (1996).
75. L. D. Zusman and D. N. Beratan, *J Phys Chem A* 101, 4136 (1997).
76. A. Okada, T. Bandyopadhyay, and M. Tachiya, *J Chem Phys* 110, 3509 (1999).
77. P. Boman, B. Eliasson, R. A. Grimm, G. S. Martin, J. T. Strnad, and S. W. Staley, *J Am Chem Soc* 121, 1558 (1999).
78. A. Soudackov and S. Hammes-Schiffer, *J Am Chem Soc* 121, 10598 (1999).
79. R. I. Cukier, *J Phys Chem.* 99, 16101 (1995).
80. J. Hirst, G. N. L. Jameson, J. W. A. Allen, and F. A. Armstrong, *J Am Chem Soc* 120, 11994 (1998).
81. J. Hirst, J. L. C. Duff, G. N. L. Jameson, M. A. Kemper, B. K. Burgess, and F. A. Armstrong, *J Am Chem Soc* 120, 7085 (1998).
82. G. Steinberg-Yfrach, J. L. Rigaud, E. N. Durantini, A. L. Moore, D. Gust, and T. A. Moore, *Nature*, 392, 479 (1998).
83. J. A. Roberts, J. P. Kirby, and D. G. Nocera, *J Am Chem Soc* 117, 8051 (1995).
84. J. P. Kirby, J. A. Roberts, and D. G. Nocera, *J Am Chem Soc* 119, 9230 (1997).
85. S. Datta, *Electronic Transport in Mesoscopic Systems*, Cambridge University Press (1995).
86. W. Schmickler, *Surf Sci* 295, 43 (1993).
87. E. P. Friis, J. E. T. Andersen, Y. I. Kharkats, A. M. Kuznetsov, R. J. Nichols, J. D. Zhang, J. Ulstrup, *Proc Natl Acad Sci (USA)* 96, 1379 (1999).
88. D. DeVault, *Photosynth Res* 10, 125 (1986).

4 Electron Transfer at Electrodes and Interfaces

Daniël Vanmaekelbergh

4.1 Scope

In the first part of this century, electrochemical research was mainly devoted to the mercury electrode in an aqueous electrolyte solution. A mercury electrode has a number of advantageous properties for electrochemical research; its surface can be kept clean, it has a large overpotential for hydrogen evolution and both the interfacial tension and capacitance can be measured. In his famous review [1], D. C. Grahame made the firm statement that “*Nearly everything one desires to know about the electrical double layer is ascertainable with mercury surfaces if it is ascertainable at all.*” At that time, electrochemistry was a self-contained field with a natural basis in thermodynamics and chemical kinetics. Meanwhile, the development of quantum mechanics led to considerable progress in solid-state physics and, later, to the understanding of electrostatic and electrodynamic phenomena at metal and semiconductor interfaces.

At present, electrochemical science is a multidisciplinary field overlapping with many other fields, such as solid-state physics and chemistry, surface science, statistical physics including molecular dynamics and quantum chemistry [2, 3, 4]. This opening-up of the field has several origins. The development of device physics, where charged interfaces between various metals and semiconductors played a key role, is an important factor. In addition, the enormous progress in experimental and theoretical investigations of inter- and intramolecular electron-transfer processes has surely promoted fundamentally new developments in electrochemical kinetics [5]. It is now recognized that electrochemical processes may proceed in completely different ways at a molecular level; in some reactions ions are transferred through the electrochemical double layer; in others, electrons tunnel through the double layer without disturbing it.

In this chapter, it is my aim to discuss electrochemical phenomena in a rather general way, starting from basic concepts derived from solid state physics and interfacial science (Sections 4.2 and 4.3). Thus, the electrochemical double layer is

discussed, with, as starting point, the electrical double layer at a metal/vacuum surface (Section 4.5). In Sections 4.8 and 4.9, electrochemical electron transfer is treated in terms of elastic tunneling events between energy levels located at both sides of the interfacial double layer. This procedure is similar to that used to describe interfacial tunneling between two metals in Section 4.6. Such an analogy is made possible if the electron energy levels are defined to correspond to a dissolved redox system; the fluctuating-energy-level model is dealt with in Section 4.4. In Section 4.7, the various mechanisms of electrochemical processes are discussed. It is shown that, at a molecular level, a clear distinction can be made between electrochemical ion transfer and simple electron transfer. In this section, the reason why current-potential characteristics may have common features despite the diversity of mechanisms is also explained. The purely phenomenological treatment is compared with microscopic models for outer-sphere electron transfer in Section 4.8.

4.2 Open Electron Systems

A steady-state current flowing in an electrical device corresponds to a net movement of electrons over macroscopic distances. Since electrical devices consist of more than one phase, there is also a net flux of electrons through the phase boundaries. Transfer of electrons through interfaces forms an important subject in surface physics and chemistry, including electrochemistry. For example, a steady-state current flow in an electrochemical cell consisting of two Pt electrodes and a solution containing the oxidized and reduced species of a redox system means that electrons are transferred from the reduced species to the Pt electrode through the electrochemical double layer at one electrode, and that electrons are transferred from the other Pt electrode to the oxidized species. The current through the solution corresponds to the movement of ions. In electrochemical language, electron flow through the cell is due to a potential difference between the two electrodes. Here, we will use the concept of electrochemical potential to discuss the conditions for electronic equilibrium in one phase and between two phases [6–8]. We also consider electron transport due to a gradient of the electrochemical potential and transfer caused by a drop of the electrochemical potential across an interface. The use of the electrochemical potential makes it easier to discuss electrochemical electron transfer in the more general framework of interfacial electron transfer.

4.2.1 The Electrochemical Potential

We consider a system of N electrons separated from the surroundings by a wall that allows work to be performed on the surroundings and heat to be exchanged. In addition, electrons may enter or leave the system through the wall (i.e., through an interface). Thus, the system is *open* with respect to electrons. The change in the internal energy, U , is accounted for by the so-called central law of thermodynamics:

$$dU = T dS - P dV + \mu dN \quad (1)$$

Here, μ is the chemical potential of the electrons in the system at a given temperature T , P is the pressure, and N is the number of electrons. The chemical potential accounts for the kinetic energy of the electrons and the potential energy due to interactions of the electrons with the other electrons and the core ions. (A microscopic theory for electrons in a solid phase is discussed in Section 4.3.) From Eq. 1 it follows that μ can be defined as the increase in internal energy of the electron system when one electron is added to the system under conditions of constant volume V and entropy S :

$$\mu = \left(\frac{\partial U}{\partial N} \right)_{S, V} \quad (2)$$

A particularly interesting relationship between the chemical potential and the Gibbs free energy, G , is found from Eq. 1 and $G = H - TS = U + PV - TS$:

$$dG = V dP - S dT + \mu dN \quad (3)$$

From Eq. 3 it follows that the chemical potential is equal to the increase in free energy of the electron system upon addition of one electron at constant pressure and temperature:

$$\mu = \left(\frac{\partial G}{\partial N} \right)_{P, T} \quad (4)$$

So far, we have considered open electron systems. We would, however, like to apply the concepts introduced above to electrical and electrochemical devices that consist of metals and/or doped insulators. Solid phases, such as metals and insulators do not contain electrons only. For instance, a metal consists of a regular array of core ions, and more or less freely moving electrons (the electron gas). However, as long as we discuss the transfer or directed motion of solely electrons, the concept of the chemical potential of the electrons in a (solid) phase remains valuable.

In solid state physics and chemistry, and in electrochemistry, an entire phase has often a potential ϕ with respect to a reference potential. The electrons in the entire phase have then an additional potential energy which forms a contribution to the free energy of the electron system. This is clear from the fact that an electron from a given phase, at potential ϕ , may perform work in an external circuit by leaving this phase and arriving in a similar phase at a higher potential. We account for this effect by writing Eq. 4 in a more general form:

$$\mu_e = \left(\frac{\partial G}{\partial N} \right)_{P, T, \phi} = \mu - e\phi \quad (5)$$

Here, μ_e is the electrochemical potential; μ accounts for the kinetic energy and the potential energy due to electron–electron and electron–core-ion interactions (“in-

ternal” contribution); $-e\varphi$ then forms the “external” contribution to the chemical potential. We will see that, in practice, a change in the electrochemical potential of the electrons in a given phase is brought about by a change in the potential energy term $-e\varphi$.

4.2.2 Electronic Equilibrium between Two Phases

We consider a system of two phases in electrical contact. For instance, this system may consist of two pieces of metal so close that electrons can tunnel between the two. In thermodynamic language, we consider a system consisting of two subsystems (A, B) separated by a boundary allowing the passage of electrons. The system is isolated from the surroundings, which means that the total internal energy is constant, that is, $U = U_A + U_B = \text{constant}$. We also assume that the subsystems are in thermal and mechanical equilibrium ($T_A = T_B$, $P_A = P_B$) and that both contain a large number of electrons (Figure 1). Our goal is now to find the condition for equilibrium with respect to electron exchange. If there is no net electron flow from one subsystem to the other, electronic equilibrium is reached and the entropy of the entire system is maximal (Figure 2):

$$S = S_A + S_B = \text{maximal} \quad (6)$$

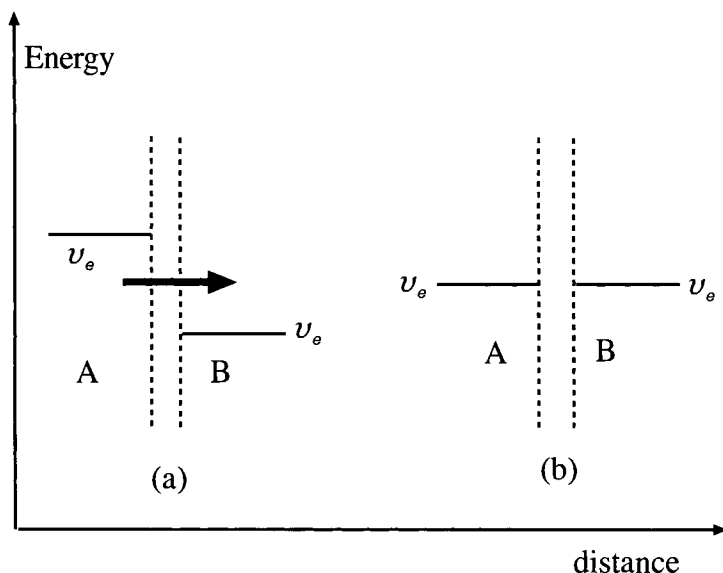


Figure 1. Two free electron systems separated by an interface through which electrons can be exchanged. (a) Situation before electronic equilibrium: the electrochemical potential in phase A is higher than in B, electrons tunnel from A to B. (b) Electronic equilibrium: the electrochemical potential has the same value in both phases.

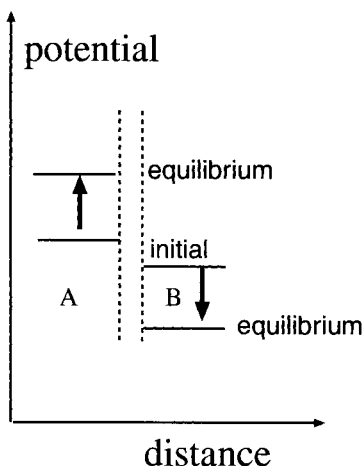


Figure 2. Change of the [electrostatic] potential of both phases due to electron flow from phase A to phase B, during equilibration. The arrows show the change of the potential, which is caused by surface charging.

We consider an infinitesimal deviation from electronic equilibrium, the transfer of a very small number, dN_A , of electrons from subsystem A to B, so that $dS = 0$. From Eq. 1, it follows that

$$0 = dS_A + dS_B = T^{-1}(dU_A + dU_B - \mu_{e,A} dN_A - \mu_{e,B} dN_B) \quad (7)$$

Since $dU_A = -dU_B$, and $dN_A = -dN_B$, it follows, under conditions of thermal and mechanical equilibrium, that electronic equilibrium is reached when the electrochemical potential of the electrons in both subsystems is equal:

$$\mu_{e,A} = \mu_{e,B} \quad (\text{given and constant } T, P) \quad (8)$$

The condition for electronic equilibrium means that there is no *net* flow of electrons from one subsystem to the other. However, there is a flux of electrons from A to B, compensated by a flux from B to A:

$$J_{A \rightarrow B}^{\text{eq}} = J_{B \rightarrow A}^{\text{eq}} = J^{\text{eq}} \quad (9)$$

J^{eq} is the interfacial exchange flux. The exchange flux (or the electrical equivalent, the exchange current density) is an important quantity. Its value is determined by the kinetics of electron exchange between the two phases (Sections 4.6 to 4.9). With a (small) deviation from equilibrium between the two subsystems, a net electron flux from one subsystem to the other occurs and is proportional to J^{eq} . It must be remarked that the condition (Eq. 8) for electronic equilibrium implies that the chemical potential is averaged over a sufficiently long time period. Time-resolved measurements may show fluctuations in the chemical potential around the equilibrium value.

We consider the equilibration between two pieces of metal (A and B) as an example. Before the pieces are in contact, the electrochemical potentials are respec-

tively $\mu_{e,A}$ (initial) and $\mu_{e,B}$ (initial). We assume that $\mu_{e,A}$ (initial) is larger than $\mu_{e,B}$ (initial). The pieces are brought in close contact so that electrons may tunnel from one phase to the other. Electrons are transferred from A to B until equilibrium is reached. At equilibrium $\mu_{e,A}^{\text{eq}}$ is equal to $\mu_{e,B}^{\text{eq}}$. However, the number of electrons which are transferred from A to B is relatively small. It can be assumed that the chemical potential of the electrons in both phases is hardly changed. The change in the electrochemical potential is caused by changes in the potential energy of both phases. Equilibration leads to changes $-e\phi_A$ (initial) \rightarrow $-e\phi_A$ (equilibrium), and $-e\phi_B$ (initial) \rightarrow $-e\phi_B$ (equilibrium) (Figure 2). These changes are due to the fact that a small amount of charge can change the potential of the entire phase considerably. Assume, for instance, that A and B are metallic cubes of 1 cm^3 in volume and 6 cm^2 surface area, and that the surface capacitance C is $10^{-5} \text{ C V}^{-1} \text{ cm}^{-2}$. In Section 4.3, it is shown that such a system contains approximately 10^{22} free electrons. The change of the electrical potential of phase A due to the transfer

of one electron is $d\phi = \frac{1.6 \times 10^{-19}}{C} \text{ V}$, which is $0.3 \times 10^{-14} \text{ V}$. The transfer of the tiny number of 10^{14} electrons from phase A to B ($1.6 \times 10^{-9} \text{ mol}$), results in a 0.3-V increase in the electrical potential of phase A, accompanied by a 0.3-eV decrease in the electrochemical potential. It is clear that the 'internal' chemical potential in the two phases is scarcely changed by the transfer of only 10^{14} of the total number of 10^{22} free electrons. In conclusion, a change in the electrochemical potential of a macroscopic phase is due to a change of the potential energy of the entire phase.

4.2.3 Deviations from Equilibrium

First, we show that electrons *tend* to flow from a region with a higher electrochemical potential to a region with a lower electrochemical potential. We consider a small, but finite departure from the equilibrium situation between the two subsystems A and B; the number of electrons is $N_A^{\text{eq}} + \Delta N$ and $N_B^{\text{eq}} - \Delta N$, respectively ($\Delta N > 0$). The entropy of the isolated system is lower than the equilibrium value. The entropy increases when the system evolves towards equilibrium by the transfer of the small excess of electrons from A to B:

$$\Delta S = T^{-1}[-\mu_{e,A}(-\Delta N) - \mu_{e,B}(\Delta N)] > 0 \quad (10)$$

Hence, it follows that electrons flow from the subsystem A with higher electrochemical potential to subsystem B with lower electrochemical potential.

In many experimental situations, a steady-state *nonequilibrium* condition between two phases (A and B) is sustained by electrical work being done on the system. For instance, the net interfacial electron flux $J_{A \rightarrow B}$ is measured as a function of the difference in the electrochemical potential $\mu_{e,A} - \mu_{e,B}$. For a sufficiently small departure from equilibrium, it is observed that the net flux is proportional to the exchange flux and increases with increasing $|\mu_{e,A} - \mu_{e,B}|$:

$$J_{A \rightarrow B} = J^{\text{eq}} f(\mu_A - \mu_B) \quad (11)$$

There is often a small region around equilibrium in which the net flux is proportional to J^{eq} and $\mu_{e,A} - \mu_{e,B}$. Experimental investigation of the precise relationship between the net current flow and the deviation from equilibrium has been a major issue in interfacial science (Section 4.6). The measurement of the relationship between the interfacial electron flux and the electrochemical potential of the electrons in an electrode, and a fundamental interpretation of it, continue to be important issues in electrochemistry (Sections 4.7 to 4.9).

When a phase is not in electronic equilibrium, electrons tend to flow from a position of higher to a position of lower electrochemical potential. A net directed flow of electrons through the phase occurs, proportional to the gradient in the electrochemical potential [9]. If we consider a phase in which there is a gradient in the electrochemical potential in the x -direction only, the net flux of electrons is given by

$$J(x) = (-1/e)[(k_B T/e)D]n(x) \left[\frac{\partial \mu_e}{\partial x} \right] \quad (12)$$

The electron flux is hence proportional to the density of electrons, $n(x)$, the mobility of the electrons $[(k_B T/e)D]$ (D being the diffusion constant) and the driving force $\left[\frac{\partial \mu_e}{\partial x} \right]$.

For instance, in a photovoltaic or a photoelectrochemical solar cell, a (small) drop in the electrochemical potential over the active phase is necessary for collecting the electrons [6, 9]. However, it leads to a decrease of the work that an electron can perform in the external circuit.

4.3 The Electronic Structure of Solids

In Section 4.2, it was shown that the electrochemical potential is the relevant state function for use in discussions of electronic equilibrium and deviations from equilibrium. Consider, for example, two metal phases (A and B) so close that electrons may tunnel from one phase to the other. The difference in the electrochemical potential of the two phases quantifies the deviation from equilibrium; this difference is very important for the rate of electron transfer. However, it is clear that thermodynamic considerations do not lead to predictions of the rate of electron transfer.

The net interfacial electron flux is the result of many discrete tunneling events between electron levels in phases A and B. Usually, electron tunneling is an elastic process; it occurs between an occupied and an empty electron level of the same energy. Hence, the probability of electron tunneling depends on the distribution of the electron levels at both sides of the interface, and on their occupancy. The electronic structure of solids is thus of primary importance for the kinetics of interfacial electron transfer. In analogy, electrochemical electron transfer can be regarded as the result of discrete tunneling events between electron levels in a solid (the elec-

trode) and the redox system in solution. For dealing with electrochemical electron transfer in a similar way as electron transfer between two solid phases, a model for the electron levels corresponding to a redox system in solution is also required. This subject will be treated in Section 4.4. First, the electronic structure of metals, semiconductors, and insulators will be discussed.

4.3.1 Free and Independent Electrons

Metals form a class of solids with characteristic macroscopic properties. They are ductile, have a silver-white luster, and they conduct electricity and heat remarkably well. An early, but still relevant microscopic model aimed at explaining the electrical conductivity, heat conductivity, and optical properties was proposed by Drude [10]. His model incorporates two important successes of modern science: the discovery of the electron in 1887 by J. J. Thomson, and the molecular kinetic gas theory put forward by Boltzmann and Maxwell in the second half of the 19th century.

Drude assumed that the macroscopic properties of metals are due to an electron gas present in the metallic phase. As in the kinetic model proposed for perfect gases, the electrons do not interact with each other, except during elastic collisions. This is called the independent electron approximation. The density of electrons in a metal is huge, 10^{22} – 10^{23} cm^{-3} , much larger than the molecular density in a perfect gas. Nevertheless, the independent electron approximation has been successfully used in modern quantum mechanical models. Drude furthermore assumed that the distribution of the kinetic energy of individual electrons is given by the Maxwell–Boltzmann distribution, and that the average kinetic energy of the electron gas is therefore $3/2k_B T$. The electrons stay in the solid phase owing to attraction by the positive background charge, which is, according to Drude, smeared out over the entire solid. Hence, the major effect of the positive background charge is to create a potential energy well at the metal surface, keeping the electrons inside (Figure 3).

The modern picture is that we have a lattice of positive core ions and more or less freely moving valence electrons. The moving valence electrons interact with the periodic potential energy field of the core ions, and this interaction must be taken into account for a complete description of the electronic structure of solids (Section 4.3.4). The wave-mechanical interaction between electrons and the lattice of ion cores is a necessary element for the understanding that the energetic distribution of electrons is not a continuous function, but is organized in energy bands, separated by forbidden gaps. The electron–lattice interaction was not incorporated in the Drude model. Even in simple quantum-mechanical models, such as that of Sommerfeld (Section 4.3.2), this interaction is completely ignored. Thus, both the Drude and Sommerfeld models are *free-electron models*, in which the interaction of freely moving valence electrons with the periodic field of core ions is neglected.

The Sommerfeld model is a simple quantum-mechanical model which takes the Pauli principle into account. It is sufficient for developing a model for the probability of electron tunneling events. It will therefore be discussed in some detail in the next section. A more detailed discussion can be found in Ref. [11].

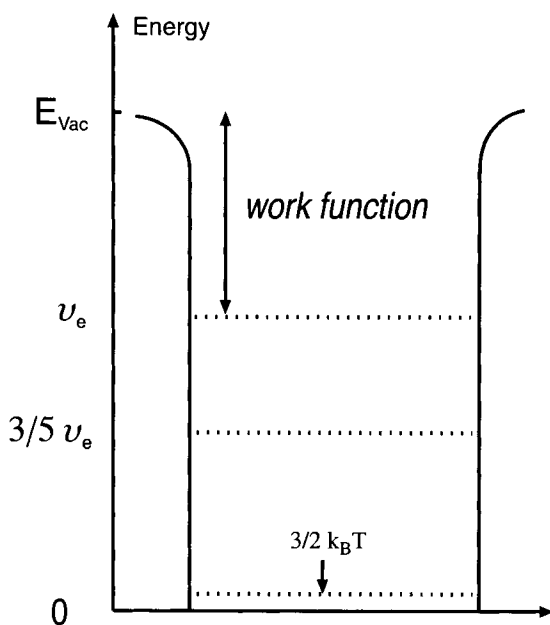


Figure 3. Energy diagram for free electrons in a metal. The positive background charge of the core ions leads to a potential energy well with respect to the energy of the electron in vacuum E_{vac} . The averaged kinetic energy of the free electrons is indicated with dashed lines: $3/2 k_B T$ according to the Drude model, and $3/5 \mu_e$ according to the Sommerfeld model. The electrochemical potential μ_e of the electrons in the metal [Fermi level] is also indicated.

4.3.2 The Sommerfeld Model for Free Electrons in a Metallic Phase

We consider a metallic phase of volume V , with N free electrons, and hence a free electron density n given by $n = N/V$. The charge of the core ions is smeared out and leads to a potential energy well keeping the free electrons in the metallic phase (Figure 3). Since in the Sommerfeld model the electrons do not interact with each other, we can describe the electron energy levels by *one-electron wave functions*. An independent electron can be described by a single-electron wave function $\psi(x, y, z)$ which satisfies

$$\begin{aligned} \frac{-\hbar^2}{2m_e} \left(\frac{\partial^2}{\partial x^2} + \frac{\partial^2}{\partial y^2} + \frac{\partial^2}{\partial z^2} \right) \psi(x, y, z) + E_p(x, y, z) \psi(x, y, z) \\ = E(x, y, z) \psi(x, y, z) \end{aligned} \quad (13)$$

In the free-electron approximation, the potential energy is position-independent; E_p is then an additive constant set here to zero, $E_p = 0$ (Figure 3); the total energy $E(x, y, z)$ is purely kinetic. A solution of Eq. 13 is

$$\psi_{\vec{k}}(\vec{r}) = \frac{1}{\sqrt{V}} e^{i\vec{k} \cdot \vec{r}} = \frac{1}{\sqrt{V}} e^{i(k_x x + k_y y + k_z z)} \quad (14)$$

The vector \vec{k} is the wave vector. The plane wave $e^{i\vec{k}\cdot\vec{r}}$ has a constant amplitude in any plane perpendicular to \vec{k} , and is periodic along lines parallel to \vec{k} , with a wavelength $\lambda = 2\pi/k$. The prefactor $\frac{1}{\sqrt{V}}$ is due to the normalization condition that the electron must be present in the volume V . The total (kinetic) energy of electrons with wave vector \vec{k} is

$$E(\vec{k}) = \frac{\hbar^2 k^2}{2m_e} = \frac{\hbar^2 (k_x^2 + k_y^2 + k_z^2)}{2m_e} \quad (15)$$

The one-electron wave functions $\psi_{\vec{k}}(\vec{r})$ should correspond to propagating rather than standing waves. The mathematical procedure for obtaining propagating waves was developed by Born and von Karman [11]. They considered a cube of volume V with sides L . The electron waves leave the metal through a face of the cube and reenter it simultaneously through the opposite face. The boundary conditions are hence periodic:

$$\left. \begin{aligned} \psi(x, y, z) &= \psi(x + L, y, z) \\ \psi(x, y, z) &= \psi(x, y + L, z) \\ \psi(x, y, z) &= \psi(x, y, z + L) \end{aligned} \right\} \quad (16)$$

The wave function presented by Eq. 14 is in accordance with the boundary condition (Eq. 16) if, $e^{ik_x L} = 1$ etc., hence if

$$\left. \begin{aligned} k_x &= m_x(2\pi/L) & m_x &= 0, \pm 1, \pm 2, \dots \\ k_y &= m_y(2\pi/L) & m_y &= 0, \pm 1, \pm 2, \dots \\ k_z &= m_z(2\pi/L) & m_z &= 0, \pm 1, \pm 2, \dots \end{aligned} \right\} \quad (17)$$

The free-electron levels described by Eqs. 15–17 can be represented in the three-dimensional k space (Figure 4). From this figure and Eq. 15 it is clear that the number of electron levels with a given energy E increases considerably with increasing E .

The occupation of the electron levels is in accordance with the Pauli exclusion principle. Two electrons per $\vec{k}(k_x, k_y, k_z)$ vector are allowed, with opposite spin. The electron levels are filled in order of increasing energy, beginning with the level of lowest energy ($E = 0$). Since we deal with a huge number of electrons, the occupied volume in k -space will form a sphere with radius k_F ; the corresponding energy is the Fermi energy $E_F = \frac{\hbar^2 k_F^2}{2m_e}$ (Figure 4). The number of electrons is equal to twice the number of k points within the sphere, hence

$$N(E \leq E_F) \equiv N = 2 \frac{(4/3)\pi k_F^3}{(2\pi/L)^3} = \frac{k_F^3}{3\pi^2} V \quad (18)$$

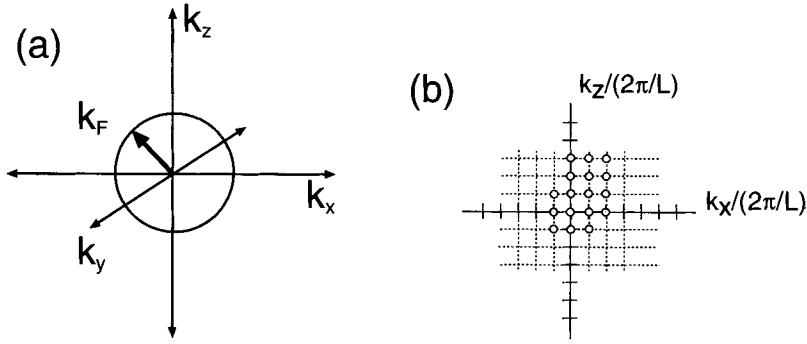


Figure 4. (a) The Fermi surface in k -space according to the free electron model of Sommerfeld. (b) The allowed free electron states are represented by discrete points (k_x, k_y, k_z) . The electrons with the highest kinetic energy are on the Fermi-surface.

The free electron density is therefore

$$n = N/V = \frac{k_F^3}{3\pi^2} \quad (19)$$

Another important quantity is the density of electron-energy levels in a small energy region between E and $E + dE$. It is found by calculation of the number of allowed k values in a shell of k -space between k and $k + dk$, being $\frac{4\pi k^2 dk}{(2\pi/L)^3}$, division by the volume, substitution of k by E in Eq. 15, and multiplication by two to account for the electron spin. The result is that the density of energy levels between E and $E + dE$ is given by

$$g(E) dE = \frac{\sqrt{2}m_e^{3/2}}{\pi^2\hbar^3} E^{1/2} dE \quad (20)$$

The average kinetic energy of a free electron follows from Eqs. 15, 19, and 20:

$$\langle E_k \rangle = \int_0^{E_F} g(E) E dE / n = 3/5 E_F \quad (21)$$

This result can be understood qualitatively by examination of Figure 4: a large fraction of the free electrons are located close to the Fermi surface. It is of interest to compare the average kinetic energy, $3/5 E_F$, with the average kinetic energy $3/2 k_B T$ of particles in the classical Maxwell-Boltzmann distribution, which was used by Drude (Figure 13). Using Eqs. 18 and 15, we can express E_F as a function of the free-electron density n . The free-electron density in most metals is between 10^{22} and 10^{23} cm^{-3} . This gives a Fermi energy of between 1.5 and 5 eV. The aver-

age kinetic energy in the Sommerfeld model is hence much larger than $3/2k_B T$ in the entire temperature range from 0 K up to room temperature.

4.3.3 Occupation of the Electron-Energy Levels

The distribution of the electron levels, $g(E)$, for a gas of independent and free electrons was calculated in the foregoing section. At 0 K, all energy levels up to the Fermi-energy level are occupied with one electron. (The spin degeneracy was accounted for in the density $g(E)$.) From the definition of chemical potential given in Section 4.2.1, $\mu = \left(\frac{\partial U}{\partial N} \right)_{S,V}$, it directly follows that the Fermi-level E_F is equal to the chemical potential μ at $T = 0$ K (and $\varphi = 0$). It can be shown quantitatively that this is true as long as $k_B T \ll E_F$ [11].

The occupation of the electron energy levels under thermal equilibrium at $T > 0$ K can be derived from statistical thermodynamics [11]. The reasoning results in the well-known Fermi–Dirac occupation function. The probability that an electron energy level at E is occupied by an electron is given by

$$f(E) = \frac{1}{1 + e^{(E - \mu_e)/k_B T}} \quad (22)$$

In the energy region $\mu_e - k_B T < E < \mu_e + k_B T$, there is a smooth transition from $f \approx 1$ to $f \approx 0$. In Figure 5, $g(E)f(E)$ is sketched for a free-electron gas.

When we add an electron to the system at a given temperature and pressure, the electron is necessarily positioned in a level close to μ_e . The increase in free energy of the electron system due to the addition of one electron is hence μ_e (Figure 5). Hence, the Fermi–Dirac occupation function is in accordance with the thermodynamic definition of the electrochemical potential.

4.3.4 The Origin of Energy Bands

In the free-electron model, the interaction of valence electrons with the lattice of core ions is neglected. As a result, the energy of the electrons varies in a continuous way with the wave vector \vec{k} (Eq. 15). Here, we discuss in a rather qualitative way how the $E(k)$ relationship is affected by the interaction of the electron waves with the periodic lattice. For simplicity, we consider electrons moving in the (positive) x

direction, hence with wave vectors $k_x = \frac{2\pi}{(L/m_x)}$ (Eq. 17) and corresponding wave-

lengths $\lambda = \frac{2\pi}{k_x} = \frac{L}{m_x}$. The distance between the centers of the core ions in the x direction is denoted by d_x . There is, hence, a modulation of the potential energy in the x direction, given by

$$E_p(x) = E_p(\text{max}) \cos(2\pi x/d_x) \quad (23)$$

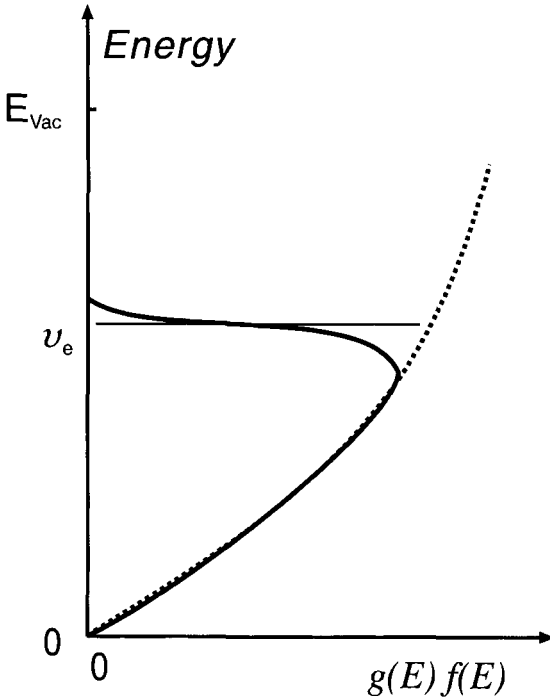


Figure 5. The density of electron states, $g(E)$, (dashed line), and the density of occupied states, $g(E)f(E)$, (full line, $T > 0$ K) as a function of the energy, according to the free electron model of Sommerfeld.

(Similar modulations hold for the y and z directions.) The electrons with low energy have wavelengths much larger than the lattice constant d_x . However, at higher energy there are free electrons with wavelengths obeying

$$\frac{\lambda}{2} \cong q \times d_x \quad (q = 1, 2, \dots) \quad (24)$$

Such electrons will be reflected backward and forward between two (adjacent) core ions (Bragg reflection). Due to the periodic lattice, electron propagation is prohibited in the x direction when the wave vector is equal (or close) to $k_x = \frac{2\pi}{\lambda} = \frac{\pi}{q \times d_x}$. This is also true for electrons moving in the negative x direction,

with $k_x = -\frac{\pi}{q \times d_x}$. Thus, propagating waves are prohibited because of Bragg reflection whenever

$$k_x = \pm \frac{\pi}{q \times d_x} \quad (q = 1, 2, \dots) \quad (25)$$

Electrons undergoing Bragg reflection correspond to standing waves. Two standing waves can be constructed by a linear combination of the waves propagat-

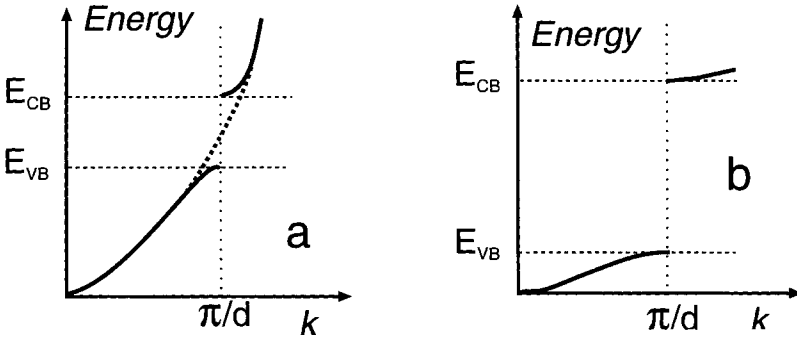


Figure 6. Sketches of the relationship between the energy E and wave vector k , when electron scattering with the periodic lattice is taken into account. (a) Nearly free electrons: the scattering is relatively weak, the free electron model is approximately valid for $k < \pi/d$. (b) Strong interaction: the free electron model is not valid. Tiny bands are separated by broad band gaps.

ing in the positive and negative x directions. The electron density corresponding to the first standing wave is centered at the core ions; the electron density corresponding to the second one is between the core ions. The two standing waves correspond to considerably different energies. With perturbation theory, it can be shown that the energy difference is equal to the amplitude of the periodic perturbation in the x direction, that is, $E_p(\text{max})$ (see Eq. 23).

It is concluded that scattering of the free-electron waves at the periodic lattice potential leads to discontinuities in the $E(k)$ relationship at k values of around

$k = \pm \frac{\pi}{q \times d}$ ($q = 1, 2, \dots$). Energy bands, separated by gaps, are formed. The first

and second energy bands, separated by a gap, are shown in Figure 6. A more elaborate treatment shows that the width of the energy bands and gaps is determined by the strength of the interaction between the valence electrons and the core ions. If the interaction is relatively weak, the energy bands extend over a large energy region (several eV), and the energy gaps are narrower than the energy bands [nearly free electrons, see Figure 6(a)]. The $E(k)$ relationship for free electrons holds

for most of the electrons in a band, except near $k = \pm \frac{\pi}{q \times d}$ ($q = 1, 2, \dots$). In

contrast, a strong interaction between valence electrons and core ions results in narrow bands, separated by broad gaps [Figure 6(b)]. The energy of the electrons increases with increasing value of k , with a much lower slope than for free electrons.

The acceleration of valence electrons due to an external force can be discussed with Newton's law ($\vec{a} = \vec{F}/m$), provided that the mass of an electron, m_e , is replaced by the effective mass, m_e^* , of an electron with given energy in a given lattice. It is found that

$$m_e^* = \hbar^2 / (d^2 E / dk^2) \quad (26)$$

From Eqs. 15 and 26 it is clear that the effective mass of free electrons is equal to the real mass. Comparison of Figures 6(a) and (b) shows that electrons strongly bound to the core ions have a larger effective mass than the (nearly) free electrons. This means that the lattice attenuates the response of electrons to an external force, in the same way that a viscous liquid moderates the movement of dissolved particles. However, close to $k = \pm \frac{\pi}{q \times d}$ ($q = 1, 2, \dots$), that is, at the top and bottom of the energy bands, quantum-mechanical features occur which have no classical counterpart. The effective mass of the electrons can be much larger and much smaller than the real mass, and can, indeed, be negative.

4.3.5 Metals, Semiconductors and Insulators

The energy levels at 0 K are filled in accordance with the Pauli principle, starting at $E = 0$. Two major classes of solids can be distinguished. When an energy band is not completely filled, the Fermi energy (chemical potential) is located in a band. There are empty electron levels available directly above the Fermi energy (Figure 5). This means that all electrons in such a band can respond to an external force (electric field) by increase of their kinetic energy. The electrical conductivity, which is the current density divided by the electrical field, is huge; this is the case of a metal. When filling of the electron levels leads to completely full energy bands, the Fermi energy lies in the gap between the highest occupied band (valence band, VB, top of the band denoted as E_{VB}) and lowest unoccupied band (conduction band, CB, bottom of the band denoted as E_{CB}). The electrons of the full valence band cannot increase their kinetic energy. The electronic conductivity is zero at 0 K, this is the case of an insulator [Figure 7(a)].

When $T > 0$ K, the population of the electron energy levels is described by the Fermi–Dirac distribution function (See Section 4.3.3, Eq. 22). At $T > 0$ K, electrons from the valence band can be thermally excited into the conduction band. As a result, the bottom of the CB becomes partly populated and the top of the VB partly depopulated [Figure 7(b)]. An empty electron level at the top of the valence band is called a (*valence-band*) *hole*. The concentration of holes, p , and of electrons, n , can be expressed as a function of the electrochemical potential with Eq. 22. We denote the density of electron levels within $k_B T$ from the top of the VB and the bottom of the CB as the effective density of valence band levels, N_{VB} , and conduction band levels, N_{CB} , respectively. The electron occupancy of the electron levels at the bottom of the CB is

$$f(E_{CB}) = \frac{n}{N_{CB}} = \frac{1}{1 + e^{(E_{CB} - \mu_e)/k_B T}} \cong e^{-(E_{CB} - \mu_e)/k_B T} \quad (27)$$

The density of holes at the top of the valence band is

$$\frac{p}{N_{VB}} = 1 - f(E_{VB}) = \frac{e^{(E_{VB} - \mu_e)/k_B T}}{1 + e^{(E_{VB} - \mu_e)/k_B T}} \cong e^{(E_{VB} - \mu_e)/k_B T} \quad (28)$$

In deriving Eqs. 27 and 28, it is assumed that $E_{CB} - \mu_e \gg k_B T$ and $\mu_e - E_{VB} \gg k_B T$.

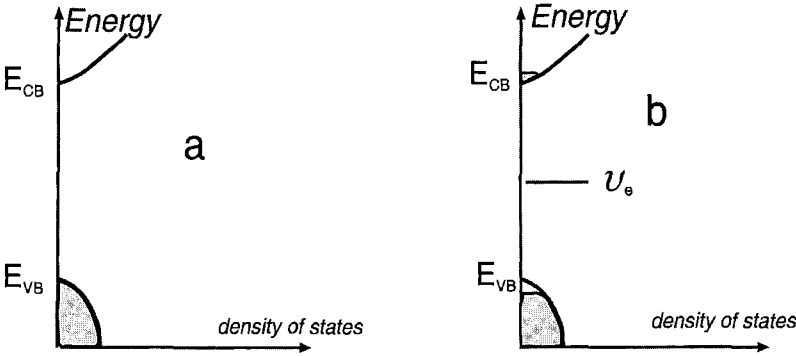


Figure 7. Sketch of the density of electron states as a function of energy for a typical intrinsic semiconductor or insulator. (a) 0 K; (b) $T > 0$ K, some electrons from the valence band are thermally excited into the conduction band in agreement with the Fermi-Dirac function. The electrochemical potential or Fermi level is located in the middle of the gap.

From Eqs. 27 and 28 it also follows that

$$\frac{np}{N_{CB}N_{VB}} = e^{-(E_{CB}-E_{VB})/k_B T} \quad (29)$$

The density of free electrons and holes is determined by the energy gap $E_{CB} - E_{VB}$ and the temperature. Solids for which $E_{CB} - E_{VB}$ is not larger than, say, $10 k_B T$ are often called intrinsic semiconductors. If the gap is much larger, the solids are classified as insulators. The distinction between intrinsic semiconductors and insulators is only quantitative.

4.3.6 Extrinsic Semiconductors

The incorporation of foreign atoms into an otherwise pure solid has important consequences for the optical and electronic properties. Here, we discuss how the electronic structure of insulators is affected by foreign atoms. Incorporation of foreign atoms usually leads to localized electron levels. A considerable effect on the opto-electronic properties is expected, when the localized levels are located in the gap between the VB and CB. For instance, P atoms can be incorporated into pure Si. This leads to localized levels just below E_{CB} . At 0 K, these levels are occupied with an electron [Figure 8(a)]. At room temperature, the localized electrons are easily excited into the CB. The density of free electrons is then approximately equal to the density of P atoms. Equations 27 to 29 are still valid. It is clear that doping of Si with P leads to a considerable increase in the electrochemical potential, which is now not far below E_{CB} [Figure 8(b)]. Doping of Si with P leads to an extrinsic *n*-type semiconductor, for which it holds that $n \gg p$. In contrast, doping of Si with Al (an atom with three valence electrons) leads to a *p*-type extrinsic semiconductor, whereby $p \gg n$ [Figure 9(a),(b)].

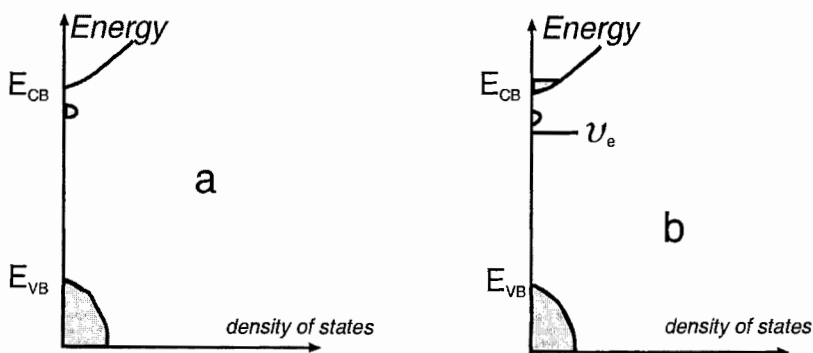


Figure 8. Sketch of the density of electron states as a function of energy for a typical *n*-type extrinsic semiconductor. (a) 0 K, the donor atoms correspond to localized filled states just below the conduction band edge; (b) $T > 0$ K, each donor atom is thermally ionized, this leads to a considerable density of electrons at the bottom of the CB; the electrochemical potential is not far below the CB edge.

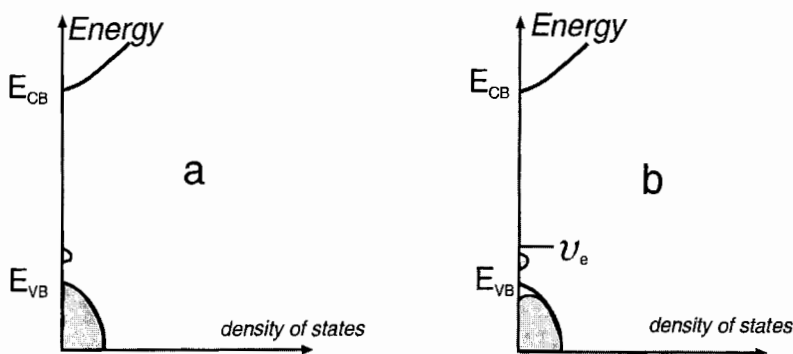


Figure 9. Sketch of the density of electron states as a function of energy for a typical *p*-type extrinsic semiconductor. (a) 0 K, the acceptors correspond to localized empty states just below the conduction band edge; (b) $T > 0$ K, each acceptor atom is thermally occupied with an electron from the valence band, this leads to a considerable density of holes at the top of the valence band. The electrochemical potential is not far above the VB edge.

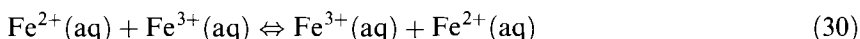
4.4 Electron-Energy Levels Corresponding to a Redox System

An important subject in this chapter on “Electron transfer at electrodes and interfaces” is to draw an analogy between electrochemical and interfacial electron transfer between two solid phases. Any theory dealing with electron transfer has a thermodynamic and a kinetic basis. In Section 4.2, it was shown that electrons flow or tunnel in the direction of decreasing electrochemical potential; the gradient of the electrochemical potential is the driving force behind a directed flow of electrons,

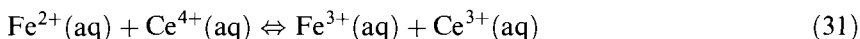
through a phase or across an interface. A net interfacial current density is the result of many elastic tunneling events between discrete electron levels on both sides of the interface. Thus, a kinetic treatment requires knowledge of the energetic distribution of electron levels, and their occupancy. Crystalline phases have been discussed in Section 4.3. Here, in Section 4.4.1, we will define the electrochemical potential of a dissolved redox system. Following the seminal work of Gerischer [12], we will discuss, in Section 4.4.2, how one can define the distribution of the empty and occupied electron energy levels corresponding to the oxidized and reduced species, respectively.

4.4.1 The Electrochemical Potential of a Dissolved Redox System

Electron transfer between oxidized and reduced species present in a liquid phase (water) is one of the simplest chemical processes. For instance,



and



In the equilibrium of Eq. 30, electrons are exchanged between the reduced species $\text{Fe}^{2+}(\text{aq})$ and the oxidized species $\text{Fe}^{3+}(\text{aq})$, and vice versa. Exchange occurs under conditions of chemical equilibrium; the reaction free energy ΔG_R is zero. In the second case, a mixture of $\text{Fe}^{2+}(\text{aq})$ and $\text{Ce}^{4+}(\text{aq})$ will spontaneously evolve to an equilibrium mixture of the oxidized and reduced species of both redox systems. The driving force, that is, the reaction free energy at any time is given by

$$\Delta G_R = N_A \{ [\mu(\text{Ce}^{3+}) - \mu(\text{Ce}^{4+})] - [\mu(\text{Fe}^{2+}) - \mu(\text{Fe}^{3+})] \} \quad (32)$$

where the chemical potentials of the reduced and oxidized species are defined per molecule, and ΔG_R is given per mole.

We can devise a galvanic cell, with two inert metal electrodes in two compartments, connected by a salt bridge in which the reaction shown in Eq. 31 evolves electrochemically. The metal electrode in the right compartment is in contact with a solution containing $\text{Fe}^{2+}(\text{aq})$ and $\text{Fe}^{3+}(\text{aq})$ ions, the other one is in contact with $\text{Ce}^{4+}(\text{aq})$ and $\text{Ce}^{3+}(\text{aq})$. A voltmeter will indicate a potential difference between the two electrodes. When they are connected by a wire (external circuit), electrons will flow from the left electrode through the external circuit to the right electrode, until equilibrium is reached. A galvanic cell allows one to monitor the chemical reaction under (nearly) reversible conditions (low rate of the reaction), if a variable resistance (load) in the external circuit is used. It is then reasonable to assume that the electrons in the left and right electrode are in equilibrium with the $\text{Fe}^{2+}(\text{aq})$, $\text{Fe}^{3+}(\text{aq})$ and $\text{Ce}^{4+}(\text{aq})$, $\text{Ce}^{3+}(\text{aq})$ redox system, respectively:

$$\mu_e(\text{left}) = \mu(\text{Fe}^{2+}) - \mu(\text{Fe}^{3+}) \quad (33)$$

$$\mu_e(\text{right}) = \mu(\text{Ce}^{3+}) - \mu(\text{Ce}^{4+}) \quad (34)$$

The reaction free energy ΔG_R is hence directly related to the electrochemical-potential difference measured between the two metal electrodes with a voltmeter (see Eqs. 32–34). Furthermore, the electrochemical potential of a redox system in solution is probed by measurement of the potential of a metal phase, in equilibrium with the redox system, with respect to a reference electrode.

We denote an electrochemical reaction more generally as



The forward process describes the transfer of an electron from a reduced species, which is in equilibrium with the solvent molecules, to a metal phase, with electrochemical potential μ_e ; this results, eventually, in an oxidized species in equilibrium with the solvent molecules. When electronic equilibrium is reached between the metallic phase and the solution, the electrochemical potential in both phases is equal and given by

$$\begin{aligned} \mu_e(\text{Ox/Red}) &= \mu(\text{Red}) - \mu(\text{Ox}) \\ &= [\mu^o(\text{Red}) - \mu^o(\text{Ox})] + k_B T \ln(c_{\text{Red}}/c_{\text{Ox}}) \end{aligned} \quad (36)$$

where the superscript indicates the standard state. Equation 36 is known as the Nernst equation.

4.4.2 The Fluctuating-Energy-Level Model Proposed by Gerischer

In Figure 10, the gradual solvation of the reduced and oxidized forms of a redox system is represented by plots of the potential energy of the ions as a function of a generalized solvation coordinate ρ . Figure 10(a) shows an overview, and (b) is more detailed. Roughly, ρ indicates the distance between the redox ions and the polar solvent molecules. The lower plot shows the potential energy of a the reduced species (Red) as a function of ρ , following

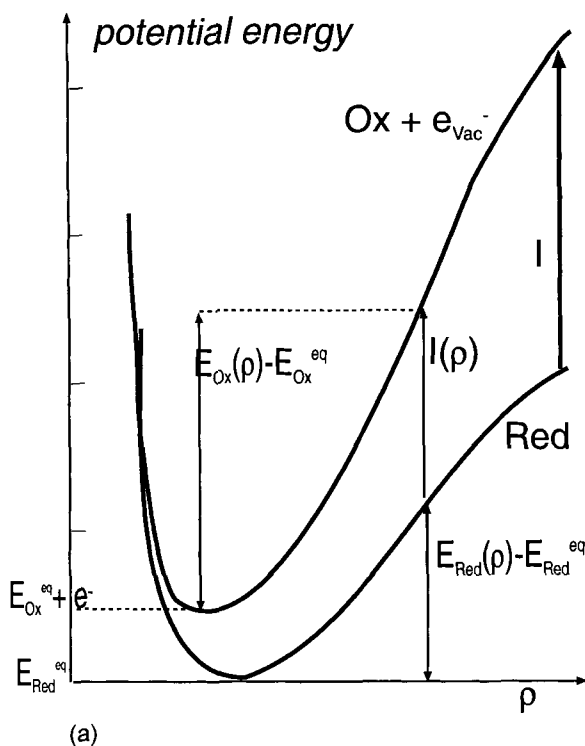


The energy of the reduced species is at a minimum when the equilibrium solvation structure $\text{Red}[\text{solv. Red}]$ is reached; this is characterized by $E_{\text{Red}}^{\text{eq}}$, $\rho = \rho_{\text{Red}}^{\text{eq}}$. The upper curve shows the potential energy of an electron in vacuum and the oxidized species which is gradually solvated:



The equilibrium structure of the solvated oxidized species is indicated as $\text{Ox}[\text{Solv. Ox}]$; the minimum energy and corresponding characteristic value of the solvation

Figure 10a. Solvation curves of the reduced (Red) and Oxidized (Ox) species of a redox system. The potential energies of Red and Ox (+ one electron in vacuum) are shown as a function of a generalized solvation coordinate ρ . I is the ionization energy in the gas phase; $I(\rho)$ is the ionization energy for a given solvation structure. The energy of a solvation structure with respect to equilibrium is indicated by $[E(\rho) - E^{\text{eq}}]$; $E_{\text{Red}}^{\text{eq}}$, and $E_{\text{Ox}}^{\text{eq}}$ correspond to equilibrium solvation. The marks on the potential energy axis are separated by 10 eV.



potential energy

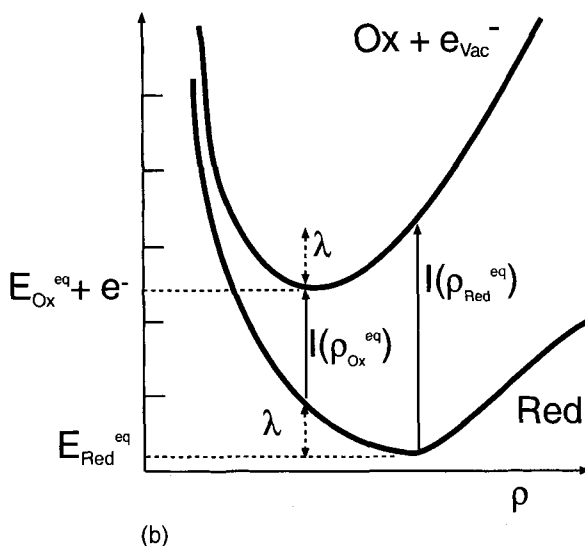


Figure 10b. Detail of Fig. 4.1 (a) showing a thermodynamic cycle involving ionization and solvent reorganization. $I(\rho_{\text{Red}}^{\text{eq}})$ is the ionization energy of the reduced species with an equilibrium solvation structure; $-I(\rho_{\text{Ox}}^{\text{eq}})$ is the electron affinity for the oxidized species with an equilibrium solvation structure. λ is the reorganization energy.

coordinate is denoted as $E_{\text{Ox}}^{\text{eq}}$ and $\rho_{\text{Ox}}^{\text{eq}}$, respectively. The solvation energy of an ion is proportional to the square of the charge of the ion and the inverse of the ion radius [8]. Solvation enthalpies can also be measured experimentally. For example, the solvation energies of the Fe^{2+} and Fe^{3+} ions in water are 20 and 45 eV, respectively.

Due to thermal movement of the solvent molecules in the solvation shell, the potential energy of the reduced and oxidized species may deviate from their equilibrium value. If we could probe the energy of an individual species over a sufficiently long time period, we would find a distribution in its energy around the minimum. The probability that the energy of the oxidized and reduced species deviates from the equilibrium value by $E(\rho) - E^{\text{eq}}$ is given by the Boltzmann distribution:

$$W_{\text{Ox}}(E - E_{\text{Ox}}^{\text{eq}}) = \frac{e^{-[E - E_{\text{Ox}}^{\text{eq}}]/k_B T}}{\int_0^\infty e^{-[E - E_{\text{Ox}}^{\text{eq}}]/k_B T} d(E - E_{\text{Ox}}^{\text{eq}})} \quad (39)$$

$$W_{\text{Red}}(E - E_{\text{Red}}^{\text{eq}}) = \frac{e^{-[E - E_{\text{Red}}^{\text{eq}}]/k_B T}}{\int_0^\infty e^{-[E - E_{\text{Red}}^{\text{eq}}]/k_B T} d(E - E_{\text{Red}}^{\text{eq}})} \quad (40)$$

The merit of Gerischer's early paper [12] is that he found a way to express these probabilities as a function of the electronic energy, whereby the standard electrochemical potential acts as a reference point. The reasoning is as follows. First, the ions in the gas phase ($\rho \rightarrow \infty$) are considered: the energy difference between the two curves is the ionization energy, I , of the reduced ion. For example, the ionization energy for $\text{Fe}^{2+}(\text{g})$ to $\text{Fe}^{3+}(\text{g})$ is 30.6 eV per ion. More generally, the vertical energy difference between the solvation curves, that is, $E[\text{Ox}(\rho) + e_{\text{Vac}}] - E_{\text{Red}}(\rho)$, is the ionization energy $I(\rho)$ of the reduced species at a given nonequilibrium solvation. In this ionization process, the nuclear coordinates remain unchanged (Franck-Condon principle). Gerischer used the vertical energy difference $-I(\rho)$ as an independent variable for further considerations. We denote

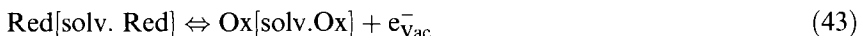
$$-I(\rho) = E_{\text{Red}}(\rho) - E_{\text{Ox}}(\rho) - E_{\text{Vac}} \quad (41)$$

Since there is a unique and continuous relationship between $-I(\rho)$ and the solvation coordinate ρ , there is also a unique and continuous relationship between the thermal deviations from equilibrium $[E_{\text{Ox}}(\rho) - E_{\text{Ox}}^{\text{eq}}$ and $E_{\text{Red}}(\rho) - E_{\text{Red}}^{\text{eq}}$] and $-I(\rho)$. This means that the probability of nonequilibrium solvation can be expressed as a function of the vertical energy difference $-I(\rho)$:

$$\left. \begin{aligned} W_{\text{Ox}}(E - E_{\text{Ox}}^{\text{eq}}) &\Rightarrow W_{\text{Ox}}[-I(\rho)], \\ \text{and} \\ W_{\text{Red}}(E - E_{\text{Red}}^{\text{eq}}) &\Rightarrow W_{\text{Red}}[-I(\rho)] \end{aligned} \right\} \quad (42)$$

To find a reference point on the $-I(\rho)$ coordinate axis, we consider the following

equilibrium:



If we compare the electrochemical equilibrium at a metal (Eq 36) with the equilibrium of Eq. 43, we see that in the latter the electron is promoted from the Fermi level in the metal to vacuum by an amount of work equal to the work function being performed, that is, $E_{\text{vac}} - \mu_e^o(\text{Ox/Red})$. Under standard conditions, it holds that, $\mu(e_{\text{vac}}^-) + \mu^o(\text{Ox, solv. Ox}) - \mu^o(\text{Red, solv. Red}) = 0$, and hence that

$$\mu(e_{\text{vac}}^-) = \mu^o(\text{Ox/Red}) + [E_{\text{vac}} - \mu^o(\text{Ox/Red})] \quad (44)$$

The energy difference $E_{\text{Red}}^{\text{eq}} - [E_{\text{Ox}}^{\text{eq}} + E_{\text{vac}}]$ corresponds to $\mu^o(\text{Red, solv. Red}) - \mu^o(\text{Ox, solv. Ox})$, hence to $\mu_e^o(\text{Ox/Red})$ on the electrochemical potential scale. The standard electrochemical potential of the redox system, $\mu_e^o(\text{Ox/Red})$, which is located by amount of energy given by $E_{\text{vac}} - \mu_e^o(\text{Ox/Red})$ below the vacuum level, forms the characteristic reference point (see Figure 12 further on). Inspection of Figure 10(a),(b) shows that

$$[E_{\text{Red}}(\rho) - E_{\text{Red}}^{\text{eq}}] + I(\rho) = [E_{\text{Ox}}(\rho) - E_{\text{Ox}}^{\text{eq}}] + [E_{\text{Ox}}^{\text{eq}} - E_{\text{Red}}^{\text{eq}}] \quad (45a)$$

Two special cases of this general relationship are also important. The first one holds for the discrete case that $\rho = \rho_{\text{Red}}^{\text{eq}}$:

$$I(\rho_{\text{Red}}^{\text{eq}}) = [E_{\text{Ox}}(\rho_{\text{Red}}^{\text{eq}}) - E_{\text{Ox}}^{\text{eq}}] + [E_{\text{Ox}}^{\text{eq}} - E_{\text{Red}}^{\text{eq}}] \quad (45b)$$

The second relationship holds for the case that $\rho = \rho_{\text{Ox}}^{\text{eq}}$:

$$[E_{\text{Red}}(\rho_{\text{Ox}}^{\text{eq}}) - E_{\text{Red}}^{\text{eq}}] + I(\rho_{\text{Ox}}^{\text{eq}}) = [E_{\text{Ox}}^{\text{eq}} - E_{\text{Red}}^{\text{eq}}] \quad (45c)$$

The energy difference $[E_{\text{Ox}}(\rho_{\text{Red}}^{\text{eq}}) - E_{\text{Ox}}^{\text{eq}}]$ is the heat output when the solvation structure around the oxidized species is reorganized, starting from the equilibrium solvation structure typical for the reduced species and ending with the equilibrium structure typical for the oxidized species. $[E_{\text{Red}}(\rho_{\text{Ox}}^{\text{eq}}) - E_{\text{Red}}^{\text{eq}}]$ has an analogous meaning for reorganization around the reduced species. The difference between the values of $[E_{\text{Ox}}(\rho_{\text{Red}}^{\text{eq}}) - E_{\text{Ox}}^{\text{eq}}]$ and $[E_{\text{Red}}(\rho_{\text{Ox}}^{\text{eq}}) - E_{\text{Red}}^{\text{eq}}]$ is small. For simplicity, it is assumed in the literature that they are equal. These reorganization energies are both denoted as λ :

$$\lambda = [E_{\text{Ox}}(\rho_{\text{Red}}^{\text{eq}}) - E_{\text{Ox}}^{\text{eq}}] = [E_{\text{Red}}(\rho_{\text{Ox}}^{\text{eq}}) - E_{\text{Red}}^{\text{eq}}] \quad (46)$$

In Figure 11, the thermal energies of nonequilibrium solvation $[E_{\text{Red}}(\rho) - E_{\text{Red}}^{\text{eq}}]$ and $[E_{\text{Ox}}(\rho) - E_{\text{Ox}}^{\text{eq}}]$ are presented as a function of the vertical energy difference (the y axis). It is clear that $[E_{\text{Red}}(\rho) - E_{\text{Red}}^{\text{eq}}]$ is zero at $-I(\rho_{\text{Red}}^{\text{eq}})$, that $[E_{\text{Ox}}(\rho) - E_{\text{Ox}}^{\text{eq}}]$ is zero at $-I(\rho_{\text{Ox}}^{\text{eq}})$, and that $[E_{\text{Red}}(\rho) - E_{\text{Red}}^{\text{eq}}]$ equals $[E_{\text{Ox}}(\rho) - E_{\text{Ox}}^{\text{eq}}]$ at the reference point $E_{\text{Red}}^{\text{eq}} - E_{\text{Ox}}^{\text{eq}}$, that is, at $\mu_e^o(\text{Ox/Red})$ (see Eqs. 45). In Figure 12, the proba-

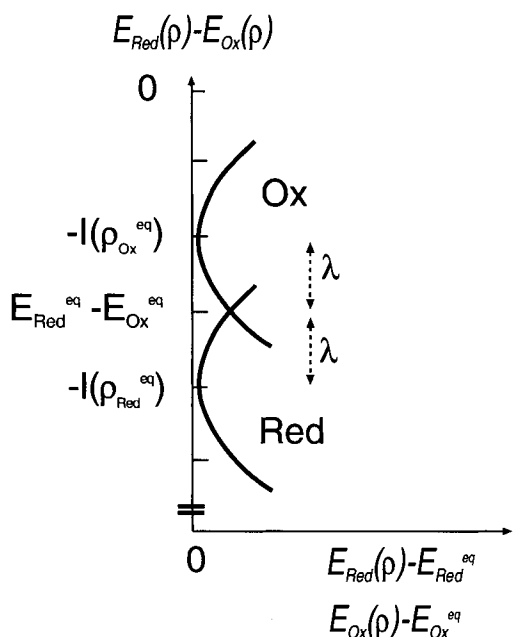


Figure 11. Plot of the thermal activation energy corresponding to non-equilibrium solvation $[E(\rho) - E^{\text{eq}}]$ of the oxidized and reduced species (horizontal axis) as a function of the ionization energy $[E_{\text{Red}}(\rho) - E_{\text{Ox}}(\rho)]$. The plot is derived from Fig. 4.1. (see section 4.2). λ is the reorganization energy of the outer sphere redox system.

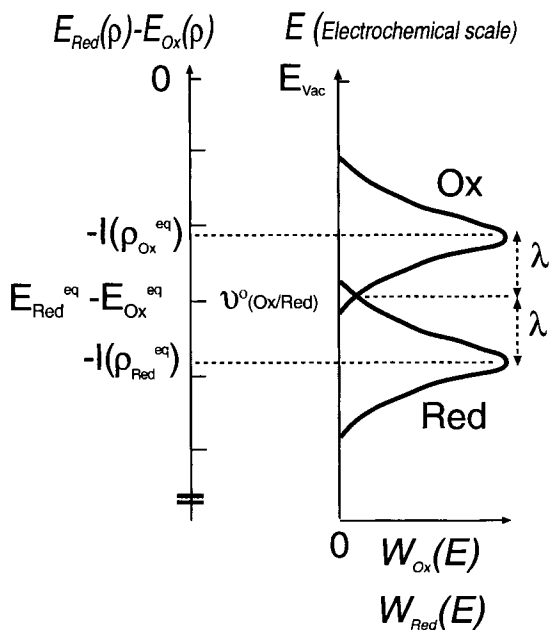


Figure 12. Sketch of the probabilities $W_{\text{Ox}}(E)$ and $W_{\text{Red}}(E)$ to find an empty or filled electron level corresponding to an oxidized and reduced ion, respectively, as a function of the electron free energy (vertical axis). The standard electrochemical potential $\mu^{\circ}(\text{Ox/Red})$ with respect to the vacuum level acts as a reference point.

bilities $W_{\text{Ox}}[-I(\rho)]$ and $W_{\text{Red}}[-I(\rho)]$ are sketched in a qualitative way (using Eqs. 39–40 and Figure 11). It is clear that $W_{\text{Ox}}[-I(\rho)]$ and $W_{\text{Red}}[-I(\rho)]$ have their maximum at $-I(\rho_{\text{Ox}}^{\text{eq}})$ and $-I(\rho_{\text{Red}}^{\text{eq}})$, respectively, and that the probabilities are equal at $\mu_e^o(\text{Ox/Red})$. From Eq. 45c, it follows that $-I(\rho_{\text{Ox}}^{\text{eq}})$ is located at $[E_{\text{Red}}^{\text{eq}} - E_{\text{Ox}}^{\text{eq}}] + [E_{\text{Red}}(\rho_{\text{Ox}}^{\text{eq}}) - E_{\text{Red}}^{\text{eq}}]$, that is, an energy λ above $\mu_e^o(\text{Ox/Red})$. Similarly, it follows from Eq. 45b that the maximum of $W_{\text{Red}}[-I(\rho)]$ is located at λ below $\mu_e^o(\text{Ox/Red})$.

The foregoing discussion makes it clear that the vertical energy difference $-I(\rho)$ forms an electronic energy coordinate axis with a characteristic reference point, $\mu_e^o(\text{Ox/Red})$, which is experimentally accessible. This means that the probability functions can be used directly in models for electrochemical electron transfer between a solid and a simple redox system (see Sections 4.8 and 4.9). In the literature, the electronic energy coordinate axis has been denoted as E , and the characteristic points as $\mu_e^o(\text{Ox/Red})$ (or E_F^o), and E_{Ox}^m and E_{Red}^m denoted the energies corresponding to the maximum $W_{\text{Ox}}(E)$ and $W_{\text{Red}}(E)$ values, respectively. For quantitative purposes (see Sections 4.8 and 4.9), the probability functions are expressed as normalized Gauss functions:

$$W_{\text{Ox}}(E) = (4\pi k_B T \lambda)^{-1/2} e^{-(E - E_{\text{Ox}}^m)^2 / 4\lambda k_B T} \quad (47)$$

and

$$W_{\text{Red}}(E) = (4\pi k_B T \lambda)^{-1/2} e^{-(E - E_{\text{Red}}^m)^2 / 4\lambda k_B T} \quad (48)$$

The density of empty and occupied electron-energy levels corresponding to a dissolved redox system are given by

$$g_{\text{Ox}}(E) = W_{\text{Ox}}(E) c_{\text{Ox}} \quad (49)$$

and

$$g_{\text{Red}}(E) = W_{\text{Red}}(E) c_{\text{Red}} \quad (50)$$

respectively. The electrochemical potential of the redox system in solution corresponds to the energy whereby $g_{\text{Ox}}(E) = g_{\text{Red}}(E)$.

4.5 Interfacial Structure

Research dealing with the atomic structure and charge distribution at crystal surfaces is a modern and fast-developing field. Metal and semiconductor surfaces show many interesting features, and this is certainly also the case for electrochemical interfaces, that is, metal (or semiconductor)/(aqueous) solution interfaces. This section is not intended to give a comprehensive overview of surface and interfacial

structures. The aim is to provide a general (but somewhat simplified) picture of electrochemical interfaces, convenient for a further discussion of electrochemical electron transfer. In the last two decades it became clear that the surface structure of the solid is a relevant factor for a better understanding of electrochemical interfaces. Therefore, this surface structure is discussed first. The metal/solution electrochemical interface can then be “constructed” by taking into account physisorption and chemisorption of water and ions.

4.5.1 Metal Surfaces

Crystals are characterized by a regular array of atoms. In the bulk, all atoms are surrounded by their neighbors in the same way. However, atoms at the surface can only interact with each other and the inner neighbors. This results in surface tension, and an inward contraction of the surface atoms (or core ions).

A second surface effect is due to the high kinetic energy and small mass of the free electrons (see Section 4.3). Electrons impinging on the surface wall may penetrate this wall; this decreases their kinetic energy and increases their potential energy. Electrons spill over the surface plane, which corresponds to the center of the core ions. A time-averaged sketch of the distribution of the electrons and ions near the surface of a metal is presented in Figure 13(a).

The free-electron model allows a more quantitative discussion of the probability of finding electrons in a limited region just outside the surface plane. Consider a metal surface in the (y, z) -plane (Figure 14). The potential energy in the crystal is set to zero. The potential energy of an electron at rest, outside the metal is denoted as E_{vac} . It is clear that the Fermi energy, E_F , of the electrons is considerably below E_{vac} ; the work function $E_{\text{vac}} - \mu_e$ is generally in the order of a few eV. From Eqs. 13–14 it follows that the component of the wave functions in the x direction is given by

$$\psi(x) = \frac{1}{\sqrt{L}} e^{ik_x x} \quad (51)$$

and the corresponding kinetic energy is by given

$$E(k_x) = \frac{\hbar^2 k_x^2}{2m_e} \quad (52)$$

The Schrödinger equation for the region outside the metal is

$$\frac{-\hbar^2}{2m_e} \frac{\partial^2 \psi(x)}{\partial x^2} + E_{\text{vac}} \psi(x) = E(x) \psi(x) \quad (53)$$

It is important to note that the energy of the electron in rest in vacuum, E_{vac} , is larger than the total energy of the impinging electron. Nevertheless, wave functions

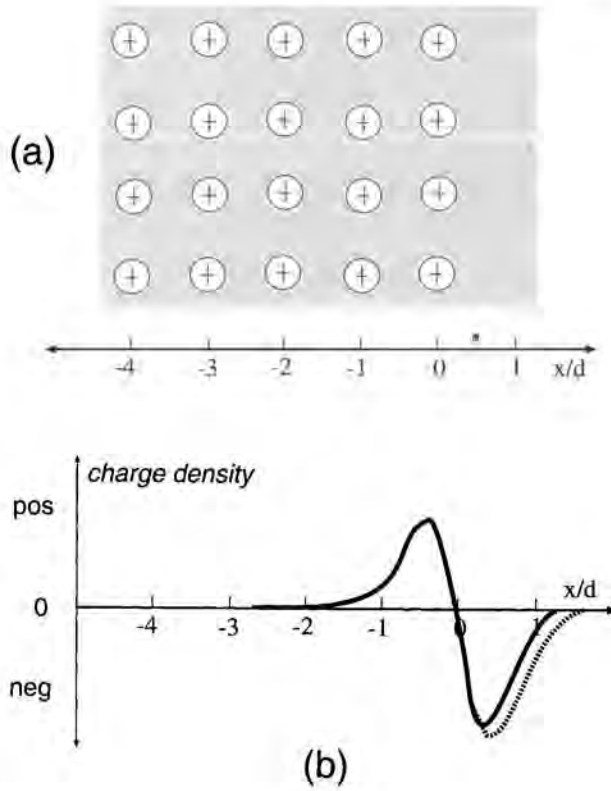


Figure 13. Schematic representation of the double layer at a metal surface. (a) Lattice of positive core ions (lattice parameter is d), the electron density is indicated with grey; electrons spill over the jellium plane (at $x/d = 0$). (b) Charge density, roughly corresponding to the jellium model. Just inside the metal, the charge density is positive, the spill-over region has a negative charge. The dashed line indicates the charge density when there is a net negative surface charge.

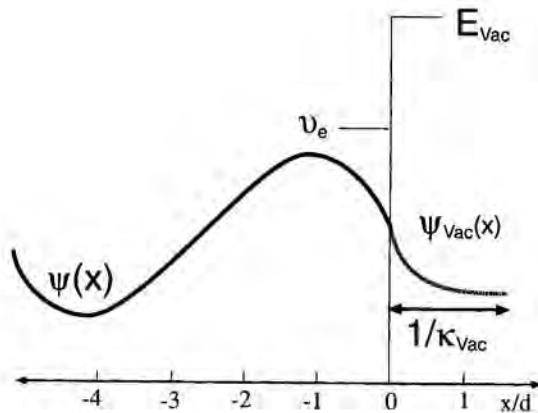


Figure 14. Free electron wave function corresponding to an electron moving in the x -direction, perpendicular to the surface. The dashed line shows the exponential decay of the wave function in vacuum; the decay length being $1/\kappa_{\text{vac}}$.

of the form

$$\psi_{\text{vac}}(x) = \frac{1}{\sqrt{L}} e^{-\kappa_{\text{vac}} x} \quad (54)$$

with

$$\kappa_{\text{vac}}(x) = \left[\frac{2m_e [E_{\text{vac}} - E(x)]}{\hbar^2} \right]^{1/2} \quad (55)$$

are solutions of Eq. 53. The wave functions of electrons impinging on the surface decay exponentially outside the metal. The decay length $1/\kappa_{\text{vac}}$ depends on the effective barrier height $E_{\text{vac}} - E(x)$. From Eq. 55, it follows that the decay length $1/\kappa_{\text{vac}}$ is 1.9 Å for a barrier height of 1 eV. The exponential decay of wave functions is a key feature in understanding electron tunneling (see Section 4.6). It is furthermore clear that there is a considerable probability of finding free electrons at the other side of the surface plane in a region extending over some unit cells (see also Figure 13).

The electron distribution at metal surfaces has been discussed with more realistic models than the free-electron model being used. The “jellium” model [13] is often used in surface science; it takes into account electron–electron interactions while the charge of the core ions is smeared out homogeneously over the crystal. It also forms a basis for realistic models of the electrochemical double layer [2]. The “jellium” model results in a picture for the double layer at the metal surface which differs from Figure 13 in details only.

The time-averaged situation is sketched in Figure 13(a). In Figure 13b, the charge density is sketched. There is an excess of positive charge just inside the metal and an excess of negative charge just outside the metal surface. Electron spill-over gives rise to an electrical double layer at the metal surface characterized by a surface dipole and a surface potential drop.

The surface double layer is important for the electrochemical potential. In Section 4.2, it was discussed that the (electro)chemical potential of the electrons depends on the potential of the metal phase. If we take the potential energy of an electron at rest outside the metal (hence E_{vac}) as a reference, the electrochemical potential can be rewritten as follows (see Eq. 56):

$$\mu_e = \mu + (-e\varphi - E_{\text{vac}}) \quad (56)$$

where μ is the contribution due to the kinetic energy of the electrons in the metal phase and $-e\varphi - E_{\text{vac}}$ is the potential energy referred to vacuum. The drop of the potential energy over the surface region is thus $-e\varphi - E_{\text{vac}}$. In Figure 15a, the situation is sketched for a metal surface where the net surface-charge density is zero. This means that the potential energy of an electron moving away from the surface reaches E_{vac} within a distance of a few unit cells from the surface plane (or jellium edge). We define the potential drop across the double layer of the metal surface as

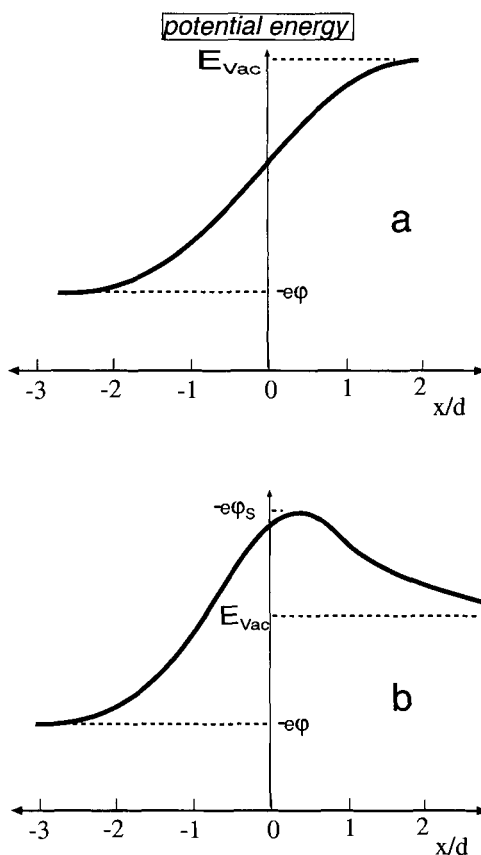


Figure 15. Drop of the potential energy (experienced by electrons) at a metal surface. (a) The nett charge density of the metal surface is zero. The drop in the potential energy corresponds to the surface dipole layer. (b) The nett charge density of the metal surface is negative. An electron approaching the metal phase experiences the nett negative charge density over a considerable distance.

$$\Delta\phi_M = \phi - \phi_S \quad (57)$$

where ϕ_S is the electrostatic potential at the outer side of the jellium double layer (Figure 15). We can say that for an *uncharged surface* the entire difference, $-e\phi - E_{vac}$, is a good approximation of the potential drop $\Delta\phi_M = \phi - \phi_S$ across the double layer. Experimentally, $\Delta\phi_M$ can be measured with a Kelvin probe [11]. Values in the region of one eV are commonly found. This makes it clear that the electrical field in the double layer is very large.

It is of interest to discuss what happens if a metal crystal is charged. A negative charge means that the metal phase contains an excess electrons compared to the neutral state; a positive charge indicates an electron deficiency. An outcome of the jellium model is that the surface-charge density, σ , mainly affects the electron spill-over region. A net negative surface charge corresponds to a spill-over region which is somewhat more extended compared to the neutral state (Figure 13(b), dashed curve); the charge of the spill-over region is then not fully compensated by the excess posi-

tive charge at the other side of the jellium edge. The profile of the potential energy is depicted in Figure 15(b). Due to the net negative charge, an electron just outside the metal has a higher potential energy. The potential energy only reaches E_{vac} at a considerable distance from the surface. Because of the negative charge density $\delta\sigma$, the surface potential drop $\Delta\phi_M = \phi - \phi_s$ increases with respect to the neutral state. Another effect of excess electrons in the metal crystal is that the electrochemical potential, μ_e , of the electrons in the metal phase increases with respect to E_{vac} . A net negative charge makes the entire potential energy drop $-e\phi - E_{\text{vac}}$ less negative than the neutral case. In other words, the thermodynamic work function $E_{\text{vac}} - \mu_e$ decreases because of an increase in the negative surface charge.

For a further discussion of the electrochemical double layer, it is of interest to define a differential capacitance, C_M , for the jellium double layer:

$$C_M = \frac{\partial\sigma}{\partial\Delta\phi_M} = \frac{\partial\sigma}{\partial(\phi - \phi_s)} \quad (58)$$

The jellium double layer is highly polarizable and should not be compared with the classical parallel-plate capacitor. For instance, the thickness of the double layer changes with the charge density. An infinitesimal negative charge density $\delta\sigma$ (<0) on the surface leads to an extension of the spill-over region and an increase in the surface potential $\partial\Delta\phi_M = \partial(\phi - \phi_s) > 0$, hence $C_M < 0$! The double layer of the metal surface has a considerable influence on the structure of the electrochemical double layer. It will also become clear that several features of the electrochemical double layer at a metal can only be understood if the metal surface dipole is taken into account.

4.5.2 Physisorption and Chemisorption

If a gas is brought into contact with a clean metal surface, molecules will absorb on the metal surface. The metal surface itself is characterized by a dipole and a large polarizability. Dipole–dipole and London interactions act between the metal surface and the molecules; hence polar and nonpolar molecules and ions may become adsorbed. Physisorption may influence the potential energy drop $-e\phi - E_{\text{vac}}$ and, hence, the chemical potential μ_e with respect to E_{vac} . The dipole–dipole interactions can lead to a preferential orientation of physisorbed polar molecules such as H_2O .

If a metal orbital and an orbital from the absorbed species overlap considerably, bonding and antibonding orbitals are formed. The bonding and antibonding orbitals correspond to surface energy levels. The occupation of these energy levels is determined by their energy with respect to the Fermi energy μ_e . The binding energy can be considerably larger than the average thermal energy at room temperature: this corresponds to chemisorption. Consider, for instance, chemisorption of a Cl atom on a metal surface. The bonding atomic orbital lies considerably below μ_e and is occupied with two electrons. Due to the electronegativity of Cl we have a strongly polar metal–Cl bond. Chemisorption of Cl leads to a local increase of the surface dipole moment and may also increase the interfacial potential drop $\Delta\phi_M = \phi - \phi_s$.

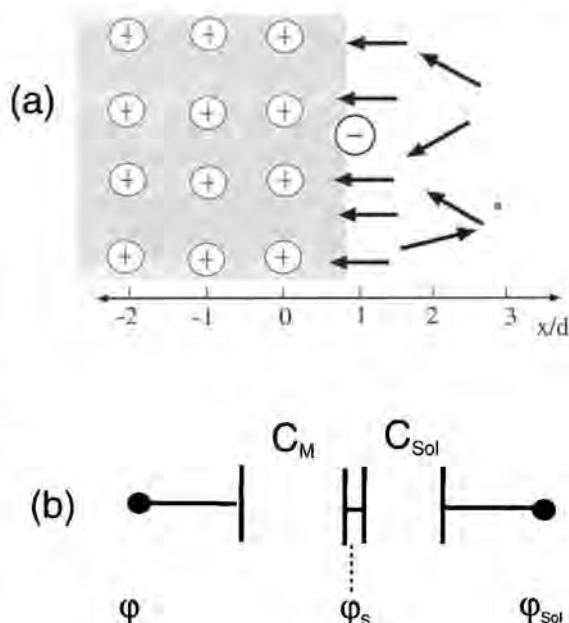


Figure 16. Schematic representation of an electrochemical double layer at a metal/electrolyte solution interface. (a) The jellium double layer (with electron spill-over region) contacts a layer of (ordered) solvent molecules, chemisorption of a negative ion is also shown. (b) Representation of the double layer capacitance as a series connection of the capacitance corresponding to the double layer of the metal surface, and the capacitance of the Helmholtz layer at the solution side.

It is clear that the interaction of molecules with the metal surface has a considerable influence on the electrochemical potential of the electrons in the metal with respect to the vacuum level.

4.5.3 The Metal/Solution Interface

Physisorption of a small number of water molecules on a clean metal surface leads to a highly oriented (sub)monolayer. If we admit more water, the molecules will interact with the first layer and hydrogen bonds will be formed. A few molecular distances away from the metal surface, the structure of the water phase becomes identical to that in the bulk. If ions are present in the water phase, they can compensate for a net charge on the metal surface. Figure 16 shows a typical structure of a metal/water electrochemical double layer. The concentration of ions in the water phase is assumed to be relatively large ($\geq 10^{-2}$ M). This means that the charge on the metal surface is compensated by ions in a narrow region, of a few Å. Figure 16(a) also shows the possibility that polarizable negative ions are chemisorbed on the metal surface.

Experimental investigations with mercury electrodes were very successful in the first half of this century [1]. Mercury has the advantage of offering a very clean surface. Moreover, with a hanging mercury drop electrode, measurement of not only the interfacial capacitance, but also the interfacial surface tension as a function of surface charge density is possible. A combination of careful experiments and subtle thermodynamic theory led to a detailed empirical picture of the mercury/

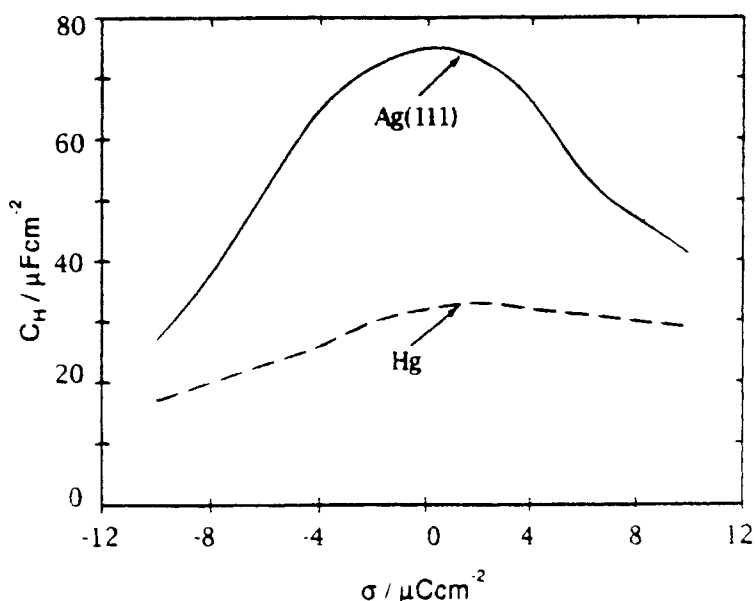


Figure 17. The double layer capacitance measured with two different metals (Ag and Hg) in an aqueous electrolyte solution as a function of the charge density at the surface. The influence of the nature of the metal phase on the total capacitance is clearest around the point of zero charge. The results are taken from W. Schmickler, *Chem. Rev.* 96, 3177 (1996).

aqueous solution interface [1]. However, the role of the metal double layer was not recognized in those days. Later measurements of the interfacial capacitance $C_{M/Sol}$ with a variety of metals and electrolyte solutions made it clear that the capacitance is determined by the nature of the metal, the solution, and the charge density. The capacitance of a Hg and a Ag electrode in aqueous solution is shown as a function of the charge density in Figure 17 [2]. It is clear that $C_{M/Sol}$ reaches a pronounced maximum near the point of zero charge ($\sigma = 0$), and that, with increasing negative and positive charge density, $C_{M/Sol}$ becomes smaller and tends to a value of about $20 \times 10^{-6} \text{ F cm}^{-2}$. The difference between the two metals is most obvious at low charge density. Measurements with different metal electrodes at the point of zero charge indicated that $C_{M/Sol}$ gradually increases with the free-electron density of the metal, and hence with the polarizability of the metal-surface double layer.

The results can be understood, at least qualitatively, if the surface double layer of the metal itself is taken into account [2]. A simple picture is presented in Figure 16; a water layer with specific orientation contacts the jellium double layer. Conceptually, the potential drop over the electrochemical double layer, $\Delta\phi_{M/Sol}$, can be separated into two contributions: a drop over the metal double layer and a drop over the first layer of solvent molecules [see Figure 16(b)]:

$$\Delta\phi_{M/Sol} = (\phi - \phi_s) + (\phi_s - \phi_{Sol}) \quad (59)$$

capacitance

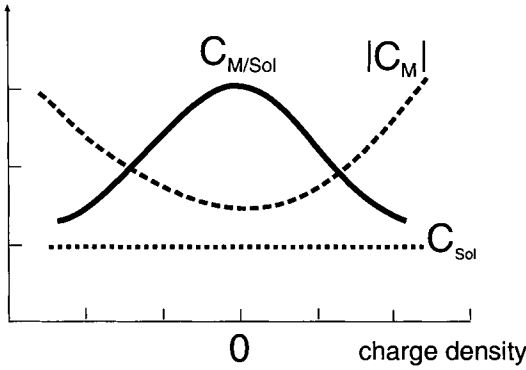


Figure 18. Estimation of the capacitance of the electrochemical double layer $C_{M/Sol}$ as a function of the charge density, using a series connection of the capacitance of the double layer of the metal surface ($C_M < 0$) and the molecular Helmholtz layer (C_{Sol}). It is found that the electrochemical double layer capacitance shows a maximum at around the point of zero charge, where the influence of the metal phase is strongest. This is in qualitative agreement with the experimental results (Fig. 17). The bars on the capacitance axis indicate 2×10^{-5} F/cm², the bars on the horizontal axis indicate 5×10^{-6} C/cm².

The capacitance of the electrochemical double layer is then

$$\frac{1}{C_{M/Sol}} = \frac{\partial(\varphi - \varphi_S)}{\partial\sigma} + \frac{\partial(\varphi_S - \varphi_{Sol})}{\partial\sigma} = \frac{1}{C_M} + \frac{1}{C_{Sol}} \quad (60)$$

where the capacitance of the jellium double layer is negative (Eq. 58). For convenience we rewrite Eq. 60 as

$$C_{M/Sol} = \frac{C_M C_{Sol}}{C_M + C_{Sol}} = \frac{|C_M| C_{Sol}}{|C_M| - C_{Sol}} \quad (61)$$

It is clear that $|C_M|$ being $\frac{-\partial\sigma}{\partial(\varphi - \varphi_S)}$ should be larger than C_{Sol} if the double layer capacitance $C_{M/Sol}$ is to be positive.

Experimental results, such as those presented in Figure 17, can be interpreted on the basis of the above model (see Figure 18). It should be realized that the jellium double layer is most easily polarizable at around the point of zero charge ($\sigma = 0$); $|\partial(\varphi - \varphi_S)|$ is then largest for a given change of the charge density $\partial\sigma$. This means that $|C_M|$ is smallest around the point of zero charge (Eq. 58). To a first approximation, C_{Sol} can be assumed to be independent of the charge density. It follows then from Eq. 61 that the double-layer capacitance $C_{M/Sol}$ has a maximum at around $\sigma = 0$; and that $C_{M/Sol}$ gradually decreases to C_{Sol} with increasing positive

or negative charge density (see Figure 18). This feature agrees with the experimental results of Figure 17. The model also explains why the influence of the nature of the metal on the electrochemical double-layer capacitance is most obvious in the region of the point of zero charge. The model used here is certainly oversimplified and the agreement between the model and experimental results is only qualitative. A further discussion can be found in Ref. [2]. It is, however, clear that the highly polarizable jellium layer cannot be neglected in modern electrochemistry. Recently, strong evidence has been found to show that this layer also plays an essential role in the kinetics of electrochemical metal dissolution [14].

4.5.4 The Semiconductor/Solution Interface

Similar to metal/solution interfaces, the potential drop at the solution side of the semiconductor/electrolyte interface, $\varphi_s - \varphi_{\text{sol}}$, is determined by chemisorption of ions (such as H^+ , OH^-) and the preferential orientation of a layer of solvent molecules. However, the density of free carriers in a semiconductor is much smaller than the free-electron density in a metal. As a result, the part of the interfacial potential difference located at the solid side of the interface, that is, $\varphi - \varphi_s$, extends much deeper into the solid than for a metal/liquid interface. Investigations in the field of semiconductor electrochemistry usually deal with large-band-gap extrinsic semiconductors, that is, with $E_{\text{CB}} - E_{\text{VB}} > 1$ eV. Here, we will focus on the interface between an n -type semiconductor and a concentrated aqueous electrolyte. A similar picture is obtained for a p -type semiconductor/electrolyte interface.

An n -type semiconductor at room temperature has free electrons in the conduction band compensated by positively charged immobile ionized donors (Section 4.3.6). The concentration of free electrons (donors), n_{bulk} , is usually between 10^{16} and 10^{19} cm^{-3} , hence $10^6 - 10^3$ smaller than in a metal. A common situation is that the electrons are transferred from the semiconductor to a redox system, so that equilibrium is achieved. The surface region of the solid is then depleted of free electrons (Figure 19); a depletion layer of width d_{sc} is formed. The concentration of free electrons in the depletion layer, $n(x)$, is much smaller than the concentration of the immobile donors n_{bulk} . Thus, the charge density in the depletion layer per unit volume is en_{bulk} . Therefore, the surface charge density at the solid side is:

$$\sigma_{\text{sc}} = e \int_0^{d_{\text{sc}}} [n_{\text{bulk}} - n(x)] dx \cong en_{\text{bulk}} d_{\text{sc}} \quad (62)$$

The charge density corresponding to the depletion layer is compensated by an excess of negative ions in the solution part of the double layer (Helmholtz layer).

With en_{bulk} for the charge density per unit volume, the Poisson equation gives

$$\frac{E_{\text{CB,bulk}} - E_{\text{CB}}(x)}{-e} \cong \frac{en_{\text{bulk}}}{2\epsilon\epsilon_0} [d_{\text{sc}} - x]^2 \quad (63)$$

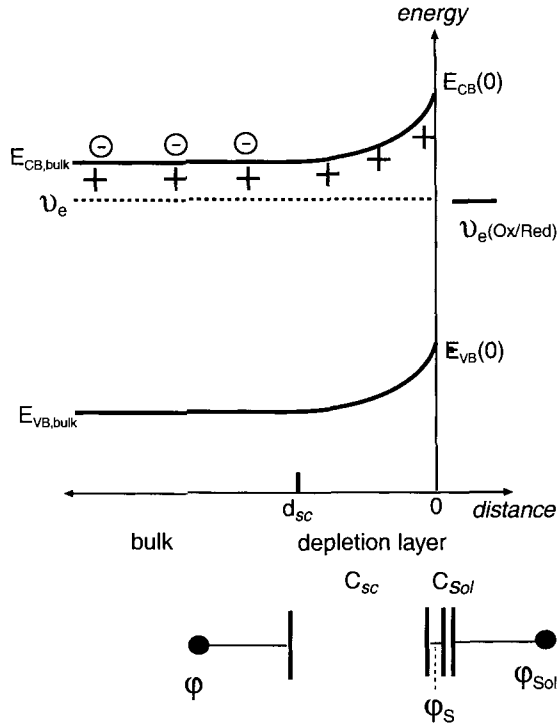


Figure 19. The electronic structure of an n-type semiconductor/electrolyte solution interface under conditions of free electron depletion at the surface. Shown are the conduction and valence band edges as a function of the distance from the surface. The interfacial potential drop is distributed over a region in the solid (depletion region, width d_{sc}) and the molecular Helmholtz layer at the liquid side (not shown). The interfacial capacitance is represented by a series connection of the capacitance of the depletion layer (C_{sc}) and the Helmholtz layer (C_{sol}).

and after two integrations

$$d_{sc} \cong \sqrt{\frac{2\epsilon\epsilon_0}{e^2 n_{bulk}}} \sqrt{E_{CB}(x=0) - E_{CB,bulk}} \quad (64)$$

The potential-energy difference over the depletion layer, $E_{CB}(x=0) - E_{CB,bulk}$, is often called the band bending. With $\epsilon = 10$, and $E_{CB}(x=0) - E_{CB,bulk} = 1$ eV, the width of the depletion layer is 1000, 100, and 10 nm for free carrier densities of 10^{15} , 10^{17} , and 10^{19} cm^{-3} , respectively. In Figure 19, the energy of the edges of the valence- [$E_{VB}(x)$] and conduction bands [$E_{CB}(x)$] are shown as a function of the distance from the solid surface; the electrochemical potential μ_e of the free electrons is also indicated. The concentration of free electrons at a given position in the depletion layer, $n(x)$, can be expressed as a function of the concentration in the bulk solid, n_{bulk} , with Fermi–Dirac statistics (see Section 4.3.5). From Eq. 27 it follows that

$$n(x) = n_{bulk} e^{-[E_C(x) - E_{C,bulk}]/k_B T} \quad (65)$$

The total potential drop over the interface, $\phi - \phi_{sol}$, is distributed over the depletion layer, $\phi - \phi_S = -[E_{CB,bulk} - E_{CB}(0)]/e$, and the solution side of the interface,

$\varphi_S - \varphi_{\text{Sol}}$ (see Figure 19). The capacitance of the electrochemical double layer is:

$$\frac{1}{C_{\text{Sc/Sol}}} = \frac{\partial[\varphi - \varphi_S]}{\partial\sigma} + \frac{\partial[\varphi_S - \varphi_{\text{Sol}}]}{\partial\sigma} = \frac{1}{C_{\text{Sc}}} + \frac{1}{C_{\text{Sol}}} \quad (66)$$

The entire electrochemical double layer can be represented by a series connection of two parallel plate capacitors. It is usually assumed that the structure of the double layer at the solution side does not differ much from that at a metal. The capacitance of the depletion layer is given by

$$C_{\text{SC}} = \frac{\epsilon\epsilon_0}{d_{\text{SC}}} \quad (67)$$

in which the width of the depletion layer is given by Eq. 64. Under conditions of depletion, C_{SC} is much smaller than C_{Sol} , hence $\frac{\partial[\varphi - \varphi_S]}{\partial[\varphi - \varphi_{\text{Sol}}]} \cong 1$. This means that a change in the surface charge density corresponds to a change in the width of the depletion layer solely, and that the band edges at the surface do not shift.

Surface atoms, crystal imperfections and adsorbed molecules can give rise to localized energy levels located in the band gap. These so-called surface states play an important role as mediators of interfacial electron transfer. The surface states may or may not be occupied by an electron; the surface-localized electrons give a contribution, σ_S , to the surface charge:

$$\sigma = \sigma_{\text{SC}} + \sigma_S \quad (68)$$

with

$$\sigma_S = -e \int_{E_{\text{VB}}}^{E_{\text{CB}}} s(E) f(E) dE \quad (69)$$

Here, the surface density of the states is denoted as $s(E)$ and they have an electron occupancy $f(E)$. If there is electronic equilibrium between the surface states and the free electrons in the solid, $f(E)$ is determined by the Fermi–Dirac function, Eq. 22. Under conditions of interfacial current flow, $f(E)$ may be determined by the rates of filling and emptying of the states [see Section 4.9]. If the change in the total surface-charge density corresponds to the change in the charge of the depletion layer, that is, $d\sigma_{\text{SC}} \gg d\sigma_S$, then $d(\varphi - \varphi_{\text{Sol}}) \cong d(\varphi - \varphi_S)$; only the potential drop over the depletion layer changes, the band edges at the surface do not shift when μ_e is changed. However, if $d\sigma_S$ cannot be neglected with respect to $d\sigma_{\text{SC}}$, the potential drop over the depletion layer as well as over the solvent layer changes: $d(\varphi - \varphi_{\text{Sol}}) = d(\varphi - \varphi_S) + d(\varphi_S - \varphi_{\text{Sol}})$. When μ_e is changed to a higher value with respect to a reference electrode, then $d\mu_e = dE_{\text{CB, bulk}}$. In the normal case in which $d\sigma_{\text{SC}} \gg d\sigma_S$, the band edges at the surface do not shift; $dE_{\text{CB}}(0)/d\mu_e \cong 0$. Where the surface state density (close to the Fermi level) is sufficiently high, it is possible that $0 < dE_{\text{CB}}(0)/d\mu_e < 1$.

The distribution of the interfacial potential drop over the semiconductor and the depletion layer is an important problem in the field of electrochemistry. It is often strongly related to the kinetics of interfacial electron transfer [15].

4.6 Electron Tunneling

Electron tunneling is an important mechanism for transporting electrons through solids, large molecules, and molecular complexes. Quantum-mechanical tunneling is the main mechanism of electron transfer through an interfacial layer between two condensed phases in intimate contact. From the previous section it is clear that metallic and semiconducting solids have a considerable potential-energy barrier at their surface, which confines the electrons within the solid. At or below room temperature, the classical, thermally activated escape of electrons over the surface barrier (thermionic emission) is a very improbable process, since the surface barrier is usually 50–100 $k_B T$ at room temperature. Quantum-mechanical tunneling of electrons can occur if the interfacial layer is sufficiently thin. Electron tunneling is a key feature in electrochemical electron transfer (See Sections 4.8 and 4.9). We will first discuss the probability of tunneling through a rectangular barrier between two free-electron systems [16]. We will use this result to derive the tunnel-current density between two metal phases. Finally, we will discuss experimental results dealing with tunneling between two metals separated by vacuum, an oxide layer, or water.

4.6.1 The Probability of Electron Tunneling

We consider two metallic free-electron systems, with atomically flat surfaces separated by vacuum over a distance Δx (Figure 20). In fact, the model system is an extension of the metal surface considered in Section 4.5. The complex potential energy barrier at a metal surface, discussed in Section 4.5 is simplified here to a rectangular barrier. We look for the quantum-mechanical probability that an electron in phase A is also present in phase B. This probability is given by the ratio of squared amplitudes, B^2 and A^2 , of the free-electron wave function in phase B and A, respectively. It is quantified by the transmission coefficient:

$$T[E(k_x, k_y, k_z), E_{\text{vac}}, \Delta x] = B^2/A^2 \quad (70)$$

Tunneling implies that the one-electron wave function $\psi(k_x, k_y, k_z)$ extends over the two metal phases and the vacuum in between. This wave function is a solution of the Schrödinger equations in phase A, the vacuum, and phase B. It should fulfil the following boundary conditions:

$$\begin{aligned} &\text{metal A/vacuum } (x = 0): \\ &\psi_A(x = 0) = \psi_{\text{vac}}(x = 0) \end{aligned} \quad (71)$$

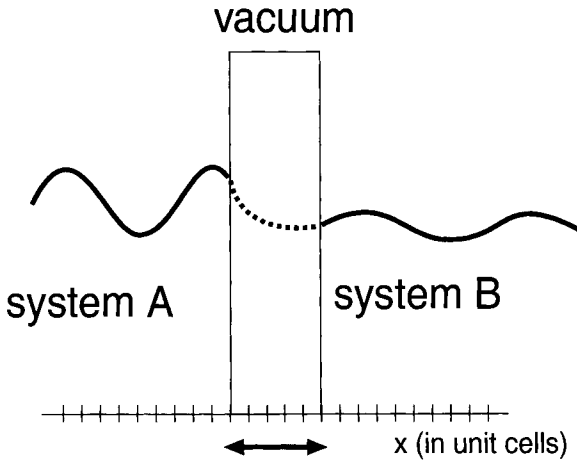


Figure 20. Elastic tunneling of an electron between two metal phases separated by vacuum (rectangular barrier). Shown are the wave functions of a free electron propagating in a direction perpendicular to the interface. The wave function decays exponentially in the vacuum. The tunneling probability is related to the amplitude of the free electron wave functions (see section 6).

$$\left. \frac{\partial \psi_A}{\partial x} \right|_{x=0} = \left. \frac{\partial \psi_{vac}}{\partial x} \right|_{x=0} \quad (72)$$

and similar conditions for the boundary vacuum/metal B, ($x = \Delta x$). A wave function corresponding to an electron with a large probability for tunneling is sketched in Figure 20. The free-electron wave functions in phases A and B are given by equations such as Eq. 14. The electron wave in vacuum does not propagate, instead, the amplitude of the wave function decays exponentially; $\psi_{vac}(x) \propto e^{-\kappa_{vac}x}$ (Eq. 54),

with $\kappa_{vac} = \left[\frac{2m_e[E_{vac} - E(x)]}{\hbar^2} \right]^{1/2}$ (Eq. 55). The mathematical solution of the problem can be found in more specialized texts [16]. In practical cases, the effective barrier height is of the order of magnitude of 1 eV. The barrier width is, usually, considerably larger than the decay length of the wave function: $\kappa_{vac} \times \Delta x \gg 1$. Under these conditions (strong attenuation), the tunneling probability is found to be:

$$T = T_o e^{-2\kappa_{vac}\Delta x} \quad (73)$$

In Eq. 73, T_o is a pre-factor close to unity, which depends weakly on the effective barrier height $E_{vac} - E(x)$. The distance dependence of the tunneling probability is determined by

$$2\kappa_{vac} = 2 \times \left[\frac{2m_e[E_{vac} - E(x)]}{\hbar^2} \right]^{1/2} \quad (74)$$

This is rationalized by the fact that the probability of finding an electron in vacuum at a distance Δx from the surface of phase A is proportional to $[\psi_{vac}(\Delta x)]^2 \propto e^{-2\kappa_{vac}\Delta x}$. For an effective barrier height of 1 eV, calculation shows that $2\kappa_{vac}$ is about 1 \AA^{-1} .

The tunneling probability over a barrier of given width Δx depends critically on the effective barrier height $E_{\text{vac}} - E(x)$. We should keep in mind that the total kinetic energy of the free electrons is given by Eq. 15; $E(\vec{k}) = \frac{\hbar^2 k^2}{2m_e} = \frac{\hbar^2 (k_x^2 + k_y^2 + k_z^2)}{2m_e}$. Thus, electrons with energy close to the Fermi energy and with $k_x^2 \gg k_y^2 + k_z^2$ have the highest tunnel probability (see also Figure 4). In contrast, electrons propagating parallel to the surface plane do not tunnel.

It should be remarked here that Eq. 73 defines a dimensionless tunneling probability, not a tunneling rate or rate constant. Above, we considered a wave function extended over two metal phases; we did not consider a measurable tunneling rate. It can be expected that the lifetime of an electron in phase A before tunneling into phase B is proportional to $1/T$. In theories of electrochemical electron transfer, tunneling rate constants defined as

$$k_T = k_{T,0} \times e^{-\beta(r-r_0)} \quad (75)$$

are often used. Here, k_T is the number of tunneling events per electron level and per second; $k_{T,0}$ is the maximum number, when the electron donor and acceptor are in closest contact (at a distance r_0); $k_{T,0}$ is often related to the frequency of a nuclear vibration directly coupled to the reaction coordinate [17]; the parameter β has a meaning similar to $2\kappa_{\text{vac}}$.

4.6.2 Interfacial Electron Tunneling Between Two Metals

Above, we calculated the tunneling probability of a free electron [characterized by a wave function $\psi(k_x, k_y, k_z)$] through a barrier of a given thickness. The total interfacial current density between two metal phases separated by a barrier is the result of many discrete tunneling events with widely varying probabilities. We start with some qualitative considerations. In Figure 21(a) and (b), the situation for very low T ($T \approx 0$ K) is sketched. The occupation of the free-electron states changes abruptly from $f(E) = 1$ for $E < \mu_e$ to $f(E) = 0$ for $E > \mu_e$. In Figure 21(a), the situation for equilibrium is shown, $\mu_{e,A} = \mu_{e,B}$. Elastic tunneling between the two phases is not possible: there are no empty electron states in phase B with the same energy as the occupied states in phase A. We conclude that in the theoretical limit case of zero temperature, the exchange current at equilibrium is zero. In Figure 21(b), a non-equilibrium situation with $\mu_{e,A} > \mu_{e,B}$ is shown. Tunneling from phase A to B can occur in the entire energy region between $\mu_{e,A}$ and $\mu_{e,B}$. It is clear that tunneling from free-electron energy levels $\psi(k_x, k_y, k_z)$ with energy close to $\mu_{e,A}$ is the most likely, since the effective barrier height is then smallest. The rate of electron tunneling from A to B per range of energy is indicated by the length of arrows. Electron tunneling from B to A does not occur.

In Figure 21(c) and (d), the situation for $T \gg 0$ K (e.g., room temperature) is sketched. The occupation of states with energy around $\mu_{e,A}$ and $\mu_{e,B}$ is given by the Fermi–Dirac function, that is, $f(E, \text{phase } A) = \{1 + e^{[E - \mu_{e,A}]/k_B T}\}^{-1}$ (Eq. 22).

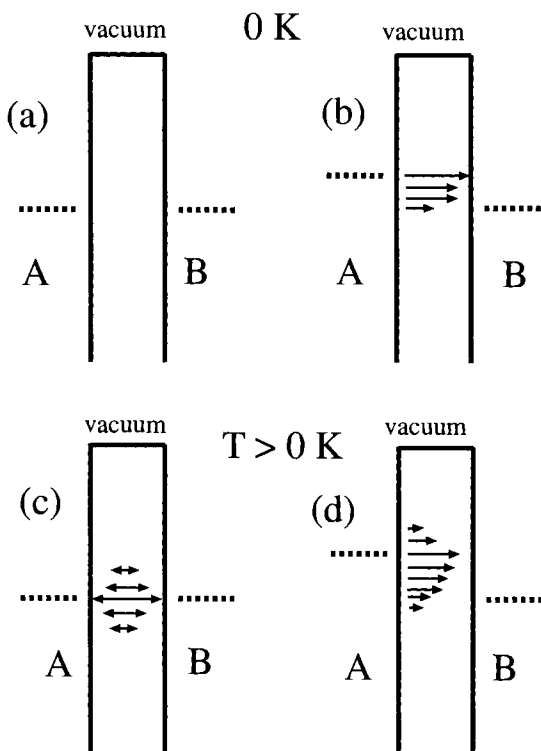


Figure 21. Electron tunneling between two metal phases at 0 K (a, b), and temperatures considerably above 0 K (c, d). The dashed lines show the position the electrochemical potential (Fermi-level) in a phase. The length of the arrows indicates the rate of electron transfer in an energy interval. The probability of a single tunneling event and the Fermi-Dirac occupation of the free electron energy levels is taken into account (see section 6).

The tunneling rate from phase A to B per energy interval is now determined by the transmission coefficient and the occupation factors of both phases, that is, $f(E, \text{phase A}) \times [1 - f(E, \text{phase B})]$. A similar reasoning holds for tunneling from B to A. In Figure 21(c), equilibrium is depicted. There is an energy range of a few $k_B T$ around μ_e in which $f(E, \text{phase A}) \times [1 - f(E, \text{phase B})]$ is nonzero, hence, in which tunneling from A to B can occur. The same statement holds for tunneling from B to A. Since $f(E, \text{phase A}) \times [1 - f(E, \text{phase B})]$ is a much stronger function of energy than the transmission coefficient, the tunneling rate per range of energy [arrows in Figure 21(c)] is determined by the function $f(E, \text{phase A}) \times [1 - f(E, \text{phase B})]$, peaking at the Fermi level. At equilibrium, there is a considerable electron-exchange flux, $J_{A \rightarrow B}^{\text{eq}} = J_{B \rightarrow A}^{\text{eq}} = J^{\text{eq}}$, which depends on the transmission coefficient $T[E(k_x, k_y, k_z), E_{\text{vac}}, \Delta x]$, the density of states in phases A and B, and the temperature. In Figure 21(d), a nonequilibrium situation at room temperature is shown. Tunneling from phase A to B occurs in the entire energy region between $\mu_{e,A} + k_B T$ and $\mu_{e,B} - k_B T$; the electron flux from A to B is considerably enhanced: $J_{A \rightarrow B} \gg J^{\text{eq}}$. The tunneling rate per range of energy is maximal at $\mu_{e,A}$. It is also clear that $J_{B \rightarrow A} \ll J^{\text{eq}}$. There will be a net current flow from phase A to B.

The relationship between the net electron flux $J = J_{A \rightarrow B} - J_{B \rightarrow A}$ and the difference in electrochemical potential $\mu_{e,A} - \mu_{e,B}$ will now be discussed more quantitatively.

The difference $\mu_{e,A} - \mu_{e,B}$ is often called the “bias” in physics, and the “overpotential” in electrochemistry. The rate of tunneling of an electron from phase A to B is proportional to $T[E(k_x, k_y, k_z), E_{\text{vac}}, \Delta x] \times g(E, \text{phase B}) \times [1 - f(E, \text{phase B})]$, written in compact form as $T[E] \times g(E, B) \times [1 - f(E, B)]$. Hence, the electron flux from A to B is:

$$J_{A \rightarrow B} = \Gamma \int_0^\infty T[E]g(E, A)f(E, A)g(E, B)[1 - f(E, B)] dE \quad (76)$$

Here Γ is a proportionality constant [$\text{J cm}^4 \text{ s}^{-1}$]. A similar equation holds for the electron flux from B to A. The net electron flux is hence given by

$$J[\mu_e(A) - \mu_e(B)] = \Gamma \int_0^\infty T[E]g(E, A)g(E, B)[f(E, A) - f(E, B)] dE \quad (77)$$

Close to equilibrium, where $\mu_e(A) - \mu_e(B)$ is sufficiently small, $T[E]g(E, A) \cdot g(E, B)$ is almost a constant, while $\int_0^\infty [f(E, A) - f(E, B)] dE$ is proportional to $\mu_{e,A} - \mu_{e,B}$. The net electron flux J is hence proportional to $\mu_{e,A} - \mu_{e,B}$. A region where the response of the system (here the electron flux) is proportional to a moderate deviation from equilibrium could be expected (see Section 4.2.3). For a stronger deviation from equilibrium, where $\mu_{e,A}$ is considerably above $\mu_{e,B}$, the total interfacial electron flux is dominated by tunneling from states close to $\mu_{e,A}$, where $f(E, B) \approx 0$. $T[E \cong \mu_{e,A}]$ increases strongly with $\mu_{e,A}$; from Eqs. 73–74 it follows that

$$\frac{\partial T(E \cong \mu_e)}{\partial \mu_e} = \frac{T(E \cong \mu_e) \times \kappa_{\text{vac}} \times \Delta x}{E_{\text{vac}} - \mu_e} \quad (78)$$

Hence, the net flux J increases more steeply than linear with $\mu_{e,A} - \mu_{e,B}$.

It is important to realize that the shape of the $J(\mu_{e,A} - \mu_{e,B})$ relationship is critically determined by the tunneling distance Δx . Consider, for instance, $T[E \cong \mu_{e,A}]$. From Eq. 78, it follows that:

$$\frac{\partial[\partial T(E \cong \mu_e)/\partial \mu_e]}{\partial \Delta x} = \frac{T(E \cong \mu_e) \times \kappa_{\text{vac}}}{E_{\text{vac}} - \mu_e} \times (1 - 2\kappa_{\text{vac}}\Delta x) \quad (79)$$

Since, for strong attenuation, $2\kappa_{\text{vac}}\Delta x > 1$, it holds that $\frac{\partial T(E \cong \mu_e)}{\partial \mu_e}$ decreases with increasing tunneling distance. This means that the slope of the J vs $\mu_{e,A} - \mu_{e,B}$ curve becomes less steep when the width of the barrier is increased.

4.6.3 Experimental Tunneling Spectroscopy

Before the invention of the scanning tunneling microscope (STM), planar metal/vacuum/metal and metal/insulator/metal junctions were used in studies of electron

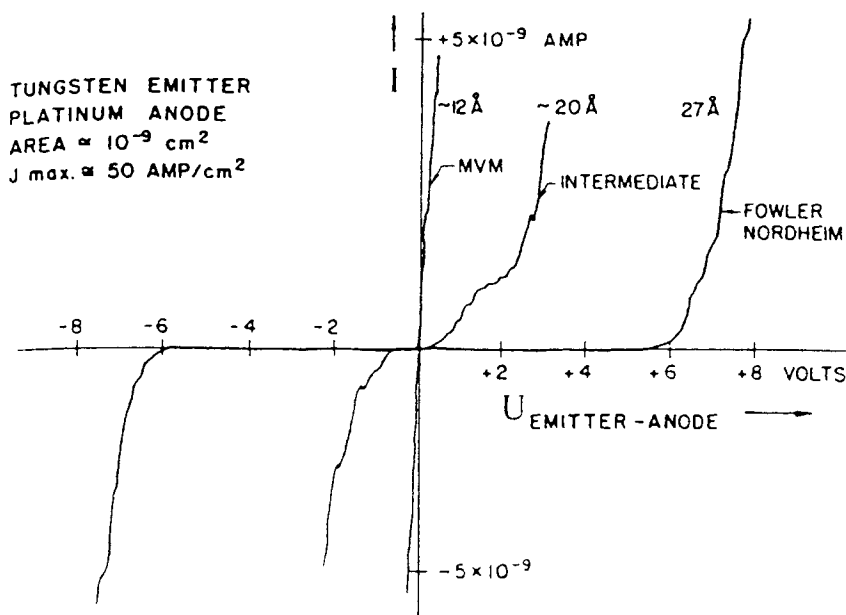


Figure 22. The tunneling current, I , measured between two metal electrodes (tungsten en platinum) separated by a vacuum barrier as a function of the difference in electrochemical potential (here denoted as $U_{\text{emitter-anode}}$); the distance between the two electrodes (12, 20, 17 Å) is indicated in the figure. Reprinted from "Scanning Probe Microscopy and Spectroscopy", R. Wiesendanger, Cambridge University Press 1994

tunneling [16]. It is a difficult task to prepare metal/vacuum/metal junctions for quantitative studies. The metal surfaces need to be smooth on an atomic scale. The distance between the two metals should be varied between 10 to 100 Å in a controlled way. Moreover, the setup should be free from vibrations. Reliable results on vacuum tunneling between two metal electrodes were first reported in 1971 [16]. Figure 22 presents J vs $\mu_{e,A} - \mu_{e,B}$ for three separations (12, 20, and 27 Å) between the electrodes. It is clear that the tunnel current at a given bias $\mu_{e,A} - \mu_{e,B}$ is strongly dependent on the separation. The net electron flux J increases linearly with $\mu_{e,A} - \mu_{e,B}$ near equilibrium (Ohmic region), and super-linearly at higher bias, in agreement with the predictions of the previous section. It is also clear that the slope of the J vs $\mu_{e,A} - \mu_{e,B}$ relationship decreases with increasing separation, as discussed above. Much experimental work was also devoted to metal oxide-metal junctions [16]. Experimental problems were due to spatial inhomogeneities in the thickness and chemical composition of the oxide layer. The introduction of STM apparatus was accompanied by a substantial development of tunneling spectroscopy, since variation of the tip-metal distance can be more easily controlled than with planar junctions. Experimental work was often focused on the determination of the effective barrier height by measurement of the net electron flux, J , vs the separation, Δx ,

at a given bias (see Eqs. 73–74). Since tunneling from states close to $\mu_{e,B}$ forms the dominant contribution to J , the effective barrier heights, between 3 and 4 eV, were found to be close to the work function $E_{\text{vac}} - \mu_e$ of the metal under investigation.

Study of electron tunneling across an electrochemical double layer between two metals is an important subject in electrochemistry. The effective barrier height of an electrochemical double layer was obtained by variation of the substrate–tip separation. Interestingly, the barrier heights were 1–2 eV, that is, 2 eV smaller than in vacuum [2]. There have been several attempts to explain this feature. The perhaps most realistic interpretation was provided by Schmickler and coworkers [2]. They assume interaction between the tunneling electron and the electrons in the H_2O molecules. This leads to a considerable reduction of the barrier height for interaction with the H atoms, and a high barrier height when the tunneling electron interacts with oxygen. According to Schmickler, the overall effect is a reduction of the effective barrier to values in reasonable agreement with those obtained from experiments. The experimental results are important for electrochemical electron transfer between an electrode and a redox system in solution. It is found that the barrier height for electrochemical electron tunneling is 1 to 2 eV, hence considerably below the work function in vacuum. Therefore, electron tunneling across an electrochemical double layer has a higher probability than through vacuum, and the distance dependence of the tunneling rate is weaker.

4.7 Electrochemical Reactions: Kinetics and Mechanism

4.7.1 The Diversity of Electrochemical Processes

In Eqs. 80–82 some typical electrochemical equilibria are presented:

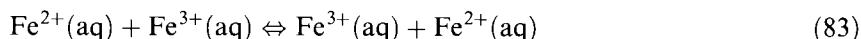


The first equation represents the equilibrium between hydrated Ag^+ ions and Ag atoms in a single-crystal configuration. Alternatively, we may say that there is a heterogeneous thermodynamic equilibrium between Ag^+ ions in the solid phase (where they are stabilized by the gas of free electrons) and Ag^+ ions in the liquid phase (stabilized by interaction with water molecules). The forward reaction step corresponds to the anodic dissolution of a silver crystal. On an atomic level, one may say that a Ag^+ core ion is transferred from the metallic phase to the liquid water phase. In an electrochemical cell, an electron flows from the Ag electrode (the working electrode) to the counter electrode each time that one Ag^+ ion is transferred from the solid to the liquid phase across the electrochemical double layer. Although the electron flow is measured in the external circuit between the working

and counter electrode, the electrochemical process itself corresponds to the transfer of an ion through the double layer. Electron transfer and tunneling are not involved.

The second equilibrium involves hydrated I^- ions in equilibrium with I_3^- complexes. In the forward step, an iodide ion donates an electron to the working electrode and is hence oxidized to a I atom. We may speculate that the I^- ion remains outside the double layer and that an electron tunnels through the double layer. However, from many experimental results and molecular dynamic simulations (see Section 4.7.2), it became clear that this is not the case. Instead, a solvated I^- ion penetrates the double layer and becomes chemisorbed as a $\text{I}^{\delta-}$ ion ($\delta < 1$) on the metal surface, losing about half of its hydration shell [18, 19]. Moreover, there is a local restructuring of the double layer. Here also, the electrochemical reaction does not involve tunneling of an electron through the double layer.

The third equilibrium involves hydrated $\text{Fe}^{2+}(\text{aq})$ and $\text{Fe}^{3+}(\text{aq})$ ions. Homogeneous electron transfer between these ions has been well studied [5]:



Here an electron is transferred from the reduced $\text{Fe}^{2+}(\text{aq})$ species to the oxidized $\text{Fe}^{3+}(\text{aq})$ species. The kinetics of this process can be followed through measurement of the concentration of $\text{Fe}^{2+}(\text{aq})$ as a function of reaction time. The fact that the homogeneous reaction in solution proceeds at a considerable rate indicates that, in the electrochemical process, the electrode acts as a sink or source of electrons only. This suggests that an electron may tunnel from an $\text{Fe}^{2+}(\text{aq})$ ion outside the double layer to an empty state in the metal, without disturbing the double layer structure. This is indeed confirmed by molecular dynamic simulations (see next section). The process shown in Eq. 82 is one of the examples where tunneling of an electron through the double layer occurs and where the reduced and oxidized species, and hence also the activated complex does not interact strongly with the electrode. This type is called an *outer-sphere electron transfer*. Since there is no breaking or formation of bonds, outer-sphere reactions are the simplest class of electrochemical reactions. For this simple class there is a sound theoretical background. Marcus was awarded with the Nobel prize in chemistry in 1992 for providing a classical model for this type of electron-transfer reaction [5]. Hopfield [20], and Levich and Doganadze have presented more elaborate quantum-mechanical models. A comprehensive review can be found in [21]. In Sections 4.8 and 4.9, we will treat simple electrochemical electron transfer similarly to electron tunneling between two metals, using the model for electron energy levels in a dissolved redox system proposed by Gerischer (see Section 4.4).

The previous discussion shows that electrochemical reactions may proceed by a variety of reaction paths. Some reactions involve transfer of ions through the double layer, in other cases an electron tunnels through the double layer without disturbing it. Many important electrochemical processes occur with bond breaking and/or bond formation; the quantitative modeling of such processes has started only recently [22]. The important reaction coordinates of electrochemical ion transfer (ECIT) reactions and electrochemical electron transfer (ECET) reactions will be discussed in the next section. In Section 4.7.3, the experimental relationship

between the rate of an electrochemical reaction and the deviation from equilibrium will be discussed. Although electrochemical processes occur by very different mechanisms, it is commonly found that the current density (hence the rate) increases exponentially with the deviation from equilibrium. This seems strange considering the large variation in mechanisms. However, a phenomenological treatment (Section 4.7.4) shows that the exponential kinetic law only implies that the energy of activation changes linearly with the deviation from equilibrium, that is, the overpotential.

4.7.2 Electrochemical Ion Transfer and Electrochemical Electron Transfer (ECIT and ECET)

Elucidation of the mechanism of an electrochemical process implies knowledge of the structure of the activated complex, and the way in which such a transition state is reached. Hence, one looks for the important reaction coordinates; these are the coordinates that critically determine the free energy of the system (molecule + electrode). Progress in this difficult field of science requires molecular dynamic simulations [18, 19], experimental data, and common sense. Here, we briefly discuss the important reaction coordinates for typical ECIT and ECET processes.

Anodic dissolution of metals (e.g., Eq. 80) has frequently been discussed in terms of electron transfer (for a review, see Ref. [14]). It is, however, clear that anodic dissolution implies the transfer of a chemical species through the electrochemical double layer. In Ref. [14], anodic dissolution was discussed as the transfer of a metal ion through the double layer, occurring in two steps. In the first step, a metal ion in the jellium plane evolves into a partially hydrated chemisorbed metal ion; this is accompanied by local restructuring of the double layer. The formation of a chemisorbed species changes the potential drop over the inner region (metal part) of the electrochemical double layer. In the second step, the partially hydrated metal ion is transferred through the outer part of the double layer, that is, the ordered layer of solvent molecules. It is shown that this model leads to a realistic relationship between anodic current density and overpotential. The model provides a microscopic interpretation of the anodic charge-transfer coefficient. The model of coupled ion transfer also explains several features of the interfacial impedance, where the classical models (based on electron transfer) failed. This work indicates that anodic dissolution can be treated more conveniently in terms of ion transfer than electron transfer.

The important reaction coordinates in ECIT and ECET processes were studied with the aid of molecular dynamic simulations together with quantum-mechanical calculations of the potential energy of the reacting system [18, 19]. This work finally leads to the free energy as a function of two important coordinates: the distance of the reacting species from the electrode surface, and the deviation of the solvation structure from equilibrium. The free-energy surface gives insight in the possible reaction pathways and transition states. As an example of an ECIT process, the oxidation of I^- to a I atom at a Pt/water interface was investigated. It was found that the distance of the ion from the electrode surface and the accompanying partial dehydration is the important reaction coordinate. The reaction proceeds via a

transition state, which strongly interacts with the metal. Finally, a chemisorbed $I^{\delta-}$ ion ($\delta < 1$) is formed.

Molecular dynamic simulations for the $Fe^{3+}(aq)/Fe^{2+}(aq)$ reaction shows that penetration of the $Fe^{2+}(aq)$ ion into the double layer leads to a huge increase of the potential energy. Penetration of a strongly hydrated $Fe^{2+}(aq)$ ion [see Section 4.4] in the double layer does not occur. Instead, an electron tunnels from an activated complex outside the double layer into an empty state of the metal. It will be shown in Section 4.8 that iso-energetic tunneling can only occur if a transition state with nonequilibrium solvation of the Fe^{2+} is formed. The formation of such a solvation structure is in many cases the rate-determining step. The time-averaged probability of nonequilibrium solvation has been considered originally by Gerischer. This “fluctuating energy level model” provides a very convenient means for treating electrochemical electron transfer similarly to interfacial electron transfer between two solids (Sections 4.8 and 4.9).

4.7.3 Current Density vs Overpotential: Experimental Results

Investigations of electrochemical kinetics are usually performed on a three-electrode electrochemical cell containing a working electrode (the electrode of interest), a counter electrode and a reference electrode. The current measured in the external circuit between working and counter electrode corresponds to the interfacial current density, j , at the working electrode multiplied with its surface area. This current density is measured as a function of the potential difference between the working and the reference electrode, $U - U_{Ref}$. In fact, the voltmeter measures the difference in electrochemical potential of the electrons in the working and reference electrodes:

$$U - U_{Ref} = -e[\mu_e - \mu_{e,Ref}] \quad (84)$$

The chemical potential of the electrons in the reference electrode does not change when the current is changed. This means that the overpotential at the working electrode can simply be controlled by $U - U_{Ref}$:

$$U - U^{eq} = (U - U_{Ref}) - (U^{eq} - U_{Ref}) = -e[\mu_e - \mu_e^{eq}] \quad (85)$$

It can be concluded that, with a conventional three-electrode electrochemical cell, the rate of the electrochemical reaction occurring at the working electrode can be measured as a function of the deviation from equilibrium.

When U is substantially more positive than U^{eq} , electrons flow from the working electrode to the counter electrode in the external circuit. This means that, at the working electrode, the anodic process prevails, that is, electrons are transferred from the reduced species to the electrode. The cathodic process occurs when $U - U^{eq}$ is negative. (By convention we take the current to be negative when a cathodic process occurs at the working electrode.) When mass transport to the working electrode does not limit the current, j changes exponentially with $U - U^{eq}$. A sketch of a typical result is shown in Figure 23. Commonly, the logarithm of the current density of the anodic and cathodic branches is plotted vs $U - U^{eq}$. In many

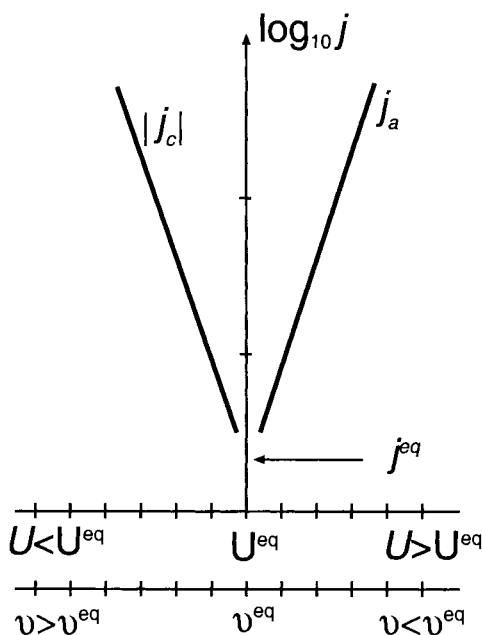


Figure 23. Schematic representation of the cathodic and anodic partial current densities at a metal electrode in contact with a simple redox system as a function of the overpotential $U - U^{\text{eq}}$. The bars on the vertical axis indicate one decade of current, the bars on the horizontal axis indicate 0.1 V (or 0.1 eV for the electrochemical potential scale).

cases, a linear relationship is found to hold over one to three orders of magnitude of current density. At larger overpotentials, $\ln|j|$ may increase less than linearly with $|U - U^{\text{eq}}|$. The exponential relationship between the current density and overpotential can be quantified as

$$\frac{\partial \ln[j/A \text{ cm}^{-2}]}{\partial (U - U^{\text{eq}})} = \frac{e \times \alpha_a}{k_B T} \quad \text{for } U - U^{\text{eq}} > 0 \text{ (anodic branch)} \quad (86)$$

and

$$\frac{\partial \ln[|j|/A \text{ cm}^{-2}]}{\partial (U - U^{\text{eq}})} = \frac{-e \times \alpha_c}{k_B T} \quad \text{for } U - U^{\text{eq}} < 0 \text{ (cathodic branch)} \quad (87)$$

The coefficients α_a and α_c are called the empirical charge-transfer coefficients. For simple outer-sphere electron-transfer processes, these coefficients are close to 1/2, and the current density is independent of the nature of the metal [21]. Extrapolation of the linear plots to $U - U^{\text{eq}} = 0$ gives the exchange current density at equilibrium, j^{eq} .

4.7.4 A Heuristic Treatment of Electrochemical Kinetics

Although there is strong evidence that electrochemical processes may proceed by very different pathways involving completely different reaction coordinates, it is

almost commonly observed that, around equilibrium, the current density and hence the rate of an electrochemical process increases exponentially with the overpotential (Figure 23). We may conclude that study of $j(U - U^{\text{eq}})$ is not sufficient for deriving the mechanism of an electrochemical reaction. In general, small-amplitude-modulation techniques are required together with structural information of the double layer under conditions of current flow [23]. However, it remains interesting to investigate why an exponential relationship between j and $U - U^{\text{eq}}$ is observed so commonly. This requires a heuristic and phenomenological treatment of electrochemical kinetics, without any reference to the precise mechanism [21].

We discuss a nonspecified electrochemical process denoted as



The reaction free energy, ΔG_R , is given by

$$\Delta G_R = \mu_{\text{Ox}} + \mu_e - \mu_{\text{Red}} \quad (89)$$

where μ_{Ox} and μ_{Red} are the chemical potentials of the oxidized and reduced species, respectively, and μ_e is the electrochemical potential of the electrons in the solid phase. The relationship between μ_e and the electrode potential is given by Eq. 85. Under conditions of thermodynamic equilibrium between the species in solution and the electrons in the solid phase, the reaction free energy is zero:

$$\Delta G_R \equiv 0 = \mu_{\text{Ox}}^{\text{eq}} + \mu_e^{\text{eq}} - \mu_{\text{Red}}^{\text{eq}} \quad (90)$$

The electrochemical potential of the electrons in the working electrode is then given by, $\mu_e^{\text{eq}} \equiv \mu_{\text{Red}}^{\text{eq}} - \mu_{\text{Ox}}^{\text{eq}}$, this corresponds to the electrode potential U^{eq} .

The net rate of the electrochemical process at the working electrode is directly related to the net current density j given by

$$j = j_a + j_c = j_a - |j_c| = e[k_a c_{\text{red}} - k_c c_{\text{Ox}}] \quad (91)$$

In Eq. 91, the concentrations of the oxidized and reduced species just outside the electrochemical double layer are used (number of molecules per cm^3); k_a and k_c are the electrochemical rate constants (cm s^{-1}) for the anodic and cathodic process, respectively. As for chemical processes, it is assumed that the forward and backward reactions proceed via an activated complex (transition state), see Figure 24. The rate constants can then be written as:

$$k_a = A_a e^{-\Delta G_a^* / k_B T} \quad (92)$$

$$k_c = A_c e^{-\Delta G_c^* / k_B T} \quad (93)$$

Since a deviation of the electrode potential from equilibrium changes the rates of the anodic and cathodic process, the activation energies must be a function of

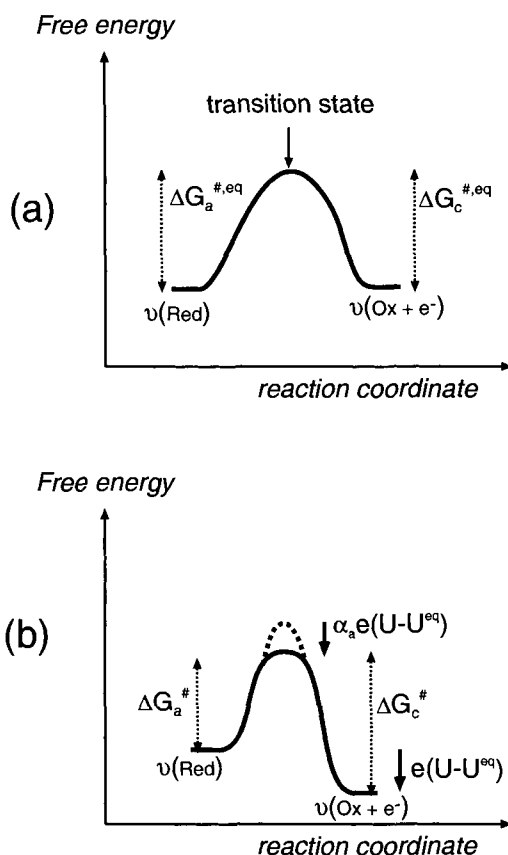


Figure 24. Free energy diagrams corresponding to the heuristic model for electrochemical reactions presented in section 7.4. The upper diagram represents the situation at electrochemical equilibrium; the lower diagram represents the situation where $U > U^{\text{eq}}$ (nett anodic current flow).

$U - U^{\text{eq}}$. We therefore write the activation energies as Taylor expansions around U^{eq} :

$$\begin{aligned} \Delta G_a^\ddagger(U - U^{\text{eq}}) &= \Delta G_a^{\ddagger, \text{eq}} + \left. \frac{\partial \Delta G_a^\ddagger}{\partial (U - U^{\text{eq}})} \right|_{\text{eq}} \times (U - U^{\text{eq}}) \\ &\quad + \frac{1}{2} \left. \frac{\partial^2 \Delta G_a^\ddagger}{\partial (U - U^{\text{eq}})^2} \right|_{\text{eq}} \times (U - U^{\text{eq}})^2 + \dots \end{aligned} \quad (94)$$

$$\begin{aligned} \Delta G_c^\ddagger(U - U^{\text{eq}}) &= \Delta G_c^{\ddagger, \text{eq}} + \left. \frac{\partial \Delta G_c^\ddagger}{\partial (U - U^{\text{eq}})} \right|_{\text{eq}} \times (U - U^{\text{eq}}) \\ &\quad + \frac{1}{2} \left. \frac{\partial^2 \Delta G_c^\ddagger}{\partial (U - U^{\text{eq}})^2} \right|_{\text{eq}} \times (U - U^{\text{eq}})^2 + \dots \end{aligned} \quad (95)$$

If the first-order partial derivatives are (nearly) independent of the overpotential

$U - U^{\text{eq}}$, we may neglect the second- and higher-order terms in the expansion. In this case we define

$$\alpha_a = \frac{-1}{e} \left. \frac{\partial \Delta G_a^\ddagger}{\partial (U - U^{\text{eq}})} \right|_{\text{eq}} \quad (96)$$

$$\alpha_c = \frac{1}{e} \left. \frac{\partial \Delta G_c^\ddagger}{\partial (U - U^{\text{eq}})} \right|_{\text{eq}} \quad (97)$$

The first-order derivatives correspond to the *charge-transfer coefficients* for the anodic and cathodic processes, respectively.

It generally holds that (see also Figure 24)

$$\Delta G_a^\ddagger - \Delta G_c^\ddagger = \mu_{\text{Ox}} + \mu_e - \mu_{\text{Red}} \quad (98)$$

and hence at equilibrium that

$$\Delta G_a^{\ddagger, \text{eq}} = \Delta G_c^{\ddagger, \text{eq}} \equiv \Delta G^{\ddagger, \text{eq}} \quad (99)$$

When the second- and higher-order terms in the Taylor's expansion of the activation energies can be neglected, we have:

$$\Delta G_a^\ddagger (U - U^{\text{eq}}) = \Delta G^{\ddagger, \text{eq}} - \alpha_a \times e(U - U^{\text{eq}}) \quad (100)$$

and

$$\Delta G_c^\ddagger (U - U^{\text{eq}}) = \Delta G^{\ddagger, \text{eq}} + \alpha_c \times e(U - U^{\text{eq}}) \quad (101)$$

From Eqs. 92–93 and 100–101, it follows that we can write the rate constants as follows

$$k_a = k_a^{\text{eq}} e^{\alpha_a \times e(U - U^{\text{eq}})/k_B T} \quad (102)$$

$$k_c = k_c^{\text{eq}} e^{-\alpha_c \times e(U - U^{\text{eq}})/k_B T} \quad (103)$$

Substitution of the rate constants in Eq. 91 gives the total current density:

$$j = j^{\text{eq}} [e^{\alpha_a \times e(U - U^{\text{eq}})/k_B T} - e^{-\alpha_c \times e(U - U^{\text{eq}})/k_B T}] \quad (104)$$

The exchange current density at equilibrium is given by

$$j^{\text{eq}} = ek_a^{\text{eq}} c_{\text{red}} = ek_c^{\text{eq}} c_{\text{ox}} \quad (105)$$

Equation 104 is known as the Butler–Volmer equation. In many cases, it agrees with the experimental $j(U - U^{\text{eq}})$ relationship, see previous section. The above treatment shows that an exponential $j(U - U^{\text{eq}})$ relationship can be explained

simply if it is assumed that the activation energy changes linearly with the overpotential. The fact that deviations from this exponential relationship occur at higher overpotentials indicate that the second-order terms in the Taylor's expansions (Eqs. 94–95) cannot be neglected. It is the task of microscopic theories to explain why the activation energy changes linearly with the overpotential in a limited region around equilibrium. For ECIT it has recently been found that the activation energy depends on the charge density on the electrode, and may vary linearly with the overpotential [19]. For outer-sphere electron transfer, there are well-established microscopic theories that explain a linear relationship between overpotential and activation energy [5, 12, 15, 21], see Sections 4.8 and 4.9.

Experimentally, it is often found that the anodic and cathodic charge transfer coefficients are about 1/2. This is typically the case for outer-sphere electron transfer. Values between zero and one are found for several more complex reactions. We now consider whether this behavior is reasonable in the framework of the phenomenological model presented here. In an outer-sphere process, the oxidized and reduced species are outside the electrochemical double layer. The chemical potential of these species is then not influenced by the electrode potential, and the following is valid:

$$\text{and } \left. \begin{array}{l} \mu_{\text{Ox}} = \mu_{\text{Ox}}^{\text{eq}} \\ \mu_{\text{Red}} = \mu_{\text{Red}}^{\text{eq}} \end{array} \right\} \quad (106)$$

Also, in the case of more complex electrochemical processes, these conditions may hold. Consider, for instance, the electrochemical equilibrium between Ag and Ag^+ (aq) (Eq. 80). The hydrated silver ion is, finally, outside the double layer; its chemical potential does not depend on the electrode potential. Since a change of the electrode potential only affects the interfacial potential drop and μ_e (see Section 4.5), it is reasonable to assume that the chemical potential of the silver atoms in the silver phase is also independent of the electrode potential. Hence, also in the case of Eq. 80, the polarization $U - U^{\text{eq}}$ leads to a change of μ_e only. In contrast, if products or reactants are chemisorbed on the electrode, their chemical potential depends on the electrode potential. If the conditions presented by Eqs. 106 are valid, it also holds that

$$\Delta G_a^\ddagger - \Delta G_c^\ddagger = \mu_e - \mu_e^{\text{eq}} = -e(U - U^{\text{eq}}) \quad (107)$$

and, since in the linear case $\Delta G_a^\ddagger = \Delta G^{\ddagger, \text{eq}} - e\alpha_a(U - U^{\text{eq}})$ and $\Delta G_c^\ddagger = \Delta G^{\ddagger, \text{eq}} + e\alpha_c(U - U^{\text{eq}})$, Eq. 107 implies that $\alpha_a + \alpha_c = 1$. In the case of an outer-sphere electron-transfer process, the transition state remains outside the double layer. Transfer coefficients of 1/2 are then made reasonable by the assumption that the electron occupation of the transition state is 1/2. The energy of the transition state then contains a contribution of 1/2 μ_e . This agrees with transition states proposed for homogeneous outer-sphere reactions [5].

4.8 Electron Transfer between a Metal and a Simple Redox System

In Section 4.8.2, we will calculate the net flow of electrons between a metal electrode and a simple redox system as a function of the difference of the electrochemical potentials in both phases. We will, therefore, consider all possible elastic tunneling events between discrete electron energy levels on both sides of the interface. The energetic distribution of electron energy levels in the metal has been discussed in Section 4.3. The distribution of electron energy levels corresponding to the redox system in solution is provided by the fluctuating-energy-level model proposed by Gerischer [12] (Section 4.4). The procedure which will be followed is similar to that used in the calculation of the net electron flux between two metals. In Section 4.8.3, we will compare the results with those obtained from an independent theory, developed by Marcus [5]. We will also consider the results of both microscopic theories with regard to the phenomenological framework developed in Section 4.7. First, some remarks on the analogy between electrochemical electron tunneling and tunneling between two metals are made in Section 4.8.1.

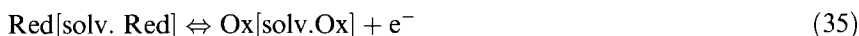
4.8.1 Comparison between Electrochemical Electron Tunneling and Tunneling between Two Metals

In Section 4.6.1, we discussed the probability of an elastic tunneling event between two electron-energy levels corresponding to free electrons (Eqs. 73–75). In electrochemical electron tunneling, we consider tunneling between free-electron levels in the metal and electronic orbitals localized on the oxidized or reduced species. When these orbitals interact weakly with the free-electron levels, expressions similar to Eqs. 73–74 are valid for the tunneling probability. In fact, in the literature, one often finds an expression similar to Eq. 75 to describe the distance dependence of the rate of electron tunneling between molecular levels [17, 21]. In the following section, it is implied that in the electrochemical case, the probability of elastic tunneling is described by equations analogous to those derived for vacuum tunneling between free-electron levels. There is experimental evidence that shows that tunneling between two metals through an electrochemical double layer is characterized by a considerably lower effective barrier height than vacuum tunneling (see Section 4.6.3). For tunneling through an electrochemical double layer, the effective barrier height is 1–2 eV [2]. Thus, the attenuation of the probability of electron tunneling with distance is less than in vacuum.

Redox ions in solution are subject to chaotic Brownian movement. In principle, a certain range of tunneling distances between the metal and the redox species should be taken into account in a kinetic theory. The tunneling probability decays exponentially with increasing distance between the metal and the redox ion. Only redox ions nearest to the metal surface are, therefore, taken into account. Then, the inner solvation shell of the ion contacts the Helmholtz layer. There is no penetration of the reacting system into the electrochemical double layer (See Section 4.7.2).

4.8.2 Current Density as a Function of Overpotential

We consider an outer-sphere electrochemical reaction between a metal and a simple redox system, once again using the reaction depicted in Eq. 35:



The electrochemical potential of a free electron system in equilibrium with the redox system is:

$$\mu_e(\text{Ox/Red}) = \mu^o(\text{Ox/Red}) + k_B T \ln(c_{\text{Red}}/c_{\text{Ox}}) \quad (108)$$

The electrochemical potential of the working electrode, μ_e , can be controlled with respect to a reference potential by use of a three-electrode electrochemical cell. One can then measure the rate of electrochemical electron transfer (by the current density j in the external circuit) as a function of the deviation from equilibrium, $\mu_e - \mu_e^{\text{eq}}$.

The energetic distribution of the electron energy levels on both sides of the electrochemical double layer is depicted in Figure 25. In Figure 25(a), the situation for electrochemical equilibrium is given, $\mu_e^{\text{eq}} = \mu(\text{Ox/Red})$; in Figure 25(b), μ_e is higher than μ_e^{eq} , thus, a net flow of electrons from the metal to the oxidized species occurs (net cathodic current flow). The energetic distribution of the electron levels corresponding to the redox system has been discussed in Section 4.4. The time-averaged

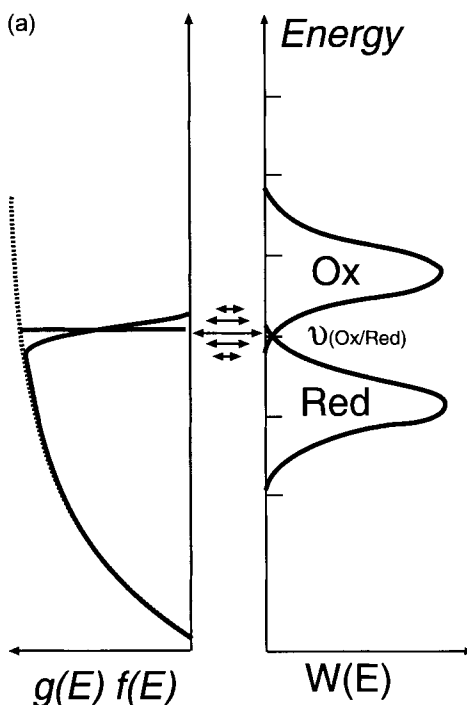


Figure 25a. Electron exchange between a metal and a simple redox system in solution under conditions of electrochemical equilibrium, $\mu_e = \mu(\text{Ox/Red})$. The energy distribution of the occupied and empty electron levels in the metal and in the redox system are depicted. Elastic tunneling occurs between occupied and empty levels on both sides of the interface. The rate of exchange is maximal at around the Fermi-level as indicated by the length of the arrows.

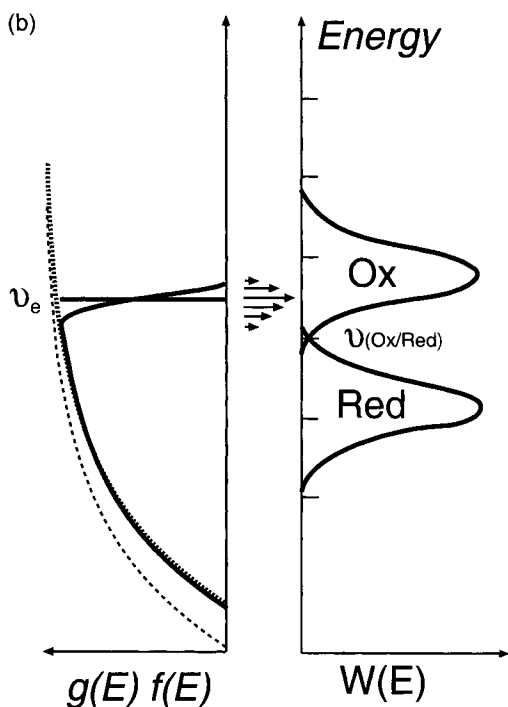


Figure 25b. Cathodic electron transfer between a metal and a simple redox system in solution for a moderate deviation from equilibrium, $\mu_e > \mu(\text{Ox/Red})$. The energy distribution of the occupied and empty electron levels in the metal and in the redox system are depicted. Elastic tunneling occurs between occupied and empty levels on both sides of the interface. The rate of exchange is maximal at around the Fermi-level in the metal (see length of arrows).

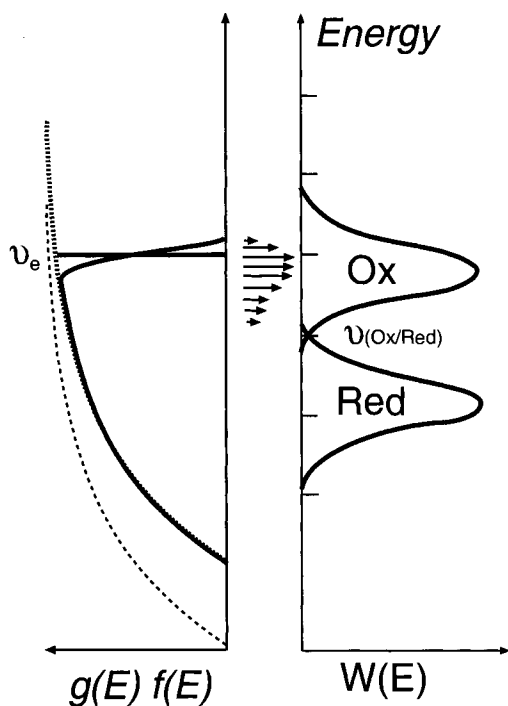


Figure 25c. Cathodic electron transfer between a metal and a simple redox system in solution under strong deviation from equilibrium, $\mu_e \geq \mu(\text{Ox/Red}) + \lambda$. The dominant contribution to the cathodic current is provided by tunneling in the energy interval at around the energy of the most probable empty state corresponding to the oxidized species (see length of arrows).

probability that an oxidized species corresponds to an empty energy level of energy E is given by $W_{\text{Ox}}(E)$; the probability of finding an occupied energy level at an energy E is given by $W_{\text{Red}}(E)$, with

$$W_{\text{Ox}}(E) = (4\pi k_B T \lambda)^{-1/2} e^{-(E - E_{\text{Ox}}^{\text{eq}})^2 / 4\lambda k_B T} \quad (47)$$

$$W_{\text{Red}}(E) = (4\pi k_B T \lambda)^{-1/2} e^{-(E - E_{\text{Red}}^{\text{eq}})^2 / 4\lambda k_B T} \quad (48)$$

In Figure 25, we took a typical value of 1 eV per molecule for the reorganization energy λ .

The net current flow through the external circuit between the working and counter electrode is given by

$$j = j_a + j_c = e(k_a c_{\text{Red}} - k_c c_{\text{Ox}}) \quad (109)$$

Here, k_a and k_c are the electrochemical rate constants (cm s^{-1}) and c_{Red} and c_{Ox} are the concentrations of the redox ions just outside the electrochemical double layer. The anodic current is due to electron transfer from the reduced species to the empty states in the working electrode, the cathodic current is due to transfer from an occupied electron level in the metal to an unoccupied level corresponding to the oxidized species. We evaluate the electrochemical rate constants by taking into account all elastic tunneling events between the energy levels in the metal, $g(E)$, and those in the electrolyte, given by $W_{\text{Ox}}(E)c_{\text{Ox}}$ and $W_{\text{Red}}(E)c_{\text{Red}}$. The procedure is similar to that described in Section 4.6.2. Thus:

$$k_a = \Gamma \int_{-\infty}^{E_{\text{vac}}} T(E) W_{\text{Red}}(E) g(E) [1 - f(E)] dE \quad (110)$$

and

$$k_c = \Gamma \int_{-\infty}^{E_{\text{vac}}} T(E) W_{\text{Ox}}(E) g(E) f(E) dE \quad (111)$$

A close inspection of Figures 25(a) and (b) shows that, under conditions of equilibrium or sufficiently small overpotential ($|\mu_e - \mu_e^{\text{eq}}| < \lambda$), electron tunneling occurs predominantly in the energy range around the Fermi level of the metal. This is because the occupancy of the electron levels in the metal and redox system are given by the Fermi–Dirac law. To a good approximation, we may confine the integration to the energy range between $\mu_e - k_B T$ and $\mu_e + k_B T$; thus

$$k_a = k_B T \times \Gamma \times T(\mu_e) \times g(\mu_e) \times W_{\text{Red}}(\mu_e) \quad (112)$$

and

$$k_c = k_B T \times \Gamma \times T(\mu_e) \times g(\mu_e) \times W_{\text{Ox}}(\mu_e) \quad (113)$$

In the equations for the probability functions $W_{\text{Red}}(\mu_e)$ and $W_{\text{Ox}}(\mu_e)$, we can use

$$\begin{aligned}\mu_e - E_{\text{Red}}^{\text{eq}} &= [\mu_e - \mu^o(\text{Ox/Red})] + \lambda = [\mu_e - \mu(\text{Ox/Red})] \\ &\quad + [\mu(\text{Ox/Red}) - \mu^o(\text{Ox/Red})] + \lambda\end{aligned}$$

and

$$\begin{aligned}\mu_e - E_{\text{Ox}}^{\text{eq}} &= [\mu_e - \mu^o(\text{Ox/Red})] - \lambda \\ &= [\mu_e - \mu(\text{Ox/Red})] + [\mu(\text{Ox/Red}) - \mu^o(\text{Ox/Red})] - \lambda\end{aligned}$$

(see Figure 12 and Eq. 46). Furthermore, $\mu_e - \mu(\text{Ox/Red})$ is $\mu_e - \mu_e^{\text{eq}}$, and the difference $\mu(\text{Ox/Red}) - \mu^o(\text{Ox/Red})$ is given by Eq. 36. Since we assumed a small overpotential, that is, $\mu_e - \mu^o(\text{Ox/Red}) < \lambda$, the exponent in the equations for $W_{\text{Red}}(\mu_e)$ and $W_{\text{Ox}}(\mu_e)$ can be simplified. It is found that

$$k_a = k_a^{\text{eq}} e^{-(\mu_e - \mu_e^{\text{eq}})/2k_B T} \quad (114)$$

with

$$k_a^{\text{eq}} = \frac{k_B T \times \Gamma \times T(\mu_e) \times g(\mu_e)}{\sqrt{4\pi k_B T \lambda}} \times \sqrt{\frac{c_{\text{Ox}}}{c_{\text{Red}}}} \times e^{-\lambda/4k_B T} \quad (115)$$

and

$$k_c = k_c^{\text{eq}} e^{(\mu_e - \mu_e^{\text{eq}})/2k_B T} \quad (116)$$

with

$$k_c^{\text{eq}} = \frac{k_B T \times \Gamma \times T(\mu_e) \times g(\mu_e)}{\sqrt{4\pi k_B T \lambda}} \times \sqrt{\frac{c_{\text{Red}}}{c_{\text{Ox}}}} \times e^{-\lambda/4k_B T} \quad (117)$$

Equations 115 and 117 satisfy the necessary condition $k_a^{\text{eq}} c_{\text{Red}} = k_c^{\text{eq}} c_{\text{Ox}}$ at electrochemical equilibrium. The activation energy is $\lambda/4$ for exchange at equilibrium. The anodic and cathodic partial current densities change exponentially with the deviation from equilibrium, $\mu_e - \mu_e^{\text{eq}}$. This holds as long as the concentrations of the reduced and oxidized species just outside the double layer are independent of the overpotential (kinetic control), and the overpotential is sufficiently small with respect to the reorganization energy, that is, $|\mu_e - \mu_e^{\text{eq}}| < \lambda$. It is clear that the current density shows a sub-exponential increase at larger overpotentials. Consider, for example, the case of cathodic electron flow, with μ_e close to the maximum of the probability function of the oxidized species, $\mu_e \approx E_{\text{Ox}}^{\text{eq}}$ [Figure 25(c)]. When we increase the overpotential further, electron tunneling in the energy range around $E_{\text{Ox}}^{\text{eq}}$ remains the dominant contribution to the cathodic current; hence, the overall cathodic current flow will tend to a constant value.

4.8.3 Marcus, Gerischer and the Phenomenological Rate Equations

In the years 1955–1960, a kinetic theory for homogeneous outer-sphere electron transfer was put forth by Marcus [5]. Marcus pointed out that simple electron transfer reactions, as described by Eqs. 30–31, cannot occur if the reaction complex has an equilibrium solvation structure. This would imply that the reacting system consisting of two ions exchanging an electron has the wrong solvation sphere after the transfer of the electron. In such a way, tunneling cannot proceed iso-energetically. Marcus proposed that, for the Franck–Condon principle to be obeyed during elastic tunneling, tunneling occurs in an activated complex characterized by a non-equilibrium solvation structure. This activated complex should have a free energy which is independent of the position of the electron in transition. With the use of classic electrostatic theory, Marcus was able to find the activated complex with the lowest free energy, and hence to predict the most probable reaction path for simple electron transfer. At a later stage, the theory was adapted for the case of electrochemical electron transfer between a metal and a simple redox system. The activation energy for anodic and cathodic electron transfer can be written as follows:

$$\Delta G_a^\# = \frac{\lambda}{4} \left(1 + \frac{\mu_e - \mu_e^{\text{eq}}}{\lambda} \right)^2 \quad (118)$$

$$\Delta G_c^\# = \frac{\lambda}{4} \left(1 - \frac{\mu_e - \mu_e^{\text{eq}}}{\lambda} \right)^2 \quad (119)$$

Here, λ is the reorganization energy composed of a component due to vibrational excitations in the ligand–metal ion bonds and a component due to the non-equilibrium solvation sphere. Using classic electrostatic theory, Marcus was able to find an expression for the reorganization energy of the solvation structure as a function of the radii of the reduced and oxidized species and the static dielectric constant of the solvent. In the decades after the appearance of the first papers, it became clear that the predictions of Marcus are in qualitative, and sometimes quantitative agreement with the results of many experiments in the field of homogeneous, intramolecular and electrochemical electron transfer. In the following, we place the predictions of the microscopic classical theories of Marcus and Gerischer in the framework of the general and phenomenological treatment presented in Section 4.7.

At equilibrium, that is, $\mu_e = \mu_e^{\text{eq}}$, the Marcus theory predicts that the activation energy for electron exchange between the metal and redox system is $\lambda/4$ (see Eqs. 118–119). This is the same as the prediction of the Gerischer theory, Eqs. 115 and 117. Moreover, it appeared that the reorganization energy λ has the same meaning in both theories. In Section 4.4, a definition for λ within the Gerischer model was given by Eq. 46. Marcus found a quantitative expression for this quantity. Experimentally, the activation energy $\lambda/4$ can be obtained from the temperature dependence of the exchange current at equilibrium (see Section 4.7.3). Values on the order of 0.1 to 0.5 eV are usually found, in qualitative agreement with the prediction from

the Marcus theory that for most redox systems λ should lie in the range 0.5–2 eV per molecule [5].

We now consider the results for a sufficiently low overpotential, that is, $|\mu_e - \mu_e^{\text{eq}}| < \lambda$. For example, we take $\mu_e > \mu_e^{\text{eq}}$ (net cathodic current flow). The Marcus theory predicts that $\Delta G_a^\# = \frac{\lambda}{4} + \frac{1}{2}(\mu_e - \mu_e^{\text{eq}})$, and $\Delta G_c^\# = \frac{\lambda}{4} - \frac{1}{2}(\mu_e - \mu_e^{\text{eq}})$ (see Eqs. 118–119). This is in complete agreement with the predictions of the Gerischer theory, described by Eqs. 114–119. This means that in the framework of the phenomenological theory (Section 4.7, Eqs. 100–101) the charge-transfer coefficients are independent of the overpotential and temperature, that is, $\alpha_a = \alpha_c = 1/2$. Charge-transfer coefficients close to 1/2 have been found for many simple redox systems [21].

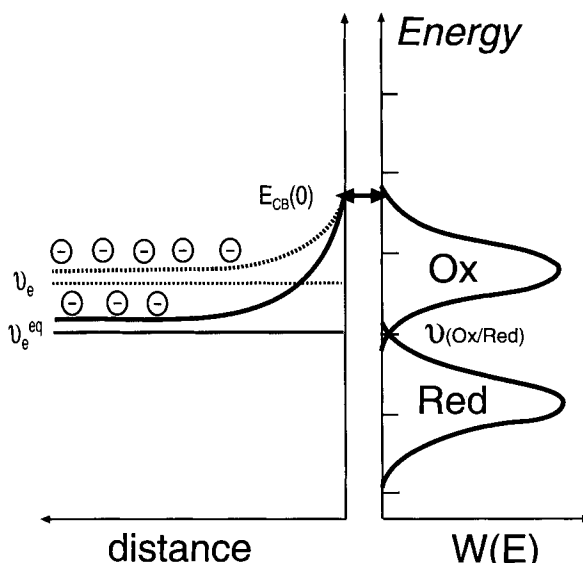
At higher overpotential, $\mu_e - \mu_e^{\text{eq}}$ can become close to, or even higher than λ . If the graphical description of the Gerischer theory is used (Figure 25), it follows that cathodic electron transfer will predominantly occur by tunneling in the energy range close to $E_{\text{Ox}}^{\text{eq}}$. It follows that the rate of cathodic transfer will increase less than exponentially with $\mu_e - \mu_e^{\text{eq}}$. If μ_e becomes equal to or higher than $E_{\text{Ox}}^{\text{eq}}$, the cathodic current will tend to a constant maximum value. The Marcus theory also predicts that the current increases less than exponentially with the overpotential if the condition $|\mu_e - \mu_e^{\text{eq}}| < \lambda$ is not fulfilled. Furthermore, it predicts that the current *decreases* with increasing overpotential if $\mu_e - \mu_e^{\text{eq}}$ becomes greater than λ . Experimental evidence for this so-called inverted region has been put forward for homogeneous and intramolecular electron transfer. It is clear from Figure 25 that an inverted regime cannot occur for electrochemical electron transfer at a metal electrode. Electron tunneling in the energy range around $E_{\text{Ox}}^{\text{eq}}$ remains the dominant contribution to the cathodic current if $\mu_e - \mu_e^{\text{eq}}$ is made higher than λ .

4.9 Comparison of Electron Transfer at a Semiconductor With Electron Transfer at a Metal Electrode

With the development of solid-state semiconductor devices (diodes, transistors), semiconductor/solution interfaces [24] became a subject of scientific interest. Since the 1960s, semiconductor electrochemistry and photo-electrochemistry has become established as an independent subdiscipline in electrochemical science. The basic principles and summaries of experimental results can be found in review papers and textbooks [25]. Here, we will introduce the subject by comparing simple electron transfer at a metal with that at a semiconductor electrode.

The main differences between the kinetics of electron transfer at a metal and that at a semiconductor electrode originate in the difference in the density of free carriers. In a typical metal, the electrochemical potential or Fermi level, μ_e , is located in a band. The free-electron density is huge, 10^{22} – 10^{23} cm⁻³. We discussed the metal/solution interface in Section 4.5; it has a rather complicated structure with a double

Figure 26. Electronic structure of an interface between an *n*-type semiconductor and an electrolyte solution containing a simple redox system. The conduction band edge is shown as a function of the distance from the surface at the left side (solid line: equilibrium, dashed line: nett cathodic current flow). At the other side, the energetic distribution of empty and occupied electron levels corresponding to the redox system is shown. Electron transfer is possible in the energy region just above the conduction band edge at the surface.



layer at the metal surface extending over a few unit cells adjacent to a molecular solvent layer. However, the width of the entire double layer is less than a nanometer. This means that free electrons in the bulk are in tunneling distance from redox ions contacting the solution part of the double layer. Moreover, the density of occupied and empty free electron states with energy close to μ_e is large. Typically, electrochemical electron tunneling occurs in the energy range between $\mu_e - k_B T$ and $\mu_e + k_B T$ (see Section 4.8). At equilibrium, isoenergetic electron tunneling may occur if the reduced or oxidized species has an electron level in this energy range. This requires a nonequilibrium solvation structure around the reacting ion, corresponding to a thermal activation energy given by one fourth of the reorganization energy of the redox system.

In bulk semiconductors, the electrochemical potential is in the gap between the valence and conduction bands (see Section 4.3.5). The density of free carriers (holes in the VB and free electrons in the CB) is 10^{16} – 10^{19} cm^{-3} , this is three to six orders of magnitude smaller than in a metal. The consequences for the structure of the semiconductor/solution interface were discussed in Section 4.5.4. In Figure 26, the interface between an *n*-type semiconductor and an electrolyte is depicted; the energetic distribution of electron levels corresponding to the redox system is also shown (see also Sections 4.4 and 4.8; for simplicity we assumed here that $c_{Ox} = c_{Red}$). In Figure 26, the situation at equilibrium is shown. The interfacial region consists of a layer in the solid, depleted of free electrons (typically 10–1000 nm in thickness), adjacent to the Helmholtz layer at the solution side. Electrons in the bulk of the semiconductor are therefore much too far from the redox ions for tunneling to be possible. Cathodic tunneling from the semiconductor to an oxidized species only involves electrons at the surface, with potential energy equal to $E_{CB}(0)$. It follows that, in such a situation, the activation energy is considerably larger than $\lambda/4$, since

an electron from the bulk has to overcome the potential-energy barrier of the depletion layer. This also becomes apparent if anodic transfer from a reduced species to the empty states in the conduction bands is considered. Tunneling is possible in the energy range above $E_{CB}(0)$ only. The probability of finding a filled level corresponding to the reduced species in this energy range is very low. Again, we conclude that the activation energy is much higher than for electron exchange between a redox system and a metal. The activation energy for electron exchange between an *n*-type semiconductor electrode and a redox system has been calculated on the basis of the fluctuating-energy-level model [15]. It is found that

$$\Delta G^{\#,\text{eq}} = \lambda/4 + \frac{E_{CB}(0) - \mu(\text{Ox/Red})}{2} + \frac{[E_{CB}(0) - \mu(\text{Ox/Red})]^2}{4\lambda} \quad (120)$$

The activation energy exceeds $\lambda/4$; the additional contributions depend on the degree of depletion at equilibrium and they can easily be as large as $\lambda/4$ itself. Hence, the exchange current density between a typical *n*-type semiconductor and a simple redox system can be orders of magnitude lower than that in a metal.

The high activation energy for direct exchange between a semiconductor and a redox system opens the gate for competitive pathways, that is, for exchange mediated by surface-electron levels located in the band gap (surface states). In Figure 27, electron exchange between an *n*-type semiconductor and a simple redox system, mediated by surface states, is shown. The exchange between surface states located at around μ_e and a simple redox system across the Helmholtz layer requires an activation energy of $\lambda/4$. The exchange of electrons between surface levels and the free electron levels (conduction band) in the bulk semiconductor requires a thermal activation energy of the order of $E_{CB}(0) - \mu(\text{Ox/Red})$. Thus, electron exchange mediated by surface energy levels is a two-step process; both steps can proceed

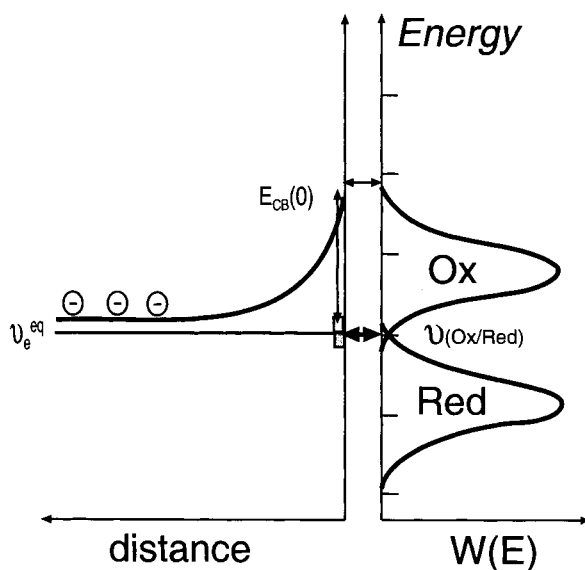


Figure 27. Representation of the competition between direct electron exchange (at around the conduction band edge at the surface) and exchange mediated by surface electron levels. Surface states may exchange electrons with the redox system in the energy interval at around the electrochemical potential. Surface states exchange electrons with the conduction band by electron capture and thermal electron excitation (vertical arrows).

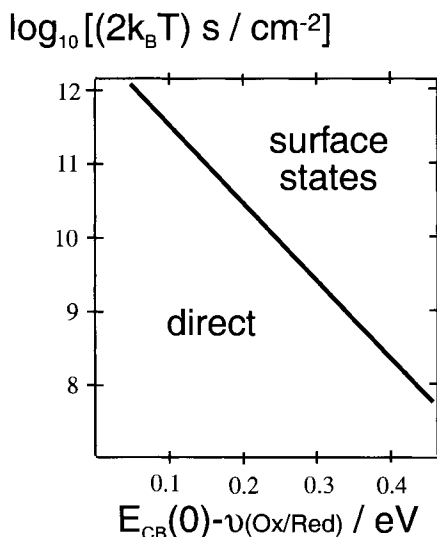


Figure 28. Diagram showing the competition between direct and surface state mediated electron exchange between an *n*-type semiconductor and a simple redox system ($\lambda = 1$ eV). The competition is determined by the effective density of surface states at around the Fermi-level [$2 k_B T s$] and the band bending at equilibrium [$E_{CB}(0) - \mu(\text{Ox/Red})$]. The demarcation line indicates equal rate of both processes.

with considerably lower activation energy than that for direct exchange given by Eq. 120. It is clear that the competition between direct and surface-state-mediated exchange depends on the reorganization energy λ of the redox system, the degree of depletion at equilibrium, that is, $E_{CB}(0) - \mu(\text{Ox/Red})$, and the density of surface energy levels as a function of energy in the band gap. A general analysis of the competition between direct and surface-state-mediated exchange is out of reach. In [15], the problem was simplified by it being pointed out that surface states at around μ_e are the most effective in electron exchange between a semiconductor and a simple redox system under equilibrium conditions. (This is not necessarily the case under net cathodic or anodic current flow). The effective density of these states is denoted as $k_B T \times s(\mu_e)$ (cm^{-2}). The competition between surface-state-mediated and direct exchange is represented in Figure 28 by the demarcation line in the diagram, with $\log_{10}[k_B T \times s(\mu_e)]$ and $E_{CB}(0) - \mu(\text{Ox/Red})$ as coordinate axes. If the depletion at equilibrium is relatively weak, say 0.1 eV, the effective density must be higher than 10^{12} cm^{-2} to make surface-state-mediated transfer competitive with direct transfer. But, for a moderate band bending of 0.3 eV, a density of surface states of 10^9 cm^{-2} suffices. Reducing the density of surface states at a semiconductor/solution interface below a value of 10^9 cm^{-2} is a difficult task. It is probably only possible with layered semiconductors and hydrogen-terminated silicon surfaces [26]. This may explain why, in so many cases, experimental results indicate that surface states are involved to a large extent in electron exchange at equilibrium and in a net cathodic or anodic current flow [15, 25].

When we make the electrochemical potential, μ_e , of a metal or semiconductor electrode different from the value at equilibrium, $\mu_e^{\text{eq}} = \mu(\text{Ox/Red})$, the interfacial potential drop $\varphi - \varphi_{\text{Sol}}$ is changed, and $\partial(\mu_e - \mu_e^{\text{eq}}) = -e\partial(\varphi - \varphi_{\text{Sol}})$. With a metal electrode, the only effect for the electrochemical kinetics is that μ_e is changed with respect to the distribution of electron levels corresponding to the redox system. As a

result, the probability of electron transfer from the metal to the oxidized species, and from the reduced species to the metal is changed (see Section 4.8.2). With a semiconductor electrode under conditions of depletion, a change of the overpotential $\partial(\mu_e - \mu_e^{\text{eq}})$ can result in a change of the potential drop over the depletion and Helmholtz layers; $\partial(\mu_e - \mu_e^{\text{eq}}) = -e[\partial(\varphi - \varphi_S) + \partial(\varphi_S - \varphi_{\text{Sol}})]$. Where the occupation of surface energy levels is not changed with the overpotential, the distribution of $\partial(\mu_e - \mu_e^{\text{eq}})$ over the interfacial layers is determined by the relative value of the capacity of the depletion and Helmholtz layers, that is, by the parameter

$\frac{C_{\text{sol}}}{C_{\text{Sc}} + C_{\text{Sol}}}$ (Section 4.5.4). If the density of free carriers is not too high (below

10^{18} cm^{-3}), it usually holds that $\frac{C_{\text{sol}}}{C_{\text{Sc}} + C_{\text{Sol}}} \cong 1$. In this case, a change in the overpotential only affects the potential drop in the depletion layer. The surface energy levels of the semiconductor remain at the same relative position with respect to the electron levels of the redox system, (see Figure 2b for an *n*-type semiconductor). The probability of tunneling through the Helmholtz layer is unaltered by a change of the overpotential, in contrast with a metal electrode. A change of the overpotential only affects the density of free carriers at the surface. Applying Eq. 62 for the surface, $x = 0$, we find for an *n*-type semiconductor that

$$n(0) = n^{\text{eq}}(0)e^{(\mu_e - \mu_e^{\text{eq}})/k_B T} \quad (121)$$

It is concluded that if $\frac{C_{\text{sol}}}{C_{\text{Sc}} + C_{\text{Sol}}} \cong 1$ holds, the anodic current density remains

equal to the exchange current density at equilibrium, and that the cathodic current density increases exponentially with $\mu_e - \mu_e^{\text{eq}}$. In the framework of the phenomenological treatment presented in Section 4.7, this would mean that $\alpha_a = 0$, and that $\alpha_c = 1$. The relationship between the current density j and the overpotential $\mu_e - \mu_e^{\text{eq}}$ is similar to that observed with a semiconductor/metal diode junction. In the literature, this is referred to as “ideal behavior”. Extensive research has been devoted to the electrochemical kinetics of semiconductor/electrolyte junctions, with a large variety of semiconductors and simple redox systems in aqueous and non-aqueous solvents being looked at. Only in a minority of cases were strong indications found for ideal behavior [15, 25, 26]. This is not unexpected, since the activation energy for electron exchange at equilibrium can be large, and even a small density of surface states may lead to an alternative pathway for exchange.

Several models have been proposed for the electrochemical kinetics if surface states are involved [15, 25]. They merely differ in their assumptions made to simplify the problem. A change in the occupation of the surface electron levels changes the potential drop over the depletion and Helmholtz layers. One should realize that then both the density of free carriers at the surface and the tunneling probability per electron changes with the overpotential. A complete treatment was presented in [15], for mono-energetic surface states, and in [27], assuming surface states distributed over the band gap. Here, we present results for surface states confined to a small energy range (Figure 29). The cathodic and anodic current density corresponding to direct and surface-state-mediated transfer are shown in Figure 29 (top

D. Vanmaekelbergh

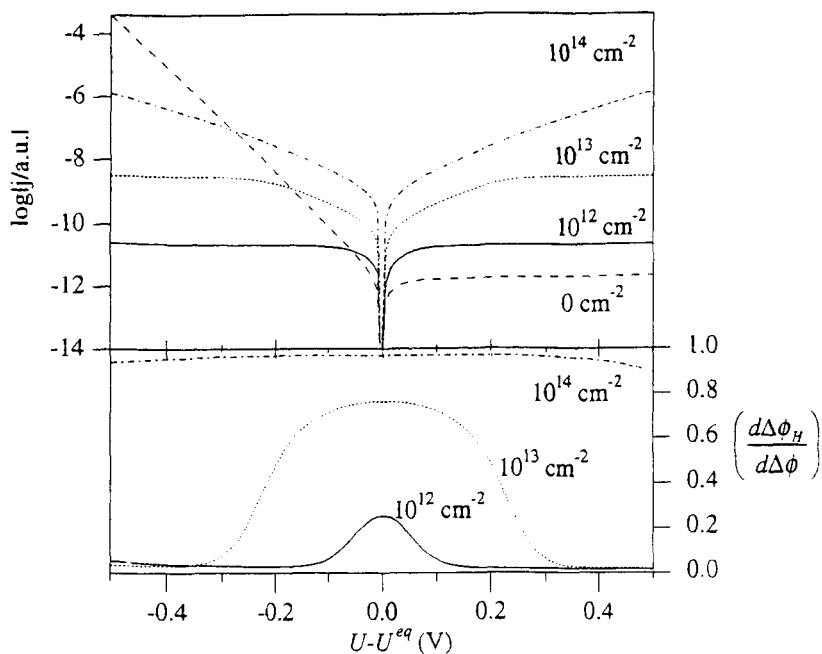


Figure 29. Calculated current-potential characteristics for direct (dashed lines, $0/\text{cm}^2$) and surface state mediated electron transfer between an n -type semiconductor electrode and a simple redox system. The plots show the transition from ideal diode behavior to metallic behavior with increasing density of surface states at around the Fermi-level of the solid (indicated in the figures). This is also clear from the plots below, which show the change of the interfacial potential drop over the Helmholtz-layer (here denoted as $\Delta\phi_H$) with respect to the total change of the interfacial potential drop (here denoted as $\Delta\phi$). Results from D. Vanmaekelbergh, *Electrochim. Acta* 42, 1121 (1997).

part) as a function of $\mu_e - \mu_e^{\text{eq}}$. In Figure 29 (bottom), the change of the potential drop over the Helmholtz layer, $\phi_S - \phi_{\text{Sol}}$, referred to the total change of the interfacial potential drop $\phi - \phi_{\text{Sol}}$ is shown. It can be seen that the j vs $\mu_e - \mu_e^{\text{eq}}$ relationship changes from ideal diode behavior to that typical for a metal electrode if the effective density of surface states is gradually increased. It is also clear that surface states enhance the rate of electron exchange at equilibrium considerably.

References

1. *The electrical double layer and the theory of electrocapillarity*. D. C. Grahame, *Chem. Rev.* 41, 441 (1947).
2. *Electronic effects in the electric double layer*. W. Schmickler, *Chem. Rev.* 96, 3177 (1996).
3. *Computer simulations of electrochemical interfaces*. E. Spohr in: *Advances in Electrochemical Science and Engineering*, vol. 6 (1999). Eds.: R. C. Alkire and D. M. Kolb, Wiley-VCH, Weinheim.
4. *Charge transfer processes at semiconductor-electrolyte interfaces in connection with problems of catalysis*. H. Gerischer, *Surface Science* 18, 97 (1969).

5. *Electron transfer reactions in chemistry: theory and experiment*. R. A. Marcus, *Angew. Chem. Int. Ed. Engl.* 32, 1111 (1993).
6. *Physik der Solarzellen*. P. Würfel, Spektrum, Heidelberg (1999).
7. *Thermal Physics*. C. B. P. Finn in: "*Physics and its Applications*", vol. 5 Eds.: S. B. Palmer and E. R. Dobbs, Chapman & Hall, New York (1993).
8. *Physical Chemistry* P. W. Atkins, Oxford University Press, Oxford (1990).
9. *Driving force for electron transport in porous nanostructured photoelectrodes*. D. Vanmaekelbergh and P. E. de Jongh, *J. Phys. Chem. B*, 103, 747 (1999).
10. P. Drude, *Annalen der Physik* 1, 566 (1900), and *Annalen der Physik* 3, 369 (1900).
11. N. W. Ashcroft and N. D. Mermin in: *Solid State Physics* Ed.: D. G. Crane, Philadelphia (1976).
12. *Über den Ablauf von Redoxreaktionen an Metallen und an Halbleitern*. H. Gerischer, *Z. Phys. Chem. N. F.* 26, 223 (1960).
13. *Theory of metal surfaces: work function* N. D. Lang and W. Kohn, *Phys. Rev. B* 3, 1215 (1970).
14. *Coupled partial ion-transfer steps in the anodic dissolution of metals*. D. Vanmaekelbergh and B. H. Erne, *J. Electrochem. Soc.* 146, 2488 (1999).
15. *Direct and surface state mediated electron transfer at semiconductor/electrolyte junctions.—A comparison of steady-state results*. D. Vanmaekelbergh, *Electrochim. Acta* 42, 1121 (1997).
16. *Scanning probe microscopy and spectroscopy*. R. Wiesendanger, Cambridge University Press, Cambridge (1994).
17. (a) *Electron transfers in chemistry and biology*. R. A. Marcus and N. Sutin, *Biochimica et Biophysica Acta* 811, 265 (1985); (b) *Contemporary issues in electron transfer research*. P. F. Barbara, T. J. Meyer, and M. A. Ratner, *J. Phys. Chem.* 100, 13148 (1996). (c) *Nature of biological electron transfer*. C. C. Moser et al, *Nature* 355, 796 (1992).
18. *A unified model for electrochemical electron transfer and ion transfer reactions*. W. Schmickler, *Chem. Phys. Letters* 237, 152 (1995).
19. *A Kramers reaction rate theory for electrochemical ion transfer reactions*. M. T. M. Koper and W. Schmickler, *Chemical Physics* 211, 123 (1996).
20. *Electron transfer between biological molecules by thermally activated tunneling*. J. J. Hopfield, *Proc. Nat. Acad. Sci. USA* 71, 3640 (1974).
21. *'Surface electron transfer processes'* R. J. Dwayne Miller, G. L. McLendon, A. J. Nozik, W. Schmickler and F. Willig. VCH, (1995) Weinheim.
22. *Large-scale computer simulation of an electrochemical bond-breaking reaction* A. Calhoun, M. T. M. Koper and G. A. Voth, *Chem. Phys. Lett.* 305, 94 (1999).
23. (a) *On the impedance of galvanic cells. I. Theory* J. H. Sluyters, *Recueil* 79, 1092 (1960); *II Experimental verification* J. H. Sluyters and J. J. C. Oomen, *Recueil* 79, 1101 (1960). (b) *Impedance spectroscopy at semiconductor electrodes. Review and recent developments*. W. P. Gomes and D. Vanmaekelbergh, *Electrochim. Acta* 41, 967 (1996). (c) *Frequency response analysis of intensity modulated photocurrents at semiconductor electrodes*. L. M. Peter et al., *Electrochim. Acta* 35, 1657 (1990). (d) *Dynamic aspects of semiconductor photoelectrochemistry*. L. M. Peter, *Chem. Rev.* 90, 753 (1990). (e) *Time and frequency resolved studies of photoelectrochemical kinetics*. L. M. Peter and D. Vanmaekelbergh in: *Advances in Electrochemical Science and Engineering*, vol. 6 (1999). Eds R. C. Alkire and D. M. Kolb, Wiley-VCH, Weinheim.
24. *Redoxvorgänge an Germanium Elektroden*. F. Beck and H. Gerischer, *Zeitschrift für Elektrochemie* 63, 943 (1959).
25. (a) *Electrochemistry at Semiconductor and Oxidized Metal electrodes*. S.R. Morrison, Plenum, New York (1980). (b) *Semiconductor Photoelectrochemistry*. Yu. V. Pleskov and Yu. Ya Gurvich, Consultants Bureau, New York (1986). (c) *Electron levels in semiconductor electrochemistry*. W. P. Gomes and F. Cardon, *Progress in Surface Science*, 12, 155 (1982).
26. (a) *Rate constants for charge transfer across semiconductor-liquid interfaces*. A. M. Fajardo and N. S. Lewis, *Science* 274, 969 (1996). (b) *In situ measurements of interface states at silicon surfaces in fluoride solutions*. G. Oskam et al., *Phys. Rev. Lett.* 76, 1521 (1996). (c) *Hole reactions from d-energy bands of layer-type group VI transition metal dichalcogenides: new perspectives for electrochemical solar energy conversion*. H. Tributsch, *J. Electrochem. Soc.* 125, 1086 (1978).
27. *Electrochemistry of homoepitaxial CVD diamond: energetics and electrode kinetics in aqueous solutions*. J. van de Lagemaat et al, *J. Electroanal. Chem.* 475, 139 (1999).

5 Proton-Coupled Electron Transfer

Sharon Hammes-Schiffer

5.1 Introduction

Proton-coupled electron transfer (PCET) reactions play a vital role in a wide range of chemical and biological processes. For example, PCET is required for the conversion of energy in photosynthesis [1] and respiration [2]. In particular, the coupling between proton motion and electron transfer is involved in the pumping of protons across biological membranes in photosynthetic reaction centers [1] and in the conduction of electrons in cytochrome c [3]. In addition to biological processes, PCET is also important in electrochemical processes [4, 5] and in solid state materials [6].

Recently, a number of experiments on model PCET systems have been performed. Nocera and coworkers designed an experimental approach to photoinduce electron transfer within an electron donor–acceptor pair juxtaposed by a proton-transfer interface [7–9]. They have studied a variety of complexes, including a system in which an electron is transferred from a Ru^{II} polypyridine complex to dinitrobenzene through an amidinium–carboxylate interface [9]. Their results indicate that the electron transfer reaction is strongly affected by the proton interface and that in some cases a proton is transferred along with the electron. Meyer and coworkers have performed kinetic isotope effect studies on a range of oxoruthenium polypyridyl complexes [10]. Their experiments indicate that reactions based on the Ru^{IV} –oxo group often involve PCET. In addition, Thorp and coworkers have studied the effects of substitutions for reactions involving oxoruthenium [11]. These types of experimental studies on model PCET systems are becoming more prevalent as the important role of PCET in chemistry and biology is recognized.

The formulation of a theory for PCET is particularly challenging because of the disparate timescales involved. The description of the solute must accurately incorporate the quantum mechanical behavior of the solute electrons involved in both proton transfer (PT) and electron transfer (ET) and the transferring proton(s). The description of the solvent must include the effects of both electronic and inertial

polarization. In this chapter, electronic polarization refers to the solvent response assumed to be instantaneous, and inertial polarization refers to the non-instantaneous solvent response (e.g., nuclear reorientation and translation). As a result of these complexities, the theory of PCET has not been developed as extensively as the theory of single ET. To date, two distinct theoretical formulations for PCET have been proposed. The first was developed by Cukier [7, 12], and the second was developed by Soudackov and Hammes-Schiffer [13, 14]. This chapter centers on the second theoretical formulation, which is based on a multistate continuum theory. The first formulation will be discussed only briefly for comparison.

In the theory of PCET developed by Soudackov and Hammes-Schiffer, the solute is described with a multistate valence bond (VB) model, the solvent is represented as a dielectric continuum, and the active electrons and transferring proton(s) are treated quantum mechanically on equal footing. This theory provides free energy surfaces that depend on a set of scalar solvent variables corresponding to the individual charge transfer reactions. Thus, this theory is a multidimensional analog of the standard Marcus theory for single electron transfer. For processes involving significant inner-sphere (i.e., solute) reorganization, the effects of solute intramolecular vibrations can be incorporated into the formulation. The input quantities required for this theory are gas phase valence bond matrix elements that can be fit to quantum chemistry calculations and solvent reorganization energy matrix elements that can be calculated with electrostatic continuum methods.

Dielectric continuum theory has been applied to single ET and single PT reactions throughout the literature [4, 5, 15–22]. The most basic description of a single-charge transfer reaction is a two state VB model. As mentioned above, in this chapter the Born–Oppenheimer approach is adopted for the separation of solvent and solute electronic timescales (i.e., the solvent electrons are assumed to respond instantaneously to the solute electrons) [23]. In this case, the free energy curves are obtained as functions of a single scalar solvent variable representing the difference in interaction energies of the VB states with the solvent inertial polarization field. Various limits of single ET and single PT reactions have been thoroughly investigated. For example, single charge transfer reactions may be electronically adiabatic or non-adiabatic, where electronically adiabatic refers to the limit in which the solute electrons respond instantaneously to the inertial polarization of the solvent. Moreover, single PT reactions may be vibrationally adiabatic or non-adiabatic, where vibrationally adiabatic refers to the limit in which the transferring proton(s) respond instantaneously to the inertial polarization of the solvent. Rate expressions have been derived for these various limits.

The application of multistate continuum theory to PCET [13] is analogous to the previous applications to single charge transfer reactions. The most basic description of a PCET reaction involving one electron and one proton is a four-state VB model derived by combination of the two-state VB models for single ET and single PT reactions. Within this four-state VB model, the mixed electronic/proton vibrational free energy surfaces are obtained as functions of two scalar solvent variables corresponding to ET and PT. The adiabatic and non-adiabatic limits with respect to the ET electrons, PT electrons, and transferring proton have been considered. Both the ET and the PT electrons correspond to valence electrons of the solute: the ET

electrons are those involved in the change in charge distribution when the electron transfers, and the PT electrons are those involved in the breaking and forming of bonds when the proton transfers. Typically PCET reactions involve electronically adiabatic PT. In this case the four-state VB model can be transformed into a two-state VB model. Even in this two-state VB model, however, the free energy surfaces depend on two scalar solvent variables corresponding to ET and PT. In the limit of electronically non-adiabatic ET, the Golden Rule may be applied to these two-dimensional free energy surfaces for obtaining rate expressions.

The multistate continuum theory may be further extended for investigations of PCET reactions involving more than two charge transfer reactions. For example, a PCET reaction involving one electron and two protons is described by an eight-state VB model. In the limit of electronically adiabatic PT, this eight-state VB model can be transformed to a two-state VB model. In either case, however, the free energy surfaces are obtained as functions of three scalar solvent variables corresponding to the ET reaction and the two PT reactions.

An outline of this chapter is as follows. In Section 5.2, the basic two-state dielectric continuum theory for single ET and single PT reactions is described. The purpose of this section is to lay the groundwork for the future sections and to point out the important issues relevant to PCET reactions. In Section 5.3, the multistate continuum theory formulation for PCET reactions is presented. First, the general four-state VB model is presented and then the two-state VB model for the specific case of electronically adiabatic PT is presented. A discussion of the incorporation of inner-sphere reorganization and the extension to more than two charge transfer reactions is also included in this section. In the last part of this section, the theory of Cukier and coworkers is briefly discussed for comparison. In Section 5.4, applications of the multistate continuum theory formulation are discussed. The procedure for calculating the required input quantities is described, and the initial application to experimentally studied PCET through asymmetric salt bridges is discussed. In Section 5.5, the effects of specific solute and solvent properties on the rates and mechanisms of PCET are summarized. Future directions are discussed in Section 5.6.

5.2 Continuum Theory for Single Charge Transfer

In dielectric continuum theory, the solute density is placed in a cavity embedded in a dielectric continuum solvent characterized by the electronic and inertial dielectric constants ϵ_∞ and ϵ_o , respectively. Typically, the solvent polarization potential field is assumed to respond linearly to the change in solute charge density. The free energy of the system for fixed solute nuclei is a functional of the solvent inertial polarization potential field $\phi_{\text{in}}(\mathbf{r})$:

$$\mathcal{U}[\phi_{\text{in}}] = \mathcal{S}[\phi_{\text{in}}] + \mathcal{W}[\phi_{\text{in}}] \quad (1)$$

where $\mathcal{S}[\phi_{\text{in}}]$ is the self-energy of the solvent inertial polarization potential and $\mathcal{W}[\phi_{\text{in}}]$ includes the gas phase solute energy and the solute–solvent interaction energy. The interaction term can be expressed in terms of the solute electronic wavefunction Ψ as

$$\mathcal{W}[\phi_{\text{in}}] = \langle \Psi | \mathcal{H} | \Psi \rangle \quad (2)$$

where the Hamiltonian operator \mathcal{H} is a sum of the gas phase solute Hamiltonian and the interaction of the solute charge density with the solvent.

For charge transfer reactions, the solute electronic wavefunction is expanded in a basis of VB (also denoted “diabatic”) charge transfer states ψ_i :

$$\Psi = \sum_i c_i \psi_i \quad (3)$$

In this case, the free energy can be expressed in terms of a set of scalar solvent variables representing the interaction energies of the densities of the VB states with the solvent. If the off-diagonal densities are neglected, the required number of scalar solvent variables is one less than the number of included VB states with linearly independent densities [20]. The remainder of this section describes the application of this general approach to single ET and single PT and points out the issues relevant to PCET.

5.2.1 Single-Electron Transfer

The most basic ET system is represented by a two-state VB model with electronic VB states defined as

$$\begin{aligned} (1) \quad & \text{D}_e^\ominus \text{A}_e \\ (2) \quad & \text{D}_e \text{A}_e^\ominus \end{aligned} \quad (4)$$

where the symbols D_e and A_e represent a general electron donor and acceptor. In this model, the free energy can be expressed in terms of a single solvent coordinate z_e , which represents the difference in interaction energy of the two VB states with the inertial polarization field $\phi_{\text{in}}(\mathbf{r})$ of the solvent. Thus,

$$z_e = \int d\mathbf{r} [\rho_{22}(\mathbf{r}) - \rho_{11}(\mathbf{r})] \phi_{\text{in}}(\mathbf{r}) \quad (5)$$

where $\rho_{ii}(\mathbf{r})$ is the total charge density of VB state i . This type of scalar solvent coordinate has been used throughout the literature for the description of single electron transfer reactions [18, 19].

The VB matrix corresponding to the free energy given in Eq. 1 is

$$\mathbf{H}(z_e) = \mathcal{S}(z_e)\mathbf{I} + \mathbf{H}_o + \begin{pmatrix} 0 & 0 \\ 0 & z_e \end{pmatrix} \quad (6)$$

The first term, $\mathcal{S}(z_e)$, is the transformed self-energy of the solvent inertial polarization and is expressed as

$$\mathcal{S}(z_e) = \frac{1}{2t'_{22}}(z_e + t'_{12})^2 - \frac{1}{2}t'_{11} \quad (7)$$

The inertial reorganization energy matrix elements t'_{ij} are defined as

$$t'_{ij} = -\int d\mathbf{r} v_{ij}(\mathbf{r})[\hat{K}(\varepsilon_o) - \hat{K}(\varepsilon_\infty)]v_{ii}(\mathbf{r}) \quad (8)$$

where $\hat{K}(\varepsilon)$ is the dielectric Green function [24] for the medium with dielectric constant ε and

$$\begin{aligned} v_{11}(\mathbf{r}) &= \rho_{11}(\mathbf{r}) \\ v_{22}(\mathbf{r}) &= \rho_{22}(\mathbf{r}) - \rho_{11}(\mathbf{r}) \end{aligned} \quad (9)$$

The second term \mathbf{H}_o has matrix elements

$$(H_o)_{ij} = (h_o)_{ij} - \frac{1}{2}t_{ii}^{(\infty)}\delta_{ij} \quad (10)$$

where h_o is the gas phase solute Hamiltonian (which includes the kinetic energy of the solute electrons) and

$$t_{ij}^{(\infty)} = -\int d\mathbf{r} \rho_{ji}(\mathbf{r})\hat{K}(\varepsilon_\infty)\rho_{ii}(\mathbf{r}) \quad (11)$$

is the electronic reorganization energy matrix element that accounts for the interaction of the solute with the electronic polarization of the solvent (within the Born–Oppenheimer approximation). The third term in Eq. 6 represents the interaction of the solute with the inertial polarization of the solvent.

The VB matrix given in Eq. 6 involves only a single solvent coordinate z_e . In the derivation of this expression, the off-diagonal densities are neglected and a coordinate transformation eliminates one of the diagonal densities. Due to this coordinate transformation, the transformed self-energy $\mathcal{S}(z_e)$ given in Eq. 7 is the sum of the actual self-energy of the solvent inertial polarization and the term $\int d\mathbf{r} \rho_{11}(\mathbf{r})\phi_{in}(\mathbf{r})$, which represents the interaction of the density of VB state 1 with the inertial polarization of the solvent. As a result, this interaction is not included in the third term of Eq. 6.

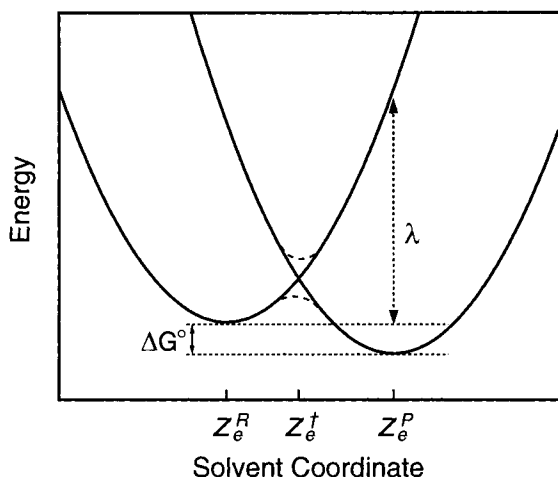


Figure 1. Schematic illustration of the diabatic (solid) and adiabatic (long-dashed) electronic free energy curves as functions of the solvent coordinate z_e for a single electron transfer reaction. The Marcus theory quantities ΔG° and λ are indicated.

The diabatic free energy curves are the diagonal elements $H_{11}(z_e)$ and $H_{22}(z_e)$ of the matrix \mathbf{H} given in Eq. 6. These curves are parabolas with minima at $z_e^R = -t'_{12}$ and $z_e^P = -t'_{12} - t'_{22}$ and an intersection point at $z_e^\ddagger = (H_o)_{11} - (H_o)_{22}$. Figure 1 is a schematic illustration of these two parabolas and indicates the standard Marcus theory parameters λ and ΔG° [4, 15]. The adiabatic free energy curves can be calculated if the matrix \mathbf{H} is diagonalized, as shown by the dashed lines in Figure 1. Although the lowest adiabatic curve is a double well in Figure 1, it could be a single well in the Marcus inverted region (defined as $-\Delta G^\circ > \lambda$) or in the limit of very large coupling between the VB states. Note that in this formulation, the reorganization energy and free energy of reaction are

$$\lambda = t'_{22}/2 \quad (12)$$

$$\Delta G^\circ = (H_o)_{22} - (H_o)_{11} + \Delta G^{\text{solv}} \quad (13)$$

where

$$\Delta G^{\text{solv}} = -\frac{1}{2}t'_{22} - t'_{12} \quad (14)$$

is the difference in the equilibrium inertial solvation energies of states 1 and 2. [Note that the electronic solvation energy is included in the term $(H_o)_{22} - (H_o)_{11}$.] It is straightforward to prove that, in the limit of weak coupling, the standard Marcus barrier formula is obtained. Rate expressions have been derived for electron transfer in both the adiabatic and non-adiabatic limits. The adiabatic limit of ET refers to the situation in which the solute electrons respond instantaneously to the inertial solvent motion, and the reaction occurs on the lowest adiabatic free energy curve. The non-adiabatic limit of ET corresponds to weak coupling between the diabatic electronic states, and the upper adiabatic curve is involved.

The non-adiabatic limit of ET is most relevant to typical PCET reactions. In the non-adiabatic limit, application of the Golden Rule to the diagonal elements of the VB matrix given in Eq. 6 leads to the rate expression [16, 17, 25, 26].

$$k_{12} = \frac{2\pi}{\hbar} |(h_o)_{12}|^2 (4\pi\lambda k_B T)^{-1/2} \exp[-(\Delta G^\circ + \lambda)^2 / (4\lambda k_B T)] \quad (15)$$

An analogous rate expression has been derived for non-adiabatic electron transfer in the presence of an inner-sphere solute mode that is not coupled to the solvent. In this case, the VB matrix is the same as that in Eq. 6, with a dependence of the diagonal gas-phase matrix elements $(h_o)_{ii}$ on an inner-sphere solute mode q . The inner-sphere vibrational wave functions are calculated for each diabatic electronic state by a solution of the Schrödinger equation:

$$[T_q + (H_o)_{ii}(q)]\phi_\mu^{(i)}(q) = \varepsilon_\mu^{(i)} \phi_\mu^{(i)}(q) \quad (16)$$

where T_q is the kinetic energy of the inner-sphere solute mode. Application of the Golden Rule to this system leads to the rate expression [27, 28]:

$$k_{12} = \frac{2\pi}{\hbar} |(h_o)_{12}|^2 (4\pi\lambda k_B T)^{-1/2} \sum_\mu \rho_{1\mu} \sum_v |\langle \phi_\mu^{(1)} | \phi_v^{(2)} \rangle_q|^2 \\ \times \exp[-(\varepsilon_v^{(2)} - \varepsilon_\mu^{(1)} + \Delta G^{\text{solv}} + \lambda)^2 / (4\lambda k_B T)] \quad (17)$$

where \sum_μ and \sum_v indicate a summation over the vibrational states for diabatic state 1 and 2, respectively, $\langle \rangle_q$ indicates integration over the inner-sphere mode q , and $\rho_{1\mu}$ is the Boltzmann factor for state 1μ . Note that this equation is valid only if the inner-sphere mode is not coupled to the solvent. In general, the transferring proton in PCET reactions is coupled to the solvent. Thus, the application of this equation with the identification of the transferring proton as the inner-sphere mode is not valid for general PCET reactions.

5.2.2 Single Proton Transfer

A single proton transfer reaction can be represented by a two-state VB model with electronic VB states defined as



where the symbols D_p and A_p represent a general proton donor and acceptor and H represents the transferring proton. For simplicity, all solute nuclei are assumed to be fixed except the transferring H atom, which has a coordinate r_p . In this model, the free energy can be expressed in terms of a single solvent coordinate z_p defined as

$$z_p = \int d\mathbf{r} [\rho_{bb}(\mathbf{r}) - \rho_{aa}(\mathbf{r})] \phi_{\text{in}}(\mathbf{r}) \quad (19)$$

The VB matrix corresponding to the free energy is

$$\mathbf{H}(r_p, z_p) = \mathcal{S}(r_p, z_p) \mathbf{I} + \mathbf{H}_o(r_p) + \begin{pmatrix} 0 & 0 \\ 0 & z_p \end{pmatrix} \quad (20)$$

where all definitions are analogous to those given for single ET except for the dependence of \mathcal{S} and \mathbf{H}_o on the proton coordinate r_p . (Again the off-diagonal densities are neglected.) The electronically diabatic surfaces $H_{ii}(r_p, z_p)$ are parabolic along the z_p coordinate. A proton transfer reaction may be electronically adiabatic or electronically non-adiabatic, where electronically adiabatic refers to the situation in which the solute electrons respond instantaneously to the proton and solvent.

In the electronically non-adiabatic limit, the proton vibrational states can be calculated for each diabatic electronic state (i.e., each diagonal element of the matrix \mathbf{H} defined in Eq. 20). If the r_p -dependence of the self energy is neglected, this leads to two sets of shifted parabolas (with the same frequencies) along z_p , corresponding to electronic states a and b . In the limit of weak coupling, the rate expression for electronically non-adiabatic proton transfer is analogous to that given in Eq. 17 [except that $(h_o)_{ab}$ may depend on r_p and thus is included in the integration over r_p as $|\langle \phi_\mu^{(a)} | (h_o)_{ab}(r_p) | \phi_\nu^{(b)} \rangle_p|^2$].

For typical PCET reactions, the proton transfer reaction is electronically adiabatic. The electronically adiabatic surface is the lowest eigenvalue of $\mathbf{H}(r_p, z_p)$, expressed as

$$E(r_p, z_p) = \mathcal{S}(r_p, z_p) + \frac{1}{2} \left\{ (H_o)_{aa}(r_p) + (H_o)_{bb}(r_p) + z_p - \sqrt{[z_p + (H_o)_{bb}(r_p) - (H_o)_{aa}(r_p)]^2 + 4(H_o)_{ab}(r_p)^2} \right\} \quad (21)$$

In general, this surface is not parabolic along the z_p coordinate.

An electronically adiabatic proton transfer reaction may be either vibrationally adiabatic or vibrationally non-adiabatic. Vibrationally adiabatic refers to the situation in which the proton responds instantaneously to the solvent, while vibrationally non-adiabatic refers to the opposite limit. The adiabatic proton vibrational wave functions are calculated if the Schrödinger equation is solved for fixed values of z_p :

$$[T_p + E(r_p, z_p)] \phi_\mu(r_p; z_p) = \varepsilon_\mu(z_p) \phi_\mu(r_p; z_p) \quad (22)$$

where T_p is the kinetic energy of the proton mode. (Note that if the dependence of the transformed self-energy \mathcal{S} on the proton coordinate r_p is negligible, the change in free energy $E(r_p, z_p)$ along r_p is nearly equivalent to the change in potential energy along r_p .) Figure 2a is a schematic illustration of the energies $\varepsilon_\mu(z_p)$ of the two lowest adiabatic proton vibrational states for a typical symmetric single proton transfer reaction. The corresponding energies along the proton coordinate r_p for specified values of z_p are depicted in Figure 2b. If the reaction is vibrationally

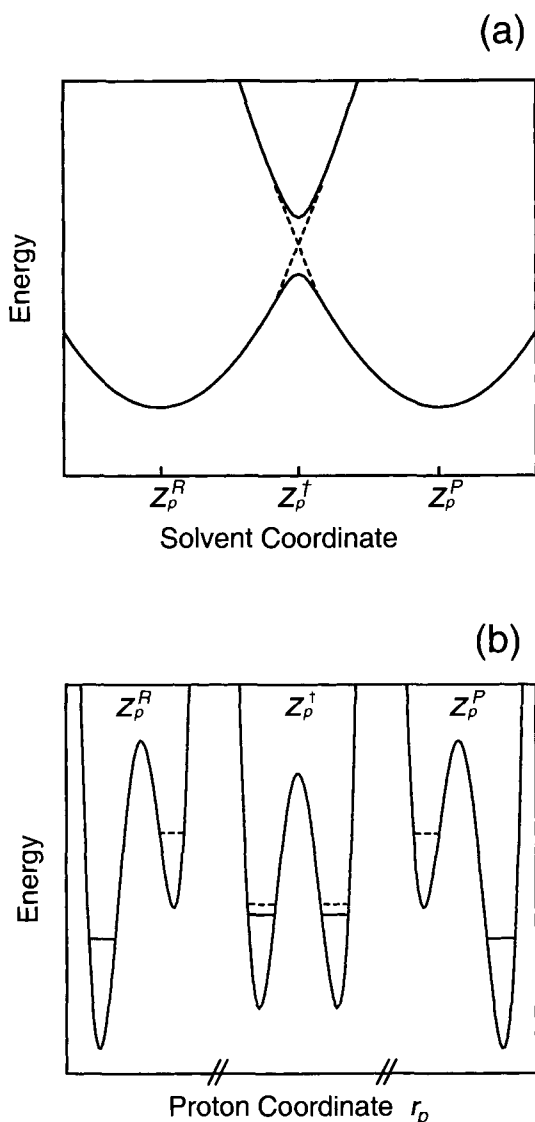


Figure 2. (a) Schematic illustration of the adiabatic (solid) and diabatic (dashed) vibrational free energy curves as functions of the solvent coordinate z_p for a symmetric single proton transfer reaction. (b) Potential energy curves as functions of the proton coordinate r_p for three specific values of the solvent coordinate z_p indicated in (a).

adiabatic, the reaction progresses on the lower curve and the rate could be calculated with an analog of the adiabatic ET rate expression. If the reaction is vibrationally non-adiabatic, the upper state is involved. The calculation of rates for vibrationally non-adiabatic reactions involves the definition of localized diabatic proton vibrational states (with energies indicated as dashed lines in Figure 2a) and the application of the Golden Rule to these vibrationally diabatic states [21].

The vibrationally adiabatic proton wave functions provide the most useful description for PCET reactions. For typical single proton transfer reactions, the lowest adiabatic vibrational state is a double well along z_p , as shown in Figure 2a. In gen-

eral, however, the lowest adiabatic vibrational state need not be a double well along z_p . For example, the lowest adiabatic vibrational state could be a single well along z_p if the potential energy along r_p is a single well. A single well potential energy along r_p could arise due to a large difference between the energies of the two VB states, a large coupling between the two VB states, or a short distance between the proton donor and acceptor. Moreover, the lowest adiabatic vibrational state could be a single well along z_p if the potential energy along r_p is a double well but the reorganization energy is very small. As will be discussed below, the free energy surfaces for PCET reactions are typically single wells along the z_p coordinate for the relevant energies. This single well character arises from the small reorganization energy for PT relative to the energy difference between the PT states.

5.3 Multistate Continuum Theory for Proton-Coupled Electron Transfer

5.3.1 Four-State Formulation

The most basic PCET system can be represented by a four-state VB model with electronic VB states defined as

$$\begin{aligned}
 (1a) \quad & D_e^\ominus - {}^\oplus D_p \text{ H} \cdots \cdots A_p^\ominus - A_e \\
 (1b) \quad & D_e^\ominus - D_p \cdots \cdots \text{H} A_p - A_e \\
 (2a) \quad & D_e - {}^\oplus D_p \text{ H} \cdots \cdots A_p^\ominus - A_e^\ominus \\
 (2b) \quad & D_e - D_p \cdots \cdots \text{H} A_p - A_e^\ominus.
 \end{aligned} \tag{23}$$

The notation for these VB states is consistent with the notation used in the above discussion of single ET and single PT. Thus, a and b indicate the proton transfer (PT) state, and 1 and 2 indicate the electron transfer (ET) state. As above, all solute nuclei are assumed to be fixed except the transferring H atom, which has a coordinate r_p .

In this model, the free energy can be expressed in terms of the proton coordinate r_p and two scalar solvent coordinates z_p and z_e corresponding to PT and ET, respectively. Each scalar solvent coordinate represents the difference in interaction energy of the two VB states involved in the charge transfer reaction with the inertial polarization field $\phi_{\text{in}}(\mathbf{r})$ of the solvent. Thus,

$$\begin{aligned}
 z_p &= \int d\mathbf{r} [\rho_{1b,1b}(\mathbf{r}) - \rho_{1a,1a}(\mathbf{r})] \phi_{\text{in}}(\mathbf{r}) \\
 z_e &= \int d\mathbf{r} [\rho_{2a,2a}(\mathbf{r}) - \rho_{1a,1a}(\mathbf{r})] \phi_{\text{in}}(\mathbf{r})
 \end{aligned} \tag{24}$$

where $\rho_{ii}(\mathbf{r})$ is the total charge density of VB state i . These scalar solvent coor-

dinates are analogous to the standard solvent coordinate used for the description of single ET and single PT reactions. In general, a four-state VB model would include three solvent coordinates, where the third solvent coordinate is defined as

$$z_{ep} = \int d\mathbf{r} [\rho_{2b,2b}(\mathbf{r}) - \rho_{1a,1a}(\mathbf{r})] \phi_{in}(\mathbf{r}) \quad (25)$$

As shown in Ref. [13], however, for the PCET four-state VB model defined in Eq. 23

$$z_{ep} = z_p + z_e \quad (26)$$

due to a linear dependency among the VB state densities. Thus, the only linearly independent scalar solvent coordinates in this model are z_p and z_e . (The off-diagonal densities are neglected.)

The VB matrix corresponding to the free energy is

$$\mathbf{H}(r_p, z_p, z_e) = \mathcal{S}(r_p, z_p, z_e) \mathbf{I} + \mathbf{H}_o(r_p) + \begin{pmatrix} 0 & 0 & 0 & 0 \\ 0 & z_p & 0 & 0 \\ 0 & 0 & z_e & 0 \\ 0 & 0 & 0 & z_p + z_e \end{pmatrix} \quad (27)$$

The transformed self-energy of the solvent inertial polarization field can be expressed as

$$\mathcal{S}(r_p, z_p, z_e) = \frac{1}{2} \sum_{i,j=1b,2a} \{ [y'_i + t'_{1a,i}(r_p)] [\mathbf{t}'_i(r_p)^{-1}]_{i,j} [y'_j + t'_{1a,j}(r_p)] \} - \frac{1}{2} t'_{1a,1a}(r_p) \quad (28)$$

where the summation runs over valence bond states $1b$ and $2a$, the truncated reorganization energy matrix \mathbf{t}'_i has dimensions 2×2 corresponding to these two states, and $(z_p, z_e) \equiv (y'_{1b}, y'_{2a})$. (The $1a$ state is eliminated through a coordinate transformation and the $2b$ state is eliminated due to the linear dependency among the solvent coordinates.) The inertial reorganization energy matrix elements t'_{ij} are defined in Eq. 8, where in this case

$$\begin{aligned} v_{1a,1a}(\mathbf{r}) &= \rho_{1a,1a}(\mathbf{r}) \\ v_{ii}(\mathbf{r}) &= \rho_{ii}(\mathbf{r}) - \rho_{1a,1a}(\mathbf{r}) \quad (i = 1b, 2a, 2b). \end{aligned} \quad (29)$$

The matrix elements of the Hamiltonian $\mathbf{H}_o(r_p)$ are defined in Eq. 10. The last term in Eq. 27 represents the interaction of the solute with the inertial polarization potential field of the solvent. (As discussed above, the transformed self-energy includes the interaction of the VB state $1a$ with the inertial polarization of the solvent.)

One important result derived from this theoretical formulation is that the reorganization energy for PCET is not simply the sum of the reorganization energies for

PT and ET. Analogous to the situation discussed above for single ET, the reorganization energy for a reaction from the reference VB state $1a$ to VB state i is

$$\lambda_i = t'_{ii}/2 \quad (30)$$

As proven in Ref. [13],

$$\lambda_{2b} = \lambda_{1b} + \lambda_{2a} + t'_{1b,2a} \quad (31)$$

where λ_{2b} , λ_{1b} , and λ_{2a} denote the reorganization energies for PCET, PT, and ET, respectively. The extra term $t'_{1b,2a}$ is due to the interaction of the density $v_{1b,1b}$ with the inertial polarization field caused by the density $v_{2a,2a}$ (or, equivalently, the reverse interaction).

The description of PCET reactions is particularly challenging due to the quantum mechanical behavior of the ET electrons, the PT electrons, and the transferring protons. The adiabatic mixed electronic/proton vibrational states are calculated when the following Schrödinger equation is solved for fixed solvent coordinates (z_p, z_e) :

$$H'(\mathbf{r}_e, r_p, z_p, z_e)\Phi_n(\mathbf{r}_e, r_p; z_p, z_e) = E_n(z_p, z_e)\Phi_n(\mathbf{r}_e, r_p; z_p, z_e) \quad (32)$$

where

$$H'(\mathbf{r}_e, r_p, z_p, z_e) = T_p + \mathcal{S} + \mathcal{H}. \quad (33)$$

Here \mathbf{r}_e represents the electron coordinates, T_p is the kinetic energy of the transferring proton, and \mathcal{S} and \mathcal{H} are defined in Eqs. 1 and 2 (and are represented in the VB basis by the matrix \mathbf{H} in Eq. 27). A convenient set of basis functions for the solution of Eq. 32 is

$$\xi_{i\mu}(\mathbf{r}_e, r_p; z_p, z_e) = \psi_i(\mathbf{r}_e; r_p, z_p, z_e)\phi_{\mu}^{(i)}(r_p; z_p, z_e) \quad (34)$$

where ψ_i is the electronic VB state i and $\phi_{\mu}^{(i)}$ is the corresponding proton vibrational state calculated if the one-dimensional Schrödinger equation is numerically solved:

$$[T_p + H_{ii}(r_p, z_p, z_e)]\phi_{\mu}^{(i)}(r_p; z_p, z_e) = \varepsilon_{\mu}^{(i)}(z_p, z_e)\phi_{\mu}^{(i)}(r_p; z_p, z_e). \quad (35)$$

Here $H_{ii}(r_p, z_p, z_e)$ is the diagonal element of the VB matrix given in Eq. 27. The matrix \mathbf{H}' for the basis set defined in Eq. 34 has matrix elements

$$H'_{i\mu, j\nu} = \delta_{ij}\delta_{\mu\nu}\varepsilon_{\mu}^{(i)}(z_p, z_e) + \langle \phi_{\mu}^{(i)} | H_{ij} | \phi_{\nu}^{(j)} \rangle_p (1 - \delta_{ij}) \quad (36)$$

where $\langle \rangle_p$ indicates integration over the proton coordinate r_p .

The adiabatic mixed electronic/proton vibrational surfaces can be calculate by the diagonalization of the matrix \mathbf{H}' along a two-dimensional grid of solvent coordinates

(z_p, z_e) . These surfaces are numerically exact solutions to Eq. 32 and include all non-adiabatic coupling among the ET electrons, the PT electrons, and the transferring proton. Furthermore, although these surfaces are electronically and vibrationally adiabatic with respect to the solvent coordinates, the non-adiabatic coupling vectors between the adiabatic mixed electronic/proton vibrational states (i.e., the electron-solvent and proton-solvent non-adiabatic couplings) can be calculated along the solvent grid [13].

If the PCET reaction involves electronically adiabatic ET and PT and is vibrationally adiabatic, the system moves on the lowest two-dimensional energy surface equivalent to the lowest eigenvalue of the matrix \mathbf{H}' . In this case, the rate could be calculated with the multidimensional generalization of the Grote-Hynes theory [29–31].

If the PCET reaction involves electronically non-adiabatic ET and PT, the system can be viewed in terms of electronically diabatic surfaces given by $\varepsilon_\mu^{(i)}(z_p, z_e)$, defined in Eq. 35. If the dependence of the self-energy on the proton coordinate r_p is neglected, these surfaces consist of four sets of shifted paraboloids (with identical frequencies) in the two-dimensional solvent space. These two-dimensional paraboloids are analogous to the one-dimensional parabolas for the two-state single ET theory described above. The coupling between a pair of paraboloids $i\mu$ and $j\nu$ is $\langle \phi_\mu^{(i)} | (h_o)_{ij} | \phi_\nu^{(j)} \rangle_p$. In the limit of small coupling, the Golden Rule can be applied when the rate expressions for reactions among these electronically diabatic states are calculated.

Typically, PCET reactions involve electronically adiabatic PT and electronically non-adiabatic ET. In this case, the mixed electronic/proton vibrational ET diabatic surfaces may be obtained if Eq. 32 is solved with the settings $(H_o)_{1a,2a} = (H_o)_{1a,2b} = (H_o)_{1b,2a} = (H_o)_{1b,2b} = 0$. The resulting surfaces consist of two sets of two-dimensional “paraboloids” (where the quotation marks indicate that these surfaces are not exactly parabolic along z_p) corresponding to ET states 1 and 2. For each ET state, the minima of the “paraboloids” are shifted slightly depending on the weights of PT states a and b . The couplings between pairs of “paraboloids” can be calculated with the aid of the full Hamiltonian matrix \mathbf{H}' with all off-diagonal elements included. In the limit of weak coupling, the Golden Rule can be used for obtaining a rate expression. A simplification of this important limit is presented in the next section.

5.3.2 Two-State Formulation

A two-state model is possible for PCET reactions that involve electronically adiabatic PT. This two-state model is convenient for the derivation of a rate expression in the limit of electronically non-adiabatic ET. The first step is to transform the VB basis set to another equivalent basis set. The new basis functions are defined to be the eigenvectors of the two matrices

$$\mathbf{H}_I(r_p, z_p) = \begin{pmatrix} (H_o)_{1a,1a}(r_p) & (H_o)_{1a,1b}(r_p) \\ (H_o)_{1b,1a}(r_p) & (H_o)_{1b,1b}(r_p) + z_p \end{pmatrix} \quad (37)$$

$$\mathbf{H}_{\text{II}}(r_p, z_p) = \begin{pmatrix} (H_o)_{2a,2a}(r_p) & (H_o)_{2a,2b}(r_p) \\ (H_o)_{2b,2a}(r_p) & (H_o)_{2b,2b}(r_p) + z_p \end{pmatrix} \quad (38)$$

If all four of the new basis states are included, the adiabatic mixed electronic/proton vibrational states are exactly the same as those obtained with the original four VB states. Moreover, the diabatic mixed electronic/proton vibrational states for the new basis states are exactly the same as the adiabatic states obtained with the settings $(H_o)_{1a,2a} = (H_o)_{1a,2b} = (H_o)_{1b,2a} = (H_o)_{1b,2b} = 0$ (as described at the end of the previous section).

If the reaction involves electronically adiabatic PT, there is a large splitting between the two eigenvalues for each of these matrices. In this case, the two basis states higher in energy are negligible, and the free energy can be described in terms of the two remaining wavefunctions

$$\Psi_{\text{I}}(r_p, z_p) = c_{1a}(r_p, z_p)\psi_{1a} + c_{1b}(r_p, z_p)\psi_{1b} \quad (39)$$

$$\Psi_{\text{II}}(r_p, z_p) = c_{2a}(r_p, z_p)\psi_{2a} + c_{2b}(r_p, z_p)\psi_{2b} \quad (40)$$

with corresponding energies

$$E_{\text{I}}(r_p, z_p) = \frac{1}{2} \left\{ (H_o)_{1a,1a}(r_p) + (H_o)_{1b,1b}(r_p) + z_p - \sqrt{[z_p + (H_o)_{1b,1b}(r_p) - (H_o)_{1a,1a}(r_p)]^2 + 4(H_o)_{1a,1b}(r_p)^2} \right\} \quad (41)$$

$$E_{\text{II}}(r_p, z_p) = \frac{1}{2} \left\{ (H_o)_{2a,2a}(r_p) + (H_o)_{2b,2b}(r_p) + z_p - \sqrt{[z_p + (H_o)_{2b,2b}(r_p) - (H_o)_{2a,2a}(r_p)]^2 + 4(H_o)_{2a,2b}(r_p)^2} \right\} \quad (42)$$

The matrix representing the free energy in this new basis set is

$$\mathbf{H}(r_p, z_p, z_e) = \mathcal{S}(r_p, z_p, z_e)\mathbf{I} + \begin{pmatrix} E_{\text{I}}(r_p, z_p) & V(r_p, z_p) \\ V(r_p, z_p) & E_{\text{II}}(r_p, z_p) \end{pmatrix} + \begin{pmatrix} 0 & 0 \\ 0 & z_e \end{pmatrix} \quad (43)$$

where the coupling is expressed as

$$V(r_p, z_p) = c_{1a}(r_p, z_p)c_{2a}(r_p, z_p)(h_o)_{1a,2a} + c_{1b}(r_p, z_p)c_{2b}(r_p, z_p)(h_o)_{1b,2b} \\ + c_{1a}(r_p, z_p)c_{2b}(r_p, z_p)(h_o)_{1a,2b} + c_{1b}(r_p, z_p)c_{2a}(r_p, z_p)(h_o)_{1b,2a} \quad (44)$$

The proton vibrational states can be calculated for each of the two electronic states by solution of the Schrödinger equation

$$[T_p + H_{JJ}(r_p, z_p, z_e)]\phi_{\mu}^J(r_p; z_p, z_e) = \varepsilon_{\mu}^J(z_p, z_e)\phi_{\mu}^J(r_p; z_p, z_e) \quad J = \text{I, II} \quad (45)$$

where H_{JJ} is the diagonal element of the matrix given in Eq. 43. The resulting mixed electronic/proton vibrational states consist of the initial states $\Psi_I \phi_\mu^I$ with energies $\varepsilon_\mu^I(z_p, z_e)$ and the final states $\Psi_{II} \phi_\nu^{II}$ with energies $\varepsilon_\nu^{II}(z_p, z_e)$.

These ET diabatic free energy surfaces are parabolic along the z_e coordinate but are not exactly parabolic along the z_p coordinate, because of the complicated z_p -dependence of E_I and E_{II} and the averaging over the r_p coordinate for the different vibrational states. For example, in general, these surfaces could be double wells along the z_p coordinate, as found for single PT reactions. For typical PCET reactions, however, these surfaces have been found to be approximately parabolic along the z_p coordinate at the energies of interest. This approximately parabolic form results from the small reorganization energy for PT relative to the difference in energies of VB states 1a and 1b and VB states 2a and 2b. Even for symmetric PT interfaces, the transferring electron introduces significant asymmetry between PT states *a* and *b*. Moreover, the reorganization energy for PT is decreased by the presence of the relatively large electron donor and acceptor.

Figures 3–5 depict the energies $\varepsilon_\mu^I(z_p, z_e)$ and $\varepsilon_\nu^{II}(z_p, z_e)$ [in parts (a)] and the associated potential energy curves along r_p [in parts (b)] for model symmetric PCET

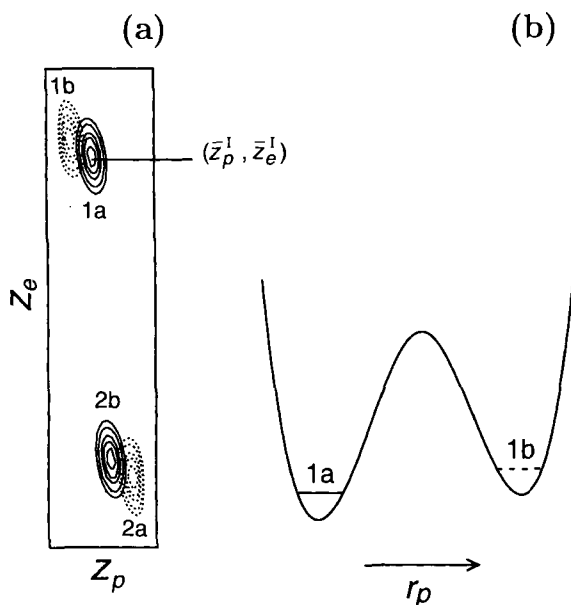


Figure 3. (a) The ET diabatic free energy surfaces as functions of the solvent coordinates z_p and z_e for a symmetric PCET reaction. For simplicity, only the lowest two mixed electronic/proton vibrational states are shown for each ET state. The two lowest energy states are solid while the two higher energy states are dashed. The free energy surfaces are labeled according to the dominant valence bond state. (b) The potential energy curve as a function of the proton coordinate r_p evaluated at $(\bar{z}_p^I, \bar{z}_e^I)$, the minimum of the lowest energy state in (a) corresponding to ET state 1. The lowest two proton vibrational adiabatic states are indicated on this potential energy curve.

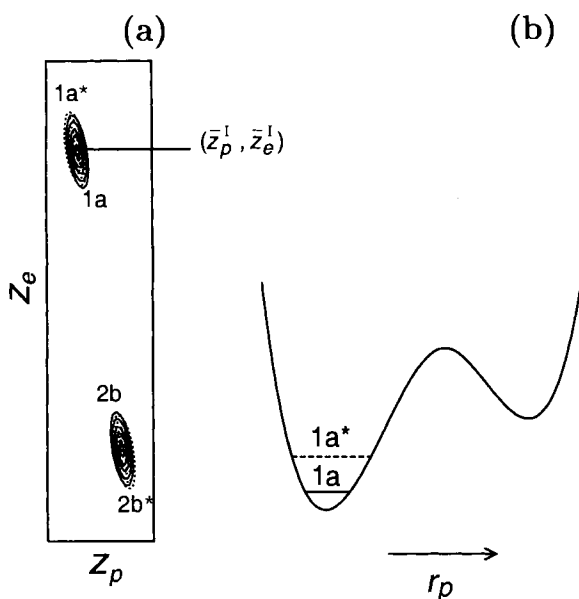


Figure 4. The same features as in Figure 3 are shown here, but for a different symmetric PCET reaction. The asterisks indicate excited vibrational states. Note that the two-dimensional plot contains four “paraboloids,” although two pairs are virtually identical.

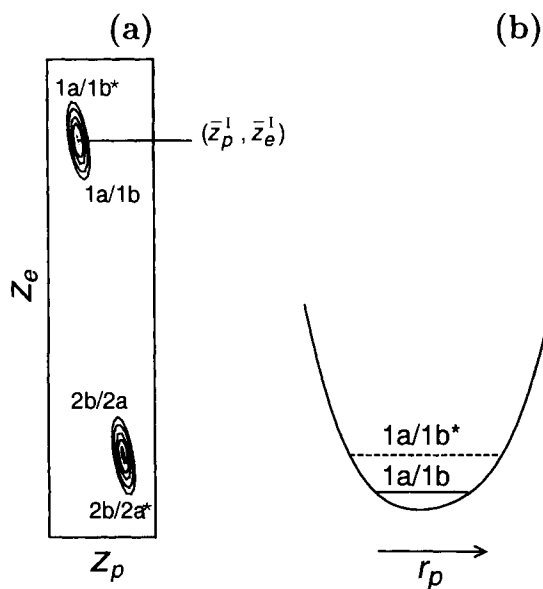


Figure 5. The same features as in Figure 4 are shown here, but for a different symmetric PCET reaction. The $1a/1b$ ($2b/2a$) notation indicates a mixture of the $1a$ and $1b$ ($2a$ and $2b$) valence bond states, and the asterisks indicate excited vibrational states. Note that the two-dimensional plot contains four “paraboloids”, although two pairs are virtually identical.

reactions. These model systems, which consist of point charges placed in an ellipsoidal cavity embedded in a dielectric continuum, are described in detail in Ref. [32]. For simplicity, in parts (a), only the lowest two mixed electronic/proton vibrational free energy surfaces are shown for each ET state. These ET diabatic free energy surfaces are labeled according to the dominant VB state. Note that the energy scales for z_p and z_e are not the same, but, rather, the z_p axis is expanded by a factor of approximately four. In other words, the disparity between the lengths of the z_p and z_e axes should be approximately four times greater. The shifts of the “paraboloids” are smaller along z_p than along z_e , because proton transfer has a smaller solvent reorganization energy than that of electron transfer. In parts (b), the potential energy curves along the proton coordinate r_p are shown only for the solvent coordinates $(\bar{z}_p^1, \bar{z}_e^1)$, the minimum of the lowest energy “paraboloid” corresponding to ET state 1.

In Figure 3a, the “paraboloids” correspond to electronic states $1a$, $1b$, $2a$, and $2b$. This situation arises when the potential along the r_p coordinate (shown in Figure 3b) is slightly asymmetric, with a high barrier so that the lowest two vibrational states are virtually pure (i.e., localized) a and b PT states. Note that the minima for the “paraboloids” corresponding to the $1a$ and $1b$ states are shifted relative to each other. A transition from $1a$ to $2a$ corresponds to ET, while a transition from $1a$ to $2b$ corresponds to EPT (where both the electron and the proton are transferred).

In Figure 4a, the “paraboloids” correspond to electronic states $1a$, $1a^*$, $2b$, and $2b^*$, where the asterisks indicate excited vibrational states. This situation arises when the potential along the r_p coordinate (shown in Figure 4b) is very asymmetric so that the lowest two vibrational states are localized on the same side of the PT interface (in this case a for electronic state 1 and b for electronic state 2). Note that the minima for the “paraboloids” corresponding to the $1a$ and $1a^*$ states are virtually identical. The slight shift between these “paraboloids” is due to somewhat less purity of the $1a^*$ state.

In Figure 5a, the “paraboloids” correspond to electronic states $1a/1b$, $1a/1b^*$, $2b/2a$, and $2b/2a^*$. This situation arises when the potential along the r_p coordinate (shown in Figure 5b) has a low barrier (or no barrier) so that all vibrational states are mixtures of a and b PT states and are delocalized. Note that the minima for the $1a/1b$ and $1a/1b^*$ states are virtually identical. These examples illustrate that the multistate continuum theory provides a valuable framework for the analysis and interpretation of the wide range of behavior exhibited by PCET reactions.

Although the matrix in Eq. 43 is of the same form as the matrix in Eq. 6, which was used in two-state ET theory, these two matrices are fundamentally different because of the dependence of the PCET matrix on the second solvent coordinate z_p and the proton coordinate r_p . In the limit that \mathcal{S} and V are independent of r_p and that E_I , E_{II} , \mathcal{S} , and V are independent of z_p , the rate expression for non-adiabatic ET is the same for PCET as for single ET with an inner-sphere mode, given in Eq. 17. This limit corresponds to no coupling between the proton and solvent and is not valid for general PCET reactions. Thus, a new rate expression must be derived by the application of the Golden Rule to the PCET system described by the Hamiltonian given in Eq. 43. This application of the Golden Rule involves transitions between pairs of two-dimensional approximate paraboloids rather than pairs of one-dimensional parabolas.

Such a rate expression has been derived for PCET reactions satisfying well-defined conditions [33]. First, all of the relevant diabatic free-energy surfaces are assumed to be exact paraboloids with identical second derivatives obtained from the self-energy (i.e., the r_p -dependence of the self-energy and the nonlinear z_p -dependence of $E_I(r_p, z_p)$ and $E_{II}(r_p, z_p)$ are neglected). Second, the coupling $V_{\mu\nu}(z_p)$ is assumed to be independent of z_p for the relevant energies. Third, the coupling $V_{\mu\nu}(z_p)$ is assumed to be much smaller than the thermal energy $k_B T$. If these three assumptions are valid, then application of the standard methodology used to derive the non-adiabatic ET rate expression given in Eq. 15 leads to

$$k = \frac{2\pi}{\hbar} \sum_{\mu} P_{\mu}^I \sum_{\nu} V_{\mu\nu}^2 (4\pi\lambda_{\mu\nu}k_B T)^{-1/2} \exp\left\{-\frac{(\Delta G_{\mu\nu}^{\circ} + \lambda_{\mu\nu})^2}{4\lambda_{\mu\nu}k_B T}\right\} \quad (46)$$

where \sum_{μ} and \sum_{ν} indicate a sum over vibrational states associated with ET state 1 and 2, respectively, and P_{μ}^I is the Boltzmann factor for state $I\mu$. In this expression, the reorganization energy is defined as

$$\lambda_{\mu\nu} = \varepsilon_{\mu}^I(\bar{z}_p^{II\nu}, \bar{z}_e^{II\nu}) - \varepsilon_{\mu}^I(\bar{z}_p^{I\mu}, \bar{z}_e^{I\mu}) \quad (47)$$

the free energy difference is defined as

$$\Delta G_{\mu\nu}^{\circ} = \varepsilon_{\nu}^{II}(\bar{z}_p^{II\nu}, \bar{z}_e^{II\nu}) - \varepsilon_{\mu}^I(\bar{z}_p^{I\mu}, \bar{z}_e^{I\mu}) \quad (48)$$

and the coupling is defined as

$$V_{\mu\nu} = \langle \phi_{\mu}^I | V(r_p, z_p^{\dagger}) | \phi_{\nu}^{II} \rangle_p \quad (49)$$

where $(\bar{z}_p^{I\mu}, \bar{z}_e^{I\mu})$ and $(\bar{z}_p^{II\nu}, \bar{z}_e^{II\nu})$ are the solvent coordinates for the minima of $\varepsilon_{\mu}^I(z_p, z_e)$ and $\varepsilon_{\nu}^{II}(z_p, z_e)$, respectively, and z_p^{\dagger} is the PT solvent coordinate at the intersection point of the two paraboloids along the straight-line reaction path connecting the two minima. Note that typically $V_{\mu\nu}$ is much smaller than the thermal energy for the EPT mechanism even in the limit of electronically adiabatic ET due to the averaging of the coupling over the proton vibrational wavefunctions. Although the three assumptions mentioned above are not rigorously valid for the PCET formulation described in this chapter, they are approximately valid for many PCET reactions of interest. Thus, this rate expression allows the calculation of approximate rates for a wide range of PCET reactions. The derivation of more general rate expressions is a direction for the future.

The previous work of Cukier and coworkers [7, 12] differs from the formulation described in this chapter in a number of fundamental ways. In contrast to the multistate continuum theory described in this chapter, Cukier and coworkers did not calculate mixed electronic/proton vibrational free energy surfaces as functions of two solvent coordinates. Instead, they calculated “solvated proton potentials” obtained by the assumption that the inertial polarization of the solvent responds instantaneously to the proton position. (This is the limit opposite to the standard adiabatic limit of the fast proton vibrational motion responding instantaneously to

the slower inertial solvent motion.) Cukier and coworkers calculated adiabatic proton vibrational wave functions for the solvated proton potentials for the two relevant diabatic electronic states and calculated values for the reorganization energy for both ET and EPT with a five-site ellipsoidal model. They used Eq. 17 in conjunction with these two different reorganization energies to calculate two separate rates for ET and EPT. Note that the derivation of Eq. 17 is for a single ET reaction described by a single solvent coordinate z_e with an inner-sphere solute mode that is not coupled to the solvent. Thus, the direct application of this equation does not accurately account for the coupling of the proton to the solvent in PCET reactions.

5.3.3 Incorporation of Inner-Sphere Reorganization

Inner-sphere reorganization (i.e. solute reorganization) is important if the solute nuclear coordinates change significantly during the charge transfer process. Inner-sphere reorganization can be incorporated into the multistate continuum theory by the introduction of one or more inner-sphere reaction coordinates and by the parametrization of the gas phase Hamiltonian as a function of these inner-sphere reaction coordinates. If a single solute mode is mainly responsible for the inner-sphere reorganization energy, this mode is treated as the inner-sphere coordinate. If many solute modes are responsible for the inner-sphere reorganization energy, one (or possibly a few) collective inner-sphere reaction coordinates are defined. The collective inner-sphere reaction coordinate(s) are determined by geometry optimizations being performed for all VB states. The gas phase matrix elements are parametrized to reproduce the calculated energies of the VB states (or the associated adiabatic states) at these optimized geometries. In the simplest case, the term $\frac{1}{2}k_i(q - q_i)^2$ is added to each gas-phase matrix element $(h_o)_{ii}$, where q is the inner-sphere reaction coordinate, q_i represents the optimized solute geometry for valence bond state i , and k_i represents a frequency that is fit so that the calculated energies for state i are obtained at the optimized geometries for the other VB states.

Once the gas phase Hamiltonian is parametrized as a function of the inner-sphere reaction coordinate(s), the free energy is calculated as a function of the proton coordinate(s), the scalar solvent coordinates, and the inner-sphere reaction coordinate(s). Note that this approach assumes that the optimized geometries of the VB states are not significantly affected by the solvent. For proton transfer reactions, the proton donor-acceptor distance may be treated as an additional solute reaction coordinate that can be incorporated into the molecular mechanical terms describing the diagonal matrix elements $(h_o)_{ii}$ and, in some cases, the off-diagonal matrix elements $(h_o)_{ij}$. If the inner-sphere reaction coordinate represents a “slow” mode, it is treated in the same way as the solvent coordinates. As discussed throughout the literature, however, often the inner-sphere reaction coordinate must be treated quantum mechanically [27, 28]. In this case, the inner-sphere reaction coordinate is treated in the same way as the proton coordinate(s), and the vibrational wave functions depend explicitly on both the proton coordinate(s) and the inner-sphere reaction coordinate(s).

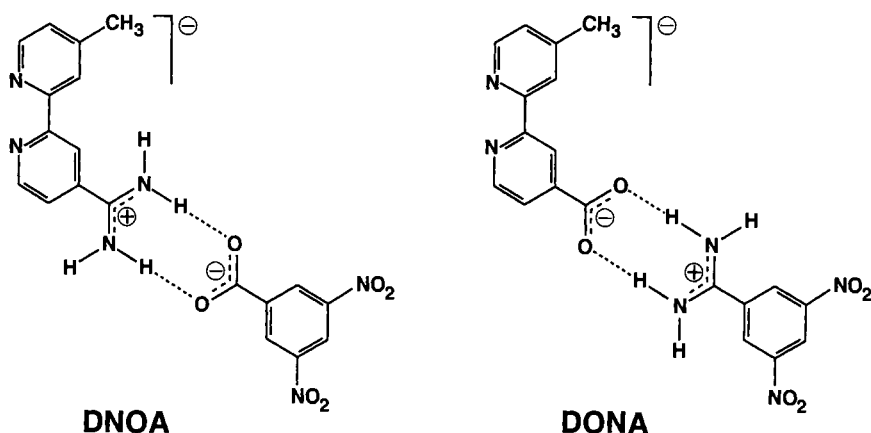


Figure 6. Model PCET systems investigated with the multistate continuum theory.

5.3.4 Extension to More than Two Charge-Transfer Reactions

This multistate continuum theory has been generalized for charge-transfer reactions involving N_e transferring electrons and N_p transferring protons. For this general case, the solute is represented by a VB model containing $2^{N_e+N_p}$ VB states. The free energies of the electronic states are expressed in terms of $N_e + N_p$ linearly independent scalar solvent coordinates and N_p proton coordinates (assuming that all other solute coordinates are fixed). The proton coordinates are treated quantum mechanically for the calculation of the adiabatic mixed electronic/proton vibrational free energy surfaces as functions of $N_e + N_p$ scalar solvent coordinates. (In this case, the calculation of the proton vibrational states may require the solution of a multi-dimensional rather than a single-dimensional Schrödinger equation.) If inner-sphere reorganization is significant, the effects of intramolecular solute vibrations are incorporated into the adiabatic states.

The systems depicted in Figure 6 are examples of PCET systems involving the transfer of one electron coupled to the motion of two protons. Although only one proton is expected to transfer in these systems, the electron transfer reaction could be coupled to the motion of both protons. These systems may be described with eight-state VB models. If the notation introduced above is used, the VB states are denoted $1aa$, $1ba$, $1ab$, $1bb$, $2aa$, $2ba$, $2ab$, $2bb$, where the first index indicates the ET state and the second and third indices indicate the PT state for the first and second proton transfer reactions, respectively. The free energy surfaces obtained with this model depend on three solvent variables, z_e , z_{p1} , and z_{p2} , corresponding to the electron transfer and the two proton transfer reactions. Another type of PCET reaction involving more than a single PT reaction is PCET along a hydrogen-bonding network (e.g., a chain of hydrogen-bonded water molecules). Such a mechanism is thought to be important in a wide range of proteins. Thus, the gen-

eralizability of the multistate continuum theory is a critical feature for the study of biologically relevant processes.

5.4 Applications of Proton-Coupled Electron Transfer in Solution

5.4.1 Calculation of Input Quantities

The input quantities required for the multistate continuum theory for PCET are the gas phase VB matrix elements, the inertial reorganization energy matrix, and the diagonal elements of the electronic reorganization energy matrix. In general, all of these quantities depend on the proton coordinate. The matrix elements of the gas phase Hamiltonian can be approximated by standard molecular mechanical terms fit to electronic structure calculations for the gas phase solute [34–36]. The reorganization energy matrix elements can be determined with standard electrostatic continuum methods for calculating the polarization potential fields resulting from a charge density in a cavity of arbitrary shape embedded in a dielectric continuum solvent [37]. Two-cavity models such as the FRCM method [38] could be utilized to obtain more accurate reorganization energy matrix elements.

5.4.2 Proton-Coupled Electron Transfer through Asymmetric Salt Bridges

The initial application of this multistate continuum theory was the investigation of PCET through asymmetric salt bridges [13]. The specific systems studied represent a donor–(amidinium–carboxylate)–acceptor salt bridge (DNOA) and the corresponding switched interface donor–(carboxylate–amidinium)–acceptor salt bridge (DONA), as shown in Figure 6. These theoretical investigations were motivated by experiments of Nocera and coworkers, who studied systems analogous to the DNOA and DONA systems depicted in Figure 6, except that the electron donors were $[(\text{tmbpy})_2\text{Ru}^{\text{II}}(\text{Mebpy}-\text{amH}^+)]^{3+}$ and $[(\text{tmbpy})_2\text{Ru}^{\text{II}}(\text{Mebpy}-\text{COO}^-)]^+$, respectively. (Here tmbpy = 3,3',4,4'-tetramethyl-2,2'-bipyridine, $\text{Mebpy}-\text{amH}^+$ = 4-methyl-2,2'-bipyridine-4'-amidinium, and $\text{Mebpy}-\text{COO}^-$ = 4-methyl-2,2'-bipyridine-4'-carboxylate.) In these experiments, the electron transfer reaction was initiated by laser excitation of the metal-to-ligand charge transfer transition of the Ru^{II} –polypyridyl complex. This photoexcitation promotes the transferring electron to the Mebpy ligand, from where it is transferred to the dinitrobenzoic acceptor through the salt-bridge interface. Nocera and coworkers found that the rate of electron transfer is approximately 10^2 times faster for the DONA interface than for the DNOA interface. This substantial difference between the rates for the two systems indicates that the proton transfer interface plays a significant role in the electron transfer reactions.

The initial theoretical studies on the DNOA and DONA systems were based on a four-state VB model, as given in Eq. 23. Thus, only one of the proton transfer

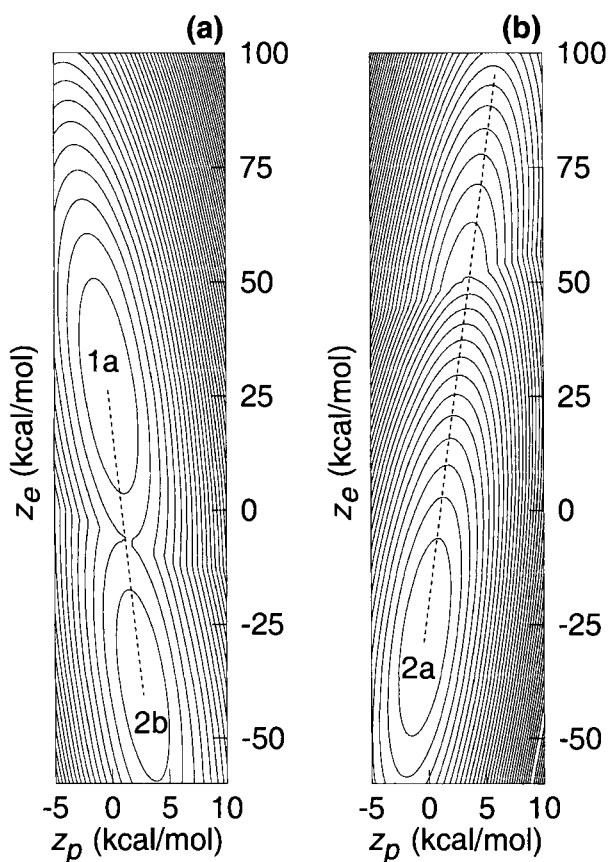


Figure 7. The two-dimensional ground state free energy surfaces for (a) DNOA and (b) DONA. The straight-line reaction paths are shown on the contour plots as dashed lines, and the minima are labeled according to the dominant VB states. Note that the z_p solvent coordinate is scaled by a factor of approximately four. (Reproduced from Ref. [14].)

reactions at the PT interface was included. The mixed electronic/proton vibrational free energy surfaces were obtained as functions of the two solvent coordinates z_p and z_e defined in Eq. 24. High-level electronic structure calculations were performed to obtain the gas phase energies of the active electronic states as functions of the proton coordinate r_p for the DNOA and DONA systems. The gas phase Hamiltonian matrix elements $(h_o)_{ij}(r_p)$ were represented as molecular mechanical terms parametrized to fit these gas phase energies. The reorganization energy matrix elements were calculated with a five-site ellipsoidal model. Figure 7 depicts the lowest-energy adiabatic surfaces for the DNOA and DONA systems, and Figure 8 depicts one-dimensional slices along a straight-line reaction path for these two-dimensional surfaces. [Note that for the DONA system, the reactant $1a$ state is so much higher in energy than the product $2a$ state that the $1a$ state does not correspond to a minimum on the lowest-energy adiabatic surface shown in Figure 7(b).]

The two-dimensional electron transfer diabatic free energy surfaces in Figure 7 have been analyzed with the Golden Rule rate expression given in Eq. 46. This analysis suggests that ET and EPT are possible for both systems, but ET is the dominant path due to significant overlap between the proton vibrational wave

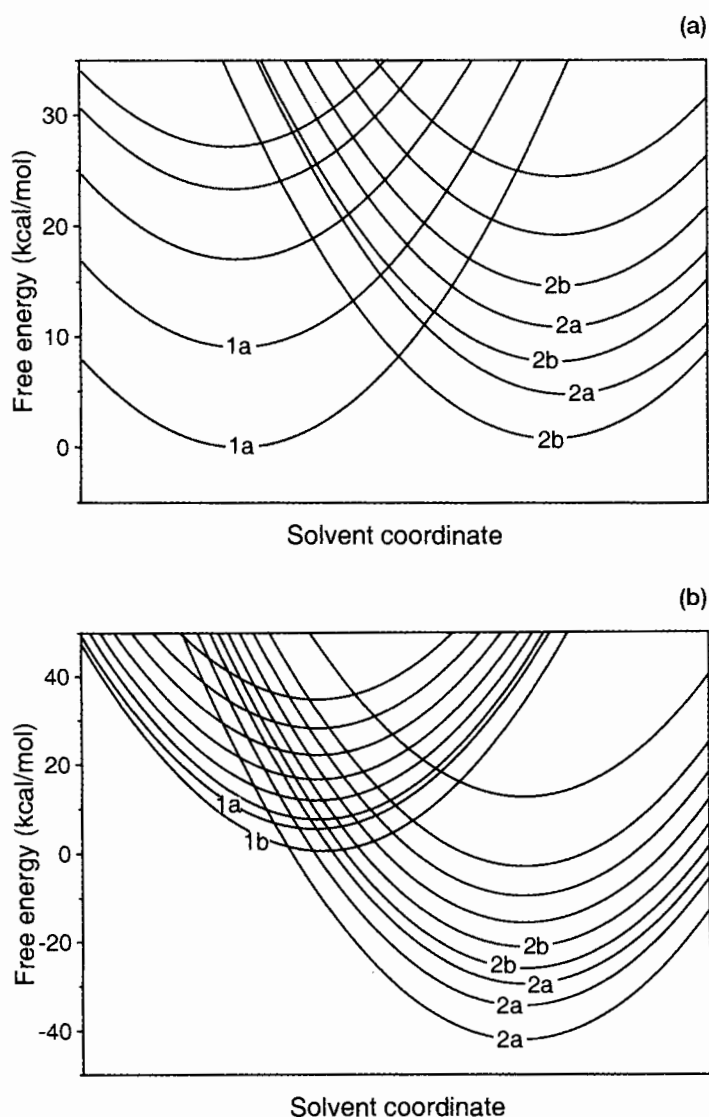


Figure 8. Slices of the two-dimensional ET diabatic free energy surfaces along the reaction path indicated in Figure 7 for (a) DNOA and (b) DONA. The ET diabatic states are labeled according to the dominant VB states.

functions for the lowest 1a and 2a vibrational states. The relevant paths are endothermic for DNOA and exothermic for DONA, and the activation energy barriers are significantly higher for DNOA than for DONA. Thus, these free energy surfaces are consistent with the experimental result that the rate is faster for DONA than for DNOA. This initial application illustrates the power of the multistate continuum theory for elucidating PCET reactions. Recently this application has

been refined by implementing the two-cavity FBCM method [38] for calculating the reorganization energy matrix elements and by including both proton transfer reactions with an eight-state VB model.

5.5 Fundamental Principles of Proton-Coupled Electron Transfer

The multistate continuum theory for PCET provides a framework for the analysis of the effects of specific solute and solvent properties on the rates and mechanisms of PCET reactions. The properties of interest include the relative energies of the gas phase solute charge transfer states, the distance between the proton donor and acceptor, the distance between the electron donor and acceptor, and the solvent polarity. In Ref. [32], a comprehensive study of the effects of these physical properties on the rates, mechanisms, and kinetic isotope effects of PCET reactions is presented. Some of the predictions obtained from this study are discussed in this section.

The most important physical properties for determining both rates and mechanisms of PCET reactions are the relative energies of the solute charge transfer states. The rate is strongly affected by the relative energies of the ET states. If the energy of ET state 2 is decreased relative to the energy of ET state 1, the barrier for reaction decreases and the rate increases. When the Marcus inverted region is reached, this trend is reversed. The mechanism of PCET is strongly affected by the relative energies of the PT states. ET is favored as the energy of the $2a$ state is decreased relative to the $2b$ state, while EPT is favored as the energy of the $2b$ state is decreased relative to the $2a$ state.

The distance between the proton donor and acceptor also affects the rates and mechanisms of PCET reactions. As this distance decreases, the barrier along the proton coordinate r_p decreases and eventually disappears. As illustrated in Figures 3–5, the height of this barrier determines the number of localized proton vibrational states. In particular, if the barrier along the proton coordinate is very low or non-existent, the proton vibrational wave functions are mixtures of a and b , so the distinction between ET and EPT is unclear. For systems in which the potential is a double well along the proton coordinate, however, the rate of EPT decreases as the barrier along the proton coordinate increases due to the decrease of the overlap of the proton vibrational wave functions for the a and b states.

The distance between the electron donor and acceptor affects the rates and mechanisms of PCET reactions in two different ways. First, an increase in this distance results in a decrease in the coupling between ET states ($1a/2a$, $1a/2b$, $1b/2a$, $1b/2b$). In the limit of electronically non-adiabatic electron transfer, a decrease in this coupling results in a decrease in the rate. Moreover, as the distance between the electron donor and acceptor increases, the interaction between the proton and the electron decreases. Thus, for a symmetric PT system with an initial state of $1a$, EPT is favorable for short electron donor–acceptor distances and ET becomes equally favorable as this distance increases.

Finally, the solvent polarity will affect the rates and mechanisms of PCET re-

2. (a) M. Wikstrom, *Nature* **1989**, 338, 776; (b) G. T. Babcock, M. Wikstrom, *Nature* **1992**, 356, 301; (c) B. G. Malmstrom, *Acc. Chem. Res.* **1993**, 26, 332.
3. (a) M. J. Therien, M. Selman, H. B. Gray, I.-J. Chang, J. R. Winkler, *J. Am. Chem. Soc.* **1990**, 112, 2420; (b) J. N. Onuchic, D. N. Beratan, *J. Chem. Phys.* **1990**, 92, 722.
4. R. A. Marcus, *Ann. Rev. Phys. Chem.* **1964**, 15, 155.
5. J. Ulstrup, *Charge-Transfer Processes in Condensed Media*; Springer: Berlin, 1979.
6. (a) R. R. Birge, *Annu. Rev. Phys. Chem.* **1990**, 41, 683; (b) H. Durr, H. Bouas-Laurent, *Photochromism: Molecules and Systems. Studies in Organic Chemistry* 40; Elsevier: Amsterdam, 1990.
7. R. I. Cukier, D. G. Nocera, *Annu. Rev. Phys. Chem.* **1998**, 49, 337.
8. (a) C. Turro, C. K. Chang, G. E. Leroy, R. I. Cukier, D. G. Nocera, *J. Am. Chem. Soc.* **1992**, 114, 4013; (b) J. A. Roberts, J. P. Kirby, D. G. Nocera, *J. Am. Chem. Soc.* **1995**, 117, 8051.
9. J. P. Kirby, J. A. Roberts, D. G. Nocera, *J. Am. Chem. Soc.* **1997**, 119, 9230.
10. (a) R. A. Binstead, B. A. Moyer, G. J. Samuels, T. J. Meyer, *J. Am. Chem. Soc.* **1981**, 103, 2897; (b) R. A. Binstead, T. J. Meyer, *J. Am. Chem. Soc.* **1987**, 109, 3287; (c) R. A. Binstead, M. E. McGuire, A. Dovletoglou, W. K. Seok, L. E. Roecker, T. J. Meyer, *J. Am. Chem. Soc.* **1992**, 114, 173; (d) R. A. Binstead, L. K. Stultz, T. J. Meyer, *Inorg. Chem.* **1995**, 34, 546.
11. B. T. Farrer, H. H. Thorp, *Inorg. Chem.* **1999**, 38, 2497.
12. (a) R. I. Cukier, *J. Phys. Chem.* **1994**, 98, 2377; (b) X. G. Zhao, R. I. Cukier, *J. Phys. Chem.* **1995**, 99, 945; (c) R. I. Cukier, *J. Phys. Chem.* **1995**, 99, 16101; (d) R. I. Cukier, *J. Phys. Chem.* **1996**, 100, 15428.
13. A. V. Soudackov, S. Hammes-Schiffer, *J. Chem. Phys.* **1999**, 111, 4672.
14. A. V. Soudackov, S. Hammes-Schiffer, *J. Am. Chem. Soc.* **1999**, 121, 10598.
15. (a) R. A. Marcus, *J. Chem. Phys.* **1956**, 24, 966; (b) R. A. Marcus, *J. Chem. Phys.* **1965**, 43, 679.
16. A. A. Ovchinnikov, M. Y. Ovchinnikova, *Soviet Physics JETP* **1969**, 29, 688.
17. S. Efrima, M. Bixon, *J. Chem. Phys.* **1976**, 64, 3639.
18. L. D. Zusman, *Chem. Phys.* **1980**, 49, 295.
19. D. F. Calef, P. G. Wolynes, *J. Phys. Chem.* **1983**, 87, 3387.
20. M. V. Basilevsky, G. E. Chudinov, M. D. Newton, *Chem. Phys.* **1994**, 179, 263–278.
21. D. Borgis, J. T. Hynes, *Chem. Phys.* **1993**, 170, 315.
22. M. V. Basilevsky, A. V. Soudackov, M. V. Vener, *Chem. Phys.* **1995**, 200, 87.
23. H. J. Kim, J. T. Hynes, *J. Chem. Phys.* **1992**, 96, 5088–5110.
24. M. D. Newton, H. L. Friedman, *J. Chem. Phys.* **1988**, 88, 4460–4472.
25. R. Kubo, Y. Toyozawa, *Progr. Theor. Phys.* **1995**, 13, 160.
26. (a) V. G. Levich, R. R. Dogonadze, *Dokl. Akad. Nauk SSSR* **1959**, 124, 123; (b) V. G. Levich, R. R. Dogonadze, *Dokl. Akad. Nauk SSSR* **1960**, 133, 158.
27. (a) N. R. Kestner, J. Logan, J. Jortner, *J. Phys. Chem.* **1974**, 78, 2148; (b) J. Ulstrup, J. Jortner, *J. Chem. Phys.* **1975**, 63, 4358; (c) J. Jortner, *J. Chem. Phys.* **1976**, 64, 4860.
28. P. F. Barbara, T. J. Meyer, M. A. Ratner, *J. Phys. Chem.* **1996**, 100, 13148.
29. R. F. Grote, J. T. Hynes, *J. Chem. Phys.* **1980**, 73, 2715.
30. H. A. Weidenmüller, Z. Jing-Shang, *J. Stat. Phys.* **1984**, 34, 191.
31. P. Hanggi, P. Talkner, M. Borkovec, *Rev. Mod. Phys.* **1990**, 62, 251.
32. H. Decornez, S. Hammes-Schiffer, *J. Phys. Chem. A* **2000**, 104, 9370.
33. A. V. Soudackov, S. Hammes-Schiffer, *J. Chem. Phys.* **2000**, 113, 2385.
34. A. Warshel, *Computer Modeling of Chemical Reactions in Enzymes and Solutions*; John Wiley: New York, 1991.
35. R. Vuilleumier, D. Borgis, *Chem. Phys. Lett.* **1998**, 284, 71.
36. U. Schmitt, G. A. Voth, *J. Phys. Chem. B* **1998**, 102, 5547.
37. J. Tomasi, M. Persico, *Chem. Rev.* **1994**, 24, 2027.
38. (a) M. V. Basilevsky, I. V. Rostov, M. D. Newton, *Chem. Phys.* **1998**, 232, 189–199; (b) M. D. Newton, M. V. Basilevsky, I. V. Rostov, *Chem. Phys.* **1998**, 232, 201–210.
39. (a) J.-Y. Fang, S. Hammes-Schiffer, *J. Chem. Phys.* **1997**, 106, 8442; (b) J.-Y. Fang, S. Hammes-Schiffer, *J. Chem. Phys.* **1997**, 107, 5727.
40. S. Hammes-Schiffer, *J. Phys. Chem. A* **1998**, 102, 10443.

6 Relationship between Electron and Electronic Excitation Transfer

Piotr Piotrowiak

6.1 Introduction

In many molecular, biological and solid-state systems electron and electronic excitation transfer processes occur alongside one another. Frequently, they offer independent competing pathways for excited-state deactivation. More importantly, in certain instances, they are linked together as crucial steps of the same photo-conversion chain, for example, in the photosynthetic reaction centers, in which the elaborate arrays of antenna chromophores collect electronic energy and rapidly transfer it to the charge-separation site. The underlying formal link between these two phenomena is even more universal: both electronic excitation transfer (EET) and electron-transfer (ET) processes can be viewed as special cases of nonradiative decay of an electronic excited state. Consequently, the rate of both of these cases can be described by the appropriate variants of the Fermi “golden rule” [1]

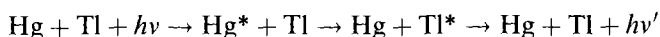
$$k = (4\pi^2/h) \cdot |V|^2 \cdot \rho \quad (1)$$

with the differences lying only in the specific description of the electronic coupling V and the Franck–Condon density of states, ρ [2]. In both cases, the electronic coupling term, V , consists of the direct donor–acceptor interaction, as well as the component mediated by the intervening material (bridge, matrix, or solvent). The latter is usually conveniently treated by numerous variants of Kramers “superexchange” scheme [3]. Similarly, as the magnitude of the donor–acceptor interaction increases, both ET and EET shift from the weakly coupled (non-adiabatic) regime treated by the “golden-rule” expressions, to the strongly coupled, or adiabatic regime. For ET and EET in molecular systems, the treatment of the density of states, ρ , is also very similar, and typically involves partitioning of the relevant Frank–Condon factors into intramolecular and medium components. The objective of this short chapter is to emphasize the similarities between electron and electronic energy transfer processes and theories, as well as bring to the attention of the reader the important

aspects in which ET and EET differ from one another and may require diverse treatments. The author does not attempt to present a comprehensive review of the energy transfer literature and apologizes if many important contributions were not included among the illustrations of the discussed principles.

Despite the obvious connection between electron and electronic excitation transfer, the two fields of research have separate origins and for the most part evolved independently from one another. Charge-transfer investigations have their roots in electrochemistry and redox-reaction studies. Electron transfer has only since relatively recently frequently been associated with photoinduced processes. The early theory of charge transfer evolved from two directions [4]: classical rate theory and quantum-mechanical tunneling [5]. Not surprisingly, electronic excitation transfer was always associated with light, or more generally, radiation-induced phenomena. Its early theory, like that of charge transfer, stems from two independent sources, in this case the phenomenological description of quenching, and the time-dependent quantum mechanics of coupled systems [7]. Excitation-transfer studies often preceded their electron-transfer counterparts in terms of concepts or experimental execution, for example, the use of donors and acceptors dispersed in amorphous glasses [8], the application of steroids [9] and oligopeptides [10] as donor-acceptor bridges, and the investigation of the through-bond versus through-space electronic coupling [11] and orientation effects [12]. In other instances, for example, in the quest for the "Marcus inverted region," the lead clearly belonged to electron transfer [13]. In general, when it comes to studies on molecular donor-acceptor systems, both areas borrowed heavily from the more developed solid-state physics.

Very elegant experiments unequivocally proving the occurrence of electronic energy transfer were performed in 1922 and 1923 by Cario and Franck [14]. When a mixed vapor of mercury and thallium was irradiated with the mercury line at 253.67 nm, the emission lines of thallium could be observed in addition to the anticipated fluorescence spectrum of mercury. Since thallium cannot absorb 253.67-nm light, it must have been "sensitized" by the excited mercury atoms in order to produce the green fluorescence



A remarkably modern quantum-mechanical model of electronic energy transfer was introduced in 1928 by Kallmann and London [7]. In their approach, two atoms with energy levels E_k and F_k are described by stationary Schrödinger equations

$$[H, u_k] = E_k u_k; \quad [G, v_k] = F_k v_k \quad (2)$$

The interaction between the atoms is represented by a time-dependent potential W . This leads to a time-dependent Schrödinger equation describing the entire weakly coupled system:

$$[H, \psi] + [G, \psi] + W \cdot \psi - \frac{\hbar}{i} \cdot \frac{\partial \psi}{\partial t} = 0 \quad (3)$$

where ψ is the time-dependent wave function describing the entire system. This wave function is expanded in terms of the stationary eigenfunctions u_k and v_k :

$$\psi = fu_kv_je^{i/h(E_k+F_j)t} + gu_jv_ke^{i/h(E_j+F_k)t} + \dots \quad (4)$$

where E_k , F_k are the energies of the respective stationary states, and f and g are slowly varying functions of time. This last assumption leads to the intrinsically adiabatic nature of this theory of electronic energy transfer.

For two local transition dipoles μ_1 and μ_2 (“virtual oscillators”) associated with two atoms or molecules of the gas, the interaction W becomes $W_{12}(R) \propto \mu_1\mu_2/R^3$ and leads to the following expression for the energy-transfer cross section:

$$q = \int_0^\infty \left(1 + \frac{\sigma}{2\mu_1\mu_2} R^6\right)^{-1} \pi R dR \quad (5)$$

where R is the distance between the dipoles and σ is the energy mismatch between the adiabatic states of the donor and acceptor. In the Kallmann–London model, the appropriate energy levels become isoenergetic (a requirement necessary for the transfer to occur) thanks to the continuous kinetic energy distribution of particles in the gas phase. When $\sigma = 0$ we have a “sharp resonance” condition and the transfer is very efficient. The efficiency of transfer drops steeply as σ increases. While certain aspects of this model may have been incorrect (e.g., the adiabaticity of the process), it clearly played a crucial role in the development of the subsequent theories. One immediately recognizes the similarity with the density-matrix treatment of coherent excitation transfer, as well as with the Fermi “golden rule” if the interaction with one sharply defined acceptor eigenstate is replaced by an integration over a continuum of final states. The close resemblance between the final Eq. 5 and the Förster expression for the rate of singlet excitation transfer is also apparent.

In the following paragraphs we will briefly discuss the mechanisms of electronic excitation transfer most frequently encountered in molecular systems, and outline the formalism most commonly used to interpret energy-transfer data. More attention will be devoted to the exchange-mediated excitation transfer processes because of their particularly close relationship to charge transfer.

6.2 Singlet Energy Transfer

The first improved theory addressing the weakly coupled, or non-adiabatic electronic excitation transfer was the semiclassical vector model proposed by Förster [15]. It was further developed and refined by Levinson [16], Kasha [17], and others [18], who sometimes referred to it as the “molecular exciton theory”. Notably, this was the first successful attempt to link the rate of electronic excitation transfer with readily available experimental parameters, such as the absorption spectrum of the

acceptor and the fluorescence spectrum of the donor. In its original version, Förster's model, like the earlier theory of "quenching spheres" of Perrin [6], described the efficiency of excitation transfer in terms of the critical donor-acceptor separation R_0 :

$$R_0 = \left\{ \frac{9000(\ln 10)\kappa^2 \Phi_D J(\nu)}{128\pi^5 N_A n^4} \right\}^{1/6} \quad (6a)$$

and

$$k_{\text{SET}} = \frac{1}{\tau_0} \left(\frac{R_0}{R} \right)^6 \quad (6b)$$

where τ_0 is the intrinsic lifetime of the donor excited state, n is the solvent's refractive index, $J(\nu)$ is the spectral overlap integral which can be obtained by use of Levshin's "mirror image" rule [19], or by direct integration of the experimental spectra. The electronic coupling is contained in the "orientation factor", κ , which is determined by the magnitude and the mutual orientation of the local transition dipoles, μ_D and μ_A , of the donor and the acceptor. One of the most commonly used variants of the Förster expression for k_{SET} is given below

$$k_{\text{SET}} = \frac{8.79 \times 10^{-25}}{n^4} \cdot \frac{[\mu_D \cdot \mu_A - 3(\mu_D \cdot \mathbf{R})(\mu_A \cdot \mathbf{R})]^2}{R^6} \cdot \frac{\Phi_D}{\tau_D} \cdot \int_0^\infty F_D(\nu) A_A(\nu) d\nu \quad (7a)$$

with

$$\kappa = |\mu_D \cdot \mu_A - 3(\mu_D \cdot \mathbf{R})(\mu_A \cdot \mathbf{R})| = |\sin \vartheta \sin \varphi \cos \omega - 2 \cos \vartheta \cos \varphi| \quad (8)$$

where ϑ and φ are the angles between the respective transition dipoles and the vector \mathbf{R} connecting their centers, while ω is the dihedral angle defined by the three vectors μ_D , μ_A , and \mathbf{R} .

Perhaps the most distinguishing feature of bimolecular singlet energy transfer in solution is the fact that it can proceed at rates substantially faster than diffusion. When the Franck-Condon factors (i.e., the spectral overlap) are favorable and the transition dipoles of the donor and the acceptor are large, singlet energy transfer is much faster than the rate of donor-acceptor encounters. For example, it was observed early on that in the case of 1-chloroanthracene serving as the donor and perylene as the acceptor [20] k_{SET} exceeds $1 \times 10^{11} \text{ M}^{-1} \text{ s}^{-1}$ both in benzene and in liquid paraffin, even though the k_{diff} values for these two solvents are on the order of 10^{10} and $10^8 \text{ M}^{-1} \text{ s}^{-1}$, respectively. This is possible because the direct electro-

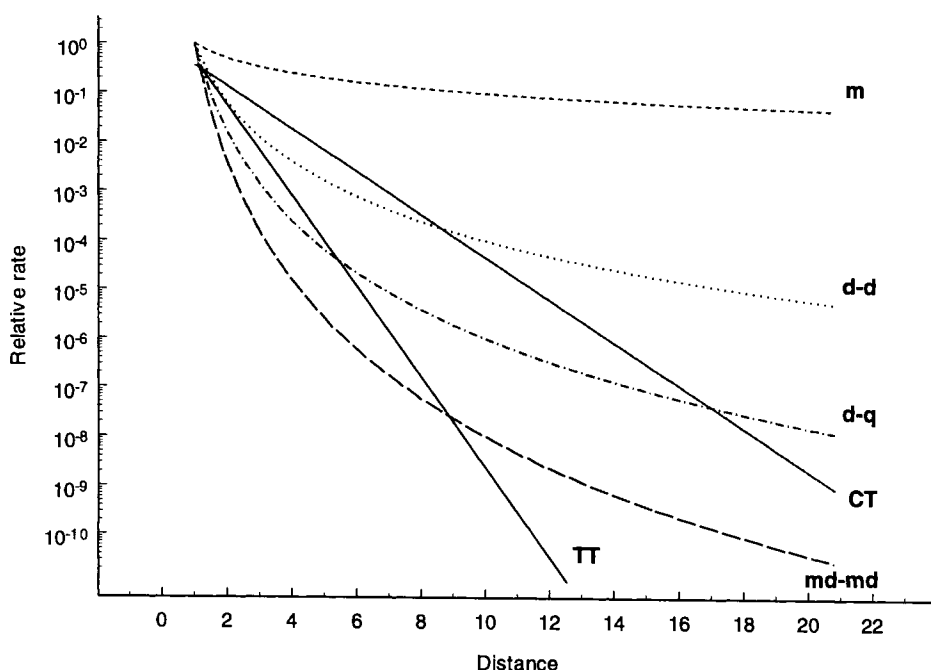


Figure 1. Theoretical dependence of the rates of various charge and excitation transfer processes on the donor–acceptor separation [21]. From top to bottom: **m**: conductivity of a metal; **d-d**: energy transfer by the electric dipole–electric dipole mechanism; **d-q**: energy transfer by the electric dipole–electric quadrupole mechanism; **CT**: superexchange-mediated charge transfer; **md-md**: energy transfer by magnetic dipole–magnetic dipole interaction; **TT**: superexchange-mediated triplet energy transfer. The curves were normalized to a common origin (this is not meant to imply that at minimum donor–acceptor separation all mechanisms lead to the same magnitude of coupling) and plotted versus distance in arbitrary units.

static coupling between the transition dipoles of the donor and the acceptor is a long-range interaction, which falls off relatively slowly with distance (Figure 1).

Electronic coupling

In 1953, Dexter presented a much broader theory of electronic energy transfer [22] and gave a detailed, quantitative description of the various electronic coupling mechanisms. He pointed out that the donor–acceptor coupling is formally described by the Coulomb and exchange integrals between the localized wave functions of the relevant electronic ground and excited states. Dexter’s treatment includes the Förster model as a special-case excitation transfer involving spin-allowed transitions of the donor and the acceptor. The electrostatic Coulomb interaction can be conveniently represented as a Taylor expansion of interactions between electrical multipoles centered on the donor and the acceptor (Eq. 9). Thus, Förster’s theory corresponds to truncating the multipole expansion after the first dipole–dipole term:

$$\begin{aligned}
 V_{\text{DA}} = & \frac{e^2}{\epsilon R^3} \cdot \left\{ \frac{\mathbf{r}_D \cdot \mathbf{r}_A - 3(\mathbf{r}_D \cdot \mathbf{R})(\mathbf{r}_A \cdot \mathbf{R})}{R^2} \right\} + \text{dipole-dipole} \\
 & + \frac{3e^2}{2\epsilon R^4} \cdot \left\{ \sum_{k=1}^3 \frac{R_i}{R} r_{Di} r_{Ai}^2 \left(-3 + \frac{5R_i^2}{R^2} \right) \right. \\
 & \quad \left. + 10 \frac{XYZ}{R^3} (x_A y_A z_D + x_A z_A y_D + y_A z_A x_D) + \dots \right\} + \dots \text{dipole-quadrupole} \\
 & - \int \phi'_D(\mathbf{r}_1) \phi_A(\mathbf{r}_2) \frac{1}{r_{12}} \phi'_A(\mathbf{r}_1) \phi_D(\mathbf{r}_2) d\tau \quad \text{exchange}
 \end{aligned} \tag{9}$$

If the local transitions of both chromophores are strongly allowed, the dipole-dipole interaction indeed dominates the expansion, and it has been shown in countless experiments that the approximation is satisfactory. Since it corresponds to the interaction between two point dipoles, the donor-acceptor center-to-center distance R (defined as the distance between the centers of mass of the local charge distributions) should be considerably larger than the length of either dipole. At short distances, the point dipole approximation should break down and either inclusion of higher-order multipoles, or explicit summation of interactions between charges assigned to individual atoms (point monopoles) of the donor and the acceptor may be necessary. Similarly, at small donor-acceptor separations, the exchange coupling (see Figure 2 further on) should also contribute significantly to singlet energy transfer. The departure from the ideal $1/R^6$ distance dependence of the rate (Figure 1) is usually taken to indicate the presence of other coupling mechanisms. However, in nearly all studied cases, including systems with closely coupled donors and acceptors, the rate of singlet energy transfer can be fully accounted for by the dipole-dipole interaction and there are only a few examples of model systems in which it was possible to achieve an appreciable contribution from the higher multipole or exchange terms [23]. Most likely, there are two main reasons for this behavior: Firstly, in many cases of flexible model compounds, the donor-acceptor separation, and even more so, the mutual orientation of the transition dipoles, are not known with a precision sufficient to make a strong case for the presence of other coupling mechanisms. More fundamentally, as was pointed out by Scholes and Ghiggino [24], the different contributions to the coupling, including the short-distance penetration term not discussed by Dexter, can carry opposite signs, thus leading to constructive and destructive interference effects somewhat analogous to the pathway interference effects familiar from electron transfer studies [25].

In general, each interaction in Eq. 9 has its own distinct orientation dependence. Nevertheless, it is possible to construct rigid donor-acceptor systems of such symmetry that all terms of the multipole expansion, as well as the exchange coupling, are rigorously equal to zero. Levy, Piotrowiak, and collaborators used spirobifluorenes (D_{2d} point group) to demonstrate that such perfect symmetry cancellation of the donor-acceptor coupling can indeed be obtained; however, it can be observed only in degenerate, or nearly degenerate bichromophoric molecules at the

bottom of the respective vibrational manifolds [26]. Populating vibrationally excited states of the donor (excess energy $\geq 600 \text{ cm}^{-1}$), or introducing a large donor–acceptor energy gap ($\Delta E \geq 1000 \text{ cm}^{-1}$) leads to efficient vibronic coupling and very rapid energy transfer ($k_{\text{SET}} \approx 1 \times 10^{12} \text{ s}^{-1}$) [27]. It is likely that vibronic mixing with higher, essentially localized excited states plays an important role in providing the interchromophore coupling. On the basis of this work, it can be generalized that vibronic coupling effects are likely to be of importance for most donor–acceptor systems used in excitation and charge-transfer studies, since the employed free-energy gaps are typically much larger than a few hundred wavenumbers [28].

Mediated singlet excitation transfer

For reasons outlined above, the donor–acceptor coupling in singlet energy transfer is usually viewed as a direct electrostatic interaction between the localized transition dipoles. The only role of the intervening medium is to screen this interaction depending on the value of ϵ^2_{∞} or n^4 . This overly simplistic view has been challenged by several groups, particularly by Paddon-Row, Scholes, and Ghiggino [23, 29], who studied, in detail, various coupling contributions to the singlet energy transfer in a well-characterized rigidly linked bichromophore. It was found that the “through-bond” exchange coupling was the dominant mechanism, followed by the direct dipole–dipole interaction, and by the “relayed Coulomb coupling”, that is, a mechanism of donor–acceptor interaction which involves the virtual excitations of the bridging moiety. This sequential donor \leftrightarrow bridge \leftrightarrow acceptor interaction is essentially a variant of the original concept of superexchange, only applied to a different type of excitation and, hence, employing a different basis set. The resulting formula for relayed Coulombic electronic coupling does, indeed, closely resemble the classic McConnell perturbation theory expression [30] for superexchange-mediated electron transfer. Treating the bridge as a single excitable unit, one obtains, within the dipole–dipole approximation that

$$V_{\text{relay}}^{\text{dd}} \approx \frac{V_{\text{donor-bridge}}^{\text{dd}} V_{\text{bridge-acceptor}}^{\text{dd}}}{\Delta E_{\text{average}}} \quad (10)$$

where $\Delta E_{\text{average}}$ is the average energy gap between the excited state of the bridge and the excited states of the donor and the acceptor, and $V_{\text{donor-bridge}}$ and $V_{\text{bridge-acceptor}}$ are expressed in terms of the standard dipole–dipole coupling. In the case of the frequently employed saturated hydrocarbon bridges, the difference between the $\Delta E_{\text{donor-bridge}}$ and $\Delta E_{\text{bridge-acceptor}}$ is negligibly small, since the $\sigma \leftrightarrow \sigma^*$ transition of the bridge lies approximately 3 eV ($24,000 \text{ cm}^{-1}$) or more above the S_1 states of typical chromophores. Interestingly, the sign of the Coulombic relay contribution was the opposite of those of exchange and dipole–dipole interactions. The importance of mixing of the orthogonally polarized local transitions of the donor and/or acceptor was also investigated. It was found that this “pre-mixing” can increase the overall coupling by more than an order of magnitude.

The most convincing demonstration of the importance of the “Coulombic relay mechanism,” or a bridge-exciton-mediated singlet energy transfer, comes from the

recent work of Albinsson et al., who investigated an elegant series of porphyrin-based bichromophores linked by bridges of equal length but with widely differing excited-state energies [39]. The $\Delta E_{\text{donor-bridge}}$ was varied over the range from 4000 to 18000 cm^{-1} and a very good linear correlation between the measured singlet energy transfer rates and $(1/\Delta E_{\text{donor-bridge}})^2$ was obtained. Importantly, the bridge-chromophore energy gap was always kept well above the average thermal energy, thus avoiding the possibility of trivial stepwise energy transfer (i.e., exciton hopping or energy migration). It is possible that the through-bond exchange coupling also makes a significant contribution in these systems.

Spectral overlap and the Franck–Condon density of states

The possibility of expressing the Franck–Condon density of states in terms of the experimentally measurable spectral overlap integral is a unique and valuable feature of the Förster theory and singlet energy transfer. The resulting density of states is free of approximations introduced in the classical or semiclassical theoretical expressions for the Franck–Condon factors used in electron-transfer studies. All familiar aspects of the Marcus and Marcus–Jortner treatments of the Franck–Condon factors, including the existence of the “inverted region” at large donor–acceptor energy gaps, are inherently present in the spectral overlap integral. This is more readily appreciated when one treats the emission band of the donor and the absorption band of the acceptor as symmetric Gaussian functions whose widths are determined by the respective Stokes parameters S_D and S_A . In this case, the spectral overlap integral can be expressed in closed form, and the expression for k_{SET} becomes virtually identical with the Marcus equation, with the sum of Stokes shifts of the donor and acceptor, $S_D + S_A$ taking the place of the reorganization energy λ :

$$k_{\text{SET}} = V_{\text{DA}}^2 \cdot \sqrt{\frac{1}{4k_B T(S_D + S_A)}} \cdot \exp \left[-\frac{[\Delta E_{\text{DA}} - (S_D + S_A)]^2}{4k_B T(S_D + S_A)} \right] \quad (11)$$

Unlike in the case of electron and triplet energy transfer, it seems that there has not been much interest in mapping out the driving-force dependence of singlet energy transfer in the highly exoergic range. The author is aware of only a few reported cases of the “inverted region” or “gap law” behavior [32].

Coherent energy transfer

Finally, we should mention the possibility of coherent excitation transfer when the donor–acceptor interaction is strong, but the coupling of the system to the thermal bath is weak. The resulting two-level weakly damped system lends itself to the time-dependent density-matrix approach [33], which is essentially identical to the familiar spin-1/2 treatment in magnetic resonance. Under certain circumstances, coherence effects can be important for singlet energy transfer, because the donor states are populated instantaneously by direct photoexcitation. With a sufficient band width of the excitation source (e.g., ultrashort femtosecond pulses), quantum superposition states can be prepared in a coherent fashion even in condensed media at room

temperature, and a broad array of polarization transfer and coherence transfer phenomena can be studied. In the case of spin-forbidden $S_0 \rightarrow T_1$ transitions, the donor T_1 state is populated by intersystem crossing from the S_1 state and any coherence of the original state is usually lost before the excitation transfer can take place. Therefore, coherence effects are very unlikely in triplet energy transfer at ambient conditions.

6.3 Triplet Energy Transfer

Förster theory and its variants have been very successful for treating energy transfer between donors and acceptors with strong allowed electronic transitions. However, this approach is not applicable to electronic energy transfer leading to spin multiplicity changes of the donor and/or acceptor unit. Such processes abound especially in organic molecular systems, in which the spin multiplicity is always well defined and the spin-orbit coupling relatively weak. However, it was the problem of excitation transfer ("sensitized luminescence") in inorganic solids that prompted further theoretical development in this area. Dexter demonstrated that triplet energy transfer (or, more generally, any electronic excitation transfer involving spin-forbidden local transitions) can proceed owing to the exchange coupling between the donor and the acceptor [22, 34]. As will be shown below, the exchange interaction can be viewed as a two-electron two-orbital analog of the one-electron two-orbital resonance integral. As a result, triplet excitation transfer is mechanistically much more closely related to charge-transfer processes than to spin-allowed singlet energy transfer.

Electronic coupling

To describe electronic energy transfer involving spin-forbidden vertical transitions, one must write the wave functions of the initial and the final state so that they explicitly contain the spin functions:

$$\Psi_I = \varphi'_D(\mathbf{r}_1)\chi'_D(\sigma_1)\varphi_A(\mathbf{r}_2)\chi_A(\sigma_2) - \varphi'_D(\mathbf{r}_2)\chi'_D(\sigma_2)\varphi_A(\mathbf{r}_1)\chi_A(\sigma_1) \quad (12a)$$

$$\Psi_F = \varphi_D(\mathbf{r}_1)\chi_D(\sigma_1)\varphi'_A(\mathbf{r}_2)\chi'_A(\sigma_2) - \varphi_D(\mathbf{r}_2)\chi_D(\sigma_2)\varphi'_A(\mathbf{r}_1)\chi'_A(\sigma_1) \quad (12b)$$

where φ_i is the spatial part of the wave function and χ_i is the spin part of the wave function. Now we can explicitly write out the matrix elements of the perturbation Hamiltonian H_1 , at the same time separating the spatial and spin integrals (the Hamiltonian $H_1 = e^2/r_{12}$ does not operate on spin functions and, therefore, such factoring out is possible):

$$\begin{aligned} V_{DA} &= \langle H_1 \rangle \\ &= \langle \varphi'_D(\mathbf{r}_1)\varphi_A(\mathbf{r}_2) | H_1 | \varphi_D(\mathbf{r}_1)\varphi'_A(\mathbf{r}_2) \rangle \times \langle \chi'_D(\sigma_1)\chi_A(\sigma_2) | \chi_D(\sigma_1)\chi'_A(\sigma_2) \rangle \\ &\quad - \langle \varphi'_D(\mathbf{r}_1)\varphi_A(\mathbf{r}_2) | H_1 | \varphi'_A(\mathbf{r}_1)\varphi_D(\mathbf{r}_2) \rangle \times \langle \chi'_D(\sigma_1)\chi_A(\sigma_2) | \chi'_A(\sigma_1)\chi_D(\sigma_2) \rangle \end{aligned} \quad (13)$$

The first term in the above expression is the Coulomb-interaction term, which vanishes, unless

$$\chi'_{\text{D}} = \chi_{\text{D}} \quad \text{and} \quad \chi_{\text{A}} = \chi'_{\text{A}}$$

that is, the Coulomb interaction allows only transitions which preserve the spin multiplicity of the donor and the acceptor units; it does, however, allow electronic-energy transfer between donor and acceptor of different spin multiplicity (this is of minor importance for organic systems, since there are very few stable compounds with ground-state spin other than 0, and the $^3\Sigma_{\text{g}}^-$ to $^3\Sigma_{\text{u}}^-$ transition of the ubiquitous molecular oxygen is symmetry-forbidden).

The second term in the above expression is the exchange integral, for which the following selection rules apply:

$$\chi'_{\text{D}} = \chi'_{\text{A}} \quad \text{and} \quad \chi_{\text{D}} = \chi_{\text{A}}$$

that is, χ does not have to be equal to χ' , so the spin functions on both chromophores can change simultaneously. Therefore, for $\chi'_{\text{D}} = \chi'_{\text{A}}$, $\chi_{\text{D}} = \chi_{\text{A}}$ and $\chi'_{\text{D}} \neq \chi_{\text{D}}$, $\chi_{\text{A}} \neq \chi'_{\text{A}}$ the expression for the donor-acceptor interaction simplifies to

$$V_{\text{DA}} = \langle H_1 \rangle = -\langle \varphi'_{\text{D}}(\mathbf{r}_1) \varphi_{\text{A}}(\mathbf{r}_2) | H_1 | \varphi'_{\text{A}}(\mathbf{r}_1) \varphi_{\text{D}}(\mathbf{r}_2) \rangle \quad (14)$$

The exchange integral is, in principle, a purely quantum-mechanical result of the antisymmetrization of the electronic wave function and, therefore, does not possess an obvious classical analogue. One may try to visualize the exchange interaction by creating two virtual charge distributions Q' and Q given by $Q'(\mathbf{r}_1) = \varphi'_{\text{D}}(\mathbf{r}_1) \varphi'_{\text{A}}(\mathbf{r}_1)$ and $Q(\mathbf{r}_2) = \varphi_{\text{D}}(\mathbf{r}_2) \varphi_{\text{A}}(\mathbf{r}_2)$ and rewriting Eq. 14 accordingly. However, more insight can be gained by rewriting the spatial portions of the excited and ground state wave functions of the donor and the acceptor in terms of the products of the corresponding localized HOMO and LUMO orbitals. In this zero-order orbital approximation, the spatial wave function of the lowest excited state (either triplet or singlet) becomes $\varphi' = \varphi^{\text{LUMO}} \varphi^{\text{HOMO}}$, and for the ground state $\varphi = \varphi^{\text{HOMO}} \varphi^{\text{HOMO}}$. In this basis set, Eq. 14 transforms into

$$|V_{\text{DA}}| = |\langle \varphi_{\text{D}}^{\text{LUMO}}(1) \varphi_{\text{A}}^{\text{HOMO}}(2) | H_1 | \varphi_{\text{A}}^{\text{LUMO}}(1) \varphi_{\text{D}}^{\text{HOMO}}(2) \rangle| \quad (15)$$

which explicitly shows that triplet energy transfer can be described as a double electron exchange between the HOMO and LUMO orbitals of the donor and the acceptor. This concept is frequently represented graphically, as shown in Figure 2. Naturally, if the HOMO orbitals are replaced by the valence band of a semiconductor, and the LUMO orbitals by the corresponding conduction band, one obtains the commonly accepted mechanism of triplet exciton migration in semiconductors. The same model can be used to explain triplet exciton mobility in molecular solids [35].

The simplification of Eq. 15 can be taken even further. Since the Hamiltonian $H_1 = 1/r_{12}$ varies very slowly with distance compared to the exponential decay of

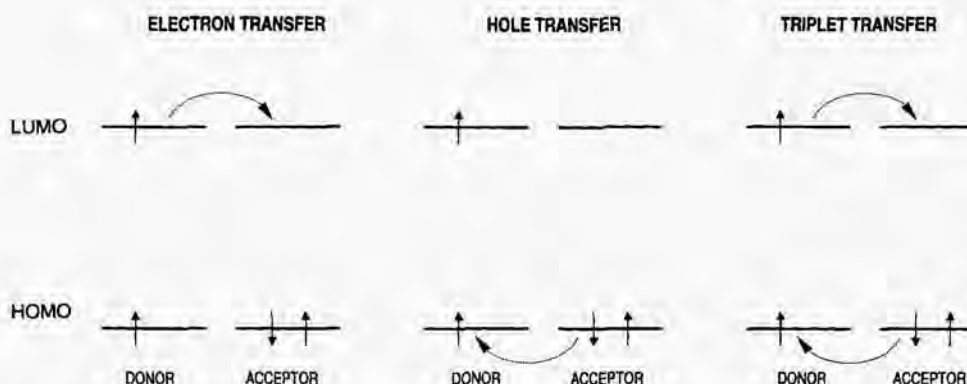


Figure 2. Schematic representation of electron, hole, and triplet energy transfer between the localized HOMO and LUMO orbitals of the donor and the acceptor. Note that the above diagram also applies to the exchange-mediated singlet excitation transfer if the spin of the electron in the LUMO orbital is reversed.

electronic wave functions, it can be, perhaps somewhat daringly, postulated that $1/r_{12}$ can be approximated by its average value, which, in turn, for weakly interacting systems will be approximately equal to the inverse of the center-to-center donor-acceptor distance, $\langle 1/r_{12} \rangle \approx 1/r_{DA} = \text{const.}$ As a result, one obtains

$$\begin{aligned}
 V_{DA}^{TT} &\approx \text{const.} \cdot \langle \phi_D^{\text{LUMO}}(1) \phi_A^{\text{HOMO}}(2) | \phi_A^{\text{LUMO}}(1) \phi_D^{\text{HOMO}}(2) \rangle \\
 &= \text{const.} \cdot \langle \phi_D^{\text{LUMO}}(1) | \phi_A^{\text{LUMO}}(1) \rangle \langle \phi_A^{\text{HOMO}}(2) | \phi_D^{\text{HOMO}}(2) \rangle \\
 &\approx \text{const}' \cdot V_{DA}^{\text{ET}} \cdot V_{DA}^{\text{HT}}
 \end{aligned} \tag{16}$$

In the approximate expression above, the two-electron two-orbital exchange integral is effectively replaced by the product of the overlap integrals between the LUMO and HOMO orbitals of the donor and the acceptor. Within the framework of the same assumption ($1/r$ varying slowly compared to the decay of the wave function), these overlap integrals can be viewed as approximations of the resonance integrals corresponding to electron transfer and hole transfer, respectively. As a consequence, the electronic coupling element responsible for triplet energy transfer becomes proportional to the product of the electronic coupling for the electron and hole transfer processes, $V^{TT} \propto V^{\text{ET}} \cdot V^{\text{HT}}$, and since the transfer rates are proportional to $|V|^2$, it can be also stated that $k^{TT} \propto k^{\text{ET}} \cdot k^{\text{HT}}$.

Furthermore, since the electronic coupling, and the rates of all three processes, fall off exponentially with distance, with characteristic slopes of β^- , β^+ , and β^{TT} :

$$\begin{aligned}
 V^{\text{ET}} &= V_0^{\text{ET}} \cdot \exp\{-[\beta^-(R_{DA} - R_0)/2]\} \\
 k^{\text{ET}} &= k_0^{\text{ET}} \cdot \exp\{-[\beta^-(R_{DA} - R_0)]\}
 \end{aligned} \tag{17a}$$

$$V^{\text{HT}} = V_0^{\text{HT}} \cdot \exp\{-[\beta^+(R_{\text{DA}} - R_0)/2]\}$$

$$k^{\text{HT}} = k_0^{\text{HT}} \cdot \exp\{-[\beta^+(R_{\text{DA}} - R_0)]\} \quad (17b)$$

$$V^{\text{TT}} = V_0^{\text{TT}} \cdot \exp\{-[\beta^{\text{TT}}(R_{\text{DA}} - R_0)/2]\}$$

$$k^{\text{TT}} = k_0^{\text{TT}} \cdot \exp\{-[\beta^{\text{TT}}(R_{\text{DA}} - R_0)]\} \quad (17c)$$

Hence it can be written that

$$V^{\text{TT}} \propto V_0^{\text{ET}} \cdot V_0^{\text{HT}} \cdot \exp\{-[\beta^-(R_{\text{DA}} - R_0)/2]\} \cdot \exp\{-[\beta^+(R_{\text{DA}} - R_0)/2]\}$$

$$= V_0^{\text{ET}} \cdot V_0^{\text{HT}} \cdot \exp\{-[(\beta^- + \beta^+)(R_{\text{DA}} - R_0)/2]\} \quad (18)$$

from which it follows directly that $\beta^{\text{TT}} = \beta^- + \beta^+$ (V_0 and k_0 correspond to the minimum donor-acceptor separation, $R = R_0$, for example, one σ -bond in a bridged system, or van der Waals contact in a glass or liquid solution).

The validity of these simple approximations in weakly coupled bridged donor-acceptor systems was tested experimentally on a carefully designed family of homologous donor-acceptor compounds [36]. The distance dependence of intramolecular triplet energy transfer was determined for the first time and compared with the corresponding electron and hole transfer distance dependencies [37]. Identical saturated hydrocarbon bridge units (cyclohexane and trans-decalin) and stereochemical attachments were used in all three series of experiments (electron [38], hole [39], and triplet [36] energy transfer). Biphenyl served as the donor and naphthalene as the acceptor in the pulse radiolysis measurements of electron and hole transfer rates [40]. For energy-transfer studies biphenyl was replaced by benzophenone as the triplet donor; however, naphthalene was retained as the acceptor. The variation of the electronic structure of the model compounds was therefore, as far as possible, kept to a minimum. The resulting correlation of transfer rates is shown in Figure 3.

It should be emphasized that the linearity of the plot in Figure 3 is merely a consequence of the rates of both charge transfer and triplet excitation transfer being exponentially distance dependent. It is the slope of the resulting line that contains the information about the relationship between the respective electronic coupling elements. In Figure 3, the slope is, within experimental error, equal to one, confirming that, indeed, $\beta^{\text{TT}} = \beta^- + \beta^+$.

A satisfactory agreement between the distance dependence of the rate of triplet energy transfer and the rate of electron transfer alone could also be obtained in these model systems, with $\beta^{\text{TT}} \approx 2\beta^{\text{ET}}$, showing that, for a comparable bridge, the rate of triplet energy transfer falls off twice as rapidly with increasing donor-acceptor separation as with electron transfer (Figure 4) [42, 43]. It is remarkable that this correlation is maintained for triplet transfer rates spanning five orders of magnitude. This behavior can be attributed to the approximately symmetric displacement of the HOMO and LUMO orbitals of aromatic donors and acceptors, which leads to approximately equal values of β^+ and β^- .

It is also worthwhile to point out that the correlation plots in Figures 3 and 4 contain systems with all possible stereochemical attachments of the donor and acceptor to the bridge (equatorial-equatorial, equatorial-axial and axial-equatorial).

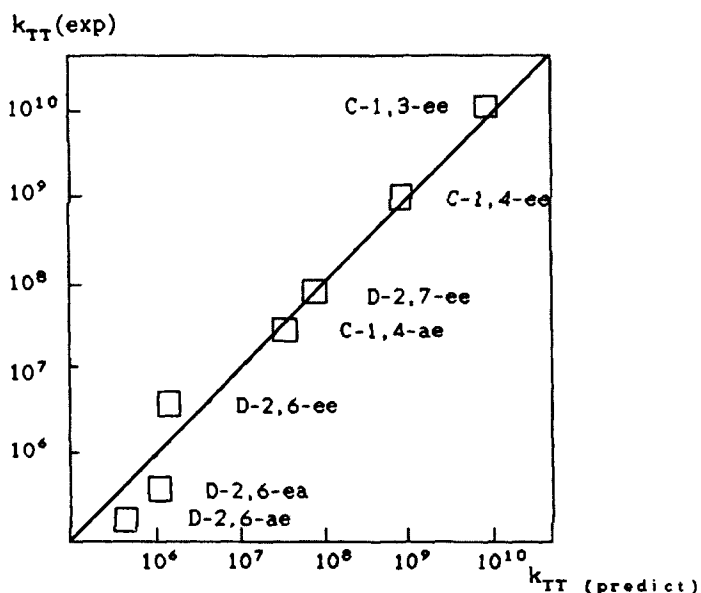


Figure 3. Correlation between the experimentally measured rates of triplet energy transfer and the scaled product of the appropriate electron and hole transfer rates [41]. The straight line indicates the slope of unity which corresponds to $\beta^{TT} = \beta^- + \beta^+$.

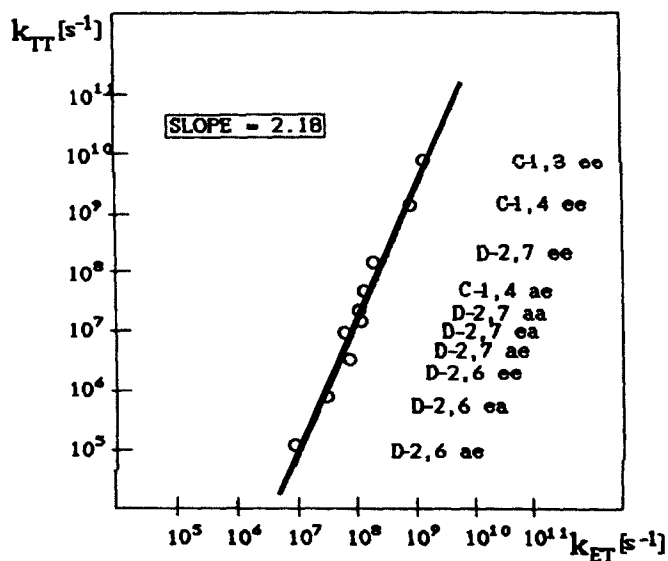


Figure 4. Correlation between the experimentally measured rates of triplet energy transfer and the electron transfer rates in analogous model compounds [41]. The fitted line indicates that $\beta^{TT} = 2.18 \cdot \beta^-$, nearly in perfect agreement with the simplified theory.

The stereochemistry of the attachment to the bridge primarily affects the corresponding V_0 , which determines only the intercept at $R = R_0$, and has a negligible influence on the slope of the distance dependence. The differences in V_0 can be large, so that different sets of stereoisomers must be analyzed separately. However, in all three processes studied (electron, hole, and triplet transfer) the dependence of V_0 on the donor–acceptor stereochemistry was the same, with the equatorial–equatorial isomers always giving the highest V_0 , and leading to a nearly constant value of $V_0^{\text{TT}}/(V_0^{\text{ET}} \cdot V_0^{\text{HT}})$, regardless of the attachment pattern. This self-cancellation effect further confirms the validity of the approximate picture.

The model compounds of Closs, Miller, and Piotrowiak were subsequently treated computationally by Morokuma and coworkers [44]. The results of their *ab initio* calculations agreed with the experimental observations and showed that the dependence of V^{TT} on the donor–acceptor separation and on the stereochemistry of the attachment to the bridge closely tracks that of the product of V^{ET} and V^{HT} .

The described relationship between charge transfer and triplet energy transfer processes is expected to be general for most donor–acceptor systems, provided that a few important criteria are met: (1) The wave functions of the excited state and the radical ions of the donors and acceptors must be well represented by the zero-order HOMO–LUMO approximations. As a consequence, the correlation is likely to break down in the presence of strong configuration interaction. (2) All involved states, that is, the reduced, oxidized, and triplet states of the donor and acceptor, must be well below the appropriate virtual states of the bridging unit, thus satisfying the conditions of weak coupling propagating by the superexchange mechanism. Strongly coupled systems, for example, those involving conjugated bridges are likely to depart from the linear correlation. (3) The spin states of all components must be well defined (this is frequently not the case if transition metal complexes serve as the donor and/or acceptor) [45].

Franck–Condon factors and the reorganization energy

The rate of triplet energy transfer in the original Dexter formulation is given by

$$k_{\text{TT}} = \frac{2\pi}{\hbar} |V_{\text{DA}}|^2 \cdot \int f_{\text{D}}(E) F_{\text{A}}(E) dE \quad (19)$$

where f_{D} is the normalized emission spectrum of the donor and F_{A} is the normalized absorption spectrum of the acceptor. In the case of triplet energy transfer they correspond to the phosphorescence and the $S_0 \rightarrow T_1$ absorption spectra, respectively. Unfortunately especially the latter, can frequently not be readily measured in organic molecules. Therefore, expressing the Franck–Condon density of states in terms of spectral overlap, which is so convenient in the analysis of singlet energy transfer processes, is generally impractical for triplet transfer. Instead, the semi-classical Marcus–Jortner formula [46] used in most electron-transfer studies can be applied here without any modification. Thus, the expression for the rate of triplet excitation transfer becomes

$$k_{\text{TT}} = \left(\frac{\pi}{\hbar^2 \lambda_{\text{s}} k_{\text{B}} T} \right)^{1/2} \cdot |V^{\text{TT}}|^2 \cdot \sum_{n=0}^{\infty} e^{-S} \cdot \frac{S^n}{n!} \cdot e^{-(\Delta G_0 + \lambda_{\text{s}} + n\hbar\nu)^2 / (4\lambda_{\text{s}} k_{\text{B}} T)} \quad (20)$$

where $S = \lambda_v/h\nu$, λ_s and λ_v are the low-frequency (classical) and high-frequency (quantized) contributions to the nuclear reorganization energy, ν is the average frequency of the vibrational mode coupled to the electronic coordinate, n is the vibrational quantum number of the final state, and all other symbols have their usual meaning.

It has been experimentally demonstrated by several groups using covalently linked organic [47] and organometallic [48] model compounds, as well as freely diffusing [49] and incarcerated [50, 51] donors and acceptors, that the Marcus–Jortner equation adequately describes the driving-force dependence of triplet energy-transfer rates, and that as for electron transfer, the highest rates occur when the Franck–Condon factors are optimized, approximately at $-\Delta G^\circ = \lambda_{\text{total}}$. When the optimum free energy of reaction is exceeded, one enters the “inverted region” and the rates begin to diminish (Figure 5).

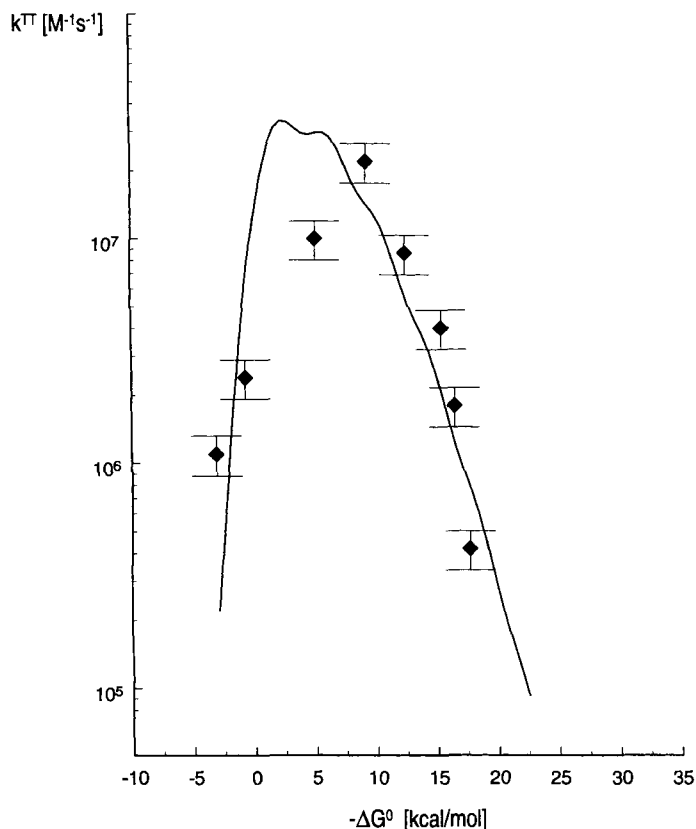


Figure 5. Free-energy dependence of triplet energy transfer from a biacetyl donor trapped within a hemicarcerand cage to several rigid aromatic acceptors in solution. Note that the curve is much narrower, and that the “inverted region” is reached at a much lower value of ΔG° than is typically observed in electron-transfer systems. The oscillations in the calculated line are artifacts of the single high frequency mode approximation (from the work of Deshayes, Piotrowiak, et al. [52]).

While the overall appearance of the above equation is the same for charge and excitation transfer, the relative importance of various terms can be very different. In the case of electron transfer, the overall reorganization energy is dominated by the solvent contribution λ_s , which, according to the simplest continuum model of solvation, depends on the effective radii of the donor and the acceptor, the separation between them, and the dielectric constant of the medium. In polar solvents, the magnitude of the solvent-reorganization energy can readily exceed 1 eV (ca. 23 kcal/mol). Consequently, a correction for the large variation in λ_s , usually based on the Born expression, must be included in the analysis electron-transfer data. The variations in the magnitude of λ_v , which is typically much smaller (typically 3–4 kcal/mol for each of the reactants) are usually ignored without much detriment to agreement with the experimental results.

The partitioning between the internal and external components of the reorganization energy in triplet transfer is the opposite of that found for electron transfer. Triplet energy transfer does not involve a major redistribution of charges between the donor and the acceptor. Indeed, often even the dipole moments of the individual moieties, and of the entire assembly, remain unchanged (e.g., among the commonly used donors and acceptors this applies to biacetyl, naphthalene, anthracene, and pyrene). Therefore, the corresponding solvent-reorganization energy is very small, typically less than 0.1 eV. As a result, λ_v is the leading component of the overall reorganization energy in triplet transfer, and the transfer rates become extremely sensitive to this parameter. The dominance of λ_v is further amplified by the fact that the absolute magnitude of the internal reorganization energy is usually considerably larger for triplet transfer than it is for electron transfer, and in some cases, primarily the olefins, it can exceed 1 eV (Table 1).

While at first it might seem counterintuitive, this effect is readily explained in terms of the simplest zero-order orbital picture of the electron and electronic excitation transfer processes. Triplet transfer to and from a typical closed-shell organic molecule involves a change in occupancy of both the HOMO and LUMO orbitals of the donor and the acceptor. For an olefinic or aromatic donor or acceptor, this can be represented as $\pi^1\pi^{*1} \rightarrow \pi^2\pi^{*0}$ (donor) and $\pi^2\pi^{*0} \rightarrow \pi^1\pi^{*1}$ (acceptor). This results in the overall bond order being changed by one. The analogous reduction and oxidation processes (either thermal or photoinduced) involve only one occupancy change, $\pi^2\pi^{*0} \rightarrow \pi^2\pi^{*1}$ (reduction) and $\pi^2\pi^{*0} \rightarrow \pi^1\pi^{*0}$ (oxidation), with the corresponding bond order change of 1/2. Table 1 contains internal reorganization energies calculated at the AM1 semi-empirical level (except where noted) for a selection of commonly used donors and acceptors [53]. While the individual values of λ_v obtained at such a low level of computation should be taken very cautiously, the overall trends are clearly visible, with the triplet reorganization energy usually being at least twice as large as that associated with the formation of the corresponding radical anion or the radical cation. The notable exceptions include molecular oxygen and biacetyl, both of which exhibit unusually low triplet reorganization energies.

The importance of structural relaxation in triplet energy transfer was recognized some time ago by Balzani [54, 55]. The dependence of triplet energy transfer rates on the magnitude of internal reorganization energy was investigated experimentally by Deshayes, Piotrowiak, and coworkers [52]. Acceptors with internal reorganiza-

Table 1. Reorganization energies (in kcal/mol) associated with the triplet formation, one-electron oxidation, and one-electron reduction of selected common organic donors and acceptors. Calculations were performed at the semi-empirical level (AM1).

Compound	$S_0 \rightarrow T$	Ox	Red	Compound	$S_0 \rightarrow T$	Ox	Red
Rigid aryls:				Olefins:			
Acenaphthene	6.1	4.0	2.8	1,3-Cyclohexadiene	18.2	5.5	3.7
Anthracene	10.1	3.3	2.5	Cycloheptatriene	22.6	9.5	6.9
Azulene	10.0	3.3	2.2	1,4-Diphenylbutadiene	18.4	7.2	6.8
Benzene	7.7	4.6	1.8	cis-Piperylene	20.5	5.5	3.8
Biphenyl	12.0	6.3	5.6	trans-Piperylene	20.6	5.8	4.0
Coronene	8.2	3.6	2.8	cis-Stilbene	30.3	9.2	8.8
Fluorene	8.4	4.0	2.9	trans-Stilbene	21.9	6.9	6.4
Naphthalene	14.0	2.7	2.9	Other donors & acceptors:			
Phenanthrene	10.6	4.3	3.5	Dimethylaniline	8.7	7.2	(-) ^b
Pyrene	6.6	3.5	2.3	Tetramethylbenzidine	19.6	10.2	9.8
Triphenylene	8.2	3.5	2.9	Tetrathiafulvalene	8.0	3.4	3.3
Ketones:				Triethylamine	26.0	15.4	(-) ^b
Acetone	5.6	0.7	3.1	Benzoquinone	12.3	15.8	4.6
Acetophenone	7.5	4.2	3.8	Nitrobenzene	7.2	4.4	4.5
Anthrone	8.8	3.8	3.1	Tetracyanoethylene	17.3	4.4	2.1
Biacetyl	1.1	(-) ^a	6.6	Tetracyanoquinodimethane	16.4	4.0	3.8
Benzophenone	7.5	4.7	4.0	Molecular oxygen:			
Fluorenone	12.7	4.0	3.5	Oxygen O_2 ($T_0 \rightarrow S_1$) ^c	0.38	2.6	11.1

^a Calculations on the radical cation of biacetyl did not converge.

^b Bound radical anion states of small amines are an artifact of the semi-empirical calculation.

^c The O_2 calculations were performed at the MP2 and UMP2 level with the 6-311G** basis set.

tion energies ranging from nearly zero to more than 1 eV were investigated. The same donor, biacetyl encapsulated in a hemicarcerand cage, was employed in all cases. It was found that quenchers with nearly identical triplet energies can lead to transfer rates differing by almost three-orders of magnitude as a result of large differences in their internal reorganization energies (Figure 6). It was concluded that a meaningful ΔG° dependence can be obtained only if the acceptors are separated into groups with similar internal reorganization energies: (a) Rigid aromatics with small geometry changes and modest internal reorganization energies (Figure 5); (b) Olefins exhibiting a large-amplitude internal relaxation and correspondingly large reorganization energies. The olefins provide an interesting example, which shows that the terms “internal” and “high-frequency” reorganization energy are not always synonymous. Not surprisingly, the major fraction of reorganization energy in an olefin is associated with the twisting of the formally double bond. However, the olefin twisting motion on the product side usually corresponds to vibrational frequencies lower than kT and, therefore, contributes to the low-frequency λ_s , rather than the high-frequency λ_v [47, 56, 57]. The study also demonstrated that molecular oxygen, with its negligibly small internal reorganization energy, is a

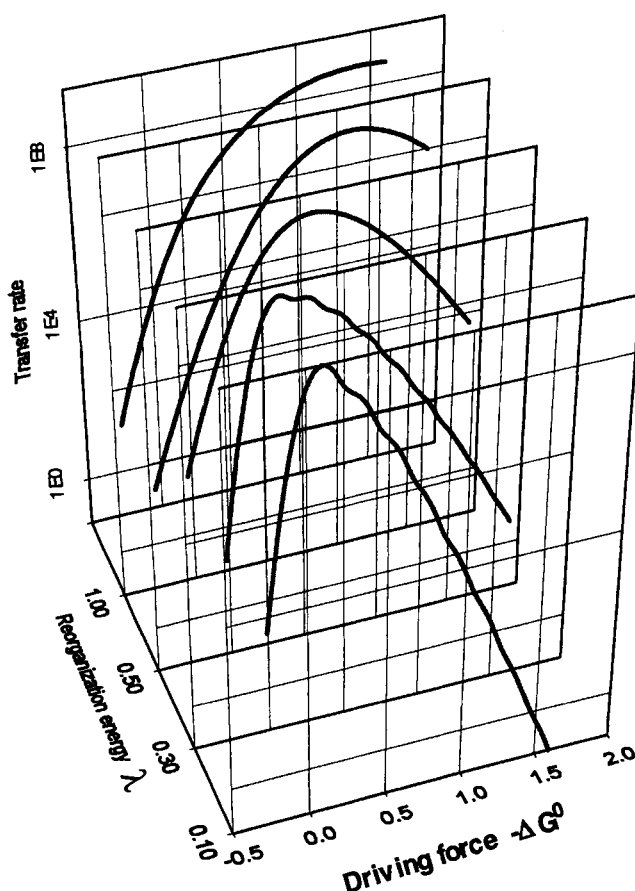


Figure 6. The driving-force (in eV) dependence of non-radiative transfer rates (in arbitrary units) predicted by the Marcus–Jortner equation for total reorganization energies of 0.1, 0.3, 0.5, 1.0, and 1.5 eV. Various ratios of λ_s and λ_v were used for the individual traces.

unique triplet energy acceptor, excelling at quenching low-energy triplets; however, because of very unfavorable Franck–Condon factors, it is not particularly efficient in quenching high-energy triplets with small reorganization energies [58].

6.4 Summary

Almost exactly 50 years ago, James Franck remarked: “Migration of excitation energy between molecules or inside a molecule from one of its groups to another is observed under many different conditions. The transferred excitation energy may be used just as the directly absorbed light energy for the promotion of chemical process, or it may be dissipated into heat. The most remarkable facts are that the excitation energy under suitable conditions can be transferred with a high yield over

distances of $\sim 50\text{--}100\text{ \AA}$ and that molecules or molecular groups which do not possess the quality to fluoresce still are able to transfer their excitation energy to energy acceptors which may not be in contact with them. There is no doubt that every example of transfer of electronic excitation energy observed so far can be understood either by an electron migration, or by exciton migration, or by the process of sensitized fluorescence, but in many cases uncertainty exists as to whether one of these three processes is solely responsible for a particular phenomenon and, if so, which one it is . . . Especially, interpretations of energy transfer by and in substances of biological importance are often based on doubtful hypotheses.” [59].

It is rather noteworthy that Franck wrote the above paragraph well before the seminal contributions of Dexter [22], Terenin, and Ermolaev [8], or Marcus [46a], Jortner [46b], Miller [13], and Closs [13b]. Most impressively, essentially all of his comments were proven correct. While we have certainly advanced beyond “doubtful hypotheses”, electronic excitation transfer in biological systems continues to be the most fascinating and challenging problem. The recent X-ray determination of the intriguing structures of the LH1 and LH2 antenna complex [60] brought a new wave of interest among theorists [61] and experimentalists [62], similar to that which followed the solution of the bacterial photoreaction center some time ago [63]. The spectroscopic behavior of the antenna arrays could not be explained in terms of the standard Förster theory and led to the development of the distributed transition dipole approach [61], which is likely to be helpful in the treatment of other complex nonbiological multichromophoric systems. Charge and excitation transfer processes mediated by non-carbon based bridges are only beginning to receive well-deserved attention, with the few available results seemingly challenging the common intuition [64]. There is also a renewed interest in charge- and energy-transfer processes in strongly coupled adiabatic systems (mixed-valence compounds and J-aggregates). Strongly coupled multichromophoric systems in which the distinction between charge and energy transfer becomes arbitrary will be particularly interesting. Among the little explored mechanisms of donor–acceptor coupling, the spin–orbit interaction, which is often viewed only as a wasteful sink accelerating the non-radiative decay to the ground state, should be studied in more detail. Indeed, artificially enhanced spin–orbit coupling has been used recently in the development of organic light emitting diodes (LEDs) with record efficiencies, nearly reaching the theoretical limit [65]. Among the more exotic applications of electronic excitation transfer one could envision the use of a sequence of weakly endoergic singlet energy transfers to increase the efficacy of laser cooling processes [66].

Acknowledgments

The research at Rutgers University is supported by a core grant from the Office of Basic Energy Sciences of the U.S. Department of Energy. Support of graduate students through a National Science Foundation Research Training Grant is acknowledged. The author thanks all friends and collaborators who have made some of the described research possible. Finally, the Faculty of Engineering of the Tokyo

Metropolitan University is thanked for generously sponsoring a visit during which the final stage of editing this section of the handbook took place.

References

1. (a) E. Fermi, *Nuclear Physics*, University of Chicago Press, Chicago, **1950**, p. 142; (b) E. Fermi, *Notes on Quantum Mechanics*, University of Chicago Press, Chicago, **1954**.
2. J. Franck, *Trans. Faraday Soc.* **1925**, *21*, 536; E. U. Condon, *Phys. Rev.* **1928**, *32*, 858.
3. H. A. Kramers, *Physica* **1934**, *1*, 182.
4. N. S. Hush, J. Ulstrup, in *Electron and Ion Transfer in Condensed Media*, A. A. Kornyshev, M. Tosi and J. Ulstrup (eds), World Scientific, Singapore, **1997**, p. 1.
5. (a) G. Wentzel, *Z. Phys.* **1926**, *38*, 518; (b) H. A. Kramers, *Z. Phys.* **1926**, *39*, 828; (c) L. Brillouin, *J. Physique* **1926**, *7*, 353.
6. J. Perrin, *Compt. r. Acad. Sci. Paris* **1927**, *184*, 1097.
7. H. Kallmann, F. London, *Z. Phys. Chem. (B)* **1928**, *2*, 207.
8. A. Terenin, V. L. Ermolaev, *Trans. Faraday. Soc.* **1956**, *52*, 1042.
9. (a) S. A. Latt, H. T. Cheung, E. R. Blout, *J. Am. Chem. Soc.* **1965**, *87*, 995; (b) R. A. Keller, L. J. Dolby, *J. Am. Chem. Soc.* **1969**, *91*, 1293.
10. L. Stryer, R. P. Haugland, *Proc. Natl. Acad. Sci.* **1967**, *58*, 720.
11. W. Amrein, K. Schaffner, *Helv. Chim. Acta* **1975**, *58*, 397.
12. R. A. Keller, *J. Am. Chem. Soc.* **1968**, *90*, 1940.
13. (a) J. R. Miller, J. V. Beitz, R. K. Huddleston, *J. Am. Chem. Soc.* **1984**, *106*, 5057; (b) J. R. Miller, L. T. Calcaterra, G. L. Closs, *J. Am. Chem. Soc.* **1984**, *106*, 3047.
14. (a) J. Franck, *Z. Phys.* **1922**, *9*, 859; (b) G. Cario, *Z. Physik* **1922**, *10*; (c) G. Cario, J. Franck, *Z. Physik* **1923**, *11*, 161; (d) G. Cario, J. Franck, *Z. Physik* **1923**, *17*, 202.
15. T. Förster, *Ann. Phys.* **1948**, *6*, 55.
16. G. L. Levinson, W. T. Simpson, W. Curtis, *J. Am. Chem. Soc.* **1957**, *79*, 4314.
17. E. G. McRae, M. Kasha, *J. Chem. Phys.* **1958**, *28*, 721; M. Kasha, *Rev. Mod. Phys.* **1959**, *31*, 162.
18. (a) W. T. Simpson, D. L. Petersen, *J. Chem. Phys.* **1957**, *26*, 588; (b) G. J. Hoijtink, *Z. Elektrochem.* **1960**, *64*, 156.
19. V. L. Levshin, *Z. Phys.* **1931**, *72*, 368.
20. E. J. Bowen, R. Livingston, *J. Am. Chem. Soc.* **1954**, *76*, 6300.
21. The terms "molecular wire" and "photonic wire" are used increasingly frequently and at times arbitrarily in the literature for describing electron and excitation transfer in bridged systems. Therefore, it is useful to juxtapose the very weak distance dependence of the conductivity of a metallic wire with the steep fall-off of most excitation and charge-transfer processes.
22. D. L. Dexter, *J. Chem. Phys.* **1953**, *21*, 836.
23. H. Oevering, J. W. Verhoeven, M. N. Paddon-Row, E. Cotsaris, N. S. Hush, *Chem. Phys. Lett.* **1988**, *143*, 488.
24. G. D. Scholes, K. P. Ghiggino, *J. Phys. Chem.* **1994**, *98*, 4580.
25. M. D. Newton, *Chem. Rev.* **1991**, *91*, 767 and references therein, also the first chapter of this part of the handbook (i.e., Volume I, Part 1, Chapter 1).
26. N. A. van Dantzig, D. H. Levy, C. Vigo, P. Piotrowiak, *J. Chem. Phys.* **1995**, *103*, 4894.
27. W. T. Yip, D. H. Levy, R. Kobetic, P. Piotrowiak, *J. Phys. Chem. A* **1999**, *103*, 10.
28. (a) A. H. Maki, J. G. Weers, E. F. Hilinski, S. V. Milton, P. M. Rentzepis, *J. Chem. Phys.* **1984**, *80*, 2288; (b) Y. Zeng, M. B. Zimmt, *J. Am. Chem. Soc.* **1991**, *113*, 5107; (c) A. M. Oliver, M. N. Paddon-Row, J. Kroon, J. W. Verhoeven, *Chem. Phys. Lett.* **1992**, *191*, 371; (d) L. D. Cola, V. Balzani, F. Barigelli, L. Flamigni, P. Belser, S. Bernhard, *Recl. Trav. Chim. Pays-Bas* **1995**, *114*, 534.
29. (a) G. D. Scholes, K. P. Ghiggino, A. M. Oliver, M. N. Paddon-Row, *J. Phys. Chem.* **1993**, *97*, 11871; (b) G. D. Scholes, *J. Phys. Chem.* **1996**, *100*, 18731; (c) E. K. L. Yeow, D. J. Haines, K. P. Ghiggino, A. M. Oliver, M. N. Paddon-Row, *J. Phys. Chem. A* **1999**, *103*, 6517.
30. H. M. McConnell, *J. Chem. Phys.* **1961**, *35*, 508.

31. (a) K. Kilså, J. Kajanus, J. Mårtensson, B. Albinsson, *J. Phys. Chem. B* **1999**, *104*, 7329; (b) K. K. Jensen, S. B. van Berlekom, J. Kajanus, J. Mårtensson, B. Albinsson, *J. Phys. Chem. A* **1997**, *101*, 2218.
32. (a) R. K. Naqvi, C. Steel, *Chem. Phys. Lett.* **1970**, *6*, 29; (b) P. S. Engel, L. D. Fogel, C. Steel, *J. Am. Chem. Soc.* **1974**, *96*, 327.
33. (a) V. May, O. Kühn, *Charge and Energy Transfer Dynamics in Molecular Systems*, Wiley-VCH, Weinheim, **2000**; (b) J. M. Jean, R. A. Friesner, G. R. Fleming, *J. Chem. Phys.* **1992**, *96*, 5827; (c) A. G. Redfield, *Adv. Mag. Res.* **1965**, *1*, 1.
34. It is worth noting that while Dexter's name became synonymous with the exchange mechanism of energy transfer, the main body of his seminal paper is devoted to spin-allowed EET mediated by the various multipole terms of the Coulomb interaction.
35. (a) R. W. Brandon, R. E. Gerkin, C. A. Hutchison, Jr. *J. Chem. Phys.* **1962**, *37*, 477; (b) G. C. Nieman, G. W. Robinson, *J. Chem. Phys.* **1962**, *37*, 2150.
36. G. L. Closs, M. D. Johnson, J. R. Miller, P. Piotrowiak, *J. Am. Chem. Soc.* **1989**, *111*, 3751.
37. For earlier qualitative comparisons of charge and excitation transfer in individual donor-acceptor systems, see H. E. Zimmerman, R. D. McKelvey, *J. Am. Chem. Soc.* **1971**, *93*, 3638 and A. L. Shain, *J. Chem. Phys.* **1972**, *56*, 6201.
38. G. L. Closs, L. T. Calcaterra, N. J. Green, K. W. Penfield, J. R. Miller, *J. Phys. Chem.* **1986**, *90*, 3673.
39. G. L. Closs, M. D. Johnson, J. R. Miller, N. J. Green, *J. Phys. Chem.* **1989**, *93*, 1173.
40. Pulse radiolysis in chlorinated solvents leads to the formation of radical cations of almost all organic compounds including aryls. In most non-halogenated solvents, pulse radiolysis results in the formation of solvated electrons and radical anions of the solute. Therefore, depending on the selected solvent, the same donor-acceptor system could be used for the electron and hole transfer studies.
41. P. Piotrowiak, Ph. D. Dissertation, University of Chicago, **1988**.
42. G. L. Closs, P. Piotrowiak, J. R. Miller, in *Photochemical Energy Conversion*, J. R. Norris, D. Meisel (eds), Elsevier, Amsterdam, **1989**, p. 23.
43. G. L. Closs, P. Piotrowiak, J. M. McInnis, G. R. Fleming, *J. Am. Chem. Soc.* **1988**, *110*, 2652.
44. N. Koga, K. Sameshima, K. Morokuma, *J. Phys. Chem.* **1993**, *97*, 13117.
45. The large spin-orbit coupling in chromophores bearing heavy atoms introduces mixing of states with different spin multiplicities. As a result, the spin of the donor and the acceptor can become ill-defined on the timescale of excitation transfer. In these cases, the sharp distinction between exchange-mediated triplet transfer versus Coulomb-mediated singlet transfer is no longer meaningful. This is of particular concern in transition metal complexes. For example, the formal triplet charge-transfer state of Os^{II} complexes has a considerable singlet character. Therefore, the conclusions regarding triplet and electron-transfer rates drawn in R. E. Holmlin, R. T. Tong, J. K. Barton, *J. Am. Chem. Soc.* **1998**, *120*, 9724 are most likely incorrect.
46. (a) R. A. Marcus, *J. Chem. Phys.* **1956**, *24*, 966; (b) J. Jortner, *J. Chem. Phys.* **1976**, *64*, 4860.
47. M. E. Sigman, G. L. Closs, *J. Phys. Chem.* **1991**, *95*, 5012.
48. D. B. MacQueen, J. R. Eyler, K. S. Schanze, *J. Am. Chem. Soc.* **1992**, *114*, 1897.
49. Z. Murtaza, D. K. Graff, A. P. Zipp, L. A. Worl, W. E. Jones, W. D. Bates, T. J. Meyer, *J. Phys. Chem.* **1994**, *98*, 10504.
50. A. Farrán, K. Deshayes, *J. Phys. Chem.* **1996**, *100*, 3305.
51. J. Parola, F. A. Pina, E. Ferreira, M. Maestri, V. Balzani, V. J. *J. Am. Chem. Soc.* **1996**, *118*, 11610.
52. I. Place, A. Farran, K. Deshayes, P. Piotrowiak, *J. Am. Chem. Soc.* **1998**, *120*, 12626.
53. Experimental values of triplet reorganization energies are, in general, difficult to obtain. The Franck-Condon triplet energies are most often derived from the extremely weak $T_1 \leftarrow S_0$ absorption induced either by a solvent containing heavy atoms or by complexation with O₂. Values obtained for molecules with $T_1 \leftarrow S_0$ spectra without a clearly defined 0-0 peak carry a large margin of error. The energies of the fully relaxed triplet states of olefins are usually obtained either from equilibria measured with species whose triplet energies are well established, or by photoacoustic experiments. These approaches tend to be less reliable than simple phosphorescence measurements, especially in the case of short-lived triplets. Some values can

- be found in: (a) A. A. Gorman, I. R. Gould, I. Hamblett, *J. Am. Chem. Soc.* **1981**, *103*, 4553; (b) A. A. Gorman, I. Hamblett, R. J. Harrison, *J. Am. Chem. Soc.* **1984**, *106*, 6952; (c) R. A. Caldwell, J. L. Goodman, K. S. Peters, H. Misawa, *J. Am. Chem. Soc.* **1986**, *108*, 6803; (d) R. A. Caldwell, N. Tuqiang, L. A. Melton, *J. Am. Chem. Soc.* **1989**, *111*, 457; (e) R. A. Caldwell, A. D. Strickland, *J. Phys. Chem.* **1993**, *97*, 13394.
54. V. Balzani, F. Bolletta, F. Scandola, *J. Am. Chem. Soc.* **1980**, *102*, 2105.
55. The early discussion of the role of nuclear reorganization in energy transfer, especially among classical photochemists, centered on the concept of "nonvertical excitation transfer". While many of the conclusions fully agree with the spirit of the Marcus–Jortner approach, the term itself is rather unfortunate as it suggests that the process may be violating the Franck–Condon principle and the Born–Oppenheimer approximation.
56. A similar situation occurs when biphenyl is used as triplet acceptor, see D. Zhang, G. L. Closs, D. D. Chung, J. R. Norris, *J. Am. Chem. Soc.* **1993**, *115*, 3670.
57. Where there is a significant change in the frequency of the relevant mode (or modes) upon crossing from the reactant to the product side, but the mode remains strongly quantized, the Franck–Condon factors can be obtained with the more general expression given by W. Siebrand, *J. Phys. Chem.* **1967**, *46*, 440. This still corresponds to a single-mode approximation, but with the final frequency ν_F being different from the initial one, ν_I . The summation over all vibrational levels n of the final state coupled to the lowest vibrational level of the initial state yields

$$k = \left(\frac{4\pi}{h\lambda_s k_B T} \right)^{1/2} \cdot |V|^2 \cdot \sum_0^{\infty} \left[\frac{(1-\xi)^{1/2} e^{-(1/4)\gamma\xi^n |H_n(x)|^2}}{n!} \right] \cdot e^{-(\lambda_s + \Delta G^\circ + n h \nu_F)^2 / (4\lambda_s k_B T)}$$

where ξ and γ are the distortion and displacement parameters defined respectively as

$$\xi = \frac{(\nu_I - \nu_F)}{(\nu_I + \nu_F)} \quad \text{and} \quad \gamma = \sqrt{k_I k_F} \cdot \frac{(q_I - q_F)^2}{h(\nu_I + \nu_F)}$$

where k_I and k_F are the force constants on the reactant and product side of the barrier, and q_I and q_F are the respective equilibrium positions. The variable x in the Hermite polynomial H_n is defined as

$$x = \sqrt{\frac{\gamma(1-\xi)}{2\xi}}$$

All the necessary excited-state parameters (frequencies, force constants, and equilibrium geometries) can be obtained from MO calculations or, in a few cases, from excited-state Raman measurements. The above rate expression, like the standard Marcus–Jortner equation, can be readily modified to include more than one vibrational mode. The difference between the two approximations should be most pronounced when $h|\nu_I - \nu_F| > k_B T$ and $h|\nu_I - \nu_F| > \lambda_s$. The second condition is more likely to be satisfied for electronic excitation transfer than for charge transfer.

58. The poor Franck–Condon factors for highly exoergic triplet energy transfer to molecular oxygen were first pointed out by L. K. Patterson, G. Porter, M. R. Topp, *Chem. Phys. Lett.* **1970**, *7*, 612.
59. J. Franck, R. Livingston, *Rev. Mod. Phys.* **1949**, *21*, 505.
60. (a) G. McDermott, S. M. Prince, A. A. Freer, A. M. Hawthornthwaite-Lawless, M. Z. Papiz, R. J. Cogdell, N. W. Isaacs, *Nature* **1995**, *374*, 517; (b) J. Koepke, X. Hu, C. Muenke, K. Schulten, H. Michel, *Structure* **1996**, *4*, 581.
61. (a) H. Sumi, *J. Phys. Chem. B* **1999**, *103*, 252; (b) K. Mukai, S. Abe, H. Sumi, *J. Phys. Chem. B* **1999**, *103*, 6096.

62. (a) R. Jimenez, S. N. Dikshit, S. Bradforth, G. R. Fleming, *J. Phys. Chem.* **1996**, *100*, 6825; (b) H. M. Wu, M. Ratsep, R. Jankowiak, R. J. Cogdell, G. J. Small, *J. Phys. Chem. B* **1997**, *101*, 7641; (c) C. De Caro, R. W. Visschers, R. van Grondelle, S. Völker, *J. Phys. Chem.* **1994**, *98*, 10584.
63. J. Deisenhofer, O. Epp, K. Miki, R. Huber, H. Michel, *Nature* **1985**, *318*, 618.
64. (a) A. Zehnacker, F. Lahmani, C.A. van Walree, L. W. Jenneskens, *J. Phys. Chem. A* **2000**, *104*, 1377; (b) C. A. van Walree, M. R. Roest, W. Schuddeboom, L. W. Jenneskens, J. W. Verhoeven, J. M. Warman, H. Kooijman, A. L. Spek, *J. Am. Chem. Soc.* **1996**, *118*, 8395.
65. (a) G. Gu, G. Parthasarathy, S. R. Forrest, *Appl. Phys. Lett.* **1999**, *74*, 305; (b) D. F. O'Brien, M. A. Baldo, M. E. Thompson, S. R. Forrest, *Appl. Phys. Lett.* **1999**, *74*, 442.
66. J. L. Clark, P. F. Miller, G. Rumbles, *J. Phys. Chem. A* **1998**, *102*, 4428.

7 Charge-Transfer Excited States of Transition Metal Complexes

John F. Endicott

7.1 Definitions and General Concepts

Charge transfer (CT) excited states are generated by the absorption of energy, usually light energy, by a molecular or supramolecular system. The distribution of electron density of these species differs from that of the ground state. The change in the charge distribution can be associated with specific atoms, or groups of atoms, and this association is the basis for classification and interpretation of the spectra and for detailed mechanistic discussions. The identification of specific groups of atoms with this charge redistribution does lead to useful simplifications in the discussion of CT spectroscopy and CT excited-state properties. The discussion of observations on specific systems later in this chapter will begin with ion-pair systems in which this concept is relatively well defined and then progress to the discussion of systems in which the simplified picture is less and less appropriate. A number of general theoretical concepts need to be mentioned and terms need to be defined before the observations are dealt with.

7.1.1 Basic Concepts

Only condensed-phase systems will be considered in this chapter. General systematic approaches to the spectroscopy and properties of CT excited states were described in detail by Mulliken [1]. Approaches to the CT spectroscopy of transition metal complexes were developed by Jørgensen [2]. Lever developed these approaches further and summarized their application to a range of transition metal complexes [3]; Solomon and Hanson [4] considered their application to metalloenzymes and model systems. Endicott [5], Hovarth and Stevenson [6], and Ferraudi [7] discussed the photochemistry and photophysics of transition metal CT systems, including the applications of the various theoretical models. These works may be consulted for

more detail than is possible here and for somewhat different perspectives than those presented here.

It is useful to first consider a system $\{D^-, A\}$, composed of a well-defined electron donor, D^- , and a well-defined electron acceptor, A . This idealized system will exhibit a simple absorption band corresponding to the process described in Eq. 1:



Here, the asterisk designates an electronically and vibrationally excited system. The CT excited state so generated, the Franck–Condon (FC) excited state, will have the same nuclear coordinates as the ground state. The nuclei in the FC state will not generally be at equilibrium with the new charge distribution. Nuclear relaxation (bond length and bond angle changes, solvent reorganization, etc.) of the FC state may generate a vibrationally equilibrated excited state (VEqES). The difference in the energy of the FC and VEqES, λ_{vib} , will appear as heat deposited in a condensed phase environment. Figure 1 qualitatively illustrates these energy relationships. The rate at which vibrational energy in the electronically excited system is converted into heat in the solvent medium appears to vary with the size of the molecular vibrational quanta and with the coupling of the vibrational motion to the solvent vibrational modes. Since many of the physical and chemical processes characteristic of CT excited states occur in very short time regimes (process lifetimes of ps or shorter), the rate of vibrational cooling can be an important factor in the discrimination between potential relaxation channels.

The simplest assumption about excited-state physical and chemical behavior is that all processes are sequential: relaxation within the excited-state potential-energy (PE) manifold to the lowest energy vibrational level of the electronic excited state (the VEqES), then a reaction to form products or crossing to lower-energy potential-energy surfaces (e.g., the ground state in Figure 1). The excited states that conform to this limit can be treated as normal chemical species, species that are at equilibrium with their environment in all but the electronic coordinates. In general, one expects some relaxation of interelectronic repulsion, ΔE_{el} , to accompany the FC to VEqES relaxation process, so that Eq. 2,

$$h\nu_{\text{max}} = E^{00} + \lambda_{\text{vib}} + \Delta E_{\text{el}} \quad (2)$$

gives the energy of the absorption maximum.

7.1.2 The Idealized Limit of Weak D/A Electronic Coupling (LWEC)

While the energy and free energy must be the same for the vertical transition, $h\nu_{\text{max}}$, the subsequent vibrational relaxation of the excited state to the VEqES may result in significant changes of solvation in a $\{D^-, A\}/\{D, A^-\}$ system. This will result in differences of the energy, E^{00} , and free energy, ΔG^{00} , of the VEqES. In the limit of very little D/A coupling that is considered here, and for the free-energy interpretation of the transition energy ($h\nu_{\text{max}} = \Delta G^{00} + \chi_{\text{vib}}^{\text{op}} + \Delta G_{\text{el}}$),

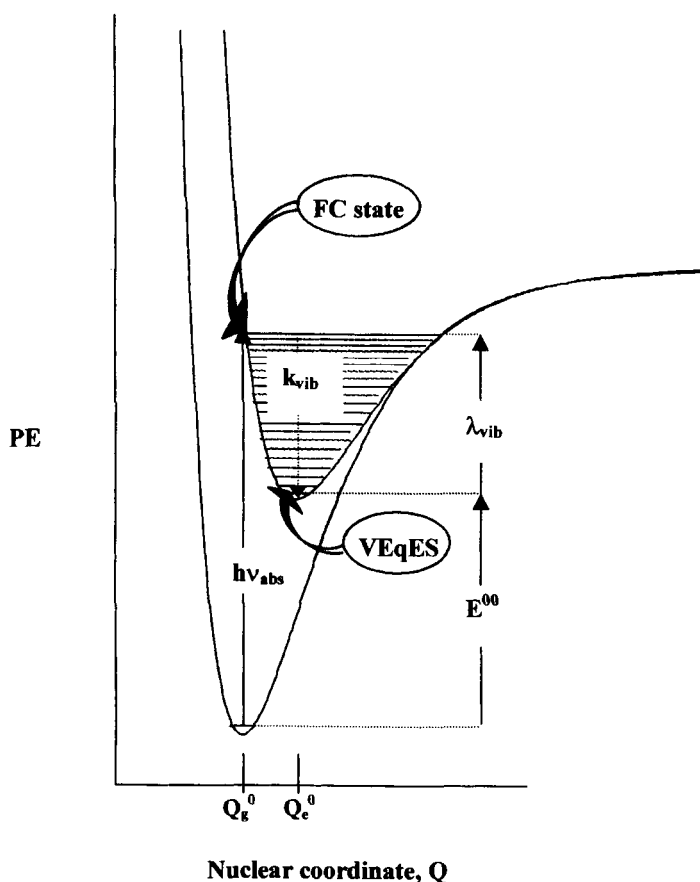
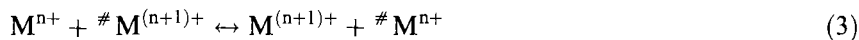


Figure 1. Qualitative illustration of the energy relationships in an idealized two-state system.

$\Delta G^{00} \cong -F[E^\circ(A/A^-) - E^\circ(D/D^-)]$, and $\Delta G_{el} = \Delta E_{el} \sim 0$; F is Faraday's constant and $E^\circ(X/X^-)$ is the standard electrode potential for the X/X^- redox couple. In this limit, the vibrational-free energy difference between the nuclear coordinates of the excited-state free energy minimum and those of the ground-state free energy minimum, χ_{vib}^{op} , has the same meaning as the reorganizational energy for the thermally activated electron-transfer reaction, χ_r^{th} : $\chi_{vib}^{op} \cong \chi_r^{th}$. Values of χ_r^{th} can be obtained as the average of the reorganization energies, χ_{exch}^{th} , for the thermally activated, self-exchange electron-transfer reactions (Eq. 3) of the donor and acceptor redox couples



(M^{x+} and $\# M^{y+}$ differ only in oxidation state and, possibly, in isotopic composition). Since the electrode potentials and the thermally activated self-exchange

electron-transfer rates are, in principle, independently measurable, this limit provides a very useful point of departure for the discussion of the charge-transfer excited states of transition metal complexes.

7.2 Charge-Transfer Absorption Spectroscopy

The characteristics of the absorption of light by matter can be used to obtain a great deal of information about the structure and properties of that matter. For the molecular substrates considered here, the observable features of the absorption process and the correlated molecular properties can be summarized as follows:

- a) The energy of the absorption maximum ($h\nu_{\max}$) is correlated with the energy difference of the two electronic configurations and the differences of molecular geometry of the vibrationally equilibrated electronic excited and ground states.
- b) The oscillator strength (or integrated intensity; proportional to $\epsilon_{\max}\Delta\nu_{1/2}$) correlates with the square of the electronic matrix element (H_{ge}), or the symmetry selection rules for the absorption.
- c) The full width at half maximum ($\Delta\nu_{1/2}$) correlates with the differences in geometry of the ground and excited state.
- d) The asymmetry (or skewness) of the absorption band can be related to vibronic progressions that result from the excited-state distortion.

If there is configurational mixing between two electronic states, the ground-state (G) wave function is given to first order by Eq. 4, the excited state (E) wave function by Eq. 5.

$$\Psi_G = (\Psi_G^0 + \alpha_{GE}\Psi_E^0)/(1 + \alpha_{GE}^2)^{1/2} \quad (4)$$

$$\Psi_E = (\Psi_E^0 - \alpha_{EG}\Psi_G^0)/(1 + \alpha_{EG}^2)^{1/2} \quad (5)$$

In these equations, $\alpha_{GE} = H_{GE}/E_{GE}^0$ is the mixing coefficient and Ψ_1^0 is the initial- or diabatic-state wave function [1]. For a well-defined charge-transfer transition, α_{GE}^2 and α_{EG}^2 are both much less than one and approximately equal. In real systems, α_{IJ}^2 can span a range of values from about zero (for the LWEC in Section 7.1.2) to about one (for highly delocalized systems). To the degree that the mixing coefficients differ from zero, factors other than those discussed in Section 7.1.2 will contribute to the transition energy.

7.2.1 The Energies of Charge-Transfer Absorptions

Equations 4 and 5 provide a simple basis for defining the energy differences between two electronic states. Thus, the dominant contribution to $h\nu_{\max}$ in solution should

be the difference in the vertical ionization energies of the vibrationally equilibrated states G and E , $IE_s^v(G)$, and $IE_s^v(E)$. In addition, state E must be generated with the nuclear coordinates of the ground state, and this leads to a correction corresponding to the differences in vibrational (including solvational) energies. This is denoted by λ_{vib} in Figure 1. Finally, there will be some electronic relaxation, ΔE_{el} , associated with the changes of nuclear coordinates in the excited state. This leads to Eq. 6 [1, 8–10],

$$h\nu_{\text{max}} = IE_s^v(G) + EA_s^v(E) + \lambda_{\text{vib}} + \Delta E_{\text{el}} \quad (6)$$

where $-IE_s^v(E) = EA_s^v(E)$. Since α_{GE} is small, and since Ψ_G^2 and Ψ_E^2 are proportional to charge densities of electrons at the different atomic or molecular subunits involved in charge-transfer transitions, $IE_s^v(D)$ and $EA_s^v(A)$ are often substituted for the first two terms in Eq. 6. These quantities are well defined only in the diabatic limit ($\alpha_{GE} = 0$). When the donor and acceptor moieties can be investigated separately, as is often the case for coordination complex systems, it is then convenient to define $IE_s^v(D)$ and $EA_s^v(A)$ in terms of these moieties and to introduce an additional term, C_{DA} , into Eq. 6 to account for the alteration of their values as a result of the covalent linkage. Gorelsky et al. [10] have tabulated values of IE_s^v for a number of transition metal complexes; however, these quantities are not generally available or readily determined.

Experimental Charge-Transfer absorption-energy correlations useful for transition metal complexes

Variations on Eq. 6 substitute “optical electronegativities”, $\chi_{\text{el}}(X)$ [2, 3, 5], or solution electrode potentials [3, 10–12] for $[IE_s^v(D) - EA_s^v(A)]$. Both approaches have been used extensively. The optical electronegativity approach has considerable appeal, since it makes use of common chemical concepts. However, the correlation of $h\nu_{\text{max}}$ with $[\chi_{\text{el}}(M) - \chi_{\text{el}}(X)]$ (for a metal center M and a ligand center X) is empirical and requires a large number of correction terms in order to apply to a variety of complexes [13]. Moreover, this approach involves orbital-based parameters, and that presumes that it is possible to identify an explicit donor orbital and an explicit acceptor orbital. This is often not straightforward, as is discussed below. Nevertheless, this approach can be a useful basis for interpreting spectra and values of $\chi_{\text{el}}(M)$ and $\chi_{\text{el}}(X)$ have been published [2, 3, 5]. The use of electrode potentials as a substitute for vertical, solution ionization energies leads to straightforward empirical correlations with $h\nu_{\text{max}}$. Such correlations employ independently measured parameters and do not require the explicit identification of the donor and acceptor orbitals, but they do introduce free-energy quantities into an energy correlation. Since the optical transitions are vertical, with the change of electronic state induced without a change of nuclear coordinates, the energy changes (Section 7.1.2) are equal to the free-energy changes for this process [14]. Assume, for $\{D^-, A\} \rightarrow \{D, A^-\}$ that $h\nu = E^{00} + \lambda_{\text{vib}} + (\text{other terms})$, as in Figure 1. Then the energy of the absorption maximum of the CT transition may be represented as in Eq. 7,

$$h\nu_{\text{max}}(DA) = F[E^\circ(A/A^-) - E^\circ(D/D^-)]_{\text{LWEC}} + \frac{1}{2}(\chi_r^D + \chi_r^A) + \gamma_{DA} \quad (7)$$

where the terms on the right-hand side are all free-energy terms (defined in Section 7.1.2; see also [15–18]) and experimentally determined for the individual A/A[−] and D/D[−] couples. The reorganizational free energies for the bimolecular M/M[−] self-exchange reactions (see Eq. 3) are represented as χ_r^M in Eq. 7 for conciseness (rather than as $\chi_{\text{exch}}^{\text{th}}$ used in Section 7.1.2; also note that $\chi_r^M = 4\Delta G^\ddagger(\text{M/M})$ [19, 20]). The deviations from the limit of weak D/A electronic coupling that arise from covalently linking the donor and acceptor are represented by γ_{DA} . The contributions to γ_{DA} can arise from charge delocalization, direct D/A covalent contributions (e. g., as in metal–metal bonding), differences in the solvation energy contributions, etc. It is useful to view γ_{DA} as a measure of the differences between the diabatic (separate fragments; no interaction between D and A) and the adiabatic (allowing for interactions between D and A) contributions to these terms. In the limit that $|\Delta G^\circ| < \chi_r$ and $|H_{\text{DA}}| < (\chi_r + \Delta G^\circ)/2$ (for χ_r and ΔG° being the respective diabatic parameters) Brunschwig and Sutin [21] have evaluated γ_{DA} for a two-state model as in Eq. 8:

$$\gamma_{\text{DA}} \cong 2H_{\text{DA}}^2 \Delta G^\circ / (\chi_r + \Delta G^\circ)^2 + 2H_{\text{DA}}^4 \Delta G^\circ (3\chi_r - \Delta G^\circ) / (\chi_r + \Delta G^\circ)^5 \quad (8)$$

Of course, this corresponds to an adiabatic potential-energy surface with two potential-energy minima separated by a well-defined barrier. Note that γ_{DA} contains anharmonicities induced into χ_r^M by D/A interactions as well as energy corrections that originate from D/A coupling. To some extent (i.e., as in first-order perturbation theory or in a Taylor's series expansion around the diabatic values of χ_r^M and ΔG°), γ_{DA} may be linearized so that $\gamma_{\text{DA}} \cong \sum_M^{D,A} [(\gamma_\chi^M(\chi_r^M) + \gamma_G^M(\Delta G^\circ))]$, $\chi_\rho^M \cong (\chi_r^M + \gamma_\chi^M)$ and $E_{1/2}^a \cong [E^\circ(\text{M/M}^-) + \gamma_G^M]$. Then Eq. 9 is an experimentally useful expression, in which the potentials for the donor and acceptor centers in the actual molecule of interest have been substituted for the standard potentials of the separate, non-interacting D and A fragments:

$$h\nu_{\text{DA}} = F[E_a^\circ(\text{A/A}^-) - E_a^\circ(\text{D/D}^-)] + \frac{1}{2}(\chi_\rho^{\text{D}} + \chi_\rho^{\text{A}}) + \dots \quad (9)$$

Additional contributions to $h\nu_{\text{max}}$ can arise from configurational mixing and from the differences in the species involved in the optical and electrochemical processes. However, the mixing between the ground and CT-excited states, described in Eqs. 4 and 5, results in smaller differences between the ground-state and excited-state nuclear coordinates; this cancels (in the harmonic-oscillator limit) the effect of the increase of their energy difference in coordinates of the unmixed (or diabatic) states. These issues will be discussed further within the context of MLCT excited states. The actual values of χ_ρ^M to be used in Eq. 9 are not generally available from an independent experimental measurement. If the contributions of γ_{DA} were small, the appropriate values of χ_ρ^M will be very similar to those of χ_r^M . In a series of closely related complexes, the variations of χ_ρ^M might be based on: a) The measured values of χ_r^M , adjusted to give the best empirical fit within the series; b) An appropriate theoretical model to estimate the γ_{DA}^M correction terms; or c) The difference

between the observed absorption maxima and $F[\Delta E_a^\circ(\text{A}/\text{A}^-) - \Delta E_a^\circ(\text{D}/\text{D}^-)]$. Examples are developed in the sections below.

Orbital based energy arguments

In the simplest case, a singlet–singlet CT transition, the electronic transition energy can be related to the energy differences, $\Delta\epsilon(\psi)$, between the molecular orbitals occupied in the ground state (HOMO – n) and in the excited state (LUMO + n). When the significant contributions are only from the highest occupied ($n = 0$) and lowest unoccupied ($n = 0$) molecular orbitals, then Eq. 10 results [9],

$$\Delta E(\psi) = \epsilon_{\text{LUMO}} - \epsilon_{\text{HOMO}} - J_{\text{HL}} + 2K_{\text{HL}} \quad (10)$$

where ϵ_{LUMO} and ϵ_{HOMO} are the LUMO and HOMO orbital energies and J_{HL} is the Coulomb integral and K_{HL} is the exchange integral. All the components of Eq. 10 must be calculated from a molecular-orbital model. The close energies and number of the diabatic states, the large number of valence shell electrons, and so forth for transition metal systems makes accurate calculations difficult and time-consuming. Simple one-electron approaches to orbital energies are sometimes used, but these need to be corrected for the interactions between electrons to be useful [9].

7.2.2 Charge-Transfer Excited-State Terms and Assignments

The electronic symmetry of the excited state is determined by the symmetries of partly occupied molecular orbitals. Since configurational mixing is most important between states of the same symmetry, the state symmetries can be determined on a relatively simple basis. Thus, if one can identify the HOMOs of the D and A molecular fragments corresponding to the excited state, then the symmetry of that state will be the result of the direct product of the fragment symmetries reduced in the point group of the molecule. For example, consider the lowest-energy ligand-to-metal charge-transfer (LMCT) excited states of $\text{Co}(\text{NH}_3)_5\text{Br}^{2+}$. The electron transferred to cobalt will be in a $d\sigma$ orbital of $a_1(d_{z^2})$ or $b_1(d_{x^2-y^2})$ symmetry in the C_{4v} point group. The bromine atom has the electronic symmetry resulting from one partly occupied p orbital, a_1 or e in C_{4v} . The resulting ligand-to-metal charge-transfer excited states have A_1 , B_1 and E symmetries. The A_1 state involves only σ -type orbitals and is often classified as a σ -LMCT state, while the E state corresponds to a hole in the $p\pi$ orbitals and is often classified as a π -LMCT state. In another example, the LUMO on pyridine has b_2 symmetry while the partly occupied orbitals of $\text{Ru}(\text{NH}_3)_5^{3+}$ will have a_2 , b_1 , and b_2 symmetry in the C_{2v} point group, and the lowest-energy metal-to-ligand charge-transfer excited states will have B_1 , A_2 , and A_1 symmetry (or B and A symmetry in the actual C_2 symmetry of the molecule). The absorption bands that dominate the observed spectrum depend on a combination of selection rules and orbital overlap. These issues are discussed in the next section.

7.2.3 The Analysis of Spectroscopic Absorption Bands

For most transition metal complexes in solution, broad and intense charge-transfer absorption bands are observed. The intensity and band shape contain information about the structure of the electronic excited state.

The oscillator strength or intensity of the absorption band

The electronic-transition dipole moment for the $G \rightarrow E$ transition is defined by $\mathbf{M}_{GE} = \langle \Psi_G | \Delta\mu_{GE} | \Psi_E \rangle$ where the Ψ_i are the state wave functions and $\Delta\mu_{GE}$ is the difference in dipole moment of the ground and excited states [22]. The intensity of the transition is proportional to $|\mathbf{M}_{GE}|^2$. The broad absorption bands usually observed in transition metal systems are composed of progressions in the vibrational modes that correlate with the differences in nuclear coordinates between the vibrationally equilibrated ground and excited state. Since the energy difference between the donor and acceptor is generally solvent-dependent, the distribution of solvent environments that is characteristic of solutions may also contribute to the bandwidth (see further discussion of this point in the sections below). If the validity of the Born–Oppenheimer approximation is assumed, the intensity of each of these vibronic components is given by Eq. 11,

$$\mathbf{M}_{G0 \rightarrow En} = \langle \mathbf{M}_{GE} \rangle S_{G0, En} \quad (11)$$

where $\langle \mathbf{M}_{GE} \rangle$ is a mean value of \mathbf{M}_{GE} , assumed to be independent of the nuclear coordinates, $S_{G0, En} = \langle \phi_{G0} | \phi_{En} \rangle$ is the vibrational-overlap integral and ϕ_{Im} are the vibrational wave functions for the m th vibrational mode of the I th electronic state [22]. The oscillator strength for the $G0 \rightarrow En$ vibronic absorption is given by Eq. 12 (for $\nu_{G0 \rightarrow En}$ in cm^{-1} ; g is a multiplicity factor).

$$\begin{aligned} f_{G0 \rightarrow En} &= \frac{8\pi^2 g m_e c \nu_{G0 \rightarrow En}}{3 h e^2} |\langle \mathbf{M}_{GE} \rangle|^2 |S_{G0, En}|^2 \\ &= 4.70 \times 10^{29} \nu_{G0 \rightarrow En} |\langle \mathbf{M}_{GE} \rangle|^2 |S_{G0, En}|^2 \end{aligned} \quad (12)$$

Summation of $f_{G0 \rightarrow En}$ over all the allowed vibronic transitions, n , gives the theoretical absorption band envelope. When one is dealing with a single excited state, the electronic absorption band energy, intensity and band shape can provide much pertinent information. The substitution of molar absorptivity, $\epsilon_{v(m)}$, for oscillator strength (for light of energy $h\nu_m$) results in Eq. 13 [23, 24] (assuming that the electronic transition dipole moment, \mathbf{M}_{GE} , is the same for all vibrational states),

$$\epsilon_{v(m)} = \frac{4\pi^2 |\mathbf{M}_{GE}|^2 \nu_m N_A}{(3 \times 10^{10} \ln 10) n h c} \sum_j \frac{\Gamma \langle \phi_E | \phi_j \rangle^2}{4\pi^2 (\nu_m - \nu_0 - \nu_j)^2 + \Gamma^2} \quad (13)$$

where n is the index of refraction, c is the speed of light, N_A is Avagadro's number,

ϕ_j are excited-state vibrational wave functions, ϕ_G is the ground-state vibrational wave function, $\langle \phi_j | \phi_G \rangle$ is a vibrational-overlap integral, $h\nu_0 = \Delta E_{GE}^{00}$, $h\nu_j$ is the correlated excited-state vibrational quantum, and Γ is the lifetime limited line width. The summation of Eq. 13 over all the allowed vibronic transitions, j , gives the theoretical band envelope. The results of such summations are usually expressed in terms of $(H_{GE}\Delta\mu_{GE})^2$. Then the intensity becomes inversely proportional to $\nu_{G0 \rightarrow Ej}$ (see definitions above, Eqs. 4 and 5 and Ref. [25]). Then the molar absorptivity at the frequency ν_m is given by equations of the form of Eq. 14 [24–27],

$$\varepsilon_{\nu_m} = \frac{8N\pi^3}{3000h^2c\nu_m \ln 10} n^3 H_{GE}^2 (\Delta\mu_{GE})^2 (FC) \quad (14)$$

in which n is the index of refraction and (FC) is a Franck–Condon factor. In the simpler models, the Franck–Condon factor is assumed to be a function of excitation of a single, quantized, high-frequency vibration (or of a single nuclear coordinate), $h\nu_h \geq 4k_B T$, and of classical low-frequency modes, $h\nu_s \leq 4k_B T$. In such a case (FC) can be represented as in Eq. 15 [24, 25].

$$(FC) = \sum_j F_j \{ \exp[-(\Delta G_{GE}^0 - h\nu_m + jh\nu_h + \lambda_s)^2 / 4\lambda_s k_B T] \} / (4\pi\lambda_s k_B T)^{1/2} \quad (15)$$

$$F_j = S^j [\exp(-S)] / j!; \quad S = \lambda_h / h\nu_h$$

For an absorption band with a Gaussian band shape and involving single configurational contributions, Eq. 16 may be used to obtain values H_{GE} [1, 19, 20]

$$H_{GE} \cong (0.0205) [\varepsilon_{\max} \Delta\nu_{1/2} h\nu_{\max}]^{1/2} / r_{GE} \quad (16)$$

In this equation, the energies are expressed in cm^{-1} , and r_{GE} , the distance between centers of charge in the ground and excited state, is expressed in Å. The value of r_{GE} is not generally available from ordinary optical or molecular structural measurements [28–35].

The absorption bandwidth

The absorption bandwidth is usually formulated as a function of the reorganizational energies that also contribute to Eq. 15. For a band with a Gaussian shape (i.e., for the reduced spectrum, $\nu_m \varepsilon(\nu_m)$ vs. ν_m), the full width at half the absorbance maximum is given by Eq. 17a [8].

$$\Delta\nu_{1/2} = 2[2(2k_B T \lambda_s + w) \ln 2]^{1/2} \quad (17a)$$

When there are coupled vibrations for which $h\nu_h > k_B T$, but with $\lambda_h < \lambda_s$, then these may contribute to the bandwidth and $w = h\nu_h \lambda_h$ [8]. When ΔG_{GE} is dependent on the solvent environment, this (in addition to λ_s) can also contribute to the bandwidth. Where δ is the standard deviation for the variation of $(|\Delta G_{GE}| + \lambda_s)$ with the distribution of solvates, and when $(|\Delta G_{GE}| + \lambda_s) > 0$ in a specific solvent,

the band width is approximately given by Eq. 17b:

$$\Delta\nu_{1/2} \cong 2\delta + 2[2(2k_B T\lambda_s + w) \ln 2]^{1/2} \quad (17b)$$

The skewness of the absorption band

As written, Eqs. 14 and 15 imply that the overall absorption band will only be Gaussian (in the limit of a system in which only two electronic states need to be considered) if $\lambda_h = 0$. As they are written, these equations are actually only correct for an idealized transition between states that each correspond to a single electronic configuration and for which the excited state will distort along a nuclear coordinate corresponding to a single high frequency vibrational mode, ν_h . Several factors, such as the superposition of the transitions to several states with different electronic configurations, the thermal population of ground state vibrational levels, the superposition of vibronic progressions in several vibrational modes, and so forth can result in near-Gaussian band shapes of the ambient reduced absorption spectrum. The “single configuration approximation” is nearly always better for low-temperature emission spectra than for ambient solution absorption spectra. More generally, Eq. 15 should be summed over the contributions of different high-frequency vibrational modes. Thermal population of vibrational excited states always contributes to the ambient absorption spectra of transition metal complexes since the metal–ligand vibrational frequencies are typically in the range of 600–100 cm^{-1} (high for stretches, low for bends) and $k_B T \approx 200 \text{ cm}^{-1}$. Thus, at 300 K one expects an approximately 5 % population of an M–L stretch with $h\nu \approx 600 \text{ cm}^{-1}$.

Despite the anticipated complications, Eq. 15 does define a useful limit, and it can be used as a basis for interpreting the non-Gaussian shapes of absorption bands. Of course, the interpretation is greatly facilitated by any resolution of the vibronic components implicit in Eq. 15. The contributing vibrational modes and their re-organizational energies can sometimes be determined from resonance Raman spectra [4, 23, 24, 26, 36], even when the absorption bands have no resolved structure. When resolution of the contributing vibrational modes is possible and λ_r values can be estimated, it is then possible to infer the molecular structure of the excited state.

7.3 Charge-Transfer Emission Spectroscopy

The interpretations of CT absorption and emission spectroscopy differ more in detail than in principle. The major distinction for transition metal systems is that while the absorption process usually occurs without a change of spin multiplicity, the emission almost always does involve a change of electronic spin multiplicity. This is the case because upper excited-state relaxation processes, including those that are nominally spin forbidden, tend to be very rapid (10^{11} s^{-1} or faster), and the only electronic excited states with lifetimes long enough to produce a significant, readily detectable emission are those that differ in spin multiplicity from the ground state. Exceptions might in principle arise for systems in which there is little or no

excited-state distortion ($\lambda_r \approx 0$), but such a situation is very unlikely for a charge-transfer process. The spin-orbit coupling is large enough for the heavier metals so that spin multiplicity distinctions cannot be made.

7.3.1 The Interpretation of Charge-Transfer Emission Spectra

The energies of charge-transfer emission bands can be treated very similarly to the absorptions, as described in Eqs. 6–8; this is done by merely replacing the reorganizational terms by their negatives: $h\nu_{\max}^{\text{em}} = E_{\text{EG}}^{00} - \lambda_{\text{vib}}'$. However, the substitution of electrode potentials for E_{EG}^{00} will also require a $T\Delta S$ correction if there is a change of spin multiplicity (ca. 230 cm^{-1} for a triplet-singlet transition at 300 K).

The intensity and shape of the emission band are treated in a closely related way. For an emission, the intensity function in the single high-frequency vibrational-mode limit is given by Eqs. 18 and 19 [24–26, 37–39].

$$I(\nu_{\text{m}}) = \frac{64\pi^4}{3h^3c^3 \ln 10} \nu_{\text{m}} n^3 H_{\text{GE}}^2 (\Delta\mu_{\text{GE}})^2 (\text{FC}) \quad (18)$$

$$(\text{FC}) = \sum_j F_j \{ \exp[-(\Delta G_{\text{GE}}^0 + h\nu_{\text{m}} + jh\nu_{\text{h}} + \lambda_{\text{s}})^2 / 4\lambda_{\text{s}}k_{\text{B}}T] \} / (4\pi\lambda_{\text{s}}k_{\text{B}}T)^{1/2} \quad (19)$$

$$F_j = S^j [\exp(-S)] / j!; \quad S = \lambda_{\text{h}} / h\nu_{\text{h}}$$

7.4 The Classification of Charge-Transfer Absorption Bands

Charge-transfer absorption bands are generally put into categories based on the general nature of the donor and of the acceptor. Within molecules, these categories are named according to the following pattern: donor-to-acceptor-charge-transfer (DACT). The most common of such intramolecular charge-transfer categories are: metal-to-ligand (MLCT), ligand-to-metal (LMCT), metal-to-metal (MMCT or MM'CT); ligand-to-ligand (LLCT or LL'CT). The common usage is a little different for charge-transfer transitions between different molecules: charge-transfer-to-solvent (CTTS), or, for charge transfer within ion pairs, ion-pair-charge-transfer (IPCT) or outer-sphere-charge-transfer (OSCT; this nomenclature could also be used for CTTS).

7.5 The Electronic States Generated by Charge-Transfer Absorptions

Excited states are, by definition, always transient. Their lifetimes vary from a few femtoseconds to more than a day, depending on the system and the conditions. The

shortest-lived excited “states” are very difficult to characterize. Two classes of electronic excited states can be reasonably well characterized and are important in discussions of excited-state chemistry or physics: a) The initial excited “state” generated by light absorption, the Franck–Condon (FC) excited state; b) Excited states that are in thermal equilibrium with their environment only in the sense that they have relaxed from the nuclear coordinates of the ground state to the nuclear coordinates characteristic of the potential-energy minimum of an excited-state electronic surface, the vibrationally equilibrated excited states (VEqES). These two states are illustrated in Figure 1 for the simplest two-state limit.

7.5.1 The Franck–Condon State in Transition Metal Complexes

Transition metal complexes typically have several electronic configurations, which differ relatively little in energy. These configurations will generally mix and give rise to several electronic excited states. These are properties that give transition metal complexes their remarkable structural and catalytic properties. However, these same properties generally make Eq. 1 and Figure 1 only useful in the definition of an idealized limit for the interpretation of the properties of actual transition metal systems. This issue is especially a problem for the interpretation of Franck–Condon-state properties. In general, the Franck–Condon excited states of transition metal complexes should be regarded as mixtures of a number of different electronic configurations. The description of Franck–Condon states is a matter of continuing investigation and some controversy. This is an issue of some importance in understanding these systems since the electronic configuration of the Franck–Condon state is likely to be an important factor in determining its relaxation pathway. Upper excited state and “prompt” chemical and physical processes are not uncommon in such systems.

7.5.2 The Vibrationally Equilibrated Excited States (VEqES)

To a significant extent, the vibrationally equilibrated excited states (VEqES) can be treated as a well-defined thermodynamic system. The molecular geometry, the solvation environment, and so forth can, in principle, be inferred from the emission band shape (e. g., as in Eqs. 17 and 18) or they can be probed by the use of resonance Raman and time-resolved Raman and infrared techniques. Typically, the VEqES is a better oxidant and reductant than the ground state, and this is a very important aspect of the chemistry of charge-transfer excited states.

7.6 Excited-State Relaxation Processes

Excited-state lifetimes constitute an important constraint on the properties and potential uses of charge-transfer excited states. The lifetime behavior of the VEqES

can be addressed in a reasonably systematic manner. The factors controlling the lifetimes of the Franck–Condon and intermediate excited states of transition metal complexes are not at all well understood.

7.6.1 Vibrationally Equilibrated Excited States Relaxation Processes

Any excited-state relaxation process necessarily involves the dissipation of energy from the electronically excited molecular system to the environment. This energy may appear as light, in emission as discussed above, as heat, as electrical energy (in some heterogeneous systems) and/or in some chemical form. The emphasis in this chapter is on the physical processes.

The heat-generating physical relaxation processes are generally referred to as “nonradiative relaxation” processes. These processes are, in principle, closely related to chemical reaction processes. The rates of the nonradiative relaxation of an excited state depend on several factors. Among these are the difference in energy between the VEqES and the ground state (the “energy gap” ΔE_{EG} , or the driving force), the density of acceptor states, the coupling to the solvent environment, and the coupling of acceptor (or product vibrational) states to the VEqES (usually expressed in terms of $S = \lambda_a/h\nu_a$ for the acceptor vibrational mode a , and for λ_a , the contribution of $h\nu_a$ to the reorganizational energy). Two limiting regimes should be considered: 1) The “high-temperature” limit, in which $h\nu_h > 4k_{\text{B}}T > h\nu_s$; 2) The “low-temperature” limit in which $4k_{\text{B}}T \ll h\nu_s < h\nu_h$. (The “classical” limit corresponds to $4k_{\text{B}}T \gg h\nu_h > h\nu_s$; this limit does not correspond well to observed excited-state relaxation processes).

In the high-temperature limit, and for a single high-frequency acceptor mode, the relaxation rate can be represented as in Eq. 20 [22, 25, 37, 38, 40–43].

$$\begin{aligned}
 k_{\text{nr}} &= \frac{4\pi^2}{h} H_{\text{GE}}^2 (\text{FC}) \\
 (\text{FC}) &= \sum_h \sum_j F_j \{ \exp[-(\Delta G_{\text{EG}}^0 + jh\nu_h + \lambda_s)^2 / 4\lambda_s k_{\text{B}}T] \} / (4\pi\lambda_s k_{\text{B}}T)^{1/2} \\
 F_j &= S^j [\exp(-S)] / j!; \quad S = \lambda_h / h\nu_h
 \end{aligned} \tag{20}$$

In effect, Eq. 20 describes a thermally activated crossing from the VEqES to the j th high-frequency (acceptor) vibrational level, for which the activation barrier is $\Delta G^\ddagger(j) = (\Delta G_{\text{EG}}^0 + jh\nu_h + \lambda_s)^2 / 4\lambda_s k_{\text{B}}T$. This limit weights the contributions of different high-frequency vibrations in proportion (through S) to their contributions to the total reorganizational energy. The same weighting is characteristic of absorption and emission. This has the effect of making the same high-frequency modes equally important in the radiative and nonradiative processes. In this limit, emission band-shape analysis can provide information about the molecular geometry of the VEqES and it can provide parameters required for the calculation of k_{nr} .

In the low temperature limit, $k_B T \ll h\nu_s < h\nu_h$. For this condition, the non-radiative relaxation rate constant is approximately temperature-independent and is given in the single-mode limit by Eq. 21 [40, 41],

$$k_{nr}^o = H_{GE}^2 [8\pi^3 / (h^3 \nu_M \Delta E_{GE}^{00})]^{1/2} \exp(-\gamma \Delta E_{GE}^{00} / h\nu_M) \quad (21)$$

$$\gamma = \ln[\Delta E_{GE}^{00} / \lambda_M] - 1$$

where $h\nu_M$ is the maximum-frequency vibrational mode that is coupled to the relaxation coordinate; $h\nu_M$ contributes λ_M to the total reorganizational energy λ_{vib} . The highest-frequency vibrational modes are strongly favored in this limit, since they provide the best vibrational overlap [40–42, 44]. In this limit, the weighted vibrational frequencies, those that make the dominant contributions to k_{nr}^o , are different for emission spectra (e. g., as in Eqs. 17 and 18) and for nonradiative relaxation [40]. The assumption that the vibrational modes that dominate the emission band shape are also the modes that dominate k_{nr}^o in the low-temperature limit can result in an error in k_{nr}^o of several orders of magnitude [40]. In this limit, isotopic substitution (for nuclei contributing to ν_M) should result in large changes of k_{nr}^o [41]. The lowest-energy, triplet MLCT excited state of the $\text{Ru}(\text{bpy})_3^{2+}$ complex is an example of a photosystem with a bound, well-characterized VEqES [7, 45]. This metal-to-ligand charge-transfer (MLCT) state has nominal triplet spin multiplicity, although spin–orbit coupling results in the splitting of this state into components [45–47], and the spin-forbidden relaxation to the singlet ground state is relatively slow (ca. 600 ns in water under ambient conditions) [7, 11]. Excitation into the $^1\text{MLCT}$ excited state has been found to produce a Franck–Condon excited state which relaxes to the vibrationally excited $^3\text{MLCT}$ state with $k_{nr} \approx 10^{13} \text{ s}^{-1}$ [48, 49]. Vibrational relaxation of the $^1\text{MLCT}$ excited states seems to be significantly slower than intersystem crossing for the $\text{Ru}(\text{bpy})_3^{2+}$ complex [48, 49].

7.6.2 Upper-Excited-State Electronic-State Relaxation

One expects events to occur so rapidly following Franck–Condon-state generation that the rates of at least some relaxation processes may be faster than the rate at which heat flows away from the relaxing molecule. This will make it difficult to apply normal kinetic models to these relaxation processes. The probability of surface crossing will depend on vibrational overlap, possibly in a manner related to that in Eqs. 20 or 21. The use of Eqs. 20 or 21 does presume some form of the simple limiting model, illustrated in Figure 1, in which vibrational relaxation is assumed to be rapid compared to the crossing between states with different electronic configurations. This presumes that the coupling matrix element is sufficiently small, so that the potential-energy surfaces of the electronic states involved in the crossing can be meaningfully distinguished. When H_{ij} is very large and/or the states are close in energy, this approach is not likely to be useful. In such instances, it may be more useful to consider the crossing to be from a vibronic state, with a wave function of the form given by Eq. 22 [48–53],

$$\Psi_{ij} \cong \psi_{ab}^{\text{el}}(\phi_{a,i} + \alpha_{ab}\phi_{b,j}) \quad (22)$$

where ψ_{ab}^{el} is an adiabatic electronic wave function, ϕ_{kl} are vibrational wave functions and α_{ab} is a mixing coefficient. This leads to a model for upper-state relaxation that is essentially a cascade through a series of vibrational states of mixed electronic parentage. In this limit, the electronic configurations are mixed and relaxation depends largely on the rate of energy flow from the molecular vibrational states to the solvent. If the molecular vibrational quanta are large, this can be a relatively slow (ca. ps) process. Very few systematic studies are available. It does seem that upper-state crossings between electronic configurations are very rapid in transition metal complexes, often with subpicosecond lifetimes [48, 50–53].

7.7 Observations on the Weak Electronic Coupling Limit: Ion-Pair Charge-Transfer Absorption Bands

One would expect the weak electronic coupling limit approach, that is, for $\gamma_{\text{DA}} \approx 0$ in Eq. 7, to apply best to systems in which the donor and acceptor are not covalently linked. Ion pairs form one class of such systems. Although D/A coupling is necessarily weak in ion pairs of transition metal complexes, it is often strong enough to give rise to an observable optical response, and systematic studies are possible. These studies amount to an experimental definition of the optical behavior of charge-transfer systems in the weak-coupling limit. Cannon [15] and Endicott and coworkers [16, 17] have reported free-energy analyses of spectra similar to those employed here. Lever and coworkers [10] have used a closely related energy analysis (to obtain vertical, solution ionization energies).

7.7.1 The Correlation of Observed Ion-Pair Charge-Transfer Energies with Experimental Electron-Transfer Parameters

If we assume that the reorganizational free-energy contributions to Eq. 7 are a linear combination of those of the constituent couples, $\chi_r^{\text{DA}} = (\chi_r^{\text{D}} + \chi_r^{\text{A}})/2$, then $h\nu_{\text{max}}$ can be factored into contributions of the donor and the acceptor. Since the electrode potentials are determined for the separated donor and acceptor species, the actual free-energy change associated with the ion pairs contains a correction for the ground state (K_0) and excited state (K_0') association (a “work term” that is written in terms of formation constants), Eq. 23.

$$\Delta G_e - \Delta G_g = FE_a^\circ(\text{D}/\text{D}^-) - FE_a^\circ(\text{A}/\text{A}^-) + RT \ln(K_0'/K_0) \quad (23)$$

The work term correction, $RT \ln(K_0'/K_0)$, is ignored in the discussion below. There have been several general treatments and discussions of ion-pair charge-transfer (IPCT) spectra [10, 15, 54–56]. In the context of Eq. 7 as a systematic basis for

interpreting charge-transfer spectra, ion-pair spectra are a plausible model for the limit of $\gamma_{\text{DA}} \cong 0$. A representative sample of IPCT spectra has been assembled in Table 1 [10, 18, 55–72]. Electrode potentials [58, 73–78] and electron-transfer reorganizational energies [58, 74, 76, 77, 79–82] for the constituent couples of these ion pairs are presented in Table 2. The reorganizational energies in Table 2 are obtained from the reported rate constants for self-exchange reactions (Eq. 3), except for the halides and NCS^- for which best-fit (to the IPCT data for Ru^{III} ion pairs) values have been used. The observed IPCT energies for Ru^{III} , Co^{III} and $\text{Fe}(\text{CN})_6^{3-}$ acceptors are reasonably predicted by the sum of the difference in electrode potentials and the average of the free energies of activation of the self-exchange reactions of the constituent couples, Figure 2. Excluding the halides, the overall correlation based on Eq. 7 has a slope of 0.87 ± 0.06 , an intercept of $(2.0 \pm 1.2) \times 10^3 \text{ cm}^{-1}$ with $r^2 = 0.91$ (including halides for all but the reference systems results in a slope of 0.95 ± 0.04 , an intercept of $(1.2 \pm 1.2) \times 10^3 \text{ cm}^{-1}$, $r^2 = 0.94$). This can be considered to be a good confirmation of this approach since the experimental parameters used in the correlation were based on measurements of three very different quantities, and the measurements were performed in about 30 different laboratories. There do seem to be some detailed deviations from the general correlation: a) The $\text{Os}(\text{CN})_6^{4-}$ donors consistently show the largest positive differences ($\Delta h\nu_{\text{max}}$) between $h\nu_{\text{max}}(\text{obsd})$ and $h\nu_{\text{max}}(\text{calcd})$; this suggests an error (of about $3 \times 10^3 \text{ cm}^{-1}$) in one or more of the parameters listed in Table 2 for this complex; b) The values of $\Delta h\nu_{\text{max}}$ are more consistently positive for $\text{Fe}(\text{CN})_6^{4-}$ and for $\text{Co}(\text{sep})^{3+}$ than for the other acceptors; c) In general, the values of $\Delta h\nu_{\text{max}}$ are more negative for Co^{III} acceptors than for $d\pi$ acceptors (by about $1 \times 10^3 \text{ cm}^{-1}$; the correlation line for all but $\text{Co}(\text{sep})^{3+}$ has a slope of 1.3 ± 0.3 and an intercept of $-10 \pm 5 \times 10^3 \text{ cm}^{-1}$). Some of these systematic deviations reflect inconsistencies and uncertainties in the parameters used (these were often obtained under different medium conditions, and some involve spectral deconvolutions of broad, weak absorption bands). The Co^{III} acceptors are particularly interesting, since the basis for their consistency with the overall correlation is not clear. The spin-allowed electronic IPCT transition will generate a low-spin (2E_g in O_h symmetry) Co^{II} complex in each case. However, the Co^{II} species involved in the electrochemical and self-exchange kinetic measurements is in each case a high-spin complex ($^4T_{1g}$ in O_h symmetry). That these systems correlate reasonably well with those of the other acceptors suggests that the half-wave potentials are more negative and the self-exchange rate constants are larger (i. e., the reorganizational energies are smaller) for the excited-state couples involving low-spin Co^{II} than for their high-spin ground states, and that these differences very nearly cancel in the correlation in Figure 2. Overall, the observations summarized here indicate that Eq. 7 is a good basis for predicting charge-transfer energies in weakly coupled systems.

7.7.2 Electronic Coupling in Ion-Pair Charge-Transfer Systems

Equation 16 in combination with data from Table 1 implies that there is a substantial difference in the electronic coupling matrix element for the Ru^{III} and Co^{III}

Table 1. Ion-pair charge-transfer spectra: $\{M^{III}L_6^{m+}, X^{n-}\} + h\nu \rightarrow * \{M^{II}L_6, X^{(n-1)-}\}$.

Acceptor	Donor	$h\nu_{\max}^{\text{obsd}}$ 10^3 cm^{-1}	ϵ_{\max} $\text{cm}^{-1} \text{ M}^{-1}$	$\Delta\nu_{1/2}$ 10^3 cm^{-1}	$h\nu_{\max}^{\text{calcd a}}$ 10^3 cm^{-1}	Ref. ^b
Ru(NH ₃) ₆ ³⁺	Cl ⁻	35.0	250		35.00 ^c	57
	Br ⁻	31.0	220	5.6	30.97 ^c	57
	I ⁻	24.9	240	6.4	23.79 ^c	57
	NCS ⁻	26.8			26.77 ^c	73
	Fe(CN) ₆ ⁴⁻	13.1	34	6.3	14.57	58
	Ru(CN) ₆ ⁴⁻	18.0	31	6	18.96	59
	Os(CN) ₆ ⁴⁻	17.4	40	9.0	16.62	58
	Mo(CN) ₈ ⁴⁻	15.2	11	4.2	17.17	58
	W(CN) ₈ ⁴⁻	13.3	20	6.0	14.99	58
Ru(en) ₃ ³⁺	I ⁻	22.2			22.4 ^c	60
	Ru(CN) ₆ ⁴⁻	14.5	7.3	6.4	17.9	61
Ru(NH ₃) ₅ py ³⁺	Br ⁻	29.5			27.39	60
	I ⁻	24.4			20.18	60
	NCS ⁻	24.3			23.19	62
	Fe(CN) ₆ ⁴⁻	11.0	33	6.3	10.97	63
	Ru(CN) ₆ ⁴⁻	15.3	40	9.0	15.4	63
	Os(CN) ₆ ⁴⁻	15.6	38	7.1	13.2	63
	Fe(CN) ₆ ⁴⁻	15.4	30	6.7		64
Ru(NH ₃) ₅ Cl ²⁺	Ru(CN) ₆ ⁴⁻	19.8	40	9.4		65
	Os(CN) ₆ ⁴⁻	19.6	20	6.6		64
	Fe(CN) ₆ ⁴⁻	12.2	28	7.9	10.7	58
Fe(CN) ₆ ³⁻	Os(CN) ₆ ⁴⁻	16.4	10	10	12.8	58
	Mo(CN) ₈ ⁴⁻	13.9	13	6.5	13	58
	Cl ⁻	47			46.7	66
Co(NH ₃) ₆ ³⁺	I ⁻	36.3	960	8.1	35.5	66, 67
	NCS ⁻	38.3			38.54	68
	Fe(CN) ₆ ⁴⁻	22.7	300		26.28	55
	Ru(CN) ₆ ⁴⁻	29.2	240		30.65	55
	I ⁻	36.2	1150	8.2	34.91	67
Co(en) ₃ ³⁺	NCS ⁻	38.3			37.32	68
	Fe(CN) ₆ ⁴⁻	24.2	195	9.0	25.1	61, 69
	Ru(CN) ₆ ⁴⁻	28.6	260	10	29.39	68
	Os(CN) ₆ ⁴⁻	27.9	195	10.2	27.13	61
	Mo(CN) ₈ ⁴⁻	25.8	53	7.0	27.7	61
	W(CN) ₈ ⁴⁻	23.4	62	8.6	25.4	61
	Cl ⁻	38.0			41.81	70
	Br ⁻	36.8			37.85	70
Co(sep) ³⁺	I ⁻	33.8	2100	9.7	30.65	67
	NCS ⁻	35.2			33.66	71
	Fe(CN) ₆ ⁴⁻	23	105		21.44	55
	Ru(CN) ₆ ⁴⁻	26.9			25.82	56
	Br ⁻	36.8	150		40.79	71
	I ⁻	34.2	220		33.58	71
Co([9]aneN ₄) ₂ ³⁺	NCS ⁻	35.1			36.60	71
	Fe(CN) ₆ ⁴⁻	20.2			24.37	113
	Ru(CN) ₆ ⁴⁻	27.2			28.9	113

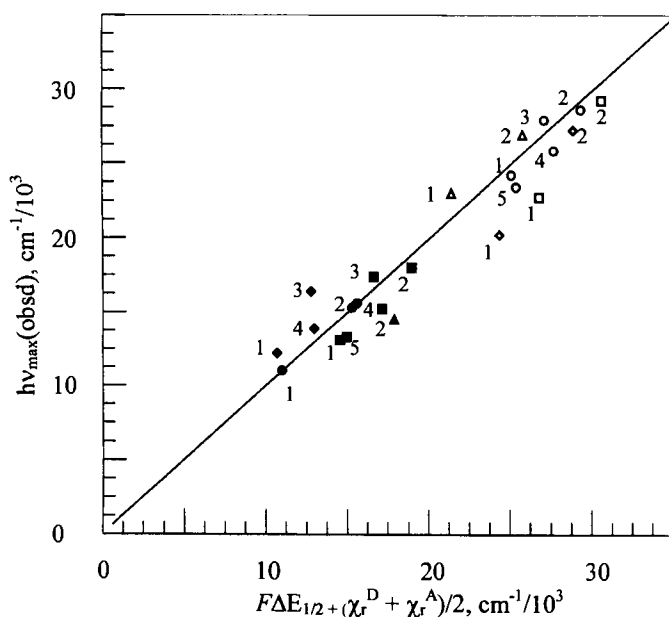
^aCalculation based on Eq. 7 and parameters in Table 2.^bFor IPCT spectra.^cIPCT spectra and thermal parameters used for the value of χ_r^D .

Table 2. Experimental and derived parameters for use in ion-pair charge-transfer correlations.^a

Couple	E_f , ^b V	χ_r^{th} , ^c 10^3 cm^{-1}	$r_{\text{D(A)}}$, ^d Å	$I_D^{\text{v}}(\text{EA}_A^{\text{v}})$, ^e eV	λ_r^{op} , ^e 10^3 cm^{-1}
$\text{Ru}(\text{NH}_3)_6^{3+,2+}$	0.06	13.64 [79]	3.35	(4.11)	9.35
$\text{Ru}(\text{en})_3^{3+,2+}$	0.21	13.31 [79]	3.7	(4.48)	3.7
$\text{Ru}(\text{NH}_3)_5\text{py}^{3+,2+}$	0.3	10.3 [80]	3.8	(4.32)	7.74
$\text{Ru}(\text{NH}_3)_5\text{Cl}^{2+,+}$	-0.04		3.4	(3.8)	10.64
$\text{Fe}(\text{CN})_6^{3-,4-}$	0.358 [58]	10.7 [74]	4.6	5.69 (4.16)	12.57
$\text{Ru}(\text{CN})_6^{3-,4-}$	0.92 [74]	10.4 [74]	4.7	6.30	12.58
$\text{Os}(\text{CN})_6^{3-,4-}$	0.63 [74]	10.4 [74]	4.7	6.18	11.94
$\text{Mo}(\text{CN})_8^{3-,4-}$	0.726 [58]	~ 10 [58]	—	5.86	8.34
$\text{W}(\text{CN})_8^{3-,4-}$	0.456 [58]	~ 10 [58]	—	5.64	11.13
$\text{Co}(\text{NH}_3)_6^{3+,2+}$	-0.06 [94]	35.11 [81]	3.3	(2.67)	31.29
$\text{Co}(\text{en})_3^{3+,2+}$	-0.21 [75]	30.32 [82]	3.65	(2.74)	25.00
$\text{Co}(\text{sep})^{3+,2+}$	-0.30 [76]	21.56 [76]	4.1	(3.04)	18.71
$\text{Co}([9]\text{aneN}_4)^{3+,2+}$	-0.40 [77]	25.81 [77]	4.4	(3.06)	16.62
$\text{Cl}^{0,1-}$	2.35 [78]	19.42 ^f		8.33	22.90
$\text{Br}^{0,1-}$	1.86 [78]	19.32 ^f		7.81	20.32
$\text{I}^{0,1-}$	1.27 [78]	14.42 ^f		7.21	22.26
$\text{NCS}^{0,1-}$	1.57 [78]	15.6 ^f		7.35	19.68

^a All values refer to aqueous solutions.^b Formal potentials referenced to NHE from tabulations in [10, 115] except as indicated.^c Values for the reorganizational free energies based on observed rate constants for self-exchange reactions (Eq. 3) of the couples noted, except (for halides) as indicated: $k_{\text{exch}} = K_0 v_{\text{eff}} \exp(-\chi_r^{\text{th}}/4k_B T)$. Values of v_{eff} vary depending on the contributions to χ_r^{th} , $v_{\text{eff}}^2 = (v_s^2 \chi_s^{\text{th}} + v_h^2 \chi_h^{\text{th}})/(\chi_s^{\text{th}} + \chi_h^{\text{th}})$ [14]. $K_0 = (4/3)\pi(r_{\text{D(A)}})^3 N_A \exp(-\delta) \times 10^3$; $\delta = (z_D z_A e^2 / \epsilon k_B T) \cdot [r_{\text{DA}}^{-1} - \kappa / (1 + \kappa r_{\text{DA}})]$; $\kappa = (8\pi N_A e^2 \mu / 10^3 \epsilon k_B T)$. Where N_A is Avagadro's number, e is the electronic charge, ϵ is the solvent dielectric constant, z_D and z_A are the formal charges of the donor and acceptor, and μ is the ionic strength.^d Values based on mean Van der Waals radii.^e Values of vertical ionization energy of donors, I_D , vertical electron affinities of acceptors, (EA_s^{v}) , and reorganizational energies, λ_r^{op} , obtained in [10]. All in aqueous solution.^f Value based on fit to the $\{\text{Ru}(\text{NH}_3)_6^{3+}, \text{X}^-\}$ IPCT absorption.

acceptors, and for the halide ($H_{\text{DA}} = 760 \pm 15$ and $2460 \pm 370 \text{ cm}^{-1}$, respectively) and $\text{M}(\text{CN})_6^{4-}$ (143 ± 45 and $590 \pm 60 \text{ cm}^{-1}$, respectively) donors. This indicates that the Co^{III} /halide systems are not really weakly coupled. However, the configurational mixing energies, ϵ_{IJ} , are only about 150 cm^{-1} and this is smaller than the uncertainties noted above. The other systems are certainly reasonable models for the weakly coupled limit. That the H_{DA} values for Co^{III} acceptors are three to four times larger than for Ru^{III} acceptors is interesting. The origin of the effect is not entirely clear. It has been suggested that the $\text{M}(\text{CN})_6^{4-}$ donors form hydrogen bonds to the amines of $\text{Ru}(\text{NH}_3)_6^{3+}$ [59, 83] and this may result in better $d\pi/d\sigma$ than $d\pi/d\pi$ overlap. Also, larger values of H_{DA} have been predicted for $\text{Co}^{\text{III}}/\text{Co}^{\text{II}}$ than for $\text{Ru}^{\text{III}}/\text{Ru}^{\text{II}}$ self-exchange reactions [84]. Whatever its origin, this ordering of H_{DA} is not often characteristic of covalently linked LMCT systems.

**Key to Acceptors:**

■ Ru(NH ₃) ₆ ³⁺	□ Co(NH ₃) ₆ ³⁺
▲ Ru(en) ₃ ³⁺	△ Co(sep) ₃ ³⁺
● Ru(NH ₃) ₅ py ³⁺	○ Co(en) ₃ ³⁺
◆ Fe(CN) ₆ ³⁻	◇ Co([9]aneN ₃) ₂ ³⁺

Figure 2. Correlation of IPCT absorption maxima with thermal parameters of the component redox couples for M(CN)₆⁴⁻ donors; M = Fe (1), Ru (2), Os (3), Mo (4), W (5). Data from Tables 1 and 2.

7.7.3 Ion-Pair Charge-Transfer Absorption Band Widths

The average of the IPCT bandwidths is slightly larger than expected based only on the $k_B T$ contributions to Eq. 17a. Experimental factors may enter into this to a significant degree, owing to the contributions of higher-order aggregates [83], the very limited solubilities of some of the ion pairs, and the deconvolution problems mentioned previously. If the deviations are significant, then the contributions of δ , Eq. 17b, would be ca. $(1.5 \pm 1) \times 10^3 \text{ cm}^{-1}$.

A different issue concerns Lever's reorganizational energies (λ_r^{op} in Table 2) for the vertical ionization processes [10]. These are best-fit energy values for the individual donors and acceptors, and they are, in principle, different from the self-exchange reorganizational free energies (χ_r^{th} in Table 2). The values of λ_r^{op} are systematically larger $[(+2.4 \pm 2.6) \times 10^3 \text{ cm}^{-1}]$ than the values of χ_r^{th} for the anionic donors, but systematically smaller $[(-5.4 \pm 3.0) \times 10^3 \text{ cm}^{-1}]$ for the cationic

onic acceptors. The values of χ_r^{th} very likely contain an entropy ($T\Delta S$) contribution, and they correspond to the average of the sum of the χ_r^{th} contributions from the donor and the acceptor. The major contributions to ΔS probably arise from solvational effects. The solvation entropy of a cation is a function of its charge and size [85], as in Eq. 24:

$$\Delta S_{\text{solv}} \cong -3.3 (Z^2/r) \text{ cm}^{-1} \text{ mol}^{-1} \text{ T}^{-1} \quad (24)$$

where Z is the ionic charge, r is the effective ionic radius in Å and the parameters are evaluated in water at 25 °C. For a one electron process the entropy change associated with an acceptor or a donor is $\Delta(\Delta S) = (3.3 \times 10^3)(2Z - 1)/r \text{ cm}^{-1} \text{ M}^{-1} \text{ T}^{-1}$, so the contributions have different signs for cations and anions. For $\text{M}(\text{CN})_6^{4-}$, Eq. 24 implies $T\Delta S = -2.0 \times 10^3 \text{ cm}^{-1}$. This is similar in magnitude to the observed differences and consistent with $\chi_r^{\text{th}} = \lambda_r^{\text{op}} - \Gamma\Delta S$. That the signs of $(\chi_r^{\text{th}} - \lambda_r^{\text{op}})$ are different for donors than for acceptors may originate from some other factor, possibly a systematic error of $(2-5) \times 10^3 \text{ cm}^{-1}$ in the reference threshold ionization energy [86]. In any event, the uncertainties in the various parameters make it difficult to evaluate these differences. Overall, the values of χ_r^{th} and λ_r^{op} do vary in similar ways, as expected.

7.8 Ligand-to-Metal Charge-Transfer (LMCT) Absorption Bands

7.8.1 Energy Correlations for Simple Systems: $\text{M}^{\text{III}}(\text{NH}_3)_5(\text{X}^-)$ Complexes

When the donor is covalently linked to the acceptor one might expect Eq. 9 to fail owing to the cross terms introduced by the covalent bonding. In addition, the covalent M–X bond can give rise to four qualitatively different configurational descriptions of charge-transfer transitions in complexes with partly filled d orbitals (for ligand p, metal d orbitals): 1) $p\sigma$ -bonding to $d\sigma^*$ -antibonding; 2) ligand $p\pi$ -nonbonding to $d\sigma^*$ -antibonding; 3) $p\sigma$ -bonding to $d\pi$ -nonbonding; and 4) $p\pi$ -nonbonding to $d\pi$ -nonbonding. The transitions observed are most often assigned as in *a* and *b* in d^6 low-spin transition metal complexes, and as in *d* in low-spin d^5 complexes. Assignments are more complicated with other metal d-orbital configurations and/or in complexes with more than one donor ligand (or acceptor metal). All else being equal, transitions of types *a* and *b* tend to be higher in energy (by ca. 10 Dq) than transitions of type *d*. The effects of covalent interactions are expected to be much larger in $p\sigma/d\sigma^*$ (*a*) than in the other types of LMCT transitions. In the limit that the M–X bond is more covalent than ionic, the corresponding $p\sigma/d\sigma^*$ transition should not exhibit the properties discussed above for IPCT absorption bands and the transition should not be classified as a charge-transfer transition.

The use of electrochemical data for the actual molecule can accommodate some of the effects of covalency. In general, the observations on LMCT absorptions in the ammine complexes suggest that nonlinear, or cross-term effects make only small contributions to the transition energies. Thus, the absorption maxima of the

Table 3. Ligand-to-metal charge-transfer spectra of simple complexes.

Complex	Donor	$h\nu_{\max}^a$ $\text{cm}^{-1}/10^3$	ϵ_{\max}^b $\text{cm}^{-1} \text{ M}^{-1}/10^3$	$\Delta\nu_{1/2}$ $\text{cm}^{-1}/10^3$	Ref.
$\text{Ru}(\text{NH}_3)_6^{3+}$	NH_3	36.36	0.475		3
$\text{Ru}(\text{NH}_3)_5\text{Cl}^{2+}$	Cl^-	30.5	1.93		87, 88
$\text{Ru}(\text{NH}_3)_5\text{Br}^{2+}$	Br^-	25.1	1.92		87, 88
$\text{Ru}(\text{NH}_3)_5\text{I}^{2+}$	I^-	18.5	2.05		88
$\text{Ru}(\text{NH}_3)_5\text{NCS}^{2+}$	NCS^-	20.2	3.02		114
$\text{Ru}(\text{NH}_3)_5\text{SCN}^{2+}$	SCN^-	19.4	2.45		114
$\text{Ru}(\text{NH}_3)_5[\text{NCFe}(\text{CN})_5]^-$	Fe^{II}	10.20	2.9		83
$\text{Ru}(\text{NH}_3)_5[\text{NCRu}(\text{CN})_5]^-$	Ru^{II}	14.57	2.5	5.18	83
$\text{Ru}(\text{NH}_3)_5[\text{NCOs}(\text{CN})_5]^-$	Os^{II}	12.15	3.1		83
$\text{Ru}(\text{NH}_3)_5[\text{NCRu}(\text{NH}_3)_5]^{4+}$	Ru^{II}	11.2	4.2	5.6	83, 90
$\text{Ru}(\text{NH}_3)_5[\text{NCRu}(\text{tpy})(\text{bpy})]^{4+}$	Ru^{II}	14.29	4.1	4.9	89, 89
$\text{Co}(\text{NH}_3)_5\text{Cl}^{2+}$	$\text{Cl}^-(\pi)$	37.1	0.6		92
	$\text{Cl}^-(\sigma)$	43.9	20		
	$\text{Br}^-(\pi)$	32.0	0.85		92
$\text{Co}(\text{NH}_3)_5\text{Br}^{2+}$	$\text{Br}^-(\sigma)$	39.5	18.5		
	$\text{I}^-(\pi)$	26.1	2.7		92
	$\text{I}^-(\sigma)$	34.9	16.5		
$\text{Co}(\text{NH}_3)_5\text{I}^{2+}$	NCS^-	33.3	3.1		
$\text{Co}(\text{NH}_3)_5[\text{NCRu}(\text{CN})_5]^-$	Ru^{II}	26.7	0.69	6.02	56
$\text{Co}(\text{tetraen})[\text{NCRu}(\text{CN})_5]^-$	Ru^{II}	26.7	0.50	8.3	93
$\text{Co}(\text{tpy})(\text{bpy})[\text{NCRu}(\text{CN})_5]^-$	Ru^{II}	17.7	1.01	4.7	93

^a Units of $\text{cm}^{-1} \cdot 10^{-3}$ ^b ($\text{cm}^{-1} \text{ M}^{-1}$)/ 10^3

$\text{X}^- \rightarrow \text{M}^{\text{III}}$ LMCT (ligand π orbital to metal $d\pi$ or $d\sigma$ acceptor orbital) transitions in $\text{M}(\text{NH}_3)_5\text{X}^{2+}$ complexes [3, 56, 83, 87–93] very strongly correlate with $h\nu_{\max}$ of the $\{\text{M}(\text{NH}_3)_6^{3+}, \text{X}^-\}$ IPCT absorptions discussed above, Table 3 and Figure 3. The deviations are systematic: the slope of the least-squares correlation line for the data in Figure 3 is 0.84 ± 0.06 and the intercept is $-1.4 \pm 1.9 \times 10^3 \text{ cm}^{-1}$. The deviations from a 1:1 correspondence are much larger when X is a halide [3, 87, 88, 92] than when X is $\text{M}(\text{CN})_6^{4-}$ [56, 83, 90, 91, 93] (6–8 compared to $3.5 \times 10^3 \text{ cm}^{-1}$, respectively). Some of the deviations arise from differences in the $\text{M}^{\text{III}}/\text{M}^{\text{II}}$ and $\text{X}^{\cdot}/\text{X}^-$ reduction potentials in the bound and ion-pair systems. The actual reduction potentials have been measured for some of the $(\text{NH}_3)_5\text{Ru}^{\text{III}}[\text{NCM}^{\text{II}}(\text{CN})_5]^-$ complexes [83] and estimated for some of the $\text{Ru}^{\text{III}}(\text{NH}_3)_5(\text{X}^-)^{2+}$ complexes. For these complexes, the effective reorganizational free energies are $\chi_p = (5.0 \pm 1.4) \times 10^3 \text{ cm}^{-1}$, independent of whether X^- is a halide or a hexacyano complex. Similarly, a plausible correlation line can be drawn through the data in Figure 3 with a slope of one and an intercept of $-5 \times 10^3 \text{ cm}^{-1}$. In the Co^{III} complexes, the coordinated halide is probably more difficult to oxidize, while the metal is easier to reduce [73, 94] than in the corresponding ion pair, and the effect of the reduction potentials may not be particularly important. A very rough estimate suggests that χ_r/χ_p may

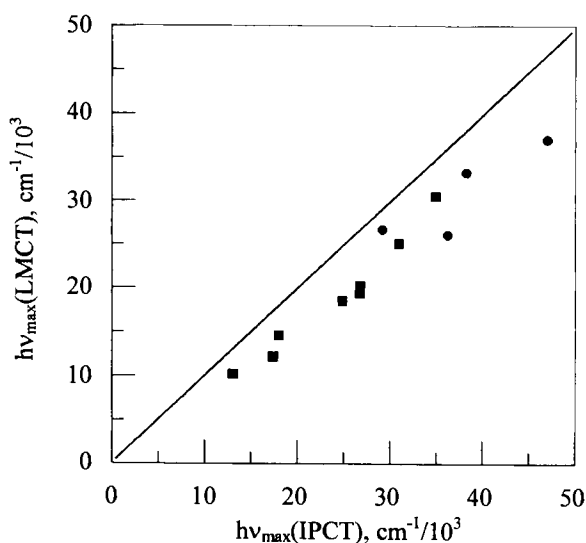


Figure 3. Correlation of charge-transfer absorption maxima for $M^{III}(L)_5X^{2+}$ complexes and $\{M^{III}(L)_6^{3+}, X^-\}$ ion pairs; closed circles for $M = Co$, closed squares for $M = Ru$. Data from Tables 1 and 3. The points correspond to compounds and ion pairs with the same M^{III} and X^- .

be about twice as large for the LMCT bands of the $Co(NH_3)_5X^{2+}$ complexes as for those of the $Ru(NH_3)_5X^{2+}$ complexes. The optical transition dipole lengths must be significantly smaller for the LMCT transitions of $M^{III}(L)_5(X^-)$ complexes than for the IPCT transitions of the related $\{M^{III}(L)_6, X^-\}$ ion pairs. A smaller solvent re-organizational energy is expected for the systems with the smaller dipole lengths, and this probably accounts for many of the observations noted.

Overall, the LMCT absorptions conform to expectation based on Eq. 9, but the effective values of χ_p are smaller than those for IPCT absorptions. Nonlinear covalent effects in γ_{DA} appear to be relatively small.

7.8.2 More Complex Ligand-to-Metal Charge-Transfer (LMCT) Systems

Thiaether complexes

A large number of complexes have been prepared with thiaether ligands [34, 77, 95–97]. These complexes typically contain several sulfur donor atoms. For example, several complexes of Cu^{II} with tetrathia macrocyclic ligands are listed in Table 4. These complexes typically exhibit two broad charge-transfer bands in the visible region of the spectrum. The energy differences of these bands average about the same as the energy differences of the σ -LMCT and π -LMCT bands of the $Co(NH_3)_5X^{2+}$ complexes in Table 3 ($7.7 \times 10^3 \text{ cm}^{-1}$). A similar assignment of these absorptions, $p\sigma \rightarrow d\sigma$ and $p\pi \rightarrow d\pi$ seems likely. However, the multiple donors of these relatively low-symmetry complexes (C_{2h} typical symmetry) should lead to several components of each of the bands ($A_g \rightarrow B_u$ and $A_g \rightarrow A_u$ components for each, in the simplest analysis of C_{2h} symmetry). Apparently these components are not resolved in ambient solutions. The copper(II) complexes differ from the ruthenium ammine

Table 4. Ligand-to-Metal Charge-Transfer (LMCT) spectra of some thiaether complexes.

Complex ^a	$h\nu_{\max}^{\text{b,c}}$	$\epsilon_{\max}^{\text{c,d}}$	Assignment
Cu([12]aneS ₄) ²⁺	25.84	6.0	σ/σ^*
	14.81	2.0	π/σ^*
Cu([13]aneS ₄) ²⁺	25.64	6.0	σ/σ^*
	16.00	1.8	π/σ^*
Cu([14]aneS ₄) ²⁺	25.64	8.2	σ/σ^*
	17.54	1.9	π/σ^*
Cu([15]aneS ₄) ²⁺	24.15	8.0	σ/σ^*
	17.7	1.14	π/σ^*
Cu([16]aneS ₄) ²⁺	22.73	6.1	σ/σ^*
	16.58	0.8	π/σ^*
Cu([15]aneS ₅) ²⁺	24.15	~7	σ/σ^*
	17.70	~2	π/σ^*
Cu([20]aneS ₆) ²⁺	23.81	~7	σ/σ^*
	18.35	~1.4	π/σ^*
Cu(EtTTu) ²⁺	24.39	6.8	σ/σ^*
	16.34	1.1	π/σ^*
Cu([9]aneS ₃) ₂ ²⁺	22.47 ^e	9.5 ^e	σ/σ^{*f}
Cu([9]aneS ₃)(aq.) ²⁺	26.74 ^e	~2 ^e	σ/σ^{*f}
Co([9]aneS ₃) ₂ ^{3+*}	30.3 ^g	22 ^g	σ/σ^{*f}

^a Ligand abbreviations: [12]aneS₄ = 1,4,7,10-tetrathiacyclododecane; [13]aneS₄ = 1,4,7,10-tetrathiacyclotridecane; [14]aneS₄ = 1,4,8,11-tetrathiacyclotetradecane; [15]aneS₄ = 1,4,8,12-tetrathiacyclopentadecane; [16]aneS₄ = 1,5,9,13-tetracyclohexadecane; [15]aneS₅ = 1,4,7,10,13-pentathiacyclopentadecane; EtTTu = 3,6,10,13-tetrathiapentadecane; [9]aneS₄ = 1,4,7-trithiacyclononane.

^b Units = cm⁻¹ 10⁻³.

^c (M⁻¹ cm⁻¹)/10³.

^d Data from [96] except as indicated.

^e [99].

^f Only one CT band reported.

^g [77].

complexes discussed above in that the $F\Delta E_a^\circ$ and χ_ρ contributions to $h\nu_{\max}$ relate to a metastable geometry of the copper(I)/(RS⁺) species rather than to the equilibrated species. This is a result of the different ligand conformations required for the Cu^{II} and Cu^I complexes and the slow rates of conformational isomerization [97, 98]. One expects that this would lead to larger values of $F\Delta E_a^\circ$ and smaller values of χ_ρ^{Cu} than for the Ru^{III} and Co^{III} ammine complexes. This point is difficult to evaluate quantitatively, since the measured values of Cu^{II}/Cu^I potentials are for the equilibrium geometries of the complexes [98]. However it can be illustrated for the [9]aneS₃ complexes.

The Co([9]aneS₃)₂^{3+/2+}, Cu([9]aneS₃)₂^{2+/+} and Cu([9]aneS₃)(aq)^{2+/+} complexes exhibit a single relatively intense RR'S/Cu^{II} LMCT absorption band [77, 97, 99]. This is most likely a $p\sigma \rightarrow d\sigma^*$ transition. The Co([9]aneS₃)₂^{3+/2+} couple has values of $E_{1/2} = 0.42$ V, $\chi_r^{\text{Co}} = 14 \times 10^3$ cm⁻¹, and $h\nu_{\max}$ (LMCT) = 30.3×10^3 cm⁻¹ [77].

These observations, the assumption that $(\chi_r^{\text{Co}} - \chi_p^{\text{Co}}) \approx 5 \times 10^3 \text{ cm}^{-1}$ (based on the comparisons in the preceding section) and Eq. 9 imply that $(FE_a^0 + \chi_p^S/2) \approx 26.7 \times 10^3 \text{ cm}^{-1}$. This, data from Table 4, values of $E_{1/2} = 0.70$ and 0.33 V [99], respectively for the $\text{Cu}([\text{9}] \text{aneS}_3)_2^{2+,+}$ and $\text{Cu}([\text{9}] \text{aneS}_3)(\text{H}_2\text{O})_n^{2+,+}$ couples, and Eq. 9 suggest values of $\chi_p^{\text{Cu}} \approx 3 \times 10^3$ and $6 \times 10^3 \text{ cm}^{-1}$, respectively, for these complexes (in the Cu^{II} conformational geometry). Extended to the macrocyclic thiaether complexes in Table 4, this argument suggests values of $E_{1/2}(\text{Cu}^{\text{II}}/\text{Cu}^{\text{I}})$ of about $0.2\text{--}0.6 \text{ V}$ for these complexes with the Cu^{II} ligand conformation. This is reasonably consistent with experimental estimates [98].

Ligand-to-Metal Charge-Transfer (LMCT) Excited States in MX_n Complexes

There have been many spectroscopic studies of high-symmetry MX_n ($n = 4, 6$ and 8) complexes [2, 3]. When the ground state has a partly filled d-orbital sub-shell, such complexes will have a very large number of LMCT excited states [3]. For example, the “ $p\pi \rightarrow d(t_2)$ ” excited-state configurations of $\text{Fe}(\text{Cl})_4^-$ give rise to $(A_1 + A_2 + 2E + 3T_1 + 3T_2)$ LMCT excited states [from the product of the $\text{Fe}^{\text{II}}(T_2)$ lowest-energy excited-state configuration with the E , T_1 , and T_2 symmetry-adapted combinations of $\text{Cl}(p\pi)$ orbitals]. The energy differences between these states depend on electron–electron repulsion terms that are not explicitly treated in this chapter. The variations of these energies as the ligands or metals are altered are expected to follow patterns similar to those discussed above.

7.8.3 Ligand-to-Metal Charge-Transfer (LMCT) Band Shapes and Intensities

As noted in Tables 3 and 4, the LMCT absorption bands of transition metal complexes tend to be broad ($\Delta\nu_{1/2} \approx 5$ to $8 \times 10^3 \text{ cm}^{-1}$) and the molar absorptivities are large ($\epsilon_{\text{max}} \approx 1$ to $20 \times 10^3 \text{ M}^{-1} \text{ cm}^{-1}$). Most of the bands are structureless in ambient solutions.

7.9 Metal-to-Ligand Charge-Transfer (MLCT) Absorption Band Energies

7.9.1 General Comments

MLCT excited states have been the subject of a vast amount of research and literature. This section will attempt a general overview of the area. More detailed accounts can be found elsewhere [45, 47, 100–102]. The overwhelming majority of the published studies involve low-valent metals with polypyridyl ligands. In fact, any ligand with relatively low-energy LUMO's will give rise to such transitions. The general features of these transitions are not different from the IPCT and LMCT transitions discussed above. Excited-state properties can be different when 1) The

electron is excited from a metal-centered nonbonding orbital (commonly a $d\pi$ orbital); and 2) The ligand-radical electron in the excited state is highly delocalized. Under such circumstances, the MLCT excited states are relatively undistorted (small λ_r), and the excited states can be long-lived under ambient conditions. As a result, they have attracted a great deal of attention. One or both of these features is usually absent in LMCT excited states, and most of these are relatively short-lived. Of course, there is a number of other properties that contribute to excited-state lifetimes and no universal generalizations are possible. Charge-transfer excited-state dynamics will be discussed briefly below.

7.9.2 Metal-to-Ligand Charge-Transfer (MLCT) Excited-State Energies

The same basic principles should be applicable to all CT transitions, and one expects Eqs. 7 and/or 9 to be at least as applicable for the MLCT absorption maxima as for the LMCT transitions. Many useful correlations of electrochemical potentials and $h\nu_{\max}$ have been found and exploited [9, 103–105]. The approaches outlined above will be used in this section.

Table 5 summarizes the MLCT spectra and electrochemical data of some simple $\text{Ru}(\text{bpy})_n(\text{Amine})_{(6-2n)}^{2+}$ complexes. There are two striking features of the MLCT spectra of these complexes: 1) The lowest-energy MLCT bands do not appear to have much of a reorganizational contribution; and 2) There are two MLCT transitions in these complexes. The first of these features is most evident in the similar values of $(h\nu_{\max} - F\Delta E_{1/2})$ in acetonitrile for the complexes with $n = 1$ and $n = 3$, despite the very large difference in the metal-centered reorganizational energies, χ_r , of these complexes (in water). The energies of the lowest energy MLCT bands of the complexes in Table 5 can be represented by Eq. 25.

$$h\nu_{\max} = F\Delta E_{1/2} + (1.3 \pm 0.2) \times 10^3 \text{ cm}^{-1} \quad (25)$$

This seems to suggest that reorganizational energies make very little contribution to $h\nu_{\max}$ for this class of complexes.

Table 5. Metal-to-ligand charge-transfer spectra: simple Ru^{II} bipyridine complexes.

Complex	MLCT ₁ ^{a,b}	MLCT ₂ ^{a,b}	χ_r^b	$E_{1/2}$, ^{a,c} V	$F\Delta E_{1/2}^b$
$(\text{bpy})_2\text{Ru}(\text{bpy})^{2+}$	21.98	—	5.2	1.210, -1.378	20.87
$(\text{bpy})_2\text{Ru}(\text{en})^{2+}$	20.53	28.99	9.2	0.876, -1.509	19.24
$(\text{bpy})_2\text{Ru}(\text{NH}_3)_2^{2+}$	20.41	28.99	9.7	0.825, -1.510	18.83
$(\text{bpy})_2\text{Ru}(\text{en})_2^{2+}$	19.42	27.40	10	0.514, -1.731	18.11
$(\text{bpy})_2\text{Ru}(\text{NH}_3)_4^{2+}$	19.16	27.32	10.4	0.455, -1.736	17.67

^a Y. Lei, Ph. D. Dissertation, Wayne State University, 1988. $E_{1/2}$ in H_2O .

^b Units = $\text{cm}^{-1} \cdot 10^{-3}$.

^c Vs. S.C.E. in CH_3CN .

The origin of the two MLCT transitions in these complexes has been recognized for some time [106, 107]. It is convenient to discuss this issue with reference to the $\text{Ru}(\text{NH}_3)_4\text{bpy}^{2+}$ complex. This complex has approximate C_{2v} symmetry, and its two MLCT bands arise from configurational mixing of the constituent pyridine moieties of the bpy ligand.

If the charge-transfer excited states of the pyridine moieties are represented by the zero-order wave functions Ψ°_{CT1} and Ψ°_{CT2} , then the resulting symmetric and anti-symmetric combinations are given in Eqs. 26a and b:

$$\Psi^\circ_{\text{CTs}} = (\Psi^\circ_{\text{CT1}} + \Psi^\circ_{\text{CT2}})/\sqrt{2} \quad (26a)$$

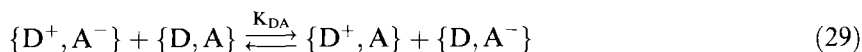
$$\Psi^\circ_{\text{CTa}} = (\Psi^\circ_{\text{CT1}} - \Psi^\circ_{\text{CT2}})/\sqrt{2} \quad (26b)$$

Of these two excited states, only the symmetric state, Ψ°_{CTs} , will mix with the symmetric ground state. Optical transitions to both states are allowed in C_{2v} symmetry. In the Hückel limit, the splitting between these two states can be represented as $2 H_{12}$, where H_{12} is the matrix element for mixing LUMOs of the two pyridines. The relative ordering of these states is not obvious. This leads to Eqs. 27 and 28 for the two transitions.

$$h\nu_l = E_{\text{pyCT}} - H_{12} + \dots \quad (27)$$

$$h\nu_u = E_{\text{pyCT}} + H_{12} + 2 H_{\text{gL}}^2/E_{\text{pyCT}} + \dots \quad (28)$$

These equations assume that only the lowest energy state mixes with the ground state, that the potential energy surfaces are harmonic and have the same force constants, and that the displacement of the ground state potential energy surface compensates for the stabilization and destabilization of the states that mix [116]. The use of electrochemical data in the evaluation of parameters that contribute to $h\nu_{\text{max}}$ leads to a significant correction term in strongly coupled donor-acceptor systems since the excited state species is not involved in the electrochemical processes [9, 116]. The optical and electrochemical processes are related by means of the electron-transfer equilibrium in Eq. 29.



This leads to Eq. 30 for the absorption maximum.

$$h\nu_{\text{max}} = F\Delta E^\circ + \chi_r^{\text{D/A}} + RT \ln K_{\text{DA}} + \dots \quad (30)$$

The contribution of the $RT \ln K_{\text{DA}}$ can be evaluated in terms of perturbation theory quantities mentioned above, and this leads to the experimentally useful expression in Eq. 31,

$$h\nu_{\text{max}} = F\Delta E_{1/2}^\circ + \chi_r^{\text{D/A}}(1 - 2\alpha_{\text{DA}}^2) + RT \ln K_{\text{el}} + \dots \quad (31)$$

where half-wave potentials have been substituted for standard potentials and K_{el} is

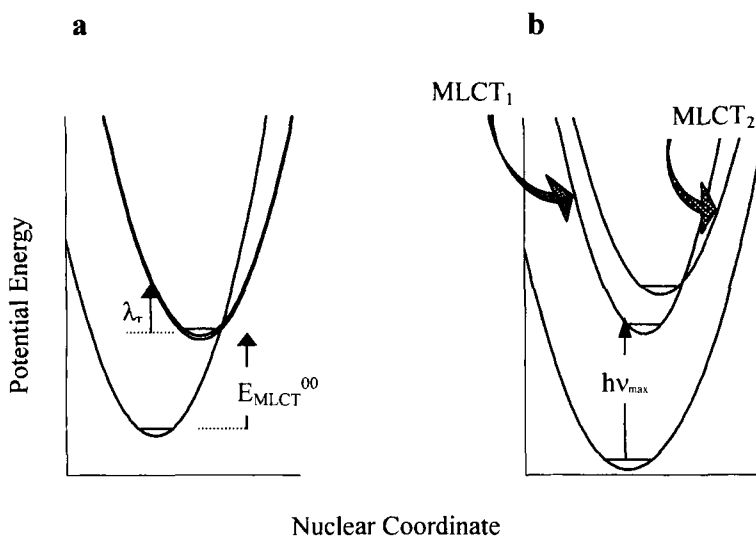


Figure 4. Qualitative illustration of the effects of configurational mixing in an A–D–A complex. a) Diabatic states with degenerate acceptors; b) Effect of mixing between the three states; it is assumed that only MLCT_1 mixes with the ground state.

a purely electrostatic term (roughly analogous to ion pair association constants) [116]. The meaning of the reorganization free energy is the same in equations 7 and 31; the argument summarized is an approach to the evaluation of γ_{DA} . This argument shows that apparent reorganizational parameters inferred from optical/electrochemical correlations are necessarily smaller than those required for a free energy correlation. The discrepancy increases with the fraction of charge delocalized as a result of donor-acceptor mixing (α_{DA}^2). When the optical/electrochemical correlations involve a comparison with constituent, thermal reorganizational parameters (as in Fig. 2 or implied in Fig. 3), then an additional correction for the fraction of charge delocalized is required and the effective “reorganizational energy” is $(h\nu_{\text{max}} - F\Delta E_{1/2}^{\text{D/A}}) \cong \chi_r^{\text{th}}(1 - 4\alpha_{\text{DA}}^2)$ [116].

In principle, this argument can be readily extended to the other bipyridine complexes in Table 5, since the energies of the two transitions would vary only in their contributions of λ_r and ϵ_s . When the electrochemical measurements are on the donor and acceptor of the covalently linked complex, as in Table 5, the success of optical electrochemical correlations appears to depend on the fortuitous cancellation of terms and the very small contributions of any variations in solvent contributions to the effective reorganizational energy. Since $\chi_r(\text{D})$ for the donor complexes considered here (Table 5) largely originates in the solvent, the negligible contribution of this quantity to the $\chi_r(\text{eff})$ for the MLCT transitions of bpy complexes is similar to the inferences about LMCT transitions in Section 7.8.1. This can be attributed to the very small dipole lengths of these transitions [31, 35].

For large differences in the energies of the ground and excited states, $h\nu_{\max} = (E_{\text{gL}} + \lambda_r) = (F\Delta E_{1/2} + \chi_p(1 - 2\alpha_{\text{gL}}^2))$, where $\epsilon_s = H_{\text{gL}}^2/E_{\text{MLCT}}^0 = H_{\text{gL}}^2/(F\Delta E_{1/2} + \chi_p)$, and the slope of a plot of $h\nu_{\max}$ vs $\Delta E_{1/2}$ is $F(1 - 2\alpha_{\text{gL}}^2)$. In practice, the variations of structural parameters that give rise to different values of $F\Delta E_{1/2}$ may also give rise to changes in χ_r . For the much studied Ru^{II} complexes, most of the contributions to χ_r arise from the solvent contributions (Table 2), and when the transition dipole length is small, as seems to be the case for polypyridyl ligands [31, 35], the variations arising from χ_r may be very small, as seems to be the case for the bipyridine ligand, and the slopes of such plots may be a measure of the electron density delocalized from the metal to the ligand (α_{gL}^2).

The above analysis raises the possibility that very different behavior, as in correlations of $h\nu_{\max}$ and $F\Delta E_{1/2}$, will be observed when the dipole length is long relative to the molecular dimensions, and/or when the effects of excited-state/excited-state (e. g., as manifested in H_{12}) configurational mixing differ greatly from the effects of excited-state/ground-state mixing (as manifested in ϵ_s in the above). The surprising result of the analysis presented here is that solvent contributions to χ_p are largely attenuated in strongly coupled systems. A perturbation-theory argument suggests that there is less attenuation of the effect of the donor and acceptor redox properties on the absorption energy. However, those properties must be evaluated in the actual complex.

7.9.3 Band Shapes and Intensities

The observed MLCT absorption bands are generally broad ($\Delta\nu_{1/2} \approx 4\text{--}6 \times 10^3 \text{ cm}^{-1}$, even for $d\pi/p\pi^*$ transitions). One would normally attribute this to an effect of the solvent reorganizational energy, as in Eq. 17. However, if the solvent reorganizational energy is as small as inferred in the preceding section, then these band widths are about twice those predicted. The implication is that the broad bands observed in fluid solution arise from the distribution of solvates and the effect of solvent on the transition energy (i. e., each differently solvated complex should have a different value of $F\Delta E_{1/2}$). This inference suggests that the evaluation of key parameters based on spectral fits to equations such as Eqs. 14, 15, 18, and 19 should be done with some caution.

7.10 Excited-State Lifetimes and Luminescence Properties

The $\text{Ru}(\text{bpy})_3^{2+}$ complex is a very good luminophore, and this and related complexes have been very extensively investigated [45, 101, 102, 108, 109]. The emission band shapes have generally been fitted to Eqs. 18, 19, or some variation of these [25, 37–39, 110]. The small solvent-reorganizational contributions, inferred above, suggest that the broad emission bands are not just a consequence of contributions of the solvent-reorganizational energy in these equations. The bandwidth is also likely

to show the effect of the distribution of solvates on the emission energy. On the other hand, some vibronic structure, arising from molecular vibrations with $h\nu_{\text{vib}} \gg k_{\text{B}}T$, is evident in the emission of the Ru^{II} polypyridyl complexes, as expected from Eqs. 18 and 19. The bandwidths of the resolved components may be more compatible with the above inferences.

A brief survey of some of the various observations on $\text{Ru}(\text{bpy})_3^{2+}$ are useful for perspective. It was noted above that $h\nu_{\text{max}}(\text{abs.}) \approx F\Delta E_{1/2}$ for this complex. It has also been reported that $[h\nu_{\text{max}}(\text{abs.}) - h\nu_{\text{max}}(\text{emission})] \approx 5 \times 10^3 \text{ cm}^{-1}$ for this complex [45, 101, 108, 109]. This energy should be approximately equal to $2\lambda_{\text{r}}$ plus the singlet/triplet MLCT excited-state energy difference, $E^{00}({}^1\text{MLCT}) - E^{00}({}^3\text{MLCT})$. Arguments presented above indicate that $h\nu_{\text{max}}(\text{abs.}) \cong (F\Delta E_{1/2} + \chi_{\rho})$ and $h\nu_{\text{max}}(\text{emission}) = [E^{00}({}^3\text{MLCT}) - H_{12}' - \lambda_{\text{r}}'] \cong (F\Delta E_{1/2} - \chi_{\rho})$. The heat generated during the Franck–Condon excited-state relaxation to the ${}^3\text{MLCT}$ state has been measured by photoacoustic-microcalorimetric methods [111, 112], and $E^{00}({}^3\text{MLCT})$ was determined to be $16.5 \pm 0.4 \times 10^3 \text{ cm}^{-1}$ in ambient aqueous solution. This is very close to $h\nu_{\text{max}}(\text{emission}) = 17.0 \times 10^3 \text{ cm}^{-1}$, observed in the same medium, and λ_{r}' (primed values for tripled state quantities) must be very small.

The relatively long excited-state lifetimes of $\text{Ru}(\text{bpy})_3^{2+}$ are readily attributed to a combination of the spin multiplicity changes that accompany relaxation, the large ground state–excited state energy difference and the small reorganizational energy that result in a relatively small nonradiative relaxation rate constant [45, 102]. In contrast, the intersystem crossing rate, from the Franck–Condon excited state to the ${}^3\text{MLCT}$ excited state is faster than the rate of vibrational relaxation within an electronic manifold, apparently a few hundred femtoseconds compared to a few picoseconds [48, 49]. Overall, it appears that the excited-state nonradiative relaxation rates depend very strongly on vibrational overlap, and a competition between state-to-state energy migration and vibrational relaxation.

7.11 Perspectives and Conclusions

This chapter has dealt largely with the information that may be obtained from the spectroscopy of charge-transfer excited states. It is an attempt to integrate several kinds of spectroscopic studies with electrochemical studies. This has led to the inference that solvent reorganizational energies often make very small contributions to the absorption (and probably emission) energies of very strongly coupled donor–acceptor complexes. This behavior limits the usefulness of standard electron-transfer formalisms in describing the energetics, band shapes, and so forth of such charge-transfer systems. In contrast, even strongly coupled donor/acceptor complexes still exhibit the electrochemical behavior characteristic of their constituent couples. Since solvation is a significant factor when electrode potentials are determined, the distribution of the solvates characteristic of the solution state will give rise to a distribution of electrode potentials and this is probably an important factor in absorption and emission bandwidths in solution.

“Pure” charge-transfer excited states are most rigorously defined in the weakly coupled limit. Simple examples of this limit are found in ion-pair complexes, complexes in which there is no covalent linkage between the donor and acceptor. Standard models work very well in this limit, and the IPCT absorption maximum is successfully described by the sum of the reduction potentials and the electron-transfer reorganizational energies of the constituent ionic partners, as in Eqs. 7 and 9 ($\gamma_{\text{DA}} \approx 0$).

When the donor and acceptor are covalently linked, the ionic contributions are no longer adequate to describe the observations. The effect of the covalent linkage can be symbolically represented by a parameter, γ_{DA} , that takes into account the changes in the parameters from their values at the ionic limit. To some degree, γ_{DA} can be linearized so that a set of modified parameters, designated in Eq. 9 as $E_{\text{a}}^{\circ}(\text{X}/\text{X}^-)$ and χ_{ρ}^{X} ($\text{X} = \text{D}, \text{A}$) can be defined for the covalently linked complex. When values of $E_{1/2}(\text{X}/\text{X}^-)$ can be directly measured in the strongly coupled complex of interest, they differ significantly from the purely ionic values. Values of χ_{ρ}^{X} can very rarely be directly measured in a covalently linked D/A complex, whereas the reorganizational parameter $\chi_{\text{r}}^{\text{X}}$ can be determined for the ionic limit from the measurement of self-exchange electron-transfer rates. The combination of the experimental correlation of $h\nu_{\text{max}}(\text{IPCT})$ with $h\nu_{\text{max}}(\text{LMCT})$ and a perturbation-theory argument for MLCT excited states demonstrates that solvent reorganizational contributions are far less in χ_{ρ}^{X} for the strongly coupled systems than in $\chi_{\text{r}}^{\text{X}}$ for the ionic limit. This appears to be a consequence of the very small dipole length for the charge-transfer transitions in covalently linked, strongly coupled D/A complexes.

Acknowledgements

Partial support of the research at Wayne State University by the Division of Chemical Sciences Office of Basic Energy Sciences, Office of Energy Research, U.S. Department of Energy is gratefully acknowledged.

References

1. R. S. Mulliken, W. B. Person, *Molecular Complexes*, Wiley-Interscience, New York 1967.
2. C. K. Jorgensen, *Orbitals in Atoms and Molecules*, Academic Press, New York 1962.
3. A. P. B. Lever, *Inorganic Electronic Spectroscopy*, Elsevier, Amsterdam 1984.
4. E. I. Solomon, M. A. Hanson, in E. I. Solomon, A. B. P. Lever (Eds.): *Inorganic Electronic Spectroscopy and Structure*, Vol. 2, Wiley, New York 1999, p. 1.
5. J. F. Endicott, in A. W. Adamson, P. D. Fleischauer (Eds.): *Concepts in Inorganic Photochemistry*, Wiley, New York 1975, p. 81.
6. O. Hovarth, K. L. Stevenson, *Charge Transfer Photochemistry of Coordination Complexes*, VCH, New York 1993.
7. G. J. Ferraudi, *Elements of Inorganic Photochemistry*, Wiley, New York 1988.
8. R. A. Marcus, *J. Phys. Chem.* **94** (1990) 4963.
9. A. B. P. Lever, E. Dodsworth, in E. I. Solomon, A. B. P. Lever (Eds.): *Electronic Structure and Spectroscopy of Inorganic Compounds*, Vol 2, Wiley, New York 1999, p. 227.

10. S. I. Gorelsky, V. Y. Kotov, A. B. P. Lever, *Inorg. Chem.* 37 (1998) 4584.
11. N. Sutin, *Accounts Chem. Res.* 15 (1982) 275.
12. C. Creutz, N. Sutin, *Inorg. Chem.* 15 (1976) 496.
13. H.-H. Schmidtke, in H. A. O. Hill, P. Day (Eds.): *Physical Methods in Advanced Inorganic Chemistry*, Wiley-Interscience, New York 1968.
14. R. A. Marcus, N. Sutin, *Comments Inorg. Chem.* 5 (1986) 119.
15. R. D. Cannon, *Adv. Inorg. Chem. Radiochem.* 21 (1979) 179.
16. J. F. Endicott, G. J. Ferraudi, J. R. Barber, *J. Phys. Chem.* 79 (1975) 630.
17. J. F. Endicott, T. Ramasami, D. C. Gaswick, R. Tamilarasan, M. J. Heeg, G. R. Brubaker, S. C. Pyke, *J. Am. Chem. Soc.* 105 (1983) 5301.
18. T. Ramasami, J. F. Endicott, *Inorg. Chem.* 23 (1984) 3324.
19. N. S. Hush, *Prog. Inorg. Chem.* 8 (1968) 391.
20. N. S. Hush, *Electrochim. Acta* 13 (1968) 1005.
21. B. S. Brunswig, N. Sutin, *Coord. Chem. Rev.* 187 (1999) 233.
22. J. B. Birks, *Photophysics of Aromatic Molecules*, Wiley-Interscience, New York 1970.
23. A. B. Myers, R. A. Mathies, in T. G. Spiro (Ed.): *Biological Applications of Raman Spectroscopy*, Vol. 2, Wiley, New York 1982, p. 1.
24. A. B. Myers, in A. B. Myers, T. R. Rizzo (Eds.): *Laser Techniques in Chemistry*, Vol. XXIII, Wiley & Sons, New York 1995, p. 325.
25. I. R. Gould, D. Noukakis, G.-J. Luis, R. H. Young, J. L. Goodman, S. Farid, *Chem. Phys.* 176 (1993) 439.
26. A. Myers, *Accts. Chem. Res.* 30 (1998) 519.
27. J. V. Casper, T. J. Meyer, *Inorg. Chem.* 22 (1983) 2446.
28. D. H. Oh, S. G. Boxer, *J. Am. Chem. Soc.* 112 (1990) 8161.
29. D. H. Oh, M. Sano, S. G. Boxer, *J. Am. Chem.* 113 (1991) 6880.
30. J. R. Reimers, N. S. Hush, *J. Phys. Chem.* 95 (1991) 9773.
31. Y. K. Shin, B. S. Brunswig, C. Creutz, N. Sutin, *J. Phys. Chem.* 100 (1996) 8157.
32. L. Karki, H. P. Lu, J. T. Hupp, *J. Phys. Chem.* 100 (1996) 15637.
33. R. J. Cave, M. D. Newton, *Chem. Phys. Lett.* 249 (1996) 15.
34. G. U. Bublitz, W. M. Laidlaw, R. G. Denning, S. G. Boxer, *J. Am. Chem. Soc.* 120 (1997) 6068.
35. B. S. Brunswig, C. Creutz, N. Sutin, *Coord. Chem. Rev.* 177 (1998) 61.
36. R. S. Czernuszewicz, T. G. Spiro, in E. I. Solomon, A. B. P. Lever (Eds.): *Inorganic Electronic Structure and Spectroscopy*, Vol. 1, Wiley, New York 1999, p. 353.
37. D. Graff, J. P. Claude, T. J. Meyer, in S. S. Isied (Ed.): *Electron Transfer Reactions*, Vol. 253, American Chemical Society, Washington, D. C. 1997, p. 183.
38. E. M. Kober, J. V. Casper, R. S. Lumpkin, T. J. Meyer, *J. Phys. Chem.* 90 (1986) 3722.
39. Z. Murtaza, D. Graff, A. P. Zipp, L. A. Worl, W. E. Jones, Jr., W. D. Bates, T. J. Meyer, *J. Phys. Chem.* 98 (1994) 10504.
40. M. Bixon, J. Jortner, J. Cortes, H. Heilte, M. E. Michel-Beyerle, *J. Phys. Chem.* 98 (1994) 7289.
41. R. Englman, J. Jortner, *Mol. Phys.* 18 (1970) 145.
42. K. F. Freed, J. Jortner, *J. Chem. Phys.* 52 (1970) 6272.
43. N. Kestner, J. Logan, J. Jortner, *J. Phys. Chem.* 64 (1974) 2148.
44. V. M. Kenkre, T. A., M. D. Fayer, *J. Chem. Phys.* 101 (1994) 10618.
45. G. A. Crosby, *Acc. Chem. Res.* 8 (1975) 231.
46. H. Reisen, E. Krausz, *Comments Inorg. Chem.* 18 (1995) 27.
47. H. Yersin, D. Braun, G. Hensler, E. Galhuber, in C. D. Flint (Ed.): *Vibronic Processes in Inorganic Chemistry*, Kluwer, Dordrecht 1989, p. 195.
48. N. H. Damarauer, G. Cerullo, A. Yeh, T. R. Boussie, C. V. Shank, J. K. McCusker, *Science* 275 (1997) 54.
49. N. H. Damarauer, J. K. McCusker, *J. Phys. Chem.* 103 (1999) 8440.
50. D. A. Sexton, L. M. Skibsted, D. Magde, P. C. Ford, *Inorg. Chem.* 23 (1984) 4533.
51. D. A. V. Tominaga, A. E. Kliner, A. E. Johnson, N. E. Levinger, P. F. Barbara, *J. Chem. Phys.* 98 (1993) 1228.
52. P. J. Reid, C. Silva, P. F. Barbara, L. Karki, J. T. Hupp, *J. Phys. Chem.* 99 (1995).

53. S. K. Doorn, D. O. Stoutland, R. B. Dyer, W. H. Woodruff, *J. Am. Chem. Soc.* **115** (1993) 6398.
54. R. Billing, *Coord. Chem. Rev.* **159** (1997) 257.
55. A. Haim, *Comments Inorg. Chem.* **4** (1985) 113.
56. A. Vogler, A. H. Osman, H. Kunkley, *Coord. Chem. Rev.* **64** (1985) 159.
57. D. Waysbort, M. Evenor, G. Navon, *Inorg. Chem.* **14** (1975) 514.
58. R. Billing, D. E. Khoshtariya, *Inorg. Chem.* **33** (1994) 4038.
59. V. G. Poupouloulou, H. Taube, *Inorg. Chem.* **36** (1997) 2240.
60. H. Elsbernd, J. K. Beattie, *Inorg. Chem.* **7** (1968) 2468.
61. R. Billing, A. Vogler, *J. Photochem. Photobiol. A* **103** (1997) 239.
62. J. C. Curtis, cited by Gorelski [10].
63. J. C. Curtis, T. J. Meyer, *Inorg. Chem.* **21** (1982) 1562.
64. S. I. Gorelski, A. P. B. Lever, cited by Gorelski [10].
65. A. Vogler, A. Kisslinger, *J. Am. Chem. Soc.* **104** (1982) 2311.
66. M. Linhard, *Z. Electrochem.* **50** (1944) 224.
67. R. Billing, R. Benedix, H. Henni, *Z. Anorg. Allg. Chem.* **600** (1991) 21.
68. K. Yoneda, *Bull. Chem. Soc. Jpn.* **28** (1955) 125.
69. R. Larsson, *Acta Chim. Scand.* **21** (1967) 257.
70. F. Pina, M. Ciano, Q. G. Mulazzani, V. M., V. Balzani, L. Moggi, *Sci. Papers I. P. C. R.* **78** (1984) 166.
71. G. Stich, cited by Gorelski [10].
72. H. Toma, *J. Chem. Soc. Dalton Trans.* (1980) 471.
73. T. Ramasami, J. F. Endicott, *Inorg. Chem.* **23** (1984) 3324.
74. H. Macartney, *Inorg. Chem.* **30** (1991) 3337.
75. A. Hammershoi, D. Geselowitz, H. Taube, *Inorg. Chem.* **23** (1984) 979.
76. I. Creaser, R. J. Gene, J. M. B. Harrowfield, A. J. Herlt, A. M. Sargeson, M. R. Snow, J. Springborg, *J. Am. Chem. Soc.* **104** (1982) 6016.
77. H.-J. Kueppers, A. Neves, C. Pomp, D. Ventur, K. Wieghardt, B. Nuber, W. J., *Inorg. Chem.* **25** (1986) 2400.
78. D. Stanbury, *Adv. Inorg. Chem.* **33** (1987) 70.
79. T. J. Meyer, H. Taube, *Inorg. Chem.* **7** (1968) 2369.
80. G. M. Brown, H. J. Krentzien, M. Abe, H. Taube, *Inorg. Chem.* **18** (1979) 3374.
81. J. F. Endicott, G. R. Brubaker, T. Ramasami, K. Kumar, K. Dwarakanath, J. Cassel, D. Johnson, *Inorg. Chem.* **22** (1983) 3754.
82. F. P. Dwyer, A. M. Sargeson, *J. Phys. Chem.* **65** (1961) 1892.
83. V. G. Poupouloulou, H. Taube, F. S. Nunes, *Inorg. Chem.* **38** (1999) 2844.
84. M. D. Newton, *J. Phys. Chem.* **92** (1988) 3049.
85. B. E. Conway, J. O. M. Bockris, in J. O. M. Bockris (Ed.): *Modern Aspects of Electrochemistry*, Butterworths, London 1954.
86. A. B. P. Lever, private communication, October, 1999.
87. H. Hartmann, C. Buschbeck, *Z. physik. Chem. Frankfurt* **11** (1957) 120.
88. E. Verdonck, L. G. Vanquickenborne, *Inorg. Chem.* **13** (1974) 762.
89. M. J. Powers, T. J. Meyer, *J. Am. Chem. Soc.* **102** (1980) 1289.
90. M. A. Watzky, *Ph. D. Dissertation*, Wayne State University, Detroit 1994.
91. M. A. Watzky, J. F. Endicott, X. S. Song, Y. Lei, A. Macatangay, *Inorg. Chem.* **35** (1996) 3463.
92. M. Linhard, M. Weigel, *Z. physik. Chem. Frankfurt* **11** (1957) 308.
93. T. Buranda, *Ph. D. Dissertation*, Wayne State University 1992.
94. T. Ramasami, J. F. Endicott, *J. Am. Chem. Soc.* **107** (1985) 389.
95. S. R. Cooper, S. C. Rawle, *Struct. Bonding (Berlin)* **72** (1990) 1.
96. T. E. Jones, D. B. Rorabacher, L. A. Ochrymowycz, *J. Am. Chem. Soc.* **97** (1975) 7485.
97. H. H. Sanaullah, C. Schoeneich, M. Morton, D. G. Van der Velde, G. S. Wilson, K.-D. Asmus, R. S. Glass, *J. Am. Chem. Soc.* (1997) 2134.
98. N. M. Villeneuve, R. R. Schroeder, L. A. Ochrymowycz, D. B. Rorabacher, *Inorg. Chem.* **36** (1997) 4475.
99. K. Krylova, *Ph. D. Dissertation*, Wayne State University, Detroit 1998.
100. V. Balzani, A. Juris, M. Venturi, S. Campagna, S. Serroni, *Chem. Rev.* **96** (1996) 759.

101. A. Juris, F. Barigelletti, S. Campagna, V. Balzani, P. Belser, A. von Zelewsky, *Coord. Chem. Rev.* **84** (1988) 85.
102. T. J. Meyer, *Prog. Inorg. Chem.* **30** (1983) 389.
103. R. de la Rosa, P. J. Chang, F. Salaymeth, J. C. Curtis, *Inorg. Chem.* **31** (1985) 4229.
104. F. Salaymeth, S. Berhaue, R. Yusof, R. de la Rosa, E. Y. Fung, R. Matamoros, K. W. Law, Q. Zheng, E. M. Kober, J. C. Curtis, *Inorg. Chem.* **32** (1993) 3895.
105. M. A. Watzky, A. V. Macatangay, R. A. Van Camp, S. E. Mazzetto, X. Song, J. F. Endicott, T. Burahda, *J. Phys. Chem.* **101** (1997) 8441.
106. W. L. Parker, G. A. Crosby, *Intern. J. Quantum Chem.* **39** (1991) 299.
107. A. M. Zwickel, C. Creutz, *Inorg. Chem.* **10** (1971) 2395.
108. K. Kalyanasundaram, *Photochemistry of Polypyridine and Porphyrin Complexes*, Academic Press, New York 1992.
109. K. Kalyanasundaram, *Coord. Chem. Rev.* **46** (1982) 159.
110. Z. Murtaza, A. P. Zipp, L. A. Worl, D. K. Graff, W. E. Jones, Jr., W. D. Bates, T. J. Meyer, *J. Am. Chem. Soc.* **113** (1991) 5113.
111. X. Song, J. F. Endicott, *Chem. Phys. Lett.* **204** (1993) 400.
112. C. D. Borsarelli, S. E. Bratalovsky, *J. Phys. Chem.* **102** (1998) 6231.
113. R. Billing, G. Stich, H. Hennig, *Z. Chem.* **30** (1990) 377.
114. A. V. Macatangay, *Ph. D. Dissertation*, Wayne State University, 1998.
115. J. F. Endicott, K. Kumar, T. Ramasami, F. P. Rotzinger, *Prog. Inorg. Chem.* **30** (1983) 141.

8 Synthetic Applications of Photocatalytic Oxidation and Reduction Reactions of Organic Reactants on Irradiated Semiconductor Surfaces

Marye Anne Fox

8.1 Introduction

Developing efficient and broadly applicable methods for controlled oxidation and reduction reactions remains a significant challenge for synthetic chemists. Electro-synthesis is more and more frequently being considered as a reliable synthetic tool in the arsenal of techniques available to the synthetic organic chemist. As a consequence of the utility of conventional electrochemistry, the related field of photo-electrochemistry has also become more interesting as a means for inducing redox reactions as a solution to problems in organic synthesis. Photoelectrochemical synthesis, like typical electrochemical transformations conducted in a standard electrochemical cell, provides a means for controlling reactivity from three venues: selective adsorption for chemoselective activation of a desired substrate, potential control for selective thermodynamic activation of one oxidant or reductant in the presence of others, and current control for producing a product at the desired oxidation level [1, 2].

One particularly appealing route for effecting controlled redox reactions involves an array of surface-mediated reactions initiated by ultraviolet irradiation of suspended semiconductor particles [3–13]. Such reactions involve band-gap excitation of the semiconductor, interfacial electron transfer, and secondary dark chemical reactions of singly oxidized and reduced adsorbates. Because the semiconductor surface is restored to its original structure and oxidation level after these transformations, these photoreactions are often called photocatalytic, leaving the light-responsive photocatalyst ready to act as initiator for another cycle. The use of such photocatalysts also obviates the need to acquire expensive electrochemical equipment.

This exciting area has been studied extensively over the last two and a half decades, primarily because of its potential as a route for solar energy conversion by production of chemical fuels [8–13] and as a means for environmental detoxification of polluted air or water streams [14–21]. Solar energy conversion by the

photocatalytic splitting of water (to its component elements hydrogen and oxygen) has been a particularly appealing goal of this research, because it represents a conceptually simple route to a combustible gas, hydrogen, which can be easily burned back to water via a highly exothermic and pollution-free reaction. Indeed, photocatalytic water splitting represents one of the “Holy Grails” of current chemistry [22]. Equally appealing, a solar-driven route for the complete mineralization of potentially toxic organic materials to simple inorganic, nontoxic compounds and salts would be a significant and important chemical achievement [23].

Although the most thoroughly investigated photoelectrochemical investigations have focused on changes in oxidation state in simple inorganic molecules (e.g., in water splitting, carbon dioxide or nitrogen reduction, or metal deposition from ionic salts), the principles developed in these studies are equally applicable to organic transformations. Photocatalytic water splitting [10–14] and advanced oxidation processes for photodetoxification [15–21] also rely on the same sequences: namely, photochemical production of an electron/hole pair, followed by interfacial photoinduced electron transfer, effecting redox half reactions on the surface of a suspended semiconductor. The oxidized and reduced species thus produced can then participate in a wide array of subsequent dark chemical transformations, and the extent to which the surface affects the course of subsequent dark reactions will dictate the feasibility of this technique in achieving synthetically useful redox transformations of organic adsorbates, at least in competition with complete oxidative mineralization of the adsorbate in question.

A specific aim of this chapter is to compare the similarities and differences in reactivity that distinguish photoelectrochemical conversions from those that take place on poised electrodes or upon treatment with homogeneously dispersed redox reagents. In this chapter, therefore, we consider specifically how reactions that take place under controlled ultraviolet irradiation on a redox-active heterogeneous suspension permit specific chemical selectivity and control of oxidation and reduction level.

Because photocatalytic redox events are driven by light, efficient interfacial electron transfer to produce singly oxidized radical ions always competes with energy-wasting electron-hole recombination. Thus, back electron transfer between the oxidized and reduced radical ion pair formed on the irradiated surface competes with diffusion of the redox intermediates from the surface into the bulk of the contacting solution and with trapping of the surface-bound radical ions by trapping reagents. The semiconductor surface itself can also influence the stability of the radical ion pair generated, producing a quite different reactivity from that observed when the same intermediates are produced in homogeneous solution. The efficiency of electron-hole recombination is an inherent limitation for practical applications of photocatalysis in synthesis, as the high drive force always makes charge recombination favorable, thus limiting the quantum efficiency of the desired reaction.

Photoelectrochemistry is inherently interdisciplinary, and it has attracted the attention of chemists who approach the various aspects of the science from quite different perspectives. Although the diversity of this approach reflects the importance of the field, it does also make it virtually impossible to include all relevant work in a summary chapter of reasonable length. Even so, the examples cited here can serve,

we believe, as a helpful introduction to those new to this field. Each year the compilation of reactions that can be initiated by photoelectrochemical activation on irradiated semiconductors grows, and a comprehensive discussion of all relevant work becomes impossible. For that reason, examples from our own research group are usually chosen as illustrative of the principle being discussed [1–7, 24, 25]. We acknowledge at the onset that this article therefore neglects many important contributions to the area, simply in the interest of maintaining a review of reasonable length that covers the principles most relevant to synthetically useful transformations. For more complete coverage, we refer the interested reader to a number of earlier reviews that present more detail about mechanisms of these, and related, conversions, and for which this treatment represents an update.

The emphasis of this article is on organic transformations, and the principles chosen here for illustration of the operative examples are chosen from organic chemistry. In illustrating these principles, we provide a compilation of many controlled redox reactions of a range of organic functional groups. In describing the guiding principles of synthetic photoelectrochemical conversions on illuminated surfaces of metal oxide and metal chalcogenide semiconductors, we show how photoelectrochemical catalysts are useful as selective activators of organic reactivity. We describe here illustrations of photocatalytic oxidations, reductions, and pericyclic reactions of a wide range of organic substrates.

8.2 Principles Governing Photoelectrochemistry

Organic photoelectrochemistry can be defined as a field in which redox reactions of carbon-based compounds are initiated or assisted by the absorption of a photon at the surface of a semiconductor particle to which the substrate of interest is adsorbed. In a photoelectrochemical conversion, the organic substrate of interest is not converted to an excited state, the activating photon having been absorbed instead by the semiconductor.

8.2.1 Redox Reactions on Irradiated Semiconductor Surfaces

By definition, a semiconductor does not have a continuum of states (as do metallic conductors) but rather a band structure. The filled levels, called the valence band, are an energetically closely spaced array of orbitals composed of the valence electrons of the material. A gap exists between the top edge of this band and the lower edge of a similar closely spaced array of orbitals that are unoccupied in the ground state, that is, the conduction band. The gap separating these bands is called the band gap.

In an intrinsic (undoped) semiconductor, the Fermi level lies at a potential exactly halfway between the bands, whereas with an *n*-type (negatively doped) or a *p*-type (positively doped) semiconductor, the Fermi level respectively lies just below the conduction band edge or just above the valence band (Figure 1).

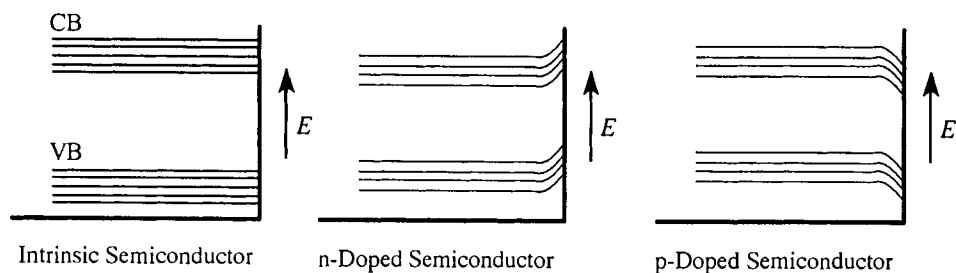


Figure 1. Band bending in *n*- and *p*-doped semiconductors. (The vertical line represents the interface between the solid semiconductor on the left and a contacting liquid on the right.)

When a semiconductor surface is brought into contact with an electrolyte containing a redox couple, interfacial electron transfer can transpire, to equilibrate the solution phase potential and the Fermi level of the bulk semiconductor. As electron exchange takes place across the interface, equilibration with the solution occurs and the bulk Fermi level moves to the solution-phase equilibrium potential, whereas the band-edge positions at the surface remain fixed at their original values. Thus, in moving inward from the semiconductor–electrolyte interface, the bands bend. Charge injection in this region of bent bands forces electrons to move in the opposite direction from holes: in an *n*-doped material, electrons move away from the surface and toward the bulk of the semiconductor while the holes move toward the surface. Thus, band bending assists in improving the efficiency of photoinduced charge separation.

As a result of band bending, the surface of an irradiated *n*-type semiconductor becomes electron-deficient and acts as a photoanode toward an oxidizable adsorbate. The conduction-band electron in an irradiated semiconductor is almost isoenergetic with the reduction potential for oxygen. In aerated solutions in which the semiconductor is saturated with adsorbed oxygen, the electron can often be trapped as superoxide, or when bound to the surface of the photocatalyst, it can trap other surface-confined reactive intermediates [26, 27].

When a semiconductor surface (whether configured as a single-crystal electrode or as a particle) is exposed to light of an energy greater than the band gap, a band-to-band transition takes place, which moves an electron from the filled valence band to the vacant conduction band (Figure 2). Every semiconductor therefore has a wavelength onset that represents an energy minimum characteristic of that particular material. The absorption of a photon thus induces charge separation, generating a highly energetic electron and creating a lower-energy vacancy in the valence band. This charge-separated species is referred to as an electron-hole pair.

Back electron transfer (recombination of the electron-hole pair) is, of course, highly favorable from a thermodynamic viewpoint. But because of the absence of states in the semiconductor band gap, quantum restrictions slow recombination by back electron transfer and the lifetime of the photogenerated electron-hole pair is sufficiently long to permit charge trapping. Thus, a valence-band hole is trapped for some period and can, at least in principle, act as an anode poised at the energy of

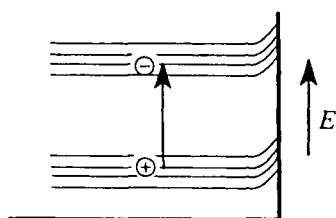


Figure 2. Photoexcitation of an *n*-type semiconductor particle.

the valence-band edge. The conduction-band electron can, in principle, act similarly, as a cathode poised at the band edge of the conduction band. Thus, we can think of the excited semiconductor surface as presenting an electron-hole pair to an adsorbed substrate or to a contacting solution including a redox-active reagent, with the charge carriers localized in the conduction and valence bands, respectively. In an *n*-type semiconductor, the surface of the semiconductor becomes electron-deficient and acts as an oxidative site toward an oxidizable organic compound. If an adsorbed reagent of the correct redox potential can trap one of the charge carriers faster than the electron and hole can recombine, new surface-mediated chemistry will be observed.

Thus, on a semiconductor, it is possible for the conduction-band electron to be captured by interfacial electron transfer to an appropriate adsorbed acceptor and for the valence-band hole to be filled by interfacial electron transfer from an adsorbed organic donor, at a rate competitive with spontaneous back electron transfer from the charge-separated pair (Figure 3).

When the valence-band hole and the conduction-band electron are both trapped by an appropriate oxidation or reduction half reaction, singly oxidized and reduced species are formed on the surface of the photocatalyst. Because these adsorbed intermediates can move about the surface, either migrating closer together or diffusing away from each other, before back-electron transfer occurs, novel chemistry is likely to ensue. It is a unique characteristic of photoelectrochemical catalysts that both oxidized and reduced species are produced on the same surface. As a result,

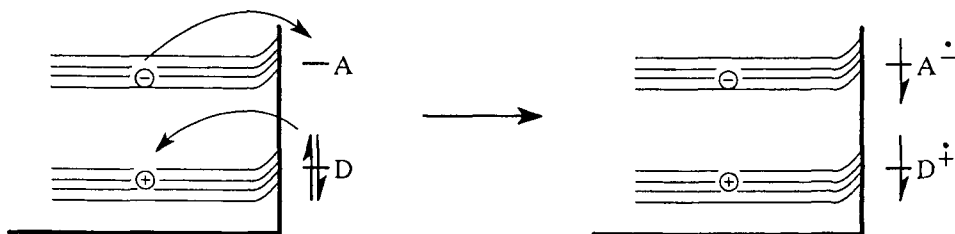


Figure 3. Interfacial electron transfer with an adsorbed electron donor D and acceptor A. (The vertical line represents the interface between the solid semiconductor on the left and a contacting liquid on the right; the horizontal lines represent the respective redox potentials of A and D.)

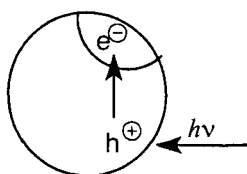


Figure 4. Charge trapping on a metalized semiconductor powder, as an analog to a short-circuited electrochemical cell.

photoelectrochemical redox reactions often differ significantly from the electrochemical transformations observed in a conventional three-electrode cell, where the surface of the working electrode is rendered either oxidizing or reducing by virtue of an imposed potential. That is, unlike in photocatalysis, the oxidizing and reducing sites are appreciably physically separated in a standard electrochemical conversion, even occurring in separate half cells in which the anode and cathode are in separate compartments divided by a membrane. In the latter arrangement, secondary reactions between the singly oxidized and reduced intermediates are unlikely.

Apart from the lack of physical separation of the anode and cathode, a suspended semiconductor particle can itself be considered to be a nanoscopic version of a miniature electrochemical cell [8–10, 28]. In photocatalysis, both the anodic and cathodic sites are produced on the same particle, whose dimensions can vary from the subcolloidal to single crystalline in size. This variation permits photocatalytic redox transformations to be performed without the standard electrochemical equipment usually employed for maintaining the potential or analyzing current flow during an electrochemical conversion. Bard [8] has shown that, for practical applications, the semiconductor photocatalyst can be considered as a “short-circuited” electrochemical cell, prepared by deposition of an inert metal with low overpotential onto the surface of the semiconductor. Such a metalized powder is shown in Figure 4. This powder thus includes regions for both photoactivated oxidation of an organic substrate adsorbed at the irradiated semiconductor–electrolyte interface and for collection of the photogenerated electrons as a pool on the metal site. As in a standard electrochemical cell, these metalized powders include sites for photo-induced oxidation and reduction, analogous to the working anode and cathode. On platinized TiO_2 powders, however, no external current flow accompanies these transformations.

Even without deposition of a metal island, wide band-gap semiconductor powders often maintain photoactivity, as long as the rates or the positions of the oxidative and reductive half reactions can be separated. Photoelectrochemical conversion on untreated surfaces also remains efficient if either the oxidation or reduction half reaction can take place readily on the dark semiconductor upon application of an appropriate potential. Metalization of the semiconductor photocatalyst will be essential for some redox couples, whereas, for others, platinization will have nearly no effect. Furthermore, because the oxidation and reduction sites on an irradiated particle are very close to each other, secondary chemical reactions can often occur readily, as the oxidized and reduced species migrate toward each other, leading either to interesting net reactions or, unfortunately, sometimes to undesired side reactions.

For photoelectrochemical conversions to proceed on untreated surfaces, either the oxidation or reduction must occur readily in the dark, thus scavenging one of the photogenerated charge carriers. That is, there must be a kinetic preference for either oxidation or reduction. An alternative explanation for the effectiveness of native powders may be the involvement of defect sites, which can act as charge accumulation centers in parallel to purposely introduced metal sites.

Obviously these powders are simpler to work with than a full electrochemical cell, in that they are easily moved and inexpensive, and do not require extensive electrochemical analytical instrumentation. Furthermore, depending on particle size, the complete development of a space-charge region at the interface of such a powder may be absent. In these films, charge separation is governed by the kinetics at the film surface, not by the electric field of the space-charge layer [8, 29].

If one conceptually considers making the particle smaller and smaller, one eventually reaches a colloidal state. Colloidal forms of metal oxide semiconductors can often be prepared by hydrolysis of an appropriate organometallic precursor, and the resulting suspension may represent the ultimate miniature photoelectrochemical cell [28]. The resulting colloid can then be used as synthesized or it can be deposited as a thin film on an inert support.

This analogy to a short-circuited electrochemical cell also explains why photoactivity is maintained as the size of the photocatalyst decreases from a single crystal or powder to the colloidal range, even if physical properties of the photocatalyst are changed. For example, the absorption characteristics, the quantum efficiency of charge separation, and the kinetics of interfacial electron transfer are often influenced by the photocatalyst particle size. On sufficiently small particles, the space-charge width needed for effective band bending may exceed the dimensions of the particle, making charge separation much less efficient. Even in this case, though, surface effects are often still observed.

When molecules or intermediates are adsorbed onto a specific surface, the conformational equilibrium can be altered from that observed in solution, because surfaces can transmit electrostatic forces to stretch bonds in the adsorbate. This, in turn, affects the relative rates of intra- and intermolecular reactivity, both in unimolecular rearrangements and in collisional transformations.

8.2.2 Comparison of a Photoelectrochemically Generated Electron-Hole Pair and a Molecular Excited State

The electron-hole pair produced by irradiation of a suspended *n*-type semiconductor particle is similar in some ways to an excited state of an organic compound. In a typical organic molecule, there is a large gap between the filled and vacant molecular orbitals, typically so large that most organic solids are insulating. Promotion of an electron from the highest occupied molecular orbital (HOMO) to the lowest-lying unoccupied molecular orbital (LUMO) by absorption of a photon in an organic ground state alters the net oxidation and reduction potentials. That is, removing or adding an electron from/to the excited state is much easier than from/to the corresponding ground state, because the promoted electron occupies a higher-

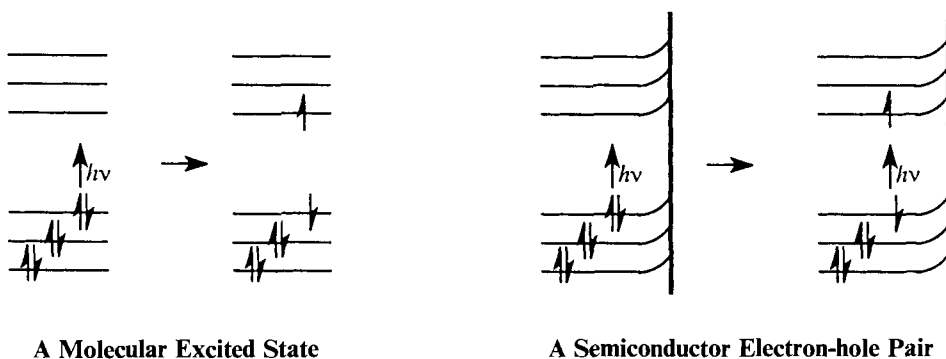


Figure 5. Comparison of a molecular excited state with a semiconductor electron-hole pair.

energy orbital and can be more easily removed because of the vacancy created in a lower-lying orbital that is normally filled in the ground state. The higher electron-transfer activity of most excited molecules thus derives from an enhanced electron affinity (from a vacancy in the HOMO) and a reduced ionization potential (from the high energy of the electron in the LUMO). Figure 5 shows the similarity of an excited state to a photogenerated electron-hole pair produced by irradiation of a semiconductor powder.

Relaxation of the highly energetic electron from the LUMO to the vacancy created in the HOMO regenerates the ground state, just as back electron transfer within the electron-hole pair restores the photocatalyst to its original state. Because charge recombination is so favorable energetically, the electron-hole pair typically lives only a few hundred picoseconds or less. In comparison, some excited states, depending on whether their multiplicity is singlet or triplet, can live for much longer periods, up to several microseconds in some cases. Thus, with either a surface-confined electron-hole pair or an excited state, subsequent chemical or electron-transfer events must be very fast to compete with relaxation to the ground state. These difficulties cause a reduction in quantum efficiency both in inducing chemical trapping of the electron-hole pair or in observing net chemical conversions from an excited organic molecule. This lower quantum yield is a practical limitation on the synthetic utility of either conversion, particularly if an undesired side reaction competes with the desired transformation.

8.2.3 Energy Considerations

The fixed potential of the band edges of a given semiconductor can be established independently by many physical or electrochemical methods. These band-edge positions define the limits of the attainable oxidation and reduction half reactions that can be achieved on this surface. As long as the oxidation potential of the adsorbed donor (hole trap) is lower than the valence band edge, and the reduction potential of the adsorbed acceptor (electron trap) is lower than the conduction-band edge,

Table 1. Band positions^a in some common semiconductors [30].

Semiconductor	E_{VB} (V, vs SCE)	E_{CB} (V, vs SCE)	E_g (V)	$A(E_g)$, (nm)
TiO ₂	3.0	0.0	3.0	410
SnO ₂	3.8	+0.3	3.5	350
ZnO	2.9	-0.1	3.0	410
SrTiO ₃	3.0	-0.2	3.2	390
CdS	2.2	-0.2	2.4	520
CdSe	1.4	-0.3	1.7	730
CdTe	1.4	0.0	1.4	890
GaAs	0.8	-0.6	1.4	890
GaP	1.4	-0.9	2.3	540
InP	1.2	-0.1	1.3	950

^a Approximate positions. Source: Ref. [5]. In water at pH 1.

electron transfer at the illuminated interface is thermodynamically favored, Figure 3. Although the band gap (E_g) in the semiconductor photocatalyst is subject to shifts with pH, solvent, and temperature, the corresponding onset wavelengths dictate the accessible energy for the trapped electron or hole. Thus, the valence-band edge (E_{VB}) represents a thermodynamic limit for the oxidation potential of the adsorbate of interest, whereas the conduction band edge (E_{CB}) represents the corresponding limit for the reduction half reaction.

Table 1 provides a list of these values for the most commonly accessible semiconductor powders suspended in aqueous acid, along with a conversion of the band gap to an absorption onset wavelength $A(E_g)$. The band-edge positions [30] can also be adjusted by control of the particle size of the irradiated semiconductor. Quantization effects can shift these values by more than 100 nm; this allows control of the onset wavelength and of the band positions of several common semiconductors.

By carefully choosing the semiconductor, one can select the onset wavelength over a range varying from the long-wavelength ultraviolet (UV) through the visible region. One can also define the available redox potentials accessed on that semiconductor. Single-electron transfer from an adsorbed donor can be expected to compete favorably with electron-hole recombination for any adsorbate whose oxidation potential is lower than the valence-band edge, and the corresponding single-electron transfer to an adsorbed acceptor whose reduction potential is lower than the conduction band edge is similarly exothermic.

A comparison of typical redox potentials for common organic functional groups with the valence band edge of TiO₂ reveals that many organic molecules and species can function exothermically as electron donors to a surface-bound photogenerated hole [5]. Because of the high positive valence-band edges in metal oxide semiconductors, many oxidative conversions can be conducted on aerated solutions in which the irradiated TiO₂ photocatalyst is suspended. Indeed, the high oxidizing power implied by the band edge (3.0 V vs SCE) permits single-electron oxidation of

virtually any organic substrate that contains either nonbonding electrons or a conjugated π system.

8.2.4 Solvent Effects

Because of the high photooxidative reactivity of TiO_2 , deriving from the high positive potential of a valence-band hole, even water can be oxidized on irradiated TiO_2 . In aqueous solutions, therefore, direct oxidation of an adsorbed substrate must compete with solvent oxidation [31]. The formation of hydroxyl radicals by single-electron oxidation of surface-bound water is usually the dominant process in water, with the radical having been detected by EPR spectroscopy [32–34] and implicated by isotope effects [35].

The hydroxyl radical is highly reactive toward many organic reactants, and high yields of oxidation and oxygenation products are often obtained in water. The high reactivity of $\cdot\text{OH}$ has a drawback, however, if the desired goal is controlled redox reactivity with synthetic utility, in that little selectivity or reaction control is possible for reactions initiated by a radical that is so active. Furthermore, if the organic substrate of interest is rather nonpolar, it is difficult to control the level of photo-induced oxidation. It effectively increases the adsorptivity of that product so that the partially oxidized substrate does not diffuse away from the irradiated surface. If the organic reactant is hydroxylated in the photocatalyzed surface-mediated reaction with a hydroxyl radical, further secondary oxidations are accelerated because the adsorptivity of the initial product is greater than that of the reactant.

Overoxidation, sometimes to the point of complete mineralization, is often observed in water. Of course, this complete destruction of organic materials is useful if the goal is a photocatalytic conversion that results in purification of a water stream, but for selective organic redox chemistry of use to the synthetic organic chemist, this lack of control can be disastrous.

By shift from a reactive solvent (e.g., water) to an inert solvent (e.g., acetonitrile), this problem can be easily solved. Acetonitrile is oxidized just outside the potential window of the band gap of common semiconductors, so the adsorbed substrate can be selectively oxidized. Without an oxidative source for producing hydroxyl radicals, however, there are fewer opportunities for the incorporation of OH groups.

In nonaqueous solvents, the band edges shift slightly from those seen in water at pH 1. In particular, the conduction band becomes sufficiently negative to cause reduction of oxygen, so that interfacial electron transfer to capture the photo-generated electron-hole pair generates an organic cation radical and a superoxide on the same surface. When these intermediates are formed at nearby sites, controlled new reactions can be observed. Therefore, most photoelectrochemical reactions that are of interest for their synthetic utility are attained by irradiation of metal oxide semiconductor suspensions (often TiO_2) in the presence of air while suspended in an inert solvent, often acetonitrile. Photocatalytic reactivity can be partially controlled, in fact, by the use of mixed solvents to control surface polarity [36].

8.2.5 Semiconductor Stability toward Catalytic Cycling

The utility of visible- or UV-sensitive semiconductors as initiators for redox chemistry is limited by the instability of the surface under irradiation while in contact with an oxidizable substrate or an electrolyte. This decreased activity is caused by the chemical reactivity of the semiconductor itself, so that an insulating (blocking) layer is formed or the electrode quickly corrodes. This lack of stability is particularly troublesome with small-band-gap semiconductors that adsorb strongly in the visible region.

Much attention has been devoted to solving this problem by the attachment of catalysts or inert conductive layers on the surface, by the chemical alteration of the surface composition of the semiconductor (e.g., by silicide formation), by change of the composition of the electrolyte, or by imbedding of the semiconductor in a protective layer or film. In principle, the modification of electrodes, powders, and films by chemical attachment of photoactive or electroactive catalysts [37, 38] could address these difficulties. By attaching a chemical catalyst, one can competitively improve the operational lifetime of a given semiconductor by suppressing photocorrosion and improving the rate of a desired redox reaction. Although the use of nonaqueous solvents can prolong the lifetime of II/VI and III/V semiconductors like CdS or GaAs, most non-oxidic semiconductors, especially those with narrow band gaps, which are thus responsive to visible light, quickly degrade upon exposure to light, and others even react with the organic materials in the dark.

For these reasons, most photoelectrochemical studies of organic transformations, have employed robust, highly stable metal oxides as the photosensitive surface. Metal oxides are often used for photocatalysis, since they withstand decomposition under most photoelectrochemical conditions, with TiO_2 , ZnO , and SnO_2 most frequently used for these applications. Nanocrystalline porous TiO_2 has such a large internal surface area that efficient light absorptivity and high reactivity are often attained [39]. Bicomponent metal oxides, such as WO_3/TiO_2 are also useful photooxidation catalysts [40, 41], and significant enhancement of redox activity has been observed in several large-and-small band gap composites [42, 43]. Unfortunately, these metal oxides possess large band gaps, making them responsive only to ultraviolet irradiation and, hence, less useful for solar energy conversion than their highly colored, but chemically unstable, narrow band-gap relatives are.

8.2.6 Photosensitization

Adsorption of dyes onto a semiconductor surface allows for another mode of photoactivation [44–48]. The dye adsorbs a photon, generating an excited state in which a sufficiently higher-energy orbital is populated to allow direct injection of an electron into the conduction band edge [1]. The dye thus becomes oxidized and can either react chemically with nucleophiles by bond formation or can be restored to its original oxidation level by electron transfer. In the latter case, the reaction partner is oxidized, regenerating the ground state of the sensitizer ready to participate in

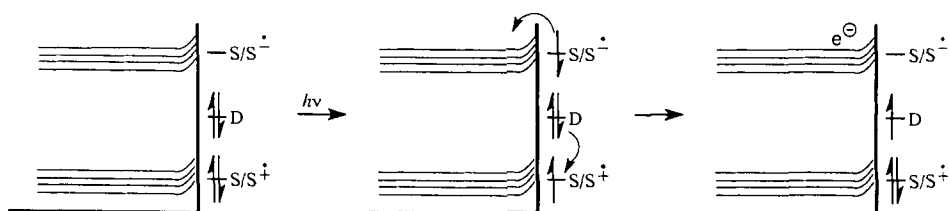
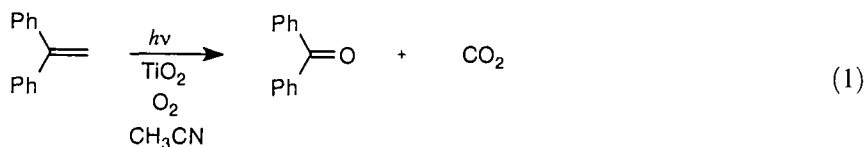


Figure 6. Oxidative electron exchange at a dye-sensitized *n*-type semiconductor electrode between the excited state of the sensitizer *S* and an adsorbed donor *D*.

another sensitization cycle and initiating permanent oxidative consumption of the donor. With dye sensitization, charge separation and oxidation of the immediately accessible donor takes place in the same manner as would have been attained by direct excitation of the semiconductor, followed by interfacial electron transfer from an adsorbed donor. (Compare Figures 3 and 6).

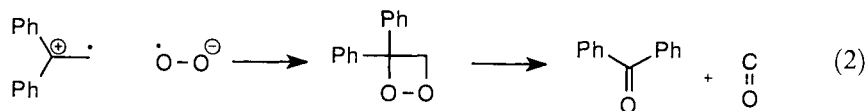
8.3 Mechanism

These arguments suggest that organic oxidations should be particularly facile on UV-irradiated TiO₂ powders suspended in CH₃CN [49]. To illustrate key mechanistic features, we will look in some detail at the oxidation of 1,1-diphenylethylene as a typical example of a photoinduced oxygenation. The products observed in this conversion are benzophenone and CO₂, Eq. 1 [50].



The thermodynamic considerations discussed earlier suggest that irradiation of a TiO₂ suspension gives rise to an electron-hole pair, with the valence-band edge at about +3.0 V vs SCE and the conduction band edge at about −0.8 V. Since the oxidation potential of 1,1-diphenylethylene is +1.8 V in acetonitrile, formation of its radical cation should be thermodynamically permissible on illuminated TiO₂. Interfacial electron transfer from an adsorbed olefin and adsorbed oxygen should thus generate an olefin cation radical and superoxide (Figure 7).

The high chemical yield of the oxidative cleavage product argues for efficient interception of a cation radical (Eq. 2), perhaps by superoxide produced by surface trapping of the conduction band electron.



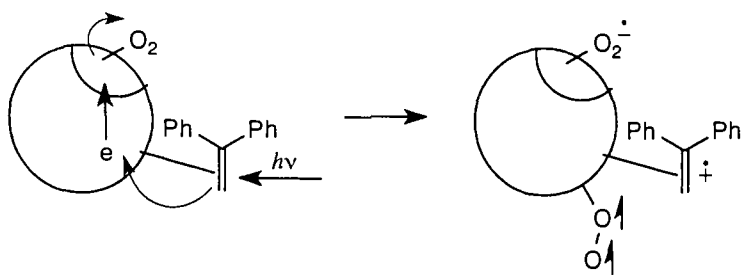


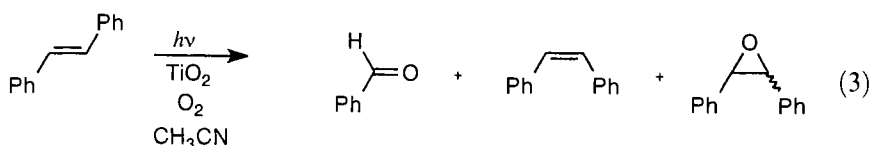
Figure 7. Trapping of the electron-hole pair to produce a cation radical and superoxide.

If so, one may expect products to result from chemical bond formation between the cation-radical-anion-radical pair, which are both paramagnetic and of opposite charge. In the latter route, there is a precedent for the formation of dioxetane intermediates of stable olefin cation radicals [51], as in the characterization by Nelsen and coworkers of a dioxetane cation radical from adamantylidene cation radical [52]. If a dioxetane is formed, either in neutral form or as a cation radical, the TiO_2 surface can function in an additional role, that is, as a Lewis acid catalyst, to induce decomposition of the dioxetane. Since no chemiluminescence could be observed in these reactions, apparently Lewis acid catalysis provides a nonradiative route for cleavage of this high-energy intermediate. That TiO_2 can indeed function in this way can be demonstrated by independent synthesis of the dioxetane derived from 1,1-diphenylethylene, which does indeed decompose to benzophenone when it is stirred in the dark on titanium dioxide.

A Hammett plot (a linear free-energy relationship) of the relative rate of oxidative cleavage of para-substituted diphenylethylenes against the σ^+ value of each substituent was indeed linear with a negative slope, consistent with the localization of positive charge in the transition state for the oxidation. Similarly, competition experiments involving mixtures of these same *p*-substituted diphenylethylenes, for which surface-adsorption equilibria can be assumed to be equivalent, showed the expected order of reactivity, consistent with formation of an intermediate involving the development of positive charge [53], that is, the more electron-donating substituent stabilized the cation radical intermediate and assisted in its formation by reducing the oxidation potential of the substituted reagent.

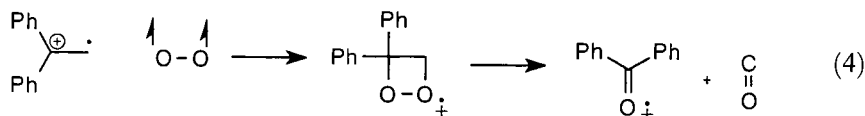
trans-Stilbene is a species that should also be exothermically oxidized by a TiO_2 valence-band hole. Indeed, direct observation of a transient radical cation from *trans*-stilbene was made when colloidal TiO_2 suspended in acetonitrile containing *trans*-stilbene was excited with a laser pulse. The observed transient was identical in absorption maximum and in lifetime to that obtained when an authentic sample of the stilbene cation radical was produced in the same medium by pulse radiolysis [54, 55]. This experiment does not necessarily prove that the cation radical is the critical intermediate in the transformation, but, since it requires the extrapolation of similar photochemical reactivity to colloids and powders, it does demonstrate that single-electron transfer can be induced by photoexcitation of the semiconductor.

Furthermore, the transient formation of cation radicals can be observed when a colloidal titanium dioxide suspension is flashed in the presence of an olefin [56]. The flash photolysis experiments also show that the surface influences the subsequent chemistry of the photogenerated intermediate. In fact, oxygenation and isomerization dominated the chemistry observed for *trans*-stilbene, with the same product distribution obtained upon starting with either the *cis* or the *trans* isomer (Eq. 3).



However, no cyclization products could be observed, in contrast to the results observed with the *cis*-stilbene cation radical produced in homogeneous solution.

A different mechanistic possibility (from the recombination of the cation radical with superoxide) is that the organic cation radical formed by oxidative capture of the photogenerated hole at the irradiated surface could be trapped by co-adsorbed triplet oxygen (Eq. 4).



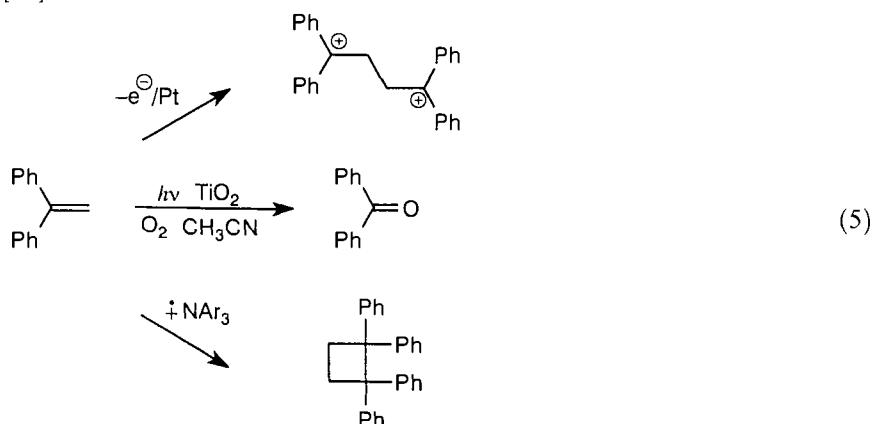
Oxygenation products would likely be formed, and it is difficult, indeed, to exclude this route, given the high concentration of adsorbed oxygen present on the photocatalyst's surface. The formation of oxidative cleavage product would at some stage require either back electron transfer from a surface-bound reduced species or direct trapping of a conduction-band electron by the oxygenated cation radical.

Superoxide (O_2^-), the expected side product produced by trapping a conduction band electron, is itself highly reactive, and we also should consider whether an alternative mechanism (superoxide + neutral DPE) might account for the observed products. However, control experiments show that superoxide solubilized in acetonitrile is unreactive toward 1,1-diphenylethylene in the dark [50]. Furthermore, added superoxide scavengers are ineffective at inhibiting the oxidative cleavage of DPE. Thus, if superoxide is formed, it never escapes from the irradiated surface. Rather, it must intercept singly oxidized intermediates generated on the irradiated semiconductor.

Back electron transfer between the olefin cation radical and superoxide would also be thermodynamically favored and would decrease the efficiency of the photochemical oxidative cleavage. It is also possible that, because spin restrictions are relaxed within the radical ion pair, the recombination could potentially generate singlet oxygen. Were it formed in this way, singlet oxygen would indeed oxidize 1,1-diphenylethylene to benzophenone. However, there is no evidence for the involvement of singlet oxygen as a general route, since the chemistry of singlet oxygen differs significantly from that observed on irradiated semiconductors. Tetramethylethylene, for example, reacts with singlet oxygen in homogeneous solution by a

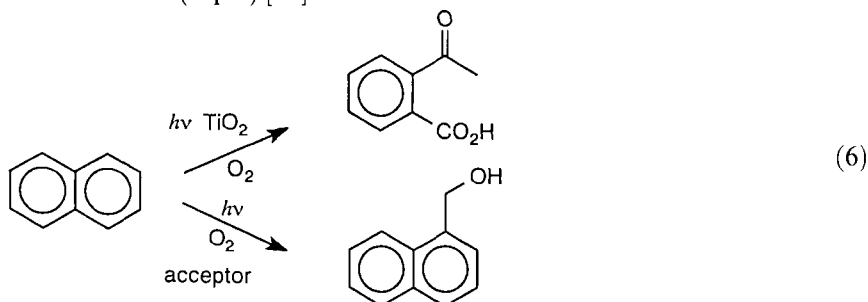
clean ene reaction, giving an allylic hydroperoxide as a major product [57]; however, when the same reagent is activated photocatalytically by irradiation of titanium dioxide in the presence of tetramethylethylene, a complex mixture is produced in which oxidative cleavage is the main pathway. Foote and coworkers have shown that singlet oxygen is unreactive toward *trans*-stilbene, unless electron-transfer pathways are involved [58]. Thus, if singlet oxygen is ever formed by reversible electron transfer on an irradiated semiconductor surface, its subsequent chemistry differs significantly from that observed in solution.

Because radical ions are known to react through a number of possible reaction pathways, [59], photoelectrochemistry provides, in principle, a possible method for choosing among competitive routes. The formation of a cation radical by hole trapping by an organic donor on an irradiated semiconductor surface often gives rise to products different from those obtained on a poised metal electrode or those derived from the same cation radical when produced in homogeneous solution (Eq. 5) [60].



Thus, the photocatalyst not only generates the radical ion but also controls its subsequent chemistry.

The selection of one preferred route for dark secondary reactions from photogenerated cation radicals can also be seen in the products derived from 1-methylnaphthalene. Although ring cleavage is observed on irradiated TiO_2 suspensions, side-chain oxidation of the corresponding radical cation takes place in homogeneous solution (Eq. 6) [61].



We conclude that photocatalysis on irradiated metal oxide surfaces is initiated by interfacial single-electron transfer to capture the photogenerated hole in a likely first step in oxidative photocatalysis. This route produces an olefin cation radical when an alkene is the substrate of interest. This species is then trapped by adsorbed oxygen, producing a strained intermediate that is opened and cleaved under the Lewis acidic conditions operative on the surface of TiO_2 . Analogous single-electron oxidations are also likely as the first step in other organic conversions observed on TiO_2 , as we will see in the following sections.

8.4 Chemical Selectivity through Photoelectrochemical Activation

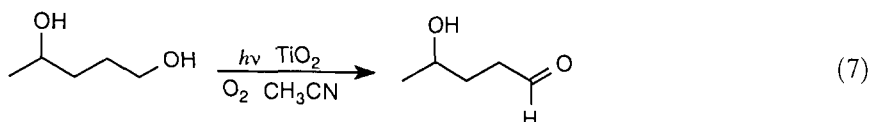
In principle, like all electrochemical reactions initiated by the transfer of an electron across an electrode–electrolyte interface, photoelectrochemical transformations offer the possibility of more precise control than can be attained with reactions that take place in homogeneous solution [62, 63]. This better selectivity derives from three features associated with reactions that take place on surfaces, and hence with the photoelectrochemical event: the applied potential (allowing for specific activation of a functional group whose oxidation potential is higher, even in a multifunctional molecule); the chemical nature of the electrode surface (and hence of the adsorption equilibrium constant of a specific molecule present in the double layer); and, finally, control of current flow (and hence a constraint on the number of electrons passed to an adsorbed reactant).

8.4.1 Adsorption and Surface Effects

Preadsorption of an active substrate has been shown from kinetic studies to be necessary for efficient photoelectrochemical activation. The factors that influence the binding constant for a substrate of interest adsorbed on the surface of metal oxide semiconductors can be quite complex. Proton exchange can take place readily at the acidic and basic sites that exist on TiO_2 [64, 65] and even without proton exchange and electrostatic effects, strong hydrogen-bonding interactions can also influence these equilibria. [66–68] Charge-transfer interactions [64, 69] have also been suggested as significant influences on adsorption equilibria. Even substrates lacking polar or ionizable groups, for example, saturated hydrocarbons, have been observed to bind to oxide surfaces, through nonspecific dispersion forces [64].

Because adsorption equilibria can produce a substantially different population at the semiconductor–liquid interface than is present in solution, interfacial charge trapping can produce specific activation of the better adsorbate from a mixture. Thus adsorption pre-equilibria are likely to be important in controlling the relative rates of photooxidation of competing substrates on semiconductor surfaces. Because adsorption equilibria can be influenced by the addition of very small amounts of co-solvent additives, higher reactivity [36] and higher selectivity can often be simulta-

neously observed in the oxidation of a more strongly adsorbed site over a less strongly adsorbed one. This preference can even be observed for preferential adsorption sites within a single molecule, for example, a 7:1 preference for oxidation of the primary site over the secondary site is observed in the photocatalytic oxidation of 1,4-pentanediol on illuminated TiO_2 (Eq. 7) [65].



Most reactions on surfaces are complicated by variations in mass transfer and adsorption equilibrium [70]. It is precisely these complexities, however, that afford an additional means of control in electrochemical or photoelectrochemical transformations. Not only does the surface assemble a nonstatistical distribution of reagents compared with the solution composition, but it also generally influences both the rates and course of chemical reactions [71–73]. These effects are particularly evident with photoactivated surfaces: the intrinsic lifetimes of both excited states and photogenerated transients and the rates of bimolecular diffusion are particularly sensitive to the special environment afforded by a solid surface. Consequently, the understanding of surface effects is very important for applications that depend on chemical selectivity in photoelectrochemical transformation.

First, it is important to recognize that the chemical character of a surface, even for those faces that are not photosensitive, can change the rates and reaction paths of chemical reactions taking place thereon [74]. The effect of the surface on the diffusional motion of adsorbates, whether they are stable species or reactive intermediates, depends sensitively on the adsorptive forces that bind the reagent to the reaction site. When a substrate of interest is adsorbed, surface confinement changes the electronic distribution in the molecule and, hence, both the accessible trajectories for interaction with another reagent and the molecule's electron density.

Even the underlying support can influence relative reaction rates [75]. For example, when a photochemical precursor to a family of benzylic radicals, for example, benzyl phenylacetate, a dibenzyl ketone, or a dibenzyl sulfone, is irradiated while adsorbed on dry silica gel [76], spectroscopic measurements can demonstrate that singlet and triplet radical pairs are produced. The details of reactions taking place through radical recombination show that local adsorption mimics many of the same characteristics of solution-phase cage effects. That is, preadsorption dictates that translational motion of the photogenerated radicals is greatly influenced by the silica gel surface. The extent to which this motion is affected by the radical-pair multiplicity and by temperature varies with the chemical character of the surface, but is rather insensitive to the state of hydration of the silica gel and the presence or absence of co-adsorbates. That no rearrangement products were formed in homogeneous solution from the same substrates implies that restricted motion indeed influences the subsequent reactivity of surface-bound reagents. For example, the yield of photo-Fries rearrangement product derived from amides on silica gel is much higher than in solution [77], with a much larger proportion of the *para* isomer.

Stereochemistry is also affected in a significant way by surface adsorption. When enone photocycloadditions are allowed to occur as adsorbates on silica gel or alumina, larger fractions of reaction product derived from attack on the more hindered β face are observed. Thus, surface adsorption apparently influences conformational inversion, enhancing the formation of *trans*-fused products. This effect is synthetically useful, for sometimes a complete reversal of stereochemistry is observed compared with that seen in methanolic solution.

The surface also presents a highly polar environment that can favor formation of polar products. In the photooxidation of basic aqueous triethanolamine sensitized by $\text{Ru}(\text{bpy})_3$ and mediated by N,N' -bis-(3-sulfonatopropyl)-2,2'-bipyridine, SiO_2 colloids stabilize intermediates that bear electrostatic charge, in contrast with the suppression of hydrogen evolution in homogeneous aqueous solution under similar conditions [78]. The surface charge of the particles assists in charge transfer within the cage, repelling the reduced bipyridinium product and thus retarding the recombination rate. Other profound shifts in reaction rate are observed upon changing the ionic strength and pH of the contacting solution, and similar effects have also been observed on other metal oxide colloids [79, 80], and when the colloids are trapped within micelles, vesicles, and so forth. The pH also affects the rate of photocatalytic degradation, presumably because of adsorption effects [81, 82].

Physical techniques for evaluating surface polarity led deMayo and coworkers to assign relative rates of reaction on silica gel particles from shifts in the absorption spectra of absorbed spiropyrans [76, 77]. Similarly, Darwent and coworkers demonstrated that kinetic salt effects correlate with surface charge and with zeta potential measurements on colloidal titanium dioxide [80].

On metal oxide and metal chalcogenide semiconductor surfaces, multiple adsorption sites are accessible. On titanium dioxide, for example, there are acidic, basic, and surface defect sites available as likely targets for adsorption. Although the applicable adsorption isotherms differ at each site, selective activation toward a desired product on a specified semiconductor surface may indeed depend on photocatalyst preparation, which may in turn influence the relative fraction of each type of adsorption site. Although the number of basic sites can be determined by titration, the total number of acidic sites is more difficult to establish experimentally because of competitive water adsorption. Roughly, there are 2.4 times more acidic than basic binding sites on several of the commercially available TiO_2 .

In most photocatalysis, Langmuir–Hinshelwood kinetics is observed, suggesting the importance of substrate adsorption in key steps of the reaction [83]. That is, the rate of photocatalysis is proportional to the concentration (or pressure) of the reactant, which in turn can be related to the surface coverage Φ by the Langmuir expression, Eq. 8,

$$\Phi = KC/(1 + KC) \quad (8)$$

where K is the adsorption coefficient and C is the initial concentration of the reactant.

Occasionally, deviations from this simple expression have been observed, with most such observations being attributed to mechanistic complexity. For example,

the relative importance of the Langmuir–Hinshelwood mechanism relies entirely on the surface association of the adsorbed species, whereas the Eley–Rideal route takes place in such a way that the reaction proceeds by collision of a dissolved reactant with surface-bound intermediates [84]. In practice, however, both kinetic descriptions show the same kinetic profiles; this makes it difficult to unambiguously delineate the specific adsorption mode. Although similar kinetic profiles are shown for both transformations, trichloroethylene adsorbs at Ti sites by a π interaction, whereas dichloroacetaldehyde, an intermediate proposed in the photocatalyzed decomposition of trichloroethylene, is dissociatively chemisorbed by attachment of the α -hydrogen to a oxide surface site [85].

This surface-binding complexity is even further complicated by photoexcitation and by the presence of other adsorbates on the same surface. Detailed kinetic investigations have shown that adsorption and photoadsorption are influenced by thermal removal of water and surface hydroxyl groups [86]. Preadsorption of other reagents on SnO_2 can produce a substantial increase in oxygen photoadsorption under sub-band-gap irradiation and can shift the photosensitivity threshold to much longer wavelengths.

Thus, surface effects and adsorption equilibria can dramatically influence the relative reactivity of photoelectrochemical transformations. Not only does the surface effectively control the movement of reagents from the electrolyte to the photo-activated surface and the desorption of products (avoiding overreaction or complete mineralization), but it also influences the stability and accessibility of photo-generated intermediates toward secondary intermolecular reactions [87]. Because the efficiency of diffusion and mass transfer to and from the photocatalyst surface depends on the solvent and catalyst pretreatment, quantitative predictions of photocatalytic reactions have proved to be difficult, although the qualitative principles governing each step of these events can be easily recognized.

Surface properties of semiconductors can vary with size of the crystal or crystallite. In large crystals, electron delocalization is so extensive that the crystal properties are collective and bear no close resemblance to the electronic states of the components. The presence of highly crystalline phases at the surface of a semiconductor particle causes profound changes in structure, bonding, and reactivity of adsorbates, so that a moderate size cluster of the individual molecules must be formed before full solid-state properties will be observable. Reducing the size of the semiconductor particle from single crystal to colloids or clusters will eventually disrupt the macroscopic characteristics of the large particle and will significantly affect the course of photoinduced electron-transfer reactions [88–93].

The use of arrested precipitation to prepare sized semiconductor particles from solution has made it possible to prepare colloidal clusters of narrow size distribution. Dramatic blue shifts in the absorption maxima of such aggregates are observed as the colloidal cluster size is reduced; this is a consequence of the kinetic energy requirement for spatially localizing the electron-hole pair at neighboring sites in a small particle. ZnS crystallites with an average diameter of 20 Å, for example, exhibit an apparent band gap that is blue-shifted by about 0.6 V from that observed in bulk crystals. Even larger shifts are observed with HgSe and PbSe semiconductors, where, with diameter sizes less than 50 Å, the optical edge is shifted

by about 2.8 V. Although the chemical consequences of these electronic changes are still not clear, such quantum size effects are bound to influence photocatalytic activity. With such shifts, the flat-band potentials become slightly more negative and the surface charge shifts.

The rate of flow of electrons across the interface from such a charged particle depends on the availability of an accessible site for this transfer. Lattice defects provide sites where conduction-band electrons can be easily transferred through solid dislocation levels. Reduction sites for electron accumulation are usually provided by metalization of the semiconductor particle. This can be achieved through in situ reduction of metal salts, resulting in metal island deposition, or by a number of vapor-transfer techniques. The existence of such sites will thus control whether single or multiple electron-transfer events can actually take place under steady-state illumination.

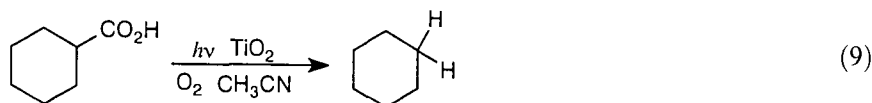
The surface crystal structure and particle size can also influence photoelectrochemical activity. The mode of pretreatment, for example, dictates whether titanium dioxide exists in the anatase phase (as is likely in samples which have been calcined at temperatures below 500 °C) or in the rutile phase (from calcination temperatures above 600 °C) or as a mixture of the two phases for pretreatments at intermediate temperature ranges. The effect of crystalline phase could be easily demonstrated in the photocatalytic oxidation of 2-propanol and reduction of silver sulfate, where anatase is active for both systems. But when the catalyst was partially covered with platinum black, alcohol oxidation was easy, but silver ion reduction was suppressed. On rutile, redox activity was observed for Ag^+ , alcohol oxidation was negligible [85].

Particle-size control can also be afforded by the colloid being constrained to vesicles, membranes, or zeolites. With small particles or clusters, a range of oxidative efficiencies is observed by spectroscopic methods [94]. The observed rates are non-Arrhenius, which the authors explain to be a function of multiphonon electron tunnelling, probably to preexistent traps. The shorter lifetimes observed at shorter emission wavelengths were thought to indicate significant Coulombic interaction between traps. An intriguing recent report achieves size limitation of semiconductor electrodes by preparation by photolithography techniques. The use of specially designed particles with controlled size, morphology, surface catalysts, and dopants can surely influence the selectivity, which can ultimately be attained in photoelectrochemical conversions. Only very few explorations of these effects in organic systems have yet been made.

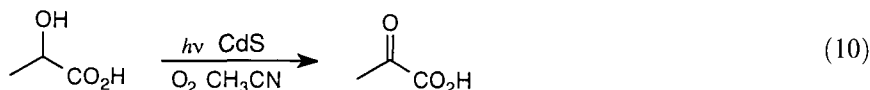
8.4.2 Potential Control

In principle, chemoselectivity should be achieved if the oxidation potential of a desired donor adsorbate lies between the valence-band edges of two possible semiconductor photocatalysts. Given that TiO_2 has a more positive valence-band edge than CdS , the former should be the more active photocatalyst. By switch of the excited photocatalyst from TiO_2 to CdS , the reactivity of the photogenerated hole toward oxidative activation is greatly changed. Consistent with this idea, decar-

boxylation of organic acids (Eq. 9) is much more efficient on irradiated suspensions of rutile than on CdS [95].



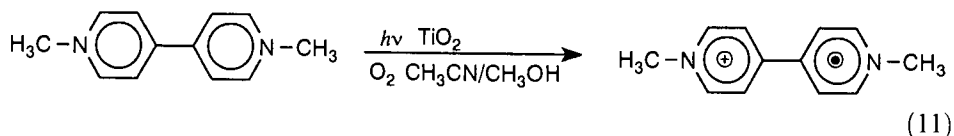
Chemical differentiation between two oxidizable sites in the same molecule can also be achieved in organic photocatalytic reactions by choice of a different semiconductor and thus adjustment of the electrochemical band-edge positions. Consistent with this idea, the photocatalytic oxidation of lactic acid on UV-irradiated platinumized-TiO₂ leads to decarboxylation, presumably through the singly oxidized carboxyl radical. In contrast, the same reagent on irradiated platinumized CdS leads to pyruvic acid by oxidation of the alcohol group (Eq. 10) [96].



Unfortunately, shifts in the valence-band edge position and in surface adsorptivity do not always give functional-group-specific oxidation or the expected order of reactivity. For example, different product distributions in oligopeptide formation were achieved by the light-responsive semiconductor being changed: diglycine is formed twice as efficiently on platinumized TiO₂ as on platinumized CdS, whereas pentaglycine is formed four times faster on CdS/Pt than on TiO₂/Pt [97]. Presumably, this imprecision reflects complicated dependence on electron-exchange reactions and kinetics governed by surface effects. For example, when potentiostatic oxidation of lactic acid was conducted in the dark on glassy carbon at +1.3, +1.5, or +1.6 V (potentials respectively less positive, nearly equivalent to, and more positive than the valence-band edge of CdS under photocatalytic reaction conditions), only decarboxylation could be observed. Furthermore, nearly equivalent current doubling was observed on both TiO₂ and CdS; this suggests no evident difference in the mechanism on these two materials, and that observed chemoselectivity may be more strongly influenced by adsorption differences on the semiconductor surface than by band-edge effects.

It is important to note that if the band edges of an illuminated semiconductor govern its photoelectrochemical reactivity, then experimental variation with solvent will take place, since the band positions of many common semiconductors [12, 20, 21] shift with changes in electrolyte. The shift of great importance in oxidative organic phototransformations is that of the conduction band edge. As the band edge moves above or below about -0.8 V, it loses or retains the ability to reduce adsorbed oxygen, for the reduction potential of oxygen in acetonitrile is -0.78 V. Thus, oxygen can assume a dual role in photocatalytic half reactions, either acting as an electron trap in generating superoxide on illuminated titania particles or as a chemical trap for singly oxidized organic intermediates produced on the photocatalytic surface.

Even though photoelectrochemical activation of rutile or anatase can thus be envisioned as a means for oxygen activation, and although most photocatalytic transformations are conducted in the presence of air, other acceptors with reduction potentials less negative than the conduction band edge can also act as electron traps. Flash photolysis of a colloidal suspension of TiO_2 in the presence of methyl viologen, for example, shows direct evidence (spectroscopic absorption) of the single-electron reduction product (Eq. 11) [98].



Thus, the band positions of the irradiated semiconductor are key thermodynamic variables for in the control of the observed redox chemistry resulting from photocatalyzed single-electron transfer (charge trapping) across the semiconductor–electrolyte interface. Whether oxygenation, rearrangement, isomerization, or other consequences follow this initial electron transfer seems to be controlled by surface effects on the relative rates of reaction.

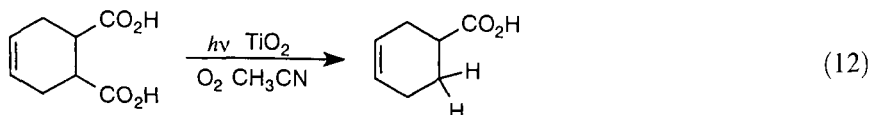
8.4.3 Current Control

Ultraviolet irradiation of a photocatalyst creates an electron-hole pair, and hence activates the semiconductor surface, thereby offering several important advantages over analogous transformations that might take place in a standard electrochemical cell. An electron-hole pair on the surface of a metal oxide is sensitive to light flux, because control of the number of incident photons will also control interfacial current flow. Upon irradiation, semiconductor particles become active centers for electron exchange, but their activity is immediately extinguished as soon as interfacial charge transfer takes place. If the number of incident photons is low, the number of photogenerated electrons and holes available to each adsorbate will also be low. In turn, the observable quantum yield of products will be decreased [99–101]. The absorption spectrum of the semiconductor will also influence reactivity because of shifts in wavelength, and the characteristics of the semiconductor particle (crystal morphology, doping densities, or surface pretreatment) will influence the kinetics for subsequent reactions and hence the distribution of products induced by photoexcitation. The quantum efficiency can be therefore be enhance by intermittent irradiation alternating with an intervening dark period [100, 101].

In a conventional electrochemical cell poised at a high positive potential, oxidation of an adsorbed donor by interfacial electron transfer occurs readily. If the product of that single-electron oxidation is itself oxidized at the applied potential, a second electron also flows. This is a relatively common occurrence for substrates that undergo a geometry change after the initial oxidation, either by bond cleavage or by a twist about a multiple bond.

In contrast, photoelectrochemical activation depends on the trapping of the photogenerated electron-hole pair, usually by the capture of a highly oxidizing, surface-confined hole. But after interfacial electron transfer from an adsorbed donor has taken place, the hole is filled and further oxidation is blocked. Thus, because the number of adsorbed molecules is much higher at any time than the number of photogenerated holes on an irradiated surface, most photocatalytic transformations proceed through single-electron oxidation, even in reactants that participate in multiple -electron oxidation in conventional electrochemical cells.

This current-control feature can be illustrated in the electrochemical decarboxylation of vicinal diacids. These reagents have long been used as protecting groups for double bonds, since electrochemical deprotection by two-electron oxidation causes bis-decarboxylation and production of a C=C double bond [60]. In contrast, when platinized titanium dioxide is irradiated in the presence of one such vicinal diacid (cyclohexenedicarboxylic acid), the major reaction pathway leads to mono-decarboxylation, rather than to benzene formation (Eq. 12).



It is likely that this reaction takes place through a surface-adsorbed radical whose further oxidation is blocked by the immediate step in surface oxidation potential that accompanies interfacial electron transfer to trap the photogenerated hole. On the surface of a photocatalyst, this radical is reduced to an anion, and protonated, producing a C-H bond.

This control, of course, depends on the surface density of photogenerated holes, which in turn depends on incident light flux. At high incident light intensities, surface charge can accumulate, sometimes to a loading that permits electrophoretic mobility even of a quite large particle [102, 103]. When appropriately prepared, colloidal TiO_2 can apparently accumulate charge to directly effect multiple quanta redox reactions. Such charge accumulation produces charge densities that are directly related to the doping level of the semiconductor. Thus, pretreatment to influence the doping level not only alters band positions but may also improve the efficiency of photoinduced electron transfer, making even very difficult reactions possible. For example, the dispersal of Fe_3O_2 into doped TiO_2 produced a material with greatly improved properties for nitrogen reduction.

8.5 Selective Photoelectrochemical Transformations

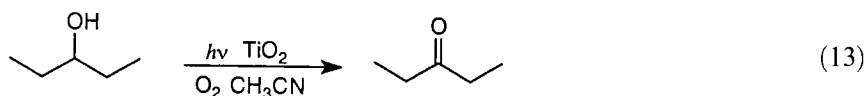
The relevant principles influencing chemical selectivity in photoelectrochemical reactions having been discussed, we can now survey the use of such techniques in

organic chemistry. Although the quantum efficiency for some photoelectrochemical transformations can be quite low, the additional modes of chemical control afforded by adsorption and surface effects, by band-edge-dependent selectivity, and by Coulombic control of interfacial electron transfer make the use of photoelectrochemical activation an attractive synthetic technique.

8.5.1 Oxidations

Most common metal oxide and metal chalcogenide semiconductors have valence-band edges that lie positive of the oxidation potentials of most organic functional groups, and thermodynamics will thus favor photocatalytic oxidation. For efficient processes to take place, an easily oxidizable donor is required, but a whole range of substrates have been shown to be useful for this application. For example, a Japanese group has shown that this purpose is served not only by pure compounds, but even by wastes such as polyvinyl chloride, algae, protein, dead insects, and animal excrement, which function as electron sources [104]. Thus, synthetic utility is attained only if this wide reactivity is controlled. In practice, selectivity is best controlled by the adsorption and oxidation potential effects [105].

Given that single-electron oxidation is mechanistically important in these reactions, the thermodynamic criteria discussed earlier can be used, together with the known reactions of cation radicals, to predict new organic oxidation products. For example, there is a wide variety of oxidations that proceed by photoelectrochemical methods. Alcohols, for example, can be oxidized to the corresponding carbonyl compounds in high yield [106–118] (Eq. 13).



In fact, primary alcohols can be selectively oxidized to the corresponding aldehydes, without appreciable overoxidation, whereas poorer yields were obtained with secondary aliphatic aromatic alcohols [106c]. Similarly, phenols can be converted to quinones [118]. The efficiency of the photocatalytic oxidation depends on the pretreatment and size of the photocatalyst [119], and analogous conversions are also obtained on heteropolyacids, which can be considered soluble analogs of TiO_2 suspensions [120].

Anatase is much more active than rutile in the liquid-phase photooxidation of 2-propanol, and the observed reactivity compared well with that of gaseous alcohol on platinized titania [106a]. Because most early studies employed the alcohol as a sacrificial reagent for the photochemical production of hydrogen, the organic product was often not analyzed and little effort was devoted to the selective activation of alcohols in the presence of other functional groups. In the oxidation of car-

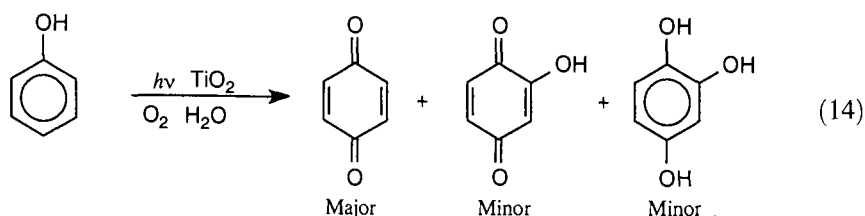
bohydrates, for example, complete oxidative conversion to hydrogen and carbon dioxide was a primary goal [109]. Even with this orientation, however, it is clear that the chemical structure of the alcohol affected the quantum yield of hydrogen, with methanol and ethanol being more efficiently oxidized than other primary alcohols, and water being oxidized as least four times less efficiently than methanol [110].

The effect of doping could be easily explored in this series. For liquid-phase alcohol photooxidations, best photoefficiency was attained with a platinum loading of TiO_2 of 0.1–1 weight %, and other noble and transition metals, when deposited on the metal oxide photocatalyst, also enhanced the photoredox reactivity, in the decreasing order $\text{Pt} > \text{Rh} > \text{Pd} > \text{Ru} > \text{In}$ [111]. Pretreatment of the photocatalysts at high temperature often enhanced hydrogen evolution, as did the presence of transition metal oxide dopants. Vanadium and molybdenum oxides present on the surface of TiO_2 , for example, increased the rate, but decreased the selectivity, in the thermal oxidation of methanol, but decreased its photocatalytic activity [112]. The addition of alkali metal salts similarly shifted the selectivity in the photooxidation of aqueous methanol toward water, and induced further oxidation of acetaldehyde and acetic acid, the partially oxidized products derived from methanol [113]. With metallic nickel as a support, 2-propanol could not be photocatalytically oxidized on SrTiO_3 , CdS , or TiO_2 without water, and no hydrogen evolved if oxygen was present [113]. A mechanism focusing on surface binding to a hydroxyl group at acidic sites was implicated.

In only a few of these studies was chemical selectivity considered. For example, primary alcohols could be selectively oxidized to the corresponding aldehydes, without appreciable overoxidation, when the platinized TiO_2 photocatalyst was suspended in benzene (Eq. 7). Poorer yields were obtained with secondary aliphatic or aromatic alcohols [106c]. In photodehydrogenation of mixtures of ethanol and D_2O , D_2 was found to be the major gaseous product, suggesting selective binding of water. In the photooxidation of sorbitol, the photocurrents produced on illuminated TiO_2 were found to depend on molecular structure (chain length and the number of OH groups). The reactions were pH dependent and the effects were ascribed to the high concentrations of OH groups at the photoactivated surface when long-chain polyols were adsorbed [116]. The photoelectrochemical oxidation of primary or secondary tertiary alcohols was much more difficult than that of primary or secondary alcohols, and primary sites could be oxidized selectively in the presence of secondary ones.

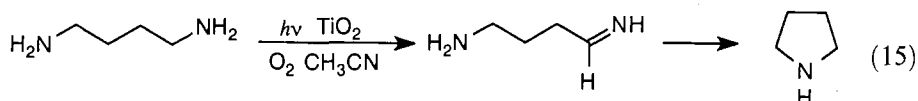
Quantum efficiencies for photooxidation were improved by platinization of the TiO_2 photocatalyst, with the observed yield increasing linearly with platinum coverage [117–121]. Acetone was the major product in the presence of air or silver ion, a result that was similar to those observed upon γ irradiation or in the Fenton reaction. This similarity was interpreted as implying hydroxyl radical mediation of the observed oxidations.

In the photooxidation of phenol on an irradiated suspension of titanium dioxide, the hydroxyl radical was also directly implicated as the reactive species [122], with oxygen incorporated in the observed organic products (Eq. 14) [118].



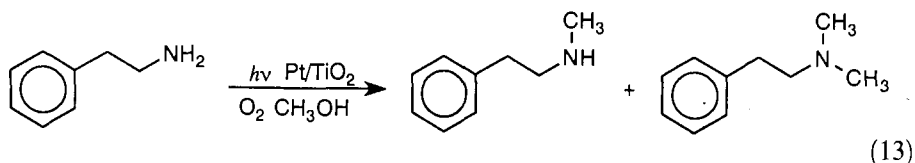
On further photolysis, aldehydes, acids, and CO_2 could be obtained. Selectivity was attained within a series of chlorinated phenols [122], and the rate of phenol oxidation depended on the coadsorption of Fe^{3+} or Ag^+ onto the surface of the photocatalyst [123].

Organic compounds bearing heteroatoms from the same column in the periodic table also react by similar paths. Photocatalytic oxidation of primary amines on irradiated semiconductor suspensions, for example, forms Schiff bases which can couple with the starting amine [124]. Two different products are formed, depending on the initial concentration of the amine and on the nature of the semiconductor catalyst (Eq. 15) [125].

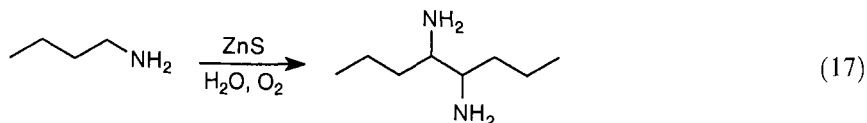


Formylation was also observed when the amine conversion was carried to high conversion. Secondary amines are obtained from primary amines, and diamines can be cyclized photoelectrochemically.

If the photocatalytic irradiation is conducted in the presence of an alcohol, *N*-alkylation is observed (Eq. 16) [126].

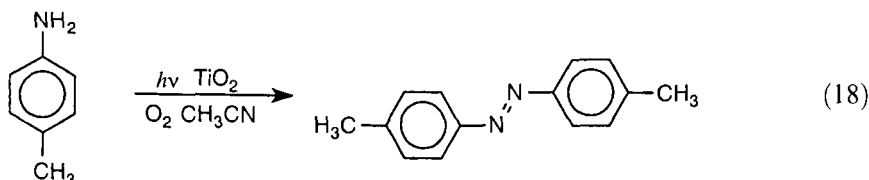


The photoefficiency varied with alcohol structure: ethanol > methanol > 2-propanol > *tert*-butanol. If the reaction is conducted under a hydrogen atmosphere, the production of amines is enhanced, a process which was inhibited by oxygen. Amines bearing α -hydrogens react by carbon-carbon coupling at the α -positions, as do ethers and some substituted alcohols [115a]. On colloidal ZnS, for example, α -coupling, presumably through a radical produced by deprotonation of the photo-generated radical cation, is observed with amines (Eq. 17) as well as with ethers and alcohols.



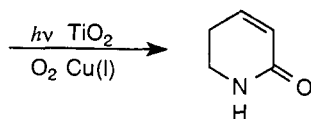
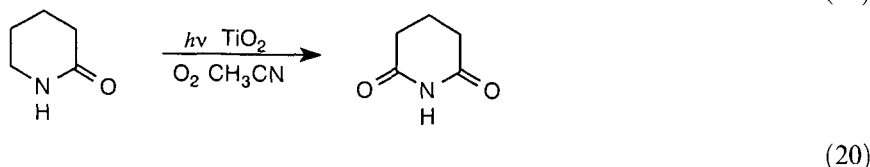
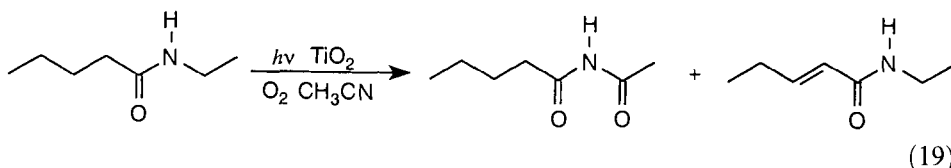
Cleavage adjacent to nitrogen was also observed in the photoelectrochemical demethylation of methyl orange [127]. Photocatalytic cleavage of an *N*-methyl group was competitive with C–N cleavage adjacent to the azo linkage.

The photoelectrochemical activation of aryl amines also produces coupling at nitrogen. With toluidines, for example, azo products are formed (Eq. 18) [128].



Formation of a nitrogen radical by N–H deprotonation must be faster than α -deprotonation of the pendant alkyl group. Similarly, pyrrole could be photopolymerized [129] and picolines could be photocatalytically degraded [130].

Amides are oxidized to either imides or α,β -unsaturated amides [131, 132], sometimes quite chemoselectively (Eq. 19). Lactams can be photocatalytically converted to imides (Eq. 20), but if the reaction is conducted in the presence of Cu(I), unsaturation is induced instead.

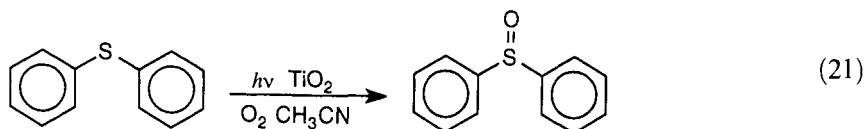


The oxidative photoelectrochemical synthesis of amino acids from simple molecules (ammonia, methane, and water) has been reported [133, 134]. Low efficiencies were observed in the conversion of mixtures of methane, ammonia, and water to several amino acids on platinized TiO_2 . Amino acids and peptides were formed when glucose replaced methane as the carbon source in a parallel experiment. Higher quantum efficiencies (20–40 %) were observed in the conversion of α -keto acids or α -hydroxy acids to the corresponding α -amino acids, and moderate levels of enantiomeric selectivity (optical yields of about 50 %) were reported when chiral starting materials were employed.

The resulting amino acids are coupled to oligopeptides on irradiated TiO_2 [97].

The molecular weight distribution of the peptides could be partially controlled by choice of the sensitizer: diglycine was formed twice as efficiently on platinized titanium dioxide as on platinized cadmium sulfide, whereas the yield of pentaglycine was four times higher on CdS/Pt than on TiO₂/Pt.

Thioethers convert cleanly to the corresponding sulfoxides [135], (Eq. 21), even in competition with other oxidizable groups [136, 137].



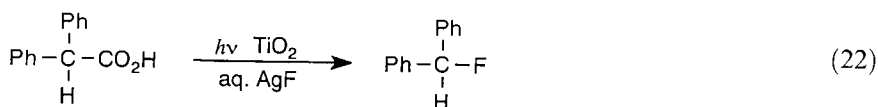
Not surprisingly, thiols can be oxidized cleanly to disulfides [138], as in the CdS-photocatalyzed conversion of cysteine to cystine, where the uptake of oxygen was pH dependent. The reaction rate was not increased in deuterium oxide nor decreased by added azide, suggesting that singlet oxygen is not involved. Superoxide dismutase did inhibit the conversion. Phosphines and phosphonic acids undergo similar oxidative transformations [139].

Photocatalyzed oxidative decarboxylation of carboxylic acid is an important oxidative degradation route [140–144]. Simple carboxylic acids suffer photo-Kolbe decarboxylation under the usual photoelectrochemical conditions (Eq. 9). In the decarboxylation of acetic acid on an irradiated *n*-TiO₂ single crystal or polycrystalline electrode, for example, ethane was formed, whereas methane was produced on irradiated TiO₂ powders. Depending on the identity of the semiconductor, the extent and identity of the adsorbed metal, and the pH of the solution, the extent of alkyl coupling as opposed to reduction could be closely controlled. The different reactivity observed on dark electrodes and illuminated powders probably derives from the different space-charge thickness developed on each surface. On a powder, a newly formed radical will persist until it is trapped by a co-adsorbate or until back electron transfer generates an anion, protonation of which allows for surface desorption. The critical involvement of alkyl radicals has been established in spin-trapping experiments, although deuterium incorporation seems to implicate the eventual protonation of an anionic intermediate.

Consistent with this idea, the photocatalyzed decarboxylation of oxalic acid was found to be controlled by surface properties and by the presence of recombination centers, which in turn depended on the photocatalyst preparation method [142]. Analogous results have been observed in the photodecarboxylation of pyruvic acid [143] and formic acid [144].

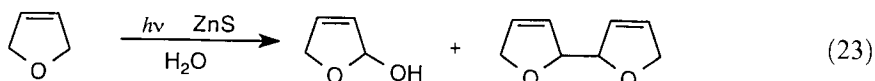
As we saw earlier [60, 145] with vicinal diacids, mono- or bis-decarboxylation occur, depending on incident light flux (Eq. 12). At low light flux, the primary product is that of monodecarboxylation. Multiple carboxylic acids such as ethylene diaminetetracarboxylic acid also suffer decarboxylation under photocatalytic oxidation conditions [146].

Carboxylic acids have also been converted to the corresponding fluoride upon irradiation of TiO₂ suspended in an aqueous solution also containing silver fluoride [147] (Eq. 22).



In the conversion of di- and triphenylacetic acid to the corresponding fluorides, laser flash photolytic investigations demonstrated that a carbocationic intermediate was trapped by fluoride in the key step. This interesting conversion was claimed to take place through a two-photon process in which the photocatalytically generated radical remains bound to the surface of the photocatalyst, then trapping a second photogenerated hole to produce a carbocation.

The surface-enhanced carbon-carbon coupling of radicals required for carbon-carbon bond formation in the photo-Kolbe reaction could also be observed with other surface-generated radicals. Cyclic allylic ethers are deprotonated at the position adjacent to oxygen under photoelectrochemical activation, producing radicals that can dimerize or be trapped with oxygen [148] (Eq. 23).



As the photocatalytic carbon-carbon bond is formed, hydrogen evolves when the photocatalytic activation is done on colloidal ZnS [149, 150]. This dehydrodimerization also takes place with saturated ethers, with reactivity related to C-H bond strength. Thus, 2,5-dihydrofuran (an allylic ether) is more easily activated than the isomeric 2,3-dihydrofuran (a vinyl ether). With the former substrate, all three diastereomeric coupling products are observed. Water is required for the reaction, and the primary photochemical product is thought to be a surface-bound hydroxyl radical.

Photocatalytic activation of allyl and benzyl ethers results either in carbon-carbon coupling or oxygenation [148-151]. The photocatalyst used for these conversions can be generated in situ, by photolysis of a zinc dithiolene salt, by pre-formed catalysts, or by particles supported within surfactant vesicles. Radical intermediates formed by hydrogen abstraction by photogenerated hydroxyl or hydroperoxyl radicals may also be important in the photoelectrochemically induced oxidation of hydrocarbons. In the TiO₂-sensitized photooxidation of toluene to cresols, for example, a photo-Fenton (radical) type mechanism has been suggested [150].

Radical cations are probably involved in the photooxidation of olefins [1-7, 24, 50-54, 56, 61, 66] (Eqs. 2 and 5). Many oxidizable arenes and dienes are, similarly, oxidatively cleaved or rearranged by routes consistent with initial formation of a radical cation. As we saw above, the observed oxidative cleavage product probably derives from the combination of a surface-bound radical cation with superoxide or adsorbed oxygen. With alkanes or simply substituted alkenes, however, the capture of a photogenerated hole is often thermodynamically forbidden. Thus, instead of radical cations, radicals formed by hydrogen atom abstraction by an activated oxygen species dominate the observed chemistry. With alkanes, oxygenation at sites

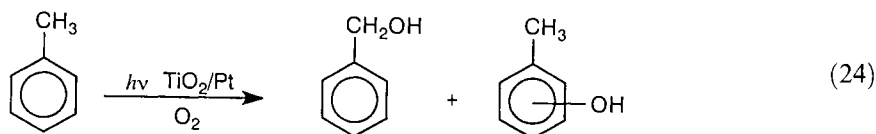
controlled by radical stability, rather than oxidative cleavage, is observed [151–153]. The relative ratio of oxygenation to complete mineralization can be controlled, at least to some extent, by careful choice of the metal oxide photocatalyst

In fact, the surface significantly affects the distribution of products observed from the initially formed radical cation [154]. Surface control of the competition between deprotonation and oxidative cleavage of a photoelectrochemically generated radical cation can be seen in the divergent chemistry attained from the 1-methylnaphthalene cation radical formed on irradiated TiO_2 powders and by homogeneously dispersed single-electron oxidants (Eq. 6) [60]. Here the semiconductor surface delivers the co-adsorbed oxygen or superoxide to the π system more rapidly than C–H deprotonation can take place.

Aromatic hydrocarbons can be oxidatively cleaved either on a side chain or in the ring (Eq. 6) [60]. Even saturated hydrocarbons can be induced to become oxygenated or to participate in isotope exchange on irradiated platinum/ titanium dioxide catalysts [151, 155, 156]. Competitive trapping of the photogenerated conduction band electron by adsorbed protons is thought to be responsible for the reduced contribution of oxygen at lower pH.

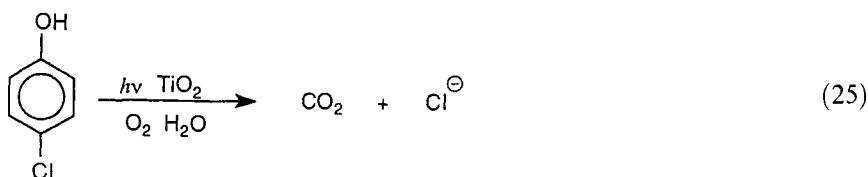
The observation of products at intermediate oxidation level in the photocatalytic reactions of hydrocarbons is consistent with a surface-bound radical intermediate [157]. Photocatalytic isotope exchange between cyclopentane and deuterium on bi-functional platinum/titanium dioxide catalysts indicates the importance of weakly adsorbed pentane at oxide sites. The platinum serves to attract free electrons, decreasing the efficiency of electron–hole recombination, and to regenerate the surface oxide after exchange. Much better control of the exchange is afforded with photoelectrochemical than thermal catalysis.

Water oxidation cannot be solely responsible for the observed chemistry, since toluene as a neat liquid can be oxidized to benzyl alcohol (Eq. 24) [151].



Here the intervention of the hydrocarbon radical cation seems possible. Hydrocarbon photocatalyzed oxidations seem to depend significantly on the relative positions of the valence-band edge of the active photocatalyst and the oxidation potential of the substrate. For example, in contrast to the photocatalytic oxidation of toluene described above, lower activity was observed in neat benzene, despite the fact that its oxidation potential lies at or slightly below the valence-band edge. This observation implies the importance of radical cation formation (by photoinduced electron transfer across the irradiated interface) as a preliminary step to hydrocarbon radical formation. If the benzene is dispersed into a benzene-saturated aqueous solution into which the semiconductor is suspended, complete mineralization is attained [158]. Thus, to observe selective photoelectrochemistry, it is necessary to avoid primary formation of the highly reactive, nonselective hydroxyl radical (formed by water oxidation) by the use of an unreactive, but polar, organic solvent.

Complete mineralization of alkyl [159, 160], vinyl [161], and aryl [162–164] halides, as shown in Eq. 25, for example, probably requires the generation of a photogenerated hydroxyl radical. These reactions figure prominently in current photocatalysis applications dealing with environmental purification.



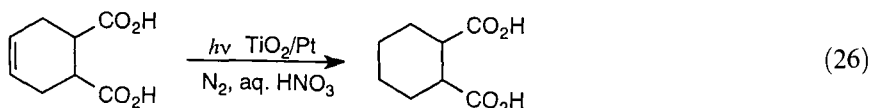
The most important class of photocatalytic transformations is the oxidation of a range of organic substrates. This reactivity follows from either trapping of an electron–hole pair to produce a photogenerated surface-adsorbed radical cation or from radicals produced by activated oxygen radicals (surface oxides or adsorbed hydroxyl, hydroperoxyl, or peroxy radicals) [165]. Thus, photoelectrochemistry is an excellent means for initiating chemoselective oxidation.

8.5.2 Reductions

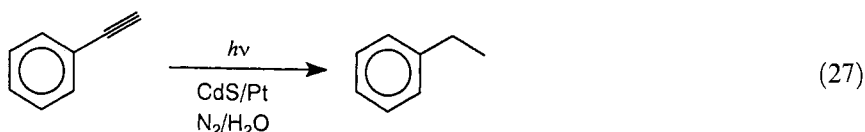
Many fewer photocatalytic organic reductions have been reported. Reductions of organic substrates are less thoroughly studied, largely because of the early emphasis on the use of organic compounds as oxidizable source for the production of hydrogen gas. Nonetheless, some examples do exist, such as the hydrogenation of olefins, vinyl ethers, and α,β -unsaturated enones and alkynes [166, 167]. Similarly, other multiple bonds can be reduced, e.g., the N=N double bond of diaryl azo compounds [168] or carbonyl C=O bonds [169, 170].

When oxygen is specifically removed from a photocatalysis mixture, other reagents can accept the photogenerated conduction-band electron. Because of the only modestly negative potential of electrons at the conduction-band edge of conveniently accessible semiconductors, few organic substrates can fill this role. Cationic organic reagents are, indeed, reduced in this potential regime, as in the photoinduced reduction of methyl viologen and comparable derivatives (Eq. 11) [171].

Catalytic hydrogenations can be induced by the reduction of protons present in aqueous acid, especially on metalized semiconductor suspensions. For example, the oxidative chemistry reported earlier for cyclohexene-4,5-bis-dicarboxylic acid (Eq. 12) is suppressed if the reaction is conducted in the absence of oxygen in aqueous nitric acid. Under those conditions, catalytic hydrogenation of the double bond becomes a major pathway (Eq. 26) [60].



Analogous photoelectrochemical hydrogenations of double and triple bonds have also been reported with other oxidizable sacrificial donors (Eq. 27) [166].



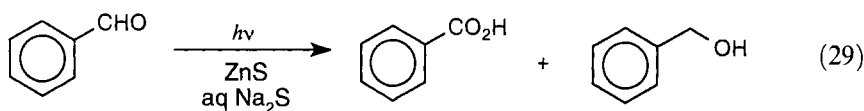
With CdS metalized with platinum or rhodium as the photocatalyst, hydrogenation was about four times more efficient than hydrogen evolution, with the observed efficiency depending on the solution-phase pH and the identity and loading of the metal catalyst.

By these same routes, olefins, vinyl ethers, and α, β -unsaturated enones could be photoelectrochemically hydrogenated on TiO_2 in the presence of ethanol as sacrificial oxidant [166–168]. With 2-methyl-2-pentene, hydrogenation occurred in 63% yield, without side products (Eq. 28).



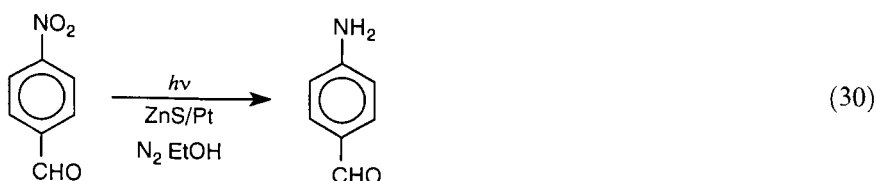
The photoelectrochemical reduction of the $\text{N}=\text{N}$ double bond of methyl orange, a diaryl azo dye, can be similarly sensitized by colloidal titanium dioxide [168]. The reaction was sensitive to pH and the identity of the organic redox reaction could be shifted by conducting the photoreaction in the presence of cationic surfactants, which increased the efficiency of oxidative cleavage by inhibiting charge recombination [127]. Reduction was favored when polyvinyl alcohol was used instead. The ambident photoactivity of methyl orange thus makes it an attractive probe for the activity of irradiated semiconductor suspensions.

Photoelectrochemical reduction of double bonds also takes place on ZnS sols. For example, efficient photodisproportionation of aldehydes, that is, a photo-Canizzaro reaction, can be observed on suspensions prepared from cold oxygen-free aqueous solutions of ZnS and Na_2S (Eq. 29) [169].



In the same way, acetaldehyde produces ethanol and acetic acid, together with smaller quantities of biacetyl and acetoin. The relative paucity of photoelectrochemically induced reductions makes this an interesting area for further investigation.

Selective reduction of a halogenated aromatic nitro compound to the corresponding hydroxylamine or amine upon irradiation of TiO_2 suspended in degassed alcohol has also been reported, as has the selective photoreduction of *p*-nitrobenzaldehyde to the corresponding aldehydic aniline (Eq. 30) [170], and alkyl azides can also be reduced to the corresponding amine.



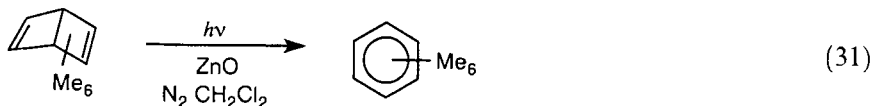
The synthesis of a benzimidazole through reductive photocatalysis has also been described [172]. Although the reduction of N_2 to ammonia was claimed to be induced by photocatalysis on TiO_2 [173], the reproducibility of this reported result was challenged [174].

The photocatalytic reduction of various metal salts has been a primary route for the preparation of metallized semiconductors, as well as in the detoxification of metal-contaminated waste streams [175], but the details of such reactions are beyond the scope of this article.

8.5.3 Cycloadditions and Retrocycloadditions

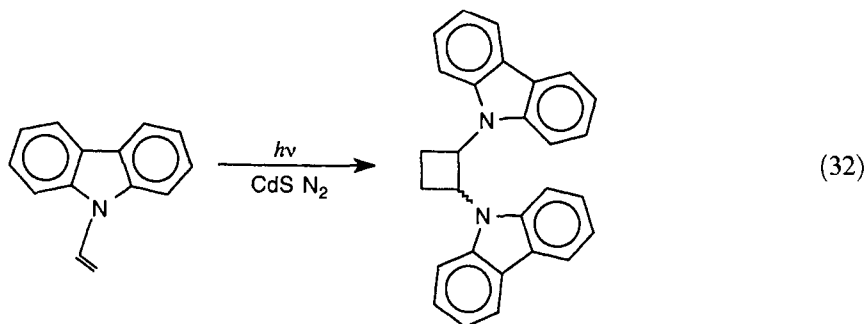
The ubiquitous and reversible formation of radical cations in photoelectrochemical transformations allows pericyclic reactions to take place upon photocatalytic activation since the barriers for pericyclic reactions are often lower in the singly oxidized product than in the neutral precursor. For example, ring openings on irradiated CdS suspensions are known in strained saturated hydrocarbons [176], and formal $[2 + 2]$ cycloadditions have been described for phenyl vinyl ether [177] and *N*-vinyl carbazole [178]. The cyclization of nonconjugated dienes, such as norbornadiene, have also been reported [179]. A recent example involves a 1,3-sigmatropic shift [180].

Several reactions that can formally be classified as cycloadditions or retrocycloadditions take place in homogeneous solution with single-electron oxidative initiation, so the observation of parallel activity on irradiated semiconductor suspensions is certainly reasonable. Photocatalysis by ZnO or CdS induces the ring-opening of several highly strained hydrocarbons, in parallel to the analogous reactions taking place in the dark upon exposure to a single-electron oxidant, ceric ammonium nitrate [76]. The observation of quantum yields greater than unity in the valence isomerization of hexamethyl(dewarbenzene) to hexamethylbenzene, Eq. 31, suggests that a surface-bound cation radical-chain mechanism may be involved.



Different pretreatment of CdS gave rates that varied only by a factor of about two. Thus, surprisingly, different surface areas, impurities, and surface structures seem to play only a minor role in this reaction. Anthracene [177] and quinolone [176] dimers could also be opened in similar fashion.

Ring formation takes place in the photodimerization of unsaturated ethers and amines, such as phenyl vinyl ether and vinyl carbazole (Eq. 32).



The presence of both stereoisomers in this dimerization implies that a stepwise process involving cation radicals is probably involved. A detailed kinetic and product study showed that when the reaction was conducted on ZnO, variations in the surface composition had a major effect on both the rate and stereochemistry. Thus, the effect of various quenchers could be explained as competitive adsorption at active sites, with or without interference with electron transfer. Neither particle size, surface area, nor crystal structure appeared to significantly influence the CdS photocatalyzed dimerization of *N*-vinylcarbazole [179].

Intramolecular cycloadditions can also be induced by photoelectrochemical activation. Norbornadiene, for example, can be cyclized upon irradiation of ZnO, ZnS, CdS, or Ge semiconductors [179].

8.5.4 Geometric Isomerizations

When exposed to CdS excited with light of an energy greater than its band gap (Eq. 3), the *cis* and *trans* isomers of substituted stilbenes achieve thermodynamic equilibrium [181]. Given that the reaction was quenched by electron donors (methoxybenzenes or pyrenes) and is affected by the ratio of substrate to catalyst, light intensity, and temperature, a radical cation is the likely intermediate, as was discussed earlier for the related styrenes. Oxygen suppressed the reaction [182], producing instead oxidative cleavage products [53]. When a Hammett plot was constructed for the rate of isomerization of *p*-substituted stilbenes, a sharp break at $\sigma = 0.19$ occurred; this indicates a change in the rate-determining step with a change of the electron-donating ability of the substituent. The two regions would represent endothermic and exothermic hole trapping, respectively, with a ρ value (-0.74) reminiscent of that previously observed for the oxidative cleavage of diphenylethylenes [53]. Surface precomplexation would be expected to diminish the observed ρ value.

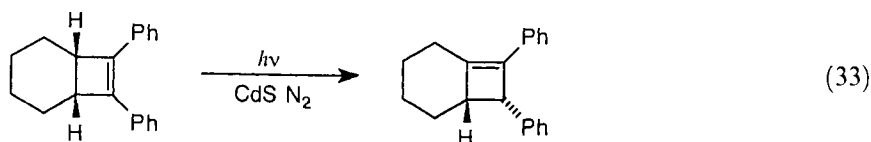
A Stern–Volmer plot for photocatalytic stilbene isomerization also has both curved and linear components [183]. This requires at least two separate mechanisms

that differ as to whether the adsorption of the quencher on the surface competes with that of the reactant or whether each species has a preferred site and is adsorbed independently. In both mechanisms, quenching of a surface-adsorbed radical cation by a quencher in solution is required. Similarly, the geometric isomerization of simple alkenes on irradiated ZnS suspensions exhibited high turnover numbers; this indicates that trapped holes derived from surface states (sulfur radicals from zinc vacancies or interstitial sulfur) play a decisive role.

Thus, as with the oxidative cleavages, transient formation of a surface-adsorbed radical cation is likely in photoelectrochemically induced geometrical isomerizations.

8.5.5 Miscellaneous Reactions

Several other notable organic transformations can be observed on irradiated semiconductor particles, but the paucity of work on organic photoelectrochemical conversions, apart from redox chemistry, shows that many possibilities remain for finding synthetically useful variants of photocatalysis. Visible-light irradiation of metal chalcogenides, for example, CdS, can induce what appears to be a symmetry-forbidden [1, 3] sigmatropic shift of hydrogen (Eq. 33) in the absence of oxygen [180].



The reaction was at least partially intramolecular, so that it is necessary to consider a radical cation-mediated hydrogen shift which would have been forbidden in the ground-state neutral precursor. In a second example, photoinduced Michael-like reactions have also been observed when α,β -unsaturated acids were used as substrates for amino acid synthesis [184].

8.6 Conclusions

Although photoelectrochemistry has been known as a field for over thirty years, its full impact on organic synthesis has yet to be revealed. This article has dealt with a variety of examples that show how chemical conversions can be induced by photoelectrochemical activation of light-sensitive semiconductor surfaces. Photoexcitation causes the promotion of an electron from the valence band to the conduction band, thus producing a surface-confined electron-hole pair. The charges represented by this pair are then trapped by interfacial electron transfer. The oxidized and reduced

species thus produced undergo dark secondary reactions which are greatly influenced by the surface on which they are produced.

Water is one possible hole trap, conceivably the dominant one in aqueous solution. The hydroxyl radical thus produced is a key intermediate in many oxidative degradations observed on irradiated metal oxide suspensions [185]. For many organic transformations, the key intermediate is the singly oxidized radical cation derived from the molecule of interest that was selectively adsorbed on the photocatalyst surface. The presence or absence of oxygen is also vitally important in defining subsequent reaction pathways.

Net chemical transformations observed in photocatalysis are thus controlled by band-edge positions, by adsorption effects, and by light-influenced current density. The surface can act to assemble co-adsorbates and can significantly influence the local polarity of photogenerated intermediates produced on that surface. Oxidations, reductions, cycloadditions, retrocycloadditions, and geometric isomerizations have been observed on these photocatalytic surfaces, often in high chemical yield. As with all such transformations, the utility of such new chemical processes lies in the chemist's ability to specify stereochemistry and regiochemistry or to activate a specific functional group in a complex molecule, or to choose a particular substrate from a mixture. It is here that a substantial challenge remains, as little is currently known about the detailed effect of the surface on secondary reactions of surface-bound intermediates. Nonetheless, photoelectrochemistry provides a useful new technique for the control of organic redox chemistry.

Applications of photoelectrochemistry in problems related to environmental issues are manifold, and have been the central focus of much work in this field conducted over the last decade. Although practical applications are still evolving, many of the transformations discussed here will represent key steps in the oxidative degradation of many contaminants. For example, the conversion of acetic acid to methane, the oxidative decomposition of biomass, and the photodegradation of organochlorine compounds, in this article discussed from the view of their synthetic utility, along with the photochemical recovery of toxic or precious metals also represent important social uses of solar energy. These reactions may also be involved in the dissolution of minerals, in the generation of biologically active oxidants or metabolites, or in the reduction of chemisorbed nitrogen on titanium-rich desert sands. The photoelectrochemical reduction of CO_2 also opens the possibility that organic feedstocks might one day be derived from aldehydes and alcohols produced by photoelectrochemical reductions [186].

Acknowledgments

Our program in organic photoelectrochemistry and chemically modified electrodes has been supported for many years by the U.S. Department of Energy, Office of Basic Energy Sciences; our investigation of surface-adsorbed radical ions has been supported by the National Science Foundation. I am also grateful to Professor James K. Whitesell for helpful discussions and assistance in illustrating this manuscript.

References

1. M.A. Fox, *Adv. Electron Transfer Chem.*, 1, 1 (1991).
2. M.A. Fox and M.T. Dulay, *Chem. Rev.*, 93, 341 (1993).
3. M. A. Fox, *Top. Org. Electrochem.*, 1, 177 (1986).
4. M. A. Fox, *Top. Curr. Chem.*, 142, 71 (1987).
5. M. A. Fox, *Accts. Chem. Res.*, 16, 314 (1983).
6. M. A. Fox and P. Pichat, in *Photoinduced Electron Transfer* (M. Chanon and M. A. Fox, eds.), Elsevier Scientific, Amsterdam, 1988, Chapter 5.2.
7. M. A. Fox, in *Photocatalysis* (N. Serpone and E. Pelizzetti, eds.), Wiley and Sons, New York, 1988, p. 524.
8. A. J. Bard, *J. Photochem.*, 10, 59 (1979).
9. A. J. Bard, *Science*, 207, 139 (1980).
10. A. J. Bard, *J. Phys. Chem.*, 86, 172 (1982).
11. R. Memming, in *Electroanalytical Chemistry* (A. J. Bard, ed.), Dekker, New York, 1979.
12. M. S. Wrighton, *Acc. Chem. Res.*, 12, 303 (1979).
13. H. O. Finklea, *J. Chem. Ed.*, 60, 325 (1983).
14. A. Hagefeldt and M. Grätzel, *Chem. Rev.*, 95, 49 (1995).
15. M.A. Fox in *Photocatalysis and Environment. Trends and Applications*, (M. Schiavello, ed.) Reidel Press, Amsterdam, 1989, Part III, Chapter 5.
16. D. Bahnemann, J. Cunningham, M.A. Fox, E. Pelizzetti, P. Pichat, and N. Serpone, *Aquatic and Surface Photochemistry* (G.R. Helz, R.G. Zepp, and D.G. Crosby, eds.) Lewis Publishers, Boca Raton, FL, 1994, p. 261.
17. D.F. Ollis and H. Al-Ekabi, eds., *Photocatalytic Purification and Treatment of Water and Air; Proceedings of the First International Conference on TiO₂ Photocatalytic Purification and Treatment of Water and Air*, Elsevier, Amsterdam, 1993.
18. M.A. Fox, in *Electroorganic Synthesis—Festschrift in Honor of Manuel M. Baizer* (R. D. Little and N. Weinberg, eds.) Marcel Dekker, New York, 1990, p. 181.
19. M.A. Fox, *Chemtech*, 11, 680 (1992).
20. M.R. Hoffmann, S.T. Martin, W. Choi, and D.W. Bahnemann, *Chem. Rev.*, 95, 69 (1995) and references cited therein.
21. O. Legrini, E. Oliveros, and A.M. Braun, *Chem. Rev.*, 93, 671 (1993).
22. A.J. Bard and M.A. Fox, *Accts. Chem. Res.*, 28, 141 (1995).
23. For an example, see E. Borgarello, N. Serpone, M. Barbeni, E. Pelizzetti, P. Pichat, J.M. Hermann, and M.A. Fox, *J. Photochem.*, 36, 373 (1987).
24. M.A. Fox in *Homogeneous and Heterogeneous Photocatalysis* (E. Pelizzetti and N. Serpone, eds.), Reidel Press, Amsterdam, 1986, Chapter 22.
25. M.A. Fox, in *Photoinduced Electron Transfer* (M. A. Fox and M. Chanon, eds.), Elsevier Scientific, Amsterdam, 1988, Chapter 4.13.
26. H. Gerischer and A. Heller, *J. Phys. Chem.*, 95, 5261 (1991).
27. H. Gerischer, *Electrochim. Acta*, 38, 3 (1993).
28. P.V. Kamat, *Prog. Reacn. Kinet.*, 19, 277 (1994).
29. A. Henglein, *Chem. Rev.*, 89, 1861 (1989).
30. A. J. Nozik, *Ann. Rev. Phys. Chem.*, 29, 189 (1978).
31. E. Pelizzetti and C. Minero, *Electrochim. Acta*, 38, 47 (1993).
32. C.D. Jaeger and A.J. Bard, *J. Phys. Chem.*, 83, 3146 (1979).
33. V. Brezova, A. Stasko, and L. Lapcik, *J. Photochem. Photobiol. A Chem.*, 59, 115 (1991).
34. M. Anpo, T. Shima, and Y. Kubokawa, *Chem. Lett*, 1799 (1985).
35. J. Cunningham and S. Srijaranai, *J. Photochem. Photobiol. A Chem.*, 43, 329 (1988).
36. D. D. Sackett and M.A. Fox, *J. Phys. Org. Chem.*, 1, 103 (1988).
37. R. M. Murray, *Accts. Chem. Res.*, 13, 135 (1980).
38. A. J. Bard, *J. Chem. Ed.*, 60, 302 (1983).
39. B. O'Regan and M. Grätzel, *Nature*, 353, 737 (1991).
40. I. Shiyonovskaya and M. Hepel, *J. Electrochem. Soc.*, 146, 243 (1999).

41. H. Yamashita, S. Kawasaki, Y. Ichihashi, M. Harada, M. Takeuchi, M. Anpo, G. Stewart, M.A. Fox, C. Louis, and M. Che, *J. Phys. Chem.*, 102, 5870 (1988).
42. B. Ohtani, H. Osaki, S. Nishimoto, and T. Kagiya, *Chem. Lett.*, 1075 (1985).
43. K.R. Gopidas, M. Bohorquez, and P.V. Kamat, *J. Phys. Chem.*, 94, 6435 (1990).
44. H. Osora, W. Li, and M.A. Fox, *J. Photochem. Photobiol.*, 43, 232 (1997).
45. W. Li, H. Osora, L. Otero, D.C. Duncan, and M.A. Fox, *J. Phys. Chem.*, 102, 5333 (1998).
46. I. Willner, Y. Eichen, A. Frank, and M.A. Fox, *J. Phys. Chem.*, 97, 7264 (1993).
47. J. Fang, L.Su, J. Wu, Y. Shen, and Z. Lu, *New J. Chem.*, 21, 1303 (1997).
48. M.K. Nazeeruddin, A. Kay, I. Rodicio, R. Humphrey-Baker, E. Muller, P. Liska, and M. Grätzel, *J. Am. Chem. Soc.*, 115, 6382 (1993).
49. M.A. Fox, in *Photocatalysis* (E. Pelizzetti and N. Serpone, eds.), Wiley Interscience, 1989, Chapter 13.
50. M.A. Fox and C. C. Chen, *J. Am. Chem. Soc.*, 103, 6757 (1981).
51. M. A. Fox and C. C. Chen, *J. Comp. Chem.*, 4, 488 (1983).
52. S. F. Nelsen, D. L. Kapp, R. Akaba, and D. H. Evans, *J. Am. Chem. Soc.*, 108, 6863 (1986).
53. M. A. Fox and C. C. Chen, *Tetrahedron Lett.*, 24, 547 (1983).
54. R. B. Draper and M.A. Fox, *Langmuir*, 6, 1396 (1990).
55. M. Anpo, M. Tomonari, and M.A. Fox, *J. Phys. Chem.*, 93, 7300 (1989).
56. M.A. Fox, B. Lindig, and C.C. Chen, *J. Am. Chem. Soc.*, 104, 5828 (1982).
57. G. O. Schenck and K. Schulte-Elte, *Liebigs Ann. Chem.*, 618, 185 (1958).
58. L. T. Spada and C. S. Foote, *J. Am. Chem. Soc.*, 102, 393 (1980).
59. A. J. Bard, A. Ledwith, and H. J. Shine, *Adv. Phys. Org.*, 13, 156 (1976).
60. M. A. Fox, C. C. Chen, K. H. Park, and J. N. Younathan, *Amer. Chem. Soc. Sympos. Ser.*, 278, 69 (1985).
61. M. A. Fox, C. C. Chen, and J. N. Younathan, *J. Org. Chem.*, 49, 1969 (1984).
62. M.A. Fox, R.B. Draper, M.T. Dulay, and K. O'Shea, in *Photochemical Conversion and Storage of Solar Energy-IPS-8* (E. Pelizzetti and M. Schiavello, eds.), Kluwer, Amsterdam, 1991, p. 323.
63. M.A. Fox, J. Muzyka, and H. Ogawa, *Symposium on Photoelectrochemistry and Electro-synthesis on Semiconducting Materials* D. Ginley, ed., Electrochemical Society, Pennington, NJ, 1988.
64. A. V. Kiselev and A. V. Uvarov, *Surf. Sci.*, 6, 399 (1967).
65. H. P. Boehm, *Disc. Faraday Soc.*, 52, 264 (1971).
66. I. Carrizosa and G. Munuera, *J. Catal.*, 49, 174 (1977).
67. Y. Suda, T. Morimoto, and M. Nagao, *Langmuir*, 3, 99 (1987).
68. G. Ramis, G. Busca, and V. Lorenzelli, *J. Chem. Soc., Faraday Trans.*, 1, 83, 1591 (1987).
69. G. Busca, H. Saussey, O. Saur, J. C. Lavalley, and V. Lorenzelli, *Appl. Catal.*, 14, 245 (1985).
70. P.V. Kamat, *Chem. Rev.*, 93, 267 (1993).
71. M.A. Fox, in *Free Radicals in Biology and Environment* (F. Minisci, ed.), Kluwer, Amsterdam, 1997, p. 437.
72. J.L. Ferry and M.A. Fox, *Langmuir*, 14, 1725 (1997).
73. M.A. Fox and M.T. Dulay, *J. Photochem. Photobiol. A, Chem.*, 98, 91 (1996).
74. P.V. Kamat, *Chem. Rev.*, 93, 267 (1993).
75. M.A. Fox, K.E. Doan, and M.T. Dulay, *Res. Chem. Intermed.*, 20, 711 (1994).
76. B. Frederick, L.J. Johnston, P. deMayo, and S.K. Wong, *Can. J. Chem.*, 62, 403 (1984).
77. M.M. Abdel-Malik and P. de Mayo, *Can. J. Chem.*, 62, 1275 (1984).
78. Y. Degani and I. Willner, *J. Am. Chem. Soc.*, 105, 6228 (1983).
79. I. Willner and Y. Degani, *Isr. J. Chem.*, 22, 163 (1982).
80. G.T. Brown, J.R. Darwent, and P.D. Fletcher, *J. Am. Chem. Soc.*, 107, 6446 (1985).
81. D.H. Kim and M.A. Anderson, *J. Photochem. Photobiol. A Chem.*, 94, 221 (1996).
82. C. Kormann, D.W. Bahnemann, and M.R. Hoffmann, *Environ. Sci. Tech.*, 25, 494 (1991).
83. C.S. Türcü and D.F. Ollis, *J. Catal.*, 122, 178 (1990).
84. H. Al-Ekabi, H. and P. deMayo, *J. Phys. Chem.*, 90, 4075 (1986).
85. A.L. Pruden and D.F. Ollis, *J. Catal.*, 82, 404 (1983).
86. P. Pichat, in *Homogeneous and Heterogeneous Photocatalysis* (E. Pelizzetti and N. Serpone, eds.), D. Reidel, Dordrecht, 1986.

87. V. Brezova, S. Vodny, M. Vesely, M. Ceppan, and L. Lapcik, *J. Photochem. Photobiol.*, **56**, 125 (1991).
88. T. Uchihara and M.A. Fox, *Inorg. Chim. Acta*, **242**, 253 (1996).
89. A.V. Barzykin and M.A. Fox, *Isr. J. Chem.*, **33**, 21 (1993).
90. T. Türk, U. Resch, M.A. Fox, and A.J. Vogler, *J. Phys. Chem.*, **96**, 3818 (1992).
91. M.A. Fox, *Res. Chem. Intermed.*, **15**, 153. (1991).
92. A. Kudo, M. Steinberg, A.J. Bard, A. Campion, M.A. Fox, T.E. Mallouk, S.E. Webber, and J.M. White, *J. Electrochem. Soc.*, **137**, 3846 (1990).
93. E.S. Smotkin, R. Malcolm Brown, Jr., L.K. Rabenberg, K. Salomon, A.J. Bard, A. Campion, M.A. Fox, T.E. Mallouk, S.E. Webber, and J.M. White, *J. Phys. Chem.*, **94**, 7543 (1990).
94. T. Torimoto, R.J. Fox, III, and M.A. Fox, *J. Electrochem. Soc.*, **143**, 3712 (1996).
95. R.E. Schwerzel, *J. Electrochem. Soc.*, **83**, 513 (1983).
96. H. Harada, T. Sakata, and T. Ueda, *J. Am. Chem. Soc.*, **107**, 1773 (1985).
97. J. Onoe, T. Kawai, and S. Kawai, *Chem. Lett.*, 1667 (1985).
98. J.L. Muzyka and M.A. Fox, *J. Photochem. Photobiol. A: Chemistry*, **57**, 27 (1991).
99. Y. Nosaka and M.A. Fox, *J. Phys. Chem.*, **90**, 6521 (1986).
100. G. Stewart and M.A. Fox, *Res. Chem. Intermed.*, **21**, 933 (1995).
101. C.J. Koval, *Photochem. Photobiol. A*, **74**, 273 (1993).
102. D. Bahnemann, A. Henglein, J. Lilie, and L. Spankel, *J. Phys. Chem.*, **88**, 711 (1984).
103. D. Duonghang, J. Ramsden, and M. Graetzel, *J. Am. Chem. Soc.*, **104**, 2977 (1982).
104. T. Kawai and T. Sakata, *Chem. Lett.*, 81 (1981).
105. M.A. Fox, S. Ruberu, A. Hadd, and Y.S. Kim, *Proc. Electrochem. Soc.*, 93-18, 104 (1993).
106. (a) R. B. Cundall, R. Rudham, and M. Salim, *J. Chem. Soc., Faraday Trans.*, **1**, 72, 1642 (1976). (b) R. H. Hussein and R. Rudham, *J. Chem. Soc., Faraday Trans.*, **1**, 80, 2817 (1984). (c) F. H. Hussein, G. Pattenden, R. Rudham, and J. J. Russell, *Tetrahedron Lett.*, 3363 (1984).
107. A. Ichou, M. Formenti, B. Pommier, and S. J. Teichner, *J. Catal.*, **9**, 293 (1985).
108. (a) M. Kawai, T. Kawai, S. Naito, and K. Tamaru, *Chem. Phys. Lett.*, **110**, 58 (1984). (b) S. Naito, *J. Chem. Soc., Chem. Commun.*, 1211 (1985).
109. (a) T. Kawai and T. Sakata, *J. Chem. Soc., Chem. Commun.*, 694 (1980). (b) T. Kawai and T. Sakata, *Nature*, **286**, 474 (1980).
110. (a) P. Pichat, J. M. Herrmann, J. Disdier, H. Bourbon, and M. N. Mozzanega, *Nouv. J. Chim.*, **5**, 627 (1981). (b) P. Pichat, M. N. Mozzanega, J. Disdier, and J. M. Herrmann, *Nouv. J. Chim.*, **6**, 559 (1982). (c) P. Pichat, J. M. Herrmann, H. Courbon, J. Disdier, and M. N. Mozzanega, *Can. J. Chem. Eng.*, **60**, 27 (1982). (d); L. T. Prahov, J. Disdier, J. M. Herrmann, and P. Pichat, *Int. J. Hydrogen Energy*, **9**, 397 (1984).
111. S. Teratani, J. Nakamichi, K. Taya, and K. Tanaki, *Bull. Chem. Soc. Jpn.*, **55**, 1688 (1982).
112. T. Carlson and G. L. Griffin, *J. Phys. Chem.*, **90**, 5896 (1986).
113. K. Domen, S. Naito, T. Ohnishi, and K. Tamaru, *Chem. Lett.*, 555 (1982).
114. (a) M. Fraser and J. R. MacCallum, *J. Chem. Soc., Faraday Trans.*, **1**, 82, 607 (1986). (b) M. Fraser and J. R. MacCallum, *J. Chem. Soc., Faraday Trans.*, **1**, 2747 (1986).
115. (a) S. Yanagida, T. A. Zuma, H. Kawakami, H. Kizumoto, and H. Sakurai, *Chem. Commun.*, 21 (1984). (b) S. Yanagida, H. Kawakami, K. Hashimoto, T. Sakata, C. Pac, and H. Sakurai, *Chem. Lett.*, 1449 (1984). (c) S. Yanagida, T. Azuma, and H. Sukurai, *Chem. Lett.*, 1069 (1982).
116. (a) O. Enea, *Electrochim. Acta.*, **31**, 405 (1986). (b) O. Enea and A. J. Bard, *Nouv. J. Chim.*, **9**, 691 (1985).
117. (a) S. Nishimoto, B. Ohtani, and T. Kagiya, *J. Chem. Soc., Faraday Trans.*, **1**, 81, 2467 (1985). (b) S. Nishimoto, B. Ohtani, H. Shirai, and T. Kagiya, *J. Chem. Soc. Perkin Trans.*, **11**, 661 (1986).
118. K. Okamoto, Y. Yamamoto, H. Tanaka, M. Tanaka, and A. Itaya, *Bull. Chem. Soc. Jpn.*, **58**, 2015 (1985).
119. H. Yamashita, Y. Ichihashi, M. Harada, M. Anpo, G. Stewart, and M.A. Fox, *J. Catal.*, **158**, 97 (1996).
120. M.A. Fox, R. Cardona, and E. Gaillard, *J. Am. Chem. Soc.*, **107**, 6347 (1987).
121. M.A. Fox, H. Ogawa, and P. Pichat, *J. Org. Chem.*, **54**, 3847 (1989).

122. N. Serpone, H. Al-Ekabi, B. Patterson, E. Pelizzetti, C. Minero, E. Pramauro, M.A. Fox, and R.B. Draper, *Langmuir*, 5, 250 (1989).
123. A. Sclafani, L. Palmisano, and E. Davi, *J. Photochem. Photobiol.*, 56, 113 (1991).
124. M.A. Fox and J.N. Younathan, *Tetrahedron*, 42, 6285 (1986).
125. M.A. Fox and M.J. Chen, *J. Am. Chem. Soc.*, 105, 4497 (1983).
126. (a) B. Ohtani, H. Osaki, S. Nishimoto, and T. Kagiya, *Tetrahedron Lett.*, 2019 (1986). (b) H. Miyama, Y. Nosaka, T. Fukushima, and H. Toi, *J. Photochem.*, 1553 (1986).
127. J. R. Darwent and A. Lepre, *J. Chem. Soc. Faraday Trans.*, 1182, 1457 (1986).
128. M.A. Hema, V. Ramakrishnan, and J.C. Kuriacose, *Ind. J. Chem.*, 16B, 619 (1978).
129. M.A. Fox and K. L. Worthen, *Chem. Mater.*, 3, 253 (1991).
130. M.A. Fox and H. Ogawa, *J. Inform. Record. Mater.*, 5/6, 351 (1990).
131. C. Maillard, C. Guillard, P. Pichat, and M.A. Fox, *New J. Chem.*, 16, 821 (1992).
132. J.W. Pavlik and S. Tantayanon, *J. Am. Chem. Soc.*, 103, 6755 (1981).
133. H. Reiche and A. J. Bard, *J. Am. Chem. Soc.*, 101, 3127 (1979).
134. W.W. Dunn, Y. Aikawa, and A. J. Bard, *J. Am. Chem. Soc.*, 103, 6893 (1981).
135. R.S. Davidson and J.E. Pratt, *Tetrahedron Lett.*, 24, 547 (1983).
136. M.A. Fox and A.A. Abdel-Wahab, *J. Catal.*, 126, 693 (1990).
137. M.A. Fox and A.A. Abdel-Wahab, *Tetrahedron Lett.*, 31, 4533 (1990).
138. J.D. Spikes, *Photochem. Photobiol.*, 34, 549 (1981).
139. K.W. Krosley, D.M. Collard, J. Adamson, and M.A. Fox, *J. Photochem. Photobiol. A*, 69, 357 (1993).
140. (a) B. Kraeutler and A. J. Bard, *J. Am. Chem. Soc.*, 100, 2339 (1978). (b) B. Kraeutler and A. J. Bard, *J. Am. Chem. Soc.*, 100, 5985 (1978). (c) H. Reiche, W. W. Dunn, K. Wilbourn, F. R. F. Fan, and A. J. Bard, *J. Phys. Chem.*, 84, 3207 (1980). (d) H. Yoneyama, Y. Takao, H. Tamura, and A. J. Bard, *J. Phys. Chem.*, 87, 1417 (1983). (e) C. D. Jaeger and A. J. Bard, *J. Phys. Chem.*, 83, 3146 (1979).
141. D. N. Furlong, D. Wells, and W. H. F. Sasse, *Aust. J. Chem.*, 39, 757 (1986).
142. J.M. Herrmann, M.N. Mozzanega, and P. Pichat, *J. Photochem.*, 22, 333 (1983).
143. K. Miyahita, K. Nakamura, T. Kawai, and T. Sakata, *Photochem. Photobiol.*, 39, 151 (1984).
144. I. Willner and Z. Goren, *Chem. Commun.*, 172 (1986).
145. J.L. Muzyka and M.A. Fox, *J. Org. Chem.*, 55, 209 (1990).
146. A.P. Davis and D.L. Green, *Environ. Sci. Tech.*, 33, 609 (1999).
147. C. Lai, Y.I. Kim, C.M. Wang, and T.E. Mallouk, *J. Org. Chem.*, 58, 1393 (1993).
148. J. Buecheler, N. Zeug, and H. Kisch, *Angew. Chem.*, 94, 792 (1982).
149. S. Yanagida, T. Azuma, Y. Midori, C. Pac, and H. Sakurai, *J. Chem. Soc. Perkin Trans.*, 11, 1487 (1985).
150. N. Zeug, J. Buecheler, and H. Kisch, *J. Am. Chem. Soc.*, 107, 1459 (1985).
151. A.A. Pincock, A.L. Pincock, and M.A. Fox, *Tetrahedron*, 1985, 41, 4107.
152. (a) M. Fujihira, Y. Satoh, and T. Osa, *Nature*, 293, 206 (1981). (b) M. Fujihira, Y. Satoh, and T. Osa, *Bull. Chem. Soc. Japan*, 55, 666 (1982). (c) M. Fujihara, Y. Satoh, and T. Osa, *J. Electroanal. Chem.*, 126, 277 (1981).
153. C.G. Giannotti, S. LeGreneur, and O. Watts, *Tetrahedron Lett.*, 24, 5071 (1983).
154. T. Kanno, T. Oguchi, H. Sakuragi, and K. Tokumaru, *Tetrahedron Lett.*, 21, 467 (1980).
155. Y. Simamura, H. Misawa, T. Oguchi, T. Kanno, H. Sakuragi, and K. Tokumaru, *Chem. Lett.*, 1691 (1983).
156. K. Takagi, T. Fujioka, Y. Sawaki, and H. Iwamura, *Chem. Lett.*, 913 (1985).
157. K. Hashimoto, T. Kawai, and T. Sakata, *J. Phys. Chem.*, 88, 4083 (1984).
158. (a) L. Izumi, W.W. Dunn, K.O. Wilbourn, F.R.F. Fan, and A.J. Bard, *J. Phys. Chem.*, 84, 3207 (1980). (b) L. Izumi, W.W. Dunn, K.O. Wilbourn, F.R.F. Fan, and A.J. Bard, *J. Phys. Chem.*, 85, 218 (1981).
159. (a) C.Y. Hsiao, C.L. Lee, and D.F. Ollis, *J. Catal.*, 82, 418 (1983). (b) D.F. Ollis, C.Y. Hsiao, L. Budiman, and C.L. Lee, *J. Catal.*, 88, 89 (1984). (c) A. Sohailuddin and D.F. Ollis, *Solar Energy*, 32, 597 (1984). (d) T. Nguyen and D.F. Ollis, *J. Phys. Chem.*, 88, 3386 (1984). (e) A.L. Pruden and D.F. Ollis, *Environ. Sci. Tech.*, 17, 628 (1983). (f) D.F. Ollis, *Environ. Sci. Tech.*, 19, 480 (1983).
160. M.A. Fox, Y.S. Kim, and M.T. Dulay, *Catal. Lett.*, 5, 369 (1990).

161. A.L. Pruden and D.F. Ollis, *J. Catal.*, **82**, 404 (1983).
162. (a) D.F. Ollis, *J. Catal.*, **97**, 569 (1986). (b) R.W. Matthews, *J. Catal.*, **97**, 565 (1986).
163. (a) X. Li, J.W. Cubbage, and W.S. Jencks, *J. Org. Chem.*, **64**, 8525 (1999). (b) X. Li, J.W. Cubbage, T.A. Tetzlaff, and W.S. Jencks, *J. Org. Chem.*, **64**, 8509 (1999).
164. M. Barbeni, E. Pramauro, E. Pelizzetti, E. Borgarello, M. Grätzel, and N. Serpone, *Nouv. J. Chim.*, **8**, 547 (1984).
165. A.A. Pincock, A.L. Pincock, and M.A. Fox, *Tetrahedron*, **41**, 4107 (1985).
166. A. J. Frank, Z. Goren, and I. Willner, *Chem. Commun.*, 1029 (1985).
167. H. Yamataka, N. Seto, J. Ichihara, T. Hanafusa, *Chem. Commun.*, 788 (1985).
168. (a) G. T. Brown and J. R. Darwent, *J. Phys. Chem.*, **88**, 4955 (1984). (b) G. T. Brown and J. R. Darwent, *J. Chem. Soc.*, **80**, 1631 (1984).
169. S. Yanagida, Y. Ishimaru, and C. Pac, *J. Am. Chem. Soc.*, **109**, 6464 (1986).
170. (a) C. Joyce-Pruden, J. Pross, and Y. Li, *J. Org. Chem.*, **57**, 5087 (1992). (b) T. Bruton, F. Mahdavi, and Y. Li, *J. Org. Chem.*, **58**, 4765 (1993). (c) H. Wang, R.E. Partch, and Y. Li, *J. Org. Chem.*, **62**, 5222 (1997).
171. Y. Nosaka and M.A. Fox, *J. Phys. Chem.*, **92**, 1893 (1988).
172. H. Wang, R.E. Partch, and Y. Li, *J. Org. Chem.*, **62**, 5222 (1997).
173. G.N. Schrauzer and T.D. Guth, *J. Am. Chem. Soc.*, **99**, 7189 (1977).
174. J.A. Davies, D.L. Boucher, and J.G. Edwards, *Adv. Photochem.*, **19**, 235 (1995).
175. W.Y. Lin, C. Wei, and K. Rajeshwar, *J. Electrochem. Soc.*, **140**, 2477 (1993).
176. (a) K. Okada, K. Hisamitsu, and T. Mukai, *Chem. Commun.*, 941 (1980). (b) K. Okada, K. Hisamitsu, Y. Takahashi, T. Hanaoka, T. Miyashi, and T. Mukai, *Tetrahedron Lett.*, **25**, 5311 (1984).
177. R. A. Barber, P. deMayo, and K. Okada, *J. Chem. Soc., Chem. Commun.*, 1073 (1982).
178. H. Al-Ekabi and P. deMayo, *Tetrahedron*, 386 (1987).
179. S. Lahiry and C. Halder, *Solar Energy*, **37**, 71 (1986).
180. P. deMayo and G. Wenska, *Tetrahedron*, 395 (1987).
181. H. Al-Ekabi and P. deMayo, *Chem. Commun.*, 1231 (1984).
182. H. Al-Ekabi and P. deMayo, *J. Phys. Chem.*, **89**, 5815 (1985).
183. T. Hasegawa and P. deMayo, *Langmuir* **2**, 362 (1986).
184. T. Sakata, *J. Photochem.*, **29**, 205 (1985).
185. M. Anpo, K. Chiba, M. Tomonari, S. Coluccia, M. Che, and M.A. Fox, *Bull. Chem. Soc. Jpn.*, **64**, 543 (1991).
186. H. Yamashita, H. Nishiguchi, N. Kamada, M. Anpo, H. Hatano, K. Kikui, Y. Teraoka, S. Kagawa, S. Ehara, L. Palmisano, A. Sclafani, M. Schiavello, and M.A. Fox, *Res. Chem. Intermed.*, **20**, 815 (1993).

9 Radiative Charge Recombination and Electrochemiluminescence

Ann-Margret Andersson and Russell H. Schmehl

9.1 Introduction

The topic of radiative charge recombination encompasses a variety of areas including decomposition of reactive organic substances by redox pathways, simple annihilation of the one electron oxidized and one electron reduced forms of a particular substance and complex charge annihilation processes in microheterogeneous environments. Luminescent charge recombination processes are attractive for analytical applications because an optical signal can be generated from chemical systems subjected to electrolysis. As a result, a rich array of applications has sprung forth from studies of electrogenerated chemiluminescence and electroluminescence.

The first observation of luminescence associated with a charge recombination process came in the early part of the 20th century in experiments involving oxidative electrolysis of aqueous halide solution at mercury anodes [1]. The report describes the observation of colored “flames” from the mercury pool surface following formation of a coating of mercury halide on the electrode surface during electrolysis and the authors relate this to flame emission of mercury halides.

Many years passed before systematic studies of luminescent charge recombination came in the 1960s from several groups [2, 3, 4, 5]. In part, the study of radiative charge recombination was limited by the difficulty posed in generating and manipulating the reactive species. Advances in techniques for handling air-sensitive materials and the development of modern electroanalytical methods made the study of emissive charge annihilation processes more straightforward. The phenomenon is of both practical and theoretical interest and the literature today on this topic is broad in scope.

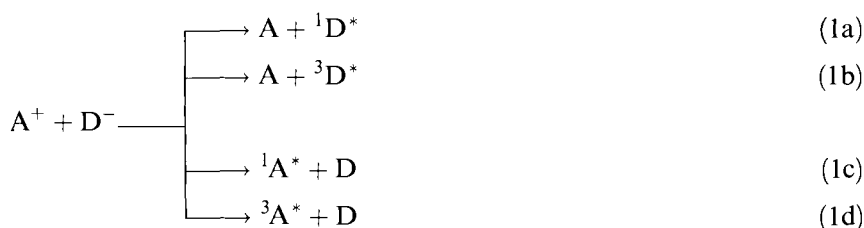
This chapter will focus on processes leading to the formation of localized excited states, excimers and exciplexes by annihilation of radical ions in solution. The article will not deal with either direct absorption or emission from intramolecular charge-transfer excited states. In addition, the voluminous literature in this area prohibits any attempt to comprehensively cover published work in the space avail-

able. The chapter will also focus on electrogenerated chemiluminescence (ECL) and electroluminescence (EL). A number of reviews present overviews of ECL [6, 7, 8, 9] and EL [10]. Additional articles exist that emphasize techniques for generation of ECL [11] and analytical applications [12]. A brief discussion of experimental aspects and applications will be presented here, but the emphasis will be on mechanistic aspects of radiative charge recombination and applications.

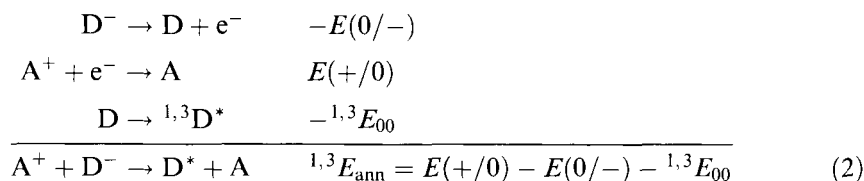
9.2 Processes Leading to Radiative Charge Recombination

9.2.1 Annihilation of Anion and Cation Radicals

To create an excited state in a charge recombination (or annihilation) process, the free energy of the process must be large enough to generate an excited state of one of the reaction products. For systems involving organic radical ion reactants (both doublet states), annihilation can result in either singlet or triplet excited states, as shown in Eq. 1.



The free energy of the annihilation reaction can be evaluated from the one-electron potentials for oxidation and reduction of the species involved and the zero-zero emission energy, E_{00} , of the luminescent product. The excited state formed can be either singlet or triplet spin multiplicity (or both). If strict spin conservation is observed in the process, the products will contain 75 % triplet and 25 % singlet; however, hyperfine interactions provide alternate avenues for angular momentum conservation [13, 14].



It is possible that some cases for which annihilation appears favored by Eq. 2 will not result in formation of an excited state. The simple expression does not account for differences in solvation energies and entropic factors for the redox processes which are generally in the range of 0.1–0.2 eV.

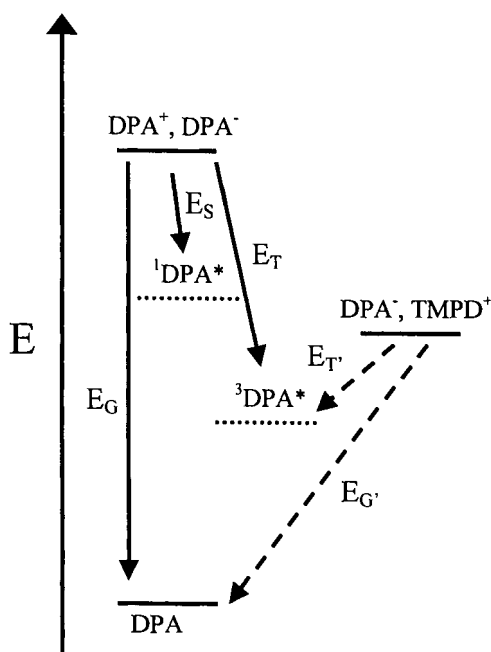


Figure 1. Energy level diagram for charge annihilation processes. Relative energies are shown for the DPA^+ , DPA^- pair, the TMPD^+ , DPA^- pair and the singlet and triplet excited states of DPA. The allowed recombination processes are indicated by the arrows.

A typical energy level diagram, with 9,10-diphenylanthracene (DPA) as an example, is shown in Figure 1. Annihilation of DPA cation and anion radicals results in the formation of the singlet excited state of diphenylanthracene, and fluorescence is observed. In general, for cases where A^+ and D^- differ, only one of the two product species has an accessible excited state. Figure 1 also depicts such a case for reaction of DPA^- with the N,N, N',N'-tetramethylphenylene diamine cation radical (TMPD^+). The energy available in the annihilation reaction is far below that required to produce either singlet state and only the DPA triplet is formed initially. However, fluorescence is also observed upon annihilation of DPA^- and TMPD^+ ; the fluorescence results from triplet-triplet annihilation (Eq. 3). Since fluorescence is observed in systems exoergic enough to populate the singlet excited state of the



chromophore directly and in systems clearly lacking sufficient energy, the former are referred to as energy-sufficient annihilation processes and the latter are energy-deficient.

9.2.2 Excimer and Exciplex Emission

Charge-annihilation processes preceding emission may occur from solvent-separated or contact ion pairs, and there is a possibility that excited-state dimers

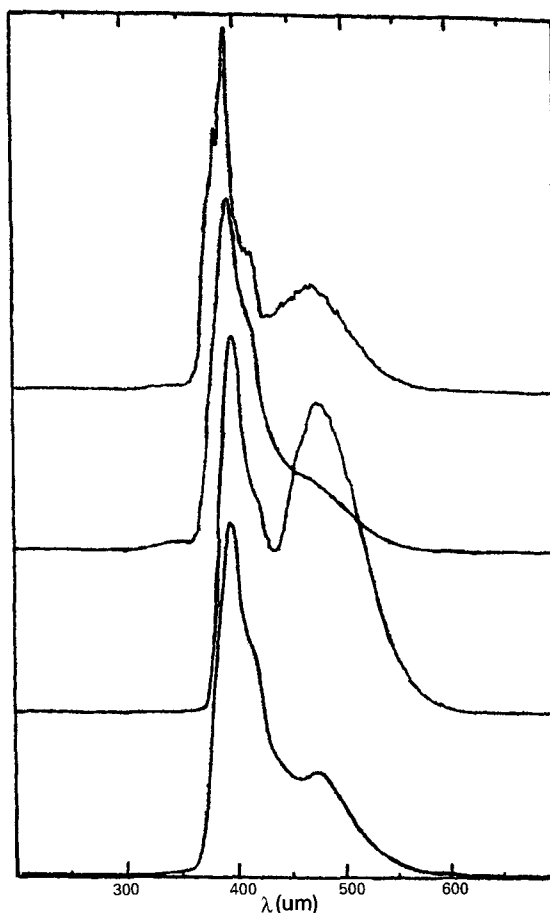
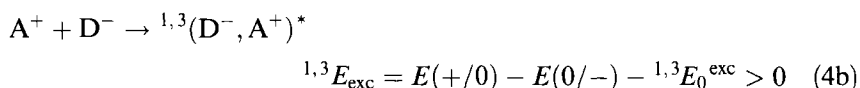
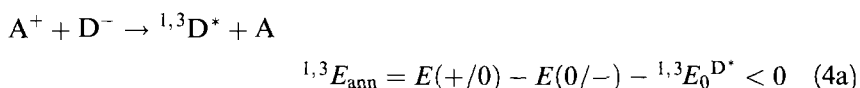


Figure 2. Emission from a solution containing pyrene (0.005 M) (top) and pyrene (0.005 M) plus TMPD (0.001 M) (lower three spectra), which show fluorescence prior to electrolysis, electrogenerated chemiluminescence and post-electrolysis fluorescence (top to bottom), (with permission of the American Chemical Society).

(excimers) or excited-state intermolecular charge-transfer complexes (exciplexes) may form [15]. Excimers and exciplexes have shallow energy minima at energies lower than the localized excited state of the luminescent chromophore, and emission can occur from this weakly bound state to the ground state. Excimer emission has been observed from pyrene dimers following reaction of TMPD^+ and pyrene anion (PY^-). It has been observed that, for the $\text{TMPD}^+/\text{PY}^-$ system, both ^1PY localized fluorescence and $^1(\text{PY})_2$ excimer emission occur, but the excimer emission is much more intense than that observed upon direct excitation of pyrene [16]. Figure 2 illustrates the emission observed following direct excitation of pyrene and following annihilation of the radical ions. The explanation for the larger fraction of excimer emission from the redox reaction can be found in the fact that triplet-triplet annihilation is required for an emitting excited state to be produced following the charge-recombination process, and this reaction requires an intimate encounter of two pyrene molecules.

Other reactions of aromatic hydrocarbon anion radicals and amine cation radicals lead to exciplex emission, particularly in nonpolar solvents [15]. Luminescence from exciplexes is most definitively observed in systems for which the redox reaction is energetically unable to yield a localized excited state. The free energy of exciplex formation, ${}^{1,3}E_{\text{exc}}$, is associated with solvation and geometry optimization in the encounter complex of D^- and A^+ .

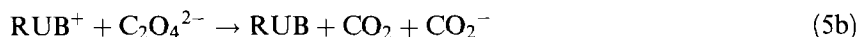


This is exemplified by the reaction of benzophenone anion with the tri(tolylamine) cation (TPTA⁺) in THF [17]. Formation of all triplet and singlet locally excited states for this system is not thermodynamically possible, yet broad, unstructured red emission is observed and was assigned to the exciplex.

Weller and Zachariasse thoroughly investigated exciplex formation and luminescence for donor acceptor systems in THF [18]. A particularly interesting result from their work came from an examination of the temperature dependence of radiative charge recombination between 9,10-dimethylantracene anion (DMA⁻) and TPTA⁺ in THF [19]. They found that both exciplex emission and fluorescence from DMA* were observed in solution at low temperature (ca. -50°C). As the solution temperature is raised, the excimer emission decreases in relative intensity, and at room temperature the emission is nearly completely DMA* fluorescence. The monomer-to-excimer emission intensity ratio as a function of temperature follows Arrhenius kinetic behavior and yields an activation barrier that is nearly the same as the energy gap between the exciplex and the ¹DMA* states. Thus, their model consisted of reaction of the solvent-separated ions to form an intimate emissive ion pair which could dissociate to yield the singlet anthracene derivative.

9.2.3 Reactions of Radical Ions with Other Reagents

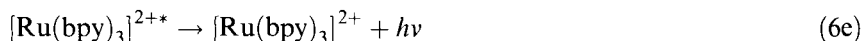
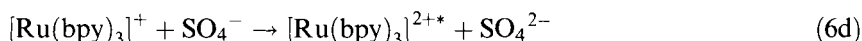
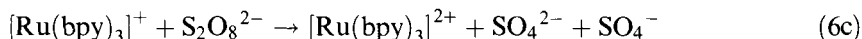
Another approach for generating excited states by charge-recombination reactions involves the generation of a single radical ion species in the presence of a substrate in solution to yield a second radical ion of opposite redox character. An early observation of such chemistry was made by Chang and Bard in studies of the electrochemical oxidation of rubrene (RUB) and other fluorophores in the presence of oxalate [20]. Oxidation of oxalate, either directly at the electrode surface or by mediated oxidation by the rubrene cation, results in decomposition of the oxalate anion radical to yield CO₂ and the CO₂⁻ radical, a strong reducing agent (Eq. 5). Reaction of the CO₂⁻ radical with the RUB⁺ results in luminescence from rubrene.





The mechanism postulated by Bard involves the steps shown in Eq. 5. Subsequent studies by others have shown that this mechanism is operative for several additional reagents that decompose to yield a strongly reducing radical following one-electron oxidation. In particular, tertiary amines with a hydrogen atom in the α position undergo deprotonation following oxidation to yield a strongly reducing radical [21]. Application of these types of systems to the detection of various organic analytes is presented in Section 9.5 of this chapter.

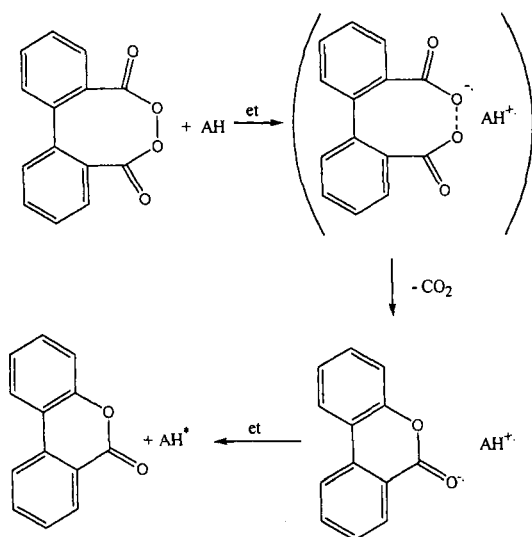
Related chemistry has been demonstrated for reactions involving initial reduction of one species and concomitant reduction of a second species that leads to production of a strong oxidizing agent. The peroxydisulfate dianion decomposes upon reduction, to produce SO_4^- , which can annihilate with an anion radical to yield a luminescent species. White and Bard demonstrated this for reduction of solutions containing tris(2,2'-bipyridine) ruthenium(II), $[\text{Ru}(\text{bpy})_3]^{2+}$, in the presence of $\text{S}_2\text{O}_8^{2-}$ as shown below [22]:



Reactions of this type involve the oxidation/reduction of a reactive intermediate for which the one-electron redox potential may not be known (CO_2^- in Eq. 5). Determination of the free energy for formation of the emissive state requires knowledge of the potentials of both ion radicals and the energy of the emitting excited state (Eq. 2). It is, in principle, possible to find approximate values for one-electron potentials of very unstable ion radicals (e.g., the $\text{CO}_2^{-/0}$ potential of Eq. 5) by use of a series of chromophores with varying potentials for forming the excited state from the radical ion (varying $\text{RUB}^{+/*}$ potentials).

9.2.4 Chemically Induced Electron-Exchange Luminescence

This class of radiative charge recombination is very similar to the processes described in Section 9.2.3, except for the fact that generation of a transient radical ion is not necessary for initiation of the process. The free energy for generation of an excited state is possessed by a chemical substance which can be isolated and stored (as some radical ions can). The most common systems of this sort involve reaction



Scheme 1.

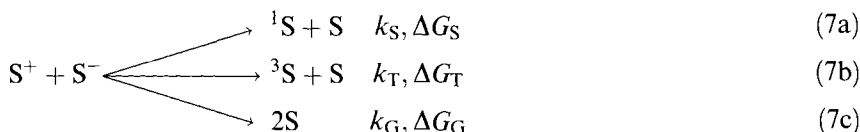
of organic peroxides with a luminescent “activator” molecule [23, 24]. For example, diphenoyl peroxide reacts with various aromatic hydrocarbons (i.e. pyrene, rubrene) to yield the excited hydrocarbon, benzocoumarin and CO₂. The mechanism postulated for the process is shown in Scheme 1.

Following oxidation of the aromatic hydrocarbon by the peroxide, the peroxide anion radical loses CO₂ and generates the product benzocoumarin anion radical, a strong reducing agent. Annihilation of this anion radical with the hydrocarbon cation radical results in generation of the hydrocarbon excited state. The final reaction is a radiative charge recombination and is directly analogous to the reactions in Eqs. 5d and 6d above. Koo and Schuster showed that the rate constant for the reaction correlated well with the one-electron oxidation potential of the aromatic hydrocarbon [25]. The relative yield of luminescence is insensitive to the presence of oxygen and generates emissive exciplexes when aromatic amines are used as reductants; both phenomena indicate the loss of CO₂ and back electron transfer occur within a solvent cage.

Examination of the above reaction sequence indicates that evaluation of the energy available to produce an excited state differs from the processes described in Sections 9.2.1–9.2.3. While the actual reaction to generate the excited state parallels those above, the energy available can be assessed from the free energy of thermal decomposition of the organic peroxide. Typical organic peroxides decompose to generate two carbonyl-containing species (in some cases CO₂) with heats of reaction between 2.5 and 3.9 V (55 and 90 kcal/mol). Thus, ample energy is available for generation of excited states in bimolecular reactions. While this class of radiative charge recombination reactions will not be discussed further in this chapter, the chemically induced electron-exchange luminescence mechanism may be the predominant mode of reaction in many bioluminescent systems.

9.3 Kinetic Aspects

From the above discussion it should be clear that annihilation of radical ions can result in production of several species. In the very simplest case of self-annihilation of one-electron oxidized and one-electron reduced forms of a particular species, S, three processes compete (Eq. 7).



As mentioned above (Figure 1, Eq. 2), as long as the processes shown in Eqs. 7a and 7b involve formation of the lowest-energy excited state, the relative free energies of the three processes will be $\Delta G_{\text{G}} \gg \Delta G_{\text{T}} > \Delta G_{\text{S}}$. Efficient radiative charge recombination requires that either k_{S} or k_{T} (or both) is significantly more rapid than k_{G} .

The relative rates of the reactions leading to formation of either ground-state or excited-state products can be evaluated in terms of formalisms developed by Marcus [26], Hopfield [27], Jortner [28], and others [29]. The development of the semiclassical and quantum-mechanical expressions for electron transfer are discussed in Chapters. 3–5 (Volume I, Part 1). A general expression for the rate constant of a non-adiabatic electron-transfer process is given below,

$$\begin{aligned}
 k_{\text{ann}} &= \sum_{j=0}^{\infty} F_j V^2 \left(\frac{4\pi^3}{h^2 \lambda_s k_B T} \right)^{1/2} \exp \left[-\frac{(j h \nu_v + \Delta G_q + \lambda_s)^2}{4 \lambda_s k_B T} \right] \\
 F_j &= \frac{\exp(-S) S^j}{j!} \\
 S &= \frac{\lambda_v}{h \nu_v}
 \end{aligned} \quad (8)$$

where F represents the Franck–Condon factor associated with overlap of the zeroth vibrational state of the ion pair with the j th state of the mode v (of frequency $h\nu_v$; $h\nu_v \gg k_B T$) of the recombination product (S , T , or G); λ_v is the internal reorganization energy associated with internal coordinates of the ions undergoing electron transfer, λ_s is the sum of low-frequency modes associated with the electron transfer, V is the electronic-coupling matrix element between the initial and final states, and ΔG_q is the free energy of the annihilation process that yields either an excited state or the ground state (Eq. 7). This expression indicates that, for a series of closely related electron-transfer reactions having nearly identical reorganization energies, the rate constant will reach a maximum when ΔG_q equals $\lambda_s + j h \nu_v$ (activationless electron transfer) and will then decrease as the free energy increases further (Figure 3). The region of decreasing electron-transfer rate constant with increasing exoer-

gonicity of the reaction is referred to as the Marcus inverted region. The observation of luminescence from charge recombination reactions represented an early (though indirect) verification of the existence of the inverted region [15, 18]. For the three reactions of Eq. 7, the solvent reorganization might be expected to be comparable if there are not large internal coordinate differences between the ground state and excited state products. For systems in which the product state is a locally excited state on either the electron donor or acceptor, internal coordinate distortions relative to the ground state are likely to be smaller than systems with a charge-transfer excited-state product. Nonetheless, assuming the difference in λ between reactions 7a–7c is small, the relative rate constants of the three annihilation reactions can be seen to depend on λ and ΔG as shown in Figure 3. When either ΔG_S or ΔG_T is relatively close to λ , the annihilation to yield ground state will be deep in the inverted region (since $\Delta G_G \gg \Delta G_S$ or ΔG_T) and the rate constant for formation of an excited state will be orders of magnitude larger than that for producing only ground state. However, if the free energy to produce an excited state is

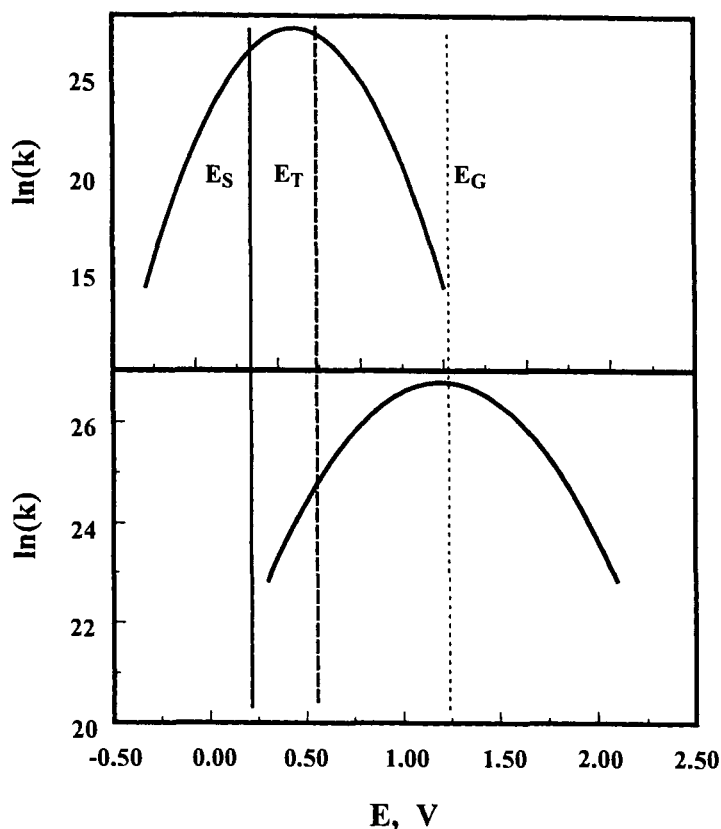


Figure 3. Free-energy dependence of electron transfer reactions for case (a) λ is approximately equal to ΔG_S (or ΔG_T) and (b) where λ is closer in energy to ΔG_G .

much smaller than λ , ground-state formation can be favored (Figure 3). From Eq. 8 it can be seen that it should be possible to predict relative yields of singlet, triplet, and ground state for particular annihilation reactions if one is able to obtain reasonable estimates of the above parameters for each reaction type.

The above account, however, does not include the possibility of direct luminescence from the intimate radical-cation–radical-anion pair, a process commonly observed when the two radicals originate from different substances (i.e., not self-annihilation). As mentioned above, Weller and Zachariasse very clearly illustrated that luminescence from ion pairs (exciplexes) is significant [18, 30]. In addition, singlet emission can result from energy-deficient systems by triplet–triplet annihilation processes. The issue of charge recombination from solvent-separated and intimate ion pairs has been addressed in detail recently in the work of Gould and Farid [31, 32, 33]. In studies of cyanoanthracene anion donors and alkylbenzene cation acceptors, they were able to examine differences in charge-recombination rate constants between contact radical ion pairs (CRIPs) formed by direct excitation of the ground-state charge-transfer complex and solvent-separated radical ion pairs (SSRIPs). Significant differences were found for the electronic coupling, V , and medium reorganization energies, λ_s , of the two ion-pair types, and luminescence is only observed from the CRIPs [31a]. Figure 4 shows the free-energy dependence of return electron transfer to the ground state from contact and solvent-separated ion pairs; the smaller λ_s for the CRIPs serves to favor radiative charge recombination over decay directly to the ground state. The authors also note that electron-transfer expressions like Eq. 8 cannot be used to describe CRIPs, since results indicate that electron transfer in the CRIP case is adiabatic (strong electronic coupling).

The authors also examined the charge-transfer luminescence in detail. In the late 1980s Marcus illustrated the relationship between charge-transfer luminescence and nonradiative recombination (i.e., radiative and nonradiative electron transfer to the ground state) [34]. Marcus pointed out that the charge-transfer luminescence of a CRIP presents radiative relaxation to the ground state over a free-energy range that is analogous to the normal and inverted regions. Thus, the charge-transfer emission can be fit by a series of Gaussian functions with spacings between the maxima of $h\nu$. The width of each Gaussian component depends on λ_s and the magnitude of each component is given by the relative Franck–Condon factors. The significance of this is that all of the adjustable parameters required to predict the rate constant of the nonradiative charge recombination process are obtained [32]. Gould and coworkers illustrated the validity of this approach by taking parameters from fits of charge-transfer luminescence of 1,2,4,5-tetracyanobenzene/hexamethylbenzene complexes in several solvents, using the parameters to calculate rate constants for nonradiative electron transfer and showing that the values obtained correlated well with experimental rate constants [35]. Like the earlier results of Bard, indicating excimer formation is more likely to result from annihilation of two triplets than from direct excitation of the chromophore, the work of Farid and Gould shows that vast differences exist between recombination processes of contact and solvent-separated ion pairs.

Localized fluorescence that results from cross-electron-transfer reactions can occur by direct singlet formation or by reaction to yield triplets that annihilate to

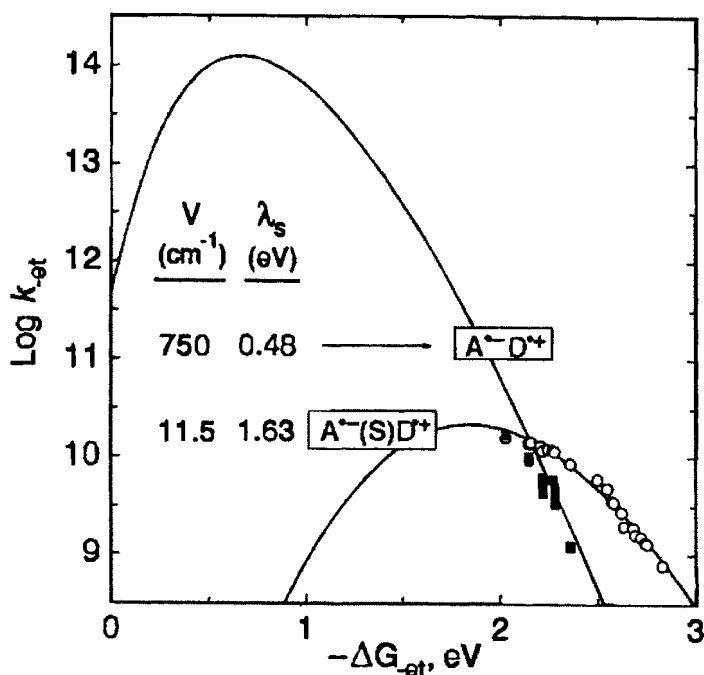


Figure 4. Free-energy dependence of return electron transfer for contact ion pairs (A^-D^+) and solvent-separated ion pairs ($A^-(S)D^+$) for recombination of dicyanonaphthalene anions with alkylbenzene cation radicals. Solid lines represent fits to the data with values for V and λ_s given. From Gould, I. R.; Farid, S. *Acc. Chem. Res.*, **1996**, 29, 522, with permission from the American Chemical Society.

produce the fluorescent excited species (Eq. 1a, Eq. 3). Recently, Wightman and coworkers used high-frequency generation of radical ions at microelectrodes to explore the dynamics of luminescence evolution in systems containing DPA and one of a group of electron donors [36]. The free energies for the reaction of DPA^+ with the donor anion radical ranged from +3.24 V to +2.41 V. Since the energies of the excited DPA singlet and triplet are 3.06 and 1.8 V, respectively, some of the reactions were energy-sufficient and others generated fluorescence by triplet-triplet annihilation. Observing the intensity-time dependence of the electrochemically generated luminescence in the 0–500 μs time regime, the authors were able to unambiguously determine the chemistry leading to DPA fluorescence by determining the reaction order for fluorescence onset and the degree of quenching by radical ions in solution. Particularly interesting was the observation that reaction of DPA^+ with the naphthyl phenyl ketone anion (NPK^-) ($E_{\text{ann}} = 3.01$ V) could occur by both mechanisms and that the predominant path depends on the concentration of DPA.

The question of the free-energy dependence of heterogeneous electron-transfer reactions at liquid-liquid interfaces was addressed by Bard and coworkers. They ex-

aminated radiative charge recombination at the water–benzonitrile interface to illustrate inverted region behavior in this type of heterogeneous electron transfer [37]. The generation of DPA^+ (and $[(\text{bpy})_3\text{Ru}]^{3+}$ and thianthrene cation) in the vicinity of a benzonitrile/aqueous $\text{C}_2\text{O}_4^{2-}$ interface resulted in luminescence, presumably by a mechanism analogous to Eqs. 5a–c. The reactions paralleling Eqs. 5b and 5d are heterogeneous; direct recombination of the cation radical and CO_2^- to yield ground-state products cannot compete effectively with formation of the excited state. Thus, they concluded the highly exoergic heterogeneous reaction to form ground-state products is in the inverted region.

9.4 Experimental Considerations: Techniques and Molecular Systems

9.4.1 Generation and Characterization of Reactive Species

Early studies of radiative charge recombination processes made use of chemical oxidation and reduction to create the reactive radical ion species. Despite the limitation of the use of chemically stable radical ions, a significant body of literature developed that discussed radiative charge recombination for cross-electron-transfer reactions. In particular, many studies involved reactions of organic radical anions with amine cation radicals [5, 15, 18, 19].

Paralleling this work was a growing body of literature illustrating electrochemical methods for the generation and investigation of luminescence by annihilation of radical ions produced either by simultaneous (two-electrode) or sequential (one-electrode) processes. Electrochemical methods made it possible for the reactive species to be formed in a controlled fashion, for the generation of either pulses of emitted light or continuous luminescence. Faulkner, Bard, and coworkers give overviews of experimental methods in excellent reviews [9, 11, 38].

Pulsed electrode techniques

One approach for obtaining electrogenerated chemiluminescence (ECL) involves sequential oxidation and reduction of a species capable of exhibiting luminescence. This is most commonly accomplished by sequential potential steps, as shown in Figures 5 and 6 [6, 11, 39]. Initial reduction of substrate for a period of time t_f results in formation of the anion radical extending some distance from the electrode surface as shown in Figure 5. At time t_f , the potential is stepped to a value capable of oxidizing the substrate (oxidation of both S and S^- to S^+ will occur) and is held at that value for a time t_r . Luminescence will be observed if the potential is switched and will continue until no S^- remains to react with S^+ (or, if t_r is short relative to t_f , until all S^+ is consumed), as shown in Figure 6. Figure 5 also shows the concentrations of S , S^- , and S^+ as a function of the distance from the electrode at some time during the oxidation of S . This figure illustrates that a reaction plane is established where S^- and S^+ annihilate and luminescence occurs. With increasing time

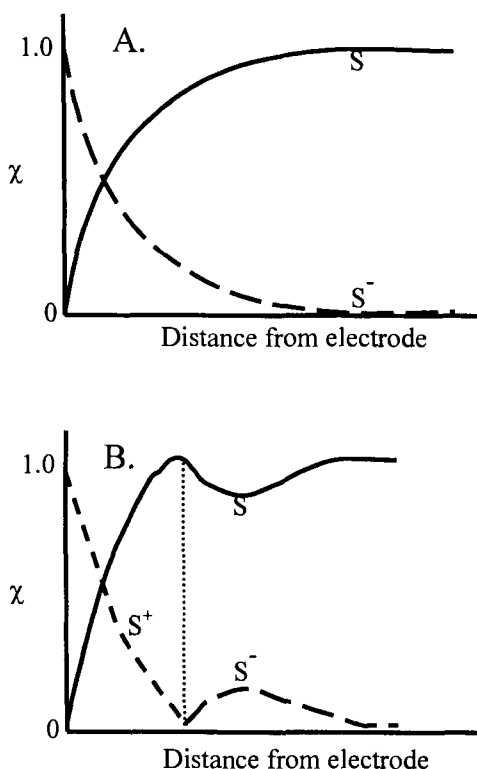


Figure 5. Concentration-distance profiles: (A) following reduction of S to S⁻ and (B) after subsequent change in potential to oxidize S to S⁺. The dotted line represents the plane where annihilation of S⁺ and S⁻ occurs.

($t > t_f$), the plane where luminescence is observed moves away from the electrode and the luminescence intensity decreases as the available S⁻ is depleted.

Analysis of the decay of luminescence intensity with time has been shown to be related to the mechanism of the annihilation process (i.e., direct fluorescence from singlets or luminescence resulting from triplet-triplet annihilation). Feldberg developed simulation techniques for intensity-time profiles from potential step experiments, relating the emission rate (photons/s) to the total redox rate N (moles/s) [40].

$$I = \phi_F \eta^* N \quad (9)$$

The parameters ϕ_F and η^* represent the fluorescence quantum yield of S^{*} and the efficiency of emitting excited states being produced in the charge recombination reaction [$k_S/(k_S + k_T + k_G)$, from Eq. 7]. Feldberg determined that a linear relationship exists between ω , a dimensionless rate parameter proportional to the emission intensity [$\omega = (It_f^{1/2})/(\phi_F AD^{1/2} C)$; A = electrode area, D = substrate diffusion coefficient, C = bulk concentration of S], and $(t_r/t_f)^{1/2}$ (Eq. 10).

$$\log(\omega) = 0.7 + \log(\phi_F \eta_*) - 1.45(t_r/t_f)^{1/2} \quad (10)$$

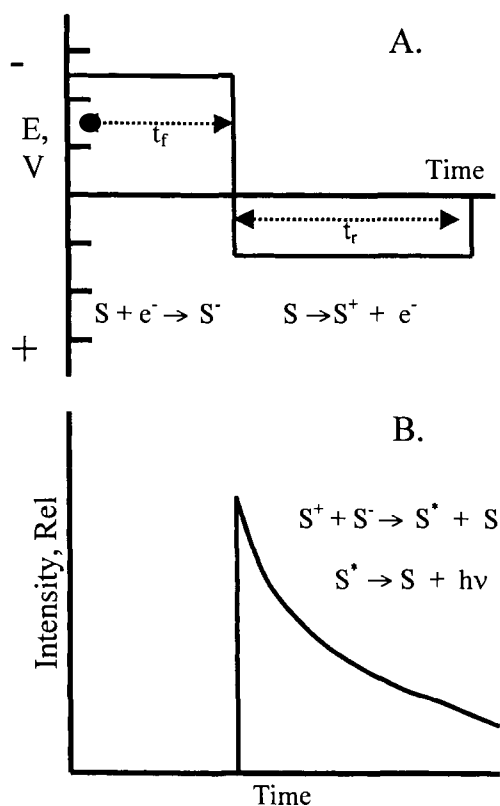


Figure 6. (A) Potential sequence for generation of ECL by double potential step methods and (B) the intensity-time profile resulting from the potential sequence of (A).

The constants of the equation were obtained from simulations and the process applies only to generation of singlet excited states at diffusion-limited annihilation rates. Nonetheless, the expression provided an experimental approach for determining efficiencies of the production of emitting excited states in annihilation reactions. Simulations for systems that react via triplet formation and subsequent triplet-triplet annihilation were also developed [40b] and they illustrated that the two mechanisms can be distinguished by analysis of intensity-time profiles.

With the advent of rapid-scan and high-frequency pulse methods, more direct approaches for evaluating annihilation mechanisms and dynamics have been developed. Early work of van Duyne, using triple potential steps with very short step times, allowed estimation of the annihilation rate constant for DPA anion and cation radicals [29]. More recently, Wightman and coworkers have used multicycle generation of ECL at microelectrodes to determine annihilation rate constants and ECL efficiencies [41, 42]. Figure 7 shows the normalized ECL intensity from DPA at a 1- μm Pt disk as a function of time (t/t_r) at different oscillation frequencies. The intensity increases rapidly after the potential is switched, and then decays as the reactants are depleted. As the oscillation frequency is increased, the annihilation occurs closer to the electrode surface, the intensity-time profile broadens and

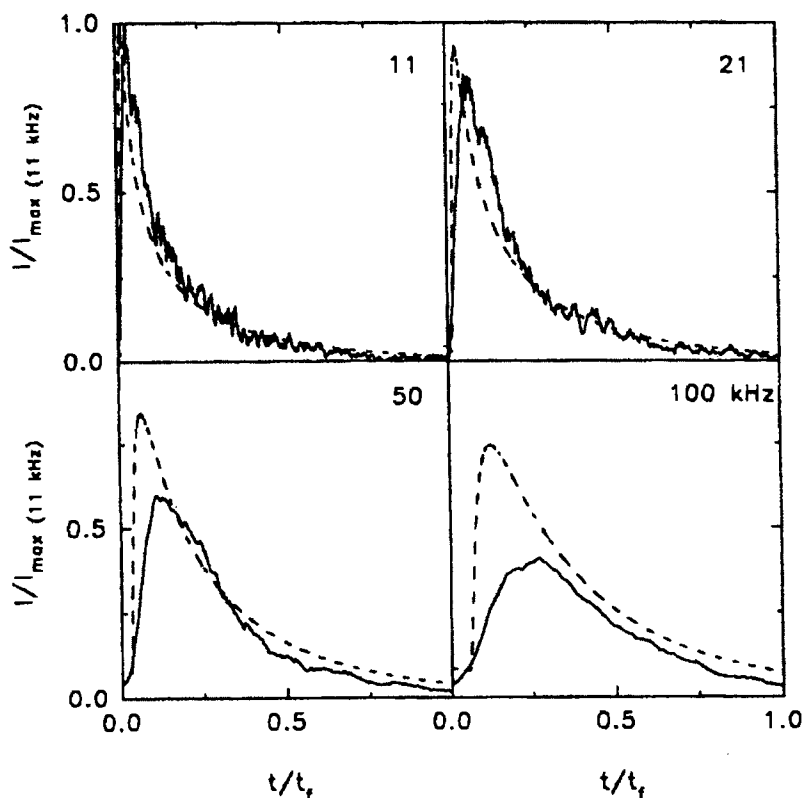


Figure 7. ECL intensity from 0.38 mM DPA in CH_3CN containing 0.1 M tetrabutylammonium hexafluorophosphate at a $1 \mu\text{m}$ Pt disk (—) and simulations of the profiles, assuming diffusion-limited annihilation of DPA^+ and DPA^- . From Collinson, M. M. et al., *J. Phys. Chem.*, **1994**, 98, 11942, with permission from the American Chemical Society.

the experimental intensities are smaller than those expected from simulations. The broadening of the emission profile with time indicates the evolution from diffusion control to kinetic control in the experiment, and provides data that can be simulated to yield ion annihilation rate constants. The decreased intensities have been attributed to quenching by the electrode [43, 44]. As mentioned in Section 9.3 above, this technique also provides a direct approach that serves to distinguish energy-sufficient and energy-deficient processes leading to fluorescence by ECL. Finally, distinct interference patterns have been observed in the ECL intensity–time profiles obtained at frequencies between 2 and 20 kHz for millimolar solutions of substrates [45]. On these timescales, the emission plane is at a distance from the electrode comparable to the wavelengths emitted by chromophores such as DPA and $[(\text{bpy})_3\text{Ru}]^{2+}$. Fourier transforms of these interference patterns produce frequency-domain spectra of the emitting chromophores. This is an interesting verification of the predicted

oscillations in chromophore emission intensity with distance from metallic electrodes [43, 44].

Steady-state electrochemical methods

The most useful electrochemical way to generate radical ion species for steady-state ECL measurements is rotating ring-disk voltammetry, RRDE. While the technique requires two potentiostats and the ring-disk electrodes, the apparatus is sold commercially and both instrumental and conceptual aspects of the technique have been described in detail by Faulkner and Bard [11]. Briefly, ring-disk electrodes consist of a disk electrode and a concentric ring electrode that is electrically insulated from the disk. The potential at each electrode can be independently controlled so that one reactant can be generated at the disk and the other at the ring. When the ring-disk electrode is potentiostatted and rotated, lamellar flow established at the planar disk electrode transports solution from the disk to the ring. In a typical RRDE experiment, annihilation of cation and anion radicals occurs at the inner ring surface and a thin ring of luminescence is generated. This steady-state experiment can be used to measure ECL quantum yields; because annihilation reactions are generally diffusion limited and an excess of the oppositely charged radical ion is generated at the ring electrode, essentially all the ion produced at the disk is trapped and thus the number of annihilations per second is given by $N = i_{\text{disk}}/n\mathfrak{F}$. If an RRDE system is calibrated to yield absolute values of the emission rate, ECL quantum yields can be determined [16, 46].

RRDE experiments are also useful for the examination of systems where multi-electron oxidation or reduction reactions are possible. An example is shown in Figure 8 for the reduction of DPA at the disk while TMPD^+ is steadily generated at the ring [46]. The emission intensity increases as the DPA is reduced at -1.8 V;

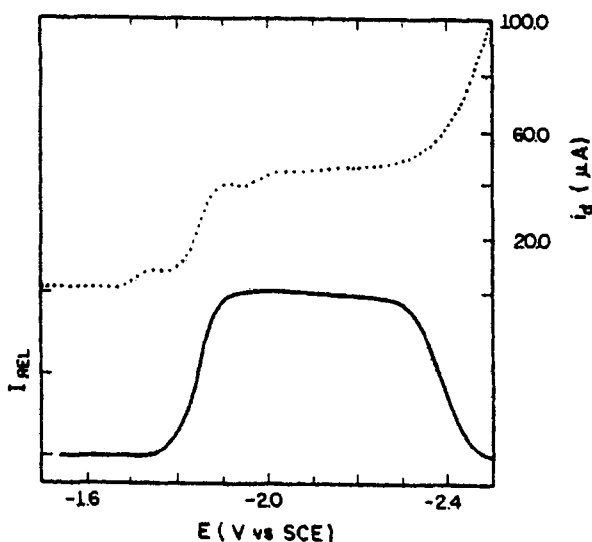


Figure 8. RRDE experiment illustrating the disk current and emission intensity as a function of the disk potential in a cell containing TMPD and DPA. The ring current is fixed at $+0.35$ V to generate TMPD^+ and the disk potential is scanned. From Maloy and Bard, *J. Am. Chem. Soc.*, **1971**, 93, 5968, with permission from the American Chemical Society.

however, the second reduction of DPA (to produce DPA^{2-}) leads to a decrease in the ECL intensity, apparently because the dianion is highly reactive and does not survive to reach the ring.

9.4.2 Molecular Systems

This section is intended to provide representative examples of particular molecular systems that have been well studied and are known to undergo either self-annihilation or cross-electron-transfer reactions to generate luminescence. The structures of organic species commonly observed to participate in radiative charge recombination reactions are shown in Figure 9 (either lumophores or ancillary reactants). Tables 1 and 2 provide data for inorganic and organic systems that undergo self-annihilation

Table 1. Inorganic complexes exhibiting ECL via self-annihilation.

Complex ^a	E^o (ox) V	E^o (red) V	$\lambda_{\text{max}}^{\text{em}}$ /nm (eV)	ϕ_{em}	Ref.	Comment
$[\text{Ru}(\text{bpy})_3]^{2+}$	+1.26 ^b	-1.28	610 (2.03)	0.07	[84, 85]	vs SSCE; $\phi_{\text{ecl}} = 0.05$
$[\text{Ru}(\text{dpphen})_3]^{2+}$	+1.09	-1.47	615 (2.01)	0.37	[85, 86]	vs NHE; $\phi_{\text{ecl}} = 0.24$
$[\text{Os}(\text{bpy})_3]^{2+}$	+0.82	-1.21	725 (1.71)	0.005	[87, 88]	vs SSCE
$[\text{Pt}_2(\text{P}_2\text{H}_2\text{O}_5)_4]^{4-}$	+0.45 ^b	—	510 (2.43)	0.5	[89, 90, 91]	$E^0(\text{ox})$ is peak potential.
$[\text{Pd}(\text{TPP})]$	+1.40 ^b	-1.45 ^b	690 (1.80)	—	[92]	
$[\text{Mo}_6\text{Cl}_{14}]^{2-}$	+1.36	-1.70	765 (1.62)	0.18	[93]	vs SCE; Cross rxn. w/ $\text{W}_6\text{Cl}_8\text{Br}_6^-$ gives ECL
$[\text{Cu}(\text{py})\text{I}]_4$	+0.28	—	690 (1.80)	—	[94, 95]	vs ferrocene

^aSee Figure 9 for ligand structures.

^bPotential vs. Ag wire quasi reference electrode.

Table 2. Organic compounds exhibiting ECL via self-annihilation.

Compound ^a	E^o (ox) V	E^o (red) V	$\lambda_{\text{max}}^{\text{em}}$ /nm (V)	ϕ_{em}	Ref.	Comment
9,10-Diphenylanthracene	+1.22	-1.92	395 (3.14)	0.95	[96]	
Luminol	+0.22	—	425 (2.92)	—	[97]	
Phenanthrene	+1.8	-2.47	495 (2.50)	—	[98]	Phosphorescence
Perylenetetracarboxylic Diimide	+1.62 ^b	-0.81 ^b	540 (2.30)	—	[99]	vs. SCE
Rubrene	+0.95	-1.37	540 (2.30)	0.98	[100]	vs. SCE
1-Methyl-2,5-diphenylindene	+1.33	-2.39 ^c	390 (3.18)	0.82	[101]	

^aSee Figure 9 for structures of compounds.

^bPeak potential for reversible CV.

^cPeak potential for irreversible CV.

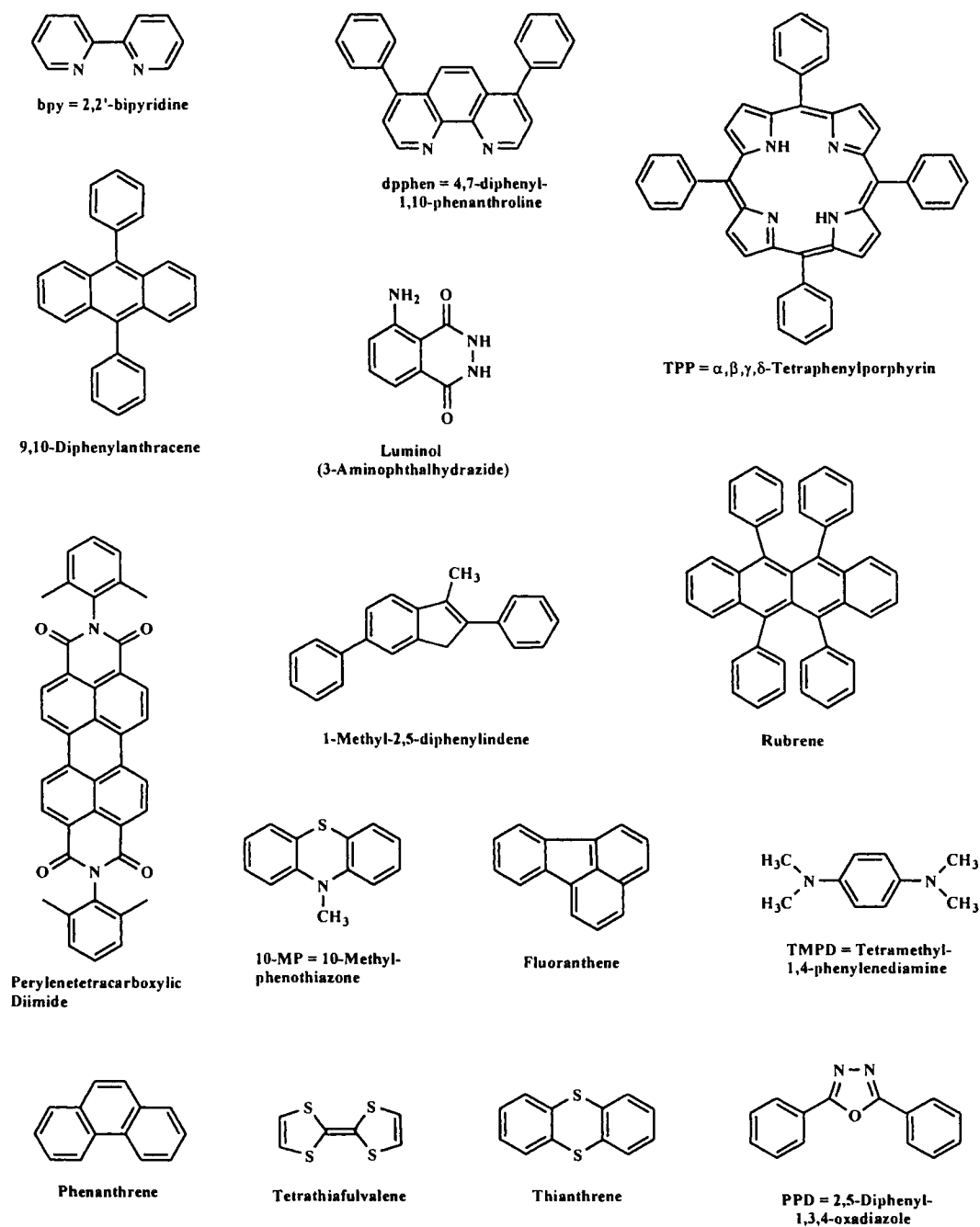


Figure 9. Structures of some of the compounds and ligands listed in Tables 1–3.

to generate luminescence. The one-electron potentials for reduction of the cation radical (or oxidized metal complex) and reduction of the compound are presented along with the emission maxima and luminescence quantum yield (not the radiative charge recombination yield). In Table 1, only a few derivatives of $[(bpy)_3Ru]^{2+}$ are presented; however, this class of chromophores makes up by far the largest and most widely studied class of ECL active molecules, and numerous applications making use of Ru^{II} complexes have been developed (vide infra). Luminescence of all Ru^{II} and Os^{II} diimine complexes originates from a triplet metal-to-ligand charge-transfer (MLCT) transition. The precise energy of the singlet MLCT state is not known, but even if annihilation could yield the singlet state, the intersystem crossing efficiency is unity [47]. The palladium(II) porphyrin, $Pd(TPP)$, exhibits only phosphorescence following reaction of $[Pd(TPP)]^+$ and $[Pd(TPP)]^-$, despite the fact that the reaction is of sufficient energy to generate the singlet, and fluorescence is observed upon photoexcitation [48]. Both the one-electron oxidized and one-electron reduced forms of $[Pt_2(P_2H_2O_5)_4]^{4-}$ are unstable; the oxidized complex disproportionates at diffusion-limited rates. Nonetheless, ECL has been observed for this strongly luminescent chromophore. Nocera and coworkers reported ECL for Mo and W clusters, including luminescence from cross-reaction of the oxidized Mo complex and reduced W complex.

The instability of either the radical cation or the radical anion of such systems limits the number of organic systems studied by direct oxidation and reduction of a chromophore. A large number of experiments have been performed on DPA and rubrene for which reversible one-electron oxidation and reduction is possible. These systems represent standards for the development of new analytical methods. For example, absolute ECL quantum yield measurements were made by Bezman and Faulkner using rubrene as substrate [49]. More recently, DPA has been used extensively in ECL investigations involving high-frequency voltage oscillations, which include intriguing observation of individual chemical reactions in solution [50]. With the development of rapid-scan (high-frequency potential step) methods, a broader range of organic systems can be investigated.

A very large number of radiative charge recombination processes involve annihilation of known cation radicals and anion radicals, CIEEL processes, or reactions involving an ion radical and a reactive substrate which will decompose to a radical ion. Table 3 provides a very brief list of well-studied cases. The literature is extensive and readers are referred to earlier reviews of this topic [15, 18, 23, 30].

9.5 Applications

9.5.1 Sensors for Organic Substrates Employing $[(bpy)_3Ru]^{2+}$ and Derivatives

There has been rapidly growing interest in the use of ECL systems in sensor development. ECL detection of analytes can be performed with the use of uncomplicated instrumentation and inexpensive materials. The observation of luminescence, par-

Table 3. Mixed systems exhibiting ECL.

Compound ^a	E_{pa} , V ^b	E_{pc} , V ^b	λ_{max}^{em}/nm (eV)	ϕ_{em}	Ref.	Comment
[Ru(bpy) ₃] ⁺ + S ₂ O ₈ ²⁻	+1.30	—	610 (2.03)	0.07	[22]	vs Ag/AgCl
[Ru(bpy) ₃] ³⁺ + C ₂ O ₄ ²⁻	+1.30	—	610 (2.03)	0.07	[102]	vs Ag/AgCl
(TMPD) ⁺⁺ + (Rubrene) ^{*-}	+0.24	-1.3	540 (2.30)	0.98	[103]	vs SCE; ecl from rubrene singlet
(10-MP) ⁺⁺ + (Fluoranthene) ^{*-}	+0.77	-1.70	405 (3.06)	0.35	[104]	vs Pt wire QRE; ecl from singlet FA
(TTF) ⁺⁺ + (Anthracene) ^{*-}	+0.33 ^c	-2.09	400 (3.10)	0.30	[105]	vs SCE; ecl from singlet AN
(Thianthrene) ⁺⁺ + (PPD) ^{*-}	+1.25	-2.17	430 (2.88)	0.04	[106]	vs SCE; ecl from singlet TH
[Cr(bpy) ₃] ³⁺ + Unknown	—	-0.26	730 (1.70)	0.005	[107, 108]	vs Ag wire; Oxidant not identified

^a See Figure 9 for structures of compounds or ligands.

^b Potentials are reported as peak potentials and are reversible unless noted otherwise.

^c $E^0(ox)$, not peak potential.

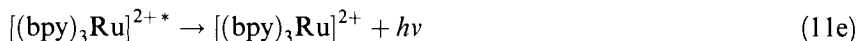
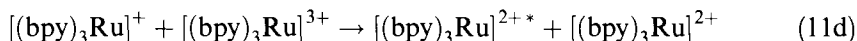
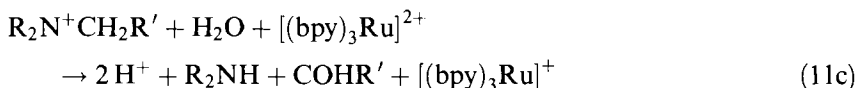
ticularly in the absence of an excitation light source, affords high sensitivity and a broad dynamic range. Since annihilation reactions often occur at near-diffusion-limited rates, signal onset and equilibration are generally limited by factors other than reaction dynamics in ECL systems. Several comprehensive reviews of analytical applications of ECL have been published in recent years [12, 51, 52] and the systems discussed below will provide illustrative examples and report some recent developments.

A vast number of ECL systems are based on luminescent Ru^{II} complexes, and the most widely studied is [(bpy)₃Ru^{II}]²⁺. Luminescence from this chromophore is from a metal-to-ligand charge-transfer triplet state, ³MLCT. This state can be created by several mechanisms, as discussed in Section 9.2.3 [52]. One approach involves reduction of the complex in the presence of persulfate anion; reduction of persulfate results in formation of SO₄⁻, a strong oxidant, which reacts with [(bpy)₃Ru]⁺ to yield the ³MLCT state. However, persulfate is the only species known to react in this way with the complex and no applications currently exist [22]. Of greater importance are systems in which the emitting species can also be obtained by oxidation of [(bpy)₃Ru]²⁺ in the presence of a substrate that generates a strong reductant following a one-electron oxidation. Analytical applications are given below.

Detection of aliphatic amines

In 1987, Noffsinger and Danielson reported the generation of ECL from the reaction of [(bpy)₃Ru]²⁺ with aliphatic amines, proposing the following mechanism

[21];

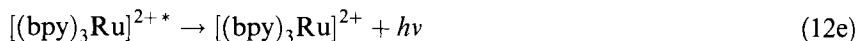
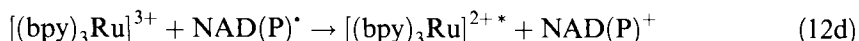


Leland and Powell [53] also studied ECL obtained from reaction of $[(\text{bpy})_3\text{Ru}]^{3+}$ with tripropylamine. There is an inverse relationship between the first ionization potential of the amine and ECL intensity and therefore $[(\text{bpy})_3\text{Ru}]^{2+}$ ECL intensity can be ordered as follows: tertiary > secondary > primary.

Bioorganic applications

With the knowledge that ECL can be generated by alkyl amines, Bobbitt et al. [54] have reported the detection of amino acids by $[(\text{bpy})_3\text{Ru}]^{2+}$ ECL. When capillary electrophoresis is employed in the separation, the presence of various amino acids, in particular proline and leucine, can then be detected directly by reaction with $[(\text{bpy})_3\text{Ru}]^{3+}$ generated in situ with up to a femtomolar sensitivity.

Jameison et al. [55] demonstrated the quantitative ECL detection of β -nicotinamide adenine dinucleotide (NADH) and the phosphate NADPH. They proposed the following mechanism, which involves direct oxidation of the NAD(P)H and the Ru complex at the electrode:



The intermediate, NAD^\bullet or NADP^\bullet , is a radical on the nicotinamide that can annihilate with $[(\text{bpy})_3\text{Ru}]^{3+}$. This system is significant, because the activity of any enzyme that produces or consumes either NADH or NADPH can be directly monitored by ECL.

Another interesting application involves use of ECL in the detection of pathogenic bacteria that produce β -lactamases, enzymes that aid the bacteria in resisting the toxic effects of clinically administered β -lactam antibiotics such as penicillins. They function by hydrolytically opening the cyclic amide of the antibiotic, thereby rendering it harmless to the bacteria (Figure 10). Liang et al. have developed a method of indirectly screening bacteria for the presence of β -lactamases by utilizing

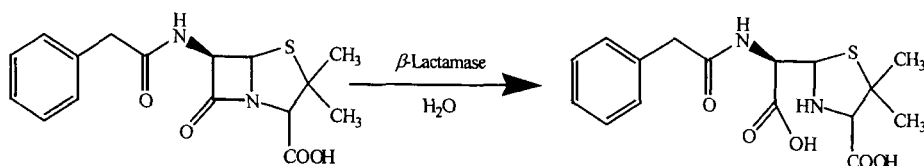


Figure 10. The hydrolysis of penicillin by β -lactamase.

the ability of β -lactam antibiotics to act as the amine-containing reductant in the $[(bpy)_3Ru]^{2+}$ ECL reaction [56].

In related work, Dong and Martin developed an assay that detects the catalytic activity of the enzymes pig liver esterase and porcine kidney leucine aminopeptidase by using substrates which have been labeled with metal-binding ligands [57]. The enzymes catalyze changes in the substrates that affect their ability to bind to non-luminescent Ru complexes to form mixed-ligand complexes capable of ECL.

Analysis of pyruvate can also be accomplished by ECL of Ru^{II} complexes. Since Ru^{III} bipyridine complexes are not strong enough oxidants to directly oxidize pyruvate (to generate a strongly reducing radical species following decarboxylation), Ce^{3+} is added. By the application of a higher electrode potential, Ce^{4+} is generated, which can mediate the oxidation of pyruvate to form intermediates which can reduce $[(bpy)_3Ru]^{3+}$, ultimately leading to luminescence from the Ru^{II} bipyridyl complex [58].

Immunoassays and DNA probe assays

Blackburn et al. reported the first use of ECL detection for the development of immunoassays and DNA probe assays [59, 60]. By modification of one of the bipyridyl ligands of $[(bpy)_3Ru]^{2+}$ with a *N*-hydroxysuccinimide, a reactive species that readily labels proteins and nucleic acids is obtained. An immunoassay device was developed by IGEN, Inc [61]; this device employs magnetic beads chemically modified in a variety of ways to promote association of immune complexes labeled with ECL-active Ru^{II} . Figure 11 illustrates various modes of association of antigen/antibody complexes and other biomolecules with magnetic beads. The beads are drawn to an electrode surface by magnetic interaction and ECL is induced from the Ru^{II} complex bound to the beads by a mechanism involving reaction of electro-generated Ru^{III} with a tertiary amine [62]. ECL methods show promise for widespread use in immunoassays since the technique offers very low detection limits and eliminates the use of radioactive isotopes employed in many current methods. The Ru labels are versatile and long-lived, and even multiple labels do not interfere with antibody immunoreactivity.

The magnetic bead / ECL approach has also been used in DNA-probe assays. Perkin Elmer Corporation has developed an ECL-based assay for post-PCR product detection [63]. (Figure 11). The method allows PCR product identification following fewer PCR cycles than other available analytical methods.

Another novel approach to identification of particular DNA fragments by ECL

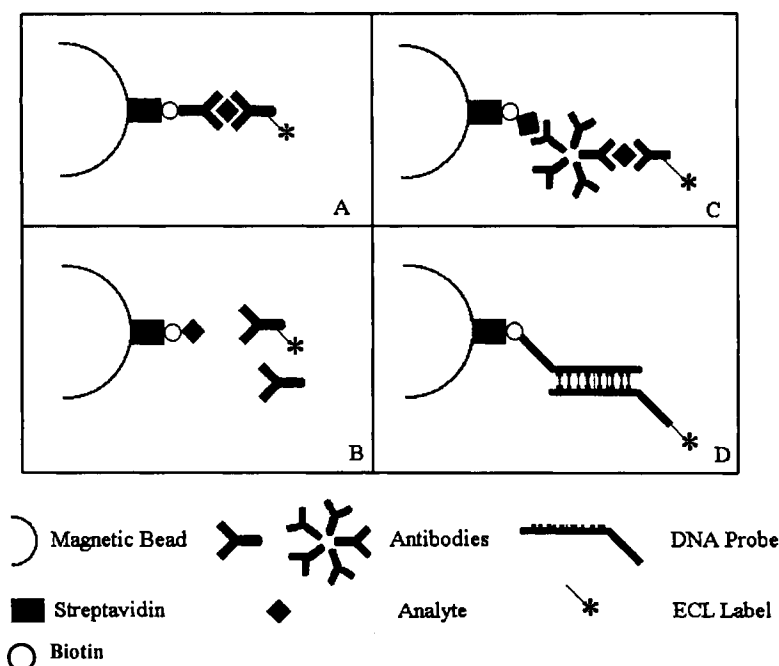


Figure 11. Modes of association of antigen/antibody complexes and other biomolecules with magnetic beads.

was recently presented by Xu and Bard [64]. The approach was to modify a Au electrode with difunctional hydrocarbon having a thiol to bind to the gold surface and a phosphonic acid moiety to ion pair with Al^{3+} in solution. The resulting modified electrode efficiently binds the phosphate group of DNA single strands (i.e., poly-dC). Exposing this electrode to $[\text{Ru}(\text{bpy})_3]^{2+}$ -labeled single strands with the complimentary sequence (i.e., poly-dG), results in ECL from the surface-bound Ru^{II} complex in the presence of tripropyl amine. The approach requires complete surface coverage by the unlabeled single strand and stability of the surface ensemble to temperature cycling required in the hybridization process.

Immobilized $[(\text{bpy})_3\text{Ru}]^{2+}$ and derivatives

There has been significant effort to develop analytical systems involving ECL-active Ru^{II} diimine complexes immobilized on electrode surfaces [65, 66]. Electrode-bound Ru^{II} complexes immobilized in Nafion films by electrostatic binding have been used in flow-injection analysis of oxalate, alkyl amines, and NADH [67]. Martin and Nieman have also employed electrode-bound Ru^{II} bipyridyl complexes in the analysis of glucose by detecting NADH produced in oxidation of glucose by glucose dehydrogenase [68]. In addition, an extremely sensitive fiber-optic-linked ECL probe for oxalate was reported by Egashira and coworkers [69].

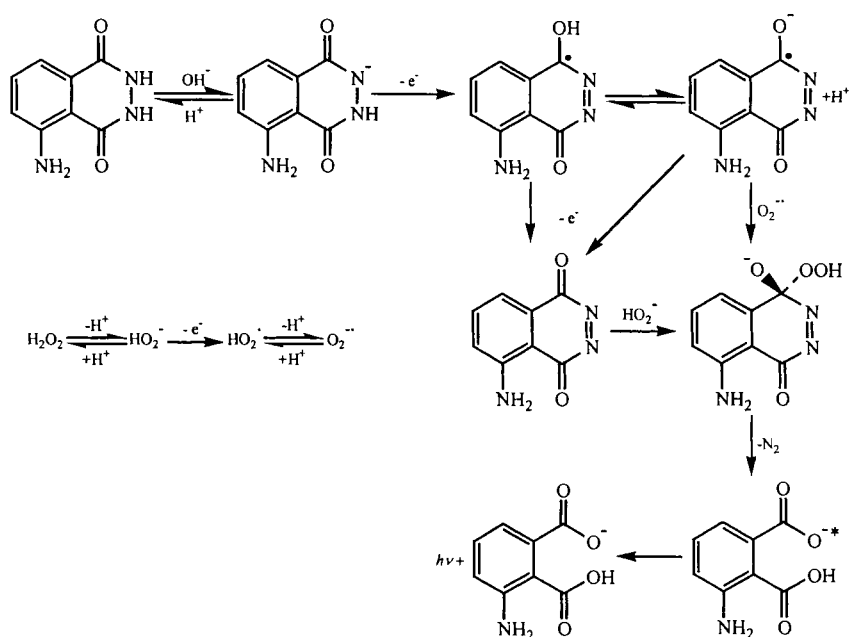


Figure 12. Proposed ECL mechanism of luminol.

9.5.2 Sensors Employing Other ECL Chromophores

Luminol-based detection of molecules

Often conventional chemiluminescence reactions can be initiated electrochemically. The luminol reaction has been studied in detail and the mechanism of the ECL reaction is believed to be similar to that of chemiluminescence. As shown in Figure 12, the luminol ion undergoes a one-electron oxidation to yield a diazaquinone, which reacts with peroxide (^-OOH) to give the excited 3-aminophthalate, which has an emission maximum of 425 nm. This reaction is particularly versatile and has been utilized in a variety of ECL assays, many of which have been summarized by Knight [12]. The luminol ECL reaction can be used for the determination of any species labeled with luminol derivatives, hydrogen peroxide, and other peroxides and enzymatic reactions which produce peroxides. A few of them are briefly described below.

Sekura and Terao reported a luminol-based ECL sensor for lipid hydroperoxides, which are of great importance since they are involved in the regulation of prostaglandin biosynthesis, which in turn can lead to cancer development, aging, and other pathological conditions [70]. In this method, there are two approaches for generation of ECL. By the application of potentials between 0.5 and 1.0 V, luminol is oxidized to a diazaquinone which reacts with free lipid hydroperoxide to yield

luminescence as in Figure 12. When the applied potential is greater than 1.0 V, both luminol and the lipid hydroperoxide are oxidized electrochemically and a more complicated emission occurs by the reaction of the diazaquinone with the oxidized product of lipid hydroperoxide.

Marquette and Blum have reported a luminol-based fiber-optic biosensor for glucose and lactate [71]. In this method, glucose oxidase or lactate oxidase is immobilized on preactivated membranes. Substrates present in solution, glucose or lactate, are oxidized by the respective enzyme, producing hydrogen peroxide. Luminol, which has been previously oxidized at a glassy carbon electrode, reacts with hydrogen peroxide, producing an ECL signal.

Other systems

There is a variety of analytical applications that involve electrochemical generation of luminescence in systems for which the chemistry is not clearly understood. A few are mentioned here.

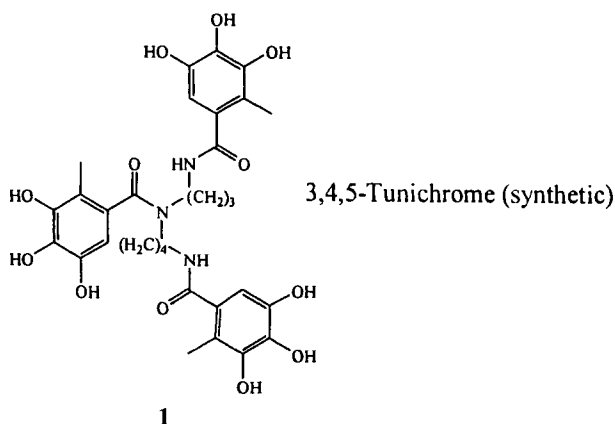
A novel ECL assay for the determination of 2,4- and 3,4- diaminotoluene (DAT) isomers is based on reaction of these molecules with Au^+ and Cu^{2+} , respectively, in aqueous solution under oxidizing conditions in buffer-containing tripropylamine [72]. Luminescence is observed upon potential ramping from 0 to +2.8 V. The nature of the emitting species was not specified, but could involve a charge-transfer excited state of the metal complex with DAT or an oxidized form of DAT. DAT isomers were screened for ECL enhancement against 32 metals; the apparent specificity of Au^+ for 2,4-DAT and Cu^{2+} for 3,4-DAT is believed to be linked to the radii of each ion. This ECL approach could lead to applications in the determination of some aminoaromatics from degradation of explosives (e.g., TNT) as well as detection and quantification of various transition metals in water supplies.

Chen et al. characterized ECL from indole and tryptophan in the presence of hydrogen peroxide under oxidizing conditions. In both cases, there is only tryptophan or indole, electrolyte, and H_2O_2 in the cell. A triangular pulse voltage was applied (1.0 V) to oxidize tryptophan or indole. Tryptophan and indole are both very weakly electrochemiluminescent in the absence of H_2O_2 , but with peroxide, the ECL signal is enhanced. The process is believed to go through a dioxetane intermediate obtained after one-electron oxidation of the substrate. The presence of seventeen other amino acids (in excess) did not interfere in the determination of tryptophan, making the method remarkably selective.

Egashira et al. observed ECL from various hydroxyl compounds; this led to the development of alcohol and sugar sensors [73, 74] ECL is observed upon voltage-cycling of basic aqueous solutions of various sugars and simple vicinal alcohols between +1.4 and -1.2 V (vs. Ag/AgCl). While the mechanism is not clear, the authors state that aldehyde excited states may be formed; no spectral data is given as the emission is very weak.

A completely new source of electrochemiluminescent compounds may have been discovered recently. Weak luminescence was observed from fluids extracted from tunicates, a type of marine invertebrate, and synthetic tunichromes (**1**; chromophore in the tunicates) upon oxidation [75]. There was a 10-fold enhancement of ECL

when the synthetic analogs of the tunichromes were complexed to Hg^{2+} . The mechanism of the luminescent enhancement is not clear.



9.5.3 Device Applications

Electroluminescent displays

The application of radiative charge recombination with the greatest commercial potential is the development of electroluminescent devices based on organic light-emitting diodes (OLEDs). The typical device consists of a sandwich arrangement of materials: an optically transparent electrode, a hole-conducting layer, a luminescent chromophore, an electron-conducting layer and a second electrode. In some devices, the hole or electron carrier may also be the luminescent chromophore and even simpler devices exist, with a single organic thin film sandwiched between two electrodes. Radiative charge recombination in solid-state devices is complicated in several ways unique to the medium. The additional issues that arise involve rates of charge transport in the electron and hole carriers, excited-state quenching in the solid state and interactions of excited states with the charged electrodes. This area has been the focus of a tremendous amount of research directed toward understanding the fundamental factors important in the operation of electroluminescent devices. Several recent reviews provide excellent overviews of these topics and even a superficial discussion of organic light-emitting displays is beyond the scope of this chapter [76, 77].

However, the link between electrogenerated chemiluminescence in solution and electroluminescence is obvious. In recent work of Armstrong, Wightman, and coworkers, the detailed aspects of ECL generation from components widely used in the construction of organic organic LED's is discussed [78]. Some of the examined systems had multiple radical ion recombination reactions and potential-emitting excited states; the results showed that emission always occurred from a single emitting excited state. In addition, electroluminescent devices containing $[(\text{bpy})_3\text{Ru}]^{2+}$, one of the most widely studied ECL-active molecules, as the emitting chromophore, have been produced [79, 80, 81].

Laser action driven by ECL

ECL for laser applications has been investigated because of the advantages it may have over conventional dye lasers. A laser operating by ECL would not require an additional pump laser, and enhanced power, tunability and range of available wavelength are additional factors. While the pumping rate achieved by ECL previously has been two orders of magnitude lower than the optimal, Horiuchi et al. have reported a device structure designed to enhance the ECL efficiency and realize laser action driven by ECL [82].

Scanning electrochemical microscopy

Light emission by ECL at scanning electrochemical microscope (SECM) tips is also under current development [83]. Visible light is generated at the SECM tip by ECL as the tip is moved in the vicinity of insulating and conductive substrates. ECL intensity decreases with both insulating and conductive substrates as the tip-substrate distance decreases. Although the resolution is still poor, the technique shows potential for applications in the studies of the kinetics and mechanisms of co-reactant ECL reactions.

9.6 Summary

The thrust of this chapter has been to provide a brief overview of this fascinating area, from the essential theoretical framework provided by electron-transfer theory to the array of potential novel device applications. From early studies of radiative charge recombination, experimental approaches developed greater sophistication and the range of chemical reaction types expanded. The ability to generate luminescence by electrochemical excitation presents a rich array of potential device applications and the future of research in this area is certainly bright.

Acknowledgments

The authors wish to thank the U.S. Department of Energy, Office of Basic Energy Sciences, for support of photochemical research in the RHS group.

References

1. Bancroft, W. D.; Weiser, H. B. *J. Phys. Chem.*, **1914**, *18*, 762.
2. Bard, A. J.; Santhanam, K. S. V. *J. Am. Chem. Soc.*, **1965**, *87*, 139.
3. Hercules, D. M. *Science*, **1964**, *145*, 808.
4. Visco, R. E.; Chandross, E. A. *J. Am. Chem. Soc.*, **1964**, *86*, 5350.
5. Weller, A.; Zachariasse, K. *J. Chem. Phys.*, **1967**, *46*, 4984.

6. Faulkner, L. R.; Glass, R. S. in "Chemical and Biological Generation of Excited States," Adam, W.; Cilento, G.; eds., Academic Press, New York, 1982, Ch. 6.
7. Faulkner, L. R.; Bard, A. J. in "Electrochemical Methods", John Wiley, New York, 1980, p. 621.
8. Park, S.-M.; Tryk, D. A. *Rev. Chem. Intermed.*, **1981**, 4, 43–79.
9. Faulkner, L. R.; Glass, R. S. in "Chemical and Biological Generation of Excited States", Adam, W.; Cilento, G.; eds., Academic Press, New York, 1982, pp. 191–227.
10. See Sheats, J. R.; Antoniadis, H.; Hueschen, M.; Leonard, W.; Miller, J.; Moon, R.; Roitman, D.; Stocking A. *Science*, **1996**, 273, 884 and Sheats, J. R.; Cheng, Y.-L.; Roitman, D. B.; Stocking, A. *Acc. Chem. Res.*, **1999**, 32, 193.
11. Faulkner, L. R.; Bard, A. J. in *Electroanalytical Chemistry*, **1977**, 10, 1–95.
12. Knight, A. W. *Trends in Analytical Chemistry*, **1999**, 47–62.
13. Hoytink, G. J. *Faraday Discuss. Chem. Soc.*, **1968**, 45, 14.
14. Hoytink, G. J. in "Chemiluminescence and Bioluminescence", Hercules, D.M.; ed., Plenum, New York, 1973, p. 147.
15. See Weller, A. in "The Exciplex", Gordon, M.; Ware, W. R.; DeMayo, P.; Arnold, D. R.; eds., Academic Press, New York, 1975, p. 23.
16. Maloy, J. T.; Bard, A. J. *J. Am. Chem. Soc.*, **1971**, 93, 5968.
17. Tachikawa, H.; Faulkner, L. R.; *J. Am. Chem. Soc.*, **1976**, 98, 5569.
18. Weller, A.; Zachariasse, K. in "Chemiluminescence and Bioluminescence", Hercules, D.M.; ed., Plenum, New York, 1973, p. 181.
19. Weller, A.; Zachariasse, K. A. *Chem. Phys. Lett.*, **1971**, 10, 590.
20. Chang, M. M.; Saji, R.; Bard, A. J. *J. Am. Chem. Soc.*, **1977**, 99, 5399.
21. Noffsinger, J. B.; Danielson, N. D. *Anal. Chem.*, **1987**, 59, 865.
22. White, H. S.; Bard, A. J. *J. Am. Chem. Soc.*, **1982**, 104, 6891.
23. Schuster, G. B. *Acc. Chem. Res.*, **1979**, 50, 4068.
24. Schuster, G. B.; Horn, K. A.; in "Chemical and Biological Generation of Excited States", Adam, W.; Cilento, G.; eds., Academic Press, New York, 1982, Ch. 7.
25. Koo, J. Y.; Schuster, G. B. *J. Am. Chem. Soc.*, **1977**, 99, 6107.
26. (a) Marcus, R. A.; Sutin, N. *Biochem. Biophys. Acta*, **1985**, 811, 265. (b) Marcus, R. A. *J. Chem. Phys.*, **1984**, 81, 4494. (c) Siders, P.; Marcus, R. A. *J. Am. Chem. Soc.*, **1981**, 103, 741.
27. Hopfield, J. J. *Proc. Nat. Acad. Sci.*, **1974**, 71, 3640.
28. Ulstrup, J.; Jortner, J. *J. Chem. Phys.*, **1975**, 63, 4358.
29. Van Duyne, R. P.; Fischer, S.F. *Chem. Phys.*, **1974**, 5, 183.
30. Beens, H.; Weller, A. in "Organic Molecular Photophysics", Birks, J. B.; Ed.; Wiley, London, 1975, vol. 2, Ch. 4.
31. (a) Gould, I. R.; Young, R. H.; Moody, R. E.; Farid, S. *J. Phys. Chem.*, **1991**, 95, 2068. (b) Gould, I. R.; Moody, R.; Farid, S. *J. Am. Chem. Soc.*, **1988**, 110, 7242.
32. Gould, I. R.; Farid, S.; Young, R. H. *J. Photochem. Photobiol. A.*, **1992**, 65, 133.
33. Gould, I. R.; Farid, S. *Acc. Chem. Res.*, **1996**, 29, 522.
34. Marcus, R. A. *J. Phys. Chem.*, **1989**, 93, 3078.
35. Gould, I. R.; Noukakis, D.; Goodman, J. L.; Young, R. H.; Farid, S. *J. Am. Chem. Soc.*, **1993**, 115, 3830.
36. Ritchie, E. L.; Pastore, P.; Wightman, R. M. *J. Am. Chem. Soc.*, **1997**, 119, 11920.
37. Zu, Y.; Fan, F.-R. F. Bard, A. J. *J. Phys. Chem. B*, **1999**, 103, 6272.
38. Tachikawa, H.; Faulkner, L. R. in "Laboratory Techniques in Electroanalytical Chemistry", Dekker, New York, 1984, Ch. 23.
39. Faulkner, L. R. *Methods in Enzymology*, **1978**, 57, 494.
40. (a) Feldberg, S. W. *J. Am. Chem. Soc.*, **1966**, 88, 390. (b) Feldberg, S.W. *J. Am. Chem. Soc.*, **1966**, 70, 3928.
41. Collinson, M. M.; Wightman, R. M. *Anal. Chem.*, **1993**, 65, 2576.
42. Collinson, M. M.; Wightman, R. M.; Pastore, P. *J. Phys. Chem.*, **1994**, 98, 11942.
43. Waldeck, D. H.; Alivisatos, A. P.; Harris, C. B. *Surf. Sci.*, **1985**, 158, 103.
44. Chance, R. R.; Prock, A.; Silbey, R. *Adv. Chem. Phys.*, **1978**, 37, 1.
45. Collinson, M. M.; Pastore, P.; Maness, K. M.; Wightman, R. M. *J. Am. Chem. Soc.*, **1994**, 116, 4095.

46. Maloy, J. T.; Prater, K. B.; Bard, A. J. *J. Am. Chem. Soc.*, **1971**, 93, 5959.
47. Demas, J. N.; Taylor, D. G. *Inorg. Chem.*, **1979**, 98, 3722.
48. Murov, S. L.; Carmichael, I.; Hug, G. L. "Handbook of Photochemistry", 2nd ed., Dekker, New York, 1993, Ch. 1.
49. Bezman, R.; Faulkner, L. R. *J. Am. Chem. Soc.*, **1972**, 94, 6324.
50. Collinson, M. M.; Wightman, R. M. *Science*, **1995**, 268, 1883.
51. Rozhitskii, N. N.; Belash, E. M.; Bykh, A. I. *J. Anal. Chem. USSR (Engl. Transl.)*, **1994**, 49, 829.
52. Lee, W.-Y. *Mikrochim. Acta*, **1997**, 127, 19.
53. Leland, J. K.; Powell, M. J. *J. Electrochem. Soc.*, **1990**, 137, 3127.
54. Bobbitt, D. R.; Jackson, W. A.; Hendrickson, H. P. *Talanta*, **1998**, 46, 565.
55. Jameison, F.; Sanchez, R. I.; Dong, L.; Leland, J. K.; Yost, D.; Martin, M. T. *Anal. Chem.*, **1996**, 68, 1298.
56. Liang, P.; Sanchez, R. I.; Martin, M. T. *Anal. Chem.*, **1996**, 68, 2426.
57. Dong, L.; Martin, M. T. *Anal. Biochem.*, **1996**, 236, 344.
58. Knight, A. W.; Greenway, G. M. *Analyst*, **1994**, 119, 879.
59. Blackburn, G. F.; Shah, H. P.; Kenten, J. H.; Leland, J.; Kamin, R. A.; Link, J.; Peterman, J.; Powell, M. J.; Shah, A.; Talley, D. B.; Tyagi, S. K.; Wilkins, E.; Wu, T. G.; Massey, R. J. *Clin. Chem.*, **1991**, 37, 1534.
60. Kenten, J. H.; Casadei, J.; Link, J.; Lupold, S.; Willey, J.; Powell, M.; Rees, A.; Massey, R. *Clin. Chem.*, **1991**, 37, 1626.
61. See the home page of IGEN for more information: <http://www.igen.com>.
62. Deaver, D. R. *Nature*, **1995**, 377, 758.
63. DiCesare, J.; Grossman, B.; Katz, E.; Picozza, E.; Ragusa, R.; Woundenburg, T. *Bio-Techniques*, **1993**, 15, 152.
64. Xu, X.-H.; Bard, A. J. *J. Am. Chem. Soc.*, **1995**, 117, 2627.
65. Abruna, H. D.; Bard, A. J. *J. Am. Chem. Soc.*, **1982**, 104, 2641.
66. Rubenstein, I.; Bard, A. J. *J. Am. Chem. Soc.*, **1980**, 102, 6641.
67. Downey, T. M.; Nieman, T. A. *Anal. Chem.*, **1992**, 64, 261.
68. Martin, A. F.; Nieman, T. A. *Anal. Chim. Acta*, **1993**, 281, 475.
69. Egashira, N.; Kumasako, H.; Ohga, K. *Anal. Sci.*, **1990**, 6, 903.
70. Sakura, S.; Terao, J. *Anal. Chim. Acta*, **1992**, 262, 59.
71. Marquette, C. A.; Blum, L. J. *Anal. Chim. Acta*, **1999**, 381, 1.
72. Bruno, J. G.; Cornette, J. C. *Microchem. J.*, **1997**, 56, 305.
73. Chen, G. N.; Lin, R. E.; Zhao, Z. F.; Duan, J. P.; Zhang, L. *Anal. Chim. Acta*, **1997**, 341, 251.
74. Egashira, N.; Nabeyama, Y.; Kurauchi, Y.; Ohga, K. *Anal. Sci.*, **1996**, 12, 793.
75. Bruno, J. G.; Collard, S. B.; Andrews, R. J. *J. Biolumin. Chemilumin.*, **1997**, 12, 155.
76. A collection of articles on the topic is presented in *Acc. Chem. Res.*, **1999**, 32, pp 191–276.
77. Salbeck, J. *Ber. Bunsenges. Phys. Chem.*, **1996**, 100, 1667.
78. Anderson, J. D.; McDonald, E. M.; Lee, P. A.; Anderson, M. L.; Ritchie, E. L.; Hall, H. K.; Hopkins, T.; Mash, E. A.; Wang, J.; Padias, A.; Thayumanavan, S.; Barlow, S.; Marder, S. R.; Jabbour, G. E.; Shaheen, S.; Kippelen, B.; Peyghambarian, N.; Wightman, R. M.; Armstrong, N. R. *J. Am. Chem. Soc.*, **1998**, 120, 9646.
79. (a) Handy, E. S.; Pal, A. J.; Rubner, M. F. *J. Am. Chem. Soc.*, **1999**, 121, 3525. (b) Lyons, C. H.; Abbas, E. D.; Lee, J.-K.; Rubner, M. F. *J. Am. Chem. Soc.*, **1998**, 120, 12100.
80. Maness, K. M.; Terrill, R. H.; Meyer, T. J.; Murray, R. W.; Wightman, R. M. *J. Am. Chem. Soc.*, **1996**, 118, 10609.
81. Elliott, C. M.; Pichot, F.; Bloom, C. J.; Rider, L. S. *J. Am. Chem. Soc.*, **1998**, 120, 6781.
82. Horiuchi, T.; Niwa, O.; Hatakenaka, N. *Nature*, **1998**, 394, 659.
83. Fan, F.-R. F.; Cliffel, D.; Bard, A. J. *Anal. Chem.*, **1998**, 70, 2941.
84. Tokel, N. E.; Bard, A. J. *J. Am. Chem. Soc.*, **1972**, 94, 2862.
85. McCord, P.; Bard, A. J. *J. Electroanal. Chem.*, **1991**, 318, 91.
86. Juris, A.; Balzani, V.; Barigelletti, F.; Campagna, S.; Belser, P.; von Zelewsky, A. *Coord. Chem. Rev.*, **1988**, 84, 85.
87. Abruna, H. D. *J. Electroanal. Chem.*, **1984**, 175, 321.
88. Kober, E. M.; Caspar, J. V.; Lumpkin, R. S.; Meyer, T. J. *J. Phys. Chem.*, **1986**, 90, 3722.

89. Kim, J.; Fan, F. F.; Bard, A. J.; Che, C.-M.; Gray, H. B. *Chem. Phys. Lett.*, **1985**, 121, 543.
90. Vogler, A.; Kunkely, H. *Angew. Chem. Int. Ed. Engl.*, **1984**, 23, 316.
91. Fordyce, W. A.; Brummer, J. G.; Crosby, G. A. *J. Am. Chem. Soc.*, **1981**, 103, 7061.
92. Tokel-Takvoryan, N. E.; Bard, A. J. *Chem. Phys. Lett.*, **1974**, 25, 235.
93. Mussell, R. D.; Nocera, D. G. *Inorg. Chem.*, **1990**, 29, 3711.
94. Ford, P. C. *Coord. Chem. Rev.*, **1994**, 132, 129.
95. Vogler, A.; Kunkely, H. *Am. Chem. Soc. Symp. Ser.*, **1987**, 333, 155.
96. Kim, J.; Faulkner, L. R. *J. Electroanal. Chem.*, **1988**, 242, 107 and 123.
97. Epstein, B.; Kuwana, T. *Photochem. Photobiol.*, **1965**, 4, 1157.
98. Zweig, A.; Maricle, D. L.; Brinen, J. S.; Maurer, A. H. *J. Am. Chem. Soc.*, **1967**, 89, 473.
99. Lee, S. K.; Zu, Y.; Herrmann, A.; Geerts, Y.; Mullen, K.; Bard, A. J. *J. Am. Chem. Soc.*, **1999**, 121, 3513.
100. Maricle, D. L.; Maurer, A. *J. Am. Chem. Soc.*, **1967**, 89, 188.
101. Wilson, J. R.; Park, S.-M.; Daub, G. H. *J. Electrochem. Soc.*, **1981**, 128, 2085.
102. Rubinstein, I.; Bard, A. J. *J. Am. Chem. Soc.*, **1981**, 103, 512.
103. Kim, J.; Faulkner, L. R. *J. Am. Chem. Soc.*, **1988**, 110, 112.
104. Bezman, R.; Faulkner, L. R. *J. Am. Chem. Soc.*, **1972**, 94, 6331.
105. Wallace, W. L.; Bard, A. J. *J. Electrochem. Soc.*, **1978**, 125, 1430.
106. Keszthelyi, C. P.; Tachikawa, H.; Bard, A. J. *J. Am. Chem. Soc.*, **1972**, 94, 1522.
107. Bolletta, F.; Ciano, M.; Balzani, V.; Serpone, N. *Inorg. Chim. Acta*, **1982**, 62, 207.
108. Kane-Maguire, N.; Guckert, J. A.; O'Neill, P. J. *Inorg. Chem.*, **1987**, 26, 2340.

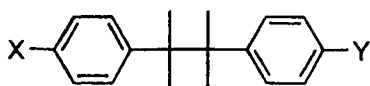
10 Electron Transfer Reactions in Organic Chemistry

Stephen F. Nelsen

10.1 Introduction

Reactions of organic compounds involving electron transfer are so common that this review cannot even attempt to be comprehensive, and I apologize in advance to the many people whose work has been omitted. Pross and Shaik especially emphasized the similarity between two-electron polar processes and single-electron-transfer processes at the level of consideration of reaction-coordinate diagrams [1]. Most bond-shift reactions can be postulated to involve sequential single-electron-transfer steps, and the single-electron-transfer formalism has been extended to a very wide range of chemistry [2]. Especially Ashby's group reformulated several reactions involving organic compounds that are usually considered to be two-electron bond-shift reactions as single-electron-transfer reactions, including Grignard additions and metal hydride reductions [3]. Some examples of these reactions very likely do involve single-electron transfer, but others may well not. Ashby [3a] has responded to criticism of the ring-opening methodology that was used as evidence for single-electron-transfer reactions in some cases [3b]. This chapter will focus on reactions that unarguably involve single-electron-transfer steps. Schmittle and Burghardt have provided a very useful review of radical cation reactions [4].

Reactive radical ions may often be generated by electrochemistry and/or photochemistry either in addition to, or instead of, independently prepared redox reagents that cause electron transfer to occur spontaneously, using thermal excitation energy. This makes it impractical to separate the types of chemistry initiated by electron transfer according to the mode of radical ion generation. Electron loss (or gain) by a neutral diamagnetic organic molecule (by far the most common kind), produces a radical cation (or anion), from loss of an electron from the highest occupied molecular orbital (or gain of one in the lowest unoccupied molecular orbital). This can result in very large changes in bond strength, frequently initiating cleavage and/or addition reactions. Nicholas and Arnold gave an important early discussion of the relationship between solution- and gas-phase measurements of the ease of electron

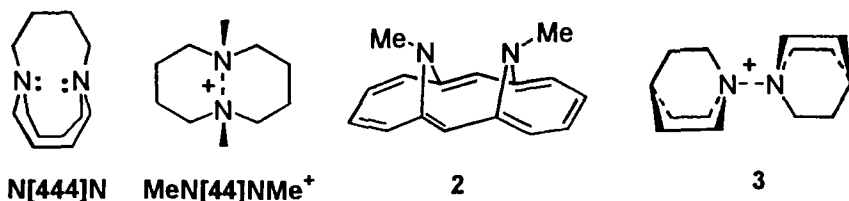
**1**

and proton transfer and bond strength. They used thermodynamic cycles to demonstrate the great acidity of toluene radical cation, and, in general, the bond-weakening that accompanies electron loss or gain [5]. Thermodynamic cycles including redox potentials and pK_A values are now often used for estimating bond dissociation energies, especially by Bordwell and coworkers [6]. As an example of bond weakening, the central C–C bond cleavage reactions of the radical ions derived from 4,4'-substituted bicumyls (**1**) have especially been studied by Maslak and coworkers [7]. Both the radical cations and radical anions of **1** have so much weakening of the central bond that spontaneous cleavage to cumyl radicals and cumyl cations or anions occurs, and substituents X and Y have been varied to bring the rate constants for cleavage into convenient ranges for measurement. Various 4'-substituted 4-Me₂N **1**^{•+} radical cations generated by chemical or photolytic oxidation have free energies of activation for central bond cleavage that average 23 kcal/mol lower than the neutral compounds, and the rate constants show little variation with solvent because of compensating enthalpy and entropy effects. The radical anions of the corresponding 4-NO₂-substituted systems average 12 kcal/mol lower free energies of activation than their neutral compounds. Later work uses radical cations generated by photo-electron transfer with tetranitromethane [7d] or chlorinated quinones [7e] to study reactions within contact ion pairs generated by irradiation into the charge-transfer band, and in solvent-separated ion pairs generated by irradiation into the quinone.

10.2 Inner- and Outer-Sphere Electron Transfer Reactions

Taube used the term inner-sphere for electron transfer between inorganic redox centers that were connected by a bridging ligand at the transition state [8], and it meant the same thing to Ebersson in 1982 [9]. Here electron transfer occurs within bonding distances between the reactants, through the first coordination sphere of the metal, and ligand transfer occurs simultaneously with electron transfer [10], (so the process might be termed L[−] transfer as well as e[−] transfer). Outer-sphere then referred to electron-transfer transition states that did not transfer a ligand along with the electron, that is, ones that lacked significant bonding between the partners, and kept the inner coordination shells for the participating metal intact in the transition state. Outer-sphere reactions are the type of electron transfer with which Marcus- and related electron-transfer theories deal (see Volume I, Part 1, Chapter 3).

The situation is somewhat different for many main-group compounds, where “three-electron σ -bonded” dimeric radical ions often exist. Thus, instead of being the transition state for electron transfer between the components, a bonded, inner-sphere species is often lower in enthalpy than the separated components, and an intermediate for electron transfer between them. Occurrence of 3e- σ -bonded species was pointed out by Pauling almost 70 years ago [11a], and examples with small substituents have been studied computationally more recently [12]. Examples in several systems are experimentally established [13], both for anions like $[\text{Cl} \cdot \cdot \text{Cl}]^-$ [14a] and $[\text{RS} \cdot \cdot \text{SR}]^-$ [14b–d]) and for cations like $[\text{R}_2\text{S} \cdot \cdot \text{SR}_2]^+$ (both in solution [13, 15a–b] and in the gas phase) [15c] and special examples of $[\text{R}_3\text{N} \cdot \cdot \text{NR}_3]^+$ [18]. In valence-bond language these species are stabilized by having resonance structures with charge on either group [11a], and in molecular orbital terms, by having two bonding electrons and only one antibonding electron in a weak σ bond, formed by end-on overlap of p-rich orbitals centered at the two heteroatoms [11b]. Only a few examples of unsymmetrical or neutral systems are well characterized, such as $\text{R}_2\text{S} \cdot \cdot \text{SR}$ [16], and Clark pointed out that the 3e- σ bond strength decreases regularly as the difference in ionization potential of the components increases [12a]. The 3e- σ -bonded radical cations can also rearrange to unsymmetrical hydrogen-bonded species that are intermediates in hydrogen-transfer reactions [12d], and the presence of both species is indicated by tandem mass spectroscopy experiments on methyl chloride [17]. Asmus especially studied geometry effects on the strength of 3e- σ bonds in $[\text{R}_2\text{S} \cdot \cdot \text{SR}_2]^+$ through studies of the absorption spectra of both acyclic and cyclic disulfides [13a, 14b]. Alder examined $[\text{R}_3\text{N} \cdot \cdot \text{NR}_3]^+$ in many examples of medium-ring bridgehead diamines [18a], finding that the triply tetramethylene bridged species **N[444]N**, which has the nitrogens pyramidalized inward, as indicated, gives the most persistent radical cation of all. **N[444]N** is isolable in all three oxidation states, with N–N distances of 2.806(6) Å (neutral), 2.295(10) Å (1+) and 1.532(6) Å (2+). Although **N[333]N**⁺ is also isolable, examples with different sized bridges, which cause the neutral form to prefer conformations with lone pair axes that are not collinear, are much less stable. When the third ring is changed to two methyl groups in **MeN[44]NMe**⁺, the radical cation formed by reduction of the dication only lasts milliseconds at room temperature; this implies that the $[\text{R}_3\text{N} \cdot \cdot \text{NR}_3]^+$ bond strength is about 15 kcal/mol, because bond cleavage to give the amine radical cation that is unstabilized by a 3e- σ bond is the rate-determining step for decomposition; the cleaved material undergoes rapid intramolecular hydrogen transfer. Oxidation of neutral diamines usually does not lead to 3e- σ -bonded species unless the nitrogens are pre-organized by their substituents to have the nitrogens rather close, and to also have their lone-pair orbital axes nearly collinear in the neutral form [18]. For example, oxidation of neutral **MeN[44]NMe** does not produce the 3e- σ -bonded cation. Vogel and Gerson have shown that the unsaturated bis(aza)-bridged cyclotetradecaheptaene system of **2** provides a rigid framework that allows the N,N'-dimethyl-substituted 3e- σ bonded compound (**2**⁺) not only to be produced from the neutral species, but to be isolated [19]. Quinuclidine gives the dimer radical cation **3** upon oxidation at low temperature [20], which we presume occurs because its bicyclic structure precludes the rapid hydrogen-atom transfer that rapidly destroys most intermolecular amine–amine radical cation pairs.



A source of confusion is that inner-sphere means different things to different people. In ET theory discussions, which overwhelmingly focus on Taube outer-sphere reactions, inner-sphere effects (sometimes used interchangeably with inner-shell) refer to large λ_{in} values, as in McLendon's definition, "changes in bond angles and bond lengths in the reactant and product molecules themselves" [21a]. Thus, for Marcus theory discussions, inner-sphere effects refer to Taube outer-sphere reactions that are slower than "expected" because the transition metal coordination complexes that are implicitly considered as the standard reactions have vanishingly small λ_{in} , and λ_{out} is expected only to depend on molecular size. As a radical ion becomes more stabilized by delocalization, the localization required to produce a $3e$ - σ -bonded dimer radical ion makes it less likely that this species will be an intermediate in electron transfer. A large inner-sphere effect in the sense of a large λ_{in} value does not necessarily promote inner-sphere electron transfer in the Taube sense. Although hydrazine radical cations have exceptionally large λ_{in} values (see Section 10.8.1), they undergo electron transfer by a Taube outer-sphere mechanism, because they enjoy more π -stabilization by delocalizing the charge over both nitrogens than they would gain by delocalizing charge in a σ -bond of a dimer radical cation. The charge-localized trialkylamine radical cations usually undergo hydrogen transfer more rapidly than they do electron transfer with their neutral forms, so "self" electron transfer is not observed, although, as pointed out above, **3** is an observed intermediate in self-ET of quinuclidine.

Especially Eberson and Shaik [22] and Kochi [23] have introduced a third different usage for inner-sphere, in attempting to more carefully consider Taube outer-sphere reactions. "Its meaning [inner-sphere] has been extended to encompass ET between D[onor] and A[cceptor] that are strongly coupled due to mutual interpenetration of their coordination spheres" [23a]. Electronic coupling between the components of an electron-transfer reaction is quantitatively measured by the parameter H_{ab} (also called J , V , and β , among other designations). Eberson and Kochi both use the criterion that, when H_{ab} is >1 kcal mol⁻¹, a reaction should be classified as inner-sphere. However, Marcus- and other electron-transfer theories do not assume that H_{ab} is small, although its size relative to λ is important. Thus, discussions of electron-transfer theory do not use inner-sphere to refer to the size of H_{ab} , instead employing the terms adiabatic and non-adiabatic for reactions having high and low H_{ab} relative to λ . Different limiting-rate equations are needed for adiabatic and non-adiabatic reactions [21]. An H_{ab} of 1 kcal/mol lies between these limits for most cases, so $H_{ab} = 1$ kcal/mol does not appear to constitute a borderline between different regions in terms of modern ET theory. Savéant considers inner- and outer-sphere as separate, well-defined reactions that can be in competition, referring to the

Taube usage of these words. Both Shaik and Fawcett discuss the inner- and outer-sphere possibilities as two ends of a mechanistic continuum, which is certainly true if by these terms one means the size of H_{ab} [24]. Other terms that might be less confusing are also used to make the distinction between negligible and non-negligible electronic interaction at the ET transition state: outer-sphere in the Ebersson-Kochi sense has also been called nonbonded and unbound, and inner-sphere called bonded and bound. Zipse has recently reviewed electronic-structure calculation work in this area [25], emphasizing that calculated transition-state structures often indicate significant interaction between the ET partners. However, the calculations do not directly address the size of H_{ab} , and are mostly on “stripped down” models that often do not very closely reflect the structures of compounds studied experimentally, and the distances calculated are for gas-phase structures lying on exceptionally “soft” energy surfaces, so their applicability to reactions in solution is not clear at this point.

Both the Ebersson and Kochi groups base their practical identification of reactions as inner-sphere upon comparison of observed rate constants for intermolecular ET reactions with calculated ones for outer-sphere reactions in their sense, that is, small H_{ab} reactions so the barrier does not depend upon H_{ab} , using some version of ET theory. When an observed reaction is significantly faster than predicted by the two-state model but with $\Delta G^* = \lambda/4$, it is deemed to have inner-sphere character, that is, to have an H_{ab} that is >1 kcal/mol, so the barrier is significantly affected. How large an effect the use of $H_{ab} = 1$ kcal/mol has depends strongly upon the vertical reorganization energy λ . For the classical two-state Marcus–Hush model, $\Delta G^* = \lambda/4 - H_{ab} + (H_{ab})^2/\lambda$, so an H_{ab} of 1 kcal/mol corresponds to 10 % lowering of the barrier from $\lambda/4$ at $\lambda = 40$ kcal/mol, 19 % lowering at $\lambda = 20$, and 38 % lowering at $\lambda = 10$ kcal/mol. Unfortunately, there is no way of experimentally dissecting H_{ab} from the other parameters that determine the rate constant for intermolecular interactions. Kochi’s group has particularly emphasized another factor than large H_{ab} (but which is not independent of the size of H_{ab}) that leads to larger than “expected” rate constants. Intermolecular ET reactions require an encounter complex formation constant (K_e , unit M^{-1}) to make the units come out right. The expressions usually used for estimating K_e implicitly assume that there is no driving force for association [21c], but this is often not the case. Kochi’s group has emphasized that large association constants do occur for good donors with good acceptors, such as alkylated aromatics with NO^+ , and amines with CBr_4 , and calls them “quasi-covalent bonded” [26]. Ebersson’s interpretation of an electron-transfer mechanism in the nitration of easily oxidized aromatics has been modified with this idea [27]. Because there is experimentally no way of separating the effect of a large K_e from that of a large H_{ab} in causing k_{ET} for intermolecular reactions to increase, and steric hindrance lowers both, these factors appear to be lumped together in discussions of Ebersson–Kochi inner-sphere reactions. Most recently, Kochi’s group has focused on the big difference between rates of charge separation upon quenching of quinone excited-state acceptors by alkylated aromatic donors, where unhindered donors (such as hexamethylbenzene) show much faster quenching, especially in less polar solvents, and are designated inner-sphere, relative to hindered donors (such as hexaethylbenzene) where steric interactions lower K_{eq} and H_{ab} [28]. Hubic and Kochi

especially emphasize that the Rehm–Weller equation was derived assuming only diffusional encounters, that is, small K_e values so that encounter complex decay as well as its formation is diffusion-controlled. They see, however, excited-state emission that requires the extended lifetime that accompanies high K_e values, but these systems still follow the Rehm–Weller equation [28b]. The estimation of H_{ab} for any intermolecular reaction from the observed rate constant seems to invite considerable speculation. Values for five other ET parameters (K_e , ΔG° [29], λ_s , λ_v , and $\tilde{\nu}_v$), none of which can typically be accurately measured independently, are required. Indeed, it appears likely that at least some intermolecular reactions may usually proceed through a variety of transition states, which presumably have a spectrum of values for H_{ab} [21], as indicated from self-electron-transfer rate-constant measurements on phenyl-substituted N,N' -bis(bicyclic) hydrazine radical cations [30].

In contrast to the experimentally based work discussed above, in the most recent comprehensive theoretical discussion [21d], Bixon and Jortner state that the question of whether non-adiabatic or adiabatic algorithms describe electron-transfer reactions was settled in the 1960s, and that the majority of outer-sphere electron-transfer reactions are non-adiabatic. This is certainly true for the reactions that occur in the Marcus inverted region in which these authors are interested, but we think the question of whether reactions in the normal region are best treated by adiabatic theory that includes an electronic transmission coefficient or by non-adiabatic equations remains to be established.

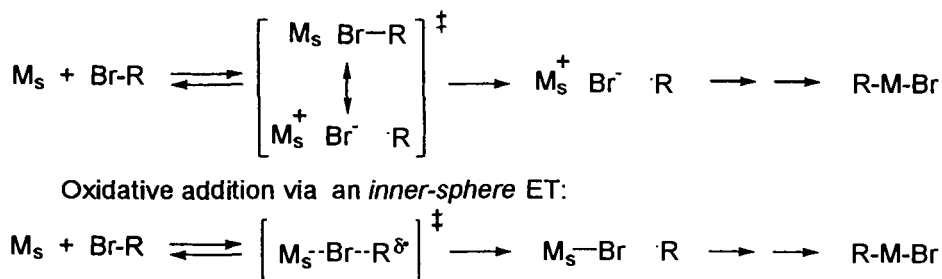
10.3 Bond Cleavage

10.3.1 Reductive Cleavage of Single Bonds

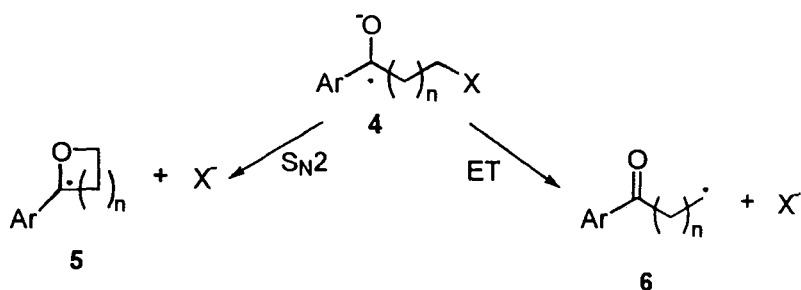
Addition of an electron to a molecule populates an antibonding orbital; this can greatly weaken bonds, even being dissociative (breaking them without thermal activation) if the orbital populated is sufficiently localized. Reductions sometimes lead to low activation energies for breaking C–C bonds even when the populated orbital is highly delocalized, as for **1**[•] [7]. The most synthetically important electron-transfer reaction is probably the production of organometallic RM from alkyl halides, RX, by reaction with metals, most recently discussed in detail by Riecke and coworkers in the context of comparing reactions of organic halides with activated zinc to those with many other reductants [31]. These reductions are argued to involve single-electron-transfer processes, from the (usual) loss of stereochemistry at the carbon being reduced, the tertiary > secondary > primary alkyl halide rate preference, and the reactivity of aryl and vinyl as well as alkyl halides. Electron addition to alkyl chlorides, bromides, and iodides (RX) is dissociative, the free energy of R^\bullet and X^- decreasing as distance increases, as discussed by Savéant and coworkers [32], who considered adiabatic theory for such reactions at electrodes [33]. The intrinsic barrier for dissociative cleavages includes, besides the solvent and inner reorganization energies, the bond-dissociation energy for the breaking bond.

Dissociative reduction reactions of the C–X bonds of alkyl halides [34], certain benzyl halides [35], α -haloacetophenones [36], C–S bonds in sulfonium salts [37], and O–O bonds in peroxides [38] were studied with the use of electrodes as well as electrochemically generated aromatic radical anions as reductants. Such reductions can be complicated by electrode material effects, reduction of the radical product in a wave not resolved from that of the starting material, and double layer effects. Maran and coworkers discuss estimating the standard potential for such irreversible electrochemical reactions [38b]. Savéant's group notes that different profiles for cyclic voltammetry peak width versus scan rate are observed for $\text{Me}_2\text{S}^+\text{CH}_2\text{Ph}$ at 293 K (broader at high and low scan rate) and 273 K (increasing width as scan rate is increased), and relates this difference to the cleavage being concerted at 293 K, but a short-lived intermediate being present at 273 K. They also discuss the theory for dissociative electron transfer that takes into account that the fragments are initially formed in a solvent cage, causing large entropy contributions [39]. Arene radical anions are intermediates in the electrochemical reduction of fluoromethylated arenes, which has been studied in detail with the use of both electrochemistry and redox catalysis [40]. In contrast to other ArCX_3 molecules, which proceed through carbenes generated by CX bond cleavage in ArCX_2^- intermediates, the $\text{X} = \text{F}$ dihalobenzyl anions protonate and reduce a second CF bond faster than they lose fluoride. The nature of Ar and solvent are both important in determining the relative rates of accepting electrons, bond cleavages, and diffusion to the electrode.

A principal mechanistic question for alkyl halide reductions has been the degree of bonding of the metal to the halide at the transition state, that is, whether the reaction is inner-sphere in the Taube sense (see Scheme 1). The M_s symbol refers to solid metal, and less is known about reactions that occur at solid surfaces than those in solution because of problems with studying kinetics (unless the surface is an electrode). Rieke and coworkers emphasize quantities that can be measured, the $\ln(k_{\text{RX}}/k_{n\text{-RX}})$ for secondary ($s\text{-RX}$) and tertiary ($t\text{-RX}$) halides relative to primary ones ($n\text{-RX}$), which they summarize for 14 reactions [31]. The $\text{Co}^{\text{II}}/\text{RI}$, $\text{Cr}^{\text{II}}/\text{RBr}$, and $\text{Cr}^{\text{II}}/\text{RCl}$ cases are completely established as Taube inner-sphere reactions [10]. They show the largest selectivity, $\ln(k_{t\text{-RX}}/k_{n\text{-RX}})$ and $\ln(k_{s\text{-RX}}/k_{n\text{-RX}})$ values of over three and one, respectively. At the other extreme, reaction of RBr with magnesium is extremely unselective [41], and is now usually accepted to be outer-sphere,



Scheme 1. Reductive cleavage of organobromides by a divalent metal M.

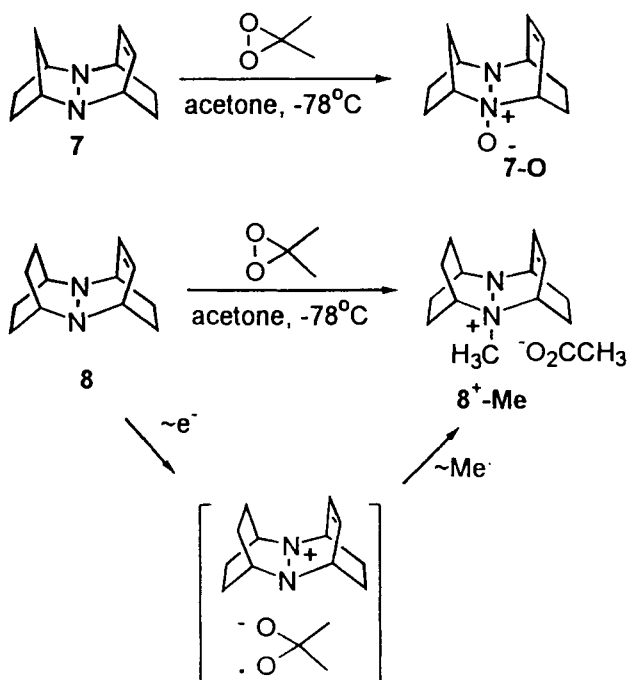


Scheme 2. Kimura and Takamuku's S_N2 , ET competition.

although stereochemical results have led to considerable speculation about whether the radical intermediates are significantly complexed to the metal surface [42]. Reaction of RBr at an inert electrode shows a spread of <0.5 for these selectivities and Ph_2CO^- , RBr shows $\ln(k_{t-RX}/k_{n-RX})$ of about one and $\ln(k_{s-RX})/k_{n-RX})$ of about zero [43]. Both are often proposed to be Taube outer-sphere, although it has also been argued that the latter might be inner-sphere, through an $[Ar_2CO \cdots Li \cdots BrR]^\ddagger$ transition state [44]. The selectivity of the activated zinc, alkyl bromide reaction most closely resembles the inner-sphere ones [31].

We now turn to the question of how “bound” the transition state for ET in alkyl halide reductions might be [24]. Zipse [25] highlights the experimental work of Kimura and Takamuku on the competition between intramolecular S_N2 at oxygen and ET in the radical anions of aroyl-haloalkanes **4** (see Scheme 2) [45], as well as theoretical studies on simplified systems [46]. For short chains ($n = 1$) only ET product **6** is observed, but when $n = 2$ or 3, mostly S_N2 reaction, producing **5** is observed when $X = Cl$. The rate of disappearance of **4** correlates well with the reduction potential of the parent ketones and solvent polarity irrespective of the ratio between substitution and electron-transfer processes, suggesting a common mechanism for these processes. In a computational study, three transition states for reaction of $MeCl$ with $H_2C=O^{\cdot-}$ have been found, an *O*-alkylation “bound-”, a *C*-alkylation “bound-”, and an ET “unbound” transition state [47]. Shaik has found that ET/ S_N2 pathway calculations are sensitive to both the coordinate system chosen and the choice of wave function; this indicates that the potential energy surfaces are very flat and will be difficult to evaluate properly [48]. The actual branching ratio in these calculations will depend on dynamics as well as energetics, and solvation effects are probably large.

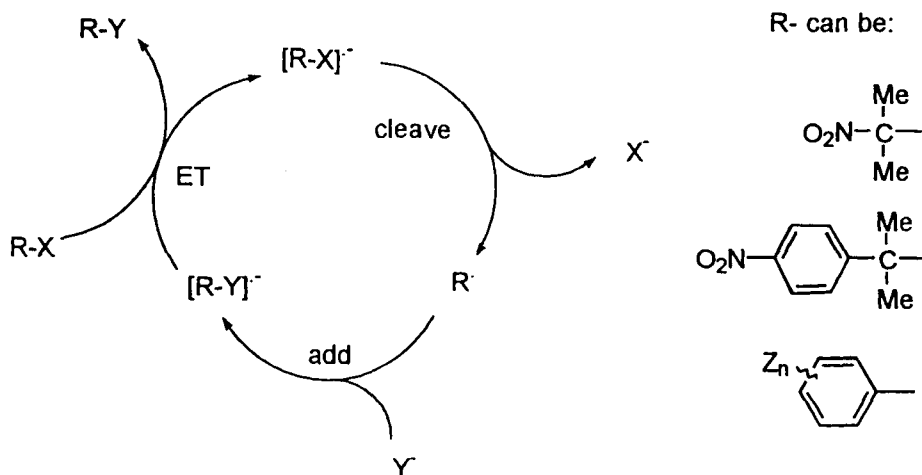
An initially puzzling switch between S_N2 and single-electron transfer chemistry occurs for reduction of dimethyldioxirane with hydrazines **7** and **8** (see Scheme 3) [49]. As expected, a nucleophilic nitrogen of **7** cleaves the $O-O$ bond and acetone is lost, producing hydrazine oxide **7-O** (which is unstable at room temperature, undergoing retro-Diels–Alder reaction). The surprise is that when one more methylene is added to the hydrazine, **8** undergoes a completely different reaction, in which a $C-CH_3$ bond of dimethyldioxirane is broken, producing **8⁺-Me**. This rather clearly involves single-electron-transfer chemistry, the O,O bond-cleaved dioxirane radical



Scheme 3. $\text{S}_{\text{N}}2$ and one-electron reduction of dimethyldioxirane by hydrazines.

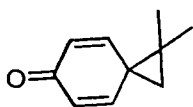
anion undergoing facile β -scission to produce acetate and a methyl radical. Ethyl transfer is favored over methyl transfer when methyl, ethyldioxirane is reduced, ruling out significant $\text{S}_{\text{N}}2$ character for the C–C bond cleavage. The methyl radical, however, cannot be generated free in solution because formation of **8⁺-Me** is rather efficient, and free methyl radicals in acetone produce methane rather rapidly. The dioxirane radical anion presumably is formed on the proper face of the hydrazine, suggesting similar transition states in this respect for the $\text{S}_{\text{N}}2$ reduction of **7** and the single-electron-transfer of **8**. The difference in oxidation potential between **7** and **8** is large enough to rationalize the switch in reaction pathways between them [49].

In contrast to the behavior of most alkyl halides, aryl halide reductions produce discrete $\text{ArX}^{\cdot-}$ intermediates, although lifetimes for cleavage of $\text{ArX}^{\cdot-}$ to aryl radicals and halides are rather short [32]. As shown in Scheme 4, heterolytic cleavage of C–X bonds of radical anions R–X, where R can stabilize a negative charge, such as the 2-nitropropyl systems studied by Russell, the *p*-nitrocumyl systems studied by Kornblum, and the aromatic systems studied by Bunnett (the $\text{S}_{\text{RN}}1$ reaction) can lead to radical chain-substitution reactions, which are synthetically valuable [50]. The entering nucleophile Y^- cannot lead to a more easily reduced R–Y product than R–X, or the ET step will fail to carry the chain. $\text{ArX}^{\cdot-}$ cleavages are also chain-carrying steps in certain radical chain dehalogenation reactions [51]. Lifetimes for $\text{ArX}^{\cdot-}$ cleavage have been measured electrochemically [52] and by pulse radiolysis [53]. The spin-bearing aromatic π system is orthogonal to the C–X σ^* bond that becomes populated to allow cleavage, making it appear that out-of-plane

Scheme 4. $S_{\text{RN}}1$ reactions.

deformation of the C–X bond will accompany the cleavage. Polyfluorinated radical anions are of particular interest in this regard because they show exceptionally large fluorine ESR splittings that are incompatible with planar π -aromatic structures [54], and are now interpreted with the aid of semi-empirical calculations as non-planar “pseudo- π ” structures that contain an admixture of σ^* orbitals [55]. Although addition of electron-withdrawing substituents usually decreases $\text{ArX}^{\bullet-}$ cleavage rates (the ground state is stabilized more than the C–X bond cleavage transition state), addition of fluorine substituents causes the opposite effect for CF cleavage. The much more easily reduced pentafluorobenzoate radical anion undergoes CF bond cleavage 2.4×10^3 times faster than the *para*-, 8.0×10^4 times faster than the *ortho*-, and more than 4×10^5 times faster than the *meta*-monofluorobenzoates [55b]. Increased σ -character in the ground state as fluorines are added is argued to be responsible, and methods for making predictions from calculations on these species (for which quite different cleavage behavior is calculated in the gas phase than is observed in solution) have been recently discussed [55b].

The cleavage of strained ring C–C bonds β,γ to the carbonyl group in ketyls (ketone radical anions) was studied quantitatively. The groups of Tanko [56] and Tanner [57] demonstrated that, in contrast to the case for neutral radicals, where it is used extensively, the cyclopropylcarbinyl, homoallyl ring opening of cyclopropyl ketone ketyls is not a good probe for detecting ketyls in a reaction sequence. Even when opening occurs, the equilibrium constant for opening is poor, in contrast to the uncharged case, so ring-closed products are isolated even when ketyls that open were intermediates. Tanko's group showed that spirocyclopropylcyclohexa-2,5-dienone **16** (cleavage rate constant 10^7 s^{-1} , and exoenergetic) does serve as a probe for detecting a ketone radical anion [58a–c]. In contrast to cyclopropylketone ketyls, which cleave much more slowly than their uncharged radical analogues (O^-

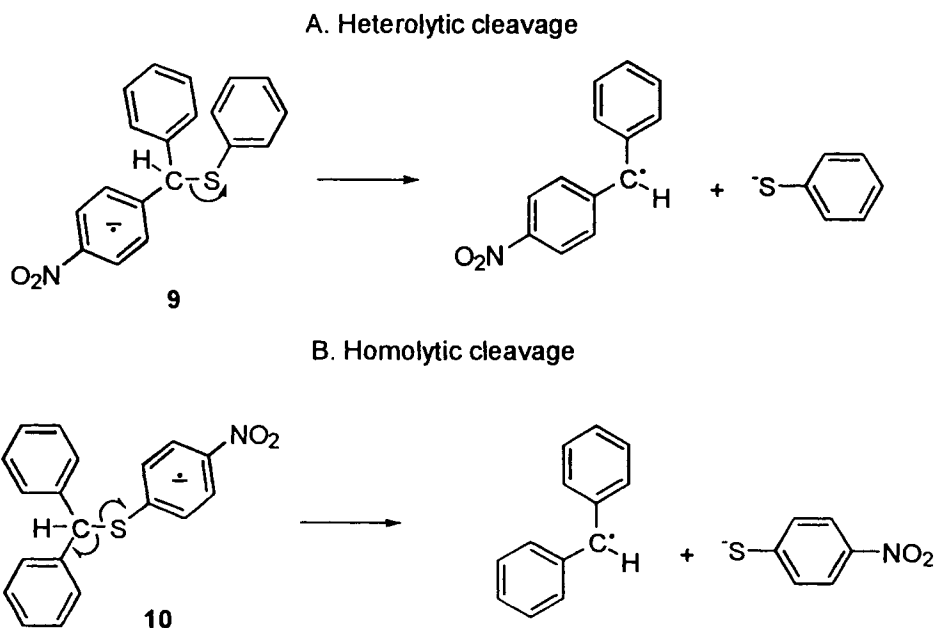


16

replaced by H), methylcyclobutylketone ketyl has a rate constant for cleavage that is probably larger than its uncharged radical analog [58d].

10.3.2 Heterolytic versus Homolytic Bond-Cleavage Reactions

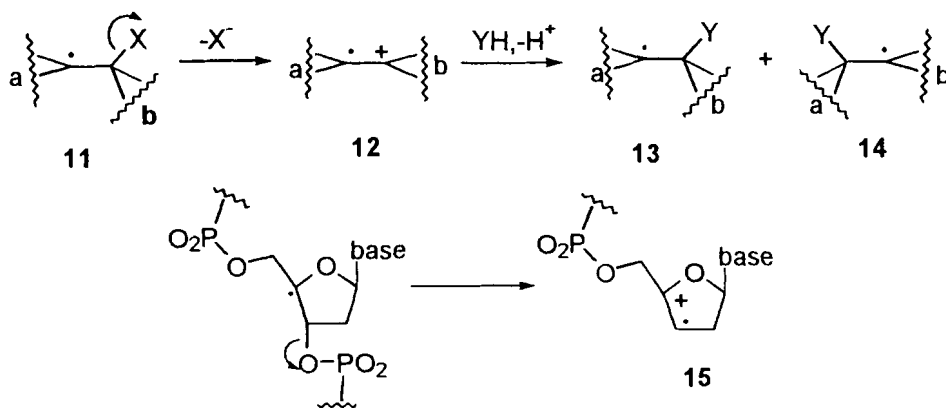
A rather subtle point concerning bond cleavages of radical ions was discussed by Guthrie and coworkers [59] emphasizing C–O bond cleavage, and later by Maslak and coworkers [60], using C–S bond cleavage. We shall consider Maslak's experiment here (see Scheme 5). The presence of the nitro group assures which component of the molecule bears the negative charge in the starting materials, **9** and **10**. Reaction A is called a heterolytic cleavage because the electron pair in the cleaving CS bond ends up on the initially neutral group, while reaction B is called a homolytic cleavage because the charge ends up on the initially charged unit, so one electron of the CS bond goes to each unit. The activation energies for cleavage of **9** and **10** are



Scheme 5. Heterolytic and homolytic C–S bond-cleavage reactions.

almost the same, but cleavage B is almost 8 kcal/mol less endoergic, so its intrinsic barrier must be significantly higher than that for cleavage A. The distribution of charge at the transition state is more delocalized for the heterolytic cleavage, A, (both the O_2NAr group and the SAr group stabilize negative charge), than for the homolytic cleavage B, where the $\text{O}_2\text{NC}_6\text{H}_4\text{S}$ group bears most of the charge both in the starting material and at the transition state. It is pointed out that most known bond cleavages of radical ions are of the heterolytic mode, as are the reverse of these cleavage reactions, the synthetically important radical anion coupling reactions that occur in $\text{S}_{\text{RN}}1$ reactions [50].

Heterolytic cleavage of a neutral radical would give a radical cation. β -Halo and other leaving-group-substituted radicals rearrange, switching the position of the leaving group and radical. These reactions were once always written as concerted reactions, proceeding through bridged transition states [61], probably because radical cations were felt to be too unstable to be intermediates. Gilbert, Norman, and Williams had already established by 1980, through identification by ESR of the radical decomposition products as a function of pH, that heterolytic cleavage to radical cations (see Scheme 6) was occurring in α -donating-group-stabilized, β -hydroxy examples of **11**, although the radical cations **12** themselves were too unstable to build up enough for detection [62]. Most recent interest in such reactions has focused on the C–O cleavage of the 3-phosphatyl substituent from 4-radicals in DNA, which gives radical cation **15** and strand cleavage, suggested as the key intermediate in the radiolytic cleavage of DNA by Schulte–Fröhlinde and coworkers [63]. Zipse has suggested, on the basis of calculations, that $\text{S}_{\text{RN}}2$ reactions, in which the radical cation intermediate is avoided by nucleophilic attack on the initial radical, are more likely than cleavage to radical cations [64]. It is not, however, clear that the great favoring of non-ionic over ionic pathways in the gas phase is completely compensated for by the current methods of trying to account for solvation. In any event, Giese's group has assembled an impressive set of data supporting the intermediacy of **15** in aqueous solution, including the solvent effect on the cleavage



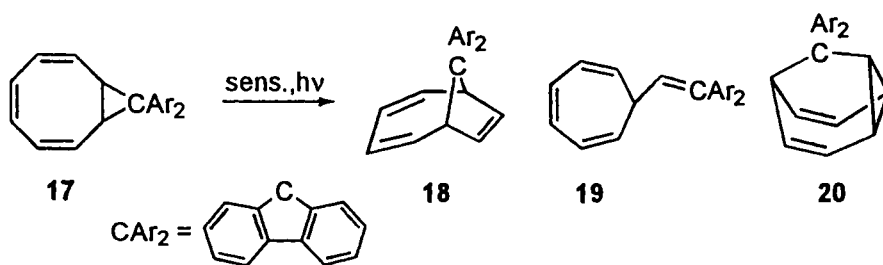
Scheme 6. $\text{C}_\beta\text{--X}$ heterolytic radical cleavage and capture.

rate [65a], observation of photocurrent upon cleavage [65b], ESR observation of the allylic radical after reduction of the allylic cation [65c], how the relative position of various bases in nucleotide oligomers affects the rate of reduction [65d], and Chemically Induced Dynamic Nuclear Polarization (CIDNP) studies on reactions proceeding through chemically generated 4-radicals [65e].

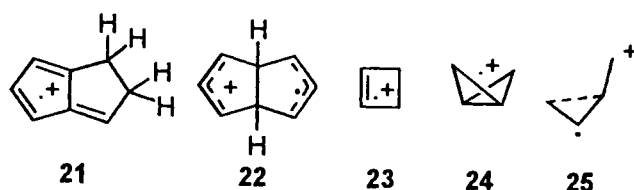
10.4 Rearrangements Initiated by Bond Cleavage in Radical Cations

Removal of an electron from a σ bond formally generates a one-electron σ bond [12], although in real compounds delocalization of the "hole" over several bonds usually occurs. Even if the hole in a radical cation is principally delocalized over a π system, as in $\mathbf{1}^+$, cleavage of a σ -bond can occur rapidly [7]. Cleavage of bonds in rings does not allow separation of the radical and ionic components formed, and can lead either to rearrangement reactions when the odd electron can be disposed of rapidly enough, or to addition of external reagents to the bond that was cleaved. Rearrangement reactions of radical cations will be considered in this section. Gassman and Hershberger found that electrochemically generated triarylamine radical cations catalyze the ring-opening isomerization of quadricyclanes to norbornadienes by an electron-transfer route. Interest here was in using this reaction to turn the exothermic isomerization on and off at will. Less fouling of the electrode was observed when the $\text{Ar}_3\text{N}^{+\bullet}$ -quadricyclane ET was endothermic, and a catalytic turnover of nearly 250 was observed for the parent compound [66].

Roth has especially emphasized the changes in bonding that occur upon electron loss, using CIDNP studies on recovered starting material and products from samples undergoing photo-electron transfer, usually initiated by photolysis of chloranil, as the principal method for deducing cation radical structure [67]. He pointed out that maxima on the neutral surface rather frequently become minima on the radical cation surface. He calls radical cations that have especially large bond-length changes relative to neutral species "nonvertical" ones. This is not the usual meaning of the term, which is that a vertical cation is one with no relaxation at all from the neutral geometry. All cations observed on the timescale of NMR are nonvertical in this sense, because both internal geometry and solvent will have relaxed during the measurement. Extensive skeletal rearrangements occur upon loss of an electron in the absence of nucleophiles from many unsaturated and strained molecules, such as those observed by Roth and coworkers for bicyclo[6.1.0]triene **17**, which gives the allylic CC bond-shift product **18**, the ring-contraction product **19**, and the more substantial rearrangement to the barbaralane derivative **20** (see Scheme 7) [68]. Energy surfaces for photochemical as well as thermal rearrangements of hydrocarbon radical ions are being studied [69]. Several isomers of dihydropentalene radical cations such as **21** have been characterized [70], including the bridgehead dihydro compound **22**, where the subtle question of whether charge is localized or delocalized has been approached through study of its ESR and optical spectra, and computationally [71]. Particularly Bally and coworkers are doing extremely detailed



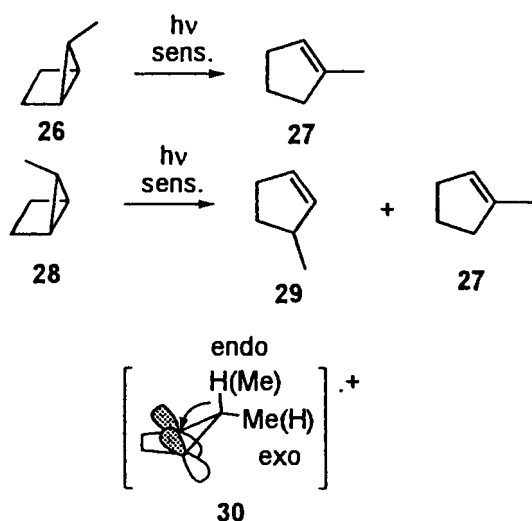
Scheme 7. Skeletal rearrangements of a bicyclo[6.1.0]nonatriene.



mapping of energy surfaces like that of C_4H_6^+ isomers, containing species such a cyclobutene radical cation, **23**, bicyclobutane radical cation, **24**, and *s*-cis- and *s*-trans-butadiene radical cation [72]; for this, they used a combination of density-functional and other calculations and optical spectroscopy on matrix-isolated species. Of special interest are their comments on calculating the structure of cyclopropylcarbinyl radical cation **25**, which lies in an exceptionally flat potential region.

Brouwer and Wilbrandt have applied resonance Raman spectroscopy and calculations to questions of structure of amine radical cations [73]. Well-resolved Raman spectra of trialkylamine radical cations that are so short-lived that their electrochemical oxidation waves are irreversible may be obtained at room temperature in solution by photoionization and time-resolved detection. Comparison of the observed spectrum with calculations for various isomers provides a powerful method of answering structural questions. Density-functional calculations prove much easier to apply to open-shell species than Hartree–Fock calculations, which require cumbersome and expensive corrections to introduce sufficient electron correlation to consider questions like the charge distribution of disubstituted piperazine (1,4-diazacyclohexane) radical cations. The dimethyl- and diphenyl-substituted piperazine radical cations are delocalized, but charge is localized on one ArN unit of the dianisyl-substituted compound [73d].

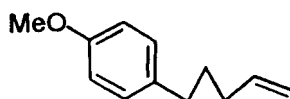
In the absence of nucleophiles, the anti- and syn-5-methyl-bicyclo[2.1.0]heptanes **26** and **28** rearrange to the isomeric methylcyclopentenenes **27** and **29** as major products under photo-ET conditions, although some crossover is detected for **28** (see Scheme 8) [74]. Matrix ESR studies show that bridging-bond stretched intermediate cations are formed, and that substituent shift from the middle carbon to form the



Scheme 8. Nonplanar bicyclo[2.1.0]-pentene radical cation.

cyclopentene radical cations occurs overwhelmingly from the endo-directed substituent (see **30**) which is far better aligned with the p-rich orbitals than is the exo-directed substituent. If the bridging CC bond cleaves, the ring flattens out and the stereochemistry is lost because the exo and endo substituents on the bridging carbon become scrambled. The more strained endo-methyl intermediate cation obtained from **28** undergoes such scrambling competitively with substituent migration. The same products are formed from the related 7-methylated 2,3-diazabicycloheptenes, but with these precursors the un-rearranged cations **30** were not detected. Bridgehead-substituted analogs were also studied [74c].

Dinnocenzo and Schmittl showed that *cis*-arylvinylcyclopropane **31** isomerizes to the *trans* isomer upon one-electron oxidation with a huge rate acceleration over that of the neutral compound (ca. 10^{24}). Both *cis* and *trans* radical cations may be detected by ESR, and the isomerization is catalytic in oxidant, because the *trans* radical cation oxidizes the *cis* neutral compound [75]. The open radical cation through which **31**⁺ and its analogs must pass to isomerize also closes to cyclopentene radical cations when substituents on the vinyl group allow significant presence of the proper conformation for closure [76]. CIDNP studies by Roth show that related cyclopropane isomerizations under photo-ET conditions proceed through the neutral triplet diradical produced by back-ET to the initially produced radical cation [77], emphasizing the importance of radical ion lifetime considerations for their reactions.

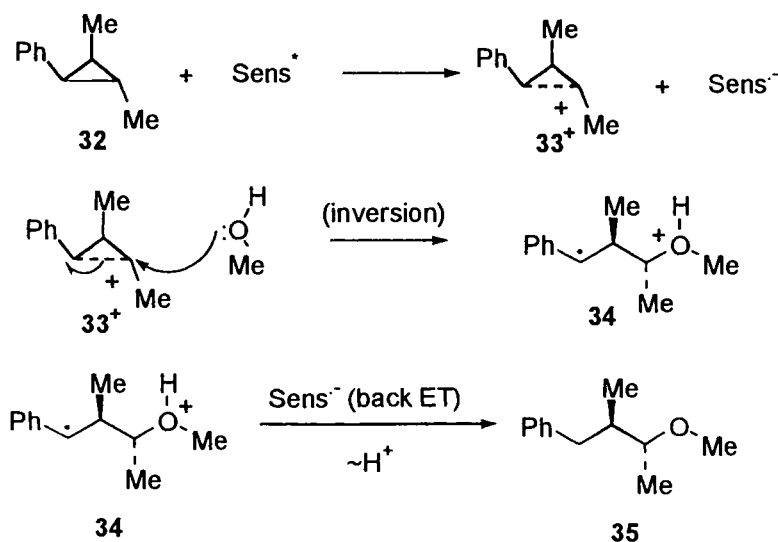


31

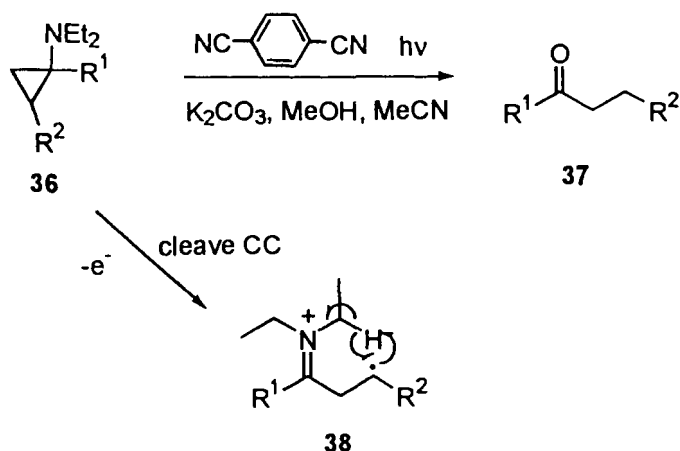
As most recently discussed by Zipse [78], 1,2-shifts and HX eliminations of β -acetoxy and β -phosphatoxyl radicals have often been formulated as proceeding through CO bond heterolysis to give alkene radical cations and delocalized acetoxy or phosphatoxy anions that bond in a second step. Calculations suggest that reactions through the radical cations are not the lowest-energy pathways (in the gas phase, for the stripped-down cases calculated, see also the discussion of Ref. [25] in Section 10.2).

10.5 Additions to Single Bonds of Radical Cations

A particularly well-studied example of an addition reaction proceeding through a radical cation involves the 1-cyanonaphthalene-initiated photocleavage of arylcyclopropanes in methanol, producing methyl ethers by addition of a hydrogen atom to the arylated carbon, and a methoxy group to the adjacent carbon. The reaction was proposed, by its discoverers, Rao and Hixson [79], to proceed through nucleophilic bond opening of the arylcyclopropane radical cation. Extensive studies, by Dinnocenzo and coworkers, involving independent generation of the arylcyclopropyl intermediates and the determination of the stereochemistry of ring opening are consistent with this mechanism, shown for conversion of **32** to **35** in Scheme 9 [80]. The reaction proceeds with extremely high inversion at the carbon attacked by methanol, and with selective cleavage of the most-substituted cyclopropane bond. Tertiary aminocyclopropanes like **36** are cleaved to ketones **37** under photo-ET



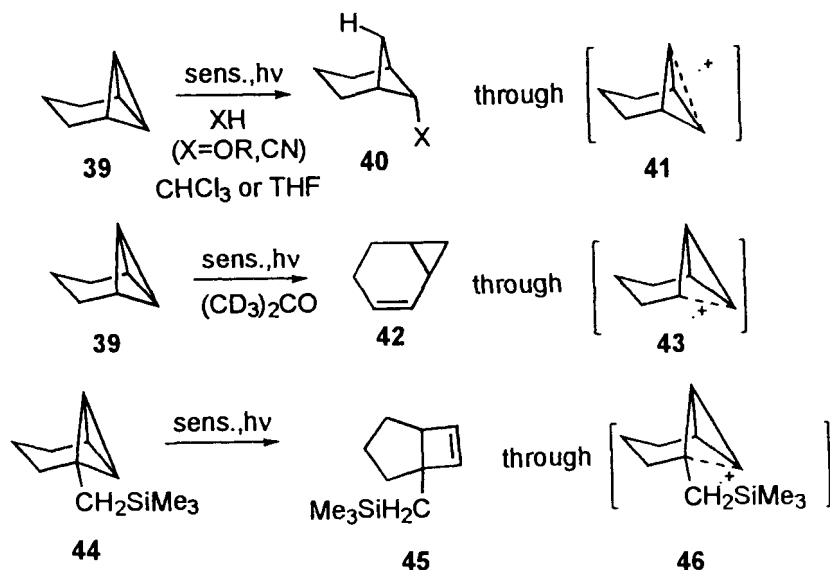
Scheme 9. Cyclopropane radical cation cleavage by methanol.



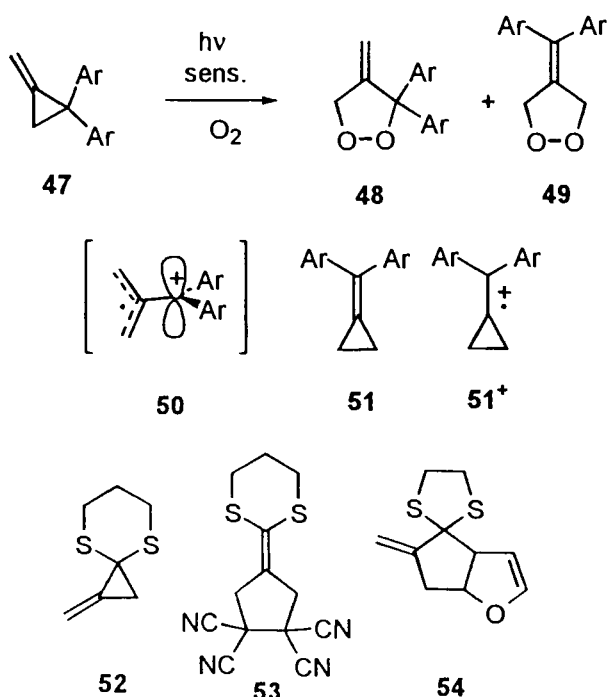
Scheme 10. Cleavage of aminocyclopropanes to ketones.

conditions (see Scheme 10) [81]. The hydrogen atom introduced at the CR^2 carbon is postulated to arise from internal hydrogen atom abstraction as in **38**.

Bicyclobutanes are also cleaved, but small changes in conditions cause different bonds to break, as shown for Moore's bridged bicyclobutane **39** and its derivative **44** in Scheme 11. Thus water, alcohols, and HCN in chloroform or THF add stereospecifically across the bridging bicyclobutane bond to form **40** [82], implying that



Scheme 11. Isomeric cleavages of bicyclobutanes.



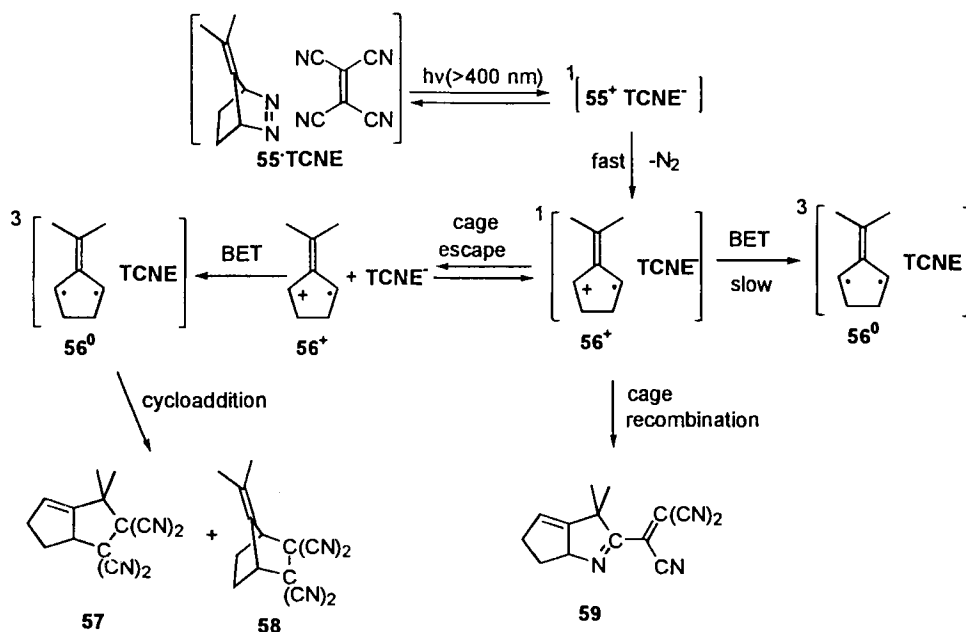
Scheme 12. Isomeric methylenecyclopropane radical cations.

the cation attacked is **41**, which is also consistent with CIDNP studies of recovered starting material [83], but in acetone- d_6 , norcar-2-ene **42** is formed, consistent with the side-bond-weakened cation **43** undergoing a 1,3-hydrogen shift. The alkylated derivative **44** produces the bicyclo[3.2.0]hept-6-ene **45**, also consistent with a side-bond-weakened cation, **46**, this time undergoing C–C bond shift [84].

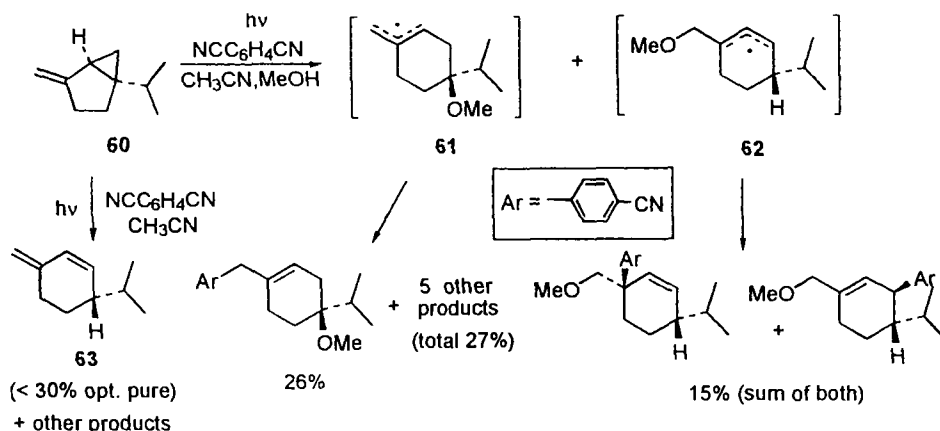
Diarylmethylenecyclopropanes can give two distinct kinds of radical cations, formally 1e- σ -bonded ones from loss of an electron from a CC σ -bond, and alkene radical cations from loss of an electron from the π bond (see Scheme 12). The cation from the saturated carbon diaryl species **47** was shown by deuterium rearrangement to open and reclose, to exchange the vinyl and saturated CH_2 groups upon photo-ET, and to add oxygen to give both the saturated carbon-substituted and alkene carbon-substituted dioxolanes (**48** and **49** respectively) in the presence of oxygen. The ring-opened bisected cation **50** was proposed as the radical cation intermediate [85]. More recently, CIDNP evidence provided further support for the bisected radical cation, and spectroscopic and photoacoustic calorimetry evidence supports back-ET prior to reformation of the three-membered ring [85c]. CIDNP and chemical studies showed that **47** adds to chloranil to give [3 + 2] adducts with the C=O bond of both the saturated-carbon- and alkene-carbon-substituted types in the absence of oxygen, with polarization patterns consistent with the alkene radical cation **50** as the intermediate. In contrast, the isomeric vinyl-carbon diaryl com-

pound **51** does not rearrange to **47** or add to chloranil, and produces a polarization pattern consistent with the cyclopropane-containing olefin cation $\mathbf{51}^+$ as the intermediate. In contrast to formation of both regioisomers of adducts from three-membered ring-cleaved radical cations of **47**, different regioisomers are produced from the thioketal-stabilized radical cation derived from **52**, upon addition to electron-poor and electron-rich double bonds. The photoadduct with tetracyanoethylene is the ketene dithioketal regioisomer **53** (in 85 % yield), but with 9,10-dicyanoanthracene sensitization, addition to furan produces the saturated thioketal regioisomer **54** [85d]. Isomeric epoxide radical cations are also formed. Depending on the alkyl substituents present, three-membered ring-cleaved (2-oxaallyl) or uncleaved oxygen-centered epoxide radical cations are generated [86].

Blackstock employed the significant triplet stabilization of an alkylated trimethylenemethane diradical to probe the photo-ET chemistry of the radical cation (see Scheme 13) [87]. Irradiation into the charge-transfer band of the azo $\mathbf{55}^+$ -TCNE complex is argued to produce the singlet radical ion pair $\mathbf{55}^+$ TCNE $^-$, which must lose nitrogen rapidly to give the singlet trimethylenemethane radical cation-TCNE $^-$ pair $^1[\mathbf{56}^+$ TCNE $^-]$. Back-ET in this pair should be slow because of the spin problem, so unless rapid cage recombination to the unprecedented cyano group adduct **59** occurs, cage escape followed by spin-allowed back-ET to $^3[\mathbf{56}^0$ TCNE] occurs, followed by coupling to the adducts **57** and **58** in the ratio known to occur from $^3\mathbf{56}^0$. In contrast to most photo-ET reactions, different products arise from $\mathbf{56}^+$ and



Scheme 13. Reactions of a substituted trimethylenemethane radical cation.



Scheme 14. Complex cyclopropane ring-opening products.

56⁰; this allows information on ion pairing and back-ET reactions to be more fully considered than usual.

Roth and coworkers' careful studies of the 1,4-dicyanobenzene and phenanthrene-sensitized photo-ET reaction of optically active (+)-sabinene (**60**) in acetonitrile/methanol points out the problem with trying to use cyclopropane cleavage reactions on more complicated systems than those used for mechanistic studies (Scheme 14) [88]. Three-quarters of the product isolated is derived from allylic radical **61**, which is formed with impressive regioselectivity for attack at the most hindered end of the most substituted cyclopropyl bond, with stereochemistry demonstrating that only inversion at the carbon attacked is observed, so methanol capture is faster than ring opening. One-quarter of the product arises from allyl radical **62**, presumably formed by regio- and stereoselective hydrogen atom shift in **60**⁺. Despite these impressive regio- and stereoselectivities, various unselective reactions of the allyl radicals, principally with the dicyanobenzene ET sensitizer, produce a plethora of products, and the major product was only formed in 26 % yield, in the presence of seven other identified compounds [88]. In the absence of methanol to trap the radical cation, the hydrogen-shift isomer **63** was formed in low yield (25 % at 40 % conversion), along with acetonitrile adducts and dimeric material. In contrast to the high stereospecificity when radical cation lifetime is limited by rapid nucleophile trapping, **63** is formed with under 30 % optical purity, indicating that racemization through the open form of intermediate(s) intervenes under these conditions [88b]. Somewhat similar results, with many products formed rather stereoselectively, are observed for reactions of norbornadiene, quadricyclane, and their 7-methylene derivatives [89]. Similar photolyses of geraniol also produce several products, including those of five-membered ring carbon-carbon bond formation and bicyclic ether formation. The product distribution, including stereochemistry, is quite dependent upon photosensitizer, and it is postulated that 1,4-dicyanobenzene provides sufficient driving force to produce solvent-separated

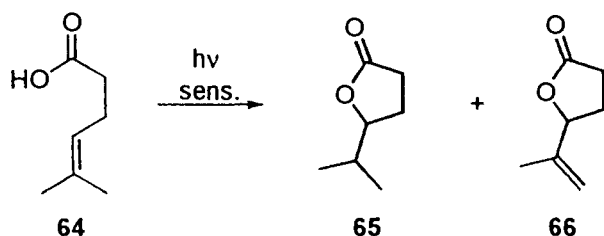
radical ion pairs, but 9,10-dicyanoanthracene is only capable of forming contact radical ion pairs [90a]. ET-photolysis of (+)-*cis*-chrysanthemol produces an oxacylohex-3-ene, formed by intramolecular attack of the hydroxyl group upon the dimethylated terminal position of the double bond, with significant retention of stereochemistry [90b].

Organosilane radical cations undergo alcohol-assisted nucleophilic Si–C cleavage that is rapid enough to compete with return ET to the sensitizer in polar solvents, and that raises quantum yield in nonpolar solvents when a nucleophile is tethered in proper position for the nucleophilic cleavage [91]. Photo-ET allows cleavage of a trimethylsilylated enol ether in the presence of a trimethylsilylated saturated alcohol, although other products are also formed, so the deprotection is not as clean as desired [92].

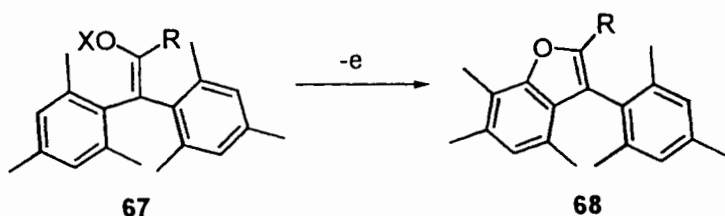
10.6 Additions to π Systems of Radical Cations

π -Radical anions generated by any means tend to capture electrophiles, and π -radical cations tend to capture nucleophiles. Addition reactions to radical ions generated by photoinduced electron transfer were reviewed by Mizuno and Otsuji [93], and photochemical cycloadditions, including radical-ion ones, by Müller and Mattay [94]. Arnold reported the use of methoxynaphthalenes as photosensitizers (S) for addition of alcohols to 1,1-diphenylethylene, a reaction presumably proceeding by electron transfer to form $S^{\bullet+}$ and $\text{Ph}_2\text{CCH}_2^{\bullet-}$, followed by protonation of the anion and back electron transfer, generating Ph_2MeC^+ , which captures the alcohol [95]. A lack of space and our interests have caused us to focus on reactions of radical cations here. Parker has reviewed the extensive work on the addition of nucleophiles to the π -radical cations from anthracenes and their 9,10-heteroatomic analogs [96]. Gassman and coworkers have especially studied photoelectron-transfer-induced closure of γ,δ -unsaturated carboxylic acids to γ -lactones, such as **64** to **65**, with cyanoaromatic compounds as sensitizers (see Scheme 15) [97]. Yields of **65** are significantly improved when steric hindrance is introduced into 1,4-dicyanobenzene sensitizers by alkylation of the other four positions of the ring, although formation of the unsaturated product **66** remains detectable.

Schmittl has both reviewed [98] and done extensive work on enol radical cations [99]. Ketones appear to oxidize both electrochemically and with many chemical

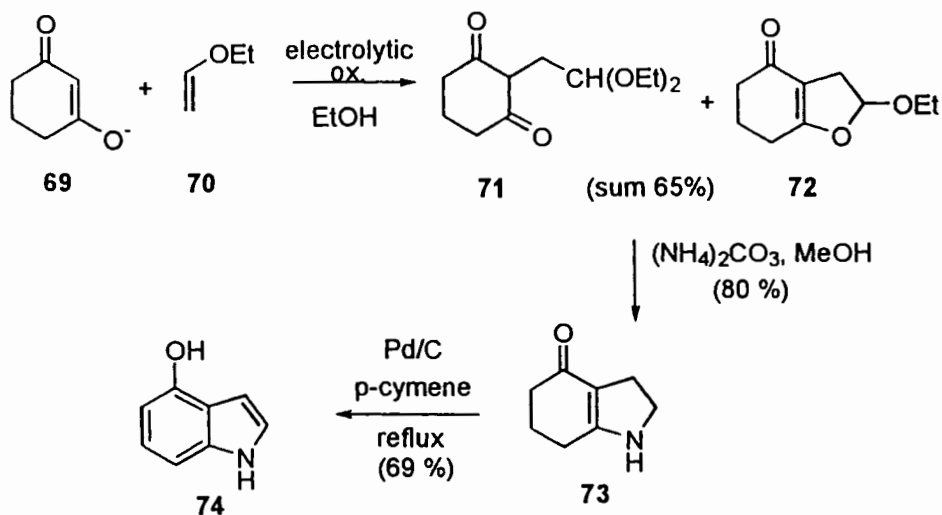


Scheme 15. Gassman's γ -lactone formation.

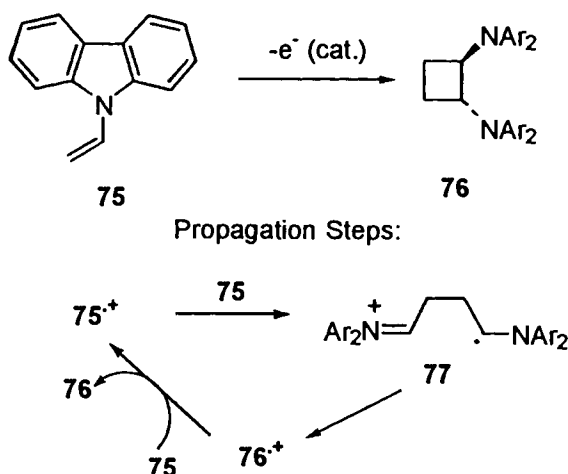


oxidants through the lower oxidation potential enol form. However, even when ionizing radiation directly oxidizes the keto form, rearrangement to produce the enol radical cation can be observed in cryogenic matrices, demonstrating that there is little barrier to the isomerization [100]. Dimesityl ketones exist exclusively in their enol form **67**, allowing less mechanistic ambiguity for their reactions. Their cations are stable enough to be detected, and can be prepared by several oxidation methods, from the enol or its derivatives, and cyclize to benzofurans **68** [99]. Electrolytic oxidation of enolates allows their addition to donor-substituted olefins [101], forming carbon-carbon bonds. Chemical oxidants such as manganese triacetate are more commonly used synthetically. A preparation of 4-hydroxyindole (**74**) that features electrolytic oxidation for the key carbon-carbon bond-forming step is shown in Scheme 16 [102]. Both compounds of the mixture **71** + **72** from the electrolytic oxidation step are converted to **73** without separation. The chemistry of electrolytically generated enol ester radical cations was especially developed by Shono and co-workers [103], who obtained α -substituted ketones as products.

Carbon-carbon bond-forming reactions form the core of synthetic organic chemistry, and cycloaddition reactions in which alkene π systems form two CC



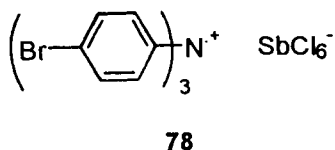
Scheme 16. Electrolytic oxidation-based preparation of 4-hydroxyindole.

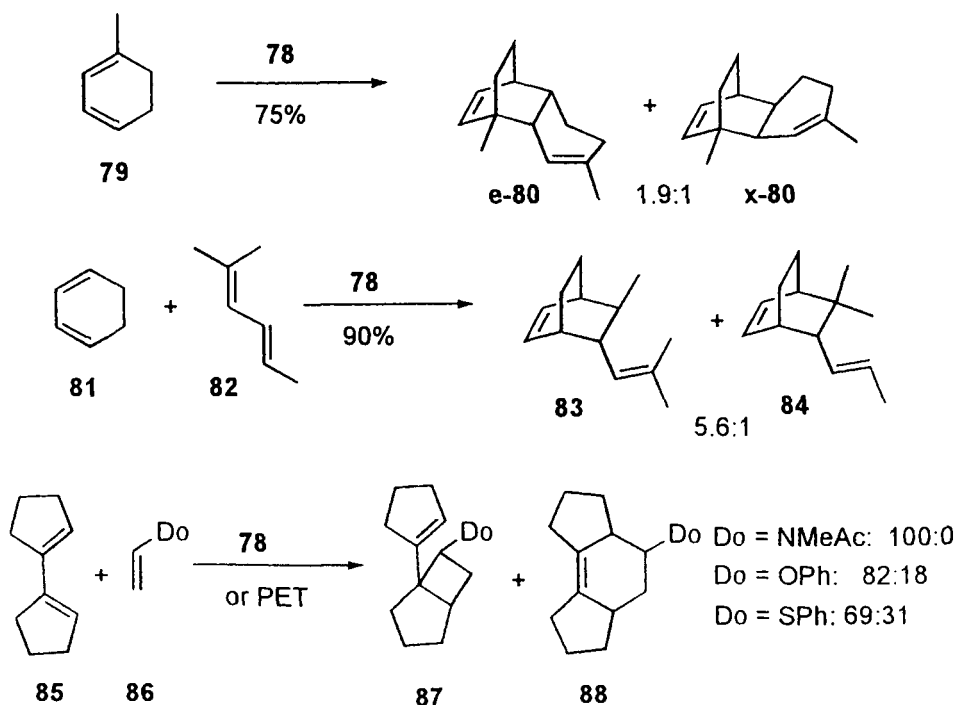


Scheme 17. Ledwith's radical cation (2 + 2) reaction.

bonds by adding to π radical cations have tantalized organic chemists since the late 1960s. Ledwith and coworkers showed that the strong donor-substituted alkene, *N*-vinylcarbazole (**75**) undergoes chain (2 + 2) dimerization to the disubstituted cyclobutane **76**, catalyzed either by metal oxidants or by photosensitization (see Scheme 17) [104]. They also postulated the currently accepted mechanism (Scheme 17), with an intermediate distonic radical cation **77** having only one of the new carbon-carbon bonds of the product.

Bauld and coworkers, especially, developed the analogous Diels-Alder (4 + 2) cycloaddition reactions. These reactions are conveniently catalyzed by tris(4-bromophenyl)aminium hexachloroantimonate (**78**) or by photosensitization with aromatic nitriles. The radical cation-catalyzed Diels-Alder reaction is far faster than the uncatalyzed one, and leads to some selectivity for attack at the least substituted double bond for the monoene component (Scheme 18, **79** \rightarrow **80**), but only modest *endo* selectivity (*e*- and *x*-**80**) [105]. Cross reactions with two dienes proved to be notably less sensitive to inhibition by steric hindrance of alkyl groups substituted on the double bonds than the uncatalyzed reactions, as cyclohexadiene adds detectably even to the trisubstituted double bond of 2-methylhexadiene (**82**), producing both **83** and **84**. Dienes such as **85** react with donor-substituted olefins (**86**) to principally give the vinylcyclobutene products **87**, but they may be thermally rearranged to the cyclohexene product **88** in good yield [105]. Schmittel and coworkers have studied the cation radical catalyzed Diels-Alder addition of both

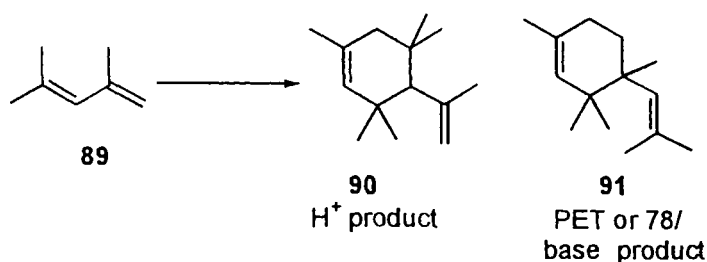




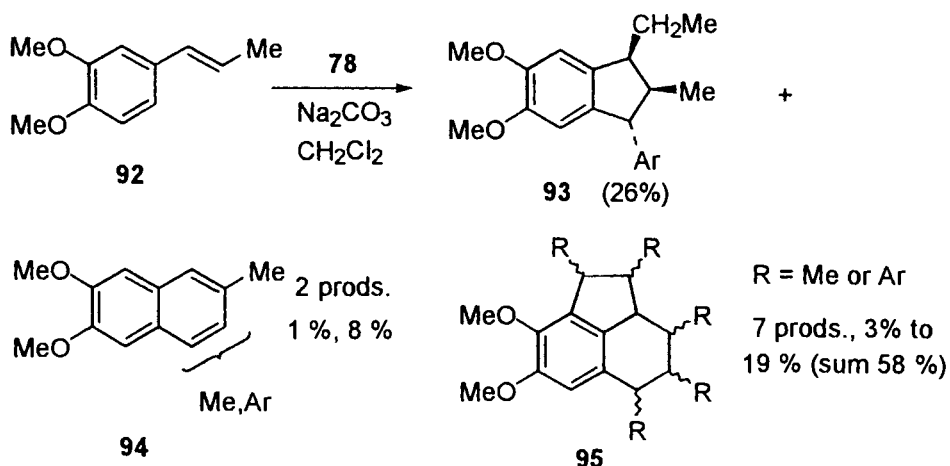
Scheme 18. Bauld's radical cation (4 + 2) and (2 + 2) reactions.

allenes and ketenes to pentamethylcyclopentadiene [106]. An interesting oxygenation of arylmethylketenes to diaryldimethylsuccinic anhydrides occurs upon treatment with triarylamine radical cations, although it was concluded that the reaction does not involve ketene radical cations [106b].

Roth and coworkers obtained CIDNP evidence for a singly bonded intermediate in the radical cation Diels–Alder dimerization of spiro[2,4]heptadiene [107]. Gassman and Singleton pointed out that acid-catalyzed (4 + 2) addition reactions can compete with the radical cation chain process when a hindered base (2,6-di-*tert*-butylpyridine) is not included. For 2,4-dimethyl-1,3-pentadiene (**89** of Scheme 19)



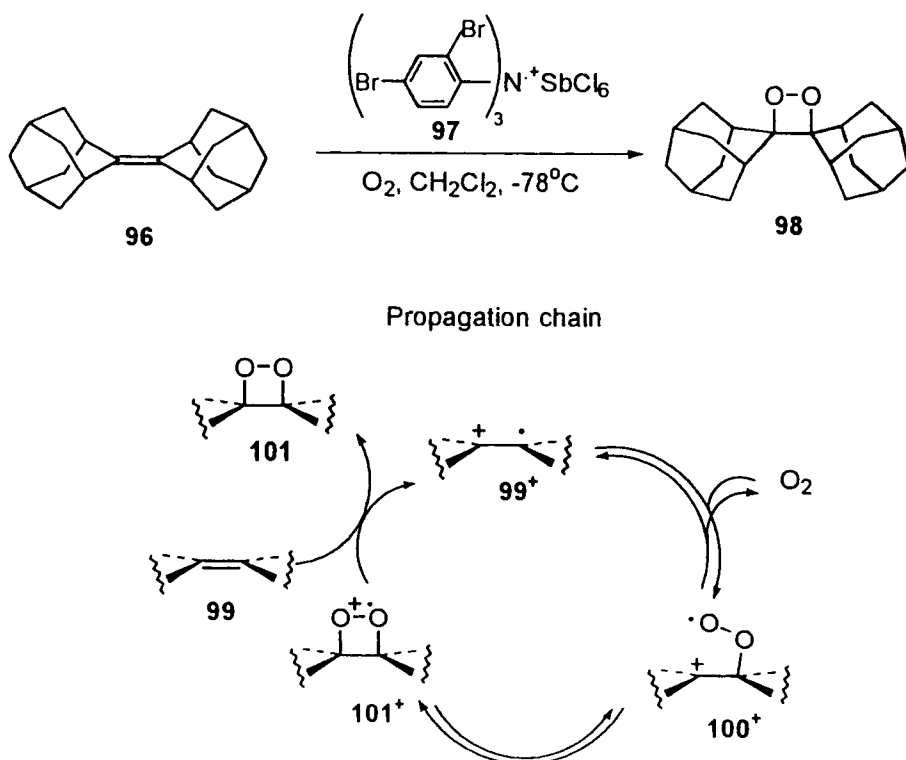
Scheme 19. Gassman's proton/radical cation dichotomy.



Scheme 20. Wilson's propenyldimethoxybenzene oligomerizations.

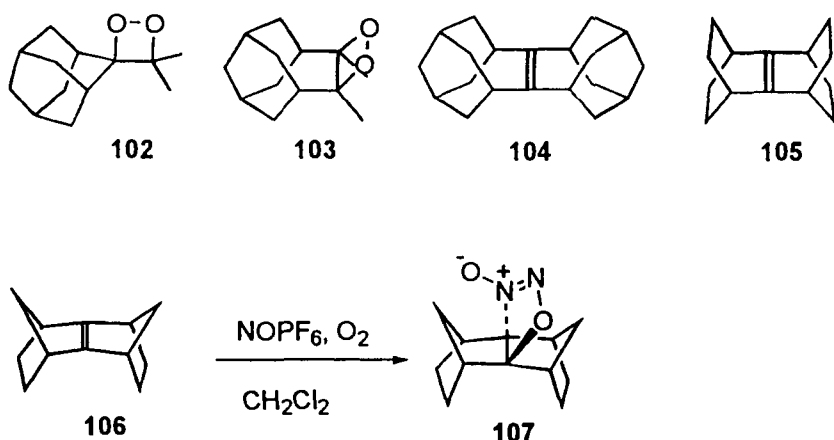
the acid-catalyzed product of addition to the trisubstituted double bond **90** was obtained with acid alone or with **78** in the absence of base, while the product of addition to the disubstituted double bond, **91**, was produced by photo-ET or from **78**/added base [108]. Wilson and coworkers found complex chemistry for **92** upon treatment with **78** in methylene chloride (see Scheme 20) [109]. Although an 86 % yield of the aromatized Diels–Alder adduct **93**, which is also the product formed upon treatment with acid, was obtained in the absence of added base, addition of sodium carbonate, which presumably switches the product mixture towards the radical-cation-initiated reaction, cut the yield of **93** to 26 %, and nine other products were formed in ≥ 1 % yield. Careful work demonstrated that the isomeric dimeric naphthalenes **94** were formed in 1 and 8 % yield, while seven regio- and stereoisomers of the trimeric products **95** were isolated in yields of 3 to 19 % (total yield of identified products, 93 %). Similar products, in slightly different ratios, were formed, starting with the cyclobutane photodimer of **92**. The number of products that form, as well as the change in types of products that form from radical cations upon change of the substitution on donor-substituted olefins make these reactions unsuitable for synthetic use.

As was noted in Scheme 12, distonic radical cations obtained from cyclopropane bond cleavages add oxygen rapidly, producing products with two CO bonds. So do some alkene radical cations. Addition of O_2 to an alkene radical cation is formally a nucleophilic attack by the single alkene π electron on O_2 , and oxidizes both carbon atoms (an alkene radical cations has formally two $\frac{1}{2}+$ carbons, and the adduct a $1+$ and an oxygen-bound carbon). The oxygenation of the radical cation of biadamantylidene (**96**) leads to dioxetanes such as **98** in chain reactions (see Scheme 21) [110]. The reactions may be initiated electrochemically or photochemically, but tris(*o,p*-dibromophenyl)amine hexafluoroantimonate, **97**, is a superior catalyst for the dark reaction of certain tetraalkylalkenes, with turnovers up to ca. 800 at



Scheme 21. Cation radical catalyzed chain oxygenation of olefins.

-78°C . The tribromo analog of **97**, **78**, is not an efficient catalyst because its oxidation potential is not high enough. High turnover is important, because **97** reacts with oxygenated compounds, including **98** and diethyl ether. These reactions are characterized by unusually shaped “E,C, backwards E” cyclic voltammetry curves because the dioxetane radical cation **101**⁺ formed from the starting alkene **99** oxidizes the electrode at a potential at which the electrode oxidizes **99**. Olefin radical cations attack oxygen to form C–O-bonded β -peroxyl radical cations (**100**⁺ of Scheme 21), as shown by isomerization about the central single bond of suitably substituted olefins. The equilibrium is poor up to the formation of **101**⁺, and the reaction only occurs efficiently because reduction of **101**⁺ by the starting alkene **99** is quite exothermic. Low temperature greatly increases catalyst turnover because of the reversibility, **101**⁺ \rightarrow **99**⁺ + O₂. These reactions make **102** and **103** available: neither can be made by ¹O₂ addition, which gives only ene products with alkenes that have abstractable α -hydrogens, or by any other published method. The olefin-face sensitivity for the chain reaction is greater for halogen substitution on the biadamantylidene ring than for the ¹O₂ reaction that produces the same dioxetanes [111]. However, the reaction of Scheme 21 is quite sensitive to alkene structure. It fails for alkenes that do not have at least two α -branched carbons, apparently be-

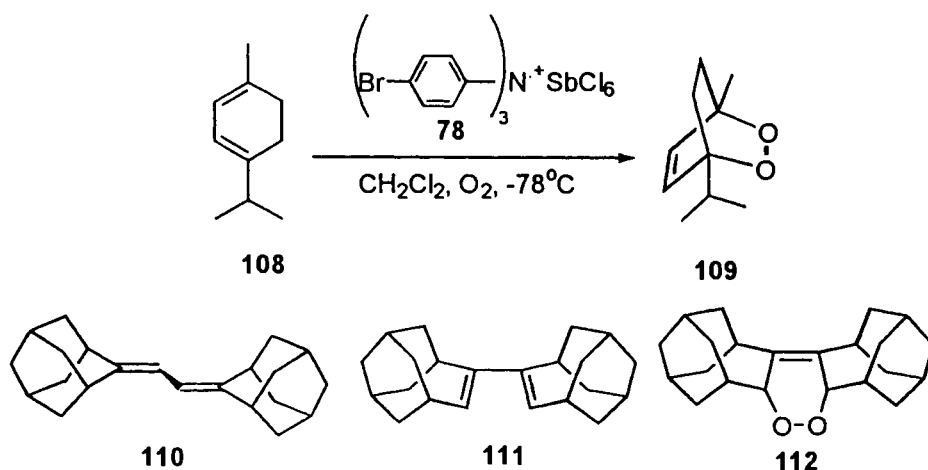


Scheme 22. Formation of a 4,5-dihydro-1,2,3-oxadiazole-3-oxide.

cause the radical cations react with themselves too rapidly, and also fails for several tetra- α -branched ones such as **104** and **105**, possibly because the $\mathbf{100}^+$ intermediates in these cases do not close rapidly enough [110].

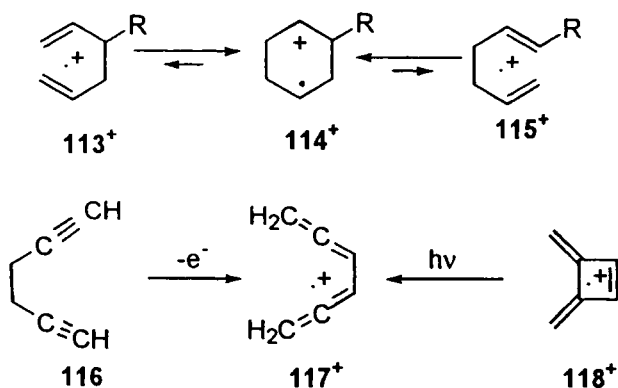
Syn-sesquinorbornene **106** fails to produce the dioxetane with either $^1\text{O}_2$, as well as after several attempts at radical cation oxygenation chain reactions, but reaction with NOPF_6 gave **107**, a derivative of a previously unreported heterocyclic ring system (see Scheme 22) [112]. No **107** was detected upon reaction of **106** with NO , and $\mathbf{106}^+$ is presumably involved in its formation.

The similar radical cation chain oxygenation of dienes to endoperoxides was discovered by Barton and coworkers, who formulated it as a Lewis acid catalyzed reaction that avoided the spin-state problem for triplet oxygen reacting with singlet starting materials to give singlet products [113]. Like the reaction of alkenes, diene-radical-cation-catalyzed oxygenation is a $^1\text{O}_2$ mimic reaction, but has a significantly different substitution pattern for substrates that are successful. The radical-cation oxygenation reactions being discussed produce radical cations that are much better oxidants than the starting compound, producing a characteristic cyclic voltammogram wave shape. However, the unhindered diene **108** has such a short radical cation lifetime, that it does not give this wave shape, although **108** produces **109** with about 260 turnovers at -78°C (see Scheme 23) [110]. The cyclic voltammogram of **110** is not noticeably affected by oxygen, and no oxygenated products were observed. The equilibrium for addition is presumably poor, with closure to form a dioxetane intermediate too slow to compete with CO bond cleavage because the cation is allylic, so Scheme 23 chemistry does not occur. An *s*-cis diene conformation is required for endoperoxide formation, and the *s*-cis form of **110** probably is too high in energy to be populated. However, **111** has enough *s*-cis diene to allow efficient formation of its endoperoxide, **112**. This material cannot be made from **111** with $^1\text{O}_2$; at least six products were formed, but only traces of **112** [110].



Scheme 23. Cation radical catalyzed chain oxygenation of dienes.

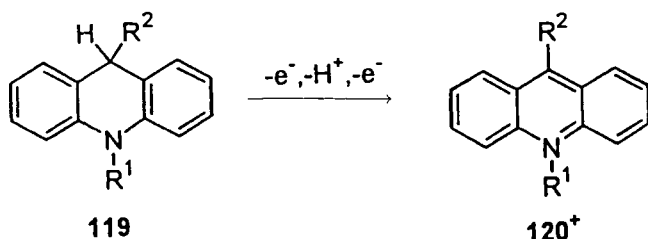
Cope rearrangements (3,3-sigmatropic shifts) catalyzed by oxidants are well known, but matrix studies and calculations suggest that the cyclohexanediyl cation **114**⁺ is usually so much more stable than the opened cations **113**⁺ and **115**⁺ that back electron transfer must occur before the CC bond cleavages that generate neutral **113** and **115** will occur (see Scheme 24) [114]. The cation from 1,5-diyne **116** is an exception, because its closed form is much less stable than its bis(allene) Cope rearrangement product **117**⁺, which was independently generated both by oxidation of neutral **117** and by photolysis of dimethylenecyclobutene radical cation, **118**⁺.



Scheme 24. Radical cation Cope rearrangements.

10.7 Trisubstituted Nitrogen Oxidations and Aminium Radical Cation Deprotonations

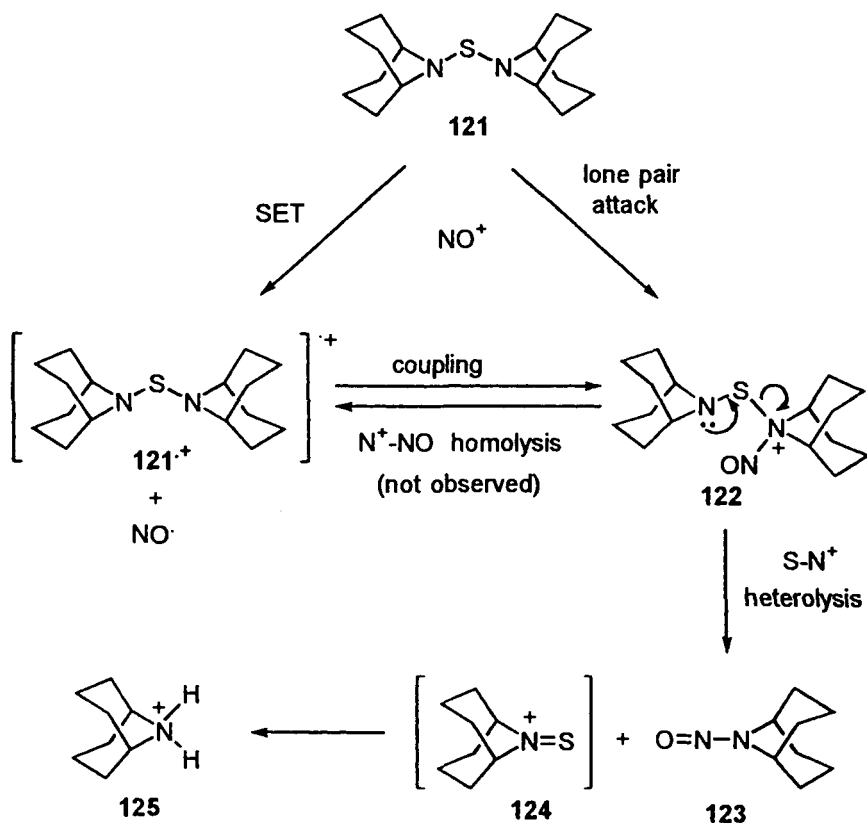
Because stable products are usually diamagnetic compounds, most reaction sequences proceeding through radical ions involve multistep sequences, and unraveling the characteristics of individual steps can be difficult. Quantitatively studying individual steps has rarely been attempted in most of the product-oriented studies described in Sections 10.3–10.5. As an instructive example of the consideration of individual steps for complex reactions, the timing of electron and hydrogen loss in oxidative amine dealkylation is a long-standing problem that has been considered with various oxidants for decades [115]. Although $R_2NCHR'_2$ is converted to $R_2N^+=CR'_2$ in the steps of interest, hydrolysis usually occurs to generate the dealkylated amine before products are isolated. The question was whether there was initial hydrogen-atom abstraction to produce $R_2NR'_2C^\bullet$, or a one-electron transfer to produce $R_2NCHR'_2\bullet^{+}$ that deprotonates to the same species. Different reagents can obviously give different results, and it would seem to be a reasonably straightforward question to answer, because the products from the oxidant (which are frequently complex) do not have to be considered. More recently, it has been fashionable to study similar questions using more complex systems that are intended to model biological systems. For example, Miwa and coworkers applied hydrogen isotope effects at the methyl group being attacked in oxidative dealkylation of methylated anilines by cytochrome P-450 [116]. They pointed out that the mechanisms should differ in the size of these isotope effects. From literature data on aniline oxidations by other reagents, it was decided that a radical cation deprotonation mechanism, an e^- , H^+ transfer (a), has a small isotope effect ($k_H/k_D \leq 4$), while an H^\bullet transfer mechanism (b), shows a big one ($k_H/k_D \geq 7$). Although it was not obvious what k_H/k_D ought to be for a third mechanism, (c) e^- , H^\bullet transfer, the small isotope effect for P-450 oxidation of *N,N*-dimethylaniline was concluded to show that mechanism (a) occurs [116]. However, later experiments demonstrate that these k_H/k_D ranges are not correct, and that the real ranges are more variable than thought. Dinnocenzo and coworkers showed that k_H/k_D is 6–9 if bases related to quinuclidine are used for deprotonation of the stable tertiary amine radical cation, dianisylmethylamine [117]. Parker and Tilsit found k_H/k_D values for $ArNMe_2$ that varied between 5 and 22 [118], and Mariano and coworkers obtained k_H/k_D values of 5–6 for photochemically generated trialkylamine radical cations by enone anion radicals [119]. Dinnocenzo and coworkers emphasized that the k_H/k_D pattern for a series of substrates with a reagent should be more reliable than the examination of only one, and that the H^\bullet transfer mechanism (b) for *tert*-butoxy radical attack on deuterated $ArN(Me)_2$ has a k_H/k_D pattern that is indistinguishable from that of P-450 attack on these compounds, and that both are significantly different from the e^- , H^+ profile (a) [120]. However, in the most recent studies on both the horseradish peroxidase compounds I ($O=Fe^{IV}por^{+}$) and II ($O=Fe^{IV}por^0$), and $O=Fe^{IV}TMP^{+}$ as a model for cytochrome P-450, both kinetic isotope effects were investigated by looking at the disappearance of oxidant and product isotope effects, to reach a rather different conclusion [121]. There is no kinetic isotope effect for the horse-



radish peroxidase compounds, consistent with the accepted e^-/H^+ -transfer mechanism (a), and it is suggested that $O=Fe^{IV}TMP^{*+}$ also involves (a), but that for this system, H-atom transfer from $ArNMe_2^{*+}$ to $O=Fe^{IV}TMP^0$ competes with back-ET, leading to the observed product isotope effects [121]. Thus, the mechanistic scheme previously considered was not extensive enough, as it ignored back-ET, which completely altered the conclusion reached from the isotope-effect data.

There has also been considerable interest in rate constants for aminium radical cation deprotonations. Dinnocenzo and Banach showed that the maximum rate constant for deprotonation of dianisylmethylamine radical cation occurs for amines whose pK_a for their protonated forms is 8 pK_a units below its pK_a of ca. 18 [117]. Savéant and coworkers have particularly studied 9-substituted *N*-alkylacridans **119**^{•+} [122], which are not only model compounds for NADH, but are especially revealing, because their deprotonated forms **119** oxidize to stable **120**⁺. This allows k_H to be measured by a combination of electrochemistry, redox catalysis, and laser flash spectroscopy, and also the thermodynamics for C–H bond cleavage (expressed as the bond dissociation free energy, BDFE) to be determined through the use of thermodynamic cycles. Marcus-like theory is used to rationalize the fact that the intrinsic barrier for deprotonation, ΔG_0^\ddagger , is little larger than $BDFE/4$, because the solvent reorganization is rather small for compounds of this size. Steric effects are important enough that ΔG_0^\ddagger becomes noticeably greater than $BDFE/4$ as the size of the R^2 group in **119** increases. It is pointed out that the $\Delta G_0^\ddagger \approx BDFE/4$ relation also fits previous work on deprotonation of alkylaromatic and dianisylmethylamine radical cations [112].

The inner-sphere character (in all three senses, see Section 10.2) for electron removal from R_2N groups will be considered next. The change in pyramidalization at nitrogen upon electron loss causes relatively large λ_{in} values for compounds containing R_2N groups [123]. Unpublished work by Trieber, Nelsen, and Kentamäa on oxidation of diaminosulfides such as **121** addresses the Taube and Ebersson/Kochi definitions of inner-sphere in R_2N oxidations. Trieber showed that oxidation of **121** electrochemically or with triarylamine **78**⁺ gives **121**^{•+}, but oxidation with NO^+ , despite the electron transfer being 11 kcal/mol exothermic, does not. As indicated in Scheme 25, the *N*-nitrosamine **123** and protonated amine **125** are isolated instead; we suggest by the S–N⁺ heterolysis of **122**. Because NO^+ is a small, powerful electrophile, it is not surprising that **121** would react with it through the S_N2 lone-pair attack shown, instead of single-electron transfer. Amines that are difficult to oxidize and even alkenes react with NO^+ by two-electron attack. NO^+ reacts with most



Scheme 25. NO^+ oxidation of a diaminodisulfide in solution.

substrates with which it undergoes exothermic single-electron transfer, by producing the single-electron-transfer products, but **121** does not, presumably because **122** undergoes more rapid $\text{S}-\text{N}^+$ heterolysis than N^+-NO homolysis. There is no proof that **122** is not formed by the SET coupling route shown. In this regard, however, the reaction of **121** with NO^+ in the gas phase (studied by Kentamäa) is particularly interesting, because only $\text{121}^{\cdot+}$ is formed, with no **123** or other cleavage product observed. This strongly suggests that **122** is not formed in the gas phase. It should be noted that this gas-phase reaction will proceed through an ion-dipole complex that is bound much more tightly than the solution reaction encounter complex would be, because solvation greatly decreases the 10–20 kcal/mol encounter complex binding energies that are typically found in the gas phase. Although Ebersson and Kochi call systems in which H_{ab} is greater than 1 kcal/mol “bonded” [22, 23], and Kochi emphasizes “bonding” in systems with large K_e values in solution [26], structures of the much stronger encounter complexes formed in the gas phase between hydrazines and their radical cations are calculated not to be intermediate between the geometries of the neutral and cation, but to clearly have neutral and

radical cation components whose geometry is only changed as expected to allow as close an approach as possible [130e]. The switch in products between gas phase and solution suggests that single-electron transfer is more rapid than S_N2 attack of the diaminosulfide nitrogen in the gas phase, which appears to be opposite to the case in solution. A principal difference between the solution- and gas-phase reactions is the obvious lack of solvation in the gas phase, and hence of λ_s , which would favor the single-electron-transfer reaction that is observed.

10.8 Studies Focusing on Electron Transfer Kinetics of Organic Systems

Savéant's electrochemical work on reductive CX bond cleavage is highlighted in Section 10.3, and Chapter 9 (Volume I, Part 1) discusses other heterogeneous electron-transfer experiments. Only homogeneous reactions will be discussed here.

10.8.1 Intermolecular Reactions

The forty-year-old Marcus cross-rate theory for calculating the rate constant for electron-transfer reactions between different species (k_{ij} of Eq. 1) was derived classically and ignores separation of λ_v and λ_s , tunneling, and variations in both the preexponential factor and K_e [21].



Most studies have been on metal coordination compounds [21, 124], where work terms are typically required to account for multiply charged species approaching each other, leading to additional parameters being required. For reactions with 0/+1 charges as shown in Eq. 1, Marcus's equations simplify to Eq. 2.

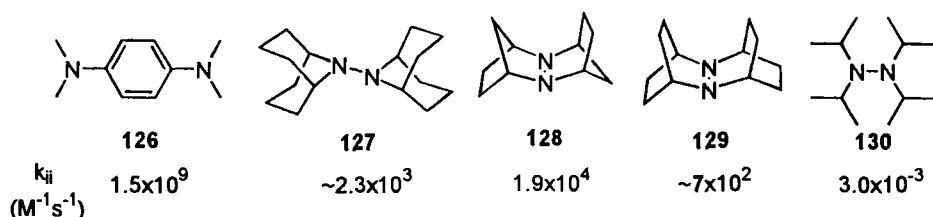
$$k_{ij}(\text{calcd}) = (k_{ii}k_{jj}K_{ij}f_{ij})^{1/2} \quad (2a)$$

$$\ln(f_{ij}) = [\ln(k_{ij})]^2 / [4 \ln(k_{ii}k_{jj}/Z^2)] \quad (2b)$$

K_{ij} and k_{ij} are the equilibrium constant and cross reaction rate constant for Eq. 2, k_{ii} and k_{jj} are the self-exchange ET rate constants, and Z is a preexponential factor usually set at 10^{11} (results are quite insensitive to its value). Because K_{ij} can be calculated from the difference in formal oxidation potentials for the components, Eq. 2 states that k_{ij} only depends upon the formal oxidation potential and intrinsic ($\Delta G^\circ = 0$, or self-ET) rate constant k_{ii} for each couple involved.

There is no transient to follow for the $\Delta G^\circ = 0$ self-ET reaction (see Eq. 3),



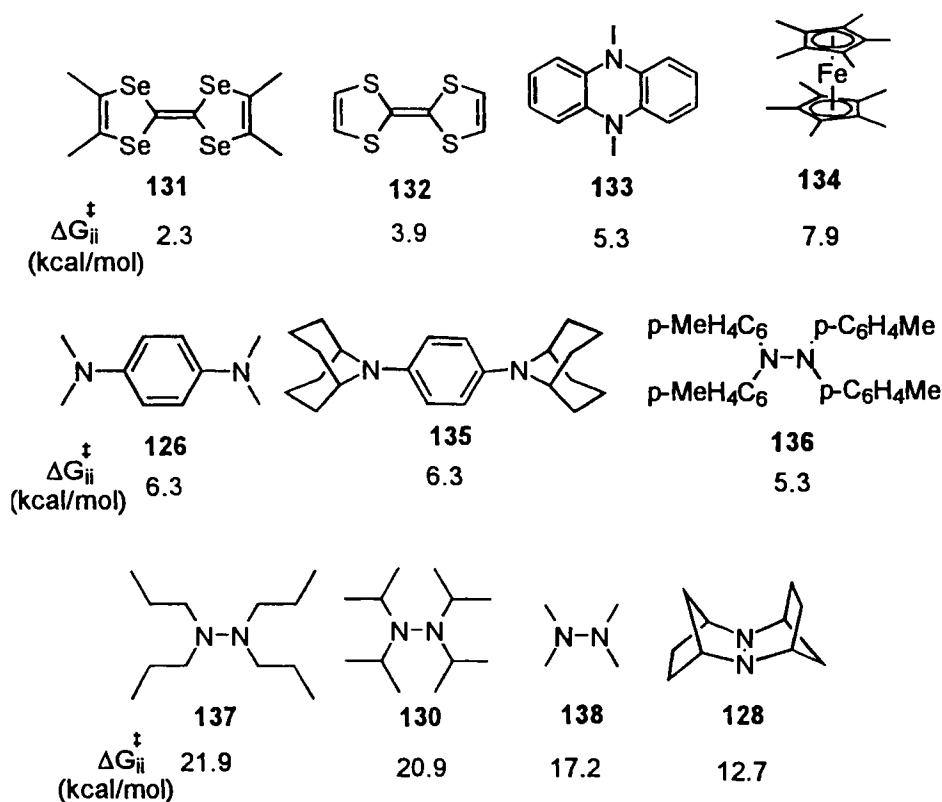


Scheme 26. Self-exchange rate constants (25 °C in acetonitrile).

so obtaining k_{ii} values for reactions that are too fast to follow on a laboratory time scale rely on magnetic-resonance line broadening, developed at about the same time as Marcus cross-rate theory. The first organic radical cation ever isolated, that from tetramethyl-*p*-phenylenediamine (**126**, Scheme 26), was used by Weissman in developing the slow-exchange region NMR line-broadening technique for determining k_{ii} , published in the same year as McConnell's similar work on organocopper compounds [125]. The slow-exchange-region NMR method is especially simple, because only the radical cation concentration needs to be known for accurate k_{ii} values to be obtained [125]. However, k_{ii} for **126**^{0/+} is too large to keep the measurements in the desired region in acetonitrile, and acid added to stabilize **126**⁺ in water resulted in the wrong k_{ii} being reported initially (protonated **126** does not electron-exchange, and hardly any neutral **126** is present at pH 5, but the equation used to calculate the rate constant assumes pseudo-first-order conditions) [126]. Grampp and Jaenicke studied *p*-phenylenediamine derivative self-ET using ESR line broadening, which is more appropriate for their large k_{ii} values ($1.5 \times 10^9 s^{-1}$ for **126**^{0/+} exchange at 25 °C in acetonitrile) [127]. Nelsen's group established that tetraalkylhydrazines have exceptionally large and substituent-dependent geometry changes upon electron loss [123], and that many examples with bis(bicyclic) substituents, such as **127**–**129**, were isolable as radical cations and give measurable slow-exchange NMR k_{ii} values, all a factor of $\geq 8 \times 10^4$ smaller than that for **126** [128]. The near-180° lone-pair–lone-pair twist angle present for *N,N*-bis(bicyclic) hydrazines like **127** and near-0° twist angle present for *N,N'*-bis(bicyclic) hydrazines like **128** and **129** (twisted 13° in crystals) greatly restrict the geometry change between neutral and cation (the cations have 3e- π bonds, and twist angles near 0/180°) [128] relative to the 90°-twist-angle acyclic hydrazines. This results in a much larger λ_v and smaller k_{ii} for **130**^{0/+}, whose k_{ii} value is a factor of 4.5×10^6 smaller than **128**^{0/+}, and 5×10^{11} smaller than **126**^{0/+} [129]. The bond-length-change, force-constant algorithm [21] used for calculating λ_v of metal-centered species is not very appropriate for nitrogen-centered organic species, where changes in bond angles and twist angles are very important. The λ_v values can be much more easily calculated without going through expressions containing force constants, from the total energies for the geometry-optimized reduced and oxidized states, and their vertical ET partners [128a].

Experimental determination of k_{ij} usually employs stopped-flow measurements, which require stability of both the diamagnetic and paramagnetic oxidation states

on the timescale of the experiment. Most studies have focused on metal-centered examples, and commented upon good agreement between Eq. 2 and experiment [21b,c]. Pladziewicz and Nelsen have studied a wide range of structural types of 0/+1 organic and substituted ferrocene cross-ET reactions [129c, 130]. Their reaction set presently includes 141 reactions between 45 compounds (91 reactions of 27 compounds in the most recent publication [130c]). The $k_{ij}(\text{calcd})$ values using E^o values measured by cyclic voltammetry and best-fit $k_{ii}(\text{fit})$ values for each couple are almost all within a factor of 0.5 to 2 of k_{obs} ; the average difference in activation barrier, $|\Delta G^{\ddagger}_{ij}|$ is 0.18 kcal/mol. Equation 2 unquestionably correlates the data successfully for a large variety of structural types. The $k_{ii}(\text{fit})$ values are systematically slightly smaller than k_{ii} values measured under self-exchange conditions, possibly because H_{ab} is more favorable for self-exchanges [129c]. The dynamic range of $k_{ii}(\text{fit})$ values is very large, 2.3×10^{14} , shown for selected compounds as relative $\Delta G^{\ddagger}_{ii}(\text{fit})$ values in Scheme 27. By pitting large and small barrier compounds against each other, $k_{ii}(\text{fit})$ values can be obtained for low barrier compounds that cannot be measured directly under self-exchange conditions (such as **131** and **132**). Grampp and Jaenicke studied **132**^{0/+} under self-exchange conditions, and showed that the

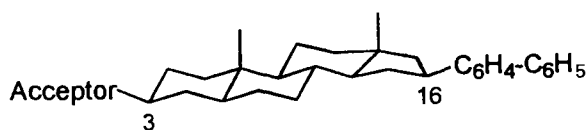


Scheme 27. Intrinsic barriers from cross-rate studies.

rate constant obtained, even after correction for diffusion, is not that to which simple Marcus theory refers, because solvent tumbling becomes the rate-limiting step [127c]. Combining very fast and very slow compounds also allows rate constants to be measured for high barrier compounds that cannot be studied under self-exchange conditions because the reactions are too slow to show even NMR line broadening, and/or the radical cations are too unstable to survive until equilibration of electron transfers occur (such as **137** and **138**). The barrier of aromatic compounds **131–133** cover a 3 kcal/mol range, and their barriers correlate well with AM1 calculations of the enthalpy portion of λ_v . Ferrocene and three methylated derivatives including decamethylferrocene **134** have $k_{ii}(\text{fit})$ values within experimental error of each other, a significantly smaller range than for k_{ii} values measured by fast-exchange NMR line broadening [131]. The $k_{ii}(\text{fit})$ value for the *p*-phenylene diamine derivative substituted with bulky alkyl groups (**135**) is within experimental error of that for the tetramethyl compound (**126**) which is not consistent with the aryl- π -system touching transition states favored by Grampp and Jaenicke for self-ET of **126** (and nearly universally assumed to represent the transition states for intermolecular ET between aromatic systems) [126]. Tetratolylhydrazine **136** has a $\Delta G^\ddagger_{ii}(\text{fit})$ value comparable to other aromatic amines, much smaller than hydrazines with alkyl substituents. Rate differences caused by differences in steric hindrance are obvious for the 2-atom π -system tetraalkylhydrazines. Larger H_{ab} for tetramethylhydrazine (**138**) than for the tetrapropyl (**137**) and tetraisopropyl (**130**) derivatives presumably is responsible for faster ET for reactions involving **138**. Even changing from methyl to ethyl substituents decreases $k_{ii}(\text{fit})$ by a factor of 2000, and in computer modeling, prevents significant direct NN π system overlap. The dynamic range in $k_{ii}(\text{fit})$ values for hydrazines is a notably large 10^{12} , indicating how important λ_v effects can be for organic compounds. The applicability of Eq. 2 to reactions involving compounds having a large range of k_{ii} indicates that the thermodynamics and intrinsic barrier indicated by the formal potential and $k_{ii}(\text{fit})$ values for each couple are in fact all that are needed to predict intermolecular electron-transfer rate constants to a surprising degree of accuracy. Because many of the reactions are non-adiabatic (Eq. 2 was derived using classical adiabatic theory), and especially because the ET parameters $\tilde{\nu}_v$ and λ_v vary very widely, this behavior is surprising. For Eq. 2 to work so well, the averaging of preexponential factors for the self-reactions must be as good an approximation as averaging of the intrinsic barriers.

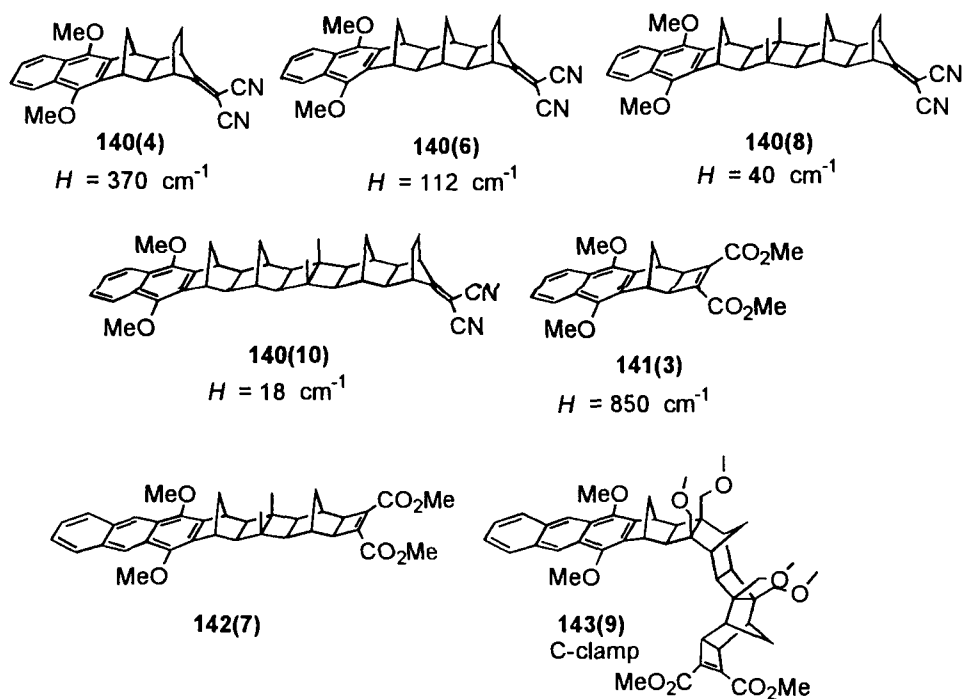
10.8.2 Intramolecular Reactions: Donor–Bridge–Acceptor Systems

ET systems consisting of an electron donor and acceptor linked by a bridge (**D–B–A** systems) have controlled geometry if the bridge is rigid enough, making it likely that there actually is a single-electron-transfer transition state, and electron transfer within them is first order, so guessing the K_e that is necessary for intermolecular systems is not necessary. Completely arbitrarily, we shall not discuss the large amount of work done on aromatic-bridged and directly bonded **D–A** systems, which will be covered in a future volume of this series. Miller, Closs, and coworkers studied ET rate constants in systems including the 5 α -androstane-3,16-diyl acceptor–

**139 (10 σ)**

biphenyl systems shown as **139** [132]. Electrons were indiscriminately added (or removed) from the acceptor and biphenyl groups by pulse radiolysis, and the rate at which the radical ion approaches its equilibrium distribution between acceptor and biphenyl units was determined by optical absorption measurements. Even with the tiny H_{ab} arising from the small electronic overlap through the 10 σ -bond shortest pathway between the units, k_{ET} proved too large to measure ($k_{ET} > 2 \times 10^9 \text{ s}^{-1}$) for the fastest system, where the acceptor is hexahydronaphthoquinon-2-yl, which has $-\Delta G^\circ \cong \lambda$. Smaller k_{ET} was observed when $-\Delta G^\circ$ exceeded λ , and this system was the first for which the long-sought “Marcus inverted region,” where making an ET reaction more exoergic makes it slower, was observed [132]. The widely quoted H_{ab} of 6.2 cm^{-1} for **139** was obtained assuming a constant H_{ab} for all examples and analysis of the rate constant using Jortner’s single averaged frequency rate expression [21d] with $\tilde{\nu}_v$ fixed at 1500 cm^{-1} for all examples (how quantitative each assumption is might be considered, because the structural changes in the acceptors used are large enough to change ΔG° for ET from biphenyl radical anion to acceptor by over 2 eV, and might be expected to cause some variation in both H_{ab} and $\tilde{\nu}_v$), and somewhat arbitrarily fixing λ_v at 0.45 eV. It was later noted that λ_v is substantially larger than 0.45 eV for biphenyl $^{\cdot-}$, but that the biphenyl rotation component has such a low frequency that it can be lumped with λ_s , so the results are presumably not affected [133]. Related systems with cyclohexane and decalin bridges as well as linked cubane bridges have also been studied, and the dependence of H_{ab} on number of bonds (n) discussed [134]. These compounds follow the predicted $e^{-\beta n}$ relationship that arises from the proportionality of H_{ab} to n and the proportionality of rate constant to $(H_{ab})^2$ for these non-adiabatic ET reactions.

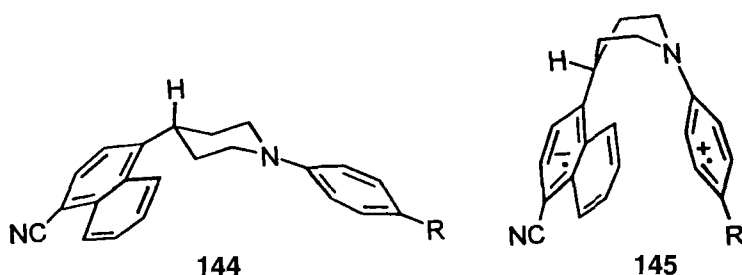
Paddon-Row and coworkers studied a revealing series of rigidly double σ -bond linked systems, where **D** = 1,4-dimethoxynaphthalene-2,3-diyl, **A** = 7-dicyanomethylene (**140**, even numbers of σ -bonds in the shortest pathway) or **A** = bis-electron-withdrawing-substituted cyclobutene (**141**, odd number of σ bonds), see Scheme 28. Photoexcitation gives the charge-separated form $^+\text{D}-\text{B}-\text{A}^-$, leading to very large dipole moments: 26 Debye for **140(4)**, 37 for **140(6)**, 55 for **140(8)**, 68 for **140(10)** [135]. Pulse radiolysis studies gave k_{ET} that was too fast to measure for all of **140(4)** to **140(12)**, but the CT bands observed gave estimates of H_{ab} of 1300, 480, and 240 cm^{-1} for **140(4)** $^{\cdot-}$, **140(6)** $^{\cdot-}$, and **140(8)** $^{\cdot-}$ respectively [136]. Fluorescence quenching allows the study of charge separation in the series **140(8)**–**140(12)**, and both emission and absorption CT bands were studied for **140(4)**. A Hush-type two-state analysis of the radiative decay rate constants gave the H_{ab} values shown in Scheme 28, which are 28 to 17 % of those quoted above for the radical anions [137a]. Charge recombination was studied with time-resolved



Scheme 28. Paddon-Row type rigidly linked D-B-A molecules.

microwave conductivity in dioxane and less polar solvents. In contrast to charge separation, k_{BET} is very dependent upon solvent polarity, and local donor excited states are populated, producing delayed donor fluorescence [138a]. Bixon, Jortner, and Verhoeven have re-analyzed the data for radiative emission from these and related compounds in terms of a three-state model, instead of the two-state model previously used [137c, 139]. The two-state model only includes the ground state, S_0 (DBA) and the first excited state, S_1 (D^+BA^-), lying ΔE above S_0 , but the next, locally excited state S_n (DBA)* lying ΔE^* above S_1 also needs to be included for these systems. It was concluded from the solvent dependence of the emission from the charge-transfer state that the three-state model is necessary, and data were re-analyzed using it, giving the result that the H_{ab} values previously extracted both from absorption and emission spectra actually refer principally to S_0 - S_n mixing, and not the S_0 - S_1 mixing to which they were attributed, so that H_{ab} for S_0 - S_1 mixing in these compounds is at least an order of magnitude smaller than previously believed.

Zimmt and coworkers have studied **D** = dimethoxyanthracene analogs of **140** and **141**, such as **142(7)** and the stereoisomeric, single cis bicyclic ring fusion compounds like **143(9)** [140]. The latter compounds have “C-clamp” shapes that place **D** and **A** fairly close but far enough apart so that solvent can get between them, and have much longer distance through-bond than through-space/solvent pathways for



ET. Fluorescence quenching studies establish that, in contrast to the all trans-fused **142(n)**, the C-clamp **143(n)** molecules show faster ET in more polar solvents, and exacting analysis in terms of modern ET theory establishes that polar solvents raise H_{ab} . Similar conclusions have been reached by Paddon-Row and coworkers for similarly-shaped species [141].

Many larger systems, having three to five charge-bearing centers of various sorts have been studied, often ones with other **D** and **A** units, including many porphyrin and quinone systems intended to mimic biological systems. This work will be covered in the subsequent volumes of this monograph.

If the bridge is flexible, various orientations of donor and acceptor are obviously possible. Verhoeven and coworkers have established a “harpooning” mechanism in which electron-transfer charge separation precedes bridge conformational change for formation of D^+, A^- exciplexes in the absence of solvent by using 4-cyanonaphthyl-*N*-arylpiperidines **144**, which have the aryl groups far apart in the ground state conformation, but can move them close together by flipping the piperidine ring to a boat conformation **145** [142]. In gas phase, jet-cooled molecules, where the aryl group is phenyl or tolyl, the threshold excess energy required to attain the emission attributed to the boat-form exciplex **145** is 4.8 kcal/mol, but it is only 2.1 kcal/mol for the compound where the aryl group is anisyl. The barrier required to flip the piperidine ring in ground state **144** is about 10 kcal/mol, but exciplex formation stabilizes the product in the charge-separated form, lowering the barrier.

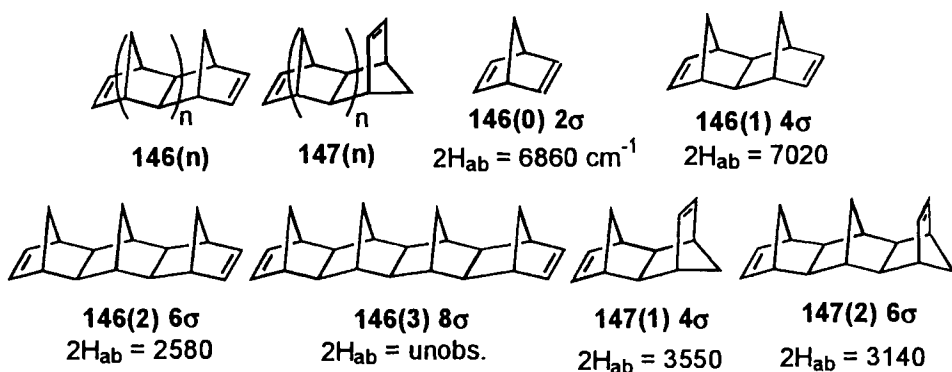
10.8.3 Intramolecular Reactions: Intervalence Compounds

Among the most revealing electron transfer systems ever devised are “symmetrical,” localized (also called Robin–Day [143] Class II) intervalence compounds, which have identical charge-bearing units (**M**) joined symmetrically by a bridge (**B**), and an overall charge that places different charges on the charge-bearing units, so they may be symbolized as “ $M-B-M^{n+1}$ ” systems. It may be seen that they are special cases of **D–B–A** systems, in which **D** and **A** only differ in charge. Such compounds fix one more ET parameter than do **D–B–A** systems; ΔG° is zero. Furthermore, as Hush pointed out, the charge-transfer band maximum transition energy (E_{op} or $\tilde{\nu}_{max}$) is equal to Marcus’s total reorganization energy λ (when vibronic coupling is ignored), and the transition dipole moment for this band allows simple calculation

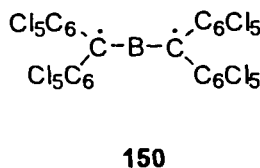
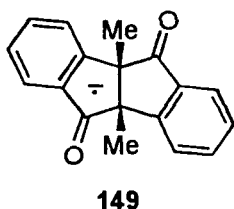
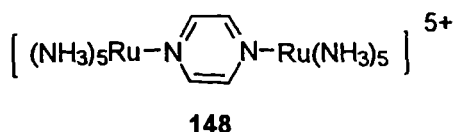
of the electronic interaction energy H_{ab} if the electron transfer distance d is known (See Volume I, Part 1, Chapter 8).

The intervalence compound concept was developed for compounds having transition metal coordination complex **M** groups, and such systems have been studied most, but we only consider organic-centered systems here. Cowan and coworkers were the first to apply the term to organic compounds, pointing out that tetrathiafulvalene (**132**, Scheme 27) is a delocalized (Robin–Day Class III) intervalence complex [143b]. So are the other species shown in Scheme 27, including the first organic radical cation ever isolated, **126**^{•+}. From Hush theory, E_{op} for a Class-III compound is equal to $2H_{ab}$, providing a far more accurate measure of H_{ab} than can be achieved for any Class-II compound, where ϵ_{max} and band width at half height must be determined as well as a value assumed for the electron-transfer distance (it cannot be easily measured). The $E_{op} = 2H_{ab}$ relationship becomes increasingly far off as direct overlap of the charge-bearing units occurs, as for hydrazine radical cations [129b]. Hush, Paddon-Row, and coworkers used this relationship to measure H_{ab} in the gas phase for Class-III bis(alkene) cations like those from the all anti-bridged **146(n)** and the less favorably aligned mono-syn-bridged **147(n)** (see Scheme 29) [144]. The separation between the symmetric and antisymmetric π -bond combination orbitals was measured by photoelectron spectroscopy and equated with $2H_{ab}$. Direct overlap makes the splitting different from $2H_{ab}$ for **146(0)**. The relatively low resolution of PE spectroscopy unfortunately makes an experimental number not determinable for **146(3)** and higher oligomers. It is not obvious how large the solvent effect on H_{ab} ought to be; solvation energies for radical cations are very large compared to H_{ab} , and electron distributions and hence solvation energies should be different for the ground- and excited-state radical cations.

For **126**^{•+} in acetonitrile, $H_{ab} = 8150 \text{ cm}^{-1}$, while for the Creutz–Taube complex, **148**, which also has a five-bond, six-membered aromatic-ring pathway between the charge-bearing centers, H_{ab} is ca. 1000 cm^{-1} , emphasizing the better overlap between the charge-bearing units and bridge in organic compounds than in transition metal coordination complexes [145]. The relatively small H_{ab} for **148** makes its



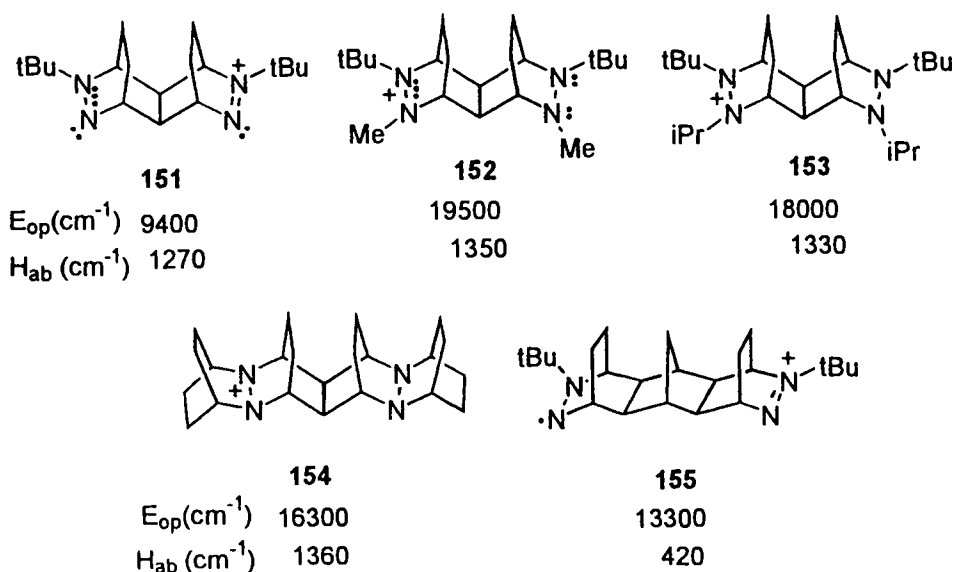
Scheme 29. Gas-phase H_{ab} values from PE spectroscopy.



Hush-type intervalence band occur in the IR region. From the $E_{\text{op}} = 2H_{ab}$ assumption for Class-III intervalence compounds in solution, consistent analyses of Class-II and Class-III compounds for both metal and organic-centered intervalence complexes are obtained in several instances [145].

Pioneering work by Mazur invoked fast-electron transfer on the infrared time scale for the anion radical **149** [146a], although later work using dynamic ESR showed that electron exchange between the keto units, which also requires counterion exchange in the nonpolar solvents in which **149** is stable, is much slower than previously thought [146b]. Considerable work has been done on dimeric perchlorotriarylmethanes connected by a bridge, **150** [147], but most interest has been in the diradical oxidation state of these systems. It has been suggested that the radical anion oxidation states should be classified by whether the diradical oxidation state is a ground-state singlet (feudal) or a triplet (allodial). Arene-bridged bis(quinone) and bis(dicarboxydiimide) radical anions that are both Class II and Class III have been prepared and studied by Miller and coworkers [148]. Optical spectra of diarylamine-centered intervalence radical cations linked *meta* to aromatic systems (minimizing H_{ab} and maximizing stability of high spin ground states for poly(radical-cations)) [149], and ones linked *para* (maximizing H_{ab}) have also been studied [150], as well as a 9-nitrogen one including both types of links [149h].

Saturated-bridged intervalence complexes were designed to use the large vibrational reorganization energies of hydrazines to obtain systems for which optical analysis could be carried out accurately and k_{ET} could also be measured [151]. Although a charge-transfer absorption band can be seen for some $\Delta G \neq 0$ **D-B-A** systems like **140(4)** and **140(6)** of Scheme 28, these systems have great intensity borrowing from a local excitation band, and the H_{ab} obtained from it, although appropriate for calculating the charge separation rate, does not really give the **D-to-A** H_{ab} value of Hush theory [139]. This problem does not arise for the dinitrogen-centered $\Delta G^\circ = 0$ compounds discussed below, which have a larger energy gap between local excitation and charge transfer, as well as a symmetry difference for the transitions. Rather small structural changes in nitrogen-centered charge-bearing



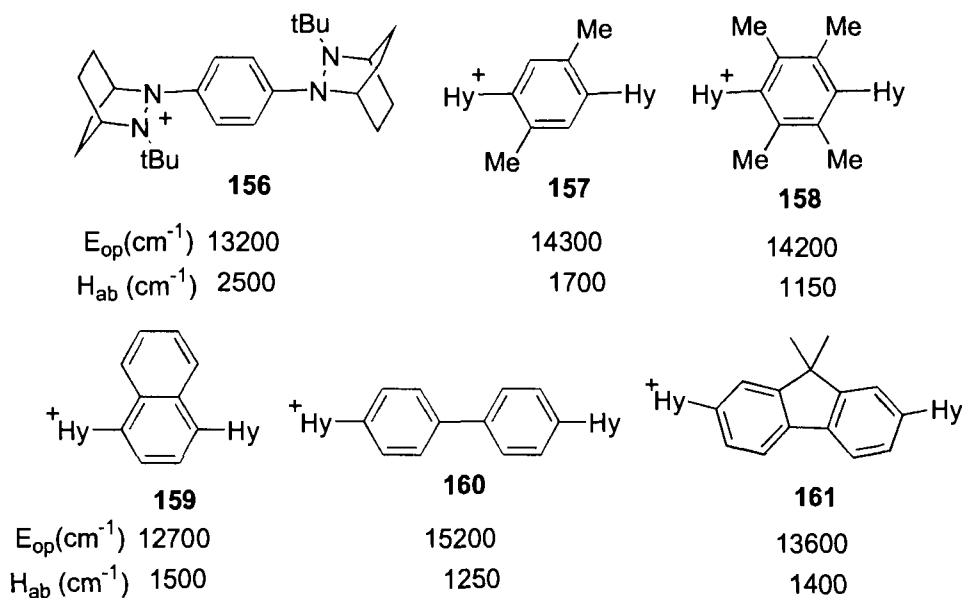
Scheme 30. Saturated-bridged bis(diazonium) and bis(hydrazine) intervalence compounds.

units cause large changes in vertical reorganization energy, as for bis(diazene) radical cation **151** and bis(hydrazine) radical cations **152** and **153**, where the vertical reorganization energy E_{op} approximately doubles upon alkylation of each dinitrogen system. Scheme 30 shows optically derived ET parameters at 25 °C in acetonitrile for each compound. The large increase in E_{op} between **151** and **152** occurs because geometry reorganization and hence λ_v is much larger in bis(hydrazine) radical cations like **152**, where the neutral hydrazine unit is strongly pyramidalized, and even the oxidized hydrazine unit is significantly pyramidalized [151a]. The diamagnetic oxidized dinitrogen unit in the bis(diazene) is planar at nitrogen, and corresponds geometrically to a doubly oxidized hydrazine, which is also planar at nitrogen [127]. It has been shown by magnetic resonance line broadening that intermolecular electron transfer between a hydrazine radical cation and its dication is significantly faster than between the neutral and the hydrazine radical cation, despite the presence of a work term for the $1+/2+$ exchange which slows down the former [128a].

Organic-centered localized intervalence compounds are of interest because they allow the accuracy of calculations of ET rate constants from optically-derived ET parameters in systems that have the maximum number of parameters well defined to be tested. The rate constant for intramolecular exchange between the dinitrogen units of bis(diazonium) and bis(hydrazine) radical cations may be accurately measured by dynamic ESR for the large nitrogen hyperfine splitting when k_{ET} is near 10^8 s^{-1} [151a]. The large λ_v of hydrazines takes the charge-transfer band maximum from the near-IR region, where it lies for transition-metal-centered systems with large λ_s and for 4σ -bond linked bis(diazonium) radical cation **151**, to the UV region, corresponding to a big increase in the ET barrier. However, k_{ET} for **152** was too

small to be measured by ESR, and that for **151** too large [151a]. Getting compounds into the right rate range by tinkering with the alkyl groups and ET distances proved possible. The diisopropyl compound **153** has a 1500 cm^{-1} smaller E_{op} than its methyl-substituted analogue **152**, causing an increase in k_{ET} that allowed its measurement in acetonitrile using the long-range splitting of hydrogens on the bridge anti to the hydrazine unit, and in methylene chloride, the smaller λ_{s} put k_{ET} into the correct range for measurement using the larger nitrogen splitting [151b]. Replacing the alkyl groups by a bicyclic ring in **154** lowered E_{op} by 3200 cm^{-1} without significantly affecting H_{ab} , putting the k_{ET} into the desired region [151c]. Unfortunately, the change of the hydrazine units from trans to cis fused also caused by the structural change of the alkyl groups apparently introduces conformational complexity that causes anomalous temperature sensitivity of the rate constant [151c,d]. Increasing the number of saturated bonds connecting the diazenium units from 4 to 6 in **155** increased E_{op} by 3900 cm^{-1} and cut H_{ab} by a factor of 3, putting its k_{ET} in the desired window for measurement by ESR [152].

Synthesis of bis(hydrazines) with aromatic bridges is much easier than that for the saturated-bridges species because *tert*-butyldiazenium salts may be added to aryl dilithiums. The *p*-phenylene-bridged radical cation **156** (see Scheme 31) is localized [153]. Although the bridge is the same as for **126**, greater delocalization of the charge in the charge-bearing unit is important for lowering H_{ab} enough so that $H_{\text{ab}} < \lambda/2$ (which causes localization); H_{ab} for untwisted **156–158** is estimated at ca. 4600 cm^{-1} from the cosine relationship for H_{ab} at each *N*-bridge connection



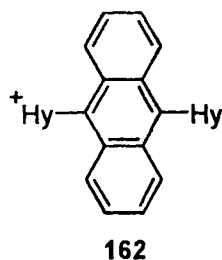
Scheme 31. ■■



[153b]. Lambert and Nöll have shown that tetraanisyl-*p*-phenylenediamine, which has a very small λ_v , as do other triarylamines, is a localized (Class II) system, although it has only a tiny ET barrier [150b]. The k_{ET} of **156** is too large to measure very accurately by ESR, but addition of methyl groups to the bridge in **157** and **158** twists the hydrazines into poorer conjugation with the ring, lowering H_{ab} and placing k_{ET} in the measurable range, as are compounds **159–161**, the latter two because of smaller H_{ab} caused by the greater number of bonds between the hydrazine units [134c].

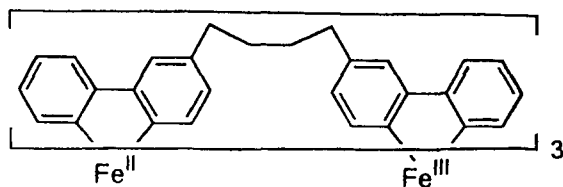
Having both rate and optical data on several compounds of Schemes 30 and 31 allowed more detailed consideration of how to best obtain optical parameters from the charge-transfer bands that accurately describe the energy surface for thermal electron transfer. The optical spectra of **156–158** are significantly broader than Hush's "high-temperature limit" (charge-transfer band width at half-height $\Delta\tilde{\nu}_{1/2}(\text{htl}) = (16RT \ln(2)E_{\text{op}})^{1/2}$, see Chapter 8 of Volume I, Part 1). The reason is apparently not principally the vibronic coupling broadening dependence of $\Delta\tilde{\nu}_v$ suggested by Hush, both because $\Delta\tilde{\nu}_{1/2}$ is quite bridge-dependent with the same hydrazine charge-bearing units (**159–161** have $\Delta\tilde{\nu}_{1/2}$ near the $\Delta\tilde{\nu}_v(\text{htl})$ value in acetonitrile, in contrast to **156–158**, which have broader bands), and because the broadening is quite sensitive to solvent, being larger in methylene chloride than in acetonitrile for all systems studied [151–153]. Vibronic coupling theory does not properly explain the charge-transfer bands of the high λ_v bis(hydrazines), as shown by failure to obtain reasonable partitioning of λ_v from λ_s using it. Rate constants calculated from optical parameters using single $\tilde{\nu}_v$ versions of vibronic coupling theory are far from those observed and have anomalous calculated temperature effects. When Hush's simple two-state treatment is used with diabatic energy surfaces that fit the charge-transfer bands [meaning that the diabatic surfaces are not exactly parabolas, because parabolas give $\Delta\tilde{\nu}_{1/2}(\text{htl})$], quite accurate predictions of the rate constants are obtained using Hush's formula for H_{ab} [154]. An experimental estimate of the electron-transfer distance d gives slightly better fit to the observed data than using the distance between any specific atoms in these molecules. Studies of k_{ET} and the optical spectra of **158**, **160**, and **161** in methylene chloride at various concentrations show that although ion-pairing effects increase E_{op} detectably and the ion-pairing equilibrium constant is a few thousand M^{-1} , calculation of k_{ET} from $\Delta G^\circ = 0$ for extraction of the optically derived parameters does not introduce much error compared to calculating it using the proper ΔG° because of compensating changes in the H_{ab} obtained [153d]. The solvent reorganizational energies for the compounds of Schemes 30 and 31 do not follow dielectric continuum theory predictions that λ_s will depend linearly upon the bulk solvent parameter $\gamma = 1/n^2 - 1/\epsilon_s$ (where n is the refractive index and ϵ_s is the static dielectric constant). The relationship between the optical spectrum of the 2+ oxidation state of **156** and its singlet, triplet splitting is that expected from a three-state model (there are two equal energy excited states because the hydrazine units are the same in the dication), and the H_{ab} values for its 1+ and 2+ oxidation states are quite similar [155].

Although the Marcus–Hush two-state system analysis of the optical spectrum gives accurate rate constants for **156–161**, adding a second benzo ring to give the anthracene-9,10-diyl-bridged compound **162** produces a k_{ET} at least a factor of 100



larger than expected from the two-state model [156]. The optical spectrum is also anomalous, and reveals why this compound is different. A band corresponding to bridge oxidation ($^+\text{Hy-B-Hy} \rightarrow \text{Hy-}^+\text{B-Hy}$) is observed at lower transition energy than the Hush-type ($^+\text{Hy-B-Hy} \rightarrow \text{Hy-B-Hy}^+$)* band, because the aromatic bridge λ_v is so much smaller than the hydrazine one that λ plus ΔG° for bridge oxidation is still smaller than λ for the Hush-type band. This occurs because the bridge oxidation state lies too close in energy to the hydrazine-oxidized ground states of the system. Application of a simple three-state model was found not to produce a $\text{Hy-}^+\text{B-Hy}$ ground-state energy minimum, so the latter is not an intermediate in the ET.

Because ϵ_{max} for the Hush-type charge-transfer band of an intervalence compound is proportional to H_{ab}^2 , ET within intervalence compounds for which the charge-transfer band may be easily seen is at least close to being adiabatic. For adiabatic reactions, H_{ab} affects the ET barrier through the relationship $\Delta G^*[(1 + 0.25C)/(1 + C)]\lambda/4 - H_{ab} + H_{ab}^2/\lambda$ ($C = 0$, using the Marcus-Hush assumption of parabolic diabatic surfaces, and C is the fitting parameter for a quartic term added to the diabatic surfaces) [154]. The preexponential factor for adiabatic reactions does not contain H_{ab} , and is only linearly dependent on $\tilde{\nu}_v$. A $\tilde{\nu}_v$ of 400 cm^{-1} is often used for metal coordination complexes, and is near 1500 cm^{-1} for aromatic compounds. AM1-based dynamics calculations on bis(hydrazines) and bis(diazonium) salts indicated intermediate values of 800 cm^{-1} and 1100 cm^{-1} are more appropriate [151d]. There has been much more interest recently in non-adiabatic electron-transfer reactions [157]. When H_{ab} is small, ΔG^* is only significantly determined by λ , and the preexponential factor is proportional to H_{ab}^2 . Using classical theory, the size of $\tilde{\nu}_v$ does not appear in the rate expression. Elliott and coworkers have studied the $\text{Fe}(\text{bpy})_3$ -centered system **163**, achieving the first



comparison of optical and thermal ET parameters for a non-adiabatic electron transfer [158]. It has k_{ET} small enough to be measured by NMR line broadening because of a small H_{ab} of about 6 cm^{-1} estimated from the optical spectrum. The charge-transfer band had a reported ϵ_{max} of $0.24\text{ M}^{-1}\text{ cm}^{-1}$, extracted by subtraction of spectra for other species in electron-transfer titrations from a region with absorption corresponding to many times this number.

References

1. (a) Pross, A.; Shaik, S.; *Acct. Chem. Res.* **1983**, *16*, 363. (b) Pross, A. *Acct. Chem. Res.* **1985**, *18*, 212.
2. Chanon, M. *Acct. Chem. Res.* **1987**, *20*, 214.
3. (a) Ashby, E. C. *Acct. Chem. Res.* **1988**, *21*, 414. (b) Newcomb, M.; Curran, D. P. *Acct. Chem. Res.* **1988**, *21*, 206.
4. Schmittel, M.; Burghart, A. *Angew. Chem. Int. Ed.* **1997**, *36*, 2550.
5. Nicholas, A.M. de P.; Arnold, D.R. *Can. J. Chem.* **1982**, *60*, 2165.
6. (a) Bordwell, F.G.; Bausch, M.J. *J. Am. Chem. Soc.* **1986**, *108*, 2473. (b) Bordwell, F. G.; Zhang, X. M. *Acct. Chem. Res.* **1993**, *26*, 510.
7. (a) Maslak, P.; Ansel, S. L. *J. Am. Chem. Soc.* **1988**, *110*, 8260. (b) Maslak, P.; Narvaez, P.; Vallombroso, T. M., Jr.; *J. Am. Chem. Soc.* **1995**, *117*, 12373. (c) Maslak, P.; Chapman, W. H., Jr.; Vallombroso, T. M., Jr.; Watson, B. A. *J. Am. Chem. Soc.* **1995**, *117*, 12380. (d) Maslak, P. *Top. Curr. Chem.* **1993**, *168*, 1. (e) Maslak, P.; Chapman, W. H., Jr. *J. Org. Chem.* **1996**, *61*, 2647.
8. Taube, H.; Gould, E. S. *Acct. Chem. Res.* **1969**, *2*, 321.
9. Ebersson, L. *Acta Chem. Scand.* **1982**, *B36*, 533.
10. Kochi, J. K. *Organometallic Mechanisms and Catalysis* Academic Press: New York, 1978, pp. 139–16, 153.
11. (a) Pauling, L. *J. Am. Chem. Soc.* **1931**, *53*, 3225. (b) Baird, N. C. *J. Chem. Educ.* **1977**, *54*, 291.
12. (a) Clark, T. *J. Am. Chem. Soc.* **1988**, *110*, 1672. (b) Gill, P. M. W.; Radom, L. *J. Am. Chem. Soc.* **1988**, *110*, 4931. (c) Hiberty, P. C.; Humbel, S.; Danovich, D.; Shaik, S. *J. Am. Chem. Soc.* **1995**, *117*, 9003. (d) Humbel, S.; Cote, I.; Hoffmann, N.; Bouquand, J. *J. Am. Chem. Soc.* **1999**, *121*, 5507.
13. (a) Asmus, K.-D. *Sulfur-Centered Reactive Intermediates in Chemistry and Biology*, Chatgililoglu, C.; Asmus, K.-D., Eds.; Plenum Press: New York, 1990, p. 155. (b) Gilbert, B. C. *Ibid.*, p. 135.
14. (a) Nishikada, K.; Williams, F. *Phys. Rev. Letters* **1975**, *34*, 302. (b) Nelson, D. J.; Peterson, R. L.; Symons, M. C. R. *J. Chem. Soc. Perkin Trans. 2* **1977**, 2005. (c) Marrignier, J. L.; Belloni, J. *J. Phys. Chem.* **1981**, *85*, 3100. (d) Surdhar, P. S.; Armstrong, D. A. *J. Phys. Chem.* **1987**, *91*, 6532.
15. (a) Gilbert, B. C.; Hodgeman, D. K.; C.; Norman, R. O. C. *J. Chem. Soc. Perkin Trans. 2* **1973**, 1748. (b) Asmus, K.-D. *Acct. Chem. Res.* **1979**, *12*, 436. (c) Deng, Y.; Illies, A. J.; James, M. A.; McKee, J. L.; Peschke, M. *J. Am. Chem. Soc.* **1995**, *117*, 420.
16. (a) Gilbert, B. C.; Marriot, P. R. *J. Chem. Soc. Perkin Trans. 2* **1979**, 1425. (b) Giles, J. R. M.; Roberts, B. P.; *J. Chem. Soc. Perkin Trans.* **1980**, 1497. (c) Fanzi, R.; Geoffroy, M.; Reddy, M. V. V. S.; Weber, J. *J. Phys. Chem.* **1987**, *91*, 3187.
17. Nichols, L. S.; McKee, M. L.; Illies, A. J. *J. Am. Chem. Soc.* **1998**, *120*, 1538.
18. (a) Alder, R. W. *Acct. Chem. Res.* **1983**, *16*, 321. (b) Nelsen, S. F.; Ippolitti, J. T.; Petillo, P. A. *J. Org. Chem.* **1990**, *55*, 3825.
19. Gerson, F.; Knöbel, J.; Buser, U.; Vogel, E.; Zehuder, M. *J. Am. Chem. Soc.* **1986**, *108*, 3781.
20. Dinocenzo, J. P.; Banach, T. E. *J. Am. Chem. Soc.* **1988**, *110*, 971.
21. (a) Guarr, T.; McLendon, G. *Coord. Chem. Rev.* **1985**, *68*, 1–52. (b) Newton, M. D.; Sutin, M. *Ann. Rev. Phys. Chem.* **1984**, *35*, 437–80. (c) Sutin, N. *Prog. Inorg. Chem.* **1983**, *30*, 441–99. (d) Bixon, M.; Jortner, J. *Adv. Chem. Phys.* **1999**, *106*, 35–202.

22. (a) Ebersson, L.; Shaik, S. S. *J. Am. Chem. Soc.* **1990**, *112*, 4484–9. (b) Ebersson, L. *New J. Chem.* **1992**, *16*, 151.
23. (a) Hubig, S. M.; Bockman, T. M.; Kochi, J. K. *J. Am. Chem. Soc.* **1996**, *118*, 3842. (b) Kochi, J. K. *Angew. Chem. Int. Ed. Engl.* **1988**, *27*, 1227. (c) Fukizumi, S.; Kochi, J. K. *Bull. Chem. Soc. Japan* **1983**, *56*, 969. (d) Fukizumi, S.; Wong, C. L.; Kochi, J. K. *J. Am. Chem. Soc.* **1980**, *102*, 2928.
24. (a) Sastry, G. N.; Danovich, D.; Shaik, S. *Angew. Chem. Int. Ed. Engl.* **1996**, *35*, 1098. (b) Fawcett, W. R.; Opallo, M. *Angew. Chem. Int. Ed. Engl.* **1994**, *33*, 2131.
25. Zipse, H. *Angew. Chem. Int. Ed. Engl.* **1997**, *36*, 1697.
26. (a) Bockman, T. M.; Karpinski, Z. J.; Sankaraman, S.; Kochi, J. K. *J. Am. Chem. Soc.* **1992**, *114*, 1970. (b) Blackstock, S. C.; Lorand, J. P.; Kochi, J. K. *J. Org. Chem.* **1987**, *52*, 1451. (c) Blackstock, S. C.; Kochi, J. K. *J. Am. Chem. Soc.* **1987**, *109*, 2484.
27. (a) Ebersson, L.; Radner, F. *Acct. Chem. Res.* **1987**, *20*, 53. (b) Kochi, J. K. *Acct. Chem. Res.* **1992**, *25*, 39.
28. (a) Hubig, S. M.; Rathore, R.; Kochi, J. K. *J. Am. Chem. Soc.* **1999**, *121*, 617–626. (b) Hubig, S. M.; Kochi, J. K. *J. Am. Chem. Soc.* **1999**, *121*, 1688–1694.
29. It seems universally accepted that ΔG° can be accurately determined by electrochemistry, but this requires the use of model compounds for most intramolecular cases, and can only be true for reactions that are slow enough to allow equilibration of solvent fluctuations. Quantitative electrochemical measurements are usually made in polar solvents like acetonitrile containing 0.1 M of a supporting electrolyte. The “corrections” for solvent changes for reactions run in other solvents are not very accurate, although widely used.
30. Nelsen, S. F.; Wang, Y.; Hiyashi, R. K.; Powell, D. R.; Neugebauer, F. A. *J. Org. Chem.* **1995**, *60*, 2981.
31. Guijarro, A.; Rosenberg, D. M.; Rieke, C. *J. Am. Chem. Soc.* **1999**, *121*, 4155.
32. (a) Andrieux, C. P.; Blocman, C.; Dumas-Bouchiat, J.-M.; M'Halla, F.; Savéant, J.-M. *J. Am. Chem. Soc.* **1980**, *102*, 3806. (b) Andrieux, C. P.; Blocman, C.; Dumas-Bouchiat, J.-M.; M'Halla, F.; Savéant, J.-M. *J. Am. Chem. Soc.* **1980**, *102*, 3432. (c) Andrieux, C. P.; Savéant, J.-M.; Zann, D. *Nouv. J. Chim.* **1984**, *8*, 107.
33. (a) Savéant, J.-M. *J. Am. Chem. Soc.* **1987**, *109*, 6788. (b) Savéant, J.-M. in *Adv. in Electron Transfer Chemistry*; Mariano, P. S., Ed.; JAI Press: Greenwich, 1994, Vol. 4, p. 53.
34. (a) Andrieux, C. P.; Gallardo, I.; Savéant, J.-M.; Su, K. B. *J. Am. Chem. Soc.* **1986**, *108*, 638. (b) Andrieux, C. P.; Gallardo, I.; Savéant, J.-M. *J. Am. Chem. Soc.* **1989**, *111*, 1620. (c) Andrieux, C. P.; Gélis, L.; Medebielle, M.; Pinson, J.; Savéant, J.-M. *J. Am. Chem. Soc.* **1990**, *112*, 3509. (d) German, E. D.; Kuznetsov, A. M.; Tikhomirov, V. A. *J. Phys. Chem.* **1995**, *99*, 9095.
35. (a) Andrieux, C. P.; Le Gorand, A.; Savéant, J.-M. *J. Am. Chem. Soc.* **1992**, *114*, 6892. (b) Huang, Y.; Wayner, D. D. M. *J. Am. Chem. Soc.* **1995**, *116*, 2157.
36. (a) Andrieux, C. P.; Savéant, J.-M.; Tallec, A.; Tardivel, R.; Tardy, C. *J. Am. Chem. Soc.* **1997**, *119*, 2420. (b) Andrieux, C. P.; Savéant, J.-M.; Tallec, A.; Tardivel, R.; Tardy, C. *J. Am. Chem. Soc.* **1996**, *118*, 9788.
37. (a) Saeva, F. G. D.; Morgan, B. P. *J. Am. Chem. Soc.* **1984**, *106*, 4221. (b) Andrieux, C. P.; Robert, M.; Saeva, F. D.; Savéant, J.-M. *J. Am. Chem. Soc.* **1994**, *116*, 7864. (c) Severin, M. G.; Farnia, G.; Vianello, E.; Arévalo, M. C. *J. Electroanal. Chem.* **1988**, *251*, 369.
38. (a) Workentin, M. S.; Maran, F.; Wayner, D. D. M. *J. Am. Chem. Soc.* **1995**, *117*, 2120. (b) Antonello, S.; Musumeci, M.; Mayner, D. M. W.; Maran, F. *J. Am. Chem. Soc.* **1997**, *119*, 9541.
39. (a) Andrieux, C. P.; Savéant, J.-M.; Tardy, C. *J. Am. Chem. Soc.* **1997**, *119*, 11546. (b) Andrieux, C. P.; Savéant, J.-M.; Tardy, C. *J. Am. Chem. Soc.* **1998**, *120*, 4167.
40. Andrieux, C. P.; Combellas, C.; Kanoufi, F.; Savéant, J.-M.; Thiébault, A. *J. Am. Chem. Soc.* **1997**, *119*, 9527.
41. Rogers, H. R.; Hill, C. L.; Figuwara, Y.; Rogers, R. J.; Mitchell, R.; Deutch, J.; Whitesides, G. M. *J. Am. Chem. Soc.* **1980**, *102*, 217, 226, 231, 239.
42. Garst, J. F. *Acct. Chem. Res.* **1991**, *24*, 95, and references therein.
43. Garst, J. F.; Smith, C. D.; *J. Am. Chem. Soc.* **1976**, *98*, 1520.
44. Lund, H.; Daasbjerg, K.; Lund, T.; Occhiliani, D.; Pedersen, S. U. *Acta Chem. Scand.* **1997**, *51*, 135.

45. (a) Kimura, N.; Takamuku, S. *Bull. Chem. Soc. Japan* **1991**, *64*, 2433. (b) Kimura, N.; Takamuku, S. *J. Am. Chem. Soc.* **1994**, *116*, 4087.
46. (a) Sastry, G. N.; Shaik, S. *J. Am. Chem. Soc.* **1995**, *117*, 3290. (b) Sastry, G. N.; Reddy, A. C.; Shaik, S. *Angew. Chem. Int. Ed. Engl.* **1995**, *34*, 1495. (c) Sastry, G. N.; Danovich, D.; Shaik, S. *Angew. Chem. Int. Ed. Engl.* **1996**, *35*, 1098.
47. Beretan, J.; Gallardo, I.; Moreno, M.; Savéant, J.-M. *J. Am. Chem. Soc.* **1996**, *118*, 5737.
48. Sastry, G. N.; Shaik, S. *J. Phys. Chem.* **1996**, *100*, 12241.
49. Nelsen, S. F.; Scamehorn, R. G.; De Felippis, J.; Wang, Y. *J. Org. Chem.* **1993**, *58*, 1657.
50. (a) Bunnett, J. F.; *Acct. Chem. Res.* **1978**, *11*, 413. (b) Kornblum, N. *Angew. Chem. Int. Ed. Engl.* **1975**, *14*, 734. (c) Rossi, R. A.; Rossi, R. H. *Aromatic Substitution by the S_{RN}1 mechanism*, American Chemical Society: Washington, DC, 1987. (d) Julliard, M. Chanon, M. *Chem. Rev.* **1983**, *83*, 425.
51. Bunnett, J. F. *Acct. Chem. Res.* **1992**, *25*, 2.
52. (a) Savéant, J.-M. *Acct. Chem. Res.* **1980**, *13*, 323. (b) Savéant, J.-M. *Adv. Phys. Org. Chem.* **1990**, *26*, 1. (c) Savéant, J.-M. *Tetrahedron* **1994**, *50*, 10117. (d) Andrieux, C. P.; Savéant, J.-M. *Investigation of Rates and Mechanisms of Reactions, Techniques of Chemistry*; Bernasconi, C. F., Ed.; Wiley: New York, 1986; Vol. VI/4E, Part 2, p. 305. (e) Andrieux, C. P.; Hapiot, P.; Savéant, J.-M. *Chem. Rev.* **1990**, *90*, 723. (f) Parker, V. D. *Adv. Phys. Org. Chem.* **1983**, *19*, 132.
53. (a) Behar, D.; Neta, P. *J. Am. Chem. Soc.* **1980**, *102*, 4798. (b) Neta, P.; Behar, D. *J. Am. Chem. Soc.* **1980**, *103*, 103. (c) Behar, D.; Neta, P. *J. Am. Chem. Soc.* **1981**, *103*, 2280.
54. (a) Yim, M. B.; Wood, D. E. *J. Am. Chem. Soc.* **1976**, *98*, 2053. (b) Starichenko, V.; F.; Shchegoleva, L. N.; Efremova, N. V.; Steingarts, V. D.; Saik, V. O.; Schastnev, P. V. *Chem. Phys.* **1985**, *100*, 79. (c) Lozovoy, V. V.; Grigoryants, V. M.; Anisimov, O. A.; Molin, Yu. N. Schastnev, P. V.; Shchegoleva, L. N.; Bilkis, I. I.; Shteingarts, V. D. *Chem. Phys.* **1985**, *112*, 1463.
55. (a) Shchegoleva, L. N.; Bilkis, I. I.; Schastnev, P. V. *Chem. Phys.* **1983**, *82*, 343. (b) Kononov, V. V.; Laev, S. S.; Beregovaya, I. V.; Shchegoleva, L. N.; Shteingarts, V. D.; Tsvetkov, Y. D.; Bilkis, I. (*submitted for publication*).
56. (a) Tanko, J. M.; Drumright, R. E. *J. Am. Chem. Soc.* **1990**, *112*, 5362. (b) Tanko, J. M.; Drumright, R. E. *J. Am. Chem. Soc.* **1992**, *114*, 1844.
57. Tanner, D. D.; Chen, J. J.; Luelo, C.; Peters, P. M. *J. Am. Chem. Soc.* **1992**, *114*, 713.
58. (a) Tanko, J. M.; Brammer, L. E., Jr. *J. Chem. Soc. Chem. Commun.* **1994**, 1165. (b) Tanko, J. M.; Brammer, L. E., Jr. *J. Chem. Soc. Perkin 2* **1994**, 1407. (c) Tanko, J. M.; Drumright, R. E.; Kamruden Suleman, N.; Brammer, L. E., Jr. *J. Am. Chem. Soc.* **1994**, *116*, 1785. (d) Tanko, J. M.; Phillips, J. P. *J. Am. Chem. Soc.* **1999**, *121*, 6078.
59. (a) Wu, F.; Guarr, T. F.; Guthrie, R. D. *J. Phys. Org. Chem.* **1992**, *5*, 7. (b) Guthrie, R. D.; Patwardhan, M.; Chateaneuf, J. E. *J. Phys. Org. Chem.* **1994**, *7*, 147.
60. Maslack, P.; Theyroff, J. *J. Am. Chem. Soc.* **1996**, *118*, 7235.
61. Skell, P. S.; Shea, K. J. *Free Radicals*, Vol. 2, Kochi, J. K., Ed., Wiley: New York, 1973, Ch. 26, p. 809.
62. Gilbert, B. C.; Norman, R. O. C.; Williams, P. S. *J. Chem. Soc. Perkin II* **1980**, 647, **1981**, 1401.
63. Behrens, G.; Koltzenburg, G.; Schulte-Fröhlinde, D. *Z. Naturforsch. C* **1982**, *37*, 1205.
64. Zipse, H. *Angew. Chem. Int. Ed. Engl.* **1994**, *33*, 1985; Curran, P. D. *Chemtrack: Org. Chem.* **1994**, *8*, 25.
65. (a) Giese, B.; Beyrich-Graf, X.; Burger, J.; Kesselheim, C.; Senn, M.; Schäfer, T. *Angew. Chem. Int. Ed. Engl.* **1993**, *37*, 1742. (b) Giese, B.; Erdmann, P.; Girard, L.; Gabel, T.; Petratta, M.; Schäfer, T. *Tetrahedron Lett.* **1994**, *35*, 2683. (c) Peukert, S.; Batra, R.; Giese, B. *Tetrahedron Lett.* **1997**, *38*, 3507. (d) Meggers, E.; Kusch, D.; Spichly, M.; Wille, U.; Giese, B. *Angew. Chem. Int. Ed. Engl.* **1998**, *37*, 460. (e) Gugger, A.; Batra, R.; Rzedek, P.; Rist, G.; Giese, B. *J. Am. Chem. Soc.* **1997**, *119*, 8740.
66. Gassman, P. G.; Hershberger, J. W. *J. Org. Chem.* **1987**, *52*, 1337.
67. Roth, *Acct. Chem. Res.* **1987**, *21*, 343, and references therein.
68. Miyashi, T.; Takahashi, Y.; Konno, A.; Mukai, T.; Roth, H. D.; Schilling, M. L.; Abelt, C. J. *J. Org. Chem.* **1989**, *54*, 1445.

69. Bally, T. *Radical Ionic Systems*, Lund, A.; Shiotani, M., Eds.; Kluwer: Dordrecht, 1991, p. 3.
70. Bally, T.; Truttman, L.; Wang, J. T.; Williams, F. *J. Am. Chem. Soc.* **1995**, *117*, 7923.
71. (a) Bally, T.; Truttman, L.; Dai, S.; Williams, F. *Ibid.* **1995**, *117*, 7916. (b) Bally, T.; Truttman, L.; Williams, F. *Theochem—J. Mol. Struct.* **1997**, *398*, 255.
72. (a) Sastry, G. N.; Bally, T.; Hrouda, V.; Cársky, P. *J. Am. Chem. Soc.* **1998**, *120*, 9323. (b) Hrouda, V.; Carsky, P.; Ingr M.; Bally, T. *J. Phys. Chem. A* **1998**, *102*, 9297. (c) Barone, V.; Rega, N.; Bally, T. *J. Phys. Chem. A* **1999**, *103*, 2217.
73. (a) Brouwer, A. M.; Langkilde, F. W.; Bajdor, K.; Wilbrandt, R. *Chem. Phys. Lett.* **1994**, *225*, 386. (b) Brouwer, A. M.; Wiering, P. G.; Zwier, J. M.; Langkilde, F. W.; Wilbrandt, R. *Acta Chem. Scand.* **1997**, *51*, 217. (c) Brouwer, A. M.; Wilbrand, R. *J. Phys. Chem.* **1996**, *100*, 9678. (d) Brouwer, A. M. *J. Phys. Chem. A* **1997**, *101*, 3626. (e) Brouwer, A. M.; Zweier, J. M.; Svendsen, O. S.; Mortensen, O. S.; Langkilde, F. W.; Wilbrandt, R. *J. Am. Chem. Soc.* **1998**, *120*, 3748.
74. (a) Adam, W.; Walter, H.; Chen, G.-F.; Williams, F. *J. Am. Chem. Soc.* **1992**, *114*, 3007. (b) Adam, W.; Walter, H.; Zang, G. *J. Am. Chem. Soc.* **1992**, *114*, 5027. (c) Adam, W.; Sahin, C.; Sendelbach, J.; Walter, H.; Chen, G.-F.; Williams, F. *J. Am. Chem. Soc.* **1994**, *116*, 2576.
75. Dinnocenzo, J. P.; Schmittel, M. *J. Am. Chem. Soc.* **1987**, *109*, 1561.
76. Dinnocenzo, J. P.; Conlon, D. A. *Tetrahedron Lett.* **1985**, *36*, 7415.
77. Roth, H. D.; Manion Schilling, M.; L. *J. Am. Chem. Soc.* **1981**, *103*, 7210 and references therein.
78. (a) Zipse, H. *J. Chem. Soc. Perkin Trans. 2* **1996**, 1797. (b) Zipse, H. *J. Am. Chem. Soc.* **1997**, *119*, 1087. (c) Zipse, H. *J. Am. Chem. Soc.* **1997**, *119*, 2889.
79. Rao, V. R.; Hixson, S. S. *J. Am. Chem. Soc.* **1979**, *101*, 6458.
80. (a) Dinnocenzo J. P.; Farid, S.; Goodman, J. L.; Gould, I. R.; Todd, W. P.; Mattes, S. L. *J. Am. Chem. Soc.* **1989**, *111*, 8973. (b) Dinnocenzo, J. P.; Todd, W. P. Simpson, T. R.; Gould, I. R. *J. Am. Chem. Soc.* **1990**, *112*, 2462. (c) Shaik, S. S.; Dinnocenzo, J. P. *J. Org. Chem.* **1990**, *55*, 3434. (d) Dinnocenzo, J. P.; Lieberman, D. R.; Simpson, T. R. *J. Am. Chem. Soc.* **1993**, *115*, 365. (e) Dinnocenzo, J. P.; Simpson, T. R.; Zuilhof, D. R.; Lieberman, D. R.; Todd, W. P. *J. Am. Chem. Soc.* **1997**, *119*, 987. (f) Dinnocenzo, J. P.; Simpson, T. R.; Zuilhof, D. R.; Lieberman, D. R. *J. Am. Chem. Soc.* **1997**, *119*, 994.
81. Lee, J.; U., J. S.; Blackstock, S. C.; Cha, J. K. *J. Am. Chem. Soc.* **1997**, *119*, 10241.
82. Gassman, P. G.; Olson, K. D. *J. Am. Chem. Soc.* **1982**, *104*, 3740.
83. Roth, H. D.; Schilling, M. L. M.; Gassman, P. G.; Smith, J. L. *J. Am. Chem. Soc.* **1984**, *106*, 2711.
84. Gassman, P. G.; Hay, B. A. *J. Am. Chem. Soc.* **1985**, *107*, 4075.
85. (a) Takahashi, Y.; Miyashi, T.; Mukai, T. *J. Am. Chem. Soc.* **1983**, *105*, 6511. (b) Miyashi, T.; Takahashi, Y.; Mukai, T.; Roth, H. D.; Schilling M. L. M. *J. Am. Chem. Soc.* **1984**, *107*, 1079. (c) Ikeda, H.; Makamura, T.; Miyashi, T.; Goodman, J. L.; Akiyama, K.; Tero-Kubota, S.; Houmam, A.; Wayner, D. D. M. *J. Am. Chem. Soc.* **1998**, *120*, 5832. (d) Nakamura, M.; Toganoh, M.; Ohara, H.; Nakamura, E. *Org. Lett.* **1999**, *1*, 7.
86. Williams, F.; Dai, S.; Snow, L. D.; Qin, X.-Z.; Bally, T.; Nitsche, S.; Haselbach, E.; Nelsen, S. F.; Teasley, M. F. *J. Am. Chem. Soc.* **1987**, *109*, 7526.
87. Painter, S. L.; Blackstock, S. C. *J. Am. Chem. Soc.* **1995**, *117*, 1441.
88. (a) Weng, H.; Sethuraman, V.; Roth, H. D. *J. Am. Chem. Soc.* **1994**, *116*, 7021. (b) Weng, H.; Sheik, Q.; Roth, H. D. *J. Am. Chem. Soc.* **1995**, *117*, 10655.
89. (a) Weng, H.; Du, X.-M.; Roth, H. D. *J. Am. Chem. Soc.* **1995**, *117*, 135. (b) Weng, H. Roth, H. D. *J. Org. Chem.* **1995**, *60*, 4136.
90. (a) Weng, H.; Scarlata, C.; Roth, H. D. *J. Am. Chem. Soc.* **1996**, *118*, 10947. (b) Herberitz, T.; Roth, H. D. *J. Am. Chem. Soc.* **1996**, *118*, 10954.
91. (a) Dinnocenzo, J. P.; Farid, S.; Goodman, J. L.; Gould, I. R.; Todd, W. P.; Mattes, S. L. *J. Am. Chem. Soc.* **1989**, *111*, 8973. (b) Dinnocenzo, J. P.; Farid, S.; Goodman J. L.; Gould, I. R.; Todd, W. P. *Mol. Cryst. Liq. Cryst.* **1991**, *194*, 151. (c) Dinnocenzo, J. P.; Farid, S.; Goodman J. L.; Gould, I. R.; Todd, W. P. *J. Am. Chem. Soc.* **1992**, *113*, 3601; Todd, W. P.; Dinnocenzo, J. P.; Farid, S.; Goodman, J. L.; Gould, I. R. *Tetrahedron Lett.* **1993**, *34*, 2863. (d) Dockery, K. P.; Dinnocenzo, J. P.; Farid, S.; Goodman, J. L.; Gould, I. R.; Todd, W. P. *J. Am. Chem. Soc.* **1997**, *119*, 1987.

92. Gassman, P. G.; Bottorff, K. J. *J. Org. Chem.* **1988**, *53*, 1097.
93. Mizuno, K.; Otsuji, Y. *Topics Curr. Chem.* **1994**, *169*, 301.
94. Müller, F.; Mattay, J. *Chem. Rev.* **1993**, *93*, 99.
95. (a) Arnold, D. R.; Maroulis, A. J. *J. Am. Chem. Soc.* **1977**, *99*, 7355. (b) Maroulis, A. J.; Arnold, D. R. *Synthesis* **1979**, 819.
96. Parker, V. D. *Acct. Chem. Res.* **1984**, *17*, 243.
97. (a) Gassman, P. G.; Bottorff, K. J. *J. Am. Chem. Soc.* **1987**, *109*, 7546. (b) Gassman, P. G.; De Silva, S. A. *J. Am. Chem. Soc.* **1991**, *113*, 9870.
98. Schmittel, M. *Topics Curr. Chem.* **1994**, *169*, 183.
99. (a) Schmittel, M.; Roeck, M. *Chem. Ber.* **1992**, *125*, 1611. (b) Schmittel, M.; Gescheidt, G.; Roeck, M. *Angew. Chem. Int. Ed. Engl.* **1994**, *33*, 1961. (c) Schmittel, M.; Levis, M. *Chem. Lett.* **1994**, 1935, 1939. (d) Schmittel, M.; Keller, M.; Burghat, A. *J. Chem. Soc. Perkin Trans. 2* **1995**, 2327. (e) Schmittel, M.; Jürgen, H.; Trenkle, H. *J. Org. Chem.* **1995**, *60*, 2736. (f) Schmittel, M.; Langels, A. *Liebigs Ann.* **1996**, 999.
100. Gebicki, J.; Bally, T. *Acct. Chem. Res.* **1997**, *30*, 477.
101. (a) Schäfer, H.; Alazrak, A. *Angew. Chem. Int. Ed. Engl.* **1968**, *7*, 474. (b) Schäfer, H.; Alazrak, A. *Chem. Ber.* **1972**, *105*, 2398. (c) Schäfer, H. *Angew. Chem. Int. Ed. Engl.* **1981**, *20*, 911.
102. Torii, S.; Uneyama, K.; Onishi, T.; Fujita, Y.; Ishiguro, M.; Nishida, T. *Chem. Lett.* **1980**, 1603.
103. (a) Shono, T.; Matsumura, Y.; Nakagawa, Y. *J. Am. Chem. Soc.* **1974**, *96*, 3532. (b) Okawa, M.; Nishiguchi, I.; Yokoyama, T.; Nitta, M. *Chem. Lett.* **1975**, 4323. (c) Shono, T.; Nishiguchi, I. *J. Am. Chem. Soc.* **1975**, *97*, 6144. (d) Shono, T.; Nishiguchi, I.; Nitta, M. *Chem. Lett.* **1976**, 1319. (e) Shono, T.; Nishiguchi, I.; Kashimura, S.; Okawa, M. *Bull. Soc. Chem. Japan* **1978**, *51*, 2181. (f) Shono, T.; Kashimura, S. *J. Org. Chem.* **1983**, *48*, 1939.
104. (a) Ledwith, A. *Acct. Chem. Res.* **1972**, *5*, 133, and references therein. (b) Shirota, Y. *Photo-induced Electron Transfer*, Fox, M.A.; Chanon, M., Eds.; Part D, Elsevier: Amsterdam, 1988, 441.
105. Bauld, N. L.; Bellville, D. A.; Harirchian, B.; Lorenz, K. T.; Pabon, R. A., Jr.; Reynolds, D. W.; Wirth, D. D.; Chiou, H.-S.; Marsh, B. K. *Acct. Chem. Res.* **1987**, *20*, 371, and references therein.
106. (a) Schmittel, M.; Soehrlé, C. *Tetrahedron Lett.* **1993**, *34*, 8431. (b) Schmittel, M.; von Seggern, H. *J. Am. Chem. Soc.* **1993**, *115*, 2162. (c) Schmittel, M.; von Seggern, H. *Liebigs Ann.* **1995**, 1815. (d) Schmittel, M.; Woehrlé, C.; Bohn, I. *Chem.—Eur. J.* **1996**, *2*, 1031.
107. Roth, H. D.; Schilling, M. L.; Abelt, C. J. *J. Am. Chem. Soc.* **1986**, *108*, 6098.
108. Gassman, P. G.; Singleton, D. A. *J. Am. Chem. Soc.* **1984**, *106*, 7993.
109. Wilson, R. M.; Dietz, J. G.; Shepherd, T. A.; Ho, D. M.; Schnapp, K. A.; Elder, R. C.; Watkins, J. W., II; Geraci, L. S.; Campana, C. F. *J. Am. Chem. Soc.* **1989**, *111*, 1749.
110. (a) Nelsen, S. F. *Acct. Chem. Res.* **1987**, *20*, 269. (b) Nelsen, S. F. *Advances in Oxygenated Processes*, Vol. 2, Baumstark, A.L., Ed.; JAI: Greenwood, CT, 1990, 153.
111. Nelsen, S. F.; Klein, S. J.; Trieber, D. A., II; Ismagilov, R. F.; Powell, D. R. *J. Org. Chem.* **1997**, *62*, 6539.
112. Nelsen, S. F.; Teasley, M. F.; Kaftory, M. *J. Org. Chem.* **1988**, *52*, 5930.
113. Barton, D. H. R.; LeClerc, G.; Magnus, P. D.; Menzies, I. D. *J. Chem. Soc. Perkin Trans. 1* **1975**, 2055.
114. (a) Dai, S.; Pappas, R. S.; Chen, G.-F.; Guo, Q.-X.; Wang, J. T.; Williams, F. *J. Am. Chem. Soc.* **1989**, *111*, 8759. (b) Williams, F.; Guo, Q. X.; Debout, D. C.; Carpenter, B. K. *J. Am. Chem. Soc.* **1989**, *111*, 4133.
115. For older work, see Chow, Y. L.; Danen, W. C.; Nelsen, S. F.; Rosenblatt, D. H. *Chem. Rev.* **1978**, *78*, 243.
116. Miwa, G. T.; Walsh, J. S.; Kedderis, G. L.; Hollenberg, P. F. *J. Biol. Chem.* **1983**, *258*, 1445.
117. Dinnocenzo, J. P.; Banach, T. E. *J. Am. Chem. Soc.* **1989**, *111*, 8646.
118. Parker, V. D.; Tilset, M.; *J. Am. Chem. Soc.* **1991**, *113*, 8778.
119. (a) Xu, W.; Mariano, P. S. *J. Am. Chem. Soc.* **1991**, *113*, 1431. (b) Xu, W.; Zhang, X.-M.; Mariano, P. S. *J. Am. Chem. Soc.* **1991**, *113*, 8863.

120. (a) Dinnocenzo, J. P.; Karki, S. B.; Jones, J. P. *J. Am. Chem. Soc.* **1993**, *115*, 7111. (b) Karki, S. B.; Dinnocenzo, J. P.; Jones, J. P.; Korzekwa, K. R. *J. Am. Chem. Soc.* **1995**, *117*, 3205. (c) Manchestyer, J. I.; Dinnocenzo, J. P.; Higgins, L. A.; Jones, J. P. *J. Am. Chem. Soc.* **1997**, *119*, 5069.
121. Goto, Y.; Watanabe, Y.; Fukuzumi, S.; Jones, J. P.; Dinnocenzo, J. P. *J. Am. Chem. Soc.* **1998**, *120*, 10762.
122. Anne, A.; Fraoua, S. Grass. V.; Moiroux, J.; Savéant, J.-M. *J. Am. Chem. Soc.* **1998**, *120*, 2951.
123. (a) Nelsen, S. F. *Acc. Chem. Res.* **1981**, *14*, 131. (b) Nelsen, S. F. in *Molecular Structures and Energetics*; Liebman, J. F.; Greenberg, A., Eds.; VCH: Deerfield Beach, FL, 1986, Vol. 3, Ch. 1, p. 1. (c) Nelsen, S. F. in *Advances in Electron Transfer Chemistry*, Vol. 3, Mariano, P. S., Ed., JAI: Greenwich, CT, 1993, p. 167.
124. For a review of work on metal-centered systems in nonaqueous solvents, see: Wherland, S. *Coord. Chem. Rev.* **1993**, *123*, 169.
125. (a) Bruce, C. R.; Noerbert, R. E.; Weissman, S. I. *J. Chem. Phys.* **1956**, *24*, 473. (b) McConnell, H. M.; Weaver, H. E. *J. Chem. Phys.* **1956**, *25*, 307. (c) McConnell, H. M.; Berger, S. B. *J. Chem. Phys.* **1957**, *27*, 230.
126. Britt, A. D. *J. Chem. Phys.* **1964**, *41*, 3069.
127. (a) Grampp, G.; Jaenicke, W. *Ber. Bunsenges. Phys. Chem.* **1984**, *88*, 325. (b) Grampp, G.; Jaenicke, W. *Ber. Bunsenges. Phys. Chem.* **1984**, *88*, 335. (c) Grampp, G.; Jaenicke, W. *Ber. Bunsenges. Phys. Chem.* **1991**, *95*, 904.
128. (a) Nelsen, S. F.; Blackstock, S. C.; Kim, Y. *J. Am. Chem. Soc.* **1987**, *109*, 677. (b) Nelsen, S. F.; Wang, Y. *J. Org. Chem.* **1994**, *59*, 1655. (c) Nelsen, S. F.; Chen, L.-J.; Ramm, M. T.; Voy, G. T.; Powell, D. R.; Accola, M. A.; Seehafer, T.; Sabelko, J.; and Pladziewicz, J. R. *J. Org. Chem.* **1996**, *61*, 1405.
129. (a) Nelsen, S. F.; Ismagilov, R. F.; Chen, L.-J.; Brandt, J. L.; Chen, X.; Pladziewicz, J. R. *J. Am. Chem. Soc.* **1996**, *118*, 1555. (b) Nelsen, S. F.; Tran, H. Q.; Ismagilov, R. F.; Ramm, M. T.; Chen, L.-J.; Powell, D. R. *J. Org. Chem.* **1998**, *63*, 2536.
130. (a) Nelsen, S. F.; Wang, Y.; Ramm, M. T.; Accola, M. A.; Pladziewicz, J. R. *J. Phys. Chem.*, **1992**, *96*, 10654. (b) Nelsen, S. F.; Ramm, M. T.; Ismagilov, R. F.; Nagy, M. A.; Trieber, D. A., II; Powell, D. R.; Chen, X.; Gengler, J. J.; Qu, Q.; Brandt, J. L.; Pladziewicz, J. R. *J. Am. Chem. Soc.* **1997**, *119*, 5900. (c) Nelsen, S. F.; Ismagilov, R. F.; Gentile, K. E.; Nagy, M. A.; Tran, H. Q.; Qu, Q.; Halfen, D. T.; Oldegard, A. L.; Pladziewicz, J. R. *J. Am. Chem. Soc.* **1998**, *120*, 8230. (d) Pladziewicz, Nelsen, and coworkers, in preparation.
131. (a) Yang, E. S.; Chan, M.-S.; Wahl, A. C. *J. Phys. Chem.* **1980**, *84*, 3094. (b) McManis, G. E.; Nielson, R. M.; Gochev, A.; Weaver, M. J. *J. Am. Chem. Soc.* **1989**, *111*, 5533. (c) Nielson, R. M.; McManis, G. E.; Safford, L. K.; Weaver, M. J. *J. Phys. Chem.* **1989**, *93*, 2152. (d) Kirchner, K.; Dang, K.-S.; Stebler, M.; Dodgen, H. W.; Wherland, S.; Hunt, J. P. *Inorg. Chem.* **1989**, *28*, 3604.
132. Closs, G. L.; Miller, J. R. *Science* **1988**, *240*, 440.
133. Miller, J. R.; Paulson, B. P.; Bal, R.; Closs, G. L. *J. Phys. Chem.* **1995**, *99*, 6923.
134. (a) Paulson, B.; Pramod, K.; Eaton, P.; Closs, G.; Miller, J. R. *J. Phys. Chem.* **1993**, *97*, 13042. (b) Paulson, B. P.; Curtiss, L. A.; Bal, B.; Closs, G. L.; Miller, J. R. *J. Am. Chem. Soc.* **1996**, *118*, 378.
135. Warman, J. M.; de Haas, M. P.; Verhoeven, J. W.; Paddon-Row, M. N. *Adv. Chem. Phys.* **1999**, *106*, 571–589 and references therein.
136. Penfield, K. W.; Miller, J. R.; Paddon-Row, M. N.; Cotsaris, E.; Oliver, A. M.; Hush, N. S. *J. Am. Chem. Soc.* **1987**, *109*, 5061.
137. (a) Oevering, H.; Verhoeven, J. W.; Paddon-Row, M. N.; Warman, J. M. *Tetrahedron* **1989**, *45*, 4751. (b) Paddon-Row, M. N.; Verhoeven, J. W. *New J. Chem.* **1991**, *15*, 107. (c) Verhoeven, J. H. *Adv. Chem. Phys.* **1999**, *106*, 603–644 and references therein.
138. Warman, J. M.; Smit, K. J.; Jonker, S. A.; Paddon-Row, M. N.; Oliver, A. M.; Kroon, J.; Oevering, H.; Verhoeven, J. W. *J. Phys. Chem.* **1991**, *95*, 1979.
139. Bixon, M.; Jortner, J.; Verhoeven, J. W. *J. Am. Chem. Soc.* **1994**, *116*, 7349.
140. (a) Zeng, Y.; Zimmt, M. B. *J. Phys. Chem.* **1992**, *96*, 8395. (b) Cave, R. J.; Newton, M. D.; Kumar, K.; Zimmt, M. B. *J. Phys. Chem.* **1995**, *99*, 17501–4. (c) Kumar, K.; Lin, Z.; Waldek,

- D. H.; Zimmt, M. B. *J. Am. Chem. Soc.* **1996**, *118*, 243. (d) Han, H.; Zimmt, M. B. *J. Am. Chem. Soc.* **1998**, *120*, 8001–8002. (e) Kumar, K.; Kurnikov, I. V.; Beratan, D. N.; Waldeck, D. H.; Zimmt, M. B. *J. Phys. Chem. A* **1998**, *102*, 5529.
141. (a) Jolliffe, K. A.; Bell, T. D. M.; Ghiggino, K. P.; Langford, S. J.; Paddon-Row, M. N. *Angew. Chem. Int. Ed.* **1998**, *37*, 916. (b) Jolliffe, K. A.; Langford, S. J.; Ranasinge, M. G.; Shepard, M. J.; Paddon-Row, M. N. *J. Org. Chem.* **1999**, *64*, 1238.
142. (a) Wegewijs, B.; Hermant, R. M.; Verhoeven, J. W.; Kunst, A. G. M.; Rettschnick, R. P. H. *Chem. Phys. Lett.* **1987**, *140*, 587. (b) Wegewijs, B.; Ng, A. K. F.; Rettschnick, R. P. H.; Verhoeven, J. W. *Chem. Phys. Lett.* **1992**, *200*, 357. (c) Wegewijs, B.; Verhoeven, J. W.; Bralavsky, S. E. *J. Phys. Chem.* **1996**, *100*, 8890.
143. (a) Robin, M. B.; Day, P. *Adv. Inorg. Radiochem.* **1967**, *10*, 247. (b) Cowan, D. O.; LeVanda, C.; Park, J.; Kaufman, F. *Acct. Chem. Res.* **1973**, *6*, 1.
144. (a) Paddon-Row, M. N.; Patney, H. K.; Brown, R. S.; Houk, K. N. *J. Am. Chem. Soc.* **1981**, *103*, 5575. (b) Paddon-Row, M. N. *Acct. Chem. Res.* **1982**, *15*, 245. (c) Hush, N. S. *Coord. Chem. Rev.* **1985**, *64*, 135.
145. Nelsen, S. F.; Tran, H. Q.; Nagy, M. A. *J. Am. Chem. Soc.* **1998**, *120*, 298.
146. (a) Schroeder, A. H.; Mazur, S. *J. Am. Chem. Soc.* **1978**, *100*, 7339. (b) Föderer, P.; Gerson, F.; Heinzer, J.; Mazur, S.; Ohya-Nishiguchi, H.; Schroder, A. H. *J. Am. Chem. Soc.* **1979**, *101*, 2275.
147. (a) Ballester, M.; Pascual, I.; Torres, J. *J. Org. Chem.* **1990**, *55*, 3035. (b) Ballester, M.; Pascual, I.; Riera, J.; Castañer, J. *J. Org. Chem.* **1991**, *56*, 217. (c) Castañer, J.; Riera, J. (c) Castañer, J.; Riera, J. *J. Org. Chem.* **1991**, *56*, 5445. (d) Ballester, M.; Pascual, I.; Carreras, C.; Vidal-Gancedo, J. *J. Am. Chem. Soc.* **1994**, *116*, 4205. (e) Veciana, J.; Rovira, C.; Crespo, M. I.; Armet, O.; Domingo, V. M.; Palacio, F. *J. Am. Chem. Soc.* **1991**, *113*, 2552. (f) Veciana, J.; Rovira, C.; Ventosa, N.; Crespo, M. I.; Palacio, F. *J. Am. Chem. Soc.* **1993**, *115*, 57.
148. (a) Jozeriak, T. H.; Almlöf, J. E.; Feyereisen, M. W.; Miller, L. L. *J. Am. Chem. Soc.* **1989**, *111*, 4105. (b) Almlöf, J. E.; Feyereisen, M. Y.; Jozefiak, T. H.; Miller, L. L. *J. Am. Chem. Soc.* **1990**, *112*, 1206. (c) Rak, S. F.; Jozeriak, T. H.; Miller, L. L. *J. Org. Chem.* **1990**, *55*, 4794. (d) Rak, S. F.; Miller, L. L. *J. Am. Chem. Soc.* **1992**, *114*, 1388.
149. (a) Bonvoisin, J.; Launay, J.-P.; Van der Auweraer, M.; De Schryver, F. J. *J. Phys. Chem.* **1994**, *98*, 5052; **1996**, *100*, 18006. (b) Bonvoisin, J.; Launay, J.-P.; Rovira, C.; Veciana, J. *Angew. Chem. Int. Ed. Engl.* **1994**, *33*, 2106. (c) Lahil, K.; Moradpour, A. Bowlas, C.; Menou, F.; Cassoux, P.; Bonvoisin, J.; Launay, J.-P.; Dive, G.; Dehareng, D. *J. Am. Chem. Soc.* **1995**, *117*, 9995. (d) Bonvoisin, J.; Launay, J.-P.; Verbouwe, W.; Van der Auweraer, M.; Dwe Schryver, F. C. *J. Phys. Chem.* **1996**, *100*, 17079. (e) Stickley, K. R.; Blackstock, S. C. *J. Am. Chem. Soc.* **1994**, *116*, 11576. (f) Stickley, K. R.; Blackstock, S. C. *Tetrahedron Lett.* **1996**, *36*, 1585. (f) Stickley, K. R.; Blackstock, S. C. *Mol. Cryst. Liq. Cryst. A* **1995**, *271*, A.81. (g) Stickley, K. R.; Shelby, T. D.; Blackstock, S. C. *J. Org. Chem.* **1997**, *62*, 1498. (h) Shelby, T. D.; Blackstock, S. C. *J. Am. Chem. Soc.* **1998**, *120*, 12155.
150. (a) Lambert, C.; Nöll, G. *Angew. Chem. Int. Ed. Engl.* **1998**, *37*, 2107. (b) Lambert, C.; Nöll, G. *J. Am. Chem. Soc.* **1999**, *121*, 8434.
151. (a) Nelsen, S. F.; Chang, H.; Wolff, J. J.; Adamus, J. *J. Am. Chem. Soc.* **1993**, *115*, 12276. (b) Nelsen, S. F.; Ramm, M. T.; Wolff, J. J.; Powell, D. R. *J. Am. Chem. Soc.* **1997**, *119*, 6863. (c) Nelsen, S. F.; Adamus, J.; Wolff, J. J. *J. Am. Chem. Soc.* **1994**, *116*, 1589. (d) Nelsen, S. F. *J. Am. Chem. Soc.* **1996**, *118*, 2047.
152. Nelsen, S. F.; Trieber, D. W., II; Wolff, J. J.; Powell, D. R.; Rogers-Crowley, S. J. *Am. Chem. Soc.* **1997**, *119*, 6873.
153. (a) Nelsen, S. F.; Ismagilov, R. F.; Powell, D. R. *J. Am. Chem. Soc.* **1996**, *118*, 6313. (b) Nelsen, S. F.; Ismagilov, R. F.; Powell, D. R. *J. Am. Chem. Soc.* **1997**, *119*, 10213. (c) Nelsen, S. F.; Ismagilov, R. F. *J. Am. Chem. Soc.* **1999**, *121*, 7108. (d) Nelsen, S. F.; Ismagilov, R. F. *J. Phys. Chem. A* **1999**, *103*, 5373.
154. Nelsen, S. F.; Ismagilov, R. F.; Trieber, D. A., II *Science* **1997**, *278*, 846.
155. Nelsen, S. F.; Ismagilov, R. F.; Teki, Y. *J. Am. Chem. Soc.* **1998**, *120*, 2200.
156. Nelsen, S. F.; Ismagilov, R. F.; Powell, D. R. *J. Am. Chem. Soc.* **1998**, *120*, 1924.
157. Barbara, P. F.; Meyer, T. J.; Ratner, M. A. *J. Phys. Chem.* **1996**, *100*, 13148.
158. Elliott, C. M.; Derr, D. L.; Matyushov, D. V.; Newton, M. D. *J. Am. Chem. Soc.* **1998**, *120*, 11714.

Volume I

Part 2

Methods and Techniques

1 Classical Methods

Andreja Bakac

1.1 Introduction

The methods described in this chapter are used to study solution reactions that take place within a wide range of timescales, from several microseconds to several days or longer. In the present context, the word “classical” is used to describe reactions between chemical species that are either stable and used as such or generated in a chemical reaction in a rapid pre-mixing step which does not use radiation, photochemical or electrochemical sources.

Standard methods and techniques are covered and examples of chemical reactions are provided to illustrate the applicability of a particular method/technique to specific chemical systems and to demonstrate the utility of the information obtained in deciphering the mechanism. It is not the purpose of this chapter to provide an in-depth review of the chemistry involved.

For the most part, the methods described allow direct observation of reactants, products, or intermediates by monitoring the change in some physical property, such as absorbance, electrical conductivity, NMR and so forth. In addition, there is a section on indirect methods and special cases to describe competition reactions and slow exchange reactions, that is, those reactions not amenable to study by NMR or ESR line broadening.

Unless stated otherwise, the rate constants are quoted at 298 K.

1.2 Mixing Methods

1.2.1 Manual Mixing

For reactions requiring more than about a minute for completion, the reactants are mixed manually, and concentration changes are monitored by spectroscopic, elec-

trochemical, or chemical methods [1]. Electron-transfer reactions often are accompanied by optical absorbance changes in the visible and/or UV range, which makes the spectrophotometric monitoring of the reaction progress especially convenient. The actual handling of the solutions, especially if an air-free atmosphere is desired, often involves the use of syringe-septa techniques. The reaction is initiated by injection of the last reagent through the septum, and the absorbance changes are followed either at a single wavelength or by use of a rapid-scan instrument which can collect data over a range of wavelengths in a short time.

The most common type of rapid-scan instruments, diode array, utilizes an array of detectors and reverse optics, that is, the light is dispersed after it passes through the sample. Such instruments can collect a spectrum in a fraction of a second, thus ensuring that the solution composition remains unchanged during the acquisition time, provided the half-time for the reaction is longer than several seconds. In the example shown in Figure 1, the spectra of a decaying Cr^{V} complex [2] were collected by use of a diode array spectrometer over a period of 30 s.

Another type of rapid-scan instrument uses a combination of a spinning grating and single detector.

Over the past two decades, spectrophotometers have become much smaller and lighter owing to the use of compact modern electronics and sturdy, but lightweight housings made of synthetic materials. The instruments are routinely operated by use of computers which also digitize the data and calculate rate constants.

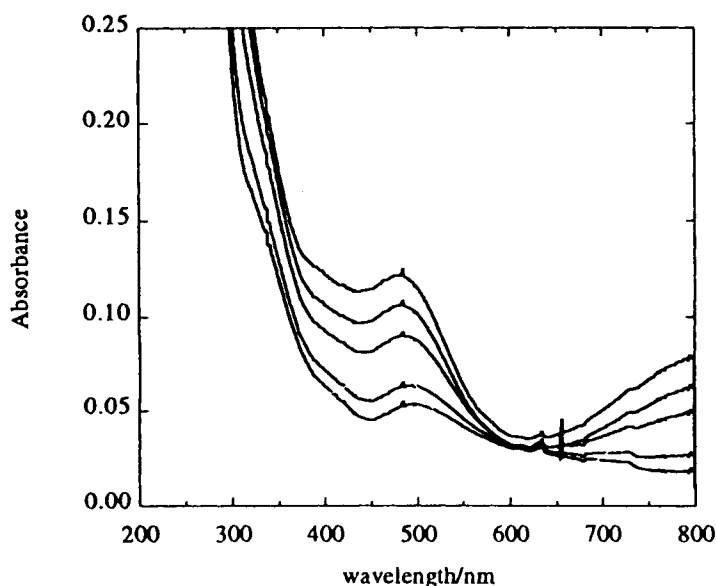


Figure 1. The decay of $[\text{14}]\text{aneN}_4\text{CrO}^{3+}$ as studied by use of a diode array spectrophotometer. The spectra, from top to bottom, were taken 3, 8, 12, 20, and 30 seconds after the initiation of the reaction. (Previously unpublished data from the author's laboratory).

The constant temperature in the cell compartment is maintained with circulating thermostatted water through the cell holder or by use of a specially designed cell holders with thermoelectric temperature control.

Data treatment consists of the fitting of single-wavelength data to appropriate kinetic equations. Global analysis is required for complicated, multistep reactions. Global analysis packages are provided these days almost routinely by instrument manufacturers.

1.2.2 Rapid Mixing

For the reactions reaching completion in less than a minute, the manual mixing of the reagents and the initiation of data acquisition would overlap with the chemical reaction. A number of rapid mixing and relaxation techniques are available to cover these shorter timescales, as described below.

Continuous flow

This method operates under steady-state conditions which makes it possible to measure high reaction rates with slow detection methods. The fast streams of two reactant solutions flow from the loading syringes into the mixing chamber. From there, the reaction solution passes through the observation chamber and is finally disposed into the waste receptacle. The reagents are continuously replenished and the spectroscopic measurements are done at selected points along the observation tube. At a constant flow rate, these points represent different times. Alternatively, the measurements can be done at a fixed point and the time variation achieved by varying the flow rate. Reactions with half-lives of 1 ms or longer can be measured by this technique owing to the availability of efficient mixing chambers [1].

One of the problems with classical continuous-flow instruments is the large volume of reactants needed for each kinetic run (10–100 mL), although this requirement has already been greatly reduced from the early days when several liters of solution was needed [1].

In a modification of the continuous-flow method known as “continuous-flow method with integrating observation (CFMIO)” [3] the mixer is incorporated into the observation tube and the reaction is monitored along the flow path rather than perpendicular to it. In this mode, the observation begins immediately after the reactants enter the mixing/observation tube; this dramatically extends the upper limit of the rate constants than can be measured. Also, the signal is improved by the increased path length.

Kinetic equations have been derived for the calculation of rate constants from measured absorbancies, the flow rate, and known spectral data for reactants and products [4]. For an ideal mixer, the expression for the first-order rate constant is given by Eq. 1,

$$k = \epsilon v/l \quad (1)$$

where v is the flow velocity, l the path length, and ε is defined in Eq. 2.

$$\frac{\text{Abs}_v - \text{Abs}_{\text{inf}}}{\text{Abs}_0 - \text{Abs}_{\text{inf}}} = \frac{1 - e^{-\varepsilon}}{\varepsilon} \quad (2)$$

Here Abs_v is the measured absorbance at a given velocity, and Abs_0 and Abs_{inf} are the absorbances corresponding to the reactants and products, respectively.

For second-order reactions with equal concentrations of the reactants, the corresponding expressions are given in Eqs 3 and 4,

$$k = \varepsilon v[A]_0/l \quad (3)$$

$$\frac{\text{Abs}_v - \text{Abs}_{\text{inf}}}{\text{Abs}_0 - \text{Abs}_{\text{inf}}} = \frac{\ln(1 + \varepsilon)}{\varepsilon} \quad (4)$$

where $[A]_0$ represents the initial concentration of the reagents.

A time resolution of approximately 10 μs is possible with the CFMIO method, although at such short times the mixing and chemical reaction take place simultaneously and the analysis becomes more complicated. Nonetheless, the method was used successfully in a study of the reactions of iron(III) and ruthenium(III) polypyridine complexes with several transition metal cyano compounds [3], but each experiment required approximately 300 mL of solution. The measured rate constants for electron transfer exceeded $3 \times 10^9 \text{ M}^{-1} \text{ s}^{-1}$.

The measuring cell which serves as a basis of the CFMIO method [3] can also be used in a stopped-flow mode by positioning of one or more observation channels perpendicular to the flow tube. This combined stopped-flow, continuous-flow method [5] was used to determine the effect of surface-active substances (sodium dodecyl sulfate or dodecyltrimethylammonium chloride) on electron-transfer reactions between metal complexes.

The technique of continuous flow was further improved and expanded with the introduction of pulsed flow, which uses short pulses of constant-velocity flow and cuts the reagent consumption to 3–4 mL per determination [6]. The combination of large flow velocities and short times was experimentally achieved by use of a special syringe ram assembly.

The instrument uses a radial mixer/observation cell shown in Figure 2. The reagents are introduced through alternating slits arranged around the observation tube and then travel through the tube at a rate of 2 m/s to 9 m/s.

This instrument was tested in a study of several electron-transfer reactions, including that between IrCl_6^{2-} and $\text{Fe}(\text{CN})_6^{4-}$ [6], $k = 4.1 \times 10^5 \text{ M}^{-1} \text{ s}^{-1}$. The data treatment according to the equations given above for pseudo-first-order conditions showed the calculated pseudo-first-order rate constants to be a function of flow velocity, the more so the higher the concentrations and reaction rates. This deviation from the expected behavior was rationalized by the effects of mixing and an empirical relationship was found between the true rate constant (k), the measured value (k_{obs}) and flow velocity, Eq. 5,

$$k_{\text{obs}} = k - (1/v)(mk/l) \quad (5)$$

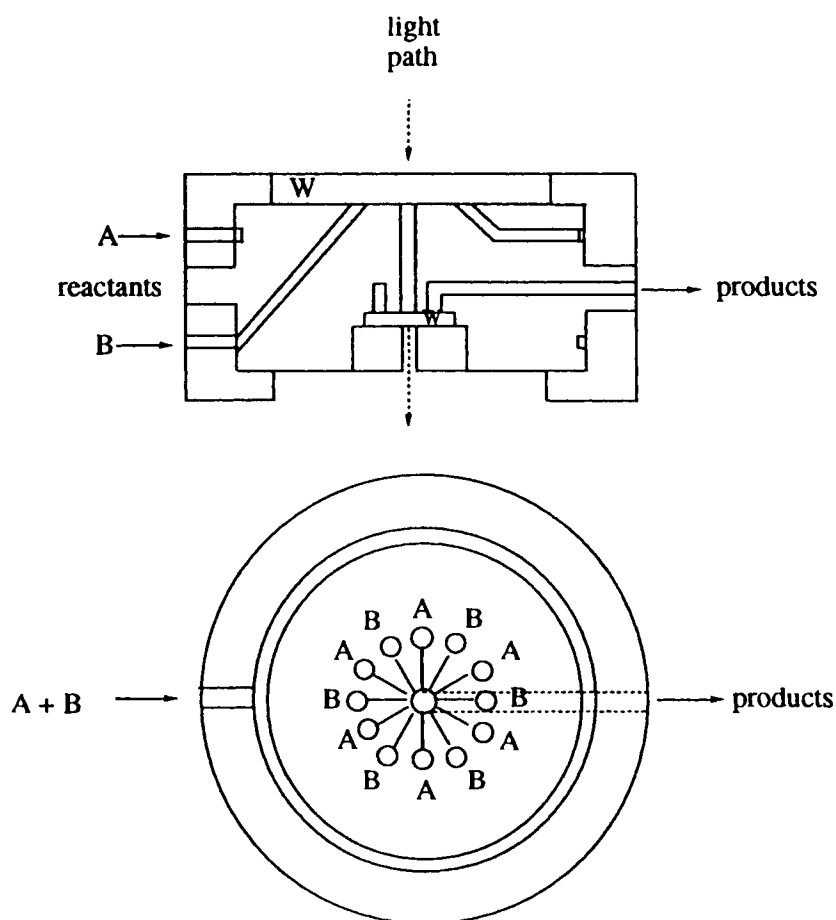


Figure 2. Top and end views of a radial mixer/observation cell used in pulse-accelerated-flow spectrometer. W, windows, A and B, reactants. Reproduced with permission from S. A. Jacobs, M. T. Nemeth, G.W. Kramer, T. Y. Ridley, and D. W. Margerum, *Anal. Chem.* 1984, 56, 1058. Copyright 1984 American Chemical Society.

such that the intercept of the k_{obs} vs $1/v$ plot gives k . In the above expression, m is a proportionality constant.

Under second-order conditions, calibration plots were necessary to extract the true rate constants from the observed values of $(\text{Abs}_v - \text{Abs}_{\text{inf}})/\text{Abs}_0 - \text{Abs}_{\text{inf}}$. The rate constants of $1.6 \times 10^9 \text{ M}^{-1} \text{ s}^{-1}$ for the reduction of $\text{Fe}(\text{phen})_3^{3+}$ by $\text{Fe}(\text{CN})_6^{4-}$ and $(0.11\text{--}2.5) \times 10^8 \text{ M}^{-1} \text{ s}^{-1}$ for a series of reactions between $\text{Cu}(\text{dmp})^+$ and copper(III) peptide complexes were obtained [6].

The pulsed-flow method evolved further into the pulsed-accelerated-flow method [7]. Here, the solutions have a range of flow velocities owing to the constant flow

acceleration during each push. Equation 6, where k_m is a mixing proportionality constant, is applicable to both pseudo-first- and second-order conditions.

$$1/k_{\text{obs}} = 1/k + 1/k_{\text{mix}} = 1/k + 1/k_m v \quad (6)$$

Rate constants as high as $1.2 \times 10^5 \text{ s}^{-1}$ and $2 \times 10^9 \text{ M}^{-1} \text{ s}^{-1}$ were measured with a special twin-path cell. Even higher rate constants (up to $5 \times 10^5 \text{ s}^{-1}$) were measured later, but data treatment became more complex, because an additional term, second-order in velocity, was found to contribute to mixing at such high rates [8].

Stopped flow

This is the most widely used of all the rapid-mixing techniques. The pistons of the drive syringes are pushed pneumatically to force the two reactant solutions through the tubing into the mixing chamber, from there into the observation chamber and finally into the stopping syringe, Figure 3. The flow is suddenly arrested as the piston hits a mechanical stop and simultaneously triggers the data-acquisition process. The observation post is perpendicular to the direction of the flow. Standard instruments mix equal volumes of the two reactant solutions, but it is possible to change the mixing ratio by use of syringes of different bore or by varying the travel distance of the two drive syringes [4].

Some of the early stopped-flow work concentrated on the oxidations of iron(II) complexes shown in Eqs. 7–9 [9, 10].

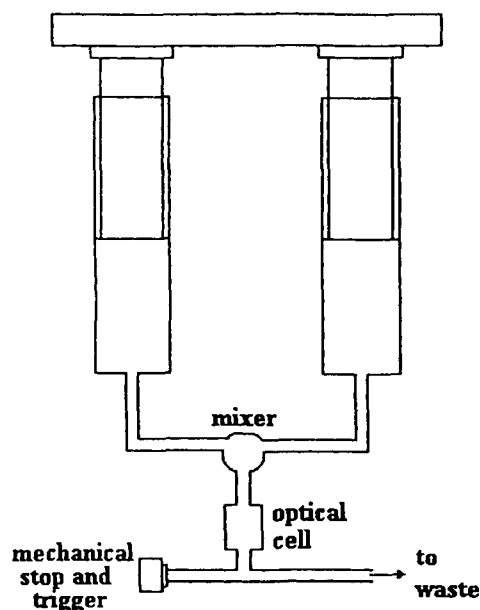
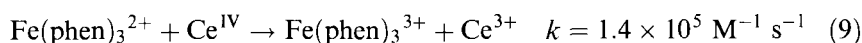


Figure 3. Schematics of a stopped-flow instrument.



The technique turned out to be extremely useful for kinetic determinations and the early home-made instruments were soon replaced by commercial products.

The limit for the measured rate constants is determined by the mixing rate and the instrument's dead time, defined as the time required for the solution to travel from the mixing chamber to the observation point. Nowadays, half-times in the millisecond range can be measured routinely. An extension of accessible rates up to 2000 s^{-1} through algebraic corrections for mixing effects was discussed [11]. Under the assumption that the behavior of the solution at short times after mixing in the stopped-flow is described by the same equations that were found applicable for pulsed-accelerated flow, the precise rate constant can be obtained from a set of experiments carried out under pseudo-first-order conditions by use of Eq. 10.

$$k_{\text{obs}} = k[\text{excess reagent}]/(1 + k[\text{excess reagent}]/k_{\text{mix}}) \quad (10)$$

The fit to this equation will provide values of k and the mixing constant k_{mix} , which is constant for a given instrument. The $\text{IrCl}_6^{2-}/\text{Fe}(\text{CN})_6^{4-}$ reaction was again used as a test case. The value, obtained by use of Eq. 10, was $4.2 \times 10^5 \text{ M}^{-1} \text{ s}^{-1}$. The good agreement with other determinations justifies and supports the assumptions made above.

In addition to standard methods of monitoring the reaction progress by UV and visible spectroscopies, other detection methods also can be used. For example, electron-transfer reactions between monomeric and dimeric metal carbonyl complexes in Eq. 11 have been studied by infrared stopped-flow spectroscopy utilizing a tunable CO laser as a source of infrared radiation and a HgCdGe detector [12].



In another study [13], rapid-scan infrared spectra were recorded over the course of the reaction between $\text{Fe}(\text{CO})_3(\text{PPh}_3)_2$ and I_2 in CHCl_3 . At a 1:1 ratio of reactants, the $\text{Fe}(\text{CO})_3(\text{PPh}_3)_2$ signal at 1878 cm^{-1} first disappeared but then slowly reappeared to the extent of 50 %. An intermediate was clearly observed in the spectrum at 2050 cm^{-1} . The data were interpreted by invoking the formation and subsequent disproportionation of a 19-electron iron(I) intermediate.

The stopped-flow mixing can be combined with a variety of detection methods in addition to spectrophotometry. A nice example is provided by a rapid-scanning EPR spectrometer in which the reagents are delivered from a stopped-flow mixer into an EPR cell. This action triggers the generation of a wave form to drive a rapid-scan unit. The rate constants are obtained from the digitized spectra [14].

The oxidation of phenol by ferrate(V) was studied by use of pre-mix (stopped-flow) pulse radiolysis [15]. To avoid complications from the thermal reaction be-

tween Fe^{VI} and phenol, the pulse was applied a short time (100 ms) after the mixing to generate Fe^{V} by reducing Fe^{VI} with hydrated electrons and hydroxyisopropyl radicals. The ensuing reaction between Fe^{V} and phenol, Eq. 12, proceeds in part by formation of an iron(III)-catechol complex and has an overall rate constant of $3.8 \times 10^5 \text{ M}^{-1} \text{ s}^{-1}$.



A combination of stopped-flow mixing and laser-flash photolysis of the newly generated species is finding increasing use in studies of biological reactions. In a recent example [16], a ferrocyanochrome $\text{a}_3\text{-CO}$ adduct was produced by the stopped-flow mixing of the fully reduced cytochrome caa_3 and CO. The follow-up photolysis caused rapid dissociation of CO. The recombination of the reduced ferrocyanochrome and CO, and the reaction with O_2 were then observed as kinetic steps.

An important development in stopped-flow spectrophotometry is sequential flow, whereby an intermediate is first generated in a pre-mix stage, and then allowed to react in the next step with the reagent of interest, as shown in Figure 4. Solutions A and B are mixed first, and the resulting mixture is allowed to flow into the aging loop. At this point, the flow is temporarily arrested to allow the reaction to go to completion. When the flow is resumed, the aged solution is mixed with reagent C from the third syringe and the observation begins. In principle, one could build a

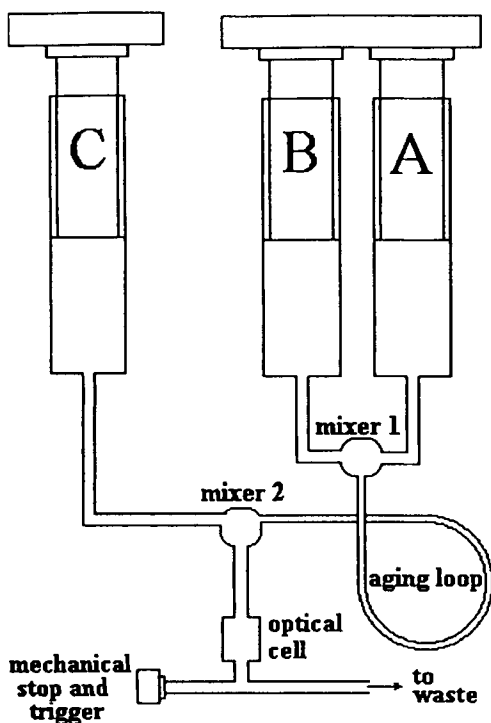
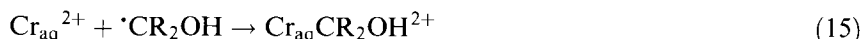
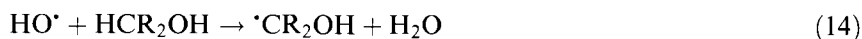
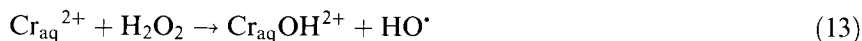


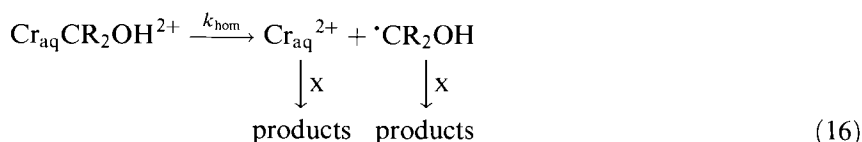
Figure 4. Schematics of a sequential stopped-flow instrument.

number of successive stages into such an instrument, and there are known examples of instruments with up to five mixers [17], but two mixers are much more typical. As an example, a detailed kinetic and thermodynamic study of the formation and subsequent homolysis of several short-lived organochromium complexes was made possible by use of three-syringe, two-mixer stopped-flow [18].

In the first stage, the organochromium complexes were generated in a Fenton-type scheme, Eqs. 13–15.



The organochromium ions were then mixed with a solution of a scavenger (X) for $\text{Cr}_{\text{aq}}^{2+}$ and/or $\cdot\text{CR}_2\text{OH}$. The rapid removal of homolysis fragments, Eq. 16, reversed the equilibrium of the reaction of Eq. 15, and led to direct measurement of k_{hom} ($\leq 300 \text{ s}^{-1}$).



1.3 Relaxation Methods

These methods are applicable to chemical reactions at equilibrium. If the equilibrium is suddenly perturbed by a change in temperature, pressure, or some other parameter, then the system will relax toward the new equilibrium position. The rate constants for the forward and reverse steps can be determined from the rate of relaxation [19, 20].

Another important source of perturbation of a chemical system is light, such as a laser flash. The irradiation can cause a rapid photochemical reaction, such as photolysis of a single bond. The reverse, thermal reaction will then regenerate the reactant(s). This method differs from the other relaxation methods mentioned above in that the relaxation process brings the system back to its initial state rather than to a new equilibrium. The amount of energy deposited with a flash is often large enough to temporarily perturb even an irreversible thermal system, which makes this technique applicable to both reversible and irreversible reactions. Flash photolytic methods are a subject of a later chapter and will not be dealt with here.

The data treatment and kinetic equations for relaxation kinetics have been developed and discussed in detail [1, 19–21]. For a set of two opposing first-order reactions, Eq. 17.



the relaxation is a first-order process and the observed rate constant is $k_1 + k_{-1}$, Eq. 18.

$$-dx/dt = (k_1 + k_{-1})x \quad (18)$$

Here x represents the displacement of the concentrations from the new equilibrium, Eq. 19.

$$x = [A] - [A]_{\text{eq}} = [P]_{\text{eq}} - [P] \quad (19)$$

In relaxation kinetics, reaction rates are often expressed in terms of relaxation time, which is the reciprocal of the rate constant, Eq. 20,

$$\tau = (k_1 + k_{-1})^{-1} \quad (20)$$

and represents the time necessary for the concentration to decrease to $1/e$ of its value.

For a system of two opposing first-order reactions one would expect first-order behavior, as experimentally observed. In relaxation kinetics, however, even non-first-order reactions will exhibit first-order kinetics provided the perturbation of the system is small enough so that higher-order terms in x can be neglected. For a system of opposing second- and first-order reactions, Eq. 21,



one can derive the rate law of Eq. 22.

$$-dx/dt = k_1 x^2 + (k_1[A]_{\text{eq}} + k_1[B]_{\text{eq}} + k_{-1})x \quad (22)$$

At small x , the term $k_1 x^2$ becomes negligible, and the relaxation time is given by Eq. 23.

$$\tau^{-1} = k_1([A]_{\text{eq}} + [B]_{\text{eq}}) + k_{-1} \quad (23)$$

In multistep reactions with n reversible steps, there will be n relaxation times, each of which will contain kinetic information on all the steps involved in the reaction.

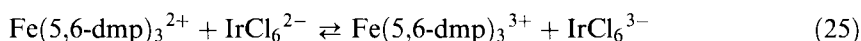
1.3.1 Temperature Jump

The size of the change in equilibrium constant with temperature is a function of ΔH° , as described by the van't Hoff equation, Eq. 24:

$$d(\ln K)/dT = \Delta H^\circ/RT^2 \quad (24)$$

In practice, a measurable change in concentration can be achieved with a temperature rise of 1–10 °C. As noted above, the concentration changes need to be small to reduce the kinetics to first-order behavior. The standard heat sources are thermostatted baths or electrical, microwave, or optical (laser) heating. The electric heating is often accomplished by a discharge of a capacitor through an electrically conducting solution ("Joule heating") [22–24], which limits the technique to polar solvents containing moderate to high concentrations of salts. Rise times of 1 μ s or less are not uncommon [23].

Temperature jump [25] with Joule heating was used in an early study of rapid outer-sphere electron-transfer reactions [22] between polypyridine metal complexes and hexachloro- and hexabromometalates, Eq. 25,



for which $k_f = 2.3 \times 10^8 \text{ M}^{-1} \text{ s}^{-1}$ and $k_r = 2.8 \times 10^9 \text{ M}^{-1} \text{ s}^{-1}$ at 10 °C. The data for this and related reactions were fitted to the Marcus equation for calculation of the reorganization energies ranging from 4 to 7 kcal/mol.

Microwave heating provides reasonable temperature jumps (≥ 1 °C) in 1 μ s, which is somewhat inferior to electrical heating. The method requires a solvent that absorbs in the microwave region of the spectrum. Most polar solvents are acceptable.

Optical heating uses a high-power pulsed laser and produces a reasonable increase in temperature in very short times (ps to μ s range). The reaction solutions must absorb at the wavelength of the laser pulse, usually in the near infrared [26]. Either the solvent or a solute can serve as the light-absorbing material. Clearly, the solute used for this purpose must not interfere with the chemical reaction being studied or with the detection method used. The absorbance of the solution has to be adjusted properly so that the temperature rise is significant, but the temperature gradient—always present when laser heating is used—not too steep. Strongly absorbing solutions cannot be used because the temperature rise is limited to a small segment of the solution at the front end of the cell. A block diagram of a laser-heated temperature-jump instrument is shown in Figure 5.

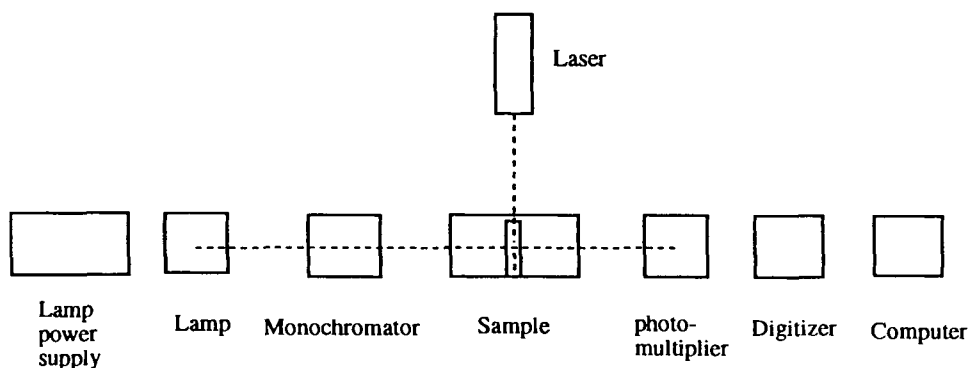
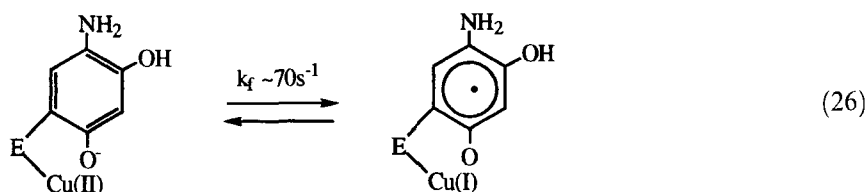


Figure 5. Block diagram of a laser-heated temperature-jump instrument.

In recent years, temperature-jump methods have been used widely in studies of enzymatic and biological electron transfer. These methods seem to be ideally suited for the task owing to the existence of finely balanced, easily perturbed equilibria in biological systems. Kinetic determinations are facilitated by the large molar absorptivities of most metalloenzymes, so that even small concentration changes provide measurable signals.

An example [27] is provided by the recent determination of the rate of intramolecular electron transfer in a copper-containing amine oxidase, $\text{Cu}^{\text{II}}\text{-topa}_{\text{NH}_2}/\text{Cu}^{\text{I}}\text{-topa}_{\text{SQ}}$, Eq. 26, where topa represents 3-(2,4,5-trihydroxyphenyl)-1-alanine.



The observed rate constant, $k_{\text{obs}} = 150 \text{ s}^{-1}$, was combined with an independently determined equilibrium constant (0.7–1) to calculate the forward rate constant $k_f \approx 70 \text{ s}^{-1}$.

To circumvent the equilibrium requirement, which is the greatest limitation of temperature jump, attempts have been made to combine this technique with some others. The stopped-flow temperature jump, for example, has found use in studies of reactions involving the formation of intermediates on not-too-short timescales ($\geq 10 \text{ ms}$) [23]. In this method, the temperature jump is applied during the course of the stopped-flow reaction. The equilibrium between the reactants and intermediates is perturbed, which permits a direct study of the fast steps occurring prior to the rate-determining step [28].

An adaptation of the temperature-jump method, named indirect laser-induced temperature jump [29], was used in studies of distance dependence of electron transfer at electrodes. A pulsed Nd:YAG laser was used to cause a sudden ($< 5 \text{ ns}$) change in temperature ($< 5 \text{ K}$) at an electrode/electrolyte interface. The increase in temperature causes a change in the open-circuit potential. The relaxation step is a function of the dissipation of thermal energy and the rate of electron transfer between the electrode and its redox partners.

The kinetics of electron transfer through ferrocene-terminated alkanethiol monolayers on a gold electrode were determined as a function of the number of methylene groups in the alkyl chain tethering the ferrocene to the electrode [29].

1.3.2 Pressure Jump

At a constant temperature, the dependence of the equilibrium constant on pressure (P) is given by Eq. 27.

$$d(\ln K)/dP = \Delta V^\circ/RT \quad (27)$$

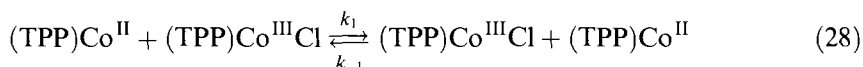
The molar volume change ΔV° is small for most reactions in solution, which requires large pressure changes (≥ 50 atm) for a measurable perturbation of an equilibrium [30]. This technique has not found much use in electron-transfer reactions, but various absorption–desorption phenomena, association–dissociation equilibria, and structural relaxations have been studied successfully. Pressure jump is also quite useful in biological studies of folding and unfolding of proteins and DNA owing to the pressure sensitivity of these processes [31].

1.3.3 Spin-Relaxation Methods

Spectroscopy and kinetics are related through the dimension of time—spectroscopy uses frequency, kinetics uses time. The interaction of the nuclear magnetic moment with an outside magnetic field forms the basis of NMR. In the closely related ESR, it is the electron's magnetic moment that interacts with the magnetic field.

NMR line broadening

Invaluable kinetic information has been obtained by NMR line broadening in exchange reactions [32] that occur on millisecond to submillisecond time scales. Not only is the technique applicable to solvent- and ligand-exchange processes, but also to electron exchange, even though paramagnetic species are involved. The nucleus that is being monitored resides on a ligand and is far removed from the metal center. This distance makes the signal reasonably sharp but shifted. The shift often facilitates the measurement by precluding the overlap between the signals for the two oxidation states. The width of the NMR signals associated with the ligand is a function of the time that the respective nucleus (^1H , ^{13}C , ^{15}N , ^{31}P , etc.) resides at a given site. The longer the residence time (i.e., the slower the electron exchange between the metals), the sharper the signals. As the temperature rises, the rate of exchange increases and the lines broaden and eventually coalesce. Finally, as the exchange rate increases even further, the signal becomes sharp once again. These changes in the appearance of the ^1H NMR spectrum with temperature are illustrated in Figure 6 [33] for an inner-sphere, chloride-bridged electron-exchange reaction (Eq. 28).



The observed signals correspond to the porphyrin methyl groups associated with Co^{II} and Co^{III} . The large downfield shift for $(\text{TPP})\text{Co}^{\text{II}}$ is caused by its paramagnetism.

There is no exchange at the lowest temperature (-32°C) and the *p*-methyl lines for both oxidation states are sharp. The second set of peaks in Figure 6 falls into the category of slow exchange where the broadening of the lines is already visible, but still much smaller than their separation. The line broadening is defined as the difference between the line width at half height between the exchange-broadened signal (W) and the signal obtained in the absence of exchange (W_0). In the slow-

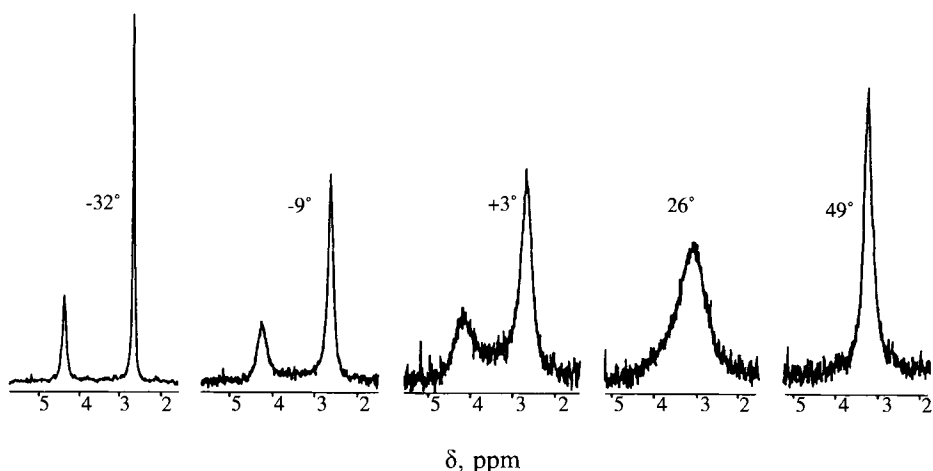


Figure 6. Temperature dependence of the *p*-methyl line shapes in 90-MHz ^1H NMR spectra of a mixture of $\text{Co}^{\text{II}}\text{TTP}$ and $\text{ClCo}^{\text{III}}\text{TTP}$ in CDCl_3 . Reproduced with permission from R. D. Chapman and E. B. Fleischer, *J. Am. Chem. Soc.* 1982, 104, 1582. Copyright 1982 American Chemical Society.

exchange region, the line broadening is directly related to the exchange rate constant by the expression in Eq. 29 (W in units s^{-1}).

$$(W - W_0) = 1/(\pi\tau) \quad (29)$$

The application of this equation to the above reaction in tetrahydrofuran gave $k_{\text{exch}} = 8.8 \times 10^3 \text{ M}^{-1} \text{ s}^{-1}$

This approach is commonly used for the determination of electron-exchange rate constants. Some of the recent examples include macrocyclic cobalt(III)/cobalt(II) couples [34] of the form $\text{LCo}(\text{OH}_2)\text{X}^{2+}/\text{LCo}(\text{OH}_2)_2^{2+}$ (L is the macrocyclic ligand, X = Cl, Br, and N_3), caged complexes $\text{Co}(\text{act})^{3+}/\text{Co}(\text{act})^{2+}$ [35], the couple $\text{Ru}(\text{en})_3^{3+}/\text{Ru}(\text{en})_3^{2+}$ [35], and copper(II)/copper(I) macrocyclic pentathiaether complexes [36].

The point of coalescence is also related to the exchange rate constants. For equal population of the two peaks, the expression is given in Eq. 30.

$$k_{\text{exch}} = \sqrt{2}\pi\omega_{1/2}^c \quad (30)$$

The term $\omega_{1/2}^c$ is the line width at half-height of the coalesced peak and is equal to the separation between the two peaks in the absence of exchange, $\delta\nu$. The exchange rate constants for the $(\text{TPP})\text{Co}^{\text{II}}/(\text{TPP})\text{Co}^{\text{III}}\text{Cl}$ reaction in CDCl_3 ($k = 2.7 \times 10^4 \text{ M}^{-1} \text{ s}^{-1}$) and C_6D_6 ($5.0 \times 10^5 \text{ M}^{-1} \text{ s}^{-1}$) were determined by this method [33].

For the fast-exchange region (following the coalescence stage), the line-shape

equation for the two-site system under steady-state conditions was derived [37] from the general line-shape equations, known as Bloch equations. In the absence of proton spin-spin coupling and in the limiting case when $2\pi(\delta\nu)\tau \ll 1$, the simplified expression in Eq. 31 applies.

$$W_{DP} = f_D W_D + f_P W_P + 4\pi f_P f_D (\delta\nu)^2 \tau \quad (31)$$

Here W_{DP} is the difference in the widths between the broadened and final lines, f_D and f_P are the proportions of the reactants present in the diamagnetic and paramagnetic states, respectively, and $\delta\nu$ is the contact shift.

This method was used to determine the rate constants from the line widths of the methyl peaks for the exchange reactions [37] of the couples $\text{Fe}(4,7\text{-Me}_2\text{phen})_3^{3+/2+}$ ($k = 1.4 \times 10^7 \text{ M}^{-1} \text{ s}^{-1}$ in acetonitrile) and $\text{Fe}(4,4'\text{-Me}_2\text{bpy})_3^{3+/2+}$ ($k = 6 \times 10^6 \text{ M}^{-1} \text{ s}^{-1}$). For $\text{Fe}(4,7\text{-ch}_2\text{phen})_3^{3+/2+}$, the line widths of the 5,6-proton peaks were used for the determination of $k_{\text{exch}} = 4.1 \times 10^5 \text{ M}^{-1} \text{ s}^{-1}$.

For several other complexes of iron and ruthenium with substituted polypyridine ligands, spin-spin coupling with nearby protons required that the line-shape analysis be done by use of Eqs. 32–36.

$$\text{AI} \propto \frac{\left(1 + \frac{\tau f_D}{T_{2P}} + \frac{\tau f_P}{T_{2D}}\right) S + QR}{S^2 + R^2} \quad (32)$$

$$Q = 2\pi\tau[\Delta\nu + (1 - f_P)\delta\nu] \quad (33)$$

$$S = \frac{\tau}{T_{2D}T_{2P}} + \frac{f_D}{T_{2D}} + \frac{f_P}{T_{2P}} - 4\pi^2\tau(\Delta\nu)(\Delta\nu + \delta\nu) \quad (34)$$

$$R = 2\pi\tau\left[\frac{(\Delta\nu + \delta\nu)}{T_{2D}} + \frac{\Delta\nu}{T_{2P}}\right] + 2\pi(\Delta\nu + f_P\delta\nu) \quad (35)$$

$$\Delta\nu = \nu_D - \nu \quad (36)$$

In these equations, AI is the absorption intensity, T_{2d} and T_{2P} are the transverse relaxation times for the two sites, ν_D is the resonance frequency of the diamagnetic site, and ν is the sweeping frequency. For a mixed second-order rate law, $\tau = 1/\{k_{\text{exch}}([D] + [P])\}$.

This treatment yielded the exchange rate constants for the couples $\text{Fe}(\text{bpy})_3^{3+/2+}$, $\text{Ru}(\text{bpy})_3^{3+/2+}$, $\text{Os}(\text{bpy})_3^{3+/2+}$, and several substituted derivatives. All the rate constants are of the order of 10^6 – $10^7 \text{ M}^{-1} \text{ s}^{-1}$ [37].

Clearly, the expressions in the fast and intermediate exchange region are complex [1, 38, 39], even when valid approximations can be made to simplify the equations. Moreover, a substantial experimental effort is sometimes required before it can be ascertained whether such simplifications are justified. The most reliable and probably the best method for the determination of exchange rate constants in nontrivial cases is the matching of experimental and calculated spectra by computer modeling.

ESR line broadening

“Heroic techniques are not required” [40] for the measurement of electron-transfer rates, even when they are close to the diffusion limit. The principles involved in ESR and NMR line broadening are very similar, but different frequencies are involved and the timescales differ. The ESR method allows the measurement of very short lifetimes (10^{-4} to 10^{-9} s).

As is the case with NMR, the ESR determinations are often carried out in the limit of slow exchange. The fast-exchange limit is difficult to reach experimentally because it requires inordinately high concentration of reagents (≥ 1 M), which exceeds the solubility limit of many compounds. Nonetheless, some electron-exchange constants, such as that between nitrobenzene radical anion and nitrobenzene have been measured in the limit of fast exchange [41]. In this example, the diamagnetic species, nitrobenzene, was used as solvent.

From the researcher’s point of view, the intermediate exchange region often provides the best conditions for line-broadening experiments [42], but data treatment requires computer simulations based on different theoretical models.

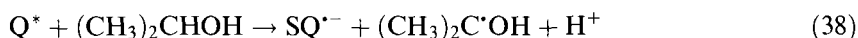
In the slow-exchange region, the rate information is obtained from the broadening of hyperfine components, as shown in Figure 7 for the reaction between $(\text{C}_6\text{H}_5\text{Cl})_2\text{Cr}^+$ and $(\text{C}_6\text{H}_5\text{Cl})_2\text{Cr}$ in dimethylsulfoxide, for which $k_{\text{exch}} = 2.0 \times 10^8 \text{ M}^{-1} \text{ s}^{-1}$ [43].

The reaction between $\text{Cr}(\text{bpy})_3^+$ and $\text{Cr}(\text{bpy})_3$, $k = 1.5 \times 10^9 \text{ M}^{-1} \text{ s}^{-1}$ in dmf, was measured [44] in the slow-exchange limit by use of Eq. 37.

$$k = 2.83 \times 10^6 \sqrt{3\pi} \Delta(\Delta H_{\text{pp}}) / [\text{Cr}(\text{bpy})_3] \quad (37)$$

where $\Delta(\Delta H_{\text{pp}})$ is the exchange-induced increase (in gauss) in the peak-to-peak line width of the first-derivative spectra. The above expression was derived in an earlier study of the electron exchange between naphthalene and naphthalene anions [45]. The factor 2.83×10^6 relates the field in oersteds to the frequency.

A study of several quinone/semiquinone reactions [46] used similar conditions (low-exchange limit) and an in situ photolysis–ESR flow instrument. The chemistry involved in the generation of semiquinones is shown in Eq. 38



where Q^* is the excited quinone and $\text{SQ}^{\bullet-}$ the corresponding semiquinone. The residence time of the solution in the cell was approximately 20 ms. The exchange rate constants k_{exch} in the range $6\text{--}20 \times 10^7 \text{ M}^{-1} \text{ s}^{-1}$ for various $\text{Q}/\text{SQ}^{\bullet-}$ couples were obtained by use of an equation that is essentially the same as that shown above except for an added line-intensity correction term.

For the examples discussed so far, continuous wave (cw) ESR was utilized, where the magnetic field is swept during the measurement. In the pulsed free induction decay attenuation method [47, 48], the sample in the applied steady field is subjected to a powerful microwave pulse which causes the tipping of the magnetization vector. This method is analogous to pulsed NMR measurements. After the pulse, the

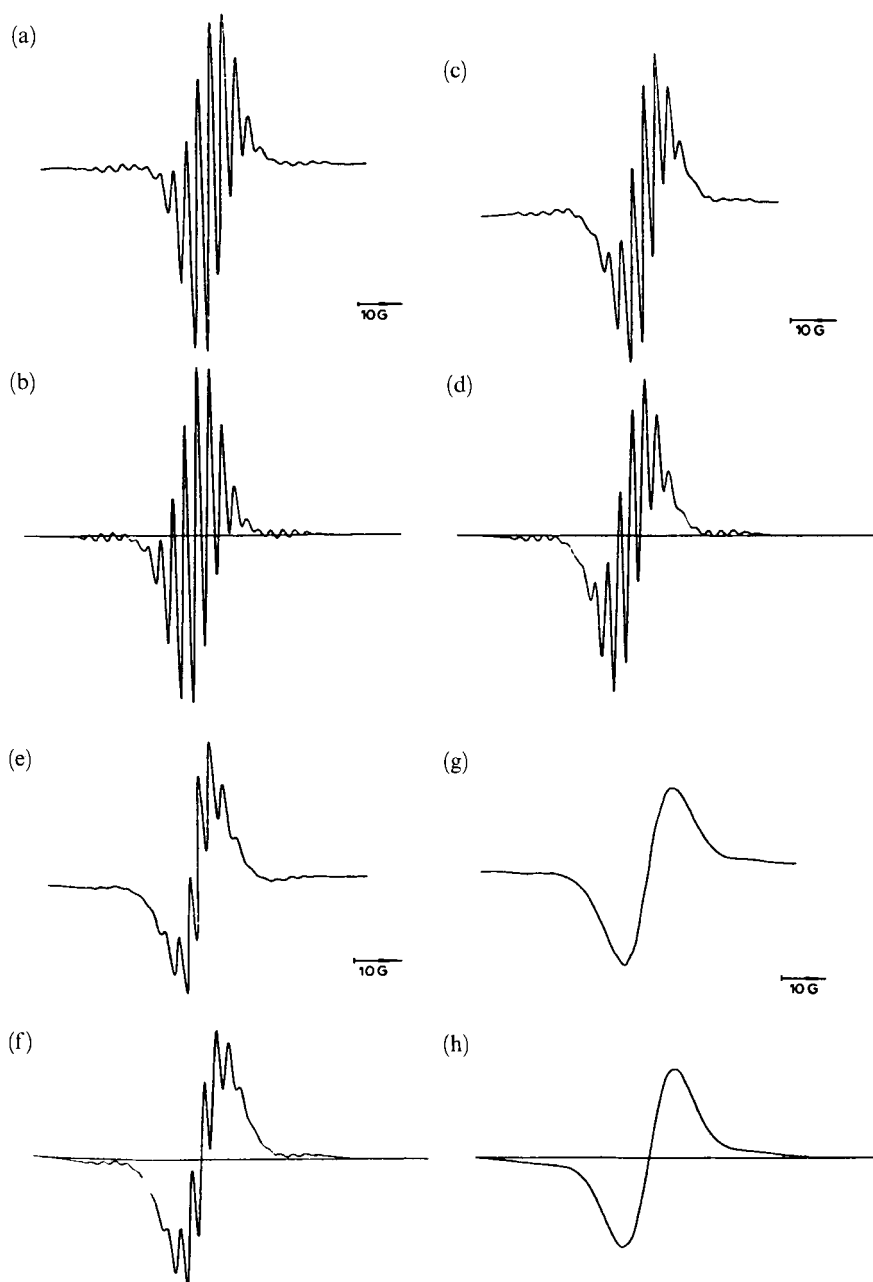
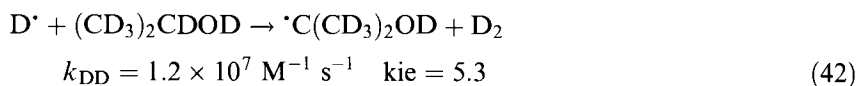
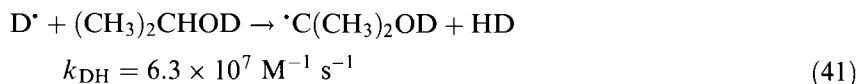
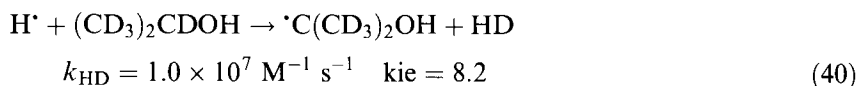
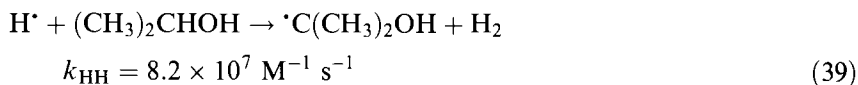


Figure 7. ESR spectra of 5.4×10^{-4} M $(\text{C}_6\text{H}_5\text{Cl})_2\text{Cr}^+$ in DMSO at 22°C . (a) No added $(\text{C}_6\text{H}_5\text{Cl})_2\text{Cr}^0$. (c) Added ca. 0.04 M $(\text{C}_6\text{H}_5\text{Cl})_2\text{Cr}^0$. (e) Added ca. 0.08 M $(\text{C}_6\text{H}_5\text{Cl})_2\text{Cr}^0$. (g) added ca. 0.1 M $(\text{C}_6\text{H}_5\text{Cl})_2\text{Cr}^0$. Panels (b), (d), (f), and (h) are computer simulations of the spectra immediately above them. Reprinted with permission from T. T.-T. Li and C. H. Brubaker, Jr., *J. Organomet. Chem.* 1981, 216, 223. Copyright 1981 Elsevier.

magnetization relaxes to its equilibrium position in a process known as free induction decay (FID). The EPR spectra are obtained by Fourier transformation of extrapolated FID's [49]. This method makes it possible to assign precise intensities and line widths [50] to each radical and was used recently in a study of hydrogen-atom abstraction from 2-propanol by hydrogen and deuterium atoms [49], produced by pulse radiolysis. The electron pulse triggered the ESR pulse unit and the detection system. The width of the microwave pulse was 40 ns, and the delay between electron pulse (duration 15 ns) and the microwave pulse was 0.4 μ s. The rate constants obtained and the associated kinetic isotope effects (kie) are summarized in Eqs 39–42.



1.4 High-Pressure Techniques

In studies of reaction kinetics at different temperatures, the enthalpies (ΔH^\ddagger) and entropies (ΔS^\ddagger) of activation are provided by the Eyring equation, Eq. 43.

$$k = \frac{k_{\text{B}}T}{h} e^{-(\Delta H^\ddagger/RT)} e^{-(\Delta S^\ddagger/R)} \quad (43)$$

These parameters are extremely useful for unraveling reaction mechanisms. The interpretation of ΔH^\ddagger for an elementary step is straightforward—it is the difference in heat contents between the reactants and transition state. The ΔS^\ddagger term, although defined clearly in the equation above, is much less tangible. It describes the change in order (or disorder) of the system and is subject to more freedom in interpretation than ΔH^\ddagger . The situation is not helped by the fact that standard deviations associated with ΔS^\ddagger are usually large, and a straightforward, reasonably quantitative interpretation is possible only at large absolute (positive or negative) values of ΔS^\ddagger .

Another parameter closely related to the disorder of a system, but easier to interpret, is the volume of activation. Also, ΔV^\ddagger can be measured much more precisely than ΔS^\ddagger [51], but special techniques, utilizing high pressure, are needed. It takes 2000–3000 atm to induce a significant change in rate constants and obtain precise

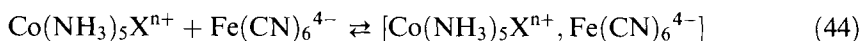
values of ΔV^\ddagger . In comparison, changing the temperature over a range of 20–30 K is sufficient to determine ΔH^\ddagger precisely.

The interpretation of ΔV^\ddagger is concerned with two major contributions to the observed values: the intrinsic changes in volume (caused by changes in bond lengths and angles) and changes in solvation.

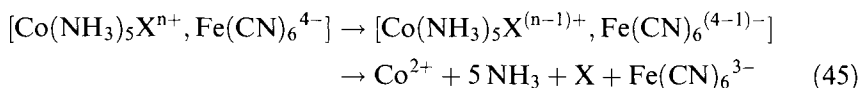
Almost every imaginable spectroscopic and electrochemical method have been used for the determination of ΔV^\ddagger . The development of a transportable high pressure unit [52] made such measurements accessible to many laboratories. High-pressure NMR work, however, is more difficult to carry out and requires special equipment [53, 54].

In the transportable unit, pressures up to 2000–4000 atm are generated with a hand-operated mechanical screw pump. Good sealing and lubrication are achieved by use of oil as the pressure medium. The reaction cell is located in a hydrostatic medium (usually water for UV/visible measurements) which is separated from the oil by a separator unit. For the stopped-flow measurements, the complete assembly (drive syringes, observation cell, and the stopping syringe) are placed inside the hydrostatic medium, in which the syringe plungers move to balance the internal and external pressure. The windows of the observation cells are usually made of sapphire or fused silica. Both materials have the required optical transparency coupled with good mechanical properties.

High-pressure effects have so far been studied for a large number of reactions, including several categories of electron transfer: outer-sphere, long-distance (utilizing biological molecules), and photochemical [51]. Surprising results were obtained in the reaction between $\text{Co}(\text{NH}_3)_5\text{X}^{n+}$ ($\text{X} = \text{Cl}^-$, N_3^- , H_2O , etc.) and $\text{Fe}(\text{CN})_6^{4-}$ [55]. Because of the large equilibrium constant for the formation of the precursor complex from the oppositely charged reactants, Eq. 44,



it was possible to separate the volume change for this stage from that for electron transfer, Eq. 45.



The ion-pair formation has an activation volume of close to zero, which is very different from the large positive ΔV^\ddagger expected for the desolvation caused by charge neutralization. The data were rationalized by the consideration of solvent-separated ion pairs.

High-pressure NMR [53, 54, 56] typically utilizes either pressurizable NMR tubes or a high-pressure probe head. The greatest advantage of the pressurizable glass tubes is that they can be used with commercial probes which makes it possible to spin the sample and thus improve the resolution. On the negative side, the thick tube walls reduce the sensitivity and lead to imperfect temperature control. Also, the pressures are usually lower than those obtained with high-pressure probe heads.

The sensitivity is much higher for high-pressure probe heads, in which the RF coil is placed close to the sample tube. A high-pressure high-resolution probe consists of the high-pressure bomb with an NMR insert holding the RF coil and the sample container [53]. Connections to the pressure-transmitting medium and access for temperature-measuring devices are built into the probe. The sample container, which is usually a standard NMR tube, allows pressure transmission and separates the sample from the pressure-transmitting fluid.

A high-pressure probe in combination with a ^{13}C NMR instrument was used recently in a study of self-exchange reactions for several cyanometalate complexes, $\text{Os}(\text{CN})_6^{3-}/\text{Os}(\text{CN})_6^{4-}$, $\text{Mo}(\text{CN})_8^{3-}/\text{Mo}(\text{CN})_8^{4-}$, and $\text{W}(\text{CN})_8^{3-}/\text{W}(\text{CN})_8^{4-}$ [57]. The rate constant k_{exch} was found to be strongly influenced by added cations. Moreover, the values of ΔV^\ddagger were inconsistent with Marcus theory. It was concluded that partially desolvated cations (Li^+ , Na^+ , K^+ , etc.) bridge the reacting anions in the transition state.

1.5 Indirect Methods and Special Cases

1.5.1 Competition Kinetics

Some reactions are difficult to study directly because the required instrumentation is not available or the changes in standard physical properties (light absorption, conductivity etc.) typically used in kinetic measurements are too small to be useful. Competition kinetics can provide important information in such cases. In some situations, the chemistry itself makes direct measurement inconvenient or even impossible. This is the case, for example, in studies of slow reactions of free radicals. Because of the ever-present radical-depleting second-order decomposition reactions, slow reactions of free radicals with added substrates are possible only at very low, steady-state radical concentrations. The standard methods of radical generation (pulse radiolysis and flash photolysis) are not useful in such cases, because they require micromolar levels of radicals for a measurable signal. The self-reactions usually have $k \geq 10^9 \text{ M}^{-1} \text{ s}^{-1}$, so that the competing reactions must have a pseudo-first-order rate constant of 10^4 s^{-1} or higher (or equivalent, if conditions are not pseudo-first order) to be observed. Competition experiments, on the other hand, can handle much lower rate constants, as described later for some reactions of $^{\bullet}\text{C}(\text{CH}_3)_2\text{OH}$ radicals with transition metal complexes.

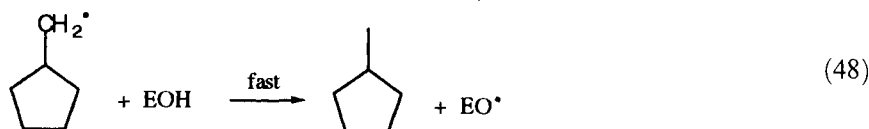
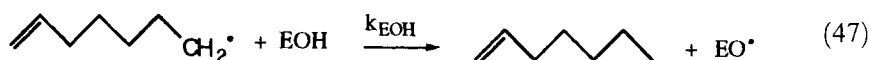
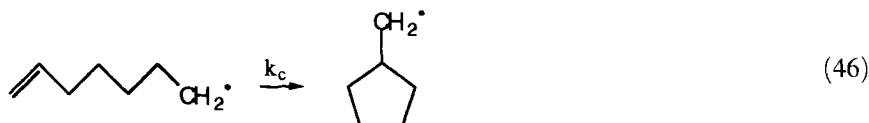
Depending on the timescales involved and the nature of the chemical reaction, the kinetic information can be obtained from product distribution, luminescence quenching, or kinetic measurements in the presence of a kinetic probe or a radical precursor. Inevitably, however, the result is obtained as a *relative* rate constant. The conversion to the absolute value requires that the rate constant for the competing process(es) be known.

Competition between intramolecular and intermolecular reactions of free radicals has been used extensively in kinetic and mechanistic studies. The rate constants for

the cyclization, ring opening, or β -scission of a number of radicals are now available. These "radical clock" [58] reactions cover a range of over 11 orders of magnitude in rate constants [58–60] and can be used to time the reactions with desired substrates on almost any timescale.

In addition to their role in kinetics, radical clocks also serve an important mechanistic function in that the formation of the rearranged product provides evidence for radical involvement in the first place. The incorporation of a ring-opening probe into the substrate, followed by product analysis—specifically, a search for rearranged product—has been used in mechanistic studies of the action of some enzymes, such as cyt P450 [61] and methane monooxygenase [62].

The cyclization of 1-hexenyl radical as a clock reaction has been used in large number of cases, including hydrogen-atom abstraction from the phenolic group of α -tocopherol (vitamin E, EOH) [63]. The radicals were generated in the presence of EOH at 70°C and the products, 1-hexene and methylcyclopentane, determined after the completion of the reaction. (See Eqs. 46–48.)

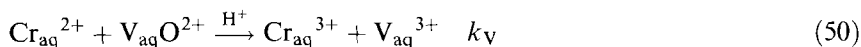


The ratio of the two products is given by Eq. 49.

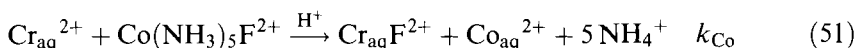
$$\frac{[\text{1-hexene}]}{[\text{methylcyclopentane}]} = \frac{k_{\text{EOH}}[\text{EOH}]}{k_c} \quad (49)$$

A plot of the left-hand side of the equation against [EOH] yielded k_{EOH}/k_c , which was combined with the known k_c ($1.1 \times 10^6 \text{ s}^{-1}$ at 70°C) to give $k_{\text{LOH}} = 1.7 \times 10^6 \text{ M}^{-1} \text{ s}^{-1}$.

Product analysis has also been utilized in studies of nonradical reactions where the competition is usually established between two bimolecular paths for the consumption of the limiting reagent. The reduction of $\text{Cr}_{\text{aq}}^{2+}$ by $\text{V}_{\text{aq}}\text{O}^{2+}$, Eq. 50, is fast and accompanied by only a small absorbance change [64].



The competing reaction of $\text{Co}(\text{NH}_3)_5\text{F}^{2+}$ with $\text{Cr}_{\text{aq}}^{2+}$, Eq. 51, has $k_{\text{Co}} = 9 \times 10^5 \text{ M}^{-1} \text{ s}^{-1}$, and produces $\text{Co}_{\text{aq}}^{2+}$, which can be conveniently determined by spectrophotometry after conversion to the intensely blue $\text{Co}(\text{NCS})_4^{2-}$.

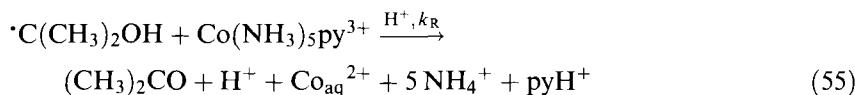
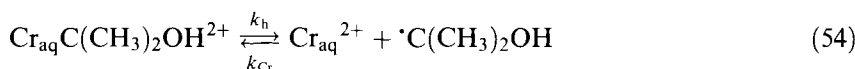
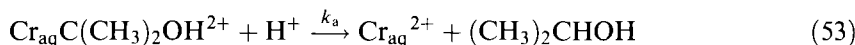


In the experiment, limited amounts of $\text{Cr}_{\text{aq}}^{2+}$ were either injected or generated in situ in the presence of large, known amounts of $\text{V}_{\text{aq}}\text{O}^{2+}$ and $\text{Co}(\text{NH}_3)_5\text{F}^{2+}$. The concentration of $\text{Co}_{\text{aq}}^{2+}$ produced was related to the total concentration of the product ($[\text{V}_{\text{aq}}^{3+}] + [\text{Co}_{\text{aq}}^{2+}] = [\text{Cr}_{\text{aq}}^{2+}]_{\text{total}}$) by Eq. 52

$$[\text{Co}_{\text{aq}}^{2+}]_{\text{inf}}/[\text{Cr}_{\text{aq}}^{2+}]_{\text{total}} = 1 + (k_{\text{VO}}/k_{\text{CoF}})([\text{V}_{\text{aq}}\text{O}^{2+}]_{\text{av}}/[(\text{NH}_3)_5\text{CoX}^{2+}]_{\text{av}}) \quad (52)$$

which yielded $k_{\text{V}} = 1.4 \times 10^6 \text{ M}^{-1} \text{ s}^{-1}$.

Controlled scission of the Cr–C bond in the presence of a substrate was used to determine the kinetics of reduction of a number of transition metal complexes with organic free radicals. The reaction scheme for $\text{Co}(\text{NH}_3)_5\text{py}^{2+}$ [65] is shown in Eqs. 53–55.



The organochromium complex disappears in two parallel processes: irreversible acidolysis (k_{a}) and reversible homolysis (k_{h}). The kinetics, Eq. 56, are determined by k_{a} and the competition for the organic radical between $\text{Co}(\text{NH}_3)_5\text{py}^{2+}$ and a controlled excess of $\text{Cr}_{\text{aq}}^{2+}$.

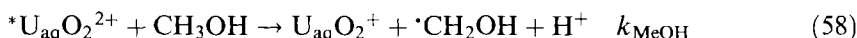
$$\begin{aligned} & -d[\text{Cr}_{\text{aq}}\text{C}(\text{CH}_3)_2\text{OH}^{2+}]/dt \\ & = \left(k_{\text{a}} + \frac{k_{\text{h}}k_{\text{R}}[\text{Co}^{\text{III}}]}{k_{\text{R}}[\text{Co}^{\text{III}}] + k_{\text{Cr}}[\text{Cr}_{\text{aq}}^{2+}]} \right) [\text{Cr}_{\text{aq}}\text{C}(\text{CH}_3)_2\text{OH}^{2+}] \end{aligned} \quad (56)$$

The fit of the data to the above equation yielded the composite rate constant $k_{\text{Cr}}/k_{\text{h}}k_{\text{R}}$, which was combined with the known values for k_{h} and k_{Cr} to yield $k_{\text{R}} = 1.2 \times 10^7 \text{ M}^{-1} \text{ s}^{-1}$. This method was used to measure rate constants as low as $5 \times 10^5 \text{ M}^{-1} \text{ s}^{-1}$ [66], which is clearly outside the range of direct determinations.

Luminescence quenching is limited to the reactions of excited states. By use of spectrofluorometers, luminescence intensities can be monitored precisely. As an example, let us consider the uranyl(VI) ion which has a long-lived, strongly luminescent excited state, $^*\text{U}_{\text{aq}}\text{O}_2^{2+}$ [67]. In the absence of added reagents, the decay to the ground state takes place by physical quenching (k_{phys}) and light emission (k_{em}), so that the quantum yield (Φ_0) is given by Eq. 57.

$$\Phi_0 = k_{\text{em}}/(k_{\text{phys}} + k_{\text{em}}) \quad (57)$$

In the presence of a quencher, say methanol, the chemical reaction of Eq. 58



contributes to the loss of $^*\text{U}_{\text{aq}}\text{O}_2^{2+}$ and diminishes the quantum yield, Eq. 59.

$$\Phi = k_{\text{em}} / (k_{\text{phys}} + k_{\text{em}} + k_{\text{MeOH}}[\text{MeOH}]) \quad (59)$$

Fluorescence intensities (F), which are related to quantum yields through the intensity of absorbed light (I_{abs}), Eq. 60,

$$F = \Phi I_{\text{abs}} \quad (60)$$

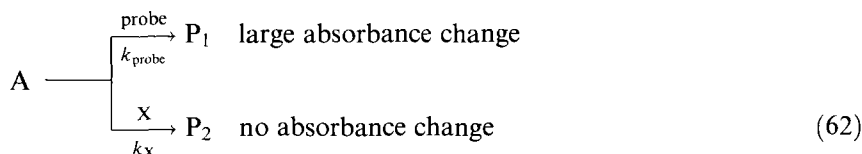
are directly related to the rate constants for all the processes involved, Eq. 61,

$$\begin{aligned} F_0/F &= (k_{\text{phys}} + k_{\text{em}} + k_{\text{MeOH}}[\text{MeOH}]) / (k_{\text{phys}} + k_{\text{em}}) \\ &= 1 + \tau_0 k_{\text{MeOH}}[\text{MeOH}] \end{aligned} \quad (61)$$

where $\tau_0 = (k_{\text{phys}} + k_{\text{em}})^{-1}$.

A plot, known as the Stern–Volmer plot, of F_0/F against $[\text{MeOH}]$ yielded $\tau_0 k_{\text{MeOH}} = 7.2$ [67]. By use of the independently known τ_0 (1.2×10^{-6} s), one obtains $k_{\text{MeOH}} = 6 \times 10^6 \text{ M}^{-1} \text{ s}^{-1}$. Similar determinations were carried out for a number of alcohols and other reducing compounds. Many of the rate constants were later determined directly by laser-flash photolysis [68]. Excellent agreement between the two methods was found.

If the reaction of interest does not have a measurable monitoring signal, a parallel reaction accompanied by a large change in the desired physical property, usually absorbance, may be employed as a kinetics tool [69, 70]. Under such conditions, the scheme in Eq. 62 applies



The expression for the loss of the limiting reagent A is given as the sum of all the contributing reactions, Eq. 63.

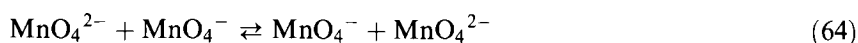
$$-d[\text{A}]/dt = (k_{\text{probe}}[\text{probe}] + k_{\text{X}}[\text{X}])[\text{A}] \quad (63)$$

In practice, the composite rate constant is corrected for the independently-measured rate constant for the probe reaction. The precision improves when the kinetic contribution from the k_{X} path is as large as possible while still retaining an acceptable absorbance change provided by the probe reaction. This approach is used widely in laser-flash photolysis studies of radical reactions, which are described in detail in one of the following chapters.

1.5.2 Exchange Reactions

Exchange reactions represent a special case in chemical kinetics, because they lead to no net chemical change. The physical properties of the system remain unchanged; this requires a special approach for the monitoring of kinetics. For fast reactions, NMR and ESR line broadening are extremely valuable for obtaining the exchange rate constant k_{exch} , as already described. For slower reactions, one of the exchanging partners is isotopically labeled. The reaction is allowed to proceed for a pre-determined period of time and is then quenched. The products are separated and the extent of label scrambling is determined experimentally.

An early example is provided by the electron-exchange reaction in Eq. 64 [71].



The permanganate ion was labeled with ^{54}Mn . The separation of MnO_4^- for kinetic determinations was achieved by co-precipitation with tetraphenylarsonium perrhenate, and the activity was determined with a scintillation counter. The rate constant, $k_{\text{exch}} = 710 \text{ M}^{-1} \text{ s}^{-1}$ at 273 K, was obtained by fitting of the data to Eq. 65

$$k_{\text{exch}} = \ln 2 / \{t_{1/2}([\text{MnO}_4^-] + [\text{MnO}_4^{2-}])\} \quad (65)$$

where $t_{1/2}$ represents the half-life for electron exchange.

In a similar study, ^{59}Fe -labeled $\text{Fe}(\text{H}_2\text{O})_6^{3+}$ was allowed to exchange with $\text{Fe}(\text{H}_2\text{O})_6^{2+}$ in the presence of chloride ions [72]. The reaction was quenched by the addition of 2,2'-bipyridine which complexes Fe^{II} , and the activity of ^{59}Fe in the complex was determined by scintillation counting. It was found that most of the exchange takes place by the reaction of Eq. 66



which has a rate constant of $57.6 \text{ M}^{-1} \text{ s}^{-1}$ at an ionic strength of 3.0 M.

The determination of the self-exchange rate for the couple $\text{O}_2/\text{O}_2^{\bullet-}$ was an important development in view of the failure of Marcus–Hush theory to yield consistent results. The values obtained by the latter approach varied with the chemical system chosen and covered a range of over 16 orders of magnitude [73].

The experimental determination was carried out by use of ^{18}O as a probe [74]. The labeled $\text{O}_2^{\bullet-}$ was allowed to exchange with $^{32}\text{O}_2$ at high pH (Eq. 67),



which ruled out the involvement of the conjugate acid HO_2 ($\text{p}K_a = 4.7$) in the exchange reaction and also slowed down the decay of $\text{O}_2^{\bullet-}$ by disproportionation. The exchange was quenched by lowering of the pH, a process that induced rapid disproportionation of $\text{O}_2^{\bullet-}$, Eq. 68.



The solution was purged with argon and catalase was added to initiate yet another disproportionation reaction, Eq. 69.



The amount of ^{18}O in the newly produced O_2 was determined by mass spectroscopy and the exchange rate constant, $k_{\text{exch}} = 450 \text{ M}^{-1} \text{ s}^{-1}$, was calculated by use of the expression in Eq. 70

$$\ln \left\{ \frac{{}^{32}\text{O}_2 + {}^{36}\text{O}_2}{{}^{36}\text{O}_2} \right\} = k_{\text{exch}}[\text{O}_2]t \quad (70)$$

where $[\text{O}_2]$ represents the concentration of $^{32}\text{O}_2$ present during the exchange reaction.

Acknowledgments

This work was supported by the U.S. Department of Energy, Office of Basic Energy Sciences, Division of Chemical Sciences under contract W-7405-Eng-82. I am indebted to Dr. Peter Metelski for insightful comments and help with some figures, and to Drs. Steve Veysey and Rudi van Eldik for helpful discussions.

Abbreviations

act = azacaptan = 8-methyl-1,3,13,16-tetraaza-6,10,19-trithiabicyclo[6.6.6]eicosane

ch₂phen = dicyclohexylphenanthroline

dmf = dimethylformamide

dmp = 2,9-dimethyl-1,10-phenanthroline

en = ethylenediamine = 1,2-diaminoethane

EPR = electron paramagnetic resonance

k_f = forward rate constant

kie = kinetic isotope effect

k_r = reverse rate constant

Me₂-phen = dimethylphenanthroline

Me₂bpy = dimethylbipyridine

NMR = nuclear magnetic resonance

phen = 1,10-phenanthroline

py = pyridine

topa = 3-(2,4,5-trihydroxyphenyl)-1-alanine

TPP = tetra-p-tolylporphine

References

1. K. A. Connors, *Chemical Kinetics. The Study of Reaction Rates in Solution*, VCH, New York 1990, Chapter 4.
2. A. Bakac, W.-D. Wang, *Inorg. Chim. Acta* **2000**, 297, 27–35.
3. J. F. Holzwarth, in W. J. Gettins, E. Wyn-Jones (Eds.): *Techniques and Applications of Fast Reactions in Solution*, D. Reidel, Boston 1979, pp. 13–24.
4. B. H. Robinson, in C. F. Bernasconi (Ed.): *Techniques of Chemistry. Volume VI. Investigation of Rates and Mechanisms of Reactions, Vol. 2*, Wiley, New York 1986, pp. 9–26.
5. H. Bruhn, J. Westerhausen, J. F. Holzwarth, J. H. Fuhrhop, in W. J. Gettins, E. Wyn-Jones (Eds.): *Techniques and Applications of Fast Reactions in Solution*, D. Reidel, Dordrecht 1979, pp. 523–534.
6. G. D. Owens, R. W. Taylor, T. Y. Ridley, D. W. Margerum, *Anal. Chem.* **1980**, 52, 130–138.
7. M. T. Nemeth, K. D. Fogelman, T. Y. Ridley, D. W. Margerum, *Anal. Chem.* **1987**, 59, 283–291.
8. C. P. Bowers, K. D. Fogelman, J. C. Nagy, T. Y. Ridley, Y. L. Wang, S. W. Evetts, D. W. Margerum, *Anal. Chem.* **1997**, 69, 431–438.
9. N. Sutin, B. M. Gordon, *J. Am. Chem. Soc.* **1961**, 83, 70–73.
10. G. Dulz, N. Sutin, *Inorg. Chem.* **1963**, 2, 917–921.
11. P. N. Dickson, D. W. Margerum, *Anal. Chem.* **1986**, 58, 3153–3158.
12. M. S. Corrairie, J. D. Atwood, *Inorg. Chem.* **1989**, 28, 3781–3782.
13. J. P. Maher, in W. J. Gettins, E. Wyn-Jones (Eds.): *Techniques and Applications of Fast Reactions in Solution*, D. Reidel, Dordrecht 1979, pp. 29–34.
14. S. A. Jacobs, G. W. Kramer, R. E. Santini, D. W. Margerum, *Anal. Chim. Acta* **1984**, 157, 117–124.
15. J. D. Rush, J. E. Cyr, Z. Zhao, B. H. J. Bielski, *Free Rad. Res.* **1995**, 22, 349–360.
16. B. C. Hill, *Biochem.* **1996**, 35, 6136–6143.
17. U. Nickel, K. Kemnitz, W. Jaenicke, *J. Chem. Soc. Perkin II* **1978**, 1188–1193.
18. G. W. Kirker, A. Bakac, J. H. Espenson, *J. Am. Chem. Soc.* **1982**, 104, 1249–1255.
19. G. H. Czerlinski, *Chemical Relaxation, Chapter 8*, Marcel Dekker, New York 1966.
20. G. Schwartz, in C. Bernasconi (Ed.): *Techniques of Chemistry. Volume VI. Investigation of Rates and Mechanisms of Reactions*, Wiley, New York 1986, pp. 27–139.
21. J. H. Espenson, *Chemical Kinetics and Reaction Mechanisms*, McGraw-Hill, New York 1995, Chapter 11.
22. P. Hurwitz, K. Kustin, *Inorg. Chem.* **1964**, 3, 823–826.
23. D. H. Turner, in C. F. Bernasconi (Ed.): *Techniques of Chemistry. Volume VI. Investigation of Rates and Mechanisms of Reactions*, Wiley, New York 1986, pp. 141–189.
24. R. F. Pasternack, K. Kustin, L. A. Hughes, E. Gibbs, *J. Am. Chem. Soc.* **1969**, 91, 4401–4404.
25. G. Czerlinski, M. Eigen, *Z. Elektrochemie* **1959**, 63, 652–661.
26. B. Marcandalli, G. Stange, J. F. Holzworth, *J. Chem. Soc., Faraday Trans. I* **1988**, 84, 2807–2819.
27. D. M. Dooley, D. E. Brown, *J. Biol. Inorg. Chem.* **1996**, 1, 205–209.
28. G. G. Hammes, *Acc. Chem. Res.* **1968**, 1, 321–329.
29. J. F. Smalley, S. W. Feldberg, C. E. D. Chidsey, M. R. Linford, M. D. Newton, Y.-P. Liu, *J. Phys. Chem.* **1995**, 99, 13141–13149.
30. W. Knoche, in C. Bernasconi (Ed.): *Techniques of Chemistry. Volume VI. Investigation of Rates and Mechanisms of Reactions*, Wiley, New York 1986, pp. 191–218.
31. M. Jacob, G. Holtermann, D. Perl, J. Reinstein, T. Schindler, M. A. Geeves, F. Schmid, *Biochem.* **1999**, 38, 2882–2891.
32. E. D. Becker, *High Resolution NMR. Theory and Chemical Applications*, Academic Press, New York 1980, Chapter 11.
33. R. D. Chapman, E. B. Fleischer, *J. Am. Chem. Soc.* **1982**, 104, 1582–1587.
34. C. L. Schwarz, J. F. Endicott, *Inorg. Chem.* **1995**, 34, 4572–4580.
35. P. D. Metelski, Y. Fu, K. Khan, T. W. Swaddle, *Inorg. Chem.* **1999**, 38, 3103–3109.
36. A. M. Q. V. Linde, K. L. Juntunen, O. Mols, M. B. Ksebati, L. A. Ochrymowycz, D. B. Rorabacher, *Inorg. Chem.* **1991**, 30, 5037–5042.

37. M. S. Chan, A. C. Wahl, *J. Phys. Chem.* **1978**, *82*, 2542–2549.
38. G. Fraenkel, in C. F. Bernasconi (Ed.): *Techniques of Chemistry. Volume VI. Investigation of Rates and Mechanisms of Reactions*, Wiley, New York 1986, pp. 547–604.
39. R. G. Wilkins, *Kinetics and Mechanism of Reactions of Transition Metal Complexes*, VCH, Weinheim 1991, Chapter 3.
40. M. T. Jones, S. I. Weissman, *J. Am. Chem. Soc.* **1962**, *84*, 4269–4274.
41. G. Grampp, Y. A. Khan, H. Larsen, *J. Chem. Soc., Perkin Trans. 2* **1997**, 2555–2557.
42. G. Grampp, *Spectrochim. Acta A* **1998**, *54*, 2349–2358.
43. T. T.-T. Li, C. H. Brubaker, Jr., *J. Organomet. Chem.* **1981**, *216*, 223–234.
44. T. Saji, S. Aoyagui, *Bull. Chem. Soc. Japan* **1973**, *46*, 2101–2105.
45. R. L. Ward, S. I. Weissman, *J. Am. Chem. Soc.* **1957**, *79*, 2086–2090.
46. D. Meisel, R. W. Fessenden, *J. Am. Chem. Soc.* **1976**, *98*, 7505–7510.
47. D. M. Bartels, M. T. Craw, P. Han, A. D. Trifunac, *J. Phys. Chem.* **1989**, *93*, 2412–2421.
48. P. Han, D. M. Bartels, *Chem. Phys. Lett.* **1989**, *159*, 538–542.
49. J. Geimer, D. Beckert, A. Jenichen, *Chem. Phys. Lett.* **1997**, *280*, 353–358.
50. T. Kausche, J. Sauberlich, E. Trobitzsch, D. Beckert, K. P. Dinse, *Chem. Phys.* **1996**, *208*, 375–390.
51. G. Stochel, R. van Eldik, *Coord. Chem. Rev.* **1999**, *187*, 329–374.
52. D. Magde, R. van Eldik, in W. B. Holzapfel, N. S. Isaacs (Eds.): *High-pressure techniques in chemistry and physics*, Oxford University Press, Oxford 1997, pp. 267–306.
53. L. Helm, A. E. Merbach, D. H. Powell, in W. B. Holzapfel, N. S. Isaacs (Eds.): *High-pressure techniques in chemistry and physics*, Oxford University Press, Oxford 1997, p. 187.
54. T. W. Swaddle, in W. B. Holzapfel, N. S. Isaacs (Eds.): *High-pressure techniques in chemistry and physics*, Oxford University Press, Oxford 1997, p. 343.
55. I. Krack, R. van Eldik, *Inorg. Chem.* **1986**, *25*, 1743–1747.
56. P. D. Metelski, PhD thesis, Department of Chemistry, University of Calgary, 1998.
57. P. D. Metelski, T. W. Swaddle, *Inorg. Chem.* **1999**, *38*, 301–307.
58. D. Griller, K. U. Ingold, *Acc. Chem. Res.* **1980**, *13*, 317–323.
59. J. H. Horner, N. Tanaka, M. Newcomb, *J. Am. Chem. Soc.* **1998**, *120*, 10379–10390.
60. M. Newcomb, C. C. Johnson, M. B. Manek, T. R. Varick, *J. Am. Chem. Soc.* **1992**, *114*, 10915–10921.
61. P. R. O. de Montellano, R. A. Stearns, *J. Am. Chem. Soc.* **1987**, *109*, 3415–3420.
62. K. E. Liu, C. C. Johnson, M. Newcomb, S. J. Lippard, *J. Am. Chem. Soc.* **1993**, *115*, 939–947.
63. C. Evans, J. C. Scaiano, K. U. Ingold, *J. Am. Chem. Soc.* **1992**, *114*, 4589–4593.
64. A. Bakac, J. H. Espenson, *Inorg. Chem.* **1981**, *20*, 953–954.
65. A. Bakac, V. Butkovic, J. H. Espenson, R. Marcec, M. Orhanovic, *Inorg. Chem.* **1986**, *25*, 341–345.
66. A. Bakac, V. Butkovic, J. H. Espenson, R. Marcec, M. Orhanovic, *Inorg. Chem.* **1986**, *25*, 2562–2566.
67. R. Matsushima, *J. Am. Chem. Soc.* **1972**, *94*, 6010–6016.
68. M. Z. Hoffman, F. Bolletta, L. Moggi, G. L. Hug, *J. Phys. Chem. Ref. Data* **1989**, *18*, 219–543.
69. H. Paul, R. D. Small, Jr., J. C. Scaiano, *J. Am. Chem. Soc.* **1978**, *100*, 4520–4527.
70. A. Bakac, *Croat. Chem. Acta* **1993**, *66*, 435–445.
71. J. C. Sheppard, A. C. Wahl, *J. Am. Chem. Soc.* **1957**, *79*, 1020–1024.
72. R. J. Campion, T. J. Conocchioni, N. Sutin, *J. Am. Chem. Soc.* **1964**, *86*, 4591–4594.
73. K. Zahir, J. H. Espenson, A. Bakac, *J. Am. Chem. Soc.* **1988**, *110*, 5059–5063.
74. J. Lind, X. Shen, G. Merenyi, B. O. Jonsson, *J. Am. Chem. Soc.* **1989**, *111*, 7654–7655.

2 Electrochemical Techniques

Steen Uttrup Pedersen and Kim Daasbjerg

2.1 Electrochemical Techniques

The distinct feature of electrochemical methods is that they can be used to obtain information about the energetics and kinetics of a wealth of reactions, including both heterogeneous and homogeneous processes. In this sense, the electrode is a unique tool, because it can be used to generate or activate molecules and at the same time detect, either directly or indirectly, intermediates formed during this electrochemical activation process. The characteristic time window of the different electrochemical techniques may range from nanoseconds to several days, so when used in combination, they offer a versatile methodology that allows the study of many kinds of chemical reactions.

In the present chapter, the main focus will be on the most common electrochemical techniques and methods used in the elucidation of reaction mechanisms. In general, it is possible from a quantitative analysis of the relation between current and potential to formulate even complex reaction mechanisms that incorporate preceding and/or follow-up reactions. A part of this text is devoted specifically to the description of the procedures used in the extraction of standard potentials and rate constants once the mechanism is known. However, before a discussion of the individual techniques can be accomplished, an introduction to the basic concepts in electrochemistry seems appropriate. For obvious reasons, this part can only be of limited length in a chapter, and for the reader who would appreciate a more detailed description of the basic principles, we recommend the book of Bard and Faulkner [1].

2.1.1 Introduction

One of the most fundamental equations used in electrochemistry is the Nernst equation (Eq. 1) that relates the electrode potential, E , with the concentrations of the two species O and R in the equilibrium process shown in Eq. 2.

$$E = E_{\text{O}}^{\circ} + \frac{RT}{nF} \ln \left(\frac{C_{\text{O,eq}}}{C_{\text{R,eq}}} \right) \quad (1)$$



The parameter R is the gas constant, T is the temperature, F is the Faraday constant and n is the number of electrons consumed in the electron transfer step (Eq. 2). The standard potential, E_{O}° of the redox couple O/R is defined as the reduction potential of O when the activity coefficients for both O and R are equal to one. Once E_{O}° is known, the electrode potential can be used to measure concentrations in solutions or to calculate equilibrium constants, K_{eq} , for redox equilibria (Eq. 3) involving two or more redox couples as shown in Eq. 4.



$$\Delta E^{\circ} = E_{\text{O}_1}^{\circ} - E_{\text{O}_2}^{\circ} = \frac{RT}{nF} \ln \left[\frac{C_{\text{R}_1,\text{eq}} C_{\text{O}_2,\text{eq}}}{C_{\text{O}_1,\text{eq}} C_{\text{R}_2,\text{eq}}} \right] = \frac{RT}{nF} \ln K_{\text{eq}} = - \frac{\Delta G^{\circ}}{nF} \quad (4)$$

A very important point in electrochemistry is that the exchange of electrons between an electrode and an reactant, that is, an oxidant or reductant, can only take place at the electrode surface. In the Nernst equation, this fact might seem to be partly obscured by the use of equilibrium concentrations, but as no net reaction occurs at equilibrium, the surface concentrations must be equal to the equilibrium concentrations. In most applications of electrochemistry, the electrode potential is varied, to achieve surface concentrations $C_{\text{O}}(0, t)$ that are different from the concentrations found far from the electrode surface, that is, in the bulk (C_{O}°). In other words, the electrode potential is used for creating a nonequilibrium situation where the dynamic response of the chemical system can be examined.

Because the exchange of electrons occurs at the electrode surface, the rate of any electrochemical process will depend on $C_{\text{O}}(0, t)$ and not the concentration in the bulk of the solution, C_{O}° . This is a distinct difference between an electrode reaction that is a heterogeneous process and a homogeneous process. Besides $C_{\text{O}}(0, t)$, the rate of an electrode reaction also depends on the electrode potential which can be varied by increase or decrease of the charge on the electrode surface. Formally, the electrode potential is defined as the work required for the transfer of a positive charge from infinity to the electrode surface. For a reduction process, the electron is always transferred from the electrode to the oxidant present at the surface, and the speed of this process can be increased by “pumping” more electrons onto the electrode surface, and in this manner raise the energy. Thus, the potential is almost always negative for a reduction process and the rate increases when the electrode potential is lowered (i.e., made even more negative). This dependency of the pertinent rate constant k_{red} on the electrode potential is, of course, also true for an oxidation process, with the modification that the rate constant k_{ox} increases if the potential becomes more positive by the “drawing away” of electrons from the electrode surface. The explicit equations for the two rate constants k_{red} and k_{ox} are given in Eqs. 5 and 6, respectively, where α denotes the so-called symmetry factor and k° is the standard heterogeneous rate constant.

$$k_{\text{red}} = k^{\circ} \exp \left[\frac{-\alpha n F}{RT} (E - E_{\text{O}}^{\circ}) \right] \quad (5)$$

$$k_{\text{ox}} = k^{\circ} \exp \left[\frac{(1 - \alpha) n F}{RT} (E - E_{\text{O}}^{\circ}) \right] \quad (6)$$

The “pump” or control unit for adjustment of the surface charge at the electrode is usually a potentiostat that is capable of keeping the electrode potential at a fixed value relative to a reference electrode. Alternatively, the amount of charge can be adjusted by control of the current rather than the potential; this can be achieved by a suitable power supply.

The current i measured at any value of the potential E for a given electrode reaction (Eq. 2) provides a direct measure of the rate of the charge-transfer process occurring at the electrode surface. It can be quantified as shown in Eq. 7

$$i = nFA D_{\text{O}} \left(\frac{\partial C_{\text{O}}}{\partial x} \right)_{x=0} = nFA [k_{\text{red}} C_{\text{O}}(0, t) - k_{\text{ox}} C_{\text{R}}(0, t)] \quad (7)$$

where A is the area of the electrode surface, D_{O} is the diffusion coefficient of O and $\left(\frac{\partial C_{\text{O}}}{\partial x} \right)_{x=0}$ is the concentration gradient of O at the surface. Note that the presence of the two opposing terms in Eq. 7 is a reflection of the fact that both a reduction and oxidation process take place in the reaction (Eq. 2). Combining Eqs. 5–7 then results in the fundamental current potential equation given in Eq. 8.

$$i = nFA k^{\circ} \left\{ C_{\text{O}}(0, t) \exp \left[\frac{-\alpha n F}{RT} (E - E_{\text{O}}^{\circ}) \right] - C_{\text{R}}(0, t) \exp \left[\frac{(1 - \alpha) n F}{RT} (E - E_{\text{O}}^{\circ}) \right] \right\} \quad (8)$$

The different parameters incorporated in Eq. 8 can be divided into two groups. The first group consists of the standard rate constant, k° , the symmetry factor α , the number of electrons transferred, n , and the standard potential E_{O}° , all of which are intrinsic parameters specifically related to the reaction system under investigation. The electrode area, A , the surface concentrations, $C_{\text{O}}(0, t)$ and $C_{\text{R}}(0, t)$, the temperature, T , and the electrode potential, E , belong to the second group of experimental parameters that can be varied externally. In particular, E has an enormous influence on the balance between the reduction and oxidation processes, as expressed mathematically by its presence with opposite signs in the exponential terms of Eq. 8. Apparently, any size of the current i can thus be obtained simply through an adjustment of E . However, this is only true within some limits. First of all, the absolute variation of the electrode potential is set by the characteristic potential window of the medium, that is, if too extreme potentials are applied, decomposition of the medium will occur either by reduction or oxidation of the solvent or the supporting electrolyte. But even at less extreme potentials and especially if k° is large, the limiting and rate-controlling step may become transport of the substrates

to and from the electrode surface rather than the electrode reaction. Thirdly, the situation may be complicated by the presence of chemical reactions involving O and R. For instance, if the species R is involved in follow-up chemistry that consumes electrons, the total number of electrons used are higher than n . In other words, the current which is proportional to the total number of electrons consumed is also dependent on the fate of R.

In summary, the current i is therefore determined by a) heterogeneous kinetics in terms of $E - E_O^\circ$, α , and k° , b) mass transport as expressed by $C_O(0, t)$ and $C_R(0, t)$, and c) homogeneous kinetics. Each of these three points is discussed in further detail in the following sections.

2.1.2 Heterogeneous Kinetics

The equilibrium situation is characterized by $E = E_{\text{eq}}$, when $i = 0$, $C_O(0, t) = C_O^*$ and $C_R(0, t) = C_R^*$, that is, the two terms in Eq. 8 become equal and cancel each other. The exchange current, i_0 , is defined as being equal to one of the two terms, as stated in Eq. 10. This equation can be rewritten as shown in Eq. 11 if the Nernst equation (Eq. 1) is employed.

$$\begin{aligned} i_0 &= nFAk^\circ C_O^* \exp\left[\frac{-\alpha nF}{RT}(E_{\text{eq}} - E_O^\circ)\right] \\ &= nFAk^\circ C_R^* \exp\left[\frac{(1-\alpha)nF}{RT}(E_{\text{eq}} - E_O^\circ)\right] \end{aligned} \quad (10)$$

$$i_0 = nFAk^\circ C_O^{*(1-\alpha)} C_R^{*\alpha} \quad (11)$$

If Eq. 11 is inserted into the current-potential equation (Eq. 8), the so-called current-overpotential equation results (Eq. 12), where the overpotential η is defined as the potential relative to the equilibrium potential, $\eta = E - E_{\text{eq}}$.

$$i = i_0 \left\{ \frac{C_O(0, t)}{C_O^*} \exp\left[\frac{-\alpha nF\eta}{RT}\right] - \frac{C_R(0, t)}{C_R^*} \exp\left[\frac{(1-\alpha)nF\eta}{RT}\right] \right\} \quad (12)$$

On the assumption that the surface concentrations of O and R will not differ significantly from the bulk concentrations, Eq. 12 can be reduced to the Butler-Volmer equation shown in Eq. 13. For very small variations of η , both exponential functions can be linearized, and the simple expression given in Eq. 14 results.

$$i = i_0 \left\{ \exp\left[\frac{-\alpha nF\eta}{RT}\right] - \exp\left[\frac{(1-\alpha)nF\eta}{RT}\right] \right\} \quad (13)$$

$$i = -i_0 \left(\frac{nF\eta}{RT} \right) \quad (14)$$

Electrode reactions are called reversible when the surface concentrations are adjusted quickly in accordance with the Nernst equation upon a change in E . In many experiments this requirement of O and R being constantly in equilibrium with the electrode is hard to fulfil, since the heterogeneous charge transfer is accompanied by both structural and solvent reorganization. The larger the reorganization energy, the slower the charge transfer process becomes, i.e. k° is diminished. The term reversible is therefore used for electrode reactions with a large k° . Another important requirement for reversibility is that the surface concentrations of O and R are not perturbed by the presence of homogeneous reactions during the electrochemical measurement.

Should the electrode reaction be associated with a low k° value, a significant overpotential is required for any reaction to be accomplished. Hence, one of the terms in Eq. 8 can be neglected, depending on the sign of the overpotential, and the electrode reaction is then referred to as an irreversible process. At low values of E , the oxidation term in Eq. 8 is negligible; this leads to Eq. 15. On the other hand, at high potentials the reduction term can be neglected, with Eq. 16 resulting.

$$\begin{aligned} i &= nFAk^\circ C_O(0, t) \exp\left[\frac{-\alpha nF}{RT}(E - E_O^\circ)\right] \\ &= i_0 \left\{ \frac{C_O(0, t)}{C_O^*} \exp\left[\frac{-\alpha nF\eta}{RT}\right] \right\} \end{aligned} \quad (15)$$

$$\begin{aligned} i &= nFAk^\circ C_R(0, t) \exp\left[\frac{(1 - \alpha)nF}{RT}(E - E_O^\circ)\right] \\ &= i_0 \left\{ \frac{C_R(0, t)}{C_R^*} \exp\left[\frac{(1 - \alpha)nF\eta}{RT}\right] \right\} \end{aligned} \quad (16)$$

Consider a reduction process, where $C_O(0, t) \approx C_O^*$; then Eq. 15 can be transformed to the Tafel equation given in Eq. 17.

$$\log i = \log i_0 - \frac{\alpha nF\eta}{2.3RT} \quad (17)$$

In a Tafel plot, the logarithm of the current is plotted against η , as illustrated in Figure 1. Note that the slope is equal to $-\alpha nF/2.3RT$ and the intercept corresponds to $\log i_0$. From these values, k° can be determined with Eq. 11. Tafel plots are often employed in corrosion studies, since k° is usually small and the condition $C_O(0, t) \approx C_O^*$ can be accomplished by simply stirring the solution. Deviations from the idealized Tafel behavior are seen at large $|\eta|$, where $C_O(0, t)$ becomes significantly smaller than C_O^* .

An intermediate situation between the reversible and irreversible cases arises for relatively slow charge-transfer processes, where the Nernst equation does not apply. On the other hand, k° is not so small that either of the two terms in Eq. 8 can be neglected. Such an electrode process is denoted quasi-reversible.

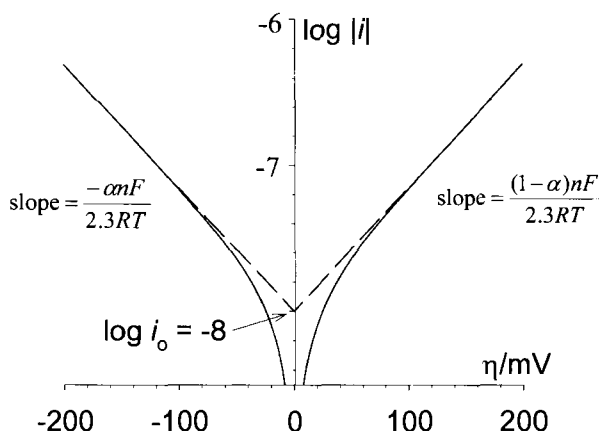


Figure 1. Tafel plot for anodic and cathodic branches of the current–overpotential curve for $O + ne \rightleftharpoons R$ ($n = 1$, $\alpha = 0.5$, $T = 25^\circ\text{C}$, and $i_0 = 10^{-8}$ A).

2.1.3 Mass Transport

The flux, $J_O(x, t)$, is defined as the transport of O per unit area ($\text{mol s}^{-1} \text{cm}^{-2}$). It can be divided into three components, diffusion, migration, and convection, as originally expressed in the Nernst–Planck equation, written for one-dimensional mass transport along the x -axis in Eq. 18.

$$\begin{aligned} J_O(x, t) &= -\frac{D_O C_O(x, t)}{RT} \nabla \mu_O^{\text{el}}(x, t) + v(x, t) C_O(x, t) \\ &= -D_O \frac{\partial C_O(x, t)}{\partial x} - \frac{z_O F}{RT} D_O C_O(x, t) \left(\frac{\partial \phi(x, t)}{\partial x} \right) + v(x, t) C_O(x, t) \end{aligned} \quad (18)$$

$$\mu_O^{\text{el}}(x, t) = \mu_O^\circ + RT \ln C_O(x, t) + z_O F \phi(x, t) \quad (19)$$

The parameter D_O is the diffusion coefficient ($\text{cm}^2 \text{s}^{-1}$), $\mu_O^{\text{el}}(x, t)$ is the electrochemical potential defined in Eq. 19, $v(x, t)$ is the velocity (cm s^{-1}) of a volume element in the solution along the x -axis, z_O is the charge of O, μ_O° is the standard chemical potential, and $\phi(x, t)$ is the potential. The convection expressed by $v(x, t) C_O(x, t)$ should be taking into account only if the solution is, for example, stirred so that it moves relative to the electrode surface. The diffusion and migration terms arise because of non-uniformity in $\mu_O^{\text{el}}(x, t)$. Specifically, the diffusion is caused by concentration gradients, that is, when $\frac{\partial C_O(x, t)}{\partial x} \neq 0$, and the migration is

caused by the potential gradient $\frac{\partial \phi(x, t)}{\partial x}$, which creates an electric field. Whereas convection can be avoided if the solution is not stirred, migration and diffusion will always take place in an electrochemical cell, although the former process pertains

only to charged species. The effect of migration on $J_O(x, t)$ can largely be eliminated by the addition of a large excess of an electroinactive salt, the supporting electrolyte. In most electroanalytical experiments, a 100-fold excess of supporting electrolyte relative to substrate, together with the absence of stirring, will ensure that the only kind of mass transport to consider is the diffusion of the electroactive material to the electrode surface. In that instance, the Nernst–Planck equation is simplified to the expression given in Eq. 20, which is better known as Fick's first law.

$$-J_O(x, t) = D_O \frac{\partial C_O(x, t)}{\partial x} \quad (20)$$

The current i is given as the flux at the electrode surface, $J_O(0, t)$, integrated over the total electrode area, A , as expressed in Eq. 21.

$$i(t) = -nFAJ_O(0, t) = nFAD_O \left(\frac{\partial C_O(x, t)}{\partial x} \right)_{x=0} \quad (21)$$

A second equation essential for the description of processes controlled by diffusion is Fick's second law (Eq. 22) which states that concentration changes occurring at a specific point in a solution depends on the difference between the fluxes in and out of this point.

$$\frac{\partial C_O(x, t)}{\partial t} = D_O \frac{\partial^2 C_O(x, t)}{\partial x^2} \quad (22)$$

In other words, the law describes the time development in the concentration profiles. Note that Fick's two laws have been written in forms that apply to one-dimensional mass transport processes, but the extension of the equations to three dimensions is straightforward.

Let us now consider the diffusion process of O in the redox couple O/R in closer details. The oxidized species O will be reduced to R at the electrode surface when the applied potential E is smaller than E_O° . This diminishes the concentration of O near the electrode surface and a so-called diffusion layer is formed where $C_O(x, t)$ is less than C_O^* . Thus, the reduction process taking place at the electrode surface creates concentration gradients in the solution. The thickness of the diffusion layer, δ , increases with time and as long as the electrode dimension is large compared to δ , the diffusion will be perpendicular to the electrode surface. Diffusion is said to be planar (or one-dimensional) and δ depends on \sqrt{t} as stated in Eq. 23.

$$\delta = \sqrt{2D_O t} \quad (23)$$

Inserting a realistic value of D_O of $10^{-5} \text{ cm}^2 \text{ s}^{-1}$ in Eq. 23 shows that the value of δ after 5 s will be 0.01 cm ($= 10^6 \text{ \AA}$), which is large on molecular scale but small compared to the normal dimensions of the electrochemical cell. The diffusion layer can never grow to infinity because natural convection in terms of vibrations, tem-

perature and density gradients will tend to preclude any further development in the concentration gradients. Under normal conditions, the maximum value of δ is attained after approximately 5 s, and from then on, a steady-state situation is reached with no further changes in the size of δ ($= 0.01$ cm) and the shape of the concentration profiles. Planar or one-dimensional diffusion will always prevail for an electrode, as long as the radius is about 10 times larger than δ (i.e., radius > 1 mm). However, for smaller electrodes, material may also diffuse to the electrode surface from other directions, and then diffusion is said to be nonplanar or spherical. Obviously, the spherical versions of Fick's two laws should then be employed in the description of the diffusion process.

The final point we would like to emphasize is that the diffusion layer should never be confused with the double layer. The double layer arises because the charge on the electrode is counterbalanced by ions of opposite charge that are specifically adsorbed at the electrode surface. Such a "construction" resembles a capacitor and gives rise to double-layer capacitance, which will be described in detail later on. The thickness of the double layer is only a few Å, much smaller than δ .

2.1.4 Homogeneous Kinetics

Homogeneous reactions preceding or following the charge-transfer process at the electrode surface may substantially influence the current measured. Obviously, if any of the species involved in the chemical reactions are electroactive and can be reduced or oxidized, the total number of electrons consumed is going to be different from the number of electrons used in the reduction of O to R. However, even if the species should be non-electroactive, the current measured at a given value of E is affected by the presence of chemical reactions, as they may shift the charge-transfer equilibrium. From a quantitative point of view, a detailed knowledge of the mechanism is required for assessing the exact influence of such reactions on the response of a given electrochemical technique. Specific examples illustrating these features will be provided along with a description of the different electrochemical techniques (see Sections 2.2 and 2.3). At this point, however, it seems appropriate to introduce the simple nomenclature used in the description of electrochemical reaction schemes where both heterogeneous and homogeneous steps are mixed. A heterogeneous step is indicated by E, whose subscript characterizes the process as being either reversible (r), irreversible (i) or quasi-reversible (q). Homogeneous reactions are denoted by the letter C, with subscript numbers and letters differentiating between first-order (1), second-order (2), reversible (r), and irreversible (i) processes. An E_rC_i mechanism thus consists of the reactions shown in Eqs. 24 and 25, where Y denotes an electroinactive species.

E_rC_i :



A C_iE_r mechanism corresponds to the reactions depicted in Eqs. 26 and 27.

C_iE_r :



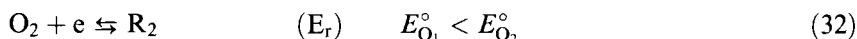
A mechanism as shown in Eqs. 28 and 29 where the electroactive substrate O is regenerated in the homogeneous step is called catalytic, and C is then marked with a prime. The reaction is not genuinely catalytic, because electrons are consumed, but it is catalytic in the sense that the redox couple O/R is not consumed.

E_rC' :



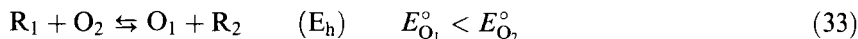
Unfortunately, this simple nomenclature is not used consistently in the electrochemical literature and it is usually discarded when more complicated mechanisms need to be distinguished. One example is the $E_rC_iE_r$ mechanism shown in Eqs. 30–32 and the related DISP mechanism depicted in Eqs. 30, 31, and 33 which both may occur if $E_{O_2}^\circ > E_{O_1}^\circ$. In general, the $E_rC_iE_r$ mechanism prevails if k_1 for Eq. 30 is larger than 10^7 s^{-1} , since O_2 is then formed so close to the electrode surface that it can be further reduced in a second heterogeneous step (Eq. 32). For smaller values of k_1 , on the other hand, O_2 will be formed so distant from the electrode that it rather reacts with R_1 in a homogeneous electron-transfer reaction (Eq. 33) [2, 3], that is, the DISP mechanism. In a few publications, the DISP mechanism has been given the abbreviation ECE_h , where the subscript “h” in E_h emphasizes the homogeneous nature of the electron-transfer step.

$E_rC_iE_r$:



DISP:

Eq. 30 + Eq. 31



Trivial names such as DIM1 and DIM2 are also often applied for mechanism EC_2 involving the formation of dimers. In the DIM1 mechanism, two R molecules dimerize, while in the DIM2 mechanism, coupling between R and O is followed by further reduction of the adduct RO by R .

2.2 Potential-Step Experiments

2.2.1 Chronoamperometry

One of the simplest experiments employed in electrochemistry is chronoamperometry (CA). In CA, the electrode potential is changed abruptly from a potential with no current flow to a potential where the surface concentration of O becomes zero. If only O is initially present in the cell, and homogeneous kinetics, migration and convection can be disregarded (i.e., the supporting electrolyte is in 100-fold excess and there is no stirring of the solution), the experiment can be described by the following equations (Eqs. 34–38).

$$\text{Fick's second law:} \quad \frac{\partial C_O(x, t)}{\partial t} = D_O \frac{\partial^2 C_O(x, t)}{\partial x^2} \quad (34)$$

$$\text{Initially:} \quad t = 0, \quad C_O(x, 0) = C_O^*; \quad C_R(x, 0) = 0 \quad (35)$$

$$\text{Far from the electrode:} \quad x \rightarrow \infty, \quad C_O(x, t) = C_O^*; \quad C_R(x, t) = 0 \quad (36)$$

$$\text{Electrode surface:} \quad x = 0, \quad C_O(0, t) = 0; \quad C_R(0, t) = C_O^* \quad (37)$$

$$\text{Fick's first law:} \quad i(t) = nFAD_O \left(\frac{\partial C_O(x, t)}{\partial x} \right)_{x=0} = -nFAD_R \left(\frac{\partial C_R(x, t)}{\partial x} \right)_{x=0} \quad (38)$$

Since the surface concentration of O becomes zero (Eq. 37), the rate of the reduction of O will be mass-transport-controlled or rather diffusion-controlled, as the migration and convection terms can be neglected. Thus, the experiment can be described by use of Fick's first and second laws (Eqs. 38 and 34, respectively). The substrate O is the only species initially present in the cell (Eq. 35) and because the electrode area A is small compared to the cell volume V in electroanalytical experiments, the bulk concentration can be assumed to be unchanged during the experiment (Eq. 36). Should a preparative conversion of O to R be the goal, a large A/V ratio would have been desirable. Equations 34–38 can be solved with the Laplace transformations; this affords the Cottrell equation (Eq. 39).

$$i = \frac{nFA\sqrt{D_O}C_O^*}{\sqrt{\pi t}} \quad (39)$$

As seen, the current i recorded depends on $t^{-1/2}$; this reflects the increase in the thickness of the diffusion layer δ as a function of $t^{1/2}$, as expressed in Eq. 23. A typical CA experiment is shown in Figure 2. When normal microdisc electrodes with diameters ranging from 0.1 to 3 mm are used in the CA technique, the useful time range is 1 ms to 5 s. For step times shorter than 1 ms, the double-layer charging current would contribute significantly to the measured current. The upper time limit is set by the point where the diffusion layer has grown so large that spherical

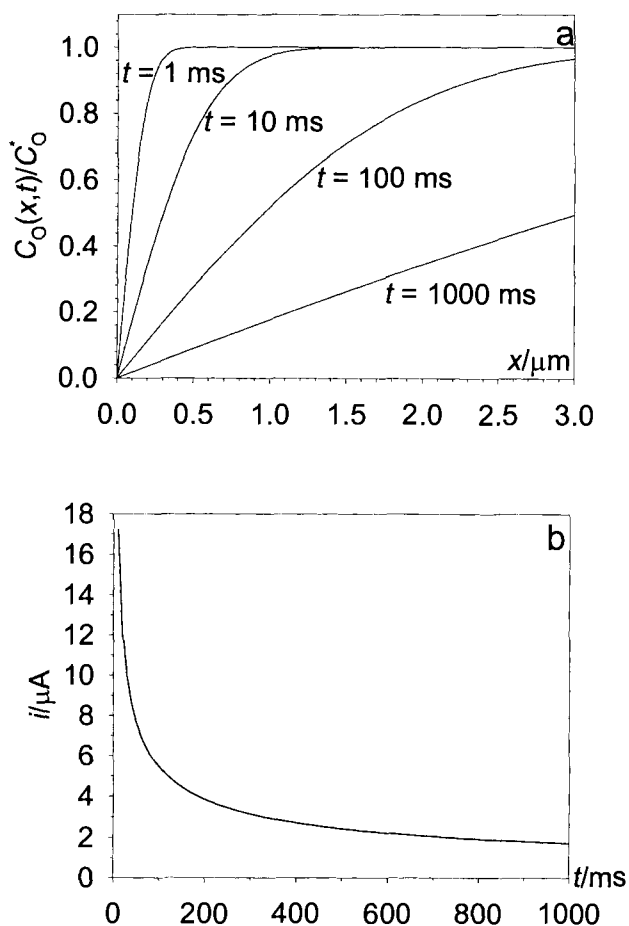


Figure 2. Chronoamperometric experiment for $O + e \rightleftharpoons R$: a) concentration profiles are shown after 1, 10, 100, and 1000 ms. The concentration gradient at the electrode surface ($x = 0$) is seen to decrease with time; b) plot of the current i vs time t is shown in the interval 0–1000 ms. The current decreases as a function of $t^{-1/2}$.

diffusion no longer can be neglected, and the current has become time-independent. Natural convection may also contribute to the mass transport for large step times.

Perhaps the most prominent feature of the CA technique is that it can be performed on any chemical system, regardless of the value of k° and α , as long as $C_O(0, t) = 0$. For a reversible electrode reaction this condition can easily be fulfilled, as $C_O(0, t)/C_O^*$ is 0.01 for $E - E_O^\circ = -118\text{ mV}$ and 0.001 for $E - E_O^\circ = -177\text{ mV}$ according to the Nernst equation (Eq. 1). While the potential applied therefore does not need to be polarized much in the case of a reversible process for achieving zero surface concentration, the potential step required for quasi-reversible and, in particular, irreversible electrode reactions will be much larger. The appropriate potential value for a given process may be determined by means of cyclic voltammetry.

The disadvantage of the CA technique is that it is a “blind” technique, which is suitable for quantitative measurements only when it is combined with more direct techniques such as cyclic voltammetry. No direct information about intermediates

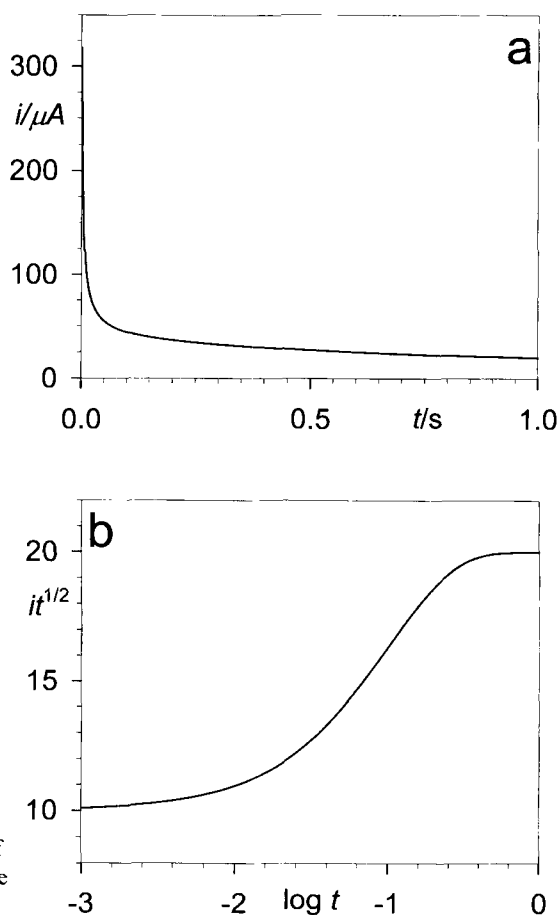


Figure 3. Chronoamperometric curve recorded for an $E_rC_iE_r$ mechanism: a) plot of current vs time, b) plot of time-normalized current ($i\sqrt{t}$) vs the logarithm of time, c) plot of number of electrons (n , see text) vs the logarithm of time, and d) plot of n vs logarithm of the dimensionless rate constant ($\lambda = k_1 t$).

can be found by CA, so it is generally of limited value for mechanistic studies. The recorded current usually depends only on the diffusion process of O to the electrode and the electron stoichiometry of the electrode process, represented by n . Almost all CA experiments lead to curves with similar shapes and only a closer examination of the curves will reveal if reliable kinetic information can be extracted. For instance, the i versus t curve for the E_rC_i mechanism (Eqs. 24 and 25) will be exactly the same as the curve for the corresponding E_iC_i mechanism. On the other hand, it will provide some information if the electron stoichiometry is dependent on the rate of a chemical step.

In Figure 3(a), the curve obtained in CA for the $E_rC_iE_r$ reaction mechanism (Eqs. 30–32) is depicted for $k_1 = 10 \text{ s}^{-1}$. A plot of $i\sqrt{t}$ versus $\log t$ as shown in Figure 3(b) can eliminate the time dependence of the current due to the growth of the diffusion layer. In the plot shown in Figure 3(c), the $i\sqrt{t}$ values are normalized by division with the constant $i\sqrt{t}$ value obtained at $t < 2 \text{ ms}$, where the influence of the follow-

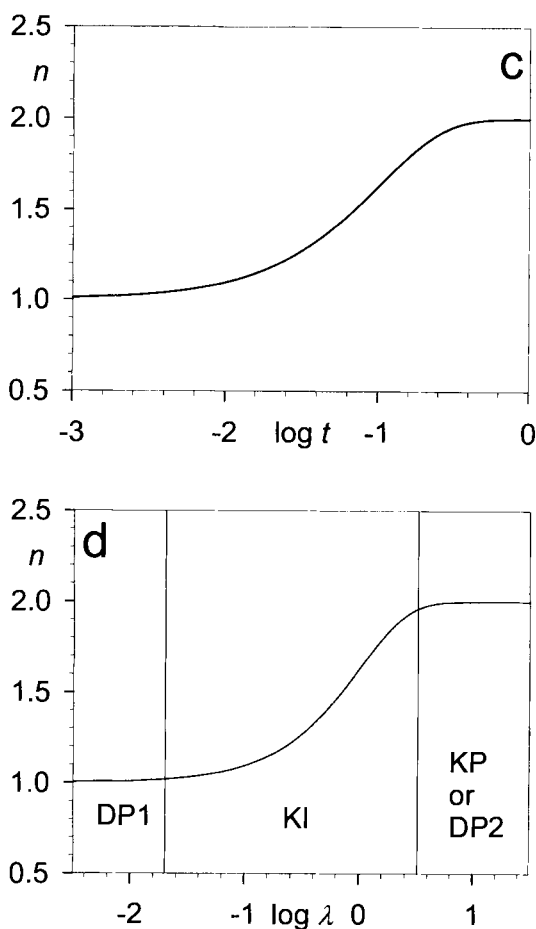
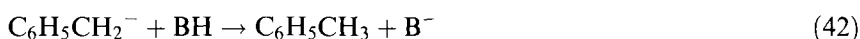
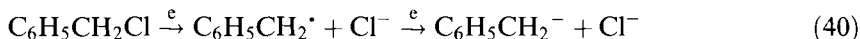


Figure 3 (continued)

up reaction is negligible. Figure 3(c) can immediately be divided into three zones according to the apparent value of n ; I: $t < 2$ ms, where $n = 1$, II: $2 \text{ ms} < t < 322$ ms, where $1 < n < 2$, and III: $t > 322$ ms, where $n = 2$. If k_1 is larger than 10 s^{-1} , the three zones would be shifted to a shorter time. A general zone diagram for the $E_r C_i E_r$ reaction mechanism can be obtained by introduction of a dimensionless rate constant $\lambda = k_1 t$. This diagram with the three zones is shown in Figure 3(d), where zone I with $n = 1$ is found at $\lambda < 0.02$. In French, this zone is called “diffusion pure 1” or DP1. In zone II ($0.02 < k_1 t < 3.22$), n is controlled by the competition between kinetics and diffusion and it is called the “kinetic intermédiaire” or the KI zone. Finally, the third zone ($\lambda > 3.22$), denoted as “kinetic pure,” or KP, is completely controlled by the follow-up process and here $n = 2$. Actually, the limits between the different zones depend on the accuracy of the current measurements. In the above discussion, the uncertainty of the current was assumed to be 2 %, but if the precision is higher, the KI zone would be further expanded at the expense of the

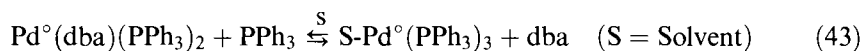
two other zones. In that case, the kinetic window of the CA technique is widened and quantitative measurements relying on the crossing between the different zones will be easier to carry out.

A simple example illustrating how the determination of n in CA could be used in a mechanistic description is the reduction of benzyl chloride in aprotic media. Suppose the value of n in the KP zone is one, unless an acid, BH, is present; then n turns out to be 2. This could be explained by the mechanism proposed in Eqs. 40–42.



In the first step, the two-electron reduction of benzyl chloride would lead to the formation of chloride and the benzyl anion (Eq. 40). The latter species may either react as a nucleophile or base. If it reacts with the starting material, benzyl chloride, in an $\text{S}_{\text{N}}2$ reaction (Eq. 42), then the flux of O is halved; this explains why the overall electron consumption corresponds to one. In the presence of an acid, on the other hand, the benzyl anion is protonated and n becomes equal to two (Eq. 43).

CA can also be used for the study of reaction schemes involving equilibrium reactions that are established prior to the heterogeneous electron-transfer step. For instance, the equilibrium constant, K_{43} , for the palladium ligand-exchange reaction shown in Eq. 43, where the ligand dba (dibenzylideneacetone) is substituted with PPh_3 (triphenylphosphine), was determined by CA [4]. Both Pd complexes can be oxidized, with $\text{S-Pd}^\circ(\text{PPh}_3)_3$ being the easiest to oxidize.



Thermodynamically, the equilibrium is positioned on the left-hand side, but when $\text{S-Pd}^\circ(\text{PPh}_3)_3$ is oxidized at the electrode, it is shifted to the right. Interestingly, in cyclic voltammetry, a plateau-shaped rather than peak-shaped voltammogram is seen, because the diffusion layer of $\text{S-Pd}^\circ(\text{PPh}_3)_3$ grows in an unusual manner as the concentration of $\text{S-Pd}^\circ(\text{PPh}_3)_3$ is buffered through the above equilibrium process. Still, it is difficult to quantify K_{43} in cyclic voltammetry on the basis of the shapes of the voltammograms. In CA, on the other hand, the situation is easier, as the current depends only on the electron stoichiometry and the amount of the substrate present. The value of K_{43} can therefore be obtained simply by measuring the ratio of the currents pertaining to the oxidation of $\text{S-Pd}^\circ(\text{PPh}_3)_3$ and $\text{Pd}^\circ(\text{dba})(\text{PPh}_3)_2$. Both oxidation processes are two-electron processes and the application of a small step time results in the equilibrium becoming “frozen” during the experiment, making only the equilibrium concentrations available for the electrode reactions.

The use of CA in combination with other techniques has also lead to a general methodology for the determination of n and D for electrode processes. Whereas the current in the CA technique for ordinary micro-electrodes is proportional to $n\sqrt{D}$

(see Eq. 39), there are other functional relationships between n and D in other techniques, i.e. in steady-state voltammetry with an ultramicroelectrode (see Section 2.4), the plateau current, i_{ss} , is directly proportional to nD . Thus, a comparison of the responses from two different techniques will allow the isolation of n and D if the areas of the electrodes used in the experiments are accurately known. This is not always the case, and reference compounds such as ferrocene (fc) or $\text{Fe}(\text{CN})_6^{4-}$ with known n ($= 1$) and D values are therefore often introduced into the cell. The procedure suggested by Amatore and coworkers is outlined below [5]: A cell containing substances O and ferrocene in known concentrations is prepared; separate CA experiments are carried out on O and ferrocene with the use of a microelectrode. The normalized current ratio a_{CA}^* is calculated according to Eq. 44.

$$a_{\text{CA}}^* = \frac{n_{\text{O}}}{n_{\text{fc}}} \left[\frac{D_{\text{O}}}{D_{\text{fc}}} \right]^{1/2} = \left(\frac{i_{\text{O}}}{i_{\text{fc}}} \right) \left(\frac{C_{\text{fc}}^*}{C_{\text{O}}^*} \right) \quad (44)$$

The microelectrode is then replaced by an ultramicroelectrode, and steady-state voltammograms of O and ferrocene are recorded; this allows calculation of the ratio between the normalized plateau currents, a_{ss}^* (Eq. 45).

$$a_{\text{ss}}^* = \frac{n_{\text{O}}}{n_{\text{fc}}} \left[\frac{D_{\text{O}}}{D_{\text{fc}}} \right] = \left(\frac{i_{\text{pl, O}}}{i_{\text{pl, fc}}} \right) \left(\frac{C_{\text{fc}}^*}{C_{\text{O}}^*} \right) \quad (45)$$

The number of electrons, n_{O} , involved in the reduction of O and the diffusion coefficient D_{O} can now easily be obtained from Eqs. 46 and 47, respectively.

$$n_{\text{O}} = \frac{(a_{\text{CA}}^*)^2 n_{\text{fc}}}{a_{\text{ss}}^*} \quad (46)$$

$$D_{\text{O}} = \left(\frac{a_{\text{ss}}^*}{a_{\text{CA}}^*} \right)^2 D_{\text{fc}} \quad (47)$$

Interestingly, n_{O} and D_{O} can also be obtained from a single CA experiment if an ultramicroelectrode is used [6]. Following the potential step, planar diffusion will initially dominate, as the diffusion layer is smaller than the radius of the electrode. The current thus follows the usual Cottrell equation (Eq. 39). Later in the CA experiment, however, the diffusion layer grows larger than the radius of the ultramicroelectrode, and spherical diffusion will now dominate. This results in a time-independent current, given by Eq. 48 if the electrode is disc shaped, or Eq. 49 for microsphere geometry.

$$\text{Disc:} \quad i_{\text{ss, disc}} = 4rn_{\text{O}}FD_{\text{O}}C_{\text{O}}^* \quad (48)$$

$$\text{Microsphere:} \quad i_{\text{ss, sphere}} = n_{\text{O}}FAD_{\text{O}}C_{\text{O}}^*/r \quad (49)$$

Combination of Eq. 48 with Eq. 39 (see also Eq. 80 in Section 2.4) results in Eq. 50

for a disc electrode, where D_O can be obtained from the slope of a plot of $i(t)/i_{ss, disc}$ versus $t^{-1/2}$.

$$\text{Disc: } i(t)/i_{ss, disc} = \left(\frac{\pi^{1/2} r}{4D_O^{1/2}} \right) t^{-1/2} + 1 \quad (50)$$

Afterwards, n_O can be calculated from Eq. 48 for a disc electrode by insertion of the value for D_O .

2.2.2 Sampled-Current Voltammetry

If the potential applied in CA is not polarized sufficiently to fulfil the condition $C_O(0, t) = 0$, the current also depends on the heterogeneous electron-transfer kinetics. The Cottrell expression given in Eq. 39 should for a reversible process then be modified according to Eq. 51, where i_{cot} denotes the Cottrell current.

$$i = \frac{i_{cot}}{1 + \left(\frac{D_O}{D_R} \right)^{1/2} \exp \left(\frac{nF}{RT} (E - E_O^\circ) \right)} \quad (51)$$

In a sampled current voltammetry experiment, small potential steps are made progressively as shown in Figure 4(a) within the typical limits of $E_O^\circ + 200$ mV and $E_O^\circ - 200$ mV for a reversible process. The i versus E curve can be constructed (Figure 4(b)) with the following characteristics for the reversible process: the limiting current, i_l , obtained at $E - E_O^\circ < -118$ mV, is proportional to C_O^* , $E_{3/4} - E_{1/4} = -\frac{56.4}{n}$ mV (Tomeš criteria) and a plot of E versus $\log[(i_l - i)/i]$ has a slope of $\frac{59.2}{n}$ mV at 25 °C.

2.2.3 Double-Potential-Step Chronoamperometry

A double-potential-step chronoamperometry (DPSC) experiment consists of two CA experiments. The potential of the second step is normally adjusted so that the R molecules formed upon reduction of O in the first step is reoxidized to O in a diffusion-controlled process, but it might also be adjusted to other values with the purpose of detecting other species formed [7]. In contrast to the CA technique, DPSC is a reversal technique, where the intermediates/products formed during the first step are probed directly in the second step. In this sense, it corresponds to a pump/probe experiment in photochemistry. While CA, in general, provides little if any information about follow-up chemistry, DPSC is a very strong tool for distinguishing between different mechanisms such as for example E, EC_i, and DIM1. It is also a good tool for the determination of the relevant rate constants.

Traditionally, a DPSC experiment on O is carried out in the following manner: Initially, the potential E_i is held at a much more positive value than E_O° , so no re-

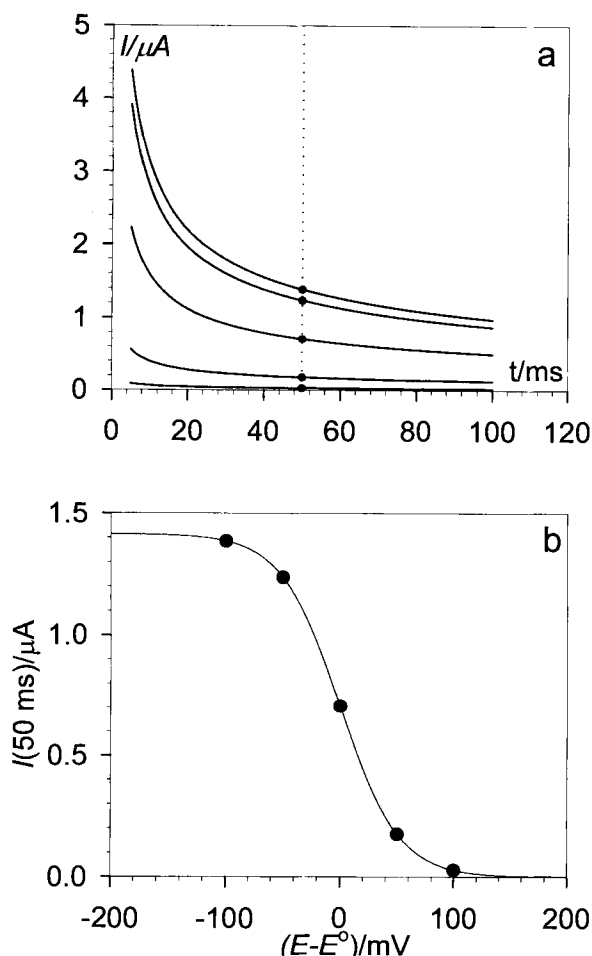


Figure 4. Sampled current voltammetry: a) Potential step experiments for E equal to $E_0^\circ + 100$ mV (lowest curve), $E_0^\circ + 50$ mV, E_0° , $E_0^\circ - 50$ mV, and $E_0^\circ - 100$ mV. b) The current recorded at 50 ms is plotted versus the step potential E as the sigmoid curve. The points shown in (a) are included in (b).

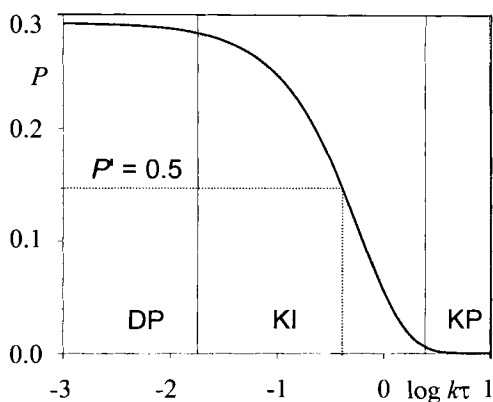
duction occurs. At $t = 0$, the potential is stepped abruptly to E_1 , a much more negative potential than E_0° ; this will generate R at a diffusion-controlled rate at the electrode surface for a period τ . At $t = \tau$ the potential is stepped to E_2 , which normally is equal to E_i , to reoxidize R to O. This potential value is maintained until $t = 2\tau$ and the current ratio $P = -\frac{i(2\tau)}{i(\tau)}$ can be evaluated. For simple reversible or

quasi-reversible heterogeneous electrode processes unaffected by kinetic follow-up reactions, P is equal to 0.293 for any value of τ and C_O^* . The reason why P is smaller than unity is that the R molecules formed at the electrode during the first step either diffuse towards the electrode surface or the bulk of the solution during the second step. In other words, only about 30 % of the generated R molecules are “recaptured” by the electrode.

Consider now an E_rC_i mechanism as shown in Eqs. 24 and 25, where, in a chemical step, R reacts further to the electroinactive species Y with a rate constant k . If this reaction proceeds on a timescale much smaller than τ , then all R is de-

Figure 5. Zone diagram for an E_rC_i mechanism based on DPSC measurements of the

current ratio $P = -\frac{i(2\tau)}{i(\tau)}$ vs the logarithm of the dimensionless rate constant, $k\tau$. The DP zone is for $k\tau < 0.018$, the KI zone for $0.018 < k\tau < 2.44$, and, finally, the KP zone for $k\tau > 2.44$. In the plot it is shown (dotted lines) how $\log k\tau_{0.5} = -0.393$ can be obtained from $P' = 0.5$.



pleted in the diffusion layer and thus $P = 0$. Should the chemical step, on the other hand, be so slow that it can be neglected, P is equal to 0.293, corresponding to a simple E_r mechanism. For the intermediate situation, where the timescale of the chemical reaction is comparable to τ , the value of P will be somewhere between 0 and 0.293. The above features are most conveniently illustrated by the construction of a zone diagram as shown in Figure 5, based on the dimensionless rate constant $\lambda = k\tau$. On the assumption that the precision of the current measurements is within 2 %, the DP zone appears for $\lambda < 0.018$ where the current response is totally unperturbed by the follow-up reaction. The KP zone, characterized by $P = 0$, is then found for $\lambda > 2.44$, and the intermediate zone KI, characterized by $0 < P < 0.293$, is observed for $0.018 < \lambda < 2.44$. From an experimental point of view, the ratio P can be varied simply by use of different step times τ in a series of experiments promoting the passage of the reaction system from one zone to another. It is difficult to accomplish the complete passage from $DP \rightarrow KI \rightarrow KP$, as it would require a variation in τ of a factor of 130 within the time window of the DPSC technique that normally ranges from 1 to 1000 ms. Fortunately, a shift between just two zones is usually sufficient for kinetic analysis; the rate constant may be extracted from a comparison between the experimental plot of P vs $\log \tau$ and the simulated curve shown in Figure 5.

The smallest first-order rate constant that can be measured in this manner from the $DP \rightarrow KI$ passage is $0.018/\tau_{\max} = 0.018 \text{ s}^{-1}$, assuming $\tau_{\max} = 1000 \text{ ms}$. Similarly, the maximum first-order rate constant that can be measured from the $KP \rightarrow KI$ passage is expected to be $2.44/\tau_{\min} = 2.4 \times 10^3 \text{ s}^{-1}$, with τ_{\min} equal to 1 ms.

For some applications, the P ratio is normalized by division by 0.293. This means that the normalized parameter $P' = P/0.293$ like P is zero in the KP zone for an E_rC_i mechanism, but one in the DP zone. A particular simple approach for the determination of rate constants by DPSC is based on the measurement of the step time $\tau_{0.5}$ at which P' is equal to 0.5 (i.e., $P = 0.1464$). For the E_rC_i mechanism, the equation $\log \lambda_{0.5} = \log(k\tau_{0.5}) = -0.393$ holds; this is illustrated by the dotted lines in Figure 5. Thus, the rate constant k can easily be calculated as $0.405/\tau_{0.5}$. Similar simple relationships have been obtained for other mechanisms, and they are included in Table 1.

Table 1. Equations for calculating rate constants for simple reaction mechanisms based on the reaction order approach for DPSC [137].

Mechanism	Rate constant, k	$\frac{\partial \log \tau_{0.5}}{\partial \log C_O^*}$
$E_r C_i$	$0.405/\tau_{0.5}$	0
DISP ($E_r C_i E_h$)	$0.272/\tau_{0.5}$	0
DIM1	$0.830/(\tau_{0.5} C_O^*)$	-1
DIM2	$0.678/(\tau_{0.5} C_O^*)$	-1

From the definition of $\lambda_{0.5}$, it follows that $\tau_{0.5}$ is inversely proportional to the rate constant of the chemical reaction. The influence of substrate concentration, proton concentration (pH), and temperature on the reaction rate can therefore be deduced simply from the variation in $\tau_{0.5}^{-1}$. For example, the reaction order of the substrate can be determined as $-\partial \log \tau_{0.5} / \partial \log C_O^*$. Likewise, apparent activation energies, E_a , may be obtained from plots of $\tau_{0.5}^{-1}$ against the inverse temperature (T^{-1}), since the slope is equal to $-E_a/R$ [8]. Kinetic isotope effects can also easily be quantified as $\frac{k_H}{k_D} = \frac{\tau_{0.5,D}}{\tau_{0.5,H}}$ [9].

A sophisticated use of DPSC has been that of the selection of step potentials for the detection of various intermediates. One such example was provided by Amatore *et al.*, showing that the formation $Cr_2(CO)_{10}^{2-}$ on a short timescale upon reduction of $Cr(CO)_6$ was by an $E_r C_i C_2$ mechanism involving the dimerization of two $Cr(CO)_5^{-\bullet}$ molecules [7]. This mechanism differs from the one observed on a longer timescale, where $Cr(CO)_5^{2-}$, formed in a two-electron reduction of $Cr(CO)_6$, can react with $Cr(CO)_6$ to yield $Cr_2(CO)_{10}^{2-}$ and CO.

The development of ultramicroelectrodes with characteristic physical dimensions below 25 μm has allowed the implementation of faster transients in recent years, as discussed in Section 2.4. For CA and DPSC this means that a smaller step time τ can be employed, while there is no advantage to a larger τ . Rather, steady-state currents are attained here, owing to the contribution from spherical diffusion for the small electrodes. However, by combination of the use of ultramicroelectrodes and microelectrodes, the useful time window of the techniques is widened considerably. Compared to scanning techniques such as linear sweep voltammetry and cyclic voltammetry, described in the following, the step techniques have the advantage that the responses are independent of heterogeneous kinetics if the potential is properly adjusted. The result is that fewer parameters need to be adjusted for the determination of rate constants.

2.3 Linear Sweep Voltammetry and Cyclic Voltammetry

In linear sweep voltammetry (LSV), the potential of the working electrode is changed linearly from an initial to a final potential in a single scan. If the potential

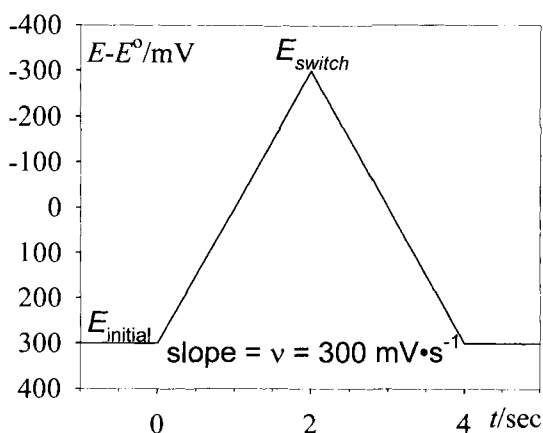


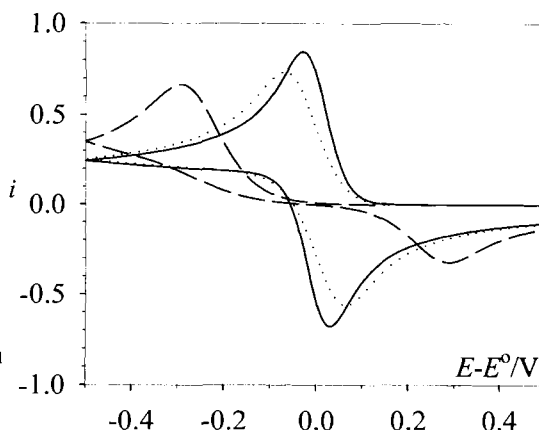
Figure 6. The potential vs time plot for cyclic voltammetry. For linear sweep voltammetry only the first linear ramp is used.

limits are adjusted so that the standard potential of the substrate O is positioned between the two limits, a reduction process will take place according to Eq. 2. In cyclic voltammetry (CV), two scans are applied, in which the potential is changed linearly from an initial potential to a switch potential and then back to the initial potential. The characteristic E vs t plot for this technique is shown in Figure 6. A linear sweep voltammogram or a cyclic voltammogram is a plot of the measured current versus the applied potential, as illustrated in Figure 7 for three specific cases, the reversible, quasi-reversible, and irreversible processes. These cases will be discussed in detail later.

In CV, substrates are generally activated during the first scan by electron transfer and the reverse scan is then used to detect the activated substrates. The formation of other electrochemically active intermediates or products can also be revealed by these scans or possibly by the performance of multiscans. The CV technique is, like DPSC, similar to the pump/probe experiment known from photochemistry, but in CV, unique knowledge about the thermodynamic properties of the intermediates

Figure 7. Simulated cyclic voltammograms pertaining to $O + e \rightleftharpoons R$ for three different values of the dimensionless heterogeneous rate constant

$\psi = \frac{\left(\frac{D_O}{D_R}\right)^{1/2} k^\circ}{[D_O \pi \nu (nF/RT)]^{1/2}}$: a) solid line, $\psi = 30$, b) dotted line, $\psi = 0.3$ and c) dashed line, $\psi = 0.03$. If $D_O = D_R = 10^{-5} \text{ cm}^2 \text{ s}^{-1}$, $\nu = 1 \text{ V s}^{-1}$ and $T = 25^\circ \text{C}$, then a) $k^\circ = 1 \text{ cm s}^{-1}$, b) $k^\circ = 0.01 \text{ cm s}^{-1}$ and c) $k^\circ = 0.001 \text{ cm s}^{-1}$. Note that the latter case with $k^\circ = 0.001 \text{ cm s}^{-1}$ is not strictly irreversible according to the definitions given for k° below.



can be obtained from the measured potentials. The time parameter in the experiment is the sweep rate, v , that is, the rate at which the potential is changed with time. The introduction of ultramicroelectrodes has extended the upper limit of sweep rates in CV to 1 MV s^{-1} , allowing the detection and characterization of intermediates with a lifetime as small as $1 \mu\text{s}$.

If O is the only species initially present in the electrochemical cell and there is no homogeneous kinetics, migration and convection, so the mass transport occurs by diffusion, the LSV experiment can be characterized mathematically by the following equations.

$$\text{Fick's second law:} \quad \frac{\partial C_{\text{O}}(x, t)}{\partial t} = D_{\text{O}} \frac{\partial^2 C_{\text{O}}(x, t)}{\partial x^2} \quad (52)$$

$$\text{Initially:} \quad t = 0, \quad C_{\text{O}}(x, 0) = C_{\text{O}}^*; \quad C_{\text{R}}(x, 0) = 0 \quad (53)$$

$$\text{Far from the electrode:} \quad x \rightarrow \infty, \quad C_{\text{O}}(x, t) = C_{\text{O}}^*; \quad C_{\text{R}}(x, t) = 0 \quad (54)$$

$$\text{Electrode surface:} \quad x = 0,$$

$$\text{Reversible:} \quad \frac{C_{\text{O}}(0, t)}{C_{\text{R}}(0, t)} = \exp\left(\frac{nF(E_i - vt - E_{\text{O}}^{\circ})}{RT}\right) \quad (55)$$

$$\begin{aligned} \text{Quasi-reversible:} \quad & D_{\text{O}} \left(\frac{\partial C_{\text{O}}(x, t)}{\partial x} \right)_{x=0} \\ &= k^{\circ} \left[\exp\left(\frac{-\alpha nF(E_i - vt - E_{\text{O}}^{\circ})}{RT}\right) C_{\text{O}}(0, t) \right. \\ &\quad \left. - \exp\left(\frac{(1 - \alpha)nF(E_i - vt - E_{\text{O}}^{\circ})}{RT}\right) C_{\text{R}}(0, t) \right] \end{aligned} \quad (56)$$

$$\begin{aligned} \text{Irreversible:} \quad & D_{\text{O}} \left(\frac{\partial C_{\text{O}}(x, t)}{\partial x} \right)_{x=0} \\ &= k^{\circ} \exp\left(\frac{-\alpha nF(E_i - vt - E_{\text{O}}^{\circ})}{RT}\right) C_{\text{O}}(0, t) \end{aligned} \quad (57)$$

$$\text{Fick's first law:} \quad i(t) = nFAD_{\text{O}} \left(\frac{\partial C_{\text{O}}(x, t)}{\partial x} \right)_{x=0} = -nFAD_{\text{R}} \left(\frac{\partial C_{\text{R}}(x, t)}{\partial x} \right)_{x=0} \quad (58)$$

Note that in the description of the conditions at the electrode surface, the exact nature of the electron-transfer process should be taken into account, that is, if it is under thermodynamic control as in the reversible case (Eq. 55) or kinetically controlled as in the quasi-reversible (Eq. 56) and irreversible cases (Eq. 57). This is contrary to the situation in a CA and DPSC experiment where the potential is usually stepped to a potential value where the surface concentration of O becomes

zero and the process thus becomes diffusion-controlled, regardless of the value of the standard heterogeneous rate constant.

For the LSV and CV techniques, the concept of reversibility/irreversibility is therefore very important. Electrochemists are responsible for some confusion about the term irreversible, since a reaction may be electrochemically irreversible, yet chemically reversible. In electrochemistry, the term irreversible is used in a double sense, to describe effects from both homogeneous and heterogeneous reactions. In both cases, the irreversible situation arises when deviations from the Nernst equation can be seen as fast changes in the electrode potential, E , are attempted and the apparent heterogeneous rate constants, k_{app} , for the O/R redox couple is relatively small. The heterogeneous rate constant can be split into two parts: a constant factor in terms of the standard rate constant, k° , and an exponential function of the overpotential ($E - E^\circ$), as expressed in Eq. 59, where only the reductive process is considered (see also Eq. 5).

$$k_{\text{app}} = k^\circ \exp \left[\frac{-\alpha n F}{RT} (E - E^\circ) \right] \quad (59)$$

Several factors, such as large structural differences between O and R or hindered access for the redox center approaching the electrode surface, can lower k° . The apparent heterogeneous rate constant might also be diminished by the potential factor when the overpotential, $E - E^\circ$, is positive, that is, $E > E^\circ$, which can be the case when the heterogeneous reaction is followed by a very fast chemical reaction. To keep these situations separate, we will first look at charge-transfer reactions where no preceding or following chemical reactions are present, and afterwards we will consider the effect of including chemical reactions.

2.3.1 Charge-Transfer Reactions

Charge-transfer reactions (Eq. 2) occurring at the electrode surface are conveniently classified as Nernstian (reversible), quasi-reversible, or irreversible, depending on the standard heterogeneous rate constant, k° . If the rate constant is large, the surface concentrations will be adjusted to the electrode potential as expressed in the Nernst equation (Eq. 1). A practical definition of reversibility is conditions where the ratio of surface concentrations of O and R is constantly in accordance with the Nernst equation. Redox reactions are quasi-reversible/irreversible when deviations from the Nernst equation can be detected. The irreversible case is characterized by the complete lack of a reverse reaction, while for the quasi-reversible case, the reverse reaction has to be considered although the electron-transfer kinetics is slow. The assignment of a given redox system to either of the three cases depends on the electrochemical technique used and the timescale of the experiment. In LSV and CV, the timescale is expressed by $\frac{RT}{Fv}$, which roughly corresponds to the time needed to scan the potential from E° to the peak potential for a reversible process.

Matsuda and Ayabe suggest the following zone boundaries for the heterogeneous kinetics when $D_O = D_R$, $\alpha = 0.5$, $T = 25^\circ\text{C}$, and ν is given in V/s [10]:

$$\text{Reversible: } k^\circ \geq 0.3\sqrt{n\nu} \text{ cm/s}$$

$$\text{Quasi-reversible: } 0.3\sqrt{n\nu} \text{ cm/s} \geq k^\circ \geq 2 \times 10^{-5}\sqrt{n\nu} \text{ cm/s}$$

$$\text{Irreversible: } k^\circ \leq 2 \times 10^{-5}\sqrt{n\nu} \text{ cm/s}$$

Thus, at high $k^\circ/\nu^{1/2}$ ratios (fast heterogeneous kinetics or low sweep rate), the cyclic voltammogram will appear reversible. Increase of the sweep rate will gradually transform it into a quasi-reversible and irreversible voltammogram. In the kV/s range of sweep rates, even the redox pair with the largest heterogeneous rate constants k° of 10 cm/s will appear quasi-reversible.

2.3.2 Nernstian Charge Transfer

The cyclic voltammogram for a Nernstian or reversible charge-transfer process, as shown in Figure 7(a), is characterized by the presence of peaks on both the forward and reverse scans. The peak shape is due to the fact that the current at first increases exponentially because of the increasing overpotential as predicted by the current-potential equation (Eq. 8), but later the mass-transport process in terms of diffusion manifests itself through $C_O(0, t)$. At sufficiently negative potentials on the forward scan and at sufficiently positive potentials on the reverse scan, compared to E° , the current becomes limited by the diffusion process and will thus be proportional to $t^{-1/2}$. In the intermediate region of mixed control, the peaks appear at positions that are independent of sweep rate and substrate concentration. The peak potential for the forward scan E_p is equal to $E_O^\circ - 1.109RT/nF = E_O^\circ - 28 \text{ mV}$ for $n = 1$ and $T = 25^\circ\text{C}$, and the separation between the oxidation and reduction peak potentials, ΔE_p , is 57 mV. (The exact value is slightly dependent on the chosen switch potential). Moreover, the half-peak width, $E_p - E_{p/2}$, is equal to -56.5 mV . The peak current is proportional to the substrate concentration and $\nu^{1/2}$, while the peak current ratio, $-i_{p, \text{ox}}/i_{p, \text{red}}$, is unity, and independent of ν [1]. Potentials of thermodynamic significance can, strictly speaking, only be obtained from reversible voltammograms.

2.3.3 Quasi-Reversible and Irreversible Charge Transfer

If k° is relatively small, the ratio of the surface concentrations, $C_O(0, t)/C_R(0, t)$ deviates from the value provided by the Nernst equation. For a reduction process this means that $C_O(0, t)$ would be higher and $C_R(0, t)$ smaller at a given value of E than predicted from Eq. 1. Expressed differently, a larger overpotential is required when k° is small if a current similar to that in the reversible case is to be obtained. The result is that the voltammograms will be displaced to lower potentials, as

Table 2. The difference between the oxidative and reductive peak potentials, ΔE_p , as a function

of the dimensionless heterogeneous rate constant, $\psi = \frac{\left(\frac{D_O}{D_R}\right)^{\alpha/2} k^\circ}{[D_O \pi \nu (nF/RT)]^{1/2}}$. The ΔE_p values were obtained from digital simulation with $D_O = D_R = 10^{-5} \text{ cm}^2 \text{ s}^{-1}$, $T = 25^\circ\text{C}$, $n = 1$, and switch potential, $E_\lambda = E_O^\circ - 400 \text{ mV}$.

ψ	$\Delta E_p/\text{mV}$	ψ	$\Delta E_p/\text{mV}$
20	58.8	0.1	216
10	60.1	0.05	284
5	62.7	0.02	378
2	70.3	0.01	450
1	82.4	0.005	520
0.5	105	0.002	620
0.2	157	0.001	690

shown in Figure 7. These are the quasi-reversible (curve b) and irreversible (curve c) cases.

For quasi-reversible charge transfer, E_p and ΔE_p are functions of ν , k° , and α . Moreover, i_p is not proportional to $\nu^{1/2}$ as found for reversible charge transfer. The cyclic voltammograms are described by the dimensionless parameters α and ψ defined in Eq. 60.

$$\psi = \frac{\left(\frac{D_O}{D_R}\right)^{\alpha/2} k^\circ}{[D_O \pi \nu (nF/RT)]^{1/2}} \quad (60)$$

The peak-potential difference ΔE_p depends mainly on the kinetic parameter ψ , as illustrated in Table 2. By measurement of ΔE_p as a function of ν for a given system, k° can be estimated. However, great care should be exerted to ensure that uncompensated resistance does not contribute to the value of ΔE_p , since this would hamper the procedure. Clearly, the use of ultramicroelectrodes can be recommended for this kind of measurements, as the ohmic drop is much smaller here compared to microelectrodes of normal size. This is particularly true when high sweep rates are required for determining large values of k° (see Section 2.4).

If k° becomes even smaller, a new limiting form is attained, that is, the irreversible case, where the backward reaction is negligible at the potentials where the forward process takes place. For the totally irreversible wave, i_p is proportional to the bulk concentration C_O^* and $\nu^{1/2}$, as was the case for the reversible charge-transfer case even though the absolute current here was larger. However, E_p is shifted in a negative direction by $30/\alpha n \text{ mV}$ for each decade change in ν , and the wave is broad with a half-peak width, $E_p - E_{p/2}$, of $-47.7/\alpha n \text{ mV}$, compared to the -56.5 mV for the reversible case. In this situation, there is no straightforward access to either k° nor E_O° , unless other techniques such as convolution are employed [11].

2.3.4 Ohmic Drop

The potential applied to the working electrode is always measured relative to a reference electrode. In organic solvents, a substantial potential drop might be included in the measurements due to the non-zero resistance, R , between the working electrode and the reference electrode. The real potential felt at the working electrode is therefore different from the applied potential. The potential drop, often referred to as the ohmic drop or iR drop, is proportional to the current, i , at the working electrode. As a result, the ohmic drop can be substantial if high sweep rates are employed for the study of high substrate concentrations at large electrodes in resistive media. For instance, in *N,N*-dimethylformamide or acetonitrile at microelectrodes (diameter ≈ 1 mm), with substrate concentrations in the millimolar range, the ohmic drop is important for sweep rates higher than 1 V s^{-1} . The ohmic drop may partly be compensated by positive feedback systems incorporated in the potentiostats, but even then this does not work if sweep rates higher than 1000 V s^{-1} are applied at normal-sized microelectrodes. For ultramicroelectrodes, the ohmic drop is less important and can be neglected for $v < 1000 \text{ V s}^{-1}$.

2.3.5 Coupled Chemical Reactions

So far we have assumed that the redox couple in the charge-transfer reaction is stable towards chemical reactions within the timescale of the LSV or CV experiments. However, in many cases the charge transfer at the electrode to or from a molecule will result in the formation of a radical species (odd-electron) or another reactive species which will react either at the electrode or in homogeneous solution to form more stable products. If R undergoes a fast homogeneous reaction, then more O has to be converted to R at the electrode surface to maintain the surface concentration ratio as required by the Nernst equation (Eq. 1). A fast follow-up reaction will therefore cause a reduction current at less extreme potentials than if no chemical reaction takes place. This is illustrated in Figure 8, where the cyclic voltammograms pertaining to an E_rC_i and an E_r mechanism are shown. The shift in potential for the E_rC_i mechanism renders the overpotential, $E - E_O^\circ$, positive ($E > E_O^\circ$); this implies that the apparent heterogeneous rate constant is diminished by the potential factor (see Eq. 59). Moreover, the shift in potential will depend on the type of follow-up reaction. For a first-order follow-up reaction, the peak potential will be shifted according to Eq. 61, while for a second-order process Eq. 62 applies.

$$\text{First order:} \quad \partial E_p / \partial \log(k/v) = 29.6 \text{ mV/decade} \quad \text{at } 25^\circ\text{C} \quad (61)$$

$$\text{Second order:} \quad \partial E_p / \partial \log(kC_O^*/v) = 19.7 \text{ mV/decade} \quad \text{at } 25^\circ\text{C} \quad (62)$$

It should be emphasized that these slopes are only valid when $n = 1$ and the wave is purely kinetic, that is, the chemical reaction is so fast that a stationary state is established by mutual compensation of the chemical reaction of the intermediate

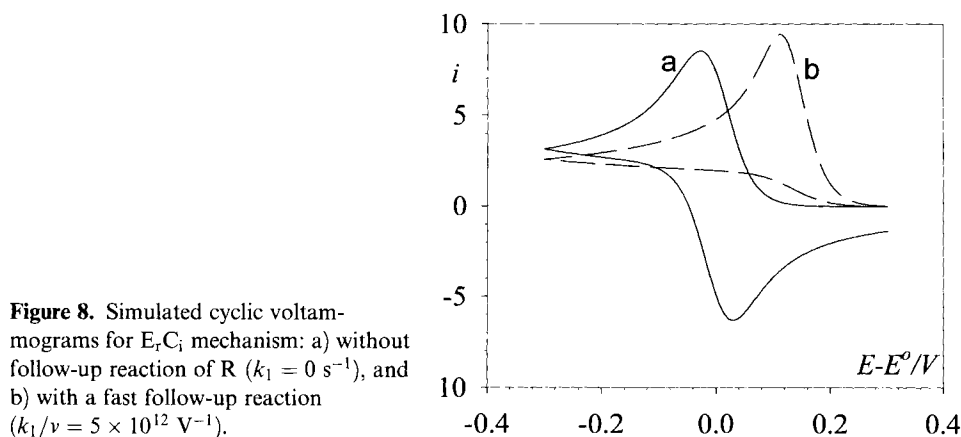


Figure 8. Simulated cyclic voltammograms for $E_r C_i$ mechanism: a) without follow-up reaction of R ($k_1 = 0 \text{ s}^{-1}$), and b) with a fast follow-up reaction ($k_1/v = 5 \times 10^{12} \text{ V}^{-1}$).

and the diffusion processes. Increasing the sweep rate will make the voltammogram appear reversible, and the pure diffusion zone is then attained.

Very thorough theoretical analyses of the theoretical LSV slopes, $\partial E_p / \partial \log v$ and $\partial E_p / \partial \log C_O^*$, for various reaction mechanisms were carried out by Nicholson and Shain [12, 13] and Savéant *et al.* [14–17]. These slopes are very useful in the elucidation of reaction mechanisms. By adaptation of the approach proposed by Parker [18], it is possible to develop simple general equations that directly relate the LSV slopes to the kinetic rate law of the process of interest. The rate law is assumed to be of the general type

$$\text{Rate} = k' C_O^o C_R^r C_I^i C_X^x \quad (63)$$

where the subscript O refers to the substrate, R is the primary intermediate, I is a secondary intermediate that may be formed during the process, and X is an additional reactant. The superscripts o, r, i, and x are the reaction orders in the participating species. The LSV slopes for mechanisms corresponding to the above rate law can be predicted directly from Eqs. 64 to 66.

$$\partial E_p / \partial \log v = \frac{-2.3RT}{nF(1+r)} \quad (64)$$

$$\partial E_p / \partial \log C_O^* = \frac{2.3RT(o+r+i-1)}{nF(1+r)} \quad (65)$$

$$\partial E_p / \partial \log C_X^* = \frac{2.3RTx}{nF(1+r)} \quad (66)$$

In Table 3, the LSV slopes for some of the most common mechanisms are listed.

As an illustrative example of the influence of homogeneous reactions on the cyclic voltammetric behavior, the oxidation of an anion R^- to the corresponding short-

Table 3. Linear sweep voltammetry slopes from reaction orders^{a,b}

No.	Mechanism	Rate	<i>r</i>	<i>o</i>	<i>i</i>	<i>x</i>	<i>S</i> ₁	<i>S</i> ₂	<i>S</i> ₃
1	$R + X \xrightarrow{k} C$	$k C_R C_X$	1	0	0	1	-1/2	0	1/2
2	$R + X \xrightarrow{k} C$ $C + R \rightleftharpoons D + O$	$k C_R C_X$	1	0	0	1	-1/2	0	1/2
3	$2R \xrightarrow{k} C + O$ $C \rightarrow D$	$k C_R^2$	2	0	0	0	-1/3	+1/3	0
4	$2R \xrightleftharpoons{K} C + O$ $C + X \xrightarrow{k} D$	$k K C_R^2 C_X / C_O$	2	-1	0	1	-1/3	0	1/3
5	$2R \xrightarrow{k} C$	$k C_R^2$	2	0	0	0	-1/3	+1/3	0
6	$R + O \xrightarrow{k} C$	$k C_R C_O$	1	1	0	0	-1/2	+1/2	0
7	$R + O \xrightleftharpoons{K} C$ $C + R \xrightarrow{k} D + O$	$k K C_R^2 C_O$	2	1	0	0	-1/3	+2/3	0
8	$R + X \xrightleftharpoons{K} C + I$ $C + R \xrightarrow{k} D$	$k K C_R^2 C_X / C_I$	2	0	-1	1	-1/3	0	1/3
9	$O + 2e \rightleftharpoons R'$ $R' + X \xrightarrow{k} F$	$k C_{R'} C_X$	1	0	0	1	-1/4	0	1/4
10	$R' + O \xrightarrow{k} G$	$k C_{R'} C_O$	1	1	0	0	-1/4	+1/4	0
11	$R' + X \xrightleftharpoons{K} F + I$ $F \xrightarrow{k} G$	$k K C_{R'} C_X / C_I$	1	0	-1	0	-1/4	-1/4	1/4

^a*S*₁, *S*₂, and *S*₃ refer to $dE_p/d \log v$, $dE_p/d \log C_O^*$, and $dE_p/d \log C_X^*$, respectively, and are expressed in units of $(\ln 10)RT/nF$. The signs of *S*₁, *S*₂, and *S*₃ change if oxidation processes are considered.

^bTable 3 is taken from Ref. [18] with slight modifications.

lived radical R^* , followed by dimerization will be treated. The DIM1 mechanism is shown in Eqs. 67–68.



Transient radicals generated directly at the electrode by reduction or oxidation of a precursor will be present adjacent to the electrode in a thin reaction layer that is much smaller than the diffusion layer. Therefore, the concentration of the radical will be of the same order as the precursor concentration and second-order reactions become likely. This is contrary to most common radical reactions involving homogeneous approaches where the steady-state concentration of the radical is very low, because of slow rate-controlling formation and fast follow-up reactions. For the DIM1 mechanism $\partial E_p / \partial \log v = 19.7$ mV and $\partial E_p / \partial \log C_{R^-}^* = -19.7$ mV in the kinetic zone, noting that Eq. 67 is an oxidation process. The rate constant for the dimerization of the radical, k_{dim} , can often be estimated or assumed to be within one or two orders of magnitude from the diffusion limit. On this basis, it is possible to correct the measured totally irreversible oxidation potentials to standard potentials by Eq. 69.

$$E^\circ = E_p^{\text{ox}} + 0.0197 \log \left(\frac{k_{\text{dim}} C_{\text{R}^-}^*}{58.4\nu} \right) - 0.0232 \text{ V} \quad \text{at } 25^\circ\text{C} \quad (69)$$

If $C_{\text{R}^-}^*$ is 1 mM and ν is 0.1 Vs⁻¹, E° will be at a potential 60 mV higher than the observed irreversible oxidation potential, E_p^{ox} , on the assumption that k_{dim} is equal to 10⁸ M⁻¹ s⁻¹. For many solvents, the diffusion-controlled rate constant k_d is close to 10¹⁰ M⁻¹ s⁻¹, so the difference between E° and E_p^{ox} can at most be 100 mV. Recent examples where this procedure have been applied can be found in Refs. [19, 141]. Often the correction procedure is used in combination with fast cyclic voltammetry at ultramicroelectrodes when the voltammogram appears totally irreversible at the highest possible sweep rate, ν_{max} . Under these circumstances, the lower limit for k_{dim} can be estimated from Eq. 70.

$$k_{\text{dim}} > \frac{31.1\nu_{\text{max}}}{C_{\text{R}^-}^*} \text{ M}^{-1} \text{ s}^{-1} \quad \text{at } 25^\circ\text{C} \quad (70)$$

If $C_{\text{R}^-}^*$ is 1 mM and the maximum sweep rate applicable experimentally is, for example, 100 kV s⁻¹, then k_{dim} is at minimum $3 \times 10^9 \text{ M}^{-1} \text{ s}^{-1}$, which narrows the range of k_{dim} to 3×10^9 to $10^{10} \text{ M}^{-1} \text{ s}^{-1}$ (i.e., k_d). With k_{dim} known within such a narrow range, E° can be estimated rather precisely by Eq. 69, if E_p^{ox} is measured accurately at low sweep rate at a normal microelectrode.

2.3.6 Mixed Charge Transfer and Kinetic Control

In the preceding chapter, the charge transfer was assumed to be so fast that it was Nernstian. However, this condition cannot always be fulfilled, either because the charge transfer is intrinsically slow (i.e., k° is small), or because the follow-up reaction causes the voltammetric wave to shift, thereby lowering the apparent heterogeneous rate constant k_{app} by the potential factor (Eq. 59). Let us consider once more the DIM1 (EC₂) mechanism, but now open for the possibility that the heterogeneous step is not necessarily reversible. It is then convenient to define two dimensionless parameters related to k° and k_{dim} :

$$A = \frac{k^\circ}{(D_O\nu)^{1/2}} \left(\frac{RT}{nF} \right)^{1/2} \quad (71)$$

$$\lambda = \frac{k_{\text{dim}} C_O^*}{\nu} \left(\frac{RT}{nF} \right) \quad (72)$$

The general behavior expected in LSV may then be computed by digital simulations [20] and the results can be conveniently visualized in a zone diagram as shown in Figure 9. For $\log \lambda < -1$, the dimerization reaction has no effect whatsoever, and the cyclic voltammetric behavior pertains to the reversible, quasi-reversible (QR), or totally irreversible charge transfer (IR), depending on the value of A . For very large

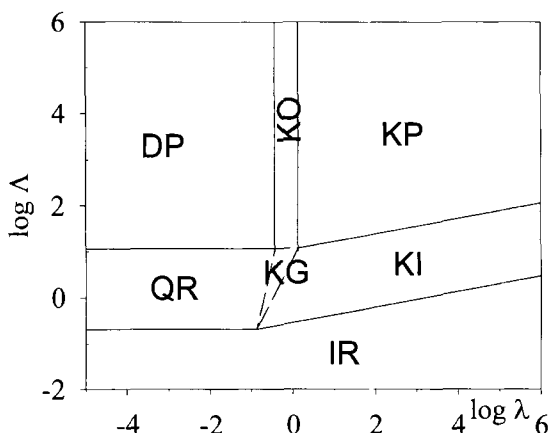
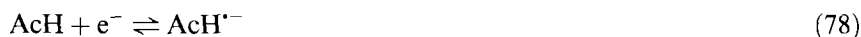


Figure 9. Zone diagram for a DIM1 (EC₂) mechanism, where the parameters λ and A are defined in the text.

values of A ($\log A > 2$) the charge transfer is always Nernstian and the wave is influenced by the follow-up reaction going from the pure diffusion zone, DP, over an intermediate region, KO, and further to the kinetically controlled zone, KP, for a large value of λ . The effects of joint electron transfer and chemical irreversibility are mainly manifested in zone KG.

The reaction-order approach and zone diagrams are very useful, as they often provide the necessary information from which a reaction mechanism can be proposed. Therefore, the first step in the elucidation of a reaction mechanism using LSV is usually the measurement of the diagnostic criteria, i.e. the peak potential and half-peak width as a function of sweep rate and concentrations of the reactants involved. Once a working scheme is set up, all the information available in the cyclic voltammograms should be considered, not just the peak potentials and peak widths, to either confirm or modify the proposed mechanism. In practice, this is done by comparison of experimental cyclic voltammograms with digitally simulated voltammograms. In recent years many simulation programs have become commercially available, and voltammograms for even rather complex mechanisms can be calculated straightforwardly. An example of this approach concerns the electrochemical reduction of 3-chloroacetophenone (AcCl) in aprotic solvents [21]. In cyclic voltammetry, a one-electron quasi-reversible system is seen at high sweep rates, showing that the reduction process leads to the formation of the radical anion in the first step. At lower sweep rates, the wave becomes irreversible due to follow-up reactions and a second peak pertaining to one of the products formed, acetophenone (AcH), appears at lower, that is, more negative potentials. This could be confirmed from a comparison with an authentic sample of AcH. The results point towards the presence of a cleavage reaction, where the carbon–chlorine bond in the radical anion of 3-chloroacetophenone is fragmented. However, measurement of the LSV slopes $\left(\frac{\partial E_p}{\partial \log v} \approx -19.7 \text{ mV} \text{ and } \frac{\partial E_p}{\partial \log C_{\text{AcCl}}^*} \approx +19.7 \text{ mV} \right)$ for similar acetophenone systems reveals that the radical anion is also involved in a dimeriza-

tion reaction (DIM1). The following reaction scheme (Eqs. 73–79) was proposed.



This scheme describes the competition between, on one hand, the dimerization process (Eq. 74) and, on the other hand, the cleavage reaction (Eq. 75) of the radical anion, followed by fast hydrogen abstraction (Eq. 76) from the solvent SH (forming AcH) and reduction (Eq. 77) of the thus generated solvent radical. The second wave observed in the voltammogram is attributed to reduction (Eq. 78) of the generated acetophenone, the radical anion of which may reduce the remaining AcCl in a homogeneous reaction (Eq. 79). We have omitted the dimerization reaction of $\text{AcH}^{\bullet-}$ and the cross reaction between $\text{AcCl}^{\bullet-}$ and $\text{AcH}^{\bullet-}$ from the above scheme for the sake of simplicity.

Figure 10 shows a comparison of the simulated and experimental cyclic voltammograms; it encompasses the waves of both the starting compound, 3-chloroacetophenone, and the acetophenone formed during the scan. While the first wave is described well theoretically, the second wave of acetophenone deviates somewhat. The fit to the second wave may be improved by introduction of new processes involving the radical anion of acetophenone besides the dimerization and cross reactions. However, since reproducible values of k_{cl} and $2k_{\text{dim}}$ could be obtained by optimization of the fit to the first cyclic voltammetric wave for the different substrate concentrations and sweep rates employed, these reactions were not considered in greater detail.

2.4 Ultra microelectrodes

Since the mid-eighties, ultramicroelectrodes (UMEs) have been developed for many different applications. At an early stage, they were employed in biological and medical research where, for example, small electrodes were implanted in rat brains. The main difference between microelectrodes and UMEs is the mode of diffusion that shifts from planar to spherical, depending on the exact thickness of the diffusion layer. As long as the diffusion layer is smaller than the dimension of the electrode, the diffusion will also be planar for an UME. UMEs could be defined as

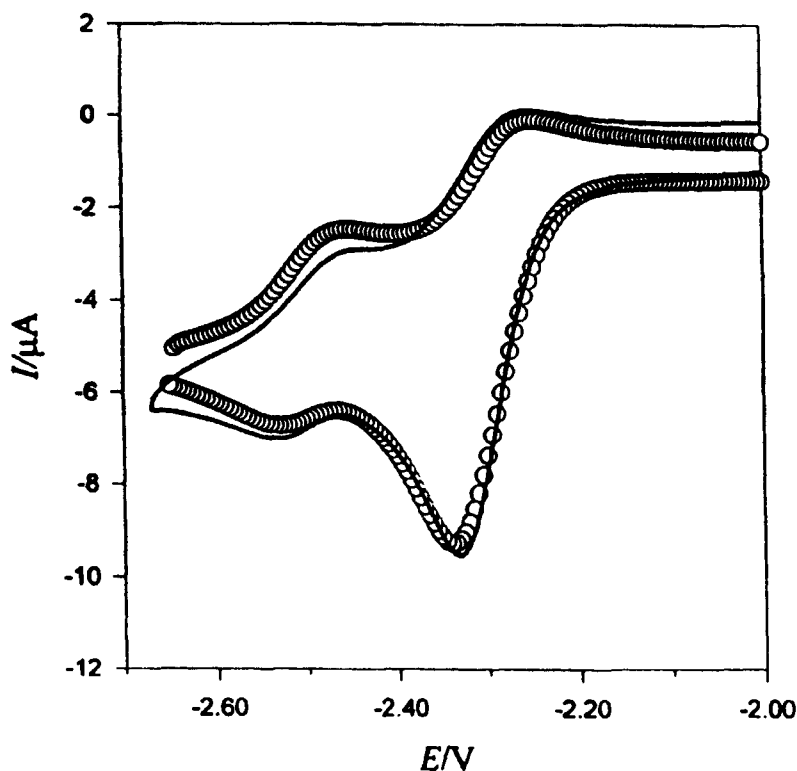


Figure 10. Cyclic voltammogram of 3-chloroacetophenone at a concentration of 2 mM, obtained at a glassy carbon electrode in THF/0.3 M Bu₄NBF₄ at a sweep rate of 0.2 V s⁻¹. The potential *E* is measured against fc⁺/fc. The simulated curve (O) is obtained with $k_c = 0.6 \text{ s}^{-1}$ and $2k_{\text{dim}} = 2 \times 10^3 \text{ M}^{-1} \text{ s}^{-1}$. Taken from H. Jensen and K. Daasbjerg, *Acta Chem. Scand.* 52:1151 (1998) [21].

electrodes where spherical diffusion dominates after 1 s in a CA experiment. Since the Cottrell equation given in Eq. 39 is valid only for planar diffusion, an extra term should be added to incorporate the contribution from spherical diffusion as stated in Eq. 80, where r is the radius of a microsphere electrode.

$$i = nFAD_0C_O^* \left[\frac{1}{(\pi D_0 t)^{1/2}} + \frac{1}{r} \right] \quad (80)$$

The second term in Eq. 80 that is proportional to r^{-1} describes the contribution from spherical diffusion; when it is 10 times larger than the planar diffusion term [i.e., $(\pi D_0 t)^{-1/2}$] after 1 s, this would lead to a definition of UMEs as stated in Eq. 81.

$$\left(\frac{r}{\pi^{1/2} D_0^{1/2}} \right) < 0.1 \quad (81)$$

In most cases, D_O is about $10^{-5} \text{ cm}^2 \text{ s}^{-1}$, and it then follows that the characteristic radius of an UME is smaller than $6 \mu\text{m}$. However, it is important to notice that D_O is sometimes appreciably smaller than $10^{-5} \text{ cm}^2 \text{ s}^{-1}$ if O is a very large molecule, or, more likely, if a viscous or glass-like medium is used; planar diffusion would then prevail even at a radius of $6 \mu\text{m}$. Note also that a microelectrode with a radius of $100 \mu\text{m}$ experiences a substantial contribution from spherical diffusion. If the geometry of the electrode differs from the simple disk or microsphere shape, the definition is less clear. In general, the characteristic behavior of a UME is observed if at least one of the dimensions is in the micrometer range. For instance, a band electrode with a width of less than $10 \mu\text{m}$ behaves as an UME even if it is several mm long.

Electrodes can be divided into four categories according to their characteristic dimensions: 1) Macroelectrodes, such as parallel plates, 2) Microelectrodes, 3) Ultramicroelectrodes, and 4) Nanoelectrodes. The four types of electrodes are illustrated in Figure 11 together with their characteristic electrical properties important for their applicability: resistance, R , double-layer capacitance, C_{dl} , and current, i .

The cell time constant, $\tau_{\text{cell}} = RC_{dl}$ expresses the ability of the cell to respond to fast changes in the electrode potential. Part of the current observed initially in a CA experiment in which the potential is changed suddenly is used to charge the double-layer capacitor and is called the capacitive current, i_c . Because this charging process passes the resistance in the cell, the current response will be the same as for a RC circuit, that is, an exponential function (Eq. 82).

$$i_c = \frac{\Delta E}{R} \exp\left(\frac{-t}{RC_{dl}}\right) \quad (82)$$

Thus, i_c decreases to zero with time and is diminished by more than 90 % when $t > 2.3RC_{dl}$. The cell time constant is a very important parameter for evaluation of the time elapsed until i_c has become insignificant compared to the faradaic current component pertaining to the electrode processes, i_f . For the LSV or CV techniques, i_c has two components, as shown in Eq. 83, since the potential is changed constantly throughout the experiment.

$$i_c = \left\{ \frac{E_i}{R} - vC_{dl} \right\} \exp\left(\frac{-t}{RC_{dl}}\right) + vC_{dl} = \left\{ \frac{E_i}{R} - vC_{dl} \right\} \exp\left(\frac{-(E - E_i)}{vRC_{dl}}\right) + vC_{dl} \quad (83)$$

There is a transient term at the beginning of the scan, with E_i denoting the initial potential applied prior to the potential sweep, and a nontransient or constant term, vC_{dl} . When the direction of the scan is reversed in CV, another transient contribution appears and the nontransient component of i_c changes sign. At high sweep rates it is difficult to separate the i_f component from i_c by use of subtraction procedures. Usually the contribution from the transient part is only acceptable within the first 100 mV of the potential scan, which leads to the expression shown in Eq. 84 for the maximum applicable sweep rate, v_{max} .

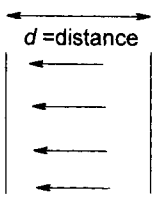

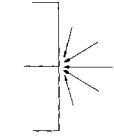
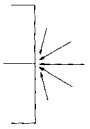
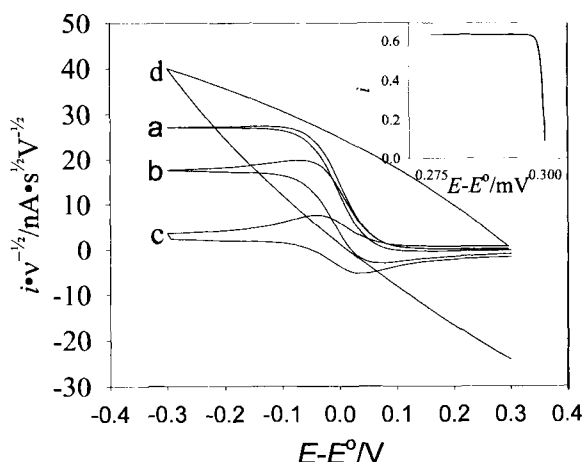
Electrode type	R	C_{dl}	i	iR	RC_{dl}
Macroelectrodes  $d = \text{distance}$ $A = \text{area}$	$\propto d/A$	$\propto A$	$\propto A$	$\propto d$	$\propto d$
Microelectrodes  $r = \text{radius}$	$\propto r^{-1}$	$\propto r^2$	$\propto r^2$	$\propto r$	$\propto r$
Ultramicroelectrodes  $r = \text{radius}$	Spherical dif. $\propto r^{-1}$	$\propto r^2$	$\propto r$	const	$\propto r$
	Planar dif. $\propto r^{-1}$	$\propto r^2$	$\propto r^2$	$\propto r$	$\propto r$
Nanoelectrodes 					

Figure 11. Electrochemical characteristics of four different types of electrodes. The expressions for the electrical properties of nanoelectrodes are complex and therefore not included.

Figure 12. Simulated cyclic voltammograms for 10- μm diameter hemi-spherical UME with $\alpha = 0.5$, $k^\circ = 10000 \text{ cm s}^{-1}$, $T = 25^\circ\text{C}$, $n = 1$, $R = 30 \text{ k}\Omega$, $C_{\text{dl}} = 20 \text{ pF}$, a) $\nu = 0.020 \text{ V s}^{-1}$, b) $\nu = 1.0 \text{ V s}^{-1}$, c) $\nu = 10^3 \text{ V s}^{-1}$, and d) $\nu = 10^6 \text{ V s}^{-1}$. The inset shows the effect of the time constant at the beginning of the scan for curve (c). Note that the current has been normalized with $\sqrt{\nu}$ and that for curve (a) the current has been divided by four.



$$\nu_{\text{max}} = \frac{4.3 \times 10^{-2}}{RC_{\text{dl}}} = \frac{4.3 \times 10^{-2}}{\tau_{\text{cell}}} \quad (\text{in V s}^{-1}) \quad (84)$$

For most electrode configurations, C_{dl} is proportional to r^2 because capacitance is a surface-related property, whereas the resistance in a cell containing a disk or hemisphere working electrode, R , is largest close to the electrode surface and proportional to ρ/r , where ρ is the specific resistivity. Thus, τ_{cell} is directly proportional to r and it is therefore smaller for ultramicroelectrodes than for microelectrodes. In LSV and CV, this means that larger sweep rates, typically up to 1 MV s^{-1} can be employed (see Eq. 84), and in CA and DPSC, the use of smaller step times becomes possible as i_c fades away much faster (see Eq. 82). For the CV technique, these properties are illustrated in Figure 12, where cyclic voltammograms for a reversible redox couple were simulated for different sweep rates at a 10- μm hemi-spherical electrode. Note also that the ohmic drop presents a smaller problem for ultra-microelectrodes, since iR is proportional to r as long as the current is due to planar diffusion. When spherical diffusion takes over on a longer timescale, that is, when smaller sweep rates are employed in CV, i is directly proportional to r and iR becomes independent of r .

In summary, the applications of UMEs can be divided into four main groups: 1) Fast-transient techniques, 2) Conditions where the iR drop would prevent the use of normal microelectrodes, 3) Detectors for monitoring bulk concentrations, and 4) Sensors, where the small dimension of the electrode is crucial.

2.4.1 Fast-Transient Techniques

The introduction of UME to the electroanalytical field has extended the applicability of techniques such as LSV, CV, CA, and DPSC. Because the cell time constant τ_{cell} as well as the iR loss are smaller for UMEs than for the normal-sized electrodes, it

becomes possible to employ larger sweep rates in LSV and CV up to 1 MV s^{-1} and smaller step times ($>1 \text{ }\mu\text{s}$) in CA and DPSC. For fast-transients experiments the diffusion mode is predominantly planar and the voltammograms recorded at a UME therefore have the same characteristics they would have had if a normal micro-electrode had been used. While the CA and DPSC techniques both enjoy the full advantage of the low τ_{cell} value offered at an UME, the LSV and CV techniques still have a problem concerning the nontransient component of i_c , that is, the constant contribution νC_{dl} (see Eqs. 82 and 83). Unfortunately, the faradaic current i_f increases only as a function of $\sqrt{\nu}$, meaning that the ratio i_f/i_c decreases with $\sqrt{\nu}$ as illustrated in Figure 12. In most situations it is possible to extract i_f from the total current, $i_{\text{total}} = i_f + i_c$. One procedure consists of subtracting the voltammogram recorded of the solution without any substrate being present ($i_{\text{total}} = i_c$) from the voltammogram obtained in the presence of the substrate. Alternatively, the contribution from i_c can be estimated from the baseline of the cyclic voltammogram recorded for the substrate, followed by a simple mathematical subtraction.

The early applications of fast CV mainly focused on the measurement of the peak-potential separation, ΔE_p , for the reduction or oxidation process of aromatic compounds, to obtain the pertinent standard heterogeneous rate constant k° from the relationship given in Table 2 [22]. The largest k° values of about 4 cm s^{-1} were found for the reduction of aromatic hydrocarbons such as anthracene at a gold electrode in acetonitrile. The peak-potential separation increased from the 58 mV expected for a reversible process at low ν to about 100 mV on going to ν values of 10 kV s^{-1} . This also shows that there is no real need for employing extremely large sweep rates in the determination of k° for the majority of compounds. Rather, it is important to ensure that the measurements at the lower sweep rates are not hampered by the contribution from spherical diffusion if a too small UME is used.

The above analysis also shows that for almost all applications of fast CV employing $\nu > 1 \text{ kV s}^{-1}$, the quasi-reversible or irreversible nature of heterogeneous electron transfer reactions must be considered. In particular, this becomes important when fast CV is used in a kinetic analysis of fast homogeneous follow-up reactions. The extraction of the relevant rate constants is complicated by the mixed kinetic control of the electrode process and the chemical reaction. As a result, the number of parameters involved in the fitting procedures is increased considerably and with it the possibility of introducing errors.

Savéant *et al.* have studied the reduction of aryl halides and 4-nitrobenzyl chloride by fast CV, and found that the mechanism follows an E_qC_i pathway, where the chemical step consists of a cleavage reaction of the radical anion generated in the first heterogeneous step [23]. To obtain the cleavage rate constant, k_c , the experimentally obtained voltammograms were compared with simulated voltammograms, which involved the adjustment of a number of parameters at the same time; E° , α , k° , k_c , and C_{dl} . The only way to lower the uncertainty on the determination of so many parameters is to carry out the procedure for a series of voltammograms recorded at different sweep rates, even though this work may be tedious and rather time-consuming.

The development of UMEs has considerably improved the possibility of detecting short-lived intermediates, no matter if they disappear in first-order or second-order

processes. In normal CV, where a sweep rate of at most 1000 V s^{-1} can be applied, electrogenerated intermediates with lifetimes larger than 1 ms can be detected directly. This corresponds to first-order rate constants smaller than 10^3 s^{-1} or second-order rate constants smaller than $10^6 \text{ M}^{-1} \text{ s}^{-1}$ on the assumption that the concentration of the substrate is in the millimolar range. In fast CV employing UME, sweep rates as high as 10^6 V s^{-1} can be applied, this lowers the detectable lifetime of intermediates to 1 μs . When converted to first- and second-order rate constants, this corresponds to values of 10^6 s^{-1} and $10^9 \text{ M}^{-1} \text{ s}^{-1}$, respectively. Should a first-order reaction proceed by a rate constant that is larger than 10^6 s^{-1} , there would be no access to its determination by fast CV. One then has to resort to an indirect method such as redox catalysis (see Section 2.7). For electrogenerated intermediates undergoing a second-order reaction, the situation is simpler, as the upper limit on the rate constant is set by the diffusion together of two species. The maximum rate constant is simply equal to the diffusion-controlled limit, k_d , given in Eq. 85, where N_A is Avogadro's number, D is the sum of the diffusion coefficients of the two reactants, and δ is the distance between the reactants at the closest approach. For many solvents, including *N,N*-dimethylformamide and acetonitrile, k_d is about $10^{10} \text{ M}^{-1} \text{ s}^{-1}$. The upper limit is thus almost within reach of the CV method when UMEs are used.

$$k_d = 4\pi N_A D \delta \quad (85)$$

Dimerization reactions are among the simplest second-order processes. In electrochemistry they are commonly observed when cationic substrates are reduced or anionic substrates are oxidized to neutral short-lived radical intermediates that are prone to fast dimerization. To determine the relevant second-order rate constant, the mechanism should be assessed first. As discussed in Section 2.3, a convenient approach consists of measuring the diagnostic criteria, $dE_p/d \log \nu$ and $dE_p/d \log C_O^*$, at an ordinary microelectrode. This often allows the various possible mechanisms to be distinguished, that is, in this case, the dimerization processes DIM1, DIM2, and DIM3. Afterwards, two different strategies based on UMEs can be adopted for evaluation of the rate constant for the dimerization process. In the first approach, the sweep rate is increased until the reaction mechanism is shifted from the KP to the KI zone where partial reversibility is observed. The rate constant can then be obtained from a comparison with simulated voltammograms. The second approach is to increase the sweep rate further until full reversibility is achieved in the DP zone. The standard potential E_O° is measured as the midpoint between $E_{p,a}$ and $E_{p,c}$. Then, from the potential displacement of E_p relative to E_O° observed at lower sweep rates, it is possible to calculate the rate constant with the appropriate equation. For instance, for a DIM1 mechanism, Eq. 69 applies. The latter method is rather uncertain, even though E_p is measured at microelectrodes at low sweep rate with a high accuracy. This is due to the appreciable uncertainty associated with the determination of E_O° ; even a small deviation in the measured potential displacement ($E_p - E_O^\circ$) such as 5 mV will result in an error of 80 % on the rate constant determined.

In the DPSC technique, the advantage of employing UMEs is that the cell time

constant $\tau_{\text{cell}} = RC_{\text{dl}}$ is diminished. For DPSC this offers a real advantage compared to the potential sweep experiments, since the capacitive current contribution is purely transient in its nature. This means that i_c is appreciable just after the potential steps, but then drops to zero as an exponential function of τ_{cell} (see Eq. 82). To ensure that the current measured is purely faradaic, the step times used should always be at least 10 times larger than τ_{cell} . As discussed for ordinary microelectrodes, it is also advantageous to adjust the potentials in DPSC so the heterogeneous electrode processes occur diffusion-controlled regardless of the value of k° and α . This reduces the number of variables and simplifies the simulation procedure considerably. While $10\tau_{\text{cell}}$ sets the lower limit of the time window, the upper limit is often set by the time at which the spherical diffusion process starts to prevail. Strictly speaking, this is so only from the point of view of convenience, since the spherical diffusion could be accounted for. On the assumption that the spherical diffusion should contribute less than 5 % to the total current, the step time should never exceed $\frac{(0.05r)^2}{\pi D_O}$. The two limits together define, for a given electrode size, the time window in which Cottrell behavior can be expected and the contribution from the capacitive and the spherical current is negligible (Eq. 86).

$$10\tau_{\text{cell}} < \tau < \frac{(0.05r)^2}{\pi D_O} \quad (86)$$

As discussed previously for the DPSC technique, a variation in τ of at least a factor of 130 is required for a complete transition from the KP to the DP zone through the KI zone. In practice, this is accomplished only if at least two different-sized UMEs are used.

The DPSC technique with UME has been employed by Savéant *et al.* [24] and Forster [25] in the study of the reduction process of various pyridinium cations. The rate constant k_{dim} for the dimerization of the radicals formed upon reduction was found by fitting to a working curve for a DIM1 mechanism as illustrated in Figure 13 for 1-methyl-4-*tert*-butylpyridinium. For this particular case, $k_{\text{dim}} = 6.4 \times 10^6 \text{ M}^{-1} \text{ s}^{-1}$. Two UME's with diameters of 5 and 17 μm were used to cover the range of step times from 3 μs to 3 ms. Note that the contribution to the flux from spherical diffusion at 3 ms for the 17- μm diameter UME becomes somewhat higher than 5 %.

Although the DPSC technique with UME has some advantages over fast CV with respect to cell time constant, ohmic drop, and slow heterogeneous kinetics, the technique has rarely been used. The main reason for this is that DPSC is a "blind" technique, where it is difficult to distinguish between a variation in the real response and experimental artefacts such as adsorption or changes in C_{dl} .

2.4.2 Applications of UME in Resistive Media and under Industrial Conditions

The ohmic drop presents a severe problem in electrochemistry, in particular when large electrodes are used. In the worst case, all the power of the potentiostat is lost

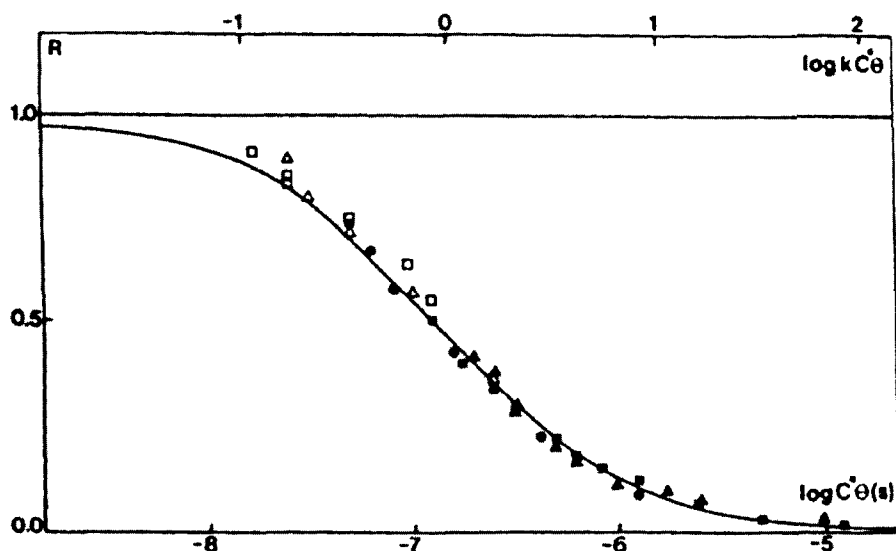


Figure 13. Double potential step chronoamperometry of 1-methyl-4-*tert*-butylpyridinium at a 5- μm (\square, \triangle) and a 17- μm ($\blacksquare, \blacktriangle$) diameter gold disk electrode. Variation of the normalized current ratio $R(=P')$ with step time $\theta(=\tau)$. From C. P. Andrieux, P. Hapiot, and J.-M. Savéant, *J. Phys. Chem.* 92:5992 (1988) [24].

in heating of the cell solution in a resistive manner. From the very early days of organic electrochemistry, this problem forced electrochemists to work in dipolar solvents. In particular, solvents like *N,N*-dimethylformamide, acetonitrile and dimethyl sulfoxide were and still are used extensively, because their aprotic nature allows the electrogeneration of relatively stable basic intermediates or products. Supporting electrolytes such as large tetraalkylammonium ions are added in high concentrations of 0.1 M, to raise the conductivity to an acceptable level for the electrochemical measurements. Still, in CV the voltage drop between the working electrode and the reference electrode becomes a severe problem at high sweep rates since the current, i , increases as a function of sweep rate. The cyclic voltammograms recorded at ordinary microelectrodes are distorted significantly when ν is larger than 1 V s^{-1} , and although different compensation procedures can be employed, the problem is never completely solved. The problem is diminished considerably if UMEs rather than microelectrodes are employed, because the iR voltage drop is proportional to r . In general, for sweep rates below 1000 V s^{-1} , no compensation is necessary when UMEs are used. However, for higher sweep rates, this is not the case, and some kind of electronic or mathematical correction of the electrode potential is needed. Moreover, a new problem arises, because the usual way of carrying out the on-line iR compensation by means of a positive feedback circuit may not function at the largest sweep rates applied in fast CV, because of band-pass limitations of the potentiostat.

Although the iR problem is therefore not completely eliminated for UMEs, there are still so many benefits from the reduced ohmic drop, that new interesting areas of applications within the electrochemical field have emerged. One such area pertains to the study of electrochemical processes in nonpolar solvents. For a long period, the use of dipolar organic solvents containing large amounts of supporting electrolytes has tended to separate organic electrochemistry from the field of classical organic chemistry where nonpolar solvents like ethers and hydrocarbons are frequently used. Also, from a mechanistic point of view, a wider selection of solvents would be desirable, so that solvent effects could be used for distinguishing between polar and nonpolar mechanisms. Finally, it would allow mechanistic investigations of ion-pairing phenomena in nonpolar solvents to be carried out.

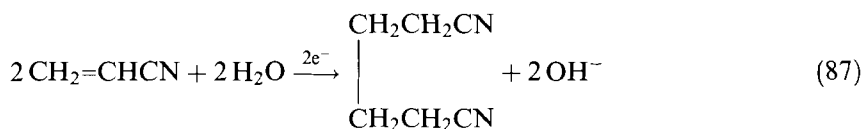
The resistivity of a medium is related to 1) the solvent polarity, 2) the concentration of the supporting electrolyte, and 3) the solvent viscosity. One of the first breakthroughs was made by Parker as early as 1977, who employed a small micro-electrode (not yet an UME) for recording cyclic voltammograms of the reduction of perylene in benzene containing 0.1 M tetrabutylammonium perchlorate [26]. This new electrochemical development was not appreciated until later in the 1980s, when the development of UMEs made detailed electroanalytical studies in nonpolar solvents such as toluene [27, 28], hexane [27], and mineral oil [29] possible. The studies were extended to glasses, gels, and other highly viscous media, with the interesting feature that the cyclic voltammograms remained transient and peak-shaped, even if small sweep rates were applied. This is explained by the very small diffusion coefficients of molecules in a highly viscous medium being inversely proportional to the solvent viscosity. As a result, the growth of the diffusion layer is slow, and the onset of spherical diffusion occurs later. The presence of supporting electrolytes in concentrations of 0.001–0.7 M was still necessary for carrying out the measurements in nonpolar solvents, and it also required the tailoring of new types of supporting electrolytes such as dinonylnaphthalenesulfonic acid/trioctylphosphine oxide and tetrahexylammonium perchlorate that could be solvated and sufficiently dissociated in these solvents [27, 30].

The diminished need for high concentrations of supporting electrolyte in electrochemical measurements with UMEs has an interesting implication on the mode of mass transfer. Normally, mass transport of the electroactive redox pair, O/R, to the electrode, is governed by diffusion, while the migrational flux is precluded by the use of a large excess of the supporting electrolyte. The current going through the cell in the bulk solution is completely based on the migration of the ions from the supporting electrolyte. If no or only little supporting electrolyte is present, ions other than the electrolyte have to take over the current transport. Suppose that O is a positively charged species, then the migration of O will increase the total mass transport of O to the electrode surface and enhance the overall reduction rate to afford the neutral R. During this reduction process, the number of ions in the diffusion layer will change significantly and further increase the migrational flux of O. In other words, there is an intimate coupling of the diffusion and migration processes for the redox pair O/R, because either O or R will be charged.

A third effect to consider is the liquid junction potential that arises between the solution and the reference electrode because of the different concentrations of elec-

trolyte at the two places. This effect, as well as the ohmic loss and the intimate coupling of migrational and diffusional fluxes may substantially distort the recorded voltammograms. In steady-state measurements of limiting currents, the problem is somewhat simplified, because the exact electrode potential is not important and only the effect of the coupled diffusional and migrational fluxes need to be solved [31–33]. In all other cases where an exact knowledge of potentials is required, all three effects should be considered [34].

The fact that the iR drop is a smaller problem for UMEs compared to microelectrodes has another straightforward advantage, the substrate concentration can be increased substantially; this makes the performance of electroanalytical studies under conditions similar to industrial conditions possible. For instance, the industrially important hydrodimerization of acrylonitrile to adiponitrile takes place at high concentrations in aqueous medium in the presence of tetraalkylammonium salts that form an aprotic medium in the vicinity of the electrode surface. The mechanism consists of a dimerization reaction of the radical anions of acrylonitrile formed upon reduction of acrylonitrile in the aprotic tetraalkylammonium layer, followed by protonation of the dimer in the aqueous phase (Eq. 87). However, at low to moderate concentrations of acrylonitrile, a change in mechanism occurs in favor of a two-electron reduction of acrylonitrile to propionitrile (Eq. 88).



Unfortunately, the industrial process depicted in Eq. 87 could not be studied by classical electroanalytical techniques due to the high concentrations of acrylonitrile employed. Rather, one had to resort to the use of other olefins as model compounds that could form relatively stable radical anions in an aprotic medium where the protonation reaction was suppressed. However, it would be reasonable to question the industrial relevance of such studies, since the olefins selected are different from acrylonitrile. Montenegro and Pletcher therefore chose another approach using a hemispherical UME as the electroanalytical tool [35]. In this manner, the substrate concentration could be raised to a level compatible with the industrial process. In Figure 14 the steady-state voltammogram of a 1.5 M aqueous solution of acrylonitrile (+ tetraalkylammonium salt) is shown; although the shape of the wave is somewhat distorted because of the presence of the nearby discharge of the medium, the plateau current, I_L could be extracted. These values of I_L were normalized by division with the different concentrations C used in the experiments according to the theoretical expression given in Eq. 89 for a hemi-spherical UME.

$$I_L = 2\pi r n F D C \quad (89)$$

From these data, a plot of I_L/C versus C could be constructed as shown in Figure 15. As seen, a gradual shift from $n = 2$ at $C < 0.5$ M to $n = 1$ at $C > 1.2$ M occurs,

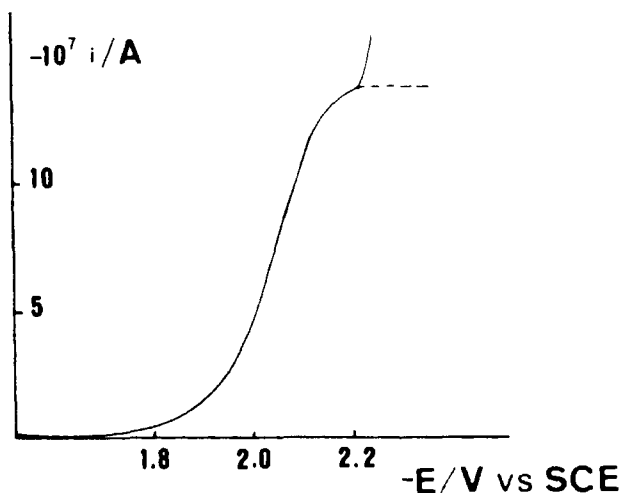


Figure 14. Plot of i - E curve recorded at a Hg ultramicroelectrode with area $8 \times 10^{-7} \text{ cm}^2$ for acrylonitrile (1.5 mol dm^{-3}) in an aqueous solution of Na_2HPO_4 (15 %)/ Bu_4NHSO_4 (0.4 %), pH 7, sweep rate 50 mV s^{-1} . From M. I. Montenegro and D. Pletcher, *J. Electroanal. Chem.* 248:229 (1988) [35].

that is the reaction shown in Eq. 88 is dominant when a low concentration of acrylonitrile is used, whereas the target reaction (Eq. 87) prevails at high concentrations. Interestingly, in the absence of the tetraalkylammonium salt, n is always two, regardless of the concentration. This shows that the formation of a hydrophobic layer by the tetraalkylammonium cations at the electrode surface is essential for creating the optimum non-acidic conditions for the production of adiponitrile in the dimerization reaction of two radical anions of acrylonitrile. The investigation confirms in a beautiful way the conclusions known already from process optimization in industry, and illustrates the prospects of using such a methodology in the investigation of other industrial processes prior to scale-up.

2.4.3 Steady-State Measurements at UMEs for Monitoring Slow Homogeneous Reactions

UV spectroscopy is often the technique of choice when relatively slow homogeneous reactions should be monitored, but sometimes the use of alternative and different approaches would be desirable. For instance, this situation arises if the species studied are without characteristic UV absorption bands or if the relevant bands are overlapped by the spectrum of other reactants, intermediates and products. In that case, electrochemical monitoring might provide an attractive alternative because of its ease and selectivity.

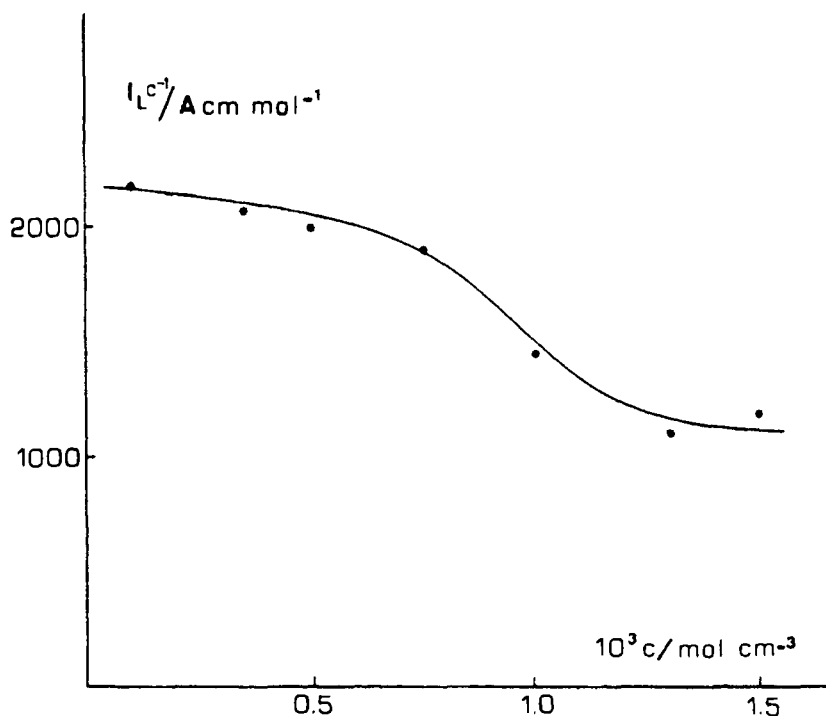


Figure 15. The normalized plateau current, I_L/C , (proportional to n) versus the concentration (C) for acrylonitrile in aqueous Na_2HPO_4 (15 %) / Bu_4NHSO_4 (0.4 %), pH 7. From M. I. Montenegro and D. Pletcher, *J. Electroanal. Chem.* 248:229 (1988) [35].

The steady-state current measured at a UME for a given electroactive species is given by Eqs. 48 and 89 for a disk and a hemi-spherical UME, respectively, that is, the plateau current is proportional to the bulk concentration. This is also true if other steady-state techniques like the rotating disk electrode (RDE) technique or polarography are employed. The monitoring of steady-state plateau currents should therefore provide the same kind of kinetic information that would have been obtained had the UV absorption of the species been monitored. While the steady-state behavior at an RDE arises because of convection due to stirring, it is attained at an UME because of spherical diffusion. The UMEs have the advantage that measurements also can be carried out in nonpolar solvents such as tetrahydrofuran or toluene. For an RDE, the larger electrode area combined with the enhanced mass transport due to convection results in larger plateau currents that are incompatible with the high resistance of nonpolar solvents.

Two strategies have been adopted for kinetic measurements. Either the electrode potential can be adjusted so that only the steady-state current is measured as a function of time, or the potential might be scanned continuously with the recording of steady-state voltammograms at certain time intervals. The first strategy outlined

has been used by the present authors to monitor the electron-transfer reaction between aromatic radical anions $A^{\bullet-}$ and alkyl halides RX [36]. The relevant reactions are depicted in Eqs. 90–92 with the rate law for the consumption of $A^{\bullet-}$ given in Eq. 93. Since the reactions shown in Eqs. 91 and 92 are always much faster than the reaction given by Eq. 90, the steady-state approximation can be applied to R^{\bullet} , to lead to the simplified differential expression shown in Eq. 94.



$$\frac{dC_{A^{\bullet-}}}{dt} = -k_{ET}C_{A^{\bullet-}}C_{RX} - (k_{91} + k_{92})C_{A^{\bullet-}}C_{R^{\bullet}} \quad (93)$$

$$\frac{dC_{A^{\bullet-}}}{dt} = -2k_{ET}C_{A^{\bullet-}}C_{RX} \quad (94)$$

$$C_{A^{\bullet-}} = C_{A^{\bullet-}}(0) \exp(-2k_{ET}C_{RX}t) \quad (95)$$

$$i = i_0 \exp(-2k_{ET}C_{RX}t) \quad (96)$$

On the assumption that $C_{A^{\bullet-}} = C_{A^{\bullet-}}(0)$ at $t = 0$ and $C_{RX} \gg C_{A^{\bullet-}}(0)$, Eq. 94 may be integrated to give Eq. 95. Substituting the concentration with the plateau current in Eq. 95 leads to the simple relationship (Eq. 96) between the observable parameter, i , and the rate constant k_{ET} . The parameter i_0 is the current measured at $t = 0$.

The first step in the experimental procedure consists of preparative electrolysis of the aromatic compound A to $A^{\bullet-}$. The preparative potentiostat is then disconnected and a UME is inserted into the cathodic compartment. The steady-state oxidation current of $A^{\bullet-}$ is recorded as a function of time for a certain time period to ascertain that the stability of $A^{\bullet-}$ is high. If this is indeed the case, the alkyl halide RX is added to the solution while it is stirred for a few seconds to assure that homogeneous conditions apply for the reaction of Eq. 90. The recorded current is observed to decay exponentially towards zero. A plot of $\ln i$ versus t is shown in Figure 16 for four different combinations of aromatic compounds and sterically hindered alkyl halides. From the slopes of the straight lines, $-2k_{ET}C_{RX}$, k_{ET} values can readily be obtained. The method is useful for the study of relatively slow reactions with $k_{ET} < 10 \text{ M}^{-1} \text{ s}^{-1}$.

The second strategy adopted for kinetic measurements involves the recording of complete voltammetric waves at certain time intervals rather than continuous measurement of the plateau current. This leads to a poorer time resolution but the advantage is that less charge is passed through the UME, and therefore the problems associated with fouling of the electrode surface should be smaller. The approach also opens the possibility of regenerating the electrode surface electrochemically by polarization of the electrode potential. This method has been used by Amatore and Pflüger in an investigation of the oxidative addition of substituted iodobenzenes (ArI) to tetrakis(triphenylphosphine)palladium(0) in toluene + 0.06 M tetrahexylammonium tetrafluoroborate [28]. In Figure 17, the i versus t curve is shown,

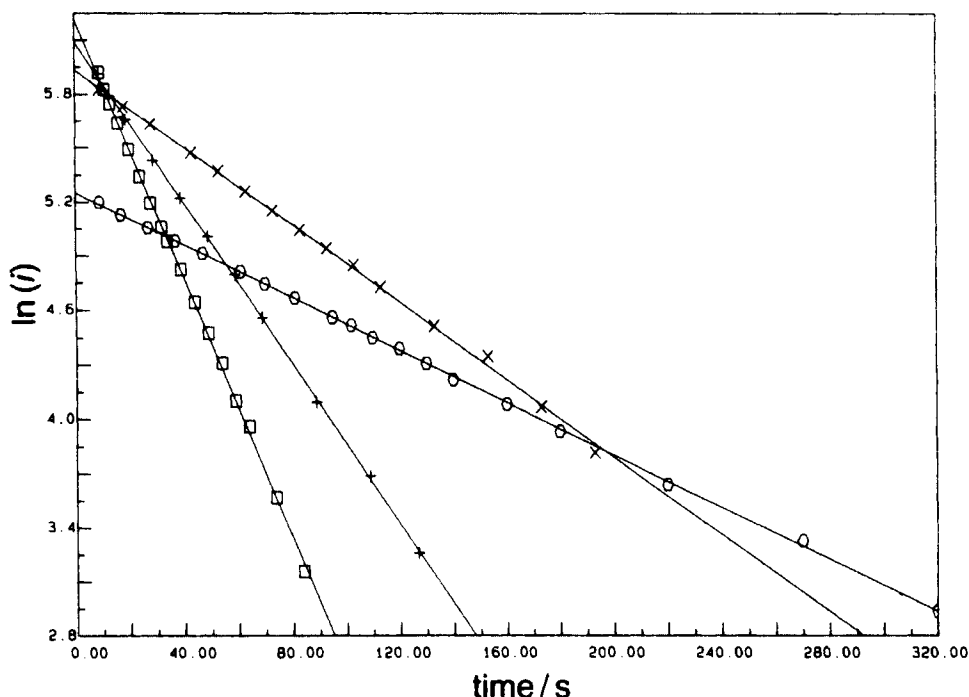


Figure 16. Current decay curves: the natural logarithm of the steady-state oxidation plateau current of radical anions (mediators) plotted against time (s) for the following four combinations of mediator/substrate: benzophenone/1-bromo-2,2-dimethylpropane (+); perylene/1-bromo-2,2-dimethylpropane (x); perylene/1-bromoadamantane (□) and quinoxaline/2-chloro-2-methylpropane (O). All measurements were obtained with a 10- μm platinum disk electrode in DMF/0.1 M Bu_4NBF_4 at 22°C. From S. U. Pedersen and K. Daasbjerg, *Acta Chem. Scand.* 43:301 (1989) [36].

where each “spike” corresponds to a potential scan at the gold disk UME in the range from -2.7 to $+0.2$ V vs Ag/Ag^+ . The plateau current is recorded at the upper potential limit. The decay of i corresponds to an overall second-order process, first order in both $\text{Pd}(0)$ and ArI .

2.4.4 Sensors

In biology and medicine, UMEs were employed at an early point, although the special features of small-sized electrodes were not recognized until later. The main motivation for using UME was the possibility of placing an electrode in biological tissue to monitor the concentrations of electroactive signal substances present in such environments. The UMEs that are used for *in vivo* studies are usually made of carbon fibers, because this electrode material is less likely to be blocked by adsorption of proteins. The carbon fiber with typical diameter of 10 μm is melted into soft glass, where the end is cut and polished. The size of the overall arrangement may amount to

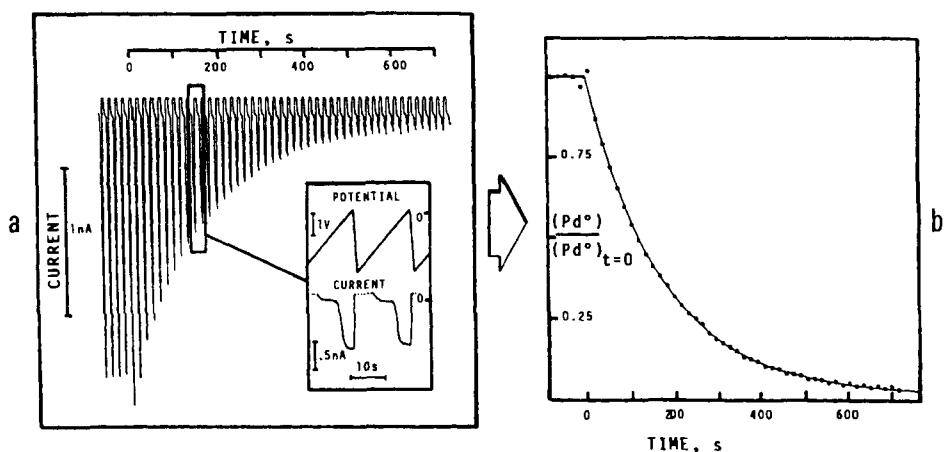


Figure 17. Variation of the concentration of $\text{Pd}^\circ(\text{PPh}_3)_4$ as a function of time during its reaction with *p*-iodotoluene in toluene/0.06 M Hex_4NBF_4 at 25°C , monitored electrochemically at a $5\text{-}\mu\text{m}$ -radius gold-disk UME: a) Display of the voltammograms recorded from -2.7 to $+0.2$ V vs Ag/Ag^+ with a sweep rate of 50 mV s^{-1} as a function of time. In the inset, two successive voltammograms are shown (the cathodic current portion is deleted for simplification) together with the picture of the potential/time scan. b) The resulting variation of the $\text{Pd}^\circ(\text{PPh}_3)_4$ concentration is depicted as a function of time, where the solid line corresponds to the calculated response. From C. Amatore and F. Pflüger, *Organometallics* 9:2276 (1990) [139].

ca. $70\text{ }\mu\text{m}$ in diameter, sufficiently small for its implantation in tissue without causing severe damage and at the same time sufficiently large to ensure that only extracellular processes are monitored. Among the substances studied in this manner are the catecholamines (dopamine, norepinephrine, and epinephrine) and their acid and alcohol metabolites, ascorbic acid, uric acid, and 5-hydroxytryptamine. As ongoing work of the Wightman group, the secretion of 5-hydroxytryptamine by neurotransmitters has been investigated, in which the timing and quantity of neurotransmitter bursts could be characterized [37].

The scanning electrochemical microscopy (SECM) technique introduced in recent years by Allen Bard is another area where the smallness of the electrode is essential [38]. The principle in SECM is a mobile UME inserted in an electrolyte solution. The UME is normally operated in a potentiostatic manner in an unstirred solution so that the current recorded is controlled solely by the spherical diffusion of the probed substance to the UME. The current can be quantified from Eqs. 48, 49, or 89 as long as the electrode is positioned far from other interfaces. However, if a solid body is present in the electrolyte solution, the diffusion of the substance to the UME is altered. For instance, when the position of the UME is lowered in the z direction, that is, towards the surface of the object, the diffusion will be partially blocked and the current decreases. By monitoring of the current while the electrode is moved in the x - y plane, the topology of the object can be graphed. The spatial resolution is about $0.25\text{ }\mu\text{m}$. In one investigation carried out by Bard *et al.*, the

typography of stomata on the surface of grass and leaves was studied. Upon stimulation of the stomatal guard cells by light radiation they were able to detect the evolution of oxygen from the individual cells from its reduction at the UME [39].

The SECM technique has also found many other applications [40]. It has been used to modify the surface of objects and in the investigation of electrode processes taking place at other electrode surfaces. In the latter case, this has made a detailed mapping of concentration profiles possible. Recent developments by Unwin *et al.* have also shown that SECM, when operated as in a DPSC experiment, can be used in the study of reactions occurring at liquid/liquid and liquid/gas interfaces [41]. During the first potential step, the substance O is reduced (or possibly oxidized), under diffusion control, to R at the UME that is placed near the interface. The R formed in this way may then interact with the interface by adsorption or a chemical reaction; the progress of these processes can be evaluated by monitoring of the current pertaining to the reoxidation of R to O during the second potential step. In this manner, the SECM-DPSC technique has been used to study the charge-transfer kinetics occurring between two immiscible electrolyte solutions. The driving force for these processes is provided by the potential difference between the two phases, and it can be adjusted by a change of the galvanic potential of the liquid junction. Rusling *et al.* have carried out extensive studies on the possibility of performing catalytic electrochemical reactions in aqueous micro-emulsions when the microphases are separated by a surfactant [42]. However, quantification is difficult because of the uncertainties associated with the characterization of the interface, unless one turns to the SECM-DPSC method. Bard *et al.* have performed similar studies on long-range electron transfer through phospholipid monolayers at the interface between two immiscible electrolyte solutions [43].

Perhaps the most astonishing achievements within the field of small electrodes are the electrochemical detection of single molecules [44], single reactions [45] or single-electron-transfer events [46] with the use of so-called nanodes with radii in the order of a few nanometers. The nanode employed in the electrochemical detection of single molecules was prepared by electrochemical sharpening of an 125 μm Pt-Ir wire. The wire was completely coated with wax or polyethylene before the electrode surface was exposed electrochemically in an STM procedure. The electrode surface of the nanodes was slightly recessed (10 nm) relative to the insulating coating, as depicted in Figure 18. It was therefore possible to trap one or two electroactive molecules such as of (trimethylammonio)methyl ferrocene, Cp_2FeTMA in the small enclosed volume (ca. 10^{-18} cm^3) formed when the nanode surface was moved close (within 10 nm) to a conductive substrate. The electroactive molecules were then able to transport electrons between the nanode and the substrate, about 10^7 times/s, resulting in a total current in the order of 1 pA.

The same authors have recently studied the effect of placing two nanodes in series in an electrolyte solution containing micromolar concentrations of an electroactive reagent such as $\text{Cp}_2\text{FeTMA}^+$. Then the *i-E* characteristics for small potential differences have a staircase shape, where the height corresponds to the transfer of one electron.

Wightman *et al.* [45] observed a single chemical reaction between two molecules. The reaction was the electron transfer between an electrogenerated aromatic radical

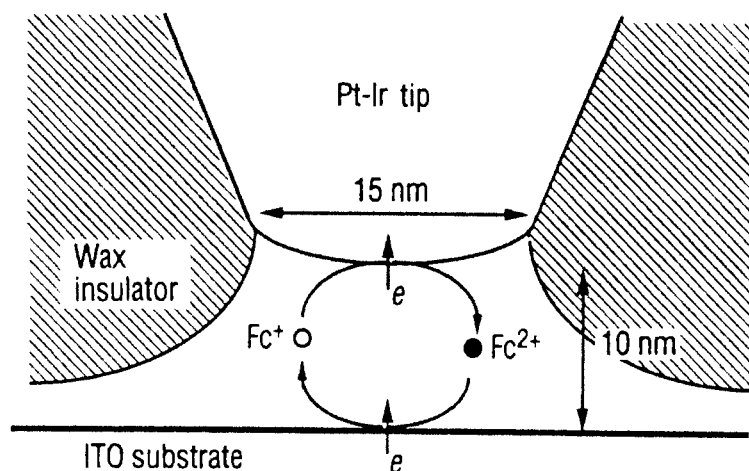


Figure 18. Idealized schematic illustration of the tip geometry and the tip-substrate configuration used. From F. F. Fan and A. J. Bard, *Science* 267:871 (1995) [44].

anion, A_1^- and an aromatic radical cation, A_2^+ , where A_1 may be the same compound as A_2 or different. When the two radical ions collide, electron transfer takes place immediately and either the non-emitting triplet state of the parent compounds or the corresponding excited singlet state that relaxes to the ground state by photo emission are formed. The substrate selected in this particular study was 9,10-diphenylanthracene (DPA), which was first oxidized to DPA^+ over 500 μ s, followed by reduction to DPA^- over the next 50 μ s. The thickness of the diffusion layer pertaining to DPA^+ , δ_{DPA^+} , is approximately 1 μ m, as calculated from Eq. 23. Since the subsequent reductive pulse is somewhat shorter, the diffusion layer of DPA^- will grow out into the diffusion layer of DPA^+ , as depicted in Figure 19, until $\delta_{DPA^-} \approx 300$ nm. This corresponds to a volume of the DPA^- diffusion layer of approximately 2×10^{-14} dm^3 , as the radius of the disk electrode is 5 μ m. The photons emitted during the 50- μ s reductive pulse were recorded with high temporal resolution and the events were shown to be stochastic. A Poisson distribution was observed, which is characteristic of discrete, random, and independent events. Recently, chemiluminiscence has also been used to monitor the shapes of small electrodes [47, 48].

2.5 Hydrodynamic Electrochemical Techniques

So far the electrochemical techniques described have been based on diffusion as the mode of mass transfer of the electroactive reactants, that is, the concentration profiles develop according to Fick's second law (Eq. 22). The thickness of the diffusion

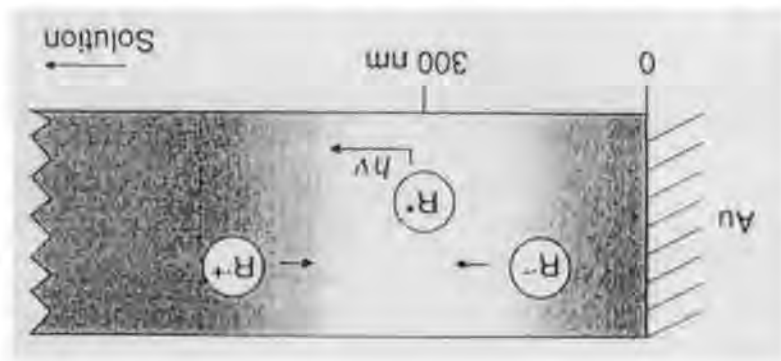


Figure 19. A radical anion of 9,10-diphenylanthracene ($R^{\bullet-} = DPA^{\bullet-}$) is electrogenerated during the cathodic potential pulse and diffuses into the layer of the radical cation of 9,10-diphenylanthracene ($R^{\bullet+} = DPA^{\bullet+}$) electrogenerated during the anodic potential pulse. From M. M. Collinson and R. M. Wighman, *Science* 268:1883 (1995) [45].

layer grows as $\sqrt{2D_0t}$ (Eq. 23) and, thus, the maximum flux of the reactant decreases as $t^{-1/2}$ (Eq. 39). The migration is eliminated by addition of an inert electrolyte to the solution and the contribution from convection can largely be neglected if the solution is not stirred. Natural convection always takes place to some extent because of vibrations and the presence of density gradients and temperature fluctuations in the solution, but these contributions to the flux are of no importance until the diffusional flux has diminished to a low level. In chronoamperometry, this happens at microelectrodes when the step time is larger than 5 s and the flux of the electroactive reactant is decreased by more than two orders of magnitude compared to the flux after 1 ms. At this point, the measured current will not be a function of $t^{-1/2}$ any longer as predicted by the Cottrell equation (Eq. 39), but rather attain a steady-state value. The contribution from spherical diffusion may help to attain this steady-state situation.

When forced convection is applied in the cell by means of, for instance, a magnetic stirrer, the flux due to convection increases and may become the dominant constituent of the total flux even after just a few ms. This results in a steady-state situation, where the diffusion layer stops growing. (If the convection is laminar, then the solution adjacent to the electrode surface will not move relative to the electrode, and diffusion becomes the only mode of mass transport in this thin layer.) Overall, the effect of convection is thus to shrink the thickness of the diffusion layer, resulting in larger concentration gradients in the diffusion layer with much more efficient mass transport of the electroactive species. In other words, the current densities that can be accomplished in stirred solutions are much higher than in unstirred.

Many modes of convection have been implemented in electrochemical cells in terms of stirring, rotation, vibration, and so forth. They may be divided into two main groups according to our ability to describe the mass transport mathematically. If a magnetic bar is used to stir the solutions as in preparative electrolysis (PE), the

mass-transport process is not well defined, owing to fluctuations. In this case, it is impossible to calculate the concentration profiles in the cell and the exact influence of the convection is unpredictable, although general and averaged effects might be discussed [49–55]. For some special convection modes, as observed for the rotating disc electrode (RDE), the development in the concentration profiles can be predicted precisely. Another example is the dropping mercury electrode used in classical polarography, where the effect of the convection (i.e., a growing drop) can also be described mathematically. In the following, PE and the RDE technique will be discussed in further details; readers interested in polarography are referred to Refs. [1, 56, 57, 58].

2.5.1 Preparative Electrolysis

Preparative electrolysis differs from electroanalytical techniques in that the aim is to electrolyze all the electroactive substance present in the solution rather than just the small fraction present in a thin diffusion layer adjacent to the electrode surface. To achieve bulk electrolysis, a large A/V (electrode area to cell volume) ratio is required in combination with enhanced mass transport; this is accomplished by the solution being stirred with a magnetic bar. Preferentially, exhaustive electrolysis on laboratory scale should provide the products in a yield that enables their identification and quantification by the common spectroscopic and chromatographic methods. Because of the continuous developments in the sensitivity of these methods, a few milligrams of the substance is often sufficient. The total charge, Q , used in exhaustive electrolysis is obtained by integration of the current with a coulometer. From Q , it is then possible to calculate the number of electrons, n , consumed by one substrate molecule in the electrogeneration of the product, on the basis of Eq. 97, where m is number of moles of the substrate in the cell.

$$n = \frac{Q}{F \cdot m} \quad (97)$$

Note that the calculated value of n might be a fraction if the current efficiency is less than 100 % or the mechanism followed is complex. Preparative electrolysis can be performed under potentiostatic or galvanostatic conditions. In the former case, the use of a potentiostat ensures that the potential of the working electrode relative to a reference electrode is held at a constant value during the whole electrolysis process independently of the current supplied. Preferentially, the potential should be selected so that the substrate can be electrolyzed without the products or the medium being reduced or oxidized at the same time. It is possible by proper potential adjustment to control the fraction of electrolysis X which is defined according to Eq. 98 as the fraction of the substrate transformed during electrolysis.

$$X = \frac{C_O^*(\text{initial}) - C_O^*(\text{end})}{C_O^*(\text{initial})} = \{1 + 10^{(E - E_O^\circ)n/59.2}\}^{-1} \quad (98)$$

If the electrode potential, E , is 118 mV smaller than E_O° for the preparative reduction of O, then X is 99 % or, expressed differently, only 1 % of O has not been transformed at the end of the electrolysis. Equation 98 is valid not only for fast (nernstian) but also for slow heterogeneous electrode reactions, since an equilibrium situation is always attained at the end of the electrolysis where the current is essentially zero. For an irreversible electrode reduction, the rate of electrolysis as expressed by the electrolysis current is, however, very low if $E - E_O^\circ$ is -118 mV. The employment of much higher overpotentials or mediated electrolysis (see Section 2.7) may then be required for achieving a reasonable rate of transformation.

The rate of transformation of O, $-\frac{\partial C_O}{\partial t}$, is proportional to $C_O(t)$. Consequently, $C_O(t)$ decreases exponentially with time during electrolysis, and the same is true for the potentiostatic electrolysis current, $i(t)$. The expression for $i(t)$ is shown in Eq. 99, where i_L is the limiting current at the start of the electrolysis ($t = 0$).

$$i(t) = i_L \exp\left(\frac{-Am_O t}{V}\right) \quad (99)$$

The time constant for the electrolysis depends on the A/V ratio and the phenomenological parameter, m_O , that describes the efficiency of the mass transport. While most small-scale electrolyses can easily be carried out under potentiostatic conditions, a galvanostatic approach is necessary for large-scale electrolysis, since it requires the use of higher current densities. Most potentiostats are not able to deliver currents higher than 2 A, but a galvanostat can be adjusted to sustain any value throughout the electrolysis. In the latter case, there is no need for the use of a reference electrode, as long as the current is used only for transforming substrate to product. The applied current, i_{ap} , should always be kept at or below the limiting current, i_L , for the substrate at any time during the electrolysis. The steady-state voltammogram of a typical galvanostatic electrolysis process is illustrated in Figure 20. The substrate O is reduced at -1.0 V to a product P which can be further reduced and, unfortunately, destroyed at -1.6 V. At -2.4 V, the medium (solvent and supporting electrolyte) discharge appears. During potentiostatic electrolysis, the potential is set to -1.2 V, which should ensure exhaustive electrolysis of O to P with an electrolysis fraction X larger than 99.9 %. If i_{ap} in the galvanostatic approach is adjusted to the limiting current of 100 mA, then soon after the onset of electrolysis, the effective potential will move from the initial -1.0 V to the second wave at -1.6 V and, as a result, some of the product P will be destroyed by the further reduction process. If i_{ap} is adjusted to 50 mA, the electrolysis takes longer, but the potential value will not move to the second wave until 50 % of O has been reduced. For $i_{ap} = 10$ mA, the selectivity is even higher, as 90 % of O can be reduced before the shift in the potential occurs; this is, however, at the cost of considerable extension of the electrolysis time. On industrial scale, where the use of galvanostatic electrolysis is obligatory, i_{ap} is normally adjusted during electrolysis according to in situ measurements of the concentration of O or some preprogrammed value. The optimal situation is attained when i_{ap} is always slightly lower than i_L . Another

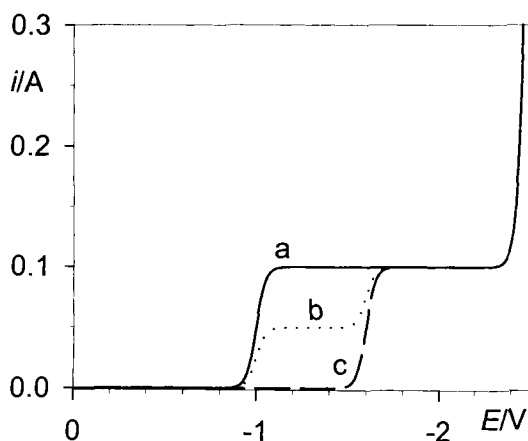


Figure 20. Example of preparative electrolysis monitored by steady-state voltammetry. The curves shown are constructed but they could have been recorded with RDE, UME, or polarography for a substrate O that is reduced reversible at $E_O^\circ = -1.0$ V to a product that is reducible at -1.6 V. The medium is reduced at $E < -2.4$ V. The different curves correspond to a) Before the preparative electrolysis, b) after 50 % of O has been electrolyzed to product, and c) after exhaustive electrolysis of O to product.

approach consists of adding starting material to the electrochemical cell during the electrolysis so the same high value of i_{ap} can be sustained for a long period.

2.5.2 Rotating Disc Electrode

The essential components constituting the RDE system are a speed controller, a motor, and an electrode. The rotation speed (rounds per second, rps) of the motor is adjusted by means of the speed controller. The electrode which is shown in Figure 21 is a 3–5 mm diameter conducting disc imbedded in an insulating rod of teflon, plastic, or glass. The electrode rod is often mounted, so it is a direct extension of the motor axle, but a drive belt can also connect it. The electrical contact to the rotating working electrode is made with brushes of carbon-silver. The flow of the solution near the spinning electrode will be laminar if the Reynolds number, $R_e = r^2\omega/v_k$ is smaller than 200 000, where r is the radius of the disc electrode, ω is the angular rotation rate (rad s^{-1}), and v_k is the kinematic viscosity. For an aqueous solution at 20°C , v_k is equal to $0.01 \text{ cm}^2 \text{ s}^{-1}$ and, thus, the rotation rate ($2\pi\omega$) should be less than 300 000 rps to ensure laminar conditions. However, the practical limit is closer to 200 rps due to non-idealities imposed by the spinning rod.

When the electrode rod rotates, the solution close to the electrode surface is forced along with it, and because of the centrifugal force, it will be thrown outwards radially from the center of the electrode. From below, new solution is dragged to the electrode surface, as indicated by the arrows shown in Figure 21. Karman and

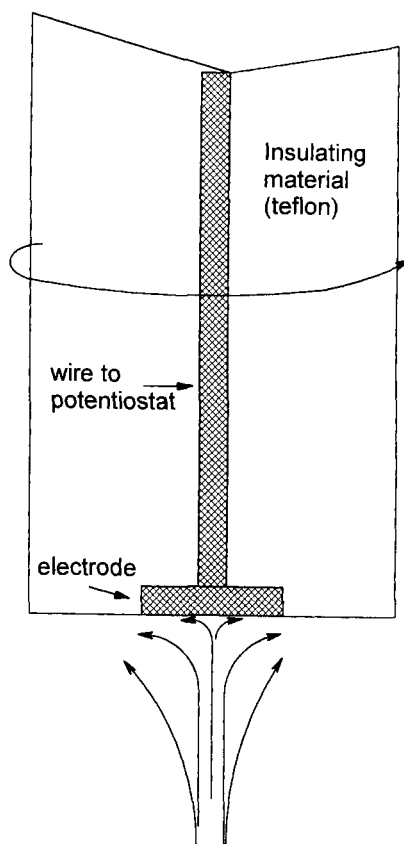


Figure 21. Schematic illustration of a rotating disc electrode (RDE). The stream arrows indicate the flow to the rotating disc.

Cochran mathematically described these movements of the solution in the cell under laminar conditions. The forced convection was included in the Nernst–Planck equation which allowed the calculation of the steady-state concentration profile depicted in Figure 22.

However, for most applications, the Nernst-approximated profile is used, in which the concentration is assumed to vary linearly in a diffusion layer with thickness, δ_{RDE} , given by Eq. 100.

$$\delta_{\text{RDE}} = 1.61 D_{\text{O}}^{1/3} \nu_k^{1/6} \omega^{-1/2} \quad (100)$$

The use of Fick's first law (Eq. 21) then provides the relation for the current i given in Eq. 101 where $C_{\text{O}}(0)$ is the concentration of O at the electrode surface.

$$i = n F A D_{\text{O}} \left(\frac{\partial C_{\text{O}}(x)}{\partial x} \right)_{x=0} = \frac{n F A D_{\text{O}} (C_{\text{O}}^* - C_{\text{O}}(0))}{\delta_{\text{RDE}}} \quad (101)$$

The plateau current, i_{pl} obtained when the polarization of the RDE is sufficient to

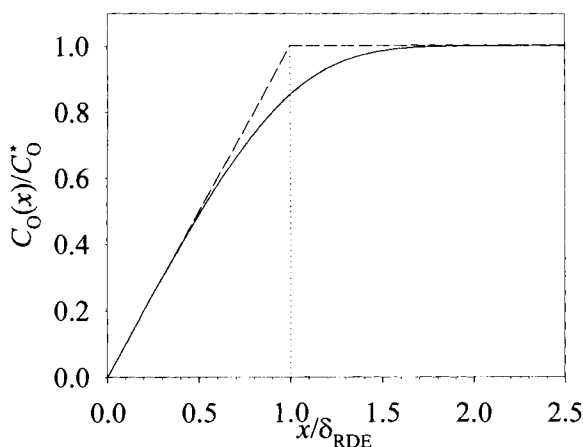


Figure 22. Concentration profile for O. The concentration of O is normalized with the bulk concentration and the distance to the electrode surface is normalized with the diffusion layer thickness $\delta_{\text{RDE}} = 1.61 D_{\text{O}}^{1/3} \nu_k^{1/6} \omega^{-1/2}$ (Eq. 100).

make $C_{\text{O}}(0) \approx 0$ can then be expressed as shown in Eq. 102 known as the Levich equation.

$$i_{\text{pl}} = \frac{0.602nFAD_{\text{O}}^{2/3}\omega^{1/2}C_{\text{O}}^*}{\nu_k^{1/6}} \quad (102)$$

Note that i_{pl} is proportional to C_{O}^* . If the electrode reaction of O is nernstian then Eq. 101 can be transformed into a relation between the applied potential, E , and i as shown in Eq. 103.

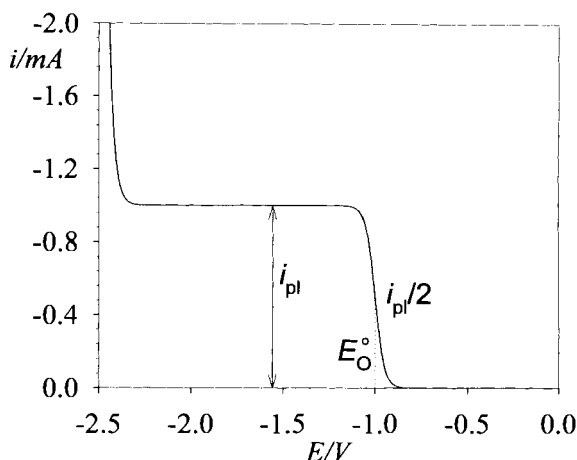
$$E = E_{\text{O}}^{\circ} + \frac{RT}{nF} \ln \frac{i_{\text{pl}} - i}{i} = E_{\text{O}}^{\circ} + \left(\frac{59.2}{n} \right) \log \frac{i_{\text{pl}} - i}{i} \text{ mV} \quad \text{at } T = 20^{\circ}\text{C} \quad (103)$$

The reversibility of a given system can be tested by plotting E against $\log \frac{i_{\text{pl}} - i}{i}$, where the slope ideally should be $59.2/n$ mV at 20°C . For quasi-reversible and irreversible electrode processes the slope will be substantially larger. A typical voltammogram for the reversible case is shown in Figure 23, where the standard potential is found at $i = i_{\text{pl}}/2$.

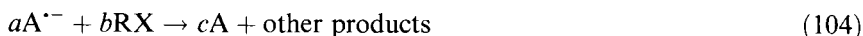
The RDE technique has found widespread use in analytical electrochemistry because of an excellent signal-to-noise ratio resulting from the enhanced mass transport. The RDE method has also been employed for monitoring concentrations in kinetic applications [59], as described for ultramicroelectrodes [60] and in the determination of the stoichiometry for electron-transfer reactions by means of redox titration [61]. The latter procedure will be described next.

Consider a reaction between an electrogenerated aromatic radical anion, $\text{A}^{\cdot-}$,

Figure 23. Typical RDE voltammogram (calculated) for the reversible reduction of O. The medium is reduced at $E < -2.3$ V. The standard potential E° for O can easily be measured at the point where the current, i is equal to half of the plateau current i_{pl} , as indicated by the dotted line. In this case $E^\circ = -1.0$ V.



and an alkyl halide, RX , where the parent aromatic compound A as well as other non-electroactive products are formed. The net reaction can be written as in Eq. 104, where the aim is to determine a , b , and c .



First, the aromatic compound A is added to an electrochemical cell equipped with an RDE. In Figure 24 the steady-state voltammogram recorded of a 50-mL solution containing $C_{\text{A},0} = 2$ mM is shown as the solid curve. The plateau current pertaining to A , $i_{\text{pl},\text{A},0}$, is -1 mA and the Levich equation, Eq. 102, can be used to relate $i_{\text{pl},\text{A},0}$ and $C_{\text{A},0}$, as shown in Eq. 105.

$$\frac{C_{\text{A},0}}{i_{\text{pl},\text{A},0}} = \frac{C_{\text{A}}}{i_{\text{pl},\text{A}}} = 2 \quad \left(\text{in } \frac{\text{M}}{\text{A}} \right) \quad (105)$$

Most of the A compound is then reduced preparatively in a one-electron process affording $\text{A}^{\bullet-}$. In Figure 24, the voltammogram recorded after passage of 9.5 C is shown as the dashed curve. To express $C_{\text{A}^{\bullet-},1}$ by the measurable $i_{\text{pl},\text{A}^{\bullet-},1}$ parameter, the ratio $D_{\text{A}}/D_{\text{A}^{\bullet-}}$ should be known. For most aromatic compounds it is close to one, and it is then possible to deduce the following relationship (Eq. 106) between the plateau currents and concentrations pertaining to both A and $\text{A}^{\bullet-}$.

$$C_{\text{A}^{\bullet-},1} = \frac{C_{\text{A},0}}{i_{\text{pl},\text{A},0}} \left(\frac{D_{\text{A}}}{D_{\text{A}^{\bullet-}}} \right)^{2/3} i_{\text{pl},\text{A}^{\bullet-},1} = 2 \left(\frac{D_{\text{A}}}{D_{\text{A}^{\bullet-}}} \right)^{2/3} i_{\text{pl},\text{A}^{\bullet-},1} \approx 2i_{\text{pl},\text{A}^{\bullet-},1} \quad \text{if } D_{\text{A}^{\bullet-}} \approx D_{\text{A}} \quad (106)$$

In this example, $i_{\text{pl},\text{A},1}$ is measured to be -0.1 mA, which means that 0.2 mM of A

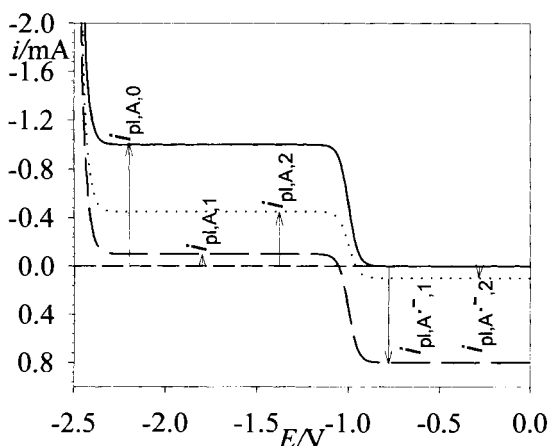
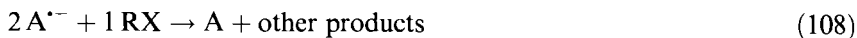
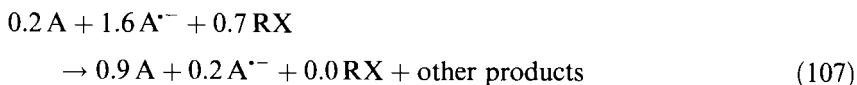


Figure 24. Constructed example of a stoichiometric determination by means of the RDE technique. The solid curve illustrates the reversible reduction of A to $A^{\bullet-}$ taking place at $E^\circ = -1.0$ V. The plateau current $i_{pl,A,0}$ is proportional to $C_{A,0} = 2$ mM. The cell volume is 50 mL. The dashed curve is a RDE voltammogram recorded after preparative reduction of A to $A^{\bullet-}$, consuming 9.5 C. Finally, the dotted-line curve is a voltammogram recorded after 0.7 mM of the alkyl halide has been added and reacted with $A^{\bullet-}$.

is left unelectrolyzed in the cell, while the $i_{pl,A^{\bullet-},1}$ value of 0.8 mA corresponds to $C_{A^{\bullet-},1} = 1.6$ mM. Note that the apparent disappearance of 0.2 mM compound in the cell is due to the formation of nonelectroactive products during the electrolysis of A.

The substrate RX is now added in a concentration ($= 0.7$ mM) that ensures that some $A^{\bullet-}$ is left in the cell after completion of the reaction. That the latter condition is fulfilled can easily be seen from the third voltammogram recorded in Figure 24, where $i_{pl,A^{\bullet-},2} > 0$. It is found that $i_{pl,A,2} = -0.45$ mA and $i_{pl,A^{\bullet-},2} = 0.1$ mA, corresponding to $C_{A,2} = 0.9$ mM and $C_{A^{\bullet-},2} = 0.2$ mM, respectively. The stoichiometry for the reaction of Eq. 104 can now easily be extracted from Eq. 107, and the result is shown in Eq. 108 with $a = 2$, $b = 1$, and $c = 1$.



Half of the amount of $A^{\bullet-}$ must therefore be transformed into a non-electroactive product. Obviously, Eqs. 105 and 106 are valid only for this specific process, but similar relations can easily be found for other reactions. The RDE technique has found many other applications, for instance, ones concerning the transient signals obtained at short time intervals. The reader interested in such subjects as well as the ring-disc technique is referred to Refs. [1, 62].

2.6 Combination of Electrochemistry and Spectroscopy

The use of spectroscopic methods such as UV, IR, and EPR spectroscopy in combination with electrochemistry is a strong tool for the detection and characterization of intermediates and products. Even the electrode/electrolyte interface may be studied in this manner. The equipment can be classified into three types according to the exact setup of the two parts. The first type (Type 1), in which the electrogeneration is separated in time and place from the spectroscopic detection, can be employed in the study of products or longer-lived intermediates. In practice, the setup often consists of a flow cell connected to a cuvette by tubes. This approach requires the construction of the electrochemical flow cell while the spectroscopic cell and the spectrometer are commercially available. In the second type of equipment (Type 2), which is very useful in the study of short-lived intermediates, the spectroscopic detection occurs simultaneously with the electrogeneration within the diffusion layer of the electrode. This combination of methods is known as spectroelectrochemistry and it requires that the light from the spectrometer is able to penetrate the diffusion layer. Therefore, the electrode surface should either reflect the light or be optically transparent in terms of fine minigrids, lithographic–galvanic structures (LIGA) [63], or thin layers of metal films such as gold or oxides of tin. In the third type of equipment (Type 3), the electrogeneration and detection take place at the same time, but with the spectroscopic cell placed outside the diffusion layer of the electrode. Techniques such as pulse radiolysis, flash photolysis, modulated photolysis and photoelectron injection in combination with electrochemical detection modes have been described recently [64] and will not be covered herein.

2.6.1 Type 1

Electrochemical flow cells

One of the essential units in the Type 1 equipment is the flow cell that can be constructed in numerous ways depending on the specific requirements concerning flow rates, conversion efficiency, electrode material, and so forth. The present authors have used a flow cell where the housing was made of inert PCTE (Kel-F). Carbon fibers were used for the working electrode, and these were pressed tightly into a porous ceramic 50-mm tube with an inner bore of 5 mm and outer bore of 16 mm. The connection to the working electrode was made with a platinum wire. The counter electrode was a platinum net placed in a compartment outside the ceramic tube. A small reference electrode was placed downstream, so the flow cell could be operated both potentiostatically and galvanostatically. The electrolyte could be forced through the flow cell with syringes or by means of an HPLC pump [65].

Flow cell and EPR

The flow cell has been used in combination with EPR spectroscopy to study self-exchange electron-transfer reactions between aromatic radical anions in line-

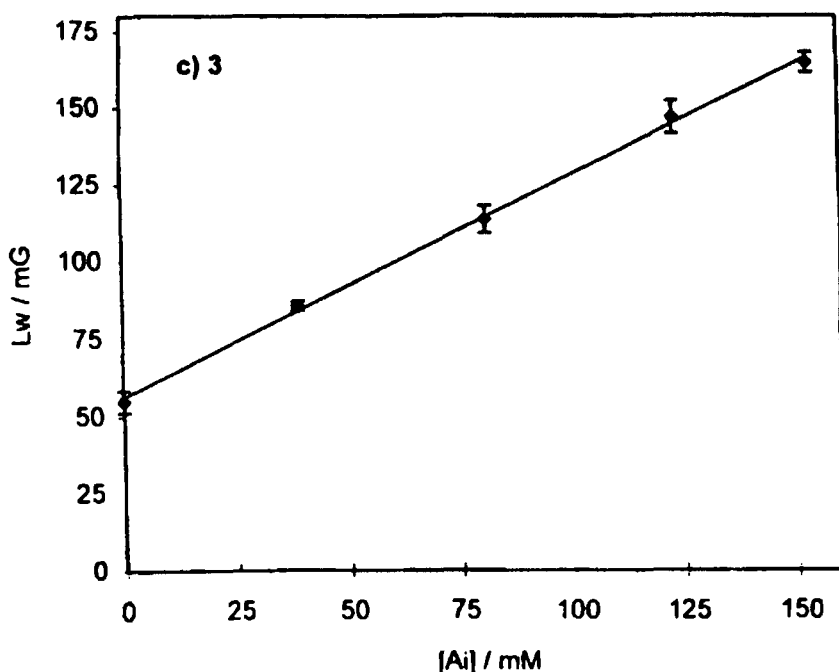


Figure 25. Corrected EPR linewidth L_w vs the concentration of 2,5-di-*tert*-butyl-1,4-dimethoxybenzene $[A_i]$, measured for the self-exchange electron-transfer reaction between the substrate and its radical cation (A^+). The concentration of the latter was in all experiments equal to 0.05 mM in acetonitrile/0.1 M Bu_4NBF_4 . From the slope, k_{ET} is calculated to be $1.1 \times 10^8 \text{ M}^{-1} \text{ s}^{-1}$; this corresponds to a self-exchange reorganisation energy of $21.2 \text{ kcal mol}^{-1}$. From D. Jürgen, S. U. Pedersen, and H. Lund, *Acta Chem. Scand.* 51:767 (1997).

broadening experiments [66, 67] to obtain self-exchange reorganization energies. For this application it is very important that the concentration of the paramagnetic species is controllable and can be kept constant. One example is given in Figure 25, where the self-exchange reorganization energy was measured for 2,5-di-*tert*-butyl-1,4-dimethoxybenzene and the corresponding radical cation. Because of the separation of the electrochemical flow cell and the ESR cuvette, there is a finite transit time between the sites of generation and detection, which means that only radicals with a certain lifetime can be detected. The excellent sensitivity of the ESR apparatus allows the measurement of very low steady-state concentrations of the radical ions and the flow rate can be varied so that the kinetics of the decay reactions can be studied.

Flow cell and IR

The same electrochemical flow cell has also been used in combination with IR spectroscopy in a stopped-flow system [68, 69]. The purpose was to study the electrogeneration of the Collman reagent $Fe(CO)_4^{2-}$ obtained from the two-electron reduction of $Fe(CO)_5$. It was possible to monitor the consumption of $Fe(CO)_5$ and

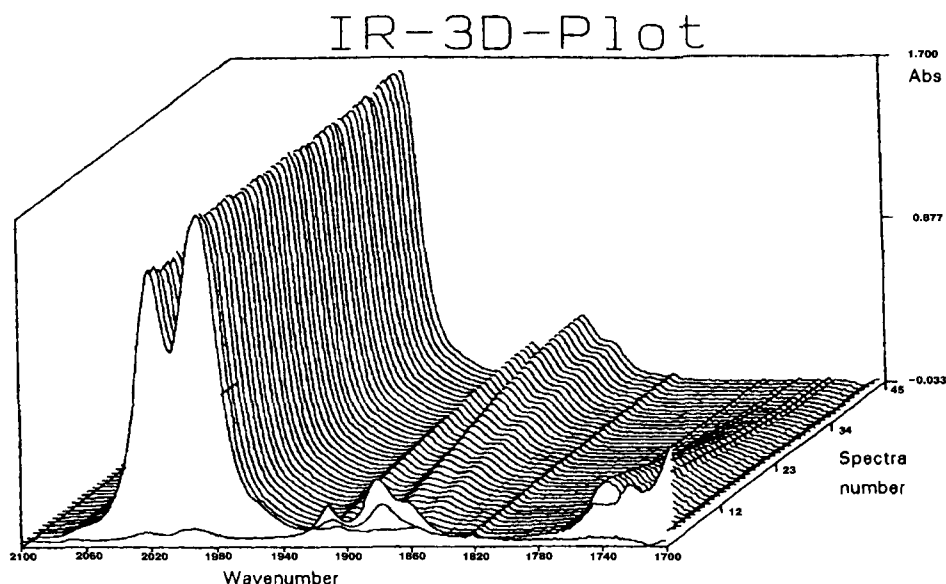


Figure 26. Application of flow-cell and IR spectroscopy to study the reaction between the electro-generated Collman reagent, $\text{Fe}(\text{CO})_4$ ($\nu = 1741 \text{ cm}^{-1}$) and $\text{Fe}(\text{CO})_5$ ($\nu = 2018$ and 1993 cm^{-1}) to generate $\text{Fe}_2(\text{CO})_8^{2-}$ ($\nu = 1914$ and 1883 cm^{-1}). $\text{Fe}(\text{CO})_5$ (1 mM) is reduced in the flow cell to $1\text{mM } \text{Fe}(\text{CO})_4^{2-}$, which is mixed with 10 mM $\text{Fe}(\text{CO})_5$ in the IR cuvette. The medium was acetonitrile/0.1 M Bu_4NBF_4 . From C. Amatore, J. N. Verpeaux, and S. U. Pedersen, in *Novel Trends in Electroorganic Synthesis* (S. Torii, Ed.), Kodansha, Tokyo, 1995, p. 205.

generation of $\text{Fe}(\text{CO})_4^{2-}$. The reactions of $\text{Fe}(\text{CO})_4^{2-}$ with $\text{Fe}(\text{CO})_5$ were also monitored by IR spectroscopy and this is shown in Figure 26. The product was easily identified as $\text{Fe}_2(\text{CO})_8^{2-}$ and the rate constants for the reaction was then obtained under pseudo-first-order conditions to be $2.3 \text{ M}^{-1} \text{ s}^{-1}$. The reaction between $\text{Fe}(\text{CO})_4^{2-}$ and alkyl halides (RX) could likewise be studied and the products $\text{RFe}(\text{CO})_4$ and $\text{RCOFe}(\text{CO})_4$ could be identified, and rate constants could be measured [9, 68].

Flow cell and UV

The electrochemical flow cell has also been used in combination with a UV spectrophotometer to obtain accurate UV spectra for a considerable number of aromatic radical anions ($\text{A}^{\cdot-}$) in *N,N*-dimethylformamide [65]. A solution of 0.1 mM of the aromatic compound (A) was pumped with a constant flow rate through the electrochemical flow cell. The latter was operated galvanostatically so that the electrolysis current could be increased steadily until the absorbance of the reduced or oxidized species attained a maximum, as illustrated in Figure 27. The maximum corresponds to the situation where all A is reduced to $\text{A}^{\cdot-}$ (or to $\text{A}^{\cdot+}$ in the case of an oxidation). When the current is increased beyond the optimum value, a further reduction of $\text{A}^{\cdot-}$ to A^{2-} takes place, leading to the decrease observed in the absorbance of $\text{A}^{\cdot-}$. This may be accompanied by the appearance of the spectrum for A^{2-} , as in

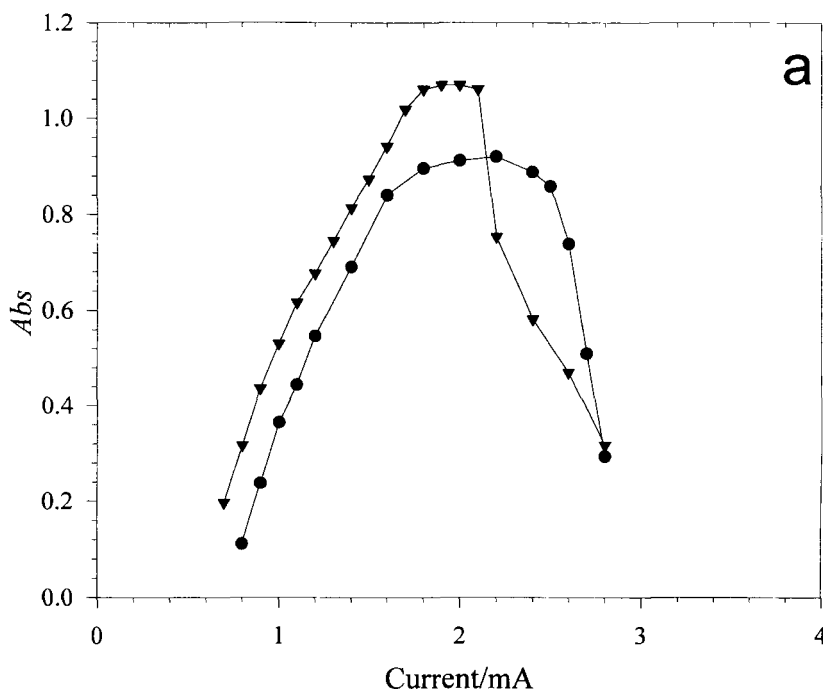


Figure 27. Application of flow cell and UV spectroscopy to study the reduction of aromatic compounds in *N,N*-dimethylformamide/0.1 M Bu₄NBF₄: a) Plot of absorbance at $\lambda_{\text{max}} = 556$ nm and 732 nm, of the products obtained in the reduction of anthraquinone (▼) and anthracene (●), respectively, as the galvanostatic current to the flow cell is increased and a continuous flow of 5 mL min⁻¹ is maintained. The substrate concentrations are both 0.1 mM and the light path is 1 cm; b) and c) The absorption spectra of the product obtained from reduction of anthraquinone and anthracene, respectively, when the galvanostatic current is increased above the maximum required for generating the radical anion. The current is increased from 2.0 to 2.8 mA in steps of 0.2 mA and the development in the spectra is indicated with arrows. Isosbestic points are also indicated. For anthraquinone, the spectra of the radical anion and the dianion could be resolved whereas for anthracene the dianion is protonated and spectra of the radical anion and 9,10-dihydroanthracen-9-ide could be resolved [65].

the case of anthraquinone. Most other dianions, including 9,10-dihydroanthracen-9-ide, are protonated immediately to AH⁻, whose spectrum is then recorded. The results obtained are summarized in Table 4.

To summarize, the type 1 equipment, in which the spectroscopic detection is combined with an electrochemical flow cell, has the advantage that the experimental setup is relatively simple. The lower limit of the time window is ca. 5 s, with the major drawback that only relatively stable intermediates can be detected. On the other hand, this ensures that homogeneous conditions are always attained. If the lifetime of the intermediates is less than 1 s, they exist in a reaction layer within the diffusion

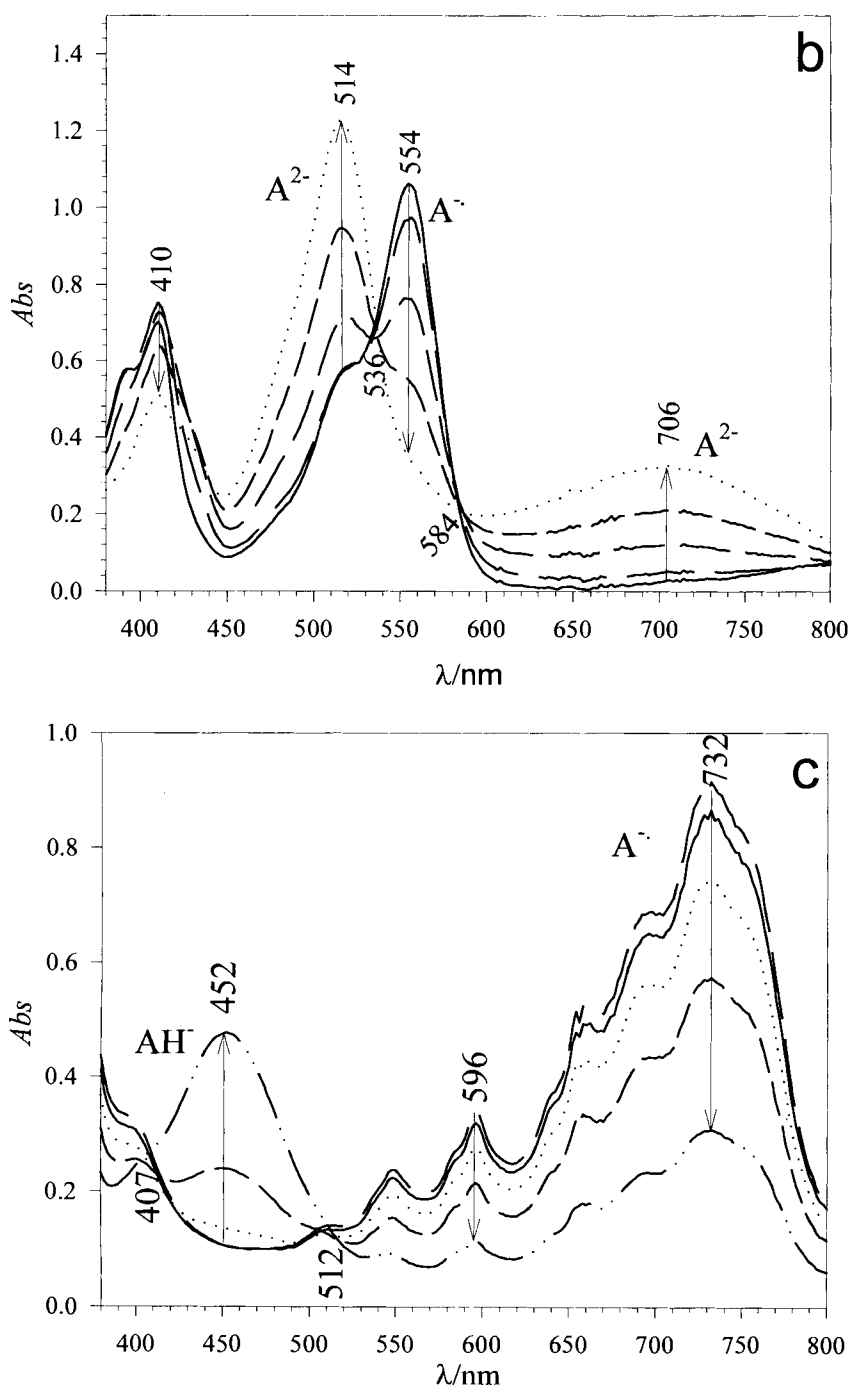
**Figure 27** (continued)

Table 4. Standard potentials of some aromatic and heteroaromatic compounds, E° , the wavelength corresponding to maximum absorption, λ_{max} , the extinction coefficients measured by means of the dip probe are given by ϵ_{probe} (see Section 2.6.3 and Ref. [65] for details), and those by the flow technique are given by ϵ_{flow} .

Substrate	$-E^\circ$, V vs SCE	λ_{max} , nm	$10^{-3} \times \epsilon_{\text{probe}}$	$10^{-3} \times \epsilon_{\text{flow}}$
Benzophenone ^a	1.707	754	8.50	8.60
		338		16.0
Fluorenone ^a	1.220	550	7.50	7.65
		378		3.37
1,4-Naphthoquinone ^a	0.575	411	8.10	8.80
		480		4.85
		574		1.42
		302		10.0
Anthraquinone ^a	0.800	556	11.6	10.7
		410		6.98
		274		22.7
1,2-Benzanthraquinone ^a	0.672	624	8.15	8.40
		415		4.45
		301		27.7
(<i>E</i>)-Stilbene ^b	2.136	496	42.0	47.7
		704		9.74
		312		7.21
Anthracene ^a	1.890	732	9.40	9.20
		662		5.35
		596		3.49
		368		20.5
		328		27.6
9,10-Diphenylanthracene ^a	1.794	614	7.70	8.30
		676		7.03
		566		6.41
		378		24.2
		332		23.0
Fluoranthene ^a	1.688	450	17.0	20.0
		516		7.22
		314		25.7
Perylene ^a	1.613	578	50.5	56.5
		682		6.30
		438		4.24
		322		16.8
Benzonitrile ^b	2.230	403	4.03	3.90
		314		15.2
<i>p</i> -Tolunitrile ^b	2.337	436	3.12	2.92
		316		14.0
1,4-Diacetylbenzene ^b	1.407	624	14.7	14.0
		394		24.7
1,4-Dicyanobenzene ^b		430	7.26	6.79
9,10-Dicyanoanthracene ^a	1.015	706	6.58	6.79
(<i>E</i>)-Azobenzene ^a	1.279	426	51.6	47.6
		290		8.48

Table 4 (continued)

Substrate	$-E^\circ$, V vs SCE	λ_{\max} , nm	$10^{-3} \times \epsilon_{\text{probe}}$	$10^{-3} \times \epsilon_{\text{flow}}$
(<i>E</i>)-4-Methoxycarbonylazobenzene ^b	1.015	480	33.0	38.8
Quinoxaline ^a	1.589	604	2.35	2.26
		323		5.17
Phenazine ^a	1.090	542	8.23	8.05
		600		3.35
		513		7.26
		372		14.0
		288		26.2

^a The lifetime is longer than 500 s.^b The lifetime is in the interval from 50 to 500 s.

layer, and spectroscopic detection would require that the light passes through the diffusion layer. Then the method of choice would be spectroelectrochemistry.

2.6.2 Type 2

Spectroelectrochemistry

In spectroelectrochemistry, spectroscopic detection in the electrochemical cell occurs simultaneously with the electrochemical generation. Often the response is also monitored electrochemically, thus providing an even more detailed description of the intermediates produced. The spectroelectrochemistry technique has found widespread use; there are excellent reviews on the subject [70].

Spectroelectrochemistry can be accomplished in different ways. If the light is passed through an optically transparent electrode (OTE), as shown in Figure 28(A), the light will go through not only the diffusion layer containing the intermediate generated at the electrode, but also through the bulk solution where no intermediate is present. In this sense, the bulk solution presents nothing but a complicating factor, in particular if it is recalled that the thickness of the diffusion layer ($\delta < 0.1$ mm) is very small compared to the size of the bulk in normal cells. This has resulted in the design of special thin layer cells with such small physical dimensions, that the diffusion layer extends to the cell wall. The combination of an optically transparent electrode and a thin-layer cell is denoted an OTTLE (optically transparent thin-layer electrode) (see Figure 28(B)). The fact that the cell volume is very small compared to the electrode area has an interesting implication. Suppose a redox pair O/R is present in the cell, then changes in the electrode potential provide a facile way of controlling the concentration ratio of O and R at the electrode surface according to the Nernst equation. Because of the smallness of the cell and the restrictions imposed thereby on the diffusion layer, the concentrations of O and R everywhere in the cell will be the same as at the surface after a short while. In other words, the spectroscopic measurements pertain to equilibrium concentrations.

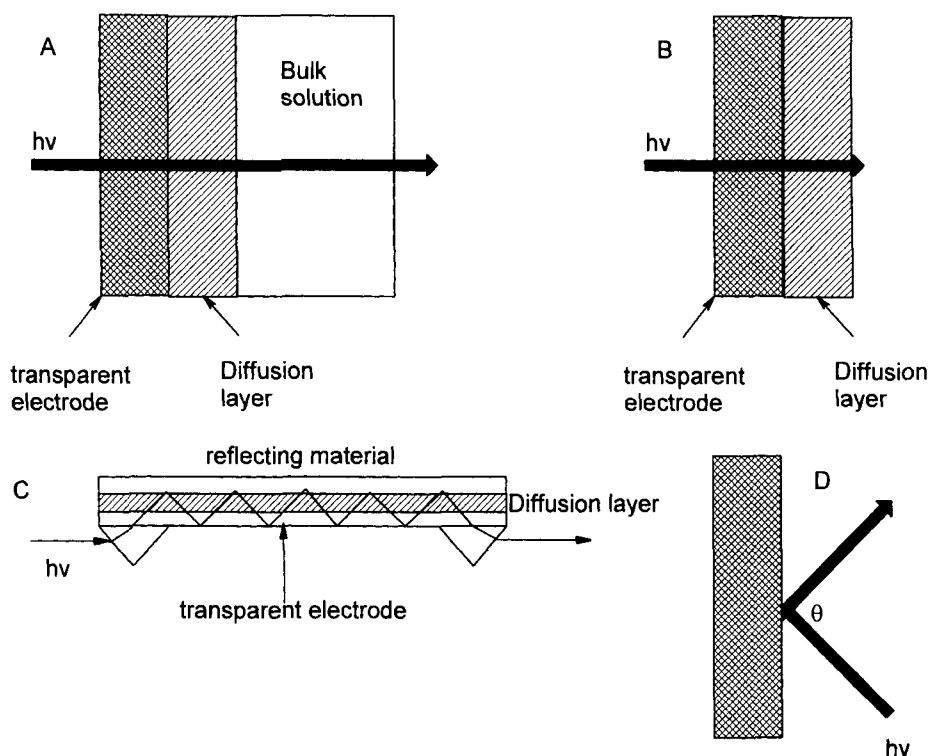


Figure 28. Configurations for spectroelectrochemistry. A) optically transparent electrode; B) optically transparent thin-layer electrode (OTTLE); C) Internal reflection spectroscopy, and D) specular reflectance spectroscopy.

Internal reflection spectroscopy

The principle underlying internal reflection spectroscopy is shown in Figure 28(C). The light beam is directed from the inside of an OTE at an angle greater than the critical angle, so that it is reflected at the electrode/electrolyte interface. The depth of the light into the solution is about $0.1\ \mu\text{m}$, which is much larger than the thickness of the double layer but smaller than the diffusion layer. For most applications such a path length is too short, and as a result, multiple reflections have to be used.

Specular reflectance spectroscopy

In specular reflectance spectroscopy, the intermediates are also monitored close to the electrode surface by spectroscopy, but here there is no need for an OTE, as ordinary well-polished disk electrodes will do the job. The light beam is directed towards the front of the electrode surface and is reflected as shown in Figure 28(D). The beam therefore transverses the diffusion layer twice, and the light path can be changed by variation of the angle of reflectance.

Diffusion-layer imaging

The diffusion-layer imaging technique which was developed by McCreery is another method for studying intermediates in the diffusion layer [71–75]. A laser beam is directed in a parallel direction through the diffusion layer of the electrode and the light is then magnified and focused on a diode-array detector. With this method, spatial resolution of the diffusion layer of 1.25 μm is achieved, and concentration profiles in the diffusion layer are mapped. A detailed description of mass transport processes as well as the kinetics and spectra of intermediates can be obtained. Diffusion coefficients and extinction coefficients for, for example, the benzophenone radical anion were measured with this technique [74, 75].

OTTLE–EPR

The use of EPR as detection mode can be a very powerful tool for the identification of radical intermediates that are electrochemically generated. Different types of electrochemical cells have been developed for that purpose. An OTTLE flat cell with an internal width of only 0.35 mm was used by McQuillan et al. for recording both UV and EPR spectra [76]. The reference and the counter electrode were placed relatively far from the platinum net working electrode; this resulted in a large resistance and made the control of the potential difficult. Such a cell is best suited for studies in highly conducting solvents such as water containing a high electrolyte concentration. McQuillan et al. studied the reduction of anthraquinone sulphonates at high pH, and found that it proceeded by a two-electron process in the presence of the alkali cations Li^+ and Na^+ , but by two one-electron reductions in the presence of tetraalkylammonium cations. It was possible to record the EPR and UV spectra of the radical anion and the UV spectrum of the dianion.

An alternative cell design developed by Allan Bond and shown in Figure 29 is now commercially available from Micro Glass Instruments [77]. The electrochemical cell built into a quartz tube of only 4 mm in outer diameter fits directly into the cavity of the EPR spectrometer. The working electrode is a curled platinum wire, while a 70- μm platinum wire electrocoated with Ag and with the outer layer further converted to AgCl by oxidation serves as a pseudo reference electrode. The advantage of this design is that the two electrodes can be placed close to each other, improving the electrochemical properties of the cell with respect to a lowering of the resistance and time constant. However, this cell is less efficient than the flat OTTLE in the electrochemical generation process because of the smaller dimensions. None of the cells can be used for quantitative investigations of kinetic and mechanistic aspects, as the EPR signal is not proportional to the charge injected into the cells. Neudeck recently proposed a modified design using a flat OTTLE with a laminated gold micromesh [63]. The exposed area of the working electrode is small (1 \times 3 mm) and can be placed completely within the EPR cavity. The connection wire to the working electrode is, furthermore, shielded because of the lamination and does not contribute to the generation of radicals.

The cells described above are all characterized by the working electrode being placed directly in a static solution in the EPR cavity. In general, exhaustive electrolysis is accomplished within 30 s, depending on the exact thickness of the cell, so

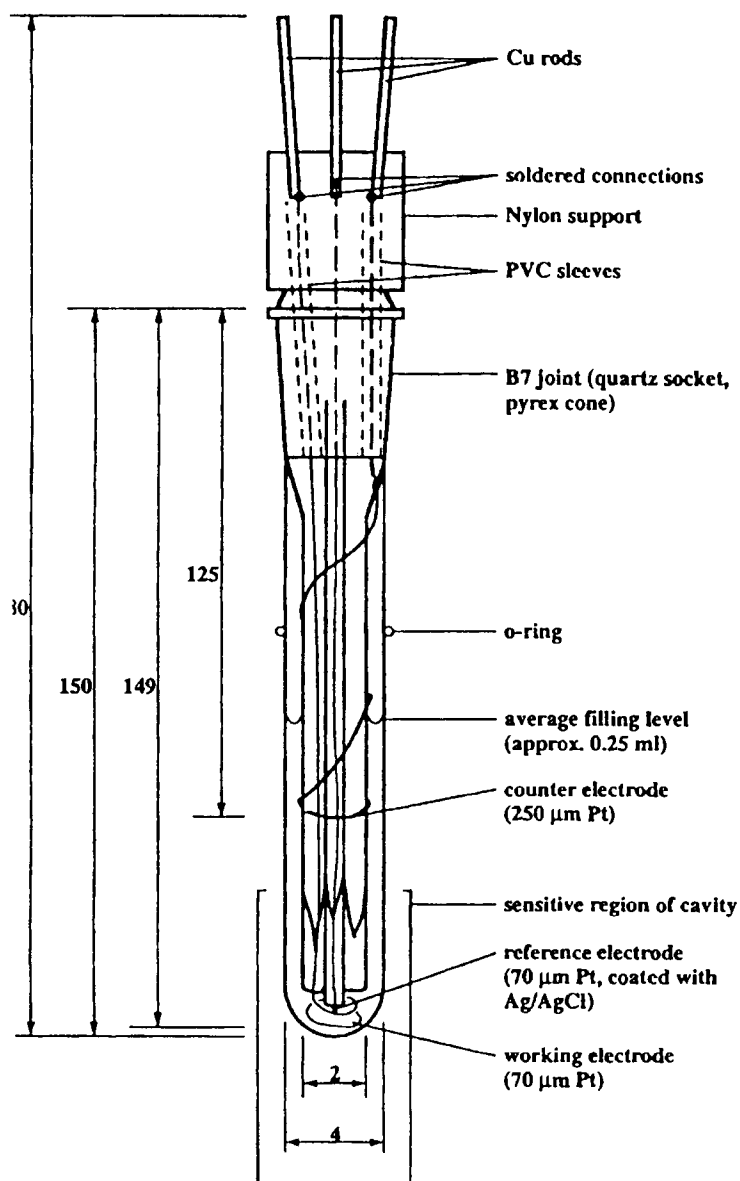


Figure 29. The small volume in situ ESR electrochemical cell shown was developed by Allan Bond and is now commercially available from Micro Glass Instruments. From D. A. Fiedler, M. Koppenol, and A. M. Bond, *J. Electrochem. Soc.* 142:862 (1995) [77].

very unstable radicals cannot be detected. A flow-through cell designed by Compton is supposed to combine the best from the flow cell and OTTLE [78]. Essentially, the cell is a dismountable channel electrode with dimensions of $0.4 \times 6 \times 30$ mm, and with applicable flow rates between 10^{-4} and 10^{-1} mL s $^{-1}$. Since the flow is laminar, a parabolic velocity profile will develop across the channel. The sensitivity of the cell is good and kinetic and mechanistic parameters may be deduced from changes occurring as a consequence of variations in the flow rates.

Charge-transfer processes occurring across the liquid–liquid interface have also been studied by EPR. The Galvani potential difference between the two immiscible solvents, water and 1,2-dichloroethane (DCE), was controlled electrochemically by means of a bipotentiostat. The water phase contained potassium ferrocyanide, which, in the DCE phase, by electrochemical polarization of the interface, can reduce a compound such as tetracyanoquinodimethane to its radical anion or oxidize a compound such as tetrathiafulvalene to its cation radical. Both radicals were detected by EPR spectroscopy [79].

OTTLE-IR

The combination of IR spectroscopy with OTTLE cells has not found as many applications as OTTLE-UV, in spite of the much better structural characterization of solution species by IR spectroscopy. OTTLE-IR suffers from the disadvantage that the extinction coefficients in the IR range are much smaller than in the UV range; this means that higher substrate concentrations are required and/or substrates with particularly strong bands need to be chosen for a high signal to noise ratio. In recent years, a number of OTTLE-IR cells have been designed for the study of, in particular, organometallic and inorganic complexes. A simple transmission IR cell can be constructed as shown in Figure 30, with a gold minigrid working electrode sandwiched between two IR transparent windows. The difficult part consists of sealing the cell properly, because normal IR windows made of NaCl or KBr are quite fragile and cannot tolerate large pressures. Polished silicon windows might be used, but unfortunately these will block some wavelength ranges of the IR light. The electrolysis time has to be long (>30 s) for a good signal to noise ratio for the weak IR absorbances.

Another kind of cell, made by Graham and Curran, was based on an internal reflection crystal [80]. A gold minigrid was mounted directly on a prism ($9 \times 9 \times 45$ mm) and on top of this was a zinc selenide prism. The distance (observation) between the minigrid and the prism is typically 13–15 μm , which results in a very short response time. For a potential-step experiment, maximum absorbance is achieved within a couple of seconds. The cell is especially well-suited for potential-scan experiments because the intermediate generated at the electrode will rapidly fill out most of the observation distance even when moderately fast sweep rates (50 mV s $^{-1}$) are applied. Some “memory” effect is, however, present, because the diffusion layer will not be completely evolved on this timescale. At smaller sweep rates (2 mV s $^{-1}$) all of the observation layer behaves like a thin layer, where the concentrations are in equilibrium with the electrode surface concentrations. The cell has been used to study the reduction process of $\text{Fe}(\text{CO})_5$ by CV, where it was pos-

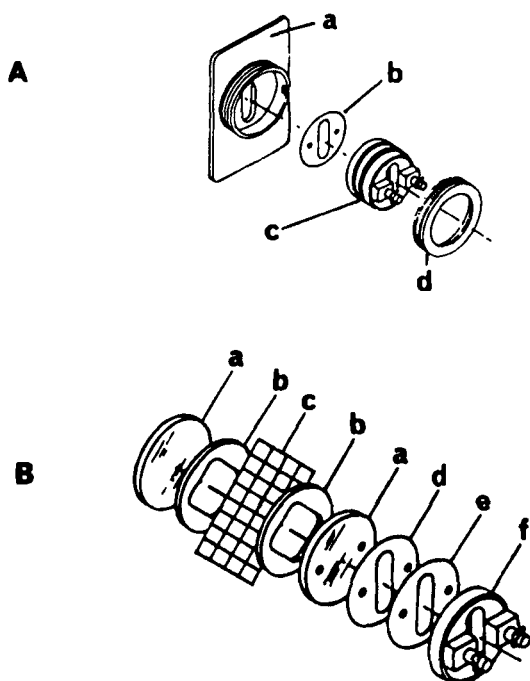


Figure 30. A) Diagram of the OTTLE-IR and cell holder: a) back plate, b) teflon gasket, c) salt plate/minigrid electrode assembly (see Fig 30 B), d) knurled end cap. B) Expanded view of the salt plate/minigrid electrode assembly: a) NaCl salt plates, b) Tefzel gaskets, c) gold minigrid electrode, d) indium gasket, e) teflon gasket, f) needle plate. From J. P. Bullock, D. C. Boyd, and K. R. Mann, *Inorg. Chem.* 26:3084 (1987) [140].

sible to identify most of the intermediates by IR, although the mechanism assigned for the dimerization was not correct [81].

OTTLE-UV (OTTLE/Nernst method)

The design and applications of OTTLE-UV cells have been discussed in details elsewhere [70], and only one important application will be discussed here, namely the construction of a Nernst plot for the determination of the formal reduction potential, $E_O^{\circ'}$, and the electron stoichiometry, n . The ratio of the surface concentrations for a given redox pair O/R can be controlled by the applied electrode potential according to the Nernst equation shown in Eq. 109. (In principle, this equation is more explicit than Eq. 1, since the formal potential incorporates the relevant activity coefficients. For most applications, however, this has no significance.) For a reversible redox pair, the adjustment of the surface concentrations occurs instantaneously whereas in the quasi-reversible case, this process might take a longer time. For some irreversible redox pairs the establishment of the equilibrium is so slow that it is not attained even after several days or years. In a thin-layer cell with its small dimensions, the ratio of concentration becomes the same everywhere in the cell within a few seconds as long as the redox pair is not involved in homogeneous reactions.

The concentration ratio of O and R can be determined by UV spectroscopy at any time by measurement of the absorbance at a wavelength where O and R absorb with different extinction coefficients. A common situation is that one of the two

species is colored with a unique absorbance in the visual range, since either O or R contains an uneven number of electrons. This provides easy access to the determination of, say, C_R , and C_O can then be calculated as $C_O = C_O^* - C_R$, where C_O^* is the initial concentration. In a typical experiment, the applied potential is changed in steps from a situation where C_O/C_R is greater than 1000 to less than 0.001 with special attention paid to the turnover range around one. At each value of the electrode potential, the OTTLE is allowed to equilibrate until no more changes are observed in the UV spectra and the current measured is zero. The latter point is important, because one of the major problems associated with OTTLE, the iR loss, may then be neglected.

The logarithm of the measured C_O/C_R ratios is plotted against the applied electrode potential in a Nernst plot, as illustrated in Figure 31. As predicted by the rearranged Nernst equation given in Eq. 110, the formal potential is then equal to the electrode potential ($E = E_O^{\circ'}$) when $\log(C_O/C_R)$ is zero and the number of electrons consumed n is obtained from the slope which is $nF/2.3RT$.

$$E = E_O^{\circ'} + \frac{RT}{nF} \ln \left(\frac{C_O(x=0)}{C_R(x=0)} \right) \quad (109)$$

$$\log \frac{C_O(x=0)}{C_R(x=0)} = \log \frac{C_O}{C_R} = \left(\frac{nF}{2.3RT} \right) (E - E_O^{\circ'}) \quad (110)$$

In this manner, it is possible to measure $E_O^{\circ'}$ with a precision of a few mV or better. Although $E_O^{\circ'}$ might be determined more easily and with a similar precision for a reversible system by the CV technique, the OTTLE/Nernst experiment is very useful for the study of quasi-reversible systems. The presence of slow heterogeneous kinetics means that the equilibrium is attained relatively slowly upon changing the potential, but this presents no problem as long as the redox pair is kinetically stable. The technique has therefore been used in the measurement of $E_O^{\circ'}$ and n for a large number of inorganic salts and enzymes [70, 82].

When the heterogeneous electron-transfer process at the electrode becomes slow and irreversible, the use of the direct OTTLE/Nernst experiment is inconvenient because of the uncertainties associated with a slow equilibration process. A mediated OTTLE/Nernst experiment should rather be considered, where a redox mediator M_{ox}/M_{red} characterized by a high heterogeneous rate constant is added to the cell (Eq. 111). The concentration ratio of the mediator couple will be adjusted quickly to the applied electrode potential E and, furthermore, it will be in a redox equilibrium (Eq. 112) with the redox pair O/R in the bulk solution, according to Eq. 113.



$$E = E_M^{\circ'} + \frac{RT}{nF} \ln \left(\frac{[M_{ox}]}{[M_{red}]}} \right) = E_O^{\circ'} + \frac{RT}{nF} \ln \left(\frac{[O]}{[R]} \right) \quad (113)$$

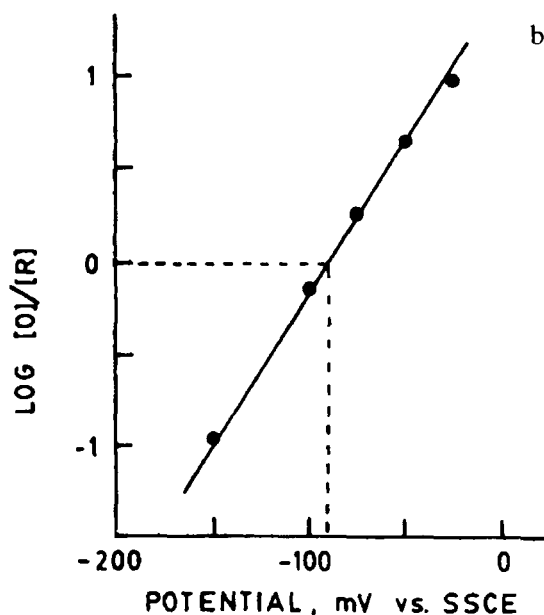
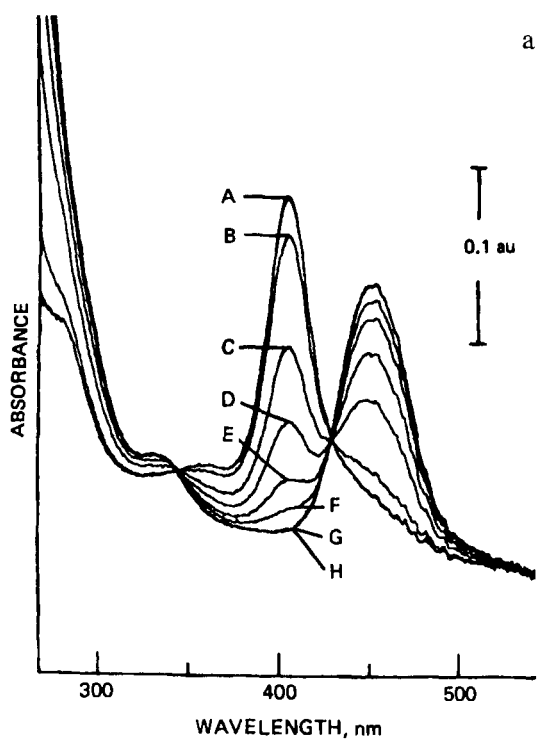


Figure 31. OTTLE spectropotentiostatic experiment on 0.87 mM $[\text{Tc}^{\text{III}}(\text{diars})_2\text{Cl}_2]^+$, 0.6 M TEAP in DMF. a) Spectra recorded during applied potentials, mV vs SSCE: A, -250; B, -150; C, -100; D, -75; E, -50; F, 25; G, 100; H, 250. From R. W. Hurst, W. R. Heineman, and E. Deutsch, *Inorg. Chem.* 20:3298 (1981) [82]; b) Plotted data from Figure 31(a), recorded at 403 nm. From W. R. Heineman, F. M. Hawkridge, and H. N. Blount, in *Electroanalytical Chemistry*, Vol. 13 (A. J. Bard, Ed.), Marcel Dekker, New York, 1984, p. 20 [70].

Again, the value of $E_O^{\circ'}$ may be extracted from a Nernst plot of the logarithm of the concentration ratio $[O]/[R]$ against E . In some cases, the measurements are made difficult by the presence of additional absorbances in the UV range due to the mediator couple.

The mediated OTTLE/Nernst method, with 2,6-dichlorophenolindophenol as mediator, was employed by Heineman *et al.* in the measurement of $E_O^{\circ'}$ for cytochrome c [83]. For enzymes, the mediated OTTLE/Nernst method is probably the method of choice, since the heterogeneous charge-transfer processes often are very slow; the electroactive metal center is insulated by the surrounding protein structure and cannot get close to the electrode surface.

2.6.3 Type 3

Fiber-optic probes for UV- and IR spectroelectrochemistry

Fiber-optic probes are now commercially available for transmission UV spectroscopy and, since recently, also for IR spectroscopy. In both cases a bifurcated cable carries the light from the source to the tip of a probe. The tip is constructed so the solution under study can freely flow through entry holes into the light path. The light is reflected at a mounted mirror and passes through the solution once more before it enters another cable that carries the attenuated light to the spectrometer.

The cuvette length is equal to the sum of the light paths to and from the mirror through the solution. The cuvette length is fixed on some probes, but can be adjusted on other probes if the mirror is moved. A commercially available solution transmission probe from Ocean Optics is shown in Figure 32. The fiber-optic probes can be inserted into the solution of an H-cell used for preparative electrolysis, which allows the recording of spectra during the progress of the electrolysis. This provides important information about the nature of the intermediates/products involved as well as about the kinetics.

2.7 Indirect Electrolysis

In the middle of the 1970s a revival of the use of indirect electrolysis in organic chemistry occurred; this was stimulated, in particular, by its advantages in lowering energy consumption and by its ability to enhance product selectivity. A number of papers published by Lund *et al.* [84–86] and Savéant *et al.* [87–89] in this period dealt with both the synthetic possibilities and the kinetics involved, especially concerning the reduction of aromatic and aliphatic halides by radical anions of aromatic and heteroaromatic compounds. In this chapter we will provide a general description of indirect reduction processes; the main emphasis will be on the principles underlying the methodology. Obviously, these principles are also directly applicable to oxidation processes. Next, we present a couple of specific examples



Figure 32. UV dip probe based on light guides, from Ocean Optics.

illustrating the sort of quantitative information that can be extracted by the indirect approach. A wealth of other examples that show the general scope of the methodology can be found in accounts and review articles already available in the literature [90–97].

A direct reduction process involves three main steps, where the substrate first diffuses to the electrode, an electron is transferred from the surface of the electrode, and the substrate then finally returns to the solution in its reduced form. If the electron-transfer process is accompanied by large structural changes in the substrate and/or substantial solvent reorganization, then k^o will be small and the electrode process will be sluggish and become the rate-controlling step. In that case, the only way to increase the reduction rate according to the current–overpotential equation (Eq. 12) is to apply a higher overpotential, although the expense might be a falling current yield due to background discharge or other unwanted side reactions.

In comparison, an indirect electrochemical reduction is based on the steps shown in Figure 33. Here, the electrode transfers an electron to a suitable mediator that diffuses into the solution and transfers the electron to the substrate. The mediator is regenerated and can diffuse back to the electrode surface for another activation cycle. The indirect approach thus combines heterogeneous electron transfer with a homogeneous redox reaction. The mediator therefore acts as an efficient three-dimensional electrode with substantial overall rate enhancement for the reduction

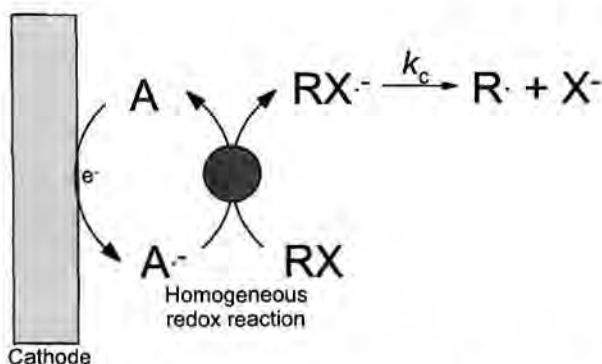


Figure 33. The principle of indirect electrolysis exemplified by a reduction process (see Eqs. 114–119 for a description of the species involved).

process to follow. In most cases this is a great advantage, since the overpotential required for carrying out the reduction of the substrate may be lowered by several hundred mV compared with the direct approach. Moreover, the lowering of the potential is usually accompanied by a gain in the selectivity of the reaction as the selectivity is dependent on the potential differences between the mediator and the various electrophores (functional groups) in the substrate. For a corresponding direct reduction process in which a high overpotential (brute force) is required, such a selective reduction cannot be obtained, in particular, if the reducibility of the different electrophores is alike. Even if the substrate contains only one electrophore, large differences may be observed in the product distributions. The rather negative potentials employed in the direct reduction process often favor the formation of anions due to further reduction of the intermediates formed in the first step; this reaction pathway is less likely in the indirect method.

The mediator is a key species in the indirect reduction (or oxidation) process as it is involved in both the homogeneous and heterogeneous reactions. The most common mediators used are inorganic ions, metal complexes, and aromatic compounds. In general, the following conditions should be fulfilled:

- a) The mediator is more easily reducible than the substrate (for a reduction process)
- b) The heterogeneous rate constant k° is high, so the heterogeneous charge transfer process at the electrode surface is fast.
- c) The homogeneous reaction taking place between the reduced (or the oxidized) form of the mediator and the substrate is fast. Electron-transfer processes are accelerated if they have inner-sphere character.
- d) Both the oxidized and reduced forms of the mediator are characterized by high chemical stability if no substrate is present.
- e) Both the oxidized and reduced forms of the mediator are sufficiently soluble in the chosen solvent. Should problems regarding solubility arise, the use of two-phase systems may be a possibility.

The indirect reduction of many organic substrates, in particular alkyl and aryl halides, by means of radical anions of aromatic and heteroaromatic compounds has been the subject of numerous papers over the last 25 years [98–121]. Many issues have been addressed, ranging from the exploration of synthetic aspects to quantitative descriptions of the kinetics involved. Savéant *et al.* coined the expression “redox catalysis” for an indirect reduction, in which the homogeneous reaction is a pure electron-transfer reaction with no chemical modification of the mediator (i.e., no ligand transfer, hydrogen abstraction, or hydride shift reactions). In the following we will consider such reactions and derive the relevant kinetic equations to show the kind of kinetic information that can be extracted.

The indirect reduction of many organic substrates by radical anions can be described by the following general reaction scheme:



The mediator A denotes a stable aromatic or heteroaromatic compound selected so its standard potential, E_A° , is positive relative to the standard potential of the substrate RX, E_{RX}° . The radical anion $A^{\bullet -}$ is generated by heterogeneous electron transfer (Eq. 114) to A at the electrode surface. The actual indirect reduction process between $A^{\bullet -}$ and RX takes place in a homogeneous step (Eq. 115) with rate constant k_{ET} . The radical anion of the substrate, $RX^{\bullet -}$, formed by this process, cleaves to the radical R^{\bullet} and the anion X^- in a fragmentation reaction (Eq. 116), which may be followed by a number of fast follow-up processes, depending on the nature of R^{\bullet} . For aryl radicals, hydrogen abstraction from the solvent HS as shown in the reaction of Eq. 117 is a potential reaction path. However, regardless of whether R^{\bullet} , a solvent-derived radical S^{\bullet} , or a mixture of them are formed in solution, their fate is determined by $A^{\bullet -}$ as indicated by the processes in Eqs. 118 and 119 [122]. Dimerization or cross-coupling reactions of R^{\bullet} and S^{\bullet} are normally not seen, owing to their low steady-state concentrations which arise because the forward electron-transfer reaction (Eq. 115) is normally the slowest and rate-controlling step. Overall, two molecules of $A^{\bullet -}$ are thus used in the reduction of one molecule of RX.

One of the interesting features of the above scheme is the presence of a competition between the first-order cleavage reaction (Eq. 116) and the second-order reverse electron-transfer process (Eq. 115). According to the overall reaction scheme, neglecting for a while the heterogeneous process (Eq. 114), the differential equation

for species $A^{\cdot-}$ can be expressed as shown in Eq. 120, where the steady-state assumption has been imposed on the intermediates $RX^{\cdot-}$, R^{\cdot} , and S^{\cdot} .

$$\frac{\partial C_{A^{\cdot-}}}{\partial t} = -\beta C_{A^{\cdot-}}, \quad \text{where } \beta = \frac{2k_c k_{ET} C_{RX}}{k_c + k_{-ET} C_A} \quad (120)$$

The competition between the cleavage reaction (Eq. 116) and the reverse electron-transfer reaction (Eq. 115), as expressed by the two terms in the denominator of the above expression, is dependent on the concentration of A, unless $k_c \gg k_{-ET} C_A$. In that case, the rate-controlling step is the forward electron-transfer process (Eq. 114) with $\beta = 2k_{ET} C_{RX}$. If $k_c \approx k_{-ET} C_A$, the reaction kinetics of $A^{\cdot-}$ becomes slower as C_A is increased, and, ultimately, the cleavage reaction is the rate-controlling step with Eq. 115 acting as a pre-equilibrium process, that is, $\beta = \frac{2k_c k_{ET} C_{RX}}{k_{-ET} C_A}$.

The fact that the competition ratio is dependent on C_A can be exploited for the determination of the rate constant k_c , but two main points have to be fulfilled. First of all, the two rate constants involved, k_c and k_{-ET} , should be of such a relative magnitude that a variation of C_A in the range accessible is actually reflected in an effect on the competition ratio of the two reactions. Secondly, if the absolute value of the rate constant k_c is to be calculated from the value of k_{-ET} , then the latter has to be known. This is the case when the reverse electron transfer is so exoergic that it is controlled by the diffusion together of the two species, and k_{-ET} can be set equal to the diffusion-controlled rate constant k_d . The rate constant k_d depends on the viscosity of the specific solvent used, but in most cases it is close to a value of $10^{10} \text{ M}^{-1} \text{ s}^{-1}$. (It should always be checked that the reaction under investigation is controlled by diffusion of the reverse process, i.e., that the rate constant k_{ET} in a plot of $\log k_{ET}$ against the driving force (proportional to $-FE_A^\circ$) is positioned in the region characterized by a slope of $1/59 \text{ mV}^{-1}$ (see below)).

Savéant and coworkers [87–89, 123–125] introduced this approach for determining k_c in linear sweep voltammetry. The experimental voltammograms were compared with simulations to determine cleavage rate constants for radical anions ranging from 10^6 to $5 \times 10^8 \text{ s}^{-1}$. The indirect approach is therefore a very useful supplement to direct techniques such as cyclic voltammetry [126–130], pulse radiolysis [131–135], and flash photolysis [136], which have proven to be convenient and effective tools when the cleavage rate constant of $RX^{\cdot-}$ is lower than 10^7 s^{-1} .

One example illustrating the indirect LSV approach pertains to the reduction of 1-chloronaphthalene with 4-methoxybenzophenone as mediator in DMSO. The experimental parameter measured in the LSV experiments is $i_p/2\zeta i_{pd}$, where ζ is the excess factor, that is, the concentration ratio of the substrate 1-chloronaphthalene and the redox catalyst 4-methoxybenzophenone, and i_p and i_{pd} are the peak currents measured for the mediator with and without the substrate being present. Note that the currents obtained are dependent on the nature of the products formed in Eqs. 118 and 119, that is, the amount of A regenerated. In many situations a reduction process is expected to dominate, but a contribution from other processes has to be looked for and specifically taken into account in the simulation procedure. In the present example, the forward electron-transfer reaction (Eq. 114) is rate-controlling

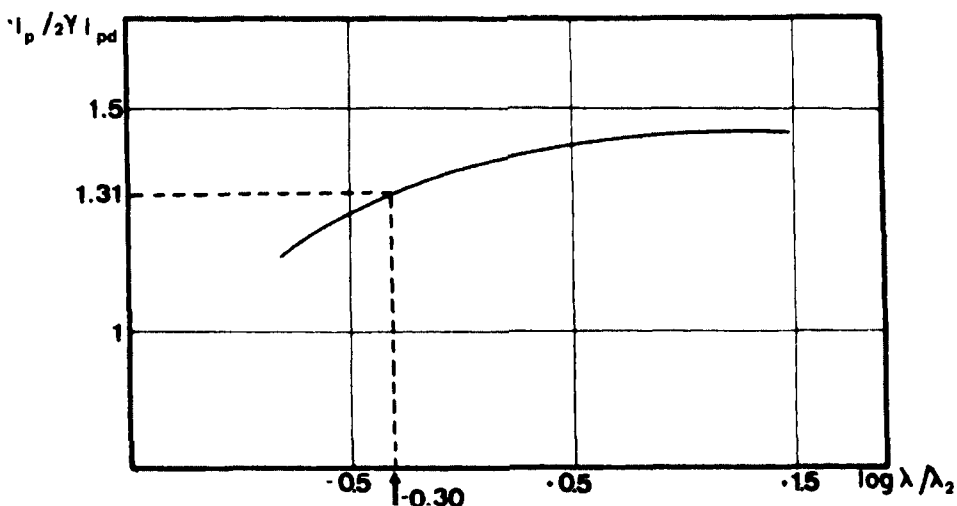


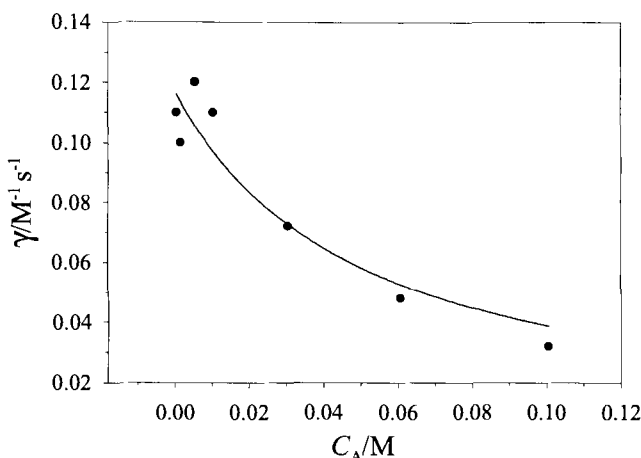
Figure 34. Reduction of 1-chloronaphthalene in DMSO as catalyzed by 4-methoxybenzophenone. Mixed kinetic control, the excess factor, ζ (denoted by γ in the plot) = 0.5, $\nu = 0.1 \text{ V s}^{-1}$, $C_A = 0.02 \text{ M}$. The abscissa $\log \lambda / \lambda_2$ corresponds to $\log k_c / k_{-ET} C_A$. Working curve for $\lambda_1 = RTk_{ET} C_A / F\nu = 0.5$. From C. P. Andrieux, C. Blocman, J. M. Dumas-Bouchiat, F. M'Halla, and J.-M. Savéant, *J. Am. Chem. Soc.* 102:3806 (1980).

for $C_A < 4 \times 10^{-3} \text{ M}$; this allows straightforward determination of k_{ET} to be $100 \text{ M}^{-1} \text{ s}^{-1}$. On the other hand, a C_A value of above $4 \times 10^{-3} \text{ M}$ shifts the system into the region of mixed kinetic control. The ratio k_c / k_{-ET} can then be determined to be 10^{-2} M by comparison of the experimental value of $i_p / 2\zeta i_{pd}$ obtained at $\nu = 0.1 \text{ V s}^{-1}$, $\zeta = 0.5$, and $C_A = 0.02 \text{ M}$ with the corresponding working curve of $i_p / 2\zeta i_{pd}$ vs $\log(k_c / k_{-ET} C_A)$, as shown in Figure 34. With $k_{-ET} = k_d = 5 \times 10^9 \text{ M}^{-1} \text{ s}^{-1}$, $k_c = 5 \times 10^7 \text{ s}^{-1}$.

In LSV, the upper limit of measurable k_c of $5 \times 10^8 \text{ s}^{-1}$ is set by the maximum C_A of about 20 mM which is tolerated without introducing migration of $A^{\cdot-}$ when the concentration of the supporting electrolyte is 0.1 M. Other techniques, however, may not have this limitation, and this would allow the range of accessible k_c values to be extended as a matter of course. Recently, we described an electrochemical method employing the RDE technique that extends the upper limit of accessible rate constants to ca. $5 \times 10^9 \text{ s}^{-1}$ [141]. The method is based on steady-state current measurements of $A^{\cdot-}$, but other techniques, such as optical detection of $A^{\cdot-}$, could also be considered. First, $A^{\cdot-}$ is generated electrochemically to a given concentration (ca. 1 mM), followed by the actual experiment where the decay in the concentration of $A^{\cdot-}$ due to the reaction with RX is recorded as a function of time for varying concentrations of RX and A. In this procedure, there is no restrictions imposed by migration on the maximum value of C_A applicable, as long as the amount of $A^{\cdot-}$ generated initially is kept low.

Figure 35. The parameter

$\gamma = \frac{\beta}{2C_{RX}}$ plotted against the concentration of the mediator 2,3-dimethylnaphthoquinone, C_A . The parameter β is the decay constant of the reaction between $A^{\cdot-}$ and diphenyl disulfide [141].



From decay kinetics, the parameter β can be obtained by Eq. 120. For the sake of convenience, the parameter γ defined in Eq. 121 is introduced.

$$\gamma = \frac{\beta}{2C_{RX}} = \frac{k_c k_{ET}}{k_c + k_{-ET} C_A} = \frac{k_{ET}}{1 + \frac{k_{-ET} C_A}{k_c}} \quad (121)$$

Thus, measurement of γ at different concentrations of mediator A will allow the parameters k_{ET} and the ratio k_c/k_{-ET} to be obtained directly in a nonlinear least-square fit of the values to Eq. 121. Alternatively the parameters may be obtained in a linear fit of $1/\gamma$ against C_A ; the intercept at the ordinate provides $1/k_{ET}$ and the slope is given by $k_{-ET}/k_c k_{ET}$. An example of this procedure is the determination of k_c for the radical anion of diphenyl disulfide, where values of γ were measured for different values of C_A , where A is 2,3-dimethylnaphthoquinone. In Figure 35, a plot of γ vs C_A is shown, where the nonlinear fit leads to the following values: $k_{ET} = 0.1 \text{ M}^{-1} \text{ s}^{-1}$ and $k_c/k_{-ET} = 0.05 \text{ M}$ (i.e., $k_c = 5 \times 10^8 \text{ s}^{-1}$ with $k_{-ET} = 10^{10} \text{ M}^{-1} \text{ s}^{-1}$).

Besides the possibility of extracting cleavage rate constants k_c for short-lived radical anions $RX^{\cdot-}$, the redox catalysis approach may also provide the standard potential of RX , E_{RX}° , from the measurements of k_{ET} . In practice, the rate constants k_{ET} are obtained for the reaction between a number of aromatic radical anions with different values of E_A° and a given substrate by means of CV, LSV, or a potentiostatic technique employing an ultramicroelectrode or RDE. According to the theoretical treatment of the above kinetic scheme, the rate constant k_{ET} can be expressed as shown in Eq. 122 [125].

$$\frac{1}{k_{ET}} = \frac{1}{k_d} + \frac{1}{k_{ET}^\circ \exp[(\alpha_{hom} F/RT)(E_{RX}^\circ - E_A^\circ)]} + \left(\frac{1}{k_d} + \frac{1}{Z_{hom}} \right) \frac{1}{\exp[(F/RT)(E_{RX}^\circ - E_A^\circ)]} \quad (122)$$

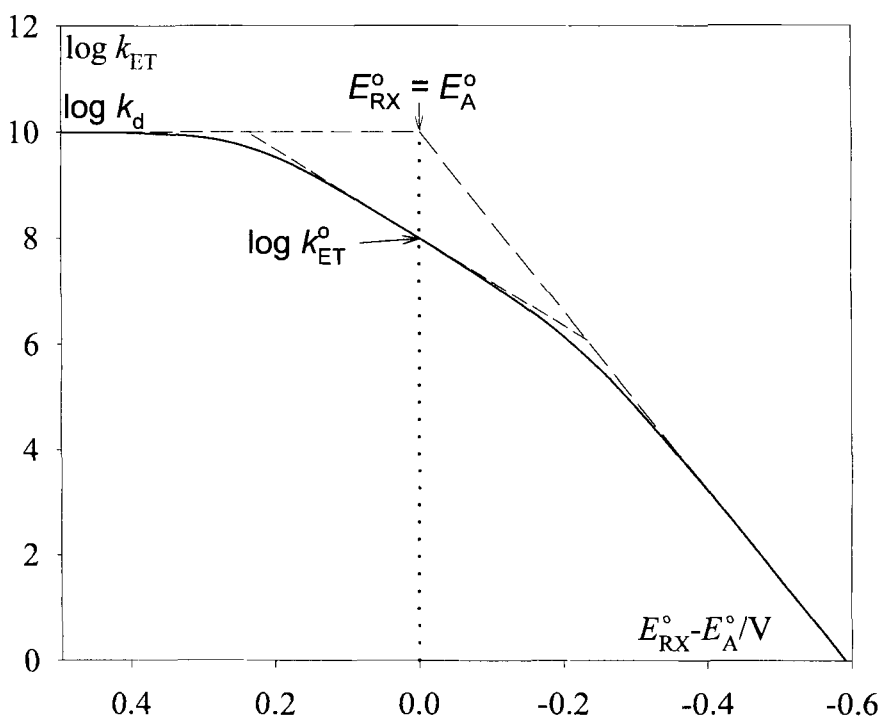


Figure 36. The dependency of the homogeneous electron-transfer rate constant, k_{ET} on the potential difference, $E_{RX}^o - E_A^o$. In the logarithmic plot, three asymptotes are noted, with slopes of 0, $-1/118 \text{ mV}^{-1}$, and $-1/59 \text{ mV}^{-1}$, representing diffusion-controlled, activation-controlled, and counter-diffusion-controlled electron-transfer reactions, respectively [125]. The transfer coefficient α_{hom} is set equal to 0.5.

The parameter Z_{hom} is the collision frequency ($= 3 \times 10^{11} \text{ M}^{-1} \text{ s}^{-1}$), k_{ET}^o is the homogeneous standard rate constant and α_{hom} is the homogeneous transfer coefficient. Depending on the magnitude of the three terms given in Eq. 122, a diagram of $\log k_{ET}$ vs E_A^o , as shown in Figure 36 can be broken down into three regions, namely from left the diffusion-controlled, the activation-controlled, and the counter-diffusion-controlled zone with $k_{-ET} = k_d$. The E_{RX}^o value can therefore be obtained from the plot by simple extension of a line of slope $-1/59 \text{ mV}^{-1}$ (the dashed line in Figure 36) from the counter-diffusion controlled zone to the diffusion-controlled limit, that is, the standard potential is calculated on the basis of the last term of Eq. 122. If $Z_{hom} \gg k_d$, $1/Z_{hom}$ can be neglected and the last term can be rewritten as shown in Eq. 123.

$$k_{ET} = k_d \exp[F/RT(E_{RX}^o - E_A^o)] \quad (123)$$

Note that the above analysis only applies if the cleavage process (Eq. 116) occurs completely outside the molecular diffusion layer. Should the cleavage process pro-

ceed faster ($k_c > 10^9 \text{ s}^{-1}$), an error of ca. 100 mV might be introduced in the determination of E_{RX}^0 . Detailed analyses of this problem have been offered elsewhere [125].

References

1. A. J. Bard and L. R. Faulkner, *Electrochemical Methods, Fundamentals and Applications*, Wiley, New York, 1980.
2. C. Amatore and J.-M. Savéant, *J. Electroanal. Chem.* **86**:227 (1978).
3. C. Amatore and J.-M. Savéant, *J. Electroanal. Chem.* **102**:21 (1979).
4. C. Amatore, A. Jutand, F. Khalil, M. A. Mbarki, and L. Mottier, *Organometallics* **12**:3168 (1993).
5. C. Amatore, M. Azzabi, P. Calas, A. Jutand, C. Lefrou, and Y. Rollin, *J. Electroanal. Chem.* **288**:45 (1990).
6. G. Denuault, M. V. Mirkin, and A. J. Bard, *J. Electroanal. Chem.* **308**:27 (1991).
7. C. Amatore, P. J. Krusic, S. U. Pedersen, and J.-N. Verpeaux, *Organometallics* **14**:640 (1995).
8. V. D. Parker, *Acta Chem. Scand., Ser. B* **B35**:51 (1981).
9. V. D. Parker and O. Hammerich, *Acta Chem. Scand., Ser. B* **B36**:133 (1982).
10. H. Matsuda and Y. Ayabe, *Z. Electrochem.* **59**:494 (1955).
11. J. C. Imbeaux and J. M. Savéant, *J. Electroanal. Chem.* **44**:169 (1973).
12. R. S. Nicholson and I. Shain, *Anal. Chem.* **36**:706 (1964).
13. R. S. Nicholson, *Anal. Chem.* **37**:667 (1965).
14. J.-M. Savéant and E. Vianello, *CR Hebd. Acad. Sci.* **256**:2597 (1963).
15. J.-M. Savéant and E. Vianello, *Electrochim. Acta* **10**:905 (1965).
16. C. P. Andrieux, L. Nadjo, and J.-M. Savéant, *J. Electroanal. Chem.* **42**:223 (1973).
17. C. P. Andrieux and J. M. Savéant, *J. Electroanal. Chem.* **53**:165 (1974).
18. V. D. Parker, in *Electroanalytical Chemistry*, Vol. 14 (A. J. Bard, Ed.), Marcel Dekker, New York, 1986, p. 1.
19. T. Lund and S. U. Pedersen, *J. Electroanal. Chem.* **362**:109 (1993).
20. L. Nadjo and J. M. Savéant, *J. Electroanal. Chem.* **48**:113 (1973).
21. H. Jensen and K. Daasbjerg, *Acta Chem. Scand.* **52**:1151 (1998).
22. J. O. Howell, W. G. Kuhr, R. E. Ensman, and R. M. Wightman, *J. Electroanal. Chem.* **209**:77 (1986).
23. C. P. Andrieux, A. Le Gorande, and J.-M. Savéant, *J. Am. Chem. Soc.* **114**:6892 (1992).
24. C. P. Andrieux, P. Hapiot, and J.-M. Savéant, *J. Phys. Chem.* **92**:5992 (1988).
25. R. J. Forster, *Phys. Chem. Chem. Phys.* **1**:1543 (1999).
26. R. Lines and V. D. Parker, *Acta Chem. Scand., Ser. B* **B31**:369 (1977).
27. L. Geng, A. G. Ewing, J. C. Jernigan, and R. W. Murray, *Anal. Chem.* **58**:852 (1986).
28. C. Amatore and F. Pflüger, *Organometallics* **9**:2276 (1990).
29. G. T. Check and R. Mowery, *Anal. Chem.* **61**:1467 (1989).
30. L. Geng and R. W. Murray, *Inorg. Chem.* **25**:3115 (1986).
31. K. B. Oldham, *J. Electroanal. Chem.* **250**:1 (1988).
32. J. C. Myland and K. B. Oldham, *J. Electroanal. Chem.* **347**:49 (1993).
33. J. B. Cooper, A. M. Bond, and K. B. Oldham, *J. Electroanal. Chem.* **331**:877 (1992).
34. M. F. Bento, L. Thouin, C. Amatore, and M. I. Montenegro, *J. Electroanal. Chem.* **443**:137 (1998).
35. M. I. Montenegro and D. Pletcher, *J. Electroanal. Chem.* **248**:229 (1988).
36. S. U. Pedersen and K. Daasbjerg, *Acta Chem. Scand.* **43**:301 (1989).
37. R. J. Wightman and D. O. Wipf, in *Electroanalytical Chemistry*, Vol. 15 (A. J. Bard, Ed.), Marcel Dekker, New York, 1989, p. 267.
38. A. J. Bard, F. F. Fan, J. Kwak, and O. Lev, *Anal. Chem.* **61**:132 (1989).
39. M. Tsionsky, Z. G. Cardon, A. J. Bard, and R. B. Jackson, *Plant Physiol.* **113**:895 (1997).
40. A. L. Barker, M. Gonsalves, J. V. Macpherson, C. J. Slevin, and P. R. Unwin, *Anal. Chim. Acta* **385**:223 (1999).

41. C. J. Slevin, J. V. Macpherson, and P. R. Unwin, *J. Phys. Chem. B* 101:10851 (1997).
42. Y. Shao, M. V. Mirkin, and J. F. Rusling, *J. Phys. Chem. B* 101:3202 (1997).
43. M. Tsionsky, A. J. Bard, and M. V. Mirkin, *J. Am. Chem. Soc.* 119:10785 (1997).
44. F. F. Fan and A. J. Bard, *Science* 267:871 (1995).
45. M. M. Collinson and R. M. Wightman, *Science* 268:1883 (1995).
46. F. F. Fan and A. J. Bard, *Science* 277:1791 (1997).
47. R. G. Maus, E. M. McDonald, and R. M. Wightman, *Anal. Chem.* 71:4944 (1999).
48. R. M. Wightman, C. L. Curtis, P. A. Flowers, and Maus, *J. Phys. Chem. B* 102:9991 (1998).
49. C. Amatore and J. M. Savéant, *J. Electroanal. Chem.* 123:189 (1981).
50. C. Amatore and J. M. Savéant, *J. Electroanal. Chem.* 123:203 (1981).
51. C. Amatore, F. M'Halla, and J. M. Savéant, *J. Electroanal. Chem.* 123:219 (1981).
52. C. Amatore, J. Pinson, J. M. Savéant, and A. Thiebault, *J. Electroanal. Chem.* 123:231 (1981).
53. C. Amatore and J. M. Savéant, *J. Electroanal. Chem.* 125:1 (1981).
54. C. Amatore and J. M. Savéant, *J. Electroanal. Chem.* 125:23 (1981).
55. C. Amatore and J. M. Savéant, *J. Electroanal. Chem.* 126:1 (1981).
56. R. Guidelli, in *Electroanalytical Chemistry*, Vol. 5 (A. J. Bard, Ed.), Marcel Dekker, New York, 1971, p. 149.
57. G. J. Patriarche, M. Chateau-Gosselin, J. L. Vandelbalck, and P. Zuman, in *Electroanalytical Chemistry*, Vol. 11 (A. J. Bard, Ed.), Marcel Dekker, New York, 1979, p. 141.
58. P. Zuman, *Topics in Organic Polarography*, Plenum Press, London, 1970.
59. U. Svanholm and V. D. Parker, *J. Am. Chem. Soc.* 98:2942 (1976).
60. K. Daasbjerg, S. U. Pedersen, and H. Lund, *Acta Chem. Scand.* 43:876 (1989).
61. K. Daasbjerg, *Acta Chem. Scand.* 47:398 (1993).
62. W. J. Albery and M. L. Hitchman, *Ring-Disc Electrodes*, Clarendon Press, Oxford, 1971.
63. A. Neudeck and L. Kress, *J. Electroanal. Chem.* 437:141 (1997).
64. K. Daasbjerg, S. U. Pedersen, and H. Lund, in *General Aspects of the Chemistry of Radicals* (Z. B. Alfassi, Ed.), Wiley, Chichester, 1999, p. 385.
65. S. U. Pedersen, T. B. Christensen, T. Thomasen, and K. Daasbjerg, *J. Electroanal. Chem.* 454:123 (1998).
66. D. Jürgen, S. U. Pedersen, J. A. Pedersen, and H. Lund, *Acta Chem. Scand.* 51:767 (1997).
67. H. Larsen, S. U. Pedersen, J. A. Pedersen, and H. Lund, *J. Electroanal. Chem.* 331:971 (1992).
68. C. Amatore, P. J. Krusic, S. U. Pedersen, and J.-N. Verpeaux, *Organometallics* 14:640 (1995).
69. C. Amatore, J.-N. Verpeaux, and S. U. Pedersen, in *Novel Trends in Electroorganic Synthesis* (S. Torii, Ed.), Kodansha, Tokyo, 1995, p. 205.
70. W. R. Heineman, F. M. Hawkridge, and H. N. Blount, in *Electroanalytical Chemistry*, Vol. 13 (A. J. Bard, Ed.), Marcel Dekker, New York, 1984, p. 1.
71. C.-C. Jan and R. L. McCreery, *Anal. Chem.* 57:1763 (1985).
72. C.-C. Jan and R. L. McCreery, *Anal. Chem.* 58:2771 (1986).
73. H. P. Wu and R. L. McCreery, *Anal. Chem.* 61:2347 (1989).
74. K. R. Walczyk, G. S. Popkirov, and R. N. Schindler, *Ber. Bunsenges. Phys. Chem.* 99:1028 (1995).
75. K. R. Walczyk, G. S. Popkirov, and R. N. Schindler, *Her. Bunsenges. Phys. Chem.* 99:1546 (1995).
76. R. S. K. A. Gamage, A. J. McQuillan, and B. M. Peake, *J. Chem. Soc. Faraday Trans.* 87:3653 (1991).
77. D. A. Fiedler, M. Koppenol, and A. M. Bond, *J. Electrochem. Soc.* 142:862 (1995).
78. B. A. Coles and R. G. Compton, *J. Electroanal. Chem.* 144:87 (1983).
79. R. D. Webster, R. A. W. Dryfe, B. A. Coles, and R. G. Compton, *Anal. Chem.* 70:792 (1998).
80. P. B. Graham and D. J. Curran, *Anal. Chem.* 64:2688 (1992).
81. D. J. Curran, P. B. Graham, and M. D. Rausch, *Organometallics* 12:2380 (1993).
82. R. W. Hurst, W. R. Heineman, and E. Deutsch, *Inorg. Chem.* 20:3298 (1981).
83. W. R. Heineman, B. J. Norris, and J. F. Goelz, *Anal. Chem.* 47:79 (1975).
84. H. Lund, M.-A. Michel, and J. Simonet, *Acta Chem. Scand.* B28:900 (1974).
85. H. Lund, M.-A. Michel, and J. Simonet, *Acta Chem. Scand.* B29:231 (1975).

86. J. Simonet, M.-A. Michel, and H. Lund, *Acta Chem. Scand.* **B29**:489 (1975).
87. C. P. Andrieux, J. M. Dumas-Bouchiat, and J.-M. Savéant, *J. Electroanal. Chem.* **88**:43 (1978).
88. C. P. Andrieux, J. M. Dumas-Bouchiat, and J.-M. Savéant, *J. Electroanal. Chem.* **87**:39 (1978).
89. C. P. Andrieux, J. M. Dumas-Bouchiat, and J.-M. Savéant, *J. Electroanal. Chem.* **87**:55 (1978).
90. H. Lund, K. Daasbjerg, T. Lund, and S. U. Pedersen, *Acc. Chem. Res.* **28**:313 (1995).
91. H. Lund, K. Daasbjerg, D. Occhialini, and S. U. Pedersen, *Russian Journal of Electrochemistry* **31**:865 (1995).
92. L. Ebersson, *Electron Transfer in Organic Chemistry*, Springer, Heidelberg, 1987.
93. C. P. Andrieux and J.-M. Savéant, in *Investigation of Rates and Mechanisms of Reactions, Part 2*, Vol. VI part 2 (C. F. Bernasconi, Ed.), Wiley, New York, 1986, p. 305.
94. C. P. Andrieux, P. Hapiot, and J.-M. Savéant, *Chem. Rev.* **90**:723 (1990).
95. J.-M. Savéant, *Acc. Chem. Res.* **13**:323 (1980).
96. J.-M. Savéant, *Acc. Chem. Res.* **26**:455 (1993).
97. E. Steckhan, *Angew. Chem. Int. Ed. Engl.* **98**:683 (1986).
98. H. Lund and J. Simonet, *J. Electroanal. Chem.* **65**:205 (1975).
99. P.-E. Hansen, A. Berg, and H. Lund, *Acta Chem. Scand.* **B30**:267 (1976).
100. H. Lund and E. Hobolth, *Acta Chem. Scand.* **B30**:895 (1976).
101. E. Hobolth and H. Lund, *Acta Chem. Scand.* **B31**:395 (1977).
102. C. Degrand and H. Lund, *Nouv. J. Chim.* **1**:35 (1977).
103. H. Lund, *Acta Chem. Scand.* **B31**:424 (1977).
104. H. Lund and C. Degrand, *Tetrahedron Lett.*:3593 (1977).
105. H. Lund and C. Degrand, *Acta Chem. Scand.* **B33**:57 (1979).
106. C. Degrand, R. Mora, and H. Lund, *Acta Chem. Scand.* **B37**:429 (1983).
107. P. Fuchs, U. Hess, H. Holst, and H. Lund, *Acta Chem. Scand.* **B35**:185 (1981).
108. U. Hess, P. Fuchs, E. Jacob, and H. Lund, *Z. Chem.*:64 (1980).
109. H. Lund and H. S. Carlsson, *Acta Chem. Scand.* **B32**:505 (1978).
110. H. S. Carlsson and H. Lund, *Acta Chem. Scand.* **B34**:409 (1980).
111. J. Eriksen, H. Lund, and A. Nyvad, *Acta Chem. Scand.* **B37**:459 (1983).
112. P. Nelleborg, H. Lund, and J. Eriksen, *Tetrahedron Lett.* **26**:1773 (1985).
113. T. Lund and H. Lund, *Acta Chem. Scand.* **B40**:470 (1986).
114. K. Daasbjerg, S. U. Pedersen, and H. Lund, *Acta Chem. Scand.* **45**:424 (1991).
115. T. Lund, S. U. Pedersen, H. Lund, K. M. Cheung, and J. H. P. Utle, *Acta Chem. Scand.* **B41**:285 (1987).
116. K. Daasbjerg and T. B. Christensen, *Acta Chem. Scand.* **49**:128 (1995).
117. K. Müllen, J. Alexander, K. U. Klabunde, F. G. Klarner, H. Lund, and T. Lund, *Chem. Ber.* **125**:505 (1992).
118. H. S. Sørensen and K. Daasbjerg, *Acta Chem. Scand.* **52**:51 (1998).
119. J.-M. Savéant, *Adv. Phys. Org. Chem.* **26**:1 (1990).
120. C. P. Andrieux, L. Gelis, M. Medebielle, J. Pinson, and J.-M. Savéant, *J. Am. Chem. Soc.* **112**:3509 (1990).
121. J.-M. Savéant, *Tetrahedron* **50**:10117 (1994).
122. D. Occhialini, J. S. Kristensen, K. Daasbjerg, and H. Lund, *Acta Chem. Scand.* **46**:474 (1992).
123. C. P. Andrieux, C. Blocman, J. M. Dumas-Bouchiat, and J.-M. Savéant, *J. Am. Chem. Soc.* **101**:3431 (1979).
124. C. P. Andrieux, C. Blocman, J. M. Dumas-Bouchiat, F. M'Halla, and J.-M. Savéant, *J. Am. Chem. Soc.* **102**:3806 (1980).
125. C. P. Andrieux and J.-M. Savéant, *J. Electroanal. Chem.* **205**:43 (1986).
126. J. G. Lawless and M. D. Hawley, *J. Electroanal. Chem.* **21**:365 (1969).
127. L. Nadjo and J.-M. Savéant, *J. Electroanal. Chem.* **30**:41 (1971).
128. B. Aalstad and V. D. Parker, *Acta Chem. Scand.*, **B36**:47 (1982).
129. C. P. Andrieux, A. Le Gorande, and J.-M. Savéant, *J. Am. Chem. Soc.* **114**:6892 (1992).
130. D. O. Wipf and R. M. Wightman, *J. Phys. Chem* **93**:4286 (1989).
131. R. K. Norris, S. D. Barker, and P. Neta, *J. Am. Chem. Soc.* **106**:3140 (1984).

- 132. P. Neta and D. Behar, *J. Am. Chem. Soc.* *102*:4798 (1980).
- 133. P. Neta and D. Behar, *J. Am. Chem. Soc.* *103*:103 (1981).
- 134. D. Behar and N. P., *J. Am. Chem. Soc.* *103*:2280 (1981).
- 135. K. Sehested and J. Holcman, *J. Phys. Chem.* *82*:651 (1978).
- 136. N. Mathivanan, L. J. Johnston, and D. D. M. Wayner, *J. Phys. Chem.* *99*:8190 (1995).
- 137. V. D. Parker, *Acta Chem. Scand.* *B38*:165 (1984).
- 138. C. P. Andrieux, P. Hapiot, and J.-M. Savéant, *J. Phys. Chem.* *92*:5987 (1988).
- 139. C. Amatore and F. Pflüger, *Organometallics* *9*:2276 (1990).
- 140. J. P. Bullock, D. C. Boyd, and K. R. Mann, *Inorg. Chem.* *26*:3084 (1987).
- 141. T. B. Christensen and K. Daasbjerg, *Acta Chem. Scand.* *51*:307 (1997).

3 Radiation-Chemical Techniques

George V. Buxton and Quinto G. Mulazzani

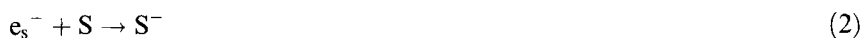
3.1 Introduction

Radiation chemistry is defined here as the chemistry ensuing from the interaction of high-energy photons and particles with matter, so-called ionizing radiation. Although the energy required to ionize a molecule is typically of the order of 10 eV, the penetration depth in the condensed phase of particles with such energy is very small. In practice, the types of radiation commonly used for general chemistry are ^{60}Co γ -rays or fast electrons from an accelerator with energies typically in the range 2–20 MeV. In each case the result of the interaction is the ejection of a single electron, which may have sufficient energy to effect ionization of further molecules, but which eventually becomes thermalized and trapped in the liquid or solid medium. In this way, stable molecules (M) are converted into highly reactive free radicals ($\text{M}^{\bullet+}$) and solvated electrons (e_s^-):



A distinguishing feature of radiation chemistry is the nonselective absorption of energy so that the molecules are ionized according to their relative abundance in the medium of interest. For example, in dilute solution ($\leq 0.1 \text{ mol dm}^{-3}$) the ionized molecules (M) are effectively those of the solvent so that a knowledge of the radiation chemistry of the solvent is of paramount importance for most studies using radiation-chemical methods.

Examples of the chemical fate of the reactants generated radiolytically in specific media are described in this chapter and, as one would expect, in many cases the reactions involve the gain or loss of a single electron. This is always true for the solvated electron which can only react by transfer into a vacant orbital of an acceptor:



In many cases the product S^- is itself a free radical ($S^{\bullet-}$), or a hyper-reduced metal ion, which in turn reacts in one-electron gain or loss processes. It is not surprising, then, that radiation-chemical methods are widely used in the study of electron-transfer processes. Of particular value is the technique of pulse radiolysis which permits reactions to be studied on timescales ranging from seconds down to picoseconds, so that even the most reactive species can be studied. It is this technique and its applications that form the subject matter of this chapter which begins with an outline of the radiation chemistry of water and other solvents. Next there is a historical view of pulse radiolysis, some of the landmark discoveries are discussed, followed by a description of the principal features of a pulse radiolysis facility and the various methods of detecting and measuring transient species. The chapter ends with some examples of data capture and analysis, and methods of sample preparation.

3.2 Interaction of Ionizing Radiation with Condensed Matter

The radiation chemistry of liquids and solids is distinguished by the nature of the energy loss suffered by the ionizing particle along its track through the medium [1]. The rate of energy loss per unit length of the track is referred to as the linear energy transfer or stopping power or, more commonly, LET. When the ionizing particle is a high-energy electron, the ionization events occur in small clusters, called spurs, that are widely separated along the track of the primary particle, and the radiation is said to be of low LET. When the particle is an energetic nuclear ion such as H^+ , He^{2+} , and so forth, the rate of energy loss is much higher; the spurs are more closely spaced and can overlap to form cylindrical columns of ionized molecules. In this case, the radiation has a high LET; the two types of radiation are compared in Figure 1. In reality, there are high LET segments in the track of an electron because the LET increases as the energy of the electron decreases, as shown in Figure 1. Thus, some of the low-energy electrons produced in the initial ionizations have sufficient energy to cause further ionizations in close proximity, forming spurs. Similarly, there are relatively low LET segments in the track of an ion with high LET caused by the ejected electrons that have sufficient energy to form their own (branch) tracks. Thus, LET actually varies along the track of the particle, but it is often sufficient just to consider LET in terms of the total energy lost by the particle divided by the length of the track. The descriptions that follow of the radiolysis of water and other solvents is for low LET radiation because almost invariably fast electrons from accelerators or ^{60}Co γ -rays, which themselves generate fast electrons by Compton scattering [1], are the sources used for the radiolytic generation of the species whose chemistry is to be studied. As will be described later (Section 3.7.1, under "Sample Cell and Flow System with Optical Detection"), the size of the sample to be irradiated is chosen to ensure that energy deposition in it is fairly uniform.

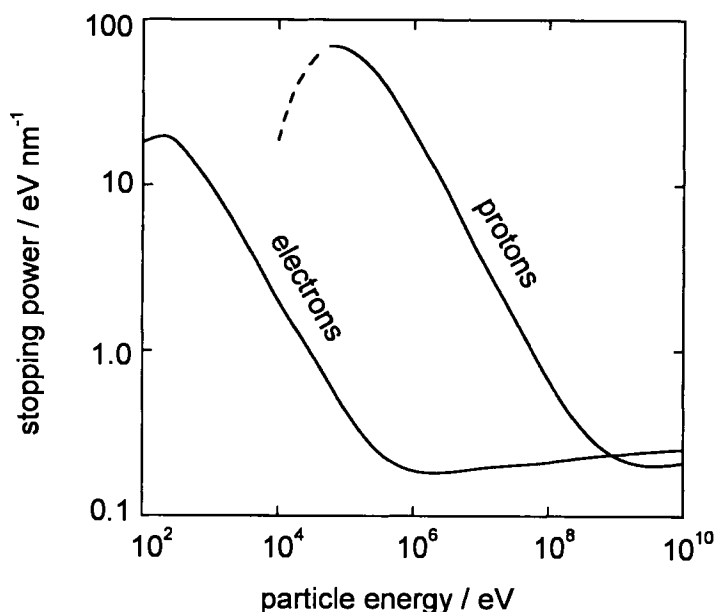
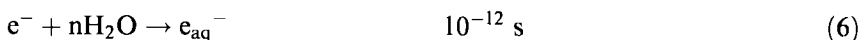
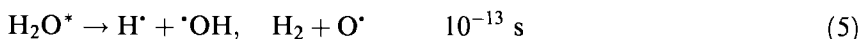
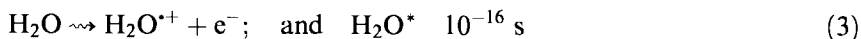


Figure 1. Stopping power of water as a function of energy of impinging electrons or protons. (Adapted from A.J. Swallow, *Radiation Chemistry*, Longman, London, 1973, p. 28).

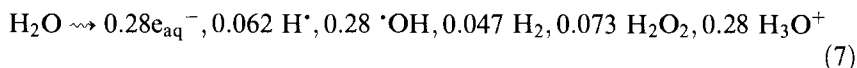
3.3 The Radiation Chemistry of Water

The sequence of events resulting from the interaction of low LET radiation with water is summarized by the following reactions (the time by which the event is estimated to be complete is also given):



The reaction given in Eq. 3 represents ionization and electronic excitation of water molecules; this occurs on the timescale of an electronic transition. The positive radical ion H_2O^{*+} is known to undergo the ion-molecule reaction (Eq. 4) in the gas phase with a rate constant of $8 \times 10^{12} \text{ dm}^3 \text{ mol}^{-1} \text{ s}^{-1}$ [2], which sets the lifetime of the ion at less than 10^{-14} s in the liquid. The electronically excited states H_2O^* are known to dissociate in the gas phase, as shown in Eq. 5, and the electron released in the ionization event is known to become thermalized and solvated in less than

10^{-12} s [3]. It is generally accepted that at about 10^{-12} s after ionization the products of Eqs. 4–6 are in thermal equilibrium with the bulk liquid and are clustered together in spurs. Next, these products begin to diffuse randomly, with the result that a fraction of them encounter one another and react together to form molecular or secondary radical products, while the remainder escape into the bulk liquid and effectively become homogeneously distributed throughout the medium. This spur expansion and reaction is complete by about 10^{-7} s, at which time the radiolysis of water can be represented by reaction (7) [4]:



where the numbers are the radiation chemical yields (G values) in units of $\mu\text{mol J}^{-1}$. In the early literature the G values are quoted as molecules/100 eV, and some authors still use these units today. The conversion factor is as follows:

$$1 \text{ molecule/100 eV} \equiv 1.036 \times 10^{-7} \text{ mol J}^{-1} \text{ (or } 0.1036 \mu\text{mol J}^{-1}\text{)}$$

Some authors quote G values without including the units, and most commonly the omitted units are molecules/100 eV, so the reader should exercise care in interpreting these numerical values.

The yields of the initial products of Eqs. 4–6 are not yet established unequivocally. The results of attempts to model the early stages of water radiolysis to match up with experimental measurements that are limited to about 10^{-10} s suggest that $G(\text{ions})$ and $G(\text{excitation})$ have values of about 0.5 and 0.1 $\mu\text{mol J}^{-1}$, respectively [5]. Thus, around 40 % of the initial yields are consumed by the spur reactions. The spur reactions are listed in Table 1.

Table 1. Spur reactions in water.

Reactions	$k [10^{10} \text{ dm}^3 \text{ mol}^{-1} \text{ s}^{-1}]^a$
$e_{\text{aq}}^- + e_{\text{aq}}^- \rightarrow \text{H}_2 + 2\text{OH}^-$	0.55
$e_{\text{aq}}^- + \cdot\text{OH} \rightarrow \text{OH}^-$	3.0
$e_{\text{aq}}^- + \text{H}_3\text{O}^+ \rightarrow \text{H}^\bullet + \text{H}_2\text{O}$	2.3
$e_{\text{aq}}^- + \text{H}^\bullet \rightarrow \text{H}_2 + \text{OH}^-$	2.5
$e_{\text{aq}}^- + \text{H}_2\text{O}_2 \rightarrow \cdot\text{OH} + \text{OH}^-$	1.1
$\text{H}^\bullet + \text{H}^\bullet \rightarrow \text{H}_2$	0.5
$\cdot\text{OH} + \cdot\text{OH} \rightarrow \text{H}_2\text{O}_2$	0.55
$\cdot\text{OH} + \text{H}^\bullet \rightarrow \text{H}_2\text{O}$	0.7
$\text{H}_3\text{O}^+ + \text{OH}^- \rightarrow 2\text{H}_2\text{O}$	14.0 ^b

^a Values taken from Ref. [7]. ^b K.J. Laidler, *Chemical Kinetics*, McGraw-Hill, New York, 1965, p. 535.

Table 2. Selected properties of the species e_{aq}^- , H^\bullet , $^{\bullet}OH$ and $O^{\bullet -}$.

	e_{aq}^-	H^\bullet	$^{\bullet}OH$	$O^{\bullet -}$
Absorption maximum, nm ^a	720	<200	~225	240
Extinction coefficient, m ² mol ^{-1a}	1900	162 ^b	54 ^b	24
G-value, $\mu\text{mol J}^{-1c}$	0.28	0.062	0.28	
Mobility, $10^3 \text{ cm}^2 \text{ V}^{-1} \text{ s}^{-1}$	1.9 ^d			
Redox potential, V ^e	-2.87	-2.2 ^d	1.9 ^f	1.8
			2.73 ^g	
p <i>K</i> _a ^d		9.6 ^h	11.9 ⁱ	

^aValues taken from Ref. [56]. ^bAt 188 nm. ^cValues taken from Ref. [4]. ^dValues taken from Ref. [7b]. ^eValues taken from Ref. [66b]. ^f($^{\bullet}OH + e^- \rightarrow OH^-$). ^g($^{\bullet}OH + e^- + H^+ \rightarrow H_2O$). ^h($H + H_2O \rightarrow e_{aq}^- + H_3O^+$). ⁱ($^{\bullet}OH + H_2O \rightarrow O^{\bullet -} + H_3O^+$).

3.3.1 Properties of the Primary Radicals

The physical properties of significance here are summarized in Table 2. The hydrated electron and the hydrogen atom are strong reducing agents and the hydroxyl radical is a powerful oxidant. Because of these properties, they are very effective in bringing about one-electron changes in molecules and ions.

The hydrated electron

The hydrated electron may be visualized as a localized electron surrounded by oriented water molecules. As mentioned earlier, it reacts by adding into a vacant orbital on the acceptor molecule or ion (Eq. 2). Rate constants for this reaction range from $19 \text{ dm}^3 \text{ mol}^{-1} \text{ s}^{-1}$ for $S = H_2O$ up to the diffusion-controlled limit, but the activation energy is invariably small ($6\text{--}30 \text{ kJ mol}^{-1}$); this indicates that the entropy of activation is the dominant kinetic parameter. This can be understood in terms of the accessibility to the electron of a vacant orbital on S. Molecules such as water, simple alcohols, ethers, and amines have no low-lying empty orbitals to accommodate an extra electron; this explains why solvated electrons have an appreciable lifetime in these solvents. On the other hand, e_{aq}^- reacts rapidly with organic compounds with low-lying vacant orbitals, for example, most aromatics, halides, aldehydes, ketones, thiols, disulfides, and nitro compounds.

In its reactions, e_{aq}^- acts as a nucleophile. Thus, its reactivity is greatly enhanced by electron-withdrawing groups next to double bonds or on aromatic rings. Although the first step in the reaction is electron addition, this is in some cases followed by rapid dissociation of an anionic fragment so that the overall process can be viewed as one of dissociative capture. This is epitomized by organic halides:



Some characteristic reactivities of e_{aq}^- are illustrated by the data in Table 3. A

Table 3. Rate constants for some reactions of e_{aq}^- .^a

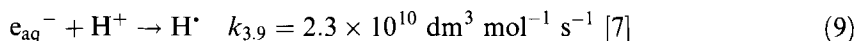
Solute (inorganic)	k [dm ³ mol ⁻¹ s ⁻¹]	Solute (organic)	k [dm ³ mol ⁻¹ s ⁻¹]
O ₂	1.9×10^{10}	(CH ₃) ₂ CO	6.5×10^9
H ₃ O ⁺	2.3×10^{10}	C ₆ H ₆	1.1×10^7
Ag ⁺	3.9×10^{10}	C ₆ H ₅ Cl	6.4×10^8
N ₂ O	9.1×10^9	C ₆ H ₅ NO ₂	3.7×10^{10}
NH ₄ ⁺	1.5×10^6	C ₆ H ₅ I	1.2×10^{10}
NO ₃ ⁻	9.7×10^9	MV ²⁺ ^b	7.2×10^{10}
Cd ²⁺	5.3×10^{10}	CH ₄	$<1 \times 10^7$
Fe ³⁺	6.0×10^{10}	CH ₃ I	1.6×10^{10}
ClO ₄ ⁻	$<1 \times 10^6$	CH ₃ OH	$<1 \times 10^4$
MnO ₄ ⁻	2.6×10^{10}	CH ₃ CN	3.7×10^7
CrO ₄ ²⁻	1.8×10^{10}	C ₂ H ₂	2.0×10^7
Fe(CN) ₆ ³⁻	3.1×10^9	C ₂ H ₄	$<3 \times 10^5$
Fe(CN) ₆ ⁴⁻	$<7 \times 10^4$	CH ₂ =CCl ₂	2.3×10^{10}
Co(NH ₃) ₆ ³⁺	8.7×10^{10}	CO ₂	7.7×10^9
H ₂ O	19	C(NO ₂) ₄	5.3×10^{10}

^a Values taken from Ref. [7]. ^b MV²⁺ = 1,1'-dimethyl-4,4'-bipyridinium.

notable feature of these data is the reactivity of e_{aq}^- with Cd²⁺ and CrO₄²⁻ where the rate constants are larger than those predicted by the Debye–Smoluchowski expression for diffusion-controlled reactions between charged reactants. It is suggested [6] that the larger than normal reaction radius for these reactions reflects the quantum-mechanical nature of e_{aq}^- and its ability to tunnel from its solvent trap to the acceptor. Tunnelling between solvent traps may also explain the mobility of e_{aq}^- (see Table 2) because it is much higher than that expected for a monovalent anion of radius 0.3 nm.

The hydrogen atom

The hydrogen atom is not an important primary radical in neutral and alkaline solution, but it is the major reducing radical at low pH where the following reaction (Eq. 9) is rapid:



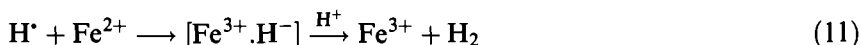
It is a less powerful reductant than e_{aq}^- (Table 2) and can be considered formally as a weak acid with $pK_a = 9.6$:



although with $k_{3,10} = 2.2 \times 10^7 \text{ dm}^3 \text{ mol}^{-1} \text{ s}^{-1}$ and $k_{-3,10} = 19 \text{ dm}^3 \text{ mol}^{-1} \text{ s}^{-1}$ [7], equilibrium is not established under normal conditions.

The hydrogen atom readily reduces cations with higher reduction potentials than itself, but generally at a slower rate than e_{aq}^- . In some cases it reacts via the for-

mation of a hydride complex and effectively becomes an oxidant:



With many organic compounds it reacts like $\cdot\text{OH}$ (see below), abstracting H from alkyl groups and adding to centers of unsaturation. Because it absorbs only in the far-UV region, many of its rate constants have been measured by competition kinetics [7].

The hydroxyl radical

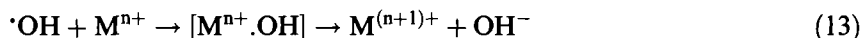
The hydroxyl radical is a powerful oxidant with a standard reduction potential of 2.73 V in acidic solution. In neutral solution where the free energy of neutralization of OH^- by the proton is not available, the reduction potential is calculated to be 1.9 V (Table 2).

Several inorganic anions and low-valent transition metal ions are readily oxidized by $\cdot\text{OH}$, and the reaction is commonly represented as a one-electron transfer process:



There are, however, a number of examples which show that the reaction actually proceeds via the formation of an adduct, followed by an inner-sphere electron transfer. In the case of halide ions, X^- , the intermediate species $\text{HOX}^{\bullet-}$ have been observed by pulse radiolysis and it has been suggested that this is the reaction path for most oxidizable inorganic anions [8].

Similarly, pulse radiolysis studies of the oxidation of metal ions by $\cdot\text{OH}$ reveal that the reaction can be represented by the following equation:



for $\text{M}^{n+} = \text{Ti}^+, \text{Ag}^+, \text{Cu}^{2+}, \text{Sn}^{2+}, \text{Fe}^{2+}, \text{Mn}^{2+}, \text{Cr}^{3+}$. It has been proposed that $\cdot\text{OH}$ is unlikely to react by simple outer-sphere electron transfer because of the large solvent reorganization energy involved in forming the hydrated hydroxide ion [8], and this does seem to be borne out by the experimental evidence.

The radical $\cdot\text{OH}$ reacts with many inorganic anions at near-diffusion-controlled rates, but with metal ions there seems to be an upper limit of about $3 \times 10^8 \text{ dm}^3 \text{ mol}^{-1} \text{ s}^{-1}$, regardless of the reduction potential of M^{n+} . There is no correlation between the measured values of $k_{3,13}$ and the rates of exchange of water molecules coordinated to M^{n+} , which rules out ligand substitution as a general mechanism; other possibilities are abstraction of H from a coordinated water molecule and $\cdot\text{OH}$ entering the coordination shell to increase the coordination number by one.

At high pH, $\cdot\text{OH}$ is rapidly converted to $\text{O}^{\bullet-}$:



with $k_{3,14} = 1.2 \times 10^{10} \text{ dm}^3 \text{ mol}^{-1} \text{ s}^{-1}$ and $k_{-3,14} = 9.3 \times 10^7 \text{ s}^{-1}$ [7] and equilib-

rium is rapidly established. $\text{O}^{\bullet-}$ is generally less reactive than $\cdot\text{OH}$ with inorganic anions, and with Br^- , CO_3^{2-} , and $\text{Fe}(\text{CN})_6^{4-}$ the rate is immeasurably slow. This property was used to establish (see below) the value of the equilibrium constant $K_{3,14}$ (Table 2).

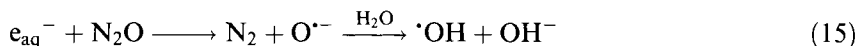
In its reactions with organic molecules, $\cdot\text{OH}$ behaves as an electrophile whereas $\text{O}^{\bullet-}$ is a nucleophile. Thus, like H^{\bullet} (see above), $\cdot\text{OH}$ readily adds to double bonds but $\text{O}^{\bullet-}$ does not; however, both forms of the radical abstract H from C–H bonds. In the case of an aromatic molecule carrying an aliphatic side chain, $\cdot\text{OH}$ adds preferentially to the aromatic ring and $\text{O}^{\bullet-}$ abstracts H from the side chain; this can result in a change of reaction mechanism when the pH is raised so that $\text{O}^{\bullet-}$ replaces $\cdot\text{OH}$ as the oxidant.

3.3.2 Generation of Secondary Radicals

Because, as shown by Eq. 7 and Table 2, the radiolysis of water produces approximately equal numbers of powerful reducing (e_{aq}^- , H^{\bullet}) and oxidizing radicals ($\cdot\text{OH}$), for its chemical applications it is desirable to create either totally reducing or totally oxidizing conditions. This is readily achieved by interconversion of the primary radicals, by conversion of the primary radicals into a single kind of secondary radical, or by removal of the unwanted primary radical by reaction to form a relatively inert secondary radical. Some useful systems that satisfy these requirements are described below.

Oxidizing conditions

A most convenient and widely used method of achieving almost totally oxidizing conditions is to saturate the water with N_2O , which converts e_{aq}^- to $\cdot\text{OH}$:



Under these conditions, the concentration of N_2O is $2.5 \times 10^{-2} \text{ mol dm}^{-3}$ and, since $k_{3,15} = 9.1 \times 10^9 \text{ dm}^3 \text{ mol}^{-1} \text{ s}^{-1}$ [7], $k_{3,15}[\text{N}_2\text{O}]$ is $2.3 \times 10^8 \text{ s}^{-1}$, so that the radical conversion is essentially complete in about 15 ns. From this it is clear that a pulse radiolysis setup with a time resolution shorter than this is of no advantage when $\cdot\text{OH}$ is generated by this method. It should also be borne in mind that the initial product of reaction (15) is $\text{O}^{\bullet-}$ and that the half-life for its protonation in water is ca. 8 ns.

The available yield of $\cdot\text{OH}$ under these conditions has been shown [9] to fit an empirical equation:

$$G(\cdot\text{OH}) = 0.54 + \frac{0.31(k[S]/\lambda)^{1/2}}{1 + (k[S]/\lambda)^{1/2}} \mu\text{mol J}^{-1} \quad (16)$$

where $\lambda = 4.7 \times 10^8 \text{ s}^{-1}$ and k is the rate constant for the reaction of $\cdot\text{OH}$ with the solute S. The hydrogen atom reacts only slowly with N_2O ($k = 2.1 \times 10^6$

Table 4. Spectral data and redox potentials of some secondary inorganic radicals.

Radical	λ_{\max} [nm] ^a	ϵ [m ² mol ⁻¹] ^a	Redox Couple	E° [V] ^b
Cl ₂ ^{•-}	340	880	Cl ₂ ^{•-} /2Cl ⁻	2.1 ^c
			Cl ₂ /Cl ₂ ^{•-}	0.4
Br ₂ ^{•-}	360	990	Br ₂ ^{•-} /2Br ⁻	1.66
			Br ₂ /Br ₂ ^{•-}	0.5
I ₂ ^{•-}	385, 750	940, 280	I ₂ ^{•-} /2I ⁻	1.05
			I ₂ /I ₂ ^{•-}	0.21
(SCN) ₂ ^{•-}	480	760	(SCN) ₂ ^{•-} /2SCN ⁻	1.33
			(SCN) ₂ /((SCN) ₂ ^{•-}	0.54
Cl [•]	320 ^d	450 ^d	Cl [•] /Cl ⁻	2.4 ^e
N ₃ [•]	277	140	N ₃ [•] /N ₃ ⁻	1.33
HS [•]			HS [•] /HS ⁻	1.15
CO ₃ ^{•-}	600	186	CO ₃ ^{•-} /CO ₃ ²⁻	1.5
ClO ₂ [•]	~360	100	ClO ₂ [•] /ClO ₂ ⁻	0.93
BrO ₂ [•]	475	100	BrO ₂ [•] /BrO ₂ ⁻	1.27
NO ₂ [•]	400	20	NO ₂ [•] /NO ₂ ⁻	1.04
NO ₃ [•]	595, 640, 675	134 ^{e,f}	NO ₃ [•] /NO ₃ ⁻	2.5 ^e
SO ₃ ^{•-}	255	100	SO ₃ ^{•-} /SO ₃ ²⁻	0.7
SO ₄ ^{•-}	450	110	SO ₄ ^{•-} /SO ₄ ²⁻	2.43
O ₃ ^{•-}	430	190	O ₃ /O ₃ ^{•-}	1.01
HO ₂ [•]	225	140	HO ₂ [•] , H ⁺ /H ₂ O ₂	1.48
O ₂ ^{•-}	245	235	O ₂ /O ₂ ^{•-}	-0.33 ^g

^a Values taken from Ref. [56]. ^b Values selected from Refs. [66a] and [66b]. ^c M. Bydder, PhD Thesis, University of Leeds (UK), 1999; G.V. Buxton, M. Bydder, G.A. Salmon, *Phys. Chem. Chem. Phys.* **1999**, 1, 269–273. ^d G.V. Buxton, M. Bydder, G.A. Salmon, J. E. Williams, *Phys. Chem. Chem. Phys.* **2000**, 2, 237–245. ^e T. Løgager, K. Sehested, J. Holcman, *Radiat. Phys. Chem.* **1993**, 41, 539–543. ^f At 635 nm. ^g Standard state: 1 atm O₂.

dm³ mol⁻¹ s⁻¹) [7] so that approximately 90 % of the radicals available in N₂O-saturated neutral solution are [•]OH and 10 % are H[•]. At pH > 11, where the reaction of Eq. 10 becomes increasingly important, G([•]OH) can increase up to 0.6 μmol J⁻¹, whereas at pH < 3 the fraction of oxidizing radicals decreases because the reaction of Eq. 9 competes with the reaction of Eq. 15.

The radical [•]OH is rather unselective when it abstracts H from C–H bonds because of the significantly larger energy of the H–OH bond being formed. More selective oxidizing radicals can be obtained by conversion of [•]OH into another inorganic radical, for example: Br₂^{•-}, I₂^{•-}, CO₃^{•-}, N₃[•], and so forth, which have different reduction potentials (see Table 4). This strategy is particularly useful for the study of redox changes in metalloproteins and organometallic complexes, because the secondary inorganic radicals are more likely to react selectively at the metal center, whereas [•]OH will also attack the organic moiety and generate a reducing radical there.

Another convenient method of creating oxidizing conditions is by the following reaction:



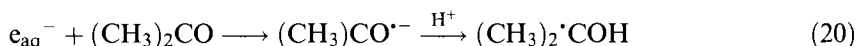
This reaction generates the strong oxidant $SO_4^{\bullet-}$, which has a reduction potential of 2.43 V (see Table 4). Thus, it is a more powerful oxidizing radical than $\bullet OH$ in neutral solution and can be used to generate other oxidants such as Cl^\bullet and NO_3^\bullet through electron-transfer reactions with Cl^- and NO_3^- , respectively [7a].

Reducing conditions

A convenient method of obtaining totally reducing conditions is to convert all the primary radicals to the same secondary reducing radical in N_2O -saturated solution containing a suitable organic solute. For example, when the solute is 2-propanol, practically all (see below) of the primary radicals e_{aq}^- , H^\bullet , and $\bullet OH$ are converted to $(CH_3)_2\bullet COH$ by the reactions shown in Eqs. 15, 18, and 19:



Alternatively, when acetone replaces N_2O , Eq. 20 replaces Eq. 15:



and the same result is achieved. Other simple alcohols such as methanol and ethanol are often used as a source of secondary reducing radicals and it is the H on the α -carbon atom that is preferentially abstracted, as shown for 2-propanol. However, $\bullet OH$ does abstract at other positions, so that, in practice, a mixture of radicals is produced where only one is desired. The distributions of radicals formed by reaction of $\bullet OH$ with a variety of simple alcohols are given in Table 5.

Table 5. Abstraction by $\bullet OH$ radicals from various positions in alcohols.^a

Compound	% Abstraction from α C-H	% Abstraction from other C-H	% Abstraction from OH
CH_3OH	93.0	—	7.0
CH_3CH_2OH	84.3	13.2	2.5
$CH_3(CH_2)_2OH$	53.4	46.0	<0.5
$(CH_3)_2CHOH$	85.5	13.3	1.2
$CH_3(CH_2)_3OH$	41.0	58.5	<0.5
$(CH_3)_3COH$	—	95.7	4.3
$(CH_2OH)_2$	100	—	<0.1
$CH_3CH(OH)CH_2OH$	79.2	20.7	<0.1
$CH_3CH(OH)CH(OH)CH_3$	71.0	29.0	<0.1

^aValues taken from Ref. [160].

Table 6. Selected properties of main radicals (see Table 5) obtained from the scavenging of $\cdot\text{OH}$ by $\text{R}_1\text{R}_2\text{R}_3\text{COH}$ species ($\text{R}_1, \text{R}_2, \text{R}_3 = \text{H}, \text{CH}_3$) and by HCO_2^- .

Radical	$\text{p}K_a^a$	$E^\circ(\text{RO}, \text{H}^+/\text{ROH}^\cdot) [\text{V}]^b$	$E^\circ(\text{RO}/\text{RO}^{\cdot-}) [\text{V}]^b$
$\cdot\text{CH}_2\text{OH}$	10.71	-1.18	-1.81
$\text{CH}_3\cdot\text{CHOH}$	11.51	-1.25	-1.93
$(\text{CH}_3)_2\cdot\text{COH}$	12.03	-1.39	-2.10
$\cdot\text{CH}_2\text{C}(\text{CH}_3)_2\text{OH}$	$>13.5^c$	-0.1 ^d	
$\text{CO}_2^{\cdot-}$	-0.2 ^{e,f}	-1.91	-1.90

^aG.P. Laroff, R.W. Fessenden, *J. Phys. Chem.* **1973**, 77, 1283–1288. ^bH.A. Schwarz, R.W. Dodson, *J. Phys. Chem.* **1989**, 93, 409–414. ^cM. Simic, P. Neta, E. Hayon, *J. Phys. Chem.* **1969**, 73, 3794–3800. ^dJ.P. Endicott in *Concepts of Inorganic Photochemistry* (Eds.: A.W. Adamson, P.D. Fleishauer), Wiley, New York, **1975**, p. 88. ^e $\text{p}K_a$ of $\text{CO}_2\text{H}^\cdot$. ^fA.S. Jeevarajan, I. Carmichael, R.W. Fessenden, *J. Phys. Chem.* **1990**, 94, 1372–1376.

The alcohol radicals contain a dissociable proton on the hydroxyl group so that the basic form will begin to be present when the pH of the solution approaches the $\text{p}K_a$ of the radical. Generally, the basic form of an alcohol radical is a stronger reductant than the undissociated form. The relevant data are collected in Table 6.

Also included in Table 6 are data for the carboxyl radical which, because of its low $\text{p}K_a$, exists in its basic form even at low pH, and is thus a very effective reductant over the whole pH range, although it is not as powerful as e_{aq}^- . It is generated in the reactions represented by Eqs. 21–23 and, unlike the alcohols, only one kind of radical is produced:



When it is required to have e_{aq}^- as the reducing agent, it is customary to add 2-methyl-2-propanol (tert-butanol) to the solution to convert $\cdot\text{OH}$ to the relatively unreactive radical $\cdot\text{CH}_2(\text{CH}_3)_2\text{COH}$. This system can be exploited to generate hyper-reduced states of metal ions, as in Eq. (24), for example:



The monovalent ions Cd^+ , Co^+ , Ni^+ , and Zn^+ are themselves strong reductants and can be used to reduce metalloproteins at sites where there is negative charge which makes them less accessible to e_{aq}^- .

It is clear from the foregoing information that the radiolysis of water provides a powerful method of generating one-electron redox agents that can be finely tuned in terms of reduction potential and electric charge. The method has been widely

exploited in general chemistry and has generated a wealth of kinetic [7a] and mechanistic information for these redox agents which can be retrieved from the bibliographic database at <http://www.rcdc.nd.edu>.

3.4 The Radiation Chemistry of Organic Liquids

Although the radiation chemistry of organic liquids is generally more complex than that of water, a substantial knowledge of electron-transfer processes in these systems has, nevertheless, been built up. The advantage of organic liquids over water is the range of solvent polarities available so that species that are insoluble in water can be studied by dissolving them in a suitable solvent, or mixture of solvents.

The principal features that distinguish organic liquids from water are the following:

- 1) Organic molecules contain more atoms and bonds than water, therefore the radiolytic products resulting from ionization and fragmentation are more numerous;
- 2) The generally lower relative permittivity of organic liquids means that the coulombic field of the positive ion (see Eq. 1) influences the thermalized electron more strongly, resulting in geminate recombination of the primary ions. A consequence of this is that there is less chance for the ions to react with solutes. Nevertheless, liquids such as simple alcohols, ethers, and ketones are sufficiently polar to solvate a large enough fraction of the thermalized electrons to make them useful media in which to study redox reactions.

For a low LET track, the distance, r_c , at which the potential energy of a separated ion pair is equal to the thermal energy (kT) is given by the Onsager equation [10]:

$$r_c = \frac{e^2}{4\pi\epsilon_0\epsilon_r kT} \quad (25)$$

where r_c is in meter, e is the electronic charge (1.602×10^{-19} C), ϵ_0 is the permittivity of free space (8.854×10^{-12} F m⁻¹), ϵ_r is the relative permittivity (dielectric constant) of the medium, k is the Boltzmann constant (1.381×10^{-23} J K⁻¹), and T is the absolute temperature. Values of r_c for a number of liquids are listed in Table 7. Depending on the value of r_c , a greater or lesser fraction of the ion pairs escape geminate recombination and become free (solvated) ions but, as with water, the free solvated ions may exist in spurs, in which case only a fraction of these free ions would escape into the bulk solution. G values of free ions in various liquids are also included in Table 7. The general trend is that G_{fi} increases as r_c decreases, but there are notable exceptions; the large values of G_{fi} for neopentane and tetramethylsilane reflect the high mobility of the electron in these liquids [10], whilst G_{fi} for ammonia

Table 7. Onsager radii and free ion yields for some liquids.

Liquid	r_c [nm] ^a	G_{fi} [$\mu\text{mol J}^{-1}$] ^b
Neopentane	32	0.1
Tetramethylsilane	31	0.074
<i>n</i> -Hexane	30	0.012
Cyclohexane	28	0.015
Cyclohexene	26	0.017
Dioxan	26	0.009
Benzene	25	0.007
Carbon tetrachloride	25	0.009
Toluene	24	0.007
Ethylamine	8.1	0.18
Tetrahydrofuran	7.7	0.064
Ammonia	2.8	0.33
<i>n</i> -Propanol	2.8	0.15
Acetone	2.8	0.12
Ethanol	2.3	0.18
Benzonitrile	2.2	0.14
Methanol	1.7	0.2
Acetonitrile	1.5	0.21
Water	0.7	$\sim 0.4^c$

^a Values taken from Ref. [10]. ^b Values selected from A.O. Allen, *Nat. Stand. Ref. Data Ser., Nat. Bur. Stand. (US)* **1976**, 57, 1–16. ^c Estimated by the authors.

may be attributable to the slowness of the reaction of e_s^- with NH_4^+ [7a]. Detailed information on the radiolytic behavior of a great variety of organic and other non-aqueous solvents, for example, ammonia, can be found at <http://www.rcdc.nd.edu>.

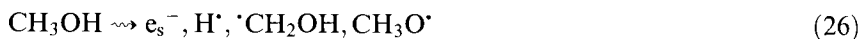
3.5 One-Electron Reduction and Oxidation in Nonaqueous Solvents

In the following section some pulse radiolysis investigations are described in which the radiolysis of nonaqueous solvents has been used to generate one-electron redox reagents and, in some cases, to characterize their involvement in electron-transfer reactions.

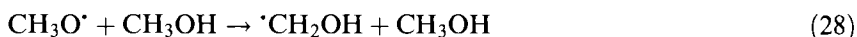
3.5.1 Alcohols

Methanol

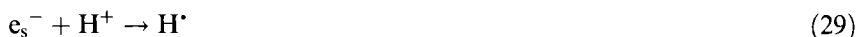
The radiolysis of methanol can be represented by Eq. 26:



Both H^\bullet and $\text{CH}_3\text{O}^\bullet$ react rapidly ($t_{1/2} = 18$ ns and 106 ns, respectively) with the solvent to produce additional $^\bullet\text{CH}_2\text{OH}$:



Thus, in argon-purged solution, the main reactive species are the one-electron reductants e_s^- and $^\bullet\text{CH}_2\text{OH}$. In alkaline solution, $^\bullet\text{CH}_2\text{OH}$ deprotonates to form $\text{CH}_2\text{O}^{\bullet-}$, which is a more powerful reductant than $^\bullet\text{CH}_2\text{OH}$ (see Table 6). In acidic solution, or neutral solution saturated with N_2O , e_s^- is converted to $^\bullet\text{CH}_2\text{OH}$ by the reactions of Eqs. 29–31:



Therefore, when the solubility of a compound is higher in methanol than in water, the radiolysis of methanol may provide a more efficient method of effecting one-electron reduction of that compound. Some illustrative examples are given below.

Transition metal complexes

The reduction of transition metals with organic ligands has been the subject of a number of studies in methanol [11]:

- 1) One-electron reduction of the following complexes: $[\text{Co}^{\text{II}}(\text{DPE})_2\text{Br}]\text{Br}$, $[\text{Co}^{\text{II}}(\text{DPE})_2\text{Cl}]\text{ClO}_4$, $[\text{Rh}^{\text{I}}(\text{DPE})_2]\text{Cl}$ or $[\text{Rh}^{\text{I}}(\text{DPE})_2]\text{ClO}_4$, and $[\text{Rh}^{\text{I}}(\text{VPP})_2]\text{Cl}$, where DPE = 1,2-bisdiphenylphosphinoethane and VPP = *cis*-1,2-bisdiphenylphosphinoethylene [11a]. The Co^{II} complexes are reduced by e_s^- , H^\bullet , and $^\bullet\text{CH}_2\text{OH}$ to give $\text{Co}(\text{DPE})_2\text{X}$ which eliminates X^- , giving $\text{Co}(\text{DPE})_2^+$. The reaction of the latter species with H_2 and CO could then be examined. The Rh^{I} complexes were reduced only by e_s^- . The products regenerated the starting compounds, presumably by reacting with CH_3OH ;
- 2) One-electron reduction of a series of hydrido complexes of iron(II)-containing organonitriles of general formula $t\text{-FeH}(\text{L})(\text{DPE})_2^+$, where $\text{L} = \text{CH}_3\text{CN}$, $\text{CH}_3\text{CH}_2\text{CN}$, CH_2CHCN , $\text{C}_6\text{H}_5\text{CN}$, and $p\text{-CH}_3\text{C}_6\text{H}_4\text{CN}$. Reduction results in the loss of L, to give the iron(I) complex $\text{FeH}(\text{DPE})_2$. On the other hand, for $\text{L} = p\text{-ClC}_6\text{H}_4\text{CN}$, reduction by e_s^- causes Cl^- to be eliminated leaving a neutral radical coordinated to the Fe^{II} center [11b]. When $\text{L} = \text{CO}$ or $\text{P}(\text{OCH}_3)_3$, reduction by e_s^- induces ring-opening of the DPE ligand [11c]. Investigations such as these complement electrochemical studies and provide mechanistic and kinetic details that are not otherwise accessible.

Quinones

Quinones, which play an important part in oxidation–reduction processes in nature, have very low solubility in water but their one-electron reduction can be readily investigated in methanol by pulse radiolysis [12]. In this way, the semiquinone radicals of 9,10-anthraquinone [12a] and quinizarin [12b], generated by e_s^- , $\cdot\text{CH}_2\text{OH}$ and $\text{CH}_2\text{O}^{\cdot-}$, have been characterized.

Oxidation in methanol

Although reducing conditions are readily achieved in methanol radiolysis, it is also possible to observe one-electron oxidation. For example, pulse radiolysis of N_2O -saturated solutions of *N,N,N',N'*-tetramethyl-*p*-phenylenediamine (TMPD) or I^- results in the formation of $\text{TMPD}^{\cdot+}$ and $\text{I}_2^{\cdot-}$, respectively. The oxidant was assigned as the methoxy radical $\text{CH}_3\text{O}^{\cdot}$, whose half-life in pure methanol was estimated to be 106 ns [13].

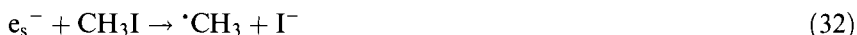
Secondary oxidizing radicals such as $\text{Br}_2^{\cdot-}$ have also been generated in methanol by the reaction of e_s^- with SF_6 [14], where the initial oxidant may be $\cdot\text{SF}_5$. The spectrum of $\cdot\text{SF}_5$ in methanol is reported to have λ_{max} at 300 nm and $\epsilon_{\text{max}} = 130 \text{ m}^2 \text{ mol}^{-1}$ [15]. In the absence of an oxidizable solute, $\cdot\text{SF}_5$ decays by mixed first- and second-order kinetics, which are attributed to its self-reaction and reaction with $\cdot\text{CH}_2\text{OH}$ and CH_3OH .

2-Propanol

The radiation chemistry of 2-propanol is analogous to that of methanol, that is, the main reactive species are e_s^- and $(\text{CH}_3)_2\cdot\text{COH}$. In alkaline solution, $(\text{CH}_3)_2\cdot\text{COH}$ deprotonates to $(\text{CH}_3)_2\text{CO}^{\cdot-}$. In the presence of N_2O or acetone, e_s^- is converted to $(\text{CH}_3)_2\cdot\text{COH}/(\text{CH}_3)_2\text{CO}^{\cdot-}$ by the reactions in Eqs. 30 and 18, or the reaction of Eq. 20, respectively. The solvated electron in 2-propanol has been utilized to study electron-transfer reactions between aromatic radical anions (donor) and aromatic molecules (acceptor) [16]. The donor–acceptor pairs studied were pyrene–anthracene, pyrene–9,10-dimethylantracene and *m*-terphenyl–*p*-terphenyl. In the first two cases an equilibrium was established and the parameters k_{forward} and k_{back} were measured; this was the first example of the measurement of an equilibrium constant by use of pulse radiolysis. The rate constants for the electron-transfer reactions were examined in terms of the Marcus theory [17].

Pulse radiolysis of 2-propanol has also been used to investigate elementary redox and radical reactions of fullerenes in solution [18]. For example, reduction of C_{60} to $\text{C}_{60}^{\cdot-}$ by e_s^- ($k \geq 10^{10} \text{ dm}^3 \text{ mol}^{-1} \text{ s}^{-1}$) and $(\text{CH}_3)_2\cdot\text{COH}$ [$k = (5 \pm 2) \times 10^8 \text{ dm}^3 \text{ mol}^{-1} \text{ s}^{-1}$] was observed, and $\text{C}_{60}^{\cdot-}$ was found to be stable for hours in the absence of oxygen. C_{60} is insoluble in water, but its reduction in this solvent by $(\text{CH}_3)_2\cdot\text{COH}$ was achieved by imbedding the fullerene in γ -cyclodextrin to form a soluble guest–host complex in a 9:1 (vol %) water:2-propanol mixture. In this case, the reaction rate was two times slower than that in neat 2-propanol. Information was also obtained [18] on the addition of $\cdot\text{CH}_3$ to C_{60} in 2-propanol by the follow-

ing reactions (Eqs. 32 and 33):

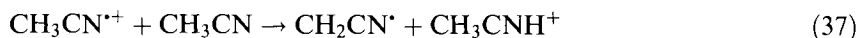
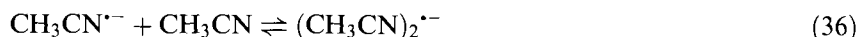
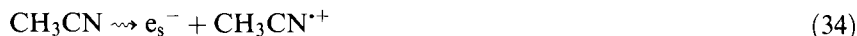


3.5.2 Acetone

One-electron oxidants can be generated by pulse radiolysis of acetone containing appropriate solutes. For example, it has been shown that solutions of KSCN and KBr produce $(\text{SCN})_2^{\cdot-}$ and $\text{Br}_2^{\cdot-}$, respectively [19], and, similarly, NO_3^\cdot and $\text{Cl}_2^{\cdot-}$ are formed in solutions of LiNO_3 and LiCl [20]. These oxidants are formed in significant yields, presumably by reaction of the corresponding anion with the solvent radical cation $(\text{CH}_3)_2\text{CO}^{\cdot+}$, and are sufficiently long-lived to permit their electron-transfer reactions to be studied in this solvent.

3.5.3 Acetonitrile

Acetonitrile is a versatile solvent for laboratory use because of its high dielectric constant and aprotic character. Studies of its radiation chemistry show that the radiolysis can be represented by the following steps [21]:



Addition of electron acceptors to acetonitrile confirmed the presence of a transient reducing species through the formation of radical anions of solutes such as biphenyl [21a, 22], pyrene, trans-stilbene, and so forth [21b]. This reducing species has a broad absorption with λ_{max} at 1450 nm, and was shown to exist in the monomeric and dimeric forms (see Eq. 36) from the effect of temperature on the absorbance at λ_{max} [21b]. The monomeric form is responsible for the 1450 nm peak, whilst the dimeric form exhibits a weak maximum at 550 nm superimposed on the tail of the monomeric band. The enthalpy change accompanying the reaction of Eq. 36 has been measured to be $-34.9 \text{ kJ mol}^{-1}$ [21b] so that $\text{CH}_3\text{CN}^{\cdot-}$ is the dominant reducing species at room temperature.

The G value of the reducing species, $G(\text{R})$, has been obtained by measurement of the yields of products of their reaction with various electron acceptors, and values in the range $0.11 \mu\text{mol J}^{-1}$ [21b] to $0.21 \mu\text{mol J}^{-1}$ [23] have been reported. The reason for the variation is likely to be due to assumptions made about the magnitudes of the molar absorption coefficients of the product radical anions. $G(\text{R}) = 0.21 \mu\text{mol J}^{-1}$ was obtained from the yield of $\text{Ru}(332)$ produced by pulse

radiolysis of acetonitrile containing Ru(333), where Ru(333) and Ru(332) represent $[\text{Ru}_3(\mu\text{-O})(\mu\text{-OAc})_6(\text{py})_3]^+$ and $[\text{Ru}_3(\mu\text{-O})(\mu\text{-OAc})_6(\text{py})_3]$, with ruthenium oxidation states of (III, III, III) and (III, III, II), respectively. Since Ru(333) and Ru(332) are stable in acetonitrile, their absorption coefficients are known, and so the reduction yield can be measured accurately. Thus $G(\text{R}) = 0.21 \mu\text{mol J}^{-1}$ is well founded.

In the presence of oxygen, $\text{CH}_3\text{CN}^{\bullet-}$ reacts to form $\text{O}_2^{\bullet-}$ in a reversible process:



with $k_{3,38} = 1.0 \times 10^{11} \text{ dm}^3 \text{ mol}^{-1} \text{ s}^{-1}$ and $k_{-3,38} = 2 \times 10^6 \text{ dm}^3 \text{ mol}^{-1} \text{ s}^{-1}$, so that $K_{3,38} = 5 \times 10^4$ [23]. Pulse radiolysis of oxygen-saturated solutions of tetracyanobenzene (TCNB) in acetonitrile showed that $\text{O}_2^{\bullet-}$ transfers an electron to TCNB with $k = 6.8 \times 10^9 \text{ dm}^3 \text{ mol}^{-1} \text{ s}^{-1}$ [21b].

Acetonitrile is a convenient solvent in which to study, by pulse radiolysis, the one-electron reduction of transition metal complexes that are not stable in water or hydroxylic media. For example, the tantalum compound $[\text{Ta}_2\text{Cl}_6(4\text{-methylpyridine})_4]$ has been shown to be reduced by $\text{CH}_3\text{CN}^{\bullet-}$ with $k = 1.2 \times 10^{11} \text{ dm}^3 \text{ mol}^{-1} \text{ s}^{-1}$ [24]. The absorption spectrum of the product shows the characteristic features of d - d transitions and it was suggested that the added electron is delocalized over the double-bonded Ta=Ta moiety. Another example is the radiolytic reduction of the vanadium(III) complex $[\text{VCl}_3(\gamma\text{-pic})_3]$, where $\gamma\text{-pic}$ is 4-methylpyridine, to the V^{I} derivative via the V^{II} complex [25]. It was shown by pulse radiolysis that the electron adduct of the V^{III} complex decayed in a first-order process with $k = 1.3 \times 10^3 \text{ s}^{-1}$ which is thought to involve loss of Cl^- . The intermediate V^{II} complex had a lifetime of ca. 4 s and decayed by second-order kinetics with $k = 2.5 \text{ dm}^3 \text{ mol}^{-1} \text{ s}^{-1}$ to form $\text{VCl}(\gamma\text{-pic})_3$, which was stable for two or three days.

3.5.4 Chlorinated Hydrocarbons

Early studies of the radiation chemistry of chlorinated hydrocarbons demonstrated the formation of molecular cations of aromatic hydrocarbons with half-lives of the order of a few microseconds [26]. In solutions containing two different aromatic solutes, it was possible to measure the rate of electron transfer from the neutral molecule to the radical cation. Some specific examples of other studies are given below.

Tetrachloromethane

Although various aspects of the radiolysis of CCl_4 are still under debate, this solvent can be used to initiate one-electron oxidation processes. The major oxidant is $^{\bullet}\text{CCl}_3$ formed in Eq. 39:



In the presence of oxygen, the reaction in Eq. 40 generates $^{\bullet}\text{O}_2\text{CCl}_3$, which is also an oxidizing radical. Some examples of the use of pulse radiolysis of CCl_4 solutions to investigate one-electron oxidation are given below.

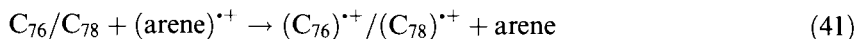
Compounds that have been shown to be oxidized under these conditions include phenol, *p*-methoxyphenol, TMPD, chlorpromazine [27], and a series of metal-tetraphenylporphyrins (M-TPP) with $\text{M} = \text{Zn}^{\text{II}}, \text{Mg}^{\text{II}}, \text{Cd}^{\text{II}}, \text{Pb}^{\text{II}}, \text{Hg}^{\text{II}}, \text{Pt}^{\text{II}}, \text{Cu}^{\text{II}}, \text{Co}^{\text{II}}, \text{Mn}^{\text{III}},$ and $\text{V}^{\text{IV}}\text{O}$ [28]. The phenols form phenoxyl radicals and the other compounds form radical cations. In the case of M-TPP, the resultant π -radical cations were found to oxidize $\text{Co}^{\text{II}}\text{TPP}$ to $\text{Co}^{\text{III}}\text{TPP}$ with rate constants of $10^5 \text{ dm}^3 \text{ mol}^{-1} \text{ s}^{-1}$ despite the driving force being in excess of 0.4 V. Addition of 1 % pyridine increased the rate constants by at least two orders of magnitude. In each system, the rate constants were fairly insensitive to variations in the driving force, and it was suggested [28] that the rate-determining steps may involve the formation of an intermediate between $\text{Co}^{\text{II}}\text{TPP}$ and $\text{M-TPP}^{\bullet+}$ rather than being a true outer-sphere electron transfer. The enhancing effect of pyridine was thought to be due to its efficiency as an electron-conduction channel rather than its effect on the redox potential.

1,2-Dichloroethane

One-electron oxidation of metalloporphyrins in this solvent is complicated by the production of HCl which rapidly demetallates these complexes. However, addition of pyridine as a base prevents this and allows the oxidation products to be investigated [29]. Under these conditions, the redox processes are similar to those observed in CCl_4 solution (see above).

Dichloromethane

Amongst the radiolysis products of dichloromethane is the highly oxidizing radical cation $\text{CH}_2\text{Cl}_2^{\bullet+}$ [30]. Examples of its use in studies of electron transfer reactions are the oxidation of the fullerenes C_{60} [18], C_{76} , and C_{78} to the corresponding fullerene radical cations $\text{C}_n^{\bullet+}$, and also arenes to $(\text{arene})^{\bullet+}$ [30]. By measurement of the rates of the reaction in Eq. 41 for several different $(\text{arene})^{\bullet+}$, clear evidence was obtained for the Marcus inverted region (see below) from a plot of $\log k$ vs $\Delta G (= \text{IP}_{\text{fullerene}} - \text{IP}_{\text{arene}})$, where IP is the ionisation potential.



3.5.5 2-Methyltetrahydrofuran and 2,2,4-Trimethylpentane

These two solvents were used to investigate the intramolecular electron transfer occurring in a homologous series of eight compounds of general structure A-Sp-B where B is 4-biphenyl, Sp is a rigid saturated hydrocarbon spacer separating A and B, and A is one of the series of eight acceptor groups [31]. Solvated electrons react in a statistical way to give $\text{A}^{\bullet-}\text{-Sp-B}$ and $\text{A-Sp-B}^{\bullet-}$. The rate constant for the electron transfer

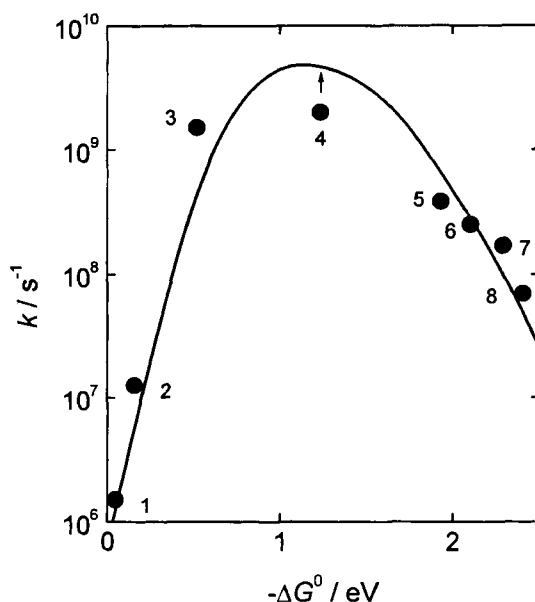


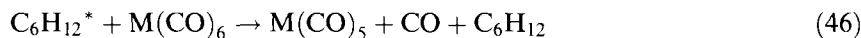
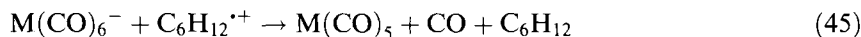
Figure 2. Dependence of rate constant on $-\Delta G^\circ$ for electron transfer from $B^{\cdot-}$ to A in $A-Sp-B^{\cdot-}$ generated pulse radiolytically in 2-methyltetrahydrofuran. B = 4-biphenyl, A = 2-naphthyl (1), 9-phenanthryl (2), 1-pyrenyl (3), hexahydronaphthoquinon-2-yl (4), 2-naphthoquinonyl (5), 2-benzoquinonyl (6), 5-chlorobenzoquinon-2-yl (7), 5,6-dichlorobenzoquinon-2-yl (8). (Adapted from Ref. [31]).



could be extracted, and showed a “bell-shaped” dependence on the driving force (see Figure 2). The authors described this as the first unambiguous demonstration of the inverted region predicted by the Marcus theory [17] for highly exoergic reactions [31]. The measurements were based on a 30-ps pulse radiolysis system; nevertheless, some of the intramolecular electron-transfer rates were too fast to be measured, and only their lower limit of $2 \times 10^9 \text{ s}^{-1}$ could be estimated.

3.5.6 Cyclohexane

Pulse radiolysis of solutions of the hexacarbonyl complexes $M(CO)_6$ of the Group-6 metals $M = \text{Cr}, \text{Mo}, \text{and W}$ has been shown to produce the corresponding pentacarbonyls, and the following mechanism was proposed [32]:



The decay of $M(CO)_5$ in the absence of additives, possibly representing addition of

a solvent molecule, and their reactivity towards H_2 , N_2 , and CO were examined [32].

3.5.7 Dimethyl Sulfoxide

Totally reducing and oxidizing conditions can be achieved by the radiolysis of dimethyl sulfoxide (DMSO) containing appropriate solutes [33]. Thus, addition of 1 % acetone or triethylamine provides a good medium for generating only reducing radicals, whilst aerated DMSO containing CCl_4 (or other halogenated hydrocarbons) provides a medium for one-electron oxidation. In each case, the yields of the radicals approach $0.4 \mu\text{mol J}^{-1}$, the sum of the primary yields of e_s^- and $\text{DMSO}^{+\bullet}$ produced by the radiolysis. These properties make DMSO a good solvent for studying one-electron redox processes when they cannot be studied in aqueous solution.

3.5.8 Ammonia

The solvated electron in liquid ammonia was discovered in 1864 by Weyl, and was identified in 1908 by Kraus as an electron, e_{am}^- , in a cavity surrounded by ammonia molecules. It is prepared when an alkali metal, for example sodium, is dissolved in ammonia, to form a stable blue color; under these conditions the electron is present in equilibrium with the metal atom and cation [34]. By contrast, e_{am}^- produced by pulse radiolysis of liquid ammonia is unstable due to its reactions with other radiolysis products; for example, in pure ammonia at -45°C , its lifetime is ca. $7 \mu\text{s}$ [35]. The major decay reactions are thought to involve the oxidizing radicals $\cdot\text{NH}_2$ and $\cdot\text{NH}$ [36], because addition of potassium ethoxide stabilizes e_{am}^- ; this is explicable, since ethoxide ion is expected to scavenge these radicals [36a].

The solvated electron in ammonia has a strong absorption band in the infrared region, and λ_{max} shifts from 1850 nm at 23°C to 1410 nm at -75°C ; this is attributed to the effect of temperature on the orientation of the ammonia molecules in the first solvation shell [37]. On the other hand, $G(e_{\text{am}}^-) = 0.32 \mu\text{mol J}^{-1}$ remains constant over the same temperature range [37]. It is relatively straightforward, therefore, to study one-electron redox reactions in liquid ammonia by pulse radiolysis, but relatively few investigations have been made.

Perkey and Farhataziz [38] have measured the rate constants for the reaction of e_{am}^- with some aromatic hydrocarbons (anthracene, nitrobenzene, phenanthrene, naphthalene, benzamide), with acetone and with dichloromethane, 1,2-dichloroethane, and 1-chloropropane. In the case of the aromatic molecules listed above, the rate constants are an order of magnitude larger than the corresponding values in water, reflecting the lower viscosity of liquid ammonia and indicating that the reactions are diffusion-controlled. In the case of biphenyl (B), the reaction of e_{am}^- was found to be reversible [39]:



with $k_{3.47}/k_{-3.47} = 8.3 \times 10^4$ and $31 \times 10^4 \text{ dm}^3 \text{ mol}^{-1}$ at 21.6 and 10.5 °C, respectively.

Examples of the reduction of metal ions by e_{am}^- include Ag^+ ($k = 1.5 \times 10^{12} \text{ dm}^3 \text{ mol}^{-1} \text{ s}^{-1}$ at 23 °C) [40] and Cu^{2+} ($k = 1.5 \times 10^{11} \text{ dm}^3 \text{ mol}^{-1} \text{ s}^{-1}$ at –50 °C [36a], and $8.3 \times 10^{11} \text{ dm}^3 \text{ mol}^{-1} \text{ s}^{-1}$ at 23 °C [41]). Absorption spectra have been reported for the transient species resulting from the reaction of e_{am}^- with these cations, and also with Ni^{2+} , Hg^{2+} , Cd^{2+} , Pb^{2+} , Zn^{2+} , Tl^{2+} , and Fe^{2+} [41]. There is also evidence that Cu^{2+} is oxidized to Cu^{3+} ($k \approx 6 \times 10^9 \text{ dm}^3 \text{ mol}^{-1} \text{ s}^{-1}$ at –50 °C) [36a] and Fe^{2+} to Fe^{3+} [41], where the oxidant is thought to be $\cdot\text{NH}_2$.

3.5.9 Solvent Mixtures

These media are essentially an extension of dilute solutions whereby the solute now comprises a significant fraction of the total volume. Nevertheless, the principle remains the same, namely to generate the required radicals. For example, one-electron reduction of the fullerene C_{84} has been effected in nitrogen-saturated toluene/2-propanol/acetone (8:1:1) [42]. Here the solvent primary radicals are converted to $(\text{CH}_3)_2\cdot\text{COH}$ by reduction of acetone and oxidation of 2-propanol.

Another example is the use of solvent mixtures to study protonation reactions. Thus, pulse radiolysis of acetone/2-propanol/carbon tetrachloride has been shown to produce HCl within approximately 100 ns, and this system has been used to measure rates of fast protonation reactions [43].

It is clear from the foregoing descriptions that pulse radiolysis provides a very versatile way of generating one-electron redox reagents under a wide range of solvent conditions that can be finely tuned to accommodate the reactions of interest.

3.6 Pulse Radiolysis

3.6.1 Historical Perspective

It was in 1960, ten years after the publication of the first detailed description of flash photolysis by Porter [44], that the analogous technique of pulse radiolysis was introduced in four separate laboratories: by McCarthy and MacLachlan at Du Pont Experimental Station, Wilmington, Delaware [45], by Matheson and Dorfman at Argonne National Laboratory, Illinois [46], by Keene et al. at AEI Ltd., Manchester [47], and by Steele and Boag at Mount Vernon Hospital, Northwood [48]. Actually, as noted by Boag [49], the idea of mimicking flash photolysis by using single pulses of high energy electrons from a linear accelerator was already being developed in 1953. The lapse in time between the advent of flash photolysis and the first experiments in pulse radiolysis was due mainly to the fact that electron accelerators able

to produce single short pulses of radiation of sufficient intensity were still under development when flash photolysis became operative. In addition to this, these machines were large, expensive, and for safety reasons, required housing in buildings designed to protect personnel from the radiation [50].

The first paper describing pulse radiolysis results was that of McCarthy and MacLachlan [45]. They gave a detailed description of the apparatus and technique, and reported on the identification of the spectrum of the benzyl radical generated from benzyl chloride dissolved in cyclohexane, ethanol, ethanol with glycerol, and glycerol. The data were in good agreement with those obtained from flash photolysis studies made by Porter and Windsor in 1957 [51]. Matheson and Dorfman [46] also identified the benzyl radical in cyclohexane and examined other systems in which transient absorption spectra were observed and tentatively attributed to the allyl radical and the inorganic radicals $I_2^{\cdot-}$, BrO^{\cdot} , BrO_3^{\cdot} . The first experiments at Mount Vernon Hospital [48] and Manchester [47] were focused mainly on the oxidation of ferrous ion to ferric ion in aqueous sulfuric acid solution, the basic process of the Fricke dosimeter [52].

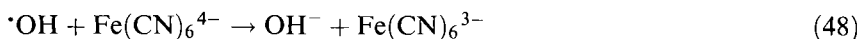
Following these first reports, pulse radiolysis studies were soon directed towards the identification of transient species and the characterization of their reaction kinetics in a variety of solvents [53]. Examples of such work are: a) Determination of the rate constants for the addition of the hydroxyl radical to benzene in aqueous solution to form the hydroxycyclohexadienyl radical and its subsequent reaction with oxygen to form the corresponding peroxy radical [54]; and b) The characterization of the transient species produced in ethanol and aqueous solutions of ethanol [55]. In the next few years, the number of laboratories with pulse radiolysis facilities grew rapidly and there was a burgeoning interest in identifying and characterizing the transient species generated by ionizing radiation. Some of the landmark discoveries in those early years are described briefly in the following paragraphs.

Absorption spectrum of the hydrated electron

The discovery in 1962 of the intense absorption band of e_{aq}^- (λ_{max} 720 nm, ϵ_{max} 1900 m² mol⁻¹) [56] in pulse radiolysis experiments on aqueous solutions was made almost simultaneously at Mount Vernon Hospital [57] and Manchester [58], and provided an extremely useful method for measuring the rate constants for the reaction of this species with a variety of compounds. As mentioned in the Introduction, reactions of the hydrated electron are electron-transfer reactions. The first paper dealing with this type of measurement appeared in 1963 [59] and contained the rate constants for the reactions of e_{aq}^- with H^+ , H_2O_2 , and O_2 . Many other rate constants for the reactions of e_{aq}^- were determined in the following years. The NDRL/NIST Solution Kinetics Database, Version 3, which covers the literature up to 1994, contains nearly two thousand entries for this type of reaction, almost all of them obtained by means of pulse radiolysis [7a]. In many cases, the rate constant for a given reaction has been determined more than once; for example, the rate constants for the reaction of e_{aq}^- with H^+ , NO_3^- , $C_6H_5NO_2$, Ag^+ , Cu^{2+} , and MV^{2+} (1,1'-dimethyl-4,4'-bipyridinium) have been determined 19, 16, 14, 11, 10, and 8 times, respectively [7a].

The hydrogen atom and hydroxyl radical

Because the H \cdot atom and the \cdot OH radical possess only small absorptions in the UV region [56], the first rate constants for their reactions with a variety of substrates were obtained by following the formation of an absorbing product or by using the competition kinetic method [60]. A prime example of the use of this method is the study of the rate of oxidation of hexacyanoferrate(II) by \cdot OH as a function of the pH of the aqueous solution [61]. By following the formation of hexacyanoferrate(III) at 420 nm, Rabani and Matheson [61] measured the value of $k_{3.48}$ and found it to decrease sharply with increasing pH at pH > 12.

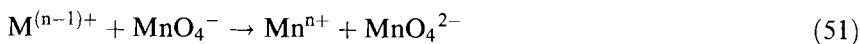


The data were interpreted (correctly) in terms of the dissociation of \cdot OH to $\text{O}^{\cdot-}$ with $\text{p}K_a(\cdot\text{OH}) = 11.9 \pm 0.2$ on the basis that $\text{O}^{\cdot-}$ is unreactive towards $\text{Fe}(\text{CN})_6^{4-}$.



In 1965, Adams et al. [62] obtained the absolute rate constants for the reaction of \cdot OH with a number of solutes, using the competition method; the reactions of \cdot OH with CO_3^{2-} , SCN^- , and SeO_3^{2-} that give the absorbing radicals $\text{CO}_3^{\cdot-}$, $(\text{SCN})_2^{\cdot-}$ and $\text{SeO}_3^{\cdot-}$, respectively, were used as references. Similarly, Thomas [63] determined the rate constant for the reaction of \cdot OH with I^- by following the formation of $\text{I}_2^{\cdot-}$ (λ_{max} 385 nm, ϵ_{max} 940 m 2 mol $^{-1}$) [56], and from that derived the rate constants for other reactions of the \cdot OH radical [63]. The NDRL/NIST Database cited above contains 1787, 715, and 171 entries for the reactions of \cdot OH, H \cdot , and $\text{O}^{\cdot-}$, respectively [7a].

In 1965, the first International Symposium on Pulse Radiolysis was held in Manchester and the scientific contributions and discussions were published in book form. One of these contributions [64] described what is probably the first determination, by means of pulse radiolysis, of rate constants for electron transfer from transient species, obtained from the reaction of e_{aq}^- with various metal ions, and MnO_4^- ; these reactions were followed by monitoring of the disappearance of the absorbance of MnO_4^- [64]:



where $\text{M}^{n+} = \text{Cr}^{3+}$, Ni^{2+} , Co^{2+} , Cd^{2+} , Cu^{2+} , Ag^+ .

Pulse radiolysis was also applied very early to the estimation of the redox potentials of transient species. By examination of the reactivity of the transient species Zn^+ , Cd^+ , and Pb^+ towards Cd^{2+} and Pb^{2+} , Zn^{2+} and Pb^{2+} , and Zn^{2+} and Cd^{2+} , respectively, Baxendale et al. [65], were able to show that $E^\circ(\text{Zn}^{2+/+}) < E^\circ(\text{Cd}^{2+/+}) < E^\circ(\text{Pb}^{2+/+})$ which is in agreement with subsequent evaluations [66a]. Since then, many redox potentials of transient species have been determined by means of pulse radiolysis and have enriched the specialized compilations [66].

In 1967, the first three-stage electron-transfer process examined by pulse radiolysis was reported [67]. Such a cascade process is of relevance to electron transport in biological systems. By irradiating an aqueous solution containing acetone (0.82 mol dm^{-3}), acetophenone ($3.34 \text{ mmol dm}^{-3}$), and benzophenone ($72 \text{ } \mu\text{mol dm}^{-3}$) at pH 13, Adams et al. [67] were able to observe, at $2 \text{ } \mu\text{s}$ after the pulse, the spectrum of the acetophenone radical anion ($\lambda_{\text{max}} 445 \text{ nm}$, $\epsilon_{\text{max}} 260 \text{ m}^2 \text{ mol}^{-1}$) [68] originating from the reduction of acetophenone by the $(\text{CH}_3)_2\text{CO}^{\bullet-}$ radical. In the following $50 \text{ } \mu\text{s}$, the acetophenone radical anion reacted with benzophenone ($k = 7.8 \times 10^8 \text{ dm}^3 \text{ mol}^{-1} \text{ s}^{-1}$) so that the absorption band at 445 nm disappeared and that of the benzophenone radical anion ($\lambda_{\text{max}} 600 \text{ nm}$, $\epsilon_{\text{max}} 480 \text{ m}^2 \text{ mol}^{-1}$) [68] was formed.

One-electron redox equilibria

The examples of redox reactions described above were measured under conditions where they went to completion in the forward direction. However, when the reduction potentials of the electron donor (D) and acceptor (A) are not very different, equilibrium conditions can be achieved where all the species in Eq. 52 are present:



The first determination of an equilibrium constant by measurement of the concentrations of the transients at equilibrium involved the system duroquinone (DQ) and oxygen [69]:



where $K_{3.53} = 2.3 \times 10^{-2}$ was obtained.

The kinetic method provides another way of obtaining equilibrium constants by the measurement of the rate of approach to equilibrium. It relies on the back reaction having a measurable effect on the forward electron-transfer reaction in a scheme comprising Eqs. 52 and 54:



where the rate equation is Eq. 55 and the integrated form is Eq. 56:

$$-d[\text{D}^-]/dt = k_{3.52}[\text{D}^-][\text{A}] - k_{-3.52}[\text{A}^-][\text{D}] + k_{3.54}[\text{X}] \quad (55)$$

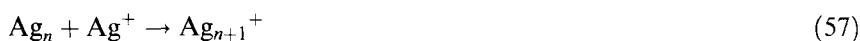
$$\ln[\text{D}^-]_t - [\text{D}^-]_e = C_1 - (k_{3.52}[\text{A}] + k_{-3.52}[\text{D}])t \quad (56)$$

Here $[\text{A}^-]_e$ is the concentration of $[\text{A}^-]$ at equilibrium and C_1 is a constant. Values of $(k_{3.52}[\text{A}] + k_{-3.52}[\text{D}])$ can be obtained from a plot of $\ln[\text{A}^-]_t - [\text{A}^-]_e$ versus t and then $k_{3.52}$, $k_{-3.52}$, and hence $K_{3.52}$, can be calculated from a plot of $(k_{3.52}[\text{A}] + k_{-3.52}[\text{D}])$ vs. $[\text{A}]$ at constant $[\text{D}]$. As mentioned in Section 3.5.1, the first

report of such a measurement was by Arai and Dorfman [16] for electron transfer from the pyrenide anion to anthracene and 9,10-dimethyl anthracene in 2-propanol.

Another example of the determination of a redox equilibrium by pulse radiolysis is the measurement of the reduction potential of silver aggregates, Ag_n , as a function of the aggregation number n . Such measurements are of intrinsic value in understanding photographic development processes [70].

The principle of the method is to produce, in the same pulse, silver atoms and an electron donor, in this case the sulfonatopropylviologen radical anion ($\text{SPV}^{\bullet-}$) for which $E^\circ(\text{SPV}/\text{SPV}^{\bullet-}) = 0.41 \text{ V}$; the aggregation of silver atoms and the decay of $\text{SPV}^{\bullet-}$ are then followed by time-resolved optical spectroscopy. After a certain time, during which $[\text{SPV}^{\bullet-}]$ remains constant, the decay of this radical and the growth of Ag_n become correlated, showing that Ag_n has reached a critical size where it is able to accept an electron from $\text{SPV}^{\bullet-}$. The proposed mechanism [70] involves autocatalytic growth of Ag_n through the following reaction sequence:



The data obtained [70] show that the reaction in Eq. 58 commences when $n = 4$ so that $E^\circ(\text{Ag}_5^+/\text{Ag}_5) \approx 0.41 \text{ V}$.

Pulse radiolysis at high pressure

Of particular interest in the radiation chemistry of water is the equilibrium (Eq. 59) between e_{aq}^- and H^\bullet since one can obtain from it the reduction potential of e_{aq}^- :



To measure the back reaction, it is necessary to generate H^\bullet in alkaline solution, and this was achieved by Matheson and Rabani [71] who developed a pulse radiolysis cell capable of operating at a pressure of 100 bar. In this way they were able to produce H^\bullet effectively during the pulse ($0.4 \mu\text{s}$) by the following reaction (Eq. 60):



Subsequently, Hentz et al. [72] were able to carry out pulse radiolysis studies at pressures up to 6.3 kbar. Some of the principal results obtained for aqueous solutions were: a) The absorption spectrum of e_{aq}^- showed only a small blue shift ($d\lambda_{\text{max}}/dP$) of 0.06 eV/kbar up to 4.88 kbar and thereafter no further change; this indicates that the cavity volume of e_{aq}^- is very small ($V = 7 \text{ ml mol}^{-1}$); and b) The diffusion coefficient of e_{aq}^- changes negligibly with pressure, in contrast to normal ions and molecules.

In liquid ammonia at 23°C , however, ($d\lambda_{\text{max}}/dP$) at low pressure is about four times greater than it is in water, consistent with the much larger cavity of e_{am}^- ($V = 98 \text{ mL mol}^{-1}$) being more compressible [73].

Pulse radiolysis at high temperature

Pulse radiolysis studies of liquids at high temperature must necessarily be carried out at pressures sufficiently high to prevent boiling. The first pulse radiolysis experiments at high temperature were conducted by Michael et al. [74] who determined the spectrum of e_{aq}^- in the temperature range -4 to 390°C which the use of small suprasil capillaries above 200°C .

It was some ten years before any systematic program of pulse radiolysis at high temperature had begun when Christensen and Sehested [75] had available a pulse radiolysis cell that enabled measurements to be made up to 320°C and 140 bar. This work focused on the radiation chemistry of water at elevated temperatures because of its relevance to the radiation chemistry occurring in the primary cooling circuits of pressurized water reactors used for electricity generation.

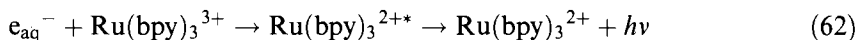
The study at elevated temperatures of reactions that are diffusion-controlled at ambient temperature, can be particularly informative, since the kinetics of a diffusion-controlled reaction reveals little information about the chemical mechanism. The general expression for a time-independent rate constant in solution is [76]:

$$1/k_{\text{obs}} = 1/k_{\text{diff}} + 1/k_{\text{react}} \quad (61)$$

where k_{obs} , k_{diff} , and k_{react} are the observed, diffusion-controlled, and activation-controlled rate constants, respectively. Thus, by raising the temperature sufficiently, it has proved possible to make the diffusion process so fast that it is no longer rate-limiting and information specific to the chemical, or activated step is revealed [77]. Such studies have shown that the reactions of: 1) e_{aq}^- with N_2O , NO_3^- , NO_2^- , SeO_4^{2-} , $\text{S}_2\text{O}_3^{2-}$, and phenol [78], and 2) $\cdot\text{OH}$ with benzene and a number of substituted benzenes [79], are all reversible. The experimental manifestation of this behavior is that Arrhenius plots for k_{obs} are nonlinear. Similarly, nonlinear Arrhenius behavior is exhibited by k_{obs} for radical-radical combination reactions because there is no energy barrier to the chemical step so that $1/k_{\text{react}}$ becomes the dominant term on the right-hand side of Eq. 61 as the temperature is raised.

General chemistry

The contribution of pulse radiolysis to general chemistry is very significant, and this is exemplified by the following studies of transition metal complexes. The reduction of tris(2,2'-bipyridine)ruthenium(III) ion by the hydrated electron was the first example of this type of reaction to show clearly the formation of a product in an electronically excited state [80]:



The spectrum of the chemiluminescence produced by this reaction corresponded closely to the emission spectrum obtained on photoexcitation of $\text{Ru}(\text{bpy})_3^{2+}$ [80].

In their reactions with transition metal complexes, free radicals may attack directly at the metal center or at a ligand to produce a coordinated free radical, which may then undergo electron transfer involving the metal center. The first observation

of a coordinated free radical was reported by Hoffman and Simic who found that the reaction of $\cdot\text{OH}$ with benzoatopentamminecobalt(III) generated a product with an absorption spectrum that was very similar to that obtained by reaction of $\cdot\text{OH}$ with benzoate/benzoic acid [81]:



The absorption spectrum of the coordinated radical was intermediate between those of $\cdot\text{C}_6\text{H}_5(\text{OH})\text{CO}_2\text{H}$ and $\cdot\text{C}_6\text{H}_5(\text{OH})\text{CO}_2^-$, in keeping with the effect of the carboxylate group being coordinated to the metal center [81]. There was no evidence in this example for electron transfer from the ligand radical to the cobalt(III) center. On the other hand, reaction of e_{aq}^- with the same complex generated Co^{II} within the time resolution ($<1 \mu\text{s}$) of the measurements. By contrast, reaction of e_{aq}^- , $\text{CO}_2^{\cdot-}$ or $(\text{CH}_3)_2\cdot\text{COH}$ with *p*-nitrobenzoatopentamminecobalt(III) resulted in the added electron being localized on the *p*-nitrobenzoato ligand [82]. This species then decayed by a first-order process ($k = 2.6 \times 10^3 \text{ s}^{-1}$), representing intramolecular electron transfer from the coordinated radical to the metal center. This was the first reported observation using pulse radiolysis of this type of process [82].

Detection methods

Optical detection in early pulse radiolysis experiments was based mainly on the spectrophotographic recording method but this was abandoned in the mid-sixties in favor of the photoelectric method. The traces on the oscilloscope screen were photographed, usually enlarged and reproduced on graph paper before being subjected to analysis. A common feature of pulse radiolysis assemblies now is the use of fast-transient digitizing recorders coupled to computers, which allow the rapid collection and manipulation of the data. Devices such as optical multichannel analyzers (OMA) [83] and streak cameras [84] can be used to get complete spectra after a single pulse. A method for the simultaneous recording of optical changes on multiple time scales has recently been described [85].

Other methods of monitoring the reactions and products were soon introduced. These included electrical conductivity in 1962 [49], magnetic resonance (EPR in 1968 [86] and NMR in 1976 [87]), polarography in 1971 [88], light scattering (Rayleigh scattering in 1974 [89] and Raman scattering in 1976 [90]), and microwave absorption in 1973 [91]. Of these methods, conductivity is the most widely used after optical measurements, and the others are all limited to specialist laboratories.

3.7 Pulse Radiolysis Facilities

In the first monograph dedicated to pulse radiolysis, published in 1969 by Matheson and Dorfman [92], which still represents a most valuable source of information on the various aspects of the technique, it is reported that by the end of 1968 at least 27

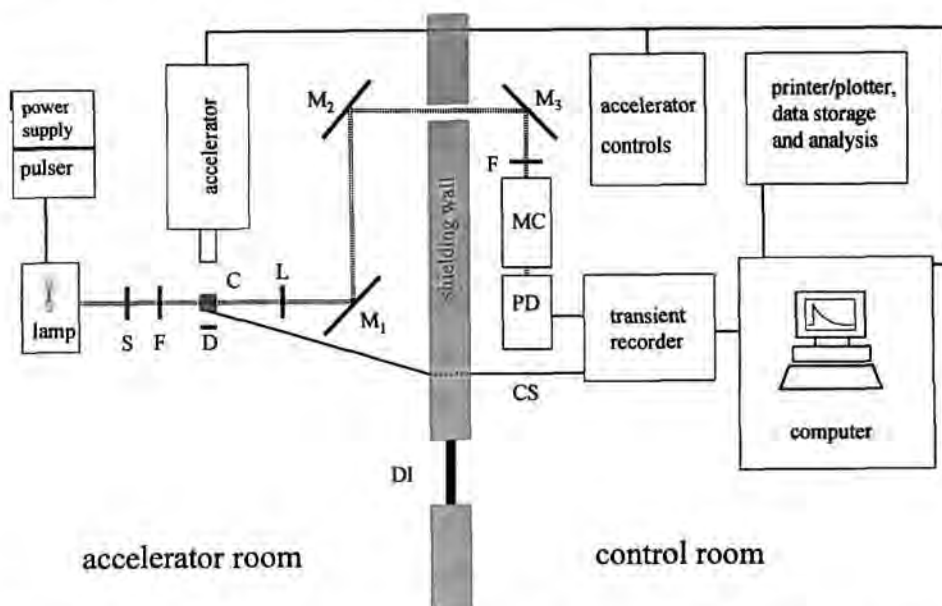


Figure 3. Schematic of a pulse radiolysis facility with optical and conductometric detection. C: cell; CS: conductivity signal; D: dose monitor; DI: door and interlock system; F: filters; L: lens; MC: monochromator; M_1 : mirrors; PD: photodetector; S: shutter.

laboratories were equipped with pulse radiolysis facilities. These laboratories were located in the US (11), UK (6), and Canada (4); Denmark, France, Germany, Israel, Switzerland, and the USSR possessed one pulse-radiolysis laboratory each. In the following years, many other institutions in Europe, Japan, and other parts of the world installed pulse radiolysis facilities. At the same time, some of the laboratories that pioneered pulse radiolysis made great improvements to their facilities and introduced other methods of detection.

3.7.1 A Typical Modern Pulse Radiolysis Facility

A typical pulse radiolysis facility with optical and conductometric detection is represented schematically in Figure 3. The essential parts of the system are: accelerator and related controls, sample cell, light source with its power supply and pulser unit, light shutter, filters, lenses, and mirrors to bring the analyzing light beam from the light source through the sample cell to the monochromator(s) and the photodetector, transient recorder (oscilloscope or transient digitizer), and computer. The computer used to control the experiment and to collect the data can be connected to a printer and/or a plotter and to other computers for storage and analysis of the data. Various components of the assembly such as the lamp pulser, shutter, filters,

lenses, dose monitor, and monochromator(s) can be computer-controlled. In Figure 3, for the sake of clarity, the connections between the computer and these components have been omitted. For the same reason, the possibility of monitoring the temperature of the sample has not been indicated. The figure shows the presence of a shielding wall of appropriate thickness that separates the accelerator room from the control room; the door connecting the two rooms is controlled by an interlock system, the complexity of which generally increases with increasing energy of the electron beam. In some laboratories, the control room is fitted with a Faraday cage surrounding the data-collection station [93]. In other cases, the Faraday cage is placed around the accelerator so that the electrical interference is contained at source [94]. In Figure 3 only one exit port of the electron beam has been indicated, which is the most common situation. In some laboratories, however, by means of bending magnets it is possible to bring the electron beam to different exit ports equipped for different types of experiments [95, 96]. In other cases, the instrumentation needed for experiments of different nature is mounted on interchangeable benches. This solution has been adopted, for example, at the FRAE Institute in Bologna, where the bench supporting the cell holder and the components of the optical detection system that reside in the accelerator room can rapidly replace the bench supporting the apparatus used for radiation processing [97]. Finally, closed-circuit television can provide useful remote visual monitoring and control of some aspects of the experiment.

A brief description of the major components of a pulse radiolysis system will be given in the following; whenever possible, references will be given to the original papers where the specific solutions adopted in the various laboratories are described in detail.

Accelerators

Almost all the work in pulse radiolysis is based on the use of three types of electron accelerators: linear accelerators (linacs), Van de Graaff accelerators, and Febetrans. The first accelerator used by Keene at Manchester was a 4-MeV linac with pulses of 0.2–2 μ s duration [47a]; this was replaced in 1967 with an 8–12-MeV linac capable of delivering pulses from 5 ns to 5 μ s duration [93]. Further improvements made to the Manchester system up to 1989 have been documented [93]. Similarly, the 13-MeV linac used at Argonne in 1960 by Matheson and Dorfman produced pulses of 0.4 to 5 μ s duration [46], whereas in 1989 the equipment comprised a 20-MeV linac, capable of producing pulses from 25 ps to 10 μ s duration, and a 3-MeV Van de Graaff accelerator, which is dedicated to EPR and magnetic resonance studies (see below) [95, 98].

The parameters that make a given accelerator more or less suitable for a specific pulse radiolysis experiment are the pulse length, the energy, the size of the beam, the dose per pulse, and the repetition rate. In general, the shorter the pulse, the better it is, since the length of the pulse usually determines the resolution time of the system. However, the cost of an accelerator increases significantly with decreasing pulse length. Many pulse radiolysis systems are based on machines that deliver pulses of some nanoseconds up to microseconds duration and this is quite adequate for many

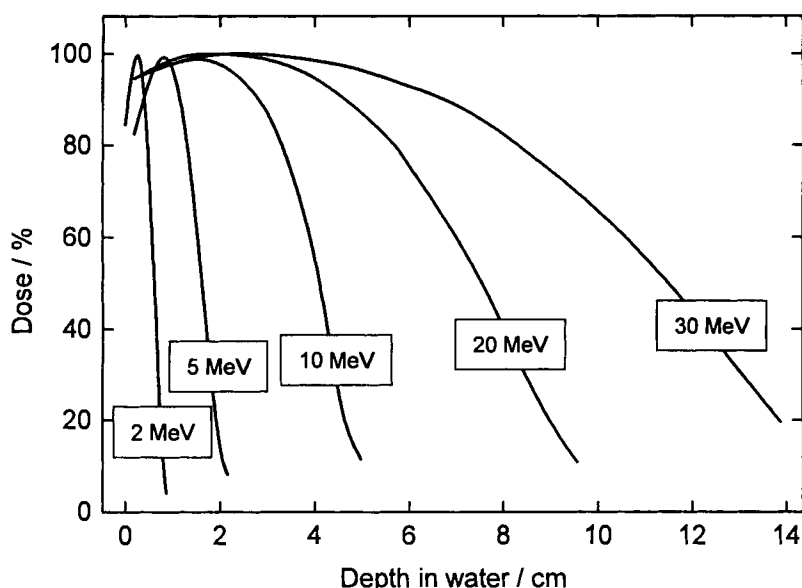


Figure 4. Dependence of dose deposition on depth in water. (Adapted from J.W. Boag in *Action Chimiques et Biologiques des Radiations*, Vol 6 (Ed.: M. Haissinsky), Masson et Cie., Paris, 1963, p. 5).

chemical applications. Some detailed information on accelerators can be found in a number of publications [92, 99–101].

The first nanosecond facility in China was installed in 1990 at the Shanghai Institute of Nuclear Research [102]. Other new accelerators for radiolysis experiments have been recently installed at the Institute of Nuclear Chemistry and Technology, Warsaw [96], at the Radiation Laboratory of the University of Notre Dame [103], and at the Chemistry Department of the Brookhaven National Laboratory [104].

Pulse radiolysis with picosecond time resolution has been developed, or is planned, in only a few laboratories. These rather special facilities are described separately in Section 3.9.

The energy of the electron has influence on the penetration of the beam, as shown in Figure 4. If the energy is very low, for example, 600 keV as it is with a Febetron 706, special care must be taken in the construction of the irradiation cell (see below). Energies higher than 20 MeV are unnecessary and may represent a problem because of induced radioactivity and additional costs for shielding. With only a few exceptions (Orsay 0.6 MeV, Osaka 28 MeV, Ottawa 35 MeV, Sapporo 45 MeV, and Amsterdam 85 MeV), the majority of the pulse radiolysis laboratories have accelerators that generate electron beams of ca. 2 to 20 MeV energy. Of the accelerators presently in operation, approximately 50 % are linacs (2–20 MeV), 25 % are Van de Graaffs (2–5 MeV) and 25 % are Febetrans (mostly Febetron 705, 2 MeV). In general terms, a beam energy of about 10 MeV gives ample flexibility as far as the assembling of a variety of experiments is concerned.

The size of the beam should match that of the cell, particularly when quantitative information is to be gained from absorbance measurements. It can be modified to some extent by means of scatter plates interposed between the exit window and the cell (if the energy of the electron beam allows this to be done) or by means of focusing magnets. In general, the beam is kept small and as uniform as possible and the optical path length is increased by use of multiple reflection cells (see below). For conductivity experiments (see below), the size of the beam should match the volume between the electrodes.

The dose per pulse that is used in pulse radiolysis experiments, for example, with aqueous solutions, can vary between a few tenths of a Gy and several hundred Gy, depending on the nature of the experiment ($1 \text{ Gy} = 1 \text{ J kg}^{-1}$ and a dose of 1 Gy generates ca. $0.6 \mu\text{mol dm}^{-3}$ of radicals in water). In general, because of the greater sensitivity of the detection method, conductivity experiments (see below) require lower doses than those needed in optical measurements. A low dose per pulse is required when radical-radical reactions are to be minimized or when pseudo-first-order conditions are to be maintained, for example, when dealing with highly absorbing substrates so that they can be used only at low concentration. Under these circumstances, which could be associated with intrinsically weak signals, averaging procedures to increase the signal-to-noise ratio may become necessary. These procedures are somewhat impractical with Febetrons since the pulse repetition rate of these accelerators is low, approximately one pulse every 1–2 minutes; with linacs and Van de Graaffs, the pulse repetition rate is not a limitation for data averaging. It is important, however, to maintain a constant dose per pulse during averaging, particularly if the study involves measuring second-order reaction kinetics.

Some experiments may require the use of different doses. Depending on the accelerator, this can be done by a change of the length of the pulse (if the experiment allows it), the focusing of the beam and/or the beam current. Alternatively, the amount of radiation that reaches the sample cell can be varied by means of scatter plates of variable thickness or, particularly with Febetrons, metal shields with holes of different sizes [105].

Sample cell and flow system with optical detection

The majority of the pulse radiolysis work deals with the monitoring of changes in absorbance and/or conductivity (see below) induced by the irradiation of solutions (in particular aqueous solutions). Many types of cells used for the measurement of transient optical absorption have been described in the literature, their shapes and sizes depending on a variety of factors such as energy and size of the electron beam, nature of the experiment to be performed, scarcity and/or cost of substrate to be examined, and so forth. The material from which the cells for optical measurements are made can vary, but the optical windows are generally made of Spectrosil quartz which does not darken when irradiated. When the energy of the electron beam is of the order of 10 MeV , there are no particular restrictions as far as the design of the irradiation cell is concerned. With electron beams of this type, rectangular or cylindrical cells with 1–3 mm-thick walls, optical path lengths of 0.5 to 5–10 cm and cross sections of less than 0.1 cm^2 up to $1\text{--}2 \text{ cm}^2$ are commonly used. A short path

length is obviously needed when the sample to be irradiated presents an intrinsically high absorbance in the spectral region to be examined or when dealing with fast (picoseconds) measurements (see Section 3.9). With non-absorbing samples, the tendency is to increase the optical path length as much as possible, to be compatible with the size of the electron beam and the sample availability. Multiple reflection cells can also be used to increase the optical path length and to keep the volume of the sample to be irradiated relatively small. A multiple reflection cell that "enabled the use of long optical paths of up to 80 cm with an actual cell length of only 4 cm" has been described [106]. When the energy of the electron beam is low, the thickness of the wall through which the electron beam enters the sample and that of the sample itself must be reduced accordingly. For example, a cell with a 0.2-mm-thick electron wall, 1-cm optical path length and a cross section of 0.05 cm² is used for pulse radiolysis experiments with 600 keV electrons from a Febetron 706 [107].

Pulse radiolysis experiments with optical and/or conductometric detection often require the solution to be changed after each irradiation pulse. As a consequence, systems have been devised to perform this operation which, in many cases, is remotely controlled. The solution to be examined, sparged with an inert gas (to remove O₂) or saturated with a specific gas, for example, nitrous oxide, is contained in a flask or a syringe (see Figure 5) which is connected to the irradiation cell. The solution is made to flow into the cell by maintenance of a small excess gas pressure in the flask or by mechanical operation of the plunger of the syringe. A motor-driven tap or an electromagnetic valve between the reservoir and the cell (or after the cell) will stop the solution flow at any required time. The cell can be drained before being refilled with fresh solution or, more simply, the irradiated solution is pushed away by fresh solution. When the experiment requires many samples of the same solution because of averaging procedures and/or multiwavelength examinations, the change of the solution can also be under computer control; in some cases, particularly when the solution is available in large amount, it is left flowing at the appropriate rate during the entire experiment. In all cases it is desirable that the solution in the cell is completely refreshed between pulses to prevent any interference from accumulated reaction products.

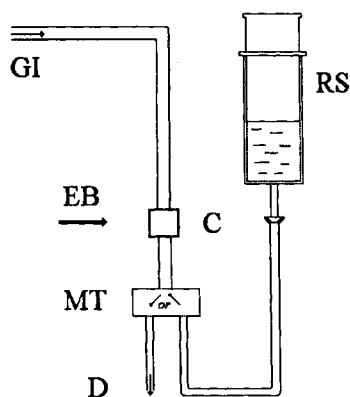


Figure 5. Schematic representation of a flow system. C: cell; D: drain; EB: electron beam; GI: gas inlet; MT: motor-driven 2-way tap; RS: reservoir syringe.

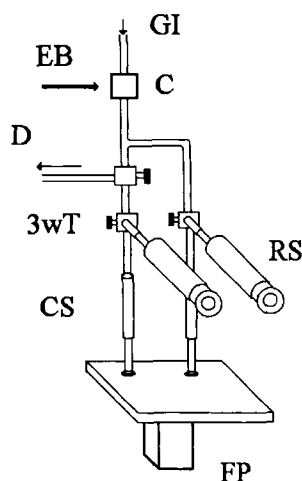


Figure 6. Schematic representation of a rapid-mixing device for pulse radiolysis. C: cell; CS: calibrated syringes (2 mL); D: drain; EB: electron beam; FP: firing piston; GI: gas inlet; RS: reservoir syringes; 3WT: 3-way tap.

In Figure 3, the electron beam and the monitoring light beam are perpendicular to each other. An alternative solution, that of the analyzing light beam being col-linear with the electron beam, has also been adopted [45, 108].

In some cases, because of decomposition phenomena, it may be necessary to prepare the solution to be irradiated “immediately” before the pulse. A procedure of this type, based on the use of a rapid-mixing device placed before the irradiation cell, has recently enabled Czapski et al. to investigate by pulse radiolysis the species HCO_3^- and H_2CO_3 in solutions that were made acidic approximately 50 ms before the pulse so that their decomposition was kept at a low level. From this study it has emerged that the HCO_3^\cdot radical is a strong acid ($\text{p}K_a < 0$) [109]. An example of a rapid mixing device for pulse radiolysis studies is shown in Figure 6.

A setup for pulse radiolysis of aggressive substances, such as anhydrous HNO_3 , has been described [110]. The all-glass flow system is designed to operate by remote control and each point where the unit has contact with the surrounding atmosphere is protected by a suitable guard tube.

Most pulse radiolysis experiments are performed with solutions at ambient temperature. In other cases, the temperature of the sample is kept constant or it is varied by means of suitable thermostatic systems. The construction details of a variable-temperature (from ca. -160 to $+150^\circ\text{C}$) cell housing adaptable to a pulse radiolysis flow system have been given [111]. An alternative method of carrying out pulse radiolysis studies on liquids at high temperature (up to 300°C) is to enclose the whole assembly of cell, reservoir syringe, and flow system in a pressure vessel [112]. Only the cell is located within a heating block and the reservoir remains at ambient temperature. With this method, the sample in the cell can be changed remotely as in conventional experiments.

A high-pressure cell, originally utilized in flash-photolysis experiments where limitations caused by low beam penetration do not exist, has been adapted for measurements up to 200 MPa in pulse radiolysis experiments to be performed at ambient temperature with a beam energy as low as 2 MeV [113].

Sometimes it can be informative to compare the permanent spectral changes induced by the pulse irradiation of a solution with those detected at the end of the longest time that is permitted by the pulse radiolysis detection system. This can be done by use of a spectrophotometric cell attached to a bulb provided with a stop-cock that allows the sample to be adequately prepared, for example, with the aid of a vacuum line. The cell is then placed in front of the accelerator and is used as a normal pulse radiolysis irradiation cell. When the pulse radiolysis experiment is complete, the cell can be transferred into a spectrophotometer, preferably a diode-array type, where spectra and/or kinetic data can be obtained. Samples irradiated in this way can also be used to examine the reactivity of the permanent products originating from the irradiation toward a specific reagent, for example O_2 . Examples of "slow" pulse radiolysis experiments of this type have been reported in the literature [114]. A "single-shot" pulse radiolysis setup, where a diode-array spectrophotometer is connected to the normal optical system by means of a fiber-optic light guide, has been used for studies over times greater than about ten seconds [93].

Another system, based on the familiar stopped-flow method, has been developed specifically to measure relatively slow reactions of the superoxide radical with molecules of biological interest [115]. One of the reactants, $O_2^{\cdot-}$, is generated by radiolysis of oxygenated formate solution in one arm of the stopped-flow apparatus before this solution is mixed with the second solution containing the solute of interest and passed into a spectrophotometer. For solutes that have suitable absorption spectra, rate constants can be determined under pseudo-first-order conditions by the fading of the solute absorbance being monitored. Rate constants of the order of 10^4 – 10^5 dm^3 mol^{-1} s^{-1} are readily measured in this way. In the case where the solute is transparent, the reaction rate can be obtained from the rate of disappearance of $O_2^{\cdot-}$ which absorbs strongly at 250 nm [56]. However, in this case it is not possible to judge whether the superoxide radical undergoes oxidation or reduction, or whether its rate of decay is the termination step of a fast chain reaction.

This difficulty can be overcome by measurement of the depletion of O_2 in the reaction with use of an oxygen electrode [115], and then four situations can be distinguished. Firstly, there may be no reaction between $O_2^{\cdot-}$ and the solute S, so that $G(-O_2) = 0.5G(O_2^{\cdot-})$ because of the stoichiometry of the reaction given by Eq. 64.



Secondly, when $O_2^{\cdot-}$ is oxidized, $G(-O_2) = 0$; thirdly, when $O_2^{\cdot-}$ is reduced, $G(-O_2) = G(O_2^{\cdot-})$; and lastly, when a chain reaction occurs by the propagating steps represented by Eqs. 65 and 66, $G(-O_2) \gg G(O_2^{\cdot-})$.



A combination of optical kinetic measurements and oxygen electrode measurements serves to evaluate rate constants and indicate the direction of electron transfer, as well as confirming the overall stoichiometry of the reaction.

Dose monitor and dosimetry

Inasmuch as the irradiation dose can change from pulse to pulse, it is desirable and often necessary to monitor the dose delivered by each pulse. This can be done by means of various devices: a toroidal coil placed around the electron beam [116], a secondary emission chamber placed just before the exit window of the accelerator [13], a charge collector placed in the proximity of the irradiation cell [117], or, electron beam energy permitting, behind the irradiation cell [118]. With these devices, a parameter is obtained representing the relative dose of each pulse; calibration against chemical dosimeters provides the knowledge of the absolute irradiation dose associated with each individual pulse.

The chemical dosimeter that is used most frequently is the thiocyanate dosimeter [119]. Other chemical dosimeters for pulse radiolysis are ferrocyanide [119], modified Fricke (Super-Fricke) [119], hydrated electron [120], O₂-saturated solutions of potassium iodide [112], and N₂O-saturated solutions of methylviologen and formate [118]. The C(NO₂)₄ (tetranitromethane, TNM) dosimeter is used in pulse radiolysis experiments with simultaneous optical and conductometric detection [121–124]. The composition and characteristics of the various chemical dosimeters used for pulse radiolysis with optical detection are listed in Table 8.

As far as possible, dosimetry should be carried out under the same conditions used for the experiments, to avoid errors due to the possible nonlinear response of the dose monitor. The choice of dosimeter depends on the following factors:

- 1) Its sensitivity, that is, the value of $G\epsilon$ (m² J⁻¹), where G (μmol J⁻¹) is the yield of product and ϵ (m² mol⁻¹) is the molar absorption coefficient at the monitoring wavelength;
- 2) The formation time of the product;
- 3) The stability of the product.

For low dose per pulse, a large value of $G\epsilon$ is desirable; when the response time of the optical detection system is slow, the product should be relatively stable.

The thiocyanate dosimeter is not suitable when the dose per pulse is large and/or the detector response time is long, because the product (SCN)₂^{•-} decays in a fast self-reaction, the rate of which increases with increasing dose. For these conditions it is better to use the ferrocyanide dosimeter for high dose and the methylviologen dosimeter for low dose, because the respective products Fe(CN)₆³⁻ and MV^{•+} are stable. The hydrated electron dosimeter is suitable for low doses; it should be used cautiously, since the G value changes with measurement time.

In pulse radiolysis experiments with optical detection, the measured quantity is optical absorbance, so any measured absorbance A can be quantified as a value of $G\epsilon$ with Eq. 67:

$$\frac{(A/V_{DM})}{(A/V_{DM})_{\text{dosimeter}}} = \frac{(G\epsilon)}{(G\epsilon)_{\text{dosimeter}}} \times \frac{\rho_{\text{dosimeter}}}{\rho} \quad (67)$$

where V_{DM} represents the reading of the dose monitor. Because the absorbed dose

Table 8. Chemical dosimeters for pulse radiolysis with optical detection.

Dosimeter	Composition	Monitored species	Monitoring wavelength [nm] and monitoring time ^a	$G\epsilon$ [m ² J ⁻¹]	Ref.
KSCN, thiocyanate	O ₂ -satd. 1×10^{-2} mol dm ⁻³ SCN ⁻	(SCN) ₂ ^{•-}	475, ca. 30 ns	2.6×10^{-4}	119
Fe(CN) ₆ ⁴⁻ , ferrocyanide	O ₂ -satd. 5×10^{-3} mol dm ⁻³ Fe(CN) ₆ ⁴⁻	Fe(CN) ₆ ³⁻	420, ca. 70 ns	3.5×10^{-5}	119
Super-Fricke	O ₂ -satd. 1×10^{-2} mol dm ⁻³ Fe ^{II} in 0.4 mol dm ⁻³ H ₂ SO ₄	FeSO ₄ ⁺	304, 16 s ^{b,c}	3.68×10^{-4}	119
e _{aq} ⁻ , hydrated electron	N ₂ , Ar or He purged 1×10^{-2} mol dm ⁻³ ethanol in 10^{-4} mol dm ⁻³ OH ⁻	e _{aq} ⁻	578, ca. 100 ns ^d 700, ca. 100 ns	3.05×10^{-4} 5.18×10^{-4}	120 120
KI, iodide	O ₂ -satd. 5×10^{-3} mol dm ⁻³ I ⁻	I ₂ ^{•-}	385, ca. 60 ns	3.2×10^{-4}	112
MV ²⁺ , methylviologen	N ₂ O-satd. 0.1 mol dm ⁻³ formate and 5×10^{-4} mol dm ⁻³ MV ²⁺	MV ^{•+}	605, ca. 1 μs	9.66×10^{-4}	118
C(NO ₂) ₄ , TNM, tetranitromethane	Ar purged or N ₂ O-satd. 1×10^{-3} mol dm ⁻³ C(NO ₂) ₄ and 0.2 mol dm ⁻³ 2-propanol at pH 4-5	C(NO ₂) ₃ ⁻	350, ca. 0.7 μs	9.0×10^{-4}	121, 123

^a Time (calculated) at which the formation of the monitored species is complete. ^b Experimental monitoring time. ^c Requires the use of a deuterium lamp. ^d Time at which spur reactions are complete.

depends on the electron density ρ (electrons g^{-1}), corrections should be made for any difference in this quantity between the test solution and the dosimeter by inclusion of the second factor on the right-hand side of Eq. 67. Since absorbance is proportional to the optical path length, it is obvious why dosimetry should be carried out in the cell used for the experiment.

Analyzing light, optical system and monitoring devices

High-pressure xenon arc lamps of various power, from 50 to 1000 W, but mostly 450 W, are the standard light sources for pulse radiolysis with optical detection. The spectrum of this type of lamp satisfactorily covers the region that is usually explored in pulse radiolysis experiments based on the use of photomultipliers and photodiodes as optical detectors. Lamps of this type with quartz or sapphire windows to extend their spectrum in the UV and NIR regions, respectively, are commercially available. Xenon lamps can be pulsed, usually for a few milliseconds, to increase their output by about 100-fold, particularly in the UV region where, in general, the light is most needed and the lamp output is weakest. Xenon lamps are not very stable in the millisecond or higher timescale region because of arc instability. For experiments in this time domain, tungsten-halogen lamps for the visible region [118] and deuterium lamps in the UV region [119] are convenient.

A shutter and cutoff filters are usually placed between the light source and the irradiation cell to minimize photolysis effects. For example, when the MV^{2+} /formate dosimeter is used (see Table 8), it is essential to exclude UV light to prevent photolytic generation of $\text{MV}^{\bullet+}$, which is also the product of this dosimeter system. Similar considerations apply to the ferrocyanide and Fricke dosimeters where photo-oxidation of Fe^{II} to Fe^{III} can occur. Different filters are sometimes mounted on a wheel that can be remotely controlled, possibly by a computer, as it is done for the shutter.

By means of lenses and mirrors, the monitoring light is transported through a hole in the shielding wall from the accelerator room into the control room, and focused onto the entrance slit of a monochromator. Two monochromators and appropriate filters are usually used to minimize the amount of scattered light that could reach the photodetector. The setting of the monochromator(s) and the in/out positioning of the filters can be computer-controlled. The light emerging from the monochromator is transformed by the photodetector (photomultiplier or photodiode) into an electrical signal which, after amplification, is gathered by a transient recorder (oscilloscope or transient digitizer) as a set of voltage-time values which are fed into the computer. In general, a so-called back-off circuit is used, which reduces to zero the large voltage generated by the high level of the continuous analyzing light, and so allows the measurement of small transient or permanent changes in light intensity superimposed on it.

Photomultipliers and photodiodes are used in the UV-Vis and in the NIR-IR regions, respectively. In general, the optical system comprises different interchangeable boxes containing different photomultipliers or photodiodes so that a wide spectral range can be covered. The response time and the sensitivity of a photodetector can be varied by appropriate changes in the electronic circuits; this can generate

“fast, low-sensitivity” and “slow, high-sensitivity” interchangeable boxes. Details on the optical monitoring techniques for transient species [125] and back-off circuits [125, 126] are available in the literature.

The optical detection system is effectively a spectrophotometer and the following should be checked regularly to ensure that it is working correctly:

- 1) The photodetector response should be linear, that is, the output current i of the detector should be proportional to the incident light intensity I ;
- 2) The wavelength settings on the monochromator(s) should be correct;
- 3) The widths of the entrance and exit slits of the monochromator(s), which determine the optical bandwidth ($\pm\delta\lambda$) at a given wavelength λ should be narrow compared to the width of the spectral features. Absorption coefficients of narrow peaks measured with too large slit widths will be too small;
- 4) The response time of the electronics should be much shorter than the time dependence of the chemical species of interest.

In many laboratories, pulse radiolysis has become, similarly to laser flash photolysis, a “one-button” operation [127]. This means that the majority of the experimental parameters are entered into the computer before the command to trigger the pulse is given. Thus, the computer will perform a number of operations such as setting the accelerator and the monochromator(s), inserting the required filters, changing the solution in the irradiation cell, resetting the monitors of the light level, dose, and temperature, triggering the lamp, opening the shutter, triggering the back-off unit and the recorder, and, finally, triggering a pulse from the accelerator. In the case of signal averaging at a fixed wavelength, these operations will be automatically repeated for a predetermined number of times, and it is important for second-order decay kinetics that the dose per pulse is kept constant during the averaging process. For running a spectrum, the initial and the final wavelengths, as well as the wavelength increment and the number of observations at each wavelength, are also entered into the computer. At the end of the experiment, a file or a set of files will be stored in the computer together with any required parameters and other information. From these files, traces representing absorbance versus time (fixed wavelength experiment) or absorption spectra as a function of time (multiwavelength experiment) will be obtained. Examples of traces and a spectrum are shown in Figure 7 and will be discussed in Section 3.10.

The pulse radiolysis setup shown in Figure 3 also represents the situation where emission from a transient species is to be measured. Under these circumstances, the monitoring light beam is unnecessary, but the optical system usually requires some adjustments in order to increase the amount of emitted light that can be transported from the sample cell onto the photodetector. A classic pulse-radiolysis-induced emission experiment is represented by Eq. 62 and is described in Section 3.6.1 (under “General chemistry”). Another example is the observation of luminescence at 1.27 μm from singlet oxygen, $\text{O}_2(^1\Delta_g)$, generated by energy transfer from the triplet excited state of benzene (68) [128]:



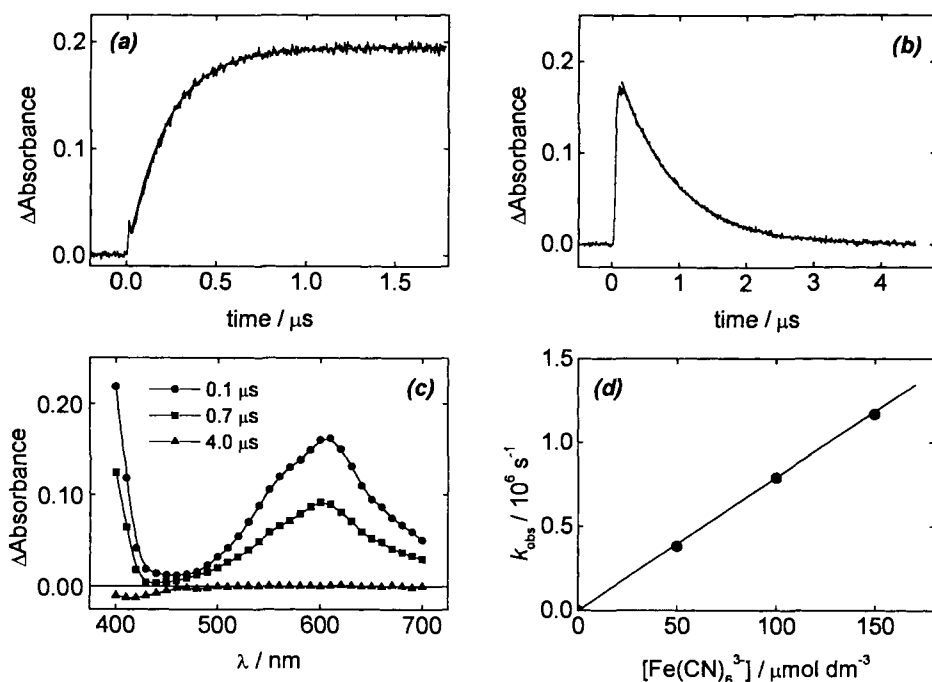


Figure 7. Examples of data obtained by pulse radiolysis with optical detection. a) Formation of $\text{MV}^{\bullet+}$ from the reaction of MV^{2+} with $\text{CO}_2^{\bullet-}$ in N_2O -saturated solution containing $5 \times 10^{-4} \text{ mol dm}^{-3} \text{ MV}^{2+}$ and $0.1 \text{ mol dm}^{-3} \text{ HCO}_2^-$. Conditions: optical path = 2.0 cm, $\lambda_{\text{mon}} = 605 \text{ nm}$, dose = 10 Gy (10-ns pulse). b) Decay of $\text{MV}^{\bullet+}$ obtained in N_2O -saturated solution containing $5 \times 10^{-3} \text{ mol dm}^{-3} \text{ MV}^{2+}$, $0.1 \text{ mol dm}^{-3} \text{ HCO}_2^-$ and $1.5 \times 10^{-4} \text{ mol dm}^{-3} \text{ Fe}(\text{CN})_6^{3-}$. Conditions same as in (a). c) Spectral changes obtained from the pulse irradiation of solution (b). Conditions same as in (a). d) Plot of k_{obs} vs $[\text{Fe}(\text{CN})_6^{3-}]$ for the decay of $\text{MV}^{\bullet+}$ obtained from the pulse radiolysis of N_2O -saturated solutions containing $0.1 \text{ mol dm}^{-3} \text{ HCO}_2^-$ and $5 \times 10^{-3} \text{ mol dm}^{-3} \text{ MV}^{2+}$. Conditions same as in (a).

In this case, a 7-m optic fiber was used for coupling the reaction cell and the photodetector.

Light-scattering measurements

Time-resolved measurements of the intensity of scattered light (Rayleigh or Raman) require the use of a sample cell with optical windows at each end and on one of its sides, together with a monochromatic analyzing light source, which is generally a laser. In the case of Rayleigh scattering, for example, by polymer molecules such as polynucleotides, it is convenient to use the 514.5-nm line from an Ar ion laser [129]. The configuration of the cell is such that the analyzing light beam crosses the sample perpendicularly to the electron beam and the light scattered is monitored at 90° to the laser beam and the electron beam by an optical system analogous to that used

for absorption/emission measurements [129]. A similar cell configuration is used for time-resolved resonance Raman spectroscopy [90, 130]. In this case the analyzing light source is usually a tunable dye laser emitting light at a wavelength within the absorption band of the transient species under examination and the detector is an optical multichannel analyzer (OMA). In each case, kinetic information is obtained from variations in the intensity of the scattered light with time. Furthermore, time-resolved resonance Raman spectroscopy can reveal mechanistic details that are not observable by absorption spectroscopy. For example, it has been shown recently [131] that a direct electron-transfer path occurs in the reaction of $\cdot\text{OH}$ with selected aromatic molecules in aqueous solution, the extent of this pathway, as opposed to addition of $\cdot\text{OH}$ to the benzene ring, being directly related to the ionization potential (IP) of the molecule. If $\text{IP} > 8 \text{ eV}$, addition is the first step, and if $\text{IP} < 7 \text{ eV}$, it is electron transfer, with both processes occurring at intermediate values of IP [131].

Conductivity measurements

The scheme shown in Figure 3 also describes the case in which optical and conductometric detection (see below) are carried out simultaneously. In the most simple arrangement, the sample cell is provided with two parallel electrodes, usually of platinum or glassy carbon which define the volume of solution that is irradiated by the electron beam and interrogated by the monitoring light beam [132]. Except for the electrodes, the cell and the flow system are essentially the same as those used for performing optical measurements. The electrical signals originating from the respective changes in conductivity and absorption, induced by the irradiation of the system, are captured by the transient recorder and fed into the computer. The final result is the generation of two traces, representing the respective time-dependence characteristics of absorbance and conductivity.

There are two conductometric methods, D.C. and A.C. In the D.C. method a constant voltage, typically in the range 100–300 V [124] is applied between the electrodes, and the conductivity is recorded as a function of time. To avoid electrolysis and polarization of the electrodes, the polarity of the applied voltage is usually reversed at a frequency of 10–100 Hz [121]. The D.C. method can be used to cover the time range 10 ns to 100 μs with intrinsic solution conductances of up to $5 \times 10^{-4} \text{ S cm}^{-1}$, that is, the solution should not contain more than about $10^{-3} \text{ mol dm}^{-3}$ of ion pairs. Higher concentrations can be tolerated for shorter time ranges, the limiting factor being baseline drift due to the intrinsic conductance of the solution.

In the A.C. method, two identical cells are used to form two arms of a Wheatstone bridge powered by an A.C. voltage from a high-frequency (10 MHz) generator [122, 133]. Both cells contain the solution to be investigated but only one of them is irradiated, thus creating a voltage difference in the two arms of the bridge, from which the change in conductance can be obtained. The advantage of the A.C. method is that conductance changes can be measured from a few microseconds to infinite time in solutions containing up to $10^{-2} \text{ mol dm}^{-3}$ ion pairs.

Detailed descriptions of state-of-the-art apparatus and experimental procedures can be found in the literature for D.C. [124] and A.C. [133] conductivity detection.

Dosimetry for conductivity detection

The chemical dosimeter used for pulse radiolysis experiments with optical and conductivity detection is the tetranitromethane (TNM) dosimeter (see Table 8). The reduction of TNM by e_{aq}^- and/or $(CH_3)_2\dot{C}OH$ generates in less than 1 μs the stable nitroform ion $C(NO_2)_3^-$, which absorbs at 350 nm (ϵ 1500 $m^2 mol^{-1}$); $G[C(NO_2)_3^-] = 0.60 \pm 0.02 \mu mol J^{-1}$. The conductivity signal arises from the formation of the $C(NO_2)_3^-/H^+$ ion pair for which the molar conductance Λ is 360 and 390 $S cm^2 mol^{-1}$ at 18 and 25 $^\circ C$, respectively [121–124].

Other calibration systems for conductivity measurements that have been described include the following [134–139]:

- 1) N_2O -saturated $1 \times 10^{-2} mol dm^{-3}$ dimethylsulfoxide (DMSO) at pH 4–5 for which $G(H^+) = G(CH_3SO_2^-) = 0.62 \mu mol J^{-1}$ and $\Lambda(H^+/CH_3SO_2^-) = 350 S cm^2 mol^{-1}$ at 18 $^\circ C$ [135].
- 2) O_2 -free $0.1 mol dm^{-3}$ tert-butanol saturated with CH_3Cl at pH 4–5. The conductivity signal is caused by H^+/Cl^- which form with $G = 0.33 \mu mol J^{-1}$ [135].
- 3) $5 \times 10^{-3} mol dm^{-3} CH_2Cl_2$ and $0.2 mol dm^{-3}$ tert-butanol at pH 4.3. The conductance increase is due to the formation of H^+ ($G = 0.28 \mu mol J^{-1}$, $\Lambda = 350 S cm^2 mol^{-1}$) and Cl^- ($G = 0.28 \mu mol J^{-1}$, $\Lambda = 76 S cm^2 mol^{-1}$) [136].
- 4) O_2 -free $2.5 \times 10^{-3} mol dm^{-3}$ acetone, $1 \times 10^{-4} mol dm^{-3} MV^{2+}$, and $0.2 mol dm^{-3}$ tert-butanol at varied pH. The conductance change results from the replacement of MV^{2+} by MV^{+} (which corresponds to $\Lambda = 40 S cm^2 mol^{-1}$) and the formation of one proton in acid solution or the removal of one OH^- ($\Lambda = 200 S cm^2 mol^{-1}$) in basic solution [137].
- 5) $0.1 mol dm^{-3}$ methanol and 0.2 – $0.5 mmol dm^{-3}$ tetranitromethane at pH 4–5 for which $G(H^+) = G(\dot{C}H_2OH) = G(\dot{O}H + H^+) = 0.68 \mu mol J^{-1}$ [138].
- 6) N_2O -saturated $1 \times 10^{-3} mol dm^{-3}$ phenol at pH 11.2 for which $G(OH^-) = 0.62 \mu mol J^{-1}$, assuming a molar conductance for the phenolate ion of $35 S cm^2 mol^{-1}$ [139].

3.8 Other Methods of Detection

3.8.1 Polarography

The principle of this method [140] is to obtain information on electron transfer between the radical and a hanging drop mercury electrode which gives rise to a polarographic current recorded as the change in voltage across a resistor. The electron transfer gives rise to a cathodic (positive) or anodic (negative) current depending on whether the radical is reduced or oxidized as in Eqs. 69 or 70:



In pulse radiolysis experiments the radicals are produced homogeneously in the solution. The polarographic current, i , is determined by the concentration of radicals at the electrode surface, the rate at which they are oxidized or reduced and the rate at which they are replaced by other radicals diffusing to the surface from the bulk solution; account also has to be taken of reactions of the radicals in the bulk solution. By measuring the current, at a fixed time after the pulse, as a function of the potential applied, one can obtain a polarogram which is characteristic of the redox behavior of the radical and so can be used to identify it. Information about the rate of electron transfer can be extracted from measurements of the time dependence of i at a fixed potential. For radicals which undergo self-reaction in the bulk solution, the appropriate relationship is given by Eq. 71, provided the time is shorter than the first half-life of the radical [140],

$$\frac{1}{i_t t^{0.5}} = \frac{\pi^{0.5}}{nFAD^{0.5}c_0} + \frac{2k_2\pi^{0.5}t}{nFAD^{0.5}} \quad (71)$$

where n is the number of electrons transferred, F is the Faraday constant, A is the surface area of the electrode, D is the diffusion coefficient, c_0 is the concentration of radicals at the electrode, and $2k_2$ is the rate constant for the self reaction in the bulk solution.

3.8.2 Microwave Detection

The microwave-detection method has been developed [141] for the study of ionic species and their reactions in nonpolar liquids on a nanosecond timescale, and relies on the fact that microwaves are attenuated in weakly conducting media. It is very useful, for example, for the study of geminate recombination of radical ions in liquid hydrocarbons. It is also more suitable than either optical or D.C. conductivity methods for the study of homogeneous ion recombination processes where problems in data analysis can arise from underlying absorptions and distortion of the kinetics due to separation of the ions, respectively.

Although it is essentially a conductivity technique, the experimental setup is very similar to that used for optical absorption measurements. In simple terms, the attenuation of the amplitude of the microwave resulting from its passage through the irradiated system is measured. Actually, the microwaves are reflected back through the medium by a metal plate at the back of the cell, but because microwaves undergo reflection at any dielectric discontinuity, such as the gas-liquid interface at the front of the cell, interference effects arise due to the coherent nature of the microwave radiation.

The primary information obtained is the transient change in the output voltage of the detector, which occurs when the sample in the cell is made conducting by a pulse of ionizing radiation. The cell is constructed of a length of metal waveguide and can be one of two types: a reflection cell or a resonant-cavity cell. With the reflection cell, microwaves pass from the source through the sample and are reflected from the rear wall of the cell back to the detector. The resonant-cavity cell, on the

other hand, acts effectively as a multiple reflection cell which results in a longer path length through the irradiated medium.

3.8.3 Magnetic Resonance

Electron paramagnetic resonance

An important property of EPR spectroscopy is the detailed information provided by the structure of the spectra so that there is higher degree of certainty of correctly identifying the radicals than is the case with optical spectroscopy. Thus, chemically similar radicals that would be expected to have similar UV absorption spectra have completely different EPR spectra. For example, in its reactions with organic molecules, $\cdot\text{OH}$ can attack at a number of different sites, either to abstract a hydrogen atom from a saturated molecule (see Table 5) or to add to an aromatic ring. Each of the product radicals has a distinctive EPR spectrum, and the relative efficiency with which reaction occurs at each site on the target molecule can be determined from the intensities of the spectra of the various radical products.

Pulse radiolysis allows time-resolved measurements to be made. The radiation pulse is guided through an axial hole in the EPR magnet to generate the radicals directly in a suitable cell located in the EPR cavity. Usually the solution under investigation flows continuously through the cell and optimum sensitivity and time resolution is achieved by repetitive pulsing combined with signal sampling and averaging.

Absorption of microwave radiation occurs when the following resonance condition,

$$h\nu = g_e\mu_B B \quad (72)$$

is fulfilled, where g_e is the magnetogyric ratio, μ_B is the Bohr magneton, and B is the magnetic field strength. Equation 72 applies when the populations of the spin-energy levels conform to the Boltzmann distribution; in time-resolved experiments, however, the transient radicals encounter one another and, depending on their spin states, either react (singlet state) or separate (triplet state), resulting in abnormal line intensities in the EPR spectrum (the equilibrium Boltzmann distribution is not attained). This phenomenon is known as chemically induced dynamic electron polarization or CIDEP.

Two different types of pulsed EPR experiments are possible: a spectrum can be measured at a fixed time after the pulse by variation of the field strength B (Eq. 72), or the time profile of a particular spectral line can be measured at constant B to give kinetic information. One variation of this kinetic method is to detect the recombination of singlet-state radical ion pairs in liquid hydrocarbons by the fluorescence of the product excited state [142]. This technique is known as fluorescence-detected magnetic resonance (FDMR) and provides information on the spin dynamics of the radical ion pair as well as the chemical kinetics.

A second variation, which is extremely useful for measuring rate constants of hydrogen atom reactions in aqueous solution, is the following: immediately after

formation of H^\bullet in the EPR cavity by radiolysis, a $\pi/2$ microwave pulse is applied and the subsequent free induction decay (FID) is recorded [143]. The information extracted from the FID signal includes the rate of scavenging of H^\bullet by the solute and any spin exchange and chemical reactions between H^\bullet and other radicals. These latter processes are second-order in radical concentration and can be minimized by the use of small radiation doses. The FID method, as applied to reactions of the hydrogen atom in water, has distinct advantages over optical detection for the following reasons. First, the absorption spectrum of H^\bullet is in a generally inaccessible region of the UV [56], and secondly, $G(\text{H}^\bullet)$ in neutral water is only $0.062 \mu\text{mol J}^{-1}$, so that the optical signals in any case tend to be rather weak.

Nuclear magnetic resonance

This method has been developed and used at the Argonne National Laboratory [144]. It is used to measure the chemically induced dynamic nuclear polarization (CIDNP) of the products of radical reactions. Because the separations of the energy levels of the nuclear spin states are a thousand times smaller than those of electron spin states, a very homogeneous magnetic field is required to detect them. It is not possible, therefore, to have an axial hole in the NMR magnet to measure the NMR signal directly inside the irradiation cell. Instead, the radicals are generated by irradiation through an axial hole in a small magnet and are then transferred by a fast flow system to the probe of the NMR spectrometer. Although the radicals will have reacted by then, any CIDNP resulting from their reactions will be contained in the products as long as the solution can be transferred to the spectrometer before nuclear spin relaxation occurs. In practice, this means that a transfer time not longer than one or two seconds is required.

3.9 Picosecond Pulse Radiolysis

Although much valuable kinetic and mechanistic information has been obtained by pulse radiolysis with pulses of lengths in the nanosecond to microsecond time range since the technique was invented, it was natural to want to achieve even shorter time resolution, for a) the direct observation of the events taking place in the early stages of radiolysis (10^{-14} – 10^{-10} s), such as electron solvation, ion recombination, spur reactions, and so forth, and b) the measurement of very fast reaction rates (see below).

The first pulse radiolysis system capable of picosecond time resolution (20 ps) was in use by 1968 at the University of Toronto [145] and others were subsequently installed at Notre Dame University, Argonne National Laboratory, Tokyo, Osaka, and Hokkaido Universities, the Hahn–Meitner Institute in Berlin, and the Institute of Chemical Kinetics and Combustion in Novosibirsk. Current developments at Brookhaven [104] and Argonne [146] National Laboratories and Tokyo University [147] are aimed at subpicosecond timescales; a new picosecond facility is also being installed at Orsay [148].

The picosecond system at the University of Toronto was based on an *S*-band linac which produced a single 35-ns pulse containing 100 fine-structure pulses of less than 10 ps spaced 350 ps apart [149]. The analyzing light was the Cerenkov radiation generated when the high-energy (40 MeV) electrons from the accelerator passed through air, and the arrival of this light pulse at the sample was delayed with respect to the electron pulse by travelling a longer distance through an optical delay system; both pulses passed coaxially through the sample cell. The delay could be varied so that the absorption signal produced by each fine structure pulse could be measured at different stages of its formation and decay and so a complete absorbance–time profile could be obtained from a train of fine-structure pulses. This stroboscopic method makes it unnecessary for the optical detector to have a particularly fast response. This system allowed a time resolution of 20 ps within the time window of 20–350 ps between one fine structure pulse and the next. However, uncertainty about the age of a primary product arises when the product does not disappear within this time window.

The stroboscopic pulse radiolysis system described above was modified at Argonne National Laboratory to use a single fine-structure pulse from a 20-MeV L-band linac [150]. This reduced the uncertainty in the age of the primary products to the width of a fine-structure pulse and allowed kinetic measurements to be extended to 3.5 ns. In practice, the time resolution of absorbance measurements was 100 ps.

Improvements in time resolution in the stroboscopic method were achieved at the University of Tokyo by use of a twin linac system in which one accelerator delivers the electron pulse to the sample and the other generates the Cerenkov light pulse used as the analyzing light [151]. Both linacs are driven by the same microwave source and delay between the electron pulse and the light pulse is achieved by phase shifters [151a]. The result is that the time interval between these two pulses is less than 3 ps.

The new accelerator at Brookhaven is based on an RF photocathode gun with one or more resonant cavities in which microwaves create transient electric fields up to 1 MeV cm⁻¹ [104]. A pulse of laser light is used for generating photoelectrons which are accelerated to 9 MeV in a distance of 30 cm. The laser pulse can also be used as the analyzing light source; this means it is closely synchronized with the electron pulse. The time resolution of the electron pulse is therefore that of the laser pulse, so that subpicosecond pulse radiolysis is possible. A similar system is planned at Argonne National Laboratory [146].

With optical detection, the overall time resolution is limited by the different velocities of fast electrons and photons in condensed media; this results in loss of synchronization as the two beams pass through the sample cell. This desynchronization is approximately 10 ps cm⁻¹ in water [145], so the optical path length has to be reduced proportionally to achieve the improved time resolution provided by subpicosecond pulses. There is thus a compromise between having short time resolution (short optical path) and high absorbance signals (long optical path).

One example of fast reaction rates measured with a picosecond system, involving intramolecular electron transfer, has already been described in Section 3.5.5. Another example is the measurement of rate constants of solvated electrons in

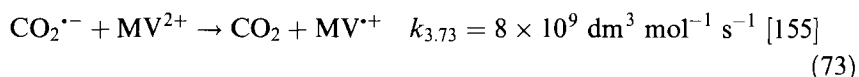
water and alcohols at high concentrations of electron acceptors, S [152]. Under these conditions, the yield of e_s^- at the end of a 20-ps pulse is markedly reduced, with $G(e_s^-) \propto -\ln[S]$. The decrease may partly be due to reaction of the electron before it becomes solvated, and partly due to it becoming solvated within the reaction distance of S so that it does not have to diffuse to react. It was found that there was a good correlation between $[S]_{37}$, the value of [S] that reduces $G(e_s^-)$ to 37 % of its value in the absence of S, with the rate constant $k(e_s^- + S)$ measured at high [S] in water, methanol, and ethanol. However, there was very poor correlation with $k(e_{aq}^- + S)$ measured at low [S] in water [152].

3.10 Data Capture and Analysis

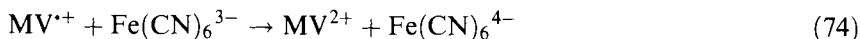
As illustrated by Figure 3, it is standard practice in pulse radiolysis experiments to capture analog signals, for example, from photodetectors or conductivity cells, with transient recorders that output these signals in digital form so that they can be fed into a computer for analysis. Of course, the time resolution of the transient digitizer must be compatible with that of the signal of interest. Once the data have been stored in the computer they can be analyzed, either “on-line” whilst the experiment is being carried out or at a later date. Unless the measurements being made are routine ones, it is good practice to carry out some critical on-line analysis to ascertain whether or not the correct experimental conditions have been chosen so that they can, if necessary, be adjusted before a lot of irrelevant data have been acquired.

The computer software used for data analysis comprises programs that are generally written “in-house” for kinetic and spectral analysis, and are developed according to the needs of the experimenters [127a]. Analytic solutions for simple reaction schemes are available [153]. For analysis of complex kinetics involving several reactions occurring simultaneously and/or sequentially, an algorithm such as FACSIMILE [154] can be used to numerically integrate the specified set of differential equations and so enable the time profile of the reactions to be modeled and compared with that observed experimentally. If all the parameters are known for the chosen reaction set, then the time profile can be simulated and the reaction set adjusted to obtain agreement with experiment. On the other hand, if some of the parameters are unknown, they can then be evaluated in a nonlinear least-squares fitting procedure.

The majority of the data analysis required in pulse radiolysis experiments is quite straightforward; this is exemplified in Figure 7 for the absorbance changes obtained from the pulse radiolysis of N_2O -saturated aqueous solutions containing $0.1 \text{ mol dm}^{-3} \text{ HCO}_2^-$, 5×10^{-4} or $5 \times 10^{-3} \text{ mol dm}^{-3} \text{ MV}^{2+}$, $0\text{--}1.5 \times 10^{-4} \text{ mol dm}^{-3} \text{ Fe(CN)}_6^{3-}$, and ionic strength $\mu = 0.1 \text{ mol dm}^{-3}$. Panel (a) shows $\text{MV}^{\bullet+}$, formed in the reaction shown in Eq. 73, and monitored at 605 nm:



The displayed signal is the average of three oscilloscope traces and the solid line shows the first-order kinetic fit to the data. Under these conditions, $MV^{•+}$ is infinitely stable and the absorbance at the plateau can be used to measure the dose-taking $G\varepsilon(MV^{•+}) = 9.66 \times 10^{-4} \text{ m}^2 \text{ J}^{-1}$ [118]. The small spike at the end of the pulse is real and is due to e_{aq}^- which disappears rapidly upon reaction with N_2O [7a]. Panel (b) shows the decay of $MV^{•+}$ at 605 nm in the presence of $1.5 \times 10^{-4} \text{ mol dm}^{-3} \text{ Fe(CN)}_6^{3-}$ as a result of the reaction shown in Eq. 74:



The displayed signal is the average of five traces and the solid line shows the first-order kinetic fit to the data. Note the rounding off of the signal at short times because of simultaneous occurrence of the reactions of Eqs. 73 and 74. The rate constant for the reduction of ferricyanide by $\text{CO}_2^{•-}$ is $k = 7 \times 10^8 \text{ dm}^3 \text{ mol}^{-1} \text{ s}^{-1}$ at $\mu = 0.1 \text{ mol dm}^{-3}$ [7a] so that, under these conditions, more than 97 % of $\text{CO}_2^{•-}$ reacts with MV^{2+} . Panel (c) shows the spectral changes observed when $[MV^{2+}] = 5 \times 10^{-3} \text{ mol dm}^{-3}$ and $[\text{Fe(CN)}_6^{3-}] = 1.5 \times 10^{-4} \text{ mol dm}^{-3}$ as the reactions in Eqs. 73 and 74 take place. The spectra at 0.1 and 0.7 μs are undoubtedly due to $MV^{•+}$ as it decays (Eq. 74), whilst the spectrum at 4 μs shows an increase of transmission in the region of 420 nm due to the removal of Fe(CN)_6^{3-} (λ_{max} 420 nm, ε_{max} 102 $\text{m}^2 \text{ mol}^{-1}$) [9] by Eq. 74. The absorbances of Fe(CN)_6^{4-} and MV^{2+} are negligible above 400 nm, so that the decay to the baseline in panel (b) is to be expected. Finally, panel (d) shows a plot of k_{obs} for Eq. 74 against $[\text{Fe(CN)}_6^{3-}]$, the slope of which gives $k_{3,74} = (7.8 \pm 0.1) \times 10^9 \text{ dm}^3 \text{ mol}^{-1} \text{ s}^{-1}$ at $\mu = 0.1 \text{ mol dm}^{-3}$. The zero intercept confirms that Eq. 74 accounts for all $MV^{•+}$.

In some cases, it is necessary to establish whether the product(s) originating from the reaction of a given radical with the solute under investigation possesses oxidizing or reducing properties and/or whether the reaction is quantitative or not. This can be done by means of so-called redox indicators, that is, species that, when acting as electron donors or acceptors, generate products that can be easily monitored and quantified. A number of redox indicators and their properties are presented in Table 9. A recent example [156] of this practice is represented by the examination of the redox properties of the product originating from the reaction of 8-bromoguanosine (8-Br-Guo) with e_{aq}^- at $\text{pH} \approx 7$; this substance was unreactive towards MV^{2+} , but generated $\text{TMPD}^{•+}$ from TMPD in nearly quantitative yield. This finding contributed substantially to the definition of the mechanism of reduction of 8-Br-Guo.

3.11 Purification of Materials and Preparation of Solutions

Purity of solvents, solutes and gases is important in pulse radiolysis experiments because very reactive species are generated in micromolar concentrations in solutions that may be saturated with a gas and contain up to molar concentrations of

Table 9. Selected redox indicators for pulse radiolysis studies with optical detection.

Compound	Monitored species	λ_{mon} [nm] (ϵ [$\text{m}^2 \text{mol}^{-1}$])	Redox potential E° (A/A ⁻) [V]
Electron acceptors, A			
C(NO ₂) ₄	C(NO ₂) ₃ ⁻	350 (1460) ^a	>0.16 ^b
Fe(CN) ₆ ³⁻	Fe(CN) ₆ ³⁻ (bleaching)	420 (102) ^c	0.36 ^d
MV ²⁺	MV ^{•+}	606 (1370) ^e 396 (4210) ^e	-0.45 ^f
PNAP	PNAP ^{•-}	545 (290) ^g 350 (1780) ^g	-0.36 ^f
Electron donors, D			
ABTS ²⁻	ABTS ^{•-}	415 (3600) ^h	>0.27 ^b
AH ₂ /AH ⁻ /2 ⁻ⁱ	AH [•] /A ^{-j}	350 (330) ^k	0.30 ^{f,l} 0.015 ^{f,m}
Fe(CN) ₆ ⁴⁻	Fe(CN) ₆ ³⁻	420 (102) ^c	0.36 ^d
PZH ⁺	PZH ^{•2+}	265 (6250) ⁿ 505 (950)	0.86 ^o
TMPD	TMPD ^{•+}	565 (1250) ^p	0.27 ^f

Abbreviations: ABTS²⁻ = 2,2'-azinobis(3-ethylbenzothiazoline-6-sulfonate ion); AH₂ = ascorbic acid; MV²⁺ = 1,1'-dimethyl-4,4'-bipyridinium; PNAP = 4-nitroacetophenone; PZH⁺ = promethazine, conjugate acid; TMPD = *N,N,N',N'*-tetramethyl-*p*-phenylenediamine.

^aRef. [106]. ^bEstimated by the authors. ^cRef. [9]. ^dK.E. Heusler, W.J. Lorenz in *Standard Potentials in Aqueous Solution* (Eds.: A.J. Bard, R. Parsons, J. Jordan), Marcel Dekker, New York, 1985, p. 408. ^eRef. [161]. ^fRef. [66b]. ^gRef. [138]. ^hB.S. Wolfenden, R.L. Willson, *J. Chem. Soc. Perkin Trans. II* **1983**, 805–812. ⁱThe p*K*_a values of ascorbic acid are 4.1 and 11.8 (*Handbook of Chemistry*, 77th edn., CRC Press, Boca Raton, 1996). ^jThe p*K*_a of oxidized ascorbate is -0.4 (G.P. Laroff, R.W. Fessenden, R.H. Schuler, *J. Am. Chem. Soc.* **1972**, *94*, 9062–9073). ^kR.H. Schuler, *Radiat. Res.* **1977**, *69*, 417–433. ^lAt pH 7. ^mAt pH 13.5. ⁿD. Bahnemann, K.-D. Asmus, R.L. Willson, *J. Chem. Soc. Perkin Trans. II* **1983**, 1661–1668. ^oD. Bahnemann, K.-D. Asmus, R.L. Willson, *J. Chem. Soc. Perkin Trans. II* **1983**, 1669–1673. ^pS. Fujita, S. Steenken, *J. Am. Chem. Soc.* **1981**, *103*, 240–2545.

scavengers, acid, alkali, buffers to control pH, and neutral salts to control ionic strength. Most commercially available gases and chemicals solutes are of sufficient quality that they can, in many cases, be used without further purification. It is important, however, to vary the concentrations of these solutes, either a) to confirm that the reactions of interest are not affected by adventitious impurities, or b) to quantify these effects so that appropriate corrections can be made. If, for example, the additive (scavenger, buffer, etc.) is 99.5 % pure, the amount of X, where X represents a generic impurity, introduced into the system could reach levels as high as millimolar, that is, comparable to, or even higher than the concentration of the solute S under investigation.

3.11.1 Purification of Solvents

The principal method of purifying solvents is by distillation under conditions where oxidizable and reducible impurities are removed. Of course, the purified solvent should not then be exposed to a polluted atmosphere or contaminated glassware; organic solvents are generally kept in an inert atmosphere after purification. One commonly used test for solvent purity is to measure the lifetime of the solvated electron in it following a small pulse of radiation. For example, the lifetime of e_s^- in the solvent system should be significantly longer than in the solution in which its reaction rate is being measured, and this condition determines the necessary level of purity. Thus, less pure solvents can be tolerated, for example, in picosecond pulse radiolysis where timescales are short compared to the time of reaction with the impurity.

Water

Nowadays water is generally purified by means of commercially available purification systems and this is adequate for most work in radiation chemistry. Previously, it was common practice to carry out triple distillation, in which distilled water was redistilled successively from alkaline permanganate and acidic dichromate solutions; in some laboratories the steam was passed through a silica tube heated to 800 °C before being condensed [157].

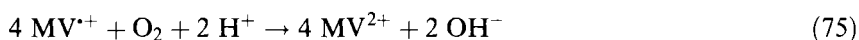
Nonaqueous solvents

Here the purpose of purification is to remove water as well as other impurities. In general, the degree of purity required depends on the conditions of the experiment; thus, the most stringent purification procedures should be adopted when radiation effects are measured in the solvent alone, but these precautions may not be necessary when solutes are to be added. The various methods for purification of these solvents are illustrated by the following specific examples taken from the literature.

- 1) Alcohols were refluxed over sodium metal and NaBH_4 , fractionally distilled and stored under argon [11a, 158]. Alternatively, they were refluxed with 2,4-dinitrophenylhydrazine and H_2SO_4 for 15 h and then distilled twice under argon [12b].
- 2) Acetonitrile was passed through a 2-m column of type-H activated alumina, refluxed for 48 h, and then fractionally distilled [21b].
- 3) Acetone was distilled from KMnO_4 and dried over molecular sieves [19].
- 4) Chlorinated hydrocarbons were washed successively with concentrated H_2SO_4 and KOH followed by distilled water, dried over barium oxide and passed through a column of alumina [26, 27].
- 5) Cyclohexane was passed through a 1-m column of activated silica gel and stored under argon [32]. Alternatively, it was bubbled with argon, shaken first with concentrated H_2SO_4 , then with KOH pellets and finally stirred over Na/K alloy under vacuum for several days [159].
- 6) Ammonia was treated with Na/K alloy and then distilled under vacuum [73].

Gases

The purity of commercially available gases is such that most can be used straight from the cylinder, but where it is essential to remove O_2 , for example, from N_2O , this can be done by passing the gas through a column of Cr^{2+} solution [160] or one of the commercially available gas purifiers. Even then it is important to know whether a solution that is required to be free of oxygen really is that. An easy test, which permits the amount of oxygen that is left in the solution after the purging procedure to be quantified, is performed by pulsing of an N_2O -saturated or any inert gas purged solution containing $5 \times 10^{-4} \text{ mol dm}^{-3} MV^{2+}$ and $0.1 \text{ mol dm}^{-3} HCO_2^-$ and then measuring the loss of the resulting MV^{+} radical cation. In the presence of micromolar amounts of O_2 , a decay of MV^{+} is observed in the millisecond time frame. If it is assumed that O_2 is the only species that reacts with MV^{+} , then the concentration of O_2 left in the solution can be calculated from the following stoichiometric equation:



The amount of MV^{+} that is destroyed can be easily calculated from ΔOD at 605 nm, the optical path of the cell, and the extinction coefficient of MV^{+} , $\epsilon_{605} = 1.37 \times 10^3 \text{ m}^2 \text{ mol}^{-1}$ [161].

3.12 Concluding Remarks

In the context of electron-transfer reactions, the contribution to the body of knowledge on the kinetics and mechanisms of these processes from pulse radiolysis studies is very significant. As has been shown above and elsewhere (see the list of "Further Reading"), pulse radiolysis is particularly well suited to the study of fast electron-transfer reactions involving free radicals and metal ions in unusual oxidation states.

Because of the high cost of setting up new pulse-radiolysis facilities, there is a need for the existing facilities to be made more available to the wider chemistry community through expanded collaboration with radiation chemists who have access to them. There is also a need to increase the awareness of the wider chemistry community of the achievements and potential of radiation-chemical methods in general chemistry; such awareness is likely to develop only by the introduction of radiation chemistry into the chemistry curriculum in higher education.

References

1. A. Chatterjee in *Radiation Chemistry: Principles and Applications* (Eds.: Farhataziz, M.A.J. Rodgers), VCH, Weinheim, **1987**, pp. 1–28.
2. F.W. Lampe, F.H. Field, J.L. Franklin, *J. Am. Chem. Soc.* **1957**, 79, 6132–6135.

3. J.M. Wiesenfeld, E.P. Ippen, *Chem. Phys. Lett.* **1980**, 73, 47–50.
4. G.V. Buxton in *Radiation Chemistry: Principles and Applications* (Eds.: Farhataziz, M.A.J. Rodgers), VCH, Weinheim, **1987**, pp. 321–349.
5. (a) S.M. Pimblott, J.A. LaVerne, *J. Phys. Chem. A* **1997**, 101, 5828–5838; (b) D. Swiatla-Wojcik, G.V. Buxton, *J. Phys. Chem.* **1995**, 99, 11464–11471.
6. E.J. Hart, M. Anbar, *The Hydrated Electron*, Wiley Interscience, New York, **1970**, pp. 170–191.
7. (a) A.B. Ross, W.G. Mallard, W.P. Helman, G.V. Buxton, R.E. Huie, P. Neta, *NDRL-NIST Solution Kinetics Database, Ver. 3*, Notre Dame Radiation Laboratory, Notre Dame, IN and National Institute of Standards and Technology, Gaithersburg, MD, **1998**; (b) G.V. Buxton, C.L. Greenstock, W.P. Helman, A.B. Ross, *J. Phys. Chem. Ref. Data* **1988**, 17, 513–886.
8. D. Meyerstein, *J. Chem. Soc. Faraday Disc.* **1977**, 63, 203–204.
9. R.H. Schuler, A.L. Hartzell, B. Behar, *J. Phys. Chem.* **1981**, 85, 192–199.
10. A.J. Swallow in *Radiation Chemistry: Principles and Applications* (Eds.: Farhataziz, M.A.J. Rodgers), VCH, Weinheim, **1987**, pp. 351–375.
11. (a) Q.G. Mulazzani, P.G. Fuochi, G. Pilloni, E. Vecchi, *Radiat. Phys. Chem.* **1977**, 10, 275–282; (b) P.G. Fuochi, Q.G. Mulazzani, G. Pilloni, G. Zotti, *J. Phys. Chem.* **1980**, 84, 2985–2989; (c) P.G. Fuochi, Q.G. Mulazzani, G. Pilloni, G. Zotti, *Inorg. Chim. Acta* **1983**, 68, 195–200.
12. (a) J. Mayer, R. Krasiukianis, *Radiat. Phys. Chem.* **1990**, 36, 169–173; (b) J. Mayer, R. Krasiukianis, *Radiat. Phys. Chem.* **1991**, 37, 273–278.
13. D.H. Ellison, G.A. Salmon, F. Wilkinson, *Proc. R. Soc. Lond. A* **1972**, 328, 23–36.
14. K.M. Bansal, R.W. Fessenden, *J. Phys. Chem.* **1976**, 80, 1743–1745.
15. D.W. Johnson, G.A. Salmon, *J. Chem. Soc. Faraday Trans. 1* **1977**, 73, 2031–2035.
16. S. Arai, L.M. Dorfman, *Adv. Chem. Ser.* **1968**, 82, 378–386.
17. (a) R.A. Marcus, *J. Chem. Phys.* **1956**, 24, 966–978; (b) R.A. Marcus, *Discuss. Faraday Soc.* **1960**, 29, 21–31.
18. D.M. Guldi, H. Hungerbühler, E. Janata, K.-D. Asmus, *J. Chem. Soc., Chem. Commun.* **1993**, 84–86.
19. M.A.J. Rodgers, *Trans. Faraday Soc.* **1971**, 61, 1029–1040.
20. R.K. Broszkiewicz, E. Kozłowska-Millner, A. Blum, *J. Phys. Chem.* **1981**, 85, 2258–2262.
21. (a) J.L. Baptista, H.D. Burrows, *J. Chem. Soc. Faraday Trans. 1* **1974**, 70, 2066–2079; (b) I.P. Bell, M.A.J. Rodgers, H.D. Burrows, *J. Chem. Soc. Faraday Trans. 1* **1977**, 73, 315–326.
22. A. Singh, H.D. Gesser, A.R. Scott, *Chem. Phys. Lett.* **1968**, 2, 271–273.
23. T. Imamura, T. Sumiyoshi, K. Takahashi, Y. Sasaki, *J. Phys. Chem.* **1993**, 97, 7786–7791.
24. A.-M. Koulkes-Pujo, B. Le Motais, L.G. Hubert-Pfalzgraf, *J. Chem. Soc. Dalton Trans.* **1986**, 1741–1742.
25. B. Le Motais, A.-M. Koulkes-Pujo, L.G. Hubert-Pfalzgraf, *Radiat. Phys. Chem.* **1987**, 29, 21–24.
26. S. Arai, H. Ueda, R.F. Firestone, L.M. Dorfman, *J. Chem. Phys.* **1969**, 50, 1072–1077.
27. J. Grodkowski, P. Neta, *J. Phys. Chem.* **1984**, 88, 1205–1209.
28. J. Grodkowski, J.H. Chambers, Jr., P. Neta, *J. Phys. Chem.* **1984**, 88, 5332–5333.
29. P. Neta, V. Grebel, H. Levanon, *J. Phys. Chem.* **1981**, 85, 2117–2119.
30. D.M. Guldi, K.-D. Asmus, *J. Am. Chem. Soc.* **1997**, 119, 5744–5745.
31. J.R. Miller, L.T. Calcaterra, G.L. Closs, *J. Am. Chem. Soc.* **1984**, 106, 3047–3049.
32. L. Flamigni, *Radiat. Phys. Chem.* **1979**, 13, 133–138.
33. M. Kumar, P. Neta, *J. Phys. Chem.* **1992**, 96, 3350–3354.
34. N.V. Klassen in *Radiation Chemistry: Principles and Applications* (Eds.: Farhataziz, M.A.J. Rodgers), VCH, Weinheim, **1987**, p. 35, and references therein.
35. J. Belloni, P. Cordier, J. Delaire, *Chem. Phys. Lett.* **1974**, 27, 241–244.
36. (a) J. Belloni, F. Billiau, P. Cordier, J.A. Delaire, M.O. Delcourt, *J. Phys. Chem.* **1978**, 82, 532–536; (b) J. Belloni, P. Cordier, J.A. Delaire, M.O. Delcourt, *J. Phys. Chem.* **1978**, 82, 537–539.
37. Farhataziz, L.M. Perkey, *J. Phys. Chem.* **1975**, 79, 1651–1654.
38. L.M. Perkey, Farhataziz, *Int. J. Radiat. Phys. Chem.* **1975**, 7, 719–730.
39. Farhataziz, L.M. Perkey, *J. Phys. Chem.* **1976**, 80, 122–126.

40. Farhataziz, P. Cordier, L.M. Perkey, *Radiat. Res.* **1976**, *68*, 23–30.
41. Farhataziz, P. Cordier, *J. Phys. Chem.* **1976**, *80*, 2635–2641.
42. P.V. Kamat, G. Sauvé, D.M. Guldi, K.-D. Asmus, *Res. Chem. Intermed.* **1997**, *23*, 575–585.
43. D. Brault, P. Neta, *J. Phys. Chem.* **1983**, *87*, 3320–3327.
44. G. Porter, *Proc. R. Soc. A* **1950**, *200*, 284–300.
45. R.L. McCarthy, A. MacLachlan, *Trans. Farad. Soc.* **1960**, *56*, 1187–1200.
46. M.S. Matheson, L.M. Dorfman, *J. Chem. Phys.* **1960**, *32*, 1870–1871.
47. (a) J.P. Keene, *Nature*, **1960**, *188*, 843–844; (b) C.W. Gilbert, J.P. Keene, P.F. Browne, T.J. Davy, *British Empire Cancer Campaign Report* **1960**, *38*, Part II, 498–499.
48. R.E. Steel, J.W. Boag, *British Empire Cancer Campaign Report* **1960**, *38*, Part II, 251–253.
49. J.W. Boag in *Early Developments in Radiation Chemistry* (Ed.: J. Kroh), Royal Society of Chemistry, Cambridge, **1989**, pp. 7–20.
50. J.P. Keene in *Pulse Radiolysis* (Eds.: M. Ebert, J.P. Keene, A.J. Swallow, J.H. Baxendale), Academic Press, London, **1965**, pp. 1–14.
51. G. Porter, M.W. Windsor, *Nature* **1957**, *180*, 187–188.
52. J.W.T. Spinks, R.J. Woods, *An Introduction to Radiation Chemistry*, 3rd edn., Wiley, New York, **1990**, pp. 97–101.
53. (a) R.L. McCarthy, A. MacLachlan, *J. Chem. Phys.* **1961**, *35*, 1625–1627; (b) R.L. McCarthy, A. MacLachlan, *Trans. Faraday Soc.* **1961**, *57*, 1107–1116; (c) A. MacLachlan, R.L. McCarthy, *J. Am. Chem. Soc.* **1962**, *84*, 2519–2524.
54. L.M. Dorfman, I.A. Taub, R.E. Bühler, *J. Chem. Phys.* **1962**, *36*, 3051–3061.
55. I.A. Taub, L.M. Dorfman, *J. Am. Chem. Soc.* **1962**, *84*, 4053–4059.
56. G.L. Hug, *Nat. Stand. Ref. Data Ser., Nat. Bur. Stand. (US)* **1981**, *69*, 1–159.
57. (a) E.J. Hart, J.W. Boag, *J. Am. Chem. Soc.* **1962**, *84*, 4090–4095; (b) J.W. Boag, E.J. Hart, *Nature* **1963**, *197*, 45–47.
58. J.P. Keene, *Nature* **1963**, *197*, 47–48.
59. S. Gordon, E.J. Hart, M.S. Matheson, J. Rabani, J.K. Thomas, *J. Am. Chem. Soc.* **1963**, *85*, 1375–1377.
60. G.V. Buxton in *General Aspects of the Chemistry of Radicals* (Ed.: Z.B. Alfassi), Wiley, Chichester, **1999**, pp. 51–77.
61. J. Rabani, M.S. Matheson, *J. Am. Chem. Soc.* **1964**, *86*, 3175–3176.
62. G.E. Adams, J.W. Boag, B.D. Michael, *Trans. Faraday Soc.* **1965**, *61*, 1417–1424.
63. J.K. Thomas, *Trans. Faraday Soc.* **1965**, *61*, 702–707.
64. J.H. Baxendale, J.P. Keene, D.A. Stott in *Pulse Radiolysis* (Eds.: M. Ebert, J.P. Keene, A.J. Swallow, J.H. Baxendale), Academic Press, London, **1965**, pp. 107–115.
65. J.H. Baxendale, J.P. Keene, D.A. Stott, *Chem. Commun.* **1966**, 715–716.
66. (a) D.M. Stanbury, *Adv. Inorg. Chem.* **1989**, *33*, 69–138; (b) P. Wardman, *J. Phys. Chem. Ref. Data* **1989**, *14*, 1637–1755; (c) S. Steenken, *Landolt-Börnstein* **1985**, *13e*, 147–293.
67. G.E. Adams, B.D. Michael, J.T. Richards, *Nature* **1967**, *215*, 1248–1250.
68. G.E. Adams, R.L. Willson, *J. Chem. Soc. Faraday Trans. 1* **1973**, *69*, 719–729.
69. K.B. Patel, R.L. Willson, *J. Chem. Soc. Faraday Trans. 1* **1973**, *69*, 814–825.
70. M. Mostafavi, J.L. Marignier, J. Amblard, J. Belloni, *Radiat. Phys. Chem.* **1989**, *34*, 605–617.
71. M.S. Matheson, J. Rabani, *J. Phys. Chem.* **1965**, *69*, 1324–1335.
72. R.R. Hentz, Farhataziz, E.M. Hansen, *J. Chem. Phys.* **1971**, *55*, 4974–4979.
73. Farhataziz, L.M. Perkey, R.R. Hentz, *J. Chem. Phys.* **1974**, *60*, 4383–4389.
74. B.D. Michael, E.J. Hart, K.H. Schmidt, *J. Phys. Chem.* **1971**, *75*, 2798–2805.
75. H. Christensen, K. Sehested, *Radiat. Phys. Chem.* **1981**, *18*, 723–731.
76. R.M. Noyes in *Progress in Reaction Kinetics, Vol. 1* (Ed.: G. Porter), Pergamon, London, **1961**, p. 129.
77. A.J. Elliot, D.R. McCracken, G.V. Buxton, N.D. Wood, *J. Chem. Soc. Faraday Trans.* **1990**, *86*, 1539–1547.
78. G.V. Buxton, S.R. Mackenzie, *J. Chem. Soc. Faraday Trans.* **1992**, *88*, 2833–2836.
79. L. Ashton, G.V. Buxton, C.R. Stuart, *J. Chem. Soc. Faraday Trans.* **1995**, *91*, 1631–1633.
80. J.E. Martin, E.J. Hart, A.W. Adamson, H. Gafney, J. Halpern, *J. Am. Chem. Soc.* **1972**, *94*, 9238–9240.
81. M.Z. Hoffman, M. Simic, *J. Am. Chem. Soc.* **1970**, *92*, 5533–5534.

82. M.Z. Hoffman, M. Simic, *J. Am. Chem. Soc.* **1972**, *94*, 1757–1759.
83. E.P.L. Hunter, M.G. Simic, B.D. Michael, *Rev. Sci. Instrum.* **1985**, *56*, 2199–2204.
84. K.H. Schmidt, S. Gordon, W.A. Mulac, *Rev. Sci. Instrum.* **1976**, *47*, 356–357.
85. G.L. Hug, Y. Wang, C. Schöneich, P.-Y. Jiang, R.W. Fessenden, *Radiat. Phys. Chem.* **1999**, *54*, 559–566.
86. B. Smaller, J.R. Remko, E.C. Avery, *J. Chem. Phys.* **1968**, *48*, 5174–5181.
87. A.D. Trifunac, K.W. Johnson, R.H. Lowers, *J. Am. Chem. Soc.* **1976**, *98*, 6067–6068.
88. J. Lilie, G. Beck, A. Henglein, *Ber. Bunsenges. Phys. Chem.* **1971**, *75*, 458–465.
89. G. Beck, J. Kiwi, D. Lindenau, W. Schnabel, *Eur. Polym. J.* **1974**, *10*, 1069–1075.
90. P. Pagsberg, R. Wilbrandt, K.B. Hansen, K.V. Weisberg, *Chem. Phys. Lett.* **1976**, *39*, 538–541.
91. J.M. Warman, M.P. De Haas, A. Hummel, *Chem. Phys. Lett.* **1973**, *22*, 480–483.
92. M.S. Matheson, L.M. Dorfman, *Pulse Radiolysis*, MIT Press, Cambridge, MA, **1969**.
93. J. Butler, B.W. Hodgson, B.M. Hoey, E.J. Land, J.S. Lea, E.J. Lindley, F.A.P. Rushton, A.J. Swallow, *Radiat. Phys. Chem.* **1989**, *34*, 633–646.
94. A. Hutton, G. Roffi, A. Martelli, *Quaderni dell'Area di Ricerca dell'Emilia Romagna* **1974**, *5*, 67–74.
95. C.D. Jonah in *Report of the Workshop on the Proposed Pulse Radiolysis Facility at Brookhaven National Laboratory*, BNL Formal Report BNL-52229, **1989**, pp. 37–41.
96. Z. Zimek, *Radiat. Phys. Chem.* **1990**, *36*, 81–83.
97. P.G. Fuochi, *Radiat. Phys. Chem.* **1994**, *44*, 431–440.
98. A.D. Trifunac in *Report of the Workshop on the Proposed Pulse Radiolysis Facility at Brookhaven National Laboratory*, BNL Formal Report BNL-52229, **1989**, pp. 32–36.
99. M.C. Sauer, Jr. in *The Study of Fast Processes and Transient Species by Electron Pulse Radiolysis* (Eds.: J.H. Baxendale, F. Busi), Reidel, Dordrecht, **1982**, pp. 35–47.
100. L.K. Patterson in *Radiation Chemistry: Principles and Applications* (Eds.: Farhatziz, M.A.J. Rodgers), VCH, Weinheim, **1987**, pp. 65–96.
101. J.F. Wishart in *Photochemistry and Radiation Chemistry: Complementary Methods for the Study of Electron Transfer* (Eds.: J.F. Wishart, D.G. Nocera), *Adv. Chem. Ser.* **254**, American Chemical Society, Washington, DC, **1998**, pp. 35–50.
102. S.D. Yao, S.G. Sheng, J.H. Cai, J.S. Zhang, N.Y. Lin, *Radiat. Phys. Chem.* **1995**, *46*, 105–109.
103. K. Witham, S. Lyons, R. Miller, D. Nett, P. Treas, A. Zante, R.W. Fessenden, M.D. Thomas, Y. Wang, *Proc. of '95 Particle Accelerator Conference and International Conference on High Energy Accelerators*, Dallas, TX, May 1–5, **1995**.
104. J.F. Wishart, *Houshasenkagaku (Biannual Journal of Japanese Society of Radiation Chemistry)* **1998**, *66*, 63–64.
105. A.M. Hutton, G. Roffi, G. Semerano, M.D. Ward, *Quaderni dell'Area di Ricerca dell'Emilia Romagna* **1972**, *3*, 61–85.
106. J. Rabani, W.A. Mulac, M.S. Matheson, *J. Phys. Chem.* **1965**, *69*, 53–70.
107. J. Delaire, P. Cordier, J. Belloni, F. Billiau, M.O. Delcourt, *J. Phys. Chem.* **1976**, *80*, 1687–1690.
108. J.K. Thomas, S. Gordon, E.J. Hart, *J. Phys. Chem.* **1964**, *68*, 1524–1527.
109. G. Czapski, S.V. Lymar, H.A. Schwarz, *J. Phys. Chem. A* **1999**, *103*, 3447–3450.
110. E. Kozłowska-Milner, R. Broszkiewicz, J. Stanikowski, *Radiochem. Radioanal. Lett.* **1975**, *22*, 269–273.
111. P. Wardman, *J. Phys. E: Sci. Instrum.* **1972**, *5*, 17–18.
112. G.V. Buxton, N.D. Wood, S. Dyster, *J. Chem. Soc. Faraday Trans. 1* **1988**, *84*, 1113–1121.
113. J.F. Wishart, R. van Eldik, *Rev. Sci. Instrum.* **1992**, *63*, 3224–3225.
114. (a) Q.G. Mulazzani, S. Emmi, M.Z. Hoffman, M. Venturi, *J. Am. Chem. Soc.* **1981**, *103*, 3362–3370; (b) Q.G. Mulazzani, M. D'Angelantonio, M. Venturi, M.-L. Boillot, J.-C. Chambron, E. Amouyal, *New J. Chem.* **1989**, *13*, 441–447.
115. B.H.J. Bielski, H.W. Richter, *J. Am. Chem. Soc.* **1977**, *99*, 3019–3023.
116. Z. Zimek, J. Grodkowski, *Proc. Tihany Symp. Radiat. Chem.* **1986**, *6*, 719–724.
117. G.E. Adams, J.W. Boag, B.D. Michael, *Trans. Faraday Soc.* **1965**, *61*, 492–505.
118. C.A. Kelly, E.L. Blinn, N. Camaioni, M. D'Angelantonio, Q.G. Mulazzani, *Inorg. Chem.* **1999**, *38*, 1579–1584.

119. G.V. Buxton, C.R. Stuart, *J. Chem. Soc. Faraday Trans.* **1995**, 91, 279–281.
120. E.J. Hart, E.M. Fielden in *Manual on Radiation Dosimetry* (Eds.: N.W. Holm, R.J. Berry), Marcel Dekker, New York, **1970**, pp. 331–335.
121. K.-D. Asmus, *Int. J. Radiat. Phys. Chem.* **1972**, 4, 417–438.
122. M. Kelm, J. Lilie, A. Henglein, E. Janata, *J. Phys. Chem.* **1974**, 78, 882–887.
123. K.-D. Asmus, E. Janata in *The Study of Fast Processes and Transient Species by Electron Pulse Radiolysis* (Eds.: J.H. Baxendale, F. Busi), Reidel, Dordrecht, **1982**, pp. 91–113.
124. B. Vojnovic, R.F. Anderson, B.D. Michael, *Radiat. Phys. Chem.* **1986**, 27, 363–373.
125. G. Roffi in *The Study of Fast Processes and Transient Species by Electron Pulse Radiolysis* (Eds.: J.H. Baxendale, F. Busi), Reidel, Dordrecht, **1982**, pp. 63–89.
126. E. Janata, *Rev. Sci. Instrum.* **1986**, 57, 273–275.
127. (a) D.C. Foyt, *Comput. Chem.* **1981**, 5, 49–54, and references therein; (b) E. Janata, *Radiat. Phys. Chem.* **1992**, 40, 437–443, and references therein; (c) E. Janata, *Radiat. Phys. Chem.* **1994**, 44, 449–454, and references therein.
128. A.A. Gorman, I. Hamblett, E.J. Land, *J. Am. Chem. Soc.* **1989**, 111, 1876–1877.
129. G.D.D. Jones, P.O'Neill, *Int. J. Radiat. Biol.* **1990**, 57, 1123–1139.
130. (a) R.F. Dallinger, S. Farquharson, W.H. Woodruff, M.A.J. Rodgers, *J. Am. Chem. Soc.* **1981**, 103, 7433–7440; (b) P.C. Lee, K. Schmidt, S. Gordon, D. Meisel, *Chem. Phys. Lett.* **1981**, 80, 242–247.
131. G.N.R. Tripathi, *J. Am. Chem. Soc.* **1998**, 120, 4161–4166.
132. K.-D. Asmus, G. Beck, A. Henglein, A. Wigger, *Ber. Bunsenges. Phys. Chem.* **1966**, 70, 869–874.
133. E. Janata, J. Lilie, M. Martin, *Radiat. Phys. Chem.* **1994**, 4, 353–356.
134. M.N. Schuchmann, E. Bothe, J. von Sonntag, C. von Sonntag, *J. Chem. Soc. Perkin Trans. 2* **1998**, 791–796, and references therein.
135. S. Steenken, J. Buschek, R.A. McClelland, *J. Am. Chem. Soc.* **1986**, 108, 2808–2813, and references therein.
136. L.P. Candias, P. Wolf, P. O'Neill, S. Steenken, *J. Phys. Chem.* **1992**, 96, 10302–10307.
137. L.P. Candias, S. Steenken, *J. Phys. Chem.* **1992**, 96, 937–944.
138. V. Jagannadham, S. Steenken, *J. Am. Chem. Soc.* **1984**, 106, 6452–6551.
139. A.J.S.C. Vieira, S. Steenken, *J. Am. Chem. Soc.* **1987**, 109, 7441–7448.
140. K.-D. Asmus, E. Janata in *The Study of Fast Processes and Transient Species by Electron Pulse Radiolysis* (Eds.: J.H. Baxendale, F. Busi), Reidel, Dordrecht, **1982**, pp. 115–128.
141. J. M. Warman in *The Study of Fast Processes and Transient Species by Electron Pulse Radiolysis* (Eds.: J.H. Baxendale, F. Busi), Reidel, Dordrecht, **1982**, pp. 129–161.
142. A.D. Trifunac, J. P. Smith in *The Study of Fast Processes and Transient Species by Electron Pulse Radiolysis* (Eds.: J.H. Baxendale, F. Busi), Reidel, Dordrecht, **1982**, pp. 179–187.
143. P. Han, D.M. Bartels, *Chem. Phys. Lett.* **1989**, 159, 538–542.
144. A.D. Trifunac in *The Study of Fast Processes and Transient Species by Electron Pulse Radiolysis* (Eds.: J.H. Baxendale, F. Busi), Reidel, Dordrecht, **1982**, pp. 163–178.
145. M.J. Bronskill, J.W. Hunt, *J. Phys. Chem.* **1968**, 72, 3762–3766.
146. C.D. Jonah, A.D. Trifunac, *Cahiers de Radiobiologie* **1998**, 8, 20–24.
147. T. Kozawa, T. Kobayashi, T. Ueda, M. Uesaka, *Nucl. Instrum. Methods Phys. Res.* **1997**, A 399, 180–184.
148. J. Belloni, J.-L. Marignier, M. Gaillard, *Cahiers de Radiobiologie* **1998**, 8, 25–28.
149. M.J. Bronskill, W.B. Taylor, R.K. Wolff, J.W. Hunt, *Rev. Sci. Instrum.* **1970**, 41, 333–340.
150. C.D. Jonah, *Rev. Sci. Instrum.* **1975**, 46, 62–66.
151. (a) H. Kobayashi, Y. Tabata, *Nucl. Instrum. Methods Phys. Res.* **1985**, B10/11, 1004–1006; (b) Y. Tabata, H. Kobayashi, M. Washio, S. Tagawa, Y. Yoshida, *Radiat. Phys. Chem.* **1985**, 26, 473–479.
152. J.W. Hunt in *Advances in Radiation Chemistry*, Vol. 5 (Eds.: M. Burton, J.L. Magee), Wiley, New York, **1976**, pp. 185–315, and references therein.
153. C. Capellos, B.H.J. Bielski, *Kinetic Systems: Mathematical Description of Chemical Kinetics in Solution*, Wiley, New York, **1972**.
154. A.R. Curtis, W.P. Sweetenham, *FACSIMILE/CHEKMAT Users' Manual*, AERE R 12805, UKAEA, Harwell, **1988**.

155. Q.G. Mulazzani, M. D'Angelantonio, M. Venturi, M.Z. Hoffman, M.A.J. Rodgers, *J. Phys. Chem.* **1986**, 90, 5347–5352.
156. M. Ioele, R. Bazzanini, C. Chatgililoglu, Q.G. Mulazzani, *J. Am. Chem. Soc.* **2000**, 122, 1900–1907.
157. E.J. Hart, *J. Am. Chem. Soc.* **1951**, 73, 68–73.
158. J.H. Baxendale, P. Wardman, *J. Chem. Soc. Faraday Trans. 1* **1973**, 69, 584–594.
159. N. Gee, G.R. Freeman, *J. Chem. Phys.* **1992**, 96, 586–592.
160. K.-D. Asmus, H. Möckel, A. Henglein, *J. Phys. Chem.* **1973**, 77, 1218–1221.
161. T. Watanabe, K. Honda, *J. Phys. Chem.* **1982**, 86, 2617–2619.

Further Reading

In addition to the references cited above, the following publications also contain descriptions of various aspects of pulse radiolysis and/or its applications.

- “Pulse Radiolysis: Experimental Features”. S. Karolczak in *Properties and Reactions of Radiation Induced Transients: Selected Topics* (Ed.: J. Mayer), Polish Scientific Publishers PWN, Warsaw, **1999**, pp. 11–37.
- “Pulse Radiolysis”. J. Butler, E.J. Land in *Free Radicals: A Practical Approach* (Eds.: N.A. Punchard, F.J. Kelly), Oxford University Press, Oxford, **1996**, pp. 47–61.
- “Pulse Radiolysis”. C. von Sonntag, H.-P. Schuchmann, *Methods Enzymol.* **1994**, 233, 3–20.
- “Pulse Radiolysis”. G.A. Salmon, A.G. Sykes, *Methods Enzymol.* **1993**, 227, 522–534.
- “Pulsed Radiation Techniques: Flash Photolysis and Pulse Radiolysis”. R.V. Bensasson, E.J. Land, T.G. Truscott, *Excited States and Free Radicals in Biology and Medicine: Contributions from Flash Photolysis and Pulse Radiolysis*, Oxford University Press, Oxford, **1993**, Chap. 3, pp. 64–100.
- “Method of Studying Radiation Chemical Processes”. *CRC Handbook of Radiation Chemistry* (Eds.: Y. Tabata, Y. Ito, S. Tagawa), CRC Press, Boca Raton, **1991**, Chap. III, pp. 97–186.
- *Pulse Radiolysis* (Ed.: Y. Tabata), CRC Press, Boca Raton, **1991**.
- “Pulse Radiolysis in Study of Oxygen Radicals”. M.G. Simic, *Methods Enzymol.* **1990**, 186, 89–100.
- “Pulse Radiolysis”. W.L. Waltz in *Photoinduced Electron Transfer, Part B. Experimental Techniques and Medium Effects* (Eds.: M.A. Fox, M. Chanon), Elsevier, Amsterdam, **1988**, Chap. 2.2, pp. 57–109.
- “Pulse Radiolysis Studies of Organic Electron Transfer Reactions”. P. Neta, A. Harriman in *Photoinduced Electron Transfer, Part B. Experimental Techniques and Medium Effects* (Eds.: M.A. Fox, M. Chanon), Elsevier, Amsterdam, **1988**, Chap. 2.3, pp. 110–162.
- “Pulse Radiolysis Equipment: A Setup for Simultaneous Multiwavelength Kinetic Spectroscopy”. M. Saran, G. Vetter, M. Erben-Russ, R. Winter, A. Kruse, C. Michel, W. Bors, *Rev. Sci. Instrum.* **1987**, 58, 363–368.
- “Sources of Ionizing Radiation, Their Interaction with Matter and Radiation Techniques”. C. von Sonntag, *The Chemical Basis of Radiation Biology*, Taylor & Francis, London, **1987**, Chap. 2, pp. 9–30.
- “Pulse Radiolysis”. M.Z. Hoffman in *Inorganic Reactions and Methods, Vol. 15* (Ed.: J.J. Zuckerman), VCH, Weinheim, **1986**, pp. 272–297.
- “Pulse Radiolysis Methodology”. K.-D. Asmus, *Methods Enzymol.* **1984**, 105, 167–178.
- “Data Acquisition and Analysis in Pulse Radiolysis”. D.C. Foyt in *The Study of Fast Processes and Transient Species by Electron Pulse Radiolysis* (Eds.: J.H. Baxendale, F. Busi), Reidel, Dordrecht, **1982**, pp. 199–225.

4 Photochemical Techniques

Kevin Henbest and Michael A. J. Rodgers

4.1 Introduction

The advantages of photochemical techniques for initiating electron-transfer reactions and measuring their kinetic features are manifold. Many excellent reviews, research monographs, and specialized books describing photoinduced electron transfer and the photochemical techniques employed have been published, and the reader is referred to them throughout this review [1–11]. In this chapter, a summary of basic principles and standard techniques is given and attention is paid to the several applications and to the limitations of the various techniques. The current availability of laser excitation sources with short duration pulses coupled with high-time-resolution diagnostic instrumentation enables the experimenter to study a large variety of photoinduced processes occurring over a wide range of timescales. There is no doubt that in the past three decades the photosciences have provided powerful and varied methods for studying electron-transfer processes and have contributed greatly to the development of the area.

An electron-transfer process can be generally represented by Eq. 1:



The reactant state is converted to the product state by the transfer of one electron. The participants in the reactant state may be individual molecules held transiently in proximity by a solvent cage; or they can be distinct parts of a supramolecular unit. Several types of chemical species can make up the reactant state; it may contain only ground-state, spin-paired entities, or electronically excited entities (singlet or other multiplicity), or reactive entities (free radicals, metal complexes in unusual oxidation states, etc.) Many combinations are possible, and a large variety of reactant states can be prepared from some precursor state by photon absorption. The chapters in this series of volumes contain an abundance of examples. In every case, however, no matter what the identity of the entities participating in the process, the

primary challenge to the investigator is to generate the desired reactant state and to measure the rate constant of the electron-transfer event within that framework. Having achieved this, the next challenge is to examine how the rate constant varies with changes in various parameters, such as molecular structure, driving force, spatial separation, orientation, solvent properties, temperature, and so forth. In this way the experimentalist builds up an array of rate data that allows testing of current theories and the formulation of new ones.

It is worth mentioning at this juncture that in a bimolecular reaction between a pair of individual reactive species in dilute homogeneous solution, the desired reactant state is achieved by normal diffusive processes. Except in those cases where there is a large energy barrier to the movement of the electron, the diffusive process itself is likely to determine the overall reaction rate constant. In those cases, the measured rate parameters provide no information on the nature of the electron transfer. The act of obtaining the proper reactive state that allows useful data to be obtained about the electron jump has proven to be a challenge of significant proportions and successful achievement of this has tested the ingenuity of the community of experimental chemists.

4.2 The Significance of Photoexcitation for Electron Transfer

The annihilation of a photon of light in an interaction with the bound electrons of a molecular system induces an electric-dipole transition with the result that a new electronic state is populated. The electronic configuration of the new state is different from that of the original (ground) state configuration, with the result that it possesses chemical properties that are different from the initial one. Energies ranging from 4.95 eV (114 kcal mol⁻¹) for 250 nm light to 1.65 eV (38 kcal mol⁻¹) for 750 nm light can be imparted to molecular arrangements by the straightforward act of light absorption. Thus, the electromagnetic energy of the photon raises the chemical potential of the absorber by amounts that are significant with respect to the energy requirements of many chemical events, including bond breakage. These energetic electronic states are intrinsically unstable and they seek to rid themselves of the excess energy. The ways to do this are diverse. Depending on the nature of the molecule itself and on the other molecules in the vicinity, reactions such as bond fission, bond formation, bond isomerization, excitation transfer, proton transfer, and electron transfer all become potential channels for energy loss. These chemical modes are in addition to the radiative (fluorescence, phosphorescence) and non-radiative deactivation channels. It is this diversity of energy-loss mechanisms that provides the richness of the photochemical sciences; photoexcitation provides a plethora of new chemical entities, the nature and reactivity of which serve to generate a great deal of intrinsic interest and research activity.

Not only does the act of photoexcitation generate interesting chemical entities; it does so with great rapidity. The duration of a single excitation event is a difficult concept to pin down because it is shrouded in the uncertainty principle. However, a

simple calculation shows that a single cycle of 300-nm light (travelling at $3 \times 10^8 \text{ ms}^{-1}$) will pass a point in space in 1 fs. If there happens to be a chromophoric residue (alkene, carbonyl) occupying that point in space, then the annihilation event might take that length of time. On the other hand if annihilation does not require the passage of a full cycle, it will occur in a correspondingly shorter time. In any case, the excitation event is intrinsically very rapid and presents little in the way of “dead time” to an experimental examination of the chemical effects of photoexcitation. The same considerations apply when light is employed to probe the consequences of photoexcitation, such as in optical absorption spectrometry and spectrofluorimetry. Again, the molecule–photon interaction time is vanishingly small and in itself imposes no instrumental time response. As will be examined later, more practical considerations such as the width of light pulses or the impedance of electronic components are the important factors that limit the investigator’s ability to obtain the desired information.

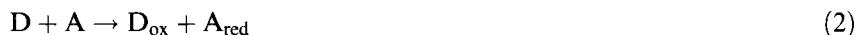
In the context of electron-transfer reactions, photoexcitation has played and continues to play a significant role. The chapters of this series of volumes contain a multitude of examples of the use of photon absorption to initiate reactions in which electrons are transferred from one molecular entity to another. The mission of the current chapter is not to exemplify the uses of photoexcitation in electron-transfer science, but to give some insight into the questions “why use photoexcitation” and “how is it best done?”

4.2.1 Advantages of Photoexcitation

There are several reasons why photoexcitation is employed in the pursuit of knowledge in the electron-transfer arena. Four of these are examined in the following segments.

Energetic considerations

Photoexcitation is able to provide the energy to drive the process in the desired direction. For example, in the schematic process



which is a slightly less generic description than was shown in Eq. 1 and where D and A represent the individual electron-donor and -acceptor species in the reactant state and the “ox” and “red” subscripts indicate the entities having undergone an electron-transfer reaction, the reaction will proceed spontaneously in the indicated direction if

$$E_{A/A_{\text{red}}} - E_{D_{\text{ox}}/D} > 0 \quad (3)$$

where the E quantities represent the one-electron reduction potentials (in volts) of the participants. Were the above inequality not true, then the indicated reaction would be difficult, at best. Suppose, however, that A (or D) is promoted to an

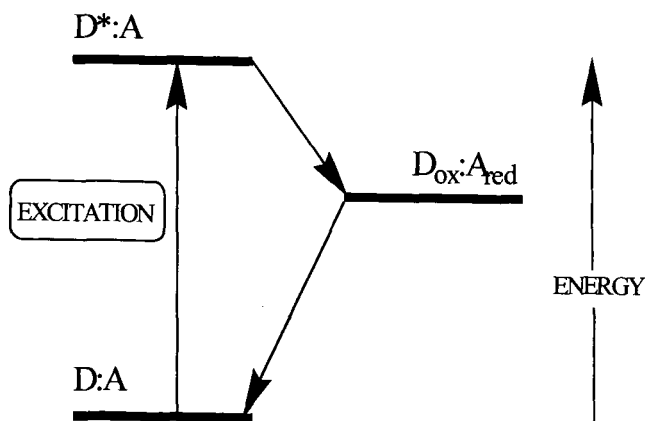
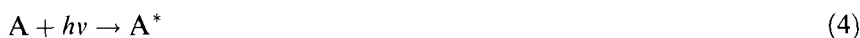


Figure 1. Schematic energy level diagram for a typical photoinduced electron transfer. Charge separation and recombination routes are shown—see text.

(unspecified) excited state by photon absorption:



Such an act provides a source of potential energy that may overcome the thermodynamic barrier of the reaction in Eq. 2, and the appropriate form of Eq. 3 is now

$$E_{A/A_{\text{red}}} + E_{00} - E_{D_{\text{ox}}/D} > 0 \quad (5)$$

Where E_{00} represents the energy of the unspecified excited state of A.

Excited-state energies are upwards of 1.5 eV above the ground state and thus it is clear that the act of photoexcitation will make a major change in the thermodynamic balance. Even significant barriers to reactions in the ground state can be overcome by photoexcitation. This situation is shown schematically in Figure 1, where it can be seen that the redox-pair product state ($D_{\text{ox}}:A_{\text{red}}$) is at an energy level that is intermediate between that of $D:A$ and $D^*:A$.

Thus, from the state $D^*:A$ the electron transfer is energetically downhill and will proceed spontaneously, as will the reaction that regenerates the ground state $D:A$. The use of light to provide the energy requirement for the reaction allows the two-electron-transfer rate constants for each reaction pair to be measured.

The scheme indicated in Figure 1 (excitation, charge separation, charge recombination) is most likely to occur when the product state has the same spin multiplicity as the reactant state, or when the product species are held together (e.g., by chemical bonds) for periods that allow intersystem crossing to occur. However, the charge separation–recombination sequence is not the only type of process that photoexcitation can achieve. An example is when the product state is held only loosely by a solvent cage and the entities therein can diffuse apart and have independent reactive identities. Such a scheme would be typified by the sequence



Here Eq. 6 represents a photoinduced charge-separation process where the product state escapes the cage prior to (or in competition with) recombination. Equation 7 shows a schematic redox reaction involving a substrate S and one of the released components of the product state. This type of sequence uses photons to prepare a redox-active species that is not an excited state of the light-absorbing component.

Control of process

A second good reason for the use of photoexcitation as a means of promoting an electron-transfer process is that it provides the opportunity for the experimenter to prepare the system looked at without any possibility that the reaction being studied will *proceed* during the preparation stage. In the chapter "Classical Methods" in this volume, Bakac points out that the time taken for the reactants to mix can be a limiting factor for rate measurements and she discusses methodologies that have been developed to minimize such problems. Photoexcitation completely circumvents this difficulty because it is not the reactants themselves that are mixed in the reaction vessel, but their ground state precursors. For example, in studies of the photoinduced electron-transfer reactions within electrostatically bound ion-pair complexes in solution, the participating ionic species that were mixed in the reaction vessel to prepare the ion pairs were energetically incapable of undergoing electron transfer [12, 13]. Subsequent photoexcitation generated an excited state of one of the components of the complex, thereby providing the driving force for the desired reaction to proceed. In this way, the sample-preparation stage can be cleanly and completely separated from the reaction stage. No electron transfer can occur until the photons have been delivered and absorbed.

Wavelength variability

Yet another reason for using of light to promote the target reaction is that it allows the wavelength to be employed as a variable parameter. A simple example of this could be applied to the schematic Eq. 2, where either A or D could serve as the absorber of radiation, for example, at different wavelengths. By this expedient, the direction of electron transfer could be reversed. This idea of using variable wavelengths can be made more complicated inasmuch as it allows delayed two-color experiments. Thus, one pulse would prepare an excited state of a precursor compound and, some time later, within the excited-state lifetime, a second color pulse would be injected to convert the primary product into a derivative state (higher excited state, free radical, etc.) This would be one of the reactants in an electron-transfer reaction with another (unexcited) compound present in the reaction mixture. Clearly the imaginative use of wavelength as a variable allows the possibility of investigating unusual situations.

Vast time window

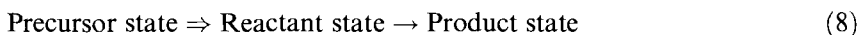
A fourth advantage of using photoexcitation to study electron-transfer reactions is the vast time window that such a technique offers. As has been indicated above, understanding the nature of the electron transfer process relies on the measurement

of rate parameters under controlled conditions. Thus, any methodology that extends the time window in which reaction rates can be studied will be advantageous. As discussed earlier, photon–molecule interactions are to all intents and purposes “instantaneous”. The present state of technology allows the experimenter to generate reactant states and product states and to record their optical signatures on sub-picosecond timescales, a fact that allows reactions occurring with lifetimes less than 10^{-14} s to be kinetically characterized.

The tremendous progress in electro-optic technology over the past 25 years has been an important enabling force that has allowed students of kinetics to explore time domains hitherto existing only in their imaginations. Readers interested in following technological developments as they occur might wish to obtain free subscriptions to trade publications such as “Laser Focus World,” “Lasers and Optronics,” and “Photonics.” The pages therein point the way to the future in photoscience.

4.3 The Methodology of Photokinetics

From the foregoing discussion it is now possible to extend the generalized electron-transfer reaction of Eq. 1 to add a light-induced process:



Where the precursor state is prepared initially by the experimenter by synthesis, mixing, and so forth in the absence of the initiating photons. The conversion of the precursor state to the reactant state is brought about by the absorption of a photon in a chromophore that is part of the precursor state. With the appropriate reactant state being thus prepared, the electron-transfer process will proceed spontaneously at a rate determined by the nature of the reaction. The experimenter’s task is simply to evaluate the rate constant of the elementary reaction that generates the product state. This is accomplished by the time-honored procedure of chemical reaction kinetics, that is, by determining the decrease in concentration of one of the reactant-state components as a function of time, or by determining the increase in concentration of one of the product-state components as a function of time. When the reaction is elementary, that is, when the reactant and product states are coupled through a transition state only, the rates of reactant decrease and product increase convey the same information, namely, the rate constant for the reaction.

There is an important proviso, however, which is that the outlined procedure will only provide the rate constant being sought if there are no competing channels that can also serve to deactivate the reactant state. If the prepared reactant state can also involve itself in a proton-transfer reaction, say, that yields a different product state, then the measured rate constant will be the sum of the rate constants of the two competing processes. The measured rate constant will only be identical to the electron-transfer rate constant if the competing side channels contribute negligibly to the total. It is never good practice to assume without evidence that the electron-

transfer process is the unique reaction path; it is always prudent to measure the stoichiometry of the electron-transfer reaction as well as the rate constant. This problem is even more significant when the rate of decrease of a reactant is the sole observable that is employed to evaluate the rate parameter, as is usually the case when emission lifetimes/quantum yields are employed to monitor the progress of a reaction. That the emission of a donor (say) excited state is quenched in the presence of a putative acceptor is a necessary but far from sufficient condition that the process causing the loss of the emissive state is an electron-transfer event.

4.3.1 Instrumentation Considerations

Having set the scene as to why the approaches of photochemical science are useful in obtaining the kinetic parameters of electron-transfer reactions and having pointed out some cautions, it remains to discuss the “nuts and bolts” of instrumentation and technology. The organization of the remainder of the chapter is that excitation sources will be discussed in a separate segment, since all photomethods largely depend on the same sources. Subsequently, the diverse methods of measuring the time profiles of declining reactant concentrations and growing product concentrations will be outlined.

4.3.2 Excitation Sources

Today the very large majority of investigations into the kinetics of electron transfer reactions employ pulsed excitation sources of one kind or another. This is largely because such sources enable a clear distinction to be made between the preparation stage and the reaction stage; they also allow elementary reactions to be followed. This is usually not the case with cw light sources. By their very nature, such sources allow the experimenter to measure loss of starting material and/or formation of a product. To convert such data into information that is relevant to elementary reactions requires mechanistic interpretations that could be fraught with uncertainty. In what follows, the discussion will be restricted to pulsed light sources. For investigators who are interested in cw light sources, an excellent review exists [14].

Pulsed excitation sources

Pulsed flashlamps

The earliest experiments in transient spectrometry used high-energy flashlamps as light sources for generating observable concentrations of short-lived species [15]. Their continued use during the 1950s and 1960s enabled the flash-photolysis technique to be used to great effect in the study of photochemically generated intermediate species [16]. However, flashlamps had their drawbacks. Pulses of useful energy were long in duration ($>1\ \mu\text{s}$), much of the input electrical energy was used for generating light at wavelengths that were not useful in the photochemical study, and the coupling of the light to the sample was difficult and resulted in many losses.

Thus, in the late 1960s, the advent of high-power, short-pulse lasers provided many advantages to the experimentalist and created a revolution in the photosciences.

Pulsed lasers [17]

With the invention of the laser in 1960 [18], and the subsequent development of pulsed lasers using Q-switching methodology, monochromatic and highly collimated light sources became available with pulse durations in the nanosecond regime. Such light sources rapidly gained popularity with photoscientists, because the collimation allowed efficient coupling to the sample, and the monochromaticity property meant that many more photons were available to pump a particular absorption band of the sample at a much lower input energy. The early pulsed lasers allowed the study of photoprocesses that occurred in nanoseconds—some 10^3 times faster than events measurable by flash photolysis with the aid of flashlamps.

It is the process of Q-switching that is responsible for the generation of controlled high-energy laser pulses of a few nanoseconds duration. In this action, the laser medium (solid crystal, gas, or liquid dye) is pumped by a flash lamp with the cavity completely closed (high Q value) so that the medium stores all the input energy and the population of lasing states builds up to a high value. At an appropriate moment during the pumping flash, the cavity is caused to drastically lower its Q value (Q is switched from high to low) and the stored energy is dumped out of the cavity as a giant, short pulse. The sequence of pumping and switching is repeated to generate another pulse, and so on. In modern laser systems, this cycle can be repeated at kHz rates, depending on the energy per pulse required. These days, the Q-switching process is usually achieved by rapidly switching the way in which the cavity transmits polarized light via a Pockels cell. Because Q-switching employs high-voltage electrical pulses to operate the Pockels cell, there is a limiting rate at which this can be achieved, because of circuit rise time characteristics (RC time constants). Q-switched pulse durations of a few nanoseconds are readily available in the year 2000.

A laser excitation source that is employed in many laboratories for nanosecond photolysis studies is the Q-switched Nd:YAG laser [19–21]. The lasing medium is an yttrium aluminum garnet crystal into which Nd^{++} ions are doped. This device typically has a pulse width of 6 ns and lases at its fundamental wavelength of 1064 nm. Output energies per pulse from the oscillator-only configuration can be as high as 0.5 J; this can be increased to multijoule per pulse by amplification. The 1064-nm line can be frequency-doubled to 532 nm, tripled to 355 nm, or quadrupled to 266 nm (with concomitant energy lowering) to give useful excitation wavelengths in the visible and ultraviolet. Frequency doubling is achieved by the beam being passed through an orientated crystal of dihydrogen phosphate (KDP) or β -barium borate (BBO) [22]. The Ruby laser [23] (694 nm, second harmonic at 347 nm) is another solid-state system that can be Q-switched and is capable of delivering high pulse energy.

High-energy ultraviolet light pulses in the 20-ns range can be produced by the transverse discharge of transmission lines through tubes containing gases such as nitrogen (337.1 nm) [24] or mixtures of halogens with rare gases (excimers) [25–27]. The XeCl excimer laser, for example, can typically produce 300 mJ of 15–20-ns

pulses at 308 nm. Gas lasers (excimer) and solid-state lasers (Nd:YAG) are commonly used as pump sources for dye lasers [22]. An advantage of dye lasers is that they are tunable to any wavelength from 340 nm to 900 nm with the suitable choice of laser dye. However, a single, specific laser dye has only a narrow lasing wavelength range, typically 20–30 nm, and the changing of wavelengths requires the insertion of a different laser dye into the cuvette and perhaps different optical elements, and subsequent realignment. There are other complications with the use of laser dyes. The dyes have uncertain stability; the Coumarin dyes for the 450-nm range are particularly susceptible to rapid degradation. The dyes are often toxic or carcinogenic, and if allowed to escape into the laboratory are hazardous to the operators. Such difficulties are avoidable by the replacement of the dye lasers with a solid-state alternative; to this end, optical parametric oscillators (OPOs) have recently been introduced [28–29]. These devices, when pumped by the 355-nm harmonic of a Q-switched Nd:YAG laser, can produce narrow-bandwidth, tunable laser wavelengths from 440 nm to the infrared. From these, UV lines can be generated by frequency doubling of the signal and idler outputs.

Mode-locked lasers

To achieve time resolution below a few nanoseconds requires other methods of generating short laser pulses. The typical method is to resort to mode-locking techniques. In a mode-locked laser, the axial modes that oscillate in the laser cavity are forced into phase-lock condition at some points. As the light pulse is propagated back and forth between the reflecting ends of the cavity, interference occurs between the modes. Where the cycles are in phase, interference is constructive and narrow intense pulses are generated; elsewhere the interference is destructive. This produces a train of pulses within the envelope of the pumping flash. The time interval between pulses (τ_p) is given by

$$\tau_p = 2L/c \quad (9)$$

Where L is the cavity length and c is the velocity of light; the τ_p parameter is the cavity round-trip time. The width of the pulse (FWHM) is given approximately by

$$\Delta\tau \cong 1/\Delta\nu_{bw} \quad (10)$$

Where $\Delta\nu_{bw}$ is the total oscillating bandwidth. The shortest pulses are therefore generated by the widest frequency distributions, that is, by arranging for a broad gain bandwidth. Only those frequencies in the emission spectrum of the laser material that can be maintained above the lasing threshold will participate in $\Delta\nu_{bw}$. Dye lasers and some solid-state lasers (titanium–sapphire) have broad spectral outputs and can produce pulse widths significantly lower than 1 ps. Gas lasers have much narrower bandwidths and typically have pulse widths closer to 100 ps. The solid-state Nd:YAG laser is intermediate at near 30 ps.

There are presently many types of lasers that produce short light pulses which have outputs that differ in wavelength, tunability, pulse length, repetition rate, energy

per pulse, average power, and peak power. In a very general way, mode-locked lasers fall into two categories, high repetition rate (about 10^8 Hz), and low repetition rate (less than about 10^3 Hz). The former class is typified by mode-locked cw lasers; the second by flashlamp-pumped solid-state (e.g., Nd:YAG) lasers.

In several laboratories, repetitively mode-locked cw ion (Ar^+ , Kr^+) or solid-state (Nd:YAG) lasers have been employed to synchronously pump dye lasers [30–31]. These latter operate at a repetition rate of close to 80 MHz and can be tuned to generate pulse widths of as short as ca. 1 ps. The dye laser can, if so desired, be acousto-optically cavity-dumped to achieve lower output rates. Dyes of the rhodamine family ($\lambda_{\text{max}} = 590$ nm) are optimally efficient, and average powers of several tens of milliwatts are achievable with high stability over long periods. This represents a few nanojoules per pulse, although in cavity-dumped mode, where energy is stored in the cavity during the dark periods, the per-pulse output energy can exceed 10^{-8} J. Such energies are very low in terms of the instantaneous concentration of excited states that can be produced. For example, the complete absorption of 10 nJ in a volume of 1 mm^3 will convert about 50 nM of the absorber into excited states. Even with differential extinction coefficients of $5 \times 10^4 \text{ M}^{-1} \text{ cm}^{-1}$, the absorbance change at the excitation wavelength (in a 1-mm path) would be only about 2.5×10^{-4} —a very small absorbance. For this reason, a high degree of signal averaging is required to extract signal from noise, hence the usefulness of a source of high repetition rates and the need for long-term pulse-to-pulse amplitude stability. An improvement on this approach is amplification of the synchronously pumped dye laser output by passing it through a multistage (three or four) dye-amplifier module [32]. The several stages of this latter can be pumped with excimer, Cu vapor, or Q-switched Nd:YAG lasers. In this way, energies of hundreds of microjoules per pulse are attainable at repetition rates in the range 30 to 200 Hz. Advances with Nd:YAG regenerative amplifiers have yielded repetition rates of 1 kHz in the dye-amplifier pump [33].

Flashlamp-pumped solid-state lasers operating at 10–30 Hz are capable of being mode-locked by combination of an active acousto-optic crystal with a passive saturable absorber. In Nd:YAG lasers, this results in pulses of duration as low as 18 ps with output energies (after amplification) of up to 100 mJ per pulse at 1064 nm. Subsequent harmonic generation steps yield pulses at 532 nm, 355 nm, or 266 nm with energies and stability that conveniently provide excitation beams for flash photolysis studies. Shorter pulses than are obtainable from Nd:YAG can be delivered by Nd:(phosphate)glass systems, which have larger $\Delta\nu_{\text{bw}}$ values. Otherwise, short-cavity dye lasers, pumped by the 18-ps 532-nm pulses from a mode-locked Nd:YAG system will produce tunable light of peak energy near 1 mJ, with pulse widths near 6 ps.

The earliest subpicosecond systems incorporated dye laser technology. Shank, Ippen, and their colleagues at the Bell Laboratories [34] were the first to develop mode-locked subpicosecond lasers and to show how to compress pulses to very short values. With the colliding-pulse mode-locked (CPM) laser they achieved reduced pulse widths well into a subpicosecond range. Two approaches based on synchronously pumped dye lasers and colliding pulse dye lasers are commonly employed to produce subpicosecond pulses. These are briefly discussed below.

The fundamental (1064-nm) line of a mode-locked cw Nd:YAG laser is of intrinsically shorter time duration (about 70 ps) than is the pulse from a mode-locked cw ion laser (>100 ps). Thus, compression of Nd:YAG pulses will achieve shorter pulses for dye pumping. Pulse compression can be achieved by the focusing of the 1064-nm line into a single-mode, optic fiber that imparts frequency chirp to the light [35–36]. Removing this chirp, with a pair of gratings, results in a markedly compressed pulse. Pulses treated in this way, followed by frequency doubling, have yielded 532-nm pulses as short as 6 ps. The pulses can be used to synchronously pump dye lasers, and have generated dye trains with pulse trains near 200 fs in duration [37], similar pulse widths can be obtained by using the normal-width 532-nm beam and a dye pump, but including a saturable absorber in the dye laser cavity, either in a separate jet system or simply as an additive to the dye laser stream [38]. The shortest pulses have been obtained from colliding-pulse dye lasers that are passively mode-locked. Coupled to optimal cavity design and component selection, these have been shown to generate light pulses of less than 100 fs in duration [39, 40]. Pulse durations less than 10 fs have also been generated [41].

The femtosecond laser systems indicated above produce high-repetition-rate (close to 10^8 Hz) pulse trains with individual pulse energies in the nanojoule range. As such, their main usefulness lies in fluorescence excitation sources. As with the low-energy picosecond pulse trains, dye amplification stages can be applied to enhance pulse energies to hundreds of microjoules [42]. The amplification produces pulse broadening owing to frequency chirp induced in the optical components (lenses, windows, liquids, etc.), through which the pulses must pass. To some extent, this can be offset by the addition of a grating pair stage to compress the pulse, although subjecting such devices to the intense peak powers involved are very likely to cause surface damage. In the late 1980s, the state of the art in terms of intense subpicosecond pulses were attained by hybrid dye-excimer laser systems [43]. These generated 80-fs pulses of 248-nm (KrF) light with energy per pulse in the region of 15 mJ.

In the 1990s, titanium–sapphire (Ti–S) based laser systems became commercially available and are currently in widespread use for subpicosecond pulse generation [44–46]. The Ti–S laser has the advantage that it is a solid-state device with an indefinitely long operational life and replaces the need for flowing laser dyes that degrade with time. The lasers are pumped either with a continuous-wave 7-W argon ion laser at 514 nm, or with a 5-W Nd:YAG diode-pumped solid-state laser, frequency-doubled to 532 nm. The Ti–S laser oscillator has tunable output in the range 750 nm to 840 nm with a maximum at 800 nm. Different optics sets can extend the tuning range. The repetition rate is close to 80 MHz. A Ti–S oscillator undergoes self-mode locking through a self-focusing mechanism; the high intensity of light in the crystal produces refractive-index changes in the crystal, most markedly along the axis of the beam waist. A variable aperture is employed to control the mode-locking mechanism. Self-mode locking circumvents the need for matching the cavity length with that of the pump laser. The output pulse from an oscillator of the above type is typically 80 fs, although shorter pulses are achievable [47, 48]. Should longer pulses be required, additional optics can be employed to generate pulses in the picosecond range [49].

The average power output of a Ti-S oscillator is in the region of 500 mW, which corresponds to a per-pulse energy of a few nanojoules. While not powerful enough for transient absorption studies, oscillators of this type have been employed as sources for fluorescence lifetime work, including two-photon excitation, and for fluorescence upconversion studies [50, 51].

For use in transient absorption studies, the output of the Ti-S oscillator can be amplified with, for example, a Ti-S regenerative amplifier operating at 1 kHz. The final output is then a 1-kHz train of pulses, typically 100 fs in duration, with a per-pulse energy of ca. 1 mJ at 800 nm (or close to it). The amplifier is typically pumped at 1 kHz with the second harmonic (527 nm) of a Q-switched Nd:YLF laser. Prior to amplification, the short pulses need to be stretched to several hundred picoseconds long, to avoid damage to the optical components in the amplifier cavity. After the amplification has occurred, the pulses are re-compressed, so that the 100-fs output pulse is obtained. The near-IR (800-nm) pulse can be frequency-doubled to 400 nm, tripled to 266 nm, or converted to tunable visible light by use of an optical parametric amplifier (OPA), so that wavelengths suitable for photoexcitation work are generated.

In the foregoing segment an attempt has been made to provide a broad survey of light sources that have proven useful to the photochemical community for studies in the area of photoinduced electron transfer. The survey is by no means comprehensive; to do so would soon exhaust the page allotment. The coverage has, rather, been aimed at the more widely used devices, examples of which are extant in the authors' laboratory.

4.4 Detection and Measurement Techniques

In the above section the photodevices that can be employed to reach the appropriate reactant state were outlined. In the remainder of the chapter, the devices and instruments for monitoring the subsequent change and determining the rate characteristics will be discussed. By far the most frequently employed diagnostic techniques are optical absorption and emission spectrometry; other less-used methodologies include light-scattering spectrometry, and the electron-spin-based spectroscopies, such as EPR, ENDOR, and CIDNP. These last three are not addressed in this review.

4.4.1 Optical Absorption Spectrometry

Principles and limitations

In electron-transfer reactions, the movement of an electron from the reactant state to the product state generates new species that have different electronic configurations. Different electronic configurations in a molecule give rise to different

electronic absorption spectra, and therefore monitoring optical absorption changes during an electron-transfer reaction has proven to be a sensitive and widely used method of following the time course of a photoinduced reaction.

When a beam of light at some wavelength λ is incident on a sample containing an absorbing compound, the logarithm of the ratio of incident light intensity (I_0) to that of the transmitted light intensity (I) is termed the absorbance (A_λ) of the sample. A_λ is related to the molar concentration (c) of the absorbing species according to

$$A_\lambda = \log(I_0/I) = \varepsilon_\lambda c l \quad (11)$$

where ε_λ is the molar decadic extinction coefficient (units of $\text{mol dm}^{-3} \text{ cm}^{-1}$) at the wavelength λ , and l is the optical path length of the sample. Thus, A_λ is directly proportional to the concentration of the absorbing species and, when the species concentration changes with time, then $dA_\lambda/dt = dc/dt$. Hence, the time profile of the change in A_λ is directly related to the time profile of the absorber concentration. Equation 11 shows that $A_\lambda(t)$ is obtained by monitoring of the time dependence of the change in the transmitted light intensity, $I(t)$, at a constant value of I_0 . When the latter cannot be kept constant, its value must also be determined for every $I(t)$ value (see below). $I(t)$ is a light-fluence quantity, which is converted to electronic charge by a photosensitive detector. The ultimate measurement is of a voltage–time profile, $V(t)$, which is referenced to V_0 , derived from I_0 . Thus

$$A_\lambda(t) = \log[V_0/V(t)] = \varepsilon_\lambda c(t) l \quad (12)$$

From the time dependence of V , thence of A_λ , and eventually of c , the rate parameters being sought can be determined.

From the above it is apparent that A is a function of two variables, namely time and wavelength. The time dependence leads to dynamics information as outlined above; the wavelength dependence provides spectral information, useful for assignment or structural purposes. When values of $A(\lambda, t)$ are obtained for a photo-initiated sample, a dynamic surface (A – λ – t) can be constructed; this contains the totality of the information available from an optical absorption experiment.

Two distinct types of experiment have been employed to generate $A(\lambda, t)$ data for transient species. One is a continuous recording method in which a photodetector (photodiode, photomultiplier tube–PMT) monitors the transmittance of the sample at fixed wavelength (λ) in a continuous manner, before, during, and after the initiating light pulse. The detector output is fed to the input amplifier of a waveform-recording device such as a digital oscilloscope, which acquires the waveform and stores it for eventual processing. Thus, recording of the $V(t)$ profile is done in real time. Repeating the process over a series of wavelengths allows the investigator to build up the dynamic surface for the light-induced transient which is, in principle, capable of providing rate data at different wavelengths and time-dependent spectra. In what follows, this type of experiment will be referred to as the continuous photoelectric method. Examples of time-resolved spectra and kinetic profiles obtained in the authors' laboratory using the photoelectric method are shown in Figure 4 (see

later on). The photoelectric method is excellent for providing kinetic information, since the time profiles from a single experiment arrive at the digitizer as analog voltage waveforms that can be digitized into as many bits of information as required. This lends itself to highly precise determinations of rate parameters. The same is not true of the spectral information, which is taken point-by-point, and the number of points taken, and hence the precision of the obtained spectrum will to some extent depend on the investigator's patience.

The major limitation of photoelectric recording is what can be thought of as the nanosecond barrier. This limitation arises because of the intrinsic time response of the electronic devices that must be used to acquire and process the photon-generated cathode current of the PMT or photodiode. All such devices have impedance, and even the best-designed circuitry has stray capacitance of typically 20 pF which, when combined with the 50- Ω industry/standard of electronic amplifiers, yields a RC time constant of 1 ns. Hence, instruments that are built up from conventional electronic units will have minimum rise times in the ns region and therefore chemical changes that have lifetimes less than 5 ns, say, will be severely deformed. Of course, other reasons may intervene (e.g. 10-ns-wide laser pulses) that make the instrument response even poorer than implied by the nanosecond barrier.

It is important to find a way around the nanosecond barrier problem if reactions occurring in the subnanosecond regime are to be investigated, and the pump-probe method provides the path. Here, two light pulses are generated; one to excite the sample (prepare the reactant state) and one to probe the system at a given time post-excitation. In the early experiments, high-energy flashlamps were used for generating observable concentrations of short-lived species and lower energy flash sources were used as interrogating beams. The two flashes were electronically delayed, one with respect to the other. This procedure stems from the methodology employed by Norrish and Porter in 1949 as part of their invention of the technique of flash photolysis which led to their being awarded the Nobel Prize in Chemistry in 1967 and which revolutionized the study of short-lived transient species inasmuch as it proved capable of generating and analyzing chemical species with lifetimes shorter than a few milliseconds [15, 52]. (It is interesting to note that some 50 years after Norrish and Porter's 1949 *Nature* paper [15] that reported the development, Ahmed Zewail was awarded the 1999 Nobel Prize in Chemistry for using Norrish-Porter concepts on the femtosecond timescale to investigate the transition-state domain.)

In the modern era, flashlamps have been superseded by pulsed laser sources which are monochromatic, highly collimated, and have a much higher repetition rate. With a single laser source, the probe pulse can be a small part that is split off from the main pump beam, to therefore be of the same wavelength. Such an arrangement is restricted to the measurement of the kinetics of repopulation of ground-state absorption removed (bleached) by the pump pulse. This method has been employed fruitfully in several laboratories [53-56].

Significantly more information is available when the probe pulse is a white-light continuum and a spectrograph is used to disperse the spectral distribution of the beam transmitted by the sample. Under these conditions, one obtains an absorption spectrum of transient species formed, or ground-state species removed by the ini-

tiating pulse. This spectrum will be registered at a time that is given by the difference in arrival times at the sample of the pump and probe pulses, and it will be an average over the temporal width of the probe pulse. An alternative method of obtaining spectral information is to employ a probe beam of a selected, but changeable wavelength. Such a beam can be isolated from a continuum by one of a set of interference filters, or it can be generated by an optical parametric amplifier (see above) which can be scanned to provide spectral coverage [57, 58]. In both these instances the detector is a commonplace photodiode.

Repetition of the spectrum acquisition sequence at different probe-pulse arrival times provides a series of spectra delayed with respect to each other. Thus, time resolution of the reaction is achieved in a point-by-point manner, from which the intensity–time–wavelength surface can be produced.

In this experiment type, the detector of the transmitted probe light behaves as a photon integrator only and the time resolution derives from the instrument's capability for measuring the difference in the time of arrival of the pump and probe pulses. This capability provides an intrinsic limitation to the pump–probe method, which depends critically on the width of the pulses being employed. As indicated earlier, exceedingly short duration pulses are commonplace these days.

A more practical limitation to this method involves the regime of large time differences. When a single laser is used as the source of both pump and probe pulses, the time difference is generated by delay of the probe with respect to the pump with an optical delay line. Such devices are excellent for delays in the subnanosecond region and up to 3 ns or so, but their alignment and operation becomes very cumbersome for delay times in excess of 10 ns or so, and they are rarely used in this regime. Investigators have used a pair of individual light sources for the longer delays. Thus, Porter and his colleagues, in their original microsecond experiments, used a pair of flashlamps, one to pump and one to probe [15, 51].

More recently, others have employed two Q-switched lasers to generate delays in the long nanosecond region [59, 60], especially where spectra and not kinetic profiles are being sought. In the above development, nothing has been stated about the analytical wavelength region employed in photoelectric spectrometry or pump–probe spectrometry. In fact, most of the work carried out to date centers on the UV–visible wavelength region, although there is increasing activity among the research community in exploring the mid-infrared (fingerprint) region; there will be more about this latter subject later on.

Examples of instrumentation

In this section, two operational instruments based on the principles discussed in the previous sections are described. One is useful for monitoring processes with reaction times in the 10^{-8} s to $>10^0$ s range—a so-called suprananosecond kinetic spectrometer. The other—an ultrafast kinetic spectrometer—is employed for reactions occurring in the range $<10^{-12}$ s to $>10^{-9}$ s. Both these spectrometers are in use in these authors' laboratory for investigating photoinduced electron-transfer reactions, *inter alia*. The use of these homegrown instruments to illustrate this chapter is not

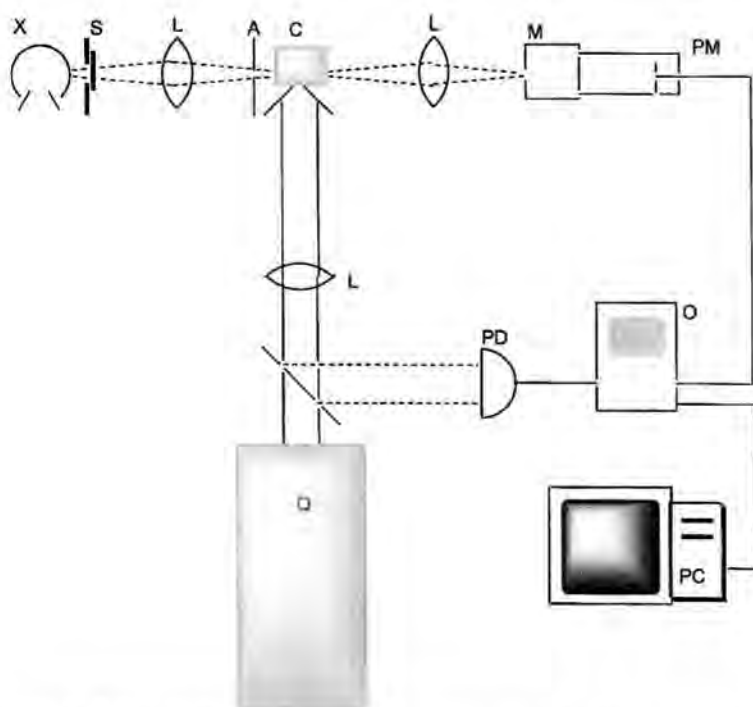


Figure 2. Schematic layout of a typical suprananosecond kinetic spectrometer: Q: Q-switched laser with harmonic generators; L: lens; X: cw monitoring lamp; S: shutter; A: aperture (see Figure 3 for detail); C: sample cuvette; M: monochromator; PM, PD: photodetectors; O: digital oscilloscope; PC: personal computer.

meant to indicate anything other than that these are typical of similar instruments found worldwide in the laboratories of the electron-transfer community.

Suprananosecond kinetic spectrometer

A suprananosecond kinetic spectrometer is schematically shown in Figure 2. The excitation source is a Q-switched Nd:YAG laser (Continuum Surelite I) which is capable of a 10-Hz repetition rate but is typically used in the “replicate-one-shot” mode. The nominal 6-ns pulse can contain up to 450 mJ at 1064 nm, which decreases after harmonic conversions to 532 nm, 355 nm, or 266 nm. In addition to these harmonic lines, the 355-nm line can be used to pump an OPO (Opotek Magicprism), which provides tunable radiation in the range 420 nm to ca. 900 nm. The selected photolysis beam is incident on one face of a 10 mm × 10 mm quartz cuvette containing the sample.

In experiments in fluid solutions where absorbance at the excitation wavelength (λ_{exc}) can be controlled, it is advantageous to arrange that the deposition of pho-

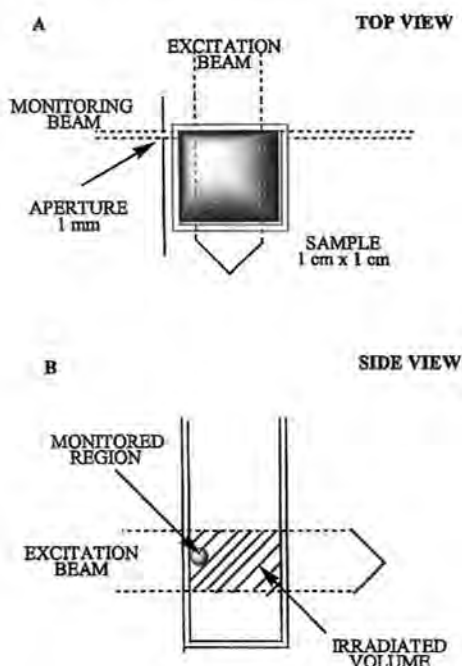


Figure 3. Detailed views of the geometrical relationships of the laser beam, the cuvette, and the monitoring beam.

tons, and thereby the production of excited states is as homogeneous as possible in the interrogated volume. The Beer–Lambert law ensures that the concentration of excited states will decline exponentially with distance from the laser input face. However, as stated below, the interrogation volume is restricted to the first mm from the laser input face and thus absorbance values at λ_{exc} of one per cm or even greater can provide close to homogeneous energy deposition.

The monitoring light source is either a 150-W xenon arc lamp [61–64] or a 100-W quartz–halogen lamp. The path of the monitoring light is at right angles to the excitation beam and it interrogates the first 1 mm of the irradiated volume behind the laser input face (see Figure 3). This is arranged by appropriate placement of lens and an aperture.

Xenon arc lamps operate at high pressure (20 atm) with a short arc configuration and require a highly stable DC power supply for low baseline ripple. The lamp output is a smooth continuum with weak superposition of lines in the visible and strong lines in the near-IR. Xenon arc lamps are prone to suffer from baseline ripple with a frequency less than ca. 1 kHz. This can be caused by power-supply fluctuations or by wandering of the arc. These ripples can cause severe distortions in the time profile of low-intensity transient absorptions on the millisecond or longer timescales. The current supply to the xenon lamp can be pulsed to high intensities [65–68] to increase the radiance. A 250-W xenon lamp with a 450-amp pulse has been reported to have a 700-times increase in radiance in the UV, 300-times increase in the visible and 50-times in the IR [65]. Tungsten and quartz–halogen

lamps [69–73] are less subject to ripple and provide much more stable outputs, albeit with much reduced intensities. Tungsten emits a continuum from the near-UV into the IR [74]. The quartz–halogen lamps have quartz filaments and are run at higher temperatures than tungsten lamps, namely at 3000 to 3200 K, which gives somewhat higher UV outputs. A quartz–halogen lamp can be used as a standard for calibrating the spectral response of spectrometers [75]. The high-wattage lamps are used with shutters, to protect the sample from undue photolysis, and the detector from unnecessary fatigue.

The lamp housing is equipped with a rear reflector and a fused-quartz, four-element, spherically corrected $f/0.7$ lens assembly (Oriel) to collect the light and transfer as much as possible through the 1-mm aperture in front of the cuvette. The exiting beam is re-collimated and focused onto the entrance slit of a 0.22-m monochromator (Spex 1681) which disperses the white light into its component wavelengths and isolates a narrow range of wavelengths at the exit slit. The grating may be either ruled [76–81] or holographic [80, 82–85]. Ruled gratings can contain periodic ruling errors that result in ghost images in the dispersion plane and holographic grating is therefore preferred. Holographic gratings are manufactured from photoresist materials that are exposed to interference fringes produced from diffracted monochromatic light. They are free of ghost images. There is a multitude of different types of monochromators with different configurations [76–78, 86, 87]. One important consideration is the f -number, defined as

$$f = f_c/d_c \quad (13)$$

where f_c is the focal length and d_c the diameter of the collimating mirror. The lower the f -number, the more light is transmitted by the device. When designing an optical system, it is important to arrange for the beam that is incident on the entrance slit of the monochromator to have a convergence that matches the f -number of the monochromator. If the f -number of the entrance optics is smaller than the f -number of the monochromator, then the grating will be overfilled and stray light may be increased. If the f -number of the entrance optics is larger than that of the monochromator, then the area of the grating that is illuminated is decreased, and the resolution of the instrument suffers [77, 80]. The grating in most frequent use is a holographic type and covers the range from 230–800 nm with a blaze at 400 nm.

The photodetector that monitors the intensity and time profile of the monochromatic light issuing from the exit slit of the monochromator is a side-on photomultiplier tube (Hamamatsu 928), which has an excellent response in the UV, visible, and near-IR to about 900 nm. Photomultiplier tubes (PMTs) are light-detection devices capable of measuring weak fluxes of light, as low as 10^{-15} W. They depend on the photoelectric effect for their function, in which electrons are emitted from the illuminated part of the active surface. It consists of a photosensitive cathode, an electron-multiplier section (dynodes), and an electron collector (anode), all sealed in a vacuum tube. When photons of the appropriate frequency are incident on the photocathode (held at a high negative potential), electrons are emitted and are directed onto the first of the dynode series where secondary emission of electrons occurs. Each dynode is held at a lower negative voltage than its predecessor so that

the arriving electrons possess about 100–200 V of energy and thus each arriving electron generates several secondary electrons, thereby producing a cascade that contributes to the multiplication process. In a typical 11-dynode stage photomultiplier tube, each stage provides an amplification of ca. 2.5, leading to an overall gain of 10^6 or so. The electrons leaving the final dynode are collected by the anode, and this charge, when run to ground through a load resistance, produces the output signal voltage. The photomultiplier tube employed in the current instrument uses just five stages of gain, with the sixth employed as the collector electrode. In this way, gain is sacrificed for improved time response [88]. Photodiode/fast amplifier combinations can replace photomultiplier tubes, and this is particularly advantageous in the near-IR where photomultiplier photocathodes tend to have poor quantum efficiencies [89]. It is important that the photodetector must respond linearly to the light intensity. This is checked by inserting neutral density filters between the lamp and the monochromator entrance slit and confirming that the detector output corresponds to that expected from the transmittance of the filter. Excellent descriptions of the comparisons between detectors and the spectral response characteristics of different photocathodes have been published [90–91].

The current waveform on the anode of the photodetector is fed to the input connector of a transient digitizer/digital oscilloscope where it is converted into digital format and read into a PC. The resulting stored data can be processed for spectral/dynamic content by one of several available commercially available data manipulation software packages.

The suprananosecond instrument described, in common with almost every other such instrument, is a single-beam spectrometer inasmuch as it records the absorbance difference between the pre-pulse and post-pulse values, that is, the combined spectra of the ground state and product state are involved. Only when the sample has zero absorbance prior to the excitation event, does the experiment provide absolute absorption spectra. An example of this is presented in Figure 4, which shows the transient difference spectrum of the triplet state of a metallophthalocyanine compound, measured point by point from absorbance–time profiles such as the one shown in the inset. The spectrum in Figure 4 has positive and negative values of difference absorbance. When the absorbance is negative, as shown at 680 nm, the ground state removed by the pulse has a higher ϵ value than the excited state generated concomitantly. When positive (530 nm), the excited state has a higher ϵ than that of the ground state. When both states absorb equally, there is a zero value in the absorbance difference spectrum.

In some laboratories [92, 93], the spectrometer outlined above has been modified to include an optical multichannel analyzer (OMA) for obtaining spectral information in a “single shot”. In this arrangement, the monitoring beam is steered into a spectrograph (“polychromator”) after the sample which disperses the white light over a diode array/CCD detector situated at its focal plane. Time resolution requires some kind of “gating” which can be provided by 1) an electromechanical shutter in the monitoring beam, 2) use of a pulsed lamp as the monitoring source, or 3) application of a gating pulse to an intensification stage on the detector. The detector thus provides a dispersed absorption spectrum of the species produced in the sample by photoexcitation, each pixel corresponding to a particular wavelength

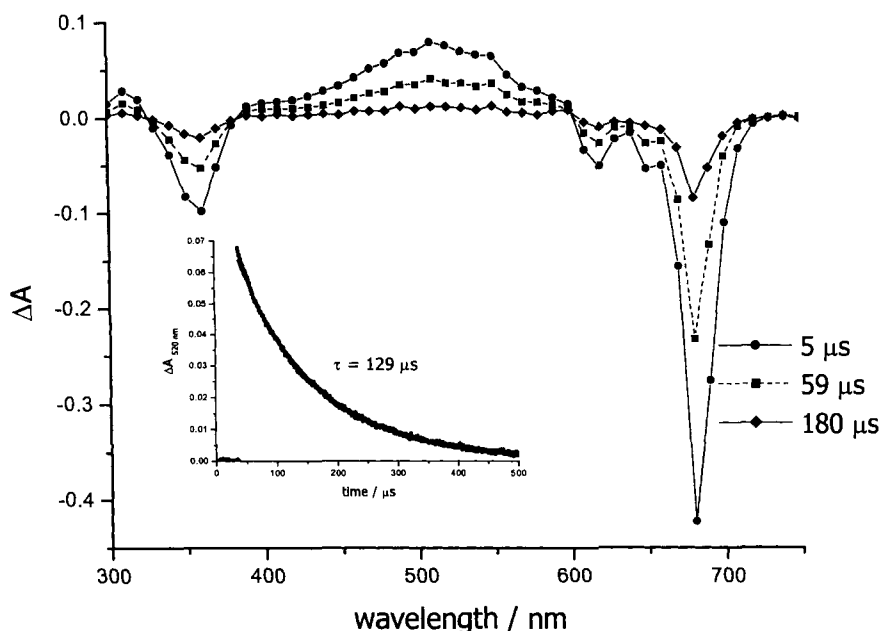


Figure 4. *Main figure:* transient absorbance spectra recorded at three-times (5, 59, and 180 μs) post-355-nm excitation of a solution of bis(trihexylsiloxy) phthalocyaninato- Sn^{IV} in toluene solution. *Inset:* the time profile of the absorption decay at 520 nm.

interval. The recorded spectrum is an average over the temporal width of the monitoring beam pulse. Kinetic information can be obtained by the spectrum collection being repeated at a series of times between arrival of the excitation and the interrogating pulses. While the OMA technique will generate a dispersed absorption spectrum from a single excitation event, in practice, multiple repetitions are employed to improve the signal-to-noise response.

The preceding narrative has focused on the UV–visible spectral region for interrogating the transient states generated. However, in recent years, there has been increasing activity in mid-infrared detection of time-resolved spectra. The major advantage that IR spectrometry brings is that it offers the possibility of structural as well as kinetic information, and it provides distinct absorption bands for some species that have only indistinct UV–visible absorptions. The major drawback to IR observations is that extinction coefficients are generally much smaller than in the visible region; this places additional demands on instrumental sensitivity. Nevertheless, several interesting reports of suprananosecond studies have appeared [94–97].

Ultrafast kinetic spectrometer

A schematic layout of the system extant in the authors' laboratory is shown in Figure 5. The laser assembly is Ti–S based with a titanium–sapphire oscillator (SpectraPhysics, Tsunami) that is pumped by a frequency-doubled, diode-pumped

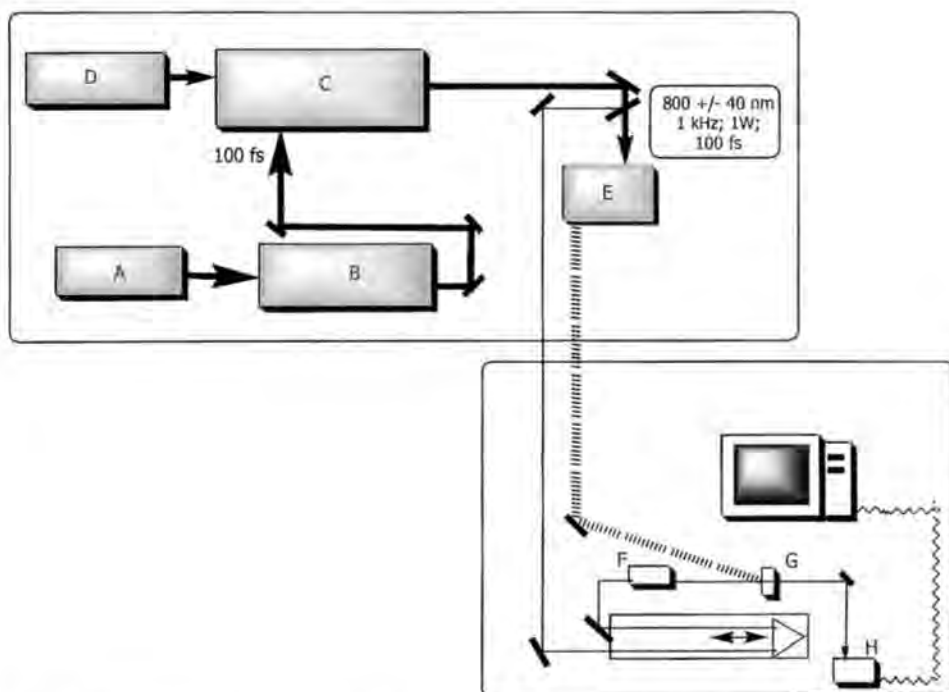


Figure 5. Schematic layout of an ultrafast pump-probe spectrometer. *Top left panel:* A: cw diode-pumped, frequency-doubled, Nd:YAG laser; B: mode-locked Ti-S oscillator; C: regenerative Ti-S amplifier; D: Q-switched, frequency-doubled Nd:YLF amplifier pump laser; E: second/third-harmonic generators or OPA. *Lower right panel:* F: continuum generation; G: sample; H: CCD spectrograph. The double arrow indicates the optical delay stage, and the dashed line indicates the pump-beam trajectory.

5-W cw Nd:YAG laser (SpectraPhysics, Millennia). The oscillator output (ca. 10 nJ, 70 fs, 80 MHz) at 800 ± 30 nm is steered into a Ti-S regenerative amplifier (Positive Light, Spitfire) which is pumped with a frequency-doubled (527 nm) Q-switched Nd:YLF laser (Positive Light, Merlin) operating at 1 kHz. Before entering the amplifier cavity, the 70-fs pulse is stretched to lower its peak power, then steered into the cavity where its amplitude is increased by ca. 10^5 . The amplified pulse is subsequently recompressed to ca. 100 fs. The output of the amplifier is typically 1 mJ per pulse at a repetition rate of 1 kHz. It can be wavelength-tuned over a range of 780 nm to 820 nm. For obtaining useful excitation wavelengths (400 nm, 266 nm), the output of the amplifier is coupled into a harmonic generator (CSX, SuperTripler). For achieving tunable excitation wavelengths in the visible and near-IR regions, the 800-nm beam is employed as pump for an optical parametric amplifier (OPA-800, SpectraPhysics).

A fraction of the amplifier output light (800 nm) is split from the main beam for continuum generation prior to harmonic generation. This is accomplished by the red light (a few tens of μ J) being focused into a 1-mm thick sapphire plate where, at

sufficiently high peak powers, nonlinear optical processes such as stimulated Raman and multiwave mixing occur within the beam waist. This process (self-phase modulation) results in the production of a coherent white-light beam along the pump-beam direction and having a similar time duration. Before continuum generation, the red-light beam traverses an optical delay line that provides an experimental time window of 1.6 ns with a step resolution of 6.6 fs. The energy of the probe pulses is ca. $5 \mu\text{J}/\text{cm}^2$ at the sample.

The pump beam is typically up to $50 \mu\text{J}$ per pulse, although with OPA output this is rarely possible. The spot size at the sample normally has a ca. 2-mm diameter, but again this varies with conditions. A mechanical chopper operating at 30 Hz is positioned in the pump beam upstream of the sample. This provides a series of pump on–pump off exposures (see below). The angle between pump and probe beam is kept as small as possible and is typically $5\text{--}7^\circ$. The liquid sample is held in a reservoir and is pumped through a flow cell (path length of 2 mm, or less). After traversing the sample, the probe beam is focused into a $400\text{-}\mu\text{m}$ fiber-optic cable and entered into a CCD spectrograph (Ocean Optics, SD1000) capable of 0.5 nm per pixel resolution over the range 400 nm to 800 nm. Spectral information is passed from the spectrograph to a PC where it is sorted according to whether it is a pump-on or pump-off sequence. The chopper sync-out signal is used by the software as an indicator of the state of the chopper. The pump-off signals provide the I_0 data, and the pump-on data provide the corresponding I values (Eq. 9). Typically, 4000 excitation pulses are averaged for the transient spectrum at a particular delay time to be generated. A PC with LabView (National Instruments) software acquires data from the CDD spectrograph and operates the delay line. Repetition of the sequence at a series of delay line settings allows the generation of a dynamic surface, and absorbance data at a particular wavelength as a function of delay time provides time profiles.

The instrument response function (10 % to 90 % of rise) of the ultrafast spectrometer is ca. 250 fs. Figure 6 shows an example of a dynamic surface and Figure 7 depicts a reaction–time profile obtained on the instrument described above. The system described is a typical example; similar spectrometers are found in laboratories around the world. There are variants, largely concerning the pump laser. For example the pump–probe technique has been used to great effect with dye-laser sources from which subpicosecond pulses are available [98–99]. Mode-locked Nd:YAG and Nd:glass lasers have similarly been employed. As described in an earlier section, pulse durations for these laser types are suprapicosecond, but they have proven very useful where reaction times are 50 ps and longer [100, 101]. As with the ultrafast systems, continua can be generated if, for example, residual near-IR light is used after the harmonic generation process and the detection system is based on diode-array spectrography [102–105]. In addition, there have been reports of streak cameras being employed as time-resolved detectors in experiments where continuum generation was avoided [106–108].

Ultrafast mid infrared detection

The majority of ultrafast instruments have employed electronic absorption spectrometry for determining the ultrafast dynamic properties of the systems of interest. However, in recent years some investigators have successfully turned their attention

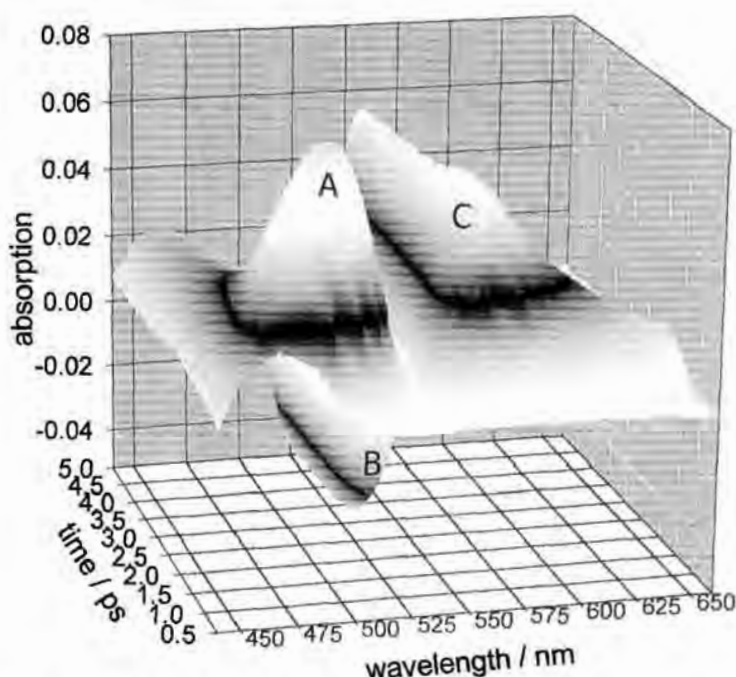


Figure 6. A dynamic surface generated by absorption of 400-nm light pulses in an aqueous solution of tetrakis(sulfonatophenyl)porphinato Ni^{II} . The positive feature indicated by "A" is an immediately formed absorption with a peak at 490 nm. This decays with fast and slow components (see Figure 7). The negative feature indicated by "B" is loss of absorption at the wavelength of the ground state due to removal of some fraction of its population upon photoexcitation. This recovers only slightly over the 5-ps time window. The positive feature labeled "C" which decays only slightly over the 5-ps time window is possibly another part of the longer-lived contributor at 490 nm. Careful scrutiny of the surface shows that the fast component at "A" has a wavelength maximum at 490 nm, whereas the slower contributor has a maximum near 460 nm. Surfaces such as this contain a wealth of information on a single page.

to the mid-IR spectral region, to measure the vibrational properties of short-lived transient states, and, hence, deduce information about structural features. Pump-probe excitation sources employed have been either amplified dye lasers or Ti-S lasers; detector systems have been based on conventional mercury cadmium telluride (MDT) technology [108–115]. Recently, Okamoto has developed detection technology based on optically heterodyned absorption anisotropy [116–117]. This provides improved signal-to-noise ratio for spectral detection, but kinetic information is difficult to obtain.

4.4.2 Light-Scattering Spectrometry

In electronic absorption spectrometry, the spectral bands are broad and often featureless, thus providing minimal information as to the structure of the absorber.

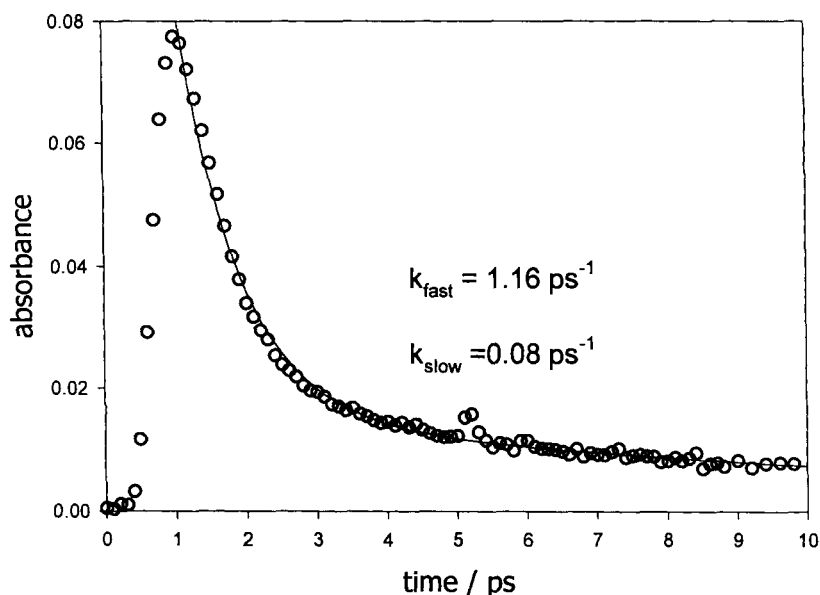


Figure 7. A two-dimensional slice from the surface shown in Figure 6 at 490 nm, allowing rate-parameter evaluation. The fast component has a lifetime of some 860 fs; the slower component has a lifetime of 12.5 ps.

The use of the mid-infrared (fingerprint) spectral region is one way of improving the information content; another depends on light-scattering methods. Inelastic scattering between visible light and molecular systems leads to energy exchanges, and the scattered photons possess energies that are different from the incident ones by an amount equal to one or more vibrational quanta (the Raman effect). The scattered light can have lower frequencies (Stokes) than the incident frequency, or higher frequencies (anti-Stokes). Thus, the frequency of the scattered radiation reports on vibrational transitions in the scattering molecule and Raman spectrometry is therefore complimentary to mid-IR spectrometry. Raman scattering is very weak and only high concentrations of scatterer can be detected in this way. When the frequency of the incident light is close to that of an electronic transition in the scatterer, however, considerable enhancement of active Raman modes can be observed (resonance Raman effect). There is a growing number of investigators who have employed time-resolved resonance Raman (TR^3) spectrometry to study electron transfer and other characteristics of excited states.

TR^3 spectrometry

Lasers are the ideal interrogation sources for TR^3 spectrometry in that they have the narrow line width necessary for discrimination between Raman radiation and elastically scattered light; they also have the high intensities required to generate sufficient signal. Some investigators have used two pulsed laser sources; one to generate the transients and the other to obtain the TR^3 data. The experiment is

therefore of the pump–probe type. Nanosecond and picosecond pulses have been employed [118, 119]. The most frequently used detectors for TR³ have been photomultiplier tubes. Detailed descriptions of picosecond time-resolved Raman apparatus have been published [120–121].

Raman spectra are specific fingerprints for individual chemical species. Clear assignments can often be made if several species are present. The Stokes and anti-Stokes intensities are compared for the determination of the vibrational population ratios and vibrational energy flow on a time-resolved basis. Isotopic Raman spectra provide information on normal modes, geometry, and chemical bonding. Molecular distortions due to solvation changes can sometimes be observed in lineshape and position changes.

The usefulness of resonance Raman spectroscopy for investigating a photo-induced electron-transfer reaction can be exemplified by the well-known oxidative quenching of the MLCT excited state of Ru(bpy)₃²⁺ by MV²⁺. Additional support that the quenching of the excited state occurs by an electron-transfer reaction is given by a resonance Raman spectroscopy study [122]. When mixtures of Ru(bpy)₃²⁺ and MV²⁺ were excited and interrogated by two lasers, detailed vibrational spectra were obtained that could be matched with the Raman spectra of the redox intermediates, including the MV^{•+} ion. No evidence for an excited state of MV^{•+} was observed; this indicates that an energy-transfer process was not occurring.

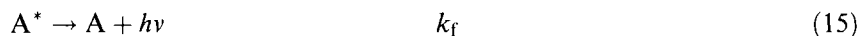
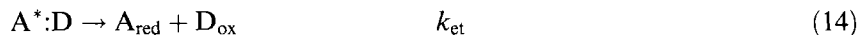
Time-resolved Raman spectroscopy also provides valuable mechanistic information on quenching reactions of molecules such as trans-stilbene [123]. The fluorescence of trans-stilbene can be quenched by tertiary amines. TR³ spectra measured 60 ns after excitation contained peaks that could be assigned to the transient anion radical of trans-stilbene [123].

4.4.3 Fluorescence Instrumentation [124–126]

Introduction

In the electron-transfer process generalized in Eq. 1, one of the components of the reactant state may be fluorescent. This spin-allowed radiative process will thus be in competition with the nonradiative electron-transfer reaction and the two processes will contribute to the overall decay of the reactant state. The intrinsic lifetimes of fluorescent molecular states range typically from 10^{−11} to longer than 10^{−8} s. The occurrence of electron transfer involving the fluorescent state will shorten its lifetime and measurement of this quantity will therefore allow computation of the rate constant for electron transfer.

The kinetic scheme describing this situation can be written as follows:



$$\text{From this, } -d[A^*]/dt = -dI_{\text{f}}/dt = [A^*]_0 \exp(-t/\tau) \quad (16)$$

$$\text{and } \tau^{-1} = k_{\text{obs}} = k_{\text{f}} + k_{\text{et}} \quad (17)$$

Measurement of τ in the absence of the electron donor will therefore yield k_f , and in its presence, k_{obs} will be obtained, from which k_{et} can be evaluated. However, the proviso discussed earlier concerning product identity still applies, and the wise investigator will be concerned with whether it is electron transfer that is actually causing the quenching process. In the past twenty years, time-resolved measurements for fluorescence lifetime determination have become highly developed and they have been much used in electron-transfer research.

Sensitivity and specificity of fluorescence detection

Fluorescence detection is a very sensitive technique, capable of measuring concentrations as low as one part in 10^{10} . In comparison, absorption spectrophotometry is ca. 10^3 times less sensitive. The superior sensitivity of fluorescence is due to the fluorescence signals being measured relative to a zero background. The photomultiplier (or other detector) measures either photon arrival or the absence of photons. In absorption spectrophotometry, the signal is determined from the difference between two light intensity measurements, one the test and one the reference. As the concentration of absorber is reduced, the test and reference signals will approach each other in magnitude, and eventually the measurement of the small difference between two nearly equal large signals will become subject to large random error.

Instrumentation

Time-correlated single-photon counting [125–131]

Time-correlated single-photon counting (TCSP) has proven to be a much-used method for measuring fluorescence lifetimes. It is highly sensitive in that it requires only one photon to be incident on the detector per excitation cycle, and statistical analysis of the experimental data gives lifetimes with well-defined error limits. Commercial systems are available which allow lifetimes from 50 ps to many tens of nanoseconds to be measured with relative ease and high precision.

Figure 8 shows a typical schematic diagram of a TCSP system. The experimental setup requires an excitation source, sample chamber, a sensitive photomultiplier detector, and electronics that allow precise timing of the interval between the arrival of the pulse from the excitation source and the arrival of first fluorescence photon at the detector. In a typical experiment, a hydrogen-flashlamp excitation source produces low-intensity light pulses of a few nanoseconds' duration. Each pulse produces a fluorescence pulse, the fluorescence photons are emitted over a range of times after excitation with more photons being emitted earlier, and fewer emitted later as the excited state decays. Single-photon counting relies on the fact that highly sensitive photomultipliers are able to give measurable current output pulses after a single photon strikes the photocathode. This allows the delay time between the excitation pulse and the arrival of individual photons to be determined. The key to the precise timing is the time-to-amplitude converter (TAC). The TAC is a device that starts to charge a capacitor linearly upon command from the start pulse generated by a photodiode that senses the excitation pulse. It ceases to charge when commanded by the arrival of the fluorescence (stop) pulse. It subsequently outputs a

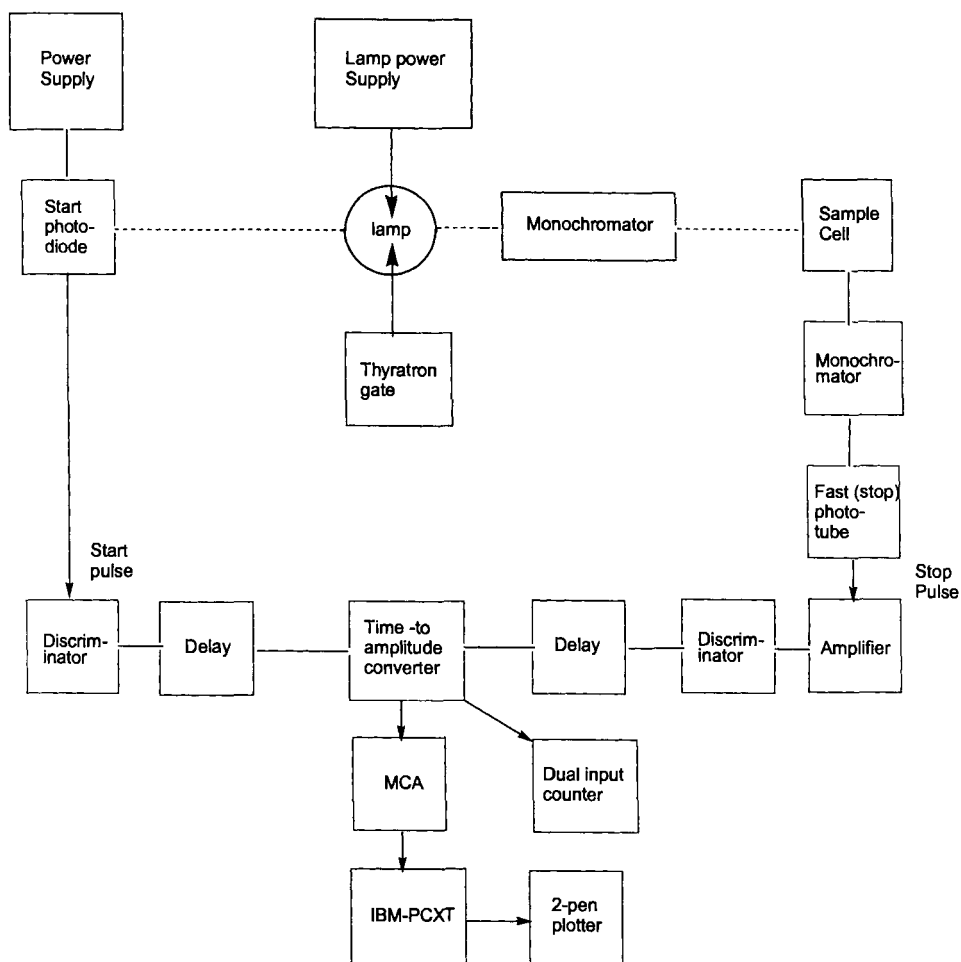


Figure 8. A schematic presentation of a time-correlated single-photon-counting instrument (see text).

voltage pulse whose amplitude is derived from the stored charge and is thus proportional to the time interval between start and stop pulses.

The voltage pulse produced by the TAC is fed to the multichannel analyzer (MCA), and is stored in a specific channel according to its amplitude, and hence time, post-excitation. The probability of a single photon event being counted is high soon after excitation and decreases with time. Repetitive operation of the TAC produces a probability histogram for the detection of fluorescence photons, which is identical to the fluorescence decay curve.

The fluorescence lifetime is obtained from this curve by an iterative curve-fitting program that deconvolutes the lifetime from the instrument-response profile (IRF). This describes the response of the instrument to scattered excitation pulses. A typical

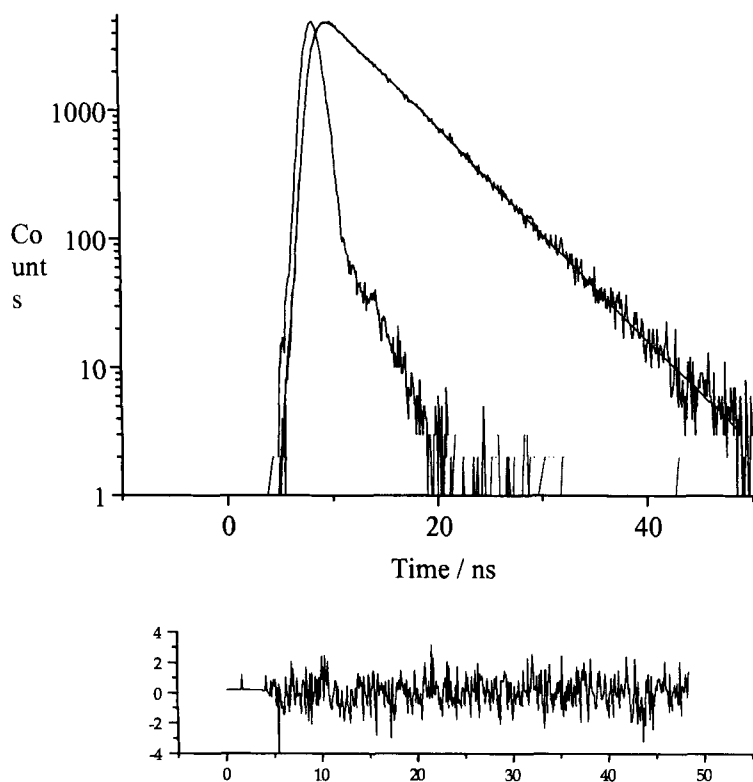


Figure 9. The time profile for the decay of fluorescence from a solution of anthracene in degassed hexane. The data were obtained with a time-correlated single-photon-counting instrument such as that shown in Figure 8. The upper panel shows the raw data with a superimposed linear fit and the instrument-response function. The extracted lifetime was 5.14 ns. The lower panel shows the residuals. (Courtesy of Dr. F. N. Castellano).

scattering solution for obtaining an IRF is colloidal silica, or even a weak suspension of coffee creamer. The results of a typical experiment are shown in Figure 9. The plot consists of three traces, the instrument-response function, the raw experimental data and the numerical fit obtained from the fitting program. The data are usually displayed with a logarithmic ordinate in order to scale the intensity response that is usually arranged to cover over four decades and to clearly show any deviations between data and fit. The plot at the bottom of the diagram shows the percentage differences between the experimental curve and the calculated fitted curve, that is, the residuals. The deviations between the experimental data and the calculated best fits are often too small to be seen by eye, and an assessment of the best fit is normally carried out with statistical tests, such as point-by-point weighted residuals and autocorrelation functions. Full details of data analysis and evaluation can be found in the relevant literature [125, 126, 131].

Fluorescence upconversion [132]

Fluorescence upconversion (also called fluorescence sum frequency mixing) is a technique for measuring fluorescence lifetimes with time resolution in the subpico-second timescale. The upconversion method allows significant improvements in time resolution over the above-discussed time-correlated single-photon-counting (TCSPC) method. The latter has time resolution (with deconvolution) approaching 20 ps. Streak cameras do not allow for time resolution much below 1 ps. Barbara and coworkers described an upconversion instrument with a minimum 300-fs full-width-half-maximum (FWHM) response function [132]. Upconversion is an all-optical method of time-resolving fluorescence, analogous to an optical boxcar and akin to the pump-probe absorption method. It involves frequency mixing of non-coherent fluorescence from a sample with a coherent probe pulse. This is accomplished in a nonlinear crystal such as KDP or LiIO_3 . Time resolution is obtained by delay of the probe pulse relative to the excitation pulse, with use of an optical delay stage.

The apparatus can be divided into three main sections, laser-pulse production, amplification, and fluorescence upconversion. The ultrafast lasers employed for upconversion are those that have been described above. The experiment is a cross-correlation between the fluorescence pulse and the laser pulse. At time $t = 0$, the sample is excited by the ultrafast laser pulse. The resulting incoherent fluorescence (frequency $= \omega_f$) is collected and mixed in a nonlinear crystal (such as KDP) with the gating pulse (frequency $= \omega_l$) derived from the excitation source and arriving at time $t = \tau$. This frequency mixing of the fluorescence and probe beams generates light at the sum frequency, ω_{sum}

$$\omega_{\text{sum}} = \omega_l + \omega_f \quad (18)$$

The theory of sum-frequency conversion of incoherent light can be found in the literature [133–134]. The intensity of the sum-frequency light at a given delay time is proportional to the correlation function of the fluorescence intensity with the intensity of the ω_l beam. A time profile of the fluorescence intensity is obtained by change of the arrival time of one of the pulses with the aid of an optical delay line.

4.4.4 Frequency-Domain (Phase-Shift) Measurements [91, 135]

Over a substantial number of years the phase-shift or frequency-domain method has been employed for the measurement of fluorescence lifetimes. The technique requires the continuous excitation of a fluorescent sample with a source of varying intensity. The fluorescence response would normally be expected to increase and decrease to reflect the changes in excitation intensity. However, in a frequency-domain experiment the excitation beam is modulated at a high frequency, $\omega = 2\pi f$, to produce a sinusoidally changing intensity given by:

$$I_0(t) = A + B \cos(\omega t) \quad (19)$$

If the fluorescence from the sample has a lifetime much shorter than a half period, the fluorescence signal will vary in a sinusoidal manner, without phase shift. If the decay time is comparable with that half period, the sinusoidal signal from the sample emission is phase-shifted with respect to the excitation. For a single exponential lifetime τ , the fluorescence response from the sample is

$$I(t) = C\tau \left[A + \frac{B}{(1 + \omega^2\tau^2)^{1/2}} \cos(\omega t - \delta) \right] \quad (20)$$

The value τ can be obtained directly from the measurement of the phase angle, δ , between excitation and fluorescence.

$$\tan \delta = \omega\tau \quad (21)$$

The modulation ratio M is another valuable parameter that describes the modulation of the fluorescence intensity relative to the excitation intensity:

$$M = \cos \delta = \frac{1}{(1 + \omega^2\tau^2)^{1/2}} \quad (22)$$

Most commercial spectrometers contain a Debye–Sears cell [136], which employs a quartz crystal oscillating at a specified frequency to modulate the intensity of the excitation beam. A cross-correlation detection technique is generally used to measure phase angles at a frequency ω with the gain of the photomultiplier modulated at a frequency $\omega + \Delta\omega$, where $\Delta\omega$ is of the order of a few hertz. The detector signal contains a component at frequency $\Delta\omega$, which is filtered and used to obtain δ with high precision using digital signal-processing techniques. At a single modulation frequency, a single δ value is obtained and only single exponential lifetimes can be determined. However, if the excitation intensity is modulated at two different frequencies in consecutive experiments, the δ and M values should yield the same lifetime if the fluorescence decay is truly exponential. Alternatively, the two sets of δ and M values can be used to obtain τ_1 and τ_2 for the sample exhibiting bi-exponential decay. The laboratories of Lakowicz and Gratton have both been very active in developing frequency-domain fluorometry [91, 137–139].

An important development in the phase-shift technique is the use of a radio-frequency synthesizer as the driver for the Pockels cell modulator. In this way, the excitation beam can be modulated at any frequency between 1 and 200 MHz [137–139]. This approach allows use of cw lasers such as the He–Cd laser and even mode-locked lasers [139] as the excitation source. If δ and M are measured at six to ten suitably spaced frequencies, least-squares curve-fitting techniques can be employed to obtain lifetimes with greatly enhanced precision. Typical data obtained by this multifrequency technique make measurement of decay times as short as 10 ps possible. Gratton and coworkers have developed other curve-fitting procedures to analyze data obtained on a multifrequency phase-shift fluorimeter. These experiments include the construction of time-resolved spectra [140], measurements of ro-

tational relaxation times from fluorescence anisotropy data [141], multi-exponential analyses [142–143], and determination of distributions of lifetimes as continuous functions [143–144]; these greatly increase the power of the phase-shift technique.

4.5 Concluding Remarks

In this chapter an attempt has been made to provide an outline of how photo-excitation methods are useful for the student of the kinetic properties of electron-transfer reactions. The emphasis has been on the practice itself, the why and the how. The authors of other chapters of this series of volumes will discuss the manifold results of such studies and put them into the context of the current theories. There is no doubt that photoinitiation of electron-transfer reactions is a powerful technique that is in widespread use. One significant reason for its popularity must be that photoinitiation allows access to timescales on which the fastest of reactions occur. For example, Xu et al. reported recently [145] that the photoinduced electron-transfer reaction between rhodamine 6G and dimethylaniline (DMA) occurs in neat DMA with a lifetime of 85 fs. Reaction lifetimes shorter than this will surely be few and far between.

Acknowledgments

We wish to express our thanks to Ms. Anna Paola Pelliccioli and Mr. Alexei V. Gusev for providing the data from which Figures 4, 6, and 7 were generated, and to Dr. F. N. Castellano for providing Figure 9 and for insightful discussions about fluorescence lifetime measurements. Experimental facilities in these laboratories have been constructed with support from the National Science Foundation, the National Institutes of Health, and the Center for Photochemical Sciences at Bowling Green State University.

References

1. M. A. Fox, M. Chanon, *Photoinduced Electron Transfer*, Vols. 1–4, Elsevier, New York, 1988.
2. J. R. Bolton, N. Mataga, G. McLendon, *Electron Transfer in Inorganic, Organic, and Biological Systems*, Advances in Chemistry Series 228, CSC Symposium Series 2, American Chemical Society, Washington, DC, 1991.
3. J. Ulstrup, *Charge transfer processes in condensed media*, Springer, Berlin, 1979.
4. R. D. Cannon, *Electron transfer reactions*, Butterworths, London, 1980.
5. V. Balzani, F. Scandola, *Supramolecular Photochemistry*, Horwood, Chichester, 1991.
6. N. Mataga, T. Okada, H. Masuhara, Eds., *Dynamics and mechanisms of photoinduced electron transfer and related phenomena*, Elsevier, Amsterdam, 1992.
7. A. Horvath, K. L. Stevenson, *Charge transfer photochemistry of coordination compounds*, VCH, New York, 1993.

8. D. Astruc, *Electron transfer and radical processes in transition metal chemistry*, VCH, New York, **1995**.
9. M. C. Petty, M. R. Bryce, D. Bloor, Eds, *Introduction to molecular electronics*, Oxford, New York, **1995**.
10. J. Jortner, M. Ratner, Eds, *Molecular electronics*, Blackwell, **1997**.
11. J. Jortner, M. Bixon, Eds, *Electron Transfer from Isolated Molecules to Biomolecules* (Advances in Chemical Physics, Vols. 106 and 107.) Wiley, **1999**.
12. M. Aoudia, M. A. J. Rodgers, *J. Am Chem Soc.* **1997**, 119, 12859–12868.
13. S. Logunov, M. A. J. Rodgers, *J. Phys Chem.* **1992**, 8697–8700.
14. I. R. Gould, in *Handbook of Organic Photochemistry*, Vol. 1 (Ed.: J. C. Scaiano), CRC Press, Boca Raton, Florida, **1987**, Chapter 5.
15. R. G. W. Norrish, G. Porter, *Nature*, **1949**, 164, 658.
16. G. Porter, M. A. West, in *Techniques of Chemistry, Part II*, Vol. 6, 3rd ed. (Ed.: G. G. Hammes), Wiley Interscience, New York, **1974**, pp. 367–462.
17. O. Svelto, *Principles of lasers*, Plenum Press, New York, **1998**.
18. T.H. Maiman, *Nature*, **1960**, 187, 493.
19. D. C. Brown, Solid State Lasers, in *Applied Optics and Optical Engineering*, Vol. 6 (Eds.: R. Kingslake, B. J. Thompson), Academic Press, New York, **1980**, Chapter 1.
20. D. Findlay, D. W. Goodwin, in *Advances in Quantum Electronics*, Vol. 1 (Ed.: D. W. Goodwin), Academic Press, New York, **1970**, p. 77.
21. R. B. Chesler, J. E. Geusic, Solid State Ionic Lasers, in *Laser Handbook*, Vol. 1 (Eds.: F. T. Arecchi, E. O. Schultz-Dubois), North-Holland, Amsterdam, **1972**, p. 325.
22. D. M. Rayner, in *Handbook of Organic Photochemistry*, Vol 1 (Ed.: J.C. Scaiano), CRC Press, Boca Raton, Florida, **1987**, Chapter 7.
23. V. Evtuhov, J. K. Neeland, in *Lasers, a Series of Advances*, Vol. 1 (Ed.: A. K. Levine), Marcel Dekker, New York, **1966**.
24. A. L. Bloom, *Gas Lasers*, Wiley, New York, **1968**.
25. H. Pummer, *Proc.SPIE*, **1986**, 38, 610.
26. C. K. Rhodes, Ed., *Excimer Lasers*, Springer, Berlin, **1979**.
27. J. J. Ewing, in *Laser Handbook*, Vol. 3 (Ed.: M. L. Stitch), North Holland, Amsterdam, **1979**, Chapter A4.
28. see OPOTEK User Manual, OPOTEK, Solana Beach, CA 92075.
29. see MOP0-730 Optical Parametric Oscillator, Spectra Physics Lasers Inc, Mountain View, CA 94039-7013.
30. P. G. May, W. Sibbett, K. Smith, J. R. Taylor J. R. Willson, *Opt. Comm.* **1982**, 42, 285.
31. G. R. Fleming, in *Chemical Applications of Ultrafast Spectroscopy* (Eds.: J. E. Baldwin, J. B. Goodenough, J. Halpern, J. S. Rowlinson), Oxford University Press, New York, **1986**.
32. D. J. Bradley in *Topics in Applied Physics*, Volume 18 (Ed.: S.L. Shapiro), Springer, Berlin, **1977**.
33. I. N. Duling III, T. Norris, T. Sizer, P. Bado, G. A. Mourou, *J. Opt. Soc. Am. B*, **1985**, 2, 616.
34. R. L. Fork, B. I. Greene, C. V. Shank, *Appl. Phys. Lett.* **1981**, 38, 671.
35. C. V. Shank, R. L. Fork, R.T. Yen, in *Picosecond Phenomena III* (Eds.: K.B. Eisenthal, R.M. Hochstrasser, W. Kaiser, A. Laubereau), Springer Series in Chemical Physics 23, Springer, Berlin, **1982**.
36. E. P. Ippen, C. V. Shank in *Ultrashort Light Pulses* (Ed.: S. L. Shapiro), Springer, Berlin, **1977**.
37. B. H. Kolner, J. D. Kafka, D. M. Bloom, T. Baer, *Ultrafast Phenomena IV*, Springer, Berlin, **1984**.
38. G. A. Mourou, T. H. Sizer, *Opt. Commun.*, **1982**, 47, 41.
39. C. V. Shank, R. L. Fork, F. Beisser, *Laser Focus*, **1983**, 59.
40. C.V. Shank, R.L. Fork, R.T. Yen, R.H. Stolen, W.J. *Appl. Phys. Lett.* **1982**, 40, 761.
41. G. R. Fleming, G. S. Beddard, *Optics Laser Technol.*, **1978**, 257.
42. T. Turner, M. Chatelet, D. S. Moore, S. C. Schmidt, *Opt. Lett.* **1986**, 11, 357.
43. S. Szatmari, F. P. Schafer, E. Muller-Horsche, W. Muckernheim, *Opt. Commun.*, **1987**, 63, 305.
44. P. Georges, T. Lepine, G. Roger, A. Brun, *J. Phys.* IV 1: (C7), **1991**, 271–274.

45. A. Rundquist, C. Durfee, Z. Chang, G. Taft, E. Zeek, S. Backus, M.M. Murnane, H. C. Kapteyn, I. Christov, V. Stoev, *Applied Physics B—Lasers and Optics*, **1997**, 65, 161–174.
46. P. M. W. French, *Reports on progress in Physics*, **1995**, 58, 169–262.
47. F. Hajiesmaeibaigi, A. Azima, *Can. J. Phys.*, **1998**, 76, 495–499.
48. A. Kasper, K. J. Witte, *J. Opt. Soc. Am. B.*, **1998**, 15, 2490–2495.
49. see Tsunami (Mode-locked Ti-sapphire laser) User's Manual, Spectra-Physics.
50. J. R. Lakowicz, I. Gryczynski, H. Malak, Z. Gryczynski, *J. Phys. Chem.*, **1996**, 100, 19406–19411.
51. D. S. English, K. Das, K. D. Ashby, J. Park, J. W. Petrich, E. W. Castner, *J. Am Chem. Soc.* **1997**, 119, 11585–11590.
52. G. Porter, *Proc. Roy. Soc., London*, **1950**, A200, 284.
53. E. P. Ippen, C. V. Shank, A. Bergman, *Chem. Phys. Lett.*, **1978**, 38, 611.
54. T. Gillbro, V. P. Sundström in *Picosecond Phenomena III* (Eds.: K. B. Eisenthal, R. M. Hochstrasser, W. Kaiser, A. Laubereau), Springer, Berlin, **1982**, 315.
55. K. G. Spears, T. H. Gray, D. Huang, in *Picosecond Phenomena III* (Eds.: K. B. Eisenthal, R. M. Hochstrasser, W. Kaiser, A. Laubereau), Springer, Berlin, **1982**, 278.
56. T. J. Chuang, G. W. Hoffman, K. B. Eisenthal, *Chem Phys. Lett.*, **1974**, 25, 201.
57. T. Kobayashi, *Bull. Chem. Soc. Jpn.*, **1997**, 70, 1211–1224.
58. G. Schweitzer, Li Xu, B. B. Craig, F. C. Deschryver, *Optics Commun.*, **1997**, 142, 283–288.
59. J. C. Scaiano, L. J. Johnston in *Organic Photochemistry*, Vol. 10 (Ed.: A. Padwa), Marcel Dekker, New York, **1989**; p. 309.
60. R. M. Wilson, K. A. Schnapp, *Chem Rev.* **1993**, 93, 223.
61. J. F. Rabek, *Experimental Methods in Photochemistry and Photophysics, Part II*, Wiley Interscience, New York, **1982**, 822–847.
62. R. E. Birr, C. N. Clark, in *SPSE Handbook of Photographic Science and Engineering* (Ed.: T. Woodlief Jr.), McGraw-Hill, New York, **1978**.
63. L. R. Koller, *Ultraviolet Radiation*, 2nd Ed., Wiley, New York, **1965**.
64. W. Elenbaas, *Light sources*, Crane, Russak, New York, **1972**.
65. B. W. Hodgson, J. P. Keene, *Rev Sci Instr.*, **1972**, 43, 493.
66. T. Hviid, S. O. Nielsen, *Rev. Sci. Instr.*, **1972**, 43, 1198.
67. L. H. Luthjens, *Rev Sci Instr.*, **1973**, 44, 1661.
68. G. Beck, *Rev. Sci. Instr.*, **1974**, 45, 318.
69. J. F. Rabek, *Experimental Methods in Photochemistry and Photophysics, Part I*, Wiley Interscience, New York, **1982**, Chapter 1.
70. G. J. Zissis, A. J. Larocca, in *Handbook of Optics, Section 3*, (Eds.: W. G. Driscoll, W. Vaughan), McGraw-Hill, New York, **1978**.
71. F. E. Clarkson, C. N. Clark, in *Applied Optics and Optical Engineering, Vol 1*. (Ed.: R. Kingslake), Academic Press, New York, **1965**.
72. J. E. Eby, R. E. Levin, in *Applied Optics and Optical Engineering, Vol 7.*, (Eds.: R. R. Shannen, J. C. Wyant), Academic Press, New York, **1979**.
73. see Light Sources, Monochromators, Detection Systems, Catalogue Vol. 2, Oriel Corporation, Stamford, CT.
74. see Incandescent Lamps catalog TP 110R2, General Electric Co., Cleveland.
75. W. H. Melhuish, in *Accuracy in Spectrophotometry and Luminescence Measurements* (Eds.: R. Mavrodineau, J. I. Schultz, O. Menis), NBS Special Publication 378, Government Printing Office, Washington D.C., **1973**, 137.
76. S. P. Davis, *Diffraction Gratings Spectrographs*, Holt, Rinehart, and Winston, New York, **1970**.
77. H. H. Willard, L. L. Merrit, J. A. Dean, F. A. Settle, *Instrumental Methods of Analysis*, 6th Ed., Wadsworth, Belmont, CA, **1988**.
78. R. Kingslake, *Optical System Design*, Academic Press, New York, **1983**.
79. D. Richardson, in *Applied Optics and Optical Engineering, Vol. 5* (Ed.: R. Kingslake), Academic Press, New York, **1969**, Chapter 2.
80. J. M. Lerner, A. Thevenon, *The Optics of Spectroscopy—A Tutorial*, Instruments SA Inc., Edison, NJ, **1986**.
81. G. W. Storke, in *Handbuch der Physik, Vol 29* (Ed.: S. Fluegge), Springer, Berlin, **1967**, 426.

82. J. Flamand, A. Grillo, G. Hayat, *American Laboratory*, **1975**, 47, 7(5).
83. M. C. Hutley, *J Phys. E.*, **1976**, 9, 513.
84. J. M. Lerner, J. Flamand, J. P. Laude, G. Passereau, A. Thevenon, *Soc. Photo-Opt. Instrum. Eng.*, **1980**, 82, 240.
85. J. M. Lerner, J. P. Laude, *Electro-Opt. (U.S.A.)*, **1983**, 31, 15.
86. R. A. Sawyer, *Experimental Spectroscopy*, 3rd Ed., Dover, New York, **1963**.
87. R. J. Meltzer, in *Applied Optics and Optical Engineering*, Vol. 5, (Ed.: R. Kingslake), Academic Press, New York, **1969**, chapter 3.
88. G. Beck, *Rev. Sci. Instrum.*, **1976**, 47, 537–41.
89. J.H. Baxendale, C. Bell, J. Meyer, *Int. J. Radiation. Phys. Chem.*, **1974**, 6, 117.
90. I. R. Gould, in *Handbook of Organic Photochemistry*, Vol. 1, (Ed.: J. C. Scaiano), CRC Press, Boca Raton, Florida, **1987**, Chapter 4.
91. J. R. Lakowicz, *Principles of Fluorescence Spectroscopy*, 2nd ed., Kluwer Academic/Plenum, New York, **1999**.
92. J. F. Rabek, *Experimental Methods in Photochemistry and Photophysics, Part II*, Wiley Interscience, New York, **1982**, p. 843.
93. L. J. Chen, J. S. Guo, J. G. Yang, *Spectroscopy and spectral analysis*, **1999**, 19, 286–288.
94. F. W. Grevels, W. E. Klotzbucher, J. Schrickel, K. Schaffner, *J. Am Chem. Soc.* **1994**, 116, 6229–6237.
95. G. W. Sluggett, C. Turro, M. W. George, I. V. Kopyug, N. J. Turro, *J. Am Chem. Soc.* **1995**, 117, 5148–5153.
96. G. A. Neyhart, C. J. Timpson, W. D. Bates, T. J. Meyer, *J. Am. Chem. Soc.* **1996**, 118, 3730–3737.
97. J. R. Schoonover, K. C. Gordon, R. Argazzi, W. H. Woodruff, K. A. Peterson, C. A. Bignozzi, R. B. Dyer, and T. J. Meyer, *J. Am Chem. Soc.*, **1993**, 115, 10996–10997.
98. S.M. Arrivo, K.G. Spears, J. Sipior, *Opt. Commun.*, **1995**, 116, 377–382.
99. N. Moritz, K. Tischhofer, A. Seilmeier, *Opt. Commun.* **1993**, 103, 461–468.
100. S. L. Logunov, M. A. J. Rodgers, *J. Phys Chem.* **1992**, 96, 2915.
101. S. Aramakis G.H. Atkinson, *J. Am Chem. Soc.* **1992**, 114, 438–444.
102. A. Déclémy, C. Rullière, *Rev. Sci. Instrum.*, **1986**, 57, 2733.
103. S. J. Atherton, S. M. Hubig, T. J. Callan, J. A. Duncanson, P. T. Snowden, M. A. J. Rodgers, *J. Phys. Chem.*, **1987**, 91, 3137.
104. J. A. Hutchinson, L. J. Noe, *IEEE J. Quantum Electron.*, **1984**, 20, 1353.
105. L. J. Noe, in *Biological Events probed by Ultrafast laser Spectroscopy* (Ed.: R. R. Alfano), Academic Press, New York, 339, **1982**.
106. N. H. Schiller, Y. Tsuchiya, E. Inuzuka, Y. Suzuki, K. Kinoshita, K. Kamiya, H. Iida, R. R. Alfano, *Optical Spectra*, June **1980**.
107. K. Yoshihara, A. Namiki, M. Sumitani, N. Nakashima, *J. Chem. Phys.*, **1979**, 71, 2892.
108. H. Kobayashi, T. Ueda, T. Kobayashi, S. Tagawa, Y. Yoshida, Y. Tabata, *Radiat. Phys. Chem.*, **1984**, 23, 393.
109. H. Okamoto, *J. Phys. Chem. A*, **1999**, 103, 5852–5857.
110. H. Okamoto, *J. Phys Chem.*, **2000**, 104, 0000.
111. E. J. Heilweil in *Ultrafast Infrared and Raman Spectroscopy*, (Ed.: M. D. Fayer), Marcell Dekker, New York, **2000**, in press.
112. T. A. Heimer, E. J. Heilweil, C. A. Bignozzi, and G. J. Meyer, *J. Phys. Chem. A* **2000**, 104, 4256.
113. L. H. Kidder, I. W. Levin, E. N. Lewis, V. D. Kleiman, and E. J. Heilweil *Optics Letters*, **1997**, 22, 742.
114. S. M. Arrivo, V. D. Kleiman, T. P. Dougherty and E. J. Heilweil. *Optics Letters* **1997**, 22, 1488.
115. T. A. Heimer and E. J. Heilweil, *J. Phys. Chem. B*, **1997**, 51, 10990.
116. H. Okamoto, *Chem Phys. Lett.* **1998**, 283, 33–38.
117. H. Okamoto, M. Tasumi, *Chem Phys Lett.* **1996**, 256, 502–508.
118. Y. Uesugi, Y. Mizutani, T. Kitagawa, *Rev. Sci. Inst.*, **1997**, 68, 4001–4008.
119. S. E. J. Bell, J. H. Rice, J. J. McGarvey, R. E. Hester, J. N. Moore, R. N. Perutz, T.Q. Ye, Y. Mizutani, T. Kitagawa, *Laser Chemistry*, **1999**, 19, 271–274.

120. A. Laubereau, M. Stockburger, Eds., *Time Resolved Vibrational Spectroscopy*, Springer, Berlin, **1986**.
121. G. Atkinson G. Ed. *Time Resolved Vibrational Spectroscopy* Academic, New York, **1983**.
122. M. Forster, and R. E. Hester, *Chem Phys. Lett.*, **1982**, 85, 287.
123. W. Hub, U. Kluter, S. Schneider, S. Dörr, J. D. Oxman, F. D. Lewis, *J. Phys. Chem.* **1984**, 88, 2308.
124. G. R. Fleming, in *Light Chemical Change and Life: a source book in Photochemistry* (Eds.: J.D. Coyle, R.R. Hill, D.R. Roberts), Open University Press, Milton Keynes, **1982**, chapter 4.
125. J. N. Demas, *Excited State Lifetime Measurements*, Academic Press, New York, **1983**.
126. D. V. O'Connor, D. Phillips, *Time-Related Single Photon Counting*, Academic Press, London, **1984**.
127. W. R. Ware, in *Creation and Detection of the Excited State, Vol. 1.*, (Ed.: A. A. Lamola), Marcel Dekker, New York, **1971**, chapter 5.
128. I. Isenberg, in *Biochemical Fluorescence, Vol. 1*, (Eds.: R.H. Chen, H. Edelhoch), Marcel Dekker, New York, **1975**, p. 43.
129. M. G. Badea, L. Brand, *Methods Enzymol.*, **1979**, 61, 378.
130. L. J. Cline Love, L. A. Shaver, *Anal. Chem.*, **1976**, 48, 364A–371A.
131. D. A. Holden, in *Handbook of Organic Photochemistry Vol. 1*. (Ed.: J. C. Scaiano), CRC Press, Boca Raton, Florida. **1989**.
132. M. A. Kahlow, W. Jarzeba, T.P. DuBrull, P. F. Barbara, *Rev. Sci. Instrum.* **1988**, 59, 1098–1109.
133. F. Zernicke, J. E. Midwinter, *Applied Nonlinear Optics*, **1973**, Wiley, New York.
134. Y. R. Shen, *The Principles of Nonlinear Optics*, **1984**, Wiley, New York.
135. F. W. Teale, *NATO Adv. Sci. Inst. Ser. A*, **1983**, 69, 59.
136. P. Debye, F. W. Sears, On the scattering of light by supersonic waves, *Proc Natl. Acad. Sci. U.S.A.*, **1932**, 18, 409.
137. E. Gratton, M. Limkeman, *Biophys. J.* **1984**, 44, 315.
138. J. R. Lakowicz, B. P. Maliwal, E. Gratton *Anal. Instrum.*, **1985**, 14, 193.
139. J. R. Alcala, E. Gratton, D. M. Jameson, *Anal. Instrum.*, **1985**, 14, 225.
140. T. Parasassi, F. Conti, E. Gratton, *Cell Mol. Biol.*, **1986**, 32, 103.
141. J. Lakowicz, H. Cherek, B. P. Maliwal, E. Gratton. *Biochemistry*, **1985**, 24, 376.
142. T. Parasassi, F. Conti, E. Gratton, *Biochemistry*, **1984**, 23, 5660.
143. T. Parasassi, F. Conti, M. Glaser, E. Gratton, *J. Biol. Chem.*, **1984**, 239, 14011.
144. E. Gratton, D. M. *Anal. Chem.*, **1985**, 57, 1694.
145. Q-H Xu, G. D. Scholes, M. Yang, G. R. Fleming. *J. Phys. Chem. A*, **1999**, 103, 10348–10358.

1 Reactivity Patterns of Radical Ions—A Unifying Picture of Radical-anion and Radical-cation Transformations

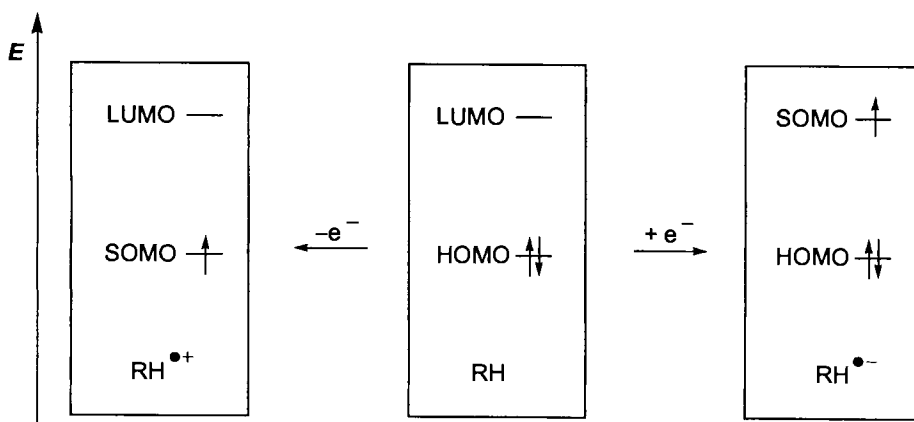
Michael Schmittle and Manas K. Ghorai

1.1 Introduction

The chemistry of charged radicals, both radical anions and radical cations [1], has attracted much attention over the last two decades [2]. Despite a growing number of electron-transfer (ET)-promoted reactions that proceed with high selectivity and with unprecedented low activation barriers, however, most preparative chemists are still hesitant to use ET concepts when mapping out strategies for interesting synthetic target molecules. The reluctance to use radical-ion chemistry is firmly founded in the common notion that ET-initiated processes are mostly extremely complex transformations involving short-lived radical-ion intermediates the reactivity of which is hard to control and to predict. In our analysis covering several hundred transformations of odd-electron charged species [1], however, the majority of reactivity patterns proves to be extremely similar, irrespective of whether radical anions or radical cations are involved, making predictions on the *primary reaction channel* very reliable. Because a large body of kinetic data has recently become available on the reactivity of radical ions, it is now possible to map out the primary reaction channels not only conceptually but also on the basis of reliable data. We hope that the following unifying treatment, although it might not do justice to every possible individual case study in the literature, provides a helpful guide to the understanding of the fascinating chances of radical-ion transformations.

1.2 A Unifying Picture of Radical-anion and Radical-cation Chemistry

Radical ions are usually generated by one-electron reduction or oxidation processes starting from neutral compounds—an electron is either injected into the LUMO or removed from the HOMO. Even a simple MO picture of this process (Scheme 1)



Scheme 1. One-electron-transfer reduction and oxidation of RH.

suggests that the two radical-ion intermediates should share, at least qualitatively, some common features that will determine their chemical fate:

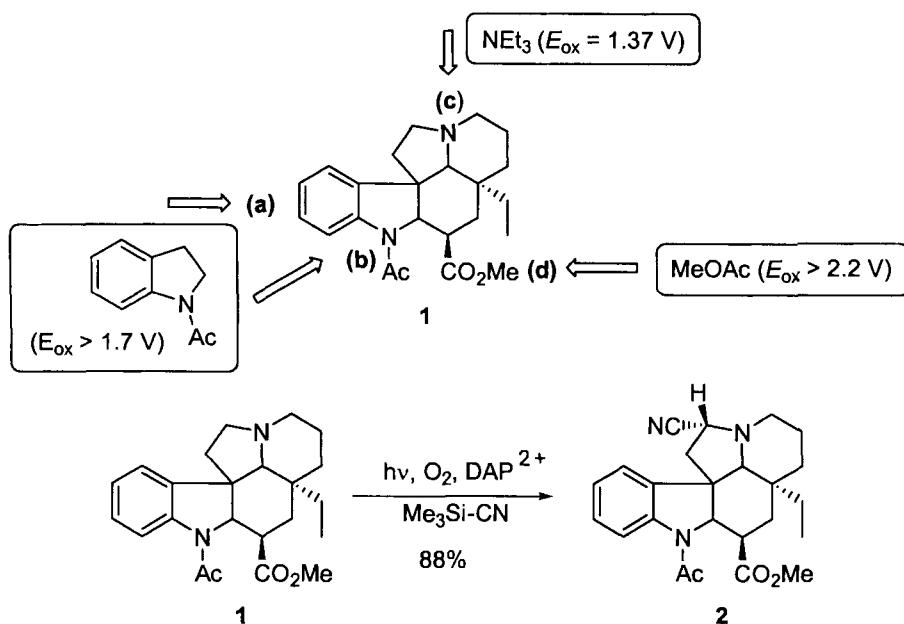
- 1) Both species carry an unpaired electron and a charge: hence, they will behave as either nucleophiles (or electrophiles) and likewise as radicals [3].
- 2) By electron injection into an antibonding orbital or electron removal from a bonding orbital characteristic bonds are weakened: as a consequence a plethora of bond cleavage processes is typical for both radical anions and cations.

To comprehend our categorization and to conceive the similarity between radical-anion and radical-cation reactivity the concept of the electrophore is of paramount importance. In simple terms, the electrophore is the ET active part of the molecule which either accepts or ejects an electron. To illustrate this concept it is helpful to analyze the reaction behavior of complex molecules after one-electron-transfer activation.

The alkaloid **1** [4] (Scheme 2), for example, has four donor functionalities (a)–(d) that could potentially be involved in the one-electron oxidation. At what site do we expect the oxidation to occur? For rapid analysis we approximate the various sub-units (a)–(d) by small, structurally related molecules the potentials of which are known. Accordingly, triethylamine and methyl acetate can serve as models for (c) and (d). As donors (a) and (b) are linked by conjugation, we treat them together and, indeed, find with *N*-acetylindoline a good approximation.

From the oxidation potentials provided above we have to conclude that oxidation will originate from the donor site (c) with the lowest E_{ox} , which is indeed observed in the selective photoinduced electron-transfer (PET) cyanation of **1** using DAP^{2+} (*N,N'*-dimethyl-2,7-diazapyreniumbistetrafluoroborate) as sensitizer [4].

As reversible redox potentials in solution are not available *in extenso* they can be replaced to a first approximation by ionization energies [5] or electron affinities [5, 6] either from experimental compilations or quantum-chemical calculations [7].



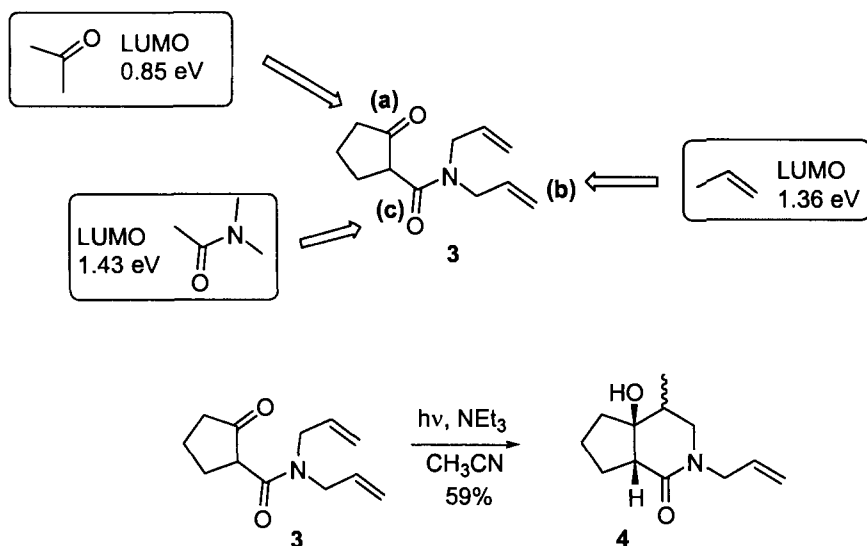
Scheme 2. Finding the relevant donor in alkaloid **1** containing several alternative electrophoric sites and the selective transformation of **1** [4] using PET.

Hence, a quick analysis might use LUMO energies from semi-empirical calculations for the analysis of the reduction of **3** (Scheme 3). Because the LUMO energy of acetone as model for site (a) in **3** is the lowest within the three electrophores, one must expect that an electron will be accepted at this site. This is indeed demonstrated in the PET reduction of **3** to a ketyl radical anionic intermediate using triethylamine as sensitizer [8].

While identification of the relevant electrophores in both examples above has enabled specification of the site at which the reaction will occur, it will be difficult for the non-expert reader to predict the primary reaction of the radical ion. Hence, we have written this review with the intention of providing *guidelines for the identification of primary reaction channels of radical ions and information about their kinetic reactivity*, which should enable the reader to set up defined ET-induced reactions even in polyfunctional molecules.

1.3 A Construction Set of Electrophores and its Relevance for Devising Selective Reactions *via* Radical Ions

The examples in Schemes 2 and 3 have illustrated the significance of identifying the electrophore with the lowest LUMO (or highest HOMO) energy for one-electron



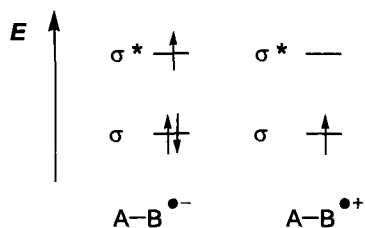
Scheme 3. LUMO energies calculated using AM1 [9a,c] and the selective transformation of **3** [4].

reduction (or oxidation) reactions. But that is not sufficient! In addition, it is necessary to categorize the relevant electrophore according to its main constituents, i.e. to check whether it has mainly σ^* or π^* (for reductions) or σ , π or n character (for oxidations). This categorization is helpful because it will enable us to make predictions on the follow-up reactions of the radical ions.

If one wishes to induce a bond-cleavage reaction at the stage of the radical ion, one must choose either an acceptor whose LUMO contains a significant σ^ component or a donor whose HOMO has high σ participation.* In both, electron transfer will lead to a significant bond weakening, resulting in bond cleavage (Scheme 4).

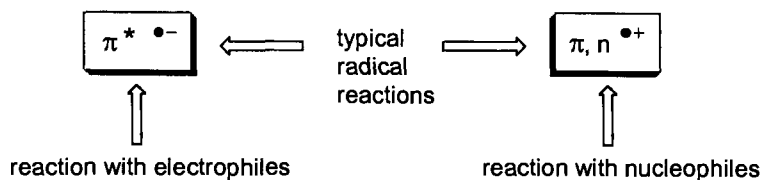
If we like to induce bond formation at the stage of the radical ion, it is advisable to select either an acceptor whose LUMO contains significant π^ character or a donor whose HOMO has a predominant π (or n) component.* Electron transfer in both will lead to either radical or ion-type bond-formation reactions (Scheme 5).

The above considerations have emphasized the need to establish the main character of the LUMO (of acceptors) and likewise of the HOMO (of donors). For that

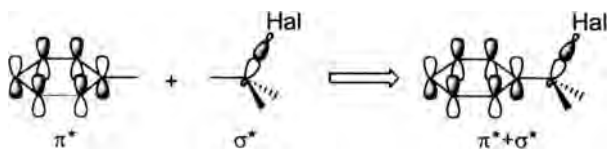


Scheme 4. Illustration of bond weakening in both σ^* radical anions and σ radical cations.

Bond formation through



Scheme 5. Illustration of the similar reactivity patterns of radical anions and radical cations in bond-formation reactions.



Scheme 6. Electrophores are often assembled from individual functional groups and bonds at the periphery.

purpose, the electrophore of interest should be analyzed with regard to the functional group(s) (halide, phenyl, carbonyl, amino etc.) and the peripheral bonds (such as C–C, C–H, C–Hal bonds) that have orbital overlap with the main functional group(s). It is indisputable that the acceptor (or donor) qualities of different groups and bonds will be different and that only those with the lowest individual LUMO (or highest individual HOMO) energies will be main contributors to the LUMO (or HOMO) of the electrophore (Scheme 6).

The main character of a composed electrophore will be determined by the character of the strongest contributor (acceptor or donor). Hence in the following, the acceptor properties of several common bonds and functional groups that are relevant for organic ET synthesis will be listed. Because of the lack of extensive electron affinity data, we have preferred to approximate the acceptor qualities by the LUMO energies as calculated by AM1 (Table 1) [9a, c, 10]. The calculations also enable categorization of acceptors as either σ^* or π^* .

Likewise, we have established a qualitative order of the donor properties of several bonds and functional groups. The ordering was based on ionization potentials [5], because these are readily accessible for many molecules (Table 2).

It is obvious that a reduction of a pure σ^* acceptor will lead to rather efficient bond weakening as much as oxidation of a σ donor will entail bond cleavage (Scheme 4). The numbers [11, 12] in Table 3 underline the drastic effect of one-electron transfer on the bond strength of appropriate σ^* acceptors and σ donors. In all cases the bond-dissociation energies (BDE) of the radical ions are much lower than those of the neutral precursors (Table 3).

As mentioned above, however, most acceptors (or donors) will not be pure σ^*

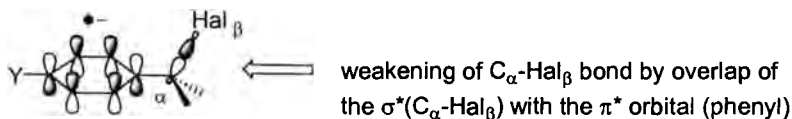
Table 1. Acceptor qualities (LUMO energies) of a variety of σ^* and π^* acceptors as determined by AM1 semi-empirical calculations [9a, c, 10].

Energy of LUMO	σ^* Acceptor (energy of LUMO, eV)	π^* Acceptor (energy of LUMO, eV)
+5 to +3 eV	C-H ethane (+4.1) C-F fluoromethane (+3.8) C-N dimethylamine (+3.5) C-O oxirane (+3.4) ^a C-O dimethyl ether (+3.2)	
+3 to +2 eV	C-C oxirane (+2.7)	C \equiv C ethyne (+2.1)
+2 to +1 eV	C-Cl chloromethane (+1.6) C-F tetrafluoromethane (+1.2)	C \equiv N acetonitrile (+1.7) C=C ethylene (+1.4) C=N acetonimine (+1.2) C=O methyl acetate (+1.1)
+1 to 0 eV	C-S dimethylsulfide (+0.9) C-Br bromomethane (+0.9) C-I iodomethane (+0.5)	C=O acetaldehyde (+0.8) Ph benzene (+0.6) C=N azirine (+0.6) Ar pyridine (+0.1)
0 to -1 eV	C-Se dimethylselenide (-0.5) ^b C-O C-S methyl mesylate (-0.7)	NO ₂ nitromethane (-0.1) Ar pyrimidine (-0.2) Ar phenanthroline (-0.7) Ar anthracene (-0.8)
-1 to -3 eV	S-S dimethyl disulfide (-1.5) C-Br tetrabromomethane (-2.1) C-O, C-S methyl triflate (-2.4)	Ar nitrobenzene (-1.1)

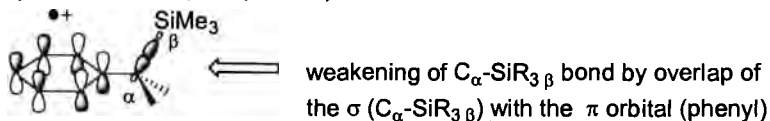
^aHigher-lying unoccupied MO.^bValue calculated by use of PM3 [9b].

acceptors (or σ donors). The relevant frontier orbital will be composed of two or more constituents, e.g. for benzyl halides and benzylsilanes (Scheme 7).

($\sigma^*+\pi^*$) radical anion (benzyl halide)

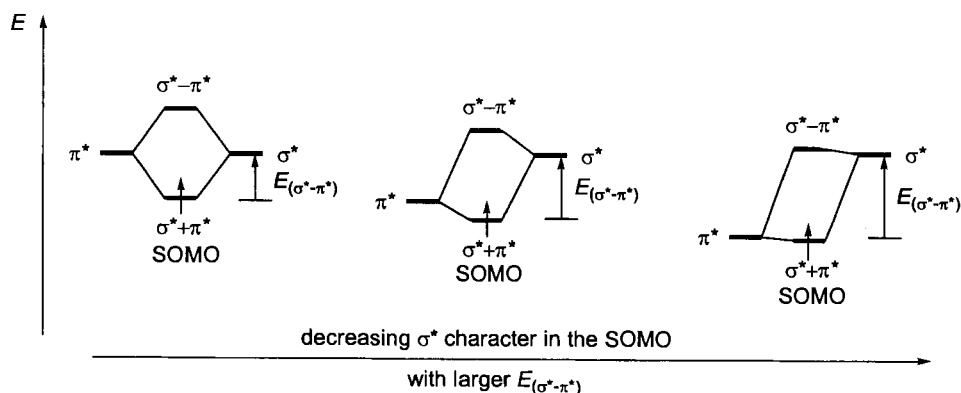


($\sigma+\pi$) radical cation (benzylsilane)

**Scheme 7.** The relevant frontier MO for benzyl halides and benzylsilane.

Let us examine the reduction of a benzyl halide, which is, according to our understanding a typical ($\sigma^* + \pi^*$) acceptor. ($\sigma^* + \pi^*$) radical anions are composed of σ^* and π^* components in the singly occupied orbital. If there is good overlap between them (stereoelectronic effect) then for a given C–X bond the weakening will be stronger the closer the energy of the σ^* and the π^* electrophore (cf. Scheme 8).

For the simplest case, i.e. compounds with the same kind of scissile bond (similar homolytic bond-dissociation energies and σ^* energies!), the splitting $E_{(\sigma^*-\pi^*)}$ provides a good measure of the bond weakening. Along this line, substituted benzyl bromide radical anions have a lower ΔG_{BDE} when the energy of the π^* LUMO is raised, because the σ^* character in the SOMO is increased [13].



Scheme 8. In a radical anion with a constant $\sigma^*(\text{C-X})$ energy $E_{(\sigma^*-\pi^*)}$ becomes larger when the energy of the π^* orbital is reduced. Hence, the σ^* character of the SOMO decreases.

A particular situation is met when the observed bond cleavage in the radical anion is not expected because of the low σ^* character of the SOMO, as observed in the reduction of aryl halides. For example, the analysis of 4-chloronitrobenzene based on AM1 [9a, c] calculations clearly indicates that the LUMO and the nLUMO do not share any $\sigma^*(\text{C-Cl})$ character. Actually, the lowest unoccupied orbital with a

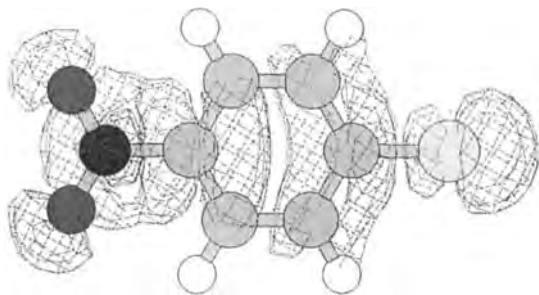


Figure 1. LUMO + 3 orbital of 4-chloronitrobenzene according to AM1 [9a, c] calculations.

Table 2. Donor qualities (HOMO energies) of a variety of σ , π , and n donors as determined by experimental ionization energies from the NIST webbook [5].

Energy of HOMO	σ donor (energy of HOMO, eV)	π or n donor (energy of HOMO, eV)
-7 to -8 eV	Sn-Sn hexamethyldistannane (-8.0)	Ar anthracene (-7.4) n_N trimethylamine (-7.9) Ar <i>p</i> -hydroquinone (-7.9)
-8 to -9 eV	Ge-Ge hexamethyldigermane (-8.1) Si-Si hexamethyldisilane (-8.3) C-Sn tetramethylstannane (-8.9)	n_P triethylphosphane (-8.1) Ar pyrrole (-8.2) Ar anisole (-8.2) n_{Se} diethylselenide (-8.3) n_S diethylsulfide (-8.4) Ar furan (-8.9)
-9 to -10 eV	C-Ge tetramethylgermane (-9.3) C-C cyclopropane (-9.9) C-Si tetramethylsilane (-9.8)	Ar benzene (-9.2) n_I iodomethane (-9.5) n_O diethyl ether (-9.5) n_{Se} H_2Se (-9.9)
-10 to -11 eV	C-H cyclopentane (-10.3)	n_N ammonia (-10.1) n_S H_2S (-10.5) n_{Br} tribromomethane (-10.5) n_{Br} bromomethane (-10.5) C=C ethene (-10.5)
-11 to -12 eV	C-H ethane (-11.5)	n_{Cl} chloromethane (-11.3) C \equiv C ethyne (-11.4) n_{Cl} tetrachloromethane (-11.5)
-12 to -13 eV	C-H fluoromethane (-12.5) C-H methane (-12.6)	n_O H_2O (-12.6)

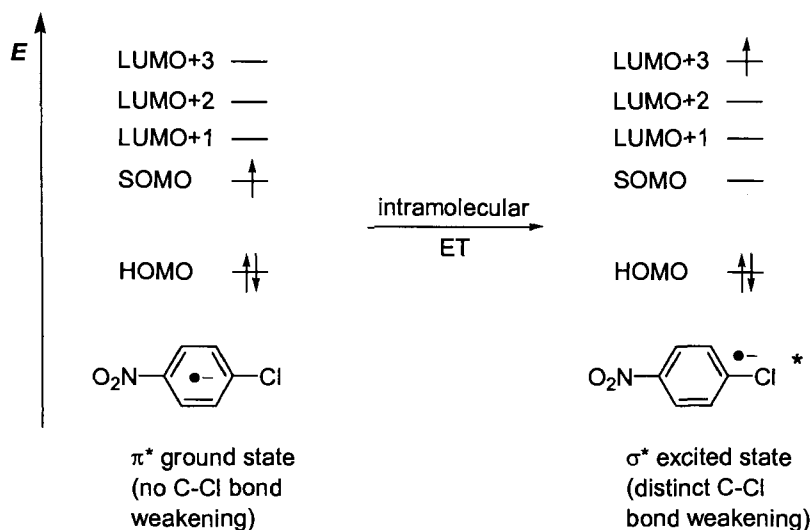
Table 3. Bond-dissociation energies (BDE) of σ^* radical anions and σ radical cations.

Radical anion	BDE (kJ mol ⁻¹) [11]	Radical cation	BDE (kJ mol ⁻¹) [12]
Cl-CCl ₃ ^{•-}	-59 (306) ^a	CH ₃ -H ^{•+}	172 (440) ^a
Cl-CHCl ₂ ^{•-}	-92 (325) ^a	CH ₃ -CH ₃ ^{•+}	215 (377) ^a
Br-CBr ₃ ^{•-}	-13 (235) ^a	(CH ₃) ₃ C-CH ₃ ^{•+}	25 (364) ^a
Br-CHBr ₂ ^{•-}	-50 (259) ^a	Cyclopropane ^{•+}	89 (251) ^a

^aValues in parentheses are the bond-dissociation energies of the neutral compounds.

sizeable $\sigma^*(C-Cl)$ component is the LUMO+3 orbital (Figure 1). Nevertheless, C-Cl bond cleavage can be initiated by first forming an aromatic π^* radical anion that undergoes activation by intramolecular ET to the LUMO+3 orbital (Scheme 9).

Conceptually seen, such an ET reaction is possible through the avoided crossing of both electronic states separated by the energy gap $\Delta E_{\sigma^*,\pi^*}$. In a more pictorial description, the π^* acceptor system serves as an intramolecular redox relay which helps to shuttle the electron to the $\sigma^*(C-Cl)$ orbital which is not accessible by direct



Scheme 9. 'Intramolecular ET' activates 4-chloronitrobenzene radical anion for bond cleavage.

reduction because of its higher energy. It is obvious that the π^* radical anion will undergo bond cleavage only in the presence of a low-lying $\sigma^*(\text{C-X})$; otherwise it will undergo typical π^* reactions, such as transformations with either electrophiles or radical species.

What we have summed up for radical anions is likewise valid for radical cations, except that they might contain, in addition to the σ and π donor sites, also n donor character. Hence, σ , $(\sigma + \pi)$, and $(\sigma + n)$ radical cations may undergo bond cleav-

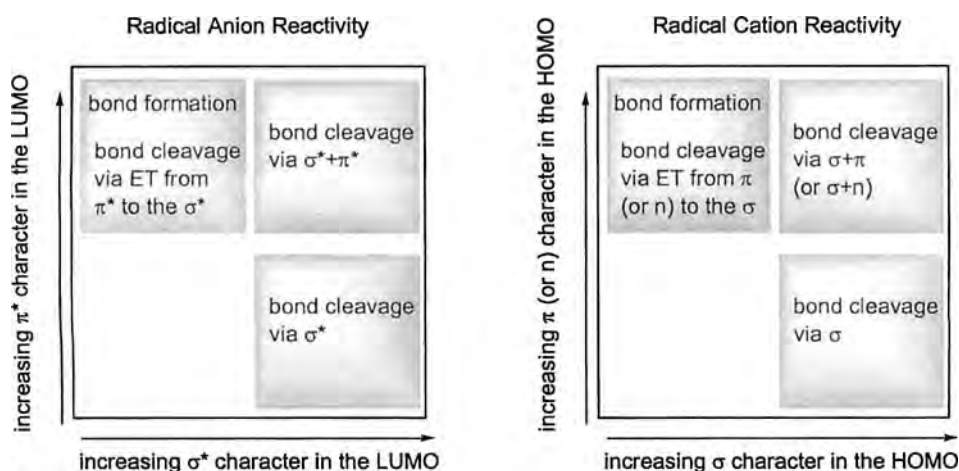


Figure 2. Radical anion and radical cation reactivity related to the character of the frontier MO of the redox-active molecule.

age because an electron is completely or partly removed from a bonding σ type orbital. In contrast, pure π and n radical cations, will undergo bond-formation reactions. Hence, to sum up the following picture of radical-ion chemistry may be sketched (Figure 2).

The above categorization emphasizes the similarities of the reactivity patterns of radical anions and radical cations. On the basis of the bond and fragment electron affinities (Table 1) or ionization potentials (Table 2), we can now devise systems that should undergo, for example, facile bond cleavage. As a prerequisite the σ^* (or σ) orbital representing the scissile bond has to be made a major contributor to the LUMO (or HOMO).

For example, C–Cl bonds can be easily cleaved by reduction because of their low-lying σ^* orbitals, whereas C–N bonds are much more difficult to cleave. Hence, it is advisable to incorporate the $\sigma^*(\text{C–N})$ into a $(\sigma^* + \pi^*)$ system by overlap of $\sigma^*(\text{C–N})$ with a low-lying π^* (e.g. from nitrobenzene). If overlap of the σ^* with a π^* is not possible, we still can set up a low-lying π^* redox relay to shuffle the electron to the σ^* by intramolecular ET.

The analogous situation can be arranged for bond cleavage in radical cations by using appropriately placed π or n donors to assist bond cleavage (Scheme 10).

To reveal the analogies in the primary reaction behavior of radical ions, we will use in this review the following structure:

- reductive and oxidative **bond-cleavage reactions**,
- reductive and oxidative **bond-formation reactions**, and
- ‘**pericyclic**’ **processes** under reducing and oxidizing conditions.

The vast body of examples covering many decades can obviously not be presented in a comprehensive manner here. Thus, we have decided to focus on a few selected examples from the recent literature; this should give the interesting reader the chance to find analogous examples through cited references. We regret that this way of presenting the material will not do justice to the numerous pioneers of radical-ion chemistry, whose work is extensively quoted in older reviews [14] or monographs [2]. The synthetic examples will be accompanied by kinetic and thermodynamic data to provide a qualitative and quantitative picture of radical-ion reactivity. When devising new synthetic schemes using these odd-electron species the combination of synthetic, kinetic, and thermodynamic aspects hopefully will serve as guide to the achievement of highly selective transformations.

1.4 Reductive and Oxidative Bond-cleavage Reactions

1.4.1 General Principles of Bond Cleavage

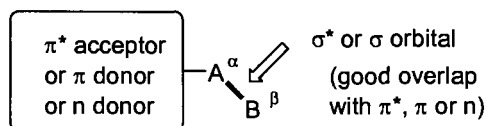
As discussed above, bond cleavage in radical ions is a result of the weakening of a single bond after electron transfer.

Bond cleavage

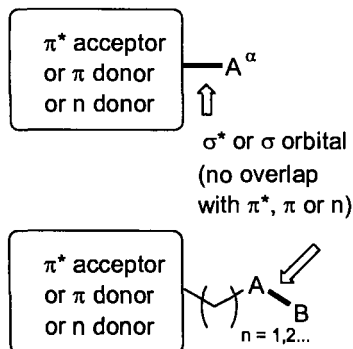
via σ^* acceptors / σ donors



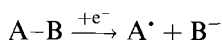
via $(\sigma^* + \pi^*)$ acceptors / $(\sigma + \pi)$ or $(\sigma + n)$ donors



via π^* acceptors / π or n donors as redox relays



Scheme 10. Schematic view of bond cleavage in radical ions.



There are three distinct cases to be recognized depending on the σ^* (or σ) character of the LUMO (or HOMO).

- 1) If we deal with a pure σ^* LUMO (or σ HOMO), electron injection (or removal) will entail the strongest bond weakening effect. ET activation of such systems will always lead to bond dissociation.
- 2) In contrast, radical ions, whose LUMO has $(\pi^* + \sigma^*)$ character (or whose HOMO has $(\pi + \sigma)$ or $(n + \sigma)$ character), will experience reduced bond weakening after ET. Nevertheless, these systems still undergo efficient bond cleavage.
- 3) Molecules with pure π^* LUMO (π or n HOMO) character might undergo—in competition to other reactions—efficient bond cleavage, if they contain σ^* (or σ) orbitals which are energetically accessible by intramolecular ET.

Table 4. Acceptor type classification of aryl halides according to PM3 [9b, d] calculations.

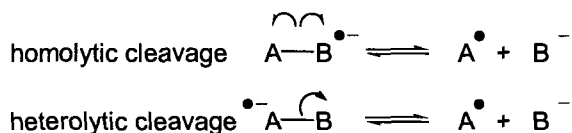
Molecule	LUMO (energy)	Energy of lowest σ^* orbital
Fluorobenzene	π^* (+0.03 eV)	+2.33 eV (LUMO + 2)
Chlorobenzene	π^* (+0.06 eV)	+1.46 eV (LUMO + 2)
Bromobenzene	σ^* (−0.05 eV)	
Iodobenzene	σ^* (−0.43 eV)	
1,4-Dibromobenzene	σ^* (−0.32 eV)	
<i>p</i> -Cyanobromobenzene	π^* (−0.86 eV)	−0.45 eV (C–Br) +1.69 eV (C–CN)
<i>p</i> -Nitrobromobenzene	π^* (−1.39 eV)	−0.72 eV (C–Br) +1.10 eV (C–NO ₂)

To realize how the acceptor character can change from a σ^* to π^* system within a seemingly analogous series of compounds it is instructive to check the classification in Table 4.

While the cartoon-like depiction of the acceptor (or donor) in Scheme 10 emphasizes the analogies in radical-ion chemistry in a rather general manner, our compilation (Scheme 11) aims at providing more insight into some relevant functionalities involved in dissociation processes.

Irrespective of the electrophoric system involved in one-electron transfer-initiated bond dissociation one can easily derive the thermodynamic driving force for a such process by use of thermochemical cycle calculations [15]. Such estimates are particularly valuable as experimental numbers, because bond-dissociation data are scarce.

The cleavage of radical ions can proceed homolytically (or heterolytically) depending on whether the scission leaves (or does not leave) the charge mainly in the same region as in the radical ion. Change-over from homolytic to heterolytic bond cleavage can even occur in the same family of compounds, and the kinetic changes seem to be simply related to the thermodynamics of the bond cleavage and *not* to the mode of scission [16].

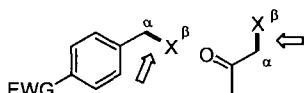


The kinetics of bond cleavage will be treated separately below according to the type of electrophore. Such data are important as cleavage rate constants can vary by more than ten orders of magnitude, depending on the nature of R and X in $\text{RX}^{\bullet-}$ [17].

The huge amount of bond-dissociation [18] examples makes this reactivity pattern one of the most prominent in radical-ion chemistry. We will therefore discuss this mode of reaction by providing thermodynamic and kinetic data along with some representative synthetic examples.

Bond cleavage via reduction**via pure σ^* acceptors**

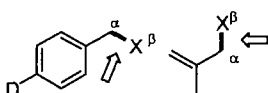
C-Hal, C-O, O-O, C-S, C-Se

via ($\sigma^*+\pi^*$) acceptors

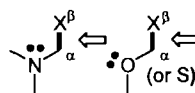
X = Hal, O, S, N, C

*the α atom is quite often carbon, but can likewise be a heteroatom, such as oxygen, nitrogen, sulfur..***Bond cleavage via oxidation****via pure σ donors**

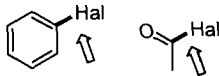
C-Si, C-Ge, C-Sn

via ($\sigma+\pi$) donors

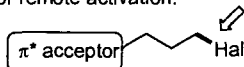
X = Si, Sn, H, C

via ($\sigma+n$) donors

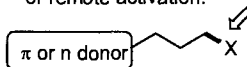
X = Si, Sn, H, C

**via intramolecular ET shuttled
by π^* acceptors**

or remote activation:

**by π donors**very rare
even with X = Sn, Si

or remote activation:

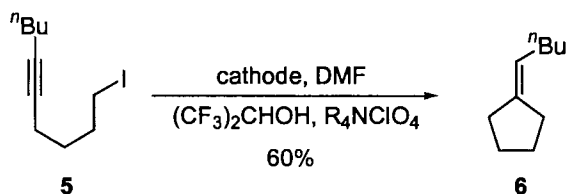
**by n donors****Scheme 11.** A compilation of scissile bonds often encountered in radical ion cleavage reactions.**1.4.2 Synthetic, Kinetic and Thermodynamic Aspects of Reductive Bond Cleavage****Bond cleavage after reduction of σ^* acceptors***Synthetic aspects*

We encounter reductive bond cleavage of σ^* acceptors when there are no readily reducible π^* acceptors, such as aryl, carbonyl, and analogous functionalities present. Hence, this reaction pattern is commonly realized in aliphatic systems containing the electrophores depicted in Scheme 12, such as in simple reductions $R-Hal \rightarrow R-H$ [19]. Equally of importance is the dehalogenation of geminal [20] and vicinal dihaloalkanes [21], which has also been described for SO_2R , SR , OAc , OMe , OH ,

Common σ^* acceptors for reductive bond cleavage

C-Hal, C-O, C-S, C-Se, O-O, Si-Hal

Scheme 12. Frequently used σ^* acceptors that undergo rapid bond cleavage after reduction.



Scheme 13. 5-*exo-dig* cyclization initiated after reductive C–I bond cleavage [25].

and other leaving groups [21]. C–Hal bond cleavage is, moreover, frequently applied in $\text{S}_{\text{RN}}1$ reactions [2b] with aliphatic halides [22], in the generation of alkyl lithium compounds [23], and in cyclization reactions (Scheme 13) [24, 25].

C–O bond cleavage is most efficiently set up in strained systems, e.g. in oxiranes [26] and oxetanes [27], whereas O–O bond cleavage in cyclic peroxides [28] and C–S [29] and C–Se [30] bond rupture occur efficiently even in unstrained compounds. Si(Ge)–Hal bond cleavage [31] has become a valuable reaction, e.g. in the preparation of network polysilanes and polygermanes [32].

Kinetic and thermodynamic aspects

Pure σ^* acceptors, e.g. aliphatic halides and peroxides, are mostly believed to undergo dissociative ET, i.e. concomitant with ET into the σ^* orbital the bond elongates until it cleaves. Hence, over years it was believed that in such processes radical anions are generally not involved as distinct intermediates, although in very few examples parent anions had been observed, e.g. for CF_3Cl , CF_3Br , CCl_4 and CBr_4 [33]. Moreover, recent femtosecond studies revealed for the $\text{Et}_2\text{S}-\text{I}_2$ system after photoinduced charge transfer that reversible ET occurs in less than 150 fs (fastest trajectory) and is followed by the rupture of the I–I bond with the release of the first I atom in 510 fs [34]. Although semi-empirical calculations found both dissociative and non-dissociative ET with polyhalogen methanes [35], one must also take into consideration that the surrounding solvent will be important. Indeed, electron-transfer reduction of CCl_4 in the gas phase is predicted to yield an intermediate radical anion [36], whereas it is dissociative in $\text{H}_2\text{O}-\text{CH}_3\text{CN}$ (36:64 % *v/v*) [35]. As a consequence, the question of dissociative or non-dissociative ET has to be answered depending on the individual molecule and the reaction conditions.

For dissociative ET reactions thermodynamic bond dissociation data are not very meaningful, because they are intrinsically interwoven with the ET step. Nevertheless, some data are available, e.g. on halomethanes [37], and polyhalomethanes [11, 38].

Seminal work by Savéant and his group [39] has contributed to our understanding of the dynamics of dissociative ET, compared with the corresponding stepwise process [40]. Obviously, bond-dissociation energy, rather than bond dissociation free energy, represents the important contribution to the intrinsic barrier [41]. One must, moreover, take into account that dissociative ET can occur in the adiabatic (e.g. *tert*-butyl bromide) and in the non-adiabatic regime (di-*tert*-butyl peroxide)

[42]. Reorganization energies of such processes have been calculated and evaluated [43].

Irrespective of the mechanistic pathway, radical anions from σ^* acceptors undergo very rapid bond cleavage, a process that might be related to the toxicity [44] and carcinogenic activity [45] of polyhalogen alkanes, and which is of huge importance in synthetic chemistry.

Bond cleavage after reduction of ($\sigma^* + \pi^*$) acceptors

Synthetic aspects

Reductive bond cleavage in ($\sigma^* + \pi^*$) radical anions can be accomplished under milder conditions than with σ^* acceptors, because the π^* component can be used to move the reduction potential towards less cathodic potentials. The most common examples involve C–Hal bond cleavage in (hetero)benzylic and (hetero)allylic positions. Even those bonds can, however, be cleaved whose σ^* orbital is very high in energy, e.g. C–O, C–N, and C–C bonds (Scheme 14).

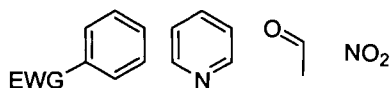
Common ($\sigma^* + \pi^*$) acceptors for reductive bond cleavage.

Combine

good σ^* acceptors : C–Hal, C–O, C–S,
C–Se, O–O, Si–Hal

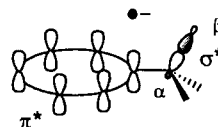
with

good π^* acceptors



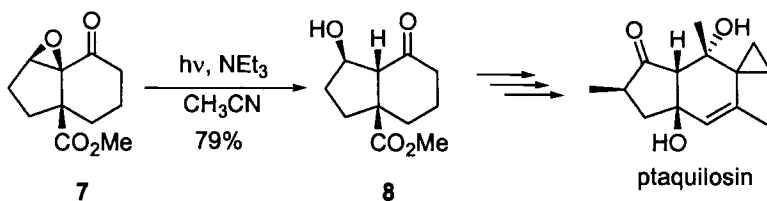
or poor σ^* acceptors: C–C, C–N

and allow for good overlap of the σ^* and π^* orbitals such as in



Scheme 14. Frequently used ($\sigma^* + \pi^*$) acceptors that undergo rapid reductive bond cleavage.

C–Hal bond cleavage is a main motif in simple reductions $\text{R–Hal} \rightarrow \text{R–H}$ [46] or for $\text{R–Hal} \rightarrow \text{R–E}$ by trapping the resulting anions with electrophiles E^+ [47]. Likewise, $\text{S}_{\text{RN}}1$ reactions [2b] involving benzyl halides [48], heteroarene methyl halides [49], and difluoromethyl quinones are frequently used [50]. Whereas bond cleavage of pure σ^* (C–N, C–O, C–C) acceptors is rather difficult, C–N [51], C–O [52], C–S [53], and C–Se bond rupture [30] can be readily realized in the corresponding ($\sigma^* + \pi^*$) systems. Even C–C bond cleavage is possible, for example in α -cyclopropylketones [54], but is restricted to a few instances. Other types of bond cleavage include rupture of the disulfide bond [55] and Se–S [56], Se–Se [56], and O–Si bond scission [52].



Scheme 15. Regioselective C–O bond cleavage as a key step in the synthesis of ptaquilosin [57].

Kinetic and thermodynamic aspects

($\sigma^* + \pi^*$) acceptors are often involved in thermal $S_{RN}1$ reactions [2b], because dissociative ET, for example between 4-nitrocumylchloride ($E^\circ_{SCE} = -1.12$ V) and 2-nitropropanate ($E^\circ_{SCE} = 0.077$ V), overcomes the sluggishness of an outer-sphere ET followed by bond dissociation (kinetic amplification through the $S_{RN}1$ process) [58].

C–Hal bond cleavage

When σ^*, π^* overlap in the radical anion is comparable within a series of compounds then thermodynamic factors will govern the kinetics. Following the trend in $\Delta G_{het}(RX^{\bullet-})$, bond cleavage in benzyl chloride $^{\bullet-}$ is dissociative, whereas the corresponding *p*-nitrobenzyl chloride $^{\bullet-}$ undergoes bond scission at 4×10^6 s $^{-1}$ [59]. The situation becomes somewhat more complicated when we compare the C–X bond cleavage of different groups X, because then the different homolytic bond-dissociation energies and σ^* energies also become important. For example, bond scission in benzyl halide $^{\bullet-}$ usually follows the order $BzBr^{\bullet-} > BzCl^{\bullet-} > BzF^{\bullet-}$ [60, 61]. Bond weakening is also responsible for the complete defluorination of trifluoromethylarenes— $NC-C_6H_4-CH_2F^{\bullet-}$ ($k = 7 \times 10^6$ s $^{-1}$) cleaves more rapidly than $NC-C_6H_4-CHF_2^{\bullet-}$ ($k = 4 \times 10^5$ s $^{-1}$) and $NC-C_6H_4-CF_3^{\bullet-}$ ($k = 3.8 \times 10^1$ s $^{-1}$) [62].

C–O bond cleavage

After one-electron reduction of cyanoanisoles the C–O bond rupture is very slow [63]. Much more rapid and in line with the driving force $\Delta G_{het}(RX^{\bullet-})$ is bond cleavage in $ArCOCH_2-OPh^{\bullet-}$: $Ar = pMeOPh$ at $k = 1.2 \times 10^7$ s $^{-1}$ compared with $Ar = Ph$ at $k = 7.0 \times 10^5$ s $^{-1}$ and $Ar = pCF_3Ph$ at $k = 1.0 \times 10^3$ s $^{-1}$ [64]. The role of the anionic leaving group Y has also been investigated in the bond scission of α -phenoxyacetophenones $PhCOCH_2OPh-Y$ [65]. Here, the rate constant correlates well with σ ($\rho = 3.1$) [66], because of the thermodynamic contribution to the activation barrier, as required by the Savéant model [17, 40, 67]. In this model the cleavage is viewed as an intramolecular dissociative ET, in which the electron is transferred from a π^* to the σ^* orbital of the bond to be cleaved.

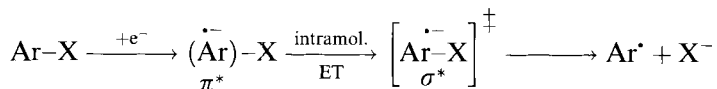
C–X bond cleavage

It has been demonstrated that in ($\sigma^* + \pi^*$) acceptors even bonds (e.g. C–C) with very high-lying σ^* orbitals, which are neither accessible in σ^* acceptors by direct

electron injection nor in π^* acceptors by intramolecular ET, can be broken. To effect such difficult processes, the ($\sigma^* + \pi^*$) acceptor must have a weak homolytic bond and a high reduction potential, and the anion produced should be very stable [68]. By following these rules, rate constants of C–C bond cleavage in 1,2-diarylethane $^{\bullet-}$ were increased from 8×10^5 to $>3 \times 10^{10} \text{ s}^{-1}$; this enabled the design of interesting self-destructive electron acceptors [68]. Analogous C–S bond scission is feasible, but much slower [69, 70].

Bond cleavage after intramolecular ET via π^* redox relays

Many compounds undergo reductive C–X bond cleavage even though the LUMO does not have observable $\sigma^*(\text{C–X})$ character; examples are aromatic and vinylic halides [72] where the C–Hal bond is located orthogonal to the LUMO. It has been proposed [71] on the basis of semi-empirical calculations [72] and experimental evidence [73] that for aryl halides an intramolecular ET from the primarily formed π^* to the $\sigma^*(\text{C–X})$ is responsible for the observed difference in cleavage rates ($k = 10^{10} \text{ s}^{-1}$ for phenyl halides compared with $k = 10^{-2} \text{ s}^{-1}$ for nitrophenylhalides). More precisely, intramolecular $\pi^* \rightarrow \sigma^*$ dissociative ET takes place when the energy of the σ^* orbital is reduced (as a result of bond stretching) to match the energy of the π^* LUMO to which the unpaired electron has initially been transferred [17].



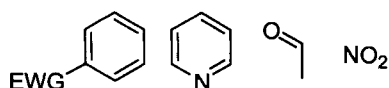
Synthetic aspects

As we have seen above, the rate of bond cleavage can be modulated very readily by the energy splitting between the π^* LUMO and the unoccupied $\sigma^*(\text{C–X})$. Usually the π^* LUMO belongs to an aromatic, heteroaromatic, vinylic, or heterovinylic (e.g. acyl groups) acceptor. Bonds that are frequently cleaved are depicted in Scheme 16.

Common π^* acceptors as redox relays for reductive bond cleavage.

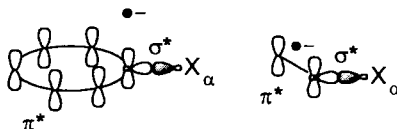
Combine

good π^* acceptors

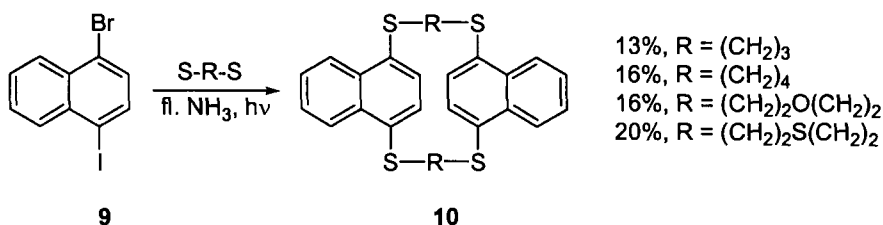


with good σ^* acceptors: C–Hal, C–O, C–S, C–Se, O–O, Si–Hal

avoiding overlap of the σ^* and π^* orbital system. Intramolecular ET from the π^* radical anion to the σ^* acceptor leads to bond cleavage. Frequent systems are



Scheme 16. Frequently used π^* acceptors that function as redox relays to shuttle electrons to the scissile C–X bonds.



Scheme 17. Four reductive C–Hal bond-cleavage reactions are used in the quadruple $\text{S}_{\text{RN}}1$ reaction to assemble **10** [80].

Frequently, bond cleavage is used for $\text{R–Hal} \rightarrow \text{R–H}$ dehalogenations [74], and the formation of carbanions [75]. More seldom encountered are reactions of π^* acceptors that have the σ^* bond spatially well separated and that depend on long-range ET. Such a situation occurs in phenyl-substituted alkyl chlorides [76], and bridgehead halides [77] with various redox relay functions (e.g. a nitroaryl group) [78].

π^* Haloacceptors and related systems play a prominent role in $\text{S}_{\text{RN}}1$ reactions [2b] of aryl halides [79, 80], hetaryl halides [79c, 81], and vinyl halides [82]. A spectacular example of the use of such acceptors is the macrocycle synthesis by a quadruple $\text{S}_{\text{RN}}1$ reaction depicted in Scheme 17 [80].

C–C bond cleavage is readily possible with nitrile radical anions as a shuttle [83]; C–N bond cleavage is rare, but has been effected in phenyl-substituted dimethylanilines [84], some benzenesulfonamides [52], and by using benzotriazole both as the π^* acceptor and as the anionic leaving group [85]. C–O or C–S bond cleavage can readily be accomplished in reductions of the type $\text{R–O} \rightarrow \text{R–H}$ [86] and lithium carbanion generation [23]. C–S bond cleavage in aromatic polysulfones [87] and alkenyl phenyl sulfones [88] can, moreover, be regarded as originating from π^* acceptors. Other bond-cleavage processes have been recognized—for example in the cathodic cleavage of S–P [89], N–S (in aryl azo sulfides) [90], and Si–O bonds [91].

Kinetic and thermodynamic aspects

C–Hal bond cleavage

Recent work [72b, d] has demonstrated that for a variety of halonitrobenzene radical anions there is a correlation between the experimental rate constants (spanning eight orders of magnitude) and $\Delta E_{\sigma^*, \pi^*}$. If the scissile bond of interest does not change its σ^* LUMO energy significantly within a series of analogous compounds, changes in the energy gap $\Delta E_{\sigma^*, \pi^*}$ can be experimentally accessed through $E_{(\text{RX}, \text{RX}^{\bullet-})}^\circ$. As a result, linear correlations between $\log k$ and $E_{(\text{RX}, \text{RX}^{\bullet-})}^\circ$ were obtained for aryl chlorides and bromides [17]. Moreover, a correlation of $\log k$ (C–Br bond cleavage) with σ was found in $\text{YC}_6\text{H}_4\text{–Br}^{\bullet-}$ ($\rho = -17.9$) [66].

With regard to different leaving groups and the substitution pattern at the aryl group several general statements are possible [71, 72a, 92]. The dissociation rate constant of $\text{Ar–X}^{\bullet-}$ varies considerably with the nature of the halogen ($\text{I} > \text{Br} > \text{Cl}$)

and its position relative to a second substituent ($o > p > m$). Comparison of cleavage rates reveals the order of reactivity $\text{CN} > \text{CH}_3\text{C}(=\text{O}) > \text{NO}_2$. For a series of compounds with similar structures the intrinsic activation barrier changes with the thermodynamic component [93], in accordance with the Savéant model [17, 40]. Solvent effects on the cleavage rate constants of π^* radical anions are much better understood, as a result of recent investigations [94]. Earlier results implied specific solvation of the transition state, but recent work has emphasized the dominant role of solvation of the leaving group. It was, moreover, shown that solvent effects, which can be described by the Pekar factor, determine the intrinsic rate constant [94].

By use of a series of 1-aryl- ω -haloalkanes [95a] and 1-aryl- ω -haloalkanes [95b] intramolecular ET between the π^* radical anion site and the distal σ^* (C–X) acceptor was evaluated for longer distances. The correlation with the acceptor number of the solvent indicates that the negative charge is more localized in the transition state than in the initial radical anion [95b]. Notably, rate constants for the dissociation of $\text{Ar-Cl}^{\cdot-}$ show the same correlation with solvent polarity as aryl- ω -haloalkanes [95b]. Experimental and theoretical investigations on ω -halo-1-alkene $^{\cdot-}$ [96] and phenyl-substituted 4-benzoyloxy-1-methylcyclohexylbromide $^{\cdot-}$ [97] shed further light on intramolecular dissociative ET processes.

C–X bond cleavage

C–O bond cleavage rates have become accessible through kinetic investigations of diphenyl ether ($k = 4 \times 10^5 \text{ s}^{-1}$) [98] and of trifluoromethoxybenzenes (4-CN: $k = 4 \times 10^3 \text{ s}^{-1}$, 4-H: $k = 3 \times 10^7 \text{ s}^{-1}$). Interestingly, when the leaving group properties of methoxide and chloride were compared [99], cleavage was rapid when attached to a phenyl ring, but much slower when attached to a 4-cyanophenyl group. The C–S thioether bond is more readily cleaved than the C–O bond [100].

Cleavage of other bonds

Rate data for cleavage of other bonds are rare. According to electrochemical investigations, S–S bond cleavage in diphenyldisulfide $^{\cdot-}$ proceeds at $5 \times 10^8 \text{ s}^{-1}$, whereas that of dialkyldisulfides is slightly slower [101].

1.4.3 Synthetic, Kinetic and Thermodynamic Aspects of Oxidative Bond Cleavage

Bond cleavage after oxidation of σ donors

In comparison with the rich chemistry of σ^* radical anions the synthetic utility of σ radical cations is quite restricted, because pure σ donors are mostly limited to Si–Si, C–Si, C–Ge, and C–Sn functionalities (Scheme 18). Only strained carbocyclic compounds [119] have low ionization energies (IE) that make them readily accessible $\sigma(\text{C–C})$ and $\sigma(\text{C–H})$ donors, but they are of limited synthetic use. In contrast, $\text{Me}_3\text{M–MMe}_3$ ($\text{M} = \text{Sn, Ge, Si}$; IE s ranging from 8.0 to 8.3 eV) [5] and Me_4M ($\text{M} = \text{Sn, Ge, Si}$; IE s ranging from 8.9 to 9.8 eV) [5] are, in general, better donors

Common σ donors for oxidative bond cleavage

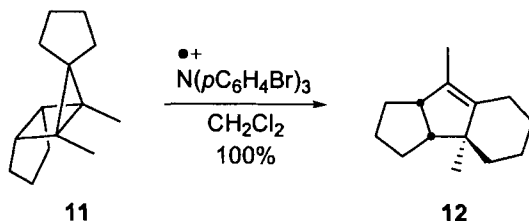
C–Si, C–Ge, C–Sn, Si–Si, C–N (in azo compounds)

Scheme 18. Frequently encountered σ donors that undergo efficient oxidative bond cleavage.

than terminal alkenes (e.g. propene has a $IE = 9.73$ eV) [5], which makes them attractive for oxidative cleavage.

Synthetic aspects

Whereas C–H bond cleavage has been used only rarely, e.g. in adamantane [103], C–C bond rupture is more common, but only in strained carbocycles [104–106]. C–N bond cleavage is observed in azoalkane $^{++}$ decomposition [106d], although little synthetic use has been elaborated [107]. In contrast, C–Sn bond cleavage in alkylstannanes has been developed into a novel alkylation of α,β -unsaturated ketones [108] and a versatile alkylation of electron-poor olefins [109]. Oxidative Si–Si [110] and Ge–Ge bond cleavage [102] have also found use.



Scheme 19. Oxidative C–C bond cleavage in housane **11** leads to the formation of diquinane **12** [106c].

Kinetic and thermodynamic aspects

Whereas the rather strong donor qualities of the above electrophores can readily be quantified by the corresponding ionization energies [5, 111], very little is known about the thermochemical data, except as a result of calculation [112, 113]. Fragmentation of Me_3MR^{++} ($M = Si, Sn$; $R = Me, i\text{-}Pr, \text{allyl}, \text{benzyl}, Ph$) is endothermic for all R and occurs in the order $i\text{-}Pr \geq Me > \text{allyl} > \text{benzyl} > \text{phenyl}$ and $M = Sn > Si$ [113]. C–Sn bonds can be cleaved efficiently through intramolecular assistance by a carbonyl group or heteroatoms [114], as is also known for Si–Si bond scission [115]. Sn–Sn [116], Sn–Ge [116], Sn–Si [116], and Ge–Ge [117] bond-cleavage reactions roughly follow the qualitative order: $Sn\text{--}C \gg Ge\text{--}Ge > Si\text{--}Si$ [117].

C–H and C–C bond cleavage in σ radical cations is feasible, but not a versatile option for synthetic use because of the very high oxidation potentials. Deprotonations in alkane radical cations have strongly negative Gibbs energies, with strong preference for tertiary over secondary or primary C–H bonds [118]. C–C bonds are selectively weakened in strained carbocycles [119].

Bond cleavage after oxidation of ($\sigma + \pi$) or ($\sigma + n$) donors

Analogous to the situation of ($\sigma^* + \pi^*$) acceptors, a donor can be composed of two interacting σ and π (or n) electrophore subunits [120]. For stereoelectronic reasons [121] bond weakening in ($\sigma + \pi$) or ($\sigma + n$) donors is most often encountered between the α and β atoms (with respect to the π or n electrophore, Scheme 10).

Synthetic aspects of ($\sigma + \pi$) donors

C–H deprotonation is frequently encountered at the benzylic position of aromatic [122] and heteroaromatic [123] systems (e.g. in deprotections [124]), in bisallylic systems [125], but less often in allylic functionalization [126]. To compete with other pathways C–C bond scission often needs an extra driving force which is available in strained cyclic systems [127]. Unstrained systems require the assistance of radical- and cation-stabilizing groups to reduce the C–C bond-dissociation energy [128].

Common ($\sigma + \pi$) donors for oxidative bond cleavage.

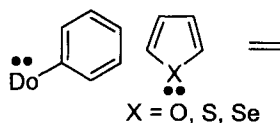
Combine

good σ donor: C–Si, C–Ge, C–Sn, Si–Si,

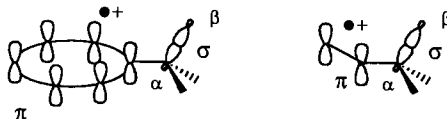
or poor σ donors: C–C, C–H

good π donors

with



and allow for good overlap of the σ and π orbitals such as in



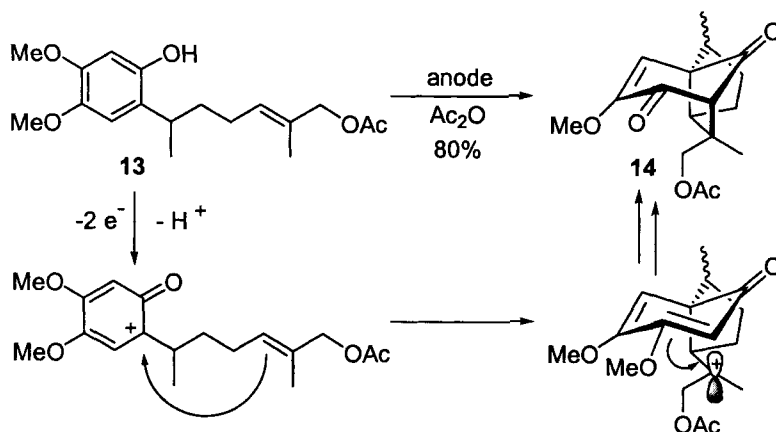
Scheme 20. Frequently used ($\sigma + \pi$) donors that undergo oxidative bond cleavage.

The proper use of a strong electrofugal group X^+ ($X = SiR_3, SnR_3, SR$) facilitates highly chemoselective bond scission [129], as in many C–Si [130, 131] and C–Sn cleavage reactions [132]. When alternatives are lacking oxidation of sulfides often results in the oxidative cleavage of the C–S bond [133]. O–H deprotonation is a key step in the oxidative transformation of phenols [134] (Scheme 21) and enols [135]. Much less used are other scissions, e.g. Si–Si bond cleavage [136].

Synthetic aspects of ($\sigma + n$) donors

C–H deprotonation plays an important role in the α -functionalization of alcohols [138], amines [139] + related N -functionalities [140], ethers [141], and sulfides [142]. N,O -acetals are versatile precursors to N -acyliminium intermediates [143].

Because cation stabilization makes an important contribution, N-, S-, and O-substituents are often used to support C–C bond cleavage [109, 144]. C–C bond scission is readily achieved in strained carbocyclic [145] or heterocyclic [146] ring systems, with many examples stemming from cyclopropyl sulfides [147].



Scheme 21. O–H Deprotonation is the key step in the oxidation of phenol **13** to the tricyclic product **14** [137].

Common ($\sigma+n$) donors for oxidative bond cleavage

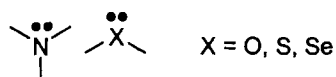
combine

good σ donor: C–Si, C–Ge, C–Sn, Si–Si,

or poor σ donors: C–C, C–H

with

good n donors

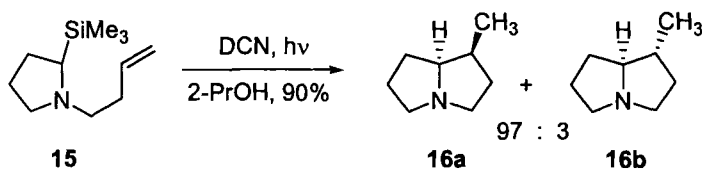


and allow for good overlap of the
 σ and n orbitals such as in



Scheme 22. Frequently used ($\sigma + n$) donors that undergo oxidative bond cleavage.

C–Sn [148] and C–Si [121, 149] bond cleavage has developed into a versatile synthetic method for adding functionality α to nitrogen, oxygen and sulfur centers. C–Si bond cleavage is known to be induced by nucleophiles such as pyridine [150] and methanol, and stereoselectivities have been interpreted as indicating that C–Si bonds can even be attacked by a double bond system [151].



Scheme 23. C–Si bond cleavage assisted by the neighboring double bond [151b].

*Kinetic and thermodynamic aspects***C–H bond cleavage**

Removal of an electron generally brings about significant thermochemical C–H bond weakening both in $(\sigma + \pi)$ radical cations (i.e. deprotonation in the benzylic position [152]) and $(\sigma + n)$ radical cations (i.e. deprotonation at the α -carbon of amines [153, 154], ethers [155], and thioethers [156]). The kinetic acidity of benzyl radical cations is rather well understood [152d, 157, 158], although occasionally an addition–elimination route was favored over direct proton transfer [159]. For alkyl arene radical cations [160] a linear relationship has been established between $\log k_{\text{dep}}$ and thermochemical acidity [157].

Likewise, the biologically important C–H deprotonation [161] of amine radical cations has been extensively studied [162], with the kinetic acidities paralleling the thermodynamic $\text{p}K_{\text{a}}$ values [163]. C–H deprotonation of thioethers has also been studied, but more rarely [164].

C–C bond cleavage

Bond dissociation data [165] indicate that C–C bond cleavage can only occur with appropriate substitution at the carbon centers (alkyl, aryl, hydroxy, siloxy, alkoxy) [166] to stabilize the resultant radical and cationic intermediates [152e]. Reasonable prediction of C–C bond cleavage of $(\sigma + \pi)$ radical cations can be made on the basis of linear correlation between kinetic and thermodynamic data for 1,2-biarylethanes [167]. Activation data correspond closely to the experimental ΔG° values [60]. Importantly, C–C bond-cleavage reactions in strained-ring systems can be induced by nucleophiles leading to inversion of configuration at the carbon center [168]. $(\sigma + n)$ radical cations equally can undergo C–C bond cleavage at a sufficiently high rate [169] (even decarboxylation [170]).

C–X bond cleavage

Monomolecular C–X bond cleavage energies are accessible by thermochemical cycle calculations; such bond dissociation processes are often induced by nucleophiles, at least with $\text{X} = \text{SiR}_3$ [163, 171]. As a consequence, rates are much faster than expected on the basis of thermochemical data. Detailed data are available for aniline radical cation desilylation [170].

C–N bond cleavage in cyclic azoalkane $^{2+}$ with expulsion of N_2 is apparently very rapid, because only follow-up products were detected [172]. In contrast, C–S bond cleavage in benzyl phenyl sulfide $^{2+}$ is rather slow with $k \approx 10^3 \text{ s}^{-1}$ [164].

O(N)–H bond cleavage

In such systems, C–H deprotonation—if feasible at all—cannot usually compete with O–H deprotonation. Whereas thermodynamic $\text{p}K_{\text{a}}$ values are available [173], kinetic data are rather scarce [174], despite the importance of such processes. Very

recently, the rate constants for deprotonation of phenol radical cations by water were measured to be $(0.6\text{--}6) \times 10^8 \text{ M}^{-1} \text{ s}^{-1}$. Consistent with the $\text{p}K_{\text{a}}$ values, the 2-methoxyphenol radical cation is more reactive than the 4-methoxy derivative [175].

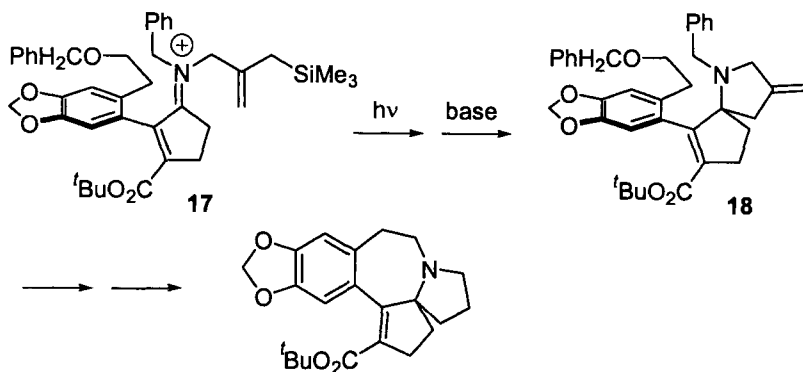
Cleavage of other bonds

Other bond cleavage (O–Si [176], O–Sn [177], O–C [178], O–P [179], O–Ti [176b, 180], O–Zr [181], S–C [182], Si–Si [183]) can be readily set up in radical cations for synthetic use and in several instances kinetic data are known. Rapid O–C bond cleavage might even occur in the antioxidant action of 7,8-diacetoxy-4-methylcoumarin [184].

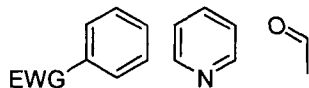
Bond cleavage after intramolecular ET via π or n redox relays

Although the analogous reaction mode is frequently observed with radical anions, at present this seems to be largely a *terra incognita* in radical-cation chemistry. We would, therefore, like to propose the combination of readily scissile σ donors, e.g. C–Sn, C–Si, and the Group IV M–M bonds ($\text{M} = \text{Si}, \text{Ge}, \text{Sn}$), with good π donors in the same molecules. Because the π donor must be more electron-rich than the σ donor, electron-rich π donors such as ferrocene-, amino-, and alkoxy-substituted phenyl groups, and larger aromatic systems might be appropriate. Such a system is, for example, realized in the C–Sn bond cleavage of trimethylphenylstannane $^{+}$ [113]. Other examples might include methylenecyclopropane [185], which is known to effect rapid cleavage of the C–C bond [186], and of the Ge–O bond in diger-moxanes [187].

The elegant synthesis of the harringtonine alkaloid skeleton might involve the photoinduced oxidation of an electron-rich phenyl group that acts as a redox relay by accepting an electron from the $\sigma(\text{C}–\text{Si})$ donor [188].



Scheme 24. Formation of parts of the harringtonine alkaloid skeleton via C–Si bond cleavage [188].

Common π^* acceptors for reductive bond formation.**Use****good π^* acceptors****but avoid any scissile bonds at the periphery of the π^* system, such as****C-Hal, C-O, C-S, C-Se, O-O, Si-Hal****Scheme 25.** Frequently used π^* acceptors for reductive bond-formation reactions.

1.5 Reductive and Oxidative Bond-formation Reactions

1.5.1 General Principles of Bond Formation

Although the bond-cleavage reactions described above might also lead to bond formation *via* a follow-up intermediate, we would like to discuss in the ensuing section bond formation right at the stage of the radical ion. Again, we recognize very similar reaction motifs in both radical-anion and radical-cation chemistry (cf. Schemes 5 and 25).

1.5.2 Synthetic, Kinetic and Thermodynamic Aspects of Reductive Bond-formation

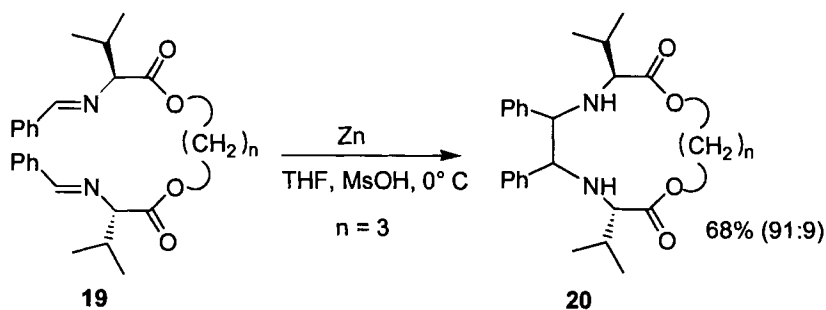
Bond formation at the radical anion stage (Scheme 25) usually occurs either by reaction with an electrophile (proton, cation, unsaturated electron-poor system) or with another odd-electron species (charged or neutral radical).

Reactions of π^* radical anions with closed-shell systems

Synthetic aspects

One of the most frequently encountered reactions is that with proton sources, as observed with arenes (Birch reduction) [189], aldehydes [190], alkynes [2d], fullerenes [191], ketones [192] (even enantioselective protonation of ketyl radical anions [193]), nitriles [194], nitro [195] and nitroso compounds [196], and olefins [197]. Protons are often replaced as electrophiles by trialkylsilyl chloride [198].

C-C bond formation in inter- or intramolecular additions starting with olefin [199, 200], ketyl [201] (generated by PET [202], chemical or cathodic [24, 203] reduction) [204, 205] or imine radical anions [206] has become a versatile method. In general, the intramolecular addition is highly suitable for the construction of five membered rings, less so for six-, and not effective for seven-membered ring formation.



Scheme 26. Stereoselective bisimine cyclization via radical anion intermediates [206b].

Kinetic and thermodynamic aspects

Protonation

Protonation becomes a rapid reaction in protic solvents and in the presence of acids, as demonstrated for, e.g., *n*-butyl acrylate in aqueous solution [207], methyl acrylate in EtOH [208], cinnamates in the presence of phenol in DMF [209], and benzaldehyde in ethanolic buffer solution [210]. Rate constants for protonation of aromatic radical anions (anthracene [211], naphthalene, 2-methoxynaphthalene, 2,3-dimethoxynaphthalene) by a number of proton donors including phenols, acetic acid, and benzoic acids in aprotic DMF were found to vary from $5.0 \times 10^4 \text{ M}^{-1} \text{ s}^{-1}$ (for anthracene, in the presence of *p*-chlorophenol) to $6.2 \times 10^7 \text{ M}^{-1} \text{ s}^{-1}$ (for anthracene, in the presence of pentachlorophenol) [212]. For dimedone, PhOH, or PhCO₂H the rate of protonation depends on the hydrogen-bond basicity of the solvent and increases in the order DMSO < DMF << MeCN [213].

When the substrate was more difficult to reduce the rate of protonation of alkyl cinnamates in the presence of phenol in DMF [209] increased. For aryl cinnamates the competing rate-determining dimerization of the radical anions is predominant [214]. In MeOH proton transfer occurs as a monomolecular reaction with the hydrogen-bonded radical anion complex (first-order rate constant k_{prot} varies from $2.9 \times 10^2 \text{ s}^{-1}$ to $3.5 \times 10^3 \text{ s}^{-1}$) [215].

Faster protonation rates were observed in the self-protonation of aromatic carboxylic radical anions ($k_{\text{prot}} > 10^6 \text{ M}^{-1} \text{ s}^{-1}$) [216] and (*R*)-(-)-1,1'-biphenyl-2,2'-diyl hydrogen phosphate radical anion ($k_{\text{prot}} = 5.7 \times 10^9 \text{ M}^{-1} \text{ s}^{-1}$) [217].

Reaction with other electrophiles

Kinetic studies of the reaction of CO₂ with radical anions generated from dialkyl fumarates and maleates showed that C–C bond formation was the rate-determining step. The pseudo first-order rate constants, k_{CO_2} , for fumarate radical anions in CO₂-saturated DMF were found to vary between 0.35 and 1.5 s⁻¹ and to decrease in the same order as observed for dimerization [218]. Rate constants for maleates (k_{CO_2} varied from 32.0 s⁻¹ to 18.0 s⁻¹) were higher. Rather slow is the coupling of CO₂ with the 4-keto isophorone^{•-} in MeCN ($k_{\text{CO}_2} = 0.35 \text{ s}^{-1}$) [219].

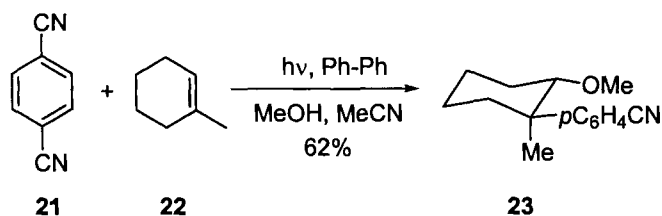
Aromatic radical anions and alkyl halides can react either by ET or direct S_N2 [95a, 220]. The S_N2 reaction depends on the steric requirements of the substrate and the magnitude of the driving force for the ET process [221]. In general, with increasing standard potential of the aromatic compound or decreasing ability of the substrate as electron acceptor, the S_N2 mechanism becomes more important.

Reactions of π^* radical anions with open-shell systems

Synthetic aspects

The coupling of two radical anions is frequently realized in the reductive dimerization of olefins with different groups R, for example R = CN (e.g. acrylonitrile [234]), C(=O)OR [198b, 237], C(=O)X [222], Ph [223], NO₂ [224], and SO₂Ph [225]. Diastereoselective and enantioselective dimerizations are reported for cinnamic esters [226] and oxazolidones [227], respectively.

On the other side, coupling of radical anions with radicals is a key step in the electrochemical reductive *t*-butylation of aromatic compounds [228], in the photo-NOCAS reaction [229], and for other combinations [87].



Scheme 27. Radical anion–radical coupling in the photo-NOCAS reaction [229].

Radical-anion and radical-cation intermediates, for example, react with each other after PET in donor–acceptor systems. After proton reorganization they undergo cyclization to provide a direct synthetic route to macrocycles and *N*-heterocycles with a variety of ring sizes [230]. Cycloadditions *via* radical ion pairs [231] and the C–C bond formation between C₆₀ and *N,O*-ketene acetals [232] also fit this category.

Kinetic and thermodynamic aspects

Intermolecular reactions of π^* radical anions with electron-poor olefins often proceed quite sluggishly. As a consequence, radical anion electrohydrodimerization (EHD) and radical anion–radical reactions are frequently encountered during electrochemical reduction when the radical concentration is rather high.

Dimerization of activated olefins

In general, the cathodic reduction of electron-deficient olefins generates a π^* radical anion which undergoes radical anion–radical anion dimerization to form the dianion dimer which undergoes protonation and/or cyclization. Several investigations

[233] have been performed on reductive dimerization; the best known example is the production of adiponitrile from acrylonitrile [234]. The initial step in the EHD is a rapidly established equilibrium between two radical anions and a dimer dianion; this has been extensively studied for cinnamates [235], fumarates [236], and maleates [237].

For dimerization of methyl and ethyl cinnamate the equilibrium constants were estimated to be 53.1 and 109.0 M⁻¹, respectively [238]. In solvents of low acidity (acetonitrile, DMF, alkaline ethanol) [235] the radical anion dimerization step was found to be rate-determining ($k \approx 5 \times 10^3$ M⁻¹ s⁻¹) depending on the structure of the alkyl group of the cinnamic ester moiety [239] (e.g., for electron-donating R = Bu^t, $k_{\text{obs}} = 4.1 \times 10^2$ M⁻¹ s⁻¹; for electron-withdrawing R = 4-NC-C₆H₅, $k_{\text{obs}} = 5.7 \times 10^4$ M⁻¹ s⁻¹). Rate studies indicate that complexation with water is crucial for the radical anion–radical anion coupling step of ethyl cinnamate ($k = 5.4 \times 10^2$ M⁻¹ s⁻¹ in DMF containing 0.28 M H₂O; $k = 1.4 \times 10^2$ M⁻¹ s⁻¹ in dry DMF [236]). As a consequence, stereoselectivity in cinnamic ester coupling could be controlled by appropriate selection of the solvent. In slightly wet DMF dimerization is relatively slow and stereoselective—involving two radical anions with a hydrogen-bonded water molecule serving as a template—whereas in MeOH two neutral radicals are involved in the rapid and unselective dimerization.

The dimerization rate constants of dialkyl fumarates ($k = 25$ – 120 M⁻¹ s⁻¹) [236] decrease with increasing steric hindrance of the alkyl group and prove to be significantly smaller than those of fumaronitrile ($k = 7 \times 10^5$ M⁻¹ s⁻¹) [240]. The electrochemically generated dimethyl maleate^{•-} undergoes rapid *cis*–*trans* isomerization to the dimethyl fumarate^{•-} then rapid radical anion dimerization [241]. In comparison, the EHD rate constant for 4-methylcoumarin ($k = 1.8 \times 10^5$ M⁻¹ s⁻¹) proved similar to that of a relatively fast cinnamate (4-cyano; $k = 5.7 \times 10^4$ M⁻¹ s⁻¹) [242].

Dimerization of arenes and heteroarenes

The dimerization of anthracene^{•-} has been studied extensively [243, 244]. With strongly electron-withdrawing substituents at position 9 the radical anions undergo reversible dimerization in aprotic solvents such as DMF, MeCN, propylene carbonate, DMSO etc. followed by rate determining σ bond formation to furnish the stable dimer dianion [245]. In DMF k_{dim} were found to decrease in the order NO₂ ($k_{\text{dim}} = 1.6 \times 10^6$ M⁻¹ s⁻¹) > CHO ($k_{\text{dim}} = 3.1 \times 10^5$ M⁻¹ s⁻¹) > CN ($k_{\text{dim}} = 1.3 \times 10^5$ M⁻¹ s⁻¹).

Reductive dimerization of benzene [246], cyano biphenyl ether [247], pyridine [248], and acridine [249] derivatives has also been investigated. Radical anions of diesters of pyridine and benzene undergo rapid reversible dimerization ($k_{\text{dim}} = 10^3$ – 10^4 M⁻¹ s⁻¹) [250].

Dimerization of aldehydes, ketones and related systems

In general, reductive generation furnishes a ketyl radical anion which undergoes radical–radical coupling to form the dimer dianion [251]. This dimerization was found to be faster than the reaction of the radical anion with the parent molecule (e.g. for of *p*-cyanobenzaldehyde: 28.6 M⁻¹ s⁻¹ compared with 1.45 M⁻¹ s⁻¹) [252].

Kinetic studies have revealed that aliphatic ketyl radical anions are very short-lived compared with aromatic (half life of acetone^{•-} in aqueous 2-propanol is 72 μ s, whereas that for acetophenone^{•-} is 1.5 ms) [253]. The reductive dimerization of simple aromatic aldehydes has been studied in aprotic solvents, with the second order rate constant being larger in acetonitrile than in DMF, because of ion-pair effects [254]. Electron-withdrawing substituents reduce the speed of dimerization (benzaldehyde^{•-}: $k = 2.4 \times 10^3 \text{ M}^{-1} \text{ s}^{-1}$, *p*-cyanobenzaldehyde^{•-}: $k = 5 \text{ M}^{-1} \text{ s}^{-1}$) [255], whereas protic solvents lead to protonation before dimerization [256].

In imine reductions rapid equilibration of dimeric dianions and the precursor radical anions leads to the thermodynamically more stable isomer [257]. In the reductive coupling of salicylideneanilines, however, rate-determining C–C bond formation is preceded by intramolecular H-bridging [258].

Reaction with neutral radicals

Few rate data have been reported for the coupling of radical anions with alkyl radicals [259]. In general, coupling is rapid with rate constants approaching the diffusion limit (1-hexenyl radical + naphthalene^{•-}: $k_2 = 2.4 \times 10^9 \text{ M}^{-1} \text{ s}^{-1}$ in 1,2-dimethoxyethane) [260]. Although the rates of coupling of alkyl radicals with aromatic radical anions are found to vary slightly in the order primary > secondary > tertiary, the small activation energy is not sensitive to structural differences between the alkyl radical and in the aromatic substrate or to variations in SOMO–SOMO energies [261].

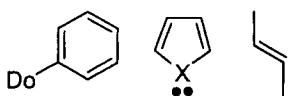
1.5.3 Synthetic, Kinetic, and Thermodynamic Aspects of Oxidative Bond-formation

Reactions of π radical cations with closed-shell systems

Common π donors for oxidative bond formation.

Use

good π donors



but avoid any scissile bonds at the periphery of the π system, such as

C–Si, C–Sn, $\overset{\cdot\cdot}{\text{X}}\text{--}\overset{\cdot\cdot}{\text{H}}$, $\overset{\cdot\cdot}{\text{X}}\text{--}\overset{\cdot\cdot}{\text{Si}}$

Sometimes even cleavage of

C–C (in strained systems) and C–H bonds

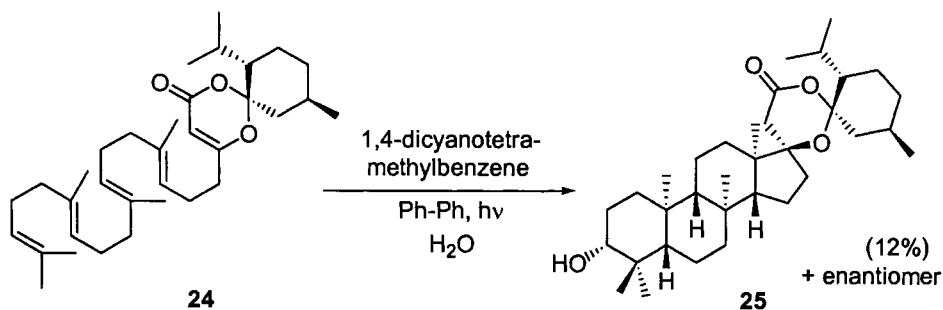
may interfere with bond formation processes

Scheme 28. Frequently used π donors for oxidative bond-formation reactions.

Synthetic aspects

Intermolecular reactions involving attack of *n*-nucleophiles (even F^-) [262] at π radical cations include reactions at alkenes [263], allenes [264], aromatic systems

[265], enol esters [266], enol ethers [267], fullerenes [268], benzofurans [269], dienes [270, 271], furans [272], pyrrolidines [273], and ketene imines [274]. These reactions usually proceed by *anti*-Markovnikov addition [275]. C–C bond formation is possible by reaction with cyanide [264]. Truly spectacular examples are derived from PET cascade cyclizations [276], as demonstrated in a short biomimetic route to the steroid system **25** (two out of 256 stereoisomers) [277].



Scheme 29. Biomimetic cascade cyclization of **24** to steroid ring system **25** [277].

Likewise, *n*-nucleophiles react well in intramolecular cyclizations to trap olefin and arene radical cations [278].

Because both radical–nucleophile and radical–radical coupling (electropolymerization [316]) can occur under anodic conditions mechanistic differentiation is often difficult. Under chemical oxidation [279b] and PET conditions [279a], however, only radical–nucleophile coupling is encountered. Intermolecular [280] and intramolecular [281] C–C bond formation used for biomimetic atroposelective coupling [282] and for natural product synthesis [283] is nowadays a well-established synthetic tool.

Kinetic and thermodynamic aspects

Although addition of a nucleophile to a π radical cation seems to be a straightforward process, several mechanistic scenarios [284] (e.g. the disproportionation, complexation, and half-regeneration pathways) that depend on the reactants need to be considered [285]. It has, moreover, been stressed that for protic nucleophiles such as alcohols and water, deprotonation of the primary adduct is important [286]. As a consequence, the rational design of bond-forming reactions requires deeper understanding of mechanistic matters.

Extensive kinetic data have been collected over the last decade especially for substituted arylanthracenes [287], dienes [288], styrenes [289], and psoralen [290]. Combinations of π radical cations and *n*-type nucleophiles are very rapid processes that approach the diffusion controlled limit for anionic nucleophiles. Primary

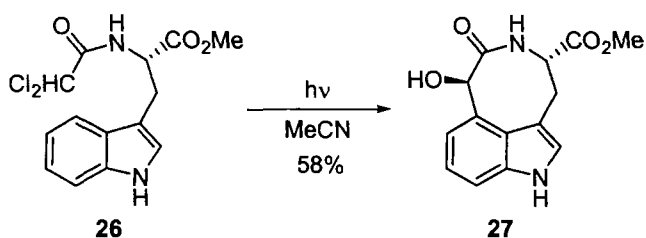
amines were found to add to 9-phenylanthracene radical cation with second-order rate constants in the range 8×10^6 to $3 \times 10^9 \text{ M}^{-1} \text{ s}^{-1}$. The rates increase with increasing amine basicity and decreasing steric requirements [287]. If, however, the amines become too strong donors (e.g. tertiary amines and anilines) they might react with the radical cation by ET [291]. Less studied are reactions with protic nucleophiles that occur according to the deprotonation mechanism. In line with nucleophilicity data [292], bond formation with water and alcohols is much slower than with amines and pyridines [286, 289].

The reaction of π radical cations with π nucleophiles usually leads to C–C bond formation, a reaction that can be very fast (cf. pericyclic reactions also), as in the oxidative dimerization of triphenylamine ($k = 1\text{--}10 \times 10^7 \text{ M}^{-1} \text{ s}^{-1}$) [293]. Hence, such a reaction mechanism can even operate in anodic oxidations (4-methoxybiphenyl [294], tetrahydrocarbazole [295], 4,4'-dimethoxystilbene [296] and 9-methoxyanthracene) [297], where the radical cation concentration is very high.

Reactions of π radical cations with open-shell systems

Synthetic aspects

π Radical cations react readily with stable radicals, e.g. oxygen [298], superoxide [299] or NO_2 [300], and short-lived radicals (as detected in the charge transfer nitration [301] of electron-rich aromatic systems with tetranitromethane) [302]. Moreover, PET in general leads to intra- [303] or intermolecular [304] radical ion pairs [305], but direct bond formation between organic radical cations and radical anions is rare. It might play a role in PET Paternò–Büchi reactions [306], and in related PET cycloadditions [307]. If the radical anion site of an intramolecular radical ion pair is designed to lose an anion, efficient protocols to radical cation–radical combinations can be installed.



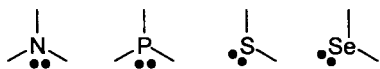
Scheme 30. Radical cation–radical coupling after intramolecular PET and loss of chloride at the radical anion site [305a].

Radical cation–radical cation coupling [308] is often observed during anodic oxidations when their concentration is sufficiently high; the capacity of π radical cations to undergo atom abstraction reactions, e.g. of fullerene $^{+\bullet}$ [309], has little significance only.

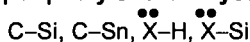
Kinetic and thermodynamic aspects

Reactions with stable radical species, e.g. oxygen and NO_2 , occur readily, although oxygenation rates of aryl olefin radical cations (ca $10^6 \text{ M}^{-1} \text{ s}^{-1}$ [310]) are two or three orders of magnitude slower than those of neutral radicals with oxygen [311]. The polar effect in such reactions is remarkable. Whereas *trans*-stilbene $^{\bullet+}$ has little reactivity towards oxygen, derivatives with a *p*-MeO group react at $k = 1.2\text{--}4.5 \times 10^7 \text{ M}^{-1} \text{ s}^{-1}$ [312]. Much more rapid is the reaction of stilbene $^{\bullet+}$ with superoxide ($k = 4.1 \times 10^{10} \text{ M}^{-1} \text{ s}^{-1}$) [310].

Reactions that include the dimerization of two radical cations are, for example, those of anethole [313], pyrroles [314], oligopyrroles [315], thiophenes [316], oligothiophenes [317], diphenylamine [318], triphenylamine [319], *N,N*-dimethylaniline [320], and diphenylpolyene [321].

Reactions of *n* radical cations with closed-shell systems**Common *n* donors for oxidative bond formation.****Use****good *n* donors**

but avoid any scissile bonds at the periphery of the π system, such as



Sometimes even cleavage of

C-C (in strained systems) and C-H bonds

may interfere with bond formation processes

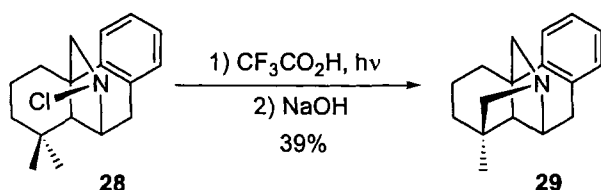
Scheme 31. Commonly used *n* donors for oxidative bond formation.

Synthetic aspects

Whereas nitrogen-centered radical cations are prone to C-H, C-C bond-cleavage reactions, $\text{R}_3\text{P}^{\bullet+}$ and $\text{R}_2\text{S}^{\bullet+}$ suffer predominantly nucleophilic attack [322, 323]; few exceptions have been reported to date. This reaction plays an important part in the formation of oxygenated derivatives (P [324], S [325]), C-S [326], S-S, and Se-Se bond formation [327], and in removing sulfur-protecting groups [328–330].

Whereas intermolecular attack of a π nucleophile is rather rare [331] (e.g. disulfide $^{\bullet+}$ + arene [332], and diselenide $^{\bullet+}$ + dienes [333]), intramolecular cyclizations of amine radical cations have been useful in the preparation of five-membered rings [334].

Hydrogen abstraction is the key factor in the intramolecular radical functionalization step of the Hofmann–Löffler–Freitag reaction (Scheme 32) [335].



Scheme 32. Successful preparation of pentacycle **29** [336] via the Hofmann–Löffler–Freitag reaction.

Kinetic and thermodynamic aspects

Kinetic data are very scarce and available mostly for amine, phosphane [337], and sulfide [338] radical cation reactions with nucleophiles. In intermolecular reactions, phosphane radical cations react with sulfur nucleophiles [339], $k = 10^5\text{--}10^7 \text{ M}^{-1} \text{ s}^{-1}$, following the same reactivity pattern as with π radical cations [289]. Cyclization rate constants for the attack at double-bond systems are faster than those of the neutral radicals, as shown for dialkylamine radical cations [340] ($k = 6 \times 10^5\text{--}1 \times 10^{10} \text{ M}^{-1} \text{ s}^{-1}$).

Reactions of n radical cations with open-shell systems

Synthetic aspects

Oxygen reacts readily with aromatic sulfides [341], *N*-methionyl peptides [342], 1,3-dithianes [343], aziridines [344], and phosphorus [345] compounds after oxidation. On the other hand, aryl radicals are involved in the ET reaction of trivalent phosphorus compounds with aromatic diazonium salts [346].

Kinetic aspects

Although the homogeneous reaction of sulfide $^{•+}$ with oxygen has been accomplished at high O_2 pressures only [347], the spontaneous reaction in a zeolite was recently monitored kinetically [348]. The very large rate constant for the reaction between dimethylsulfide $^{•+}$ and superoxide, $k = 2.3 \times 10^{11} \text{ M}^{-1} \text{ s}^{-1}$, can be interpreted in terms of rapid ET rather than radical–radical coupling [349]. Rates are also known for the reaction of phosphane $^{•+}$ with oxygen [339].

1.6 Pericyclic Reactions

1.6.1 General Principles of Pericyclic Reactions

Per definitionem, pericyclic reactions proceed in a concerted manner, i.e. bond cleavage and bond formation occur simultaneously. Recent high-level calculations

on radical cation Diels–Alder reaction have, however, put the stepwise [350] and concerted [351] cycloadditions close in energy whereas experimental evidence (mostly [352] stereospecific! [353]) argues for concertedness. Stereospecific retro-Diels–Alder fragmentation has, moreover, been observed in the gas phase [354].

1.6.2 Synthetic, Kinetic and Thermodynamic Aspects

Radical anion pericyclic processes

Synthetic aspects

Although cycloadditions have frequently been observed in radical-cation chemistry, this reaction mode is apparently very rare in radical-anion chemistry because of the electron repulsion term. Few examples are known of Diels–Alder dimerizations [355], [2 + 2] cycloadditions [356], retro-[2 + 2] cycloadditions [357], and cyclo-trimerizations [358]. Equally, little is known about electrocyclic reactions, despite their interesting stereochemical course [359].

Although the synthetic utility of radical anion pericyclic processes is still to be explored, the recently disclosed intermediacy of radical anions in metathesis reactions with Grubb's catalyst [360] should ignite the search for further examples of this interesting class of reactions.

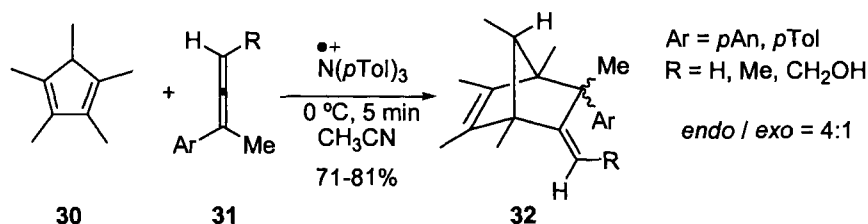
Kinetic and thermodynamic aspects

To the best of our knowledge no experimental kinetic and thermodynamic studies have been performed on radical anion pericyclic processes. Interesting structural information has, however, been obtained for some [2 + 2] cycloadduct^{•−}, e.g. 4N/5e radical anions [361].

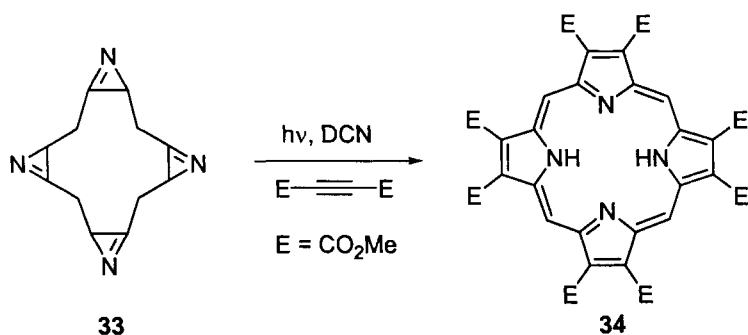
Radical cation pericyclic processes

Synthetic aspects

Since their original discovery [362] pericyclic radical cation reactions have been developed for various synthetic formats. The methodology nowadays is most advanced for intra- [363] and intermolecular Diels–Alder cycloadditions [364], and



Scheme 33. Only two out of 32 possible isomers of **32** are formed in this highly peri-, chemo-, regio- and stereoselective radical cation Diels–Alder cycloaddition [365b, c].



Scheme 34. Preparation of porphyrin **34** initiated through electrocyclic ring opening of four azirine radical cations to 2-azaallenyl radical cations [373c].

wide variations in the dienophile [365] (cf. allene **31**) and the diene [366] have been realized. Likewise, several examples are known of other cycloadditions ([2 + 2] [367], with diazomethane [368] or osmium tetroxide [369], epoxidation [370], cyclopropanations [371]) and cycloreversions [372].

An exciting cycloaddition which is not pericyclic in nature has been developed on the basis of PET opening of azirines to 2-azaallenyl radical cations [373]; these add readily to substrates such as imines and acetylenes. This paves the way for the synthesis of imidazoles [373a, e], heterophanes [373b, e], and even porphyrins (cf. the preparation of **34**) [373c, e].

Many classical pericyclic reactions, for example the Cope [374, 375], Claisen [376], vinylcyclobutane [377], vinylcyclopropane [378], and vinylcyclobutanone [365a] rearrangements and the [1, 16] hydrogen shift in an A/D *seco* corrin radical cation [379], can be translated into the radical cation format equally easily. The stereochemical course of these rearrangements has been described as stereospecific in the vinylcyclobutane [377, 380] and Cope [374b] rearrangements but with retention, inversion, and partial loss of the stereochemical integrity in the rearrangement of vinylcyclopropane [381] and vinylcyclobutanone [365a] radical cations.

Kinetic aspects

Recent studies [382] have provided rate data for cycloaddition reactions. Accordingly, steric effects at the electrophile site, and the capacity of the added unsaturated component $\text{RCH}=\text{CH}_2$ to stabilize radicals and cations, play a vital role, the importance of which is reflected in a rate decrease for $\text{R} = \text{Ph} \approx \text{OR} > \text{vinyl} > \text{alkyl}$ by a factor of 100–300. In principle, the observed trends follow those for addition of carbocations to alkenes [292]. A study of the [2 + 1] cycloaddition of 4-methoxystyrene also emphasizes the importance of the rapid one-electron reduction of the intermediate dimer radical cation [383]. A direct view of 4-center 3-electron cyclobutane [384] and bisdiazene-oxide [385] radical cations has been obtained with polycyclic, rigid systems.

1.7 Conclusion

In this brief review we have outlined a unifying concept to promote understanding of primary reaction pathways of radical ions in solution. From the analysis in this review, which is based on (i) identifying the electrophore in a complex molecule and (ii) identifying the character of the electrophore, it has become clear that both radical anions and radical cations undergo analogous reactions with regard to the electrophoric system. Our heuristic concept of relating the reactivity of a radical ion to the relevant electrophore is closely connected to the principle of localized charge as used in mass spectroscopy [386]. Hence, the interested reader will find many analogies in radical ion gas-phase chemistry, an area which unfortunately could not be covered in our present analysis [387].

It is hoped that our guide for predicting the reactivity of radical ions, whether generated by electrolysis, or by chemical or photochemical ET processes, will encourage scientists to devise novel radical-ion reactions for synthetic applications. Because our analysis has aimed at covering synthetically relevant radical-ion transformations, it should be noted that less frequently used reactions, such as *cis-trans* isomerizations, and ET oxidation or reduction of radical ions are not included. One should, moreover, bear in mind that the reactivity of radical ionic intermediates might be heavily influenced by counterion effects [388], a research area which still deserves major attention.

Finally, it can be stated that many reactivity patterns of free radical ions are equally found in oxidative and reductive transformations involving initial inner-sphere ET, such as in reactions with samarium iodide [389], low valent titanium [390] and titanocene complexes [391], manganese(III) [392], and CAN [393].

Acknowledgments

M. K. G. is deeply indebted to the Alexander von Humboldt Stiftung, and M. S. would like to thank all his coworkers whose commitment has made possible the joint contributions in the field of electron transfer activation. Generous financial support over many years from the Deutsche Forschungsgemeinschaft (SFB 347, Schwerpunkt Normalverfahren, Graduiertenkolleg), the Volkswagen-Stiftung, and the Fonds der Chemischen Industrie is gratefully acknowledged.

References

1. T. Linker, M. Schmittel, *Radikale und Radikationen in der Organischen Synthese*, Wiley-VCH, Weinheim, **1998**.
2. (a) *Photoinduced Electron Transfer*, (Eds.: M. Chanon, M.-A. Fox), Parts A–D, Elsevier, Amsterdam, **1981**; (b) R. A. Rossi, R. H. de Rossi, *Aromatic Substitution by the $S_{RN}1$ Mechanism*, ACS 178, Washington DC, **1983**; (c) L. Eberson, *Electron Transfer Reactions in Organic Chemistry*, Springer, Berlin, **1987**; (d) *Organic Electrochemistry*, (Eds.: H. Lund, M. M. Baizer) Marcel Dekker, New York **1991**; (e) T. Shono, *Electroorganic Synthesis*, Acad. Press,

- London, **1991**; (f) G. J. Kavarnos, *Fundamentals of Photoinduced Electron Transfer*, VCH, New York, **1993**; (g) K. Yoshida, *Electrooxidation in Organic Chemistry*, Krieger, Malabar, **1993**; (h) D. Kyriacou, *Modern Electroorganic Chemistry*, Springer, Berlin, **1994**; (i) J. Volke, F. Liška, *Electrochemistry in Organic Synthesis*, Springer, Berlin, **1994**.
3. V. D. Parker, *Acta Chem. Scand.* **1998**, 52, 145–153.
 4. J. Santamaria, M. T. Kaddachi, J. Rigaudy, *Tetrahedron Lett.* **1990**, 31, 4735–4738.
 5. NIST Chemistry WebBook by P. J. Linstrom; General Editor W. G. Mallard, NIST Standard Reference Database No 69 (November 1998 Release), [http://webbook.nist.gov/chemistry/]
 6. P. Kebarle, S. Chowdhury, *Chem. Rev.* **1987**, 87, 513–534.
 7. J. A. Pople, *Angew. Chem.* **1999**, 111, 2014–2023; *Angew. Chem. Int. Ed.* **1999**, 38, 1894–1902.
 8. J. Cossy, D. Belotti, J. P. Pete, *Tetrahedron Lett.* **1987**, 28, 4545–4546.
 9. (a) M. J. S. Dewar, E. G. Zoeibisch, E. F. Healy, J. J. P. Stewart, *J. Am. Chem. Soc.* **1985**, 107, 3902–3909; (b) J. J. P. Stewart, *J. Comput. Chem.* **1989**, 10, 221–264; (c) A comparison of calculated and experimental electron affinity data [5] indicates that AM1 [9a] performs somewhat better than PM3. [9b] d) As ionization potentials and electron affinity data of iodo compounds are much better calculated by PM3 [9b] than by AM1 [9a] we used the PM3 semi-empirical method for the data in Table4.
 10. A comparison of calculated and experimental ionization energies shows that AM1 [9a] and PM3 [9b] perform better than ab initio (STO-3G, 3–21 G, 6–31G*, 6–31+G**) and DFT (B3PW91, BLYP, B3LYP, B3P86) calculations, see P. Politzer, F. Abu-Awwad, *Theor. Chem. Acc.* **1998**, 99, 83–87.
 11. J.-P. Cheng, Z. Zheng, *Tetrahedron Lett.* **1996**, 37, 1457–1460.
 12. Determined by thermochemical cycle calculations using ionization energies from reference [5].
 13. K. Daasbjerg, *J. Chem. Soc., Perkin Trans. 2* **1994**, 1275–1277.
 14. Electrochemistry I–VI, Ed. E. Steckhan, *Top. Curr. Chem.* **1987**, 142; **1988**, 148 and 143; **1990**, 152; **1994**, 170; **1997**, 185; Electron Transfer I–II, Ed. J. Mattay, *Top. Curr. Chem.* **1994**, 169; **1996**, 177.
 15. D. D. M. Wayner, V. D. Parker, *Acc. Chem. Res.* **1993**, 26, 287–294.
 16. Z.-R. Zheng, D. H. Evans, E. S. Chan-Shing, J. Lessard, *J. Am. Chem. Soc.* **1999**, 121, 9429–9434.
 17. J.-M. Savéant, *Tetrahedron* **1994**, 50, 10117–10165.
 18. T. W. Greene, P. G. M. Wuts, *Protective Groups in Organic Synthesis*, Wiley, New York, **1999**.
 19. M. S. Mubarak, D. G. Peters, *J. Electrochem. Soc.* **1996**, 143, 3833–3838; T. Fuchigami, M. Kasuga, A. Konno, *J. Electroanal. Chem.* **1996**, 411, 115–119; A. A. Pud, G. S. Shapoval, O. E. Mikulina, L. L. Gervits, *Russ. J. Electrochem.* **1996**, 32, 337–342; A. Kotsinaris, G. Kyriacou, C. Lambrou, *J. Appl. Electrochem.* **1998**, 28, 613–616.
 20. A. J. Fry, J. Touster, *Electrochim. Acta* **1997**, 42, 2057–2063.
 21. J. Simonet, *L'Actualité Chimique* **1998**, 4–42.
 22. Some recent examples providing access to older references: M. Médebielle, M. A. Oturan, J. Pinson, J. M. Savéant, *J. Org. Chem.* **1996**, 61, 1331–1340; M. A. Nazareno, R. A. Rossi, *J. Org. Chem.* **1996**, 61, 1645–1649; M. C. Murguia, R. A. Rossi, *Tetrahedron Lett.* **1997**, 38, 1355–1358; A. N. Santiago, A. E. Stahl, G. L. Rodriguez, R. A. Rossi, *J. Org. Chem.* **1997**, 62, 4406–4411; A. E. Lukach, A. N. Santiago, R. A. Rossi, *J. Org. Chem.* **1997**, 62, 4260–4265; Z. Y. Long, Q. Y. Chen, *J. Fluor. Chem.* **1998**, 91, 95–98; E. Delli, S. Kouloumtzoglou, G. Kyriacou, C. Lambrou, *Chem. Comm.* **1998**, 1693–1694; A. E. Lukach, R. A. Rossi, *J. Org. Chem.* **1999**, 64, 5826–5831.
 23. M. Yus, *Chem. Soc. Rev.* **1996**, 25, 155–161.
 24. R. D. Little, M. K. Schwaebe, *Top. Curr. Chem.* **1997**, 185, 1–48.
 25. R. Shao, D. G. Peters, *J. Org. Chem.* **1987**, 52, 652–657.
 26. E. Bartmann, *Angew. Chem.* **1986**, 98, 629–631; *Angew. Chem. Int. Ed. Engl.* **1986**, 25, 653–655; T. Cohen, I.-H. Jeong, B. Mudryk, M. Bhupathy, M. A. Awad, *J. Org. Chem.* **1990**, 55, 1528–1536.
 27. B. Mudryk, T. Cohen, *J. Org. Chem.* **1989**, 54, 5657–5659.
 28. Y. Chen, J.-M. Zheng, S.-M. Zhu, H.-Y. Chen, *Electrochimica Acta* **1999**, 44, 2345–2350.
 29. W. E. Truce, D. P. Tate, D. N. Burdge, *J. Am. Chem. Soc.* **1960**, 82, 2872–2876.

30. A. Krief, A. Nazih, *Tetrahedron Lett.* **1995**, 36, 8115–8118.
31. Z. J. Jedliński, A. Stolarzewicz, Z. Grobelny, M. Szwarc, *J. Phys. Chem.* **1994**, 88, 6094–6095.
32. M. Okano, H. Fukai, M. Arakawa, H. Hamano, *Electrochem. Comm.* **1999**, 1, 223–226.
33. A. Hasegawa, F. Williams, *Chem. Phys. Lett.* **1977**, 46, 66–68; C. E. Clots, R. N. Compton, *J. Chem. Phys.* **1977**, 67, 1779–1780; A. Kühn, E. Illenberger, *J. Phys. Chem.* **1989**, 93, 7060–7061; A. Kühn, E. Illenberger, *J. Chem. Phys.* **1990**, 93, 357–364; H. Muto, K. Nunome, *J. Chem. Phys.* **1991**, 94, 4741–4748; R. A. Popple, X. D. Finch, K. A. Smith, F. B. Dunning, *J. Chem. Phys.* **1996**, 104, 8485–8489.
34. D. P. Zhong, A. H. Zewail, *Proc. Natl. Acad. Sci.* **1999**, 96, 2602–2607.
35. V. A. Tikhomirov, E. D. German, *J. Electroanal. Chem.* **1998**, 450, 13–20.
36. E. D. German, V. A. Tikhomirov, *J. Mol. Struct. (Theochem)* **1998**, 423, 251–261.
37. (a) R. Benassi, F. Bernardi, A. Bottoni, M. A. Robb, F. Taddei, *Chem. Phys. Lett.* **1989**, 161, 79–84; (b) T. Tada, R. Yoshimura, *J. Am. Chem. Soc.* **1992**, 114, 1593–1595; (c) J. Bertran, I. Gallardo, M. Moreno, J.-M. Savéant, *J. Am. Chem. Soc.* **1992**, 114, 9576–9583.
38. S. Roszak, W. S. Koski, J. J. Kaufman, K. Balasubramanian, *J. Chem. Phys.* **1997**, 106, 7709–7713.
39. J.-M. Savéant, *J. Am. Chem. Soc.* **1987**, 109, 6788–6795; J.-M. Savéant, in *Advances in Electron Transfer Chemistry*, ed. P. S. Mariano, JAI Press, Greenwich, **1994**, Vol. 4, p. 53–116.
40. J.-M. Savéant, *Acc. Chem. Res.* **1993**, 26, 455–461.
41. C. P. Andrieux, J.-M. Savéant, C. Tardy, *J. Am. Chem. Soc.* **1998**, 120, 4167–4175.
42. R. L. Donkers, F. Maran, D. D. M. Wayner, M. S. Workentin, *J. Am. Chem. Soc.* **1999**, 121, 7239–7248.
43. E. D. German, A. M. Kuznetsov, V. A. Tikhomirov, *J. Electroanal. Chem.* **1997**, 420, 235–241.
44. C. G. Fraga, B. E. Leibovitz, A. L. Tappel, *Free Rad. Biol. Med.* **1987**, 3, 119–123.
45. Y. T. Woo, D. Y. Lai, J. C. Arcos, M. F. Argus, in *Chemical Induction of Cancer*, Vol. IIIb, p. 71, Academic Press, New York, **1985**; J. J. Kaufman, W. S. Koski, S. Roszak, K. Balasubramanian, *Chem. Phys.* **1996**, 204, 233–237.
46. M. F. Semmelhack, R. J. de Franco, J. Stock, *Tetrahedron Lett.* **1972**, 1371–1374; P. Martigny, H. Lund, *Acta. Chem. Scand.* **1979**, B33, 575–579; J. I. Lozano, F. Barba, *Electrochim. Acta* **1997**, 42, 2173–2176.
47. I. Chiarotto, M. Feroci, C. Giomini, A. Inesi, *Bull. Soc. Chim. Fr.* **1996**, 133, 167–175; E. Oguntoye, S. Szunerits, J. H. P. Utley, P. B. Wyatt, *Tetrahedron* **1996**, 52, 7771–7778; G. Montero, G. Quintanilla, F. Barba, *Electrochim. Acta* **1997**, 42, 2177–2180; K. Uneyama, G. Mizutani, *Chem. Comm.* **1999**, 613–614; B. Batanero, M. J. Perez, F. Barba, *J. Electroanal. Chem.* **1999**, 469, 201–205.
48. M. P. Crozet, A. Gellis, C. Pasquier, P. Vanelle, J. P. Aune, *Tetrahedron Lett.* **1995**, 36, 525–528; D. Witt, J. Rachon, *Heteroatom Chem.* **1996**, 7, 359–364; S. A. Dandekar, S. N. Greenwood, T. D. Greenwood, S. Mabic, J. S. Merola, J. M. Tanko, J. F. Wolfe, *J. Org. Chem.* **1999**, 64, 1543–1553.
49. C. Roubaud, P. Vanelle, J. Maldonado, M. P. Crozet, *Tetrahedron* **1995**, 51, 9643–9656; A. Gellis, P. Vanelle, M. Kaafarani, K. Benakli, M. P. Crozet, *Tetrahedron* **1997**, 53, 5471–5484; P. Vanelle, P. Rathelot, J. Maldonado, M. P. Crozet, *Heterocycles* **1997**, 45, 1519–1528; V. Beraud, P. Perfetti, C. Pfister, M. Kaafarani, P. Vanelle, M. P. Crozet, *Tetrahedron* **1998**, 54, 4923–4934.
50. A. Giraud, L. Giraud, M. P. Crozet, P. Vanelle, *Synlett* **1997**, 1159–1160.
51. J. Almena, F. Foubelo, M. Yus, *Tetrahedron Lett.* **1993**, 34, 1649–1652; J. Almena, F. Foubelo, M. Yus, *J. Org. Chem.* **1994**, 59, 3210–3215; E. W. Oliver, D. H. Evans, J. V. Caspar, *J. Electroanal. Chem.* **1996**, 403, 153–158.
52. J. F. Gil, D. J. Ramón, M. Yus, *Tetrahedron* **1993**, 49, 9535–9546; J. F. Gil, D. J. Ramón, M. Yus, *Tetrahedron* **1994**, 50, 3437–3446; J. F. Gil, D. J. Ramón, M. Yus, *Tetrahedron* **1994**, 50, 7307–7314; J. M. Saa, P. Ballester, P. M. Deya, M. Capo, X. Garcias, *J. Org. Chem.* **1996**, 61, 1035–1046; U. Azzena, S. Demartis, G. Melloni, *J. Org. Chem.* **1996**, 61, 4913–4919; J. F. Bunnett, J. Jenvey, *J. Org. Chem.* **1996**, 61, 8069–8073; E. Alonso, D. J. Ramon, M. Yus, *Tetrahedron* **1997**, 53, 14355–14368.

53. E. M. Kaiser, C. G. Edmonds, S. D. Grubb, J. W. Smith, D. Tramp, *J. Org. Chem.* **1971**, *36*, 330–335; T. Mandai, H. Irei, M. Kuwada, J. Otera, *Tetrahedron Lett.* **1984**, *25*, 2371–2374; S. D. Rychnovsky, A. J. Buckmelter, V. H. Dahanukar, D. J. Skaltitzky, *J. Org. Chem.* **1999**, *64*, 6849–6860; K. Wakamatsu, J. Dairiki, T. Etoh, H. Yamamoto, S. Yamamoto, Y. Shige-tomi, *Tetrahedron Lett.* **2000**, *41*, 365–369.
54. M. Fagnoni, P. Schmoltdt, T. Kirschberg, J. Mattay, *Tetrahedron* **1998**, *54*, 6427–6444.
55. E. Shouji, N. Oyama, *J. Electroanal. Chem.* **1996**, *410*, 229–234; J. Ludvik, B. Nygard, *J. Electroanal. Chem.* **1997**, *423*, 1–11.
56. V. Jouikov, L. Grigorieva, *Electrochim. Acta* **1996**, *41*, 2489–2491.
57. J. Cossy, S. Ibhi, P. H. Kahn, L. Tacchini, *Tetrahedron Lett.* **1995**, *36*, 7877–7880.
58. C. Costentin, P. Hapiot, M. Médebielle, J.-M. Savéant, *J. Am. Chem. Soc.* **1999**, *121*, 4451–4460.
59. C. P. Andrieux, A. Le Gorande, J.-M. Savéant, *J. Am. Chem. Soc.* **1992**, *114*, 6892–6904.
60. P. Maslak, *Top. Curr. Chem.* **1993**, *168*, 1–46.
61. N. Kimura, S. Takamuku, *Bull. Chem. Soc. Jpn.* **1993**, *66*, 3613–3617.
62. C. P. Andrieux, C. Combella, F. Kanoufi, J.-M. Savéant, A. Thiébault, *J. Am. Chem. Soc.* **1997**, *119*, 9527–9540.
63. M. D. Koppang, N. F. Woolsey, D. E. Bartak, *J. Am. Chem. Soc.* **1984**, *106*, 2799–2805.
64. M. L. Andersen, W. Long, D. D. M. Wayner, *J. Am. Chem. Soc.* **1997**, *119*, 6590–6595.
65. M. L. Andersen, N. Mathivanan, D. D. M. Wayner, *J. Am. Chem. Soc.* **1996**, *118*, 4871–4879.
66. J. S. Jaworski, *J. Chem. Res. (S)* **1997**, 412–413.
67. J.-M. Savéant, *J. Phys. Chem.* **1994**, *98*, 3716–3724.
68. P. Maslak, J. Kula, J. E. Chateaufneuf, *J. Am. Chem. Soc.* **1991**, *113*, 2304–2306.
69. P. Maslak, J. Therooff, *J. Am. Chem. Soc.* **1996**, *118*, 7235–7236.
70. P. Maslak, J. N. Narvaez, T. M. Vallombroso, Jr. *J. Am. Chem. Soc.* **1995**, *117*, 12373–12379.
71. D. Behar, P. Neta, *J. Phys. Chem.* **1981**, *85*, 690–693; P. Neta, D. Behar, *J. Am. Chem. Soc.* **1981**, *103*, 103–106.
72. (a) J.-M. Savéant, *Adv. Phys. Org. Chem.* **1990**, *26*, 1; (b) A. B. Pierini, J. S. Duca, Jr. *J. Chem. Soc., Perkin Trans. 2* **1995**, 1821–1828; (c) T. Underwood-Lemons, G. Sághi-Szabó, J. A. Tossell, J. H. Moore, *J. Chem. Phys.* **1996**, *105*, 7896–7903; (d) A. B. Pierini, J. S. Duca, Jr., D. M. A. Vera *J. Chem. Soc., Perkin Trans. 2* **1999**, 1003–1009.
73. D. D. Clarke, C. A. Coulson, *J. Chem. Soc. A* **1969**, 169–172; M. C. R. Symons, *Pure Appl. Chem.* **1981**, *53*, 223–229; R. Dressler, M. Allan, E. Haselbach, *Chimia* **1985**, *39*, 385–389; M. C. R. Symons, *Acta Chem. Scand.* **1997**, *51*, 127–134.
74. M. S. Mubarak, D. G. Peters, *J. Electroanal. Chem.* **1997**, *425*, 13–17; C. Ji, D. G. Peters, *J. Electroanal. Chem.* **1998**, *455*, 147–152; A. I. Tsyganok, K. Otsuka, *Appl. Cat. B*, **1999**, *22*, 15–26; A. Profumo, E. Fasani, A. Albini, *Heterocycles* **1999**, *51*, 1499–1502; E. Fasani, F. F. Barberis Negra, M. Mella, S. Monti, A. Albini, *J. Org. Chem.* **1999**, *64*, 5388–5395.
75. D. J. Ramón, M. Yus, *Tetrahedron Lett.* **1993**, *34*, 7115–7118; A. Bachki, F. Foubelo, M. Yus, *Tetrahedron Lett.* **1994**, *35*, 7643–7646; F. F. Huerta, C. Gómez, M. Yus, *Tetrahedron* **1995**, *51*, 3375–3388.
76. J. S. Duca, M. H. Gallego, A. B. Pierini, R. A. Rossi, *J. Org. Chem.* **1999**, *64*, 2626–2629.
77. M. C. Harsanyi, P. A. Lay, R. K. Norris, P. K. Witting, *Aust. J. Chem.* **1996**, *49*, 581–597.
78. M. C. Harsanyi, P. A. Lay, R. K. Norris, P. K. Witting, *J. Org. Chem.* **1995**, *60*, 5487–5493.
79. (a) R. Beugelmans, M. Chbani, *Bull. Soc. Chim. Fr.* **1995**, *132*, 290–305; (b) C. G. Ferrayoli, S. M. Palacios, R. A. Alonso, *J. Chem. Soc., Perkin Trans. 1*, **1995**, 1635–1638; (c) J. W. Wong, K. J. Natalie, G. C. Nwokogu, J. S. Pisipati, P. T. Flaherty, T. D. Greenwood, J. F. Wolfe, *J. Org. Chem.* **1997**, *62*, 6152–6159; (d) M. Médebielle, J. Pinson, J.-M. Savéant, *Electrochim. Acta* **1997**, *42*, 2049–2055; (e) M. T. Baumgartner, M. H. Gallego, A. B. Pierini, *J. Org. Chem.* **1998**, *63*, 6394–6397.
80. R. Beugelmans, M. Chbani, M. Soufiaoui, *Tetrahedron* **1996**, *37*, 1603–1604.
81. M. Chbani, J. P. Bouillon, J. Chastanet, M. Soufiaoui, R. Beugelmans, *Bull. Soc. Chim. Fr.* **1995**, *132*, 1053–1060; M. Médebielle, M. A. Oturan, J. Pinson, *New J. Chem.* **1995**, *19*, 349–352.
82. A. N. Santiago, G. Lassaga, Z. Rappoport, R. A. Rossi, *J. Org. Chem.* **1996**, *61*, 1125–1128.

83. S. D. Rychnovsky, S. S. Swenson, *J. Org. Chem.* **1997**, *62*, 1333–1340.
84. U. Azzena, F. Dessanti, G. Melloni, L. Pisano, *Tetrahedron Lett.* **1999**, *40*, 8291–8293.
85. Y. H. Kang, K. Kim, *Tetrahedron* **1999**, *55*, 4271–4286.
86. S. M. A. Jorge, N. R. Stradiotto, *J. Electroanal. Chem.* **1997**, *431*, 237–241.
87. P. Cauliez, M. Benaskar, A. Ghanimi, J. Simonet, *New J. Chem.* **1998**, 253–261.
88. S. Prigent, P. Cauliez, J. Simonet, D. G. Peters, *Acta Chem. Scand.* **1999**, *53*, 892–900.
89. J. F. Pilard, J. Simonet, *Tetrahedron Lett.* **1997**, *38*, 3735–3738.
90. C. Dell'Erba, M. Novi, G. Petrillo, C. Tavani, *Gazz. Chim. Ital.* **1997**, *127*, 361–366.
91. S.-H. Chen, V. Farina, D. M. Vyas, T. W. Doyle, B. H. Long, C. Fairchild, *J. Org. Chem.* **1996**, *61*, 2065–2070.
92. J. G. Lawless, M. D. Hawley, *J. Electroanal. Chem.* **1969**, *21*, 365–375; J. C. Stellhammer, W. E. Wentworth, *J. Chem. Phys.* **1969**, *51*, 1802–1814; F. M'Halla, J. Pinson, J.-M. Savéant, *J. Electroanal. Chem.* **1978**, *89*, 347–361; G. J. Gores, C. E. Koeppe, D. E. Bartak, *J. Org. Chem.* **1979**, *44*, 380–385; F. M'Halla, J. Pinson, J.-M. Savéant, *J. Am. Chem. Soc.* **1980**, *102*, 4120–4127; V. D. Parker, *Acta Chem. Scand. Ser. B.* **1981**, *35*, 595–599 and 655–660.
93. J. S. Jaworski, P. Leszczynski, S. Filipek, *J. Electroanal. Chem.* **1997**, *440*, 163–167.
94. J. S. Jaworski, P. Leszczynski, J. Tykarski, *J. Chem. Res. (S)* **1995**, 510–511; J. S. Jaworski, *Tetrahedron Lett.* **1999**, *40*, 5771–5772; J. S. Jaworski, P. Leszczynski, *J. Electroanal. Chem.* **1999**, *464*, 259–262.
95. (a) N. Kimura, S. Takamuku, *J. Am. Chem. Soc.* **1994**, *116*, 4087–4088; (b) N. Kimura, S. Takamuku, *J. Am. Chem. Soc.* **1995**, *117*, 8023–8024.
96. T. Underwood-Lemons, G. Sághi-Szabó, J. A. Tossell, J. H. Moore, *J. Chem. Phys.* **1996**, *105*, 7896–7903.
97. S. Antonello, F. Maran, *J. Am. Chem. Soc.* **1998**, *120*, 5713–5722.
98. M. D. Koppang, N. F. Woolsey, D. E. Bartak, *J. Am. Chem. Soc.* **1986**, *108*, 6497–6502.
99. C. Combella, F. Kanoufi, A. Thiébault, *J. Electroanal. Chem.* **1997**, *432*, 181–192.
100. A. Maercker, *Angew. Chem.* **1987**, *99*, 1002–1019; *Angew. Chem. Int. Ed.* **1987**, *26*, 972–989.
101. T. B. Christensen, K. Daasbjerg, *Acta Chem. Scand.* **1997**, *51*, 307–317.
102. K. Mochida, H. Watanabe, S. Murata, M. Fujitsuka, O. Ito, *J. Organomet. Chem.* **1998**, *568*, 121–125.
103. A. Bewick, J. M. Mellor, B. S. Pons, *J. Chem. Soc., Chem. Commun.* **1978**, 738; M. Mella, M. Freccero, A. Albini, *J. Chem. Soc., Chem. Commun.* **1995**, 41–42; M. Mella, M. Freccero, A. Albini, *Tetrahedron* **1996**, *52*, 5533–5548.
104. P. G. Gassman, B. A. Hay, *J. Am. Chem. Soc.* **1985**, *107*, 4075–4076; P. G. Gassman, B. A. Hay, *J. Am. Chem. Soc.* **1986**, *108*, 4227–4228; P. G. Gassman, S. J. Burns, *J. Org. Chem.* **1988**, *53*, 5576–5678.
105. C. J. Abelt, H. D. Roth, M. L. M. Schilling, *J. Am. Chem. Soc.* **1985**, *107*, 4148–4152; K. I. Booker-Milburn, *Synlett* **1992**, 809–810; M. Abe, A. Oku, *J. Org. Chem.* **1995**, *60*, 3065–3073; G. Maier, H. Rang, R. Emrich, S. Gries, H. Irngartinger, *Liebigs Ann.* **1995**, 161–167; B. Hong, M. A. Fox, G. Maier, C. Hermann, *Tetrahedron Lett.* **1996**, *37*, 583–586; M. Abe, M. Nojima, A. Oku, *Tetrahedron Lett.* **1996**, *37*, 1833–1836.
106. (a) W. Adam, H. Walter, G.-F. Chen, F. Williams, *J. Am. Chem. Soc.* **1992**, *114*, 3007–3014; (b) W. Adam, C. Sahin, J. Sendelbach, H. Walter, G.-F. Chen, F. Williams, *J. Am. Chem. Soc.* **1994**, *116*, 2576–2584; (c) W. Adam, T. Heidenfelder, C. Sahin, *Synthesis* **1995**, 1163–1170; (d) W. Adam, T. Heidenfelder, *Chem. Soc. Rev.* **1999**, *28*, 359–365.
107. T. Karatsu, Y. Ichino, A. Kitamura, W. H. Owens, P. S. Engel, *J. Chem. Res. (S)* **1995**, 440–441.
108. M. Fagnoni, M. Mella, A. Albini, *J. Phys. Org. Chem.* **1997**, *10*, 777–780.
109. M. Mella, M. Fagnoni, M. Freccero, E. Fasani, A. Albini, *Chem. Soc. Rev.* **1998**, *27*, 81–89.
110. Y. Nakadaira, N. Komatsu, H. Sakurai, *Chem. Lett.* **1985**, 1781–1782; H. Watanabe, M. Kato, E. Tabei, H. Kuwabara, N. Hirai, T. Sato, Y. Nagai, *J. Chem. Soc., Chem. Commun.* **1986**, 1662–1663; S. Kyushin, Y. Ehara, Y. Nakadaira, M. Ohashi, *J. Chem. Soc., Chem. Commun.* **1989**, 279–280.
111. J. M. White, *Aust. J. Chem.* **1995**, *48*, 1227–1251; H. Bock, B. Solouki, *Chem. Rev.* **1995**, *95*, 1161–1190.
112. C. Carra, F. Fiussello, G. Tonachini, *J. Org. Chem.* **1999**, *64*, 3867–3877.

113. G. L. Borosky, A. B. Pierini, *J. Mol. Struct. Theochem* **1999**, 466, 165–175.
114. J. Yoshida, M. Izawa, *J. Am. Chem. Soc.* **1997**, 119, 9361–9365.
115. Y. Nakadaira, S. Otani, S. Kyushin, M. Ohashi, H. Sakurai, Y. Funada, K. Sakamoto, A. Sekiguchi, *Chem. Lett.* **1991**, 601–602.
116. S. Fukuzumi, T. Kitano, K. Mochida, *J. Am. Chem. Soc.* **1990**, 112, 3246–3247.
117. K. Mochida, C. Hodota, R. Hata, S. Fukuzumi, *Organomet.* **1993**, 12, 586–588.
118. M. Mella, M. Freccero, A. Albini, *J. Chem. Soc., Chem. Commun.* **1995**, 41–42; M. Mella, M. Freccero, A. Albini, *Tetrahedron* **1996**, 52, 5533–5548.
119. P. G. Gassman, R. Yamaguchi, G. F. Koser, *J. Org. Chem.* **1978**, 43, 4392–4393.
120. Actually, there is an alternative option that is frequently encountered when a σ donor is flanked on one side by a π donor, on the other by an n donor. In our analysis, we have included this option by assigning such systems either to the $(\sigma + \pi)$ or $(\sigma + n)$ donor class based on the better donor (either π or n).
121. J. Yoshida, K. Nishiwaki, *J. Chem. Soc., Dalton Trans.* **1998**, 2589–2596.
122. A. J. Bagdaley, R. Brettell, *J. Chem. Soc., Chem. Commun.* **1966**, 108; K. Ponsold, H. Kasch, *Tetrahedron Lett.* **1979**, 4463–4464; D. P. DeCosta, A. K. Bennett, J. A. Pincock, *J. Am. Chem. Soc.* **1999**, 121, 3785–3786.
123. T. Thyran, D. A. Lightner, *Tetrahedron Lett.* **1996**, 37, 315–318.
124. W. Schmidt, E. Steckhan, *Angew. Chem.* **1978**, 90, 717; *Angew. Chem., Int. Ed. Engl.* **1978**, 17, 673–674; W. Schmidt, E. Steckhan, *Angew. Chem.* **1979**, 91, 850–851; *Angew. Chem., Int. Ed. Engl.* **1979**, 18, 801–802; W. Schmidt, E. Steckhan, *Angew. Chem.* **1979**, 91, 851–852; *Angew. Chem., Int. Ed. Engl.* **1979**, 18, 802–803.
125. Z. Yang, B. X. Wang, H. W. Hu, S. M. Zhu, *Syn. Commun.* **1998**, 28, 3163–3171.
126. T. Shono, Y. Matsumura, Y. Nakagawa, *J. Am. Chem. Soc.* **1974**, 96, 3532–3536; T. Chiba, M. Okimoto, H. Nagai, Y. Takata, *J. Org. Chem.* **1979**, 44, 3519–3523; R. M. Borg, D. R. Arnold, T. S. Cameron, *Can. J. Chem.* **1984**, 62, 1785–1802.
127. Y. Takahashi, H. Ohaku, S. Morishima, T. Suzuki, T. Miyashi, *Tetrahedron Lett.* **1995**, 36, 5207–5210; C. Gaebert, J. Mattay, *Tetrahedron* **1997**, 53, 14297–14316; W. Bergmark, S. Hector, G. Jones II, C. Oh, T. Kumagai, S. Hara, T. Segawa, N. Tanaka, T. Mukai, *Photochem. Photobiol.* **1997**, 109, 119–124; T. Herbertz, H. D. Roth, *J. Am. Chem. Soc.* **1998**, 120, 11904–11911; T. Herbertz, H. D. Roth, *J. Org. Chem.* **1999**, 64, 3708–3713; R. S. Glass, *Top. Curr. Chem.* **1999**, 205, 1–87.
128. A. L. Perrott, H. J. P. deLijser, D. R. Arnold, *Can. J. Chem.* **1997**, 75, 384–397; M. Suzuki, T. Ikeno, K. Osoda, K. Narasaka, T. Suenobu, S. Fukuzumi, A. Ishida, *Bull. Chem. Soc. Jpn.* **1997**, 70, 2269–2277; A. Anne, S. Fraoua, J. Moiroux, J.-M. Savéant, *J. Phys. Org. Chem.* **1998**, 11, 774–780; J. L. Faria, R. A. McClelland, S. Steenken, *Chem. Eur. J.* **1998**, 4, 1275–1280; W. Zhang, L. Yang, L.-M. Wu, Y. C. Liu, Z. L. Liu, *J. Chem. Soc., Perkin Trans. 2* **1998**, 1189–1193.
129. J. Yoshida, T. Murata, S. Isoe, *Tetrahedron Lett.* **1986**, 27, 3373–3376; T. Koizumi, T. Fuchigami, T. Nonaka, *Bull. Chem. Soc. Jpn.* **1989**, 62, 219–225.
130. P. S. Mariano, *Acc. Chem. Res.* **1983**, 16, 130–137; A. J. Y. Lan, S. L. Quillen, R. O. Heuckeroth, P. S. Mariano, *J. Am. Chem. Soc.* **1984**, 106, 6439–6440.
131. M. Freccero, E. Fasani, A. Albini, *J. Org. Chem.* **1993**, 58, 1740–1745; K. Mizuno, G. Konishi, T. Nishiyama, H. Inoue, *Chem. Lett.* **1995**, 1077–1078; M. Kako, K. Hatakenaka, S. Kakuma, M. Ninomiya, Y. Nakadaira, M. Yasui, F. Iwasaki, M. Wakasa, H. Hayashi, *Tetrahedron Lett.* **1999**, 40, 1133–1136.
132. S. Fukuzumi, K. Yasui, S. Itoh, *Chem. Lett.* **1997**, 161–162.
133. T. Yoshiyama, T. Fuchigami, *Chem. Lett.* **1992**, 1995–1998; T. Fuchigami, T. Fujita, *J. Org. Chem.* **1994**, 59, 7190–7192; E. Baciocchi, C. Crescenzi, O. Lanzalunga, *Tetrahedron* **1997**, 53, 4469–4478.
134. K. Chiba, M. Fukuda, S. Kim, Y. Kitano, M. Tada, *J. Org. Chem.* **1999**, 64, 7654–7656; H. Takakura, S. Yamamura, *Tetrahedron Lett.* **1999**, 40, 299–302.
135. M. Schmittel, A. Abufarag, O. Luche, M. Levis, *Angew. Chem.* **1990**, 102, 1174–1176; *Angew. Chem. Int. Ed. Engl.* **1990**, 29, 1144–1146; M. Schmittel, M. Levis, *Chem. Lett.* **1994**, 1935–1938.
136. M. Kako, H. Takada, Y. Nakadaira, *Tetrahedron Lett.* **1997**, 38, 3525–3528; Y. Tajima, H. Ishikawa, Y. Shimanuki, T. Miyazawa, N. Mikami, M. Kira, *Chem. Lett.* **1998**, 415–416.

137. S. Yamamura, Y. Shizuri, H. Shigemori, Y. Okuno, M. Ohkubo, *Tetrahedron* **1991**, *47*, 635–644.
138. R. Suau, F. Nájera, R. Rico, *Tetrahedron* **1999**, *55*, 4019–4028.
139. G. Pandey, P. Y. Reddy, U. T. Bhalerao, *Tetrahedron Lett.* **1991**, *32*, 5147–5150; Furuta S, Fuchigami T, *Electrochim. Acta* **1998**, *43*, 3183–3191.
140. A. G. M. Barrett, D. Pilipauskas, *J. Org. Chem.* **1991**, *56*, 2787–2800; A. Papadopoulos, B. Lewall, E. Steckhan, K.-D. Ginzel, F. Knoch, M. Nieger, *Tetrahedron* **1991**, *47*, 563–572; K. D. Moeller, L. D. Rutledge, *J. Org. Chem.* **1992**, *57*, 6360–6363; V. N. Belevskii, D. A. Tyurin, N. D. Chuvylkin, *High Ener. Chem.* **1998**, *32*, 305–315; T.-S. Kam, T.-M. Lim, Y.-M. Choo, *Tetrahedron* **1999**, *55*, 1457–1468; J. Yoshida, S. Suga, S. Suzuki, N. Kinomura, A. Yamamoto, K. Fujiwara, *J. Am. Chem. Soc.* **1999**, *121*, 9546–9549.
141. V. N. Belevskii, S. I. Belopushkin, D. A. Tyurin, N. D. Chuvylkin, *High Ener. Chem.* **1999**, *33*, 77–86.
142. T. Fuchigami, K. Yamamoto, A. Konno, *Tetrahedron* **1991**, *47*, 625–634; T. Fuchigami, A. Konno, K. Nakagawa, M. Shimojo, *J. Org. Chem.* **1994**, *59*, 5937–5941.
143. F. Cornille, U. Slomczynska, M. L. Smythe, D. D. Beusen, K. D. Moeller, G. R. Marshall, *J. Am. Chem. Soc.* **1995**, *117*, 909–917; P. Brungs, K. Danielmeier, J. Jakobi, C. Nothhelfer, A. Stahl, A. Zietlow, E. Steckhan, *J. Chim. Phys.* **1996**, *93*, 575–590.
144. M. Kimura, N. Saitoh, H. Kawai, Y. Sawaki, *Novel Trends in Electroorganic Synthesis*, Ed. S. Torii, Springer, Tokyo **1998**, p. 73–76; W. A. McHale, A. G. Kutateladze, *J. Org. Chem.* **1998**, *63*, 9924–9931; M. Nakamura, M. Toganoh, H. Ohara, E. Nakamura, *Org. Lett.* **1999**, *1*, 7–9.
145. Y. Takemoto, T. Ohra, S. Furuse, H. Koike, C. Iwata, *J. Chem. Soc., Chem. Commun.* **1994**, 1529–1530.
146. A. P. Schaap, G. Prasad, S. D. Gagnon, *Tetrahedron Lett.* **1983**, 3047–3050; E. Hasegawa, S. Koshii, T. Horaguchi, T. Shimizu, *J. Org. Chem.* **1992**, *57*, 6342–6344; A. J. Highton, T. N. Majid, N. S. Simpkins, *Synlett* **1999**, 237–239.
147. Y. Takemoto, S. Furuse, H. Koike, T. Ohra, C. Iwata, H. Ohishi, *Tetrahedron Lett.* **1995**, *36*, 4085–4088; M. Kimura, H. Kawai, Y. Sawaki, in *Novel Trends in Electroorganic Synthesis*, Ed. S. Torii, Springer, Tokyo **1998**, p. 77–78.
148. J. Yoshida, Y. Ishichi, S. Isoe, *J. Am. Chem. Soc.* **1992**, *114*, 7594–7595; K. Narasaka, Y. Kohno, *Bull. Chem. Soc. Jpn.* **1993**, *66*, 3456–3463; K. Narasaka, Y. Kohno, S. Shimada, *Chem. Lett.* **1993**, 125–128; S. Kyushin, S. Otani, Y. Nakadaira, M. Ohashi, *Chem. Lett.* **1995**, 29–30; T. Ikeno, M. Harada, N. Arai, K. Narasaka, *Chem. Lett.* **1997**, 169–170; K. Narasaka, *Pure Appl. Chem.* **1997**, *69*, 601–604; T. Mikami, M. Harada, K. Narasaka, *Chem. Lett.* **1999**, 425–426.
149. Y. S. Jung, W. H. Swartz, W. Xu, P. S. Mariano, N. J. Green, A. G. Schultz, *J. Org. Chem.* **1992**, *56*, 6037–6047; E. Meggers, E. Steckhan, S. Blechert, *Angew. Chem.* **1995**, *107*, 2317–2319; *Angew. Chem. Int. Ed. Engl.* **1995**, *34*, 2137–2139; E. Le Gall, J.-P. Hurvois, S. Sinbandhit, *Eur. J. Org. Chem.* **1999**, 2645–2653.
150. J. Yoshida, S. Suga, K. Fuke, M. Watanabe, *Chem. Lett.* **1999**, 251–252.
151. (a) G. Pandey, G. Kumaraswamy, U. T. Bhalerao, *Tetrahedron Lett.* **1989**, *30*, 6059–6062; (b) G. Pandey, G. D. Reddy, *Tetrahedron Lett.* **1992**, *33*, 6533–6536; (c) G. Pandey, G. D. Reddy, G. Kumaraswamy, *Tetrahedron* **1994**, *50*, 8185–8194.
152. (a) F. G. Bordwell, J.-P. Cheng, M. J. Bausch *J. Am. Chem. Soc.* **1988**, *110*, 2872–2877; (b) F. G. Bordwell, J.-P. Cheng, *J. Am. Chem. Soc.* **1989**, *111*, 1792–1795; (c) F. G. Bordwell, A. V. Satish, *J. Am. Chem. Soc.* **1992**, *114*, 10173–10176; (d) M. Bietti, E. Baciocchi, S. Steenken, *J. Phys. Chem. A* **1998**, *102*, 7337–7342; (e) C. X. Zhao, Y. F. Gong, H. Y. He, X. K. Jiang, *J. Phys. Org. Chem.* **1999**, *12*, 688–694.
153. X. Zhang, F. G. Bordwell, *J. Org. Chem.* **1992**, *57*, 4163–4168.
154. M. Bietti, A. Cuppoletti, C. Dagostin, C. Florea, C. Galli, P. Gentili, H. Petride, C. R. Caia, *Eur. J. Org. Chem.* **1998**, 2425–2429.
155. E. Fasani, M. Mella, A. Albini, *J. Chem. Soc. Perkin Trans. 2* **1995**, 449–452.
156. J. Mönig, R. Goslich, K.-D. Asmus, *Ber. Bunsen Ges. Phys. Chem.* **1986**, *90*, 115–121.
157. E. Baciocchi, T. Del Giacco, F. Elisei, *J. Am. Chem. Soc.* **1993**, *115*, 12290–12295.
158. P. Hapiot, J. Moiroux, J.-M. Savéant, *J. Am. Chem. Soc.* **1990**, *112*, 1337–1343; A. Anne, P. Hapiot, J. Moiroux, P. Neta, J.-M. Savéant, *J. Phys. Chem.* **1991**, *95*, 2370–2377; G. N. R.

- Tripathi, *Chem. Phys. Lett.* **1992**, *199*, 409–416; A. Anne, P. Hapiot, J. Moiroux, P. Neta, J.-M. Savéant, *J. Am. Chem. Soc.* **1992**, *112*, 4694–4701; V. D. Parker, Y. X. Zhao, Y. Lu, G. Zheng, *J. Am. Chem. Soc.* **1998**, *120*, 12720–12727.
159. V. D. Parker, E. T. Chao, G. Zheng, *J. Am. Chem. Soc.* **1997**, *119*, 11390–11394.
160. E. Baciocchi, M. Bietti, S. Steenken, *Chem. Eur. J.* **1999**, *5*, 1785–1793.
161. R. B. Silverman, *Adv. Electr. Trans. Chem.* **1992**, *2*, 177–213.
162. C. G. Shaefer, K. S. Peters, *J. Am. Chem. Soc.* **1980**, *102*, 7566–7567; A. Sinha, T. C. Bruice, *J. Am. Chem. Soc.* **1984**, *106*, 7291–7292; S. Das, C. von Sonntag, *Z. Naturforsch.* **1986**, *41b*, 505–513; F. D. Lewis, *Acc. Chem. Res.* **1986**, *19*, 401–405; J. P. Dinnocenzo, T. E. Banach, *J. Am. Chem. Soc.* **1989**, *111*, 8646–8653; W. Xu, X.-M. Zhang, P. S. Mariano, *J. Am. Chem. Soc.* **1991**, *113*, 8863–8878; W. Xu, P. S. Mariano, *J. Am. Chem. Soc.* **1991**, *113*, 1431–1432; M. Goez, I. Sartorius, *J. Am. Chem. Soc.* **1993**, *115*, 11123–11133; M. Goez, I. Sartorius, *Chem. Ber.* **1994**, *127*, 2273–2276; O. Brede, D. Beckert, C. Windolph, H. A. Göttinger, *J. Phys. Chem. A* **1998**, *102*, 1457–1464; K. S. Peters, A. Cashin, P. Timbers, *J. Am. Chem. Soc.* **2000**, *122*, 107–113.
163. X. Zhang, S.-R. Yeh, S. Hong, M. Freccero, A. Albini, D. E. Falvey, P. S. Mariano, *J. Am. Chem. Soc.* **1994**, *116*, 4211–4220.
164. M. Ioele, S. Steenken, E. Baciocchi, *J. Phys. Chem. A* **1997**, *101*, 2979–2987.
165. D. M. Camaioni, *J. Am. Chem. Soc.* **1990**, *112*, 9475–9483.
166. J. H. Penn, D.-L. Deng, K.-J. Chai, *Tetrahedron Lett.* **1988**, *29*, 3635–3638; D. R. Arnold, L. J. Lamont, *Can. J. Chem.* **1989**, *67*, 2119–2127; R. Popielarz, D. R. Arnold, *J. Am. Chem. Soc.* **1990**, *112*, 3068–3082; D. R. Arnold, L. J. Lamont, A. L. Perrott, *Can. J. Chem.* **1991**, *69*, 225–233; S. Perrier, S. Sankararaman, J. K. Kochi, *J. Chem. Soc. Perkin Trans. 2* **1993**, 825–837.
167. P. Maslak, T. M. Vallombroso, W. H. Chapman, Jr., J. N. Narvaez, *Angew. Chem.* **1994**, *106*, 110–113; *Angew. Chem. Int. Ed. Engl.* **1994**, *33*, 73–75.
168. J. P. Dinnocenzo, W. P. Todd, T. R. Simpson, I. R. Gould, *J. Am. Chem. Soc.* **1990**, *112*, 2462–2464; J. P. Dinnocenzo, D. R. Lieberman, T. R. Simpson, *J. Am. Chem. Soc.* **1993**, *115*, 366–367.
169. L. A. Lucia, R. D. Burton, K. S. Schanze, *J. Phys. Chem.* **1993**, *97*, 9078–9080; J. W. Leon, D. G. Whitten, *J. Am. Chem. Soc.* **1993**, *115*, 8038–8043.
170. Z. Su, P. S. Mariano, D. E. Falvey, U. C. Yoon, S. W. Oh, *J. Am. Chem. Soc.* **1998**, *120*, 10676–10686.
171. J. P. Dinnocenzo, S. Farid, J. L. Goodman, I. R. Gould, W. P. Todd, S. L. Mattes, *J. Am. Chem. Soc.* **1989**, *111*, 8973–8975; W. P. Todd, J. P. Dinnocenzo, S. Farid, J. L. Goodman, I. R. Gould, *Tetrahedron Lett.* **1993**, *34*, 2863–2866.
172. W. Adam, T. Kammel, M. Toubartz, S. Steenken, *J. Am. Chem. Soc.* **1997**, *119*, 10673–10676.
173. L. Qin, G. N. R. Tripathi, R. H. Schuler, *Z. Naturforsch.* **1985**, *40a*, 1026–1039; F. G. Bordwell, X.-M. Zhang, J.-P. Cheng, *J. Org. Chem.* **1993**, *58*, 6410–6416; J.-P. Cheng, Y. Zhao, *Tetrahedron* **1993**, *49*, 5267–5276; M. Jonsson, J. Lind, T. E. Eriksen, G. Merényi, *J. Am. Chem. Soc.* **1994**, *116*, 1423–1427.
174. O. Hammerich, V. D. Parker, A. Ronlán, *Acta Chem. Scand.* **1976**, *B30*, 89–90; V. D. Parker, Y. Chao, B. Reitsöen, *J. Am. Chem. Soc.* **1991**, *113*, 2336–2338; M. Schmittel, G. Gescheidt, M. Röck, *Angew. Chem.* **1994**, *106*, 2056–2058; *Angew. Chem. Int. Ed. Engl.* **1994**, *33*, 1961–1963.
175. T. A. Gadosy, D. Shukla, L. J. Johnston, *J. Phys. Chem. A* **1999**, *103*, 8834–8839.
176. (a) M. Schmittel, M. Keller, A. Burghart, *J. Chem. Soc. Perkin Trans. 2*, **1995**, 2327–2333; (b) M. Schmittel, A. Burghart, H. Werner, M. Laubender, R. Söllner, *J. Org. Chem.*, **1999**, *64*, 3077–3085.
177. Y. Kohno, K. Narasaka, *Bull. Chem. Soc. Jpn.* **1995**, *68*, 322–329.
178. M. Schmittel, J. Heinze, H. Trenkle, *J. Org. Chem.* **1995**, *60*, 2726–2733.
179. M. Schmittel, J.-P. Steffen, A. Burghart, *Acta Chem. Scand.* **1999**, *53*, 781–791.
180. M. Schmittel, R. Söllner, *Angew. Chem.* **1996**, *108*, 2248–2250, *Angew. Chem. Int. Ed. Engl.* **1996**, *35*, 2107–2109.
181. M. Schmittel, R. Söllner, *J. Chem. Soc., Perkin Trans. 2*, **1999**, 515–520.

182. E. Baciocchi, E. Fasella, O. Lanzalunga, M. Mattioli, *Angew. Chem.* **1993**, *105*, 1110–1112; *Angew. Chem. Int. Ed. Engl.* **1993**, *32*, 1071–1073.
183. K. Mizuno, T. Tamai, I. Hashida, Y. Otsuji, *J. Org. Chem.* **1995**, *60*, 2935–2937.
184. H. G. Raj, V. S. Parmar, S. C. Jain, K. I. Priyadarsini, J. P. Mittal, S. Goel, S. K. Das, S. K. Sharma, C. E. Olsen, J. Wengel, *Bioorg. Med. Chem.* **1999**, *7*, 2091–2094.
185. H. J. P. de Lijser, T. S. Cameron, D. R. Arnold, *Can. J. Chem.* **1997**, *75*, 1795–1809.
186. K. Komaguchi, M. Shiotani, A. Lund, *Chem. Phys. Lett.* **1997**, *265*, 217–223.
187. K. Mochida, K. Takekuma, H. Watanabe, S. Murata, *Chem. Lett.* **1998**, 623–624.
188. R. W. Kavash, P. S. Mariano, *Tetrahedron Lett.* **1989**, *30*, 4185–4188.
189. P. W. Rabideau, Z. Marcinow, *Org. React.* **1992**, *23*, 1–334.
190. T. Guena, D. Pletcher, *Acta Chem. Scand.* **1998**, *52*, 23–31.
191. G. E. Lawson, A. Kitaygorodskiy, Y.-P. Sun, *J. Org. Chem.* **1999**, *64*, 5913–5920.
192. D. C. de Azevedo, J. F. C. Boodts, J. C. M. Cavalcanti, A. E. G. Santana, A. F. dos Santos, E. S. Bento, J. Tonholo, M. O. F. Goulart, *J. Electroanal. Chem.* **1999**, *466*, 99–106.
193. G. Asensio, A. Cuenca, P. Gaviña, M. Medio-Simón, *Tetrahedron Lett.* **1999**, *40*, 3939–3940.
194. J. Volke, V. Skála, *J. Electroanal. Chem.* **1972**, *36*, 383–388.
195. F. Marken, S. Kumbhat, G. H. W. Sanders, R. G. Compton, *J. Electroanal. Chem.* **1996**, *414*, 95–105; P. A. Lay, R. K. Norris, P. K. Witting, *Aust. J. Chem.* **1997**, *50*, 999–1007.
196. F. Williot, M. Bernard, D. Lucas, Y. Mugnier, J. Lessard, *Can. J. Chem.* **1999**, *77*, 1648–1654.
197. A. Arranz, S. F. deBetoño, J. M. Moreda, A. Cid, J. F. Arranz, *Anal. Chim. Acta* **1997**, *351*, 97–103.
198. (a) T. Ohno, H. Nakahiro, K. Sanemitsu, T. Hirashima, I. Nishiguchi, *Tetrahedron Lett.* **1992**, *33*, 5515–5516; (b) S. Kashimura, Y. Murai, M. Ishifune, H. Masuda, H. Murase, T. Shono, *Tetrahedron Lett.* **1995**, *36*, 4805–4808.
199. D. A. Tyssee, M. M. Baizer, *J. Org. Chem.* **1974**, *39*, 2819–2823; T. Ohno, Y. Ishino, Y. Tsumagari, I. Nishiguchi, *J. Org. Chem.* **1995**, *60*, 458–460; T. Ohno, H. Aramaki, H. Nakahiro, I. Nishiguchi, *Tetrahedron* **1996**, *52*, 1943–1952; G. Pandey, M. K. Ghorai, S. Hajra, *Tetrahedron Lett.* **1998**, *39*, 8341–8344; N. Kise, Y. Hirata, T. Hamaguchi, N. Ueda, *Tetrahedron Lett.* **1999**, *40*, 8125–8128.
200. H. E. Bode, G. Sowell, R. D. Little, *Tetrahedron Lett.* **1990**, *31*, 2525–2528; S. P. Chavan, K. S. Ethiraj, *Tetrahedron Lett.* **1995**, *36*, 2281–2284; G. Pandey, S. Hajra, M. K. Ghorai, K. Ravikumar, *J. Am. Chem. Soc.* **1997**, *119*, 8777–8787; G. Pandey, M. K. Ghorai, S. Hajra, *Tetrahedron Lett.* **1998**, *39*, 1831–1834; S. Kashimura, Y. Murai, M. Ishifune, H. Masuda, M. Shimomura, H. Murase, T. Shono, *Acta Chem. Scand.* **1999**, *53*, 949–951.
201. (a) G. Pattenden, G. M. Robertson, *Tetrahedron Lett.* **1983**, *24*, 4617–4620; (b) J. Cossy, S. Bouzbou, C. Mouza, *Synlett* **1998**, 621–622.
202. J. Cossy, J.-P. Pete, *Adv. Electron Transfer Chem.* **1996**, *5*, 141–195.
203. S. Hintz, A. Heidbreder, J. Mattay, *Top. Curr. Chem.* **1996**, *177*, 77–124.
204. D. P. Fox, R. D. Little, M. M. Baizer, *J. Org. Chem.* **1985**, *50*, 2202–2204; D. Beloti, J. Cossy, J. P. Pete, C. Portella, *J. Org. Chem.* **1986**, *51*, 4196–4200; R. D. Little, D. P. Fox, L. Van Hijfte, R. Dannecker, G. Sowell, R. L. Wolin, L. Moëns, M. M. Baizer, *J. Org. Chem.* **1988**, *53*, 2287–2294; N. Kise, T. Suzumoto, T. Shono, *J. Org. Chem.* **1994**, *59*, 1407–1413; G. H. Lee, E. B. Choi, E. Lee, C. S. Pak, *J. Org. Chem.* **1994**, *59*, 1428–1443; G. Pandey, S. Hajra, M. K. Ghorai, K. Ravikumar, *J. Org. Chem.* **1997**, *62*, 5966–5973; G. H. Lee, S. J. Ha, I. K. Yoon, C. S. Pak, *Tetrahedron Lett.* **1999**, *40*, 2581–2584.
205. R. Gorny, H. J. Schäfer, R. Fröhlich, *Angew. Chem.* **1995**, *107*, 2188–2191; *Angew. Chem. Int. Ed. Engl.* **1995**, *34*, 2007–2009.
206. (a) T. Shono, N. Kise, E. Shirakawa, H. Matsumoto, E. Okazaki, *J. Org. Chem.* **1991**, *56*, 3063–3067; (b) N. Kise, H. Oike, E. Okajaki, M. Yoshimoto, T. Shono, *J. Org. Chem.* **1995**, *60*, 3980–3992.
207. P. Kujawa, N. Mohid, C. K. Zaman, W. Manshol, P. Ulanski, J. M. Rosiak, *Radiat. Phys. Chem.* **1998**, *53*, 403–409.
208. G. Sun, J. Wu, X. Qin, X. Fang, W. Wang, *Radiat. Phys. Chem.* **1999**, *55*, 409–416.
209. V. D. Parker, *Acta. Chem. Scand.* **1981**, *B35*, 295–301.
210. C. P. Andrieux, M. Grzeszczuk, J.-M. Savéant, *J. Am. Chem. Soc.* **1991**, *113*, 8811–8817.

211. M. F. Nielsen, O. Hammerich, *Acta. Chem. Scand.* **1992**, 46, 883–896.
212. M. F. Nielsen, O. Hammerich, *Acta. Chem. Scand.* **1987**, B 41, 668–678.
213. M. F. Nielsen, H. Eggert, O. Hammerich, *Acta. Chem. Scand.* **1991**, 45, 292–301.
214. O. Hammerich, M. F. Nielsen, *Acta. Chem. Scand.* **1998**, 52, 831–857.
215. I. Fussing, O. Hammerich, A. Hussain, M. F. Nielsen, J. H. P. Utley, *Acta. Chem. Scand.* **1998**, 52, 328–337.
216. A. S. Mendkovich, O. Hammerich, T. Y. Rubinskaya, V. P. Gulyai, *Acta. Chem. Scand.* **1991**, 45, 644–651.
217. L. C. T. Shoute, *J. Phys. Chem.* **1997**, 101, 5335–5542.
218. L.-S. R. Yeh, A. J. Bard, *J. Electrochem. Soc.*, **1977**, 124, 355–360.
219. A. R. de Andrade, J. F. C. Boodts, *J. Brazil. Chem. Soc.*, **1998**, 9, 257–261.
220. Y. Huang, D. D. M. Wayner, *J. Am. Chem. Soc.* **1994**, 116, 2157–2158.
221. H. S. Sørensen, K. Daasbjerg, *Acta Chem. Scand.* **1998**, 52, 51–61.
222. F. Barba, J. L. de la Fuente, M. Galakhov, *Tetrahedron*, **1997**, 53, 5831–5838; S. Kashimura, M. Ishifune, Y. Murai, H. Murase, M. Shimomura, T. Shono, *Tetrahedron Lett.* **1998**, 39, 6199–6202; J. Gruber, F. F. Camilo, A. C. M. Arantes, *Helv. Chim. Acta* **1999**, 82, 389–393.
223. M. Kimura, N. Moritani, Y. Swaki, *Electroorg. Synth.*, M. M. Baizer Mem. Symp., Dekker, New York **1991**, p. 61.
224. P. Mikesell, M. Schwaebe, M. DiMare, R. D. Little, *Acta Chem. Scand.* **1999**, 53, 792–799.
225. J. Delaunay, A. Orliac, J. Simonet, *J. Electrochem. Soc.* **1995**, 142, 3613–3619.
226. J. H. P. Utley, M. Güllü, M. Motevalli, *J. Chem. Soc. Perkin Trans I* **1995**, 1961–1970.
227. N. Kise, M. Echigo, T. Shono, *Tetrahedron Lett.* **1994**, 35, 1897–1900; N. Kise, S. Mashiba, N. Ueda, *J. Org. Chem.* **1998**, 63, 7931–7938.
228. C. Degrand, H. Lund, *Acta Chem. Scand.* **1977**, B31, 593–598; C. Degrand, D. Jacquin, P.-L. Compagnon, *J. Chem. Res. (S)* **1978**, 246–247.
229. D. R. Arnold, K. A. McManus, *Can. J. Chem.* **1998**, 1238–1248 and cited references.
230. M. Machida, H. Takechi, Y. Kanaoka, *Chem. Pharm. Bull.* **1982**, 30, 1579–1587; W. Xu, P. S. Mariano, *J. Am. Chem. Soc.* **1991**, 113, 1431–1432; U. C. Yoon, P. S. Mariano, *Acc. Chem. Res.* **1992**, 25, 233–240; A. G. Griesbeck, A. Henz, J. Hirt, *Synthesis* **1996**, 1261–1276; T. Hasegawa, Y. Yamazaki, *Tetrahedron* **1998**, 54, 12223–12232.
231. D. R. Arnold, P. C. Wong, A. J. Maroulis, T. S. Cameron, *Pure Appl. Chem.* **1980**, 52, 2609–2619; N. E. Polyakov, A. I. Kruppa, V. S. Bashurova, R. N. Musin, T. V. Leshina, L. D. Kispert, *J. Photochem. Photobiol. A* **1999**, 128, 65–74.
232. Y. Rubin, P. S. Ganapathi, A. Franz, Y.-Z. An, W. Qian, R. Neier, *Chem. Eur. J.* **1999**, 5, 3162–3184.
233. M. M. Baizer in *Organic Electrochemistry*, eds. H. Lund and M. M. Baizer, New York, Marcel Dekker, **1991**, chapter 22, 879–948.
234. M. M. Baizer *Chemtech* **1980**, 10, 161–164; D. E. Danly *Chemtech* **1980**, 10, 302–311.
235. E. Lamy, L. Nadjo, J.-M. Savéant *J. Electroanal. Chem.* **1973**, 42, 189–221.
236. M. J. Hazelrigg Jr., A. J. Bard, *J. Electrochem. Soc.* **1975**, 122, 211–220.
237. E. A. Casanova, M. C. Dutton, D. J. Kalota, J. H. Wagenknecht, *J. Electrochem. Soc.*, **1993**, 140, 2565–2567.
238. B. M. Bezilla Jr., J. T. Maloy, *J. Electrochem. Soc.* **1979**, 126, 579–583.
239. I. Fussing, M. Güllü, O. Hammerich, A. Hussain, M. F. Nielson, J. H. P. Utley, *J. Chem. Soc., Perkin Trans. 2* **1996**, 649–658.
240. V. J. Puglishi, A. J. Bard, *J. Electrochem. Soc.* **1972**, 119, 829–833.
241. A. P. Doherty, K. Scott, *J. Electroanal. Chem.* **1998**, 442, 35–40.
242. M. F. Nielsen, B. Batanero, T. Löhl, H. J. Schäfer, E.-U. Würthwein, R. Fröhlich, *Chem. Eur. J.* **1997**, 3, 2011–2024.
243. O. Hammerich, V. D. Parker, *Acta. Chem. Scand.* **1981**, B 35, 341–347; O. Hammerich, V. D. Parker, *Acta. Chem. Scand.* **1983**, B37, 379–392.
244. C. Z. Smith, J. H. P. Utley, *J. Chem. Res. (S)* **1982**, 18–19; C. Amatore, J. Pinson, J.-M. Savéant, *J. Electroanal. Chem.* **1982**, 137, 143–148; C. Amatore, D. Garreau, M. Hammi, J. Pinson, J.-M. Savéant, *J. Electroanal. Chem.* **1985**, 184, 1–24; A. S. Mendkovich, L. V. Michalchenko, V. P. Gulyai, *J. Electroanal. Chem.* **1987**, 224, 273–275.
245. R. Eliason, O. Hammerich, V. D. Parker, *Acta. Chem. Scand.* **1988**, B46, 7–10.

246. M. Sertel, A. Yildiz, R. Gambert, H. Baumgärtel, *Electrochim. Acta* **1986**, *31*, 1287–1292.
247. M. D. Koppang, N. F. Woolsey, D. E. Bartak, *J. Am. Chem. Soc.* **1985**, *107*, 4692–4700.
248. C. Degrand, D. Jacquin, P.-L. Compagnon, *J. Chem. Res. (S)* **1978**, 246–247; C. Degrand, D. Jacquin, P.-L. Compagnon, *J. Chem. Res. (M)* **1978**, 3272–3282.
249. R. M. Crooks, A. J. Bard, *J. Electroanal. Chem.* **1988**, *240*, 253–279.
250. R. D. Webster, *J. Chem. Soc., Perkin Trans. 2* **1999**, 263–269.
251. A less common route involves the further reduction of the ketyl radical anion to the corresponding dianion and subsequent nucleophilic addition to a carbonyl group.
252. L.-S. R. Yeh, *J. Electroanal. Chem.* **1977**, *84*, 159–168.
253. M. Grätzel, A. Henglein, K. M. Bansal, *Ber. Bunsenges. Phys. Chem.*, **1973**, *77*, 6–11.
254. W. R. Fawcett, T. M. Krygowski, *Can. J. Chem.* **1976**, *54*, 3283–3292; W. R. Fawcett, A. Lasia, *Can. J. Chem.* **1981**, *59*, 3256–3260.
255. N. R. Armstrong, N. E. Vanderborgh, R. K. Quinn, *J. Electrochem. Soc.* **1975**, *122*, 615–619.
256. C. P. Andrieux, M. Grzeszczuk, J.-M. Savéant, *J. Am. Chem. Soc.* **1991**, *113*, 8811–8817.
257. J. G. Smith, C. D. Veach, *Can. J. Chem.* **1966**, *44*, 2497–2502; J. H. Smith, I. Ho, *J. Org. Chem.* **1972**, *37*, 653–656.
258. A. A. Isse, A. M. Abdurahman, E. Vianello, *J. Electroanal. Chem.* **1997**, *431*, 249–255.
259. S. U. Pedersen, T. Lund, K. Daasbjerg, M. Pop, I. Fussing, H. Lund, *Acta Chem. Scand.* **1998**, *52*, 657–671.
260. J. F. Garst, F. E. Barton, *Tetrahedron Lett.* **1969**, 587–590.
261. C. Chatgililoglu, K. U. Ingold, J. C. Scaiano, *J. Am. Chem. Soc.* **1981**, *103*, 7739–7742; S. U. Pedersen, T. Lund, *Acta Chem. Scand.* **1991**, *45*, 397–402.
262. M. S. W. Chan, D. R. Arnold, *Can. J. Chem.* **1997**, *75*, 1810–1819.
263. M. Kojima, A. Ishida, S. Takamuku, Y. Wada, S. Yanagida, *Chem. Lett.* **1994**, 1897–1900; H. Weng, H. D. Roth, *J. Org. Chem.* **1995**, *60*, 4136–4145; H. J. P. de Lijser, D. R. Arnold, *J. Org. Chem.* **1997**, *62*, 8432–8438; H. J. P. de Lijser, D. R. Arnold, *J. Chem. Soc. Perkin Trans. 2* **1997**, 1369–1380; S. Swansburg, K. Janz, G. Jocys, A. Pincock, J. Pincock, *Can. J. Chem.* **1998**, *76*, 35–47; V. Nair, L. G. Nair, *Tetrahedron Lett.* **1998**, *39*, 4585–4586; V. Nair, S. B. Panicker, *Tetrahedron Lett.* **1999**, *40*, 563–564.
264. D. R. Arnold, K. A. McManus, M. S. W. Chan, *Can. J. Chem.* **1997**, *75*, 1055–1075.
265. C. P. Butts, L. Eberson, M. P. Hartshorn, W. T. Robinson, D. J. Timmerman-Vaughan, *Acta Chem. Scand.* **1997**, *51*, 73–87; L. Eberson, M. P. Hartshorn, J. O. Svensson, *Acta Chem. Scand.* **1997**, *51*, 279–288; F. Ciminale, A. Ciardo, S. Francioso, A. Nacci, *J. Org. Chem.* **1999**, *64*, 2459–2464.
266. T. Shono, S. Kashimura, *J. Org. Chem.* **1983**, *48*, 1939–1940.
267. L. Lopez, V. Calò, F. Stasi, *Synthesis* **1987**, 947–948.
268. G. Lem, D. I. Schuster, S. H. Courtney, Q. Lu, S. R. Wilson, *J. Am. Chem. Soc.* **1995**, *117*, 554–555; I. G. Safonov, S. H. Courtney, D. I. Schuster, *Res. Chem. Intermed.* **1997**, *23*, 541–548.
269. M. Cariou, J. Simonet, *Tetrahedron Lett.* **1991**, *32*, 4913–4916; C. P. Butts, L. Eberson, M. P. Hartshorn, W. T. Robinson, B. R. Wood, *Acta Chem. Scand.* **1996**, *50*, 587–595.
270. D. R. Arnold, M. S. W. Chan, K. A. McManus, *Can. J. Chem.* **1996**, *74*, 2143–2166.
271. H. Baltes, L. Stork, H. J. Schäfer, *Justus Liebigs Ann. Chem.* **1979**, 318–327.
272. As a keystone in the synthesis of a) maltol: T. Shono, Y. Matsumura, *Tetrahedron Lett.* **1976**, 1363–1364; (b) rethrolones: T. Shono, Y. Matsumura, H. Hamaguchi, K. Nakamura, *Chem. Lett.* **1976**, 1249–1252; (c) the flavouring agent cyclotene: T. Shono, Y. Matsumura, H. Hamaguchi, *J. Chem. Soc., Chem. Commun.* **1977**, 712–713.
273. T. Shono, Y. Matsumura, K. Tsubata, Y. Sugihara, S. Yamane, T. Kanazawa, T. Aoki, *J. Am. Chem. Soc.* **1982**, *104*, 6697–6703.
274. J. Y. Becker, E. Shakkour, J. A. P. R. Sarma, *J. Chem. Soc., Chem. Commun.* **1990**, 1016–1017; J. Y. Becker, E. Shakkour, J. A. P. R. Sarma, *J. Org. Chem.* **1992**, *57*, 3716–3720.
275. R. A. Neunteufel, D. R. Arnold, *J. Am. Chem. Soc.* **1973**, *95*, 4080–4081; M. Kojima, A. Ishida, Y. Kuriyama, Y. Wada, H. Takeya, *Bull. Chem. Soc. Jpn.* **1999**, *72*, 1049–1055.
276. K. D. Warzecha, X. C. Xing, M. Demuth, *Pure Appl. Chem.* **1997**, *69*, 109–112; C. Heineemann, M. Demuth, *J. Am. Chem. Soc.* **1997**, *119*, 1129–1130; X. Xing, M. Demuth, *Synlett* **1999**, 987–990.

277. C. Heinemann, M. Demuth, *J. Am. Chem. Soc.* **1999**, *121*, 4894–4895.
278. G. Pandey, M. Sridar, U. T. Bhalerao, *Tetrahedron Lett.* **1990**, *31*, 5373–5376; A. K. Panfilov, G. V. Cherkaev, T. V. Magdesieva, N. M. Przhiyalgovskaya, *Zh. Org. Khim.* **1992**, *28*, 691–699; Y. Inoue, T. Okano, N. Yamasaki, A. Tai, *J. Chem. Soc., Chem. Commun.* **1993**, 718–720; A. Goosen, C. W. McClelland, F. C. Rinaldi, *J. Chem. Soc., Perkin Trans. 2* **1993**, 279–281; F. D. Lewis, G. D. Reddy, B. E. Cohen, *Tetrahedron Lett.* **1994**, *35*, 535–538.
279. (a) M. Fujita, A. Shindo, A. Ishida, T. Majima, S. Takamuku, S. Fukuzumi, *Bull. Chem. Soc. Jpn.* **1996**, *69*, 743–749; (b) V. Nair, J. Mathew, P. P. Kanakamma, S. B. Panicker, V. Sheeba, S. Zeena, G. K. Eigendorf, *Tetrahedron Lett.* **1997**, *38*, 2191–2194.
280. K. McMahon, D. R. Arnold, *Can. J. Chem.* **1993**, *71*, 450–468; D. R. Arnold, X. Du, H. J. P. de Lijser, *Can. J. Chem.* **1995**, *73*, 522–530; M. Tanaka, H. Nakashima, M. Fujiwara, H. Ando, Y. Souma, *J. Org. Chem.* **1996**, *61*, 788–792; T. Douadi, M. Cariou, J. Simonet, *Tetrahedron* **1996**, *52*, 4449–4456.
281. B. B. Snider, T. Kwon, *J. Org. Chem.* **1992**, *57*, 2399–2410; A. Heidbreder, J. Mattay, *Tetrahedron Lett.* **1992**, *33*, 1973–1976; G. Pandey, A. Krishna, K. Girja, M. Karthikeyan, *Tetrahedron Lett.* **1993**, *34*, 6631–6634; D. G. New, Z. Tesfai, K. D. Moeller, *J. Org. Chem.* **1996**, *61*, 1578–1598; H. E. Zimmerman, K. D. Hoffacker, *J. Org. Chem.* **1996**, *61*, 6526–6534; F. Ciminale, L. Lopez, G. M. Farinola, *Tetrahedron Lett.* **1999**, *40*, 7267–7270.
282. D. A. Evans, C. J. Dinsmore, D. A. Evrard, K. M. DeVries, *J. Am. Chem. Soc.* **1993**, *115*, 6426–6427.
283. R. B. Herbert, A. E. Kattah, A. J. Murtagh, P. W. Sheldrake, *Tetrahedron Lett.* **1995**, *36*, 5649–5650.
284. O. Hammerich, V. D. Parker, *Adv. Phys. Org. Chem.* **1984**, *20*, 55–189.
285. M. Schmittel, A. Burghart, *Angew. Chem.* **1997**, *109*, 2659–2699; *Angew. Chem. Int. Ed. Engl.* **1997**, *36*, 2550–2589.
286. M. Oyama, K. Nozaki, T. Nagaoka, S. Okazaki, *Bull. Chem. Soc. Jpn.* **1990**, *63*, 33–41; M. Oyama, K. Nozaki, S. Okazaki, *J. Electroanal. Chem.* **1991**, *304*, 61–73.
287. V. D. Parker, B. Reitstøen, M. Tilset, *J. Phys. Org. Chem.* **1989**, *2*, 580–584; F. Norrsell, K. L. Handoo, V. D. Parker, *J. Org. Chem.* **1993**, *58*, 4929–4932; M. S. Workentin, L. J. Johnston, D. D. M. Wayner, V. D. Parker, *J. Am. Chem. Soc.* **1994**, *116*, 8279–8287; H. J. Wang, G. Zheng, V. D. Parker, *Acta Chem. Scand.* **1995**, *49*, 311–312; M. S. Workentin, V. D. Parker, T. L. Morkin, D. D. M. Wayner, *J. Phys. Chem. A* **1998**, *102*, 6503–6512.
288. C. S. Q. Lew, J. R. Brisson, L. J. Johnston, *J. Org. Chem.* **1997**, *62*, 4047–4056.
289. L. J. Johnston, N. P. Schepp, *J. Am. Chem. Soc.* **1993**, *115*, 6564–6571; L. J. Johnston, N. P. Schepp, *Pure Appl. Chem.* **1995**, *67*, 71–78.
290. P. D. Wood, L. J. Johnston, *Photochem. Photobiol.* **1997**, *66*, 642–648.
291. M. S. Workentin, L. J. Johnston, D. D. M. Wayner, V. D. Parker, *J. Am. Chem. Soc.* **1994**, *116*, 8279–8287.
292. H. Mayr, M. Patz, *Angew. Chem.* **1994**, *106*, 990–1010; *Angew. Chem., Int. Ed. Engl.* **1994**, *33*, 938–958.
293. T. Sumiyoshi, *Chem. Lett.* **1995**, 645–646.
294. V. D. Parker, *Acta Chem. Scand.* **1983**, *B37*, 393–401.
295. C. L. Kulkarni, B. J. Scheer, J. F. Rusling, *J. Electroanal. Chem.* **1982**, *140*, 57–74.
296. B. Aalstad, A. Ronl  n, V. D. Parker, *Acta Chem. Scand.* **1981**, *B35*, 247–257.
297. K. Nozaki, M. Oyama, H. Hatano, S. Okazaki, *J. Electroanal. Chem.* **1989**, *270*, 191–204.
298. L. Lopez, *Top. Curr. Chem.* **1990**, *156*, 117–166.
299. A. P. Schaap, K. A. Zaklika, B. Kaskar, L. W.-M. Fung, *J. Am. Chem. Soc.* **1980**, *102*, 389–391; L. T. Spada, C. S. Foote, *J. Am. Chem. Soc.* **1980**, *102*, 391–393; K. E. O'Shea, S. H. Jannach, I. Garcia, *J. Photochem. Photobiol. A* **1999**, *122*, 127–131.
300. E. Bosch, J. K. Kochi, *J. Am. Chem. Soc.* **1996**, *118*, 1319–1329.
301. M. Lehnig, *J. Chem. Soc., Perkin Trans. 2* **1996**, 1943–1948.
302. C. Amatore, J. K. Kochi, *Adv. Electron Transfer Chem.* **1991**, *1*, 55–148.
303. K. Mizuno, M. Ikeda, Y. Otsuji, *Tetrahedron Lett.* **1985**, *26*, 461–464.
304. R. J. Sundberg in *Organic Photochemistry*, Ed. A. Padwa, Marcel Dekker, New York, Vol. 6, p 121–176, **1983**.

305. M. Mascal, C. J. Moody, J. Chem. Soc., Chem. Commun. **1988**, 587–588; M. Mascal, C. J. Moody, *J. Chem. Soc., Chem. Commun.* **1988**, 589–590.
306. (a) J. Mattay, J. Gersdorf, K. Buchkremer, *Chem. Ber.* **1987**, 120, 307–318; (b) J. Gersdorf, J. Mattay, H. Görner, *J. Am. Chem. Soc.* **1987**, 109, 1203–1209; D. Sun, S. M. Hubig, J. K. Kochi, *J. Org. Chem.* **1999**, 64, 2250–2258.
307. K. Maruyama, T. Otsuki, S. Tai, *J. Org. Chem.* **1985**, 50, 52–60.
308. V. D. Parker, *Acta Chem. Scand.* **1998**, 52, 154–159.
309. C. Siedschlag, H. Luftmann, C. Wolff, J. Mattay, *Tetrahedron* **1997**, 53, 3587–3592; C. Siedschlag, H. Luftmann, C. Wolff, J. Mattay, *Tetrahedron* **1999**, 55, 7805–7818.
310. M. Tsuchiya, T. W. Ebbesen, Y. Nishimura, H. Sakuragi, K. Tokumaru, *Chem. Lett.* **1987**, 2121–2124.
311. Although the bimolecular rate constant of radical cations with superoxide anion is higher, this process most often results in electron transfer rather than in oxygenation, see ref. [310].
312. S. Tojo, K. Morishima, A. Ishida, T. Majima, S. Takamuku, *J. Org. Chem.* **1995**, 60, 4684–4685.
313. C. Demaille, A. J. Bard, *Acta Chem. Scand.* **1999**, 53, 842–848.
314. C. P. Andrieux, P. Audebert, P. Hapiot, J.-M. Savéant, *J. Phys. Chem.* **1991**, 95, 10158–10164.
315. P. Audebert, J. M. Catel, V. Duchenet, L. Guyard, P. Hapiot, G. Le Coustumer, *Syn. Met.* **1999**, 101, 642–645; A. Merz, J. Kronberger, L. Dunsch, A. Neudeck, A. Petr, L. Parkanyi, *Angew. Chem.* **1999**, 111, 1533–1538; *Angew. Chem. Int. Ed.* **1999**, 38, 1442–1446.
316. A. F. Diaz in *Organic Electrochemistry*, H. Lund, M. M. Baizer, Eds., Chapter 33, Marcel Dekker, New York, **1991**; P. Hapiot, L. Gaillon, P. Audebert, J. J. E. Moreau, J. P. Lère-Porte, M. W. C. Man, *J. Electroanal. Chem.* **1997**, 435, 85–94; J. J. Apperloo, R. A. J. Janssen, *Syn. Met.* **1999**, 101, 373–374.
317. E. Levillain, J. Roncali, *J. Am. Chem. Soc.* **1999**, 121, 8760–8765.
318. H. Yang, A. J. Bard, *J. Electroanal. Chem.* **1991**, 306, 87–109.
319. S. C. Creason, J. Wheeler, R. F. Nelson, *J. Org. Chem.* **1972**, 37, 4440–4446; R. F. Nelson, R. H. Philp Jr., *J. Phys. Chem.* **1979**, 83, 713–716.
320. D. Larumbe, I. Gallardo, C. P. Andrieux, *J. Electroanal. Chem.* **1991**, 304, 241–247.
321. A. Smie, J. Heinze, *Angew. Chem.* **1997**, 109, 375–379; *Angew. Chem. Int. Ed. Engl.* **1997**, 36, 363–367.
322. G. Pandey, D. Pooranchand, U. T. Bhalariao, *Tetrahedron* **1991**, 47, 1745–1752.
323. H. J. Shine, *Phosphorus Silicon* **1994**, 95–6, 429–430.
324. S. Yasui, K. Shioji, A. Ohno, M. Yoshihara, *J. Org. Chem.* **1995**, 60, 2099–2105.
325. T.-L. Ho, *Synthesis* **1973**, 347–354.
326. A. Houmam, D. Shukla, H.-B. Kraatz, D. D. M. Wayner, *J. Org. Chem.* **1999**, 64, 3342–3345; W. K. Lee, B. Liu, C. W. Park, H. J. Shine, I. Y. Guzman-Jimenez, K. H. Whitmire, *J. Org. Chem.* **1999**, 64, 9206–9210.
327. V. Jouikov, D. Fattahova, *Electrochim. Acta* **1998**, 43, 1811–1819.
328. A. Lebouc, J. Simonet, J. Gelas, A. Debhi, *Synthesis* **1987**, 320–321; H. J. Cristau, B. Chabaud, C. Niangoran, *J. Org. Chem.* **1983**, 48, 1527–1529.
329. M. Kimura, S. Matsubara, Y. Sawaki, H. Iwamura, *Tetrahedron Lett.* **1986**, 27, 4177–4178.
330. T. Mandai, H. Yasunaga, M. Kawada, J. Otera, *Chem. Lett.* **1984**, 715–716; T. Mandai, H. Irei, M. Kawada, J. Otera, *Tetrahedron Lett.* **1984**, 25, 2371–2374.
331. K. Narasaka, T. Okauchi, *Chem. Lett.* **1991**, 515–518.
332. H. Takeuchi, T. Hiyama, N. Kamai, H. Ōya, *J. Chem. Soc., Perkin Trans. 2* **1997**, 2301–2305.
333. G. Pandey, R. Sochanchingwung, S. K. Tiwari, *Synlett* **1999**, 1257–1258.
334. M. Newcomb, T. M. Deeb, D. J. Marquardt, *Tetrahedron* **1990**, 46, 2317–2328; S. Karady, E. G. Corley, N. L. Abrahamson, J. S. Amato, L. M. Weinstock, *Tetrahedron* **1991**, 47, 757–766; M. Newcomb, K. A. Weber, *J. Org. Chem.* **1991**, 56, 1309–1313; U. Jahn, S. Aussieker, *Org. Lett.* **1999**, 1, 849–852.
335. M. Kimura, Y. Ban, *Synthesis*, **1976**, 201–202; M. W. Wolff, *Chem. Rev.* **1963**, 63, 55–64.
336. Y. Shibazuma, T. Okamoto, *Chem. Pharm. Bull.* **1985**, 33, 3187–3194.
337. B. Merzougui, Y. Berchadsky, P. Tordo, G. Gronchi, *Electrochim. Acta* **1997**, 42, 2445–2453; S. Yasui, K. Shioji, M. Tsujimoto, A. Ohno, *J. Chem. Soc., Perkin Trans. 2* **1999**, 855–862.

338. H. Yokoi, A. Hatta, K. Ishiguro, Y. Sawaki, *J. Am. Chem. Soc.* **1998**, *120*, 12728–12733.
339. S. Yasui, K. Shioji, M. Tsujimoto, A. Ohno, *Chem. Lett.* **1995**, 783–784.
340. J. H. Horner, F. N. Martinez, O. M. Musa, M. Newcomb, H. E. Shahin, *J. Am. Chem. Soc.* **1995**, *117*, 11124–11133.
341. P. H. Sackett, J. S. Mayausky, T. Smith, S. Kalus, R. L. McCreery, *J. Med. Chem.* **1981**, *24*, 1342–1347.
342. B. L. Miller, K. Kuczera, C. Schöneich, *J. Am. Chem. Soc.* **1998**, *120*, 3345–3356.
343. M. Kamata, M. Sato, E. Hasegawa, *Tetrahedron Lett.* **1992**, *35*, 5085–5088.
344. A. P. Schaap, G. Prasad, S. D. Gagnon, *Tetrahedron Lett.* **1983**, *24*, 3047–3050; A. P. Schaap, G. Prasad, S. Siddiqui, *Tetrahedron Lett.* **1984**, *25*, 3035–3038.
345. S. Yasui, K. Shioji, M. Tsujimoto, A. Ohno, *Tetrahedron Lett.* **1996**, *37*, 1625–1628.
346. S. Yasui, M. Fujii, C. Kawano, Y. Nishimura, A. Ohno, *Tetrahedron Lett.* **1991**, *32*, 5601–5604; S. Yasui, M. Fujii, C. Kawano, Y. Nishimura, K. Shioji, A. Ohno, *J. Chem. Soc., Perkin Trans. 2* **1994**, 177–183; S. Yasui, K. Shioji, A. Ohno, *Tetrahedron Lett.* **1994**, *35*, 2695–2698.
347. D. P. Riley, M. R. Smith, P. E. Correa, *J. Am. Chem. Soc.* **1988**, *110*, 177–180.
348. W. Zhou, E. L. Clennan, *Chem. Commun.* **1999**, 2261–2262.
349. B. L. Miller, T. D. Williams, C. Schöneich, *J. Am. Chem. Soc.* **1996**, *118*, 11014–11025.
350. U. Haberl, O. Wiest, E. Steckhan, *J. Am. Chem. Soc.* **1999**, *121*, 6730–6736.
351. M. Hofmann, H. F. Schaefer, III *J. Am. Chem. Soc.* **1999**, *121*, 6719–6729.
352. N. L. Bauld, J. Yang, *Tetrahedron Lett.* **1999**, *40*, 8519–8522.
353. N. L. Bauld, J. Yang, *Org. Lett.* **1999**, *1*, 773–774.
354. (a) G. Bouchoux, J. Y. Salpin, *Rapid Commun. Mass Spectrom.* **1994**, *8*, 325–328; (b) C. Denekamp, A. Weisz, A. Mandelbaum, *J. Mass Spectr.* **1996**, *31*, 1028–1032; (c) N. Morlender-Vais, A. Mandelbaum, *J. Mass Spectr.* **1998**, *33*, 229–241.
355. D. W. Borhani, F. D. Greene, *J. Org. Chem.* **1986**, *51*, 1563–1570.
356. J. Delaunay, G. Mabon, A. Orliac, J. Simonet, *Tetrahedron Lett.* **1990**, *31*, 667–668; R. G. Janssen, M. Motevalli, J. H. P. Utley, *Chem. Commun.* **1998**, 539–540.
357. A. Pezeshk, I. D. Podmore, P. F. Heelis, M. C. R. Symons, *J. Phys. Chem.* **1996**, *100*, 19714–19718; A. A. Voityuk, M.-E. Michel-Beyerle, N. Rösch, *J. Am. Chem. Soc.* **1996**, *118*, 9750–9758; R. Epple, E.-U. Wallenborn, T. Carell, *J. Am. Chem. Soc.* **1997**, *119*, 7440–7451.
358. A. S. Kurbatova, Y. V. Kurbatov, *Russ. J. Org. Chem.* **1997**, *33*, 1050.
359. N. L. Bauld, J. Cessac, C.-S. Chang, F. R. Farr, R. Holloway, *J. Am. Chem. Soc.* **1976**, *98*, 4561–4567; M. A. Fox, J. R. Hurst, *J. Am. Chem. Soc.* **1984**, *106*, 7626–7627.
360. V. Amir-Ebrahimi, J. G. Hamilton, J. Nelson, J. J. Rooney, J. M. Thompson, A. J. Beaumont, A. D. Rooney, C. J. Harding, *Chem. Commun.* **1999**, 1621–1622.
361. K. Exner, D. Hunkler, G. Gescheidt, H. Prinzbach, *Angew. Chem.* **1998**, *110*, 2013–2016; *Angew. Chem. Int. Ed.* **1998**, *37*, 1910–1913.
362. F. A. Bell, R. A. Crellin, N. Fujii, A. Ledwith, *J. Chem. Soc., Chem. Commun.* **1969**, 251–252; A. Ledwith, *Acc. Chem. Res.* **1972**, *5*, 133–139.
363. D. B. Rusterholz, D. B. Gorman, P. G. Gassman, *Molecules* **1997**, *2*, 80–86.
364. N. L. Bauld, *Adv. Electron Transfer Chem.* **1992**, *2*, 1–66.
365. (a) M. Schmittel, H. von Seggern, *J. Am. Chem. Soc.* **1993**, *115*, 2165–2177; (b) M. Schmittel, C. Wöhrle, I. Bohn, *Chem. Eur. J.* **1996**, *2*, 1031–1040; (c) M. Schmittel, C. Wöhrle, *J. Org. Chem.* **1995**, *60*, 8223–8230; (d) U. Haberl, E. Steckhan, S. Blechert, O. Wiest, *Chem. Eur. J.* **1999**, *5*, 2859–2865; N. L. Bauld, J. Yang, D. Gao, *Perkin Trans. 2* **2000**, 207–210.
366. C. F. Gürtler, E. Steckhan, *S. Blechert, J. Org. Chem.* **1996**, *61*, 4136–4143; C. F. Gürtler, S. Blechert, E. Steckhan, *Chem. Eur. J.* **1997**, *3*, 447–452; T. Peglow, S. Blechert, E. Steckhan, *Chem. Eur. J.* **1998**, *4*, 107–112; J. Botzem, U. Haberl, E. Steckhan, S. Blechert, *Acta Chem. Scand.* **1998**, *52*, 175–193; T. Peglow, S. Blechert, E. Steckhan, *Chem. Commun.* **1999**, 433–434.
367. Y. Takahashi, M. Ando, T. Miyashi, *J. Chem. Soc., Chem. Commun.* **1995**, 521–522; L. Brancaleon, D. Brousmiche, V. J. Rao, L. J. Johnston, V. Ramamurthy, *J. Am. Chem. Soc.* **1998**, *120*, 4926–4933M; N. L. Bauld, D. Gao, *Perkin Trans. 2* **2000**, 191–192.
368. K. Ishiguro, M. Ikeda, Y. Sawaki, *J. Org. Chem.* **1992**, *57*, 3057–3066.
369. W. B. Motherwell, A. S. Williams, *Angew. Chem.* **1995**, *107*, 2207–2209; *Angew. Chem., Int. Ed. Engl.* **1995**, *34*, 2031–2033.

370. N. L. Bauld, G. A. Mirafzal, *J. Am. Chem. Soc.* **1991**, *113*, 3613–3614.
371. N. L. Bauld, G. W. Stufflebeme, K. T. Lorenz, *J. Phys. Org. Chem.* **1989**, *2*, 585–601.
372. R. Herges, F. Starck, T. Winkler, M. Schmittel, *Chem. Eur. J.* **1999**, *5*, 2965–2970; G. D. Reddy, O. Wiest, T. Hudlický, V. Schapiro, D. Gonzalez, *J. Org. Chem.* **1999**, *64*, 2860–2863.
373. (a) F. Müller, J. Mattay, *Angew. Chem.* **1991**, *103*, 1352–1353; *Angew. Chem., Int. Ed. Engl.* **1991**, *30*, 1336–1337; (b) F. Müller, J. Mattay, *Angew. Chem.* **1992**, *104*, 207–208; *Angew. Chem., Int. Ed. Engl.* **1992**, *31*, 209–210; (c) F. Müller, A. Karwe, J. Mattay, *J. Org. Chem.* **1992**, *57*, 6080–6082; (d) F. Müller, J. Mattay, S. Steenken, *J. Org. Chem.* **1993**, *58*, 4462–4464; (e) F. Müller, J. Mattay, *Chem. Ber.* **1993**, *126*, 543–549.
374. (a) K. Lorenz, N. L. Bauld, *Catalysis* **1985**, *95*, 613–616; (b) T. Miyashi, A. Konno, Y. Takahashi, *J. Am. Chem. Soc.* **1988**, *110*, 3676–3677; (c) H. Ikeda, T. Oikawa, T. Miyashi, *Tetrahedron Lett.* **1993**, *34*, 2323–2326.
375. H. Ikeda, T. Minegishi, H. Abe, A. Konno, J. L. Goodman, T. Miyashi, *J. Am. Chem. Soc.* **1998**, *120*, 87–95; H. Ikeda, T. Takasaki, Y. Takahashi, A. Konno, M. Matsumoto, Y. Hoshi, T. Aoki, T. Suzuki, J. L. Goodman, T. Miyashi, *J. Org. Chem.* **1999**, *64*, 1640–1649.
376. S. Dhanalekshmi, C. S. Venkatachalam, K. K. Balasubramanian, *J. Chem. Soc., Chem. Commun.* **1994**, 511–512.
377. D. W. Reynolds, B. Harirchian, H.-S. Chiou, B. K. Marsh, N. L. Bauld, *J. Phys. Org. Chem.* **1989**, *2*, 57–88.
378. J. P. Dinnocenzo, D. A. Conlon, *J. Am. Chem. Soc.* **1988**, *110*, 2324–2326.
379. B. Kräutler, A. Pfaltz, R. Nordmann, K. O. Hodgson, J. D. Dunitz, A. Eschenmoser, *Helv. Chim. Acta* **1976**, *59*, 924–937.
380. N. L. Bauld, *J. Comput. Chem.* **1990**, *11*, 896–898.
381. J. P. Dinnocenzo, D. A. Conlon, *Tetrahedron Lett.* **1995**, *36*, 7415–7418.
382. S. Tojo, S. Toki, S. Takamuku, *J. Org. Chem.* **1991**, *56*, 6240–6243; N. P. Schepp, L. J. Johnston, *J. Am. Chem. Soc.* **1994**, *116*, 6895–6903; N. P. Schepp, L. J. Johnston, *J. Am. Chem. Soc.* **1994**, *116*, 10330–10331; O. Brede, F. David, *Radiat. Phys. Chem.* **1996**, *47*, 53–58; N. P. Schepp, D. Shukla, H. Sarker, N. L. Bauld, L. J. Johnston, *J. Am. Chem. Soc.* **1997**, *119*, 10325–10334.
383. L. J. Johnston, N. P. Schepp, *Pure Appl. Chem.* **1995**, *67*, 71–78.
384. H. Prinzbach, G. Gescheidt, H. D. Martin, R. Herges, J. Heinze, G. K. S. Prakash, G. A. Olah, *Pure Appl. Chem.* **1995**, *67*, 673–682; G. Gescheidt, H. Prinzbach, A. G. Davies, R. Herges, *Acta Chem. Scand.* **1997**, *51*, 174–180; M. Etzkorn, F. Wahl, M. Keller, H. Prinzbach, F. Barbosa, V. Peron, G. Gescheidt, J. Heinze, R. Herges, *J. Org. Chem.* **1998**, *63*, 6080–6081.
385. K. Exner, H. Prinzbach, G. Gescheidt, B. Grossmann, J. Heinze, *J. Am. Chem. Soc.* **1999**, *121*, 1964–1965.
386. F. W. McLafferty, F. Turecek, *Interpretation of Mass Spectra*, 4th Ed., University Science Books, Mill Valley, 1993, Chapter 4.3.
387. M. Born, S. Ingemann, N. M. M. Nibbering, *Mass Spectr. Rev.* **1997**, *16*, 181–200.
388. F. Casado, L. Pisano, M. Farriol, I. Gallardo, J. Marquet, G. Melloni, *J. Org. Chem.* **2000**, *65*, 322–331.
389. G. A. Molander, *Org. React.* **1994**, *46*, 211–367; G. A. Molander, C. R. Harris, *Chem. Rev.* **1996**, *96*, 307–338; R. J. Enemærke, K. Daasbjerg, T. Skrydstrup, *Chem. Commun.* **1999**, 343–344.
390. J. E. McMurry, *Chem. Rev.* **1989**, *89*, 1513–1524.
391. A. Gansäuer, T. Lauterbach, H. Bluhm, M. Noltemeyer, *Angew. Chem.* **1999**, *111*, 3112–3114; *Angew. Chem. Int. Ed.* **1999**, *38*, 2909–2910 and cited references.
392. G. G. Melikyan, *Org. React.* **1996**, *49*, 427–675; B. B. Snider, *Chem. Rev.* **1996**, *96*, 339–363; T. Linker, *J. Prakt. Chem.* **1997**, *339*, 488–492.
393. V. Nair, J. Mathew, J. Prabhakaran, *Chem. Soc. Rev.* **1997**, 127–132.

2 Electron Transfer from Aliphatic and Alicyclic Compounds

Heinz D. Roth

2.1 Introduction

Electron-transfer processes have attracted considerable attention because of their central role in the chemistry of life and as a method for generating interesting intermediates, in the gas phase, in solution, or in the solid state. Photo-induced electron transfer is one of the very few fundamental reaction types known in excited-state organic chemistry. It occurs in the solid state, in solution, and in the gas phase, including the Earth's atmosphere and outer space. The products generated by electron transfer vary with the nature of the substrate and with the medium in which the reaction is conducted. They can be macromolecular 'charge-separated' entities (in the photosynthesis of the green plant), zwitterions, ion pairs, or 'free' radical ions, carrying a positive or negative charge in addition to an unpaired spin. These intermediates can be characterized by a range of spectroscopic techniques and their reactions can be studied conveniently. This chapter deals with electron transfer from saturated chain- or cyclic hydrocarbons, and the structures and reactions of their positively charged radical ions.

Alkanes (Section 2.2) are among the least reactive compounds; their C–H bonds are among the least acidic moieties (highest pK_a values) known. Likewise, *n*-alkanes have very low electron affinities and very high ionization potentials; thus, they are poor electron acceptors and electron donors; it takes significant energies to activate them. For the small-ring compounds, cyclopropane and cyclobutane (Section 2.3), electron transfer occurs with relief of ring strain; these systems are more reactive. Strained bicyclic systems, particularly bicyclo[1.1.0]butane and bicyclo[2.1.0]pentane (Section 2.4), are more reactive still.

Electron transfer from methane is significant because it seems likely that the radical cation and secondary intermediates derived from it (CH_3^\bullet , CH_3^+) played a significant role in the chemical evolution preceding the origins of life. Methane is a probable constituent of early planetary atmospheres and its radical cation has potential significance as an interstellar species.

2.2 Electron-transfer Reactions of Aliphatic Compounds

Alkanes are among the least reactive classes of compound; their C–H bonds are among the least acidic moieties (highest pK_a values) known. Likewise, *n*-alkanes have very low electron affinities and very high ionization potentials; thus, they are poor electron acceptors and electron donors. The molecular anions of *n*-alkanes are even less stable than are those of cycloalkanes (Section 2.3) and their temporary anion states are even shorter lived [1]. Non-dissociative electron attachment requires the dissipation of excess energy by radiation or collision; for simple alkanes, methane through butane, negative ion yields are ca 10^4 times lower than positive ion yields. Typically, electron impact does not result in molecular ions; instead, small fragment ions such as CH^- , CH_2^- , CH_3^- , C_2H^- predominate [2–4]. The adiabatic ionization potentials of *n*-alkanes decrease from 12.61 eV for methane and 11.52 eV for ethane to 10.25 eV for *n*-pentane and 10.13 eV for *n*-hexane and to 9.80 eV for *n*-octane and 9.65 eV for *n*-decane [5]. As a consequence, it takes significant energies to activate these compounds.

In the gas phase, *n*-alkanes are readily ionized upon electron impact (mass spectrometry, MS) or upon He_x impact (photoelectron spectroscopy, PES). The resulting spectra provide information about the molecular ions, for example, on their ease of fragmentation and their fragmentation patterns (MS) [6, 7], whereas the PE spectra reveal the ordering and energies of their molecular orbitals [8]. In solution the high oxidation potentials of *n*-alkanes pose significant difficulties for the generation of their radical cations and render the resulting species highly reactive, although the electron-donor properties improve somewhat with increasing branching (vide infra). Accordingly, these radical cations were long thought to be unstable and decompose by instantaneous deprotonation. Radical cations have become readily accessible only with the advent of halocarbon and noble gas matrix-isolation techniques. The development of these techniques was crucial for the detailed study of *n*-alkane radical cations.

2.2.1 High-energy Irradiation of Matrices

The pioneering work of W. H. Hamill and co-workers established that high-energy photons, such as X-rays or γ -rays, can eject electrons from halogen-containing matrix materials, viz., tetrachloromethane, chlorobutanes, and several Freon mixtures [9–11]. High-energy photons interact with these materials by generating ‘holes’ while ejecting electrons into the matrix (Eq. 1). In the presence of solute molecules (S) of lower oxidation potential than the host (*n*-alkane guests at low concentrations; ca 1 in 10^3), the holes are unstable. A host molecule transfers an electron to the ‘hole’, regenerating the matrix material (Eq. 2). The ejected electrons are ‘solvated’ in the matrix or attach themselves to a halogen-containing molecule (Eq. 3), causing its fragmentation to a halide ion and a free radical (Eq. 4). These processes are without direct consequence for the radical cation; they are mentioned here because they can interfere with the observation of the species chosen for study, or because the halide

ions can scavenge the radical cations to form free radicals (Eq. 5).



The overall procedure, based on a combination of cryogenic techniques, matrix isolation, ionizing radiation, and ESR detection, has become the method of choice for generating and studying alkane radical cations. One note of caution is in order, however. It is generally recognized that the barriers to the rearrangements of radical cations are considerably lower than are those on the parent energy surfaces. Accordingly, some radical cations are unstable in solid matrices and rearrange instantaneously under the conditions of radiolytic generation in frozen matrices. Applications of optical spectroscopy to the study of alkane radical cations are limited. Although this technique is of great importance for studying many organic radical ions, the spectra of alkane radical cations do not fall into an accessible spectral range.

An alternative method of radical cation generation involves photo- or electron-impact ionization of substrates at high dilution (ca 1 in 10^6) during vapor deposition in neon matrices at (ca 5 K) [12]. The radical cations deposited in the matrix owe their stability to the high ionization potential of the matrix material, which is more difficult to oxidize than are *n*-alkanes. This technique has found significant applications and has provided invaluable insights in special cases (Section 2.3); it is not, however, generally accessible and offers only a very limited temperature range for study. Finally, some of the more stable radical cations of highly branched alkanes can be generated in zeolites.

The application of matrix isolation methods has facilitated the generation and study of many radical cations. Early examples of alkane radiolysis generating radical cations include *n*-octane, which produced a species '*n*-C₈H₁₈^{•+}' [13, 14], and the well characterized radical cation of hexamethylethane, reported independently by three different groups in 1980/81 [15–18]. Although the ESR spectrum of '*n*-C₈H₁₈^{•+}' provided little specific information about its structure and the latter might be considered a 'special case', the time was ripe for systematic investigation of electron transfer from alkanes. Thus, when Iwasaki and co-workers reported clear information on the structure of ethane radical cation, the study of alkane radical cations became a significant area of scientific investigation [19].

2.2.2 Electron Spin Resonance

Among the techniques available for the study of free radicals or radical ions in solution, electron spin resonance (ESR) stands out as a technique with sufficient

resolution to provide detailed information about the identity of the intermediate in question. In an external magnetic field the unpaired electron of such a species can adopt either of two spin orientations, parallel or antiparallel to the field H_0 . The two orientations are of slightly different energies. Transitions between the corresponding spin levels can be stimulated by applying radiation of a frequency satisfying the resonance condition:

$$h\nu = g\mu H_0 \quad (6)$$

where h is the Planck constant, g is a parameter characteristic for the radical under scrutiny, μ is the Bohr magneton, and H_0 is the applied magnetic field strength [20, 21].

Experimentally, resonance is approached by sweeping the field in the range near 3400 G while holding the frequency constant, typically at ca 9.6 GHz. A key contribution to the identification of the radical (ion) is due to the interaction of the unpaired spin with nearby magnetic nuclei, the so called hyperfine interaction. This gives rise to a pattern of signals characteristic for the radical (ion). The spacing of the signals and their relative intensities identify the magnitude of the interaction between the electron and a group of equivalent nuclei as well as the nuclei so coupled; these results reveal the spin-density distribution in the paramagnetic intermediate under study [20, 21].

The hyperfine coupling constants of magnetic nuclei in organic radicals range from essentially 0 to 200 G (0 to 20 mT). The resulting spectra appear in absorption with intensities determined by the Boltzmann population of the states at thermal equilibrium. This feature limits the sensitivity of the ESR method and has restricted its application to relatively stable species with lifetimes greater than a few milliseconds. Another limitation has its origin in the tendency of free radicals to dimerize, thereby annihilating the unpaired spins. Nevertheless, this method has been the method of choice for the study of numerous families of radicals and radical ions; it has proved invaluable for probing their spin-density distributions and has provided detailed insights into many structures.

Appropriate modification of the ESR spectrometer and generation of free radicals by flash photolysis enables time-resolved (TR) ESR spectroscopy [22]. Spectra observed under these conditions are remarkable for their signal directions and intensities. They can be enhanced as much as one-hundredfold and appear as absorption, emission, or a combination of both. Effects of this type are a result of chemically induced dynamic electron polarization (CIDEP); these spectra indicate the intermediacy of radicals whose sublevel populations deviate substantially from equilibrium populations. Significantly, the splitting pattern characteristic of the spin-density distribution of the intermediate remains unaffected; thus, the CIDEP enhancement not only facilitates the detection of short-lived radicals at low concentrations, but also aids their identification. Time-resolved ESR techniques cannot be expected to be of much use for electron-transfer reactions from alkanes, because their oxidation potentials are prohibitively high. Even branched alkanes have oxidation potentials well above the excited-state reduction potential of typical photo-

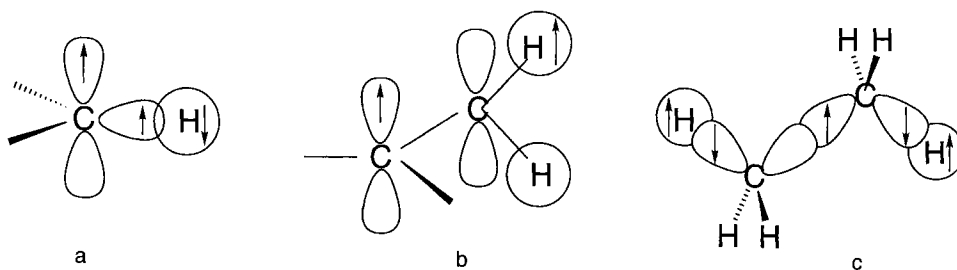


Figure 1. (a, left) Preferred configuration of electron spins in the σ orbital connecting a ^1H nucleus to an sp^2 -hybridized C atom bearing unpaired π spin density (π, σ -polarization); (b, center) “molecular π orbital” consisting of two carbon p_z orbitals and an H_2 “group orbital” due to hyperconjugation between an sp^2 -hybridized C atom bearing unpaired spin and a $\text{CH}_2\text{-R}$ group (π, σ -delocalization); (c, right) delocalization of an unpaired electron throughout the C–C σ -frame and extending directly into two chain-end in-plane C–H bonds (σ -delocalization).

sensitizers (see Section 2.3.3). They have, however, proved useful for some strained ring compounds (below).

The ^1H hyperfine coupling constants are related to carbon spin densities by different mechanisms of interaction. For π radicals, there are two principal mechanisms involving either induction (π, σ -polarization) or delocalization (π, σ -delocalization, hyperconjugation). Protons attached directly to carbon atoms bearing positive spin-density have negative hyperfine coupling constants because of the preferred exchange interaction between the unpaired π spin-density and the carbon σ electron (Figure 1a). Positive hyperfine coupling constants, on the other hand, are usually observed for protons which are one C–C bond removed from a carbon bearing positive spin-density. The positive sign is a result of a hyperconjugative interaction which delocalizes the π spin-density on carbon into an H_n ‘group-orbital’ (cf. Figure 1b). Finally, the radical cations formed upon electron transfer from n -alkanes are typically σ radicals, in which the unpaired electron is delocalized throughout the carbon framework and extends directly into the two chain-end in-plane C–H bonds, resulting in large positive hyperfine coupling constants for these ^1H nuclei (Figure 1c).

In the next section we discuss the radical cations generated upon electron transfer from simple n -alkanes to holes generated in various matrices upon radiolysis. The ESR spectra observed in these matrices reveal many interesting structural details. We will begin with the special case of the long-elusive methane radical cation, followed by the radical cations of n -alkanes and those of branched alkanes.

2.2.3 Electron-transfer Reactions of Methane

Electron transfer from methane is significant because it seems likely that $\text{CH}_4^{\bullet+}$ and secondary intermediates derived from it (CH_3^\bullet , CH_3^+) played a significant role in

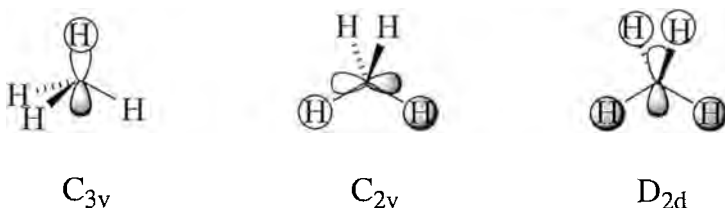


Figure 2. Possible Jahn-Teller distorted geometries for methane radical cation.

the chemical evolution preceding the origins of life. Methane is a likely constituent of early planetary atmospheres and its radical cation has potential significance as an interstellar species [23]. In the laboratory, however, the ESR spectrum of this species has long been elusive, probably because methane is the alkane most difficult to oxidize and its radical cation is least stable. For example, radiolysis experiments in SF_6 only gave complexes of methyl radical with a fluorinated compound [24]. In 1984, Knight and co-workers succeeded in the ESR detection of $\text{CH}_4^{+\bullet}$ in a neon matrix at 4 K [25]. Neon discharge ionization of methane ($IP = 12.6$ eV) gave rise to a quintet ($a_{\text{H}} = 5.48$ mT) whereas methane- D_2 gave rise to a 1:2:1 triplet ($a_{\text{H}} = 12.17$ mT) of 1:2:3:2:1 quintets ($a_{\text{D}} = 0.222$ mT). The a_{D} splitting corresponds to an a_{H} splitting of 1.4 mT.

For a species with tetrahedral symmetry (T_d), Jahn–Teller distortion upon ionization can lead to radical cations of C_{3v} , C_{2v} , or D_{2d} symmetry (Figure 2). The ESR spectrum observed for $\text{CH}_4^{+\bullet}$ suggests the presence of four equivalent protons, i.e., a species with D_{2d} symmetry. On the other hand, the spectrum of $\text{CH}_2\text{D}_2^{+\bullet}$ clearly shows the presence of two non-equivalent pairs, i.e., a species with C_{2v} symmetry. C_{2v} symmetry was, therefore, assigned to both $\text{CH}_4^{+\bullet}$ and $\text{CH}_2\text{D}_2^{+\bullet}$; the perprotio species, $\text{CH}_4^{+\bullet}$, is assumed to undergo dynamic Jahn–Teller distortion (fluxional behavior), so that the spectrum reflects an averaged geometry. The 5.48 mT splitting of $\text{CH}_4^{+\bullet}$ is essentially equal to the average splitting of the C_{2v} species, $[a_{\text{H}} + (a_{\text{D}} \times 6.5)]/2 = (12.17 - 1.46)/2 = 5.36$ [25].

Ab initio calculations on $\text{CH}_4^{+\bullet}$ at the UHF/6-31G* level indicated the presence of two elongated (116.4 pm) and two shortened (107.5 pm) C–H bonds with hyperfine coupling constants, $a_{\text{H}} = 13.7$ mT and $a_{\text{H}} = -1.7$ mT, respectively. For $\text{CH}_2\text{D}_2^{+\bullet}$, the deuterons preferentially occupy the shorter bonds [25]. The C_{2v} symmetry assigned to $\text{CH}_4^{+\bullet}$ is the same as that of BH_4^+ [26, 27], with which it is isoelectronic. The radical cation of C_{2v} symmetry (two different types of C–H bond) was probed by Eriksson and collaborators by a wide range of different calculation methods; the results are summarized in Table 1 [28]. The nature of the (large amplitude) tunneling among Jahn–Teller distorted structures was elucidated in a group theoretical study [29] and by results obtained with various isotopomers [30].

It is noteworthy, that ab initio calculations even for small molecules give substantially different results depending on the basis set and the method used to take electron correlation into account. These difficulties are illustrated here with the results from three different calculations on two different methane radical cations. At

Table 1. Structures and isotropic hyperfine coupling constants (Gauss) of the methane radical cation.

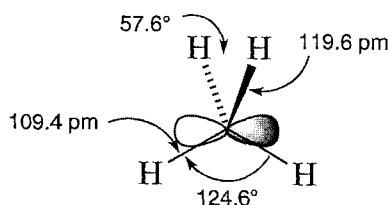
Species		Method ^a					
		LDA	BP	PWP	LDA//PF//D2P	CISP	Experiment
C_{2v}	C	4.1	14.7	23.3	—	—	—
	H _a	118.3	128.7	133.6	121.1	137.0	121.7
	H _b	−16.4	−20.1	−18.6	−16.3	−17.0	−14.6

^a According to [28].

different levels of theory the relative energies of the different SOMOs change along with the structure parameters. Accordingly, the global minimum can depend on the method of calculation and more than one species might become local minima. For the methane radical cation calculations with the 6-31G* basis set at different levels of electron correlation gave considerably different results. At the UHF/6-31G* level, a C_s species reported earlier [25] was the global minimum, whereas the D_{2d} structure had one negative frequency. Using UB3LYP/6-31G*, the D_{2d} structure was the global minimum, whereas the C_s structure showed one negative frequency. Finally, the UMP2/6-31G* level gave both D_{2d} and C_s species as minima with similar energies, but different hyperfine coupling patterns (Table 1; Figure 3) [31]. The ^1H nuclei connected by long bonds have strong positive hyperfine coupling constants. Aside from the different ^1H hyperfine coupling patterns (which might be masked in the experiment by dynamic Jahn–Teller effect) the two structures have significantly different isotropic ^{13}C hyperfine couplings. The D_{2d} structure has a very small ^{13}C hyperfine coupling (−0.36 to 0.42 mT), whereas the C_s species has a more significant interaction (1.8–3.3 mT) [31]. Accordingly, the actual structure should be identified unambiguously by the isotropic ^{13}C hyperfine splitting. Unfortunately, the spectra of $^{13}\text{CH}_4^{+\bullet}$ are anisotropic, and the isotropic coupling is not known unambiguously [30].

2.2.4 Electron-transfer Reactions of *n*-Alkanes

The ESR spectrum of ethane radical cation at 4 K in SF_6 contained a 1:2:1 triplet because of two strongly coupled protons (15.25 mT), corresponding to a spin-

**Figure 3.** Possible Jahn-Teller distorted geometries for methane radical cation.

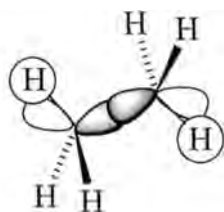


Figure 4. Schematic representation of the SOMO for ethane radical cation.

density of 0.3 in the H_{1s} orbital. The hyperfine coupling of the remaining four protons is smaller than the linewidth (≤ 1 mT) [19]. The coupling documents an unambiguous example of σ -delocalization. Another important result is the direct detection of static Jahn–Teller distortion. These effects are usually based on indirect detection, i.e., via the temperature-dependence or isotope effects on hyperfine coupling [32–34]. In a few special cases, the distortion is believed to be introduced by the matrix [35, 36]. However, for most alkane radical cations (with the notable exception of $C_3H_8^{*+}$, *vide infra*), the coordinate of distortion is independent of the matrix; the mode of distortion appears to be intrinsic to the radical cations. The matrix only serves to stabilize the distorted form [37].

These results suggest that the C_2H_6 molecule (D_{3d} symmetry) is distorted to D_{3d} symmetry in the electron-transfer process generating $C_2H_6^{*+}$. The mode of deformation was associated with a Jahn–Teller active rocking vibration (e_g) of the methyl groups (Figure 4) [38]. The structure of the resulting radical cation resembles diborane, B_2H_6 , rather than the diborane anion, $B_2H_6^-$, with which it is isoelectronic [39].

Upon raising the temperature to 77 K, the spectrum changes to a septet with a splitting of 5.04 mT, one third of the value at 4 K. This change was ascribed to a dynamic Jahn–Teller effect, viz., rapid equilibration of three equivalent distorted forms, each with two strongly coupled 1H nuclei. An apparent activation energy, $E_a = 250$ cal mol $^{-1}$, was derived for the exchange; this value is one order of magnitude smaller than that for methyl rotation in the gas phase ($E_a = 2.8$ kcal mol $^{-1}$) [19].

Detailed calculations using *ab initio* or density functional theory methods revealed two different structures for $C_2H_6^{*+}$, a ‘diborane-type’ structure and a ‘long-bond’ structure. In the diborane structure, the unpaired electron is delocalized between the C–C bond and two ‘bridging’ C–H bonds; whereas in the long-bond structure it resides principally in the C–C bond. The large positive hyperfine coupling constant observed at low temperatures [19] is reproduced well by the results of B3LYP calculations on the diborane structure [40].

The next higher homolog, propane, C_3H_8 , poses an additional interesting problem. Electron transfer from C_3H_8 gave rise to three different radical cations, depending on the matrix [41]. Different structures obtained in different matrices are ascribed to the fact that the energies of several high-lying orbitals are very close to each other. Therefore, even small perturbations as a result of the matrix can alter the relative energies of these levels.

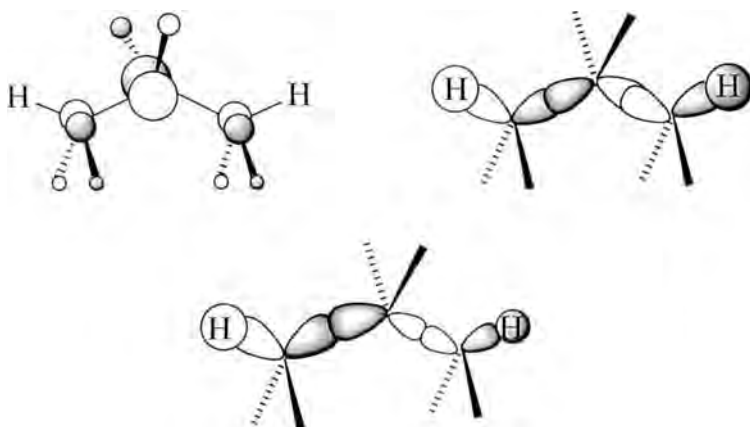


Figure 5. Schematic representation of three SOMOs corresponding to three different propane radical cations observed by ESR.

The species observed in F113 has two strong hyperfine interactions (10.5 mT) and four weaker ones (5.25 mT). This spectrum was assigned to a delocalized $\text{C}_3\text{H}_8^{+\bullet}$ species with a pseudo π orbital, resulting from the antibonding combination of three pseudo π - CH_2 orbitals. The ^1H nuclei of the center carbon are most strongly coupled whereas the two protons in the C–C–C plane have negligible hfcs. The magnitude of the strong hfcs (C-2) relative to the weaker ones (C-1,3) reflects the orbital coefficient at the corresponding carbons (Figure 5) [41].

Electron transfer from C_3H_8 in SF_6 generated a different ESR spectrum—a 1:2:1 triplet with two strongly coupled protons (9.8 mT). This spectrum is compatible with a SOMO consisting of two C–H orbitals, lying in the plane of two C–C σ -orbitals. The two in-plane ^1H nuclei at C-1 and C-3 are strongly coupled [42]; the hyperfine interactions of the remaining protons were derived from line-shape analysis at higher temperatures. The out-of-plane ^1H nuclei at C-1 and C-3 have a splitting constant, $a = -0.3$ mT, whereas those at C-2 are coupled less strongly. Compared with the parent, C_3H_8 , the probable structure of the radical cation is one in which the rotational axes of the CH_3 groups are bent toward the central carbon and the two in-plane C–H bonds are lengthened (4b_1 symmetry).

A third structure type of $\text{C}_3\text{H}_8^{+\bullet}$ was obtained in C_3F_8 ; the ESR spectrum of this species has only one strongly coupled ($a = 8.4$ mT) and one moderately coupled proton ($a = 1.8$ mT); the other splittings are considerably weaker ($a = 0.9, 0.6$ mT). Deuteration at C-2 identified the 0.6 mT splitting as due to the protons at C-2. The spectrum was assigned to a radical cation with one lengthened C–C bond. The two major splittings were assigned to the in-plane terminal protons at the lengthened bond and at the shorter one, respectively [43, 44].

Eriksson and colleagues used the 4b_1 species as a test case for a wide range of different calculation methods (Figure 5; Table 2) [28]. More recent detailed calculations revealed two different minima on the $\text{C}_3\text{H}_8^{+\bullet}$ potential surface, corresponding to the structure types with either two or one lengthened C–C bonds (Table 2).

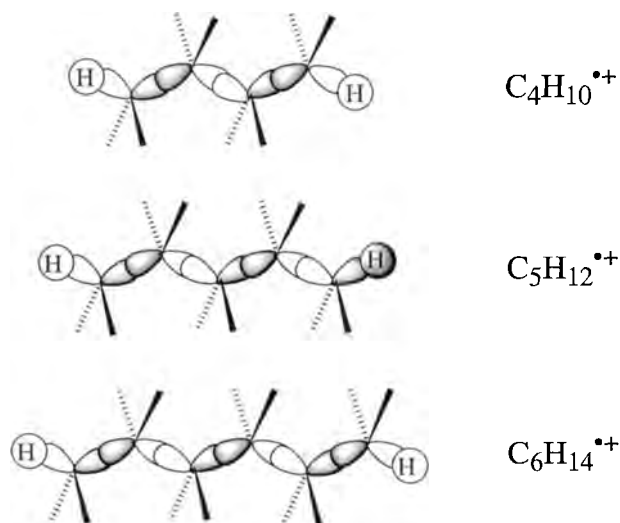
Table 2. Structure and isotropic hyperfine coupling constants (Gauss) of propane radical cations.

Species	Method ^a					
	LDA	BP	PWP	LDA//PF//D2P	CISP	Experiment
C ₃	C1,3	16.1	16.7	20.3	—	—
	C2	−3.3	−2.9	−0.11	—	—
	H1,3 _{long}	123.3	129.0	130.4	114.0	88.6
	H1,3 _{short}	−2.7	−4.2	−4.1	−3.9	−5.8
	H2	−5.1	−6.9	−6.2	−5.2	−7.1

^a According to [28].

Electron-transfer reactions of the longer *n*-alkanes generated the higher homologs of the σ -delocalized radical cation, C₃H₈^{•+} observed in F113. The resulting radical cations also have 1:2:1 ESR triplets with two strongly coupled protons [41, 45–47]. The splitting decreases sharply from 5.5 mT for C₄H₁₀^{•+} to 1.0 mT for C₁₀H₂₂^{•+}. By analogy to the C₃H₈^{•+} structure in F113, the SOMOs are σ -orbitals spread over fully extended planar C–C systems; two C–H group-orbitals at the terminal carbons contain the strongly coupled ¹H nuclei (Figure 6). The steadily diminishing hfcs with increasing chain length can be attributed to the distribution of the unpaired electron spin over an ever-increasing number of carbons (Figure 7). The hyperfine coupling constants of the inner protons and the out-of-plane methyl protons are typically small and are resolved only in special cases [42, 48].

Actually, the ESR spectra are more complex than the above simple description based on the exclusive formation of fully extended radical cations. In most frozen matrices, depending on the chain length, radical cations in *gauche* conformations were also detected [41, 49–53]. In the *gauche* forms, the spin delocalization is ter-

**Figure 6.** Schematic representation of the SOMOs for butane through hexane radical cations.

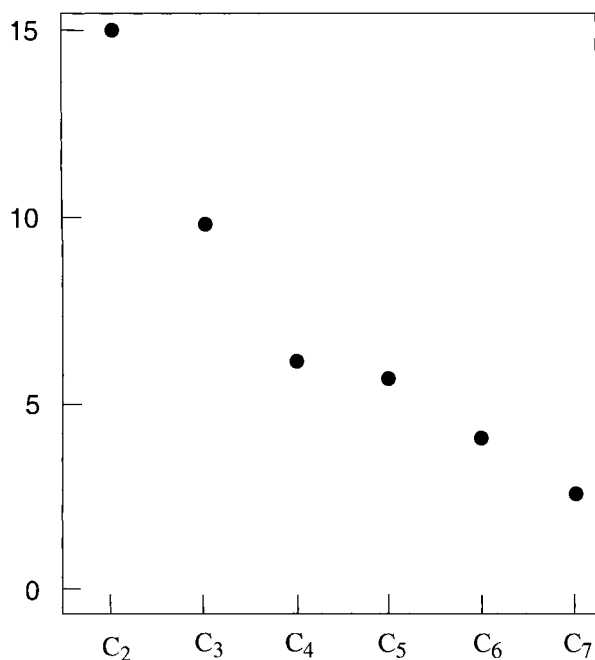


Figure 7. Hyperfine coupling constants (mT) of the in-plane chain-end ^1H nuclei for extended σ radical cations of ethane through heptane.

minated at the *gauche* carbon and the unpaired electron is confined mostly to the longer fragment. Therefore, the hfc's of the in-plane ^1H nuclei become larger than for the fully extended conformers. The strongly coupled protons are one chain-end ^1H nucleus and an additional in-plane ^1H nucleus at the *gauche* carbon; the latter has a slightly larger hfc because the *gauche* carbon has slightly greater spin-density [41, 50]. The co-existence of two conformers is illustrated for *n*-pentane, which can exist in the *s-trans,trans,trans*- and the *s-trans,trans,gauche*-conformation (Figure 8). The observed ESR spectrum was dissected into two independent contributions, a

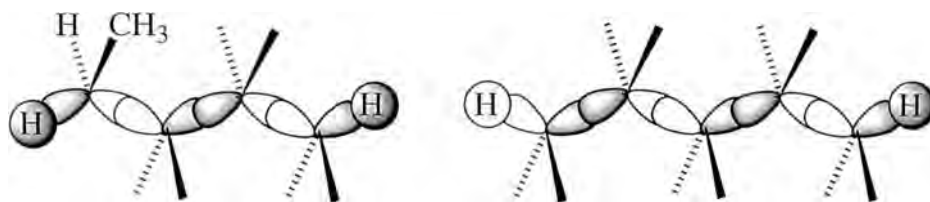
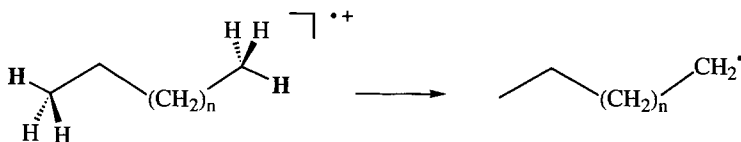


Figure 8. Schematic representation of the SOMOs for two conformers of pentane radical cation.

narrower one for the linear conformer and a spectrum with wider extension for the kinked one. The different spin and charge densities at the chain-end and the *gauche* carbon causes the ^1H nuclei attached 'in-plane' to have different reactivities (see Section 2.2.5).

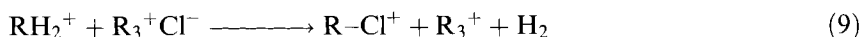
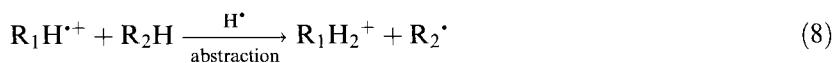
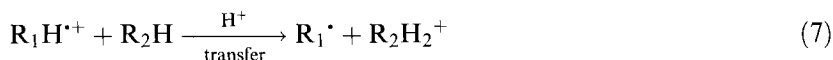
An interesting extension of these results was observed upon radiolysis inside pentasil zeolite (ZSM-5) [54]. The oxidation potentials of alkanes are too high to enable oxidation by the zeolite; indeed, incorporation of alkanes into Na- or HZSM-5 does not give rise to any absorption above 260 nm (cf. Section 2.2.6). Therefore, the neutral hydrocarbon molecules undergo electron transfer to holes generated in the zeolite upon radiolysis. At low alkane concentration (loading 0.5 % by weight), only the characteristic triplets of the extended radical cations, ($n = 3,5$), were observed (*n*-hexane, $a = 3.9$ mT; *n*-octane, $a = 2.9$ mT). Comparison of these spectra with those obtained in SF_6 and chlorofluorocarbons [19] revealed that only the fully extended conformers of the alkane radical cations are present in the zeolite enforced by the geometry of the zeolite channels [19].

Radiolysis at higher substrate loadings (3.0 % by weight), yielded different spectra, which were assigned to the corresponding primary alkyl radicals, ($n = 3,5$). Because the appearance of the new species was concentration-dependent, their formation was ascribed to an ion-molecule reaction, generating a protonated *n*-alkane, at the same time [54].



2.2.5 Deprotonation of *n*-Alkane Radical Cations

The reaction of the *n*-hexane and *n*-octane radical cations with their diamagnetic parents to generate alkyl radicals and protonated *n*-alkanes is one of the few reactions observed for *n*-alkane radical cations. Under the limited range of conditions in which they can be generated, only a limited range of reagents is available. The bimolecular H-atom transfer seems to be a general reaction for *n*-alkane radical cations. This reaction is not limited to zeolite media but occurs in halogen-containing matrices also. The mechanism of these conversions poses several interesting questions. The key step can involve transfer of a proton to the neutral *n*-alkane (Eq. 7) or abstraction of hydrogen atom from the *n*-alkane (Eq. 8). Additional questions concern the donor site, from which H^{\cdot} or H^+ originate, and the acceptor site to which H^{\cdot} or H^+ is transferred. The mechanism of this conversion was elucidated by Ceulemans and coworkers in elegant studies of *n*-heptane and *n*-octane in CCl_3F [55, 56].



The prevailing conformers of alkane radical cations depend on specific interactions between the host matrix and the guest alkane. For example, γ -irradiation of *n*-heptane in CCl_3F generated an extended all-*trans* conformer of $n\text{-C}_7\text{H}_{16}^{*+}$, whereas *n*-octane gave rise to the *gauche* at-C2 conformer of $n\text{-C}_8\text{H}_{18}^{*+}$. In experiments with $n\text{-C}_7\text{H}_{16}$ containing small amounts of $n\text{-C}_8\text{D}_{18}$, the spectrum of 1-heptyl radical, $n\text{-C}_7\text{H}_{15}\cdot$, was superimposed on that of $n\text{-C}_7\text{H}_{16}^{*+}$; this finding was ascribed to H^+ transfer from $n\text{-C}_7\text{H}_{16}^{*+}$ to $n\text{-C}_8\text{D}_{18}$. The preferential formation of primary heptyl radical during the early phase of the reaction identified a chain-end carbon as the donor site. This conclusion is in agreement with the reactivity expected for a σ -delocalized radical cation; a proton of a lengthened and weakened C–H bond should be donated preferentially. This is the same proton which also has a strong hyperfine coupling constant. The formation of secondary heptyl radicals appearing at higher *n*-heptane concentrations was explained as a result of intermolecular radical site transfer.

Analogous experiments with *n*-octane revealed that the secondary octyl radical, $2\text{-C}_8\text{H}_{17}\cdot$, was present from the very onset of proton transfer, suggesting the 2-position as the donor site. γ -Irradiation of *n*-octane generates the *gauche* at-C2 conformer of $n\text{-C}_8\text{H}_{18}^{*+}$, a species with large unpaired electron density on one in-plane chain-end C–H bond and on the in-plane C–H bond at C2 [55]. The formation of secondary octyl radical clearly supports significant donor site selectivity for H^+ transfer from *n*-alkane radical cations to *n*-alkanes. The *gauche* at-C2 conformer of $\text{C}_8\text{H}_{18}^{*+}$ reacted at the site of greater electron spin (and positive hole) density (C2) and generated the more stable free radical. Thus, this mode of reaction is favored by both kinetic and thermodynamic principles.

Deprotonation from the carbon of highest spin-density has been suggested as a general rule. This is strongly supported by the deprotonation of the propane radical cation in different matrices. The $\text{C}_3\text{H}_8^{*+}$ species observed in F113, which has high spin-density on C-2 (Figure 5) and strongly coupled secondary protons (10.5 mT) gave rise to 2-propyl radical. In contrast, the $\text{C}_3\text{H}_8^{*+}$ species formed in SF_6 , which has high spin-density on C-1 and C-3 and in which the chain-end in-plane ^1H nuclei are strongly coupled, generated the 1-propyl radical [41]. Additional strong evidence for this principle was derived from the deprotonation of isobutane radical cation (Section 2.2.6). On the other hand, it has been noted that the spin-density–reactivity correlation might not hold universally [41, 46, 49, 51].

The H^+ acceptor site was identified by experiments on $n\text{-C}_7\text{H}_{16}$ containing different amounts of $n\text{-C}_8\text{D}_{18}$ and a small percentage of 1-chlorohexane (e.g. Eq. 9). These experiments revealed the formation of small amounts of chlorooctanes, presumably via neutralization of protonated octane molecules by chloride ions. Among

the resulting chlorooctanes, the 2-isomer predominates, identifying C2 as the primary H^+ acceptor site [55].

2.2.6 Electron-transfer Reactions of Branched Alkanes

Branched alkanes are somewhat more easily oxidized than *n*-alkanes, although typically still quite unreactive. Their ionization potentials are barely lower than those of *n*-alkanes, ranging from 10.68 eV for 2-methylpropane to 9.89 eV for 2,2,4-trimethylpentane. As typical saturated hydrocarbons they are unreactive in the potential range that is experimentally accessible in non-aqueous solvents. Some branched alkanes with especially weak C–H bonds can, however, be oxidized under these conditions. For example, oxidation potentials (relative to the Ag/Ag^+ electrode) were assigned to 2,2-dimethylbutane (ca 3.3 V) or 2-methylpentane (ca 3.0 V) [57]. The radical cations of branched alkanes have interesting structural features. Electron transfer from the simplest branched alkane, 2-methylpropane, to electron holes generated in a halocarbon or SF_6 matrix gave rise to two different radical cations, of C_s and C_{3v} symmetry. Radiolysis in SF_6 at 4 K generated a radical cation, whose ESR spectrum contained a triplet ($a_H = 5.8$ mT). In this radical cation the unpaired spin is localized largely in one C–C bond (C_s symmetry); two *trans*- β -protons, one on each adjacent methyl group, are strongly coupled [19, 41]. This species is deprotonated to form *iso*-butyl free radical by loss of H^+ from a methyl group. Radiolysis in Freon at 4 K generated the same C_s radical cation. However, warming to 77 K caused irreversible conversion to a different species (C_{3v} symmetry), in which the spin is localized largely in the tertiary C–H bond, causing the tertiary proton to be strongly coupled ($a_H = 25.0$ mT) (Figure 9) [41]. This species is deprotonated to form *t*-butyl free radical.

It was the oxidation of 2,2,3,3-tetramethylbutane (hexamethylethane), studied independently in three different laboratories, which might have signaled the onset of systematic investigation of electron-transfer reactions from alkanes and of the structures of the resulting radical cations. Oxidation of hexamethylethane generated a radical cation with a seven-line ESR spectrum with $a_H = 2.9$ mT. The unpaired spin of this radical cation is localized in the central C–C bond; six *trans*- β -protons, one on each adjacent methyl group, are strongly coupled by hyperconjugation [17]. The hyperfine couplings of the *gauche* β -hydrogens were also assigned ($a_H =$

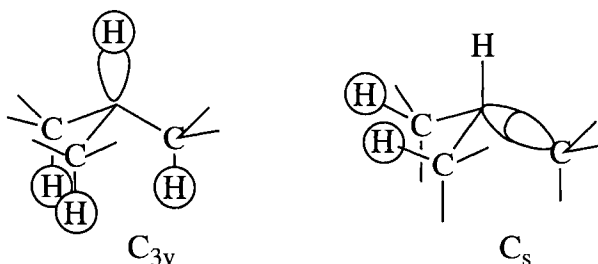


Figure 9. Schematic representation of σ - and π -SOMOs considered for isobutane radical cation.

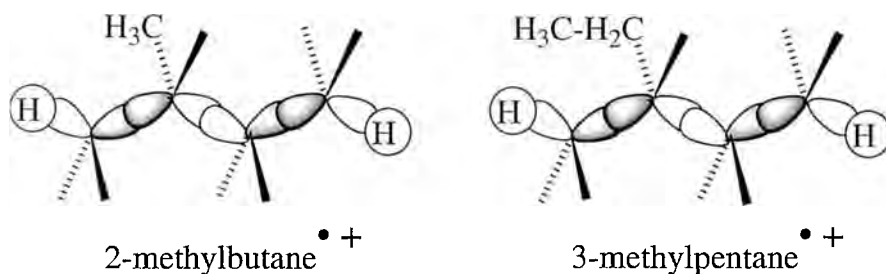


Figure 10. Schematic representation of SOMOs for *s-trans,trans*-2-methylbutane and *s-trans,trans*-3-methylpentane radical cations.

0.42 mT) [18]. Interestingly, the six methyl groups remain static even at 77 K [18] in considerable contrast to the facile rotation of the methyl groups of the ethane radical cation. The reason for the pronounced hindrance of methyl rotation must lie in the significant steric congestion of the tetramethylbutane framework.

Electron transfer from 2-methylbutane [58] and 3-methylpentane [58, 59] generated remarkably similar ESR spectra—both donors gave rise to four-line spectra with $a_H \approx 4.5$ mT. These patterns were rationalized in terms of radical cations, with the unpaired spin localized in the C3–C4 bond; the large hfcs arise from one proton in each of three methyl groups (Figure 10) [58, 59]. Radiolysis of specific deuterated derivatives and spectral simulations led Shiotani and coworkers to a refined assignment [58]. Details go beyond the scope of this review.

Many other branched alkanes undergo electron-transfer reactions in cryogenic matrices. Although the ESR spectra of the resulting radical cations reveal interesting structural features [60–62], detailed discussion would exceed the scope of this review.

2.2.7 Electron Transfer from Alkanes to Zeolites

Zeolites were introduced as catalysts for large-scale heterogeneous reactions in petrochemistry, because they have significant advantages for processes such as cracking, aromatic isomerization, or disproportionation [63–68]. One of the most intriguing properties of acid zeolites is their spontaneous generation of organic radical cations on adsorption of organic electron donors [69]. Molecules containing strained rings are especially readily converted to their radical cations on incorporation into zeolites [70], although radical cations have also been obtained from selected alkanes. Because radical cations sequestered in zeolite pores are protected from reagents that typically would cause their decay in solution, their lifetimes are increased so that they can be studied by conventional spectroscopic techniques. Also, the limiting geometry of the zeolite pores can manifest itself in two ways: (i) it might selectively incorporate substrates with suitable geometries (shape selectivity); and (ii) it might restrict the geometry (conformation) of a sequestered intermediate. Thus, *trans*-1,2-diphenylcyclopropane was incorporated readily into ZSM-5 where-

as the *cis* isomer was not [70]. On the other hand, radiolysis of *n*-hexane and *n*-octane in pentasil zeolite generated solely the EPR spectra of the 'extended' radical cations (*vide supra*) [54].

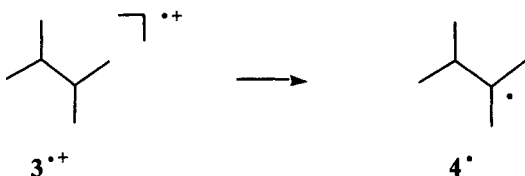
Radical cations are also generated efficiently upon γ -radiolysis of appropriate 'guests' sequestered in zeolites. In this experiment, a 'hole' and a free electron are generated in the zeolite, and the guest transfers an electron to the 'hole'. Given the redox- and acid-base-active nature of zeolites it is not obvious whether the original substrate or a rearranged product is oxidized by interaction with the newly created 'hole'. In fact, many alkenes undergo significant reactions before the onset of radiolysis.

Chen and Fripiat succeeded in generating radical ions from saturated hydrocarbons, e.g., 3-methylpentane (**1**), upon sequestering them into H-mordenite and heating for several hours [71]. The resulting species were identified by their EPR spectra [72]. Adsorption of **1** and heating to 100 °C for 4 h produced a 'nine-line spectrum' ($a = 17.3$ G, $g = 2.003$), which was identified by Roduner and Crockett as that of the 2,3-dimethylbutene radical cation (**2** $^{+\bullet}$) [72]. Although an electron-transfer step must be involved at some stage of this conversion, it is not clear at what stage electron transfer to the zeolite occurs.



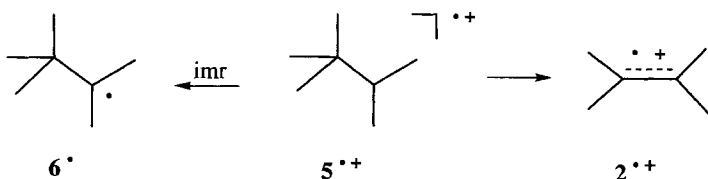
Significant applications of γ -radiolysis in the study of electron-transfer processes and radical cations in zeolites have emanated from the radiation group at Argonne National Laboratories [73]. For example, Barnabas et al. studied the fate of highly branched alkanes, 2,3-dimethylbutane, 2,2,3-trimethylbutane, and 2,2,3,3-tetramethylbutane, upon γ -radiolysis in pentasil zeolite (ZSM-5) [74, 75].

γ -Radiolysis of 2,3-dimethylbutane (**3**) in pentasil zeolite at 4 K forms the corresponding radical cation (**3** $^{+\bullet}$; a broad quintet, $a = 3.7$ mT); by analogy with typical radical cations of branched hydrocarbons, the quintet is caused by coupling of a single proton per methyl group. In addition, 2,3-dimethyl-2-butyl free radical (**4** $^\bullet$), recognized as a septet ($a = 2.34$ mT) of doublets ($a = 0.55$ mT), is formed to a lesser extent [75].



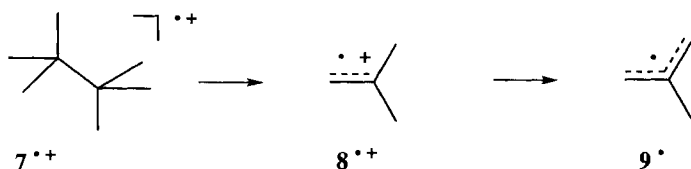
Radiolysis of ZSM-5 containing 2,2,3-trimethylbutane (**5**) at 77 K yielded a six-line spectrum characteristic of **5** $^{+\bullet}$ ($a = 3.1$ mT, 5H) [76]. Upon raising the temperature, in the range 120–200 K, the well known 2,3-dimethyl-2-butene radical

cation (2^{++}) was observed ($a = 1.7$ mT, nine lines observed, 12H). Its formation was ascribed to “thermal elimination of methane”, a reaction similar to the above-mentioned elimination of H_2 [72].



Above 200 K, an additional seven-line pattern ($a = 2.25$ mT, 6H) appeared, which was ascribed to 2,3,3-trimethyl-2-butyl radical, 6^{\bullet} , apparently as a result of deprotonation of 5^{++} . Because the abundance of this species increased with substrate loading, its formation was ascribed to an ion–molecule reaction (Section 2.2.5).

γ -Radiolysis of tetramethylbutane (7) in pentasil zeolite gave rise to a ‘seven-line’ spectrum ($a = 3.1$ mT, 6H; outer lines not distinct), identified as that of 7^{++} [72, 74]. The splitting is, once again, caused by a single (in-plane) proton per methyl group. An additional weak quartet ($a = 2.2$ mT) indicated formation of methyl radical, most probably formed by fragmentation of 7^{++} . Upon annealing at 125 K, a new spectrum appeared ($a = 1.49$ mT, 2H; $a = 1.38$ mT, 2H; $a = 0.33$ mT, 3H); this was assigned to 2-methylpropenyl free radical, 7^{\bullet} . This species was explained by rapid deprotonation of 2-methylallyl radical cation (8^{++} , not observed). This reaction, assigned by the authors to “scission of the central C–C bond” of 9^{++} [74], amounts to ‘elimination’ of 2-methylpropane (C_4H_{10}), similar to the loss of CH_4 [76] and H_2 [72] mentioned above.



Among the various conversions discussed in this section, deprotonation is clearly a general reaction of alkane radical cations. The interesting elimination or fragmentation reactions, on the other hand, seem to be zeolite-specific reactions without precedent in halogen containing matrices.

2.3 Electron-transfer Reactions of Cycloalkanes

Similar to alkanes most cycloalkanes also are quite unreactive and have very high pK_a values and low electron affinities, making them poor electron acceptors. Although the molecular anions of cycloalkanes are very unstable, temporary anion

states with lifetimes shorter than picoseconds have been observed. The four smallest ring systems, cyclopropane through cyclohexane have temporary anion states at 5.29, 5.80, 6.14, and 4.11 eV [1]. The ionization potentials of cycloalkanes are somewhat lower than those of the low *n*-alkanes (the *IP* of cyclopropane through cyclooctane lie between 9.75 and 9.90 eV); they are still poor electron donors and are difficult to oxidize in solution or in solid matrices. The molecular ions are accessible in the gas phase (electron or He_x impact ionization), as documented by their mass and photoelectron spectra. Also, simple cycloalkanes and their derivatives readily undergo electron transfer to 'holes' generated upon radiolysis of halogen-containing matrices [9–11]. Some substituted cyclopropanes and cyclobutanes undergo photo-induced electron transfer to photo-excited electron acceptors in solution, generating radical cation–radical anion pairs (Section 2.3.3).

The basic cycloalkanes with three to eight carbons (*c*-C₃H₆–*c*-C₈H₁₆) undergo electron transfer upon radiolysis in halogen-containing matrices, generating the radical cations (*c*-C₃H₆^{•+}–*c*-C₈H₁₆^{•+}). The ESR spectra observed in these systems reveal interesting structural details. Some properties of these species are discussed below. Common features include delocalization of the unpaired electron throughout the molecular frame and a noticeable positive *g*-shift relative to alkane and aromatic radical cations. In addition, the overall width of the ESR spectra, i.e., the sum of all hyperfine coupling constants, increases with increasing ring size (Figure 11). In marked contrast, a steady decrease in spectral width with increasing chain length is observed for aliphatic radical cations (cf., Figure 7). For the typical σ -delocalized linear aliphatic radical cations, only C–H bonds in the molecular plane contribute to delocalizing the unpaired electron spin. Only the in-plane ¹H nuclei are strongly coupled; typically, two terminal protons satisfy this requirement. Because the spin-density in the terminal C–H bond decreases with increasing numbers of carbons delocalizing the electron spin, so does the magnitude of the ¹H hyperfine coupling.

Among the simple cycloalkanes, we first discuss electron transfer from the three- to eight-membered cycloalkane prototypes to electron holes generated by radiolysis in different matrices, giving rise to the simple cycloalkane radical cations. Because of the significant interest they have attracted, the electron-transfer reactions of cyclopropane and, to a lesser extent, cyclobutane derivatives will be treated separately. Finally, electron transfer from some bicyclic hydrocarbons and the resulting radical cations will be discussed in a separate section (Section 2.4).

2.3.1 Electron Transfer from C₃–C₈ Prototype Cycloalkanes

Several of the simple cycloalkane radical cations, generated by electron transfer, are Jahn–Teller active. Apart from the interesting small-ring radical cations, *c*-C₃H₆^{•+} and *c*-C₄H₈^{•+}, one common-ring radical cation, *c*-C₆H₁₂^{•+}, and one medium-ring species, *c*-C₈H₁₆^{•+}, also show this interesting phenomenon. On the other hand, *c*-C₅H₁₀^{•+} and *c*-C₇H₁₄^{•+} seem to be Jahn–Teller inactive.

Cyclopropane, the simplest strained ring system, continues to be subject to intense and detailed scrutiny by a variety of techniques. Its photoelectron spectrum,

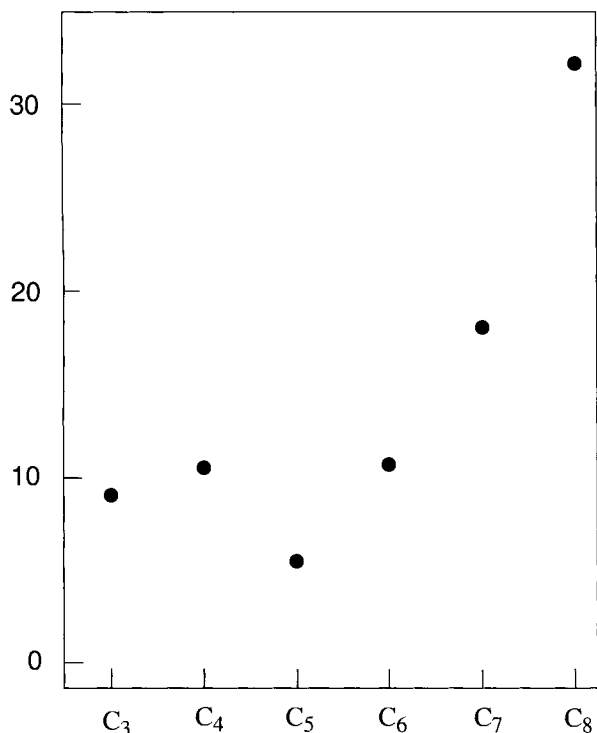


Figure 11. Sum of all hyperfine coupling constants (mT) for radical cations of C₃–C₈ cycloalkanes; the strained rings (C₃, C₄) clearly deviate from the trend of C₅–C₈.

investigated over thirty years ago, showed Gaussian shaped bands without fine structure. Molecular-orbital calculations suggest that the first two bands, a double peak centered near 11 eV, be assigned to a $^2E'$ state. The large splitting of these bands (0.8 eV), also observed for many derivatives, is ascribed to Jahn–Teller distortion of the ionic ground state [77]. The two states resulting from the distortion, 2B_2 and 2A_1 , (C_{2v} symmetry) correspond to two different molecular structures (Figure 12). In rigid matrices, cyclopropane readily undergoes electron transfer upon γ -radiolysis at 4.2 K; the ESR spectrum of the resulting radical cation has two strongly coupled ^1H nuclei ($a_{\text{H}} = 2.04$ mT) and four less strongly coupled nuclei ($a_{\text{H}} = -1.17$ mT). These splittings were assigned to the β - and α -protons, respectively, of a trimethylene (2A_1)-type radical cation structure, an equilibrium structure with one lengthened C–C bond, because of static Jahn–Teller distortion of the cyclopropane ring (D_{3h} symmetry) [78, 79]. At higher temperatures, an averaged spectrum, consisting of only a single line (FWHH = 1.5 mT), was observed. This spectrum was ascribed to an averaged structure resulting from dynamic Jahn–Teller distortion, interconverting three equivalent 2A_1 structures with three equivalent 2B_2

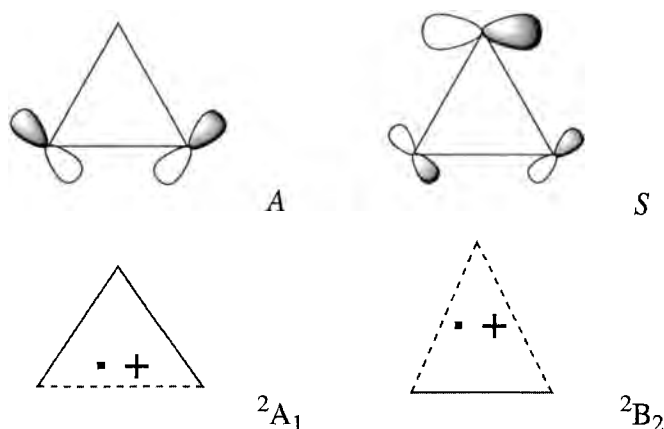


Figure 12. The degenerate pair of cyclopropane HOMOs, *S* and *A*, and schematic radical cation structures, *A* and *B*, resulting from removing an electron from one of the orbitals.

structures as transition states [37, 78–80]. The magnitude of a_β (2.04 mT) and a_α (–1.17 mT) fortuitously averages to $a_{\text{avg}} \approx 0$ [80].

The structure of the cyclobutane radical cation also is of major interest. The parent cyclobutane system is known to have a puckered ring with D_{2d} symmetry [81]. Electron transfer from one of the cyclobutane e orbitals is expected to lead to a Jahn–Teller unstable radical cation, which might distort to structures of D_{2d} and C_{2v} symmetry [81]. Ushida et al. studied the EPR spectra obtained upon X-irradiation of cyclobutane in frozen CFCl_3 solution [82]. At 4 K, a triplet of triplets appeared with hyperfine coupling constants, $a_{\text{H1}} = 4.9$ mT (2H), $a_{\text{H2}} = 1.4$ mT (2 H), and four weakly coupled protons ($a_{\text{H1}} = 0.5$ mT), suggesting an intermediate with C_{2v} symmetry. These findings were interpreted in terms of a radical cation that had undergone static Jahn–Teller distortion to a rhombic structure of C_{2v} symmetry (Figure 13, type D) [82]. Upon annealing the sample at 77 K, the spectrum changed irreversibly to a five-line pattern (measured at 4 K). This result was ascribed to an irreversibly reduced barrier to ring puckering and/or flattening. Finally, at temperatures above 77 K, a nearly isotropic nine-line spectrum with a hyperfine coupling constant, $a_{\text{H}} = 1.33$ mT was observed. This change was ascribed to a dynamic Jahn–Teller effect via pseudorotation. Additional structure types can be envisaged that are compatible with the low-temperature ESR pattern and cannot be rigorously eliminated [82].

The cyclobutane radical cation was calculated by several groups, who evaluated Jahn–Teller distorted structures potentially arising upon ionization of cyclobutane [79, 83–87]. Four distorted local minima were considered (Figure 13). A rectangular structure with two weakened C–C bonds (type A) and a rhomboidal structure with four weakened C–C bonds (type B) result from first order Jahn–Teller distortion. Two further structures, a trapezoidal one (one weakened C–C bond; type C), and an irregular structure shaped like a kite (two lengthened C–C bonds; type D) can be envisaged as a consequence of second-order Jahn–Teller distortion [86]. A detailed recent study also considered puckered equivalents of the planar structure types, A–D

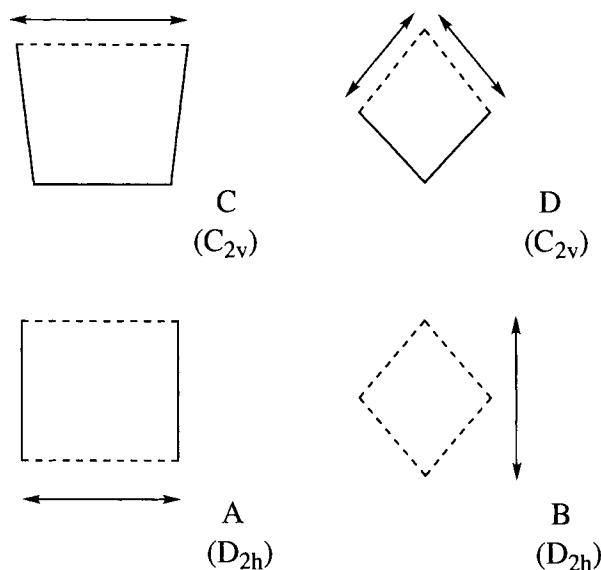


Figure 13. Possible structure types of cyclobutane radical cations.

[86]. At the QCISD-(T)/6-31G**/UMP2/6-31G* level of theory a rhombic structure, quite flexible to ring-puckering, emerged as the most stable.

The most recent study, using UHF, MP2, BLYP and B3LYP methodologies, reached somewhat different conclusions. Density functional theory calculations showed one imaginary frequency for the rhombic structure (four equivalent bonds, 157.3 pm), suggesting that it is a (very low-lying) transition structure between two parallelograms (two pairs of equivalent bonds, 149.5 and 169.5 pm, respectively) [87]. A calculation of the hyperfine coupling constants for the minimum yielded values, $a = 2.09, 0.29$ mT; the rather poor agreement with the experimental splittings, $a = 4.9, 1.4$ mT, is unsettling, particularly because hyperfine coupling constants calculated for many strained-ring systems are in significantly better agreement with experiment. Because hyperfine coupling patterns (and the related CIDNP patterns) are the only experimental data available for many strained ring systems, closer reproduction of these data by calculation seems desirable.

In contrast to the radical cations of strained-ring cycloalkanes, the cyclopentane radical cation, $c\text{-C}_5\text{H}_{10}^{+\bullet}$, formed by electron transfer to radiolysis-induced holes in halocarbon matrices, had a simpler spectrum. A triplet with $a_{\text{H}} = 2.5$ mT (2H) was attributed to a localized species with C_s symmetry. The unpaired electron was assigned to a W-shaped σ -orbital, involving C5–C1–C2, and the two equatorial protons at C5 and C2 [80, 88, 89]. At temperatures above 77 K, all ring protons become equivalent, most probably as a result of processes such as ring inversion, or pseudo-rotation around the C5-axis [89].

Five-membered rings typically have non-planar conformers, either a puckered C_2 ‘envelope’ or a C_s ‘half chair’ (Figure 14). The conformers are readily interconverted by flipping one CH_2 from above the approximate ring plane to below. Ring inversion converts the molecule into its mirror image, interchanging equatorial and

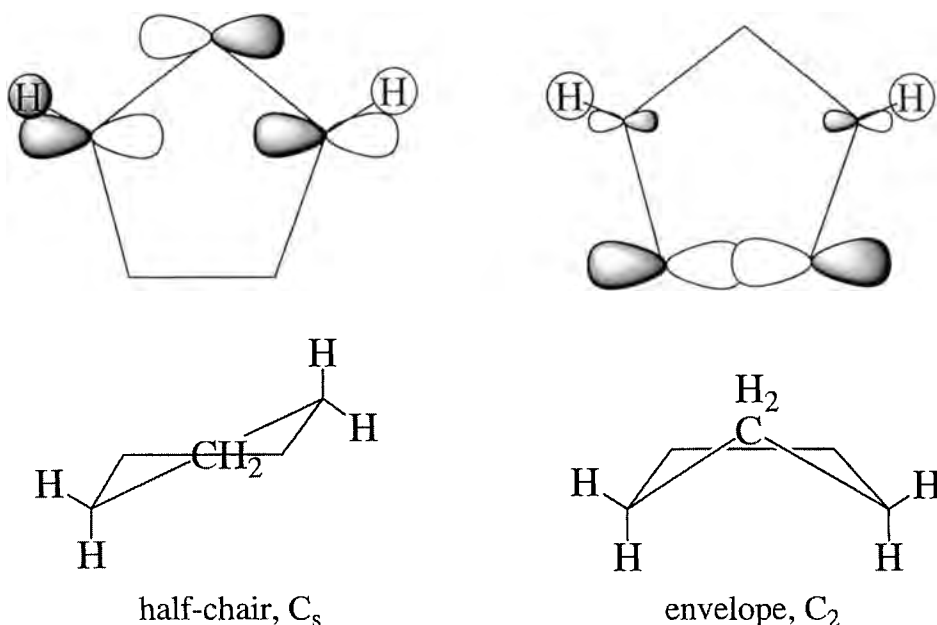


Figure 14. Conformers of cyclopentane and schematic representation of possible singly occupied molecular orbitals (SOMOs) of cyclopentane radical cation.

axial ^1H nuclei at a given carbon, whereas pseudo-rotation would move the unpaired electron spin to an adjacent set of carbon atoms. Spectra simulation led to estimates of $1.2 \text{ kcal mol}^{-1}$ for the barrier of ring inversion and $3.6 \text{ kcal mol}^{-1}$ for the barrier to pseudo-rotation [84]. The observed ESR pattern is consistent with either the C_s or the C_2 structure. Ab initio calculations carried out at the time supported a $^2A''$ state with the σ -type W shaped SOMO [80, 88]; however, an element of ambiguity persisted, because the calculations did not reproduce the radical cation well. Alternatively, the unpaired electron may be localized mainly in one C–C bond (Figure 14) interacting mainly with two quasi-equatorial β hydrogens. Recent ab initio calculations (6-31G* basis set, UHF, UB3LYP, or UMP2) favored the alternative structure. The C3–C4 bond was significantly lengthened (ca 210 pm) and the electron spin-density was almost entirely localized at C3,4 ($\rho_{3,4} = 0.46$, UB3LYP) [31]. At this level, only the quasi-equatorial ^1H nuclei had large hyperfine coupling constants ($a_{2,5} = 1.98 \text{ mT}$), although still somewhat different from the experimental values.

Interestingly, the averaged hyperfine coupling of the eleven-line spectrum changes significantly in different matrices, ranging from 0.59 mT in C_6F_{12} to 0.77 mT in CFCl_3 . This result might suggest that the electronic ground state is influenced by the nature of the matrix. Other matrix-dependent ESR spectra will be discussed for the radical cations of the bicyclo[4.4.0]decane isomers (Section 2.4.2).

Electron transfer from *c*- C_6H_{12} was studied by many groups as a convenient and simple target for pulse radiolysis [37, 90–93]. Radiolysis of *c*- C_6H_{12} in Freon-113

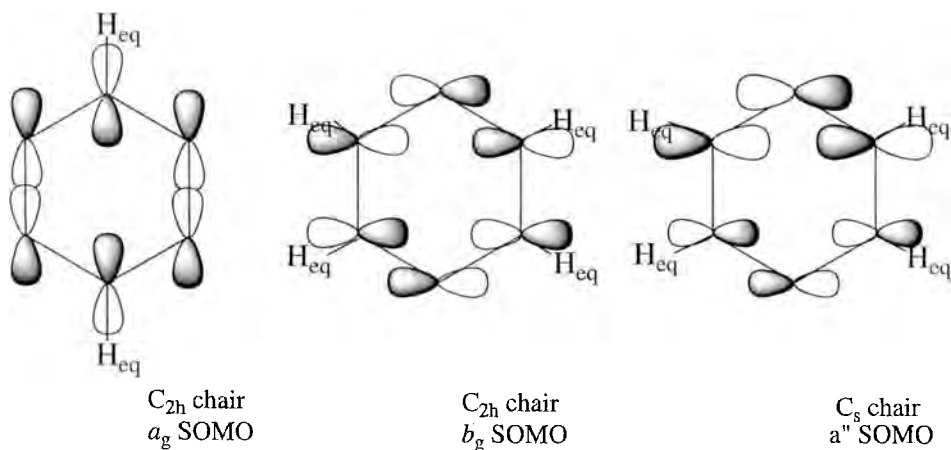


Figure 15. Possible SOMOs of cyclohexane radical cations. Because the a_g and b_g SOMOs are incompatible with the observed hyperfine coupling pattern, further distortion of the b_g SOMO to an a'' SOMO was suggested [94, 95].

produced a Jahn–Teller active radical cation, $c\text{-C}_6\text{H}_{12}^{+\bullet}$. The spectra observed at 4 or 77 K were broad and difficult to analyze. The ESR spectrum at 4 K contained three pairs of equivalent protons, $a_{\text{H}} = 8.5$ mT, $a_{\text{H}} = 3.4$ mT, $a_{\text{H}} = 1.4$ mT. Jahn–Teller distortion of the degenerate E_g structure (a D_{2d} chair) might lead to either a 2A_g or a 2B_g state (C_{2h} symmetry; Figure 15) [92, 93]. The observed spectrum was assigned to a radical cation of 2A_g structure, with two elongated C–C bonds and the splitting to the six equatorial protons of $c\text{-C}_6\text{H}_{12}^{+\bullet}$ [37, 92]. The simple species fitting this description would have four equivalent protons, however; an additional distortion, twisting two ${}^1\text{H}$ nuclei ‘out of plane’, must, therefore, be invoked to account for the spectrum [94, 95]. At temperatures ≥ 140 K a well resolved seven-line spectrum appeared ($a_{\text{H}} = 4.3$ mT); this is readily explained as the average of three rapidly equilibrating 2A_g structures with an estimated activation barrier between 170 and 240 cal mol $^{-1}$ [37].

Electron-transfer reactions of higher cycloalkanes were also studied. Electron transfer from $c\text{-C}_7\text{H}_{14}$ to unstable holes generated by radiolysis in Freon-113 gave rise to a stable radical cation, $c\text{-C}_7\text{H}_{14}^{+\bullet}$; its spectrum was interpreted in terms of a twisted chair form with C_2 symmetry [37]. Finally, radiolysis of $c\text{-C}_8\text{H}_{16}$ in a Freon-113 matrix generated a Jahn–Teller-active radical cation, $c\text{-C}_8\text{H}_{16}^{+\bullet}$, with three sets of non-equivalent protons [37]. A detailed discussion of these species exceeds the scope of this review.

2.3.2 Cyclopropane Radical Cations

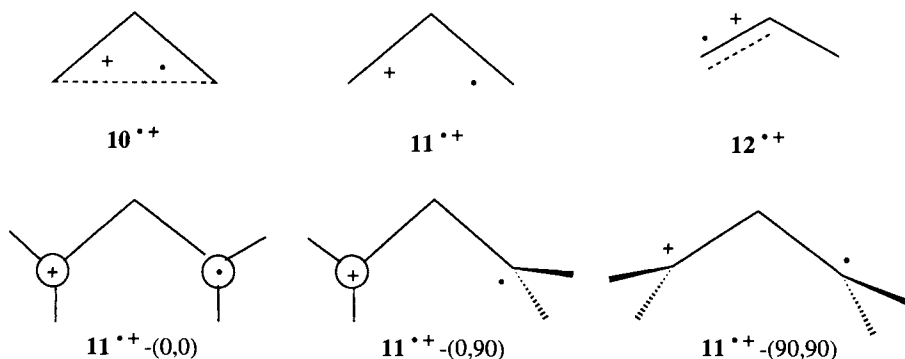
Cyclopropane has a degenerate pair of in-plane e' orbitals (S, A). Accordingly, vertical ionization leads to a doubly degenerate ${}^2E'$ state. Jahn–Teller (JT) distor-

tion of this state results in two non-degenerate electronic states, 2A_1 and 2B_2 (C_{2v} symmetry) [96–104]. The 2A_1 component (orbital S singly occupied) relaxes to an equilibrium structure with one lengthened C–C bond, which is the lowest energy species for many cyclopropane radical cations (Figure 12). This assignment is based unambiguously on ESR [78, 105, 106] and nuclear spin polarization (CIDNP) studies (cf. below) [107–110]. The two structure-types considered for the cyclopropane radical cation, 2B_2 ('type **B**') and 2A_1 ('type **A**') pose several interesting questions. Which structure is of lower energy? Can the 2A_1 species undergo ring-opening to trimethylene radical cation? How is the ring-opened species related to propene radical cation? How do substituents affect the relative stabilities of the 2B_2 and 2A_1 structures? These questions have been pursued in theoretical and experimental studies. We will review some molecular orbital calculations and discuss them in the light of experimental results.

Molecular orbital calculations

The radical cations of cyclopropane have long been the target of theoretical investigations) [96–104]. Here, we will discuss mainly a thorough *ab initio* study by Borden and co-workers [101], dealing with the cyclopropane radical cation, 10^{*+} , its potential ring opening to trimethylene radical cation, 11^{*+} , and the further rearrangement to propene cation radical 12^{*+} . In addition, we will briefly mention a study by Krogh-Jespersen and Roth [103], dealing specifically with the existence of the 2B_2 structure type and its potential stabilization by appropriate substituents, and two papers dealing with the ring-opened species [102, 104].

In view of the significant ring-strain of the cyclopropane system, it is hardly surprising, that the propene radical cation, 12^{*+} was found to be the lowest energy isomer on the $C_3H_6^{*+}$ potential surface. At the unrestricted Hartree–Fock (UHF/6-31G*/MP2/6-31G*) level (C_s symmetry), 12^{*+} lies ca 10 kcal mol $^{-1}$ below the 2A_1 radical cation with only one lengthened C–C bond ' 10^{*+} '. A vibrational analysis of this structure showed only positive frequencies, thus identifying this species as a local minimum. In contrast, the ring-opened trimethylene radical cation, 11^{*+} , does not appear to be a minimum, because vibrational analysis in C_{2v} symmetry showed one imaginary and one low frequency.

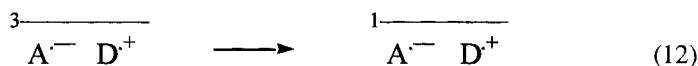
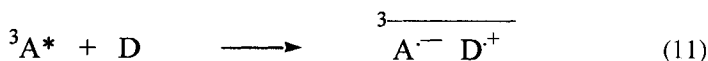
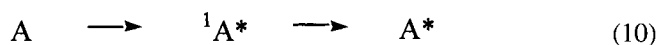


Additional geometries in which the terminal CH₂ groups were rotated relative to the plane of the three-carbon unit from orientation '0' (in plane) to orientation '90' (perpendicular) likewise failed to qualify as local minima. The calculations failed to indicate a chemically significant barrier for the conversion of 11^{*+} to 12^{*+} . The essence of these findings was confirmed by UMP2/6-31G* calculations of Skancke [104], who identified the conversion of 10^{*+} (2A_1) to 12^{*+} as a one-step reaction with a barrier of ca 30 kcal mol⁻¹, approximately one half that measured for the parent system [111, 112]. In summary, these calculations argue against the opening of 10^{*+} to 11^{*+} reported to occur in CF₂Cl-CFCl₂ matrices, even at cryogenic temperatures [105, 106]. On the other hand, it is possible that matrix forces affect the prevailing structure. We will discuss several examples of effects of this nature (*vide infra*).

Photoinduced electron transfer of cyclopropane systems

The ring-strain inherent in cyclopropane makes it a significantly better electron donor than non-strained cyclic hydrocarbons. Accordingly, a wide range of cyclopropane derivatives undergo electron transfer upon interacting with acceptor excited states. The resulting 'photoinduced electron transfer' (PET) is a mild and versatile method for the generation of radical cation-radical anion pairs in solution (Scheme 1) [113–115]. The PET method utilizes the fact that the oxidative power of an acceptor and the reductive power of a donor are substantially enhanced by photoexcitation. Thus, donor-acceptor pairs with negligible or weak interactions in the ground state, can readily undergo electron transfer, generating radical ion pairs, if either reactant is excited electronically. For the study of radical cations it is advantageous to excite the acceptor (Eq. 10). Depending on the nature of the acceptor and its lifetime, it will be quenched before or after intersystem crossing to the triplet state.

In Scheme 1, the reaction is formulated for triplet quenching (Eq. 11), which generates radical ion pairs of triplet spin multiplicity. Even so, the resulting radical ions have limited lifetimes, because the pairs readily undergo intersystem crossing



Scheme 1.

(Eq. 12), followed by recombination of the singlet pairs (Eq. 13); alternatively, separation by diffusion (Eq. 14) might generate 'free' radical ions.

The most common triplet-state electron acceptors are ketones and quinones, whereas aromatic hydrocarbons, often bearing one or more cyano groups, are the most frequently used singlet-state electron acceptors. For the generation of radical cations from a given donor it is important that the exothermicity of electron-transfer reactions can be adjusted to fall within an appropriate range, typically between 0.2 and 1.0 eV. The change in free energy (ΔG) for an electron-transfer reaction is given by the Rehm Weller equation (Eq. 11) [116]

$$\Delta G = -E_T - E_{\text{red}} + E_{\text{ox}} - e^2/\epsilon a \quad (15)$$

where E_T is the excited state energy (0–0 transition), E_{ox} is the one-electron oxidation potential of the donor, E_{red} is the one-electron reduction potential of the acceptor, and a is the distance (Å) between donor and acceptor. The term $e^2/\epsilon a$ (Coulomb term) takes account of ion pairing. Alternatively, one can define the reduction potential of the acceptor excited state as

$$^*E_{\text{red}} = -E_T + E_{\text{red}} \quad (16)$$

The application of PET is limited to the oxidation of substrates with oxidation potentials well below the threshold value defined by $^*E_{\text{red}}$. According to Eq. 16 the change in free energy of the reaction can be tuned by variation of the solvent (polarity) and of the acceptor (reduction potential, excited-state energy). For a given class of acceptors the excited state energies typically vary over a narrow range, whereas the reduction potentials can be altered substantially by the introduction of appropriate substituents (Table 3). It is not, therefore, generally a problem to adjust the exothermicity to an appropriate range.

The parent cyclopropane system does not, in fact, readily undergo electron transfer in solution; apparently, the excited state reduction potentials of most sensitizers are too low (Table 3). However, introducing simple alkyl substituents increases the donor capacity of the cyclopropane system. This is aptly shown by the (gas-phase) ionization potential of 1,1-dimethylcyclopropane (9.0 eV) compared with that of cyclopropane (9.87 eV). PET from a series of methyl-substituted cyclopropanes to photoexcited chloranil was probed in solution. These experiments failed to provide evidence for electron transfer from *cis*- or *trans*-1,2-dimethylcyclopropane. On the other hand, 1,1,2-trimethyl- and 1,1,2,2-tetramethylcyclopropane were oxidized [108, 109].

Conjugation with one or two phenyl groups also converts the cyclopropane ring to an excellent electron donor. Although 1-phenyl- and 1,2-diphenylcyclopropane arguably belong into the category of aromatic compounds, their electron-transfer chemistry is included here, because their reactions are essentially those of cyclopropane compounds.

Two types of competing reaction pose potential drawbacks to the PET method. First, the principal types of electron acceptor are ketones and quinones, the triplet states of which are known to abstract hydrogen atoms with formation of neutral radicals. Second, many of the radical cations generated by PET are potential proton

Table 3. Excited state reduction potentials of selected electron acceptors.

	E_{A/A^-} ^a	$E_{(0,0)}$ ^b	$^3E^{*c}$	$^*E_{A/A^-}$ ^d
<i>Singlet acceptors</i>				
2,4,6-Triphenylpyrylium tetrafluoroborate (TTF)	-0.29 ^e	2.8		2.5
2,6,9,10-Tetracyanoanthracene (TCA)	-0.45	2.82		2.35
1,2,4,5-Tetracyanobenzene (TCB)	-0.65	3.83		3.2
9,10-Dicyanoanthracene (DCA)	-0.89	2.88		2.0
1,4-Dicyanonaphthalene (DCN)	-1.28	3.45		2.15
9-Cyanoanthracene (CA)	-1.39	2.96		1.55
<i>p</i> -Dicyanobenzene (<i>p</i> -DCB)	-1.60	4.29 ^f		2.7
9-Cyanophenanthrene (CP)	-1.88 ^g	3.42		1.55
1-Cyanonaphthalene (1-CN)	-1.98 ^h	3.75		1.75
2-Cyanonaphthalene (2-CN)	-2.13 ^h	3.68		1.55
Naphthalene (N)	-2.50 ⁱ	3.97		1.45
Phenanthrene (P)	-2.45 ⁱ	3.58		1.15
Anthracene (A)	-1.96 ⁱ	3.28		1.3
<i>Triplet acceptors</i>				
Chloranil (CA)	+0.02 ⁱ		2.7 ^j	2.7
Benzoquinone	-0.54 ⁱ		2.95 ^j	2.4
Naphthoquinone	-0.60 ⁱ			
Anthraquinone	-0.94 ^k		2.72 ^k	1.8
Benzil	-1.50 ^k		2.36 ^k	0.85
Benzophenone	-2.16 ^k		2.95 ^k	0.8

^a Half wave reduction potential (V) vs. SCE; from Ref. [98], except as noted otherwise.^b Singlet energy (eV) from the 0,0 transition of the fluorescence spectrum; from Ref. [98], except as noted otherwise.^c Triplet energy (eV).^d Excited state reduction potential.^e 48. Saeva, F. D., Olin, G. R. *J. Am. Chem. Soc.* **1980**, 102, 299.^f Arnold, D. R., Maroulis, A. J. *J. Am. Chem. Soc.* **1976**, 98, 5931.^g Park, S.-M. Caldwell, R. A. *J. Electrochem. Soc.* **1977**, 124, 1859.^h McCullough, J. L., Miller, R. C., Fung, D., Wu, W.-S. *J. Am. Chem. Soc.* **1975**, 97, 5942.ⁱ Mann, C. K., Barnes, K. K. *Electrochemical Reactions in Nonaqueous Systems*, Marcel Dekker, Inc., New York, **1970**.^j Kavarnos, G. L., Turro, N. *J. Chem. Rev.* **1986**, 86, 40.^k Gersdorf, L., Mattay, L., Görner, H. *J. Am. Chem. Soc.* **1987**, 109, 1203.

donors (Section 2.2.5) and the radical anions are comparably strong bases. Accordingly, proton transfer in the geminate radical ion pair might produce neutral radicals, and the potential involvement of two or more competing reactions might introduce mechanistic ambiguities. On the other hand, this feature has made it possible to study interesting electron-transfer-proton-transfer sequences.

Electron transfer of cyclopropane systems—the CIDNP method

As mentioned earlier, the cyclopropane radical cation, prepared by γ -radiolysis in rigid matrices, had an ESR spectrum compatible with the trimethylene structure (2A_1) [78, 79]. Irradiation of several methyl-substituted derivatives at 77 K gave rise

to a family of radical cations of the same structure type (type A) [105], which had been identified previously on the basis of chemically induced dynamic nuclear polarization (CIDNP) results [107, 110]. Because of the significance of this method for the study of electron-transfer reactions and for assigning radical cation structures, we briefly discuss the underlying basic principles.

Chemically induced dynamic nuclear polarization (CIDNP) is a nuclear magnetic resonance method based on the observation of transient signals, typically substantially enhanced, in either absorption or emission. These effects are induced as a result of magnetic interactions in radical or radical ion pairs on the nanosecond time scale. This method requires acquisition of an NMR spectrum during (or within a few seconds of) the generation of the radical ion pairs. The CIDNP technique is applied in solution, typically at room temperature, and lends itself to modest time resolution. The first CIDNP effects were reported in 1967, and their potential as a mechanistic tool for radical pair reactions was soon recognized [117, 118]. Nuclear spin polarization effects were discovered in reactions of neutral radicals and experiments in the author's laboratory established that similar effects could also be induced in radical ions [119–121].

The theory underlying this effect depends critically on two selection principles: the nuclear spin-dependence of intersystem crossing in a radical pair, and the electron spin-dependence of the rates of radical pair reactions. The combination of these selection principles causes a 'sorting' of nuclear spin states into different products, formed by geminate recombination (allowed for singlet pairs but spin-forbidden for triplet pairs) or by free-radical ('escape') products (whose formation is electron spin-independent). As a result, geminate reaction products are formed with characteristic non-equilibrium populations of nuclear spin levels, whereas 'escape' products show complementary non-equilibrium spin level populations.

The transitions between levels with non-equilibrium populations will be in the direction towards restoring the normal Boltzmann population; their signal intensities will depend on the extent of non-equilibrium population. The observed effects are optimal for radical pairs with lifetimes in the nanosecond range. On a shorter time-scale, hyperfine induced intersystem crossing is negligible whereas on a longer time-scale the polarization decays owing to spin–lattice relaxation in the radicals.

The quantitative theory of CIDNP enables one to compute the intensity ratios of CIDNP spectra on the basis of reaction and relaxation rates and characteristic parameters of the radical pair (initial spin multiplicity, μ), the individual radicals (electron g factors, hyperfine coupling constants, a), and the products (spin–spin coupling constants, J) [122–126]. Conversely, the patterns of signal directions and intensities observed for different nuclei of a reaction product can be interpreted in terms of the hyperfine coupling constants of the same nuclei in the radical cation intermediate. This feature has proved significant for the assignment of radical cation structures.

In a well designed experiment, the pattern of CIDNP signal directions and intensities observed for a diamagnetic product reveal the relative magnitude and the absolute sign of the hyperfine coupling constants of the corresponding nuclei in the paramagnetic intermediate. The hyperfine coupling constants, in turn, can be interpreted in terms of carbon spin densities and these reveal important structural features of the intermediates. These results often are quite unambiguous, because

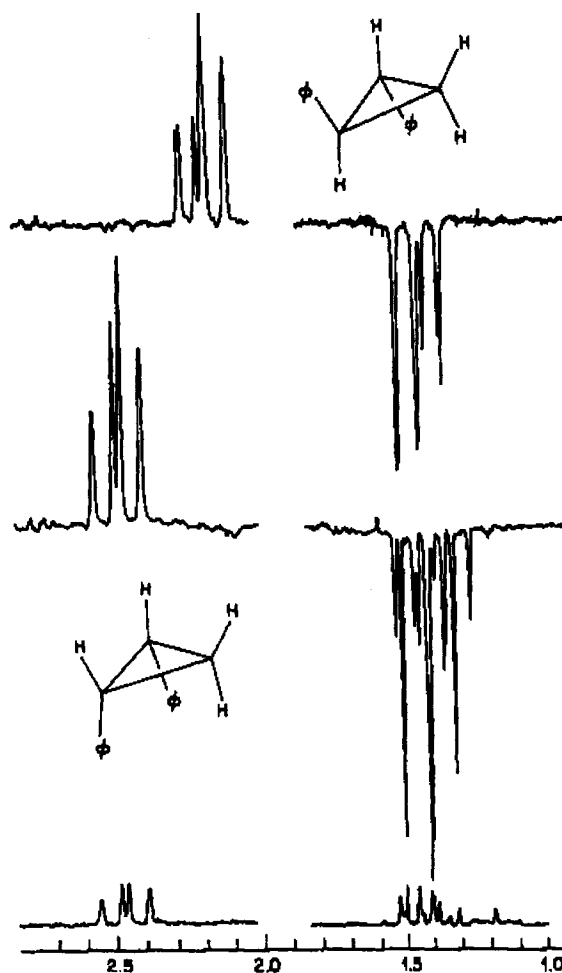
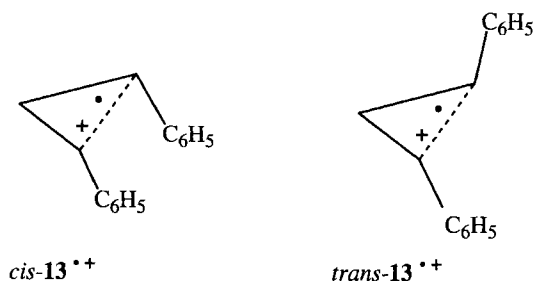


Figure 16. PMR spectra (90 MHz) observed during the irradiation of chloranil in acetonitrile- d_3 solutions containing *trans*- (top) or *cis*-1,2-diphenylcyclopropane (bottom), respectively [107].

NMR chemical shifts are usually well understood, and the identity of the coupled nuclei is clearly established. Combined with PET as a method of radical ion generation, the CIDNP technique has been the key to elucidating mechanistic details of important reactions and provided insight into many short-lived radical cations with unusual structures, many of which had previously eluded any other technique.

The nature of the cyclopropane radical cation was first characterized unambiguously by CIDNP effects of a 1,2-disubstituted derivative. The pattern of benzylic and geminal polarization observed during the reaction of chloranil with *cis*- and *trans*-1,2-diphenylcyclopropane (Figure 16) supported radical ions with spin-density on the benzylic carbons [107].

Strictly, the results do not differentiate a priori between a 'closed' and an 'open' radical cation. The 'closed' structure was assigned because the reaction did not cause geometric isomerization, suggesting that the stereochemistry at the key car-



bonds is preserved in the intermediate. These results establish local minima on the radical cation potential surface but do not eliminate the possibility of the existence of additional minima with different stereochemistry and allow no conclusions concerning the global minimum on the radical ion energy surface.

'Standard' structure types of cyclopropane radical cations

In this context we consider the potential effects of substituents on the structure of the cyclopropane radical cation. For molecules with a pair of degenerate HOMOs suitable substitution might be expected to lift the degeneracy and favor one structure over the other. Qualitative predictions of the favored structure can be based on a frontier (F) MO/perturbational (P) MO approach [110, 127]. The substrates are dissected into molecular fragments and the potential interactions of the component FMOs are considered. According to PMO theory [127] the strength of the fragment perturbation is approximately proportional to $S^2/\Delta E$, where S is the overlap integral between the components and ΔE is the difference between the FMO orbital energies. For the S^2 term, three factors will be of primary importance: the FMO orbital symmetry (where present); the magnitude of the coefficients at the point(s) of union; and the orientation of the fragments relative to each other [110].

For cyclopropane, substituents at a single carbon might most effectively stabilize the anti-symmetrical HOMO, whereas substitution at two carbons is expected stabilize the symmetrical orbital. The radical ions of many derivatives also belong to the general structure type **A**. On the other hand, cyclopropane radical cations with the alternative, anti-symmetrical singly occupied (SO) MO should be of particular interest. The reversal of the ordering of structure types **A** and **B** can be envisaged via three different mechanisms, involving stabilization of structure type **B** by conjugation, homoconjugation, or hyperconjugation.

Because a structure of 2A_1 symmetry was established for the prototype [78], it is hardly surprising that the radical ions of many derivatives also belong to that general structure type. Radical cations of the same structure type as those derived from *cis*- and *trans*-1,2-diphenylcyclopropane were established for numerous cyclopropane derivatives, including 1,2-di-, 1,1,2-tri- and 1,1,2,2-tetramethylcyclopropane (Table 4) [104, 109]. Two of these systems provide a direct comparison between the results of CIDNP and ESR experiments. In both instances the ESR spectra observed by Williams and coworkers after γ -irradiation in frozen solutions [105, 106] contain splitting patterns supporting the presence of spin-density on two car-

Table 4. ^1H Hyperfine coupling patterns constants for radical cations of selected cyclopropane systems.

Radical cation	Calculation	CIDNP	ESR
		No result	a - 12.5 b + 21.0
		No result	a (-) 10.4 b (+) 20.5 c (+) 20.5
		No result	a (-) 11.9 b (+) 21.8 c (+) 21.8
		a - b + c + d +	a (-) 9.8 b (+) 14.5 c (+) 20.6 d (+) 17.9
		a + b +	a (+) 15.0 b (+) 18.7
		a - b +	
		a - b +	
	a (-) 10.5 b (+) 7.9 c (-) 4.0	a - b + c -	a (-) 5.1 b (+) 6.6 c (-) 2.0
	a (-) 10.6 b (+) 9.9 c (+) 12.6	a - b + c +	

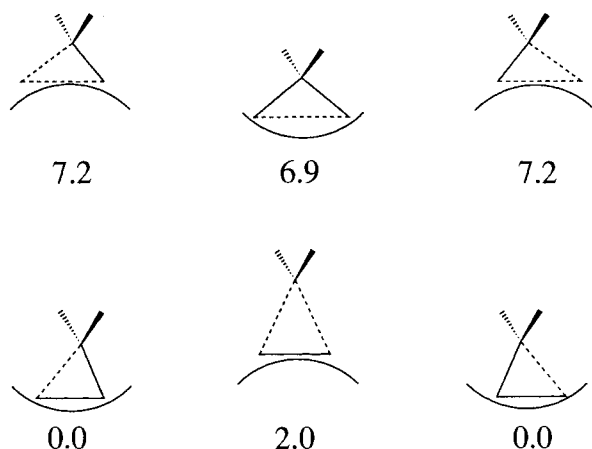


Figure 17. Minima and transition states on the potential energy surface of radical cation states of 1-methylcyclopropane (PMP4/6-311G*//UMP2/6-31G* + Δ ZPE; relative energies in kcal/mol) [103].

bon centers and, thus, fully confirm the structure type (A) assigned on the basis of CIDNP results.

Stabilization by hyperconjugation was probed by ab initio calculations on the radical cations of methyl- and 1,1-dimethylcyclopropane [103]. Two sets of structures reflect the first-order Jahn–Teller distortion of the parent cation from the doubly degenerate $^2E'$ (D_{3h} symmetry) ground state to non-degenerate states 2A_1 and 2B_2 . States of type A (one long and two short ring C–C bonds) are always minima. For methyl and 1,1-dimethyl derivatives, type B structures are the preferred first-order Jahn–Teller type distorted structures. Although their energies lie below the type A structures, the type B structures are, however, transition states, undergoing second-order Jahn–Teller type distortions to unsymmetrical (scalene) structures with one very long C–C bond. These structures represent the absolute minima for 1-methyl- and 1,1-dimethylcyclopropane radical cations (Figure 17) [103]. The ‘scalene’ structures can be viewed as distorted type B structures or as unsymmetrical type A structures with substituents at one ‘terminal’ carbon.

The calculated hyperfine coupling constants (B3LYP/6-31G*//MP2/6-31G*) for the type B transition state and the distorted minimum clearly show that this species must be considered a type A structure. The hyperfine coupling pattern of the lowest-energy minimum ($a_2 = -1.43$ mT; $a_3 = 1.98$ mT) shows a trend similar to the experimental splittings of the *trans*-1,2-dimethylcyclopropane radical cation ($a_{1,2} = -1.19$ mT; $a_3 = 2.18$ mT), whereas the pattern calculated for the transition state ($a_{2,3} = 0.55$ mT) is incompatible with that model (Figure 18). The distorted structure type calculated for the methyl-substituted systems seems to prevail also under other conditions (see below).

Although the results indicated some stabilization for the type B structures, they clearly indicate that hyperconjugation is not sufficient to alter the ‘natural’ preference of cyclopropane radical cations for the type A structure. On the other hand, both conjugation and homoconjugation have been shown to reverse the stabilities

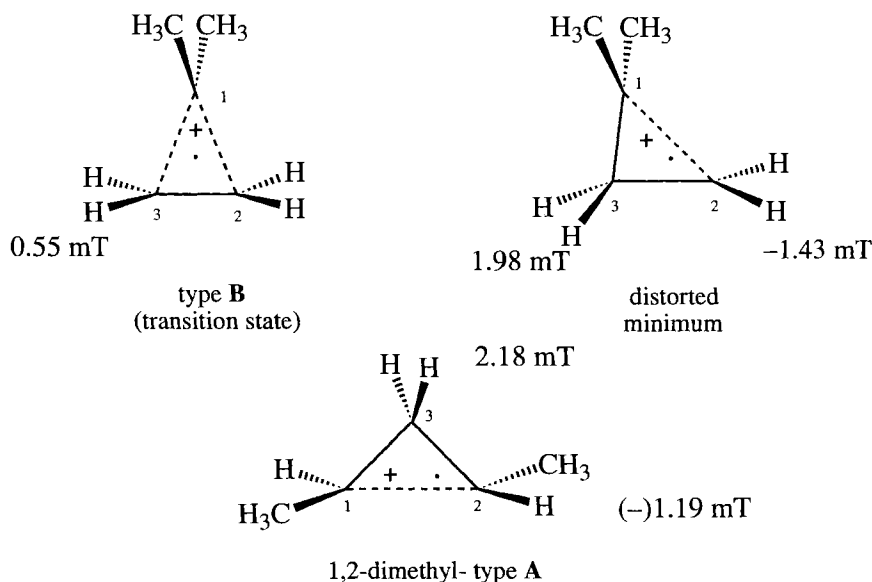
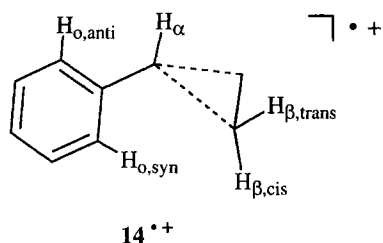


Figure 18. Comparison between the hyperfine coupling constants calculated for the type **B** radical cation (top, left) and the distorted minimum (top, right), respectively, of 1,1-dimethylcyclopropane [31] and the experimental hyperfine coupling constants [105, 106] of 1,2-dimethylcyclopropane (bottom).

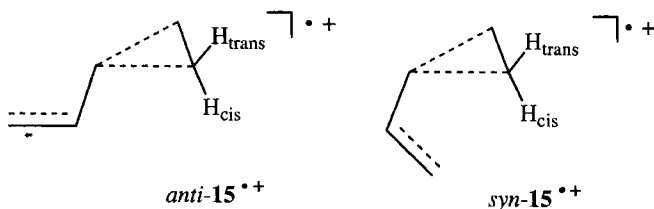
of the 'natural' structure types 2B_2 and 2A_1 . Conjugation with a suitable π -system, either a vinyl [128] or a phenyl group [129, 130], is sufficient to stabilize structures of type **B**, whereas homoconjugation stabilized type **B** radical cations for substrates, such as norcaradiene and derivatives [108, 131] and spiro[cyclopropane-1,9'-fluorene] [110, 132]. These assignments are based on experimental results and born out by ab initio calculations.

The structure of the phenylcyclopropane radical cation, $14^{+\bullet}$, was based on CIDNP effects observed during the electron-transfer reaction from **14** to photo-excited chloranil. The results indicated that the unpaired electron spin was delocalized between the aromatic ring and the benzylic cyclopropane carbon [129]. π,σ -Polarization induces negative hyperfine coupling (hfc) constants in the aromatic *ortho* and *para* protons and in the benzylic cyclopropane protons. The secondary cyclopropane protons had significantly divergent hyperfine coupling constants, because of a pronounced stereoelectronic effect. The strongly polarized secondary protons confirm the presence of spin-density on the benzylic carbon; the emission supports positive hfc's, which arise typically via π,σ -delocalization (hyperconjugation) of spin-density on to the ^1H nuclei. These results support a radical cation, $14^{+\bullet}$, $\text{R} = \text{H}$, in which spin and charge are delocalized between the phenyl ring and the benzylic cyclopropane carbon; two cyclopropane bonds are lengthened and weakened (type **B**). These conclusions are in full accord with the results of ab initio calculations (B3LYP/6-31G*), which delineated the principal structural features and the charge density distribution in the radical cation, $14^{+\bullet}$ [129, 130].



The vinylcyclopropane radical cation, $15^{\bullet+}$, is another radical cation of structure type **B**, which is stabilized by conjugation. Its proposed structure was based exclusively on ab initio calculations (B3LYP/6-31G*) because the electron-transfer photochemistry of this species failed to provide clear-cut CIDNP effects [128]. In this context it is worth noting that product studies cannot, in principle, establish the cyclopropane radical cation structure type. Irrespective of the structure, nucleophilic capture is expected to result in the cleavage of the strained ring.

Calculations using the 6-31G* basis set and employing UB3LYP//UB3LYP and UMP2//UB3LYP methodologies, respectively, indicated the existence of two conformers, *s-anti-1* $^{\bullet+}$ and *s-syn-1* $^{\bullet+}$. Both have structures of type **B**, resembling a π -complex between vinylmethylene and ethene. The calculated bond lengths for the two conformers show similar trends; the allylic cyclopropane bonds are lengthened (+6 %) whereas the bond between the secondary carbons C2–C3 is shortened (–4 %). Also, the distinct difference between the (vinyl) double bond (134.0 pm) and the bond linking the cyclopropane and ethene functions (147.5 pm) is reduced; these bonds are of essentially equal length (139.8); in essence, the array, C β –C α –C1, has been converted to an allyl moiety [128].



The calculated spin densities of the two conformers support the conclusions derived from the bond lengths—most of the unpaired electron density is located on the tertiary cyclopropane carbon (C1) and the terminal vinyl carbon (C β). The general type of spin-density distribution calculated for the two conformers of $15^{\bullet+}$ has precedent in several vinylcyclopropane systems with 'locked' geometries (vide infra) [134, 135].

Perhaps the most interesting mechanism stabilizing radical cations of type **B** involves homoconjugation. The interaction with the butadiene frontier molecular orbital (FMO) can lift the degeneracy of the cyclopropane in-plane e' orbitals (*S*, *A*) and favor the type **B** structure. This principle was shown to stabilize substrates such as norcaradiene and derivatives [110, 131] and, to a lesser extent,

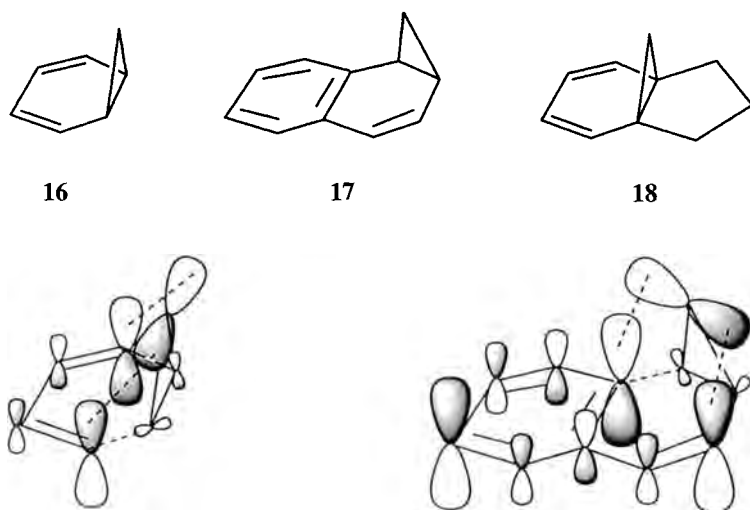


Figure 19. Structures of norcaradiene, **16**, and two derivatives, **17**, **18**, and schematic illustration of homoconjugation between the frontier molecular orbitals of butadiene (bottom left) and styrene (bottom right), respectively, with the anti-symmetrical cyclopropane HOMO.

spiro[cyclopropane-1,9'-fluorene] [110, 132]. The assignments are based on *ab initio* calculations on the parent system (**16**) and two derivatives, on CIDNP results observed for a benzo-annulated system (benzonorcaradiene, **17**), and on the electron-transfer photochemistry of a bridged tricyclic derivative, tricyclo[4.3.1.0^{1,6}]deca-2,4-diene (**18**) in the presence of methanol. This study identified **18** as a unique probe elucidating mechanistic features of the nucleophilic capture of radical cations (Figure 19).

The norcaradiene radical cation, **16**^{•+}, has *C_s* symmetry and a ²A'' electronic ground state. The bond lengths offer limited support for homoconjugation. Although the internal cyclopropane bond of **16**^{•+} (C1–C6 = 153.8 pm) is slightly longer than the two lateral bonds (C1–C7 = C6–C7 = 153.3 pm), it is actually shortened upon ionization (–3.4 pm) while the lateral bonds are lengthened (+2.8 pm). The bonds between the pairs of olefinic carbons (C2–C3 = C4–C5 = 139.5 pm) are only marginally shorter than the intervening bond (C3–C4 = 140.5 pm). However, the delocalization of spin-density to C7 clearly supports the effect of homoconjugation. Although the (UMP2) spin-density at C7 ($\rho_7 = 0.246$) is lower than that at the terminal butadiene carbons, ($\rho_{2,5} = 0.359$), the delocalization of spin and charge on to C7 supports a structure of type **B**. The extent of delocalization depends on the level of perturbation theory; calculations at the UHF level show significantly less delocalization ($\rho_{2,5} = 0.61$, $\rho_7 = 0.231$) than do the UMP2 calculations. The hyperfine coupling pattern also reflects a type **B** structure. Two alkene protons (H2,5) and the geminal cyclopropane protons have significant negative coupling constants ($a_{2,5} = -0.091$ mT; $a_{7\text{syn}} = -0.057$ mT; $a_{7\text{anti}} = -0.063$ mT); sizeable positive cou-

pling constants ($a_{1,6} = 1.36$ mT) are observed for the bridgehead carbons; the alkene protons near the nodal plane have negligible coupling constants ($a_{3,4} = -0.04$ G) [131].

Benzobicyclo[4.1.0]hepta-2,4-diene radical cation, $17^{+\bullet}$ (no symmetry), was optimized at the UHF/6-31G* level of theory. The cyclopropane C–C bonds are subtly different; the lateral bond conjugated with the ethene function (C1–C7, 152.4 pm) is longer, whereas that conjugated with the benzene ring is shorter (C6–C7, 149.1 pm), than the internal bond (C1–C6, 151.3 pm). The bonds linking the strained ring to the styrene moiety are slightly longer (C1–C2, 145.4 pm; C5–C6, 148.5 pm) than those of the styrene function (C2–C3 138.5 pm; C4–C5 143.8 pm; C3–C4 139.9 pm) [131].

The assignment of an antisymmetric cyclopropane SOMO to the radical cation, $17^{+\bullet}$, was based on a comparison of CIDNP effects (Figure 20) with those for *cis*-1,2-diphenylcyclopropane. While the nuclei of the aromatic segments showed identical or very similar polarization, the cyclopropane protons show characteristic differences. This suggests significantly different spin-density distributions for the cyclopropane moieties of the two species and, thus, different structures [108]. The benzonorcaradiene radical cation should owe its structure to the symmetry of the fragment FMOs at the points of union. The styrene HOMO is antisymmetric at the positions of attachment, suggesting preferred interaction with the antisymmetric cyclopropane HOMO (Figure 19).

The calculated carbon spin densities of $17^{+\bullet}$ document the extent of homoconjugation; most of the spin is located on C2 ($\rho_2 = 0.355$), significantly less on C5 and C7 ($\rho_5 = 0.153$, $\rho_7 = 0.149$), whereas the tertiary cyclopropane carbons, C1 and C6 ($\rho_1 = -0.009$, $\rho_6 = -0.007$), have negative spin-density. The calculated hfcs are in qualitative agreement with the CIDNP effects observed during the electron transfer from benzonorcaradiene, **17**, to photo-excited chloranil [108]. The tertiary cyclopropane ^1H nuclei, H1 and H6, have large positive hfcs ($a_1 = 0.93$ mT, $a_6 = 1.06$ mT), whereas the geminal cyclopropane nuclei ($\text{H}_{7\text{s,a}}$), have negative hfcs of moderate magnitude ($a_{7\text{s}} = -0.34$ mT, $a_{7\text{a}} = -0.28$ mT) [131].

Tricyclo[4.3.1.0^{1,6}]deca-2,4-diene radical cation, $18^{+\bullet}$, also has a $^2A''$ electronic ground state. When optimized at the UHF/6-31G* level of theory with imposed C_s symmetry. The C–C bond lengths of the cyclopropane ring are slightly more divergent than are those of $16^{+\bullet}$; the internal bond (C1–C6 = 153.9 pm) is 3 pm longer than the lateral bonds (C1–C10 = C6–C10 = 150.8 pm). Both types of bonds are lengthened upon ionization, perhaps due to the release of strain. The bonds between the olefinic carbons are essentially equal in length (C2–C3 = C4–C5 = 139.3 pm; C3–C4 = 139.1 pm) [131].

The carbon spin-density on the bridge carbon is lower than that of $16^{+\bullet}$ ($\rho_{10} = 0.203$), even considering the lower level of theory, whereas the terminal butadiene carbons have correspondingly higher spin densities ($\rho_{2,5} = 0.383$). The hyperfine coupling pattern of $18^{+\bullet}$ shows minor changes relative to $16^{+\bullet}$: increased coupling constants for the olefinic protons $\text{H}_{2,5} = -0.96$ mT) and decreased coupling constants for the cyclopropane protons ($a_{10\text{syn}} = -0.54$ mT; $a_{10\text{anti}} = -0.48$ mT). These data support a radical cation related to structure type **B**. The extent of homoconjugation, as judged by the extent of delocalization, is less than for $16^{+\bullet}$, possibly

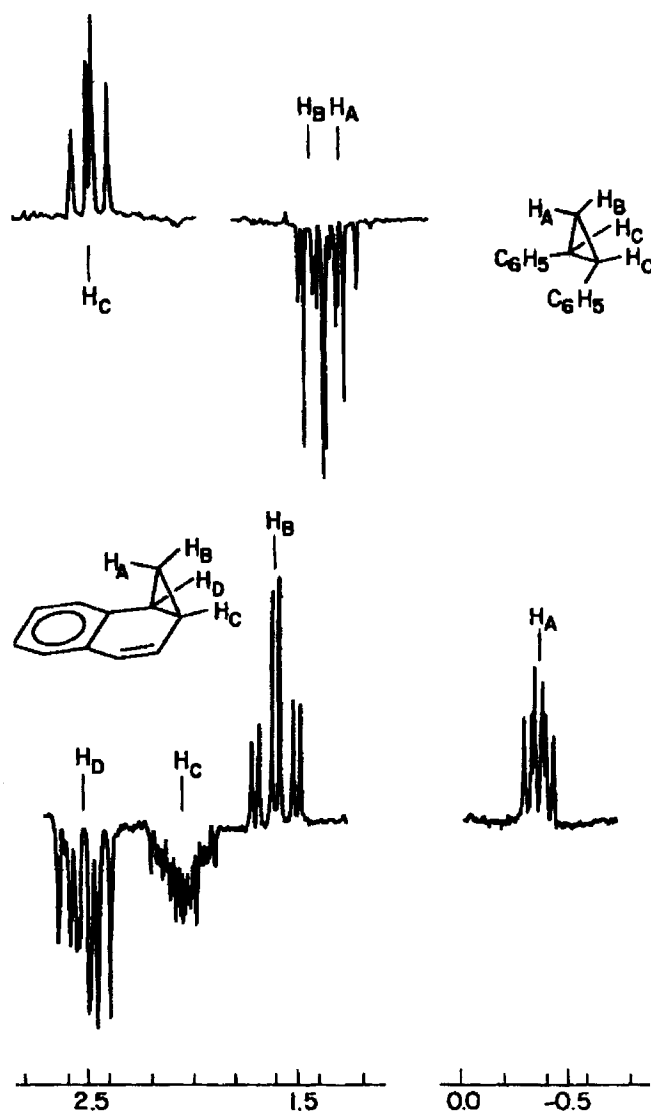
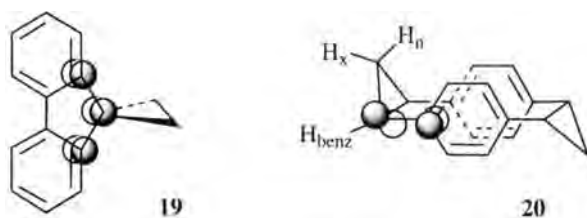


Figure 20. ^1H CIDNP spectra (cyclopropane resonances only) observed during the photo-reaction of chloranil with *cis*-1,2-diphenylcyclopropane (top) and benzonorcaradiene (bottom). The opposite signal directions observed for analogous protons provide evidence that the two radical cations belong to two different structure types [107, 108].

because of strain introduced by the trimethylene bridge. This feature, though crucial for enforcing the norcaradiene structure, might limit the extent of homoconjugation because of steric factors. Still, the calculations predict a significant role of homoconjugation in the radical cations, $16^{\bullet+}$ and $18^{\bullet+}$.

The radical cation of spirofluorene, **19**, is mentioned only in passing. The orientation of the fragments allows only the second highest MO of the biphenyl moiety to interact with a cyclopropane FMO (the *A* HOMO). Thus, the type B structure should be stabilized to a lesser extent. The extent of homoconjugation also is expected to be weak because of a more serious mismatch in orbital energies [110, 127].



The interaction between a cyclopropane group and olefinic or aromatic systems conjugated to it depends on their relative orientation. Although the 3°,3°-cyclopropane bond of benzonorcaradiene (**17**) lies in a plane perpendicular to the aromatic π system, [1:2,9:10]bismethano[2.2]paracyclophane (**20**) features a parallel arrangement of these elements [133]. The photoreaction of this obviously strained compound with chloranil gives rise to CIDNP effects not unlike those observed for *cis*-diphenylcyclopropane (*cis*-**13**). The relative signal intensities of **20** are, however, noticeably distorted (Figure 21). The (secondary) endo proton (1.2 ppm) is more strongly enhanced (indicating a larger hyperfine coupling) than both the *exo* (2.0 ppm) and the benzylic protons.

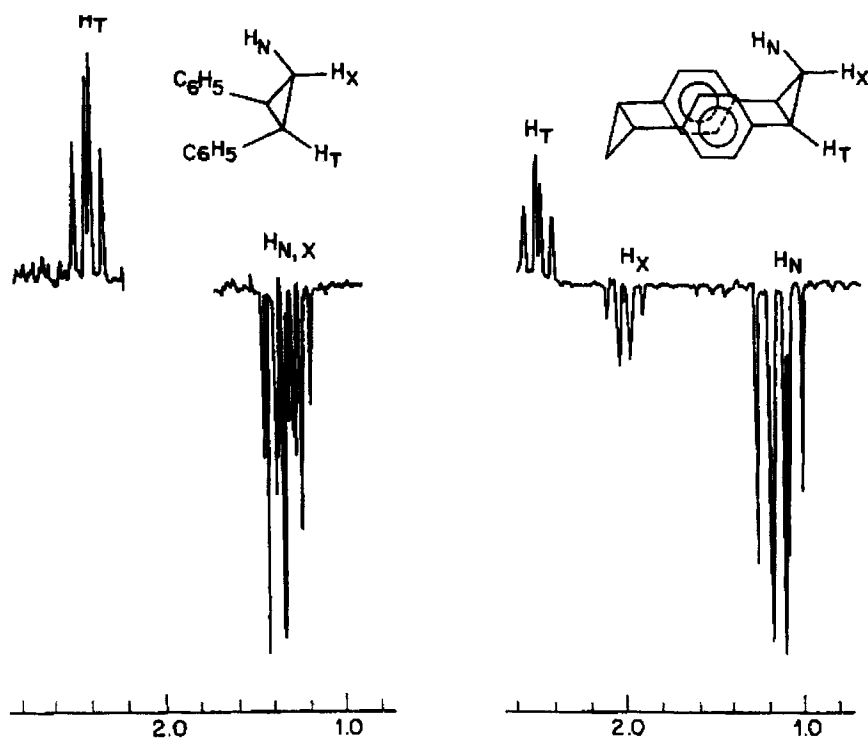


Figure 21. A comparison of the CIDNP effects observed for the cyclopropane protons of *cis*-diphenylcyclopropane (left) and [1:2,9:10]bismethano[2.2]paracyclophane (right) [133].

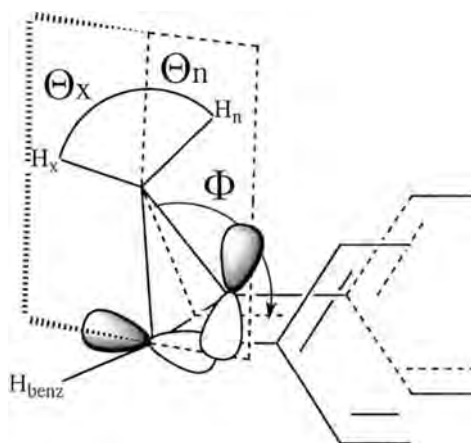


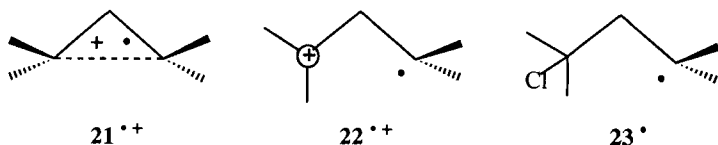
Figure 22. Partial view of [1:2.9:10] bismethano[2.2]paracyclophane showing the angles Φ and Θ discussed in the text.

This finding was interpreted in terms of different dihedral angles, Θ_x and Θ_n , between the singly occupied orbital and the two geminal C–H bonds. Non-identical dihedral angles for the secondary cyclopropane protons can result if the angle, Φ (Figure 22), and the distance between the benzylic cyclopropane carbons is increased in the radical cation relative to the parent hydrocarbon. The endo proton, which in the diamagnetic molecule lies in the shielding cone of the aromatic moieties, has in the radical cation the smaller dihedral angle Θ , with the benzylic ‘ π ’ orbital (Figure 22) and, therefore, the greater hyperfine coupling [133].

The comparably weak enhancement of the benzylic protons and the relatively strong ^{13}C polarization for the benzylic carbons are indicative of a pyramidal benzylic carbon. Although radicals containing pyramidal carbon are reasonably rare, existing examples are derived from strained ring systems [136–139]. For the radical cation $20^{+\bullet}$, the change in the angle, Φ , the stretching of the doubly benzylic bond, and the adoption of a pyramidal structure apparently relieve some of the strain in the carbon skeleton, yet maintain reasonable overlap between the benzylic carbons and the benzene rings [133]. Possibly, the sum of these changes may amount to a ‘ring-opened’ cyclopropane radical cation (*vide infra*).

Electron transfer and ring-opening—trimethylene radical cation

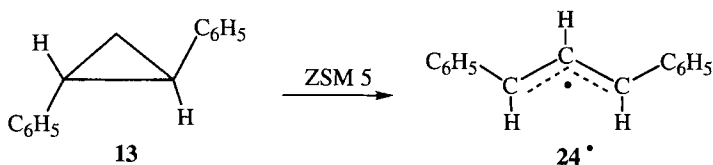
The potential ‘ring-opening’ of cyclopropane radical cations, ‘breaking’ the weakened bond of type A radical cations ($21^{+\bullet}$), has been a subject of both interest and controversy. The ESR spectra of cyclopropane radical cation and its methyl-substituted derivatives decayed at temperatures near 100 K. They were replaced by secondary spectra, in which the protons at one cyclopropane center do not interact with the electron spin. This coupling pattern was interpreted as evidence for a ring-opened trimethylene species ($22^{+\bullet}$) in which one terminal carbon has rotated into an orthogonal orientation [105, 106, 140].



Similar species were postulated to explain the geometric isomerization of 1-aryl-2-vinylcyclopropanes upon reaction with aminium radical cations [141]. As mentioned above, *ab initio* calculations fail to support the existence of this structure type for the parent system and simple derivatives. Another potential argument against the existence of species such as **22^{•+}** lies in its failure to undergo a hydrogen shift, generating the known and stable propene radical cation [142]. Hydrogen shifts have been observed in numerous electron-transfer-induced reactions [143–147], including in matrices at cryogenic temperatures, under the very conditions that give rise to the putative **22^{•+}** [143–146]. These considerations have led several authors to advance alternative explanations. They include structures, such as **23[•]** [99–101, 148], in which a chloride ion has captured the cationic center of either **21^{•+}** or **22^{•+}**. Although interaction of **21^{•+}** or **22^{•+}** with one or more matrix molecules might form a chloronium-substituted free radical or a matrix cluster [149], ESR spectra failed to furnish direct evidence for coupling to the matrix.

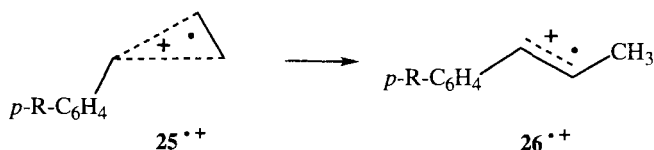
Interestingly, the rearrangement was found to be limited to two matrices, $\text{CFCl}_2\text{CF}_2\text{Cl}$ and $\text{CF}_2\text{ClCF}_2\text{Cl}$, suggesting a major role of the matrix in the conversion. The putative nucleophilic ring opening by chloride ion, generating the β -chloroalkyl radical (**23[•]**), has precedent in many substitution of cyclopropane radical cations in solution (Section 2.4.3). In this instance the matrix might prevent the approach of the ion. Comparison of radical cation structures or reactions in matrices and in solution can, however, be misleading. Matrix forces are responsible for several reactions unprecedented in solution, such as the series of ‘fragmentations’ in zeolites (Section 2.2.7). Matrix forces have been invoked also to account for a ‘reordering’ of electronic states in matrices (Section 2.2.6) or zeolites (Section 2.4.2). In view of these considerations the discrepancy between the postulated structure (**22^{•+}**) and the *ab initio* calculations is unsettling but not irreconcilable.

In this context, we mention two zeolite-induced conversions of cyclopropane derivatives. Incorporation of *trans*-1,2-diphenylcyclopropane (*trans*-**13**) and its 3,3-D₂-isotopomer into the channels of a redox-active pentasil zeolite (Na-ZSM-5) generated *exo,exo*-1,3-diphenylallyl radical (**24[•]**) and its 2-D₁-isotopomer. This conversion is a zeolite-specific reaction; it requires a series of reactions, including oxidation, ring opening, and deprotonation [70].



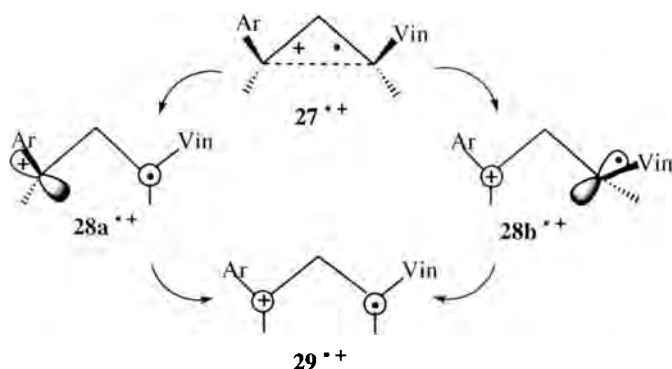
Incorporation of arylcyclopropanes (**25**, R = H, OCH₃) into ZSM-5 also caused a matrix-specific conversion, generating *trans*-propenylbenzene radical cations

($26^{+\bullet}$, $R = H, OCH_3$) [70]. The formation of $26^{+\bullet}$ requires a series of reactions, including oxidation, ring opening, and a hydrogen shift. Interestingly, the 2,2- d_2 -isotopomer of **25** ($R = OCH_3$) gave rise to three different isotopomers of $26^{+\bullet}$ ($R = OCH_3$), containing two, one or no deuterium. This observation requires several competing mechanisms, including one proceeding with two D vs. H exchanges. This reaction also is zeolite-specific.



Ring-opened cyclopropane radical cations have been postulated also to account for the stereochemistry of the aminium radical cation-catalyzed rearrangement of 1-aryl-2-vinylcyclopropanes (**27**) [141]. These systems, of course, contain substituents that might veil the ‘true’ nature of the cyclopropane radical cation by delocalizing spin and charge.

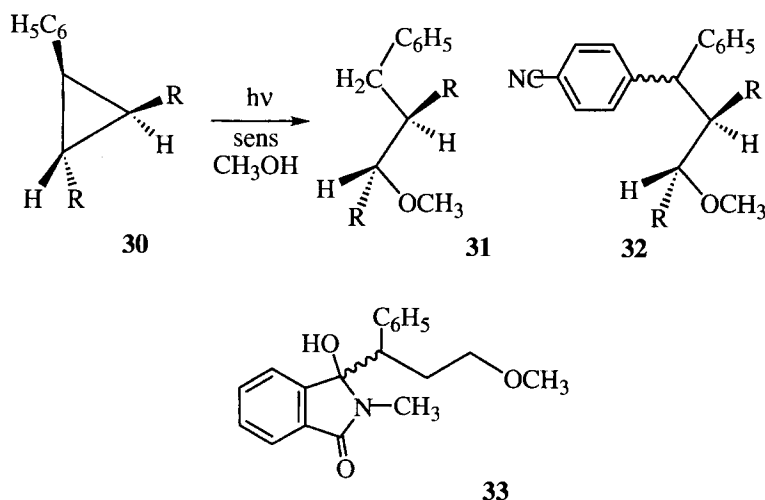
The potential surface of the radical cations derived from **27** might contain several minima separated by low barriers; the ultimate reaction products might afford little information about any one minimum. Even ESR results might not differentiate unambiguously between a planar ring-opened radical cation ($29^{+\bullet}$) and a rapidly equilibrating pair of orthogonal bifunctional intermediates (e.g., $28^{+\bullet}$). Perhaps the most likely explanation involves a pair of isomeric cyclopropane radical cations with one very weak bond, viz., $27^{+\bullet}$, which might enable either or both tertiary carbon atoms to rotate. The bifunctional structures shown below, either orthogonal (e.g. $28^{+\bullet}$) or planar ($29^{+\bullet}$) might signify minima or transition structures.



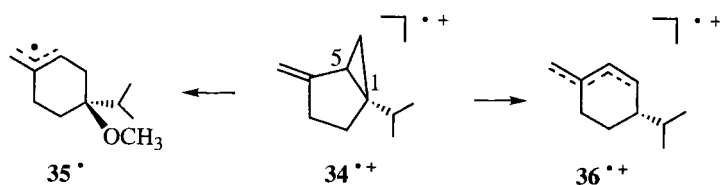
Additional insight into the ‘ring-closed’ or ‘ring-opened’ structure of cyclopropane radical cations can be derived unambiguously from the stereochemical course of their reactions. These reactions are discussed in detail in Section 2.4; here we briefly mention several illuminating examples of cyclopropane radical cation reactivity, chosen solely to illuminate the structure of cyclopropane radical cations.

Various substituted cyclopropanes undergo electron-transfer-induced nucleophilic addition of alcoholic solvents. For example, the electron-transfer reaction of phenylcyclopropane (**30**, $R = H$) with *p*-dicyanobenzene resulted in a ring-opened ether, **31** [150]. This reaction also produced an aromatic substitution product (**32**, $R = H$) formed by coupling with the sensitizer anion [150–152]. A related pair of products (**31**, **33**, $R = H$) was obtained upon photo-induced electron transfer between phenylcyclopropane and *N*-methylphthalimide [153].

More recently, Dinnocenzo and colleagues showed that a 2,3-dimethyl derivative (**30**, $R = CH_3$) and several 1-phenyl- and 1,1-diphenyl-2-alkyl-substituted cyclopropanes are captured with complete inversion of configuration [154, 155]. The observed stereochemistry requires an intermediate radical cation, $30^{+\bullet}$, with the unperturbed stereochemistry of the parent molecule. This result unambiguously rules out a ring-opened cyclopropane radical cation in solution.



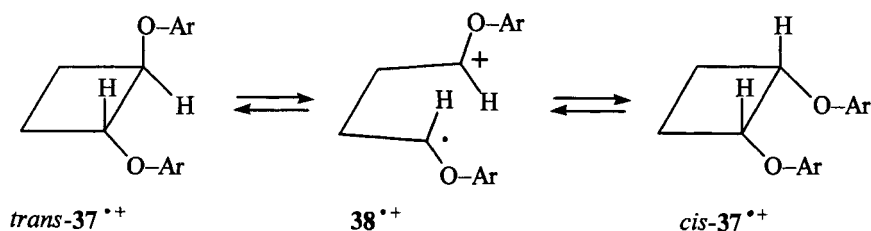
The nature of vinylcyclopropane radical cation was elucidated via the electron-transfer photochemistry of a simple vinylcyclopropane system, in which the two functions are locked in the *anti* configuration, viz. 4-methylene-1-isopropylbicyclo-[3.1.0]hexane (sabinene, **34**) [156]. The electron-transfer reaction of (1*R*, 5*R*)-(+)-**34** with 1,4-dicyanobenzene–phenanthrene in acetonitrile–methanol produced various optically active ring-opened products. The stereochemical relationship between **34** and the products requires that the radical cation, $34^{+\bullet}$, retain the three-dimensional integrity of **34**, i.e., that significant bonding is maintained in the three-membered ring. Any ring-opened radical cation, in which C1 would be planar, is clearly eliminated. Nucleophilic capture of $34^{+\bullet}$ by methanol generated free radical **35** $^{\bullet}$ in stereoselective fashion. In competition with this intermolecular reaction, an intramolecular hydride shift from C6 to C1 produced β -phellandrene radical cation, $36^{+\bullet}$, which is also captured by the nucleophile.



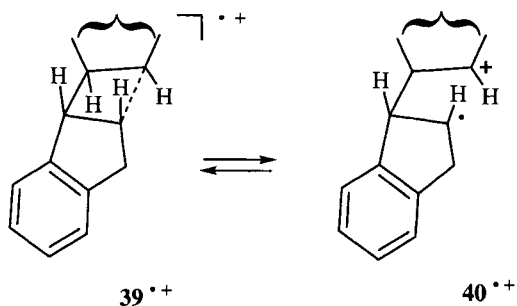
2.3.3 Electron-transfer Reactions of Substituted Cyclobutane Systems

Having discussed the electron-transfer reactions of cyclopropane derivatives in some detail, we only touch briefly on the related reactions of the larger ring systems. Cyclobutane, cyclohexane, and cyclooctane have degenerate HOMOs (Section 2.3.1); thus, their radical cations are Jahn–Teller active. It is reasonable to expect that suitable substitution will lift the degeneracy and favor one radical cation structure over the other. Qualitative predictions of the preferred structure are readily derived.

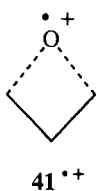
Considering cyclobutane, one might expect that 1,2-disubstituted derivatives favor structure type C, in which the doubly substituted cyclobutane bond is weakened (and lengthened), or a related structure type, in which this bond is actually broken. Ab initio calculations at the QCISD-(T)/6-31G*//UMP2/6-31G* level of theory showed that the radical cation of *trans*-1,2-dimethylcyclobutane has a trapezoidal structure [86]. Although ESR results on simple derivatives are not available, this expectation is born out by several experimental observations.



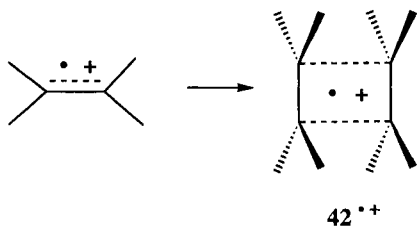
For example, the electron-transfer-induced geometric isomerization of 1,2-diaryloxycyclobutane, **37**, can be rationalized via the bifunctional radical cation, **38**^{•+}, formed by ring opening of a type C radical ion [157]. Similarly, the fragmentation of the *anti*-head-to-head dimer of dimethylindene might involve consecutive cleavage of two cyclobutane bonds in a type C radical ion. Because of the low ionization potential of the aryl substituents (*IP* 9.25 eV) [8], the primary ionization is expected to occur from one of the aryl groups. CIDNP results observed during the dimer cleavage were rationalized in terms of an equilibrium between ring-closed (**39**^{•+}) and ring-open (**40**^{•+}) radical cations [158].



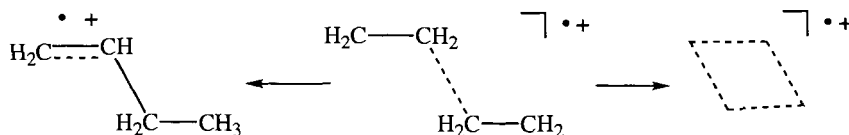
By analogy with substituent effects discussed for the cyclopropane system (Section 2.3.2), one might expect that 1,1-disubstitution might stabilize cyclobutane radical cations of the structure type resembling a kite (type D). As far as we are aware such a structure has not yet been established unambiguously, although the oxetane radical cation (**41**^{•+}) clearly belongs to that structure type. The unpaired electron is localized on the oxygen and the adjacent ¹H nuclei are strongly coupled ($a = 6.6$ mT, $a = 1.1$ mT) [159, 160].



Cyclobutane radical cations can also be formed by addition of ethylene radical cations to a neutral ethylene. For example, vinyl amines [161] and other electron-rich alkenes [162] undergo [1 + 2] cycloadditions, which even might proceed as chain reactions [163]. Fluorescence-detected magnetic resonance effects observed during the pulse radiolysis of anthracene-d₁₀ in the presence of tetramethylethene generated an ESR spectrum compatible with eight equivalent methyl groups; the splitting, $a_d = 0.82$ mT, was approximately one half that of the monomer splitting, $a_m = 17.1$ mT [164–167]. The data were interpreted as evidence for a ‘sandwich’ dimer; higher cluster cations were also invoked [167]. Although the ESR spectrum is compatible with a radical cation with two weakened C–C bonds (type A; **42**^{•+}), they do not rule out other structures.



Ab initio calculations at the QCISD-(T)/6-31G**/UMP2/6-31G* level of theory failed to furnish evidence for the ‘sandwich-type’ π -complex; rather, they support the formation of an ‘*anti*’- π -complex between ethylene and its radical cation, in which the two components are connected by one long (190 pm) bond only. This complex is connected to two different transition states leading to the (rhombic) cyclobutane radical cation or, by 1,3-H-shift, to 1-butene radical cation [167].

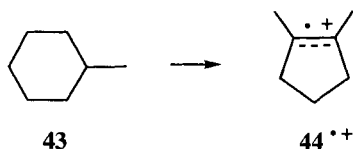


The density functional theory calculations mentioned earlier also modeled the ring-opening of cyclobutane radical cation [87]. This reaction proceeded via a distorted trapezoid transition state with two shorter (142.2, 147.1 pm) and two longer bonds (187.7, 208.4 pm), forming the ‘*anti*’-complex (one long bond; 227.6 pm), similar to that calculated earlier [168].

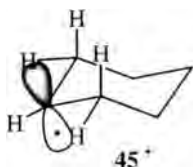
As for derivatives of unstrained ring systems, we mention—in passing—the electron-transfer oxidation of various mono-, di-, or trialkylcyclohexanes, which were studied in significant detail. Interestingly, the radical cations of 1-alkyl and 1,1-dialkyl derivatives have been assigned a SOMO resembling the a_g SOMO of the cyclohexane radical cation [169–171]. A more detailed discussion would exceed the scope of this review.

2.3.4 Electron-transfer Reactions of Cycloalkanes in Zeolites

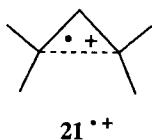
Similar to linear and branched alkanes, cycloalkanes also give rise to radical cations in zeolites, spontaneously or upon γ -radiolysis. This brief discussion of selected examples is intended only to give a flavor of the work being done. Thus, a 13-line radical cation spectrum ($a = 0.17$ mT, $g = 2.003$) obtained upon incorporation of 1-methylcyclohexane, **43**, into zeolites [71] was identified as 1,2-dimethylcyclopentene radical cation, **44** $^{\bullet+}$ (two sets of protons with hyperfine coupling constants in the ratio of ca 2:1; $a = 1.67$ mT, 2 CH_3 ; $a = 3.42$ mT, 4H) [72]. The formation of **44** $^{\bullet+}$ was rationalized by protonation of the 3° carbon of **43**, followed by loss of H_2 . Loss of a proton from a rearranged carbocation may generate **44**, which is oxidized to **44** $^{\bullet+}$ by a Lewis site.



γ -Irradiation of cyclohexane on Na-ZSM-5 at 77 K generated the EPR spectrum of cyclohexyl free radical, **45** \cdot [172]. The clear difference between two sets of β -protons ($a = 2.2$ mT, $1H_{\alpha}$; $a = 4.0$ mT, $2H_{ax}$; $a = 0.5$ mT, $2H_{eq}$) indicates that at 77 K **45** \cdot is conformationally rigid. A cyclohexane radical cation (Section 2.3.1) is a probable intermediate, but no evidence for this species was observed. The formation of **45** \cdot was ascribed to 'spontaneous' proton transfer to the zeolite matrix, in contrast with previously discussed deprotonations (Section 2.2.5), which proceeded by ion-molecule reactions.



γ -Radiolysis of 1,1,2,2-tetramethylcyclopropane, **21**, in zeolite Na-Y produced an EPR spectrum that was simulated with the known hyperfine coupling parameters of radical cation, **21** \cdot^+ , with one lengthened cyclopropane bond (Section 2.3.4; $a = 1.87$ mT, $2H$; $a = 1.49$ mT, $12H$) [173]. In contrast with *trans*-1,2-diphenylcyclopropane (*trans*-**13**), which is spontaneously oxidized and undergoes ring opening and deprotonation (below), **45** \cdot^+ remains unchanged. Apparently, its bulky shape isolates it from other molecules as well as precluding migration in the channels.



2.4 Electron-transfer Reactions of Bicyclic Systems

Many bicycloalkanes are as unreactive as alkanes or unstrained cycloalkanes. They have very high pK_a values and their low electron affinities make them poor electron acceptors. The ionization potentials of unstrained bicycloalkanes are somewhat lower than those of unstrained cycloalkanes—bicyclo[2.2.2]octane (*IP* 9.47 eV), bicyclo[4.3.0]nonane (*IP* 9.46 eV), or bicyclo[4.4.0]decane (*IP* 9.32 eV) lie below the 9.75–9.90 eV range characteristic of cycloalkanes [5]. As a result, they are somewhat easier to oxidize in solution or in solid matrices. Strained bicycloalkanes have even lower ionization potentials (bicyclo[1.1.0]butane, *IP* 8.7 eV); the ring strain

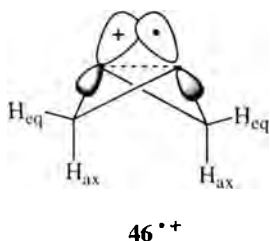
present in these systems provides an additional driving force for their oxidation, making them significantly better electron donors. As a result, they readily undergo photo-induced electron transfer to excited electron acceptors in solution. All bicycloalkanes are readily ionized upon electron or He_α impact in the gas phase. Because of the difference in reactivity, we will discuss strained bicycloalkanes separately from those with little or no strain.

2.4.1 Electron Transfer of Strained Bicyclic Systems

Bicyclic ring systems containing three or four-membered rings have special bonding forces, which are reflected in their unusual chemistry. Their electron-transfer reactions have been studied in the gas, liquid, and solid phases, and the structure and reactivity of their radical cations have been the target of intense scrutiny.

Bicyclobutane radical cations

The unique bonding in bicyclobutane, **46**, and its unusual chemistry resulted in early interest in its radical cation. The structure and reactivity of the parent radical cation and of various derivatives have been studied by ESR–ENDOR spectroscopy and CIDNP effects, by identification of representative reaction products, and by MNDO and ab initio calculations. The structure of the bicyclobutane radical cation was characterized by ESR–ENDOR spectroscopy [174–176]. The ESR spectrum contained a triplet (7.7 mT) of quintets (1.14 mT). These results were interpreted in terms of a radical cation, **46** $^{\bullet+}$, in which the bridgehead carbons bear spin-density and the transannular bond is lengthened. Given this spin-density distribution, the large hyperfine coupling was assigned to the axial protons (H_{ax}); the smaller quintet splitting suggests that the remaining two pairs of protons have identical hyperfine couplings. The bridgehead protons have negative coupling constants, because they are adjacent to centers of major spin-density, whereas the axial and equatorial protons (H_{eq}) must have positive hyperfine couplings, as a result of ' π, σ -delocalization'. The large difference between axial and equatorial hyperfine coupling indicates a non-planar, puckered geometry for the radical cation. No evidence for interconversion is apparent up to 160 K; this finding requires an inversion barrier of at least 12 kJ mol $^{-1}$.



MNDO calculations [174, 175] identified the highest occupied MOs (Figure 23). The key feature of the HOMO is a bonding contribution to the transannular link-

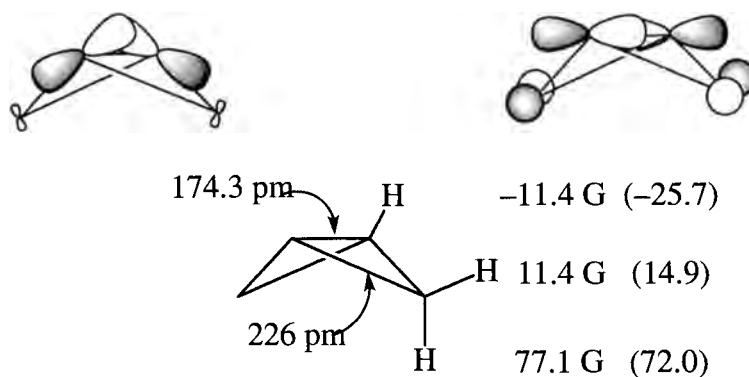


Figure 23. Schematic representation of two high lying MOs for bicyclobutane (top) and structure parameters of the bicyclobutane radical cation.

age. Removal of an electron from this HOMO yields radical cation, $46^{+\bullet}$, with a lengthened transannular bond (178.6 pm, MNDO; 174.3 pm, B3LYP/6-31G*//MP2/6-31G*) and an increased flap angle (132° , MNDO; 133.6° , B3LYP/6-31G*//MP2/6-31G*; Figure 23). Coupling constants calculated at different levels of theory are summarized in Table 5.

The photoreactions of electron acceptors with several bridged bicyclobutane systems, e.g., tricyclo[4.1.0.0^{2,7}]heptane, $47^{+\bullet}$, give rise to CIDNP effects supporting negative hfcs for H1 and H7 and positive hfcs for H2 and H6 and for H3,3' and H5,5'. These results would place electron spin-density at C1 and C7, in agreement with the involvement of the A_1 type HOMO (Figure 23) [77, 177]. The axial 'flag-pole' ^1H nuclei of $46^{+\bullet}$ are replaced in $47^{+\bullet}$ by the trimethylene bridge. This structure type has been confirmed by CIDNP results for several derivatives [177, 178].

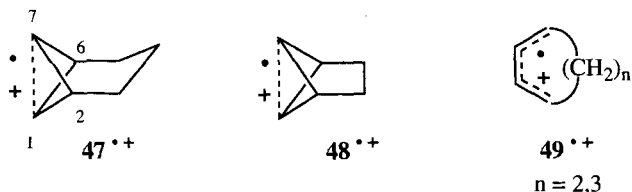
Although radical cation $47^{+\bullet}$ is persistent in solution on the nanosecond time-scale, both $47^{+\bullet}$ and dihydrobenzvalene radical cation, $48^{+\bullet}$, the lower homolog

Table 5. Isotropic hyperfine coupling constants (Gauss) of the bicyclo[1.1.0]butane radical cation.

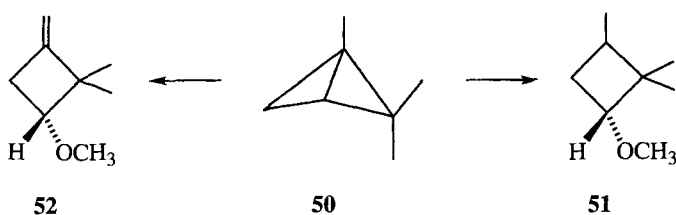
Nucleus	Calculation method			Experiment ^a
	B3LYP	MP2	MP2/B3LYP	
H _{1,3}	-10.88	-27.04	-11.6	-11.4
H _{2,4ax}	79.83	76.35	79.28	77.1
H _{2,4eq}	12.98	13.76	11.65	11.4

^a ESR/ENDOR [174–176].

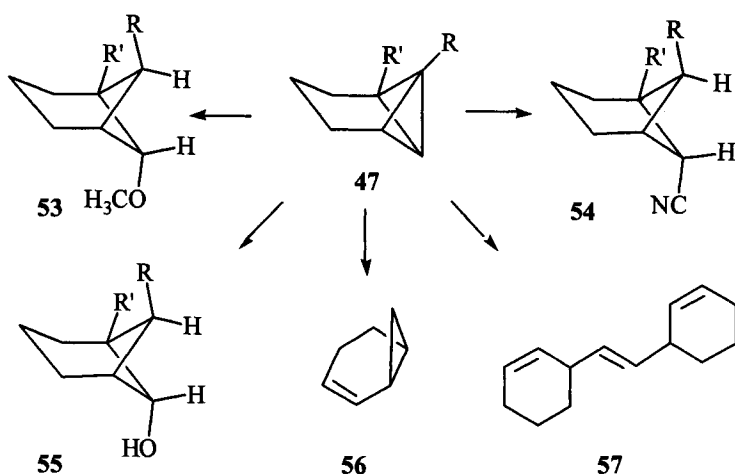
with a dimethylene bridge, undergo ring opening in cryogenic matrices, forming the radical cations of cycloheptadiene and cyclohexadiene, respectively ($49^{+\bullet}$; $n = 2, 3$). The identity of the product radical cations was established unambiguously by ENDOR, which gives particularly rich information about the cycloalkadiene radical cations [175, 176]. The formation of $49^{+\bullet}$ in cryogenic matrices stands in interesting contrast to the rearrangements of $47^{+\bullet}$ and of a benzolog of a dehydro derivative in solution (*vide infra*).



The electron-transfer-induced chemistry of bicyclobutane systems offer a rich variety of reactions. Irradiation of naphthalene in the presence of **46** resulted in rapid fluorescence quenching without rearrangement. In contrast, irradiation with either 1-cyanonaphthalene or 9,10-dicyanoanthracene in solutions containing derivatives of **46** resulted in product formation. The product distribution obtained under electron-transfer conditions is compatible with radical cations of structure type $46^{+\bullet}$, which is firmly established by ESR and CIDNP results. Nucleophilic capture of the 1,2,2-trimethyl derivative, $50^{+\bullet}$, led to cleavage of the transannular bond. The initial capture is followed by net addition, producing **51**, or dehydrogenation, yielding **52** [179].

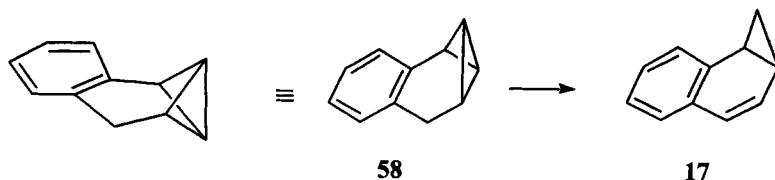


The most thoroughly studied bicyclobutane system is a bridged derivative, tricyclo[4.1.0.0^{2,7}]heptane (Moore's hydrocarbon, **47**), which has revealed many facets of radical cation reactivity. Nucleophilic solvents (CH_3OH , H_2O) or ionic nucleophiles (CN^-) capture $47^{+\bullet}$, leading to products formally derived by addition across the transannular bond (**53**, **54**, **55**). Significantly, each product is derived by back-side attack, as indicated clearly for the monomethyl derivative (**54**, **55**, $R = CH_3$) [180]. In the absence of nucleophiles, a (dimeric) rearrangement product (**57**) was obtained (Scheme 2) [180, 181].



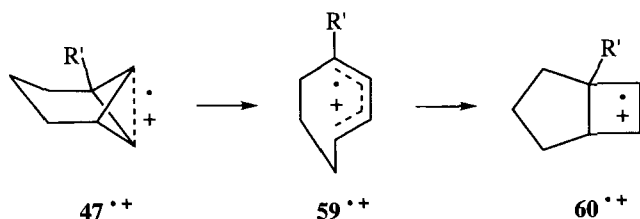
Scheme 2.

The bridged bicyclobutane, **47**, and the benzolog, **58**, of a dehydro derivative undergo an interesting rearrangement to norcarene systems; these conversions require a 1,3-hydrogen (hydride) migration or their intermolecular equivalent [177, 178]. The rearrangement products, **56** and **17** are well known and their NMR features are unmistakable. These results establish a striking difference between the rearrangements in cryogenic matrices [175, 176] and in solution [177, 178].

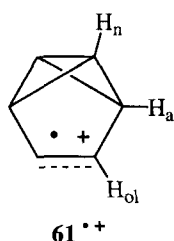


Two tricycloheptane derivatives carrying a bulky substituent in the 2-position [(**47**), $R' = -CH_2-Si(CH_3)_3$, $1-CH_3-cyclo-C_3H_4-$] undergo yet another electron-transfer-induced rearrangement to bicyclo[3.2.0]hept-6-enes, whereas other similarly substituted derivatives [(**47**), $R' = -C(CH_3)_3$, $-Si(CH_3)_3$] gave the unexceptional methanol adducts only [182, 183]. The rearrangement was ascribed originally to a complex mechanism, involving four consecutive radical cations. We have proposed that this reorganization might be interpreted, by analogy with the conversion of the neutral parent molecule [184], as a conrotatory ring-opening, generating $59^{+\bullet}$, followed by conrotatory ring-closure, yielding $60^{+\bullet}$ [185, 186]. Alternatively, the key intermediate $59^{+\bullet}$ might be trapped by electron-return, generating *cis,trans*-cycloheptadiene, a structure type which has been invoked as an intermediate in several bicyclobutane-to-cyclobutene rearrangements [187]. Although the revised explanation was accepted by the original authors [188], it remains to be established whether orbital symmetry plays a definite role in this radical cation reaction. Altogether, **47**

and derivatives undergo at least three types of rearrangement. Although the identity of the products is established beyond doubt, the mechanistic details remain to be established.



Benzvalene (**61**) is a tricyclic benzene isomer containing a bicyclobutane ring system bridged by an ethene moiety. The radical cation of this system is accessible by photo-induced electron transfer in solution or by radiolysis in cryogenic matrices. A CIDNP study indicated negative hfc's for the olefinic protons (H_{ol}), strong positive hfc's for the (non-allylic) bridgehead protons (H_n), and negligible hfc's for the allylic bridgehead protons (H_a) [189]. These results suggest that benzvalene radical cation has spin and charge essentially localized in the olefinic moiety, although with efficient spin delocalization on to the non-allylic bridgehead 1H nuclei. The strong positive hfc's of the non-allylic bridgehead protons are evidence for a strong hyperconjugative interaction between these protons and the π -orbitals bearing the unpaired spin. These assignments were confirmed by the ESR spectrum of **61^{•+}**, a triplet (+2.79 mT; H_{ol}) of triplets (−0.835 mT; H_n). A third triplet splitting, from the allylic β -protons (−0.158 mT; H_n), is revealed in the ENDOR spectrum [190]. The small negative value of the coupling constant reflects the position of the β -protons in the nodal plane of the π -system. This allows only spin polarization (inefficient for β - 1H -nuclei) as a coupling mechanism.



The above data are consistent with a radical cation corresponding to the HOMO established by photoelectron spectroscopy and simple theoretical models [191–193]. This assignment is also supported by theoretical calculations [31, 193]. Ab initio molecular orbital calculations at the MP2/6-31G* level support two low-lying radical cationic states of **61^{•+}**, 2B_1 and 2A_1 in C_{2v} symmetry [31]. The hyperfine coupling constants calculated for the 2B_1 state (B3LYP/6-31G**//MP2/6-31G*; Figure 24) are fully compatible with the observed CIDNP and ESR/ENDOR results. In contrast, those for the 2A_1 state (a single point calculation at the MP2/6-31G**//UHF/6-31G* level) show irreconcilable differences with the experimental findings. Cal-

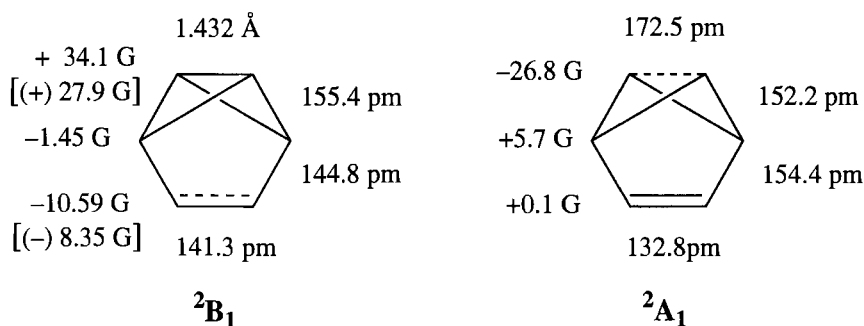
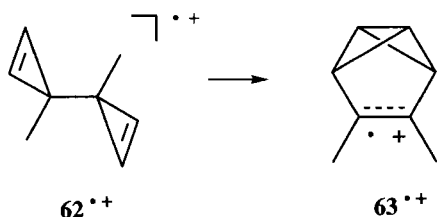


Figure 24. Two structure types of benzvalene radical cation with spin and charge located mainly in the ethylene (2B_1 ; left) or the bicyclobutane function (2A_1 ; right). Hyperfine coupling constants calculated for the 2B_1 structure (B3LYP/6-31G*//MP2/6-31G*) agree well with the experimental values (in brackets) and signs; in contrast, the 2A_1 structure (MP2/6-31G*//UHF/6-31G*) shows irreconcilable differences.

culations at the UMP2/6-31G* level in general show excellent agreement for the positive hyperfine coupling constants but overestimate the negative ones significantly. Clearly, the 2B_1 state is the ground state of $61^{+\bullet}$; the bicyclobutane moiety is a ‘pendant’ group. Although spin-density is efficiently delocalized on to the γ - ${}^1\text{H}$ nuclei, no spin-density is found in the γ -carbons, and the transannular C–C bond is slightly shortened relative to the parent molecule.

In this context, we mention the formation of a derivative of **61** by rearrangement of 3,3'-dimethylbicyclopropenyl (**62**). The electron-transfer chemistry of bicyclopropenyl was of interest, because its radical cation might be an intermediate in the rearrangement of prismane (vide infra), and also as a potential adduct between cyclopropenium cation and cyclopropenyl radical. For reasons of practicality the 3,3'-dimethyl-derivative, **62**, was chosen for study because it is not subject to prototropic rearrangements.

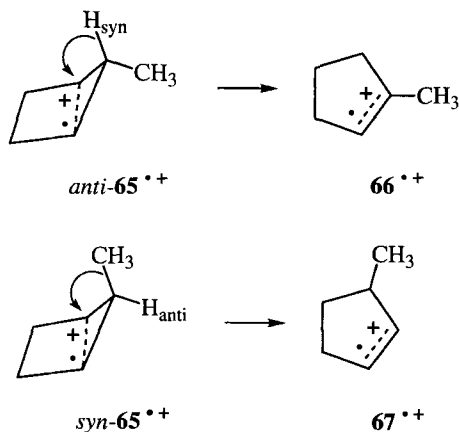


CIDNP results indicate that the radical cation, **62** $^{\bullet+}$, is exceedingly short-lived and undergoes selective rearrangement to one dimethylbenzvalene radical cation (**63** $^{\bullet+}$). This species was identified by its unmistakable chemical shift and polarization pattern. Because the CIDNP effects reflect the spin-density distribution of **63** $^{\bullet+}$, any intermediate(s) preceding it cannot have lifetimes exceeding (fractions of) nanoseconds [194]. The interesting mechanistic challenge posed by this rearrangement exceeds the scope of this review.

Bicyclopentane radical cation

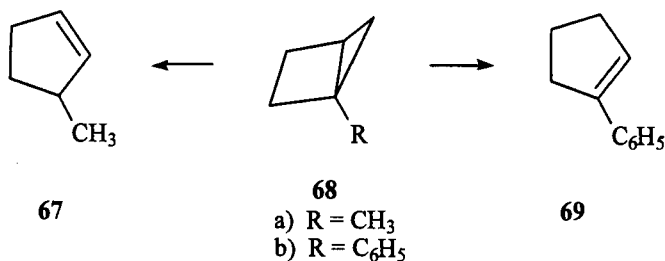
The highly strained bicyclo[2.1.0]pentane, **64**, undergoes electron transfer readily in solution and in cryogenic matrices. Electron transfer to radiolytically generated holes in CF_3CCl_3 generated an ESR spectrum with several strongly coupled nuclei, $a_1 = 4.49$ mT (1H), $a_2 = 3.35$ mT (2H), $a_3 = 1.17$ mT (2H). These data, especially the single strongly coupled proton, suggest a puckered conformation for the resulting radical cation, **64**^{•+} [195, 196]. This assignment is unlikely to be compatible with planar radical centers at the bridgehead carbons. Ab initio calculations indicate that the transannular bond of **64**^{•+}, similar to numerous cyclopropane systems, remains bonding and that the bridgehead carbons are still pyramidal [31]. Upon annealing the sample above 90 K, **64**^{•+} rearranges to cyclopentene radical cation [195], a conversion previously believed to be spontaneous [196].

Additional support for the puckered structure of **64**^{•+} comes from the interesting stereochemistry of the hydrogen or methyl migration in *syn*- and *anti*-5-methyl-**64**; the radical cation of *anti*-**65**^{•+} rearranged to 1-methylcyclopentene radical cation, **66**^{•+}, via a H-shift of the strongly coupled 'flagpole' *syn*-5-hydrogen [145]. In contrast, *syn*-**65**^{•+} generated 3-methylcyclopentene, **67**, via a methyl shift, under identical conditions.



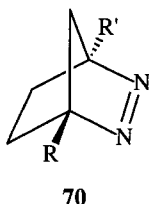
Derivatives of **64** with a single bridgehead substituent rearranged with significant regioselectivity. Thus, the 1-methyl derivative, **68a**, yielded **67** exclusively, whereas the 1-phenyl derivative, **68b**, gave mainly 1-phenylcyclopentene, **69**. Radiolysis in cryogenic matrices failed to provide any evidence for the primary radical cations, **68**^{•+}; only the ESR spectra of the cyclopentene radical cations were observed. In these systems, the rearrangement of the bicyclobutane radical cations may, indeed, be spontaneous [197].

These rearrangements have been probed by CASSCF calculations [198]. They show that the rearrangements have two components, bond breaking and atom or group migration. Although these are discussed as two separate steps, there is only



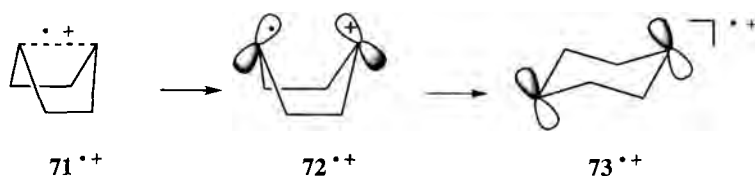
one minimum after the rate-determining transition state. In this respect, the potential surface of bicyclopentane radical cation is similar to that of cyclopropane radical cation, which also failed to show a minimum after the rate-determining transition state [148]. In view of this analogy, one might consider the rearrangements of *anti*- $\text{65}^{\bullet+}$ to $\text{66}^{\bullet+}$ and of *syn*- $\text{65}^{\bullet+}$ to $\text{67}^{\bullet+}$ as non-synchronous 1,3-sigmatropic shifts. All experimental results are fully compatible with this proposed assignment.

Radical cations of derivatives of $\text{64}^{\bullet+}$ are accessible also by irradiation of azobicycloalkanes, **70**. For a detailed description of the rich chemistry of **64** and its derivatives, and of a large family of azobicyclo[2.2.1]alkanes the reader is referred to a recent review [199].

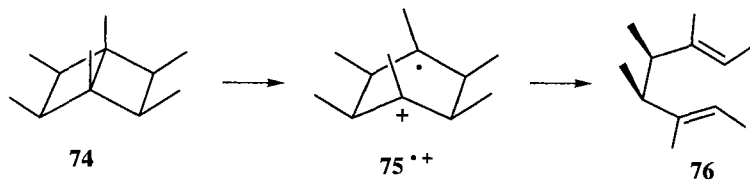


Bicyclo[2.2.0]hexane

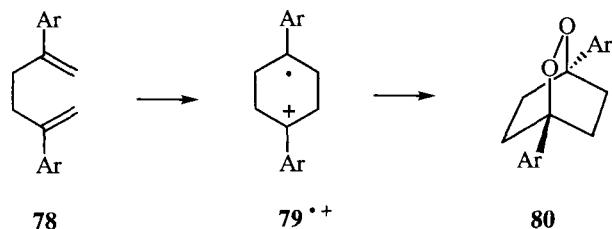
Although less strained than bicyclobutane (**46**) and bicyclopentane (**64**), bicyclo[2.2.0]hexane, **71**, undergoes electron transfer not only in cryogenic matrices but also in solution. Electron transfer from this strained ring system to holes generated in halocarbon matrices, CFCl_3 or CF_3CCl_3 , gave rise to an ESR spectrum ($g = 2.0026$; $a = 1.2 \text{ mT}$), indicating the presence of six equivalent nuclei. This spectrum was identified as that of the ring-opened chair conformer of cyclohexane-1,4-diyl radical cation, $\text{73}^{\bullet+}$, a species in which the unpaired spin is delocalized between two 2p-orbitals at C1 and C4; two α -protons and four axial β -protons strongly interact with the unpaired spin [145]. No evidence was obtained for either the bicyclo[2.2.0]hexane radical cation, $\text{71}^{\bullet+}$, or the boat conformer of cyclohexane-1,4-diyl radical cation, $\text{72}^{\bullet+}$, which is the necessary intermediate, however fleeting, in the ring opening of $\text{71}^{\bullet+}$. At temperatures above 90 K, the spectrum of $\text{73}^{\bullet+}$ is replaced by that of cyclohexene radical cation, a conversion readily explained by a 1,3-H shift of an axial hydrogen.



Some chemical evidence for the existence of a boat conformer was obtained in the electron-transfer reaction of hexamethylbicyclo[2.2.0]hexane, **74**. This reaction formed the *erythro*-(*E,E*)-diene, **76**, along with lower yields of hexamethylcyclohexene formed by hydrogen migration [200]. These results are compatible with the initial generation of the 1,4-diy radical cation, **75**^{•+}, which is partitioned between stereospecific ring opening, yielding **76**, and hydrogen migration, generating hexamethylcyclohexene. The cleavage of **75**^{•+} should be favored by the repulsive interaction between the four all-*cis* methyl groups. Of course, these results provide only indirect evidence for the boat conformer, **75**^{•+}.



The 1,4-diy species, **73**^{•+}, is obtained also upon electron transfer from 1,5-cyclohexadiene, **77**, both in cryogenic matrices [143] and in solution [201]. Solution experiments provided chemical evidence for the cyclohexane-1,4-diy structure type in an elegant study of the electron-transfer-initiated photochemistry of 2,5-diphenylhexa-1,5-diene, **78**, and derivatives in the presence of molecular oxygen [201–203]. The intermediate 1,4-cyclohexanediyls, **79**^{•+}, were intercepted by O₂; the stereochemistry of the *endo*-peroxide products, **80**, showed that the initial cycloaddition occurred in the same stereospecific manner established for the thermal rearrangement of the neutral parent [204].



The formation of **79**^{•+} could be viewed as a stepwise Cope rearrangement, which is ‘arrested’ after the first (ring-closing) step. Radical cations of different hexadiene systems constitute an interesting family of intermediates, related to the potential mechanistic extremes of the Cope rearrangement. Possible pathways include an associative mechanism (addition precedes cleavage), a dissociative mechanism (cleav-

age precedes addition) and a concerted mechanism (addition and cleavage proceed in coordinated fashion). Radical cations corresponding to the three mechanistic extremes have been characterized, illustrating remarkable differences between the potential surfaces of radical cations and neutral precursors. On the precursor potential surface, states of intermediate geometry are saddle points (transition structures), whereas they are pronounced minima on the radical cation potential surface. In essence, the parent molecules undergo a concerted Cope rearrangement via a transition structure, whereas the radical cations undergo cycloaddition or cleavage reactions, which are 'arrested' at intermediate geometries [205–214].

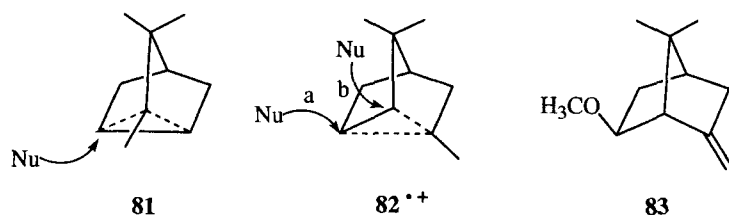
It is an interesting question whether intermediates of type $79^{+\bullet}$ cleave to hexa-1,5-diene radical cations, i.e., whether they complete the radical cation Cope rearrangement. The hydrogen shift in cryogenic matrices [143] efficiently competes (and suppresses) any Cope rearrangement. On the other hand, the photoinduced electron-transfer reaction of **78** in polar solvents results in exchange of a deuterium label between the terminal olefinic and the allylic positions. These results are compatible with a cycloreversion [201]. Recent results suggest that the second, ring-opening step does not involve the radical cation, $79^{+\bullet}$, but occurs in a biradical, $79^{\bullet\bullet}$, generated by triplet recombination (Section 2.4.4) [202, 203].

Bicyclo[*n*.1.0]alkane systems

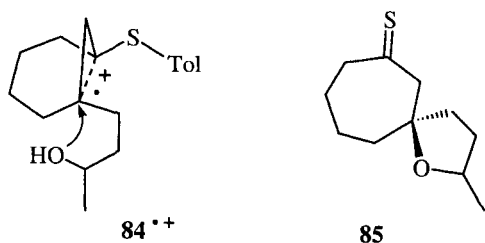
Although bicyclo[3.1.0]hexane and bicyclo[4.1.0]heptane are modestly efficient electron donors, the main value of these ring systems lies in the rigid framework they offer for the elucidation of the stereochemical course of radical cation reactions. We will mention several vinylcyclopropane systems and several tricyclic cyclopropane derivatives.

The tricyclanes, **81** and **82**, readily undergo electron transfer in solution to sensitizers in either the excited singlet [215] or triplet states [216]. The resulting radical cations undergo interesting ring-opening substitution reactions in the presence of nucleophiles. For $81^{+\bullet}$, the attack occurred exclusively at the tertiary, rather than quaternary, carbon [215]. The chiral isomer, **82**, has two 3° – 4° bonds, either of which might be the site of spin and charge, possibly in an equilibrium. The attack of the nucleophile is less hindered at the carbon further removed from the (neopentyl type) dimethyl-substituted bridge (approach a). The isolated product, **83**, is optically active, and formed by backside attack on the less hindered carbon [216]. These results show that the nucleophilic substitution at the cyclopropane one-electron bond is subject to 'conventional' steric hindrance and does not proceed with 'inverse' steric effects [154].

An interesting electron-transfer reaction was observed for a bicyclo[4.1.0]heptane



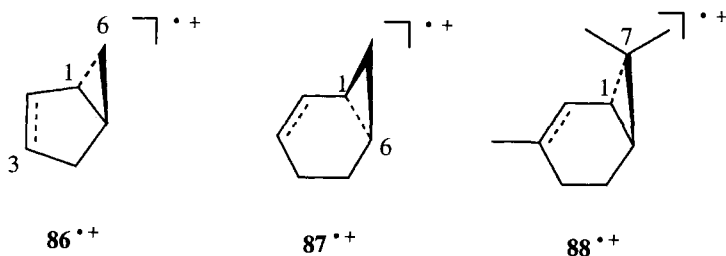
system, **84**, bearing a (3-hydroxybutyl) substituent and a *p*-tolylthio moiety in the 1- and 6-positions, respectively. The compound readily undergoes electron transfer and the resulting radical cation, **84**^{•+}, generates the spiro product **85** by regiospecific intramolecular nucleophilic capture [217]. This attack corresponds to a backside 'substitution' of an intramolecular leaving group.



The CIDNP method was used to probe the hyperfine coupling patterns and structures of several rigid vinylcyclopropane radical cations, in which the two functionalities are locked in either the *syn*- (**86–88**) or the *anti*- (**35**) configuration. Spin polarization effects observed during electron-transfer reactions of these systems suggest significantly different structure types, in which either the internal cyclopropane bond or a lateral one is involved in delocalizing spin and charge [218]. In view of the fixed orientations of the vinyl group relative to the cyclopropane moiety and the different substitution patterns in these substrates, these findings elucidate the electronic and stereochemical requirements for conjugation between the two functionalities. They probe the significance of such factors as orbital overlap and charge stabilization in the radical cations and the release of ring strain in their formation or in their reactions. Three structure types were considered for the radical cations: the well-documented structure with one lengthened C–C bond (type **A**), the structure with two lengthened bonds (type **B**), and the ring-opened bifunctional structure.

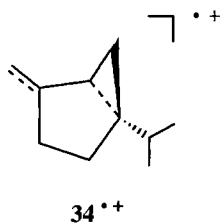
The effects observed for bicyclo[3.1.0]hex-2-ene, **86**, were particularly clear-cut, because the ¹H spectrum is fully resolved [218]. The polarization pattern supported a species with spin-density on C3 and C6, indicating the delocalization of spin and charge into the lateral cyclopropane bond. The bicyclohexene system has limited mobility, enabling more significant orbital overlap of the lateral cyclopropane bond with the alkene p-orbitals (**86**^{•+}). The participation of the lateral bicyclohexene bond is supported by ab initio calculations, carried to the MP2/6-31G* level of theory. The lateral cyclopropane bond is lengthened (C1–C6 = 1.748 Å), and carbons C3 and C6 carry prominent spin densities, whereas lower spin densities were found at C2 and C1 [220].

CIDNP effects observed for norcarene [147, 178] supported a radical cation, **87**^{•+}, which spin and charge are delocalized between the olefinic group and the Walsh orbital of the (more highly substituted) internal cyclopropane bond. The bicycloheptene system, **87**^{•+}, appears to be more flexible than **86**^{•+}; either the internal or the lateral cyclopropane bond can align with the alkene p-orbitals. Delocalization of spin and charge into the more highly substituted bond is preferred.



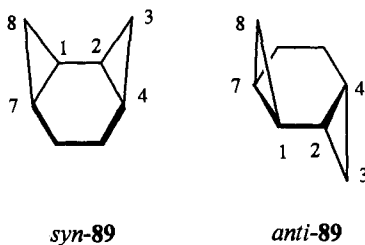
The spin polarization effects upon electron transfer from carene suggested a radical cation structure, **88^{•+}**, in which spin and charge are delocalized between the olefinic group and the Walsh orbital of the adjacent lateral cyclopropane bond. The change in structure (**87^{•+}** compared with **88^{•+}**), caused by the geminal methyl groups at C7, reflects stabilization of the radical cation as a result of hyperconjugative interaction with the methyl groups. For both **87^{•+}** and **88^{•+}**, the more highly substituted cyclopropane bonds are involved in delocalizing spin and charge.

4-Methylene-1-isopropylbicyclo[3.1.0]hexane (sabinene, **34**) contains an alkene and a cyclopropane function locked in the *anti* orientation. CIDNP effects for **34** support a radical cation, in which the electron spin is delocalized between the olefinic π -system and the internal cyclopropane bond. The results are compatible with a vinylcyclopropane radical cation, **34^{•+}**, with one weakened cyclopropane bond, which has retained the steric integrity of the parent molecule [219].



Systems containing two adjacent cyclopropane rings

Some tri- and tetracyclic alkanes contain two cyclopropane moieties locked into a fixed orientation. These arrangements might give rise to interesting stereoelectronic effects in the interaction between the cyclopropane rings. For example, CIDNP effects during electron-transfer reactions of *syn*- and *anti*-tricyclo[5.1.0.0^{2,4}]octane (*syn*-, *anti*-**89**) indicate significantly different structures for their radical cations.



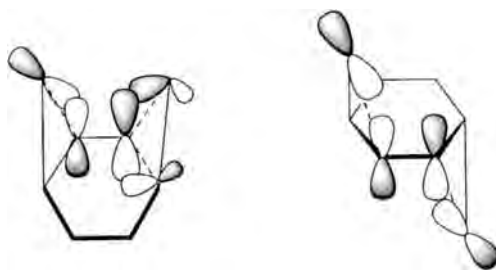


Figure 25. Schematic representation of cyclopropane MOs combining to form the SOMOs of *syn*- (left) and *anti*-tricyclo [5.1.0.0^{2,4}]octane (right) radical cations.

The polarization pattern for *anti*-**89** fits a structure, *anti*-**89**^{•+}, in which spin and charge are localized in the lateral bonds (C1–C8, C2–C3; cf., Figure 25). The less substituted lateral bonds are involved because the orientation of the cyclopropane rings enables overlap between the Walsh orbitals of two lateral cyclopropane bonds [220]. Ab initio calculations (B3LYP/6-31G*/MP2/6-31G*) support this assignment. The carbons of the lateral cyclopropane bonds, C1,2 and C3,8, bear most of the spin-density ($\rho_{1,2} = 0.192$; $\rho_{3,8} = 0.322$) and the 3° cyclopropane protons (H4,7) show large positive hyperfine couplings ($a = 2.0$ mT). The geminal protons, H3,8s and H3,8a ($a_s = -0.72$ mT; $a_a = -0.05$ mT) have significantly different hyperfine coupling constants. The structure suggested for *anti*-**89**^{•+} has precedent in that of **86**^{•+}.

The CIDNP spectrum of *syn*-**89** supported a quite different, although not obvious, structure. Ab initio calculations indicated a structure with dissimilar cyclopropane fragments and 12 distinct ¹H nuclei. A lengthened internal bond (C1–C7) and spin densities $\rho_1 = 0.2$ and $\rho_7 = 0.31$ support a type **A** structure for one cyclopropane ring whereas lengthened C2–C3 and C2–C4 bonds and spin densities $\rho_2 = 0.24$, $\rho_3 = 0.15$, and $\rho_4 = 0.17$ suggest a type **B** structure for the second cyclopropane ring (Figure 25). The barrier between the structure shown and its mirror image is very low so rapid equilibrium between two equivalent structures is probable.

No discussion of cyclopropane radical cations would be complete without reference to the quadricyclane radical cation, **90**^{•+}, and its valence isomer, the norbornadiene radical cation, **91**^{•+}. These valence isomers have attracted considerable attention; one features two rigidly arranged adjacent cyclopropane rings, whereas the other contains two ethene π systems uniquely suited to the probing of through-space interactions [221–225]. In addition, the potential energy surface of these radical cations poses the interesting question of whether there are two discrete minima or a single minimum, accessible upon oxidation of either parent. Although other methods had failed to provide evidence for more than one intermediate [225], the CIDNP technique furnished clear-cut evidence for the existence of two distinct species with characteristic spin-density distributions [226, 227]. This result is compatible with molecular orbital considerations, which suggest the antisymmetric combination of two ethene π orbitals or cyclopropane Walsh orbitals as respective HOMOs of the two parent molecules (Figure 26). The radical ions have different state symmetries and their SOMOs have different orbital symmetries.

The structures of these ions (Table 6) rest on detailed CIDNP spectra delineating the hyperfine patterns of both ions [226, 227], ab initio calculations on both ions

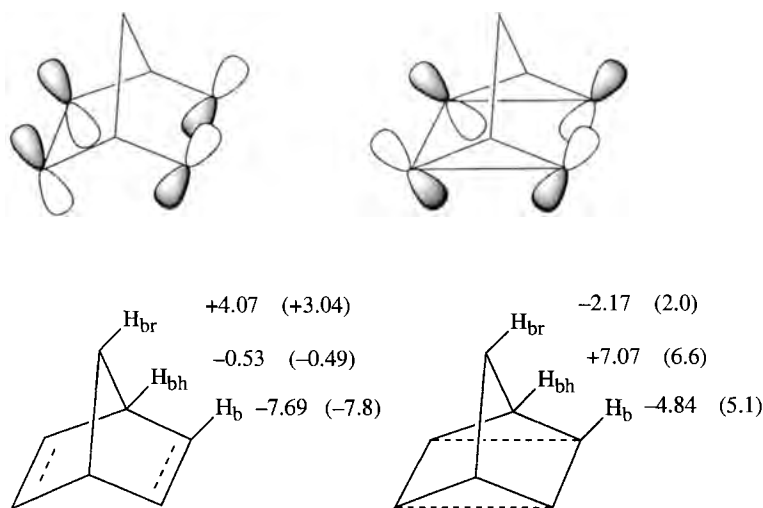


Figure 26. Schematic representation of SOMOs of bicyclo[2.2.1]heptadiene (**91**) and quadricyclane (**90**) and calculated hyperfine coupling constants (Gauss; B3LYP/6-31G*/MP2/6-31G*) [31]. Experimental values [230, 231] are given in parentheses.

[31, 228], and ESR and ENDOR data for norbornadiene [229, 230] and quadricyclane radical cations [231]. Early calculations at the UMP2/6-31G* level [228] showed excellent agreement for the positive hyperfine coupling constants but overestimated the negative ones significantly. More recent calculations, using the MP2 structure and calculating spin densities and hyperfine coupling constants with density functional methods (B3LYP/6-31G*/UMP2/6-31G*), produce plausible values for both positive and negative hyperfine interactions [31]. The CIDNP results indicate the absolute signs and relative magnitude of the hyperfine coupling constants; comparison with the calculated values (Table 6) shows satisfactory agreement [228].

Table 6. Hyperfine coupling constants (Gauss) of bicyclo[2.2.1]heptadiene and quadricyclane radical cations.

Species	Quadricyclane			Norbornadiene			
	CIDNP ^a	Calc ^b	ESR ^c	CIDNP ^a	Calc ^b	ESR ^d	ESR ^e
H_{ol}	-1	-4.84	-5.1	-1	-7.69	-7.8	8
H_{bh}	+1	+7.07	+6.6	-vs	-0.53	-0.49	
H_b	-m	-2.17	-2.0	+s	+4.07	+3.04	3.3

^a According to [226, 228]; l = large, m = medium, s = small, vs = very small.

^b B3LYP/6-31G*/MP2/6-31G* [31].

^c According to [231].

^d ESR/ENDOR [230].

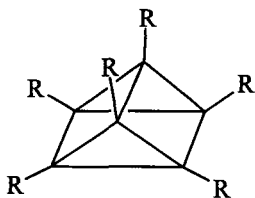
^e According to [229].

The calculations indicate that each radical cation is related uniquely to the geometry of one of the precursors.

For both species the unpaired spin-density resides on four equivalent carbons; ^1H nuclei attached to these centers (H_{ol}) have sizeable hfc's, because of the familiar π, σ spin polarization (cf. Figure 1a). The CIDNP effects of the bridgehead (β) protons (H_{bh}) indicate major differences—a sizeable positive hfc of $\mathbf{90}^{+\cdot}$ can be ascribed to hyperconjugation (π, σ spin delocalization; cf. Figure 1b); in contrast only very weak and negative hyperfine coupling constants were observed for $\mathbf{91}^{+\cdot}$. Because the β protons of $\mathbf{91}^{+\cdot}$ lie in the nodal plane of its SOMO, the hyperconjugative interaction is inefficient; the observed sign of the β protons was, therefore ascribed to 'residual' π, σ polarization [230]. This type of interaction is usually obscured by the typically much stronger hyperconjugative interaction.

The CIDNP effects for the protons of the methylene bridge (H_b) again are quite different, suggesting a sizeable positive hyperfine coupling for $\mathbf{91}^{+\cdot}$ and an even larger negative one for $\mathbf{90}^{+\cdot}$. The positive sign for the γ hyperfine coupling of $\mathbf{91}^{+\cdot}$ can be ascribed reasonably to a 'long-range' π, σ spin delocalization which is aided by an approximate W arrangement of the γ C–H bond relative to the p-orbitals at the olefinic carbons. The bridge (γ) protons of $\mathbf{90}^{+\cdot}$ lie in the nodal plane of the SOMO, rendering the π, σ spin delocalization mechanism inefficient. The relatively large negative hyperfine coupling indicated by the CIDNP results might suggest a σ, σ polarization mechanism operating between the bridgehead (β) and bridge (γ) protons. The dihedral angle ($\text{H}-\text{C}\beta-\text{C}\gamma-\text{H} \approx 60^\circ$) is compatible with a sizeable interaction. This interesting assignment was confirmed independently by an ESR study [231].

Another system with two adjacent cyclopropane rings is prismane, **92**, the highly strained quadricyclic isomer of benzene first considered by Ladenburg [232]. Its radical cation has proved elusive. Even hexamethylprismane, **93**, is rapidly rearranged by chloranil in polar solvents at room temperature. CIDNP experiments provided tentative evidence for the fleeting existence of $\mathbf{93}^{+\cdot}$ during the electron-transfer reaction of **93** with anthraquinone. The prismane polarization is very weak; apparently, only a small fraction of $\mathbf{93}^{+\cdot}$ reverts back to **93**. The predominant reaction is ring opening to hexamethyl-Dewar-benzene, **94** [233]. In essence, **94** is related to **93** as **91** is related to **90**. Because of the high symmetry of **93**, the CIDNP results do not offer clues about the structure of the intermediate; the polarization observed for **94** implicates a radical cation in which spin and charge is located on four equivalent carbons.



92, R = H

93, R = CH₃

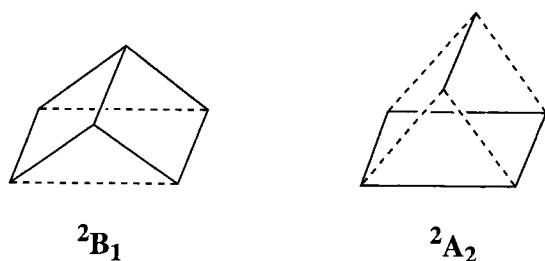


Figure 27. Schematic representation of two radical cation structures derived from prismane.

Ab initio calculations for 92^{++} support the existence of 93^{++} and help to delineate its structure. The highest occupied molecular orbital in prismane is e'' , which has significant bonding character in the cyclopropane bonds and antibonding character in the transannular bonds connecting them. The next lower orbital (e') has bonding character mainly in the three transannular bonds. Removal of an electron from the e'' orbital gives rise to a ${}^2E''$ state which undergoes Jahn–Teller distortion, yielding a 2A_2 and a 2B_1 state (in C_{2v} symmetry).

Calculations (MP2/6-31 G) identified the 2B_1 state as lowest in energy. Two of its cyclopropane bonds are lengthened to 1.73 Å whereas the transannular bonds are shortened to 1.48 Å (Figure 27). These changes reflect the bonding pattern in the e'' orbital. The 2A_2 state lies close in energy to the 2B_1 state; four equivalent cyclopropane bonds are stretched to 1.63 Å and one transannular bond is shortened to 1.46 Å. This state has an imaginary b_1 frequency that converts it to the 2B_1 state through C_s pathways. In essence, the 2A_2 state is a transition state in the pseudorotation interconverting two equivalent 2B_1 states [233].

The lowest state of prismane (2B_1) radical cation lies 16 kcal mol^{−1} above the 2B_2 state of the Dewar benzene radical cation (at the MP2/6-31G* level); the energy difference is considerably less than that between the ground states of the corresponding neutral systems (37 kcal mol^{−1}) [234]. The ground electronic states of prismane and Dewar benzene ions do not correlate; their interconversion is forbidden from both state-symmetry and orbital-symmetry considerations. Nevertheless, the CIDNP experiments indicate that the actual barrier is quite small [233].

The prismane system exemplifies several characteristics of strained-ring radical cations, including the low barrier to isomerization and the fact that its ion apparently has less strain energy than the parent molecule. Additional investigations of 92^{++} or even 93^{++} will be difficult, because of its kinetic instability and its high symmetry (one might expect a 13-line ESR spectrum showing an unexceptional coupling constant near 1.0 mT),

2.4.2 Electron Transfer of Unstrained Bicyclic Systems

In contrast with the highly strained bicyclic hydrocarbons containing three- and four-membered rings, the radical cations of bicyclic hydrocarbons containing five-membered or larger rings undergo electron transfer only reluctantly. As for simple

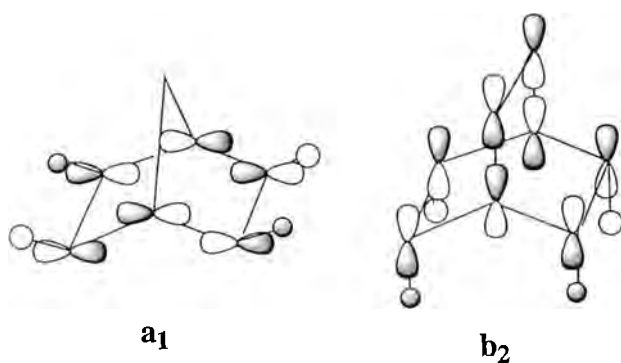
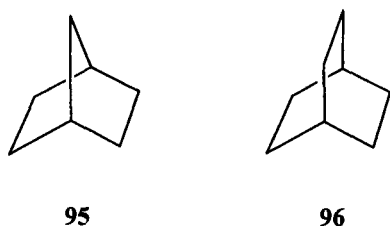


Figure 28. Schematic representation of SOMOs for bicyclo[2.2.1]heptane, **95**, and bicyclo[2.2.2]octane, **96**.

alkanes or cycloalkanes and their derivatives, electron transfer can be achieved in halogen-containing matrices upon radiolysis. Few systems are selected here; they were chosen to give a flavor of the research that has been performed. Among the species studied we mention bicyclo[2.2.1]heptane, **95**, and bicyclo[2.2.2]octane, **96**. Radiolysis of **95** generated the corresponding radical cation, **95**^{•+}. The ESR spectrum contained a five-line pattern, $a_{\text{H}} = 6.5$ mT, indicating the presence of four equivalent strongly coupled protons. The spectrum was interpreted in terms of a structure in which the unpaired electron spin is delocalized over the four *exo*-C-H bonds (Figure 28) [229, 235].

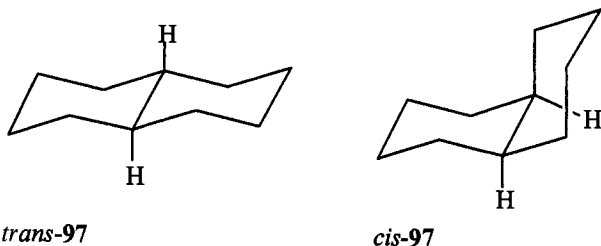


Radiolysis of **96** resulted in an interesting, temperature-dependent spectrum. At 4 K, the species is Jahn–Teller-active and exhibits a static distortion from D_{3h} to C_{2v} symmetry. In contrast to the bicyclo[2.2.1]heptane radical cation, the SOMO of **96**^{•+} involves four *endo*-C-H bonds, $a_{\text{H}} = 3.8$ mT. At 77 K in perfluorocyclohexane or Freon-113, the radical cation is dynamically averaged, with splitting from 12 equivalent protons [235].

We note that the simple symmetrical structures might be an over-simplified or idealized view of the structures of **95**^{•+}, at least. More recent detailed investigations in other matrices and using line-shape analysis furnished evidence for less symmetrical species with several modes of distortion. For details, the reader is referred to a recent detailed description [236].

Two bicycloalkane isomers, *cis*- and *trans*-bicyclo[4.4.0]decane (decalin; *cis*-, *trans*-**97**) have been the focus of investigation by both radiolysis [237] and photo-

lysis [238]. Radiolysis of *cis*-bicyclo[4.4.0]decane also gave rise to a five-line spectrum with $a_{\text{H}} = 5.0$ mT. Most of the spin-density is confined to the central C–C bond [237, 238]; the four protons in *trans* positions are strongly coupled [239]. Interestingly, significant matrix dependence was observed for the hyperfine pattern of the *trans* radical cation (*trans*-97 $^{\bullet+}$) in halocarbon matrices [239]. Radiolysis of *cis*- and *trans*-97 in several synthetic zeolites also gave rise to significantly different ESR spectra. Depending on the nature of the zeolite host and the temperature, the hyperfine splitting of the resulting spectra showed variations of a magnitude that supported the stabilization of two different structure types ('electronic states') for both *cis*- and *trans*-97 $^{\bullet+}$ [240]. In some zeolites a single structure was observed whereas in others both structures were found.



For *cis*-97 $^{\bullet+}$, the authors discussed two radical cation structures, one corresponding to the 2A_1 state ($a = 4.95$ mT, 4H, in silicalite, 45 K), the other corresponding to the 2A_2 state ($a = 2.8$ mT, 4H, in silicalite, 95 K). Calculations predict the 2A_2 state to be higher in energy. For *trans*-97 $^{\bullet+}$, they assigned radical cation structures corresponding to a (lower-energy) 2A_g state, ($a = 5.05$ mT, in silicalite) and a higher-energy 2B_g state ($a = 2.85$ mT, in Na–Y), respectively. The spectra contain five-line patterns, because of coupling with four equatorial protons, either those at the α -carbons (adjacent to the transannular bond; 2A_1 , 2A_g), or those at the β -carbons, one C–C bond further removed (2A_2 , 2B_g) [240]. Even more unusual is the interpretation of a nine-line spectrum ($a = 3.0$ mT) of *cis*-97 $^{\bullet+}$ in offretite, which was interpreted in terms of a fast equilibrium between structures corresponding to the 2A_1 and 2A_2 states, a most interesting assignment.

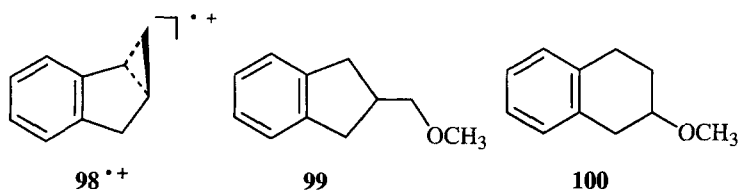
2.4.3 Electron-transfer Chemistry of Bicyclic and Higher Ring Systems

Many radical cations derived from cyclopropane (or cyclobutane) systems undergo bond formation with nucleophiles, typically neutralizing the positive charge and generating addition products via free-radical intermediates [140, 147]. In one sense, these reactions are akin to the well known nucleophilic capture of carbocations, which is the second step of nucleophilic substitution via an S_N1 mechanism. The capture of cyclopropane radical cations has the special feature that an sp^2 -hybridized carbon center serves as an (intramolecular) leaving group, which changes the reaction, in essence, to a second-order substitution. Whereas the S_N1 reaction involves two electrons and an empty p-orbital and the S_N2 reaction occurs with redistribution of four electrons, the related radical cation reaction involves three electrons.

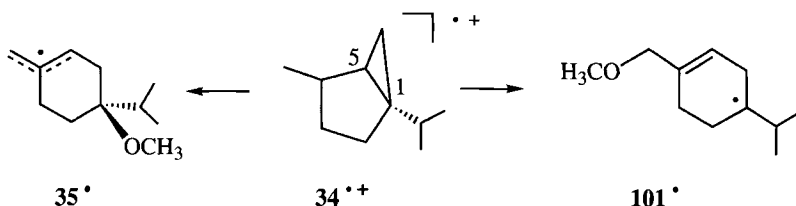
The high regio- and stereoselectivity in the nucleophilic capture of the 'one-electron bonds' of 30^{*+} and 34^{*+} (above) was interpreted as significant because it indicated that the radical cations had retained the three-dimensional integrity of the parent molecules. Clearly, a significant degree of bonding is maintained in the three-membered ring. These results also established the second-order nature of nucleophilic capture. Further, because the substitution reaction occurred even at cyclopropane sites carrying bulky alkyl groups [154, 155], an early transition state was indicated for the nucleophilic substitution–ring opening on cyclopropane radical cations.

In this section, we consider the electron-transfer photochemistry of bi-, tri-, and quadricyclic cyclopropane systems to illuminate the general factors affecting the stereo- and regiochemistry of radical cation nucleophilic capture. Experimental results were interpreted in support of several governing factors. These include: (i) the spin and charge density distribution in the radical cation (the educt); (ii) the extent of conjugation in the educt and the free-radical formed (the product); (iii) the release of ring strain upon forming the product; (iv) steric factors; and (v) the selectivity (reactivity) of the nucleophile.

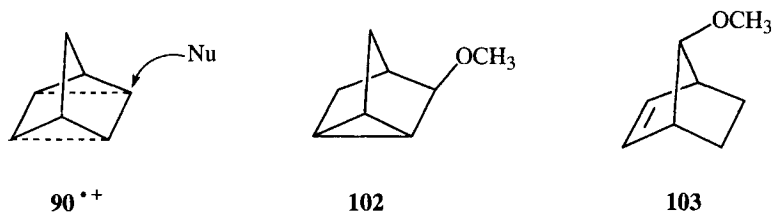
The spin and charge density distribution of the radical cation is an obvious (perhaps trivial) consideration, because it delineates the singly occupied molecular orbital (SOMO), which must be involved in the reaction. For example, the regio-selective capture of 30^{*+} and 34^{*+} occurs at positions of high spin and charge density. The reduced regioselectivity for benzobicyclo[3.1.0]hexene, **98** (comparable yields of **99** and **100**), suggests that both C5 and C6 have significant spin-density [241]. These results are compatible with a radical cation in which the Walsh orbitals of both the 3° – 3° and the 3° – 2° cyclopropane bonds overlap the benzene π system [241].



The thermodynamic changes in the nucleophilic capture, i.e., the extent of conjugation in radical cation educt and free-radical product and the release of ring strain in forming the product are also of obvious importance. For example, 34^{*+} generates a conjugated radical cation, 36^{*+} , via a sigmatropic shift, and forms an allyl radical, 35^\bullet , upon nucleophilic attack [156]. Both reactions form fully conjugated 'products' with full relief of ring strain. Similarly, nucleophilic attack on 1-aryl-2-alkylcyclopropanes, 30^{*+} , forms benzyl radicals [154, 155]. The high regioselectivity in the nucleophilic capture of the 'one-electron bonds' of 30^{*+} or 34^{*+} reflects the unfavorable energetics for the formation of alternative products. Thus, attack at the benzylic position of 30^{*+} or the *exo*-methylene position of 34^{*+} (yielding **101** $^\bullet$) is energetically disfavored. Similarly, the nucleophilic attack on 98^{*+} is regio-random, because it generates two benzyl radicals of comparable stability.



The nucleophilic addition of methanol to quadricyclane radical cation, $90^{\bullet+}$, produced two methanol adducts, **102**, having a 3-*exo*-methoxy group, and **103**, bearing a 7-*anti*-methoxy group. The stereochemistry of the methoxy groups in these structures identified the direction of nucleophilic attack upon $90^{\bullet+}$ as exclusively from the *exo* position [242]. It can be viewed as a backside attack of the nucleophile on the weakened cyclopropane bond with inversion of configuration. 7-Methylenequadricyclane also was attacked exclusively from the *exo* face [243].

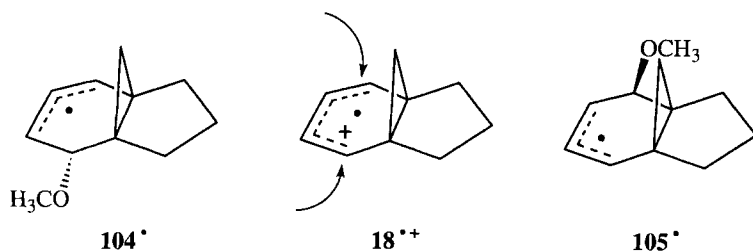


The regiospecific intramolecular capture of the internal cyclopropane bond of the bicyclo[4.1.0]heptane radical cation, $84^{\bullet+}$, by the pendant hydroxyalkyl group also amounts to backside 'substitution' of an intramolecular leaving group [217].

Steric factors have been mentioned; they are not expected to play a major role. In fact, several radical cations have been captured by attack on highly congested centers [154, 156]. The ring-opening substitution of tricyclane radical cation, $81^{\bullet+}$, occurred exclusively at the tertiary carbon [215] whereas that of $82^{\bullet+}$ occurred at the tertiary carbon further removed from the dimethyl-substituted bridge, i.e., at the less hindered of two tertiary carbons, not at the quaternary carbon [216]. These results clearly show that the nucleophilic substitution at the cyclopropane one-electron bond is subject to 'conventional' steric hindrance and is not subject to 'inverse' steric effects [154].

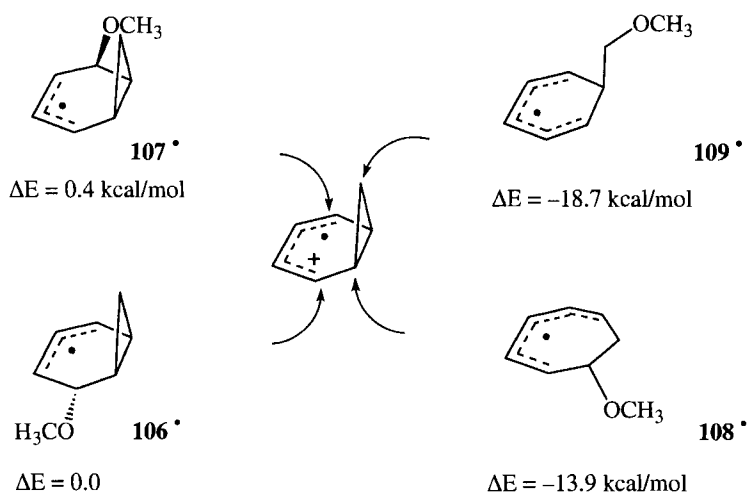
The selectivity (reactivity) of the nucleophile may play a role. Methanol seems to be a selective reagent, as it captures β -phellandrene radical cation, $36^{\bullet+}$, with high regiospecificity at the *exo*-methylene carbon, and sabinene radical cation, $35^{\bullet+}$, exclusively at the quaternary carbon [156].

Significant insights into the nature of the nucleophilic capture of radical cations is provided by the regiochemistry of the attack on the bridged norcaradiene radical cation, $18^{\bullet+}$. The products suggested regiospecific attack of methanol on $18^{\bullet+}$ with capture at C2 and C5 generating 104^\bullet and 105^\bullet . The attack occurs with limited stereoselectivity, because products derived from 104^\bullet and 105^\bullet were formed in comparable yields [131].



Interestingly, no products were derived by nucleophilic attack on the cyclopropane ring of $18^{\bullet+}$, even though ab initio calculations suggest that spin and charge are delocalized on to the strained ring, notably on to C10 (Section 2.3.2) [131]. Contrary to ample precedent suggesting release of ring strain is important in radical cation reactions [154–156], particularly when leading to delocalized free-radicals or radical cations, $18^{\bullet+}$ failed to generate products implying nucleophilic attack at the cyclopropane ring. While the failure of the nucleophile to attack at C1/C6 can be explained by the fact that the bridgehead carbons are nodal centers, attack at C10 remains feasible.

To eliminate unforeseen energetic issues, the relative energies of the four methoxy-substituted free radicals were confirmed by calculations on the free radicals, 106^{\bullet} – 109^{\bullet} , derived from the truncated parent system, $16^{\bullet+}$. The results (UHF/6-31G*) confirmed the expected ordering of energies (relative to the *anti*-methoxynorcarenyl radical, 106^{\bullet}). The bicyclic radicals, 106^{\bullet} and 107^{\bullet} , retaining the strained ring lie significantly above the monocyclic ring-opened radicals, methoxycycloheptadienyl, 108^{\bullet} , and methoxymethylcyclohexadienyl, 109^{\bullet} (Scheme 3).



Scheme 3.

Because the factors considered above cannot explain the failure of $18^{+\bullet}$ to undergo nucleophilic capture at the strained ring, we sought the key to the reactivity in the nature of its orbitals which might be involved in the reaction, i.e. its SOMO and LUMO. This approach has precedent in several theoretical treatments. Pross probed the capture of radical cations by nucleophiles with curve-crossing methodologies. The excited state involved in the curve crossing requires 'double excitation' [244]. Later, Shaik and Pross showed that the excitation energy could be small and the resulting barrier low [245]. This prediction was confirmed by results of Eberson and coworkers; nucleophiles attack the dibenzofuran radical cation at the site of the highest LUMO coefficient, which coincides with the site of highest spin-density in the dibenzofuran triplet state [246–248]. Similarly, Shaik and collaborators explained the well-documented stereochemical course of nucleophilic displacement of a σ bond (with inversion of configuration) [156, 180, 181, 242, 243, 249–253] by involvement of the σ^* orbital (the LUMO) of the weakened bond [254, 255].

The bridged norcaradiene, $18^{+\bullet}$, is well suited to probing the orbitals involved in the nucleophilic capture of radical cations. This becomes evident when considering the combined effects of free energy and molecular orbital contributions. We have mentioned the significant free energy differences between attack at the strained ring and addition to the diene moiety (cf., Scheme 3). Perhaps more importantly, the two MOs potentially involved in the reaction have a substantially different distribution of orbital coefficients. The SOMOs of $16^{+\bullet}$ and $18^{+\bullet}$ have large orbital coefficients at C2,5 and C7 (C10), which are reflected in the hyperfine pattern of these species (cf., Figure 29, bottom). In contrast, the principal orbital coefficients of the LUMOs are located at C2,5 and C3,4 and the orbital lobes at C7 (C10) offer no target for attack by the nucleophile (Figure 29, top). Because the orbital coefficients of SOMO and LUMO differ, the norcaradiene system will elucidate whether the regioselectivity of nucleophilic capture is governed by the SOMO, or by the nature and topology of the LUMO. The products derived from $18^{+\bullet}$ are clearly formed by attack at a center where both SOMO and LUMO have significant orbital coefficients. This assignment seems persuasive, because the reaction of $18^{+\bullet}$ fails to follow the direction of a significant advantage in driving force. For the norcaradiene system, molecular orbital arguments and free energy considerations predict different regioselectivities. Obviously, the molecular orbital requirements outweigh the significant free energy differences, because of the relief of ring strain and extended conjugation.

The product-determining involvement of the LUMO can also explain the regioselective capture of many other radical cations, including the nucleophilic attack on 1-aryl-2-alkylcyclopropanes, $30^{+\bullet}$. The high regioselectivity in the nucleophilic capture of the 'one-electron bonds' of $30^{+\bullet}$ was originally cited as evidence of inverse steric effects [154, 155]. However, the SOMO and LUMO of disubstituted cyclopropane radical cations (e.g. 1,2-dimethylcyclopropane; Figure 30) clearly suggest that the observed regioselectivity reflects electronic rather than steric factors. Capture at the unsubstituted cyclopropane carbon cannot be expected, because neither SOMO nor LUMO have orbital coefficients at that carbon [31].

A detailed discussion of the reactivity of organic radical ions is presented in the contribution of Schmittel and Ghorai (Volume II, Part 1, Chapter 1 in this handbook).

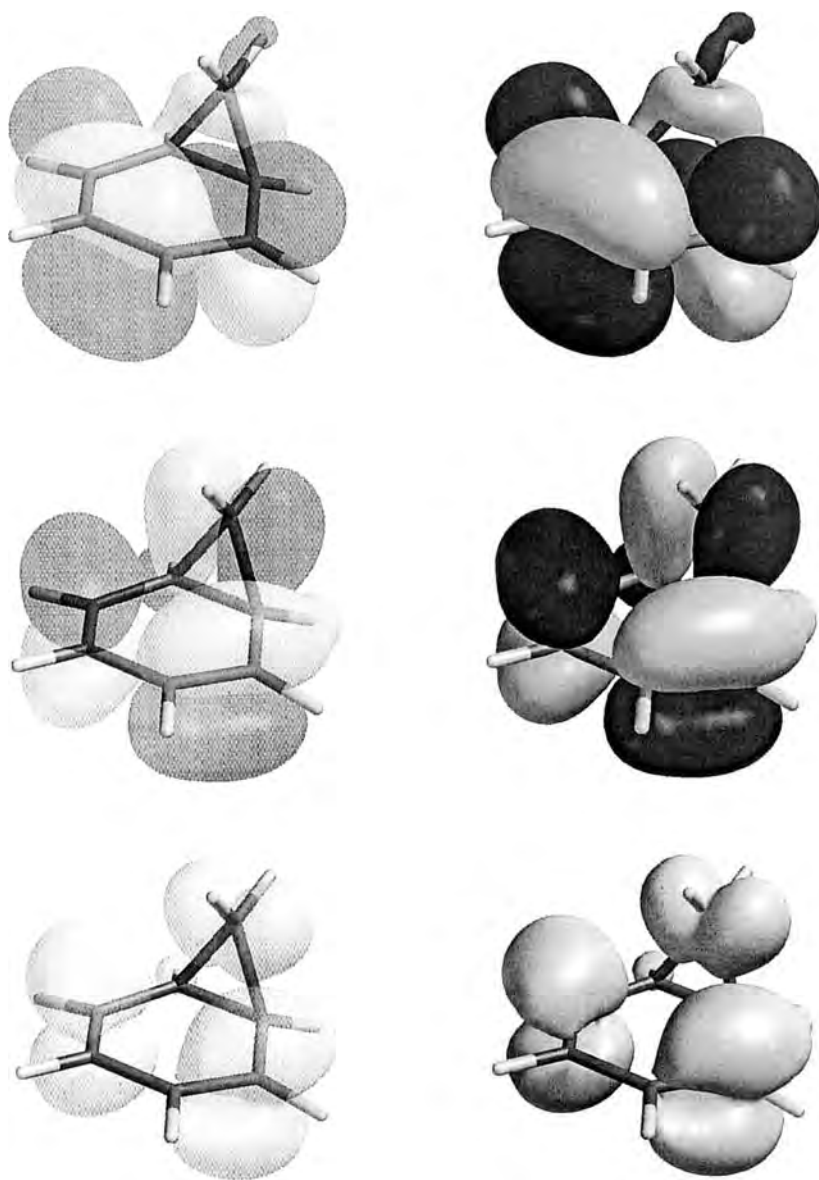


Figure 29. Pictorial representation (calculated by Spartan) of the spin density distribution of norcaradiene radical cation, $18^{+\bullet}$, (bottom), and its SOMO (center) and LUMO (top).

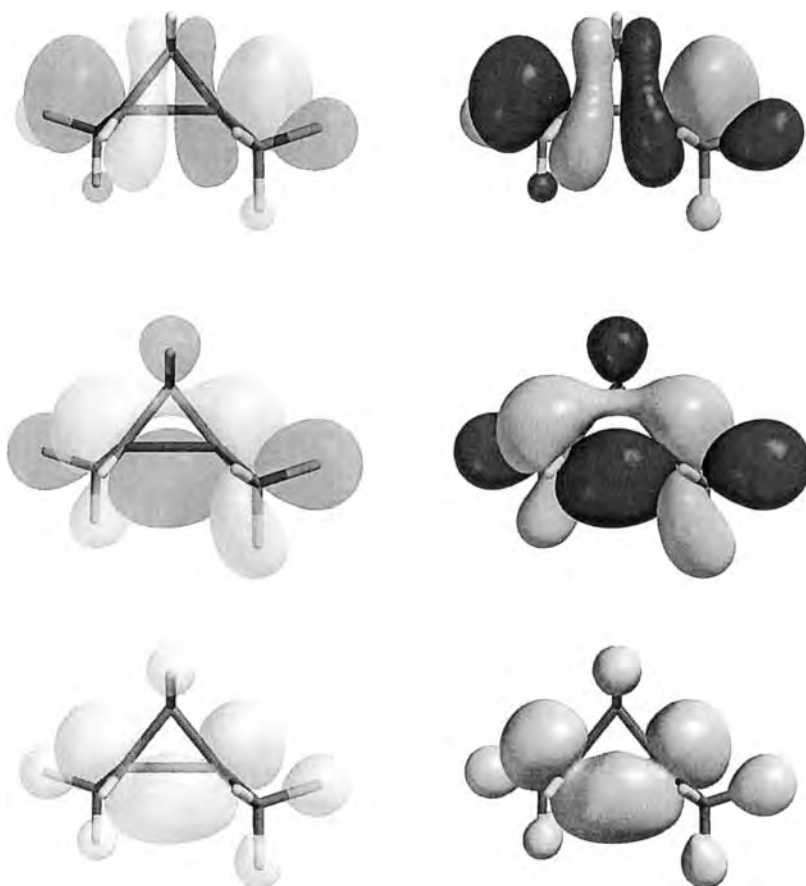
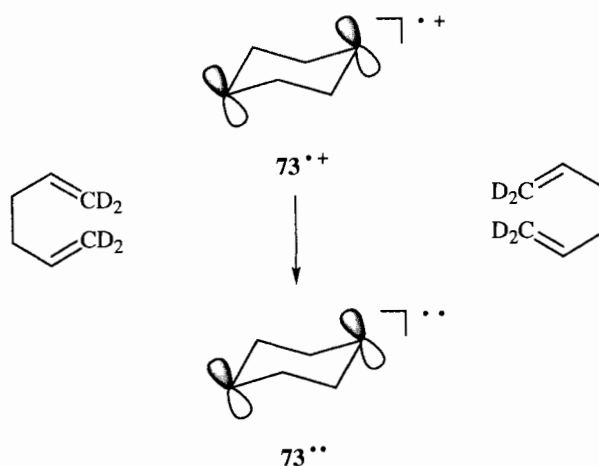


Figure 30. Pictorial representation (calculated by Spartan) of the spin density distribution of *trans*-1,2-dimethylcyclopropane radical cation (bottom), and its SOMO (center) and LUMO (top).

2.4.4 Triplet Recombination of Radical Ion Pairs

In the context of the potential Cope rearrangement of hexa-1,5-diene radical cations (Section 2.4.1), we mentioned the triplet recombination of radical ion pairs generating a biradical [202, 203]. Because of continuing interest in this type of reaction we briefly mention two additional examples involving radical cationic systems discussed in this review, viz., the isomeric 1,2-diphenylcyclopropane radical cations, *cis*- and *trans*-**13**^{•+}, and norbornadiene radical cation, **91**^{•+}.

The steric integrity of *cis*- and *trans*-**13**^{•+} is established clearly; it is a key argument for their ring-closed structure [223]. *cis*- and *trans*-**13**, however, undergo geometric isomerization when reacted with photo-excited singlet acceptors, such as 1,4-dicyanonaphthalene. The electron-transfer-induced conversion was ascribed to



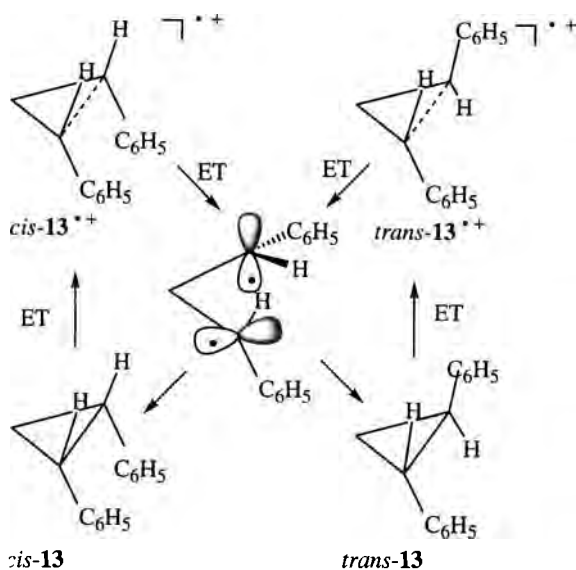
Scheme 4.

reverse electron transfer in pairs of triplet spin multiplicity, a process that populates a triplet state of **13** [107, 227]; accordingly, the overall reaction involves two consecutive intermediates, a radical cation and a triplet state.

The triplet recombination of cyclohexanediyl radical cations with a sensitizer radical anion (above) generates a triplet biradical with similar geometry. This conversion requires only that the biradical energy lies below the radical ion pair energy. The key structural changes amounting to a Cope rearrangement occur in two separate steps, the formation of $73^{+\bullet}$ and the conversion of $73^{\bullet\bullet}$ to the hexadienes. The detailed pathway of the formation of $73^{+\bullet}$ is not known. The conversion of $73^{\bullet\bullet}$ to the hexadiene isomers requires breaking one of two essentially equivalent doubly allylic C–C bonds (Scheme 4).

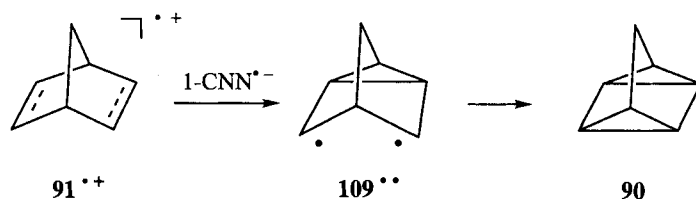
The rearrangements of **13** and **91** require specific energetic and structural features: (i) the energy of the radical ion pair must lie above an accessible triplet state and (ii) a mismatch must exist between the potential surfaces of ground and triplet state. Both requirements seem to be fulfilled. Because of the relatively high negative reduction potential of dicyanonaphthalene ($E_{\text{A}^-/\text{A}} \approx -1.6$ V relative to the SCE), the free energy of the radical ion pair generated by reaction with *cis*- or *trans*-**13** ($E_{\text{D/D}^+} \approx 1.5$ V relative to the SCE; $\Delta G > 3.1$ eV) lies above an accessible triplet state of **13**. A ring-opened triplet state with two orthogonal p-orbitals, $13^{\bullet\bullet}$, was postulated [107, 227]; as its structure lies between those of *cis*- and *trans*-**13**, it can decay to either isomer. The geometry of minimum energy of the intermediate, $13^{\bullet\bullet}$, corresponds to (or lies near) a saddle point on the potential surface of the parent molecule, enabling decay to either isomer (Scheme 5). The biradical was observed recently and its free energy determined [256], confirming the mechanism previously assigned [107, 227]. Because a (partial) bond is broken in this step, the recombination was called ‘dissociative’ [256].

Another example of triplet recombination involves the formation of quadricyclane upon electron transfer from norbornadiene to 1-cyanonaphthalene (1-CNN) [226]. Once again, the radical ion pair energy lies above 3 eV, so an intermediate on the



Scheme 5.

norbornadiene triplet potential surface is postulated. This species probably has a nortricyclanediyl structure, **109^{••}** [228], which enables decay to quadricyclane, **90**. By analogy with the nomenclature used above [256], the recombination of **91^{•+}** would be 'associative'.



The net conversion of **91** to **90** by triplet recombination of the radical ion pair, **91^{•+}**–**1-CNN^{•-}**, occurs in very low quantum yield, illustrating the potential problem associated with triplet recombination as a preparative method. Because the product, **90**, is a better electron donor than the starting material, **91**, it will undergo electron transfer preferentially. The resulting radical cation, **90^{•+}**, undergoes the well-known ring opening to **91^{•+}**, causing the rapid loss of any product formed.

2.4.5 Concluding Remarks

The electron-transfer processes discussed in this chapter constitute an interesting facet of the overall field. Although the substrates discussed here do not play a role

in the important chemistry of life, they do occur in the Earth's atmosphere and in outer space. Electron-transfer reactions of alkanes and cycloalkanes generate a plethora of interesting intermediates, and their study has revealed a wide range of interesting reactions. Some (unrecognized) electron-transfer reactions preceded the actual discovery of the electron [257], and some radical ions were observed long before their nature was recognized [258]. Given these early beginnings, the field of electron-transfer chemistry is well over one hundred years old. It is safe to predict significant and vigorous advances in this field for at least the first decade of the new century. In particular, time-resolved spectroscopic methods and their extension to as yet inaccessible spectral regions is expected to facilitate major new contributions.

References

1. Jordan KD, Burrow PD, *Chem. Rev.* **1987**, 87, 557–588.
2. Melton CE, in *Mass Spectrometry of Organic Ions*, McLafferty FW, Ed, Academic Press, **1963**, 163–205.
3. Melton CE, in *Principles of Mass Spectrometry and Negative Ions*, Marcel Dekker, New York, **1970**, 163–205.
4. Janousek BK, Brauman JI, in *Gas Phase Ion Chemistry*, Bowers MT, Ed, Academic Press, **1979**, Vol II, 53–86.
5. Lias SG, Ed., *J. Phys. Chem. Ref. Data* **1988**.
6. Howe I, Williams DH, Bowen RD, *Mass Spectrometry Principles and Applications*, Wiley, New York, **1981**.
7. Lehman TA, Bursey MM *Ion Cyclotron Resonance Spectrometry*, **1976**.
8. Turner DW, Baker AD, Baker C, Brundle CR, *Molecular Photoelectron Spectroscopy*, Wiley–Interscience, New York, **1970**.
9. Rao PS, Nash JR, Guarino JP, Ronayne MR, Hamill WH, *J. Am. Chem. Soc.* **1962**, 84, 500–501.
10. Guarino JP, Ronayne MR, Hamill WH *J. Am. Chem. Soc.* **1962**, 84, 4230–4235.
11. Louwrier PWF, Hamill WH, *J. Phys. Chem.* **1970**, 74, 1418–1421.
12. Knight LB Jr, *Accounts Chem. Res.* **1986**, 19, 313–321.
13. Nauwelaerts F, Ceulemans J, *Chem. Phys. Lett.* **1976**, 38, 354–356.
14. Nauwelaerts F, Lemahieu M, Ceulemans J, *J. Chem. Phys.* **1977**, 66, 140–142.
15. Smith IG, Symons MCR, *J. Chem. Res.* **1989**, 382.
16. Symons MCR, *Chem. Phys. Lett.* **1980**, 69, 198–200.
17. Wang JT, Williams F, *J. Phys. Chem.* **1980**, 84, 3156–3159.
18. Shida T, Kubodera H, Egawa Y, *Chem. Phys. Lett.* **1981**, 79, 179–182.
19. Toriyama K, Nunome K, Iwasaki M, *J. Am. Chem. Soc.* **1981**, 103, 3591–3592.
20. Carrington A, McLachlan AD, *Introduction to Magnetic Resonance*, Harper & Row, New York, **1967**.
21. Wertz JE, Bolton JR, *Electron Spin Resonance: Elementary Theory and Practical Applications*, McGraw–Hill, New York, **1972**.
22. McLauchlan KA, Stevens DG, *Accounts Chem Res.* **1988**, 21, 54–59.
23. Miller SL, Urey HC, *Science* **1959**, 130, 245.
24. Toriyama K, Nunome K, Iwasaki M, *J. Phys. Chem.* **1988**, 92, 5097–5103.
25. Knight LB, Jr, Steadman J, Feller D, Davidson ER, *J. Am. Chem. Soc.* **1984**, 106, 3700–3701.
26. Symons MCR, Chen T, Glidewell C, *J. Chem. Soc. Chem. Commun.* **1983**, 326–328.
27. Claxton TA, Chen T, Symons MCR, *Faraday Disc. Chem. Soc.* **1984**, 78, 1.
28. Eriksson LE, Malkin VG, Malkina OL, Salahub DR, *Int. J. Quant. Chem.* **1994**, 52, 879–901.
29. Matsushita M, Momose T, Shida T, Knight LB, Jr, *J. Chem. Phys.* **1995**, 103, 3367–3376.
30. Knight LB, Jr, King GM, Petty JT, Matsushita M, Momose T, Shida T, *J. Chem. Phys.* **1995**, 103, 3377–3385.

31. Herberzt T, Roth HD, **2000**, unpublished results.
32. Carter MK, Vincow G, *J. Chem. Phys.* **1967**, 47, 292–302.
33. Kira M, Watanabe M, Sakurai H, *Chem. Letters* **1979**, 973–976.
34. Clark T, Chandrasekhar J, Jr, Schleyer PvR, *J. Chem. Soc., Chem. Commun.* **1980**, 26.
35. Liebling GR, McConnel HM, *J. Chem. Phys.* **1965**, 42, 3931–3934.
36. Closs GL, Redwine OD, *J. Am. Chem. Soc.* **1986**, 108, 506–507.
37. Iwasaki M, Toriyama K, Nunome K, *Faraday Disc. Chem. Soc.* **1984**, 78, 19.
38. Herzberg G, *Electronic Spectra and Electronic Structure of Polyatomic Molecules*, Van Nostrand Reinhold, New York, **1966**, p. 50.
39. Claxton TA, Overill RE, Symons MCR, *Mol. Phys.* **1974**, 27, 701–706.
40. Zuilhof H, Dinnocenzo JP, Reddy AC, Shaik SS, *J. Phys. Chem.* **1996**, 100, 15774–15784.
41. Toriyama K, Nunome K, Iwasaki M, *J. Chem. Phys.* **1982**, 77, 5891–5912.
42. Matsuura K, Nunome K, Toriyama K, Iwasaki M, *J. Phys. Chem.* **1989**, 93, 149–154.
43. Toriyama K, *Chem. Phys. Lett.* **1991**, 177, 39–44.
44. Toriyama K, Okazaki M, Nunome K, *J. Chem. Phys.* **1982**, 77, 3955–3963.
45. Toriyama K, Nunome K, Iwasaki M, *J. Am. Chem. Soc.* **1987**, 109, 3591–3592.
46. Toriyama K, Nunome K, Iwasaki M, *J. Phys. Chem.* **1981**, 85, 2149–2152.
47. Wang JT, Williams F, *Chem. Phys. Lett.*, **1981**, 82, 177–181.
48. Iwasaki M, Toriyama K, *J. Am. Chem. Soc.* **1986**, 108, 6441–6443.
49. Tabata M, Lund A, *Rad. Phys. Chem.* **1984**, 23, 545.
50. Lindgren M, Lund A, Dolivo G, *Chem. Phys.* **1985**, 99, 103–110.
51. Lund A, Lindgren M, Dolivo G, Tabata M, *Rad. Phys. Chem.* **1985**, 26, 491.
52. Dolivo G, Lund A, *J. Phys. Chem.* **1985**, 89, 3977–3984.
53. Dolivo G, Lund A, *Z. Naturforsch.* **1985**, 40a, 52–65.
54. Toriyama K, Nunome K, Iwasaki M, *J. Am. Chem. Soc.* **1987**, 109, 4496–4500.
55. Demeyer A, Stienlet D, Ceulemans J, *J. Phys. Chem.* **1994**, 98, 9530–9543.
56. Ceulemans J, *Spectrochim. Acta A* **1998**, 54, 2359–2372.
57. Fleischmann M, Pletcher D, *Tetrahedron Lett.* **1968**, 6255–6258.
58. Toriyama K, Nunome K, Iwasaki M, *Chem. Phys. Lett.* **1986**, 132, 456–458.
59. Shiotani M, Yano A, Ohta N, Ichikawa T, *Chem. Phys. Lett.* **1988**, 147, 38–42.
60. Cochran EL, Adrian FJ, Bowers, J. *Chem. Phys.* **1964**, 40, 213–220.
61. Muto H, Iwasaki M, Takahashi Y, *J. Chem. Phys.* **1977**, 66, 1943–1952.
62. Hulme R, Symons MCR, *J. Chem. Soc.* **1965**, 1120.
63. Wojciechowski BW, Corma A, *Catalytic Cracking, Catalysts Kinetics and Mechanisms*, Marcel Dekker: New York, **1984**.
64. Venuto PB, *Adv. Catal.* **1968**, 18, 259–371.
65. Venuto PB, *Microporous Mater.* **1994**, 2, 297–411.
66. Hölderich WF, Hesse M, Nümann F, *Angew. Chem., Int. Ed. Engl.* **1988**, 27, 226–246.
67. Hölderich WF, *Stud. Surf. Sci. Catal.* **1989**, 49, 69.
68. Corma A, García H, *Catal. Today* **1997**, 38, 257–308.
69. Corma A, García H, *Top. Catal.* **1998**, 6, 127–140.
70. Herberzt T, Lakkaraju PS, Blume F, Blume M, Roth HD, *Eur. J. Org. Chem.* **2000**, 467–472.
71. Chen FR, Fripiat JJ, *J. Phys. Chem.* **1993**, 97, 5796–5797.
72. Roduner E, Crockett R, *J. Phys. Chem.* **1993**, 97, 11853–11854.
73. Trifunac AD, Qin X-Z, *Appl. Magn. Resonance* **1990**, 1, 29–40.
74. Barnabas MV, Werst DW, Trifunac AD, *Chem. Phys. Lett.* **1993**, 204, 435–439.
75. Werst DW, Tartakovsky EE, Piocos EA, Trifunac AD, *J. Phys. Chem.* **1994**, 98, 10249–10257.
76. Shiotani M, Lund A, *Radical Ionic Systems*, Lund A, Shiotani M, Eds; Kluwer Academic: Dordrecht, **1991**, p. 151–176.
77. Gleiter R, *Top. Curr. Chem.* **1980**, 86, 197–285.
78. Iwasaki M, Toriyama K, Nunome K, *J. Chem. Soc. Chem. Comm.* **1984**, 202–203.
79. Shida T, Takemura Y, *Radiat. Phys. Chem.* **1983**, 21, 157.
80. Ohta K, Nakatsuji H, Kubodera H, Shida T, *Chem. Phys.* **1983**, 76, 271–281.
81. Almennigen A, Bastiansen O, Skancke PN, *Acta Chim. Scand.* **1961**, 15, 711.

82. Ushida K, Shida T, Iwasaki M, Toriyama K, Numone K, *J. Am. Chem. Soc.* **1983**, *105*, 5496–5497.
83. Bauld NL, Bellville DJ, Pabon R, Chelsky R, Green G, *J. Am. Chem. Soc.* **1983**, *105*, 2378–2382.
84. Bouma WJ, Poppinger D, Radom L, *Isr. J. Chem.* **1983**, *23*, 21–36.
85. Dewar MS, Merz KM, Jr, *J. Mol. Struct. THEOCHEM* **1985**, *122*, 59–65.
86. Jungwirth P, Carsky P, Bally T, *J. Am. Chem. Soc.* **1993**, *115*, 5776–5782.
87. Wiest O, *J. Phys. Chem. A* **1999**, *103*, 7907–7911.
88. Sjöquist L, Lund A, Maruani J, *Chem. Phys.* **1988**, *125*, 293–298.
89. Huang MB, Lunell S, Lund A, *Chem. Phys. Letters* **1983**, *99*, 201–205.
90. Tabata M, Lund A, *Chem. Phys.* **1983**, *75*, 379–388.
91. Shida T, Takemura Y, *Rad. Phys. Chem.* **1983**, *21*, 157.
92. Toriyama K, Nunome K, Iwasaki M, *J. Chem. Soc., Chem. Commun.* **1984**, 143–145.
93. Lunell S, Huang MB, Claesson O, Lund A, *J. Chem. Phys.* **1985**, *82*, 5121–5126.
94. Shiotani M, Ohta N, Ichikawa T, *Chem. Phys. Letters* **1988**, *149*, 85–88.
95. Toriyama K, Nunome K, Iwasaki M, *J. Phys. Chem.* **1986**, *90*, 6836–6842.
96. Haselbach E, *Chem. Phys. Lett.* **1970**, *7*, 428–430.
97. Rowland CG, *Chem. Phys. Lett.* **1971**, *9*, 169–173.
98. Collins JR, Gallup GA, *J. Am. Chem. Soc.* **1982**, *104*, 1530–1533.
99. Wayner DDM, Boyd RJ, Arnold DR, *Can. J. Chem.* **1985**, *63*, 3283–3289.
100. Wayner DDM, Boyd RJ, Arnold DR, *Can. J. Chem.* **1983**, *61*, 2310–2315.
101. Du P, Hrovat DA, Borden WT, *J. Am. Chem. Soc.* **1988**, *110*, 3405–3412.
102. Lunell S, Yin L, Huang M-B, *Chem. Phys.* **1989**, *139*, 293–299.
103. Krogh-Jespersen K, Roth HD, *J. Am. Chem. Soc.* **1992**, *114*, 8388–8394.
104. Skancke A, *J. Phys. Chem.* **1995**, *99*, 13886–13889.
105. Qin XZ, Snow LD, Williams F, *J. Am. Chem. Soc.* **1984**, *106*, 7640–7641.
106. Qin XZ, Williams F, *Tetrahedron* **1986**, *42*, 6301–6314.
107. Roth HD, Schilling MLM, *J. Am. Chem. Soc.* **1980**, *102*, 7956–7958.
108. Roth HD, Schilling MLM, *Can. J. Chem.* **1983**, *61*, 1027–1035.
109. Roth HD, Schilling MLM, *J. Am. Chem. Soc.* **1983**, *105*, 6805–6808.
110. Haddon RC, Roth HD, *Croat. Chem. Acta* **1984**, *57*, 1165–1176.
111. Rabinovitch BS, Schlag EW, Wiberg K, *J. Chem. Phys.* **1958**, *28*, 504–505.
112. Schlag EW, Rabinovitch BS, *J. Am. Chem. Soc.* **1960**, *82*, 5996–6000.
113. Mattes SL, Farid S, *Org. Photochem.* **1983**, *6*, 233–326.
114. Mattay J, Vondenhof M, *Topics Curr. Chem.* **1991**, *159*, 219–255.
115. *Photoinduced Electron Transfer*, Fox MA, Chanon M, Eds, Elsevier, Amsterdam, **1988**.
116. Knibbe H, Rehm D, Weller A, *Ber. Bunsenges. Phys. Chem.* **1969**, *73*, 839–845.
117. Bargon J, Fischer H, Johnson U, *Z. Naturforsch.* **1967**, *A 22*, 1551–1556.
118. Ward HR, Lawler RG, *J. Am. Chem. Soc.* **1967**, *89*, 5518–5519.
119. Roth HD, Lamola AA, *J. Am. Chem. Soc.* **1972**, *94*, 1013–1014.
120. Roth HD, Lamola AA, *J. Am. Chem. Soc.* **1974**, *96*, 6270–6275.
121. Lamola AA, Roth HD, Schilling MLM, Tollin G, *Proc. Nat. Acad. Sci. USA* **1975**, *72*, 3265–3269.
122. Closs GL, *Adv. Magn. Reson.* **1974**, *7*, 157–229.
123. Kaptein R, *Adv. Free Radical Chem.* **1975**, *5*, 319–380.
124. Adrian FJ, *Rev. Chem. Intermed.* **1979**, *3*, 3–43.
125. Freed JH, Pedersen JB, *Adv. Magn. Reson.* **1976**, *8*, 2–84.
126. Roth HD, in *Encyclopedia of Nuclear Magnetic Resonance*, Grant DM, Harris RK, Eds, **1996**, vol. 2, 1337–1350.
127. Dewar MJS, Dougherty RC, *The PMO Theory of Organic Chemistry*, Plenum Press, N.Y. **1975**.
128. Herbertz T, Roth HD, *J. Am. Chem. Soc.* **1998**, *120*, 11904–11911.
129. Herbertz T, Lakkaraju PS, Roth HD, Sluggett G, Turro NJ, *J. Phys. Chem. A* **1999**, *103*, 11350–11354.
130. Dinnocenzo JP, Zuilhof H, Lieberman DR, Simpson TR, McKechney MW, *J. Am. Chem. Soc.* **1997**, *119*, 994–1004.

131. Herbertz T, Blume F, Roth HD, *J. Am. Chem. Soc.* **1998**, *120*, 4591–4599.
132. Roth HD, Schilling MLM, Schilling FC, *J. Am. Chem. Soc.* **1985**, *107*, 4152–4158.
133. Roth HD, Schilling MLM, Hutton RS, Truesdale EA, *J. Am. Chem. Soc.* **1983**, *105*, 153–157.
134. Roth HD, Herbertz T, *J. Am. Chem. Soc.* **1993**, *115*, 9804–9805.
135. Roth HD, Weng H, Herbertz T, *Tetrahedron*, **1997**, *53*, 10051–10070.
136. Kawamura T, Tsumura M, Yokomichi Y, Yonegawa T, *J. Am. Chem. Soc.* **1977**, *99*, 8251–8256.
137. Fessenden RW, *J. Phys. Chem.* **1967**, *71*, 74.
138. Ohta K, Nakatsuji H, Hirao K, Yonezawa T, *J. Chem. Phys.* **1980**, *73*, 1770–1776.
139. Behrens G, Schulte-Frohlinde D, *Angew. Chem.* **1973**, *85*, 993.
140. Qin X-Z, Williams F, *Chem. Phys. Lett.* **1984**, *112*, 79–83.
141. Dinnocenzo JP, Schmittel M, *J. Am. Chem. Soc.* **1987**, *109*, 1561–1562.
142. Shiotani M, Nagata Y, Sohma J, *J. Phys. Chem.* **1984**, *88*, 4078–4082.
143. Guo QX, Qin XZ, Wang JT, Williams F, *J. Am. Chem. Soc.* **1988**, *110*, 1974–1976.
144. Williams F, Guo QX, Petillo PA, Nelsen SF, *J. Am. Chem. Soc.* **1988**, *110*, 7887–7888.
145. Williams F, Guo QX, Bebout DC, Carpenter BK, *J. Am. Chem. Soc.* **1989**, *111*, 4133–4134.
146. Adam W, Walter H, Chen G-F, Williams F, *J. Am. Chem. Soc.* **1992**, *114*, 3007–3014.
147. Roth HD, Schilling MLM, Gassman PG, Smith JL, *J. Am. Chem. Soc.* **1984**, *106*, 2711–2712.
148. Du P, Hrovat DA, Borden WT, *Chem. Phys. Lett.* **1986**, *123*, 337–340.
149. Symons MCR, *Chem. Phys. Lett.* **1978**, *117*, 381–382.
150. Rao VR, Hixson SS, *J. Am. Chem. Soc.* **1979**, *101*, 6458–6459.
151. Mizuno K, Ogawa J, Kagano H, Otsuji Y, *Chem. Lett.* **1981**, 437–438.
152. Mizuno K, Ogawa J, Otsuji Y, *Chem. Lett.* **1981**, 741–744.
153. Mazzocchi PH, Somich C, Edwards M, Morgan T, Ammon HL, *J. Am. Chem. Soc.* **1986**, *108*, 6828–6829.
154. Dinnocenzo JP, Todd WP, Simpson TR, Gould IR, *J. Am. Chem. Soc.* **1990**, *112*, 2462–2464.
155. Dinnocenzo JP, Lieberman DR, Simpson TR, *J. Am. Chem. Soc.* **1993**, *115*, 366–367.
156. Weng H, Sethuraman V, Roth HD, *J. Am. Chem. Soc.* **1994**, *116*, 7021–7025.
157. Evans TR, Wake RW, Jaenicke O, The Exciplex, Academic Press, New York, **1975**, 345–358.
158. Roth HD, Hutton RS, *J. Phys. Org. Chem.* **1990**, *3*, 119–125.
159. Symons, MCR, Wren BW, *Tetrahedron Lett.* **1983**, *24*, 2315–2318.
160. Snow LD, Wang JT, Williams F, *Chem. Phys. Lett.* **1983**, *100*, 193–197.
161. Ledwith A, *Accounts Chem. Res.* **1972**, *57*, 133–139.
162. Mattes SL, Farid S, *Accounts Chem. Res.* **1982**, *15*, 80–86.
163. Bauld NL, *Tetrahedron*, **1989**, *45*, 5307–5363.
164. Ichikawa T, Ohta N, Kajioaka H, *J. Phys. Chem.* **1979**, *83*, 284–295.
165. Saik VO, Anisimov OA, Lozovoy VV, Molin YuN, *Z. Naturforsch.* **1985**, *40a*, 239–245.
166. Barnabas MW, Trifunac AD, *Chem. Phys. Lett.* **1992**, *193*, 298–304.
167. Desrosiers MF, Trifunac AD, *J. Phys. Chem.* **1986**, *90*, 1560–1564.
168. Jungwirth P, Bally T, *J. Am. Chem. Soc.* **1993**, *115*, 5783–5789.
169. Lindgren M, Shiotani M, Ohta N, Sjoquist L, Lund A, *Chem. Phys. Lett.* **1989**, *161*, 127–130.
170. Shiotani M, Lindgren M, Ichikawa T, *J. Am. Chem. Soc.* **1990**, *112*, 967–973.
171. Lindgren M, Shiotani M, in *Radical Ionic Systems*, Lund A, Shiotani M, Eds; Kluwer Academic: Dordrecht, **1991**, 125–150.
172. Werst DW, Piosos EA, Tartakovsky EE, Trifunac AD, *Chem. Phys. Lett.* **1994**, *229*, 421–428.
173. Qin X-Z, Trifunac AD, *J. Phys. Chem.* **1990**, *94*, 4751–4754.
174. Gerson F, Qin X-Z, Ess C, Kloster-Jensen E, *J. Am. Chem. Soc.* **1989**, *111*, 6456–6457.
175. Arnold A, Burger U, Gerson F, Kloster-Jensen E, Schmidlin SP, *J. Am. Chem. Soc.* **1993**, *115*, 4271–4281.
176. Gerson F, *Accounts Chem. Res.* **1994**, *27*, 63–69.
177. Roth HD, Schilling MLM, Gassman PG, Smith JL, *J. Am. Chem. Soc.* **1984**, *106*, 2711–2712.
178. Abelt CJ, Roth HD, Schilling MLM, *J. Am. Chem. Soc.* **1985**, *10*, 4148–4152.
179. Gassman PG, Carroll GT, *Tetrahedron* **1986**, *42*, 6201–6206.
180. Gassman PG, Olson KD, Walter L, Yamaguchi R, *J. Am. Chem. Soc.* **1981**, *103*, 4977–4979.
181. Gassman PG, Olson KD *J. Am. Chem. Soc.* **1982**, *104*, 3740–3742.
182. Gassman PG, Hay BA, *J. Am. Chem. Soc.* **1985**, *107*, 4075–4078.

183. Gassman PG, Hay BA, *J. Am. Chem. Soc.* **1986**, *108*, 4227–4228.
184. Wiberg KB, Szeimies G, *Tetrahedron Letters* **1968**, 1235–1239.
185. Roth HD, *Accounts Chem. Res.* **1987**, *20*, 343–350.
186. Roth HD, *Topics Curr. Chem.* **1992**, *163*, 131–245.
187. Woodward RB, Hoffmann R, *The Conservation of Orbital Symmetry*, Verlag Chemie, Weinheim, **1971**.
188. Gassman PG (1988) in *Photoinduced Electron Transfer*, Fox MA, Chanon M, Eds, Elsevier, Amsterdam, **1988**, Vol. C, 70.
189. Abelt CJ, Roth HD, Schilling MLM, *J. Am. Chem. Soc.* **1985**, *107*, 4148–4152.
190. Gerson F, Arnold A, Burger U, *J. Am. Chem. Soc.* **1991**, *113*, 4359–4360.
191. Bischof P, Gleiter R, Mueller E, *Tetrahedron* **1976**, *32*, 2769–2773.
192. Harman PJ, Kent JE, Gan TH, Peel JB, Willett GD, *J. Am. Chem. Soc.* **1977**, *99*, 943–944.
193. Gleiter R, Gubernator K, Eckert-Maksic M, Spanget-Larsen J, Bianco B, Gandillion G, Burger U, *Helv. Chim. Acta* **1981**, *64*, 1312–1313.
194. Abelt CJ, Roth HD, *J. Am. Chem. Soc.* **1985**, *107*, 3840–3843.
195. Williams F, Guo QX, Kolb TM, Nelsen SF, *J. Chem. Soc., Chem. Commun.* **1989**, 1835–1836.
196. Ushida K, Shida T, Walton JC, *J. Am. Chem. Soc.* **1986**, *108*, 2805–2808.
197. Adam W, Sahin C, Sendelbach J, Walter H, Chen G-F, Williams F, *J. Am. Chem. Soc.* **1994**, *116*, 2576–3584.
198. Blancafort L, Adam W, González D, Olivucci M, Vreven T, Robb MA, *J. Am. Chem. Soc.* **1999**, *121*, 10583–10590.
199. Adam W, Heidenfelder T, *Chem. Soc. Rev.* **1999**, *28*, 359–365.
200. Tsuji T, Miura T, Sugiura K, Nishida S, *J. Am. Chem. Soc.* **1990**, *112*, 1998–1999.
201. Miyashi T, Konno A, Takahashi Y, *J. Am. Chem. Soc.* **1988**, *110*, 3676–3677.
202. Ikeda H, Minegishi T, Abe H, Konno A, Goodman JL, Miyashi T, *J. Am. Chem. Soc.* **1998**, *120*, 87–95.
203. Miyashi T, Ikeda H, Takahashi Y, *Accounts Chem. Res.* **1999**, *32*, 815–824.
204. Doering WvE, Roth WR, *Tetrahedron* **1962**, *18*, 67–74.
205. Roth HD, *Proc. IUPAC Symp. Photochem.* **1984**, *10*, 455–456.
206. Roth HD, Schilling MLM, *J. Am. Chem. Soc.* **1985**, *107*, 716–718.
207. Roth HD, Schilling MLM, Abelt CJ, *Tetrahedron* **1986**, *42*, 6157–6166.
208. Roth HD, Schilling MLM, Abelt CJ, *J. Am. Chem. Soc.* **1986**, *108*, 6098–6099.
209. Momose T, Shida T, Kobayashi T, *Tetrahedron* **1986**, *42*, 6337–6342.
210. Dai S, Wang JT, Williams F, *J. Am. Chem. Soc.* **1990**, *112*, 2835–2836.
211. Dai S, Wang JT, Williams F, *J. Am. Chem. Soc.* **1990**, *112*, 2837–2837.
212. Abelt CJ, *J. Am. Chem. Soc.* **1986**, *108*, 2013–2019.
213. Roth HD, *Z. Phys. Chem.* **1993**, *180*, 135–158.
214. Williams F, *J. Chem. Soc., Faraday Trans.*, **1994**, *90*, 1681–1687.
215. Arnold DR, Du X, *Can. J. Chem.* **1994**, *72*, 403–414.
216. Wlostowski M, Roth HD, unpublished results.
217. Takemoto Y, Ohra T, Koike H, Furuse S-I, Iwata C, Ohishi H, *J. Org. Chem.* **1994**, *59*, 4727–4729.
218. Roth HD, Herberzt T, *J. Am. Chem. Soc.* **1993**, *115*, 9804–9805.
219. Roth HD, Weng H, Zhou D, Herberzt T, *Pure Appl. Chem.* **1997**, *69*, 809–814.
220. Herberzt T, Roth HD, *J. Am. Chem. Soc.* **1997**, *119*, 9574–9575.
221. Hoffmann R, Heilbronner E, Gleiter R, *J. Am. Chem. Soc.* **1970**, *92*, 706–707.
222. Hoffmann R, *Accounts Chem. Res.* **1971**, *4*, 1–9.
223. Dewar MJS, Wasson JS, *J. Am. Chem. Soc.* **1970**, *92*, 3506–3508.
224. Heilbronner E, Schmelzer A, *Helv. Chim. Acta* **1975**, *58*, 936–967.
225. Haselbach E, Bally T, Lanyiova Z, Baertschi P *Helv. Chim. Acta* **1979**, *62*, 583–592.
226. Roth HD, Schilling MLM, Jones G, *J. Am. Chem. Soc.* **1981**, *103*, 1246–1248.
227. Roth HD, Schilling MLM *J. Am. Chem. Soc.* **1981**, *103*, 7210–7217.
228. Raghavachari K, Haddon RC, Roth HD, *J. Am. Chem. Soc.* **1983**, *105*, 3110–3114.
229. Toriyama K, Nunone K, Iwasaki M, *J. Chem. Soc., Chem. Commun.* **1983**, 1346–1347.
230. Gerson F, Qin X-Z, *Helv. Chim. Acta* **1989**, *72*, 383–390.

231. Ishiguro K, Khudyakov IV, McGarry PF, Turro NJ, Roth, HD, *J. Am. Chem. Soc.* **1994**, *116*, 6933–6934.
232. Ladenburg A, *Chem. Ber.* **1869**, *2*, 140.
233. Raghavachari K, Roth HD, *J. Am. Chem. Soc.* **1989**, *111*, 7132–7136.
234. Oth JMF, *Ang. Chem.* **1968**, *79*, 1102; *Ang. Chem. Int. Ed. Engl.* **1968**, *7*, 646.
235. Nunome K, Toriyama K, Iwasaki M, *Tetrahedron* **1986**, *42*, 6315–6323.
236. Toriyama K, Okazaki M, *Radiat. Phys. Chem.* **1989**, *33*, 505.
237. Lotais BC, Jonah CD, *Radiat. Phys. Chem.* **1989**, *33*, 505.
238. Sauer MCJ, Schmidt KH, *Scand. Chem. Acta.* **1996**, *51*, 167–173.
239. Melekhov VI, Anisimov OA, Sjoquist L, Lund A, *Chem. Phys. Lett.* **1990**, *174*, 95–102.
240. Barnabas MV, Trifunac AD, *Chem. Phys. Lett.* **1991**, *187*, 565–570.
241. Hixson SS, Xing Y, *Tetrahedron Lett.* **1991**, *32*, 173–174.
242. Weng H, Roth HD, *J. Org. Chem.* **1995**, *60*, 4136–4145.
243. Weng H, Du X-M, Roth HD, *J. Am. Chem. Soc.* **1995**, *117*, 135–140.
244. Pross A, *J. Am. Chem. Soc.* **1986**, *108*, 3537–3538.
245. Shaik SS, Pross A, *J. Am. Chem. Soc.* **1989**, *111*, 4306–4312.
246. Eberson L, Radner F, *Acta. Chem. Scand.* **1992**, *46*, 312–314.
247. Eberson L, Radner F, *Acta. Chem. Scand.* **1992**, *46*, 802–804.
248. Eberson L, Hartshorn MP, Radner F, Merchan M, Roos BO, *Acta. Chem. Scand.* **1993**, *47*, 176–183.
249. Dinnocenzo JP, Simpson TR, Zuilhof H, Todd WP, Heinrich T, *J. Am. Chem. Soc.* **1997**, *119*, 987–993.
250. Arnold DR, Humphreys RWR, *J. Am. Chem. Soc.* **1979**, *101*, 2743–2744.
251. Weng H, Sheik Q, Roth HD, *J. Am. Chem. Soc.* **1995**, *117*, 10655–10661.
252. Herbertz T, Roth HD, *J. Am. Chem. Soc.* **1996**, *118*, 10954–10962.
253. Gassman PG, Olson KD, *Tetrahedron Lett.* **1983**, *1*, 19–22.
254. Shaik SS, Dinnocenzo JP, *J. Org. Chem.* **1990**, *55*, 3434–3436.
255. Shaik SS, Reddy AC, Ioffe A, Dinnocenzo JP, Danovich D, Cho JK, *J. Am. Chem. Soc.* **1995**, *117*, 3205–3222.
256. Karki SB, Dinnocenzo JP, Farid S, Goodman JC, Gould I, Zona TA, *J. Am. Chem. Soc.* **1997**, *119*, 431–432.
257. Roth HD, *Topics Curr. Chem.* **1990**, *156*, 1–19.
258. Roth HD, *Tetrahedron* **1986**, *42*, 6097–6100.

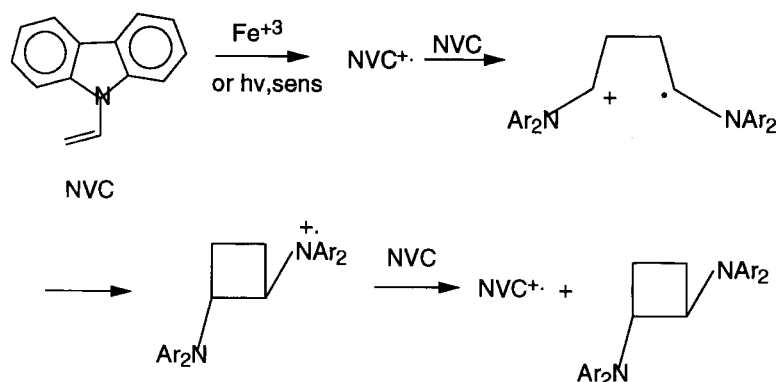
3 The Electron-transfer Chemistry of Carbon–Carbon Multiple Bonds

Nathan L. Bauld and Daxin Gao

3.1 Introduction

The research of the Ledwith group at Liverpool on the cyclodimerization of *N*-vinylcarbazole (NVC) is the key to much of the modern electron transfer chemistry of carbon–carbon multiple bonds (Scheme 1) [1].

Not only was the overall reaction novel in its *connectivity*, i.e., the formation of cyclobutane rings (cyclobutanation), which is unusual outside of photochemistry, but even more importantly, the *cation radical chain mechanism* which was proposed and demonstrated for the reaction represented a fundamentally new reaction mechanism. Significantly for the present context, this mechanism involved not one but two electron transfer (ET) steps. The first, ionization of NVC to the corresponding cation radical ($\text{NVC}^{+\bullet}$) was effected by either a metal ion oxidant (e.g. Fe^{3+}) or by photosensitized electron transfer (PET) to excited state chloranil. This step is followed by cycloaddition of $\text{NVC}^{+\bullet}$ to neutral NVC to yield, in Ledwith's formulation, an acyclic 1,4-butanediyl cation radical. The latter then cyclizes to the cyclobutane cation radical, which is subsequently reduced to the neutral cyclobutane product by electron transfer from neutral NVC, thereby also regenerating $\text{NVC}^{+\bullet}$ and setting up the chain mechanism. Following the suggestion of Farid, this type of dimer is referred to more specifically as a *cyclobutadimer*. These latter three steps thus constitute a chain process. Although this mechanism *might* be valid in the case of NVC, one aspect of it appears to require revision for the cyclobutadimerizations of many other substrates. In particular, many of the cyclodimerizations appear to proceed in a concerted manner, directly forming a cyclobutane cation radical, and avoiding the formation of an intermediate acyclic cation radical (*vide infra*). This latter mechanism, in its simplest form, consists essentially of a *substrate ionization* step followed by a propagation cycle consisting of alternating *cation radical/neutral cycloaddition* and *electron transfer* steps. Incidentally, a *catalytic* (as opposed to a chain) *version* of this mechanism is also potentially available and can be realized when the cyclobutadimer cation radical is neutralized by the reduced form of



Scheme 1. The cation radical chain cyclodimerization of *N*-vinylcarbazole.

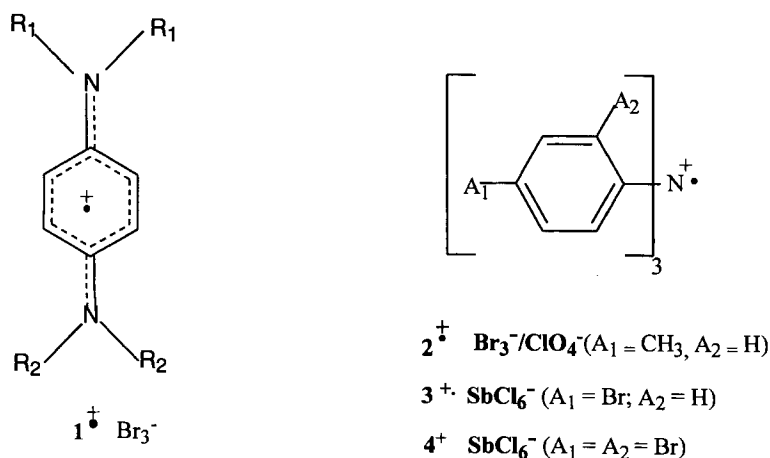
the species which initially oxidizes the substrate, instead of being neutralized by the substrate itself. It is evident that cation radicals (or radical cations) are key reactive intermediates in these ET reactions. However, analogous mechanisms exist, at least on paper, for the case in which the substrate accepts an electron to form an *anion radical* (radical anion). The ET chemistry of both organic cation and anion radicals will be considered in this chapter, beginning with the more abundant ET chemistry of cation radicals.

3.2 Electron Transfer Chemistry Involving C–C Multiple Bonds as Single-electron Donors

3.2.1 Discovery of Cation Radicals

The first stable cation radical salts (**1**) were obtained by Würster in 1879, simply by reacting the corresponding diamine with bromine in methanol/acetic acid solvent (Scheme 2) [2].

A stable triarylaminium salt (**2**) was isolated by Wieland in 1907 [3]. Neither **1** nor **2** was recognized as a cation radical salt, since this concept had not yet even begun to emerge. It was not until 1926 that Weitz formulated the corresponding perchlorate salt of **2** as a delocalized cation which is also a ‘free ammonium radical’ [4]. Michaelis then made Weitz’s interpretation more certain via electrochemical oxidation studies, and he coined the term ‘cationic free radical’, which is the appropriate antecedent of the current term ‘cation radical’ [5]. Since that time, many other cation radical salts have been prepared, but the salts **3**⁺⁺ and **4** have an especially important role in the electron transfer chemistry of cation radicals [6, 7].

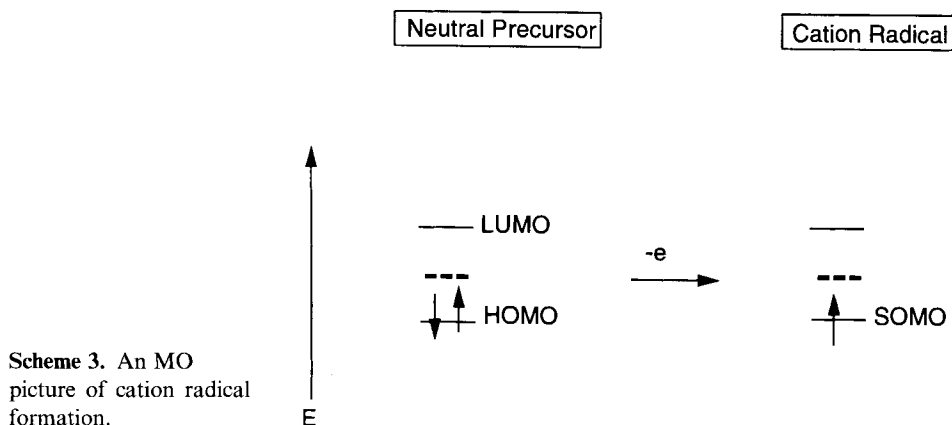


Scheme 2.

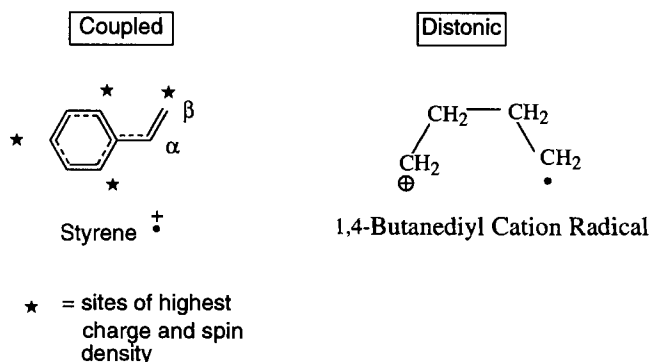
3.2.2 A Molecular-orbital Picture of Cation Radical Formation

Conceptually, cation radicals are related to the corresponding neutral molecules through removal (ionization) of one electron (Scheme 3).

In contrast to carbocation, radical, or carbanion formation, no bonds are broken in cation radical formation, although bonding is diminished by removal of an electron from a bonding MO. If the geometry of the resulting cation radical is not very different from that of the neutral precursor (by no means always the case!), the ground state cation radical can be considered to result from the removal of an electron from the highest energy MO (i.e., the HOMO) of the precursor, which MO then becomes the SOMO (singly occupied MO) of the cation radical. This latter MO then predominantly controls the spin distribution in the cation radical. If, in



Scheme 3. An MO picture of cation radical formation.



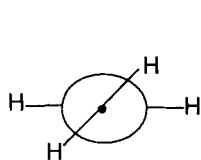
Scheme 4. Spin and Charge Coupling/Uncoupling in Cation Radicals.

addition, the original precursor molecule was nonpolar or at least not very polar, the same SOMO also primarily controls the (positive) charge density in the cation radical. For this reason, the spin and charge in many pi hydrocarbon cation radicals are said to be ‘coupled’. Thus, to a first approximation, the spin and charge density at a given carbon atom are equal. We may say that spin and charge ‘travel together’. We may even consider this spin/charge density to be ‘hole density’, which term implies both spin and positive charge. However, if the neutral precursor has substantial charge separation, the net charge density is a composite of the effects of the SOMO electron density and the density contributed by other occupied MOs. The spin and the charge densities are then said to be ‘uncoupled’. A cation radical in which the spin and charge are essentially completely separated (i.e., uncoupled) is termed a ‘distonic’ cation radical. An example of a distonic cation radical which is particularly relevant to the reactions of cation radicals with pi bonds is the 1,4-butanediyl cation radical (Scheme 4).

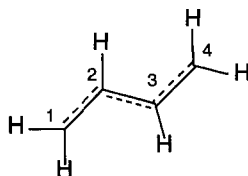
In terms of reactivity, the importance of the spin density is that radicals, including cation radicals, tend to react at the position(s) of highest spin density, especially in coupling reactions with other radicals, but also in abstractions of atoms from neutral molecules. The importance of charge density is, of course, that in their reactions with nucleophiles (neutral or negatively charged), cation radicals tend to react at the position of highest charge density. For hydrocarbon cation radicals, in which spin and charge are coupled, both types of reaction tend to occur at the same position(s). This scenario also holds even for many non-hydrocarbon cation radicals. However, it should also be noted that when a neutral molecule is significantly dipolar, the charge distribution in the cation radical does not arise exclusively from the SOMO, so that spin and charge are partially uncoupled.

3.2.3 Cation Radical Structures

The geometric structures of cation radicals are often considered to be similar to those of the corresponding neutral molecules from which they are generated. Such



Ethene Cation Radical

Non-planar (dihedral angle = 27°)*s-trans*-1,3-Butadiene Cation Radical

(planar; C2-C3 bond order increased)

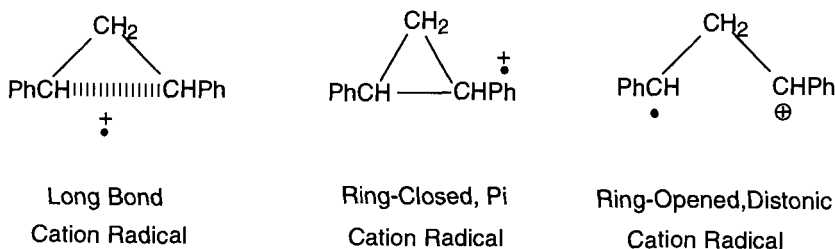
Scheme 5. Ethene and butadiene cation radicals.

an approximation serves best when the charge and spin density (hole density) is extensively delocalized, so that no individual bond is sharply weakened. However, cation radical structures can and often do differ in very important ways from those of the corresponding neutrals. We will focus here upon just a few of the structural adjustments which are most pertinent to the ET chemistry of carbon-carbon multiple bonds.

Pi cation radicals

Pi cation radicals, that is cation radicals in which the SOMO is a pi type orbital, are obviously key intermediates in the ET chemistry of alkenes and alkynes. The ethene cation radical, which has the novel twisted structure shown in Scheme 5, provides an excellent example of a significant structural adjustment which can accompany the loss of an electron [8].

Since in a planar ethene cation radical of the pi type the SOMO would be completely localized in one bond (the pi bond), the latter is substantially weakened. Torsion around this weakened carbon-carbon bond relieves torsional strain (eclipsing of the C–H bonds) and allows additional delocalization of the SOMO to the C–H bonds via hyperconjugation. However, if the SOMO is delocalized over two pi bonds, as in the case of diene cation radicals (which are especially important intermediates in the ET chemistry of interest), the ground state cation radical structure remains planar [9]. Evidently neither of the pi bonds is weakened sufficiently to occasion torsion around the formal pi bonds. In the case of diene cation radicals, an important consequence of cation radical formation is the strengthening of the central (C2–C3) bond, so that torsion around this bond becomes much more difficult than in the parent diene. Although net bonding is diminished in the cation radical, the C2–C3 bond is actually strengthened when an electron is removed from the HOMO, which is antibonding between these two atoms. On the other hand, the C1–C2 and C3–C4 bonds are more strongly attenuated. The consequence is that all three C–C bonds in the butadiene cation radical have nearly equal stretching force constants [9]. *A direct consequence of this is that cation radicals corresponding to the s-cis and s-trans forms of the diene are not readily interconvertible.*



Scheme 6. The long, one-electron bond.

Sigma cation radicals

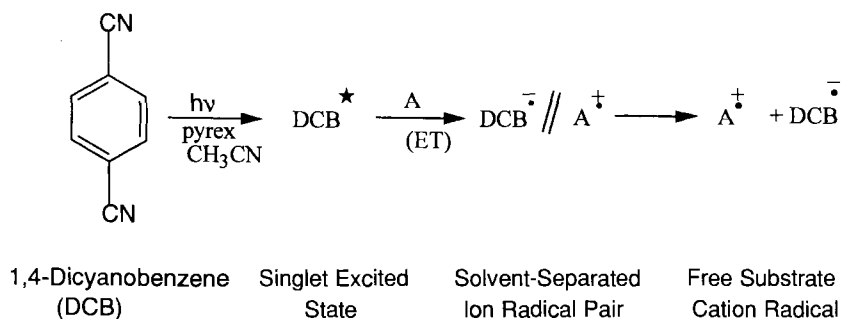
The second type of structural adjustment which is pertinent to the present chemistry is the ‘long bond’. An especially good example of this phenomenon is available in the case of the 1,2-diphenylcyclopropane cation radical [10]. Any of the three possible structures of this cation radical illustrated in Scheme 6 might be considered to be plausible, *a priori*.

The distonic cation radical appears plausible because in it a strained cyclopropane bond is broken and both the spin and charge are delocalized benzylically. The ring-closed structure in which the (pi) SOMO (i.e., the cation radical moiety) resides on one of the aryl rings is also plausible, since delocalization of the SOMO over an aromatic ring tends to stabilize it. However, the long bond structure, in which the SOMO is somewhat concentrated in a specific, much-lengthened cyclopropane bond, but with additional benzylic delocalization of the SOMO onto both phenyl rings, is preferred. This long, one electron bond is nevertheless sufficiently strong that the *cis* and *trans* isomers of this cation radical are not interconverting on the relevant time scale (the CIDNP time scale). Nevertheless, all three types of cation radical structure—ring-opened distonic, ring closed pi, and long bond—may play a role in the relevant ET chemistry and all deserve consideration. It should be noted that the long bond (or trapezium) structure is particularly favored by a symmetrical 1,2-disubstitution pattern, which is usually encountered in cation radical cyclobutanation reactions. This is especially the case if the substituents are cation stabilizing substituents, such as aryl or vinyl, but even 1,2-dimethylcyclobutane appears to favor the long bond structure [11]. The cyclobutane cation radical itself, however, has a novel rhomboid structure [11].

3.2.4 The Generation of Cation Radicals in Solution

The photosensitized electron transfer (PET) method

In their pioneering research on the cyclodimerization of *N*-vinylcarbazole, the Ledwith group used both metal ion oxidants (e.g., Fe^{3+}) and photosensitized electron transfer (PET) to generate substrate cation radicals. This latter method, previously



Scheme 7. Photosensitized electron transfer ionization.

used by Ellinger in his own research on *N*-vinylcarbazole [12], has remained rather popular, and the basic processes involved in it are therefore briefly illustrated in Scheme 7.

Essentially, the photoexcited state of an electron deficient photosensitizer becomes a potent single electron acceptor (SEA), in part because of the electronic excitation energy available to drive the reaction, and in part because the electron withdrawing groups on the sensitizer strongly stabilize the resulting sensitizer anion radical. Although Ledwith's group used chloranil as a sensitizer, many other sensitizers are now in common use, including 1,4-dicyanobenzene (DCB), cyanonaphthalene (CN), dicyanonaphthalenes (DCN), and di- and tetracyanoanthracene (DCA and TCA, respectively). A key requirement in the PET method is that the ultraviolet light must be exclusively absorbed by the sensitizer, and not significantly by the substrate, so that direct photochemistry is circumvented. For many substrates it is sufficient merely to carry out the reaction in a Pyrex reaction vessel, but for substrates which have significant absorption at or above 290 nm appropriate filters (e.g., uranium filters) are required. Traditionally, these PET reactions are carried out in dry acetonitrile solvent, even though it is known that cation radicals sometimes react with such polar solvents. Further, hydrocarbon substrates may not be soluble in acetonitrile. To avert reactions of the ion radical intermediates with the solvent, and to provide solubility for most organic substrates, dichloromethane may sometimes be a preferable solvent. The efficiency of PET reactions in dichloromethane and other relatively less polar solvents can be substantially improved through the use of a cationic photosensitizer such as an *N*-methylacridinium salt [13]. When the excited state of such a cation accepts an electron from the substrate, a radical/cation radical pair is formed in contrast to the more usual anion radical/cation radical pair. In the latter case but not in the former, diffusive separation of the cation radical is retarded by coulombic attractions. Slower diffusive separation, in turn, leads to more back electron transfer and to less efficient generation of free cation radicals. This would be especially true if the solvent is a relatively nonpolar one, such as dichloromethane. Another variation in the PET method consists of using a *co-sensitizer*, i.e., one which does not absorb the ultraviolet light but which,

when present in excess, acts as the primary electron donor, forming a co-sensitizer cation radical [14]. The co-sensitizer, often biphenyl, is chosen so that the subsequent electron transfer from the ultimate substrate molecule is exergonic. A consequence of this method of generating substrate cation radicals is that presumably only free substrate cation radicals are formed, thus minimizing the chances of reaction with the anion radical of the sensitizer. Further, the ionization of a substrate or a mixture of substrates is considerably more selective in the much less exergonic process involving a co-sensitizer cation radical.

The aminium salt method

In 1981, Bauld and Bellville demonstrated that substrate cation radicals can be generated at a rate sufficient to produce efficient ET cycloaddition chemistry by using triarylamminium salts such as 3^{+} in catalytic amounts [15]. Since 3^{+} is commercially available and shelf-stable, this chemical method of oxidation is a particularly convenient method for generating cation radicals of substrates which have oxidation potentials up to about 1.6 V vs SCE and for studying their unique ET chemistry in solution. The oxidation potential of **3** is 1.05 V vs. SCE [7]. Other triarylamminium salts such as 4^{+} which have even higher oxidation potentials (the oxidation potential of **4** is 1.59 V [7]) are also available and have been employed in many successful ET reactions of less readily oxidizable substrates. A particular advantage of 4^{+} is its much greater solubility than 3^{+} , in dichloromethane, so that reactions can be run at temperatures as low as -78°C or even lower.

Electrochemical and other methods

Anodic electrochemical (EC) oxidation is also a very attractive procedure for inducing ET chemistry of pi cation radicals [16], and a variety of other ionization methods have also been employed, many of which involve the generation of cation radicals on surfaces. Examples include zeolites [17], clays [18], semiconductors [19], and cation radical polymer surfaces [20]. The generation of cation radicals in solution by photoionization and photosensitized electron transfer, in conjunction with time-resolved spectroscopic studies of the reactions of the cation radical represents a particularly powerful method for the quantitative study of cation radical chemistry, which will be extensively noted in this review [14, 21]. Finally, the generation of cation radicals in rigid matrices by gamma radiolysis has proved to be an excellent way of not only studying the structures of cation radicals, but even of revealing their intramolecular chemistry [22].

General mechanisms of substrate ionization

Using a familiar method of classifying the mechanisms of intermolecular electron transfers, the mechanism of substrate ionization may be of the *inner sphere* or the *outer sphere* type. *Outer sphere electron transfer* involves the transfer of an electron between two chemical species without the development of any significant covalent interaction between them, i.e., through space or through another molecule or mol-

ecules. In contrast, *inner sphere electron transfer* occurs with the assistance of at least some significant degree of covalent interaction. Typically, photosensitized electron transfer is highly exergonic and the ET is of the outer sphere variety. Evidence strongly suggest that, at least in acetonitrile, the most common solvent for PET reactions, the cation radical/anion radical pair is initially formed as a *solvent separated ion pair* [23]. In solvents which are much less polar, as for example dichloromethane, it is not certain whether solvent-separated or contact ion pairs are formed. A reliable method of generating contact ion pairs is available for instances in which the sensitizer and the substrate form a ground state donor/acceptor complex. Irradiation of this complex at the charge transfer frequency generates the contact cation radical/anion radical pair [23]. In the case of chemical ionization by an agent such as an aminium salt, which is typically an endergonic process, recent evidence indicates that many of these electron transfers occur by an inner sphere process which involves strong covalent interaction, the more precise details of which will be discussed further on [24].

Electron transfer and hole transfer

The term ‘hole transfer’ is frequently used to describe the specific type of electron transfer which occurs between a cation radical and a neutral molecule. The cation radical is considered to have a missing electron or ‘hole’, and transfers this to the neutral molecule, which then becomes a cation radical, while the original cation radical is neutralized. Hole transfer is of one of the simplest and most common types of reaction between cation radicals and neutral molecules.

3.2.5 Cation Radical Cyclobutanation

Scope of the cation radical chain cyclobutanation reaction

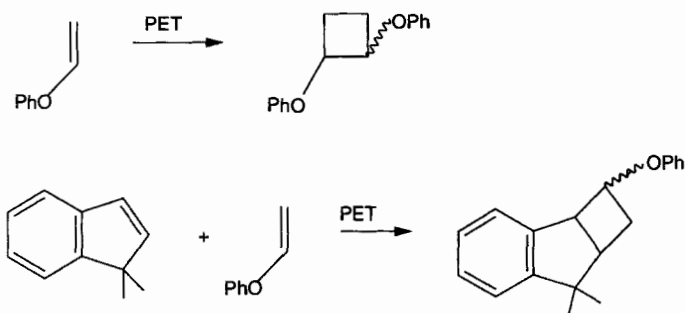
Subsequent to the work of the Ledwith group, cation radical cyclobutanation was extended to a variety of relatively readily ionizable substrates, including styrenes, indenenes, and phenyl vinyl ether (Scheme 8) [25, 26].

Farid also reported the first example of an efficient cross addition, that occurring between dimethylindene and phenyl vinyl ether [27]. Essentially all of these reactions were carried out using the PET method.

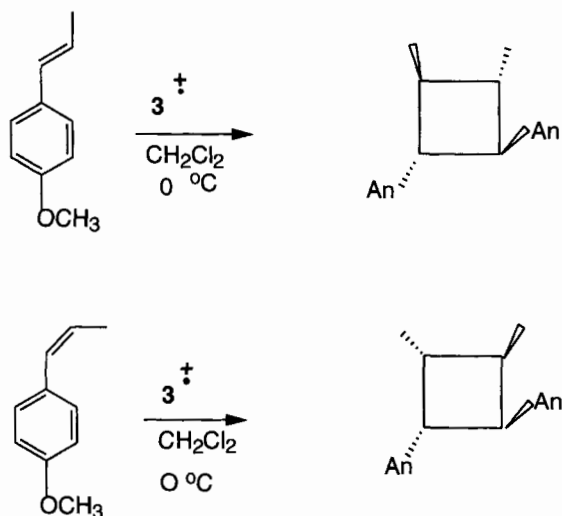
The mechanism of cation radical cyclobutanation

The stereochemistry of cyclobutanation was first studied using the aminium salt (3^{+}) method. The cyclobutadimerizations of both *trans*- and *cis*-anethole were found (Scheme 9) to be stereospecific [28].

Subsequently the same reactions were studied using the PET method (acetonitrile solvent), and confirmed to be stereospecific [29]. The mechanistic significance of these results is that a mechanism analogous to the one proposed by Ledwith for the cyclobutadimerization of *N*-vinylcarbazole which involves a distonic cation radical,



Scheme 8. Other early examples of cyclobutanation.

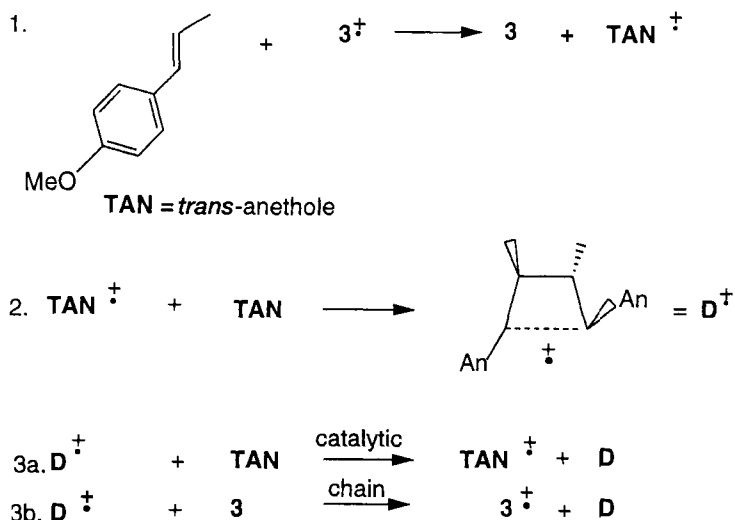


An = *p*-Anisyl = 4-Methoxyphenyl

Scheme 9. The cyclobutadimerization of *trans*- and *cis*-anethole.

is difficult to reconcile with stereospecificity. Since the cycloadditions were found to be completely stereospecific in both a polar (acetonitrile) and a relatively non-polar (dichloromethane) solvent, a more plausible mechanism involves the concerted addition of the *trans*-anethole cation radical to neutral *trans*-anethole (Scheme 10).

The resulting dimer cation radical could conceivably be of either the ring-closed, π type or the long bond type. By analogy to the known structure of the 1,2-

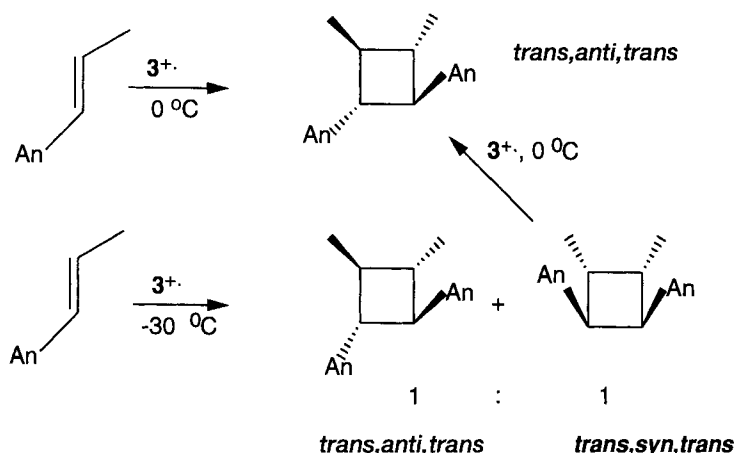


Scheme 10. Mechanism of the aminium-salt induced cation radical cyclobutadimerization of *trans*-anethole.

diphenylcyclopropane cation radical and in view of the calculational results for the 1,2-dimethylcyclobutane cation radical, this dimer cation radical has been assumed to be of the long bond type.

Selectivity characteristics of cation radical cyclobutane

In every case, including those of *trans*-anethole and phenyl vinyl ether, cyclobutadimerization has proved to be completely head to head regiospecific. This is eminently plausible since in the case of either a styrene or an enol ether type cation radical, there is much more spin and charge density on the carbon beta to the aryl or alkoxy group than alpha to it. Reaction therefore preferentially occurs at the beta position. This tendency is further reinforced by the circumstance that when the covalent bond is established at the beta position of the cation radical, positive charge and/or spin will be generated at the alpha position, where it can be effectively stabilized by the aryl or heteroatom substituent. The cation radical also tends to add to the beta carbon of the neutral molecule for this latter reason. Although the thermodynamically more stable *anti* cyclobutane isomer is often favored over the *syn* isomer, *anti* diastereoselectivity is not necessarily high in all cases. An interesting case is that of *trans*-anethole dimerization. When the reaction is carried out at 0 °C, using the aminium salt catalyst, only the *trans,anti,trans* cyclobutadimer is obtained. However, if the reaction is carried at –40 °C, an approximately 50:50 mixture of this isomer along with the *trans,syn,trans* isomer is obtained (Scheme 11) [28].



Scheme 11. *Syn/anti* diastereoselectivity in the dimerization of *trans*-anethole.

When the latter mixture is treated with the aminium salt at 0 °C, the mixture isomerizes completely to the more stable *trans,anti,trans* isomer. Evidently, the cyclodimerization is reversible at the higher temperature. It is also noteworthy that even the reversal is stereospecific, since none of the other possible diastereoisomers are formed. This result is nicely interpreted in terms of the ionization of the *trans,syn,trans* cyclobutadimer to a long bond cation radical, followed by concerted fragmentation to *trans*-anethole and the *trans*-anethole cation radical, avoiding the formation of any *cis*-anethole. The cyclodimerization of phenyl vinyl ether gives both *trans* (or *anti*) and *cis* (or *syn*) isomers initially, but subsequent reaction induces some isomerization of the less stable *cis* isomer to the more stable *trans* isomer. This is believed to occur through the intervention of a distonic 1,4-butanediyl type cation radical.

Comparison of the selectivity of cation radical cyclobutadimerization with direct photocyclodimerization

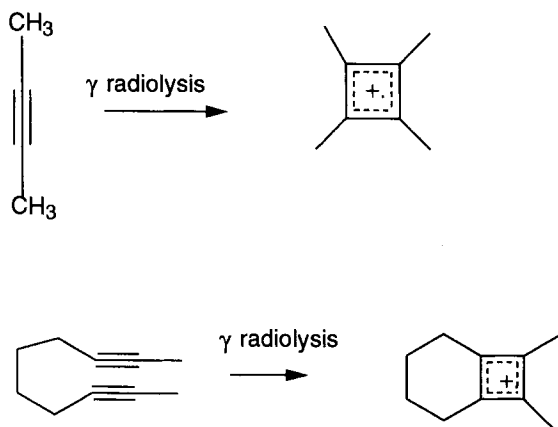
The reaction of singlet excited *trans*-anethole with ground state *trans*-anethole is considered to occur *via* an excited state dimer (excimer), in a process which selectively gives rise to the *trans,syn,trans* cyclobutadimer, in direct contrast to the cation radical process [30]. This appears to be a rather general result for direct photodimerization *via* singlet excited states. In further contrast, triplet excited states of *cis* and *trans* isomers undergo extensive *cis/trans* isomerization (of the starting alkene), and moreover the cycloaddition is stepwise. Both of these processes are inconsistent with stereospecific addition. However, head-to-head regiospecificity is often the strong preference in both singlet and triplet photocyclodimerizations as well as in cation radical cyclodimerizations.

Rates of cation radical cyclobutanation reactions

The cation radicals of a substantial number of styrene derivatives have been generated both by photoionization and by photosensitized electron transfer and the absolute rates of their reactions with a variety of neutral styrenes, dienes, and electron rich alkenes measured by means of time resolved UV–visible spectroscopy. As an example, the rate of cycloaddition of the *p*-methoxystyrene cation radical to *p*-methoxystyrene is $1.4 \times 10^9 \text{ M}^{-1} \text{ s}^{-1}$, only about a factor of ten less than the diffusion controlled rate in acetonitrile [31]. Incidentally, the rate of the reverse of this reaction is also rather high, at 8×10^7 . The authors conclude, in agreement with the findings of both the Bauld and Lewis groups, that there is no evidence for a distonic cation radical intermediate, suggesting that the evidence is most consistent with the concerted formation of a long bond cyclobutane cation radical intermediate. Incidentally, the rate constant for the electron transfer reduction of this long bond cyclobutane cation radical is found to be $1.5 \times 10^{10} \text{ M}^{-1} \text{ s}^{-1}$, i.e., essentially the diffusion controlled rate. That terminal methyl groups attached to the double bond have a substantial steric effect on cation radical cycloadditions is evident from the rate constant for the cycloaddition of the *trans*-anethole cation radical to *trans*-anethole, which is only $8 \times 10^7 \text{ M}^{-1} \text{ s}^{-1}$. This steric effect is also evident in the relative rates of addition of the vinylnisole and *trans*-anethole cation radicals to various alkenes, enol ethers, and styrenes [32]. The profound stabilizing effect of the *p*-methoxy function upon the cation radical moiety is also evident in comparing the relative rates of addition of the parent styrene cation radical and the vinylnisole cation radical to alkenes and enol ethers. Whereas the styrene cation radical reacts even with cyclohexene with a rate constant of 1.2×10^9 , the reaction of the vinylnisole cation radical with this simple alkene is too slow to measure ($< 5 \times 10^5$).

Kinetics of the cyclobutadimerization of *trans*-anethole

A kinetic study has been reported for the cyclodimerization of *trans*-anethole as initiated by 3^{++} in dichloromethane solution [33]. The kinetic rate law which applies over a range of concentrations and for four different temperatures ranging from 0 to 25°C is second order in the concentration of *trans*-anethole and first order in the aminium salt concentration. These kinetics are consistent with a chain mechanism in which termination is a unimolecular reaction of the *trans*-anethole cation radical, quite possibly *via* de-protonation. The initiation step consists of the ionization of *trans*-anethole by the aminium salt. The second molecule of *trans*-anethole enters the rate law through the first propagation step, in which the *trans*-anethole cation radical reacts with *trans*-anethole. The activation parameters derived for the reaction are $\Delta G_a = 10.6 \text{ kcal mol}^{-1}$, $\Delta H_a = 2.1 \text{ kcal mol}^{-1}$, and $\Delta S_a = -29.85 \text{ e.u.}$. The unusually low value of ΔH is reflected in the circumstance that the rate decreases by less than a factor of 2 from the highest to the lowest temperature studied. As expected for a reaction involving the generation of *trans*-anethole cation radicals, the reaction rate is slowed by the addition of large amounts of the neutral triarylamine **3**, revealing either reversal of the ionization step under these conditions or conversion of the more efficient chain mechanism, in part, to a catalytic one by



Scheme 12. Cation radical cyclo-additions of alkynes.

neutralizing the dimer cation radical with **3** instead of with *trans*-anethole. However, the effect is small, the addition of 100 mol % of **3** producing only a rate diminution of at most a factor of 4.

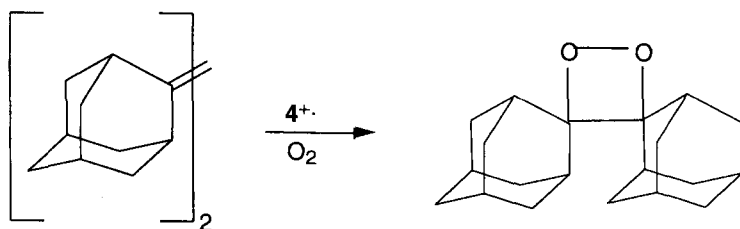
Cation radical cyclobutanation reactions of alkynes, ketenes, and allenes

The cation radical cyclodimerization of 2-butyne has been observed by ESR spectroscopy under matrix isolation conditions (Scheme 12) [34].

When the cation radical of this alkyne is generated by γ radiolysis in a solid matrix at 77 K and then warmed to 150 K, the ESR spectrum of the 1,2,3,4-tetramethyl-1,3-butadiene cation radical is observed. An analogous intramolecular reaction was also observed even in a rigid matrix at 77 K. The feasibility of the cycloaddition step itself is therefore indicated, but little work has yet been done in respect of the aminium salt or PET induced cycloadditions of alkynes in solution at ambient or near-ambient temperatures. Whether a chain or catalytic alkyne cyclodimerization can be effected is yet unclear, as is the potential fate of the cyclobutadiene products.

Theoretical considerations in cyclobutanation

A unique aspect of cation radical cycloaddition is the ability to form cyclobutane rings in a thermal reaction of amazing facility. The corresponding reaction on the neutral potential surface is extremely difficult for most unsaturated systems. Like the latter reaction, which is formally a $[2 + 2]$ cycloaddition, the cation radical cyclobutanation reaction, which is a $[2 + 1]$ cycloaddition, is formally symmetry forbidden [35]. The kinetic driving force for cation radical cycloadditions, in general, as contrasted to neutral cycloadditions will be discussed in detail further on. Reaction path calculations suggest that cation radical cyclobutanations, in the simpler cases, have little or no activation energy and proceed via non-synchronous but, at



bis(adamantylidene)

Scheme 13. Oxetane formation by cation-radical cycloaddition to dioxygen.

least in some cases, concerted reaction paths. For example, the cycloaddition of the ethene cation radical both to ethene and to ethyne involves the formation of a loose, T-shaped ion/molecule complex intermediate which collapses smoothly to the cyclobutane or cyclobutene cation radical, respectively [11, 36]. Further results indicate that the ethyne cation radical also adds to neutral ethyne via an effectively concerted path [36]. In none of these cases do the calculations reveal the intervention of a distonic cation radical intermediate.

3.2.6 Formation of 1,2-Dioxetanes by Cation Radical Additions to Triplet Dioxygen

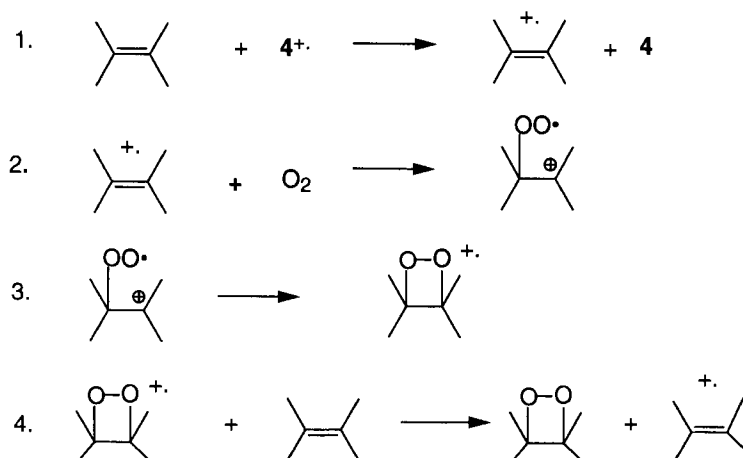
In a reaction quite analogous to cation radical cyclobutanation, cation radicals of some relatively ionizable, but sterically hindered alkenes have been found to add to ground state dioxygen in a very efficient cation radical chain process (Scheme 13) [37].

The reaction is somewhat limited in scope because cyclobutadimerization is a potentially competing reaction for substrates which are ionizable but not sterically hindered, and conjugated dienes react with oxygen under these same conditions to give 1,4-endoperoxides (vide infra). The reaction is best carried out using the more potent, hexabromo salt at -78°C , and has been found to be incompletely stereospecific. Consequently, a distonic cation radical intermediate has been postulated to play a role in the mechanism (Scheme 14).

3.2.7 Cation Radical Diels–Alder Cycloadditions

Historical

The γ radiolysis of 1,3-cyclohexadiene was reported, in 1969, to yield two sets of dimers [38]. One set was the familiar pair of *syn* and *anti* cyclobutane dimers which had previously been obtained via triplet sensitized photodimerization. The other set



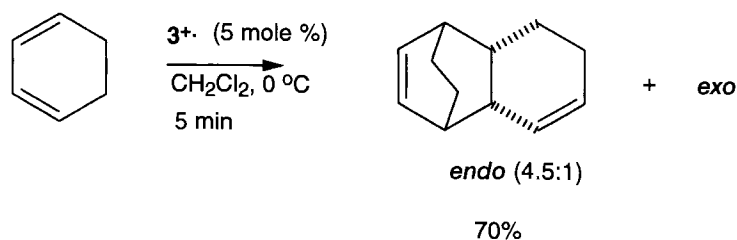
Scheme 14. Cation radical chain mechanism for oxetane formation.

of dimers was the *endo/exo* Diels–Alder dimer pair. The Diels–Alder dimers were shown to arise primarily through a cation radical chain mechanism, which was highly periselective for Diels–Alder cycloaddition as opposed to cyclobutanation. The cyclobutane dimers and a portion of the Diels–Alder dimers (primarily the *exo* dimer) were produced by triplet 1,3-cyclohexadiene chemistry.

The aminium salt catalyzed cation radical Diels–Alder reaction

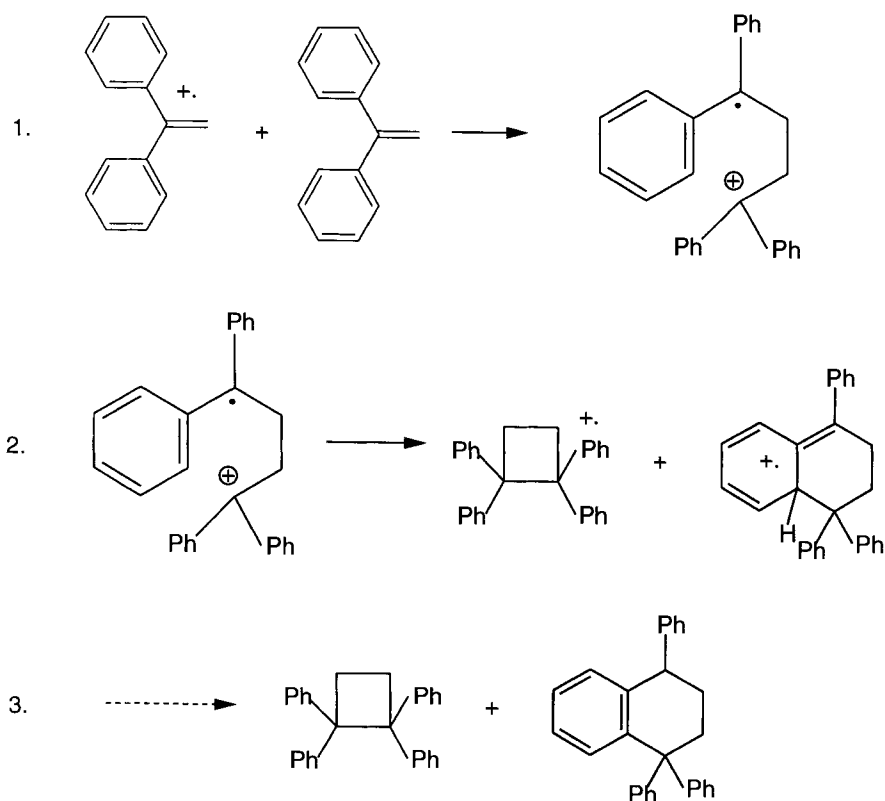
In 1981, this cation radical Diels–Alder cyclodimerization of 1,3-cyclohexadiene was shown to be more cleanly (only 1 % of the cyclobutane dimers is produced), conveniently (in a synthetic organic context), and efficiently (70 % yield) carried out by chemical ionization of the diene, using $3^{+•}$ (Scheme 15) [39].

The reaction was carried out in dichloromethane solvent at 0 °C for 5 min, using 5 mol % of the initiator. The *endo/exo* ratio (4.5:1) was similar to that found in the thermal Diels–Alder cyclodimerization of this same diene. This encouraging result and the convenience of the procedure led to the extensive study of the cation radical Diels–Alder reaction and its utility in synthetic organic chemistry [40]. It is of further note that the same cyclodimerization was subsequently carried out by the PET



Scheme 15. The aminium salt initiated cation radical Diels–Alder reaction.

method, and the rate constant for the cycloaddition of the 1,3-cyclohexadiene cation radical to the neutral diene was estimated to be $2 \times 10^8 \text{ s}^{-1}$, only a factor of sixty less than the diffusion controlled rate [41]. Other relatively ionizable 1,3-cyclohexadiene derivatives have more recently been found to undergo facile cation radical Diels–Alder cyclodimerization. These include 1-methyl-1,3-cyclohexadiene and 1-methoxy-1,3-cyclohexadiene. Readily ionizable acyclic dienes such as 2,4-dimethyl-1,3-pentadiene and 1,1'-dicyclohexenyl also undergo such cyclodimerization, but dienes which ionize with more difficulty, such as 1,3-butadiene, isoprene, 2,3-dimethyl-1,3-butadiene, and 1,3-cyclopentadiene do not. Another very early development in cation radical cycloaddition chemistry was the photosensitized electron transfer cyclodimerization of 1,1-diphenylethene first reported in 1973 by Neunteufel and Arnold [42]. These authors reported the efficient (70 %) formation of a Diels–Alder type adduct using methyl 4-cyanobenzoate as the sensitizer. Subsequently, Mattes and Farid observed the formation of both the cyclobutadimer and Diels–Alder type dimers, and proposed a common distonic cation radical intermediate (Scheme 16) [43].



Scheme 16. The pet induced cyclodimerization of 1,1-diphenylethene.

Note that the DA dimers are formed in an unusual way, in effect, by using a dienic moiety which includes one of the benzene ring bonds. Additional important observations of Diels–Alder reactions induced under PET conditions were reported by Libman [44] and by Mizuno [45].

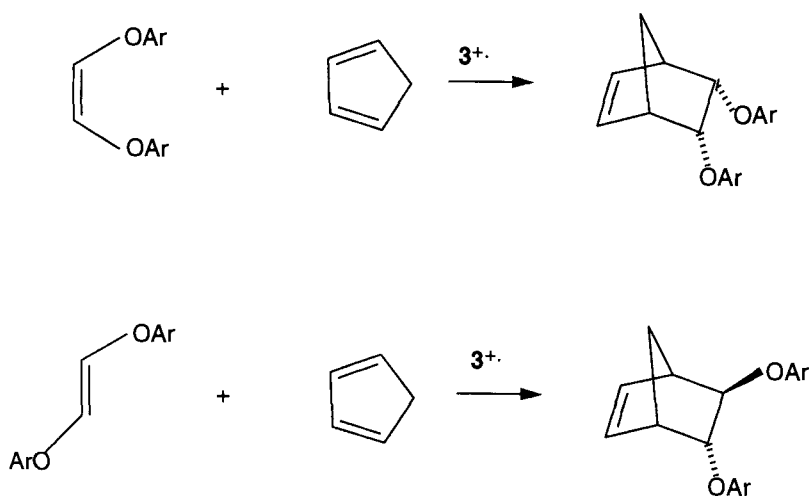
Stereochemistry of the cation radical Diels–Alder reaction

The uncatalyzed Diels–Alder reaction is well known to be highly stereospecific, preferentially occurring via syn addition to both the diene and dienophilic components. Stereochemical studies of the cation radical Diels–Alder reaction have confirmed an analogous stereospecificity in two distinctly different systems. The initial study was carried out using the cycloaddition of the three geometric isomers of 2,4-hexadiene as dienophilic components and 1,3-cyclohexadiene as the diene component [39]. Each of the three isomers of the acyclic diene was found to add stereospecifically to cyclohexadiene. In a more recent study, the *cis* and *trans* isomers of 1,2-diaryloxyethenes were found to add stereospecifically to 1,3-cyclopentadiene (Scheme 17) and also to 2,3-dimethyl-1,3-butadiene [46].

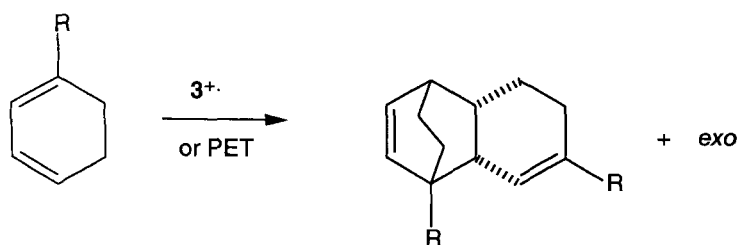
Regiochemistry of the cation radical Diels–Alder reaction

In most cases the cation radical Diels–Alder reaction has proved to be highly regiospecific with respect to the reaction of an unsymmetrical dienophile with an unsymmetrical diene. As examples, the cyclodimerizations of both 1-methyl-1,3-cyclohexadiene and 1-methoxy-1,3-cyclohexadiene are essentially regioexclusive (Scheme 18) [47–49].

It is noteworthy that the latter cyclodimerization cannot be carried out using the aminium salt method, because both the reactant and the Diels–Alder product react with the aminium salt in a destructive manner.



Scheme 17. The stereospecificity of the cation radical Diels–Alder reaction.



R = Me, OMe

Scheme 18. Regiospecificity of the cation radical Diels–Alder.

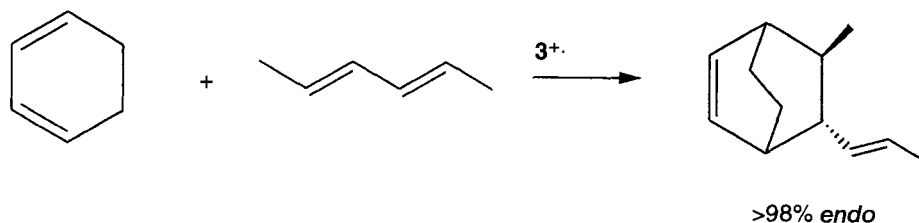
endo/exo Diastereoselectivity

Besides being essentially 100 % stereospecific, the reaction of *trans,trans*-2,4-hexadiene with 1,3-cyclohexadiene is at least 98 % *endo* diastereoselective (Scheme 19) [39, 47, 48].

However, the cyclodimerization of 1,3-cyclohexadiene and also the addition of the *cis,cis* isomer of 2,4-hexadiene to 1,3-cyclohexadiene are only modestly stereoselective. The addition of *cis,trans*-2,4-hexadiene to 1,3-cyclohexadiene is highly stereoselective for the addition to the *trans*-propenyl group, but only modestly stereoselective for the addition to the *cis*-propenyl group. Further, the addition of a dienophile having a pendant, unsubstituted vinyl double bond to this diene is also highly *endo* stereoselective. The installation of a *cis* group at the terminus of the dienophilic moiety consistently appears to reduce the *endo* stereoselectivity to a more modest level. It has been proposed that the *cis* substituent attenuates the secondary interaction involving the *endo* double bond in the transition state for cycloaddition [47, 48]. The effect has been termed the ‘*cis*-propenyl effect’. The addition of the *trans*-anethole cation radical to both 1,3-cyclohexadiene and 1,3-cyclopentadiene is, however, only moderately diastereospecific (ca 3:1) [49].

Scope of the cation radical Diels–Alder reaction

Although the (neutral) Diels–Alder reaction is one of the most useful in the repertoire of synthetic organic chemistry, it has, like any other reaction, some well



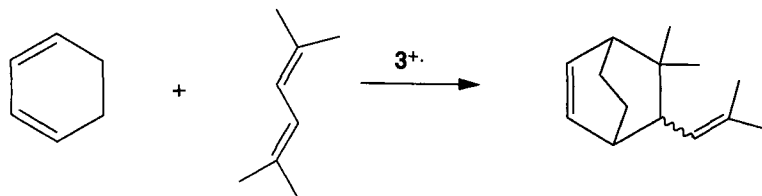
Scheme 19. *endo* Diastereoselectivity of the cation radical Diels–Alder.

defined limitations. In particular, it is rather sensitive to steric effects in both the dienophilic and dienic components, and it tends to work much more efficiently with electron deficient dienophiles than with electron rich ones. Although the cation radical Diels–Alder reaction has its own set of limitations, it is nicely complementary to the neutral Diels–Alder in being far less sensitive to steric effects, and in being most readily applicable to electron rich dienophiles. The range of substrate molecules which have oxidation potentials appropriate for use in cation radical cycloadditions induced by $3^{+\bullet}$ would appear to be approximately from about 1.2 V to about 1.6 V vs. SCE. Where the oxidation potential is substantially less than 1.2 V, the substrate ionization may be too rapid, resulting in cation radical/cation radical reactions (especially coupling). *Trans*-1,2-di-*p*-anisylethene ($E_{\text{ox}} = 1.20$ V vs SCE), which is readily ionized but fails to undergo either cyclodimerization or Diels–Alder addition, appears to be such a case. Stilbene, which has an ionization potential of 1.59 V, reacts cleanly but rather slowly, taking hours instead of the usual minutes to react when $3^{+\bullet}$ is used as the catalyst. Classes of ionizable substrates include many conjugated dienes (but not 1,3-butadiene and 1,3-cyclopentadiene, the oxidation potentials of which are much too high), electron rich styrene derivatives (especially those with beta alkyl substitution), aryl vinyl sulfides, aryl vinyl and aryl propenyl ethers, and 1,2-diaryloxyethenes. It appears to be rather generally the case that in cross additions (as opposed to dimerizations) the substrate which has the lower oxidation potential preferentially reacts as the cation radical component of the cation radical Diels–Alder reaction. Under PET and anodic oxidation conditions, enol alkyl ethers, *N*-vinylamides (enamides), and vinylindoles are also potentially viable substrates.

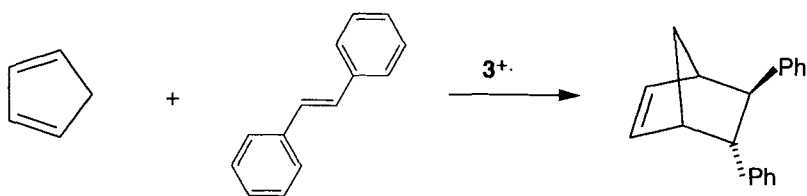
Additions to sterically hindered dienophiles

With respect to the matter of steric sensitivity, the reaction of 2,5-dimethyl-2,4-hexadiene with 1,3-cyclohexadiene is instructive [39]. Apparently, no Diels–Alder additions of this sterically hindered acyclic diene, either as the dienophilic or dienic component, have ever been reported. However, the cation radical Diels–Alder cycloaddition referred to above (Scheme 20) occurs smoothly, the readily ionizable acyclic diene serving as the dienophilic component.

Of further interest is the observation that the same reaction is not observed at all under PET conditions, which should reliably furnish the same diene cation radical [50]. Further, the normally efficient cation radical cyclodimerization of 1,3-cyclohexadiene is completely inhibited in the presence of the hindered diene, so that



Scheme 20. Diels–Alder addition of a sterically hindered dienophile.



Scheme 21. Diels–Alder addition of stilbenes.

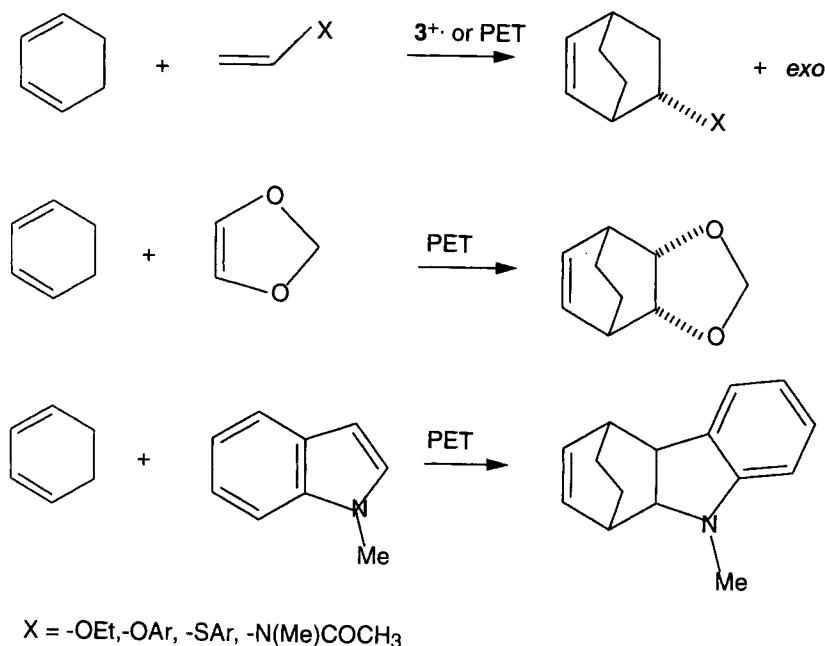
no cycloaddition at all occurs, even though the cation radicals of both dienes should be formed in the highly exergonic electron transfer to the excited state sensitizer. Evidently the rate of cycloaddition of the acyclic diene cation radical to the cyclic diene is indeed relatively slow as a result of steric repulsions, and the lifetime of this cation radical is therefore great enough that it is quenched by back electron transfer from the sensitizer anion radical more rapidly than it can add to 1,3-cyclohexadiene. The cation radical of the latter diene, assuming that it is indeed produced, evidently must undergo rapid, probably diffusion controlled, electron transfer from (hole transfer to) the acyclic diene, which has a much lower oxidation potential. Another reaction system which highlights the relatively lower level of sensitivity of the cation radical Diels–Alder reaction to steric effects is the stilbene/1,3-cyclopentadiene system (Scheme 21).

Although neutral Diels–Alder reactions of stilbene as a dienophile are unknown, the cation radical Diels–Alder reaction cited above occurs smoothly [51]. *Trans* stilbenes yields only *trans* adducts, while *cis*-stilbenes yield primarily, but not exclusively, *cis* adducts. The stereospecificity of the cycloaddition step in the latter reaction system was, however, not readily evaluated because of the occurrence of competing *cis* to *trans* isomerization of the starting material. It was established, however, that at low conversions, the reaction tends toward stereospecificity. Since *cis*-stilbene is much less readily ionizable than *trans*-stilbene, the Diels–Alder cycloadditions in the *cis*-stilbene system were studied using the *p,p'*-dimethyl derivative.

Electron-rich alkenes as dienophiles in the cation radical Diels–Alder reaction

In the present context, the term electron rich alkenes refers primarily to enol ethers, enol sulfides, and *N*-vinylamides or *N*-vinylamines. Such alkenes are typically much more readily ionizable than are simple alkenes. The conversion of these substrates to the corresponding (highly electron deficient) cation radicals represents a sharp Umpolung. The Diels–Alder additions of *trans*-anethole, phenyl vinyl ether, phenyl vinyl sulfide, 1,3-dioxole, and *N*-methylindole to 1,3-cyclohexadiene have been reported (Scheme 22) [49, 52].

It should also be born in mind that electron rich alkenes are also especially reactive neutral components of cation radical cycloaddition reactions, since they are also highly nucleophilic. Consequently, in appropriate instances, either role sense of the cation radical Diels–Alder reaction may be operative, i.e. either the diene or the electron rich alkene could be reacting as the cation radical.



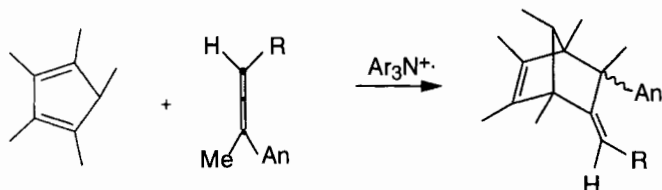
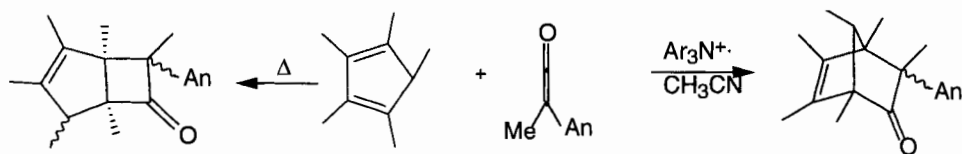
Scheme 22. Diels–Alder additions to electron rich alkenes.

Diels–Alder cycloadditions to ketenes and allenes

The facile Diels–Alder addition of certain ketenes and allenes to a relatively readily ionizable diene, 1,2,3,4,5-pentamethylcyclopentadiene, initiated by $3^{+\bullet}$ has also been observed (Scheme 23) [53, 54].

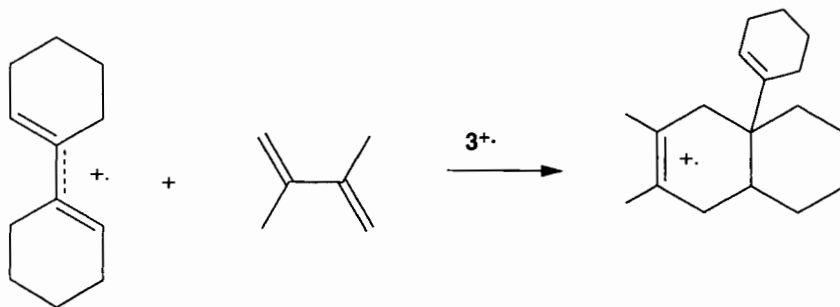
Role-selectivity in the cation radical Diels–Alder reaction

In view of the demonstrated stereospecificity of at least some cation radical Diels–Alder reactions, it is at least possible that these reactions, like the neutral Diels–Alder, are true pericyclic reactions, i.e., they may occur via a concerted cycloaddition. The results of a variety of calculations, however, make clear that the cycloadditions must at least be highly non-synchronous, so that the extent of the formation of the second bond, which completes the cyclic transition state, is no more than slight [55, 56]. If the cation radical Diels–Alder reaction is nevertheless interpreted as pericyclic and the concept of orbital correlation diagrams is applied to them, it emerges that the cycloaddition is symmetry allowed if the ionized (cation radical) component is the dienophile, but forbidden if it is the diene [39, 55]. The former mode of reaction has been referred to as the $[4 + 1]$ mode, and the latter as the $[3 + 2]$ mode. Interestingly, the great majority of cation radical Diels–Alder reactions thus far observed seem to represent the formally allowed $[4 + 1]$ mode. An interesting case in point is the reaction of 1,1'-dicyclohexenyl with 2,3-dimethylbutadiene (Scheme 24) [57].



Ar = 4-methylphenyl
An = 4-methoxyphenyl

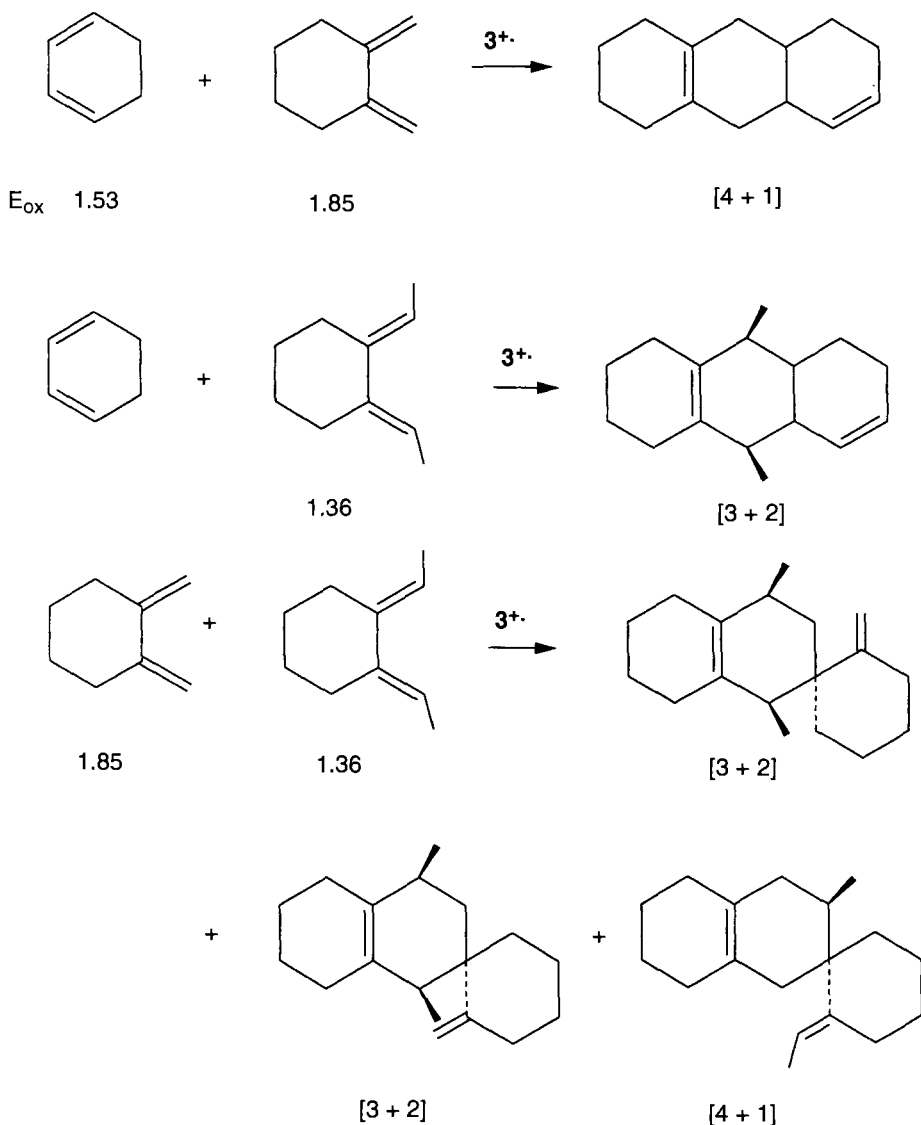
Scheme 23. Cation radical cycloadditions of ketenes and allenes.



Scheme 24. Role preferences in the cation radical Diels–Alder.

Both of these dienes are conformationally flexible as regards the adoption of an *s-cis* conformation, but the former apparently has a somewhat higher *s-cis* content and might therefore be expected to preferentially adopt the dienic role. However, the product corresponds to the use of 2,3-dimethyl-1,3-butadiene in the dienic role. Since this latter diene is by far the more difficult to ionize of the two dienes, the observed reaction must be of the allowed $[4+1]$ type. The possibility that this empirically observed sense of role selectivity has its origin in orbital symmetry allowedness/forbiddenness was tested in the manner shown in Scheme 25.

In each case the ionized component is readily identified by the large difference in oxidation potentials of the two reactants, but there is little, if any, preference for the



Scheme 25. Test of orbital symmetry effects on role specificity.

ionized component to participate as the dienophilic as opposed to the dienic component. For instance, in the final example of Scheme 25, the ratio of [4 + 1]/[3 + 2] products is 1:1.2. This result is not especially surprising since, as mentioned previously, the highly non-synchronous transition state can have but little pericyclic character. It is of further interest that cation radical cyclobutane, a formally [2 + 1] cycloaddition, is also formally symmetry forbidden, but is nevertheless ex-

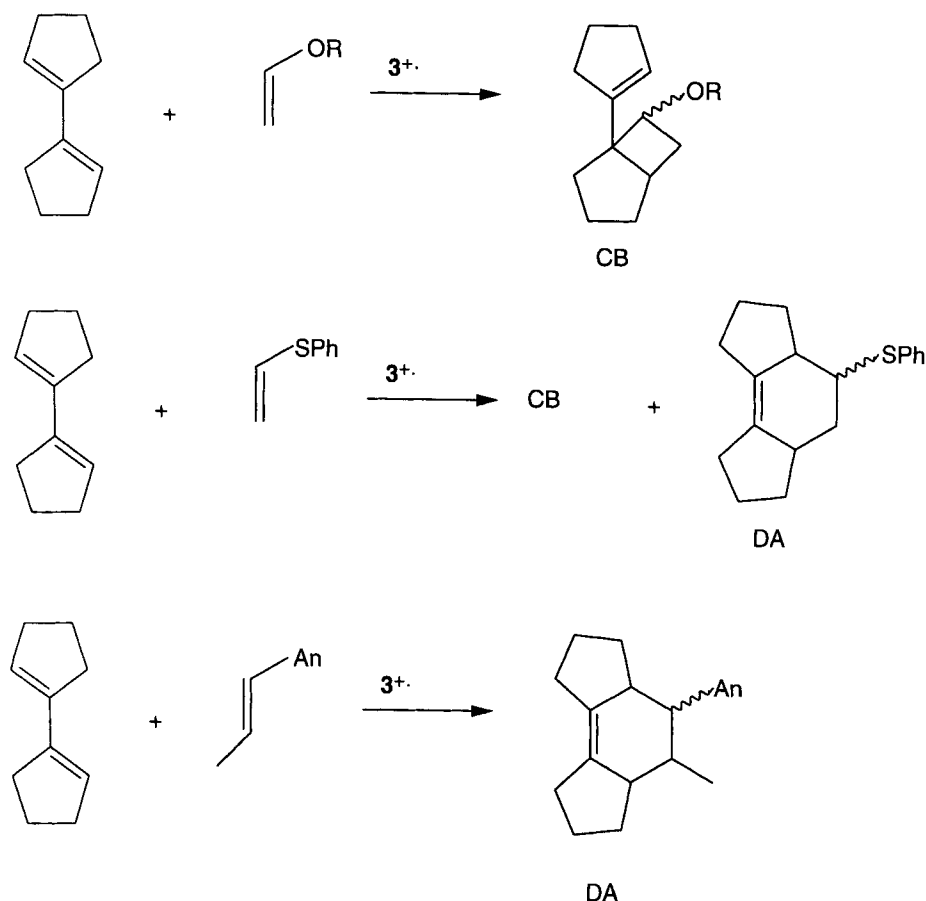
tremely rapid in appropriate cases. A more appropriate explanation for the preference for $[4 + 1]$ cycloaddition over $[3 + 2]$ cycloaddition, based upon conformational effects, will be proposed further on.

Periselectivity

An intriguing competition arises in the context of cation radical cycloadditions (as in the context of Diels–Alder cycloadditions) which involve at least one conjugated diene component. Since both cyclobutanation and Diels–Alder addition are extremely facile reactions on the cation radical potential energy surface, it would not be surprising to find a mixture of cyclobutane (CB) and Diels–Alder (DA) addition to the diene component in such cases. Even in the cyclodimerization of 1,3-cyclohexadiene, *syn* and *anti* cyclobutadimers are observed as 1 % of the total dimeric product. Incidentally, the DA dimers have been shown not to arise indirectly via the CB dimers in this case [58]. The cross addition of *trans*-anethole to 1,3-cyclohexadiene also proceeds directly and essentially exclusively to the Diels–Alder adducts (*endo* > *exo*). Similarly, additions to 1,3-cyclopentadiene yield essentially only Diels–Alder adducts. However, additions to acyclic dienes, which typically exist predominantly in the *s-trans* conformation which is inherently unsuitable for Diels–Alder cycloaddition, can yield either exclusively CB adducts, a mixture of CB and DA adducts or essentially exclusively DA adducts (Scheme 26) [59].

Although clearly the *s-cis* conformational content of the diene component has a major effect on the CB/DA periselectivity, a second effect related to role specificity also appears to represent a significant factor (Scheme 27).

If an *s-trans* diene component is ionized to the corresponding cation radical, it cannot participate in a Diels–Alder cycloaddition directly, and the large bond order between C2–C3 of the diene cation radical strongly prohibits equilibration with the *s-cis* diene cation radical. When proceeding in this role sense, only CB adducts can result. In contrast, if the dienophilic component is ionized, either DA or CB adducts can result, since the *s-trans* neutral diene, at least in some cases, may be able to equilibrate with the *s-cis* conformer at a rate faster than the cycloaddition rate. As a further illustration, the reaction of 1,1-dicyclopentenyl with phenyl vinyl sulfide yields an initial adduct distribution corresponding to a CB/DA ratio of 3.02. The excess of CB products is plausible in view of the slightly lower oxidation potential of this diene (1.34) than phenyl vinyl sulfide (1.42). If the oxidation potential of the vinyl sulfide is increased by using a *p*-bromo substituent, the CB/DA ratio is increased to 8.74. On the other hand, if the oxidation potential is decreased by the use of a *p*-ethyl substituent, the CB/DA is decreased to 0.85. This type of effect could also explain, at least in part, the tendency toward the prevalence of $[4 + 1]$ over $[3 + 2]$ cycloadditions. In each of the three cases described above, the rearrangement of the CB adducts to DA adducts via a cation radical mechanism (*vide infra*) is relatively rapid, so that the initial product ratio at very low conversions must be evaluated [60]. Finally, in connection with the CB vs DA competition represented in Scheme 26, it should be noted that the oxidation potentials are in the order *trans*-anethole (lowest) and vinyl ethers (highest), with phenylvinyl sulfide and 1,1-

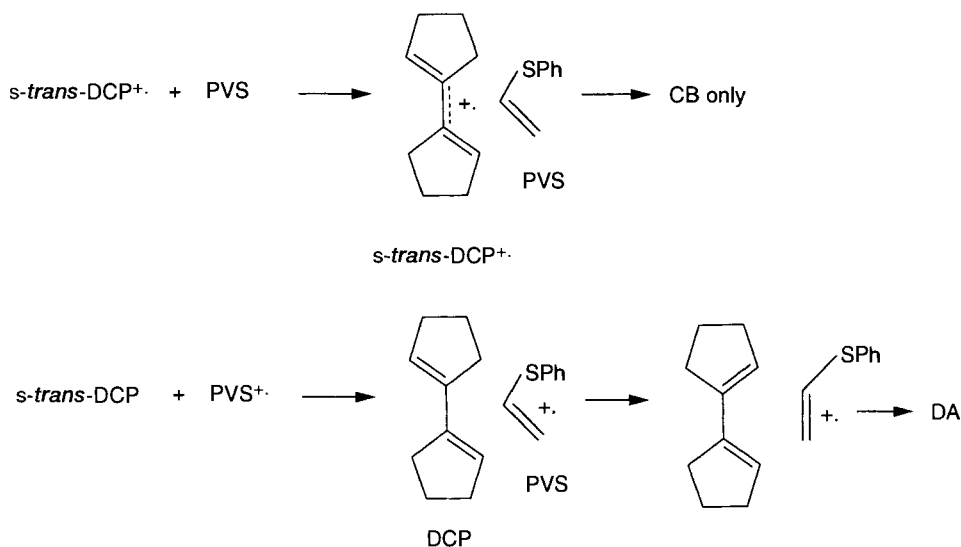


Scheme 26. Competition between Diels–Alder and cyclobutanation paths for acyclic diene components.

dicyclopentenyl being intermediate. This order of oxidation potentials is thus consistent with the expectation that if an acyclic diene is the more ionizable component, cyclobutanation (i.e. [2 + 1] addition) is the predominant result, and a [3 + 2] Diels–Alder addition is unlikely. On the other hand, if the dienophilic component is more oxidizable, the [4 + 1] Diels–Alder product is likely to predominate.

Periselectivity in cycloadditions of electron-rich alkenes

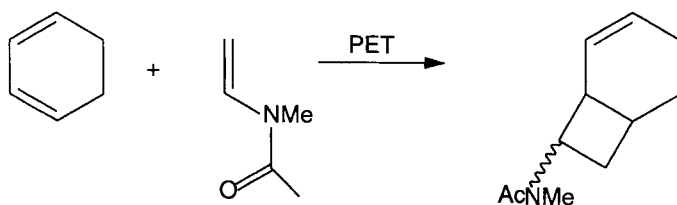
The cation radical cycloaddition reactions of conjugated dienes which can adopt either the *s-cis* or *s-trans* conformation with a dienophile can proceed to yield either CB or DA adducts or an admixture of both, as noted above. In the case where the dienophile is an electron rich alkene, the tendency toward CB adduct formation appears to be even more pronounced than in the case of a dienophile of the diene or



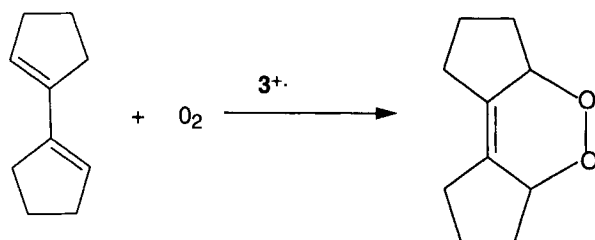
Scheme 27. Conformational effects on CB vs DA periselectivity.

styrene type [59a]. As will be noted further on, the tendency of these initially formed vinylcyclobutane adducts to quickly rearrange via a cation radical mechanism to the cyclohexene (i.e., Diels–Alder) adducts is also more pronounced. In the case of a very highly electron rich substrate such as *N*-methyl-*N*-vinylacetamide, even the reaction with the rigidly *s-cis*-1,3-cyclohexadiene is CB periselective (Scheme 28) [61].

Observations such as this tend to suggest that the TS for cation radical cyclobutanation has the positive charge either more localized or more highly developed than in the Diels–Alder TS, so that strongly carbocation stabilizing functions tend to favor the cyclobutanation reaction over Diels–Alder addition. It is important to note that many electron rich alkenes are incompatible with the aminium salt catalyst, requiring that their cation radical cycloadditions be carried out using the PET method or anodic oxidation. Vinyl sulfides and enol phenyl ethers such as phenyl vinyl ether or phenyl propenyl ether are exceptions to this generalization, and can be used effectively in the context of aminium salt catalysis.



Scheme 28. Cyclobutane periselectivity in electron rich alkenes.



Scheme 29. Cation radical chain dioxygenation of conjugated dienes.

3.2.8 Cation Radical Diels–Alder Cycloadditions to Dioxygen

The cycloaddition of an *s-cis* conjugated diene to ground state (triplet) dioxygen to give the hetero Diels–Alder adduct, a 1,4-*endo* peroxide, in its ground electronic state is spin forbidden. In an early, ingenious attempt to break down the ‘spin barrier’ toward the addition of a singlet molecule to triplet oxygen, the triarylamminium salt was successfully employed as a catalyst (Scheme 29) [62].

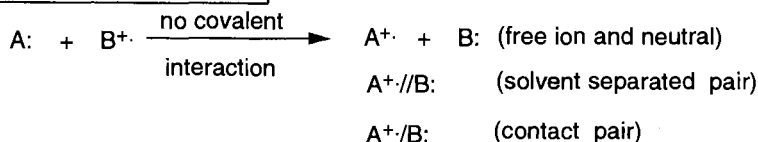
Although a cation radical mechanism was not initially proposed, it was later established that these reactions proceed via a cation radical chain process involving the cation radical of the conjugated diene [63]. Since the *s-trans* cation radical can not directly undergo cyclization to the *endo* peroxide cation radical, the reaction either must proceed via the *s-cis* cation radical or perhaps, in the case of conformationally flexible dienes, indirectly via the vinyl dioxetane cation radical (the CB type product), which subsequently rearranges to the *endo* peroxide (the DA type product).

3.2.9 Mechanisms of Formation of Substrate Cation Radicals from the Aminium Salt

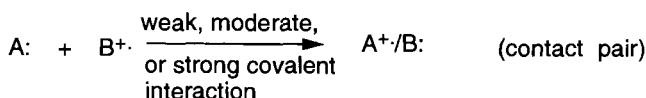
General considerations

The question of the nature of the process whereby substrate cation radicals are generated from the neutral substrate by electron transfer to an aminium salt (or other *chemical* agents) is of fundamental mechanistic interest. Moreover it is relevant to the *stereochemical outcome* of the reaction, as well as to the *selectivity* in ionizing one of two dissimilar reacting neutral molecules (as in the cation radical Diels–Alder reaction or in cross cyclobutanations) or when two or more functional groups are present in a single substrate molecule. Since substrate ionization via the aminium salt $3^{+\bullet}$ is virtually always endergonic, it is considered highly *unlikely* that solvent separated pairs would be formed directly, i.e. that electron transfer would occur through a solvent molecule. This conclusion follows because solvent reorganization and thus the intrinsic activation energy for the latter type of electron transfer is typically much greater than for electron transfers yielding intimate (i.e., contact) pairs. Thus, if electron transfer is of the outer sphere type, i.e., involves no

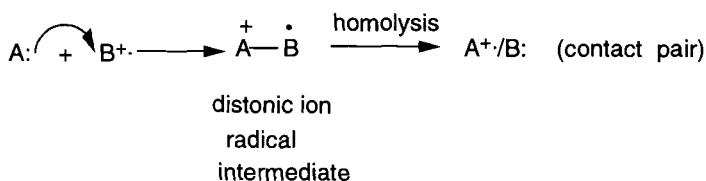
Outer Sphere Electron Transfer:



Inner Sphere Electron Transfer:



Polar Mechanism of Electron Transfer:

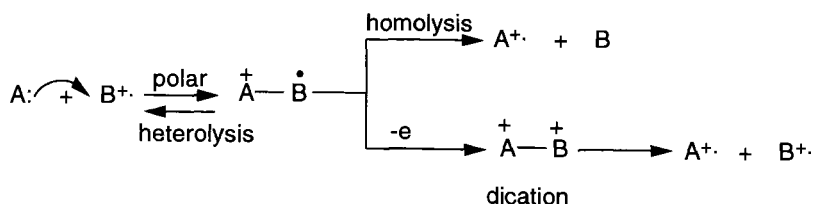


Scheme 30. Inner and outer sphere electron transfer mechanisms.

significant covalent interaction between the substrate and the aminium salt, it must presumably generate contact pairs. On the other hand, the range of possible inner sphere mechanisms is quite large, encompassing covalent interactions ranging from very weak to quite strong (Scheme 30).

The limit of the strong interaction case is presumably a stepwise electrophilic reaction establishing a full covalent bond in a distonic cation radical intermediate, followed by homolysis of this bond to yield the substrate cation radical and the neutral triarylamine (Scheme 31).

A plausible variation of this latter theme is the oxidation of the distonic cation



Scheme 31. Variants of the polar or limiting inner sphere et mechanism.

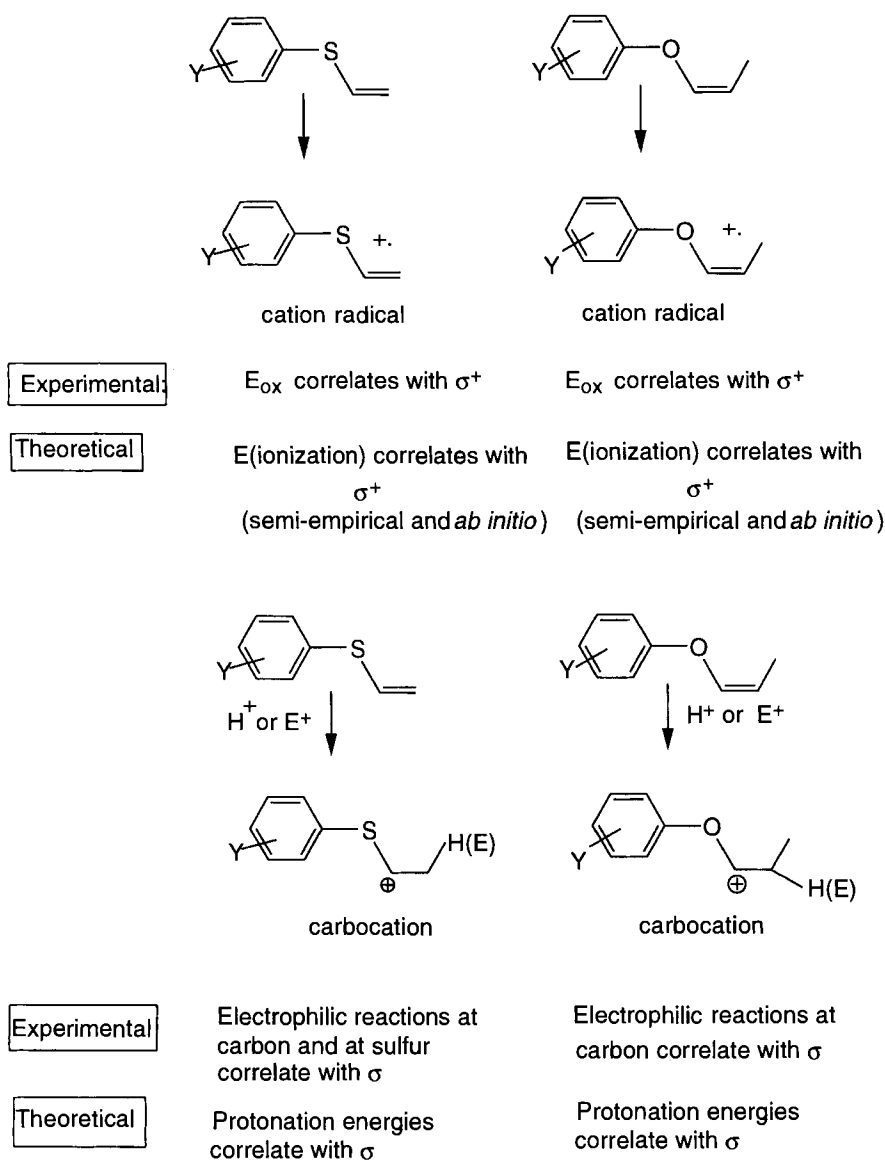
radical produced by the electrophilic mechanism by another aminium ion to give a di-cation, followed by homolysis of the latter to yield a substrate cation radical and an aminium ion [64]. In the case of the cleavage of a distonic cation radical intermediate, it might be thought that this should preferentially cleave to the aminium ion and a neutral substrate molecule, since this process is typically exergonic, than cleavage to the substrate cation radical. However, it should be noted that the latter process involves a bond heterolysis, whereas the former one involves homolysis. Since the redistribution of charge is much smaller in a homolysis, it is conceivable that the endergonic homolytic route could be kinetically favored over the exergonic heterolytic route.

Mechanistic criteria for the substrate ionization step

The mechanism of ionization of the two substrate molecules phenyl vinyl sulfide and phenyl *cis*-1-propenyl ether by the aminium salt 3^{++} has been studied in detail and a mechanistic criterion established for distinguishing outer sphere and inner sphere ionization in these and analogous substrate molecules [65]. Using this criterion, which is designated the σ/σ^+ criterion, it is also possible to distinguish between weak and strong inner-sphere ionization. The method takes advantage of the circumstance that the ionization of *meta* and *para* substituted derivatives of these two types of substrate to the corresponding cation radicals correlates extremely well with the Hammett–Brown substituent parameters σ^+ whereas the addition of an electrophile to the double bond to yield an α -aryloxy or α -arylthiocarbocation, or to the heteroatom to yield an onium ion, correlates with the Hammett σ substituent parameters (Scheme 32).

This dichotomy has been rigorously established by both theoretical methods (semi-empirical and *ab initio* calculations) and by experimental measurements for both cation radical and carbocation formation (Scheme 32) [66]. The kinetics of aminium salt-induced cation radical Diels–Alder reactions of these substrates were then studied, and an excellent correlation with the Hammett σ values was observed for both the enol ethers and the enol sulfides. The reactions of the aryl propenyl ethers involved 2,3-dimethyl-1,3-butadiene as the dienic component [64], while the reactions of the aryl vinyl sulfides involved cyclopentadiene as the dienic component (Scheme 33) [65].

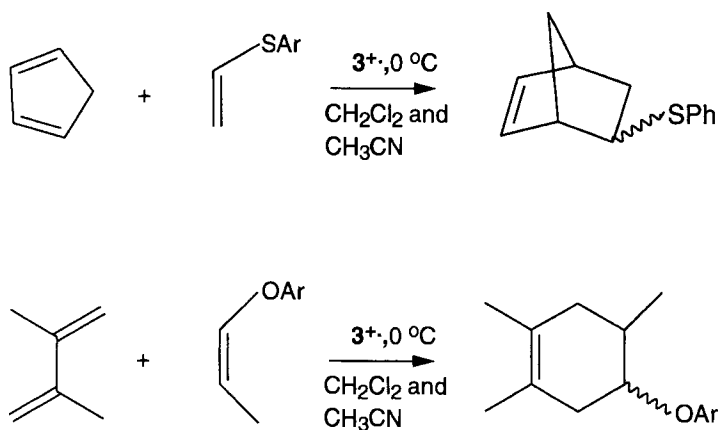
The distinctions between the correlations with σ and σ^+ were both statistically significant at well above the 95 % confidence level. *These results suggest that the transition state for the ionization step, which was established as rate determining, closely resembles that for an electrophilic attack and has little if any cation radical (outer sphere) character.* This and other supporting evidence suggests that the transition states for these two reaction series closely resembles a *distonic* cation radical. Whether the site of the electrophilic attack is on the heteroatom or upon the β -carbon of the double bond is less certain, but stereochemical evidence (stereo-specific addition in the case of *cis*- β -deutero phenyl vinyl sulfide) is more consistent with attack at sulfur in the case of the aryl vinyl sulfides. In any case, these results are most consistent with a polar mechanism for ET, which involves a distonic cation radical intermediate (Scheme 34).



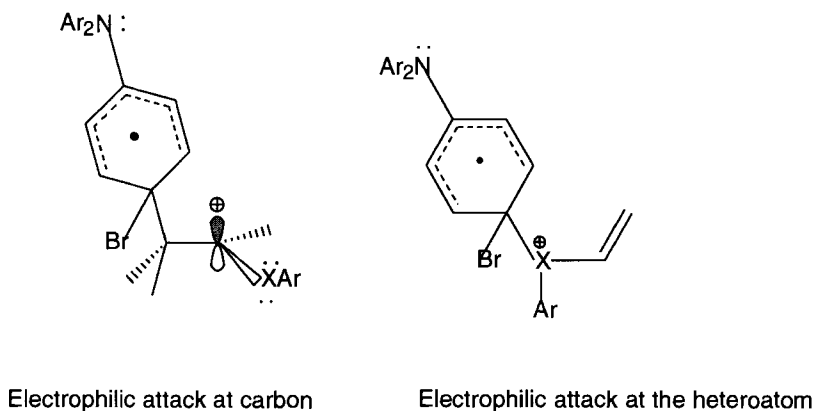
Scheme 32. The σ/σ^+ criterion for inner sphere vs. outer sphere ionization.

3.2.10 Neutralization of the Product Cation Radical

An electron transfer process is also involved in the second propagation step of a cation radical chain reaction, i.e., the step in which the product cation radical is neutralized by electron transfer from the neutral substrate molecule. For an efficient chain reaction, this step should, of course, be exothermic. If the assumption is made

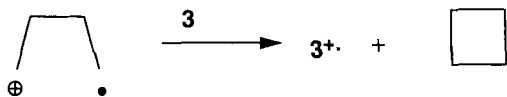


Scheme 33. Kinetic studies of the cation radical Diels–Alder reactions of aryl vinyl sulfides with cyclopentadiene and of aryl propenyl ethers with 2,3-dimethyl-1,3-butadiene. In both solvents, both extended reaction series have rates which correlate excellently with the Hammett σ parameters and poorly with the Hammett–Brown σ^+ values. The preference is statistically significant at or above the 95 % confidence level.



Scheme 34. Possible structures of the distonic cation radical intermediate.

that the cation radical cycloaddition step is concerted, i.e., it does not proceed via an intermediate distonic cation radical, this requirement is relatively easily met, since the net conversion of a pi bond to a sigma bond usually will assure that the cation radical moiety (hole) is delocalized over a less extensive pi system and is therefore less stable in the cycloadduct than in the reactant. Interestingly, this is not necessarily the case if a distonic cation radical intermediate is involved. It has been plausibly argued by both D’Innocenzo [67] and by Nelsen [68] that the (vertical) neutralization of the carbocation site of a distonic cation radical, which would generate a diradical intermediate, is generally endothermic. Therefore, if a distonic



Scheme 35. Hypothetical neutralization of a distonic cation radical by the bond-coupled electron transfer mechanism.

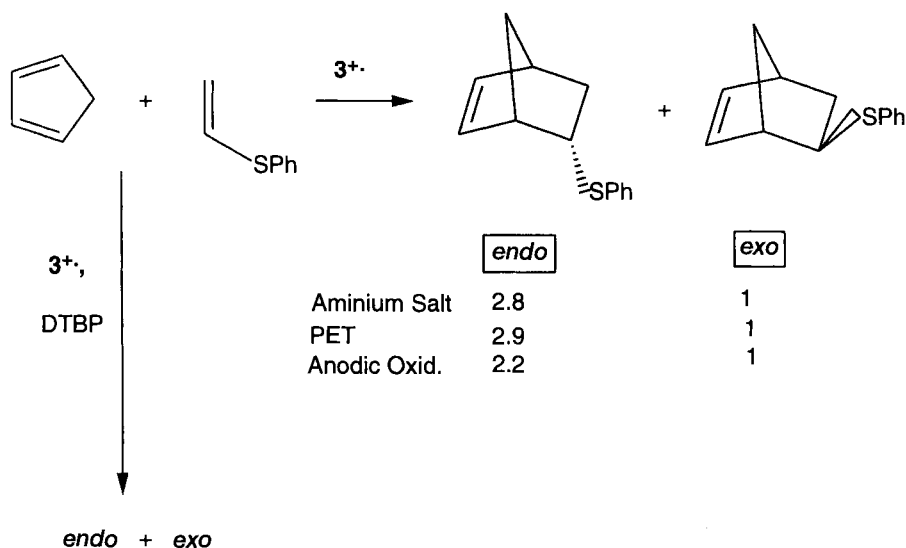
cation radical intermediate is involved, it appears reasonable to assume that it must first cyclize to the ring-closed product cation radical before it can be neutralized by exothermic hole transfer. This was considered to be a plausible scenario in the cation radical chain addition to triplet oxygen to yield dioxetanes, which is a non-stereospecific but highly efficient chain process, and also in the vinylcyclopropane rearrangement [68]. More recently, the possibility of *bond-coupled electron transfer* has been considered for the neutralization of distonic cation radical intermediates [69]. Since concerted electron transfer and bond fragmentations have now been established, it appears quite reasonable to consider the possibility of bond-coupled electron (hole) transfer to neutralize the distonic cation radical intermediate, i.e., a step in which the neutral product is generated directly by simultaneous ET and covalent bond formation. This mechanism, which is at this point still hypothetical, is illustrated in Scheme 35 for a cation radical cyclobutanation reaction.

3.2.11 Mechanistic Diagnosis of Cation Radical Cycloadditions

Qualitative diagnosis

Evidence for the operation of cation radical mechanisms for cycloaddition has often been provided by means of a comparison of the results obtained for various methods of generating cation radicals. For example, in the Diels–Alder cycloaddition of phenyl vinyl sulfide to 1,3-cyclopentadiene (Scheme 36) the same adducts are formed whether the cation radicals are generated by chemical ionization (aminium salt), photochemical ionization (the PET method), or electrochemical ionization (anodic oxidation) [65].

No other adducts are formed, and the *endo/exo* diastereomeric ratio is essentially the same for all of these methods. Further, the existence of an acid catalyzed mechanism for cycloaddition can be explicitly excluded by using an excess of a hindered amine base (2,6-di-*tert*-butylpyridine, DTBP) in the aminium salt induced reaction and by examining the results of an authentic acid catalyzed reaction (using, for example, triflic acid). In the former case, the same *endo* and *exo* adducts are formed in virtually the same relative amounts, but in the latter case neither of these adducts is formed. It is worth noting that acid catalyzed reactions have indeed sometimes been observed under typical aminium salt conditions [70], but these have never been observed, nor would they be expected, under PET conditions. Finally, in the instance where cation radicals are generated by the aminium salt method, the intervention of substrate cation radicals can usually be verified by the addition of the reduced form of the catalyst, i.e., the neutral triarylamine, to the reaction mixture.



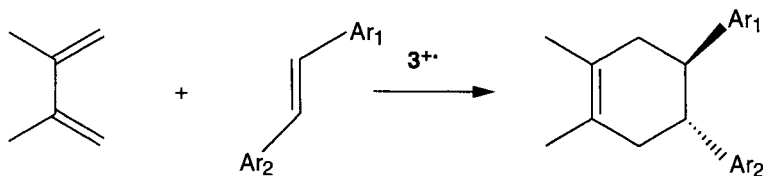
Scheme 36. Mechanistic diagnosis of cation radical cycloadditions.

The substrate ionization step, if it is not already reversible, often becomes reversible under these conditions, resulting in a modest to very pronounced rate diminution [40].

Quantitative diagnosis

A more quantitative criterion for the operation of a cation radical cycloaddition mechanism has been carried out for a Diels–Alder reaction system consisting of various substituted derivatives of *trans*-stilbene (as the ionizable dienophile) and 2,3-dimethyl-1,3-butadiene (Scheme 37) [71].

The criterion relies on the proposal that *for a symmetrical pi system (such as trans-stilbene), the development of a full unit of positive charge distributed symmet-*



Scheme 37. The symmetry criterion for cation radical formation via outer sphere electron transfer. Substituent effects in mono- and disubstituted stilbenes are multiplicative; $\log k_{\text{rel}}$ correlates with σ^+ with $\rho = -4.16$; the oxidation potentials of these same stilbene derivatives correlate with the same substituent parameters with $\rho = -5.02$.

rically over the system is a unique and positive indication of cation radical formation. The symmetrical distribution of charge in the TS was established by a competition kinetic study which reveals that both mono- and disubstituted stilbenes are nicely incorporated on the same Hammett–Brown plot, and that substituent effects are essentially multiplicative for substitutions on one or both rings. The magnitude of the positive charge development was assessed via the Hammett–Brown ρ value and a comparison with the ρ value for the complete ionization of these same substrates, in the same solvent, to the corresponding cation radicals. Thus the oxidation potentials for these substituted stilbenes correlate nicely with Hammett–Brown σ^+ values, and the slope corresponds to a ρ value of -5.02 . In the same solvent (acetonitrile) the ρ value for the plot of the log of the relative rate constants for the Diels–Alder cycloadditions vs σ^+ is -4.16 , i.e., approximately 83 % of a unit of positive charge is present in this transition state. It is of further interest that similar studies have been carried out for the cation radical cyclopropanation of these same substrates, and the ρ value (-4.56) represents 91 % of the full unit of positive charge [72]. The rate determining step of these reactions has been found to be the cycloaddition step, so that even in the TS of cycloadditions, 83–91 % of the charge remains on the stilbene moiety, consistently with a reaction having an early transition state. Incidentally, *cis*-stilbene has a much higher oxidation potential than *trans*-stilbene (1.70 V vs 1.59 V vs SCE), so that its addition to dienes under these same conditions is too slow to observe. However, 4,4'-dimethyl-*cis*-stilbene has been observed to undergo the cation radical Diels–Alder reaction [73].

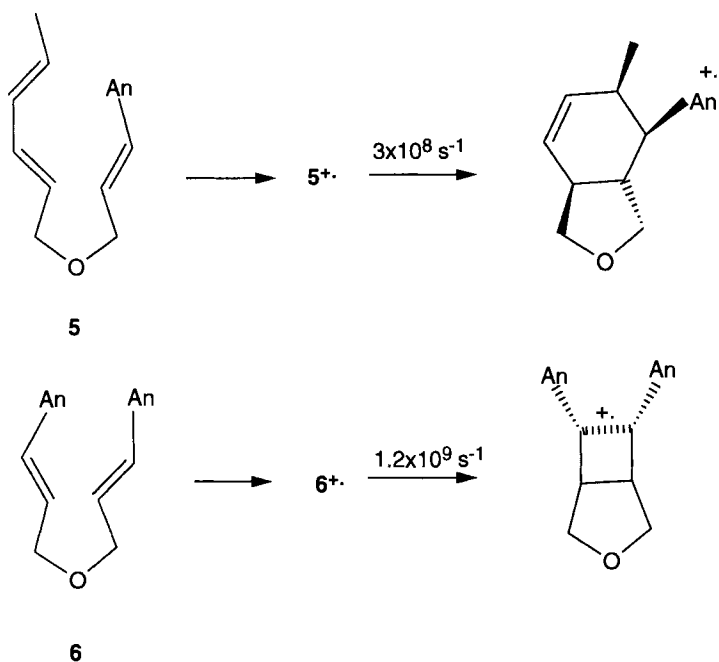
3.2.12 Absolute Reaction Rates and Cation Radical Probes

The rate constant for the Diels–Alder cyclization of substrate **5**, generated by photoionization and by photosensitized electron transfer, has been determined to be $3 \times 10^8 \text{ s}^{-1}$ (Scheme 38) [31].

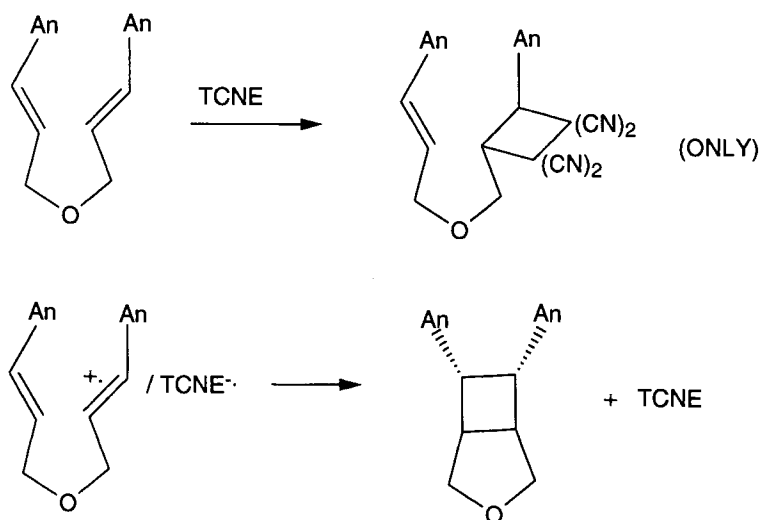
This substrate, along with the corresponding substrate **6**, which has a cyclobutanation rate of 1.2×10^9 , have been proposed as sensitive cation radical probes, for detecting the presence of cation radical intermediates in various reactions [74]. An interesting example is the reaction of tetracyanoethylene (TCNE) with electron rich alkenes, a reaction for which an electron transfer mechanism had been considered (Scheme 39) [75].

The reaction of **6** with TCNE yields only the conventional adduct corresponding to the uncyclized probe and none of the product expected from the cation radical cyclization. That the probe cyclization of the cation radical of **6** would have been observed in the context of an ET mechanism, if it had been involved, was demonstrated by generating the contact ion radical pair of $\mathbf{6}^{+\bullet}/\text{TCNE}^{\bullet-}$ via excitation of the charge transfer complex of **6** and TCNE. The cyclobutane cyclization product of the probe reaction was easily detected under these conditions. Consequently, an ET mechanism for this reaction can be confidently excluded. In a similar manner, the epoxidation of **5** and **6** by oxidized metalloporphyrins provides strong evidence against a cation radical mechanism for these reactions [76].

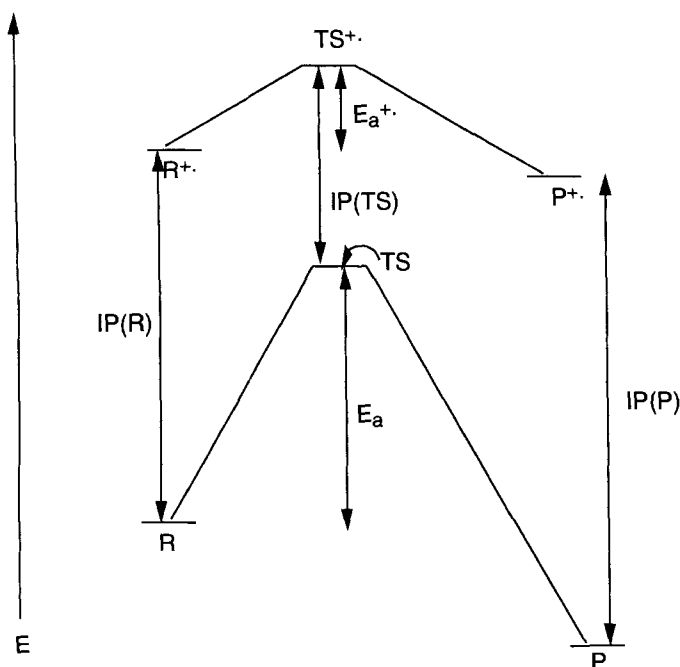
CATION RADICAL PROBES



Scheme 38. Cation radical probes.



Scheme 39. Cation radical probes quantitatively rule out an et mechanism for the addition of tetracyano-ethylene to electron rich alkenes.



Scheme 40. The kinetic impetus for cation radical cycloadditions. R = reactant, P = product, $R^{+\cdot}$ = reactant cation radical, $P^{+\cdot}$ = product cation radical, IP = ionization potential, E_a = activation energy.

3.2.13 General Theoretical Considerations in Cation Radical Cycloadditions

The facility of many cation radical cycloadditions is impressive, and it is clear that this is not primarily the result of a powerful thermodynamic driving force. In fact, the thermodynamic driving force for cation radical cycloadditions is often less than that for the corresponding neutral reactions [35, 77]. Thus, although cation radicals are indeed relatively high energy intermediates compared to the corresponding neutral compounds, both the reactants and the products of cation radical cycloadditions exist upon the same high energy potential surface. It is therefore necessary to look for a transition state effect not related to product development as the common and primary basis for the rapidity of these reactions. One such effect is evident upon examination of the potential surface given in Scheme 40.

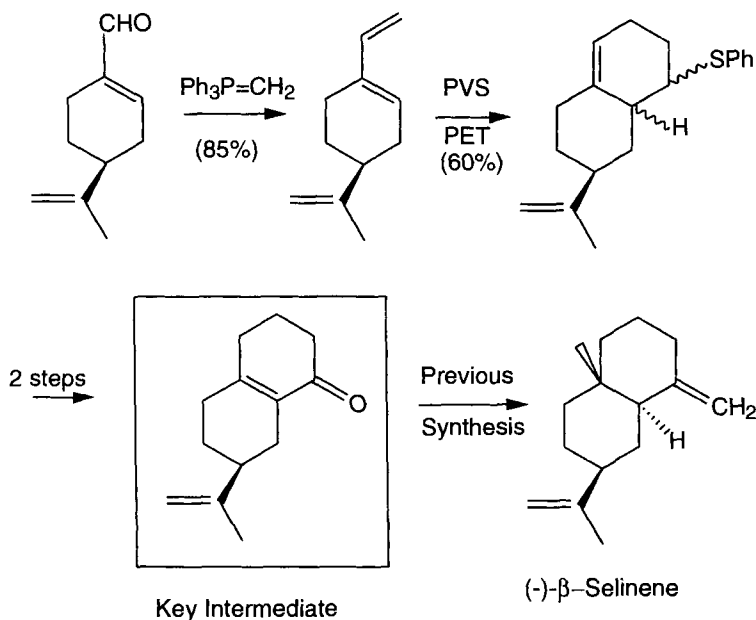
From this perspective, it emerges that *the kinetic driving force for the cation radical cycloaddition relative to the corresponding neutral one can be expressed as the difference in the ionizabilities of the reactant and the transition state*. As a specific example, we may consider a highly non-synchronous TS for cation radical Diels–Alder cycloaddition—which is supported by theoretical calculations (vide infra). This transition state is essentially a distonic cation radical, the radical site of which is easily ionized because the odd electron is in a non-bonding MO. In contrast, the

ionization of the reactant involves the removal of an electron from an orbital which is strongly bonding. Further, transition states in general, because they are relatively less bonding and relatively higher in energy than reactant states, can be expected to have lower oxidation potentials. It also appears likely that the diminished electronic repulsions in a cation radical transition state are another intrinsic factor favoring these reactions not only over the corresponding neutral reactions, but also over the corresponding anion radical reactions.

Additional insights follow from an inspection of the curve shown in Scheme 40. First, for an effective chain process, *the oxidation potential of the product should be higher than that of the reactant*, so that the hole transfer process involved in the propagation cycle will be exergonic. This is normally the case in cycloadditions because the product typically has one less pi bond than the reactants, so that the former has a less highly delocalized cation radical moiety (hole) than the latter. Also, the use of the exergonicity associated with the neutralization of the product cation radical to ionize the reactant is relatively much more efficient than quenching the product by a molecule of the neutral triarylamine, followed by the ionization of the substrate by the aminium salt. This follows because in the latter scenario the difference in the oxidation potentials of the product cation radical and the neutral triarylamine represents wasted energy. Consequently, *the catalytic mechanism, which involves an endergonic ionization step, is intrinsically less energy efficient than the chain mechanism*, which involves an exergonic substrate ionization step. On the other hand, it also follows that *substrate ionization is more selective in the context of a catalytic mechanism than in the chain mechanism*.

3.2.14 Computational Results

All calculations presented to date, including both semi-empirical and ab initio results, indicate that the cation radical DA reaction transition state is at least highly non-synchronous, somewhat resembling a distonic cation radical [35, 56]. The question of whether the reaction is even weakly concerted, i.e., whether the second C–C bond has begun to form at all in the transition state is of special interest in relation to reaction stereospecificity. Early results based upon MP2/6-31G* calculations for the DA reaction of the *s-cis*-1,3-butadiene cation radical with ethene suggested that the reaction might well be concerted [56], but more recent, and more sophisticated, calculations suggest that the reaction may be stepwise, involving a short-lived distonic cation radical intermediate which has essentially no covalent interaction between the distonic termini [78]. On the other hand, experimental results for three distinct cation radical DA reaction systems reveal highly stereospecific reactions [79]. Of course, the reaction systems studied experimentally are not those for which the reaction path was calculated, nor are solvation effects included in the calculations. Further, it is formally possible that a distonic cation radical intermediate could cyclize to the DA adduct cation radical at a rate faster than bond rotation, and thus be stereospecific. It is also relevant to note that an intermediate distonic cation radical has been detected in the DA cyclodimerization of spiro[2,4]heptadiene, although it can not be definitely determined that this is the



Scheme 41. The cation radical Diels–Alder reaction in a formal total synthesis of beta selinene.

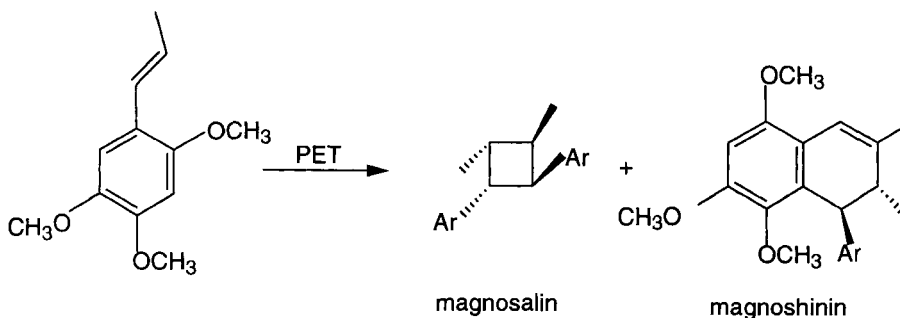
sole or even the major pathway for this reaction [80]. Consequently, it is reasonable to assume a certain mechanistic diversity in the cation radical DA reaction with respect to its concerted vs. stepwise nature. Nevertheless, the observations of stereospecificity in three structurally very different systems continues to support the concept of concerted cation radical Diels–Alder reactions.

3.2.15 Natural Product Synthesis and Synthetic Methodology using Cation Radical Cycloaddition Reactions

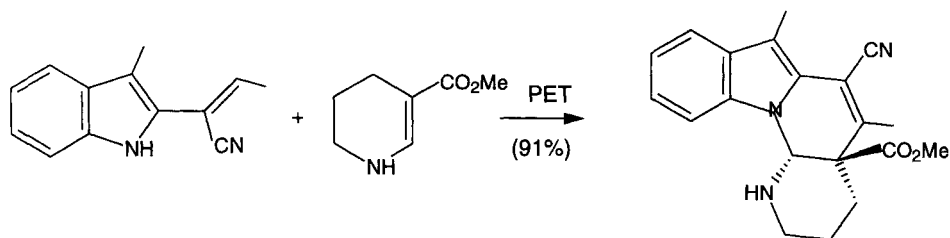
The usefulness of the cation radical Diels–Alder reaction for natural product synthesis has been illustrated in the synthesis of β -selinene (Scheme 41) [81], which utilizes phenyl vinyl sulfide as a Diels–Alder dienophile and the photosensitized electron transfer method as the preferable method for generating the corresponding cation radical.

It was demonstrated that the use of phenyl vinyl sulfoxide or sulfone in a thermal Diels–Alder reaction was highly unsatisfactory as an alternate route. The synthesis of the neolignins galbulin, isogalbulin [82], magnoshinin, and magnosalin [83] have all been accomplished by means of a cation radical cycloaddition (Scheme 42).

The syntheses of galbulin, isogalbulin, and magnoshinin involve cation radical Diels–Alder reactions, while that of magnosalin involves a cation radical cyclobutanation. The galbulin and isogalbulin syntheses involve aminium salt induced cycloadditions, whereas the magnoshinin and magnosalin syntheses were carried



Scheme 42. Cation radical cycloadditions in the synthesis of magnosalin and magnoshinin.



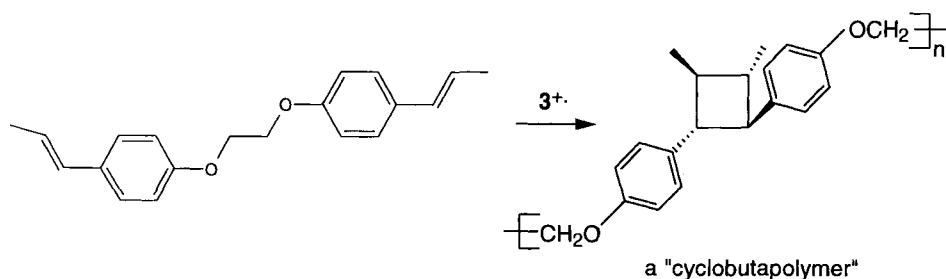
Scheme 43. Construction of the goniomitine skeleton using vinylindoles as diene components.

out using the PET method. Another especially impressive synthetic use of cation radical cycloadditions is the use of 2-vinylindoles as Diels–Alder dienes for the construction of alkaloid skeletons. As an example, the Goniomitine framework has been generated in this way, using the PET method (Scheme 43) [84].

3.2.16 Cation Radical Polymerization

The cation radical intermediate and the process of electron (hole) transfer have recently been shown to constitute the basis for a fundamentally new addition to the repertoire of polymerization methods [85]. Both cation radical chain cyclobutana-tion polymerization (Scheme 44) and Diels–Alder polymerization have been demonstrated under the typical aminium salt conditions.

Cycloaddition polymers having average molecular weights of up to 200 000 have been generated in this way using appropriately constituted difunctional monomers. The mechanistic advantage of polymerization over the familiar cycloaddition reactions of monofunctional substrates is considered to be that in the propagation cycle electron (hole) transfer is intramolecular in the difunctional context, but intermolecular in the monofunctional context. An intriguing aspect of these novel polymers is that they retain ionizable end groups, such that the polymerization process can be ‘resurrected’. The ability to rather efficiently produce cyclobuta-



Scheme 44. Cation radical chain cycloaddition polymerization.

polymers under very mild thermal conditions is an especially novel aspect of this polymerization method.

3.2.17 The Cation Radical Vinylcyclobutane (VCB) Rearrangement

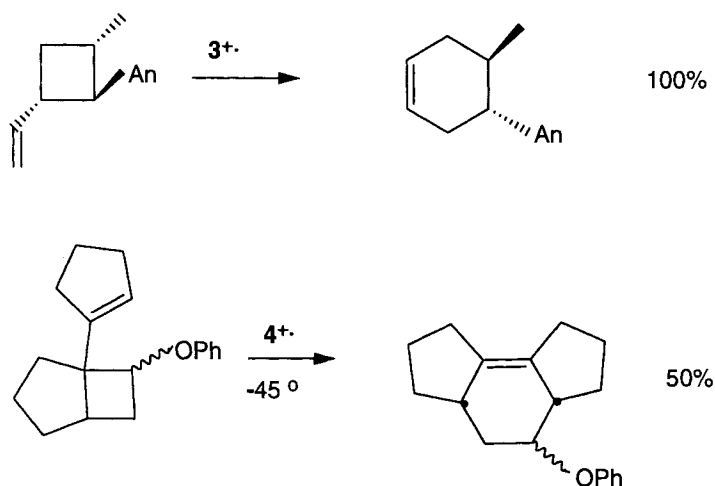
Scope and occurrence

A further complication in cation radical cycloadditions involving at least one conjugated diene component is the often facile rearrangement of initially formed cyclobutane (CB) adducts to cyclohexene (i.e., DA) adducts. However, this can also provide a synthetically useful route for *indirect, net Diels–Alder cycloaddition* to acyclic dienes [86]. Further, the cation radical vinylcyclobutane (VCB) rearrangement can usually be suppressed by carrying out the reaction using $3^{+\bullet}$ for a very short period of time at 0°C , for a somewhat longer time at -30°C , or at -78°C with the corresponding tris(2,4-dibromophenyl)aminium hexachloroantimonate salt ($4^{+\bullet}$) which is much more soluble than $3^{+\bullet}$. In this way, either the CB rich mixture or the DA adducts may be obtained. For example, the CB adduct strongly predominates in the cycloaddition of *trans*-anethole with 1,3-butadiene at -30°C , but this is rapidly rearranged at 0°C in the presence of $3^{+\bullet}$ or by the PET method to the corresponding Diels–Alder adduct (Scheme 45).

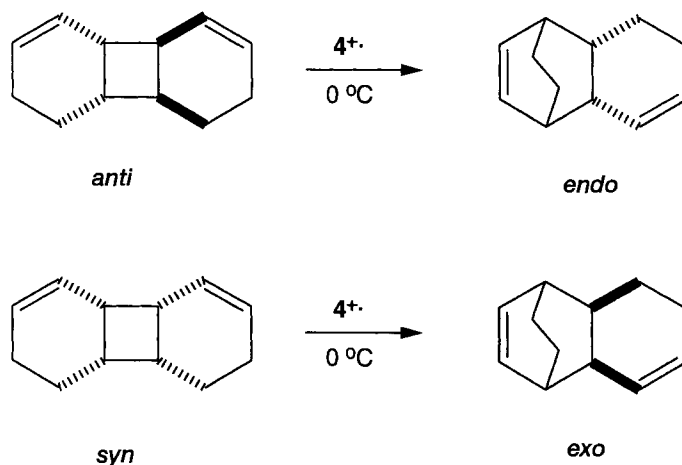
Similarly, the cyclobutane adducts of phenyl vinyl ether and 1,1'-dicyclopentenyl are the predominant products under PET conditions, but these rearrange smoothly at -45°C in the presence of $4^{+\bullet}$ to Diels–Alder adducts.

Mechanism of the cation radical VCB rearrangement

The cation radical VCB rearrangement has been found, at least in several cases, to occur intramolecularly, rather than by dissociation/recombination [86]. An especially interesting case is the rearrangement of the CB dimers of 1,3-cyclohexadiene generated by triplet sensitized photochemistry. In the presence of the usual aminium salt catalyst ($3^{+\bullet}$), these CB dimers are quite stable, but if the more powerful hexabromo aminium salt, $4^{+\bullet}$, is used, these individual dimers rearrange to the DA dimers via a stereospecific VCB rearrangement (Scheme 46).



Scheme 45. The cation radical vinylcyclobutane (VCB) rearrangement.



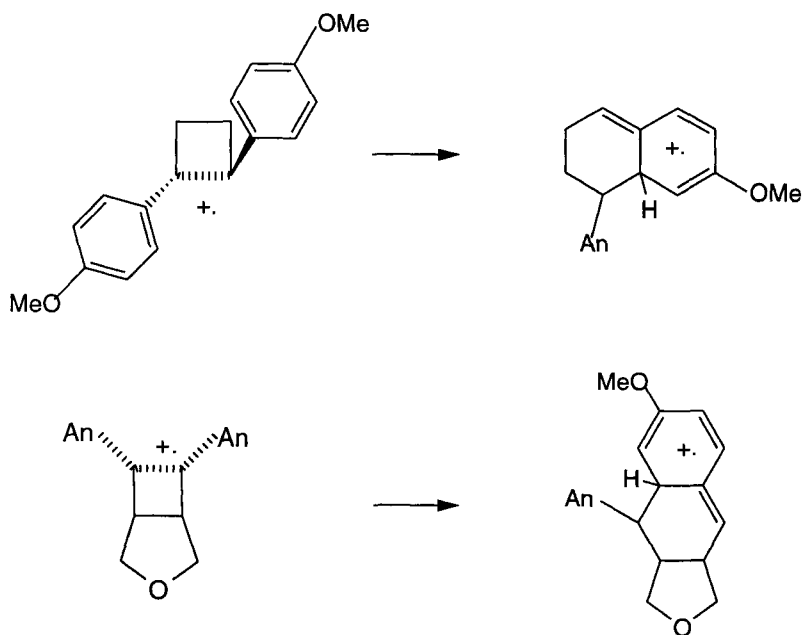
Scheme 46. Intramolecular vs. dissociation/recombination mechanisms for the VCB rearrangement.

Thus, the *anti* CB dimer rearranges to the *endo* DA dimer, and the *syn* CB dimer rearranges to the *exo* DA dimer by a 1,3-sigmatropic shift which occurs suprafacially with retention of configuration. The necessity for using the more powerful aminium salt is inherent in the difficulty of ionizing the CB dimers, which have only simple alkene moieties available for ionization. More generally, the feasibility of an efficient cation radical VCB rearrangement depends upon the presence of a readily ionizable functionality on the cyclobutane ring carbon vicinal to the carbon bearing the vinyl group. The anisyl, arylthio, and aryloxy groups are especially effective in

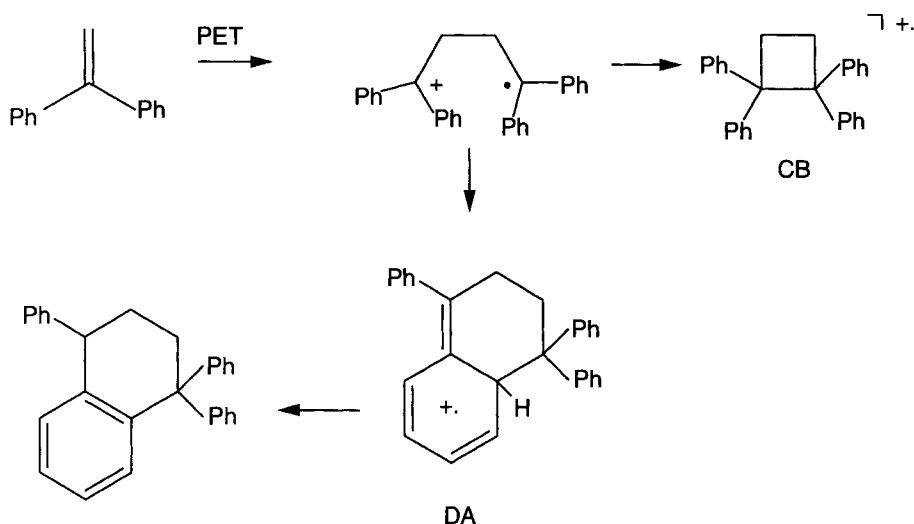
this context. In the rearrangement of the CB adduct of *trans*-anethole and 1,3-butadiene it was further shown that the highly efficient rearrangement to the DA adduct did not involve dissociation/recombination. Thus, the addition of 800 mol % of 2,3-dimethyl-1,3-butadiene, which is three times as reactive toward the *trans*-anethole cation radical as is 1,3-butadiene, to the reaction mixture prior to the addition of the initiator, fails to generate even a trace of the adduct of *trans*-anethole and 2,3-dimethyl-1,3-butadiene.

3.2.18 The Cation Radical ‘Phenylcyclobutane’ Rearrangement

A reaction which is formally analogous to, and in a sense much more surprising than, the vinylcyclobutane rearrangement is a reaction in which one of the unsaturated bonds of an aryl ring fulfills the same role as an alkene double bond in the latter rearrangement. In view of the close analogy to the vinylcyclobutane rearrangement, it might be appropriate to designate this type of rearrangement as the phenylcyclobutane rearrangement. An example of this latter type of rearrangement which has been studied especially carefully occurs in the cyclobutadimerization of vinylanisole [87]. The initial cation radical cyclobutanation reaction occurs with a rate constant of $1.4 \times 10^9 \text{ s}^{-1}$ to give the long bond cyclobutane cation radical. The latter is able to rearrange, via a phenylcyclobutane rearrangement, to a hexatriene type cation radical in which the aromaticity of one of the aryl rings has been disrupted (Scheme 47).



Scheme 47. Cation radical “phenylcyclobutane” rearrangements.



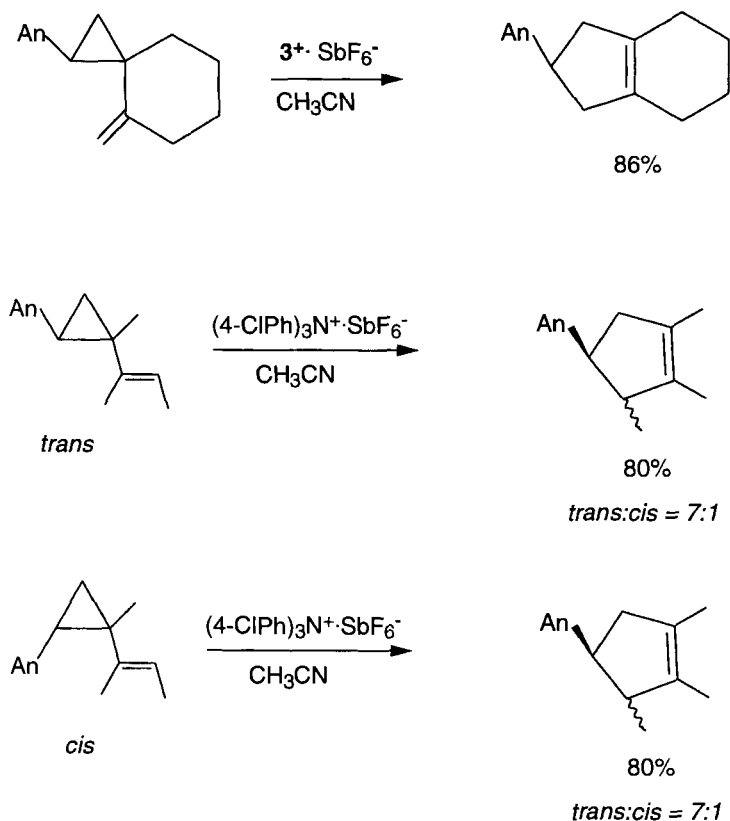
Scheme 48. The cyclodimerization of 1,1-diphenylethene.

A similar reaction has been observed in the case of an intramolecular cation radical cyclobutane, and in this case the cyclized product having a re-aromatized aryl ring was isolated and characterized [31]. Although these reactions appear to be concerted rearrangements, not involving a distonic cation radical intermediate, analogous products could be formed from a distonic cation radical intermediate. The photosensitized cation radical cyclodimerization of 1,1-diphenylethene, originally reported by Arnold's group [42], and subsequently scrutinized by Farid [43], appears to involve an intermediate distonic cation radical which can close to give a cyclobutane or a hexatriene cation radical (Scheme 48).

3.2.19 The Cation Radical Vinylcyclopropane Rearrangement

Efficient and facile rearrangements analogous to the cation radical vinylcyclobutane rearrangement have also been identified in the vinylcyclopropane (VCP) series (Scheme 49).

In rather marked contrast to the vinylcyclobutane series, neither *cis*- nor *trans*-2-*p*-anisyl vinylcyclopropane undergoes ring expansion in the presence of aminium salts. However, several more highly alkylated derivatives undergo the reaction with impressive efficiency [88]. Evidently a stepwise pathway is involved in at least some cases, since non-stereospecificity has been demonstrated in one instance (Scheme 49) [89]. Interestingly, the intermediate distonic cation radical, in this latter case, does not re-cyclize to regenerate the original vinylcyclopropane cation radical, since the latter does not undergo *cis*–*trans* isomerization under the relevant conditions. In view of the cation radical cyclopropanation reaction to be discussed below, the



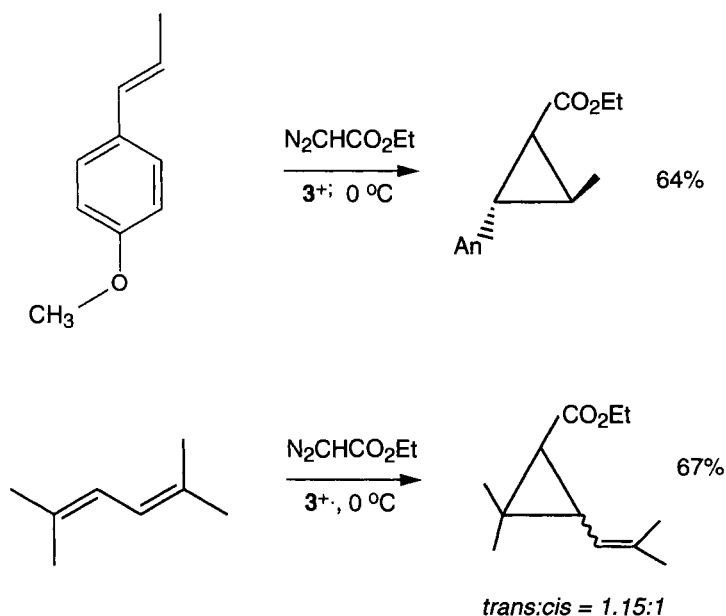
Scheme 49. The cation radical vinylcyclopropane rearrangement.

cation radical vinylcyclopropane rearrangement is of further interest because it formally makes available cation radical routes to all ring sizes from three to six.

3.2.20 Cation Radical Chain Cyclopropanation

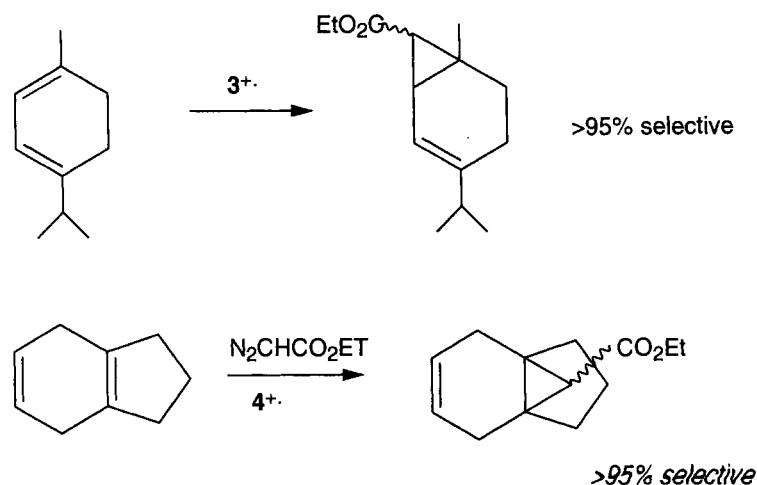
The chain addition of cation radicals of conjugated dienes and electron rich styrenes to ethyl diazoacetate has been found to be a relatively efficient method of generating cyclopropane derivatives (Scheme 50) [90].

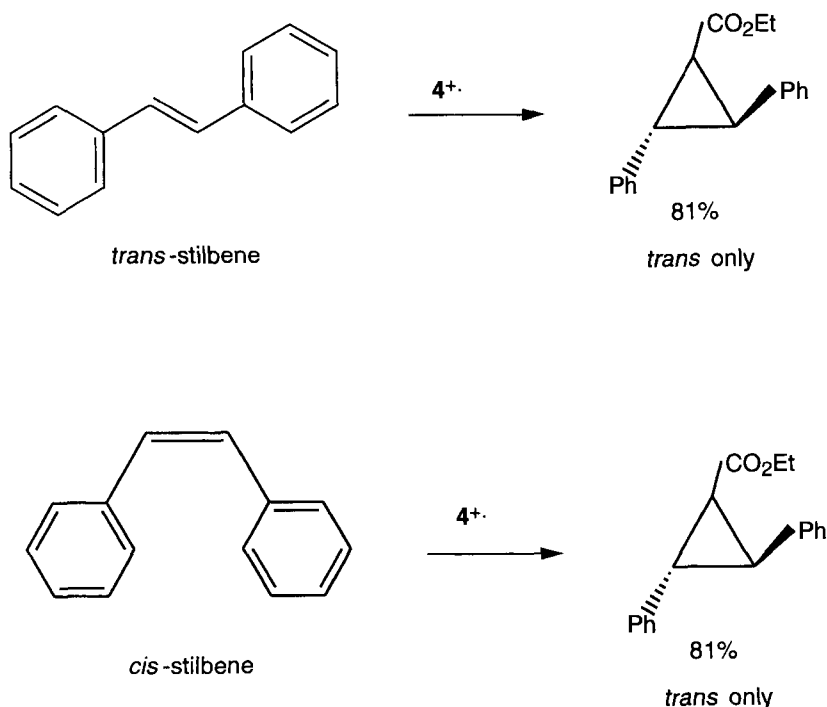
An excess (5:1 mole ratio) of ethyl diazoacetate is used in these reactions to suppress cyclobutadimerization or Diels–Alder cyclodimerization. In difunctional molecules which have non-equivalent ionizable functionalities, cyclopropanation is highly selective for the more easily oxidized functionality. The latter selectivity is perhaps the most attractive aspect of the reaction. In contrast to transition metal (e.g. rhodium) catalyzed cyclopropanations, cation radical additions to electron deficient alkene moieties do not occur at all. The reaction is relatively sensitive to

**Scheme 50.** Cation radical chain cyclopropanation.

steric effects, since α -terpinene is cyclopropanated at the less sterically hindered double bond with a very high degree of selectivity (Scheme 51).

Similarly, tetrasubstituted alkene functions can be cyclopropanated selectively in the presence of less highly substituted alkene moieties. These latter reactions require the more potent aminium salt 4^{++} as the initiator, since simple alkene functions are

**Scheme 51.** Selectivity in cyclopropanation.



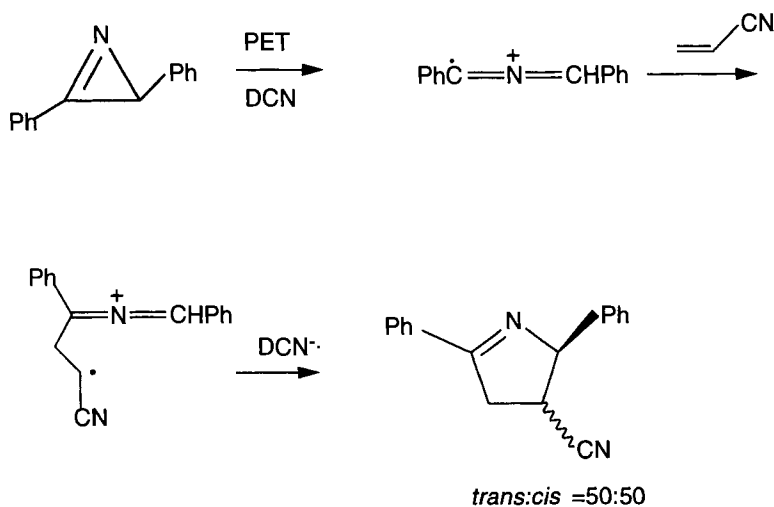
Scheme 52. Stereochemistry of cyclopropanation.

extremely difficult to ionize. The use of this more potent initiator also allows the reactions to be performed at -78°C , thus enhancing the selectivity. Stilbenes and even tetrasubstituted alkenes can be cyclopropanated (Scheme 52).

The cyclopropanation of *cis*- and *trans*-stilbene is completely non-stereospecific, suggesting a stepwise process involving a distonic cation radical intermediate. In accord with this supposition, a long bond cyclopropane cation radical structure would seem to be rather unfavorable in this system, because of the presence of the electron withdrawing ester function at the site of the hypothetical long bond. Similarly, a ring closed structure for the cyclopropane cation radical would not appear to be especially appealing. This gives rise to the interesting question of how this distonic cation radical is neutralized, since electron transfer to the non-bonding orbital of a carbocation site would not appear to be energetically favorable. *In this case, it might be reasonable to postulate a bond-coupled ET process, in which ET is concerted with the formation of the cyclopropane bond of the neutral product.*

3.2.21 Cation Radical Cycloadditions Forming Five-membered Rings

When 2,3-diphenylazirine is ionized by the PET method, the resulting cation radical apparently undergoes rapid cleavage to a distonic cation radical (Scheme 53) [91].



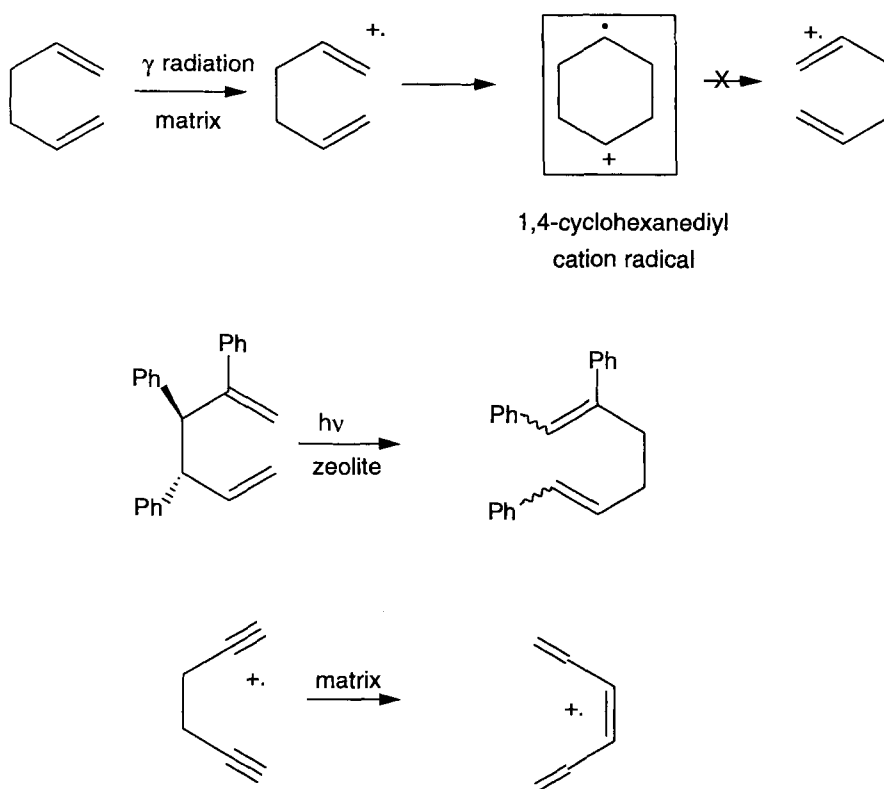
Scheme 53. [3 + 2] Cycloadditions with azirine cation radicals.

The cationic site is of the immonium type, and is relatively unreactive, but the radical site is reactive toward electron deficient alkenes such as acrylonitrile, yielding a 50:50 mixture of the diastereoisomeric pyrrolines, after being neutralized by back electron transfer from the sensitizer anion radical. The net result is an interesting example of a net 1,3-dipolar cycloaddition which, in the Huisgen method of classification of cycloadditions, is of the [3 + 2] type. The same general reaction had previously been carried out by Padwa, using direct photochemical excitation, a procedure which, in contrast, was highly diastereoselective (90:10, in favor of the *trans* isomer) [92].

3.2.22 The Cation Radical Cope Reaction

The cation radical version of the familiar Cope reaction has also received substantial attention. Semi-empirical calculations predict that the cation radical of 1,5-hexadiene should undergo cyclization to a 1,4-cyclohexanediyl cation radical with little or no activation, but that the subsequent ring opening cleavage in the opposite sense would necessarily be highly endothermic [55]. Consequently, the full Cope reaction can presumably not be realized in the simple case of 1,5-hexadiene. This prediction has been amply verified by generating this cation radical via gamma radiolysis in a rigid matrix and observing its closure to the expected 1,4-cyclohexanediyl cation radical, which is relatively stable under the conditions of its generation (Scheme 54) [93].

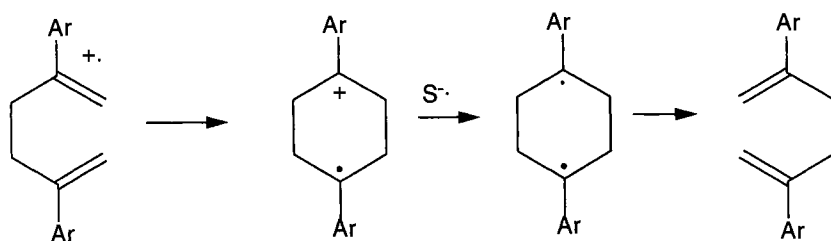
The difficulty in completing the full Cope reaction can, however, be circumvented by installing cation radical stabilizing groups at the 3 and 4 positions of a 1,5-hexadiene derivative [94] or by providing for the delocalization of the cation radical



Scheme 54. The cation radical cope reaction.

moiety of the product over a conjugated system consisting of the original C1, C2, C5, and C6 atoms (Scheme 54) [95]. Although the former case may well proceed by a stepwise, distonic cation radical, mechanism, the latter one does appear to be a bona fide example of a concerted [3,3] sigmatropic shift. An especially interesting way to bring about the final stage of the Cope reaction, that is the cleavage of an intermediate cyclohexanediyl cation radical to a 1,5-hexadiene derivative, has been discovered by Miyashi (Scheme 55) [96].

When the PET method is used to generate the 1,5-hexadiene-type cation radical, the latter cyclizes to the 1,4-cyclohexanediyl cation radical, which is then reduced by electron transfer from the sensitizer anion radical to the 1,4-cyclohexanediyl diradical. The cleavage of the latter to a neutral 1,5-hexadiene derivative is then thermodynamically favorable. The course of these reactions has been followed by the scrambling of deuterium from the 1- and 6-positions of the diene to the 3- and 4-positions, by trapping the intermediate cation radical with dioxygen, and by studying the corresponding reactions of the meso- and dl-3,4-dimethyl compounds. The latter reactions have been found to be stereospecific.



$S^{\bullet-}$ = sensitizer anion radical in the PET method

Ar = phenyl or 4-methoxyphenyl

Scheme 55. An indirect version of the cation radical cope reaction.

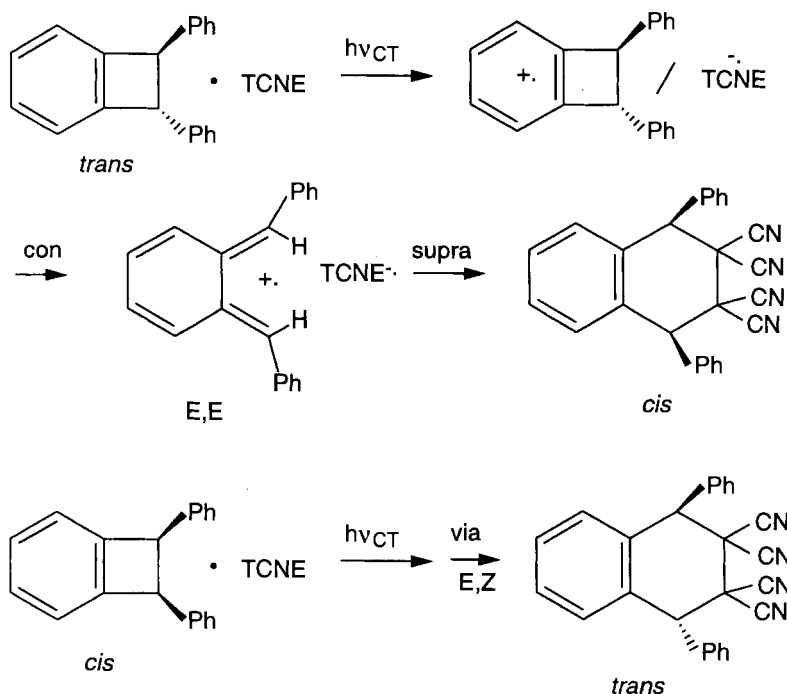
3.2.23 A [1,16] Sigmatropic Shift

One of the earliest, and certainly one of the more impressive examples of apparent cation radical sigmatropic shifts involves the corrin series [97]. Electrochemical oxidation of a nickel(II)-A/D-secocorrinate in acetonitrile containing a trace of water was found to provide an almost quantitative yield of a secocorrin oxide in which a [1,16] hydrogen shift, from the methylene group at C19 in the D ring to the methylenide carbon in the A ring, had occurred in the intermediate cation radical.

3.2.24 Electrocyclic Reactions of Cation Radicals

The retroelectrocyclic ring opening of cyclobutene cation radicals to the 1,3-butadiene type cation radicals has been studied both in the gas phase and in solution. A particularly elegant experiment is the demonstration of conrotatory stereospecificity in the ring opening of the *cis*- and *trans*-1,2-diphenylbenzocyclobutene cation radicals, generated by charge transfer excitation of the electron donor–acceptor complexes of the corresponding neutral substrates with tetracyanoethylene [98]. The formation of the tetracyanoethylene adducts of the *o*-xylylene type cation radical (Scheme 56) is stereospecific, the *cis* benzocyclobutene derivative yielding the *trans* adduct, and the *trans*-benzocyclobutene derivative yielding the *cis* adduct.

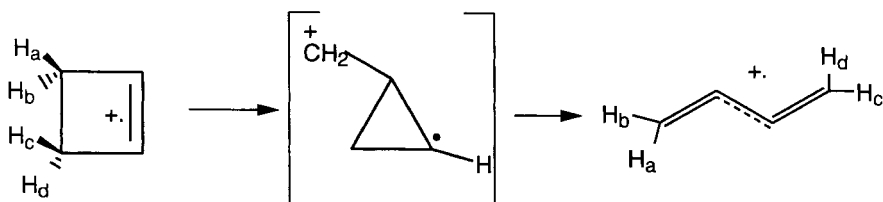
Interestingly, the retroelectrocyclic cleavage of the anion radicals of the same substrates had also been found to be symmetry allowed in the conrotatory mode, which was also experimentally observed (*vide infra*). The stereochemistry of both of these ring openings is the same as that found in the neutral molecules (conrotatory). The retroelectrocyclic cleavage of the parent cyclobutene cation radical, generated by gamma radiolysis of matrix isolated cyclobutene, has also been studied in elegant detail [99]. Very interestingly, the reaction does not appear to generate the *s-cis*-1,3-butadiene cation radical as would be naively expected, but appears to proceed directly to the *s-trans*-1,3-butadiene cation radical, which can be authentically gen-



Scheme 56. Electrocyclic reactions of cation radicals.

erated directly from 1,3-butadiene. This result had previously been predicted by low level *ab initio* calculations which envisioned the formation of an intermediate distonic cyclopropylcarbiny cation radical [100]. Subsequently, much more sophisticated calculations have revealed that a reaction path proceeding via the cyclopropylcarbiny cation radical is indeed the preferred one (Scheme 57) [101].

However, the calculations indicate that this species is not an actual energy minimum but a flat portion of the potential surface. This reaction path, which has been termed a *non-electrocyclic reaction*, somewhat surprisingly is also predicted to be conrotatorily stereospecific.

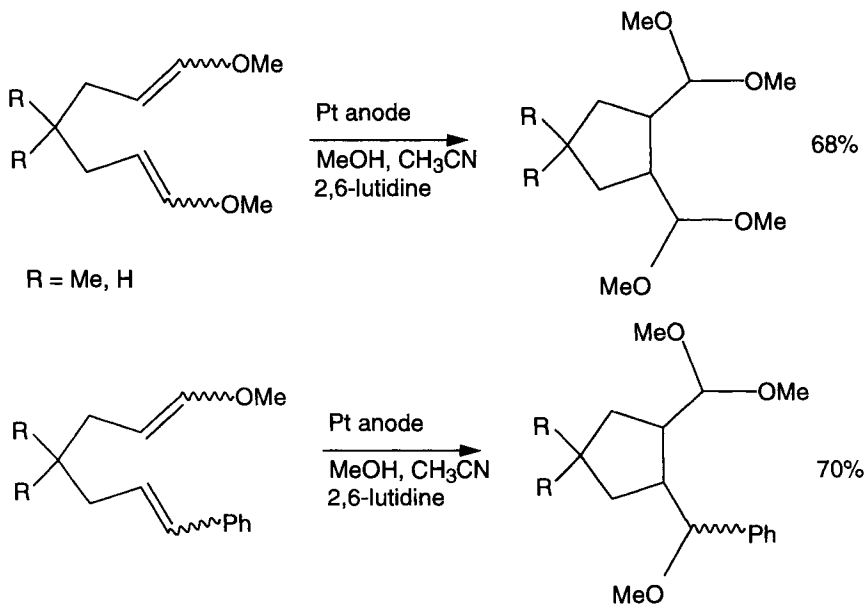


Scheme 57. The conrotatory, nonelectrocyclic path from the cyclobutene cation radical to 1,3-butadiene cation radical.

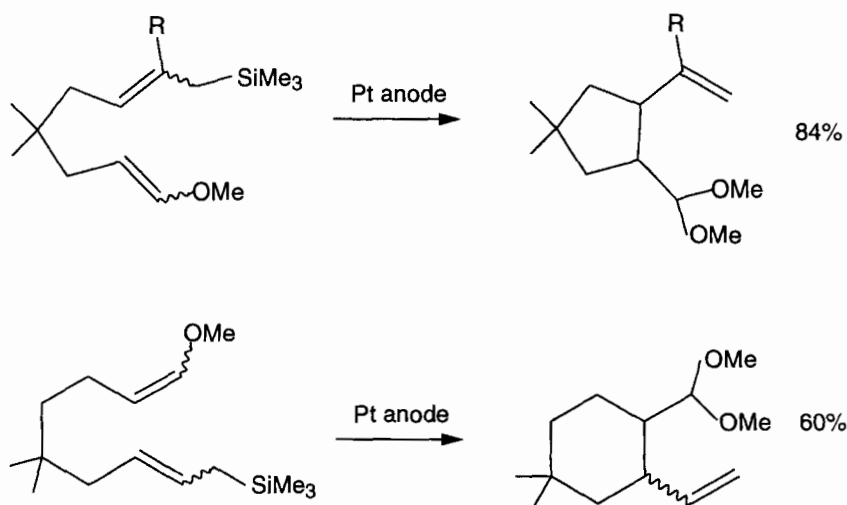
3.2.25 Cation Radical Cyclizations

Scope and general aspects of cation radical cyclizations

The distinction between the two terms ‘cycloaddition’ and ‘cyclization’ should be noted. In contrast to cycloadditions, in which a ring is formed by generating two new bonds either in an intermolecular or an intramolecular context, cyclization is an intramolecular reaction in which a ring is formed by generating only one new bond. The Diels–Alder reaction is a cycloaddition, while the cyclization of the 1,5-hexadiene cation radical to give the 1,4-cyclohexanediyl cation radical represents a cation radical cyclization. Moeller’s group has been especially ingenious in developing the synthetic potential of cation radical cyclization reactions [102]. It should be born in mind that, unlike most of the previously discussed cycloadditions, these cyclization reactions are typically neither chain nor catalytic processes, but require the stoichiometric oxidation of an appropriate substrate to its cation radical. For this reason, among others, most of the efficient cyclizations already reported have involved the generation of substrate cation radicals by anodic oxidation. Normally the substrate is bifunctional, and contains one functionality which is especially easily oxidizable and one to which the cation radical moiety may readily add by an electrophilic or radical addition mode. The vinyl ether function plays an especially prominent role in much of the anodic cyclization chemistry reported thus far, especially as the oxidizable function, but also in some cases as the neutral component of the cyclization reaction (Scheme 58).



Scheme 58. Cation radical cyclization reactions.



Scheme 59. Cation radical cyclizations using allylsilanes as neutral components.

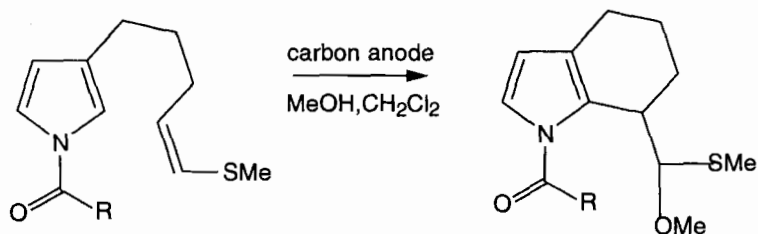
As neutral components, simple styryl and even alkene functions have been employed in cyclizations generating 5–7 membered rings. Vinylsilane and allylsilane functionality have also been ingeniously employed, the silyl group providing an effective electrofugal leaving group (Scheme 59).

Most of these reactions take place in good yield and using relatively simple electrochemical apparatus. It is especially important in this context to note the initial example of such cation radical cyclizations, especially under anodic oxidation conditions, which was provided by Shono (Scheme 60) [103].

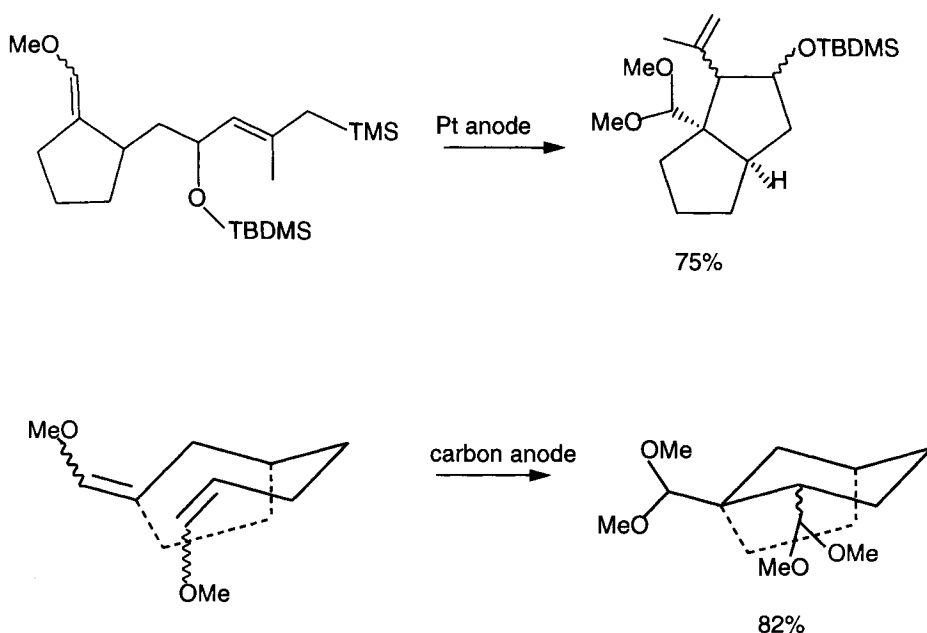
Although this reaction proceeded in a relatively low yield, it provides not only the prototype example, but an interesting exemplification of the use of a vinyl sulfide moiety as the ionizable group, and of an electron rich aromatic ring as the neutral moiety.

Cation radical cyclizations in natural product synthesis

The effective potential use of cation radical cyclization reactions for natural product synthesis has been proposed, and the syntheses of Crinipellin B and Scopadulcic



Scheme 60. The precedent for anodic cation radical cyclizations.



Scheme 61. Cation radical approaches to crinipellin B and scopadulcic acid B.

Acid B appear to be well underway, as illustrated by the published model studies illustrated in Scheme 61 [104].

3.2.26 Other Reactions of Cation Radicals

Coupling reactions

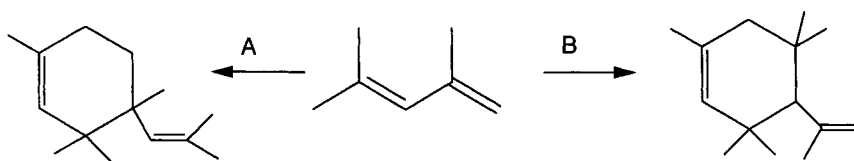
It is abundantly clear that *electron transfer*, *cycloaddition*, *cyclization*, and *re-arrangement* are characteristic and facile reactions of pi cation radicals. Equally as characteristic, even if not quite as useful, are the coupling reactions which frequently occur between cation radicals when they are generated in higher concentrations, e.g., at anodes or when an aminium salt initiator is used which too readily oxidizes the substrate. As radical species, cation radicals would be expected to participate in coupling reactions which afford di-cations. An especially interesting case of this type involves the coupling of vinylcarbazole cation radicals under certain conditions to give di-cations, which then propagate addition polymerization from both cationic sites [105]. Many other such couplings have been observed.

Cation radicals as Brønsted acids and electrophiles

As electrophilic species, cation radicals react readily with a variety of nucleophiles. The rates of such reactions, in fact, often approach diffusion control. For example,

the 4-vinylanisole cation radical reacts with azide ion in trifluoroethanol solution at the diffusion controlled rate ($7 \times 10^9 \text{ M}^{-1} \text{ s}^{-1}$) [106]. Even the *trans*-anethole cation radical reacts at a rate which is only a factor of two less than the diffusion controlled rate. Finally, cation radicals which have allylic hydrogens are highly acidic, often being in the category of superacids, so that acid catalyzed chemistry is a potential concomitant of cation radical chemistry, especially under aminium salt conditions. Further, the di-cations which may be generated by cation radical/cation radical coupling may de-protonate to yield strong acids. This appears to be an especial caveat for aminium salt initiated chemistry, which can however, be controlled in many cases by the addition of a hindered amine base. Acid catalyzed, electrophilic chemistry appears not to be problematic in the case of the PET method of generating cation radicals, because the corresponding anion radicals of the sensitizer sweep out any protonic species. Further, it has not yet become evident that acid catalyzed processes are problematic under anodic oxidation conditions. A classic instance of the intrusion of acid-catalyzed electrophilic chemistry in the context of an aminium salt catalyzed reaction is available in the Diels–Alder cyclodimerization of 2,4-dimethyl-1,3-pentadiene (Scheme 62) [70].

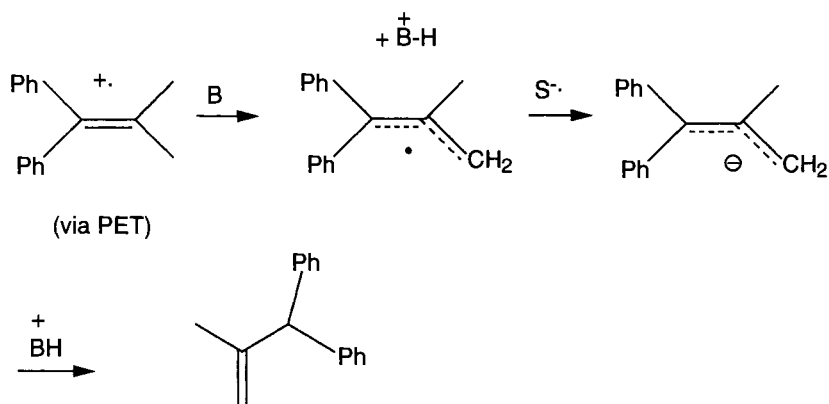
The DA dimer obtained in the aminium salt reaction differs from that obtained by the PET method and from that obtained using the aminium salt/hindered base method, but is the same as that obtained by the Brønsted acid catalyzed reaction of this diene. The addition of insoluble bases like sodium carbonate is not sufficient to suppress the extremely facile, acid-catalyzed cyclodimerization of this particular diene, which yield a highly stabilized tetramethylallyl carbocation intermediate. Nevertheless, this results demonstrates the necessity for caution in assigning a cation radical mechanism to a cyclodimerization reaction observed under aminium salt conditions.



A = PET induced reaction of cation radicals or
aminium salt induced reaction in the presence
of a hindered base: cation radical mechanism

B = aminium salt induced reaction in the absence of
soluble, hindered base or triflic acid catalyzed reaction:
Brønsted acid catalyzed, carbocation mediated reaction.

Scheme 62. Cation radical vs. carbocationic Diels–Alder cycloaddition reactions.



Scheme 63. Contrathermodynamic isomerization of alkenes.

Contrathermodynamic alkene isomerization

Arnold's group has exploited the acidity of alkene cation radicals which have allylic hydrogens to isomerize an alkene function from a position in conjugation with an aryl ring to the position once removed from its original placement (Scheme 63) [107].

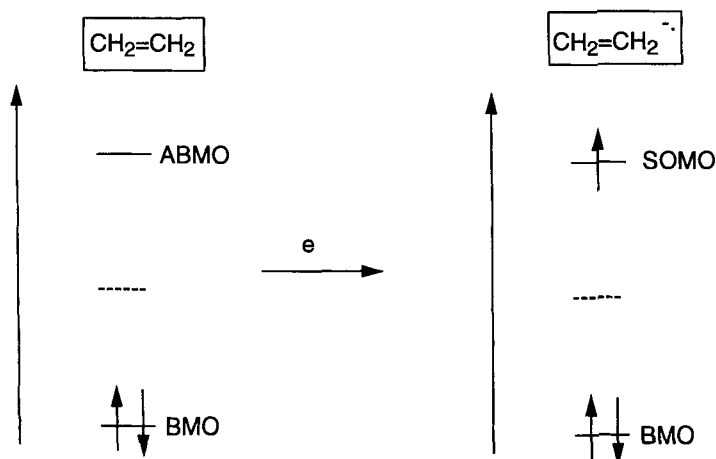
This reaction presumably relies upon the relative ease of ionization of the styrene type system to the corresponding cation radical using the PET method. This can be rapidly deprotonated by an appropriate base to the corresponding allylic radical, which is then reduced by the sensitizer anion radical to the corresponding allylic anion. This anion, in turn, can be protonated at either allylic terminus by the conjugate acid of the base which de-protonated the cation radical. When the non-conjugated alkene is generated, it is relatively much less ionizable by the excited state sensitizer, so that the photostationary state favors the less thermodynamically stable, non-conjugated alkene function.

3.3 Electron Transfer Chemistry Involving C–C Multiple Bonds as Single Electron Acceptors

3.3.1 The Three-electron Bond of the Ethene Anion Radical

The structure of the ethene anion radical remains unknown, but a simple HMO picture of this species (Scheme 64) reveals a three electron bond loosely analogous to those found in some radicals, such as the nitroxyl radicals.

Not only does the addition of an electron to the π^* MO of ethene inherently greatly decrease the extent of bonding relative to the two electron bond present in ethene, but it also appears highly likely that because of the additional electronic



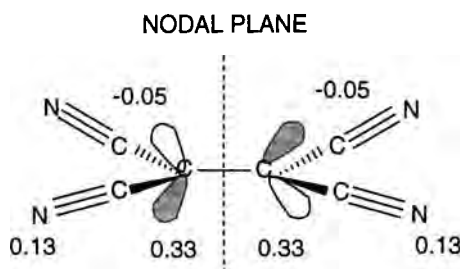
Scheme 64. The three electron bond of the ethene anion radical.

repulsions in a three electron pi system the bond energy is far less than that of even a one electron pi bond (as in the ethene cation radical). The severely weakened pi bond could thus be amenable to twisting in order to decrease the torsional strain present in a planar species, just as was the case with the corresponding cation radical. On the other hand, the cationic hyperconjugative interactions with the CH bonds which are present in the twisted but not in the planar form of the ethene cation radical are also likely to be less favorable in the anionic case. What does appear clear is that not only is ethene relatively difficult to reduce to the corresponding anion radical, in contrast to, e.g. benzene, but the resulting anion radical is also highly reactive and unstable.

3.3.2 The Shape of the SOMO of a Pi Anion Radical

The energy of the SOMO of an ethene derivative which is substituted with conjugating, electron withdrawing substituents is of course much lower than that of ethene itself. An extreme case of such an anion radical is that of tetracyanoethylene (TCNE), which has been isolated as the tetrabutylammonium salt. A reasonably direct, experimental examination of the SOMO distribution of this anion radical was possible through polarized single crystal neutron diffraction studies [108]. Interestingly, the pi SOMO was found not to be centered directly around the two alkene carbon nuclei, but rather to be bent back, away from the alkene C–C bond, as is theoretically expected for an MO which is anti-bonding between these two carbons (Scheme 65).

The spin densities found on the central alkene carbons, the cyano group carbons, and the terminal nitrogens are 0.33, -0.05 , and 0.13 , per atom, respectively. These experimental findings are in good agreement with the results of density functional



Scheme 65. Shape and spin densities in the SOMO of the TCNE anion radical.

theoretical (DFT) calculations. Thus, the alkene carbons have a total of 66 % of the spin, while the remainder of the positive spin is delocalized onto the terminal nitrogens of the cyano groups.

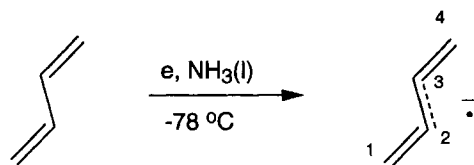
3.3.3 The Butadiene Anion Radical

The LUMOs of conjugated pi systems are typically much lower in energy than that of ethene, so that the reduction of these systems to the corresponding anion radicals is more facile. The electrochemical reduction of 1,3-butadiene in liquid ammonia solution at $-78\text{ }^{\circ}\text{C}$, in fact, yields an anion radical which is stable enough to permit observation by ESR spectroscopy (Scheme 66) [109].

The hyperfine splitting arising from the four protons at the terminal carbon atoms is found to be -0.76 mT , while that of the two other protons is -0.28 mT , indicating that, as theory predicts, the SOMO of this diene anion radical is more heavily concentrated on C1 and C4, as opposed to C2 and C3. In contrast, the cation radical of 1,3-butadiene is apparently too short-lived in *fluid* solution to be observed by ESR spectroscopy.

3.3.4 Disproportionation of Anion Radicals to Dianions and Neutrals

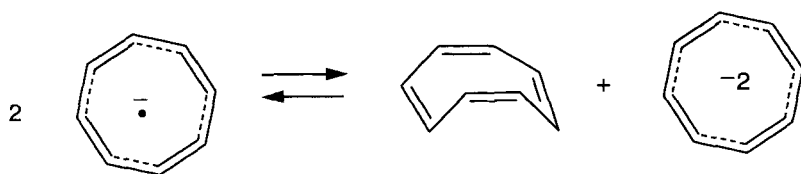
The tendency of anion radicals to undergo an electron transfer reaction yielding a neutral molecule and a dianion (Scheme 67) is especially noteworthy.



$$a_{1,4} = -0.76\text{ mT (4H)}$$

$$a_{2,3} = -0.28\text{ mT (2H)}$$

Scheme 66. Formation and hyperfine couplings in the 1,3-butadiene anion radical.

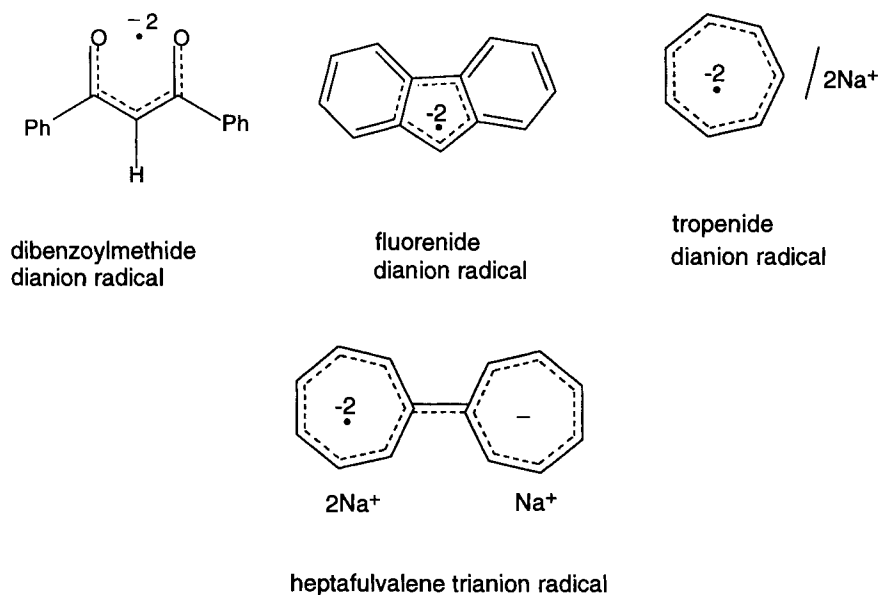


Scheme 67. Disproportionation of anion radicals.

Though this tendency to disproportionate is especially marked in relatively non-polar solvents, it can occur to a significant extent even in polar solvents. Apparently, the additional electronic repulsions incurred by adding a second electron to the SOMO of an anion radical are negated by the even stronger electrostatic attraction of the dianion to two unipositive metal ions. Besides the coordination of metal ions to the dianion, substantial structural changes incurred in converting the neutral species to the anion radical or in converting the anion radical to the dianion may affect the extent of disproportionation. In the cyclooctatetraene case, for example, the neutral molecule is tub-shaped, with the four alkene pi bonds essentially perpendicular to each other [110]. Formally, this molecule has a very high energy LUMO, comparable to that in ethene. However, the anion radical which is actually formed is planar, and the SOMO of this anion radical occupies a very low energy, non-bonding orbital. Consequently, the conversion from a tub shaped anion radical to a planar structure is highly favored by the dramatic lowering of the energy of the SOMO. On the other hand, the planar octagonal shape of the anion radical has a substantial amount of angle strain, owing to the wider than normal bond angles, along with some additional torsional strain. In contrast, the conversion of the anion radical to the dianion takes advantage of the lower SOMO energy without having to compensate for any additional strain, since the dianion is also planar. To put the argument more succinctly, on the anion radical side of the equilibrium, two species have ring strain, whereas on the dianion side, only one does. The tetraphenylethylene anion radical is another persistent anion radical for which disproportionation has been found to be extensive [111]. In this instance, a possible incremental contributing reason is the release of steric effects in the dianion, which could reasonably be expected to have a twisted structure in which the two trigonal planes of the alkene carbons are by no means coincident, and possibly might even be perpendicular.

3.3.5 Dianion Radicals, Trianion Radicals, and Multianion Radicals

Just as the one electron reduction of a neutral molecule produces an anion radical, the one electron reduction of an organic anion can yield a dianion radical, assuming that the LUMO of the anion is not too high in energy. Two anions familiar in organic chemistry are the dibenzoylmethide (an enolate of a β -diketone) [112] and fluorenone anions [113] (Scheme 68).

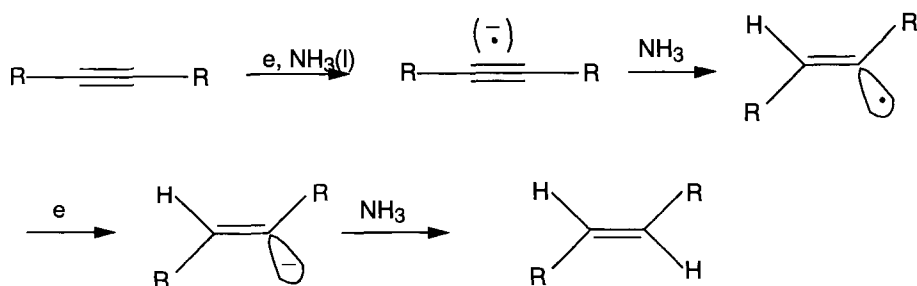


Scheme 68. Stable dianion radicals and trianion radicals.

These anions have both been converted to the corresponding persistent dianion radicals by alkali metal reduction. In the latter case, the agreement of the ESR hyperfine splitting constants with those predicted from the LUMO of the fluorenyl anion were confirmed by deuterium labeling experiments. A simple hydrocarbon dianion radical was prepared by the reduction of the tropenyl anion to the corresponding dianion radical [114]. In the case of the sodium salt of this dianion radical, the dianionic nature of the radical species was confirmed additionally by the observation of two equivalent sodium hyperfine splittings. A trianion radical was prepared by the alkali metal reduction of sesquifulvalene [115]. Unlike the corresponding anion radical, the trianion radical has the spin localized on only one of the seven-membered rings, presumably because of tight ion pairing of the other ring (which contains the dianion moiety) with two metal ions, while the ring which contains the anion radical moiety is ion paired to just one of the three metal ions.

3.3.6 Methods for Generating Anion Radicals

From the earliest times, anion radicals have been generated by the reaction of an appropriate neutral molecule with metals, especially, with sodium, potassium, or lithium in ethereal solvents. In sharp contrast to the corresponding cation radicals, these anion radicals have often proved to be quite persistent in the absence of moisture or air. This is particularly true for anion radicals of aromatic systems such



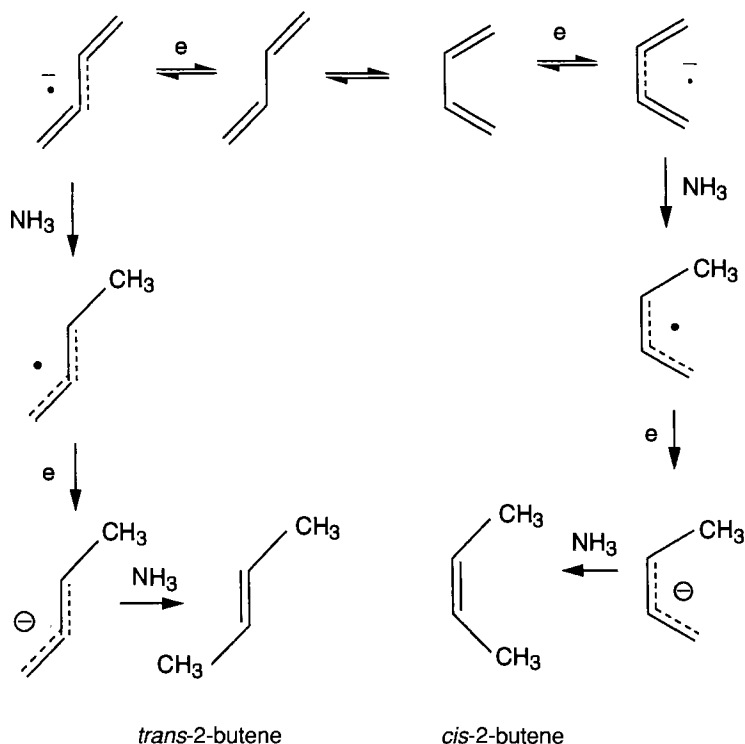
Scheme 69. Birch reduction of alkynes to trans-alkenes.

as naphthalene and biphenyl. The latter have often been prepared and used as single electron transfer (SET) agents for the homogeneous reduction of other substrates to their anion radicals. Further, there is a rich corpus of anion radical chemistry deriving from electroreduction of neutral organic substrates, which will be discussed further on. More recently, anion radicals have also been generated by the PET method, using excited states of electron rich sensitizers to reduce substrate molecules. Finally, anion radical/cation radical pairs can be generated in appropriate instances by SET between neutral, ground state molecules. Each of the above methods will be illustrated in the course of the following discussions of the ET chemistry of anion radicals.

3.3.7 The Birch Reduction of Non-Terminal Alkynes

Although alkali metal/liquid ammonia reductions (Birch reductions) of simple alkenes is difficult, presumably as a result of the very high energy of an ethene type LUMO, the corresponding reduction of non-terminal alkynes to *trans*-alkenes is an efficient and useful synthetic tool for accessing *trans*-alkenes [116]. The mechanism for this reaction (Scheme 69), involves the homogeneous reduction of the alkyne to the corresponding anion radical by the solvated electrons present in liquid ammonia solutions of alkali metals.

The anion radicals undergo protonation to give a vinyl radical, followed by homogeneous reduction of the latter to the corresponding vinyl anion, which is then protonated. The step in which the product stereochemistry is established is still not certain, but it is clear that both the vinyl radical and carbanion are bent species which should have a preference for *trans* R groups. More likely is the possibility that the vinyl radical is either initially formed with a preference for the *trans* bent structure in the protonation of the anion radical or that it rapidly equilibrates to this more favorable structure prior to reduction to the vinyl anion. The vinyl anion might be expected to be configurationally more stable than is the radical, but it is also possible that rapid equilibration of the anion yields the more stable *trans*-vinyl anion.



Scheme 70. Birch reduction of conjugated dienes.

3.3.8 Birch Reduction of Conjugated Dienes

The reaction of 1,3-butadiene with the solvated electrons of liquid ammonia results in homogeneous electron transfer to yield the diene anion radical, which is ultimately converted to a mixture of *cis*- and *trans*-2-butene [117]. The mechanism of this reduction (Scheme 70) involves protonation of the anion radical at C1 or C4 of the diene, where most of the negative charge resides, followed by homogeneous reduction of the resulting allylic radical by the solvated electrons and finally protonation of the allylic carbanion at the primary carbanion site.

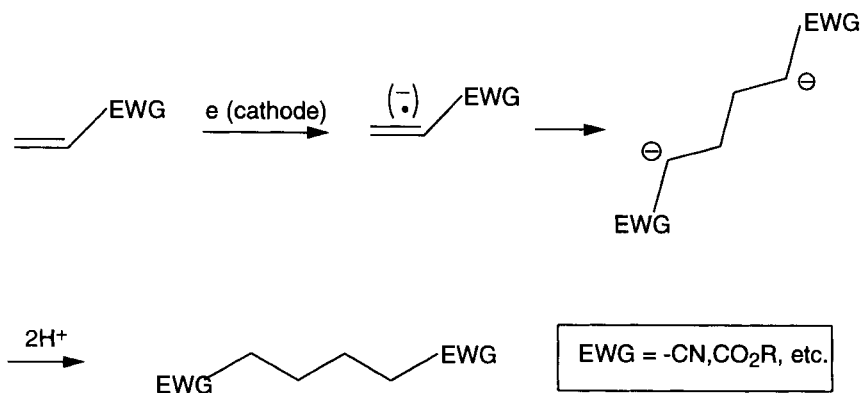
An interesting aspect of this reaction is the formation of substantial amounts of *cis*-2-butene, which would appear to require the intermediacy of the *s-cis*-1,3-butadiene anion radical, even though butadiene exists almost exclusively in the *s-trans* conformation (98 %). At -33°C , 13 % of the 2-butene mixture is the *cis* alkene, and at -78°C 50 % of the mixture is *cis*-2-butene. In the case of 1,3-pentadiene, 68 % of the 2-pentene is the *cis* isomer. The most plausible explanation for these stereochemical results appears to be the reversible reduction of the diene to the diene anion radical at -78°C by the pool of solvated electrons, which yields an equilibrium mixture of the *s-cis* and *s-trans*-anion radicals (ca. 50:50), which are

then protonated by ammonia to yield the *cis*- or *trans* allylic radical. An alternative equilibration mechanism involving unimolecular *trans*-to-*cis* isomerization appears unlikely since the C2–C3 bond order is greatly increased in the anion radical. That the protonation of the diene anion radical by ammonia might be slow enough to permit equilibration is supported by the weak acidity of ammonia (pK_a 38) and the soft basicity of the delocalized anion radical. It appears likely that once the allylic radical is formed, equilibration between the *cis* and *trans* allylic radicals or anions is highly unlikely, since this would involve the loss of allylic resonance. At -33°C , the protonation of the anion radical may be fast enough to prevent the complete equilibration of the *cis* and *trans* anion radicals.

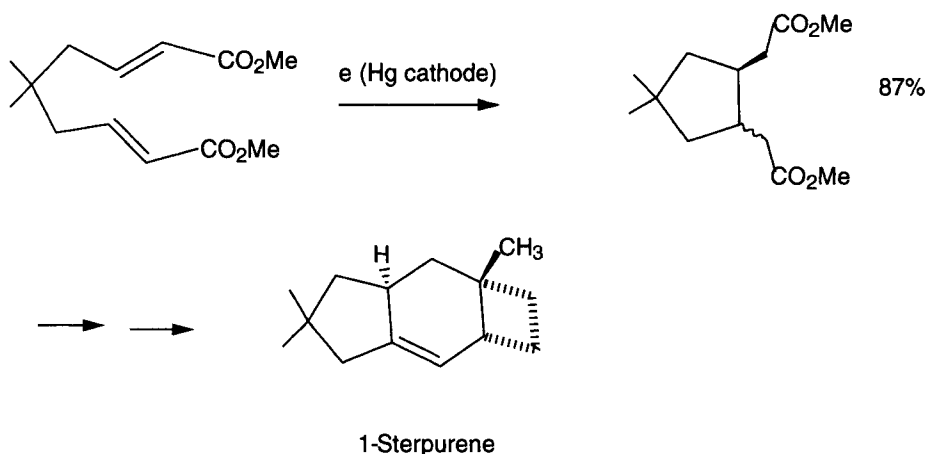
3.3.9 Coupling of Anion Radicals

In the previously described reactions, the basicity of anion radicals and their reactions with proton donors was emphasized. In the absence of viable proton donors or even in their presence, if the anion radical is relatively stable, radical coupling may be the dominant reaction. Thus even in aqueous solution, the anion radicals of alkenes substituted with strongly electron withdrawing moieties may undergo coupling in preference to protonation. The synthesis of adiponitrile from acrylonitrile (Scheme 71) is an outstanding example [118].

This kind of reaction is effective with acrylate esters and even with 4-vinylpyridine. Somewhat surprisingly, it works well even with some terminally disubstituted acrylate esters. Intramolecular versions involving cyclization to five-membered rings are especially effective. Mechanistically, these reactions could involve the coupling of two anion radicals or the addition of an anion radical to a corresponding neutral, followed by reduction of the distonic anion radical to the dianion, which is then protonated twice, yielding the hydrodimer. Apparently, the distinction between these two plausible mechanistic types has not yet been decisively made in most cases (however, please see the discussion on intramolecular cyclizations immediately



Scheme 71. The hydrodimerization of electron deficient alkenes.



Scheme 72. Total synthesis of sterpurene.

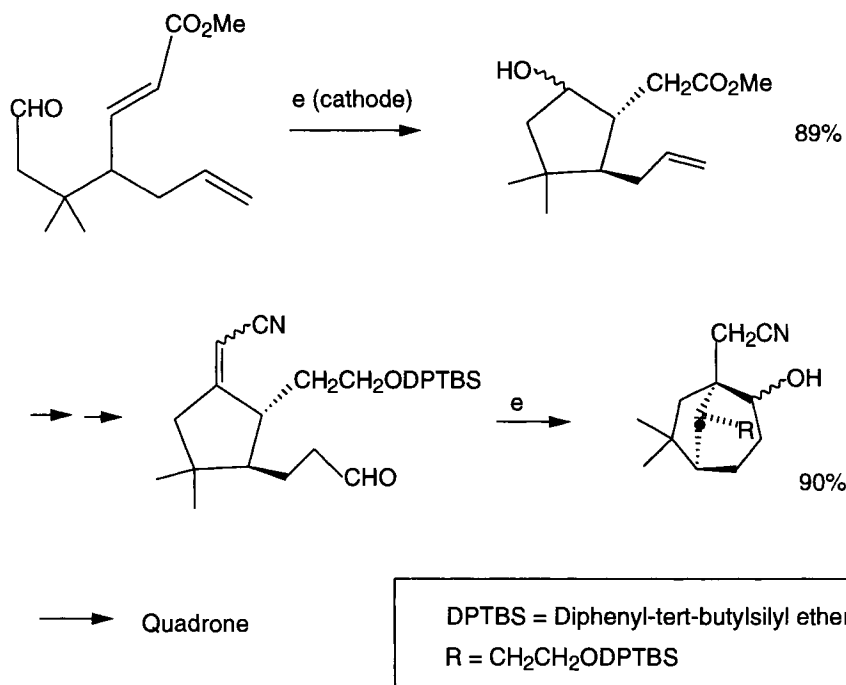
below). When substrates are reduced in the absence of any viable proton donor, as in the case of reactions carried out in an ethereal solvent, the dianion is the usual product. In the case of styrene, this dianion has been employed to propagate anion polymerization of styrene at both anionic centers of the dianion [119].

3.3.10 Intramolecular Cyclizations Involving Anion Radicals

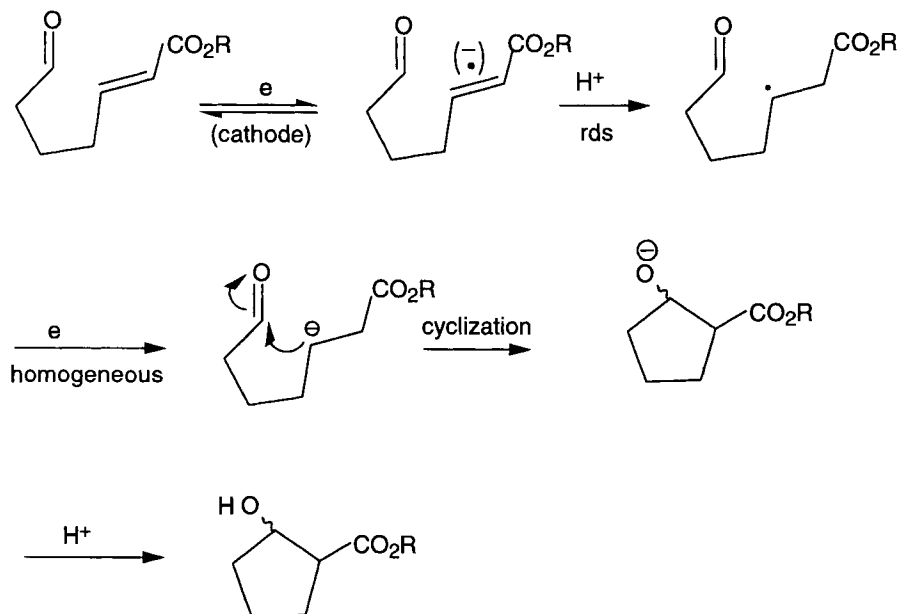
An intramolecular version of the hydrodimerization reaction discussed in the preceding section has proved to be especially attractive and efficient for natural product synthesis. A total synthesis of the sesquiterpene sterpurene exploits just such a reaction, at a very early stage of the synthesis, for the closure of the five-membered ring (Scheme 72) [120].

The anion radicals were generated by cathodic reduction, providing yields of cyclized product as high as 87 %. In a total synthesis of quadrone, efficient reductive cyclizations were used at two different stages of the synthesis (Scheme 73) [121].

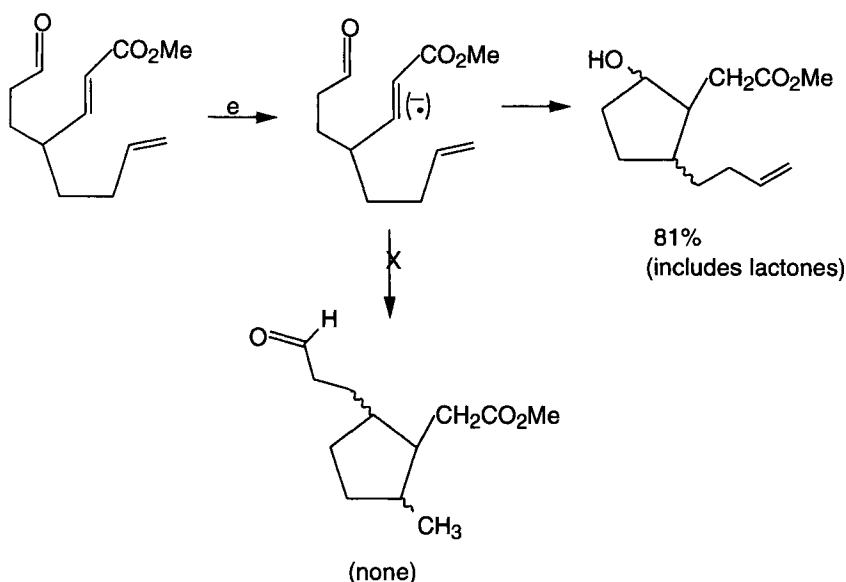
These cyclizations both involve the reductive intramolecular addition of an electron deficient alkene function to an aldehyde carbonyl function, and both are effected in ca 90 % yields. The mechanism of this latter type of electrochemically induced cyclizations of carbon–carbon double bonds to carbonyl double bonds have been studied rather extensively, with especial attention to the fundamental mechanistic question of whether the cyclization step involves an anion radical, radical, or anionic mechanism [122]. The latter two mechanisms would involve the protonation of the initially formed anion radical intermediate to form a radical, which could then cyclize or, alternatively, be further reduced to an anion, which could then cyclize. Extensive and elegant electrochemical and chemical studies have led to the formulation of these reactions as involving anionic cyclization (Scheme 74).



Scheme 73. Formal total synthesis of quadrone.



Scheme 74. The proposed anionic mechanism for cyclizations involving anion radical intermediates.



Scheme 75. A probe for distinguishing the radical and anionic mechanisms of cyclization.

Indeed, radical probe studies have very decisively excluded the radical cyclization mechanism in at least one typical case. This experiment relies upon the circumstance that the cyclization of a carbon-centered radical to an aldehyde carbon group is known to occur at approximately the same rate as the *exo*-trig cyclization of such a radical to a carbon–carbon double bond. In a probe molecule designed to provide an opportunity for a hypothetical radical intermediate to add to either or both of these functionalities, no addition to the vinyl double bond was observed (Scheme 75).

This indicates that the reaction must involve either the cyclization of an anionic intermediate, which obviously would add more rapidly to a carbonyl group than to an alkene double bond, or of the initially formed anion radical intermediate, which because of Umpolung might also prefer addition to the carbonyl group. The latter possibility was considered to be effectively ruled out because the electrochemical studies revealed that protonation of an intermediate was involved at or before the rate determining step. Thus, if cyclization had occurred at the anion radical stage, it would, according to this reasoning, be expected that this (cyclization) step would be rate determining, not the subsequent protonation of the cyclized intermediate, which would be an alkoxide anion. It might be considered, however, that if the anion radical cyclization were rapid and reversible and thermodynamically unfavorable (as appears likely), the subsequent protonation (especially by a weak acid or even a strong acid present at low concentration) could indeed be rate determining. The rapid, reversible, and selective cyclization of a delocalized and thus rather stabilized anion radical to a carbonyl group would not appear to be implausible. One further point should be made in relation to the proposed anionic cyclization mechanism.

The protonation of the anion radical intermediate proposed in Scheme 74 would appear to be highly unlikely to give the indicated radical as the primary product of protonation. Instead, protonation on oxygen would appear to be favored not only by the higher partial negative charge on oxygen, but also by the circumstance that such a protonation would yield a stabilized, allylic radical, in contrast to the simple primary radical proposed in Scheme 74. Moreover, the rearrangement of an initially formed allylic radical to the primary radical intermediate proposed would appear to be thermodynamically unfavorable, as well as kinetically and mechanistically unlikely. Of course, the allylic radical intermediate could be reduced to the corresponding allylic anion, which might then cyclize to give the (ester) enol form of the expected product. Consequently, it would appear reasonable, if the anionic cyclization mechanism is to be retained, to modify the structures of the proposed radical and anionic intermediates in this cyclization. On the other hand, as was noted above, it may be desirable to more rigorously examine the possibility of an anion radical cyclization mechanism.

3.3.11 Pericyclic Reactions of Anion Radicals

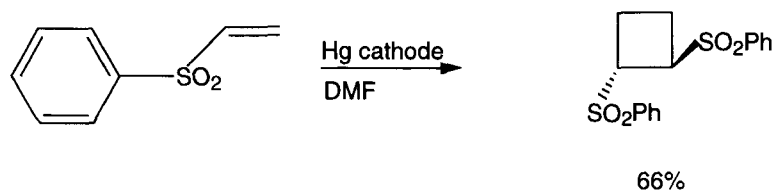
General aspects of anion radical pericyclic additions

Although the pericyclic chemistry of anion radicals has been much slower to emerge than that of cation radicals, the number of intriguing examples now available suggests that this could be an attractive area for future development in electron transfer chemistry. Reaction types which have been exemplified include cyclobutanation, retrocyclobutanation, Diels–Alder addition, electrocyclic reactions, and retroelectrocyclic reactions.

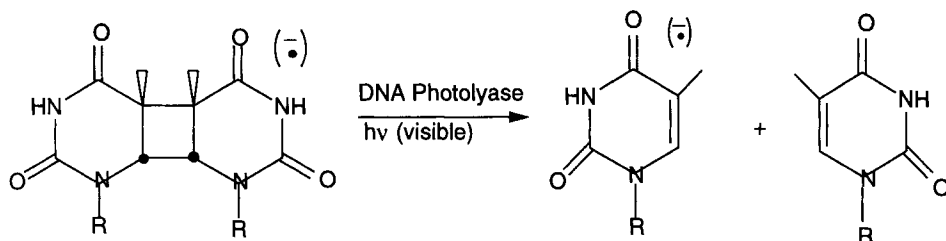
Anion radical cyclobutanation

An especially clean example of electron transfer chemistry involving carbon–carbon multiple bonds as electron acceptors, i.e., proceeding via anion radicals is the cyclobutanation of phenyl vinyl sulfone induced by reduction at a mercury pool cathode (Scheme 76) [122].

That the reaction is electrocatalytic is shown by the observation that only 0.2 F mol^{-1} of electricity is consumed. The dimer is isolated in 66 % yield. The interesting question of whether the addition of the anion radical to the neutral sulfone is con-



Scheme 76. Anion radical cyclobutanation.



Scheme 77. Anion radical retrocyclobutane in the repair of DNA.

certed or stepwise has not yet been addressed. Other examples of this type of reaction appear not to have been observed, but clearly this is an area where additional research efforts would be justified.

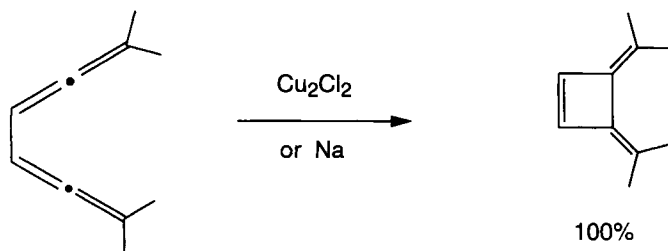
Anion radical retrocyclobutane

The reversal of cyclobutane, i.e., retrocyclobutane has also been observed in the context of a reaction of substantial biological importance (Scheme 77) [123].

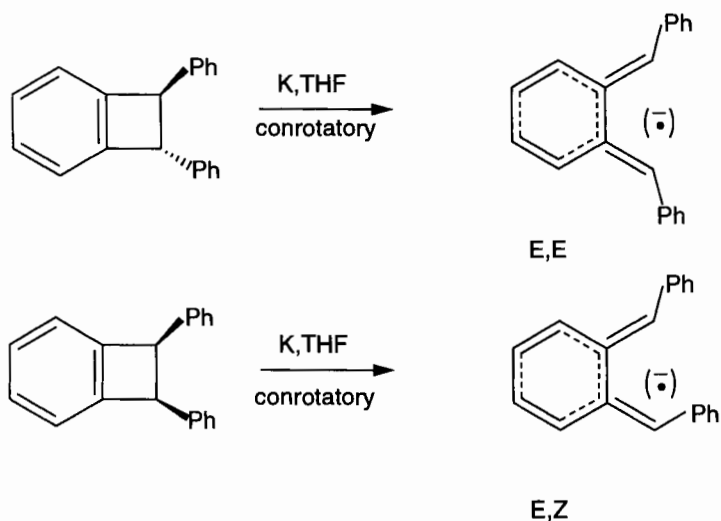
The predominant DNA photolesion engendered by long wave length UV light is pyrimidine cyclodimerization, a cyclobutane reaction involving an excited state of the pyrimidine moiety. One of the processes available for the repair of such photolesions is an enzymatic retrocyclobutane catalyzed by the enzyme DNA photolyase in the presence of visible light and one or more cofactors. Elegant work by Begley's group has demonstrated that this cleavage involves electron transfer to the pyrimidine dimer moiety to form the anion radical, which rapidly cleaves the dimer, giving one anion radical moiety and a neutral moiety.

Anion radical electrocyclic reactions

An unusually efficient example of an electron transfer catalyzed electrocyclic reaction proceeding via anion radicals has also been established [124]. The conversion of the bis(allene) shown in Scheme 78 to the corresponding cyclobutene derivative



Scheme 78. An anion radical chain electrocyclic reaction.



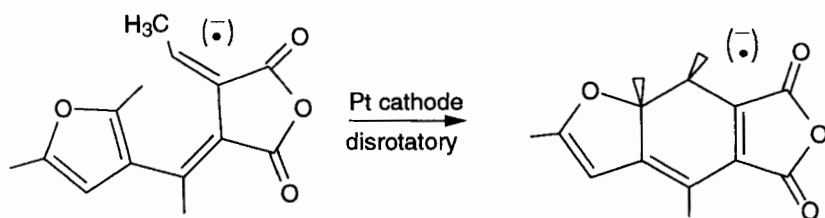
Scheme 79. A symmetry allowed anion radical retroelectrocyclic reaction.

proceeds in quantitative yield in the presence of cuprous chloride, sodium metal, or the naphthalene anion radical, and is inhibited by molecular oxygen, indicating that it proceeds via a chain mechanism.

The retroelectrocyclic cleavage of the *cis*- and *trans*-diphenylbenzocyclobutene anion radicals, generated by alkali metal reduction, has been shown to occur in a conrotatorily stereospecific manner (Scheme 79) [125].

An electrocyclic closure to a six-membered ring system has also been reported (Scheme 80) [126].

Perhaps the most interesting reaction of all of the possible anion radical pericyclic reactions, a Diels–Alder cycloaddition, has not been definitively exemplified, but one potential example of such a reaction has been proposed [127].



Scheme 80. A 1,3,5-hexatriene to 1,3-cyclohexadiene-type anion radical electrocyclic reaction.

3.4 Electron Transfer Reactions of C–C Multiple Bonds Which Involve Both Single Electron Donation and Acceptance

3.4.1 Reactions Involving both Anion Radicals and Cation Radicals

Reactions which involve thermal electron transfer (TET) between two neutral substrate molecules in their respective ground states are still relatively rare in the chemistry of alkenes and alkynes. An especially intriguing example has been provided, however, the reaction of nitroalkenes and other highly electron deficient alkenes with certain methylenecyclopropanone acetals [128]. Electron transfer between two such substrates appears to generate the anion radical/cation radical pair, the cation radical of which undergoes ring opening to form a dialkoxytrimethylenemethane cation radical. The latter then reacts with its anion radical partner in a *non-stereospecific manner* to yield largely *exo*-methylenecyclopentanone acetals. With less strongly electron deficient alkenes, e.g., those having a single ester substituent, a different reaction course is followed, in which the methylenecyclopropanone ketal initially cleaves to a zwitterion, which subsequently reacts in a *stereospecific manner* to yield only cyclopentanone ketal products.

Acknowledgment

The authors wish to acknowledge the support of the Robert A. Welch Foundation (F-149) and the National Science Foundation (CHE-9610227).

References

1. (a) F. A. Bell, A. Ledwith, D. C. Sherrington, *J. Chem. Soc.* **1969**, 2719; (b) R. A. Crellin, M. C. Lambert, A. Ledwith, *J. Chem. Soc., Chem. Commun.* **1970**, 682; A. Ledwith, *Accts. Chem. Res.* **1972**, 5, 133.
2. C. Wurster, R. Sendtner, *Ber.* **1879**, 12, 1803 and 2071.
3. H. Wieland, *Ber.* **1907**, 40, 4260.
4. (a) E. Weitz, H. W. Schwechthin, *Ber.* **1926**, 59, 2307; (b) *ibid.* **1927**, 60, 545.
5. L. Michaelis, *Chem. Rev.* **1935**, 16, 243.
6. R. I. Walter, *J. Am. Chem. Soc.* **1966**, 88, 1923.
7. W. Schmidt, F. Steckhan, *Chem. Ber.* **1980**, 113, 577.
8. (a) R. S. Mulliken, C. C. J. Roothan, *Chem. Rev.* **1947**, 41, 219; (b) A. J. Meerer, L. Schoonveld, *J. Chem. Phys.* **1968**, 48, 522; (c) H. Koppel, W. Domcke, L. S. Cederbaum, W. von Niessen, *J. Chem. Phys.* **1978**, 69, 4252; (d) D. J. Bellville, N. L. Bauld, *J. Am. Chem. Soc.* **1982**, 104, 294.
9. (a) W. Tang, X.-L. Zhang, T. Bally, *J. Phys. Chem.* **1993**, 97, 4373; (b) T. Keszthelyi, R. Wilbrandt, J.-L. Roulin, T. Bally, *ibid.* **1996**, 100, 16850.
10. H. D. Roth, M. L. Mannion, *J. Am. Chem. Soc.* **1981**, 103, 7210.
11. P. Jungwirth, T. Bally, *J. Am. Chem. Soc.* **1993**, 115, 5783–5789.
12. L. P. Ellinger, *Polymer* **1964**, 5, 559.
13. W. P. Todd, J. P. Dinnocenzo, S. Farid, J. L. Goodman, I. R. Gould, *J. Am. Chem. Soc.* **1991**, 113, 3601.

14. S. L. Mattes, S. Farid in *Organic Photochemistry*, Vol. 6 (Ed.: A. Padw (a), Marcel Dekker, New York, **1983**, p. 233.
15. D. J. Bellville, D. D. Wirth, N. L. Bauld, *J. Am. Chem. Soc.* **1981**, *103*, 718.
16. L. Cedheim, L. Eberson, *Acta Chem. Scand.* **1976**, *B30*, 527–532.
17. (a) D. Ghosh, N. L. Bauld, *J. Catalysis* **1985**, *95*, 300–304; (b) K. Lorenz, N. L. Bauld, *J. Catalysis* **1985**, *95*, 613–616.
18. P. Laszlo, J. Lucchetti, *Tetrahedron Lett.* **1984**, *25*, 1567.
19. M. A. Fox, D. D. Sackett, J. N. Younathan, *Tetrahedron* **1987**, *43*, 7.
20. N. L. Bauld, D. J. Bellville, S. A. Gardner, Y. Migron, G. Cogswell, *Tetrahedron Lett.* **1982**, *8*, 825–828.
21. N. P. Schepp, L. J. Johnston, *J. Am. Chem. Soc.* **1994**, *116*, 6895–6903.
22. T. Bally, *Chimia* **1994**, *48*, 378.
23. I. R. Gould, S. Farid, *Acct. Chem. Res.* **1996**, *29*, 522–528.
24. (a) N. L. Bauld, J. T. Aplin, W. Yueh, S. Endo, A. Loving, *J. Phys. Org. Chem.* **1998**, *11*, 15–24; (b) N. L. Bauld, J. T. Aplin, W. Yueh, A. Loinaz, *J. Am. Chem. Soc.* **1997**, *119*, 11381–11389.
25. (a) S. Kuwata, Y. Shigemitsu, Y. Odaira, *J. Org. Chem.* **1973**, *21*, 3803; S. Farid, S. E. Hartman, T. R. Evans in *The Exciplex* (Eds.: M. Gordon, T. R. Ware), Academic Press, New York, **1975**, p. 317.
26. T. R. Evans, R. W. Wake, O. Jaenicke, *ibid.*, p. 345.
27. S. Farid, S. E. Shealer, *J. Chem. Soc. Chem. Commun.* **1973**, 677.
28. N. L. Bauld, R. Pabon, *J. Am. Chem. Soc.* **1983**, *105*, 633–634.
29. F. D. Lewis, M. Kojima, *J. Am. Chem. Soc.* **1988**, *110*, 8664–8670.
30. H. Nozaki, I. Otani, R. Noyori, M. Kawanisi, *Tetrahedron* **1968**, *24*, 2183.
31. N. P. Schepp, D. Shukla, H. Sarker, N. L. Bauld, L. J. Johnston, *J. Am. Chem. Soc.* **1997**, *119*, 10325–10334.
32. (a) N. P. Schepp, L. J. Johnston, *J. Am. Chem. Soc.* **1996**, *118*, 2872–2881; (b) N. P. Schepp, L. J. Johnston, *ibid.* **1994**, *116*, 6895–6903.
33. K. T. Lorenz, N. L. Bauld, *J. Am. Chem. Soc.* **1987**, *109*, 1157–1160.
34. J. L. Courtneidge, A. G. Davies, S. M. Tollerfield, J. Rideout, M. C. R. Symons, *J. Chem. Soc. Chem. Commun.* **1985**, 1092–1093.
35. N. L. Bauld, D. J. Bellville, R. Pabon, R. Chelsky, G. Green, *J. Am. Chem. Soc.* **1983**, *105*, 2378–2382.
36. (a) G. N. Sastry, V. Hrouda, M. Ingr, P. Carsky, T. Bally, *J. Phys. Chem. A* **1998**, *102*, 9297; (b) V. Hrouda, M. Roeselova, *J. Phys. Chem. A* **1997**, *101*, 3925.
37. S. F. Nelsen, *Accts. Chem. Research* **1987**, *20*, 276.
38. (a) G. O. Schenck, S.-P. Mannsfeld, G. Schomburg, C. H. Krauch, *Z. Naturforsch.* **1964**, *19B*, 18; (b) R. Schutte, G. R. Freeman, *J. Am. Chem. Soc.* **1969**, *91*, 3715; (c) T. L. Penner, D. G. Whitten, G. S. Hammond, *J. Am. Chem. Soc.* **1970**, *92*, 2861.
39. D. J. Bellville, D. D. Wirth, N. L. Bauld, *ibid.* **1981**, *103*, 718–720.
40. (a) N. L. Bauld, D. J. Bellville, B. Harirchian, K. T. Lorenz, R. A. Pabon, Jr., D. W. Reynolds, D. D. Wirth, H.-S. Chiou, B. K. Marsh, *Accts. Chem. Research* **1987**, *20*, 371–378; (b) N. L. Bauld, *Tetrahedron* **1989**, *45*, 5307–5363; (c) N. L. Bauld in *Advances in Electron Transfer Chemistry*, Vol. 2 (Ed. P. S. Mariano), JAI Press, Greenwich, **1992**, pp. 1–65.
41. G. C. Calhoun, G. B. Schuster, *J. Am. Chem. Soc.* **1984**, *106*, 6870.
42. (a) R. A. Neunteufel, D. R. Arnold, *J. Am. Chem. Soc.* **1973**, *95*, 4080; (b) A. J. Maroulis, D. R. Arnold, *J. Chem. Soc. Chem. Commun.* **1979**, 351.
43. S. L. Mattes, S. Farid, *J. Am. Chem. Soc.* **1983**, *105*, 1386.
44. J. Libman, *J. Chem. Soc. Chem. Commun.* **1976**, 361.
45. K. Mizuno, R. Kaji, H. Okada, Y. Otsuji, *ibid.* **1978**, 594.
46. N. L. Bauld, J. Yang, unpublished work.
47. D. J. Bellville, N. L. Bauld, *J. Am. Chem. Soc.* **1982**, *104*, 2665–2667.
48. D. J. Bellville, N. L. Bauld, R. Pabon, S. A. Gardner, *ibid.* **1983**, *105*, 3584–3588.
49. R. A. Pabon, D. J. Bellville, N. L. Bauld, *J. Am. Chem. Soc.* **1983**, *105*, 5158–5159.
50. C. R. Jones, B. J. Allman, A. Mooring, B. Spahic, *ibid.* **1983**, *105*, 652.
51. (a) W. Yueh, N. L. Bauld, *J. Chem. Soc. Perkin Trans. 2*, **1995**, 871–873; (b) W. Yueh, N. L. Bauld, *ibid.*, **1996**, 1761–1766.

52. J. Mattay, J. Gersdorf, J. Mertes, *J. Chem. Soc. Chem. Commun.* **1985**, 1088.
53. M. Schmittel, C. Wöhrle, I. Bohn, *Chem. Eur. J.* **1996**, 2, 1031–1040.
54. M. Schmittel, H. von Seggern, *Angew. Chemie Intl. Ed. Eng.* **1991**, 8, 999–1001.
55. N. L. Bauld, D. J. Bellville, R. Pabon, R. Chelsky, G. Green, *J. Am. Chem. Soc.* **1983**, 105, 2378–2382.
56. N. L. Bauld, *J. Am. Chem. Soc.* **1992**, 114, 5800–5804.
57. Reference 40c, p. 15.
58. Reference 40c, pp. 5–7.
59. (a) R. A. Pabon, D. J. Bellville, N. L. Bauld, *J. Am. Chem. Soc.* **1984**, 106, 2730–2731; (b) D. W. Reynolds, N. L. Bauld, *Tetrahedron* **1984**, 42, 6189–6194.
60. T. Kim, J. Pye, N. L. Bauld, *J. Am. Chem. Soc.* **1990**, 112, 6285–6290.
61. N. L. Bauld, B. Harirchian, D. W. Reynolds, J. C. White, *ibid.* **1988**, 110, 8111–8117.
62. D. H. R. Barton, G. Leclerc, P. D. Magnus, I. D. Menzies, *J. Chem. Soc. Chem. Commun.* **1972**, 447.
63. R. Tang, H. J. Yue, J. F. Wolf, F. Mares, *J. Am. Chem. Soc.* **1978**, 100, 5248.
64. J. F. Evans, H. N. Blount, *J. Am. Chem. Soc.* **1978**, 100, 4191–4196.
65. (a) N. L. Bauld, J. T. Aplin, W. Yueh, A. Loving, S. Endo, *J. Chem. Soc. Perkin Trans. 2* **1998**, 2733–2776; (b) N. L. Bauld, J. T. Aplin, W. Yueh, A. Loinaz, *J. Am. Chem. Soc.* **1997**, 119, 11381–11389.
66. N. L. Bauld, J. T. Aplin, W. Yueh, S. Endo, A. Loving, *J. Phys. Org. Chem.* **1998**, 11, 15–24.
67. J. P. Dinnocenzo, M. Schmittel, *J. Am. Chem. Soc.* **1987**, 109, 1561–1562.
68. S. F. Nelsen, *Accounts Chem. Research* **1987**, 269–276.
69. S. B. Karki, J. P. Dinnocenzo, S. Farid, J. L. Goodman, I. R. Gould, T. A. Zona, *J. Am. Chem. Soc.* **1997**, 119, 431–432.
70. (a) P. G. Gassman, D. A. Singleton, *ibid.*, **1984**, 106, 7993; (b) D. W. Reynolds, K. T. Lorenz, H.-S. Chiou, D. J. Bellville, R. A. Pabon, Jr., N. L. Bauld, *J. Am. Chem. Soc.* **1987**, 109, 4960.
71. W. Yueh, N. L. Bauld, *J. Chem. Soc. Perkin. Trans. 2* **1995**, 871–873.
72. W. Yueh, N. L. Bauld, *J. Am. Chem. Soc.* **1995**, 117, 5671–5676.
73. W. Yueh, N. L. Bauld, unpublished results.
74. G. A. Mirafzal, T. Kim, J. Liu, N. L. Bauld, *J. Am. Chem. Soc.* **1992**, 114, 10968–10969.
75. T. Kim, G. A. Mirafzal, N. L. Bauld, *Tetrahedron Lett.* **1993**, 34, 7201–7204.
76. G. A. Mirafzal, T. Kim, J. Liu, N. L. Bauld, *J. Am. Chem. Soc.* **1992**, 114, 10968–10969.
77. Reference 40c, pp. 62–63.
78. U. Haberl, O. Wiest, E. Steckhan, *J. Am. Chem. Soc.*, **1999**, 121, in press.
79. The three systems are: (1) 1,3-cyclohexadiene with all three geometric isomers of 2,4-hexadiene (2) 1,3-cyclopentadiene with *cis*- and *trans*-diaryloxyethenes and (3) 2,3-dimethyl-1,3-butadiene with *cis*- and *trans*-1,2-diaryloxyethenes. Further, stereospecific cyclobutanation has been observed in two distinct systems: (1) cyclobutadimerization of *cis*- and *trans*-anethole (in both dichloromethane and acetonitrile) and (2) 2,3-dimethyl-1,3-butadiene with *cis*- and *trans*-1,2-diaryloxyethanes.
80. H. D. Roth, M. L. Schilling, C. Abelt, *J. Am. Chem. Soc.* **1986**, 108, 6098.
81. B. Harirchian, N. L. Bauld, *ibid.* **1989**, 111, 1826–1828.
82. R. M. Wilson, J. G. Dietz, T. A. Shepherd, D. M. Ho, K. A. Schnapp, R. C. Elder, J. W. Watkins II, L. S. Geraci, C. F. Campana, *J. Am. Chem. Soc.* **1989**, 111, 1749–1754.
83. S. Kadota, K. Tsubono, K. Makino, M. Takeshita, T. Kibuchi, *Tetrahedron Lett.* **1987**, 28, 2857.
84. C. F. Gurtler, S. Blechert, E. Steckhan, *J. Org. Chem.* **1996**, 61, 4136–4143.
85. N. L. Bauld, J. T. Aplin, W. Yueh, H. Sarker, D. J. Bellville, *Macromolecules* **1996**, 29, 3661–3662.
86. D. W. Reynolds, B. Harirchian, H.-S. Chiou, B. K. Marsh, N. L. Bauld, *J. Phys. Org. Chem.* **1989**, 2, 57–88.
87. N. P. Schepp, L. J. Johnston, *J. Am. Chem. Soc.* **1994**, 116, 6895–6903.
88. J. P. Dinnocenzo, D. A. Conlon, *ibid.* **1988**, 110, 2324–2326.
89. J. P. Dinnocenzo, D. A. Conlon, *Tetrahedron Lett.* **1995**, 41, 7415–7418.
90. (a) G. Stufflebeme, K. T. Lorenz, N. L. Bauld, *J. Am. Chem. Soc.* **1986**, 108, 4234–4235; (b) G. A. Mirafzal, A. M. Lozeva, J. A. Olson, *Tetrahedron Lett.* **1998**, 39, 9323–9326.

91. F. Müller, J. Mattay, *Angew. Chem. Int. Ed. Eng.* **1991**, *103*, 1336–1337.
92. A. Padwa, J. Smolanoff, *J. Am. Chem. Soc.* **1971**, *93*, 548.
93. Q.-X. Guo, X.-Z. Quin, J. T. Wang, F. Williams, *J. Am. Chem. Soc.* **1988**, *110*, 1974–1976.
94. K. Lorenz, N. L. Bauld, *J. Catalysis* **1985**, *95*, 613–616.
95. S. Dai, R. S. Pappas, G.-F. Chen, Q.-X. Guo, J. T. Wang, *J. Am. Chem. Soc.* **1989**, *111*, 8759–8761.
96. T. Miyashi, A. Konno, Y. Takahashi, *J. Am. Chem. Soc.* **1988**, *110*, 3676.
97. B. Krautler, A. Pfaltz, R. Nordmann, K. O. Hodgson, J. D. Dunitz, A. Eschenmoser, *Helv. Chim. Acta* **1976**, *59*, 924–937.
98. Y. Takahashi, J. K. Kochi, *Chem. Berichte* **1988**, *121*, 253–259.
99. F. Gerson, X. Z. Qin, T. Bally, J. N. Aebischer, *Helv. Chim. Acta* **1988**, *71*, 1069.
100. D. J. Bellville, R. Chelsky, N. L. Bauld, *J. Comput. Chem.* **1982**, *3*, 548.
101. (a) G. N. Sastry, T. Bally, V. Hrouda, P. Carsky, *J. Am. Chem. Soc.* **1998**, *120*, 9323–9334; (b) V. Barone, N. Rega, G. N. Sastra, T. Bally, *J. Phys. Chem. A* **1998**, *102*, in print.
102. (a) C. M. Hudson, M. R. Marzabadi, K. D. Moeller, D. G. New, *J. Am. Chem. Soc.* **1991**, *113*, 7372–7385; (b) K. D. Moeller, L. V. Tinao, *ibid.* **1992**, *114*, 1032–1041; (c) K. D. Moeller, *Top. Curr. Chem.* **1997**, *185*, 49–86.
103. T. Shono, I. Nishiguchi, S. Kashimura, M. Okawa, *Bull. Chem. Soc. Jpn* **1978**, *51*, 2181.
104. K. D. Moeller, D. Frey, L. Matson-Beal, S. H. K. Reddy, Y. Tong in *Novel Trends in Electroorganic Synthesis* (Ed.: S. Torii), Springer Verlag, Tokyo, **1998**, pp. 51–54.
105. H. Scott, G. A. Miller, M. M. Labes, *Tetrahedron Lett.* **1963**, *17*, 1073.
106. M. S. Workentin, N. P. Schepp, L. J. Johnston, D. D. M. Wayner, *J. Am. Chem. Soc.* **1994**, *116*, 1141.
107. D. R. Arnold, S. A. Mines, *Can. J. Chem.* **1987**, *65*, 2312–2314.
108. A. Zedulev, A. Grand, E. Ressouche, J. Schweizer, B. G. Morin, A. J. Epstein, D. A. Dixon, J. S. Miller, *J. Am. Chem. Soc.* **1994**, *116*, 7243.
109. D. H. Levy, R. J. Myers, *J. Chem. Phys.* **1964**, *41*, 1062.
110. (a) T. J. Katz, H. L. Strauss, *J. Chem. Phys.* **1960**, *32*, 1873; (b) H. L. Strauss, T. J. Katz, G. K. Fraenkel, *J. Am. Chem. Soc.* **1963**, *85*, 2360.
111. J. F. Garst in *Free Radicals* (Ed.: J. K. Kochi), Vol. 1, John Wiley & Sons, New York, **1973**, pp. 518–519.
112. N. L. Bauld, M. S. Brown, *J. Am. Chem. Soc.* **1967**, *89*, 5413–5417.
113. N. L. Bauld, J. H. Zoeller, Jr., *Tetrahedron Lett.* **1967**, *10*, 885–889.
114. (a) N. L. Bauld, M. S. Brown, *J. Am. Chem. Soc.* **1967**, *89*, 5417–5429; (b) F. Farr, Y. S. Rim, N. L. Bauld, *ibid.* **1971**, *93*, 6888–6890.
115. N. L. Bauld, C.-S. Chang, J. H. Eilert, *Tetrahedron Lett.* **1973**, *2*, 153–154.
116. H. O. House, *Modern Synthetic Reactions*, W. A. Benjamin, Menlo Park, **1972**, pp. 206–209.
117. N. L. Bauld, *J. Am. Chem. Soc.* **1962**, *84*, 4347.
118. (a) M. M. Baizer, *Tetrahedron Lett.* **1963**, 973; (b) M. M. Baizer, *J. Electrochem. Soc.* **1964**, *111*, 215.
119. M. Swarz in *Progress in Physical Organic Chemistry* Vol. 6 (Eds.: A. Streitwieser, Jr., R. W. Taft) Interscience, New York, **1968**, 323–438.
120. L. Moens, M. M. Baizer, R. D. Little, *J. Org. Chem.* **1986**, *51*, 4497.
121. (A) H. E. Bode, C. G. Sowell, R. D. Little, *Tetrahedron Lett.* **1979**, 2525; (b) R. D. Little, M. K. Schwaebe, *Top. Curr. Chem.* **1997**, *185*, 1–48.
122. J. Delaunay, G. Mabon, A. Orliac, J. Simonet, *Tetrahedron Lett.* **1990**, *31*, 667–668.
123. M. Witmer, E. Altmann, H. Young, A. Sancar, T. P. Begley, *J. Am. Chem. Soc.* **1989**, *111*, 9264.
124. D. J. Pasto, S.-H. Yang, *J. Org. Chem.* **1989**, *54*, 3544–3549.
125. (a) N. L. Bauld, C.-S. Chang, F. R. Farr, *J. Am. Chem. Soc.* **1972**, *94*, 7164; (b) N. L. Bauld, J. Cessac, C.-S. Chang, F. R. Farr, R. Holloway, *J. Am. Chem. Soc.* **1976**, *98*, 4561–4567.
126. M. A. Fox, J. R. Hurst, *J. Am. Chem. Soc.* **1984**, *106*, 7626–7627.
127. D. W. Borhani, F. D. Greene, *J. Org. Chem.* **1986**, *51*, 1563–1570.
128. S. Yamago, S. Ejiri, M. Nakamura, E. Nakamura, *J. Am. Chem. Soc.* **1993**, *115*, 5344.

4 Electron-transfer Reactions of Aromatic Compounds

Georg Gescheidt and Md. Nadeem Khan

4.1 Introduction

Aromatic molecules are inclined to undergo electron-transfer reactions. The additional charges introduced by the electron-transfer process are efficiently stabilized by delocalization. Nevertheless rearrangements of the molecular skeleton or follow-up reactions can occur. The course of the electron-transfer reactions and the properties of the species thus formed are the subject of this section.

In particular, we concentrate on the species formed after an one-electron transfer reaction. Starting from closed-shell diamagnetic precursors, paramagnetic stages, i.e. radical cations or radical anions are formed in this first step. To understand the properties and reactivity of these species, detailed knowledge in terms of charge and spin delocalization and electronic structure is an important prerequisite. This information is preferably derived from electronic and paramagnetic resonance (EPR and electron-nuclear multiple resonance-techniques such as ENDOR or Triple spectroscopy). It has recently been shown that the experimental results can be substantiated by the use of quantum-chemical calculations. In addition to Hartree–Fock-based *ab initio* procedures, calculations on the density-functional level of theory have been established as rather efficient tools. Therefore, before representing examples of electron-transfer-generated radicals a short survey of the computational methods is given.

Another substantial factor directing the kinetic and thermodynamic stability of charged radicals is ion pairing. This phenomenon, although well established for many years, is often not directly distinct in experiments. To establish the importance of ion pairing, or, in other words, supramolecular interactions, a separate introductory chapter is dedicated to these aspects.

The references are selected particularly from recent publications, without, however, ignoring some ‘classical’ contributions. In some sections topics are included which do not strictly represent aromatic molecules but involve interactions of π -type orbitals.

4.2 Computational Methods for Organic Radicals

The calculation of radical hyperfine properties has received enormous attention in recent years [1–4]. With rapid improvement in computer technology, combined with increasingly accurate computational schemes, theoretical predictions of radical hyperfine structures (hfs) are today serving an important role in the understanding of the properties of radicals and their reactions. Comparison of observed and computed hyperfine coupling constants (hfcc) leads to the assignment of plausible geometries and the identification of reaction products. Further analysis of the theoretical data also provides answers to questions about reaction barriers, transition states, charge and spin distributions, and a variety of other properties [1, 2, 5–7].

Of the many conventional *ab initio* approaches, multireference configuration interaction (MRCI), quadratic configuration interaction (QC1), and coupled cluster (CC) techniques, in conjunction with large basis sets, that consistently have proven able to generate hfcc of high accuracy [8–12]. Unfortunately, one problem with such approaches is that they are computationally quite expensive even for moderately sized systems, hence restricting studies to date to relatively small molecules. An alternative approach for calculating hfcc is represented by Density Functional Theory (DFT) [13], for which the computational cost and memory requirements are considerably less than those of conventional correlated *ab initio* procedures. As a consequence, the number of basis functions, and hence atoms, is not nearly as limiting a factor at the DFT level as it is for the earlier approaches. The use of DFT has increased tremendously as a serious and competitive alternative to more conventional *ab initio* approaches to elucidate molecular electronic structures. This increased interest has been further stimulated by the formulation of a ‘Hartree–Fock type’ formalism for DFT [13], by the development of accurate gradient correction schemes [14–19], and by the incorporation of DFT into widely used computational quantum chemistry programs [20, 21].

The performance of various exchange and correlation functions has been extensively tested [22–27] and number of books that review various applications of DFT has appeared in last few years [28–30]. The consensus at present appears to be that for the so-called hybrid or adiabatic connection method (ACM), functions containing a mixture of different exchange terms and gradient-corrected correlation constitutes the most accurate forms of DFT currently at hand. Method for converting DFT energies to enthalpies of formation is described and its performance, in conjunction with six DFT methods, are examined for 23 stable hydrocarbons [31]. The B3LYP atom equivalents of carbon and hydrogen are used without adjustment to calculate the enthalpies of formation of some free radicals and carbocations. The mean deviation between calculated and experimental results is found to be around 2 kcal mol^{–1}, which is of the same order as experimental uncertainties for these highly reactive species. In search of the optimal combination of basis set and exchange–correlation potential, the dependence of atomization energies (D_0) and reaction enthalpies (ΔH) for a set of 44 molecules using gradient-corrected DFT has been investigated [32]. Of the six functions tested, those that include a portion of the exact (Hartree–Fock) exchange performed best and yielded D_0 values within 3–

5 kcal mol⁻¹ of the experimental value. The thermal motion of the •CCH radical embedded in matrix of solid argon is simulated at 4 and 40 K, using hybrid DFT–molecular dynamics (DFT–MD) approach [33]. The results reveal that •CCH when embedded in the argon matrix favors an oscillating, slightly bent geometric structure, whereas in vacuum the molecule is linear. The geometries and ¹⁷O hyperfine coupling constants in several alkyl peroxy radicals is determined by DFT [34]. Results comparable to experimental values are obtained for all the alkyl peroxy radicals but erratic and strongly fluctuating results are noticed for the fluoro peroxy radicals, apart from considerable spin contamination, multireference, and matrix effects are proposed for observed deviation. A total of 22 substituted benzene radicals are investigated, two different functional schemes, the B3LYP hybrid DFT–HF functional and the ‘pure’ gradient corrected DFT functional PWP86 are employed [35]. The mechanism of degenerate [5,5]-sigmatropic rearrangements of 5,5a,10,10a-tetrahydroheptalene and (z,z)-1,3,7,9-decatetraene are explored with restricted and unrestricted Becke 3LYP/6-31G* hybrid HF–DFT calculations [36]. Calculations predicted that the [5,5]-sigmatropic rearrangements occur via stepwise diradical mechanism with activation barriers of 29.1 and 34.3 kcal mol⁻¹, respectively. The [3,3]- (cope) rearrangement of 3,6-bismethylene-1,7-octadiene is also predicted to occur by a stepwise diradical mechanism. The barrier for this reaction is much less than those for the [5,5]- rearrangements due to greater stability of its constituent radical moieties and lack of unfavorable steric interactions in the transition state. The fully optimized potential energy curves for the unimolecular decomposition of the lowest singlet and triplet states of nitromethane through the C–NO₂ bond dissociation pathway is calculated using various DFT and high level ab initio electronic structure methods [37]. For the most simple (H₂O)₂⁺ system, previous theoretical studies using Post Hartree–Fock methods [38], have shown that proton-transferred OH–H₃O⁺ isomer is the ground state structure of the ionized water dimer, however, recent density functional calculation with exchange correlation gradient corrections predict the three-electron bond isomer to be the ground-state structure [39].

This anomaly is attributed to overestimation by the exchange functions of the self-interaction part of the exchange energy in the hemi-bond ion due to its delocalized electron hole [40]. It is cautioned that this behavior of the density functions for exchange, if unrecognized, may lead to wrong predictions for ground-state structures of systems with a three-electron bond. Corrected calculations showed that the proton-transferred OH–H₃O⁺ isomer to be the ground state structure of the (H₂O)₂⁺ dimer ion. The mechanism for the 1,3-dipolar cycloaddition of trifluoromethyl azomethine ylide with acetonitrile has been characterized using DFT methods with B3LYP functional and the 6-31G* and 6-31⁺G** basis sets [41]. Density functional calculations at the B3LYP/6-31G* theory level provided data on transition-state energies for this 1,3-dipolar cycloaddition in full agreement with the stereo chemical outcome. More recently uncertainties in configurations of camphene hydrochloride and isobornyl chloride are laid to rest by a comparison of computed and experimental ¹³C and methyl proton chemical shifts [42]. There has been great deal of interest in short-strong or low-barrier hydrogen bonds [43–45], recently high level ab initio and DFT calculations have been employed to investigate these sys-

tems with reasonable accuracy [46]. The Hartree–Fock method failed to predict the relative energies of the non-ionized amino acid conformers correctly [47], however, recently DFT and MP2 methods are successfully employed for relative stability calculations of non-ionized Valine conformers [48]. Extensive density functional calculations are reported for the geometrical structures, thermochemistry, infrared, and hyperfine parameters of representative carbon-centered π -radicals [49]. In short, the merits of DFT, by far the most useful non-empirical alternative to conventional post Hartree–Fock methods for studying physicochemical properties of molecules, is now well recognized. Gradient-corrected functions have significantly increased the reliability of DFT methods, small modifications of the functional form or partial inclusion of the Hartree–Fock exchange provides even better results and contrary to methods based on an Hartree–Fock zero-order wave function, DFT approaches appear equally reliable for closed and open shell systems.

4.3 Ion Pairing

The fact that ions of opposite charges tend to pair is of great importance for the course of organic reactions [50]. Evidence for such an ion pairing is provided by hyperfine splittings from paramagnetic nuclei of alkali-metal cations associated with organic radical anions. EPR spectroscopy represents a method of choice for the study of ion-pairs. Since the first observation of a ^{23}Na -hyperfine splitting in the EPR spectrum of naphthalene reduced to its radical anion with sodium in tetrahydrofuran (THF) or 2-methyltetrahydrofuran (MTHF) [51], a large number of papers describing similar findings appeared. The largest coupling constants of alkali-metal nuclei in counterions or organic radical anions were reported therein for cation attached in a chelate-like fashion to the lone electron pairs of the oxygen atoms in the radical anion. In this respect, alkali-metal cations associated with the radical anion of *o*-dimesitylbenzene in 1,2-dimethoxyethane and THF served as a paradigm [52]. With 1,2-dimethoxyethane at room temperature the ^7Li -, ^{23}Na -, ^{39}K -, ^{85}Rb -, ^{87}Rb -, and ^{133}Cs -coupling constants amounted there to 0.375 [52], 0.695 [52], 0.491 [53], 1.66 [53], and 1.02 [52] mT respectively; such ion pairs are denoted as ‘tight’ or ‘contact’ ones. On the other hand, ion-pairs of alkali-metal cations associated with radical anions of hydrocarbons are considered as ‘loose’ or ‘solvent-separated’ ones, because the molecules of the ether solvent successfully compete with the radical anion for the positively charged counterion. Accordingly, in these ion-pairs, the hyperfine splittings from alkali-metal nuclei are smaller by 1–2 orders of magnitude than the values described above in the case of the *o*-dimesitylbenzene radical anion [54]. Typically for the ion pairs of the naphthalene radical anion in DME at room temperature, the ^7Li -, ^{23}Na -, ^{39}K -, ^{85}Rb -, ^{87}Rb -, and ^{133}Cs -coupling constants amounted to <0.01, <0.0405, <0.01, 0.0095, 0.0316, and 0.1071 mT, respectively [55]. In addition to EPR, the ENDOR technique is successfully applied to study ion-pairing of some very persistent organic radical anions with alkali-metal cations [53, 56], the relative signs of the coupling constants of proton and metal

nuclei could be determined by general triple resonance [57]. Absolute signs of these values are accessible by NMR spectroscopy also used for such studies [58], although the high concentration of the radical anion salts required by this method led to some deviations from the corresponding results obtained by EPR and ENDOR spectroscopy.

In ion pairs consisting of two radicals, the exchange interaction (J) is usually negative, however there have been reports that J is positive in some radical ion pairs [59a,b]. A conflicting mechanism has also been proposed [59c]. Tero-Kubota et al. discussed indications of a positive J for the radical ion pairs of benzophenone radical anions with the radical cation of DABCO (1,4-diazabicyclo[2,2,2]-octane) [59b]. They studied the effects of Lewis acid on the sign of J of the radical ion pair as the charge of the radical pair seems to be an important factor in the inter-radical interactions. A recent FTEPR study revealed that the sign of the exchange interaction of the radical ion pair including the 4,4'-dimethoxybenzophenone radical anion and DABCO radical cation changes from positive to negative by addition of BF_3 [59d].

The strength of association with the counterion depends on several factors, such as solvating power of the solvent, the temperature, and the radius of the cation. The ion-pairing tightens and the coupling constant of alkali-metal nucleus increases with the decreasing solvating power parallel to raising the temperature [60], however, the dependence on the radius of the cation is less clear. For tight ion-pairs of radical anions containing heteroatoms, the association tends to weaken with increase in cation radius, in the order Li^+ , Na^+ , K^+ , Rb^+ , and Cs^+ , because the contact of the counter ion with the lone electron pairs of the heteroatom diminishes in the same order. On the other hand, for loose ion pairs of radical anions without heteroatoms, an opposite sequence seems to prevail as the solvation of the counterion decreases with increasing radius of the cation. This behavior mirrors the hard-soft relationships between the radical ion, the counterion, and the solvent. The radical anion of buta-1,3-diene, 2,3-dimethylbuta-1,3-diene, and 1,1,4,4-tetramethylbuta-1,3-diene were generated from their neutral precursors by electrolytic reduction with THF replacing liquid ammonia as the solvent [61]. The buta-1,3-diene radical anion was also generated by electrolytic reduction of parent molecule at a Pt-wire cathode in liquid ammonia at 195 K [62]. A similar method is employed for 2-methylbuta-1,3-diene, 2,3-dimethylbuta-1,3-diene, and cyclohexa-1,3-diene radical anions [63]. However, in these experiments, a tetraalkylammonium cation served as the counterion, the nuclei of which did not give rise to additional hyperfine splittings in the EPR spectra. In general, reaction of buta-1,3-diene and its derivatives with an alkali-metal mirror in an ether as solvent failed to yield a persistent radical anion, because of rapid polymerization to rubber-like products [64]. EPR and ENDOR study of the radical anions of the 1,4-di-*tert*-butylbuta-1,3-diene, 2,3-di-*tert*-butylbuta-1,3-diene, its 1,1-dideutero derivative and of 1,4-di-*tert*-butylcyclohexa-1,3-diene is recently reported by Gerson et al. [65]. Characteristic of the hyperfine patterns of 1,4- and 2,3-di-*tert*-butylbuta-1,3-diene radical anions are very large coupling constants of the alkali-metal nuclei in the counter ion: $a(^{39}\text{K}) = 0.12\text{--}0.15$, $a(^{85}\text{Rb}) = 0.40\text{--}0.84$, $a(^{87}\text{Rb}) = 1.4\text{--}2.8$ and $a(^{133}\text{Cs}) = 0.70\text{--}2.6$ mT. Values of this magnitude, unusual for counterions of hydrocarbon radical anions, points to a tight or contact

ion pairing. In addition to large hyperfine splittings, a striking feature of the tight ion pair of 2,3-di-*tert*-butylbuta-1,3-diene, is the coupling constant of two protons in the 1,4-positions.

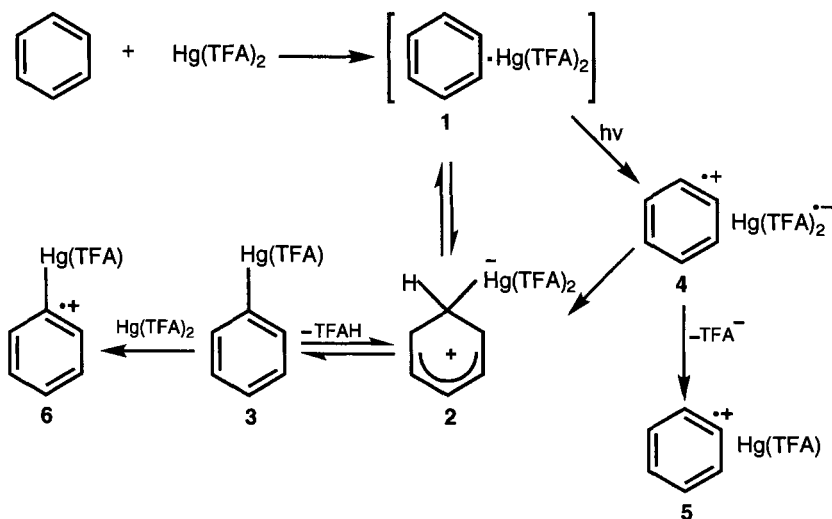
The dynamic processes in tetrahydrofuran (THF) solutions of 2,5-di-*tert*-butyl-*p*-benzoquinone^{•-}, Na⁺ ion pairs obtained by reduction with a sodium mirror is investigated by two-dimensional (2D) exchange Fourier Transformation (FT) EPR [66]. Results indicate two types of ion pairs, in first the intramolecular Na⁺ hopping is slow while in other it is fast and results in a selective smearing of some of the hyperfine lines. The origin of the latter is tentatively ascribed to complexation with OH⁻ generated by water impurity. The work demonstrates the efficiency of the 2D exchange FT EPR method in elucidating mechanisms of dynamic processes and determining kinetic parameters, in particular when several such processes occur simultaneously. Radical anions and radical cations of tetraphenylethane and its cyclophane derivatives were generated by chemical methods and characterized by their EPR and simultaneously recorded optical spectra [67]. In radical anions no specific complexation of alkali-metal counterions, K⁺ and Li⁺, by the crown-ether moieties could be observed. The solution structures of the radical cations closely matched the geometry established by X-ray diffraction analysis of crystalline tetraanisylethene [68] where the ethenic bond is twisted by 30.5° and phenyl-ring torsion amounts to 33°.

The effect of Zeeman levels crossing in spin-correlated radical ion pairs (naphthalene)^{•+}/(hexafluorobenzene)^{•-} was monitored as the influence of an external magnetic field on the solution fluorescence under X-irradiated (MARY spectrum) [69]. The results show the possibility of observing hyperfine structures of a counterion in short-lived radical ion pairs using level crossing technique. Increasing the technique sensitivity will certainly open new prospects for employing the level crossing phenomenon in studying hyperfine structures in short-lived radical ion-pairs.

4.4 Radical Cations

4.4.1 π Systems

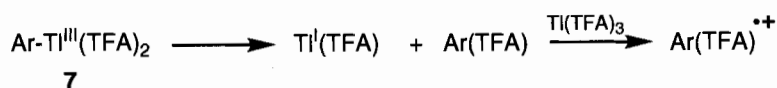
One-electron oxidation of aromatic compounds (ArH) leads primarily to corresponding radical cation which exist either in monomeric (ArH^{•+}) or dimeric form [(ArH)₂^{•+}] the latter usually formulated as π -dimer [70]. However, radical cations are reactive species and can undergo further reaction yielding more persistent radical cations e.g. oxidation of *tert*-butylbenzene or of toluene or *o*-xylene yielded radical cation of 4,4'-di-*tert*-butyl biphenyl, 4,4'-bitoluene or 3,3',4,4'-tetramethyl biphenyls, products of further σ -coupling, proton loss and further one-electron oxidation [71]. This is a well-known pathway of biaryl dehydrodimerization, explored in anodic and metal-ion oxidation of ArH [72, 73]. Other compounds with high reactivity in σ -coupling are alkoxy and amino substituted ArH [73]. Thus a risk with characterization of radical cations is that “hardy survivors and not primary radical



Scheme 1.

cations are detected” for example oxidation of 1-methoxynaphthalene by tetranitromethane [74]. Radical cations from oxidation of methylnaphthalenes are characterized by EPR spectroscopy [75] either as monomer $\text{ArH}^{\bullet+}$ or $(\text{ArH})_2^{\bullet+}$ or radical cations (derived from perylene structure) resulting from the occurrence of the Scholl reaction [76]. Results from oxidation of 1-methyl-, 1,2-, 1,3-, 1,4-, 1,5-, 1,7-, 1,8-dimethylnaphthalene, and acenaphthene is reported [77]. Except in cases where the permethyl group can interfere (1,4-, 1,5-dimethylnaphthalene) with σ -coupling at the 1-position, oxidation yielded radical cations of the corresponding 1,1'-binaphthalenes. A number of reactions can occur on oxidation of arene, represented by benzene in Scheme 1, on treatment with mercury(II) bis(trifluoroacetate) (TTFA) in trifluoroacetic acid (TFAH). The various possibilities are charge transfer complexation 1 [78], Wheeland complex 2, giving rise to arylmercury(II) trifluoroacetate 3 [79]. If charge transfer complex 1 is irradiated in its absorption band it may lead to radical cation 5 [80].

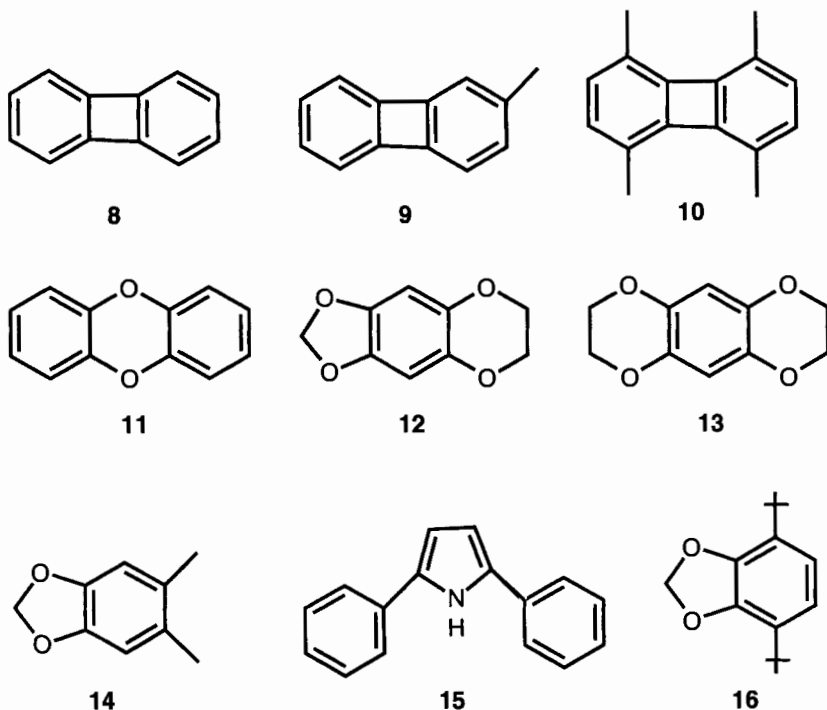
However, in certain cases under photolytic conditions, spectra of the corresponding arylmercury radical cations 6 developed, whereas no mercuriation occurred in dark [81] signifying collapse of the $\text{ArH}^{\bullet+}, \text{Hg}(\text{TFA})_2^{\bullet-}$ radical ion pair 4, provides an alternative path way to Wheeland complex 2 and hence to $\text{ArHg}(\text{TFA})^{\bullet+}$ 6. Arene radical cations can also be generated from arene and thallium(III) tris(trifluoroacetate) in trifluoroacetic acid [82], but with a different mechanism proposed by Ebersson et al. [83]. Oxidation of anthracene showed 9-trifluoroacetoxy and 9,10-bis(trifluoroacetoxy)anthracene [84, 85], benzo[*a*]pyrene, 7-methylbenzo[*a*]pyrene and 12-methylbenzo[*a*]pyrene yielded radical cations of 7- and/or 12-trifluoroacetates [86], triptycene (9,10-dihydro-9,10-[1,2]benzanthracene) showed



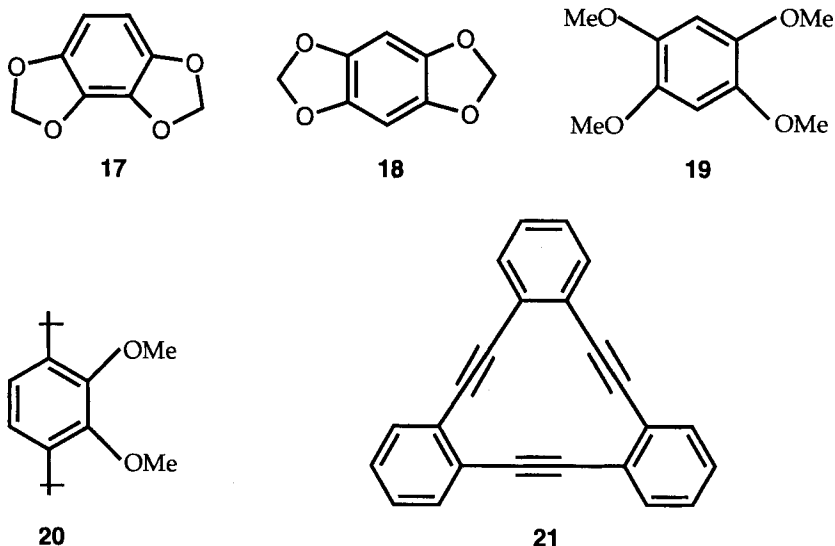
Scheme 2.

tris(trifluoroacetoxy) triptycene radical cation [85], and it is suggested that these trifluoroacetates are formed via thalliated intermediate 7 (Scheme 2).

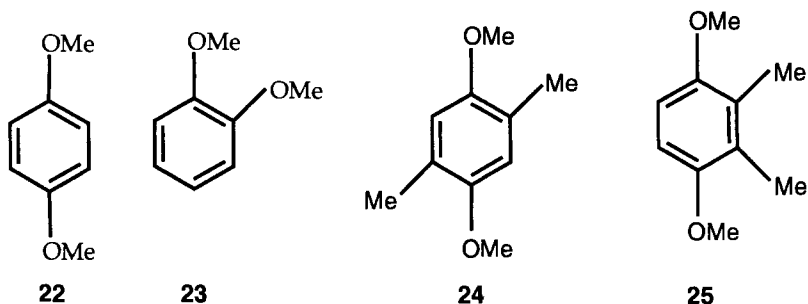
To date the mercurated arene radical cation is known for biphenylene [87], acenaphthene, pyracene, hexahydropyrene, triptycene, *p*-terphenyl, tetramethylnaphthopyran, anthracene, dibenzodioxin [89], and 4-*tert*-butylanisole [88]. In certain cases multiple mercuration is observed, for example in case of diphenylene [87] and dibenzodioxin [89]. Mercuration causes a decrease in *g*-value and always occurs at the site where the local coefficient of the Hückel HOMO of the hydrocarbon is greatest, and there is a constant ratio of about 20.6 between the hyperfine couplings by the ^{199}Hg ($I\frac{1}{2}$, abundance 16.84 %) which has been introduced, and by the proton which has been displaced [89]. EPR spectroscopic evidence is reported for 8, 9, 10, 11, 12, 13, 14, 15 and 16 as new examples of recently recognized alternative mechanism of arene mercuration in which collapse of $\text{ArH}^{\bullet+}\text{Hg}(\text{TFA})_2^{\bullet-}$ radical ion pair leads to arylmercury trifluoroacetate $\text{ArHg}(\text{TFA})^{\bullet+}$ [90].



Spectra of 17^{+} and 18^{+} have been reported by Fleischhauer et al. using a cerium(IV) flow system [91], 19^{+} by Sullivan and co-workers using $\text{AlCl}_3\text{-MeNO}_2$ [92] and 20^{+} by Bubnov by using $\text{Tl}(\text{TFA})_3\text{-TFAH}$ reagent [93].

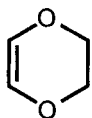
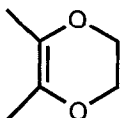
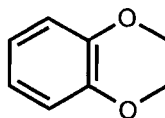


Dialkyl alkylene cations react with their parents to give tetraalkylcyclobutadiene cation [94] but diaryl alkynes on oxidation showed triarylazulene radical cations [95]; the radical anions of diaryl alkynes on the other hand do not rearrange. Reduction of **21** with potassium and small amount of benzo-18-crown-6 in THF gave septet of septet spectra with $a(6\text{H})$ 1.38, $a(6\text{H})$ 0.10 G, g 2.0026, while oxidation gave simple septet spectrum with $a(6\text{H})$ 1.29 G [90]. It is proposed that the small hyperfine coupling to aromatic protons in 12^{+} , 13^{+} , 14^{+} , 18^{+} , 19^{+} , and relatively large coupling to aromatic protons in 16^{+} and 20^{+} , reveal that the *ortho* oxygen substituents from the dioxine ring break the degeneracy of the orbitals of the benzene ring to confer ψ_A character on the SOMO. Reaction between aromatic compounds, **22–25**, and several others with halogenating agents in 1,1,1,3,3,3-hexafluoropropan-

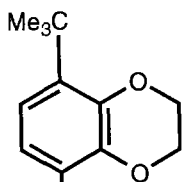
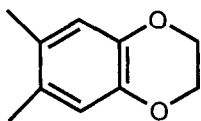
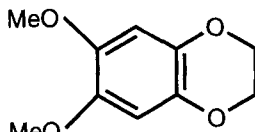
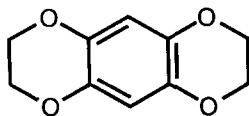
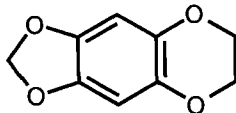
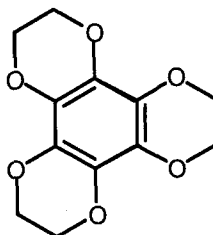


2-ol (HFP) was studied by Eberson et al. [96]. Results show that halogenating agents ICl , Cl_2 , Br_2 , I_2 , *N*-bromosuccinimide and *N*-chlorosuccinimide gave persistent radical cations and their persistency in HFP is discussed.

Recently, HFP a non-nucleophilic and strongly hydrogen bonding solvent [97] is extensively employed in several cation studies, as it increases the stability of the cations in an unprecedented manner. To a large extent this effect is assumed to be due to the strong attenuation of reactivity experienced by many nucleophiles [98]. Dihydro[1,4]dioxines can readily be converted into their radical cations, the ring inversion occurs at a rate which can be measured by monitoring line shape effects on signals of axial and equatorial protons over a range of temperatures. Computer simulations provide rate constants and, hence the activation parameters for these reactions. This study is reported for **26–28** [99].

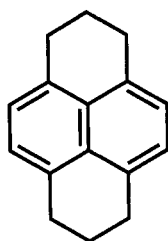
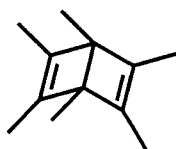
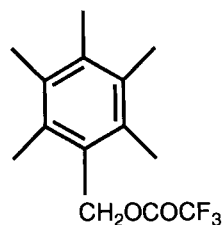
**26****27****28**

The same technique was employed to determine the kinetics of the inversion of the dioxine ring in the radical cations of **29–34** [100].

**29****30****31****32****33****34**

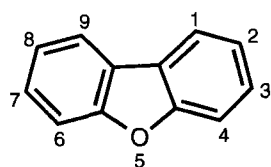
The factors in determining the barriers to ring-inversion in the spin paired and odd-electron molecules are proposed to be different bond lengths and angles associated with the oxygen atoms, related stretching and bending force constants, tor-

sional and Van der Waals interactions and the nature of the wave function in the studied systems. Iwaizumi et al. considered two factors that might account for the barrier in the hexahydropyrene radical anion $35^{\cdot-}$ being less than its radical cation. First, in the radical cation, the positive charge caused a contraction of the electron distribution, resulting in smaller overlap integrals and a decrease in the bending and stretching force constants. Second, hyperconjugative stabilization by the methylene groups, which was expected to be more important in the transition state than in the reactants, should be larger in the radical cations than in the anions [101].

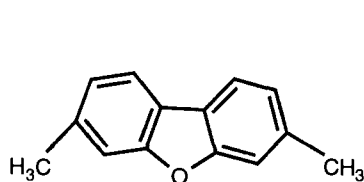
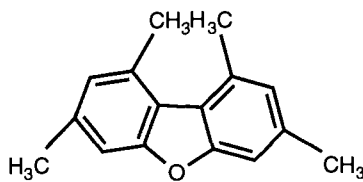
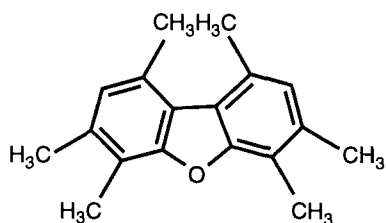
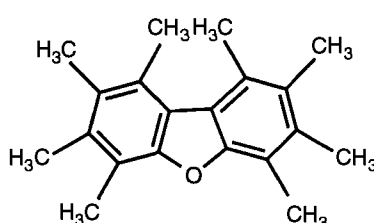
**35****36****37**

Several attempts have been made to characterize hexamethyl (Dewar benzene) radical cation $36^{\cdot+}$ [102]. A 13-line EPR spectrum with hyperfine splitting constant of 0.98 mT was assigned [103] to the 2B_2 state of $36^{\cdot+}$, but as pointed out later [104], other interpretations are also possible. The reaction between Dewar benzene and TTFA in TFAH is investigated in detail by Ebersson et al. [105]. It is proposed that the reaction involves a slow acid-catalyzed conversion of **36** into hexamethyl benzene (HMB) which is then oxidized by TTFA to pentamethylbenzyl trifluoroacetate **37**. Oxidation of benzene in Freon (CCl_3F) matrices at 4 K showed removal of orbital degeneracy and the unpaired electron occupied the b_{2g} orbital with D_{2h} symmetry, giving major spin densities on the C(1) and C(4) atoms [106]. Radical cations of a series of fluorinated benzenes, generated by γ -irradiation in halocarbon solid matrices were studied [107]. The ab initio results reveal that an unambiguous deformation in geometry is brought about by cationization and it is concluded that structure and symmetry of the SOMO of these radical cations are affected not only by the number of substitutions by fluorine but also by the position of the substitution.

An important step in making photochemically generated phenyl cations visible, is achieved by their addition to aromatics [108]. On the basis of their absorption spectra and their reactivity with typical bases/nucleophiles such as halides, alcohols, and ethers, the transients are identified as cyclohexadienyl cations formed from the photo produced 'invisible' phenyl cations by addition to the ring of added aromatics. With respect to both spectral and reactivity properties, the 'phenyl adducts' are very similar to the corresponding 'proton adducts' [109, 110]. Electrophilic reagents generally attack dibenzofuran **38** predominantly at 2-position [111], while nucleophiles such as acetate [112], cyanide [113] and trinitromethanide ion [114] attack at the 3-position, thus providing a tool for the testing of the Pross-Shaik CM model [115].

**38**

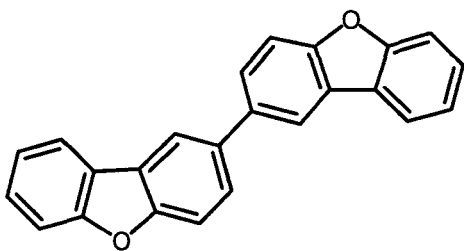
Radical cations of dibenzofuran and variety of symmetrically methylated dibenzofurans have been studied by cyclic voltammetry (CV) and EPR spectroscopy [116]. $38^{\bullet+}$ could not be generated in fluid solution due to its high reactivity however, monomeric compounds with 3- and 7-positions blocked, **39–42**, gave persistent cations.

**39****40****41****42**

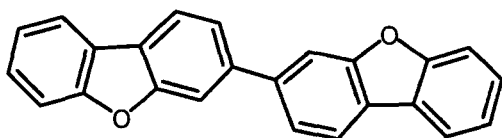
Both dehydro dimers **43**, **44** gave fairly persistent cations, whereas that of **45** could not be detected, presumably due to oligomerization.

Detailed investigation of the kinetic stability and electronic structure of **46a–d** is carried out by using EPR/ENDOR, CV and UV techniques [117].

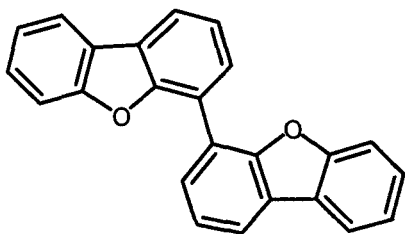
The persistent benzofuran $46c^{\bullet+}$ and $46d^{\bullet+}$ showed reduced amount of spin population in the benzofuran π -systems due to delocalization into the aromatic substituents. This reduces the deprotonation reactions or nucleophilic attack [118]. Conjugative and homo conjugative interactions between strained ring moieties and olefinic fragments in organic radical cations have been the focus of much interest in recent years [119]. Changes in molecular geometry caused by one electron oxidation has been delineated for various substrates and the spin and charge density distributions in the resulting radical cations have been assessed [120]. Typically, the reactions of these species proceed with release of ring strain [121, 122], while in some



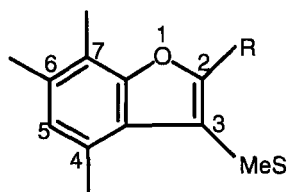
43



44



45



46

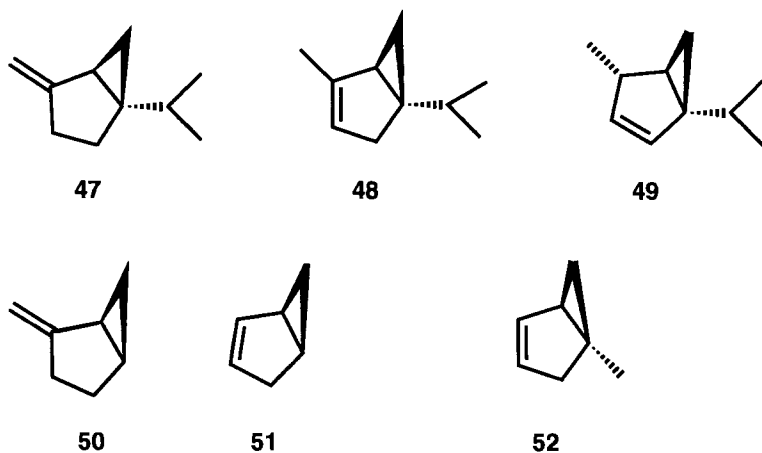
a R = CH₃ b R = Bu^t

c R = Ph d R = MeS = mesityl = 2,4,6-trimethylphenyl

systems ring opening is assisted by a nucleophile [123, 124]. Vinylcyclopropane radical cation, the simplest radical cation containing olefinic moiety and a cyclopropane ring has not been characterized adequately, although several derivatives have been studied in recent years [125]. The ring opening and isomerization of cyclopropane is shown by ab initio calculations to be catalyzed by complexation

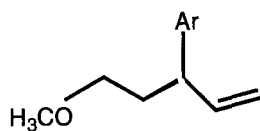
with Be^{++} [126]. Only corner attack by the metal is found in the ring-opening of cyclopropane and a reactive metacyclic intermediate is suggested. Investigations showed a facile reaction pathway, for the catalysis of the ring-opening and isomerization of cyclopropane with group II metal radical cations. The mass spectrum of vinylcyclopropane showed evidence for ring opening to penta-1,3-diene radical cation [127]. Theoretical approaches include an early STO-3G calculation for a vinylcyclopropane radical cation with seriously restricted geometry [128], and more recent INDO, MP2/6-31G*, and B3LYP/6-31G* approaches [129]. Radical cations of bicyclo [3.1.0]hex-2-ene and bicyclo [4.1.0] hept-2-ene system, are characterized by CIDNP experiments [130].

Radical cations of three terpenes, sabinene **47**, α -thujene **48**, and β -thujene **49**, containing vinylcyclopropane functions held rigidly in either an *anti*- or *syn*-orientation, are elucidated by CIDNP results observed during there electron transfer reactions with photoexcited (triplet) chloranil [131].

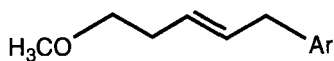


The resulting hyperfine couplings and spin densities are compared with the results of ab initio calculations for radical cations **50**, **51** and **52** [132]. In gas phase, the vinylcyclopropane radical cation, rearranges to the penta-1,3-diene radical cations [127]. Related rearrangements are documented for two rigidly linked vinylcyclopropane systems in solution: the electron-transfer-induced rearrangements of sabinene to β -phellandrene, and of α -thujene to α -phellandrene, are interpreted as novel examples of sigmatropic shifts in radical cations [133]. Products of **53**–**55**, generated by electron-transfer photochemistry of vinylcyclopropane are rationalized by attack of methanol on the radical cation, either at a secondary or the terminal vinyl carbon.

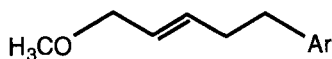
The potential surface of radical cations probed by ab initio calculations showed two minima, both belong to an unusual structure type with two lengthened cyclopropane bonds. Radical cations of **56**–**60** are studied by γ -irradiation in Freon matrices [134], the bicyclic cation **56**^{•+}, **57**^{•+} and **58**^{•+} were persistent and were characterized by EPR and ENDOR experiments. Tricyclic radical cations **59**^{•+} and **60**^{•+} readily underwent rearrangement to **61** and **62** respectively.



53



54



55



56

(R = H; R = D)

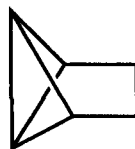


57

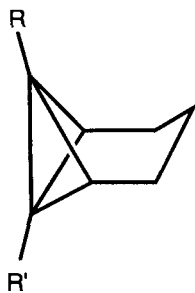


58

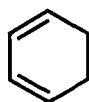
(R = H; R = D)



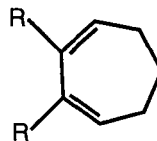
59



60

$$\begin{pmatrix} R = R' = H \\ R = D, R' = H \\ R = R' = D \end{pmatrix}$$


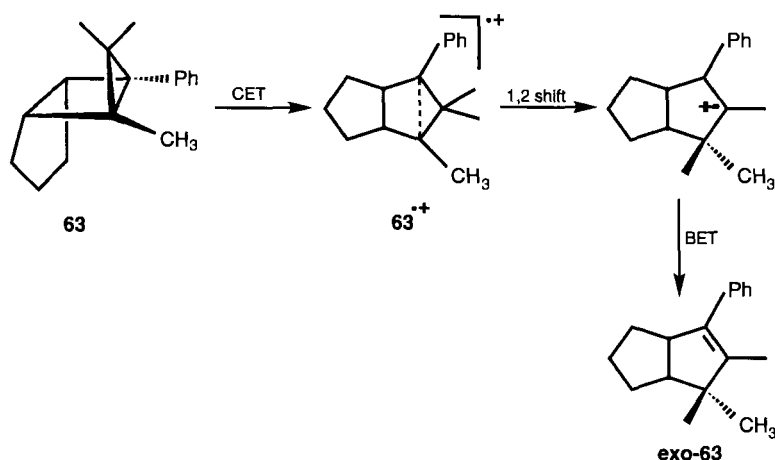
61



62

(R = H, R = D)

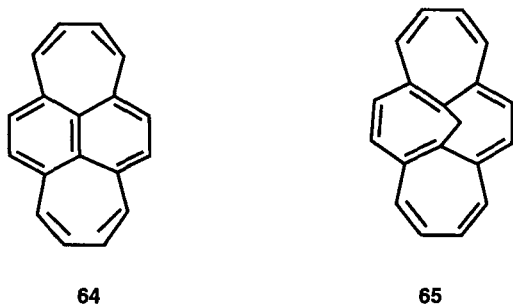
Photoinduced electron transfer (PET) is of current interest and numerous electron transfer sensitizers have been employed not only for mechanistic but also for synthetic purposes [135], effectiveness of PET being further improved by cosensitization technique [136]. PET and Chemical Electron Transfer (CET) have been conducted in solution and within zeolite cavities for the bicyclo [2.1.0] pentanes [137]. The results indicated the CET method to be comparatively better and providing mechanistic insights on the regioselectivity (effective charge localization) and



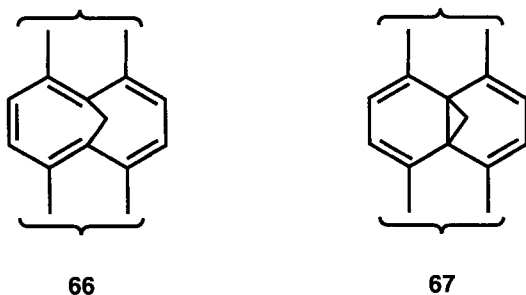
Scheme 3.

diastereoselectivity (conformational memory effect) in the rearrangement of the intermediary 1,3-diyl radical cations to the corresponding cyclopentenes. A study carried by Adam and coworkers [138] showed that 1,3-diyl radical cations generated from bicyclo [2.1.0] pentane derivatives, exhibit a high propensity to rearrange by 1,2-shift to the corresponding 1,2 radical cations, which after electron back-transfer yield cyclopentenes. The tricyclo [3.3.0.0] octane (housane) [138, 139] **63** affords only the cyclopentene *exo*-**63** upon electron transfer oxidation, and thus, the 1,2 migration in the intermediary radical cation $\text{63}^{\bullet+}$ occurs exclusively to the methyl terminus (Scheme 3).

Further investigation by the Adam group [140] showed electronic substituent effects on the diyl sites profoundly influences the regioselectivities of the 1,2 shift. The data obtained illustrate the distinct electronic character of the cationic intermediates involved in the electron transfer oxidation vs acid catalysis of the housanes. The radical anions and cations of dipleiadiene **64** and its 12b,12c-homo derivatives **65** are characterized by EPR and ENDOR spectroscopy [141]. The π -spin distribution over the perimeter is similar in the radical cations $\text{64}^{\bullet+}$, $\text{65}^{\bullet+}$, and an analogous statement holds for the corresponding radical anions.



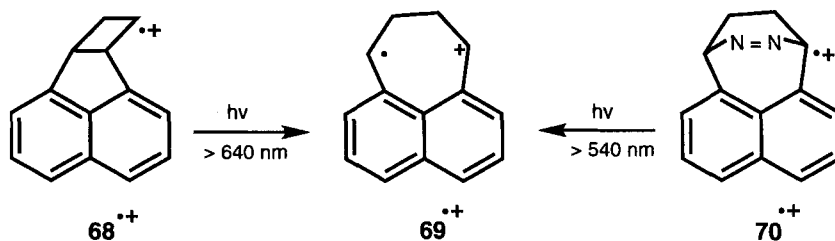
From the coupling constants of CH_2 protons, it is concluded that the cation $\mathbf{65}^{+\bullet}$ exists in the methano-bridged form $\mathbf{66}$ of the neutral $\mathbf{64}$, whereas the anion $\mathbf{65}^{\bullet-}$ adopts the bisnorcaradiene form $\mathbf{67}$ of the dianion $\mathbf{65}^{2-}$.



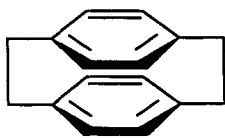
Pioneering work of Dowd on trimethylene methane [142], 1,8-naphthoquinodi-methane diradicals were among the first examples of non-Kekule π,π -diradicals that were found to be persistent in their triplet ground state at cryogenic temperatures and were thoroughly characterized by various spectroscopic methods [143]. Time resolved studies of diradicals have provided lifetimes and reactivities of numerous diradical intermediates in solution [144]. γ -irradiation of CAN, $\mathbf{68}$, in haloalkane glasses at 77 K yielded radical cation $\mathbf{68}^{+\bullet}$; its electronic absorption spectrum has been obtained and represents first report of absorption spectrum of an ionized di-radical [145]. Irradiation at >640 nm converted it into an isomer identical with that formed by ionization of 1,4-dihydro-1,4-ethanonaphtho[1,8-*de*][1,2]diazepine $\mathbf{70}$, and subsequent irradiation of the radical cation at $\lambda > 540$ nm. Results identified the photo isomer of $\mathbf{68}^{+\bullet}$ to be $\mathbf{69}^{+\bullet}$ (Scheme 4).

The molecular and electronic structures are discussed on the basis of B3LYP and CASPT2 quantum chemical calculations. Paracyclophanes are attractive model compounds for studying specific intramolecular interactions [146, 147]. Gerson et al. [148] showed the radical anion of [2,2] paracyclophane $\mathbf{71}$ is an unassociated specie, with the unpaired electron being equally distributed over both π -systems.

A range of paracyclophane radical cations has recently been studied by EPR and ENDOR spectroscopy [149]. The [5,5] and [7,7]paracyclophane showed localized radical cation at low temperatures, however at room temperature the higher molec-



Scheme 4.



71

ular flexibility leads to a fast (EPR time scale) intramolecular electron transfer. In this series radical cations in which two terminal 1,4-dimethoxy benzene units are anellated to [2,2] paracyclophane, [2,2](1,4) naphthalenophane and anthracene bridges have been studied by the same group employing EPR and ENDOR spectroscopic techniques [150].

Single electron transfer (SET) oxidation seems to be the most important pathway for propellanic σ_{C-C} bond interactions with NO_2^+ , the same reactivity is expected for nitrosonium reagent (NO^+) which are effective in SET oxidations of organic sulfides [151], urazines [152], aromatic compounds [153] and cyclopropanes [154]. NO^+ containing reagents are also reactive towards saturated hydrocarbons [155]. Chemical ($\text{NO}^+\text{BF}_4^-/\text{EtOAc}$, $\text{NO}^+\text{OAc}^-/\text{Ac}_2\text{O}$, and $\text{NO}^+\text{BF}_4^-/\text{CH}_3\text{CN}$), photochemical (photoexcited 1,2,4,5-tetracyanobenzene), and electrochemical (Pt anode, CH_3CN , NH_4BF_4) oxidation of 3,6-dehydrohomoadamantane **72** is elucidated [156].



72

Results indicated that the activation of propellane σ_{C-C} bonds with strong oxidizing electrophiles occurs by a sequence of SET steps. Ab initio {density functional theory (BLYP) and Møller–Plesset perturbation theory (MP2)} computations utilizing standard basis sets, 6-31G* and 6-311+G* (single-point energy evaluations), agreed with the experimental results implicating the involvement of the same radical cation intermediates in the activation process. Pagodane and (seco) dodecahedrane cage structures [157] allowed the study of unusual electronic phenomena [158] and of unusual molecular species (e.g. valence isomeric 4C/3e radical cations [159] and σ -bishomoaromatic 4C/2e dications [160]). The ionization and detection of [1.1.1.1] pagodane is successfully carried out by time-resolved fluorescence detected magnetic resonance [161], the first example in which the rate of conversion of two valence isomeric radical cations has been directly measured. The discovery of highly persistent 4C/3e radical cation [162], σ -bishomoaromatic 4C/2e dication [163] on oxidation of [1.1.1.1] pagodane triggered modification of the cage skeleton surrounding the central cyclobutane ring with respect to stability, persistence, and behavior of the respective radical cations and dications [164]. Synthesis, one and two electron

oxidation of [2.2.2.2] pagodane is reported by Gescheidt et al. [165]. For the quantification of the factors determining the transannular electronic interactions, a continuous search for model structures with well-defined molecular dimensions is on the way [166].

Spontaneous generation of long-lived organic cation radicals on zeolite surfaces is known for over three decades [167], however, only during the last few years has this phenomenon been widely recognized and the technique has been developed into a routine laboratory tool to generate stable cation radicals [168]. Stable and ultra-stable carbocations from 4-vinylanisole are generated within Zeolites, these reactive intermediates are found to be stable for several weeks within the confirmed environments of zeolites [169]. Results reveal that zeolites, when properly prepared, can generate and stabilize 'reactive' intermediates from neutral molecules. A new method for elucidating elementary reaction steps in zeolite catalysis is demonstrated for reactions of isobutene and other mono olefins on HZSM5 [170], one of the most active zeolite catalyst. Because of its strong Brønsted acidity it has found many critical applications in petroleum cracking, benzene alkylation, xylene isomerization and in aromatization of alkanes and alkenes [171]. The study demonstrates the use of EPR to detect and identify radiolytically generated radical cations and neutral radicals of product molecules of hydrocarbon catalysis on HZSM5. For isobutene on HZSM5, dimerization and isomerization even at cryogenic temperatures was shown [172]. Aromatic radical cations e.g. benzene^{•+}, biphenyl^{•+}, and naphthalene^{•+} being difficult to stabilize and studied in solution, are prepared in rigid matrices of certain halocarbons or on surfaces of zeolites or silica gel [173], however in certain cases EPR spectra from these disordered samples suffer from limited resolution. For biphenyl^{•+} the higher resolution of ENDOR greatly facilitated investigations of the ring proton hyperfine tensors in disordered solids [174].

The naphthalene radical cation generated by UV- or X-irradiation on HZSM5 zeolite and in frozen CFCl₃ is investigated by EPR, ENDOR and ESEEM spectroscopic methods [175]. Analysis of powder EPR line shape was made possible by the simultaneous use of ENDOR and ESEEM spectroscopies. The *g* and ring-proton hyperfine (hf) tensors were determined and were found identical in the two media, within experimental error. Iwasaki et al. [176], stabilized benzene radical cations in a CFCl₃ matrix and obtained EPR evidence for the Jahn–Teller distortion at 4.2 K, with the unpaired electron density in the ²b_{2g} orbital. EPR investigation of the benzene radical cation adsorbed on the HY molecular sieve at 203 K resulted in spectra characterized by axially symmetric *g* and *A* tensors with *g* = 2.00238, *A*_{||} = −14.00 MHz and *A*_⊥ = −11.34 MHz, suggesting rapid rotation of the benzene cation about the molecular sixfold symmetry axis [177]. EPR, ENDOR and ESEEM studies of C₆H₆^{•+} and C₆H₅D^{•+} absorbed on HY molecular sieve and silica gel suggested that C₆H₆^{•+} undergoes pseudorotation at 3.5 K, whereas C₆H₅D^{•+} on silica gel showed slowing down of the molecular motion to a rigid or semi-rigid state [178]. Recent ENDOR and EPR investigations by Lund et al. [179] yielded evidence for a Jahn–Teller distortion of monomeric benzene radical cation C₆H₆^{•+} in a CFCl₃ matrix at 30 K, with unpaired electron density predominantly in the ²b_{2g} orbital. Better resolution in case of ENDOR as compared to EPR enabled precise measurement of isotropic and dipolar hyperfine coupling constants in the

Jahn–Teller distorted state. ENDOR results of dimeric benzene cation formed after warming in CFCl_3 and present in CF_3CCl_3 at all temperatures indicate that the dimer had a sandwich structure in both matrices. An EPR study of the benzene radical cation in argon matrix generated by fast electron irradiation at 16 K showed favorable stabilization of $^2b_{1g}$ state rather than $^2b_{2g}$ state, in contrast to previous results found in Freon matrices [180].

Substitution of hydrogen by weakly perturbing alkyl groups like the methyl group in toluene and xylene anions, removes the twofold orbital degeneracy of the ground state of benzene radical cations/anions artificially [181]. The radical cations of toluene and xylene in silica gel and halocarbon matrices are reported [182], however hyperfine coupling constants determined in these investigations were different and detailed assignment of spectra is lacking. Komatsu et al. [183] studied toluene and partly deuterated toluene (toluene $\alpha\text{-d}_3$) on silica gel and Vycor glass and provided unambiguous evidence for the formation of toluene radical cation. EPR and ENDOR results on radical cations of methyl-substituted benzene, *p*-xylene, *o*-xylene, *m*-xylene and their deuterated analogs generated in CFCl_3 and CF_3CCl_3 matrices by X-ray irradiation at 77 K are investigated by Lund et al. [184]. Spectra in the radical cations are dominated by large axially symmetric hyperfine splitting due to methyl group protons. Experiments and theoretical calculations supported the stabilization of $^2b_{2g}$ type of state for the radical cations of toluene and *p*-xylene compared with the stabilization of $^2b_{1g}$ type of ground state for *o*-xylene and *m*-xylene due to lifting of the orbital degeneracy of the e_{1g} orbital by lowering the symmetry obtained after substitution of hydrogen by methyl groups.

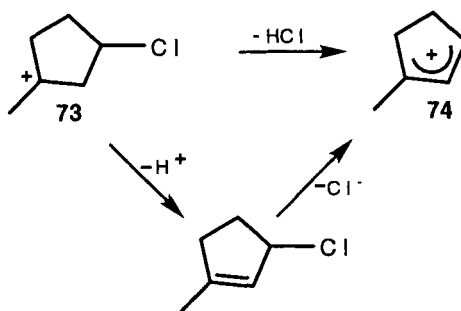
Eriksson [185] studied radiolytic reduction of acetylene adsorbed on HZSM5. Observance of hydrocarbon radical anion is a rare finding and contrasts with results for other unsaturated hydrocarbons adsorbed on HZSM5, for which radical cations are only observed. An EPR spectrum revealed radical anion to be in the *cis*-bent form. The energies, geometries, and hyperfine coupling constants are calculated for the acetylene, vinylidene, cyclobutadiene and butatriene radical anions and radical cations, using different levels of theory, including gradient-corrected density functional theory. Variable-temperature EPR study of various olefin radical cations, 1,4-cyclohexadiene, 1,3-cyclohexadiene, 3,3-dimethyl-1-butene, 2,3-dimethyl-1-butene and tetramethyl ethylene, generated radiolytically in non-acidic and acidic ZSM-5 zeolites showed isomerization reactions even at 4 K [186]. The observation of H-addition-type radicals indicates Brønsted acid-catalyzed rearrangements prior to irradiation on more acidic zeolites. Radical cations of *cis*- and *trans*-decalin are studied in Freon matrices and zeolites by EPR [187], in hydrocarbon solutions by ODEPR in CW [188] and time resolved variants [189]. ODEPR of *cis*-decalin radical cation in dilute cyclohexane and squalane [190] solution were observed at temperatures up to ambient, but signal of *trans*-decalin could be observed only below 40 K [189]. ODEPR and MARY (magnetic field effect on recombination luminescence yield) spectroscopy of spin-correlated radical ion pairs were used to study *cis*- and *trans*-decalin radical cations in nonpolar medium [191]. The analysis demonstrates that the peculiarities of the *trans*-decalin ODEPR and MARY spectra at high temperatures root in the quasi-degeneracy of electron levels and the related dynamic transitions and spin relaxation due to strong spin–orbital interactions.

4.4.2 Olefins

Radical cations of alkanes are extensively studied both in Freon matrices by EPR [192] and in hydrocarbon solutions by ODEPR technique in CW [193] and time-resolved FDMR [194] variants. An alkane with higher ionization potential is used as a matrix, and the substance of interest is added in small ($<10^{-2}$ M) concentrations as an admixture. ODEPR spectra of *cis*-decalin radical cation in cyclohexane [195] are observed for dilute solutions but efforts to observe signals of solvent radical cations (holes) in non-dilute solutions failed. This resulted in the assumption that some fast hole decay is responsible for the absence of any signal [196]. It has been demonstrated that the effect of level crossing in spin-correlated radical ion pairs [197] permits EPR spectra of radical cations without microwave pumping [198]. Recently Tadjikov et al. [199] succeeded in detecting squalane radical cation (hole) formed under the action of ionizing radiation at room temperature in a non-dilute solution by employing MARY-EPR technique. The spectrum showed one single line, homogeneously narrowed due to resonance charge transfer over the solute molecules with the rate constant exceeding the diffusion-controlled limit. The technique of radical ion pair level crossing spectroscopy revealed EPR spectrum parameters of solvent radical cations for a series of non-viscous alkanes, *n*-pentane, *n*-hexane, *n*-octane, *n*-decane, *n*-dodecane and *n*-hexadecane [200]. The rate constant for squalane hole scavenging by a diphenyl sulfide molecule is directly obtained using quantum-beats technique [201]. Results are in good agreement with that of pulse-radiolysis experiments [196], providing stronger background to the hypothesis about the hole nature of the highly mobile solvent cation in squalane. A number of EPR and theoretical studies are carried out for the cyclohexane and related radical cations [202], however, static and dynamic structures are not yet completely understood. Combined with theoretical calculations employing *ab initio* and DFT [203] methods, the radical cation is concluded to take an 2A_g electronic ground state in C_{2h} symmetry, in which two C–C bonds are elongated and other four compressed. An EPR study of radical cations of selectively deuterated cyclohexanes in a cC_6F_{12} matrix, revealed that the geometrical structure of the radical cation is distorted into a C_{2h} symmetry from the original D_{3d} symmetry. The temperature-dependent EPR line shapes are analyzed in terms of dynamical averaging among the C_{2h} structures with different zero-point vibrational energies due to deuterium mass effects under the assumption of Boltzmann distribution.

Photoheterolysis of benzylic chlorides [204] yielded results signifying that simple benzyl cations, such as cumyl and 1-phenylethyl cations, can exist in the solution as free ions; radicals arising from a competing photohomolysis are also observed frequently. Haloalkyl-carbocations are studied by heterolysis of the corresponding dihalides in super acid media [205]. ^{13}C NMR chemical shifts are interpreted as evidence for an interaction between the vacant orbital of cationic center of the haloalkyl carbocations with a lone electron pair of the halogen atom. 3-chloro-1-methylcyclopentyl cation **73**, thermally eliminates hydrogen chloride and yields 1-methyl-2-cyclopentyl cation **74**, a similar behavior reported for γ -chloroalkyl carbocations [206] (Scheme 5).

Flash photolysis experiments [207] of 1,3-dichloro-1,3-diphenyl propane **75** in

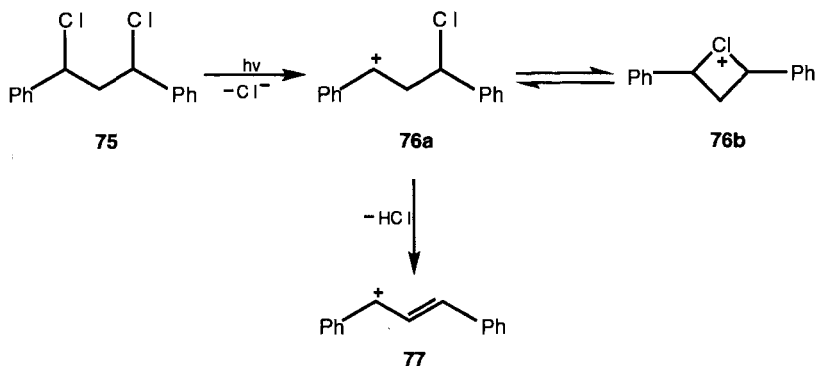


Scheme 5.

2,2,2-trifluoroethanol at 266 nm lead to γ -chloropropyl cation **76a**, kinetic results showed interconversion between the open chain cation and corresponding cyclic chloronium ion **76b**; loss of HCl yielded 1,3-diphenyl-2-propenyl cation **77** (Scheme 6).

Two-laser two-photon results revealed photoisomerization of the cation *E,E*-**77** to its stereoisomer *Z,E*-**77**, which undergoes thermal reversion with a lifetime of 3.5 μs at room temperature. Absolute rate constants for reaction of styrene, 4-methylstyrene, 4-methoxystyrene and β -methyl-4-methoxystyrene radical cation with a series of alkanes, dienes and enol ethers are measured by Laser flash photolysis [208]. The addition reactions are sensitive to steric and electronic effects on both the radical cation and the alkene or diene. Reactivity of radical cations follows the general trend of $4\text{-H} > 4\text{-CH}_3 > 4\text{-CH}_3\text{O} > 4\text{-CH}_3\text{O}-\beta\text{-CH}_3$, while the effect of alkyl substitution on the relative reactivity of alkenes toward styrene radical cations may be summarized as $1,2\text{-dialkyl} < 2\text{-alkyl} < \text{trialkyl} \leq 2,2\text{-dialkyl} < \text{tetraalkyl}$.

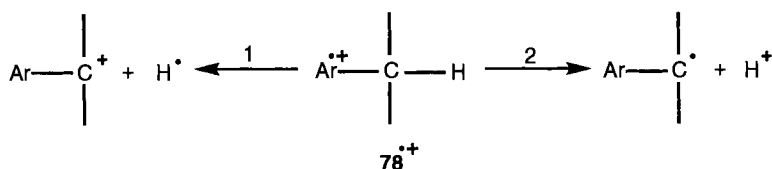
There is a considerable current interest in synthetic applications of radical cation chemistry. Alkene radical cations have been studied extensively, notable examples include the *anti* Markovnikov addition of nucleophiles [209], and the photo-NO-CAS reaction [210]. The synthetic utility of radical cation mediated chemistry, and



Scheme 6.

in particular cyclobutanation and Diels–Alder reactions, is well noted [211]. Radical cation cycloaddition can be carried out under relatively mild conditions and frequently results in product yields, stereoselectivity, and regioselectivity that equal or surpass their thermal counterparts. However, it should be noted that the rational design of synthetic strategies based on this chemistry requires detailed kinetic and mechanistic information for all the potential reaction pathways of the various intermediates. A number of conjugated diene radical cations have been generated photochemically by either photoionization or photosensitized electron transfer and have been spectroscopically and kinetically characterized using laser flash photolysis. Measured rate constants for addition to methanol demonstrate that the more highly alkyl-substituted radical cations are substantially less reactive toward nucleophilic addition reactions [212].

Fluorine substitution in the organic molecules has a significant effect on their geometry and electronic structure [213], in particular for the benzene derivatives, the structure and the symmetry of the radical cation are affected not only by the number of substitutions by fluorine but also by the position of the substitution [214]. Other examples studied are pyridine [215], butadiene [216], and ethylene [217]. Although the geometrical structure of neutral olefins are planar at the ground electronic state, non-polar structures in bent form or in twist form have been suggested for their radical cations and anions by EPR [218], photoelectron spectroscopy, and theoretical calculations [219]. EPR spectrum from γ -irradiated $\text{CCl}_2\text{FCCl}_2\text{F}$ solution containing C_2H_4 , was attributed to ethylene radical cation with a torsional angle of 45° about the C–C bond [220a]. However, Fujisawa et al. [220b] suggested that the spectrum should be attributed to a propagating radical cation of $^+\text{CH}_2-(\text{CH}_2)_n-\text{CH}_2$. Lunell and group calculated the isotropic ^1H hf splitting by an accurate CI study and concluded that the splitting of $(-)0.3$ mT corresponds to the torsional angle of 28° [221]. Based on EPR results of the propene radical cation, $\text{CH}_2=\text{CH}-\text{CH}_3^+$ produced in a CCl_3F matrix at 77 K, Toriyama et al. [222] analyzed that the rotation of the CH_3 group is hindered. However, study of partially deuterated propene $\text{CH}_3\text{CH}=\text{CD}_2$ revealed that the CH_3 group rotates freely even at 77 K [223]. INDO calculations suggested an energy minimum with a twist angle of 45° . On comparing the observed hf splitting of 0.70 mT for the CH proton and calculated value, it is concluded that the propene cation might interchange between two configurations corresponding to the energy minimum rapidly enough to give the apparent planarity on the EPR time scale because of its low barrier. Toriyama et al. reinvestigated propene cation, in addition to a study on a trimethylethylene cation, $(\text{CH}_3)_2\text{C}=\text{CH}(\text{CH}_3)^+$. Using a twisted model along the C=C bond and the bent structure in the group of CHCH_3 or CH_2 of the cations, they interpreted the observed hf splittings of 0.6 mT for the CH proton of the propene cation as well as a large non-equivalence of the two CH_2 proton coupling constants of 2.35 and 1.1 mT [224]. Radical cation of a series of fluorinated ethylenes and propenes, generated by irradiation with γ -rays in halocarbon solid matrices is recently being studied by Hasegawa et al. [225]. EPR spectra obtained for trifluoro olefin cations, $\text{CF}_2=\text{CFX}^+$ ($\text{X} = \text{H}, \text{CH}_3$ or CF_3) are successfully analyzed in terms of three ^{19}F nuclei with coaxial parallel components, thus suggesting a planar structure. The optimized geometry of the radical cations was calculated by ab initio MO method.



Scheme 7.

In contrast with the ethylene cation and the propene cation, having non-planar twisted structures, the fluorinated ethylene and propene cations are concluded to have planar structures. The cleavage of the C–H bond of alkyl aromatic radical cations usually occurs in a heterolytic fashion in solution, however, homolytic cleavage is equally possible [226] (Scheme 7).

Path 2 is generally observed in solution [227], and accordingly, radical cations $78^{\bullet+}$ represent a very interesting class of strong carbon acids, whose kinetic and thermodynamic acidity is the object of continuous investigation [228]. The possibility of the alternative path 1 involving a hydrogen atom transfer reaction is rarely observed [229]. Recently photoinduced electron transfer of bis(4-methoxyphenyl)-methane, sensitized by chloranil in CH_3CN clearly indicated the occurrence of a hydrogen atom transfer from the radical cation to the chloranil radical anion ($\text{CA}^{\bullet-}$) [230] (Scheme 8).

The low basicity of $\text{CA}^{\bullet-}$ in CH_3CN ($\text{p}K_a = 6.8$) and the substantial spin density on the oxygen atoms probably play a fundamental role in this respect, as well as, of course, the reduction potential of the formed carbocation. Trimethyl methane (TMM) is one of the most attractive organic molecules, investigated with respect to electronic structure because it is a rather small fundamental molecule with a high symmetry and a triplet ground state with a doubly degenerate HOMO [231]. The 4.2 K EPR showed a septet with isotropic ^1H hf splittings of 0.93 mT (6H) in $\text{CF}_2\text{ClCF}_2\text{Cl}$ matrix. Ab initio MO calculations predicted that $\text{TMM}^{\bullet+}$ is a $^2\text{A}_2$ state in a distorted C_{2v} structure, and the unpaired electron mainly resides in the P_z orbitals of the two equivalent terminal carbons [232]. The spectra is explained by intramolecular dynamics between the three energetically equivalent C_{2v} structures to average the structural distortion giving an apparent D_{3h} structure even at low temperatures. Pulsed EPR technique is employed to measure electron spin–lattice (T_1) and spin–spin relaxation times (T_2) for the tetramethyl ethylene radical cation in ZSM5 zeolite [233]. Major conclusions are (a) methyl rotation is hindered by radical cation interactions with co-adsorbed argon, (b) the rotational potential of the methyl group is affected by radical cation–matrix interactions, (c) $\text{TME}^{\bullet+}$ –TME interactions do not appear to occur to an appreciable extent at TME loadings less than 3 uc^{-1} (molecules per unit cell), but a change in the TME loading causes a



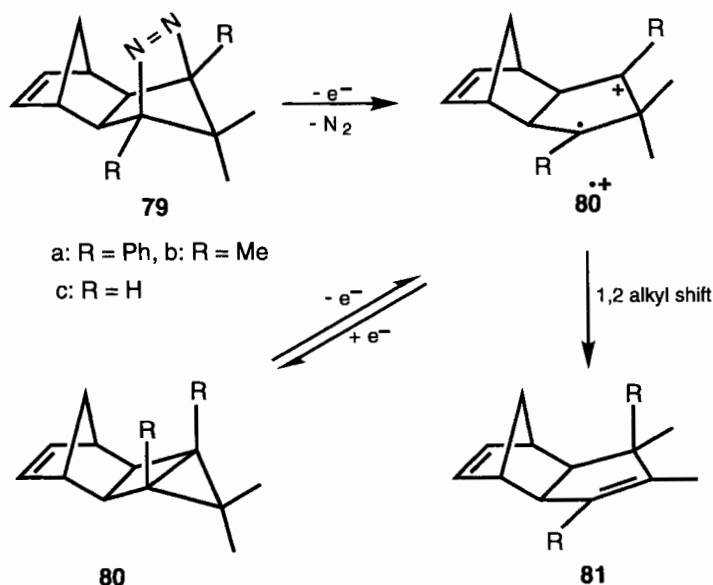
Scheme 8.

change in the radical cation–matrix interactions due to site heterogeneity and/or sorbate-induced lattice distortions.

4.4.3 Heteronuclear Radical Cations

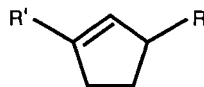
Ground-state azoalkanes can serve as electron donors and thereby be converted to radical cations [234], a method frequently used to induce electron transfer in photosensitization [235]. Azoalkane radical cations have been studied by EPR directly under matrix isolation, e.g. 2,3-diazabicyclo[2.2.2]oct-2-ene [234a], and in solution, e.g. *trans*-*N,N'*-di(1-norbornyl)diazene [234b], however some azoalkanes experience rapid loss of nitrogen upon one-electron oxidation [234c–f]. Well known for N_2 extrusion upon direct and triplet-sensitized photolysis [236], 2,3-diazabicyclo[2.2.1]hept-2-ene (DBH) and its derivatives denitrogenate effectively upon electron transfer to yield carbon-centered radical cations [234e, 234f, 237]. The azoalkanes **79a–c** showed nitrogen extrusion upon photosensitized electron transfer (PET) to yield 1,3-radical cation intermediate **80**^{•+}, reverse electron transfer (RET) affords the unrearranged housanes **80**, but significant rearrangement to dicyclopentadiene derivative **81** was observed prior to RET [238] (Scheme 9).

The housanes **80a,b** are also oxidized by PET, but are more reluctant to rearrange, results illustrating the intriguing chemical fate of radical cations derived from dicyclopentadienes and their isomers. In continuation of their investigation, Adam et al. [239] studied oxidation of 2,3-diazabicyclo[2.2.1]hept-2-enes, **82a–d**,



Scheme 9.

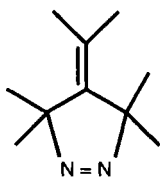
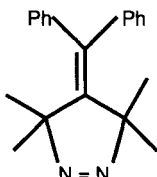
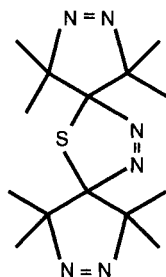
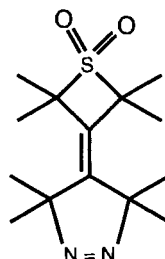
and bicyclo[2.1.0]pentanes, **83a–d**, with catalytic amounts of tris(aryl)aminium hexachloroantimonates afforded the corresponding cyclopentenes, **84a–d**.

**82****83****84**

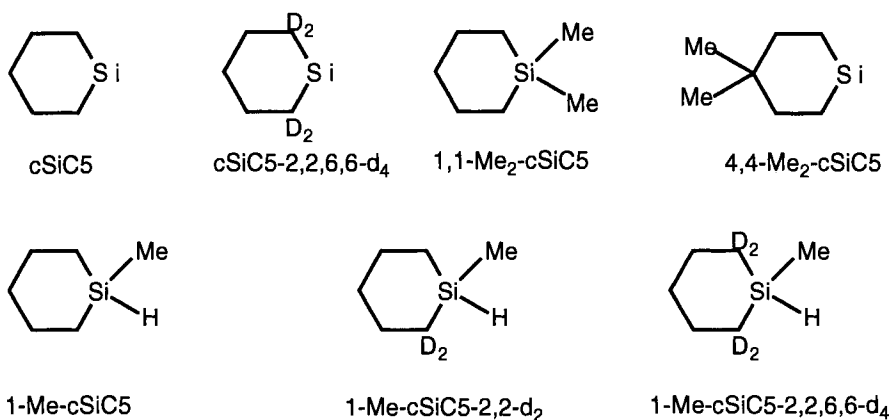
a ($R = R' = H$); b ($R = Me$; $R' = H$)

c ($R = Ph$; $R' = H$); d ($R = R' = Me$)

A reversal in the regioselectivity of the 1,2-migration was observed for the unsymmetrical derivative **80b**, **80c**, proposed to be due to delocalization of the positive charge into the aromatic ring for the 1,3-diyl radical cation, as corroborated by AM1 calculations. EPR spectra are reported for radical anion and for the first time radical cation derivatives of pyrazolines **85–88** [240].

**85****86****87****88**

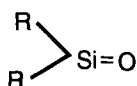
The radical anion spectra are consistent with the unpaired electron being localized principally in the $N=N$ π^* -orbital, however, for the radical cation of 4-alkylidenepyrazolines, the near degeneracy of the $N=N$ n and $C=C$ π -orbitals made the distribution of the unpaired electron difficult to predict. The radical cations of cyclopentane- and urazole-annulated azoalkanes and housanes were generated by pulse radiolysis and the intermediates characterized spectrally and kinetically by time-resolved optical monitoring. For the bridgehead-substituted diphenyl derivatives only the corresponding proximate 1,2-radical cation is detected, generated from the initially formed and too short-lived ($<1 \mu s$) distonic 1,3-radical cation by 1,2-methyl migration [241]. Triazenes increasingly find application as initiators of radical polymerization [242] and promoters of polymer ablation by ultraviolet irradiation [243]. The decomposition of symmetrical dialkyltriazenes in acidic aqueous solution proceeds with formation of alkylamines and alkyl alcohols, whereas, asymmetric 1,3-dialkyltriazenes preferably form different alkyl diazonium ions and alkyl amines due to two tautomeric forms in the starting triazenes [244]. In



Scheme 10.

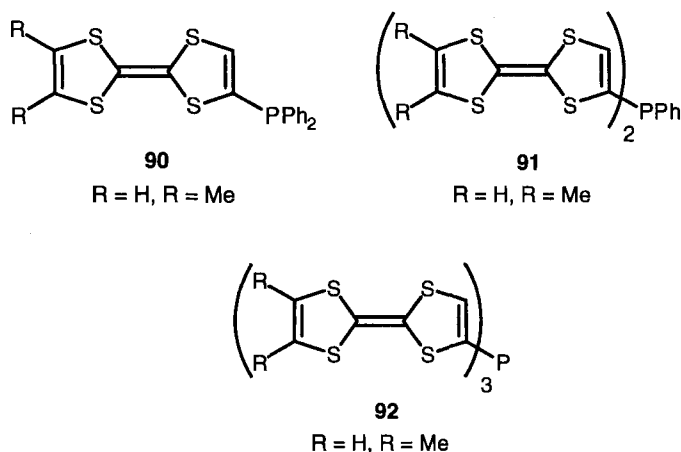
electrochemical oxidation of 1,3-diphenyltriazenes, intermediate formation of the triazene cation radical is assumed, which after protonation with residual water rearranges to aniline and finally converts to *p*-aminoazobenzene [245]. Redox properties of asymmetric 1-phenyl-3-alkyltriazenes and their corresponding triazenidoplatinum complexes are characterized by CV and the structure of the radical intermediates formed in electrolytic reactions and in oxidation with peroxy compounds is investigated [246]. Hydrazines linked by a *p*-phenylene bridging unit are charge localized in the intervalence oxidation state, proper choosing of substituents allows the isolation of compounds in 0, 1⁺, and 2⁺ oxidation states which are stable enough for variety of physical studies [247]. The structure, dynamics and thermal reactions of the radical cation of silacyclohexanes (cSiC_5) containing one Si atom in the six-membered ring have been studied by EPR and *ab initio* MO calculations. The cations were generated in perfluoromethylcyclohexane matrix by ionization radiation at low temperatures. Results suggest that cSiC_5 radical cation takes an asymmetrically distorted C_1 structure with one of the Si–C bonds elongated in which the unpaired electron resides, supported by *ab initio* MO calculations (Scheme 10).

At temperatures above 140 K, the cSiC_5 radical cations were converted into the neutral radicals via geoselective deprotonations. In recent years, a number of compounds which show multiple bonding to silicon has been isolated and studied [248]. Monomeric silanones, **89**, have as yet been observed only in solid matrices [249], apparently the presence of two bulky groups is not sufficient to prevent oligomeri-

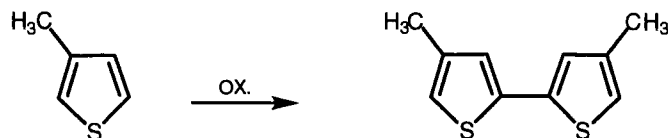
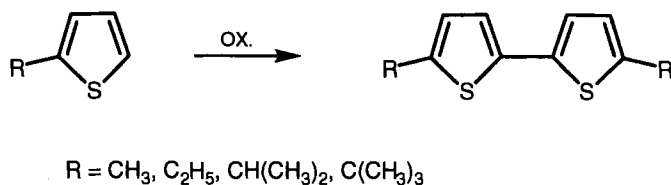


zation in fluid solutions, but formation of the silanones can be inferred from their reactions with traps such as dienes [250].

However, there is good evidence from EPR experiments for the existence of sterically stabilized silanone radical anions in solution [251]. EPR study of tris(trimethylsilyl)methylsilyl radicals $(\text{Me}_3\text{Si})_3\text{CSiH}_{n-1}\text{R}_{3-n}$ ($\text{R} = \text{H}$, Et or F, $n = 1, 2$ or 3), prepared by hydrogen abstraction from the corresponding tris(trimethylsilyl)methylsilanes is reported [252]. Hydrogen abstraction from silanols $(\text{Me}_3\text{Si})_3\text{CSiH}(\text{R})\text{OH}$ ($\text{R} = \text{H}$, Me, Et, Bu, Ph, F) under neutral conditions yielded spectra of the corresponding hydroxysilyl radicals $(\text{Me}_3\text{Si})_3\text{CSi}(\text{R})\text{OH}^\bullet$, while reaction with potassium *tert*-butoxide gave silanone radical anions $(\text{Me}_3\text{Si})_3\text{CSi}(\text{R})=\text{O}^{\bullet-}$. The electronic absorption spectra of polysilane radical ions have been studied by Ban et al. [253], Irie et al. [254] and by Ushida et al. [255]. They observed a UV band assigned to the HOMO \rightarrow LUMO transition of neutral polysilanes (SOMO \rightarrow LUMO for the cation and HOMO \rightarrow SOMO for the anion). Ushida et al. assigned the near IR band as due to charge resonance band arising from the interaction between adjacent σ -conjugated polymer segments. Ichikawa et al. [256] studied the electronic structure of polysilane and oligosilane radical anions by electronic absorption and EPR spectroscopy. They concluded that the SOMO is a pseudo- π orbital composed of antibonding Si-Si and Si-C orbitals and the unpaired electron is not delocalized all over the polymer chain but is confined to a part of the chain. A similar study of oligosilane radical cations suggested that the unpaired electron of polymer radical cation is also not delocalized all over the Si-Si main chain [257]. Tetrathiafulvalene (TTF) and its derivative represents the most popular donor π -systems and have been used for the last two decades in conducting and supraconducting radical cation salts [258]. Radical cations of **90–92** are studied by CV, EPR and ENDOR spectroscopic techniques [259].



During stepwise oxidation, each of the tetrathiafulvalene (TTF) or 4,5-dimethyltetrathiofulvalene (o-DMTTF) moieties in **90–92** donates two electrons so that exhaustive oxidation at potentials below IV (vs. SCE) leads to dications **90**²⁺, the tetracations **91**⁴⁺ and hexacations **92**⁶⁺. In the initially formed radical cations,



Scheme 11.

the electron hole is delocalized over all the TTF or *o*-DMTTF moieties, two in $\mathbf{91}^{\bullet+}$ and three in $\mathbf{92}^{\bullet+}$. On the other hand, in the paramagnetic species produced by further oxidation, also giving rise to well defined EPR and ENDOR spectra, the unpaired electron appears localized in only one donor moiety on the hyperfine time-scale. The dications $\mathbf{91}^{2+}$ and $\mathbf{92}^{2+}$, as well as the tetracations $\mathbf{92}^{4+}$ are proposed to have a triplet ground state, while the trications $\mathbf{92}^{3+}$ are able to form quartet states. Oxidation of 2-alkylthiophenes by thallium(III) tris(trifluoroacetate) in HFP yielded the corresponding persistent 5,5'-dialkyl-2,2'-bithiophene radical cations, while 3-methylthiophene showed 3,3'-dimethyl-2,2'-bithiophene [260] (Scheme 11).

A combination of collisional activation, neutralization–reionization, and ion–molecule reaction experiments has been used to characterize various $[\text{C}_2\text{H}_4\text{OS}]^{\bullet+}$ radical cations derived from *s*-alkyl thiaformate precursors, and the results suggest the occurrence of distonic ions and ion–molecular complexes [261]. Experimental evidence for the existence of isomeric distonic $\text{HC}^+(\text{SH})\text{OCH}_2^{\bullet}$ species is not found, but the calculation of the related $[\text{C}_2\text{H}_4\text{OS}]^{\bullet+}$ potential energy surface suggests that the latter ion is stable and likely to play a role in the fragmentation processes. Investigation by Asmus et al. showed that the radical cations of aliphatic sulfides are stabilized by forming the sulfur–sulfur two-center three-electron bonded dimers [262]. The nature of such 2C–3e S–S bonds has attracted considerable interest as possible intermediates in many enzymatic oxidations of organic sulfides [263]. However, radical cations of aromatic sulfides [264] are believed not to form any dimers because of the delocalization of positive charge/spin density over the aromatic rings. Recently, Sawaki et al. [265] studied aromatic sulfides by photochemical one-electron oxidation in acetonitrile. Irradiation of dicyanonaphthalene and thioanisole with nanosecond laser flash (308 nm), revealed two types of dimer radical cations at 470 (σ -type) and 800 (π -type) nm, at the expense of the monomer radical cation (520 nm). The density functional BLYP/6-31*G calculations on thioanisole predicted the existence of σ - and π -type dimer radical cations, in accordance with the experimental observation of approximately equal stability. In recent years, special interest has been given to cumulenes containing one or two atoms of

Group VB [266] (e.g. $\text{RP}=\text{C}=\text{PR}$), mainly due to considerable progress made in synthetic chemistry, especially in field of phosphorus-containing compounds [267], and to a better understanding of the redox properties of these compounds [268]. Crystal structure of diphosphaalenes stabilized by bulky substituents ($\text{Ar} = 2,4,6\text{-(Bu}^t)_3\text{C}_6\text{H}_2$), have shown that the $\text{P}-\text{C}-\text{P}$ sequence is not linear and that these molecules adopt a structure close to C_2 symmetry with the substituents on the opposite sides of the PCP plane [269]. The structure of the first term of the series, HPCPH, has been the subject of several *ab initio* studies [270], all of which reproduce the characteristics of the X-ray measurements. Electrochemical oxidation of $\text{ArP}=\text{C}=\text{PAr}$ and $\text{ArP}=\text{}^{13}\text{C}=\text{PAr}$ is studied by EPR in tetrahydrofuran [271]. Taking HPCPH as a model compound, the structure of the radical cation assessed by extensive *ab initio* calculations revealed two rotamers with HPPH dihedral angles of 45° and 135° .

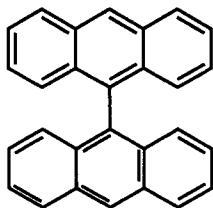
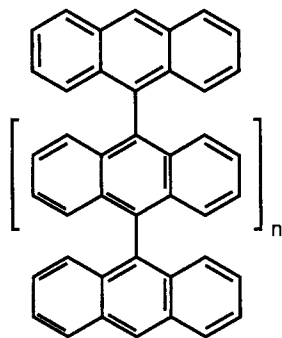
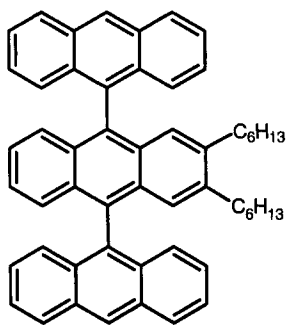
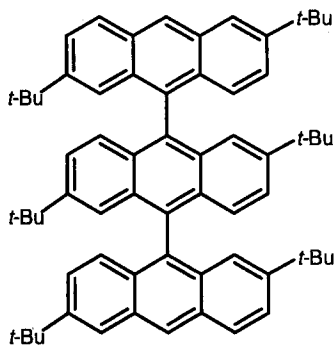
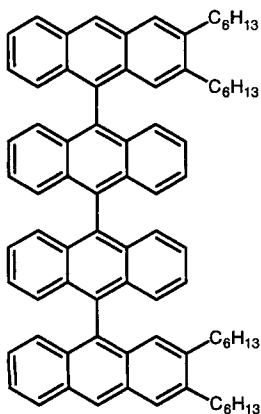
4.5 Radical Anions

4.5.1 π Systems

Radical anions of organic compounds have received much attention due to several reasons. The transition into a radical anion state activates organic molecules with respect to various transformations, which often are not typical for the starting systems and opens up new ways of their functionalization [272]. In particular, one electron reduction enhances nucleophilic and protophilic properties of organic compounds, facilitates their reactions with free radicals and makes their fragmentation and dimerization possible. There has been considerable interest in the design of organic materials that are suited in terms of electron transfer and electron storage [273]. An important aspect in the redox behavior of bis- and poly-electrophoric systems with vanishing conjugative interactions of π -subunits involves the possibility of intramolecular electron-hopping processes upon photoexcitation or upon thermal activation of a monocharged state [274]. Another factor controlling the electron transfer is the number of extra charges since successive reduction to di-, tri-, or even tetra-anion effects not only the prevailing ion-pair structure but also the spin multiplicity of the species and relative spatial arrangement of the subunits [275]. For charge storage purpose, a conjugative barrier with nearly independent redox active behavior of the subunits and density of localized charges is particularly favorable. Vanishing conjugative interaction of π -units and, thus, strongly inhibited spin-spin pairing, on the other hand also occur in organic high-spin systems, which play a central role in the search for organic ferromagnets [276]. While the 'unpairing' of the individual spins has usually been sought in π -conjugative compounds with the so-called 'non-Kekule' structures [276, 277], approaches towards high-spin molecules include the almost orthogonal alignment of spin-carrying subunits [278]. In agreement with theoretical studies [278b, 278c, 279], ferromagnetic coupling should be possible in the triplet dianion of **93** and in the polyanions of poly(9,10-

anthrylenes) **94** as long as orthogonality ($85\text{--}90^\circ$) of the subunits is retained upon charging [280].

EPR and ENDOR studies of the radical anions of **95**, **96** and **97** generated by chemical reduction are reported [281].

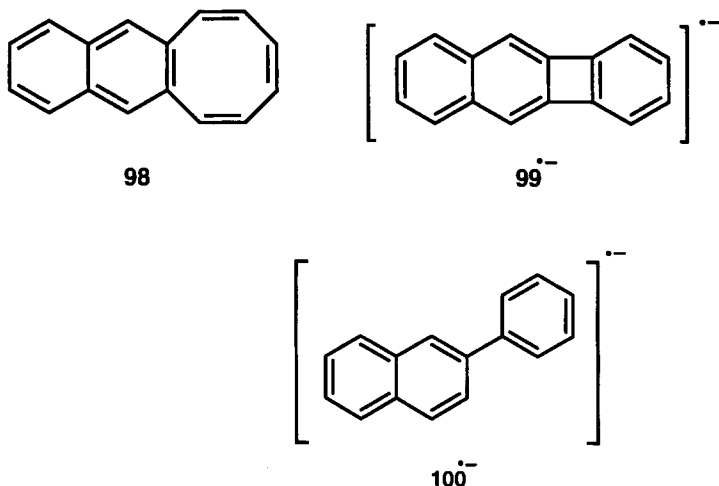
**93****94****95****96****97**

The intramolecular electron transfer in mono charged species of oligo(9,10-anthrylene)s between anthracene moieties sensitively depends on the special substitution pattern, on the radical concentration, and thus on the ion-pair conditions. The trianion of **95** and tetra anion of **96** are found in a quartet state and a quintet state. Temperature dependent EPR measurements of the dimer dianion revealed that the triplet state is thermally excited and the zero-field splitting loses its axial character (typically for orthogonal alignment) at low temperatures, pointing to increased orthorhombicity with decreasing temperature. The higher spin states of the oligomers are found to be thermally activated with 120 cal mol^{-1} for the doublet-quartet ($S = 3/2$) transition and 180 cal mol for the quintet-singlet ($S = 2$) transitions. Electrochemically generated 9,9'-bianthryl (BA) and 10,10'-dimethoxy-9,9'-bianthryl (DA) radical anions have been investigated by means of UV-Vis and EPR spectroscopy. Unpaired electron of the radical anion is localized on one of the anthracene subunits with large counter ions, tetrabutyl ammonium. The rate constants for the intramolecular electron exchange reactions were measured by EPR line-broadening effects, $(4.2 \pm 0.3) \times 10^7 \text{ s}^{-1}$ and $(2.2 \pm 0.3) \times 10^7 \text{ s}^{-1}$ for $\text{BA}^{\bullet-}$ and $\text{DA}^{\bullet-}$ in DMF at 298 K, respectively [282].

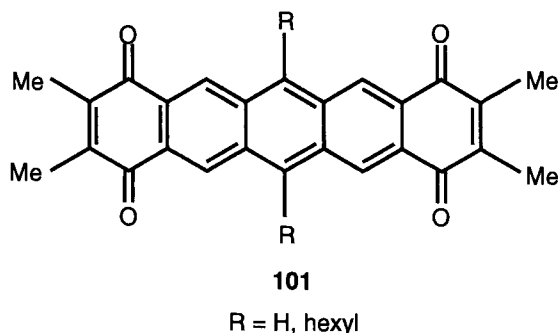
UV-Vis, ^1H and ^{13}C NMR study of monometallic salts of 9,10-dihydroanthracene and its 9,10-disubstituted derivatives in THF, showed lithium 9-phenyl-9,10-dihydroanthracene-9-ide, lithium 9,10-dimethyl-9,10-dihydroanthracenide and lithium 9,10-diphenyl-9,10-dihydroanthracenide exist as a solvent separated ion pair (SSIP). Sodium, potassium, rubidium and cesium 9,10-dihydroanthracenides, 9-methyl-9,10-dihydroanthracene-10-ides and 9-cyano-9,10-dihydroanthracenides exist as contact ion pairs (CIP) in solution. A model, taking into account the geometry and charge distribution, for the transition of CIP of alkali metal salts of 9,10-dihydroanthracene and its derivatives into SSIP is proposed [283].

Reduction of cyclooctatetraenes by electrolysis or with alkali metals yields essentially planar radical anions [284], and dianions. X-ray crystallographic structure determination of the potassium salt of 1,3,5,7-tetramethylcyclooctatetraene dianion in diglyme revealed the eight membered ring in a planar conformation with an average C-C bond length of 1.407 \AA [285], further substantiated by ^1H NMR results [286]. In the electroreduction of dibenzo[*a,e*]cyclooctene [287], the first reduction step (corresponding to the conversion of the tub-shaped parent to planar radical anion) was found to be slower than the second step leading to the planar dianion. The ^1H NMR spectra of the dianion in solution showed the protons at the cyclooctatetraene ring, shifted to lower field than the corresponding proton peaks in the neutral compound [288], behavior characteristic of an induced ring current in the cyclooctatetraene ring, as occurs in aromatic molecules and suggests strong electron delocalization over the ring. EPR and thermodynamic studies for the reduction of benzocyclooctene and cycloocta[*b*]naphthalene [289], with potassium in hexamethylphosphoric triamide (HMPA), also point to the planarity of the corresponding radical anions and dianions. A set of structurally different radicals has been detected by EPR in the reduction of cycloocta[*b*]naphthalene **98** by potassium in 1,2-dimethoxyethane [290]. In the first step, an apparently symmetry-forbidden ring closure leads to benzo[*b*]biphenylene **99** $^{\bullet-}$, subsequent reduction leads to 2-phenylnaphthalene radical anion **100** $^{\bullet-}$. Finally, the EPR spectrum of the radical anion of

a compound tentatively proposed to be dipotassium salt of dibenzoheptafulvene was observed.



Several EPR investigations of the radical anion of double-layered [2.2]paracyclophane for the study of electron transfer between the two aromatic rings and the effects of the counter ions on the spin distribution is reported [291]. In a thorough EPR study of conjugated quinone and imide radical anions, Miller et al. [292] generated electrochemically the alkyl substituted 1,4,8,11-pentacenetetron radical anions **101**^{•-} in dimethylformamide and dichloromethane solutions containing 0.1 M tetrabutylammonium tetrafluoroborate. Results indicate that at room temperature the unpaired electron is equally displaced over both quinone units (electrophores) however, EPR spectra at lower temperature clearly indicated a localization of the unpaired electron on one quinone unit of the planar conjugated pentacene skeleton. As a result of this and other findings the question of whether these radical anions might be thought of as mixed-valence species was considered.

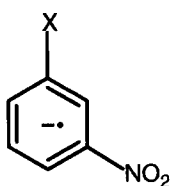
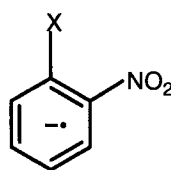


The CV of the paracyclophanes containing one quinone unit showed reversible one-electron reduction step similar to the reference compound 2,5-dimethyl-1,4-

benzoquinone. The higher reduction potential of the paracyclophane compared to the parent quinone indicates that the linked 1,4-phenylene moiety acts as an additional electrophore [293]. Three types of tetrone radical anions in which two 1,4-benzoquinone units are connected by ethane, [2.2]paracyclophane, and anthracene bridges are studied by EPR and ENDOR spectroscopy. The displacement of the unpaired electron over the two π moieties in the [2.2]cyclophane radical anions and a marked differences between the first and the second reduction potentials, are evidence for substantial intramolecular electronic interactions between the two electrophores. The existence of several types of ion pairs obtained by reduction of benzo-phenone and its derivatives by different methods has been evidenced by EPR [294]. In 4,4'-dinitrobenzophenone (DNBF) two types of anion radicals, characterized by different electron distributions have been observed [295]. A radical anion with delocalized odd electron is observed when the parent neutral molecule is reduced by the electrochemical method and by chemical methods with sodium methoxide in DMSO, on the other hand radical anion with localized electron (*p*-nitrophenyl fragment) is observed when the concentration of sodium methoxide is larger than 10^{-1} M in the same solvent and when the alkali metals in ethereal solution is employed. On the other hand, a mixture of electronically symmetric and asymmetric ion pairs is obtained by adding dimethylsulfoxide (40 %) to a solution of the ion-pair $\text{DNBF}^{\bullet-}, \text{K}^+$ in 1,2-dimethoxyethane and the superposition of the corresponding EPR spectra is observed. Radical anions of benzophenone, 4,4'-dinitrobenzophenone and 4-nitrobenzophenone generated by reduction with alkali metals (Li, Na, K) showed hindered rotation of the two rings on the EPR time-scale in the temperature range explored [296]. A four-site exchange model is employed to obtain the best fit of the experimental spectra for systems with symmetric spin distribution while a two-site exchange model is used for systems with spin-distribution localized only on one *p*-nitrophenyl fragment. Electron self-exchange rate constants of the nitrobenzene–nitrobenzene radical anion couple and their temperature dependence is measured by EPR-line broadening effects. The first order rate constants of these diffusionless reactions vary between 2.8×10^8 and $9.7 \times 10^8 \text{ s}^{-1}$ within a temperature range of 296–353 K [297]. Electron self-exchange reactions are good examples for the application of Marcus theory, since for this type of reaction the driving force $\Delta G^\circ = 0$ and activation energy in the sense of Marcus reduces to $\lambda/4$ (λ is the total reorganization energy). Different redox couples with radical cations [298] and radical anions [299] are known.

Radical anions of haloaromatic compounds are proposed to be intermediates in different type of reactions. Their fragmentation rates, determined electrochemically [300] or by pulse radiolysis [301] range from 10^{10} s^{-1} for phenyl halides to 10^{-2} s^{-1} for some halonitrobenzenes. The rate of the reaction for some aryl halide radical anions is too high to be measured electrochemically, the fragmentation of more stable radical anions such as those of 1-bromo- and 1-iodoanthraquinone [302], *p*-[303] and *m*-bromo- [304] and *p*- [303] and *m*-chloronitrobenzenes [304] occurs at considerably lower rates and the reaction is favored from their photoexcited state. Aryl halide radical anions may present σ – π 'orbital isomerism' depending on the orbital symmetry of their singly occupied molecular orbital [305], a proposal derived from theoretical and experimental evidences [306]. The isomerism is possible

when the excitation of the unpaired electron from the singly occupied to a low lying unoccupied MO of different symmetry, give rise to a species that differ in geometry from the initial state, both being different local minima on the ground state surface [307]. The π - σ isomerization of these radical anions is interpreted in terms of an intramolecular electron transfer (intra-ET) from the π -system, corresponding to the generally more stable and initially formed radical anions, to the σ^* C-halogen bond. From the two possible radical anions, it is proposed that only the σ dissociates into an aromatic radical and the anion of the leaving group [306a]. A relatively limited number of theoretical studies are known for haloaromatic radical anions [308], recently, a theoretical inspection of the potential surface of the radical anions of halobenzenes, halobenzonitriles and *o*-, *m*-, and *p*-haloacetophenones is reported [309]. It is proposed that the difference in the energy between both radical anions could be correlated with their experimental fragmentation rates, considering the intra-ET from the π to the σ system as the limiting step of the cleavage reaction. An AM1 study of the radical anions of *o*-, *m*-, and *p*-halonitrobenzenes in relation to their σ - π orbital isomerism and energy of their interconversion is carried out by Pierini et al. [310]. Based on the calculated energy of their interconversion, the intramolecular thermal electron transfer from the π -system to the $\sigma^*_{\text{C-X}}$ bond involved in the fragmentation of the intermediates into an aromatic radical and the anion of the leaving group occurs with considerable energy for the *p*-, *m*-, and *o*-chloronitrobenzenes (**102a-c**) and the *p*- and *m*-bromo (**103a,b**) derivatives. On the other hand, the intramolecular thermal electron transfer is favored for the *p*-, *m*-, *o*-iodo (**104a-c**) and *ortho* bromo (**103c**) derivatives.

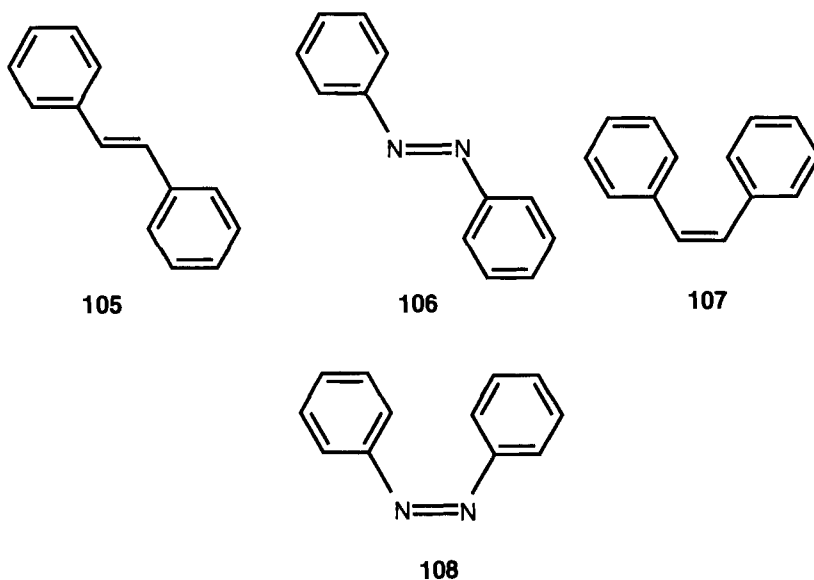
**102a** X = Cl**103a** X = Br**104a** X = I**102b** X = Cl**103b** X = Br**104b** X = I**102c** X = Cl**103c** X = Br**104c** X = I

The loss of the halide anion from *p*-chloronitrobenzene and *p*-bromonitrobenzene is accomplished by dual photochemical and electrochemical activation [303], the mechanism being absorption of light by electrogenerated anion radicals $[\text{X-C}_6\text{H}_4\text{-NO}_2]^{·-}$ (X = Br, Cl) followed by halide loss and, ultimately, the formation of nitrobenzene radical via photo ECE mechanism [311]. In contrast the dual activation of *p*-cyanonitrobenzene, *p*-dinitrobenzene, phenyl 4-nitrophenyl sulfone, methyl 4-nitrophenyl sulfone, phenyl 4-nitrophenyl sulfoxide or methyl 4-nitrophenyl sulfoxide failed to induce the leaving of any substituent [304]. It is presumed that in cases where no fragmentation occurs, the excitation energy of the radical anion is lost through collisional deactivation by the solvent. An interesting controversy has

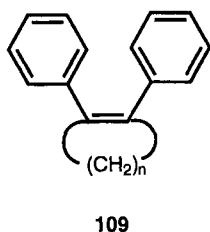
appeared concerning (in part) the mechanism of nucleophilic aromatic substitution reactions of aromatic compounds, as dinitrobenzenes, nitrobenzophenones, nitrobenzonitriles, polyfluoronitrobenzenes etc., able to stabilize radical anions [312]. Abe and Ikegami [313] observed radical anions in reaction of dinitrobenzenes with OH^- in aqueous DMSO that led to the postulation of radical anions as intermediates. Sammes et al. [314] studied the displacement of nitro groups from *p*-dinitrobenzene and other nitro compounds by various phenoxide in DMSO and concluded the radical nature of these reactions. Shein et al. [315] demonstrated the formation of *p*-dinitrobenzene radical anion on reaction with a series of anion nucleophiles, among them phenoxide ion. Electrochemical studies by Gallardo et al. [316] indicate that the reactions of *p*-dinitrobenzene and *p*-nitrobenzonitrile with phenolate or phenol in DMF show radical features and cannot be attributed to the direct reaction of the nucleophile on the substrate radical anion. Reductive activation is feasible in reaction of *p*-dinitrobenzene with phenol, however, substrate radical anion formation is not responsible for it. In radicals derived from 2,4-dinitrophenol, the localization of the spin density is found to change from the *ortho* nitro group to the *para* nitro group on charging from the radical anion to radical dianion [317]. A significant change in electronic structure of radical anion may occur in transition from aprotic to protic media. In radical anions of 1,3-dinitrobenzenes [318] and 2,7-dinitronaphthalene [319] in protic solvents, the strong solvation of one nitro group through hydrogen bonding causes an asymmetric distribution of the spin densities on the nitrogen atoms, inducing slow intramolecular electron exchange between the two nitro groups. The rate constants determined from line broadening effects are in the fast region range ($K \approx 10^9 \text{ s}^{-1}$) in aprotic solvents while in alcohols the exchange is slow ($K \approx 10^6 \text{ s}^{-1}$) on the EPR time scale [318, 319]. The position of the OH group is a decisive factor in the variation of the rate constant with the deprotonation of the radical anion, variation being large when the OH group is in the *ortho* position to one nitro group. The EPR spectra of radicals derived from 4,6-dinitrobenzene-1,3-diol showed no line-broadening effects in the experimental range of temperatures [320]. In the radical-anion and radical-dianion, the electron is localized mainly in one nitro group, while in the radical trianion the spin density is evenly distributed over the two nitro groups. ΔG^* values range from 12.6 kJ mol^{-1} for radical dianion of 2,6-dinitrophenol to 46.0 kJ mol^{-1} for radical dianion of 3,5-dinitrophenol.

Stilbenes are an important class of compounds with a broad range of applications in basic and applied research [321]. The isoelectronic (*E*)-stilbene **105** and (*E*)-azobenzene **106** belong to the basic organic compounds of which radical anions were first investigated by EPR 30 years ago [322], and since then repeatedly studied by EPR and ENDOR techniques [323]. Radical anions of **107** and **108** are not persistent because they rapidly isomerize to **105** and **106** respectively. Nevertheless, **107** $^{\cdot-}$ could be characterized by hyperfine data under specific conditions [324], whereas its azo counterpart **108** $^{\cdot-}$ has hitherto escaped detection by EPR.

Sterically congested stilbenes such as 2,2,5,5-tetramethyl-3,4-diphenylhex-3-ene has received growing attention [325]. The preparation and characteristic properties of the radical anion and dianion is investigated by EPR and the spectra analyzed using DFT techniques [326]. In radical anion the steric effect (steric repulsion of *tert*-butyl groups) and electronic effects just about balance as rotation occurs about

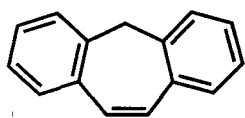


the central double bond, on the other hand, on addition of a second electron, no residual electronic stabilization exists and the most stable conformation is dictated by the steric effect to be the 90° twisted form. In 1,2-diphenylcycloalkene **109**, when the alkene is propene ($n = 1$) [327], butene ($n = 2$) [328], pentene ($n = 3$) [328b], or hexene ($n = 4$) [329], the (*Z*) configuration of $n = 3$ is fixed by incorporation of the central C=C bond into the cycloalkene ring.

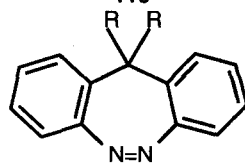


The π -spin distribution in the radical anions of stilbene series is only moderately sensitive to deviations of the π -system from planarity, the radical anions of the azobenzene series respond to steric strain by shifting the π -spin population from the benzene rings to the azo group. This is impressively demonstrated by similar hyperfine data for **110** $^{\cdot-}$ and **111** $^{\cdot-}$ which contrast with the strongly differing one for their azo counterparts **112** $^{\cdot-}$ and **113** $^{\cdot-}$, as well as by the corresponding values for sterically highly hindered **114** $^{\cdot-}$ [330].

The redox properties of free radicals are essential parameters for predicting whether electron transfer to molecules may trigger radical or ionic chemistry [331]. If these redox properties can be converted into standard potentials, that may then

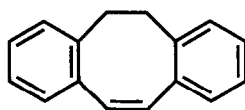


110

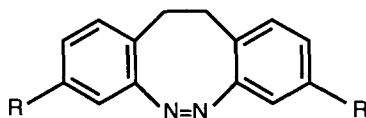


112

R = H, D

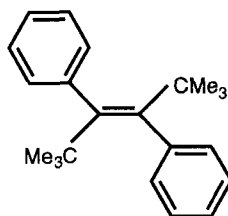


111



113

R = H, D

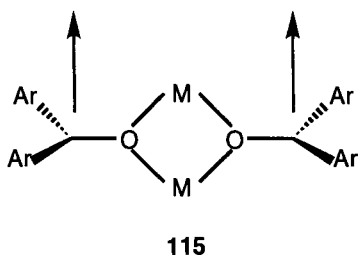


114

be used to estimate other thermodynamic parameters, such as pK_a and bond-dissociation free energies [332]. Several direct or indirect electrochemical methods are used for investigating reduction characteristics of free radicals, the simplest ones involve the recording of the oxidation wave of the anion in steady-state or CV [333]. An indirect electrochemical method, based on redox catalysis [334] has also been applied to determine reduction potentials of transient radicals [335]. Two photo-electrochemical methods have been proposed for investigating the reduction characteristics of transient free radicals [336]. One may also produce the radicals by continuous irradiation and use fast electrochemical techniques, such as normal and reverse pulse voltammetry at an ultramicro electrode to obtain the radical standard potential, at least in favorable cases, such as the oxidation of the diphenylmethyl radical and the reduction of the diphenyl cyanomethyl radical [337]. However, one limitation of this method is the possible superposition of large photocurrents arising from the photo injection of electrons from the electrode into the solution. Theoretical expressions are known that relate half-wave potential and shape of the radical polarograms to the thermodynamics and kinetics of various reactions in which the radical and the anion resulting from its reduction may be engaged. The 9-anthrylmethyl, diphenylmethyl, benzyl, and 4-methylbenzyl radicals were generated by reduction of the corresponding chlorides by electron photoinjection in laser pulse experiments. The variation of the half-wave potential with time is used as a source

of mechanism and reactivity information, and the shape of the polarograms was used as an additional diagnostic criterion. The results are compared with data obtained by other techniques and the reactivity parameters are discussed with the help of density functional quantum chemical calculations [338].

Organic high-spin molecules are basic materials for the design of organic ferromagnets [339]. Unfortunately, most of the known stable high-spin molecules are not suitable for obtaining organic based ferromagnetic materials due to antiferromagnetic intermolecular interactions which compensate the intramolecular spin alignment in the bulk material. A promising category of compounds for the development of macroscopic high-spin systems is the class of aromatic ketone radical anions of type **115**, since both intra- and intermolecular high-spin coupling seems possible.



Hou et al. [340] confirmed earlier conclusions arrived at by Hirota and Weissman [341], that alkali metal aromatic ketone radical anions form strongly coupled biradicals in which the metal acts as a spin-carrying center. The combination of fluorenone and benzophenone entities within a molecule seems attractive in this regard, because of their well known tendency to form stable radical anions. The mono- and poly-anions of some mono-, di-, and tetraketones containing fluorenone and benzophenone moieties have been studied by NMR and CV [342]. Alkali metal anion radicals of fluorenone generated by electron transfer from an alkali metal naphthalene radical anion exhibit markedly lower molar paramagnetic solvent shifts than those generated by direct reduction with an alkali metal. NMR data combined with those obtained by CV, indicate that polyketones possessing fluorenone moieties connected through isophthaloyl 'spacers' are promising system for the preparation of high-spin organics and electrophores.

Electron transfer to endoperoxides and peroxides results in the cleavage of the weak oxygen–oxygen bond [343]. This process proceeds in peroxides and endoperoxides, generally by dissociative ET mechanism, in which ET and O–O bond fragmentation are concerted. However, in case of *tert*-butyl-*p*-cyanoperbenzoate there is evidence for transition to a stepwise mechanism with formation of the intermediate radical anion [343c]. Such mechanistic studies are important because ET processes of peroxides and endoperoxides play a key role in their activity in chemical and biological systems [344], for example, Fe^{III}-promoted electron transfer reduction of the O–O bond in the antimalarial endoperoxide artemisinin, its semi-synthetic derivatives has recently been shown to be the key step in its antimalarial activity [345]. A first report of the observed reactivity from the alkoxy radical in the 'O–R–O[•]' distonic radical anion formed in a heterogeneous dissociative ET, namely 1,2-phenyl

migration (*o*-neophyl rearrangement), has appeared recently [346]. This *o*-neophyl-type rearrangement of a phenyl group to the alkoxy radical fragment occurs in the distonic radical anion formed by electrochemical single ET to the O–O bond in the endoperoxide 9,10-diphenyl-9,10-epidioxyanthracene. This rearrangement occurs at the expense of the reduction of the alkoxy radical portion of the distonic radical anion. Systems such as these can be developed as kinetic probes of the rate of second heterogeneous ET. Kinetics of both intra and intermolecular electron transfer reactions are of much interest and importance, as these are the fundamental chemical steps in numerous biological processes. In particular, the understanding of intramolecular ET has evolved to a high degree [347]. Most of the studies of intramolecular ET focus on photoinduced charge separation, involving different donor and acceptor moieties to achieve a suitable driving force ΔG° [348]. Nelsen et al. [349] studied the self-exchange within various hydrazine derivatives by optical and EPR methods. The kinetics of intramolecular electron exchange (IEE) in the radical anions of 1,3-dinitrobenzene (1,3-DNB) is studied by EPR spectroscopy. The rate constants, K , determined are ca 10^6 s^{-1} in alcohols and 10^9 s^{-1} in aprotic solvents and the reaction was found to be adiabatic and uniform in the sense of classic transition state theory [350]. It is usually believed that the absence of direct resonance between the donor and the acceptor is necessary for the occurrence of alternating line-broadening effects caused by IEE in the EPR spectra of free radicals. The examples known in the literature, where the two groups are either in non-conjugative *meta* positions, as in the radical anions of 1,3-dinitrobenzene and 2,7-dinitronaphthalene [351], or sterically forced out of planarity, as in the radical anion of dinitroindurene [352], seems to confirm this behavior. Line broadening effects due to intramolecular electron exchange are recently observed in the EPR spectra of 2,6-dinitrophenolate radical dianion, where the resonance structures can be drawn delocalizing the electron through the two nitro groups [353]. The rate constants of the intramolecular electron exchange reaction in the 1,4-dinitrobenzene radical anion (1,4-DNB) in linear alcohols are determined from the alternating line-broadening effects in EPR spectra [354]. Results demonstrate the role of solvent dynamics on the kinetics of intramolecular electron exchange in 1,4-DNB radical anion. It obeys a diffusive adiabatic regime, while the same reaction in the isomeric 1,3-DNB radical anion in alcohol follows a uniform adiabatic reaction behavior. This difference reflects a faster reaction in the 1,4-DNB radical, the ET occurs on a time scale where solvent-relaxation processes controls the reaction rate. On the other hand in 1,3-DNB radical, solvent relaxation being much faster than the ET step, does not effect the reaction dynamics, 1,4-DNB radical anion in aprotic solvents do not show evidence of alternating line broadening effects [355]. In aprotic medium, the fraction of transferred charge is substantially lower than in alcohols, due to a lower specific solvation. Since, in most aprotic solvents, the values of $1/\Gamma$ (where Γ is the Longitudinal correlation time) are higher than in alcohols, the reaction is too fast to exert discernible alternating line-broadening effects on the EPR spectra.

Despite the simmering debate within the community of physical organic chemists over the scope and importance of electron transfer in nucleophilic aliphatic substitution [356], evidence continues to accumulate that electron transfer may play a role

in the mechanism for this substitution [357], particularly when the electrophiles are sterically hindered alkyl iodides. Although S_N^2 mechanisms are known to exhibit significant steric constraints, of which Walden inversion is the most profound, evidence exists that electron transfer processes may have steric components as well [357c]. For methyl iodide and 9-phenylfluorenyl anion, backside approach is sterically feasible; whereas with the same nucleophile and neopentyl iodide, it is not, and photo activation is required. Conversely, for the 9-mesitylfluorenyl anion, backside approach is possible but not to within an S_N^2 bonding distance. Spectral evidence for single electron transfer in Nucleophilic aliphatic substitution is recently observed by Tolbert et al. [358]. The photochemical generation of closed-shell ions is a topic of current interest in organic photochemistry [359]. Carbanions are one of the most common reactive intermediates in organic synthesis [360], and hence the photo-generation of such ionic species contributes to progress in mechanistic organic chemistry. Only a few examples are known for the photochemical formation of carbanions [361], most of which are based on the photodissociation of carboxylic acids. A related reaction is the anodic oxidation of carboxylate ions (RCO_2^-), i.e. the Kolbe reaction [362], in which carbon centered radicals (R^\cdot) are formed via decarboxylation of carboxyl radicals (RCO_2^\cdot). These carbon radicals undergo dimerization or further oxidation, yielding R-R or R^+ , respectively. Photoinduced electron transfer reaction of carboxylic acids also gives carbon-centered radicals via decarboxylation [363]. In this reactions, carbon radicals are formed together with sensitizer radical anion, and hence the formation of carbanion might be expected if an effective electron transfer between them takes place. However, the reported photoinduced electron transfer reactions yielded a mixture of radical-sensitizer adducts and other radical coupling products [364]. Direct photolysis of carboxylate anions yielded carbanions [365] but their spectroscopic observation has been achieved only for carbanions stabilized by electron-withdrawing substituents e.g. *p*-nitrobenzyl anion [366] or by resonance with a carbonyl group [367]. In order to develop a novel method for the photochemical generation of carbanions, photo-induced electron transfer reactions of carboxylate salts is recently studied by Sawaki et al. [368]. They succeeded in generating carbanion from carboxylate ions by photoinduced electron transfer. This reaction is potentially useful in the conversion of arylacetic acids (RCO_2H) to RH and also as a method to generate carbanions photochemically. The key process in the formation of carbanion is the electron transfer from sensitizer anion radical to radical intermediates proceeding in-cage and depending on the free energy changes. The influence of the solute-solvent interaction through hydrogen bonding was reported recently by Chan and Chan [369] and Tominaga et al. [370]. They reported that the hydrogen bonding between the OH or NH_2 group of a solute molecule and polar solvents makes the diffusion process very slow. Radicals are interesting systems for diffusion studies as well as for elucidating the mechanism [371] and dynamics [372] of chemical reactions. Unfortunately, until recently, only a few diffusion constants (D) of radicals have been reported [373], because of technical difficulties. However, Terazima et al. [374] succeeded in measuring the D values of many intermediate radicals which appear during photochemical reactions by the transient grating (TG) method. Results indicate that transient neutral radicals created by photo induced hydrogen abstraction of quinones and *N*-heteroaromatic molecules diffuse much slower than their parent

molecules. The same group also investigated the viscosity (η) dependence [374a], the solute radius (r) dependence [374c] and the temperature (T) dependence [374d] of the D values of such radicals. The difference in D between the radicals and the parent molecules became larger with increasing η , $1/r$, or $1/T$, tendency similar to those of ions [375]. Slow diffusion of radicals was observed not only in polar solvents but also in non-polar solvents and in aprotic solvents [374b], and hence hydrogen bonding between the OH or NH group of the radical and the solvents cannot be the origin of the slow diffusion. Therefore, contrary to ions or hydrogen bonding systems, the origin of the slow diffusion remains unclear. The mobilities of the photochemically produced intermediate radical cations and anions probed by the time of flight (TOF) technique is reported by Houser and Jarnagin [376], Freeman and coworkers [377], and Albrecht and coworkers [378]. Study revealed that D of the ion radicals are smaller than those of neutral molecules of similar shapes and sizes. Freeman and coworkers attributed the origin of the slow diffusion to the electrostrictive drag by the charged species and dimerization for some compounds. Albrecht and coworkers found that D of the charged radicals can be well reproduced by the Stokes–Einstein (SE) equation. The result is in good agreement with the SE relation and is similar to that found for neutral radicals. However, if one wants to extract the effect of the charge or the unpaired electron by comparison of D of the charged radicals determined by this method with those of closed shell molecules, one should use D of closed shell molecules measured by other methods under different conditions. Since D is very sensitive to environmental and experimental conditions, it makes accurate comparisons very difficult. With the use of the TG method, D values of stable molecules can be measured simultaneously with those of the transient species. For example, Terazima et al. determined D of a cation radical and its parent molecule, N,N,N',N' -tetramethyl-*p*-phenylenediamine (TMPD), by the TG method under exactly the same conditions [379]. The results showed that the cation radicals diffuse only half as quickly as the parent molecule in ethanol, the contribution of the charge and the unpaired electron could not be separated from this measurement. The translational diffusion constants of the ketyl anion radicals, the neutral radicals, and the parent stable molecules is successfully measured under same conditions by the transient grating method [380]. Both the neutral and anion radicals diffuse slower than the parent molecules. The values are compared in detail in wide range of solvent viscosities, solute sizes and temperatures.

Reverse electron transfer (RET) process in photo induced ET is typically viewed as undesirable energy-wasting steps. Indeed, a considerable amount of work has been directed towards strategies to increase the efficiencies of photoinduced electron transfers by decreasing the rate of RET, or increasing the rates of useful competing processes such as ion-pair separation or follow-up ion radical interactions [381]. Recently an alternative approach enabling RET to give useful products, namely dissociative reverse electron transfer (DRET), is much under investigation. For efficient DRET, a triplet ion radical pair would be more useful than a singlet pair, several examples of reactions via triplet ion radical pairs are described in literature [382]. On the basis of CIDNP experiments, Wong and Arnold [383] proposed a mechanism involving ring opening of 1,2-diphenylcyclopropane (DPC) radical cation to a 1,3-cation radical, followed by RET to a triplet 1,3-biradical, with subsequent intersystem crossing and ring closure. On the basis of additional CIDNP

experiments, Schilling and Roth showed that configurationally stable *cis* and *trans*-DPC cation radicals are involved in these reactions and that the isomerization involves RET in the triplet ion radical pair leading to formation of the triplet biradical [384]. However, biradical formation could occur by RET leading to a locally excited triplet DPC, which subsequently undergoes bond breaking to form the triplet biradical or alternatively, the biradical could be the direct product of RET. These two fundamentally different mechanisms cannot be distinguished by CIDNP. Recently Farid et al. provided direct identification of the intermediates involved in the electron transfer photosensitized isomerization of DPC and demonstrated that the isomerization occurs by DRET with several triplet sensitizers and bond fragmentation can occur with 100 % quantum efficiency [385].

In bimolecular ET between freely diffusing donors and acceptors in solution, the nuclear prearrangement of the reactants in the transition state with its critical donor/acceptor distance and orbital overlap-limits the intrinsic rate of the electron exchange [386]. As a result all theoretical calculations of ET rate constants invoke far-reaching assumptions on the relative orientation and electronic interaction of the donor and acceptor in the transition state [387]. Owing to intrinsic life time of transition states, their direct (spectroscopic) observation constitutes an experimental challenge [388]. However, attempts have been made to predict structures and degrees of donor/acceptor bonding in various ET transition states by different theoretical methods [389]. Electronic coupling that promotes electron transfer between redox partners is revealed experimentally by charge-transfer interactions extent in the donor/acceptor precursor or encounter complex prior to ET, and the degree of charge transfer as defined by Mulliken theory can be taken as a measure of the donor/acceptor bonding [390]. For example, electron transfer from arene donors to photoactivated quinones occurs via encounter complexes with substantial charge transfer bonding, postulated by the observation of near-IR absorption bands and relatively high formation constants [391]. Steric effects on the kinetics of ET from hindered and unhindered arene donors to quinone acceptors and their temperature, solvent, and driving-force dependence reveal a structure-induced (mechanistic) changeover [392]. Unhindered donors undergo inner-sphere electron transfer owing to the strong electronic coupling of donor and acceptor in a well defined encounter complex preceding the ET transition state. On the other hand, hindered donors show no (kinetic or spectroscopic) evidence for a discrete encounter complex in the preequilibrium step, and the kinetics follows outer-sphere ET behavior expected for weakly coupled donors and acceptors. Although the comparative study of hindered and unhindered electron donors establishes a clear cut (experimental) distinction between outer-sphere and inner-sphere electron transfers, we believe that there will generally be a broad borderline region between the two mechanisms.

4.5.2 Alkenes

The radical anions of buta-1,3-diene and its methyl substituted derivatives are studied electrolytically in liquid ammonia [393] or in tetrahydrofuran [394]. In general, reaction of these compounds with an alkali metal in ethereal solvents fails to

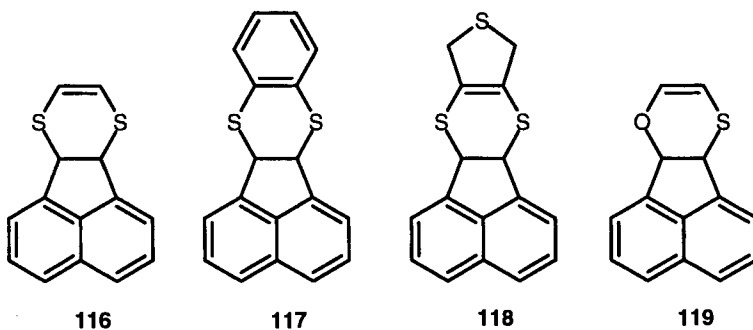
yield a persistent radical anion, because of rapid polymerization to rubber-like products [395]. However, it has been shown recently [396] that these processes can be avoided by bulky substituents. Radical anions of various aliphatic α -substituted nitro compounds have been proposed as reactive intermediates in radical-radical-anion chain-substitution reaction. The mechanism was termed S_{RN}^1 (substitution radical-nucleophilic, first order) by Bunnett [397] in his studies on aromatic substrates, while the same mechanism for aliphatic nitro compounds was elaborated by Russell [398] and Kornblum [399]. A growing number of anions have been shown to participate in S_{RN}^1 reactions with α -substituted nitro compounds e.g. $R_2CNO_2^-$, RSO_2^- , RS^- , N_3^- , SO_2^{2-} [400], $(RO)_2PO^-$ [401], and carbanions. Other mechanisms including these radical-anion intermediates have also been reported e.g. S_{ET}^2 (substitution, electron transfer, second order) [402], and reduction by dihydrobenzyl nicotinamide [403], trialkyltin hydride [404], or methane thiolate [405]. All these mechanisms have an initial step of electron capture by the α -substituted nitro compounds to yield an intermediate radical-anion, with sufficient life time to allow reaction with other species. From the viewpoint of EPR, electron capture by RNO_2 (R = alkyl, aryl) molecules to give $RNO_2^{\bullet-}$ radical anion is well established, both in solid state [406] and liquid phase [407] studies. A range of radical-anions, $[Me_2C(X)NO_2]^{\bullet-}$ with X = Br, Cl, SCN, NO_2 , CN, PO_3Et_2 , CO_2Et , COMe, SO_2Me , SO_2Ar , and Me have been identified by EPR and are found to be long lived at low temperatures [408]. Results indicate that one or more of at least three pathways are followed on the reaction of $Me_2C(X)NO_2$ with electrons; (a) electron-capture to yield a stable radical anion, $[Me_2C(X)NO_2]^{\bullet-}$, (b) dissociative electron capture to yield $Me_2C^{\bullet}NO_2$ and X^- (for X = Br, Cl, SCN), (c) dissociative electron-capture to yield $Me_2C^{\bullet}X$ and NO_2^- (for X = CN, NO_2 , PO_3Et_2 and CO_2Et).

It has been proposed that the reactions which occur remote from and uninfluenced by the charge center (charge-remote reactions) can occur following collisional activation of even electron organic anions in the gas phase [409]. Charge remote loss of a radical from an $(M-H)^-$ ion is sometimes observed when the product formed is a stable radical anion [410], however, evidence in favor of the loss of (even electron) neutrals commonly occurring by charge-remote processes from even electron anions is not strong [411]. Acetylene, with its linear structure in the ground state is expected to have a *trans*-bent structure in its electronically excited state [412]. Theoretical calculations have predicted that the acetylene radical anion has a *trans*-bent structure, but the energy difference between the *trans* and *cis* is as small as $7.4 \text{ kcal mol}^{-1}$ [413]. Muto and his collaborators first reported the acetylene radical anion trapped in a 3-methylpentane matrix at 77 K. Consistent with the theoretical predictions, the *trans*-bent structure was concluded based on the EPR data [414]. On the other hand Manceron and Andrews reported an IR study on an Li-acetylene complex anion radical generated in an argon matrix and found that the acetylene moiety has a *cis*-bent structure [415]. Kasai observed the EPR spectrum of the same complex anion and confirmed the *cis*-bent structure [416]. An EPR and MO study by Itagaki et al. [417] to elucidate the electronic structure of methylacetylene radical anion generated in glassy 2-methyltetrahydrofuran matrix by ionization radiation at 77 K. The spectrum was dominated by a large and slightly anisotropic 1H hyperfine splitting of ca 4.53 mT due to one ethynyl proton.

With the help of a selectively deuterated methylacetylene, the anisotropic hyperfine couplings are determined. Comparison of experimental values with the theoretical ones calculated by *ab initio* MO and INDO methods, a *trans*-bent structure is concluded. The formation of methylacetylene radical anion is also confirmed by an electron absorption spectroscopic study.

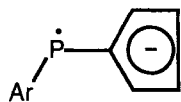
4.5.3 Heteronuclear Radical Anions

Polycyclic arenes, e.g. perylene, have been widely studied in the preparation of molecular conductors, some of the radical cations show semiconducting or metallic behavior [418]. Introduction of one or more sulfur atoms at the periphery of such systems, i.e. thia arene derivatives, generally imparts greater stability to the radical-cation salts, coupled with increase conductivity [419]. For compound **116**, X-ray structure studied have been reported on the pure donor and some radical-ion salts [420].



Radical cations and anions of compounds **116**–**119** are characterized by EPR and ENDOR techniques [421]. The *g*-factors of the radical cations comply with the values for oxidized S-donors, whereas those of the corresponding anions are typically of reduced π -systems without heteroatoms. The new derivative 8,9-bis(methylsulfanyl)-acenaphtho[1,2-*b*][1,4]dithiine has emerged as a promising electron donor for the formation of crystalline charge-transfer complexes and radical ion salts, X-ray crystal structures have been obtained for its 1:1 complexes with TCNQ and Br₂TCNQ. In his extensive study of the UV spectra of organic thiocarbonyl compounds, Janssen [422] included some sodium dithiocarbamates based on primary and secondary aliphatic amines. The spectra in ethanol showed one weak band near 350 nm and stronger bands at 288 and 253 nm. The bands were interpreted with aid of calculations of Hückel type as an $n \rightarrow \pi^*$ and two $\pi \rightarrow \pi^*$ transitions. Multiple $n \rightarrow \pi^*$ transitions have been observed in 1,2- and 1,3-dithiones, and up to four bands assignable to $n \rightarrow \pi^*$ transitions were observed in UV spectra of tetra-thiaoxalates [423] and in CD spectra of chiral dithiooxamides [424]. In an attempt to locate $n_+ \rightarrow \pi^*$ transition in the dithiocarbamate anion and to obtain information about the polarization of the $\pi \rightarrow \pi^*$ transitions, Sandström et al. [425] studied UV and CD spectra of chiral dithiocarbamates. The UV spectrum is interpreted

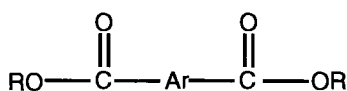
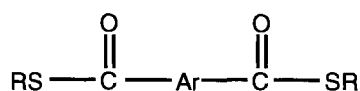
with the aid of CNDO/S calculations, and the CD spectrum with calculations by the Schellman matrix method. The CD spectrum showed a medium–strong positive band at 230 nm, however, the theoretical calculation predicted a negative sign for this band, and consequently no assignment for the 230 nm band was made. Except for 230 nm band, the calculations predict correct signs and qualitatively correct intensities for the CD bands between 200 and 400 nm in a narrow range of orientations of the 1-phenylethyl group with respect to the dithiocarbamate ion, and it is expected that the favored conformation falls in this conformational range. Low-coordinated trivalent phosphorus continues to attract attention in several fields of chemistry [426]. Reduction of systems containing a phenyl ring linked to the phosphalkene carbon [427], leads to radical anion whose phosphorus spin density is <0.5 , the unpaired electron being delocalized on both the phosphoethylenic bond and the phenyl ring. Owing to resonance stabilization of the cyclopentadienide ion, it is expected that incorporation of the phosphalkenic carbon in a cyclopentadiene ring appreciably modified the spin distribution by increasing the contribution of the phosphinyl mesomeric structure **120**.

**120**

EPR spectra of phosphafulvene and dibenzophosphafulvene radical anions, formed by electrochemical reduction or by reaction on a potassium mirror are studied [428]. Ab initio calculations on model phosphalkene and phosphafulvene radical anions show that, in accord with the experimental results, the electronic structures of these two species are quite different; whereas the unpaired electron is delocalized on the whole $P=C(H)R$ moiety in the phosphalkene anion, it is markedly localized on the phosphorus atom in the phosphafulvene anion. The isotropic coupling constants obtained for diphosphaallenic radical anion $ArP=C=PAR^{*-}$ ($Ar = 2,4,6-(Bu^t)_3C_6H_2$) reflects the probability of unpaired electron mainly localized on two equivalent phosphorus atoms [429]. The interpretation is substantiated by considering the coupling constants calculated for the *trans*-like and *cis*-like isomers at the MP2 and MCSCF optimized geometries. In light of experimental and theoretical results it is proposed that the reduction of diphosphaallene gives a slightly asymmetric *trans*-like radical anion, which rapidly interconverts between two equivalent structures. Here, a comparison with the corresponding radical cation is worthwhile to be mentioned: Diphosphaallene derivatives [430] $RP=C=PR$ are electrochemically oxidized to radical cations with the unpaired electron located in a *p*-orbital with a spin population of ca 20 % at each phosphorus (ca. 20 %). Ab initio calculation on HPCPH revealed that oxidation is accompanied by a modification of the molecular geometry. Whereas the HPPH dihedral angle, θ_{HPPH} , is equal to 90° in the neutral molecule, the radical cation has two possible θ_{HPPH} values of ca 45° and ca 135° , corresponding to two isomers of similar energy.

Recently Alberti et al. [431] applied a multi-disciplinary approach involving CV, EPR, pulse radiolysis and MO calculations to investigate the radical ions resulting from the one-electron oxidation and one-electron reduction of bis(2,4,6-tri-*tert*-butylphenyl)-1,3-diphosphaallene. Results showed significant differences from those reported by Geoffroy et al. [429, 430] at both experimental (EPR) and theoretical (MO calculation) levels, the disagreement being particularly severe in the case of the reduction. A higher spin density on the phosphorus atoms is observed in the anion than in the cation, in agreement with the different nature of the SOMO in the two species predicted by UB3LYP calculations on the model compound diphenyl-1,3-diphosphaallene, which also predict for both ions the existence of *cis* and *trans* geometrical isomers, the latter being more stable. In both radical ions the unpaired electron is found mainly localized in the PCP moiety, namely in a π -allylic type MO in the cation and in a σ MO in the anion. The paramagnetic species detected by EPR upon electrochemical reduction of bis(2,4,6-tri-*tert*-butylphenyl)-1,3-diphosphaallene in THF has been identified as the bis(2,4,6-tri-*tert*-butyl-phenyl)-1,3-diphosphaallyl radical, the identification is supported by DFT calculations [432]. One and two electron reduction of bisdiazenes has provided access to non-classical, cyclically delocalized 4N/5e radical anions and 4N/6e dianions of high persistence [433]. EPR investigation on the relatively facile one-electron reduction of cycloaliphatic monodiazenes is reported [434]. Neutral and anionic cyanocarbons and azacyanocarbons show interesting optical, electrical and/or magnetic properties [435]. Although a great deal of chemistry is known for cyanocarbanions but their exist very few reports on azacyanocarbanions [436]. Electrochemical, spectrochemical and structural characterization of the tetraalkyl ammonium salts of the 1,1,2,5,6,6-hexacyano-3,4-diazahepta-1,5-dienedide anion $[(R_4N)_2(C_{10}N_8)]^-$; R = Et, Bu is reported [437]. 2,3-diazabicyclo[2.2.1]hept-2-ene and its derivatives have been the focus of numerous mechanistic studies concerned with the extrusion step (dinitrogen loss) and fragmentation, giving rise to radicals, diradicals and radical ions. The radical anions of both *E*- and cyclic *Z*-azoalkanes proved to be much more resistant to the extrusion of dinitrogen and so have been amply investigated by EPR and ENDOR spectroscopy [438]. Unlike azoarenes, such as azobenzene with a half-wave reduction potential of -1.38 V relative to the SCE, conversion of azoalkanes to their radical anions requires a highly negative voltage [439]. Radical anions of 2,3-diazabicyclo[2.2.1]hept-2-ene and its 18 substituted and tricyclic derivatives are characterized by EPR and ENDOR [440]. Structural modification reported lead to only minor changes in the geometry of the carbon framework of radical anion and do not substantially alter the π -spin distribution.

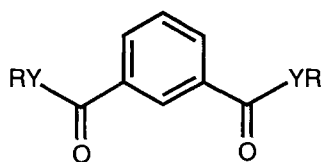
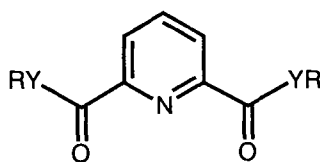
The voltammetric behavior of disubstituted alkyl pyridine and benzene esters **121** and several of their dithioic *S,S'*-diesters **122** analogs have recently been reported

**121****122**

Ar = pyridine or benzene, R = Me, Et or Pr

[441], as well as the identity and yields of the products obtained by bulk controlled potential electrolysis experiments in acetonitrile [442].

Bulk controlled-potential electrolysis experiments have shown that most of the (O) ester anion radicals decay via a simple bond cleavage mechanism to form carboxylate anions in very high yield, while the (S) ester radicals decay via a very complicated mechanism often involving aromatic substitution reactions [442]. Using CV, many of the compounds are shown to display chemically (and electrochemically) reversible behavior at slow scan rates, in the sense that the $i_p^{\text{ox.}}/i_p^{\text{red.}}$ ratios were close to one, indicating that the anion radicals formed were stable for at least several seconds and existence confirmed by EPR [442] and UV-Vis spectroscopy [443]. In contrast, other compounds, including the *meta*-substituted (O) and (S) diesters **123** and **124**, appeared to show chemically irreversible behavior at slow scan rates suggesting that the associated anion radicals of these compounds were much less stable and quickly decompose to other products.

**123****124**

Y = O, R = Me, dimethyl benzene-1,3-dicarboxylate

Y = S, R = Pr, S,S'-dipropyl benzene-1,3-dicarbothioate

Y = O, R = Me, dimethyl pyridine-2,6-dicarboxylate

Y = O, R = Pr, dipropyl pyridine-2,6-dicarboxylate

Y = S, R = Pr, S,S'-dipropyl pyridine-2,6-dicarbothioate

Cyclic voltammograms (CV) obtained at various concentrations and scan rates from several *meta*-disubstituted (O) and (S) diesters of pyridine and benzene [444]. The CV and EPR experiments revealed that a likely explanation for the surprising stability of the anion radicals of dialkylbenzene-1,3-dicarboxylates, dialkylpyridine-2,6-dicarboxylates, and their corresponding dithioic S,S'-diesters is due to a reversible dimerization mechanism. The cyclic voltammetric data were complicated and digital simulation for an EC_{dim} mechanism required several homogeneous and heterogeneous rate constants in order to obtain a good theoretical match to the experimental data. Rate constants evaluated by simulation at scan rates between 0.1–50 V s⁻¹ and substrate concentrations between 0.2 and 10 mM were estimated to be ca 10³–10⁴ L mol⁻¹ s⁻¹ for the dimerization reaction and ca 10⁻¹–10⁰ s⁻¹ for the monomerization reaction. Only approximate rate constants could be derived from the experimental curves because a large number of variables needed to be included in the simulations, meaning that no unique combination of variables would give a reasonable data fit.

4.6 So what?—Conclusions and Outlook

So what? This is an often-asked question after listening to a lecture or reading a publication about a topic, which is not too familiar to ones own field of work. Our answer contains the following aspects:

The aim of this contribution is to represent the widespread occurrence of π -type radical ions in a variety of electron-transfer processes; it should help to illustrate the state of the art in terms of the identification and characterizations of aromatic compounds in a variety of redox stages predominately by spectroscopic techniques. Aromatic (radical) polyions were upon the first species inspected by such techniques. Their structures were generally interpreted by the simplistic Hückel model and, in many cases, an astonishing agreement between the experimental results and models were found.

Nowadays, sophisticated experimental techniques and quantum-mechanical calculations allow generating and describing even rather short-lived molecules and their reactivity. Spectroscopic methods allow the detection of radicals on the ns time scale (magnetic resonance) and beyond (optical spectroscopy). Thus, it is becoming more and more practicable to establish electron-transfer generated species as intermediates in a variety of reactions. This is quite rewarding since many chemical, biochemical, and technical transformations involve electron-transfer steps: Several examples exist in which π systems undergo electron transfer and form key intermediates, e.g., in coupling reactions or isomerizations. Extensive studies exist in which quinone radical anions are established as substantial participants in photosynthesis, as taking part in the NADH pathways, or being involved in radiation damage of tissue. Moreover reduced or oxidized π systems are shown to be able to work as (semi)conductors or serve as building blocks of molecular magnets. Such systems are very helpful to gain information about electron delocalization and (para)magnetic coupling. These highly charged systems, yet, have to become considerably more stable to be useful for technical applications; even the fullerenes which are able to accept up to six electrons (C_{60} , C_{70}), do not form salts which are stable enough to be used as materials [445].

For essentially all π systems, electron transfer is connected with particular changes in the electronic absorption spectra. Thus, the usefulness of aromatic (poly)-anions and cations should particularly come to pass in cases when electron-transfer generated stages occur as short-lived mediators or as optoelectronic devices and sensors.

The references given below should serve as a guide to the fields mentioned above when connected with an appropriate online data base. Moreover, some of the above aspects are covered in the other chapters of this series.

References

1. A. Lund, M. Lindgren, S. Lunell, J. Maruani, *Molecules in Physics, Chemistry and Biology* (Ed.: J. Maruani), Kluwer Academic Publishers, Dordrecht, 1989, Vol. 3.
2. D. Feller, E. R. Davidson, *Theoretical Models of Chemical Bonding* (Ed.: Z. B. Maksic), Springer, Berlin, 1991, Part 3.

3. V. G. Malkin, O. L. Malkina, D. R. Salahub, L. A. Eriksson, *Theoretical and Computational Chemistry* (Eds.: P. Politzer, J. M. Seminario), Elsevier, Amsterdam, 1995, Vol. 2.
4. D. M. Chipman, *Quantum Mechanical Electronic Structure Calculations With Chemical Accuracy* (Ed.: S. R. Langhoff), Kluwer Academic Publishers, Dordrecht, 1995.
5. A. Lund, M. Shiotani, *Radical Ionic Systems. Properties In Condensed Phases*, Kluwer, Dordrecht, 1991.
6. L. B. Knight, Jr., *Acc. Chem. Res.* **1986**, 19, 313.
7. V. Barone, *Recent Advances In Density Functional Methods* (Ed.: D. P. Chong), World Scientific, Singapore 1995, Part 1.
8. (a) B. Engels, *Chem. Phys. Lett.* **1991**, 179, 398; (b) K. Funken, B. Engels, S. D. Peyerimhoff, F. Grein, *Chem. Phys. Lett.* **1990**, 172, 180; (c) J. Kong, R. J. Boyd, L. A. Eriksson, *J. Chem. Phys.* **1995**, 102, 3674; (d) B. Engels, S. D. Peyerimhoff, *J. Phys. B.* **1988**, 21, 3459.
9. (a) D. Feller, *J. Chem. Phys.* **1990**, 93, 579; (b) D. Feller, E. Glendening, E. A. McCullough Jr., R. J. Miller, *J. Chem. Phys.* **1993**, 99, 2829.
10. V. Barone, C. Adamo, A. Grand, R. Subra, *Chem. Phys. Lett.* **1995**, 242, 351.
11. (a) I. Carmichael, *J. Phys. Chem.* **1991**, 95, 6198; **1991**, 95, 108; *J. Chem. Phys.* **1990**, 93, 863; (b) D. M. Chipman, I. Carmichael, D. Feller, *J. Phys. Chem.* **1991**, 95, 4702; (c) I. Carmichael, *ibid.* **1994**, 98, 5044; **1995**, 99, 6832.
12. S. A. Perera, J. D. Watts, R. J. Barlett, *J. Chem. Phys.* **1994**, 100, 1425.
13. (a) P. Hohenberg, W. Kohn, *Phys. Rev. B* **1964**, 136, 864; (b) W. Kohn, L. Sham, *J. Phys. Rev. A* **1965**, 140, 1133.
14. A. D. Becke, *Phys. Rev. A* **1988**, 38, 3098; *J. Chem. Phys.* **1992**, 96, 2155.
15. J. P. Perdew, Y. Wang, *Phys. Rev. B* **1986**, 33, 8800.
16. J. P. Perdew, J. A. Chevary, S. H. Vosko, K. A. Jackson, M. R. Pederson, J. D. Singh, C. Fiolhas, *Phys. Rev. B* **1992**, 46, 6671; (b) *ibid* **1992**, 48, 4978; (c) J. P. Perdew, *Physica B* **1991**, 172, 1.
17. A. D. Becke, *J. Chem. Phys.* **1993**, 98, 1372; **1993**, 98, 5684.
18. C. Lee, W. Yang, R. G. Parr, *Phys. Rev. B* **1988**, 37, 785.
19. G. J. Laming, V. Termath, N. C. Handy, *J. Chem. Phys.* **1993**, 99, 8765.
20. M. J. Frisch, G. W. Trucks, H. B. Schlegel, P. M. W. Gill, B. G. Johnson, M. A. Robb, J. R. Cheeseman, T. A. Keith, A. G. Peterson, J. A. Montgomery, K. Raghavachari, M. A. Al-Laham, V. G. Zakrevski, J. V. Ortiz, J. B. Foresman, J. Cioslowski, B.B. Stefanov, A. Nanayakkara, M. Challacombe, C. Y. Peng, P. Y. Ayala, W. Chen, M. W. Wong, J. L. Andres, E. S. Replogle, R. Gomperts, R. L. Martin, D. J. Fox, J. S. Binkley, D. J. Defrees, J. Baker, J. P. Stewart, Head-M. Gordon, Gonzalez, J. A. Pople, *GAUSSIAN 94, Revision A.1*, Gaussian Inc., Pittsburgh, PA, 1995.
21. R. D. Amos, I. L. Alberts, J. S. Andrews, S. M. Colwell, N. C. Handy, D. Jayatilaka, P. J. Knowles, R. Kobayashi, G. J. Laming, A. M. Lee, P. E. Maslen, C. W. Murray, P. Palmieri, J. E. Rice, E. D. Simandiras, A. J. Stone, M. D. Su, D. J. Tozer, *The Cambridge Analytic Derivatives Package Issue 6.0*, University of Cambridge, Cambridge, U.K 1995.
22. (a) J. Andzelm, E. Wimmer, *J. Chem. Phys.* **1992**, 96, 1280; (b) B. G. Johnson, P. M. W. Gill, J. A. Pople, *J. Chem. Phys.* **1993**, 98, 5612.
23. N. Oliphant, R. J. Barlett, *J. Chem. Phys.* **1994**, 100, 6550.
24. (a) C. W. Bauschlicher, Jr., *Chem. Phys. Lett.* **1995**, 246, 40; (b) C. W. Bauschlicher, Jr., H. Patridge, *ibid* **1995**, 240, 533.
25. R. Neumann, N. C. Handy, *Chem. Phys. Lett.* **1995**, 246, 381.
26. (a) L. A. Eriksson, L. G. M. Pettersson, P. E. M. Siegbahn, U. Wahlgren, *J. Chem. Phys.* **1995**, 102, 872; (b) P. A. Stewart, P. W. M. Gill, *J. Chem. Soc. Faraday Trans.* **1995**, 91, 4337; (c) J. A. Altmann, N. C. Handy, V. E. Ingamells, *Int. J. Quantum Chem.* **1996**, 57, 533; (d) E. I. Proynov, E. Ruiz, A. Vela, D. R. Salahub, *Int. J. Quantum Chem. Symp.* **1995**, 29, 61.
27. V. Barone, C. Adamo, F. Mele, *Chem. Phys. Lett.* **1996**, 249, 290.
28. *Density Functional Methods in Chemistry* (Eds.: J. Labanowski, J. Andzelm), Springer, New York, 1991.
29. *Theoretical and Computational Chemistry, Modern Density Functional Theory—A Tool for Chemistry* (Eds.: J. M. Seminario, P. Politzer), Elsevier, Amsterdam 1995, Vol. 2.

30. *Density Functional Methods: Applications in Chemistry and Materials Science* (Ed.: M. Springborg), Wiley, New York 1996.
31. S. J. Mole, X. Zhou, R. Liu, *J. Phys. Chem.* **1996**, *100*, 14665–14671.
32. J. M. Martell, J. D. Goddard, L. A. Eriksson, *J. Phys. Chem. A* **1997**, *101*, 1927–1934.
33. L. A. Eriksson, A. Laaksonen, *J. Chem. Phys.* **1996**, *105*, 8195–8202.
34. S. D. Wetmore, R. J. Boyd, L. A. Eriksson, *J. Chem. Phys.* **1997**, *106*, 7738–7748.
35. L. A. Eriksson, *Molecular Physics* **1997**, *91*, 827–833.
36. B. R. Beno, J. Fennen, K. N. Houk, H. J. Lindner, K. Hafner, *J. Am. Chem. Soc.* **1998**, *120*, 10490–10493.
37. (a) A. M. Mebel, A. Luna, M. C. Lin, K. Morokuma, *J. Chem. Phys.* **1996**, *105*, 6439; (b) E. Sicilia, M. Toscano, T. Mineva, N. Russo, *Int. J. Quantum Chem.* **1997**, *61*, 571; (c) J. J. Queral, V. S. Safont, V. Moliner, J. Andres, *Theor. Chim. Acta* **1996**, *94*, 247; (d) A. Irigoras, J. M. Ugalde, X. Lopez, C. Sarasola, *Can. J. Chem.* **1996**, *74*, 1824; (e) M. R. Manaa, L. E. Fried, *J. Phys. Chem. A* **1998**, *102*, 9884–9889.
38. (a) P. M. Gill, L. Radom, *J. Am. Chem. Soc.* **1988**, *110*, 4931; (b) M. Sodupe, A. Oliva, J. Bertran, *J. Am. Chem. Soc.* **1994**, *116*, 8249.
39. R. N. Barnett, U. Landman, *J. Phys. Chem.* **1995**, *99*, 17305; *J. Phys. Chem. A* **1997**, *101*, 164.
40. M. Sodupe, J. Bertran, L. Rodriguez-Santiago, E. J. Baerends, *J. Phys. Chem. A* **1999**, *103*, 166–170.
41. L. R. Domingo, *J. Org. Chem.* **1999**, *64*, 3922–3929.
42. W. B. Smith, *J. Org. Chem.* **1999**, *64*, 60–64.
43. (a) M. Garcia-Viloca, A. Gonzalez-Lafont, J. M. Lluch, *J. Am. Chem. Soc.* **1997**, *119*, 1081; (b) M. E. Tuckerman, D. Marx, M. L. Klein, M. Parrinello, *Science* **1997**, *275*, 817; (c) S. Shan, D. Herschlag, *J. Am. Chem. Soc.* **1996**, *118*, 5515; (d) B. Schwartz, D. G. Drueckhammer, *J. Am. Chem. Soc.* **1995**, *117*, 11902; (e) J. A. Gerlt, M. M. Kreevoy, W. W. Cleland, P. A. Frey, *Chem. Biol.* **1997**, *4*, 259.
44. (a) J. A. Gerlt, P. G. Gassman, *J. Am. Chem. Soc.* **1993**, *115*, 11552; (b) J. P. Guthrie, *Chem. Biol.* **1996**, *3*, 163; (c) Y. Kato, L. M. Toledo, J. Rebek Jr., *J. Am. Chem. Soc.* **1996**, *118*, 8575; (d) G. A. Jeffrey, *An Introduction to Hydrogen Bonding*, Oxford University Press, New York 1997.
45. (a) Y. Pan, M. A. McAllister, *J. Am. Chem. Soc.* **1997**, *119*, 7561; (b) M. A. McAllister, *Can. J. Chem.* **1997**, *75*, 1195; (c) Y. Pan, M. A. McAllister, *J. Org. Chem.* **1997**, *62*, 8176; (d) C. J. Smallwood, M. A. McAllister, *J. Am. Chem. Soc.* **1997**, *119*, 11277.
46. Y. Pan, M. A. McAllister, *J. Am. Chem. Soc.* **1998**, *120*, 166–169.
47. A. Császár, *J. Mol. Struct.* **1995**, *346*, 141; *J. Am. Chem. Soc.* **1992**, *114*, 9568.
48. S. G. Stepanian, I. D. Reva, E. D. Radchenko, L. Adamowicz, *J. Phys. Chem. A* **1999**, *103*, 4404–4412.
49. C. Adamo, V. Barone, A. Fortunelli, *J. Chem. Phys.* **1995**, *102*, 384–393.
50. *Ions and Ion Pairs in Organic Reactions* (Ed.: M. Szwarc), Wiley–Interscience, New York, 1972, Vol. 1; 1974, Vol. 2.
51. N. M. Atherton, S. I. Weissman, *J. Am. Chem. Soc.* **1961**, *83*, 1330–1334.
52. B. J. Herold, A. F. Neiva Correia, J. dos Santos Veiga, *J. Am. Chem. Soc.* **1965**, *87*, 2661–2665.
53. H. Van Willigen, M. Plato, R. Biehl, K. P. Dinse, K. Möbius, *Mol. Phys.* **1973**, *26*, 793–809.
54. (a) F. Gerson, J. Jachimowicz, M. Nakagawa, M. Iyoda, *Helv. Chim. Acta* **1974**, *57*, 2141–2148; (b) W. Huber, *ibid* **1985**, *68*, 1140–1148.
55. C. L. Dodson, A. H. Reddoch, *J. Chem. Phys.* **1968**, *48*, 3226–3234.
56. H. Kurreck, B. Kirste, W. Lubitz, *Electron Nuclear Double Resonance Spectroscopy of Radicals in Solution*, VCH, New York, 1988, Ch. 4.7, 99–100.
57. H. Kurreck, B. Kirste, W. Lubitz, *Electron Nuclear Double Resonance Spectroscopy of Radicals in Solution*, VCH, New York, 1988, Ch. 2.2, 20–24.
58. E. De Boer, J. L. Sommerdijk, In *Ions and Ion Pairs in Organic Reactions* (Ed.: M. Szwarc), Wiley–Interscience, New York, 1972, Vol. 1, Ch. 7, 289–309.
59. (a) S. N. Batchelor, H. Heikkilä, C. W. M. Kay, K. A. McLauchlan and I. A. Shkrob, *Chem. Phys.* **1992**, *162*, 29; (b) S. Sekiguchi, K. Akiyama, S. Tero-Kubota, *Chem. Phys. Lett.* **1996**, *263*, 161; (c) N. J. Avdievich, A. S. Jeevarajan, M. D. E. Forbes, *J. Phys. Chem.* **1996**, *100*,

- 5334; (d) S. Sekiguchi, K. Akiyama, S. Tero-Kubota, *J. Chem. Soc., Perkin Trans. 2*, **1997**, 1619–1620.
60. (a) J. H. Sharp, M. C. R. Symons, *Ions and Ion Pairs in Organic Reactions* (Ed.: M. Szwarc), Wiley-Interscience, New York, 1972, Vol. 1, Ch. 5, 177–262; (b) F. Gerson, *High-Resolution ESR Spectroscopy*, Wiley and Verlag Chemie, New York and Weinheim, 1970, appendix 2.2, 137–143.
61. W. M. Tolles, D. W. Moore, *J. Chem. Phys.* **1967**, *46*, 2102–2106.
62. D. H. Levy, R. J. Myers, *J. Chem. Phys.* **1964**, *41*, 1062–1065.
63. D. H. Levy, R. J. Myers, *J. Chem. Phys.* **1966**, *44*, 4177–4180.
64. N. Sommer, *Kautsch. Gummi Kunstst.* **1975**, *28*, 131–135.
65. F. Gerson, H. Hopf, P. Merstetter, C. Mlynek, D. Fischer, *J. Am. Chem. Soc.* **1998**, *120*, 4815–4824.
66. S. Kababya, Z. Luz, D. Goldfarb, *J. Am. Chem. Soc.* **1994**, *116*, 5805–5813.
67. F. Barbosa, V. Péron, G. Gescheidt, A. Fürstner, *J. Org. Chem.* **1998**, *63*, 8806–8814.
68. R. Rathore, S. V. Lindeman, A. S. Kumar, J. K. Kochi, *J. Am. Chem. Soc.* **1998**, *120*, 6931.
69. B. M. Tadjikov, D. V. Stass, Yu. N. Molin, *Chem. Phys. Lett.* **1996**, *260*, 529–532.
70. (a) O. Hammerich, V. D. Parker, *Adv. Phys. Org. Chem.* **1994**, *20*, 1; (b) A. J. Bard, A. Ledwith, H. J. Shine, *Adv. Phys. Org. Chem.* **1976**, *12*, 155.
71. (a) J. K. Kochi, R. T. Tang, T. Bernath, *J. Am. Chem. Soc.* **1973**, *95*, 7114; (b) I. H. Elson, J. K. Kochi, *J. Am. Chem. Soc.* **1973**, *95*, 5060.
72. (a) K. Nyberg, *Acta Chem. Scand.* **1970**, *24*, 1609; **1971**, *25*, 2499; **1971**, *25*, 2983; **1971**, *25*, 3770; **1971**, *25*, 534; (b) L. Ebersson, K. Nyberg, H. Sternerup, *Acta Chem. Scand.* **1973**, *27*, 1679; *Acc. Chem. Res.* **1973**, *6*, 106; (c) A. McKillop, A. G. Turrell, D. W. Young, E. C. Taylor, *J. Am. Chem. Soc.* **1980**, *102*, 6504; (d) L. Ebersson, F. Radner, *Acta Chem. Scand.* **1992**, *46*, 630; (e) R. Sebastiano, J. D. Krop, J. K. Kochi, *J. Chem. Soc., Chem. Commun.* **1991**, 1481.
73. (a) A. Ronlan, K. Bechgaard, V. D. Parker, *Acta Chem. Scand.* **1973**, *27*, 2375; (b) R. N. Adams, *Acc. Chem. Res.* **1966**, *2*, 175.
74. (a) J. K. Kochi, *Acc. Chem. Res.* **1992**, *25*, 39; (b) L. Ebersson, M. P. Hartshorn, F. Radner, J. O. Svensson, *J. Chem. Soc., Perkin Trans. 2* **1994**, 1719.
75. (a) A. Terahara, H. Ohya-Nishiguchi, N. Hirota, A. Oku, *J. Phys. Chem.* **1986**, *90*, 1564; (b) M. G. Bakker, R. F. Claridge, C. M. Kirk, *J. Chem. Soc., Perkin Trans. 2*, **1986**, 1735.
76. A. T. Balaban, C. D. Nenitzescu, *Friedel–Crafts and Related Reactions* (Ed.: G. A. Olah), Wiley, New York, 1963–1965, Vol. II, Ch. 23.
77. L. Ebersson, M. P. Hartshorn, O. Persson, *J. Chem. Soc., Perkin Trans. 2* **1995**, 409–416.
78. W. Lau, J. C. Huffman, J. K. Kochi, *J. Am. Chem. Soc.* **1982**, *104*, 5515.
79. R. Taylor, *Electrophilic Aromatic Substitution*, Wiley, Chichester, 1990.
80. (a) W. Lau, J. K. Kochi, *J. Org. Chem.* **1986**, *51*, 1801; (b) A. G. Davies, *Chem. Soc. Rev.* **1993**, 299.
81. (a) J. L. Courtneidge, A. G. Davies, P. S. Gregory, D. C. McGuchan, S. N. Yazdi, *J. Chem. Soc., Chem. Commun.* **1987**, 1192; (b) A. G. Davies, C. J. Shields, J. C. Evans, C. C. Rowlands, *Can. J. Chem.* **1989**, *67*, 1748.
82. I. H. Elson, J. K. Kochi, *J. Am. Chem. Soc.* **1973**, *95*, 5060.
83. L. Ebersson, M. P. Hartshorn, O. Persson, J. O. Stevensson, *J. Chem. Soc., Perkin Trans. 2* **1995**, 1253.
84. (a) P. D. Sullivan, E. M. Menger, A. H. Reddoch, D. H. Paskovich, *J. Phys. Chem.* **1978**, *82*, 1158; (b) J. Eloranta, S. Kasa, *Acta Chem. Scand., Ser. A* **1985**, 399, 63.
85. A. G. Davies, D. C. McGuchan, *Organometallics*, **1991**, *10*, 329.
86. X. H. Chen, P. D. Sullivan, *J. Magn. Reson.* **1989**, *83*, 484.
87. J. L. Courtneidge, A. G. Davies, D. C. McGuchan, S. N. Yazdi, *J. Organomet. Chem.* **1988**, *341*, 63.
88. L. Ebersson, M. P. Hartshorn, O. Persson, *J. Chem. Soc., Perkin Trans. 2* **1995**, 1735.
89. D. V. Avila, A. G. Davies, *J. Chem. Soc., Perkin Trans. 2* **1991**, 1111.
90. A. G. Davies, K. M. Ng, *J. Chem. Soc., Perkin Trans. 2*, **1998**, 2599–2607.
91. J. Fleischhauer, S. Ma, W. Schleker, K. Gersonde, H. Twilfer, F. Dallacker, *Z. Naturforsch., Teil A*, **1982**, *37*, 680.

92. P. D. Sullivan, N. A. Brette, *J. Phys. Chem.* **1975**, 79, 474.
93. N. A. Malysheva, A. I. Prokof'ev, N. N. Bubnov, S. P. Solodovnikov, T. I. Prokof'ev, V. B. Vol'eva, V. V. Ershov, M. I. Kabachnik, *Izvest. Akad. Nauk SSSR, Ser. Khim.* **1988**, 1040.
94. (a) J. L. Courtneidge, A. G. Davies, E. Lisztyk, J. Luszyk, *J. Chem. Soc., Perkin Trans. 2* **1984**, 155; (b) J. L. Courtneidge, A. G. Davies, S. M. Tollerfield, J. Rideout, M. C. R. Symons, *J. Chem. Soc., Chem. Commun.* **1985**, 1092.
95. C. J. Cooksey, J. L. Courtneidge, A. G. Davies, J. C. Evans, P. S. Gregory, C. C. Rowlands, *J. Chem. Soc., Perkin Trans. 2* **1988**, 807.
96. L. Eberson, M. P. Hartshorn, F. Radner, O. Persson, *J. Chem. Soc., Perkin Trans. 2* **1998**, 59–70.
97. (a) L. Eberson, M. P. Hartshorn, O. Persson, *J. Chem. Soc., Chem. Commun.* **1995**, 1131; *J. Chem. Soc., Perkin Trans. 2* **1995**, 1735; *Angew. Chem. Int. Ed. Engl.* **1995**, 34, 2268; *Res. Chem. Intermed.* **1996**, 22, 799; (b) L. Eberson, M. P. Hartshorn, O. Persson, F. Radner, *J. Chem. Soc., Chem. Commun.* **1996**, 2105.
98. (a) L. Eberson, M. P. Hartshorn, O. Persson, *J. Chem. Soc., Perkin Trans. 2* **1996**, 141; (b) L. Eberson, M. P. Hartshorn, O. Persson, F. Radner, *J. Chem. Soc., Chem. Commun.* **1996**, 215.
99. A. G. Davies, C. J. Shields, J. C. Evans, C. C. Rowlands, *Can. J. Chem.* **1989**, 67, 1748.
100. D. V. Avila, A. G. Davies, R. Lapouyade, K. M. Ng, *J. Chem. Soc., Perkin Trans. 2* **1998**, 2609–2615.
101. M. Iwaizumi, T. Isobe, *Mol. Phys.* **1975**, 29, 549.
102. (a) H. Hogeveen, H. C. Volger, *Recl. Trav. Chim. Pays-Bas* **1968**, 87, 385; (b) L. A. Paquette, G. R. Krow, J. M. Bollinger, G. A. Olah, *J. Am. Chem. Soc.* **1968**, 90, 7147; (c) T. R. Evans, R. W. Wake, M. M. Sifain, *Tetrahedron Lett.* **1973**, 701; (d) N. Peacock, G. B. Schuster, *J. Am. Chem. Soc.* **1983**, 105, 3632.
103. (a) C. J. Rhodes, *J. Am. Chem. Soc.*, **1988**, 110, 4446; (b) X. Z. Qin, D. W. Werst, A. D. Trifunac, *J. Am. Chem. Soc.* **1990**, 112, 2026; (c) F. Williams, Q. X. Guo, S. F. Nelsen, *J. Am. Chem. Soc.* **1990**, 112, 2028.
104. (a) H. D. Roth, *Top. Curr. Chem.* **1992**, 163, 131; (b) H. D. Roth, P. Lakkaraju, J. Zhang, *J. Chem. Soc., Chem. Commun.* **1994**, 1969.
105. L. Eberson, M. P. Hartshorn, O. Persson, J. O. Svensson, *J. Chem. Soc., Perkin Trans. 2* **1995**, 1253–1262.
106. (a) M. Iwasaki, K. Toriyama, K. Nunome, *J. Chem. Soc., Chem. Commun.* **1983**, 320–322; (b) K. Raghavachari, R. C. Haddon, T. A. Miller, V. E. Bondybey, *J. Chem. Phys.* **1983**, 79, 1387.
107. A. Hasegawa, Y. Itagaki, M. Shiotani, *J. Chem. Soc., Perkin Trans. 2* **1997**, 1625–1631.
108. S. Steenken, M. Ashokkumar, P. Maruthamuthu, R. A. McClelland, *J. Am. Chem. Soc.* **1998**, 120, 11925–11931.
109. (a) H. J. Bakoss, R. J. Ranson, R. M. G. Roberts, A. R. Sadri, *Tetrahedron* **1982**, 38, 623; (b) G. P. Smith, A. S. Dworkin, R. M. Pagni, S. P. Zingg, *J. Am. Chem. Soc.* **1989**, 111, 525; (c) For Review see: V. A. Koptiuk, *Arenium Ions—Structure and Reactivity*, In *Topics in Current Chemistry* (Ed.: F. L. Boschke), Springer, Berlin, **1984**, 122, 96.
110. S. Steenken, R. A. McClelland, *J. Am. Chem. Soc.* **1990**, 112, 9648.
111. M. V. Sargent, F. M. Dean, *Comprehensive Heterocyclic Chemistry* (Eds.: A. J. Boulton, A. McKillop), Pergamon Press, Oxford, **1984**, 3, 599.
112. L. Eberson, F. Radner, *Acta Chem. Scand.* **1992**, 46, 802.
113. L. Eberson, F. Radner, *Acta Chem. Scand.* **1992**, 46, 312.
114. L. Eberson, M. P. Hartshorn, F. Radner, M. Merchán, B. O. Roos, *Acta Chem. Scand.* **1993**, 47, 176.
115. (a) S. S. Shaik, A. Pross, *J. Am. Chem. Soc.* **1989**, 111, 4306; (b) S. S. Shaik, E. J. Canadell, *ibid* **1990**, 112, 1452; (c) S. S. Shaik, *J. Org. Chem.* **1990**, 55, 3434.
116. L. Eberson, M. P. Hartshorn, O. Persson, F. Radner, C. J. Rhodes, *J. Chem. Soc., Perkin Trans. 2* **1996**, 1289–1295.
117. M. Schmittel, G. Gescheidt, L. Eberson, H. Trenkle, *J. Chem. Soc., Perkin Trans. 2* **1997**, 2145–2150.
118. L. Eberson, R. González-Luque, M. Merchán, F. Radner, B. O. Roos, S. Shaik, *J. Chem. Soc., Perkin Trans. 2* **1997**, 463.

119. (a) R. A. Forrester, K. Ishizu, G. Kothe, S. F. Nelsen, H. Ohya-Nishiguchi, K. Watanabe, W. Wilker, *Organic Cation Radicals and Polyradicals. In Landolt Börnstein, Numerical Data and Functional Relationships in Science and Technology*, Springer, Heidelberg, 1980, IX, Part d2; (b) K. Yoshida, *Electrooxidation in Organic Chemistry: The Role of Cation Radicals as Synthetic Intermediates*, Wiley, New York, 1984; (c) *Radical Ionic Systems* (Eds.: A. Lund, M. Shiotani), Kluwer Academics, Dordrecht, 1991; (d) H. D. Roth, *Top. Curr. Chem.* **1992**, 163, 133.
120. (a) A. Ledwith, *Acc. Chem. Res.* **1972**, 5, 133; (b) T. Shida, E. Haselbach, T. Bally, *Acc. Chem. Res.* **1984**, 17, 180–186; (c) S. F. Nelsen, *Acc. Chem. Res.* **1987**, 20, 269–276; (d) H. D. Roth, *Acc. Chem. Res.* **1987**, 20, 343–350; (e) G. A. Mirafzal, J. Liu, N. Bauld, *J. Am. Chem. Soc.* **1993**, 115, 6072; (f) F. Gerson, *Acc. Chem. Res.* **1994**, 27, 63.
121. (a) H. D. Roth, M. L. M. Schilling, G. Jones II, *J. Am. Chem. Soc.* **1981**, 103, 1246–1248; (b) H. D. Roth, M. L. M. Schilling, *J. Am. Chem. Soc.* **1981**, 103, 7210–7217; (c) Y. Takahashi, T. Mukai, T. Miyashi, *J. Am. Chem. Soc.* **1983**, 105, 6511–6513.
122. (a) P. G. Gassman, B. A. Hay, *J. Am. Chem. Soc.* **1985**, 107, 4075; (b) A. Arnold, U. Burger, F. Gerson, E. Kloster-Jensen, S. P. Schmidlin, *J. Am. Chem. Soc.* **1993**, 115, 4271–4281; (c) J. P. Dinnocenzo, M. Schmittel, *J. Am. Chem. Soc.* **1987**, 109, 1561–1562; (d) J. P. Dinnocenzo, D. A. Conlon, *J. Am. Chem. Soc.* **1988**, 110, 2324–2326.
123. (a) J. P. Dinnocenzo, W. P. Todd, T. R. Simpson, I. R. Gould, *J. Am. Chem. Soc.* **1990**, 112, 2462–2464; (b) S. S. Hixson, Y. Xing, *Tetrahedron Lett.* **1991**, 32, 173–174; (c) J. P. Dinnocenzo, D. R. Lieberman, T. R. Simpson, *J. Am. Chem. Soc.* **1993**, 115, 366–367.
124. P. G. Gassman, K. D. Olson, *J. Am. Chem. Soc.* **1982**, 104, 3740.
125. (a) H. D. Roth, T. Herbertz, *J. Am. Chem. Soc.* **1993**, 115, 9804–9805; (b) D. R. Arnold, X. Du, H. J. P. de Lijser, *Can. J. Chem.* **1995**, 73, 522; (c) H. D. Roth, H. Weng, T. Herbertz, *Tetrahedron* **1997**, 53, 10051–10070 and references therein.
126. A. Alex, T. Clark, *J. Am. Chem. Soc.* **1992**, 114, 10897–10902.
127. C. Dass, D. A. Peake, M. L. Gross, *Org. Mass. Spectrom.* **1986**, 21, 741–746.
128. L. T. Scott, I. Erden, W. R. Brunsvold, T. H. Schultzu, K. N. Houk, M. N. Paddon-Row, *J. Am. Chem. Soc.* **1982**, 104, 3659.
129. I. Yu. Shchapin, V. I. Fel'dman, V. N. Belevskii, N. A. Donskaya, N. D. Chuvylkin, *Russ. Chem. Bull.* **1995**, 44, 203–227.
130. H. D. Roth, T. Herbertz, *J. Am. Chem. Soc.* **1993**, 115, 9804–9805.
131. H. D. Roth, H. Weng, T. Herbertz, *Tetrahedron* **1997**, 53, 10051–10070.
132. W. J. Hehre, L. Radom, J. A. Pople, P. V. R. Schleyer, *Ab Initio Molecular Orbital Theory*, Wiley Interscience, New York, 1986.
133. H. Weng, Q. Sheik, H. D. Roth, *J. Am. Chem. Soc.* **1995**, 117, 10655–10661.
134. A. Arnold, U. Burger, F. Gerson, E. Kloster-Jensen, S. P. Schmidlin, *J. Am. Chem. Soc.* **1993**, 115, 4271–4281.
135. (a) G. J. Kavarnos, N. J. Turro, *Chem. Rev.* **1986**, 86, 401–449; (b) T. Oguchi, T. Arai, H. Sakuragi, K. Tokumaru, *Bull. Chem. Soc. Jpn.* **1987**, 60, 2395–2399; (c) *Photoinduced Electron Transfer* (Eds.: M. A. Fox, M. Chanon), Elsevier, Amsterdam, 1988; (d) G. J. Kavarnos, *Top. Curr. Chem.* **1990**, 156, 21–58.
136. (a) T. Majiama, C. Pac, A. Makasone, H. Sakurai, *J. Am. Chem. Soc.* **1981**, 103, 4499–4508; (b) M. Julliard, In *Photoinduced Electron Transfer* (Eds.: M. A. Fox, M. Chanon), Elsevier, Amsterdam, 1988, Part B, 216–313; (c) I. R. Gould, D. Ege, J. E. Mooser, S. Farid, *J. Am. Chem. Soc.* **1990**, 112, 4290–4301.
137. W. Adam, A. Corma, M. A. Miranda, M. Sabater-Picot, C. Sahin, *J. Am. Chem. Soc.* **1996**, 118, 2380–2386.
138. (a) W. Adam, C. Sahin, J. Sendelbach, H. Walter, G. F. Chen, F. Williams, *J. Am. Chem. Soc.* **1994**, 116, 2576; (b) W. Adam, T. Heidenfelder, C. Sahin, *Synthesis* **1995**, 1163; (c) W. Adam, A. Corma, M. A. Miranda, M. J. Sabater-Picot, C. Sahin, *J. Am. Chem. Soc.* **1996**, 118, 2380.
139. W. Schmidt, E. Steckhan, *Chem. Ber.* **1980**, 113, 577.
140. W. Adam, V. Handmann, F. Kita, T. Heidenfelder, *J. Am. Chem. Soc.* **1998**, 120, 831–832.
141. R. Bachmann, F. Gerson, P. Merstetter, E. Vogel, *Helvetica Chem. Acta* **1996**, 79, 1627–1634.

142. (a) P. Dowd, *J. Am. Chem. Soc.* **1966**, 88, 2587; (b) P. Dowd, M. Chow, *Tetrahedron* **1982**, 38, 799.
143. (a) M. S. Platz In *Diradicals* (Ed.: W. T. Borden), Wiley, New York, **1982**; (b) J. Wirz, *Pure Appl. Chem.* **1984**, 56, 1289.
144. M. C. Biewer, M. S. Platz, M. Roth, J. Wirz, *J. Am. Chem. Soc.* **1991**, 113, 8069.
145. Z. Zhu, T. Bally, J. Wirz, M. Fülischer, *J. Chem. Soc., Perkin Trans. 2* **1998**, 1083–1091.
146. (a) W. Rebafka, H. A. Staab, *Angew. Chem.* **1973**, 85, 831–832; *Chem. Ber.* **1977**, 110, 3333–3350; (b) H. A. Staab, C. P. Herz, C. Krieger, M. Rentea, *Chem. Ber.* **1983**, 116, 3813–3830; (c) H. A. Staab, A. Döhling, C. Krieger, *Liebigs Ann. Chem.* **1981**, 1052–1064.
147. (a) H. A. Staab, B. Starker, C. Krieger, *Chem. Ber.* **1983**, 116, 3831–3845; (b) F. Gerson, *Top. Curr. Chem.* **1983**, 115, 57–105.
148. F. Gerson, W. B. Martin, *J. Am. Chem. Soc.* **1969**, 91, 1883–1891.
149. A. R. Wartini, J. Valenzuela, H. A. Staab, F. A. Neugebauer, *Eur. J. Org. Chem.* **1998**, 139–148.
150. A. R. Wartini, H. A. Staab, F. A. Neugebauer, *Eur. J. Org. Chem.* **1998**, 1161–1170.
151. (a) L. Eberson, F. Radner, *Acc. Chem. Res.* **1988**, 20, 53–60; (b) B. Boduszek, H. J. Shine, *J. Org. Chem.* **1988**, 53, 5142–5147.
152. S. F. Nelsen, Y. Kim, *J. Org. Chem.* **1991**, 56, 1045–1049.
153. (a) E. K. Kim, J. K. Kochi, *J. Am. Chem. Soc.* **1991**, 113, 4962–4967; (b) M. Lehning, K. Schürmann, *Eur. J. Org. Chem.* **1998**, 913–917.
154. K. Mizuno, N. Ichinose, T. Tamai, Y. Otsuji, *J. Org. Chem.* **1992**, 57, 4669–4673.
155. G. A. Olah, P. Ramaiah, C. B. Rao, G. Sandford, R. Golam, N. J. Trivedi, J. A. Olah, *J. Am. Chem. Soc.* **1993**, 115, 7246–7249.
156. A. A. Fokin, P. A. Gunchenko, S. A. Peleshanko, P. V. R. Schleyer, P. R. Schreiner, *Eur. J. Org. Chem.* **1999**, 855–860.
157. H. Prinzbach, K. Weber, *Angew. Chem.* **1994**, 106, 2329; *Angew. Chem. Int. Ed. Engl.* **1994**, 33, 2239.
158. (a) H. D. Martin, B. Mayer, K. Weber, H. Prinzbach, *Liebigs Ann.* **1995**, 2019; (b) K. Weber, G. Lutz, L. Knothe, J. Mortensen, J. Heinze, H. Prinzbach, *J. Chem. Soc., Perkin Trans. 1* **1995**, 1991; (c) H. Prinzbach, G. Gescheidt, H. D. Martin, R. Herges, J. Heinze, G. K. S. Prakash, G. A. Olah, *Pure Appl. Chem.* **1995**, 67, 673.
159. A. D. Trifunac, D. W. Werst, R. Herges, H. Neumann, H. Prinzbach, M. Etzkorn, *J. Am. Chem. Soc.* **1996**, 118, 9444.
160. (a) R. Herges, P. von R. Schleyer, M. Schindler, W. D. Fessner, *J. Am. Chem. Soc.* **1991**, 113, 3649; (b) G. K. S. Prakash in *Stable Carbocation Chemistry* (Eds.: G. K. S. Prakash, P. von R. Schleyer), Wiley, New York, 1996.
161. A. D. Trifunac, D. W. Werst, *J. Am. Chem. Soc.* **1996**, 118, 9444–9445.
162. H. Prinzbach, B. A. R. C. Murty, W. D. Fessner, J. Mortensen, J. Heinze, G. Gescheidt, F. Gerson, *Angew. Chem. Int. Ed. Engl.* **1987**, 26, 457.
163. G. K. S. Prakash, V. V. Krishnamurthy, R. Herges, R. Bau, H. Yuan, G. A. Olah, W. D. Fessner, H. Prinzbach, *J. Am. Chem. Soc.* **1988**, 110, 7764.
164. A. D. Trifunac, D. W. Werst, R. Herges, H. Neumann, H. Prinzbach, M. Etzkorn, *J. Am. Chem. Soc.* **1996**, 118, 9444.
165. M. Etzkorn, F. Wahl, M. Keller, H. Prinzbach, F. Barbosa, V. Peron, G. Gescheidt, J. Heinze, R. Herges, *J. Org. Chem.* **1998**, 63, 6080–6081.
166. (a) M. Bertau, F. Wahl, A. Weiler, K. Scheumann, J. Wörth, M. Keller, H. Prinzbach, *Tetrahedron* **1997**, 53, 10029–10040; (b) K. Scheumann, E. Sackers, M. Bertau, J. Leonhardt, D. Hunkler, H. Fritz, J. Wörth, H. Prinzbach, *J. Chem. Soc., Perkin Trans. 2* **1998**, 1195–1210.
167. D. N. Stamires, J. Turkevich, *J. Am. Chem. Soc.* **1964**, 86, 749.
168. (a) P. S. Lakkaraju, D. Zhou, H. D. Roth, *Chem. Commun.* **1996**, 2605; (b) E. A. Piosos, D. W. Werst, A. D. Trifunac, *J. Phys. Chem.* **1996**, 100, 8408; (c) V. Ramamurthy, J. V. Caspar, D. R. Corbin, *J. Am. Chem. Soc.* **1991**, 113, 594; **1991**, 113, 600.
169. V. J. Rao, N. Prevost, V. Ramamurthy, M. Kojima, L. J. Johnston, *Chem. Commun.* **1997**, 2209–2210.
170. E. A. Piosos, P. Han, D. W. Werst, *J. Phys. Chem.* **1996**, 100, 7191–7199.

171. (a) G. T. Kerr, *Sci. Am.* **1989**, 100; (b) A. Corma, *Chem. Rev.* **1995**, 95, 559; (c) F. R. Ribeiro, F. Alvarez, C. Henriques, F. Lemos, J. M. Lopes, M. F. Ribeiro, *J. Mol. Catal. A* **1995**, 96, 245.
172. J. P. Lange, A. Gutsze, H. G. Karge, *J. Catal.* **1988**, 114, 136.
173. (a) T. Komatsu, A. Lund, *J. Phys. Chem.* **1972**, 76, 1727; (b) A. M. Volodin, V. A. Boloshov, T. A. Konovalova, *Radicals on Surfaces* (Eds.: A. Lund, C. Rhodes), Kluwer, Dordrecht, **1995**, 201–226.
174. R. Erickson, A. Lund, M. Lindgren, *Chem. Phys.* **1995**, 193, 89.
175. R. Erickson, N. P. Benetis, A. Lund, M. Lindgren, *J. Phys. Chem. A* **1997**, 101, 2390–2396.
176. M. Iwasaki, K. Toriyama, K. Nunoma, *J. Chem. Soc., Chem. Commun.* **1983**, 320.
177. T. Komatsu, A. Lund, *J. Phys. Chem.* **1972**, 76, 1727.
178. R. Erickson, M. Lindgren, A. Lund, L. Sjöqvist, *Colloids Surf. A* **1993**, 72, 207.
179. R. M. Kadam, R. Erickson, K. Komaguchi, M. Shiotani, A. Lund, *Chem. Phys. Lett.* **1998**, 290, 371–378.
180. V. I. Feldman, F. F. Sukhov, A. Yu. Orlov, *Chem. Phys. Lett.* **1999**, 300, 713–718.
181. (a) T. R. Tuttle, S. I. Weissman Jr., *J. Am. Chem. Soc.* **1958**, 80, 5342; (b) C. D. Stevenson, E. P. Wagner, R. C. Reiter, *J. Phys. Chem.* **1993**, 97, 10587.
182. (a) M. C. R. Symons, L. Harris, *J. Chem. Res. (S)* **1982**, 268; (b) M. Tabata, A. Lund, *Chem. Phys.* **1983**, 78, 379.
183. T. Komatsu, A. Lund, *J. Phys. Chem.* **1972**, 76, 1721.
184. R. M. Kadam, Y. Itagaki, R. Erickson, A. Lund, *J. Phys. Chem. A* **1999**, 103, 1480–1486.
185. E. A. Pioscos, D. W. Werst, A. D. Trifunac, L. A. Eriksson, *J. Phys. Chem.* **1996**, 100, 8408–8417.
186. D. W. Werst, E. E. Tartakovsky, E. A. Pioscos, A. D. Trifunac, *J. Phys. Chem.* **1994**, 98, 10249–10257.
187. (a) T. Shida, Y. Takemura, *Radiat. Phys. Chem.* **1983**, 21, 157; (b) M. Iwasaki, K. Toriyama, K. Nunome, *Faraday Discuss. Chem. Soc.* **1984**, 78, 19; (c) M. V. Barnabas, A. D. Trifunac, *Chem. Phys. Lett.* **1991**, 187, 565.
188. (a) V. I. Melekhov, O. A. Anisimov, A. V. Veselov, Yu. N. Molin, *Chem. Phys. Lett.* **1986**, 127, 97; (b) B. M. Tadjikov, V. I. Melekhov, O. A. Anisimov, Yu. N. Molin, *Radiat. Phys. Chem.* **1989**, 34, 353.
189. (a) D. W. Werst, L. T. Percy, A. D. Trifunac, *Chem. Phys. Lett.* **1988**, 153, 45; (b) D. W. Werst, M. G. Bakker, A. D. Trifunac, *J. Am. Chem. Soc.* **1990**, 112, 40.
190. D. W. Werst, A. D. Trifunac, *J. Phys. Chem.* **1988**, 92, 1093.
191. B. M. Tadjikov, D. V. Stass, Y. N. Molin, *J. Phys. Chem. A* **1997**, 101, 377–383.
192. (a) T. Shida, Y. Takemura, *Radiat. Phys. Chem.* **1983**, 21, 157; (b) M. Iwasaki, K. Toriyama, K. Nunome, *Faraday Discuss. Chem. Soc.* **1984**, 78, 19; (c) V. I. Melekhov, O. A. Anisimov, L. Sjöqvist, A. Lund, *Chem. Phys. Lett.* **1990**, 174, 95.
193. (a) V. I. Melekhov, O. A. Anisimov, A. V. Veselov, Yu. N. Molin, *Chem. Phys. Lett.* **1986**, 127, 97; (b) B. M. Tadjikov, V. I. Melekhov, O. A. Anisimov, Yu. N. Molin, *Radiat. Phys. Chem.* **1989**, 34, 353.
194. (a) A. D. Trifunac, D. W. Werst, L. T. Percy, *Radiat. Phys. Chem.* **1989**, 34, 547; (b) D. W. Werst, M. G. Bakker, A. D. Trifunac, *J. Am. Chem. Soc.* **1990**, 112, 40.
195. D. W. Werst, A. D. Trifunac, *J. Phys. Chem.* **1988**, 92, 1093.
196. I. A. Shkrob, M. C. Sauer, A. D. Trifunac, *J. Phys. Chem.* **1996**, 100, 5993.
197. D. V. Tass, B. M. Tadjikov, Yu. N. Molin, *Chem. Phys. Lett.* **1995**, 235, 511.
198. B. M. Tadjikov, D. V. Tass, Yu. N. Molin, *Chem. Phys. Lett.* **1996**, 260, 529.
199. B. M. Tadjikov, D. V. Tass, O. M. Usov, Yu. N. Molin, *Chem. Phys. Lett.* **1997**, 273, 25–30.
200. F. B. Sviridenko, D. V. Tass, Yu. N. Molin, *Chem. Phys. Lett.* **1998**, 297, 343–349.
201. O. M. Usov, D. V. Tass, B. M. Tadjikov, Yu. N. Molin, *J. Phys. Chem. A* **1997**, 101, 7711–7717.
202. (a) M. Lindgren, M. Shiotani In *Radical Ionic Systems* (Eds.: A. Lund, M. Shiotani), Kluwer, Dordrecht, **1991**, 115; (b) M. Lindgren, M. Matsumoto, M. Shiotani, *J. Chem. Soc., Perkin Trans. 2* **1992**, 1397; (c) P. V. Schastnev, L. N. Shchegoleva, *Molecular Distortions in Ionic and Excited States*, CRC Press, Boca Raton, FL, 1995.
203. T. Fängström, S. Lunell, B. Engels, L. Eriksson, M. Shiotani, K. Komaguchi, *J. Chem. Phys.* **1997**, 107, 297.

204. (a) T. L. Amyes, J. P. Richard, *J. Am. Chem. Soc.* **1990**, *112*, 9507; (b) J. P. Richard, T. L. Amyes, L. Bei, V. Stubblefield, *J. Am. Chem. Soc.* **1990**, *112*, 9513.
205. P. M. Henrichs, P. E. Peterson, *J. Am. Chem. Soc.* **1973**, *95*, 7449; *J. Org. Chem.* **1976**, *41*, 362.
206. D. Farcasiu, *J. Chem. Soc., Chem. Commun.* **1977**, 394.
207. M. A. Miranda, J. Péret-Prieto, E. Font-Sanchis, K. Kónya, J. C. Scaiano, *J. Phys. Chem. A* **1998**, *102*, 5724–5727.
208. N. P. Schepp, L. J. Johnston, *J. Am. Chem. Soc.* **1996**, *118*, 2872–2881.
209. (a) K. Mizuno, I. Nakanishi, N. Ichinose, Y. Otsuji, *Chem. Lett.* **1989**, 1095–1098; (b) D. R. Arnold, X. Du, K. M. Hensleit, *Can. J. Chem.* **1991**, *69*, 839–852; (c) D. R. Arnold, X. Du, J. Chen, *Can. J. Chem.* **1995**, *73*, 307–318.
210. K. A. McManus, D. R. Arnold, *Can. J. Chem.* **1994**, *72*, 2291–2304; *ibid* **1995**, *73*, 2158–2169.
211. (a) F. D. Lewis In *Photoinduced Electron Transfer* (Eds.: M. A. Fox, M. Chanon), Elsevier, Amsterdam, 1988, Part C, Ch. 4.1; (b) N. L. Bauld, *Tetrahedron* **1989**, *45*, 5307–5363; (c) N. L. Bauld, *Adv. Electron Transfer Chem.* **1992**, Vol. 2, 1–66; (d) D. A. Connor, D. R. Arnold, P. K. Bakshi, T. S. Cameron, *Can. J. Chem.* **1995**, *73*, 762–771.
212. C. S. Q. Lew, J. R. Brisson, L. J. Johnston, *J. Org. Chem.* **1997**, *62*, 4047–4056.
213. (a) C. R. Brundle, M. B. Robin, N. A. Kuebler, H. Basch, *J. Am. Chem. Soc.* **1972**, *94*, 1451; (b) C. R. Brundle, M. B. Robin, N. A. Kuebler, *J. Am. Chem. Soc.* **1972**, *94*, 1466.
214. A. Hasegawa, Y. Itagaki, M. Shiotani, *J. Chem. Soc., Perkin Trans. 2* **1997**, 1625.
215. M. Shiotani, H. Kawazoe, J. Sohma, *J. Phys. Chem.* **1984**, *88*, 2220.
216. M. Shiotani, H. Kawazoe, J. Sohma, *Chem. Phys. Lett.* **1984**, *111*, 254.
217. K. Ohta, M. Shiotani, J. Sohma, *Chem. Phys. Lett.* **1987**, *140*, 148.
218. A. Hasegawa, M. C. R. Symons, *J. Chem. Soc., Faraday Trans. 1* **1983**, *79*, 1565.
219. (a) S. Marry, C. Thomson, *Chem. Phys. Lett.* **1981**, *82*, 373; (b) M. Kira, H. Nakagawa, H. Sakurai, *J. Am. Chem. Soc.* **1983**, *105*, 6983.
220. (a) M. Shiotani, Y. Nagata, J. Sohma, *J. Am. Chem. Soc.* **1984**, *106*, 4640; (b) J. Fujisawa, S. Sato, K. Shimokoshi, *Chem. Phys. Lett.* **1986**, *124*, 391.
221. S. Lunell, M. B. Huang, *Chem. Phys. Lett.* **1990**, *168*, 63.
222. K. Toriyama, K. Nunome, M. Iwasaki, *J. Chem. Phys.* **1982**, *77*, 5981.
223. M. Shiotani, Y. Nagata, J. Sohma, *J. Phys. Chem.* **1984**, *88*, 4078.
224. K. Toriyama, K. Nunome, M. Iwasaki, *Chem. Phys. Lett.* **1984**, *107*, 86.
225. Y. Itagaki, M. Shiotani, A. Hasegawa, H. Kawazoe, *Bull. Chem. Soc. Jpn.* **1998**, *71*, 2547–2554.
226. E. Baciocchi, *Acta Chem. Scand.* **1990**, *44*, 645 and references therein.
227. X. M. Zhang, F. G. Bordwell, *J. Am. Chem. Soc.* **1994**, *116*, 904–908 and references therein.
228. (a) A. Anne, P. Hapiot, J. Moiroux, P. Neta, J. M. Savéant, *J. Am. Chem. Soc.* **1992**, *114*, 4694–4701; (b) E. Baciocchi, T. Del Giacco, F. Elisei, *J. Am. Chem. Soc.* **1993**, *115*, 12290.
229. A. Anne, J. Moiroux, J. M. Savéant, *J. Am. Chem. Soc.* **1993**, *115*, 10224–10230.
230. E. Baciocchi, T. D. Giacco, F. Elisei, O. Lanzalunga, *J. Am. Chem. Soc.* **1998**, *120*, 11800–11801.
231. (a) J. H. Davis, W. A. Goddard III, *J. Am. Chem. Soc.* **1977**, *99*, 4242; (b) H. J. P. Lijser, D. R. Arnold, *J. Phys. Chem.* **1996**, *100*, 3996.
232. K. Komaguchi, M. Shiotani, A. Lund, *Chem. Phys. Lett.* **1997**, *265*, 217–223.
233. S. D. Chemerisov, D. W. Werst, A. D. Trifunac, *Chem. Phys. Lett.* **1998**, *291*, 262–268.
234. (a) F. Gerson, X. Z. Qin, *Helv. Chim. Acta* **1988**, *71*, 1498; (b) G. Gescheidt, A. Lamprecht, C. Rüchardt, M. Schmittel, *Helv. Chim. Acta* **1992**, *75*, 351; (c) P. S. Engel, D. M. Robertson, J. N. Scholz, H. J. Shine, *J. Org. Chem.* **1992**, *57*, 6178; (d) J. L. Goodman, T. A. Zona, *Tetrahedron Lett.* **1992**, 6093–6096; (e) W. Adam, G. F. Chen, H. Walter, F. Williams, *J. Am. Chem. Soc.* **1992**, *114*, 3007; (f) W. Adam, U. Denninger, R. Finzel, F. Kita, H. Platsch, H. Walter, G. Zang, *J. Am. Chem. Soc.* **1992**, *114*, 5027.
235. (a) N. J. Turro, G. J. Kavarnos, *J. Chem. Rev.* **1986**, *86*, 401; (b) G. J. Kavarnos, *Top. Curr. Chem.* **1990**, *156*, 20.
236. W. Adam, S. Grabowski, R. M. Wilson, *Acc. Chem. Res.* **1990**, *23*, 165.
237. (a) W. Adam, M. Dörr, *J. Am. Chem. Soc.* **1987**, *109*, 1570; (b) W. Adam, M. A. Miranda, *J. Org. Chem.* **1987**, *52*, 5498.

238. W. Adam, J. Sendelbach, *J. Org. Chem.* **1993**, 58, 5310–5315.
239. W. Adam, C. Sahin, *Tetrahedron Lett.* **1994**, 35, 9027–9030.
240. R. J. Bushby, K. M. Ng, *J. Chem. Soc., Perkin Trans. 2* **1996**, 1053–1056.
241. W. Adam, T. Kammel, M. Toubartz, S. Steenken, *J. Am. Chem. Soc.* **1997**, 119, 10673–10676.
242. F. A. Benson, *The High Nitrogen Compounds*, Wiley, New York, **1984**.
243. M. Bolle, K. Luther, *J. Troe. Appl. Surf. Sc.* **1990**, 46, 279.
244. R. H. Smith Jr., B. D. Władkowski, J. A. Herling, T. D. Pfaltzgraff, B. Pruski, J. Klose, Ch. J. Michejda, *J. Org. Chem.* **1992**, 57, 654.
245. (a) J. Huguët, M. Libert, C. Caullet, *Bull. Soc. Chim. Fr.* **1972**, 12, 4860; (b) L. Dunsch, B. Gollas, A. Neudeck, A. Petr, B. Speiser, H. Stahl, *Chem. Ber.* **1994**, 127, 2423.
246. P. Rapta, L. Omelka, A. Stasko, J. Dauth, B. Deubzer, J. Weis, *J. Chem. Soc., Perkin Trans. 2* **1995**, 255–261.
247. K. Komaguchi, M. Shiotani, *J. Phys. Chem. A* **1997**, 101, 6983–6990.
248. (a) Y. Apeloig In *The Chemistry of Organosilicon Compounds* (Eds.: S. Patai, Z. Rappoport), Wiley, Chichester, 1989, 57–225; (b) J. Chojnowski, W. Stanczyk, *Adv. Organomet. Chem.* **1990**, 30, 243; (c) N. C. Norman, *Polyhedron* **1993**, 12, 2431.
249. V. N. Khabashesku, Z. A. Kerzina, A. K. Maltsev, O. M. Nefedov, *J. Organomet. Chem.* **1989**, 364, 301.
250. (a) G. Manuel, G. Bertrand, F. El Anba, *Organometallics* **1983**, 2, 391; (b) C. A. Arrington, R. West, J. Michl, *J. Am. Chem. Soc.* **1983**, 105, 6176; (c) V. N. Khabashesku, Z. A. Kerzina, E. G. Baskir, A. K. Maltsev, O. F. Nefedov, *J. Organomet. Chem.* **1988**, 347, 277.
251. A. G. Davies, A. G. Neville, *J. Organomet. Chem.* **1992**, 436, 255.
252. A. G. Davies, C. Eaborn, P. D. Lickiss, A. G. Neville, *J. Chem. Soc., Perkin Trans. 2* **1995**, 163–169.
253. H. Ban, A. Tanaka, N. Hayashi, S. Tagawa, Y. Tabata, *Radiat. Phys. Chem.* **1989**, 34, 587.
254. (a) S. Irie, K. Oka, R. Nakao, M. Irie, *J. Organomet. Chem.* **1990**, 388, 253; (b) S. Irie, M. Irie, *Macromolecules* **1992**, 25, 1766.
255. K. Ushida, A. Kira, S. Tagawa, Y. Yoshida, H. Shibata, *Polym. Mater. Sci. Eng.* **1992**, 66, 299.
256. J. Kumagai, H. Yoshida, H. Koizumi, T. Ichikawa, *J. Phys. Chem.* **1994**, 98, 13117.
257. J. Kumagai, H. Yoshida, T. Ichikawa, *J. Phys. Chem.* **1995**, 99, 7965–7969.
258. (a) M. Adam, K. Müllen, *Adv. Mater.* **1994**, 6, 439; (b) M. R. Bryce, *J. Mater. Chem.* **1995**, 5, 1481.
259. F. Gerson, A. Lamprecht, M. Fourmigué, *J. Chem. Soc., Perkin Trans. 2* **1996**, 1409–1414.
260. F. Barbosa, L. Ebersson, G. Gescheidt, S. Gronowitz, A. Hörnfeldt, L. Juliá, O. Persson, *Acta Chem. Scand.* **1998**, 52, 1275–1284.
261. D. Lahem, R. Flammang, H. T. Le, T. L. Nguyen, M. T. Nguyen, *J. Chem. Soc., Perkin Trans. 2* **1999**, 821–826.
262. (a) *Sulfur-Centered Reactive Intermediates in Chemistry and Biology* (Eds.: C. Chatgililoglu, K. D. Asmus), Plenum Press, New York 1990; (b) S. A. Chaudhri, H. Mohan, E. Anklam, K. D. Asmus, *J. Chem. Soc., Perkin Trans. 2* **1996**, 383–390.
263. (a) C. von Sonntag, *The Chemical Basis of Radiation Biology*, Taylor and Francis, London, **1987**; (b) P. Wardman, In *Sulfur-Centered Reactive Intermediates in Chemistry and Biology* (Eds.: C. Chatgililoglu, K. D. Asmus), NATO Ser. A, 197, Plenum Press, New York **1990**, 415; (c) C. Schöneich, K. D. Asmus, M. Bonifacic, *J. Chem. Soc., Faraday Trans.* **1995**, 91, 1923–1930.
264. (a) L. Engman, J. Lind, G. Merényi, *J. Phys. Chem.* **1994**, 98, 3174–3182; (b) M. Ioele, S. Steenken, E. Baciocchi, *J. Phys. Chem. A* **1997**, 101, 2979–2897.
265. H. Yokoi, A. Hatta, K. Ishiguro, Y. Sawaki, *J. Am. Chem. Soc.* **1998**, 120, 12728–12733.
266. (a) N. J. Fitzpatrick, D. F. Brougham, P. J. Goarke, M. T. Nguyen, *Chem. Ber.* **1994**, 127, 969; (b) K. Toyota, M. Shibata, M. Yoshifuji, *Bull. Chem. Soc. Jpn.* **1995**, 68, 2633.
267. *Multiple Bonds and Low Coordination in Phosphorus Chemistry* (Eds.: M. Regitz, O. Scherer), Thieme, New York, **1990**.
268. (a) A. Jouaiti, M. Geoffroy, G. Terron, G. Bernardinelli, *J. Am. Chem. Soc.* **1995**, 117, 2251; (b) W. W. Schoeller, W. Haug, J. Strutwolf, T. Busch, *J. Chem. Soc., Faraday Trans.* **1996**, 92, 1751.

269. H. H. Karsh, H. U. Reisacher, G. Müller, *Angew. Chem. Int. Ed. Engl.* **1994**, 23, 618.
270. M. T. Nguyen, A. F. Hegarty, *J. Chem. Soc., Perkin Trans. 2* **1985**, 2005.
271. M. Chentit, H. Sidorenkova, A. Jouaiti, G. Terron, M. Geoffroy, Y. Ellinger, *J. Chem. Soc., Perkin Trans. 2* **1997**, 921–925.
272. I. I. Bilkis, V. D. Shteingarts, *Izv. SO Akad. Nauk. SSSR, Ser. Khim. Nauk*, **1987**, 5, 105.
273. (a) A. Bohnen, J. Räder, K. Müllen, *Synth. Met.* **1992**, 47, 37; (b) M. Baumgarten, U. Müller, K. Müllen, *AIP Conf. Proc. Ser.*, St. Thomas **1992**, 68.
274. (a) A. Farazdel, M. Dupuis, E. Clementi, A. Aviram, *J. Am. Chem. Soc.* **1990**, 112, 4206; (b) N. Liang, J. R. Miller, G. L. Closs, *J. Am. Chem. Soc.* **1990**, 112, 5353.
275. (a) J. Fielder, W. Huber, K. Müllen, *Angew. Chem., Int. Ed. Engl.* **1986**, 25, 443; (b) G. L. Closs, P. Piotrowiak, J. M. MacInnes, G. R. Flemming, *J. Am. Chem. Soc.* **1988**, 110, 2652.
276. (a) J. S. Miller, A. J. Epstein, *Angew. Chem., Int. Ed. Engl.* **1994**, 33, 385; (b) M. Baumgarten, K. Müllen, *Top. Curr. Chem.* **1994**, 169, 1; (c) A. Rajca, *Chem. Rev.* **1994**, 94, 871.
277. *Proceedings of the Symposium on Chemistry and Physics of Molecular Based Magnetic Materials* (Eds.: H. Iwamura, J. S. Miller), *Mol. Cryst. Liq. Cryst.* **1993**, Vol. 232, 1–360; Vol. 233, 1–366.
278. (a) D. A. Dougherty In *Research Frontiers in Magnetochemistry* (Ed.: C. O. Connor), World Scientific Publishing, River Edge, NJ, 1992; (b) M. Baumgarten, U. Müller, A. Bohnen, K. Müllen, *Angew. Chem., Int. Ed. Engl.* **1992**, 31, 448; (c) M. Baumgarten, U. Müller, *Synth. Met.* **1993**, 57, 4755.
279. (a) M. H. Whangbo, *Acc. Chem. Res.* **1983**, 16, 95; (b) L. Salem, C. Rowland, *Angew. Chem., Int. Ed. Engl.* **1972**, 11, 91.
280. (a) M. Dietrich, J. Mortensen, J. Heinze, *Angew. Chem., Int. Ed. Engl.* **1985**, 24, 508; (b) K. Meehrholtz, J. Heinze, *J. Am. Chem. Soc.* **1990**, 112, 5142.
281. U. Müller, M. Baumgarten, *J. Am. Chem. Soc.* **1995**, 117, 5840–5850.
282. G. Grampp, A. Kapturkiewicz, J. Salbeck, *Chem. Phys.* **1994**, 187, 391–397.
283. R. E. Hoffman, M. Nir, I. O. Shapiro, M. Rabinovitz, *J. Chem. Soc., Perkin Trans. 2*, **1996**, 1225–1233.
284. J. H. Hammons, C. T. Kresge, L. A. Paquette, *J. Am. Chem. Soc.* **1976**, 98, 8172.
285. S. Z. Goldberg, K. N. Raymond, C. A. Harmon, D. H. Templeton, *J. Am. Chem. Soc.* **1974**, 96, 1348.
286. T. J. Katz, *J. Am. Chem. Soc.* **1960**, 82, 3784.
287. H. Kojima, A. J. Bard, H. N. C. Wong, F. Sondheimer, *J. Am. Chem. Soc.* **1976**, 98, 5560.
288. T. J. Katz, M. Yoshida, L. C. Siew, *J. Am. Chem. Soc.* **1965**, 87, 4516.
289. G. R. Stevenson, M. Colón, I. Ocasio, J. G. Concepcion, A. McB. Block, *J. Phys. Chem.* **1975**, 79, 1685.
290. M. Celina, R. L. R. Lazana, M. Luisa T. M. B. Franco, B. J. Herold, *J. Chem. Soc., Perkin Trans. 2* **1991**, 1791–1795.
291. M. Iwaizumi, S. Kita, T. Isobe, M. Kohna, T. Yamamoto, H. Horita, T. Otsubo, S. Misumi, *Bull. Chem. Soc. Jpn.* **1977**, 50, 2074–2083.
292. S. F. Rak, L. L. Miller, *J. Am. Chem. Soc.* **1992**, 114, 1388–1394.
293. A. R. Wartini, J. Valenzuela, H. A. Staab, F. A. Neugebauer, *Eur. J. Org. Chem.* **1998**, 221–227.
294. (a) K. Maruyama, T. Otsuki, *Bull. Chem. Soc. Jpn.* **1968**, 41, 444; (b) T. Takeshita, N. Hirota, *J. Chem. Phys.* **1969**, 51, 2146.
295. M. Barzaghi, P. L. Beltrame, A. Gamba, M. Simonetta, *J. Am. Chem. Soc.* **1978**, 100, 251.
296. M. Barzaghi, S. S. Mlertus, C. Oliva, E. Ortoleva, M. Simonetta, *J. Phys. Chem.* **1983**, 87, 881–888.
297. G. Grampp, Y. A. Khan, H. Larsen, *J. Chem. Soc., Perkin Trans. 2* **1997**, 2555–2557.
298. (a) G. Grampp, W. Jaenicke, *Ber. Bunsenges. Phys. Chem.* **1991**, 95, 904; (b) G. Grampp, W. Jaenicke, *J. Chem. Soc., Faraday Trans. 2* **1985**, 81, 1035.
299. (a) M. J. Weaver, *Chem. Rev.* **1992**, 92, 463; (b) H. Larsen, St. U. Pedersen, J. A. Pedersen, *J. Electroanal. Chem.* **1992**, 331, 971; (c) C. D. Stevenson, C. V. Rice, *J. Am. Chem. Soc.* **1995**, 117, 10551.
300. J. M. Savéant, *Adv. Phys. Org. Chem.* **1990**, 26, 1.
301. (a) P. Neta, D. Behar, *J. Am. Chem. Soc.* **1981**, 103, 103; (b) M. MeotNer, P. Neta, R. K. Norrish, K. Wilson, *J. Phys. Chem.* **1986**, 90, 168.

302. D. Bethell, R. G. Compton, R. G. Welling, *J. Chem. Soc., Perkin Trans. 2* **1992**, 147.
303. (a) R. G. Compton, R. A. W. Dryfe, A. C. Fisher, *J. Electroanal. Chem.* **1993**, 361, 275; *J. Chem. Soc., Perkin Trans. 2* **1994**, 1581; (b) R. G. Compton, R. A. W. Dryfe, *J. Electroanal. Chem.* **1994**, 375, 247.
304. R. G. Compton, R. A. W. Dryfe, J. C. Eklund, S. D. Page, J. Hirst, L. B. Nei, G. W. J. Fleet, K. Y. Hsia, D. Bethell, L. Martingale, *J. Chem. Soc., Perkin Trans. 2* **1995**, 1673.
305. M. J. S. Dewar, S. Kirschner, H. W. Kollmar, *J. Am. Chem. Soc.* **1974**, 96, 5242.
306. (a) R. Dressler, M. Allan, E. Haselbach, *Chimia* **1985**, 39, 385; (b) M. C. R. Symons, *Acta Chem. Scand.* **1997**, 51, 127; *Pure Appl. Chem.* **1981**, 53, 223.
307. M. J. S. Dewar, A. H. Pakiari, A. B. Pierini, *J. Am. Chem. Soc.* **1982**, 104, 3242.
308. (a) H. Villar, E. A. Castro, R. A. Rossi, *Can. J. Chem.* **1982**, 60, 2525; *Z. Naturforsch. Teil A* **1984**, 39, 49; (b) R. Benassi, C. Bertarini, F. Taddei, *Chem. Phys. Lett.* **1996**, 257, 633.
309. A. B. Pierini, J. S. Duca, Jr., *J. Chem. Soc., Perkin Trans. 2* **1995**, 1821.
310. A. B. Pierini, J. S. Duca, Jr., D. M. A. Vera, *J. Chem. Soc., Perkin Trans. 2* **1999**, 1003–1009.
311. R. G. Compton, R. A. W. Dryfe, J. Hirst, *J. Phys. Chem.* **1994**, 98, 10497.
312. (a) J. F. Bunnett, E. Mitchell, C. Galli, *Tetrahedron* **1985**, 41, 4119; (b) C. Galli, *ibid* **1988**, 44, 5205; (c) D. B. Denney, D. Z. Denney, *ibid* **1991**, 47, 6577; (d) D. B. Denney, D. Z. Denney, A. J. Perez, *ibid* **1993**, 49, 4463; (e) X. M. Zhang, D. L. Yang, X. Q. Jia, Y. C. Liu, *J. Org. Chem.* **1993**, 58, 7350.
313. T. Abe, Y. Ikegami, *Bull. Chem. Soc. Jpn.* **1976**, 49, 3227; **1978**, 51, 196.
314. P. G. Sammes, D. Thetford, M. Voyle, *J. Chem. Soc., Perkin Trans. 1* **1988**, 3229.
315. (a) S. M. Shein, L. V. Bryukhovetskaya, F. V. Pishchugin, V. F. Starichenko, V. N. Panfilov, V. V. Voevodskii, *J. Struct. Chem.* **1970**, 11, 228; (b) I. I. Bilkis, S. M. Shein, *Tetrahedron* **1975**, 31, 969.
316. M. Mir, M. Espin, J. Marquet, I. Gallardo, C. Tomasi, *Tetrahedron Lett.* **1994**, 35, 9055–9058.
317. I. I. Bilkis, V. D. Shteingarts, *Zh. Org. Khim.* **1982**, 18, 359.
318. G. Grampp, M. C. B. L. Shohoji, B. Herold, S. Steenken, *Ber. Bunsenges. Phys. Chem.* **1990**, 94, 1507.
319. J. P. Telo, M. C. B. L. Shohoji, B. J. Herald, G. Grampp, *J. Chem. Soc., Faraday Trans.* **1992**, 88, 47.
320. J. P. Telo, M. C. B. L. Shohoji, *J. Chem. Soc., Perkin Trans. 2* **1998**, 711–714.
321. (a) H. Meier, *Angew. Chem., Int. Ed. Engl.* **1992**, 31, 1399–1420; (b) H. Goerner, H. J. Kuhn In *Ad. Photochem.* (Eds.: D. C. Neckers, D. H. Volman, G. V. Von Buenau), Wiley, New York, **1995**, Vol. 19, 1–118 and references cited therein.
322. (a) R. Chang, C. S. Johnson, *J. Chem. Phys.* **1965**, 43, 3183; (b) N. M. Atherton, F. Gerson, N. J. Ockwell, *J. Chem. Soc. A* **1966**, 109.
323. (a) J. Higuchi, K. Ishizu, F. Nemoto, K. Tajima, H. Suzuki, K. Ogawa, *J. Am. Chem. Soc.* **1984**, 106, 5403; (b) U. Buser, C. H. Ess, F. Gerson, *Magn. Reson. Chem.* **1991**, 29, 721.
324. F. Gerson, H. Ohya-Nishiguchi, M. Szwarc, G. Levin, *Chem. Phys. Lett.* **1977**, 52, 587.
325. (a) J. E. Gano, G. Subramaniam, R. Birnbaum, *J. Org. Chem.* **1990**, 55, 4760–4763; (b) K. K. Laali, J. E. Gano, D. Lenoir, C. W. I. Gundlach, *J. Chem. Soc., Perkin Trans. 2* **1994**, 2169–2173 and references therein.
326. J. E. Gano, E. J. Jacob, P. Sekher, G. Subramaniam, L. A. Eriksson, D. Lenoir, *J. Org. Chem.* **1996**, 61, 6739–6743.
327. S. Konishi, A. H. Reddoch, *J. Magn. Reson.* **1978**, 29, 113.
328. F. Gerson, W. B. Martin, Jr., C. Wydler, *Helv. Chim. Acta* **1979**, 62, 2517.
329. F. Gerson, W. B. Martin, Jr., *Helv. Chim. Acta* **1987**, 70, 1558.
330. F. Gerson, A. Lamprecht, M. Scholz, H. Troxler, D. Lenoir, *Helv. Chim. Acta* **1996**, 79, 307–318.
331. C. P. Andrieux, I. Gallardo, J. M. Savéant, *J. Am. Chem. Soc.* **1989**, 111, 1620.
332. (a) D. M. Wayner, V. D. Parker, *Acc. Chem. Res.* **1993**, 26, 287; (b) F. G. Bordwell, X. M. Zhang, *ibid* **1993**, 26, 510.
333. (a) F. G. Bordwell, M. J. Bausch, *J. Am. Chem. Soc.* **1986**, 108, 1985; (b) C. P. Andrieux, P. Hapiot, J. Pinson, J. M. Savéant, *ibid* **1993**, 115, 7783.
334. (a) C. P. Andrieux, J. M. Savéant In *Electrochemical Reactions in Investigation of Rates and Mechanisms of Reactions, Techniques of Chemistry* (Ed.: C. F. Bernasconi), Wiley, New York,

- 1986, VI/4E, Part 2, 305–390; (b) C. P. Andrieux, P. Hapiot, J. M. Savéant, *Chem. Rev.* **1990**, 90, 723.
335. H. Lund, K. Daasbjerg, T. Lund, D. Occhialini, S. U. Pedersen, *Acta Chem. Scand.* **1997**, 51, 135.
336. (a) T. Nagaoka, D. Griller, D. D. M. Wayner, *J. Phys. Chem.* **1991**, 95, 6264; (b) D. D. M. Wayner, A. Houman, *Acta Chem. Scand.* **1998**, 52, 377.
337. P. Hapiot, V. V. Kononov, J. M. Savéant, *J. Am. Chem. Soc.* **1995**, 117, 1428 and references therein.
338. J. Gonzalez, P. Hapiot, V. Kononov, J. M. Savéant, *J. Am. Chem. Soc.* **1998**, 120, 10171–10179.
339. (a) J. S. Miller, A. J. Epstein, *Angew. Chemie.* **1994**, 106, 399; *Angew. Chemie Int. Ed. Engl.* **1994**, 33, 385; (b) M. Baumgarten, K. Müllen, *Top. Curr. Chem.* **1994**, 169, 1.
340. Z. Hou, A. Fujita, H. Yamazaki, Y. Wakatsuki, *J. Am. Chem. Soc.* **1996**, 118, 2503.
341. (a) N. Hirota, S. I. Weissman, *Mol. Phys.* **1962**, 5, 537; (b) N. Hirota, *J. Am. Chem. Soc.* **1967**, 89, 32.
342. A. Behrendt, C. G. Screttas, D. Bethell, O. Schieman, B. R. Steele, *J. Chem. Soc., Perkin Trans. 2* **1998**, 2039–2045.
343. (a) M. S. Workentin, R. L. Donkers, *J. Am. Chem. Soc.* **1998**, 120, 2664; *J. Phys. Chem. B* **1998**, 102, 4061; (b) S. Antonello, M. Musumeci, D. D. M. Wayner, F. Maran, *J. Am. Chem. Soc.* **1997**, 119, 9541; (c) S. Antonello, F. Maran, *J. Am. Chem. Soc.* **1997**, 119, 12595.
344. (a) *Organic Peroxides* (Ed.: W. Ando), Wiley, Chichester, England, 1992; (b) *Active Oxygen in Chemistry, Search Series* (Eds.: C. S. Foote, J. S. Valentine, A. Greenberg, J. F. Lieban), Blackie, New York, 1995, Vol. 2; (c) *Active Oxygen in Biochemistry, Search Series* (Eds.: C. S. Foote, J. S. Valentine, A. Greenberg, J. F. Lieban), Blackie, New York, 1995, Vol. 3.
345. (a) W. M. Wu, Y. Wu, Y. L. Wu, Z. J. Yao, C. M. Xhou, Y. Li, F. Shan, *J. Am. Chem. Soc.* **1998**, 120, 3316; (b) J. N. Cumming, D. Wang, S. B. Park, T. A. Shapiro, G. H. Posner, *J. Med. Chem.* **1998**, 41, 952 and references therein; (c) A. Robert, B. Meunier, *Chem. Soc. Rev.* **1998**, 27, 273.
346. R. L. Donkers, J. Tse, M. S. Workentin, *Chem. Commun.* **1999**, 135–136.
347. M. J. Weaver, *Chem. Rev.* **1992**, 92, 463.
348. P. F. Barbara, F. J. Meyer, M. A. Ratner, *J. Phys. Chem.* **1996**, 100, 13148.
349. (a) S. F. Nelsen, R. F. Ismagilov, D. R. Powell, *J. Am. Chem. Soc.* **1997**, 119, 10213; (b) S. F. Nelsen, R. F. Ismagilov, D. A. Trieber II, *Science* **1997**, 278, 846.
350. G. Grampp, M. C. B. L. Shohoji, B. Herold, S. Steenken, *Ber. Bunsenges. Phys. Chem.* **1990**, 94, 1507.
351. J. P. Telo, M. C. B. L. Shohoji, B. J. Herold, G. Grampp, *J. Chem. Soc., Faraday Trans.* **1992**, 88, 47.
352. S. Mahmood, B. J. Tabner, V. A. Tabner, *J. Chem. Soc., Faraday Trans.* **1990**, 86, 3253.
353. J. P. Telo, M. C. B. L. Shohoji, *J. Chem. Soc., Perkin Trans. 2* **1998**, 711.
354. J. P. Telo, G. Grampp, M. C. B. L. Shohoji, *Phys. Chem. Chem. Phys.* **1999**, 1, 99–104.
355. *Landolt-Börnstein New Series, Magnetic Properties of Free Radicals*, Springer, Berlin, **1980**, group II, 9d1, 634–639.
356. (a) M. Newcomb, D. Curran, *Acc. Chem. Res.* **1988**, 21, 206; (b) M. Newcomb, T. R. Varick, S. Y. Choi, *J. Org. Chem.* **1992**, 57, 373.
357. (a) M. Ahbala, P. Hapiot, A. Houman, M. Jouini, J. Pinson, J. M. Savéant, *J. Am. Chem. Soc.* **1995**, 117, 11488; (b) K. Daasbjerg, T. B. Christensen, *Acta Chem. Scand.* **1995**, 49, 128; (c) E. C. Ashby, *Acc. Chem. Res.* **1988**, 21, 414.
358. L. M. Tolbert, J. Bedlek, M. Terapane, J. Kowalik, *J. Am. Chem. Soc.* **1997**, 119, 2291–2292.
359. (a) P. K. Das, *Chem. Rev.* **1993**, 93, 119–144; (b) R. A. McClelland, *Tetrahedron* **1996**, 52, 6823–6858 and references therein.
360. E. Buncl, T. Durst, *Comprehensive Carbanion Chemistry*, Elsevier, Amsterdam, 1980.
361. D. Budac, P. Wan, *Can. J. Chem.* **1996**, 74, 1447–1464.
362. (a) S. Torii, *Electro-Organic Syntheses*, Kodansha, Tokyo, **1985**, Ch. 2, 51–74; (b) T. Ohno, T. Fukumoto, T. Hirashima, I. Nishiguchi, *Chem. Lett.* **1991**, 1085–1088.
363. P. R. Bowers, K. A. McLauchlan, R. C. Sealy, *J. Chem. Soc., Perkin Trans. 2* **1976**, 915–921.

364. (a) J. Libman, *J. Am. Chem. Soc.* **1975**, *99*, 4139–4141; (b) M. Novak, A. Miller, T. C. Bruice, *ibid* **1980**, *102*, 1465–1467; (c) Y. Kurauchi, H. Nobuhara, K. Ohga, *Bull. Chem. Soc. Jpn.* **1986**, *59*, 897–905; (d) K. Tsujimoto, N. Nakao, M. Ohashi, *J. Chem. Soc., Chem. Commun.* **1992**, 336–337; (e) M. Mella, M. Freccero, T. Soldi, E. Fasani, A. Albini, *J. Org. Chem.* **1996**, *61*, 1413–1422.
365. (a) T. O. Meiggs, S. I. Miller, *J. Am. Chem. Soc.* **1972**, *94*, 1989–1996; (b) J. D. Coyle, *Chem. Rev.* **1978**, *78*, 97–123.
366. J. D. Margerum, *J. Am. Chem. Soc.* **1965**, *87*, 3772–3773.
367. J. L. Martinez, J. C. Scaiano, *J. Am. Chem. Soc.* **1997**, *119*, 11066–11070.
368. H. Yokoi, T. Nakano, W. Fujita, K. Ishiguro, Y. Sawaki, *J. Am. Chem. Soc.* **1998**, *120*, 12453–12458.
369. M. L. Chan, T. C. Chan, *J. Phys. Chem.* **1995**, *99*, 5765.
370. T. Tominaga, S. Tenma, H. Watanabe, *J. Chem. Soc., Faraday Trans.* **1996**, *92*, 1863.
371. (a) M. Lezni, H. Schuh, H. Fischer, *Int. J. Chem. Kinet.* **1979**, *11*, 705; (b) M. Sitariski, *ibid* **1981**, *13*, 125; (c) M. Lezni, H. Fischer, *ibid* **1983**, *15*, 733.
372. (a) H. J. Werner, Z. Schulten, K. Schulten, *J. Chem. Phys.* **1977**, *67*, 646; (b) R. Kaptein, *J. Am. Chem. Soc.* **1972**, *94*, 6251.
373. (a) R. D. Burkhart, R. J. Wong, *J. Am. Chem. Soc.* **1973**, *95*, 7203; (b) P. P. Levin, I. V. Khudyakov, V. A. Kuzumin, *J. Phys. Chem.* **1989**, *93*, 208.
374. (a) M. Terazima, K. Okamoto, N. Hirota, *Laser Chem.* **1994**, *13*, 169; (b) M. Terazima, K. Okamoto, N. Hirota, *J. Phys. Chem.* **1993**, *97*, 13387; (c) *J. Chem. Phys.* **1995**, *102*, 2506; (d) K. Okamoto, M. Terazima, N. Hirota, *J. Chem. Phys.* **1995**, *103*, 10445.
375. (a) F. D. Evans, C. Chan, B. C. Lamartine, *J. Am. Chem. Soc.* **1977**, *28*, 6492; (b) D. F. Evans, T. Tominaga, C. Chan, *J. Solution Chem.* **1979**, *8*, 461.
376. N. Houser, R. C. Jarnagin, *J. Chem. Phys.* **1970**, *52*, 1069.
377. (a) J. P. Dodelet, G. R. Freeman, *Can. J. Chem.* **1975**, *53*, 1263; (b) S. S. Sam, G. R. Freeman, *J. Chem. Phys.* **1979**, *70*, 1538; **1980**, *72*, 1989.
378. (a) S. K. Lim, M. E. Burba, A. C. Albrecht, *Chem. Phys. Lett.* **1993**, *216*, 405; (b) *J. Phys. Chem.* **1994**, *98*, 9665.
379. M. Terazima, T. Okazaki, N. Hirota, *J. Photochem. Photobiol.* **1995**, *92*, 7.
380. K. Okamoto, N. Hirota, M. Terazima, *J. Chem. Soc., Faraday Trans.* **1998**, *94*, 185–194.
381. I. R. Gould, S. Farid, *Acc. Chem. Res.* **1996**, *29*, 522.
382. (a) H. D. Roth, M. L. M. Schilling, *J. Am. Chem. Soc.* **1980**, *102*, 4303; (b) H. D. Roth, M. L. M. Schilling, G. Jones, *J. Am. Chem. Soc.* **1981**, *103*, 1246.
383. P. C. Wong, D. R. Arnold, *Tetrahedron Lett.* **1979**, 2101.
384. M. L. M. Schilling, H. D. Roth, *J. Am. Chem. Soc.* **1980**, *102*, 7956; **1981**, *103*, 7210.
385. S. B. Karki, J. P. Dinnocenzo, S. Farid, J. L. Goodman, I. R. Gould, T. A. Zona, *J. Am. Chem. Soc.* **1997**, *119*, 431–432.
386. (a) H. Eyring, M. Z. Polanyi, *Phys. Chem.* **1931**, *B12*, 279; (b) K. Wynne, C. Galli, R. M. Hochstrasser, *J. Chem. Phys.* **1994**, *100*, 4797; (c) T. Hannappel, B. Burfeindt, W. Storck, F. Willig, *J. Phys. Chem.* **1997**, *B101*, 6799.
387. (a) L. Ebersson, *New J. Chem.* **1992**, *16*, 151; (b) H. Zipse, *Angew. Chem. Int. Ed. Engl.* **1997**, *36*, 1697; (c) H. Tributsch, L. Pohlmann, *Science* **1998**, *279*, 1891.
388. D. Zhong, A. H. Zewail, *J. Phys. Chem.* **1998**, *A102*, 4031.
389. (a) G. N. Sastry, S. Shaik, *J. Am. Chem. Soc.* **1998**, *120*, 2131; (b) J. T. Su, A. H. Zewail, *J. Phys. Chem.* **1998**, *A102*, 4082.
390. (a) R. S. Mulliken, *J. Am. Chem. Soc.* **1950**, *72*, 600; (b) R. S. Mulliken, W. M. Person, *Molecular Complexes*, Wiley, New York, 1969; (c) M. Tamres, M. Brandon, *J. Am. Chem. Soc.* **1960**, *82*, 2134.
391. R. Rathore, S. M. Hubig, J. K. Kochi, *J. Am. Chem. Soc.* **1997**, *119*, 11468.
392. S. M. Hubig, R. Rathore, J. K. Kochi, *J. Am. Chem. Soc.* **1999**, *121*, 617–626.
393. D. H. Levy, R. J. Myers, *J. Chem. Phys.* **1964**, *41*, 1062; **1966**, *44*, 4177.
394. W. M. Tolles, D. W. Moore, *J. Chem. Phys.* **1967**, *46*, 2102.
395. N. Sommer, Kautschuk, *Gummi Kunstst.* **1975**, *28*, 131.
396. F. Gerson, H. Hopf, P. Merstetter, C. Mlynec, D. Fischer, *J. Am. Chem. Soc.* **1998**, *120*, 4815.

397. J. K. Kim, J. F. Bunnett, *J. Am. Chem. Soc.* **1970**, 92, 7463.
398. (a) G. A. Russell, W. C. Danen, *J. Am. Chem. Soc.* **1966**, 88, 5663; **1968**, 90, 347; (b) G. A. Russell, *Chem. Soc. Special Publication* **1970**, No. 24, 271; *Pure Appl. Chem.* **1971**, 4, 67.
399. (a) N. Kornblum, R. E. Michael, P. C. Kerber, *J. Am. Chem. Soc.* **1966**, 88, 5660; (b) N. Kornblum, *Angew. Chem., Int. Ed. Engl.* **1975**, 14, 734.
400. G. A. Russell, A. R. Metcalfe, *J. Am. Chem. Soc.* **1979**, 101, 2359.
401. G. A. Russell, J. Hershberger, *J. Chem. Soc., Chem. Commun.* **1980**, 216.
402. G. A. Russell, M. Jawdoskiuk, M. Makosza, *J. Am. Chem. Soc.* **1979**, 101, 2355.
403. N. Ono, R. Tamura, A. Kagi, *J. Am. Chem. Soc.* **1980**, 102, 2851.
404. D. D. Tanner, E. V. Blackburn, G. E. Diaz, *J. Am. Chem. Soc.* **1981**, 103, 1557.
405. N. Kornblum, S. C. Carlson, R. G. Smith, *J. Am. Chem. Soc.* **1979**, 101, 647.
406. (a) C. Chacaty, *Compt. Rend. Ser. C* **1966**, 262, 680; (b) M. C. R. Symons, J. H. Sharp, *Nature* (London) **1969**, 224, 5226.
407. (a) G. A. Russell, R. K. Norris, E. J. Panek, *J. Am. Chem. Soc.* **1971**, 93, 5839; (b) H. Sayo, M. Masui, *Tetrahedron* **1968**, 24, 5075.
408. W. R. Bowman, M. C. R. Symons, *J. Chem. Soc., Perkin Trans. 2* **1983**, 25.
409. (a) J. Adams, M. L. Gross, *J. Am. Chem. Soc.* **1989**, 111, 435; (b) M. L. Gross, *Int. J. Mass Spectrom. Ion Process* **1992**, 118/119, 137; (c) J. Adams, *Mass Spectrom. Rev.* **1990**, 9, 141.
410. P. C. H. Eichinger, J. H. Bowie, *Int. J. Mass Spectrom. Ion Process* **1991**, 110, 123.
411. (a) V. H. Wysocki, M. H. Bier, R. G. Cooks, *Org. Mass. Spectrom.* **1988**, 23, 627; (b) V. H. Wysocki, M. M. Ross, S. R. Horning, R. G. Cooks, *Rapid Commun. Mass. Spectrom.* **1988**, 2, 214; (c) V. H. Wysocki, M. M. Ross, *Int. J. Mass Spectrom. Ion Process* **1991**, 104, 179.
412. (a) C. K. Ingold, G. W. King, *J. Chem. Soc.* **1953**, 2702; (b) K. K. Innes, *J. Chem. Phys.* **1954**, 22, 863.
413. S. Sakai, K. Morokuma, *J. Phys. Chem.* **1987**, 91, 3661.
414. (a) K. Matsuura, H. Muto, *J. Chem. Phys.* **1991**, 94, 4078; (b) *J. Phys. Chem.* **1993**, 97, 8842.
415. (a) L. Manceron, L. Andrews, *J. Am. Chem. Soc.* **1985**, 107, 563; (b) *J. Phys. Chem.* **1985**, 89, 4094.
416. (a) P. H. Kasai, *J. Phys. Chem.* **1982**, 86, 4092; (b) *J. Am. Chem. Soc.* **1992**, 114, 3299.
417. Y. Itagaki, M. Shiotani, H. Tachikawa, *Acta Chem. Scand.* **1997**, 51, 220–223.
418. (a) C. Krohnke, V. Enkelmann, G. Wegner, *Angew. Chem., Int. Ed. Engl.* **1980**, 19, 912; (b) M. Almeida, R. T. Henriques In *Handbook of Organic Conductive Molecules and Polymers* (Ed.: H. S. Nalwa), John Wiley and Sons, Chichester, 1997, Vol. 1, Ch. 2, 87.
419. (a) K. Bechgaard In *Structure and Properties of Molecular Crystals* (Ed.: M. Pierrot), Elsevier, Amsterdam, 1990, 235; (b) C. Heywang, S. Roth, *Angew. Chem., Int. Ed. Engl.* **1991**, 30, 176; (c) J. Morgado, I. C. Santos, L. F. Veiros, R. T. Henriques, M. T. Duarte, M. Almeida, L. Alcácer, *J. Mater. Chem.* **1997**, 7, 2387.
420. H. Tani, Y. Kamada, N. Azuma, N. Ono, *Tetrahedron Lett.* **1994**, 35, 7051; *Mol. Cryst. Liq. Cryst.* **1996**, 278, 131.
421. M. R. Bryce, A. K. Lay, A. Chesney, A. S. Batsanov, J. A. K. Howard, U. Buser, F. Gerson, P. Merstetter, *J. Chem. Soc., Perkin Trans. 2* **1999**, 755–763.
422. (a) M. J. Janssen, *The Electronic Structure of Organic Thione Compounds*, Thesis, Utrecht University, 1959; (b) *Recl. Trav. Chim. Pays-Bas* **1960**, 79, 454, 464, 1067.
423. L. Fälvh, U. Håkansson, J. Sandström, *J. Mol. Struct. (THEOCHEM)* **1989**, 185, 239.
424. A. Mannschreck, A. Talvitie, W. Fischer, G. Snatzke, *Monatsh. Chem.* **1983**, 114, 101.
425. K. Rang, J. Sandström, *J. Chem. Soc., Perkin Trans. 2* **1999**, 827–832.
426. (a) D. Bourissou, G. Bertrand, *C. R. Acad. Sci. Paris* **1996**, 322, 489; (b) M. Yoshifuji, Y. Ichikawa, K. Toyota, E. Kasashima, Y. Okamoto, *Chem. Lett.* **1997**, 87.
427. M. Geoffroy, A. Jouaiti, G. Terron, M. Cattani-Lorente, Y. Ellinger, *J. Phys. Chem.* **1992**, 96, 8241.
428. A. Al Badri, M. Chentit, M. Geoffroy, A. Jouaiti, *J. Chem. Soc., Faraday Trans.* **1997**, 93, 3631–3635.
429. H. Sidorenkova, M. Chentit, A. Jouaiti, G. Terron, M. Geoffroy, Y. Ellinger, *J. Chem. Soc., Perkin Trans. 2* **1998**, 71–74.

430. M. Chentit, H. Sidorenkova, A. Jouaiti, G. Terron, M. Geoffroy, Y. Ellinger, *J. Chem. Soc., Perkin Trans. 2* **1997**, 921.
431. A. Alberti, M. Benaglia, M. D' Angelantonio, S. S. Emmi, M. Guerra, A. Hudson, D. Macciantelli, F. Paolucci, S. Roffia, *J. Chem. Soc., Perkin Trans. 2*, **1999**, 309–323.
432. A. Alberti, M. Benaglia, M. Guerra, A. Hudson, D. Macciantelli, *J. Chem. Soc., Perkin Trans. 2*, **1999**, 1567–1568.
433. K. Exner, D. Hunkler, G. Gescheidt, H. Prinzbach, *Angew. Chem. Int. Ed.* **1998**, 37, 1910–1912.
434. (a) C. H. Ess, F. Gerson, W. Adam, *Helv. Chim. Acta* **1992**, 75, 335; (b) S. F. Gerson, A. Lamprecht, M. Scholz, H. Troxler, *ibid* **1996**, 79, 307; (c) G. Gescheidt, A. Lamprecht, C. Rüchardt, M. Schmittel, *ibid* **1992**, 75, 351.
435. (a) A. J. Fatiadi, *The Chemistry of Triple Bonded Groups*, Wiley, New York, **1983**; *Synthesis* **1986**, 249; **1987**, 749, 959; (b) W. Kaim, M. Moscherosch, *Coord. Chem. Rev.* **1994**, 129, 157; (c) W. E. Buschmann, A. M. Arif, J. S. Miller, *J. Chem. Soc., Chem. Commun.* **1995**, 2343; (d) H. Yamochi, S. Horiuchi, G. Saito, M. Kusunoki, K. Sakaguchi, T. Kikuchi, S. Sato, *Synth. Met.* **1993**, 56, 2096.
436. (a) J. E. Lind Jr., R. M. Fuoss, *J. Am. Chem. Soc.* **1961**, 83, 1828; (b) A. L. Farragher, F. M. Page, *Trans. Faraday Soc.* **1967**, 63, 10; (c) M. L. Bruce, R. C. Wallis, B. W. Skelton, A. H. White, *J. Chem. Soc., Dalton Trans.* **1981**, 1205.
437. M. Decoster, F. Conan, M. Kubicki, Y. Le Mest, P. Richard, J. S. Pala, L. Toupet, *J. Chem. Soc., Perkin Trans. 2*, **1997**, 265–271.
438. (a) G. Gescheidt, A. Lamprecht, C. Rüchardt, M. Schmittel, *Helv. Chim. Acta*, **1991**, 74, 2094; (b) R. J. Bushby, K. M. Ng, *J. Chem. Soc., Perkin Trans. 2* **1996**, 1053, 1525.
439. U. Buser, C. H. Ess, F. Gerson, *Magn. Reson. Chem.* **1991**, 29, 721.
440. F. Gerson, C. Sahin, *J. Chem. Soc., Perkin Trans. 2* **1997**, 1127–1132.
441. R. D. Webster, A. M. Bond, R. G. Compton, *J. Phys. Chem.* **1996**, 100, 10288.
442. (a) R. D. Webster, A. M. Bond, T. Schmidt, *J. Chem. Soc., Perkin Trans. 2* **1995**, 1365; (b) R. D. Webster, A. M. Bond, *J. Org. Chem.* **1997**, 62, 1779; *J. Chem. Soc., Perkin Trans. 2* **1997**, 1079.
443. R. D. Webster, A. M. Bond, D. C. Coomber, *J. Electroanal. Chem.* **1998**, 422, 217.
444. R. D. Webster, *J. Chem. Soc., Perkin Trans. 2* **1999**, 263–269.
445. see, e.g., D. M. Guldi, *Chem. Commun.* **2000**, 321–327; L. Echegoyen, L. E. Echegoyen, *Acc. Chem. Res.* **1998**, 593–601.

5 Electron-transfer Chemistry of Fullerenes

Shunichi Fukuzumi and Dirk M. Guldi

5.1 Introduction

The spherical shape of buckminsterfullerenes (C_{60}) makes these carbon allotropes ideal probes for the investigation of electron-transfer reactions, especially in relation to Marcus's electron-transfer theory [1]. In the reduction of C_{60} , the first electron is added to a triply degenerate t_{1u} unoccupied molecular orbital resulting in a maximum delocalization [2]. In fact, the remarkable cyclic voltammogram and differential pulse voltammogram of C_{60} reveal six reversible reduction steps, all equally separated from each other by ca 450 mV (Figure 1) [3–5]. When, however, C_{60} is derivatized by, for example, introducing suitable addends to the fullerene core, the multi-electron reduction usually becomes thermodynamically more difficult than for the non-derivatized C_{60} [2]. Nonetheless the multi-electron reduction of C_{60} derivatives (i.e. up to six electrons) has still been observed [6–9]. Multi-electron reduction is also possible for higher fullerenes including C_{70} , C_{76} , C_{78} , and C_{84} , but the reduction becomes thermodynamically easier as the HOMO–LUMO gap gradually decreases for the higher fullerenes [10–12]. Thus, fullerenes have quite different electron acceptor abilities—the higher fullerenes are markedly better electron acceptors than, for example, C_{60} . Encapsulating metals inside the skeleton of fullerenes to form endohedral fullerene metal complexes further attenuates the oxidizing behavior of fullerenes [13–15].

In comparison with the facile reduction of C_{60} , the oxidation of C_{60} is rendered more difficult with a reported one-electron oxidation potential of 1.26 V relative to ferrocene/ferricenium [16]. Nonetheless the electrochemical oxidation of C_{60} has shown that multi-electron oxidation occurs at ambient potentials [17]. As for $C_{60}^{•+}$, the charge of C_{60}^{*+} is highly delocalized, because the five HOMO orbitals of C_{60} (h_u) are degenerate [2]. Both reductive and oxidative electron transfer to or from C_{60} are expected to be quite efficient because minimal changes of structure and solvation are associated with the respective electron-transfer events.

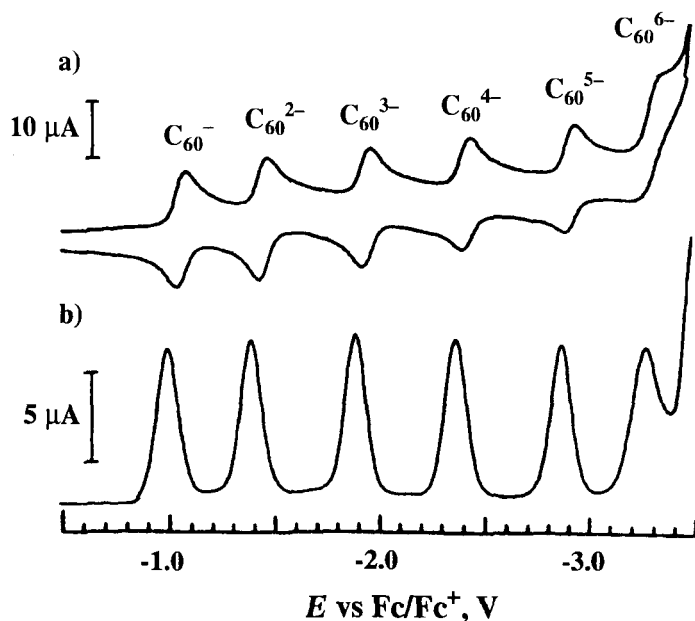


Figure 1. Cyclic voltammogram and differential pulse voltammogram of C_{60} [3].

Use of photoexcited fullerenes (i.e., the singlet or triplet excited state) widens the scope of electron-transfer reactions. This assumption is because excitation of fullerenes enhances both the electron-acceptor and -donor behavior of the photoexcited fullerenes. For example, the triplet excited state of C_{60} , which is formed by efficient intersystem crossing (i.e. with a quantum yield close to unity) [18, 19] has a reduction potential of $E^{\circ}_{\text{red}} = 1.14$ V relative to the SCE [18, 19]. This potential is clearly more positive than the reduction potential of the ground state (-0.43 V) [20]. Thus, the triplet excited state of C_{60} can be reduced with a variety of organic compounds yielding the C_{60} radical anion and the oxidized donor [18].

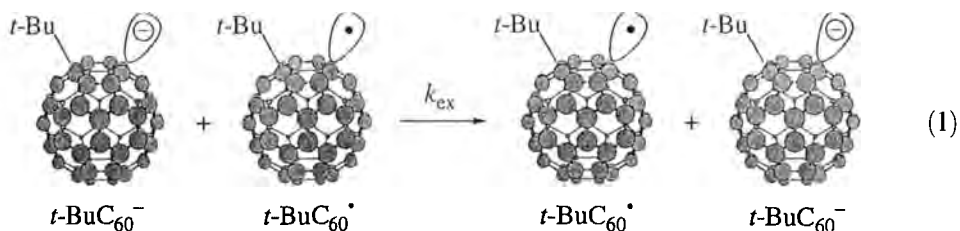
The rich redox properties of fullerenes and their derivatives, in the ground and excited states, have rendered them important three-dimensional components for the design of novel artificial photosynthesis systems. This chapter focuses on both the fundamental electron-transfer properties of fullerenes and the chemical processes associated with their electron-transfer reactions. Recent advances in time-resolved spectroscopic techniques, including laser flash photolysis and pulse radiolysis, provide a means of monitoring fast electron-transfer reactions and detecting unstable reactive intermediates of fullerene radical anions and cations as typically produced during the electron-transfer reactions. In the first part, the fundamental electron-transfer properties of fullerenes are highlighted. This section is then followed by a detailed description of the mechanistic viability of electron-transfer reactions by summarizing the numerous kinds of research currently ongoing in the electron-transfer chemistry of fullerenes.

5.2 Fundamental Electron-transfer Properties of Fullerenes

Photoinduced electron transfer from different electron donors to the triplet excited states of C_{60} and C_{70} occurs efficiently and is typically associated with a small reorganization energy [18, 19, 21–27]. Consequently, the occurrence of fast electron-transfer events involving the fullerene excited states has been well established as giving rise to small intrinsic barriers. In contrast with the fast electron-transfer reactions of the triplet excited state of C_{60} , an extremely slow electron-transfer reaction has been reported for the reaction of C_{60} in its ground state with 1,8-diazabicyclo[5.4.0]undec-7-ene (DBU) to produce $C_{60}^{\bullet-}$ in benzonitrile. The latter can be followed even by conventional Vis–NIR spectroscopy [28]. In this instance, however, it is not clear whether the generation of $C_{60}^{\bullet-}$ is directly related to electron transfer from DBU to C_{60} , or if $C_{60}^{\bullet-}$ evolves from the product of a secondary reaction.

The efficiency of electron-transfer reduction of C_{60} can be expressed by the self-exchange rates between C_{60} and the radical anion ($C_{60}^{\bullet-}$), which is the most fundamental property of electron-transfer reactions in solution. In fact, an electrochemical study on C_{60} has indicated that the electron transfer of C_{60} is fast, as one would expect for a large spherical reactant. This conclusion is based on the electroreduction kinetics of C_{60} in a benzonitrile solution of tetrabutylammonium perchlorate at ultramicroelectrodes by applying the ac admittance technique [29]. The reported standard rate constant for the electroreduction of C_{60} (0.3 cm s^{-1}) is comparable with that known for the ferricenium ion (0.2 cm s^{-1}) [22], whereas the self-exchange rate constant of ferrocene in acetonitrile is reported as $5.3 \times 10^6 \text{ M}^{-1} \text{ s}^{-1}$, far smaller than the diffusion limit [30, 31].

In general, linewidth variations of the ESR signal of radical anions in the presence of the corresponding neutral compounds at different concentrations are typically used to determine fast exchange rate constants, which are close to the diffusion limit [32, 33]. Unfortunately, this method cannot be applied to $C_{60}^{\bullet-}$, because of the absence of hyperfine structure in its ESR spectrum [34–37]. In contrast, spin polarization and hyperconjugative effects in mono-alkyl adduct radicals of the type RC_{60}^{\bullet} give rise to resolvable hyperfine interactions between R and RC_{60}^{\bullet} [38–42]. The linewidth of the ESR spectrum of $t\text{-Bu}C_{60}^{\bullet}$ increases with increasing concentration of $t\text{-Bu}C_{60}^{\bullet-}$ added to a benzonitrile solution of RC_{60}^{\bullet} , due to the electron-exchange reaction between $t\text{-Bu}C_{60}^{\bullet}$ and $t\text{-Bu}C_{60}^{\bullet-}$ (Eq. 1) [43].



The rate constant (k_{ex}) of the electron-exchange reaction between $t\text{-BuC}_{60}^-$ and $t\text{-BuC}_{60}^\bullet$ was determined as $1.9 \times 10^8 \text{ M}^{-1} \text{ s}^{-1}$ at 298 K by analyzing the linewidth variations of the ESR spectra [43]. Although C_{60} is perturbed by the $t\text{-Bu}$ addend, the much larger k_{ex} value, compared with the value for the ferrocene/ferricenium exchange ($5.3 \times 10^6 \text{ M}^{-1} \text{ s}^{-1}$), corroborates the high efficiency of electron transfer of C_{60} .

The electron transfer reactivity of C_{60} has been compared with that of p -benzoquinone which has a slightly more negative one-electron reduction potential (E°_{red} relative to the SCE = -0.50 V) [44] than C_{60} ($E^\circ_{\text{red}} -0.43 \text{ V}$). The rate constants of electron transfer from $\text{C}_{60}^{\bullet-}$ and C_{60}^{2-} to electron acceptors such as allyl halides and manganese(III) dodecaphenylporphyrin [45] correlate well with those from semiquinone radical anions and their derivatives. Linear correlations are obtained between logarithms of rate constants and the oxidation potentials of $\text{C}_{60}^{\bullet-}$, C_{60}^{2-} and semiquinone radical anions for the different electron acceptors [43]. Such correlations clearly indicate that the reorganization energies for the electron-transfer reactions of $\text{C}_{60}^{\bullet-}$ and C_{60}^{2-} are essentially the same as those of semiquinone radical anions. The self-exchange rate constants (k_{ex}) between p -benzoquinone (Q) and the semiquinone radical anion ($\text{Q}^{\bullet-}$) in benzonitrile have been determined independently at different temperatures by analyzing the linewidth variations of the ESR spectra [43]. Arrhenius plots of $\log k_{\text{ex}}$ against $1/T$ gave the activation enthalpy (ΔH^\ddagger) and activation entropy (ΔS^\ddagger) which are $3.0 \text{ kcal mol}^{-1}$ and $-3.9 \text{ cal K}^{-1} \text{ mol}^{-1}$, respectively [43]. The small ΔS^\ddagger value is consistent with adiabatic outer-sphere electron transfer [1]. The reorganization energy (λ) of the $\text{Q}^{\bullet-}/\text{Q}$ system in benzonitrile at 298 K is obtained as $16.9 \text{ kcal mol}^{-1}$; this can be regarded as the λ value for electron exchange between $\text{C}_{60}^{\bullet-}$ and C_{60} (Eq. 2) and between C_{60}^{2-} and $\text{C}_{60}^{\bullet-}$.



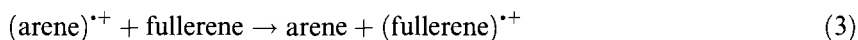
This λ value is larger than the value reported for the $\text{Q}^{\bullet-}/\text{Q}$ system in DMF ($13.1 \text{ kcal mol}^{-1}$) but smaller than the value in $\text{DMF-H}_2\text{O}$ (9:1; $17.7 \text{ kcal mol}^{-1}$) [46]. Because the larger λ value in $\text{DMF-H}_2\text{O}$ is ascribed to the larger solvation of $\text{Q}^{\bullet-}$ in the presence of H_2O [46], the solvation of $\text{Q}^{\bullet-}$ in benzonitrile might be slightly smaller than that in $\text{DMF-H}_2\text{O}$ (9:1).

The reorganization energy (λ) consists of (i) the reorganization of the inner coordination spheres (λ_i) associated with the structural change upon the electron-transfer reduction of C_{60} in the gas phase and (ii) the solvent reorganization of the outer coordination spheres (λ_o) [1]. The λ_i value for the one-electron reduction of C_{60} has been calculated theoretically as $0.001 \text{ kcal mol}^{-1}$ [43]. Thus, the small λ_i value as compared with the observed λ values, which include the solvent reorganization energy, indicate that the solvent reorganization plays a major role in determining the intrinsic barrier to the electron-transfer reduction of C_{60} .

When the reorganization energy (λ) of electron transfer is small, the Marcus inverted region ($\lambda < -\Delta G^\circ_{\text{et}}$) where the rate constant of electron transfer decreases with increasing driving force ($-\Delta G^\circ_{\text{et}}$) is reached at smaller $-\Delta G^\circ_{\text{et}}$ values [1, 47]. To date, experimental verification of the existence of such an inverted region has

only been achieved by investigating highly exergonic ($-\Delta G^\circ_{\text{et}} \gg 0$) electron-transfer reactions [48–61]. The maximum value of the rate constant for electron transfer is obtained when $-\Delta G^\circ_{\text{et}}$ equals λ . Thus, the λ value of electron transfer can be evaluated from the dependence of the rate constant (k_{et}) for electron transfer on the driving force ($-\Delta G^\circ_{\text{et}}$) provided that the λ value is constant for a series of electron-transfer reactions. To obtain the accurate reorganization energy it is, however, necessary to study a system with a small λ value and the driving-force range sufficiently wide to probe the behavior far in the inverted region ($\lambda < -\Delta G^\circ_{\text{et}}$). For this purpose the electron-transfer reactions of fullerenes seem to be an ideal system, because the λ value is small.

In fact, a Marcus inverted type dependence of the rate constants on $-\Delta G^\circ_{\text{et}}$ has been reported for electron-transfer oxidation of C_{76} and C_{78} with a series of arene radical cations produced upon radiolysis of the $\text{C}_{76}/\text{C}_{78}$ -arene systems [62]. A series of arene radical cations was generated as electron acceptors, and probed in intermolecular electron-transfer reactions with different fullerenes with ionization potentials between 7.59 and 7.1 eV (Eq. 3) [62, 63].



The kinetic studies make use of the unequally sized reaction partners (e.g. a large electron donor and a small electron acceptor couple) and benefit from the low viscosity of dichloromethane (DCM), both of which elevate the diffusion-controlled limit. To study the electron transfer, deoxygenated DCM solutions of, for example, *m*-terphenyl at high concentrations (0.02 M) were irradiated in the presence of different concentrations of fullerene (ca 10^{-5} M) [62]. This resulted in accelerated decay of $(\text{arene})^{*\cdot+}$ UV-Vis absorption, with rates linearly depending on fullerene concentration [62]. Formation of the electron-transfer product, fullerene $^{*\cdot+}$, was confirmed spectroscopically by measurement of the NIR fingerprint ($\lambda_{\text{max}} = 1080$ nm) [62, 65].

The rate constants for the investigated arenes vary between 7.8×10^8 and $4.5 \times 10^{10} \text{ M}^{-1} \text{ s}^{-1}$ [62]. The driving forces ($-\Delta G^\circ_{\text{et}}$) calculated on the basis of the difference in the respective arene and fullerene ionization potentials ($-\Delta G^\circ_{\text{et}} = \Delta IP = IP_{\text{arene}} - IP_{\text{fullerene}}$) have a pronounced parabolic dependency on the measured rate constants for the electron-transfer reactions, as shown in Figure 2.

It is important to note that the different solvation of the arene radical cation and the fullerene radical cation is largely canceled out. It is interesting to note that these results indicate a decrease of the rate constant with larger free energy towards the highly exothermic region. From the maximum value of the rate constant of electron-transfer oxidation of C_{76} and C_{78} is obtained the λ value ($13.8 \text{ kcal mol}^{-1}$) [62]. These relatively low values and minor vibrational differences between the fullerene oxidized and ground states are both consequences of the rigid structure and extensive delocalization within the resonance structure of the fullerene π -system. The λ value for the electron-transfer oxidation of fullerenes in dichloromethane ($13.8 \text{ kcal mol}^{-1}$) is smaller than that for the electron-transfer reduction of C_{60} ($16.9 \text{ kcal mol}^{-1}$) [43]. This difference might result from the smaller solvent reorganization energy in dichloromethane compared with that in benzonitrile, because

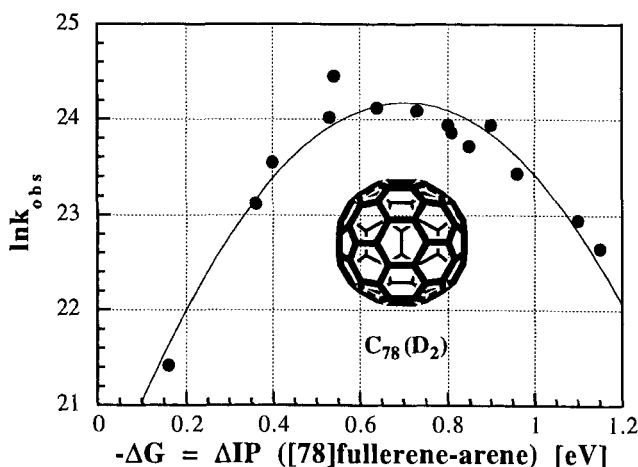


Figure 2. Plot of $\ln k_{obs}$ for electron transfer from [78]fullerene (D₂) to (arene)^{•+}, in dichloromethane at room temperature, as a function of the free energy change.

the reorganization of inner coordination spheres (λ_i) associated with the structural change upon the electron-transfer reduction or oxidation of fullerenes should be close to zero (vide supra).

5.3 Thermal Electron Transfer

5.3.1 Radiolytically Generated Radical Species

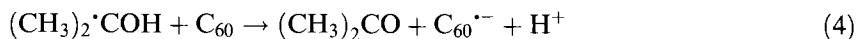
Non-aqueous media

Suitable conditions for the study of radiation-induced reduction experiments are usually found in alcohols (α -hydroxyl radicals) or aqueous solutions (hydrated electrons). Fullerenes are, however, poorly soluble in polar alcohols and almost insoluble in aqueous solutions. As a consequence of dissolving fullerenes in polar solvents, the spontaneous and irreversible formation of variable-sized clusters and aggregates is observed. Thus to perform radiation-induced reduction studies toluene was employed as a fullerene-dissolving medium [65, 66]. Methodical fullerene reduction was then achieved by addition of adequate co-solvents, namely acetone and 2-propanol. Acetone was chosen as an efficient electron scavenger to avoid generation of excited states, stemming from a reaction between solvated electrons and toluene. After the fast protonation of the initially formed $(CH_3)_2\dot{C}O^-$ species the $(CH_3)_2\dot{C}OH$ radical is produced; this has exclusively reducing properties and is identical with the main product of the radiolysis of the second co-solvent (2-propanol). Upon pulse radiolysis of an oxygen-free solution of C₆₀ in 8:1:1 (v/v) toluene–acetone–2-propanol a characteristic NIR spectrum was obtained [65, 66]. In particular, the detection of a maximum around 1080 nm is in excellent agreement

Table 1. Redox potentials, rate constants for the radiolytic reduction and π -radical anion absorption maxima of fullerenes [11, 65, 66, 68–70].

Compound	$E_{1/2}$ fullerene/fullerene $^{\cdot-}$ (V, relative to Fc/Fc $^+$ [11])	k ((CH $_3$) $_2$ $^{\cdot}$ COH) (M $^{-1}$ s $^{-1}$)	λ_{\max} (nm)
[60]fullerene	−1.06	8.5×10^8	1080
[70]fullerene	−1.02	8.0×10^8	880
[76]fullerene	−0.83	1.3×10^9	905
[78]fullerene	−0.77	1.6×10^9	975
[78]fullerene	−0.67	1.0×10^9	960

with an independently performed CNDO/S calculation of the electronic structure of the fullerene π -radical anion (i.e., C $_{60}^{\cdot-}$) [67]. This suggests successful fullerene reduction as a result of a nearly diffusion-controlled reaction between the fullerene core and (CH $_3$) $_2$ $^{\cdot}$ COH radicals with an intermolecular rate constant of 8.5×10^8 M $^{-1}$ s $^{-1}$ (Eq. 4) [65, 66]:



A qualitative similar picture was established for the reduction of higher fullerenes (e.g., C $_{70}$, C $_{76}$, C $_{78}$, and C $_{84}$) [68–70]. The associated symmetries of these higher fullerenes were expected to have an impact on the reduction potentials and, equally important, on the relative position of the corresponding π -radical anion absorption bands (Table 1).

The faster rate constants of 1.3×10^9 and 1.6×10^9 M $^{-1}$ s $^{-1}$, respectively, for the radiation-induced reduction of C $_{76}$ and C $_{78}$ with (CH $_3$) $_2$ $^{\cdot}$ COH radicals [70] compared with that for C $_{60}$ (8.5×10^8 M $^{-1}$ s $^{-1}$) [65, 66] support the view that higher fullerenes are better electron-acceptor moieties than C $_{60}$. Also, the position of the absorption maxima was effected by the absolute fullerene size [68–70].

Fullerene reduction was also studied by study of electron transfer from a series of reduced metalloporphyrin π -radical anions at high porphyrin concentrations (ca 5×10^{-4} M) [63]. This enables the fine-tuning of the reducing strength of the reducing radical species, with reduction potentials typically varying between −1.35 V relative to the SCE (ZnP/ZnP $^{\cdot-}$ couple) and −0.8 V relative to the SCE (SnP/SnP $^{\cdot-}$ couple). In this study the same solvent mixture as described above for the direct reduction of fullerenes (i.e. 8:1:1 (v/v) toluene–acetone–2-propanol) was used [65, 66, 68–70]. Again, the solely reducing species is the (CH $_3$) $_2$ $^{\cdot}$ COH radical, which reduces a number of metalloporphyrins at the macrocyclic ligand to yield the corresponding metalloporphyrin π -radical anions (MP $^{\cdot-}$). Whereas in the absence of an electron acceptor (i.e. fullerene) the MP $^{\cdot-}$ decay slowly via a sequence of disproportionation and protonation reactions, addition of various concentrations of C $_{60}$ (0.2 – 5×10^{-5} M) resulted in an accelerated decay of the absorption between 600 and 800 nm. The linear dependence of the observed rates on the C $_{60}$ concentration support the view that the MP $^{\cdot-}$ indeed react with C $_{60}$ via electron transfer [63]. To confirm the possible fullerene reduction, the formation of the NIR absorption

around 1080 nm was monitored. Most importantly, the grow-in rate of the $C_{60}^{\bullet-}$ absorption at different wavelengths in the 980–1100 nm range was nearly identical with the decay rate of the $MP^{\bullet-}$ absorption between 600 and 800 nm. For example, for $ZnP^{\bullet-}$ an intermolecular rate constant of $(2.5 \pm 1.0) \times 10^9 \text{ M}^{-1} \text{ s}^{-1}$ was derived from the $ZnP^{\bullet-}$ decay and $(1.4 \pm 1.0) \times 10^9 \text{ M}^{-1} \text{ s}^{-1}$ from the $C_{60}^{\bullet-}$ formation [63]. These two values are in reasonable agreement and confirm unmistakably the following electron transfer from the one-electron reduced metalloporphyrin π -radical anion to the fullerene (Eq. 5):



Surprisingly, the rate constants for electron transfer between all the investigated $MP^{\bullet-}$ and C_{60} were found to be in the range $(1\text{--}3) \times 10^9 \text{ M}^{-1} \text{ s}^{-1}$, despite the large variation in the one-electron reduction potentials of the examined metalloporphyrins [63]. The lack of dependence of the rate constant on the free energy change of the reaction has been ascribed to weak electronic interactions between the metalloporphyrins and C_{60} in the ground state. It should be noted, however, that no ground state charge-transfer interactions were detectable.

With the objective of oxidizing the fullerene core, radiolysis of any chlorinated hydrocarbon solvent provides the means of forming strongly oxidizing radical species [71]. For example, the radiation-induced ionization of dichloroethane (DCE) yields the short-lived and highly reactive solvent radical cation. In general, the electron affinity of $[DCE]^{\bullet+}$ is sufficient to initiate one-electron oxidation of the fullerene moiety (Eq. 6) [72–76].



Pulse radiolytic experiments with C_{60} in nitrogen-saturated or aerated DCE solutions yielded a doublet with maxima at 960 and 980 nm [64, 65]. This fingerprint is identical with that computed in CNDO/S calculations [66]. Because of the short-lived nature of the $[DCE]^{\bullet+}$ radical, the rate constants for the C_{60} oxidation could only be estimated; values were ca $2 \times 10^{10} \text{ M}^{-1} \text{ s}^{-1}$ [64, 65].

Aqueous media

Viable means of overcoming the insolubility of pristine fullerenes in polar solvents involve (i) incorporation of pristine fullerenes into the hydrophobic cavity of water-soluble host structures (e.g. cyclodextrin [77, 78], surfactants [79–82], and vesicles [81, 83, 84], or (ii) functionalization of the fullerene core with hydrophilic addends (e.g. $C_{60}C(COO^-)_2$, $C_{60}[C(OCH_2CH_2)_3CH_3]_2$, $C_{60}(C_4H_{10}N^+)$, etc.) [2]

Cyclodextrin

Cyclodextrins are water-soluble cyclic oligosaccharides with hydrophilic cavities of different sizes. For incorporation of C_{60} , thereby facilitating its dissolution in aqueous media, γ -CD is the most promising candidate. Molecular modeling (i.e., balancing of cavity radius and fullerene size) suggests that a full inclusion in the

form of a C_{60}/γ -CD 1:1 complex is almost impossible to achieve [77, 78]. Despite this apparent size mismatch, incorporation of a single C_{60} molecule between the cavities of two γ -CD molecules has been unequivocally demonstrated by use of different spectroscopic techniques [77, 78]. On the other hand, incorporation of C_{60} into the smaller analogs of the cyclodextrin family (α - and β -CD) failed; attempts to host the slightly larger C_{70} were similarly unsuccessful. Reaction of the 1:2 C_{60}/γ -CD complex with radiolytically generated hydrated electrons (e^-_{aq}) led to strong NIR changes, with the $C_{60}^{\bullet-}$ fingerprint absorption at 1080 nm [64, 85, 86] (Eq. 7) resembling those described for reduction experiments in 8:1:1 (*v/v/v*) toluene–2-propanol–acetone [65, 66].

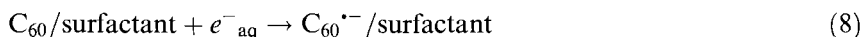


To obtain further evidence of the fullerene reduction, different α -hydroxyl radicals (i.e. $\cdot\text{CH}_2\text{OH}$, $\text{CH}_3\cdot\text{CHOH}$ and $(\text{CH}_3)_2\cdot\text{COH}$) were probed, as were hydrated electrons [65, 66, 85, 86]. In this context the different reducing strength of the generated radicals should be considered. In fact, the rate constants associated with the C_{60}/γ -CD reduction track the strength of these α -hydroxyl radicals. In addition, the reduction experiments disclose a noticeable slow-down of the C_{60}/γ -CD reduction ($2.7 \times 10^8 \text{ M}^{-1} \text{ s}^{-1}$) [85, 86], initiated by the bulky $(\text{CH}_3)_2\cdot\text{COH}$ radicals, relative to the intermolecular reduction in homogeneous systems ($8.5 \times 10^8 \text{ M}^{-1} \text{ s}^{-1}$) [65, 66]. This clearly points to the heterogeneity of the C_{60}/γ -CD 1:2 complex in which the fullerene core is separated from the surrounding aqueous phase. It is notable that the shielding is not complete and, as a matter of fact, efficient fullerene reduction occurs via hydrated electrons and significantly larger α -hydroxyl radicals.

Surfactants

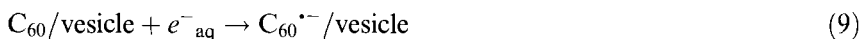
In contrast with cyclodextrins, amphiphilic micellar assemblies are a class of host molecules with flexible cavities. In a simple view, these molecules bear a hydrophilic head group and a hydrophobic tail and aggregate as 3-dimensional surface-active assemblies. To dissolve fullerenes in aqueous solutions it is important to note that surfactants create hydrophobic micro-domains capable of accommodating water-insoluble entities. A very intriguing aspect of micellar assemblies is their structural flexibility, which enables them to host not only C_{60} but also the larger C_{70} , C_{76} and C_{78} . A variety of surfactants, e.g. Triton X-100, Tween 20, BRIJ 35, and cetyltrimethylammonium chloride, were successfully shown to host hydrophobic fullerene moieties [80–82, 87]. This assumption is based on (i) the well-resolved absorption bands, which are in excellent resemblance with those reported for organic solutions (e.g., cyclohexane and dichloromethane) and (ii) the lack of any significant light scattering [80–82, 87]. These are attributes that point to the monomeric dissolution of the fullerene moieties within freshly prepared surfactant ensembles. The pulse radiolytically induced reduction of the fullerene was investigated in aqueous solution containing the respective fullerene–surfactant assembly [87]. The differential absorption spectrum recorded after reaction with hydrated electrons (i.e. a NIR fingerprint maximum at 1075 nm) suggests formation of the $C_{60}^{\bullet-}$ radical

anion generated with an intermolecular rate constant of $2.6 \times 10^{10} \text{ M}^{-1} \text{ s}^{-1}$ [87]. Complementary reduction experiments with $(\text{CH}_3)_2\text{COH}^\bullet$ radicals led to spectral changes superimposable on those described for the hydrated electrons (Eq. 8). In the absence of oxygen $\text{C}_{60}^{\bullet-}$ is stable on the experimental time scale.



Vesicular systems

Incorporation of C_{60} into different vesicular media was confirmed by monitoring the characteristic absorption bands at 220, 260, and 340 nm [81, 83, 88]. Surprisingly, all lipid bilayer membrane solutions in, for example, toluene or DCM were yellow–brownish in color rather than the magenta color of C_{60} . The UV bands are generally red-shifted with increasing fullerene concentration and the spectral shifts are accompanied by light scattering and significantly decreasing extinction coefficients [81, 88]. All these observations point to the same phenomenon—fullerene aggregation within the interior of the lipid bilayer membranes. Measurements of the fullerene triplet lifetime in positively charged DODAB, negatively charged DHP and zwitterionic lecithin systems revealed significantly reduced triplet lifetimes ($<0.2 \mu\text{s}$), relative to that of the fullerene monomer (ca $100 \mu\text{s}$) [88]. Because these triplet lifetimes are strongly effected by triplet–triplet or triplet–singlet ground-state annihilation, the shorter lifetimes provide further proof of the proposed aggregation concept. Detection of a NIR band for C_{60} , incorporated into the three types of vesicle discussed, confirms the successful reduction, for example, via hydrated electrons (e^-_{aq}) (Eq. 9) [81, 88].



Interestingly, the characteristic NIR band of $\text{C}_{60}^{\bullet-}$ within these lipid materials has a blue shift with a maximum centered at ca 1020 nm [88]; for organic solutions of C_{60} the maximum was recorded at 1080 nm [65, 66]. In addition, the 1020 nm band is substantially broadened, which again suggests fullerene aggregation.

In summary, the incorporation of C_{60} into artificial bilayer membranes, despite being successful in principle, gives rise to a number of unexpected complications. In consideration of the strong aggregation forces among fullerene cores, it is imperative to separate the individual fullerene moieties. Only the adequate hydrophilic–hydrophobic balance of the host matrix is an appropriate means to hinder the spontaneous cluster formation [88].

Monofunctionalized fullerene derivatives

Experiments on the radiation-induced reduction of the functionalized fullerene carboxylate, $\text{C}_{60}\text{C}(\text{COO}^-)_2$, in aqueous media were unsuccessful, despite the use of a concentration range that should guarantee rapid fullerene reduction (e.g., as found for $\text{C}_{60}\text{--}\gamma\text{-CD}$, $\text{C}_{60}\text{--surfactant}$, and $\text{C}_{60}\text{--vesicle}$) [89, 90]. In particular, the absorption at ca 700 nm, attributable to the initially generated hydrated electron, remained

virtually unaffected on addition of $\text{C}_{60}\text{C}(\text{COO}^-)_2$ and the characteristic NIR absorption of the fullerene radical anion was completely lacking.

Micellar aggregation of the $\text{C}_{60}\text{C}(\text{COO}^-)_2$ derivative in water, a consequence of its amphiphilic structure (i.e., hydrophobic fullerene core and hydrophilic carboxylates), is responsible for the lack of reduction [89, 90]. These clusters are considered to contain an inward oriented hydrophobic fullerene moiety and a hydrophilic layer of carboxylate head groups, which prevent the negatively charged electrons from approaching the fullerene core.

Evidence of clustering in aqueous and alcoholic systems is also provided by the ground state spectra [89, 90]. In particular, the visible region is dominated by strong dynamic light scattering and significant broadening of the absorption bands. An elegant way of avoiding aggregation of $\text{C}_{60}\text{C}(\text{COO}^-)_2$ implies the incorporation of the functionalized fullerene into a water-soluble host molecule (e.g., γ -cyclodextrin, surfactants, or vesicle [77–83]). The ground-state spectrum of this guest–host complex contains the same narrow bands as, for example, those of monomeric $\text{C}_{60}\text{C}(\text{COOEt})_2$ or C_{60} - γ -CD and clearly differs from the presumed $\{\text{C}_{60}\text{C}(\text{COO}^-)_2\}_n$ cluster. The resulting non-aggregated fullerene complex, $\text{C}_{60}\text{C}(\text{COO}^-)_2$ - γ -CD, gives rise to a rapid reduction via hydrated electrons and other reducing α -hydroxyl radicals (i.e., $\cdot\text{CH}_2\text{OH}$, $\text{CH}_3\cdot\text{CHOH}$ and $(\text{CH}_3)_2\cdot\text{COH}$) [89, 90].

Varying the fullerene concentration always resulted in accelerated decay of the hydrated electron absorption at ca 700 nm. In addition, the characteristic fullerene π -radical anion absorption, which maximizes for $\text{C}_{60}\text{C}(\text{COO}^-)_2$ at 1040 nm, grows in simultaneously. The rate constant for the fullerene reduction discloses an interesting observation: the value $9.8 \times 10^9 \text{ M}^{-1} \text{ s}^{-1}$ [89, 90] is slightly lower than that for the C_{60} - γ -CD complex ($1.8 \times 10^{10} \text{ M}^{-1} \text{ s}^{-1}$) [85, 86], paralleling the trend noted for the electrochemically determined reduction potentials of C_{60} ($E_{1/2} = -0.55 \text{ V}$ relative to the SCE; in 4:1 (v/v) toluene–acetonitrile) [91] and various mono-functionalized fullerene derivatives ($E_{1/2} = -0.64 \text{ V}$ relative to the SCE; in 4:1 (v/v) toluene–acetonitrile) [91]. It is also in line with the observation that mono-functionalization increases the LUMO energy and, in turn, shifts the reduction potentials to more negative values [92].

A fullerene derivative, $\text{C}_{60} [\text{C}(\text{OCH}_2\text{CH}_2)_3\text{CH}_3]_2$, bearing a non-ionic triethylene glycol chain rather than carboxylates, was investigated to discover potential contributions from repelling effects between the hydrated electrons and the negatively charged fullerene core [93]. It turned out, however, that clustering has the strongest effect on the fullerene reactivity. This conclusion was drawn from strong light scattering noticed in the ground state absorption spectrum; very short triplet excited state lifetimes substantiate fullerene clustering. Only the surfactant-embedded or γ -CD-incorporated complex revealed the expected ease of radiolytic reduction [93].

In the next step a positively charged pyrrolidinium salt ($\text{C}_{60}(\text{C}_4\text{H}_{10}\text{N}^+)$) was probed, not only to overcome the Coulombic charge repulsion, but, more importantly, to attract a reaction with the hydrated electrons (Eq. 10) [90, 93, 94].

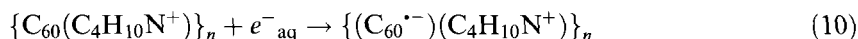


Table 2. Redox potentials and rate constants for the radiolytic reduction of some water-soluble fullerene derivatives [95].

Compound	$E_{1/2}$ fullerene/fullerene ^{•-} (V, relative to SCE)	$k_{(\text{hydrated electrons})}$ (M ⁻¹ s ⁻¹) ^a
C ₆₀	-0.35 ^b	1.8×10^{10}
C ₆₀ C(COO ⁻) ₂	-0.46 ^{c,d}	9.8×10^9
C ₆₀ [C(OCH ₂ CH ₂) ₃ CH ₃] ₂	-0.46 ^e	Not measured
C ₆₀ (C ₄ H ₁₀ N ⁺)	-0.29 ^b	3.5×10^{10}

^a Measured for the γ -CD-incorporated complexes [85, 86, 89, 94].^b Measured in THF solutions [95].^c Recalculated from values, determined in toluene-acetonitrile (4:1 v/v) [91].^d Measured for the analogous C₆₀C(COOEt)₂ [91].^e Unpublished result.

Despite the also unequivocally occurring clustering in aqueous media, attachment of a pyrrolidinium group facilitated the reduction of these clusters by hydrated electrons, compared with the negatively charged system {C₆₀C(COO⁻)₂}_n. Comparison of the NIR fingerprints of the reduced cluster ({(C₆₀^{•-})(C₄H₁₀N⁺)})_n and the reduced γ -CD-incorporated monomer ((C₆₀^{•-})(C₄H₁₀N⁺)- γ -CD) revealed several significant differences [94]. Most importantly, the spectral features of the fullerene cluster are much broader. This is further accompanied by lower yields of the reduced cluster compared with the reduced monomer.

In conclusion, reduction of monomeric fullerenes in aqueous media (e.g. γ -CD-incorporated or surfactant-embedded [77–83]) by hydrated electrons and uncharged (CH₃)₂•COH radicals reveals significant rate enhancement for the pyrrolidinium salt C₆₀(C₄H₁₀N⁺) [94] compared with C₆₀ [85, 86] and negatively charged carboxylates C₆₀C(COO⁻)₂ [89, 90]. This suggests, in line with independently determined quenching rates, an anodic shift of the reduction potential of C₆₀(C₄H₁₀N⁺) relative to C₆₀C(COO⁻)₂, C₆₀ [C(OCH₂CH₂)₃CH₃]₂, and C₆₀ (Table 2).

Bisfunctionalized fullerene derivatives

Because monofunctionalization of fullerenes shows that a single hydrophilic addend is insufficient to prevent the strong hydrophobic interactions among the compounds [89, 90, 93, 94], multiple functionalized derivatives were examined as water-soluble probes. In particular, introduction of a second hydrophilic ligand (e.g., pyrrolidinium salts or carboxylates) to the fullerene core enhances the surface coverage of the hydrophobic fullerene surface. In turn, it was expected that fullerene aggregation might be suppressed. It should be stated that these water-soluble derivatives are important alternatives to the γ -CD-incorporated and surfactant-embedded fullerenes.

A series of water-soluble bis-carboxylates and bis-pyrrolidinium salts (e.g. C₆₀ [C(COO⁻)₂]₂ and C₆₀(C₄H₁₀N⁺)₂) were studied in aqueous solutions and compared

with $[(C_{60})C(COO^-)_2]_n$ and $[(C_{60}^{*-})(C_4H_{10}N^+)]_n$ clusters [96–98]. In the ground state, the fact that none of these derivatives deviates significantly from the Lambert–Beer law has been used as a first argument in support of the absence of fullerene clusters [96]. Furthermore, triplet lifetimes of ca 40 μ s [96–98] compared with 0.4 μ s and less (i.e. for fullerene clusters) [89, 90, 94] is extra evidence for the truly monomeric occurrence of these bis-functionalized fullerenes in aqueous solutions.

Radiation-induced reduction of bis-carboxylates or bis-pyrrolidinium salts in N_2 -purged aqueous solution showed that the expected formation of the diagnostic NIR transition band occurs synchronously with the decay of the hydrated electron absorption at ca 700 nm [96]. The bis-carboxylates $(C_{60}[C(COO^-)_2]_2)$ were reduced by hydrated electrons and $(CH_3)_2\dot{C}OH$ radicals with rate constants of $(0.75 - 3.4) \times 10^9$ and $(0.9 - 2.2) \times 10^8 \text{ M}^{-1} \text{ s}^{-1}$, respectively [96]. These values are, nevertheless, significantly lower than those for the reduction of C_{60} –surfactant, $C_{60}C(COO^-)_2$ –surfactant, and the respective γ -CD-incorporated complexes. Such an effect reflects the perturbation of the fullerene π -system caused by placing two functional negatively charged appendices on to the fullerene core. Because of the electron-withdrawing nature of the pyrrolidinium groups, the electron-acceptor properties of the bis-pyrrolidinium salts $(C_{60}(C_4H_{10}N^+)_2)$ [97] are markedly improved relative to the bis-carboxylates $(C_{60}[C(COO^-)_2]_2)$ [96] and also relative to pristine C_{60} [85, 86]. For example, the rate constants for the fullerene reduction with hydrated electrons $((0.88 - 2.2) \times 10^{10} \text{ M}^{-1} \text{ s}^{-1})$ and $(CH_3)_2\dot{C}OH$ radicals $((4.7 - 7.1) \times 10^8 \text{ M}^{-1} \text{ s}^{-1})$ [97] are clearly faster than those noted for any other functionalized fullerene derivative. In conclusion, the extended and highly delocalized π -system experiences gradual destruction. Specifically, perturbation is observed which depends strongly on (i) the extent of functionalization, (ii) the relative distance of the individual addends from each other, and (iii) the electronic structure of the substituent.

5.3.2 Electron-transfer Reactions of Fullerene Anions

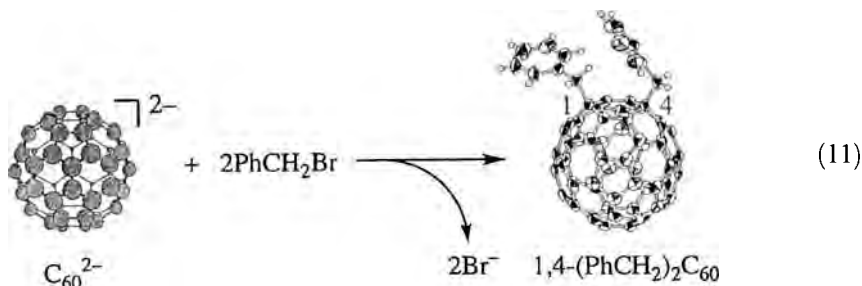
Derivatization of fullerene anions

Fullerenes such as C_{60} are easy to reduce [1], but difficult to oxidize electrochemically [2], and thus are generally regarded as electrophiles, or electron acceptors, rather than nucleophiles or electron donors. The derivatization of fullerenes has therefore been achieved by polar reactions with a variety of nucleophiles [99–104], e.g. electron-rich olefins [105–114], carbenes [115–122], carbanions [123–129], alkoxides [130, 131], and organometallic reagents [132–138]. When, on the other hand, electrons are chemically or electrochemically added to C_{60} , the resulting anions are expected to behave as strong nucleophiles or electron donors.

The two-electron reduction of C_{60} to produce C_{60}^{2-} can be achieved electrochemically in the presence of methyl iodide to yield the dimethyl adduct, Me_2C_{60} [139]. In this context, catalytic currents are observed for the electrochemical reduction of C_{60} or C_{70} to produce C_{60}^{2-} or C_{70}^{2-} , respectively, in the presence of vicinal dibromides [140] or α,ω -dihaloalkanes [141, 142]. Electrosynthesis of methanofullerenes has been achieved by the reaction of C_{60}^{2-} with *ipso*-brominated and

iodinated reagents [143]. The reaction of C_{60}^{2-} with halogenated compounds was performed with no potential applied after the completion of the electrochemical conversion of C_{60} to C_{60}^{2-} [143].

The dianion, C_{60}^{2-} , is also been produced by chemical reduction of C_{60} with thiolate anions [144] or with the trimethyl-*p*-benzoquinone dianion [145]. For example, the reaction of C_{60}^{2-} with two equivalents of benzyl bromide yields the dibenzyl adduct, $(PhCH_2)_2C_{60}$ (Eq 11).

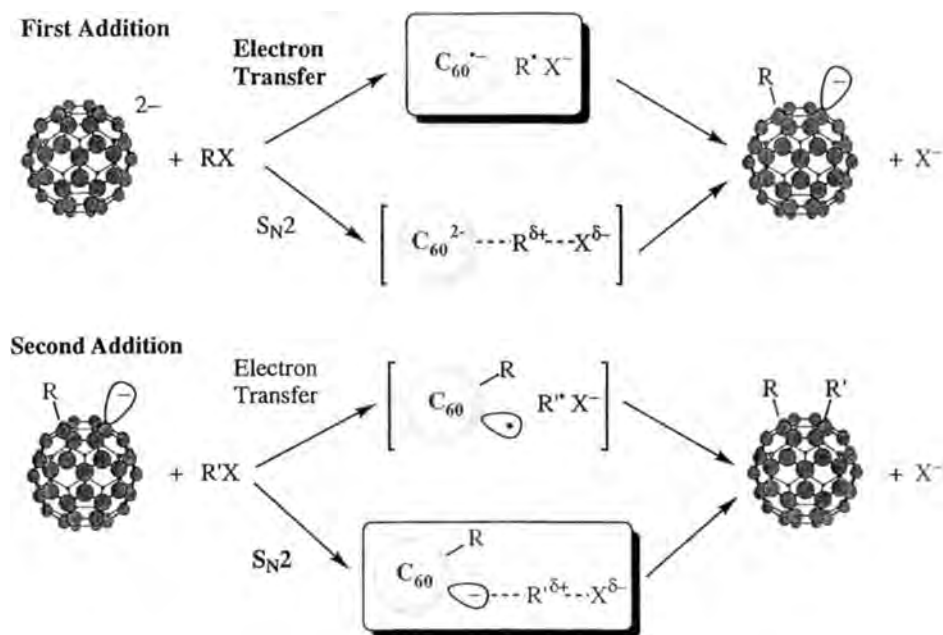


The major isomer isolated, and characterized by single-crystal X-ray diffraction, was found to be the 1,4 isomer rather than the 1,2 isomer (Eq. 11) [145]. In a 1,4 adduct of C_{60} the double bond in a pentagon increases the energy of the C_{60} cage by about 8 kcal mol⁻¹ compared with that of the 1,2 adduct [146, 147]. However, this disfavored energy increase is compensated by a decrease in steric hindrance when two bulky groups are placed in a 1,4-position. Thus, 1,4 adducts are usually the dominant products when bulky groups are added to C_{60} [145, 148]. It has been shown that the 1,2 and 1,4 adducts of C_{60} can be identified from their different absorption spectra [148]—the 1,2 adducts have a weak spike at ca 432 nm [149] and the 1,4 adducts have a broad absorption band at ca 445 nm [145, 148, 150].

A small amount of 1,2 adduct for the reaction of C_{60}^{2-} with benzyl bromide was isolated and also characterized spectroscopically [151]. The mono- and dianions of the 1,2- and 1,4- $(PhCH_2)_2C_{60}$ derivatives were then generated by controlled-potential electrolysis of the organofullerenes in benzonitrile. The visible and near-IR spectrum of $[1,2-(PhCH_2)_2C_{60}]^{+}$ has a strong absorption band at 1030 nm and a weaker band at 906 nm, whereas that of $[1,4-(PhCH_2)_2C_{60}]^{+}$ has two well-defined moderate absorption bands at 1498 and 989 nm and much weaker bands at 874 and 1237 nm [151]. Doubly reduced 1,2- $(PhCH_2)_2C_{60}$ has one strong absorption band at 905 nm and weaker bands at 801 and 1028 nm, whereas doubly reduced 1,4- $(PhCH_2)_2C_{60}$ has two strong absorption bands at 1294 and 903 nm and two much weaker bands at 806 and 1087 nm [151]. These spectroscopic data can be used to differentiate between the 1,2 and 1,4 isomers of C_{60} .

Electron transfer or the S_N2 pathway

The conversion of C_{60}^{2-} to R_2C_{60} passes through a RC_{60}^- intermediate [145]. This alkylation could proceed via two probable mechanistic pathways. One is an electron



Scheme 1.

transfer mechanism where C₆₀²⁻ acts as an electron donor and the other is an S_N2 mechanism where C₆₀²⁻ acts as a nucleophile (Scheme 1).

Such an electron-transfer rather than nucleophilic process has been one of the most central propositions in reaction mechanism [152–160]. The second step in the formation of the final bis-adduct may also proceed by an electron transfer or alternatively by an S_N2 reaction (Scheme 1). An electron transfer from C₆₀²⁻ to RX would give a radical pair (C₆₀^{•-} R[•] X⁻) where the R–X bond is cleaved upon dissociative electron transfer [160]. A facile radical coupling in the radical pair may subsequently afford the same RC₆₀[•] product as expected also from the alternative S_N2 pathway shown in the first R group addition step of Scheme 1. The addition of a second alkyl group to RC₆₀[•] may also proceed via electron transfer from RC₆₀[•] to a different alkyl halide (R'X) to give a radical pair (RC₆₀[•] R'X⁻), followed by a fast radical coupling to yield the final product, RR'C₆₀. As shown in Scheme 1, the electron transfer and S_N2 pathways in each step would give the same products. However, the operating mechanism has been distinguished by evaluating the reactivity of RX in each step [161].

The reactivity of RX toward C₆₀²⁻ is found to be insensitive to the steric hindrance of the alkyl group of RX. This is however in contrast to the normal reactivity in S_N2 reactions [162]. For example, the largest rate constant is seen for a sterically hindered CCl₄, while the also sterically hindered *t*-BuI gives rise to a larger *k*_{obs} value (4.7 × 10⁻² M⁻¹ s⁻¹) than the much less sterically hindered MeI (3.5 × 10⁻² M⁻¹ s⁻¹) [161]. Such an insensitivity of the rate on the steric hindrance

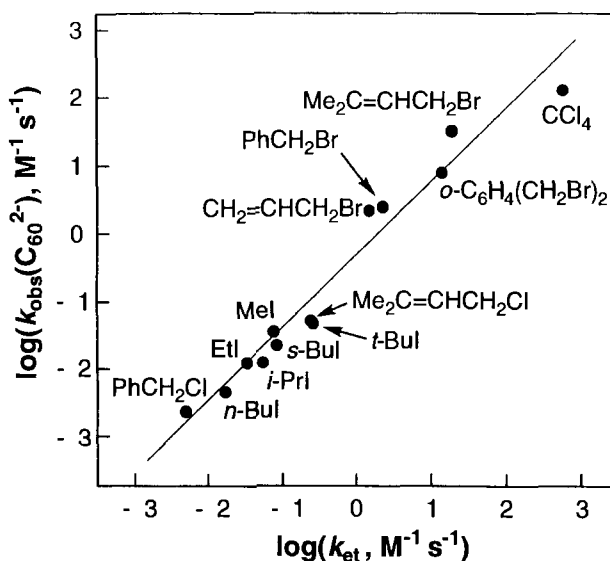


Figure 3. Correlation between $\log k_{\text{obs}}$ for the reaction of C_{60}^{2-} with alkyl halides and $\log k_{\text{et}}$ for the electron-transfer reaction of $\text{Me}_4\text{Q}^{\cdot-}$ with the same alkyl halides in degenerated PhCN at 298 K [161].

of RX is a known characteristic of electron-transfer reductions of RX [163–165]. The electron transfer pathway in the reaction of C_{60}^{2-} with RX was confirmed by comparing the observed rate constants (k_{obs}) for formation of RC_{60}^- and the rate constants (k_{et}) of electron-transfer reactions from tetramethylsemiquinone radical anion ($\text{Me}_4\text{Q}^{\cdot-}$) to the same series of RX [161]. The radical anion $\text{Me}_4\text{Q}^{\cdot-}$ was chosen to model the electron-transfer reactions of C_{60}^{2-} with RX, since $\text{Me}_4\text{Q}^{\cdot-}$ has nearly the same oxidation potential ($E_{1/2} = -0.84$ V relative to the SCE in MeCN) [166] as that of C_{60}^{2-} ($E_{1/2} = -0.87$ V relative to the SCE in PhCN) [20]. The plot between the experimentally determined $\log k_{\text{obs}}(\text{C}_{60}^{2-})$ and $\log k_{\text{et}}$ values in Figure 3 shows a good linear correlation with a slope of unity. This is a clear demonstration that a reaction of C_{60}^{2-} with RX proceeds via the rate-determining electron transfer from C_{60}^{2-} to RX as the authentic electron-transfer reaction of $\text{Me}_4\text{Q}^{\cdot-}$ with the same series of RX [161].

The reactivity order of RX for the second addition step to yield a dialkyl adduct of C_{60} is quite different from that for the first addition step [161]. For example, CCl_4 is the most reactive RX group in the first addition step, but it is much less reactive in the second addition step. For example, the k_{obs} value of $3.0 \times 10^{-5} \text{ M}^{-1} \text{ s}^{-1}$ is three orders of magnitude smaller than the most reactive $\text{Me}_2\text{C}=\text{CHCH}_2\text{Br}$ ($2.7 \times 10^{-2} \text{ M}^{-1} \text{ s}^{-1}$) [161]. The sterically hindered *t*-Bul and *s*-Bul reveal both good reactivities in the first R group addition, but show no reactivity at all in the second R group addition. Such sensitivity to the steric hindrance of the RX alkyl groups is characteristic of $\text{S}_{\text{N}}2$ reactions involving RX and nucleophiles. A typical example for this reaction type is the conversion of cobalt(I) tetraphenylporphyrin anion, $\text{Co}^{\text{I}}\text{TPP}^-$, to the σ -bonded complex, RCoTPP [162]. A good linear correlation with a slope of unity is observed between $\log k_{\text{obs}}$ of *t*-Bu C_{60}^- and $\log k_{\text{S}_{\text{N}}2}$ of CoTPP^-

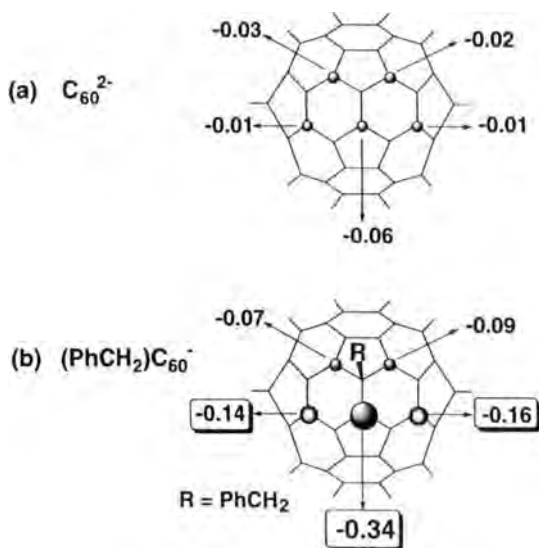


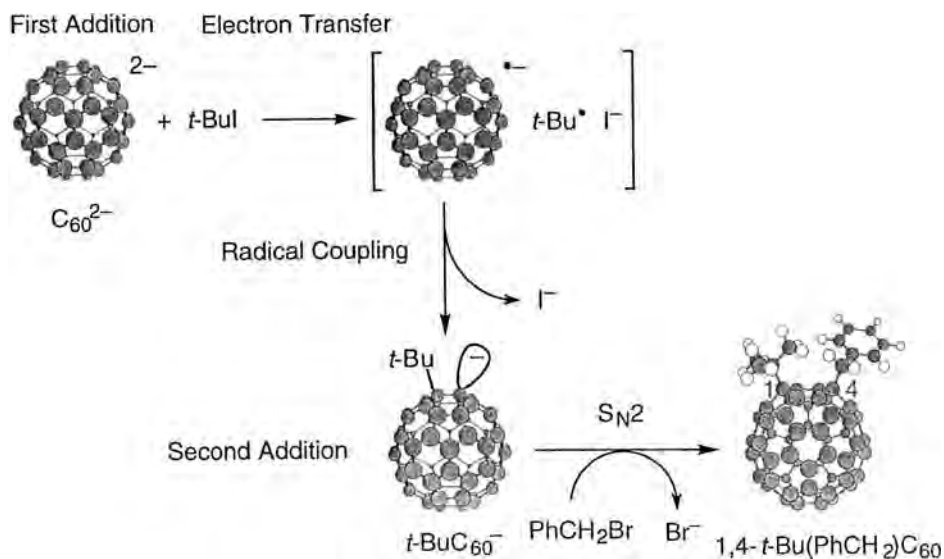
Figure 4. Calculated charge distribution on (a) C_{60}^{2-} and (b) $(PhCH_2)C_{60}^-$ [145].

[162]. Such a correlation clearly indicates that the alkylation of $t\text{-Bu}C_{60}^-$ with RX proceeds via an S_N2 pathway rather than via an electron transfer pathway.

It is interesting to discuss the reason why the reactions of C_{60}^{2-} and $t\text{-Bu}C_{60}^-$ with RX proceed via two different mechanisms, namely, an electron transfer or an S_N2 , respectively. The high delocalization of negative charge on the C_{60} skeleton should be noted with the most negative charge (i.e. -0.06) at a C_{60}^{2-} carbon atom (see for illustration Figure 4) [145].

C_{60}^{2-} with such a small negative charge at each carbon cannot act, however, as an effective nucleophile in the reaction with RX . In such a case, an electron transfer pathway is the only choice for the reaction of C_{60}^{2-} to proceed. A nucleophile, which is also an electron donor, is generally forced to undergo an electron transfer pathway when the steric hindrance at the reaction center prevents the nucleophile from interacting strongly enough to undergo an S_N2 reaction [152–160, 167]. Thus, the C_{60}^{2-}/RX system provides a unique example for an electron transfer pathway of a nucleophile which has a highly delocalized negative charge. In contrast to C_{60}^{2-} , the negative charge on $(PhCH_2)C_{60}^-$ becomes significantly localized at the C(2) position (-0.34) as well as at the C(4) and C(11) positions (-0.15) [145]. Such a localization of negative charge is also observed for $t\text{-Bu}C_{60}^-$ [168]. Addition at the C(2) position may be difficult because of steric repulsion between the proximate benzyl or $t\text{-Bu}$ groups and the nucleophilic addition of RX may then occur at the C(4) or C(11) positions, where the negative charge is the second largest [156].

In conclusion, the drastic difference in charge distribution between C_{60}^{2-} and RC_{60}^- causes significant differences in their nucleophilic reactivities so that the reactions of C_{60}^{2-} and RC_{60}^- with $R'X$ proceed via different pathways, namely, an electron transfer in the first step and an S_N2 pathway in the second step. A summary of the mechanism is shown in Scheme 2 for the formation of $t\text{-Bu}(PhCH_2)C_{60}$ as a typical example [161].



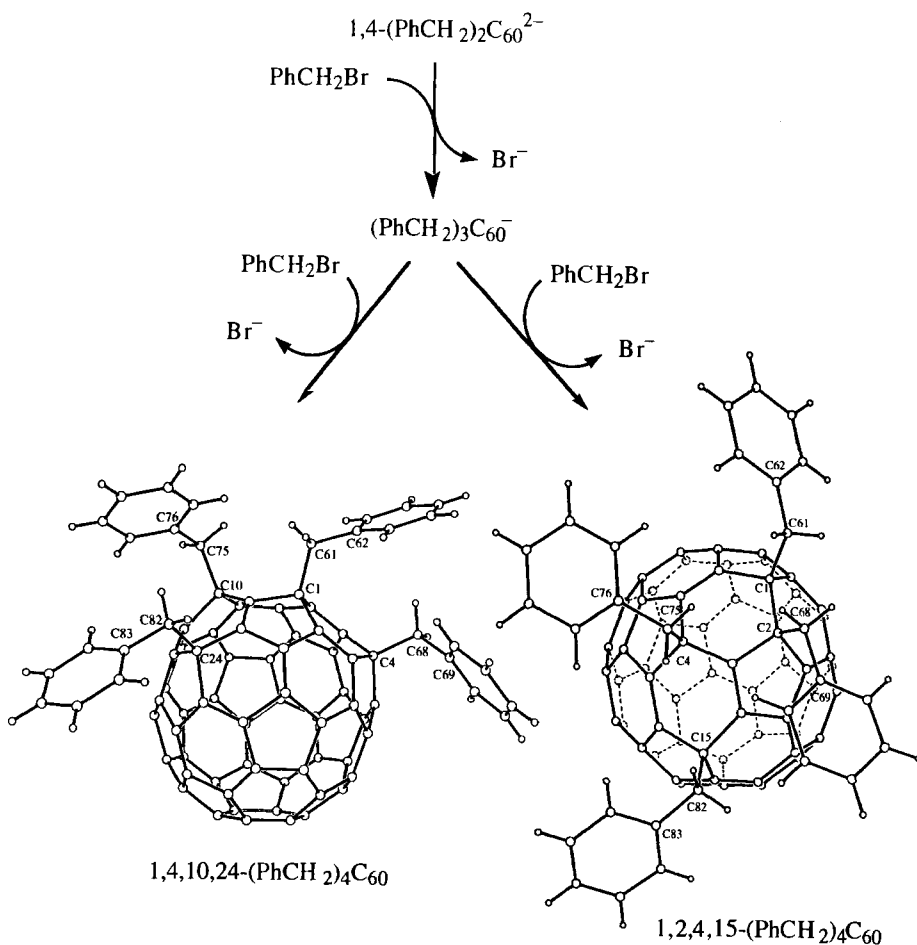
Scheme 2.

The initial electron transfer from C_{60}^{2-} to $t\text{-BuI}$ gives the $C_{60}^{\bullet-}/t\text{-Bu}^{\bullet}$ radical pair following an instantaneous cleavage of the C–I bond upon the dissociative electron-transfer reduction of $t\text{-BuI}$. A fast radical coupling between $C_{60}^{\bullet-}$ and $t\text{-Bu}^{\bullet}$ occurs in the radical pair to produce the monoadduct anion, $t\text{-BuC}_{60}^{\bullet-}$. The further addition of a second sterically hindered group does not occur via an $\text{S}_{\text{N}}2$ reaction. $t\text{-BuC}_{60}^{\bullet-}$ then undergoes an $\text{S}_{\text{N}}2$ reaction with less sterically hindered PhCH_2Br to yield the final product with two different alkyl groups such as $t\text{-Bu(PhCH}_2)_2\text{C}_{60}$ [161]. Such a sequential process for the derivatization of C_{60} is made possible by differences in alkyl halide reactivity in the first electron transfer and the second $\text{S}_{\text{N}}2$ step of the reaction.

Only a few examples of organofullerenes with multiple addends involving a 1,4-addition pattern have been reported [133, 169, 170]. The electron transfer and $\text{S}_{\text{N}}2$ sequence in Scheme 2 can be repeated by starting from the dianion of 1,4- $(\text{PhCH}_2)_2\text{C}_{60}$ to produce the corresponding tetrakisadduct, $(\text{PhCH}_2)_4\text{C}_{60}$ (Scheme 3) [148, 171].

The two isomers were isolated by HPLC from the products and the X-ray crystal structure of each isomer is shown in Scheme 3, while a schematic representation of each compound is illustrated in Figure 5 [171].

Each isomer has four benzyl groups on the C_{60} cage, with a 1,4;1,4-addition pattern for one compound (Figure 5a) and a 1,4;1,2-addition pattern for the other (Figure 5b). The positions of the two benzyl groups in the starting compound are labeled as 'A' and 'B' while the two added benzyl groups in the products are labeled as 'C' and 'D' (see Figure 5). The two isomers have three benzyl groups at identical positions. The regiochemistry of the two isomers can be rationalized by the initial

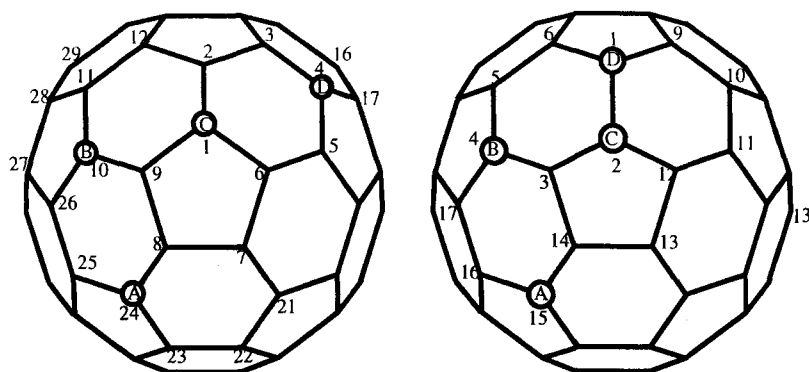


Scheme 3.

formation of a $[(\text{PhCH}_2)_3\text{C}_{60}]^-$ intermediate followed by either a 1,4- or 1,2-addition relative to the third benzyl group [172].

The monoanions of each $(\text{PhCH}_2)_4\text{C}_{60}$ isomer were also generated by bulk electrolysis (e.g., at a controlled potential) in PhCN containing 0.2 M TBAP [171]. The monoanion of the 1,4;1,4 isomer absorbs at both 801 and 1374 nm and this result contrasts with the monoanion of the 1,4;1,2 isomer which exhibits only a single absorption band at 1084 nm [171].

The I_h symmetry of the parent C_{60} is lowered by the introduction of two benzyl groups to C_{60} to give $1,4-(\text{C}_6\text{H}_5\text{CH}_2)_2\text{C}_{60}$, which leads to the larger g value (2.0004) of $1,4-(\text{C}_6\text{H}_5\text{CH}_2)_2\text{C}_{60}^{\bullet-}$ than that of $\text{C}_{60}^{\bullet-}$ ($g = 1.9984$) and a much smaller line-width ($\Delta H_{\text{msl}} = 2.5$ G at 213 K) which is temperature independent [172]. An even smaller ΔH_{msl} value (0.17 G) and a larger g value (2.0011) are observed for the



(a) 1,4,10,24-(PhCH₂)₄C₆₀ (1,4;1,4-isomer) (b) 1,2,4,15-(PhCH₂)₄C₆₀ (1,4;1,2-isomer)

Figure 5. Schematic representations of (a) the 1,4;1,4 isomer and (b) the 1,4;1,2 isomer of (PhCH₂)₄C₆₀. The positions of substitution on the C₆₀ molecule are indicated by the circles A, B, C, and D. Selected carbon atoms are labeled in accordance with IUPAC numbering [171].

tetrabenzyl C₆₀ adduct radical anion, 1,4,10,24-(C₆H₅CH₂)₄C₆₀^{•−} [172]. This is ascribed to a large splitting of the degenerate *t*_{1u} orbitals as a result of introducing four benzyl groups to C₆₀ [172]. In this case a hyperfine structure due to two non-equivalent protons of only one benzyl group (*a*H₁ = 0.31 G, *a*H₂ = 0.11 G) is observed. This is consistent with the predicted localized spin density at the C2 position next to the C1 carbon to which a benzyl group is attached [172].

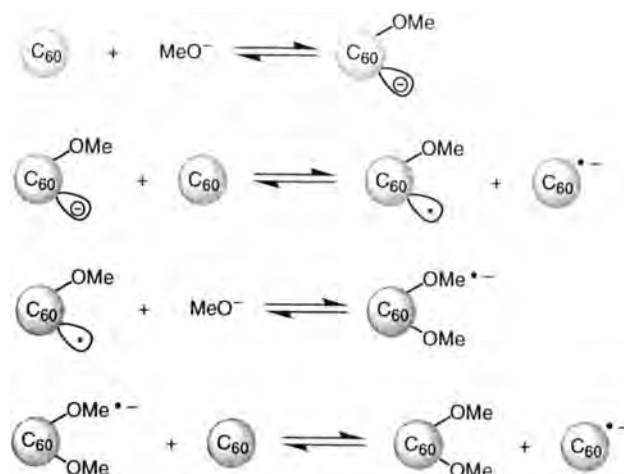
Dibenzyl adducts of C₇₀ were also electrosynthesized from C₇₀^{2−} in the presence of PhCH₂Br and purified by HPLC [173]. Mass spectral results for the largest HPLC fraction confirm formation of the [(PhCH₂)₂C₇₀] compound while ¹H NMR spectroscopy suggests that a mixture of three isomers is present in this fraction, all of which are 1,4-addition products [173].

Base-induced electron transfer

C₆₀ is known to undergo reduction to C₆₀^{•−} by addition of a MeO[−] solution. This reduction is, nevertheless, accompanied by the formation of the adduct anions, C₆₀(OMe)_{*n*}[−] (*n* = 1, 3, 5, 7) [174]. Electron transfer from MeO[−] to C₆₀ is thought to result in the formation of C₆₀^{•−} and the corresponding adduct anions [174]. *p*-Benzoquinone is also known to be reduced to semiquinone radical anion in a reaction with OH[−] in acetonitrile [175, 176]. The hydroxide ion is a much stronger electron donor in aprotic solvents such as acetonitrile than in water, since the solvation energy for OH[−] is less in aprotic solvents than in water [175]. However, no oxidized products of OH[−] were found in the reaction of *p*-benzoquinone with OH[−] [176]. The only oxidized product detected evolved from *p*-benzoquinone itself, namely, the rhodizionate dianion that is the ten-electron oxidized product of *p*-benzoquinone [176]. Thus, the one-electron reduction of ten equivalents of *p*-benzoquinone is accompanied by the ten electron oxidation of one equivalent of *p*-benzoquinone. In this case

OH^- is not the electron donor, but instead *p*-benzoquinone itself acts as the electron donor in the presence of OH^- . The addition of OH^- to *p*-benzoquinone initiates an electron transfer from the OH^- adduct of *p*-benzoquinone to *p*-benzoquinone leading to the noble disproportionation. This yields ten equivalents of semiquinone radical anion and rhodizonate dianion [176].

In the reaction of C_{60} with MeO^- , the ultimate electron source to reduce C_{60} should be C_{60} itself, since C_{60} is oxidized to $\text{C}_{60}(\text{OMe})_n^-$ accompanied by the reduction of C_{60} to $\text{C}_{60}^{\bullet-}$ [174]. The detailed spectroscopic and kinetic studies have revealed that a methoxy adduct anion of C_{60} is the true electron donor and that MeO^- is acting as a very strong base or nucleophile rather than an electron donor in PhCN [177]. The reaction sequence is shown in Scheme 4 [177]. $(\text{MeO})\text{C}_{60}^-$ becomes a much stronger reductant than the parent C_{60} once the methoxide ion adduct is formed. Then, an electron transfer from $(\text{MeO})\text{C}_{60}^-$ to C_{60} occurs to give a methoxy adduct radical of C_{60} ($(\text{MeO})\text{C}_{60}^{\bullet}$) and $\text{C}_{60}^{\bullet-}$. Although the electron transfer from $(\text{MeO})\text{C}_{60}^-$ ($E_{\text{ox}}^{\text{p}} = 0.14 \text{ V}$) to C_{60} ($E_{\text{red}}^{\circ} = -0.43 \text{ V}$) [20] is thermodynamically unfavorable as indicated by the difference in the redox potentials the follow-up reaction involving an addition of the second MeO^- to $(\text{MeO})\text{C}_{60}^{\bullet}$, is a highly exothermic process to give $(\text{MeO})_2\text{C}_{60}^{\bullet-}$. Since $(\text{MeO})_2\text{C}_{60}^{\bullet-}$ is a much stronger electron donor than the parent $\text{C}_{60}^{\bullet-}$, an electron transfer from $(\text{MeO})_2\text{C}_{60}^{\bullet-}$ to C_{60} occurs readily to yield the dimethoxy adduct of C_{60} [$(\text{MeO})_2\text{C}_{60}$] and $\text{C}_{60}^{\bullet-}$ [177] (Scheme 4).



Scheme 4.

5.4 Intermolecular Photoinduced Electron Transfer

Since the absorption features of fullerenes extend over the UV and visible spectrum, light of different frequency can be used to excite fullerenes [19, 178]. Depending on

the light frequency used, vibrational levels of the first singlet excited state or higher singlet excited states are populated. After a series of ultra-fast, cascade-like relaxation processes, the population of the lowest vibrational level of the first singlet excited state is completed before a quantitative intersystem crossing ($\tau \approx 1.3$ ns) to the triplet excited state takes place [179]. The latter is then the starting point for a slow regeneration ($\tau \approx 100$ μ s) of the singlet ground state [19]. Promoting an electron from a low-energy bonding orbital to a high-energy anti-bonding orbital leads to two profound effects. It increases the electron affinity ($C_{60}/C_{60}^{\bullet-} = -0.43$ V relative to the SCE; in benzonitrile) [20] and, at the same time, reduces the oxidation potential of the fullerene ($C_{60}/C_{60}^{\bullet+} = 1.76$ V relative to the SCE; in benzonitrile) [16, 92] by precisely the amount of the excited state energy. Thus, it makes the fullerene excited states stronger oxidants ($E_{1/2} (^1C_{60}^*/C_{60}^{\bullet-}) = 1.56$ V relative to the SCE; $E_{1/2} (^3C_{60}^*/C_{60}^{\bullet-}) = 1.13$ V relative to the SCE) and stronger reductants ($E_{1/2} (^1C_{60}^*/C_{60}^{\bullet+}) = -0.23$ V relative to the SCE; $E_{1/2} (^3C_{60}^*/C_{60}^{\bullet+}) = 0.19$ V relative to the SCE). In principle, both excited states can be probed in inter- and intramolecular charge transfer reactions with adequate electron acceptor and electron donor moieties. An intermolecular reaction with the initially formed singlet excited state stands, however, in direct competition with the rapidly occurring intersystem crossing and is, in essence, overshadowed by the latter. Thus, intermolecular electron-transfer reactions, as outlined in the following section, usually occur with the much longer-lived triplet excited state. An intermolecular electron-transfer reaction, yielding a charge separated radical pair, involves a sequence of events. In particular, the initial photoexcitation process is succeeded by a diffusion- or activation-controlled intermolecular electron transfer, which, in turn, creates a primary contact radical pair. In the current context, it is the one-electron reduced fullerene π -radical anion (or the one-electron oxidized fullerene π -radical cation) and the oxidized form of the applied electron donor (or the reduced form of the applied electron acceptor). In the final step the diffusional break-up of the contact pair to give the products completes the sequence. The dissociation depends on the ability of the solvent to retard the exergonic back electron transfer to the ground state or excited state reactant pair and stabilize the radical pair, for example, via strong dipole–dipole interactions.

5.4.1 Formation of Fullerene Radical Anions

The high reduction potential of the fullerene triplet excited state permits an efficient reductive quenching with a large number of tertiary amines to produce $C_{60}^{\bullet-}$ (Eq. 12) [18, 23, 180–191].



Selection of a polar solvent, such as different alcohols or benzonitrile, is crucial in view of accomplishing an efficient charge separation, which is, under these circumstances, typically confirmed through formation of $C_{60}^{\bullet-}$ at $\lambda_{\text{max}} = 1080$ nm [65]. In contrast, the low dielectric constant of toluene prevents the successful

charge separation. Ferrocene (Fc) [192, 193], tetrathiafulvalene (TTF) [194, 195], bis-(ethylenedithio)tetrathiafulvalene (BEDT-TTF) [194, 208], aromatic thiols [196], tetra-selenafulvalenes [197], tetraethoxyethene [198], phenothiazines [199], 3,3',5,5'-tetramethylbenzidine (NTMB) [26, 200–202], 1,4-diazabicyclo[2.2.2]octane (DABCO) [190, 203], stable nitroxide radicals [204], tetraphenylborate [205], triphenylbutylborate [205], retinol [205–207], β -carotene [209, 210], polysilane [201, 211], polygermane [201, 212], oligo-thiophene [213–216], tetrathiophene [213–216], zinc tetraphenyl porphyrin (ZnP) [217, 218] and zinc phthalocyanine (ZnPc) [27], to name a few representative cases, are all excellent electron donors. These compounds have therefore been probed as sacrificial electron donors in intermolecular quenching reactions with triplet excited fullerenes. Again, polar solutions play a central role in creating conditions which support an efficient charge separation and give rise to diffusion-controlled charge recombination ($\approx 10^{10} \text{ M}^{-1} \text{ s}^{-1}$).

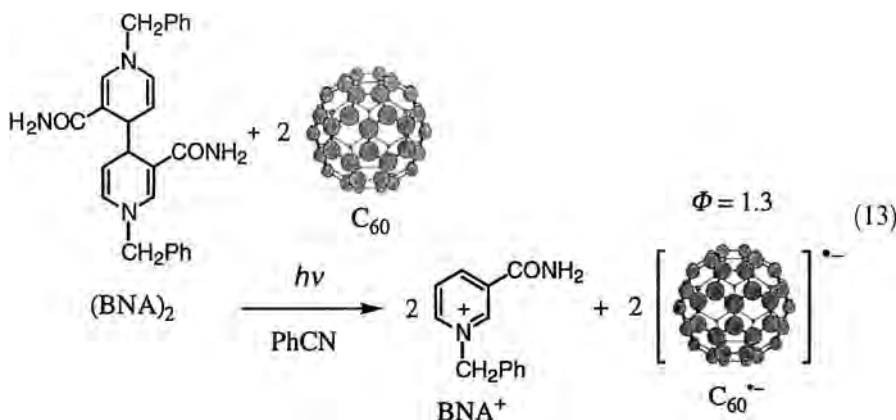
Beside the photoinduced electron transfer in homogeneous solutions, fullerenes have also been shown to play a key function in mediating electron transfer through an artificial lipid bilayer membrane [84, 219, 220]. For example, the fullerene moiety was embedded in form of aggregates within the membrane interior of a three-component cell [220]. A strong electron donor (e.g., ascorbate) was placed on one side of the lipid bilayer, while the three-component cell was completed with an adequate electron acceptor on the other side of the membrane (e.g., an aqueous solution containing anthraquinone 2-sulfonate). In an oxygen-free environment, illumination generated a measurable photocurrent between the two aqueous phases [220]. To confirm a possible electron hopping mechanism or, alternatively, a diffusion of an one-electron reduced fullerene moiety, the same studies were carried out in blank experiments without a bilayer incorporated fullerene moiety and without removal of oxygen. While the earlier set-up is meant to interrupt the redox gradient across the cell, oxygen quenches the excited and reduced states. Indeed, no photocurrent was observed in the two blanks [220]. A similar across-membrane electron transport was reported focusing on an intermolecular electron transport between a porphyrin, attached to the bilayer-water interface, and fullerenes, embedded in the lipid bilayer membrane.

ZnO or TiO_2 semiconductor clusters are excellent probes to perform electron transfer experiments since their conduction bands ($E_{\text{CB}} = -0.5 \text{ V}$ relative to the NHE) favor only one-electron reduction of, for example, C_{60} , avoiding, however, multiple reduction steps [221–223]. Pioneering experiments focusing on the reduction of C_{60} were conducted via exclusive excitation of ZnO colloids.

As an alternative to an intermolecular quenching reaction involving the fullerene triplet excited state, strong interactions between the fullerene and a donor, in form of a ground state complex or excited state complex ('exciplex'), are also an appropriate means to accelerate transfer dynamics evolving from the singlet excited state [23, 180–183, 188]. Formation of fullerene charge transfer complexes has been reported for a large variety of substrates, such as *N,N*-dimethylaniline (DMA) [180, 188], *N,N*-diethylaniline (DEA) [180, 183, 188], diphenylamines (DPA) [23], triphenylamine (TPA) [23], triethylamine (TEA) [23, 181, 182], and a number of substituted naphthalenes [224]. Generally, the resulting complexes are weak and high amine concentrations are required to study the characteristics and properties of

fullerene containing charge-transfer complexes. In aliphatic hydrocarbon solvents such as hexane or methylcyclohexane, the quenching of the monomer excited states occurs via the transient formation of 'exciplexes'.

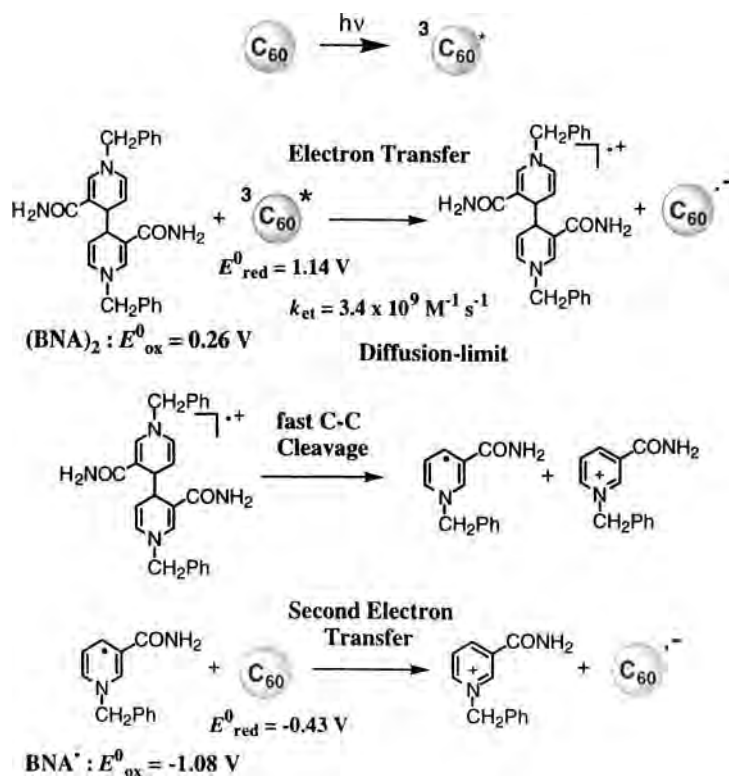
A long-lived transient of $C_{60}^{\bullet-}$ is formed in photoinduced electron transfer from ZnO or TiO₂ semiconductor colloids to C_{60} [222]. In homogeneous systems described above, however, the lifetime of the generated $C_{60}^{\bullet-}$ is generally extremely short due to fast back electron transfer to the reactant pair, resulting in no net formation of $C_{60}^{\bullet-}$. This is not the case for a photoinduced electron-transfer reaction from an NADH analog, 1-benzyl-1,4-dihydronicotinamide (BNAH), and the dimer analog [(BNA)₂] to the triplet excited state of C_{60} ($^3C_{60}^*$). A stable $C_{60}^{\bullet-}$ was found in benzonitrile solution with a surprisingly high quantum yield exceeding unity in the latter case; $\Phi_{\infty} = 1.3$ (Eq. 13) [225].



A quantum yield exceeding unity is consistent with the stoichiometry in Eq. 13, where $(BNA)_2$ can reduce two equivalents of C_{60} . The reaction mechanism for the formation of a stable $C_{60}^{\bullet-}$ is shown in Scheme 5 [225].

The triplet excited state, namely, $^3C_{60}^*$ generated by the efficient intersystem crossing upon photoexcitation of C_{60} , is quenched by electron transfer from $(BNA)_2$ to $^3C_{60}^*$ to give the radical ion pair [$(BNA)_2^{\bullet+}$ and $C_{60}^{\bullet-}$] in competition with the decay to the ground state. This step is followed by a fast cleavage of the C–C bond of the dimer (k_c) to produce *N*-benzylnicotinamide radical (BNA^{\bullet}) and BNA^+ [226]. The subsequent second electron transfer from BNA^{\bullet} to C_{60} should be by far faster than the first, as BNA^{\bullet} is a strong reductant ($E^{\circ}_{ox} = -1.08$ V relative to the SCE) [44]. Thus, once photoinduced electron transfer from $(BNA)_2$ to $^3C_{60}^*$ occurs, two $C_{60}^{\bullet-}$ molecules are produced. The generation of stable $C_{60}^{\bullet-}$ in the photoreduction of C_{60} by BNAH also proceeds via photoinduced electron transfer from BNAH to $^3C_{60}^*$ [225]. In this case, the deprotonation of $BNAH^{\bullet+}$ gives BNA^{\bullet} , which can further reduce C_{60} to $C_{60}^{\bullet-}$ [225].

The selective one-electron reduction of C_{70} to $C_{70}^{\bullet-}$ is also attained through photoinduced electron transfer from BNAH or $(BNA)_2$ to the triplet excited state of C_{70} [227]. The limiting quantum yields for formation of $C_{70}^{\bullet-}$ in the photoreduction

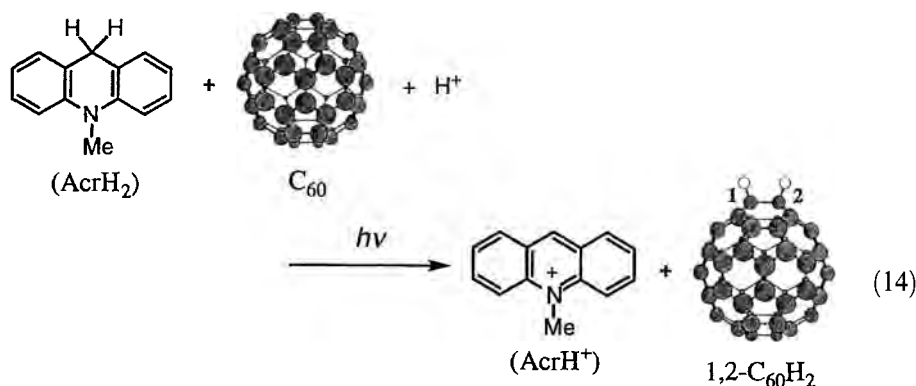


Scheme 5.

of C_{70} by BNAH and $(\text{BNA})_2$ exceed unity; $\Phi_{\infty} = 2.0$ and 1.9. Both values are larger than the corresponding values for formation of $\text{C}_{60}^{\cdot-}$ ($\Phi_{\infty} = 1.3$ and 0.80, respectively) [227]. The formation of stable $\text{C}_{70}^{\cdot-}$ is readily detected by the typical NIR spectrum ($\lambda_{\text{max}} = 1374 \text{ nm}$) [228, 229]. The enhanced reactivity of C_{70} as compared to C_{60} is ascribed to a more localized unpaired electron and negative charge in $\text{C}_{70}^{\cdot-}$ due to loss of symmetry. This facilitates the follow-up reaction in competition with the back electron transfer to the ground state reactant pair.

5.4.2 Selective Two-electron Reduction

The reduction of C_{60} and C_{70} has normally been achieved by the use of strong reductants such as BH_3 , which yield not only C_{60}H_2 and C_{70}H_2 but also polyhydride mixtures [104, 230–237]. The use of the triplet excited state of C_{60} has made it possible to attain the selective two-electron reduction of C_{60} to 1,2- C_{60}H_2 by 10-methyl-9,10-dihydroacridine (AcrH_2) which is a mild hydride donor (Eq. 14) [225, 238].



Irradiation of a deaerated PhCN solution of C_{60} , AcrH_2 and CF_3COOH with a Xe lamp equipped a UV-cut filter ($\lambda < 540 \text{ nm}$) resulted in exclusive formation of $\text{1,2-C}_{60}\text{H}_2$ in approximately 70 % yield [238]. In the dark, however, no reaction occurred even at high temperatures (e.g., 373 K) [238]. The transient absorption spectra of the radical ion pair ($\text{AcrH}_2^{\bullet+} \text{C}_{60}^{\bullet-}$) in the visible and near-IR region are observed by laser flash photolysis of a deaerated PhCN solution of C_{60} in the presence of AcrH_2 and CF_3COOH with 532 nm laser light as shown in Figure 6 [225].

The absorption band at 640 nm in the visible region agrees with that reported for $\text{AcrH}_2^{\bullet+}$ observed as a transient spectrum in the electron-transfer oxidation of AcrH_2 by $\text{Fe}(\text{phen})_3^{3+}$ (phen = 1,10-phenanthroline) [239]. The decay of the ab-

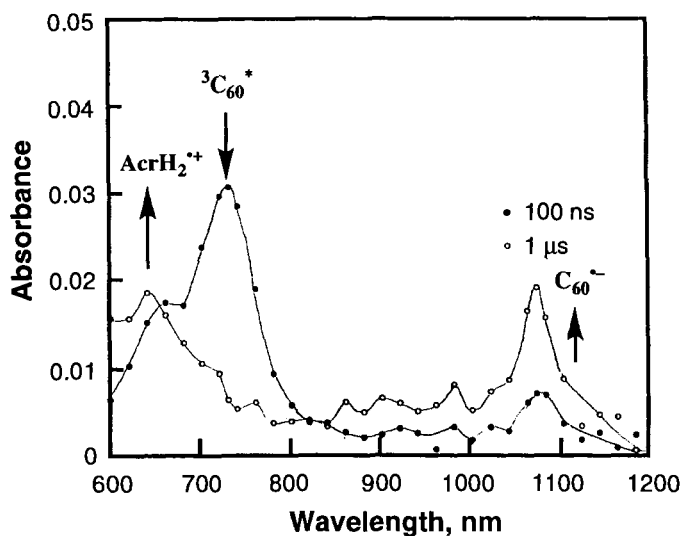
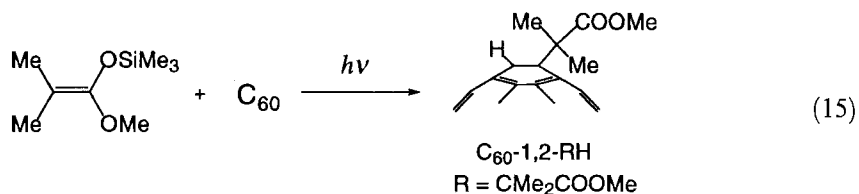


Figure 6. Transient absorption spectra observed in the photoreduction of C_{60} ($1.0 \times 10^{-4} \text{ M}$) by AcrH_2 ($1.0 \times 10^{-3} \text{ M}$), 100 ns (●) and 1 μs (○) after laser excitation in deaerated PhCN at 295 K [225].

sorbance at 740 nm due to ${}^3\text{C}_{60}^*$ coincides with the rise of the absorbance at 640 nm due to AcrH_2^{*+} as well as the absorbance at 1080 nm due to $\text{C}_{60}^{\bullet-}$ [64, 225]. Thus, the photochemical two-electron reduction of C_{60} by AcrH_2 proceeds via electron transfer from AcrH_2 to ${}^3\text{C}_{60}^*$, which gives the radical ion pair ($\text{AcrH}_2^{*+}\text{C}_{60}^{\bullet-}$) in competition with the decay to the ground state. The $\text{p}K_a$ of singly reduced C_{60} ($\text{C}_{60}\text{H}^\bullet$) encapsulated in γ -cyclodextrin (γ -CD) and dissolved in water/propan-2-ol has been determined as 4.5 on the basis of a specific IR absorption band for $\text{C}_{60}^{\bullet-}$ - γ -CD [85]. On the other hand, the $\text{p}K_a$ of AcrH_2^{*+} in water has previously been determined as 2.0 [44, 239]. The proton transfer from AcrH_2^{*+} to $\text{C}_{60}^{\bullet-}$ is therefore exergonic, and it should occur efficiently in the radical ion pair in competition with the back electron transfer to the reactant pair to give $\text{C}_{60}\text{H}^\bullet$ which is converted to 1,2- C_{60}H_2 by the fast electron transfer from AcrH^\bullet in the presence of CF_3COOH . Thus, the selective two-electron reduction of C_{60} to C_{60}H_2 occurs via sequential electron-proton-electron-proton transfer.

5.4.3 C–C Bond Formation via Photoinduced Electron Transfer

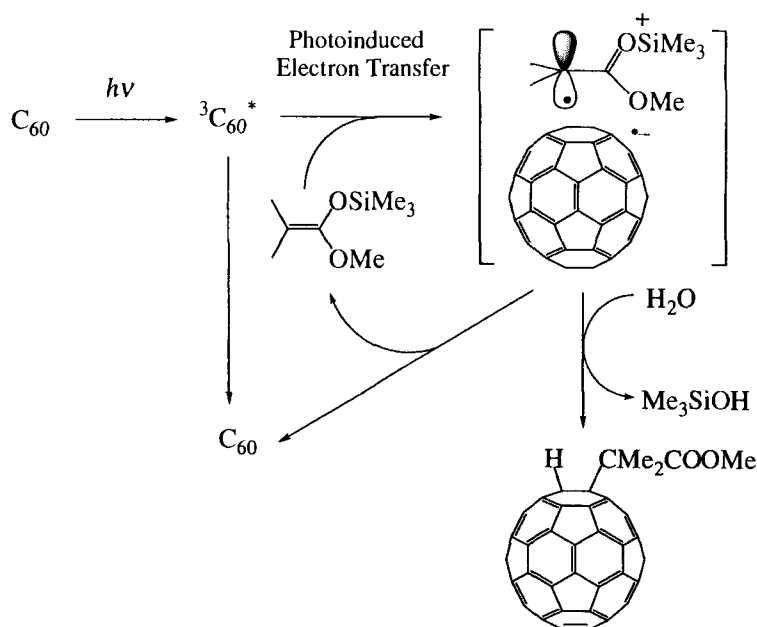
The carbon-carbon bond formation via photoinduced electron transfer has recently attracted considerable attention from both synthetic and mechanistic viewpoints [240–243]. In order to achieve efficient C–C bond formation via photoinduced electron transfer, the choice of an appropriate electron donor is essential. Most importantly, the donor should be sufficiently strong to attain efficient photoinduced electron transfer. Furthermore, the bond cleavage in the donor radical cation produced in the photoinduced electron transfer should occur rapidly in competition with the fast back electron transfer. Organosilanes that have been frequently used as key reagents for many synthetically important transformations [244–247] have been reported to act as good electron donors in photoinduced electron-transfer reactions [248, 249]. The one-electron oxidation potentials of ketene silyl acetals (e.g., E°_{ox} relative to the SCE = 0.90 V for $\text{Me}_2\text{C}=\text{C}(\text{OMe})\text{OSiMe}_3$) [248] are sufficiently low to render the efficient photoinduced electron transfer to ${}^3\text{C}_{60}^*$ [22], which, after the addition of ketene silyl acetals, yields the fullerene with an ester functionality (Eq. 15) [250, 251].



The initial monoadduct reacts further to give the corresponding bisadduct at prolonged irradiation times particularly at higher concentration of the ketene silyl acetal (10 equiv.) [22]. When the unsubstituted ketene silyl acetal ($\text{H}_2\text{C}=\text{C}(\text{OEt})\text{OSiMe}_3$) is employed, only the monoadduct, ethyl 1,2-dihydro[60]fullerene-1-acetate, is ob-

tained in quantitative yields based on recovered C_{60} [22]. Under these conditions, no polyadducts were obtained even after prolonged reaction times [22]. Such a difference in the reactivity between $Me_2C=C(OMe)OSiMe_3$ and $H_2C=C(OEt)OSiMe_3$ can be well accounted for by the decrease in the electron donor ability of the latter [248]. The laser flash photolysis study showed that the disappearance of the band due to $^3C_{60}^*$ at 740 nm is accompanied by the appearance of a new absorption band at 1080 nm due to $C_{60}^{\bullet-}$ and that the decay rate of $^3C_{60}^*$ coincides completely with the rate of formation of $C_{60}^{\bullet-}$ [252]. The reaction mechanism of the photoaddition of ketene silyl acetals to C_{60} can be summarized as shown in Scheme 6 which is essentially the same as that of the photoaddition of ketene silyl acetals to 10-methylacridone [22, 249, 253]. The photoinduced electron transfer from the ketene silyl acetal to $^3C_{60}^*$ gives the radical ion pair in competition with the decay to the ground state. The spin density of the ketene silyl acetal radical cation thus produced is nearly localized on the terminal carbon atom [248]. Thus, the ketene silyl acetal radical cation is coupled efficiently with the C_{60} radical anion in competition with the back electron transfer to the reactant pair. The resulting zwitterionic intermediate converts eventually to the product after an efficient protonation step is completed (Scheme 6) [22, 252].

The photoinduced electron-transfer reactions are usually performed in polar solvents such as acetonitrile and benzonitrile, in which the solvation energy of free ions is greatly increased compared to non-polar solvents such as benzene. Such a difference in the solvation energy of ketene silyl acetal radical cation in benzene and



Scheme 6.

benzonitrile has been estimated as 0.86 eV [248, 249]. On the other hand, the difference in the solvation energy of $C_{60}^{\bullet-}$ in benzene and benzonitrile may be negligible because of the highly delocalized negative charge. The overall difference in the free energy change of electron transfer to produce free ions in benzene and benzonitrile is thereby estimated as 0.86 eV [22]. The difference of 0.86 eV in the ΔG°_{et} values between benzene and benzonitrile may well be canceled by the large Coulombic interaction in benzene as compared with that in benzonitrile, since the difference in the values in benzene and benzonitrile with the mean separation of 6.7 Å is equal to 0.86 eV [22]. Thus, the photoinduced electron transfer from ketene silyl acetals to ${}^3C_{60}^*$ can also occur in benzene leading to the same product as obtained in benzonitrile, although the rate becomes slower [22].

There is an interesting case in which a C–C bond formation via photoinduced electron transfer yields a product which gives rise to a different regioselectivity than that predicted for a thermal polar reaction [254]. The selective γ -addition of prenyltributyltin with 10-methylacridinium ion proceeds via a polar mechanism in which the C–C bond formation should occur prior to the cleavage of the Sn–C bond. In contrast, the selective α -addition instead of γ -addition occurs through a photoinduced electron transfer from prenyltributyltin to the singlet excited state of 10-methylacridinium ion [254]. The photoinduced electron transfer from prenyltributyltin to ${}^3C_{60}^*$ also leads to the selective formation of C_{60} -1,2-(H)CH₂CH=CMe₂ in which the allylic group is introduced selectively at the α position and no γ adduct has been formed [255]. In an electron-transfer reaction, the Sn–C bond may be significantly lengthened in the prenyltributyltin radical cation generated upon the electron transfer [256]. In such a case the C–C bond formation may occur after the elongation or the cleavage of the Sn–C bond. This leads to the more favorable α -addition than the γ -addition because of the steric hindrance of two methyl groups of prenyltributyltin radical cation as shown in Scheme 7.

The free energy change of photoinduced electron transfer from electron donors to ${}^3C_{60}^*$ (ΔG°_{et}) is given by Eq. 16:

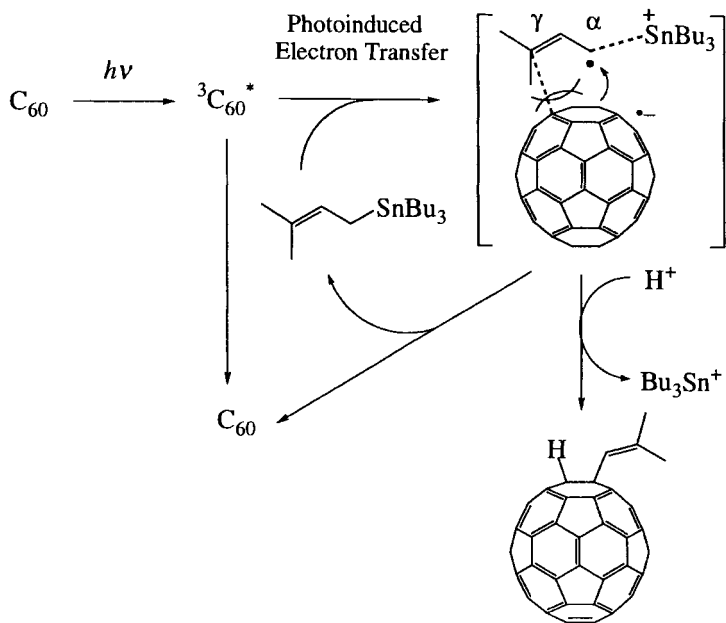
$$\Delta G^\circ_{et} = F(E^\circ_{ox} - E^\circ_{red}) \quad (16)$$

where E°_{ox} and E°_{red} are the one-electron oxidation potentials of the electron donor and the one-electron reduction potential of ${}^3C_{60}^*$, respectively. The dependence of the activation free energy of photoinduced electron transfer ΔG^\ddagger on the free energy change of electron transfer (ΔG°_{et}) has well been established as given by the Rehm–Weller free energy relation, Eq. 17:

$$\Delta G^\ddagger = (\Delta G^\circ_{et}/2) + [(\Delta G^\circ_{et}/2)^2 + (\Delta G^\ddagger_0)^2]^{1/2} \quad (17)$$

where ΔG^\ddagger_0 is the intrinsic barrier that represents the activation free energy when the driving force of electron transfer is zero, i.e., $\Delta G^\ddagger = \Delta G^\ddagger_0$ at $\Delta G^\circ_{et} = 0$ [257]. The ΔG^\ddagger values are related to the rate constant of electron transfer (k_{et}) as given by Eq. 18:

$$\Delta G^\ddagger = 2.3RT \log[Z(k_{et}^{-1} - k_{diff}^{-1})] \quad (18)$$



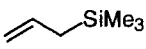
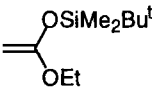
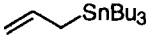
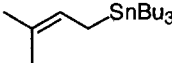
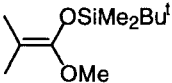
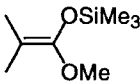
Scheme 7.

where Z is the collision frequency (i.e., $1 \times 10^{11} \text{ M}^{-1} \text{ s}^{-1}$) and k_{diff} is the diffusion rate constant (i.e., $5.6 \times 10^9 \text{ M}^{-1} \text{ s}^{-1}$) in benzonitrile. The k_{et} values can be calculated from the $\Delta G^{\circ}_{\text{et}}$ and ΔG°_0 values by using Eqs. 16 and 17. The k_{et} values of photoinduced electron transfer from 14 different organometallic electron donors are listed in Table 3, together with the free energy change of electron transfer ($\Delta G^{\circ}_{\text{et}}$), observed rate constants k_{obs} derived from the dependence of quantum yields on the donor concentration, the quenching rate constants k_{q} of ³C₆₀^{*}, and the limiting quantum yields (Φ_{∞}).

The k_{et} value increases with an increase in the driving force ($-\Delta G^{\circ}_{\text{et}}$) and they agree with the k_{q} and k_{obs} values (Table 3). Such agreement confirms the validity of the photoinduced electron transfer mechanisms shown in Schemes 6 and 7.

As mentioned earlier, organometallic reagents which are strong nucleophiles have usually been used for the alkylation of fullerenes [132–138]. On the other hand, 4-alkylated NADH analogs can be used as a mild alkylating reagent in the photochemical reactions with C₆₀ and C₇₀ [225, 227]. The one-electron oxidation of 4-*tert*-butylated BNAH (*t*-BuBNAH) results in the selective C(4)–C bond cleavage of *t*-BuBNAH^{•+} [258, 259]. Although there are two possible modes of the carbon–carbon bond cleavage in such reactions to generate (i) *t*-Bu[•] and BNA⁺ or (ii) *t*-Bu⁺ and BNA[•], the formation of *t*-Bu[•] in the one-electron oxidation of *t*-BuBNAH has been confirmed by applying a rapid mixing flow ESR technique [259]. Thus, the photoinduced electron transfer from *t*-BuBNAH to ³C₆₀^{*} is followed by the facile C(4)–C bond cleavage of *t*-BuBNAH^{•+}. The resulting *t*-Bu[•] is coupled immediately

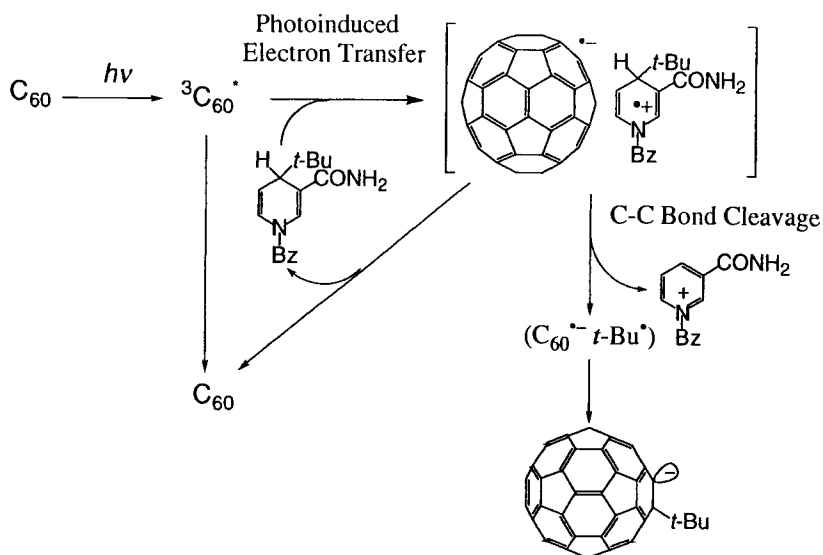
Table 3. Free energy change, $\Delta G^\circ_{\text{et}}$, and rate constants, k_{et} , of photoinduced electron transfer from group 14 organometallic electron donors to $^3\text{C}_{60}^*$, observed rate constants, k_{obs} , triplet quenching rate constants, k_{q} , and limiting quantum yields, Φ_∞ , in the photoaddition of the donors to C_{60} in benzonitrile at 298 K [212].

Electron donor	$\Delta G^\circ_{\text{et}}$ (kcal mol ⁻¹)	k_{obs} (M ⁻¹ s ⁻¹)	k_{q} (M ⁻¹ s ⁻¹)	k_{et} (M ⁻¹ s ⁻¹)	Φ_∞
	8.3	No reaction	No reaction	2.3×10^3	No reaction
	3.2	2.5×10^6	—	1.3×10^6	0.14
	-1.8	5.0×10^7	7.8×10^7	4.5×10^7	0.13
	-5.8	9.8×10^8	—	1.7×10^9	0.13
	—	2.1×10^8	3.7×10^8	—	0.19
	-5.5	2.2×10^8	4.0×10^8	4.7×10^8	0.26

with $\text{C}_{60}^{\bullet-}$ to yield the final product ($t\text{-BuC}_{60}^-$) in competition with the back electron transfer as shown in Scheme 8 [225].

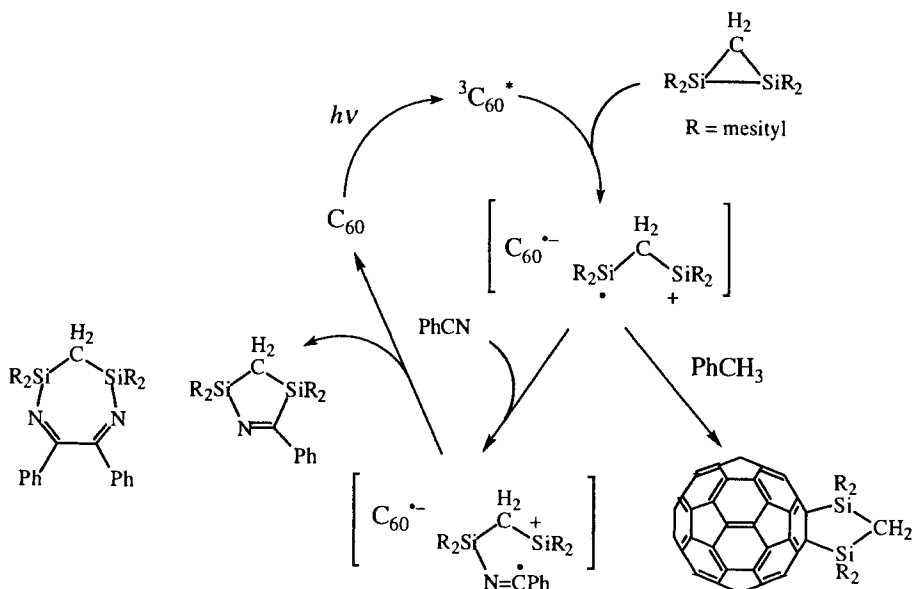
The formation of $\text{C}_{60}^{\bullet-}$ produced as a reactive intermediate in the photochemical reaction of C_{60} with $t\text{-BuBNAH}$ is also detected by the laser flash photolysis of a deaerated PhCN solution of C_{60} in the presence of $t\text{-BuBNAH}$ [225]. This type of photochemical reaction provides a unique and new way to prepare $t\text{-BuC}_{60}^-$ by using $t\text{-BuBNAH}$, which is a mild alkylating reagent under neutral conditions. The subsequent trap of the photoproduct by CF_3COOH and PhCH_2Br gave 1,2- $t\text{-BuC}_{60}\text{H}$ and 1,4- $t\text{-Bu(PhCH}_2\text{)C}_{60}$, respectively as reported for the reactions of $t\text{-BuC}_{60}^-$ with electrophiles [260–262].

Strained Si–Si σ bonds are also known to act as good electron donors [263–265]. Photoinduced electron transfer from strained disiliranes such as 1,1,2,2-tetramesityl-1,2-disilirane to $^3\text{C}_{60}^*$ occurs in benzonitrile to give a transient absorption spectrum at 1080 nm due to $\text{C}_{60}^{\bullet-}$ obtained by 532 nm laser flash photolysis of C_{60} in the presence of disilirane [266]. The photochemical reaction of C_{60} with the disilirane in benzonitrile afforded the 1:1 and 1:2 adducts of disilirane and benzonitrile in good yields. The structures of the corresponding adducts were determined by X-ray crystallographic analysis [266]. These adducts were also obtained in good yields in the presence of catalytic amounts of C_{60} . Thus, C_{60} acts as a photoinduced electron-transfer catalyst as shown in Scheme 9.



Scheme 8.

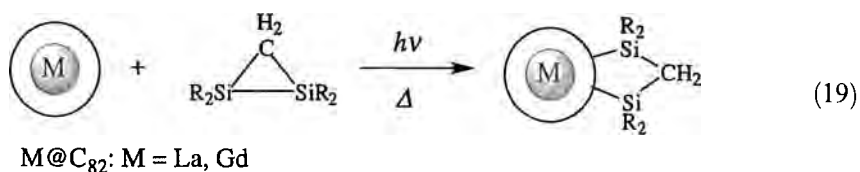
Photoinduced electron transfer from the silirane to $^3C_{60}^*$ gives the radical ion pair of $C_{60}^{\bullet-}$ and the disilirane radical cation. The Si-Si bond of the disilirane radical cation may be cleaved and trapped by benzonitrile. This sequence is followed by back electron transfer from $C_{60}^{\bullet-}$ to the adduct cation to yield the corre-



Scheme 9.

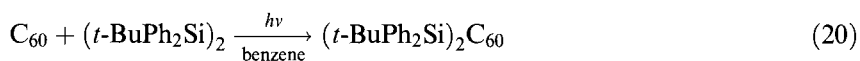
sponding adducts when C_{60} is regenerated (Scheme 9). Irradiation of a toluene solution of the disilirane and C_{60} with a high-pressure mercury lamp ($\lambda > 300$ nm) resulted, however, in the formation of 1,1,3,3-tetramesityl-1,3-disilolane [$1,2-(\text{Mes}_4\text{Si}_2\text{CH}_2)_2C_{60}$] (Scheme 9) [267]. In a nonpolar solvent, the transient absorption band due to $C_{60}^{\bullet-}$ was not observed although appreciable acceleration of the decay of ${}^3C_{60}^*$ at 740 nm was observed [266]. This suggests that the decay of the radical ion pair due to the Si–C bond formation is too fast to be detected or alternatively ${}^3C_{60}^*$ forms an exciplex with the disilirane.

When endohedral metallofullerenes which are fullerenes with metal(s) inside the hollow spherical cage are employed, the addition of disilirane to $\text{La}@C_{82}$ and $\text{Gd}@C_{82}$ (Eq. 19) occurs in both thermal and photochemical ways [268, 269].



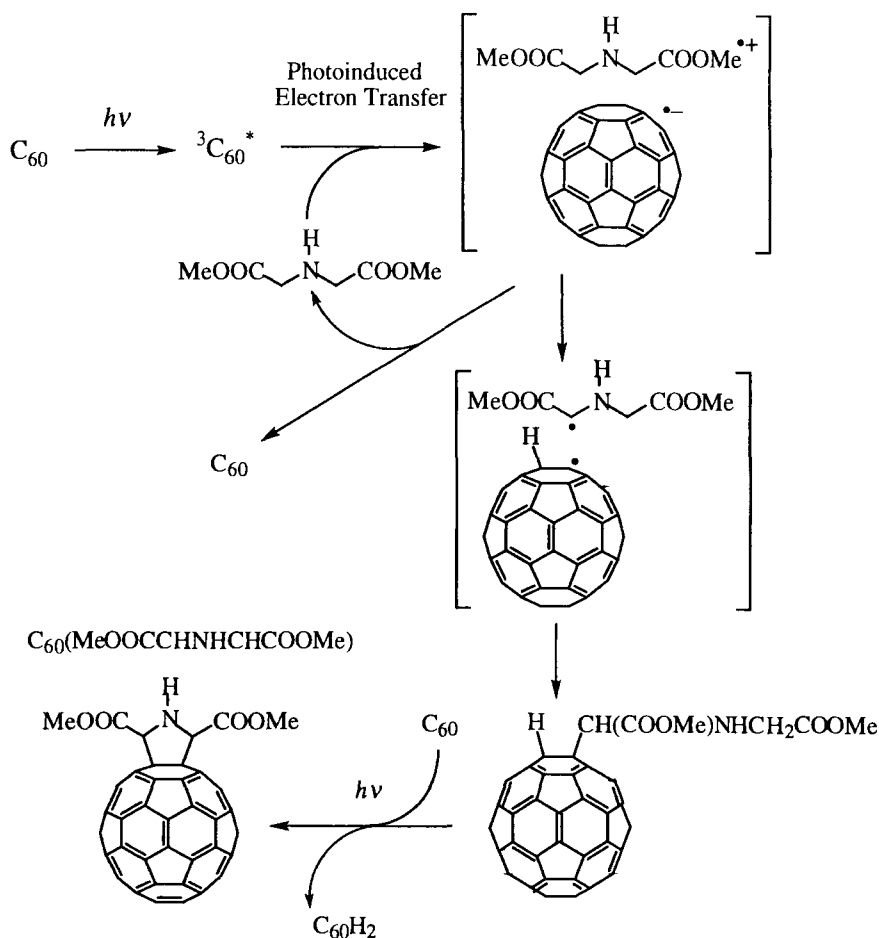
The thermal addition of digermirane to $\text{La}@C_{82}$ has been reported to occur even at 20 °C [270]. This is in sharp contrast with the fact that empty fullerenes react only photochemically. Such an enhanced reactivity of endohedral metallofullerenes may be ascribed to a significantly larger electron affinity (3.22 eV) of $\text{La}@C_{82}$ as compared to C_{60} (2.57 eV) and C_{70} (2.69 eV) [271].

Irradiation of a benzene solution of 1,1,2,2-tetraphenyl-1,2-di-*tert*-butyl-1,2-disilane and C_{60} with a low-pressure mercury lamp in a quartz tube resulted in formation of the bissilylated adduct (Eq. 20) [272].



In this case the decay of ${}^3C_{60}^*$ was not accelerated upon the addition of the disilane. The electron transfer from the disilane to ${}^3C_{60}^*$ may not occur because of the higher oxidation potential of disilanes and the large reorganization energy associated with electron-transfer reaction of disilanes [273] as compared with the strained disilirane. Thus, the bissilylated adduct is suggested to be formed via the intermediacy of $t\text{-BuPh}_2\text{Si}^\bullet$ radical generated by the photochemical Si–Si cleavage of the disilane. The UV photolysis of the disilane is known to produce the $t\text{-BuPh}_2\text{Si}^\bullet$ radical almost exclusively [274]. In fact, none of the bissilylated adducts were produced upon irradiation at $\lambda > 300$ nm where the cleavage of the disilane does not take place [272].

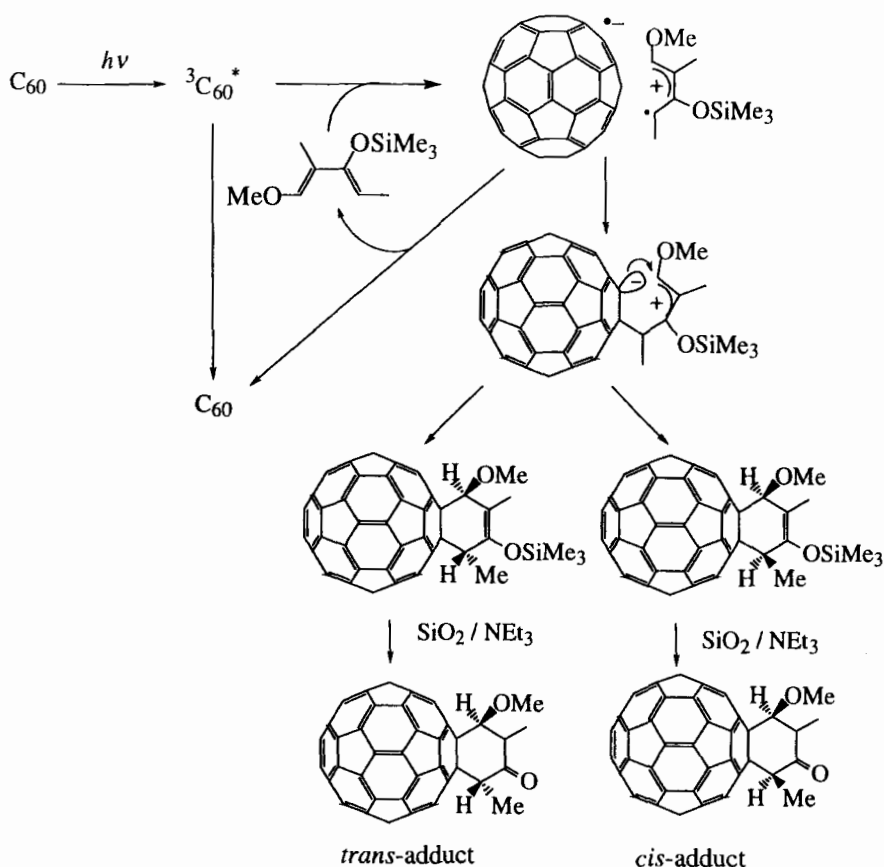
Fullerene amino acid derivatives have merited special attention in relation with the biological application [275–280]. The photochemical reactions of C_{60} with amino acid esters have been utilized to obtain fullerene amino acid derivatives [281, 282]. For example, the photochemical addition of iminodiacetic methyl ester to C_{60} provides a pyrrolidine ring-fused fullerene carboxylate, $C_{60}(\text{MeOOCCHNHCHCOOMe})$ [281]. Although the mechanistic detail has yet to be elucidated, a possible sequence



Scheme 10.

of reactions via photoinduced electron transfer from iminodiacetic methyl ester to $^3C_{60}^*$ is suggested, as shown in Scheme 10. The key step is the formation of the α -carbon-centered radical produced by photoinduced electron transfer followed by the deprotonation [281, 282]. The radical coupling between the α -carbon-centered radical and $C_{60}H^{\bullet}$ gives a 1,2 adduct which may be oxidized by C_{60} photochemically to yield the final product, $C_{60}(MeOOCCHNHCHCOOMe)$ in Scheme 10.

Diels–Alder reactions of C_{60} are generally believed to proceed via a thermally allowed concerted (suprafacial) process or a photochemical concerted (antarafacial) process [283–286]. However, an alternative stepwise (open-shell) mechanism for the Diels–Alder reaction has recently merited increasing attention [287–294]. Along this line several reports describe an electron transfer with the formation of radical ion pairs as primary step of the Diels–Alder reactions, followed by a stepwise bond formation [295–301]. The photochemical Diels–Alder reaction of C_{60} with an-



Scheme 11.

thracenes proceeds in the solid state via a photoinduced electron transfer within a charge-transfer complex comprising C₆₀ and anthracene [302]. Also the thermal Diels-Alder reaction of C₆₀ with condensed aromatics has been reported. Interestingly, in the solid state, using a high-speed vibration milling technique, the reaction is clearly accelerated [303].

The photoinduced electron transfer pathway has been unequivocally demonstrated in a photochemical Diels-Alder reactions between C₆₀ and Danishefsky's dienes (Scheme 11) [304, 305].

The transient spectra of C₆₀^{•-} at λ_{max} = 1080 nm formed in photoinduced electron transfer from Danishefsky's diene to ³C₆₀^{*} have been detected, accompanied by the decay of ³C₆₀^{*} in a laser flash photolysis of the reaction system [305]. The observed rate constant agrees well with the predicted rate constant on the basis of an electron transfer mechanism shown in Scheme 11 [305]. In the photochemical Diels-Alder reaction of C₆₀, a stereochemically defined (1*E*,3*Z*)-1,4-disubstituted Danishefsky's diene is used as a stereochemical probe. In the photochemical Diels-

Alder reaction the major Diels–Alder product is the *trans* adduct rather than the *cis* adduct (Scheme 11). Such a stereochemistry indicates that the Diels–Alder reactions proceed by a stepwise mechanism rather than a concerted mechanism. The photo-induced electron transfer from Danishefsky's diene to ${}^3\text{C}_{60}^*$ gives the triplet radical ion pair. The triplet radical ion pair is then converted to the singlet radical ion pair to give a zwitterionic intermediate (or a diradical intermediate) in competition with the back electron transfer to the reactant pair. The bond formation occurs stepwise with no symmetry restriction for the bond formation. Thus, both *trans* and *cis* adducts were obtained as the final products [305].

5.5 Intramolecular Photoinduced Electron Transfer

The most important classes of monofunctionalized fullerene derivatives give rise to a cancellation of the fivefold degeneration of their HOMO and threefold degeneration of their LUMO levels [92, 306]. In view of electron transfer processes, it should be noted that functionalization leads to wider HOMO–LUMO gaps and, consequently, to more negative reduction potentials [306]. Typically, saturation of a double bond causes a negative shift of ≈ 100 mV relative to pristine C_{60} . Similarly the excited states energies are shifted to lower energies. Taken the reduction potentials and the excited state energies in concert, significant consequences for the reduction potentials of the excited states are expected. For example, for methano- and pyrrolidinofullerenes values of +1.16 and +0.86 V relative to the SCE are reported for the ${}^1\text{C}_{60}\text{-R}^*/\text{C}_{60}\text{-R}^{\bullet-}$ and ${}^3\text{C}_{60}\text{-R}^*/\text{C}_{60}\text{-R}^{\bullet-}$ couples, respectively [307].

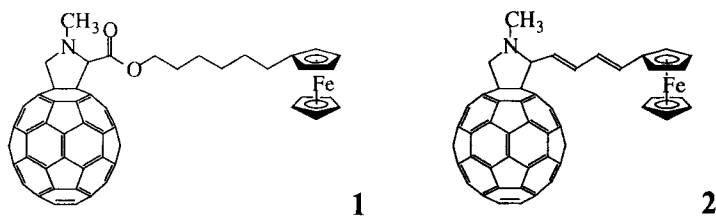
5.5.1 Fullerene Electron-donor Systems

More negative reduction potentials [306] and lower excited state energies of the functionalized fullerene derivatives [307] effect the activation energy for an intramolecular electron transfer. Despite this general disadvantage, methano- and pyrrolidinofullerenes have been employed as an electron acceptor unit. In line with the concept of using the fullerene core as the primary photosensitizer, a series of C_{60} -donor dyads have been reported [306, 308–312]. The general reaction scheme in these fullerene systems can be summarized as follows: Excitation of the fullerene core in the respective dyad yields the fullerene singlet excited state, from which an intramolecular electron transfer process evolves.

Ferrocene

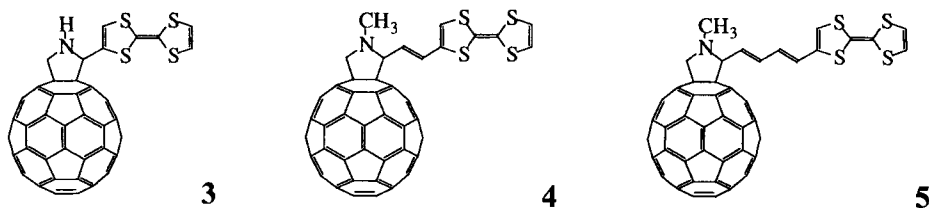
A systematic fluorescence and flash photolytic investigation of a series of covalently linked C_{60} -based ferrocene dyads (**1**, **2**) is reported as a function of the nature of the bridge (i.e., flexible or rigid) and the separation (i.e., relative distance between the donor and acceptor site) [192, 193]. The fate of the fullerene singlet excited state was

found to be governed by rapid intramolecular electron transfer, an assumption that was supported by monitoring the characteristic fullerene π -radical anion band in the NIR [192, 193]. The nature of the hydrocarbon bridge, weak electronic ground state interactions, steady-state fluorescence, picosecond-resolved photolysis and thermodynamic relation suggest two different quenching mechanisms, namely, a 'through-bond' electron transfer for rigidly-spaced dyads (**2**) and formation of a transient intramolecular 'exciplex' for flexibly-spaced dyads (**1**). With the view to improving the lifetime of the charge-separated radical pair, the flexibly-spaced dyads, in which the fullerene is connected to a ferrocene donor by extended hydrocarbon chains containing either ten σ -bonds or six σ -bonds deserve special mentioning [192, 193]. In polar solvents, the charge-separated radical pair is then regarded to diffuse semi-freely, almost like two different entities in solution. The general flexibility in these dyads promotes lifetimes of up to 2.6 μ s and 3.6 μ s in polar benzonitrile solutions for the C_{60} -donor dyad with 10 σ -bonds (**1**) and 6 σ -bonds (not shown), respectively [192, 193]. Non-polar solvents lack the beneficial role of stabilizing the radical pair. Therefore, charge recombination to yield the singlet ground state or an excited state product is usually very fast.



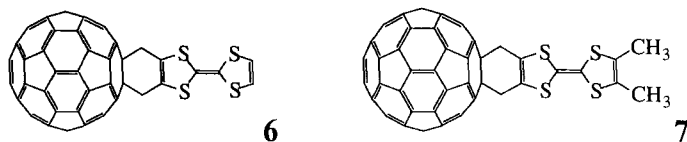
Tetrathiafulvalene

The organic donor tetrathiafulvalene (TTF) is an appealing compound as it is a π -electron donor in the field of organic molecular materials [313]. More importantly, TTF is a non-aromatic molecule in its singlet ground state configuration. In contrast to most of the donor units used in the preparation of fullerene containing dyads, it converts into the thermodynamically very stable 6 π -electron heteroaromatic 1,3-dithiolium cation upon oxidation [313]. C_{60} -based dyads (**3–5**), in which the fullerene is covalently linked to the electron donor TTF, have been synthesized by 1,3-dipolar cycloadditions of 'in situ' generated TTF-containing azomethine ylides to C_{60} [6, 306, 314–317].



Steady-state and time-resolved photolysis reveal that the fullerene singlet excited states in C_{60} -TTF dyads are subject to rapid intramolecular electron-transfer events yielding a charge-separated radical pair, namely, $C_{60}^{\cdot-}$ -TTF $^{\cdot+}$ [306, 314, 315]. The gain of aromaticity, as a result of the formation of the TTF radical cation, is a promising concept to increase the stabilization of the charge-separated state. In fact, the lifetime of the charge-separated state in C_{60} -TTF dyads was increased by a factor of ≈ 4 relative to comparable systems that do not contain TTF (e.g., ferrocene, aniline, etc.) [306, 314]. A radical pair lifetime of ca 2 ns was observed for the closely spaced C_{60} -TTF dyad (**3**), while much shorter lifetimes of 0.526 ns, 0.045 ns and 0.294 ns are reported for similarly spaced Carotene- C_{60} , ZnP- C_{60} (**22**) and H_2P - C_{60} dyads (**23**) (see Section 5.5.3), respectively.

In contrast to C_{60} -ferrocene and C_{60} -aniline dyads, back electron transfer proceeds mainly via formation of the fullerene triplet excited state [306, 314, 315]. The energy level of the latter (ca. 1.50 eV) is still sufficient to activate a second, intramolecular electron transfer, as noticed in an intermolecular quenching between the triplet excited state of C_{60} and TTF. In a different family of C_{60} -TTF dyads (**6** and **7**) ESR values and ^{32}S hyperfine coupling constants give rise to a spin density distribution located on the TTF and fullerene moieties, for the cationic and anionic species, respectively [318]. Complementary performed flash photolysis substantiates the rapid quenching of the fullerene excited states yielding long-lived ($\tau \approx 75 \mu\text{s}$) charge-separated states with an open-shell character [318].

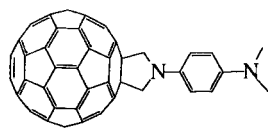


Aniline

One of the first examples regarding the design of C_{60} -based donor-acceptor dyads encompasses an electron donating *N,N*-dimethylaniline (DMA) group [186, 319–322]. In polar solvents, a significant quenching of the fullerene fluorescence was interpreted in terms of an intramolecular electron transfer process along a saturated heterocyclic bridge. In non-polar solvents, this deactivation route is, however, not observed, a consequence that stems from an overall less exergonic reaction [319].

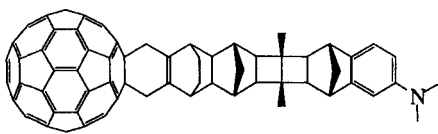
Replacing the weak electron donor DMA with a *N,N,N',N'*-tetramethyl-*p*-phenylenediamine (TMPD) donor increases the energy gap between the fullerene singlet excited state and the charge-separated state [323]. As a consequence of a more exergonic electron transfer, the C_{60} -TMPD dyad (**8**) gives rise to fast intramolecular charge separation, irrespective of the solvent polarity (i.e., non-polar methylcyclohexane and polar benzonitrile) [323].

With the scope to retard the energy-wasting back electron transfer the separation between the two redox active moieties (i.e., fullerene and aniline) was systematically increased up to a 11- σ -bond containing 'norbornylogous' bridge (**9**) [323–325]. The reactivity of this 11- σ -bonds system followed the first class of shorter DMA hybrids



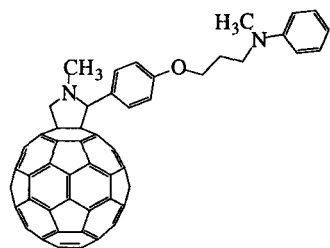
8

[319]. Successful electron transfer occurs, however, with much slower dynamics, and furthermore only in polar solutions. On the other hand, the 11- σ -bond 'norbornyl-ogous' bridge has a remarkable effect on the back electron transfer kinetics ($\tau \approx 250$ ns) [323]. Strong electron coupling between the hydrocarbon bridge and the fullerene HOMO facilitates the fast charge separation, while the relevant electronic coupling with the fullerene LUMO, which determines the back electron transfer dynamics, remains small [323].

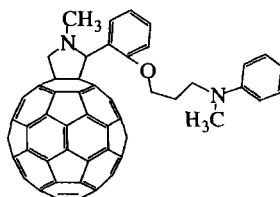


9

A topographically controlled electron transfer process was the subject in another generation of *ortho*- and *para*-substituted fullerene-aniline dyads (**10** and **11**) [326]. Minimum energy conformations yielded a folded configuration for the *ortho*-substituted dyad **11** (e.g., minimum separation between the fullerene and aniline) while the *para*-substituted analog **10** adapts a stretched one (e.g., maximum separation between the fullerene and aniline) [326]. The implemented decrease in the spatial separation between the electron donating aniline and electron accepting fullerene was beneficial in light of an efficient electron transfer. Dynamics of the singlet excited state deactivation and quantum yield of charge separation supports the computational view: In particular, the close proximity between the aniline group and the fullerene π -system in the *ortho*-substituted dyad (**11**) accelerates the electron transfer process and enhances its efficiency relative to the *para*-substituted dyad (**10**) [326].



10



11

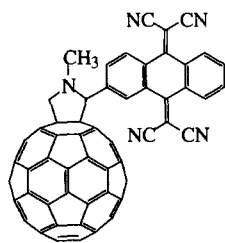
A different objective was pursued in a recent work that reported the cluster formation of a C_{60} -based aniline dyad (**10**) [327]. The feasibility to enhance the electron

delocalization from a single fullerene molecule to a fullerene cluster was probed under the aspect of improving charge-separation. For example, the *para*-substituted fullerene–aniline dyad **10** (i.e., the one that lacks any electron transfer activity) [327] forms stable clusters in polar solvents. The latter give rise to a strong quenching of the fullerene fluorescence. Identification of the fullerene π -radical anion in the NIR provides unambiguous evidence for the charge-transfer interactions between the photoexcited fullerene and aniline moieties [327]. Far more important is, however, the lifetime of the charge-separated state, being on the order of several hundred nanoseconds. This documents that formation of fullerene clusters is a viable alternative for the stabilization of charge-separated radical-pairs.

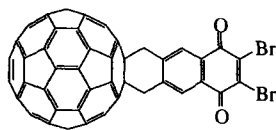
5.5.2 Fullerene Electron-acceptor Systems

The well-documented feature of fullerenes to form stable multi-anions is in sharp contrast to the poor ability to generate a stable cationic species [92]. Nevertheless, along the last several years preparation of fullerene derivatives in which C_{60} is covalently attached to an electron acceptor unit have been reported [315, 328].

Linking the fullerene core to a tetracyanoanthraquinodimethane (TCAQ) ($E_{1/2} = -0.38$ V relative to the SCE) (**12**) or a 2,3-dibromonaphthoquinone acceptor ($E_{1/2} = -0.21$ V relative to the SCE) [315] (**13**) afforded two rare examples of dyads in which an organic addend is covalently attached to the fullerene core that exhibits better electron-acceptor properties than the parent fullerene core [329].



12



13

In the light of a possible electron transfer from the photoexcited fullerene to the adjacent electron acceptor, the fullerene emission was probed in a variety of solvents. Only a moderate fluorescence quenching was noted in non-polar toluene and polar benzonitrile. Considering the energetics ($E_{1/2} (^1C_{60}\text{-R}^*/C_{60}\text{-R}^{+}) = -0.15$ relative to the SCE) of the charge-separated radical pair small thermodynamic driving forces for an associated electron transfer were determined [315]. The main reason therefore lies in the unfavorable oxidation potential of the electron donor (i.e., fullerene). Further confirmation for the inadequate mixing of redox potentials and the inefficient quenching resulting therefrom, stems from complementary pico- and nanosecond resolved photolysis. Similar to the reference compound, illumination of the C_{60} -acceptor dyads (**12** and **13**) leads to the instantaneous formation of the fullerene singlet excited state absorption [315]. These transients exhibit shortened singlet lifetimes, which fall in line with the above trend of the fluorescence

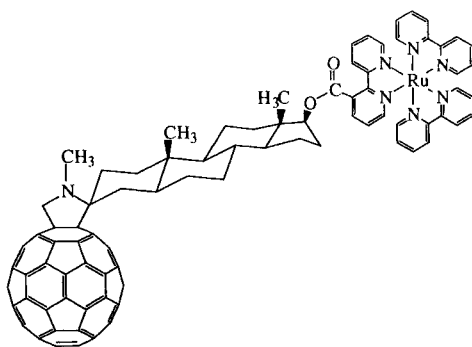
intensities [315]. Despite the shorter singlet excited state lifetimes, the differential absorption spectrum, recorded after the completion of the reaction, shows spectral characteristics of the fullerene triplet excited state, rather than those of a transient product that evolves from a possible intramolecular electron transfer.

5.5.3 Fullerene Chromophore Systems

The moderate visible absorption of C₆₀-donor dyads (see above) prompts to C₆₀-chromophore systems as suitable models for the mimicry of the primary events in natural photosynthesis [330–332]. To enhance the absorption of the fullerene containing dyads in the visible region strong chromophoric units, such as (i) ruthenium(II) polypyridyl complexes or (ii) metalloporphyrins have been implemented as antenna systems. In these C₆₀-chromophore systems the role of the fullerene changed dramatically, namely, it only accepts an electron or energy from the photoexcited chromophore.

Ruthenium complexes

Ruthenium(II) polypyridyl complexes are employed as antenna molecules [311, 333–337] for a variety of reasons: [338, 339]: Ruthenium(II) polypyridyl complexes (i) are photostable under illumination, (ii) have strong metal-to-ligand-charge-transfer absorption (MLCT) in the visible, (iii) have high lying MLCT excited states ($E^\circ_0 \approx 2.0$ eV), and (iv) are powerful electron donors in the MLCT excited state ($E_{1/2} (^*[Ru(bpy)_3]^{2+}/[Ru(bpy)_3]^{3+}) = -0.63$ V relative to the SCE; in dichloromethane). Thus, the latter should be able to generate the one-electron reduced fullerene π -radical anion ($E_{1/2} = -0.41$ V relative to the SCE; in dichloromethane) [338, 339].

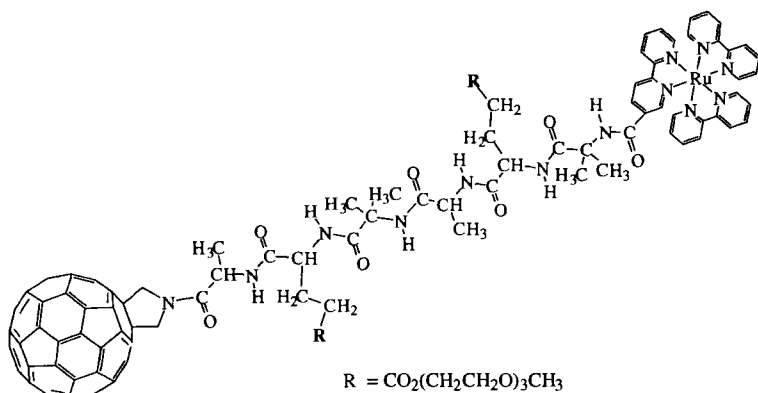


14

Since a general principle predicts that a larger separation evokes a slow-down of the back electron transfer, an androstane bridge was selected to separate the fullerene core from a $[Ru(bpy)_3]^{2+}$ complex (bpy = 2,2'-bipyridine) with an edge-to-edge distance of 11.5 Å (dyad **14**) [336]. The ruthenium MLCT excited state was found to convert, upon excitation, into the $[Ru(bpy)_3]^{3+}-C_{60}^{\bullet-}$ state with intra-

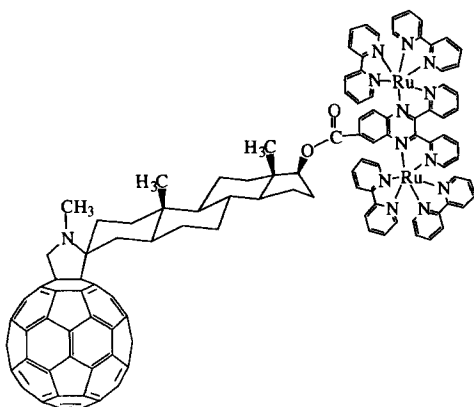
molecular rates of $0.69 \times 10^9 \text{ s}^{-1}$ (DCM–toluene, 1:1, *v/v*) and $5.1 \times 10^9 \text{ s}^{-1}$ (CH_3CN) [336]. The photochemically formed radical pair displays the superimposed features of the oxidized ruthenium complex ($[\text{Ru}(\text{bpy})_3]^{3+}$) and of the reduced fullerene moiety ($\text{C}_{60}^{\bullet-}$). Lifetimes of 304 and 169 ns in deoxygenated DCM and CH_3CN [336], respectively, are good indicators for the usefulness of this C_{60} -chromophore system.

Molecular recognition has been utilized as a motif to control the dynamics of intra- and intermolecular electron-transfer events and the efficiency of charge separation in a $[\text{Ru}(\text{bpy})_3]^{2+}$ – C_{60} donor acceptor assembly (**15**) [337]. Specifically, hydrogen bonding in polypeptide systems, with a 3_{10} α -helix supporting α -butyric acid is selected to ensure tunable separations of the donor (i.e. $[\text{Ru}(\text{bpy})_3]^{2+}$) and acceptor (i.e., fullerene) moieties. This factor is expected to have profound effects on intramolecular electron transfer dynamics between the photoexcited $[\text{Ru}(\text{bpy})_3]^{2+}$ and the electron accepting fullerene. Structures, such as the 3_{10} α -helix in non-protic solvents, are prone to configurational changes upon addition of protic solvents (i.e., a denaturation of the helical structure is observed). In non-protic solvents the two redox active moieties are locked in well-defined positions, with an edge-to-edge distance of ca 12 Å, and electron transfer occurs from the ruthenium MLCT excited state to the electron accepting fullerene [337]. In contrast, protic solvents interfere with the intramolecular hydrogen bonding of the peptide backbone and, in turn, the relative distance between the $[\text{Ru}(\text{bpy})_3]^{2+}$ and fullerene is markedly increased. Despite the general flexibility of the peptide backbone, the encountered scenario prevents either a ‘through-bond’ or ‘exciplex’ mechanism to support the electron transfer. This deactivation is reversible and repetitive addition or removal of the protic component interrupts or activates the electron transfer mechanism, respectively.



15

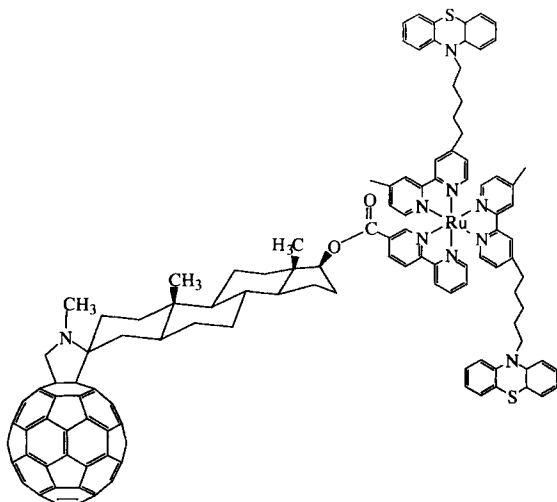
The design of a dinuclear ruthenium chromophore, in which the mononuclear $[\text{Ru}(\text{bpy})_3]^{2+}$ antenna molecule was replaced by a dinuclear $[(\text{bpy})_2\text{Ru}(\text{BL})\text{Ru}(\text{bpy})_2]^{4+}$ complex (BL = 2,3-bis-(2-pyrididyl)quinoxaline) led to a red-shift of the MLCT transition from 460 nm to 625 nm [311]. The luminescence quantum yield of the dinuclear dyad **16** gives rise to a very inefficient intramolecular



16

quenching reaction. In line with the luminescence quenching, picosecond and nanosecond resolved experiments revealed that the photoexcited MLCT $[(bpy)_2Ru(BL)Ru(bpy)_2]^{4+}$ state transforms slowly ($4.5 \times 10^7 \text{ s}^{-1}$) into the fullerene triplet excited state [311]. The difference in reactivity relative to the $[Ru(bpy)_3]^{2+}$ dyad stems from the markedly different MLCT excited state energies of the $[(bpy)_2Ru(BL)Ru(bpy)_2]^{4+}$ antenna molecule.

The systematic extension of the dyad concept aimed at the design of a molecular triad by attaching an additional electron donor to the C_{60} -chromophore dyad [340]. Selection of the second electron donor should guarantee an electron relay along a vertical energy gradient before charge recombination takes over to dominate the fate of the first couple. As a secondary electron donor unit phenothiazine (PTZ) was chosen and covalently linked to the ruthenium complex (PTZ- $[Ru(bpy)_3]^{2+}$ - C_{60}) 17. In CH_3CN solutions, first the formation of the PTZ- $[Ru(bpy)_3]^{3+}$ - $C_{60}^{\bullet-}$ pair



17

develops with intramolecular kinetics ($2.8 \times 10^9 \text{ s}^{-1}$) that are virtually identical to those of the precursor dyad. After its completion a follow-up process leads to the grow-in of the charge-separated state $\text{PTZ}^{\bullet+}\text{-}[\text{Ru}(\text{bpy})_3]^{2+}\text{-C}_{60}^{\bullet-}$. The lifetimes observed (1.29 μs in DCM and 304 ns in CH_3CN) point to a significant improvement over the dyad system **14** and corroborate the value of the synthetic strategy [340].

Metalloporphyrins

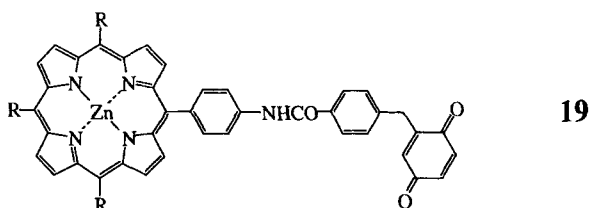
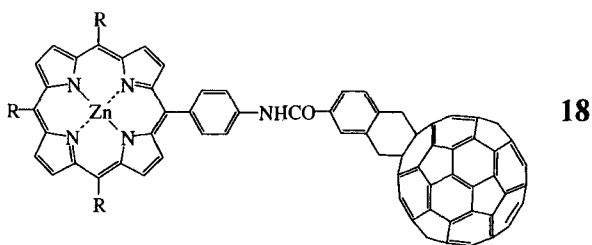
By far the largest number of C_{60} -based donor–acceptor systems studied to date utilize porphyrins as antennas for efficient light capture in the visible region of the spectrum [306, 308–310, 324, 329, 341]. In the following section systems are presented for which time-resolved and steady-state absorption and emission measurements are available, which document the intramolecular electron transfer processes under a variety of experimental conditions. But we also like to acknowledge the purely synthetic work, for which no experimental data is obtainable [342–351].

Up front, a general comment seemed necessary: Photophysical studies indicate that, when structurally possible, dyads adopt conformations in which the porphyrin and fullerene moieties are in close proximity, thus facilitating through-space interactions of photoexcited porphyrins with the fullerenes. A similar conclusion stems from a recent work that demonstrates impressively weak ligand interactions between C_{60} and a hard metal such as iron(III) in an iron(III)tetraphenylporphyrin π -radical cation ($\text{FeP}^{\bullet+}$) [352].

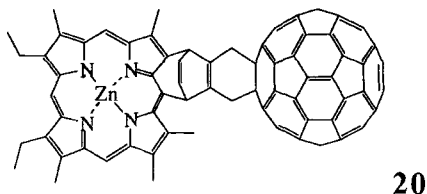
Dyads

The first direct evidence for photoinduced electron transfer in donor-linked fullerenes comes from photophysical studies regarding a ZnP-C_{60} dyad (**18**), in which two chromophores are separated by a phenyl spacer including an amido group, using picosecond time-resolved transient absorption spectroscopy [353]. As the singlet excited state absorption of the porphyrin decayed after excitation of the porphyrin, simultaneous rise and decay of the transient bands due to $\text{ZnP}^{\bullet+}$ and $\text{C}_{60}^{\bullet-}$ were observed clearly. In summary, photoinduced electron transfer evolves from the excited singlet state of the porphyrin to C_{60} in dyad **18**. To evaluate the three-dimensional effect of C_{60} in photoinduced electron transfer, a porphyrin–quinone dyad **19** (ZnP-Q) was prepared which gives rise to driving forces and electronic coupling interactions that are quite similar to the ZnP-C_{60} dyad [354]. In THF photoinduced charge separation and charge recombination in the ZnP-C_{60} dyad (**18**) is accelerated and retarded, respectively, compared to that of the ZnP-Q (**19**). The acceleration and deceleration effect of C_{60} in intramolecular electron transfer has been attributed to the smaller reorganization energy of C_{60} relative to those of typical two-dimensional acceptors such as quinones and imides [308, 309, 353–356, 358]. A combination of small reorganization energy of fullerenes with multistep electron transfer strategy is a fascinating proposal for the construction of artificial photosynthesis.

One of the first reported C_{60} -based donor–acceptor systems is also the $\text{H}_2\text{P-C}_{60}$ and the analog ZnP-C_{60} dyad (**20**), in which H_2P denotes the metal-free base tetraphenyl porphyrin and ZnP is the corresponding zinc tetraphenylporphyrin

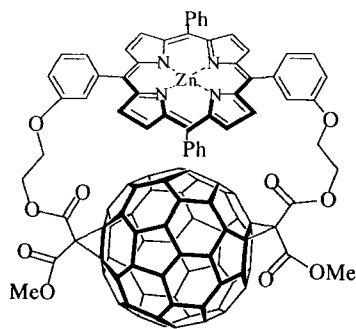


complex [360]. In polar benzonitrile the singlet excited porphyrin undergoes photo-induced electron transfer to give $\text{H}_2\text{P}^{*+}-\text{C}_{60}^{*-}$ and $\text{ZnP}^{*+}-\text{C}_{60}^{*-}$, with intramolecular rates of $\approx 2 \times 10^{11} \text{ s}^{-1}$ [360]. Unfavorable thermodynamics render an electron transfer in non-polar toluene difficult. While the lower oxidation potential of ZnP ($\approx 200 \text{ mV}$) still facilitates an electron transfer, the markedly shifted oxidation potential of H_2P gives rise to singlet-singlet energy transfer in $\text{H}_2\text{P}-\text{C}_{60}$ from the porphyrin to the fullerene.



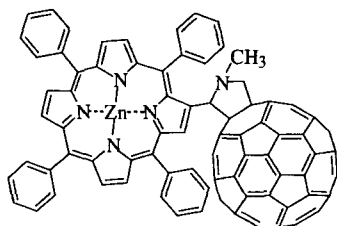
As a leading example for short-spaced dyads, a π - π stacked porphyrin-fullerene dyad ($\text{ZnP}-\text{C}_{60}$) **21** should be mentioned, which was probed in light of their electron transfer and back electron transfer dynamics [361, 362]. The close van der Waals contact ($\approx 3.0 \text{ \AA}$) is responsible for pronounced electronic interactions in the ground state between the two π -chromophores. For example, the ZnP Soret- and Q-bands in the π - π stacked dyad **21** show a bathochromic shift and lower extinction coefficients compared to free ZnP [361]. In the π - π stacked dyad **21** the linkage of the two bridging units occurs in the *trans*-2 position at the fullerene. A charge-separated radical pair evolves from a rapid intramolecular electron transfer ($\approx 35 \text{ ps}$) between the photoexcited metalloporphyrin and the fullerene core in a variety of solvents (i.e., ranging from toluene to benzonitrile). Remarkably, the lifetimes in tetrahydrofuran ($\tau = 385 \text{ ps}$) and DCM ($\tau = 122 \text{ ps}$) are markedly increased relative to the more polar solvents dichloromethane ($\tau = 61 \text{ ps}$) and benzonitrile ($\tau = 38 \text{ ps}$) [362]. This dependency prompts to an important conclusion:

The rates of the back electron transfer processes, from the $\text{ZnP}^{*+}-\text{C}_{60}^{\bullet-}$ state to the ground state, are clearly in the 'Marcus-inverted' region. This is one of the important examples that provide experimental support to electron transfer kinetics clearly occurring in the inverted region. Using the same synthetic methodology, a similar family of $\pi-\pi$ stacked porphyrin–fullerene dyads (i.e., $\text{ZnP}-\text{C}_{60}$ and $\text{H}_2\text{P}-\text{C}_{60}$), in which the porphyrin chromophore is attached by a malonate bridge to the *trans*-1 position of the fullerene sphere, has been reported [363].

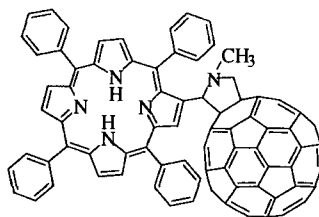


21

Increasing the distance between the donor and acceptor, by means of using spacer units of increasing size, is one approach to slow down the charge recombination [364, 365]. In this context, a fulleropyrrolidine should be mentioned which is been attached to one of the pyrrole units of H_2P (**23**) or alternatively ZnP (**22**) [365]. Based on the close proximity between the donor and acceptor efficient through-space interactions are postulated. In benzonitrile intramolecular electron-transfer events prevail yielding the $\text{H}_2\text{P}^{*+}-\text{C}_{60}^{\bullet-}$ and $\text{ZnP}^{*+}-\text{C}_{60}^{\bullet-}$ pairs with a quantum efficiency near unity and lifetimes of 290 ps and 50 ps, respectively [364]. The spatial separation impacts, at the same time, the thermodynamic driving force ($-\Delta G^\circ_{\text{et}}$) for an intramolecular electron transfer. In particular, increasing the donor acceptor separation lowers the driving force. Thus, an electron transfer that is exothermic in a closely spaced dyad becomes less exothermic in a widely spaced dyad and, in turn, is deactivated. For example, in toluene a rapid singlet–singlet energy transfer governs the deactivation of the photoexcited chromophore complex [364].



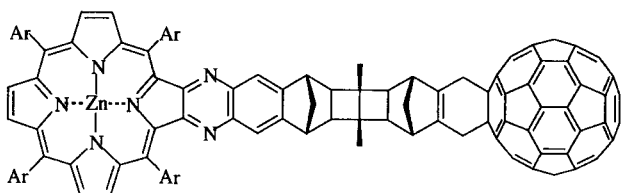
22



23

Further advances with respect to the separation principle were made via some work that reports on a long-range photoinduced electron transfer in a $\text{ZnP}-\text{C}_{60}$ dyad **24**, in which the two redox active moieties are separated by a saturated nor-

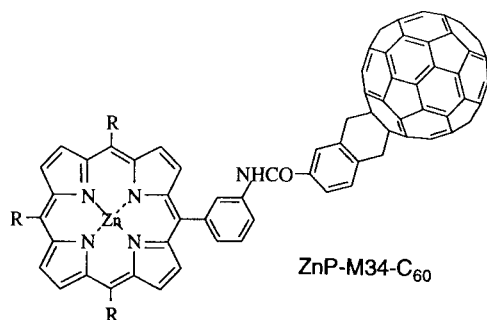
bornylogous bridge nine sigma bonds in length [324, 366]. The lifetime of the radical ion pair in the 'norbornylogous' bridged dyad is impressive (420 ns) [366] and clearly discloses a significant improvement relative to the short-spaced analogs (π - π stacked dyad: 38 ps [362]; pyrrole-linked dyad: 50 ps [364]).



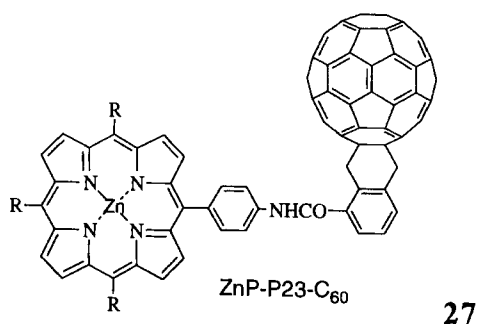
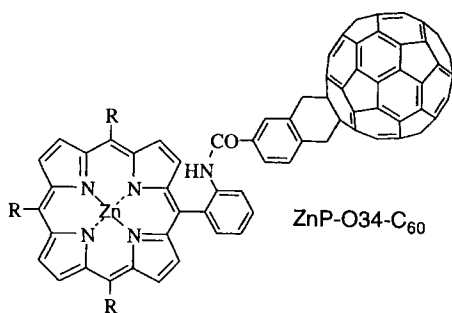
24

A phenyl group has also been employed to link the electron acceptor (C_{60}) to a ZnP, which, in addition, enabled a systematic variation of the linkage (e.g., in *ortho* (**26**), *meta* (**25**) or *para* position (**27**) of the phenyl group) [353–359]. Regardless of the specific position, the initial photoexcitation event is followed by a rapidly occurring charge separation to yield the $ZnP^{*+}-C_{60}^{\cdot-}$ with rates between $2.2 \times 10^{10} \text{ s}^{-1}$ and $0.45 \times 10^{10} \text{ s}^{-1}$ [355]. The final step in the sequence is the charge recombination process, which results in the complete restoration of the ground state. For example, in THF the radical ion pair evolves from the singlet excited state of both moieties (i.e., fullerene and porphyrin). On the other hand, in nonpolar solvents such as benzene the charge-separated state, generated by photoinduced electron transfer from the $^1ZnP^*$ to the C_{60} , recombines to yield the $^1C_{60}^*$ or energetically equilibrates with the $^1C_{60}^*$. The photodynamic behavior in nonpolar solvents is in sharp contrast with that in the other porphyrin- C_{60} dyads where direct singlet-singlet energy transfer takes place from the porphyrin to the C_{60} [360, 364, 366, 376]. In light of the intramolecular dynamics (i.e., forward and back electron transfer), it is important to note that both processes are markedly slowed-down by the *meta*-linkage (**25**) [355].

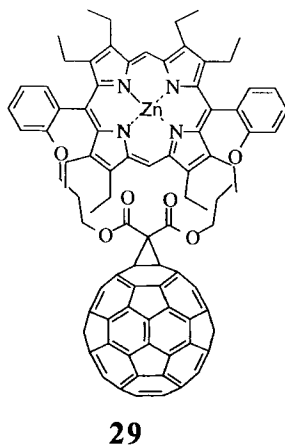
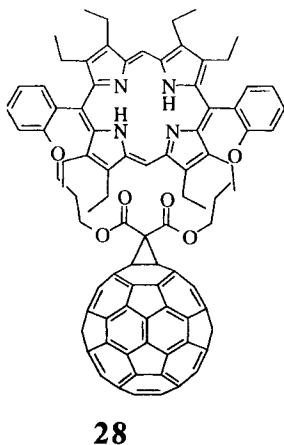
Work from a different laboratory focuses on the synthesis and photophysical properties of C_{60} -based porphyrin dyads with a variety of linkers [367–371]. These include new types of flexible polyether linkers (**30**) [367, 368], rigid steroid linkers [370] as well as novel doubly linked porphyrins [369, 371], which provide the means for a parachute-shaped dyad (e.g., $ZnP-C_{60}$ (**29**) and H_2P-C_{60} (**28**)). In both para-

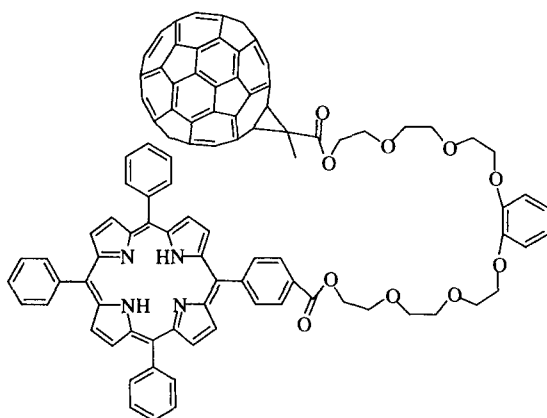


25



chute compounds, the porphyrin fluorescence is almost completely quenched with fluorescence lifetimes of 13 ps ($^1\text{ZnP}^*-\text{C}_{60}$) and 23 ps ($^1\text{H}_2\text{P}^*-\text{C}_{60}$) [369, 371]. It should be noted that in the $\text{ZnP}-\text{C}_{60}$ (**29**) and $\text{H}_2\text{P}-\text{C}_{60}$ dyads (**28**) the porphyrin is enforced in close proximity to the fullerene core. With the help of transient absorption studies the dynamics of the interactions in these systems were elucidated, especially to differentiate between electron and energy transfer as the primary process. The unique orientation of the porphyrin and fullerene moieties in the parachute-shaped dyad (**28** and **29**) seems to facilitate electron transfer in both non-polar

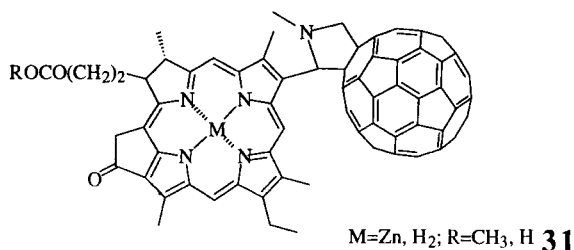


**30**

and polar media to yield the $\text{ZnP}^{\bullet+}-\text{C}_{60}^{\bullet-}$ and $\text{H}_2\text{P}^{\bullet+}-\text{C}_{60}^{\bullet-}$ pair, respectively. It is curious that, for example, the lifetime of the $\text{ZnP}^{\bullet+}-\text{C}_{60}^{\bullet-}$ state is longer in toluene ($\tau = 1015$ ps) than in the more polar solvents THF ($\tau = 99$ ps) or benzonitrile ($\tau = 69$ ps) [371]. It has been concluded that these solvent effect results from changes in the energetics of the ion pair state as well as the reorganization energy in these three solvents, being well in the Marcus inverted region. The same quenching effect is also seen in a series of flexible-linked dyads (**30**), indicating that non-covalent interaction between the porphyrin and fullerene moieties bring them into close proximity [367, 368].

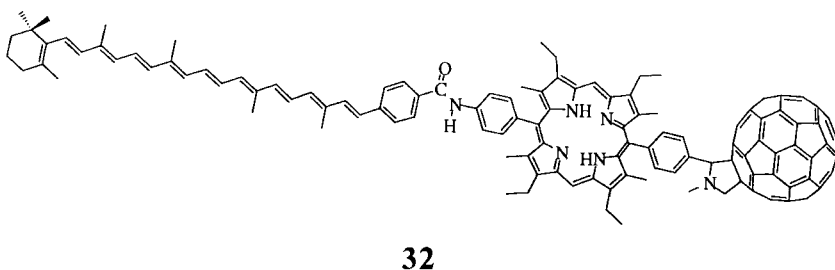
A fundamental challenge addresses the question to what extent the choice of a higher fullerene impacts the electron transfer dynamics in fullerene-based donor–acceptor systems [372]. To shed light onto this important aspect and to evaluate the intrinsic properties of C_{70} in electron-transfer reactions a $\text{ZnP}-\text{C}_{70}$ dyad was designed, resembling the basic features of the analogous $\text{ZnP}-\text{C}_{60}$ system [372]. In this context, the reduction potentials of fullerenes should be considered: In general higher fullerenes become better electron acceptors as the fullerene size increases. Despite this general trend, the difference between C_{60} and C_{70} is reported to be marginally small. Still, the intramolecular electron transfer dynamics in $\text{ZnP}-\text{C}_{70}$ ($3.5 \times 10^{10} \text{ s}^{-1}$) following the initial excitation of the ZnP chromophore, were found to be nearly twice as fast as in $\text{ZnP}-\text{C}_{60}$ ($1.9 \times 10^{10} \text{ s}^{-1}$) [372]. This has been ascribed to the inherent size and shape effect of the rugby ball-shaped C_{70} resulting in a somewhat smaller reorganization energy of this larger fullerene moiety [372].

The photophysical properties of a C_{60} -linked phytychlorin (**31**) [344, 373], a porphyrin analog, are quite different from those of conventional C_{60} -linked porphyrins. The phytychlorin– C_{60} exciplex is formed in both toluene and benzonitrile via either the singlet excited states of the phytychlorin or the C_{60} . The exciplex relaxes directly to the ground state in toluene, whereas it undergoes a conversion to the charge-separated state, followed by the decay to the ground state in benzonitrile. A similar proposal for the exciplex formation has been forwarded by the report on a free-base porphyrin C_{60} dyad [374, 375].



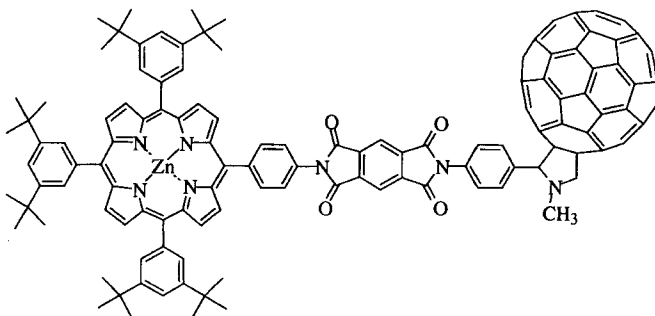
Triads

Using the above-summarized C_{60} -based porphyrin dyads as a work base, a carotenoid polyene (C) [331, 332] has been covalently linked to a $\text{H}_2\text{P}-\text{C}_{60}$ dyad, constituting the first molecular triad **32** published (e.g., $\text{C}-\text{H}_2\text{P}-\text{C}_{60}$) [376, 377]. Upon photoexcitation, a sequence of intramolecular electron-transfer events were found for $\text{C}-\text{P}-\text{C}_{60}$ triad **32**, tracking the energy gradient $\text{C}-\text{H}_2\text{P}^*-\text{C}_{60} \rightarrow \text{C}-(\text{H}_2\text{P}^+)-(\text{C}_{60}^{\bullet-}) \rightarrow (\text{C}^+)-\text{H}_2\text{P}-(\text{C}_{60}^{\bullet-})$. The final $(\text{C}^+)-\text{H}_2\text{P}-(\text{C}_{60}^{\bullet-})$ pair, which was produced with an overall quantum yield of 0.14 decays via charge recombination ($\tau = 170$ ns) to afford the carotenoid triplet state, rather than the singlet ground state [376]. Even in a glassy matrix at 77 K the radical pair is generated with a still remarkable quantum yield of 0.1. Spectral support for this recombination route was presented in terms of time-resolved EPR spectroscopy (i.e., correlating the spin-polarized radical pair and carotenoid triplet state) [377]. The sequence of (i) generating a long-lived charge separated state and (ii) forming a triplet state via charge recombination is a phenomenon heretofore observed almost exclusively in photosynthetic reaction centers.

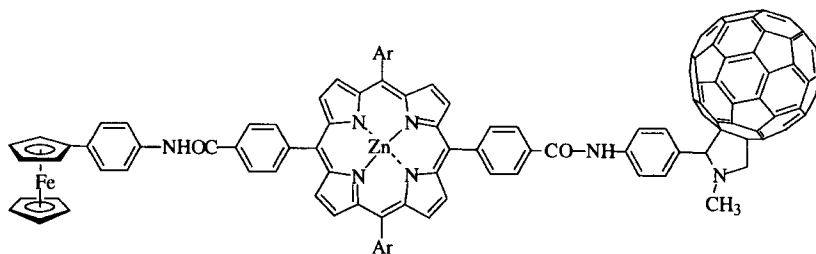


A viable alternative to the $\text{C}-\text{H}_2\text{P}-\text{C}_{60}$ triad **32** [376, 377] is the design of a sequential electron transfer relay system in which the porphyrin–fullerene pair ($\text{ZnP}-\text{C}_{60}$) is bridged via an electroactive pyromellitimide functionality (In) (**33**) [358, 378]. The photochemical results clearly show a photoinduced two-step electron transfer sequence. Starting with the initial excited porphyrin state the bridging pyromellitimide accepts an electron from the photoexcited ZnP chromophore affording a charge-separated radical pair. This transient state subsequently transfers the accepted charge from the pyromellitimide to the end terminus, namely, the fullerene moiety. The resulting spatially separated $(\text{ZnP}^+)-\text{In}-(\text{C}_{60}^{\bullet-})$ radical,

formed with an overall quantum yield of 0.46, undergoes a remarkably slow back electron transfer with a rate of $7.7 \times 10^8 \text{ s}^{-1}$ [378].

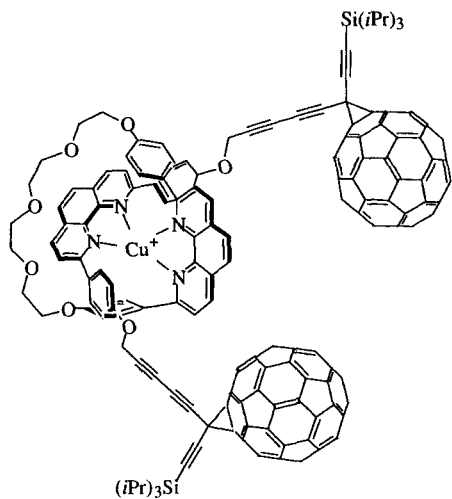
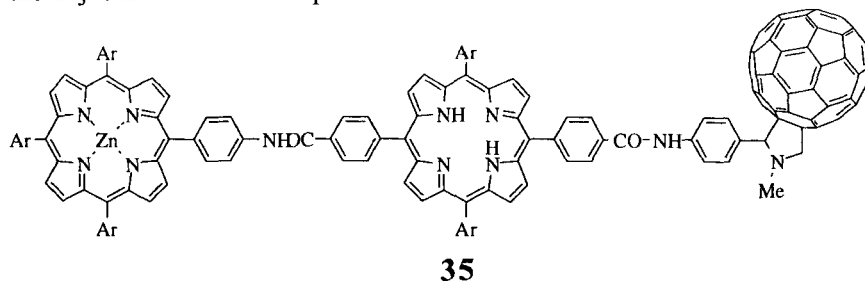
**33**

Stabilization of the charge-separated state is the focus of a more recent study regarding a Fc–ZnP–C₆₀ triad **34**, whose conceptional idea is similar to that described for the C–P–C₆₀ triad **32** [376, 377] (i.e., a controlled redox gradient $\text{Fc}^*-\text{ZnP}-\text{C}_{60} \rightarrow \text{Fc}-(\text{ZnP}^+)-(\text{C}_{60}^{\bullet-}) \rightarrow (\text{Fc}^+)-\text{ZnP}-(\text{C}_{60}^{\bullet-})$ [358, 379–381]. The improvement is, however, based on increasing the spatial separation between the individual building blocks (e.g., Fc–ZnP and ZnP–C₆₀ couples, respectively). Via utilizing of a nearly rigid bridge, comprising two phenyl groups linked by an amide functionality, a center-to-center distance of $\approx 18 \text{ \AA}$ is achieved between each of the two couples [358, 380]. Upon excitation, efficient multi-step electron transfer governs the deactivation of the photoexcited ZnP chromophore, producing a long-lived charge-separated state $(\text{Fc}^+)-\text{ZnP}-(\text{C}_{60}^{\bullet-})$ with a center-to-center distance of 34.2 \AA . In DMF a remarkable lifetime of $15.6 \mu\text{s}$ is observed [358, 380].

**34**

A novel molecular triad **35**, representing an artificial reaction center, was synthesized via linking a fullerene moiety to an array of two porphyrins (i.e., ZnP and H₂P) [382, 383]. In this ZnP–H₂P–C₆₀ triad **35**, the ZnP performs as an antenna molecule, mediating its singlet excited state energy to the energetically lower lying H₂P. This energy transfer ($k = 1.49 \times 10^{10} \text{ s}^{-1}$) is followed by a sequential electron transfer relay evolving from the generated singlet excited state of H₂P to yield $\text{ZnP}-(\text{H}_2\text{P}^+)-(\text{C}_{60}^{\bullet-})$ and subsequently $(\text{ZnP}^+)-\text{H}_2\text{P}-(\text{C}_{60}^{\bullet-})$ with rate constants of $6.99 \times 10^9 \text{ s}^{-1}$ and $2.15 \times 10^9 \text{ s}^{-1}$, respectively [383]. The final charge-separated state, formed in high yield (0.4), gives rise to a remarkable lifetime of $21 \mu\text{s}$ in

deoxygenated benzonitrile and decays directly to the singlet ground state [383]. In contrast, in non-polar toluene solutions the deactivation of the porphyrin chromophores (ZnP and H₂P) takes place via singlet–singlet energy transfer leading to the fullerene singlet excited state. This stems from the unfavorable free energy changes for an intramolecular electron-transfer event from the singlet excited state of H₂P to the adjacent fullerene acceptor.



A novel bis-fullerene rotaxane **36** structure was successfully synthesized via oxidative coupling between two methanofullerenes and a Cu(I)–bisphenanthroline complex [384]. This supramolecular assembly (**36**) provides well-defined inter-component separations. Interestingly, perturbation of the absorption spectrum of rotaxane, relative to the sum of the individual moieties, indicates strong electronic communication between the two components in the ground state [384]. More importantly, the excited states of the two fullerenes and also the Cu(I)–bisphenanthroline complex are subject to a rapid deactivation. In particular, a sequence of energy and electron-transfer events lead to a low-lying charge-separated state. However, no clear evidence for the charge-separated state is been found and its existence is only been inferred. The lack of spectral identification has been rationalized in terms of a fast back electron transfer prevailing over a slower forward electron transfer [384].

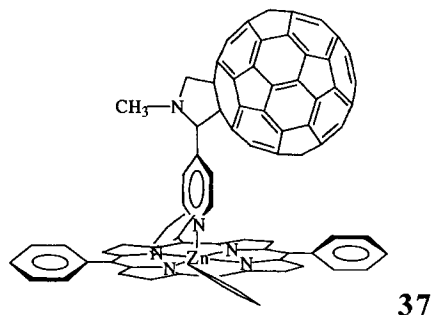
Hexad

The idea of an artificial reaction center (e.g., the sequence of energy and electron transfer) was realized in a recent report of a C_{60} -based hexad, $(ZnP)_3-ZnP-H_2P-C_{60}$, employing an array of star-shaped aligned porphyrins (i.e., four zinc porphyrins linked to a free base porphyrin) as a multichromophoric antenna system [385]. Excitation of the peripheral zinc porphyrins lead to rapid singlet-singlet energy transfer to the central zinc porphyrin (≈ 50 ps) [385]. This excited state energy is passed on to the free porphyrin, yielding the singlet excited state, which, in turn, decays via an intramolecular electron-transfer event to the adjacent fullerene moiety (3 ps). The charge-separated state formed (i.e., $(ZnP)_3-ZnP-(H_2P^{+})-(C_{60}^{*-})$) has a lifetime of 1330 ps and is generated with a quantum yield of 0.70 based on light absorbed by the ZnP antenna [385].

Supramolecular complexes

The following summarizes recent studies, whose aim is to retard the fast back electron transfer, commonly observed in supermolecular systems [386–389]. In this context, a reversible coordination of the acceptor moiety (ligand or substrate) to the donor (coordination center or receptor) rather than a covalent linkage was pursued [386–389]. This was expected to enable the diffusional splitting of the charge-separated radical pair after the initial electron transfer takes place.

Photoprocesses associated with the complexation of a pyridine-functionalized fullerene derivative to a ruthenium tetraphenyl porphyrin ($Ru(CO)P$) and to a ZnP, yielding the $ZnP-C_{60}$ (37) and $RuP-C_{60}$ dyads, respectively, have been studied by time resolved optical and transient EPR spectroscopies [386–389].



It is found that, upon irradiation in toluene, a highly efficient triplet-triplet energy transfer governs the deactivation of the RuP, while electron transfer from the porphyrin to the fullerene ($RuP^{+}-C_{60}^{*-}$) prevails in polar solvents [389]. Complexation of ZnP by the fullerene derivative is reversible and, following excitation of the ZnP, gives rise to very efficient charge separation. In fluid polar solvents like THF and benzonitrile radical ion pairs ($ZnP^{+}-C_{60}^{*-}$) are generated both by intramolecular electron transfer in the complex and by intermolecular electron transfer in the uncomplexed form [386]. In the latter case radical pairs live about 10 μ s in THF and about 50 μ s in benzonitrile at room temperature [386]. Thus, com-

plexation of the donor–acceptor couple appears a viable alternative to supermolecular polyads (e.g., triads, tetrads, etc.) involving covalent links between the components for increasing the lifetime of the charge-separated state. The coordination concept, namely, complexation of a fullerene–pyridine ligand by a macrocyclic π -system that bears a potential utilization as a chromophore system, is very general and can be employed successfully to metallophthalocyanines and structural porphyrin isomers as has been demonstrated recently [310, 388].

5.6 Oxidation of Fullerenes

5.6.1 Gas-phase Oxidation

The oxidation of fullerenes is much more difficult than their reduction because of the highly positive oxidation potentials (1.26 V relative to Fc/Fc^+ for C_{60}) [16]. Since the five HOMO orbitals of C_{60} (h_u) are degenerate and fully occupied, C_{60} may be oxidized up to C_{60}^{10+} . The formation of C_{60}^{7+} in which 7 electrons were removed from the ocean of 240 valence electrons that surround its hollow cage of C_{60} has been detected in the mass spectrum [390]. This has been achieved in an ion source that delivers high electron currents at high electron energies. Singly, doubly and triply charged C_{60}^{n+} ($n = 1, 2, 3$) cations can be readily formed in the conventional electron-impact ion source that delivers ions into a selected-ion flow tube (SIFT) apparatus [391]. C_{60}^{+} is generally quite unreactive towards nucleophiles such as alcohols under SIFT conditions in the gas phase [392, 393]. Electron transfer is rare because of the low electron recombination energy of C_{60}^{+} (7.6 eV) [394]. Addition of nucleophiles such as ammonia, amines and iron pentacarbonyl to C_{60}^{+} has been observed rather than electron transfer [395, 396]. Diels–Alder additions of 1,3-cyclopentadiene, 1,3-cyclohexadiene, anthracene and corannulene to C_{60}^{+} have also been reported to form the C_{60} adduct radical cation [397]. C_{60}^{2+} is much more reactive than C_{60}^{+} in both electron transfer and addition reactions [388]. Electron transfer becomes a dominant process only when C_{60}^{+} reacts with molecules with sufficiently low ionization energies and it must be exothermic by at least 1.8 eV due to the Coulombic repulsion between the charged products in order to compete with the addition pathway effectively [398, 399]. Electron transfer with C_{60}^{3+} becomes even more competitive than with C_{60}^{2+} . However, the ionization-energy threshold for electron transfer to C_{60}^{3+} lies 4.4 eV below the thermodynamic threshold of the electron recombination energy of C_{60}^{3+} (15.6 eV) because of the larger Coulombic repulsion between the charged products as compared with the case of C_{60}^{2+} [400].

5.6.2 Oxidation of Fullerenes in Solution

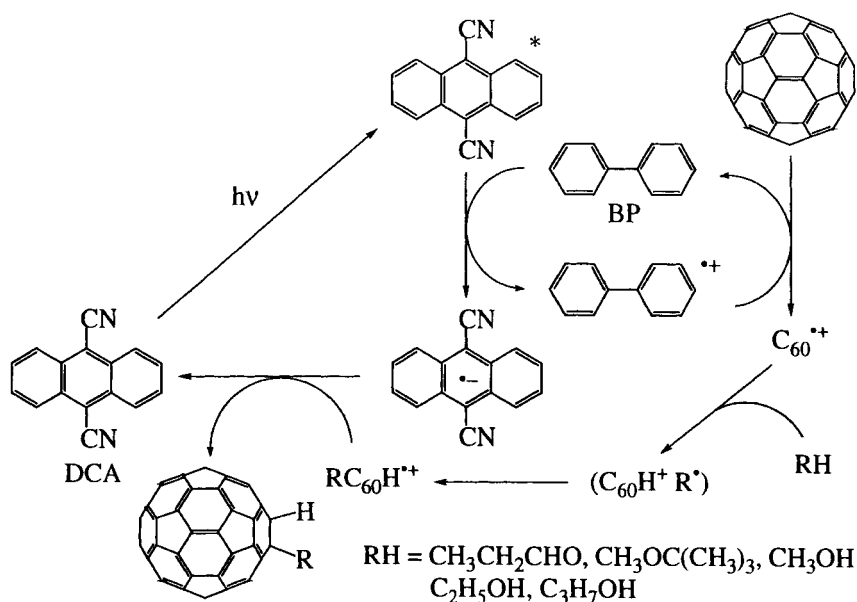
Electron acceptors such as tetracyanoquinodimethane (TCNQ) [401–404], tetracyanoethylene (TCNE) [405, 407] and chloroaniline (CIA) [24, 406] have been em-

ployed in photolysis experiments regarding the oxidative quenching of triplet excited fullerenes. In general, very fast quenching reactions are reported, but these processes are not accompanied by the separation of the free radical pairs. A triplet 'exciplex' formation has been proposed as a possible mechanism, which, in turn, would prevent the escaping from the cage. Only, in the case of TCNE the 'exciplex' has been considered as an ion-radical pair [405, 406]. Alternatively, semiconductor supports (i.e., TiO_2) have been used to initiate photochemical processes on their surfaces, including oxidation of surface-adsorbed substrates [408, 409]. In this context, the reader is reminded of that band-gap excitation of anatase TiO_2 ($E_g = 3.2$ eV) requires highly energetic UV light. On the other hand, illumination of the adsorbed substrate with visible light avoids direct excitation of the semiconductor support. Irreversible chemical changes are reported following the fullerene excitation on a TiO_2 support [408, 409]. The photoejection of electrons from the photoexcited C_{60} into the TiO_2 semiconductor is considered to be the primary step of the photooxidation process. The oxidation potential of the fullerene singlet excited state renders an electron injection from the singlet excited state into TiO_2 particles thermodynamically impossible. Rationalization of the experimental observation was forwarded in form of a hypothesis that suggests a biphotonic process (Eq. 21). In support of this hypothesis is the linear dependence of the transient oxidation product formed on the TiO_2 surface on the square of the laser dose.



The one-electron oxidation potential of C_{60} is highly positive ($E^\circ_{\text{ox}} = 1.26$ V relative to ferrocene/ferricenium, which is equivalent to 1.63 V relative to the SCE) [16]. The singlet excited states of 9,10-dicyanoanthracene ($^1\text{DCA}^*$: $E^\circ_{\text{red}} = 1.91$ V relative to the SCE) [410] and 10-methylacridinium ion ($^1\text{AcrH}^{*+}$: $E^\circ_{\text{red}} = 2.32$ V relative to the SCE) [411, 412] have both higher one-electron reduction potentials than that of C_{60} . Thus, both of them can be used as effective electron acceptors to oxidize C_{60} by photoinduced electron transfer [413]. The strong oxidizing ability of $^1\text{AcrH}^{*+}$ in the photoinduced electron-transfer reactions with a variety of electron donors has been well established [409, 410, 414–417]. Although C_{60}^{*+} is unreactive toward alcohols in the gas phase (vide supra) [390, 391], C_{60}^{*+} produced by photoinduced electron transfer from C_{60} to $^1\text{DCA}^*$ or $^1\text{AcrH}^{*+}$ can react with alcohols and hydrogen donors to afford the alkylated fullerenes [418–420]. Such a different reactivity of C_{60}^{*+} (i.e., gas phase or solution) can be ascribed to the strong solvation of the product cation. The addition of biphenyl (BP) as a cosensitizer to the $\text{DCA}-\text{C}_{60}$ system in the presence of a hydrogen donor resulted in a significant increase in the reaction efficiency via the electron transfer catalysis as shown in Scheme 12 [417, 418].

The photochemical reaction is started by a photoinduced electron transfer from BP (used in excess to C_{60}) to $^1\text{DCA}^*$ producing $\text{DCA}^{\bullet-}$ and BP^{*+} . Since electron transfer from C_{60} to BP^{*+} is exothermic, C_{60}^{*+} is formed as a free ion by electron transfer from C_{60} to BP^{*+} to regenerate BP. Without BP the facile back electron transfer from $\text{DCA}^{\bullet-}$ to C_{60}^{*+} in the radical ion pair produced direct electron transfer between C_{60} and $^1\text{DCA}^*$ would proceed leading to no product formation. In contrast



Scheme 12

to nucleophilic attacks of alcohols to the radical cation as expected from a common reaction of radical cations with nucleophiles [421, 422], the C–C bond formation with the alcohol takes place rather than the C–O bond formation (Scheme 12). Such a bizarre reaction of $\text{C}_{60}^{+\bullet}$ may be ascribed to the low electrophilicity of $\text{C}_{60}^{+\bullet}$ due to the highly delocalized positive charge. This reactivity is reminiscent of the low nucleophilicity of C_{60}^{2-} due to the highly delocalized negative charge in the reactions with alkyl halides in Scheme 2. As is the case of C_{60}^{2-} , the only reaction pathway left for $\text{C}_{60}^{+\bullet}$ is an electron transfer from RH to $\text{C}_{60}^{+\bullet}$ to give $\text{RH}^{+\bullet}$ and C_{60} . This may be followed by a rapid deprotonation of $\text{RH}^{+\bullet}$ to produce R^\bullet , since $\text{RH}^{+\bullet}$ becomes an extremely strong acid as compared to RH [423]. The addition of R^\bullet to C_{60} followed by back electron transfer from $\text{DCA}^{\bullet-}$ leads to the final product, namely, 1-substituted 1,2-dihydro [60]fullerene (Scheme 12).

5.7 Summary

This review has described the fundamental electron-transfer properties of fullerenes together with a variety of electron-transfer reactions of fullerenes, which often lead to a new type of derivatization of fullerenes. The small reorganization energy of fullerenes, especially in electron-transfer reactions, and the long triplet excited state lifetimes has rendered fullerenes as useful components in the design of novel elec-

tron transfer systems in both the ground and excited states. Most studies have so far dealt with C_{60} and a variety of C_{60} derivatives, the electron-transfer chemistry of higher fullerenes and endohedral metallofullerenes has remained to be explored further. There are many common mechanistic aspects in electron-transfer chemistry of fullerenes with that of other organic compounds described in other chapters. However, the highly delocalized negative and positive charges of fullerene anions and cations produced in the electron-transfer reduction and oxidation result in peculiar reactivities. Therefore fullerene anions and cations react in favor of an electron transfer pathway rather than a polar two-electron pathway. There have been cases where the regio- and stereo-selectivities in the reactions of fullerenes via electron transfer are different from those expected from the concerted reactions. Thus, electron-transfer chemistry of fullerenes provides an unique opportunity to synthesize new fullerene derivatives which would otherwise be impossible to obtain. It is hoped that this overview of electron-transfer chemistry of fullerenes facilitates to expand this area from both fundamental and applicational points of view.

The systematic investigation of fullerene chemistry has led to the development of useful molecular donor acceptor dyads. The selected examples are a clear demonstration of the continuing interest in fullerenes as novel, multifunctional electron storage moieties in well-ordered multicomponent composites. In this context, the unique delocalization, provided by the fullerene core, in combination with the small reorganization energy are key factors that prevent a fast back electron transfer process in fullerene-containing systems. Thus, the contributed systems are promising candidates for the design of artificial photosynthetic systems with efficient and long-lived charge separation but fewer electron transfer steps and less energy loss.

Acknowledgment

The authors are deeply indebted to the work of all collaborators and co-workers whose names are listed in the references of this chapter (in particular, S.F.: Prof. K. M. Kadish, Prof. K. Mikami and Prof. O. Ito; DMG: Prof. K.-D. Asmus, Prof. M. Maggini, Prof. N. Martin and Prof. M. Prato). S.F. acknowledges continuous support of his study on electron-transfer chemistry by a Grant-in-Aid from the Ministry of Education, Science, Culture and Sports, Japan. D.M.G. acknowledges the support by the Office of Basic Energy Sciences of the Department of Energy. This is document NDRL-4267 from the Notre Dame Radiation Laboratory). We would like to thank Drs. H. Imahori and C. Luo for their helpful discussion.

References

1. R. A. Marcus, *Annu. Rev. Phys. Chem.* **1964**, *15*, 155; R. A. Marcus, *Angew. Chem. Int. Ed. Engl.* **1993**, *32*, 1111.
2. A. Hirsch, *The Chemistry of the Fullerenes*, Thieme, New York, **1994**.
3. Q. Xie, E. Perez-Cordero, L. Echegoyen, *J. Am. Chem. Soc.* **1992**, *114*, 3978
4. Y. Ohsawa, T. Saji, *J. Chem. Soc. Chem. Commun.* **1992**, 781.
5. F. Zhou, C. Jehoulet, A. J. Bard, *J. Am. Chem. Soc.* **1992**, *114*, 11004.

6. M. Prato, M. Maggini, C. Giacometti, G. Scorrano, C. Sandona, G. Farnia, *Tetrahedron* **1996**, 52, 5221.
7. M. Keshavarz-K., B. Knight, R. C. Haddon, F. Wudl, *Tetrahedron* **1996**, 52, 5149.
8. S. Yamago, M. Yanagawa, H. Mukai, E. Nakamura, *Tetrahedron* **1996**, 52, 5091.
9. H. Nagashima, M. Saito, Y. Kato, H. Goto, E. Osawa, M. Haga, K. Itoh, *Tetrahedron*, **1996**, 52, 5053.
10. Q. Li, F. Wudl, C. Thilgen, R. L. Whetten, F. Diederich, *J. Am. Chem. Soc.* **1992**, 114, 3994.
11. Y. Yang, F. Arias, L. Echegoyen, L. P. F. Chibante, S. Flanagan, A. Robertson, L. J. Wilson, *J. Am. Chem. Soc.* **1995**, 117, 7801.
12. M. D. Diener, J. M. Alford, *Nature* **1998**, 393, 668.
13. T. Suzuki, Y. Maruyama, T. Kato, K. Kikuchi, Y. Achiba, *J. Am. Chem. Soc.* **1993**, 115, 11006.
14. K. Kikuchi, Y. Nakao, S. Suzuki, Y. Achiba, T. Suzuki, Y. Maruyama, *J. Am. Chem. Soc.* **1994**, 116, 9367.
15. T. Suzuki, K. Kikuchi, F. Oguri, Y. Nakao, S. Suzuki, Y. Achiba, K. Yamamoto, H. Funasaka, T. Takahashi, *Tetrahedron* **1996**, 52, 4973.
16. Q. Xie, F. Arias, L. Echegoyen, *J. Am. Chem. Soc.* **1993**, 115, 9818.
17. D. Dubois, K. M. Kadish, S. Flanagan, L. J. Wilson, *J. Am. Chem. Soc.* **1991**, 113, 7773.
18. J. W. Arbogast, C. S. Foote, M. Kao, *J. Am. Chem. Soc.* **1992**, 114, 2277.
19. C. S. Foote, *Top. Curr. Chem.* **1994**, 169, 347.
20. D. Dubois, G. Moninot, W. Kutner, M. T. Jones, K. M. Kadish, *J. Phys. Chem.* **1992**, 96, 7137.
21. T. Osaki, Y. Tai, M. Tazawa, S. Tanemura, K. Inukai, K. Ishiguro, Y. Sawaki, Y. Saito, H. Shinohara, H. Nagashima, *H. Chem. Lett.* **1993**, 789.
22. K. Mikami, S. Matsumoto, A. Ishida, S. Takamuku, T. Suenobu, S. Fukuzumi, *J. Am. Chem. Soc.* **1995**, 117, 11134.
23. H. N. Ghosh, H. Pal, A. V. Sapre, J. P. Mittal, *J. Am. Chem. Soc.* **1993**, 115, 11722.
24. C. A. Steren, H. van Willigen, L. Biczók, N. Gupta, H. Linschitz, *J. Phys. Chem.* **1996**, 100, 8920.
25. L. Biczók, N. Gupta, H. Linschitz, *J. Am. Chem. Soc.* **1997**, 119, 12601.
26. O. Ito, Y. Sasaki, Y. Yoshikawa, A. Watanabe, *J. Phys. Chem.* **1995**, 99, 9838.
27. T. Nojiri, M. M. Alam, H. Konami, A. Watanabe, O. Ito, *J. Phys. Chem. A* **1997**, 101, 7943.
28. A. Skiebe, A. Hirsch, H. Klos, B. Gotwschy, *Chem. Phys. Lett.* **1994**, 220, 138.
29. W. R. Fawcett, M. Opallo, M. Fedurco, J. W. Lee, *J. Am. Chem. Soc.* **1993**, 115, 196.
30. E. S. Yang, M.-S. Chan, A. C. Wahl, *J. Phys. Chem.* **1980**, 84, 3094.
31. S. Fukuzumi, S. Mochizuki, T. Tanaka, *Inorg. Chem.* **1989**, 28, 2459.
32. K. S. Cheng, N. Hirota, In *Investigation of Rates and Mechanisms of Reactions*, (Ed: G. G. Hammes), Wiley-Interscience, New York, **1974**, Vol. VI, p 565.
33. R. Chang, *J. Chem. Educ.* **1970**, 47, 563.
34. C. A. Reed, R. D. Bolskar, *Chem. Rev.* **1999**, 99, 1075.
35. P.-M. Allemand, G. Srdanov, A. Koch, K. Khemani, F. Wudl, Y. Rubin, F. Diederich, M. M. Alvarez, S. J. Anz, R. L. Whetten, *J. Am. Chem. Soc.* **1991**, 113, 2780.
36. D. Dubois, K. M. Kadish, S. Flanagan, R. E. Haufler, L. P. F. Chibante, L. J. Wilson, *J. Am. Chem. Soc.* **1991**, 113, 4364.
37. J. Stinchcombe, A. Pénicaud, P. Bhyrappa, P. D. W. Boyd, C. A. Reed, *J. Am. Chem. Soc.* **1993**, 115, 5212.
38. J. R. Morton, F. Negri, K. F. Preston, *Acc. Chem. Res.* **1998**, 31, 63.
39. J. R. Morton, K. F. Preston, P. J. Kruisic, S. A. Hill, E. Wasserman, *J. Am. Chem. Soc.* **1992**, 114, 5454.
40. J. R. Morton, K. F. Preston, P. J. Kruisic, S. A. Hill, E. Wasserman, *J. Phys. Chem.* **1992**, 96, 3576.
41. P. J. Kruisic, E. Wasserman, P. N. Keizer, J. R. Morton, K. F. Preston, *Science* **1991**, 254, 1183.
42. P. J. Kruisic, E. Wasserman, B. A. Parkinson, B. Malone, E. R. Holler Jr., P. N. Keizer, J. R. Morton, K. F. Preston, *J. Am. Chem. Soc.* **1991**, 113, 6274.
43. S. Fukuzumi, I. Nakanishi, T. Suenobu, K. M. Kadish, *J. Am. Chem. Soc.* **1999**, 121, 3468.

44. S. Fukuzumi, K. Koumitsu, K. Hironaka, T. Tanaka, *J. Am. Chem. Soc.* **1987**, *109*, 305.
45. S. Fukuzumi, I. Nakanishi, J.-M. Barbe, R. Guillard, E. Van Caemelbecke, G. Ning, K. M. Kadish, *Angew. Chem. Int. Ed. Engl.* **1999**, *38*, 964.
46. T. Layloff, T. Miller, R. N. Adams, H. Föh, A. Horsfield, W. Proctor, *Nature* **1965**, *205*, 382.
47. R. A. Marcus, N. Sutin, *N. Biochim. Biophys. Acta* **1985**, *811*, 265.
48. J. R. Miller, L. T. Calcaterra, G. L. Closs, *J. Am. Chem. Soc.* **1984**, *106*, 3047.
49. G. L. Closs, J. R. Miller, *Science* **1988**, *240*, 440.
50. N. Liang, J. R. Miller, G. L. Closs, *J. Am. Chem. Soc.* **1990**, *112*, 5353.
51. N. Mataga, T. Asahi, Y. Kanda, T. Okada, T. Kakitani, *Chem. Phys.* **1988**, *127*, 249.
52. I. R. Gould, S. Farid, *Acc. Chem. Res.* **1996**, *29*, 522.
53. J. R. Winkler, H. B. Gray, *H. B. Chem. Rev.* **1992**, *92*, 369.
54. I. R. Gould, J. E. Moser, B. Armitage, S. Farid, *J. Am. Chem. Soc.* **1989**, *111*, 1917.
55. L. S. Fox, M. Kozik, J. R. Winkler, H. B. Gray, *Science* **1990**, *247*, 1069.
56. P. Chen, R. Duesing, G. Tapolsky, T. J. Meyer, *J. Am. Chem. Soc.* **1989**, *111*, 8305.
57. E. H. Yonemoto, R. L. Riley, Y. I. Kim, S. J. Atherton, R. H. Schmehl, T. E. Mallouk, *J. Am. Chem. Soc.* **1992**, *114*, 8081.
58. M. R. Wasielewski, M. P. Niemczyk, W. A. Svec, E. B. Pewitt, *J. Am. Chem. Soc.* **1985**, *107*, 1080.
59. D. B. MacQueen, K. S. Schanze, *J. Am. Chem. Soc.* **1991**, *113*, 7470.
60. T. M. McCleskey, J. R. Winkler, H. B. Gray, *J. Am. Chem. Soc.* **1992**, *114*, 6935.
61. C. Turro, J. M. Zaleski, Y. M. Karabatsos, D. G. Nocera, *J. Am. Chem. Soc.* **1996**, *118*, 6060.
62. D. M. Guldi, K.-D. Asmus, *J. Am. Chem. Soc.* **1997**, *119*, 5744.
63. D. M. Guldi, P. Neta, K.-D. Asmus, *J. Phys. Chem.* **1994**, *98*, 4617.
64. D. R. Lawson, D. L. Feldheim, C. A. Foss, P. K. Dorhout, C. M. Elliot, C. R. Martin, B. Parkinson, *J. Electrochem. Soc.* **1992**, *139*, L68.
65. D. M. Guldi, H. Hungerbühler, E. Janata, K. D. Asmus, *J. Phys. Chem.* **1993**, *97*, 11258.
66. D. M. Guldi, H. Hungerbühler, E. Janata, K. D. Asmus, *J. Chem. Soc. Chem. Commun* **1993**, *6*, 84.
67. T. Kato, T. Kodama, T. Shida, T. Nakagawa, Y. Matsui, S. Suzuki, H. Shiromaru, K. Yamauchi, Y. Achiba, *Chem. Phys. Lett.* **1991**, *180*, 446.
68. P. V. Kamat, G. Sauvé, D. M. Guldi, K.-D. Asmus, *Res. Chem. Intermed.* **1997**, *23*, 575.
69. D. M. Guldi, H. Hungerbühler, M. Wilhelm, K.-D. Asmus, *J. Chem. Soc. Faraday Trans.* **1994**, *90*, 1391.
70. D. M. Guldi, D. Liu, P. V. Kamat, *J. Phys. Chem. A* **1997**, *101*, 6195.
71. N. E. Shank, L. M. Dorfman, *J. Chem. Phys.* **1970**, *52*, 4441.
72. N. M. Dimitrijevic, *Chem. Phys. Lett.* **1992**, *194*, 457.
73. Z. R. Lian, S. D. Yao, W. Z. Lin, W. F. Wang, N. Y. Lin, *Radiat. Phys. Chem.* **1997**, *50*, 245.
74. H. Hou, C. Luo, Z. Liu, D. Mao, Q. Qin, Z. R. Lian, S. Yao, W. Wang, J. Zhang, N. Lin, *Chem. Phys. Lett.* **1993**, *203*, 555.
75. S. D. Yao, Z. R. Lian, W. F. Wang, J. S. Zhang, N. Y. Lin, H. Hou, Z. Zhang, Q. Qin, *Chem. Phys. Lett.* **1995**, *239*, 112.
76. S. D. Yao, W. Z. Lin, Z. R. Lian, W. F. Wang, N. Y. Lin, *Radiat. Phys. Chem.* **1997**, *50*, 249.
77. M. Sundahl, T. Andersson, K. Nilsson, O. Wennerstrom, G. Westman, *Synth. Met.* **1993**, *55*, 3252.
78. T. Andersson, K. Nilsson, M. Sundahl, G. Westman, O. Wennerström, *J. Chem. Soc. Chem. Commun.* **1992**, 604.
79. A. Beeby, J. Eastoe, E. R. Crooks, *Chem. Commun.* **1996**, 901.
80. J. Eastoe, E. R. Crooks, A. Beeby, R. K. Heenan, *Chem. Phys. Lett.* **1995**, *245*, 571.
81. H. Hungerbühler, D. M. Guldi, K.-D. Asmus, *J. Am. Chem. Soc.* **1993**, *115*, 3386.
82. Y. N. Yamakoshi, T. Yagami, K. Fukuhara, S. Sueyoshi, N. Miyata, *J. Chem. Soc. Chem. Commun.* **1994**, 517.
83. R. V. Bensasson, E. Bienvenue, M. Dellinger, S. Leach, P. Seta, *J. Phys. Chem.* **1994**, *98*, 3492.
84. S. Niu, D. Mauzerall, *J. Am. Chem. Soc.* **1996**, *118*, 5791.
85. V. Ohlendorf, A. Willnow, H. Hungerbühler, D. M. Guldi, K.-D. Asmus, *J. Chem. Soc. Chem. Commun.* **1995**, 759.

86. K. I. Priyadarsini, H. Mohan, J. P. Mittal, D. M. Guldi, H. Hungerbühler, K.-D. Asmus, *J. Phys. Chem.* **1994**, *98*, 9565.
87. D. M. Guldi, *J. Phys. Chem. B* **1997**, *101*, 9600.
88. D. M. Guldi, H. Hungerbühler, *Res. Chem. Intermed.* **1999**, *25*, 615.
89. D. M. Guldi, H. Hungerbühler, K.-D. Asmus, *J. Phys. Chem.* **1995**, *99*, 13487.
90. D. M. Guldi, *Res. Chem. Intermed.* **1997**, *23*, 653.
91. D. M. Guldi, H. Hungerbühler, K.-D. Asmus, *J. Phys. Chem.* **1995**, *99*, 9380.
92. L. Echegoyen, L. E. Echegoyen, *Acc. Chem. Res.* **1998**, *31*, 593.
93. D. M. Guldi, *J. Phys. Chem. A* **1997**, *101*, 3895.
94. D. M. Guldi, H. Hungerbühler, K.-D. Asmus, *J. Phys. Chem. A* **1997**, *101*, 1783.
95. T. Da Ros, M. Prato, M. Carano, P. Ceroni, F. Paolucci, S. Roffia, *J. Am. Chem. Soc.* **1998**, *120*, 11645.
96. D. M. Guldi, H. Hungerbühler, K.-D. Asmus, *J. Phys. Chem. B* **1999**, *103*, 1444.
97. D. M. Guldi, *J. Phys. Chem. A* **2000**, *104*, 1484.
98. D. M. Guldi, M. Prato, *to be published*.
99. F. Wudl, *Acc. Chem. Res.* **1992**, *25*, 157.
100. (a) F. Diederich, C. Thilgen, *Science* **1996**, *271*, 317; (b) A. Hirsch, *Angew. Chem. Int. Ed. Engl.* **1993**, *32*, 1138.
101. R. Taylor, D. R. M. Walton, *Nature* **1993**, *363*, 685.
102. P. J. Fagan, J. C. Calabrese, B. Malone, *Science* **1991**, *252*, 1160.
103. P. J. Fagan, J. C. Calabrese, B. Malone, *Acc. Chem. Res.* **1992**, *25*, 134.
104. C. C. Henderson, P. A. Cahill, *Science* **1993**, *259*, 1885.
105. R. Schwenninger, T. Müller, B. Kräutler, *J. Am. Chem. Soc.* **1997**, *119*, 9317.
106. J. Llacyay, M. Mas, E. Molins, J. Veciana, D. Powell, C. Rovira, *Chem. Commun.* **1997**, 659.
107. M. Ohno, T. Azuma, S. Kojima, Y. Shirakawa, S. Eguchi, *Tetrahedron* **1996**, *52*, 4983.
108. B. Kräutler, T. Müller, J. Maynollo, K. Gruber, C. Kratky, P. Ochsenbein, D. Schwarzenbach, H.-B. Bürgi, *Angew. Chem. Int. Ed. Engl.* **1996**, *35*, 1204.
109. L. Isaacs, R. F. Haldimann, F. Diederich, *Angew. Chem. Int. Ed. Engl.* **1994**, *33*, 2339.
110. P. Belik, A. Gügel, J. Spickermann, K. Müllen, *Angew. Chem. Int. Ed. Engl.* **1993**, *32*, 78.
111. S. Yamago, A. Takeichi, E. Nakamura, *J. Am. Chem. Soc.* **1994**, *116*, 1123.
112. M. Prato, H. Suzuki, H. Foroudian, Q. Li, K. Khemani, F. Wudl, J. Leonetti, R. D. Little, T. White, B. Rickborn, S. Yamago, E. Nakamura, *J. Am. Chem. Soc.* **1993**, *115*, 1594.
113. P. Belik, A. Gügel, J. Spickermann, K. Müllen, *Angew. Chem. Int. Ed. Engl.* **1993**, *32*, 78.
114. A. Gügel, A. Kraus, J. Spickermann, P. Belik, K. Müllen, *Angew. Chem. Int. Ed. Engl.* **1994**, *33*, 559.
115. T. Suzuki, Q. Li, K. C. Khemani, F. Wudl, Ö. Almarsson, *Science* **1991**, *254*, 1186.
116. T. Suzuki, Q. Li, K. C. Khemani, F. Wudl, *J. Am. Chem. Soc.* **1992**, *114*, 7300.
117. S. Shi, K. C. Khemani, Q. Li, F. Wudl, *J. Am. Chem. Soc.* **1992**, *114*, 10656.
118. R. Sijbesma, G. Srdanov, F. Wudl, J. A. Castoro, C. Wilkins, S. H. Friedman, D. L. DeCamp, G. L. Kenyon, *J. Am. Chem. Soc.* **1993**, *115*, 6510.
119. M. Prato, Q. Li, F. Wudl, V. Lucchini, *J. Am. Chem. Soc.* **1993**, *115*, 1148.
120. J. E. Chateaufneuf, *J. Am. Chem. Soc.* **1995**, *117*, 2677.
121. M. Eiermann, F. Wudl, M. Prato, M. Maggini, *J. Am. Chem. Soc.* **1994**, *116*, 8364.
122. A. F. Kiely, R. C. Haddon, M. S. Meier, J. P. Selegue, C. P. Brock, B. O. Patrick, C.-W. Wang, Y. Chen, *J. Am. Chem. Soc.* **1999**, *121*, 7971.
123. P. J. Fagan, P. J. Krusic, D. H. Evans, S. A. Lerke, E. Johnston, *J. Am. Chem. Soc.* **1992**, *114*, 9697.
124. A. Hirsch, A. Soi, H. R. Karfunkel, *Angew. Chem. Int. Ed. Engl.* **1992**, *31*, 766.
125. A. Hirsch, T. Grösser, A. Skiebe, A. Soi, *Chem. Ber.* **1993**, *126*, 1061.
126. K. Komatsu, Y. Murata, N. Takimoto, S. Mori, N. Sugita, T. S. M. Wan, *J. Org. Chem.* **1994**, *59*, 6101.
127. Y. Murata, K. Motoyama, K. Komatsu, T. S. M. Wan, *Tetrahedron*, **1996**, *52*, 5077.
128. H. Nagashima, H. Terasaki, E. Kimura, K. Nakajima, K. Itoh, *J. Org. Chem.* **1994**, *59*, 1246.
129. H. Nagashima, M. Saito, Y. Kato, H. Goto, E. Osawa, M. Haga, K. Itoh, *Tetrahedron* **1996**, *52*, 5053.
130. S. R. Wilson, Y. Wu, *J. Am. Chem. Soc.* **1993**, *115*, 10334.

131. G.-W. Wang, L.-H. Shu, S.-H. Wu, H.-M. Wu, X.-F. Lao, *J. Chem. Soc. Chem. Commun.* **1995**, 1071.
132. J. M. Hawkins, *Acc. Chem. Res.* **1992**, 25, 150.
133. M. Sawamura, H. Iikura, E. Nakamura, *J. Am. Chem. Soc.* **1996**, 118, 12850.
134. G.-W. Wang, Y. Murata, K. Komatsu, T. S. M. Wan, *Chem. Commun.* **1996**, 2059.
135. M. Maggini, A. Karlsson, G. Scorrano, G. Sandona, G. Farnia, M. Prato, *J. Chem. Soc. Chem. Commun.* **1994**, 589.
136. S. Ballenweg, R. Gleiter, W. Krätschmer, *J. Chem. Soc. Chem. Commun.* **1994**, 2269.
137. A. L. Balch, V. J. Catalano, J. W. Lee, M. M. Olmstead, *J. Am. Chem. Soc.* **1992**, 114, 5455.
138. A. L. Balch, V. J. Catalano, L. W. Lee, M. M. Olmstead, S. R. Parkin, *J. Am. Chem. Soc.* **1991**, 113, 8953.
139. C. Caron, R. Subramanian, F. D'Souza, J. Kim, W. Kutner, M. T. Jones, K. M. Kadish, *J. Am. Chem. Soc.* **1993**, 115, 8505.
140. Y. Huang, D. D. M. Wayner, *J. Am. Chem. Soc.* **1993**, 115, 367.
141. F. D'Souza, J.-p. Choi, W. Kutner, *J. Phys. Chem. B* **1997**, 102, 4247.
142. F. D'Souza, J.-p. Choi, Y.-Y. Hsieh, K. Shriver, W. Kutner, *J. Phys. Chem. B* **1998**, 102, 212.
143. P. L. Boulas, Y. Zuo, L. Echegoyen, *Chem. Commun.* **1996**, 1547.
144. R. Subramanian, P. Boulas, M. N. Vijayashree, F. D'Souza, M. T. Jones, K. M. Kadish, *J. Chem. Soc. Chem. Commun.* **1994**, 1847.
145. R. Subramanian, K. M. Kadish, M. N. Vijayashree, X. Gao, M. T. Jones, M. D. Miller, K. L. Krause, T. Suenobu, S. Fukuzumi, *J. Phys. Chem.* **1996**, 100, 16327.
146. N. Matsuzawa, D. Dixon, T. Fukunaga, *J. Phys. Chem.* **1992**, 96, 7594.
147. P. A. Cahill, C. M. Rohlfing, *Tetrahedron* **1996**, 52, 5247.
148. K. M. Kadish, X. Gao, E. Van Caemelbecke, T. Hirasaka, T. Suenobu, S. Fukuzumi, *J. Phys. Chem.* **1998**, 102, 3898.
149. A. B. Smith, III, M. Strongin, L. Brard, G. T. Furst, J. Romanow, K. G. Owens, R. J. Goldschmidt, R. C. King, *J. Am. Chem. Soc.* **1995**, 117, 5492.
150. S. Miki, M. Kitao, K. Fukunishi, *Tetrahedron Lett.* **1996**, 37, 2042.
151. K. M. Kadish, X. Gao, E. Van Caemelbecke, T. Suenobu, S. Fukuzumi, *J. Phys. Chem. A* **2000**, 104, 3878.
152. L. Ebersson, *Electron-transfer reactions in Organic Chemistry*, Springer, Tokyo, **1987**.
153. N. Kornblum, *Angew. Chem. Int. Ed. Engl.* **1975**, 14, 734.
154. J. F. Bunnett, *Acc. Chem. Res.* **1992**, 25, 2.
155. M. Chanon, M. L. Tobe, *Angew. Chem. Int. Ed. Engl.* **1982**, 21, 1.
156. S. Fukuzumi, in *Advances in Electron-transfer chemistry*, Vol. 2, (Ed.: P. S. Mariano), JAI Press, Greenwich, CT, **1992**, p. 65.
157. M. Patz, S. Fukuzumi, *J. Phys. Org. Chem.* **1997**, 10, 129.
158. J. K. Kochi, *Angew. Chem. Int. Ed. Engl.* **1988**, 27, 1227.
159. E. C. Ashby, *Acc. Chem. Res.* **1988**, 21, 414.
160. M. Chanon, M. Rajzmann, F. Chanon, *Tetrahedron* **1990**, 46, 6193.
161. S. Fukuzumi, T. Suenobu, T. Hirasaka, R. Arakawa, K. M. Kadish, *J. Am. Chem. Soc.* **1998**, 120, 9220.
162. S. Fukuzumi, J. Maruta, *Inorg. Chim. Acta* **1994**, 226, 145.
163. M. Ishikawa, S. Fukuzumi, *J. Am. Chem. Soc.* **1990**, 112, 8864.
164. J.-M. Savéant, *J. Am. Chem. Soc.* **1990**, 109, 6788.
165. C. P. Andrieux, A. L. Gorande, J.-M. Savéant, *J. Am. Chem. Soc.* **1990**, 114, 6892.
166. S. Fukuzumi, T. Yorisue, *Bull. Chem. Soc. Jpn.* **1992**, 65, 715.
167. S. Fukuzumi, T. Kitano, M. Ishikawa, Y. Matsuda, *Chem. Phys.* **1993**, 176, 337.
168. Y. Murata, K. Komatsu, T. S. M. Wan, *Tetrahedron Lett.* **1996**, 37, 7061.
169. Y. Murata, M. Shiro, K. Komatsu, *J. Am. Chem. Soc.* **1997**, 119, 8117.
170. P. R. Birkett, A. G. Avent, A. D. Darwish, H. W. Kroto, R. Taylor, D. R. M. Walton, *J. Chem. Soc. Perkin Trans. 2* **1997**, 457.
171. K. M. Kadish, X. Gao, E. Van Caemelbecke, T. Suenobu, S. Fukuzumi, *J. Am. Chem. Soc.* **2000**, 122, 563.
172. S. Fukuzumi, T. Suenobu, X. Gao, K. M. Kadish, *J. Phys. Chem. A* **2000**, 104, 2908.

173. K. M. Kadish, X. Gao, O. Gorelik, E. Van Caemelbecke, T. Suenobu, S. Fukuzumi, *J. Phys. Chem. A* **2000**, *104*, 2902.
174. S. R. Wilson, Y. Wu, *J. Am. Chem. Soc.* **1993**, *115*, 10334.
175. D. T. Sawyer, J. L. Roberts, Jr. *Acc. Chem. Res.* **1988**, *21*, 469.
176. S. Fukuzumi, T. Yorisue, *J. Am. Chem. Soc.* **1991**, *113*, 7764.
177. S. Fukuzumi, I. Nakanishi, J. Maruta, T. Yorisue, T. Suenobu, S. Itoh, R. Arakawa, K. M. Kadish, *J. Am. Chem. Soc.* **1998**, *120*, 6673.
178. Y.-P. Sun, in *Molecular and Supramolecular Photochemistry*, Vol. 1, (Eds.: V. Ramamurthy, K. S. Schanze), Marcel Dekker, New York, **1997**, p. 325–389.
179. T. W. Ebbesen, K. Tanigaki, S. Kuroshima, *Chem. Phys. Lett.* **1991**, *181*, 501.
180. R. Seshadri, C. N. R. Rao, H. Pal, T. Mukherjee, J. P. Mittal, *Chem. Phys. Lett.* **1993**, *205*, 395.
181. B. Ma, G. E. Lawson, C. E. Bunker, A. Kitaygorodskiy, Y.-P. Sun, *Chem. Phys. Lett.* **1995**, *247*, 51.
182. Y.-P. Sun, B. Ma, G. E. Lawson, *Chem. Phys. Lett.* **1995**, *233*, 57.
183. Y. Wang, *J. Phys. Chem.* **1992**, *96*, 764.
184. E. Schaffner, H. Fischer, *J. Phys. Chem.* **1993**, *97*, 13149.
185. M. Fujitsuka, C. Luo, O. Ito, *J. Phys. Chem. B* **1999**, *103*, 445.
186. C. Luo, M. Fujitsuka, C.-H. Huang, O. Ito, *J. Phys. Chem. A* **1998**, *102*, 8716.
187. C. Luo, M. Fujitsuka, C.-H. Huang, O. Ito, *Phys. Chem. Chem. Phys.* **1999**, *1*, 2923.
188. M. C. Rath, H. Pal, T. Mukherjee, *J. Phys. Chem. A* **1999**, *103*, 4993.
189. S. Komamine, M. Fujitsuka, O. Ito, *Phys. Chem. Chem. Phys.* **1999**, *1*, 4745.
190. D. M. Guldi, R. E. Huie, P. Neta, H. Hungerbühler, K.-D. Asmus, *Chem. Phys. Lett.* **1994**, *223*, 511.
191. V. A. Nadochenko, F. F. Brazgun, *Russ. Chem. Bull. (Transl. of Izv. Akad. Nauk, Ser. Khim)* **1997**, *46*, 1074.
192. D. M. Guldi, M. Maggini, G. Scorrano, M. Prato, *Res. Chem. Intermed.* **1997**, *23*, 561.
193. D. M. Guldi, M. Maggini, G. Scorrano, M. Prato, *J. Am. Chem. Soc.* **1997**, *119*, 974.
194. M. M. Alam, A. Watanabe, O. Ito, *J. Photochem. Photobiol. A: Chem.* **1997**, *104*, 59.
195. A. Graja, M. A. Tanatar, Y. L. Li, D. B. Zhu, *Polish J. Chem.* **1998**, *72*, 869.
196. M. Alam, M. Sato, A. Watanabe, T. Akasaka, O. Ito, *J. Phys. Chem. A* **1998**, *102*, 7447.
197. A. Alam, O. Ito, N. Sakurai, H. Moriyama, *Fullerene Science Technology* **1998**, *6*, 1007.
198. O. Ito, Y. Sasaki, A. Watanabe, R. Hoffmann, C. Siedschlag, J. Mattay, *J. Chem. Soc. Perkin Trans. 2* **1997**, 1007.
199. H. N. Ghosh, D. K. Palit, A. V. Sapre, J. P. Mittal, *Chem. Phys. Lett.* **1997**, *265*, 365.
200. Y. Sasaki, Y. Yoshikawa, A. Watanabe, O. Ito, *J. Chem. Soc. Faraday Trans.* **1995**, *91*, 2287.
201. O. Ito, *Res. Chem. Intermed.* **1997**, *23*, 389.
202. S. Michaeli, V. Meiklyar, B. Endeward, K. Möbius, H. Levanon, *Res. Chem. Intermed.* **1997**, *23*, 505.
203. M. Fujitsuka, O. Ito, Y. Maeda, M. Kako, T. Wakahara, T. Akasaka, *Phys. Chem. Chem. Phys.* **1999**, *1*, 3527.
204. A. Samanta, P. V. Kamat, *Chem. Phys. Lett.* **1992**, *199*, 635.
205. T. Konishi, Y. Sasaki, M. Fujitsuka, Y. Toba, H. Moriyama, O. Ito, *J. Chem. Soc. Perkin Trans. 2* **1999**, 551.
206. M. Fujitsuka, C. Luo, O. Ito, Y. Murata, K. Komatsu, *J. Phys. Chem. A* **1999**, *103*, 7155.
207. Y. Sasaki, T. Konishi, M. Yamazaki, M. Fujitsuka, O. Ito, *Phys. Chem. Chem. Phys.* **1999**, *1*, 4555.
208. A. Alam, O. Ito, N. Sakurai, H. Moriyama, *Res. Chem. Intermed.* **1999**, *25*, 323.
209. Y. Sasaki, M. Fujitsuka, A. Watanabe, O. Ito, *J. Chem. Soc. Faraday Trans.* **1997**, *93*, 4275.
210. C. Luo, M. Fujitsuka, A. Watanabe, O. Ito, L. Gan, Y. Huang, C.-H. Huang, *J. Chem. Soc. Faraday Trans.* **1998**, *94*, 527.
211. A. Watanabe, O. Ito, *J. Phys. Chem.* **1994**, *98*, 7736.
212. A. Watanabe, O. Ito, K. Mochida, *Organometallics* **1995**, *14*, 4281.
213. M. Bennati, A. Grupp, M. Mehring, K. P. Dinse, J. Fink, *Chem. Phys. Lett.* **1992**, *200*, 440.
214. M. Bennati, A. Grupp, P. Bäuerle, M. Mehring, *Chem. Phys.* **1994**, *185*, 221.
215. M. Bennati, A. Grupp, P. Bäuerle, M. Mehring, *Mol. Cryst. Liq. Cryst.* **1994**, *256*, 751.

216. M. Bennati, A. Grupp, M. Mehring, *J. Chem. Phys.* **1995**, *102*, 9457.
217. J.-I. Fujisawa, Y. Ohba, S. Yamauchi, *Chem. Phys. Lett.* **1998**, *294*, 248.
218. J.-I. Fujisawa, Y. Ohba, S. Yamauchi, *Chem. Phys. Lett.* **1998**, *282*, 181.
219. K. C. Hwang, D. Mauzerall, *J. Am. Chem. Soc.* **1992**, *114*, 9705.
220. K. C. Hwang, D. C. Mauzerall, *Nature* **1993**, *361*, 138.
221. P. V. Kamat, I. Bedja, S. Hotchandani, *J. Phys. Chem.* **1994**, *98*, 9137.
222. P. V. Kamat, *J. Am. Chem. Soc.* **1991**, *113*, 9705.
223. A. Stasko, V. Brezova, S. Biskupic, K.-P. Dinse, P. Schweitzer, M. Baumgarten, *J. Phys. Chem.* **1995**, *99*, 8782.
224. R. D. Scurlock, P. R. Ogilby, *J. Photochem. Photobiol. A: Chem.* **1995**, *91*, 21.
225. S. Fukuzumi, T. Suenobu, M. Patz, T. Hirasaka, S. Itoh, M. Fujitsuka, O. Ito, *J. Am. Chem. Soc.* **1998**, *120*, 8060.
226. M. Patz, Y. Kuwahara, T. Suenobu, S. Fukuzumi, *Chem. Lett.*, **1997**, 567.
227. S. Fukuzumi, T. Suenobu, T. Hirasaka, N. Sakurada, R. Arakawa, M. Fujitsuka, O. Ito, *J. Phys. Chem. A* **1999**, *103*, 5935.
228. D. R. Lawson, D. L. Feldheim, C. A. Foss, P. K. Dorhout, C. M. Elliot, C. R. Martin, B. Parkinson, *B. J. Phys. Chem.* **1992**, *96*, 7175.
229. A. Watanabe, O. Ito, M. Watanabe, H. Saito, M. Koishi, *J. Phys. Chem.* **1996**, *100*, 10518.
230. L. Becker, T. P. Evans, J. L. Bada, *J. Org. Chem.* **1993**, *58*, 7630.
231. S. Ballenweg, R. Gleiter, W. Krätschmer, *Tetrahedron Lett.* **1993**, *34*, 3737.
232. T. F. Guarr, M. S. Meier, V. K. Vance, M. Clayton, *J. Am. Chem. Soc.* **1993**, *115*, 9862.
233. D. Mandrus, M. Kele, R. L. Hettich, G. Guiochon, B. C. Sales, L. A. Boatner, *J. Phys. Chem. B* **1997**, *101*, 123.
234. M. S. Meier, B. R. Weedon, H. P. Spielmann, *J. Am. Chem. Soc.* **1996**, *118*, 11682.
235. R. G. Bergosh, M. S. Meier, J. A. L. Cooke, H. P. Spielmann, B. R. Weedon, *J. Org. Chem.* **1997**, *62*, 7667.
236. M. S. Meier, P. S. Corbin, V. K. Vance, M. Clayton, M. Mollman, *Tetrahedron Lett.* **1994**, *35*, 5789.
237. H. P. Spielmann, G.-W. Wang, M. S. Meier, B. R. Weedon, *J. Org. Chem.* **1998**, *63*, 9865.
238. S. Fukuzumi, T. Suenobu, S. Kawamura, A. Ishida, K. Mikami, *Chem. Commun.* **1997**, 291.
239. S. Fukuzumi, Y. Tokuda, T. Kitano, T. Okamoto, J. Otera, *J. Am. Chem. Soc.* **1993**, *115*, 8960.
240. M. A. Fox, N. Chanon, (Eds.), *Photoinduced Electron Transfer*, Elsevier, Amsterdam, **1988**.
241. S. Fukuzumi, S. Itoh, in *Advances in Photochemistry*, Vol. 25, (Eds.: D. Volman, G. S. Hammond, D. C. Neckers), Wiley, New York, **1998**, pp 107–172.
242. F. Müller, J. Mattay, *Chem. Rev.* **1993**, *93*, 99.
243. G. J. Kavarnos, N. J. Turro, *Chem. Rev.* **1986**, *86*, 401.
244. T. Mukaiyama, *Org. React.* **1982**, *28*, 203.
245. A. Hosomi, *Acc. Chem. Res.* **1988**, *21*, 200.
246. I. Fleming, *Comprehensive Organic Synthesis*, Vol. 2, Pergamon, London, **1991**.
247. H. Sakurai, *Synlett* **1989**, 1.
248. S. Fukuzumi, M. Fujita, J. Otera, Y. Fujita, *J. Am. Chem. Soc.* **1992**, *114*, 10271.
249. S. Fukuzumi, M. Fujita, J. Otera, *J. Org. Chem.* **1993**, *58*, 5405.
250. H. Tokuyama, H. Isobe, E. Nakamura, *J. Chem. Soc. Chem. Commun.* **1994**, 2753.
251. K. Mikami, S. Matsumoto, *Synlett* **1995**, 229.
252. S. Fukuzumi, T. Suenobu, M. Fujitsuka, O. Ito, T. Tono, S. Matsumoto, K. Mikami, *J. Organomet. Chem.* **1999**, *574*, 32.
253. S. Fukuzumi, *Res. Chem. Intermediat.* **1997**, *23*, 519.
254. S. Fukuzumi, M. Fujita, J. Otera, *J. Chem. Soc. Chem. Commun.* **1993**, 1536.
255. K. Mikami, S. Matsumoto, T. Tono, T. Suenobu, A. Ishida, S. Fukuzumi, *Synlett* **1997**, 85.
256. E. Butcher, C. J. Rhodes, M. Standing, R. S. Davidson, R. Bowser, *J. Chem. Soc. Perkin Trans. 2* **1992**, 1469.
257. A. Rehm, A. Weller, *Isr. J. Chem.* **1970**, *8*, 259.
258. A. Anne, J. Moiroux, J.-M. Savéant, *J. Am. Chem. Soc.* **1993**, *115*, 10224.
259. N. Takada, S. Itoh, S. Fukuzumi, *Chem. Lett.* **1996**, 1103.
260. A. Hirsch, A. Soai, H. R. Karfunkel, *Angew. Chem. Int. Ed. Engl.* **1992**, *31*, 766.

261. T. Kitagawa, T. Tanaka, Y. Takata, K. Takeuchi, *J. Org. Chem.* **1995**, *60*, 1490.
262. T. Tanaka, T. Kitagawa, K. Komatsu, K. Takeuchi, *J. Am. Chem. Soc.* **1997**, *119*, 9313.
263. H. Sakurai, M. Kira, T. Uchida, *J. Am. Chem. Soc.* **1973**, *95*, 6826.
264. Y. F. Traven, R. West, *J. Am. Chem. Soc.* **1973**, *95*, 6824.
265. W. Ando, M. Kako, T. Akasaka, S. Nagase, *Organometallics* **1993**, *12*, 1514.
266. Y. Maeda, T. Wakahara, T. Akasaka, M. Fujitsuka, O. Ito, M. Kato, Y. Nakadaira, K. Kobayashi, S. Nagase, *Proceedings of 45th Symposium on Organometallic Chemistry*, Tolyo, **1998**, pp 42–43.
267. T. Akasaka, W. Ando, K. Kobayashi, S. Nagase, *J. Am. Chem. Soc.* **1993**, *115*, 10366.
268. T. Akasaka, T. Kato, K. Kobayashi, S. Nagase, K. Yamamoto, H. Funasaka, T. Takahashi, *Nature* **1995**, *374*, 600.
269. T. Akasaka, S. Nagase, K. Kobayashi, *J. Syn. Org. Chem. Jpn.* **1996**, *54*, 580.
270. T. Akasaka, K. Kato, S. Nagase, K. Kobayashi, K. Yamamoto, H. Funasaka, T. Takahashi, *Tetrahedron* **1996**, *52*, 5015.
271. S. Nagase, K. Kobayashi, *J. Chem. Soc. Chem. Commun.* **1994**, 1837.
272. T. Akasaka, T. Suzuki, Y. Maeda, M. Ara, T. Wakahara, K. Kobayashi, S. Nagase, M. Kako, Y. Nakadaira, M. Fujitsuka, O. Ito, *J. Org. Chem.* **1999**, *64*, 566.
273. S. Fukuzumi, T. Kitano, K. Mochida, *Chem. Lett.* **1990**, 1741.
274. F. W. Sluggett, W. J. Leigh, *Organometallics* **1992**, *11*, 3731.
275. Y. Z. An, L. J. Anderson, Y. Rubin, *J. Org. Chem.* **1993**, *58*, 4799.
276. M. Prato, A. Bianco, M. Magini, G. Scorrano, C. Toniolo, F. Wudl, *J. Org. Chem.* **1993**, *58*, 5578.
277. A. Skiebe, A. Hirsch, *J. Chem. Soc. Chem. Commun.* **1994**, 335.
278. L. Isaacs, A. Wehrsig, F. Diederich, *Helv. Chim. Acta* **1993**, *76*, 1231.
279. L. Isaacs, F. Diederich, *Helv. Chim. Acta* **1993**, *76*, 2454.
280. D. J. Zhou, L. B. Gan, L. B. Xu, C. P. Luo, C. H. Huang, *Fullerene Sci. Technol.* **1995**, *3*, 127.
281. L. Gan, D. Zhou, C. Luo, H. Tan, C. Huang, M. Lü, J. Pan, Y. Wu, *J. Org. Chem.* **1996**, *61*, 1954.
282. L. Gan, J. Jiang, W. Zhang, Y. Su, Y. Shi, C. Huang, J. Pan, M. Lü, Y. Wu, *J. Org. Chem.* **1998**, *63*, 4240.
283. M.-J. Arce, A. L. Viado, Y.-Z. An, S. I. Khan, Y. Rubin, *J. Am. Chem. Soc.* **1996**, *118*, 3775.
284. M. J. Arce, A. L. Viado, S. I. Khan, Y. Rubin, *Organometallics*, **1996**, *15*, 4340.
285. S. R. Wilson, Q. Y. Lu, J. R. Cao, Y. H. Wu, C. J. Welch, D. I. Schuster, *Tetrahedron* **1996**, *52*, 5131.
286. M. Ohno, N. Koide, H. Sato, S. Eguchi, *Tetrahedron* **1997**, *53*, 9075.
287. K. N. Houk, J. González, Y. Li, *Acc. Chem. Res.* **1995**, *28*, 81.
288. K. N. Houk, J. D. Evanseck, *Angew. Chem. Int. Ed. Engl.* **1992**, *31*, 682.
289. M. J. S. Dewar, C. Jie, *Acc. Chem. Res.* **1992**, *25*, 537.
290. B. A. Horn, J. L. Herek, A. H. Zewail, *J. Am. Chem. Soc.* **1996**, *118*, 8755.
291. R. Sustmann, S. Tappanchai, H. Bandmann, *J. Am. Chem. Soc.* **1996**, *118*, 12555.
292. B. R. Beno, S. Wilsey, K. N. Houk, *J. Am. Chem. Soc.* **1999**, *121*, 4816.
293. J. S. Chen, K. N. Houk, C. S. Foote, *J. Am. Chem. Soc.* **1998**, *120*, 12303.
294. E. Goldstein, B. Beno, K. N. Houk, *J. Am. Chem. Soc.* **1996**, *118*, 6036.
295. S. Fukuzumi, J. K. Kochi, *Tetrahedron* **1982**, *38*, 1035.
296. R. Sustmann, K. Lücking, G. Kopp, M. Rese, *Angew. Chem. Int. Ed. Engl.* **1989**, *28*, 1713.
297. R. Sustmann, H.-G. Korth, U. Nüchter, I. Siangouri-Feulner, W. Sicking, *Chem. Ber.* **1991**, *124*, 2811.
298. S. Fukuzumi, T. Okamoto, *J. Am. Chem. Soc.* **1993**, *115*, 11600.
299. S. Yamago, S. Ejiri, M. Nakamura, E. Nakamura, *J. Am. Chem. Soc.* **1993**, *115*, 5344.
300. D. L. Boger, C. E. Brotherton, in *Advances in Cycloaddition*, Vo. 2, (Ed.: D. P. Curran), JAI Press, Greenwich, CT, **1990**, p. 147.
301. M. Schmittel, C. Wöhrle, I. Bohn, *Chem. Eur. J.* **1996**, *2*, 1031.
302. K. Mikami, S. Matsumoto, T. Tonoi, Y. Okubo, T. Suenobu, S. Fukuzumi, *Tetrahedron Lett.* **1998**, *39*, 3733.
303. Y. Murata, N. Kato, K. Fujiwara, K. Komatsu, *J. Org. Chem.* **1999**, *64*, 3483.
304. K. Mikami, S. Matsumoto, Y. Okubo, T. Suenobu, S. Fukuzumi, *Synlett* **1999**, 1130.

305. K. Mikami, S. Matsumoto, Y. Okubo, M. Fujitsuka, O. Ito, T. Suenobu, S. Fukuzumi, *J. Am. Chem. Soc.* **2000**, *122*, 2236.
306. N. Martin, L. Sánchez, B. Illescas, I. Pérez, *Chem. Rev.* **1998**, *98*, 2527.
307. D. M. Guldi, K.-D. Asmus, *J. Phys. Chem. A* **1997**, *101*, 1472.
308. H. Imahori, Y. Sakata, *Adv. Mater.* **1997**, *9*, 537.
309. H. Imahori, Y. Sakata, *Eur. J. Org. Chem.* **1999**, 2445.
310. D. M. Guldi, *Chem. Commun.* **2000**, 321.
311. D. M. Guldi, M. Maggini, N. Martin, M. Prato, *Carbon* **2000**, *38*, 1615.
312. F. Diederich, M. Gomez-Lopez, *Chem. Soc. Rev.* **1999**, *28*, 263.
313. M. R. Bryce, W. Devonport, L. M. Goldenberg, C. Wang, *Chem. Commun.* **1998**, 945.
314. N. Martin, L. Sanchez, M. A. Herranz, D. M. Guldi, *J. Phys. Chem. A* **2000**, *104*, 4648.
315. N. Martin, L. Sanchez, B. Illescas, S. Gonzalez, M. A. Herranz, D. M. Guldi, *Carbon* **2000**, *38*, 1577.
316. K. B. Simonsen, V. V. Konovalov, T. A. Konovalov, T. Kawai, M. P. Cava, L. D. Kispert, R. M. Metzger, J. Becher, *J. Chem. Soc. Perkin Trans. 2* **1999**, 657.
317. N. Martin, L. Sanchez, C. Seoane, R. Andreu, J. Garin, J. Orduna, *Tetrahedron Lett.* **1996**, *37*, 5979.
318. J. Llacay, J. Veciana, J. Vidal-Gancedo, J. L. Bourdelande, R. Gonzalez-Moreno, C. Rovira, *J. Org. Chem.* **1998**, *63*, 5201.
319. R. M. Williams, J. M. Zwier, J. W. Verhoeven, *J. Am. Chem. Soc.* **1995**, *117*, 4093.
320. K. George Thomas, V. Biju, M. V. George, D. M. Guldi, P. V. Kamat, *J. Phys. Chem. A* **1998**, *102*, 5341.
321. S.-G. Liu, L. Shu, J. Rivera, H. Liu, J.-M. Raimundo, J. Roncali, A. Gorgues, L. Echegoyen, *J. Org. Chem.* **1999**, *64*, 4884.
322. S. I. Khan, A. M. Oliver, M. N. Paddon-Row, Y. Rubin, *J. Am. Chem. Soc.* **1993**, *115*, 4919.
323. R. M. Williams, M. Koeberg, J. M. Lawson, Y.-Z. An, Y. Rubin, M. N. Paddon-Row, J. W. Verhoeven, *J. Org. Chem.* **1996**, *61*, 5055.
324. M. N. Paddon-Row, *Fullerene Science Technology* **1999**, *7*, 1151.
325. M. J. Shephard, M. N. Paddon-Row, *Aust. J. Chem.* **1996**, *49*, 395.
326. K. George Thomas, V. Biju, D. M. Guldi, P. V. Kamat, M. V. George, *J. Phys. Chem. A* **1999**, *103*, 10755.
327. K. George Thomas, V. Biju, M. V. George, D. M. Guldi, P. V. Kamat, *J. Phys. Chem. B* **1999**, *103*, 8864.
328. M. Iyoda, F. Sultana, S. Sasaki, M. Yoshida, *J. Chem. Soc. Chem. Commun.* **1994**, 1929.
329. M. Diekers, A. Hirsch, S. Pyo, J. Rivera, L. Echegoyen, *Eur. J. Org. Chem.* **1998**, 1111.
330. D. Gust, T. A. Moore, A. L. Moore, *Pure Appl. Chem.* **1998**, *70*, 2189.
331. A. L. Moore, T. A. Moore, D. Gust, J. J. Silber, L. Sereno, F. Fungo, L. Otero, G. Steinberg-Yfrach, P. A. Liddell, S. -C. Hung, H. Imahori, S. Cardoso, D. Tatman, A. N. Macpherson, *Pure Appl. Chem.* **1997**, *69*, 2111.
332. H. Imahori, S. Cardoso, D. Tatman, S. Lin, L. Noss, G. R. Seely, L. Sereno, J. C. de Silber, T. A. Moore, A. L. Moore, D. Gust, *Photochem. Photobiol.* **1995**, *62*, 1009.
333. D. Armspach, E. C. Constable, F. Diederich, C. E. Housecroft, J.-F. Nierengarten, *J. Chem. Soc. Chem. Commun.* **1996**, 2009.
334. D. Armspach, E. C. Constable, F. Diederich, C. E. Housecroft, J.-F. Nierengarten, *Chem. Eur. J.* **1998**, *4*, 723.
335. M. Maggini, A. Dono, G. Scorrano, M. Prato, *J. Chem. Soc. Chem. Commun.* **1995**, 845.
336. M. Maggini, D. M. Guldi, S. Mondini, G. Scorrano, F. Paolucci, P. Ceroni, S. Roffia, *Chem. Eur. J.* **1998**, *4*, 1992.
337. A. Polese, S. Mondini, A. Bianco, C. Toniolo, G. Scorrano, D. M. Guldi, M. Maggini, *J. Am. Chem. Soc.* **1999**, *121*, 3456.
338. A. Juris, V. Balzani, F. Barigelletti, S. Campagna, P. Belser, A. Zelewsky, *Coord. Chem. Rev.* **1988**, *84*, 85.
339. V. Balzani, A. Juris, M. Venturi, S. Campagna, S. Serroni, *Chem. Rev.* **1996**, *96*, 759.
340. M. Maggini, D. M. Guldi, S. Mondini, G. Scorrano, F. Paolucci, P. Ceroni, S. Roffia, unpublished results.
341. D. Gust, T. A. Moore, A. L. Moore, *Res. Chem. Intermed.* **1997**, *23*, 621.

342. H. Imahori, Y. Sakata, *Chem. Lett.* **1996**, 199.
343. J.-F. Nierengarten, C. Schall, J.-F. Nicoud, *Angew. Chem. Int. Ed.* **1998**, 37, 1934.
344. J. Helaja, A. Y. Tauber, Y. Abel, N. V. Tkachenko, H. Lemmetyinen, I. Kilpeläinen, P. H. Hynninen, *J. Chem. Soc. Perkin Trans. 1* **1999**, 2403.
345. H. Maruyama, M. Fujiwara, K. Tanaka, *Chem. Lett.* **1998**, 805.
346. K. Tashiro, T. Aida, J.-Y. Zheng, K. Kinbara, K. Saigo, S. Sakamoto, K. Yamaguchi, *J. Am. Chem. Soc.* **1999**, 121, 9477.
347. E. Dietel, A. Hirsch, J. Zhou, A. Rieker, *J. Chem. Soc. Perkin Trans. 2* **1998**, 1357.
348. J.-F. Nierengarten, L. Oswald, J.-F. Nicaud, *Chem. Commun.* **1998**, 1545.
349. M. Wedel, F.-P. Montforts, *Tetrahedron Lett.* **1999**, 40, 7071.
350. X. Camps, E. Dietel, A. Hirsch, S. Pyo, L. Echegoyen, S. Hackbarth, B. Röder, *Chem. Eur. J.* **1999**, 5, 2362.
351. S. Higashida, H. Imahori, T. Kaneda, Y. Sakata, *Chem. Lett.* **1998**, 605.
352. D. R. Evans, N. L. P. Fackler, X. Zuowei, C. E. F. Rickard, P. D. W. Boyd, C. A. Reed, *J. Am. Chem. Soc.* **1999**, 121, 8466.
353. H. Imahori, K. Hagiwara, T. Akiyama, S. Taniguchi, T. Okada, Y. Sakata, *Chem. Lett.* **1995**, 265.
354. H. Imahori, K. Hagiwara, T. Akiyama, M. Aoki, S. Taniguchi, T. Okada, M. Shirakawa, Y. Sakata, *Chem. Phys. Lett.* **1996**, 263, 545.
355. H. Imahori, K. Hagiwara, T. Akiyama, M. Aoki, S. Taniguchi, T. Okada, M. Shirakawa, Y. Sakata, *J. Am. Chem. Soc.* **1996**, 118, 11771.
356. Y. Sakata, H. Imahori, H. Tsue, S. Higashida, T. Akiyama, E. Yoshizawa, M. Aoki, K. Yamada, K. Hagiwara, S. Taniguchi, T. Okada, *Pure Appl. Chem.* **1997**, 69, 1951.
357. K. Yamada, H. Imahori, Y. Nishimura, I. Yamazaki, Y. Sakata, *Chem. Lett.* **1999**, 895.
358. H. Imahori, K. Tamaki, H. Yamada, K. Yamada, Y. Sakata, Y. 'Nishimura, I. Yamazaki, M. Fujitsuka, O. Ito, *Carbon*, **2000**, 1599.
359. N. V. Tkachenko, C. Guenther, H. Imahori, K. Tamaki, Y. Sakata, H. Lemmetyinen, S. Fukuzumi, *Chem. Phys. Lett.* **2000**, 326, 344.
360. P. A. Liddell, J. P. Sumida, A. N. MacPherson, L. Noss, G. R. Seely, K. N. Clark, A. L. Moore, T. A. Moore, D. Gust, *Photochem. Photobiol.* **1994**, 60, 537.
361. E. Dietel, A. Hirsch, E. Eichborn, A. Rieker, S. Hackbarth, B. Röder, *Chem. Commun.* **1998**, 1981.
362. D. M. Guldi, C. Luo, M. Prato, E. Dietel, A. Hirsch, *Chem. Commun.* **2000**, 373.
363. J.-P. Bourgeois, F. Diederich, L. Echegoyen, J.-F. Nierengarten, *Helv. Chim. Acta* **1998**, 81, 1835.
364. D. Kuciauskas, S. Lin, G. R. Seely, A. L. Moore, T. A. Moore, D. Gust, T. Drovetskaya, C. A. Reed, P. D. W. Boyd, *J. Phys. Chem.* **1996**, 100, 15926.
365. T. Drovetskaya, C. A. Reed, P. Boyd, *Tetrahedron Lett.* **1995**, 36, 7971.
366. T. D. M. Bell, T. A. Smith, K. P. Ghiggino, M. G. Ranasinghe, M. J. Shephard, M. N. Paddon-Row, *Chem. Phys. Lett.* **1997**, 268, 223.
367. I. G. Safonov, P. S. Baran, D. I. Schuster, *Tetrahedron Lett.* **1997**, 38, 8133.
368. P. S. Baran, R. R. Monaco, A. U. Khan, D. I. Schuster, S. R. Wilson, *J. Am. Chem. Soc.* **1997**, 119, 8363.
369. P. Cheng, S. Wilson, D. I. Schuster, *Chem. Commun.* **1999**, 89.
370. R. II Fong, D. I. Schuster, S. R. Wilson, *Organic Letters* **1999**, 1, 729.
371. D. I. Schuster, P. Cheng, S. R. Wilson, V. Prokhorenko, M. Katterle, A. R. Holzwarth, S. E. Braslavsky, G. Klihm, R. M. Williams, C. Luo, *J. Am. Chem. Soc.* **1999**, 121, 11599.
372. K. Tamaki, H. Imahori, Y. Nishimura, I. Yamazaki, A. Shimomura, T. Okada, Y. Sakata, *Chem. Lett.* **1999**, 227.
373. N. V. Tkachenko, L. Rantala, A. Y. Tauber, J. Helaja, P. H. Hynninen, H. Lemmetyinen, *J. Am. Chem. Soc.* **1999**, 121, 9378.
374. H. Imahori, S. Ozawa, K. Ushida, M. Takahashi, T. Azuma, A. Ajavakom, T. Akiyama, M. Hasegawa, S. Taniguchi, T. Okada, Y. Sakata, *Bull. Chem. Soc. Jpn.* **1999**, 72, 485.
375. T. Akiyama, H. Imahori, A. Ajavakom, Y. Sakata, *Chem. Lett.* **1996**, 907.
376. P. A. Liddell, D. Kuciauskas, J. P. Sumida, B. Nash, D. Nguyen, A. L. Moore, T. A. Moore, D. Gust, *J. Am. Chem. Soc.* **1997**, 119, 1400.

377. D. Carbonera, M. Di Valentin, C. Corvaja, G. Agostini, G. Giacometti, P. A. Liddell, D. Kuciauskas, A. L. Moore, T. A. Moore, D. J. Gust, *J. Am. Chem. Soc.* **1998**, *120*, 4398.
378. H. Imahori, K. Yamada, M. Hasegawa, S. Taniguchi, T. Okada, Y. Sakata, *Angew. Chem. Int. Ed. Engl.* **1997**, *36*, 2626.
379. H. Imahori, H. Yamada, S. Ozawa, K. Ushida, Y. Sakata, *Chem. Commun.* **1999**, 1165.
380. M. Fujitsuka, O. Ito, H. Imahori, K. Yamada, H. Yamada, Y. Sakata, *Chem. Lett.* **1999**, 721.
381. H. Imahori, H. Yamada, Y. Nishimura, I. Yamazaki, Y. Sakata, *J. Phys. Chem. B*, **2000**, *104*, 2099.
382. K. Tamaki, H. Imahori, Y. Nishimura, I. Yamazaki, Y. Sakata, *Chem. Commun.* **1999**, 625.
383. C. Luo, D. M. Guldi, H. Imahori, K. Tamaki, Y. Sakata, *J. Am. Chem. Soc.* **2000**, *122*, 6535.
384. N. Armaroli, F. Diederich, C. O. Dietrich-Buchecker, L. Flamigni, G. Marconi, J.-F. Nierengarten, J.-P. Sauvage, *Chem. Eur. J.* **1998**, *4*, 406.
385. D. Kuciauskas, P. A. Liddell, S. Lin, T. E. Johnson, S. J. Weghorn, J. S. Lindsey, A. L. Moore, T. A. Moore, D. Gust, *J. Am. Chem. Soc.* **1999**, *121*, 8604.
386. T. Da Ros, M. Prato, D. Guldi, E. Alessio, M. Ruzzi, L. Pasimeni, *Chem. Commun.* **1999**, 635.
387. N. Armaroli, F. Diederich, L. Echegoyen, T. Habicher, L. Flamigni, G. Marconi, J.-F. Nierengarten, *New J. Chem.* **1999**, *23*, 77.
388. F. D'Souza, G. R. Deviprasad, M. S. Rahman, J. P. Choi, *Inorg. Chem.* **1999**, *1999*, 2157.
389. T. Da Ros, M. Prato, D. M. Guldi, M. Ruzzi, L. Pasimeni, *Chem. Eur. J.* **2000**, *6*, in press.
390. P. Scheier, B. Düner, R. Wörgötter, S. Matt, D. Muigg, G. Senn, T. D. Märk, *Int. Rev. Phys. Chem.* **1996**, *15*, 93.
391. D. K. Böhme, *Can. J. Chem.* **1999**, *77*, 1453.
392. G. Javahery, S. Petrie, J. Wang, H. Wincel, D. K. Böhme, *J. Am. Chem. Soc.* **1993**, *115*, 9701.
393. G. Javahery, S. Petrie, H. Wincel, J. Wang, D. K. Böhme, *J. Am. Chem. Soc.* **1993**, *115*, 6295.
394. D. L. Lichtenburger, M. E. Rempe, S. B. Gogosha, *Chem. Phys. Lett.* **1992**, *198*, 454.
395. G. Javahery, S. Petrie, H. Wincel, J. Wang, D. K. Böhme, *J. Am. Chem. Soc.* **1993**, *115*, 5716.
396. V. Baranov, D. K. Böhme, *Int. J. Mass Spect. Ion Processes* **1997**, *165/166*, 249.
397. H. Becker, G. Javahery, S. Petrie, D. K. Böhme, *J. Phys. Chem.* **1994**, *98*, 5591.
398. S. Petrie, G. Javahery, J. Wang, D. K. Böhme, *J. Am. Chem. Soc.* **1992**, *114*, 6268.
399. S. Petrie, J. Javahery, J. Wang, D. K. Böhme, *J. Phys. Chem.* **1992**, *96*, 6162.
400. D. K. Böhme, *Int. Rev. Phys. Chem.* **1994**, *13*, 163.
401. V. A. Nadochenko, N. N. Denisov, I. V. Rubtsov, A. S. Lobach, A. P. Moravskii, *Chem. Phys. Lett.* **1993**, *208*, 431.
402. V. A. Nadochenko, I. V. Vasil'ev, N. N. Denisov, I. V. Rubtsov, A. S. Lobach, A. P. Moravskii, A. F. Shestakov, *J. Photochem. Photobiol., A* **1993**, *70*, 153.
403. V. A. Nadochenko, N. N. Denisov, I. V. Rubtsov, A. S. Lobach, A. P. Moravsky, *Russ. Chem. Bull.* **1993**, *42*, 1171.
404. V. A. Nadochenko, N. N. Denisov, A. S. Lobach, A. P. Moravskii, *Zh. Fiz. Khim.* **1994**, *68*, 228.
405. C. A. Steren, H. Van Willigen, *Proc. Indian Acad. Sci., Chem. Sci.* **1994**, *106*, 1671.
406. C. A. Steren, P. R. Levstein, H. van Willigen, H. Linschitz, L. Biczok, *Chem. Phys. Lett.* **1993**, *204*, 23.
407. S. Michaeli, V. Meiklyar, M. Schulz, K. Möbius, H. Levanon, *J. Phys. Chem.* **1994**, *98*, 7444.
408. P. V. Kamat, M. Gevaert, K. Vinodgopal, *J. Phys. Chem. B* **1997**, *101*, 4422.
409. M. Gevaert, P. V. Kamat, *J. Chem. Soc. Chem. Commun.* **1992**, 1470.
410. J. Eriksen, C. S. Foote, *J. Phys. Chem.* **1978**, *82*, 2659.
411. S. Fukuzumi, T. Tanaka in *Photoinduced Electron Transfer, Part C* (Eds.: M. A. Fox, M. Chanon), Elsevier, Amsterdam, **1988**, pp. 578.
412. S. Fukuzumi, S. Kuroda, T. Tanaka, *J. Chem. Soc. Chem. Commun.* **1986**, 1533.
413. S. Nonell, J. W. Arbogast, C. S. Foote, *J. Phys. Chem.* **1992**, *96*, 4169.
414. S. Fukuzumi in *Advances in Electron-transfer chemistry, Vol. 2* (Ed.: P. S. Mariano), JAI Press, Greenwich, **1992**, pp. 67–175.
415. M. Fujita, S. Fukuzumi, *J. Chem. Soc. Perkin Trans. 2* **1993**, 1915.
416. M. Fujita, A. Ishida, S. Takamuku, S. Fukuzumi, *J. Am. Chem. Soc.* **1996**, *118*, 8566.

- 417. S. Fukuzumi, T. Kitano, T. Tanaka, *Chem. Lett.* **1989**, 1231.
- 418. G. Lem, D. I. Schuster, H. Courtney, Q. Lu, S. R. Wilson, *J. Am. Chem. Soc.* **1995**, *117*, 554.
- 419. C. Siedschlag, H. Luftmann, C. Wolff, J. Mattay, *Tetrahedron* **1997**, *53*, 3587.
- 420. C. Siedschlag, H. Luftmann, C. Wolff, J. Mattay, *Tetrahedron* **1999**, *55*, 7805.
- 421. A. J. Maroulis, D. R. Arnold, *Synthesis* **1979**, 819.
- 422. D. R. Arnold, X. Du, J. Chen, *Can. J. Chem.* **1995**, *73*, 307.
- 423. F. G. Bordwell, J.-P. Cheng, M. J. Bausch, J. E. Bases, *J. Phys. Org. Chem.* **1988**, *1*, 209.

6 Electron-transfer Reactions of Heteroaromatic Compounds

Angelo Albini and Maurizio Fagnoni

6.1 Introduction

Most practitioners of heterocyclic chemistry will concur with the statement by Newkome and Paudler that “the chemistry of heterocyclic compounds encompasses most, if not all, of the general reactions of organic chemistry. The presence of heteroatoms merely endows the heterocyclic systems with some *additional*, theoretical predictable properties” [1]. Thus we have here the whole body of organic chemistry, plus something peculiar to this (very large) class of compounds.

Indeed this is true also for the class of reactions treated in this book, viz. electron-transfer reactions, which also with these compounds already have an important role and are expected to have a much larger one in the near future. The number of chemical reactions more or less unambiguously characterized as electron-transfer processes in heteroaromatic chemistry in the current literature is so large that an exhaustive presentation is far beyond the space allotted for this contribution. This is, therefore, limited to discussion of the most characteristic chemical paths—or at least those which seem to answer this requirement in the opinion of these authors—with a choice of appropriate examples.

Because it is felt that particular attention should be given to the electron-transfer step, after a brief discussion of the structure of the radical ions of heteroaromatic molecules, the reactions are discussed in two sections, the first concerning the reactions in which the heterocycle is the donor, the latter reactions in which it is the acceptor. When both donor and acceptor are heterocycles, the reaction is presented in the most appropriate section.

The discussion is limited to the reactions of heteroaromatic molecules, non-aromatic heterocycles are discussed elsewhere in this book in accordance with the appropriate heteroatom-containing functionality. The most important electron-transfer phenomena involving heteroaromatics are to be found on the one hand in biochemistry, where some heterocycles have a key role in metabolism, and on the other in material science, the applications of conductive polymers derived from

heterocycles. Neither of these topics is discussed in this chapter, which is rather concerned with typical 'organic' reactions. Furthermore, many electrochemical reaction involving a two (or $2n$)-electron oxidation or reduction of heterocycles are skipped or barely mentioned (while being exhaustively discussed in electrochemistry textbooks and in some reviews quoted in this text) and the attention is concentrated on processes where the key chemical step occurs after single-electron transfer and involves odd-electron species.

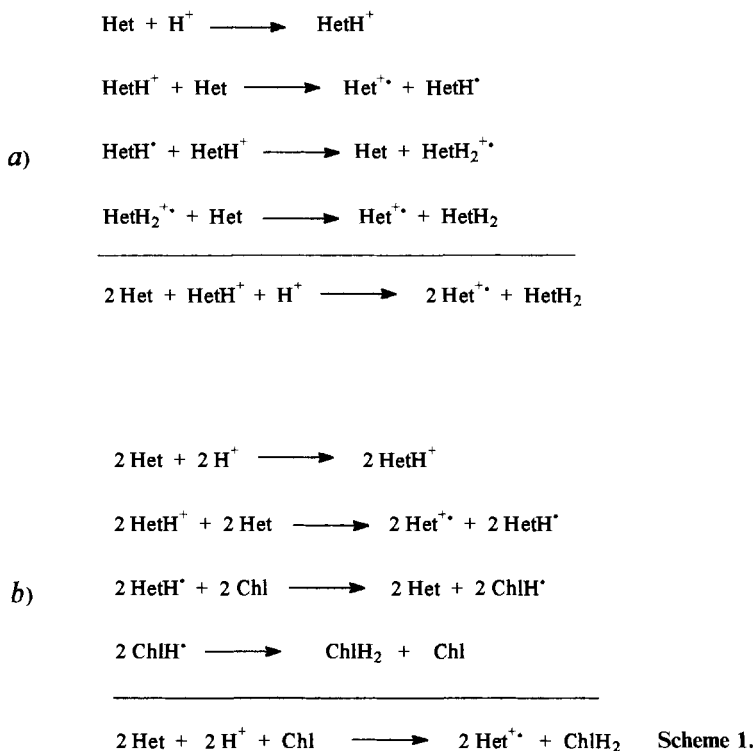
6.2 Structure of the Radical Ions of Heteroaromatic Compounds

The generation and structure of heterocyclic radical ions has been discussed previously [2] and needs not be addressed at length in this context, because the main concern here is with reactivity. A few examples of the main structural differences are, however, reported in this section to facilitate subsequent discussion of chemical reactions.

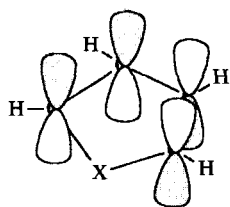
6.2.1 Radical Cations

Ionization potentials have been measured for all reasonably simple heterocycles by photoelectron spectroscopy, and the bands have been assigned by comparison with calculated molecular orbital energies. Photoelectron angular distribution studies gave further support for the assignment. A more detailed description of the structure can be obtained by EPR spectroscopy of the relaxed radical cation in matrices or fluid solutions. Many heterocycles are good donors, and radical cations are often formed by mere dissolution in a Brønsted acid (e.g. standing of alkylthiophenes in hexafluoropropanol–3 % methanesulfonic acid leads to the development of the EPR spectra of the corresponding radical cations) [3]. The process occurring is illustrated in Scheme 1a. Quantitative conversion can be obtained in the presence of an oxidant, e.g. by dissolving the heterocycle in methanesulfonic acid in the presence of chloranil, according to Scheme 1b [4]. Convenient methods for the characterization of radical cations are ^{60}Co γ irradiation (in matrix) or, in solution, UV irradiation in acids (trifluoroacetic acid, sulfuric acid) or protic media (e.g. hexafluoropropan-2-ol, HFP), if appropriate in the presence of Hg(II) or Tl(III) salts [5] or thermal oxidation by thallium(III) or mercury trifluoroacetates or nitrosonium tetrafluoroborate [6, 7] or by strong organic oxidants such as 2,3-dichloro-4,5-dicyanobenzoquinone (DDQ) in trifluoroacetic acid or in HFP [8, 9].

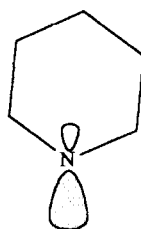
As expected from simple MO considerations, the radical cations of five-membered heterocycles, e.g. the blue species formed from furan, pyrrole, thiophene, and their alkyl derivatives, are π ions. The semi-occupied orbital is the π orbital with the heteroatom in the nodal plane (a_1), see Scheme 2, structure 1. In radical cations of α,ω -bis-(1-pyrrolyl) alkanes the charge remains localized on a single ring, rather than being delocalized over both units [5, 10, 11].



Interestingly, it has been observed that the ionization potentials (determined by the electron-impact technique) of several substituted five-membered heterocycles correlate with the σ_p^+ constants. The slopes obtained give a value of $\rho = -20.2$ for furan, -18.2 for pyrrole, -16.5 for thiophene, and a value close to the last for selenophene. Thus, the sensitivity of ionization to substituent effects is larger than for benzene ($\rho = -14.7$) and larger than that measured for the most sensitive electrophilic substitution (bromination in acetic acid, which gives $\rho = -10.0$ for thiophene). As pointed out by Linda et al. [12], the sensitivity to substituent effects



1



2

Scheme 2.

varies in the reverse order to that of the ground state aromaticity of the heterocycles.

With azines the situation is varied. In the radical cations of pyridine and diazines the semi-occupied orbital is largely confined to the n_N orbital(s) (see Scheme 2, structure **2**), while the radical cation is of the π type with monoazanaphthalenes, -phenanthrenes and -anthracenes. The situation might change with substitution. As an example, alkylpyridine radical cations are of the n type, like the parent compound, whereas for the 2,5-dimethyl, 2-chloro, and 2-bromo derivatives the structure is of the π type [13]. Likewise, with benzo[*c*]cinnoline the parent compound and its alkyl derivatives give an n radical cation, but with some dimethoxy derivatives a π structure is found [14] and a switch from n to π structure occurs also in passing from 1,2,4,5-tetrazine to its 3,6-diamino derivatives [15].

Illustrative examples of the ionization potential of heteroaromatics and of the structure of the corresponding radical cations are reported in Table 1 [5, 16–24].

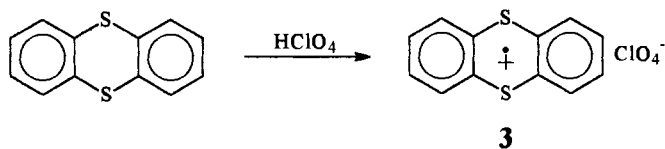
6.2.2 Radical Anions

The radical anions have been likewise characterized by methods ranging from the various electrochemical techniques supplemented by EPR/ENDOR measurements to electron transmission spectroscopy. Radical anions can be conveniently generated in a matrix by ^{60}Co γ irradiation, e.g. in CD_3OD , or in the liquid phase by potassium metal reduction in solvents such as hexamethylphosphoric triamide or dimethoxyethane. These ions have the π^* structure expected from calculations [14, 15, 25, 26].

Table 1. Ionization potential and structure of the radical cations of some representative heteroaromatic compounds.

Compound	Ionization potential, eV ^a	Structure	Other methods of generation
Furan	8.77 [16]	π	γ irradiation [17]; UV irradiation in $\text{CF}_3\text{CO}_2\text{H}$ [5]
Pyrrole	8.90 [18]	π	γ irradiation [17]; irradiation in $\text{CF}_3\text{CO}_2\text{H}/\text{Hg}(\text{CF}_3\text{CO}_2)$ [5]
Thiophene	8.91 [19]	π	γ irradiation [17]; irradiation in H_2SO_4 [5]
Oxazole	9.83 [20]	π	
Isoxazole	10.15 [21]	π	
Indole	8.20 [22]	π	
Pyridine	9.23 [19]	n	γ irradiation [13]
Pyridazine	9.31 [23]	n	γ irradiation [24]
Pyrimidine	9.73 [23]	n	γ irradiation [24]
Pyrazine	9.63 [23]	n	γ irradiation [24]
Quinoline	8.62 [25]	π	γ irradiation [24]
Isoquinoline	8.50 [25]	π	γ irradiation [24]

^a Measured by photoelectron spectroscopy.



Scheme 3.

Comparison of the π^* electron affinities of pyridine, phospho-, arsa-, and stilba-benzenes showed that these quantities, and the ionization potentials, are correlated both with heteroatom electronegativities and with the lengths of the C–X bonds, in keeping with the expectation that lengthening of the bond destabilizes the b_1 (π) orbital and stabilizes the b_1 (π^*) orbital [27].

6.2.3 Stable Radical Ions

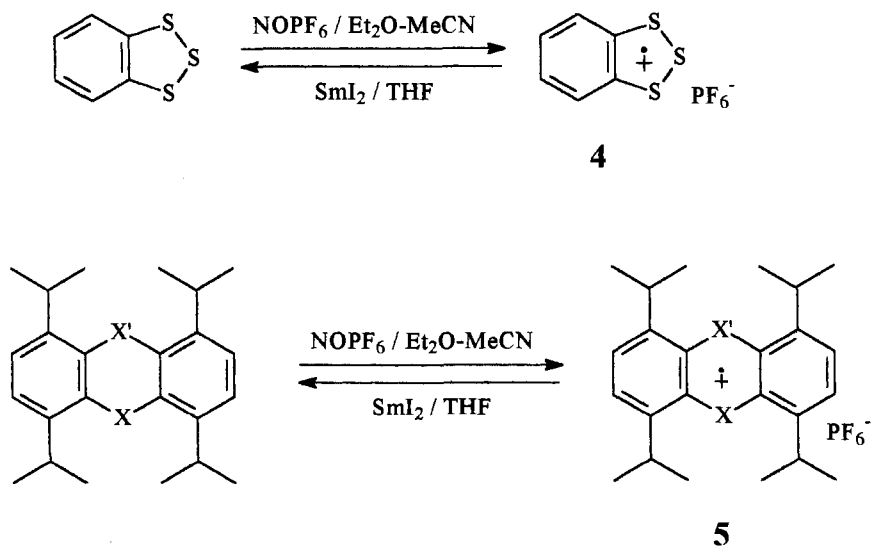
Finally, one should mention that several heteroaromatic radical cations have been prepared as stable, crystalline salts with weakly nucleophilic anions. Some of these count among the earliest known examples—for example the dark red phenothiazine radical cation tribromide obtained, and correctly identified, at the beginning of the 20th century [28]. The electrochemical or chemical preparation of the radical cations of related heterocycles such as phenoxathiin, thianthrene [7], and selenium analogs [29] have afforded many well-characterized examples (*caution*: preparation of these salts might be not free from hazard: the explosion of a dry sample of thianthrenium radical cation perchlorate (**3**, Scheme 3), apparently caused by friction, has been reported) [30]. Other chalcogen heterocycles also give stable derivatives, such as the purple or blue hexafluorophosphates of the radical cations of some benzotrithiols, **4** (see Scheme 4) [31], benzotriselenols [32], and phenanthrotrithiol [33]. Both with these compounds and with six-membered heterocycles (**5**), the one-electron redox process can be performed either electrochemically, with close to 100 % efficiency, or equally well by chemical means, oxidizing with nitrosonium hexafluorophosphate and reducing by means of samarium iodide.

Examples of stable salts of heteroaromatic radical anions isolated as crystalline compounds are the lithium, sodium, and potassium salts of 2,4,6-triphenylpyridine (**6**, Scheme 5) [34].

6.3 Chemical Reactions via Electron Transfer—The Heteroaromatic Compound is the Donor

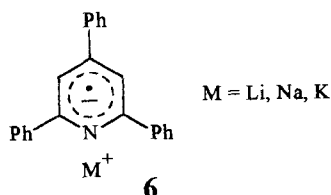
6.3.1 General Scheme

Radical cations are produced under a variety of conditions, from gas-phase to rigid matrix or to solution, and obviously their chemical behavior varies accordingly. The main preparative interest is centered on the solution phase, although the reac-



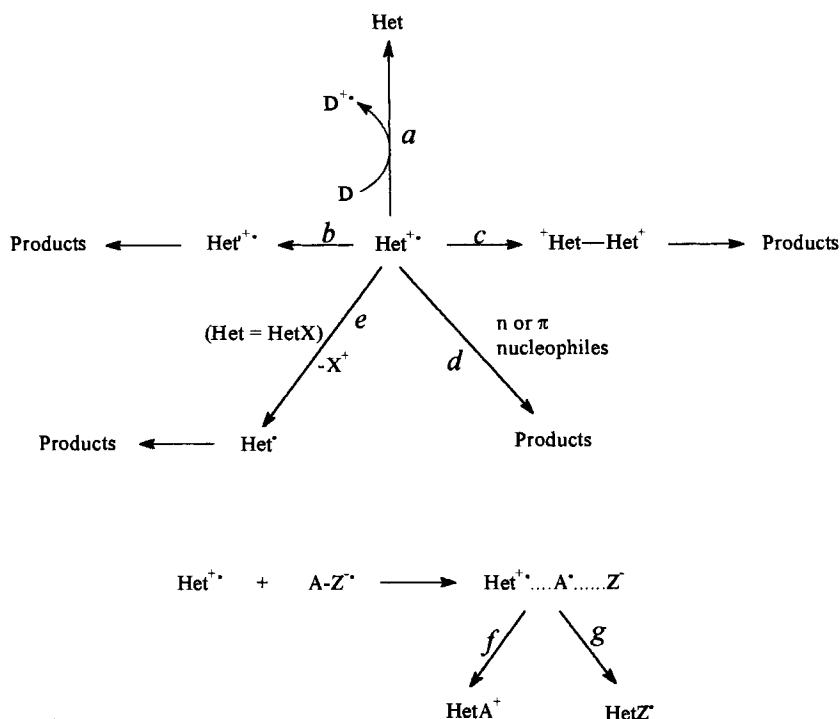
5a $X = X' = \text{S}$, **5b** $X = X' = \text{Se}$

Scheme 4.



Scheme 5.

tivity of the radical cations also depends on the mode of generation and on the medium characteristics. One-electron oxidation occurs either at the anode, or chemically by reaction with a variety of species, including Ti^{III} , Hg^{II} , PhI^{III} , NOBF_4 , persistent organic radical cations such as amminium cations or hydroquinone radical cations, or by the action of acids or light. The general pattern of reactivity of radical cations is discussed elsewhere in this book, and certainly includes useful processes. Quite appealing are electron transfer catalytic processes, although, particularly with (hetero)aromatic substrates, it is not trivial to distinguish reactions involving radical cations as the key species from processes where a diamagnetic proton adduct is involved, i.e. 'traditional' acid catalysis. As recently pointed out by Kochi, apart from not being readily identified, paramagnetic radical cations and diamagnetic cations are at any rate expected to have a similar chemistry, and the two classes of reaction might not be completely clearly differentiated. It also true that non-acidic media in which radical cations have longer lifetimes are now avail-



Scheme 6.

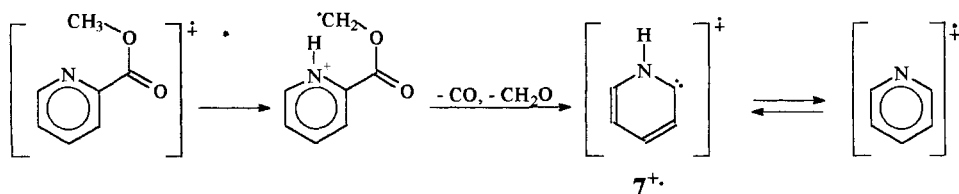
able, and this enables deeper investigation of such species and their involvement in chemical reactions [35, 36].

The main mechanistic paths for heteroaromatic radical cations are shown in Scheme 6. Besides electron transfer regenerating the starting material and rearrangement (paths *a* and *b*), these involve radical reactions, such as coupling (path *c*), cationic reactions, viz. reaction with a nucleophile (path *d*), and cleavage of an electrofugal group giving a heteroaryl radical (path *e*). An important group of reactions involves fragmentation of the radical anion concomitantly formed in the initial electron-transfer (ET) step, followed by recombination of the heteroaryl radical cation either with the radical or with the anion fragment (paths *f* and *g*, see Scheme 6, bottom).

These mechanistic alternatives are recognized in the reactions discussed below, which are, however, grouped according to overall chemical transformation occurring rather than to the specific mechanism involved.

6.3.2 Electron and Proton Transfer

An important aspect of rationalization of the reaction between the radical cations of aromatics and nucleophiles (see below) is the possibility of an electron-transfer



Scheme 7.

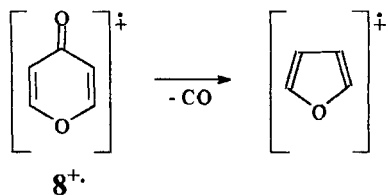
step. As an example the role of an ET step in the interaction between dibenzodioxin and thianthrene radical cation with aromatic donors such as anisole and anthracene has been evaluated through kinetic studies [37].

A related question is proton transfer, where two aspects are relevant, viz. proton transfer from a heterocyclic radical cation after an ET step (e.g. after photoinduced ET from indole to anthracenes or pyrene) [38] and the possible role of ET in proton transfer from aromatic radical cations and heterocyclic nucleophiles, in particular to pyridine derivatives [37b, 39].

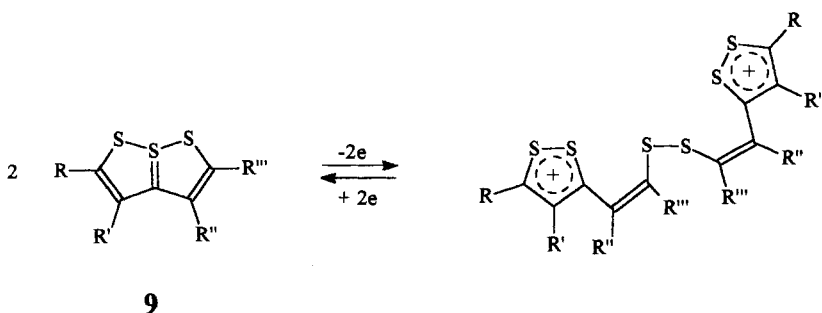
6.3.3 Ring Opening and Rearrangement

The form of the potential hypersurface for a molecular species changes drastically upon ionization. As an example, whereas azacyclohexatriene-2-ylidene **7** is largely destabilized (by ca 50 kcal mol⁻¹) relative to isomeric pyridine, it has been calculated that the difference is reduced to a few kcal mol⁻¹ for the corresponding radical cation **7**^{•+} (see Scheme 7) [40]. Isomerization of the ions is prohibited by an energy barrier, evaluated at 40–60 kcal mol⁻¹, which is lower, however, than the dissociation threshold, so interconversion does occur under mass spectrometric conditions. The effect of aromaticity even at the radical cation stage can, on the other hand, be evaluated because the furan radical cation is the main fragment formed (along with a minor amount of vinylketene) from the decarbonylation of the 2- and 4-pyrone radical cation (**8**^{•+}, see Scheme 8) [41].

Fragmentation of 2,3-diazabicyclo[2.2.1]hept-2-enes via photoinduced electron transfer offers a convenient route to cyclopentane-1,3-diyl radical cations, in turn undergoing interesting and selective rearrangements [42].



Scheme 8.



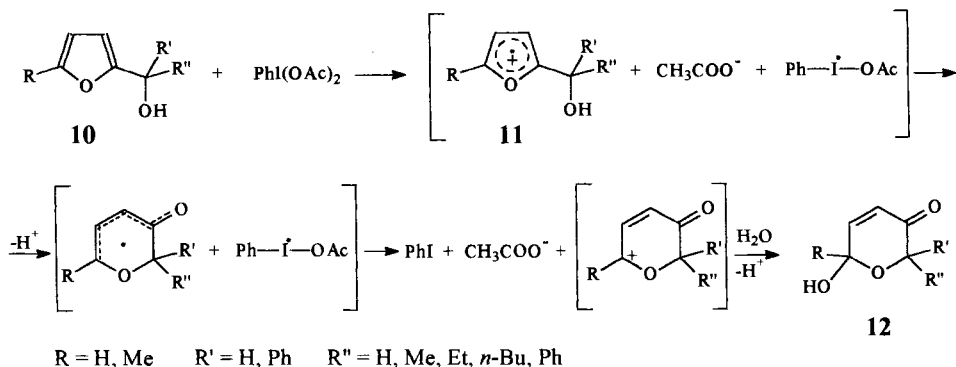
Scheme 9.

Ring-opening then dimerization to give bis (dithiolyum) di-cations linked by a disulfide bond occurs upon anodic oxidation of some 1,6,6aλ⁴-trithiapentalenes (**9**) and the starting material can be regenerated upon reduction (see Scheme 9) [43].

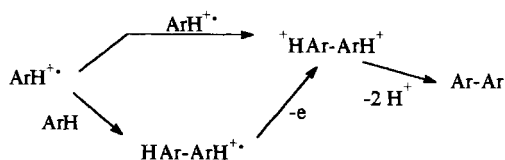
A single electron transfer- (SET) induced ring enlargement has been found in the conversion of substituted 2-furylmethanols (**10**) into 6-hydroxytetrahydropyran-3-ones (**12**) by the action of the binary reagent $\text{PhI}(\text{OAc})_2\text{-Mg}(\text{ClO}_4)_2$; it has been suggested that the reaction occurs via a furan radical cation (**11**) as illustrated in Scheme 10 [44].

6.3.4 Coupling, Dimerization, and Polymerization

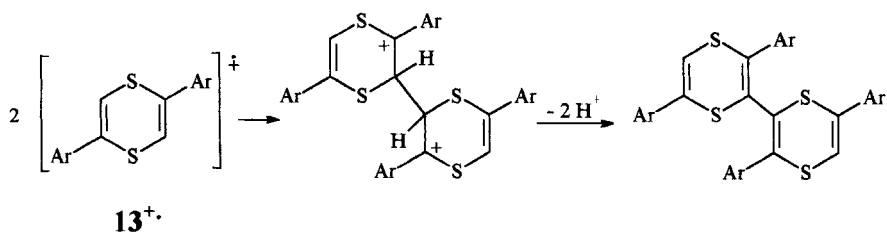
As mentioned in Section 6.3.1, the radical cations of many heteroaromatics have been formed anodically, thermally, or photochemically. With electron-rich heterocycles, one-electron oxidation is often followed by dimerization, either via coupling of two radical cations or via radical cation–substrate reaction, which in turn is most often followed by a second electron-transfer step leading to the same non-radical dication formed by the previous mechanism (see Scheme 11). The course of the reac-



Scheme 10.



Scheme 11.

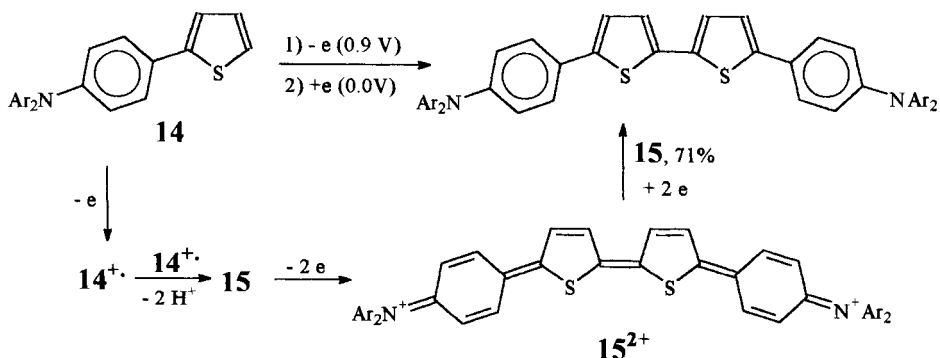


Scheme 12.

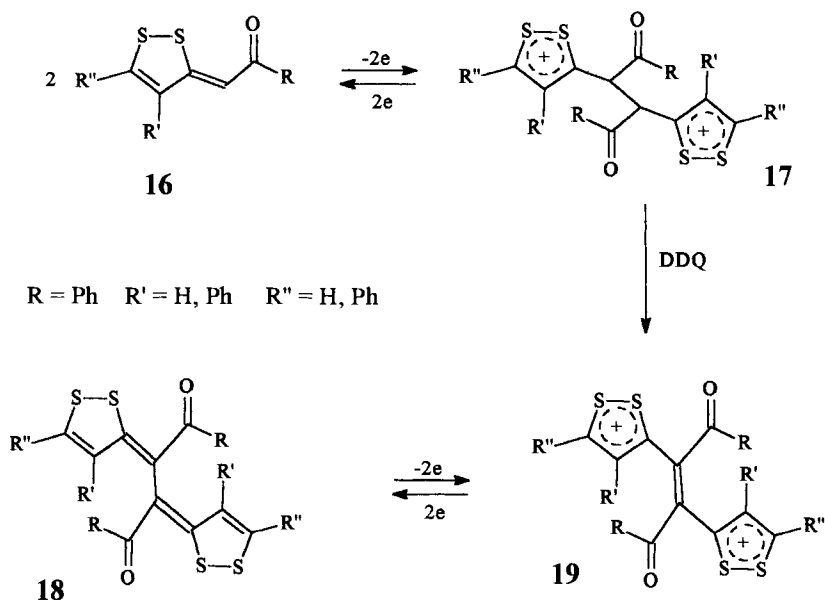
tion then depends on the paths enabling proton transfer. The mechanism of anodic dimerization has long been a subject of extensive investigation [45].

A typical example in heteroaromatic chemistry is the preparative electrolysis of some 2,5-diaryl-1,4-dithiins **13**, which give two well resolved quasi-reversible one-electron transfer waves to the radical cation and the di-cation, respectively, in cyclic voltammetry. The electrolysis gives low yields of the 2,2' dimers (see Scheme 12) via the radical cation coupling mechanism [46].

The 2-(4'-aminophenyl)thiophene **14** is converted in 71 % yield to dimer **15** by preparative electrolysis. The process is effected by oxidation at 0.9 V (1.5 F mol⁻¹), involving formation of the radical cation of the substrate (**14⁺**) dimerization, deprotonation, and further oxidation of dimer **15** (occurring at a potential lower than the applied potential), followed by controlled cathodic reduction at 0.0 V of the resulting di-cation (0.5 F mol⁻¹, see Scheme 13) [47].



Scheme 13.

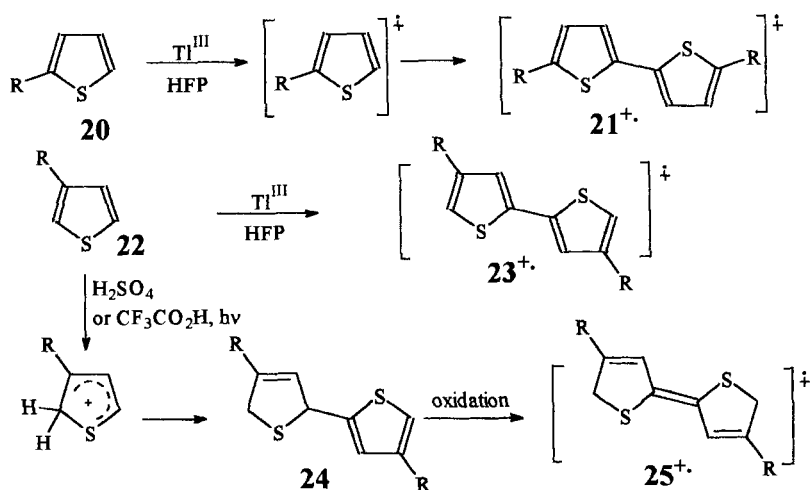


Scheme 14.

Coupling can also occur via a substituent, as for 1,2-dithiol-3-thiones, which are anodically oxidized to bis(dithiolylium)disulfides [48]. The related α -(1',2'-dithiol-3'-ylidene)acetophenones **16** are analogously oxidized to a di-cation (**17**) that deprotonates to give the uncharged dimer **18**. When, however, the electrolysis was conducted in the presence of an oxidant such as DDQ, or by further oxidizing dimer **18**, a new di-cation (**19**) was formed (Scheme 14) [49].

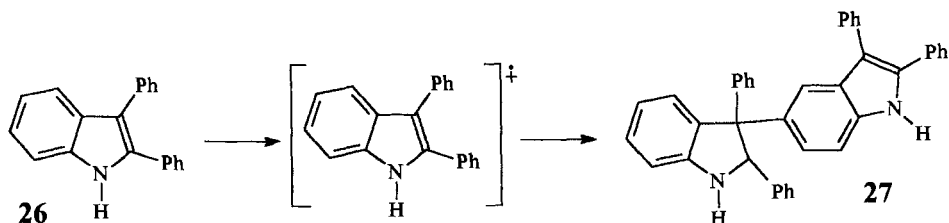
Most chemical or photochemical oxidations were initially conducted under acidic conditions, but use of other non-nucleophilic protic solvents such as HFP enables the oxidation to be performed under neutral conditions. The result of coupling reactions depends on conditions. As an example, oxidation of 2-alkylthiophenes (**20**) by thallium tris(trifluoroacetate) leads to the corresponding 5,5'-dialkyl-2,2'-bithiophene radical cations (**21**⁺), which are quite persistent species (hours) [3]. Unsubstituted thiophene and 3-alkyl derivatives (**22**) react in the same way, although the dimeric radical cations (**23**⁺), are short-lived (see Scheme 15). This is in line with expectation, because these radical cations have a free α position and fast follow-up reactions can occur, leading to oligomers or to polymers. In fact, in reactions starting from authentic 4,4'-dialkyl-2,2'-thiophene EPR spectra attributed to a tetrathiophene were observed. Under acidic conditions, however, different radical cations are obtained. Structure **25**⁺ has been attributed to these species and these have been suggested to arise from oxidation of the thiophene dimer **24** formed under acid catalysis (see Scheme 15) [3]. The final product from oxidation is a dark powder with considerable electrical conductivity and semiconductivity when doped with iodine [50]. EPR evidence suggests that 2,5-dialkylthiophenes give 3,3'-bithiophenes (mixture of *cis* and *trans* isomers).

With the radical cations of benzoannulated heterocycles, various paths are



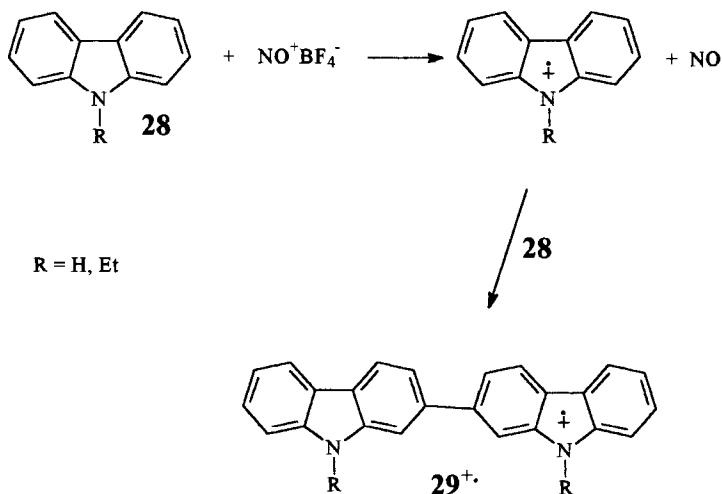
R = Me, Et, *i*-Pr, *t*-Bu

Scheme 15.

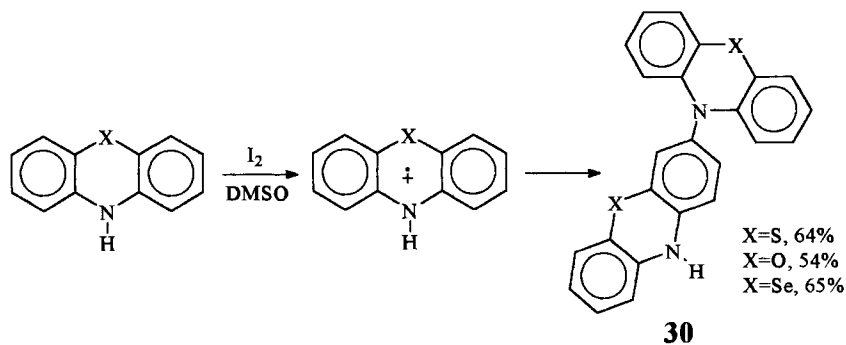


Scheme 16.

followed and C–C coupling is occasionally observed. As an example, it has been reported that a 5-[3'-(2',3'-dihydroindolyl)]indole (**27**) is formed from 2,3-diphenylindole (**26**) [51]. 3,3'-Dimers (**29**) are efficiently formed as the corresponding radical cation tetrafluoroborates by treatment of carbazole and *N*-ethylcarbazole (**28**) with nitrosonium tetrafluoroborate (97–98 %; Scheme 17) [52]; electrochemically, the *N,N'* dimer seems to be formed initially, but the 3,3' isomer is finally obtained [53]. Likewise, it has been suggested that dibenzothiophene gives the 2,2' dimer [54], but the heterocycle often functions as a heteroatom-centered nucleophile. As an example, phenothiazine, phenoxazine, and phenoselenine all give the 3,10' dimers (**30**) as the main products on oxidation by I_2 in dimethyl sulfoxide. The intermediate radical cation has been characterized; it reacts with the substrate which behaves as an *N* nucleophile (Scheme 18) [55]. Similar reactions have been performed on the same substrates under different oxidizing conditions [56]. With 1,2-dihydro-2,2-dialkyl-3-oxo-3*H*-indoles (indoxyl), a class of derivatives the radical



Scheme 17.



Scheme 18.

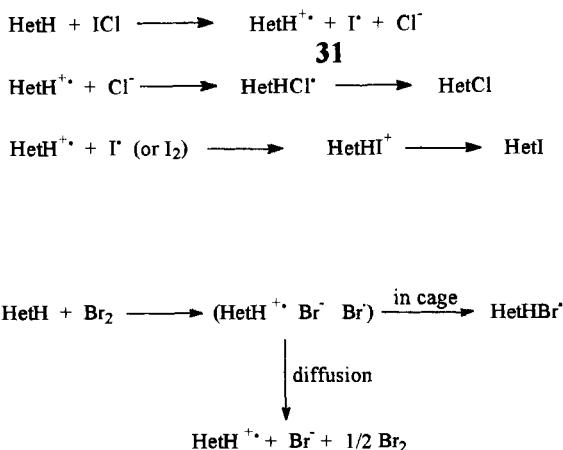
cations of which have been thoroughly characterized, C–C, C–N, and N–N bond formation have been all observed [57].

Finally, one should at least mention the all important heterocycle-based conducting materials, which are most often obtained by oxidative polymerization, e.g. of pyrrole [58].

6.3.5 Functionalization of the Ring

Halogenation

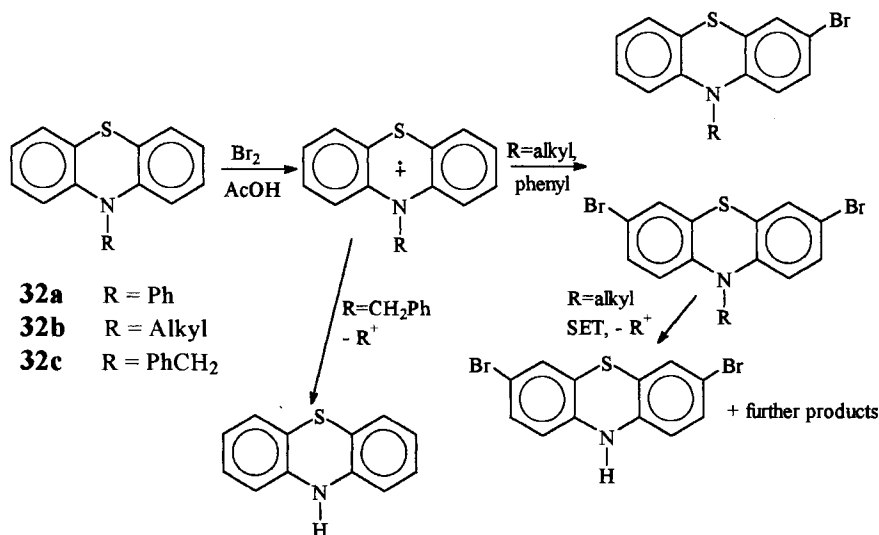
The possibility that some electrophilic aromatic substitutions occur via a SET mechanism has long been debated in the recent literature, as reported in more detail elsewhere in this book.



Scheme 19.

The halogenation of electron-rich heteroaromatics, as an example, can proceed either via the normal addition–elimination mechanism via a cation or via a SET mechanism, because the halogen, or a mixed halogen, e.g. ICl, can act as an oxidant, and the radical cation then add the halide anion. Indeed, in HFP heteroaromatics with E° ($\text{Het}^{+\bullet}/\text{Het}$) < 1.5 V relative to Ag/AgCl, e.g. thianthrene ($E^\circ = 1.32$ V), are oxidized by ICl, and the radical cation can be expediently characterized by EPR. The same holds for chlorine, bromine, and iodine with heterocycles with E° ($\text{Het}^{+\bullet}/\text{Het}$) < 1.0, 1.4, and 1.1 V, respectively, as observed for *N*-methylbenzothiazine ($E^\circ = 0.73$ V). Under these conditions, electron transfer is followed by fragmentation of the reduced acceptor to give a triad (e.g. **31**). The final course of the substitution reaction depends on the structure, involving, e.g., ionic or radical coupling within the triad (Scheme 19), and on conditions, which affect the competition between coupling within the triad or diffusion out of cage and subsequent coupling of the free solvated species (Scheme 19, bottom) [59].

Bromination of 10-phenylphenothiazine (**32a**; Scheme 20) and 10-phenylphenoxazine with bromine in acetic acid gives the corresponding 3-bromo and 3,7-dibromo derivatives via the radical cation, whereas the use of a milder reagent such as pyridinium bromide perbromide gives predominantly the 4'-bromo derivative via electrophilic substitution [60]. The preformed phenothiazine radical cation indeed adds bromide (and the nitrite and thiocyanate anions) to give the corresponding 3-substituted derivatives [56]. With 10-alkylphenothiazines (**32b**) the brominated derivatives are further oxidized to the radical cations and these undergo dealkylation. In the limiting case, 10-benzylphenothiazine (**32c**) is debenzylated, rather than brominated, apparently because of the combined effect of retardation of ring-bromination by the bulky substituent and easy detachment of the good electrofugal group (Scheme 20) [61]. The kinetic role of the radical cations of thianthrene, phenoxathiin, and phenothiazine derivatives has been investigated in detail and reviewed [7]. It should also be considered that the heterocycle itself can act as a nucleophile, leading to dimers, as mentioned in Section 6.3.4 The view has been



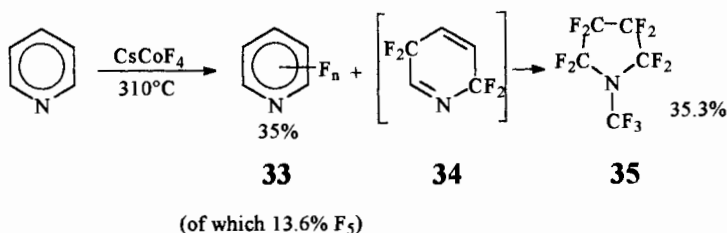
Scheme 20.

expressed that, particularly with *N*-heterocycles, the localization of the charge on the nitrogen atom makes reaction with nucleophiles slower than for the radical cations arising from the carbocyclic analogs, thus making coupling more important; this is certainly true with indoxyl (for example) [62].

Iodination of thiophene occurs quite cleanly (92 % of the 2-substituted, 2 % of the 2,5-disubstituted derivatives) in the presence of nitrosonium tetrafluoroborate [63]. The oxidative fluorination of heterocycles is of some interest, because of the limited accessibility of such compounds, despite the fact that mixtures are usually obtained. Anodic oxidation in a mixture of triethylamine and hydrogen fluoride, for example, leads to unstable dihydrodifluoro derivatives from furan and benzofuran. If, however, 1,10-phenanthrolines are used the dihydrodifluoro adducts can be conveniently dehydrofluorinated by bases; repeating the oxidation–rearomatization sequence eventually furnishes 5,6-dihydro-5,5,6,6-tetrafluoro-1,10-phenanthroline in 34 % yield. High-valence metal fluorides can also be used. As an example, fluorination of pyridine by cesium cobalt(III) fluoride leads to polyfluoropyridines (**33**) and a perfluoropiperidine (**35**) arising via 2,5-dihydro-2,2,5,5-tetrafluoropyridine (**34**; Scheme 21). Similar results are obtained with benzofuran [64].

Nitration

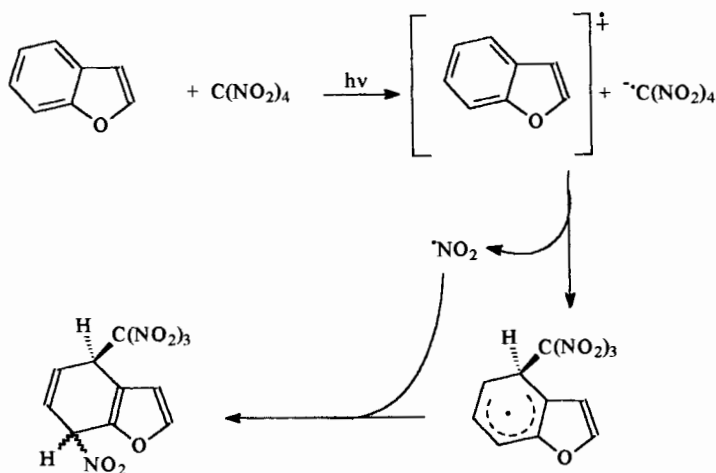
The intervention of a SET path in (hetero)aromatic nitration has been the subject of an extended debate [65]. The evidence is usually based either on the detection of intermediates or on the regioselectivity of the attack in relation to the spin and charge density on the radical cation. Limiting the attention to heteroaromatic substrates, it should be noted that the radical cations were detected spectroscopically [66] or even isolated as a salt [67] during nitration of, e.g., phenothiazine, phenox-



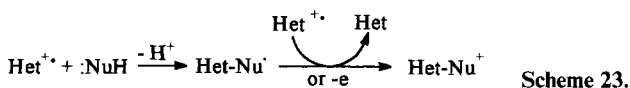
Scheme 21.

azine, or dibenzo-1,4-dioxin with HNO₃. With the last substrate, and use of 0.3–0.5 mol of the acid, the blue radical cation is the final product in 90 % yield whereas the use of 2 mol leads to isomeric dinitrodibenzodioxins [68]. With *N*-methylphenoxazine the use of a milder reagent such as tetranitromethane enables monitoring of the conversion of the initially formed radical cation into the nitro derivative [69].

When thermal reaction with tetranitromethane is too slow, photochemical excitation in the CT band induces the SET step and dihydroaromatics arising from the addition of the nitro and the trinitromethyl groups are formed (although the final products can result from further transformations). The first step here is attack of the trinitromethanide ion on the aromatic radical cation and the regioselectivity is in keeping with theoretical predictions, e.g. with predominant attack of the trinitromethide ion on positions 1 and 3 in dibenzofuran [70]. The regiochemistry of the reactions of benzofuran (Scheme 22) [71] and dibenzothiophene [72] has been similarly rationalized. Another method for SET nitration is the reaction of preformed, or in-situ formed, radical cations with NO₂. In this reaction the regiochemistry is



Scheme 22.

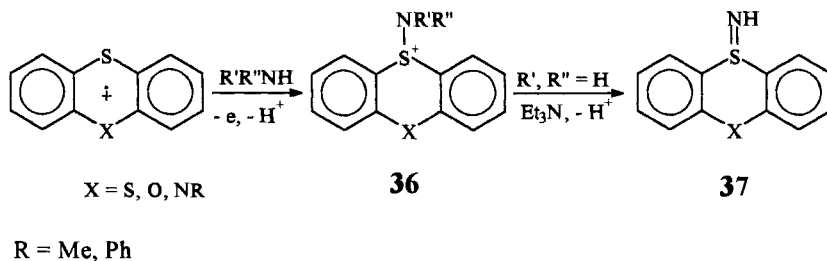


controlled by the spin density distribution in the radical cation, because this is a coupling between two radicals, as indeed has been shown for some compounds (e.g. benzofuran [71] and phenothiazine, where the main product is, however, the *S*-oxide [73]).

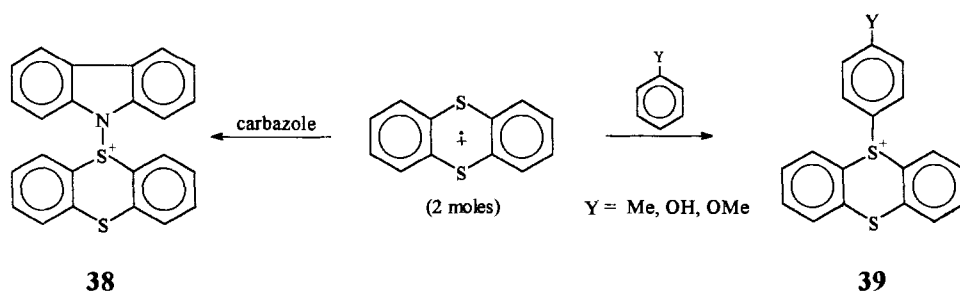
Reaction with heteroatom- or carbon-centered nucleophiles

A variety of functional groups has been obtained by reaction of radical cations with neutral nucleophiles. The initial reaction produces a radical more easily oxidized than the substrate from which the radical cation arises. A further oxidation then intervenes leading to the final cationic product (Scheme 23). When the reaction is performed electrochemically, a further ET occurs at the anode, whereas in homogenous solution the oxidant is usually a second equivalent of cation radical that is reduced to the starting substrate. The stoichiometry of the reaction thus generally requires 2 mol of the radical cation, although the mechanism might actually be different from the oversimplified delineation of the scheme and involve further intermediates, e.g. di-cations.

Many reactions involving formation of a sulfur heteroatom or a sulfur-carbon bond have been developed with the radical cations of thianthrene and analogs. As an example, anodic oxidation of phenoxathiin [74] or of thianthrene in wet acetonitrile or reaction with water of the preformed thianthrene radical cation [30, 75, 76] lead to formation of the corresponding *S*-oxides. The same is true of phenoxathiin derivatives, as has been shown for the drug chlorpromazine [77]. When treated with ammonia and amines, the thianthrene, phenoxathiin, and phenoxazine radical cation perchlorates give the corresponding sulfinimine perchlorates (**36**; Scheme 24). With ammonia, these can be deprotonated to give the neutral sulfinimines (**37**); if ammonia is slowly added to the initial radical cation salt the dimeric iminum salt can be prepared [52, 78]. Thianthrene radical cation salts have been similarly reacted with a variety of nucleophiles. Carbazole reacts at the nitrogen atom to give



Scheme 24.



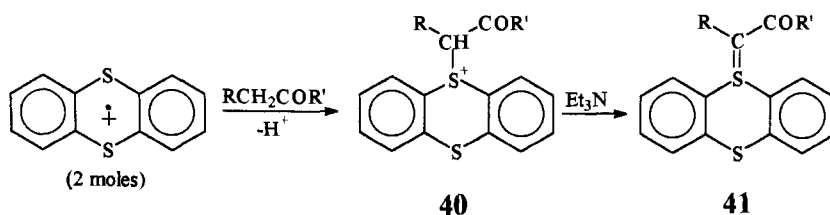
Scheme 25.

product **38** (Scheme 25) [79], but with phenol [80], toluene, and anisole [81] the reaction is at the *para* carbon atom and yields products **39**. A second mole of the thianthrene radical cation always participates into the reaction as an oxidant (compare Scheme 23).

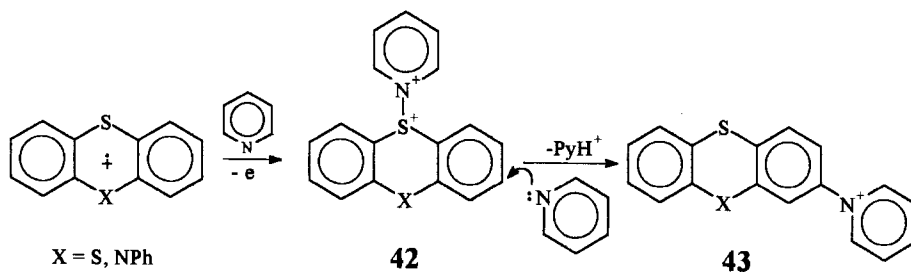
Further interesting examples of C–S bond formation involve the reaction of previously prepared (or in situ anodically generated) thianthrene or phenothiazine radical cations with alkenes or alkynes, to give 1,2-bis(hetaryl) alkanes (or the respective alkenes) [82]. With cyclooctene a 1:1 adduct is obtained instead. Another valuable application is the smooth reaction with ketones (Scheme 26). The thianthrenium salts (**40**) now obtained are readily deprotonated to the corresponding ylides (**41**) [83]. The latter compounds are directly obtained when β -dicarbonyls are used.

A ring carbon can also be involved, however, as in the reaction of the thianthrene and phenothiazine radical cations in neat pyridine or with pyridine in an anhydrous solvent. In this reaction the 1-pyridinium group is inserted on to the benzo ring (**43**), apparently via nucleophilic attack on di-cations **42**, in turn resulting from oxidation of the initially formed radical cation adducts (Scheme 27). In the presence of moisture the sulfoxides are again formed [84].

Other reactions such as the anodic cyanation or alkoxylation of electron-rich heterocycles such as pyrroles and indoles [85] or of electron-donating substituted azines [86] are important, but are not discussed in detail here, because this subject is well covered in electrochemistry textbooks.



Scheme 26.



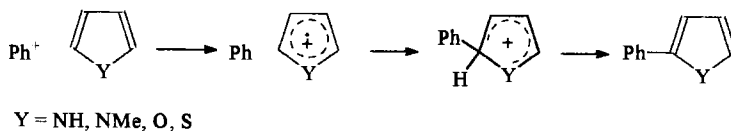
Scheme 27.

Alkylation and arylation via ET

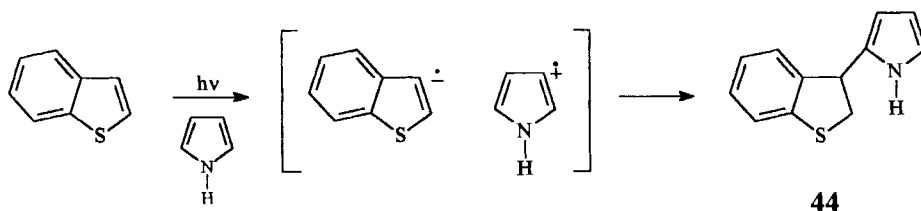
In the gas phase, alkylation of five-membered heterocycles by alkyl cations usually occurs via the usual addition–elimination mechanism of aromatic electrophilic substitution. The phenyl cation behaves differently, however; although its substrate discrimination is limited, in accord with its exceedingly high reactivity, it has marked selectivity for the α position, which does not conform with the ‘hard’ character of this cation. It has, therefore, been suggested that an electron-transfer mechanism is followed; this is thermodynamically allowed for the phenylum, and likewise for the methyl cation, but not for other alkyl cations (Scheme 28). This SET mechanism applies also for acyl cations [87].

Solution-phase studies are more important preparatively. Two main mechanisms seem to operate in solution. The first is attack of the radical cation of a heteroaromatic donor on a π nucleophile, as happens in the arylation reactions reported above. Other examples include photochemical reactions in which the heterocycle participates as a donor—for example the formation of 2- and 3-(1,2-diphenylethyl)pyrroles (yield 44 and 10 %, respectively) from the irradiation of (*E*)-stilbene in the presence of pyrrole, a reaction which evidence implies is initiated by SET from pyrrole [88]. 2-(2',2'-Diphenylethyl)furans are cleanly formed on irradiation of the corresponding furans in the presence of 1,1-diphenylethylene and an electron-accepting sensitizer [89]. Likewise, irradiation of naphthalene and benzothiophene in the presence of pyrrole results in electron transfer from the latter and leads eventually to pyrrolyldihydronaphthalene or benzothiophene, **44**, respectively (Scheme 29) [90].

A partially related reaction is the photochemical synthesis of bis(pyrrolyl)- and bis(indolyl)methanes by irradiation of (hetero)aryl aldehydes in the presence of the



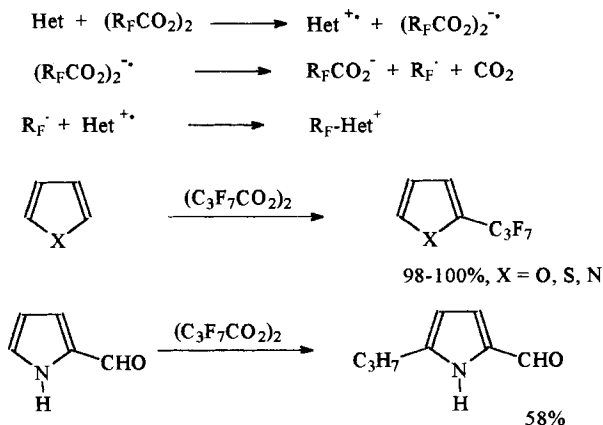
Scheme 28.



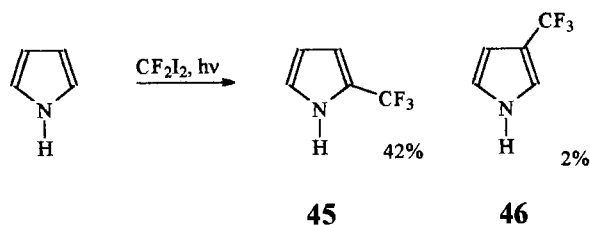
Scheme 29.

respective heterocycles; it is suggested that this involves SET to the excited aldehyde then coupling of the radical ions [91].

The second mechanism involves radical or ionic coupling when at least one of the radical ions formed by thermal or photoinduced electron transfer fragments with sufficient efficacy (compare paths *f* and *g* in Scheme 6). In this case, coupling of the radical or charged species can lead to the formation of a new bond. A typical example is the addition of tetranitromethane fragments across a (hetero)aromatic molecule; for convenience this was mentioned above along with the nitration reaction. Other processes resulting in alkylation or arylation of the heterocyclic ring are reported below. A synthetically useful reaction of this class is the perfluoroalkylation of heterocycles by use of bis(perfluoroalkanoyl)peroxides. The radical anion of the peroxide formed in the initial SET step decomposes to give a perfluoroalkyl radical, perfluoroalkanoate, and carbon dioxide. The radical couples with the donor radical cation leading to the alkylated compound (Scheme 30). In this way 2-perfluoropropylfuran and thiophene are obtained smoothly (40 °C, degassed Freon solution) in quantitative yield [92]. The reaction is equally effective with pyrrole at a lower temperature (−30 °C), with some substituted pyrroles, and with indole (with increased selectivity for the 2 position at −80 °C). The reaction fails with pyridine, but is successful with 2-pyridone or when the nitrogen lone pair is shielded, as in 2,6-di-*tert*-butylpyridine [93].



Scheme 30.

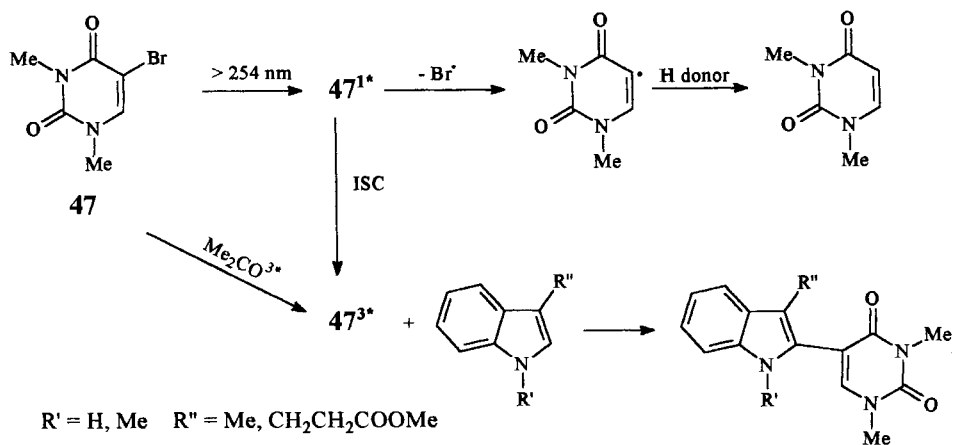


Scheme 31.

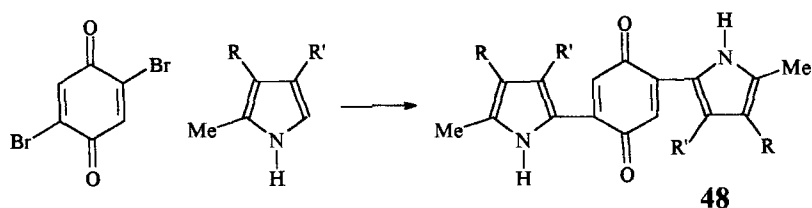
Trifluoromethylation of pyrrole (and indole and imidazole) occurs on irradiation of a mixture of the compound with difluorodiodomethane, again via a SET mechanism involving fragmentation of the radical anion (Scheme 31). The presence of the CF_3 group in the final products, **45** and **46**, is a result either of secondary decomposition of the initially formed—but not isolated—difluoroiodomethyl derivatives, or of formation of the CF_3 anion or radical in situ [94]. Perfluoroalkylation of pyrroles can also be achieved by an $\text{S}_{\text{RN}}1$ mechanism—by reaction with perfluoroalkyl iodides in the presence of magnesium or zinc [95]. Indole, on the other hand, gives a mixture of the seven possible alkylated derivatives when irradiated in the presence of ethyl chloroacetate [96].

Examples of related photochemical (hetero)arylations are the pentafluoroalkylation of pyrroles and indoles by irradiation in the presence of pentafluoroiodobenzene or of pentafluorophenyl perfluoroalkanesulfonates [97], and presumably also the acetone-sensitized photocoupling of 5-bromo-1,3-dimethyluracil (**47**) with indoles. The latter reactions apparently follow an ET path, rather than the homolytic debromination which occurs on direct irradiation (Scheme 32) [98]. A different arylation leads to 2,5-dihydro-2-(4'-cyanophenyl)-5-methoxyfuran on irradiation with 1,4-dicyanobenzene in methanol [99].

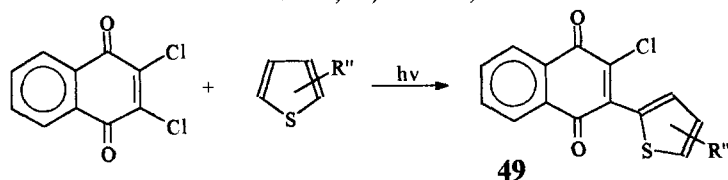
An important reaction is that with haloketones. 2,5-Dibromo-1,4-benzoquinone



Scheme 32.



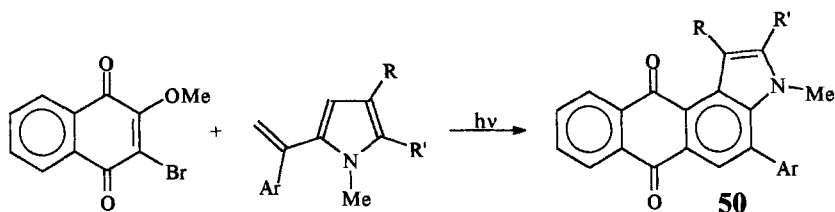
R = H, Et; R' = Me, Et



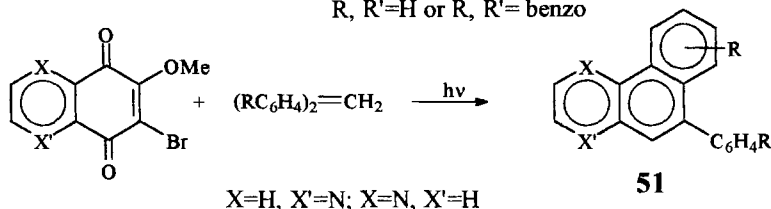
Scheme 33.

gives dyes of structure **48** (Scheme 33) smoothly on addition to pyrrole solutions; the reaction can be envisaged as being initiated by a SET step [100] (it should be noticed that 3,4,5,6-tetrachloro-1,2-benzoquinone gives enolic adducts rather than eliminating hydrogen chloride, a reaction which is envisaged as Michael addition [101]).

Analogous reactions occur smoothly upon photochemical excitation with haloquinones; these have much greater scope. As an example, furans, thiophenes, indoles, and pyrroles are readily functionalized by irradiation in the presence of haloquinones (see, e.g., product **49** in Scheme 33) [102]. Maruyama's group has also used the SET photoinduced reaction between halonaphthoquinones (or halo-methoxynaphthoquinones) and 1,1-diarylethylenes for the synthesis of a variety of heterocycles, for example compounds **50** and **51** in Scheme 34 [103].

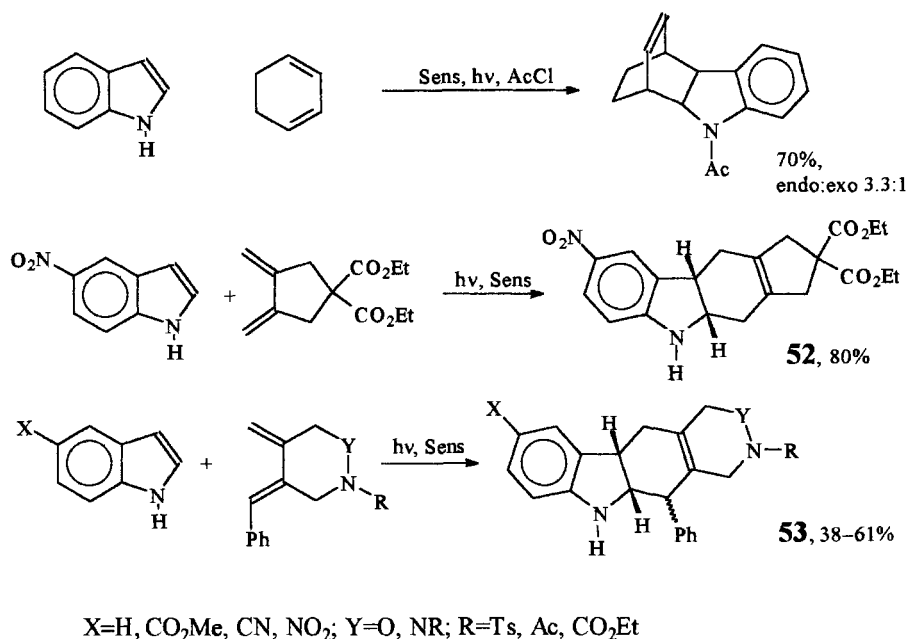


R, R' = H or R, R' = benzo



X = H, X' = N; X = N, X' = H

Scheme 34.



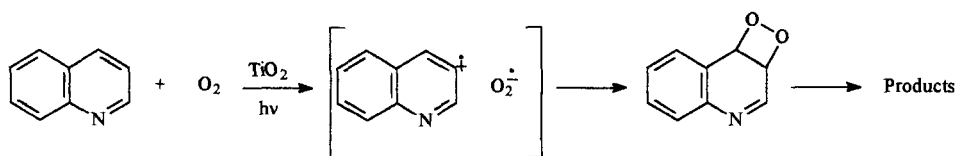
Scheme 35.

6.3.6 Cycloadditions

The radical cation Diels–Alder reaction has been the subject of many mechanistic and theoretical investigations and has been shown to have much synthetic potential. With regard to heteroaromatics, the reaction has been exploited by Steckhan in the cycloaddition of indoles and 1,3-dienes. This reaction occurs smoothly upon photosensitization by triarylpyrrium tetrafluoroborates. The reaction is satisfactory rationalized as involving addition of the indole radical cation to electron-rich dienes [104]. The reaction with exocyclic dienes has been developed for the synthesis of carbazole derivatives such as **52** and **53** [105].

6.3.7 Oxygenation

The possibility that an electron-transfer path is involved in photo-sensitized oxygenation has been considered on several occasions. This is relevant in several fields of application, from the biomimetic oxygenation of indole and flavin derivatives [106] to pollutant control. With reference to latter, it has been suggested that SET occurs in heterogeneous photosensitized oxidation by solid semiconductors, in which the adsorbed substrate donates an electron to the photogenerated hole and



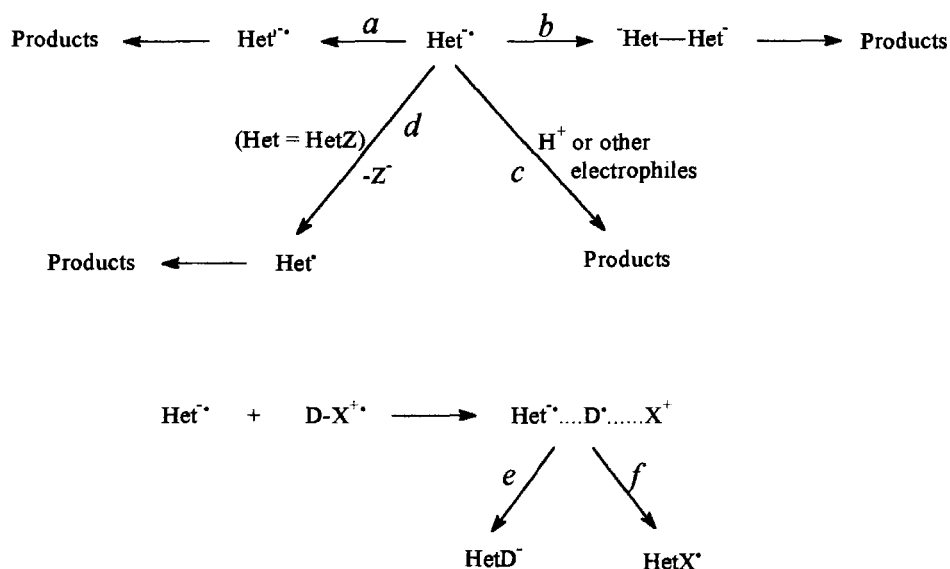
Scheme 36.

oxygen is reduced to the superoxide anion. This mechanism has been probed, e.g. by use of quinoline as a model (Scheme 36) [107].

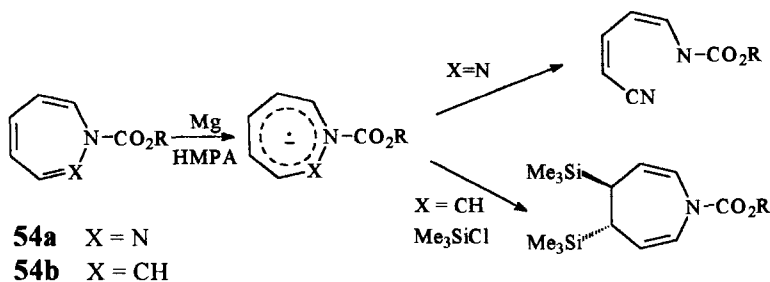
6.4 Chemical Reactions via Electron Transfer—The Heteroaromatic is the Acceptor

6.4.1 General Scheme

The general pattern of reactions is quite similar (with inverted charge) to that occurring after electron transfer in the reverse direction (see Scheme 37). Thus, apart from electron transfer and rearrangement or ring cleavage (path *a*), the reactions are those expected from radical (coupling, path *b*), from an anion (addition of an



Scheme 37.



Scheme 38.

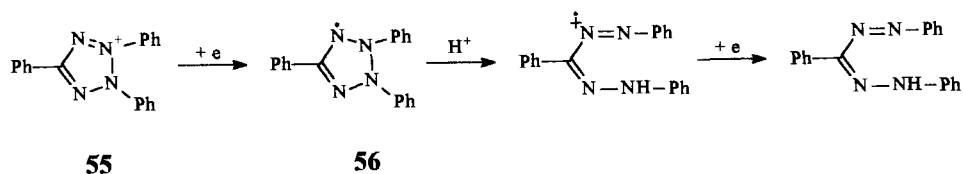
electrophile, here quite often the proton, path *c*), or cleavage of a nucleofugal group (path *d*). Here again, fragmentation of the concomitantly formed radical cation can lead to addition of the heteroaromatic radical anion either with a radical (path *e*) or with a cation (path *f*).

6.4.2 Ring Opening and Rearrangement

The ET-induced desulfurization of thiophene and related sulfur heteroaromatics by the action of metal naphthalenides [108], metal hydride-metal complexes [109], or transition metals [110] is a process with high practical significance, in view of its implication in the desulfurization of coal.

Many 1,2-diazines undergo N–N-bond cleavage upon electroreduction, eventually resulting either in reductive ring opening or in ring contraction, e.g. of the type pyridazine \rightarrow pyrrole [111] or phthalazine \rightarrow isoindole [112].

1*H*-1,2-Diazepinecarboxylates (**54a**) undergo ring cleavage upon reduction by magnesium in hexamethyl phosphoramide, whereas the corresponding azepines (**54b**) preserve the ring and are reduced under these conditions, as evidenced by the formation of a disilyl derivative (Scheme 38) [113]. The 2,3,5-triphenyltetrazolium cation (**55**) undergoes one-electron reduction by electrolysis in a strictly apolar medium, but in the presence of water the resulting radical (**56**) undergoes protonation and ring-opening to yield a formazane in an overall 2-electron process (Scheme 39) [114].



Scheme 39.

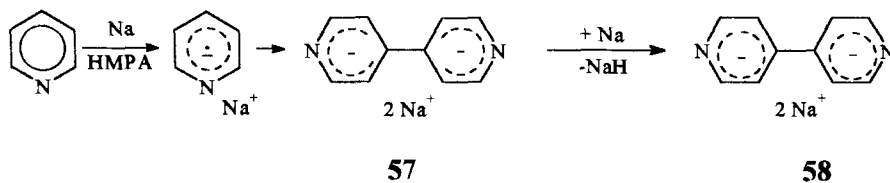
6.4.3 Coupling, Dimerization and Polymerization

With some heterocycles, separated one-electron waves are observed upon cathodic reduction, an important phenomenon i.a. with sensitizing dyes such as porphyrins [115] and cyanins. Occasionally dimers may be formed by preparative electroreduction competitively with the formation of partially or totally ring-hydrogenated heterocycles. This happens, e.g., with acridine (giving biacridane) [116], pyrimidine [117], phthalazine [118], quinazoline [119], 4-cinnolinone [116], and 4-quinazoline [120]. Cathodic coupling of 2- and 4-vinylpyridine gives the corresponding 1,4-dipyridylbutanes in good yield [121]. The dehalogenative coupling of pentafluoropyridine is discussed below.

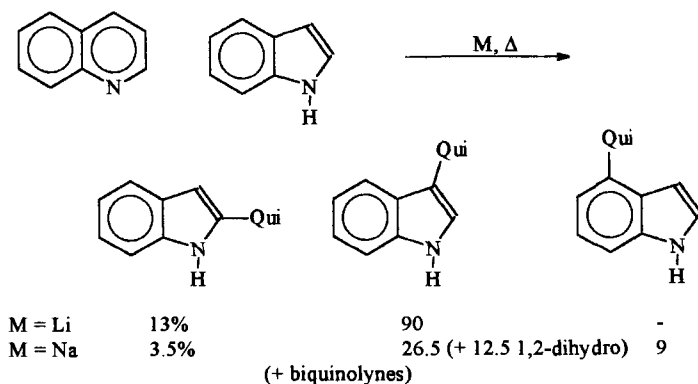
The quaternary salts of *N*-heterocycles are readily reduced and often give reversible one-electron reduction waves, as, for example, with pyridium salts [122]. Dimers have been obtained by this pathway e.g. from acridizinium and benzothiazolium salts [116]. Such processes are particularly important both with biological substrates (e.g. NAD is reported to give essentially 4,4'-dimers on reduction) [123] and in the monoelectronic reduction of di-cations such as dipyridinium and a variety of diaza polycyclic aromatic di-cations [124].

Alternatively, the radical anions of pyridine and other azines are obtained on reduction by metals or other reducing agents, e.g. lithium diethylamide. Under suitable conditions the salts of the radical anions can be obtained as crystalline materials (Section 6.2.3). Alternatively, dimerization follows; as an example, treatment of pyridine and other azines with 1 equiv. sodium in HMPA gives the well characterized radical anion, whereas in tetrahydrofuran the dimeric dianion is formed [125]. A later study with pyridine showed that treatment with sodium leads to a tetrahydro-4,4'-bipyridine dianion (**57**), which is rearomatized to yield **58** in the presence of excess sodium (Scheme 40) [126]. Treatment with LiNEt_2 gives 2,2'-bipyridine, however, possibly because of stronger coordination with the lithium cation [127]. 2,2'-Biquinoline and 1,1'-biisoquinoline are similarly obtained [128].

The procedure has been extended to heterocoupling. As an example, heating quinoline and indole in the presence of a metal gives biquinolines and indolylquinolines (occasionally accompanied by the corresponding 1,2-dihydroderivatives; Scheme 41). The result depends on the metal chosen, e.g. with copper only 2,2'-biquinoline is formed whereas with lithium a 2-(3-indolyl)quinoline is by far the main product [129]. A SET step might be involved in other hetero-coupling reactions via metalated heterocycles [130].



Scheme 40.



Scheme 41.

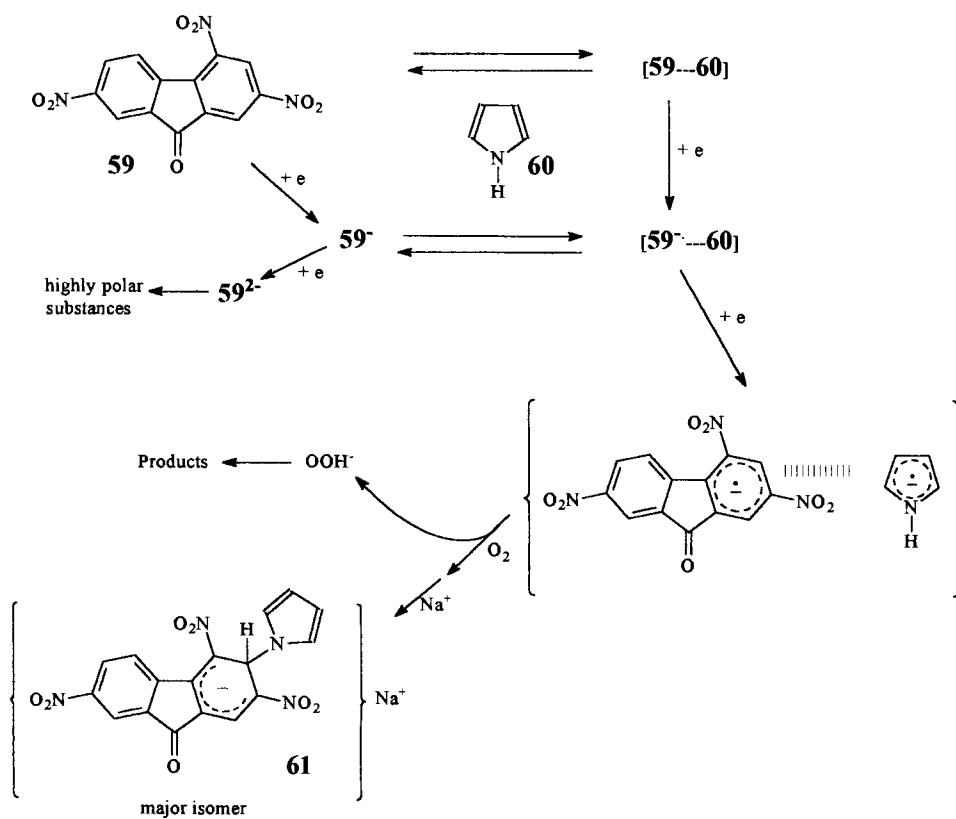
A peculiar example of heterocoupling has been found in the electroreduction of a mixture of pyrrole (**60**) and 2,4,7-trinitrofluoren-9-one (**59**), which leads to the formation of two Meisenheimer anions (the major isomer (structure **61**) from attack at position 3, the minor one from attack at position 1) arguably via coupling of the two radical anions (see Scheme 42) [131]. Electro-oxidation of such anions gives a black polypyrrole film which differs from that obtained by the normal electro-oxidative polymerization of pyrrole (compare Section 6.3.4).

6.4.4 Direct Ring Functionalization

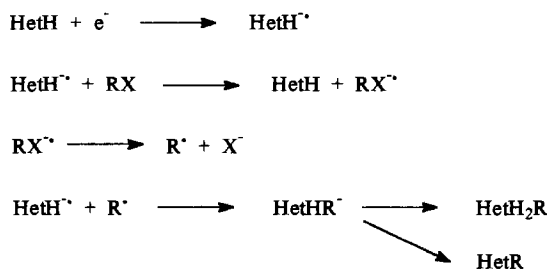
ET-initiated alkylation of azines in the presence of alkyl halides has been found to occur under electrochemical conditions according to Scheme 43. Either alkylated dihydroheterocycles or the rearomatized products are obtained. As an example, electroreduction of quinoline in the presence of 1-bromoadamantane gives alkylated quinolines (10 % in position 2, 5 % in position 7) and 2-methyl- and 2-methoxyquinoline give the 7-adamantyl derivative in 20 and 23 % yield, respectively. 1,10-Phenanthroline gives bis(adamantyl) derivatives, whereas isoquinoline and phenanthridine give the 6-adamantyl-5,6-dihydro and the 9-adamantyl-9,10-dihydro derivatives, respectively [132]. Reaction with *tert*-butyl chloride also gives alkylated dihydroheterocycles [133]. Arylation has also been performed, e.g. in the synthesis of pyrazolophenanthridines (**62**, Scheme 44) [134].

Pyridinium and related cations are well known as excellent radical traps, yielding, e.g., conveniently alkylated derivatives by addition of radicals generated by oxidants from the appropriate precursors [135]. Arylation of such derivatives can be efficiently performed at the cathode, as shown in Scheme 45 with an intermolecular example affording a precursor of cularine (**63**) [136] and with an intramolecular example giving a porphine (**64**) [137].

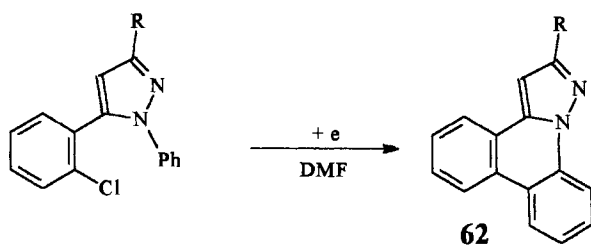
Under irradiation the cation itself can function as acceptor and generate the radicals. Addition of the radicals, particularly bulky *tert*-butyl radicals, is reversible and the yield of the end-products depends on competition between subsequent re-



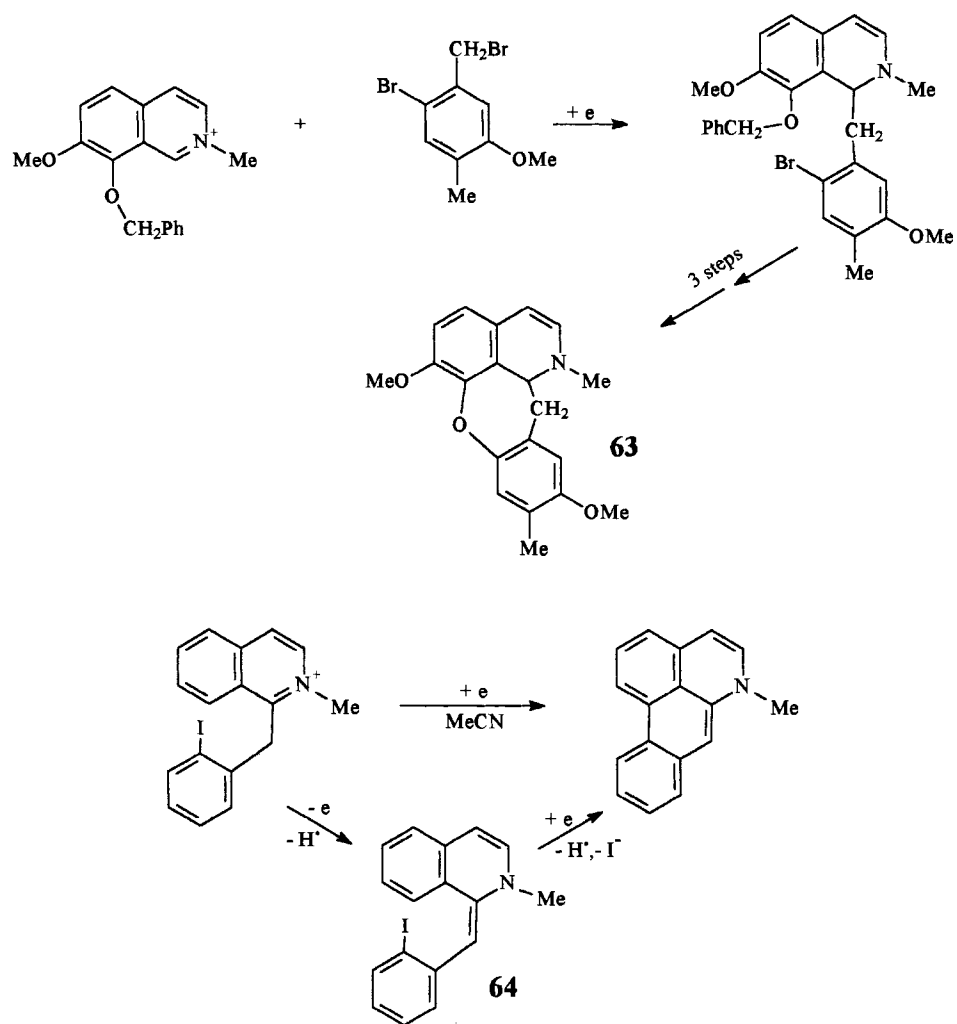
Scheme 42.



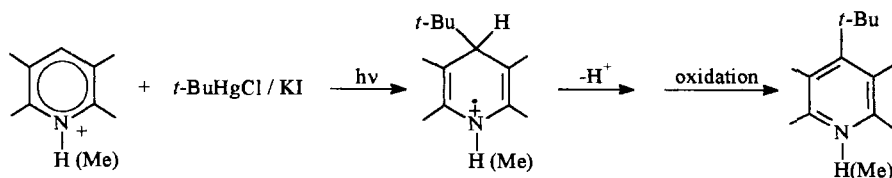
Scheme 43.



Scheme 44.



Scheme 45.



Scheme 46.

actions, viz. proton loss and oxidation of the resulting radical to give the rearomatized heterocycle or reduction to give a dihydroheterocycle. Under these conditions good yields of alkylated pyridines, quinolines, isoquinolines, or acridines have been obtained from the heterocycles by irradiation in the presence of alkyl (usually *tert*-butyl) mercury halides and acids (Scheme 46) [138]. Interestingly, 4-vinylpyridine gives 2-(2-alkylethyl) derivatives under these conditions. Pyrilyum salts are also conveniently alkylated to the corresponding 2- or 4-alkylpyrans by irradiation in the presence of Group-4 organometallic compounds [139].

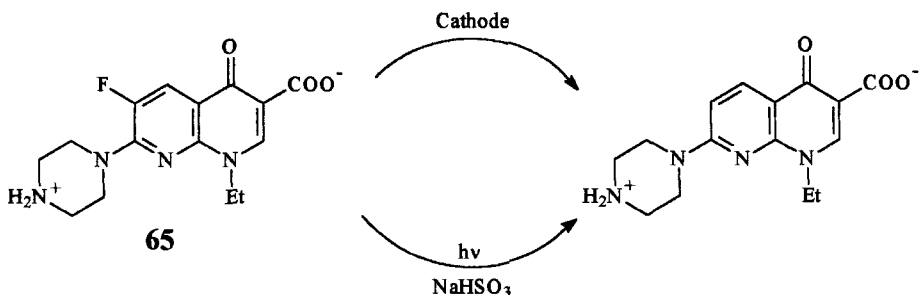
It has been suggested that the photochemical hydroxyalkylation of pyridine and other azines in acidic alcohols likewise proceeds through an ET path [140].

6.4.5 Cleavage of a Group

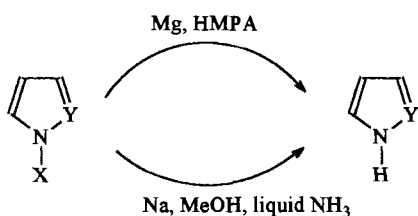
SET promoted dehalogenation is occasionally of interest. Treatment of 2-chloro-, 2-bromo- or 2-iodopyridine with sodium in liquid ammonia gives directly the EPR-detectable radical anion of the parent molecule, dehalogenation being rapid on the time-scale of the experiment [141]. The same is true for a variety of dichloro- and dibromopyridines and pyrimidines, but with 2-fluoropyridine the radical anion is more persistent and only the spectrum of the starting material is registered. For the cathodic reduction of pentachloropyridine, see Section 6.4.6.

In this connection it is noteworthy that smooth defluorination of some fluoroquinolones (used as antibacterial drugs) is obtained both at the cathode and by photolysis in the presence of sodium sulfite in aqueous solution, as it is shown for enoxacin (**65**) in Scheme 47 [142]. The 6,8-difluoro derivative lomefloxacin is selectively defluorinated at position 8 by cathodic reduction. Electron capture of electrons by 5-halouracils in neutral organic and aqueous glasses leads to species characterized as σ^* radical anions (more advanced in the path towards cleavage) with the iodo and bromo derivatives, whereas π^* radical anions are formed from the chloro and fluoro derivatives [143]. The radical anion of 2-chlorothiophene (obtained by irradiation in the crystal state) is of the σ^* type [144].

The cleavage of a side-chain can be useful. As an example, alkyl 1-pyrrolicarboxylates and the corresponding pyrazoles (**66a, b**; Scheme 48) lose the alkoxy-carbonyl group upon reduction by magnesium [145] and the corresponding trityl derivatives (**66c**) are conveniently dealkylated upon Birch reduction [146]. The latter group has an important protecting-directing role on the chemistry of pyrrole derivatives; thus the availability of simple deprotections is preparatively useful.



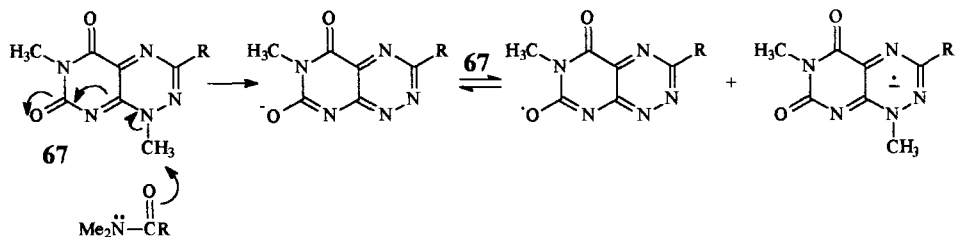
Scheme 47.



Scheme 48.

An interesting fragmentation process involving an ET step is the reaction of the antibiotic toxoflavine (**67**) and some analogs with nucleophiles. This involves transfer of an *N*-methyl group to the nucleophile and formation in equilibrium of the toxoflavine radical anion, which has been characterized by EPR (see Scheme 49) [147].

A particular example of reductive group elimination is elimination of a *N*-oxide function. Because of the rich chemistry of azine *N*-oxide it is often expedient to carry over useful functionalizations at the *N*-oxide level and then to reduce such a



Scheme 49.

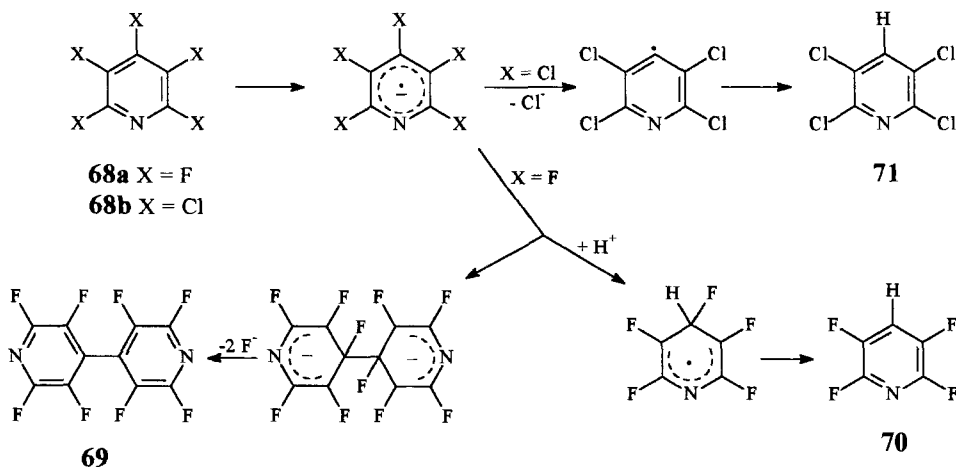
function selectively. One expedient method for *N*-deoxygenation is photoinduced ET to a donor such as an aliphatic amine, an alkene, or triethyl phosphite, a quite general procedure that usually leaves unchanged ring substituents, including the nitro group and suppresses the ring rearrangement otherwise observed on irradiation of the *N*-oxides [148].

6.4.6 Substitution of a Group

Most reactions involve halogen substitution. Many preparatively useful reactions are initiated by reductive dehalogenation of heterocycles. Cathodic reduction leads to different results with the pentafluoro- (**68a**) and pentachloropyridine (**68b**). In the first, radical anion coupling at the position of highest spin density ensues and finally gives octafluoro-4,4'-bipyridine (**69**), although in the presence of a proton source (hydroquinone) dehalogenation to **70** results (Scheme 50). With the latter substrate, fragmentation of the weaker C–Cl bond is the fastest process and thus 2,3,5,6-tetrachloropyridine (**71**) is the main product, although trapping by carbon dioxide is successful [149].

The $S_{RN}1$ reaction has been applied to heterocycles. Among five-membered ring compounds, halothiophenes have been the most studied; they have been shown to be susceptible to both electron-stimulated and photostimulated reactions, and have been converted to the corresponding acetonitriles [150], acetones [151], and phenyl-sulfides [152] in low to medium yields. In the study with the benzenethiolate anion it has been shown that the yield is low because of fragmentation of the adduct radical anion; it can be increased by adding an electron acceptor, e.g. benzonitrile which prevents decomposition. Further applications include the thermally activated $S_{RN}1$ reaction between 3-iodobenzothiophene and enolates [153] and the photo-stimulated reaction of 3-halo-2-aminobenzothiophenes [154].

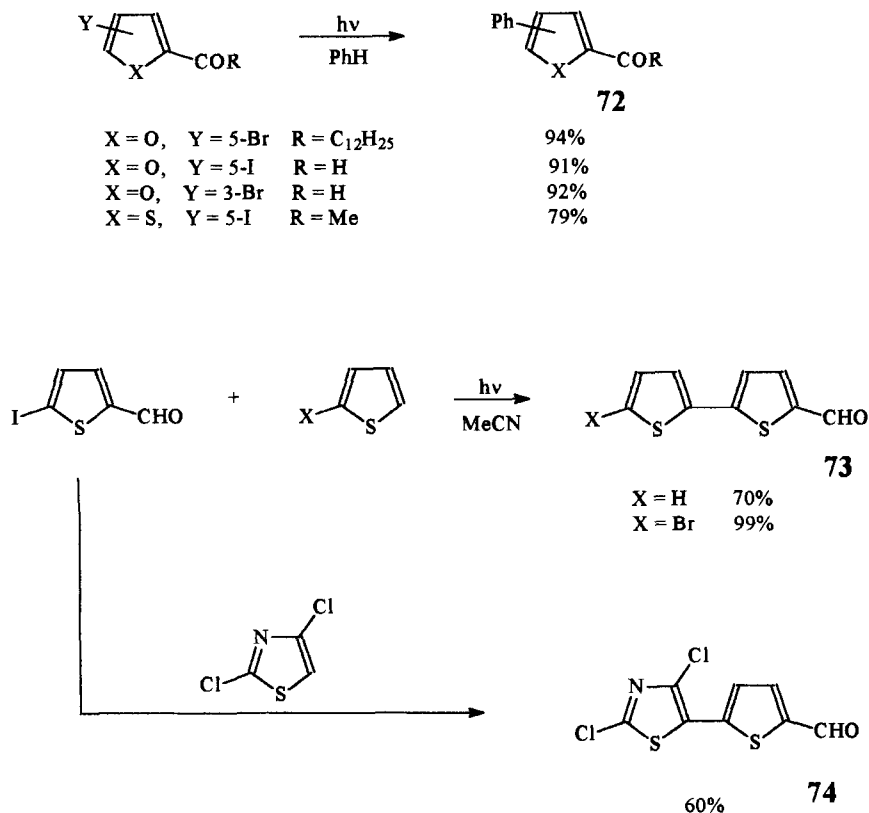
The reaction has been more extensively used for azines, however. As an example,



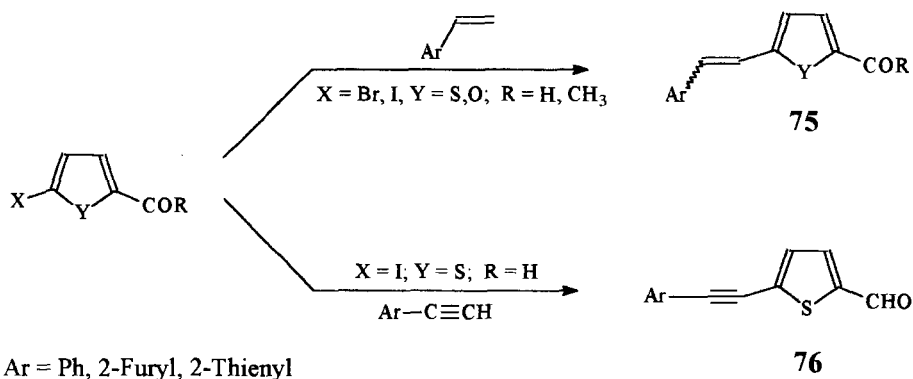
Scheme 50.

medium to good yields of substituted pyridylmethyl ketones are obtained by photo-stimulated reaction of 2-chloro-, 2-bromo-, and (although at a much lower rate) 2-fluoropyridine with the corresponding enolates [155]. Photostimulation is also effective in promoting the reaction of 2-chloroquinoline with enolates [156]. Heteroarylketones have been similarly prepared from chloropyrimidines [157] and pyrazines [158] and phenylsulfides and selenides have been prepared similarly from haloquinolines [159] and haloisoquinolines [160] via an $S_{RN}1$ reaction.

Non-chain functionalization of five-membered heterocycles to halogen derivatives via photoinduced SET has been developed by an Italian group [161]. In a typical reaction, irradiation of acylhalofurans [162], thiophenes [163], and pyrroles [164] in the presence of aromatic substrates gives rise to the corresponding arylated heterocycles (**72**; Scheme 51). The reaction is thought to involve SET and fragmentation of the heteroaryl radical anion. Heteroarylation is also effective through this path and offers an expedient entry to bithiophenecarboxyaldehydes (**73**), in turn useful synthons for naturally occurring bithiophenes [165] and for other coupled heterocycles such as compound **74** [166] (Scheme 51).



Scheme 51.



Scheme 52.

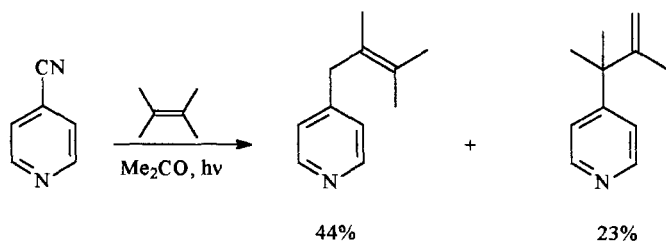
Irradiation of the same acylhaloheterocycles in the presence of (hetero)-arylalkenes and alkynes (**75**) leads to the corresponding bis(hetero)arylalkenes and alkynes (**76**) (Scheme 52) [167].

An ET mechanism is involved in the photochemical reaction of 2- and 4-cyanopyridine and other cyanoazines with alcohols, alkenes, or amines; substitution products are usually obtained. As an example, allylpyridines (and quinolines) are obtained from the acetone-sensitized reaction of the corresponding cyanoheterocycles in the presence of alkenes (Scheme 53). The reactions of various dicyanopyridines have also been studied in detail and the distribution of the products obtained is well rationalized with an ET mechanism [168].

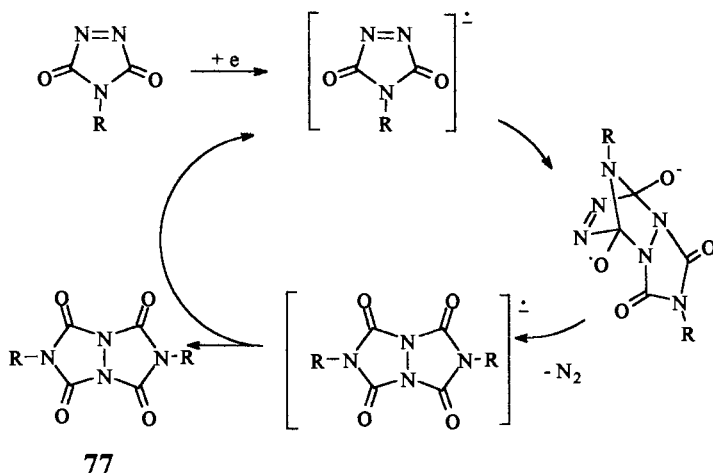
Other good acceptors are functionalized by a similar mechanism when irradiated in the presence of donors; as an example, aminonitrophenazines are formed when nitrophenazines are irradiated in the presence of aliphatic amines [169].

6.4.7 Cycloaddition

Single electron donors such as sodium metal, sodium iodide, or sodium naphthalenide (the last in an amount as low as 5 % molar) convert triazolinodiones to deaza dimers **77** via a reaction that has been formulated as a radical anion chain



Scheme 53.



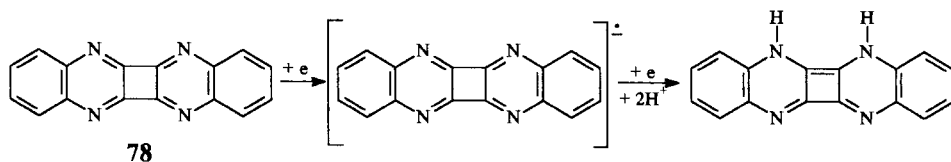
Scheme 54.

process based on a radical anion Diels–Alder reaction (Scheme 54). A similar reaction occurs with azadicarboxylates [170].

6.4.8 Ring Reduction

Selective cathodic reduction of pyridines is a process of great industrial significance [171]. As an example, dimethyl pyridinedicarboxylates undergo a highly selective electroreduction in methanol by use of a divided cell. The product obtained depends on the position of the substituents. Thus, the 2,3- and 2,5-dicarboxylates give the 1,2-dihydropyridines whereas the 2,6-, 3,4- and 2,4-dicarboxylates the 1,4-dihydropyridines [172]. Many other ring reductions of azines (often with dimerization as a side-reaction, see Section 6.4.3) are discussed in electrochemistry texts and reviews [116]. Attempts have been made to rationalize the herbicidal properties of dipyridinium salts in terms of their cathodic behavior [173].

Another process worth mentioning is the cathodic reduction of the bis-(quinoxalino)cyclobutane **78** (Scheme 55) [174].



Scheme 55.

6.5 Conclusions and Outlook

We believe it is apparent from the discussion above that heteroaromatic compounds are in no way minor players in the field of electron transfer. These compounds are more variable in their redox properties than their homocyclic counterparts and the presence of heteroatoms has a substantial effect on the electron distribution of the resulting odd-electron species, and this is an important source of selectivity in the ensuing chemical reactions. Perhaps in this field more than in any other field of organic chemistry it is apparent that the study of reactions involving electron transfer has been confronted in different laboratories and times, with different techniques and intellectual approaches, hardly realizing the benefit of an interdisciplinary approach. It is hoped that this contribution centered on the reactions of organic molecules, coupled with other, more physically oriented, contributions in this book, might help foster new interest in this topic. The impression is that we are under-exploiting the possibilities of electron transfer in the chemistry of heterocyclic compounds and this should be one of the main topics of development in the near future, not least because of its relevance to biological systems and its technical application.

Acknowledgment

We are grateful to Drs L. Cermenati and M. G. Uggetti for their help in the literature search. The work from our laboratory quoted here was supported by CNR, Rome, and MURST, Rome).

References

1. G. R. Newkome, W. W. Paudler, *Contemporary Heterocyclic Chemistry*, Wiley, New York, **1982**, p. 1.
2. (a) P. Hanson, *Adv. Heterocycl. Chem.* **1979**, 25, 205–301; (b) P. Hanson, *ibid.* **1980**, 27, 31–149; (c) A. S. Morkovnik, O. Y. Okhlobystin, *Khim. Geterotsikl. Soedin.* **1980**, 1011–1029.
3. F. Barbosa, L. Ebersson, G. Gescheidt, S. Gronowitz, A. B. Hörnfeldt, L. Julia, O. Persson, *Acta Chem. Scand.* **1998**, 52, 1275–1284.
4. R. Rathore, J. K. Kochi, *Acta Chem. Scand.* **1998**, 52, 114–130.
5. A. G. Davies, L. Julia, S. N. Yazdi, *J. Chem. Soc., Perkin Trans. 2* **1989**, 239–244.
6. A. S. Markovnick, *Zh. Obshsh. Khim.* **1982**, 52, 1877–1883.
7. (a) A. J. Bard, A. Ledwith, H. J. Shine, *Adv. Phys. Org. Chem.* **1976**, 13, 155–278; (b) H. J. Shine, *ACS Symp. Ser.* **1978**, 69, 359–375.
8. W. Lau, J. K. Kochi, *J. Am. Chem. Soc.* **1984**, 106, 7100–7112.
9. L. Ebersson, M. P. Hartshorn, O. Persson, *J. Chem. Soc., Perkin Trans. 2* **1995**, 1735–1744.
10. A. G. Davies, *Chem. Soc. Rev.* **1993**, 22, 299–304.
11. L. Ebersson, M. P. Hartshorn, O. Persson, F. Radner, *Chem. Commun.* **1996**, 2105–2112.
12. P. Linda, G. Marino, S. Pignataro, *J. Chem. Soc. (B)* **1971**, 1585–1587.
13. D. N. R. Rao, G. W. Eastland, M. C. R. Symons, *J. Chem. Soc., Faraday Trans. 1* **1984**, 80, 2803–2815.
14. H. Fischer, F. A. Neugebauer, H. Chandra, M. C. R. Symons, *J. Chem. Soc., Perkin Trans. 2* **1989**, 727–730.

15. H. Fischer, T. Müller, I. Umminger, F. A. Neugebauer, H. Chandra, M. C. R. Symons, *J. Chem. Soc. Trans. 2* **1988**, 413–421.
16. C. Aussems, S. Jaspers, G. Leroy, F. Van Remoortere, *Bull. Soc. Chim. Belges* **1969**, 78, 407–420.
17. D. N. Ramakrishna Rao, M. C. R. Symons, *J. Chem. Soc., Perkin Trans. 2* **1983**, 135–137.
18. D. W. Turner, *Adv. Phys. Org. Chem.* **1966**, 4, 31–71.
19. K. Watanabe, *J. Chem. Phys.* **1957**, 26, 542–547.
20. M. H. Palmer, R. H. Findlay, R. G. Edgell, *J. Mol. Struct.* **1977**, 40, 191–210.
21. T. Kobayashi, T. Kubota, K. Ezumi, C. Utsunomiya, *Bull. Chem. Soc. Jpn.* **1982**, 55, 3915–3919.
22. C. Aussems, S. Jaspers, G. Leroy, F. Van Remoortere, *Bull. Soc. Chim. Belges* **1969**, 78, 479–485.
23. J. R. Gleiter, E. Heilbronner, V. Hornung, *Helv. Chim. Acta* **1972**, 55, 255–274.
24. F. Brogli, E. Heilbronner, T. Kobayashi, *Helv. Chim. Acta* **1972**, 274–288. T. Kato, T. Shida, *J. Am. Chem. Soc.* **1979**, 101, 6879–6876.
25. J. Chaudhuri, S. Kuhe, J. Jagur-Grodzinski, M. Szwarc, *J. Am. Chem. Soc.* **1968**, 90, 6421–6425.
26. A. Modler-Spreitzer, A. Mannschreck, M. Scholz, G. Gescheidt, H. Spreitzer, J. Daub, *J. Chem. Res. (S)* **1995**, 180–181, (*M*), 1229–1251.
27. P. D. Burrow, A. J. Ashe III, D. J. Bellville, K. D. Jordan, *J. Am. Chem. Soc.* **1982**, 104, 425–429.
28. (a) R. Pummerer, S. Gaßner, *Ber. Dtsch. Chem. Ges.* **1913**, 46, 2310–2327; (b) F. Kehrmann, L. Diserens, *Ber. Dtsch. Chem. Ges.* **1915**, 48, 318–328.
29. S. Ogawa, M. Sugawara, Y. Kawai, S. Niizuma, T. Kimura, R. Sato, *Tetrahedron Lett.* **1999**, 40, 9101–9106.
30. Y. Murata, H. J. Shine *J. Org. Chem.* **1969**, 34, 3368–3372.
31. S. Ogawa, S. Saito, T. Kikuchi, Y. Kawai, S. Niizuma, R. Sato, *Chem. Lett.* **1995**, 321–322.
32. (a) S. Ogawa, S. Nobuta, R. Nakayama, Y. Kawai, S. Niizuma, R. Sato, *Chem. Lett.* **1996**, 757–758. (b) S. Ogawa, T. Ohmiya, T. Kikuchi, Y. Kawai, S. Niizuma, R. Sato, *Heterocycles* **1996**, 43, 1843–1846.
33. S. Ogawa, T. Kikuchi, S. Niizuma, R. Sato, *J. Chem. Soc., Chem. Commun.* **1994**, 1593–1594.
34. (a) K. Lühder, *Z. Chem.* **1967**, 7, 198–199; (b) K. Lühder, H. Langanke, *ibid.* **1970**, 10, 74–75.
35. R. Rathore, J.–K. Kochi, *Acta Chem. Scand.* **1998**, 52, 114–130.
36. L. Eberson, M. P. Hartshorn, O. Persson, F. Radner, *Chem. Commun.* **1996**, 2105–2112.
37. (a) U. Svanholm, V. D. Parker, *J. Chem. Soc., Perkin Trans. 2* **1976**, 1567–1574; (b) V. D. Parker, *Acc. Chem. Res.* **1984**, 17, 243.
38. (a) A. I. Novaira, C. D. Borsarelli, J. J. Cosa, C. M. Previtali, *J. Photochem. Photobiol. A*, **1998**, 115, 43–47; (b) C. D. Borsarelli, H. A. Montejano, J. J. Cosa, C. M. Previtali, *ibid.* **1995**, 91, 13–19; (c) H. A. Montejano, J. J. Cosa, H. A. Garrera, C. M. Previtali, *ibid.* **1995**, 86, 115–120.
39. (a) V. D. Parker, Y. T. Chao, G. Zheng, *J. Am. Chem. Soc.* **1997**, 119, 11390. (b) B. Reitstöen, V. D. Parker, *J. Am. Chem. Soc.* **1991**, 113, 6954–6958; (c) V. D. Parker, Y. Zhao, Y. Lu, G. Zheng, *ibid.* **1998**, 120, 12720–12727.
40. D. Lavorato, J. K. Terlouw, T. K. Dargel, W. Koch, G. A. McGibbon, H. Schwartz, *J. Am. Chem. Soc.* **1996**, 118, 11898–11904.
41. J. H. Holmes, J. K. Terlouw, *J. Am. Chem. Soc.* **1979**, 101, 4973–4975.
42. (a) W. Adam, C. Sahin, J. Sendelbach, H. Walter, G. F. Chen, F. Williams, *J. Am. Chem. Soc.* **1994**, 116, 2576–2584; (b) W. Adam, U. Denninger, R. Finzel, F. Kita, H. Platsch, H. Walter, G. Zang, *J. Am. Chem. Soc.* **1992**, 114, 5027–5035; (c) W. Adam, T. Heidenfelder, *Chem. Soc. Rev.* **1999**, 28, 359–365.
43. C. T. Pedersen, O. Hammerich, V. D. Parker, *J. Electroanal. Chem.* **1972**, 38, 479–481.
44. A. De Mico, R. Margarita, G. Piancatelli, *Tetrahedron Lett.* **1995**, 36, 3553–3556.
45. (a) C. P. Andrieux, L. Nadjo, J. M. Savéant, *J. Electroanalytical. Chem.* **1970**, 26, 147–186; (b) L. Nadjo, J. M. Savéant, *J. Electroanal. Chem.* **1973**, 44, 327–366.
46. M. L. Andersen, M. F. Nielsen, O. Hammerich, *Acta Chem. Scand.* **1997**, 51, 94–107.
47. I. Tabakovic, Y. Kunugi, A. Canavesi, L. L. Miller, *Acta Chem. Scand.* **1998**, 52, 131–136.

48. C. T. Pedersen, V. D. Parker, *Tetrahedron Lett.* **1972**, 771–772.
49. C. T. Pedersen, V. D. Parker, O. Hammerich, *Acta Chem. Scand.* **1976**, B 30, 478–84.
50. J. Tormo, F. J. Moreno, J. Ruiz, L. Fajari, L. Julia, *J. Org. Chem.* **1997**, 62, 878–884.
51. G. T. Cheek, R. F. Nelson, *J. Org. Chem.* **1978**, 43, 1230–1232.
52. B. K. Bandlish, H. J. Shine, *J. Org. Chem.* **1977**, 42, 561–563.
53. J. F. Ambrose, R. F. Nelson, *J. Electrochem. Soc.* **1968**, 115, 1159–1164.
54. L. Eberson, M. P. Hartshorn, O. Persson, F. Radner, *Acta Chem Scand.* **1997**, 51, 492–500.
55. Y. Tsujino, *Tetrahedron Lett.* **1969**, 763–766.
56. (a) H. J. Shine, S. M. Wu, *J. Org. Chem.* **1979**, 44, 3310–3316; (b) H. Musso, *Chem. Ber.* **1959**, 92, 2862–2873; (c) H. Musso, *ibid.* **1959**, 92, 2873–2871; (d) Y. Tsujino, *Tetrahedron Lett.* **1968**, 4111–4114.
57. C. Berti, L. Greci, R. Andruzzi, A. Trazza, *J. Org. Chem.* **1985**, 50, 368–373.
58. (a) A. F. Diaz, K. K. Kanazawa, G. P. Gardini, *J. Chem. Soc., Chem. Commun.* **1979**, 635–636; (b) K. K. Kanazawa, A. F. Diaz, R. H. Geiss, W. D. Gill, J. F. Kwak, J. A. Logan, J. F. Rabolt, G. B. Street, *ibid.* **1979**, 854–855.
59. L. Eberson, M. P. Hartshorn, F. Radner, O. Persson, *J. Chem. Soc., Perkin Trans. 2* **1998**, 59–70.
60. M. V. Jovanovic, E. R. Biehl, *J. Org. Chem.* **1984**, 49, 1905–1908.
61. H. Chiou, P. C. Reeves, E. R. Biehl, *J. Heterocycl. Chem.* **1976**, 13, 77–82.
62. P. Carloni, E. Damiani, L. Greci, P. Stipa, *Acta Chem. Scand.* **1998**, 52, 137–140.
63. F. Radner, *J. Org. Chem.* **1988**, 53, 3548–3553.
64. J. Burden, I. W. Parsons *Tetrahedron* **1980**, 36, 1423–1433.
65. (a) J. H. Ridd, *Chem. Soc. Rev.* **1991**, 20, 149–165; (b) A. S. Morkovnik, *Uspekhi Khimii* **1988**, 57, 254–280; (c) L. Eberson, F. Radner, *Acta Chem. Scand.* **1984**, B 38, 861–870; (d) L. G. Gorb, I. A. Sbroni, L. Korsukov, G. M. Zhidemirov, J. P. Litvinov, *Isv. Ak. Nauk SSSR, Ser. Khim.*, **1984**, 1079–1085.
66. (a) A. S. Morkovnick, N. M. Dobaeva, V. B. Panov, O. Y. Okhlobystin, *Dokl. Akad. Nauk SSSR* **1980**, 251, 125–8; (b) V. G. Koshechko, A. N. Inozemtsev, V. D. Pokhodenko, *Zhur. Org. Khim.* **1981**, 17, 2608–2612.
67. A. S. Morkovnick, N. M. Dobaeva, O. Y. Okhlobystin, *Khim. Geterotsikl. Soedin.* **1981**, 1214–1216.
68. A. S. Morkovnick, E. Y. Belinskii, N. M. Dobaeva, O. Y. Okhlobystin, *Zhur. Org. Khim.* **1982**, 18, 378–386.
69. A. S. Morkovnick, N. M. Dobaeva, O. Y. Okhlobystin, *Khim. Geterotsikl. Soed.* **1983**, 122–123.
70. (a) C. P. Butts, L. Eberson, M. P. Hartshorn, W. T. Robinson, B. R. Wood, *Acta Chem. Scand.* **1996**, 50, 587–595; (b) C. P. Butts, L. Eberson, M. P. Hartshorn, F. Radner, B. R. Wood, *ibid.* **1997**, 51, 476–482.
71. C. P. Butts, L. Eberson, R. Gonzalez-Luque, C. M. Hartshorn, M. P. Hartshorn, M. Merchant, W. T. Robinson, B. O. Roos, C. Vallance, B. R. Wood, *Acta Chem. Scand.* **1997**, 51, 984–999.
72. C. P. Butts, L. Eberson, M. P. Hartshorn, F. Radner, W. T. Robinson, B. R. Wood, *Acta Chem. Scand.* **1997**, 51, 839–848.
73. A. S. Morkovnik, E. Y. Belinski, O. Y. Okhlobystin, *Zhur. Org. Khim.* **1979**, 15, 1565.
74. C. Barry, G. Cauquis, M. Maurey, *Bull. Soc. Chim. Fr.* **1966**, 2510–2516.
75. H. J. Shine, Y. Murata, *J. Am. Chem. Soc.* **1969**, 91, 1872–1874.
76. V. D. Parker, L. Eberson, *J. Am. Chem. Soc.* **1970**, 92, 7488–7489.
77. H. J. Cheng, P. H. Sackett, R. L. McCreery, *J. Am. Chem. Soc.* **1978**, 100, 962–967.
78. S. R. Mani, H. J. Shine, *J. Org. Chem.* **1975**, 40, 2756–2758.
79. K. Kim, H. J. Shine, *J. Org. Chem.* **1974**, 39, 2537–2539.
80. U. Svanholm, V. D. Parker, *J. Am. Chem. Soc.* **1976**, 98, 997–1001.
81. J. J. Silber, H. J. Shine, *J. Org. Chem.* **1971**, 36, 2923–2926.
82. (a) K. Iwai, H. J. Shine, *J. Org. Chem.*, **1981**, 46, 271–276; (b) H. J. Shine, B. K. Bandlish, S. R. Mani, A. G. Padilla, *ibid.*, **1979**, 44, 915–917; (c) W. K. Lee, B. Liu, C. W. Park, H. J. Shine, J. Y. Guzman-Jimenez, K. H. Whitmire, *ibid.*, **1999**, 64, 9206–9210, (d) A. Hoomam, D. Shukla, H. B. Kraatz, D. D. M. Wayner, *ibid.* **1999**, 64, 3342–3345.

83. K. Kim, H. J. Shine, *Tetrahedron Lett.* **1974**, 4413–4416.
84. (a) H. J. Shine, J. J. Silver, R. J. Bussey, T. Okuyama, *J. Org. Chem.* **1972**, *37*, 2691–2697; (b) J. F. Evans, H. N. Blount, *ibid.* **1977**, *42*, 976–982; (c) J. F. Evans, J. R. Lenhard, H. N. Blount, *ibid.* **1977**, *42*, 983–988.
85. K. Yoshida, *J. Am. Chem. Soc.* **1979**, *101*, 2116–2121.
86. N. L. Weinberg, E. A. Brown, *J. Org. Chem.* **1966**, *31*, 4054–4058.
87. (a) A. Filippi, G. Occhiucci, M. Speranza, *Can. J. Chem.* **1991**, *69*, 732–739; (b) A. Filippi, G. Occhiucci, C. Sparapani, M. Speranza, *Can. J. Chem.* **1991**, *69*, 740–748.
88. (a) T. Kubota, H. Sakurai, *Chem. Lett.* **1972**, 923–926; (b) T. Kubota, H. Sakurai, *ibid.* **1972**, 1249–1250.
89. K. Mizuno, M. Ishii, Y. Otsuji, *J. Am. Chem. Soc.* **1981**, *103*, 5570–5572.
90. (a) J. J. McCullough, W. S. Wu, C. W. Huang, *J. Chem. Soc., Perkin Trans. 2* **1972**, 370–375; (b) P. Grandclaude, A. Lablache-Combier, C. Parkanyi, *Tetrahedron* **1973**, *29*, 651–658.
91. (a) M. D'Auria, E. De Luca, V. Esposito, G. Mauriello, R. Racioppi, *Tetrahedron* **1997**, *53*, 1157–1166; (b) M. D'Auria, *Tetrahedron* **1991**, *47*, 9225–9230.
92. H. Sawada, M. Yoshida, H. Hagii, K. Aoshima, M. Kobayashi, *Bull. Chem. Soc. Jpn.* **1986**, *59*, 215–219.
93. M. Yoshida, T. Yoshida, M. Kobayashi, N. Kamigata, *J. Chem. Soc., Perkin Trans. 1* **1989**, 909–914.
94. Q. Y. Chen, Z. T. Li, *J. Chem. Soc., Perkin Trans. 1* **1993**, 645–648.
95. (a) Q. Y. Chen., Z. M. Qiu, *J. Fluorine Chem.* **1988**, *39*, 289–292; (b) Q. Y. Chen, Z. M. Qiu, *Hyaxue Xuebao*, **1988**, *46*, 258–263 through *Chem. Abstr.* **1989**, *110*, 75218a.
96. S. Naruto, O. Yonemitsu, *Tetrahedron Lett.* **1971**, 2297–2300.
97. (a) Q. Y. Chen, Z. T. Li, *J. Chem. Soc., Perkin Trans. 1* **1993**, 1705–1710; (b) Q. Y. Chen, Z. T. Li, *J. Org. Chem.* **1993**, *58*, 2599–2604.
98. S. Ito, I. Saito, T. Matsuura, *J. Am. Chem. Soc.* **1980**, *102*, 7535–7541.
99. T. Majima, C. Pac, A. Nakasone, H. Sakurai, *J. Am. Chem. Soc.* **1981**, *103*, 4499–4508.
100. H. Fischer, A. Treibs, E. Zaucker, *Chem. Ber.* **1959**, *92*, 2026–2029.
101. K. Saito, Y. Horie, *Heterocycl.* **1986**, *24*, 579–582.
102. (a) K. Maruyama, T. Otsuki, *Chem. Lett.* **1977**, 851–852; (b) K. Maruyama, T. Otsuki, *Bull. Chem. Soc. Jpn.* **1977**, *50*, 3429–3430; (c) K. Maruyama, T. Otsuki, H. Tamiaki, *ibid.* **1985**, *58*, 3049–3050.
103. (a) K. Maruyama, K. Mitsui, T. Otsuki, *Chem. Lett.* **1978**, 323–324; (b) K. Maruyama, T. Otsuki, S. Tai, *J. Org. Chem.* **1985**, *50*, 52–60.
104. (a) A. Gieseler, E. Steckhan, O. Wiest, F. Knoch, *J. Org. Chem.* **1991**, *56*, 1405–1411; (b) O. Wiest, E. Steckhan, F. Grein, *ibid.* **1992**, *57*, 4034–4037; (c) A. Gieseler, E. Steckhan, O. Wiest, *Synlett.* **1990**, 275–277.
105. O. Wiest, E. Steckhan, *Tetrahedron Lett.* **1993**, 6391–6394; T. Peglow, S. Blechert, E. Steckhan, *Chem. Commun.* **1999**, 433–434.
106. Y. Yoshioka, S. Yamanaka, S. Yamada, T. Kawakami, M. Nishino, K. Yamaguchi, A. Nishinag, *Bull. Chem. Soc. Jpn.* **1996**, *69*, 2701–2722.
107. L. Cermenati, P. Pichat, C. Guillard, A. Albin, *J. Chem. Phys. B* **1997**, *101*, 2650–2658.
108. (a) T. Ignasiak, A. V. Kemp-Jones, O. P. Stausz, *J. Org. Chem.* **1977**, *42*, 312–320; (b) K. Chatterjee, L. M. Stock, M. L. Gorbaty, G. N. George, S. R. Kelemen, *Energy Fuels* **1991**, *5*, 771–773.
109. J. J. Eish, L. E. Hallenbeck, K. I. Han, *J. Am. Chem. Soc.* **1986**, *108*, 7763–7767.
110. (a) A. N. Statrsev, *Kinetic Catal.* **1995**, *36*, 471–478; (b) S. W. Oliver, T. D. Smith, J. R. Pilbrow, K. C. Pratts, V. Christov, *J. Catal.* **1988**, *111*, 88–93.
111. H. Lund, P. Lunde, *Acta Chem. Scand.* **1967**, *21*, 1067–1080.
112. H. Lund, E. T. Jensen, *Acta Chem. Scand.* **1970**, *24*, 1867–1877.
113. K. Saito, H. Kojima, T. Okudaira, K. Takahashi, *Bull. Chem. Soc. Jpn.* **1983**, *56*, 175–179.
114. I. Tabakovic, M. Trkovnik, Z. Grujic, *J. Chem. Soc., Perkin Trans. 2*, **1979**, 166–171.
115. A. Stanienda, G. Biebl, *Z. Phys. Chem.* **1967**, *52*, 254–275.
116. (a) H. Lund, *Adv. Heterocycl. Chem.* **1970**, *12*, 213–316; (b) H. Lund, I. Tabakovic, *ibid.* **1984**, *36*, 237–316.
117. D. L. Smith, P. J. Elving, *J. Am. Chem. Soc.* **1962**, *84*, 2741–2747.

118. H. Lund, *Österr. Chemiker Z.* **1967**, 68, 43–53.
119. H. Lund, *Acta Chem. Scand.* **1964**, 18, 1984–1995.
120. P. Pfügel, G. Wagner, *Z. Chem.* **1969**, 9, 151–152.
121. T. Nonaka, T. Kato, T. Fuchigani, T. Sekine, *Electrochim. Acta* **1981**, 26, 887–92.
122. S. I. Zhdanov, L. S. Mirkin, *Coll. Czech. Chem. Commun.* **1961**, 26, 370–379.
123. H. Jaegfeldt, *Bioelectrochem. Bioenerg.* **1981**, 8, 355–370.
124. S. Hünig, J. Gross, *Tetrahedron Lett.* **1968**, 2599–2604.
125. J. Chaudhuri, S. Kume, J. Jagur-Grodzinski, M. Szwarc, *J. Am. Chem. Soc.* **1968**, 90, 6421–6425.
126. K. Lühder, H. Füllbier, *Z. Chem.* **1988**, 28, 402–404.
127. G. R. Newkome, D. C. Hager, *J. Org. Chem.* **1982**, 47, 599–601.
128. A. J. Clarke, S. McNamara, O. Meth-Cohn, *Tetrahedron Lett.* **1974**, 2373–2376.
129. A. K. Sheinkman, V. A. Ivanov, N. A. Klyuev, G. A. Mal'tseva, *Zhur. Org. Khim.* **1973**, 9, 2550–2560.
130. T. Kauffmann, *Angew. Chem. Int. Ed. Engl.* **1979**, 18, 1–19.
131. K. Oshino, N. Ozawa, H. Kokado, H. Seki, T. Tokunaga, T. Ishikawa, *J. Org. Chem.* **1999**, 64, 4572–4573.
132. U. Hess, D. Huhn, H. Lund, *Acta Chem. Scand.* **1980**, B34, 413–417.
133. C. Degrand, H. Lund, *Acta Chem. Scand.* **1977**, B31, 593–598.
134. J. Grimshaw, J. Trocha-Grimshaw, *Tetrahedron Lett.* **1974**, 993–996; *ibid.* **1975**, 2601–2604.
135. (a) F. Minisci, R. Galli, M. Cecere, V. Malatesta, T. Caronna, *Tetrahedron Lett.* **1968**, 5609–5612; (b) F. Minisci, A. Citterio, C. Giordano, *Acc. Chem. Res.* **1983**, 16, 27–32.
136. T. Shono, T. Miyamoto, M. Mizukami, H. Hamaguchi, *Tetrahedron Lett.* **1981**, 2385–2388.
137. R. Gottlieb, J. L. Neumeyer, *J. Am. Chem. Soc.* **1976**, 98, 7108–7109.
138. (a) G. A. Russel, R. Rajaratnam, L. Wang, B. Z. Shi, B. H. Kim, C. F. Yao, *J. Am. Chem. Soc.* **1993**, 115, 10596–10604; (b) G. A. Russel, D. Guo, W. Baik, S. J. Herron, *Heterocycl.* **1989**, 28, 143–146.
139. (a) S. Kyushin, Y. Nakadaira, M. Ohashi, *Chem. Lett.* **1990**, 2191–2194; (b) E. Baciocchi, G. Doddì, M. Ioele, G. Ercolani, *Tetrahedron* **1993**, 49, 3793–3800.
140. (a) A. Castellano, J. P. Catteau, A. Lablache-Combier, *Tetrahedron* **1975**, 31, 2255–2261; (b) A. Albini, G. F. Bettinetti, M. De Bernardi, S. Pietra, *Gazz. Chim. Ital.* **1970**, 100, 700–702.
141. A. R. Buick, T. J. Kemp, G. T. Neal, T. J. Stone, *J. Chem. Soc. (A)* **1969**, 666–669.
142. (a) A. Profumo, E. Fasani, A. Albini, *Heterocycl.* **1999**, 51, 1499–1502; (b) E. Fasani, F. F. Barberis Negra, M. Mella, S. Monti, A. Albini, *J. Org. Chem.* **1999**, 64, 5388–5395.
143. H. Riederer, J. Hüttermann, M. C. R. Symons, *J. Chem. Soc., Chem. Commun.* **1978**, 313–314.
144. S. Nagai, T. Gillbro, *J. Phys. Chem.* **1977**, 81, 1793–1794.
145. K. Saito, Y. Horie, T. Murase, K. Takahashi, *Heterocycl.* **1989**, 29, 1545–1550.
146. D. J. Chadwick, S. T. Hodgson, *J. Chem. Soc., Perkin Trans. 1*, **1983**, 93–102.
147. F. Yoneda, T. Nagamatsu, *J. Am. Chem. Soc.* **1973**, 95, 5735–5737.
148. (a) E. Fasani, A. M. Amer, A. Albini, *Heterocycl.* **1994**, 37, 985–992; (b) S. Pietra, G. F. Bettinetti, A. Albini, E. Fasani, R. Oberti, *J. Chem. Soc., Perkin Trans. 2* **1978**, 185–189.
149. R. D. Chambers, W. K. R. Musgrave, C. R. Sargent, F. G. Drakesmith, *Tetrahedron* **1981**, 37, 591–595.
150. Y. L. Goldfarb, A. P. Yakubov, L. I. Belen'kii, *Khim. Geterotsikl. Soedin.* **1979**, 1044–1046.
151. J. F. Bunnet, B. F. Gloor, *Heterocycl.* **1976**, 5, 377–399.
152. M. Novi, G. Garbarino, G. Petrillo, C. Dell'Erba, *J. Org. Chem.* **1987**, 52, 5382–5386.
153. M. Prats, C. Galvez, L. Beltran, *Heterocycl.* **1992**, 34, 1039–1046.
154. L. Beltran, C. Galvez, M. Prats, J. Salgado, *J. Heterocycl. Chem.* **1992**, 29, 905–909.
155. A. P. Komin, J. F. Wolfe, *J. Org. Chem.* **1977**, 42, 2481–2486.
156. (a) J. V. Hay, T. Hulicky, J. F. Wolfe, *J. Am. Chem. Soc.* **1975**, 97, 374–377; (b) J. V. Hay, J. F. Wolfe, *ibid.* **1975**, 97, 3702–3706.
157. E. A. Oostreen, H. C. van der Plas, *Rec. Trav. Chim. Pays-Bas* **1979**, 98, 441–444.
158. D. R. Carver, A. P. Komin, J. S. Hubbard, J. F. Wolfe, *J. Org. Chem.* **1981**, 46, 294–299.
159. (a) A. B. Pierini, R. A. Rossi, *J. Org. Chem.*, **1979**, 44, 4667–4673; (b) R. A. Rossi, S. M. Palacios, *ibid.* **1981**, 46, 5300–5304.
160. J. A. Zoltewicz, T. M. Oestreich, *J. Am. Chem. Soc.* **1973**, 95, 6863–6864.

161. M. D'Auria, *Gazz. Chim. It.* **1989**, *119*, 419–433.
162. (a) R. Antonioletti, M. D'Auria, A. De Mico, G. Piancatelli, A. Scettri, *Tetrahedron* **1985**, *41*, 3441–3446; (b) R. Antonioletti, M. D'Auria, A. De Mico, G. Piancatelli, A. Scettri, *J. Chem. Soc., Perkin Trans. 1* **1985**, 1285–1288; (c) M. D'Auria, R. Antonioletti, A. De Mico, G. Piancatelli, *Heterocycl.* **1986**, *24*, 1575–1578.
163. R. Antonioletti, M. D'Auria, F. D'Onofrio, G. Piancatelli, A. Scettri, *J. Chem. Soc., Perkin Trans. 1* **1986**, 1755–1758.
164. M. D'Auria, E. De Luca, V. Esposito, G. Mauriello, R. Racioppi, *Tetrahedron* **1997**, *53*, 1157–1166.
165. (a) M. D'Auria, A. De Mico, F. D'Onofrio, G. Piancatelli, *J. Org. Chem.* **1987**, *52*, 5243–5247; (b) M. D'Auria, A. De Mico, F. D'Onofrio, G. Piancatelli, *J. Chem. Soc., Perkin Trans. 1* **1987**, 1777–1780.
166. M. D'Auria, A. De Mico, F. D'Onofrio, G. Piancatelli, *Gazz. Chim. It.* **1989**, *119*, 381–384.
167. M. D'Auria, G. Piancatelli, T. Ferri, *J. Org. Chem.* **1990**, *55*, 4019–4025.
168. (a) R. Bernardi, T. Caronna, D. Coggiola, F. Ganazzoli, *J. Org. Chem.* **1986**, *51*, 1045–1050; (b) R. Bernardi, T. Caronna, S. Morrocchi, P. Traldi, B. M. Vittimberga, *J. Chem. Soc., Perkin Trans. 1* **1981**, 1607–1609; (c) T. Caronna, B. M. Vittimberga, M. E. Kernn, W. G. McGimpsey, *J. Photochem. Photobiol. A* **1995**, *90*, 137–140; (d) R. Bernardi, T. Caronna, S. Morrocchi, M. Ursini, B. M. Vittimberga, *J. Chem. Soc., Perkin Trans. 1* **1990**, 97–100; (e) R. Bernardi, T. Caronna, G. Poggi, B. M. Vittimberga, *J. Heterocycl. Chem.* **1994**, *31*, 903–908.
169. A. Albini, G. F. Bettinetti, E. Fasani, G. Minoli, *J. Chem. Soc., Perkin Trans. 1*, **1978**, 299–303.
170. D. W. Borhani, F. D. Greene, *J. Org. Chem.* **1986**, *51*, 1563–1570.
171. J. E. Toomey, *Adv. Heterocycl. Chem.* **1984**, *37*, 167–215.
172. Y. Kita, H. Maekawa, Y. Yamasaki, I. Nishiguchi, *Tetrahedron Lett.* **1999**, *40*, 8587–8590.
173. J. Volke, *Collect. Czech. Chem. Commun.* **1968**, *33*, 3044–3048.
174. K. Hesse, S. Hünig, H. J. Bestmann, G. Schmid, E. Wilhelm, G. Seitz, R. Matusch, K. Mann, *Chem. Ber.* **1982**, *115*, 795–797.

7 Electron-transfer Reactions of Amines

Suresh Das and V. Suresh

7.1 Introduction

Amines and their derivatives are more widely distributed in nature than any other functional group family. This combined with the ease of oxidation of amines because of the lone pair of electrons on the nitrogen atom makes electron-transfer reactions of amines important in several electrochemical [1–3], photochemical [4–14], and biochemical [15–18] redox processes. One-electron oxidation of amines leads to the formation of radical intermediates that can be used for the synthesis of amino acids, alkaloids, and several other nitrogen-containing compounds of biological and pharmaceutical importance [19–23]. Electron-transfer reactions of amines are also important in several technological applications such as imaging [24], photopolymerization [25–27], and fading of textile dyes [28]. More recently the electron-donating capacity of the amino functionality has been extensively used for designing new materials such as fluoroionophores [29, 30], organic conductors [31], electroluminescent materials [32–34], photovoltaics [35, 36], and materials with non-linear optical activity [37–39].

In this chapter, we focus on the mechanistic and synthetic aspects of electron-transfer reactions of amines. The role of electron transfer of amines in enzyme-catalyzed oxidations of amines is also briefly discussed.

7.2 Mechanistic Studies

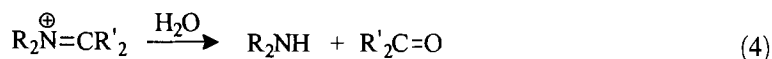
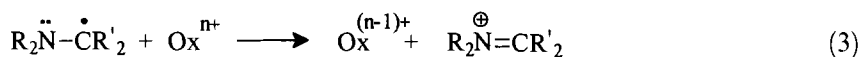
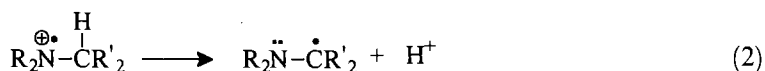
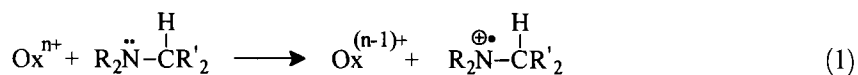
The mechanism of electron-transfer reactions of amines has been studied by different methods, including the thermochemical, electrochemical, photochemical, and radiation chemical techniques.

7.2.1 Thermal Oxidation

Electron-transfer reactions of amines can be initiated by a variety of chemical oxidants. One-electron oxidation has been observed, for example, in the reactions of amines with metal salts such as ceric ammonium nitrate (CAN) [23, 40–42], manganese oxalate [23], alkaline ferricyanide [43–46], phenanthroline complexes of iron [46], octacyanomolybdate [45]. The mechanism of electron-transfer-catalyzed reactions of amines by chlorine dioxide [45, 47] and permanganate [48] have been intensively investigated in aqueous solution. In non-aqueous solvents, *N*-bromosuccinimide in carbon tetrachloride [49] and *N*-chlorobenzotriazole in benzene [50] are reported to react with amines via single-electron transfer (SET). Metal ion-catalyzed oxidation of vinyl amines by molecular oxygen [51, 52] and of aromatic amines by nitrogen dioxide have been reported [53]. In the presence of transition metal ions, hydrogen peroxide and peracids are known to liberate hydroxyl radicals [54–58] which can react with amines either via electron transfer or hydrogen-atom transfer. It has been proposed that oxidation of amines catalyzed by enzymes such as amine oxidases [16] and cytochrome P-450 [18] occurs via single-electron-transfer processes. Reagents such as hydrogen peroxide, peroxy acid [22], and ozone [22] bring about two-electron oxidation of amines, usually resulting in the formation of amine oxides or hydroxylamines.

Mechanistic studies of the chemical oxidation of aliphatic amines have been reviewed extensively by Chow et al. [22]. Many studies of the mechanism of oxidation of amines have been performed with chlorine dioxide or ferricyanide as oxidants, because they have absorption bands with maxima at 357 and 420 nm, respectively. Changes in the absorbance at these wavelengths for the respective oxidants can be conveniently used to follow the kinetics of the reactions. On the basis of these studies, the electron-transfer mechanism shown in Scheme 1 has been proposed for amine oxidation.

The amine radical cation formed in the initial one-electron-transfer process deprotonates at the α -carbon and the amino alkyl radical formed is oxidized to the iminium salt which hydrolyzes to the dealkylated amine and a carbonyl compound. With the use of benzoyl peroxide as oxidant the aminium radical is also believed to



Scheme 1.

be formed. In many of these reactions hydrogen-atom abstraction to yield the aminoalkyl radical directly is also feasible. Chlorine dioxide, for example, reacts with dibenzyl amine by 35 % hydrogen abstraction and 65 % electron transfer [59]. Permanganate, on the other hand, reacts with triethylamine solely by electron transfer [48], whereas it reacts with benzyl amine predominantly via hydrogen-atom abstraction [60].

In the oxidation of benzylamines, apart from formation of the dealkylated amine and benzaldehyde [61–64], formation of imines [65, 66], benzonitrile [64], diazines [62] anilines [67], and *N*-benzylidene benzyl amines [64, 66, 67] has also been observed.

7.2.2 Electrochemical Oxidation

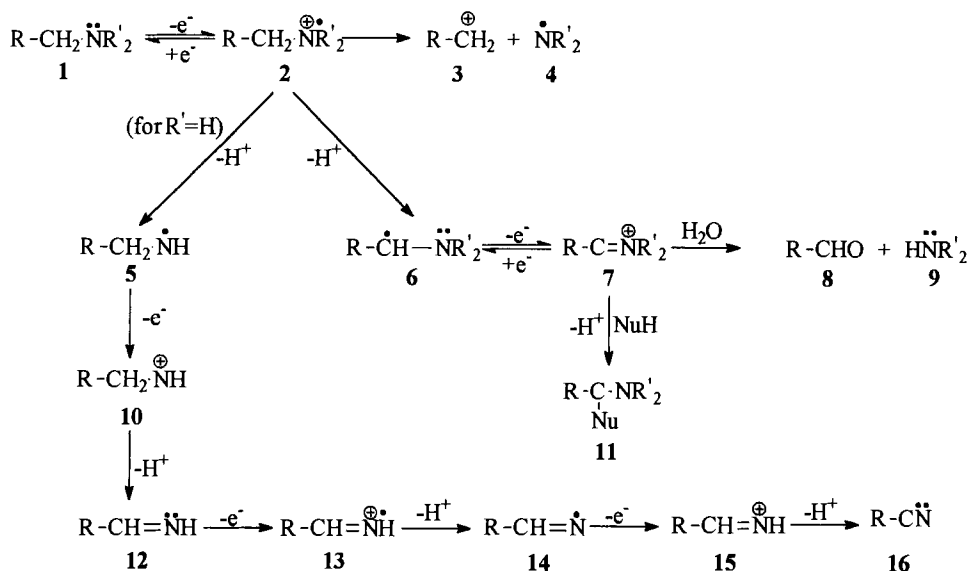
Electrochemical techniques are a convenient means of studying one-electron oxidations of amines. The reaction pattern of the anodic oxidation of amines depends greatly on the reaction conditions, including the nature of the electrode and the nucleophilicity of the solvent [1–3]. A major drawback of electrode oxidations is that unwanted secondary electron-transfer reactions can occur at the electrode surface. Also in electrochemical processes the effective reaction volume is limited at the electrode surface, thereby creating a high local concentration of reactive intermediates which can lead to dimerization and disproportionation reactions. These factors have to some extent, limited the synthetic utility of the anodic oxidation of amines. Because of this the anodic oxidation of amines has been intensively studied, although mainly from a mechanistic standpoint.

Aliphatic amines

Electrolytic oxidation of amines results in the formation of an amine radical cation by one-electron transfer to the electrode. Scheme 2 shows the various reaction pathways observed on electrochemical oxidation of aliphatic amines [1–3, 68–71]. The radical cation **2** can undergo C–N bond cleavage yielding a relatively stable carbonium ion **3**, which can undergo solvolysis, add to a nucleophile, or polymerize. As observed in the thermal oxidation reaction deprotonation at the α -carbon to yield the α -aminoalkyl radical, followed by its rapid oxidation to the iminium ion **7**, forms a major reaction pathway. The iminium ion can undergo hydrolysis or addition to a nucleophile to yield substituted product (**11**). Under strongly basic conditions, nitrogen deprotonation can occur in primary and secondary amines. The resulting nitrogen-centered radicals can couple to form dimers or can undergo further oxidation to yield nitrenium ions ($>\text{N}^{\cdot+}$). In the presence of silver [70] or nickel [71] electrodes, the nitrogen-centered radicals can be further oxidized to yield the nitrile **16**.

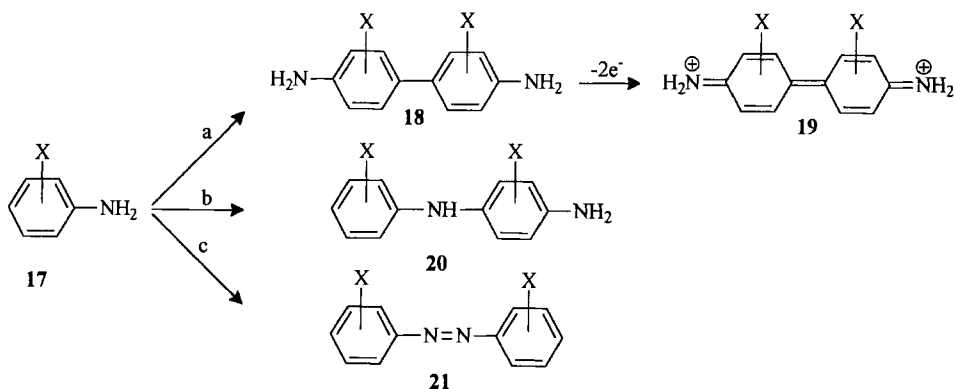
Aromatic amines

Anodic oxidation of aromatic amines has been well studied [1–3, 68, 72, 73]. These reactions are rather complex and are substantially affected by the reaction condition.

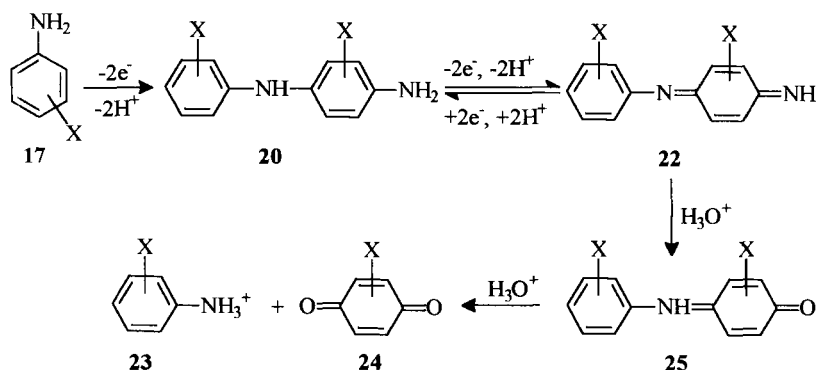


Scheme 2.

Scheme 3 shows the different reaction pathways observed in the anodic oxidation of aniline and its derivatives [74]. The cation radical formed initially can undergo dimerization or deprotonation. Dimerization is favored under strongly acidic conditions and high current densities. Subsequent deprotonation of the dimer yields the benzidine **18**. Benzidine, being more easily oxidizable than the parent amine, is converted to the diimine species. In basic solutions at low current densities and high concentrations of the starting material, deprotonation is favored, yielding a resonance-stabilized radical. This undergoes C–N coupling with a parent molecule,



Scheme 3.



Scheme 4.

leading to the formation of 4-aminodiphenylamine **20**. Further oxidation of **20** yields p -benzoquinone and the parent amine as shown in Scheme 4.

In basic solution head-to-head coupling of the deprotonated radicals result in the formation of azo compounds (**21**) from N -unsubstituted anilines. This occurs via the formation of hydrazo derivatives. p -Substituted anilines also preferentially undergo head-to-head coupling to yield azo derivatives.

The influence of reaction conditions on the electrochemical oxidation of anilines and N -alkylanilines is shown in Table 1 [74]. It has been proposed that electrochemical formation of the conducting polyaniline polymers occurs via the formation of p -aminodiphenylamine [31, 75–77].

Diphenylamines on electrooxidation also undergo aryl–aryl, N -aryl or N – N coupling as shown in Scheme 5 [1–3].

Tail-to-tail coupling of radicals obtained in the anodic oxidation of triphenylamines results in the formation of tetraphenylbenzidines. Oxidation of triarylamines to the di-cation results in the formation of the carbazoles, as observed for N -alkyl- p,p' -disubstituted diphenylamines [1–3, 78]. The cation radicals of triarylamines with substituents in the *para* position of the aryl groups, which can protect them against nucleophilic attack, are very stable and can be used as organic redox catalysts for indirect electrochemical oxidation reactions. Depending on the substitution pattern on the phenyl group the oxidation potentials of the triarylamines can be tuned over a wide range ($E_{ox} = 0.7$ – 2.0 V) and many of these have been used as redox catalysts in numerous indirect electrochemical reactions [1–3, 79–83].

7.2.3 Radiation Chemical Studies of Amines

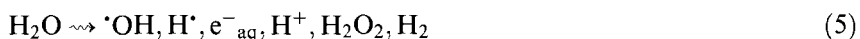
The mechanistic details of amine oxidation has also been extensively studied by use of radiation chemical methods [84–90]. In the radiolysis of dilute solutions, interaction of the ionizing radiation occurs predominantly with the solvent molecules resulting in the formation of reactive intermediates derived from the solvent [91].

Table 1. Influence of electrolysis conditions on product distribution in the anodic oxidation of aniline and *N*-alkylanilines.^{a,b}

Compound	Electrolysis conditions	Products (%) ^c
Aniline	MeCN–TEAP, low current density	4-Aminodiphenylamine (40)
Aniline	0.05 M H ₂ SO ₄ , high or low current density	<i>p</i> -Benzoquinone (90–100)
Aniline	6 M H ₂ SO ₄ , high current density	<i>p</i> -Benzoquinone (80–90) Benzidine (10–20)
<i>N</i> -Ethylaniline	MeCN–TEAP, low current density, low parent concentration	<i>N,N'</i> -Diethylbenzidine (60–70)
<i>N</i> -Ethylaniline	MeCN–TEAP, high current density	<i>N,N'</i> -Diethylbenzidine (70–80)
<i>N</i> -Ethylaniline	MeCN–TEAP, low current density, high parent concentration	<i>N</i> -Ethyl-4-ethylaminodiphenylamine (70)
<i>N</i> -Ethylaniline	6 M H ₂ SO ₄ , high current density	<i>p</i> -Benzoquinone (40) <i>N,N'</i> -Diethylbenzidine (60)
<i>N-tert</i> -Butylaniline	MeCN–TEAP, high current density	<i>N,N'</i> -di- <i>tert</i> -Butylbenzidine (100)

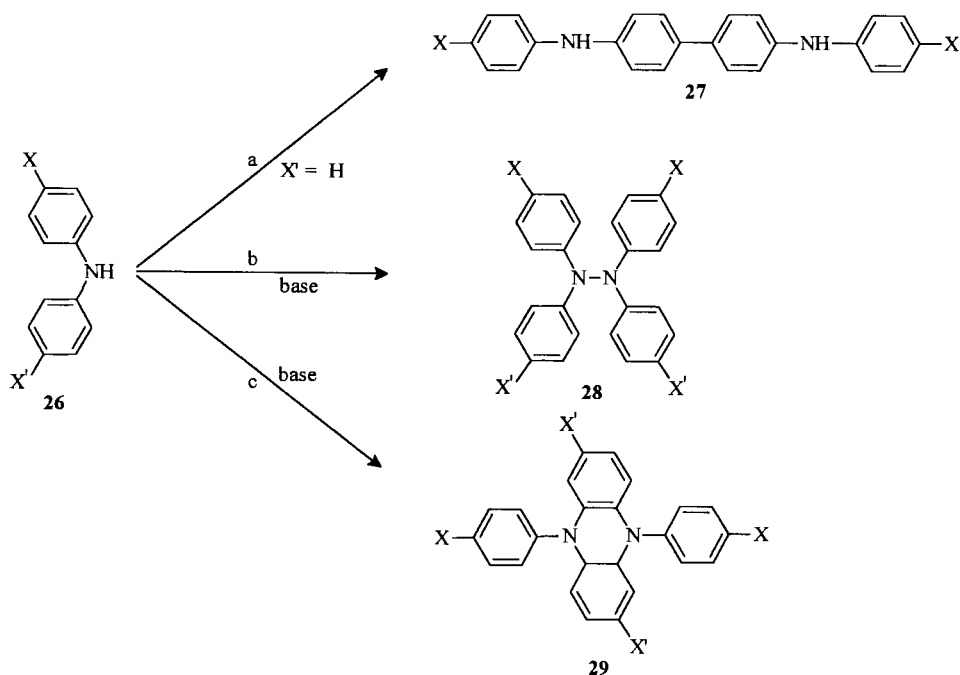
^aControlled-potential electrolyses.^bAccording to [1].^cBased on consumed parent compound.

Thus, the radiolysis of dilute aqueous solutions results in the formation of solvated electrons (e_{aq}^-) hydroxyl radicals, and hydrogen atoms (Eq. 5). In neutral and alkaline solutions, H atom formation is negligible.



Oxidizing or reducing conditions can be created by selective scavenging of the intermediates. In nitrous oxide saturated solutions, for example, reaction of the solvated electron with N₂O leads to further generation of hydroxyl radicals. Alternatively, reducing conditions can be achieved by using tertiary butanol radicals to scavenge the hydroxyl radicals. Oxidizing species other than hydroxyl radicals that have normally been generated in aqueous solutions to study amine oxidation reactions include the azide radical (N₃·) [88] and halogen radicals [89]; these are normally generated by reaction of hydroxyl radicals with azide and halogen ions. Sulfate radicals (SO₄·⁻) generated by reaction of electrons with persulfate anions, have also been used to study the oxidation of amines [92]. An oxidizing environment can also be generated in non-aqueous solvents. Radiolysis of dichloromethane solutions, for example, results in the formation of CH₂ClO₂· and CHCl₂O₂· radicals, both of which are oxidizing in nature [89].

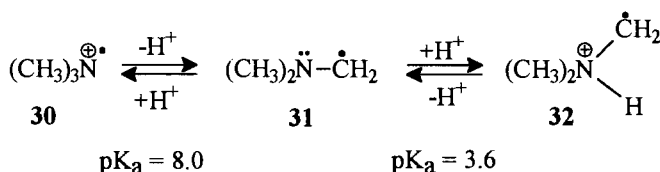
The formation and subsequent reaction of amine radical cations by radiolysis can be studied by pulse radiolysis in combination with optical [84, 87–90], conductivity



Scheme 5.

[85], and ESR [93–95] detection techniques. A major advantage of these methods over flash photolysis is that the transient signals from the amine radicals are not complicated by the presence of radical anions, which are normally generated along with amine radical cations in photoinduced electron-transfer processes. Aminoalkyl radical intermediates formed in the process can be monitored optically, because of strong absorption in the 220–450 nm region.

Apart from being good electron donors, the lability of the hydrogen atoms attached to the α -carbon of amines also make the amines very good hydrogen-atom donors. The very high rate constant ($k = 1.2 \times 10^{10} \text{ M}^{-1} \text{ s}^{-1}$) for the reaction of hydroxyl radicals with amines is, however, strongly indicative of a predominantly electron-transfer mechanism [84]. Rate constants for normal hydrogen-atom-abstraction reactions of OH^\bullet with good hydrogen-atom donors such as formate ($k = 3 \times 10^9 \text{ M}^{-1} \text{ s}^{-1}$) and isopropanol ($k = 3 \times 10^9 \text{ M}^{-1} \text{ s}^{-1}$) [96] are generally much lower. The radical cation formed in the electron-transfer reaction is an oxidizing species whereas the α -aminoalkyl radical formed via hydrogen abstraction is reducing in nature. Formation of substantial amounts of oxidizing amine radical cation even at high pH (>10.0) in the reaction of hydroxyl radicals with the amine was indicated by the reaction of the radical intermediates with *N,N'*-tetramethyl-*p*-phenylenediamine (TMPD), which results in the formation of $\text{TMPD}^{+\bullet}$. This confirms that the reaction of hydroxyl radicals with amine occurs predominantly via electron transfer [84].



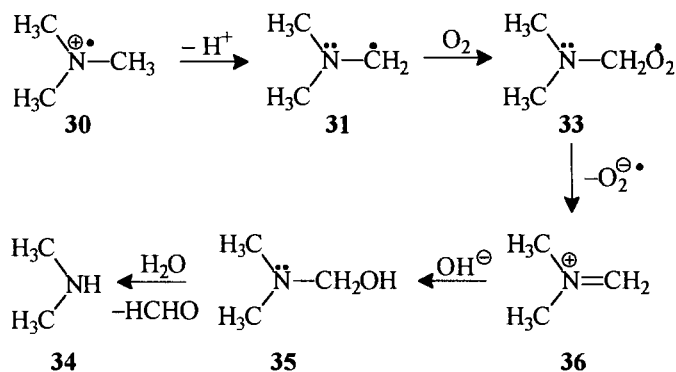
Scheme 6.

The amine radical cation of triethylamine formed in these reactions can exist in an acid–base equilibrium, as shown in Scheme 6.

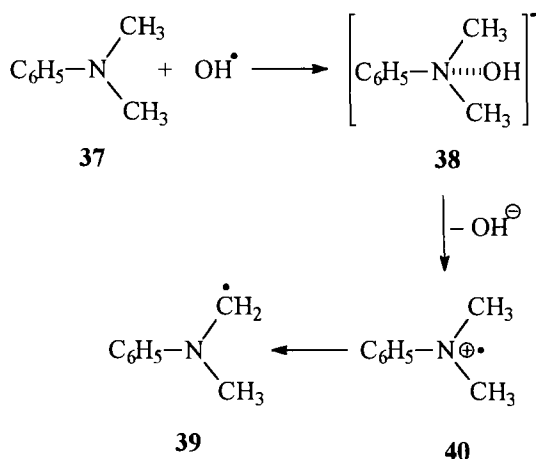
Pulse radiolysis studies using optical detection suggested the main species in equilibrium to be the α -aminoalkyl radical (**31**) and the *N*-protonated α -aminoalkyl radical (**32**) whereas results from ESR studies were indicative of protonation at the α -carbon site to form the *N*-centered radical cation (**30**). A subsequent study showed that these results could be attributed to kinetic and thermodynamic factors [84]. Thus *N*-protonation resulting in the formation of **32** is kinetically favored and is hence observed in the short time-scales involved in pulse-radiolysis systems. In the longer times involved in ESR measurements the thermodynamically more stable *N*-centered radical cation will be observed. The pK_a of **30** and **32** were estimated as 8.0 and 3.6 by use of pulse radiolysis [84]. Using the equation for similar keto \leftrightarrow enol tautomerism of barbituric acid [97], the ratio of **30/32** was estimated to be $10^{-3.6}/10^{-8} = 10^{4.4}$, indicating the *N*-centered radical (**30**) to be the predominant protonated species.

The rate constants for deprotonation of the trimethylamine radical cation by the parent amine and by hydroxyl radicals were estimated as 1×10^9 and $1 \times 10^{10} \text{ M}^{-1} \text{ s}^{-1}$, respectively [84]. The rate constants for the different steps involved in the reaction of oxygen with α -aminoalkyl radical **31** (Scheme 7) were determined by pulse radiolysis with conductivity detection [85].

The α -aminoalkyl radical (**31**) reacts rapidly with oxygen ($k = 3.5 \times 10^9 \text{ M}^{-1} \text{ s}^{-1}$) to form $\text{O}_2^{\bullet-}$ possibly via a short-lived ($\tau = 10^{-6} \text{ s}$) peroxy radical **33**. Elimination



Scheme 7.



Scheme 8.

of peroxide ion from **33** will lead to **36** (Scheme 7). The dimethyl iminium ion (**36**) adds OH^- to form (hydroxymethyl)dimethylamine (**35**) ($k = 2.8 \times 10^8 \text{ M}^{-1}\text{s}^{-1}$). This is hydrolyzed much more slowly ($k_{\text{obs}} = 4.0 \text{ s}^{-1}$) to yield formaldehyde and the dealkylated amine (**34**).

One-electron oxidation of aniline by hydroxyl radicals yields the anilinium radical $[\text{C}_6\text{H}_5\text{NH}_2]^{+\bullet}$, which loses a proton over several microseconds to give the neutral radical $\text{C}_6\text{H}_5\text{NH}^\bullet$ [98, 99]. The deprotonation was followed at 400–440 nm where the radical cation absorbs more strongly than the neutral radical. Because the $\text{p}K_{\text{a}}$ of parent aromatic amines are generally lower than those of the corresponding radical cations, an external base is required to effect deprotonation of the anilinium radical.

On the basis of studies using nanosecond time resolution, Holcman and Sehested suggested that the reaction of hydroxyl radicals with dimethylaniline occurs via the intermediate formation of a hydroxyl radical–amine adduct [100], as described in Scheme 8.

The transient absorption spectrum of the OH adduct of dimethylaniline has a broad band centered at ca 380 nm. Decay of this species results in a growth of absorption in the 450 nm region where the radical cation has a strong absorption. Assignment of the radical cation spectrum was supported by comparison with the spectra obtained in the electron-transfer reaction of sulfate radicals with DMA, and with $\text{DMA}^{+\bullet}$ spectra generated by flash photolysis and electrochemical methods [101, 102]. The spectral characteristics of the observed transient species are summarized in Table 2.

The mechanism of hydroxyl-radical-mediated oxidation of aromatic amines has recently been reinvestigated by Tripathi and Sun, who used time-resolved Raman spectroscopy as a diagnostic tool. Their studies suggest that the initial transient formed in the reaction of hydroxyl radicals with the neutral *p*-phenylene diamine is the amine radical cation and not the OH-adduct of the amine as originally believed.

Table 2. Spectral characteristic of the radicals formed in the reaction of H and OH radicals with DMA.^a

Radical	λ_{\max} (nm)	ϵ (M ⁻¹ cm ⁻¹)
[C ₆ H ₅ N(CH ₃) ₂]H [•]	380	6500 ± 1000
[C ₆ H ₅ N(CH ₃) ₂]OH [•]	380	
	<270	
C ₆ H ₅ N(CH ₃)CH ₂ [•]	330	10500 ± 500
	450	1400 ± 100
[C ₆ H ₅ N(CH ₃) ₂] ⁺⁺	270	4500 ± 400
	465	

^a According to [100].

An adduct-mediated electron-transfer pathway was, however, observed for the protonated amine [103].

The electronic absorption maxima of the few other aminium ions that have been investigated are given in Table 3 [22, 56].

The acidities of aminium ions derived from primary and secondary amines have also been measured; a few representative examples are listed in Table 4, with the acidities of the parent compounds.

The p*K*_a of the aminium ions is generally lower than those of the corresponding amine. The greater acidity of the aminium ion can be attributed to the greater amount of 's' character in the lone-pair orbital of the amine radical, (CH₃)₂N[•], which is sp²-hybridized compared, with the more basic lone pair orbital in (CH₃)₂NH, which is sp³-hybridized. In contrast, the p*K*_a of the anilinium radical is much higher than that of the protonated aniline. The basicity of the anilinium radical is comparable with that of (CH₃)₂NH⁺⁺, reflecting the sp²-hybrid character of the N–H bonds in the two species. The low basicity of the parent aniline results from

Table 3. Electronic absorption spectra of radical cations.^a

Radical cation precursor	Solvent	λ_{\max} (nm)
(CH ₂) ₅ NH (piperidine)	Acidic water	295
DABCO	Aqueous acetonitrile	465 ($\epsilon = 2000$)
HONH ₂	Acidic water	220
Aniline	Water or EPA	425 ($\epsilon = 2000$)
<i>N</i> -Methylaniline	Acidic water	455
<i>N,N'</i> -Dimethylaniline	Water or Acetonitrile	460
Diphenylamine	Acetonitrile	660
Triphenylamine (TPA)	Acetonitrile or EPA	655 ($\epsilon = 10^4$)
<i>tris-p</i> -Methoxy TPA	Acetonitrile	714
2-Aminonaphthalene	Water	525

^a According to [12].

Table 4. Acidities of radical cations and protonated parent compounds.^a

Radical cation precursor	p <i>K</i> _a value	
	–N ^{•+}	–N–H ⁺
Ammonia	6.7	9.2
Diethylamine	7.0	10.7
Hydroxylamine	4.2	6.1
Methoxylamine	2.9	4.6
Aniline	7.0	4.6

^a According to [12].

delocalization of the lone-pair electrons and the loss in resonance stabilization upon protonation.

ESR spectra of a wide variety of aminium radicals have been studied [22, 93–95, 104–114]. The radical cations were generated for this purpose by UV photolysis or γ -radiolysis in strongly acidic solutions for unstable radical cations [93–95, 104–106]. More stable radical cations such as those of triisopropylamine and 9-*tert*-butylazabicyclo(3.3.1)nonane were prepared by oxidation in dichloromethane by SbF₅ or (*p*-BrC₆H₄)₃N⁺/SbCl₆[–] [107–109]. γ -Radiation in Freon matrices at 77 K has also been used to study the ESR spectra of amine radical cations [109–114]. With the exception of a few oligocyclic amines, for which flattening is impaired by the rigid molecular framework, aminoalkyl radicals are generally planar. Various parameters related to the structure and reactivity of aminoalkyl radical cations have been extensively reviewed [22].

7.2.4 Photoinduced Electron Transfer

Photoinduced electron transfer (PET) processes can be used to bringing about one-electron oxidation and reduction of organic molecules [115–118]. In these processes, photoexcitation of an electron acceptor or donor leads to enhancement of their electron-accepting and -donating properties, respectively. When the excited state molecule comes into contact with a ground-state electron donor or acceptor within the excited state lifetime, electron transfer can occur. The feasibility of producing radical ions via these processes can be predicted by use of the Rehm–Weller equation [119], which is given in Eq. 6 [120]:

$$\Delta G^\circ = -23.06[E^\circ_{A/A^\ominus\bullet} - E^\circ_{D/D^{\oplus\bullet}}] - \frac{e_o^2}{\epsilon_A} - \Delta E_{0,0} \quad (6)$$

where ΔG° is the change in free energy associated with the electron transfer. The figure 23.06 enables ΔG° to be expressed in kcal, $E^\circ_{A/A^\ominus\bullet}$ is the reduction potential in volts of the acceptor A in the ground state, $E^\circ_{D/D^{\oplus\bullet}}$ is the oxidation potential of the donor; ϵ_A is the dielectric constant of the solvent and the term e_o^2/ϵ_A represents

Table 5. Redox potentials and free energy changes for electron transfer between the ground state of selected group of amines and the excited states of anthraquinone and dicyanoanthracene.^a

Donor (D)	Acceptor (A)	$\Delta E_{0,0}(A)$	$E_0(D/D^{+\bullet})^b$	$E_0(A/A^{\bullet-})^b$	ΔG_{el}
<i>N,N</i> -Diethylaniline	Anthraquinone	3.1	0.76	-0.94	36.10
<i>N,N</i> -Dimethylaniline	Anthraquinone	3.1	0.81	-0.94	37.26
Diethylamine	Anthraquinone	3.1	0.78	-0.94	36.56
Triethylamine	Anthraquinone	3.1	0.76	-0.94	36.10
Triphenylamine	Anthraquinone	3.1	0.98	-0.94	41.18
<i>N,N</i> -Diethylaniline	Dicyanoanthracene	2.86	0.76	-0.89	35.19
<i>N,N</i> -Dimethylaniline	Dicyanoanthracene	2.86	0.81	-0.89	36.34
Diethylamine	Dicyanoanthracene	2.86	0.78	-0.89	35.65
Triethylamine	Dicyanoanthracene	2.86	0.76	-0.89	35.19
Triphenylamine	Dicyanoanthracene	2.86	0.98	-0.89	40.26

^aAccording to [13].^bRedox potentials are reported relative to SCE in polar solvents.

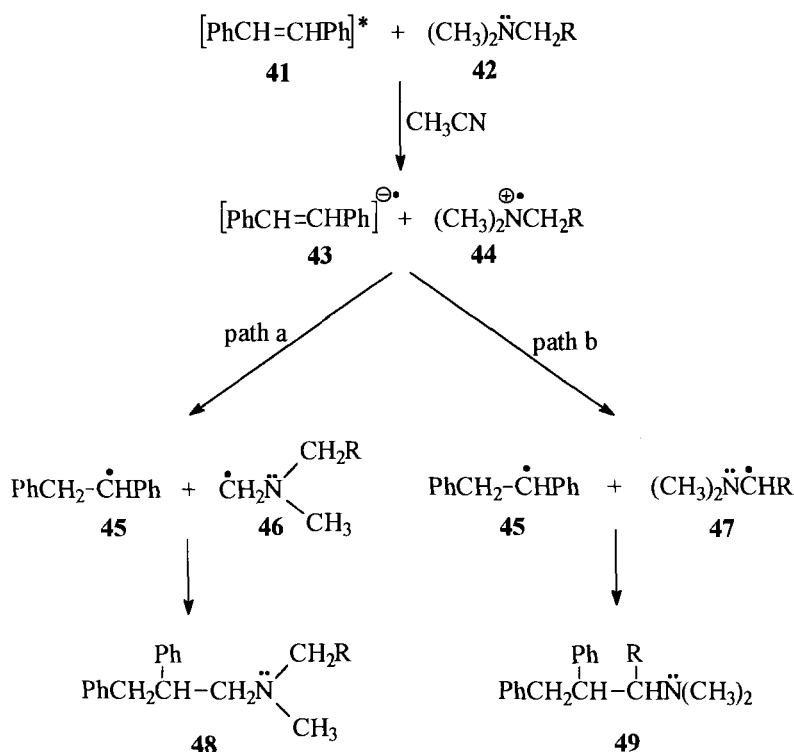
the free enthalpy associated with the Coulombic interaction between D and A. $\Delta E_{0,0}$ is the electronic excitation energy of the partner whose redox properties have been enhanced by excitation.

The Coulombic term in Eq. 6 becomes negligible in polar solvents owing to 'shielding' of the electrostatic interaction between the radical ions generated. Table 5 lists representative redox potentials and free energies for photo-mediated electron transfer between a selected group of amines and photosensitizers such as anthraquinone (AQ) and dicyanoanthracene (DCA).

The problem of secondary electron transfer normally observed in thermal and electrochemical oxidation can be partially circumvented by using photo- and radiation chemical methods, because in such processes the oxidizing species is generated as a transient and the steady-state concentration of radical intermediates is usually very low ($\leq 10^{-6}$ M).

Deprotonation at the α -carbon of aminium radicals produced in SET reactions

As discussed earlier, deprotonation of α -carbon forms a major reaction pathway for the disappearance of the amine radical cation. Studies of photoinduced electron-transfer reactions of tertiary amines by Lewis [7, 11] and by Mariano [5, 10] have contributed significantly towards our understanding of the factors that control this process. Lewis and coworkers used product-distribution ratios of stilbene-amine adducts to elucidate the stereoelectronic effects involved in the deprotonation process [5, 10, 121, 122]. In non-polar solvents, the singlet excited state of *trans*-stilbene forms non-reactive but fluorescent exciplexes with simple trialkylamines. Increasing solvent polarity brings about a decrease in the fluorescence intensity and an increase in adduct formation. For non-symmetrically substituted tertiary amines two types of stilbene-amine adduct can be formed, as is shown in Scheme 9, depending on whether the aminoalkyl radical adding to the stilbene radical is formed by de-



Scheme 9.

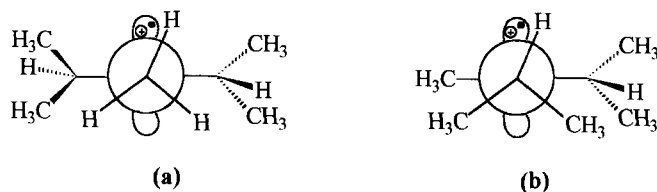
protonation of the less substituted (path a) or more substituted (path b) α -CH bond. The yields and ratios of the two types of adduct formed from a variety of unsymmetrical amines are summarized in Table 6 [122].

These studies indicate that the selectivity of α -aminoalkyl radical formation is $\text{Me} > \text{Et} \gg i\text{-Pr}$, which is the opposite of that expected on the basis of radical stability. For example, in diisopropylmethylamine, methyl adducts are formed exclusively. Similar selectivity has been observed for oxidation of unsymmetrical amines by ferricyanide [43, 123] and in anodic processes [124]. This selectivity has been attributed to requirement of overlap between the half-vacant nitrogen p orbital and the α -CH orbital of the α -carbon. From the Newman projections below it can be seen that the conformation necessary for methyl deprotonation (a) is lower in energy than that for the isopropyl deprotonation (b) [5, 122].

Selective formation of the more substituted α -aminoalkyl radical was, however, observed for amines of the type $\text{Me}_2\text{NCH}_2\text{R}$, where R is a radical stabilizing group with minimal steric requirements ($\text{R}=\text{CH}_2=\text{CH}-$, $\text{Ph}-$, $\text{HC}\equiv\text{C}-$, and $\text{C}_2\text{H}_5\text{CO}_2$) [125]. It has been proposed that the base strength can also affect the selectivity of deprotonation, as observed in the formation of the less substituted alkene as the base strength is increased in E1 elimination reactions [122, 126, 127].

Table 6. *trans*-Stilbene–amine adduct yields and ratios.^a

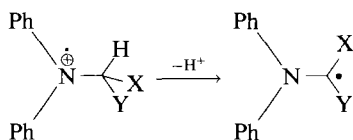
Amine	% of 48	% of 49	48/49 corrected
Diisopropylmethyl	>95	<5	>20
Isopropyl dimethyl	>95	<5	>20
Ethyl diisopropyl	92	8	12
Diethylmethyl	63	37	2.3
<i>n</i> -Butyl dimethyl	86	14	2.0
Ethyl dimethyl	84	16	1.8
Dimethylbenzyl	77	23	1.1
Dimethylallyl	87	13	2.2
Dimethylglycine ethyl ester	49	51	0.48
1-(Dimethylamine)-2-butyne dimethyl propargyl	<5	>95	<0.01

^a According to [122].**Chart 1**

Mariano and coworkers have investigated the effect of substituents on the α -CH kinetic acidity of several tertiary aromatic amine radical cations generated by electron transfer from the parent amines to the excited state of dicyanobenzene [128]. Laser excitation of 60:40 methanol–acetonitrile solutions of dimethylaniline (DMA) and dicyanobenzene (DCB) result in the formation of the DMA cation radical with an absorption maximum at ca 460 nm and the DCB radical anion with an absorption maximum at ca 340 nm, which decay by back-electron-transfer at diffusion-controlled rates ($k = 1.1 \times 10^{10} \text{ M}^{-1} \text{ s}^{-1}$). Bases such as tetrabutylammonium acetate ($n\text{-Bu}_4\text{NOAc}$) and tetrabutylammonium trifluoroacetate ($n\text{-Bu}_4\text{NOCCF}_3$) were observed to deprotonate the DMA radical cation with rate constants of 3.1×10^5 and $8 \times 10^4 \text{ M}^{-1} \text{ s}^{-1}$ respectively.

The rate constant for $n\text{-Bu}_4\text{NOAc}$ -catalyzed deprotonation increases with *para*-substitution of the amine in the order $p\text{-OMeC}_6\text{H}_4\text{NMe}_2 < p\text{-MeC}_6\text{H}_4\text{NMe}_2 < p\text{-CF}_3\text{C}_6\text{H}_4\text{NMe}_2$, which is consistent with the effects of *para* substituents, because electron-donating groups stabilize the radical cation leading to an increase in its $\text{p}K_a$. The effects of α -substituents on the rates of $n\text{-Bu}_4\text{NOAc}$ -induced α -CH deprotonation of tertiary amines was studied for the amines $\text{Ph}_2\text{N}(\text{CHR}^1\text{R}^2)$ (Table 7).

The results of these studies were compared with those obtained earlier for the stilbene amine photoaddition [7, 11] and amine–enone photoelectron-transfer-catalyzed cyclizations (Table 7). The effects of α -substituents on the α -CH deprotonation rates of aminium radicals measured in the stilbene–amine photoaddition

Table 7. Relative rates of deprotonation of the α -substituted tertiary amine cation radical from product distribution and laser spectroscopic studies.^a

Entry	X	Y	From stilbene– amine SET system	From enone– amine SET photocyclizations	From rate constant for acetate promoted deprotonation of diphenylaminium radical (laser spectroscopy)
a	H	H	1.1	1.1	0.3
b	H	CH ₃	0.5	0.2	0.1
c	CH ₃	CH ₃	<0.05	–	0.05
d	H	Ph	1.0	1.0	1.0
e	H	CH=CH ₂	0.5	1.9	0.8
f	H	C≡CH	111	3.9	22

^a According to [128].

reactions and by laser spectroscopic methods show the same trend, although in the stilbene–amine photoaddition the steric effect on α -CH deprotonation is much more pronounced. It has been suggested that the difference might arise from the different nature of the deprotonation in the two systems [129]. Proton transfer in the stilbene–amine system occurs within the contact ion-pair [7, 121, 122], the structure of which might be governed by the need for charge stabilization. This effect could make kinetic factors more important in such systems than those determined by the acetate-promoted deprotonation of the free radical cation. The differences could also be attributed to the weak nature of the base used in the laser spectroscopic studies. The second-order rate constants for the deprotonation of the aminium radical catalyzed by acetate are, in fact, much lower than diffusion-controlled processes. Thus in this instance electronic factors, i.e. the capacity of the substituents to stabilize the resulting α -amino radical could play a greater role in deciding the nature of the α -CH deprotonation.

For enone–amine photocyclization reactions the α -CH kinetic acidity seems to be mainly dependent on electronic factors and this has been attributed to the intramolecular nature of proton transfer in the enone–amine zwitterionic radicals (diagram below), which would disfavor overlap of the half vacant ‘p’ orbital on nitrogen with the α -CH bond [128, 130, 131].

Photoinduced bond-cleavage reactions

More recently, Mariano and coworkers have investigated the effects of substituents and medium on desilylation, decarboxylation, and retro-aldol cleavage reactions

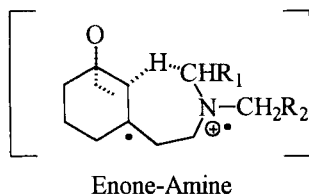
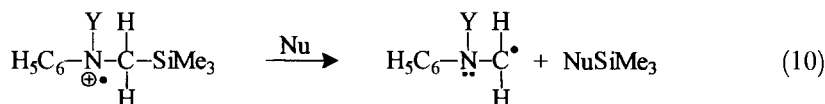
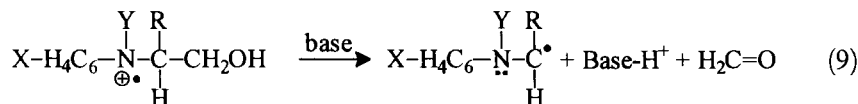
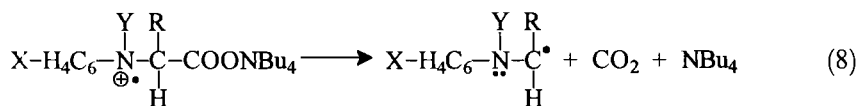
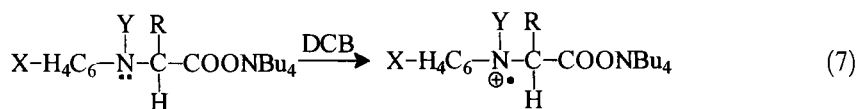


Chart 2

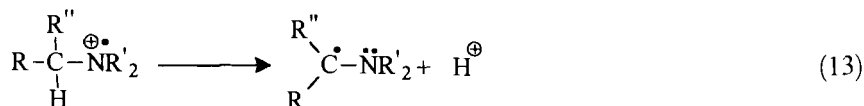
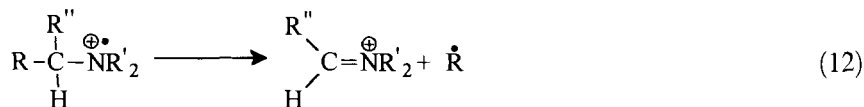
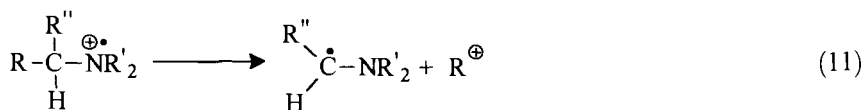
(Scheme 10) of anilinium radicals by laser-flash photolysis [129]. 308-nm laser excitation of the anilincarboxylate in the presence of dicyanobenzene leads to electron transfer from the excited state of anilincarboxylate to the ground state of DCB (Eq. 7) as evidenced by the transient absorption maxima at 340 nm ($\text{DCB}^{\cdot-}$) and 450–480 nm (anilinium radical). The decay of the anilinium radical occurs at a much faster rate than that of $\text{DCB}^{\cdot-}$ indicating that back-electron-transfer is not a major reaction pathway unlike in the SET reaction of dimethyl aniline. The fast decay of the anilinium radical has been attributed to unimolecular α -decarboxylation, as shown in Eq. 8 (Scheme 10).

The unimolecular rates of reactions (Eqs. 8 and 9) were found to depend on solvent polarity and substituents on the aniline ring, nitrogen, and α -carbon. The second-order rate constants for methanol-promoted desilylation (Eq. 10) of the aminium radical generated via SET reactions of α -anilinosilanes increased tenfold on changing the substituent on nitrogen from an alkyl group to acyl group.

The competition between fragmentation of the C–C bond and deprotonation (Scheme 11) of the aminium radical has been extensively probed by Whitten and others [132–139]. Cleavage of the C–C bond can occur to produce either carbocations (Eq. 11) or radicals (Eq. 12).



Scheme 10.



Scheme 11.

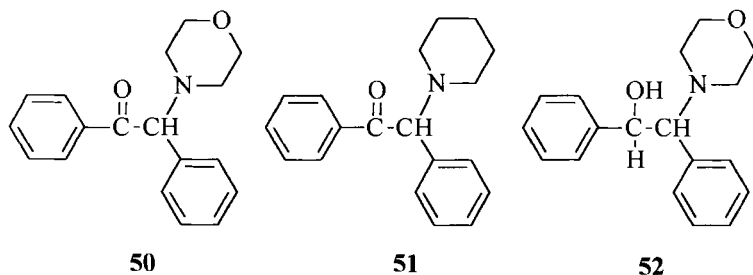
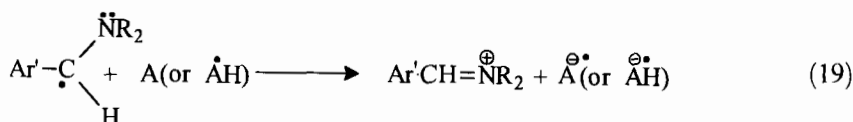
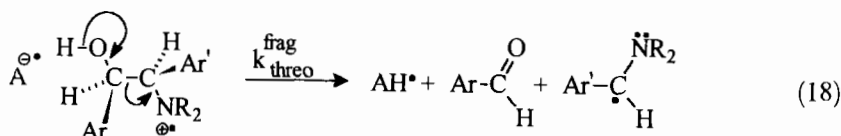
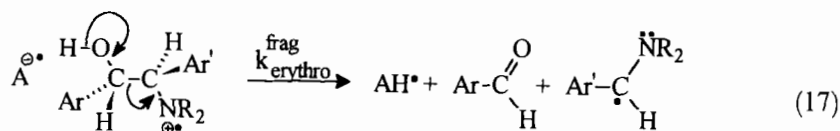
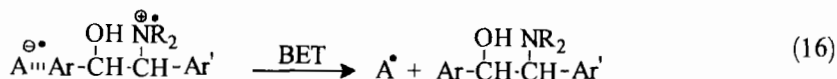
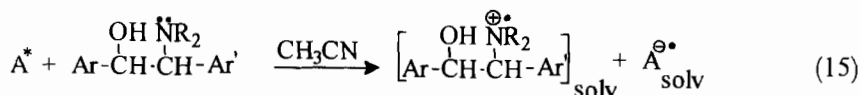
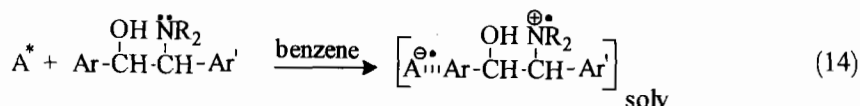


Chart 3

Photoinduced oxidation of the aminoketones **50** and **51** results predominantly in the formation of benzoyl radicals indicating Eq. 12 in Scheme 11 to be the predominant reaction pathway for the corresponding aminium radicals.

A general mechanism for fragmentation of aminium radicals derived from β -aminoalcohols in the presence of an electron acceptor (A^*) has been proposed (Scheme 12) on the basis of studies of a variety of substituted 2-morpholino-1,2-diphenylethanol derivatives.

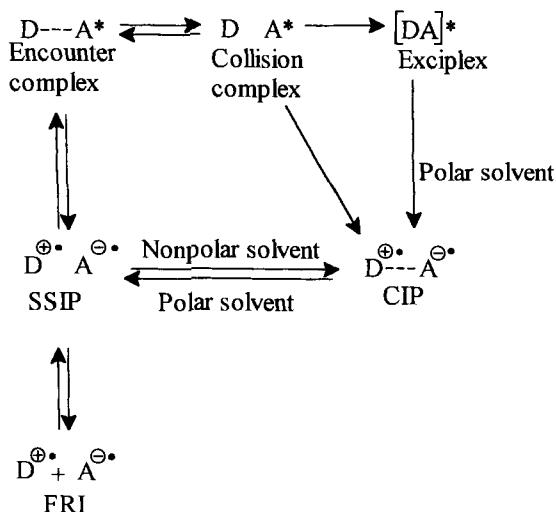
The fragmentation has been proposed to occur via proton loss from the alcohol. Studies of diastereomeric isomers of 2-morpholino-1,2-diphenyl ethanol **52** indicated a striking preference for the reaction of the *erythro* over *threo* isomers. This has been attributed to two factors. The first is the different efficiency of the quenching step (Eq. 15, Scheme 12)—it has been suggested that efficient intramolecular hydrogen-bonding of the *threo* isomer reduces the electron-donating capacity of the amine. A second and more important factor explaining the different yields is the competition between fragmentation (Eqs 17 and 18) and back-electron-transfer (Eq. 16), which yields the starting compounds. It has been proposed that the requirement of a coplanar, *anti*-parallel relationship between the alcohol, C–C bond, and amine radical cation is more easily obtained in the *erythro* isomer than for the *threo* compound.



Scheme 12.

Study of excited-state and radical-ion intermediates in SET reactions using time-resolved techniques

Nanosecond and picosecond laser-flash photolysis techniques have been used by different groups to elucidate the various intermediate stages involved in the photo-induced reactions of amines. The overall mechanism involving the electron-transfer process in a fluid medium is illustrated in Scheme 13. The dynamics of the process involve the formation of an encounter complex between the excited-state molecule and the ground-state molecule [117, 140, 141]. The encounter complex can be described as an intermolecular ensemble of excited- and ground-state molecules, separated by a small distance (ca 7 Å) and surrounded by solvent molecules. During



Scheme 13.

the lifetime of the encounter complex, the reactants undergo mutual collisions inside the solvent cage and as a result of these collisions, a stage is reached where the reactants are in contact to form what is called the collision complex. If the interaction between the reactants is strong enough (ca $5\text{--}20 \text{ kcal mol}^{-1}$), the collision complex can rapidly change to a new intermediate called an exciplex, which has partial charge transfer character and a large dipole moment. Electron transfer can occur at any of these stages [117]. Electron transfer from the collision complex or from the exciplex leads to the charge-transfer species called a contact ion pair (CIP). The contact ion pair can undergo slight separation in the solvent cage to generate a solvent-separated ion pair (SSIP). Alternatively, electron transfer from the encounter complex can directly lead to the SSIP. The solvent-separated ion pairs can then diffuse apart from the solvent cage and become separated to form the free solvated radical ions (FRI), which are analogous to free radicals and can undergo chemical reactions to yield products.

All these processes, namely, the formation of the encounter complex, collision complex, contact ion pairs, solvent-separated ion pairs, and free-radical ion pairs, are reversible. For generation of free radicals in good yields, forward electron-transfer processes have to compete efficiently with the energy wasting back-electron-transfer processes [142].

Picosecond and nanosecond transient spectroscopic studies to elucidate the nature of various intermediates formed in the photoinduced electron-transfer reaction of amines have been most extensive for the ketone–amine systems. These studies have been described in detail in a recent review by Yoon et al. [10]. Some aspects of these studies are briefly described here. In the earlier studies of Cohen and coworkers, the photochemical reactions of benzophenone with aliphatic amines were probed by fluorescence quenching, determination of product quantum yields, and nanosecond laser-flash photolysis [143–147]. They proposed that the reactions of amines with

the triplet states of benzophenone proceed via the formation of an intermediate charge-transfer complex ($^3\text{CTC}^*$), although no direct evidence for the formation of such complexes was available from their studies. Laser-flash photolysis of benzophenone in the presence of a variety of aliphatic amines indicates the formation of ketyl radicals (λ_{max} 555 nm) with a quantum yield of unity. Ketyl radicals could be generated via hydrogen-atom abstraction from amines rather than via electron transfer followed by proton transfer between the radical ion pair. However the extremely fast reaction between amine and the triplet excited state of benzophenone ($k = 5 \times 10^{10} \text{ s}^{-1}$) supports the view that electron-transfer reactions are involved. Direct proof of the electron-transfer mechanism was obtained from their studies on the flash photolysis of benzophenone–DABCO systems [146]. In these systems the formation of the ketyl radical anion as a transient species (λ_{max} 660 nm) could be observed, because of the increased stability of DABCO^{+*} and because deprotonation of the α -CH is not facile for this constrained amine [147].

Photoreduction of benzophenone by primary and secondary amines leads to the formation of benzpinacol and imines [145]. Quantum yields greater than unity for reduction of benzophenone indicated that the α -aminoalkyl radical could further reduce the ground state of benzophenone. Bhattacharyya and Das confirmed this in a laser-flash photolysis study of the benzophenone–triethylamine system, which showed that ketyl radical anion formation occurs by a fast and a slow process wherein the slow process corresponds to the reaction of α -aminoalkyl radical in the ground state of benzophenone [148]. Direct evidence for similar secondary reduction of benzil [149] and naphthalimides [150] by the α -aminoalkyl radical have also been reported. The secondary dark reaction of α -aminoalkyl radicals in photo-induced electron-transfer reactions with a variety of quinones, dyes, and metal complexes has been studied by Whitten and coworkers [151].

Formation of the ketyl radical anion in photoinduced electron-transfer reactions of benzophenone with butylamine and triethylamine was observed by Shizuka and coworkers in neat amines at low temperatures [14, 152]. At room temperatures they observed the formation of the ketyl radical (λ_{max} 555 nm), whereas on reducing the temperature to 120 K the transient absorption spectrum showed a decrease in intensity at 555 nm and a subsequent increase at 660 nm. This has been attributed to the slowing down of proton transfer between the radical ion-pairs at low temperatures, making it possible to measure ketyl radical anion absorption at 660 nm [152]. At very low temperatures however (ca 120 K) only the triplet state of benzophenone was observed (λ_{max} 525 nm), indicating thereby that under these conditions the triplet state of benzophenone does not undergo electron-transfer reactions with amines.

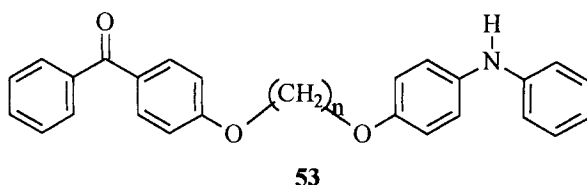
Direct evidence for the formation of radical ion intermediates in the benzophenone–amine system was also obtained by Peters et al. [153–156]. Pico-second laser-flash photolysis studies have indicated the formation of ketyl radical anions concomitant with the decay of the benzophenone triplet. For 1.0 M dimethylaniline and diethylaniline the rate of electron transfer to the benzophenone triplet was 3.6×10^{10} and $4.2 \times 10^{10} \text{ M}^{-1} \text{ s}^{-1}$, respectively. On the basis of their studies Peters et al. proposed a mechanism in which a solvent-separated ion pair

(SSIP) is formed first; this subsequently collapses into a contact ion pair (CIP). This mechanism was based on the observation of a blue shift of the absorption maximum of the ketyl radical anion from 715 to 690 nm which occurs with a half-life of 200 ± 50 ps. The SSIP, being more solvated than the CIP, is expected to have its absorption spectrum red-shifted compared with that of CIP. Subsequent studies by Devadoss and Fessenden on the benzophenone–DABCO system indicated, however, that the spectrum of initial transient has an absorption maximum at 700 nm, which shifts to the red (720 nm) in the picosecond time domain [157, 158]. These results seem to suggest that the initial species to be formed is the CIP which eventually separates to yield the SSIP and proton transfer occurs in the SSIP.

They also observed that the species absorbing at 720 nm which decays on the microsecond time-scale by first-order kinetics is a long-lived SSIP. Evolution of the SSIP to free-radical ions was ruled out, because free-radical ions should decay by second-order kinetics. Later observations by Mataga [159, 160] and by Haselbach [161], on the basis of photoconductivity measurements and transient absorption spectroscopy of the benzophenone–DABCO system, showed that the species absorbing at 710 nm decays not by first-order kinetics but by second-order kinetics; this is consistent with the formation of free-radical ions.

The mechanism of the photoreduction of benzophenone by dimethylaniline (DMA) has subsequently been probed by Mataga and coworkers by use of femto-second and picosecond absorption spectroscopy [160]. For the first time they considered the role in the photoreduction process of the first excited singlet state ($^1\text{BP}^*$) and the triplet excited state ($^3\text{BP}^*$) of benzophenone. Mataga's investigation revealed that three radical ion pairs are formed in the reduction process. In the ground state, benzophenone forms a ground state charge-transfer complex with dimethylaniline. Thus 355 nm irradiation leads to excitation of both benzophenone and the charge-transfer complex. The charge-transfer complex on excitation directly forms the contact ion pair, with an absorption maximum at 740 nm; this decays by back-electron-transfer in 85 ps to reform the ground-state reactants. During the decay process, there is no change in the absorption maximum, and proton transfer does not occur. Excitation of the uncomplexed benzophenone produces $^1\text{BP}^*$, which undergoes intersystem crossing to $^3\text{BP}^*$ with a rise time of 9 ± 2 ps. Both $^1\text{BP}^*$ and $^3\text{BP}^*$ are quenched by electron transfer to form the singlet radical ion pair and triplet radical ion pair with absorption maximum at 710 nm. These studies suggest that the electron-transfer process produces the SSIP, and that it is within the ^1BP and ^3BP SSIP that proton transfer occurs. There is no evidence based on spectral shifts for the conversion of CIP to SSIP or SSIP to CIP. Recent studies by Peters and coworkers support Mataga's results [162, 163].

Mataga and coworkers have also confirmed that ion-pair separation was highly dependent on the energy gap of charge separation ($-\Delta G_{\text{cs}}$) [164]. With increasing $-\Delta G_{\text{cs}}$, proton transfer rates within the radical ion-pair decreased rapidly, whereas the rates for dissociation increased slightly. These results indicated that the charge-separation process occurred at larger encounter distances for larger $-\Delta G_{\text{cs}}$ leading to a decrease in proton transfer within the radical ion pair and increase in ion-pair dissociation.

**Chart 4**

The effects of chain-length, solvent, and temperature on the intramolecular photoreduction of benzophenone linked to diphenylamine (**53**) has also been explored in detail [165, 166].

For these systems, direct hydrogen abstraction by benzophenone triplets was observed in benzene whereas in a polar solvent electron transfer and hydrogen-atom abstraction were observed. Electron transfer followed by an intramolecular proton transfer was observed in these systems although such proton-transfer reactions are not observed in unlinked systems of primary and secondary amines. The observed differences between the linked and unlinked systems have been attributed to the dependence of electron transfer, proton transfer, and hydrogen transfer on mutual distance and orientation. In the unlinked systems, rotational and translational motion of two reacting molecules are usually much faster than those in linked systems.

In the benzophenone-photosensitized reactions of *N,N'*-dialkyl-1-naphthylamines (DANA) in acetonitrile, Kiyota et al. observed that the initial process was a triplet energy transfer, both in the absence and presence of water or methanol [167]. The triplet aminonaphthalene so formed reacts with ground-state benzophenone to yield a triplet exciplex $^3(\text{DANA-BP})^*$. In the absence of water or methanol, the exciplex decays back to DANA and benzophenone. In the presence of water or methanol however, charge separation to yield $\text{DANA}^{+\bullet}$ and $\text{BP}^{-\bullet}$ was observed. It has been proposed that the driving force for intra-exciplex electron transfer is the enlarged reduction potential of benzophenone in the exciplex, because of hydrogen-bonding by water or methanol to the carbonyl group.

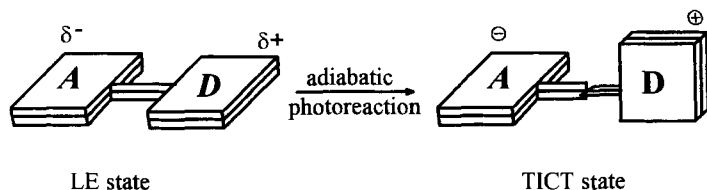
Hamanoue et al. have investigated electron-transfer reactions of several amines with the triplet state of anthraquinones [168, 169]. The photochemistry of anthraquinone is expected to vary depending on the nature of the lowest excited state. It has been observed that the lowest $n-\pi^*$ state abstracts a hydrogen atom, whereas the lowest $\pi-\pi^*$ state reacts via electron transfer. By introducing substituents on the anthraquinone chromophore, the nature of the lowest triplet state can be changed from $n-\pi^*$ to $\pi-\pi^*$. Picosecond laser-flash photolysis studies of the mixtures of anthraquinone and 1-chloroanthraquinone with amines reveal that the anthraquinone triplet forms a triplet exciplex with triethylamine. In polar solvents the exciplex changes to a contact ion pair which disappears by proton exchange between the radical ions. In acetonitrile, two transients from the SSIP and the triplet exciplex were observed. Among these transients, the SSIP is assumed to be produced by electron transfer from triethylamine to a higher triplet (T_2) of anthraquinone upon laser excitation, whereas the exciplex is produced by the reaction of the lowest triplet (T_1) of anthraquinone with triethylamine. It was proposed that

deprotonation of the aminium cation, produced after the electron-transfer reaction with anthraquinone, occurred in the contact ion pair. Recent CIDNP studies of the deprotonation of the aminium cation, generated from the anthraquinone sensitized electron-transfer reaction reveal that the relative group reactivity or substituent effect plays a key role in determining the time of proton elimination [170]. These studies show that deprotonation of the methyl, ethyl and isopropyl substituents occurs exclusively in the solvent-separated ion pair whereas the deprotonation of the allyl substituents occurs within the contact ion pair. This difference in behavior can be explained on the basis of an increase in the rate of in-cage proton transfer relative to cage life with increasing ΔG of the reaction.

The photoreduction of 9,10-anthraquinone-1,5-disulfonate by 2,2,6,6-tetramethyl piperidine in aqueous media has been studied in the nanosecond and microsecond time domains by use of time-resolved optical and ESR measurements [171]. Electron transfer from the amine to the excited state of the anthraquinone derivative occurs with a rate constant of $5.7 \times 10^8 \text{ M}^{-1} \text{ s}^{-1}$. The aminyl radicals formed via deprotonation of the aminium radicals are long-lived (ca 0.5 ms), because the steric hindrance of these radicals slows down recombination reactions. The aminyl radicals formed in these systems have been characterized by ESR.

Another area where the mechanism of intramolecular photoinduced charge separation involving amines has attracted much attention is the phenomenon of dual luminescence observed in dimethylaminobenzonitrile (DMABN) and related molecules. Dual luminescence of DMABN, first observed by Lippert [172, 173] has been extensively studied [174–183]. Grabowski proposed that the anomalous long-wavelength emission of DMABN and related molecules could be assigned to a rotational isomer namely a twisted intramolecular charge-transfer state (TICT), in which a full charge is transferred from the dimethylamino moiety to benzonitrile. The process is depicted in Scheme 14 where A and D represent the acceptor and donor moieties, respectively. It is proposed that in this state the amine and benzonitrile orbitals are completely decoupled in a 90° twisted conformation. Although many other mechanisms have been proposed to explain the phenomenon of dual luminescence, the TICT model has attracted most attention. Since then the idea of TICT has been extended to other classes of molecule with anomalous dual fluorescence [174, 179].

Recently Zachariasse and coworkers have questioned the role of TICT in DMABN and related molecules [180–183]. They observed an absence of a linear correlation between the energy of the anomalous fluorescence band and the redox potential of the donor and acceptor groups and also observed dual emission in



Scheme 14.

derivatives where 90° twist of the amino group is not possible. Zachariasse et al. propose a new model, involving a planar intramolecular charge-transfer state (PICT). They proposed that the dual fluorescence in these classes of molecules arise as a result of two close-lying excited states [S_1 and S_2 (CT)], which have an energy gap small enough to enable vibronic coupling of the two states. It has been suggested that *N*-inversion of the amino group acts as a promoting mode between the two levels.

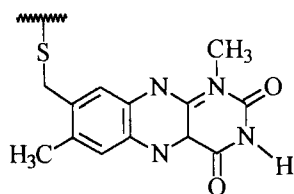
7.2.5 Electron-transfer Reactions of Amines in Biochemical Systems

Electron-transfer reactions of amines are of significant importance in biochemical systems. Enzymes known to catalyze the oxidative dealkylation of amines include monoamine oxidase [16, 17], cytochrome-P450 [18, 184–186], horseradish peroxidase [187], hemoproteins [188, 189], and chloroperoxidase [187, 188]. *N*-dealkylation of amines by peroxidases are generally accepted to occur via one-electron transfer, whereas the role of electron transfer in reactions catalyzed by enzymes such as monoamine oxidase [16, 17] and cytochrome P-450 [18, 184, 185] is currently a topic of debate.

Amine oxidations catalyzed by monoamine oxidase

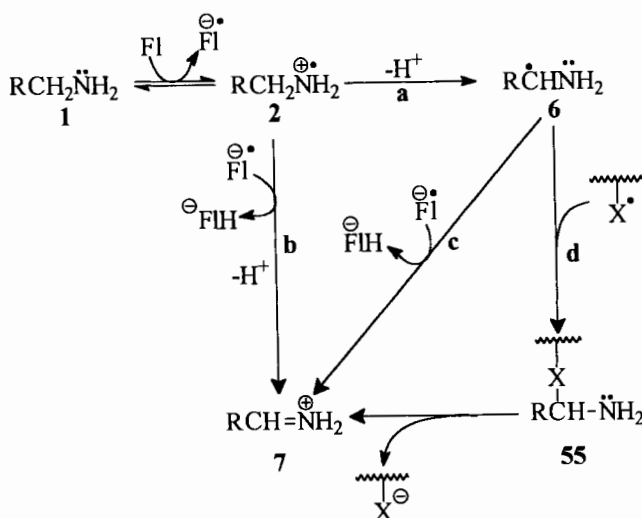
Monoamine oxidase, which exists in two distinct forms, referred to as MAO A and MAO B, is one of the enzymes responsible for the degradation of biologically important amines. Compounds that block the catalytic action of MAO A, which is selective for the degradation of norepinephrine and serotonin, have antidepressant effects whereas compounds that inhibit MAO B, which degrades dopamine in the brain, are useful for treating Parkinson's disease [190, 191]. Both MAO A and MAO B contain flavin co-enzyme attached at the 8- α -position to an enzyme-active cysteine residue (**54**). A one-electron transfer mechanism (Scheme 15) for the oxidations catalyzed by MAO was first proposed by Silverman [192] and Krantz [193, 194].

One-electron transfer from the substrate amino group to flavin (Fl) results in the formation of the aminium radical and the flavin radical anion ($Fl^{\cdot-}$) (Scheme 15). Deprotonation of the aminium radical to yield an α -aminoalkyl radical followed by a second electron transfer to the flavin radical anion will result in the formation of the reduced flavin and iminium ion. Alternatively the iminium ion can be formed by path d in Scheme 15; this involves formation of a covalent adduct which can



54

Chart 5



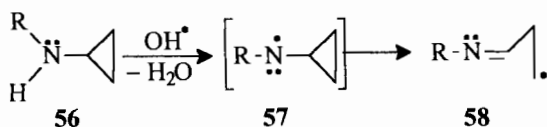
Scheme 15.

subsequently decompose to give the iminium ion. The 'X' in Scheme 15 can be the flavin radical anion or an amino acid radical formed by hydrogen-atom abstraction from the amino acid by the flavin radical anion. Instead of deprotonation the aminium radical could also undergo hydrogen abstraction by the flavin radical anion (path b) which would directly result in the formation of the iminium ion.

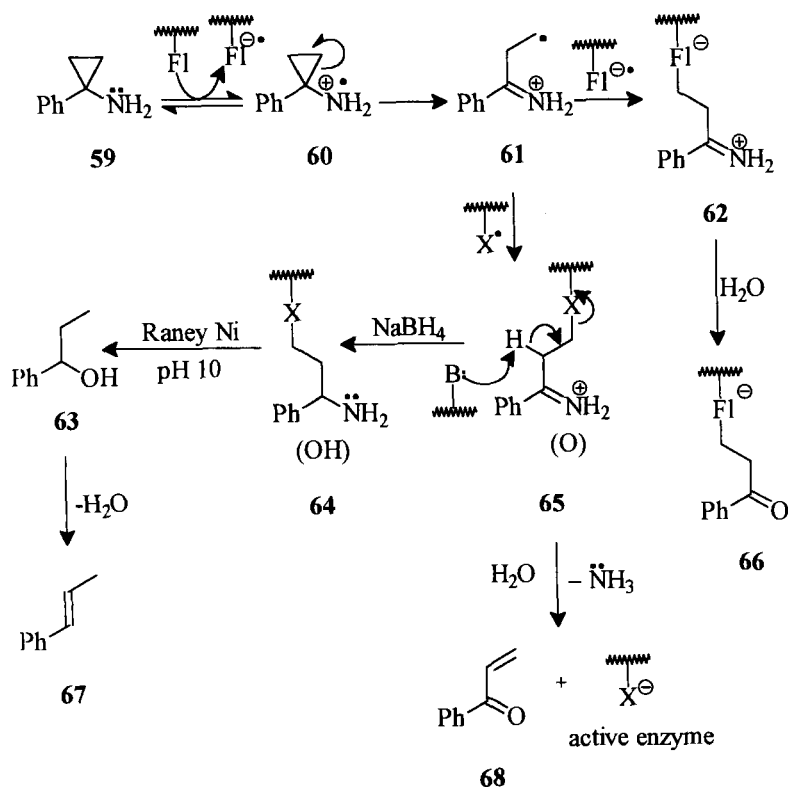
The transfer of a first electron from amine to the flavin is a thermodynamically uphill process, being endothermic by about 1.75 V for a primary amine. It has been proposed that intrinsic binding, which could distort the bonds of the amine and flavin, results in a lowering of the redox potentials of the amines and the flavin, making electron transfer feasible [16, 17].

Extensive studies by Silverman and coworkers on the mechanism of inactivation of the enzyme have provided strong support for the role of electron transfer in the catalytic mechanism of MAO [16, 17]. Laser-flash photolysis of cyclopropylamine **56** showed that its aminyl radical undergoes a very fast ring opening ($>5 \times 10^8 \text{ M}^{-1} \text{ s}^{-1}$) to yield the primary radical **58** (Scheme 16) [195].

Using similar systems Silverman and coworkers have explored the oxidation of a variety of cyclopropyl amine substrates by MAO [16, 17, 196, 197]. Involvement of electron transfer in such processes would lead to the formation of the ring-opened alkyl radical and subsequent attachment of the resultant alkyl radical to the enzyme would result in its inactivation. Scheme 17 shows the proposed mechanism for enzyme deactivation by 1-phenylcyclopropylamine.



Scheme 16.

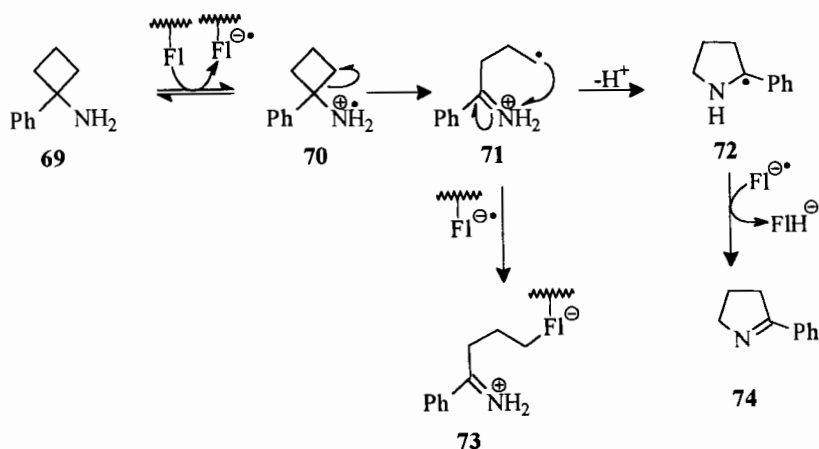


Scheme 17.

Electron transfer from the amine to flavin would result in the aminium radical which is expected to rearrange rapidly to radical **61**. Inactivation of the enzyme would then occur via coupling of the radical with the flavin radical anion resulting in the formation of **66**. Coupling of the aminium radical with an amino acid radical would result in the formation of **65**. By use of radioactive labeling techniques Silverman et al. have confirmed the formation of **65** and **66**; this confirms the role of electron transfer in the oxidation process. Similar studies have been performed using 1-phenylcyclobutylamine (Scheme 18) [198].

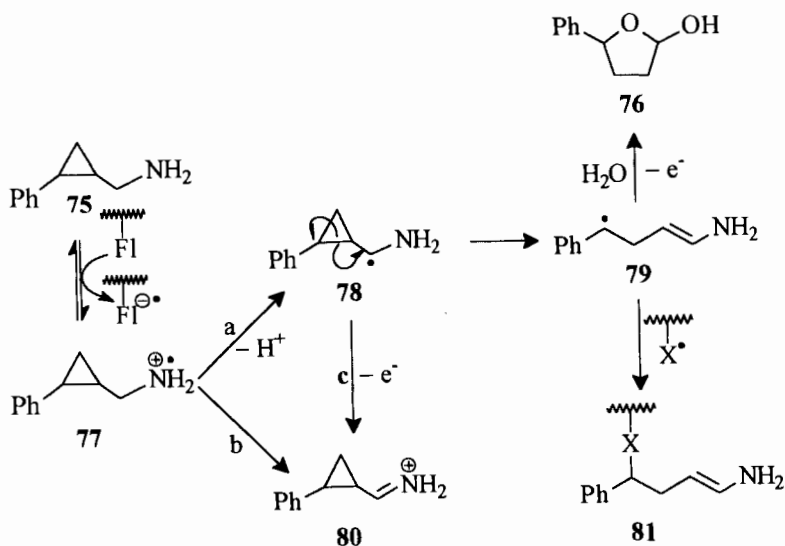
Identification of **74** on incubation of MAO with **69** confirmed the initial formation of the 1-phenylcyclobutylaminium radical. That a variety of cyclopropylamines and cyclobutylamines inactivate MAO and result in ring-opened adducts is consistent with the intermediacy of the aminyl radicals. These results strongly suggest that the MAO-catalyzed oxidation of amines involves one-electron transfer as the first step.

As discussed earlier, the aminium radical formed in this process can either undergo deprotonation and subsequent electron transfer (path a, Scheme 15) or lose a hydrogen atom (path c, Scheme 15). To differentiate between these processes

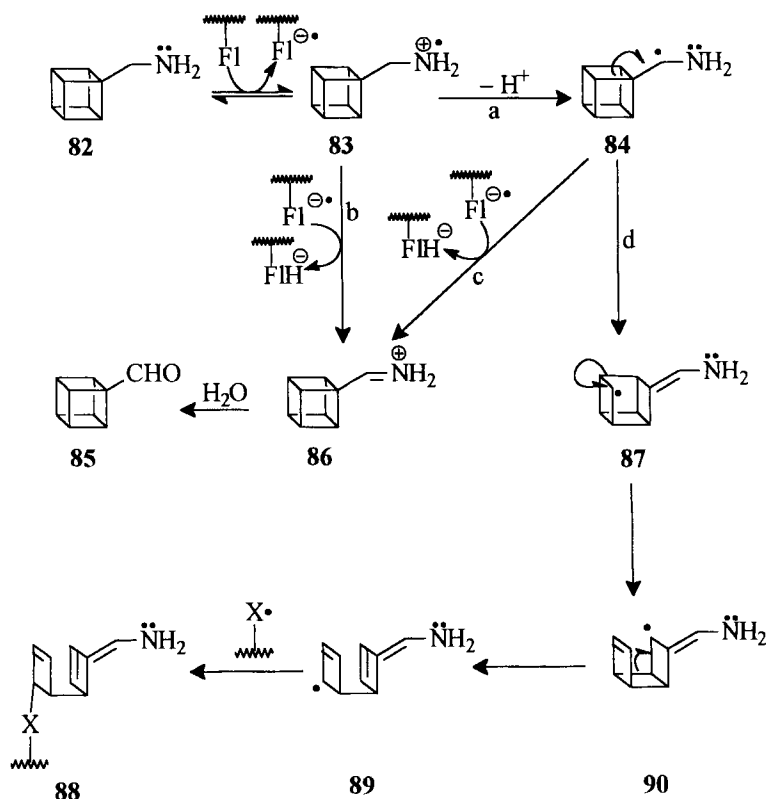


Scheme 18.

Zelevich and Silverman [199] incubated MAO with *trans*-1-aminomethyl-2-phenylcyclopropane (**75**) (Scheme 19). Newcomb et al. had previously shown that the *trans*-2-phenyl(cyclopropenyl)carbinyl radical undergoes very fast ring cleavage ($k = 3 \times 10^{11} \text{ s}^{-1}$) [200]. By comparison the α -aminoalkyl radical (**78**) if generated in these systems would be expected to form 2-hydroxy-5-phenyltetrahydrofuran (**76**). However **76** could not be detected, suggesting that the reaction occurred by path b (Scheme 19) or that the second electron transfer (path c) was much faster than the ring-opening reaction. It has been proposed that the cleavage reaction of



Scheme 19.

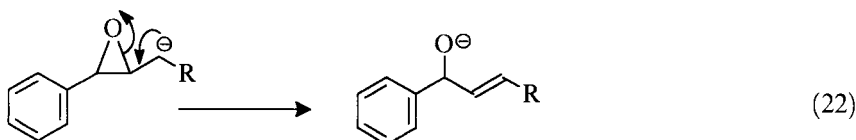
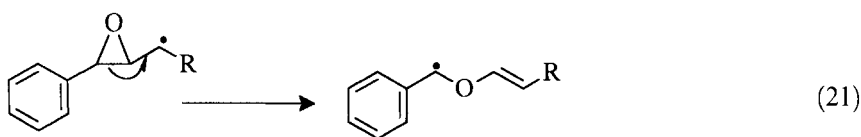


Scheme 20.

78 (Scheme 19) could be slowed because of stabilization by the amine group and during enzyme binding the free rotation of the molecule is frozen preventing overlap of the α -carbon radical orbital and the cyclopropyl radicals.

The occurrence of deprotonation/second electron transfer in such systems was confirmed by use of aminomethylcubane **82** (Scheme 20) [201]. Treatment of MAO with aminomethylcubane led to time-dependent inactivation of the enzyme and the formation of products arising from ring cleavage. If the hydrogen abstraction by flavinium radical anion (path b) is the predominant pathway the major product formed would be iminium ion **86**. Ring cleavage products cannot arise from the iminium ion **86**, because cubyl carbonyl cations are well known to undergo exclusive rearrangement to homocubanes. Decomposition of the cubane nucleus indicates that deprotonation of the aminium radical (path d) is the major reaction pathway in MAO catalyzed oxidation of amines.

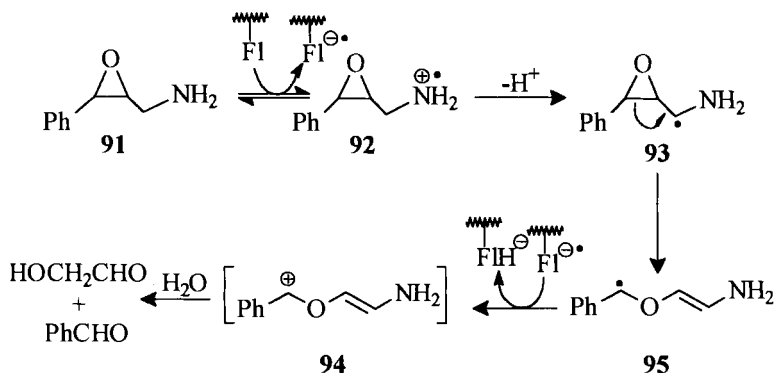
Destruction of the cubane structure could also however occur via carbanion intermediates. To rule out this possibility Silverman et al. studied the MAO-catalyzed reactions of cinnamylamine-2,3-oxide [202].



Scheme 21.

1-Substituted-2,3-epoxy-3-phenylpropyl radicals have been reported to cleave the C–C bond exclusively (Eq. 21, Scheme 21) whereas, the corresponding carbanion undergoes exclusive C–O bond cleavage (Eq. 22, Scheme 21) [203, 204]. Formation of benzaldehyde and glycolaldehyde and the absence of cinnamaldehyde, a product expected via C–O bond cleavage supports the mechanism shown in Scheme 22 for the MAO catalyzed oxidation of cinnamylamine-2,3-oxide (**91**).

Silverman's studies on mechanism based MAO inactivation have provided overwhelming support for the role of electron transfer in the MAO catalyzed dealkylation of amines. It must be mentioned however that spectroscopic attempts for detecting the radical ion intermediates have hitherto been unsuccessful. Yasanobu and coworkers could not find EPR spectral evidence for radical intermediates in MAO-catalyzed oxidation of benzylamine [205]. Miller et al. failed to observe the flavin semiquinone or an amine–flavin adduct in rapid-scan-stopped flow spectroscopy [206]. The only time-dependent absorption change observed in this study was the bleaching of the oxidized flavin. Furthermore, no influence of a magnetic field up to 6500 G was observed on the rate of MAO B reduction. The reaction rates of systems with kinetically significant radical pair intermediates are known to be altered



Scheme 22.

by exogenous magnetic fields ($B = 10\text{--}3000\text{ G}$) [207, 208]. A possible explanation proposed by Silverman for the lack of observation of the flavin semiquinone is that the first electron transfer is reversible and that the back-electron-transfer is much faster than the forward reaction leading to very short lifetimes for the flavin semiquinone. In the ESR measurements this would lead to very low steady state concentrations of the free radicals and hence would not be observable.

Search for new mechanism based investigations for deducing the mechanism of the enzyme catalyzed activity continues to be active area of research. Mariano and coworkers have used activated flavins such as 5-ethylflavinium perchlorate, whose ground state reduction potentials are high enough to promote oxidative dealkylation of amines, as enzyme models [209]. Studies on the inactivation of the model enzymes by cyclopropylamines and α -silylamines suggest a polar mechanistic model. Silverman attributes this result to the drastically altered nature of the flavin used in these studies, which could favor a nucleophilic mechanism [16].

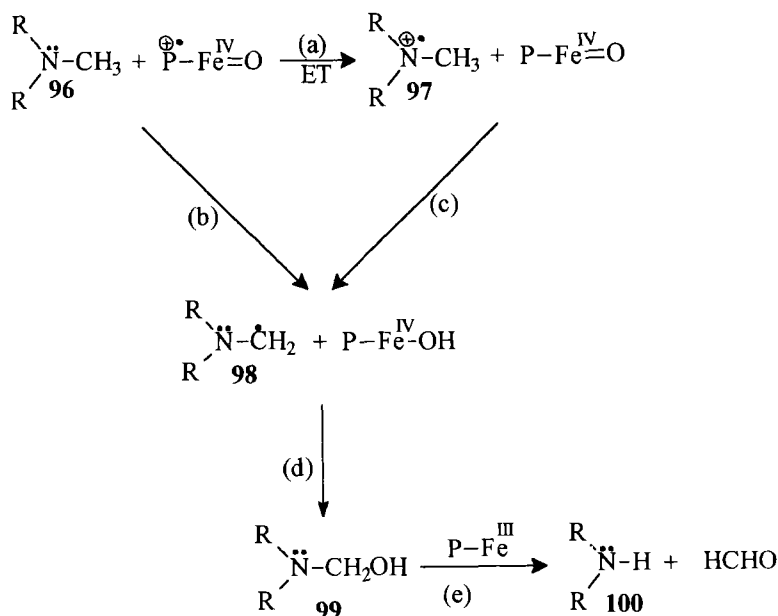
In a more recent study, Mariano and coworkers have probed the use of the reported retro-aldol type fragmentation of aminium radicals generated from *tert*- β -allylic and -propargylic β -aminoalcohols as MAO inactivators [210]. Photoexcitation of a model flavin, [3-methylflumiflavin (3MLF)], generates the triplet excited state of 3MLF which undergoes SET reactions with β -aminoalcohols. Analysis of the photoproducts, namely 4a adducts of 3MLF are indicative of the formation of aminium radicals which undergo facile retro-aldol-like fragmentation. These studies as well as the studies on MAO A inactivation by the β -hydroxylamines suggest that the enzymatic sequence is most likely initiated by one-electron transfer within the enzyme-inactivator complex which is then followed by a retro-aldol fragmentation of the intermediate tertiary aminium radical.

Amine oxidations catalyzed by cytochrome P-450

Cytochrome P-450 and hemoproteins are known to be involved in the oxidation of a broad variety of drugs, pesticides, carcinogens, steroids and fat soluble vitamins [18, 184, 185]. Amine oxidation by P-450 has been proposed to proceed either via electron/proton transfer mechanism or via hydrogen-atom abstraction mechanism (Scheme 23).

Studies using isotopic labeling as well as mechanism based on inactivation such as 4-alkyldihydropyridines and cycloalkylamines have supported the view that the first step involves an electron-transfer process (path a, Scheme 23) [18, 184–186, 211]. Deprotonation of the resultant aminium radical would yield the α -aminoalkyl radical. The formation of the dealkylated amine and carbonyl derivative has been proposed to occur via a second electron transfer to the enzyme and a nonenzymatic hydrolysis of the imine formed. In the P-450 catalyzed reaction, however this process is proposed to occur via a radical recombination process to yield a carbinolamine (**99**) which then decomposes to the dealkylated amine and the corresponding carbonyl derivative. Evidence for this was obtained by the incorporation of label from $^{18}\text{O}_2$, into the carbonyl derivative [212–214].

In a recent study, Dinnocenzo and coworkers have questioned the role of electron



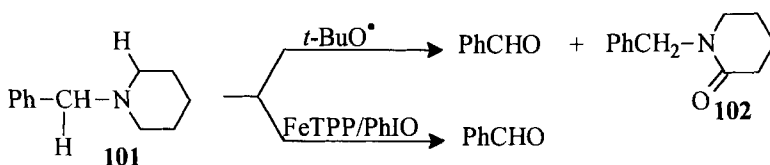
Scheme 23.

transfer in these processes [215, 216]. They have studied the isotope effect profiles for *para*-substituted *N*-methyl-*N*-(trideuteriomethyl)aniline cation radicals by pyridine and for the hydrogen abstraction from their parent amines by *tert*-butoxyl radicals. The isotope effect profiles for the P-450 catalyzed oxidation of these amines (increased isotope effects with increasing electronegativity of the *para*-substituent) were found to be indistinguishable from the hydrogen abstraction profile and distinctly different from the deprotonation profile.

In a subsequent study Guengerich et al. did not observe a continuous trend for an increase in isotopic effects with increase in electron withdrawing nature of the *para* substituent [217]. The larger value observed in their study for the 4-nitro derivative has been attributed to either a reversible electron transfer step proceeding to deprotonation or to a hydrogen-atom abstraction mechanism for this molecule. The higher oxidation potential of 4-nitro-*N,N*-dimethylaniline could be a contributing factor.

Recent studies by Baciocchi et al. on kinetic deuterium isotope effect profiles and substituent effects in the oxidizing *N*-demethylation of *N,N*-dimethylanilines catalyzed by tetrakis (pentafluorophenyl)porphyrin also supports the electron-transfer mechanism and exclude the hydrogen-atom transfer mechanism in such processes [218].

Evidence in favor of the electron-transfer mechanism has also come from studies on substrates such as *N*-ethyl-*N*-methylaniline which show a demethylation/



Scheme 24.

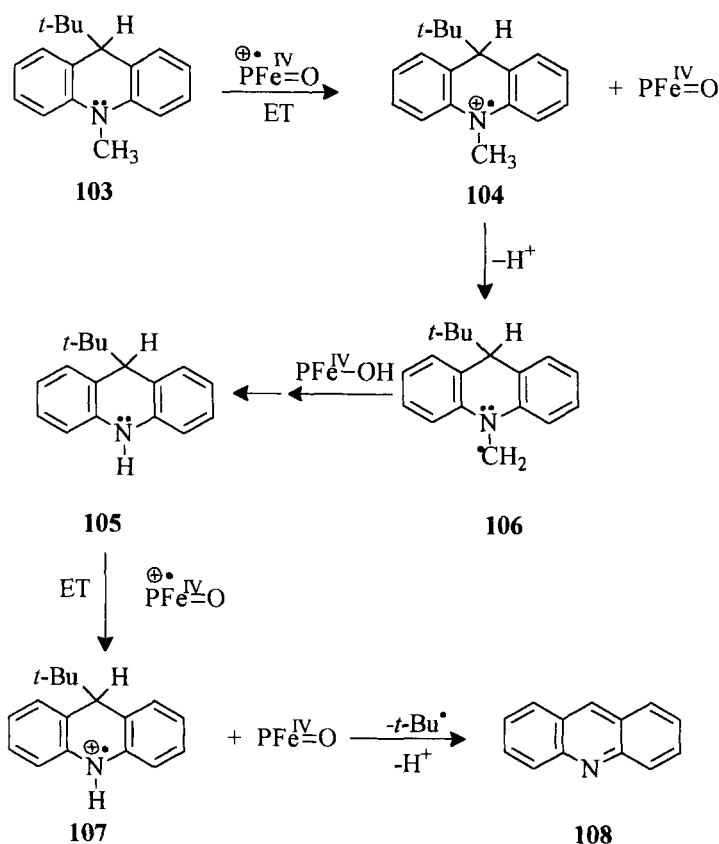
deethylation ratio of 16 to 20 [219, 220]. These results can be attributed to steric preference for deprotonation of the methyl proton [7, 221] of the aminium radicals. In *tert*-butoxyl radical systems the rate of hydrogen-atom abstraction was twice as that for the *N*-methyl group [222].

Recently Bietti et al. have investigated the use of *N*-benzylpiperidine for differentiating between the electron transfer and hydrogen-atom transfer (HAT) mechanisms [223]. Reaction of the substrate with $t\text{-BuO}^\bullet$ produced benzaldehyde and 1-benzyl-2-piperidone indicating hydrogen-atom abstraction both from the benzylic and piperidine ring α -methylene groups (Scheme 24). From the product ratio a relative rate of $k_{\text{benzyl}}/k_{\text{alkyl}}$ of 1.4 was obtained taking into account the number of equivalent positions. Under biomimetic conditions using iodosobenzene and tetraphenylporphyrin iron (III) chloride as the catalyst only benzaldehyde was obtained (Scheme 24). These differences can be attributed to the preferential deprotonation of the benzylic proton from aminium radicals, for stereoelectronic reasons, thereby confirming the electron-transfer mechanism for the reaction.

Baciacchi and Lapi have investigated the oxidation of *N*-methyl-9-*t*-butylacridane **103** by iodosylbenzene catalyzed by tetrakis(pentafluorophenyl)porphyrin iron (III). (FeTPFP) [224]. It has been reported earlier by Anne and coworkers that the radical cation of **103** generated electrochemically undergoes a very fast C–C bond cleavage to form the *t*-butyl radical and *N*-methylacridinium cation [225, 226]. In the presence of a very strong base such as 2,4,6-trimethylpyridine ($\text{p}K_{\text{a}} \sim 15.6$) deprotonation of the *N*-methyl group occurs leading to the formation of acridine. The biomimetic oxidation of **103** with iodosylbenzene in the presence of FeTPFP in CH_2Cl_2 at room temperature using a substrate/oxidant/catalyst ratio of 50:10:1 led exclusively to the formation of 9-*t*-butylacridane and formaldehyde [224]. On decreasing the substrate oxidant ratio, formation of acridine was also observed. The mechanism shown in Scheme 25 was proposed to explain the results observed.

The low kinetic isotope effect using *N*-tri-deuteromethyl-9-*t*-butylacridane indicated that a hydrogen-atom abstraction was not operative in this case.

Dealkylation of the *N*-methyl group indicates that the initially formed radical cation **104** (Scheme 25) undergoes preferential deprotonation of the *N*-methyl group instead of C–C bond cleavage. In view of the earlier report on electrochemical oxidation of **104**, this would suggest that P-Fe(IV)=O is a relatively strong base ($\text{p}K \geq 16$). This observation is interesting in view of the earlier studies where significant basicity of P-Fe(IV)=O has been implied [227].



Scheme 25.

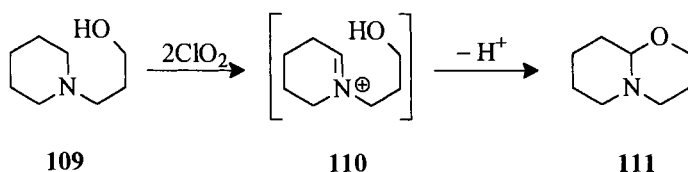
7.3 Synthetic Applications

The α -aminoalkyl radicals as well as iminium ions generated as intermediates in electron-transfer reactions of amines can be used for bringing about synthetically useful transformations of amines. The synthetic applications of amine oxidation reactions brought about by thermal, electrochemical and photochemical methods as discussed below.

7.3.1 Thermal Methods

Chemical oxidation

Because of the relative instability of amine radicals, their synthetic applications in thermal one-electron-catalyzed reactions are rare. In contrast free radicals generated in the oxidation of amides are more common [19–23, 228]. Aminium radicals gen-



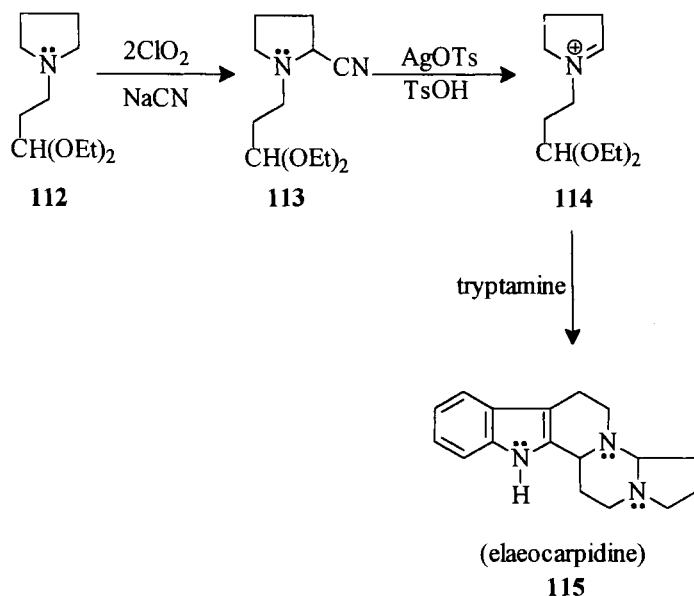
Scheme 26.

erated via metal catalyzed degradation of chloro- and hydroxylamines can undergo a variety of synthetically useful reactions such as inter- and intramolecular addition to olefins and in aromatic amination reactions [22, 55].

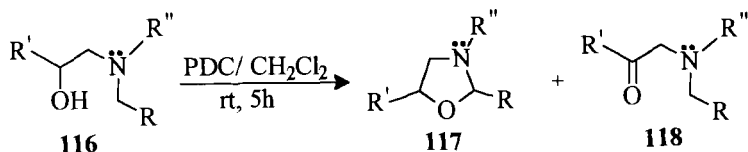
Chlorine dioxide catalyzed cyclization of tertiary aminoalcohols (Scheme 26) to oxazolidines and tetrahydro-1,3-oxazines in basic aqueous media have been reported [229].

Similar reactions, were earlier reported by Audeh and Lindsay Smith in ferricyanide catalyzed reactions [44], although in much lower yields. The ClO_2 catalyzed cyclization showed a greater regiochemical tendency for ring closure to occur at the less substituted α -carbon of the piperidine moiety compared to $\text{Hg}(\text{OAc})_2$ catalyzed reactions of the same compounds.

α -Cyanoamines are powerful synthons for the preparation of a variety of substituted piperidines. Reactions of ClO_2 with tertiary amines in the presence of 5–7 mol equivalent of aqueous sodium cyanide afforded 53–88 % of the α -cyano-substituted tertiary amine. This strategy has been utilized for the synthesis of the alkaloid (\pm)-elaecarpidine (**115**) in moderate yields (Scheme 27) [229].



Scheme 27.

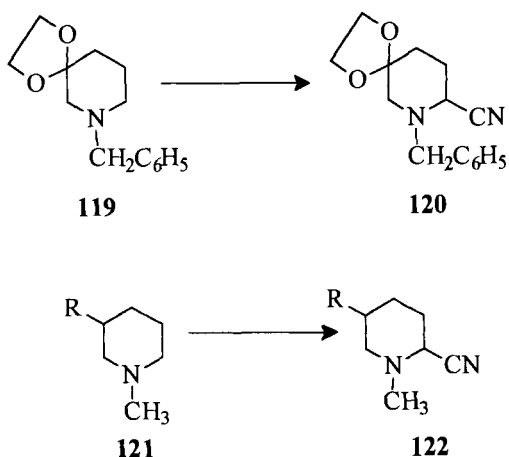


Where $\text{R} = \text{H}$
 $\text{R}' = \text{Ph-CH}_2$; alkyl
 $\text{R}'' = \text{aryl}$

Scheme 28.

Oxidation of *N*-aryl-*N*-methyl-substituted β -aminoalcohols using pyridinium dichromate (PDC) has recently been reported to give moderate to excellent yields of oxazolidines (Scheme 28) [230].

Hoornaert and coworkers have used the regioselective oxidation of piperidine-3 derivatives by mercuric acetate for the preparation of α -cyanoamines [231]. Mercuric acetate oxidation of cyclic amines to enamines is believed to occur with a two electron reduction of mercuric ion to metallic mercury which is subsequently oxidized to mercuric ion by mercurous ions [232, 233]. 1-Benzyl-3,3-(ethylenedioxy)piperidine (**119**) and 3- CO_2Et and 3- CH_2OH -substituted piperidines (**121**) were regioselectively oxidized at the α -position and trapping of the resulting 6-iminium ions with cyanide yielded the corresponding 5-substituted-2-piperidinecarbonitriles (**120**, **122**) (Scheme 29).



Where $\text{R} = \text{CO}_2\text{Et}$; CH_2OH

Scheme 29.

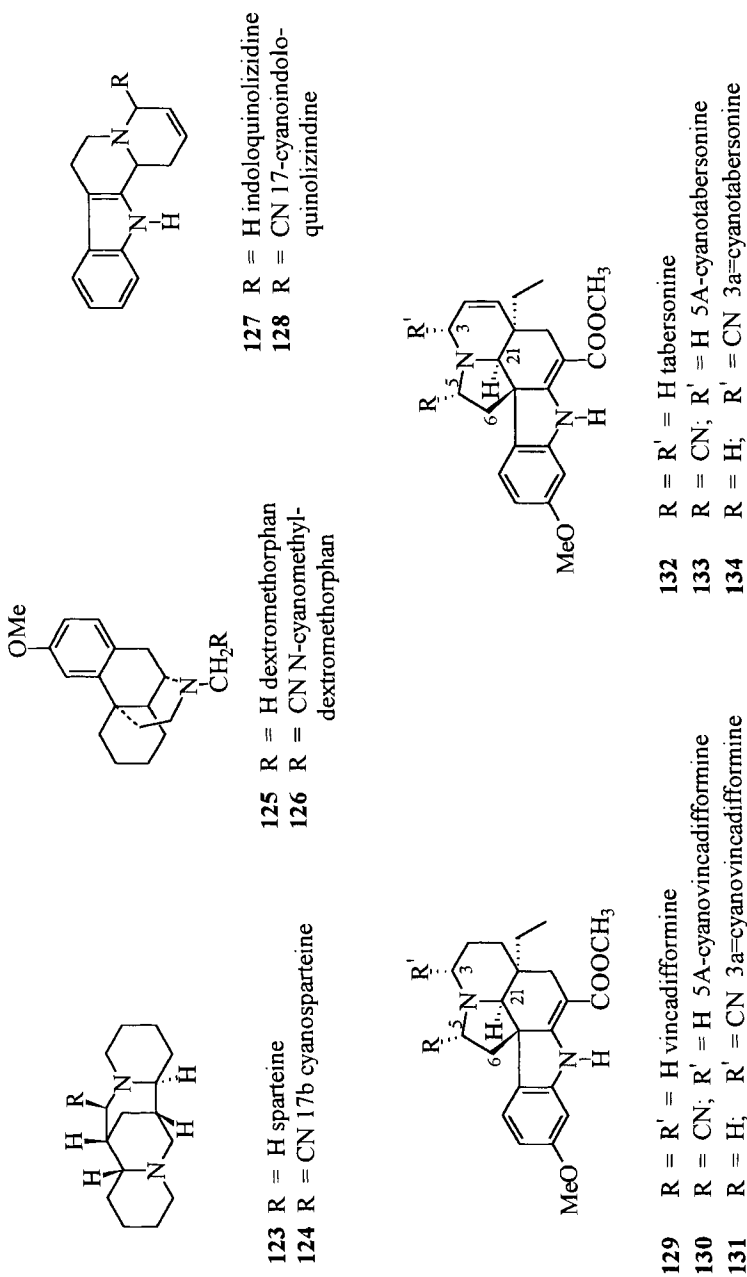
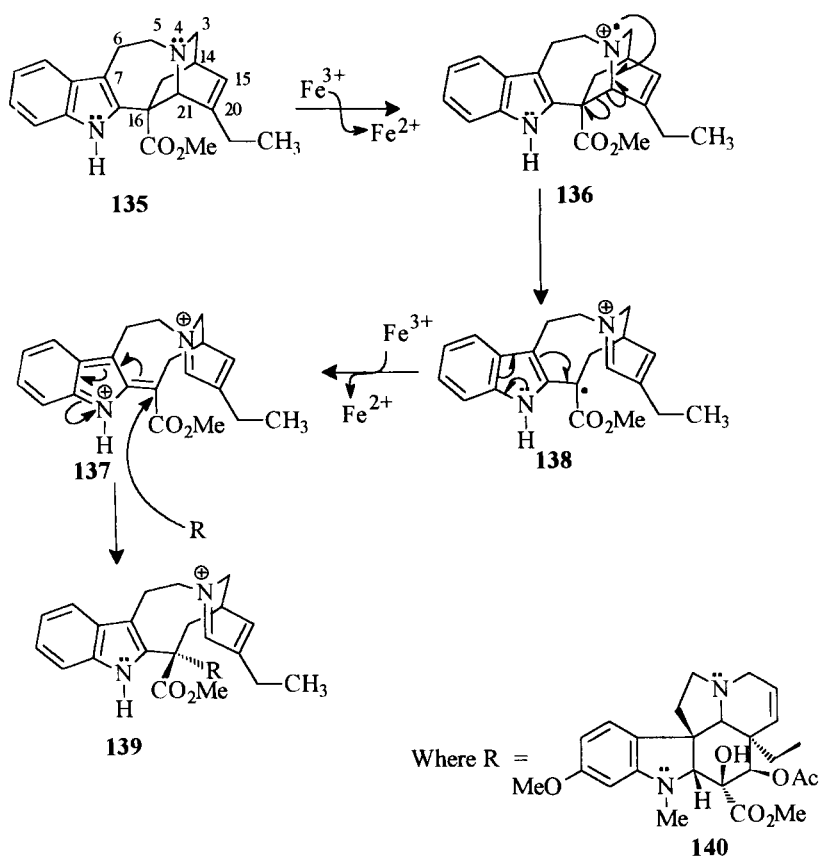


Chart 6

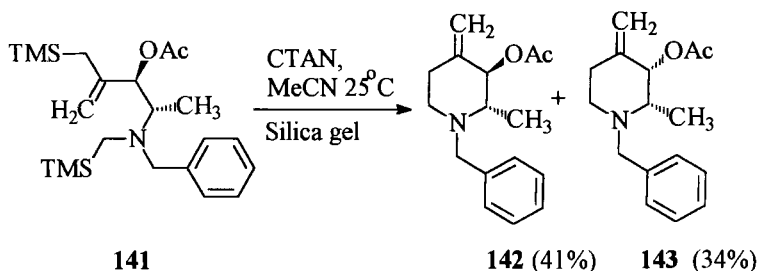
The observed regioselectivity was attributed to a transition state in which the mercuric ion is coordinated to both the N atom and the axially oriented O atom. Using this method Hoornaert and coworkers have synthesized several substituted piperidines and their bicyclic piperazine analogs [231, 234, 235].

Singlet oxygen has been reported to react with amines via an electron-transfer mechanism [236]. Electron-transfer-catalyzed reactions of alkaloids in the presence of cyanide ions, by singlet oxygen generated thermally from 1,4-naphthaleneendoperoxide led to the formation of the corresponding α -cyano-aminated products in good yields [237].

Ferric ion-induced coupling of catharanthine (**135**) and vindoline (**140**) in aqueous acidic media to produce 3,4'-anhydrovinblastine has been proposed to occur via the formation of a cation radical (**136**) of the tertiary amine of catharanthine (Scheme 30). Rearrangement and subsequent fragmentation between C16 and C21 leads to ring opening. A second oxidation followed by nucleophilic attack of the diiminium (**137**) by vindolene (**140**) results in the formation of iminium (**139**), which on borohydride reduction yields 3,4'-anhydrovinblastine (77 %) [238].



Scheme 30.



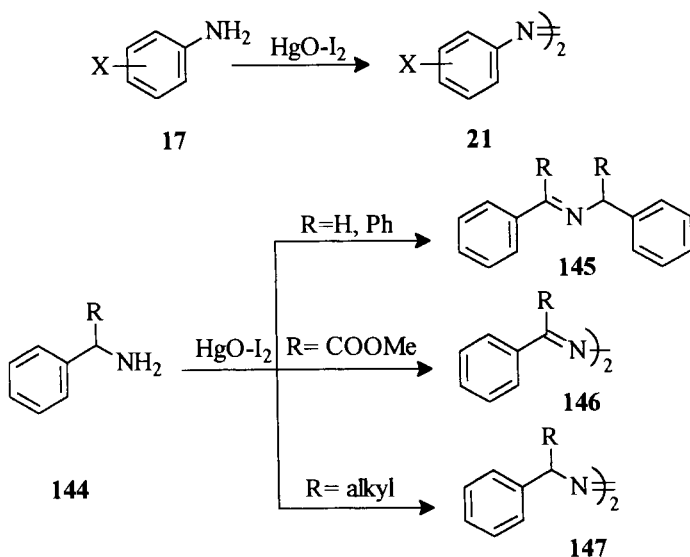
Scheme 31.

Fragmentation of the C16–C21 bond of catharanthine following formation of the radical cation has also been proposed in the oxidation reaction with dichlorodicyanoquinone [239].

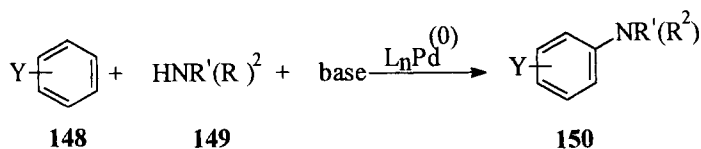
Ceric ammonium nitrate (CAN) and ceric tetrabutylammonium nitrate (CTAN) [40–42, 240] oxidation of α -silylamine and α -silylamide have been utilized for the synthesis of tetrahydropyridines (Scheme 31).

Unlike the amine analogs α -silylamido (*E*)-vinylsilanes undergo cyclization to produce tetrahydropyridines with retention of absolute and relative stereochemistry. This method has been utilized for the synthesis of the aza-sugars, (–)-1-deoxymannojirimycin and (+)-1-deoxyallonojirimycin.

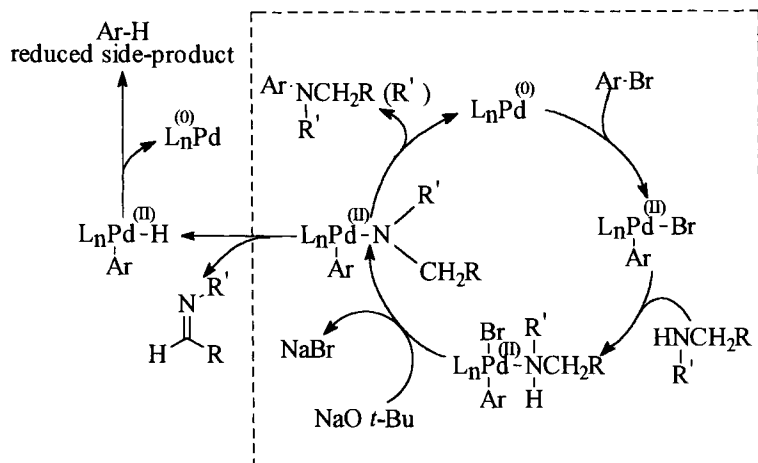
Metal oxide catalyzed reactions of anilines and benzylamines have been utilized to synthesize azobenzenes and *N*-benzylidenebenzyl amines in good yields (Scheme 32) [67, 241, 242].



Scheme 32.



Scheme 33.



Scheme 34.

Palladium catalyzed aminations of aryl halides and triflates have become a very efficient and useful method for the synthesis of aromatic amines (Scheme 33) [243–248].

The currently accepted mechanism for these transformations is shown in Scheme 34.

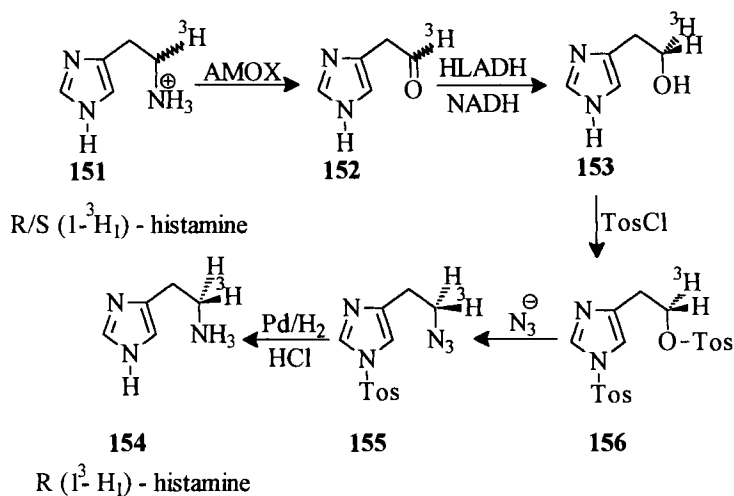
Oxidative addition of the aryl bromide to L_nPd^0 gives the Pd^{II} complex. Metathesis of amine from bromide gives the aryl amido intermediate. This can reductively eliminate to produce the aniline and regenerate Pd^0 . Current research efforts in this area have concentrated on improving the nature of the palladium catalyst.

Enzyme-catalyzed reactions

Enzyme catalysis also provides a convenient method for bringing about synthetically useful oxidizing transformations of amines [249].

Scheme 35 shows the multistep synthesis of optically pure tritium-labeled histamine, which involves an amine oxidase-catalyzed reaction as the first step [250].

Diamine oxidase (DAMOX) from pea seedlings catalyze the oxidative deamination of diamines. DAMOX-catalyzed reactions of diamines in the synthesis of phenacyl azaheterocycles is shown in Scheme 36 [251–255].



AMOX = Amine Oxidase
 HLADH = Horse liver alcohol dehydrogenase

Scheme 35.

Enantioselective oxidation of the D-amino acid by D-amino acid oxidase has been utilized to transform racemic mixtures of methionine and thionine to the corresponding L-amino acid [256, 257]. The separation of L-amino acid from a racemic β -hydroxyamino acid mixture using D-amino acid oxidase (D-ASOX), was used as a key step in the synthesis of bleomycine (Scheme 37) [258].

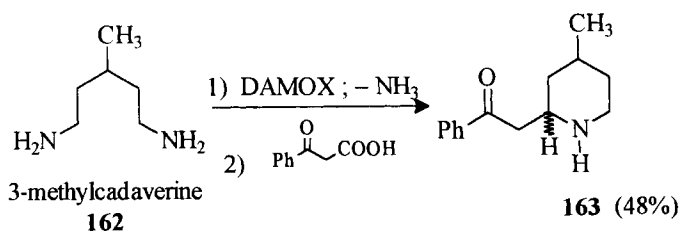
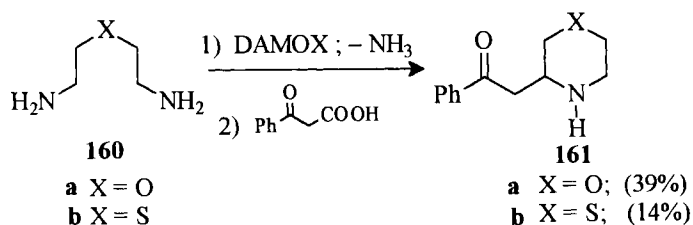
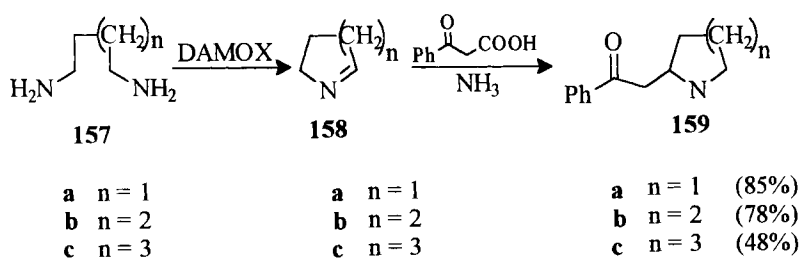
The resolution of racemic mixtures by amino acid oxidases also forms an important step in the synthesis of isotope labeled sugars and amino acids [259].

7.3.2 Electrochemical Methods

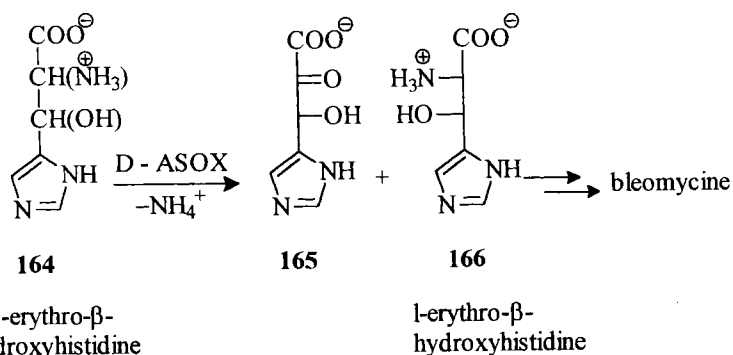
Dehydrogenation of primary amines to yield nitriles can be carried out with high efficiency at nickel hydroxide electrodes [1–3, 260]. Short chain and reactive amines are easily oxidized at low temperatures, whereas higher temperatures are required for long-chain amines (Table 8) [260].

The electrochemical dealkylation of aliphatic amines is a useful way of mimicking enzymatic dealkylation. This has been effectively used for the synthesis of *N*-dealkylated metabolites of drugs with much better efficiencies than the enzyme catalyzed reactions (Scheme 38) [2].

Nucleophilic substitution of the iminium ions formed in the electrochemical process provides a convenient route for the synthesis of α -substituted amino derivatives. For example the anodic oxidation of *N,N*-dimethylbenzylamine in methanol containing tetrabutyl ammonium fluoroborate or potassium hydroxide gives rise to methoxylated products (Scheme 39) [261].



Scheme 36.

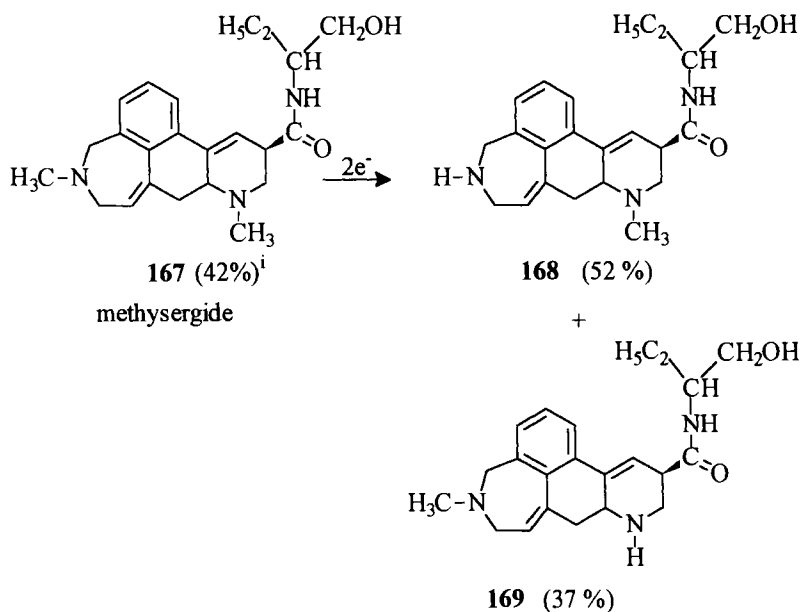


Scheme 37.

Table 8. Oxidation of primary α -unbranched amines to nitriles at the nickel hydroxide electrode.^a

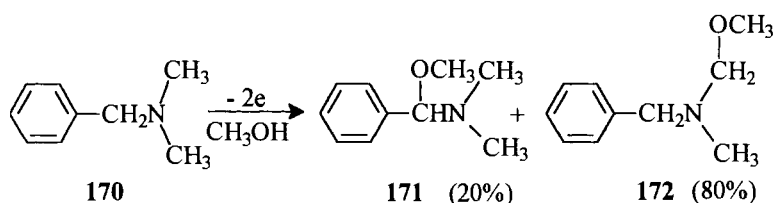
$$\text{RCH}_2\text{NH}_2 \xrightarrow{\text{NiOOH}, -e^-} \text{RC}\equiv\text{N}$$

Amine	Electrolyte ^b	T (°C)	Yield (%) of nitrile or dinitrile
Ethylamine	—	—	68
1-Propylamine	—	—	84
1-Butylamine	A	30	85
1-Hexylamine	B	5	72
1-Octylamine	C	40	95
1-Decylamine	C	60	91
Benzylamine	C	40	90
Furfurylamine	A	5	86
1,6-Diaminohexane	C	40	93
1,10-Diaminododecane	C	40	90
1,12-Diaminododecane	C	40	88
6-Aminohexanoic acid	D	40	97

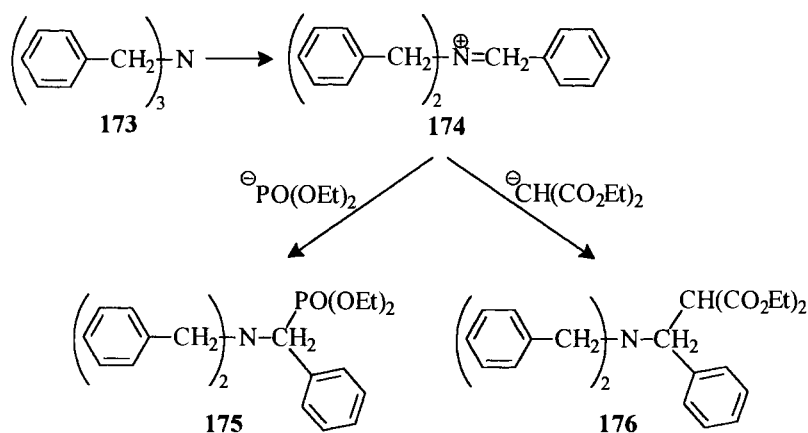
^a According to [260].^b A = 0.1 M aqueous potassium hydroxide; B = 0.1 M potassium hydroxide in acetonitrile–water (1:1, v/v); C = 0.1 M potassium hydroxide in *t*-butanol–water (1:1, v/v); D = 0.3 M potassium hydroxide in *t*-butanol–water (1:1, v/v).

(i) Percentage of starting material consumed

Scheme 38.



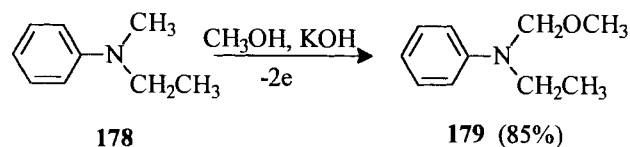
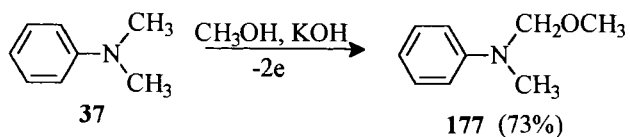
Scheme 39.



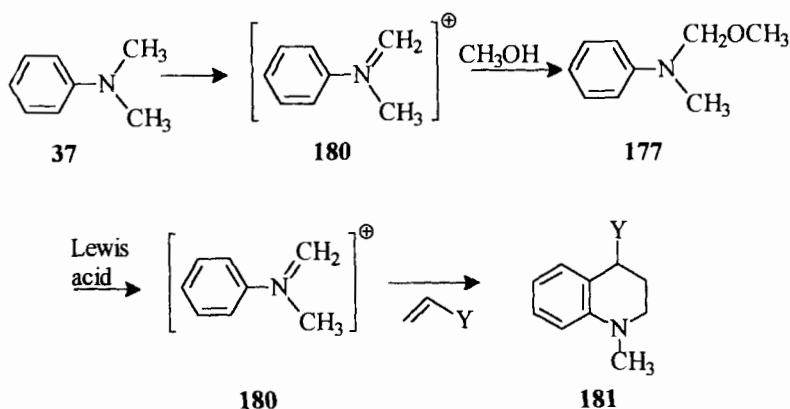
Scheme 40.

The iminium cation can also react with nucleophiles such as diethyl malonate or diethyl phosphonate as shown in Scheme 40 for tribenzylamine [262].

Anodic oxidation of *N,N*-dimethyl, or *N*-methyl-*N*-alkylanilines in basic methanol leads predominantly to the methoxylation of the *N*-methyl group (Scheme 41) [263–265].



Scheme 41.

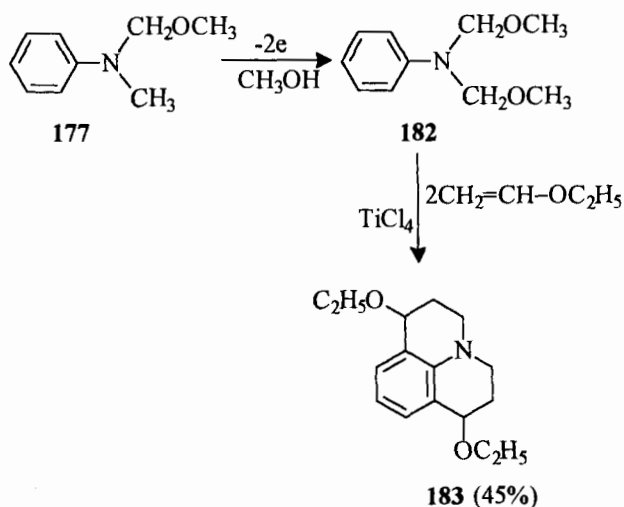


Scheme 42.

α -Methoxylated amines serve as useful synthons as they can be converted to iminium cations by Lewis acid, which can be trapped in situ by nucleophiles such as electron rich olefins as shown in Schemes 42 and 43, for the synthesis of tetrahydroquinolines and julolidine derivatives (Table 9) [265].

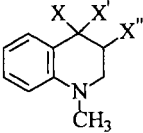
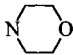
The nucleophilic addition of cyanide ions to the electrochemically generated iminium cation is a synthetically very useful reaction and has been studied for a variety of symmetric and unsymmetric ions (Table 10) [266].

In unsymmetrical amines this process generally leads to α -cyanation of the less substituted carbon. It was earlier proposed that the regioselectivity of cyanation was decided by the conformation of the amine adsorbed on the anode. However



Scheme 43.

Table 9. Synthesis of tetrahydroquinolines from *N*-methoxymethyl-*N*-methylaniline using TiCl_4 as a catalyst.^a

Electron-rich olefin	Product				Yield (%)
		X	X'	X''	
$\text{C}_6\text{H}_5\text{CH}=\text{CH}_2$	C_6H_5	H	H	H	84
$\text{C}_6\text{H}_5\text{C}(\text{CH}_3)=\text{CH}_2$	C_6H_5	CH_3	H	H	89
$\text{C}_6\text{H}_{13}\text{CH}=\text{CH}_2$	C_6H_{13}	H	H	H	58
$\text{C}_2\text{H}_5\text{OCH}=\text{CH}_2$	OC_2H_5	H	H	H	64
$\text{C}_2\text{H}_5\text{OCH}=\text{CHOSi}(\text{CH}_3)_3$	$\text{OSi}(\text{CH}_3)_3$	H	C_2H_5	H	61
$(\text{CH}_3)_3\text{SiO}$ $\quad \quad \quad \diagup$ $\quad \quad \quad \text{C}=\text{CH}_2$ $\quad \quad \quad \diagdown$ $\quad \quad \quad \text{C}_6\text{H}_5$	$\text{OSi}(\text{CH}_3)_3$	C_6H_5	H	H	31
C_4H_9 $\quad \quad \quad \diagup$ $\quad \quad \quad \text{C}=\text{CH}_2$ $\quad \quad \quad \diagdown$ $(\text{CH}_3)_3\text{SiO}$	$\text{OSi}(\text{CH}_3)_3$	C_4H_9	H	H	29
	OCH_3	C_4H_9	H	H	11
	OH	C_4H_9	H	H	21
$\text{C}_6\text{H}_5\text{CH}=\text{CH}-\text{N} \begin{array}{c} \diagup \quad \diagdown \\ \text{O} \end{array}$		H	C_2H_5	H	81
$\text{CH}_2=\text{CHOAc}$	OCH_3	H	H	H	11
	OH	H	H	H	69

^a According to [265].

efficiency of deprotonation depending upon the ability of $\alpha\text{-CH}$ orbitals to overlap with the half vacant 'p' orbitals of the aminium radical is better able to explain the observed results [7, 9, 121, 122].

Recently Le Gall et al. have been able to bring about *regio*- and *diastereo*-selective synthesis of α -cyanoamines by anodic oxidation of cyclic α -silylamines (Scheme 44) [267].

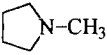
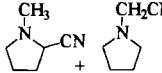
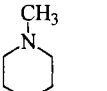
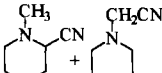
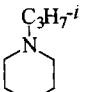
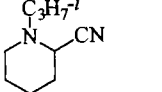
Anodic cyanation of aromatic amines can lead to cyanation on the phenyl or methyl groups as shown in Scheme 45 [268, 269].

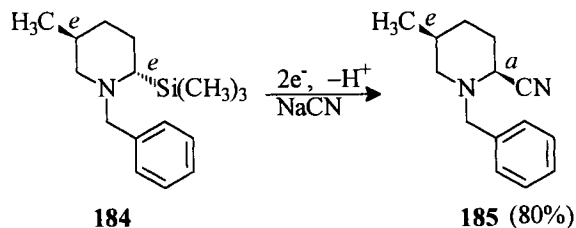
Anodic oxidation of amides and carbamates on the other hand are far more useful than those of amines. Scheme 46 shows the synthesis of a pharaoh ant trail pheromone in which the anodic oxidation of 2-pyrrolidone is an important step [270].

The use of electrochemical oxidations of amides and carbamates as a key step in the synthesis of alkaloidal compounds has been recently reviewed by Shono [271].

The electrochemical oxidations of several fluorinated amines have been investigated with a view to synthesizing fluoroorganic compounds [272]. Substitution of the hydrogen on the carbon of amines by chloromethyl and fluoromethyl groups slightly increases their oxidation potential [273]. Anodic oxidation of fluoromethyl

Table 10. Anodic cyanation of tertiary amines.^{a,b}

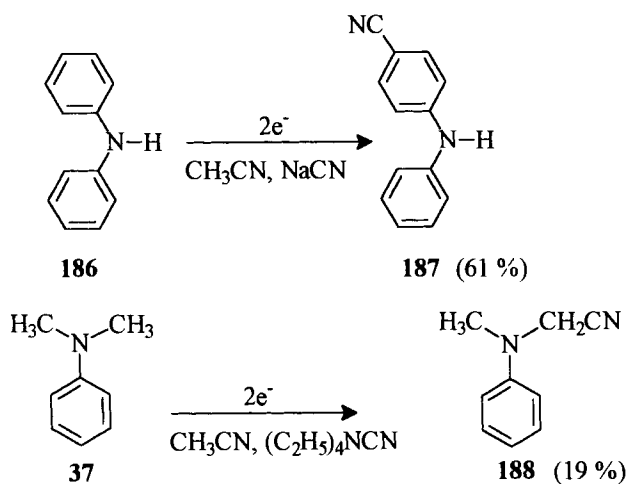
Amine	Anode potential (V vs SCE)	Product	Yield (%) ^c
(CH ₃) ₃ N	1.2–1.4	(CH ₃) ₂ NCH ₂ CN	53
(C ₂ H ₅) ₃ N	1.1–1.2	(C ₂ H ₅) ₂ NCH(CH ₃)CN	53
(C ₂ H ₅) ₂ NCH ₃	1.0–1.2	(C ₂ H ₅) ₂ N(CH ₂)CN + $\begin{array}{c} \text{H}_5\text{C}_2 \\ \diagup \\ \text{N}-\text{CHCN} \\ \diagdown \\ \text{H}_3\text{C} \quad \text{CH}_3 \end{array}$	37
(<i>i</i> -C ₃ H ₇) ₂ NCH ₃	0.9–1.1	(<i>i</i> -C ₃ H ₇) ₂ NCH ₂ CN	55
	1.0–1.3	 +	59
	1.1–1.4	 +	66
	1.0–1.2		62

^a According to [266].^b Analyte: amine (0.10 mol) + NaCN (0.15 mmol) in CH₃OH–H₂O (1:1, 75 mL).^c GLC.**Scheme 44.**

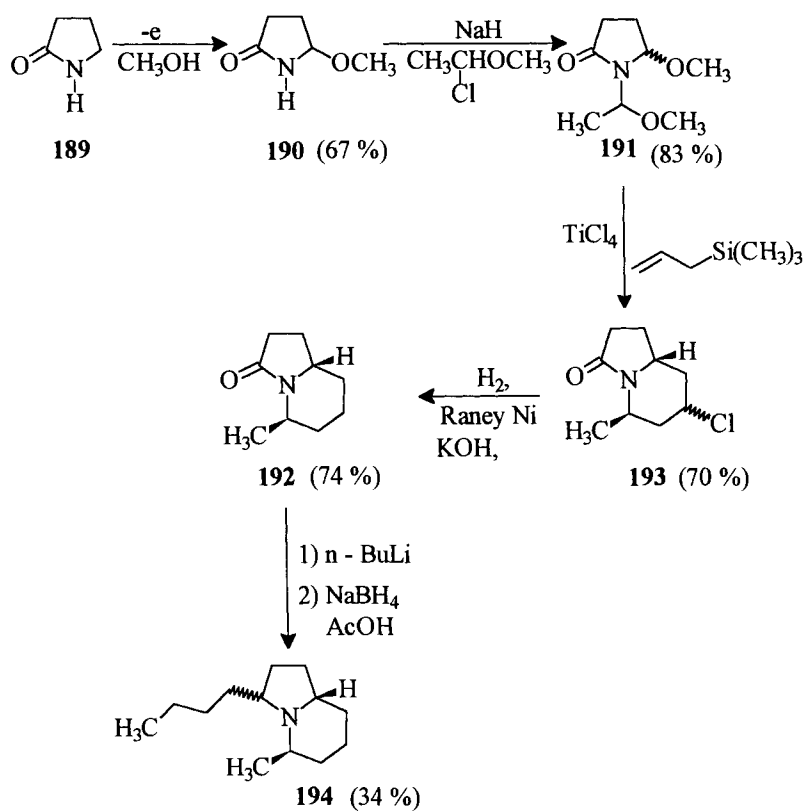
amines, such as ArN(R)CH₂X (X = CF₃, CHF₂, CH₂F) in alkaline methanol leads to preferential addition of a methoxy group at a position α to the fluoromethyl group, as shown in Scheme 47 for an *N*-methylaniline derivative [265, 273, 274].

Whereas in *N*-ethyl and *N*-methylaniline methoxylation occurs only on the methyl groups in the fluoromethyl substituted compounds, the regioselectivity is drastically changed. The α -methoxylated fluoroalkylamines have been used as precursors for the synthesis of fluorinated amino acids and dihydroquinolines [272].

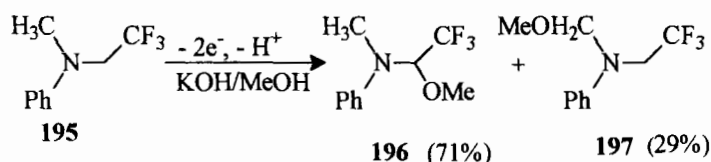
In contrast to the anodic methoxylation of *N*-(2,2,2-trifluoroethyl)amines, anodic cyanation does not occur at the position α to the trifluoroalkyl group (Scheme 48) [275].



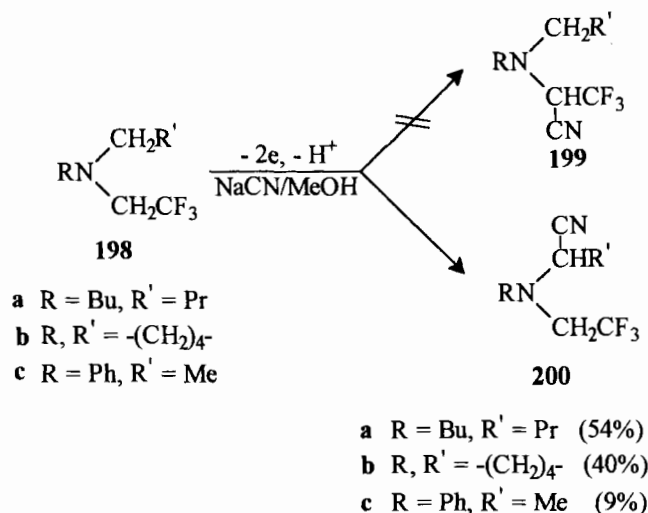
Scheme 45.



Scheme 46.

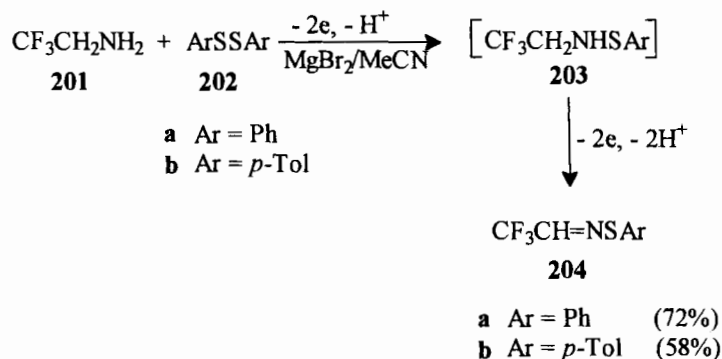


Scheme 47.



Scheme 48.

Trifluoromethylated sulfenimines which are useful starting materials for the preparation of *N*-fluoroalkylamines, aminoketones and aminoalkanoates, have been prepared by the anodic oxidation of 2,2,2-trifluoroethylamine and diaryl sulfides in MeCN/Et₄NClO₄ with MgBr₂ as the redox mediator (Scheme 49) [276].



Scheme 49.



Both direct and sensitized photoelectron-transfer reactions of amines have been utilized for bringing about synthetically useful transformations of amines.

The synthetic and mechanistic aspects of photoaddition reactions of amines with excited states of arenes and aryl olefins have been extensively investigated [10–12, 277].

The reactions of excited states of arenes and arenealkenes with primary and secondary amines result in products arising out of aminyl radical addition, whereas α -aminoalkyl radical addition occurs with tertiary amines [11, 278, 279].

N-Heteroarenes such as pyridine however photochemically add amines to yield α -aminoalkyl substituted products even with secondary amines (Scheme 50) [280].

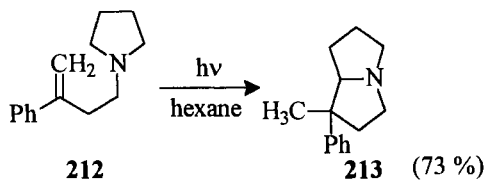
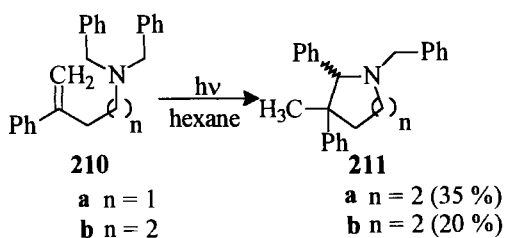
Intramolecular photoaddition reactions of aminoarenes which are of interest from the synthetic point of view, was first reported by Bryce-Smith et al., for (*N,N*-dimethylaminoalkyl)benzenes (Scheme 51) [281].

Aoyama and coworkers have synthesized several pyrrolidine and piperidine derivatives via intramolecular photoaddition reactions of tertiary (aminoalkyl) styrene (Scheme 52) [282, 283].

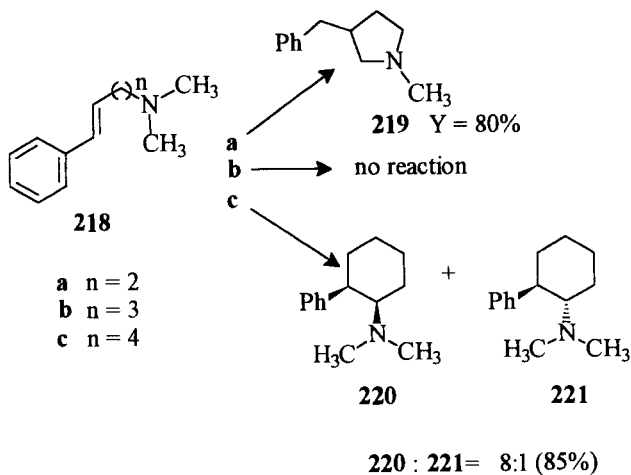
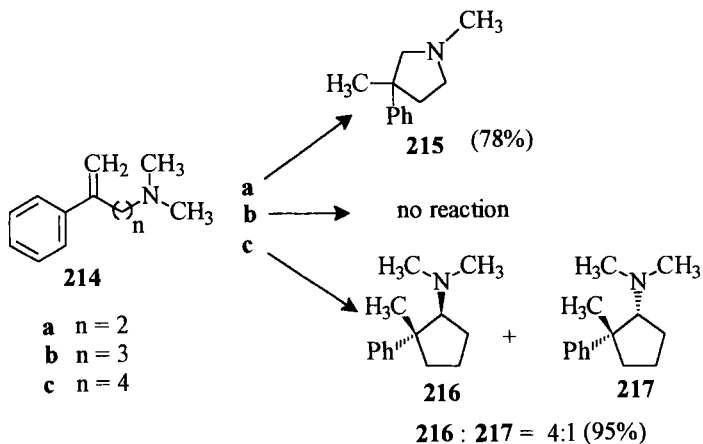
Similar intramolecular photoaddition reactions of styrylamides have also been reported by Aoyama and coworkers [282–286].

Lewis and coworkers have also observed efficient intramolecular photoaddition for several (*N,N*-dimethylaminoalkyl)styrenes, leading to the formation of nitrogen heterocycles or aminocycloalkanes (Scheme 53) [287].

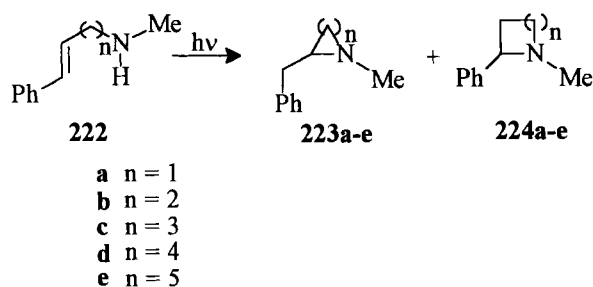




Scheme 52.



Scheme 53.



Scheme 54.

Intramolecular photoaddition reactions of secondary amines linked to styrenes can result in the formation of C–N bonds at the α - or β -carbon (Scheme 54) [288–290]. The product yields and the ratio of the two products are shown in Table 11.

Intramolecular photoaddition of secondary amines linked to various other arenes and stilbenes also provide an efficient method for the synthesis of *N*-heterocycles (Scheme 55) [291–293].

Recently, Lewis et al. have reported the synthesis of larger rings via the photo-induced intramolecular addition of (aminoalkyl)styrylamides and *N*-(aminoalkyl)-2-stilbene carboxamides (Scheme 56) [294, 295].

Intramolecular photoaddition reactions of amines for the construction of *N*-heterocycles has also been successfully explored by Sugimoto and coworkers (Scheme 57) [296–302].

Mariano and coworkers have shown that photoreactions of silylated tertiary amines such as **242**, with a cyclohexenone derivative **241** give two types of adduct, the trimethylsilyl (TMS) containing adduct **243** and the non-TMS adduct **244** (Scheme 58) [303–305].

The distribution of **243** and **244** varied, depending on the nature of the solvent [306]. The TMS adduct was found to predominate in less polar aprotic solvents

Table 11. Product yields for *N*-methyl ω -styrylaminoalkenes.^a

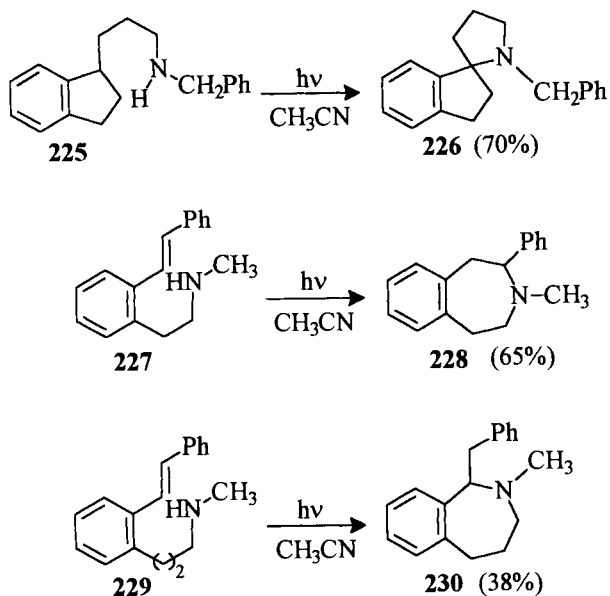
Styrylamine	Φ_{add} ^b	Yield (%) ^c	224/223 ^d
222a	–	15	>10
222b	0.024	63	14
t-222c	0.011	57	2.4
c-222c	0.019	62	2.0
222d	0.050	82	0.15
222e	–	30	>10

^a According to [291].

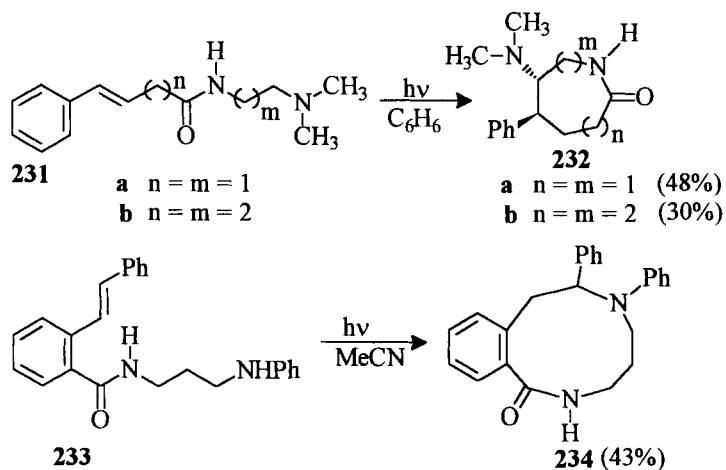
^b Quantum yield for total adduct formation using monochromatic 288 nm irradiation of 0.005 M styrylamine in nitrogen-purged acetonitrile solution.

^c Yield of the major adduct (**223** or **224**) determined by GC analysis at conversion less than 20 %.

^d Product ratio determined by GC analysis.



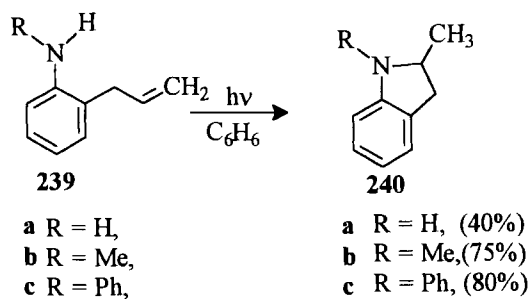
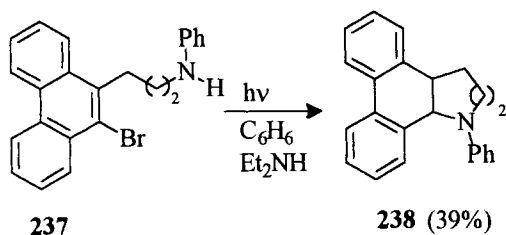
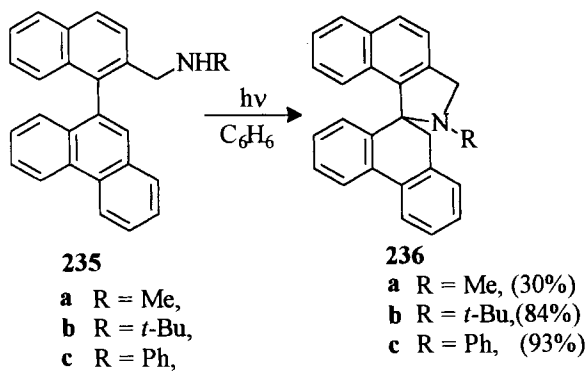
Scheme 55.



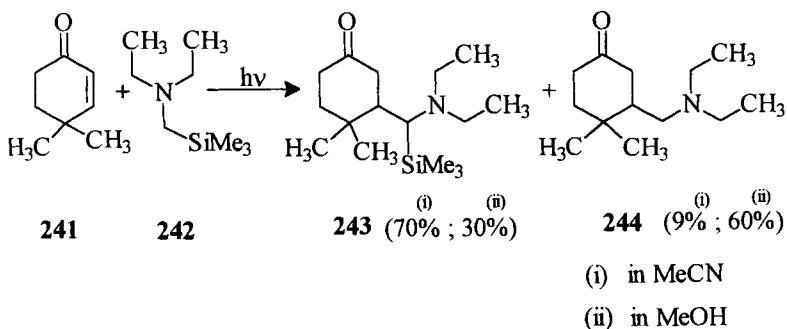
Scheme 56.

such as acetonitrile, whereas, the non-TMS adduct was formed in higher yields in polar protic solvents such as methanol.

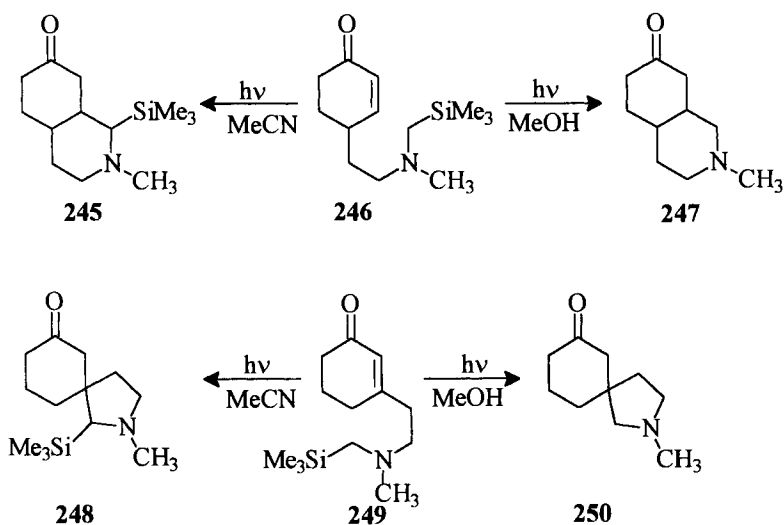
A higher chemoselectivity was obtained in the intramolecular photoreaction of α -silylamines (Scheme 59). Irradiation of **246** and **249** in methanol leads to the cyclized non-TMS products **247** and **250**, respectively, whereas, TMS containing



Scheme 57.



Scheme 58.



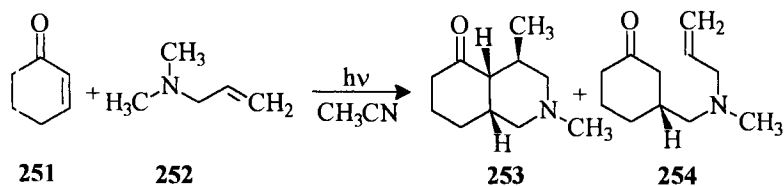
Scheme 59.

products **245** and **248** were formed when irradiation was performed in acetonitrile [131].

Mattay and coworkers reported that direct irradiation ($\lambda > 300$ nm) of 2-cyclohexene-1-one (**251**) in the presence of *N,N*-dimethylallylamine (**252**) leads to 2,4 β -dimethyl-*cis*-decahydro-5-isoquinolineone (**253**) in yields up to 20 % along with trace amounts of **254** (Scheme 60), depending on the polarity of the medium (Table 12) [307]. In polar solvents like acetonitrile containing 10 % water the PET promoted addition-cyclization process competes efficiently with the [2 + 2] cycloaddition pathway leading to dimers (Table 12). Irradiation in the presence of PET sensitizer such as dicyanonaphthalene (DCN) led to only trace amounts of products.

Sensitized photoreactions of amines

In photosensitized reactions, electron transfer occurs between the excited state of the sensitizer and amine resulting in the formation of the radical ion-pair. The sen-



Scheme 60.

Table 12. Solvent effect on the product yields in various photoaddition of *N,N*-dimethylallylamine (**252**) to 2-cyclohexen-1-one (**251**).^a

Solvent	253	254	[2 + 2] dimer	Cyclohexanone
Cyclohexene	2.6 %	traces	3.5 %	
THF	8.2 %	3.9 %	2.9 %	–
MeOH, 20 °C	7.6 %	traces	5.5 %	–
MeOH, 25 °C	5.8 %	3.3 %	2.4 %	–
CH ₃ CN	3.7 %	10.4 %	traces	–
CH ₃ CN, 0.1 eq. LiClO ₄	7.4 %	traces	traces	7.5 %
CH ₃ CN, DCN	traces	3.8 %	2.2 %	–
CH ₃ CN–10 % H ₂ O	20 %	traces	traces	–

^a According to [307].

sitizer is used in low concentrations as it is usually regenerated during the course of the reaction and hence acts in a catalytic manner. The commonly used sensitizers for the generation of aminium ions are cyanoaromatics such as dicyanobenzene (DCB), dicyanonaphthalene (DCN) and dicyanoanthracene (DCA). Ketonic sensitizers such as anthraquinone and benzophenone have also been used.

Mariano and coworkers have investigated the DCA sensitized photocyclization of silylamino–enone derivatives (Scheme 61) [130, 131, 308]. DCA-sensitized photo-reactions of **255** in acetonitrile–methanol mixture gave the substituted piperidines **256** in high yields along with the pyrrolidine ester **257** in the case of **255b**. DCA sensitized reaction of **246** resulted in the formation of a diastereomeric mixture (6:1) of hydrosoquinolines [212, 213] and <2 % of the hydrosoindoline, **258**.

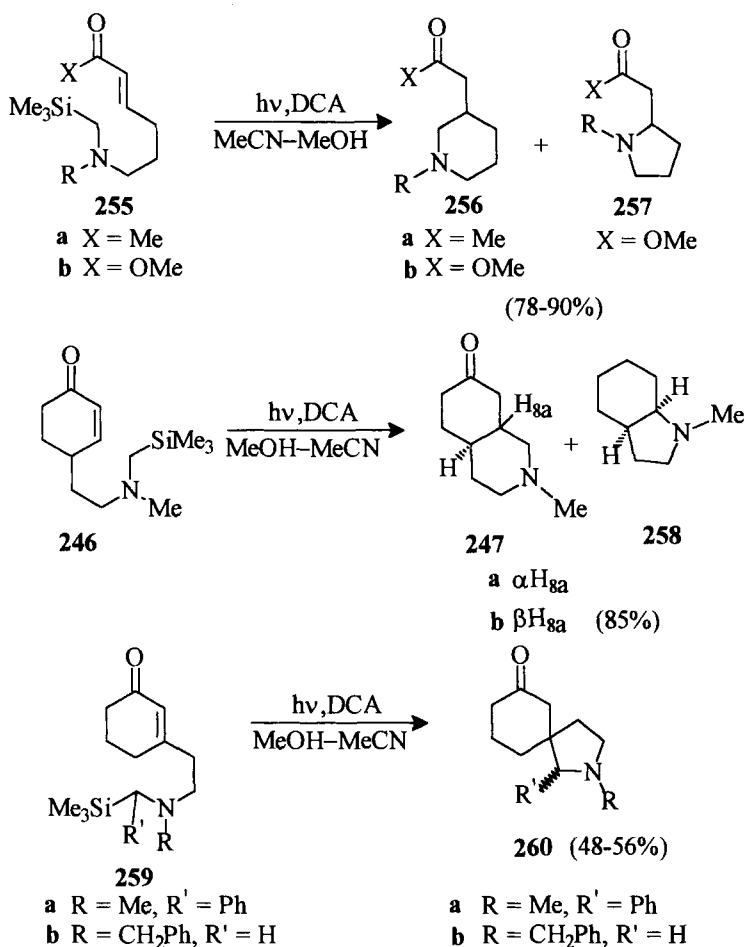
Khim and Mariano have used the same strategy for the synthesis of several functionalized piperidines (Scheme 62) [309].

Sensitized photocyclization was used as a key step in the synthesis of the *E*-ring functionalized alkaloid, yohimbane **267** (Scheme 63) [310].

Pandey and coworkers have reported several DCN-sensitized photocyclization of α -silylamines connected to unactivated olefins [311–314]. Thus, the silyl amines **268** (Scheme 64) were reported to proceed in a *regio*- and *stereo*-selective manner yielding the cyclized products **269** and **270** [311].

Similarly the biologically active natural products (\pm)-epilupine (**273**) and (\pm)-isoretronecanol (**276**) were formed in the DCN-sensitized photoreactions of the silyl amines **271** and **274**, respectively (Scheme 64) [312].

Mariano and coworkers have shown that DCN sensitized photoreaction of **268b** in non-deoxygenated solutions leads to the efficient formation (75 %) of the corresponding pyrrolidone and not the azabicyclic product [315]. Earlier studies by Padwa et al. have shown that α -aminoalkyl radicals, unlike their α -amido analogs, do not add efficiently to unactivated olefins (Scheme 65) [316]. The α -silyl amines **277** connected to electron deficient olefins on the other hand, were found to undergo efficient DCN photosensitized cyclization in deaerated solutions to yield **278** and

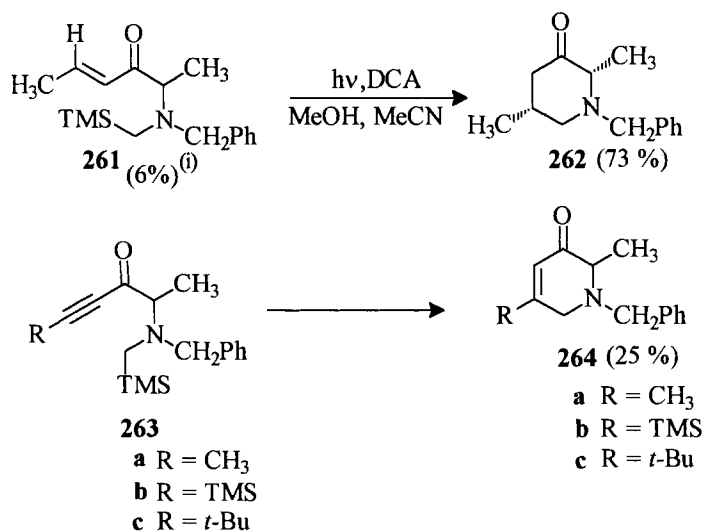


Scheme 61.

279 [315]. The synthesis of (\pm)-epilupine was achieved by Mariano et al. by a two step chemical transformation of **278b**.

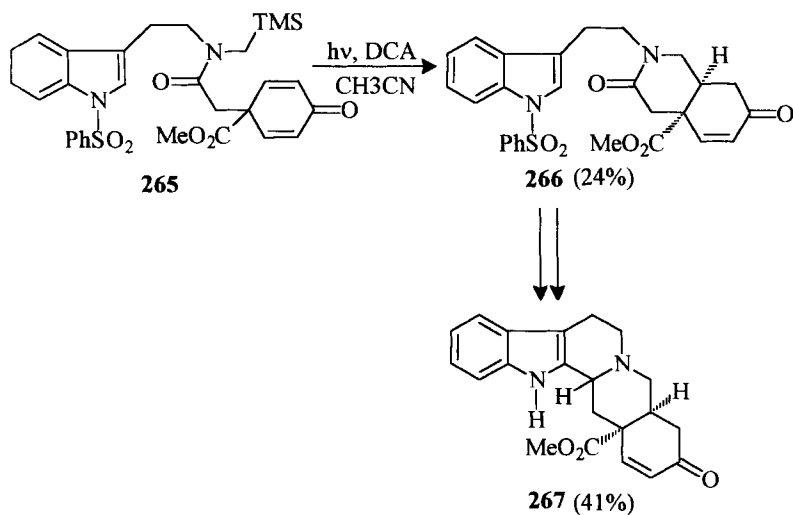
Pandey and coworkers have studied the DCN-sensitized oxidation of *N*-hydroxyamines without prior removal of dissolved oxygen, to nitron intermediates. Trapping the nitrones by dimethylfumarate (**282**) gave the corresponding cycloadducts in good yields (Scheme 66) [317].

Synthesis of oxazabicycloalkanes and related products was achieved by a one pot electron-proton-electron (EPE) transfer mediated reactions of the amine moiety [317]. Here the iminium cation is formed from the second electron oxidation of the α -aminoalkyl radical, generated via the α -deprotonation of the planar aminium radical owing to their low ionization potential. The iminium cation thus formed can

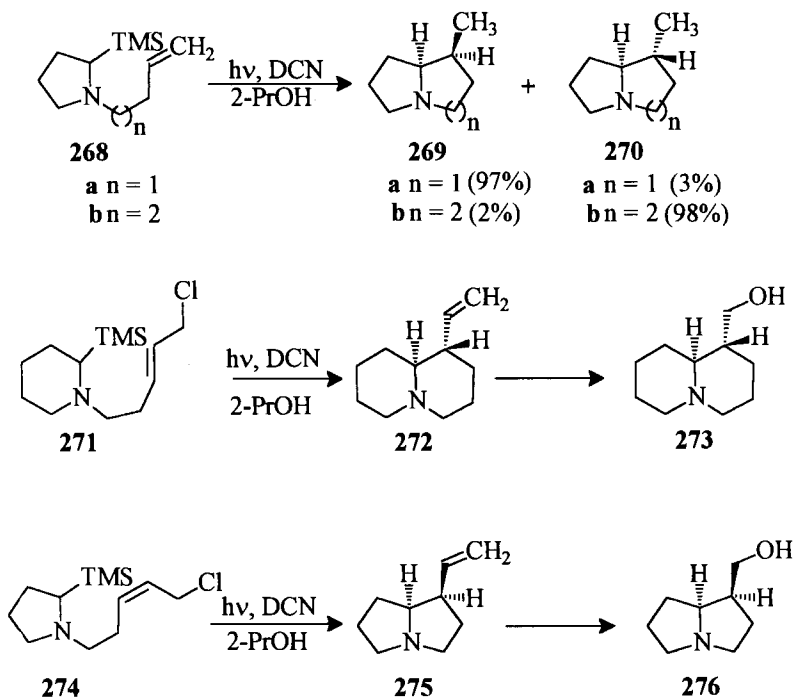


(i) Percentage of starting material consumed

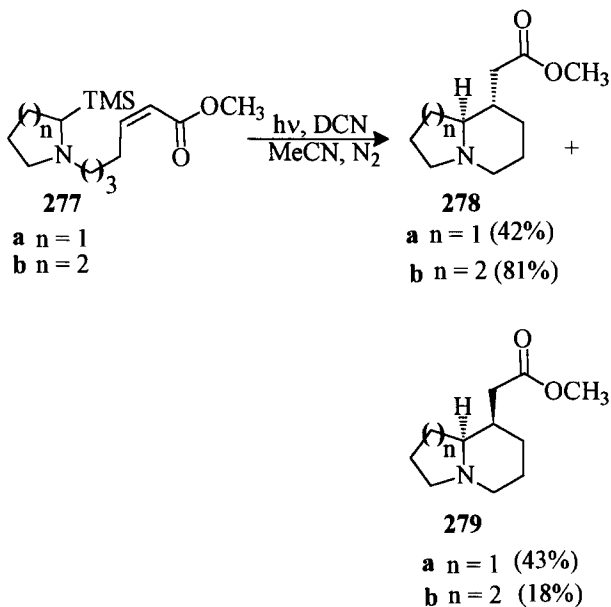
Scheme 62.



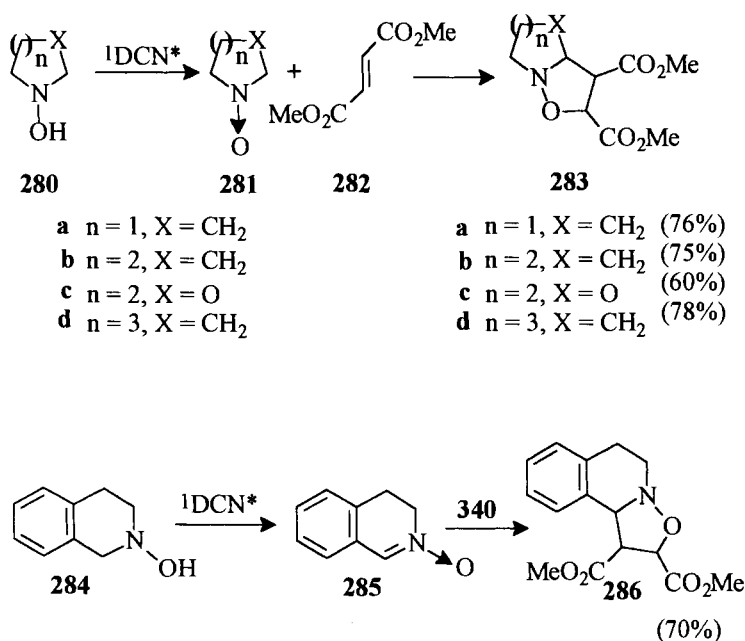
Scheme 63.



Scheme 64.



Scheme 65.



Scheme 66.

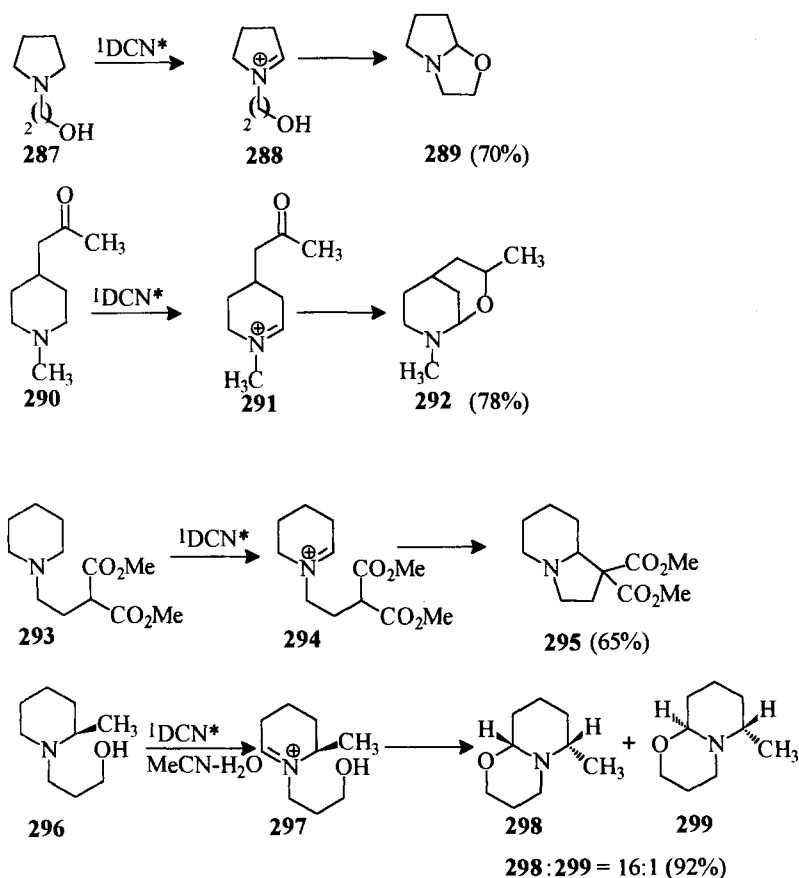
undergo nucleophilic intramolecular cyclization to form the corresponding bicyclic products (Scheme 67) [318].

Lewis and coworkers have studied the sensitized photocyclization of stilbene-linked primary amines **300** which gave **302**, in good yields (Scheme 68) [293].

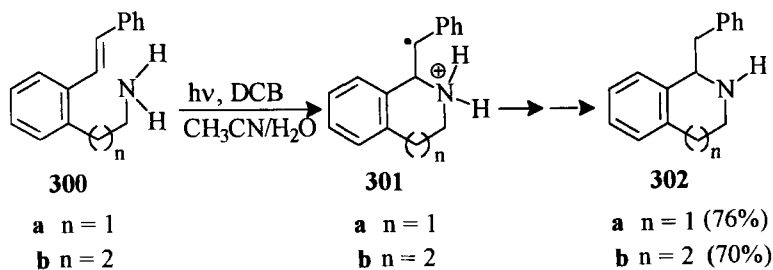
Similarly, the photosensitized electron transfer mediated reactions of several 1- and 9-(aminoalkyl)phenanthrenes using DCB have been investigated by Lewis and coworkers (Scheme 69) [319]. These reactions provide an efficient method of construction of skeletal structures of aporphine, phenanthropiperidine, phenanthroazepine and related alkaloids. The mechanism of these reactions involves an initial electron transfer from the ground state amine to the singlet arene followed by N–H proton transfer and biradical cyclization.

Photoamination of a variety of aromatic compounds with ammonia and alkylamines under photosensitized electron transfer mediated reaction conditions has been extensively investigated by Yasuda and coworkers (Scheme 70) [320–324]. The photoamination reactions of stilbene derivatives with ammonia have been utilized for the synthesis of a variety of isoquinoline derivatives [324]. The photoamination is initiated by photochemical electron transfer from the arenes to the electron acceptor followed by nucleophilic attack of ammonia or primary amines on the aromatic radical cations (Scheme 70).

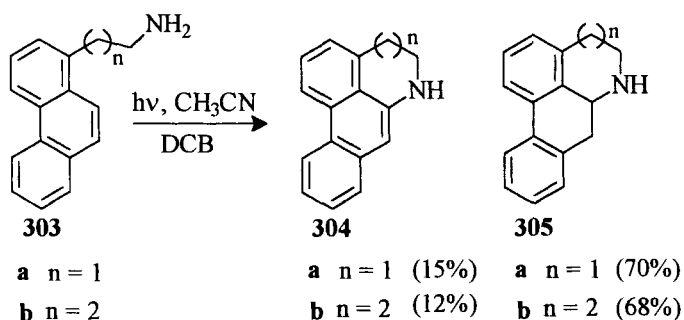
Anthraquinone photosensitized intermolecular carbon–carbon bond forming reactions of several primary, secondary and tertiary amines with electron deficient olefins have been investigated. The addition of α -aminoalkyl radical, generated



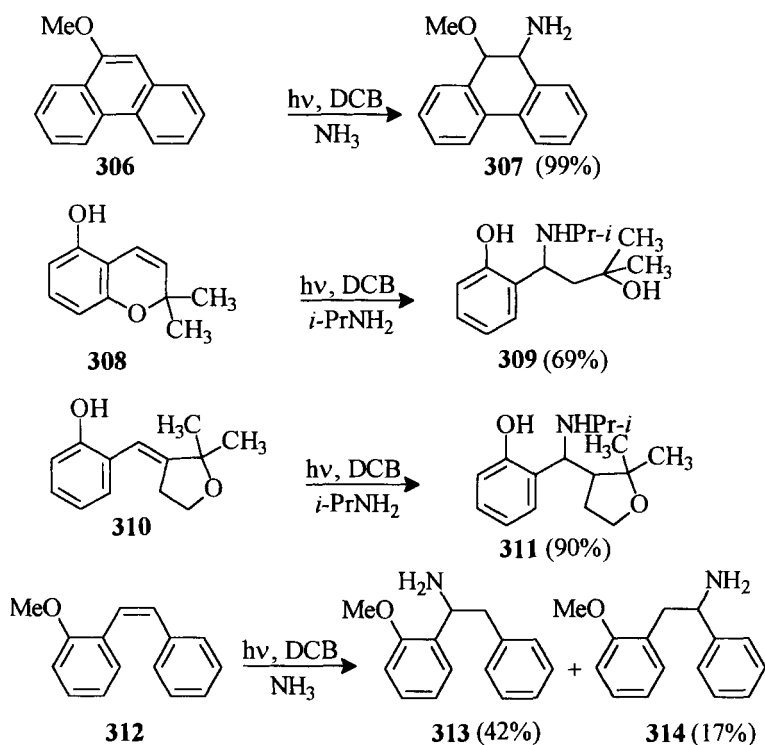
Scheme 67.



Scheme 68.



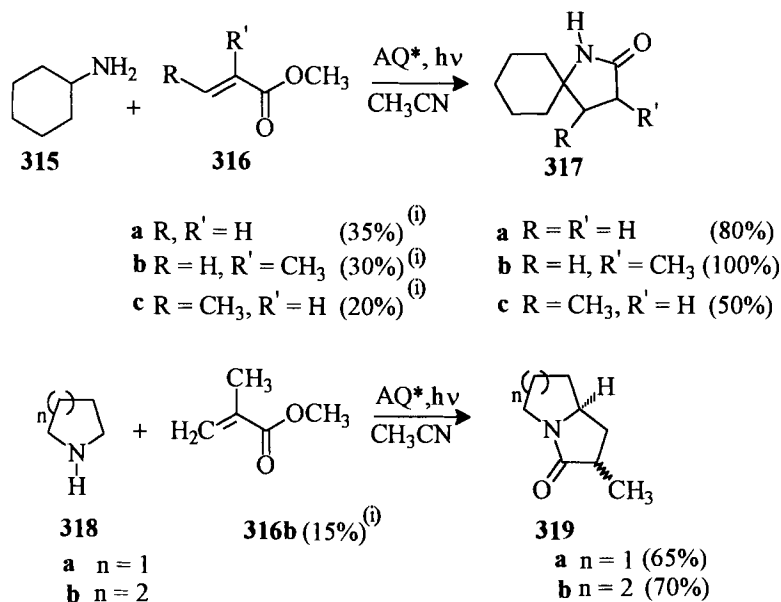
Scheme 69.



Scheme 70.

from triethylamine to electron deficient olefins, is followed by an intramolecular 1,5-hydrogen abstraction of the adduct radical. These reactions lead to the formation of products arising out of multiple addition of the olefinic substrate [325].

In the anthraquinone photosensitized reactions of primary and secondary amines with methyl methacrylate, the adducts formed undergo thermal cyclization to the corresponding bicyclic lactams and spiro lactams (Scheme 71) [325].



(i) Percentage of starting material consumed

Scheme 71.

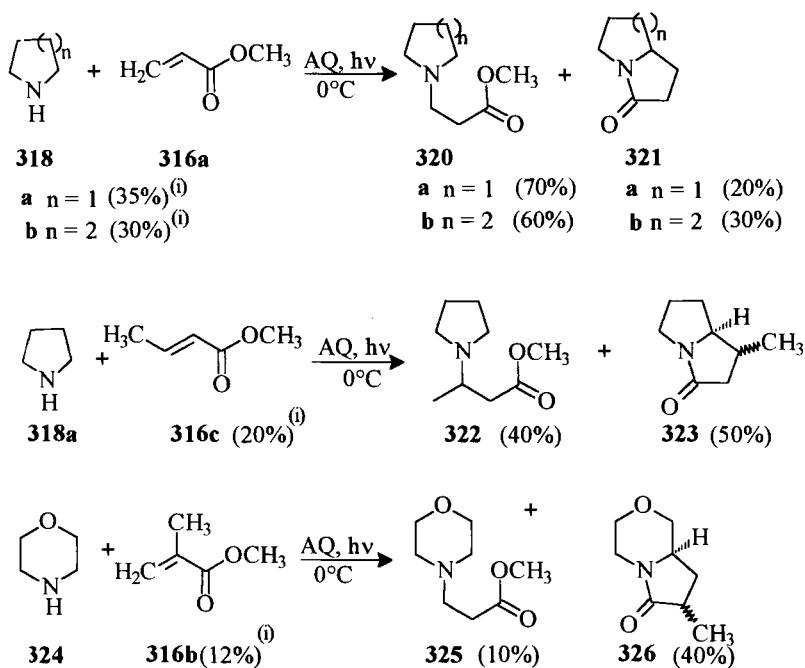
Most, α,β -unsaturated esters other than methyl methacrylate undergo facile Michael type addition with primary and secondary amines to yield *N*-addition products. By carrying out the anthraquinone photosensitized addition of several secondary amines with α,β -unsaturated esters at low temperatures ($\sim 0^\circ\text{C}$), the thermal reactions could be controlled without adversely affecting the photochemical free radical reactions. Using this procedure, indolizidone, pyrrolizidone and a mixture of heliotridone and pseudoheliotridone was synthesized (Scheme 72) [326].

Sensitizers such as benzophenone, anthrone and xanthene were also observed to catalyze these reactions [327]. Anthraquinone sensitized photoreactions of *N*-allylamines with α,β -unsaturated esters also yield lactams as the main product. Minor amounts of tandem radical addition products were also formed [328].

Recently Betrand et al. have reported the sensitized intermolecular addition of tertiary amines derived from pyrrolidines to (5*R*)-5-menthyloxy-2[5*H*]-furanone (**328**) using ketonic sensitizers (Scheme 73, Table 13) [329].

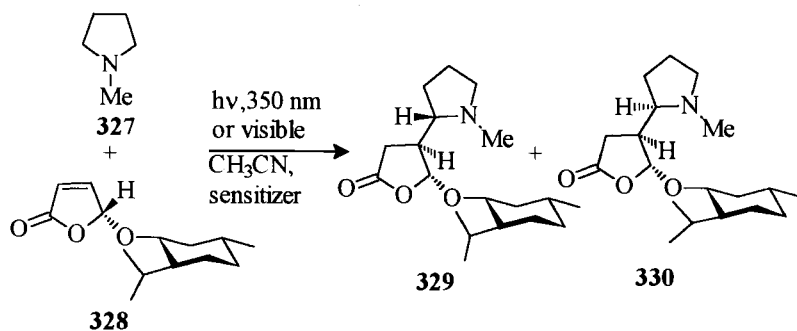
The addition occurs with complete facial selectivity on the furanone ring. The method has been generalized to the addition of tertiary amines and *N*-protected secondary amines to electron-deficient olefins (Table 13).

The electron donating ability of amines, has been utilized in several photochemical reactions for the generation of reactive radical ions which can subsequently undergo synthetically important reactions.



(i) Percentage of starting material consumed

Scheme 72.

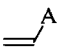
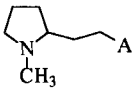
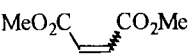
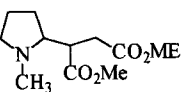
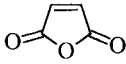
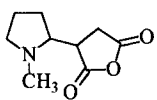
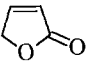
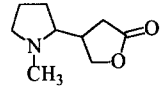
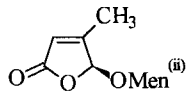
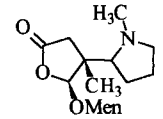
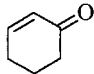
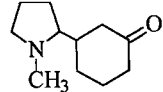


Sensitizer = 4,4'-Dimethoxybenzophenone

Scheme 73.

Cossy and coworkers have reported the stereoselective synthesis of several bicyclic pentanols in good yields, by the intramolecular addition of the ketyl radicals of δ,ϵ -unsaturated ketones, generated via photoinduced electron transfer, using triethylamine (TEA) or hexamethylphosphonic triamide (HMPA), as donors in acetonitrile

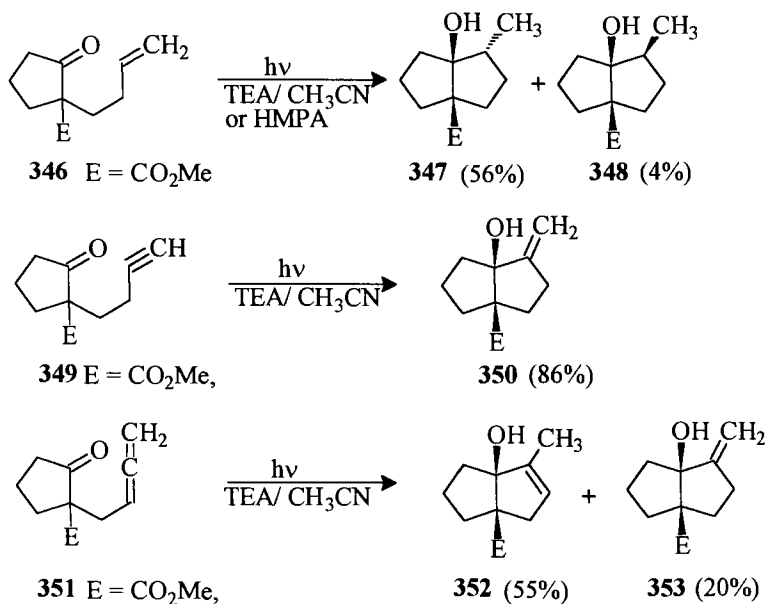
Table 13. Addition of **327** to electron-deficient alkenes.^a

Alkene	Irradiation Time (min)	Product	Yield (%)
 331 A = CN 332 A = CO ₂ Me	60	 333 A = CN 334 A = CO ₂ Me	80 ^b 87 ^b
 335 = <i>cis</i> 336 = <i>trans</i>	10	 337	69 73
 338	7	 339	76
 340	5	 341	86
 342	120	 343	71 ^d
 344	180	 345	90

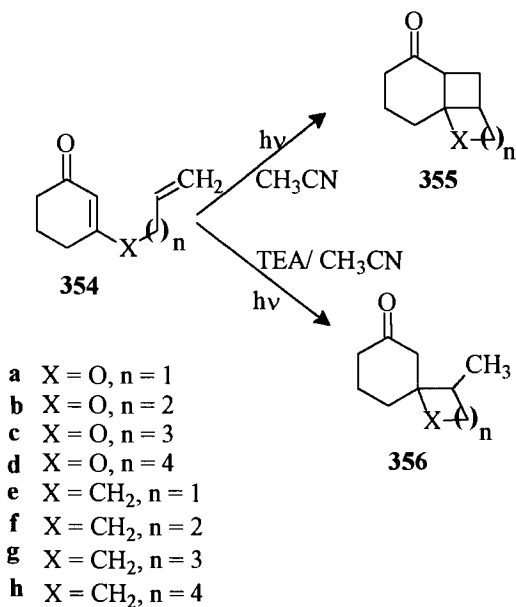
^a According to [329].^b The reaction was performed in pure *N*-methylpyrrolidine.^c Men = 1*R*-(+) = menthyl.^d Conversion = 55 %.

(Scheme 74) [330]. The use of photoreductive cyclization for the total synthesis of actinidine and isooxyskytanthine has been reported [331].

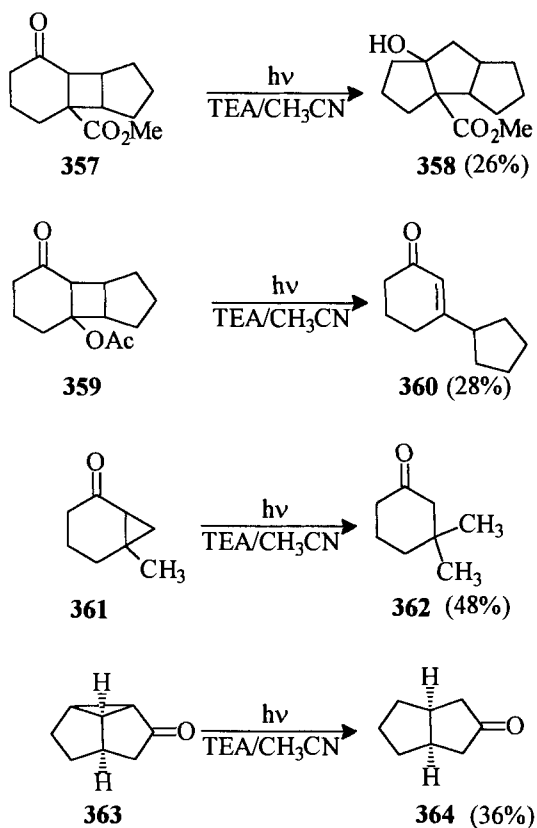
Bischof and Mattay have shown that radical anion cyclization leading to spirocyclic products compete effectively with intramolecular [2 + 2]-cycloaddition on photoexcitation of olefinic enones in the presence of triethylamine [332, 333]. The [2 + 2] cycloadducts could be converted to the corresponding spiro compounds under PET conditions (Scheme 75) [307].



Scheme 74.



Scheme 75.



Scheme 76.

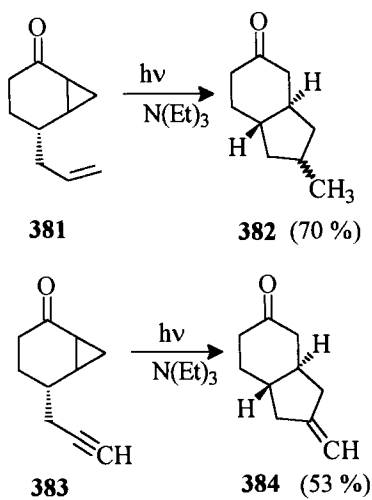
The opening of adjacent strained rings of ketyl radical anions generated in reductive photoinduced electron transfer has been explored by Mattay and coworkers (Schemes 76 and 77) [334].

Tandem fragmentation–cyclization of bicyclic ketones connected to unsaturated side chains have been used to construct bi-, tri-, and spirocyclic ketones [334].

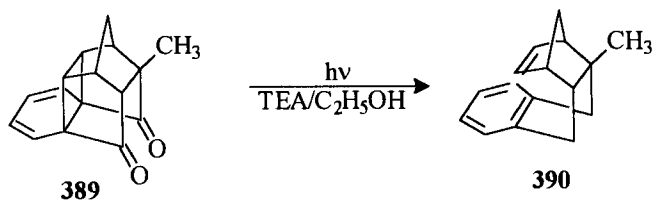
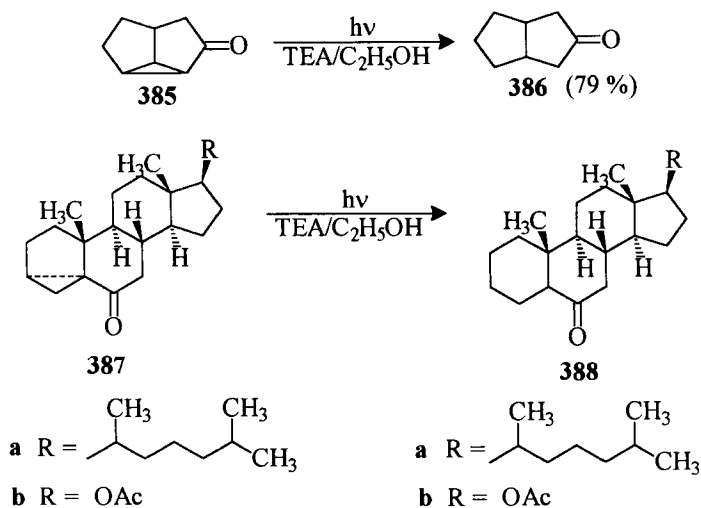
Cossy et al. have shown that depending upon the substitution pattern, ketyl radical anions obtained from photochemically induced electron transfer from amines to cyclopropylketones lead either to the formation of 3-substituted cycloalkanones or to ring expanded products (Scheme 78) [335].

Intramolecular trapping of the radical produced by the PET fragmentation was utilized by Cossy et al. for the construction of bicyclic ring systems (Scheme 79) [335].

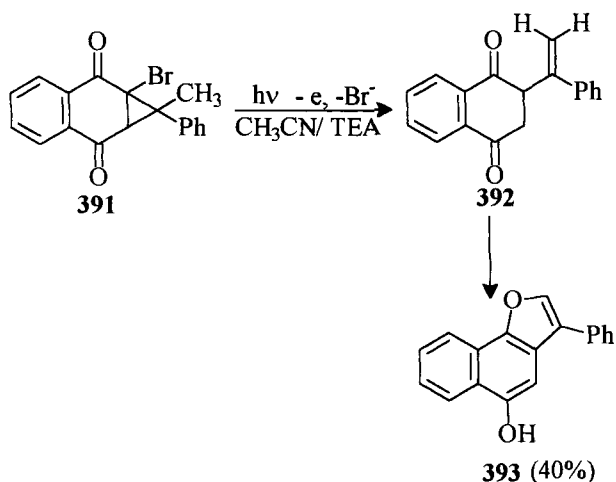
Bond cleavage reactions of cyclopropyl and cyclobutyl rings by adjacent ketyl radical anions generated via photoinduced electron transfer from amines have also been reported by Pandey and coworkers (Scheme 80) [336, 337].



Scheme 79.



Scheme 80.

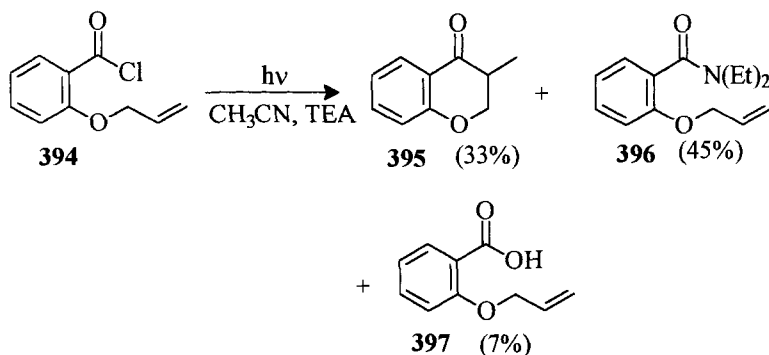


Scheme 81.

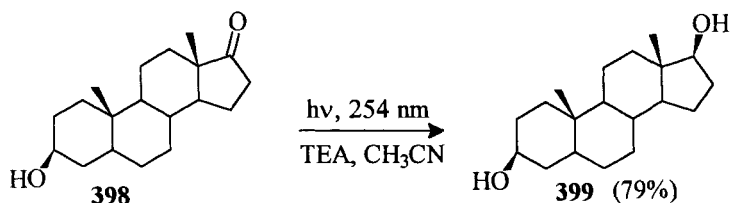
Reductive ring opening of the cyclopropyl ring in the homonaphthaquinone (**391**), gave the naphthafuran derivative **393** via the photocyclization of the intermediate 2-(α -phenylvinyl)-1,4-naphthaquinone (**392**) (Scheme 81) [338].

Photoinduced electron transfer from tertiary amines to aromatic acid chlorides leads to the formation of acyl radicals. Acyl radicals generated from *O*-allyl salicyloyl chloride (**394**) undergoes intramolecular cyclization to form 3-methyl-4-chromanone (**395**) along with formation of the amide and *O*-allylsalicylic acid (Scheme 82) [339].

Wu et al. have reported that direct excitation of amines in the presence of 3, β -hydroxy-5- α -androstan-17-one, under conditions where light is exclusively absorbed by the amine leads to the reduction of the 17-keto group with high stereoselectivity (Scheme 83) [340].



Scheme 82.



Scheme 83.

Acknowledgment

Financial support from the Council of Scientific and Industrial Research, Government of India and the Volkswagen Foundation, Germany is gratefully acknowledged. This is the contribution No. RRLT-PRU-122 from the Regional Research Laboratory (CSIR), Trivandrum.

References

1. E. Steckhan, in *Organic Electrochemistry* (Ed.: H. Lund, M. M. Baizer) **1990**, 581–613.
2. T. Shono in *Electroorganic Chemistry as a New Tool in Organic Synthesis*, Springer, Berlin, **1984**, 54–62.
3. Albert J. Fry in *Synthetic Organic Chemistry II nd Ed.*, **1989**, 274–287.
4. J. Mattay, *Synthesis* **1989**, 233–252.
5. P. S. Mariano, J. L. Stavinocha, in *Synthetic Organic Photochemistry* (Ed.: W. M. Horspool) Plenum Press, New York **1983**, 145–147.
6. U. C. Yoon, P. S. Mariano, *Acc. Chem. Res.* **1992**, 25, 233–240.
7. F. D. Lewis, *Acc. Chem. Res.* **1986**, 19, 401–405.
8. G. Pandey, *Synlett.* **1994**, 546–552.
9. A. Albini, M. Mella, M. Freccero, *Tetrahedron* **1994**, 50, 575–607.
10. U. C. Yoon, P. S. Mariano, R. S. Givens, R. W. Atwater, in *Advances in Electron Transfer Chemistry* (Ed.: P. S. Mariano) Vol. 4, JAI Press, Greenwich, CT, **1994**, 117–205.
11. F. D. Lewis, in *Advances in Electron Transfer Chemistry* (Ed.: P. S. Mariano) Vol. 5, JAI Press, Greenwich, CT, **1996**, 1–40.
12. N. J. Pienta, in *Photoinduced Electron Transfer Part C* (Ed.: M. A. Fox, M. Chanon) Elsevier, Amsterdam, **1988**, 421–486.
13. J. S. D. Kumar, S. Das, *Res. Chem. Intermed.* **1997**, 23, 755–800.
14. M. Hoshino, H. Shizuka, in *Photoinduced Electron Transfer Part C* (Ed.: M. A. Fox, M. Chanon) Elsevier, Amsterdam **1988**, 313–371.
15. J. Stubbe, W. A. van der Donk, *Chem. Rev.* **1998**, 98, 705–762.
16. R. B. Silverman, *Acc. Chem. Res.* **1995**, 28, 335–342.
17. R. B. Silverman, in *Advances in Electron Transfer Chemistry* (Ed.: P. S. Mariano) Vol. 2, JAI Press, Greenwich, Connecticut **1992**, 177–213.
18. F. P. Guengerich, T. L. MacDonald, in *Advances in Electron Transfer Chemistry* (Ed.: P. S. Mariano) Vol. 3, JAI Press, Greenwich, Connecticut **1993**, 191–241.
19. C. J. Easton, *Chem. Rev.* **1997**, 97, 53–82.
20. P. Renaud, L. Giruad, *Synthesis* **1996**, 913–926.
21. B. Giese in *Radicals in Organic Synthesis: Formation of Carbon–Carbon Bonds*, Pergamon Press, New York, **1986**.

22. Y. L. Chow, W. C. Danen, S. F. Nelson, D. H. Rosenblatt, *Chem. Rev.* **1978**, 78, 243–274.
23. P. I. Dalko, *Tetrahedron* **1995**, 51, 7579–7653.
24. R. D. Theys, G. Sosnovsky, *Chem. Rev.* **1997**, 97, 83–132.
25. L.-A. Linden, *Proc. Indian Acad. Sci. (Chem. Sci.)* **1993**, 105, 405–419.
26. N.S. Allen, G. Pullen, M. Edge, I. Weddell, R. Swart, F. Catalina, *J. Photochem. Photobiol. A: Chem.* **1997**, 109, 71–75.
27. G.K. Pullen, N.S. Allen, M. Edge, I. Weddell, R. Swart, F. Catalina, S. Navaratnam, *European Polymer Journal* **1996**, 32, 943–955.
28. K. Venkataraman, *The Chemistry of Synthetic Dyes Vol. I–VIII 1953–1978*.
29. A. P. de Silva, H. Q. N. Gunaratne, T. Gunnlaugsson, A. J. M. Huxley, C. P. McCoy, J. T. Rademacher, T. R. Rice, *Chem. Rev.* **1997**, 97, 1515–1566.
30. A. W. Czarnik, in *Fluorescent Chemosensors for Ion and Molecule Recognition* American Chemical Society, Washington D. C. **1992**.
31. P. Novák, K. Müller, K. S. V. Santhanam, O. Haas, *Chem. Rev.* **1997**, 97, 207–281.
32. T. Tsutsui, C. Adachi, S. Saito, *Electroluminescence in Organic Thin Films*, in *Photochemical Progress in Organized Molecular Systems* (Ed.: K. Honda) Elsevier Science Publishers, B. V., Amsterdam **1991**, 437–450.
33. J. Kido, M. Kimura, K. Nagai, *Science* **1996**, 275, 1267–1332.
34. K. Sakanoue, M. Motoda, M. Sugimoto, S. Sakaki, *J. Phys. Chem. A* **1999**, 103, 5551–5556.
35. D. L. Morel, E. L. Stogryn, A. K. Ghosh, T. Feng, P. E. Purwin, R. F. Shaw, C. Fishman, G. R. Bird, A. P. Piechowski, *J. Phys. Chem.* **1984**, 88, 923–933.
36. A. P. Piechowski, G. R. Bird, D. L. Morel, E. L. Stogryn, *J. Phys. Chem.* **1984**, 88, 934–950.
37. S. R. Marder, J. E. Sohn, G. D. Stucky in *Materials for Nonlinear Optics: Chemical Perspectives*, *ACS Symp. Ser.*, **1991**.
38. D. S. Chemla, J. Zyss in *Non-linear Optical Properties of Organic Molecules and Crystals, Vol. 1 and 2*, Academic Press, New York, **1987**.
39. D. J. Williams in *Nonlinear Optical Properties of Organic and Polymeric Materials*, *ACS Symp. Ser.*, Vol. 233, Washington D. C., **1983**, 251pp.
40. X-D. Wu, S-K. Khim, X. Zhang, E. M. Cederstrom, P. S. Mariano, *J. Org. Chem.* **1998**, 63, 841–859.
41. H. J. Kim, U. C. Yoon, Y-S Jung, N. S. Park, E. M. Cederstrom, P. S. Mariano, *J. Org. Chem.* **1998**, 63, 860–863.
42. X. Zhang, Y-S Jung, P. S. Mariano, M. A. Fox, P. S. Martin, J. Merkert, *Tetrahedron Lett.* **1993**, 34, 5239–5242.
43. C. A. Audeh, J. R. Lindsay Smith, *J. Chem. Soc. B* **1970**, 1280–1285.
44. C. A. Audeh, J. R. Lindsay Smith, *J. Chem. Soc. B* **1971**, 1745–1747.
45. L. A. Hull, G. T. Davis, D. H. Rosenblatt, *J. Am. Chem. Soc.* **1969**, 91, 6247–6250.
46. K. S. Shukla, P. C. Mathur, O. P. Bansal, *J. Inorg. Nucl. Chem.* **1973**, 35, 1301–1307.
47. G. T. Davis, M. M. Demek, D. H. Rosenblatt, *J. Am. Chem. Soc.* **1972**, 94, 3321–3325.
48. D. H. Rosenblatt, G. T. Davis, L. A. Hull, G. D. Forberg, *J. Org. Chem.* **1968**, 33, 1649–1650.
49. H. J. Dauben Jr, L.L. McCoy, *J. Am. Chem. Soc.* **1959**, 81, 5404–5409.
50. J. R. Lindsay Smith, J. S. Sadd, *J. Chem. Soc. Perkin Trans. 2* **1976**, 741–747.
51. S. K. Malhotra, J. J. Hostynek, A. F. Lundin, *J. Am. Chem. Soc.* **1968**, 90, 6565–6566.
52. H. Weingarten, J. S. Wager, *J. Org. Chem.* **1970**, 35, 1750–1753.
53. L. Horner, C. Betzel, *Justus Leibigs Ann. Chem.* **1953**, 579, 175–192.
54. J. K. Kochi, in *Free Radicals* (Ed.: J. K. Kochi) Vol. 2, John Wiley and Sons, New York **1973**, 665–710.
55. J. K. Kochi, in *Free Radicals* (Ed.: J. K. Kochi) Vol. 1, Interscience, New York **1973**, 591–683.
56. Y. L. Chow in *Reactive Intermediates*, Plenum Press, **1980**, 417–441.
57. Y. L. Chow, *Acc. Chem. Res.* **1973**, 6, 354–360.
58. D. H. Rosenblatt, E. P. Burrows, in *Chemistry of Amino, Nitroso, Nitro Compounds and Their Derivatives* (Ed.: S. Patai) Vol. 2, Wiley, New York **1982**, 1085–1149.
59. L. A. Hull, G. T. Davis, D. H. Rosenblatt, H. K. R. Williams, R. C. Weglein, *J. Am. Chem. Soc.* **1967**, 89, 1163–1170.

60. M. Wei, R. Stewart, *J. Am. Chem. Soc.* **1966**, *88*, 1974–1979.
61. H. Firouzabadi, A. R. Sardarian, M. Naderi, B. Vessal, *Tetrahedron* **1984**, *40*, 5001–5004.
62. H. Firouzabadi, B. Vessal, M. Naderi, *Tetrahedron Lett.* **1982**, *23*, 1847–1850.
63. H. Firouzabadi, Z. Mostafavipoor, *Bull. Chem. Soc. Jpn.* **1983**, *56*, 914–917.
64. L. Castedo, R. Riguera, M. J. Rodriguez, *Tetrahedron* **1982**, *38*, 1569–1570.
65. D. S. Kashdan, J. A. Schwartz, H. Rapoport, *J. Org. Chem.* **1982**, *47*, 2638–2643.
66. R. Neumann, M. Levin, *J. Org. Chem.* **1991**, *56*, 5707–5710.
67. K. Orito, T. Hataakeyama, M. Takeo, S. Uchiito, M. Tokuda, H. Suginome, *Tetrahedron* **1998**, *54*, 8403–8410.
68. C. K. Mann, K. A. Barnes in *Electrochemical Reactions in Nonaqueous Systems*, Dekker, New York, **1970**, 259–296.
69. K. K. Barnes, C. K. Mann, *J. Org. Chem.* **1967**, *32*, 1474–1479.
70. N. A. Hampson, J. B. Lee, J. R. Morley, K. I. MacDonald, B. F. Scanlon, *Tetrahedron* **1970**, *26*, 1109–1114.
71. P. M. Robertson, F. Swager, N. Ibl, *Electrochim. Acta.* **1973**, *18*, 923–924.
72. R. F. Nelson, *Tech. Electroorg. Synth. Part 2*, in *Tech. Chem.* (Ed.: N. L. Weinberg) Vol. V, Wiley-Interscience, New York **1974**, 269–395.
73. N. L. Weinberg, H. R. Weinberg, *Chem. Rev.* **1968**, *68*, 449–523.
74. R. L. Hand, R. F. Nelson, *J. Am. Chem. Soc.* **1974**, *96*, 850–860.
75. D. M. Mohilner, R. N. Adams, W. J. Argersinger Jr., *J. Am. Chem. Soc.* **1962**, *84*, 3618–3622.
76. M. Breitenbach, K. H. Heckner, *J. Electroanal. Chem. Interfacial Electrochem.* **1971**, *29*, 309–323.
77. J. Heinze, *Top. Curr. Chem.* **1990**, *152*, 1–47.
78. R. Reynolds, L. L. Line, R. F. Nelson, *J. Am. Chem. Soc.* **1974**, *96*, 1087–1092.
79. E. Steckhan, *Angew. Chem.* **1986**, *25*, 681–699.
80. E. Steckhan, *Top. Curr. Chem.* **1987**, *142*, 1–69.
81. W. Schmidt, E. Steckhan, *Angew. Chem. Int. Ed. Engl.* **1978**, *17*, 673–674.
82. N. Schultz, S. Töteberg-Kaulen, S. Dapperheld, J. Heyer, M. Platen, K. Schumacher, E. Steckhan, in *Recent Advances in Electro Organic Synthesis, Proceedings of the 1st International Symposium on Electroorganic Synthesis* (Ed.: S. Torii) Elsevier, Amsterdam **1987**, 127–135.
83. K.-H. Grosse Brinkhaus, E. Steckhan, D. Degner, *Tetrahedron* **1986**, *42*, 553–560.
84. S. Das, C. von Sonntag, *Z. Naturforsch.* **1986**, *41b*, 505–513.
85. S. Das, M. N. Schuchmann, H.-P. Schuchmann, C. von Sonntag, *Chem. Ber.* **1987**, *120*, 319–323.
86. S. Das, O. J. Mieden, X.-M. Pan, M. Pepas, M. N. Schuchmann, H.-P. Schuchmann, C. von Sonntag, H. Zegota, in *Oxygen Radicals in Biology and Medicine* (Ed.: M. G. Simic, K. A. Taylor, J. F. Ward, C. von Sonntag) Plenum Press, New York **1988**, 55–58.
87. M. Simic, P. Neta, E. Hayon, *Int. J. Radiat. Phys. Chem.* **1971**, *3*, 309–320.
88. Z. B. Alfassi, R. H. Schuler, *J. Phys. Chem.* **1985**, *89*, 3359–3363.
89. Z. B. Alfassi, S. Mosseri, P. Neta, *J. Phys. Chem.* **1989**, *93*, 1380–1385.
90. S. Solar, W. Solar, N. Getoff, *Radiat. Phys. Chem.* **1986**, *28*, 229–234.
91. J. W. T. Spinks, R. J. Woods in *An Introduction to Radiation Chemistry*, John Wiley and Sons, New York, **1990**, 592pp.
92. S. Das, P. V. Kamat, S. Padmaja, V. Au, S. A. Madison, *J. Chem. Soc. Perkin Trans. 2* **1999**, 1219–1223.
93. R. O. C. Norman, N. H. Anderson, *J. Chem. Soc. B* **1971**, 993–1003.
94. R. W. Fessenden, P. Neta, *J. Phys. Chem.* **1972**, *76*, 2857–2859.
95. P. Wardman, D. R. Smith, *Can. J. Chem.* **1971**, *49*, 1880–1887.
96. Farhataziz, A. B. Ross, *U. S. Department of Commerce Washington NSRDS-NBS* **1977**, *59*, 113pp.
97. M. Eigen, G. Ilgenfritz, W. Kruse, *Chem. Ber.* **1965**, *98*, 1623–1638.
98. L. Qin, G. N. R. Tripathi, R. H. Schuler, *Z. Naturforsch.* **1985**, *40a*, 1026–1039.
99. P. S. Rao, E. Hayon, *J. Phys. Chem.* **1975**, *79*, 1063–1066.
100. J. Holcman, K. Sehested, *J. Phys. Chem.* **1977**, *81*, 1963–1966.
101. J. Wheeler, R. Nelsen, *J. Phys. Chem.* **1973**, *77*, 2490–2492.

102. E. Zador, J. M. Warman, A. Hummel, *J. Chem. Soc. Faraday Transactions 1* **1976**, 72, 1368–1376.
103. G. N. R. Tripathi, Q. Sun, *J. Phys. Chem. A* **1999**, 103, 9055–9060.
104. W. C. Danen, R. C. Rickard, *J. Am. Chem. Soc.* **1972**, 94, 3254–3256.
105. V. Malatesta, K. U. Ingold, *J. Am. Chem. Soc.* **1973**, 95, 6400–6404.
106. W. C. Danen, R. C. Rickard, *J. Am. Chem. Soc.* **1975**, 97, 2303–2304.
107. H. Bock, I. Goebel, Z.-Havlas, S. Liedle, H. Oberhammer, *Angew. Chem. Int. Ed. Engl.* **1991**, 30, 187–190.
108. S. F. Nelsen, C. R. Kessel, *J. Chem. Soc. Chem. Commun.* **1977**, 30, 490–491.
109. A. de Meijere, V. Chaplinski, F. Gerson, P. Merstetter, E. Haselbach, *J. Org. Chem.* **1999**, 64, 6951–6959.
110. T. Shida, E. Haselbach, T. Bally, *Acc. Chem. Res.* **1984**, 17, 180–186.
111. M.C.R. Symons, *Chem. Soc. Rev.* **1984**, 13, 393–439.
112. X.-Z. Qin, F. Williams, *J. Phys. Chem.* **1986**, 90, 2292–2296.
113. A. de Meijere, V. Chaplinski, H. Winsel, M. A. Kusnetsov, P. Rademacher, R. Boese, T. Haumann, M. Traetteberg, P. V. Schleyer, T. Zyweitz, H. Jiao, P. Merstetter, F. Gerson, *Angew. Chem. Int. Ed. Engl.* **1999**, 38, 2430–2433.
114. M. B. Khusidman, V. P. Vyatkin, N. V. Grogor'eva, S. L. Dobychin, *Zh. Prikl. Khim. (Leningrad)* **1983**, 56, 222–224 [Chem. Abstr. **1983**, 98, 160106r].
115. *Photoinduced Electron Transfer Part A–D*, (Ed.: M. A. Fox, M. Chanon) Elsevier, New York **1988**.
116. M. Julliard, M. Chanon, *Chem. Rev.* **1983**, 83, 425–506.
117. G. J. Kavarnos, N. J. Turro, *Chem. Rev.* **1986**, 86, 401–449.
118. J. Mattay, M. Vondenhof, *Top. Curr. Chem.* **1991**, 219–255.
119. D. Rehm, A. Weller, *Isr. J. Chem.* **1970**, 8, 259–271.
120. M. Chanon, M. D. Hawley, M. A. Fox, in *Photoinduced Electron Transfer Part A* (Ed.: M. A. Fox, M. Chanon) **1988**, 1–59.
121. F. D. Lewis, T.-I. Ho, J. T. Simpson, *J. Am. Chem. Soc.* **1982**, 104, 1924–1929.
122. F. D. Lewis, T.-I. Ho, J. T. Simpson, *J. Org. Chem.* **1981**, 46, 1077–1082.
123. J. R. Lindsay Smith, L. A. V. Mead, *J. Chem. Soc. Perkin Trans. 2* **1973**, 206–210.
124. P. J. Smith, C.K. Mann, *J. Org. Chem.* **1969**, 34, 1821–1826.
125. F. D. Lewis, J. T. Simpson, *J. Am. Chem. Soc.* **1980**, 102, 7593–7595.
126. H. C. Brown, I. Moritani, *J. Am. Chem. Soc.* **1955**, 77, 3607–3610.
127. D. J. Cram, M. R. V. Sahyun, *J. Am. Chem. Soc.* **1963**, 85, 1257–1263.
128. X. Zhang, S.-R. Yeh, S. Hong, M. Freccero, A. Albini, D. E. Falvey, P. S. Mariano, *J. Am. Chem. Soc.* **1994**, 116, 4211–4220.
129. Z. Su, P. S. Mariano, D. E. Falvey, U. C. Yoon, S. W. Oh, *J. Am. Chem. Soc.* **1998**, 120, 10676–10686.
130. W. Xu, P. S. Mariano, *J. Am. Chem. Soc.* **1991**, 113, 1431–1432.
131. W. Xu, X. M. Zhang, P. S. Mariano, *J. Am. Chem. Soc.* **1991**, 113, 8863–8878.
132. E. R. Gaillard, D. G. Whitten, *Acc. Chem. Res.* **1996**, 292–297.
133. X. Ci, D. G. Whitten, *J. Phys. Chem.* **1991**, 95, 1988–1993.
134. C. M. Haugen, W. R. Bergmark, D. G. Whitten, *J. Am. Chem. Soc.* **1992**, 114, 10293–10297.
135. X. Ci, M. A. Kellet, D. G. Whitten, *J. Am. Chem. Soc.* **1993**, 113, 3893–3904.
136. X. Ci, D. G. Whitten, *J. Am. Chem. Soc.* **1989**, 111, 3459–3461.
137. X. Ci, D. G. Whitten, *J. Am. Chem. Soc.* **1987**, 109, 7215–7217.
138. L. A. Lucia, R. D. Burton, K. S. Schanze, *J. Phys. Chem.* **1993**, 97, 9078–9080.
139. Y. Wang, B. T. Hauser, M. M. Rooney, R. D. Burton, K. S. Schanze, *J. Am. Chem. Soc.* **1993**, 115, 5675–5683.
140. N. Sutin, *Acc. Chem. Res.* **1982**, 15, 275–282.
141. *Electron-transfer Reactions*, (Ed.: R. D. Cannon) Butterworths, Sevenoaks, London **1981**, 368pp.
142. M. D. Mauzerall, in *Photoinduced Electron Transfer Part A*, (Ed.: M. A. Fox, M. Chanon) Elsevier, Amsterdam **1988**, 228–244.
143. S. G. Cohen, J. I. Cohen, *J. Phys. Chem.* **1968**, 72, 3782–3793.
144. S. Inbar, S. G. Cohen, *J. Am. Chem. Soc.* **1978**, 100, 4490–4495.

145. S. G. Cohen, H. M. Chao, *J. Am. Chem. Soc.* **1968**, *90*, 165–173.
146. S. Inbar, H. Linschitz, S. G. Cohen, *J. Am. Chem. Soc.* **1980**, *102*, 1419–1421.
147. S. Inbar, H. Linschitz, S. G. Cohen, *J. Am. Chem. Soc.* **1981**, *103*, 1048–1054.
148. K. Bhattacharyya, P. K. Das, *J. Phys. Chem.* **1986**, *90*, 3987–3993.
149. J. C. Scaiano, *J. Phys. Chem.* **1981**, *85*, 2851–2855.
150. A. Demeter, L. Biczók, T. Bérces, V. Wintgens, P. Valat, J. Kossanyi, *J. Phys. Chem.* **1993**, *97*, 3217–3224.
151. X. Ci, D. G. Whitten, in *Photoinduced Electron Transfer Part C* (Ed.: M. A. Fox, M. Chanon) Elsevier, Amsterdam **1988**, 553–577.
152. M. Hoshino, H. Shizuka, *J. Phys. Chem.* **1987**, *91*, 714–718.
153. J. D. Simon, K. S. Peters, *J. Am. Chem. Soc.* **1981**, *103*, 6403–6406.
154. J. D. Simon, K. S. Peters, *Acc. Chem. Res.* **1984**, *17*, 277–283.
155. J. D. Simon, K. S. Peters, *J. Am. Chem. Soc.* **1982**, *104*, 6542–6547.
156. K. S. Peters, E. Pang, J. Rudzki, *J. Am. Chem. Soc.* **1982**, *104*, 5535–5577.
157. C. Devadoss, R. W. Fessenden, *J. Phys. Chem.* **1990**, *94*, 4540–4549.
158. C. Devadoss, R. W. Fessenden, *J. Phys. Chem.* **1991**, *95*, 7253–7260.
159. H. Miyasaka, K. Morita, K. Kamada, N. Mataga, *Chem. Phys. Lett.* **1991**, *178*, 504–510.
160. H. Miyasaka, K. Morita, K. Kamada, N. Mataga, *Bull. Chem. Soc. Jpn.* **1990**, *63*, 3385–3397.
161. E. Haselbach, P. Jacques, D. Pilloud, P. Suppan, E. Vauthey, *J. Phys. Chem.* **1991**, *95*, 7115–7117.
162. K. S. Peters, J. Lee, *J. Phys. Chem.* **1993**, *97*, 3761–3764.
163. K. S. Peters, J. Lee, *J. Phys. Chem.* **1992**, *96*, 8941–8945.
164. H. Miyasaka, K. Morita, K. Kamada, T. Nagata, M. Kiri, N. Mataga, *Bull. Chem. Soc. Jpn.* **1991**, *64*, 3229–3244.
165. H. Miyasaka, M. Kiri, K. Morita, N. Mataga, Y. Tanimoto, *Chem. Phys. Lett.* **1992**, *199*, 21–28.
166. H. Miyasaka, M. Kiri, K. Morita, N. Mataga, Y. Tanimoto, *Bull. Chem. Soc. Jpn.* **1995**, *68*, 1569–1821.
167. T. Kiyota, M. Yamaji, H. Shizuka, *J. Phys. Chem.* **1996**, *100*, 672–679.
168. K. Hamanoue, K. Yokoyama, Y. Kajiwara, M. Kimoto, T. Nakayama, H. Teranishi, *Chem. Phys. Lett.* **1985**, *113*, 207–212.
169. M. Hamanoue, K. Sawada, K. Yokoyama, T. Nakayama, S. Hirase, H. Teranishi, *J. Photochem.* **1986**, *33*, 99–111.
170. M. Goez, I. Frisch, *J. Photochem. Photobiol. A: Chem.* **1994**, *84*, 1–12.
171. D. Beckert, R. W. Fessenden, *J. Phys. Chem.* **1996**, *100*, 1622–1629.
172. E. Lippert, W. Lüder, H. Boos, in *Advances in Molecular Spectroscopy* (Ed.: A. Mangini) Pergamon Press, Oxford **1962**, 443–457.
173. E. Lippert, W. Lüder, F. Moll, W. Naegle, H. Boos, H. Prigge, I. S. Blankenstein, *Angew. Chem.* **1961**, *73*, 695–706.
174. Z. R. Grabowski, J. Dobkowski, *Pure. Appl. Chem.* **1983**, *55*, 245–252.
175. K. Rotkiewicz, K. H. Grellmann, Z. R. Grabowski, *Chem. Phys. Lett.* **1973**, *19*, 315–318.
176. W. Rettig, *Angew. Chem.* **1986**, *98*, 969–976.
177. E. Lippert, W. Rettig, V. B. Koutecky, F. Heisel, J. A. Miehe, *Adv. Chem. Phys.* **1987**, *68*, 1–173.
178. W. Rettig, W. Baumann, J. F. Rabek, in *Photochem. Photophys.* (Ed.: J. F. Rabek) Vol. 6, CRC Press, Boca Raton **1992**, 79–134.
179. K. Bhattacharyya, M. Chowdhury, *Chem. Rev.* **1993**, *93*, 507–535.
180. K. A. Zachariasse, Th. von der Haar, A. Hebecker, U. Leinhos, W. Kuhnle, *Pure. Appl. Chem.* **1993**, *65*, 1745–1750.
181. Th. von der Haar, A. Hebecker, Y. V. Il'ichev, Y. B. Jiang, W. Kuhnle, K. A. Zachariasse, *Recl. Trav. Chim. Pays-Bas* **1995**, *114*, 430–442.
182. K. A. Zachariasse, M. Grobys, Th. von der Haar, A. Hebecker, Y. V. Il'ichev, Y.-B. Jiang, O. Morawski, W. Kuhnle, *J. Photochem. Photobiol. A: Chem.* **1996**, *102*, 59–70.
183. K. A. Zachariasse, M. Grobys, Th. von der Haar, A. Hebecker, Y. V. Il'ichev, O. Morawski, I. Ruckert, W. Kuhnle, *J. Photochem. Photobiol. A: Chem.* **1997**, *105*, 373–383.
184. F. P. Guengerich, T. L. MacDonald, *Acc. Chem. Res.* **1984**, *17*, 9–16.

185. F. P. Guengerich, *Crit. Rev. Biochem. Mol. Biol.* **1990**, 25, 97–153.
186. *Cytochrome P-450: Structure, Mechanism and Biochemistry*, Plenum Press, New York **1995**.
187. G. L. Kedderis, P. F. Hollenberg, *J. Biol. Chem.* **1983**, 258, 8129–8138.
188. G. L. Kedderis, D. R. Koop, P. F. Hollenberg, *J. Biol. Chem.* **1980**, 255, 10174–10182.
189. B. W. Griffin, P. L. Ting, *Biochemistry* **1978**, 17, 2206–2211.
190. V. W. Tetrud, J. W. Langston, A. J. Rittenber, *Science* **1989**, 245, 519–532.
191. K. F. Tipton, P. Dostert, M. S. Ben, in *Monoamine Oxidase and Disease* Academic Press, New York **1984**.
192. R. B. Silverman, S. J. Hoffman, W. B. Catus III, *J. Am. Chem. Soc.* **1980**, 102, 7126–7128.
193. J. T. Simpson, A. Krantz, F. D. Lewis, B. Kokel, *J. Am. Chem. Soc.* **1982**, 104, 7155–7161.
194. A. Krantz, B. Kokel, Y. P. Sachdeva, J. I. Salach, K. Detmer, A. Claesson, C. Sahlberg, in *Monoamine Oxidase: Struct. Funct. Altered Funct. (Proc. Symp.)* (Ed.: T. P. Singer, R. W. von Korff, D. L. Murphy) Academic Press, New York **1979**, 51–70.
195. Y. Maeda, K. U. Ingold, *J. Am. Chem. Soc.* **1980**, 102, 328–331.
196. R. B. Silverman, S. J. Hoffman, *Biochem. Biophys. Res. Commun.* **1981**, 101, 1396–1401.
197. R. B. Silverman, J. M. Cesarone, X. Lu, *J. Am. Chem. Soc.* **1993**, 115, 4955–4961.
198. R. B. Silverman, P. A. Zeiske, *Biochemistry* **1986**, 25, 341–346.
199. Y. Zelechunok, R. B. Silverman, *J. Org. Chem.* **1992**, 57, 5787–5790.
200. M. Newcomb, C. C. Johnson, M. B. Manek, T. R. Varick, *J. Am. Chem. Soc.* **1992**, 114, 10915–10921.
201. R. B. Silverman, J. P. Zhou, P. E. Eaton, *J. Am. Chem. Soc.* **1993**, 115, 8841–8842.
202. R. B. Silverman, X. Lu, J. J. P. Zhou, A. Swihart, *J. Am. Chem. Soc.* **1994**, 116, 11590–11591.
203. J. M. Dickinson, J. A. Murphy, C. W. Patterson, N. F. Wooster, *J. Chem. Soc. Perkin Trans. I* **1990**, 1179–1184.
204. A. Johns, J. A. Murphy, C. W. Patterson, N. F. Wooster, *J. Chem. Soc. Chem. Commun.* **1987**, 1238–1240.
205. A. Tan, M. D. Glantz, L. H. Piette, K. T. Yasunobu, *Biochem. Biophys. Res. Commun.* **1983**, 117, 517–523.
206. J. R. Miller, D. Edmondson, C. B. Grissom, *J. Am. Chem. Soc.* **1995**, 117, 7830–7831.
207. C. B. Grissom, *Chem. Rev.* **1995**, 95, 3–24.
208. J. C. Scaiano, F. L. Cozens, J. McLean, *Photochem. Photobiol.* **1994**, 59, 585–589.
209. J.-M. Kim, S. E. Hoegy, P. S. Mariano, *J. Am. Chem. Soc.* **1995**, 117, 100–105.
210. K. A. Van Houten, J.-M. Kim, M. A. Bogdan, D. C. Ferri, P. S. Mariano, *J. Am. Chem. Soc.* **1998**, 120, 5864–5872.
211. J. R. Lindsay Smith, D. N. Martimer, *J. Chem. Soc. Perkin Trans. 2* **1986**, 1743–1749.
212. H. Kurebayashi, *Arch. Biochem. Biophys.* **1989**, 270, 320–329.
213. C. J. Parli, N. Wang, R. E. McMahon, *Biochem. Biophys. Res. Commun.* **1971**, 43, 1204–1209.
214. R. E. McMahon, H. W. Culp, J. C. Craig, N. Ekwuribe, *J. Med. Chem.* **1979**, 22, 1100–1103.
215. J. P. Dinnocenzo, S. B. Karki, J. P. Jones, *J. Am. Chem. Soc.* **1993**, 115, 7111–7116.
216. S. B. Karki, J. P. Dinnocenzo, J. P. Jones, K. R. Korzekwa, *J. Am. Chem. Soc.* **1995**, 117, 3657–3664.
217. F. P. Guengerich, C.-H. Yun, T. L. MacDonald, *J. Biol. Chem.* **1996**, 271, 27321–27329.
218. E. Baciocchi, O. Lanzalunga, A. Lapi, L. Manduchi, *J. Am. Chem. Soc.* **1998**, 120, 5783–5787.
219. T. Shono, T. Toda, N. Oshino, *J. Am. Chem. Soc.* **1982**, 104, 2639–2641.
220. Y. Seto, F. P. Guengerich, *J. Biol. Chem.* **1993**, 268, 9986–9997.
221. V. D. Parker, M. Tilset, *J. Am. Chem. Soc.* **1991**, 113, 8778–8781.
222. D. Griller, J. A. Howard, P. R. Mariott, J. C. Scaiano, *J. Am. Chem. Soc.* **1981**, 103, 619–623.
223. M. Bietti, A. Cuppoletti, C. Dagastin, C. Florea, C. Galli, P. Gentili, H. Petride, C. R. Caia, *Eur. J. Org. Chem.* **1998**, 2425–2529.
224. E. Baciocchi, A. Lapi, *Tetrahedron Lett.* **1999**, 40, 5425–5428.
225. A. Anne, S. Fraoua, J. Moiroux, J. M. Saveant, *J. Phy. Org. Chem.* **1998**, 11, 774–780.
226. A. Anne, S. Fraoua, J. Moiroux, J. M. Saveant, *J. Am. Chem. Soc.* **1996**, 118, 3938–3945.
227. O. Okazaki, F. P. Guengerich, *J. Biol. Chem.* **1993**, 268, 1546–1552.
228. F. E. McDonald, A. K. Chatterjee, *Tetrahedron Lett.* **1997**, 38, 7687–7690.

229. C-K. Chen, A. G. Hortmann, M. R. Marzabadi, *J. Am. Chem. Soc.* **1988**, *110*, 4829–4831.
230. J. T. Yli-Kauhaluoma, C. W. Harwig, P. Wentworth Jr., K. D. Janda, *Tetrahedron Lett.* **1998**, *39*, 2269–2272.
231. F. Compennolle, M. A. Saleh, S. Van den Branden, S. Toppet, G. Hoornaert, *J. Org. Chem.* **1991**, *56*, 2386–2390.
232. N. J. Leonard, D. F. Morrow, *J. Am. Chem. Soc.* **1958**, *80*, 371–375.
233. N. J. Leonard, R. R. Sauers, *J. Am. Chem. Soc.* **1957**, *79*, 6210–6214.
234. F. Compennolle, M. A. Saleh, S. Toppet, G. Hoornaert, *J. Org. Chem.* **1991**, *56*, 5192–5196.
235. S. Van den Branden, F. Compennolle, G. Hoornaert, *Tetrahedron* **1992**, *48*, 9753–9766.
236. A. P. Darmanyan, W. S. Jenks, P. Jardon, *J. Phys. Chem.* **1998**, *102*, 7420–7426.
237. C. Ferroud, P. Rool, J. Santamaria, *Tetrahedron Lett.* **1998**, *39*, 9423–9426.
238. J. Vukovic, A. E. Goodbody, J. P. Kutney, M. Misawa, *Tetrahedron* **1988**, *44*, 325–331.
239. R. J. Sundberg, P. J. Hunt, P. Desos, K. G. Gadamasetti, *J. Org. Chem.* **1991**, *56*, 1689–1692.
240. S-K. Khim, X. Wu, P. S. Mariano, *Tetrahedron Lett.* **1996**, *37*, 571–574.
241. M. Hirano, S. Yakabe, H. Chikamori, J. H. Clark, T. Morimoto, *J. Chem. Res. (S)* **1998**, 770–771.
242. M. Hudlicky, *Oxidations in Organic Chemistry*, in *ACS Monograph Vol. 186*, **1990**, 234–242.
243. J. P. Wolfe, S. Wagaw, J.-F. Marcoux, S. L. Buchwald, *Acc. Chem. Res.* **1998**, *31*, 805–818.
244. D. W. Old, J. P. Wolfe, S. L. Buchwald, *J. Am. Chem. Soc.* **1998**, *120*, 9722–9723.
245. J. P. Wolfe, S. Wagaw, S. L. Buchwald, *J. Am. Chem. Soc.* **1996**, *118*, 7215–7216.
246. V. V. Grushin, H. Alper, *Chem. Rev.* **1994**, *94*, 1047–1062.
247. B. C. Hamann, J.F. Hartwig, *J. Am. Chem. Soc.* **1998**, *120*, 7369–7370.
248. I. P. Beletskaya, A. G. Bessmertnykh, R. Guillard, *Tetrahedron Lett.* **1999**, *40*, 6393–6397.
249. *Enzyme Catalysis in Organic Synthesis, A Comprehensive Handbook*, (Ed. K. Drauz, H. Waldman) *Vol. II*, VCH, **1995**, 774–780.
250. A. R. Battersby, in *Ciba Foundation Symposium* **1985**, 22–30.
251. J. E. Cragg, R. B. Herbert, M. M. Kgaphola, *Tetrahedron Lett.* **1990**, *31*, 6907–6910.
252. W. D. Fessner, G. Sinerius, *Angew. Chem. Int. Ed. Engl.* **1994**, *33*, 209–212.
253. G. Hilt, E. Steckhan, *J. Chem. Soc. Chem. Commun.* **1993**, 1706–1707.
254. A. M. Equi, A. M. Brown, A. Cooper, S. K. Ner, A. B. Watson, D. J. Robins, *Tetrahedron* **1991**, *47*, 507–518.
255. E. Santaniello, A. Manzocchi, P. A. Bondi, C. Secchi, T. Simanic, *J. Chem. Soc. Chem. Commun.* **1984**, 803–804.
256. R. Parkin, H. O. Hultin, *Biotech. Bioeng.* **1979**, 939–953.
257. N. Nakajima, D. Conrad, H. Sumi, K. Suzuki, N. Esaki, C. Wandrey, K. Soda, *Ferment. and Bioeng.* **1990**, *70*, 322–325.
258. S. M. Hecht, K. M. Rupprecht, P. M. Jacobs, *J. Am. Chem. Soc.* **1979**, *101*, 3982–3983.
259. Y. Asada, K. Tanizawa, S. Sawada, T. Suzuki, H. Misono, K. Soda, *Biochemistry* **1981**, *20*, 6881–6886.
260. H. J. Schäfer, *Top. Curr. Chem.* **1987**, *142*, 101–129.
261. J. E. Barry, M. Finkelstein, E. A. Mayeda, S. D. Ross, *J. Org. Chem.* **1974**, *39*, 2695–2699.
262. G. Bidan, M. Genies, *Tetrahedron* **1981**, *37*, 2297–2301.
263. N. L. Weinberg, E. A. Brown, *J. Org. Chem.* **1966**, *31*, 4054–4058.
264. N. L. Weinberg, T. B. Reddy, *J. Am. Chem. Soc.* **1968**, *90*, 91–93.
265. T. Shono, Y. Matsumura, K. Inoue, H. Ohimzu, S. Kashimura, *J. Am. Chem. Soc.* **1982**, *104*, 5753–5757.
266. T. Chiba, Y. Takata, *J. Org. Chem.* **1977**, *42*, 2973–2977.
267. E. Le Gall, J-P. Hurvois, S. Sinbandhit, *Eur. J. Org. Chem.* **1999**, 2645–2633.
268. S. Andreades, E. W. Zahnow, *J. Am. Chem. Soc.* **1969**, *91*, 4181–4190.
269. K. Yoshida, T. Fueno, *J. Org. Chem.* **1976**, *41*, 731–732.
270. T. Shono, Y. Matsumura, K. Uchida, H. Kobayashi, *J. Org. Chem.* **1985**, *50*, 3243–3245.
271. T. Shono, *Top. Curr. Chem.* **1988**, *148*, 131–151.
272. T. Fuchigami, in *Advances in Electron Transfer Chemistry* (Ed.: P. S. Mariano) *Vol. 6*, JAI Press Inc., Stanford, Connecticut **1999**, 41–130.
273. M. Kimura, K. Koie, S. Matsubara, Y. Sawaki, H. Iwamura, *J. Chem. Soc. Chem. Commun.* **1987**, 122–123.

274. S. Furuta, T. Fuchigami, *Electrochim. Acta*. **1998**, *43*, 3153–3157.
275. A. Konno, T. Fuchigami, Y. Fujita, T. Nonaka, *J. Org. Chem.* **1990**, *55*, 1952–1954.
276. T. Fuchigami, S. Ichikawa, A. Konno, *Chem. Lett.* **1992**, 2405–2408.
277. N. J. Bunce, in *Handbook of Organic Photochemistry and Photobiology* (Ed.: W. M. Horspool, P.-S. Song) CRC Press, Boca Raton FL **1995**, 266–279.
278. F. D. Lewis, T.-I. Ho, *J. Am. Chem. Soc.* **1977**, *99*, 7991–7996.
279. R. C. Cookson, S. M. de B. Costa, J. Hudec, *J. Chem. Soc. D* **1969**, 753–754.
280. A. Gilbert, S. Krestnosich, *J. Chem. Soc. Perkin Trans. 1* **1980**, 2531–2534.
281. D. Bryce-Smith, A. Gilbert, G. Klunklin, *J. Chem. Soc. Chem. Commun.* **1973**, 330–331.
282. H. Aoyama, Y. Arata, Y. Omote, *J. Chem. Soc. Chem. Commun.* **1985**, 1381–1382.
283. H. Aoyama, J. Sugiyama, M. Yoshida, H. Hatori, A. Hosomi, *J. Org. Chem.* **1992**, *57*, 3037–3041.
284. H. Aoyama, Y. Inoue, Y. Omote, *J. Org. Chem.* **1991**, *46*, 1965–1967.
285. H. Aoyama, Y. Arata, Y. Omote, *J. Chem. Soc. Perkin Trans. 1* **1986**, 1165–1169.
286. H. Aoyama, Y. Arata, Y. Omote, *J. Org. Chem.* **1987**, *52*, 4639–4640.
287. W. Hub, S. Schneider, F. Doerr, J. D. Oxman, F. D. Lewis, *J. Am. Chem. Soc.* **1984**, *106*, 701–708.
288. F. D. Lewis, G. D. Reddy, D. Bassani, S. Schneider, M. Gahr, *J. Photochem. Photobiol. A: Chem.* **1992**, *65*, 205–220.
289. F. D. Lewis, D. M. Bassani, *J. Photochem. Photobiol. A: Chem.* **1992**, *66*, 43–52.
290. F. D. Lewis, G. D. Reddy, S. Schneider, M. Gahr, *J. Am. Chem. Soc.* **1991**, *113*, 3498–3506.
291. F. D. Lewis, D. M. Bassani, G. D. Reddy, *J. Org. Chem.* **1993**, *58*, 6390–6393.
292. F. D. Lewis, D. M. Bassani, E. L. Burch, B. E. Cohen, J. A. Engleman, G. D. Reddy, S. Schneider, W. Jaeger, P. Geddeck, M. Gatr, *J. Am. Chem. Soc.* **1995**, *117*, 660–669.
293. F. D. Lewis, G. D. Reddy, *Tetrahedron Lett.* **1992**, *33*, 4249–4252.
294. F. D. Lewis, J. M. Wagner-Brennan, J. M. Denari, *J. Photochem. Photobiol. A: Chem.* **1998**, *112*, 139–143.
295. F. D. Lewis, S. G. Kultgen, *J. Photochem. Photobiol. A: Chem.* **1998**, *112*, 159–164.
296. A. Sugimoto, R. Sumida, N. Tamai, H. Inoue, Y. Oytsuji, *Bull. Chem. Soc. Jpn.* **1981**, *54*, 3500–3504.
297. A. Sugimoto, S. Yoneda, *J. Chem. Soc. Chem. Commun.* **1982**, 376–377.
298. A. Sugimoto, K. Sumi, K. Urakawa, M. Ikemura, S. SaKamoto, S. Yoneda, Y. Otsuji, *Bull. Chem. Soc. Jpn.* **1988**, *56*, 3118.
299. A. Sugimoto, R. Hiraoka, H. Inoue, T. Adachi, *J. Chem. Soc. Perkin Trans. 1* **1992**, 1559–1560.
300. A. Sugimoto, N. Fukada, T. Adachi, H. Inoue, *J. Chem. Soc. Perkin Trans. 1* **1995**, 1597–1602.
301. A. Sugimoto, R. Hiraoka, N. Fukada, H. Kosaka, H. Inoue, *J. Chem. Soc. Perkin Trans. 1* **1992**, 2871–2875.
302. A. Sugimoto, J. Yamano, K. Suyuma, S. Yonada, *J. Chem. Soc. Perkin Trans. 1* **1989**, 483–487.
303. U. C. Yoon, J. U. Kim, E. Hasegawa, P. S. Mariano, *J. Am. Chem. Soc.* **1987**, *109*, 4421–4423.
304. E. Hasegawa, W. Xu, P. S. Mariano, U. C. Yoon, J. U. Kim, *J. Am. Chem. Soc.* **1988**, *110*, 8099–8111.
305. X.-M. Zhang, P. S. Mariano, *J. Org. Chem.* **1991**, *56*, 1655–1660.
306. U. C. Yoon, Y. C. Kim, J. Choi, D. U. Kim, P. S. Mariano, I. S. Cho, Y. T. Jeon, *J. Org. Chem.* **1992**, *57*, 1422–1428.
307. J. Mattay, A. Banning, E. W. Bischof, A. Heidbreder, J. Runsink, *Chem. Ber.* **1992**, *125*, 2119–2127.
308. Y. T. Jeon, C. P. Lee, P. S. Mariano, *J. Am. Chem. Soc.* **1991**, *113*, 8847–8863.
309. S. K. Khim, P. S. Mariano, *Tetrahedron Lett.* **1994**, *35*, 999–1002.
310. Y. S. Jung, P. S. Mariano, *Tetrahedron Lett.* **1993**, *34*, 4611–4614.
311. G. Pandey, G. R. Reddy, *Tetrahedron Lett.* **1992**, *33*, 6533–6536.
312. G. Pandey, G. D. Reddy, D. Chakrabarti, *J. Chem. Soc. Perkin Trans. 1* **1996**, 219–224.
313. G. Pandey, D. Chakrabarti, *Tetrahedron Lett.* **1996**, *37*, 2285–2288.

314. G. Pandey, D. Chakrabarti, *Tetrahedron Lett.* **1998**, 39, 8371.
315. S. E. Hoegy, P. S. Mariano, *Tetrahedron Lett.* **1994**, 35, 8319–8322.
316. A. Padwa, H. Nimmesgern, G.S.K. Wong, *J. Org. Chem.* **1985**, 50, 5620–5627.
317. G. Pandey, G. Kumaraswamy, *Tetrahedron Lett.* **1988**, 29, 4153–4156.
318. G. Pandey, G. D. Reddy, U. T. Bhalerao, *Tetrahedron Lett.* **1991**, 32, 5147–5150.
319. F. D. Lewis, G. D. Reddy, B. E. Cohen, *Tetrahedron Lett.* **1994**, 35, 535–538.
320. M. Yasuda, C. Pac, H. Sakurai, *J. Org. Chem.* **1981**, 46, 788–793.
321. M. Yasuda, T. Yamashita, K. Shima, *J. Org. Chem.* **1987**, 52, 753–759.
322. M. Yasuda, Y. Watanabe, K. Tanabe, K. Shima, *J. Photochem. Photobiol. A: Chem.* **1994**, 79, 61–65.
323. M. Yasuda, T. Isami, J.-I. Kubo, M. Mizutani, T. Yamashita, *J. Org. Chem.* **1992**, 57, 1351–1354.
324. M. Yasuda, T. Sone, K. Tanabe, K. Shima, *Chemistry Lett.* **1994**, 453–456.
325. S. Das, J.S.D. Kumar, K. George Thomas, K. Shivaramayya, M. V. George, *J. Org. Chem.* **1994**, 59, 624–628.
326. S. Das, J.S.D. Kumar, K. Shivaramayya, M. V. George, *J. Chem. Soc. Perkin Trans. 1* **1995**, 1797–1799.
327. S. Das, J.S.D. Kumar, K. Shivaramayya, M. V. George, *Tetrahedron* **1996**, 52, 3425–3434.
328. S. Das, J.S.D. Kumar, K. Shivaramayya, M. V. George, *J. Photochem. Photobiol. A: Chem.* **1996**, 97, 139–150.
329. S. Bertrand, C. Glapski, N. Hoffmann, J. P. Pete, *Tetrahedron Lett.* **1999**, 40, 3169–3172.
330. D. Belotti, J. Cossy, J. P. Pete, C. Portella, *J. Org. Chem.* **1986**, 51, 4196–4200.
331. J. Cossy, D. Belotti, C. Leblanc, *J. Org. Chem.* **1993**, 58, 2351–2354.
332. E. W. Bischof, J. Mattay, *Tetrahedron Lett.* **1990**, 31, 7137–7140.
333. E. W. Bischof, J. Mattay, *J. Photochem. Photobiol. A: Chem.* **1992**, 63, 249–251.
334. T. Kirschberg, J. Mattay, *J. Org. Chem.* **1996**, 61, 8885–8891.
335. J. Cossy, N. Furet, S. BouzBouz, *Tetrahedron* **1995**, 51, 11751–11764.
336. B. Pandey, A. T. Rao, P. V. Dalvi, P. Kumar, *Tetrahedron* **1994**, 50, 3835–3842.
337. B. Pandey, A. T. Rao, P. V. Dalvi, P. Kumar, *Tetrahedron* **1994**, 50, 3843–3848.
338. H. Moriwaki, T. Oshima, T. Nagai, *J. Chem. Soc. Perkin Trans. 1* **1995**, 2517–2523.
339. S. Das, C. S. Rajesh, T. L. Thanulingam, D. Ramaiah, M. V. George, *J. Chem. Soc. Perkin Trans. 2* **1994**, 1545–1547.
340. Z.-Z. Wu, G. L. Hug, H. Morrison, *J. Am. Chem. Soc.* **1992**, 114, 1812–1816.

8 Electron-Transfer Reactions of Carbonyl Compounds

Axel G. Griesbeck and Stefan Schieffer

8.1 Generation of Carbonyl Radical Ions by Electron Transfer

The carbonyl group and other organic functional groups which can be described as analogous (imines, iminium salts, thiocarbonyls) often behave as chromophores and at the same time as electrophores. Because of the functional group, most of these compounds have moderate to strong absorption in the UV to visible region of the electromagnetic spectrum and can be electronically excited to give singlet and (subsequently) triplet states with a broad range of excitation energies and lifetimes. These compounds usually also have relatively low reduction potentials and can be reduced either by chemical methods (metals, solvated electron, organic electron donors), photochemical methods (direct or mediated photoinduced electron transfer), or electrochemically by cathodic reduction. These two distinct properties make carbonyl and carbonyl analogous compounds reducible even in their ground states and even more efficiently reducible in their first electronically excited singlet and triplet states. Many processes proceed with full electron transfer, although partial electron transfer might also be responsible for modified reactivity, e.g. in Lewis acid–base interactions, charge-transfer complex formation in ground state chemistry, or contact ion pair formation in photoinduced electron-transfer processes.

Single electron oxidation of the non-activated carbonyl group, e.g. in aliphatic or aromatic aldehydes, ketones and carboxylic acid derivatives, is, on the other hand, much less feasible and only a handful of methods and synthetic applications are known. Useful methods for synthetic applications are chemical modifications to lower the oxidation potentials by peripheral donor substitution and α -silylation, or redox umpolung via oxidation of the corresponding carbonyl enols or enol ethers.

8.1.1 Electrochemical Generation of Carbonyl Radical Anions

The electrophoric carbonyl group present in all compounds makes these substrates electroreducible under a broad variety of conditions [1]. Aliphatic ketones have very

Table 1. Reduction potentials of some aliphatic ketones in EtOH–H₂O.^a

Ketone	Reduction potential (V, relative to SCE)
Acetone	–2.57
Cyclopentanone	–2.46
Cyclohexanone	–2.40

^a According to [2].

high reduction potentials and can hardly be selectively reduced in aprotic solvents (Table 1).

Under protic conditions, however, the potentials are somewhat lower and selective reduction can be achieved. The control of the pH is critical for the chemoselectivity of the reduction: at low pH pinacols are often formed because of hydroxycarbonyl radical coupling, a process which is also favored by high substrate concentrations and high hydrogen overvoltage cathodes. Alkaline solutions, on the other hand, favor the formation of alcohols as the primary reduction products. Further reduction to give hydrocarbons can be achieved in acidic media [3]. The intermediacy of pinacols, which are further reduced at more negative potentials, has been demonstrated for several aromatic ketones. Aliphatic ketones are *preferentially* reduced to the hydrocarbons via the corresponding alcohols (Scheme 1). Protonated carbonyl substrates have much lower reduction potentials, e.g. acetone has a reduction potentials of –1.2 V in 0.5 M sulfuric acid whereas the unprotonated substrate has a reduction potential of –2.57 V (relative to the SCE).

The various stages of reduction and protonation during the course of the electrochemical reduction have been carefully investigated and are described in several

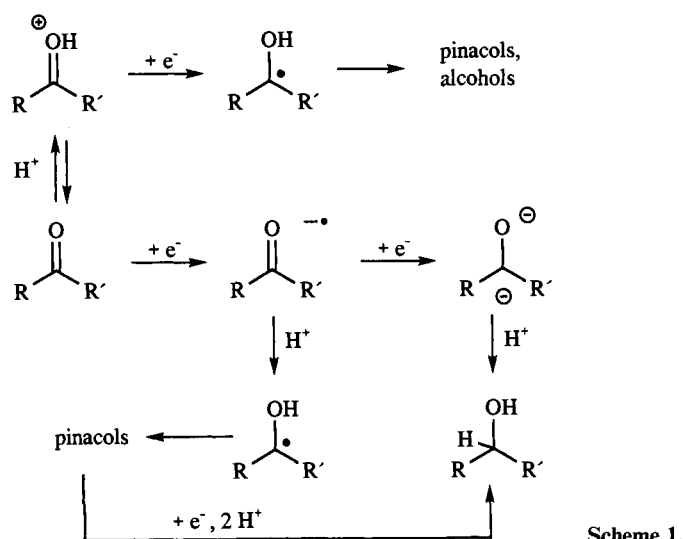


Table 2. Reduction potentials of some saturated and unsaturated aliphatic aldehydes and ketones.^a

Compound	Reduction potential (V, relative to SCE)
CH ₃ CH ₂ CHO	-1.8
PhCH ₂ CH ₂ CHO	-1.8
CH ₂ CH ₂ COCH ₃	-2.25
Cyclohexanone	-2.45
Acrolein	-1.5
Cinnamyl aldehyde	-0.8
Vinyl methyl ketone	-1.42
Cyclohex-2-enone	-1.55

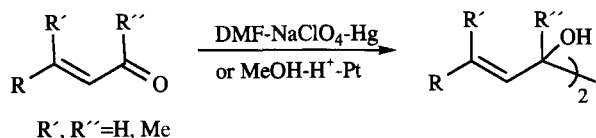
^a According to [7].

reviews. The reduction to give alcohols from ketones can be used for preparative purposes with the use of trialkylammonium halides as electrolytes in mixtures of organic solvents and water [4, 5]. Cyclohexanone and alkylated derivatives are reduced at a potential of ca -2.9 V (relative to the SCE) to give the corresponding alcohols and pinacols in good yields [6]. Aliphatic aldehydes have much lower reduction potentials than ketones and these can be further reduced by conjugation to double bonds (Table 2).

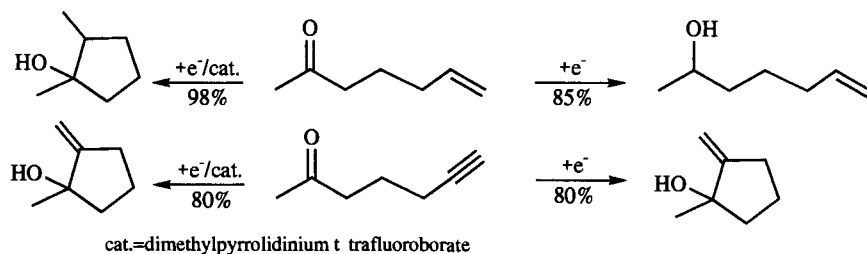
The effective electroreductive pinacolization has been exemplified in the terpene series, i.e. aldehydes such as retinal and ketones such as α - or β -ionone give the corresponding pinacols in good yields when electrolyzed in a DMF-sodium perchlorate-Hg system or with a Pt cathode in the presence of tin [8, 9].

The intermediacy of carbonyl radical ions in electrochemical reductions can be demonstrated by trapping reactions, e.g. by intramolecular cyclization of unsaturated ketones. These ring formations can occur at the electrode surface (graphite cathode) or at a mercury cathode in the presence of catalytic amounts of dimethylpyrrolidinium salts. The cyclization of 6-heptene-2-one to give *cis*-1,2-dimethylcyclopentan-1-ol was the first example in this series. These reactions have been thoroughly investigated and stereochemical features, in particular, have been elucidated by the groups of Shono, Pattenden, and Kariv-Miller [10–15]. Ketones with arene substituents at position C4 can be electrochemically cyclized to give hexahydronaphthalenes in good yields [12]. In the absence of the catalyst, the corresponding alcohols were formed with good chemoselectivity.

The structure of the tetraalkylammonium electrolyte salt is crucial to the result of the reaction, i.e. the control of two-electron-transfer steps rather than one-electron-transfer steps followed by subsequent non-reductive reactions. The alkenone



Scheme 2.



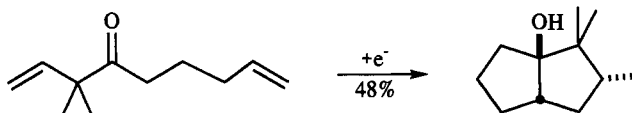
Scheme 3.

(Scheme 3) was preferentially reduced to the alcohol in the absence of the pyrrolidinium catalyst whereas in the presence of this salt, 5-*exo-trig* cyclization prevailed. The corresponding alkyneone, on the other hand, gave the 5-*exo-dig* cyclization product in 80 % yield even in the absence of the catalyst [6]. To achieve multiple cyclization reactions, *bis*-unsaturated ketones were cathodically reduced to give the bicyclo[3.3.0]octane skeleton. The electrolyses were performed in one-compartment cells in DMF with several allyl pentenyl ketones as substrates. The first reductive step is followed by two subsequent 5-*exo-trig* cyclizations to give stereoselectively the corresponding *cis*-fused bicyclooctanols in good yields (Scheme 4) [16].

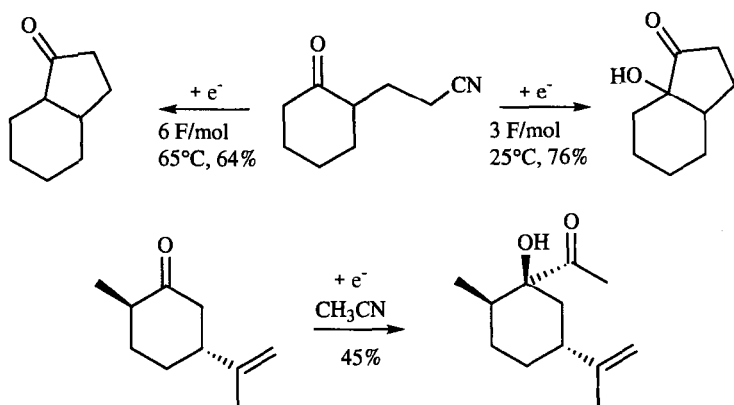
Intramolecular trapping of the electroreduced carbonyl group is also possible with cyano substituents; when γ - and δ -cyano ketones are reduced in *i*-PrOH with a Sn cathode the corresponding α -hydroxy ketones are formed in high yields. This reaction proceeds via two subsequent electron-transfer steps generating the ketyl dianions which act as highly reactive nucleophiles and attack the cyano group. The imine intermediate can be hydrolyzed to give the α -hydroxy ketone or dehydrated and subsequently electroreduced to give the corresponding ketone. Thus, the overall reaction can be described as cyclization coupled with 1,2-carbonyl transposition (Scheme 5) [17].

Likewise, intermolecular reactions are possible and lead to coupling products which correspond retrosynthetically to the addition of an acyl anion synthon to a ketone. The presence of a proton-donor cosolvent is crucial, otherwise β -hydroxy nitriles are formed preferentially. The nitrile addition reaction proceeds with good stereoselectivity, e.g. preferentially one diastereoisomer is formed from the electroreductive addition of acetonitrile (which can advantageously be used as solvent) to dihydrocarvone.

The inherent problem of electrochemical reduction (and oxidation) of carbonyl and carbonyl-analogous compounds is that the electron transfer constitutes an



Scheme 4.



Scheme 5.

heterogeneous step and large overpotentials often have to be applied to effect the reaction [18]. A solution to this problem can sometimes be the use of an indirect electrocyclic synthesis, i.e. two coupled heterogeneous–homogeneous electron-transfer steps [19]. In the first electron-transfer step, a catalyst is cathodically reduced (or anodically oxidized) and then diffuses into the reaction medium. In the second, homogeneous, step the catalyst is regenerated and transfers an electron (or a hole) to the substrate. The catalyst thus acts as electron-transfer *mediator* and can also be used in photoinduced electron-transfer reactions (vide infra). A series of aromatic mono- and polycyclic hydrocarbons has been intensively investigated as mediators for indirect reductive electrocyclic synthesis; their reduction potentials are given in Table 3.

Table 3. Reduction potentials of some aromatic compounds.

Compound	Reduction potential (V, relative to SCE)
Perylene	−1.67
Phthalonitrile	−1.69
Anthracene	−1.96
Pyrene	−2.09
Methyl benzoate	−2.17
Benzonitrile	−2.24
Chrysene	−2.24
3-Toluonitrile	−2.27
4-Toluonitrile	−2.34
Phenanthrene	−2.45
Naphthalene	−2.50
Biphenyl	−2.70

^a According to [20–22].

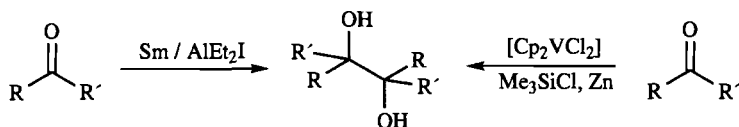
8.1.2 Chemical Generation of Carbonyl Radical Anions

The classical method of chemical one-electron reduction of carbonyl substrates is treatment with low-valent metals, e.g. alkali metals, in inert solvents. Less reactive radical anions can be characterized by UV absorption and emission spectroscopy, e.g. the benzophenone radical anion. This species has been generated also by low-temperature γ -ray irradiation and absorbs visible light in the region of 630 nm (in ethanol) to 800 nm (in 2-methyltetrahydrofuran) [23]. The benzophenone radical anions generated by reduction with alkali metals in tetrahydrofuran have similar absorption peaks at 654 nm (for the lithium compound) up to 714 nm (for the potassium compound) [24]. In hydrogen-donating solvents, the ketyl radical anions (λ_{max} ca 620–660 nm) are rapidly protonated to give the corresponding ketyl radicals (λ_{max} ca 540 nm). The role of active metals in reductive processes involving carbonyl and carbonyl analogous compounds has been extensively investigated in recent decades and is summarized in excellent reviews [25–27].

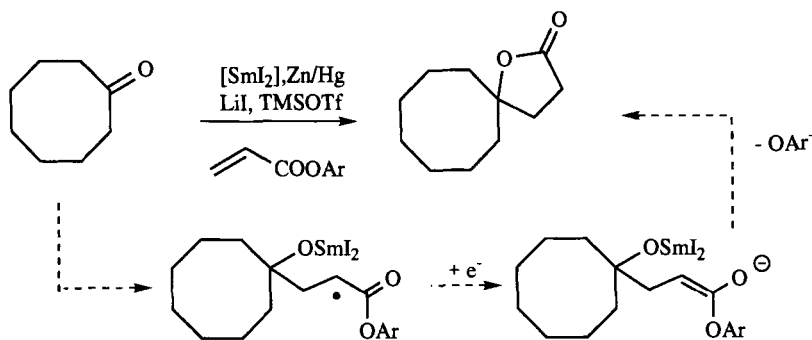
The reductive coupling of aldehydes and ketones to give 1,2-diols (pinacol coupling) is an important reactivity pathway for ketyl radical anions and an important method for C–C bond formation. A multitude of reagents has recently been developed for stoichiometric reductive dimerization, e.g. diverse alkali and earth alkali metals, low-valent metal complexes with Ce, Ti, V, Zr, Sn, Nb or Sm. Some of these reagents are prepared before use, others in situ [28, 29]. Stereoselective pinacol coupling is often achieved when chelating interactions direct the C–C formation steps. The homocoupling of aromatic carbonyl groups can be directed to high D,L-selectivities when performed with samarium metal in the presence of diethyl aluminum iodide [30]. The latter reagent generates the samarium (II) species active in electron transfer and probably also serves as chelating element in the C–C coupling step (Scheme 6).

To avoid secondary reductive steps, low concentrations of the active low-valent metal are advantageous, i.e. the use of catalytic one-electron reduction cycles [31]. Low-valent vanadium species are efficient catalysts for pinacolization. After the primary electron transfer, the oxidized vanadium catalyst can be reduced by Zn(0) or by aluminum [32]. Trialkylsilanes have to be added to decomplex the oxidized vanadium catalyst from the pinacol [33]. The same catalytic system can also be used for the synthesis of 1,2-diamines via coupling of aldimines [34]. Alternatively, a titanium (II)–samarium system gives the 1,2-diamines with moderate D,L-selectivity [35].

Ketyl radical anions can be easily trapped by electron-deficient alkenes, e.g. acrylates, to give enolate radicals. Further reduction of these species results in enolates which can be used as nucleophiles in alkylation reactions. A multi-component



Scheme 6.



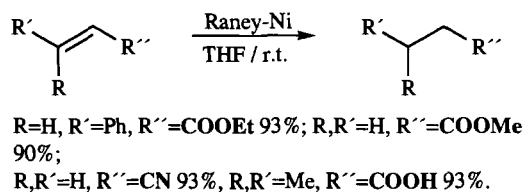
Scheme 7.

catalytic reductive system consisting of samarium (II), Zn/Hg (for reduction of the consumed samarium reagent), LiI, and TMSOTf has been developed by Corey and Zheng for the spirocyclization of cycloalkanones (Scheme 7) [36].

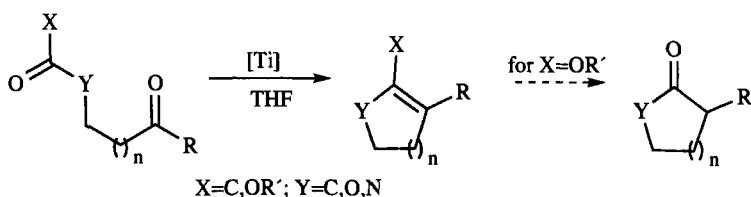
Raney nickel can be used for the chemoselective reduction of α,β -unsaturated ketones, esters, acids, nitriles, and nitroalkenes to give the corresponding saturated carbonyl compounds and carbonyl analogs in excellent yields. From trapping experiments it became evident that electron transfer from nickel to give the enone radical anion initiates the reaction which then proceeds via proton transfer and second electron-proton transfer cycle (Scheme 8) [37].

The reductive coupling of carbonyl compounds with formation of C-C double bonds was developed in the early seventies and is now known as McMurry reaction [38, 39]. The active metal in these reactions is *titanium* in a low-valent oxidation state. The reactive Ti species is usually generated from Ti(IV) or Ti(III) substrates by reduction with Zn, a Zn-Cu couple, or lithium aluminum hydride. A broad variety of dicarbonyl compounds can be cyclized by means of this reaction, unfunctionalized cycloalkenes can be synthesized from diketones, enolethers from ketone-ester substrates, enamines from ketone-amide substrates [40-42]. Cycloalkanones can be synthesized from external keto esters ($X = OR'$) by subsequent hydrolysis of the primary formed enol ethers (Scheme 9).

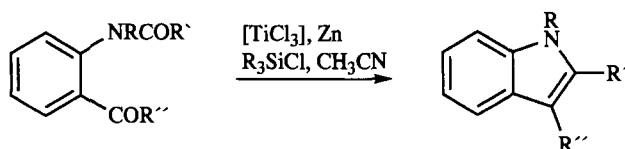
Several variations of this exceedingly important reaction have been reported in recent years, e.g. the use of *titanium-graphite* from Ti(III) and C_8K , especially



Scheme 8.



Scheme 9.



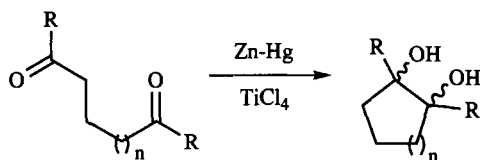
Scheme 10.

for the synthesis of unsaturated heterocycles [43–46]. Catalytic versions of the McMurry reaction have been developed for the synthesis of carbo- and heterocyclic ring systems. As in the samarium- and vanadium-catalyzed pinacolizations, Zn is used as the electron source for reloading the low-valent titanium catalyst, e.g. titanium trichloride, in the presence of trialkyl silylchlorides (Scheme 10) [47].

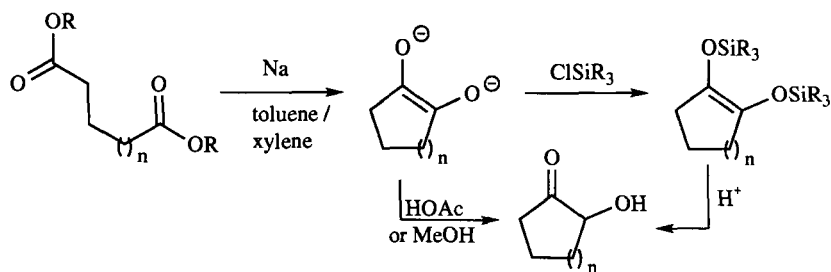
By use of weaker reductants, the C–C coupling can be stopped at the stage of the pinacols [48]. The best metals for achieving chemical pinacolization from ketones are magnesium in the form of its amalgam and mixtures of *Zn–Hg* with titanium tetrachloride (Scheme 11). In the latter reaction the Ti(II) species presumably initiates electron transfer [49].

Another important coupling reaction uses esters as the electron-accepting species and leads to α -hydroxy ketones (acyloin coupling). *Sodium*, *potassium* (less frequently) or *sodium–potassium alloys* are commonly used as electron donors in non-polar solvents such as toluene or xylene. The first detectable reaction intermediate after the primary reductive step is the enediolate which can be trapped with trialkylsilyl chloride. This method is widely used to synthesize highly nucleophilic alkenes and/or protected acyloins (Scheme 12) [50, 51].

In the acyloin protocol, the alkoxides serve as leaving groups after the C–C coupling step. If appropriate leaving groups (OR, SR, Hal) are localized at the α -



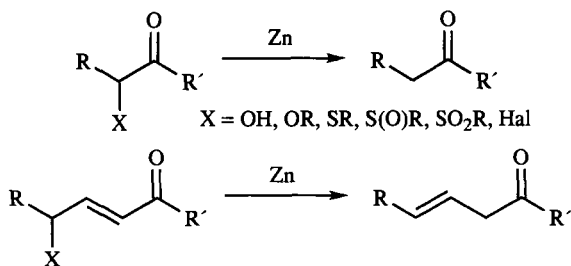
Scheme 11.



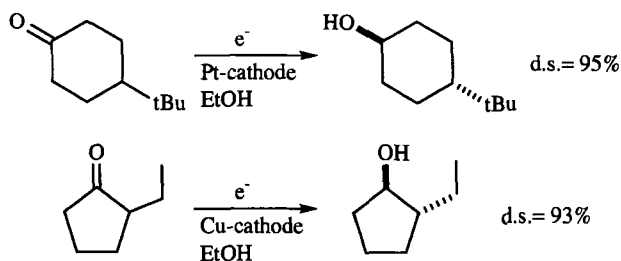
Scheme 12.

position with respect to the carbonyl group, they eliminate rapidly after two-electron transfer reduction and the corresponding enolates are formed [52]. Acyloins can also be used as substrates for this route; they are usually transformed into ketones with reductive elimination of the α -hydroxy group. As reductant, metallic *zinc* is usually used as the ideal two-electron donor. The vinylogous substrates (γ -activated α,β -unsaturated carbonyl compounds) can also be reductively cleaved with possible migration of the double bond (Scheme 13) [53]. Lactones acylated at the ω -position (e.g. γ -acyl γ -butyrolactones) are cleaved into the corresponding dicarboxylic acids [54].

Solvated electrons can be generated by dissolving alkali metals in liquid ammonia or similar solvents [55]. They are widely used for the reduction of organic compounds, e.g. in the Birch reduction of aromatic substrates. Alternatively, by using larger current densities than in direct cathodic reductions, solvated electrons can also be generated under electrochemical conditions. This methodology is useful for avoiding side-reactions derived from the use of alkali metals and electrode reactions. Even benzene can be hydrogenated by solvated electrons, a process which is not possible by direct cathodic reduction. Chiral and prochiral carbonyl substrates can be reduced to alcohols by solvated electrons with high diastereofacial selectivity. This behavior was reported for cyclic alkanones which were reduced in ethanol predominantly to give the *trans* products [56]. The selectivities are higher than those obtained from direct electroreduction of the ketones and thus the process via solvated electrons is advantageous (Scheme 14) [57].



Scheme 13.

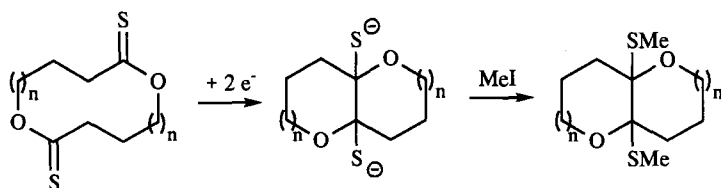


Scheme 14.

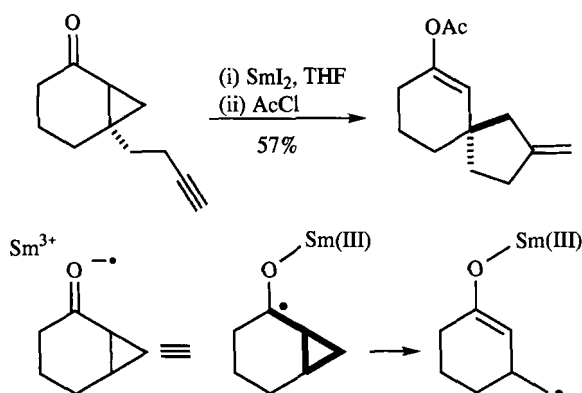
An intramolecular coupling reaction of macrodithionolactones has been developed by analogy with the C=O–C=O coupling reactions after the acyloin and McMurry protocols. *Sodium naphthalide* (vide infra), used as chemical reductant, subsequently generates two thiocarbonyl radical anions. After C–C coupling the resulting dithiolate is alkylated with methyl iodide. The methylthio groups are easily replaced by hydrogen via elimination–hydrogenation or direct substitution (Scheme 15) [58].

One of the synthetically most powerful and versatile homogeneous reductants is *samarium diiodide* (SmI_2); it was first described by Kagan et al. [59] and in recent decades has acquired the status of miracle reagent. Carbonyl compounds are ideal candidates for reductive activation by SmI_2 , because of its enormous reducing power. Reactions initiated by SmI_2 can be described as Sm(III) radical anion chemistry, i.e. the samarium (III) can alter the reactivity by complexation with other heteroatoms and eventually is destroyed by hydrolysis of the Sm(III) alkoxide. This means, on the other hand, that stoichiometric amounts of the SmI_2 reagent must be used in nearly all the applications yet developed, because of deactivation of the reagent by the product, e.g. two-electron reduction of β -hydroxy ketones with three equivalents of SmI_2 gives the corresponding 1,3-diols with high *anti*-selectivities and excellent yields [60]. In recent years, however, several regeneration systems for SmI_2 have been developed: Mg for reductive pinacolizations [61], Zn–Hg for spirolactonization [36], and Sm/Mischmetall (an alloy of light lanthanides) for Barbier reactions, pinacolization, and acyloin coupling reactions [62].

The ring-opening reaction of three-membered rings (cyclopropanes and oxiranes, respectively) adjacent to the carbonyl group is a straightforward process for the



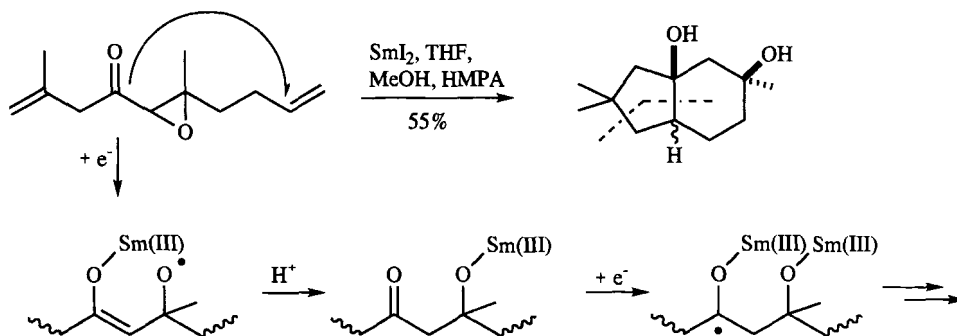
Scheme 15.



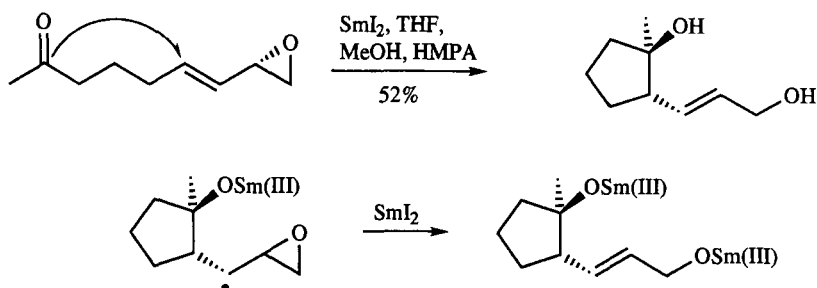
Scheme 16.

generation of alkyl radicals which can undergo further radical cyclization reactions [63–65]. Five-membered rings are easily formed via a *5-exo-trig* or *5-exo-dig* process. The resulting alkyl or vinyl radicals are subsequently reduced by SmI_2 to give the corresponding carbanions which are eventually protonated. The enolate anion, on the other hand, formed after ring-opening can be trapped by electrophiles to give enol ethers or enol acetates (Scheme 16).

By analogy, the ring-opening of epoxy ketones gives rise to 1,3-alkoxy radical anions which are stabilized by Sm(III) [66–68]. These reactions are performed in the presence of protic solvents and thus, after enolate protonation, the reformed carbonyl group is reduced again to give the reactive species which initiates radical reactions. As typical of free radical cyclizations, *5-exo-trig* or *6-exo-trig* reactions dominate the course of the reaction and further reductive steps lead to the formation of five-membered or six-membered monocyclic or annulated ring systems (Scheme 17).



Scheme 17.



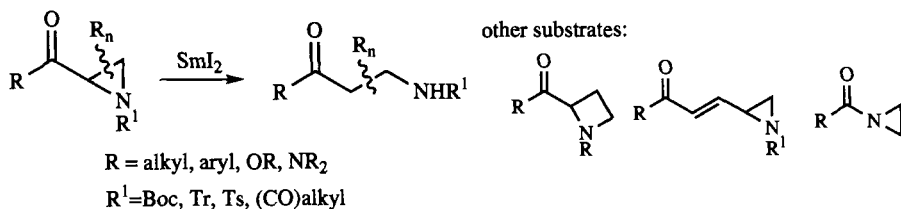
Scheme 18.

The termination step in these sequences turns out to be the second reduction step of the ultimate carbon radical. The carbanions formed thereby can be protonated or, in the presence of an appropriate leaving group, undergo β -elimination to give alkenes. Acetate, halide, and alkoxide have been reported to be appropriate leaving groups [69, 70]. Oxirane ring opening can also terminate the cyclization sequence to give hydroxyalkyl-substituted ring systems (Scheme 18) [71].

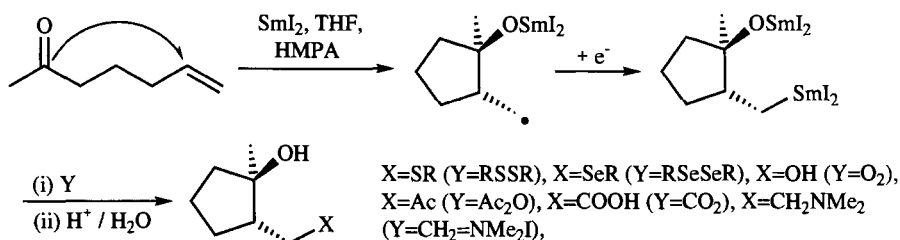
By analogy with cyclopropanes and oxiranes, 2-acylaziridines, aziridine-2-carboxylic esters and amides, are also suitable substrates for one-electron reductive ring cleavage. This is an efficient and highly regioselective method for the synthesis of β -amino carbonyl compounds. Vinylogous substrates are, furthermore, transformed into δ -amino β,γ -unsaturated carbonyl derivatives; azetidines can also be used to achieve γ -amino functionalization (Scheme 19) [72].

The secondary reduction of the terminal radical by SmI_2 generates samarium alkyl species which are suitable for classical organometallic reactions, e.g. protonation, acylation, reactions with carbon dioxide, disulfides, diselenides, or the Eschenmoser salt. A broad variety of products is available (hydroxy-substituted alkanes, esters, carboxylic acids, thioethers, selenoethers, tertiary amines) by use of the double-redox four-step (reduction–radical reaction–reduction–anion reaction) route (Scheme 20) [73].

The chain linking the carbonyl group and the alkenyl part can also be functionalized with heteroatoms. Thus, ether-linked δ,ε - or ε,ζ -unsaturated carbonyl substrates are converted into tetrahydrofurans and tetrahydropyrans, respectively, via 5-*exo-trig* or 6-*exo-trig* cyclizations [74]. The radicalophilic part of the molecule can



Scheme 19.

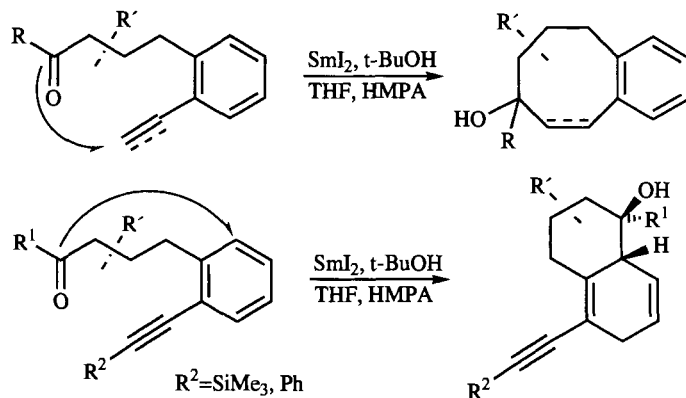


Scheme 20.

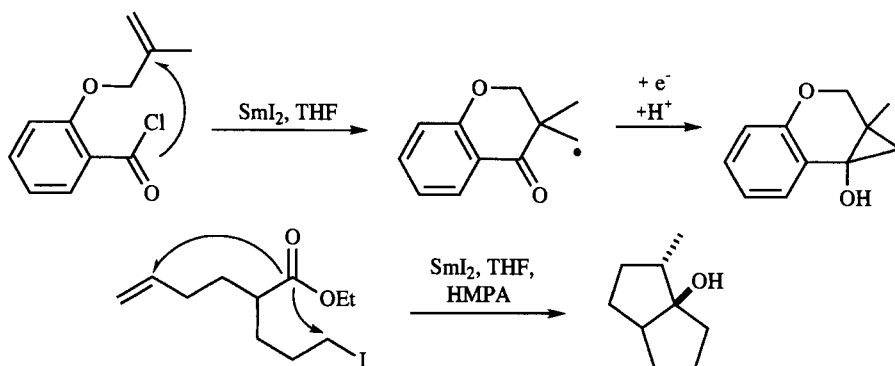
also be in conjugation with an arene group, i.e. vinyl- or alkynyl-substituted benzene rings are attacked by the ketyl radical anions [75]. The regioselectivity of this reaction, however, depends on the substituent at the alkene-alkyne termini—unsubstituted alkenes and alkynes underwent 8-*endo-trig* and 8-*endo-dig* cyclizations, respectively, whereas alkynes with substituents at the termini gave Birch-type products derived from radical attack at the *ortho'* position of the arene skeleton, with very high stereoselectivity (Scheme 21) [76].

Carbonyl substrates with appropriate leaving groups can be reduced with SmI_2 to give acyl radicals. In the presence of radical-trapping reagents these reactive intermediates can be transformed into stable products, e.g. via cyclization to give mono- or bicyclic ring systems [77]. In the absence of trapping reagents further reduction of the acyl radicals leads to acyl anions which are capable of nucleophilic addition reactions [78]. Fine tuning of the reaction conditions enables the sequential reaction of acyl anion and ketyl radical anion. Thus, bicyclization via anionic and subsequent radical reactions can be induced and proceed highly stereoselectively (Scheme 22) [79].

The mechanism of the intramolecular samarium-initiated Barbier reaction is still a matter of debate [80–82]. One of several mechanistic possibilities is primary reductive generation of the ketyl radical anion which can subsequently initiate a second



Scheme 21.

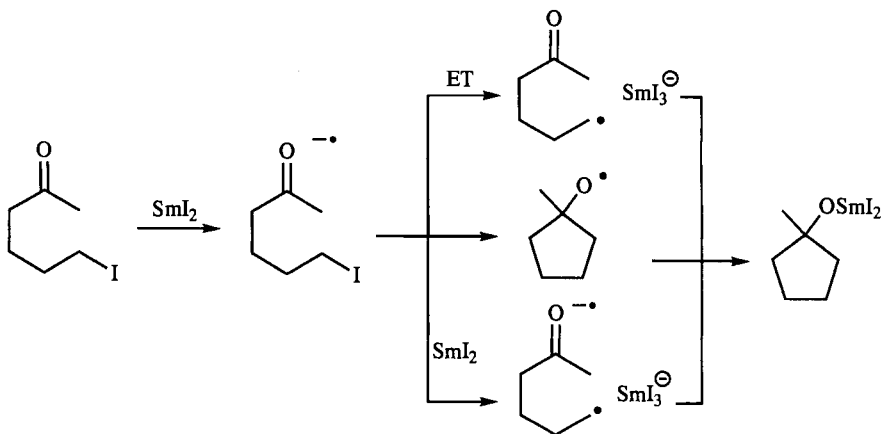


Scheme 22.

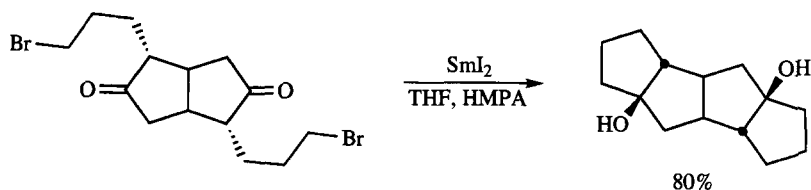
electron transfer to give the primary alkyl radical, or direct attack with substitution of the iodide leaving group (Scheme 23).

The classical (Grignard-like) mechanism for Barbier reactions involves the primary formation of an Sm-alkyl species via halogen abstraction and subsequent reduction of the alkyl radical formed after the first electron transfer. Be that as it may, the Barbier reaction can be used to construct complex polycyclic target molecules, e.g. the synthesis of tetraquinanes from diquinane precursors by two independent intramolecular cyclization steps (Scheme 24) [83].

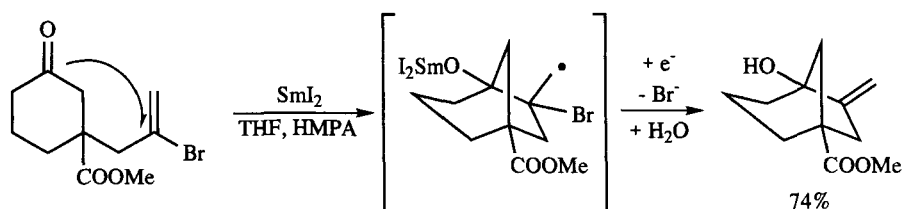
Intramolecular coupling of carbonyl groups with vinylbromides after an addition-elimination sequence involves two electron-transfer steps. In the first step the ketone is reduced to the ketyl radical anion. After 5-*exo-trig* radical addition of the vinylbromide group, a primary radical is generated which is subsequently reduced to give an alkyl samarium species which eliminates bromide. This reaction



Scheme 23.



Scheme 24.



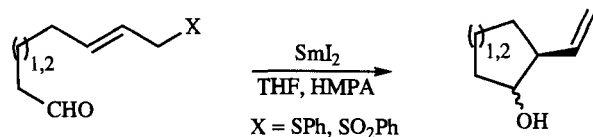
Scheme 25.

is equivalent to the intramolecular addition of the ketyl radical anion to an alkyne group (Scheme 25) [84].

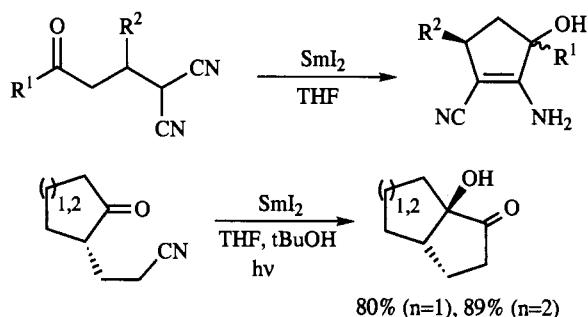
Allylic substituents ($\text{X} = \text{SR}, \text{SO}_2\text{R}$) at the radical trapping alkene can be used for radical coupling–elimination sequences leading to vinyl-substituted cycloalkanes [85]. Even non-activated aliphatic aldehydes can be reduced with SmI_2 and 5-*exo-trig* and 6-*exo-trig* radical cyclizations, respectively, (Scheme 26) and tandem cyclization processes can also be initiated by this route, leading to polyquinane structures [86].

An intramolecular reductive coupling of ketones with nitriles has been reported for acyclic and monocyclic substrates; β -amino nitriles were isolated from acyclic malononitrile adducts [87]. The SmI_2 -initiated reductive cyclization of cyclic α -cyanoalkyl-substituted ketones leads to acyloin products in high yields. In this instance further irradiation of the reaction mixtures was performed to afford complete conversion (Scheme 27) [88]. More applications have been collected in several excellent reviews [89–92].

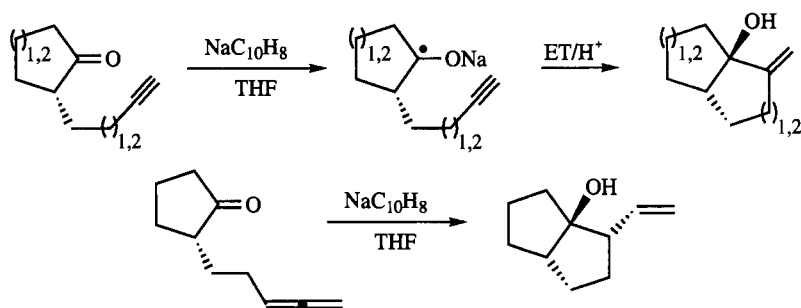
Another versatile chemical reductant which has not been widely applied in electron-transfer chemistry is sodium naphthalide. This arene radical anion is easy to generate and capable of reducing carbonyl compounds to the corresponding ketyl



Scheme 26.



Scheme 27.



Scheme 28.

radical anions under mild conditions. In this reaction the naphthalene serves as electron-transfer mediator. Applications have been reported for 5-*exo-dig* cyclizations in polyquinane and steroid syntheses (Scheme 28) [93, 94].

Allenyl-substituted cycloalkanones have also been studied; the one-electron reduction of these resulted in 5-*exo-trig* or 5-*endo-trig* cyclizations (depending on the relative position of the allene group) [95]. The reductive cyclization of ketones in the presence of acrylate side-chains have been investigated; the reductant was magnesium metal in methanol [96].

8.1.3 Photochemical Generation of Carbonyl Radical Anions

One of the most important means of inducing electron-transfer processes is photoexcitation of a substrate or a catalyst molecule in the presence of appropriate electron donor or acceptor molecules (PET = photoinduced electron transfer) [97–108].

In the simplest example, a donor and acceptor pair is activated by electronic excitation of either the donor or the acceptor. In addition to photophysical deactivation or energy transfer, two processes can proceed subsequently—the electronically excited donor donates an electron from its SOMO' into the acceptor LUMO or the

electronically excited acceptor takes up an electron from the donor HOMO into the acceptor SOMO. The free energy change for these photoinduced electron-transfer processes can be calculated from the Weller equation (Eq. 1) [109, 110]:

$$\Delta G_{\text{ET}} = \Delta E_{1/2}(\text{Donor}) - \Delta E_{1/2}(\text{Acceptor}) - \Delta E_{00} + \Delta E_{\text{coul}}. \quad (1)$$

The rates of electron transfer correlate with the free energy change as a parabolic relationship and approach the maximum values (i.e. diffusion-controlled rates for bimolecular PET reactions) for exergonic processes with negative free energy changes larger than the reorganization energy (following the Marcus equation) and decreasing rate constants in the Marcus inverted region [111]. This quadratic free energy relationship has been found for numerous photoinduced electron-transfer processes and serves nowadays as a useful tool for predicting reactivity and selectivity in PET chemistry. The secondary processes after the electron-transfer step can be categorized into three principle types:

Type I: Acceptor radical anion and donor radical cation undergo subsequent reactions leading to uncharged closed-shell molecules which cannot be photoexcited again.

Type II: Either the acceptor radical anion or the donor radical cation is retransformed into its original state during subsequent reaction steps. If this molecule corresponds to the light-absorbing species, it serves as *sensitizer* for PET processes and can be used in catalytic amounts.

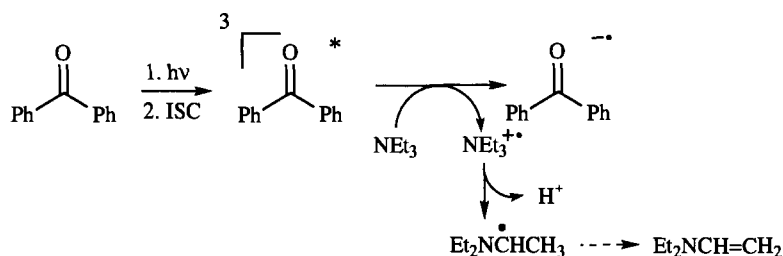
Type III: A non-absorbing molecule transports the electron or the hole after the first electron-transfer step to the target species and thus enable separation of the originally formed acceptor radical anion–donor radical cation pair. This *mediator* is often used in catalytic amounts but can also be consumed during the PET reaction. In many of these cases, mediators serve as the terminal proton–hydrogen donors.

Simple carbonyl compounds such as *aliphatic aldehydes or ketones* have singlet excitation energies of ca 3.2 to 3.5 eV and reduction potentials of ca -2.0 to -2.5 V (see Tables 1 and 2). Thus, the first singlets of these species have excited state reduction potentials of ca 0.7 to 1.5 V. Conjugation of the carbonyl group to arenes, C–C multiple bonds, and additional C=O or C=X groups reduce the corresponding excitation energies and the ground-state reduction potentials. Tuning of chromophoric and electrophoric groups enables the design of electron-accepting substrates with reduction potentials as large as 2 V. Thus, PET with these electron acceptors can lead to oxidation of organic substrates with oxidations potentials of +2 V or even higher (Table 4).

A broad variety of organic functionality has been described as donor groups—heteroatoms (N, O, S, Se), C–C double bonds (donor-substituted or conjugated), alkynes, and arenes. The oxidation potentials of the electron donor can be altered by modification of possible leaving groups for mesolytic bond cleavage, e.g. the use of silyl or stannyl groups instead of protons as electrofugs. In carbonyl photochemistry, amines have been thoroughly investigated as efficient electron donors. The photoreduction of triplet benzophenone by triethylamine leads to a caged radical ion pair which rapidly undergoes mesolytic bond cleavage of the amine radical cation to give an α -amino radical and the benzhydrol radical (Scheme 29) [113].

Table 4. Reduction potentials and triplet energies of aromatic carbonyl compounds.^a

Compound	Reduction potential, E_{red} (V, relative to SCE)	Triplet energies, $E(T_1)$ (eV)
Benzophenone	-2.16	2.95
Benzil	-1.50	2.36
Anthraquinone	-0.94	2.72

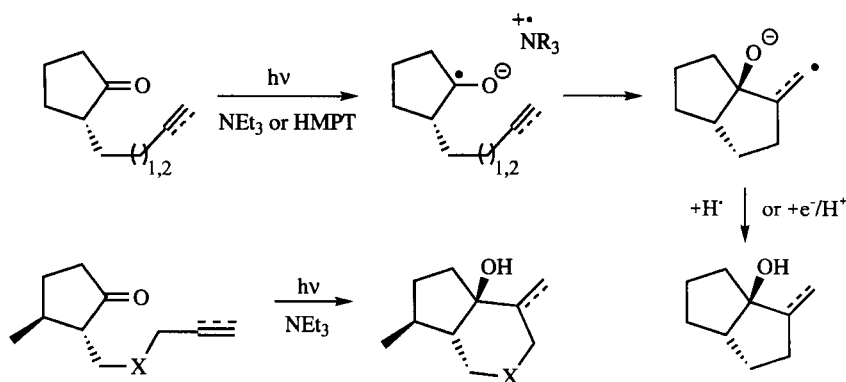
^a According to [112].**Scheme 29.**

The α -amino radical can undergo cage-combination with the hydroxyalkyl radicals but can also transfer a hydrogen atom which leads to neutral photoreduction products. This procedure enables the reductive photocyclization of simple carbonyl compounds in the presence of radicalophilic groups. This has been described for a series of γ,δ - and δ,ϵ -unsaturated ketones. These substrates were irradiated in the presence of electron-donating amines such as triethylamine or in neat HMPT. This methodology has been used for the synthesis, in moderate to high yields, of natural products and interesting unnatural biologically active molecules such as diquinanes [114], triquinanes [115], and heteroindanes such as actinidine [116] and iridoids [117] (Scheme 30).

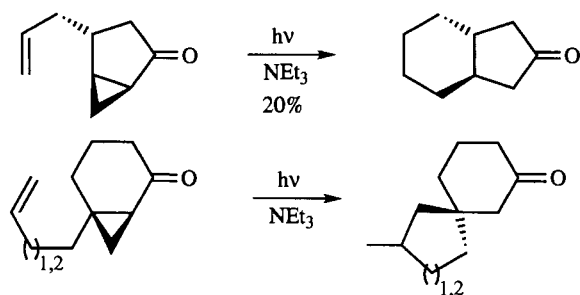
Cyclopropyl-substituted ketones are suitable substrates for generating distonic radical anions from ketyl radical anions. A series of cycloalkanone substrates with unsaturated side-chains, to trap the primary radical formed after cyclopropylcarbinyl ring opening, has been investigated (Scheme 31) [118, 119]. For the first electron-transfer step triethylamine is used as electron donor. The reaction sequence is terminated by proton or hydrogen transfer from the solvent or the α -amino radical formed after deprotonation of the amine radical cation.

The radical anions of carbonyl groups can also be generated via PET from activated alkenes, e.g. allylic silanes or stannanes. Triplet excited aromatic ketones, α -dicarbonyls and Michael systems are suitable substrates for oxidizing allylic Group 14 organometallic compounds with subsequent formation of homoallylic alcohols or β -allylated ketones (Scheme 32) [120–122].

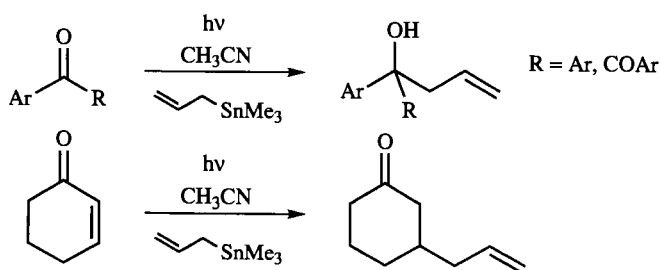
The nitrile group serves as an universal electron-accepting substituent, activating olefinic and aromatic substrates for electron-transfer steps. Cyano-substituted



Scheme 30.

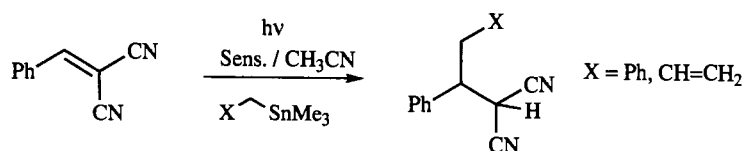


Scheme 31.



Scheme 32.

alkenes are easily alkylated in the presence of Group 14 organometallic reagents such as benzylic or allylic silanes and stannanes (Scheme 33) [123–125]. The radical anion formed after PET from an electron-donating substrate to a cyano-substituted aromatic hydrocarbon can be highly stabilized by spin- and ion-dilution or by steric effects of arene substituents. This enables the generation of long-lived radical anions



Scheme 33.

Table 5. Reduction potentials and singlet energies of cyanoaromatic compounds.^a

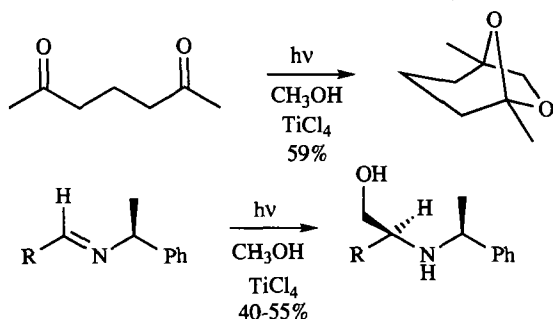
Compound ^b	Reduction potential, E_{red} (V, relative to SCE)	Singlet energies, $E(\text{S}_1)$ (eV)
2,6,9,10-TCA	-0.45	2.82
1,2,4,5-TCB	-0.65	3.83
9,10-DCA	-0.89	2.88
1,4-DCN	-1.28	3.45
9-CA	-1.39	2.96
1,4-DCB	-1.60	4.29

^a According to [126].^b TCA = tetracyanoanthracene, TCB = tetracyanobenzene, DCA = dicyanoanthracene, DCN = dicyanonaphthalene, CA = cyanoanthracene, DCB = dicyanobenzene.

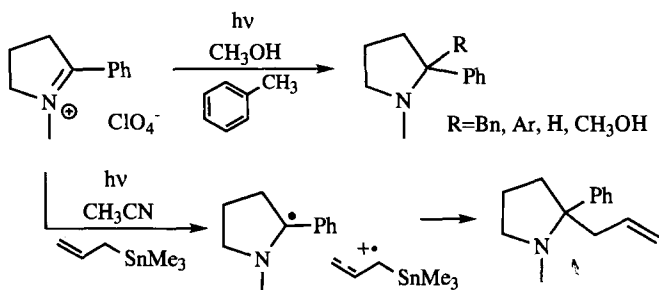
which are chemically reluctant, and thus serve as electron source in subsequent reaction steps. These compounds are often used as electron-accepting sensitizers in PET processes (Table 5). The sensitizers most often used are 9,10-dicyanoanthracene (DCA) and 1,4-dicyanonaphthalene (DCN).

Radical anions of carbonyl groups and imines also seem to be produced in the presence of *titanium(IV) chloride* in methanol as solvent. Consecutive oxidation and deprotonation of methanol leads to hydroxymethyl radicals which combine with the carbonyl radical anions to give 1,2-diols and 1,2-aminoalcohols, respectively. The synthesis of the pheromone frontalin has been achieved in a one-pot reaction by hydroxy-methylation of a diketone [127–129]. Likewise triplet sensitizers [130] can be used for direct excitation of the substrate in methanol [131]. Chiral aldimines can be conveniently hydroxymethylated with moderate diastereoselectivity by irradiation of methanolic solutions in the presence of an excess TiCl_4 (Scheme 34) [132].

The high negative reduction potentials of ketones can be substantially changed by transforming them into *iminium salts*. These carbonyl derivatives absorb light in similar wavelength regions but are much more easily reduced to neutral α -amino radicals. A multitude of electron-donating reagents has been investigated [133–136]. Arenes are oxidized by electronically excited iminium salts to give arene radical cations. When benzylic CH groups are present deprotonation to give benzylic radicals is rapid and subsequent radical combination occurs. Pyrrolidinium salts are attractive building blocks for syntheses of heterocyclic target molecules (Scheme 35) [137]. The fluorescence quenching of singlet excited iminium salts by allylsilanes or



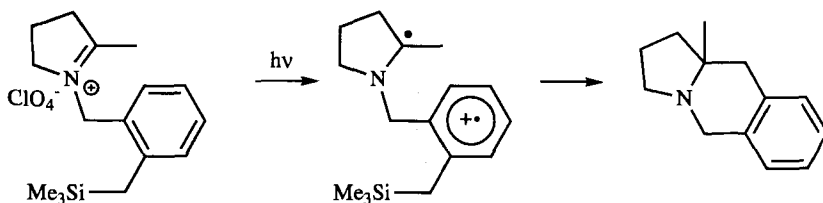
Scheme 34.



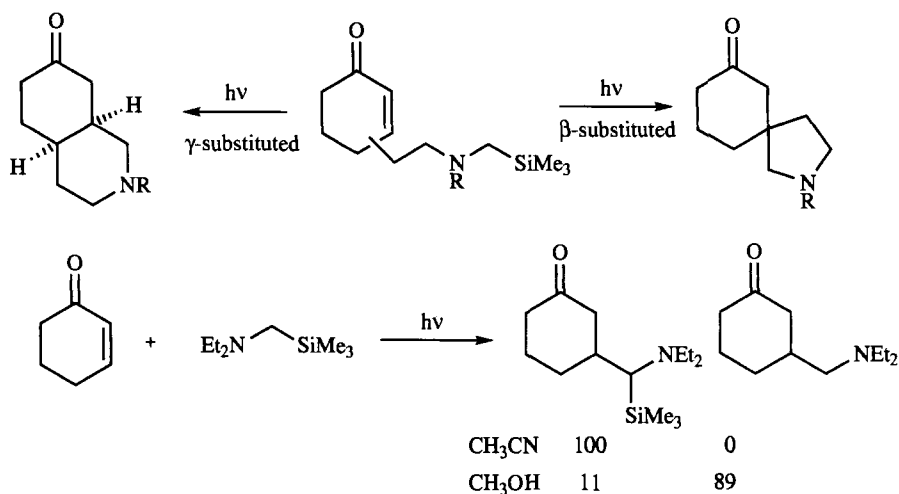
Scheme 35.

allylstannanes indicates rapid electron transfer to give the alkene radical cations. In the presence of nucleophilic solvents, allylic radicals are produced via mesolytic cleavage of the radical cations and combine with the α -amino radicals [138, 139].

These two concepts can be combined by using benzyl trialkylsilanes as electron donors in intramolecular PET-reactions. Excitation of the iminium chromophore and electron transfer leads to arene radical cations which rapidly cleave the C–Si bond to give a 1,6-biradical which combines to give the indolizidine skeleton (Scheme 36) [140].



Scheme 36.



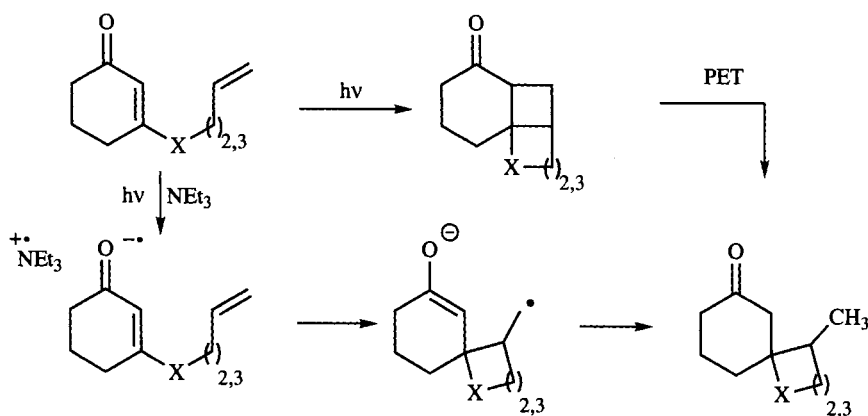
Scheme 37.

Conjugated carbonyl groups can also serve as electron acceptors in intramolecular PET reactions. Tertiary amines are versatile donor groups and can be additionally activated by α -silylation. Cyclohexene-2-ones can be coupled at the 3- or 4-position with alkylamino groups. After direct excitation of this donor–acceptor pair, electron transfer generates the enone radical anion–amine radical cation pair. Starting with the β -branched cyclohexenone, after desilylation a 1,5-biradical anion is formed which combines to give the spiro heterocyclic product. Likewise, the 1,6-biradical from the γ -branched cyclohexenone gives a perhydroisoquinoline [141, 142]. An electron transfer sensitizer such as DCN can also be used to initiate the N-oxidation. An important feature is the regiochemistry of the mesolytic bond cleavage step after the oxidation of α -trialkylsilyl amines—in methanol desilylation dominates whereas in acetonitrile only deprotonation is observed (Scheme 37).

In the presence of alkenyl side chains, electronically excited cycloalkene-3-ones readily undergo intramolecular [2 + 2] cycloadditions [143]. If, however, the radical anion of the enone is generated via electron transfer, 5- or 6-*exo-trig* cyclizations can be induced; these lead to primary carbon radicals which can be trapped by hydrogen donors or reduced to the corresponding carbanions which are subsequently protonated to give spirocyclic products. Alternatively, the photocycloadducts can be reductively cleaved by cyclobutylcarbonyl ring-opening (Scheme 38) [144, 145].

An elegant electron relay system has been developed which uses triphenylphosphine as the electron source and dicyanoanthracene as PET-sensitizer. The DCA radical anion subsequently transfers an electron to a Michael system which eventually undergoes radical cyclization chemistry [146].

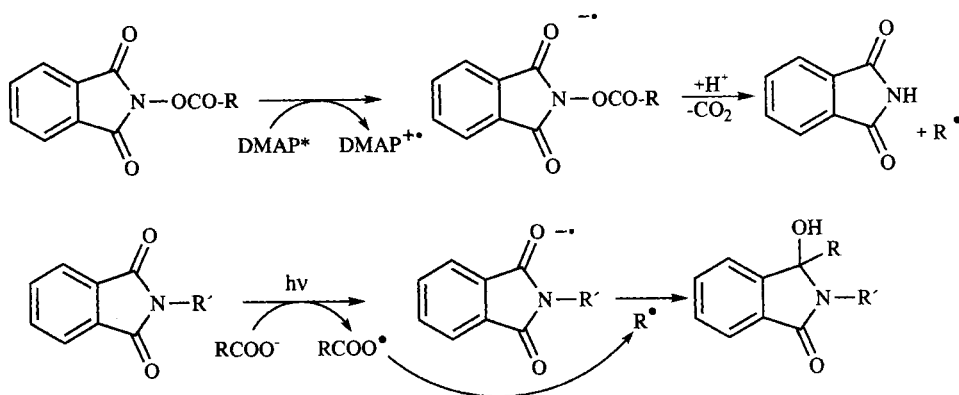
Aliphatic and aromatic *imides* have relatively low reduction potentials (e.g. *N*-methylphthalimide: -1.4 V relative to the SCE [147]) and absorb in the near ultraviolet region (260–320 nm). These properties have been widely used in synthetic transformations of imides and in catalytic processes in which imides serve as redox



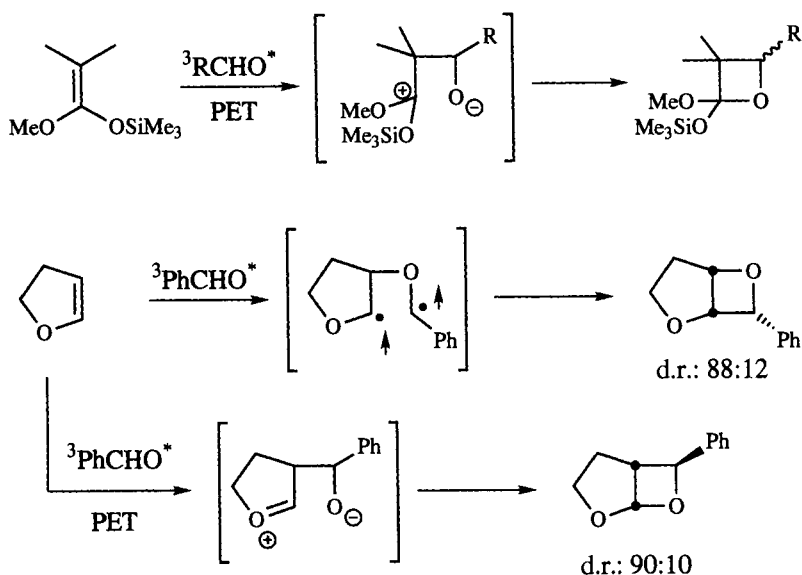
Scheme 38.

sensitizers or mediators. A photodecarboxylation protocol has been developed for *N*-acyloxyphthalimides [148, 149]. The light-absorbing species in this process is 1,6-bis(dimethylamino)pyrene which is oxidized by the phthalimide to give the phthalimide radical anion. Mesolytic cleavage results in the carboxylate radical and the phthalimide anion. Alternatively, *phthalimides* can be electronically excited directly in the presence of external alkylcarboxylates and give PET with formation of the phthalimide radical anion and the carboxylate radical [150, 151]. In both reactions decarboxylation results in the formation of free radicals which can be trapped by hydrogen-donating reagents, alkenes, solvent molecules, or phthalimide radical anions (Scheme 39).

Cycloadditions with electronically excited carbonyl groups (or homologs) usually follow biradical mechanisms. Alternatively, PET-pathways can be observed either for energetically favorable donor-acceptor situations or in highly polar solvents. For



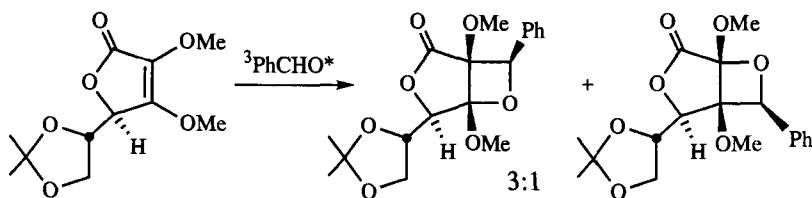
Scheme 39.



Scheme 40.

Paternò-Büchi reactions [152] this competition has been investigated for electron-rich alkene substrates for several combinations of carbonyl compounds and electron-donors, e.g. α -diketones and ketene acetals [153], aromatic aldehydes and silyl ketene acetals, and enol ethers. In polar solvents, the assumption of a 1,4-zwitterion as decisive intermediate is reasonable. This situation then resembles the sequence observed for ET-induced thermal [2 + 2]-cycloaddition reactions [154]. Both regio- and diastereoselectivity are influenced by this mechanistic scenario. The regioselectivity is now a consequence of maximum charge stabilization and no longer a consequence of the primary interaction between excited carbonyl compound and alkene. Whereas 3-alkoxyoxetanes are preferentially formed from triplet excited aldehydes and enolethers, 2-alkoxyoxetanes result from the reaction of triplet excited ketones or aldehydes and highly electron-rich ketene silylacetals (Scheme 40) [155].

In the latter reaction photoinduced electron transfer (PET) to give the carbonyl radical anion and the ketene acetal radical cation is energetically feasible [156]. PET might be followed by ISC and formation of a highly stabilized 1,4-zwitterion intermediate (aldol intermediate). C–O bond formation eventually leads to the oxetanes with correct (in respect of the experimental results) regiochemistry. Substituent tuning is not the only possibility of influencing the regioselectivity of the Paternò-Büchi reaction. If the photocycloaddition is performed in a highly polar solvent which reduces the Coulombic term in the Rehm–Weller equation, PET becomes compatible with radical pathways. This effect was observed with 2,3-dihydrofuran as electron-rich substrate which gave selectively the 3-alkoxyoxetane when added to triplet excited aliphatic aldehydes in non-polar solvents. In acetonitrile, however,



Scheme 41.

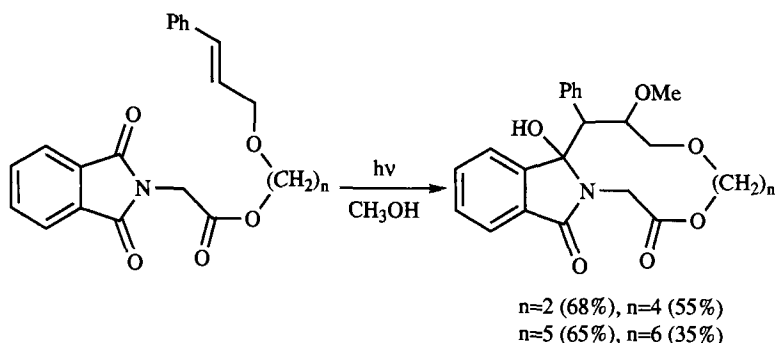
the corresponding 2-alkoxyoxetane was also detected. The relative amount of this product correlated with solvent polarity parameters thus indicating PET as the mechanism responsible [157].

Abe and coworkers have also observed this stereochemical effect in the Paternò-Büchi reaction of aromatic aldehydes with cyclic ketene acetals [158]. The addition of benzaldehyde to the 5-silyloxy-substituted 2,3-dihydrofuran resulted in the *exo*-phenyl product, albeit in low yields. Higher yields and selectivity were obtained with naphthaldehydes and acceptor-substituted benzaldehydes as carbonyl addends. Interesting substrates in this context were also the 2,3-dialkylated ascorbic acid acetonides investigated by Kulkarni and coworkers [159]. Photocycloaddition of benzaldehyde with these substrates resulted in the formation of two regioisomeric products (Scheme 41).

Both oxetanes were formed with exclusively the *exo*-phenyl configuration. The regio- and diastereoselectivity observed are in accord with the assumption of a PET process involving the oxidation of the ascorbic acid derivatives and the formation of the carbonyl radical anions. In these special instances 1,4-biradical and 1,4-zwitterion stabilization result in similar product regiochemistry. The relative configuration of the products favors the assumption of a PET-process.

Macrocyclization reactions are an important class of reactions involving photo-induced electron-transfer steps. Donor-acceptor pairs linked by a flexible hydrocarbon chain are used as starting materials. Mesolytic cleavage of a CH bond proximate to the radical cation (i.e. oxidized heteroatom, alkene, or arene group) usually precedes the primary electron transfer [160]. The resulting (1,*n*)-biradicals combine to give medium- to large-sized ring systems. A very useful carbonyl chromophore which has been intensively investigated in the last two decades is the phthalimido group [161, 162]. The reduction potential (vide supra) is remarkably low in comparison with aromatic carbonyl compounds [163]. In the presence of electron-donor groups (thioether, amines, alkenes, arenes) exergonic electron transfer can occur after electronic excitation. Applications of these PET-macrocyclizations are described with reference to the electron-donating groups.

The course of the intramolecular photoreaction of carbonyl compounds with electron-rich *alkenyl- or aryl-substituents* in the side-chain is dictated essentially by the thermodynamics of the electron-transfer step. This relationship has been intensively studied for phthalimides. When $\Delta G^\circ_{\text{ET}}$ is positive, $[\pi^2 + \sigma^2]$ cycloaddition reactions were observed with alkenyl substituents and classical Norrish II chemistry for aryl-substituted substrates. When $\Delta G^\circ_{\text{ET}}$ was negative, electron transfer prod-

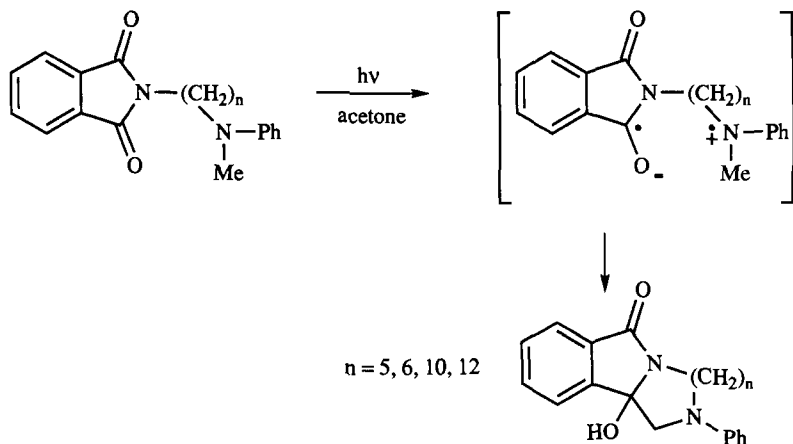


Scheme 42.

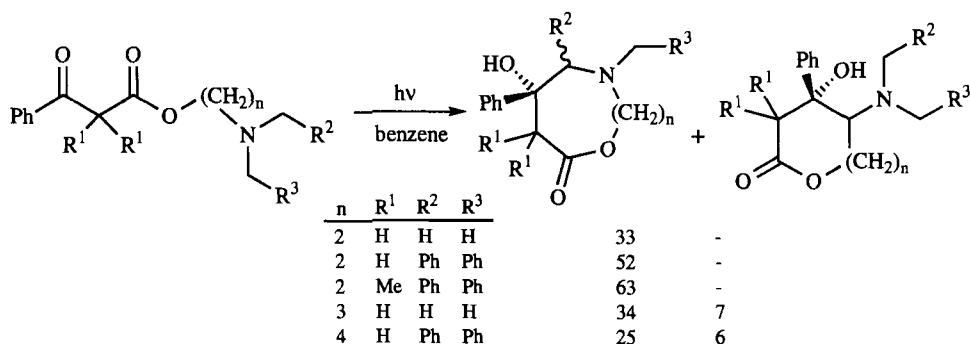
ucts predominate. Macrocyclization reactions of phthalimides with remote styryl-substituents were studied by Kubo and coworkers (Scheme 42) [164–166].

When the photolyses were performed in methanol as solvent the styrene radical cations were trapped by methanol in an *anti*-Markovnikov fashion and the resulting biradicals combined to give macrocyclic lactones in moderate to good yields. Spiroannulated products were formed by irradiation of the corresponding indenyl-substituted starting materials in methanol [167]. The yields for the heterocyclic products were excellent even for the 13-membered representative (86 %).

Intramolecular PET cyclizations of *aminoalkyl-substituted* phthalimides were investigated by the groups of Kanaoka and Coyle [168–171]. Because of the relatively low oxidation potentials of tertiary amines, these electron-transfer reactions are highly exergonic [172, 173]. The regioselectivity of the CH-activation step was remarkably high for the *N*-methyl, *N*-phenyl substituted substrates (Scheme 43).



Scheme 43.



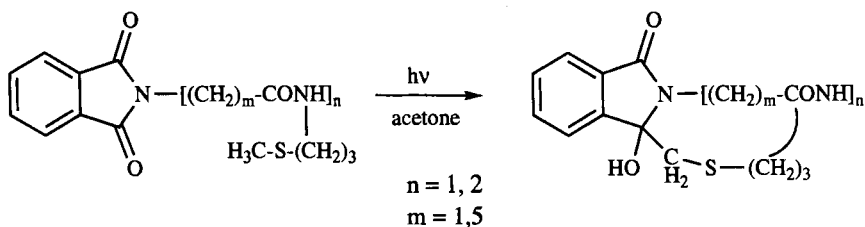
Scheme 44.

This effect has been rationalized by the higher kinetic acidity of *N*-methyl compared with *N*-methylene groups in amine radical cations. The chemical yields for the hydroxyisoindolinones were, however, always relatively poor (ring sizes between 5 and 16). The yields of these cyclization reactions could be improved by use of aromatic carbonyl groups as electron acceptors instead of phthalimides. Hasegawa and coworkers used aromatic β -oxoesters as substrates. Thus, medium-sized azalactones and lactones were available via photolysis of *N,N*-benzylaminoalkyl benzoylacetates in moderate yields [174]. Charge-transfer complexes were postulated as precursors and quenching experiments showed that the $\pi\pi^*$ triplet states are the reactive species. The regioselectivity of these cyclization reactions could be improved by use of twofold *N*-benzyl-substituted substrates which were exclusively activated by CH mesolysis of one of the benzylic C–H bonds (Scheme 44) [175].

PET-activation using the widely investigated cyclohexenone chromophore as the electron accepting group has been developed with remote amino substituents as electron-donor groups [176]. The regioselectivity of the mesolytic CH-cleavage was again controlled by use of the *N,N*-dimethylamino group. In contrast to the reactions described above, conjugate addition was observed.

N-alkyl substituted phthalimides with *alkylthio groups* in the side chain undergo facile photocyclization to give a variety of azathiacyclics. This reaction is, in contrast to the analogous transformations described above, remarkably efficient and tolerates many different functional groups in the hydrocarbon spacer. The scope and limitation of this important method were intensively investigated by Kanaoka and coworkers [177–182]. Limitations concerning the maximum ring size of the macrocycles have not yet been exactly determined. The chemical yields of unbranched azathiacyclics decreased significantly with increasing spacer length in the substrates (Scheme 45).

This process enabled the synthesis of cyclopeptide [183] and macrolide [184] model compounds with ring sizes up to 37. The acyclic starting materials were conveniently cyclized, with yields between 25 and 50 %. One major problem connected with this thioether method is the incorporation of the electron-donating group into the macrocyclic ring systems. A practical way of overcoming this dis-

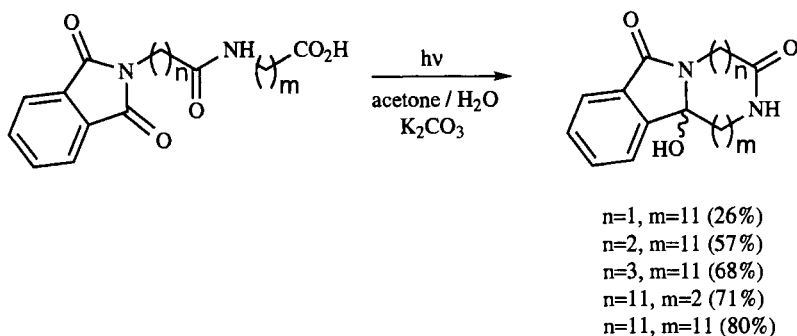


Scheme 45.

advantage was developed by Kanaoka et al. using the 1,3-dithiolanyl group as electron-donor substituent; this could be removed to give the sulfur-free compounds by treatment with Raney Ni [185]. PET-induced cyclization reactions were also investigated with enantiomerically pure phthalimides from the amino acid pool [186].

The molecular systems for the remote photocyclizations, as described in the previous chapters, consist of an electron-accepting and an electron-donating group connected by a flexible hydrocarbon chain. Both donor and acceptor group are inserted into the newly formed macrocyclic ring system and must be eliminated in a second reaction step. This detour makes these reactions less attractive for C–C coupling steps, e.g. for macrolide synthesis. An improved route has been developed using ω -aminocarboxylic acids as substrates [187]. The photodecarboxylation of *N*-phthaloyl α -aminocarboxylic acids is an efficient reaction when conducted in acetone ($\lambda = 300$ nm), in acetonitrile, and even when solid state irradiation is used [188]. This reaction also proceeds with high regioselectivity in the presence of another carboxyl group in the β - or γ -position, i.e. aspartic and glutamic acid derivatives. Electron-transfer activation from remote positions became possible when the corresponding potassium carboxylates were used (Scheme 46).

That the electron-transfer step occurs predominantly in an *intramolecular* fashion is probably because of complexation effects in the ground state of the substrates. The synthesis of cyclopeptide model compounds was intensively investigated by use of this photo-decarboxylation route. The yields of these macrocyclizations did not depend on spacer length but on the position of the amide group relative to



Scheme 46.

Table 6. Oxidation potentials of some aliphatic and aromatic ketones.^a

Ketone	Oxidation potential (V, relative to SCE)
Acetone	3.06
Cyclohexanone	2.71
Propiophenone	2.86
Acetophenone	2.82
<i>p</i> -Methoxyacetophenone	2.09

^a According to [190, 191].

the phthalimide chromophore. The maximum yield (80 %) was achieved for a 26-membered cyclopeptide from the acyclic dipeptide [189].

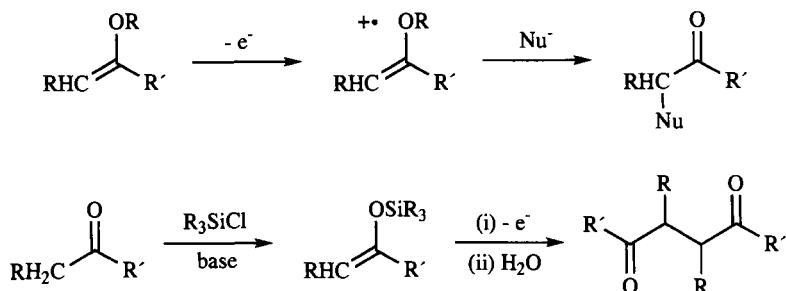
8.1.4 Generation of Carbonyl Radical Cations

In general, the electrochemical oxidation potentials of carbonyl compounds are very high (Table 6) and oxidative activation of aliphatic or aromatic carbonyl compounds is problematic whether by anodic oxidation or by photochemical methods. Oxidation at very high positive potentials is circumvented by at least three chemical modifications of the carbonyl group which enable the subsequent oxidation by chemical, electrochemical, or photoinduced electron-transfer processes.

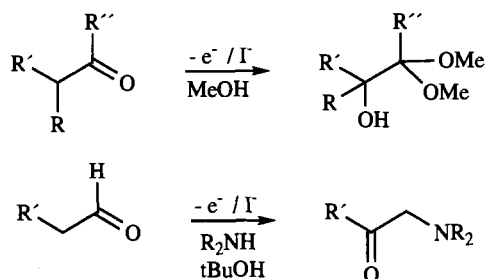
The first modification is peripheral substitution to reduce the oxidation potential of the carbonyl group—a method which often switches the reactivity because of hole localization at positions remote with respect to the C=O group (e.g. acetophenone or 4-methoxyacetophenone). Actually, the electrophore is extended by additional conjugation which reduces the oxidation potential and the HOMO–LUMO energy gap (i.e. the effect of auxochromic groups on the chromophore skeleton).

The second modification is *Umpolung* of the carbonyl group via conversion into the corresponding enol ethers or enols and subsequent oxidation to give the radical cations of enol ether and enol, respectively [192]. The oxidation potentials of these substrates are approximately 1 V (relative to the SCE) and thus oxidation is feasible even with moderately active oxidants or via anodic oxidation. Subsequent reactions of the enol radical cations and radical cations of enol ethers can result in α -substitution products (e.g. by running the reaction in the presence of nucleophiles) and re-formation of the carbonyl group (Scheme 47). Thus, the overall process corresponds to α -activation of carbonyl substrates via intermediate tautomeric enols (and sometimes also enolates) [193, 194].

The corresponding silyl enol ethers are likewise readily available carbonyl *umpolung* substrates which can be oxidized by a variety of chemical oxidants and also by cathodic oxidation. If not trapped by nucleophiles, the radical cations can dimerize and subsequently hydrolyze to give 1,4-dicarbonyl (homo)coupling products [195].



Scheme 47.

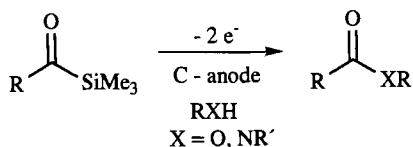


Scheme 48.

Intermediate enols can also be oxidized by indirect electrosynthesis (*vide supra*); halide anions are used as oxidation mediators. A multistep reaction converts ketones into α -hydroxylated acetals when oxidized electrochemically in the presence of iodine as the redox catalyst (Scheme 48) [196].

An analogous process has been developed for unbranched aldehydes which can be transformed into α -amino ketones when oxidized in the presence of a secondary amine and iodine, as the mediator, in aqueous *tert*-butanol. The actual reactive species is probably the enamine which is attacked by iodine cations and subsequently by water. Carbonyl transposition reaction releases iodine anions which can be anodically reoxidized [197].

A third possibility of chemical modification is conversion into an acylsilane which reduces the oxidation potential of the corresponding ketone by approximately 1 V. A peak potential of 1.45 V (relative to Ag/AgCl) for the oxidation of undecanoyltrimethylsilane has been reported. Preparative electrochemical oxidations of acylsilanes proceed in methanol to give the corresponding methyl esters. A two-step oxidation process must be assumed because of the reaction stoichiometry—oxidation of the acylsilane results in the carbonyl radical cation which is mesolytically cleaved to give the silyl cation and the acyl radical, which is subsequently oxidized to give the acyl cation as ultimate electrophile which reacts with the solvent. A variety of other nucleophiles have been used and a series of carboxylic acid derivatives are available via this pathway (Scheme 49) [198].



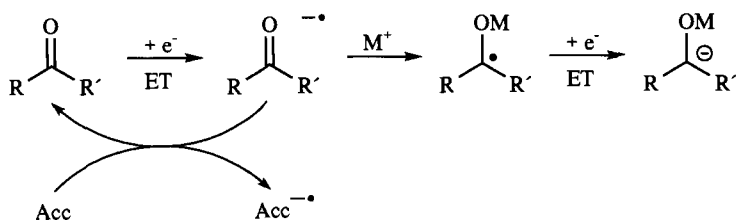
Scheme 49.

8.2 Reactivity Pattern of Carbonyl Radical Ions

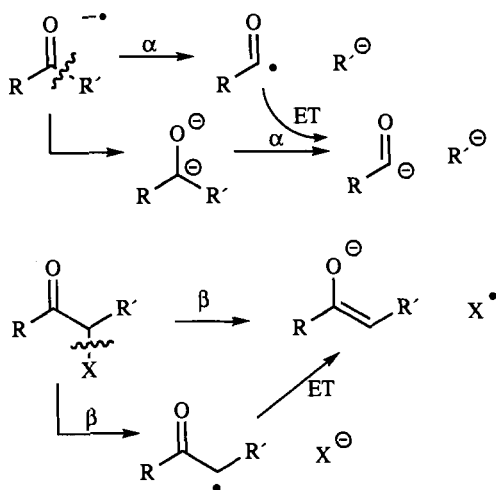
This section summarizes the reactivity pattern of carbonyl radical ion reactions which are described in numerous applications in Section 8.1. After the first one-electron-transfer step, the carbonyl radical ions can, in principle, undergo three modes of reaction—second electron transfer, bond cleavage, and bond formation.

Carbonyl radical anions are potential *electron donors* and are capable of reducing other carbonyl groups, electron acceptors with lower reduction potentials, or the primary electron source which was oxidized during the first electron-transfer step. The latter reaction is an important side-reaction in photoinduced electron-transfer processes, reconstituting the original electron donor–acceptor pair. Also carbon radicals can be reduced by carbonyl radical anions to give carbanions which can be protonated in the termination step of complex reaction cycles [199]. Further reduction of carbonyl radical anions can also proceed under strong reducing conditions to give 1,2-dianions (Scheme 50).

Bond cleavage reactions are important unimolecular processes for carbonyl radical anions which lead to radical–anion separation and stabilization. Two important cleavage modes are known: α - and β -cleavage. In the presence of good anionic leaving groups, mesolytic cleavage leads to acyl radicals which can be further reduced to acyl anions. The latter can also be directly formed via heterolytic cleavage from carbonyl dianions. In the presence of good radical leaving groups X in α -position with respect to the C=O group, rapid mesolytic cleavage leads to enolate anions and X radicals which can undergo further radical reactions. This reaction is synthetically highly useful in its intramolecular version, e.g. in cyclopropyl- or cyclobutylcarbinyl ring opening reactions. In the presence of good anionic leaving



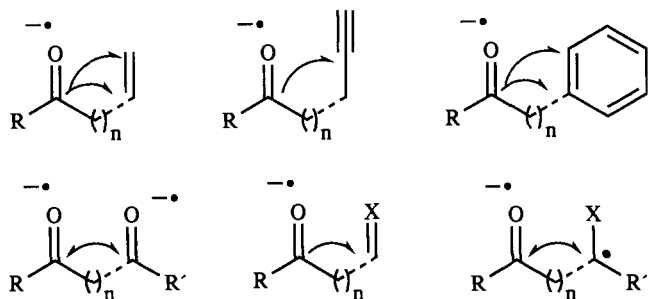
Scheme 50.



Scheme 51.

groups X in the β position, the mesolysis leads to enolate radicals which can be further reduced to enolate anions or undergo radical addition reactions (Scheme 51). Bond-cleavage reactions of radical anions and of the corresponding radical cations are often coupled, especially in photoinduced electron-transfer reactions where radical ion pairs are produced in the first electron-transfer step [200, 201].

From a synthetic point of view, *bond forming steps* are the most important reactions of radical ions [202]. Several principle possibilities have been described in Section 8.1 and are summarized in Scheme 52. Many carbo- and heterocyclic ring systems can be constructed by (inter- and intramolecular) radical addition to alkenes, alkynes, or arenes. Coupling of carbonyl radical anions leads to pinacols either intra- or inter-molecular which can be further modified to give 1,2-diols, acyloins or alkenes. Radical combination reactions with alkyl radicals afford the opportunity to synthesize macrocyclic rings. These radical ion–radical pairs can be generated most efficiently by inter- or intramolecular photoinduced electron transfer.



Scheme 52.

References

1. H. Lund, M. M. Baizer in *Organic Electrochemistry*, 3. ed. (Eds.: H. Lund, M. M. Baizer), Marcel Dekker, New York, **1991**, 433.
2. P. Kabasakalian, J. McGlotten, *Anal. Chem.* **1959**, 31, 1091.
3. M.-A. Michel, J. Simonet, G. Mousset, H. Lund, *Electrochim. Acta* **1975**, 20, 143.
4. J. P. Coleman, R. J. Holman, J. H. P. Utley, *J. Chem. Soc., Perkin Trans. II* **1976**, 879.
5. R. J. Holman, J. H. P. Utley, *J. Chem. Soc., Perkin Trans. II* **1976**, 884.
6. E. Kariv-Miller, T. J. Mahachi, *J. Org. Chem.* **1986**, 51, 1041.
7. J. W. Hayes, I. Ruzic, D. E. Smith, G. L. Booman, J. R. Delmastro, *J. Electroanal. Chem.* **1974**, 51, 269.
8. D. W. Sopher, J. H. P. Utley, *J. Chem. Soc., Perkin Trans. II* **1984**, 1361.
9. K. Uneyama, T. Tokunaga, S. Torii, *Bull. Chem. Soc. Jpn.* **1987**, 60, 3427.
10. T. Shono, M. Mitani, *J. Am. Chem. Soc.* **1971**, 93, 5284.
11. T. Shono, I. Nishiguchi, H. Ohmizu, M. Mitani, *J. Am. Chem. Soc.* **1978**, 100, 545.
12. T. Shono, N. Kise, T. Suzumoto, T. Morimoto, *J. Am. Chem. Soc.* **1986**, 108, 4676.
13. G. Pattenden, G. M. Robertson, *Tetrahedron Lett.* **1983**, 24, 4617.
14. G. Pattenden, G. M. Robertson, *Tetrahedron* **1985**, 41, 4001.
15. J. E. Swartz, E. Kariv-Miller, S. J. Harrold, *J. Am. Chem. Soc.* **1989**, 111, 1211.
16. E. Kariv-Miller, H. Maeda, F. Lombardo, *J. Org. Chem.* **1989**, 54, 4022.
17. T. Shono, N. Kise, T. Fujimoto, N. Tominaga, H. Morita, *J. Org. Chem.* **1992**, 57, 7175.
18. E. Kariv-Miller, R. I. Pacut, G. K. Lehmann, *Top. Curr. Chem.* **1988**, 148, 97.
19. E. Steckhan, *Top. Curr. Chem.* **1987**, 142, 2.
20. C. K. Mann, K. K. Barnes, in *Electrochemical Reactions in Nonaqueous Systems*, Marcel Dekker: New York, **1970**.
21. C. P. Andrieux, C. Blocman, J. M. Dumas-Bouchiat, J. M. Savéant, *J. Am. Chem. Soc.* **1979**, 101, 3431.
22. C. P. Andrieux, C. Blocman, J. M. Dumas-Bouchiat, F. M'Halla, J. M. Savéant, *J. Am. Chem. Soc.* **1980**, 102, 3806.
23. M. Hoshino, S. Arai, M. Imamura, A. Namiki, *Chem. Phys. Lett.* **1974**, 26, 582.
24. B. J. McClelland, *Trans. Faraday Soc.* **1961**, 57, 1458.
25. A. Fürstner, *Angew. Chem.* **1993**, 105, 171.
26. P. W. Rabideau, Z. Marcinow, *Org. React.* **1992**, 42, 1.
27. A. Fürstner (ed.), *Active Metals—Preparation, Characterization, Applications*, VCH: Weinheim, New York, **1996**.
28. T. Wirth, *Angew. Chem. Int. Ed. Engl.* **1996**, 35, 61.
29. A. Gansäuer, *Synlett*, **1998**, 801.
30. Y. Nishiyama, E. Shinomiya, S. Kimura, K. Itoh, N. Sonoda, *Tetrahedron Lett.* **1998**, 39, 3705.
31. T. Hirao, *Synlett* **1999**, 175.
32. T. Hirao, B. Hatano, Y. Imamoto, A. Ogawa, *J. Org. Chem.* **1999**, 64, 7665.
33. T. Hirao, B. Hatano, M. Asahara, Y. Muguruma, A. Ogawa, *Tetrahedron Lett.* **1998**, 39, 5247.
34. B. Hatano, A. Ogawa, T. Hirao, *J. Org. Chem.* **1998**, 63, 9421.
35. P. Liao, Y. Huang, Y. Zhang, *Synth. Commun.* **1997**, 27, 1483.
36. E. J. Corey, G. Z. Zheng, *Tetrahedron Lett.* **1997**, 38, 2045.
37. A. F. Barrero, E. J. Alvarez-Manzaneda, R. Chahboun, R. Meneses, *Synlett* **1999**, 1663.
38. J. E. McMurry, M. P. Fleming, *J. Am. Chem. Soc.* **1974**, 96, 4708.
39. T. Mukaiyama, T. Sato, J. Hanna, *Chem. Lett.* **1973**, 1041.
40. J. E. McMurry, *Chem. Rev.* **1989**, 89, 1513.
41. J. E. McMurry, *Acc. Chem. Res.* **1983**, 16, 405.
42. D. Lenoir, *Synthesis* **1989**, 883.
43. A. Fürstner, H. Weidmann, *Synthesis* **1987**, 1071.
44. G. P. Boldrini, D. Savoia, E. Tagliavini, C. Trombini, A. Umani-Ronchi, *J. Organomet. Chem.* **1985**, 280, 307.

45. P. Burger, H. H. Brintzinger, *J. Organomet. Chem.* **1991**, 407, 207.
46. D. L. J. Clive, C. Zhang, K. S. K. Murthy, W. D. Hayward, S. Daigneault, *J. Org. Chem.* **1991**, 56, 6447.
47. A. Fürstner, A. Hupperts, *J. Am. Chem. Soc.* **1995**, 117, 4468.
48. E. J. Corey, R. L. Danheiser, S. Chandrasekaran, *J. Org. Chem.* **1976**, 41, 260.
49. J. E. McMurry, N. O. Siemers, *Tetrahedron Lett.* **1993**, 34, 7891.
50. J. J. Blomfield, D. C. Owsley, J. M. Nelke, *Org. React.* **1976**, 23, 259.
51. K. Rühlmann, *Synthesis* **1971**, 236.
52. A. C. Cope, J. W. Barthel, R. D. Smith, *Org. Synth.* **1963**, IV, 218.
53. L. E. Overman, C. Fukaya, *J. Am. Chem. Soc.* **1980**, 102, 1454.
54. P. A. Grieco, E. Williams, H. Tanaka, S. Gilman, *J. Org. Chem.* **1980**, 45, 3537.
55. N. M. Alpatova, L. I. Krishtalik, Y. V. Pleskov, *Top. Curr. Chem.* **1987**, 138, 149.
56. J. P. Coleman, R. J. Kobylecky, J. H. P. Utley, *Chem. Commun.* **1971**, 104.
57. S. E. Zabusova, A. P. Tomilov, L. F. Filimonova, N. M. Alpatova, *Elektrokhimiya* **1980**, 16, 970.
58. K. C. Nicolaou, C.-K. Hwang, M. E. Duggan, K. B. Reddy, B. E. Marron, D. G. McGarry, *J. Am. Chem. Soc.* **1986**, 108, 6800.
59. P. Girard, J. L. Namy, H. B. Kagan, *J. Am. Chem. Soc.* **1980**, 102, 2693.
60. G. E. Keck, C. A. Wagner, T. Sell, T. T. Wager, *J. Org. Chem.* **1999**, 64, 2172.
61. R. Nomura, T. Matsuno, T. Endo, *J. Am. Chem. Soc.* **1996**, 118, 11666.
62. F. Hélon, J.-L. Namy, *J. Org. Chem.* **1999**, 64, 2944.
63. R. A. Batey, W. B. Motherwell, *Tetrahedron Lett.* **1991**, 32, 6649.
64. R. A. Batey, J. D. Harling, W. B. Motherwell, *Tetrahedron* **1996**, 52, 11421.
65. G. A. Molander, C. Alonso-Alija, *Tetrahedron* **1997**, 53, 8067.
66. G. A. Molander, C. P. Losada, *J. Org. Chem.* **1997**, 62, 2935.
67. G. A. Molander, J. A. McKie, *J. Org. Chem.* **1995**, 60, 872.
68. J. L. Chiara, S. Martinez, M. Bernabé, *J. Org. Chem.* **1996**, 61, 6488.
69. G. A. Molander, J. A. McKie, *J. Org. Chem.* **1994**, 59, 3186.
70. G. A. Molander, S. R. Shakya, *J. Org. Chem.* **1996**, 61, 5885.
71. D. P. Curran, B. Yoo, *Tetrahedron Lett.* **1992**, 33, 6931.
72. G. A. Molander, P. J. Stengel, *Tetrahedron* **1997**, 53, 8887.
73. G. A. Molander, J. A. McKie, *J. Org. Chem.* **1992**, 57, 3132.
74. G. A. Molander, G. Hahn, *J. Org. Chem.* **1986**, 51, 2596.
75. F. A. Khan, R. Czerwonka, R. Zimmer, H.-U. Reißig, *Synlett* **1997**, 995.
76. C. U. Dinesh, H.-U. Reißig, *Angew. Chem. Int. Ed. Engl.* **1999**, 38, 789.
77. M. Sasaki, J. Collin, H. B. Kagan, *Tetrahedron Lett.* **1988**, 29, 6105.
78. J. Collin, F. Dallemer, J.-L. Namy, H. B. Kagan, *Tetrahedron Lett.* **1989**, 30, 7407.
79. G. A. Molander, J. A. McKie, *J. Org. Chem.* **1993**, 58, 7216.
80. P. Girard, J. L. Namy, H. B. Kagan, *J. Am. Chem. Soc.* **1980**, 102, 2693.
81. D. P. Curran, T. L. Fevig, C. P. Jasperse, M. Tottleben, *Synlett* **1992**, 943.
82. D. P. Curran, X. Gu, W. Zhang, P. Dowd, *Tetrahedron* **1997**, 53, 9023.
83. G. Lannoye, K. Sambasivarao, S. Wehrli, J. Cook, *J. Org. Chem.* **1988**, 53, 2327.
84. D. P. Curran, B. Yoo, *Tetrahedron Lett.* **1992**, 33, 6931.
85. T. Kan, S. Nara, S. Ito, F. Matsuda, H. Shirahama, *J. Org. Chem.* **1994**, 59, 5111.
86. T. L. Fevig, R. L. Elliott, D. P. Curran, *J. Am. Chem. Soc.* **1988**, 110, 5064.
87. L. Zhou, Y. Zhang, D. Shi, *Tetrahedron Lett.* **1998**, 39, 8491.
88. G. A. Molander, C. N. Wolfe, *J. Org. Chem.* **1998**, 63, 9031.
89. G. A. Molander, C. R. Harris, *Tetrahedron* **1998**, 54, 3321.
90. M. Sasaki, J. Collin, H. B. Kagan, *New J. Chem.* **1992**, 16, 89.
91. G. A. Molander, C. R. Harris, *Chem. Rev.* **1992**, 92, 29.
92. G. A. Molander, *Acc. Chem. Res.* **1998**, 31, 603.
93. G. Pattenden, S. J. Teague, *Tetrahedron Lett.* **1982**, 23, 4571.
94. G. Pattenden, G. M. Robertson, *Tetrahedron* **1985**, 41, 4001.
95. G. Pattenden, G. M. Robertson, *Tetrahedron Lett.* **1983**, 24, 4617.
96. G. H. Lee, E. B. Choi, E. Lee, C. S. Pak, *J. Org. Chem.* **1994**, 59, 1428.
97. K. Mizuno, Y. Otsuji, *Top. Curr. Chem.* **1994**, 169, 301.

98. G. Pandey, *Top. Curr. Chem.* **1993**, 168, 175.
99. M. Chanon, M. D. Hawley, M. A. Fox, in *Photoinduced Electron Transfer*, (Eds.: M. A. Fox, M. Chanon), Part A, Elsevier: Amsterdam, **1988**, 1.
100. M. Chanon, L. Eberson, in *Photoinduced Electron Transfer*, (Eds.: M. A. Fox, M. Chanon), Part A, Elsevier: Amsterdam, **1988**, 409.
101. G. J. Kavarnos, *Fundamentals of Photoinduced Electron Transfer*, VCH: Weinheim, New York, **1993**.
102. H. D. Roth, *Top. Curr. Chem.* **1990**, 156, 1.
103. J. Mattay, *Top. Curr. Chem.* **1991**, 159, 219.
104. J. Mattay, *Angew. Chem. Int. Ed. Engl.* **1987**, 26, 825.
105. S. L. Mattes, S. Farid, *Org. Photochem.* **1983**, 6, 233.
106. M. Chanon, M. Rajzmann, F. Chanon, *Tetrahedron* **1990**, 46, 6193.
107. J. K. Kochi, *Angew. Chem. Int. Ed. Engl.* **1988**, 27, 1227.
108. G. J. Kavarnos, N. J. Turro, *Chem. Rev.* **1986**, 86, 401.
109. D. Rehm, A. Weller, *Ber. Bunsenges. Phys. Chem.* **1969**, 73, 834.
110. D. Rehm, A. Weller, *Z. Phys. Chem.* **1970**, 69, 183.
111. I. R. Gould, J. E. Moser, B. Armitage, S. Farid, J. L. Goodman, M. S. Herman, *J. Am. Chem. Soc.* **1989**, 111, 1917.
112. J. Gersdorf, J. Mattay, H. Görner, *J. Am. Chem. Soc.* **1987**, 109, 1203.
113. J. B. Guttenplan, S. G. Cohen, *J. Am. Chem. Soc.* **1972**, 94, 4040.
114. D. Belotti, J. Cossy, J. P. Pete, C. Portella, *J. Org. Chem.* **1986**, 51, 4196.
115. J. Cossy, D. Belotti, J. P. Pete, *Tetrahedron Lett.* **1987**, 28, 4545.
116. J. Cossy, D. Belotti, *Tetrahedron Lett.* **1988**, 29, 6113.
117. J. Cossy, *Tetrahedron Lett.* **1989**, 30, 4113.
118. T. Kirschberg, J. Mattay, *Tetrahedron Lett.* **1994**, 35, 7217.
119. M. Fagnoni, P. Schmoldt, T. Kirschberg, J. Mattay, *Tetrahedron* **1998**, 54, 6427.
120. K. Maruyama, H. Imahori, A. Osuka, A. Takuwa, H. Tagawa, *Chem. Lett.* **1986**, 1719.
121. A. Takuwa, Y. Nishigaichi, K. Yamashita, H. Iwamoto, *Chem. Lett.* **1990**, 639.
122. A. Takuwa, Y. Nishigaichi, H. Iwamoto, *Chem. Lett.* **1991**, 1013.
123. K. Mizuno, M. Ikeda, Y. Otsuji, *Chem. Lett.* **1988**, 1507.
124. K. Mizuno, K. Nakanishi, A. Tachibana, Y. Otsuji, *J. Chem. Soc., Chem. Commun.* **1991**, 344.
125. K. Mizuno, Y. Otsuji, *Top. Curr. Chem.* **1994**, 169, 301.
126. S. L. Mattes, S. Farid, in *Organic Photochemistry* (Ed.: A. Padwa), Marcel Dekker: New York, **1983**, 6, 233.
127. T. Sato, G. Izumi, T. Imamura, *Tetrahedron Lett.* **1975**, 2191.
128. T. Sato, S. Yamaguchi, H. Kaneko, *Tetrahedron Lett.* **1979**, 21, 1863.
129. T. Sato, H. Kaneko, S. Yamaguchi, *J. Org. Chem.* **1980**, 45, 3778.
130. B. Fraser-Reid, R. C. Anderson, D. R. Hicks, D. L. Walker, *Can. J. Chem.* **1977**, 55, 3986.
131. N. Reineke, N. A. Zaidi, M. Mitra, D. O'Hagan, A. S. Batsanov, J. A. K. Howard, D. Y. Naumov, *J. Chem. Soc., Perkin Trans 1* **1996**, 147.
132. A. G. Griesbeck, S. Buhr, J. Lex, *Tetrahedron Lett.* **1998**, 39, 2535.
133. P. S. Mariano, *Acc. Chem. Res.* **1983**, 16, 130.
134. P. S. Mariano, J. L. Stavinoha, in *Synthetic Organic Photochemistry*, (Ed.: W. M. Horspool), Plenum Press: New York, **1983**, 145.
135. U. C. Yoon, P. S. Mariano, *Acc. Chem. Res.* **1992**, 25, 233.
136. P. S. Mariano, in *Photoinduced Electron Transfer*, (Eds.: M. A. Fox, M. Chanon), Part C, Elsevier: Amsterdam, **1988**, 372.
137. R. M. Borg, R. O. Heuckeroth, A. J. Y. Lan, S. L. Quillen, P. S. Mariano, *J. Am. Chem. Soc.* **1987**, 109, 2728.
138. K. Ohga, P. S. Mariano, *J. Am. Chem. Soc.* **1982**, 104, 617.
139. R. M. Borg, P. S. Mariano, *Tetrahedron Lett.* **1986**, 27, 2821.
140. A. J. Y. Lan, S. L. Quillen, R. O. Heuckeroth, P. S. Mariano, *J. Am. Chem. Soc.* **1984**, 106, 6439.
141. W. Xu, Y. T. Jeon, E. Hasegawa, U. C. Yoon, P. S. Mariano, *J. Am. Chem. Soc.* **1989**, 111, 406.

142. W. Xu, X. M. Zhang, P. S. Mariano, *J. Am. Chem. Soc.* **1991**, *113*, 8863.
143. M. T. Crimmins, *Chem. Rev.* **1988**, *88*, 1453.
144. E. W. Bischof, J. Mattay, *Tetrahedron Lett.* **1990**, *31*, 7137.
145. J. Mattay, A. Banning, E. W. Bischof, A. Heidbreder, J. Runsink, *Chem. Ber.* **1992**, *125*, 2119.
146. G. Pandey, S. Hajra, *Angew. Chem. Int. Ed. Engl.* **1994**, *33*, 1169.
147. D. W. Leedy, D. L. Muck, *J. Am. Chem. Soc.* **1971**, *93*, 4264.
148. K. Okada, K. Okamoto, M. Oda, *J. Am. Chem. Soc.* **1988**, *110*, 8736.
149. K. Okada, K. Okamoto, N. Morita, M. Oda, K. Okubo, *J. Am. Chem. Soc.* **1991**, *113*, 9401.
150. A. G. Griesbeck, M. Oelgemöller, *Synlett* **1999**, 492.
151. A. G. Griesbeck, W. Kramer, M. Oelgemöller, *Synlett* **1999**, 1169.
152. J. Mattay, R. Conrads, R. Hoffmann, in *Methoden der Organischen Chemie* (Houben-Weyl) (Eds.: G. Helmchen, R. W. Hoffmann, J. Mulzer, E. Schaumann), Thieme Verlag: Stuttgart, **1995**, E21c, 3133.
153. J. Mattay, J. Gersdorf, K. Buchkremer, *Chem. Ber.* **1987**, *120*, 307.
154. T. Kim, H. Sarker, N. L. Bauld, *J. Chem. Soc. Perkin Trans. 2* **1995**, 577.
155. M. Abe, Y. Shirodai, M. Nojima, *J. Chem. Soc., Perkin Trans. 1* **1998**, 3253.
156. D. L. Sun, S. M. Hubig, J. K. Kochi, *J. Org. Chem.* **1999**, *64*, 2250.
157. A. G. Griesbeck, S. Buhr, M. Fiege, H. Schmickler, J. Lex, *J. Org. Chem.* **1998**, *63*, 3847.
158. M. Abe, I. Masayuki, M. Nojima, *J. Chem. Soc., Perkin Trans. 1* **1998**, 3261.
159. R. S. Thopate, M. G. Kulkarni, V. G. Puranik, *Angew. Chem. Int. Ed. Engl.* **1998**, *37*, 1110.
160. P. Maslak, J. N. Navaraz, *Angew. Chem. Int. Ed. Engl.* **1990**, *29*, 302.
161. Y. Kanaoka, *Acc. Chem. Res.* **1978**, *11*, 407.
162. A. G. Griesbeck, H. Mauder in *CRC Handbook of Organic Photochemistry and Photobiology* (Eds.: W. M. Horspool, P.-S. Song), CRC Press: New York, **1995**, 513.
163. H. Hoshino, H. Shizuka, in *Photoinduced Electron Transfer*, (Eds.: M. A. Fox, M. Chanon), Part C, Elsevier: Amsterdam, **1988**, 313.
164. K. Maruyama, Y. Kubo, *J. Am. Chem. Soc.* **1978**, *100*, 7772.
165. K. Maruyama, Y. Kubo, *Chem. Lett.* **1978**, 851.
166. K. Maruyama, Y. Kubo, M. Machida, K. Oda, Y. Kanaoka, K. Furuyama, *J. Org. Chem.* **1978**, *43*, 2303.
167. M. Machida, K. Oda, Y. Kanaoka, *Tetrahedron* **1985**, *41*, 4995.
168. M. Machida, H. Takechi, Y. Kanaoka, *Heterocycles* **1980**, *14*, 1255.
169. M. Machida, H. Takechi, Y. Kanaoka, *Heterocycles* **1977**, *7*, 273.
170. J. D. Coyle, G. L. Newport, *Tetrahedron Lett.* **1977**, 899.
171. J. D. Coyle, G. L. Newport, *J. Chem. Soc. Perkin Trans. 1* **1980**, 93.
172. M. Machida, H. Takechi, Y. Kanaoka, *Chem. Pharm. Bull.* **1982**, *30*, 1579.
173. M. Machida, H. Takechi, Y. Kanaoka, *Heterocycles* **1980**, *14*, 1255.
174. T. Hasegawa, K. Miyata, T. Ogawa, N. Yoshihara, M. Yoshioka, *J. Chem. Soc. Chem. Commun.* **1985**, 363.
175. T. Hasegawa, T. Ogawa, K. Miyata, A. Karakizawa, M. Komiyama, Y. Nishizawa, M. Yoshioka, *J. Chem. Soc. Perkin Trans. 1* **1990**, 901.
176. G. A. Kraus, L. Chen, *Tetrahedron Lett.* **1991**, *32*, 7151.
177. Y. Kanaoka, H. Migita, Y. Sato, H. Nakai, *Tetrahedron Lett.* **1973**, 51.
178. Y. Hatanaka, Y. Sato, H. Nakai, M. Wada, T. Mizoguchi, Y. Kanaoka, *Liebigs Ann. Chem.* **1992**, 1113.
179. Y. Sato, H. Nakai, T. Mizoguchi, Y. Kanaoka, *Tetrahedron Lett.* **1976**, 1889.
180. H. Takechi, S. Tateuchi, M. Machida, Y. Nishibata, K. Aoe, Y. Sato, Y. Kanaoka, *Chem. Pharm. Bull.* **1986**, *34*, 3142.
181. Y. Sato, H. Nakai, M. Wada, T. Mizoguchi, Y. Hatanaka, H. Migita, Y. Kanaoka, *Liebigs Ann. Chem.* **1985**, 1099.
182. Y. Sato, H. Nakai, M. Wada, T. Mizoguchi, Y. Hatanaka, Y. Kanaoka, *Chem. Pharm. Bull.* **1992**, *40*, 3174.
183. Sato, Y.; Nakai, H.; Mizoguchi, T.; Hatanaka, Y.; Kanaoka, Y. *J. Am. Chem. Soc.* **1976**, *98*, 2349.

184. M. Wada, H. Nakai, K. Aoe, K. Kotera, Y. Sato, Y. Hatanaka, Y. Kanaoka, *Tetrahedron* **1983**, 39, 1273.
185. M. Wada, H. Nakai, Y. Sato, Y. Hatanaka, Y. Kanaoka, *Tetrahedron* **1983**, 39, 2691.
186. A. G. Griesbeck, H. Mauder, I. Müller, E.-M. Peters, K. Peters, H. G. von Schnering, *Tetrahedron Lett.* **1993**, 34, 453.
187. A. G. Griesbeck, A. Henz, K. Peters, E.-M. Peters, H. G. von Schnering, H. G. *Angew. Chem. Int. Ed. Engl.* **1995**, 34, 474.
188. A. G. Griesbeck, A. Henz, *Synlett* **1994**, 931.
189. A. G. Griesbeck, A. Henz, W. Kramer, J. Lex, F. Nerowski, M. Oelgemöller, K. Peters, E.-M. Peters, *Helvetica Chim. Acta*, **1997**, 80, 912–933.
190. F. G. Bordwell, J. A. Harrelson, Jr., *Can. J. Chem.* **1990**, 68, 1714.
191. J. Y. Becker, L. L. Miller, T. M. Siegel, *J. Am. Chem. Soc.* **1975**, 97, 849.
192. M. Schmittel, *Top. Curr. Chem.* **1994**, 169, 183.
193. M. Schulz, R. Kluge, L. Sivilai, B. Kamm, *Tetrahedron* **1990**, 46, 2371.
194. M. Schmittel, A. Abufarag, O. Luche, M. Levis, *Angew. Chem. Int. Ed. Engl.* **1990**, 29, 1144.
195. H. J. Schäfer, *Angew. Chem. Int. Ed. Engl.* **1981**, 20, 911.
196. T. Shono, Y. Matsumura, K. Inoue, F. Iwasaki, *J. Chem. Soc., Perkin Trans. I* **1986**, 73.
197. T. Shono, Y. Matsumura, J. Hayashi, M. Usui, S. Yamane, K. Inoue, *Acta Chem. Scand. B* **1983**, 491.
198. J. Yoshida, M. Itoh, S. Matsunaga, S. Isoe, *J. Org. Chem.* **1992**, 57, 4877.
199. J.-P. Soumilion, *Top. Curr. Chem.* **1993**, 168, 93.
200. N. J. Pienta, in *Photoinduced Electron Transfer*, (Eds.: M. A. Fox, M. Chanon), Part C, Elsevier: Amsterdam, **1988**, 421.
201. F. D. Saeva, *Top. Curr. Chem.* **1990**, 156, 59.
202. S. Hintz, A. Heidbreder, J. Mattay, *Top. Curr. Chem.* **1996**, 177, 77.

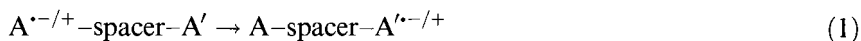
9 Electron Transfer in Radicals

Massimo Bietti and Steen Steenken

9.1 Introduction

Radical chemistry has long been an exotic (and allegedly ‘dirty’) area of chemistry. However, because of (i) contributions to the understanding of radical *reaction mechanisms*, mainly from *radiation-chemical* studies in aqueous solution [1–7], (ii) growing awareness of the occurrence and importance of *radical reactions in biological systems* such as enzymes [8, 9] or photosystem II [10–12] or *biological processes* such as diseases, cancer, or aging [13, 14], and, finally, (iii) the recognition of the *synthetic potential* of radicals [15–20] radical chemistry has succeeded in gaining legitimacy as a proper area of chemistry.

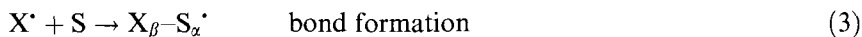
A particularly simple approach with respect to synthetic applications of radical reactions is ‘electron transfer activation’ which consists in producing radical *ions* as the reactive species. The activation can proceed by electron *addition* to the molecule to be activated, when a radical *anion* is produced, or by electron *removal* which leads to a radical *cation*. If there is more than one electron or hole trap on a molecule, such as in A–spacer–A′, the electron or hole can transfer to the other (secondary) trap.



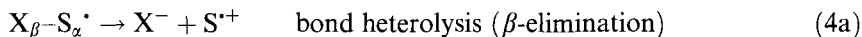
Intramolecular electron- or hole-transfer processes of this type have been intensively studied [21–23], because of their obvious relevance to photosynthesis [24–26] or to ET processes in other biological systems such as proteins [27–32] or DNA [33–35]. These reactions as well as *intermolecular* electron transfer (ET) processes, which consist just in *exchange* of charge between the reaction partners, will *not* be discussed here, although radicals do have a strong tendency to engage in one-electron transfer processes (since this is the simplest way for these species to lose their radical nature, i.e. to become closed-shell molecules) [36]. What *will* be discussed (in Sections 9.2 and 9.3) are reactions where a radical X[•] oxidizes or reduces a substrate S, Eq. 2, in which charged species are *produced de novo*:



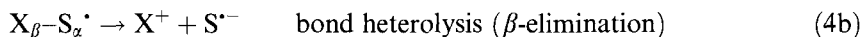
In reactions of this type, the *direction* of the electron flow between the radical X[•] and the substrate molecule S depends, of course, on the oxidizing or reducing properties of X[•] and the ability of S either to donate or to accept an electron. Irrespective of electron flow *direction*, transfer between X[•] and S can proceed by the ‘outer-sphere’ mechanism [37], Eq. 2, or by ‘inner-sphere’ or ‘bonded’ paths (Eqs 3 and 4) [38, 39]. The stoichiometry in Eqs 3 and 4 is the same as in Eq. 2. In the bonded mechanism, however, a heterolytic fragmentation of the bond joining X and S is the step in which the electron transfer actually occurs:



S is oxidized



S is reduced



For the heterolysis reactions, Eq. 4, to occur it is, of course, irrelevant *how* X–S[•] was *formed*; e.g., rather than by addition (Eq. 3), it can be produced by H-abstraction from X–S–H:



The reaction depicted by Eq. 5 can be called ‘activation by H-abstraction’, which is often analogous to ‘electron-transfer activation’. Examples of the latter (in which X–S^{•+} or X–S^{•-} are produced) will also be presented (Section 9.5) but only in heterolysis is ET taking place between X and S [40, 41].

9.2 Oxidation of S by X[•] (ET by Addition–Elimination (The ‘ad-el’ Mechanism))

Condition: (E(X[•]/X⁻) > E(S^{•+}/S))

9.2.1 S = alkene

The reaction starts with addition to the double bond (rate constant k_{ad} (M⁻¹ s⁻¹)):



If the so-formed β -X-alk-(α)yl radical undergoes rapid C-X heterolysis with the rate constant k_{het} (s^{-1}) (Eq. 7):



the reaction will *seem* as if it is electron transfer to all detection methods whose time resolution τ is larger than $1/k_{\text{het}}$. In Eqs 6 and 7 the stoichiometry is such that the electrophilic radical X^\cdot is the electron *acceptor* (which yields X^-) and the alkene is the electron *donor* (which is thereby converted to the alkene radical cation). On the basis of this concept it can be predicted that the rate of X^\cdot addition, k_{ad} , and the rate of X^- elimination, k_{het} , should increase with increasing reduction potential of X^\cdot , $E(\text{X}^\cdot/\text{X}^-)$, and, of course, with increasing ease of oxidation of the alkene, which should depend strongly on the kind and number of substituents on the alkene function.

As shown in the next section, these ideas are borne out by the reactions of alkenes with the strong oxidizing radical $\text{SO}_4^{\cdot-}$ ($E(\text{SO}_4^{\cdot-}/\text{SO}_4^{2-}) = 2.4\text{--}3.1\text{ V}$) [42–44].

$\text{X} = \text{SO}_4^{\cdot-}$

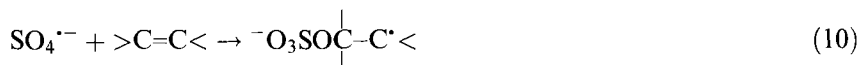
The oxidation of alkenes by $\text{SO}_4^{\cdot-}$ has been studied in aqueous acetonitrile solution, using time-resolved (a) optical and (b) conductance methods [45]. $\text{SO}_4^{\cdot-}$ was produced in the presence of the alkenes by (i) laser photolysis (20 ns pulse, $\lambda_{\text{excitation}} = 248\text{ nm}$)



or (ii) pulse radiolysis



In (a), the optical experiments, the reaction of $\text{SO}_4^{\cdot-}$ with the alkenes was studied by monitoring the rate of decay of $\text{SO}_4^{\cdot-}$ as a function of the concentration of alkene. It was found that the bimolecular rate constant for reaction of $\text{SO}_4^{\cdot-}$ (obtained from the plot of $k_{\text{obs(erved)}}$ as a function of [alkene]) increases strongly with increasing water content of the solvent, as shown in Figure 1, where allyl alcohol is used as an example. This indicates that the transition state for the reaction (which consists in addition to the C=C double bond, Eq. 10; see later and Refs [46] and [47]) is highly ionic [48].



It was observed that, after $\text{SO}_4^{\cdot-}$ had completely disappeared, due to reaction with the alkene (using concentrated or saturated solutions of the alkenes), with electron-rich alkenes, there was a first-order increase of conductance of the aqueous

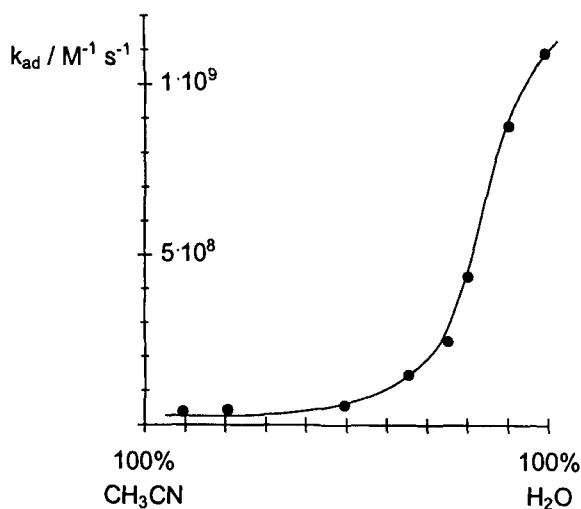
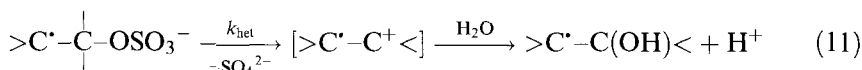


Figure 1. Rate constant k_{ad} (M⁻¹ s⁻¹) for the reaction $\text{SO}_4^{\bullet-} + \text{HOCH}_2\text{CH}=\text{CH}_2 \rightarrow \text{HOCH}_2\text{C}^+\text{HCH}_2\text{OSO}_3^-$ as a function of solvent (CH₃CN-H₂O) composition.

solution at pH 4–6. The rate of this conductance increase (which could be reversibly changed into a conductance *decrease* in basic solution, indicating that the conductance change is due to the production of H⁺) was independent of [alkene] and pH but dependent on temperature. The reaction responsible is identified [49] in terms of β -fragmentation (heterolysis) of the SO_4^- adduct to give a (short-lived) [50] alkene radical cation, followed by its rapid reaction with water.



An example is the cyclohexene derivative shown below. Figure 2 depicts the dependence of the rate of heterolysis k_{het} on solvent composition for this system. The fact that k_{het} increases strongly with increasing water content is indicative of the strongly ionic nature ($\text{S}_{\text{N}}1$ -type) of the transition state of the C–O heterolysis.

Table 1 lists the rate constants for reaction 11 in aqueous solution measured via the first-order conductance increase in H₂O at pH 4–6 and $20 \pm 2^\circ\text{C}$.

As is apparent from Table 1, the rate of heterolysis is drastically *increased* by introducing methyl groups at C=C. If, in contrast, the electron density is somewhat *reduced*, e.g. by the inductive effect of an OH group at C_γ, C_δ, or even C_ε, k_{het} decreases [51].

These results indicate that the reaction of $\text{SO}_4^{\bullet-}$ with alkenes changes from pure addition to what *seems* to be electron transfer, followed by, or concerted with, addition of water to the radical cation, as the electron density of the olefinic bond is increased. One consequence is that at the one extreme (characterized by *low* electron density), the reaction $\text{SO}_4^{\bullet-} + \text{alkene}$ stops at the *adduct* stage. At the other extreme (high electron availability) the reaction probably proceeds by outer-sphere ET. In the in-between situation, addition is followed by elimination (rates strongly depen-

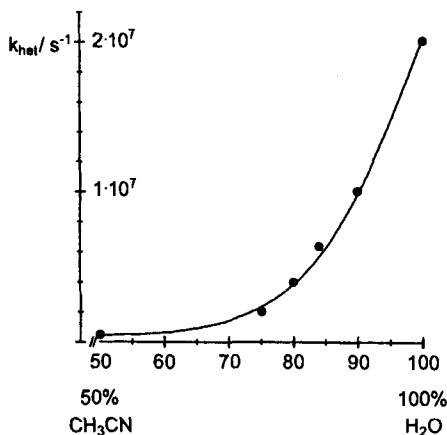
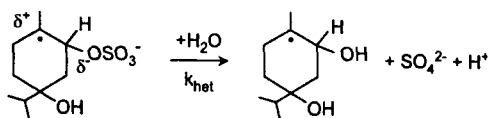


Figure 2. Effect of solvent ($\text{CH}_3\text{CN-H}_2\text{O}$) composition on the rate constant for heterolysis, k_{het} , of the α -methyl- β -sulfatocyclohexyl-type radical shown above.

dent on solvent), and this constitutes an inner-sphere ET mechanism. The solvent has an analogous effect: in(de)creasing the polarity of the solvent (dis)favors the 'electron transfer' path.

Concerning (semi)quantitative conclusions from the data in Table 1, the following statements can be made:

- 1) A methyl group at C_α increases k_{het} by ca 4000 (a consequence is that extrapolation to 1,2-dimethylcyclohexenes leads to the prediction that for these compounds $k_{\text{het}} \approx 2 \times 10^{11} \text{ s}^{-1}$) [52];
- 2) CH_2OH is more electron-donating than H;
- 3) OH (at C_γ or further removed from the reaction center ($\text{C}_\alpha/\text{C}_\beta$)) reduces k_{het} (−I effect); and
- 4) the cyclopentyl system is less 'electron rich' than the cyclohexyl.

X = Cl[•]

A further example of Eqs 6 and 7 has been studied using the time-resolved conductance technique [53]. It involves the addition to alkenes of Cl^\bullet , e.g. Scheme 1, in which the intermediate β -chloroalkyl radical undergoes C–Cl heterolysis with $k_{\text{het}} = 3.1\text{--}3.5 \times 10^4 \text{ s}^{-1}$ to give the short-lived ($\tau < 20 \text{ ns}$) alkene-type radical cation $>\text{C}^+-\text{C}^\bullet\text{H}_2$ which is trapped by the nucleophile water yielding $>\text{C}^\bullet-\text{CH}_2\text{OH}/\text{HO}-\text{C}-\text{CH}_2^\bullet$ and H^+ . It is noteworthy that in this system, Cl^- is a much better leaving group than SO_4^{2-} (see Table 1, entry 2), as reflected by the ratio of the two heterolysis rate constants, $k_{\text{het}}(\text{Cl}^-)/k_{\text{het}}(\text{SO}_4^{2-}) \geq 300$ [53]. Further examples of C–Cl heterolysis reactions will be presented in Section 9.2.2.

Table 1. The dependence of $k_{\text{het}}^{\text{a}}$ on alkene structure for the reaction depicted by Eq. 11.

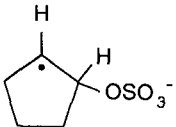
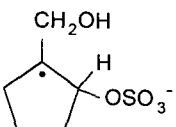
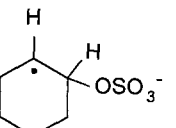
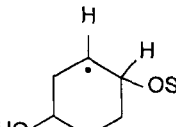
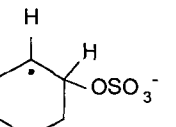
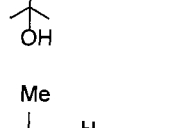
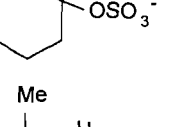
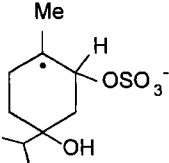
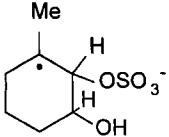
$>\text{C}^{\bullet}-\text{C}-\text{OSO}_3^-$	$k_{\text{het}} \text{ (s}^{-1}\text{) at } 20^\circ\text{C}$
$\text{HOCH}_2\text{C}^{\bullet}\text{HCH}_2\text{OSO}_3^-$	$<10^2$
$\text{Me}_2\text{C}^{\bullet}\text{CH}_2\text{OSO}_3^-$	$\leq 10^3$
$\text{Me}_2\text{C}^{\bullet}\text{CH}(\text{OSO}_3^-)\text{CH}_2\text{OH}$	4×10^4
	9.3×10^3
	2.9×10^5
	$3.0 \times 10^4^{\text{b}}$ $\Delta H^\ddagger = 17 \text{ kJ mol}^{-1\text{c}}$, $\Delta S^\ddagger = -103 \text{ J mol}^{-1} \text{ K}^{-1\text{c}}$
	1.4×10^3
	8.4×10^3
	$\geq 5 \times 10^7$
	4×10^7

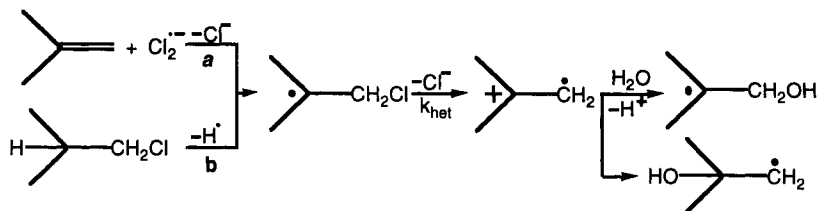
Table 1 (continued)

$>\text{C}^{\cdot}-\text{C}-\text{OSO}_3^-$	$k_{\text{het}} \text{ (s}^{-1}\text{) at } 20^\circ\text{C}$
	2×10^7
	8.4×10^4

^a Measured using the time-resolved AC or DC (time resolution ≤ 10 ns) conductance technique. In all cases the concentration of the alkene was varied to make sure that the *formation* of the $\text{SO}_4^{\cdot-}$ adduct was *not* rate-limiting.

^b The β -sulfatoalkyl radical was produced independently from the cyclohexylsulfate by abstraction of H by OH^{\cdot} (see Eq. 5).

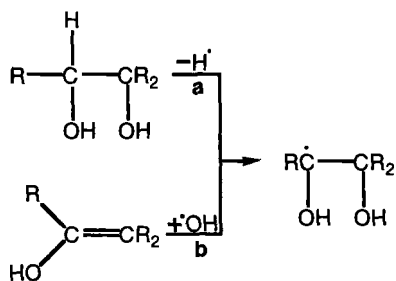
^c The activation parameters were determined by measuring the rate constants in the temperature range 5–50°C (in 5° steps). Good Arrhenius behavior was observed.



Scheme 1.

$\text{X} = \text{OH}^{\cdot}$

The hydroxyl radical reacts with alkenes predominantly [54] by addition to give β -hydroxyalkyl radicals. Because of the bad leaving-group properties of OH^- , these radicals do *not* usually undergo spontaneous β -elimination of OH^- . If, however, the leaving group OH is changed by protonation into the better leaving group H_2O , radical cations can be produced, indicating that electron transfer has proceeded. Examples of this type of reaction will be given in Section 9.2.2, because the β -hydroxyalkyl radicals involved are more readily accessible by H-abstraction reactions from aliphatic systems.



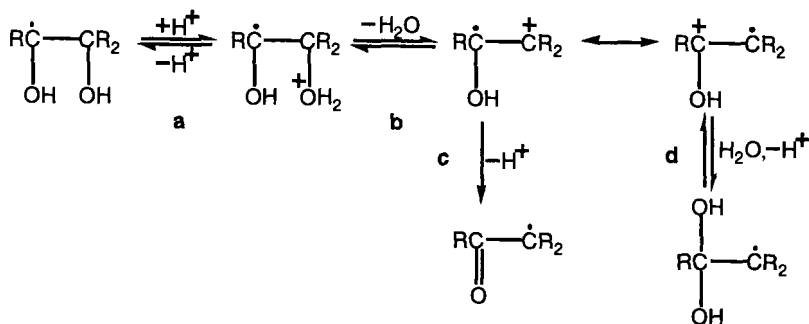
Scheme 2.

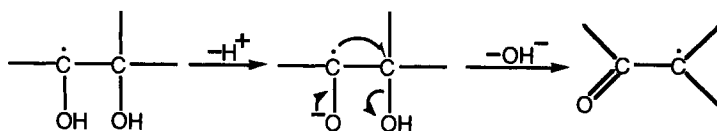
9.2.2 S = X- $\overset{|}{\underset{|}{\text{C}}}$ - $\overset{|}{\underset{|}{\text{C}}}$ -H (activation by H-abstraction)

X = OH

The reactions of polyhydric alcohols with the hydroxyl radical in aqueous solution have been extensively studied (e.g. in radiolytic and biomimetic systems), mainly because of their suitability as models for more complicated carbohydrate substrates [55] or enzymatic systems involving glycol-type radicals [56, 57]. Because there are no double bonds to which $\cdot\text{OH}$ could add, only H-abstraction reactions are possible. Because the C-H bond energy is significantly lower than the O-H bond energy, it is the carbons from which H are abstracted and not the alcohol function. In this type of reaction, α,β -dihydroxyalkyl radicals are formed. The same radicals could, in principle, be produced by *addition* of $\cdot\text{OH}$ to enols, see Scheme 2, lower part. This shows the complementarity of H-abstraction and OH-addition and thereby the relevance of the former to one-electron oxidation of olefinic bonds (Scheme 2).

A particularly important finding, first revealed by ESR studies on ethane-1,2-diol (R = H) at low pH [58, 59], and confirmed by product analysis [55, 60] and pulse-radiolysis studies [61], is that the initial α,β -dihydroxyalkyl radical from this substrate undergoes an acid-catalyzed dehydration reaction to give the carbonyl-conjugated radical $\cdot\text{CH}_2\text{CHO}$. It has been suggested [61, 62] on the basis of a wide range of experiments that this process occurs via a radical-cation (Scheme 3).

Scheme 3. H⁺-catalyzed dehydration.



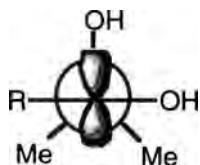
Scheme 4. OH^- -catalyzed dehydration.

A related base-catalyzed reaction has been shown to give the same carbonyl-conjugated radical, via a radical–anion intermediate [61, 63] (Scheme 4), and rate constants for the loss of OH^- (Scheme 4) have been determined [63].

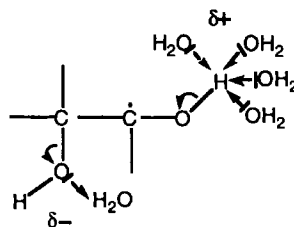
The presence of alkyl substituents can markedly increase the rate of the acid-catalyzed reaction [64] (cf. second-order rate constants for dehydration of the radicals from ethane-1,2-diol [61] and butane-2,3-diol [65] of 9×10^6 and $1.3 \times 10^8 \text{ M}^{-1} \text{ s}^{-1}$, respectively). Alkyl substituents also increase the rate of loss of OH^- in their ionized counterparts (Scheme 4) [63].

To rationalize the effect of structure and substituents on the acid- or base-catalyzed loss of water from α,β -dihydroxy-substituted radicals, the complementary techniques of pulse-radiolysis and ESR spectroscopy have been employed in a kinetic study of the dehydration of a variety of α,β -dihydroxyalkyl radicals [$\cdot\text{CR}^1(\text{OH})\text{CR}^2\text{R}^3\text{OH}$] into the corresponding carbonyl-conjugated radicals [$\cdot\text{CR}^2\text{R}^3\text{C}(\text{O})\text{R}^1$]. The overall rates of proton-catalyzed dehydration, as revealed by steady-state (ESR) and time-resolved (pulse-radiolysis) experiments, indicate the importance of the electronic effects of substituents (contrast values of 1.2×10^9 and $9.8 \times 10^8 \text{ M}^{-1} \text{ s}^{-1}$ for the radicals from cyclohexane-1,2-diol and butane-2,3-diol, respectively, with that for the radicals from erythritol of $4.2 \times 10^6 \text{ M}^{-1} \text{ s}^{-1}$). Time-resolved experiments enable information to be obtained about the generation of the protonated species [$\cdot\text{CR}^1(\text{OH})\text{CR}^2\text{R}^3\text{OH}_2^+$] and the loss of water from this intermediate.

For $\cdot\text{CR}(\text{OH})\text{CMe}_2\text{OH}$ ($\text{R} = \text{H}$ and Me) a rapid *uncatalyzed* dehydration reaction occurs, ($k = 1\text{--}2 \times 10^4 \text{ s}^{-1}$), which is believed to be assisted by the steric effect of the *gem*-dimethyl group and the polarity of the solvent. For the latter substrate, the reaction is characterized by a strongly negative activation entropy ($-93 \text{ J mol}^{-1} \text{ K}^{-1}$). These results have been interpreted in terms of Schemes 5 and 6 [66], the latter providing an explanation of the negative activation entropy of the spontaneous dehydration in terms of ‘freezing’ of water molecules in the transition state, because of solvation of the (incipient) H^+ and OH^- ions:



Scheme 5.



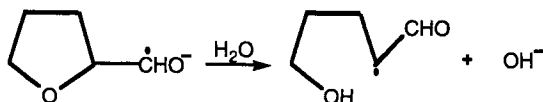
Scheme 6.

Mechanistically, the acid-catalyzed dehydration, Scheme 3, involves conversion of a *bad* nucleofugal leaving group, i.e. OH[−], into the much better one, H₂O. This difference is (quantitatively) reflected in the corresponding p*K*_a values, i.e. p*K*_a(H₃O⁺) = −1.7 compared with p*K*_a(H₂O) = 15.7. Qualitatively, protonation of the β-OH group increases the *pull* on the C_β–O bond, such that the H₂O molecule is ‘pulled out’. The opposite of this happens when the α-OH group is *deprotonated* by a Brønsted base such as OH[−], as in the *base*-catalyzed dehydration [63], Scheme 4. Here, the increased electron density at C_α caused by deprotonation at C_α–OH finally ends up *pushing* the OH group out from C_β. The rate constants for elimination of OH[−] from the ionized 1,2-dihydroxyalkyl radicals R₁C[•](O[−])CH(OH)R₂ are between 3 × 10⁶ s^{−1} (for R₁ = R₂ = H and R₁, R₂ = H or hydroxyalkyl) and ≥ 8 × 10⁶ s^{−1} (for R₁ = R₂ = Me). Clearly, the *spontaneous* dehydration, Scheme 6, should contain elements of both push and pull.

It may not be surprising that α,β-dihydroxyalkyl radicals are able to achieve one-electron reduction of oxidants such as benzoquinone or methyl viologen, with the rate constants strongly dependent on the nature of the substituents, whereby reducing power of the radical and its rate of dehydration are correlated with each other [66]. This indicates that the push-component might be more important than the pull-component.

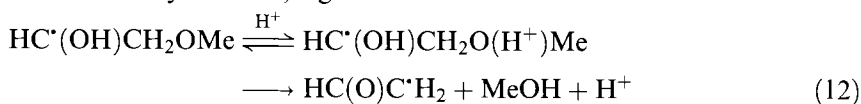
X = Oalk

A β-elimination reaction also occurs with linear and cyclic glycol mono-alkyl *ether* radicals. In this case the nucleofugal leaving group is the alkoxy function, RO, as shown in Scheme 7 for base catalysis and a cyclic system in which alkoxide elimination leads to ring-opening [63]:



Scheme 7.

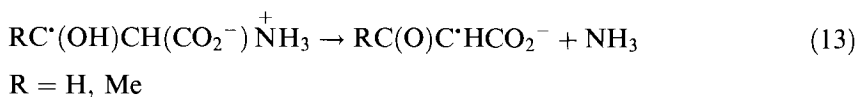
The reciprocal [67] mechanism for ring-opening is H⁺-catalysis, in which the oxygen at C_β is protonated, resulting in enhancement in the nucleofugal leaving-group properties of the alkoxy function, e.g.



As the leaving group properties of X are enhanced (equivalent to reducing the p*K*_a values of the conjugate acids H–X) compared with X = OH or OR (Schemes 1–7), the rates of β-elimination increase considerably such that support of heterolysis by deprotonation of C_α–OH or by protonation of X to achieve complete reaction tends to become unnecessary (see later).

X = NH₃

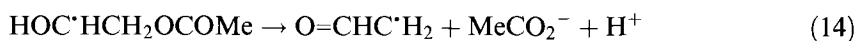
Examples with NH₃ as the leaving group are α-hydroxyalkyl-type radicals from β-amino alcohols [68] or from serine (R = H) or threonine (R = Me):



When $\text{R} = \text{Me}$ (threonine), the breakage of the C–N bond proceeds from the *neutral* α -hydroxyalkyl, as in Eq. 13; however, with the less electron-rich serine radical ($\text{R} = \text{H}$), elimination of NH_3 requires prior deprotonation from OH, i.e., the ketyl radical, $>\text{C}^*-\text{O}^-$, is needed to *push* the NH_3 group out [69].

X = OAc

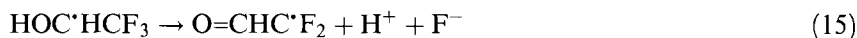
An example of further increase in the acidity of H–X are β -acetato radicals [70]:



where the rate of C–O heterolysis in aqueous solution at room temperature has been determined as $5.5 \times 10^5 \text{ s}^{-1}$ [71–74].

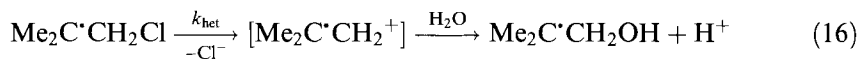
X = Hal

An acid of roughly similar strength as acetic acid is HF. In fact, elimination of F^- from α -hydroxy- β -fluoroalkyl radicals has been observed [69], e.g.:



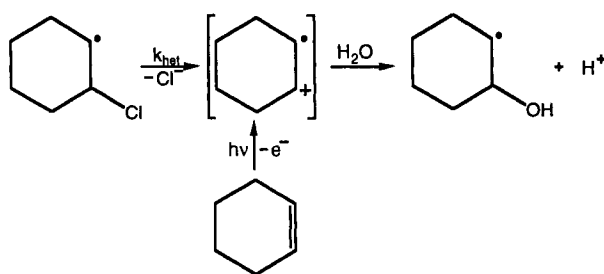
Moving from fluorine to chlorine, the acidity of H–X is drastically increased ($\text{p}K_{\text{a}}(\text{HF}) = 3.16$, $\text{p}K_{\text{a}}(\text{HCl}) = -7$). As a reflection of this, the rate constant for C_{β} –Cl bond heterolysis in $\text{HOC}^*\text{HCH}_2\text{Cl}$ in aqueous solution is very fast, $k_{\text{het}} \geq 10^6 \text{ s}^{-1}$ [71].

As a matter of fact, Cl^- is such an excellent nucleofugal leaving group (from C_{β}) that activation at the adjacent carbon (i.e., at C_{α}) by an electron-donating substituent (such as OH) is not necessary for the reaction to occur rapidly and efficiently. For instance, the β -chloroalkyl radical formed by H-abstraction from 1-chloro-2-methylpropane, $\text{Me}_2\text{C}^*\text{CH}_2\text{Cl}$ (this is the same radical as that formed in Scheme 1, Section 9.2.1), undergoes C–Cl heterolysis in aqueous solution with $k_{\text{het}} = 3.4 \times 10^4 \text{ s}^{-1}$ [75].



This rate is ca 5×10^6 times larger [75] than that for the C–Cl heterolysis from the analogous ('classical') *non*-radical system, i.e. Me_3CCl , the cornerstone of $\text{S}_{\text{N}}1$ mechanistic chemistry. This demonstrates the dramatic acceleration of heterolysis as a result of radical formation at the site adjacent to the leaving group [76]. With this species, as with *t*-BuCl, the 'hydrolysis' is of the $\text{S}_{\text{N}}1$ -type which means that the reaction proceeds via a cationic intermediate, a *radical* cation, which, however, was not *directly* seen, because its lifetime is too short.

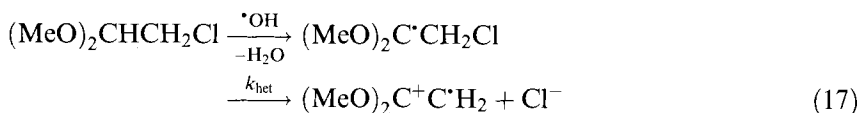
Of the many interesting examples of these heterolysis reactions [75], that involving a *cyclic* system should be specifically mentioned, with $k_{\text{het}} \geq 10^6 \text{ s}^{-1}$, as derived



Scheme 8.

from time-resolved conductance measurements [77]. This is an example of the relevance of the olefin-type radical cation intermediate in one-electron oxidation of alkenes (Scheme 8).

It should be possible to make visible the radical cation-type intermediate postulated as in Eq. 16 by stabilizing the positive charge on the carbon skeleton. This was successfully done [78, 79] by introducing *two* alkoxy substituents at that position, e.g.:



with $k_{\text{het}} \geq 5 \times 10^7 \text{ s}^{-1}$ [80].

The ESR spectrum of a cyclic and methylated derivative of the enol ether-type radical cation formed in Eq. 17 is shown in Figure 3.

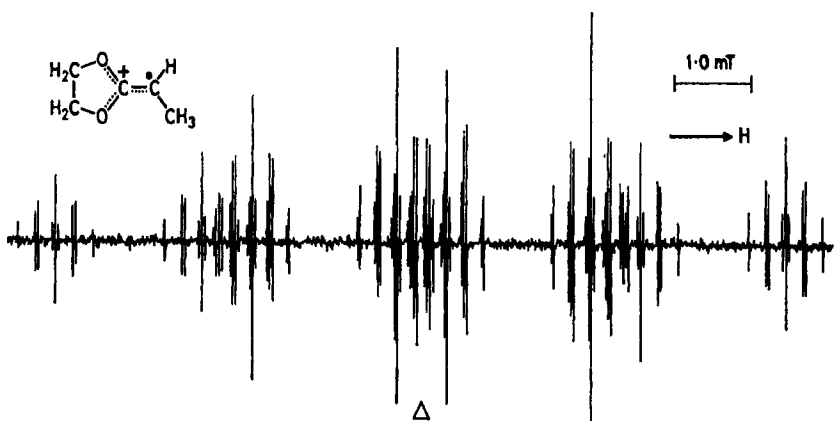
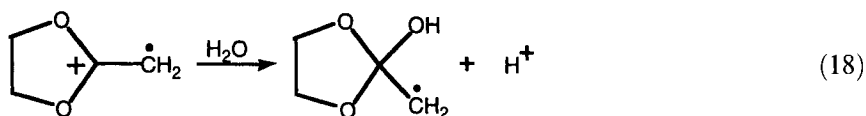


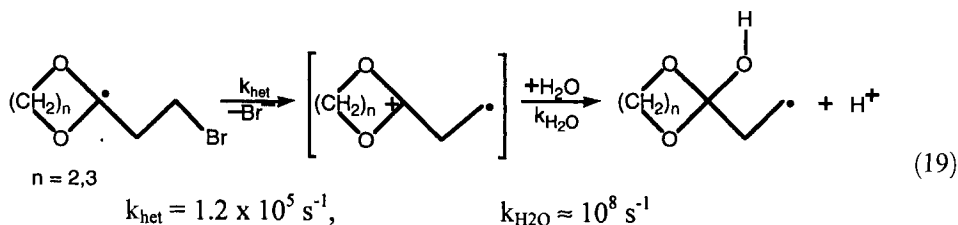
Figure 3. ESR spectrum of the 2-ethylidene-1,3-dioxolan radical cation; center indicated by a triangle. The radical cation has large CH_3 splittings; note, e.g., the well resolved second-order components. The size of the CH_3 coupling, 2.511 mT, indicates that the unpaired spin resides mainly on the carbon atom next to the CH_3 group. Experimental conditions: photolytic flow system, aqueous solutions of pH 5 at 3 °C containing 0.3 M acetone, 0.02 M $\text{K}_2\text{S}_2\text{O}_8$, and 0.03 M 2-(1-bromoethyl)-1,3-dioxolan. From Ref. [79].

Many of the radical cations studied [79] are very long-lived (ms range), because they decay only bimolecularly (by disproportionation or dimerization). Occasionally, however, a first-order reaction with water was observed, with k between 10^2 and 10^4 s^{-1} [79]; this involves (nucleophilic) *addition* of water to the radical cation, e.g.:



Nucleophiles stronger than water, e.g., OH^- or HPO_4^{2-} , react with the radical cations, with $k = 0.2\text{--}6 \times 10^9$ or 2×10^6 to $3 \times 10^8 \text{ M}^{-1} \text{ s}^{-1}$, producing alkoxy-carbonylalkyl radicals or $(\text{RO})_2\text{P}(\text{O})\text{OC}-\text{C}^\bullet\text{H}_2$ -type radicals, respectively [81, 82]. These radical cations seem to be exceptional in so far as they show a relatively high reactivity with O_2 ($k > 10^8 \text{ M}^{-1} \text{ s}^{-1}$) [79].

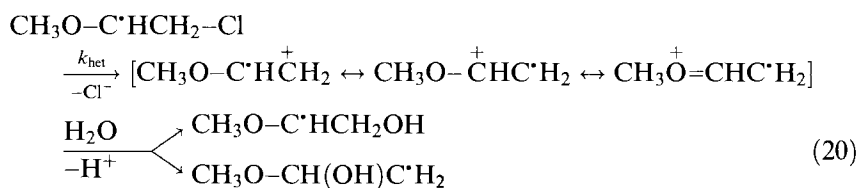
Heterolytic β -fragmentation reactions of the type in Eq. 17 have also been observed for the leaving groups F^- and Br^- [82]. For the latter, elimination is fast even when there is a methylene group in-between the radical site ($\equiv\text{C}_\alpha$) and the leaving group, i.e., if the reaction is a γ -elimination, e.g.:



which gives rise to a *distonic* radical cation with a characteristically *short* lifetime compared with the *delocalized* type radical cation produced in, e.g., Eq. 17.

α -Monoalkoxy- β -chloroalkyl radicals

The reactions of these radicals in aqueous solution are particularly interesting, because of their model character with respect to deoxyribose-derived radicals in DNA [83], which lead to strand breaks of this macromolecule. These model reactions have been studied in detail [84], by use of a large number of substrates, with the help of in-situ photolysis ESR, time-resolved conductance, and product-analysis techniques. From the results it is evident that the primarily formed α -alkoxy- β -chloroalkyl radicals in aqueous solution undergo heterolysis of the β -C-Cl bond with rates $k_{\text{het}} > 10^8 \text{ s}^{-1}$ to give rise, finally, to the β -OH-substituted analogs which were identified by ESR.



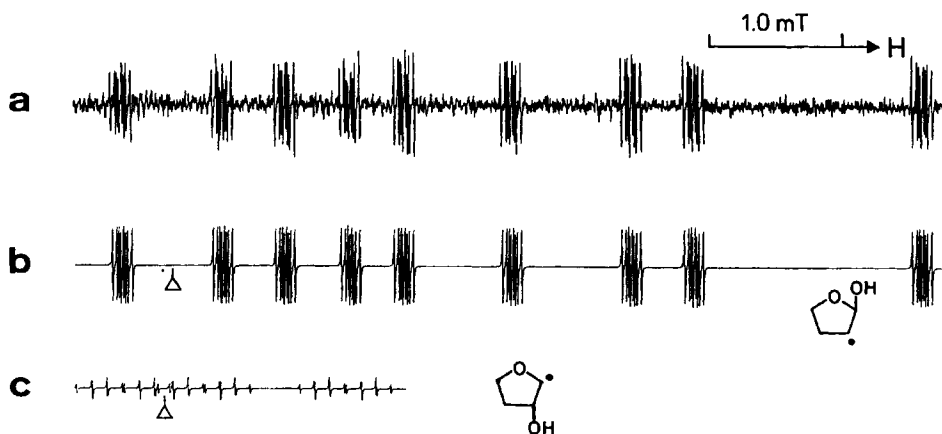


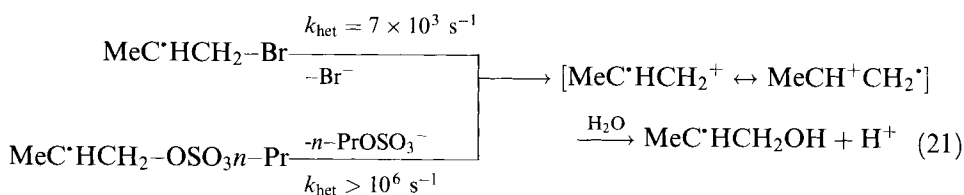
Figure 4. (a) High-field part of an ESR spectrum obtained after H-abstraction from 3-chlorotetrahydrofuran, 0.1 M, in aqueous solution, at pH 4, upon UV irradiation in a flow system at 276 K, 3 mM K₂S₂O₈, and 0.3 M acetone as sensitizer; (b) and (c) are simulated spectra calculated with a line width of 0.005 mT, centers marked by triangles [84].

Analogous results are shown in Figure 4 for the 2-yl radical derived from 3-chlorotetrahydrofuran.

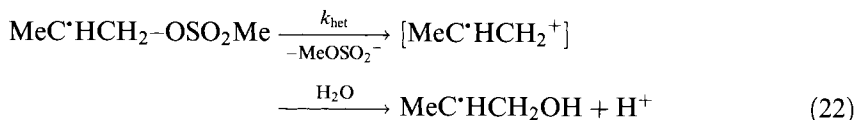
From substituent and solvent effects on reactions such as Eq. 20 it was concluded [84] that these reactions are of the S_N1 type, i.e. that alkoxyalkene (enol ether) type *radical cations* are intermediates. The lifetimes of these radical cations were estimated [84] to be of the order of nanoseconds, *much* shorter than those [78, 79, 81] of the corresponding 1,1-*di*-alkoxyalkene radical cations. This shows the importance of the additional (second) alkoxy group in stabilizing the positive charge on the carbon skeleton. On the basis of these mechanistic model studies, very detailed suggestions could be made [84] regarding the deoxyribose-derived radical reactions that lead to chain breaks in DNA (see below).

X = OSO_n[−] (n = 2, 3)

The results described in this chapter are complementary to those given above. On the basis of the acidity of sulfuric acid, the sulfonate group ROSO₃[−] is a leaving group at least as efficient as Cl[−] or Br[−]. This is reflected in the rate constants for C_β-OSO₃R heterolysis of alkyl radicals [75], e.g.:

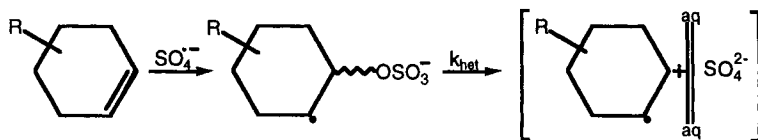


On the basis of 193 nm photoionization experiments [45], the lifetime of the propene radical cation formed in the heterolysis step is <20 ns. As expected on the basis of the lower acidity of sulfonic acid compared with sulfuric, sulfonates are weaker leaving groups than sulfates, e.g.:



$k_{\text{het}} = 2 \times 10^5 \text{ s}^{-1}$ [75], compared with $k_{\text{het}} > 10^6 \text{ s}^{-1}$ for the reaction depicted by Eq. 21.

The one-electron oxidation of cyclohexenes by $\text{SO}_4^{\cdot-}$ in aqueous solution has been studied from kinetic and stereochemical standpoints [49]. It was found that the alkene oxidation proceeds by an addition–elimination mechanism with $\text{SO}_4^{\cdot-}$ adding to the C=C double bond in the first step followed by $\text{C}_\beta\text{-OSO}_3^-$ heterolysis to give a solvent-separated alkene radical cation–sulfate ion pair ($\text{S}_{\text{N}}1$ mechanism) (Scheme 9).



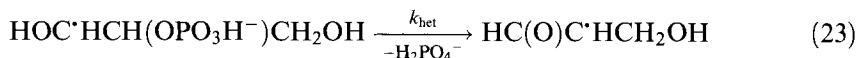
Scheme 9.

Attack of water on the radical cation occurs before the sulfate group has completely departed, the sulfate group hindering the approach of water from one side of the cyclohexene skeleton. The lifetime of the solvent-separated radical cation was estimated to be in the 10–100 ps range [49].

The rate constant for heterolysis of the ‘ SO_4^- adduct’ depends on the nature of R (Scheme 9) and it increases with additional alkyl (methyl) groups on the double bond from $k_{\text{het}} = 3 \times 10^4 \text{ s}^{-1}$ for $\text{R} = \text{H}$ and *no* methyl groups to $>5 \times 10^6 \text{ s}^{-1}$ for $\text{R} = \text{Me}_2\text{COH}$ and 1 or 2 methyl groups, in agreement with the $\text{S}_{\text{N}}1$ -character of the reaction.

X = OP(O)(OR)₂ (phosphate as leaving group) [85]

The reactions of alkyl radicals carrying phosphate as substituent in the β -position are particularly interesting because they are close models for those deoxyribose radicals that cause strand breaks in DNA [83, 86]. Historically speaking, the compounds studied first were β -phosphato *alcohols*, where H-abstraction (by $\cdot\text{OH}$) from C atoms leads to α -hydroxy- β -phosphatoalkyl radicals, e.g. for glycerol-2-phosphate, to $\text{HOC}^*\text{HCH}(\text{OPO}_3\text{H}^-)\text{CH}_2\text{OH}$ which was found to undergo a rapid elimination of (inorganic) phosphate ($k_{\text{het}} > 10^6 \text{ s}^{-1}$) to yield a β -oxoalkyl radical, Eq. 23 [87, 88]:



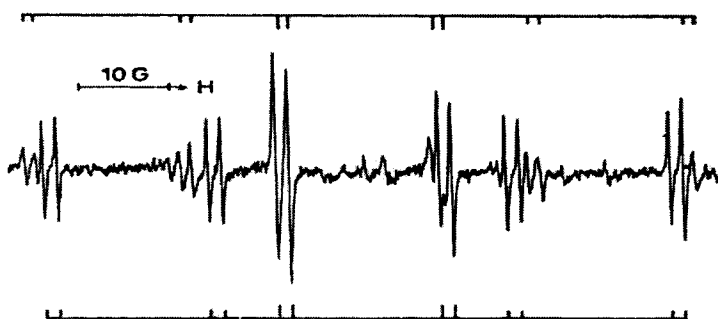
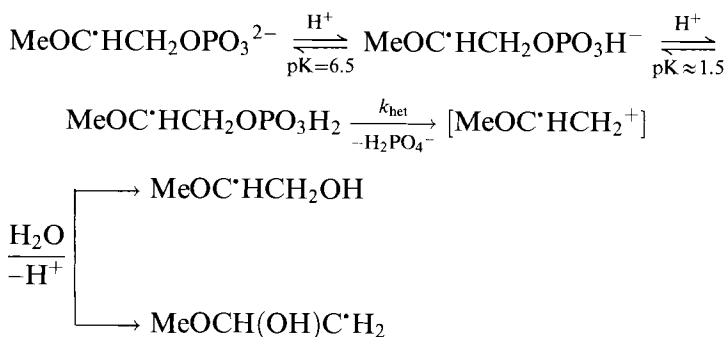


Figure 5. Spectra obtained on UV irradiation (at 2°C) of an aqueous solution of H₂O₂ (3 %) in the presence of 0.04 M glycerol-2-phosphate, pH 1.6. Lines not assigned by the stick spectra are from impurity radicals. The spectrum assigned by the upper lines is from the *cis* form of HOCH₂C[•]HCHO; that assigned by the lower lines is from the *trans* form [88].

which exists as *cis* and *trans* forms, owing to partial double bond character around the C_α–C_β bond, as shown in Figure 5. It is likely that in this fragmentation reaction a radical cation is formed which should, however, be extremely short-lived because of very rapid deprotonation from the α-OH group.

To obtain an even better model compound for the corresponding deoxyribose-centered radical in DNA, *ether* phosphates were used instead of the *alcohol* phosphates described in reaction 23. For example, on reaction of [•]OH with 2-methoxyethylphosphate at pH 4.5 the 2-yl radical is the most prominent species (see Scheme 10), as observed by ESR [89]. By measuring the coupling constants as a function of pH, the pK_a of the radical was determined to be 6.5. On reducing the pH, the 2-yl radical disappeared giving rise to two product radicals, as shown below (Scheme 10).

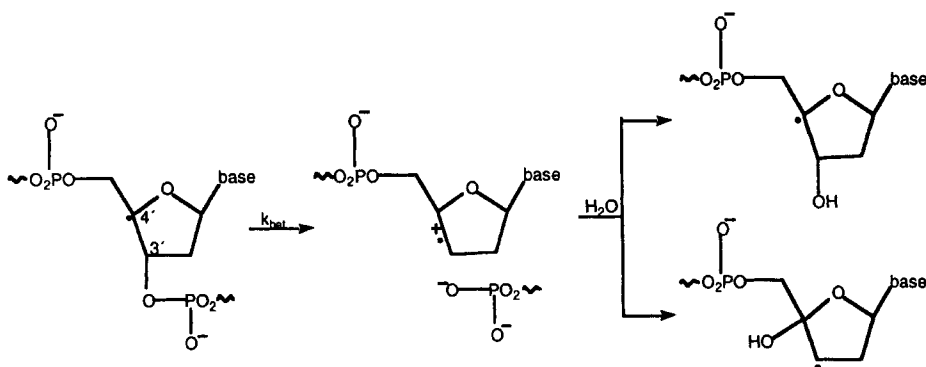
This mechanism is analogous with that described for the 2-methoxyethyl chloride 2-yl radical (Eq. 20). By performing product-analysis studies under conditions of radical scavenging with O₂ it was possible to arrive at the rate constants for heterolysis of the C–OPO₃ bond as a function of the protonation state of the phosphate leaving group, from –OPO₃H₂ to –OPO₃H[–] to –OPO₃^{2–}. The rate constants



Scheme 10.

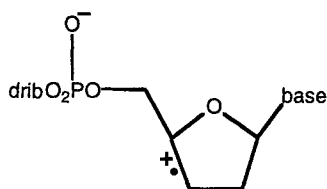
obtained (at 0 °C) are 3×10^6 , 10^3 , and $0.1\text{--}1\text{ s}^{-1}$, respectively [89]. H_2PO_4^- is thus seen to be a *much* better (by a factor of ca 10^7) leaving group than PO_4^{3-} , which reflects the difference between the $\text{p}K_{\text{a}}$ values of the conjugate acids, i.e., $\text{p}K_{\text{a}}(\text{H}_3\text{PO}_4) = 2.1$, $\text{p}K_{\text{a}}(\text{HPO}_4^{2-}) = 12.7$. The effect of alkylation of the phosphate group is similar to that of protonation, thus, for the relevant *model* reaction (that mimicking the C4' radical of DNA (Scheme 11)) [83], i.e., the reaction which constitutes the breakage of the DNA chain, the rate k_{het} is $10^3\text{--}10^4\text{ s}^{-1}$ [90]. Of course, it would be interesting to know the *rate* of this type of reaction *in DNA*. In this polymer, the deoxyribose and the phosphate groups protrude into the aqueous phase and, correspondingly, they are strongly hydrogen-bonded to the adjacent water molecules, but they are *not immersed* in the aqueous phase. Thus, their environment is not identical with that of bulk water. The expected effect (by analogy with the α -methoxy- β -chloroalkyl radicals such as in Eq. 20, see also Ref. [73]) of a decrease of polarity of the environment is a *decrease* of the rate constant of heterolysis. This is, however, probably compensated by the effect of *alkylation* on C_{α} and C_{β} : Alkylation leads to a drastic (≥ 2 orders of magnitude) *increase* of the heterolysis rate [89]. On the basis of the experiments of Giese et al [91], this type of reaction also occurs from the C4' radical of a nucleotide containing the thymine moiety dissolved in acetonitrile, in which the rate constant k_{het} can be estimated to be ca $1.8 \times 10^6\text{ s}^{-1}$ [92].

Going one step further in the direction of DNA one arrives at *oligonucleotides* [86, 93] where, again, the C4'-type radical is found to undergo rapid $\text{C}_{\beta}\text{--OPO}_3^-\text{R}$ heterolysis ($k_{\text{het}} \geq 10^2\text{--}10^3\text{ s}^{-1}$) [93] to yield the enol ether-type (deoxy)ribose-derived radical cation already suggested [83, 94] for the DNA *polymer*. Concerning the further fate of this radical cation, two major reaction channels have been suggested: (i) reaction as an *electrophile*, whereby the solvent water acts as the nucleophile, which attacks at either position of the 'olefinic' bond, see Scheme 11, and (ii) electron transfer from an 'adjacent' [95] guanine moiety in the DNA chain.

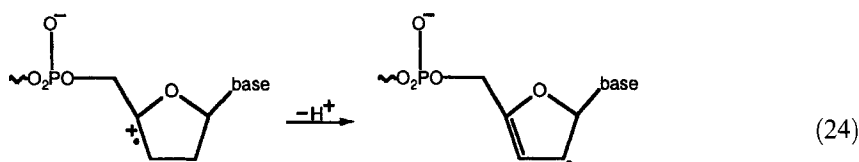


Scheme 11.

From scavenging experiments, the *rate* of electron transfer from a guanine moiety (G) in oligonucleotides to the enol ether-type radical cation (see below) can be estimated to be $\geq 10^6\text{ s}^{-1}$ [96]. This is apparently fast enough to compete with the



electrophilic reaction of the radical cation with water. It is interesting that a *third* characteristic [62] reaction of enol ether-type radical cations, i.e. deprotonation to yield an allyl-type radical, Eq. 24, has (so far) *not* been observed [86, 94].



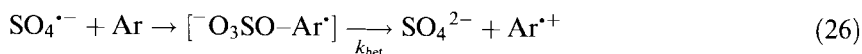
9.2.3 S = Aromatic (Ar)

X = OSO₃⁻

The strongly oxidizing radical SO₄^{•-} is often considered to be a ‘natural’ one-electron (outer-sphere) oxidant, Eq. 25:



mainly, because the final (non-radical) products of its reaction with aromatics are derived from the *radical cations* of the aromatics [97–99]. This mechanistic assumption is in fact supported by time-resolved studies in which the expected radical cations (or their characteristic neutral (radical-type) reaction products) could be identified [46, 100–102]. In principle, however, and by analogy to the olefinic systems discussed above (Section 9.2.1), there is the possibility that the reaction proceeds by an *inner-sphere* path, i.e.:



If this is the mechanism, to explain the results presently available [46, 100, 101] it is necessary to assume that k_{het} (Eq. 26) $\geq 10^7 \text{ s}^{-1}$. Rates of this order of magnitude are difficult to measure (under conditions of bimolecular formation of the hypothetical adduct $[\text{O}_3\text{SO-Ar}^{\bullet}]$), and it would therefore be desirable to *reduce* k_{het} , e.g. by decreasing the electron density of Ar. As long as experiments of this type have not been reported the question of the outer- or inner-sphere nature of oxidation of Ar by SO₄^{•-} remains unanswered.

In addition to reactions of $\text{SO}_4^{\bullet-}$ with *homocyclic* Ar, those with *heterocyclic* systems have also been studied [103–105]. For these systems also, however, solid evidence for adduct formation has *not* been obtained [106]. In sharp contrast to this are the results with the strong oxidant $\cdot\text{OH}$ (below).

X = OH

The OH radical is (one of) the most reactive species around. The reaction of $\cdot\text{OH}$ usually leads to the one-electron *oxidation* of the substrate, so a common impression is that $\cdot\text{OH}$ reacts by electron transfer. This is understandable because thermodynamically the OH radical is a very powerful one-electron oxidant. Its reduction potential at pH 0 is 2.7 V relative to the NHE [107, 108], and at pH 7 it is still 2.3 V. That this number indicates strong oxidizing power is evident on comparing it with those of some well known oxidants such as IrCl_6^{2-} (0.87 V) or Ti^{2+} (2.2 V). Despite this, $\cdot\text{OH}$ does usually *not* react by electron transfer but by addition, not only with organic substrates (containing double bonds) [109], but also with anions [110] and even metal ions [111].

This tendency to add rather than to oxidize is probably a result of stabilization of the transition state for addition by contributions from bond *making*, whereas electron transfer requires pronounced bond and solvent reorganization with a correspondingly large free energy change to reach the transition state.

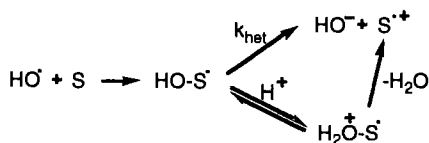
Addition of $\cdot\text{OH}$ to a substrate S leads to the ‘OH-adduct’ $\text{HO-S}\cdot$ (Scheme 12).

For $\text{HO-S}\cdot$ to yield electron transfer products, heterolysis of the bond joining HO and Y must occur. Because OH^- is a very bad leaving group (as evidenced by the high $\text{p}K_a$ (15.7) of its conjugate acid, H_2O), however, the rate of the spontaneous heterolysis, k_{het} (Scheme 12, upper part), is very low (very often $\ll 10^2 \text{ s}^{-1}$). As a consequence, the final (non-radical) products from $\cdot\text{OH}$ reactions with S are typically derived from dimerization or disproportionation of $\text{HOS}\cdot$.

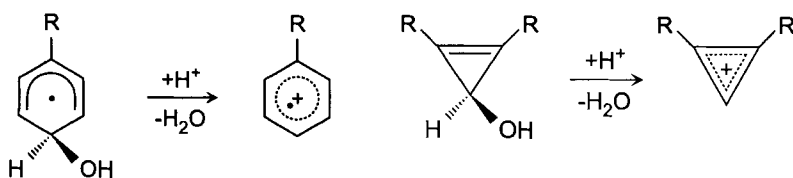
One-electron oxidation of S by $\cdot\text{OH}$ is, however, possible if the leaving group capacities of the adduct components, HO– and $\text{S}\cdot$ are changed. As for aliphatic systems (Scheme 3), protonation of HO– to give H_2O^+ – converts the bad leaving group OH^- into the excellent H_2O ($\text{p}K_a(\text{H}_3\text{O}^+) = -1.7$). If it is assumed that the Brønsted catalysis law is applicable and that the Brønsted coefficient, α , is equal to 0.5, a rate enhancement of $10^{8.7}$ induced by protonation of the leaving group –OH is calculated from the difference in the $\text{p}K_a$ values of H_2O and H_3O^+ . A somewhat similar number (10^7) is obtained by considering the difference in the reduction potentials of $\cdot\text{OH}$ at pH 7 and at pH 0 [4].

Protonation is a very effective means of improving the *nucleofugacity* of the leaving group OH. It is not restricted to *radical* systems, as shown below (Scheme 13).

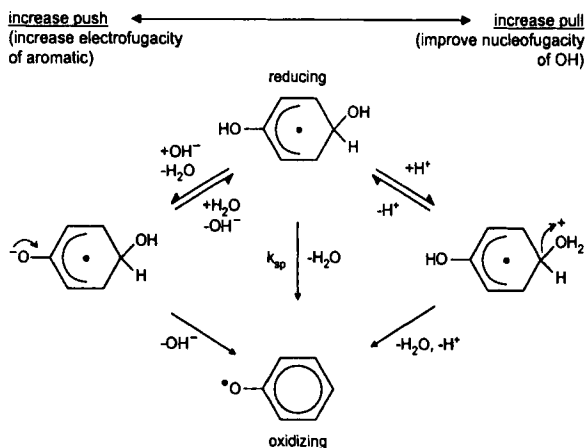
The alternative method, which can be even more efficient, is to improve the *electrofugacity* of $\text{S}\cdot$. A means of achieving this is to put electron-donating sub-



Scheme 12.



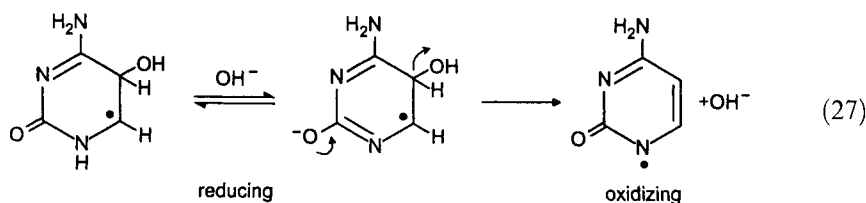
Scheme 13.



Scheme 14.

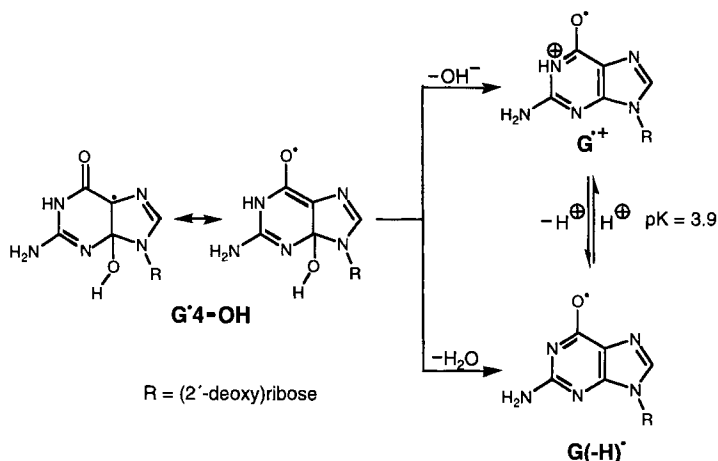
stituents into *S*[•]. An elegant method (of practical importance) is to increase the electron density on *S*[•] by ionization of a substituent which is a Brønsted acid. An example of this, which serves also to summarize the mechanisms of H^+ - and OH^- -supported dehydration, is shown in Scheme 14. This scheme is analogous to Schemes 3 and 4 which represent the situation in the ‘aliphatic–olefinic world’ [112].

Another example relates to OH^- -aided one-electron oxidation of cytosine. With cytosine, the OH reaction proceeds by addition to C5, a process that has a selectivity of 90 % [113]. The 5-hydroxy-6-yl radical is an excellent *reductant*, and the same is true for the ionized 6-yl radical formed by deprotonation from N1. This radical anion now contains sufficient electron density to eliminate the OH group at C5 as OH^- . (This is analogous to Scheme 4, as an example from the aliphatic world). The result is the cytosine-1-yl radical which is *oxidizing*, probably because of appreciable spin density on the hetero atoms N1 and O2 [113].



Schemes 14 and 15 and Eq. (27) are examples for the general phenomenon of 'redox-inversion' [4] by dehydration of OH adducts.

Another example from heterocyclic chemistry is the one-electron oxidation of guanine-derivatives by the OH-radical.

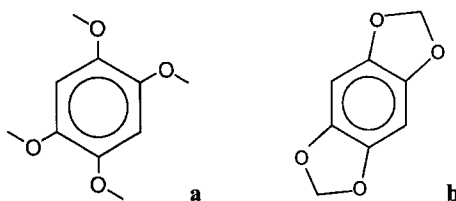


Scheme 15.

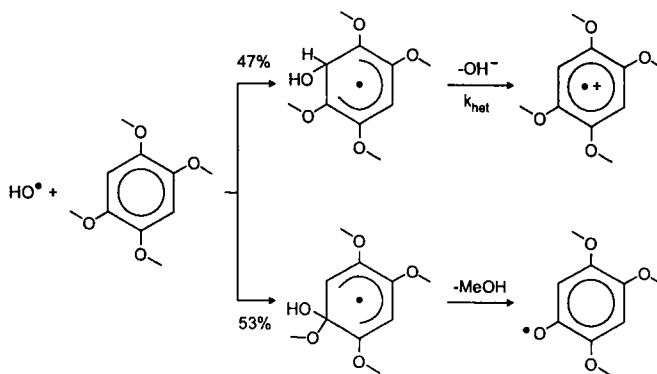
The reaction between $\cdot\text{OH}$ and phenol (see Scheme 14) can be analyzed in terms of its thermochemistry. On the basis of the potential at pH 7, $E_7(\cdot\text{OH}) = 2.3$ V relative to the NHE and $E_7(\text{PhO}\cdot) = 0.97$ V [114], the formation of $\text{PhO}\cdot$ and H_2O via an electron-transfer mechanism is exothermic by 1.33 V = 31 kcal mol $^{-1}$. Despite this, the reaction proceeds by addition, as outlined in Scheme 14. Thus, again, the propensity of $\cdot\text{OH}$ to add rather than to oxidize can be understood in terms of the transition state for addition being stabilized by contributions from bond *making*, in contrast to electron transfer which requires pronounced bond and solvent reorganization which results in a large (entropy-caused) free energy change.

It might be expected that not only the rate of addition of $\cdot\text{OH}$ [115] to the substrate S but also, particularly, the rate of heterolysis of $\text{HO-S}\cdot$ will increase with increasing electron density of S. So, as one goes to the extreme of *very electron-rich* aromatics, the ad-el mechanism might become indistinguishable from an outer-sphere ET mechanism. Examples where one is close to this situation are the *tetra-alkoxybenzenes* **a** and **b** (Scheme 16).

On the basis of pulse radiolysis experiments in aqueous solution [45], the rate constant for reaction of $\cdot\text{OH}$ with **a** has the very high value 1.5×10^{10} M $^{-1}$ s $^{-1}$. If performed in *basic* solution (pH ≈ 10), an *increase* of conductance is observed which results from the formation of OH^- (this ion is neutralized in *acidic* solution by H^+ which leads to a *decrease* of the conductance). From the *rate* of conductance increase it is evident that if an OH adduct is formed in the reaction, it eliminates OH^- with $k_{\text{het}} > 1.5 \times 10^6$ s $^{-1}$ (to give rise to the radical cation, as seen by optical detection), the yield being 47 %. The results are explained in terms of Scheme 17 which contains also the *ipso*-addition [116] at the methoxylated positions.



Scheme 16.



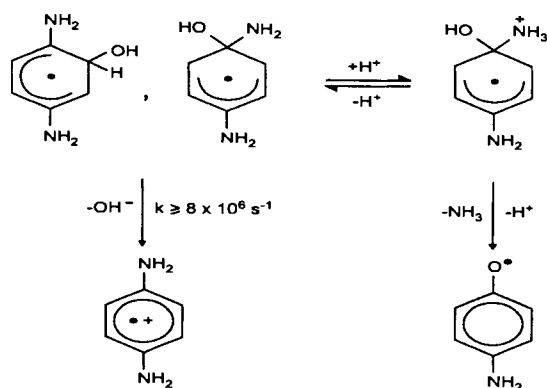
Scheme 17.

The ESR spectrum of the radical cation of the tetraalkoxy-type benzene **b**, as produced by reaction with $\cdot\text{OH}$ at pH 2, is shown in Figure 6.

An analogous, possibly even more extreme example has recently been studied by time-resolved Raman spectroscopy [117]; it was concluded that addition of $\cdot\text{OH}$ [118] and elimination of OH^- from all the ring positions are equally fast. This in effect means that the reaction is indistinguishable from an outer-sphere ET (Scheme 18) [119].



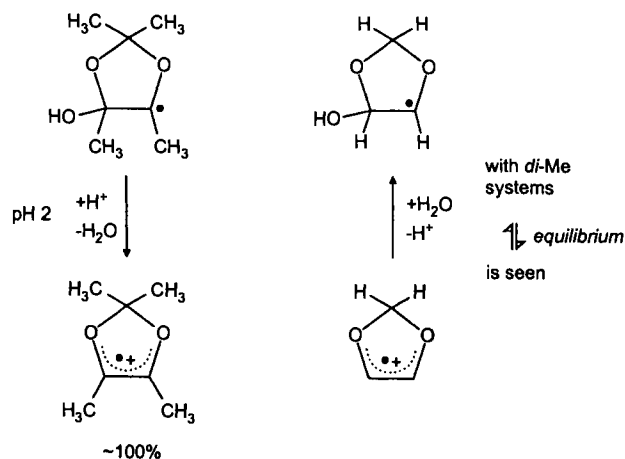
Figure 6. ESR spectrum recorded on reaction of $\cdot\text{OH}$ with 0.2 mM compound **b** in an N_2O -saturated aqueous solution at pH 2 and ca 5°C . The experimental spectrum from the four equivalent methylene hydrogens and the two equivalent aromatic hydrogens is shown in the lower part; the upper part contains the lines from ^{13}C in natural abundance. S. Steenken, unpublished material.



Scheme 18.

Other electron-rich systems are 1,3-dioxols and dioxenes. With the former, $\cdot\text{OH}$ adds to the 4,5-C-C bond to give α -alkoxy- β -hydroxyalkyl radicals, Scheme 19. With the fully methylated system (left side of Scheme 19), at pH 2 the OH adduct is quantitatively converted (by H^+ -induced dehydration) to the radical cation, as judged by ESR, whereas with only hydrogens as substituents (right side), at pH 2 dehydration is too slow to lead to a visible decrease of the (stationary) concentration of the OH adduct (Scheme 19) [45].

Even a small increase in the electron density of the system, by introducing a methylene group, i.e., by going from the 1,3-dioxol to the 1,4-dioxene system, leads, however, to complete H^+ -induced conversion of the OH adduct into the radical cation (Figure 7 and Scheme 20) [45].



Scheme 19.

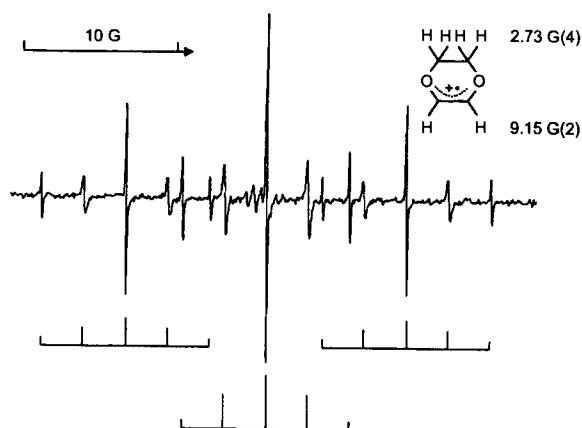
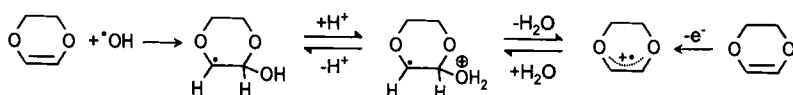


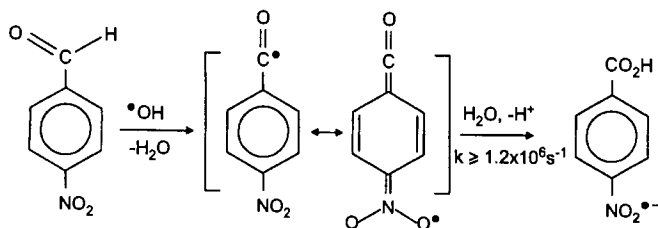
Figure 7. ESR spectrum observed on photolysis of an aqueous 0.1 M H_2O_2 solution containing ca 1 mM 1,4-dioxene at pH 2. In the quintet, there are line-broadening effects caused by partial non-equivalence of the four methylene protons.



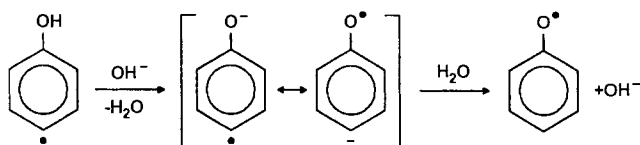
Scheme 20.

9.3 Intramolecular Electron Transfer with Bond Formation

There are so far only a few examples belonging to this category. By use of pulse radiolysis with optical and with ESR detection it was found [45] that the reaction of $\cdot\text{OH}$ with 4-nitrobenzaldehyde in aqueous solution leads quantitatively to the radical *anion* of 4-nitrobenzoate, which is explained in terms of H-abstraction from the CHO function followed by rapid addition of water ($k \geq 1.2 \times 10^6 \text{ s}^{-1}$) (Scheme 21).



Scheme 21.



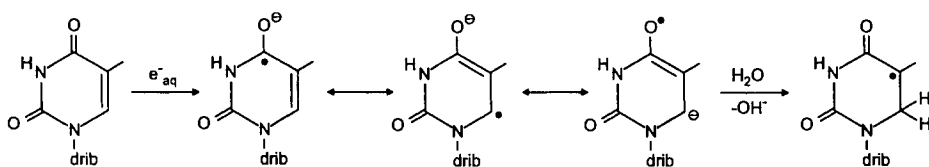
Scheme 22.

Possibly, the reaction is driven by the electrophilicity of the ketenic and nitroxide-type mesomer. In effect, it leads to the *oxidation* of the aldehyde and the *reduction* of the nitro function.

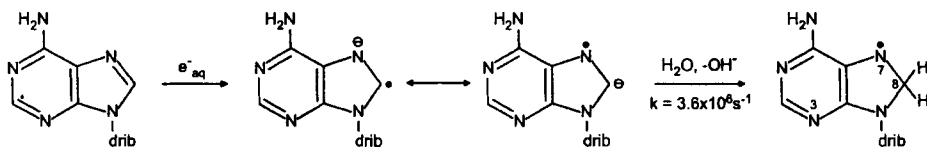
Another example of solvent-assisted intramolecular ET has been reported by Schuler [120]. It involves the transformation of a (σ -type) phenyl radical into a much more stable (π -type) phenoxyl radical (Scheme 22).

Protonation by water of the ring carbon occurs only if the phenol function is *de*-protonated, apparently because only then is the electron density at the ring sufficient for protonation by the weak acid H_2O .

In Scheme 22 another reaction is described in which a C–H bond is *formed* by proton transfer from the solvent (H_2O) to a carbon atom of the substrate. For this reaction to occur, a *high* electron density is required at the site of protonation. This reaction is the opposite to proton-transfer reactions that electron *deficient* species (e.g. radical cations) undergo, namely proton transfer *from a carbon to* the solvent water, as discussed in Section 9.5.1. There are some interesting examples, of biological relevance, of proton transfer *to* carbon from heterocyclic systems (Schemes 23 and 24):



Scheme 23. Electron addition to thymidine followed by protonation on carbon [121, 122].



Scheme 24. Electron addition to 2'-deoxyadenosine [123, 124].

9.4 Reduction of S by X[•], X = E–C[•] (E = Hetero Atom)

The examples so far described always involve a carbon-centered radical which is substituted at C_α by a hetero atom such as O, S, or N. S is always a functional group that contains a double bond, usually an oxygen, i.e. the group =O. X[•] then adds to S according to:

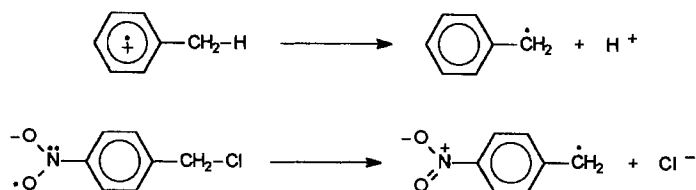


As in the opposite (or complementary) case (Eq. 4a), the mechanism thus involves the formation of X–S[•] by covalent bond formation between X[•] and S, with the second-order rate constant k_{ad} , followed by heterolysis of X–S[•] with the first-order rate constant k_{het} , to give X⁺ and S^{•-}. As described above, the kinetic condition for the detection of X–S[•] is $k_{\text{het}} < k_f [\text{S}]$ (under the (usual) condition that $[\text{X}^{\bullet}] \ll [\text{S}]$). If $k_{\text{het}} > k_{\text{ad}} [\text{S}]$, the reaction will appear to be ‘non-bonded’ (i.e. outer-sphere ET). Since k_{ad} is bimolecular (i.e. $10^9 \text{ M}^{-1} \text{ s}^{-1}$) and almost always $[\text{S}] < 1 \text{ M}$, k_{het} values $\geq 10^9 \text{ s}^{-1}$ are not usually experimentally accessible.

The conditions to be fulfilled for the heterolysis of X–S[•] to be rapid can easily be defined: the reduction potential of X⁺, $E(\text{X}^{+}/\text{X}^{\bullet})$ should be negative whereas that of S, $E(\text{S}/\text{S}^{\bullet-})$ should be positive. A prediction is that above some (large) value for the *difference* in redox potentials of X⁺ and S the species X–S[•] will be difficult to detect, because of the rapid rate of its heterolysis. Under these conditions the reaction will *seem* to proceed by outer-sphere electron transfer. Again, as in Eq. 4a, although X–S[•] is a radical and the overall reaction results in the transfer of a *single* electron, in the actual electron-transfer step an electron *pair* is transferred (heterolysis or electron pair transfer), rather than a single electron. Examples—in many cases involving molecules relevant for biological systems—of reduction of S by carbon-centered radicals substituted at C_α by a hetero atom, in most cases O or N, have already been discussed in detail [53]. The reader is referred to this literature.

9.5 Intramolecular Electron Transfer Accompanied by Bond Cleavage in Radical Ions

Although a previous chapter in this volume provides a broader perspective on the reactivity of radical cations, in this section we will examine intramolecular electron-transfer reactions coupled with or followed by cleavage of a bond in odd electron species such as radical cations, radical zwitterions and radical anions. In particular, this paragraph will be divided in oxidative and reductive bond-cleavage processes. Because this field is however too large to be covered extensively here, the discussion will be limited to selected examples—for oxidative cleavages, side-chain fragmentation reactions of alkylaromatic radical cations and decarboxylation reactions of radical zwitterions derived from benzoic and arylalkanoic acids, and for reductive



Scheme 25.

cleavages, fragmentation reactions of radical anions, such as those derived from aryl and benzyl halides and 1,2-diphenylethanes.

The occurrence of intramolecular electron transfer in radical ion bond cleavage reactions is probably not straightforward and in this respect, two examples may help the reader—C–H deprotonation in the toluene radical cation and C–Cl bond cleavage in the 4-nitrobenzyl chloride radical anion (Scheme 25).

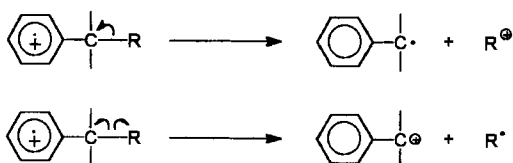
In the toluene radical cation the electron hole is delocalized over the π -system and the deprotonation reaction is coupled with intramolecular electron transfer from the scissible bond to the aromatic ring, leading to the benzyl radical. In the 4-nitrobenzyl chloride radical anion, the unpaired electron resides in a π^* orbital that does not belong to the leaving group and C–Cl bond cleavage occurs simultaneously with an intramolecular electron transfer from this orbital to the σ^* orbital of the scissible bond.

9.5.1 Oxidative Bond-cleavage Processes

Alkylaromatic radical cations

The one-electron oxidation of side-chain-substituted aromatics to give alkylaromatic radical cations often leads to oxidative transformation of the side-chain even though the primary oxidation step involves removal of an electron from the aromatic part of the molecule. Side-chain reactions of alkylaromatic radical cations mostly involve the cleavage of bonds between the α and β atoms, because the considerable overlap achievable between these bonds and the π -orbitals of the aromatic ring results in their significant weakening as compared with the neutral substrate. Many side-chain reactions are thus possible depending on the nature of the bond being cleaved—C–H bond cleavage is the most common fragmentation pattern of these reactive intermediates but fragmentation of C–C and C–X bonds (X = S, Si, Sn) can also occur. This discussion will be limited to the cleavage of side-chain C–H and C–C bonds in aromatic radical cations [125].

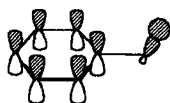
Usually the initially generated radical cations have the electron hole delocalized over the π -system and the fragmentation reaction is accompanied by an intramolecular electron transfer from the scissible bond to the aromatic ring, ultimately resulting in two formal ways of electron apportionment between the fragments, which depends on their relative thermodynamic stability. In the *heterolytic* mode the charge is transferred through the scissible bond while in the *homolytic* mode the spin is transferred across the bond being cleaved (Scheme 26) [126]. Such cleavage modes have been named *mesolytic* to account for both mechanistic possibilities [127].



Scheme 26.

The free energy for radical cation bond cleavage, ΔG_f , can be estimated by means of simple thermodynamic cycles [126, 128], where, regardless of the cleavage mode, ΔG_f depends on the free energy of homolysis of the radical cation precursor (ΔG_h) and the difference between the reduction potentials (ΔE) of the radical cation and the ionic fragment formed— $\Delta G_f = \Delta G_h - \Delta E$.

The rate of side-chain fragmentation of an alkylaromatic radical cation can be influenced by the relative orientation of the scissible bond and the aromatic π system (stereoelectronic effect). The orientation most suited for cleavage is that where the dihedral angle between the plane of the π system and the plane defined by the scissible bond and the atom of the π system to which this bond is connected is 90° . Scheme 27 shows the conformation most suited for C–H bond cleavage.

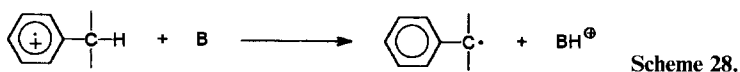


Scheme 27.

In such conformation the scissible bond is collinear with the π orbitals of the aromatic system bearing the unpaired electron, and the best orbital overlap for intramolecular ET, required for bond cleavage, can be achieved. Interestingly, when competition between C–H and C–C bond cleavage is possible, stereoelectronic effects generally play a significant role, because the former process is depressed owing to its steric requirements, which are much smaller than those of a C–C bond. In such circumstances, therefore, the conformation with the latter bond collinear with the π system is the most favored (see later).

C–H bond cleavage

The most simple and common side-chain reaction of alkylaromatic radical cations is the cleavage of a C_x –H (from now on simply indicated as C–H) bond. These reactions have features of great theoretical interest, because C–H bond cleavage must be accompanied by extensive electronic reorganization, because one of the electrons of the σ C–H bond has to be transferred to the aromatic π system. In solution such a cleavage generally occurs via the heterolytic mode, owing to the relative stability of the benzyl radical and the large negative free energy of solvation of the proton (in water $\Delta H(H^+_{\text{gas}} \rightarrow H^+_{\text{soln}}) = 260 \text{ kcal mol}^{-1}$ [129]). Accordingly, alkylaromatic radical cations behave as carbon acids with a carbon radical as the conjugate base (Scheme 28; where B is a Brønsted base, including the solvent).



Scheme 28.

$\text{p}K_{\text{a}}$ values for alkylaromatic radical cations can be calculated by the use of appropriate thermodynamic cycles and by this approach a $\text{p}K_{\text{a}}$ value between -11 and -13 has been estimated in acetonitrile for the deprotonation of the toluene radical cation [130]. On the basis of extrapolation to this radical cation, the acidities of methylbenzene radical cations have been estimated and show the expected decrease in acidity on increasing radical cation stability; this is reflected in the values of E°_{Ar} which progressively decrease with increasing number of methyl substituents. Accordingly, the difference of 440 mV in E°_{Ar} between *p*-xylene and hexamethylbenzene [131], corresponds to $\text{p}K_{\text{a}}$ values for the two radical cations of -8 and $+1$ respectively [132]. The same trend is observed for the kinetic acidity, the rate constants for deprotonation of methylbenzene radical cations in acidic aqueous solution decreasing by three orders of magnitude as the number of methyl groups increases from one to five (Table 2) [133, 134].

When considering the rate constants for deprotonation reported in Table 2 one should, however, take into account that in methylbenzene radical cations with ≤ 3 methyl groups, nucleophilic attack of water on the aromatic ring can compete efficiently with side-chain deprotonation. An elegant explanation which accounts for this competition has been provided for the toluene radical cation on the basis of the three-electron three-orbital three-configuration approach [135, 136]. Three electrons are involved in the deprotonation reaction—the unpaired electron delocalized over

Table 2. Rate constants for the deprotonation of methylbenzene radical cations in acidic aqueous solution.

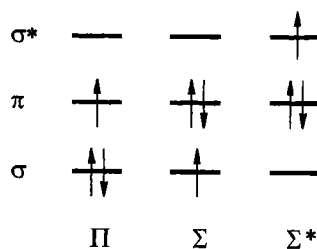
Radical cation	$k \text{ (s}^{-1}\text{)}^{\text{a}}$	$k \text{ (s}^{-1}\text{)}^{\text{b}}$
Toluene	1.0×10^7	$\geq 5 \times 10^7^{\text{c}}$
<i>o</i> -Xylene	2.0×10^6	1.3×10^7
<i>m</i> -Xylene	2.0×10^6	3.9×10^7
<i>p</i> -Xylene	1.4×10^6	$2.1 \times 10^{6\text{d}}$
Mesitylene	1.5×10^6	$\geq 5 \times 10^7$
Hemimellitene	1.5×10^6	$\geq 5 \times 10^7$
Isodurene	1.0×10^5	—
Durene	2.7×10^4	4.3×10^4
Pentamethylbenzene	1.6×10^4	—

^aRadical cations generated by pulse radiolysis (PR) (Section 9.2.3), $\text{pH} \leq 3$. Conditions under which exclusive side-chain deprotonation is reported to occur [133].

^bRadical cations generated by laser-flash photolysis (LFP), $\text{pH} = 4.5$. Conditions under which water addition to the radical cation competes with side-chain deprotonation [134].

^cAddition $> 90\%$.

^dDeprotonation $> 60\%$.



Scheme 29.

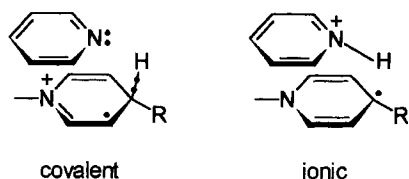
the aromatic ring and the two σ electrons of the scissible C–H bond, while the orbitals of interest are the SOMO of the phenyl ring (π) and the bonding and antibonding orbitals of the C–H bond (σ and σ^*).

Three configurations are important for description of the cleavage (Scheme 29): Π , representing the reactant radical cation, and Σ and Σ^* which make little contribution to the ground state of the radical cation but become important as the C–H bond elongates, accounting for the significant weakening of this bond compared with neutral toluene.

According to this picture the toluene radical cation should react predominantly by nucleophilic attack at the aromatic ring, side-chain deprotonation being a minor reactive pathway, in full agreement with the experimental results (Table 2). Interestingly, substitution of electron-donating groups at the *para* position will stabilize the Π state more than Σ and Σ^* , leading to an overall decrease in reactivity which is, however, associated with an increase in the relative importance of the deprotonation pathway, as clearly shown by comparing the experimental results for toluene and *p*-xylene radical cations in Table 2.

The kinetic acidity of alkylaromatic radical cations has received great attention. Savéant and his associates studied the C–H deprotonation of NADH analog radical cations and showed that the intrinsic *kinetic* acidities of the radical cations do not correlate with the *thermodynamic* acidities while a good correlation is instead observed between the intrinsic barrier and the homolytic C–H bond dissociation energy [137–139]. Thus, in such radical cations the dynamics of proton transfer are governed by the homolytic cleavage of the C–H bond, suggesting that C–H deprotonation of an aromatic radical cation can be better described as a concerted H-atom electron transfer rather than a direct proton transfer. Intrinsic barriers as high as 0.5–0.6 eV have been determined; these are comparable with those generally observed for acid–base reactions involving carbon acids [140, 141]. The behavior of NADH analog radical cations can be explained in terms of the mesomeric structures shown in Scheme 30 for the transition state of proton transfer from the radical cation to a pyridine base, where the positive charge is delocalized from the departing proton and is mostly borne by the nitrogen atom.

Whereas within the precursor complex the presence of the base does not influence the covalent state of the radical cation when the C–H bond elongates, the ionic state is highly stabilized by the presence of the base as the C–H distance increases [137]. This model implies that formation of the N–H bond does not interfere to a large extent in the dynamics of the reaction, the deprotonation of the radical cation



Scheme 30.

involving three concerted steps—homolytic cleavage of the C–H bond, electron transfer, and heterolytic formation of the N–H bond, and proceeding through an early transition state in which the N–H distance is larger than the C–H distance [139].

Interestingly, such a model leads to similar results when applied to the deprotonation reactions of methylarene radical cations by a series of pyridine bases [132] and to the deprotonation of the $(4\text{-MeOC}_6\text{H}_4)_2\text{NCH}_3$ radical cation by a series of quinuclidine bases [142].

An early transition state has also been suggested for the side-chain deprotonation of alkylaromatic radical cations in the seminal studies of Kochi [132, 143, 144] and Baciocchi [145]. Kochi determined the rates of proton transfer from various methylarene radical cations to substituted pyridine bases in acetonitrile generating the radical cations by oxidation with *tris*(phenanthroline)iron complexes [132], or charge-transfer excitation of the electron donor–acceptor complex of the methylarenes with tetranitromethane [146]. The former method leads to an indirect evaluation of the rate constants for deprotonation of the radical cations whereas the latter enables direct measurement by observation of the radical cation by means of time-resolved techniques. The deprotonation rate constants follow a general Brønsted relationship leading to β values between 0.30 and 0.15 [143, 144]. If this free energy relationship for proton transfer is considered in the context of the Marcus equation, the magnitude of these Brønsted coefficients corresponds to an overall free energy change lying in the exoergonic region of the driving force. The same conclusion is obtained from deuterium kinetic isotope effects which decrease by increasing driving force (base strength). These observations are in line with an early transition state in which proton transfer has not proceeded beyond the symmetrical situation. Such a qualitative description is also in agreement with the relatively low sensitivity of proton transfer rates to the steric effects of the pyridine bases. The Marcus approach leads to an intrinsic barrier of 0.6 eV for deprotonation of methylarene radical cations by substituted pyridine bases [147].

Similar results have been obtained by Baciocchi for the deprotonation of α -substituted 4-methoxytoluenes by 2,6-lutidine and NO_3^- in acetonitrile [145]. In this study, the same values of the Brønsted coefficient ($\alpha = 0.24$), and of the deuterium kinetic isotope effect ($k_{\text{H}}/k_{\text{D}} = 2.0$ for 4-methoxytoluene radical cation) have been obtained with the two bases; these results point again towards a highly asymmetric transition state with a very small amount of C–H bond cleavage. Moreover, values of 0.53 and 0.66 eV have been calculated for the intrinsic barrier of the reactions of the radical cations with NO_3^- and 2,6-lutidine, respectively, again comparable with those observed for acid–base reactions involving carbon acids [140, 141].

Table 3. Relative reactivities for the deprotonation of 4-MeOC₆H₄CH₂X and 4-MeC₆H₄CH₂X radical cations.

X	4-MeOC ₆ H ₄ CH ₂ X ^{•+} ^a		4-MeC ₆ H ₄ CH ₂ X ^{•+} ^b
	(NO ₃ ⁻)	(2,6-Lutidine)	<i>k</i> (CH ₂ X)/ <i>k</i> (CH ₃)
CN	183	—	9.3
OMe	20.5	13.3	>100
OH	15	19	>100
OAc	3.4	11.7	1.8
Me	2.4	2	14.1
H	1	1	1
D	0.5	0.5	—
<i>t</i> Bu	—	—	0.01

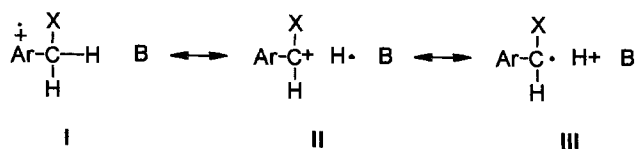
^a Intermolecular, from LFP in MeCN, *T* = 22 °C [145].^b Intramolecular, from anodic oxidations in AcOH–MeCN (3:1), *T* = 25 °C [148].

Useful information about the structure of the transition state for C–H deprotonation can be obtained by comparing the relative reactivities of two series of alkylaromatic radical cations 4-MeOC₆H₄CH₂X^{•+} [145] and 4-MeC₆H₄CH₂X^{•+} [148] (Table 3). In both instances all α -substituents (with the exception of X = *t*Bu, see later) increase the deprotonation rate compared with X = H, although there are some discrepancies between the two series of radical cations— α -substituents of the +R type (OH, OMe, Me) have a much larger kinetic effect in the deprotonation of 4-MeC₆H₄CH₂X^{•+} than in that of 4-MeOC₆H₄CH₂X^{•+}, whereas the opposite behavior is observed with a –I, –R substituent such as CN.

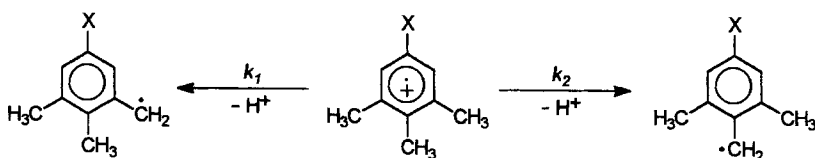
It is possible to interpret these results in terms of the model proposed by Savéant for the deprotonation of NADH analog radical cations, where the dynamics of the deprotonation process in the radical cation are controlled by the homolytic C–H bond dissociation energy [137, 139].

The transition state for the deprotonation of an alkylaromatic radical cation might be described in terms of the mesomeric structures in Scheme 31. In structure **I** the positive charge is delocalized on the aromatic ring whereas structures **II** and **III** represent the homolytic and heterolytic C–H bond cleavage modes, respectively.

If the homolytic bond-dissociation energy (BDE) is the main factor governing the dynamics of proton transfer, the transition state is better represented by structures **I** and **II**. In an alkylaromatic radical cation the build-up of positive charge at the α -carbon requires extensive charge delocalization from the aromatic ring and this is likely to occur with greater efficiency in 4-Me rather than 4-MeO substituted radical



Scheme 31.



Scheme 32.

cations, because the latter group is very effective in stabilizing a positive charge. In 4-MeOC₆H₄CH₂X^{•+}, the favorable kinetic effect of +R α -substituents in reducing the homolytic BDE might be compensated by the presence of the 4-MeO group which opposes charge transfer from the ring to the α -carbon, thus explaining the higher relative reactivities observed with 4-MeC₆H₄CH₂X^{•+}. On the other hand, whereas the α -CN group is again expected to reduce the homolytic BDE, resulting in an increase of the deprotonation rate [145], this favorable effect is likely to be felt less in the reaction of 4-MeC₆H₄CH₂CN^{•+}, because of the larger fraction of positive charge residing on the α -carbon in the transition state.

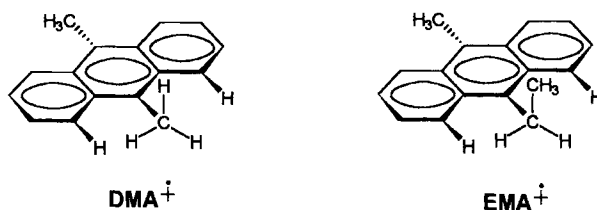
The intramolecular selectivity in the deprotonation of alkylaromatic radical cations has been investigated in a series of 5-X-1,2,3-trimethylbenzene radical cations; the results showed that spin and/or charge density at the scissible C–H bond can strongly influence the kinetic acidity, which is, accordingly, very sensitive to the nature and position (*meta* or *para*) of ring substituents (Scheme 32) [149].

Very high selectivity (k_2/k_1) is observed in the presence of +R substituents (X = Br, Me, OAc, *t*-Bu, OMe), deprotonation at the 2-methyl (*para* to the X group, the site bearing the largest charge/spin density) being strongly favored over that at the methyl groups in the 1 and 3 positions (Table 4).

As remarked previously, the deprotonation rate of an alkylaromatic radical cation can be influenced by the stereoelectronic effect (Scheme 27). In this respect, Tolbert provided convincing evidence for the operation of stereoelectronic effects in the deprotonation of 9-alkylanthracene and 9,10-dialkylanthracene radical cations

Table 4. Intramolecular selectivities (k_2/k_1) in the deprotonation of 5-X-1,2,3-trimethylbenzene radical cations generated by anodic or CAN-promoted oxidation in acetic acid.

X	k_2/k_1	
	CAN	Anodic
COOMe	2.0	1.5
H	3.4	3.0
<i>t</i> -Bu	24	16
Br	42	31
Me	55	37
OAc	110	59
OMe	>200	–

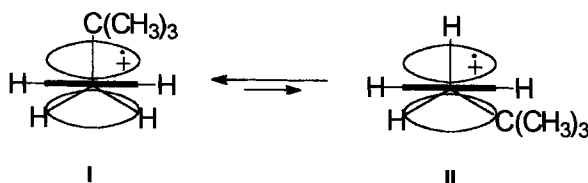


Scheme 33.

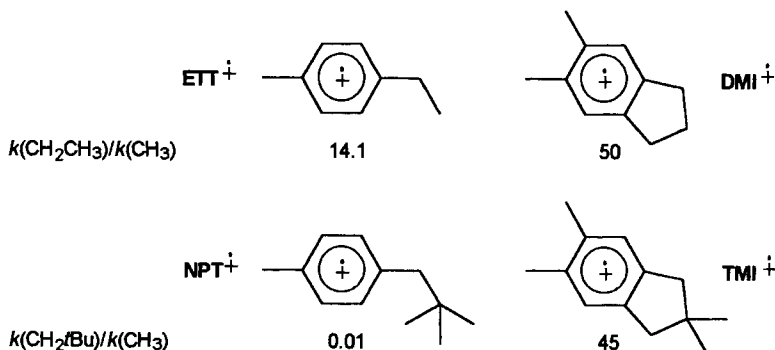
[150, 151]. Whereas the 9,10-dimethylantracene (DMA) radical cation undergoes side-chain deprotonation leading to the oxidized product 9-hydroxymethyl-10-methylantracene [152], the 9-ethyl-10-methylantracene (EMA) radical cation forms 9-ethyl-10-hydroxymethylantracene as the exclusive deprotonation product and no deprotonation products are observed with the 9,10-diethylantracene (DEA) radical cation [151], despite the relatively high thermodynamic acidity of these species ($pK_a = -6$ for $\text{DMA}^{+\bullet}$ [150]). These observations can be explained in terms of stereoelectronic control of the deprotonation reaction—whereas in $\text{DMA}^{+\bullet}$ the C–H bond can easily assume the conformation required for deprotonation, where the scissible C–H bond is collinear with the π orbitals of the aromatic system, in the presence of an ethyl substituent as in $\text{EMA}^{+\bullet}$ the analogous conformation is prevented by the unfavorable interactions with the *peri* hydrogens, which force the $\text{CH}_2\text{--CH}_3$ bond in a conformation perpendicular to the anthracene plane (Scheme 33, in which the unpaired electron is not shown).

Interestingly, when the C–H bond is forced into a conformation in which it is almost collinear with the π -system as in 1,9-ethanoanthracene (EA), a ratio for deprotonation of 28:1 is observed between the ethano group in $\text{EA}^{+\bullet}$ and the methyl group in 9-methylantracene radical cation [150].

Additional information on the role of stereoelectronic effects comes from the anodic oxidation of α -substituted *p*-xylenes [148], and from the oxidation of alkyl- and 1,4-dialkylbenzenes with a variety of one-electron oxidants [153]. The *p*-neopentyltoluene radical cation, generated by anodic oxidation, undergoes deprotonation almost exclusively at the methyl group, a behavior which has been attributed to the greater stability of the conformation having the *t*Bu group perpendicular to the plane of the aromatic ring (Scheme 34, structure I) compared with that suitable for C–H bond cleavage from the CH_2tBu group (structure II), which is destabilized by the interaction of the *t*Bu group with the *ortho* hydrogens of the ring [148].



Scheme 34.

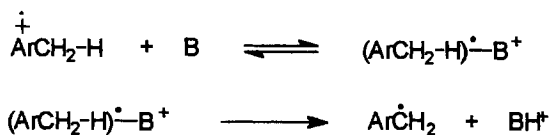


Scheme 35.

The importance of stereoelectronic effects has been assessed quantitatively by comparing the $\text{CH}_3/\text{CH}_2\text{CH}_3$ and $\text{CH}_3/\text{CH}_2t\text{Bu}$ reactivity ratios (statistically corrected) in the radical cations of *p*-ethyltoluene (ETT), *p*-neopentyltoluene (NPT), 5,6-dimethylindane (DMI), and 2,2,5,6-tetramethylindane (TMI) (Scheme 35) [148]. In the two indane derivatives the methylene groups in positions 1 and 3 bear a substituent which resembles an ethyl and a *t*-butyl group, respectively. In the *p*-xylene series, on going from $\text{ETT}^{\dot{+}}$ to $\text{NPT}^{\dot{+}}$ a dramatic 1400-fold decrease in reactivity is observed for deprotonation from the methylene position, behavior which is readily explained on the basis of a stereoelectronic effect (see above and Scheme 34).

This effect disappears as we move to the indane system, where comparable relative reactivities (50 and 45, respectively) are observed for $\text{DMI}^{\dot{+}}$ and $\text{TMI}^{\dot{+}}$, in which stereoelectronic effects cannot operate, because the scissible C–H bonds in the 1- and 3-positions are kept almost collinear with the aromatic system, because of the rigidity imposed by the cyclopentane ring. It thus seems, by comparing $\text{NPT}^{\dot{+}}$ with $\text{TMI}^{\dot{+}}$, that stereoelectronic control of deprotonation determines a decrease in the deprotonation rate from the CH_2tBu as large as 4500-fold. Interestingly, comparison of $\text{ETT}^{\dot{+}}$ and $\text{DMI}^{\dot{+}}$ shows that a stereoelectronic effect is operating in the former radical cation also. An important conclusion that comes from the study of the indane system is that steric hindrance to the approach of the base is of limited importance, a result which is in line with the early transition state proposed for deprotonation of alkylaromatic radical cations. Because stereoelectronic effects always operate in the direction of depressing the deprotonation rate, the observation that for all X substituents $k(\text{CH}_2\text{X})/k(\text{CH}_3)$ is always greater than unity (Table 3) clearly indicates a major role for electronic effects.

In another study, tertiary:secondary:primary relative reactivity data (TSP selectivity) for the deprotonation reactions of alkylbenzene radical cations [153] showed that with both intra- and intermolecular TSP selectivity the order $\text{S} > \text{T} > \text{P}$ is usually observed, suggesting that the combination of steric and stereoelectronic effects makes an *i*Pr group less reactive than Et, but still more reactive than Me.



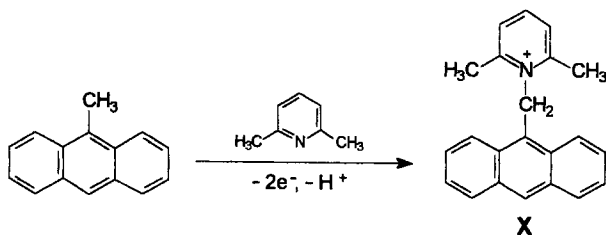
Scheme 36.

The mechanism discussed above for the deprotonation of alkylaromatic radical cations, involving a bimolecular reaction between the radical cation and the base (B), leading to a carbon centered neutral radical and the conjugated acid of the base (BH⁺) as described in Scheme 28, has been recently questioned by Parker who provided evidence for an alternative mechanism in proton-transfer reactions between methylantracene radical cations and pyridine bases [154]; this involved reversible covalent adduct formation between the radical cation and the base followed by elimination of BH⁺ (Scheme 36).

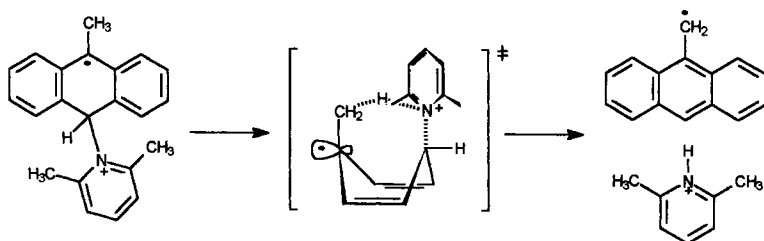
Resolution of the rate constants for the individual steps of this mechanistic scheme under non-steady-state conditions was also achieved [155].

Product studies of the reaction of the 9-methylantracene radical cation with 2,6-lutidine in acetonitrile show X to be the exclusive reaction product; it results from proton transfer from the methyl substituent (Scheme 37).

An Arrhenius activation energy, E_a , of $-1.3 \text{ kcal mol}^{-1}$ has been measured for this process. Substitution of the hydrogen at the 10-position with deuterium leads to a characteristic inverse deuterium kinetic isotope effect— $k_H/k_D = 0.83$. Both values are typical of radical cation–nucleophile combination reactions [156], and the latter is inconsistent with direct deprotonation from the 9-methyl group. Replacement of the 9-methyl with CD₃ results, moreover, in a primary deuterium kinetic isotope effect, $k_H/k_D = 5.9$. A mechanism which can account for all these observations involves nucleophilic attack of 2,6-lutidine at the 10-position of 9-methylantracene radical cation followed by a unimolecular elimination of the 2,6-lutidinium ion from the adduct leading to the 9-anthracenylmethyl radical from which the observed reaction product can be formed after oxidation. Observation of an inverse deuterium kinetic isotope effect implicates concerted bond breaking and formation, with an early transition state for the elimination reaction; this is also supported by the large primary deuterium kinetic isotope effect observed on deuterium substitution at the 9-methyl group. The transition state for the elimination reaction is thus suggested to involve a boat-like conformation of the central ring of the anthracene moiety bearing both the 9-methyl and 10-lutidinium groups in axial positions (Scheme 38, showing in the transition state only the central anthracene ring).



Scheme 37.



Scheme 38.

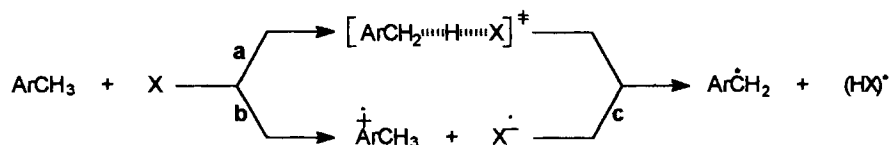
According to this picture, the elimination reaction occurs from a distonic radical cation in which the positive charge is localized on the nitrogen atom and is maintained at this site throughout the reaction. Thus, the formal deprotonation step can be described as an hydrogen-atom transfer from the 9-methyl group to an incipient 2,6-lutidine radical cation.

Comparison of the reactivities of both 9-methylanthracene and 9,10-dimethylanthracene radical cations with those of pyridine and 2,6-lutidine shows that in the absence of severe steric effects radical cation–nucleophile combination is kinetically favored over direct proton transfer, even though the latter process is highly exergonic. Because the addition step cannot usually be readily detected, however, experimental evidence does not usually enable distinction between addition–elimination and direct proton transfer mechanisms.

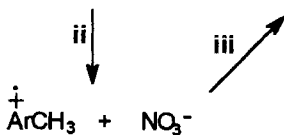
Another mechanistic ambiguity which has attracted considerable interest is the possible intermediacy of radical cations in the oxidative functionalization of alkylaromatic substrates with different organic and inorganic oxidants, a process involving C–H bond cleavage which can occur in a single step by direct hydrogen-atom transfer (HAT) from the neutral substrate to the oxidant (Scheme 39, path **a**) or by deprotonation of a first-formed aromatic radical cation (paths **b** and **c**).

Whereas in organic solvents the oxidation of toluene with permanganate (MnO_4^-) and chromyl chloride (CrO_2Cl_2) has been established to occur by HAT [157], Kochi showed that in the reaction of methylarenes with photoactivated quinones such as chloranil intermediate aromatic radical cations are formed which then undergo side-chain deprotonation [158].

Primary deuterium kinetic isotope effects have always been observed, ruling out their use as a mechanistic tool to distinguish between the two possibilities. The different behavior observed with these systems can be explained on the basis of the



Scheme 39.



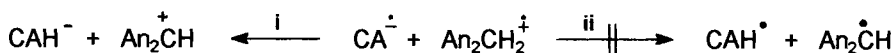
Scheme 40.

much higher oxidizing power of photoactivated chloranil (for which $E^*_{\text{red}} = 2.38$ V relative to the NHE in MeCN [159];) compared with inorganic oxidants (i.e. for MnO_4^- $E^\circ = 0.56$ V in H_2O [160]), and also by considering the hydrogen-abstrating strength of both MnO_4^- and CrO_2Cl_2 [157].

A different mechanistic picture has been proposed for the oxidation of alkylbenzenes by NO_3^* generated by LFP in MeCN; this involves reversible formation of a weak adduct between the aromatic compound and NO_3^* (Scheme 40) [161].

With monoalkylbenzenes and *m*-xylene no evidence has been obtained for formation of an intermediate radical cation, the complex decomposing to a benzyl radical (path **i**) either by a direct HAT or via a concerted electron–proton transfer mechanism. The latter seems more likely on the basis of the observation of the order of reactivity ethylbenzene > isopropylbenzene > toluene (statistically corrected) for reaction **i**, in line with the stereoelectronic effects observed for the deprotonation of alkylbenzene radical cations [153]. With more readily oxidizable substrates such as *p*-xylene and methylbenzenes with ≥ 3 methyl groups, an analogous complex is formed; this, however, is characterized by a lifetime of ≤ 20 ns and decomposes into the intermediate radical cation (experimentally observed) from which the benzyl radical is formed by deprotonation (paths **ii** and **iii**).

Along this line, much effort has been devoted to understanding the mechanism of hydroxylation of organic substrates promoted by cytochrome P-450 [162]. Whereas for unactivated alkanes experimental evidence is strongly in favor of a HAT mechanisms [163], for alkylaromatic compounds an electron-transfer mechanism can, in principle, occur, because of the similar oxidation potentials of these compounds [131, 164] and the active oxidant of cytochrome P-450, for which a value of 1.7–2.0 V relative to the SCE has been estimated [165]. Given the experimental difficulties in the direct detection of reactive intermediates in enzymatic reactions, valuable mechanistic information can be obtained, considering that with suitably chosen substrates, reactions involving radical ions can have intramolecular or intermolecular selectivity or lead to product patterns which differ from those obtained in HAT processes. Thus, by comparing the products and selectivity of the enzymatic reactions of these compounds with those obtained using well known electron transfer oxidants it is possible to distinguish between the two mechanistic pathways described in Scheme 39 [166]. When this approach was applied to a study of the cytochrome P-450-promoted oxidation of alkylaromatic compounds such as 4-substituted 1,2-dimethylbenzenes [167], 1,2-dialkylbenzenes [153], and α -alkyl-4-methoxybenzyl alcohols [168], no evidence was found for the occurrence of an



Scheme 41.

electron-transfer mechanism; the results obtained suggested that these reactions proceed through a HAT mechanism.

Whereas in solution alkylaromatic radical cations undergo predominantly heterolytic C–H bond cleavage, evidence for homolytic fragmentation has recently been provided by a LFP study of the photoinduced electron-transfer reaction of *bis*(4-methoxyphenyl)methane (An_2CH_2) sensitized by chloranil (CA) in MeCN [169]. 355-nm laser excitation results in the formation of the excited triplet chloranil, $^3\text{CA}^*$; this reacts with An_2CH_2 by electron transfer leading to $\text{An}_2\text{CH}_2^{\cdot+}$ and CA^\cdot . Quite surprisingly, from this radical ion pair An_2CH^+ and CAH^- are formed indicating the occurrence of a HAT reaction (Scheme 41, path i).

ΔG° for this reaction has been determined, on the basis of the appropriate thermodynamic cycle, to be $\leq -29 \text{ kcal mol}^{-1}$ a value which is significantly more negative than that ($\Delta G^\circ = -16 \text{ kcal mol}^{-1}$) calculated for the alternative deprotonation reaction (heterolytic C–H bond cleavage) which leads to CAH^\cdot and $\text{An}_2\text{CH}^\cdot$ (path ii), thus suggesting that homolytic C–H bond cleavage reactions of alkylaromatic radical cations might be more frequent than hitherto thought.

Comparison of oxygen and carbon acidity

A major achievement in the study of the acidity of aromatic radical cations is the recent discovery of a pH-dependent mechanistic dichotomy for 1-arylalkanol radical cations in water. Whereas in acidic solution ($\text{pH} \leq 5$) these species undergo C–H deprotonation, in basic media deprotonation of the alcoholic O–H group is observed. Clear evidence in this respect has been provided by a study of the reactivity of the radical cations of 4-methoxybenzyl alcohol (MBA) and its methyl ether (MBAME) generated by pulse radiolysis in aqueous solution [170, 171]. At $\text{pH} \leq 5$, both radical cations decay at the same rate by an H_2O -induced C–H deprotonation process, well supported by primary deuterium kinetic isotope effects ($k_{\text{H}}/k_{\text{D}}$ between 4.5 and 5.0) measured with the corresponding α -deuterated substrates (Table 5). Interestingly, whereas the effect of an α -OH group on the rate of deprotonation of alkylaromatic radical cations is clearly shown by comparing the reactivity of $\text{MBA}^{\cdot+}$ with that of 4-methoxytoluene (MT) radical cation—a 40-fold difference—[172], there is no significant difference between the α -OH- and α -OMe-substituted radical cations.

In alkaline solution $\text{MBA}^{\cdot+}$ reacts instead with ^-OH at a diffusion-controlled rate and is at least 50 and 210 times more reactive than $\text{MBAME}^{\cdot+}$ and $\text{MT}^{\cdot+}$, respectively, differences which cannot be explained on the basis of the electronic effects of the α -OH and α -OMe groups. Moreover, no deuterium kinetic isotope effect is observed for $\text{MBA}^{\cdot+}$ under these conditions, in line with the diffusion control of the reaction, whereas a $k_{\text{H}}/k_{\text{D}}$ value of 1.8 has been measured for $\text{MBAME}^{\cdot+}$. These observations point towards a key role of the α -OH group in the

Table 5. Rate constants for the uncatalyzed (k_{dec}) and ^-OH -catalyzed (k_{-OH}) decay of $\text{ArCH}_2\text{X}^{+\cdot}$ ($\text{Ar} = 4\text{-MeOC}_6\text{H}_4$, $3,4\text{-(MeO)}_2\text{C}_6\text{H}_3$; $\text{X} = \text{H}$, OH , OMe) generated by pulse radiolysis of the parent substrate in aqueous solution, measured at $T = 25^\circ\text{C}$.

Substrate	Radical cation	$k_{\text{dec}} (\text{s}^{-1})$	$k_{-OH} (\text{M}^{-1} \text{s}^{-1})$
$4\text{-MeOC}_6\text{H}_4\text{CH}_2\text{OH}^{\text{a}}$	$\text{MBA}^{+\cdot}$	1.5×10^4	1.2×10^{10}
$4\text{-MeOC}_6\text{H}_4\text{CD}_2\text{OH}^{\text{a}}$	$\text{MBA-}d_2^{+\cdot}$	3.3×10^3	1.1×10^{10}
$4\text{-MeOC}_6\text{H}_4\text{CH}_2\text{OMe}^{\text{a}}$	$\text{MBAME}^{+\cdot}$	1.5×10^4	2.5×10^8
$4\text{-MeOC}_6\text{H}_4\text{CD}_2\text{OMe}^{\text{a}}$	$\text{MBAME-}d_2^{+\cdot}$	3.0×10^3	1.4×10^8
$4\text{-MeOC}_6\text{H}_4\text{CH}_3^{\text{b}}$	$\text{MT}^{+\cdot}$	4.0×10^2	5.5×10^7
$3,4\text{-(MeO)}_2\text{C}_6\text{H}_3\text{CH}_2\text{OH}^{\text{c}}$	$\text{VA}^{+\cdot}$	17	1.3×10^9
$3,4\text{-(MeO)}_2\text{C}_6\text{H}_3\text{CH}_2\text{OMe}^{\text{c}}$	$\text{VAME}^{+\cdot}$	20	2.0×10^7
$3,4\text{-(MeO)}_2\text{C}_6\text{H}_3\text{CH}_3^{\text{c}}$	$\text{DMT}^{+\cdot}$	1.1	2.1×10^6

^a According to [170].

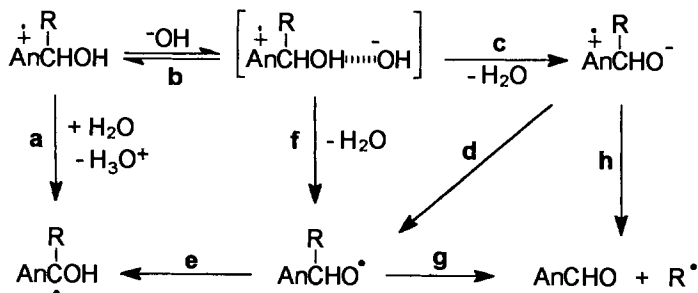
^b According to [172].

^c According to [102].

deprotonation of 1-arylalkanol radical cations in alkaline aqueous solution, as described in Scheme 42 ($\text{An} = 4\text{-MeOC}_6\text{H}_4$).

At $\text{pH} \leq 5$, where H_2O is the proton-abstracting base, $\text{MBA}^{+\cdot}$ undergoes C–H deprotonation (path **a**) whereas when the base is ^-OH deprotonation from the alcoholic O–H group occurs, the radical cation behaving as an oxygen acid. Because under the latter conditions the rate constant for deprotonation is diffusion controlled, formation of the encounter complex (path **b**) is the rate-determining step [173]. Proton transfer occurs within the complex leading either directly (intramolecular electron transfer coupled with deprotonation, path **f**) or via an intermediate radical zwitterion (paths **c** and **d**), to a benzyloxyl radical which eventually undergoes a formal 1,2-H atom shift (path **e**) leading to the same α -hydroxy-4-methoxybenzyl radical observed at $\text{pH} \leq 5$. The mechanism is the same [170, 171] when $\text{R} = \text{Me}$, but for $\text{R} = \text{Et}$, $i\text{Pr}$, C–C bond cleavage (see later) starts to compete (paths **g** and **h**).

This shift from carbon to oxygen acidity is particularly interesting, because only the C–H but not the O–H bond can overlap efficiently with the π system of the



Scheme 42.

aromatic radical cation and, moreover, C–H deprotonation is largely favored thermodynamically over O–H deprotonation.

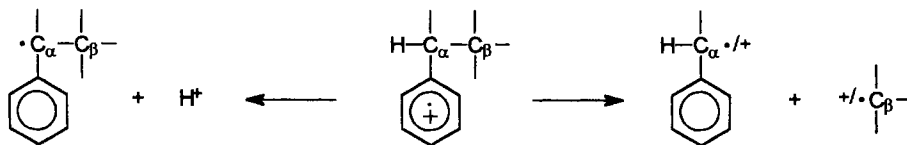
It is, however, well known that carbon acids have much larger intrinsic barriers for proton transfer than oxygen acids [140, 141, 173], thus when a base such as H_2O is involved, the much larger driving force predominates and C–H deprotonation is observed. When, on the other hand, the base is stronger (^-OH) both deprotonations are thermodynamically feasible and O–H deprotonation, characterized by a smaller intrinsic barrier, is favored over C–H deprotonation. An explanation in terms of the hard and soft acids and bases concept is also possible—O–H is a much *harder* acid center than C–H, thus in the presence of the charged *hard* base ^-OH an effective electrostatic interaction might be particularly favorable. With the uncharged and weaker base H_2O , no favorable electrostatic interaction can occur and reaction takes place at the *softer* acid center. Evidence in this respect has been provided by MO calculations showing that in $\text{MBA}^{+\bullet}$ the hydrogen bound to the oxygen atom bears a large fraction of the positive charge whereas the benzylic hydrogens are characterized by relatively large spin densities [174].

Analogous behavior is also observed with the corresponding 3,4-dimethoxy derivatives [102]; with these derivatives, however, because of the increased stability of the radical cations, in acidic solution a decrease in reactivity of three orders of magnitude for the deprotonation reaction is observed on going from $\text{MBA}^{+\bullet}$ to the 3,4-dimethoxybenzyl alcohol radical cation (veratryl alcohol, VA). In the presence of ^-OH the deprotonation site shifts from carbon to oxygen, as previously described for the 4-methoxy derivatives, and a dramatic increase in reactivity is observed, $\text{VA}^{+\bullet}$ reacting with ^-OH with $k = 1.3 \times 10^9 \text{ M}^{-1} \text{ s}^{-1}$ (Table 5), a value which is lower than the diffusion limit and which, compared with that measured for $\text{MBA}^{+\bullet}$, rather than the decreased O–H acidity of $\text{VA}^{+\bullet}$, presumably reflects the increased electron density on the aromatic system which disfavors the intramolecular (side-chain to nucleus) electron transfer eventually leading to the benzyloxyl radical.

Comparison of C–H and C–C bond cleavage

When an α -carbon is bonded to both an hydrogen atom and a saturated carbon, $\text{C}_\alpha\text{--C}_\beta$ (from now on indicated as C–C) bond cleavage can start to compete with C–H deprotonation (Scheme 43).

Thermodynamically cleavage of a C–H bond in an alkylaromatic radical cation is strongly favored over C–C fragmentation due to the much higher solvation free energy of the proton as compared to a carbocation. However, the former process is characterized by significantly higher intrinsic barriers (0.5–0.6 eV for C–H

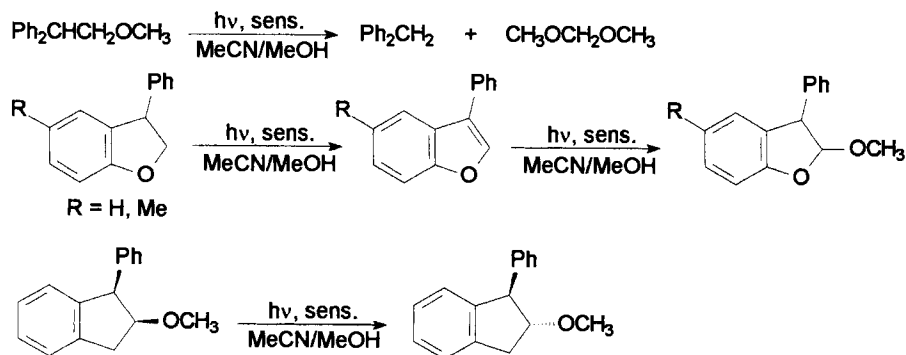


Scheme 43.

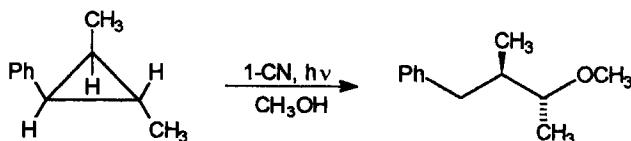
(see above), compared with 0.1–0.2 eV for C–C bond cleavage [175, 176]) and this difference may play a major role in the competition between the two cleavages. As an example, whereas in solution $\text{PhCH}_2\text{--CH}_2\text{Ph}^{+\bullet}$ undergoes exclusive deprotonation [177–179], C–C bond cleavage is the only fragmentation pathway for $\text{Ph}_2\text{CH--CHPh}_2^{+\bullet}$, in spite of the fact that for this radical cation the C–C BDE (9.3 kcal mol⁻¹ [180]) is still much higher than that for cleavage of the C–H bond (–17 kcal mol⁻¹ [128]). This behavior may be rationalized in terms of the differences in intrinsic barriers discussed above, and also by considering that the rate of C–H bond cleavage can be strongly depressed by stereoelectronic effects, which always disfavor this process when in competition with the cleavage of other bonds. Evidence in favor of stereoelectronic control of fragmentation in C–C bond cleavage reactions of alkylaromatic radical cations has been provided by Arnold for a variety of systems. Accordingly, while 2,2-diphenylethyl methyl ether radical cation undergoes C–C bond cleavage [181], no products deriving from this pathway but only from a reversible C–H deprotonation reaction are observed with the radical cations of the cyclic analogs 3-phenyl-2,3-dihydrobenzofuran, 5-methyl-3-phenyl-2,3-dihydrobenzofuran, *cis*- and *trans*-2-methoxy-1-phenylindane, all incorporating the β,β -diphenylethyl methyl ether moiety, where collinearity of the scissible C–C bond with the π -system (Scheme 27) is prevented by the presence of the five-membered ring (Scheme 44) [182].

Additional evidence comes from the study of the radical cations of *trans*- and *cis*-methyl-2-phenylcyclopentyl ether and *trans*- and *cis*-1-methyl-2-phenylcyclopentane, where only the first radical cation undergoes C–C bond cleavage since in this case in addition to the overlap between the scissible bond and the π -system, the conformation of the methoxy group allows interaction of a nonbonding electron pair on the oxygen with the σ^* orbital of this bond [183, 184].

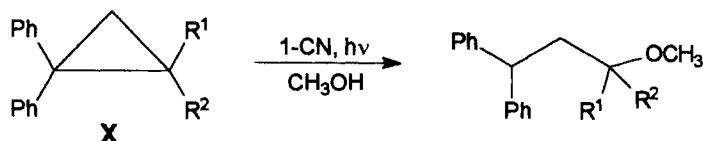
In contrast with these findings are however the similar rates of C–C bond cleavage calculated for the radical cations of $\text{PhCH}_2\text{CH}_2\text{OH}$ and 2-indanol [185, 186], indicating that further studies are needed in order to assess the importance of stereoelectronic effects on C–C bond fragmentation reactions of alkylaromatic radical cations.



Scheme 44.



Scheme 45.



Scheme 46.

Interestingly, C–C bond cleavage can successfully compete with C–H deprotonation in systems where fragmentation leads to a very stable fragment, as in the one electron oxidation of phenylacetic acids followed by rapid decarboxylation (see for example ref [187].).

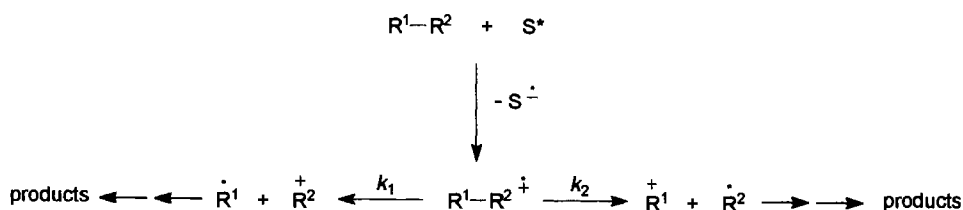
C–C bond cleavage reactions are in most cases unimolecular processes, however, the possibility that C–C bond fragmentation occurs through a nucleophilically assisted pathway has been clearly shown in the three-electron S_N2 reactions between arylcyclopropane radical cations and nucleophiles which proceed stereospecifically with inversion of configuration at the carbon atom undergoing nucleophilic substitution (Scheme 45, 1-CN = 1-cyanonaphthalene) [188, 189].

Quite surprisingly, substitution occurs at the more hindered carbon atom (Scheme 46), even when this atom bears a *tert*-butyl or two methyl substituents.

A quantitative evaluation of the steric effects has been obtained by measuring the rate constants for reaction of MeOH with $X^{\bullet+}$ (Table 6), which decrease on going from $R^1 = H$ to $R^1 = tBu$, showing however effects that are much smaller than those generally observed in four electron S_N2 reactions [190, 191]. Moreover, an increase in rate constants is observed with increasing alkyl substitution at the reaction center.

Table 6. Rate constants for reaction of MeOH with $X^{\bullet+}$ in CH_2Cl_2 at $T = 22^\circ C$.

R^1	R^2	k ($M^{-1} s^{-1}$)	k_{rel}
H	H	1.7×10^7	1
Me	H	1.5×10^8	8.8
Et	H	8.3×10^7	4.9
<i>i</i> Pr	H	3.0×10^7	1.8
<i>t</i> Bu	H	4.8×10^6	0.3
Me	Me	3.2×10^8	18.8



Scheme 47.

From these results it appears that the substitution regiochemistry is not determined by steric effects but rather by the ability of the alkyl group at C_β to stabilize a positive charge in the substitution transition state, indicating that three-electron S_N2 reactions of arylcyclopropane radical cations are dominated by electronic rather than steric effects (see later).

Evidence for nucleophile-assisted C–C bond cleavage has also been found in the nitrate-induced fragmentation reaction of 2-X-2-(4-methoxybenzyl)-1,3-dioxolane (X = H, Me) radical cations [192].

C–C bond cleavage can be heterolytic or homolytic depending on whether the charge or the spin is transferred across the scissible bond (Scheme 26). In this respect, Arnold studied the regioselectivity of the C–C bond-cleavage process in radical cations of diphenylethane derivatives (tri- and tetraarylalkanes) generated by photoinduced electron transfer (PET), showing that C–C bond cleavage may occur if the radical cation BDE is $\leq 15 \text{ kcal mol}^{-1}$ (with higher BDE values fragmentation cannot efficiently compete with back electron transfer within the radical ion pair) and that the product distribution is dependent upon the relative oxidation potentials of the two fragments formed, the carbocation deriving from the radical fragment which has the lower oxidation potential [193]. Since different products arise from the alternative fragmentation pathways of the radical cation, and given that the product distribution is determined within the radical ion pair (Scheme 47), if the product ratio from the cleavage reaction can be measured, the relative oxidation potentials of the two radical fragments can be determined.

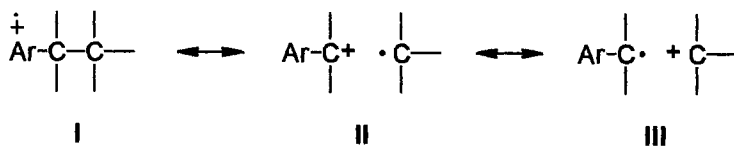
It has been suggested that the extent of charge delocalization in the transition state may be greater for the heterolytic than for the homolytic fragmentation mode, since in the former the departing fragment is predisposed to accommodate a net charge [126]. If charge delocalization decreases the transition state energy, the heterolytic cleavage may have an intrinsic kinetic advantage over the homolytic one. However, Savéant proposed that for endoergonic cleavages, C–C bond fragmentation is reversible with the rate kinetically controlled by the diffusion of the two fragments from the solvent cage rather than by activation parameters, a behavior associated with small intrinsic barriers ($\leq 0.2 \text{ eV}$), indicating that the reorganization energies for these processes are small [175]. Therefore, the reactivity of the fragments may be important with respect to the C–C bond cleavage rate.

The importance of through bond delocalization in C–C bond cleavage reactions of alkylaromatic radical cations has been established in both theoretical and experi-

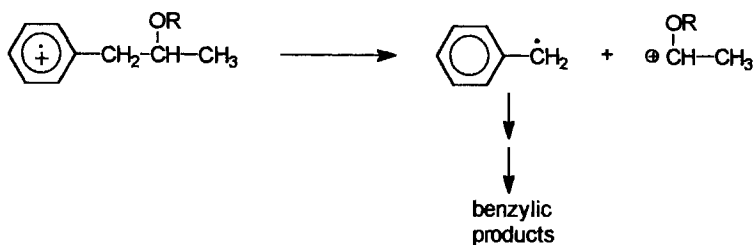
mental studies. In a MO-theoretical investigation, Kikuchi showed that a drastic change in the electronic structure of phenylethane radical cation occurs during (homolytic) C–C bond cleavage, discussing the results in terms of the three electron three orbital three configuration approach, as described in Scheme 29 [136]. In the radical cation both charge and spin are highly localized on the aromatic ring; as the C–C bond elongates a change in electronic structure occurs (attributed to the avoided crossing between the Π and Σ states), the unpaired electron density rapidly decreases on the phenyl ring, increases at C_β (due to the contribution of the Σ^* state) and transiently increases at C_α . Transient accumulation of positive charge at C_β is also observed, irrespective of the homolytic cleavage, finally leading to a benzyl cation and a methyl radical. Substitution of electron releasing groups at C_α and/or C_β stabilizes both Σ and Σ^* states favoring C–C bond cleavage, while substitution of electron releasing groups at the *para* position will mainly stabilize the Π state decreasing the importance of this reaction.

In another study, Camaioni showed that bibenzylic radical cations are π -type structures with the charge mainly localized in one of the aromatic rings and that the barrier for C–C bond cleavage is mainly associated with establishing orbital overlap between the π - and σ -systems by stretching the ethylenic bond, thus enabling through bond delocalization [194]. When sufficient overlap is achieved, the charge developing on C_α and C_β can be stabilized by delocalization on the aromatic rings as well as on the side-chain substituents. The presence of electron releasing groups such as OH and Me on the phenyl ring does not stabilize significantly the long bond structure, while substitution on the ethylenic bond leads to a change in the potential energy surface for C–C bond cleavage. Accordingly, bibenzyl, 4-methylbibenzyl and 4-hydroxybibenzyl radical cations have similar BDEs, and long-bond structures with charge and spin delocalized through the scissible C–C bond are not predicted to be stable minima. On the other hand, the presence of α -methyl or α -hydroxy groups leads to a significant decrease in radical cation BDE, and accordingly C–C bond cleavage in bicumyl radical cation is predicted to be exothermic with an early transition state and only partial delocalization into the β -ring, with fragmentation occurring when the C–C bond is elongated by 10 % of its equilibrium length. Within bicumyl radical cations, where C–C bond cleavage is the only possible fragmentation pathway, an increase in ring electron density is predicted to result in later transition states characterized by a larger extent of through bond delocalization [194].

Taken together, these studies suggest that the transition state for C–C bond cleavage in alkylaromatic radical cations can be conveniently described by the following mesomeric structures (Scheme 48), where the contribution of structure I is



Scheme 48.



Scheme 49.

predominant for exothermic scissions with early transition states, while structures **II** and **III**, accounting for through bond delocalization, give an increasing contribution as the transition states become later.

These *theoretical* studies fully support the *experimental* results obtained for side-chain fragmentation reactions of aromatic radical cations. Accordingly, product studies have shown that while bibenzyl, 4-methyl-, 4-methoxy- and 4,4'-dimethoxybibenzyl radical cations undergo exclusive C–H bond cleavage [177–179, 195], C–C bond cleavage is favored by α substitution of electron releasing groups [179], as well as by β substitution [196].

Additional information on the importance of through bond delocalization and on the competition between C–H and C–C bond cleavage comes from studies on arylalkane radical cations bearing OH or OR substituents at C_β , generated under a variety of conditions. While fragmentation of $\text{PhCH}_2\text{CH}(\text{OR})\text{CH}_3^{+\bullet}$ ($\text{R} = \text{H, Me}$) [98, 180, 196, 197] and $\text{PhCH}_2\text{CH}(\text{OEt})_2^{+\bullet}$ [198] lead to predominant or exclusive formation of benzylic products deriving from heterolytic C–C bond cleavage (Scheme 49), a different reactivity pattern is observed with the corresponding ring methoxylated radical cations. $4\text{-MeOC}_6\text{H}_4\text{CH}_2\text{CH}(\text{OMe})\text{CH}_3^{+\bullet}$ undergoes exclusive C–H deprotonation, while the product distribution changes with conditions for $4\text{-MeOC}_6\text{H}_4\text{CH}_2\text{CH}(\text{OH})\text{CH}_3^{+\bullet}$ [196]. At 50°C , in the absence of added base only products of C–H bond cleavage have been observed, the importance of the C–C bond cleavage pathway increasing in the presence of base. At 110°C in the absence of base C–H fragmentation is still predominating but C–C bond cleavage competes significantly.

On the basis of these results several conclusions can be drawn:

The relative importance of C–C bond cleavage significantly decreases by adding a 4-methoxy substituent to the ring, which indicates the existence of different electronic requirements for C–C and C–H bond cleavage. Probably, the extent of positive charge which has to accumulate on the scissible bond in the transition state (through bond delocalization), is larger for C–C than for C–H bond cleavage, as also suggested by the early transition state of the latter process. Thus, in the radical cation, the presence of the 4-methoxy group, which stabilizes the positive charge on the aromatic ring, opposing the intramolecular side-chain to nucleus electron transfer, may exert an unfavorable effect more on C–C than on C–H bond cleavage.

Replacement of the β -OMe group by OH has no influence on the reactivity of the

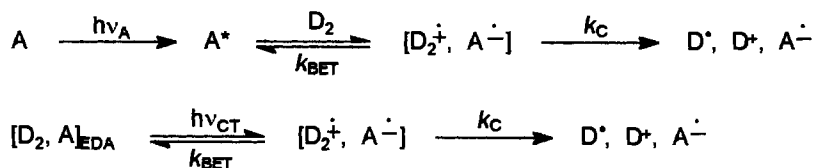
ring-unsubstituted radical cations, while it leads to a significant increase in the importance of the C–C bond cleavage pathway in the corresponding ring methoxylated ones, this reaction however being favored by the presence of a base (see later).

C–C bond cleavage can be thermally activated, as also shown by Arnold in the fragmentation of 1,1,2,2-tetraphenylethane radical cation [181]. In this respect, Maslak measured the activation parameters for a series of bicumene radical cations showing that activation enthalpies (ΔH^\ddagger) for mesolysis are between 8 and 16 kcal mol⁻¹, i.e. 30–35 kcal mol⁻¹ lower than the values for homolysis of the corresponding neutral substrate, while activation entropies (ΔS^\ddagger) are very small or negative (between 2 and –27 eu) in spite of the production of fragments in the cleavage process, suggesting the involvement of a highly ordered solvation of the transition state [199, 200]. A similar trend has been observed for C–C bond fragmentation in a series of 4-methoxybenzylic radical cations (4-MeOC₆H₄CH₂R^{•+}), where, moreover, the study of the temperature effect on the competition between C–H and C–C bond cleavage has lead to the conclusion that ΔS^\ddagger contributes more to the C–C than to the C–H fragmentation pathway while the opposite holds for ΔH^\ddagger [192].

In the same study it has also been shown that when the nucleophilicity of the system (neat MeCN) is increased by addition of NO₃⁻, certain radical cations which in the absence of NO₃⁻ undergo C–C fragmentation with $\Delta G^\ddagger > 11$ kcal mol⁻¹ (R = CMe₂OMe, CPh₂OMe, 1,3-dioxolan-2-yl), change their reactivity pattern to C–H deprotonation, suggesting that this process requires a more efficient base than the solvent. Attack of NO₃⁻ is expected to depend on the charge density (Q) at the reaction center (benzylic hydrogens or β -carbon) and accordingly calculations show that while on the benzylic hydrogens Q is almost constant for all radical cations (between 0.12 and 0.16), different values are obtained for the β -carbon depending on the nature of R: $Q \leq -0.02$ for R = CMe₂OMe and CPh₂OMe, $Q = 0.16$ for R = 1,3-dioxolan-2-yl, thus providing a rationale for the observed reactivity.

The presence of electron releasing groups on both C _{α} and C _{β} as in pinacols, pinacol ethers and bicumyls strongly favors C–C bond cleavage in the corresponding radical cation. Kochi studied the mesolytic C–C bond cleavage in pinacol radical cations, (ArC(OH)R)₂^{•+}, generated by PET [201, 202], or charge transfer excitation of the EDA complexes between the pinacol donor (D₂) and an acceptor (A = quinones [201, 202], or A = methyl viologen di-cation (MV²⁺) [203]) (Scheme 50, where D₂ = (ArC(OH)R)₂).

Direct kinetic measurements by time-resolved fs spectroscopy, following charge-transfer activation with MV²⁺ as the acceptor, lead to k_C values between 3×10^9



Scheme 50.

Table 7. Unimolecular rate constants for C–C bond cleavage of $(\text{ArC}(\text{OH})\text{R})_2^{*+}$ generated by charge-transfer activation of EDA complexes in MeCN at $T = 25^\circ\text{C}$.

Ar	R	k_C (s^{-1})
C_6H_5	C_6H_5	1.4×10^{10}
3- C_6H_5 - C_6H_4	Me	3×10^9
4- C_6H_5 - C_6H_4	Me	5×10^9
4-MeOC $_6\text{H}_4$	Me	5.3×10^{10}
4-MeOC $_6\text{H}_4$	C_6H_5	4.9×10^{10}
4-MeOC $_6\text{H}_4$	4-MeOC $_6\text{H}_4$	8.0×10^{10}

and $8.0 \times 10^{10} \text{ s}^{-1}$ (Table 7), indicating ultrafast fragmentation rate constants for all radical cations with activation energies $< 5 \text{ kcal mol}^{-1}$ [203].

The rate of fragmentation is enhanced by electron-releasing ring substituents as shown by the analysis of two series of structurally related pinacol radical cations: $(\text{X-C}_6\text{H}_4\text{C}(\text{OH})\text{Me})_2^{*+}$ with $\text{X} = 3\text{-Ph}, 4\text{-Ph}, \text{OMe}$ (Table 7), from which a Hammett correlation is observed between $\log k_C$ and σ with $\rho = -3.8$ [203]; and $(\text{X-C}_6\text{H}_4\text{C}(\text{OSiMe}_3)\text{Me})_2^{*+}$ with $\text{X} = 2,4\text{-(MeO)}_2, 4\text{-MeO}, \text{H}, 4\text{-Br}$ showing the following relative reactivities, 5000, 70, 1.0, 0.2, respectively [201]. A behavior which has been attributed to the increased stability of the fragmentation products as the ring substituents are changed, pointing towards a late transition state for the C–C bond cleavage reaction which can be described by structures **II** and **III** in Scheme 48.

Similar behavior has been observed by Maslak in the C–C bond cleavage of 4-methoxy- [204–206] and 4-dimethylaminobicumene [199, 200] radical cations (4MBC^{*+} and 4DMABC^{*+} , respectively, Scheme 51).

Accordingly, p^+ values of -2.2 and -0.8 have been obtained for mesolytic C–C bond cleavages of 4MBC^{*+} [205], and 4DMABC^{*+} [200], respectively, indicating buildup of a partial positive charge on C_β in the transition state.

Moreover, the unimolecular rate constants for mesolytic cleavage (k_m) for both 4MBC^{*+} [204], and 4DMABC^{*+} [199, 200] significantly increase by substitution of electron releasing groups at the 4-position of the β -phenyl ring as well as by replacing the side-chain Me groups with Et, while electron withdrawing substituents ($\text{X} = \text{CF}_3, \text{CN}$) slow down the fragmentation reaction (Table 8). These observations point again towards a polarized transition state in which a substantial amount of positive charge has been transferred across the scissible bond (Scheme 48).

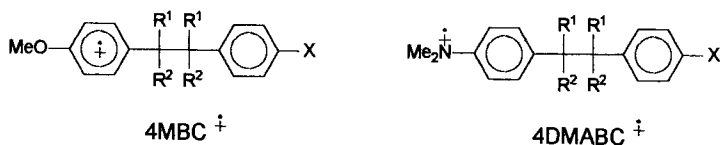
**Scheme 51.**

Table 8. Unimolecular rate constants for mesolytic cleavage of 4MBC^{•+} and 4DMABC^{•+} in CH₂Cl₂-MeOH^a at room temperature.

R ¹	R ²	X	<i>k_m</i> (s ⁻¹)
<i>4MBC^{•+}</i> ^b			
Me	Me	H	2.4×10^7
Me	Me	MeO	6.0×10^8
Me	Me	Me	1.2×10^8
Me	Me	CF ₃	1.6×10^6
Me	Me	CN	2.6×10^6
Me	Et	MeO	1.2×10^9
Et	Et	MeO	4.4×10^9
<i>4DMABC^{•+}</i> ^c			
Me	Me	H	0.7
Me	Et	H	20
Et	Et	H	1.6×10^5

^a MeOH 0.5–5 %.^b According to [204].^c According to [199].

On the basis of the comparison between the reactivities of the different series of pinacol and bicumyl radical cations discussed above (Tables 7 and 8), some conclusions can be drawn:

Increased electron density on the aromatic ring bearing the unpaired electron allows a smaller extent of charge transfer to the scissible C–C bond (compare the ρ^+ values for 4DMABC^{•+} and 4MBC^{•+}), by opposing intramolecular electron transfer, reflected in a dramatic decrease in k_m (Table 8).

Increased electron density on the β -aromatic ring (not bearing the unpaired electron) favors through bond delocalization ($\rho^+ < 0$) enhancing the fragmentation rate.

Increased electron density on both aromatic rings enhances the fragmentation rate, suggesting that in such cases stabilization of the transition state by through bond delocalization is more important than stabilization of the reactant radical cation.

Replacement of side-chain Me groups by Et or OH leads to an increase in the rate of C–C bond cleavage, as clearly shown by comparing the reactivities of three structurally related radical cations: (4-MeOC₆H₄CMe₂)₂^{•+}, (4-MeOC₆H₄CEt₂)₂^{•+}, undergoing fragmentation with $k_m = 6.0 \times 10^8$ and 4.4×10^9 s⁻¹, respectively (Table 8) and (4-MeOC₆H₄C(OH)Me)₂^{•+}, for which $k_m = 5.3 \times 10^{10}$ s⁻¹ (Table 7), in line with ability of these groups in stabilizing a positive charge on the adjacent carbon atom. Interestingly, this rate enhancement is significantly more pronounced when the β -ring lacks electron releasing substituents.

However, in partial contrast with these conclusions are the results obtained by Whitten for the fragmentation of substituted pinacol radical cations (ArC(OH)R)₂^{•+},

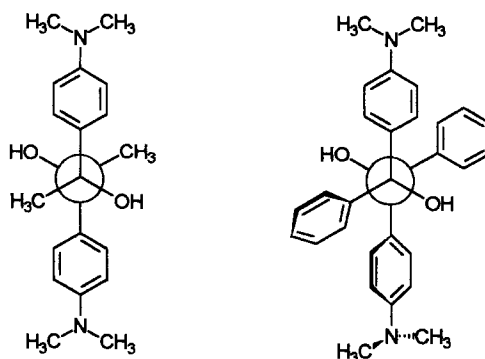
Table 9. Unimolecular rate constants for C–C bond cleavage of $(\text{ArC}(\text{OH})\text{R})_2^{*+}$ generated by PET in MeCN at room temperature.

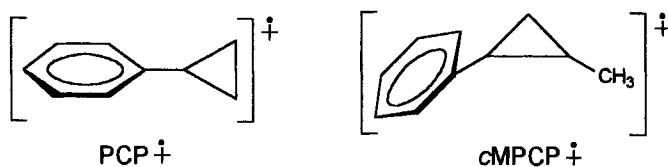
Ar	R	E_p (V relative to the NHE)	k_{BF} (s^{-1})
4-MeOC ₆ H ₄	Me	1.49	$>1 \times 10^7$
2,4-(MeO) ₂ C ₆ H ₃	Me	1.27	7.5×10^6
2,5-(MeO) ₂ C ₆ H ₃	Me	1.24	4.5×10^6
2,4,5-(MeO) ₃ C ₆ H ₂	Me	0.99	2.5×10^6
4-Me ₂ NC ₆ H ₄	H	0.95	$<5 \times 10^3$
4-Me ₂ NC ₆ H ₄	Me	0.81	1.8×10^5
4-Me ₂ NC ₆ H ₄	Ph	0.95	4×10^4

where the rate constants for C–C bond cleavage (k_{BF}) follow the stability of the corresponding radical cation (Table 9) [207–209].

An explanation accounting for the different behavior observed is not easy, but a more conclusive characterization of the radical cations by time-resolved spectroscopic techniques is certainly needed [203, 208]. It is moreover important to consider that if the reduced sensitizer is sufficiently basic, deprotonation from the side-chain OH group could also occur, followed by C–C fragmentation from an intermediate oxyl radical (see later) [201, 210].

The unexpected decrease in reactivity observed on going from $(4\text{-Me}_2\text{NC}_6\text{H}_4\text{C}(\text{OH})\text{Me})_2^{*+}$ to $(4\text{-Me}_2\text{NC}_6\text{H}_4\text{C}(\text{OH})\text{Ph})_2^{*+}$, has been instead attributed to conformational requirements in the transition state for C–C bond cleavage, based on the negative ΔS^\ddagger values (-6.9 and -10.6 eu, respectively) determined for this process, which suggest an ordered transition state [209]. Accordingly, calculations have shown that for $(4\text{-Me}_2\text{NC}_6\text{H}_4\text{C}(\text{OH})\text{Me})_2$ and $(4\text{-Me}_2\text{NC}_6\text{H}_4\text{C}(\text{OH})\text{Ph})_2$ the most stable conformations are those depicted in Scheme 52 (which should reasonably hold also for the corresponding radical cations), where the dimethylaminophenyl groups are in the correct orientation for C–C bond cleavage (face to face, where the π orbitals are collinear with the scissible σ bond) only in the former substrate.

**Scheme 52.**



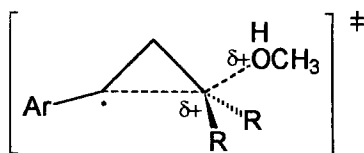
Scheme 53.

An analogous trend has been observed by Kochi for the corresponding ring methoxylated pinacols [203], where however the effects are much smaller (Table 7). Replacing the side-chain phenyl groups with 4-MeOC₆H₄ results however in a significant increase in reactivity, suggesting that in this case electronic effects overcome the steric ones.

It is also interesting to examine the nucleophilically assisted C–C bond cleavage in substituted arylcyclopropane radical cations previously described, in terms of the concepts discussed above. The experimental data obtained have shown that three-electron S_N2 reactions of arylcyclopropane radical cations are dominated by electronic rather than steric effects, the substitution regiochemistry being determined by the ability of the alkyl group at C_β to stabilize a positive charge in the transition state [188, 189, 191]. Accordingly, quantum chemical calculations have shown that phenylcyclopropane radical cation (PCP^{•+}) adopts a delocalized bisected conformation with two equally lengthened C–C bonds (Scheme 53) characterized by a significant interaction between the phenyl and cyclopropyl moieties [190, 211]. Addition of methyl groups at C_β leads to a significant increase in the C_α–C_β bond length and to a change in the relative orientation of the two rings, with the plane of the phenyl ring almost completely aligned with the C_α–C_γ bond (Scheme 53, showing *cis*-1-methyl-2-phenylcyclopropane (*c*MPCP) radical cation), allowing efficient overlap between the π-orbitals and the long C_α–C_β bond.

Alkyl substitution also leads to a significant redistribution of the positive charge which decreases on the phenyl ring simultaneously increasing at C_β. Semi-empirical calculations of the transition state structures for backside nucleophilic attack of methanol on PCP^{•+} predict a significant increase in the C_α–C_β bond length and of the charge at C_β at the expense of the charge on the phenyl ring, on going from the reactants to the transition state. In agreement with this shift in charge is the value of $\rho^+ = 2.2$ obtained from the correlation between σ^+ and the rate constants for nucleophilic substitution on *para*-substituted PCP^{•+}, reflecting the decreased ease of intramolecular electron transfer as the ring electron density increases [190]. Moreover, the C_β–O distance is predicted to decrease by increasing alkyl substitution, accompanied by charge increase at both C_β and O, a behavior which suggests that transition states for these processes become later with increasing alkyl substitution.

A product-like transition state has been proposed by Tanko for the nucleophile-induced ring opening of 1- and 2-cyclopropylnaphthalene radical cations, with the spin density delocalized over C_α and the aromatic system, and a large fraction of positive charge localized at both C_β and O (Scheme 54) [212], suggesting that stabilization of the positive charge by the naphthyl group is of limited importance. Thus, the aromatic system is expected to stabilize the reactant radical cation sig-



Scheme 54.

nificantly more than the transition state for nucleophilic substitution. In agreement with this hypothesis is the observation that no direct cyclopropyl ring opening is observed in the reaction of 9-cyclopropylanthracene radical cation with MeOH [213, 214].

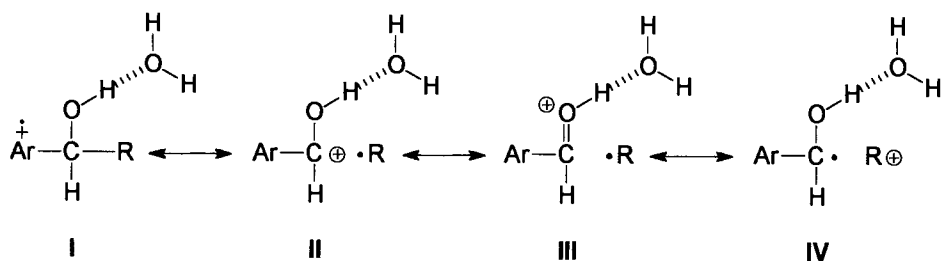
Oxygen acidity and C–C bond cleavage

The favorable effect of side-chain OH groups on the C–C bond cleavage reactions of alkylaromatic radical cations has been shown in a number of studies (see above) [179, 186, 196, 203, 207]. Along this line, in acidic aqueous solution both 4-MeOC₆H₄CH(OH)CH₂C₆H₅^{•+} and 4-MeOC₆H₄CH₂CH(OH)C₆H₅^{•+} undergo C–C bond cleavage as the major reaction pathway with similar rate constants ($k = 3.2 \times 10^4$ and 2.0×10^4 s⁻¹, respectively) suggesting that at least for these systems the position of the OH group (α or β) does not play a significant role [196]. In both fragmentation reactions a small solvent kinetic isotope effect ($k(\text{H}_2\text{O})/k(\text{D}_2\text{O})$ between 1.2 and 1.4) and negative activation entropies have been observed, suggesting that hydrogen bonding plays a major role in the α - and β -OH assisted C–C bond cleavage. Moreover, the OH group is much more effective than OMe in promoting C–C bond cleavage, as clearly shown by the observation that in acidic aqueous solution 4-MeOC₆H₄CH(OH)*t*Bu^{•+} undergoes exclusive C–C bond cleavage with a rate ($k = 1.5 \times 10^5$ s⁻¹) which is about four orders of magnitude higher than that of the corresponding methyl ether, in spite of the fact that both radical cations are characterized by very similar values of C–C BDE. As a matter of comparison, under identical conditions no difference in the rate of C–H deprotonation was observed between the radical cations of 4-methoxybenzyl alcohol and its methyl ether (Table 5) [170].

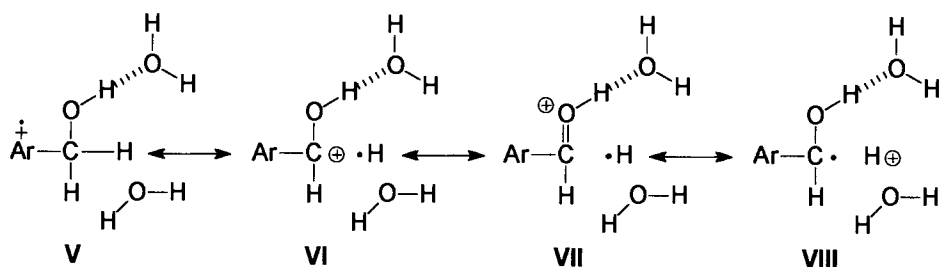
On the basis of these observations, the transition state for C–C bond cleavage in 1-arylalkanol radical cations can be conveniently described by mesomeric structures **I**–**IV** (Scheme 55, Ar = 4-MeOC₆H₄), where structure **III**, with the positively charged oxygen and the fully formed C=O double bond, strongly contributes to the transition state structure, profiting from stabilization by hydrogen bonding with the solvent water.

In contrast, in the transition state for C–H deprotonation (Scheme 56, also showing the proton-accepting base H₂O), the most important structure is now **VIII**, representing heterolytic C–H bond cleavage, whereas structure **VII** (corresponding to **III** in Scheme 55) should be of minor importance, since it involves the very unfavorable homolytic C–H bond cleavage.

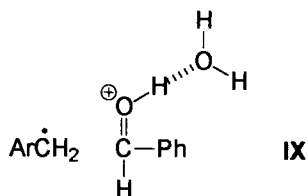
A similar transition state stabilization by hydrogen bonding can be envisaged also for 2-arylalkanol radical cations, as described by structure **IX** (Scheme 57).



Scheme 55.

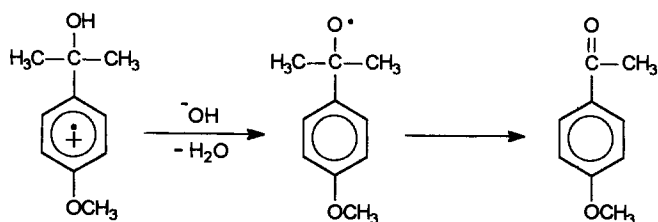


Scheme 56.



Scheme 57.

In both 1- and 2-(4-methoxyphenyl)-alcohol radical cations, C–C bond cleavage is strongly favored by the presence of ^-OH . Accordingly, pulse radiolysis studies have shown that $4\text{-MeOC}_6\text{H}_4\text{CH}(\text{OH})\text{R}^{+\bullet}$ ($\text{R} = \text{Et}, i\text{Pr}$) undergo exclusive or predominant C–H bond cleavage at $\text{pH} \leq 5$, while in the presence of ^-OH C–C bond cleavage becomes the major reaction pathway [170]. Under these conditions, base-induced C–C bond cleavage occurs with a diffusion controlled rate ($k_{-\text{OH}} \approx 1 \times 10^{10} \text{ M}^{-1} \text{ s}^{-1}$) an observation which suggests that this reaction proceeds through an analogous mechanism as that proposed for the deprotonation of 4-methoxybenzyl alcohol radical cations (Scheme 42). Namely, $4\text{-MeOC}_6\text{H}_4\text{CH}(\text{OH})\text{R}^{+\bullet}$ behave as oxygen acids undergoing O–H deprotonation leading to an intermediate oxyl radical ($4\text{-MeOC}_6\text{H}_4\text{CH}(\text{R})\text{O}^\bullet$), which can follow two reactive pathways: C–C bond cleavage and/or 1,2-H atom shift, depending on the nature of R (Scheme 42, paths e and g). When $\text{R} = \text{H}$ or Me , the 1,2 shift is the exclusive pathway, whereas when



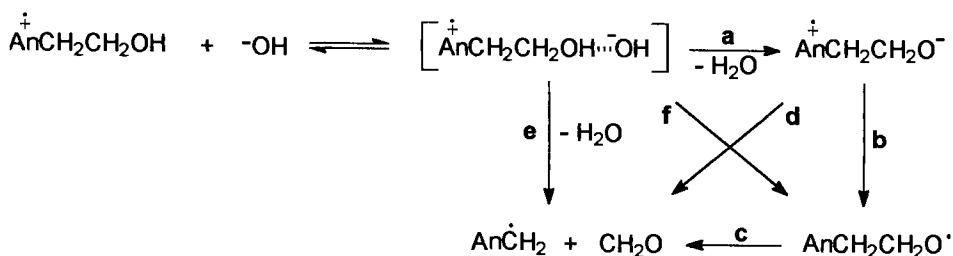
Scheme 58.

R = *t*Bu, only β -cleavage occurs. Intermediate situations apparently hold for R = Et and *i*Pr. Formation of an intermediate oxyl radical followed by β -fragmentation has been proposed in the reactions of photogenerated pinacol radical cations [201, 210].

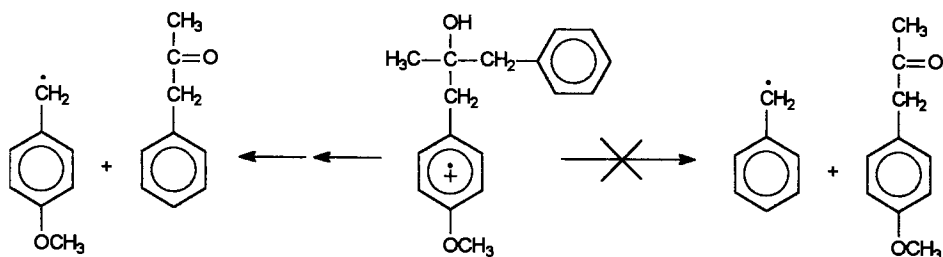
Direct evidence for the formation of the oxyl radical was indeed obtained in a pulse radiolysis study of the $^{\cdot}\text{OH}$ -induced decay of 4-methoxycumylalcohol radical cation where, accordingly the 4-methoxycumyloxyl radical was observed by time-resolved UV-Vis spectroscopy on its way to form 4-methoxyacetophenone (Scheme 58) [215].

It is however important to point out that in this case the oxyl radical is relatively long-lived, since fragmentation leads to 4-methoxyacetophenone and Me^{\cdot} , the least stable alkyl radical. In the presence of alkyl groups which can produce, after β -fragmentation, radical fragments more stable than Me^{\cdot} , one cannot exclude that such process proceeds through a mechanism involving concerted C-C bond cleavage and intramolecular electron transfer in the radical zwitterion (Scheme 42, path **f**).

When the OH group is in the β position, the mechanistic dichotomy between carbon and oxygen acidity is again observed. Accordingly, while at $\text{pH} \leq 5$, 4-MeOC₆H₄CH₂CH₂OH $^{\cdot+}$ undergoes exclusive α -C-H deprotonation with $k = 5.2 \times 10^2 \text{ s}^{-1}$, a rate constant very similar to that observed for 4-methoxytoluene radical cation (Table 5), in the presence of $^{\cdot}\text{OH}$ only C-C bond cleavage is observed with $k_{\text{OH}} = 8.3 \times 10^9 \text{ M}^{-1} \text{ s}^{-1}$, a value very close to the diffusion limit [172]. Thus, in the presence of $^{\cdot}\text{OH}$, a mechanism resembling the one described in Scheme 42 for 1-arylalkanol radical cations can be proposed also for 2-arylalkanol radical cations (Scheme 59: An = 4-MeOC₆H₄).



Scheme 59.



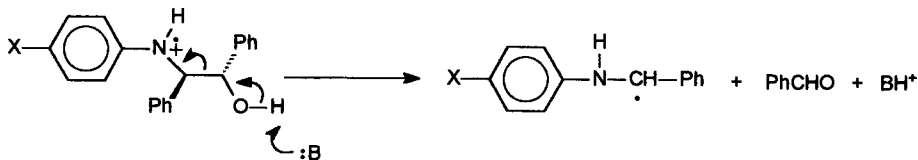
Scheme 60.

Proton transfer in the encounter complex may lead, either directly (path **f**) or via a radical zwitterion (paths **a** and **b**), to an alkoxy radical which then undergoes C–C bond β -cleavage (path **c**). As an alternative, two concerted processes are also possible; involving O–H deprotonation and C–C bond cleavage (E2 mechanism, path **e**) or C–C bond cleavage and intramolecular electron transfer in the radical zwitterion (E1cB mechanism, paths **a** and **d**).

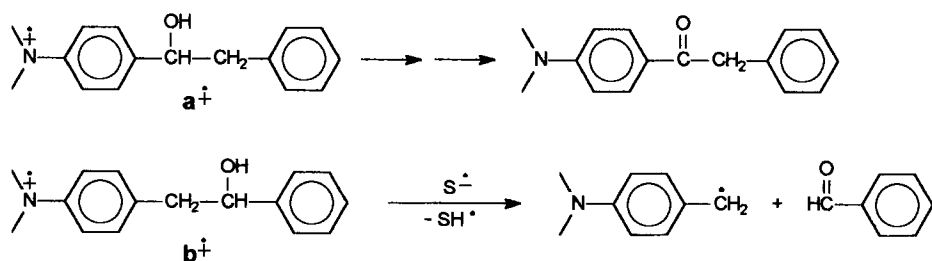
Useful information in this respect has been obtained through the product study of the ^-OH -induced decay of $4\text{-MeOC}_6\text{H}_4\text{CH}_2(\text{Me})\text{C}(\text{OH})\text{CH}_2\text{Ph}^{+\bullet}$ [172]. If alkoxy radicals are involved in the fragmentation process, products deriving from both the benzyl and 4-methoxybenzyl radical should be observed (Scheme 60). Since only products deriving from the latter radical have been observed, the intermediacy of the alkoxy radical in the ^-OH -induced fragmentation of β -OH substituted alkylaromatic radical cations can be reasonably excluded, thus the reaction proceeds through one of the concerted processes (paths **d** or **e**) described in Scheme 59.

These two mechanisms (E1cB and E2) have been proposed by Schanze and Whitten, respectively to rationalize the effect of the β -OH group on the side-chain C–C bond cleavage in the radical cations of 2-(arylamino)-1,2-diphenylethanols [216], 1,2-aminoalcohols [217], and 2-(4-*N,N*-dimethylaminophenyl)-1-phenylethanol [218].

In particular, Schanze proposed that the mechanism of base-catalyzed fragmentation in 2-(4-*X*-phenylamino)-1,2-diphenylethanol radical cations (Scheme 61) changes with the oxidation potential of the substrate, going from an E1cB-like mechanism (as in Scheme 59, paths **a** and **d**) with the more stable radical cations ($X = \text{OMe}$ and Me), to an E2-like mechanism (as in Scheme 59, path **e**) when $X = \text{H}$, Cl , CN .



Scheme 61.



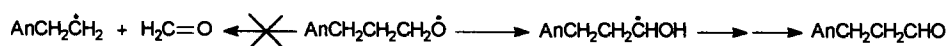
Scheme 62.

Moreover, a Brønsted correlation with $\alpha = 0.62$ has been obtained for 2-phenyl-amino-1,2-diphenylethanol radical cation [219]. Comparison of this value with that obtained for the C–C bond cleavage of 4-MeOC₆H₄CH(OH)*t*Bu^{•+} catalyzed by a series of bases in aqueous solution ($\beta = 0.4$) [170], suggests that localization of the positive charge at nitrogen results in a significantly later transition state for fragmentation.

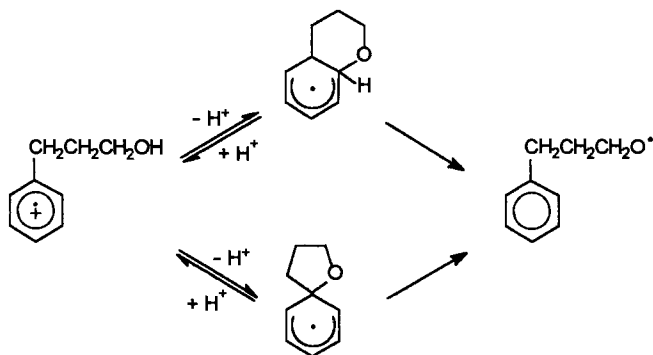
It is also interesting to compare the results for 4-MeOC₆H₄CH(OH)CH₂C₆H₅^{•+} and 4-MeOC₆H₄CH₂CH(OH)C₆H₅^{•+}, undergoing C–C bond cleavage as the major or exclusive reaction pathway in both acidic and basic aqueous solution [170, 172], with those obtained by Whitten for the fragmentation of structurally related aminoalcohol radical cations: 4-Me₂NC₆H₄CH(OH)CH₂C₆H₅^{•+} (**a**^{•+}) and 4-Me₂NC₆H₄CH₂CH(OH)C₆H₅^{•+} (**b**^{•+}), in MeCN or benzene [218]. While **a**^{•+} undergoes C–H bond cleavage leading to the corresponding aminoketone, **b**^{•+} gives clean C–C fragmentation (Scheme 62, S = sensitizer).

This peculiar behavior can be explained in terms of the already discussed through bond delocalization. Positive charge development at C_β seems to be a prerequisite for C–C bond cleavage to occur. In aminoalcohol radical cations, the positive charge is strongly localized on the dimethylamino moiety thus opposing intramolecular electron transfer from the side-chain scissible bond. In **a**^{•+}, the presence of a phenyl group at C_β is not sufficient to stabilize an incipient positive charge and accordingly no homolytic C–C fragmentation is observed. On the other hand, the presence of an additional β-OH group as in **b**^{•+} promotes through bond delocalization, making heterolytic (O–H assisted) C–C bond cleavage an efficient process. In line with this picture is the lower reactivity observed for N-aromatic substituted amino alcohol radical cations, as compared to N-alkyl substituted ones [217].

Finally, oxygen acidity extends also to 3-arylalkanol radical cations as clearly shown by 4-MeOC₆H₄(CH₂)₃OH^{•+} which undergoes α-C–H deprotonation at pH ≤ 5 and O–H deprotonation in the presence of [–]OH, with a rate constant, $k_{\text{-OH}} = 1.7 \times 10^9 \text{ M}^{-1} \text{ s}^{-1}$, which is 25 times higher than that measured for the corresponding methyl ether [172]. In basic solution, no products of C–C bond cleavage are observed, but only 3-(4-methoxyphenyl) propanal, deriving from 1,2-H shift in the intermediate oxyl radical, since β-cleavage would lead to a relatively unstable primary alkyl radical (Scheme 63, An = 4-MeOC₆H₄).



Scheme 63.



Scheme 64.

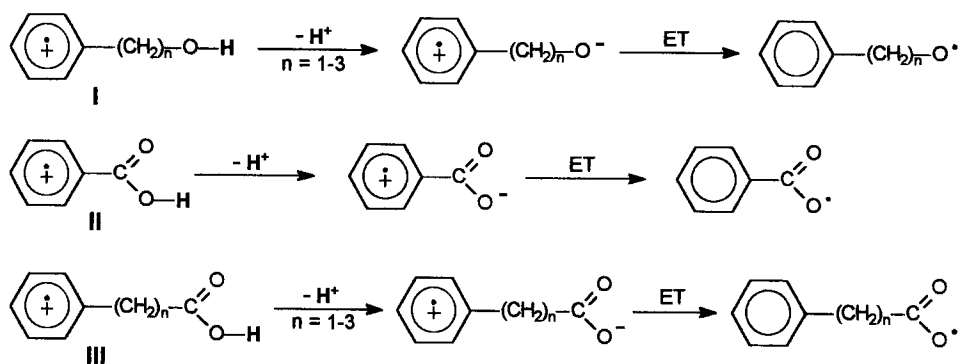
The value of $k_{-\text{OH}}$ is significantly below the diffusion limit and thus of the values measured for 1- and 2-arylalkanol radical cations, indicating that formation of the encounter complex is no longer the rate determining step. This behavior reflects the decreased oxygen acidity as well as the decreased ease of intramolecular electron transfer as the distance between the OH group and the aromatic ring bearing the positive charge is increased. An alternative mechanism has been however proposed by Gilbert accounting for the observed reactivity of 3-phenylalkanol radical cations in acidic solution, where intramolecular electron transfer proceeds through an inner-sphere mechanism by ring-closure via intramolecular nucleophilic attack of the γ -OH followed by ring opening, leading to the oxyl radical (Scheme 64) [186, 220].

Clearly, with this radical cation oxygen acidity is observed at much lower pH (between 1 and 3) suggesting that in the presence of a 4-MeO group, intramolecular electron transfer can efficiently occur only if the O-H group is deprotonated.

If the distance between the aromatic ring and the side-chain OH function is further increased as with 4-MeOC₆H₄(CH₂)₄OH, oxygen acidity in the corresponding radical cation is no longer observed [172].

Aromatic radical zwitterions

As previously discussed, removal of an electron from the π -system of alkylaromatic substrates leads to a dramatic increase in the acid strength of the $\text{C}_x\text{-H}$ bonds, as clearly shown by the $\text{p}K_{\text{a}}$ between -11 and -13 estimated for the deprotonation of toluene radical cation in acetonitrile [130]. The presence of a positive charge on the aromatic ring can also influence, however to a much smaller extent, the acidity of groups which are further spaced from the aromatic ring such as OH and CO₂H as



Scheme 65.

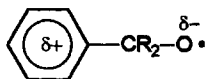
in arylalkanols, benzoic and arylalkanoic acids. Where possible, side-chain $\text{C}_\alpha\text{-H}$ deprotonation in the corresponding radical cations is strongly favored thermodynamically over O-H deprotonation. However, carbon acids exhibit much larger intrinsic barriers for proton transfer than oxygen acids [140, 141, 173] and thus, in the presence of a sufficiently strong base which overcomes the thermodynamic gap, O-H deprotonation can take over (see above). No C-H deprotonation is usually observed with aryloethanoic acid radical cations (in Scheme 65: structure **III** with $n = 1$), since in this case C-C bond cleavage leads to a very stable fragment (CO_2) and a relatively stable benzyl radical (see later).

O-H deprotonation of arylalkanol (**I**), benzoic acid (**II**) and arylalkanoic acid (**III**) radical cations eventually leads to radical zwitterions where the electron hole is localized on the aromatic system and the negative charge resides on the oxygen atom originally bonded to the acidic proton (Scheme 65). From the radical zwitterions an oxygen centered radical can be formed by intramolecular electron transfer from the side-chain $-\text{O}^-$ to the aromatic π -system, whose chemistry will be discussed below.

Since in these systems intramolecular electron transfer involves orbitals which cannot directly overlap, a point which has attracted great interest is whether or not the radical zwitterion and the oxygen centered radical are different representations of a single species. In addition, the mechanistic picture can be further complicated since intramolecular electron transfer in the radical zwitterion can be coupled with or followed by other processes (i.e. $\text{C}_\alpha\text{-C}_\beta$ bond cleavage or 1,2-carbon to oxygen H atom shift with **I**, and decarboxylation with **II** and **III**). Finally, it is also interesting to understand if in systems such as **II** and **III**, decarboxylation requires or not initial O-H deprotonation.

The mechanistic implications of carbon and oxygen acidity in arylalkanol radical cations have been discussed extensively in the previous section and will not be further considered here [170, 172, 185, 186, 215].

In this respect however, one point should be briefly considered. It has been suggested that some internal charge transfer may occur in arylcarbinyloxyl radicals, accounting for the very pronounced red-shift (≈ 100 nm) observed for the visible



Scheme 66.

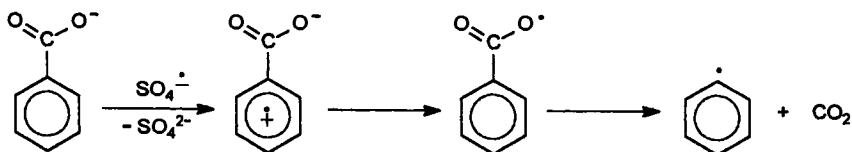
absorption band of these radicals by replacement of H with a 4-MeO group [221]. Moreover, calculations indicate that the unpaired electron is largely localized in the oxygen 2p orbital which is perpendicular to the plane of the aromatic ring and that in the ground state the oxygen atom of the benzyloxy radical bears a significant amount of negative charge, which is increased by the $\pi \rightarrow \pi^*$ transition responsible for the visible absorption band [222]. These results suggest that arylcarbinyloxy radicals display a certain zwitterionic character (Scheme 66), which should increase in the presence of electron releasing groups on the aromatic ring.

Radical zwitterions derived from benzoic acids

The reaction of benzoate anion with $\text{SO}_4^{\bullet-}$ has been established to proceed by electron transfer from the aromatic ring leading to the corresponding radical zwitterion [223], followed by decarboxylation of an intermediate benzoyloxy radical to yield the phenyl radical (Scheme 67). Both benzoyloxy and phenyl radicals have been identified by ESR spectroscopy through their adducts with CH_2NO_2^- [224, 225], and in particular, in the case of polycarboxylated benzenes, the (carboxylated) phenyl radicals have been *directly* seen by ESR [224].

For the 4-methyl derivatives, the different nature of the radical zwitterion and the neutral benzoyloxy radical, generated by $\text{SO}_4^{\bullet-}$ oxidation of 4-methylbenzoate and reaction of Ti(III) with 4-methylperoxybenzoic acid, respectively, has been clearly shown, since the former undergoes deprotonation and the latter hydrogen atom abstraction (by 4-methylbenzoyloxy and/or 4-methylphenyl radicals) from the 4-methyl group. Moreover, in the presence of a 4-MeO substituent, decarboxylation is observed only in the Ti(III)–4-methoxyperoxybenzoic acid system, while in the $\text{SO}_4^{\bullet-}$ –4-methoxybenzoate one this reaction becomes too slow and reduction of the radical zwitterion can take over, suggesting that this group significantly stabilizes the radical zwitterion by opposing intramolecular electron transfer leading to the 4-methoxybenzoyloxy radical [223].

This hypothesis is supported by the results of a pulse radiolysis and ESR study of methoxylated benzoic acids in water, where again no decarboxylation was observed from the corresponding radical zwitterions [226]. The zwitterionic nature of these radicals, with no contribution from an aroyloxy radical structure was shown on the



Scheme 67.

Table 10. Rate constants for the decarboxylation of ArCO_2^\bullet in CCl_4 at $T = 24^\circ\text{C}$.

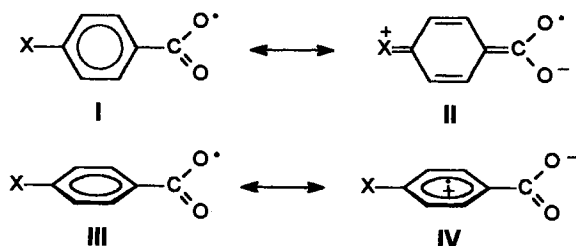
Ar	$k \text{ (s}^{-1}\text{)}$
C_6H_5	2.0×10^6
$4\text{-ClC}_6\text{H}_4$	1.4×10^6
$4\text{-MeOC}_6\text{H}_4$	3.4×10^5

basis of the following observations. The coupling constants for the one-electron oxidized methoxylated benzoic acids are very similar to those obtained from the corresponding methoxybenzene radical cations and are constant between pH 2 and 10, pointing towards an analogous charge and spin distribution in the two series of radical cations, and indicating moreover that the ionization state is the same over this pH range and thus that the carboxyl group of methoxylated benzoic acid radical cations is ionized at $\text{pH} \geq 2$.

Additional information on the nature of the radical zwitterion and the oxyl radical comes from a kinetic study of the decarboxylation of aryloxyl radicals (ArCO_2^\bullet) generated by LFP of the parent diaryl peroxide in CCl_4 [227], showing that the presence of a 4-MeO substituent leads to a significant decrease in the rate of decarboxylation (Table 10).

This behavior has been rationalized in terms of the relative arrangement of the aryl and CO_2 moieties, pointing towards a situation where these groups are coplanar (Scheme 68, structures **I** and **II**, where the unpaired electron is localized on the oxygen atom) rather than perpendicular (structures **III** and **IV**, where the arrangement of the two moieties allows through space electron transfer). Electron releasing substituents contribute to structure **II** increasing the double bond character of the Ar-CO_2^\bullet bond thus decreasing the decarboxylation rate. However, theoretical studies suggest that there is no strong preference for either the planar or perpendicular structure [227], and thus that intermediate structures may play a role in the behavior of aryloxyl radicals.

It is to be expected that the solvent should exert a strong influence on the decarboxylation rate via stabilization of (zwitter)ionic structures (**II** and **IV**). As mentioned above [226], in water no decarboxylation was observed from the radical zwitterion of 4-methoxybenzoic acid (i.e. $k \leq 10^2 \text{ s}^{-1}$).

**Scheme 68.**



Scheme 69.

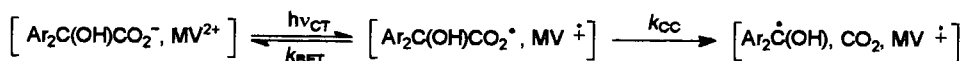
Radical zwitterions derived from arylalkanoic acids

The intermediacy of aromatic radical cations in the oxidative decarboxylation of aryloethanoic acids has been supported by a number of studies [228–231]. Direct evidence for the involvement of radical cations in these processes has been provided by a LFP study where the radical cations of the parent acids have been produced in aqueous solution by photoionization or by reaction with $\text{SO}_4^{\bullet-}$ [187]. 4-Methylphenylethanoic acid radical cation undergoes decarboxylation leading to the 4-methylbenzyl radical with $k = 1.5 \times 10^7 \text{ s}^{-1}$ at pH = 0.3 (Scheme 69, X = Me).

Interestingly, the rate constant increases by increasing pH ($k \geq 5 \times 10^7 \text{ s}^{-1}$ at pH ≥ 2.5), indicating that decarboxylation is faster when the carboxyl group is ionized. A similar reactivity has been observed with 4-methoxyphenylethanoic acid, where the corresponding radical zwitterion undergoes decarboxylation with $k \geq 5 \times 10^7 \text{ s}^{-1}$ (Scheme 69, X = MeO). Unfortunately, instrumental limits did not allow a direct comparison between the reactivities of the methyl and methoxy substituted radical zwitterions.

When the reactions of 1- and 2-naphthylethanoic acids with $\text{SO}_4^{\bullet-}$ have been studied analogously, a characteristic naphthalene-type radical cation spectrum with absorption bands centered at 310, 380, 630 and 680 nm has been observed only for the radical cation derived from the latter acid, while the former gives a spectrum with a main absorption at 330 nm attributed to the 1-naphthylmethyl radical formed by decarboxylation ($k = 5 \times 10^5 \text{ s}^{-1}$ at pH = 3.5) of a first formed radical zwitterion [187]. This behavior has been explained in terms of the much larger positive charge density at position 1 rather than 2 in the naphthalene radical cation (0.1809 and 0.0691, respectively from HMO calculations). Thus, the relatively larger accumulation of positive charge on the ring carbon atom bonded to the $\text{CH}_2\text{CO}_2\text{H}/\text{CO}_2^-$ group in 4-X-phenylethanoic acid radical cations as compared with 1-naphthylethanoic acid radical cation, reasonably accounts for the much faster rates of decarboxylation measured for the former.

More recently, Kochi studied the decarboxylation of acyloxyl radicals generated by PET in charge transfer ion pairs between benzilate anions ($\text{Ar}_2\text{C}(\text{OH})\text{CO}_2^-$) and a cationic acceptor (methylviologen di-cation (MV^{2+}) or *N*-methyl-4-cyanopyridinium (NCP^+)) in aqueous solution (Scheme 70) [232, 233].



Scheme 70.

Table 11. Rate constants for decarboxylation of MV^{2+} -benzilate and MV^{2+} -arylacetate ion pairs in aqueous solution.

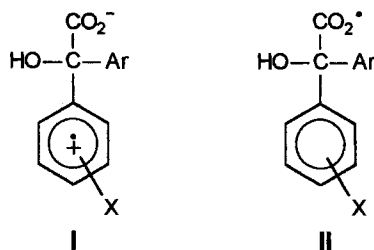
Donor	k_{CC} (s^{-1})
<i>Benzilate</i>	
Benzilate	8×10^{11}
4,4'-Dimethylbenzilate	5×10^{11}
4-Methoxybenzilate	1×10^{11}
4,4'-Dimethoxybenzilate	2×10^{11}
2,2',5,5'-Tetramethoxybenzilate	4×10^{10}
<i>Arylacetate</i>	
Diphenylacetate	6.1×10^9
Phenylacetate	1.8×10^9
4-Chlorophenylacetate	1.6×10^9
4-Methoxyphenylacetate	1.5×10^9
4-Biphenylacetate	1.5×10^9
1-Naphthylacetate	$<2 \times 10^8$

The rate constants for decarboxylation of $Ar_2C(OH)CO_2^{\cdot}$ (k_{CC}) are collected in Table 11 together with those obtained analogously for a series of aryloxy radicals ($ArCH_2CO_2^{\cdot}$).

Benziloxyl radicals undergo very fast decarboxylation ($k_{CC} > 10^{10} s^{-1}$) indicating activation barriers for C–C bond cleavage of only 1–2 kcal mol⁻¹. Interestingly, the presence of electron donating substituents on the aromatic ring leads to a decrease in k_{CC} .

To explain this observation, it has been suggested that the benziloxyl radical can be thought of as a resonance hybrid between the two structures depicted in Scheme 71: a radical zwitterion (**I**) where the electron hole is localized on the aromatic ring, and the acyloxyl radical (**II**) having the unpaired electron on the carboxyl group [232]. In the presence of electron releasing substituents (X) on the aromatic ring, the relative importance of structure **I** increases and such structure is expected to be less prone than **II** to undergo decarboxylation.

However, the possibility that **I** and **II** are different species, with the benziloxyl radical deriving from intramolecular electron transfer in a first formed radical



Scheme 71.

zwitterion cannot be ruled out, the observed differences in reactivity reflecting in this case the decreased ease of intramolecular electron transfer induced by the presence of electron releasing substituents on the aromatic ring. An additional possibility is that in the least stabilized systems, intramolecular electron transfer in the zwitterion (**I**) is coupled with decarboxylation.

With arylacetoxyl radicals, relatively slower decarboxylation rate constants have been measured (Table 11), pointing in this case towards higher activation barriers. Two main factors have been suggested to account for such behavior:

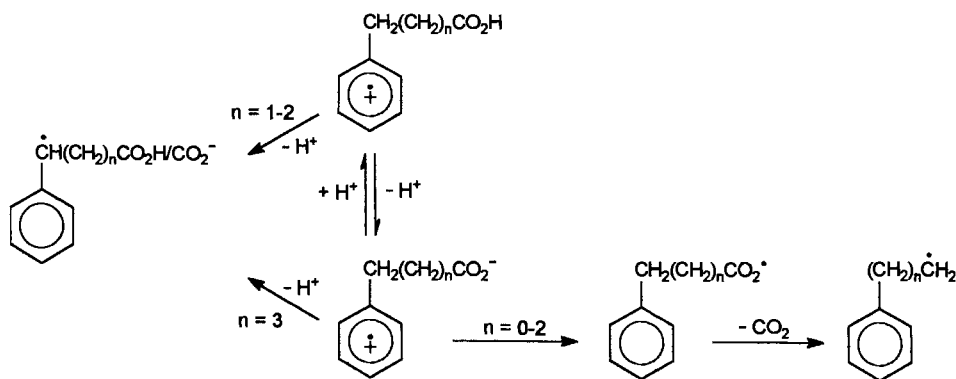
- 1) the stability of the radical formed by decarboxylation (ketyl, $\text{Ar}_2\text{C}(\text{OH})^\bullet$, relative to benzyl, ArCH_2^\bullet), because the presence of two aromatic rings rather than one allows a more extensive delocalization of the incipient radical resulting in a greater stabilization of the transition state for decarboxylation (also compare in Table 11 phenylacetate with diphenylacetate). In this respect, the presence of an α -OH group also appears to play a major role as shown by the 130-fold increase in k_{CC} on going from diphenylacetate to benzilate.
- 2) Positive charge stabilization by the aromatic system, as shown in Scheme 71, structure **I**, which disfavors decarboxylation, reflected in the relatively low k_{CC} values observed for 2,2',5,5'-tetramethoxybenzilate and 1-naphthylacetate [232].

The former explanation contrasts however, especially in the benzilate system, with the very early transition state of the decarboxylation process and thus positive charge stabilization by the aromatic system (factor **ii**) rather than the stability of the radical formed by decarboxylation (factor **i**) may play a greater role. On the other hand the very similar values of k_{CC} measured for the phenylacetoxyl radicals may reflect a relatively later transition state and a self-compensating stabilization by ring substituents of both reactant and product along the series.

When the distance between the carboxyl group and the aromatic ring is increased by the presence of additional methylene groups, as in 3-phenylpropanoic ($\text{Ph}(\text{CH}_2)_2\text{CO}_2\text{H}$) and 4-phenylbutanoic ($\text{Ph}(\text{CH}_2)_3\text{CO}_2\text{H}$) acids, decarboxylation from the radical zwitterion is still observed but $\text{C}_\alpha\text{-H}$ deprotonation can now compete efficiently. Accordingly, when $\text{Ph}(\text{CH}_2)_2\text{CO}_2\text{H}^{+\bullet}$ is generated by reaction with $\text{SO}_4^{\bullet-}$ in aqueous solution, the ESR signals of $\text{PhCH}_2\text{CH}_2^\bullet$ are observed between pH 2 and 9, which are replaced below pH = 2 by those of $\text{PhCH}^\bullet\text{CH}_2\text{CO}_2\text{H}$ [220, 228]. Similar results are obtained for $\text{Ph}(\text{CH}_2)_3\text{CO}_2\text{H}^{+\bullet}$ where, however, decarboxylation is observed at pH ≥ 3 . Interestingly, no decarboxylation is observed with $\text{Ph}(\text{CH}_2)_4\text{CO}_2\text{H}^{+\bullet}$ but only $\text{C}_\alpha\text{-H}$ deprotonation, a result which confirms that electron transfer to $\text{SO}_4^{\bullet-}$ takes place from the aromatic ring leading to an aromatic radical cation (zwitterion) which can then undergo deprotonation and for shorter chains (in Scheme 72, $n = 0-2$) decarboxylation.

If decarboxylation occurs following intramolecular electron transfer, via an acyloxy radical, this is more likely to occur from the radical zwitterion rather than the radical cation, in line with the change in mechanism observed as the pH is reduced (Scheme 72).

Rate constants for overall side-chain to nucleus electron transfer and decarboxylation (Scheme 72, $n = 0-2$) have been calculated as $k \geq 10^9 \text{ s}^{-1}$ [228].

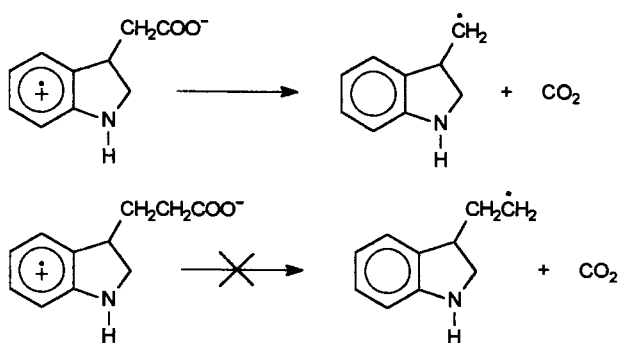


Scheme 72.

A somewhat different behavior has been instead observed for the radical zwitterions of indol-3-ylacetic and 3-indol-3-ylpropionic acids generated by pulse radiolysis in aqueous solution (through $\text{Br}_2^{\cdot-}$ oxidation), the former undergoing decarboxylation in acidic solution with $k = 1.6 \times 10^4 \text{ s}^{-1}$, while no decarboxylation has been observed with the latter (Scheme 73) [234].

An explanation can be found in terms of the much lower reduction potential of the indole-type radical cations as compared to the phenylalkanoic acid ones, which results in a greater stabilization of the positive charge on the aromatic system thus opposing intramolecular electron transfer. In other words, a later transition state is expected in the decarboxylation of indole-type radical zwitterions as compared to the phenylalkanoic acid ones, with an increased importance of the stability of the carbon centered radical.

Interestingly, when the reactivity of phenylalkanoic acid radical cations was studied in non-aqueous solvents such as acetonitrile and acetic acid, decarboxylation is still the major path for $\text{Ph}(\text{CH}_2)_2\text{CO}_2\text{H}^{+\cdot}$ while exclusive C-H deprotonation is observed with $\text{Ph}(\text{CH}_2)_3\text{CO}_2\text{H}^{+\cdot}$ [230, 235], a behavior which could

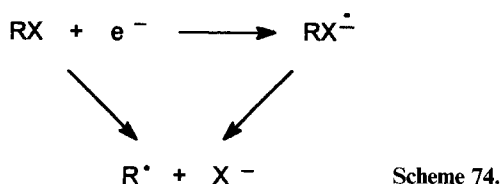


Scheme 73.

indicate a change in the acid-base properties of the radical cations under these conditions.

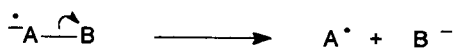
9.5.2 Reductive Bond-Cleavage Processes

Electron transfer to a neutral organic molecule is often accompanied by the cleavage of a bond, a process which can be coupled to or follow the electron transfer step (Scheme 74).

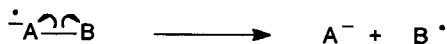


In the former case, the initial electron transfer process is dissociative, directly leading to the radical and anionic fragmentation products, a typical example being the reduction of unstrained aliphatic halides where the electron is added to the σ^* orbital of the carbon-halogen bond [236, 237]. In the latter case, an intermediate radical anion is formed which then undergoes fragmentation coupled with intramolecular electron transfer (i.e. dissociative intramolecular electron transfer). With molecules containing π^* orbitals, able to host transitorily the unpaired electron, the question which arises is whether reductive cleavage occurs via a concerted or stepwise mechanism. Distinction between these two possibilities is not easy when the lifetime of the intermediate radical anion is too short to allow detection, i.e. the kinetics of fragmentation are controlled by the initial electron transfer of the stepwise pathway or by the dissociative electron transfer of the concerted pathway. On the other hand, when the intermediate is sufficiently long lived, recognition of a stepwise mechanism is relatively straightforward. It is however important to point out that a change in the driving force of the reaction can induce a transition between the two mechanisms.

The problem of distinguishing between stepwise and concerted mechanisms has been addressed by Sav  ant who provided a thorough description of the dynamics of dissociative electron transfer by developing a model based on a Morse potential for the cleaving bond in the reactant, and on the assumption that the repulsive interaction of the two fragments formed upon electron transfer is the same as the repulsive part of the reactant potential [238, 239]. An expression where activation and reaction free energies (ΔG^\ddagger and ΔG_0) follow a quadratic Marcus type relationship [$\Delta G^\ddagger = \Delta G^\ddagger_0(1 + \Delta G_0/4\Delta G^\ddagger_0)^2$] is thus obtained, where however, in addition to the solvent reorganization free energy term (λ_0), as in the Marcus-Hush model of outer-sphere electron transfer, the intrinsic barrier ΔG^\ddagger_0 also contains a contribution of bond breaking from the bond dissociation enthalpy of the scissible bond (BDE) [$\Delta G^\ddagger_0 = (\text{BDE} + \lambda_0)/4$]. The quadratic character of the activation-driving force relationship implies that the transfer coefficient α varies with the driving force:



Scheme 75.



$\alpha = \partial\Delta G^\ddagger / \partial\Delta G_0$, and thus, the value of α may allow discrimination between the concerted and stepwise mechanisms. In the former case, a value of α significantly lower than 0.5 is expected. On the other hand, in the stepwise mechanism, given that the electron transfer step is fast compared to the following fragmentation step, α values close to or larger than 0.5 are expected [238, 240, 241].

Along these lines, new insights into the dynamics of dissociative electron transfer have been recently provided by a number of studies [240, 242–246].

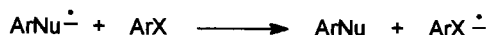
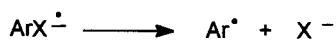
In this section we will examine selected examples of reductive fragmentation processes, namely the reductive C–X bond cleavage accompanying reduction of aryl and benzyl halides and C–C bond cleavage in the radical anions of diphenyl-ethane derivatives. In this respect, in analogy with the side-chain fragmentation reactions of alkylaromatic radical cations previously described (Scheme 26), when an intermediate radical anion is formed, fragmentation leading to radical and anionic fragments can occur in two formal ways: a heterolytic and a homolytic mode (Scheme 75) [126].

The following discussion will be focused on the effect of structural variations on the kinetics of fragmentation, the cleavage mode, and the stepwise or concerted nature of the process. Similar concepts have also been applied to the reductive cleavage reactions of other series of substrates, i.e. α -substituted acetophenones [246–250], perbenzoates [240, 251], peroxides [242, 252–256], sulfides [244, 257, 258], sulfonium salts [259–263], nitrocumenes [264, 265], arylmethyl aryl ethers and thioethers [266–270].

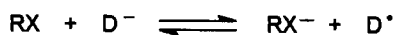
Even though fragmentation of radical anions represents a key step in $S_{RN}1$ reactions (Scheme 76) and in aliphatic nucleophilic substitution reactions (S_N2) proceeding via single electron transfer (Scheme 77), such processes and their mechanistic implications will not be discussed in this section (several reviews are available [271–277]).

Reductive dehalogenation of aryl and benzyl halides

One-electron reduction of aryl (ArX) and benzyl halides (ArCH_2X) bearing electron withdrawing ring substituents eventually produces the corresponding radical



Scheme 76.



Scheme 77.

anion which can undergo an intramolecular electron transfer process coupled to fragmentation leading to the halide anion and the aryl or benzyl radical (Scheme 74). The intramolecular electron transfer can be conveniently described in terms of a σ - π radical anion isomerism with the initially formed π radical anion (π RA) undergoing intramolecular electron transfer from the π system to the σ^* orbital of the C-X bond leading to a σ RA (a three-electron bond radical anion) which dissociates in a carbon centered radical and the anion of the leaving group (X^-) (Scheme 78) [278].

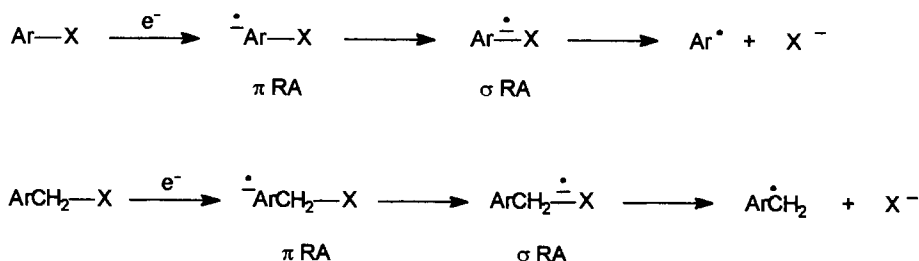
In this respect, theoretical studies have shown that in halobenzenes, halobenzonitriles, haloacetophenones and halonitrobenzenes, by considering the intramolecular electron transfer as the rate limiting step of the cleavage reaction, the energy difference between the two isomeric radical anions ($\Delta E_{\sigma\pi}$) correlates with the experimental fragmentation rates [279, 280].

Neta and Behar measured the rate constants for intramolecular electron transfer for an extended series of aryl (ArX) and benzyl halide (ArCH_2X) radical anions bearing an electron withdrawing ring substituent (NO_2 , CN , COCH_3), generated by pulse radiolysis in aqueous solution (Table 12), conditions under which spectroscopic evidence for formation of the intermediate radical anions was obtained [281–284].

By comparing the data reported in Table 12 several conclusions can be drawn:

The rates of dehalogenation strongly depend on the nature of the halogen, increasing with decreasing C-X bond strength ($\text{I} > \text{Br} > \text{Cl}$).

The relative position of the two ring substituents (the electron withdrawing Z group and the X or CH_2X group) has a strong influence on the rate of fragmentation. The *ortho* isomer reacts always faster than the *para* isomer, a behavior which suggests the occurrence, at least in part, of a direct (through space) electron transfer from the Z group to the scissible bond in the former radical anions. In this respect, it has been suggested that in the radical anions of *ortho*-nitroarylhalides steric effects,



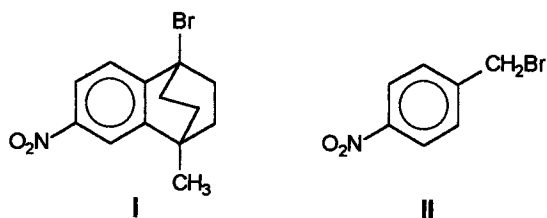
Scheme 78.

Table 12. Rate constants for fragmentation of $\text{ArX}^{\cdot-}$ and $\text{ArCH}_2\text{X}^{\cdot-}$ in aqueous solution at room temperature.

Ar	pH	$k \text{ (s}^{-1}\text{)} \text{ (X = Cl)}$	$k \text{ (s}^{-1}\text{)} \text{ (X = Br)}$	$k \text{ (s}^{-1}\text{)} \text{ (X = I)}$
<i>ArX^{·-}</i>				
4-CNC ₆ H ₄	12	5×10^6	$>3 \times 10^7$	—
3-CNC ₆ H ₄	12	4.2×10^4	8×10^6	—
2-CNC ₆ H ₄	12	9×10^6	—	—
4-CH ₃ COC ₆ H ₄	12	$\sim 10^2$	5×10^3	1.4×10^5
	7	—	—	4×10^3
3-CH ₃ COC ₆ H ₄	12	—	$\sim 10^2$	—
2-CH ₃ COC ₆ H ₄	12	1.5×10^3	5×10^5	—
	7	—	9×10^3	—
4-NO ₂ C ₆ H ₄	7	<1	—	<1
3-NO ₂ C ₆ H ₄	7	—	<1	—
2-NO ₂ C ₆ H ₄	7	—	—	<1
<i>ArCH₂X^{·-}</i>				
4-CNC ₆ H ₄	12	$>3 \times 10^7$	$>6 \times 10^7$	—
3-CNC ₆ H ₄	12	—	1.3×10^7	—
3-CH ₃ COC ₆ H ₄	12	1.5×10^4	—	—
	7	4×10^3	1.7×10^5	5.7×10^5
4-NO ₂ C ₆ H ₄	2	—	2×10^4	—
	0.6	—	3×10^3	—
3-NO ₂ C ₆ H ₄	7	<5	60	3×10^3
2-NO ₂ C ₆ H ₄	7	1.0×10^4	4.0×10^5	—

which progressively increase with the size of the halogen atom, prevent conjugation of the nitro group with the aromatic ring thus reducing the stabilization of the π^* orbital, favoring dehalogenation (see later) [285, 286]. On the other hand, fragmentation from the *meta* isomer is always significantly slower than from the *para*, because of the very low spin density at the *meta* position which disfavors intramolecular electron transfer to the halide.

Aryl halide radical anions ($^{\cdot-}\text{ArX}$) undergo fragmentation much more slowly than the homologous benzyl halide ones ($^{\cdot-}\text{ArCH}_2\text{X}$) in spite of the increased availability of the unpaired electron to the halogen in the former ones, due to reduced distance of the halogen from the ring. Such behavior reflects the importance of the C–X bond strength (which is significantly lower for ArCH_2X as compared to ArX [287, 288]) and thus the stability of the carbon centered radical formed by fragmentation. Interestingly, recent thermodynamic calculations have shown that while the C–X BDE is lowered by a factor of ca 4 on going from $\text{C}_6\text{H}_5\text{-Br}$ to the corresponding radical anion, a 14-fold decrease is instead observed in the case of $\text{C}_6\text{H}_5\text{CH}_2\text{-Cl}$ [289]. An additional factor accounting for this difference in reactivity is represented by the orientation of the C–X bond, since only in the benzyl halide radical anions the most favorable conformation for dissociative intramolecular electron transfer, where the C–X bond is perpendicular to the plane of the aromatic ring, allowing the most efficient orbital overlap, can be achieved [290]. In this re-



Scheme 79.

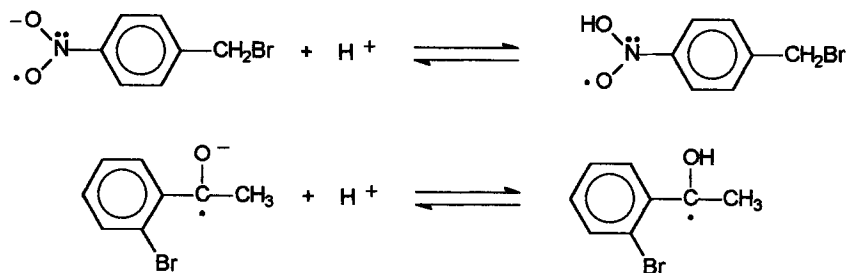
spect, it has been suggested that the transition state for cleavage of $\cdot^- \text{ArX}$ must include a large intramolecular $\pi^* \rightarrow \sigma^*$ electron transfer component [291].

Clear evidence for orbital symmetry restrictions in dissociative intramolecular electron-transfer reactions has been provided by Savéant [292], by comparing the cleavage kinetics of radical anions generated from substrates **I** and **II** in DMF (Scheme 79).

In **I** $^{\cdot-}$, the rigid bicyclooctane structure precludes overlap between the π^* orbital, bearing the unpaired electron, and the C–Br σ^* orbital where the electron should be transferred concertedly with bond cleavage and moreover, fragmentation leads in this case to a bridgehead unconjugated sp^3 radical which is significantly less stable than the conjugated 4-nitrobenzyl radical formed by cleavage of **II** $^{\cdot-}$. Accordingly, **I** $^{\cdot-}$ undergoes cleavage with $k = 9.3 \times 10^{-3} \text{ s}^{-1}$, a value which is dramatically lower than that estimated for **II** $^{\cdot-}$ ($k \geq 7.9 \times 10^8 \text{ s}^{-1}$) [292, 293].

No evidence for C–X bond cleavage has been found for the halonitrobenzene radical anions [283], while relatively fast dehalogenation occurs when $\text{Z} = \text{CN}$ and COCH_3 [281, 282], due to the much higher electron affinity of the NO_2 group as compared to CN and COCH_3 , which diminishes to a larger extent the overall ring charge density. Accordingly, the following order of reactivity is observed for dehalogenation of $\cdot^- \text{ArX}$: $\text{NO}_2 < \text{COCH}_3 < \text{CN}$ (Table 12).

Protonation of the radical anion (Scheme 80) results in a significant decrease in the fragmentation rate, as clearly shown for 4-BrC₆H₄CH₂NO₂ $^{\cdot-}$ (for which a $\text{p}K_{\text{a}} = 2.8$ has been determined [284]), 2-Br- and 4-IC₆H₄COCH₃ $^{\cdot-}$ [281].



Scheme 80.

Table 13. Rate constants for fragmentation of 4-RC₆H₄NO₂^{•−} in aqueous solution at room temperature.

R	k (s ^{−1})
CH ₂ Cl	4×10^3
CH(CH ₃)Cl	9.7×10^4
CH(C(CH ₃) ₃)Cl	4.0×10^2
CH ₂ Br	1.7×10^5
CH(CH ₃)Br	3.5×10^6
CH(C(CH ₃) ₃)Br	6.2×10^4
CH ₂ CH ₂ Br	<1
COCH ₂ Br	4.2×10^4
CH=CHBr	≤4
CH=CHCH ₂ Br	1×10^5

Structural effects

To gain additional information on these fragmentation reactions, the reactivity of a wide variety of structurally modified nitrobenzyl halide radical anions has been investigated (Table 13) [283, 290, 294].

Addition of an α -methyl substituent to 4-XCH₂C₆H₄NO₂^{•−} (X = Cl, Br) reduces the C–X bond dissociation energy by stabilizing the resulting benzyl radical thus increasing the dehalogenation rate by a factor of ≈ 20 –25 [294].

On the other hand, α -substitution with a *tert*-butyl group decreases the rate by a factor of ≈ 3 –10, indicating that this group exerts a steric effect on the orientation of the C–X bond by preventing the system from assuming a conformation in which the C–X bond is perpendicular to the plane of the aromatic ring [290]. Interestingly, the presence of an α -*tert*-butyl group appears also to decrease the rate of intramolecular through space electron transfer as shown by the ≈ 50 -fold decrease in reactivity observed on going from 2-ClCH₂C₆H₄NO₂^{•−} to 2-ClCH(C(CH₃)₃)C₆H₄NO₂^{•−}.

The presence of an additional methylene group as in 4-BrCH₂CH₂C₆H₄NO₂^{•−} disfavors intramolecular electron transfer by isolating the halogen from the unpaired electron, and accordingly for this radical anion fragmentation is estimated to occur with $k < 1$ s^{−1} [283]. When the additional methylene group is replaced by a carbonyl group (4-BrCH₂COC₆H₄NO₂^{•−}), C–Br bond cleavage is much more efficient occurring with $k = 4.2 \times 10^4$ s^{−1} [283], due to weakening of the scissible bond and increased ease of intramolecular electron transfer (as compared to 4-BrCH₂CH₂C₆H₄NO₂) provided by the presence of the carbonyl spacer.

It is also interesting to compare the reactivity of radical anions bearing a vinyl and an allyl spacer with that of 4-BrCH₂C₆H₄NO₂^{•−} (Table 13). While with 4-BrCH=CHC₆H₄NO₂^{•−} a dramatic decrease in reactivity is observed, reflecting the relatively high C–Br bond strength and thus the reduced stability of a vinyl radical as compared with benzylic; with 4-BrCH₂CH=CHC₆H₄NO₂^{•−} no significant decrease is observed indicating the effectiveness of the allyl group in channeling the electron to bromine [294].

In a later study, the temperature dependence on the unimolecular dehalogenation reaction of nitrobenzyl halide and haloacetophenone radical anions has been investigated [278], showing that the variation of the unimolecular rate constant with substrate structure depends in a complex way on the combination of E_a and $\log A$, suggesting that comparisons between rate constants for fragmentation measured at a single temperature may lead to fortuitous conclusions. Interestingly, α -substitution with methyl increases A while ethyl and *tert*-butyl decrease it, suggesting that the presence of bulky substituents prevents the system from assuming a conformation suitable for intramolecular electron transfer [290].

Comparison of concerted and stepwise cleavage

The problem of distinguishing between concerted and stepwise mechanisms in the reductive cleavage of both aryl and benzyl halides has been addressed by Savéant. While aliphatic halides undergo dehalogenation through the concerted pathway, with aryl halides intermediate radical anions are generally formed [274, 295]. This different behavior finds an explanation in the higher C–X bond dissociation energy of aryl rather than alkyl halides [287]. Moreover, in aryl halides, the incoming electron can be accommodated transitorily in the relatively low energy π^* orbital of the aromatic moiety, while with simple aliphatic halides the C–X σ^* orbital energy is so high that electron transfer concerted with bond cleavage is energetically more favorable. However, in a recent electrochemical study it has been found that the reductive cleavage of aromatic iodides in acetonitrile or DMF may follow a concerted mechanism at low driving forces [241]. For both iodobenzene and 3-methyliodobenzene an increase in the transfer coefficient α is observed on increasing the potential scan rate in cyclic voltammetry (CV) experiments, a behavior which indicates a transition from a concerted mechanism to a stepwise one as the driving force is increased [296]. An analogous behavior is observed at higher temperature, a condition which can play in favor of the concerted pathway [260]. Interestingly, no evidence for a change of mechanism has been observed with bromobenzene which undergoes a stepwise reductive cleavage even at the lower end of the scan rate domain. Such behavior has been explained in terms of the intrinsic barrier for cleavage since the concerted pathway is favored for iodobenzene as compared to bromobenzene by ca 0.17 eV [241]. From this example it follows that what governs the nature of the reductive cleavage is not the existence or non-existence of the radical anion but rather the energetic advantage offered by one mechanism over the other.

A borderline case is instead represented by benzyl halides, where a π^* orbital is available for the incoming electron as in aryl halides, but the C–X bond is now significantly weaker. In this respect, Savéant studied the kinetics of the electrochemical reduction of a series of benzyl halides in acetonitrile and DMF, showing that while nitrobenzyl halides undergo a stepwise reductive cleavage via an intermediate radical anion, with weaker electron withdrawing ring substituents such as CN and CO_2CH_3 , as well as with benzyl chloride and bromide or 9-anthracenylmethyl chloride, the reaction occurs via a concerted pathway [243, 293]. Apparently with nitrobenzyl halides, the π^* orbital is too low in energy to allow a transition to a

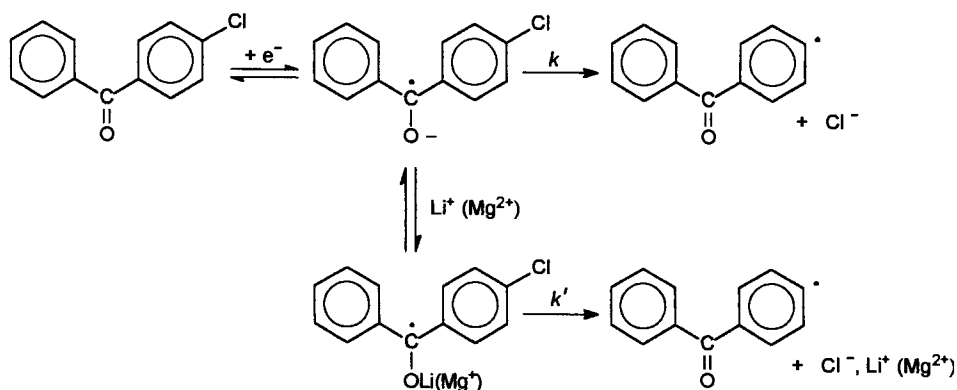
concerted mechanism at low CV scan rates (low driving forces), while the opposite situation holds for the cyanobenzyl halides where the π^* energy is too high to allow a transition to a stepwise mechanism at high scan rates (high driving forces). In contrast with these conclusions is however the suggestion that, in the reaction of benzyl chloride with photoexcited SmI_2 in THF, reductive dehalogenation leading to a benzyl radical and Cl^- occurs via a stepwise mechanism with formation of an intermediate radical anion [297].

Effects of the medium

It is also interesting to compare the kinetic data for reductive dehalogenation in DMF obtained by Savéant ($k = 80$ and $4.0 \times 10^6 \text{ s}^{-1}$ for 3-nitro- and 4-nitrobenzyl chloride, respectively and $k \gg 4.0 \times 10^6 \text{ s}^{-1}$ for 4-nitrobenzyl bromide) [293] and Danen ($k = 8 \times 10^4 \text{ s}^{-1}$ for 2-nitroiodobenzene measured chronoamperometrically) [286] with those obtained by Neta in aqueous solution for the same radical anions (Table 12: $k < 5 \text{ s}^{-1}$, $k = 4 \times 10^3 \text{ s}^{-1}$, $k = 1.7 \times 10^5 \text{ s}^{-1}$ and $k < 1 \text{ s}^{-1}$, respectively) [284], showing that the radical anions are significantly longer lived in water than in DMF. In nitrobenzyl and nitroaryl halide radical anions, the negative charge can be localized on the oxygen atoms of the nitro group, thus allowing a strong interaction with water. Two main consequences result from this stabilization: a lowering in the energy of the π^* orbital, corresponding to a decrease in driving force of the cleavage reaction, and a large solvent reorganization energy, since solvation of the negatively charged nitro group has to be rearranged into solvation of the leaving halide anion. Accordingly, very large pre-exponential factors ($\log A$ between 12.8 and 17.1) have been measured for the dehalogenation of a series of nitrobenzyl halide radical anions in water, pointing towards a positive activation entropy [278, 293].

Moreover, 3-cyanobenzyl bromide radical anion has been *directly* observed by UV-Vis spectroscopy following pulse radiolytic generation in water, and a fragmentation rate constant $k = 1.3 \times 10^7 \text{ s}^{-1}$ has been measured (Table 12) [282]; whereas, during electrochemical reduction in DMF, electron transfer and bond cleavage appear to be concerted. This different behavior can be explained on the basis of the solvation effect discussed above and also by considering that the driving force of the reaction (i.e. the energy of the incoming electron) is much larger when the radical anion is generated radiolytically [261, 293].

Solvation effects thus appear to play an important role in governing the dichotomy between concerted and stepwise mechanisms. In this respect, a detailed study of solvation and ion-pairing effects on the dynamics of intramolecular dissociative electron transfer in the cleavage of radical anions, generated by CV in MeCN or DMF, has been carried out [298]. Two families of compounds have been studied: the first one (group A) includes 4-chlorobenzophenone, 3-nitrobenzyl chloride and bromide, where the negative charge in the corresponding radical anions is localized on the oxygen atoms; the second one (group B) instead includes 2-chloro-, 9-fluoro- and 9-chloroanthracene, where the negative charge is delocalized over the entire system. In group A, the addition of water or of cations such as Li^+ or Mg^{2+} strongly stabilizes the radical anion (corresponding to an increase in $E^\circ_{\text{RX}/\text{RX}\cdot-}$), thereby significantly decreasing its fragmentation rate constant. The effect of



Scheme 81.

the addition of ion pairing cations is shown in Scheme 81 in the case of 4-chlorobenzophenone. Formation of the $RX^{\bullet-}Li^+$ adduct leads to a decrease in the π^* orbital energy and thus in cleavage driving force, and for 4-chlorobenzophenone radical anion a ratio $k/k' = 20$ can be estimated. Even higher k/k' ratios can be instead expected for cleavage of nitrobenzyl halide radical anions where, due to the weaker C–X bond as compared to aryl halides, smaller intrinsic barriers for cleavage are predicted.

In group B a slight increase in the fragmentation rate constant but no significant change in $E^\circ_{RX/RX^{\bullet-}}$ is observed as the water concentration is raised, reflecting a specific solvation and thus a greater stabilization of the halide ion (corresponding to an increase in $E^\circ_{X^-/X^-}$) which results in a decrease in the standard free energy of the reaction. On the other hand, addition of Li^+ has in this case no noticeable effect on the cleavage rate.

It is important to point out that stabilization of the halide ion by the presence of water occurs also in group A radical anions where, however, it is overcompensated by the lower energy of the π^* orbital (reflected in the less negative $E^\circ_{RX/RX^{\bullet-}}$) which disfavors intramolecular electron transfer to the σ^* orbital of the scissible bond.

These observations clearly indicate that (in these cases) solvation and ion pairing effects on the cleavage reactivity of radical anions strongly depend upon the localization of the negative charge.

In another study, the reductive C–F bond cleavage of fluoromethylarenes has been investigated in liquid ammonia and DMF by CV and/or redox catalysis [299]. Within a series of 4-cyanotoluenes where the α -carbon bears one, two or three fluorine atoms, the rate of radical anion cleavage increases on going from the trifluoro to the monofluoro derivative, a behavior which reflects the decrease in both C–F BDE and standard potential, $E^\circ_{RX/RX^{\bullet-}}$, as the number of fluorine atoms is diminished (Table 14).

Along this line, within a series of trifluoromethylarenes, the cleavage rate constants are mainly governed by $E^\circ_{RX/RX^{\bullet-}}$ which varies substantially as the aryl moiety is changed.

Table 14. Standard potentials ($E^\circ_{\text{RX/RX}\cdot-}$) and cleavage rate constants (k) for 4-cyanofluorotoluenes (4-CNC₆H₄X) and trifluoromethylarenes (4-XC₆H₄CF₃). Standard free energies (ΔG°) and intrinsic barrier free energies (ΔG^\ddagger_0) for 4-CNC₆H₄X.

X	DMF ($T = 20^\circ\text{C}$)				NH ₃ ($T = -38^\circ\text{C}$)			
	$E^\circ{}^a$	k (s ⁻¹)	ΔG° (eV)	ΔG^\ddagger_0 (eV)	$E^\circ{}^b$	k (s ⁻¹)	ΔG° (eV)	ΔG^\ddagger_0 (eV)
4-CNC₆H₄X								
CH ₂ F	-2.020	7×10^6	-0.93	0.85	-1.540	2.2×10^7	-1.35	0.91
CHF ₂	-1.890	4×10^5	-0.68	0.75	-1.450	1×10^6	-1.14	0.88
CF ₃	-1.785	3.8×10^1	-0.41	0.805	-1.345	3.5×10^2	-0.88	0.92
4-XC₆H₄CF₃								
CN	-1.785	3.8×10^1			-1.345	3.5×10^2		
CO ₂ CH ₃					-1.330	7.5		
CO ₂ <i>t</i> Bu					-1.405	2.5×10^1		
CO ₂ ⁻					-1.835	1.1×10^4		
H					-2.075	2.8×10^8		

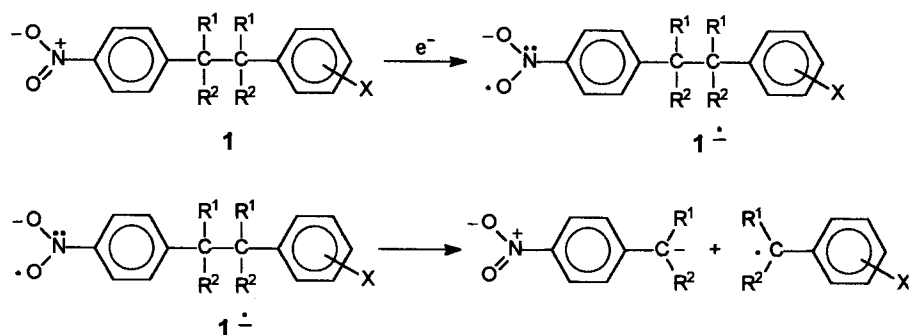
^a V relative to SCE.^b V relative to 0.01 M Ag⁺/Ag.

The cleavage rate constants for the 4-cyanofluorotoluenes measured in NH₃ are higher than those measured in DMF, in spite of the much lower temperature of the former system, reflecting the better stabilization of F⁻ by this solvent as compared to DMF, as also indicated by the activation free energies (ΔG°). Interestingly, the intrinsic barrier free energies (ΔG^\ddagger_0) are similar in the two solvents, due to a compensation between two contributions: nuclear reorganization, which is more important in DMF and solvent reorganization, which is instead more costly in NH₃.

Mesolytic cleavage in radical anions of 1,2-diphenylethane derivatives

Diphenylethane derivatives bearing electron withdrawing ring substituents are suitable compounds for the study of mesolytic C–C bond fragmentation reactions in the corresponding radical anions. This problem has been addressed by Maslak using a series of sterically crowded 4-nitrodiphenylethane derivatives, **1** [300], where the incoming electron is added to the π -system of the nitrophenyl moiety leading to a radical anion (**1**^{•-}), which can then undergo homolytic C–C bond cleavage to give an α,α -dialkyl-4-nitrobenzyl anion and an α,α -dialkylbenzyl radical (Scheme 82, X = H).

X-ray studies on strained 1,2-diphenyltetraalkyldiphenylethanes have shown that due to steric crowding, these molecules have a significantly elongated central C–C bond, and in the solid state they adopt a conformation where the torsional angles between this bond and the aromatic ring planes are very close to 90° [301], allowing the best overlap between the σ^* orbitals of this bond and both aromatic π -systems. ESR studies suggest that an analogous conformation is also observed for the corresponding radical anions [291], thus allowing delocalization of the electron density



Scheme 82.

(initially localized over the nitroaryl moiety on one side of the scissible bond) over the entire molecule as the reaction progresses.

The unimolecular rate constants for C–C bond cleavage of $1^{\bullet-}$ measured by ESR in DMSO are collected in Table 15, together with the corresponding activation free energies for mesolytic cleavage, ΔG_m^\ddagger [300].

The decay rates of the radical anions have been found to depend on the steric crowding. No fragmentation products but only that deriving from reduction of the parent compound has been detected from the relatively unstrained $1a^{\bullet-}$ which decays with a measurable rate only at $T \geq 80^\circ\text{C}$, exhibiting however second-order kinetics, a behavior attributed to disproportionation of $1a^{\bullet-}$. The importance of C–C bond cleavage increases with increasing steric crowding and accordingly, while $1b^{\bullet-}$ undergoes cleavage in competition with reduction, exclusive unimolecular C–C fragmentation has been observed for all the other radical anions in the series.

All cleavages are endoergonic and the activation free energies of mesolysis are on average $12.5 \text{ kcal mol}^{-1}$ lower than those for homolysis indicating significant C–C

Table 15. Unimolecular rate constants (k_m) and activation free energies (ΔG_m^\ddagger) for mesolytic cleavage of 4-nitrodiphenylethane derivative radical anions $1^{\bullet-}$ ($X = \text{H}$), in DMSO at $T = 27^\circ\text{C}$.

Radical anion	R^1	R^2	$k_m \text{ (s}^{-1}\text{)}$	$\Delta G_m^\ddagger \text{ (kcal mol}^{-1}\text{)}$
$1a^{\bullet-}$	Me	Me	^b	≥ 30.0
$1b^{\bullet-a}$	Me	Et	4.4×10^{-8}	28.0
$1c^{\bullet-a}$	Me	Pr	1.0×10^{-7}	26.5
$1d^{\bullet-a}$	Me	<i>i</i> Bu	2.0×10^{-5}	23.5
$1e^{\bullet-}$	Et	Et	6.3×10^{-4}	21.4
$1f^{\bullet-}$	Pr	Pr	2.0×10^{-3}	20.6
$1g^{\bullet-}$	Bu	Bu	3.1×10^{-3}	20.6

^a *Erythro* diastereoisomer.

^b Second-order kinetics.

Table 16. Unimolecular rate constants (k_m) for mesolytic cleavage of $2^{\cdot-}$ (Scheme 82, $R^1 = R^2 = Et$), in DMSO at $T = 20^\circ C$.

Radical anion	X	k_m (s^{-1})
2a $^{\cdot-}$	4-CN	2.3×10^{-2}
2b $^{\cdot-}$	4-CF ₃	9.3×10^{-3}
2c $^{\cdot-}$	4-CH ₃ CO	9.3×10^{-3}
2d $^{\cdot-}$	4-NMe ₃ ⁺	4.0×10^{-3}
2e $^{\cdot-}$	3-CF ₃	2.3×10^{-3}
2f $^{\cdot-}$	3-CN	1.8×10^{-3}
2g $^{\cdot-}$	4-Cl	1.3×10^{-3}
2h $^{\cdot-}$	H	6.5×10^{-4}
2i $^{\cdot-}$	4-Me ₂ N	5.4×10^{-4}
2j $^{\cdot-}$	4-F	4.5×10^{-4}
2k $^{\cdot-}$	4-OMe	3.8×10^{-4}

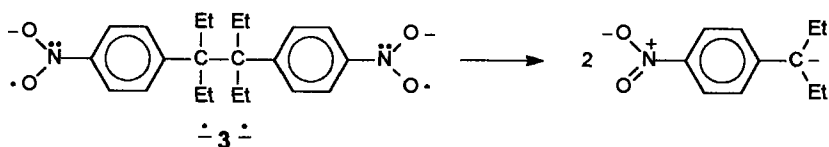
bond activation upon one-electron reduction. Such large activation has been shown to have thermodynamic origins, i.e. the transition state for mesolysis is lowered in energy as compared to that for homolysis by the difference in their free energies ($\Delta G^\ddagger_h - \Delta G^\ddagger_m \approx \Delta G_h - \Delta G_m$).

The progress of charge delocalization on going from the radical anion to the cleavage transition state can be evaluated from the effect of ring substituents X on the rate of unimolecular C–C bond cleavage. The pertinent rate constants k_m for a series of 4-nitrodiphenylethane derivative radical anions $2^{\cdot-}$ (Scheme 82, $R^1 = R^2 = Et$), measured by ESR in DMSO, are reported in Table 16 [291, 302].

The rate of C–C bond cleavage is increased by electron withdrawing X substituents while electron releasing ones determine a slight retarding effect. The very similar values of activation and reaction free energies (ΔG^\ddagger_m and ΔG_m , respectively) observed for cleavage of $2^{\cdot-}$, point towards a late product-like transition state, suggesting that the relative cleavage rates reflect the radical stabilizing effect of the X substituent.

Quite surprisingly, however, no correlation has been observed between the relative cleavage rates and σ^+ while a good correlation with σ^- exists for the radical anions bearing strongly electron withdrawing substituents, a trend which is consistent with the development of a significant amount of negative charge on the β -carbon, in contrast with the predictions based on the thermodynamic stability of the fragments.

These results indicate that the fragmentation is kinetically controlled by the ability of the system to delocalize the negative charge across the scissible bond, suggesting that the transition state for C–C bond cleavage in $2^{\cdot-}$ can be described in terms of two electronic configurations: one, corresponding to relatively early transition states, where the β -carbon supports a significant amount of negative charge, becomes important with strongly electron withdrawing X substituents (**2a-e** $^{\cdot-}$); and



Scheme 83.

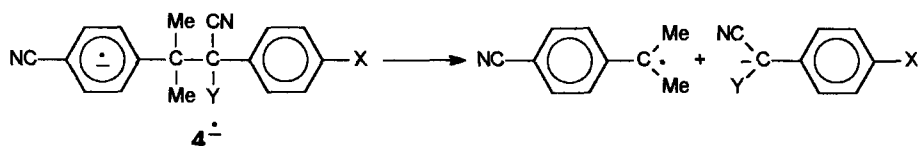
a second one represented by a σ^* radical anion (three electron C–C bond) where the additional electron is shared by both benzylic carbons, which becomes increasingly important as the ability of the radical anions to delocalize the negative charge across the scissible bond is decreased, corresponding to progressively later transition states ($2f-k^-$).

Along this line, the importance of through bond delocalization has been clearly shown for the dinitro derivative $(4\text{-O}_2\text{NC}_6\text{H}_4\text{CEt}_2)_2$ (**3**) [291, 303], whose reduction leads to a dianion ($^-\mathbf{3}^-$) having each of the two unpaired electrons delocalized over one nitroaryl moiety (Scheme 83). $^-\mathbf{3}^-$ undergoes a bimolecular fragmentation reaction (rationalized in terms of disproportionation of $\mathbf{3}^-$ followed by cleavage of $^-\mathbf{3}^-$) which is at least 3 orders of magnitude faster than that (unimolecular) from $2a^-$.

In contrast with $2a^-$ for which all of the thermodynamic advantage is expressed in the lowering of transition state energy (i.e. $\Delta G_m \approx \Delta G_m^\ddagger$), the driving force for cleavage of $^-\mathbf{3}^-$ is more negative by ca 14 kcal mol⁻¹ exhibiting however a significantly larger intrinsic barrier, suggested to derive from the inability of the dianion to delocalize the negative charge across the scissible bond due to charge repulsion. As a result, for $^-\mathbf{3}^-$ $\Delta G_m \ll \Delta G_m^\ddagger$, which shows that the possibility of through bond delocalization constitutes a kinetic advantage in the cleavage reactions of diphenylethane derivative radical anions.

Additional information comes from the study of the heterolytic C–C bond cleavage reactions of 4-cyanodiphenylethane derivative radical anions ($\mathbf{4}^-$) generated by PET in MeCN (Scheme 84) [304]. The rate constants for fragmentation are collected in Table 17.

A dramatic increase in reactivity is observed on going from $\mathbf{1}^-$ and $\mathbf{2}^-$ (Tables 15 and 16, respectively) to $\mathbf{4}^-$, indicating that the presence of an electron withdrawing substituent on the β -carbon strongly stabilizes the incipient negative charge which develops on this atom in the transition state for heterolytic fragmentation.



Scheme 84.

Table 17. Unimolecular rate constants (k_m) for mesolytic cleavage of 4^{*-} , in MeCN at $T = 27^\circ\text{C}$.

Radical anion	X	Y	k_m (s^{-1})
4a$^{*-}$	OMe	Me	8×10^5
4b$^{*-}$	H	Me	9×10^6
4c$^{*-}$	CF ₃	Me	4×10^{8a}
4d$^{*-}$	OMe	CN	4×10^{9a}
4e$^{*-}$	H	CN	$>3 \times 10^{10a}$

^a Estimated value.

References

1. P. Neta, *Adv. Phys. Org. Chem.* **1976**, 12, 223–297.
2. A. Henglein, *Electroanal. Chem.* **1976**, 9, 163–244.
3. A. J. Swallow, *Progr. Reaction Kin.* **1978**, 9, 195–366.
4. S. Steenken, *J. Chem. Soc., Faraday Trans. 1* **1987**, 83, 113–124.
5. Farhataziz, M. A. J. Rodgers, VCH Publishers, Weinheim 1987.
6. S. Steenken, *Chem. Rev.* **1989**, 89, 503–520.
7. C. von Sonntag, H. P. Schuchmann, *Angew. Chem. Int. Ed. Engl.* **1991**, 30, 1229–1253.
8. J. A. Stubbe, W. A. van der Donk, *Chem. Rev.* **1998**, 98, 705.
9. H. Eklund, M. Fontecave, *Structure With Folding & Design* **1999**, 7, R257–R262.
10. B. A. Andersson, S. Styring, in C. P. Lee (Ed.): *Current Topics in Bioenergetics*, Vol. 16, Academic Press, San Diego, CA 1991, p. 1–81.
11. C. W. Hoganson, M. Sahlin, B.-M. Sjöberg, G. T. Babcock, *J. Am. Chem. Soc.* **1996**, 118, 4672–4679.
12. S. Kim, B. A. Barry, *Biochemistry* **1998**, 37, 13882–13892.
13. H. Sies, *Oxidative Stress*, Academic Press, Orlando, FL 1985.
14. K. C. Cundy, R. Kohen, B. N. Ames, in M. G. Simic, K. A. Taylor, J. F. Ward, C. von Sonntag (Eds.): *Oxygen Radicals in Biology and Medicine*, Vol. 49, Plenum Press, New York, London 1988, p. 479–482.
15. B. Giese, *Radicals in Organic Synthesis: Formation of Carbon–Carbon Bonds*, Pergamon Press, Oxford 1986.
16. M. Regitz, B. Giese, in Houben–Weyl (Ed.): *Methoden der Organischen Chemie*, Vol. E19a, Georg Thieme Verlag, Stuttgart 1989.
17. W. B. Motherwell, D. Crich, *Free Radical Chain Reactions in Organic Synthesis*, Academic Press, London 1992.
18. M. J. Perkins, *Radical Chemistry*, Ellis Horwood, New York 1994.
19. J. Fossey, D. Lefort, J. Sorba, *Free Radicals in Organic Chemistry*, Wiley, Chichester 1995.
20. T. Linker, M. Schmittl, *Radikale und Radikationen in der Organischen Synthese*, Wiley–VCH, Weinheim 1998.
21. B. Paulson, K. Pramod, P. Eaton, G. Closs, J. R. Miller, *J. Phys. Chem.* **1993**, 97, 13042–13045.
22. J. W. Verhoeven, in J. Jortner, M. Bixton (Eds.): *Electron Transfer—From Isolated Molecules To Biomolecules*, Pt 1, Vol. 106, John Wiley & Sons, New York Et Al. 1999, P. 603–644.
23. J. M. Warman, M. P. De Haas, J. W. Verhoeven, M. N. Paddon-Row, in J. Jortner, M. Bixton (Eds.): *Electron Transfer—From Isolated Molecules To Biomolecules*, Pt 1, Vol. 106, John Wiley & Sons, New York Et Al. 1999, P. 571–601.
24. A. J. Bard, M. A. Fox, *Acc. Chem. Res.* **1995**, 28, 141–145.
25. T. J. Meyer, *Acc. Chem. Res.* **1989**, 22, 163–170.
26. M. Grätzel, *Acc. Chem. Res.* **1981**, 14, 376.
27. G. McLendon, *Acc. Chem. Res.* **1988**, 21, 160–167.

28. S. S. Isied, M. Y. Ogawa, J. F. Wishart, *Chem. Rev.* **1992**, 92, 381–394.
29. R. J. P. Williams, *J. Biol. Inorg. Chem.* **1997**, 2, 373–377.
30. S. S. Skourtis, D. N. Beratan, *J. Biol. Inorg. Chem.* **1997**, 2, 378–386.
31. C. C. Moser, C. C. Page, X. Chen, P. L. Dutton, *J. Biol. Inorg. Chem.* **1997**, 393–398.
32. J. R. Winkler, H. B. Gray, *J. Biol. Inorg. Chem.* **1997**, 2, 399–404.
33. E. D. A. Stemp, J. K. Barton, *Metal Ions in Biol. Systems* **1996**, 33, 325–365.
34. J. Jortner, M. Bixon, T. Langenbacher, M. E. Michel-Beyerle, *Proc. Natl. Acad. Sci. USA* **1998**, 95, 12759–12765.
35. B. Giese, S. Wessely, M. Spormann, U. Lindemann, E. Meggers, M. E. Michel-Beyerle, *Angew. Chem. Int. Ed. Engl.* **1999**, 38, 996–998.
36. Also (electron transfer) disproportionation is a way for radicals to lose their radical nature. With respect to disproportionation, the reader is referred to Alfassi, Z.B. (ed), *General Aspects of the Chemistry of Radicals*, Wiley, New York 1999.
37. R. A. Marcus, *Ann. Rev. Phys. Chem.* **1964**, 15, 155–196.
38. J. S. Littler, In R. O. C. Norman (Ed.): *Essays On Free-Radical Chemistry, Special Publication 24*, The Chemical Society, London 1970.
39. L. Eberson, *Electron-transfer reactions in Organic Chemistry*, Vol. 25, Springer, Berlin 1987.
40. Homolytic β -eliminations are also known, see, e.g., Kim, S.; Cheong, J. H. *Chem. Commun.* **1998**, 1143–1144 and references therein.
41. The reverse of eq 3 is an example of a homolytic reaction.
42. L. Eberson, *Adv. Phys. Org. Chem.* **1982**, 18, 79.
43. D. M. Stanbury, *Adv. Inorg. Chem.* **1989**, 33, 69–138.
44. R. E. Huie, C. L. Clifton, P. Neta, *Radiat. Phys. Chem.* **1991**, 38, 477–481.
45. S. Steenken, unpublished material.
46. O. P. Chawla, R. W. Fessenden, *J. Phys. Chem.* **1975**, 79, 2693–2700.
47. M. J. Davies, B. C. Gilbert, *J. Chem. Soc. Perkin Trans. 2* **1984**, 1809–1815.
48. The rate constants also increase with alkyl substitution at the C=C double bond (see Table 1), again evidence for the polar nature of the transition state of the interaction of $\text{SO}_4^{\cdot-}$ with C=C.
49. G. Koltzenburg, E. Bastian, S. Steenken, *Angew. Chem. Int. Ed. Engl.* **1988**, 27, 1066–1067.
50. The lifetime of the radical cation is <20 ns, as deduced from 193 nm photoionization experiments of the cyclohexene in aqueous solution.
51. If there are two methyl groups at C=C, the reaction with $\text{SO}_4^{\cdot-}$ leads 'directly', i.e. with a delay of <10 ns, to the β -hydroxyalkyl radical and H^+ .
52. With this number for k_{het} , the distinction between addition–elimination and outer-sphere electron transfer becomes a borderline case.
53. S. Steenken, in J. Mattay (Ed.): *Topics in Current Chemistry 177, Electron Transfer II*, Springer, Berlin **1996**, p. 125–145.
54. H-abstraction, particularly from allylic positions, is also observed, but is typically a minor (<10 %) process.
55. C. von Sonntag, *Adv. Carbohydr. Chem. Biochem.* **1980**, 37, 7–77.
56. J. Stubbe, W. A. Van der Donk, *Chemistry & Biology* **1995**, 2, 793–801.
57. R. Lenz, B. Giese, *J. Am. Chem. Soc.* **1997**, 119, 2784–2794.
58. A. L. Buley, R. O. C. Norman, R. J. Pritchett, *J. Chem. Soc. (B)* **1966**, 849–852.
59. R. Livingston, H. Zeldes, *J. Am. Chem. Soc.* **1966**, 88, 4333–4336.
60. C. von Sonntag, E. Thoms, *Z. Naturf. B* **1970**, 25b, 1405.
61. K. M. Bansal, M. Grätzel, A. Henglein, E. Janata, *J. Phys. Chem.* **1973**, 77, 16–19.
62. B. C. Gilbert, R. O. C. Norman, P. S. Williams, *J. Chem. Soc. Perkin Trans. 2* **1980**, 647–656.
63. S. Steenken, *J. Phys. Chem.* **1979**, 83, 595–599.
64. B. C. Gilbert, J. P. Larkin, R. O. C. Norman, *J. Chem. Soc. Perkin Trans. 2* **1972**, 794–802.
65. C. Walling, R. A. Johnson, *J. Am. Chem. Soc.* **1975**, 97, 2405.
66. S. Steenken, M. J. Davies, B. C. Gilbert, *J. Chem. Soc., Perkin Trans. 2* **1986**, 1003–1010.
67. B. C. Gilbert, R. O. C. Norman, R. C. Sealy, *J. Chem. Soc. Perkin Trans. 2* **1974**, 824–830.
68. T. Foster, P. R. West, *Can. J. Chem.* **1973**, 51, 4009–4017.
69. G. Behrens, G. Koltzenburg, *Z. Naturforsch.* **1985**, 40c, 785–797.

70. A computational study on the mechanism of rearrangements of β -acyloxyalkyl radicals has been performed: Zipse, H. *J. Am. Chem. Soc.* **1997**, *119*, 1087.
71. T. Matsushige, G. Koltzenburg, D. Schulte-Frohlinde, *Ber. Bunsenges. Phys. Chem.* **1975**, *79*, 657–661.
72. G. Koltzenburg, T. Matsushige, D. Schulte-Frohlinde, *Z. Naturforsch.* **1976**, *31b*, 960–964.
73. G. Behrens, D. Schulte-Frohlinde, *Ber. Bunsenges. Phys. Chem.* **1976**, *80*, 429–436.
74. A further example for heterolysis of the acetate function are radicals from glycerol esters, see ref 75.
75. G. Koltzenburg, G. Behrens, D. Schulte-Frohlinde, *J. Am. Chem. Soc.* **1982**, *104*, 7311–7312.
76. This is certainly related to the fact that in the (*non*-radical) reaction involving *t*-BuCl a localized carbocation (Me_3C^+) is formed, whereas in the radical system (Eq. 16) the electro-fuge is the delocalized radical cation, $\text{Me}_2\text{C}^+\text{CH}_2^\cdot$.
77. The radical cation formed in the heterolysis can also be produced by 193 nm photoionization of cyclohexene in aqueous solution, see Scheme 8: S. Steenken, unpublished material.
78. G. Behrens, E. Bothe, J. Eibenberger, G. Koltzenburg, D. Schulte-Frohlinde, *Angew. Chem.* **1978**, *90*, 639.
79. G. Behrens, E. Bothe, G. Koltzenburg, D. Schulte-Frohlinde, *J. Chem. Soc. Perkin Trans. 2* **1980**, *3*, 883–889.
80. $(\text{MeO})_2\text{C}^+\text{CH}_2^\cdot$ is able to oxidize N,N,N',N'-tetramethyl-*p*-phenylenediamine (TMPD) to $\text{TMPD}^{+\cdot}$ with the rate constant $2.9 \times 10^9 \text{ M}^{-1} \text{ s}^{-1}$: S. Steenken, unpublished.
81. G. Behrens, E. Bothe, G. Koltzenburg, D. Schulte-Frohlinde, *J. Chem. Soc. Perkin Trans. 2* **1981**, 143–154.
82. G. Koltzenburg, G. Behrens, D. Schulte-Frohlinde, *Angew. Chem. Int. Ed. Engl.* **1983**, *22*, 500–1.
83. M. Dizdaroglu, C. von Sonntag, D. Schulte-Frohlinde, *J. Am. Chem. Soc.* **1975**, *97*, 2277–2278.
84. G. Behrens, G. Koltzenburg, D. Schulte-Frohlinde, *Z. Naturforsch.* **1982**, *37c*, 1205–1227.
85. A computational study of the mechanism of fragmentation of β -phosphatoalkyl radicals has been published: Zipse, H. *J. Am. Chem. Soc.* **1997**, *119*, 2889. See also Newcomb, M.; Horner, J.H.; Whitted, P.O.; Crich, D.; Huang, X.; Yao, Q.; Zipse, H. *J. Am. Chem. Soc.* **1999**, *121*, 10685.
86. B. Giese, X. Beyrich-Graf, P. Erdmann, M. Petretta, U. Schwitter, *Chemistry and Biology* **1995**, *2*, 367–375.
87. A. Samuni, P. Neta, *J. Phys. Chem.* **1973**, *77*, 2425–2429.
88. S. Steenken, G. Behrens, D. Schulte-Frohlinde, *Int. J. Radiat. Biol.* **1974**, *25*, 205–210.
89. G. Behrens, G. Koltzenburg, A. Ritter, D. Schulte-Frohlinde, *Int. J. Radiat. Biol.* **1978**, *33*, 163–171.
90. In oligonucleotide C4'-type radicals, the rate of heterolytic phosphate elimination has been estimated as 10^2 – 10^3 s^{-1} : B. Giese, A. Dussy, E. Meggers, M. Petretta, U. Schwitter, *J. Am. Chem. Soc.* **1997**, *119*, 11130. On the other hand, with the diethyl *ester* of phosphoric acid, the rate constant for β -elimination from a 4-methyl-2'-deoxyribos-4'-yl radical is $\geq 3 \times 10^9 \text{ s}^{-1}$: A. Gugger, R. Batra, P. Rzađek, G. Rist, B. Giese, *J. Am. Chem. Soc.* **1997**, *119*, 8740.
91. B. Giese, P. Erdmann, L. Giraud, T. Göbel, A. M. Petretta, T. Schäfer, M. Von Raumer, *Tetrahedron. Lett.* **1994**, *35*, 2683–2686.
92. The number is taken from Figure 2 of ref. 91.
93. A. Gugger, R. Batra, P. Rzađek, G. Rist, B. Giese, *J. Am. Chem. Soc.* **1997**, *119*, 8740–8741.
94. C. von Sonntag, U. Hagen, A. Schön-Bopp, D. Schulte-Frohlinde, *Adv. Radiat. Biol.* **1981**, *6*, 109–142.
95. The base may be on the same ('intra-strand') or the complementary ('inter-strand' electron transfer) strand or it may be up to 5 nucleotide units below or above the radical cation [35].
96. The ET rates are distance-dependent, for details see E. Meggers, A. Dussy, T. Schäfer, B. Giese, *Chem. Eur. J.* **2000**, *6*, 485.
97. C. Walling, D. M. Camaioni, *J. Am. Chem. Soc.* **1975**, *97*, 1603.
98. C. Walling, G. M. El-Taliawi, C. Zhao, *J. Org. Chem.* **1983**, *48*, 4914–4917.
99. C. Walling, C. X. Zhao, G. M. El-Taliawi, *J. Org. Chem.* **1983**, *48*, 4910–4914.

100. P. O'Neill, S. Steenken, D. Schulte-Frohlinde, *J. Phys. Chem.* **1975**, 79, 2773–2779.
101. P. Neta, V. Madhavan, H. Zemel, R. W. Fessenden, *J. Am. Chem. Soc.* **1977**, 99, 163–164.
102. M. Bietti, E. Baciocchi, S. Steenken, *J. Phys. Chem. A* **1998**, 102, 7337–7342.
103. K. M. Bansal, R. W. Fessenden, *Radiat. Res.* **1978**, 75, 497–507.
104. H. M. Novais, S. Steenken, *J. Phys. Chem.* **1987**, 91, 426–433.
105. D. J. Deeble, M. N. Schuchmann, S. Steenken, C. von Sonntag, *J. Phys. Chem.* **1990**, 94, 8186–8192.
106. The assignment of the reaction products of $\text{SO}_4^{\cdot-}$ with N1-alkylated thymine in aqueous solution in terms of SO_4^- adducts (Lomoth, R.; Naumov, S.; Brede, O. *J. Phys. Chem. A* **1999**, 103, 6571) is in disagreement with the conductance results reported in ref 105.
107. H. A. Schwarz, R. W. Dodson, *J. Phys. Chem.* **1984**, 88, 3643–3647.
108. U. K. Kläning, K. Schested, J. Holcman, *J. Phys. Chem.* **1985**, 89, 760–763.
109. The tendency of $\cdot\text{OH}$ to add to double bonds has recently been confirmed by MO calculations: M. Peräkylä, T. A. Pakkanen, *J. Chem. Soc. Perkin Trans. 2* **1995**, 1405.
110. P. Fournier de Violet, *Rev. Chem. Intermediates* **1981**, 4, 121–169.
111. K.-D. Asmus, M. Bonifacic, P. Toffel, P. O'Neill, D. Schulte-Frohlinde, S. Steenken, *J. Chem. Soc. Faraday Trans. 1* **1978**, 74, 1820–1826.
112. A further example for the ad-el mechanism is the reaction of $\cdot\text{OH}$ with the strong reductant ascorbic acid. This reaction, which leads to the oxidation of ascorbic acid to yield the ascorbate radical, proceeds by addition to the olefinic bond of the reductone function followed by elimination of OH^- : Abe, A.; Okada, S.; Nakao, R.; Horii, T.; Inoue, H.; Taniguchi, S.; Yamabe, S. *J. Chem. Soc. Perkin Trans. 2* **1992**, 2221.
113. D. K. Hazra, S. Steenken, *J. Am. Chem. Soc.* **1983**, 105, 4380–4386.
114. J. Lind, X. Shen, T. E. Eriksen, G. Merenyi, *J. Am. Chem. Soc.* **1990**, 112, 479–482.
115. M. Anbar, D. Meyerstein, P. Neta, *J. Phys. Chem.* **1966**, 70, 2660–2662.
116. P. O'Neill, D. Schulte-Frohlinde, S. Steenken, *J. Chem. Soc. Faraday Disc.* **1977**, 63, 141–148.
117. G. N. R. Tripathi, *J. Am. Chem. Soc.* **1998**, 120, 4161–4166.
118. The formation of the 4-aminophenoxyl radical (see Scheme 18) *proves* that addition has occurred. The protonated amino function is expected to be a powerful leaving group, cf eq 13. If, alternatively, OH^- was the leaving group, the radical cation would be formed.
119. In order to explain the results, the term 'adduct-mediated electron transfer' (AMET) was introduced. This term implies that it is the adduct which *mediates* electron transfer. However, the adduct does not *mediate* ET but its heterolysis *constitutes* the ET. Furthermore, the allegation of a distinction between ET and 'AMET' creates a mechanistic dichotomy which is unnecessary. It is possible to explain all the results on the basis of a single (unified), i.e., the ad-el mechanism.
120. R. H. Schuler, P. Neta, H. Zemel, R. W. Fessenden, *J. Am. Chem. Soc.* **1976**, 98, 3825–3831.
121. D. J. Deeble, S. Das, C. von Sonntag, *J. Phys. Chem.* **1985**, 89, 5784–5788.
122. H. M. Novais, S. Steenken, *J. Am. Chem. Soc.* **1986**, 108, 1–6.
123. L. P. Candeias, S. Steenken, *J. Phys. Chem.* **1992**, 96, 937–944.
124. L. P. Candeias, P. Wolf, P. O'Neill, S. Steenken, *J. Phys. Chem.* **1992**, 96, 10302–7.
125. For a discussion on side-chain fragmentation reactions involving other C–X β -bonds, a number of reviews are available (E. Baciocchi, M. Bietti, O. Lanzalunga, *Acc. Chem. Res.* **200**, 33, 243–251. K. Mizuno, T. Tamai, A. Sugimoto, H. Maeda, *Advances in Electron Transfer Chemistry* **1999**, 6, 131–165. R. S. Glass, *Topics in Current Chemistry* **1999**, 205, 1–87. M. Schmittle, A. Burghart, *Angew. Chem. Int. Ed. Engl.* **1997**, 36, 2550–2589. E. Baciocchi, *Acta Chem. Scand.* **1990**, 44, 645–652.
126. P. Maslak, *Topics in Current Chemistry* **1993**, 168, 1–46.
127. P. Maslak, J. N. Narvaez, *Angew. Chem. Int. Ed. Engl.* **1990**, 29, 283–285.
128. D. D. M. Wayner, V. D. Parker, *Acc. Chem. Res.* **1993**, 26, 287–294.
129. H. L. Friedman, C. V. Krishnan, in E. Franks (Ed.): *Water, A Comprehensive Treatise*, Plenum Press, New York **1973**.
130. A. M. D. Nicholas, D. R. Arnold, *Can. J. Chem.* **1982**, 60, 2165–2179.
131. J. O. Howell, J. M. Goncalves, C. Amatore, L. Klasinc, R. M. Wightman, J. K. Kochi, *J. Am. Chem. Soc.* **1984**, 106, 3968–3976.
132. C. J. Schlesener, C. Amatore, J. K. Kochi, *J. Am. Chem. Soc.* **1984**, 106, 7472–7482.

133. K. Sehested, J. Holcman, *J. Phys. Chem.* **1978**, 82, 651–653.
134. C. Russo-Caia, S. Steenken, to be published.
135. M. Schmittl, A. Burghart, *Angew. Chem. Int. Ed. Engl.* **1997**, 36, 2551–2589.
136. O. Takahashi, O. Kikuchi, *Tetrahedron Lett.* **1991**, 32, 4933–4936.
137. A. Anne, S. Fraoua, V. Grass, J. Moiroux, J.-M. Savéant, *J. Am. Chem. Soc.* **1998**, 120, 2951–2958.
138. A. Anne, S. Fraoua, P. Hapiot, J. Moiroux, J.-M. Savéant, *J. Am. Chem. Soc.* **1995**, 117, 7412–7421.
139. A. Anne, P. Hapiot, J. Moiroux, P. Neta, J.-M. Savéant, *J. Am. Chem. Soc.* **1992**, 114, 4694–4701.
140. R. A. Marcus, *J. Phys. Chem.* **1968**, 72, 891–899.
141. A. O. Cohen, R. A. Marcus, *J. Phys. Chem.* **1968**, 72, 4249–4256.
142. J. P. Dinnocenzo, T. E. Banach, *J. Am. Chem. Soc.* **1989**, 111, 8646–8653.
143. C. Amatore, J. K. Kochi, *Advances in Electron Transfer Chemistry* **1991**, 1, 55–148.
144. C. J. Schlesener, C. Amatore, J. K. Kochi, *J. Phys. Chem.* **1986**, 90, 3747–3756.
145. E. Baciocchi, T. Del Giacco, F. Elisei, *J. Am. Chem. Soc.* **1993**, 115, 12290–12295.
146. J. M. Masnovi, S. Sankararaman, J. K. Kochi, *J. Am. Chem. Soc.* **1989**, 111, 2263–2276.
147. This value was determined by Savéant (A. Anne, S. Fraoua, V. Grass, J. Moiroux, J.-M. Savéant, *J. Am. Chem. Soc.* **1998**, 120, 2951–2958) using Kochi's data, while Kochi obtained 0.3 eV.
148. E. Baciocchi, M. Mattioli, R. Romano, R. Ruzziconi, *J. Org. Chem.* **1991**, 56, 7154–7160.
149. E. Baciocchi, A. Dalla Cort, L. Ebersson, L. Mandolini, C. Rol, *J. Org. Chem.* **1986**, 51, 4544–4548.
150. L. M. Tolbert, Z. Z. Li, S. R. Sirimanne, D. G. Vanderveer, *J. Org. Chem.* **1997**, 62, 3927–3930.
151. L. M. Tolbert, R. K. Khanna, A. E. Popp, L. Gelbaum, L. A. Bottomley, *J. Am. Chem. Soc.* **1990**, 112, 2373–2378.
152. L. M. Tolbert, R. K. Khanna, *J. Am. Chem. Soc.* **1987**, 109.
153. E. Baciocchi, F. D'Acunzo, C. Galli, O. Lanzalunga, *J. Chem. Soc., Perkin Trans. 2* **1996**, 133–140.
154. V. D. Parker, E. T. Chao, G. Zheng, *J. Am. Chem. Soc.* **1997**, 119, 11390–11394.
155. V. D. Parker, Y. X. Zhao, Y. Lu, G. Zheng, *J. Am. Chem. Soc.* **1998**, 120, 12720–12727.
156. B. Reitstoen, V. D. Parker, *J. Am. Chem. Soc.* **1991**, 113, 6954–6958.
157. J. M. Mayer, *Acc. Chem. Res.* **1998**, 31, 441–450.
158. T. M. Bockman, S. M. Hubig, J. K. Kochi, *J. Am. Chem. Soc.* **1998**, 120, 2826–2830.
159. S. M. Hubig, R. Rathore, J. K. Kochi, *J. Am. Chem. Soc.* **1999**, 121, 617–626.
160. K. A. Gardner, L. L. Kuehnert, J. M. Mayer, *Inorganic Chemistry* **1997**, 36, 2069–2078.
161. T. Delgiacco, E. Baciocchi, S. Steenken, *J. Phys. Chem.* **1993**, 97, 5451–56.
162. P. R. Ortiz De Montellano, *Cytochrome P-450: Structure, Mechanism And Biochemistry*, Plenum Press, New York **1995**.
163. T. G. Traylor, K. W. Hill, W. P. Fann, S. Tsuchiya, B. E. Dunlap, *J. Am. Chem. Soc.* **1992**, 114, 1308–1312.
164. L. Ebersson, *J. Am. Chem. Soc.* **1983**, 105, 3192–3199.
165. T. L. Macdonald, W. G. Gutheim, R. B. Martin, F. P. Guengerich, *Biochemistry* **1989**, 28, 2071–2077.
166. E. Baciocchi, *Xenobiotica* **1995**, 25, 653–666.
167. R. Amodeo, E. Baciocchi, M. Crescenzi, O. Lanzalunga, *Tetrahedron Lett.* **1990**, 31, 3477–3480.
168. E. Baciocchi, S. Belvedere, M. Bietti, O. Lanzalunga, *Eur. J. Org. Chem.* **1998**, 299–302.
169. E. Baciocchi, T. Del Giacco, F. Elisei, O. Lanzalunga, *J. Am. Chem. Soc.* **1998**, 120, 11800–11801.
170. E. Baciocchi, M. Bietti, S. Steenken, *Chem. Eur. J.* **1999**, 5, 1785–1793.
171. E. Baciocchi, M. Bietti, S. Steenken, *J. Am. Chem. Soc.* **1997**, 119, 4078–4079.
172. E. Baciocchi, M. Bietti, L. Manduchi, S. Steenken, *J. Am. Chem. Soc.* **1999**, 121, 6624–6629.
173. M. Eigen, *Angew. Chem., Int. Ed. Engl.* **1964**, 3, 1–19.
174. V. Bachler, E. Baciocchi, M. Bietti, S. Steenken, to be published.

175. A. Anne, S. Fraoua, J. Moiroux, J.-M. Savéant, *J. Am. Chem. Soc.* **1996**, *118*, 3938–3945.
176. P. Maslak, T. M. Vallombroso, W. H. Chapman, Jr., J. N. Narvaez, *Angew. Chem. Int. Ed. Engl.* **1994**, *33*, 73–75.
177. L. Bardi, E. Fasani, A. Albini, *J. Chem. Soc. Perkin Trans. 1* **1994**, 545–549.
178. E. Baciocchi, D. Bartoli, C. Rol, R. Ruzziconi, G. V. Sebastiani, *J. Org. Chem.* **1986**, *51*, 3587–3593.
179. D. M. Camaioni, J. A. Franz, *J. Org. Chem.* **1984**, *49*, 1607–1613.
180. D. R. Arnold, L. J. Lamont, *Can. J. Chem.* **1989**, *67*, 2119–2127.
181. A. Okamoto, M. S. Snow, D. R. Arnold, *Tetrahedron* **1986**, *42*, 6175–87.
182. D. R. Arnold, B. J. Fahie, L. J. Lamont, J. Wierzchowski, K. M. Young, *Can. J. Chem.* **1987**, *65*, 2734–2743.
183. A. L. Perrott, D. R. Arnold, *Can. J. Chem.* **1992**, *70*, 272–279.
184. D. R. Arnold, L. J. Lamont, A. L. Perrott, *Can. J. Chem.* **1991**, *69*, 225–233.
185. M. J. Davies, B. C. Gilbert, *Advances In Detailed Reaction Mechanisms* **1991**, *1*, 35–81.
186. B. C. Gilbert, C. J. Warren, *Res. Chem. Intermediat.* **1989**, *11*, 1–17.
187. S. Steenken, C. J. Warren, B. C. Gilbert, *J. Chem. Soc. Perkin Trans. 2* **1990**, 335–342.
188. J. P. Dinnocenzo, T. R. Simpson, H. Zuilhof, W. P. Todd, T. Heinrich, *J. Am. Chem. Soc.* **1997**, *119*, 987–993.
189. J. P. Dinnocenzo, W. P. Todd, T. R. Simpson, I. R. Gould, *J. Am. Chem. Soc.* **1990**, *112*, 2462–2464.
190. J. P. Dinnocenzo, H. Zuilhof, D. R. Lieberman, T. R. Simpson, M. W. Mckechney, *J. Am. Chem. Soc.* **1997**, *119*, 994–1004.
191. J. P. Dinnocenzo, D. R. Lieberman, T. R. Simpson, *J. Am. Chem. Soc.* **1993**, *115*, 366–367.
192. M. Freccero, A. Pratt, A. Albini, C. Long, *J. Am. Chem. Soc.* **1998**, *120*, 284–297.
193. R. Popielarz, D. R. Arnold, *J. Am. Chem. Soc.* **1990**, *112*, 3068–3082.
194. D. M. Camaioni, *J. Am. Chem. Soc.* **1990**, *112*, 9475–9483.
195. However, when bibenzyl radical cations are generated by photoinduced electron transfer, no deprotonation is observed since this process is relatively inefficient compared to back electron transfer (R. Popielarz, D. R. Arnold, *J. Am. Chem. Soc.* **1990**, *112*, 3068–3082. H. F. Davis, P. K. Das, L. W. Reichel, G. W. Griffin, *J. Am. Chem. Soc.* **1984**, *106*, 6968–6973).
196. E. Baciocchi, M. Bietti, L. Putignani, S. Steenken, *J. Am. Chem. Soc.* **1996**, *118*, 5952–5960.
197. E. Baciocchi, C. Rol, G. V. Sebastiani, L. Taglieri, *J. Org. Chem.* **1994**, *59*, 5272–5276.
198. S. Steenken, R. A. McClelland, *J. Am. Chem. Soc.* **1989**, *111*, 4967–4973.
199. P. Maslak, W. H. J. Chapman, T. M. J. Vallombroso, B. A. Watson, *J. Am. Chem. Soc.* **1995**, *117*, 12380–12389.
200. P. Maslak, S. L. Asel, *J. Am. Chem. Soc.* **1988**, *110*, 8260–8261.
201. S. Perrier, S. Sankararaman, J. K. Kochi, *J. Chem. Soc. Perkin Trans. 2* **1993**, 825–837.
202. S. Sankararaman, S. Perrier, J. K. Kochi, *J. Am. Chem. Soc.* **1989**, *111*, 6448–6449.
203. T. M. Bockman, S. M. Hubig, J. K. Kochi, *J. Am. Chem. Soc.* **1998**, *120*, 6542–6547.
204. P. Maslak, W. H. Chapman, *J. Org. Chem.* **1996**, *61*, 2647–2656.
205. P. Maslak, W. H. Chapman, *J. Org. Chem.* **1990**, *55*, 6334–6347.
206. P. Maslak, W. H. Chapman, *Tetrahedron* **1990**, *46*, 2715–2724.
207. E. R. Gaillard, D. G. Whitten, *Acc. Chem. Res.* **1996**, *29*, 292–297.
208. L. H. Chen, M. S. Farahat, E. R. Gaillard, S. Farid, D. G. Whitten, *J. Photochem. Photobiol. A: Chem.* **1996**, *95*, 21–25.
209. H. Gan, U. Leinhos, I. R. Gould, D. G. Whitten, *J. Phys. Chem.* **1995**, *99*, 3566–3573.
210. A. Albini, M. Mella, *Tetrahedron* **1986**, *42*, 6219–6224.
211. J. P. Dinnocenzo, M. Merchan, B. O. Roos, S. Shaik, H. Zuilhof, *J. Phys. Chem. A* **1998**, *102*, 8979–8987.
212. Y. H. Wang, J. M. Tanko, *J. Am. Chem. Soc.* **1997**, *119*, 8201–8208.
213. Y. H. Wang, J. M. Tanko, *J. Chem. Soc. Perkin Trans. 2* **1998**, 2705–2711.
214. Y. H. Wang, K. H. Mclean, J. M. Tanko, *J. Org. Chem.* **1998**, *63*, 628–635.
215. E. Baciocchi, M. Bietti, O. Lanzalunga, S. Steenken, *J. Am. Chem. Soc.* **1998**, *120*, 11516–11517.

216. R. D. Burton, M. D. Bartberger, Y. Zhang, J. R. Eyler, K. S. Schanze, *J. Am. Chem. Soc.* **1996**, *118*, 5655–5664.
217. X. H. Ci, M. A. Kellett, D. G. Whitten, *J. Am. Chem. Soc.* **1991**, *113*, 3893–3904.
218. X. Ci, D. G. Whitten, *J. Am. Chem. Soc.* **1989**, *111*, 3459–3461.
219. L. A. Lucia, R. D. Burton, K. S. Schanze, *J. Phys. Chem.* **1993**, *97*, 9078–9080.
220. M. J. Davies, B. C. Gilbert, C. W. McClelland, C. B. Thomas, J. Young, *J. Chem. Soc. Chem. Commun.* **1984**, 966–967.
221. D. V. Avila, J. Luszytk, K. U. Ingold, *J. Am. Chem. Soc.* **1992**, *114*, 6576–6577.
222. D. V. Avila, K. U. Ingold, A. A. Di Nardo, F. Zerbetto, M. Z. Zgierski, J. Luszytk, *J. Am. Chem. Soc.* **1995**, *117*, 2711–2718.
223. B. Ashworth, B. C. Gilbert, R. G. G. Holmes, R. O. C. Norman, *J. Chem. Soc., Perkin Trans. 2* **1978**, 951–956.
224. H. Zemel, R. W. Fessenden, *J. Phys. Chem.* **1975**, *79*, 1419–1427.
225. B. C. Gilbert, J. P. Larkin, R. O. C. Norman, *J. Chem. Soc. Perkin Trans. 2* **1972**, 1272–1279.
226. S. Steenken, P. O'Neill, D. Schulte-Frohlinde, *J. Phys. Chem.* **1977**, *81*, 26–30.
227. J. Chateaufneuf, J. Luszytk, K. U. Ingold, *J. Am. Chem. Soc.* **1988**, *110*, 2877–2885.
228. B. C. Gilbert, C. J. Scarratt, C. B. Thomas, J. Young, *J. Chem. Soc. Perkin Trans. 2* **1987**, *2*, 371–80.
229. L. Jönsson, *Acta Chem. Scand.* **1983**, *B37*, 761–768.
230. R. M. Dessau, E. I. Heiba, *J. Org. Chem.* **1975**, *40*, 3647–3649.
231. W. S. Trahanowsky, J. Cramer, D. W. Brixius, *J. Am. Chem. Soc.* **1974**, *96*, 1077–1081.
232. T. M. Bockman, S. M. Hubig, J. K. Kochi, *J. Org. Chem.* **1997**, *62*, 2210–2221.
233. T. M. Bockman, S. M. Hubig, J. K. Kochi, *J. Am. Chem. Soc.* **1996**, *118*, 4502–4503.
234. L. K. Mehta, M. Porssa, J. Parrick, L. P. Candeias, P. Wardman, *J. Chem. Soc., Perkin Trans. 2* **1997**, 1487–1491.
235. C. Walling, G. M. El-Taliawi, K. Amarnath, *J. Am. Chem. Soc.* **1984**, *106*, 7573–7578.
236. J.-M. Savéant, *J. Am. Chem. Soc.* **1992**, *114*, 10595–10602.
237. J.-M. Savéant, *J. Am. Chem. Soc.* **1987**, *109*, 6788–6795.
238. J.-M. Savéant, In P. S. Mariano (Ed.): *Advances In Electron Transfer Chemistry*, Vol. 4, Jai Press Inc., Greenwich, Connecticut and London, England 1994, P. 53–116.
239. J.-M. Savéant, *Acc. Chem. Res.* **1993**, *26*, 455–461.
240. S. Antonello, F. Maran, *J. Am. Chem. Soc.* **1999**, *121*, 9668–9676.
241. L. Pause, M. Robert, J. M. Saveant, *J. Am. Chem. Soc.* **1999**, *121*, 7158–7159.
242. R. L. Donkers, F. Maran, D. D. M. Wayner, M. S. Workentin, *J. Am. Chem. Soc.* **1999**, *121*, 7239–7248.
243. C. Costentin, P. Hapiot, M. Medebielle, J.-M. Savéant, *J. Am. Chem. Soc.* **1999**, *121*, 4451–4460.
244. K. Daasbjerg, H. Jensen, R. Benassi, F. Taddei, S. Antonello, A. Gennaro, F. Maran, *J. Am. Chem. Soc.* **1999**, *121*, 1750–1751.
245. C. P. Andrieux, J.-M. Savéant, C. Tardy, *J. Am. Chem. Soc.* **1998**, *120*, 4167–4175.
246. C. P. Andrieux, J.-M. Savéant, A. Tallec, R. Tardivel, C. Tardy, *J. Am. Chem. Soc.* **1997**, *119*, 2420–2429.
247. M. L. Andersen, W. Long, D. D. M. Wayner, *J. Am. Chem. Soc.* **1997**, *119*, 6590–6595.
248. M. L. Andersen, N. Mathivanan, D. D. M. Wayner, *J. Am. Chem. Soc.* **1996**, *118*, 4871–4879.
249. C. P. Andrieux, J.-M. Savéant, A. Tallec, R. Tardivel, C. Tardy, *J. Am. Chem. Soc.* **1996**, *118*, 9788–9789.
250. D. D. Tanner, J. J. Chen, L. Chen, C. Luelo, *J. Am. Chem. Soc.* **1991**, *113*, 8074–8081.
251. S. Antonello, F. Maran, *J. Am. Chem. Soc.* **1997**, *119*, 12595–12600.
252. R. L. Donkers, J. Tse, M. S. Workentin, *Chem. Commun.* **1999**, 135–136.
253. M. S. Workentin, R. L. Donkers, *J. Am. Chem. Soc.* **1998**, *120*, 2664–2665.
254. R. L. Donkers, M. S. Workentin, *J. Phys. Chem. B* **1998**, *102*, 4061–4063.
255. S. Antonello, M. Musumeci, D. D. M. Wayner, F. Maran, *J. Am. Chem. Soc.* **1997**, *119*, 9541–9549.
256. M. S. Workentin, F. Maran, D. D. M. Wayner, *J. Am. Chem. Soc.* **1995**, *117*, 2120–2121.

257. S. Jakobsen, H. Jensen, S. U. Pedersen, K. Daasbjerg, *J. Phys. Chem. A* **1999**, *103*, 4141–4143.
258. M. G. Severin, G. Farnia, E. Vianello, M. C. Arevalo, *J. Electroanal. Chem.* **1988**, *251*, 369–382.
259. X. Z. Wang, F. D. Saeva, J. A. Kampmeier, *J. Am. Chem. Soc.* **1999**, *121*, 4364–4368.
260. C. P. Andrieux, J.-M. Savéant, C. Tardy, *J. Am. Chem. Soc.* **1997**, *119*, 11546–11547.
261. C. P. Andrieux, M. Robert, F. D. Saeva, J.-M. Savéant, *J. Am. Chem. Soc.* **1994**, *116*, 7864–7871.
262. F. D. Saeva, In P. S. Mariano (Ed.): *Advances In Electron Transfer Chemistry*, Vol. 4, Jai Press Inc., Greenwich, Connecticut and London, England 1994, P. 1–25.
263. F. D. Saeva, *Top. Curr. Chem.* **1990**, *156*, 59–92.
264. Z. R. Zheng, D. H. Evans, E. S. Chan-Shing, J. Lessard, *J. Am. Chem. Soc.* **1999**, *121*, 9429–9434.
265. F. F. Wu, T. F. Guarr, R. D. Guthrie, *J. Phys. Org. Chem.* **1992**, *5*, 7–18.
266. P. Maslak, J. Theroff, *J. Am. Chem. Soc.* **1996**, *118*, 7235–7236.
267. R. D. Guthrie, M. Patwardhan, J. E. Chateaufneuf, *J. Phys. Org. Chem.* **1994**, *7*, 147–152.
268. R. D. Guthrie, B. C. Shi, *J. Am. Chem. Soc.* **1990**, *112*, 3136–3139.
269. P. Maslak, R. D. Guthrie, *J. Am. Chem. Soc.* **1986**, *108*, 2637–2640.
270. P. Maslak, R. D. Guthrie, *J. Am. Chem. Soc.* **1986**, *108*, 2628–2636.
271. H. Lund, K. Daasbjerg, T. Lund, S. U. Pedersen, *Acc. Chem. Res.* **1995**, *28*, 313–319.
272. J.-M. Savéant, *Tetrahedron* **1994**, *50*, 10117–10165.
273. R. A. Rossi, A. B. Pierini, S. M. Palacios, *Advances In Free Radical Chemistry* **1990**, *1*, 193–252.
274. J.-M. Savéant, *Adv. Phys. Org. Chem.* **1990**, *26*, 1–130.
275. R. A. Rossi, R. H. De Rossi, *Aromatic Substitution By The $S_{\text{N}}1$ Mechanism*, Vol. 178, American Chemical Society, Washington D.C. 1983.
276. R. A. Rossi, *Acc. Chem. Res.* **1982**, *15*, 164–170.
277. J. F. Bunnett, *Acc. Chem. Res.* **1978**, *11*, 413–420.
278. M. Meot-Ner, P. Neta, R. K. Norris, K. Wilson, *J. Phys. Chem.* **1986**, *90*, 168.
279. A. B. Pierini, J. S. Duca, D. M. A. Vera, *J. Chem. Soc., Perkin Trans. 2* **1999**, 1003–1009.
280. A. B. Pierini, J. S. Duca, *J. Chem. Soc., Perkin Trans. 2* **1995**, 1821–1828.
281. D. Behar, P. Neta, *J. Am. Chem. Soc.* **1981**, *103*, 2280–2283.
282. P. Neta, D. Behar, *J. Am. Chem. Soc.* **1981**, *103*, 103–106.
283. D. Behar, P. Neta, *J. Phys. Chem.* **1981**, *85*, 690–693.
284. P. Neta, D. Behar, *J. Am. Chem. Soc.* **1980**, *102*, 4798–4802.
285. C. Galli, *Tetrahedron* **1988**, *44*, 5205–5208.
286. W. C. Danen, T. T. Kensler, J. G. Lawless, M. F. Marcus, M. D. Hawley, *J. Phys. Chem.* **1969**, *73*, 4389–4391.
287. *Handbook of Chemistry and Physics*, CRC Press, Boca Raton, FL 1998–1999.
288. D. A. Pratt, J. S. Wright, K. U. Ingold, *J. Am. Chem. Soc.* **1999**, *121*, 4877–4882.
289. C. Galli, T. Pau, *Tetrahedron* **1998**, *54*, 2893–2904.
290. R. K. Norris, S. D. Barker, P. Neta, *J. Am. Chem. Soc.* **1984**, *106*, 3140–3144.
291. P. Maslak, J. N. Narvaez, J. Kula, D. S. Malinski, *J. Org. Chem.* **1990**, *55*, 4550–4559.
292. W. Adcock, C. P. Andrieux, C. I. Clark, A. Neudeck, J.-M. Savéant, C. Tardy, *J. Am. Chem. Soc.* **1995**, *117*, 8285–8286.
293. C. P. Andrieux, A. Le Gorande, J.-M. Savéant, *J. Am. Chem. Soc.* **1992**, *114*, 6892–6904.
294. J. P. Bays, S. T. Blumer, S. Baral-Tosh, D. Behar, P. Neta, *J. Am. Chem. Soc.* **1983**, *105*, 320–324.
295. J.-M. Savéant, *J. Phys. Chem.* **1994**, *98*, 3716–3724.
296. The driving force for $\text{R-X}^{\cdot-}$ bond cleavage may be expressed as a function of the bond dissociation energy of the neutral compound, BDE_{RX} , the standard potentials for radical anion formation and oxidation of the leaving anion X^- , $E_{\text{RX}/\text{RX}^{\cdot-}}^0$ and $E_{\text{X}^{\cdot-}/\text{X}^-}^0$, respectively, and an entropic term, $\Delta S = S_{\text{R}^{\cdot}} + S_{\text{X}^-} - S_{\text{RX}}^{\cdot}$: $\Delta G^0 = \text{BDE}_{\text{RX}} + E_{\text{RX}/\text{RX}^{\cdot-}}^0 - E_{\text{X}^{\cdot-}/\text{X}^-}^0 - T\Delta S$.
297. W. G. Skene, J. C. Scaiano, F. L. Cozens, *J. Org. Chem.* **1996**, *61*, 7918–7921.
298. C. P. Andrieux, M. Robert, J.-M. Savéant, *J. Am. Chem. Soc.* **1995**, *117*, 9340–9346.

- 299. C. P. Andrieux, C. Combella, F. Kanoufi, J.-M. Savéant, A. Thiebault, *J. Am. Chem. Soc.* **1997**, *119*, 9527–9540.
- 300. P. Maslak, J. N. Narvaez, T. M. Vallombroso, *J. Am. Chem. Soc.* **1995**, *117*, 12373–12379.
- 301. P. Maslak, J. N. Narvaez, M. Parvez, *J. Org. Chem.* **1991**, *56*, 602–607.
- 302. P. Maslak, J. N. Narvaez, *J. Chem. Soc., Chem. Commun.* **1989**, 138–139.
- 303. P. Maslak, J. Kula, J. N. Narvaez, *J. Org. Chem.* **1990**, *55*, 2277–2279.
- 304. P. Maslak, J. Kula, J. E. Chateaneuf, *J. Am. Chem. Soc.* **1991**, *113*, 2304–2306.

Volume II

Part 2

Organometallic and Inorganic Molecules

1 Reflections on the Two-state Electron-transfer Model

Bruce S. Brunschwig and Norman Sutin

1.1 Introduction

There is general agreement that the two most important factors determining electron transfer rates in solution are the degree of electronic interaction between the donor and acceptor sites, and the changes in the nuclear configurations of the donor, acceptor, and surrounding medium that occur upon the gain or loss of an electron [1–5]. The electronic interaction of the sites will be very weak, and the electron transfer slow, when the sites are far apart or their interaction is symmetry or spin forbidden. Since electron motion is much faster than nuclear motion, energy conservation requires that, prior to the actual electron transfer, the nuclear configurations of the reactants and the surrounding medium adjust from their equilibrium values to a configuration (generally) intermediate between that of the reactants and products. In the case of electron transfer between two metal complexes in a polar solvent, the nuclear configuration changes involve adjustments in the metal–ligand and intra-ligand bond lengths and angles, and changes in the orientations of the surrounding solvent molecules. In common with ordinary chemical reactions, an electron transfer reaction can then be described in terms of the motion of the system on an energy surface from the reactant equilibrium configuration (initial state) to the product equilibrium configuration (final state) via the activated complex (transition state) configuration.

This chapter will focus on the predictions of the traditional two-state electron transfer model. Only the ground and lowest excited state of the system are considered and contributions from higher electronic states are ignored. Thermal and optical electron transfers in both weakly and strongly interacting systems are discussed. The treatment is not intended to be exhaustive but instead will focus on certain features of the model that may be less familiar but which nevertheless have important implications.

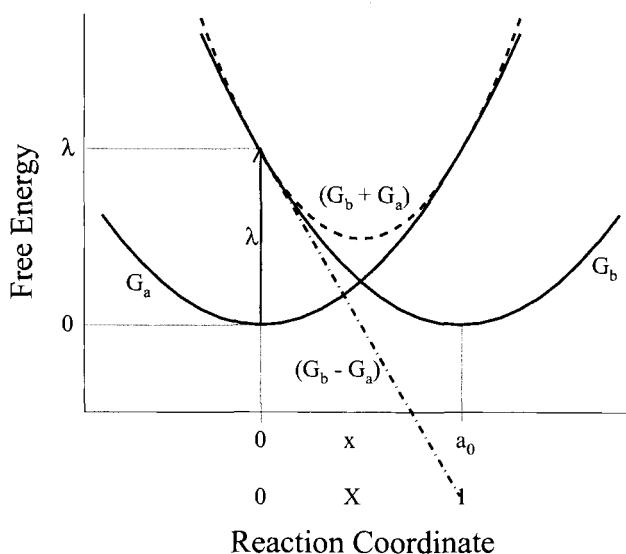
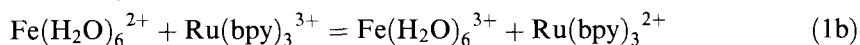
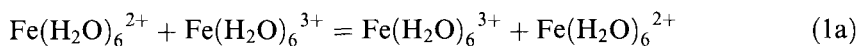


Figure 1. Plot of the diabatic free-energies of the reactants (left-hand curve, G_a) and products (right-hand curve, G_b) against the reaction coordinate for an electron transfer reaction with $\Delta G^\circ = 0$. The sum (dashes) and difference (dot-dash) of the reactant and product free-energies are also plotted.

1.2 Zero-order Energy Surfaces

Provided a hypothetical change in the charge on the reactants produces a proportional change in the dielectric polarization of the surrounding medium, the distortions of the reactants and products from their equilibrium configurations can be described in terms of displacements on harmonic free-energy curves with identical force constants [1–5]. This is illustrated in Figures 1 and 2 where the free energy of the close-contact reactants plus surrounding medium (Curve G_a) and the free energy of the close-contact products plus surrounding medium (Curve G_b) are plotted against the reaction coordinate for a self-exchange reaction.

The free-energy curves depict the zero-order or diabatic states of the system. Figure 1 shows the diabatic free-energy curves for a self-exchange reaction (Eq. 1a, $\Delta G^\circ = 0$) and Figure 2 the curves for an electron transfer reaction accompanied by a net chemical change (Eq. 1b, $\Delta G^\circ < 0$ for an exergonic reaction).



The curves have identical force constants f and their minima are separated by a_0 . The vertical difference between the free energies of the reactants and products of a self-exchange reaction at the reactants' (or products') minimum (equilibrium configuration) is the reorganization parameter $\lambda = fa_0^2/2$. Denoting the displacement along the reaction coordinate by x , a dimensionless reaction coordinate X may be defined as x/a_0 ; X varies from 0 to 1 as the reaction proceeds and, with X as the

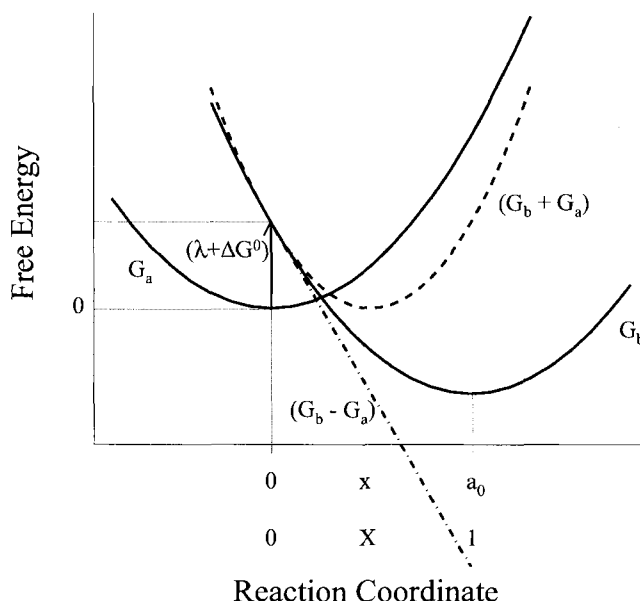


Figure 2. Plot of the diabatic free-energies of the reactants (G_a) and products (G_b) against the reaction coordinate for an electron transfer reaction with $\Delta G^\circ < 0$. The sum (dashes) and difference (dot-dash) of the reactant and product free-energies are also plotted.

coordinate, the force constants of the parabolas are equal to 2λ .

$$G_a = \frac{f}{2} x^2 = \lambda X^2 \quad (2a)$$

$$G_b = \frac{f}{2} (x - a_0)^2 + \Delta G^\circ = \lambda (X - 1)^2 + \Delta G^\circ \quad (2b)$$

The sum and difference of the zero-order free energies are given by:

$$G_b + G_a = 2\lambda (X - 1/2)^2 + \lambda/2 + \Delta G^\circ \quad (3a)$$

$$G_b - G_a = \lambda(1 - 2X) + \Delta G^\circ \quad (3b)$$

and the free-energy curves defined by these equations are included in Figures 1 and 2. The sum of the free energies of the reactants and products is a parabola [6] with force constant 4λ centered at $X = 1/2$ with its minimum vertically displaced relative to the reactant minimum by $\lambda/2 + \Delta G^\circ$. Similarly, the dependence of the average diabatic energy $(G_b + G_a)/2$ on X also is harmonic but with force constant 2λ , identical to that of the separated reactants and product curves. The parabola defined by the average energies is *still centered at $X = 1/2$* but with its minimum vertically displaced relative to the reactant minimum by $\lambda/4 + \Delta G^\circ/2$. Since the difference between the diabatic free-energies of the reactants and products ($G_b - G_a$) is linearly related to X , this difference affords a measure of the progress of the reaction [7, 8] and, as a consequence, it provides an alternate definition of the

reaction coordinate. For both self-exchange reactions and reactions accompanied by a net chemical change, the slope of a plot of $(G_b - G_a)$ against X is -2λ .

The free energy of activation for the electron transfer is the difference between the free energies of the transition-state configuration and the equilibrium configuration of the reactants.

$$\Delta G^* = G_X^* - G_{a,eq} \quad (4)$$

The equilibrium configuration of the reactants in the zero-interaction limit is located at $X = 0$ with $G_{a,eq} = 0$. At the transition state, $G_a^* = G_b^*$ so that X^* and the free energy of activation in the zero-interaction limit are given by Eqs 5a and 5b, respectively.

$$X^* = \frac{1}{2} \left(1 + \frac{\Delta G^\circ}{\lambda} \right) \quad (5a)$$

$$\Delta G^* = \lambda (X^*)^2 = \frac{\lambda}{4} \left(1 + \frac{\Delta G^\circ}{\lambda} \right)^2 \quad (5b)$$

Evidently $\Delta G^* = \lambda/4$ for $\Delta G^\circ = 0$. Three free-energy regimes can be distinguished depending on the relative magnitudes of λ and ΔG° . When $-\Delta G^\circ < \lambda$ the reaction is in the normal regime where ΔG^* decreases, and the rate constant increases, with increasing driving force. The reaction becomes barrierless ($\Delta G^* = 0$) when $-\Delta G^\circ = \lambda$ and ΔG^* is then insensitive to changes in ΔG° . If the driving force is increased even further then $-\Delta G^\circ > \lambda$ and ΔG^* increases, and the rate constant decreases, with increasing driving force. This is the counter-intuitive inverted regime.

By using the Gibbs–Helmholtz equations, it follows from Eq. 5b that the activation enthalpy and entropy are given by:

$$\Delta H^* = \frac{\Delta H_\lambda}{4} \left[1 - \left(\frac{\Delta G^\circ}{\lambda} \right)^2 \right] + \frac{\Delta H^\circ}{2} \left(1 + \frac{\Delta G^\circ}{\lambda} \right) \quad (6a)$$

$$\Delta S^* = \frac{\Delta S_\lambda}{4} \left[1 - \left(\frac{\Delta G^\circ}{\lambda} \right)^2 \right] + \frac{\Delta S^\circ}{2} \left(1 + \frac{\Delta G^\circ}{\lambda} \right) \quad (6b)$$

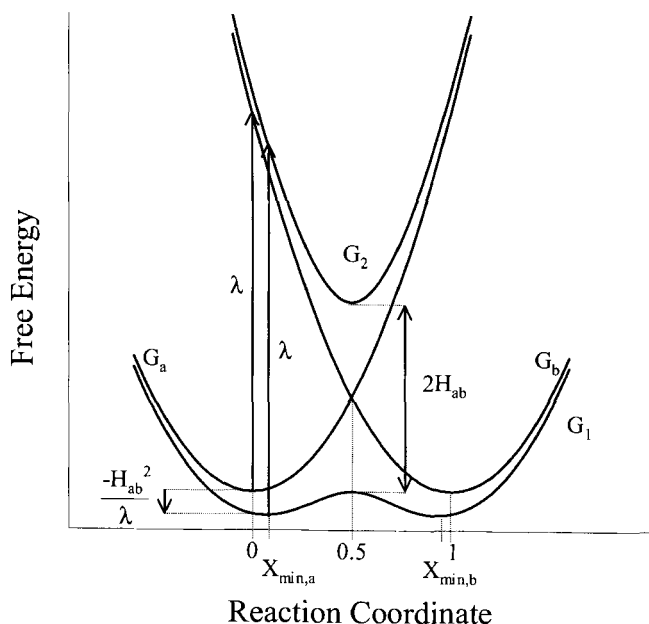
where $\Delta H_\lambda = \partial(\lambda/T)/\partial(1/T)$ and $\Delta S_\lambda = \partial(\lambda)/\partial(T)$ [9]. Eq. 5b for the free energy of activation can be rewritten as:

$$\Delta G^* = \frac{\lambda}{4} \left[1 - \left(\frac{\Delta G^\circ}{\lambda} \right)^2 \right] + \frac{\Delta G^\circ}{2} \left(1 + \frac{\Delta G^\circ}{\lambda} \right) \quad (6c)$$

which is the same form as the activation enthalpy and entropy expressions.

The above equations give the activation parameters derived for the classical model. Departures are expected, and observed, for non-parabolic surfaces that are

Figure 3. Plot of the diabatic (G_a, G_b) and adiabatic (G_1, G_2) free-energies of the reactants and products against the reaction coordinate for an electron transfer reaction with $\Delta G^\circ = 0$. H_{ab} is the electronic coupling element between the diabatic states of the reactants and products and λ is the reorganization energy for the reaction.



very weakly coupled and/or when the experimental activation parameters contain contributions from other sources [10].

1.3 Semiclassical Treatment

Electronic interaction of the reactants gives rise to the first-order energy surfaces shown as G_1 and G_2 in Figure 3. The splitting at the intersection of the zero-order energy surfaces in Figure 3 is equal to $2H_{ab}$, where H_{ab} is the electronic matrix element. We will treat H_{ab} as a positive quantity.

1.3.1 First-order Energy Surfaces

If ψ_a and ψ_b denote the wave functions of the zero-order initial (reactant) and final (product) states, their interaction gives rise to two linear combinations, the first-order or adiabatic states

$$\psi_1 = c_a\psi_a + c_b\psi_b \quad (7a)$$

$$\psi_2 = c_a\psi_b - c_b\psi_a \quad (7b)$$

where ψ_1 is the wave function for the lower (ground) and ψ_2 is the wave function for the upper (excited) adiabatic state (energies G_1 and G_2 , respectively) when the

overlap integral S_{ab} is neglected (or is zero by construction [11]), and the mixing coefficients are normalized, i.e., $c_a^2 + c_b^2 = 1$. The energies of the adiabatic states are obtained by solving the two-state secular determinant

$$\begin{vmatrix} G_a - G & H_{ab} \\ H_{ab} & G_b - G \end{vmatrix} = 0 \quad (8)$$

where, as before, $G_a = H_{aa} = \langle \psi_a | H | \psi_a \rangle$ and $G_b = H_{bb} = \langle \psi_b | H | \psi_b \rangle$ are the energies of the diabatic states. H is the total Hamiltonian operator of the system including the interaction terms. The roots of the determinant are

$$G_1 = \frac{1}{2} \{ (G_b + G_a) - [(G_b - G_a)^2 + 4H_{ab}^2]^{1/2} \} \quad (9a)$$

$$G_2 = \frac{1}{2} \{ (G_b + G_a) + [(G_b - G_a)^2 + 4H_{ab}^2]^{1/2} \} \quad (9b)$$

The difference between the adiabatic energies is given by Eq. 10 while their sum is given by Eq. 11.

$$(G_2 - G_1) = [(G_b - G_a)^2 + 4H_{ab}^2]^{1/2} \quad (10a)$$

$$= \lambda \left[\left(1 - 2X + \frac{\Delta G^\circ}{\lambda} \right)^2 + \frac{4H_{ab}^2}{\lambda^2} \right]^{1/2} \quad (10b)$$

$$(G_2 + G_1) = (G_b + G_a) \quad (11a)$$

$$= \frac{\lambda}{2} [(2X - 1)^2 + 1] + \Delta G^\circ \quad (11b)$$

Evidently the average adiabatic energy $(G_2 + G_1)/2$, like the average diabatic energy, is described by a parabola with force constant 2λ centered at $X = 1/2$ with its minimum vertically displaced by $\lambda/4 + \Delta G^\circ/2$ relative to the diabatic minimum.

The product of the adiabatic energies is given by Eq. 12a, the product of the mixing coefficients is given by Eq. 12b, and $(1 - 2c_b^2)$ is given by Eq. 12c [11].

$$G_1 G_2 = G_a G_b - H_{ab}^2 \quad (12a)$$

$$c_a c_b = H_{ab} / (G_2 - G_1) \quad (12b)$$

$$(1 - 2c_b^2) = \left(\frac{G_b - G_a}{G_2 - G_1} \right) \quad (12c)$$

The dependence of c_b^2 on the reaction coordinate is given by:

$$c_b^2 = \frac{1}{2} \left[1 - \frac{(1 - 2X)}{\{ [(1 - 2X) + \Delta G^\circ / \lambda]^2 + 4H_{ab}^2 / \lambda^2 \}^{1/2}} \right] \quad (13)$$

The squares of c_a and c_b are the fraction of the charge of the transferring electron that is on the donor and acceptor, respectively, at any given nuclear configuration.

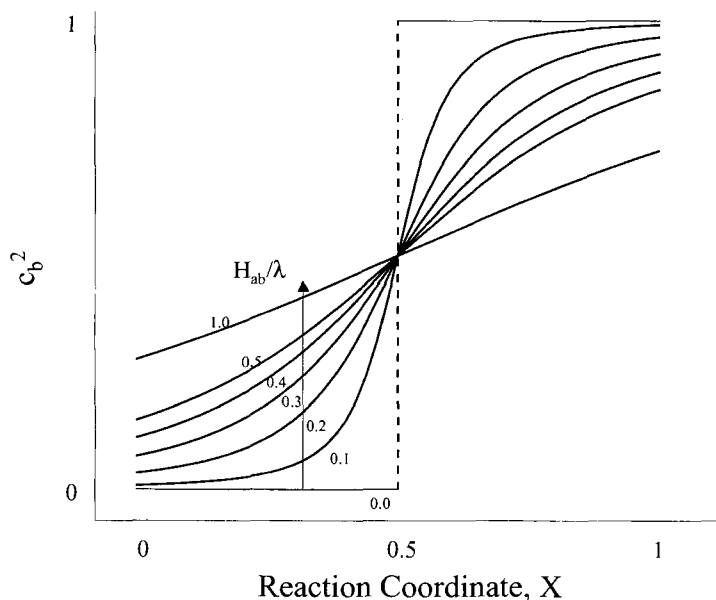


Figure 4. Plot of c_b^2 against the reaction coordinate using Eq. 13 with H_{ab}/λ varying from 0 to 0.5.

Thus c_b^2 also provides a measure of the progress of the electron transfer. *However, unlike X , which is a nuclear configuration coordinate, c_b^2 is an electronic configuration coordinate.* Figure 4 shows plots of c_b^2 vs X for various values of H_{ab}/λ and $\Delta G^\circ = 0$. As is evident from Eq. 13 and Figure 4, the two coordinates are not linearly related except at very large H_{ab} . In the very weak interaction limit (diabatic curves, $H_{ab} = 0$) no electron density is transferred until $X = 0.5$ when the electron ‘suddenly’ jumps from the donor to the acceptor. In this case c_b^2 is not a continuous function of X : instead $c_b^2 = 0$ for all $X < 1/2$ and $c_b^2 = 1$ for $X > 1/2$. As H_{ab} increases, charge density is transferred more gradually (with more delocalization present in the initial reactant configuration) and c_b^2 approaches linearity in X when $H_{ab} \geq \lambda$. Figure 4 shows that for typical symmetrical Class II systems most of the charge density is transferred between $X = 0.4$ – 0.6 .

Symmetrical systems

As shown in Figure 3, the splitting at the intersection of the diabatic energy curves lowers the barrier by H_{ab} . Further, as H_{ab} increases, the reactant and product minima of the adiabatic curves move closer together. The positions of the minima (reactant’s and product’s equilibrium configurations) are given by

$$X_{\min,a} = \frac{1}{2} \left[1 - \left(1 - \frac{4H_{ab}^2}{\lambda^2} \right)^{1/2} \right] \quad (14a)$$

$$X_{\min, b} = \frac{1}{2} \left[1 + \left(1 - \frac{4H_{ab}^2}{\lambda^2} \right)^{1/2} \right] \quad (14b)$$

and their energies are lowered by H_{ab}^2/λ relative to the diabatic minima [4]. In view of these changes the free energy of activation for a self-exchange reaction with appreciable coupling of the reactants is given by

$$\Delta G^* = \lambda/4 - H_{ab} + H_{ab}^2/\lambda \quad (15a)$$

$$= \frac{\lambda}{4} \left(1 - \frac{2H_{ab}}{\lambda} \right)^2 \quad (15b)$$

The second and third terms on the right of Eq. 15a are due to the lowering of the barrier and the stabilization of the reactants, respectively [4].

Three classes of symmetrical systems may be distinguished depending on the magnitude of the electronic coupling of the donor and acceptor sites [12–14]. In Class I systems the coupling is very weak (Figure 1) and the properties of Class I systems are essentially those of the separate reactants (i.e., the adiabatic energy curves are very close to the diabatic curves). Activated electron transfer either does not occur at all or it occurs only very slowly (because of its high non-adiabaticity) with $\Delta G^* = \lambda/4$ and optical electron transfer can not occur. Class II systems ($0 < H_{ab} < \lambda/2$, Figure 3) possess new optical and electronic properties in addition to those of the separate reactants. They remain valence trapped or charge localized: the electron transfers range from non-adiabatic ($H_{ab} < 10 \text{ cm}^{-1}$) to strongly adiabatic ($H_{ab} > 200 \text{ cm}^{-1}$) with ΔG^* given by Eq. 15. Eqs 14 and 15 hold as long as the self-exchange reaction is described by a double-well potential, i.e., as long as the system remains valence trapped. In Class III systems the interaction of the donor and acceptor sites has become so large that two separate minima are no longer discernible and the lower energy surface features a single well at $X = 1/2$ (Figure 5, bottom curve). This is the delocalized case which occurs when $H_{ab} \geq \lambda/2$. The latter condition follows readily from the zero barrier limit ($\Delta G^* = 0$) of Eq. 15.

From Eq. 3b the vertical difference between the *diabatic* energies at the equilibrium configuration (adiabatic minimum) of the reactants for $\Delta G^\circ = 0$ is given by

$$(G_b - G_a)_{\text{eq}} = \lambda(1 - 2X_{\min}) \quad (16a)$$

$$= \lambda \left(1 - \frac{4H_{ab}^2}{\lambda^2} \right)^{1/2} \quad (16b)$$

It therefore follows from Eq. 10a that the vertical difference between the adiabatic energies at the reactants' equilibrium configuration for $\Delta G^\circ = 0$ is given by:

$$(G_2 - G_1)_{\text{eq}} = \lambda \quad (17)$$

This result is independent of H_{ab} for $H_{ab} \leq \lambda/2$. In other words, the vertical difference between the free energies of the reactants and products of a symmetrical reaction remains equal to λ at the equilibrium configuration of the reactants (or

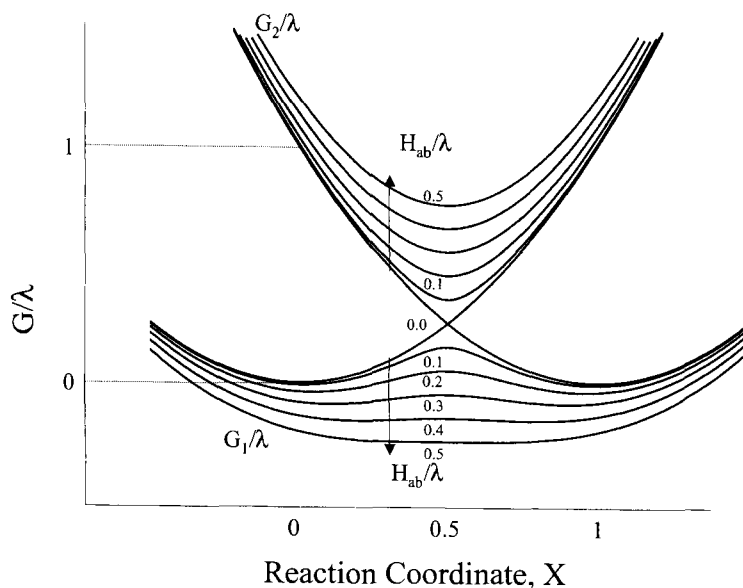


Figure 5. Plot of the adiabatic free-energy surfaces against the reaction coordinate for an electron transfer reaction with $\Delta G^\circ = 0$ and H_{ab}/λ varying from 0 to 0.5.

products) *regardless of the magnitude of the electronic coupling* as long as the system remains valence trapped [11]. Although the repulsion of the reactant and product curves increases with increasing H_{ab} , this is compensated for by the reactant and product minima moving closer together [15]. The net effect is that the adiabatic energy difference at X_{\min} remains equal to λ .

It follows from Eqs 12c and 17 that, for $H_{ab} \leq \lambda/2$, $(c_b^2)_{\text{eq}}$ is given by:

$$(c_b^2)_{\text{eq}} = \frac{1}{2} \left[1 - \left(1 - \frac{4H_{ab}^2}{\lambda^2} \right)^{1/2} \right] \quad (18)$$

Comparison with Eq. 14a shows that, for a symmetrical system with $H_{ab} > 0$, $(c_b^2)_{\text{eq}} = X_{\min, a}$. For $H_{ab}/\lambda = 0.3$ this corresponds to $X_{\min, a} = 0.10$. Moreover, at the transition state for a symmetrical system $c_b^2 = X^* = 1/2$. The equilibrium and transition-state configurations are the only configurations at which X and c_b^2 for a symmetrical system are equal.

Values of $(G_2 - G_1)/\lambda$ calculated from Eq. 10b are plotted against X for various H_{ab}/λ values in Figure 6. The adiabatic energy difference flattens with increasing H_{ab} and becomes essentially independent of X when $H_{ab} \geq 2\lambda$. Under these conditions the system is deeply into the Class III regime. Further, it is evident from Eq. 9 that, except for extreme values of X , the force constants of the vertically aligned *adiabatic* surfaces in very strongly coupled symmetrical systems ($H_{ab} \geq 2\lambda$) are equal to that of the original *diabatic* parabolas (c.f. discussion of Eq. 11).

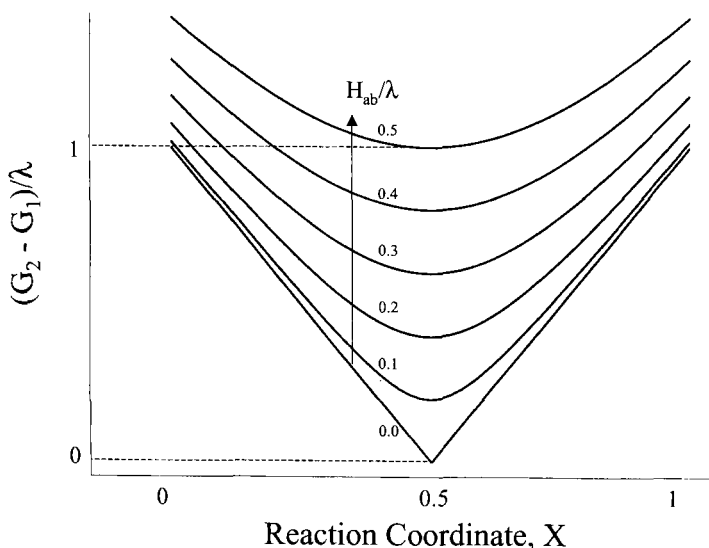


Figure 6. Plot of the differences between the adiabatic free-energy curves shown in Figure 5 vs the reaction coordinate for an electron transfer reaction with $\Delta G^\circ = 0$ and H_{ab}/λ varying from 0 to 0.5.

Unsymmetrical systems

As for symmetrical systems, the properties of an unsymmetrical Class I system are essentially those of the separate reactants. Although Class II systems are valence trapped, sufficiently endergonic reactions can exhibit a single minimum close to the non-interacting reactant minimum. This minimum shifts to $X^* = 0.5$ only when H_{ab} becomes very large. Provided that $H_{ab} < (\lambda + \Delta G^\circ)/2$ and $|\Delta G^\circ| < \lambda$, the positions of the reactant and product minima are given by Eqs 19a and 19b, while the location of the transition state is given by Eq. 19c.

$$X_{\min, a} = \frac{H_{ab}^2/\lambda^2}{(1 + \Delta G^\circ/\lambda)^2} \quad (19a)$$

$$X_{\min, b} = 1 - \frac{H_{ab}^2/\lambda^2}{(1 - \Delta G^\circ/\lambda)^2} \quad (19b)$$

$$X^* = \frac{(1 + \Delta G^\circ/\lambda - 2H_{ab}/\lambda)}{2(1 - 2H_{ab}/\lambda)} \quad (19c)$$

The free energy of activation is given by

$$\Delta G^* = \frac{\lambda}{4} + \frac{\Delta G^\circ}{2} + \frac{(\Delta G^\circ)^2}{4(\lambda - 2H_{ab})} - H_{ab} + \frac{H_{ab}^2}{(\lambda + \Delta G^\circ)} \quad (20)$$

In the above equations $-\Delta G^\circ$ is the driving force in the *non-interacting* ($H_{ab} = 0$) system [15].

1.3.2 Rate Constant Expressions

The first-order rate constant for intramolecular electron transfer or for electron transfer within the precursor complex formed from the reactants in a bimolecular reaction is given by

$$k_{el} = \kappa_{el} \nu_n \exp(-\Delta G^*/RT) \quad (21)$$

where κ_{el} is the electronic transmission coefficient, ν_n is the nuclear vibration frequency that takes the system through the intersection region and ΔG^* is the free energy of activation for the electron transfer [4].

The electronic transmission coefficient is the probability that electron transfer will occur once the system has reached the intersection region (transition state). Provided that the electronic interaction of the reactants is sufficiently strong $\kappa_{el} \approx 1$ and the electron transfer will occur with near unit probability in the intersection region: the electron transfer reaction is *adiabatic* with the system remaining on the lower energy surface on passing through the intersection region. Under these conditions k_{el} is given by

$$k_{el} = \nu_n \exp(-\Delta G^*/RT) \quad (22)$$

On the other hand, for a *non-adiabatic* reaction, $\kappa_{el} \ll 1$, $\kappa_{el} \nu_n = \nu_{el}$ and the rate constant is given by Eq. 23 where ν_{el} is the electron hopping frequency in the activated complex. The Landau–Zener treatment yields Eq. 24 for ν_{el} [16, 17].

$$k_{el} = \nu_{el} \exp(-\Delta G^*/RT) \quad (23)$$

$$\nu_{el} = \frac{2H_{ab}^2}{h} \left(\frac{\pi^3}{\lambda RT} \right)^{1/2} \quad (24)$$

In effect, the adiabatic and non-adiabatic limits of the transition state formalism correspond to $\nu_{el} \gg \nu_n$ and $\nu_{el} \ll \nu_n$, respectively.

The frequency of electron hopping in the activated complex may be estimated from $2H_{ab}/h$, the oscillating frequency of the two degenerate diabatic states [16]. Evidently $\nu_{el} \approx 10^{13} \text{ s}^{-1}$ for interaction energies of only a few hundred cal. A similar estimate is obtained from the Landau–Zener treatment of the intersection region [16]. Since the system typically spends about 10^{-13} s in the intersection region (i.e., $\nu_n \approx 10^{13} \text{ s}^{-1}$), the electron transfer will generally be adiabatic for interaction energies larger than about 100–300 cal ($30\text{--}100 \text{ cm}^{-1}$).

1.3.3 Reorganization Parameters

The reorganization parameter is usually broken down into inner-shell (vibrational) and outer-shell (solvational) components.

$$\lambda = \lambda_{\text{in}} + \lambda_{\text{out}} \quad (25)$$

The inner-shell reorganization energy is generally treated within an harmonic approximation [18]. The outer-shell reorganization energy depends upon the properties of the solvent. When a continuum model for the solvent is used λ_{out} is a function of the dielectric properties of the medium, the distance separating the donor and acceptor sites, and the shape of the reactants.

Inner-shell reorganization energy

To illustrate the approach used to calculate the inner-shell contribution to the reorganization barrier we consider the symmetrical stretching vibrations of the two reactants in the $\text{Fe}(\text{H}_2\text{O})_6^{2+} - \text{Fe}(\text{H}_2\text{O})_6^{3+}$ self-exchange reaction (Eq. 1a). The inner-shell reorganization term is the sum of the reorganization parameters of the individual reactants, i.e.:

$$\lambda_{\text{in}} = \lambda_2(d_2^\circ \rightarrow d_3^\circ) + \lambda_3(d_3^\circ \rightarrow d_2^\circ) \quad (26a)$$

The first term on the right of Eq. 26a is the energy required to change the Fe–O distance in $\text{Fe}(\text{H}_2\text{O})_6^{2+}$ from its equilibrium value d_2° to the equilibrium value d_3° in $\text{Fe}(\text{H}_2\text{O})_6^{3+}$ and the second term is the energy required to change the Fe–O distance in $\text{Fe}(\text{H}_2\text{O})_6^{3+}$ from d_3° to d_2° . Denoting $(d_2^\circ - d_3^\circ)$ by Δd° , the vertical reorganization energy is given by Eqs 26b and 26c where f_2 and f_3 are the respective breathing force constants.

$$\lambda_{\text{in}} = \frac{6f_2(\Delta d^\circ)^2}{2} + \frac{6f_3(\Delta d^\circ)^2}{2} \quad (26b)$$

$$= 3(f_2 + f_3)(\Delta d^\circ)^2 \quad (26c)$$

Evidently the contributions of the $\text{Fe}(\text{H}_2\text{O})_6^{2+}$ and $\text{Fe}(\text{H}_2\text{O})_6^{3+}$ breathing modes to λ_{in} are *directly* proportional to their respective force constants.

In the activation process, the energy required to reach the transition state configuration is given by:

$$\Delta G_{\text{in}}^* = 3f_2(d_2^\circ - d_2^*)^2 + 3f_3(d_3^\circ - d_3^*)^2 \quad (27a)$$

Energy conservation requires that the Fe–O distances in the $\text{Fe}(\text{H}_2\text{O})_6^{2+}$ and $\text{Fe}(\text{H}_2\text{O})_6^{3+}$ adjust to a common value d^* before electron transfer.

$$d_2^* = d_3^* = d^* \quad (27b)$$

Minimizing the resulting reorganization energy expression yields Eq. 27c and substitution into Eq. 27a gives Eq. 27d.

$$d^* = \frac{f_2 d_2^\circ + f_3 d_3^\circ}{f_2 + f_3} \quad (27c)$$

$$\Delta G_{in}^* = \frac{3f_2 f_3 (\Delta d^\circ)^2}{f_2 + f_3} \quad (27d)$$

$$(d_2^\circ - d^*) = \frac{f_3 \Delta d^\circ}{f_2 + f_3} \quad (27e)$$

$$(d^* - d_3^\circ) = \frac{f_2 \Delta d^\circ}{f_2 + f_3} \quad (27f)$$

The ratio of the amounts that the $\text{Fe}(\text{H}_2\text{O})_6^{2+}$ and $\text{Fe}(\text{H}_2\text{O})_6^{3+}$ ions reorganize is equal to f_3/f_2 i.e., *inversely* proportional to their force constants. Since f_3 is larger than f_2 , the $\text{Fe}(\text{H}_2\text{O})_6^{2+}$ ion reorganizes more than the $\text{Fe}(\text{H}_2\text{O})_6^{3+}$ ion. Note also that $\Delta G_{in}^* < \lambda_{in}/4$ because the free-energy surfaces are not harmonic along the reaction coordinate [15].

Considerable simplification results from using a common, reduced value f_{in} for the force constant of the $\text{Fe}(\text{H}_2\text{O})_6^{2+}$ and $\text{Fe}(\text{H}_2\text{O})_6^{3+}$ symmetrical stretching vibrations.

$$f_{in} = \frac{2f_2 f_3}{(f_2 + f_3)} \quad (28)$$

Under these conditions:

$$d^* = \frac{(d_2^\circ + d_3^\circ)}{2} \quad (29a)$$

$$\Delta G_{in}^* = \frac{3f_{in} (\Delta d^\circ)^2}{2} \quad (29b)$$

$$\bar{\lambda}_{in} = 2\bar{\lambda}_2 = 2\bar{\lambda}_3 = 6f_{in} (\Delta d^\circ)^2 \quad (29c)$$

where $\bar{\lambda}_2 = \bar{\lambda}_3 = 3f_{in} (\Delta d^\circ)^2$ with the two reactants now reorganizing to the same extent and $\Delta G_{in}^* = \bar{\lambda}_{in}/4$. Moreover, $\bar{\lambda}_{in} = 4\lambda_2 \lambda_3 / (\lambda_2 + \lambda_3)$.

The relationship between the vertical reorganization parameter and the activation energy and the effect of using different criteria for the inner-shell reorganization have recently been considered in some detail [15]. The reorganization energy and the contributions of the individual reactants turn out to be quite sensitive to the model used.

Solvent reorganization energy

Because of Coulomb interaction terms the solvent reorganization energy is not as readily broken down into contributions from the separate reactants. We illustrate

the approach used to calculate the solvent reorganization energy by using the zero-electronic-interaction, two-sphere model developed by Marcus [1, 19, 20].

The familiar Born expression for the free energy of equilibrium solvation of a charged sphere is

$$\Delta G_{\text{eq}} = -\frac{(qe)^2}{2a} \left[1 - \frac{1}{D_s} \right] \quad (30)$$

where qe is the charge on the ion, a is its radius and D_s is the static dielectric constant of the medium. The equilibrium solvation energy can be resolved into two contributions

$$\Delta G_{\text{eq}} = -\frac{(qe)^2}{2a} \left[1 - \frac{1}{D_{\text{op}}} \right] - \frac{(qe)^2}{2a} \left[\frac{1}{D_{\text{op}}} - \frac{1}{D_s} \right] \quad (31)$$

where the first contribution is the equilibrium solvation due to the electronic polarization of the medium and the second is the contribution from its orientational–vibrational polarization. D_{op} is the optical dielectric constant of the medium. Note that the orientational–vibrational polarization term contains the Pekar factor $(1/D_{\text{op}} - 1/D_s)$. The electronic polarization is assumed to be rapid and capable of keeping up with the transferring electron. The orientational–vibrational polarization is much slower and lags behind. Energy conservation requires that the orientation–vibrational polarization adjust to a nonequilibrium value prior to the electron transfer.

Marcus devised a two-step path for calculating the reversible work required to establish a nonequilibrium orientational–vibrational polarization of the medium. In the first step the orientational–vibrational and electronic polarization of the medium is changed from being in equilibrium with the initial charges q_2° and q_3° to being in equilibrium with the (hypothetical) charges q_2^* and q_3^* . In the second step the orientational–vibrational polarization remains appropriate to q_2^* and q_3^* but the electronic polarization is changed back to being in equilibrium with q_2° and q_3° . The energy required to reorganize the solvent to the nonequilibrium configuration appropriate to charges q_2^* and q_3^* is then the sum of the work done in these two paths.

$$\Delta G_{\text{out}}^* = e^2 \left(\frac{[q_2^* - q_2^\circ]^2}{2a} + \frac{[q_3^* - q_3^\circ]^2}{2a} + \frac{(q_2^* - q_2^\circ)(q_3^* - q_3^\circ)}{r} \right) \left(\frac{1}{D_{\text{op}}} - \frac{1}{D_s} \right) \quad (32)$$

The reactants are treated as rigid spheres and their radii are not allowed to change during the reorganization process: the radii in Eq. 32 are the average radii defined by $1/a = (1/a_2 + 1/a_3)/2$ and r is the distance between the centers of the spheres. *Note that the numerators in Eq. 32 contain the square of the difference of the charges (or, in the case of the electrostatic interaction term, the product of charge differences) and are not simply differences between the squares of charges, as might have been expected on the basis of the Born equation.*

Analogous to the case of the inner-shell reorganization, energy conservation requires that the transition-state charges for the solvent reorganization be equal.

$$q_2^* = q_3^* = q^* \quad (33a)$$

Minimizing the resulting solvent reorganization expression yields:

$$q^* = (q_2^\circ + q_3^\circ)/2 \quad (33b)$$

and substitution into Eq. 32 yields Eq. 34a for the free energy of activation:

$$\Delta G_{\text{out}}^* = \frac{e^2}{4} \left(\frac{1}{2a_2} + \frac{1}{2a_3} - \frac{1}{r} \right) \left(\frac{1}{D_{\text{op}}} - \frac{1}{D_s} \right) \quad (34a)$$

where it has been assumed that the zero-interaction donor and acceptor sites differ by a single electron, i.e., $(q_3^\circ - q_2^\circ) = 1$. Similarly, substitution into Eq. 32 of $q_2^* = q_3^\circ$ and $q_3^* = q_2^\circ$ yields Eq. 34b for the solvent reorganization energy in a vertical one-electron transition with $\lambda_{\text{out}} = 4\Delta G_{\text{out}}^*$.

$$\lambda_{\text{out}} = e^2 \left(\frac{1}{2a_2} + \frac{1}{2a_3} - \frac{1}{r} \right) \left(\frac{1}{D_{\text{op}}} - \frac{1}{D_s} \right) \quad (34b)$$

If there is appreciable delocalization in the initial (equilibrium) state, then less than a unit of charge will be transferred from the donor to the acceptor. In terms of the mixing coefficients, the zero-interaction charge difference $(q_2^\circ - q_3^\circ)$ needs to be scaled by $(c_a^2 - c_b^2)_{\text{eq}} = (1 - 2c_b^2)_{\text{eq}}$ to obtain the ‘real’ charge transferred. We thus obtain

$$\Delta q = (c_a^2 - c_b^2)_{\text{eq}} = (1 - 2c_b^2)_{\text{eq}} \quad (35)$$

At the minimum of the adiabatic curve, i.e., at the equilibrium configuration of the reactants, $(c_b^2)_{\text{eq}}$ is given by Eq. 18, so that:

$$[(1 - 2c_b^2)_{\text{eq}}]^2 = \left(1 - \frac{4H_{\text{ab}}^2}{\lambda^2} \right) \quad (36)$$

Electron delocalization in the initial state thus scales the solvent activation barrier by $(1 - 4H_{\text{ab}}^2/\lambda^2)$.

The vertical reorganization parameter λ is a property of the diabatic states, ($H_{\text{ab}} = 0$) and λ_{out} continues to be given by Eq. 34b *regardless of the degree of initial state delocalization*. When appreciable delocalization is present, we add a prime to indicate that λ has been modified to allow for the reduction in the charge transferred [15, 21]. In other words, λ' denotes a reorganization energy that has been scaled by $(1 - 4H_{\text{ab}}^2/\lambda^2)$. (The parameter λ' used here and in [15] corresponds to λ_{mod} introduced earlier [21].)

$$\lambda'_{\text{out}} = \lambda_{\text{out}} \left(1 - \frac{4H_{\text{ab}}^2}{\lambda^2} \right) \quad (37a)$$

Similar considerations apply to the inner-shell reorganization. When initial-state delocalization is present ($d_2^\circ - d_3^\circ$) is scaled by $(1 - 2c_b^2)_{\text{eq}}$ giving

$$\lambda'_{\text{in}} = \lambda_{\text{in}} \left(1 - \frac{4H_{\text{ab}}^2}{\lambda^2} \right) \quad (37b)$$

Consequently:

$$\lambda' = \lambda'_{\text{in}} + \lambda'_{\text{out}} = \lambda \left(1 - \frac{4H_{\text{ab}}^2}{\lambda^2} \right) \quad (37c)$$

In a sense the primed (scaled) quantities are the ‘actual’ vertical reorganization energies since their values are determined by the actual charge transferred. While it would be convenient if λ' was the separation between the diabatic energy curves at the reactant’s equilibrium configuration (X_{min}), it is not. The diabatic curves ($H_{\text{ab}} = 0$) correspond to a charge transfer of one electron with this charge abruptly transferring at the transition state: delocalization is *not* incorporated into the diabatic surfaces. This topic is discussed further under optical charge transfer in Section 1.3.4.

Time-scales for solvent electronic polarization and electron transfer

The above treatment is based upon the traditional Born–Oppenheimer approximation which states that, when nuclei move, the electrons can almost instantaneously adjust to their new positions. Another relevant time frame is the time required to establish the electronic polarization of the medium. To characterize this time frame, Kim and Hynes consider the ratio of ν_{el} , the electron hopping frequency, to ν_{ep} , the frequency characteristic of the solvent electronic polarization. The Born–Oppenheimer-based treatment is valid provided that this ratio is much less than unity, i.e., the time scale for the adjustment of the electronic polarization is much shorter than that for the transferring electron [22–26].

The electron hopping frequency may be estimated from time-dependent perturbation theory. If H_{ab} is treated as a constant perturbation, the system will start to oscillate between the two diabatic states once the perturbation is turned on. In a bimolecular reaction, for example, the perturbation is turned on upon formation of the precursor complex, while in a covalently attached (bridged) binuclear system it can be turned on upon reduction (oxidation) of one end of the fully oxidized (reduced) system by an external reagent or by photoexcitation. If the system is in the diabatic reactant state at $t = 0$, then the probability of it being in the product state at some later time t is given by the Rabi formula [27].

$$P_2 = \left[\frac{4H_{\text{ab}}^2}{(G_2 - G_1)^2} \right] \sin^2 \left[\frac{(G_2 - G_1)}{h} \pi t \right] \quad (38)$$

Consider first the case where the system is initially at the nuclear configuration of the adiabatic minimum, i.e. $(G_2 - G_1) = \lambda$. The system will start to oscillate between the two diabatic states with a frequency equal to λ/h which corresponds to $\sim 5 \times 10^{14} \text{ s}^{-1}$ for $\lambda = 40 \text{ kcal mol}^{-1}$. The maximum value of the probability of finding the system in the product state is $4H_{ab}^2/\lambda^2$ or 2×10^{-3} for $H_{ab}/\lambda = 2 \times 10^{-2}$. There is thus only a very small probability that weak coupling will drive the system into the product state at a nuclear configuration near the initial state minimum. Since the frequency with which the system oscillates under the influence of the perturbation is λ/h , the maximum frequency of attaining the product state (i.e., the maximum probability per unit time) is $4H_{ab}^2/h\lambda$. In other words, v_{el} at the adiabatic minimum is estimated to be $\approx 10^{12} \text{ s}^{-1}$ for a moderately coupled Class II system ($H_{ab} \approx 100 \text{ cm}^{-1}$, $\lambda \approx 10 \text{ kcal mol}^{-1}$). Since $v_{ep} \approx 10^{15} \text{ s}^{-1}$ or higher for most colorless solvents [25], the ratio v_{el}/v_{ep} is much less than unity for a weakly or moderately coupled Class II system near the adiabatic minimum.

We turn next to the frequency of electron hopping in the transition state. As is evident from Eq. 38 with $(G_2 - G_1) = 2H_{ab}$, the frequency of electron hopping in the transition state is equal to $2H_{ab}/h$ (see also the discussion following Eq. 24. Thus the transition-state hopping frequency v_{el} is $\leq 10^{13} \text{ s}^{-1}$ for a weakly or moderately coupled Class II system and $v_{el}/v_{ep} \ll 1$ at the transition state. Thus the condition for the validity of the Born–Oppenheimer approximation will be satisfied by most weakly and moderately coupled Class II systems. For symmetrical Class II systems, the free energy of activation will then be given by the traditional Eq. 15 [22–26] except that a correction for the so-called exchange field may be needed under certain circumstances. The exchange field arises from the overlap charge distribution ($e\psi_a\psi_b$) and serves to lower λ_{out} (more correctly, to stabilize the transition state) and to reduce the effective H_{ab} [22, 25]. However, there is no exchange field when the diabatic wave functions are appropriately chosen, i.e., when they are based on the exchange dipole moment (μ_{ab} , see below) being zero [28] and no exchange-field correction to the traditional expression for the free energy of activation is then required.

In the Born–Oppenheimer limit, the electrons of the surrounding medium equilibrate to the instantaneous position of the transferring electron while the orientations of the medium dipoles, which occur much more slowly, adjust to the smeared-out charge distribution of the transferring electron. When the time scale for electronic polarization is slower than, or comparable to, the time scale of the transferring electron, it becomes necessary to use a self-consistent treatment in which both the electronic polarization and the orientational polarization respond to the smeared-out charge distribution of the transferring electron [25]. Including the interaction of this charge distribution with the electronic polarization gives rise to a nonlinear Schrödinger equation in which the Hamiltonian depends on the wave function for the donor–acceptor pair. Such a treatment becomes increasingly important as the electronic interaction increases and introduces terms into the free energy of activation that have the net effect of *increasing* the activation energy beyond that given by the Born–Oppenheimer limit [25]. In the limit that the time scale for the solvent electronic polarization becomes very long the electronic polarization can no longer keep up with the transferring electron and the electronic polarization will contribute

to the activation barrier in much the same way as the orientational–vibrational polarization.

1.3.4 Optical Charge Transfer

In addition to thermal activation, electron transfer between the donor and acceptor sites can also be effected by the absorption of light. As a consequence, λ and H_{ab} can be obtained from spectroscopic properties.

Transition energies

The energy of the light-induced charge-transfer transition in a symmetrical double-well system is given by Eq. 39 [29, 30].

$$h\nu_{\max} = \lambda \quad (39)$$

Because λ for a symmetrical localized system is *independent* of H_{ab} , Eq. 39 holds throughout the double-well regime [11]. Further insight into Eq. 39 can be obtained by noting that $h\nu_{\max}$ is also given by:

$$h\nu_{\max} = \lambda' + 4H_{ab}^2/\lambda \quad (40)$$

The first term on the RHS is the scaled reorganization energy and the second term is a further quantum-mechanical contribution to the transition energy. Although the scaled reorganization energy associated with the charge transfer is reduced by the delocalization, and reaches zero when $2H_{ab} = \lambda$, the decrease in the reorganization energy is compensated for by the repulsion of the curves. The net effect is that $h\nu_{\max}$ remains constant and equal to λ for a symmetrical system in the double-well regime. Thus, even when appreciable delocalization is present, $h\nu_{\max}$ will still exhibit the full solvent dependence predicted for the very weakly interacting system.

The energy of the optical transition in a symmetrical Class III system is given by

$$h\nu_{\max} = 2H_{ab} \quad (41)$$

so that H_{ab} for symmetrical Class III complexes can be obtained directly from the energy of the optical transition [29]. Note that the optical transition in a Class III system no longer involves charge transfer: the transition occurs between delocalized molecular orbitals of the complex and is not accompanied by a net dipole-moment change.

The energy of the charge transfer transition in an unsymmetrical double-well system is given by:

$$h\nu_{\max,a} = (\lambda + \Delta G^\circ) \left[1 + \frac{2H_{ab}^2 \Delta G^\circ}{(\lambda + \Delta G^\circ)^3} \right] \quad (42)$$

assuming $H_{ab} < (\lambda + \Delta G^\circ)/2$ [15]. When the H_{ab}^2 contribution may be neglected, the energy of the charge transfer transition in an unsymmetrical double-well system is given by the familiar Eq. 43:

$$h\nu_{\max, a} = \lambda + \Delta G^\circ \quad (43)$$

Finally, although $h\nu_{\max}$ for a symmetrical double-well system is independent of the degree of electronic interaction, the free energy of activation does depend on H_{ab} . Thus when ΔG° may be neglected, the ratio $h\nu_{\max}/\Delta G^*$ for a double-well system is given by:

$$\frac{h\nu_{\max, a}}{\Delta G^*} = \frac{4}{(1 - 2H_{ab}/\lambda)^2} \quad (44a)$$

while, when the electronic interaction may be neglected, the ratio is given by

$$\frac{h\nu_{\max, a}}{\Delta G^*} = \frac{4}{1 + \Delta G^\circ/\lambda} \quad (44b)$$

Evidently $h\nu_{\max}/\Delta G^*$ is ≤ 4 for a weakly coupled, endergonic charge-transfer reaction and ≥ 4 for a weakly coupled, exergonic charge-transfer reaction or for charge transfer in a moderately coupled symmetrical double-well system. The value of $h\nu_{\max}/\Delta G^*$ can thus provide information about the degree of electronic interaction. However, in practice the latter is more readily obtained from the intensity of the charge transfer transition.

Intensities and dipole-moment changes

Using the Mulliken formalism, Hush [29] showed that the electronic coupling element is related to the intensity of the charge transfer transition by:

$$H_{ab} = 2.06 \times 10^{-2} \frac{(v_{\max} \epsilon_{\max} \Delta v_{1/2})^{1/2}}{r_{ab}} \quad (45)$$

where v_{\max} and $\Delta v_{1/2}$ are the band maximum and width in wave numbers, r_{ab} is the distance separating the donor and acceptor charge centroids in Ångströms, and the band is Gaussian shaped [11]. *Equation 45 is exact within a two-state model and is applicable to both symmetrical and unsymmetrical Class II and Class III systems [11].*

The Mulliken–Hush expression is a particular form of the more general equation

$$H_{ab} = \left| \frac{v_{\max} \mu_{12}}{\mu_b - \mu_a} \right| \quad (46)$$

where μ_{12} is the transition dipole and $(\mu_b - \mu_a)$ is the difference between the dipole moments of the initial and final diabatic (localized) states [11, 31]. In the general-

ized Mulliken–Hush treatment formulated by Cave and Newton [32, 33], the diabatic states are obtained by applying the transformation that diagonalizes the adiabatic dipole-moment matrix. Because μ_{ab} , the transition moment connecting the diabatic states, is zero, the value of $(\mu_b - \mu_a)$ is maximized. With this definition of the diabatic states, the diabatic dipole-moment difference is related to the measured dipole-moment change $(\mu_2 - \mu_1)$ by Eq. 47. The diabatic dipole-moment difference can thus be obtained from measurable quantities [32].

$$\mu_b - \mu_a = [(\mu_2 - \mu_1)^2 + 4\mu_{12}^2]^{1/2} \quad (47)$$

Equation 45 follows from Eq. 46 by noting that $r_{ab} \equiv |(\mu_b - \mu_a)/e|$ and that the transition dipole is given by Eq. 48:

$$\mu_{12} = \sqrt{\frac{f_{os}}{1.08 \times 10^{-5} \nu_{\max}}} \quad (48a)$$

$$f_{os} = 4.61 \times 10^{-9} (\epsilon_{\max} \Delta \nu_{1/2}) \quad (48b)$$

where f_{os} is the oscillator strength of the transition [11, 31]. Eq. 41 is obtained by noting that $(\mu_2 - \mu_1)$ is zero for a delocalized system and therefore, from Eq. 47, $(\mu_b - \mu_a) = 2\mu_{12}$. Finally, because the adiabatic and diabatic dipole-moment changes are related by:

$$(\mu_2 - \mu_1) = (\mu_b - \mu_a)(1 - 2c_b^2) \quad (49)$$

it follows from Eq. 12c that:

$$\frac{\mu_2 - \mu_1}{\mu_b - \mu_a} = \frac{G_b - G_a}{G_2 - G_1} \quad (50)$$

There is thus an inverse relationship between the ratio of the adiabatic and diabatic dipole-moment changes and the ratio of the corresponding free-energy differences within the two-state model.

Optical band shapes

In the high-temperature or classical limit the molar absorptivity at a given transition energy is obtained by weighting the transition probability [34, 35], p , by the number of systems, $n(\nu)$, having a nuclear configuration appropriate to the particular transition energy.

$$\epsilon_{cl}(\nu) = pn(\nu) \quad (51)$$

The transition probability is assumed to be energy independent with $p = \epsilon_{\max}/n_0$ where n_0 is the population of the ground-state energy minimum. Assuming a

Boltzmann distribution over the energies of the ground-state configurations gives:

$$\varepsilon_{cl}(v) = \varepsilon_{\max} \exp[-(G_1 - G_{1,eq})/RT] \quad (52a)$$

where G_1 is the energy of the system on the lower (ground-state) free-energy surface.

We first consider systems in the zero-interaction limit i.e., $H_{ab} = 0$, $G_a = G_1$ and $G_b = G_2$. Substituting Eq. 2a into Eq. 52a yields Eq. 52b for the molar absorptivity for an optical transition at the nuclear configuration defined by X .

$$\varepsilon_{cl}(v) = \varepsilon_{\max} \exp[-\lambda X^2/RT] \quad (52b)$$

From Eq. 3b the ground- excited-state energy difference ($G_2 - G_1$) is related to X^2 by

$$X^2 = [\lambda + \Delta G^\circ - (G_2 - G_1)]^2 / 4\lambda^2 = [\lambda + \Delta G^\circ - hv]^2 / 4\lambda^2 \quad (53)$$

Substituting into Eq. 52b and recalling that $\lambda + \Delta G^\circ = hv_0$ gives

$$\varepsilon_{cl}(v) = \varepsilon_{\max} \exp \left[\frac{-(hv_0 - hv)^2}{4\lambda RT} \right] \quad (54)$$

Eq. 54 predicts a Gaussian shape for the band obtained by plotting $\varepsilon(v)$ against hv . The band maximum occurs at $hv_0 = hv_{\max} = \lambda + \Delta G^\circ$. The half-width of the band is given by:

$$\Delta v_{1/2} = [16 \ln(2) \lambda RT]^{1/2} \quad (55a)$$

so that the expression for the molar absorptivity in terms of the band width is:

$$\varepsilon_{cl}(v) = \varepsilon_{\max} \exp[-4 \ln(2) (hv_0 - hv)^2 / (\Delta v_{1/2})^2] \quad (55b)$$

From a semiclassical viewpoint the assumption underlying Eq. 51 is not correct. It can be shown [36] that:

$$\varepsilon_{sc}(v)/v = \frac{hn(v)B}{cn_t} \quad (56a)$$

where B , c , and n_t are the Einstein coefficient of stimulated absorption, the speed of light and the total concentration of absorbers, respectively. The Einstein coefficient is given by [37]:

$$B = \frac{2\pi|\mu_{12}|^2}{3\hbar^2} \quad (56b)$$

where μ_{12} is the transition dipole moment. The above two equations yield:

$$\varepsilon_{\text{sc}}(\nu)/\nu = \frac{4\pi^2|\mu_{12}|^2 n(\nu)}{3\hbar c n_t} = p_{12}n(\nu) \quad (56c)$$

Again assuming a Boltzmann distribution for $n(\nu)$ over the ground-state energies and that p_{12} is energy independent (i.e., that the transition dipole moment $\mu_{12} = \langle \psi_2 | \mu | \psi_1 \rangle$ does not depend on the vibrational levels) yields Eq. 57 for the optical band shape in the zero-interaction limit

$$\varepsilon_{\text{sc}}(\nu) = \left(\frac{\varepsilon}{\nu} \right)_{\text{max}} \nu \exp[-(\lambda + \Delta G^\circ - h\nu)^2 / 4\lambda RT] \quad (57a)$$

$$= \left(\frac{\varepsilon}{\nu} \right)_{\text{max}} \nu \exp[-(h\nu_0 - h\nu)^2 / 4\lambda RT] \quad (57b)$$

where $h\nu_0$ now corresponds to the maximum in the plot of $\varepsilon(\nu)/h\nu$ against $h\nu$ and is again the energy of the vertical transition from the ground-state minimum.

To the extent that $\Delta\nu_{1/2} \ll \nu_0$ the classical and semiclassical approaches yield the same results since then:

$$\frac{\varepsilon_{\text{sc}}(\nu)}{\nu} \approx \frac{\varepsilon_{\text{sc}}(\nu)}{\nu_0}$$

However, in practice the band width is about 20 % of the energy of the maximum and so the two approaches yield different results. In the classical formalism a plot of ε_{cl} against $h\nu$ is Gaussian shaped while in the semiclassical formalism (Eq. 56), a plot of $\varepsilon_{\text{sc}}/h\nu$ against $h\nu$ is Gaussian with a maximum at $\lambda + \Delta G^\circ$; however, a plot of ε_{sc} against $h\nu$ is not Gaussian and its maximum occurs at higher energy.

The situation is more complicated when the electronic coupling is appreciable. As discussed earlier, the energy surfaces are then no longer parabolic and the minimum of the initial state no longer occurs at $X = 0$. Moreover, the low energy side of the absorption band is cut off at $h\nu = 2H_{\text{ab}}$, the minimum difference between the energies of the ground and excited states. The relevant energy expressions for a symmetrical system are:

$$\frac{G_1}{\lambda} = \left(\frac{2X^2 - 2X + 1}{2} \right) - \frac{\left[(1 - 2X)^2 + \left(\frac{2H_{\text{ab}}}{\lambda} \right)^2 \right]^{1/2}}{2} \quad (58a)$$

$$\frac{G_{1,\text{eq}}}{\lambda} = -\frac{H_{\text{ab}}^2}{\lambda^2} \quad (58b)$$

and

$$\frac{G_2 - G_1}{\lambda} = \left[(1 - 2X)^2 + \left(\frac{2H_{\text{ab}}}{\lambda} \right)^2 \right]^{1/2} \quad (58c)$$

Assuming a Boltzmann distribution over the energies on the adiabatic ground-state surface yields the following expression for the band shape

$$\begin{aligned}\varepsilon_{\text{cl}}(\nu) &= \varepsilon_{\text{max}} \exp \left[-\frac{(h\nu_0 - [(h\nu)^2 - 4H_{\text{ab}}^2]^{1/2})^2}{4\lambda RT} \right] \\ \varepsilon_{\text{sc}}(\nu) &= \left(\frac{\varepsilon}{\nu} \right)_{\text{max}} \nu \exp \left[-\frac{(h\nu_0 - [(h\nu)^2 - 4H_{\text{ab}}^2]^{1/2})^2}{4\lambda RT} \right]\end{aligned}\quad (58\text{d})$$

where ν_0 is defined above.

Plots of ε_{cl} and ε_{sc} vs $h\nu$ are presented in Figure 7 for $\Delta G^\circ = 0$ and in Figure 8 for $\Delta G^\circ/\lambda = 2$. One sees that the maximum of ε_{sc} is always at higher energy than the maximum of ε_{cl} . For the zero driving force case, as H_{ab} increases the spectrum becomes truncated at low energy. For $H_{\text{ab}}/\lambda > 1/2$ the truncated spectrum starts to shift to higher energy and becomes narrower; finally, at $H_{\text{ab}}/\lambda \gg 1$ only a sharp line remains at $h\nu = 2H_{\text{ab}}$. When $\Delta G^\circ > 0$ the spectra do not show the low energy cut-off. However, when $H_{\text{ab}}/\lambda > 1/2$ the absorption maximum shifts to higher energy and narrows. Ultimately, for $H_{\text{ab}}/\lambda \gg \Delta G^\circ/\lambda$, the spectrum again becomes a sharp line at $h\nu = 2H_{\text{ab}}$.

1.4 Quantum Mechanical Treatment

Although the semiclassical expressions work well at high temperatures, they break down at low temperatures and/or at high reaction exergonicities. Nuclear tunneling contributions to the rate can become very important under such conditions. Although corrections for nuclear tunneling can be introduced into the semiclassical treatment, tunneling enters naturally into a quantum mechanical treatment.

The quantum mechanical treatment of non-adiabatic electron transfers are normally considered in terms of the formalism developed for multiphonon radiationless transitions. This formalism starts from Fermi's golden rule for the probability of a transition from a vibronic state A_v of the reactant (electronic state A with vibrational level v) to a set of vibronic levels $\{B_w\}$ of the product

$$W_{A_v} = \frac{4\pi^2 H_{\text{ab}}^2}{h} \rho_w \quad (59\text{a})$$

$$\rho_w = \sum_w |\langle \chi_{A_v} | \chi_{B_w} \rangle|^2 \delta(\varepsilon_{A_v} - \varepsilon_{B_w}) \quad (59\text{b})$$

where ρ_w is the density of final states, ε_{A_v} and ε_{B_w} are the unperturbed energies of the vibronic levels and δ is the delta function that ensures energy conservation. To

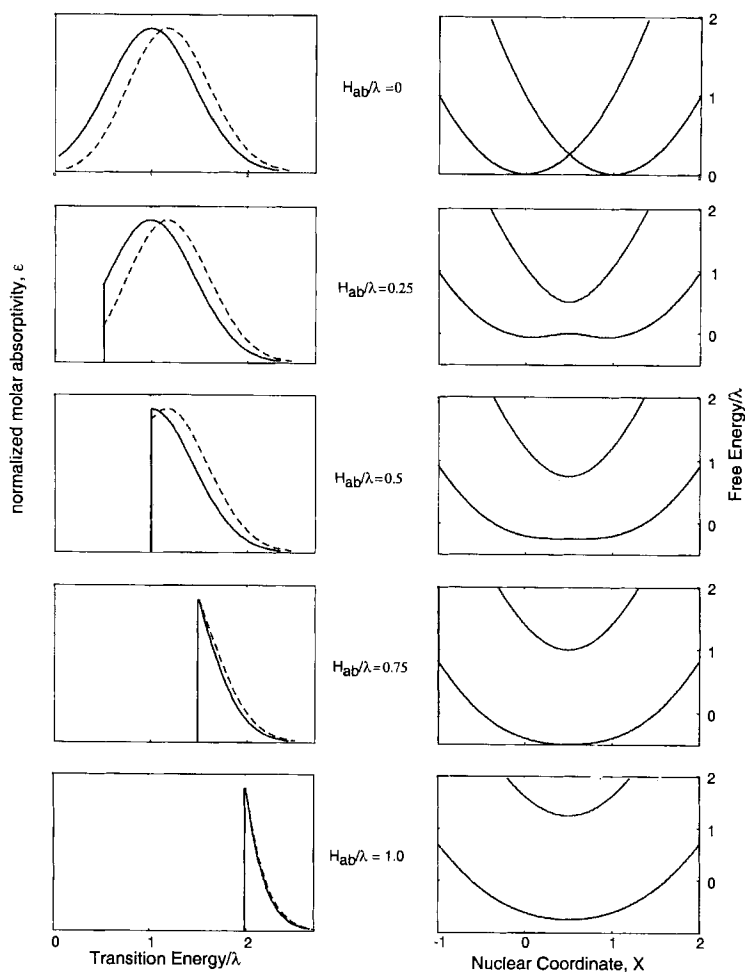


Figure 7. On the left side of the figure are plots of the normalized molar absorptivities, ϵ_{cl} (solid line) and ϵ_{sc} (dashed line), vs transition energy/ λ for $\Delta G^\circ = 0$ and H_{ab}/λ values of 0, 0.25, 0.5, 0.75 and 1, respectively. On the right side are plots of the free energy/ λ vs the nuclear coordinate x for the same values of ΔG° and H_{ab}/λ .

obtain the thermally averaged probability per unit time, k , of passing from a set of vibrational levels $\{A_v\}$ of the reactant to a set of vibrational levels $\{B_w\}$ of the product we assume a Boltzmann distribution over the vibrational levels of the reactants and sum over these levels

$$k = \frac{4\pi^2 H_{ab}^2}{h} (FC) \quad (60a)$$

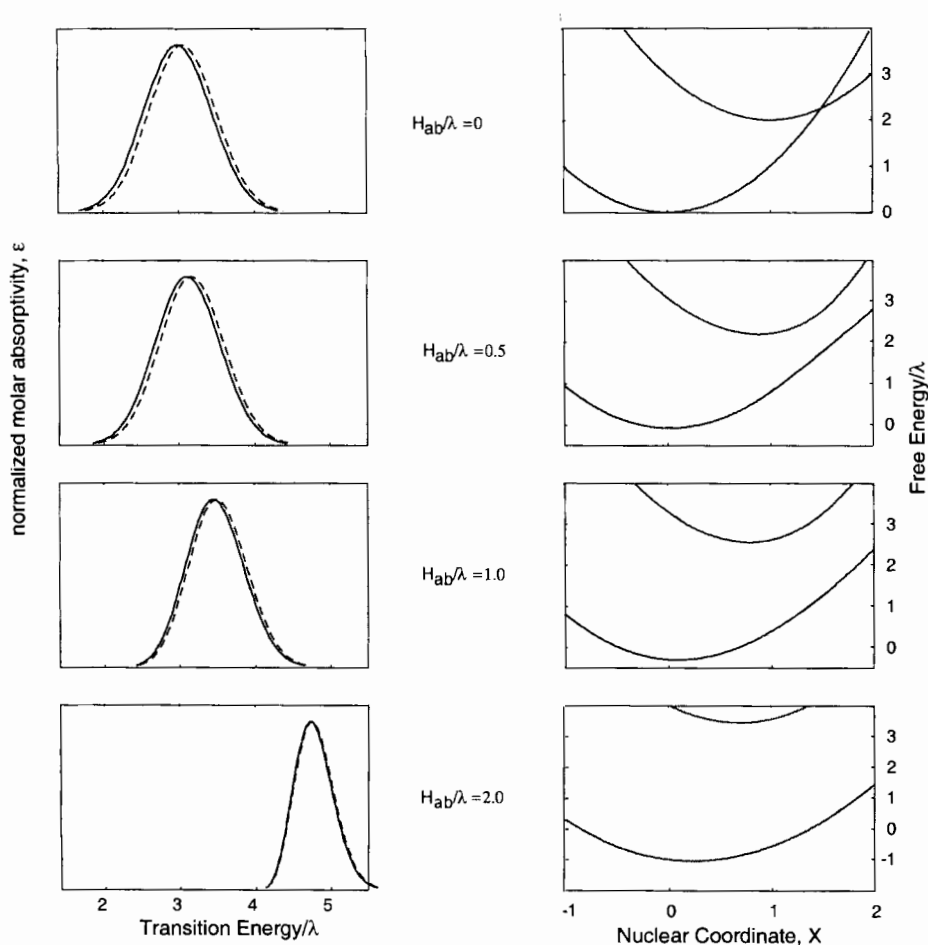


Figure 8. On the left side of the figure are shown plots of the normalized molar absorptivities, ϵ_{cl} (solid line) and ϵ_{sc} (dashed line), vs energy for $\Delta G^\circ/\lambda = 2$ and H_{ab}/λ values of 0, 0.5, 1.0 and 2, respectively. On the right side are plots of the free energy/ λ vs the nuclear coordinate x for the same values of $\Delta G^\circ/\lambda$ and H_{ab}/λ .

$$FC = \frac{1}{Q} \sum_v \sum_w \exp\left(\frac{-\epsilon_{A_v}}{RT}\right) S_{A_v, B_w}^2 \delta(\epsilon_{A_v} - \epsilon_{B_w}) \quad (60b)$$

$$Q = \sum_v \exp\left(\frac{-\epsilon_{A_v}}{RT}\right) \quad (60c)$$

where FC is the thermally averaged Franck–Condon factor and S_{A_v, B_w}^2 is the square of the overlap integral of the vibration wavefunctions of the reactants and products. If the reactant and product energy surfaces are approximated as harmonic functions, the FC factors can be explicitly calculated [38, 39].

In the following discussion we first consider the form of H_{ab} and then expressions for the thermally averaged Franck–Condon factor, FC .

1.4.1 The Electronic Coupling Element

In the present context the rate constant defined by Eq. 60 refers to a radiationless transition within a supramolecular complex that includes the precursor complex (donor–acceptor pair or excited molecule) and the surrounding solvent. Two limiting classes of radiationless transitions are of interest. The first involves the redistribution of charge within the supramolecular complex so that the transition is accompanied by a dipole-moment change. This is the type of CT (charge transfer) process that we have been considering. In the second class, there is no net charge transfer from one part of the supramolecular complex to another and thus there is no significant dipole-moment change in the transition. This type of radiationless transition is observed in the deactivation of excited states in aromatic molecules ($\pi^* \rightarrow \pi$) and in spin conversion systems. For example, in d^6 Fe(II) octahedral complexes, either a low- or high-spin isomer is more stable depending on the whether the ligand-field splitting or the interelectronic repulsion energies are larger. Interconversions between such spin states are generally not accompanied by appreciable charge transfer and so are not considered as CT transitions.

In a radiationless CT transition, the transferring charge initially strongly interacts with the donor's nuclear charge (and electrons) and only weakly interacts with that of the acceptor; at the end of the transition, the transferred charge strongly interacts with the acceptor's nuclear charge (and electrons) and only weakly with that of the donor [40]. Thus the perturbation that promotes the radiationless transition is the coulombic interaction between the transferring charge and the acceptor nuclei (and electrons), $V_{e,ac}$. The diabatic potential energies and wavefunctions constitute the zero-order states for the perturbation calculation. Unfortunately, the two diabatic wavefunctions are not solutions of the same zero-order Hamiltonian, H^o , but rather solve Hamiltonians that ignore the interaction of the transferring charge with either the acceptor or the donor and are thus not orthogonal [40, 41]. Despite this complication [11] the perturbation is just the $V_{e,ac}$ interaction (or the coulombic interaction between the oxidized donor and the transferred charge, $V_{e,do}$) and H_{ab} is given by

$$H_{ab} = \langle \psi_b | V_{e,ac} | \psi_a \rangle = \langle \psi_a | V_{e,dc} | \psi_b \rangle \quad (61a)$$

We note that, for CT transitions, the expression for H_{ab} is not needed if the Mulliken–Hush approach is used to calculate H_{ab} from experimental quantities as discussed in Section 1.3.4. Also, the generalized Mulliken–Hush treatment [32, 33] allows the calculation of H_{ab} from the adiabatic wavefunctions and the complete Hamiltonian; the extension of Eq. 56 to include more than two states is then used to obtain H_{ab} .

In the non-CT radiationless transition the change in electronic charge interacts with the nuclei in a similar manner both before and after the transition. Two types of processes can be identified: internal conversion processes in which the transition is between spin states of the same multiplicity and intersystem crossing process in which the transition is between states of different spin multiplicity. For non-CT internal conversion processes the full BO (Born–Oppenheimer) adiabatic wavefunctions for the supramolecular complex are used as the zero-order basis [42–44]. The perturbations that cause the transition are the vibronic coupling between the nuclear and electron motions. These are just the terms that are neglected in the BO approximation [45]. The terms are expanded (normally to first order) in the normal vibrational coordinates of the nuclei as is customarily done for optical vibronic transitions. Thus one obtains Eq. 61b for cases when only one normal mode couples the two states

$$H_{ic} = \frac{\langle \psi_2 | (\partial U / \partial Q)_0 | \psi_1 \rangle}{(E_2 - E_1)} \quad (61b)$$

In this equation the ψ_i and E_i are the adiabatic BO wavefunctions and energies (at the a particular nuclear configuration), respectively, U is the electronic potential energy and Q is the normal coordinate for the vibration that couples the electronic states ψ_2 and ψ_1 .

By contrast, the pure spin BO states need to be mixed for intersystem crossing or spin-conversion processes. The BO wavefunctions are mixed by the spin–orbit coupling operator, H_{so}

$$\psi'_j = \psi_j + \sum_{k \neq j} \frac{\langle \psi_k | H_{so} | \psi_j \rangle}{E_j - E_k} \psi_k \quad (61c)$$

where the ψ'_j are the mixed wavefunctions, the ψ_j are the pure spin wavefunctions and the energies and spin–orbit matrix element are evaluated at the equilibrium configuration of the initial (or final) state. The spin–orbit coupling also promotes the radiationless transition between the ψ'_j states with the intersystem crossing Hamiltonian is given by [46]:

$$\begin{aligned} H_{sc} &= \langle \psi'_1 | H_{so} | \psi'_2 \rangle \\ &\approx \langle \psi_1 | H_{so} | \psi_2 \rangle \\ &\quad + \sum_{j \neq 1,2} \langle \psi'_1 | H_{so} | \psi'_j \rangle \langle \psi'_j | H_{so} | \psi'_2 \rangle \left(\frac{1}{E_1 - E_j} + \frac{1}{E_2 - E_j} \right) \end{aligned} \quad (61d)$$

We note that for spin conversion processes that involve the flip of a single electron ($\Delta S = 1$) the first term in Eq. 61d is dominant whereas for processes in which the spins of several electrons change ($\Delta S > 1$) the first term is zero.

For most charge transfer reactions the electronic coupling element is simply given by the coulomb matrix element defined by Eq. 61a.

1.4.2 The Thermally Averaged Franck–Condon Factor

Three broad classes of vibrational modes may contribute to the thermally averaged Franck–Condon factor: the high-frequency (fast) modes ($h\nu > 1000 \text{ cm}^{-1}$) which are mainly intraligand vibrations, intermediate modes ($1000 \text{ cm}^{-1} > h\nu > 100 \text{ cm}^{-1}$) that typically include the metal–ligand stretching vibrations and higher frequency solvent orientational–vibrational modes, and the low-frequency (slow) modes ($h\nu < 100 \text{ cm}^{-1}$) which are primary solvent modes but can include low-frequency intramolecular modes. At ordinary temperatures $h\nu_v \gg kT \approx h\nu_c \gg h\nu_s$ and the low-frequency modes can be treated using classical (continuum) expressions.

Two-mode systems

We first consider the case with one high-frequency mode and one low-frequency mode. When the high-frequency mode (ν_v , with reorganization energy of λ_v) is in the low temperature limit and the low-frequency mode (ν_s, λ_s) is treated classically, the rate constant for electron transfer is given by:

$$k_{\text{el}} = \frac{H_{\text{ab}}^2}{h} \left(\frac{4\pi^3}{\lambda_s RT} \right)^{1/2} \sum_{j=0}^{\infty} F_j \exp \left[-\frac{(j h \nu_v + \Delta G^\circ + \lambda_s)^2}{4 \lambda_s RT} \right] \quad (62)$$

where $F_j = e^{-S} S^j / j!$, $S = \lambda_v / h \nu_v$ is the Huang–Rhys factor and $F_j H_{\text{ab}}^2 < h \nu_s \sqrt{\lambda_s RT} / \pi^3$ [41, 47, 48]. Because the solvent (or other low-frequency) mode behaves classically while the high-frequency mode can tunnel it is most efficient for the solvent modes to use enough of the driving force to reduce the solvent barrier significantly with the remaining driving force absorbed by the high-frequency modes. Moreover, since $h \nu_v \gg kT$ all of the reaction occurs from the lowest vibrational level of the initial state, i.e., only $A_0 \rightarrow \{B_j\}$ vibronic transitions are considered. The exponential term in Eq. 62 is a Gaussian that describes the rate constant reduction deriving from the solvent reorganization. The Gaussian is peaked at $(j h \nu_v + \Delta G^\circ + \lambda_s) \approx 0$ and has a width of $2\sqrt{4\lambda_s RT}$. The transition with $j^* \approx -(\Delta G^\circ + \lambda_s) / h \nu_v$ will normally dominate the sum. The rate constant will be maximized when the solvent reorganization is barrierless. This occurs when the effective driving force for the solvent reorganization, $-(\Delta G^\circ + j h \nu_v)$ is approximately equal to λ_s , i.e., when $j^* \approx -(\Delta G^\circ + \lambda_s) / h \nu_v$. The effective energy gap for the high-frequency mode is $-(\Delta G^\circ + \lambda_s)$. The energy change of the reactant/product and the solvent for the single largest term in the sum of Eq. 62 is plotted against driving force is illustrated in Figure 9. The solvent accepts an amount of energy that is close to the λ_s for the system while the high-frequency mode will accept no energy for very low driving forces and the majority of the energy change when $|\Delta G^\circ| \gg \lambda_s + \lambda_v$.

A convenient closed-form expression for the rate can be derived using Eq. 62

$$k_{\text{el}} = \frac{4\pi^2 H_{\text{ab}}^2 F_{j^*}}{h^2 \nu_v} \exp \left[-\frac{(j^* h \nu_v + \Delta G^\circ + \lambda_s)^2}{4 \lambda_s RT} \right] \quad (63a)$$

where

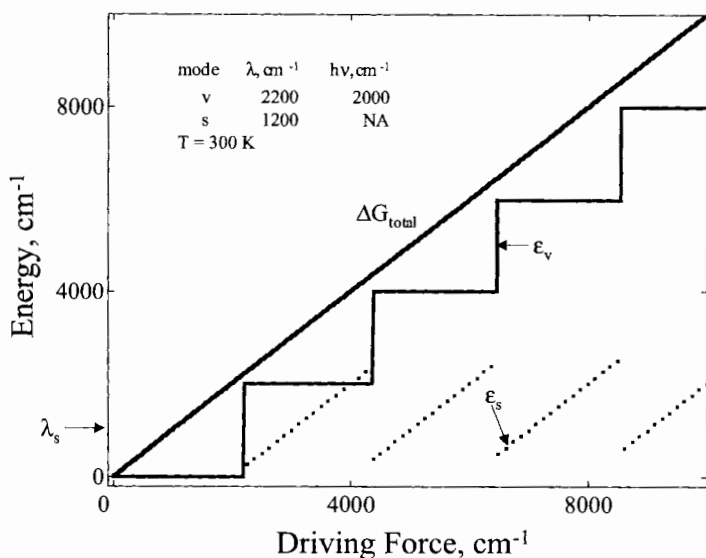


Figure 9. Plot of the energy in a particular mode for an electron transfer reaction with two active modes. $\Delta\epsilon_v$ and $\Delta\epsilon_s$ are the differences between the energies of the products and reactants in the high- and low-frequency modes, respectively; λ_i , (cm^{-1}) and $h\nu_i$ (cm^{-1}) are (2000, 2000) and (1200, -) for the high- and low-frequency modes and the temperature is 300 K. The calculations were done using Eq. 62. The straight line, the stepped solid line and the dotted lines are the total energy difference (ΔG°) and the differences between the energies of the products and reactants in the high- and low-frequency modes, respectively.

$$j^* \approx -\frac{(\Delta G^\circ + \lambda_s)}{h\nu_v} - \frac{2\lambda_s RT(\gamma + 1)}{(h\nu_v)^2} \quad (63b)$$

$$\gamma = \ln \left[-\frac{(\Delta G^\circ + \lambda_s)}{\lambda_v} \right] - 1 \quad (63c)$$

The rate constants in the inverted region calculated from Eq. 59 are almost independent of temperature and decrease much less rapidly with driving force than predicted by classical models [49].

Three-mode systems

Next we consider a reaction that contains an active mode in each of the regions outlined above. The expression for the three-mode case is:

$$k_{\text{el}} = \frac{H_{\text{ab}}^2}{h} \left(\frac{4\pi^3}{\lambda_s RT} \right)^{1/2} \exp \left[-S_c \coth \left(\frac{h\nu_c}{2kT} \right) \right] \sum_{j_v=0}^{\infty} \sum_{j_c=-\infty}^{\infty} F_{j_v} \exp \left(\frac{j_c h\nu_c}{2kT} \right) \\ \times I_{j_c} \left(S_c \operatorname{csch} \left(\frac{h\nu_c}{2kT} \right) \right) \exp \left[-\frac{(\Delta G^\circ + \lambda_s + j_v h\nu_v + j_c h\nu_c)^2}{4\lambda_s RT} \right] \quad (64)$$

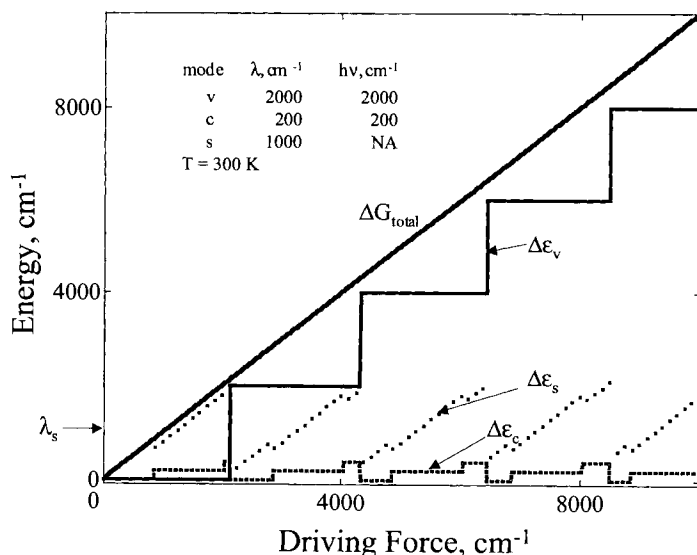


Figure 10. Plot of the energy in a particular mode for an electron transfer reaction with three active modes. $\Delta\epsilon_v$, $\Delta\epsilon_c$ and $\Delta\epsilon_s$ are the differences between the energies of the products and reactants in the high-, intermediate- and low-frequency modes, respectively; λ_i , (cm^{-1}) and $h\nu_i$ (cm^{-1}) are (2000, 2000); (200, 200); and (1000, –) for the high-, intermediate- and low-frequency modes and the temperature is 300 K. The calculations were done using Eq. 64. The straight line, the stepped solid line, the dashed line and the dotted lines are the total energy difference (ΔG°) and the differences between the energies of the products and reactants in the high-, intermediate- and low-frequency modes, respectively.

where j_v and j_c are the changes in the vibrational quantum numbers for the high and intermediate frequency modes, respectively [49]. Again the last exponential term in Eq 64 is Gaussian peaked at $(\Delta G^\circ + \lambda_s + j_v h\nu_v + j_c h\nu_c) = 0$ with a width of $2\sqrt{4\lambda_s RT}$. In this case energy sharing can take place between the high-, intermediate- and low-frequency modes; the possibility of energy borrowing is increased but again the low-frequency mode is required to pass over its barrier while the other two modes can tunnel. Figures 10 and 11 show the energy distribution for the dominant contribution to the double sum. The low-frequency mode receives $\sim \lambda_s$ of energy to minimize its barrier; the intermediate mode receives $\sim \lambda_c$, and the bulk of the energy for large driving forces is deposited in the high-frequency mode. Only very seldom is the low or intermediate-frequency energy of the product less than that of the reactant. This is shown in Figure 11 where $\Delta\epsilon_s$ is negative.

These expressions show that normally most of the excess energy is acquired by the high-frequency mode and that the intermediate-frequency mode receives an amount of energy that is less than one high-frequency vibrational quantum. Only when $\lambda_c \gg \lambda_s$ does the intermediate-frequency mode receive significantly more than a single high-frequency quantum. The effect of an intermediate mode on the rate constant for the reaction is relatively modest in the normal region but becomes important in the inverted region where the initial state needs to dispose of significantly more energy (Figure 12). In this region systems that have both high- and interme-

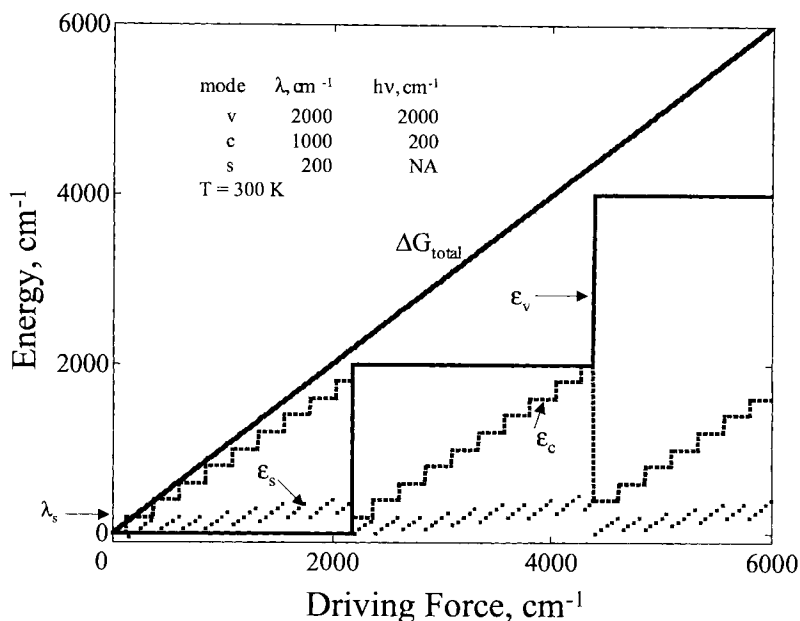


Figure 11. Plot of the energy in a particular mode for an electron transfer reaction with three active modes. $\Delta\epsilon_v$, $\Delta\epsilon_c$ and $\Delta\epsilon_s$ are the difference between the energies of the products and reactants in the high-, intermediate- and low-frequency modes λ_i , (cm^{-1}) and $h\nu_i$ (cm^{-1}) are (2000, 2000); (1000, 200); and (200, —) for the high-, intermediate- and low-frequency modes, respectively, and the temperature is 300 K. The calculations were done using Eq. 64. The straight line, the stepped solid line, the dashed line and the dotted lines are the total energy difference (ΔG°) and the differences between the energies of the products and reactants in the high-, intermediate- and low-frequency modes, respectively.

intermediate-frequency modes exhibit significant rate enhancements due to tunneling and the decrease of the rate constant with increasing driving force is attenuated. Also, due to the intermediate-frequency mode the sinusoidal quantum beat effect observed for the dependence of the rate constant on driving force in the inverted region is significantly attenuated.

The three-mode expression is most useful when discussing the rates of non-radiative deactivation of excited states in the inverted region. In this region, where $-\Delta G^\circ \gg \lambda_v + \lambda_c + \lambda_s$, a much simpler expression can be used since the product is created with a high vibrational quantum number in the high-frequency mode. This expression is Eq. 65 provided that $5\lambda_c$ and $10\lambda_s$ are each $< |\Delta G^\circ|$.

$$k_{\text{el}} = \frac{4H_{\text{ab}}^2}{h} \left[-\frac{\pi^3}{2h\nu_v(\Delta G^\circ + \lambda_c + \lambda_s)} \right]^{1/2} \times \exp \left(-\frac{\lambda_v - (\gamma_0 + 1)(\lambda_c + \lambda_s) - \gamma_0 \Delta G^\circ - \frac{(\gamma_0 + 1)^2}{h\nu_v} \left(\lambda_s RT + \frac{\lambda_c h\nu_c}{2} \coth \left(\frac{h\nu_c}{2kT} \right) \right)}{h\nu_v} \right) \quad (65a)$$

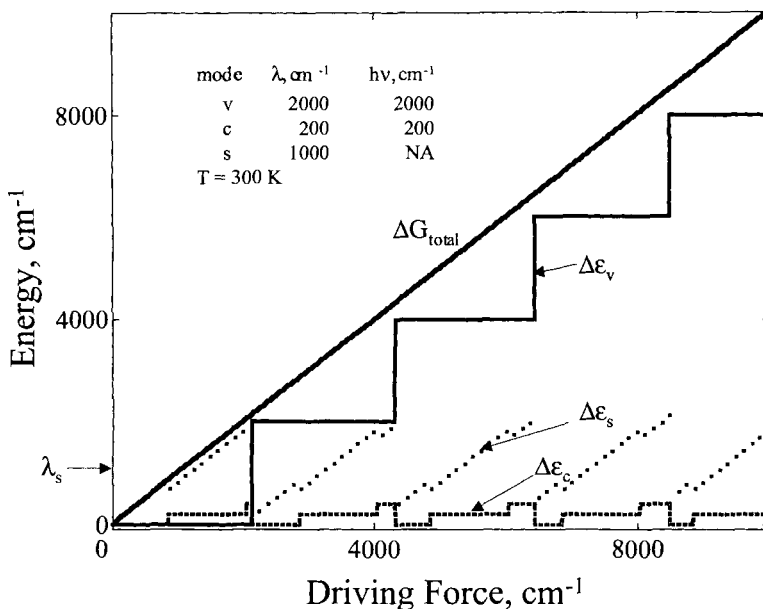


Figure 12. Plot of the logarithm of the Franck–Condon factors for the electron transfer reaction calculated using the classical expression, Eq. 23; two-mode expression, Eq. 62; three-mode expression, Eq. 64; and the approximate three-mode expression, Eq. 65 vs driving force. The parameters used ($\lambda_s, \lambda_c, h\nu_c, \lambda_h, h\nu_h$ in cm^{-1}) for the calculations are classical: (3200); two-mode, (1200, 2000, 600); three-mode (600, 600, 200, 2000, 600) and the temperature is 80 K. The solid line (inverted parabola), dotted line, oscillating solid line and the dashed line are for the classical expression, Eq. 23, the two-mode expression, Eq. 62, the full three-mode expression, Eq. 64, and the approximate three-mode expression, Eq. 65, respectively.

where

$$\gamma_0 = \ln\left(\frac{-\Delta G^\circ}{\lambda_v}\right) - 1 \quad (65b)$$

The above three-mode expression approximates the more exact expression Eq. 54 very well, but does not show the quantum beat effect.

1.5 Conclusions

The expressions derived from the traditional two-state model are useful in rationalizing a variety of electron transfer processes. Both thermal and optical charge transfer can be treated and, although not discussed here, electrochemical processes

as well. The two-state model neglects contributions from higher electronic states in calculating the energies of the zero-order ground states of the reactants and products. Contributions from higher electronic states are, however, frequently needed in calculating electronic coupling elements. Mixing with such states leads to modification of the ground-state energies when the excited states are sufficiently low lying. Such perturbations are absent in the zero-interaction limit.

Some key features of the two-state model are summarized here:

- (1) Although the reaction coordinate for charge transfer is not uniquely defined, the vertical difference between the zero-order reactant and product free energies is related to the degree of nuclear reorganization and consequently this difference provides a useful measure of the progress of the reaction (Section 1.2).
- (2) The degree of charge transfer is *not* linearly related to the reaction coordinate defined above (Section 1.3.1).
- (3) The splitting at the intersection of the adiabatic curves for a self-exchange reaction, $2H_{ab}$, enters into the expression for the free energy of activation for the exchange reaction analogous to the manner in which the driving force, $-\Delta G^\circ$, enters into the expression for the free energy of activation for a marginally adiabatic net reaction (Section 1.3.1).
- (4) The vertical difference between the free energies of the reactants and products of a self exchange reaction remains equal to λ at the equilibrium configuration of the reactants (or products) regardless of the magnitude of the electronic coupling as long as the system remains valence trapped (Sections 1.3.1 and 1.3.4).
- (5) The frequency of electron hopping in the transition state is equal to $2H_{ab}/h$ (Section 1.3.3).
- (6) The electron transfer distance is defined by the difference between the dipole moments of the localized (diabatic) reactant and product states (Section 1.3.4).
- (7) The electronic coupling element for a charge transfer reaction H_{ab} is equal to $\langle \psi_a | V_{e,ac} | \psi_b \rangle$ where $V_{e,ac}$ is the coulomb interaction between the transferring electron (initially on the donor) and the acceptor (Section 1.4.1).
- (8) At low temperatures and/or at high reaction exergonicities nuclear tunneling contributions to the rate and other quantum effects become important. Two- and three-mode expressions are presented that allow for tunneling of the higher frequency modes (Section 1.4.2).

Overall, the two-state model is remarkably successful in interpreting electron transfer and related properties and forms the cornerstone for interpreting a variety of complex physical, photosynthetic, catalytic and biological processes.

Acknowledgments

We wish to acknowledge helpful discussions with Rudolph A. Marcus. This research was carried out at Brookhaven National Laboratory under contract DE-AC02-98CH10886 with the U.S. Department of Energy and was supported by its Division of Chemical Sciences, Office of Basic Energy Sciences.

References

1. R. A. Marcus, *J. Chem. Phys.* **1957**, 26, 867–871.
2. R. A. Marcus, *Disc. Faraday. Soc.* **1960**, 29, 21–31.
3. R. A. Marcus, *Rev. Modern Phys.* **1993**, 65, 599–610.
4. N. Sutin, *Prog. Inorg. Chem.* **1983**, 30, 441–498.
5. R. A. Marcus, N. Sutin, *Biochim. Biophys. Acta* **1985**, 811, 265–322.
6. The sum of any two parabolas gives a parabola that has a force constant equal to the sum of the force constants of the two original parabolas and with its minimum located above the two original minima and horizontally between them.
7. J.-K. Hwang, A. Warshel, *J. Am. Chem. Soc.* **1987**, 109, 715–720.
8. G. King, A. Warshel, *J. Chem. Phys.* **1990**, 93, 8682–8692.
9. R. A. Marcus, N. Sutin, *Inorg. Chem.* **1975**, 14, 213–216.
10. L. W. Ungar, M. D. Newton, G. A. Voth, *J. Phys. Chem. B* **1999**, 103, 7367–7382.
11. C. Creutz, M. D. Newton, N. Sutin, *J. Photochem. Photobiol. A: Chem.* **1994**, 82, 47–59.
12. M. B. Robin, P. Day, *Adv. Inorg. Chem. Radiochem.* **1967**, 10, 247–422.
13. C. Creutz, *Prog. Inorg. Chem.* **1983**, 30, 1–73.
14. R. J. Crutchley, *Adv. Inorg. Chem.* **1994**, 41, 273–325.
15. B. S. Brunshawig, N. Sutin, *Coord. Chem. Rev.* **1999**, 187, 233–254.
16. N. Sutin, in *Bioinorganic Chemistry*, Vol. 2, (Ed.: G. L. Gunther), Elsevier, New York **1973**, pp. 611–653.
17. B. S. Brunshawig, J. Logan, M. D. Newton, N. Sutin, *J. Am. Chem. Soc.* **1980**, 102, 5798–5809.
18. R. A. Marcus, *Ann. Rev. Phys. Chem.* **1964**, 15, 155–196.
19. R. A. Marcus, *J. Chem. Phys.* **1956**, 24, 966–978.
20. R. A. Marcus, *J. Chem. Phys.* **1965**, 43, 679–701.
21. B. S. Brunshawig, C. Creutz, N. Sutin, *Coord. Chem. Rev.* **1998**, 177, 61–79.
22. H. J. Kim, J. T. Hynes, *J. Chem. Phys.* **1990**, 93, 5194–5210.
23. J. N. Gehlen, D. Chandler, H. J. Kim, J. T. Hynes, *J. Phys. Chem.* **1992**, 96, 1748–1753.
24. R. A. Marcus, *J. Phys. Chem.* **1992**, 96, 1753–1757.
25. H. J. Kim, J. T. Hynes, *J. Chem. Phys.* **1992**, 96, 5088–5110.
26. J. N. Gehlen, D. Chandler, *J. Chem. Phys.* **1992**, 97, 4958–4963.
27. P. W. Atkins, R. S. Friedman, *Molecular Quantum Mechanics*, Oxford University Press, New York **1997**, p. 187.
28. H. J. Kim, R. Bianco, B. J. Gertner, J. T. Hynes, *J. Phys. Chem.* **1993**, 97, 1723–1728.
29. N. S. Hush, *Prog. Inorg. Chem.* **1967**, 8, 391–444.
30. N. S. Hush, *Electrochim. Acta* **1968**, 13, 1005–1023.
31. Y.-G. K. Shin, B. S. Brunshawig, C. Creutz, N. Sutin, *J. Phys. Chem.* **1996**, 100, 8157–8169.
32. R. J. Cave, M. D. Newton, *Chem. Phys. Lett.* **1996**, 249, 15–19.
33. R. J. Cave, M. D. Newton, *J. Chem. Phys.* **1997**, 106, 9213–9226.
34. C. Lambert, G. Nöll, *J. Am. Chem. Soc.* **1999**, 121, 8434–8442.
35. S. F. Nelsen, R. F. Ismagilov, D. A. T. II, *Science* **1997**, 278, 846–849.
36. P. W. Atkins, R. S. Friedman, *Molecular Quantum Mechanics*, Oxford University Press, New York **1997**, p. 509.
37. P. W. Atkins, R. S. Friedman, *Molecular Quantum Mechanics*, Oxford University Press, New York **1997**, p. 196.
38. The overlap integrals S_{A_V, B_W} can be calculated if the reactant and produce surfaces are assumed to be harmonic with the same force constants.
39. T. Terasaka, T. Matsushita, *Chem. Phys. Lett.* **1981**, 80, 306–310.
40. N. R. Kestner, J. Logan, J. Jortner, *J. Phys. Chem.* **1974**, 78, 2148.
41. J. Ulstrup, *Charge Transfer Processes in Condensed Media*, Springer, New York **1979**, pp. 71–79.
42. M. Bixon, J. Jortner, *J. Chem. Phys.* **1968**, 48, 715–726.
43. K. F. Freed, J. Jortner, *J. Chem. Phys.* **1970**, 52, 6272–6291.
44. R. Englman, J. Jortner, *Mol. Physics* **1970**, 18, 145–164.

45. P. W. Atkins, R. S. Friedman, *Molecular Quantum Mechanics*, Oxford University Press, Oxford **1997**, 241.
46. E. Buhks, G. Navon, M. Bixon, J. Jortner, *J. Am. Chem. Soc.* **1980**, *102*, 2918–2923.
47. J. Ulstrup, J. Jortner, *J. Chem. Phys.* **1975**, *63*, 4358–4368.
48. J. Jortner, *J. Chem. Phys.* **1976**, *64*, 4860–4867.
49. B. S. Brunshawig, N. Sutin, *Comments Inorg. Chem.* **1987**, *6*, 209–235.

2 Charge-transfer Interactions and Electron-transfer-activated Reactions of Organometallic Complexes

Stephan M. Hubig and Jay K. Kochi

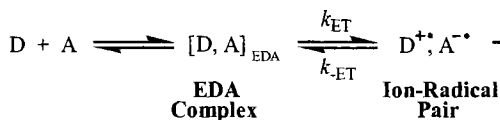
2.1 Introduction

Organometallic complexes display a rich electron-transfer chemistry as a consequence of their unique redox properties [1–3]. First, owing to their manifold oxidation states, the metal centers can undergo a variety of redox transformations involving single to multiple electron transfers that depend on the redox counterpart and the reaction conditions. Second, the coordination of the metal with various organic ligands (of different donor or acceptor properties) allows the selective stabilization of certain oxidation levels and a fine-tuning of their redox potentials. Thus, depending on their oxidation states and the ligand environment, organometallic complexes may act as electron donors or acceptors, which is discussed in detail in Section 2.2. Accordingly, they are ideal redox reagents to promote electron-transfer activated reactions of organic substrates which are (a) directly bound to the metal as ligands or (b) encounter the organometallic complex in a bimolecular (diffusional) reaction mode [4–6].

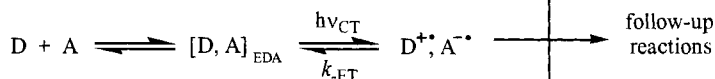
Bimolecular electron-transfer (ET) reactions in solution require the freely diffusing donor and acceptor molecules to achieve a nuclear pre-arrangement in the precursor or encounter complex [7–9] which enables electron exchange from the HOMO of the donor to the LUMO of the acceptor moiety. The distance and relative orientation of the ET partners in this precursor complex control the degree of orbital overlap or electronic coupling [10] of the redox partners in the ET transition state, which limits the rate of the intrinsically ultrafast electron jump [11–13]. As such, electron donor–acceptor (EDA) complexes represent precursor complexes with a rather strong electronic (charge-transfer) coupling [14–16] and thus play a critical role in the predisposition of redox reactants toward electron transfer. A variety of such EDA complexes involving organometallic donors and acceptors are introduced in Section 2.3 and their crystal structures and spectroscopic properties are discussed.

Depending on the energetic conditions, electron transfer may occur spontaneously in the EDA complex as a *thermal* reaction (see reaction path A in Scheme 1), or

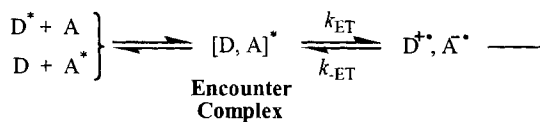
(A) Thermal ET:



(B) CT Activated ET:



(C) Sensitized ET:



Scheme 1.

it may require additional (light) energy in a *photoactivated* reaction (see reaction **B** in Scheme 1) [5, 17]. In the latter case, irradiation of the charge-transfer (CT) absorption band of the (thermally unreactive) EDA complex effects a spontaneous electron transfer from the donor HOMO to the acceptor LUMO [18], which represents the initial step in a *CT-activated* photoreaction.

An alternative possibility to initiate electron transfer between two unreactive substrates is the photoactivation of one of the redox partners. In such a *photo-sensitized* reaction (path **C** in Scheme 1), photoexcitation of one of the redox partners enhances its oxidation or reduction potential substantially. As a consequence, the reactant in the excited state is now able to undergo spontaneous electron transfer upon the formation of an encounter complex (or exciplex) [19, 20] with a suitable redox partner. Owing to the enhanced redox potentials, the encounter complex exhibits even stronger charge-transfer character as compared to the (ground-state) EDA complex [20] and facilitates electron transfers that do not occur in the ground state owing to unfavorable (endergonic) energetics. Most importantly, all three types of electron transfer described above, viz. thermal, sensitized, and CT activated pathways, ultimately lead to ion–radical pairs as the critical reaction intermediates [21] that subsequently undergo various follow-up reactions to the final products. The various methods to generate and detect organometallic ion radicals will be described in Section 2.4.

Ion–radical pairs may undergo back electron transfer [22–24] (k_{-ET} in Scheme 1) in competition with the desired follow-up reactions, which limits the yields of the final reaction products. In fact, the more endergonic the initial electron-transfer step (k_{ET} in Scheme 1) is, the faster is the corresponding (exergonic) back electron transfer, which shifts the ET equilibrium towards the precursor (EDA) complex. However, even in such cases of highly endergonic electron transfer, a net chemical reaction to the final products may still be observed if the rate of the follow-up reaction is competitive with that of the back electron transfer in Scheme 1 [25]. This

is demonstrated with many examples of follow-up reactions of organometallic ion radicals in Section 2.4.

Kinetic studies and the resulting correlation between the rate constants and the free energy change of the reaction are useful tools to elucidate mechanistic aspects of the electron-transfer step. Traditionally, electron-transfer reactions are classified as outer-sphere or inner-sphere processes [26–30]. Marcus theory [7, 8] describes the free-energy correlation of outer-sphere ET rate constants. Accordingly, free-energy correlations may be used to distinguish between outer-sphere and inner-sphere reactions [31–33]. This concept is demonstrated for various electron-transfer reactions of organometallic complexes in Section 2.5. Most importantly, steric effects introduced by bulky ligands [32, 33] are shown to induce a changeover between the two electron-transfer mechanisms as observed in organic electron transfers involving sterically encumbered electron donors [31].

This review illustrates the above delineated characteristics of electron-transfer activated reactions by analyzing some representative thermal and photoinduced organometallic reactions. Kinetic studies of thermal reactions, time-resolved spectroscopic studies of photoinduced reactions, and free-energy correlations are presented to underscore the unifying role of ion-radical intermediates [29] in—at first glance—unrelated reactions such as additions, insertions, eliminations, redox reactions, etc. (Photoinduced electron-transfer reactions of metal porphyrin and polypyridine complexes are not included here since they are reviewed separately in Chapters 2.2.16 and 2.2.17, respectively.)

2.2 Organometallic Complexes as Electron Donors or Acceptors

Because metals have low electronegativities and most frequently exist in low oxidation states when coordinated with organic ligands, organometallic complexes are most commonly employed as donors in electron-transfer reactions (see Section 2.2.1.). However, if the metal center is oxidized to its cationic state or (formally) promoted to a high oxidation level by coordination with electronegative ligands, the organometallic complex is transformed to an electron acceptor (see Section 2.2.2). A quantitative classification of organometallic complexes according to their electron donor or acceptor strength is generally based on measurements of their (vertical) ionization potentials (*IP*) and electron affinities (*EA*) in the gas phase or oxidation (E°_{ox}) and reduction (E°_{red}) potentials in solution. Thus, *IP* and E°_{ox} values represent measures for the energy required to detach an electron from a donating substrate (Eq. 1):



and electron affinities and reduction potentials are measures for the energetics of electron attachment to an acceptor (Eq. 2):



2.2.1 Organometallic Donors

Alkylmetals

The coordination of alkyl groups R around a metal center M generates a simple organometallic complex MR_n the electron-donor properties of which are readily accounted for by the electron-richness of the metal center due to the positive inductive effect of R. The (vertical) ionization potentials and (irreversible) oxidation potentials (vide infra) listed in Table 1 for a variety of polyalkyl complexes of Group IV and Group IIb metals establish the donor strength of these organometallic substrates to be comparable with those of organic aromatic donors such as naphthalene [34] or alkyl-substituted benzenes [36]. The data in Table 1 clearly show that with decreasing electronegativity of the (Group IV) metals (e.g., $C \gg Ge > Sn > Pb$) and with increasing electron donicity of the alkyl ligand (e.g., $CH_3 < C_2H_5 < i-C_3H_7 < t-C_4H_9$), the donor properties of the coordination complex improve substantially as illustrated by the ionization potentials which vary by more than 1 eV. In addition, stepwise substitution of methyl ligands by ethyl groups (see entries 1–5 in Table 1) results in incremental decrease of the ionization potential. The latter two observations are in excellent agreement with the MO description

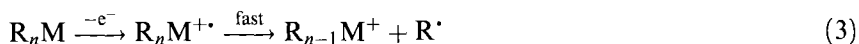
Table 1. Vertical ionization potentials (IP) and oxidation (peak) potentials (E_{ox}) of alkylmetals (R_nM).

R_nM	IP (eV)	Ref.	E_{ox} (V relative to the SCE)	Ref.
PbMe ₄	8.90	38	0.98	39
PbMe ₃ Et	8.65	38	0.84	39
PbMe ₂ Et ₂	8.45	38	0.73	39
PbMeEt ₃	8.26	38	0.63	39
PbEt ₄	8.13	38	0.55	39
SnMe ₄	9.70	40	1.42	39
SnEt ₄	8.93	40	1.65	41
Sn(<i>n</i> -)Pr ₄	8.82	42		
Sn(<i>n</i> -)Bu ₄	8.83	40	0.90	39
Sn(<i>neo</i> -)Pent ₄	8.67	42		
GeEt ₄	9.41	42		
Neopentane ^a	10.90	43		
ZnMe ₂	9.4	44		
ZnEt ₂	8.6	44		
CdMe ₂	8.8	44		
CdEt ₂	8.2	44		
Cd(<i>n</i> -)Pr ₂	8.2	44		
HgMe ₂	9.33	42	1.46	42
	9.30	44		
HgEt ₂	8.45	42	0.97	42
	8.90	44		
Hg(<i>n</i> -)Bu ₂	8.35	42		

^aFor comparison.

of alkylmetal complexes which derives the HOMO from the σ_{M-C} bonding orbitals [37].

Electrochemical oxidations of alkylmetal donors are irreversible in all cases studied owing to rapid homolytic cleavage of the metal–carbon bond at the cation-radical stage (Eq. 3):



The facile metal–carbon bond cleavage upon one-electron oxidation is not surprising considering the σ_{M-C} character of the HOMO (vide supra) [37], and the irreversible fragmentation of the cation radical allows even highly endergonic oxidations of alkylmetals to occur at reasonable rates and with good yields. In other words, even electron-transfer equilibria shifted far toward the side of the starting materials can be effectively ‘drained’ towards the electron-transfer products as demonstrated by the efficient insertion of tetracyanoethylene into the metal–carbon bond of various tetraalkyltin compounds (see Section 2.5).

Metalloenes and (arene) metal sandwich complexes

Metalloenes are useful electron donors as judged by their low (vertical) ionization potentials in the gas phase and oxidation potentials in solution (see Table 2). In fact, the electron-rich ($19 e^-$) cobaltocene with an oxidation potential of $E^\circ_{\text{ox}} = -0.9$ V relative to the SCE [45] is commonly employed as a very powerful reducing agent in solution. Unlike the alkylmetals (vide supra), the HOMOs of metalloenes reside at the metal center [46] which accounts for two effects: (i) Removal of an electron from the HOMO requires minimal reorganization energy which explains the facile oxidative conversion from metalloene to metalloenium. (ii) The metal–carbon bonding orbitals are little affected by the redox process, and thus the resulting metalloenium ions are very stable and can be isolated as salts.

Replacing cyclopentadienyl ligands in the metalloenes by arene ligands results in

Table 2. Vertical ionization potentials (IP) and oxidation potentials (E°_{ox}) of metalloenes and (arene) metal sandwich complexes.

Sandwich complex	IP (eV)	Ref.	E°_{ox} (V relative to the SCE)	Ref.
Cp_2Fe	6.86	47	0.41	48
Cp_2Co	5.55	45	−0.90	45
Cp_2Ru	7.45	45		
$(\eta^6\text{-C}_6\text{H}_6)_2\text{Cr}$			−0.80	49, 50
$\text{CpFe}(\text{HMB})^a$	4.68	45	−1.41	45
$(\eta^6\text{-C}_6\text{H}_6)\text{Cr}(\text{CO})_3$			0.84	51
			0.71	52
$(\eta^6\text{-TOL})\text{Cr}(\text{CO})_3^b$			0.82	51
			0.68	52

^a HMB = hexamethylbenzene.

^b TOL = toluene.

Table 3. Vertical ionization potentials (*IP*) and oxidation (peak) potentials (*E*_{ox}) of metal carbonyls.

Metal carbonyl	<i>IP</i> (eV)	Ref.	<i>E</i> _{ox} (V relative to the SCE)	Ref.
Cr(CO) ₆	8.40	55	1.53	53
			1.09 ^a	53
Mo(CO) ₆	8.50	55	1.53	53
Co(CO) ₆	8.56	55	1.53	53
Fe(CO) ₅	8.60	56	1.51	53
Ni(CO) ₄	8.93	56	1.26	53
Mn ₂ (CO) ₁₀	8.02	55	1.55	53
Re ₂ (CO) ₁₀	8.07	55	1.55	53

^aReversible potential in trifluoroacetic acid.

metal sandwich complexes with enhanced reducing properties (see entries 1 and 5 in Table 2). On the other hand, removal of one arene ligand and replacement by carbonyl ligands results in half-sandwich complexes with substantially higher oxidation potentials and thus diminished reducing capabilities.

Metal carbonyls

The ionization and oxidation (peak) potentials [53] of metal carbonyls listed in Table 3 establish their mild donicity despite their (formally) neutral oxidation state. However, partial replacement of carbonyls by stronger donor ligands (such as phosphine, sulfide, etc.) effects an incremental increase in their reducing properties [54]. Such a fine-tuning of the oxidation potentials of structurally similar organometallic donors is ideal for studies of the correlation between rate constants and the electron-transfer driving force (see Section 2.5).

Metal hydrides

Metal hydrides represent another type of electron donating organometallic complexes which exhibit ionization and oxidation potentials similar to alkyl or aryl coordinated metals (compare entries 2 and 3 or 2 and 4 in Table 4).

Enhanced donicity in anionic organometallic complexes (metallates)

The electron donicity of alkylmetal complexes is strongly enhanced when a negative charge is introduced. Thus, polyalkylmetallates such as borates or aurates exhibit oxidation (peak) potentials much lower than neutral polyalkylmetal complexes (compare Tables 1 and 5). An extreme case represents dimethylaurate(I) with an oxidation (peak) potential of 0.1 V (relative to the SCE) [64] which is more than 1 V lower than that of the isoelectronic dimethylmercury(II) complex (*E*_{ox} = 1.46 V relative to the SCE) [42]. Similarly, the oxidation potential of tetramethylborate (*E*_{ox} = 0.58 V relative to the SCE) [65] is substantially lower than that of the isoelectronic neopentane which exceeds 3 V [66].

Table 4. Vertical ionization potentials (*IP*) and oxidation potentials (E°_{ox}) of metal hydrides.

Metal hydride	<i>IP</i> (eV)	Ref.	E_{ox} (V relative to the SCE)	Ref.
Cp ₂ WH ₂	6.4	57	0.01	58
Cp ₂ MoH ₂	6.4	57	0.13	58
Cp ₂ MoH(C ₆ H ₆)			−0.06	59
Cp ₂ Mo(CH ₃) ₂	6.1	57		
Et ₃ SnH	9.06	60		
<i>n</i> -Bu ₃ SnH	8.72	61		
<i>n</i> -Bu ₃ GeH	9.62	61		
Re(CO) ₅ H	8.89	62		
Co(CO) ₄ H	8.90	63		

Table 5. Oxidation (peak) potentials (E_{ox}) of alkylmetallates.

Alkyl metallate	E_{ox} (V relative to the SCE)	Ref.
BMe ₄ [−]	0.58	65
BMePh ₃ [−]	0.96	65
BPh ₄ [−]	0.99	65
	0.76 ^a	67
BTol ₄ [−]	0.55 ^a	67
AuMe ₂ [−]	0.10	64
AuMe ₄ [−]	0.42	64

^a E°_{ox} values calculated from electron-transfer rate constants [67].

Similarly, the mild reducing power of metal carbonyls can be effectively enhanced by conversion of the neutral complex to the corresponding carbonylmetallate. For example, hexacarbonylvandate and pentacarbonylmanganate exhibit oxidation potentials about 1 V lower than those of the isoelectronic hexacarbonylchromium and pentacarbonyliron complexes, respectively (see Table 6). Similar trends apply to neutral and negatively charged half-sandwich complexes such as the isoelectronic CpCr(CO)₃[−] and CpMn(CO)₃ in Table 6.

The increase in the donor strength of negatively charged organometallic complexes as compared to their isoelectronic neutral counterparts is readily explained by also considering the different Coulombic work terms (ω) involved in the one-electron oxidation processes. The removal of an electron from an anion generates a neutral oxidation product which does not attract the leaving electron ($\omega = 0$), whereas electron detachment from a neutral donor requires additional energy to overcome the strong Coulombic (attractive) forces ($\omega = e^2/r$) in the resulting electron–cation pair. The opposite effect on the donicity is observed when positive charges are introduced. Thus, neutral organometallic donors lose their reducing power when oxidized to the cationic state, and therefore cationic organometallic complexes are rarely used as electron donors in electron-transfer reactions [73].

Table 6. Comparison of isoelectronic neutral and anionic metal carbonyl complexes.

Neutral complex	E_{ox} (V relative to the SCE)	Ref.	Isoelectronic metallate	E_{ox} (V relative to the SCE)	Ref.
$\text{Cr}(\text{CO})_6$	1.09	53	$\text{V}(\text{CO})_6^-$	0.23	68
$\text{Fe}(\text{CO})_5$	1.5	53	$\text{Mn}(\text{CO})_5^-$	0.08	69
$\text{CpMn}(\text{CO})_3$	0.79	53	$\text{CpCr}(\text{CO})_3^-$	−0.18	70
$\text{CpCo}(\text{CO})_2$	−0.06	71	$\text{CpFe}(\text{CO})_2^-$	−1.18	72

2.2.2 Organometallic Acceptors

Both the low electronegativity of the metallic core and the generally low (formal) oxidation state of the metal center make most organometallic complexes unsuitable as electron *acceptors*. In fact, *neutral* organometallic acceptors are very rare, however the few complexes which all contain metals in high (formal) oxidation states are very powerful oxidants. For example, $[(\text{CF}_3)_4\text{C}_2\text{S}_2]_2\text{Ni}(\text{IV})$ and Cp^*VCl_3 have reduction potentials of $E^\circ_{\text{red}} = 1.0 \text{ V}$ [74] and 0.6 V [75], respectively, relative to the SCE. Thallium(III) trifluoroacetate and mercury(II) trifluoroacetate readily oxidize arenes (see Section 2.4.2), and we wish to mention several other high-valent metal complexes, e.g. OsO_4 , SnCl_4 , TiCl_4 , which do not classify as organometallic acceptors, but act as acceptors in various electron-transfer reactions with organic donors and thus form organometallic donor–acceptor complexes (see Section 2.3) and covalently bound intermediates (see Section 2.4).

Most organometallic acceptors are positively charged complexes which show highly increased reduction potentials as compared to the isoelectronic neutral complexes. Several examples of such cationic organometallic acceptors (obtained by ‘umpolung’) and their isoelectronic neutral counterparts which act as donors are summarized in Table 7.

2.3 Electron Donor–Acceptor Interactions

The formation of charge-transfer complexes between organic electron donors and acceptors has been studied in great detail [85–87]. Similarly, the organometallic donors and acceptors introduced in Section 2.2 form electron donor–acceptor (EDA) complexes among themselves or when mixed together with an appropriate (organic or inorganic) donor or acceptor [88–90]. This association of electron donor and acceptor is critical for facilitating electron transfer between the two redox partners since it affects both the thermodynamics as well as the kinetics of the electron transfer. In fact, the formation of the EDA complex in Eq. 4, i.e.:



Table 7. Redox potentials of cationic electron acceptors and their isoelectronic neutral counterparts.

Cationic complex ^a	E°_{red} (V relative to the SCE)	Ref.	Isoelectronic neutral complex	E° (V relative to the SCE)	Ref.
Cp_2Co^+	-0.90	79	Cp_2Fe	$E^\circ_{\text{ox}} = 0.41$	48
$(\eta^6\text{-MES})_2\text{Fe}^{2+}$	-0.08	81	$(\eta^6\text{-C}_6\text{H}_6)_2\text{Cr}$	$E^\circ_{\text{red}} = -2.8$	80
$(\eta^6\text{-DUR})_2\text{Fe}^{2+}$	-0.17	81		$E^\circ_{\text{ox}} = -0.8$	49
$(\eta^6\text{-HMB})_2\text{Fe}^{2+}$	-0.27	81			
$\text{CpFe}(\text{C}_6\text{H}_6)^+$	-1.4	82	$\text{CpMn}(\text{C}_6\text{H}_6)$	$E^\circ_{\text{ox}} = 0.79$	53
				$E^\circ_{\text{red}} < -2.4$	53
$(\text{CpCF}_3)_2\text{Fe}^+$	+1.05	76			
Cp_2Fe^+	+0.41	48			
Cp^*Fe^+	-0.18	6			
$(\text{phen})_3\text{Fe}^{3+}$	+0.98	77			
$(\text{phen})_3\text{Ru}^{3+}$	+1.28	78			
$\text{CpCo}(\text{C}_6\text{H}_6)^{2+}$	+0.4	83			
$\eta^5\text{-cyclohexadienyl Fe}(\text{CO})_3^+$	-0.31	84			

^a MES = mesitylene, DUR = durene, HMB = hexamethylbenzene.

effects a predisposition of the donor–acceptor couple toward electron transfer which can be quantified by the degree of charge transfer [91] or the orbital overlap [10] in the complex (see Section 2.3.2). In the following sections, we will first discuss the formation of organometallic EDA complexes and its energetics, and then present spectroscopic and structural evidence for charge-transfer interactions involving organometallic donors or acceptors.

2.3.1 Formation of Organometallic EDA Complexes

Organometallic EDA complexes can be roughly divided into two types based on the nature of the forces that stabilize the donor–acceptor association. In *molecular (outer-sphere or second-sphere)* [88–90] complexes with neutral organometallic donors and/or acceptors, the complex formation is caused by weak Coulombic interactions such as dipole–dipole [94], induced dipole [95], or dispersion forces [96] between readily polarizable substrates. In addition, hydrogen bonding may also play a stabilizing role [97]. Since the charge-transfer interactions occur between the ligated metal center and a donor (or acceptor) that is *not* a ligand in the first (or inner) coordination sphere of the metal, such weak complexes are commonly referred to as outer-sphere or second-sphere complexes [88–90]. The weak stabilization of these complexes is reflected in the rather low formation constants (K_{EDA} in Eq. 4) which typically cover a range between 0.1 and 10 M^{-1} . Such low formation constants translate into free formation enthalpies of $-2 \text{ kcal mol}^{-1} < \Delta G^\circ_{\text{f}} < +2 \text{ kcal mol}^{-1}$. Extreme cases of such weak interactions are complexes with formation

constants of K_{EDA} approaching 0.01 M^{-1} . If diffusion-limited rates are assumed for the association of donor and acceptor, the low equilibrium constants of about 0.01 indicate lifetimes of about 0.5 ps for the EDA complex, which is in the time domain of molecular collisions. Thus, such weak complexes are also referred to as collision complexes [98] or contact charge-transfer complexes [99, 100].

Various examples for molecular complexes including organometallic donors or acceptors are listed in Tables 8 and 9, respectively, together with their formation constants (which are usually determined by spectrophotometric methods [101]). EDA complexes between organometallic donors and tetracyanoethylene (TCNE) may exhibit formation constants $K_{\text{EDA}} \gg 10$ (see entry 8 in Table 8) [110]. In these cases, the strong acceptor TCNE effects a high degree of charge transfer in the ground state, and thus EDA complexes containing TCNE are stabilized not only by the above mentioned dipole and dispersion forces, but also by charge resonance, i.e. $[\text{D}, \text{A}] \leftrightarrow [\text{D}^+, \text{A}^-]$ [102]. Such charge resonance in the ground state is frequently evidenced by (i) unusual bond lengths in the X-ray structure of the (crystalline) EDA complex as compared to the structures of the single (uncomplexed) donor or

Table 8. Molecular EDA complexes with organometallic donors.

Organometallic donor	Acceptor ^a	$K_{\text{EDA}} (\text{M}^{-1})$	Ref.
$\text{Co}(\text{acac})_2(\text{py})_2$	CHCl_3	3.7	88
$\text{Co}(\text{acac})_2(\text{py})_2$	CH_2Cl_2	3.0	106
$\text{Fe}(\text{acac})_3$	CH_3CN	0.6	107
Cp_2Fe	CCl_4	1.5	108
Cp_2Fe	CH_2I_2	0.1	109
Cp_2MoH_2	MA	5.6	58
$(\text{C}_6\text{H}_6)\text{Cr}(\text{CO})_3$	TNB	0.42	110
$(\text{C}_6\text{H}_6)\text{Cr}(\text{CO})_3$	TCNE	1070	110
Et_4Sn	I_2	3.6	111
Et_4Pb	I_2	3.1	111
$n\text{-Pr}_2\text{Hg}$	I_2	1.5	111

^aMA = maleic anhydride; TNB = trinitrobenzene; TCNE = tetracyanoethylene.

Table 9. Molecular EDA complexes with organometallic acceptors.

Organometallic acceptor	Donor	$K_{\text{EDA}} (\text{M}^{-1})$	Ref.
$\text{Ni}[\text{S}_2\text{C}_2(\text{CF}_3)_4]_2$	Perylene	^b	112
$\text{Hg}(\text{O}_2\text{CCF}_3)_2$	Mesitylene	5.1	113
OsO_4^{a}	Durene	0.47	114
SnCl_4^{a}	Mesitylene	0.4	115
SnCl_4^{a}	1-Methoxynaphthalene	1.3	115
TiCl_4^{a}	Naphthalene	0.34	116

^aHigh-valent metals that form organometallic EDA complexes.

^bUnknown.

Table 10. Dissociation constants of charge-transfer ion pairs in different solvents.

Donor anion	Acceptor cation	Solvent	K_{diss} (m)	Ref.
$\text{Co}(\text{CO})_4^-$	Cp_2Co^+	MeCN	0.011	118
		CH_2Cl_2	0.00015	118
$\text{Co}(\text{CO})_4^-$	$\text{Q}^{+\text{a}}$	MeCN	0.081	118
		THF	0.00012	118
		CH_2Cl_2	0.000015	118
		THF	0.000094	119
$\text{Co}(\text{CO})_4^-$	$\text{PPN}^{+\text{b}}$	THF	0.00012	119
$\text{V}(\text{CO})_6^-$	PPN^+	THF	0.00012	119
BPh_4^-	PPN^+	THF	0.000091	119
$\text{C}(\text{CN})_3^-$	$(\text{HMB})_2\text{Fe}^{2+\text{c}}$	CH_3CN	0.01^{d}	120

^a *N*-methyl-1-quinolinium.^b *Bis*-(triphenylphosphoranylidene)ammonium.^c HMB = hexamethylbenzene.^d Equilibrium constant ($K_{\text{EDA},2}$) for *association* of the second $\text{C}(\text{CN})_3^-$ ion to form the 2:1 complex, i.e. $\{(\text{HMB})_2\text{Fe}^{2+}, 2\text{C}(\text{CN})_3^-\}$. See [120].

acceptor components (see Section 2.3.3), (ii) unusual electrical and magnetic properties, and (iii) substantial changes in the UV–Vis and IR spectra (see Section 2.3.2).

The second type of EDA complexes involving organometallic donors or acceptors includes pairs of opposite charged ions in close contact, which are referred to as *contact ion pairs* (CIP) [103, 104] or *charge-transfer ion pairs* (CTIP) [105]. Since negative charges improve the donicity and positive charges enhance the acceptor strength, CT ion pairs usually consist of an anionic donor and a cationic acceptor, which are held together by strong Coulombic forces. Since Coulombic attraction between ions in solution strongly depends on the solvent polarity [104], the formation constants K_{EDA} (see Eq. 4) for charge-transfer ion pairs may vary over orders of magnitude in solvents as different as water ($K_{\text{EDA}} \approx 1\text{--}100 \text{ M}^{-1}$) and dichloromethane ($K_{\text{EDA}} > 10^5 \text{ M}^{-1}$). The selected examples in Table 10 illustrate this dramatic solvent dependence for the equilibrium constant (K_{diss}) of the reverse process, viz., dissociation of the contact (charge-transfer) ion pairs into free (solvated) ions [117] (Eq. 5):



2.3.2 UV–Vis Spectroscopic Evidence for Charge-transfer Interactions in Organometallic EDA Complexes

The Mulliken correlation

The most characteristic spectroscopic features of electron donor–acceptor complexes are the new absorption bands in the electronic (UV–Vis) spectra, which are

not found in the spectra of the single (donor or acceptor) components. Such absorption bands are universally observed with organic [85–87], inorganic [121], and organometallic substrates [122], for both molecular complexes [85] and contact ion pairs [103, 104], and even in the case of short-lived collision complexes with $K_{\text{EDA}} \ll 1$ (vide supra) [98]. Mulliken theory [14–16] provides the theoretical basis for the assignment of these new electronic transitions via the description of the wave function Ψ_{EDA} of the EDA complex as the sum of a no-bond (D, A) and a dative (D^+ , A^-) wave function (in first approximation), (Eq. 6):

$$\Psi_{\text{EDA}} = \mathbf{a} \psi_0(\text{D}, \text{A}) + \mathbf{b} \psi_1(\text{D}^+, \text{A}^-) + \cdots \quad (6)$$

For weakly interacting electron donors and acceptors, the wave function Ψ_{EDA} for the *ground state* basically describes a no-bond situation between donor and acceptor (D, A) in which the charge-transfer state (D^+ , A^-) does not play a significant role, i.e. $\mathbf{a} \gg \mathbf{b}$. In contrast, the ratio of the mixing coefficients \mathbf{a} and \mathbf{b} for no-bond and dative wave function is inverted in the *excited state*, i.e. the charge-transfer state (D^+ , A^-) is now predominant. The new absorption bands in the UV–Vis spectra of the EDA complexes are assigned to the electronic transition from the ground state (no-bond) to the excited (charge-transfer) state, and they are thus referred to as charge-transfer (CT) transitions. In other words, the population of the excited state of the EDA complex by photoexcitation of its CT absorption band is tantamount to a photoinduced electron transfer from a donor (HOMO) orbital to an acceptor (LUMO) orbital which yields the ion-pair state, (Eq. 7):



According to Mulliken theory [14–16], the energy gap (E_{CT}) of the charge-transfer transition from the ground state to the excited ion-pair state determines the wavelength position of the CT absorption band (λ_{CT}), i.e. $E_{\text{CT}} = h\nu_{\text{CT}} = hc/\lambda_{\text{CT}}$. This energy gap directly depends on the ionization potential (*IP*) of the donor and the electron affinity (*EA*) of the acceptor, (Eq. 8):

$$E_{\text{CT}} = h\nu_{\text{CT}} = IP - EA + \omega + \text{const.} \quad (8)$$

where ω represents the Coulombic work term for the association of D^+ and A^- to form an ion pair, and the constant term includes orbital-coupling energies which are negligible in weak EDA complexes. For a series of EDA complexes of various donors with the same acceptor, the Mulliken correlation in Eq. 8 predicts a unit slope for plots of E_{CT} against the ionization potentials of the donors. This is demonstrated in Figure 1 for the EDA complexes of *bis*(durene)iron(II) acceptor with ferrocene and a series of organic donors [124]. Similarly, the charge-transfer absorption bands of EDA complexes of Ni(IV)dithiolene [112] with various (organic and organometallic) donors follow the Mulliken correlation in Eq. 8. The linearity of the plot of E_{CT} against the ionization potentials of the donors has also been confirmed for a variety of other organometallic EDA complexes including ferrocene–alkyl halide [109], alkylmetal–iodine [111], alkylmetal–TCNE [123], metal hydride–TCNE [123], and (arene)metal tricarbonyl–nitroarene complexes [110].

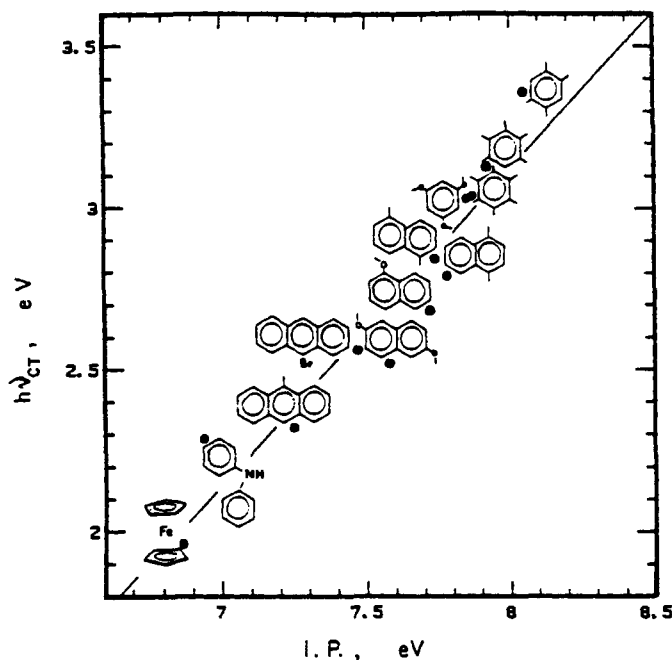


Figure 1. Mulliken correlation of the charge-transfer transition energy ($E_{CT} = h\nu_{CT}$) with the ionization potential (IP) of ferrocene and arene donors in *bis(durene)iron(II)* complexes. The straight line is arbitrarily drawn with a slope of unity [124].

Since ionization potentials of anionic donors and electron affinities of cationic acceptors are not readily available, Mulliken correlations for charge-transfer ion pairs are generally presented in a modified form using electrochemical oxidation or reduction potentials, respectively. A typical example of such a modified Mulliken plot with unit slope is shown in Figure 2 for the CT ion pairs of TpMo(CO)_3^- [$\text{Tp} = \text{hydrido-tris-(3,5-dimethylpyrazolyl)borate}$] as the donor and various pyridinium acceptors [127]. Similar (modified) Mulliken correlations with unit slopes have been found for numerous other ion pairs with pyridinium acceptors and Mn(CO)_5^- [126], Co(CO)_4^- [118], or V(CO)_6^- [118] as donors. It is important that the Coulombic work term (ω) in Eq. 8 is explicitly included in all Mulliken evaluations of ion pairs with different structures since ω reflects the electrostatic energy of the (ground-state) ion pair which strongly depends on the inter-ionic distance [125].

Solvatochromism of charge-transfer absorption bands

Molecular EDA complexes as well as charge-transfer ion pairs show (negative) solvatochromism [128], i.e. the charge-transfer absorption maxima (λ_{CT}) undergo hypsochromic shifts with increasing solvent polarity. The solvatochromic effect is readily explained on the basis of the Marcus correlation for charge-transfer energies in solution [129], (Eq. 9):

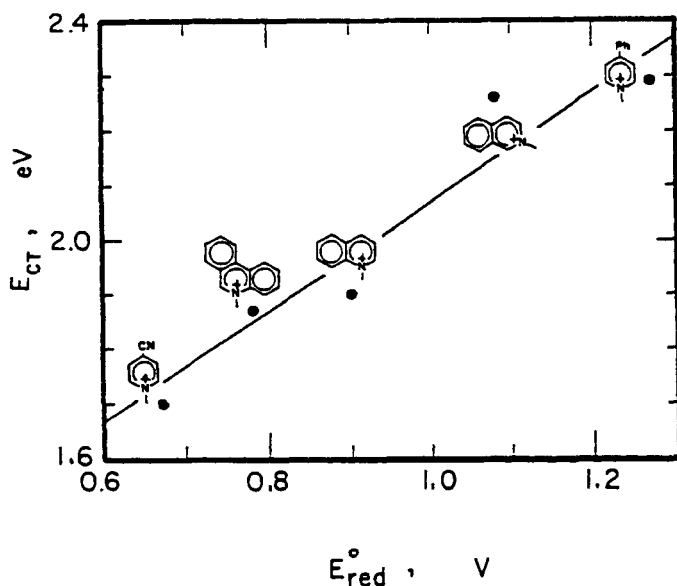
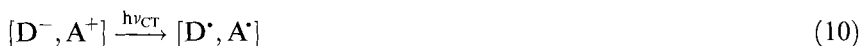


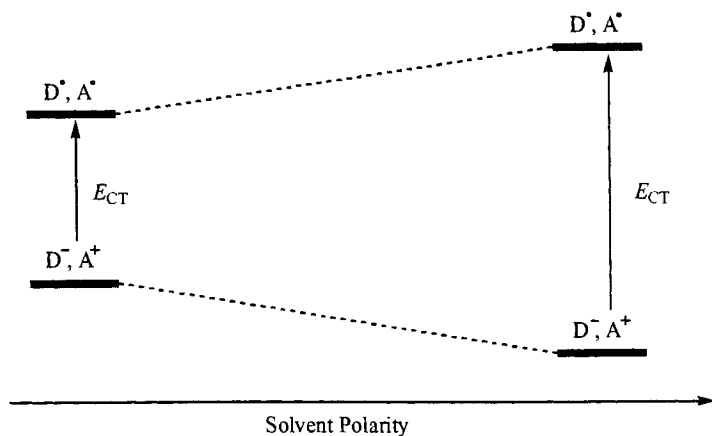
Figure 2. Variation of the charge-transfer transition energy (E_{CT}) with the reduction potential (E°_{red}) of pyridinium acceptors in CT ion pairs with $TpMo(CO)_3^-$ as the donor [127].

$$E_{CT} = \lambda_p + \lambda_i + \lambda_o + \Delta G_0 \quad (9)$$

with λ_p being the energy of first-shell solvation of the ion-pair state, λ_i the vibrational reorganization energy of the ion pair, λ_o the solvent reorganization energy excluding first-shell solvent molecules, and ΔG° the free energy gap for the transition from the ground state to the ion-pair state in Eq. 7. Since λ_p and λ_o increase with increasing polarity of the solvent [129], E_{CT} also increases with the solvent polarity which causes moderate, but sizable blue-shifts of the CT absorption bands of molecular EDA complexes [130].

In CT ion pairs the solvent-dependent color changes are much more pronounced as compared to molecular EDA complexes and hypsochromic shifts of more than 100 nm are frequently observed on going from a nonpolar solvent such as diethyl ether to the polar solvent acetonitrile. For example, the color of *N*-methylquinolinium tetracarbonylcobaltate [118] changes from green to purple to orange in diethyl ether, tetrahydrofuran, and acetonitrile, respectively. Such a strong (negative) solvatochromism is comparable with that of betaine dyes which are used as indicators to quantify solvent polarity [128]. In fact, the zwitterionic ground state of the betaine dye—like the contact ion pair—is more stabilized in polar solvents, and the biradical excited state of the dye—like the radical pair generated by CT excitation of the contact ion pair, (Eq. 10):

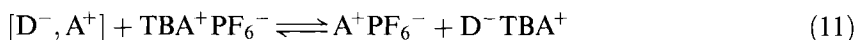




Scheme 2.

is more destabilized in polar environment. Thus the energy gap between charged ground state and biradical excited state increases with increasing solvent polarity as illustrated in Scheme 2 [131].

Since contact ion pairs can be separated by the deliberate addition of an inert salt (such as tetra-*n*-butylammonium perchlorate or hexafluorophosphate) [132], (Eq. 11):



the charge-transfer absorption bands of contact ion pairs are very sensitive to the presence of added salt. In other words, CT ion pairs are readily identified by the bleaching of their color due to added 'inert' salt [118].

2.3.3 Structural Changes due to Charge Transfer and/or Ion Pairing in Organometallic EDA Complexes

A number of the above described molecular complexes and CT ion-pair salts have been isolated in crystalline form for X-ray crystallographic studies. In general, the observation of significant changes in the structures of such charge-transfer crystals (as compared to the crystal structures of the separate components) will depend on the degree of charge transfer [91] between donor and acceptor in the ground state.

Weak molecular complexes

Weak (molecular) complexes in solution do not show any IR or NMR spectroscopic evidence for charge-transfer, i.e. the spectra of the complexes represent merely the superposition of the spectra of the separate (uncomplexed) donor and acceptor components [133]. Accordingly, X-ray crystal structures show the donors and acceptors with unperturbed bond lengths and angles [134, 135]. However, a

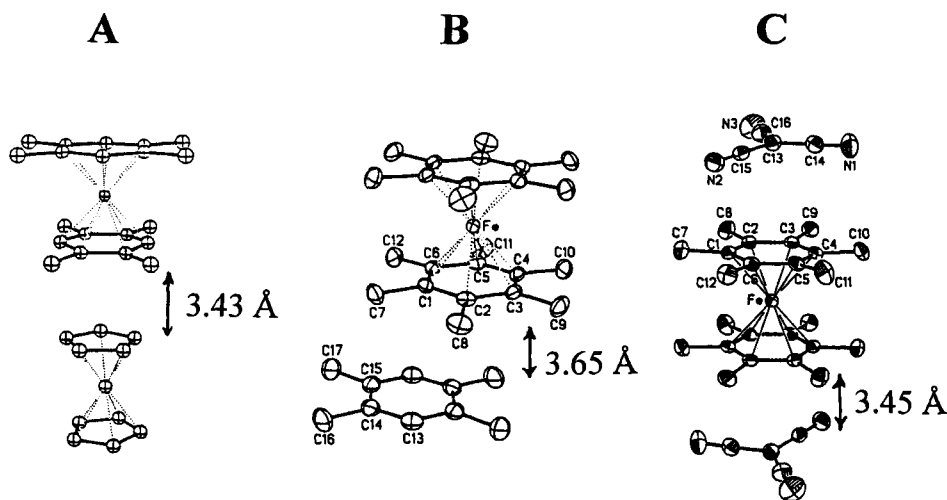


Figure 3. ORTEP diagrams of donor–acceptor pairs in charge-transfer crystals of (A) ferrocene and *bis*(durene)iron(II) [124], (B) durene and *bis*(hexamethylbenzene) iron(II) [124], and (C) tricyanomethide and *bis*(hexamethylbenzene)iron(II) [120].

characteristic crystal packing is generally observed which allows close (van der Waals) contact between the donor and acceptor molecules. For example, the distance between the Cp ring of ferrocene and the durene ring of *bis*-(durene)iron(II) in the 1:1 charge-transfer crystal (see Figure 3A) amounts to 3.43 Å [124], which is comparable to the interplanar distance of 3.65 Å between the hexamethylbenzene ring of *bis*-(hexamethylbenzene)iron(II) and durene in the CT crystal structure in Figure 3B [124]. Both distances lie within the range of donor–acceptor distances found in crystalline organic (π, π) EDA complexes [134, 135]. Similarly, tricyanomethide donor and the hexamethylbenzene ring of *bis*-(hexamethylbenzene)iron(II) in the $[(\text{HMB})_2\text{Fe}^{2+}, 2\text{C}(\text{CN})_3^-]$ CT crystal are separated by about 3.45 Å (see Figure 3C) [120]. The intermolecular distance of about 3.5 Å is very critical for charge-transfer interactions to occur between the π -orbitals of cofacially stacked donors and acceptors. A recent study shows that a mere increase by 1 Å in the closest interplanar distance between π -donors and acceptors (due to steric encumbrance) results in the charge-transfer interactions to be completely suppressed [136].

In contrast, the charge-transfer interactions in the charge-transfer salt of cationic ferrocenyl donor ($\text{CpFeCpCH}_2\text{NMe}_3^+$) with polyoxomolybdate ($\text{Mo}_6\text{O}_{19}^{2-}$) [137], as revealed by diffuse-reflectance UV–Vis spectroscopy, are not readily ‘localized’ in the crystal structure. Thus, the closest donor–acceptor contacts are located between three hydrogen atoms of the cyclopentadienyl ligands and (mostly bridged) oxygen atoms of the molybdate ion ($d = 2.66\text{--}2.76$ Å), whereas the closest distance between the iron redox center and the molybdate ion is about 4.2 Å (see Figure 4) [137]. Although the oxygen–hydrogen distances correspond to tight (van der Waals) contacts, the question remains open as to which orbitals are involved in the charge-transfer interactions.

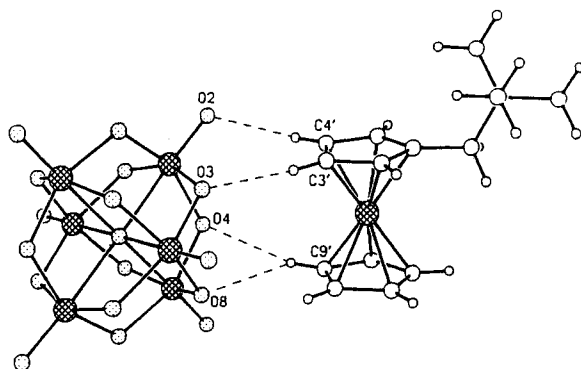


Figure 4. ORTEP diagram of the CT salt of ferrocenyl donor ($\text{FeCpCH}_2\text{N}^+\text{Me}_3$) with polyoxomolybdate ($\text{Mo}_6\text{O}_{19}^{2-}$) showing the closest donor–acceptor contacts [137].

Charge-transfer ion pairs

In CT ion pairs, a wide variety of donor–acceptor interactions is observed—from weak interactions with little structural evidence for charge transfer, as observed in methylviologen dithiolene metallate salts [138, 139], to strong interactions in pyridinium carbonyl metallate salts which are readily recognized by the significant changes in the IR spectra and X-ray structures. In fact, carbonyl metallates themselves show varying degrees of charge-transfer depending on the acceptor strength of the cationic moiety in the ion-pair salt. For example, the infrared spectrum of the ion-pair salt of the weak tetraphenylphosphonium acceptor with tetracarbonylcobaltate does not show any distortion of the tetrahedral symmetry of the cobaltate anion [140]. However, contact ion pairs derived from strong acceptors such as cobaltocenium or pyridinium with tetracarbonylcobaltate exhibit a strong distortion of the tetrahedral structure of the cobaltate anion as revealed by IR spectroscopy in solution and X-ray crystallography in the crystalline state [118]. Generally, the smaller and stronger the acceptor is, the greater are the structural changes induced by the formation of intimate ion pairs. For example, the X-ray structures in Figure 5A and 5B show the close approach of the carbonyl ligands perpendicular to the aromatic plane of the pyridinium acceptor, which allows optimal orbital overlap. In fact, the cationic acceptor clearly penetrates into the carbonyl ligand shell and causes a significant distortion of the symmetry of the metallate complex. A similar penetration of the pyridinium acceptor into the ligand shell of the metallate is observed in the crystal structure of cyanopyridinium tetraphenylborate (see Figure 5C) [65]. Such *inner-sphere* charge-transfer ion pairs are clearly to be distinguished from the *outer-sphere* complexes [88–90] frequently observed between weakly coupling uncharged donors and acceptors (vide supra). Similarly, the CT ion-pair salt of *N*-methyl-4-cyanopyridinium with $\text{TpMo}(\text{CO})_3^-$ shows significant distortion of the octahedral symmetry of the molybdate ion due to contact ion pairing (see Figure 5D) [127]. It is worth mentioning that the effects of contact ion pairing strongly depend on the solvent environment as illustrated with thallium(I) tetracarbonylco-

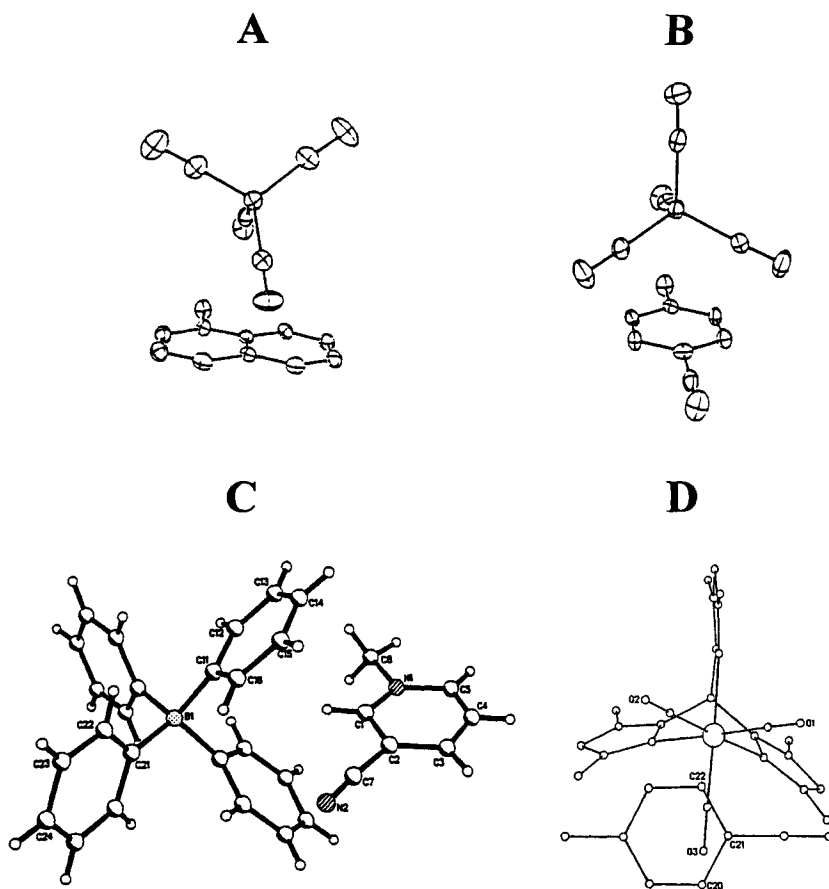


Figure 5. Intimate donor–acceptor orientation in the *inner-sphere* CT salts of (A) quinolinium with tetracarbonylcobaltate [118], (B) *N*-methyl-4-cyanopyridinium with tetracarbonylcobaltate [118], (C) *N*-methyl-3-cyanopyridinium with tetraphenylborate [65], and (D) *N*-methyl-4-cyanopyridinium with TpMo(CO)₃⁻ [127].

baltate [141], for which a solvatotropic collapse of the CT ion pair (in dichloromethane) to a covalently-linked thallium–cobalt compound (in benzene) is observed.

Strong charge-transfer interactions

In coordinately saturated donor–acceptor complexes, the formation of new bonds as described with the thallium(I) tetracarbonylcobaltate (*vide supra*) is not readily accomplished. However, strong charge-transfer interactions between donor and acceptor moiety may lead to partial or complete electron transfer, which can be revealed by (UV–Vis or IR) spectroscopic and X-ray crystallographic techniques. For example, CT crystals of nitrosonium (NO⁺) with aromatic donors show various degrees of charge transfer as detected by gradual shifts in the N–O stretch (IR)

frequencies of the nitrosyl moiety approaching those of the NO radical, as well as by several X-ray crystallographic studies which clearly demonstrate the distortions of the aromatic ring of the donor that approach bond lengths and angles of the corresponding arene cation radical [142–145]. Tetracyanoethylene (TCNE) with a reduction potential of $E^\circ_{\text{red}} = +0.24$ V relative to the SCE [146] represents a similarly strong and compact electron acceptor capable of fully oxidizing various electron donors to the cation-radical state. As a result, ion-pair salts of the type $[\text{D}^{+\cdot}, \text{TCNE}^{\cdot-}]$ have been isolated in crystalline form, and the crystal structures clearly confirm complete electron transfer. For example, the X-ray structure of CT crystals prepared from Cp^*Fe and tetracyanoethylene reveals one-dimensional stacks of $\text{Cp}^*\text{Fe}^{+\cdot}$ and $\text{TCNE}^{\cdot-}$ units in cofacial orientation [147]. Interestingly, the corresponding CT crystals of TCNE with the weaker donor ferrocene (Cp_2Fe) crystallize as molecular complexes in indefinite stacks of uncharged ferrocene and TCNE [148, 149], owing to the endergonic ($\Delta G_{\text{ET}} = +0.17$ eV) energetics of the electron transfer from ferrocene ($E^\circ_{\text{ox}} = 0.41$ V relative to the SCE) [48] to TCNE ($E^\circ_{\text{red}} = 0.24$ V relative to the SCE) [146, 150]. The ion-pair character of the crystalline Cp^*Fe –TCNE complex is quite similar to that in the CT crystals of Cp^*Fe with 7,7,8,8-tetracyano-*p*-quinodimethane (TCNQ) as acceptor [151]. Both ion-pair salts show ferromagnetic properties (as revealed by Mössbauer spectroscopy), which is due to strong orbital overlap and spin coupling in the intimate ion-pairs [147, 151]. It is noteworthy that strong orbital interactions similar to those observed between oxidized organometallic donors and $\text{TCNE}^{\cdot-}$ anion radical (generated in a *thermal* electron-transfer reaction) are also found in *photogenerated* ion–radical pairs observed upon CT excitation of EDA complexes of TCNE with olefinic donors [152]. The intimate (‘inner-sphere’) character of the latter ion–radical pairs is manifested in the ultrafast rates ($k \cong 5 \times 10^{11} \text{ s}^{-1}$) of back electron transfer (to restore the original molecular EDA complex) and their lack of driving-force dependence [152].

2.4 Electron-transfer Intermediates in Organometallic Reactions

In the previous section, we have shown that—owing to their unique donor or acceptor properties—organometallic compounds readily form electron donor–acceptor complexes in the presence of a suitable counterpart. Depending on the nature of the complex (*viz.*, molecular complex or ion-pair salt) and the extent of charge transfer, the structures of these donor–acceptor assemblies reveal various degrees of predisposition to electron transfer between the two redox centers. Whether or not electron transfer occurs spontaneously in the EDA complex will depend on the free energy and the activation energy of the redox process. Favorable energetics will result in rapid thermal electron transfer which generally initiates a series of subsequent reactions. In this case, EDA complex formation and the generation of (usually short-lived) electron-transfer intermediates often evades its observation, and the electron-transfer mechanism in Scheme 1(A) can merely be inferred to on the basis of the donor–acceptor properties of the reactants and the

nature of the final products. Time-resolved spectroscopy [153, 154] applying ultra-short laser pulses makes it possible to generate and observe electron-transfer intermediates on an ultrafast (fs, ps) time scale in accord with Mulliken's charge-transfer formulation [14–16] in Eqs 6 and 7. However, to observe EDA complex formation and photoactivated electron transfers, the thermal electron transfer must be brought to a standstill or at least, its rate needs to be substantially diminished, which can be achieved by lowering of the temperature. The electron transfer in the thermally stable EDA complex can then be *photoactivated* by deliberate irradiation of the charge-transfer absorption band (as described in Scheme 1(B)). The steady-state charge-transfer irradiation will lead to photoproducts which are unambiguously the result of an initial photoinduced electron transfer from the donor to the acceptor moiety in the EDA complex as monitored by time-resolved (laser) spectroscopy.

Depending on the starting materials, different electron-transfer intermediates may be observed. Thus, CT excitation of a molecular complex leads to the generation of an ion–radical pair, (Eq. 12):



whereas CT excitation of an ion-pair salt generates a geminate radical pair, (Eq. 13):



There are also several mixed (charged–neutral) organometallic EDA complexes known, the CT excitation of which results in the formation of ion-radical–radical pairs, (Eq. 14):



Electron transfer induced by charge-transfer irradiation (Eqs 12–14) might or might not lead to permanent chemical transformations that yield isolable photoproducts. The fate of the initial electron-transfer intermediate (viz., ion–radical pair or radical pair) is mainly determined by the competition of two pathways, i.e. back electron transfer or the follow-up reaction (see Scheme 1). If the former pathway predominates and the follow-up reaction cannot efficiently compete, the ion-radical or radical pair returns back to the original EDA complex and no net reaction is observed. On the other hand, if the rate of the follow-up reaction is in the same range as that of the back electron transfer, new intermediates and ultimately photoproducts will be formed that do not convert back to the starting materials, and thus an electron-transfer activated reaction is obtained.

2.4.1 Charge-Transfer Excitation of Organometallic EDA Complexes Followed by Efficient Back Electron Transfer

There are many examples of organometallic EDA complexes that are thermally stable and do not show permanent chemical transformations even after prolonged

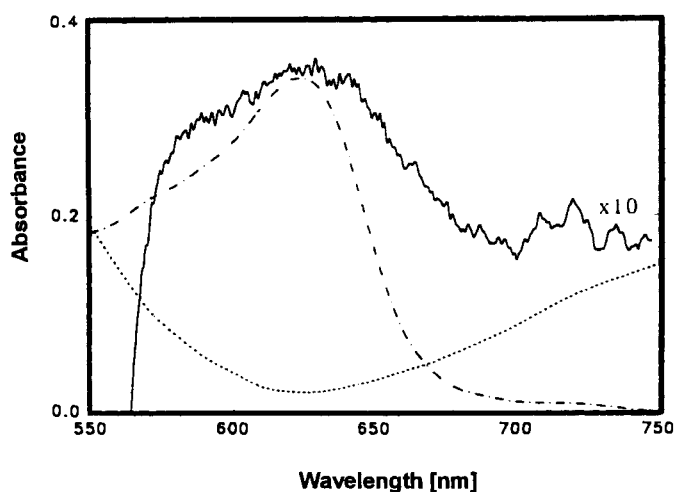
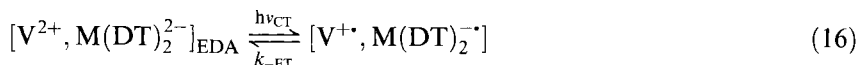


Figure 6. Transient (diffuse-reflectance) absorption spectrum (—) obtained at 25 ps following the 532-nm laser excitation of charge-transfer crystals of $[\text{CpFeCpCH}_2\text{N}^+\text{Me}_3]_2 \text{Mo}_6\text{O}_{19}$ dispersed in neutral alumina (10 %). The spectrum is deconvoluted as the (1:1) sum of reduced hexamolybdate acceptor ($\text{Mo}_6\text{O}_{19}^{3-}$, ----) and oxidized ferrocenyl donor $\text{CpFe}^+\text{CpCH}_2\text{N}^+\text{Me}_3$, - · - · -) [137].

charge-transfer irradiation. In these cases, CT excitation generates an ion-radical or radical pair which solely decays by back electron transfer to restore the original EDA complex, (Eq. 15):



Typical examples are the CT ion pairs of bipyridinium di-cations (viologens, V^{2+}) with metal ($\text{M} = \text{Zn}, \text{Cd}, \text{Hg}$) dithiolene (DT) anions [155], which form reduced viologen ($\text{V}^{+\bullet}$) and oxidized metal dithiolene complex upon CT excitation in dimethylsulfoxide, (Eq. 16):



The ion-radical pair subsequently decays as a result of back electron transfer ($k_{-\text{ET}}$, Eq. 16), which restores the original CT ion pair. In polar solvents such as dimethyl sulfoxide, dissociation of the ion-radical pair into free, solvated ion radicals can somewhat compete with the rapid back electron transfer ($k_{-\text{ET}} \approx 10^{10} \text{ s}^{-1}$). Thus, ion radicals are observed in small yields ($\Phi_{\text{ion}} \approx 0.05$) on the μs time scale upon 10-ns laser excitation [155]. They ultimately decay by (diffusional) back electron transfer.

Complete back electron transfer upon charge-transfer excitation has also been observed in crystalline EDA complexes. For example, laser excitation of the charge-transfer crystals of ferrocenyl donor and polyoxomolybdate acceptor results in short-lived (ps) transients the diffuse-reflectance absorption spectrum of which is shown in Figure 6 [137]. This transient spectrum can be deconvoluted as the sum of the absorption spectra of the oxidized ferrocenyl donor (ferrocenium) and the re-

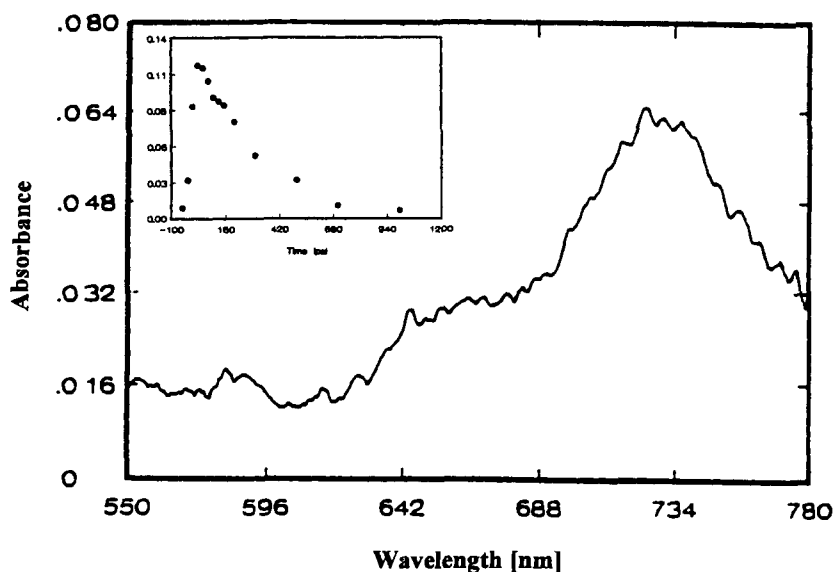
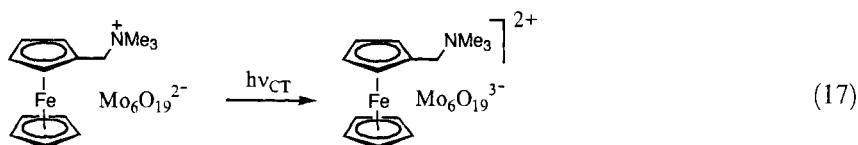


Figure 7. Transient absorption spectrum of 9-bromoanthracene cation radical obtained at 25 ps following the 532-nm CT excitation of the bromoanthracene–TiCl₄ complex in cyclohexane. The inset shows the complete decay of the cation radical within 1 ns due to back electron transfer [116].

duced hexamolybdate acceptor, which confirms the photoinduced electron transfer predicted by Mulliken theory, (Eq. 17):



Most organometallic EDA complexes of arenes with titanium tetrachloride [116] in solution also follow the general reaction scheme in Eq. 15 in that no net chemical reaction is observed upon charge-transfer irradiation due to rapid back electron transfer ($k_{\text{ET}} \approx 10^{10} \text{ s}^{-1}$). For example, the transient absorption spectrum of bromoanthracene (BrAnt) cation radical generated by 532-nm laser excitation of the [BrAnt, TiCl₄] complex in cyclohexane (see Figure 7) decays completely to the spectral baseline within about 1 ns (see inset) due to back electron transfer [116], (Eq. 18):

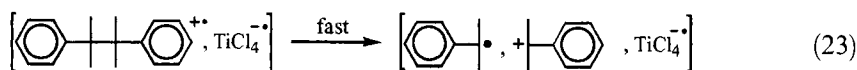
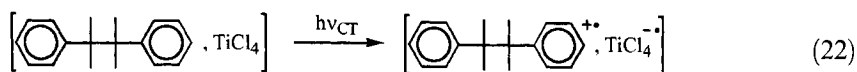
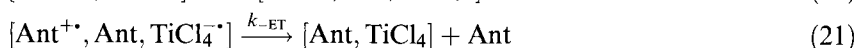


However, if 9,10-anthracene dimer (dianthracene) or bicumene is used as the aromatic donor, the simple reaction scheme in Eq. 15 does not apply any longer, but a follow-up reaction is observed that efficiently competes with back electron transfer. Various examples for this case are described in the following section.

2.4.2 Charge-Transfer Activated Reactions of Organometallic EDA Complexes

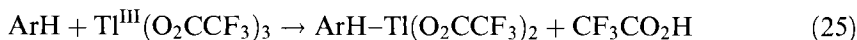
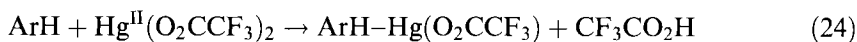
Arene fragmentation via TiCl_4 complexes

A net chemical reaction upon charge-transfer irradiation of [arene, TiCl_4] complexes is obtained if rapid fragmentation of the arene cation radical competes with the back electron transfer in Eq. 18 [116]. Thus, dianthracene (Ant_2) cleaves into two anthracene moieties (Eqs 19–21) and bicumene cation radical fragments into cumyl cation and cumyl radical (Eqs. 22, 23), which ultimately form cumene and 1-phenyl-1,3,3-trimethylindane, respectively, as final products [116].

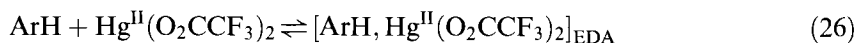


Mercuration and thallation of benzenes

Methyl-substituted benzenes react with mercury(II) and thallium(III) electrophiles in thermal reactions to yield mercuration and thallation products, respectively [113], (Eqs 24, 25):



During these reactions, transient charge-transfer absorption is observed; this is ascribed to the EDA complexes of the arene donors with the metal trifluoroacetate [113], (Eq. 26):



Accordingly, a reaction mechanism has been proposed [113] which includes one-electron transfer from the arene donor to the high-valent metal within the EDA complex as the critical first step toward mercuration or thallation, (Eq. 27):



In fact, the postulated arene cation-radical intermediate ($\text{ArH}^{+\bullet}$) has been observed recently [156] by picosecond time-resolved spectroscopy following the 355-nm laser excitation of the EDA complex of pentamethylbenzene with

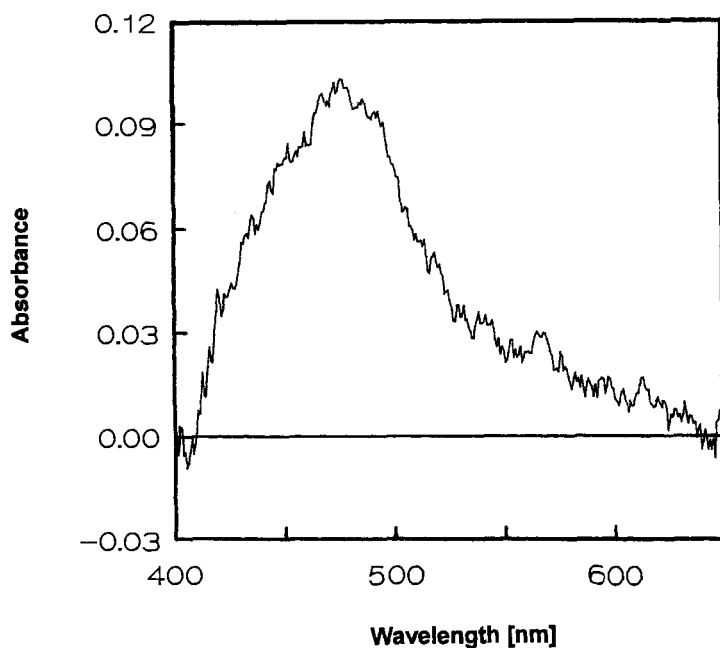
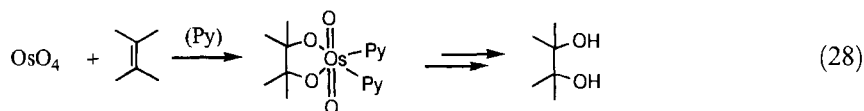


Figure 8. Transient absorption spectrum of pentamethylbenzene cation radical obtained at 25 ps following the 355-nm charge-transfer excitation of the pentamethylbenzene– $\text{Hg}(\text{CF}_3\text{CO}_2)_2$ complex in dichloromethane– CF_3COOH (2 %) mixture at -50°C [156].

$\text{Hg}^{\text{II}}(\text{O}_2\text{CCF}_3)_2$ in dichloromethane (containing 2 % (v/v) trifluoroacetic acid) at low (-50°C) temperature at which the thermal reaction is sufficiently suppressed (see Figure 8).

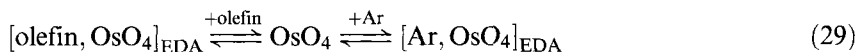
Osmylation with osmium(VIII) tetroxide

Osmium(VIII) tetroxide is an efficient reagent for *cis*-hydroxylations of alkenes [157, 158] via the osmium(VI) cycloadduct [159], which is stabilized by bases such as pyridine (pyr) [157, 160], (Eq. 28):

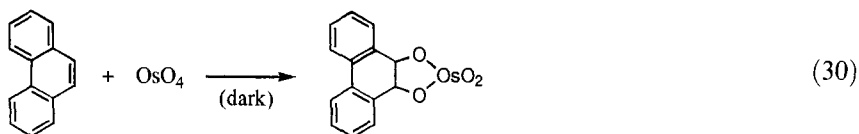


In contrast, aromatic compounds are in general not oxidized by the high-valent osmium oxide despite their lower oxidation potentials as compared to those of olefinic substrates. Thus, the donor strength of the hydrocarbon is apparently not a critical factor for efficient oxidation or oxygen transfer. In fact, olefinic and aromatic donors (Ar) behave very similarly in the formation of organometallic EDA

complexes [114], (Eq. 29):



Molecular complexes of OsO_4 with various substituted benzenes, naphthalenes, and anthracenes have been identified by their charge-transfer absorption, which follows the Mulliken correlation in Eq. 8 [114, 161]. The arene- OsO_4 complexes are quite stable when kept in the dark and only very slowly form osmium(VI) cycloadducts by thermal osmylation (Eq. 30).



On the other hand, charge-transfer irradiation of the same molecular complexes in *n*-hexane solution rapidly yields dark brown solids which—after dissolving in pyridine—have been identified by X-ray crystallography (see Figure 9), IR and NMR spectroscopy as the pyridine-ligated analogs of the osmium(VI) cycloadduct in Eq. 30 [114, 161], (Eq. 31):

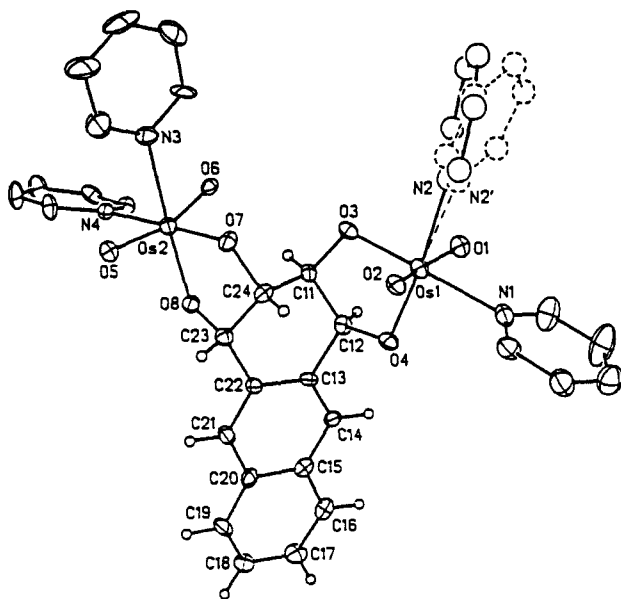
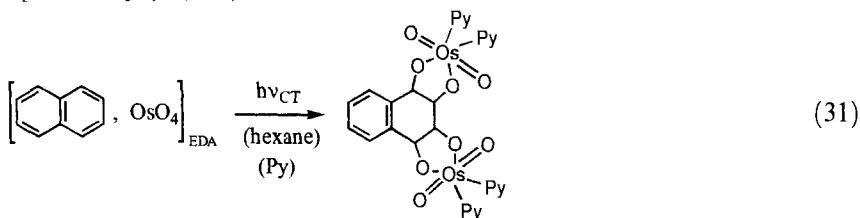
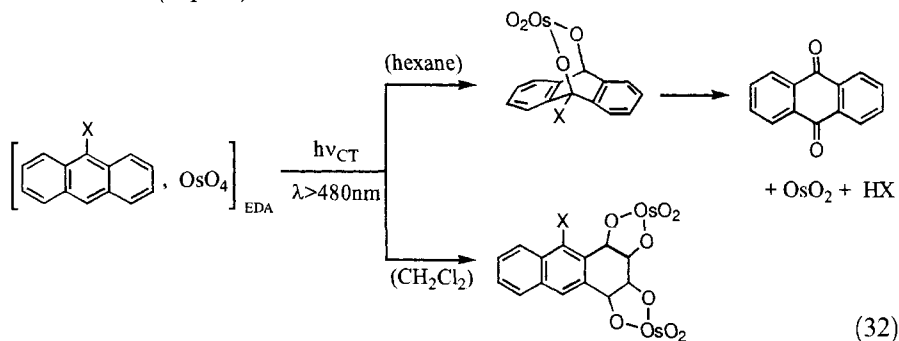


Figure 9. ORTEP diagram of the 2:1 adduct of pyridine-ligated OsO_4 with anthracene [161].

Interestingly, substituted anthracenes show different oxidation products depending on the solvent (Eq. 32):



To identify the reactive intermediates in charge-transfer activated osmylations (Eqs 30–32), the EDA complexes of OsO_4 with various arene donors are photoexcited with the 25-ps laser pulse of a mode-locked Nd:YAG laser [161]. For example, the second harmonic laser output at 532 nm solely excites the charge-transfer absorption of the anthracene– OsO_4 complex and local excitation of (complexed or uncomplexed) anthracene or osmium tetroxide is avoided. The resulting transient absorption spectrum at 20 ps after the laser pulse (see Figure 10) shows a strong, narrow ab-

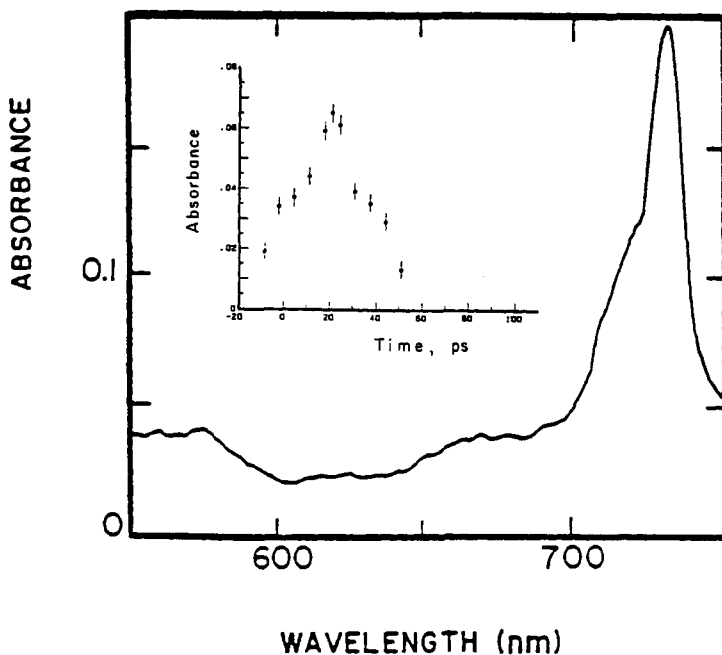
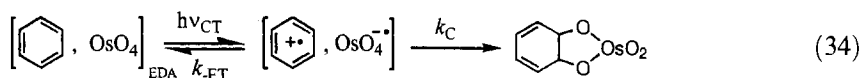


Figure 10. Transient absorption spectrum of anthracene cation radical obtained at 35 ps following the 532-nm CT excitation of the anthracene– OsO_4 complex in dichloromethane. The inset shows the formation and decay of the cation radical within about 30 ps [161].

sorption band centered at 740 nm which has been assigned to the cation radical of anthracene by comparison with the spectrum of the electrochemically generated authentic species. Similar laser photolysis experiments with other arenes (Ar) result in the observation of the corresponding cation radicals ($\text{Ar}^{+\bullet}$) on the picosecond time scale. As such, charge-transfer excitation of the $[\text{Ar}, \text{OsO}_4]$ complexes effects a spontaneous ($\tau < 20$ ps) electron transfer from the arene donor to the OsO_4 acceptor, which results in the formation of an ion–radical pair in accord with Mulliken theory [14–16] (Eq. 33):



(Note that the spectral absorption of the reduced acceptor $\text{OsO}_4^{-\bullet}$ is obscured by the arene absorption.) This ion–radical pair is formed unambiguously as the first reactive intermediate upon charge-transfer excitation, and its collapse ultimately leads to the formation of the osmium(VI) cycloadduct observed upon steady-state CT irradiation (vide supra), as depicted for the simple benzene donor in Eq. 34:



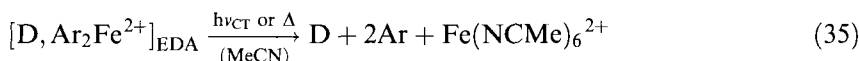
The coupling of the ion pair to form the cycloadduct is a very fast process as judged by the ultrashort lifetimes found for various arene ion radicals ($\tau \approx 20$ ps, see inset in Figure 10). However, the low quantum efficiencies ($\Phi_{\text{C}} < 0.01$) [114, 161] of the cycloadditions indicate that the predominant decay pathway of the ion radical pair in Eq. 34 is not the coupling step (k_{C}), but back electron transfer (k_{ET}) to restore the original EDA complex. Quantitative evaluation of kinetics and quantum efficiencies yields the relatively fast cycloaddition rate constants of $k_{\text{C}} \approx 10^9 \text{ s}^{-1}$ characteristic for highly exergonic bond formation.

The electron-transfer mechanism (Eq. 34) also explains the various regioselectivities observed for different arenes as the direct result of the symmetry of the arene HOMOs involved [161]. Moreover, the solvent effect on the oxidation products (Eq. 32) is now explicable on the basis of MO considerations. Thus, the ion–radical pair is very short-lived in hexane and collapses at the 9,10-positions where the anthracene HOMO is centered. The 9,10-cycloadduct is subsequently further oxidized to the anthraquinone product. In the more polar dichloromethane, the ion–radical pair is better stabilized and its longer lifetime allows relaxation of the original HOMO ion–radical pair to the subjacent (HOMO-1) ion–radical pair which leads to cycloaddition on the terminal ring (Eq. 32) [161].

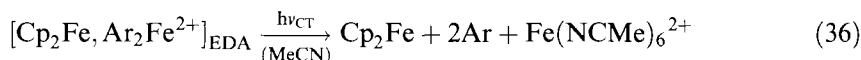
Most importantly, both in the thermal and the charge-transfer osmylation of anthracene, identical cycloadducts on the terminal ring are observed, which underscores the close relationship between the two reaction modes. Thus, a unifying electron-transfer mechanism is proposed for both thermal and photoactivated osmylation, which reveals the ion–radical pair $[\text{Ar}^{+\bullet}, \text{OsO}_4^{-\bullet}]$ as the common (primary) reactive intermediate [161].

Deligation of bis(arene)iron(II) acceptors

Organometallic acceptors of the type $\text{Ar}_2\text{Fe}^{2+}$ (Ar = mesitylene, durene, hexamethylbenzene, etc.) form EDA complexes with various organic and organometallic donors including molecular complexes with benzenes, naphthalenes, anthracenes, and ferrocene [124] and charge-transfer salts with tricyanomethide, tetraphenylborate, and tetracarbonylcobaltate (see Figure 3) [120]. As observed with OsO_4 complexes (vide supra), thermal and charge-transfer activation of the *bis*(arene)iron(II) complexes with donors (D) effect the same chemical transformations. Thus, a deligation process is observed in which the aromatic ligands of the acceptor are replaced by solvent (acetonitrile) molecules (Eq. 35).

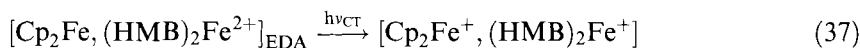


Whether the deligation process occurs spontaneously in a thermal reaction or requires photoactivation depends on the donors employed. For example, most EDA complexes of *bis*(arene)iron(II) acceptors with aromatic donors such as anthracene or durene or with ferrocene are thermally stable and can be isolated in crystalline form (see Figure 3) [124]. Photoactivation of these complexes in acetonitrile by the selective irradiation of their charge-transfer absorption bands uniformly results in the deligation of the acceptor moiety (Eq. 36).



The reactive intermediates leading to the (charge-transfer) photodecomposition of the *bis*(arene)iron(II) acceptor are revealed by picosecond time-resolved spectroscopy. For example, photoexcitation of the CT absorption band of the ferrocene-(HMB) $_2\text{Fe}^{2+}$ complex (HMB = hexamethylbenzene) with the second harmonic output (at 532 nm) of a mode-locked Nd:YAG laser (25-ps pulse width) generates a transient spectrum with an absorption maximum at 580 nm (see Figure 11A). Careful deconvolution of this absorption spectrum reveals the superposition of the absorption bands of ferrocenium ($\lambda_{\text{max}} = 620 \text{ nm}$, $\epsilon = 360 \text{ M}^{-1} \text{ cm}^{-1}$ [162]) and (HMB) $_2\text{Fe}^+$ ($\lambda_{\text{max}} = 580 \text{ nm}$, $\epsilon = 604 \text{ M}^{-1} \text{ cm}^{-1}$ [163]).

The two intermediates are clearly the result of photoinduced electron transfer from the ferrocene donor to the *bis*(arene)iron(II) acceptor, which constitutes the first reaction step toward deligation (Eq. 37).



Similar electron-transfer intermediates are observed with other (aromatic) donors that promote deligation of $\text{Ar}_2\text{Fe}^{2+}$ acceptors. For example, charge-transfer laser excitation of the EDA complex of (HMB) $_2\text{Fe}^{2+}$ with 9-methylantracene (MeANT) generates the 9-methylantracene cation radical with its characteristic absorption centered at 700 nm (see Figure 11B; Eq. 38).



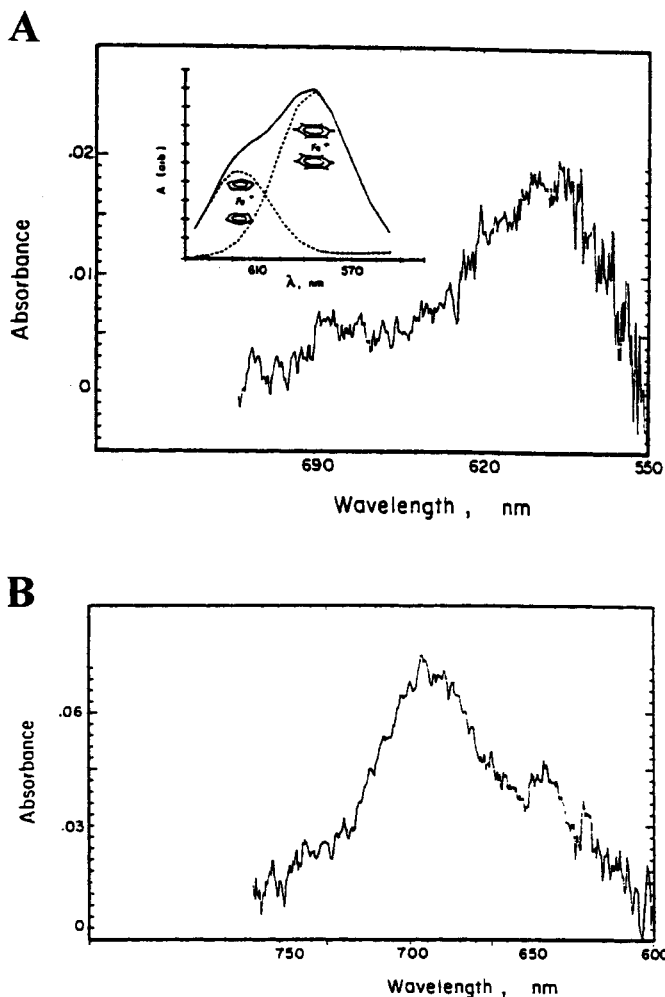
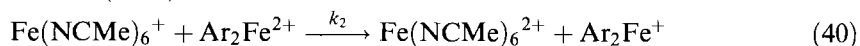
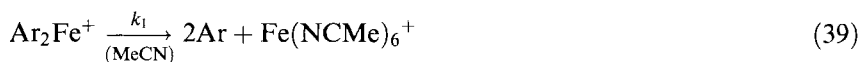


Figure 11. Transient absorption spectra obtained at 40 ps following the 532-nm CT excitation of the EDA complexes of *bis*(hexamethylbenzene) iron(II) with (A) ferrocene and (B) 9-methylanthracene. The spectrum in (A) is deconvoluted as the sum of reduced acceptor (HMB)₂Fe⁺ and oxidized donor Cp₂Fe⁺ (see inset) [124].

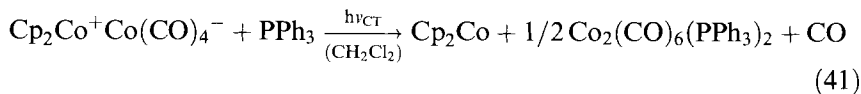
The monocationic intermediate Ar₂Fe⁺ subsequently loses its two aromatic ligands by replacing them with solvent (acetonitrile) molecules (*k*₁), and then reacts (*k*₂) with another *bis*(arene)iron(II) acceptor in an electron-transfer chain (ETC) process which results in a catalytic deligation of Ar₂Fe²⁺ [164, 165] (Eqs 39, 40).



Whereas most EDA complexes with $\text{Ar}_2\text{Fe}^{2+}$ acceptors are stable in the dark, there are some examples where spontaneous thermal reactions are observed. For example, the color of the EDA complex of ferrocene with the strongest acceptor (mesitylene)₂iron(II) with $E^\circ_{\text{red}} = -0.06$ V relative to the SCE [124] bleaches within 15 min upon mixing of the components, whereas the corresponding complexes with the weaker acceptors (durene)₂Fe²⁺ ($E^\circ_{\text{red}} = -0.16$ V relative to the SCE) and (HMB)₂Fe²⁺ ($E^\circ_{\text{red}} = -0.26$ V relative to the SCE) are thermally stable [124]. Moreover, replacing ferrocene ($E^\circ_{\text{ox}} = 0.41$ V relative to the SCE [48]) by even stronger donors such as tetracarbonylcobaltate ($E^\circ_{\text{ox}} = 0.32$ V relative to the SCE [118, 166]) or pentacarbonylmanganate ($E^\circ_{\text{ox}} = 0.05$ V relative to the SCE [167]) also results in rapid thermal deligation of the (HMB)₂Fe²⁺ acceptor. In fact, the complete kinetics of the catalytic electron-transfer activated deligation of (HMB)₂Fe²⁺ (Eqs 39, 40) in the presence of the cobaltate and the manganate donor has been analyzed recently by digital simulation of the concentration–time profiles of the monocationic (HMB)₂Fe⁺ intermediate for varying initial concentrations of the reactants [120].

Ion-pair annihilation in carbonylmetallate salts

The anionic carbonylmetallate donors tetracarbonylcobaltate [$\text{Co}(\text{CO})_4^-$], hexacarbonylvandate [$\text{V}(\text{CO})_6^-$], and pentacarbonylmanganate [$\text{Mn}(\text{CO})_5^-$] form a variety of (charge-transfer) ion-pair salts with cationic (organic or organometallic) acceptors the structures and spectroscopic properties of which have been described in Section 2.3. Most of these charge-transfer salts are thermally stable in dichloromethane solution, and even prolonged irradiation of their CT absorption bands does not result in any chemical transformations [118]. For example, the CT salt $\text{Cp}_2\text{Co}^+\text{Co}(\text{CO})_4^-$ does not show any chemical change after 8 h irradiation at wavelengths $\lambda > 520$ nm where the single cationic and anionic components do not absorb. However, in the presence of triphenylphosphine, CT irradiation effects spontaneous evolution of carbon monoxide accompanied by the disappearance of the cobaltate anion as monitored by IR spectroscopy [118]. Thus, the characteristic carbonyl absorption at $\nu_{\text{CO}} = 1887$ cm⁻¹ of the cobaltate decays, and concomitantly the growth of a new IR absorption band is observed at $\nu_{\text{CO}} = 1958$ cm⁻¹ which is assigned to the dimeric $\text{Co}_2(\text{CO})_6(\text{PPh}_3)_2$ [118]. The complete stoichiometry of the reaction is described in Eq. 41.



Similar photoinduced dimerizations and ligand substitutions in the presence of additives such as triphenylphosphine are observed with ion-pairs salts of $\text{Mn}(\text{CO})_5^-$ and $\text{V}(\text{CO})_6^-$ with cobaltocenium or other cationic acceptors such as Ph_2Cr^+ , pyridinium, quinolinium, etc [118]. Most importantly, all photochemical transformations of the various carbonyl metallate salts are initiated by actinic light that solely excites the charge-transfer absorption bands of the contact ion pairs whereas local excitation of the separate ions is deliberately excluded.

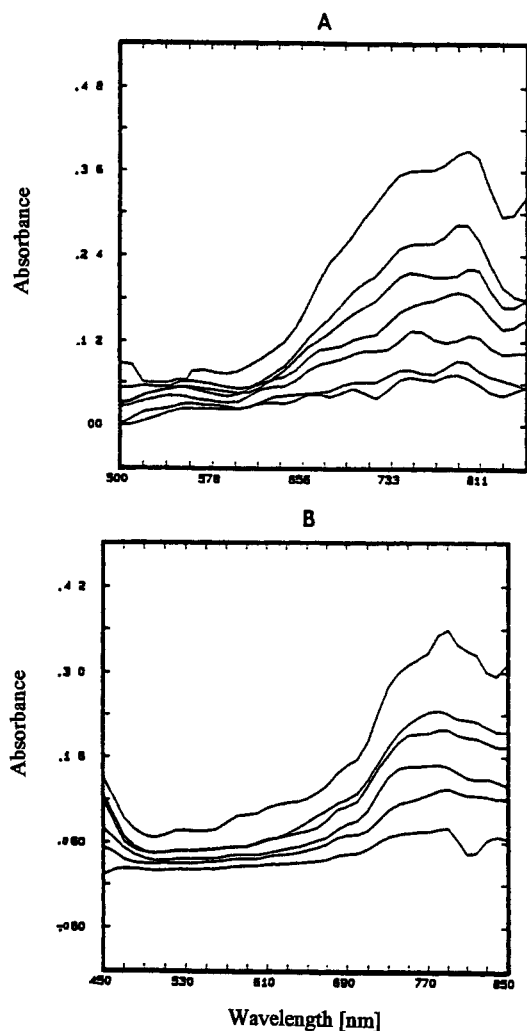


Figure 12. Transient absorption spectra of (A) Mn(CO)_5^\bullet and (B) Co(CO)_4^\bullet radicals recorded on the microsecond time scale upon 532-nm CT excitation of the cobaltocenium salts of Mn(CO)_5^- and Co(CO)_4^- , respectively [118].

The reactive intermediates in the charge-transfer photoreactions of carbonyl metallate salts are examined by time-resolved spectroscopy applying a 10-ns pulse of a Q-switched Nd:YAG laser at 532 nm [118]. Thus, the charge-transfer excitation of various manganate and cobaltate salts results in the formation of intense transient absorption centered at 800 nm and 780 nm, respectively, which are readily assigned to the 17-electron radicals Mn(CO)_5^\bullet and Co(CO)_4^\bullet , respectively (see Figure 12) [168–170].

Moreover, when pyridinium or quinolinium is used as the cationic partner of the carbonyl metallates, additional absorption bands (at shorter wavelengths) are observed which are readily assigned to the pyridinyl [171] and quinolinyl [172] radicals, respectively (see Figure 13).

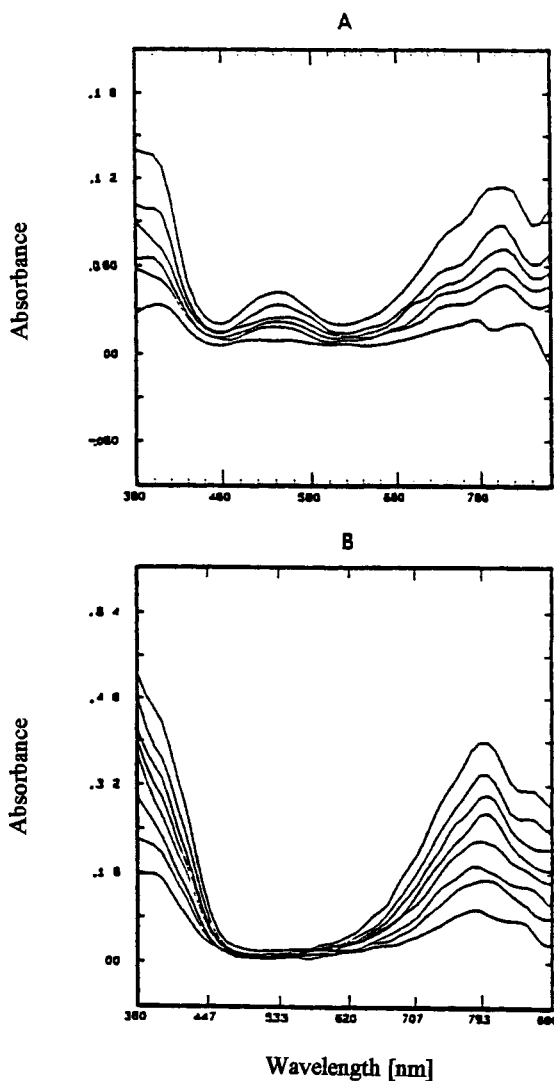
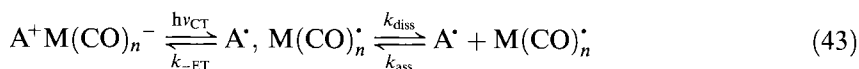


Figure 13. Transient absorption spectra recorded on the microsecond time scale upon 532-nm CT excitation of (A) quinolinium tetracarbonylcobaltate and (B) *N*-methyl-4-cyanopyridinium tetracarbonylcobaltate in acetone showing $\text{Co}(\text{CO})_4^{\bullet}$ radical (at 790 nm) and quinolinyl (at 540 nm) or cyanopyridinyl (at 370 nm) radicals, respectively [118].

All laser experiments point uniformly to an initial photoinduced electron transfer from the carbonylmetallate donor $[\text{M}(\text{CO})_n]^-$ to the cationic acceptor A^+ which results in the formation of a radical pair (Eq. 42).

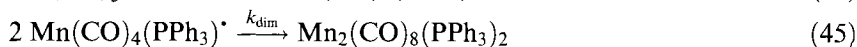
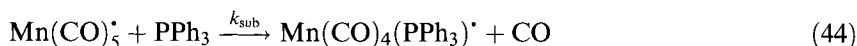


In the absence of triphenylphosphine, the photogenerated radicals undergo back electron transfer ($k_{-\text{ET}}$) either within the solvent cage of the geminate radical pair or upon diffusional encounter (k_{ass}) of the cage-escaped free radicals (Eq. 43).



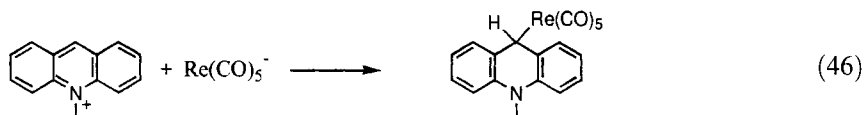
The latter process results in an overall second-order annihilation of the radicals as observed in the complete decays of the transient absorption to the spectral baseline on the microsecond time scale (see Figures 12 and 13). Since dimerization of the 17-electron radicals is orders of magnitude slower than the highly exothermic back electron transfer, no net photochemical transformations are observed even after prolonged charge-transfer irradiation.

However, even small amounts of additives (L) such as triphenylphosphine induce permanent photochemical changes due to redox processes, ligand exchange, and dimerization reactions [118]. The critical reaction step common to all these photo-reactions is the incorporation of the additive L as a ligand in the metal complex. This process must occur in a reactive stage of the metal complex since carbonyl metallates (in the ground state) do not undergo thermal ligand substitutions [173–175]. The time-resolved spectroscopic studies reveal the 17-electron radical $M(CO)_n^*$ as the reactive intermediate that rapidly undergoes ligand substitution (k_{sub}) and other subsequent reactions such as homolytic dimerization (k_{dim}) (Eqs 44, 45).



Thus, a careful analysis of the rate constants for back electron transfer, ligand substitution, and dimerization leads to the conclusion that ligand exchange in the 17-electron radical (k_{sub} in Eq. 44) lowers the rate of back electron transfer from the acceptor radical (A^*) (k_{-ET} in Eq. 43) to such an extent that dimerizations (and other possible follow-up reactions [118]) now become competitive and effect permanent photochemical transformations. The decrease of the back electron transfer rates is due to the attenuated reduction potentials of the phosphine-substituted radicals [176].

The isostructural pentacarbonyl metallates $Mn(CO)_5^-$ and $Re(CO)_5^-$ form a series of thermally or photochemically unstable charge-transfer salts with *N*-methylpyridinium cations. For example, *N*-methylacridinium reacts with pentacarbonylrhenate immediately upon mixing in acetonitrile to form the (*N*-methyl-9-acridanyl)pentacarbonylrhenium(I) adduct in 90 % yield [126] (Eq. 46).



X-ray crystallographic examination of the adduct reveals a folded acridanyl structure and a distorted square-pyramidal orientation of the carbonyl ligands around the rhenium(I) center (see Figure 14).

This adduct is very stable at room temperature and only decomposes upon heating at 80 °C in benzene to form dirheniumdecacarbonyl and biacridanyl [126] (Eq. 47).

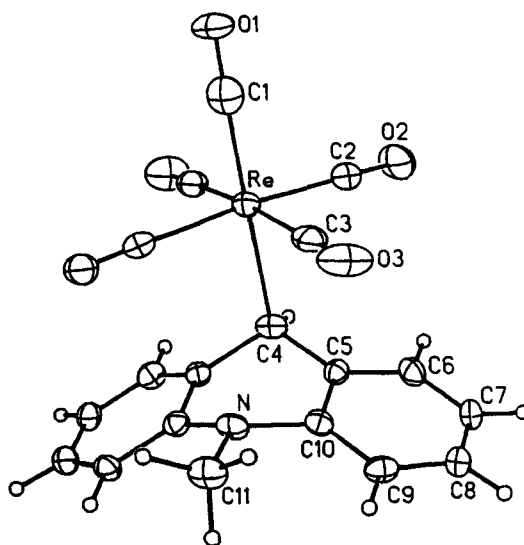
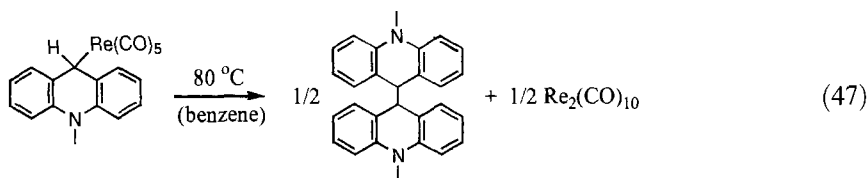
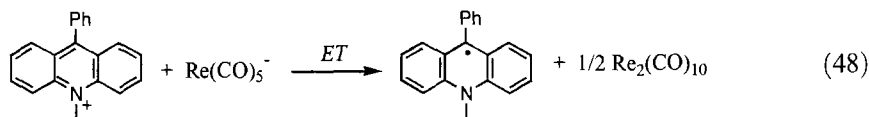


Figure 14. ORTEP diagram of (N-methyl-9-acridanyl)pentacarbonylrhenium(I) adduct [126].

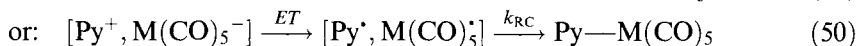
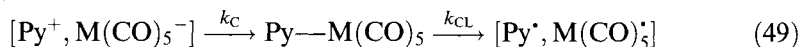


In contrast, the 9-phenylacridinium acceptor undergoes a thermal electron-transfer reaction upon mixing with the pentacarbonylrhenate(I) donor in acetonitrile to form dirheniumdecacarbonyl and the stable 9-phenylacridanyl radical (Eq. 48).



Other pyridinium acceptors yield either products of nucleophilic coupling (Eq. 46) or of electron transfer (Eq. 48). The partitioning between the two pathways is different for the two metal centers, and also strongly depends on the stereochemistry and electronic structure of the pyridinium substrate. Rhenate donors prefer adduct formation (Eq. 46), and pyridinium acceptors that form stable, delocalized pyranil radicals favor the electron-transfer pathway (Eq. 48) [126]. The rate constants for both reactions correlate with the electron-transfer driving force in the same way, and electron transfer and nucleophilic addition cannot be distinguished on the basis of their linear free-energy relationships [177], which indicates that the transition states of both pathways are closely related. Accordingly, the question arises as to whether (i) the electron-transfer products are formed as secondary products via a metastable adduct that undergoes homolytic cleavage (k_{CL} in Eq. 49) or (ii) adduct

formation is the result of radical–radical coupling (k_{RC}) as the secondary step following an initial electron transfer (k_{ET} in Eq. 50), i.e.



First, the inner-sphere formulation [26–30] for the net electron transfer in Eq. 49 seems unlikely in light of the relative rates of electron transfer and adduct decomposition. For example, biacridanyl and $\text{Re}_2(\text{CO})_{10}$ are formed immediately as a 5 % by-product to the formation of the acridanylpentacarbonylrhenium(I) adduct in Eq. 46; however, the adduct itself is very stable at room temperature (*vide supra*). Thus, electron transfer and nucleophilic addition do not seem to be sequential, but rather concurrent reaction steps. However, the linear free-energy correlations [177] with slopes substantially less than the value of unity predicted for purely outer-sphere electron transfer do indicate strong inner-sphere character for the electron-transfer step [126]. On the other hand, the inverted reaction sequence in Eq. 50 is experimentally confirmed by laser flash photolysis experiments with the isoquinolinium–pentacarbonylmanganate ion pair. Charge-transfer excitation of the ion pair with a 10-ns laser pulse at 532 nm generates initially the $\text{Mn}(\text{CO})_5^\bullet$ radical with its characteristic absorption at 780 nm (see Figure 15) [168–170]. The absorption band of

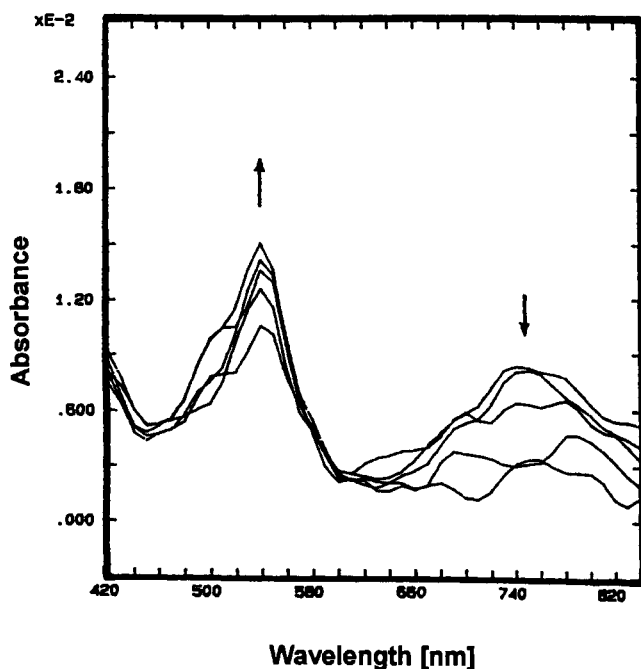
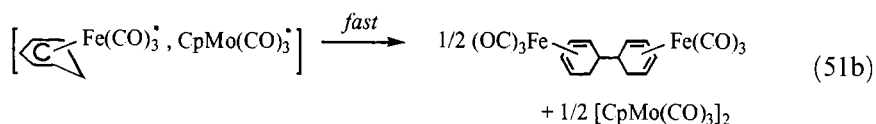
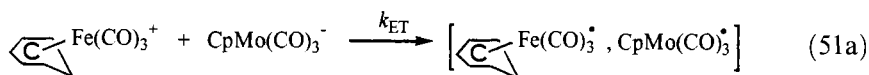


Figure 15. Transient absorption spectra recorded on the microsecond time scale upon 532-nm CT excitation of the isoquinolinium pentacarbonylmanganate ion pair showing the decay of $\text{Mn}(\text{CO})_5^\bullet$ radical (at 750 nm) and the formation of the (1:1) σ -adduct (at 540 nm) [126].

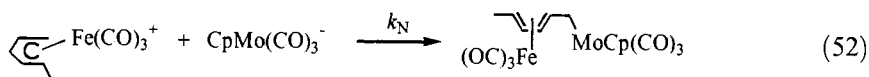
the 17-electron radical decays on the microsecond time scale and a new absorption band appears (centered at 540 nm) which is readily assigned to the radical–radical coupling product based on the comparison with the spectrum of the acridanyl-analog adduct. However, the quinolyl adduct is very unstable and ultimately cleaves again to form the electron-transfer products [126].

In general, nucleophilic addition and electron transfer require the same structural changes in the pentacarbonyl metallate anion from its original trigonal-bipyramidal geometry to the square-pyramidal shape of both the 17-electron radical and the adduct (see Figure 14). A partial disposition toward this structural change is already apparent in the precursor charge-transfer ion pair which shows significant inner-sphere character as revealed by the distortion of the carbonyl metallate symmetry [178] similar to those described for cobaltate ion pairs (see Section 2.3.3). The distorted carbonyl metallate is thus activated towards both electron transfer and nucleophilic addition since both pathways exhibit structurally and energetically similar transition states. As a consequence, the final outcome of the reaction mostly depends on the energetics of the bond formation leading to the adduct.

A similar case of concurrence of one-electron transfer and nucleophilic addition is observed in the thermal ion-pair annihilation of CpMo(CO)_3^- anion with (dienyl) Fe(CO)_3^+ cations [84, 179]. Thus, spontaneous electron transfer (k_{ET}) occurs upon mixing of (η^5 -cyclohexadienyl) Fe(CO)_3^+ with CpMo(CO)_3^- in acetonitrile to afford the transient 19-electron iron radical and the 17-electron molybdenum radical which both rapidly dimerize (Eq. 51).



In contrast, the open-chain analog (η^5 -hexadienyl) Fe(CO)_3^+ mainly (75 %) forms the nucleophilic adduct with the molybdate anion (Eq. 52).



Interestingly, the new bond in the adduct is formed at the terminal carbon of the dienyl ligand as established by X-ray crystallography (see Figure 16).

At room temperature, this adduct readily decomposes by homolytic cleavage to the 19-electron–17-electron radical pair which subsequently forms homodimers of the iron and the molybdenum complexes similar to those in Eq. 51. An overall electron transfer via the nucleophilic adduct as intermediate is observed as the favored pathway of iron complexes with acyclic dienyl ligands. However, the formation of the electron-transfer products, viz., homodimers of iron and molybdenum complexes, are also obtained directly (in 25 % yield) during the reaction. The nucleophilic adduct is not a prerequisite for the electron transfer from the molybdate

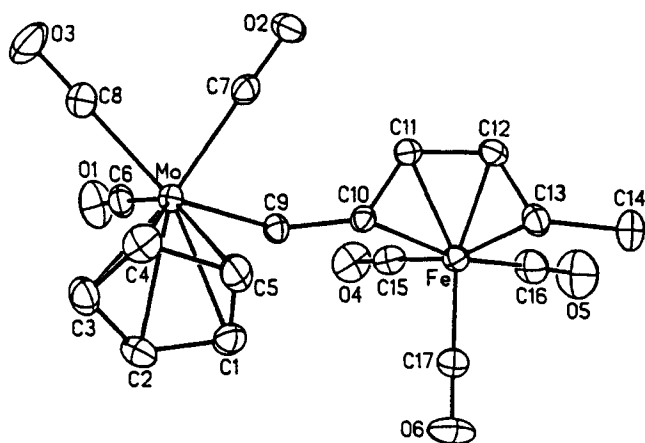
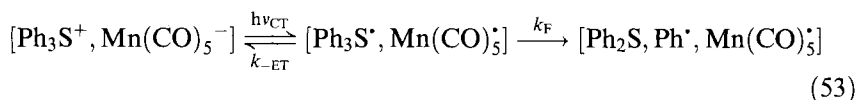


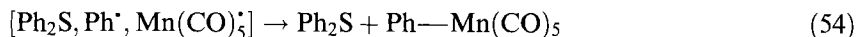
Figure 16. ORTEP diagram of the σ -adduct $\text{CpMo(CO)}_3\text{Fe(CO)}_3(\eta^4\text{-hexadiene})$ [84].

donor to the cationic iron acceptor. In other words, direct *outer-sphere* electron transfer (Eq. 51) and *inner-sphere* electron transfer via the nucleophilic adduct (Eq. 52) are concurrent rather than sequential processes, and the partitioning between the two pathways is controlled by stereochemistry and the reorganization energies involved in the transformation from the charge-transfer ion pair to the radical pair [179].

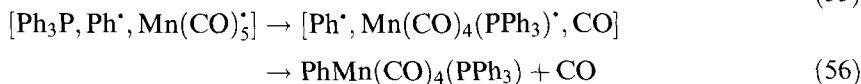
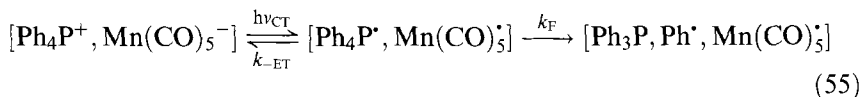
In contrast to the inner-sphere charge-transfer salts of pyridinium acceptors with carbonyl metallates (*vide supra*), contact ion pairs of tetraphenylphosphonium or triphenylsulfonium acceptors with Co(CO)_4^- , Mn(CO)_5^- , and HFe(CO)_4^- donors do not exhibit any distortions in the (T_d , D_{3h} , or C_{3v}) symmetry of the carbonyl metallate as confirmed by IR spectroscopy in solution and in the solid state [140]. Moreover, the strongly blue-shifted (as compared to the pyridinium analogs) CT absorption bands of these typical *outer-sphere* charge-transfer salts point to very weak donor-acceptor interactions owing to the rather low reduction potentials ($E_{\text{red}}^{\text{p}} \approx -2$ V relative to the SCE [140]) of the onium acceptors. Nonetheless, a rich photochemistry is observed upon charge-transfer activation of these salts, which is the direct result of the spontaneous fragmentation (k_F) of the labile sulfuranyl and phosphoranyl radicals [180] upon photoinduced electron transfer from the carbonylmallate (Eq. 53).



As a result, the energy-wasting back electron transfer (to regenerate the original charge-transfer salt) is partially suppressed, and the reactive phenyl radical couples with the 17-electron carbonylmall radical within the solvent cage to form the phenyl-substituted metal complex (Eq. 54).

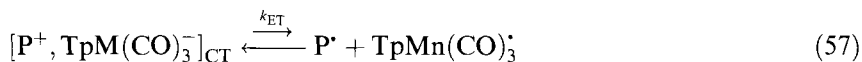


Similar homolytic combinations also apply to the radical pair photogenerated from the phosphonium salt. However, triphenylphosphine as a highly effective σ -donor replaces a CO ligand in the metal complex prior to phenyl coupling (Eqs 55, 56).



The photochemical activation of the phosphonium salt (Eq. 55) has its *thermal* counterpart in the facile (dark) conversion of the iodonium salt $\text{Ph}_2\text{I}^+ \text{Mn}(\text{CO})_5^-$. Owing to the greatly enhanced reduction potential of diphenyliodonium ($E_{\text{red}}^{\text{P}} \approx 0$ V relative to the SCE [181]) as compared to tetraphenylphosphonium ($E_{\text{red}}^{\text{P}} \approx -2.3$ V relative to the SCE [140]), electron transfer in the iodonium–metallate ion pair is now energetically feasible ($\Delta G_{\text{ET}} \approx 0$ eV). As a result, complete conversion of the charge-transfer salt to the electron-transfer products $\text{Mn}_2(\text{CO})_{10}$ and $\text{PhMn}(\text{CO})_5$ is observed within minutes upon mixing of the two components [140].

The formation of 17-electron radicals as the result of *thermal* electron transfer from a carbonyl metallate to a cationic pyrylium acceptor (P^+) is also observed with the charge-transfer salts of $[\text{TpM}(\text{CO})_3^-]$ (Tp = hydrido-*tris*-(3,5-dimethylpyrazolyl)-borate; $\text{M} = \text{Mo}, \text{W}, \text{Cr}$) [127]. Owing to the stability of the $\text{TpM}(\text{CO})_3^\bullet$ radical [182], electron-transfer equilibria (K_{ET}) are established by UV–Vis and IR spectroscopy which generally favor the intimate ion-pair state (see Structure **D** in Figure 5) in accord with the electron-transfer energetics [127] (Eq. 57).



However, with triarylpyrylium acceptors the stable 17-electron radicals are generated in high yields due to a shift of the endergonic equilibrium by the homolytic dimerization of the pyranil radicals ($2 \text{P}^\bullet \rightarrow \text{P}_2$) [183, 184].

Hydrometallation and hydrogenation of olefins with metal hydrides

Metal catalysis of olefin and arene hydrogenation is critically dependent on the reactive hydridometal intermediates. However, little is known about the mechanism of hydrogen transfer and hydrometallation and the reactive intermediates involved. The observation of transient charge-transfer absorption during hydrogenation and hydrometallation of olefins with tungsten or molybdenum hydrides [185], opens up the question of a possible electron-transfer mechanism in which the overall hydrogen-atom transfer is the result of a two-step electron-transfer–proton-transfer (ET–PT) process (Eq. 58).



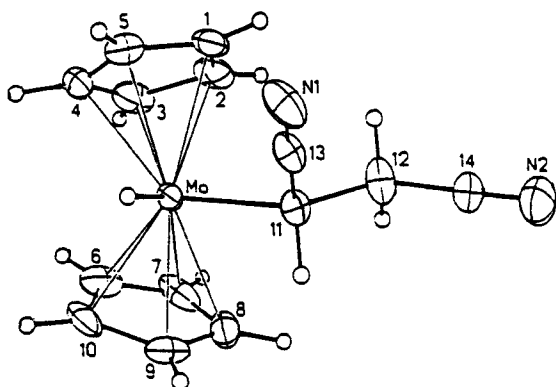
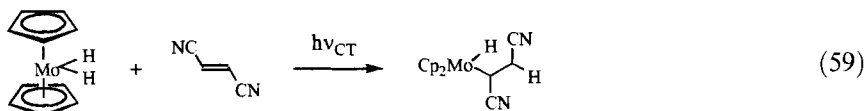
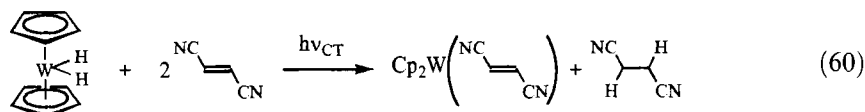


Figure 17. ORTEP diagram of the σ -adduct formed upon charge-transfer irradiation of the Cp_2MoH_2 –fumaronitrile complex in toluene [58].

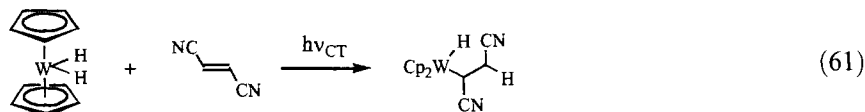
In this context, the transition metal hydrides Cp_2MoH_2 , Cp_2WH_2 , and Cp_2ReH_2 are of particular interest since they are excellent electron donors (see Table 4, Section 2.2.1) [57–59], and they form EDA complexes with various activated olefins such as fumaronitrile or maleic anhydride [58]. Charge-transfer activation of these EDA complexes in toluene by the deliberate irradiation of their charge-transfer absorption bands leads to either hydrometallation or hydrogenation [58]. For example, irradiation of the Cp_2MoH_2 –fumaronitrile complex with visible light ($\lambda > 550 \text{ nm}$) where neither the metal complex nor the olefin absorbs, yields the σ -adduct (see Figure 17) in excellent (95 %) yield (Eq. 59).



Under the same conditions, the analogous tungsten hydride reacts with fumaronitrile to form succinonitrile (95 %) and a mixture of fumaronitrile and maleonitrile complexed with tungstenocene (Eq. 60).

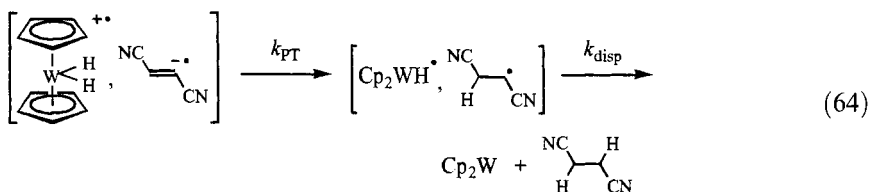
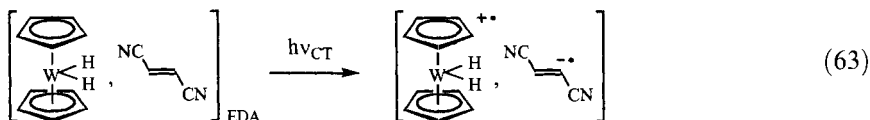


The two reaction pathways are not unique to the corresponding molybdenum or tungsten centers. For example, both metal hydrides effect hydrogenation of maleic anhydride [58]. Thus, the hydrogenation path may involve prior hydrometallation followed by reductive elimination of the hydridoalkyltungsten adduct (Eqs 61, 62).





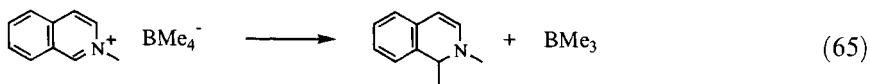
Alternatively, hydrogenation is simply explained by the sequential electron-transfer-proton-transfer reaction followed by disproportionation of the resulting radical pair (Eqs 63, 64).



Deprotonation of $\text{Cp}_2\text{WH}_2^{+\bullet}$ and $\text{Cp}_2\text{MoH}_2^{+\bullet}$ clearly occurs upon electrochemical generation of the cation radicals, and subsequent dimerization of the resulting hydridometallocene radicals has been observed [59]. Finally, the *charge-transfer* hydrogenation and hydrometallation of olefins closely parallels the *thermal* pathways in that the same type of σ -adducts are found [185].

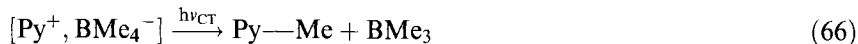
Alkylation with organoborates

Tetraalkylborates are mild and selective alkylation reagents [186, 187], and they are commonly considered as sources of nucleophilic alkyl groups (R^-) just as borohydrides are depicted as hydride (H^-) sources. However, since organoborates represent excellent electron donors (see Table 5, Section 2.2.1), the question arises as to what role electron donor-acceptor interactions play in the nucleophilic alkyl transfer. Phenyl- and alkyl-substituted borate ions form highly colored charge-transfer salts with a variety of cationic pyridinium acceptors [65], which represent ideal substrates to probe the methyl-transfer mechanisms. Most pyridinium borate salts are quite stable in crystalline form (see for example Figure 5C), but decompose rapidly when dissolved in tetrahydrofuran to yield methylated hydroypyridines (Eq. 65).



In some cases (e.g., 3-cyano-*N*-methylpyridinium tetramethylborate), this formal methide transfer is so fast that the ion-pair precursor cannot be isolated as a crystalline salt. Other charge-transfer salts such as 4-phenyl-*N*-methylpyridinium tetra-

methylborate do not react at all at room temperature. In these cases, methylation can still be achieved by deliberate irradiation of the charge-transfer absorption band of the ion-pair salt in solution (Eq. 66).

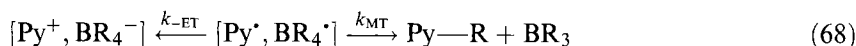


Charge-transfer activated alkyl transfer can also be carried out with the thermally unstable salts at low (-78°C) temperature at which the thermal decomposition is suppressed. In these cases, the similarity in the regioselectivity of photoinduced and thermal alkyl transfer points to the critical role of the donor-acceptor orientation in the ion-pair precursor which ultimately determines the alkylation site. In mixed alkylborates containing methyl, *n*-butyl, and *sec*-butyl groups, the alkyl transfer rates are found to increase substantially from methyl to *sec*-butyl transfer, the latter being 67 times faster than the former [65].

Charge-transfer activation of the charge-transfer salts effects a spontaneous electron transfer [18] from the borate donor to the pyridinium acceptor which results in the formation of a radical pair (Eq. 67).



The unstable BR_4^\bullet radical subsequently either transfers (k_{MT}) an alkyl radical to the pyridinyl radical or undergoes back electron transfer ($k_{-\text{ET}}$) to restore the original charge-transfer salt (Eq. 68).



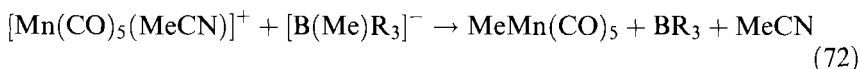
It is the competition between these two pathways that determines the thermal and photostability of the charge-transfer salt. For example, no photochemistry is observed even after prolonged CT irradiation of the charge-transfer salt of *tetrakis*[3,5-*bis*(trifluoromethyl)phenyl]borate with 4,4'-bipyridinium cation [188], which leads to the conclusion that the transfer of a *bis*(trifluoromethyl)-substituted phenyl group is too slow to efficiently compete with the (generally ultrafast [22–24]) back electron transfer. However, the photoinduced alkylations described above demonstrate that alkyl-transfer rates can be comparable or even faster than back electron transfer rates, which can only be explained by considering the alkyl transfer as an in-cage process. (The fact that no pyridine dimers are found, which readily form by coupling of free pyridinyl radicals, also supports the conclusion that no cage escape has taken place.) Accordingly, a complete mechanism for charge-transfer activated alkyl transfer can be formulated in three steps including photoinduced electron transfer ($h\nu_{\text{CT}}$) from the borate donor to the pyridinium acceptor followed by fragmentation (k_{F}) of the boranyl radical followed by coupling (k_{C}) of the alkyl and the pyridinyl radicals (Eqs 69–71).



The thermal reactions of the pyridinium borate salts are likely to follow the same electron-transfer path. Experimental evidence for this conclusion is the fact that the *sec*-butyl transfer is substantially faster than methyl transfer although a nucleophilic substitution mechanism would predict the less hindered group to be transferred preferentially. The fast rates of *sec*-butyl transfer can be readily explained on the basis of the electron-transfer mechanism (Eqs. 69–71) by considering the different boron–carbon bond strength [189, 190] for the various alkylborates. The boron–carbon bond cleavage (Eq. 70) is apparently the critical step, and its relative rate [191] as compared to that of the back electron transfer determines the overall rate for thermal alkyl transfers in pyridinium tetraalkylborate salts.

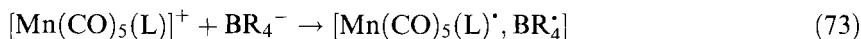
Alkyl transfer is also observed as the result of ion-pair annihilation of organoborate anions by carbonylmanganese(I) cations [192]. Thus, the manganese cations $[\text{Mn}(\text{CO})_5(\text{L})]^+$ (L = acetonitrile, pyridine, triphenylphosphine, methyldiphenylphosphine) readily react with tetramethylborate, methyltriphenylborate, and tetraphenylborate in tetrahydrofuran to yield a mixture of alkylmanganese carbonyls and/or dimanganese carbonyls and hydridomanganese carbonyls. Since in more polar solvents no such thermal reactions are observed, ion-pairing is apparently critical for all these chemical transformations. The fact that tetramethylborate (with the lowest oxidation potential) and the manganese cations $[\text{Mn}(\text{CO})_5(\text{acetonitrile})]^+$ and $[\text{Mn}(\text{CO})_5(\text{pyridine})]^+$ (with the highest reduction potentials) are the most reactive substrates, points to a redox-driven reaction scheme.

However, a general electron-transfer mechanism as formulated for the pyridinium borate salts (*vide supra*) is not applicable in this case owing to the difference in the redox products with varying manganese ligands (L). For example, the acetonitrile-substituted manganese cation affords methylmanganese pentacarbonyl as the sole product upon reaction with tetramethylborate or methyltriphenylborate (Eq. 72).



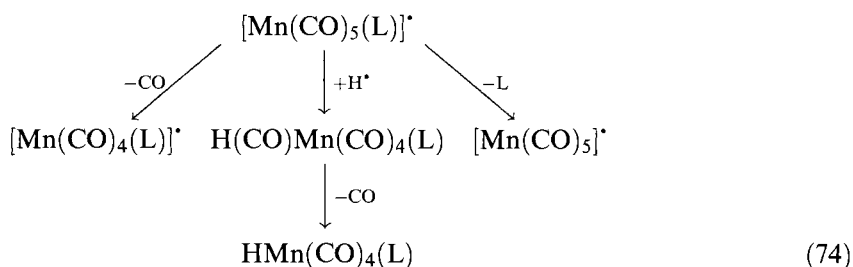
Similarly, tetraphenylborate transfers a phenyl group to form the phenyl-substituted manganese carbonyl as the only product. In contrast, pyridine- or phosphine-ligated manganese cations form dimanganese carbonyls and hydrido-manganese products besides varying amounts of alkylated manganese carbonyls depending on the manganese ligand (L). Interestingly, methyltriphenylborate does not form any alkylated or phenylated manganese carbonyls at all when reacted with pyridine- or phosphine-ligated manganese cations, and tetraphenylborate yields phenyl-substituted manganese carbonyl, dimanganese carbonyl, and hydrido manganese carbonyl in about equal amounts [192].

At first glance, all manganese products observed can readily be derived from the 19-electron carbonyl manganese radical $[\text{Mn}(\text{CO})_5(\text{L})]^\bullet$ which is generated by electron transfer from the borate donor (Eq. 73).

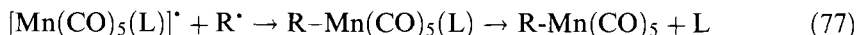


The 19-electron species either loses a CO or L ligand to form the corresponding 17-electron radical or abstracts hydrogen from the solvent and then extrudes a CO

ligand to yield the hydridotetracarbonyl product (Eq. 74).



Alternatively, both $[\text{Mn}(\text{CO})_5]^\bullet$ or $[\text{Mn}(\text{CO})_5(\text{L})]^\bullet$ radicals may couple with an alkyl or phenyl radical (R^\bullet) which are present due to the fragmentation of the unstable boranyl radical (Eqs 75–77).



Thus, all products may be derived from the primary radical pair generated by the initial electron transfer (Eq. 73). However, the acetonitrile-ligated carbonylmanganese cation yields $\text{CH}_3\text{Mn}(\text{CO})_5$ and $\text{C}_6\text{H}_5\text{Mn}(\text{CO})_5$ as the only carbonyl manganese products, and no other typical products from a 17-electron radical such as the dimer are observed. Moreover, butyltrimethyl borate transfers preferentially a methyl group to the manganese center and not the more stable butyl radical which would be the expected fragmentation product of the butyltrimethylboranyl radical. Both observations cannot be reconciled with the above delineated electron-transfer mechanism, but are satisfactorily explained on the basis of a direct nucleophilic attack of the borate anion on the manganese cation. Thus partitioning between the two pathways, i.e. electron transfer or nucleophilic addition, is controlled by the manganese ligand (L) which affects the electrophilicity of the carbonyl ligands as well as the electron affinity of the manganese center as follows [192]: acetonitrile as a poor σ -donor and a good π -acceptor withdraws electron density from the carbonyl ligands which enhances the nucleophilic attack of the borate anion on the carbonyl carbon atom. In contrast, pyridine and phosphine ligands are good σ -donors and poor π -acceptors and thus partially transfer electron density to the carbonyl ligands which decreases their electrophilicity to the point that electron transfer is a viable alternative to nucleophilic addition. Thus, manganese pentacarbonyl cations, which follow both electron-transfer and nucleophilic reaction pathways for ion-pair annihilation, are ideal substrates to demonstrate the dichotomy of the two related reactivities.

Metal–carbon bond cleavage of dimethylaurate(I) and tetramethylaurate(III)

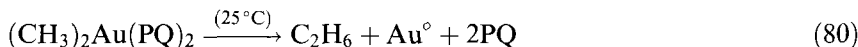
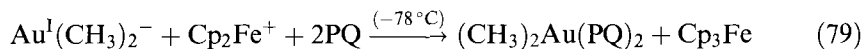
The mechanistic dichotomy between nucleophilic addition and electron transfer may also apply to alkylmetallates derived from transition metals. For example, an

electron-transfer mechanism has been discussed for alkylations with alkylcuprates [193, 194]. However, general mechanistic conclusions for transition alkylmetallates are hampered by the fact that thermal instability and air-sensitivity greatly limit their electron-transfer reactivity. Since alkylaurates act as alkylating reagents [195], but rapidly decompose under oxidative conditions [196], a detailed mechanistic study of the oxidative decomposition of dimethylaurate(I) and tetramethylaurate(III) has been undertaken recently [64].

Dimethylaurate(I) which can be isolated as the tetrabutylammonium salt, reacts with one-electron oxidants such as ferrocenium, decamethylferrocenium, or 2,4,6-trichlorobenzene diazonium in tetrahydrofuran to yield metallic gold and ethane [64] (Eq. 78).



In the presence of 9,10-phenanthrenequinone (PQ), a chelating ligand with good σ -donor and π -acceptor properties, oxidation with ferrocenium at low temperature (-78°C) leads to the formation of a green solid which decomposes at room temperature to form ethane, metallic gold, and two equivalents of phenanthrenequinone [64] (Eqs 79, 80).



The ESR spectrum of the trapped dimethylgold intermediate indicates that the unpaired electron is primarily localized on the quinone ligand, which suggests the polar formula $(\text{CH}_3)_2\text{Au}^+(\text{PQ}^{\cdot-})(\text{PQ})$ for the green adduct [64]. The trapping experiment points to the following mechanism of oxidative decomposition of dimethylaurate(I) (Eqs 81–83).

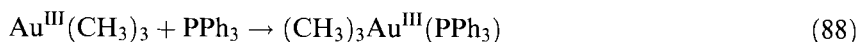
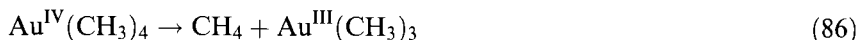
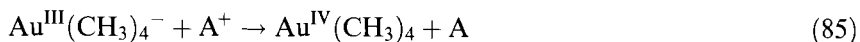


The analogous oxidation of tetramethylaurate(III) with the same one-electron oxidants (A^+) yields methane, ethane, and metallic gold in the following stoichiometry (Eq. 84).



In the presence of triphenylphosphine, a stable trimethylgold adduct $(\text{CH}_3)_3\text{Au}(\text{PPh}_3)$ is formed. The stoichiometry in Eq. 84, which is applicable to various one-electron oxidants, and the phosphine-ligated $\text{Au}(\text{III})$ intermediate strongly suggest the following electron-transfer mechanism with a tetramethylgold(IV) species as the initial (putative) reactive intermediate, which undergoes rapid homolytic

cleavage to form trimethylgold(III) (Eqs 85–88).



Thus, dimethylaurate(I) and tetramethylaurate(III) exhibit an interesting difference in the fragmentation pattern upon one-electron oxidation which clearly requires further (theoretical) exploration.

2.5 Inner-sphere and Outer-sphere Mechanisms for Electron Transfer

The distinction between inner-sphere and outer-sphere electron transfer (ET) is originally based on redox reactions of inorganic coordination complexes [26]. *Inner-sphere* electron transfer is accompanied by ligand exchange and the formation of bridged intermediates, whereas no bond formation or breakage is observed in *outer-sphere* electron transfers [2, 26–30]. However, because this chemically based differentiation has often proved ambiguous [2, 197], we refer to a more general definition of inner-sphere and outer-sphere electron transfer [31] which considers the degree of electronic coupling of the donor and acceptor orbitals in the ET transition state as sole criterion. Owing to the technical difficulties in directly observing and characterizing of transition states [198, 199], we focus on the electron donor–acceptor precursor complex prior to electron transfer (which is assumed to be structurally and electronically similar to the ET transition state [7–9]) in which the electronic coupling (or charge-transfer interaction) is experimentally confirmed by X-ray structural and (UV–Vis or IR) spectroscopic evidence.

According to Mulliken theory [14–16], the degree of charge-transfer [91] in the precursor complex is critically dependent on the intermolecular donor–acceptor distance and is a direct measure of the bonding or electronic coupling of the electron-transfer partners, which is quantitatively described by the electronic coupling matrix element V (or H_{AB}) [10]. Thus, *outer-sphere* electron transfer implies weak coupling ($V < 1 \text{ kcal mol}^{-1}$ or 350 cm^{-1} [200]) of the donor and acceptor orbitals in the ET transition state, whereas *inner-sphere* mechanisms should be considered whenever strong charge-transfer complexes (with $V > 1 \text{ kcal mol}^{-1}$ or 350 cm^{-1}) are observed as reaction intermediates [29, 201, 202].

Organometallic donors and acceptors are particularly suitable to elucidate outer-sphere and inner-sphere ET processes as follows: First, they exist as neutral molecules as well as cationic or anionic species, and thus form both molecular EDA complexes and ion-pair salts (see Section 2.3). Molecular complexes with organometallic donors and acceptors exhibit a wide range of donor–acceptor interaction from very

weak (contact) charge-transfer complexes such as the ferrocene–diiodomethane complex to the strong ionic character of TCNE complexes (see Section 2.3). In general, weak charge-transfer interaction is observed between ligated metal centers and donors (or acceptors) that are *not* ligands in the first (inner) coordination sphere of the metals. Such complexes are referred to as *outer-sphere* complexes [88–90]. In contrast, strong charge-transfer interaction is accompanied by partial penetration of the donor (or acceptor) into the inner coordination sphere of the metal. Such effects are most frequently observed in ion-pair salts. For example, the distortions in the symmetry of tetracarbonylcobaltate, tetraphenylborate, or $\text{TpMo}(\text{CO})_3^-$ by ion pairing with pyridinium or metallocenium (see Section 2.3.3) are clear signs of a penetration of the cationic acceptor into the inner coordination sphere of the organometallic donor. The resulting inner-sphere character of such charge-transfer salts is highly solvent dependent and can in its extreme develop into a covalent bond as observed with thallium(I) tetracarbonylcobaltate in benzene [141].

Inner-sphere and outer-sphere electron transfers are not only distinguishable by the structures and charge-transfer interactions of the corresponding donor–acceptor precursor complexes, but also by the free-energy correlation of the ET rate constants. The free energy change (ΔG_{ET}) accompanying outer-sphere electron transfers is simply defined by the potential gap between electron donor and acceptor and a coulombic work term (ω) [203] (Eq. 89).

$$\Delta G_{\text{ET}} = E^\circ_{\text{ox}} - E^\circ_{\text{red}} + \omega \quad (89)$$

According to Marcus theory [7, 8], the activation free energy (ΔG^\ddagger) of outer-sphere electron transfers depends on the free energy (ΔG_{ET}) and the reorganization energy (λ) as follows (Eq. 90).

$$\Delta G^\ddagger = \lambda/4[1 + \Delta G_{\text{ET}}/\lambda]^2 \quad (90)$$

As a consequence, the rate constants for *outer-sphere* electron transfers depend on the free energy of the reaction as a characteristic (quadratic) function, and *inner-sphere* ET reactions are readily revealed by substantial deviations from the Marcus behavior described in Eq. 90.

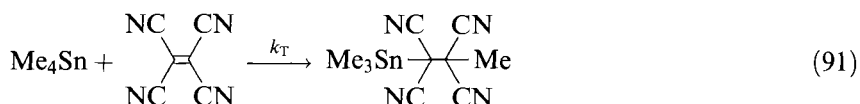
The charge-transfer concept for organic donors and acceptors derived from Mulliken theory [14–16] and the free-energy correlation of electron transfers in inorganic redox systems based on Marcus theory [7–9] are historically and methodologically separate theoretical approaches. Thus, Mulliken theory explains electronic (charge-transfer) transitions in EDA complexes, but does not consider their chemical consequences. On the other hand, Marcus theory predicts the correlation of kinetics and thermodynamics in electron-transfer reactions in the limit of weak coupling of donor and acceptor orbitals, but does not take into account energetic and electronic predisposition to electron transfer due to charge-transfer interactions in the precursor complex. However, both theoretical approaches find a common ground in the inner-sphere–outer-sphere distinction which applies to charge-transfer complexes as well as electron-transfer processes. The close relationship between charge transfer and electron transfer becomes most obvious in the study of sterically

encumbered donors and acceptors. Thus, the increase in the donor–acceptor distance caused by steric hindrance effects a diminution of the donor–acceptor orbital overlap to such an extent that a changeover from an inner-sphere to an outer-sphere mechanism of electron transfer is obtained [29, 31–33].

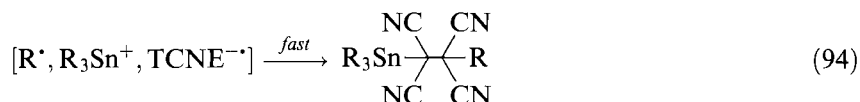
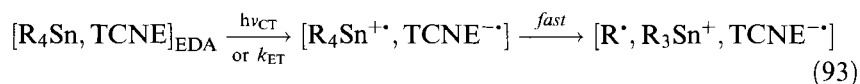
Organometallic donors and acceptors are particularly suitable to demonstrate this mechanistic changeover since (i) their steric encumbrance can be readily modulated by the introduction of bulky ligands around the metal centers, and (ii) their oxidation and reduction potentials can be easily tuned over a wide range by varying the ligands (see Section 2.2), which is important for free-energy correlation studies. As a typical example, electron-transfer reactions of alkylmetals are discussed in Section 2.5.1. However, the steric control of electron-transfer mechanisms is not limited to organometallic redox systems, and examples of purely organic electron-transfer reactions are given in Section 2.5.2 for comparison.

2.5.1 Electron-transfer Reactions of Alkylmetals

Tetraalkyltin compounds (R_4Sn) react with tetracyanoethylene (TCNE) to form an insertion product [33] (Eq. 91).



This reaction is rather slow in the absence of light ($k_T \approx 10^{-4} \text{ M}^{-1} \text{ s}^{-1}$ [33]), but can be photoactivated by deliberate irradiation of the charge-transfer absorption band of the EDA complex which forms upon mixing of the reactants in solution. The thermal as well as the photochemical pathway for TCNE insertion have been shown to occur via an initial electron transfer from the alkylmetal donor to the TCNE acceptor followed by rapid fragmentation of the resulting alkylmetal cation radical (see Section 2.2.1) (Eqs 92–94).

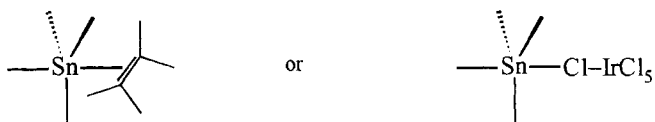


Both, the fragmentation of $R_4Sn^{+\cdot}$ (Eq. 93) and the in-cage collapse of the triad (Eq. 94) are fast processes which allows the back electron transfer within the ion–radical pair to be omitted in Eq. 93 and the electron transfer (k_{ET} (Eq. 93)) to be considered as the rate-determining step [33]. As a result, the rate constants for TCNE insertion can be directly compared with rate constants of other electron-

transfer activated cleavages of alkyl tin donors, and in all cases the rate constants reflect the rate-determining initial electron transfer. Thus, a series of tetraalkyltin compounds of different donor strengths and steric encumbrance are reacted with TCNE, hexachloroiridate(IV) and *tris*(phenanthroline)-iron(III), (FeL_3^{3+}) as oxidants, and the second-order rate constants are determined by UV-Vis spectroscopic observation of the disappearance of TCNE and IrCl_6^{2-} and the appearance of *tris*(phenanthroline)iron(II), respectively [32]. Moreover, the temperature dependence of the rate constants is obtained to calculate activation free energies (ΔG^\ddagger) for the various electron-transfer reactions. The logarithms of the rate constants are plotted against the ionization potentials of the SnR_4 donors in Figure 18. Whereas the rate constants with the iron(III) acceptor (FeL_3^{3+}) are linearly correlated with the ionization potentials, the TCNE and IrCl_6^{2-} data do not follow a linear relationship. In the case of the iron(III) acceptor, the linear correlation of $\log k$ with the ionization potentials also includes sterically encumbered alkyltin compounds such as di-*tert*-butyldimethyltin or tetra-*neo*-pentytin (data points 17 and 18 in Figure 18). In contrast, the strongest deviations from the linear correlation are observed for electron transfer from the most sterically encumbered tetraalkyltin donors to TCNE and iridate(IV) acceptors. A similar trend applies to the activation free energies (ΔG^\ddagger). Thus, the ΔG^\ddagger values for FeL_3^{3+} reactions increase linearly with increasing ionization potentials of the tetraalkyltin donors, whereas the free activation enthalpies of the TCNE and iridate(IV) acceptors do not vary significantly with the ionization potentials.

A quasi-linear correlation of $\log k$ or ΔG^\ddagger with the ionization potentials of the electron donors as observed in the FeL_3^{3+} reactions is predicted by Marcus theory for *outer-sphere* electron transfers. Accordingly, the free-energy dependence of ΔG^\ddagger can be satisfactorily simulated with the Marcus equation (Eq. 90), taking a (constant) value of $\lambda = 41 \text{ kcal mol}^{-1}$ as reorganization energy for all tetraalkyltin compounds (see Figure 19A) [32].

In contrast, similar plots of ΔG^\ddagger against ΔG_{ET} for the oxidants TCNE and hexachloroiridate(IV) deviate substantially from the simulated curve for outer-sphere electron transfer (see Figures 19B, C). Moreover, the most pronounced deviations are observed with the least hindered tetraalkyltin donors. The fact that steric effects are only observed in the latter cases, but not with the FeL_3^{3+} acceptor, leads to the conclusion that the inner coordination spheres of the tetraalkyltin donors are perturbed by TCNE and hexachloroiridate in the ET transition state. In other words, the electron transfers to TCNE and iridate(IV) exhibit strong inner-sphere character and thus occur from *quasi*-five-coordinate precursor complexes reminiscent of a variety of trigonal-bipyramidal structures known for tin(IV) derivatives, i.e.



In contrast, the outer-sphere iron(III) oxidant with its bulky phenanthroline ligands does not form such intimate precursor complexes owing to steric hindrance.

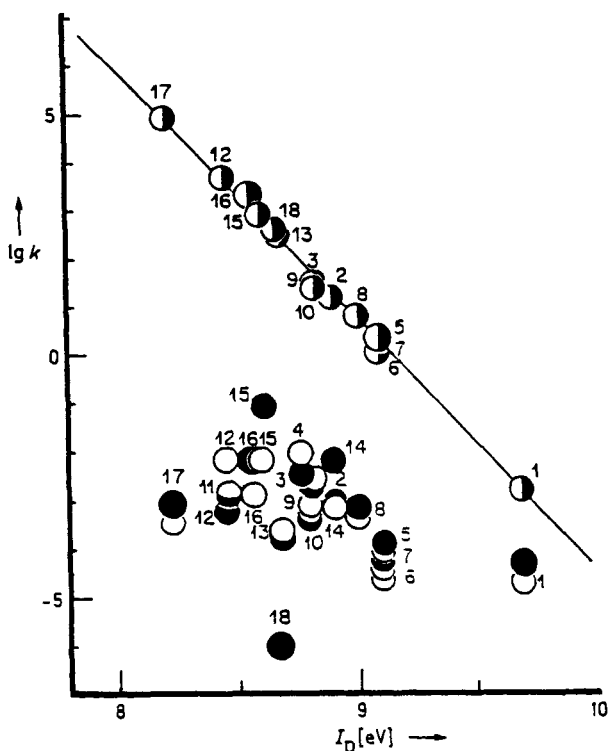


Figure 18. Contrasting behavior of IrCl_6^{2-} (●) and TCNE (○) relative to *tris*(phenanthroline) iron(III) (○) acceptors in the correlation of the rates of oxidation with the ionization potentials of various alkylmetal donors: 1 = Me_4Sn , 2 = Et_4Sn , 3 = $n\text{Pr}_4\text{Sn}$, 4 = $n\text{Bu}_4\text{Sn}$, 5 = EtSnMe_3 , 6 = $n\text{PrSnMe}_3$, 7 = $n\text{BuSnMe}_3$, 8 = Et_2SnMe_2 , 9 = $n\text{Pr}_2\text{SnMe}_2$, 10 = $n\text{Bu}_2\text{SnMe}_2$, 11 = $i\text{Pr}_4\text{Sn}$, 12 = $s\text{Bu}_4\text{Sn}$, 13 = $i\text{Bu}_4\text{Sn}$, 14 = $i\text{PrSnMe}_3$, 15 = $t\text{BuSnMe}_3$, 16 = $i\text{Pr}_2\text{SnMe}_2$, 17 = $t\text{Bu}_2\text{SnMe}_2$, 18 = $(t\text{BuCH}_2)_4\text{Sn}$ [32].

The inner-sphere complexes of tetraalkyltin donors with TCNE are spectroscopically manifested in the charge-transfer absorption bands observed for the EDA complexes such as in Eq. 92 [32, 33]. Quantitative evaluation of the charge-transfer energies according to Mulliken theory (Eq. 8) [14–16] leads to the determination of the coulombic work terms (ω) and their dependence on steric encumbrance [39]. If the electron-transfer rate constants are corrected for the coulombic work terms of sterically more or less hindered donors [39], the corresponding free-energy correlations are linear for all three acceptors, however with different Brønsted slopes which point to different degrees of charge-transfer or inner-sphere character of the donor–acceptor pairs [32, 39]. In other words, the inner-sphere–outer-sphere distinction based on electronic coupling of donor and acceptor orbitals allows for a continuum of intermediate cases to exist between the two idealized extremes, which depends on the donor–acceptor distance and thus on the degree of steric hindrance [32, 204].

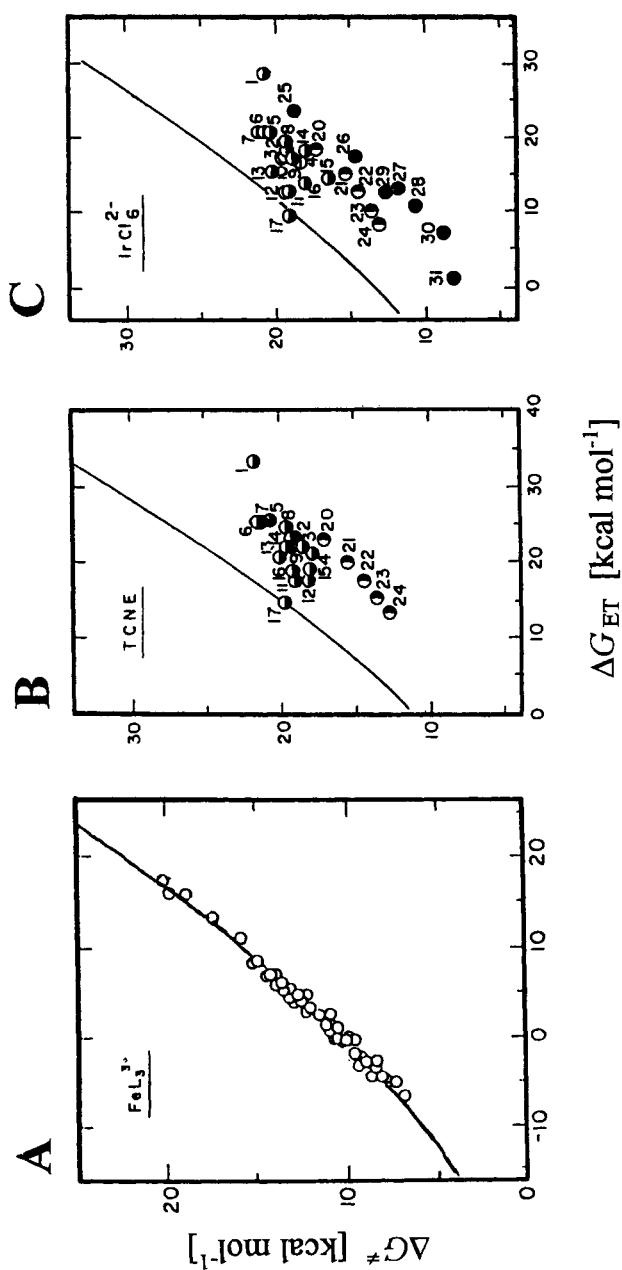


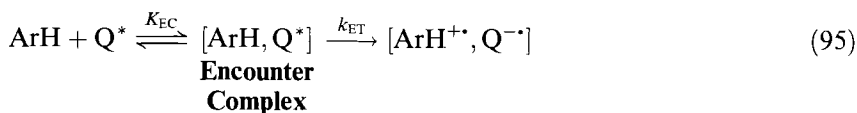
Figure 19. Correlation of the activation energy (ΔG^\ddagger) with the free energy (ΔG_{ET}) for electron transfer from alkylmetals (as identified in Figure 18) to (A) *tris*(phenanthroline) iron(III), (B) TCNE, and (C) IrCl_6^{2-} acceptors. The solid lines represent the correlations for outer-sphere electron transfer according to Marcus theory [32].

2.5.2 Steric Control of Inner-sphere or Outer-sphere Electron Transfers

The general distinction of inner-sphere and outer-sphere electron transfers on the basis of electronic coupling of the donor and acceptor orbitals [31] goes beyond its original definition that is largely based on inorganic coordination complexes [26], and thus provides a universal terminology for electron-transfer mechanisms in all branches of chemistry including inorganic, organic, and organometallic chemistry. Accordingly, the examples of steric effects on the mechanism of organometallic electron transfers are to be complemented by analogous phenomena in organic chemistry [29]. Again, the comparison of electron transfers from sterically hindered and unhindered redox partners is the method of choice to reveal the relationship between electron transfer and charge transfer and to characterize inner-sphere and outer-sphere electron transfers in organic chemistry.

Thus, electron transfers from a series of unhindered, partially hindered, and heavily hindered aromatic electron donors (with matched oxidation potentials) to photoactivated quinone acceptors are kinetically examined by laser flash photolysis, and the free-energy correlations of the ET rate constants are scrutinized [31]. The second-order rate constants of electron transfers from hindered donors such as hexaethylbenzene or tri-*tert*-butylbenzene strongly depend on the temperature, the solvent polarity and salt effects, and they follow the free-energy correlation predicted by Marcus theory (see Figure 20A). Moreover, no spectroscopic or kinetic evidence for the formation of encounter complexes (exciplexes) with the photoactivated quinones prior to electron transfer is observed.

In contrast, electron transfers from unhindered (or partially hindered) donors such as hexamethylbenzene, mesitylene, di-*tert*-butyltoluene, etc. to photoactivated quinones exhibit temperature-independent rate constants that are up to 100 times faster than predicted by Marcus theory, poorly correlated with the accompanying free-energy changes (see Figure 20A), and only weakly affected by solvent polarity and salt effects. Most importantly, there is unambiguous (NIR) spectroscopic and kinetic evidence for the pre-equilibrium formation (K_{EC}) of long-lived encounter complexes (exciplexes) between arene donor (ArH) and photoexcited quinone acceptor (Q^*) prior to electron transfer (k_{ET}) [20] (Eq. 95).



The encounter complexes exhibit high degrees of charge-transfer [20, 91], and on the basis of absorption and emission data electronic coupling matrix elements for similar complexes (exciplexes) have been determined [205] which are comparable to those of mixed-valence metal complexes commonly used as prototypical models for the bridged-activated complex in inner-sphere electron transfers [2, 26, 197]. Accordingly, we ascribe the unusually high rate constants, their temperature-independence, and their *non*-Marcus behavior to an *inner-sphere* electron transfer process [31].

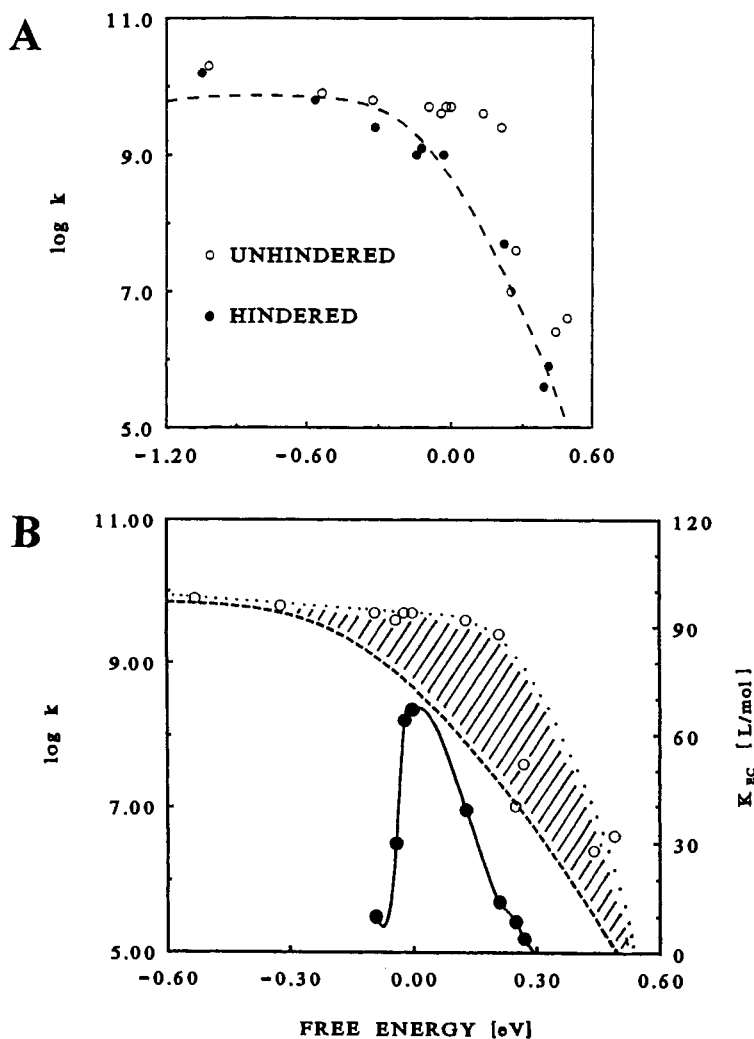


Figure 20. (A) Free-energy dependence of the second-order rate constants ($\log k$) of the electron transfer from hindered (●) and unhindered (○) arene donors to photo-activated quinones. The dashed line represents the best fit of the data points of the hindered donors to the Marcus correlation [31]. (B) Superposition of (A) and the free-energy dependence of the formation constants (K_{EC}) for encounter complexes of unhindered arenes with photoactivated quinones showing the coincidence of maximum encounter-complex formation (●) and maximum deviation of the electron-transfer rate constants of the unhindered donors (○) from Marcus behavior [31].

The difference in the ET mechanisms of hindered and unhindered donor–acceptor pairs is most evident in the comparison of the free-energy correlations in Figure 20A. Thus, the rate constants of the unhindered donors are faster than those of the hindered analogs, and they are faster than predicted by Marcus theory. In fact, the greatest deviations from Marcus behavior is observed for donor–acceptor couples that form the strongest encounter complexes (exciplexes) as gauged by their formation constants (K_{EC} in Eq. 95). Figure 20B illustrates this finding by the superposition of the Marcus-type plots and the free-energy dependence of the formation constants K_{EC} . It is evident that the strongest complex formation is obtained in the isergonic and slightly endergonic free-energy region in which also the greatest deviations of the rate constants from Marcus behavior are observed. We note that the tight encounter complexes with strong charge-transfer character must experience a significant predisposition to electron transfer [20] which allows even endergonic electron transfers to occur at diffusion-limited rates (see Figure 20). In contrast, sterically encumbered donor–acceptor couples undergo ‘loose’ diffusive encounters for electron transfer which do not exhibit any detectable charge-transfer character. Thus, the latter redox partners are good models for the weak coupling limit in *outer-sphere* electron transfers [31].

In analogy to the findings for organometallic electron transfers (*vide supra*), we establish steric encumbrance as the critical effect in controlling the changeover from the outer-sphere to the inner-sphere pathway in electron transfers of organic donors. Both pathways ultimately lead to same electron-transfer products (*viz.* ion–radical pairs (Eq. 95)) without any overall changes in the intermolecular chemical bonds. Thus, the mechanistic difference between the two pathways solely lies in the degree of bonding in the precursor complex immediately preceding the ET transition state. Although this comparative study of hindered and unhindered organic donors suggests a clear-cut (experimental) distinction between inner-sphere and outer-sphere electron transfers, we believe there will generally be a broad borderline region between the two mechanisms. Thus, the idealized inner-sphere–outer-sphere descriptions should be taken as the two extremes in a continuum of electron transfer behaviors that are tuned by the magnitude of electronic coupling in the donor–acceptor pairs [28, 29, 32, 204].

2.6 Concluding Remarks

Owing to their remarkable redox properties, organometallic compounds readily form donor–acceptor assemblies with various organic, inorganic, and other organometallic substrates. X-ray crystallographic and UV–Vis or IR spectroscopic studies show that these donor–acceptor complexes cover a wide spectrum of varying degrees of charge transfer—from weakly-bound (outer-sphere) molecular complexes to strongly-bound (inner-sphere) ion pairs. This review identifies the effects of such donor–acceptor association on the chemical reactivity. Thus, high degrees of charge transfer imply an effective predisposition toward electron transfer which is

recognized as the common (initial) step in various different organometallic reactions such as adduct formations, insertions, eliminations, or redox transformations. Depending on the energetic conditions, the critical electron transfer occurs either spontaneously in a thermal reaction or requires photoactivation, however both activation methods generally lead to identical products. Time-resolved (laser) spectroscopy is a powerful tool to detect the relevant (short-lived) reaction intermediates and to reveal the crucial role of ion-radical species in various organometallic reactions.

Most importantly, the organometallic donor–acceptor complexes and their electron-transfer activated reactions discussed in this review are ideal subjects to link together two independent theoretical approaches, viz. the charge-transfer concept derived from Mulliken theory [14–16] and the free-energy correlation of electron-transfer rates based on Marcus theory [7–9]. A unifying point of view of the inner-sphere–outer-sphere distinction applies to charge-transfer complexes as well as electron-transfer processes in organometallic chemistry.

Acknowledgment

We thank the National Science Foundation and the Robert A. Welch Foundation for financial support.

References

1. J. K. Kochi, *Organometallic Mechanisms and Catalysis*, Academic Press, New York, **1978**.
2. D. Astruc, *Electron Transfer and Radical Processes in Transition-Metal Chemistry*, VCH, New York, **1995**.
3. T. M. Bockman, J. K. Kochi in *Photosensitization and Photocatalysis Using Inorganic and Organometallic Compounds* (Eds.: K. Kalyanasundaram, M. Grätzel), Kluwer Academic, Amsterdam, **1993**, p. 407.
4. K. H. Dötz, R. W. Hoffmann (Eds.), *Organic Synthesis via Organometallics*, Vieweg, Braunschweig, **1991**.
5. J. K. Kochi, *Adv. Phys. Org. Chem.* **1994**, 29, 185.
6. N. G. Connelly, W. E. Geiger, *Chem. Rev.* **1996**, 96, 877.
7. R. A. Marcus, *J. Chem. Phys.* **1956**, 24, 966.
8. R. A. Marcus, *Angew. Chem. Int. Ed. Engl.* **1993**, 32, 1111, and references therein.
9. N. Sutin, *Acc. Chem. Res.* **1968**, 1, 225.
10. Orbital overlap is commonly described by the electronic coupling matrix element V (or H_{AB}), which is assumed (within the limit of weak coupling) to exhibit an exponential falloff with the donor–acceptor distance. See: J. F. Endicott, K. Kumar, T. Ramasami, F. P. Rotzinger, *Prog. Inorg. Chem.* **1983**, 30, 141, and references therein.
11. K. Wynne, C. Galli, R. M. Hochstrasser, *J. Chem. Phys.* **1994**, 100, 4797.
12. T. Asahi, N. Mataga, *J. Phys. Chem.* **1989**, 93, 6575.
13. T. Hannappel, B. Burfeindt, W. Störck, F. Willig, *J. Phys. Chem.* **1997**, B101, 6799.
14. R. S. Mulliken, *J. Am. Chem. Soc.* **1950**, 72, 600.
15. R. S. Mulliken, *J. Am. Chem. Soc.* **1952**, 74, 811.
16. R. S. Mulliken, W. M. Person, *Molecular Complexes*, Wiley, New York, **1969**.
17. J. K. Kochi in [4], p. 95.
18. Charge-transfer excitation of an electron donor–acceptor complex effects the transfer of an electron from the donor to the acceptor in less than 500 fs [11, 12].

19. G. J. Kavarnos, N. J. Turro, *Chem. Rev.* **1986**, 86, 401.
20. R. Rathore, S. M. Hubig, J. K. Kochi, *J. Am. Chem. Soc.* **1997**, 119, 11468.
21. Note that the ion-radical pairs may have different degrees of solvation depending on the electron-transfer pathway in Scheme 1. Thus, they may exist as contact ion pairs, solvent-separated ion pairs, or fully solvated ion radicals.
22. S. Ojima, H. Miyasaka, N. Mataga, *J. Phys. Chem.* **1990**, 94, 7534.
23. K. Kikuchi, Y. Takahashi, K. Koike, K. Wakamatsu, H. Ikeda, T. Miyashi, *Z. Phys. Chem. N. F.* **1990**, 167, 27.
24. I. R. Gould, S. Farid, *Acc. Chem. Res.* **1996**, 29, 522.
25. D. C. Mauzerall in *Photoinduced Electron Transfer, Part A* (Eds.: M. A. Fox, M. Chanon), Elsevier, New York, **1988**, p. 228.
26. H. Taube, *Electron-Transfer Reactions of Complex Ions in Solution*, Academic, New York, **1970**.
27. R. D. Cannon, *Electron-Transfer Reactions*, Butterworth, London, **1980**.
28. L. Ebersson, *Adv. Phys. Org. Chem.* **1982**, 18, 79.
29. J. K. Kochi, *Angew. Chem. Int. Ed. Engl.* **1988**, 27, 1227.
30. H. Zipse, *Angew. Chem. Int. Ed. Engl.* **1997**, 36, 1697.
31. S. M. Hubig, R. Rathore, J. K. Kochi, *J. Am. Chem. Soc.* **1999**, 121, 617.
32. S. Fukuzumi, C. L. Wong, J. K. Kochi, *J. Am. Chem. Soc.* **1980**, 102, 2928.
33. S. Fukuzumi, K. Mochida, J. K. Kochi, *J. Am. Chem. Soc.* **1979**, 101, 5961.
34. The ionization potential of naphthalene is $IP = 8.12$ [35].
35. R. C. Weast (Ed.), *CRC Handbook of Chemistry and Physics*, CRC Press, Boca Raton, FL, **1989**, p. E-87, and references therein.
36. Ionization potentials of polyalkylbenzenes lie between 7.8 and 8.8 [35].
37. See [1], p. 451.
38. H. C. Gardner, J. K. Kochi, *J. Am. Chem. Soc.* **1975**, 97, 1855.
39. S. Fukuzumi, J. K. Kochi, *Bull. Chem. Soc. Jpn.* **1983**, 56, 969.
40. V. F. Traven, R. West, *J. Gen. Chem. USSR* **1974**, 44, 1803.
41. R. J. Klingler, J. K. Kochi, *J. Am. Chem. Soc.* **1981**, 103, 5839.
42. See [32].
43. G. Bieri, F. Burger, E. Heilbronner, J. P. Maier, *Helv. Chim. Acta* **1977**, 60, 2213.
44. D. K. Creber, G. M. Bancroft, *Inorg. Chem.* **1980**, 19, 643.
45. S. Evans, J. C. Green, P. J. Joachim, A. F. Orchard, D. W. Turner, J. P. Maier, *J. Chem. Soc., Faraday Trans. 2* **1972**, 68, 905.
46. T. A. Albright, J. K. Burdett, M.-H. Whangbo, *Orbital Interactions in Chemistry*, Wiley, New York, **1985**, p. 393.
47. J. W. Rabalais, L. O. Werme, T. Bergmark, L. Karlsson, M. Hussain, K. Siegbahn, *J. Chem. Phys.* **1972**, 57, 1185.
48. A. M. Stolzenberg, M. T. Stershic, *J. Am. Chem. Soc.* **1988**, 110, 6391.
49. N. Ito, T. Saji, K. Suga, S. Aoyagui, *J. Organomet. Chem.* **1982**, 229, 43.
50. L. P. Yureva, L. N. Peregudova, L. N. Nekrasov, A. P. Korotkov, N. N. Zaitseva, N. V. Zakarin, A. Yu. Vasilkov, *J. Organomet. Chem.* **1981**, 219, 43.
51. J. O. Howell, J. M. Goncalvez, C. Amatore, L. Klasinc, R. M. Wightman, J. K. Kochi, *J. Am. Chem. Soc.* **1984**, 106, 3968.
52. M. K. Lloyd, J. A. McCleverty, J. A. Connor, E. M. Jones, *J. Chem. Soc., Dalton Trans.* **1973**, 1768.
53. Metal carbonyls are irreversibly oxidized in solution. See: C. J. Pickett, D. Pletcher, *J. Chem. Soc., Dalton Trans.* **1976**, 636.
54. S. Evans, A. F. Orchard, D. W. Turner, *Int. J. Mass Spectrom. Ion Phys.* **1971**, 7, 261. See also: C. Amatore, D. J. Kuchynka, J. K. Kochi, *J. Electroanal. Chem.* **1988**, 241, 181.
55. B. R. Higginson, D. R. Lloyd, P. Burroughs, D. M. Gibson, A. F. Orchard, *J. Chem. Soc., Faraday Trans. 2* **1973**, 69, 1659.
56. D. R. Lloyd, E. W. Schlag, *Inorg. Chem.* **1969**, 8, 2544.
57. J. C. Green, S. E. Jackson, B. Higginson, *J. Chem. Soc., Dalton Trans.* **1975**, 403.
58. J. J. Ko, T. M. Bockman, J. K. Kochi, *Organometallics* **1990**, 9, 1833.
59. R. J. Klingler, C. J. Huffman, J. K. Kochi, *J. Am. Chem. Soc.* **1980**, 102, 208.

60. T. P. Fehlner, J. K. Kochi, unpublished results.
61. B. R. Higginson, D. R. Lloyd, S. Evans, A. F. Orchard, *J. Chem. Soc., Faraday Trans. 2* **1975**, 71, 1913.
62. S. Craddock, E. A. V. Ebsworth, A. Robertson, *J. Chem. Soc., Dalton Trans.* **1973**, 23.
63. R. J. Klingler, K. Mochida, J. K. Kochi, *J. Am. Chem. Soc.* **1979**, 101, 6626.
64. D. Zhu, S. V. Lindeman, J. K. Kochi, *Organometallics* **1999**, 18, 2241.
65. D. Zhu, J. K. Kochi, *Organometallics* **1999**, 18, 161.
66. L. L. Miller, G. D. Nordblom, E. A. Mayeda, *J. Org. Chem.* **1972**, 37, 916.
67. S. Murphy, G. B. Schuster, *J. Phys. Chem.* **1995**, 99, 511.
68. A. M. Bond, R. Colton, *Inorg. Chem.* **1976**, 15, 2036.
69. D. J. Kuchynka, J. K. Kochi, *Inorg. Chem.* **1989**, 28, 855.
70. T. Madach, H. Vahrenkamp, *Z. Naturforsch.* **1979**, 34b, 573.
71. C. S. Ilenda, N. E. Schore, R. G. Bergman, *J. Am. Chem. Soc.* **1976**, 98, 255.
72. D. Miholova, A. A. Vlcek, *Inorg. Chim. Acta* **1980**, 41, 119.
73. For example, the cationic $[\text{Co}_2(\text{fulvalene})_2]^+$ complex is readily oxidized to the dication by carbon tetrachloride. See: S. F. Clark, R. J. Watts, D. L. Dubois, J. S. Connolly, J. C. Smart, *Coord. Chem. Rev.* **1985**, 64, 273.
74. J. A. McCleverty, *Prog. Inorg. Chem.* **1968**, 10, 49.
75. D. B. Morse, D. N. Hendrickson, T. B. Rauchfuss, S. R. Wilson, *Organometallics* **1988**, 7, 496.
76. P. G. Gassman, C. H. Winter, *J. Am. Chem. Soc.* **1986**, 108, 4228.
77. C. L. Wong, J. K. Kochi, *J. Am. Chem. Soc.* **1979**, 101, 5593.
78. K. L. Rollick, J. K. Kochi, *J. Am. Chem. Soc.* **1982**, 104, 1319.
79. W. E. Geiger, Jr., D. E. Smith, *J. Electroanal. Chem. Interfac. Electrochem.* **1974**, 50, 31.
80. Y. Mugnier, C. Moise, J. Tirouflet, E. Laviron, *J. Organomet. Chem.* **1980**, 186, C49.
81. Z. J. Karpinski, J. K. Kochi, *J. Organomet. Chem.* **1992**, 437, 211.
82. D. Astruc, *Top. Curr. Chem.* **1991**, 160, 49.
83. U. Koelle, B. Fuss, M. V. Rajasekharan, B. L. Ramakrishna, J. H. Ammeter, M. C. Böhm, *J. Am. Chem. Soc.* **1984**, 106, 4152.
84. R. E. Lehmann, T. M. Bockman, J. K. Kochi, *J. Am. Chem. Soc.* **1990**, 112, 458.
85. L. J. Andrews, R. M. Keefer, *Molecular Complexes in Organic Chemistry*, Holden-Day, San Francisco, **1964**.
86. R. Foster, *Organic Charge-Transfer Complexes*, Academic, New York, **1969**.
87. G. Briegleb, *Elektronen-Donator-Acceptor Komplexe*, Springer, Heidelberg, **1961**.
88. V. M. Nekipelov, K. I. Zamaraev, *Coord. Chem. Rev.* **1985**, 61, 185.
89. M. T. Beck, *Coord. Chem. Rev.* **1968**, 3, 91.
90. V. Balzani, N. Sabbatini, F. Scandola, *Chem. Rev.* **1986**, 86, 319.
91. On the basis of Mulliken theory [14–16], the degree of charge transfer is defined as the ratio $(b/a)^2$ of the mixing coefficients **a** and **b** of the no-bond and the dative wave functions, respectively. For the experimental determination of $(b/a)^2$, see [87, 92, 93].
92. J. A. A. Ketelaar, *J. Phys. Radium* **1954**, 15, 197.
93. M. Tamres, M. Brandon, *J. Am. Chem. Soc.* **1960**, 82, 2134.
94. P. Debye, *Z. Physik* **1920**, 21, 178.
95. W. J. Duffin, *Electricity and Magnetism*, McGraw Hill, New York, **1973**, p. 79.
96. F. London, *Trans. Faraday Soc.* **1937**, 33, 8.
97. See, for example: J. P. Fackler, T. S. Davis, I. D. Chawla, *Inorg. Chem.* **1965**, 4, 130.
98. N. Mataga, T. Kubota, *Molecular Interactions and Electronic Spectra*, Dekker, New York, **1970**, p. 219.
99. M. Tamres, R. L. Strong in *Molecular Association Vol. 2* (Ed.: R. Foster), Academic, London, **1979**, p. 331.
100. D. F. Evans, *J. Chem. Soc.* **1953**, 345.
101. H. A. Benesi, J. H. Hildebrand, *J. Am. Chem. Soc.* **1949**, 71, 2703.
102. The term 'charge resonance' is adopted from studies with mixed-valence metal complexes and cation-radical-neutral π -dimers ($\text{D}^+, \text{D} \leftrightarrow \text{D}, \text{D}^+$) [150].
103. C. W. Davis, *Ion Association*, Butterworth, London, **1962**.
104. M. Szwarc (Ed.), *Ions and Ion Pairs in Organic Reactions, Vols. 1 and 2*, Wiley, New York, **1972, 1974**.

105. A. Vogler, H. Kunkely, *Top. Curr. Chem.* **1990**, 158, 1.
106. K. I. Zamaraev, A. N. Kitaigorodskii, *Coord. Chem.* **1980**, 6, 563.
107. O. V. Nesterov, V. M. Nekipelov, Yu. N. Chirkov, A. N. Kitaigorodskii, S. G. Entelis, *Kinet. Katal.* **1980**, 21, 1238.
108. J. C. D. Brand, W. Snedden, *Trans. Faraday Soc.* **1957**, 53, 894.
109. F. K. Velichko, L. V. Balabanova, T. T. Vasileva, O. P. Bondarenko, G. A. Shvakhgimer, *Izv. Akad. Nauk. SSSR, Ser. Khim.* **1988**, 711.
110. H. Kobayashi, M. Kobayashi, Y. Kaizu, *Bull. Chem. Soc. Jpn.* **1973**, 46, 3109.
111. S. Fukuzumi, J. K. Kochi, *J. Am. Chem. Soc.* **1980**, 102, 2141.
112. R. D. Schmitt, R. M. Wing, A. H. Maki, *J. Am. Chem. Soc.* **1969**, 91, 4394.
113. W. Lau, J. K. Kochi, *J. Am. Chem. Soc.* **1986**, 108, 6720.
114. J. M. Wallis, J. K. Kochi, *J. Org. Chem.* **1988**, 53, 1679.
115. K. Brüggermann, J. K. Kochi, *J. Org. Chem.* **1992**, 57, 2956.
116. K. Brüggermann, R. S. Czernuszewicz, J. K. Kochi, *J. Phys. Chem.* **1992**, 96, 4405.
117. Note that the Drago–Rose determination (R. S. Drago, N. J. Rose, *J. Am. Chem. Soc.* **1959**, 81, 6138) of K_{diss} does not distinguish as to whether the products of the dissociation are free ions or solvent-separated ion pairs. See: H. C. Wang, G. Levin, M. Szwarc, *J. Am. Chem. Soc.* **1978**, 100, 6137.
118. T. M. Bockman, J. K. Kochi, *J. Am. Chem. Soc.* **1989**, 111, 4669.
119. M. Darensbourg, H. Barros, C. Bormann, *J. Am. Chem. Soc.* **1977**, 99, 1647.
120. J. K. Kochi, C. H. Wei, *J. Organomet. Chem.* **1993**, 451, 111.
121. See [105].
122. A comprehensive list of charge-transfer absorption bands of various organometallic EDA complexes is given in [3].
123. H. C. Gardner, J. K. Kochi, *J. Am. Chem. Soc.* **1976**, 98, 2460.
124. R. E. Lehmann, J. K. Kochi, *J. Am. Chem. Soc.* **1991**, 113, 501.
125. R. Billing, D. Rehorek, H. Hennig, *Top. Curr. Chem.* **1990**, 58, 166.
126. T. M. Bockman, J. K. Kochi, *J. Phys. Org. Chem.* **1997**, 10, 542.
127. T. M. Bockman, J. K. Kochi, *New J. Chem.* **1992**, 16, 39.
128. C. Reichardt, *Solvents and Solvent Effects in Organic Chemistry*, VCH, 2nd ed., Weinheim, **1988**.
129. R. A. Marcus, *J. Phys. Chem.* **1989**, 93, 3078.
130. S. M. Hubig, J. K. Kochi, *J. Phys. Chem.* **1995**, 99, 17578.
131. C. Reichardt, *Chem. Soc. Rev.* **1992**, 147.
132. A. Loupy, B. Tchoubar, *Effets de Sel en Chimie Organique et Organometallique*, Dunod, Paris, **1988**.
133. J. Yarwood, R. Arndt in *Molecular Association Vol. 2* (Ed.: R. F. Foster), Academic, New York, **1979**, p. 267.
134. Z. G. Soos, D. J. Klein in *Molecular Association Vol. 1* (Ed.: R. F. Foster), Academic, New York, **1975**, p. 2.
135. C. K. Prout, B. Kamenar in *Molecular Complexes Vol. 1* (Ed.: R. F. Foster), Elek, London, **1969**, p. 49.
136. R. Rathore, S. V. Lindeman, J. K. Kochi, *J. Am. Chem. Soc.* **1997**, 119, 9393.
137. P. L. Veya, J. K. Kochi, *J. Organomet. Chem.* **1995**, 488, C4.
138. H. Kisch, A. Fernández, Y. Wakatsuki, H. Yamazaki, *Z. Naturforsch.* **1985**, 40b, 292.
139. M. Lemke, F. Knoch, H. Kisch, J. Salbeck, *Chem. Ber.* **1995**, 128, 131.
140. C.-H. Wei, T. M. Bockman, J. K. Kochi, *J. Organomet. Chem.* **1992**, 428, 85.
141. C. Schramm, J. I. Zink, *J. Am. Chem. Soc.* **1979**, 101, 4554.
142. E. K. Kim, J. K. Kochi, *J. Am. Chem. Soc.* **1991**, 113, 4962.
143. S. Brownstein, E. Gabe, F. Lee, A. Piotrowski, *Can. J. Chem.* **1986**, 64, 1661.
144. R. Rathore, S. V. Lindeman, J. K. Kochi, *Angew. Chem. Int. Ed. Engl.* **1998**, 37, 1585.
145. G. I. Borodkin, I. R. Elanov, M. M. Shakirov, V. G. Shubin, *J. Phys. Org. Chem.* **1993**, 6, 153.
146. M. E. Peover, *Trans. Faraday Soc.* **1966**, 62, 3535.
147. J. S. Miller, J. C. Calabrese, A. J. Epstein, J. H. Zhang, W. M. Reiff, *J. Chem. Soc., Chem. Commun.* **1986**, 1026.

148. E. Adman, M. Rosenblum, S. Sullivan, T. N. Margulis, *J. Am. Chem. Soc.* **1967**, 89, 4540.
149. M. Rosenblum, R. W. Fish, C. Bennett, *J. Am. Chem. Soc.* **1964**, 86, 5166.
150. Note that the CT absorption band of the complex in solution and in the solid state at $\lambda_{CT} \approx 1100$ nm [149] is in the same wavelength range as that of charge-resonance transitions in π -dimers of aromatic cation radicals with their neutral counterparts, which points to an electron-transfer driving force close to zero. See: B. Badger, B. Brocklehurst, *Trans. Faraday Soc.* **1969**, 65, 2576, 2582, 2588.
151. J. S. Miller, J. H. Zhang, W. M. Reiff, D. A. Dixon, L. D. Preston, A. H. Reis, Jr., E. Gebert, M. Extine, J. Troup, A. J. Epstein, M. D. Ward, *J. Phys. Chem.* **1987**, 91, 4344.
152. S. M. Hubig, T. M. Bockman, J. K. Kochi, *J. Am. Chem. Soc.* **1996**, 118, 3842.
153. W. Kaiser, *Ultrashort Laser Pulses and Applications*, Springer, New York, **1988**.
154. J.-L. Martin, A. Migus, G. A. Mourou, A. H. Zewail, *Ultrafast Phenomena VIII*, Springer, New York, **1993**.
155. H. Kisch, W. Dümmler, C. Chiorboli, F. Scandola, J. Salbeck, J. Daub, *J. Phys. Chem.* **1992**, 96, 10323.
156. S. M. Hubig, unpublished results.
157. R. Criegee, *Liebigs Ann. Chem.* **1936**, 522, 75.
158. R. Criegee, B. Marchand, H. Wannowius, *Liebigs Ann. Chem.* **1942**, 550, 99.
159. R. J. Collin, J. Jones, W. P. Griffith, *J. Chem. Soc., Dalton Trans.* **1974**, 1094.
160. R. L. Clark, E. J. Behrmann, *Inorg. Chem.* **1975**, 14, 1425.
161. J. M. Wallis, J. K. Kochi, *J. Am. Chem. Soc.* **1988**, 110, 8207.
162. G. Wilkinson, M. Rosenblum, M. C. Whiting, R. B. Woodward, *J. Am. Chem. Soc.* **1952**, 74, 2125.
163. E. O. Fischer, F. Röhrscheid, *Z. Naturforsch.* **1962**, 17b, 483.
164. Z. J. Karpinski, J. K. Kochi, *J. Organomet. Chem.* **1992**, 437, 211.
165. Z. J. Karpinski, J. K. Kochi, *Inorg. Chem.* **1992**, 31, 2767.
166. Y. Mugnier, P. Reeb, C. Moise, E. Laviron, *J. Organomet. Chem.* **1983**, 254, 111.
167. D. J. Kuchynka, J. K. Kochi, *Inorg. Chem.* **1989**, 28, 855.
168. W. L. Waltz, O. Hackelberg, L. M. Dorfman, A. Wojcicki, *J. Am. Chem. Soc.* **1978**, 100, 7259.
169. S. P. Church, M. Poliakoff, J. A. Timney, J. J. Turner, *J. Am. Chem. Soc.* **1981**, 103, 7515.
170. H. W. Walker, R. S. Herrick, R. J. Olsen, T. L. Brown, *Inorg. Chem.* **1984**, 23, 3748.
171. M. Itoh, S. Nagakura, *Bull. Chem. Soc. Jpn.* **1966**, 39, 369.
172. R. F. Cozzens, T. A. Gover, *J. Phys. Chem.* **1970**, 74, 3003.
173. J. A. S. Howell, P. M. Burkinshaw, *Chem. Rev.* **1983**, 83, 557.
174. A. Davison, J. E. Ellis, *J. Organomet. Chem.* **1971**, 31, 239.
175. F. Ungváry, A. Wojcicki, *J. Am. Chem. Soc.* **1987**, 109, 6848.
176. D. J. Kuchynka, C. Amatore, J. K. Kochi, *J. Organomet. Chem.* **1987**, 328, 133.
177. F. G. Bordwell, M. J. Bausch, *J. Am. Chem. Soc.* **1986**, 108, 1979.
178. N. M. Boag, H. D. Kaesz in *Comprehensive Organometallic Chemistry Vol. 4* (Eds.: G. Wilkinson, F. G. A. Stone, E. W. Abel), Pergamon, Oxford, **1982**, p. 1161.
179. R. E. Lehmann, J. K. Kochi, *Organometallics* **1991**, 10, 190.
180. F. D. Saeva, *Top. Curr. Chem* **1990**, 156, 59.
181. A. N. Nesmeyanov, Yu. A. Chapovsky, I. V. Polovnyanyuk, L. G. Makarova, *J. Organomet. Chem.* **1967**, 7, 329.
182. M. D. Curtis, K. B. Shiu, W. M. Butler, J. C. Huffman, *J. Am. Chem. Soc.* **1986**, 108, 3335.
183. A. T. Balaban, C. Bratu, C. N. Rentea, *Tetrahedron* **1964**, 20, 265.
184. V. Wintgens, J. Pouliquen, J. Kossanyi, M. Heintz, *Nouv. J. Chim.* **1986**, 10, 345.
185. A. Nakamura, S. Otsuka, *J. Am. Chem. Soc.* **1973**, 95, 7262 and **1972**, 94, 1886.
186. E. Negishi, *J. Organomet. Chem.* **1976**, 108, 281.
187. R. Hunter, J. P. Michael, G. D. Tomlinson, *Tetrahedron* **1994**, 50, 871.
188. T. Nagamura, *Pure & Appl. Chem.* **1996**, 68, 1449.
189. S. Chatterjee, P. D. Davis, P. Gottschalk, M. E. Kurz, B. Sauerwein, X. Yang, G. B. Schuster, *J. Am. Chem. Soc.* **1990**, 112, 6329.
190. G. B. Schuster, *Pure & Appl. Chem.* **1990**, 62, 1565.
191. Cleavage rates for the boron-carbon bond in boranyl radicals have been estimated to exceed $k = 10^{11} \text{ s}^{-1}$ [189, 190].

- 192. D. Zhu, J. K. Kochi, *J. Organomet. Chem.* **1999**, 580, 295.
- 193. H. O. House, *Acc. Chem. Res.* **1976**, 9, 59.
- 194. G. Hallnemo, C. Ullenius, *Tetrahedron* **1983**, 39, 1621.
- 195. D. Zhu, unpublished results.
- 196. S. Komiya, T. A. Albright, R. Hoffmann, J. K. Kochi, *J. Am. Chem. Soc.* **1977**, 99, 8440.
- 197. A. Haim, *Prog. Inorg. Chem.* **1983**, 30, 273.
- 198. J. C. Polanyi, A. H. Zewail, *Acc. Chem. Res.* **1995**, 28, 119.
- 199. D. Zhong, A. H. Zewail, *J. Phys. Chem.* **1998**, A102, 4031.
- 200. W. L. Reynolds, R. W. Lumry, *Mechanisms of Electron Transfer*, Ronald Press, New York, **1966**, p. 12.
- 201. M. Juillard, M. Chanon, *Chem. Rev.* **1983**, 83, 425.
- 202. L. Eberson, *Electron Transfer Reactions in Organic Chemistry*, Springer, New York, **1987**, p. 18.
- 203. The free energy (ΔG_{ET}) for the transfer of an electron from a single donor to an acceptor molecule is given in eV, and thus the Faraday constant is omitted in Eq. 89.
- 204. D. R. Rosseinsky, *Chem. Rev.* **1972**, 72, 215.
- 205. I. R. Gould, R. H. Young, L. J. Mueller, A. C. Albrecht, S. Farid, *J. Am. Chem. Soc.* **1994**, 116, 8166.

3 The Thermodynamics of Organometallic Systems Involving Electron-transfer Paths

Mats Tilset

3.1 Introduction

Kochi's book from 1978 [1a] helped to establish electron-transfer and radical reactions as a crucial part of mainstream organometallic chemistry. The importance of such reactions is evident from Astruc's book [1b], still the most comprehensive and authoritative book in the area, and from several reviews and review collections [2] on aspects of organometallic electron-transfer reactivity. This chapter will be fully devoted to the use of electrochemical techniques to obtain bond-energy data for organometallic complexes, a topic that has not been previously reviewed. Aspects of the energetics of redox-induced structural changes and isomerizations, a thoroughly pursued topic, has been reviewed [2o] and will not be included here.

Bonding energetics is of fundamental importance to modern chemistry, as will be apparent from any contemporary general, organic, or inorganic chemistry text book. Knowledge of bond energies between metal and ligands and between atoms within ligands in organotransition-metal complexes is crucial to the understanding of stoichiometric and catalytic reactions. Insight into the often complex reaction mechanisms based on a quantitative understanding of strengths of bonds being formed and broken in the reaction steps involved might ultimately help in the design of new and improved processes [3]. Numerous methods, all with their particular scopes and limitations, are available for experimental estimation of the energetics of homolytic and heterolytic bond-cleavage reactions.

Electrochemical techniques, in particular cyclic voltammetry, have proven valuable for obtaining the electrode-potential data needed to obtain bond-energy data from thermochemical cycles. In a cyclic voltammetry experiment, a species generated at an electrode surface during the forward scan is detected again at the same electrode on the reverse scan. For a Nernstian, or nearly Nernstian, chemically reversible or partially reversible cyclic voltammogram, the midpoint between the anodic and cathodic peak potentials is a good estimate of the standard redox potential, E° . The time window of the experiment is adjustable through the voltage

scan rate ν (V s^{-1}). In principle, ν can be varied by many orders of magnitude and, therefore, E° can be determined for very stable and for rather short-lived species. Further details about this experimental technique will not be discussed here, because it is well covered in electrochemistry textbooks [4].

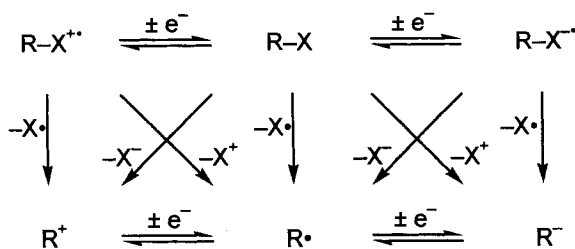
3.2 Introduction to Thermochemical Cycles in the Study of Bond-cleavage Reactions of Molecules and Ions

A covalently bonded species R-X can be envisaged as undergoing cleavage of the R-X bond by the three modes depicted in Eqs 1–3. Here, Eq. 1 represents the homolytic cleavage reaction in which the X group departs as X^\bullet , along with the corresponding homolytic bond-dissociation energy (BDE) which is normally enthalpy-based. On the other hand, in Eqs 2 and 3, X departs as X^+ or X^- , respectively. The energetics of these three reactions are interrelated by the electron affinities (EA) and ionization potentials (IP) of the R^\bullet and X^\bullet radicals, and this relationship has formed the basis of extensive studies of species in the gas phase by mass spectrometric techniques [5]. In solution, the electron affinities and ionization potentials can be replaced by the corresponding standard electrode potentials (E°) for the pertinent redox processes.

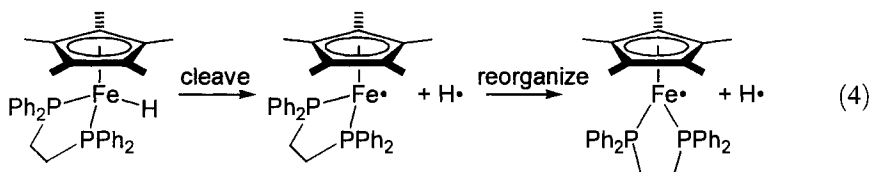
Reaction	Energy change	
$\text{R-X} \rightarrow \text{R}^\bullet + \text{X}^\bullet$	$\text{BDE}(\text{R-X})$	(1)
$\text{R-X} \rightarrow \text{R}^- + \text{X}^+$	$\text{BDE}(\text{R-X}) - EA(\text{R}^\bullet) + IP(\text{X}^\bullet)$	(2)
$\text{R-X} \rightarrow \text{R}^+ + \text{X}^-$	$\text{BDE}(\text{R-X}) + IP(\text{R}^\bullet) - EA(\text{X}^\bullet)$	(3)

The concept ‘bond-dissociation energy’ is used to describe the energy change that accompanies the breakage of a specific bond in a molecule while the remaining molecular fragments are allowed to relax to their equilibrium geometries. Thus, the bond-dissociation energy includes two important terms. The first is the energy needed to cleave the bond and remove the two fragments from each other while retaining their respective geometries exactly as they were in the molecule. The second is the ‘reorganization energy’, a term that is necessarily exothermic, which is the energy that is gained when both fragments are allowed to attain their equilibrium geometries by relaxation of bond distances and angles [6]. This term can amount to a significant fraction of the total bond-dissociation energy. It is important to keep this in mind when bond-dissociation energies and trends are discussed in terms of the molecular structures and properties of the molecules that undergo cleavage. The contributions from reorganization energies might be particularly important for sterically encumbered systems, where the spatial demands of the ligands perturb the structure away from an otherwise ideal bonding geometry. As an example, consider the homolytic cleavage of the Fe-H bond in the organometallic

Scheme 1. Relationship between homolytic and heterolytic bond cleavage and electron-transfer reactions.



complex $\text{Cp}^*\text{Fe}(\text{dppe})\text{H}$. The deuteride analog $\text{Cp}^*\text{Fe}(\text{dppe})\text{D}$ was characterized by X-ray crystallography [7a] and has a three-legged piano-stool structure. Homolysis of the Fe–H bond, Eq. 4, generates a hydrogen atom and the $\text{Cp}^*\text{Fe}(\text{dppe})^{\bullet}$ radical with the same bond angles and distances as in the original molecule. This fragment then relaxes to the ground-state structure, which is a two-legged piano stool structure with the Fe and P atoms and the Cp^* centroid lying in one plane, as verified by X-ray crystallography [7b].



It is easy to envisage homolytic and heterolytic processes analogous to those in Eqs 1–3 that involve the substrate R-X in other oxidation states, i.e. its cation, dication, anion, etc. Wayner and Parker [8] have summarized the relationships between homolytic and heterolytic bond energies and redox processes. A mnemonic that shows available R-X cleavage patterns for a substrate R-X in three different oxidation states is shown in Scheme 1. Horizontal reactions involve the transfer of an electron, vertical reactions involve transfer of an X^{\bullet} radical, and diagonal reactions involve the transfer of X^{+} or X^{-} . The energy changes for any given reaction can be written as the sum of the changes for other reactions that add up to the same overall reaction. The use of thermochemical cycles based on this scheme will usually lead to *relative* rather than *absolute* bond energies. Absolute values can, however, be obtained when one or more reliable ‘anchoring points’ are available (see Section 3.3).

In a landmark paper, Breslow and coworkers described the determination of $\text{p}K_{\text{a}}$ values of weak hydrocarbon acids by use of thermochemical cycles involving electrochemical reduction data for triarylmethyl, cycloheptatrienyl, and triphenyl- and trialkylcyclopropenyl cations and radicals [9a]. Later, they derived $\text{p}K_{\text{a}}$ data from standard oxidation potentials and bond-dissociation energies [9b, c]. The methodology was further developed by Nicholas and Arnold [10a] for the determination of cation radical acidities, and later modified and extensively used by Bordwell and coworkers [10b, c] so that homolytic bond-dissociation energies and cation radical

acidities could be determined in solution from a knowledge of pertinent electrode potential and pK_a data. Since then the application of thermochemical cycles that incorporate electrode-potential data as a means of determining *absolute or relative bond energies* that are difficult or impossible to obtain by direct methods has gained widespread popularity. Electrochemical methods have been employed to determine bond-dissociation energy, acidity, and related data for organic molecules, radicals, ions, and ion radicals, and the methods and results have been thoroughly reviewed [8, 11].

During the last decade, extensive use has also been made of such thermochemical cycles to probe the bonding energetics in organometallic complexes. The rest of this chapter will describe efforts made by us and others towards this goal. We will first describe a thermochemical cycle that can be successfully used to determine *absolute* bond-dissociation energies for M–H and C–H bonds of coordinated ligands. Thereafter, the effects of single-electron-transfer processes on the energetics of homolytic and heterolytic bond-cleavage reactions will be described.

3.3 Absolute Bond-dissociation Energies for M–H, Coordinated Ligand C–H, and M–M Bonds

Many transition-metal hydrides exhibit significant equilibrium acidities [12]. This applies in particular to those that have electron-withdrawing ancillary ligands and/or a positive charge. This section presents a thermochemical cycle that uses these acidity (pK_a) data, when available, as an anchoring point to derive absolute BDE data. In principle the method is applicable to the investigation of BDEs of any M–X bond. In practice, applications have been limited to M–H because data on the prerequisite equilibrium dissociation of M–X to M^- and X^+ in solution have been limited to metal hydrides.

3.3.1 Thermochemical Cycle for Determination of Absolute M–H Bond-dissociation Energies

By adapting the method of Bordwell for determination of C–H BDEs [10b], we arrived at a very useful method for estimating M–H bond-dissociation energies in solution (Scheme 2) [13]. The combined reactions represented by Eqs 5–9 give that depicted by Eq. 10 and constitute a thermochemical cycle which gives M–H BDE_G expressed as Eq. 11. The subscript signifies that the derived BDE_G quantity is *free-energy-based*, rather than enthalpy-based. Here, $pK_a(M-H)$ is the Brønsted acidity of the metal hydride in the chosen solvent (solv), and $E^\circ_{ox}(M^-)$ is the standard electrode potential for the oxidation of the conjugate base M^- of the metal hydride. The electrode reaction depicted by Eq. 7 refers to the reduction of H^+ in the solvent to which all other reactions are referred.

reaction	free energy change ΔG°
$M-H(solv) \longrightarrow M^-(solv) + H^+(solv)$	$2.301RTpK_a(M-H, solv)$ (5)
$M^-(solv) \longrightarrow M^\bullet(solv) + e^-$	$-FE^\circ_{ox}(M^-, solv)$ (6)
$H^+(solv) \longrightarrow 0.5H_2(g)$	$FE^\circ(H^+/H_2, solv)$ (7)
$0.5H_2(g) \longrightarrow H^\bullet(g)$	$\Delta G^\circ_f(H^\bullet, gas)$ (8)
$H^\bullet(g) \longrightarrow H^\bullet(solv)$	$\Delta G^\circ_{solv}(H^\bullet, solv)$ (9)
$M-H(solv) \longrightarrow M^\bullet(solv) + H^\bullet(solv)$	BDE_G (10)
$BDE_G = 2.301RTpK_a(M-H, solv) + F[E^\circ_{ox}(M^-, solv) - E^\circ(H^+/H_2, solv)] + \Delta G^\circ_f(H^\bullet, gas) + \Delta G^\circ_{solv}(H^\bullet, solv)$	
$BDE_G = 2.301RTpK_a(M-H, solv) + FE^\circ_{ox}(M^-, solv) + C_G$	
$BDE = 2.301RTpK_a(M-H, solv) + FE^\circ_{ox}(M^-, solv) + C$	

Scheme 2. Thermochemical cycle for determination of metal–hydride bond-dissociation energies.

It is convenient to gather all the constant terms in Eq. 11 to a constant C_G to yield the simplified Eq. 12. The value of C_G depends on the solvent chosen and on the reference electrode against which $E^\circ_{ox}(M^-, solv)$ and $E^\circ(H^+/H_2, solv)$ are referred. Compilations of metal-hydride pK_a data in acetonitrile, mostly determined by Norton and coworkers, are available [14]. Acetonitrile is also an excellent solvent for many organometallic complexes, unreactive towards many (but far from all!) hydrides, and is also a superb solvent for non-aqueous electrochemistry. The high dielectric constant of this solvent ensures that ion-pairing effects do not strongly influence acid–base or electrochemical measurements. For these reasons, it was our preferred solvent. The free energy of solvation for the hydrogen atom, $\Delta G^\circ_{solv}(H^\bullet)$, was assumed to be equal to that of the hydrogen molecule, which varies very little in several organic solvents [15]. This term was taken to be $+21.4 \text{ kJ mol}^{-1}$ in acetonitrile as calculated from reported ΔH° and ΔS° values [16]. The value for $\Delta G^\circ_f(H^\bullet)_g$ was taken as $203.3 \text{ kJ mol}^{-1}$ [17]. In practice, the H^+/H_2 electrode, whether aqueous (NHE) or non-aqueous, is rarely used as an experimental reference. We therefore adhere to the recommended [18] use of the $Fc/Fc^+(solv)$ system where Fc refers to ferrocene. When Fc is used as the reference, a quantity $FE^\circ(Fc/Fc^+, solv)$ must be added to the constant terms in Eq. 11. Two presumably reliable values for $E^\circ(Fc/Fc^+, MeCN)$ relative to $E^\circ(H^+/H_2, MeCN)$ are $+0.034$ and $+0.068 \text{ V}$ [19]. Using the average value, 4.9 kJ mol^{-1} must be added to C_G . This leads to $C_G = 229.7 \text{ kJ mol}^{-1}$ for *free-energy-based data* when acetonitrile is the solvent for electrochemical and pK_a measurements, and the electrochemical reference is Fc .

To convert the free energy data to enthalpy-based values that can be directly compared with quantities determined by calorimetric methods, the entropy contri-

bution to the M–H cleavage reaction must be included. This contribution amounts to the entropy of the hydrogen atom in solution if one assumes that the entropies of solvation for M–H and M[•] are equal. (This approximation should be valid if the two species have nearly identical shapes and charge distributions, and has been found to hold well for organic radicals R[•] compared with hydrocarbons R–H [20]). The entropy of the hydrogen atom in solution, $\Delta S^\circ(\text{H}^\bullet, \text{solv})$, is the sum of the entropy of formation of the hydrogen atom in the gas phase ($114.6 \text{ J K}^{-1} \text{ mol}^{-1}$ [17]) and the entropy of solvation of the hydrogen atom, taken to equal that of the H₂ molecule ($-49.8 \text{ J K}^{-1} \text{ mol}^{-1}$ [16]). Thus, $\Delta S^\circ(\text{H}^\bullet, \text{solv}) = 64.9 \text{ J K}^{-1} \text{ mol}^{-1}$, and $T\Delta S^\circ(\text{H}^\bullet) = 19.3 \text{ kJ mol}^{-1}$ at 298.15 K. This quantity must be added to the free-energy-based BDE_G, and thence to the constant C_G, to obtain enthalpy-based BDE data. When acetonitrile is the solvent for electrochemical and pK_a measurements and the electrochemical reference is Fc, this gives $C = 249 \text{ kJ mol}^{-1}$ for *enthalpy-based data*, Eq. 14. Similar treatment can be used for other solvents. For example [13b], $C = 308 \text{ kJ mol}^{-1}$ in DMSO, Eq. 15.

$$\begin{aligned} \text{BDE} &= 2.301RT\text{p}K_{\text{a}}(\text{M–H, MeCN}) \\ &+ FE^\circ_{\text{ox}}(\text{M}^-, \text{MeCN}) + 249 \text{ kJ mol}^{-1} \end{aligned} \quad (14)$$

$$\begin{aligned} \text{BDE} &= 2.301RT\text{p}K_{\text{a}}(\text{M–H, DMSO}) \\ &+ FE^\circ_{\text{ox}}(\text{M}^-, \text{DMSO}) + 308 \text{ kJ mol}^{-1} \end{aligned} \quad (15)$$

Many assumptions go into the calculation of C in Eq. 13 as described above, and the validity of these, and estimates of their uncertainties, have been discussed in detail [13b]. It is, however, desirable to have an independent check of the validity of the resulting data. Fortunately, M–H bond strengths have been directly determined by calorimetric investigation of the heat of hydrogenation of CpCr(CO)₃[•] and related persistent radicals [21]. These systems are also amenable to the electrochemical determination of the Cr–H BDEs. Combining the calorimetrically determined BDEs and measured pK_a(M–H) and $E^\circ_{\text{ox}}(\text{M}^-)$ data for M–H = CpCr(CO)₃H and CpCr(CO)₂(PPh₃)H led, by insertion into Eq. 13, to calculated C values of 248 and 250 kJ mol^{−1}, respectively. There is perfect agreement between the average of these values and the independently determined C value of 249 kJ mol^{−1} described above. This suggests that very reliable M–H BDE data can be obtained from this thermochemical cycle when pK_a data in acetonitrile are available and accurate $E^\circ_{\text{ox}}(\text{M}^-)$ data can be obtained from reversible voltammograms recorded in acetonitrile. If other solvents are used, great care must be taken to eliminate errors caused by conversion of pK_a scales for different solvents and reference-electrode systems. It is always desirable to have independent verification of some data when making approximations or assumptions such as these.

3.3.2 M–H Bond-dissociation Energies Determined in Acetonitrile

We have applied the thermochemical cycle that results in Eq. 13 to a wide range of organotransition-metal hydrides that have thermodynamic acidities suitable for de-

Table 1. Metal-hydride acidities, oxidation potentials, and bond-dissociation energies in acetonitrile.

Entry	Compound MH	$pK_a(\text{MH})^a$	$E_{\text{ox}}(\text{M}^-)^b$ (V relative to Fc)	BDE(MH) ^c (kJ mol ⁻¹)
1	CpCr(CO) ₃ H	13.3	-0.69	257
2	CpCr(CO) ₂ [P(OMe) ₃]H	21.1 ^e	-1.11	262 ^f
3	CpCr(CO) ₂ (PPh ₃)H	21.8 ^g	-1.29	250
4	CpCr(CO) ₂ (PEt ₃)H	25.8 ^e	-1.51	251 ^f
5	Cp*Cr(CO) ₃ H	16.1 ^e	-0.83	261 ^f
6	TpCr(CO) ₃ H	<8 ^g	-0.82	<215
7	Tp'Cr(CO) ₃ H	- ^g	-0.86	-
8	CpMo(CO) ₃ H	13.9	-0.50 ^d	290
9	Cp*Mo(CO) ₃ H	17.1	-0.71 ^d	287
10	TpMo(CO) ₃ H	10.7 ^h	-0.52	260
11	Tp'Mo(CO) ₃ H	9.7 ^h	-0.58	248
12	CpW(CO) ₃ H	16.1	-0.49 ^d	303
13	CpW(CO) ₂ (PMe ₃)H	26.6	-1.23 ^d	291
14	CpW(CO) ₂ (PMe ₃)H ₂ ⁺	>9	0.16	>316
15	TpW(CO) ₃ H	14.4 ^h	-0.58	275
16	Tp'W(CO) ₃ H	12.9 ^h	-0.65	260
17	Mn(CO) ₅ H	14.1	-0.56 ^d	285
18	Mn(CO) ₄ (PPh ₃)H	20.4	-0.87 ^d	286
19	Re(CO) ₅ H	21.1	-0.69 ^d	313
20	CpFe(CO) ₂ H	19.4	-1.35 ^d	239
21	Fe(CO) ₄ H ₂	11.4	-0.40 ^d	283
22	CpRu(CO) ₂ H	20.2	-1.06 ^d	272
23	Cp* ₂ OsH ⁺	9.9 ⁱ	-0.06	298
24	Co(CO) ₄ H	8.3	-0.27 ^d	278
25	Co(CO) ₃ (PPh ₃)H	15.4	-0.72 ^d	272
26	Co(CO) ₃ [P(OPh) ₃]H	11.3	-0.49 ^d	273

^a According to [14] unless otherwise noted.^b E° data estimated from reversible cyclic voltammograms unless otherwise noted.^c Calculated from Eq. 14 unless otherwise noted.^d Oxidation peak potentials from irreversible voltammograms [13a]. Kinetic potential shifts were applied before use of Eq. 14, as discussed elsewhere [13].^e pK_a data were calculated [22a] from calorimetrically determined BDE data [21] by use of Eq. 14.^f According to [21].^g According to [13b].^h According to [22b].ⁱ According to [22c].

termination by proton-transfer equilibrium measurements in acetonitrile [13, 22]. Table 1 lists the results currently available. Note that *reversible* voltammograms were obtained for entries 1–7, 10–11, 14–16, and 23 only. For the other species, irreversible peak potentials were measured for the anion oxidations, and the E° values were estimated by correcting for the kinetic potential shift that is caused by the rapid follow-up reactions of the electrode-generated metalloradicals. These re-

actions are, under these conditions, second-order dimerization processes, often at rates approaching diffusion-control. Although kinetic potential shift corrections can easily be applied [23], the occurrence of irreversible oxidation waves does introduce an added uncertainty into the measurements. If electron transfer itself is not rate-limiting, i.e. the electron-transfer step is Nernstian, the maximum kinetic potential shift is $E_p - E^\circ = 128 \text{ mV}$ for a diffusion-controlled ($10^{10} \text{ M}^{-1} \text{ s}^{-1}$) second-order dimerization at a substrate concentration of 10^{-3} M and a voltage scan rate v of 1 V s^{-1} which is quite typical of cyclic voltammetry experiments. The kinetic shift for an anodic wave will be to a potential less positive than E° . The 128 mV shift therefore results in the BDE being underestimated by 12 kJ mol^{-1} unless a correction is applied. These and other complicating factors, such as non-Nernstian behavior arising from irreversible cyclic voltammograms, have been thoroughly discussed in this context [13b].

After the first systematic study of M–H BDEs [13a], we noted trends that seemed particularly interesting: (i) BDEs always *increase* when going down a group in the periodic table, i.e. in the order 1st row metal < 2nd row < 3rd row when ligands are equal; (ii) BDEs are relatively insensitive to a simple ligand substitutions in which a two-electron donor CO ligand is replaced by a tertiary phosphine; and (iii) BDEs are essentially unaffected when a Cp ligand is replaced by a Cp* ligand. The first trend is in accord with a substantial amount of accumulated data [3]. The ligand effects will be further discussed in Section 3.3.4.

A compilation of absolute BDE data is valuable in that the data might provide ‘anchoring points’ for relative BDEs available from other measurements. For example, Nolan and coworkers used the BDE for $\text{CpRu}(\text{CO})_2\text{H}$ (entry 22 in Table 1) with the assumption that Ru–H BDEs in $\text{CpRu}(\text{CO})_2\text{H}$ and $\text{Cp}^*\text{Ru}(\text{CO})_2\text{H}$ are nearly equal, to estimate absolute Ru–X ($\text{X} = \text{Cl}, \text{Br}, \text{I}$) BDEs in $\text{Cp}^*\text{Ru}(\text{CO})_2\text{X}$ complexes from calorimetry data that alone would have provided relative BDEs only [24].

3.3.3 M–H Bond-dissociation Energies Determined in Solvents other than Acetonitrile

Despite the favorable properties of acetonitrile as a solvent, its use for equilibrium acidity measurements has its definite limitations. The $\text{p}K_a$ range that is tolerable is limited at the high end by onset of solvent deprotonation, and at the low end by substrate autodissociation, as has been implicated for $\text{HCo}(\text{CO})_4$ [14a] and $\text{TpCr}(\text{CO})_3\text{H}$ [22b]. These limitations can be overcome by the choice of a less polar solvent, e.g. 1,2-dichloroethane (DCE), dichloromethane, or THF. To make reliable, quantitative comparisons of thermodynamic data obtained in different solvents, it is necessary to link the acidity scales and electrode potential references in the different solvents. This has all too often proven to be a far from trivial task. Although, in principle, 1:1 relationship between the acidity scales in different solvents never exists, $\text{p}K_a$ differences between closely related compounds are often almost constant when compared in different solvents. This is because their solvation properties are similar, because of similarities in size and charge distribution. In less

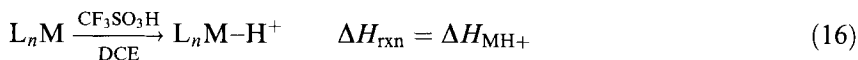
polar solvents, further complications result from extensive ion-pairing effects that will perturb acidity and electrochemical measurements. Further errors, unfortunately abundant in the literature, sometimes arise when electrode potentials measured against a certain reference in a certain solvent are converted to potentials referred against another reference, perhaps in another solvent. IUPAC has recommended [18] the use of Fc as an internal reference standard—it is commonly used not because its oxidation potential is solvent-independent (it is not!) but rather out of convenience—Cp₂Fe is inexpensive, readily available, stable in two oxidation states, and soluble in most solvents. Ruiz and Astruc [25] have recently convincingly argued that decamethylmetallocenes and Cp*Fe(C₆Me₆) would be better choices for standards, because their interactions with different solvents will be much more similar, simply because these permethylated transition-metal sandwiches are much bigger and the charge in the corresponding cations is better shielded against solvent interactions.

Heat of protonation and electrochemical measurements in 1,2-dichloroethane

Angelici [26] has reviewed a systematic study of relative acidities of *cationic* metal hydrides in DCE by measurement of the heats of protonation (ΔH_{MH^+}) of neutral metal precursors with triflic acid, Eq. 16. More recently, Wang and Angelici have used these data in a thermochemical cycle derived from Eq. 13 to obtain BDE data for these hydrides [27]. The advantage of the reaction calorimetry technique is that relative acidities can be obtained for compounds that are far too weakly acidic to be studied by proton-transfer equilibrium measurements in acetonitrile. Calorimetry does not, however, provide thermodynamically significant $\text{p}K_{\text{a}}$ data directly. We have determined the acidity of *one* of the compounds investigated calorimetrically by Angelici, Cp*₂OsH⁺, in acetonitrile [22c]. Differences between $\text{p}K_{\text{a}}$ values in acetonitrile for this compound and others for which calorimetry data are available can be approximated by use of the relationship $2.301RT\Delta\text{p}K_{\text{a}} = -\Delta\Delta H_{\text{MH}^+} + T\Delta\Delta S_{\text{MH}^+}$. With the assumption that $\Delta\Delta S_{\text{MH}^+} = 0$, this gives $\Delta\text{p}K_{\text{a}} = -\Delta\Delta H_{\text{MH}^+}/2.301RT$, or $-\Delta\Delta H_{\text{MH}^+} = 5.70 \text{ p}K_{\text{a}} \text{ kJ mol}^{-1}$ at 25 °C. This relationship predicts a slope of 5.70 for a plot of heat of protonation against $\text{p}K_{\text{a}}$ data; a slope of 6.36 (1.52 on a kcal mol⁻¹ basis) was found for such a correlation of data for a series of nitrogen bases with known aqueous $\text{p}K_{\text{a}}$ values.

This might be an indication that $\Delta\Delta S_{\text{MH}^+} \neq 0$ in DCE, perhaps as a consequence of systematic covariance of ΔH_{MH^+} and ΔS_{MH^+} because of ion pairing in DCE. It is not known whether the same applies to metal-hydride data. Nevertheless, a systematic study of ΔH_{MH^+} and $E^{\circ}_{\text{ox}}(\text{M})$ was undertaken for a wide range of complexes. On the assumption that the ideal linear relationship with a slope of 5.70 exists between ΔH_{MH^+} (DCE) and $\text{p}K_{\text{a}}$ (acetonitrile) data, the complex Cp*₂OsH⁺ can be used as an ‘anchoring point’ to relate DCE calorimetry data to acetonitrile $\text{p}K_{\text{a}}$ data. Eq. 17 was empirically derived using this ‘anchor’ and gives the relationship between BDE, ΔH_{MH^+} (in DCE), and $E^{\circ}_{\text{ox}}(\text{M})$ (V relative to the SCE in DCE) [27]. Electrochemical measurements were obtained by cyclic voltammetry, second harmonic AC voltammetry, and/or Osteryoung square-wave voltammetry. For more than half of the compounds irreversible voltammograms were obtained

and because little is quantitatively known about the nature of the follow-up reactions, no kinetic corrections have been applied to the measured potentials.

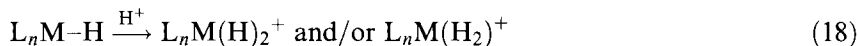


$$\text{BDE}(\text{MH}^+) = -\Delta H_{\text{MH}^+} + FE^\circ_{\text{ox}}(\text{M}) + 139 \text{ kJ mol}^{-1} \quad (17)$$

The resulting bond-energy data [27] are summarized in Table 2. As in Table 1, there is an unambiguous trend that BDEs increase down a group in the periodic table. Ligand effects are less clear-cut and will be discussed in Section 3.3.4.

Aqueous pK_a and electrochemical measurements in THF, dichloromethane, and acetone

Morris and coworkers have described the protonation reactions of a wide range of Group 8 metal hydrides, Eq. 18, as part of their investigation of cationic metal dihydride and dihydrogen complexes [28]. The relative acidities of a series of cationic dihydride or dihydrogen complexes were determined by proton-transfer equilibrium measurements in dichloromethane, THF, and acetone [29]. The absolute pK_a of $\text{CpRu}(\text{PPh}_3)_2\text{H}_2^+$ was estimated by measuring the proton-transfer equilibrium constant between $\text{CpRu}(\text{PPh}_3)_2\text{H}$ and HPCy_3^+ in dichloromethane and THF. The results were converted into a pseudo-aqueous pK_a scale by assuming constant acidity differences between $\text{CpRu}(\text{PPh}_3)_2\text{H}_2^+$ and HPCy_3^+ in the solvents used [29a], with the aqueous $pK_a = 9.7$ of HPCy_3^+ as the anchoring point. The constant-acidity-difference assumption was then applied to the whole series of complexes.



A C value of 247 kJ mol^{-1} for the use in Eq. 13, referring to the aqueous pK_a scale and electrode potentials relative to the Fc in the organic solvents, was originally used, apparently [29d] on the assumption that Ru-H BDEs of 272 kJ mol^{-1} were reasonable estimates [29b, c]. We later presented evidence that the Ru-H BDE of $\text{CpRu}(\text{PPh}_3)_2\text{H}_2^+$ might be substantially higher [30], and Morris and coworkers revised the value of C under these conditions to be 276 kJ mol^{-1} [29d]. This C value is based on assumed constant acidity differences between HPCy_3^+ and the structurally very different cationic metal dihydrides in water and THF or dichloromethane. Therefore, in our view it is highly desirable to have a direct link to BDE data independently determined under different conditions, preferably the acetone-trile-based data in Table 1. Unfortunately, thus far no such anchoring point exists.

The oxidation potentials for the conjugate bases, the neutral monohydrides, were obtained by cyclic voltammetry in THF or dichloromethane. Irreversible waves were often reported, also for $\text{CpRu}(\text{PPh}_3)_2\text{H}$, $\text{CpRu}(\text{dppe})\text{H}$, and $\text{CpRu}(\text{dppp})\text{H}$ for which other workers had reported reversible voltammetry [27, 30, 31]. It is not clear to what extent, if any, these differences will affect the calculated BDEs, and for the sake of internal consistency of data we will mostly use Morris's data. The data

Table 2. Heats of protonation, oxidation potentials, and bond-dissociation energies of metal hydrides in DCE [26].

Entry	Compound M	$-\Delta H_{\text{MH}^+}$ (kJ mol ⁻¹)	$E^\circ_{\text{ox}}(\text{M})^a$ (V relative to the SCE)	BDE(MH ⁺) ^b (kJ mol ⁻¹)
1	Cr(CO) ₂ (dppm) ₂	107	-0.12	234
2	Mo(CO) ₂ (arphos) ₂	100	0.28	266
3	Mo(CO) ₂ (dppe) ₂	115	0.24	277
4	Mo(CO) ₂ (dppm) ₂	124	0.18	281
5	W(CO) ₃ (PMePh ₂) ₃	63	0.48 ^c	249
6	W(CO) ₃ (PEtPh ₂) ₃	71	0.45 ^c	254
7	W(CO) ₃ (PEt ₂ Ph) ₃	77	0.41 ^c	255
8	W(CO) ₃ (PMe ₃) ₃	82	0.40 ^c	259
9	W(CO) ₃ (PEt ₃) ₃	105	0.28 ^c	271
10	W(CO) ₂ (dppm) ₂	132	0.14	285
11	W(CO) ₃ (tripod)	44	0.72	253
12	W(CO) ₃ (triphos)	70	0.63	270
13	Cp*Re(CO) ₂ (PMe ₂ Ph)	77	0.84 ^c	297
14	Cp*Re(CO) ₂ (PMe ₃)	84	0.80 ^c	300
15	Fe(CO) ₃ (PPh ₃) ₂	59	0.55 ^c	251
16	Fe(CO) ₃ (PMePh ₂) ₂	74	0.49 ^c	260
17	Fe(CO) ₃ (PMe ₂ Ph) ₂	89	0.45 ^c	272
18	Fe(CO) ₃ (PMe ₃) ₂	97	0.41 ^c	277
19	Fe(CO) ₃ (dppp)	88	0.31 ^c	257
20	Fe(CO) ₃ (dppm)	100	0.40 ^c	278
21	Cp* ₂ Ru	79	0.68 ^c	285
22	CpRu(PMe ₃) ₂ I	86	0.56	279
23	CpRu(dppm)H	121	0.37	296
24	CpRu(dppe)H	121	0.31	290
25	CpRu(PPh ₃) ₂ H	124	0.23 ^c	286
26	Cp* ₂ Os	111	0.51 ^c	300
27	CpOs(PPh ₃) ₂ Br	68	0.59 ^c	264
28	CpOs(PPh ₃) ₂ Cl	82	0.58 ^c	278
29	CpOs(PPh ₂ Me) ₂ Br	85	0.51 ^c	273
30	CpOs(PMe ₃) ₂ Br	123	0.34 ^c	295
31	CpOs(PPh ₃) ₂ H	156	0.13 ^c	308
32	CpIr(CO)[P(<i>p</i> -C ₆ H ₄ CF ₃) ₃]	117	0.60	314
33	CpIr(CO)[P(<i>p</i> -C ₆ H ₄ F) ₃]	125	0.53	315
34	CpIr(CO)(PPh ₃)	126	0.50	313
35	CpIr(CO)(PPh ₂ Me)	132	0.45	315
36	CpIr(CO)(PMe ₂ Ph)	136	0.41	315
37	CpIr(CO)(PMe ₃)	139	0.37	314
38	CpIr(CO)(PEt ₃)	138	0.35	311
39	CpIr(CO)(PCy ₃)	137	0.35	310
40	CpIr(CS)(PPh ₃)	111	0.51	300
41	CpIr(COD)	95	0.69	301
42	(C ₅ H ₄ Me)Ir(COD)	101	0.61	299
43	(1,2,3-C ₅ H ₂ Me ₃)Ir(COD)	110	0.54	302
44	(C ₅ Me ₄ H)Ir(COD)	115	0.47	300

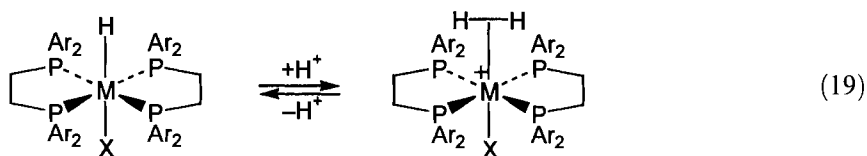
Table 2 (continued)

Entry	Compound M	$-\Delta H_{\text{MH}^+}$ (kJ mol ⁻¹)	$E^\circ_{\text{ox}}(\text{M})^a$ (V relative to the SCE)	BDE(MH ⁺) ^b (kJ mol ⁻¹)
45	Cp*Ir(COD)	119	0.45	302
46	Cp*Ir(CO)[P(<i>p</i> -C ₆ H ₄ CF ₃) ₃]	141	0.30	310
47	Cp*Ir(CO)[P(<i>p</i> -C ₆ H ₄ Cl) ₃]	154	0.20	313
48	Cp*Ir(CO)(PPh ₃)	155	0.09	303
49	Cp*Ir(CO)(PPh ₂ Me)	155	0.08	303
50	Cp*Ir(CO)(PMe ₃)	159	0.07	305
51	Cp*Ir(CO) ₂	90	0.72	298

^aIrreversible voltammograms unless otherwise noted.^bCalculated from Eq. 17.^cReversible voltammogram.

were originally used in conjunction with a rearranged Eq. 13 to discuss correlations between oxidation potentials and acidities of metal hydrides on the assumption that M–H BDEs were constant for a series of CpRu(PR₃)₂H₂⁺ complexes and the Cp* analogs [29a, c]. We have now discarded this assumption and instead used the published pK_a(MH₂⁺) and E_{ox}(MH) data to derive the corresponding BDE values for a number of derivatives of CpRu(PR₃)₂H₂⁺. Morris' revised value [29d] for C of 276 kJ mol⁻¹ in Eq. 14 is used. The data are shown in Table 3.

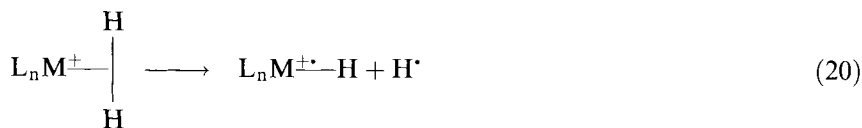
Morris also investigated dihydrogen complexes of the type (diphosphine)₂M(X)(H₂)⁺, obtained by protonation of *trans*-(diphosphine)MHX, Eq. 19 [29d–f]. Acidity and electrochemical measurements were performed under conditions identical to those above, and BDE determinations were performed analogously. These data are also included in Table 3.



Finally, electrode potential and acidity data were used by Ng et al. to study ligand effects on CpM(PR₃)₂H₂⁺ and TpM(PPh₃)₂(η²-H₂)⁺ (M = Ru, Os) complexes under similar conditions [31]; these data are included in Table 3. The Ru–H BDE determined by Ng for CpRu(PPh₃)₂H₂⁺ (Table 3, entry 19; 289 kJ mol⁻¹) is in near perfect agreement with that of Angelici (Table 2, entry 25; 286 kJ mol⁻¹) but somewhat different from the value derived from Morris' data (Table 3, entry 1; 303 kJ mol⁻¹). The source of the discrepancy might partly be the assumptions and conversions made to align the pK_a and electrochemical reference scales of the different solvents used.

Table 3. Pseudo-aqueous pK_a data and metal-hydride oxidation potential data in THF or dichloromethane.^a

Entry	Compound MH_2^+	$pK_a(MH_2^+)$	$E_{ox}(MH)$ (V relative to Fc)	BDE(MH_2^+) (kJ mol ⁻¹)
1	CpRu(PPh ₃) ₂ H ₂ ⁺	8.0	−0.20	303
2	CpRu(dppe)H ₂ ⁺	7.5	−0.09	310 ^b
3	CpRu(dtfpe)H ₂ ⁺	4.6	0.17	319 ^b
4	CpRu(dppp)H ₂ ⁺	8.6	−0.22	304 ^b
5	CpRu(dape)H ₂ ⁺	9.0	−0.22	306 ^b
6	Cp [*] Ru(PMe ₃) ₂ H ₂ ⁺	16.3	−0.62	310 ^b
7	Cp [*] Ru(PMe ₂ Ph) ₂ H ₂ ⁺	14.3	−0.57	303 ^b
8	Cp [*] Ru(PMePh ₂) ₂ H ₂ ⁺	12.2	−0.49	299 ^b
9	Cp [*] Ru(PPh ₃) ₂ H ₂ ⁺	11.1	−0.46	295 ^b
10	Cp [*] Ru(dppm)H ₂ ⁺	8.8	−0.25	302
11	Cp [*] Ru(dppm)(η^2 -H ₂) ⁺	9.2	−0.25	306
12	Cp [*] Ru(dppp)H ₂ ⁺	10.4	−0.44	293 ^b
13	<i>trans</i> -CpOs(dppm)H ₂ ⁺	10.0	−0.16	318 ^c
14	<i>cis</i> -CpOs(dppm)H ₂ ⁺	10.9	−0.16	323 ^c
15	<i>trans</i> -CpOs(dppe)H ₂ ⁺	11.8	−0.17	327 ^c
16	<i>cis</i> -CpOs(dppe)H ₂ ⁺	9.9	−0.17	316 ^c
17	<i>trans</i> -CpOs(dppp)H ₂ ⁺	13.4	−0.35	319 ^c
18	<i>trans</i> -CpOs(PPh ₃) ₂ H ₂ ⁺	13.4	−0.38	316 ^c
19	CpRu(PPh ₃) ₂ H ₂ ⁺	8.3	−0.36	289 ^c
20	TpRu(PPh ₃) ₂ (η^2 -H ₂) ⁺	7.6	−0.12	308 ^c
21	TpOs(PPh ₃) ₂ (η^2 -H ₂) ⁺	8.9	−0.22	306 ^c
22	<i>trans</i> -HRu(dtfpe) ₂ (η^2 -H ₂) ⁺	10.0	0.40	372
23	<i>trans</i> -HRu(dppe) ₂ (η^2 -H ₂) ⁺	15.0	−0.20	343
24	<i>trans</i> -ClRu(dppe) ₂ (η^2 -H ₂) ⁺	6.0	−0.12	299
25	<i>trans</i> -HRu(depe) ₂ (η^2 -H ₂) ⁺	17.5	−0.40	338
26	<i>trans</i> -HRu(dppf) ₂ H ₂ ⁺	4.4	−0.63	240
27	<i>trans</i> -HOS(dtfpe) ₂ (η^2 -H ₂) ⁺	9.2	0.10	339
28	<i>trans</i> -HOS(dppe) ₂ (η^2 -H ₂) ⁺	13.6	−0.20	335
29	<i>trans</i> -(MeCN)Os(dppe) ₂ (η^2 -H ₂) ²⁺	−2.0	0.58	321
30	<i>trans</i> -ClOs(dppe) ₂ (η^2 -H ₂) ⁺	7.4	−0.13	306
31	<i>trans</i> -BrOs(dppe) ₂ (η^2 -H ₂) ⁺	5.4	−0.11	296
32	<i>trans</i> -HOS(depe) ₂ (η^2 -H ₂) ⁺	17.3	−0.60	317

^a Data from [29] unless otherwise noted.^b Calculated from E_{ox} and pK_a data [29a, c] as mentioned in the text.^c Data from [31].

The variations in M–H BDEs for *dihydrogen* species are particularly intriguing. When a hydrogen atom is removed from a dihydrogen (η^2 -H₂) ligand, Eq. 20, it is

not only the M–H bond that is broken. The H–H bond to the other hydrogen atom in the η^2 -H₂ ligand is also cleaved. Simultaneously, the M–H bond strength to the hydrogen atom that remains on the metal will change (this is part of the reorganization process, see Section 3.2).

The H–H BDE in H₂(g) is 435 kJ mol^{−1} [17]. Inspection of the data for η^2 -H₂ species in Table 3 reveals that the H–H bond is always considerably weakened as a result of the complexation. This is in agreement with spectroscopic and structural data for η^2 -H₂ complexes [28, 32], i.e. ¹H NMR J_{HD} coupling constants, $r_{\text{H-H}}$ distances inferred from T_1 measurements, IR $\nu_{\text{H-H}}$ stretching frequencies, etc. The data in Table 3 show that the BDE values for η^2 -H₂ complexes are *strikingly lower* for most of the Os complexes than for the Ru analogs, contrasting the trends for ‘normal’ M–H bonds. This result might be readily understood by taking into account that these η^2 -H₂ BDE data reflect the combined effect of M–H and H–H bonding. It is well established that H–H cleavage is more pronounced for 3rd row metals than for 2nd row metals in η^2 -H₂ complexes, where the ancillary ligands are identical. This is because the 3rd row metals are generally more capable of donating electron density to the σ^* orbital of the H₂ ligand, ultimately leading to H–H cleavage and the formal oxidative addition of H₂ to the metal [28, 32]. It might, therefore, be argued that there is more H–H bonding left in Ru(η^2 -H₂) complexes than in analogous Os(η^2 -H₂) complexes. The compromise between a stronger M–H component and a weaker H–H component for Os can cause the apparent reversal of expected BDEs seen in Table 3.

3.3.4 Discussion of Ligand Effects on M–H BDE Data

The data in Tables 1–3 probably constitute the most extensive overview available for solution M–H BDE data that have been obtained by a single method. The effect of ancillary ligands on the M–H BDEs in series of related complexes can be studied in some detail. It was pointed out in Section 3.3.1 that the BDEs are remarkably insensitive to certain changes in the ligands. For example, within each of the following groups from Table 1, BDE differences are smaller than 8 kJ mol^{−1}: CpCr(CO)₂(L)H (entries 1–4); CpW(CO)₂(L)H (entries 12 and 13); Mn(CO)₄(L)H (entries 17 and 18); Co(CO)₃(L)H (entries 24–26); CpM(CO)₃H compared with Cp*M(CO)₃H (M = Cr, entries 1 and 5; Mo, entries 8 and 9). Similar effects are found in Table 2: less than 5 kJ mol^{−1} differences within the series CpIr(CO)(L)H⁺ (entries 32–39); Cp'Ir(COD)H⁺ (entries 41–45); Cp*Ir(CO)(L)H⁺ (entries 46–51, where the dicarbonyl differs somewhat more from the substituted compounds).

The essential lack of ligand effects in the above series can be qualitatively appreciated by considering that from Eq. 13 the BDE depends on contributions from the hydride pK_a and the oxidation potential of the corresponding anion. The introduction of a better donor ligand will make $E^\circ_{\text{ox}}(\text{M}^-)$ less positive and contribute to a lower BDE, but will normally also lead to a pK_a increase contributing to a higher BDE. Judging from the BDE data for the series mentioned above, these two opposing factors tend to cancel each other almost exactly.

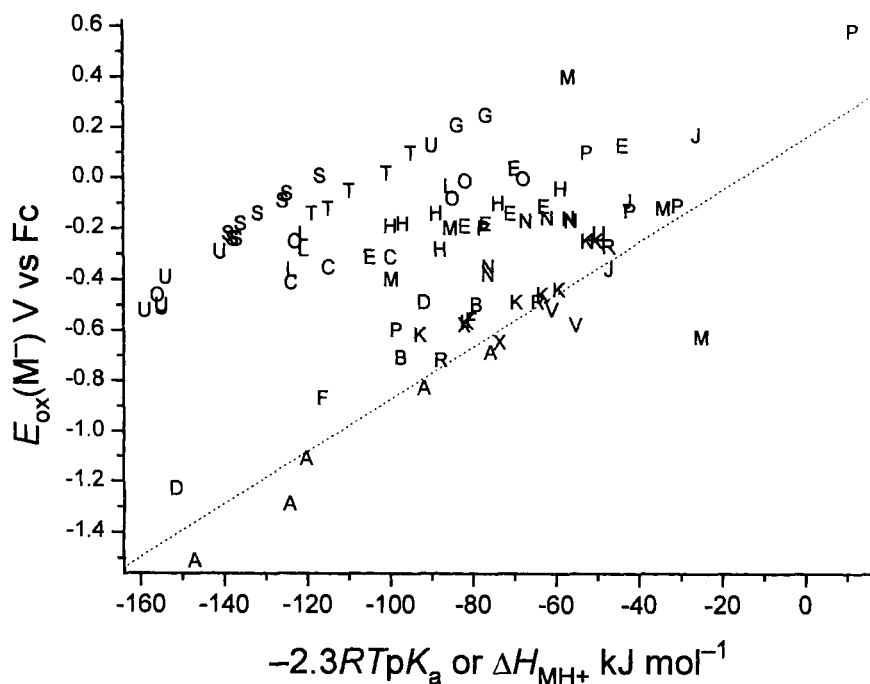


Figure 1. Plot of metal hydride acidity against oxidation potentials of their conjugate base. Legend (where L = CO or tertiary phosphine, P = tertiary phosphine, X = H or halide or MeCN⁺, Cp'' = substituted or unsubstituted Cp, Tp'' = unsubstituted or substituted Tp): A = Cp''Cr(CO)₂(L)H (Table 1, 1–5); B = Cp''Mo(CO)₃H (Table 1, 8 and 9); C = Mo(CO)₂(P₂)₂H⁺ (Table 2, 2–4); D = CpW(CO)₂(L)H (Table 1, 12 and 13); E = W(CO)₃(P₃)H⁺ (Table 2, 5–9, 11, 12); F = Mn(CO)₄(P)H (Table 1, 17 and 18); G = Cp*Re(CO)₂(P)H⁺ (Table 2, 13 and 14); H = Fe(CO)₃(P₂)H⁺ (Table 2, 15–20); J = CpRu(P₂)H₂⁺ (Table 3, 2–5, 19); K = Cp*Ru(P₂)H₂⁺ (Table 3, 6–12); L = CpRu(P₂)(L)H⁺ (Table 2, 23–25); M = Ru(P₂)₂(X)(H₂)⁺ (Table 3, 22–26); N = CpOs(P₂)H₂⁺ (Table 3, 13–18); O = CpOs(P₂)(X)H⁺ (Table 2, 27–31); P = Os(P₂)₂(X)(H₂)⁺ (Table 3, 27–32); R = Co(CO)₃(P)H (Table 1, 24–26); S = CpIr(CO)(P)H⁺ (Table 2, 32–39); T = Cp''Ir(COD)H⁺ (Table 2, 42–45); U = Cp*Ir(CO)(P)H⁺ (Table 2, 46–51); V = Tp''Mo(CO)₃H (Table 1, 10 and 11); X = Tp''W(CO)₃H (Table 1, 13 and 14).

In an attempt to shed additional light on the observed ligand effects, Figure 1 summarizes many of the data in Tables 1–3. It shows a plot of $E_{\text{ox}}(\text{M}^-)$ against $2.3RTpK_a(\text{M-H})$ (or, for Table 2, $-\Delta H_{\text{MH}^+}$) for compounds that can be more or less reasonably grouped together according to metal and ligand similarities. The energy scales are different for data from the three different tables—for Tables 1 and 3 because pK_a values refer to a different solvent, and for Table 2 because the data are enthalpy-based. Therefore, absolute energy values cannot be compared. This not important here, because the following discussion will focus on the *slope* of lines connecting data points for related complexes evaluated under the same

conditions. (The slopes should be comparable and this was the basis, through the constant-entropy-assumption, for determining the BDEs in Table 2). The electrode-potential data from Table 2 were converted from the SCE to the Fc scale by addition of 0.59 V [27]. The dotted line in Figure 1 has the slope $1/F = 0.01036$ that would result if the ligand-induced changes in $E^\circ_{\text{ox}}(\text{M}^-)$ and $\text{p}K_{\text{a}}$ contributions in Eq. 13 to the BDE data exactly cancelled each other, i.e. the BDEs within a series of related compounds remain completely insensitive to ligand variations. Data series with slopes smaller than that of the dotted line therefore show BDE variations that originate from large variations of M–H acidity rather than of M^- oxidation potentials. To a first approximation this effect might be expected for sterically demanding complexes. Protonation or deprotonation of a metal, generating or removing a coordination site, will be more sensitive to steric effects than the removal or addition of an electron where no change in coordination number is involved. Stereoelectronic effects might, of course, perturb this rather simplistic picture.

In Figure 1, it is evident that the data for the series with BDEs that were insensitive to modest changes in the ligand environment are aligned in parallel with the dotted line. All these complexes are sterically relatively unencumbered species with no more than one phosphine ligand.

The other series presented in Figure 1 represent complexes that are sterically more crowded. With an exception for the Tp-substituted complexes (V and X labels) all contain at least two tertiary phosphine ligands, or at least one diphosphine. The data points for several of these series have a smaller slope than the dotted line, and for many there is much more scatter in the data than for the sterically undemanding complexes. It is possible that this pronounced difference between ligand sensitivity for mono-phosphine derivatives and the more highly substituted congeners might be traced to steric and/or ring-strain (for chelating diphosphines) effects. The BDE variations that result might then be traced to significant differences between the contributions of reorganization energies to the BDEs.

The complexes $\text{LM}(\text{CO})_3\text{H}$ ($\text{L} = \text{Cp}$, Tp , Tp' ; $\text{M} = \text{Cr}$, Mo , W) in Figure 2 constitute an interesting series of related complexes which can be compared [22b,

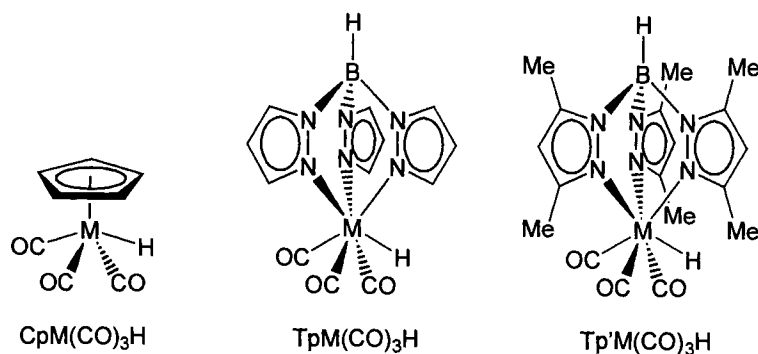


Figure 2. Cp, Tp, and Tp' metal carbonyl hydrides of the Group 6 metals.

33]. The Tp and Cp ligand types are both monoanionic, six-electron donors that occupy three coordination sites [34]. Anion oxidation potential data (Table 1) and IR ν_{CO} data show that ligand donor power decreases in the order $\text{Tp}' > \text{Tp} > \text{Cp}$. Metal-hydride acidity data determined by proton-transfer equilibrium measurements in acetonitrile suggest the opposite trend, however, because $\text{p}K_{\text{a}}$ decreases in the order $\text{Cp} > \text{Tp} > \text{Tp}'$. Thus, the better donor ligand—which should provide the least stable anion—nevertheless provides the stronger acid. As a result, the contributions from $\text{p}K_{\text{a}}$ and $E_{\text{ox}}(\text{M}^-)$ to Eq. 13 do not compensate. In fact, the slopes connecting the data points in Figure 1 (X–X—nearby D for W; V–V—nearby B for Mo) are negative, and significant C–H bond weakening is seen in the series, $\text{Cp} > \text{Tp} > \text{Tp}'$. Although the origin of this bond weakening can in principle be electronic (the Tp system is considered to be an ‘octahedral enforcer’ ligand [35]) or steric in nature, we consider the latter to be the predominant effect because it offers the best explanation for the distinct difference between Tp and Tp' . The added steric demand of Tp' causes destabilization of the hepta-coordinate hydrides $\text{Tp}'\text{M}(\text{CO})_3\text{H}$ relative to the hexa-coordinate radical $\text{Tp}'\text{M}(\text{CO})_3^\cdot$ and the anion $\text{Tp}'\text{M}(\text{CO})_3^-$ that is not as strongly felt in the Tp series, and even less in the Cp series.

Other ligand effects may be interpreted by use of Figure 1 on the basis of ring-strain effects, *cis/trans* geometry effects, halide effects, and so on, but will not be further discussed here.

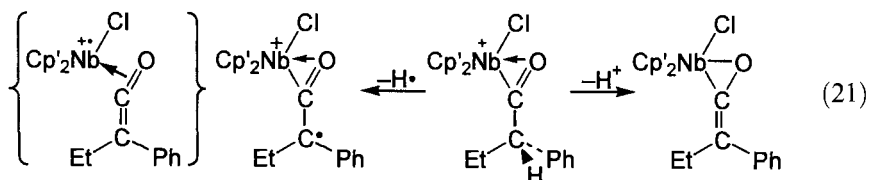
3.3.5 C–H Bond-dissociation Energies of Coordinated Ligands

One important reason that organotransition-metal chemistry has reached the importance it has today is that the binding of a ligand at a metal center alters the properties of the ligand. The coordination of a ligand can alter bond strengths within a ligand significantly, and this will have a pronounced effect on the reactivity of the ligand. The thermochemical cycle that led to Eq. 13 was a modification of one that was originally used to investigate C–H BDEs in hydrocarbons. The method is, of course, also well suited to investigation of the effects of metal coordination on the C–H BDEs of coordinated compared with free ligands. Although there are very few systematic, quantitative studies of this type in the literature, a few interesting examples that demonstrate its usefulness will be discussed.

α -C–H bonds in an η^2 -acyl complex

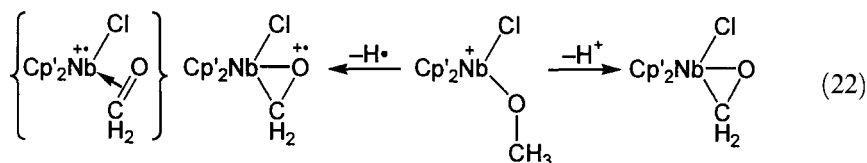
Bruno and coworkers [36] probed the heterolytic ($\text{p}K_{\text{a}}$) and homolytic (BDE) bond energy of the α -C–H bond in the η^2 -acyl complex $\text{Cp}'_2\text{NbCl}(\eta^2\text{-COCHEtPh})^+$. Its acetonitrile $\text{p}K_{\text{a}}$ of 10.4 demonstrates that it is much more acidic than regular ketones. The deprotonation, Eq. 21, yields the $\eta^2(\text{C},\text{O})$ -ketene complex $\text{Cp}'_2\text{NbCl}(\eta^2\text{-COCETPh})$. The irreversible oxidation of the ketene complex occurred at 0.24 V relative to the Fc in acetonitrile, and application of Eq. 14 led to an estimated C–H BDE in $\text{Cp}'_2\text{NbCl}(\eta^2\text{-COCHEtPh})^+$ of 343 kJ mol^{-1} , with some uncertainty be-

cause of the unknown kinetic potential shift. This value is in the range of C–H BDEs for comparably substituted ketones [37]. Thus, although the metal fragment has significantly changed the ligand acidity, it has hardly influenced the BDE of the C–H bond, and the stability of the radical at the α carbon is comparable with that of radicals derived from phenyl alkyl ketones. One possible interpretation is that delocalization of unpaired spin density on to Nb, the left structure in Eq. 21, is insignificant in the cation radical.



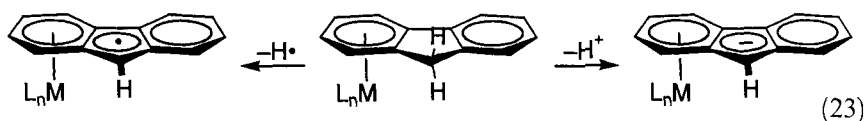
α -C–H bonds in an alkoxide complex

The methoxide complex $\text{Cp}'_2\text{Nb}(\text{Cl})(\text{OCH}_3)^+$ has a $\text{p}K_{\text{a}}$ of 10.1 in acetonitrile. It is ca 50 $\text{p}K_{\text{a}}$ units more acidic than the model compound PhOCH_3 , demonstrating a dramatic metal effect on the heterolytic C–H cleavage [36]. The methoxide complex is obtained by protonation of the formaldehyde complex, Eq. 22. The formaldehyde complex was reversibly oxidized at $E^{\circ}_{\text{ox}} = -0.07$ V relative to the Fc. The C–H BDE of the methoxy group is obtained from Eq. 14 as 301 kJ mol^{-1} . Because the C–H bond in methanol has a BDE of 393 kJ mol^{-1} [38], the cationic Nb center has weakened the C–H bond by a substantial 92 kJ mol^{-1} . The cation radical that results from H^{\bullet} cleavage gains additional stability through the formation of a Nb–C bond that was not present in the methoxide; resonance stabilization by delocalization of spin density on to Nb, the left structure in Eq. 22, was considered less important. The new Nb–C bond can be viewed as an extreme form of contribution to the *reorganization energy* discussed in Section 3.2.

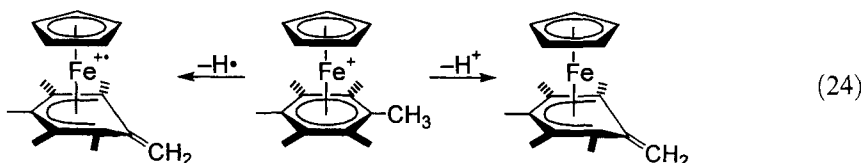


Benzylic C–H bonds in coordinated arenes

Zhang and Bordwell [39] looked at the effects of η^6 π -coordination on the acidities and C–H BDEs of fluorene ligands at the $\text{Cr}(\text{CO})_3$, $\text{Mn}(\text{CO})_3^+$, and CpFe^+ metal fragments in DMSO, Eq. 23. The metals increased the fluorene C–H acidity by 5.6, 16.9, and 8.0 $\text{p}K_{\text{a}}$ units, respectively, but application of Eq. 15 had no discernible effect on C–H BDE, which remained relatively constant at 335 kJ mol^{-1} and are unchanged from that of the free ligand.



Astruc and co-workers [40] obtained similar results in an extensive study on how benzylic C–H acidities and BDEs are affected by arene complexation to the CpFe^{n+} and $\text{Cp}^*\text{Fe}^{n+}$ fragments in DMSO, Eq. 24. The effects on the coordinately saturated, 18-electron complex $\text{CpFe}(\text{C}_6\text{Me}_6)^+$ will be briefly mentioned here; the full investigation will be more thoroughly discussed in Section 3.8., and all data are summarized in Scheme 8. Coordination of hexamethylbenzene at the CpFe^+ fragment led to an estimated 14-unit increase in acidity compared with free hexamethylbenzene. The C–H BDE was calculated as 362 kJ mol^{-1} from Eq. 15. This represents essentially no change when compared with the C–H BDE for free hexamethylbenzene.



3.3.6 Metal–Metal BDEs from Redox Equilibrium and Electrode Potential Measurements

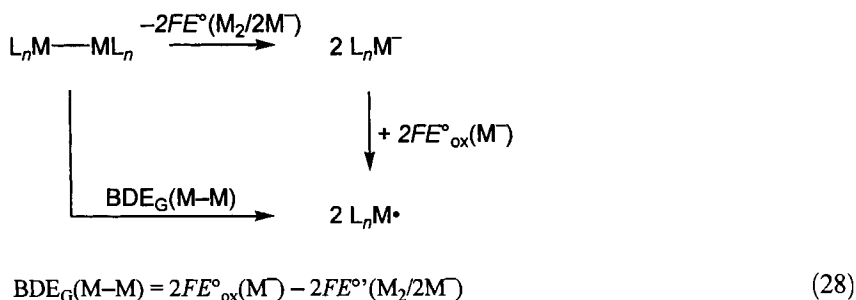
Dinuclear complexes such as $\text{Mn}_2(\text{CO})_{10}$, $\text{Cp}_2\text{Mo}_2(\text{CO})_6$, and $\text{Cp}_2\text{Fe}_2(\text{CO})_4$ serve as precursors for many organometallic complexes via reaction sequences involving formal oxidative addition across the M–M bonds, Eq. 25. Access to M–M BDE data can provide a convenient anchoring point for the determination of other M–X data. Pugh and Meyer [41] have used a redox equilibration technique that enables the determination of M–M bond strengths.



The thermochemical cycle in Scheme 3 was used for this purpose for the Mn, Mo, and Fe dimers. The formal potentials $E^{\circ'}(\text{M}_2/2\text{M}^-)$ were derived from equilibrium constant measurements of the redox equilibria, Eqs 26 and 27, by use of suitable reducing agents. When these formal potentials were combined with the anion oxidation potentials, the M–M BDE_G could be calculated from Eq. 28 as 117 kJ mol^{-1} for $\text{Mn}_2(\text{CO})_{10}$, 92 kJ mol^{-1} for $\text{Cp}_2\text{Mo}_2(\text{CO})_6$, and 105 kJ mol^{-1} for $\text{Cp}_2\text{Fe}_2(\text{CO})_4$. For the Mn dimer, estimates for the entropy change were available and eventually led to an estimated Mn–Mn BDE of ca 159 kJ mol^{-1} in enthalpy terms.



$$E^{\circ'}(\text{M}_2/2\text{M}^-) = E^{\circ}(\text{Red}/\text{Red}^+) + (RT/2F) \ln K_{\text{eq}} \quad (27)$$



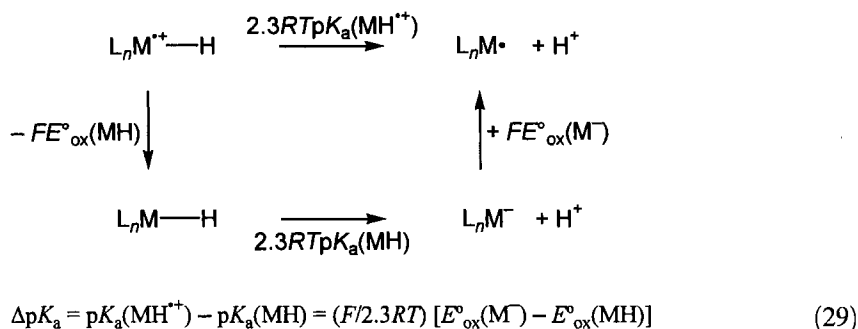
Scheme 3. Thermochemical cycle for the determination of M–M bond energies.

3.4 Metal–Hydride Cation Radical Acidities

The thermochemical cycle in Scheme 4 can be used to estimate the effect of one-electron oxidation on metal-hydride acidities. The method is analogous to one that has been extensively used to investigate organic cation radicals [10c]. Eq. 29 shows that measurements of $E^\circ_{\text{ox}}(\text{MH})$ and $E^\circ_{\text{ox}}(\text{M}^-)$ provide *relative* $\text{p}K_{\text{a}}$ data for metal hydrides and their cation radicals. Absolute values for $\text{p}K_{\text{a}}(\text{MH}^{+\bullet})$ are obtained if the acidities of the neutral hydrides are known. The oxidation potentials of 18-electron hydrides can be readily obtained by cyclic voltammetry. In our experience, the waves that are obtained are frequently chemically irreversible, even at rather high scan rates. Consequently, the oxidation peak potentials will be kinetically shifted and represent *minimum* values for the true $E^\circ_{\text{ox}}(\text{MH})$ data, the estimates for $\text{p}K_{\text{a}}(\text{MH}^{+\bullet})$ represent *maximum* values, and calculated $\Delta\text{p}K_{\text{a}}$ are *minimum* values.

We have applied Eq. 29 to a series of Cp and Tp Group 6 metal carbonyl hydrides in acetonitrile, mostly on the basis of irreversible metal-hydride oxidation

51



Scheme 4. Thermochemical cycle for the determination of metal-hydride cation radical acidities.

Table 4. pK_a and BDE data for selected metal hydrides and their cation radicals in acetonitrile.

Compound MH	$pK_a(\text{MH})$	$pK_a(\text{MH}^{+\bullet})$	ΔpK_a	BDE(MH)	BDE(MH ^{•+})	ΔBDE
CpCr(CO) ₃ H ^a	13.3	−9.5	22.8	257	233	24
CpCr(CO) ₂ [P(OMe) ₃] ₂ H ^b	21.1	−2.4	23.5	262	216	46
CpCr(CO) ₂ (PEt ₃)H ^b	25.8	0.5	25.3	251	213	38
CpCr(CO) ₂ (PPh ₃)H ^b	21.8	−2.1	23.9	250	208	42
Cp*Cr(CO) ₃ H ^b	16.1	−7.2	23.3	261	227	34
TpCr(CO) ₃ H ^c	<8	—	—	<215	—	—
Tp'Cr(CO) ₃ H ^c	<8	—	—	<212	—	—
CpMo(CO) ₃ H ^a	13.9	−6.0	19.9	290	—	—
TpMo(CO) ₃ H ^c	10.7	−8.2	18.9	260	233	27
Tp'Mo(CO) ₃ H ^c	9.7	−9.5	19.2	248	223	25
CpW(CO) ₃ H ^a	16.1	−3.0	19.1	303	—	—
CpW(CO) ₂ (PMe ₃) ₂ H ^a	26.6	5.1	21.5	291	—	—
TpW(CO) ₃ H ^c	14.4	−5.4	19.8	275	241	34
Tp'W(CO) ₃ H ^c	12.9	−6.7	19.6	260	231	29
<i>trans</i> -Cr(CO) ₂ (dppm) ₂ H ⁺ ^d	—	—	30.0	—	—	—
<i>trans</i> -Cr(CO) ₂ (dppe) ₂ H ⁺ ^d	—	—	29.5	—	—	—
<i>trans</i> -Mo(CO) ₂ (dppm) ₂ H ⁺ ^d	—	—	27.9	—	—	—
<i>trans</i> -Mo(CO) ₂ (dppe) ₂ H ⁺ ^d	—	—	26.2	—	—	—
<i>trans</i> -W(CO) ₂ (dppm) ₂ H ⁺ ^d	—	—	28.8	—	—	—
<i>trans</i> -W(CO) ₂ (dppe) ₂ H ⁺ ^d	—	—	25.4	—	—	—
Cp*Fe(dppe)H ^e	—	—	—	—	—	51

^a According to [42].^b According to [22a].^c According to [22b].^d According to [43].^e According to [48].

waves [22a, b, 42]. Bond and coworkers [43] more recently determined the effects of oxidations of Group 6 *trans*-M(CO)₂(diphosphine)₂H⁺ (M = Cr, Mo, W) cations to di-cations, on the basis of *reversible* electrode processes in acetonitrile. The pertinent acidity data derived from Eq. 29 are summarized in Table 4 and, when absolute values are available, graphically represented in Figure 3. The data establish that the 17-electron cation radicals are more acidic than their 18-electron neutral parents by a relatively constant difference of 19–23 pK_a units, translating to ca 120 kJ mol^{−1} in bond weakening with respect to deprotonation. For the 17-electron di-cations, the bond activation is somewhat greater, 25–30 pK_a units. Interestingly, many of these cation radicals can be termed *organometallic superacids*. (Acids are generally less acidic in acetonitrile than in water, primarily as a consequence of the significantly poorer solvation of the proton in acetonitrile, which alone corresponds to 7.8 pK_a units [19]).

As might be expected, the 17-electron metal-hydride cation radicals typically undergo proton-transfer reactions [30, 42–44]. The 17-electron radical that results from the deprotonation is usually oxidized, presumably via solvent coordination, to

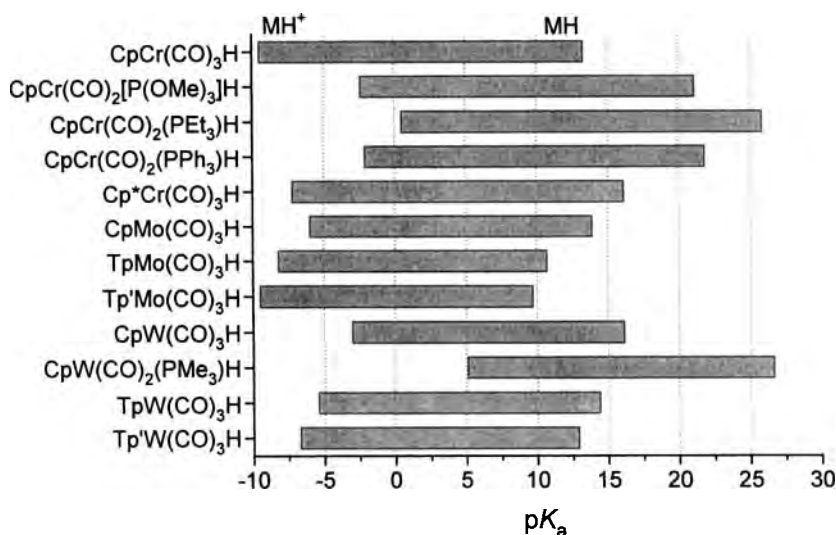
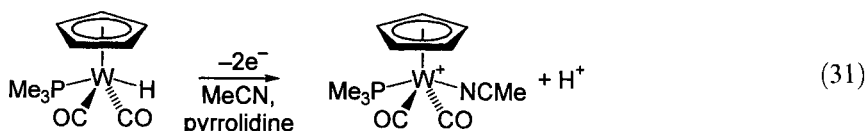
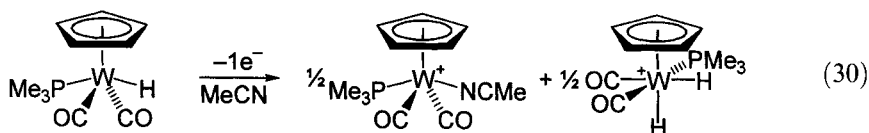


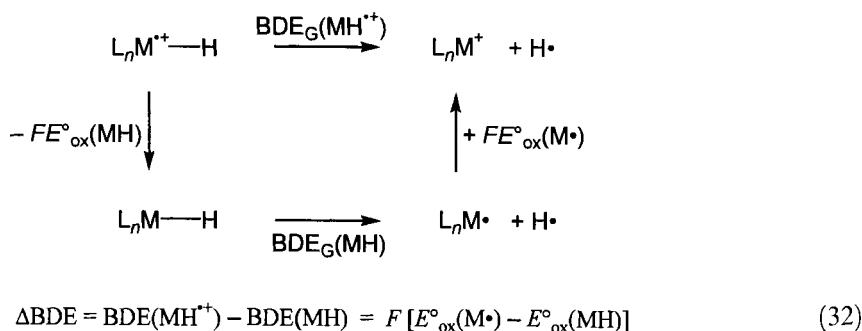
Figure 3. Acetonitrile pK_a data for selected neutral 18-electron hydrides (right end of bars) and their 17-electron cation radicals (left end).

generate a more readily oxidized [45] 19-electron radical [1b, 2c-e] to give cationic 18-electron solvento complexes. The solvent/electrolyte system is often sufficiently basic. For the less acidic species, the unoxidized metal hydride can function as the base, Eq. 30. Alternatively, external bases such as amines can be added, as in Eq. 31. Note that the change of base changes the stoichiometry from 1 faraday mol^{-1} in Eq. 30 to 2 faraday mol^{-1} in Eq. 31.



3.5 Metal-Hydride Bond-dissociation Energies in Cation Radicals

Scheme 5 depicts a thermochemical cycle which can be used to determine metal-hydride cation radical BDEs. Adding the energy terms in the cycle gives Gibbs energy BDE_G data. If the assumption is made that the solvation properties of $\text{MH}^{+\bullet}$



Scheme 5. Thermochemical cycle for the determination of metal-hydride cation radical bond-dissociation energies.

and M^{+} are essentially identical, as are those of MH and M^{\bullet} (this apparently works well for organic molecules [20]) then the solvation entropy terms will cancel and Eq. 32 applies to the desired enthalpy-based calculations. In the absence of BDE data for the parent metal hydride, Eq. 32 still provides useful insight into *relative* BDEs for the cation radical and the neutral parent.

Unfortunately, it is far from trivial to obtain oxidation potentials for commonly encountered 17-electron metalloradicals M^{\bullet} , because many such radicals dimerize at rates approaching diffusion-control, rendering it nearly impossible to observe such species by cyclic voltammetry. The use of ultramicroelectrodes was shown [41] to give a reversible signal for the oxidation of $\text{Mn}(\text{CO})_5^{\bullet}$ at scan rates of ca 5000 V s^{-1} , but the further oxidation of this radical to the 16-electron cation was not reported. There are, however, certain frequently encountered systems for which such radicals are stable at least on the time-scale of normal voltammetric measurements. Figure 4 shows an example, the oxidation of $\text{CpCr}(\text{CO})_3^{\bullet}$ in acetonitrile.

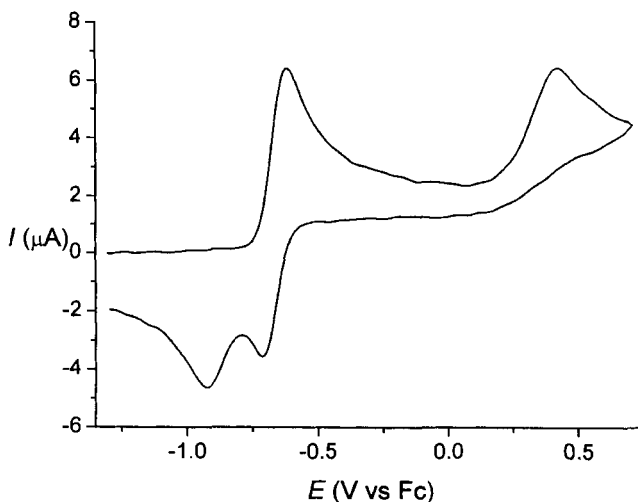


Figure 4. Cyclic voltammogram of the oxidation of $\text{CpCr}(\text{CO})_3^{\bullet}\text{Et}_4\text{N}^{+}$ in acetonitrile/ $0.1 \text{ M Bu}_4\text{N}^{+}\text{PF}_6^{-}$ at $\nu = 1.0 \text{ V s}^{-1}$.

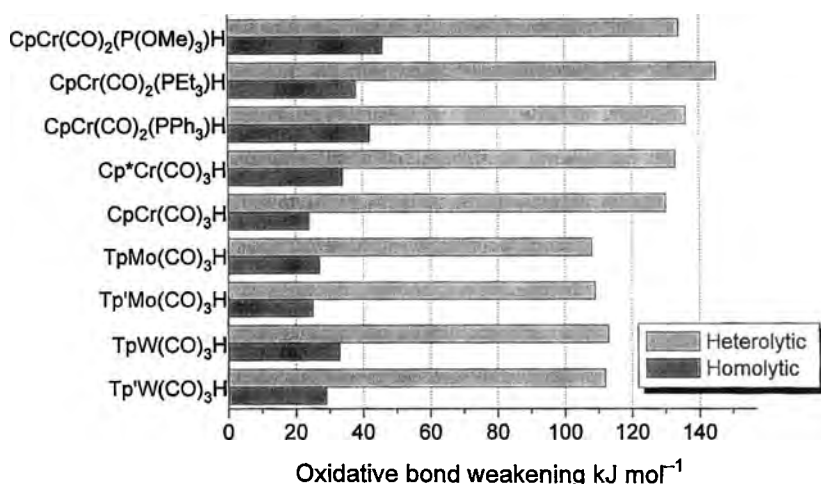


Figure 5. Oxidative activation of M–H bonds toward heterolytic and homolytic cleavage.

The anion is reversibly oxidized to the radical $\text{CpCr(CO)}_3^{\cdot}$ at -0.68 V relative to the Fc. Furthermore, an irreversible oxidation occurs at $+0.42$ V. The irreversibility is caused by the extremely fast reaction of the unsaturated, 16-electron cation CpCr(CO)_3^+ with the solvent to give $\text{CpCr(CO)}_3(\text{NCMe})^+$. The latter is reduced at -0.92 V during the reverse scan. Analogous behavior has been observed for several other complexes.

Table 4 includes $\text{p}K_a$ and BDE data for several metal hydrides and their cation radicals. In all instances where ΔBDE data are given, except for $\text{Cp}^*\text{Fe}(\text{dppe})\text{H}$, oxidation of MH and M^{\cdot} was irreversible and therefore subject to unknown kinetic potential shifts. From these data it seems a consistent trend that the one-electron oxidation leads to a bond weakening with respect to homolytic M–H cleavage. Homolytic activation is much less pronounced than heterolytic, as depicted in Figure 5. This might not come as a surprise, because proton removal from a cationic species should be more facile than from a closely related neutral species. Heterolytic bond activation of organic molecules is usually even more pronounced, as seen in references cited in Refs [8] and [11]. Heterolytic bond weakening can be expressed as $-\Delta\Delta G_{\text{het}}^{\circ} = 2.3RT\Delta\text{p}K_a = F[E_{\text{ox}}(\text{MH}) - E_{\text{ox}}(\text{M}^-)]$ and homolytic as $-\Delta\Delta G_{\text{hom}}^{\circ} = -\Delta\text{BDE} = F[E_{\text{ox}}(\text{MH}) - E_{\text{ox}}(\text{M}^{\cdot})]$. Subtraction gives the difference between heterolytic and homolytic bond weakening, $-(\Delta\Delta G_{\text{het}}^{\circ} - \Delta\Delta G_{\text{hom}}^{\circ}) = F[E_{\text{ox}}(\text{M}^{\cdot}) - E_{\text{ox}}(\text{M}^-)]$. Thus, heterolytic bond weakening will exceed homolytic bond weakening if $E_{\text{ox}}(\text{M}^{\cdot}) > E_{\text{ox}}(\text{M}^-)$. This will generally be true, because the electron-rich 18-electron anion M^- should be more readily oxidized than the electron-deficient 17-electron radical M^{\cdot} . This does not, however, explain why bond weakening (rather than a strengthening!) occurs for the homolytic process. Oxidatively-induced bond weakening for a pure σ donor ligand like the hydride can be naively rationalized in terms of the oxidation-state formalism. M–H homolysis constitutes a formal 1-electron reduction of the metal center and should be favored

by a higher oxidation state. This is, however, probably too much of a simplification, as suggested by a recent contribution from Poli and coworkers [46].

The homolytic bond activation energies given in Table 4 for the Group 6 metal complexes were based on irreversible electrode processes. It is therefore conceivable that kinetic potential shifts might have reversed the order of the $M^{0/+}$ and $MH^{0/+}$ redox couples (note that a 30 kJ mol^{-1} difference corresponds to as much as 0.3 V). This would have reversed what should have been a bond strengthening to an apparent bond weakening. Poli has argued [46], on MO and electrostatic grounds, that the oxidation processes should lead to bond strengthening, rather than bond weakening, for a $M-H^{\delta-}$ system with a very electron-rich metal fragment when the bonding energetics are dominated by the covalent component. Such an effect was inferred from an observed increase in the IR ν_{M-H} stretching frequencies when $Cp^*M(dppe)H_3$ ($M = Mo, W$) were oxidized to their relatively stable cation radicals. The inferred bond strengthening was further supported by results from DFT calculations. It has not yet been possible to apply thermochemical cycles to these systems. We recently investigated the effects of the oxidation of $Cp^*Fe(dppe)H$, for which the $M^{0/+}$ and $MH^{0/+}$ redox couples are both reversible [47]. The thermochemical cycle is indicative of homolytic bond *weakening* of 51 kJ mol^{-1} in this instance. The bond weakening has been supported by DFT calculations (J.-Y. Saillard and K. Costuas, personal communication). These results are not necessarily at odds with each other because they arise from quite different molecules; rather, they tell us that our picture of bonding even in relatively simple $M-H$ bonds is not yet complete.

3.6 Metal–Halide Bond Energies

The thermochemical cycle, Scheme 5, for determination of relative BDEs in metal hydrides in different oxidation states can be extended in a straightforward manner to any σ -bonded ligand X in any two adjacent oxidation states as shown in Scheme 6 and Eq. 32. We have recently [47] investigated the energetics of metal-halide bonding in $Cp^*Fe(dppe)X$ compounds ($X = F, Cl, Br, I$) in addition to the hydride that was discussed in Section 3.5. The sterically crowded and electron-rich $Cp^*Fe(dppe)X$ moiety supports metal complexes in a great number of oxidation states, with electron counts ranging from 15 to 19 [48]. Cyclic voltammetry in THF/ $0.2 \text{ M Bu}_4N^+PF_6^-$ shows that the couples $Cp^*Fe(dppe)^{0/+}$ and $Cp^*Fe(dppe)^{+/2+}$ are chemically reversible on the measurement time scale, as are $Cp^*Fe(dppe)X^{0/+}$ and $Cp^*Fe(dppe)X^{+/2+}$ for $X = F, Cl, Br$, and I . The electrode-potential data and the derived ΔBDE data are listed in Table 5.

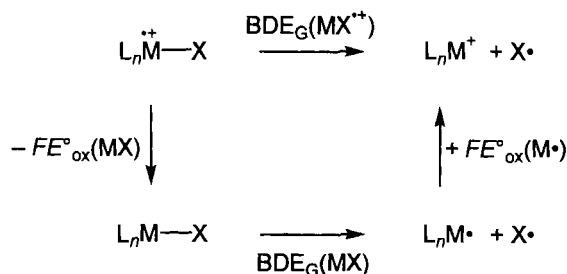
In the electrode-potential data for the halides, it is noteworthy that *the first oxidation is most facile for the most electronegative halide* and becomes increasingly more difficult in the series $F < Cl < Br < I$, with a particularly large jump (greater than 0.2 V) from F to Cl . The fluoride is also easiest to oxidize to a di-cation. The

Table 5. Electrode potential and Δ BDE data for $\text{Cp}^*\text{Fe}(\text{dppe})$ derivatives.

Compound MX	$E^\circ(\text{MX}/\text{MX}^+)^a$	$E^\circ(\text{MX}^+/\text{MX}^{2+})^a$	$\Delta\text{BDE}(\text{MX}/\text{MX}^+)$ (kJ mol ⁻¹)	$\Delta\text{BDE}(\text{MX}^+/\text{MX}^{2+})$ (kJ mol ⁻¹)
$\text{Cp}^*\text{Fe}(\text{dppe})^\cdot$	-1.27	-0.29	—	—
$\text{Cp}^*\text{Fe}(\text{dppe})\text{H}$	-0.75	0.75 ^b	51	100
$\text{Cp}^*\text{Fe}(\text{dppe})\text{F}$	-0.82	0.69	43	94
$\text{Cp}^*\text{Fe}(\text{dppe})\text{Cl}$	-0.62	0.82	63	107
$\text{Cp}^*\text{Fe}(\text{dppe})\text{Br}$	-0.58	0.81	67	106
$\text{Cp}^*\text{Fe}(\text{dppe})\text{I}$	-0.54	0.78	71	103

^aV relative to Fc in THF/0.2 M $\text{Bu}_4\text{N}^+\text{PF}_6^-$. Reversible voltammograms unless otherwise noted.^bPeak potential for irreversible oxidation.

trend is the opposite of that predicted on the basis of halide electronegativities alone. The electrode-potential data translate to an oxidatively induced bond weakening for all X. The weakening is smallest for $\text{X} = \text{F}$ and increases in the order $\text{F} < \text{Cl} < \text{Br} < \text{I}$. A further weakening occurs as a consequence of the second oxidation. The origins of these effects are not yet well understood. Recent studies have shown that the nature of the bonding between organotransition-metal centers and electronegative σ -bonded ligands such as halide, alkoxide, and amido groups is more complex than usually thought [49]. Such ligands form not only ‘normal’ covalent $\text{M}-\text{X}$ bonds, but can also act as π donors towards the metal. A ligand p_π to metal d_π electron-pair donation might destabilize electronically saturated complexes via repulsive filled–filled interactions, whereas electronically unsaturated species might be stabilized by partial π bond formation. IR ν_{CO} spectroscopy data, electrode potentials, theoretical calculations, and other evidence cited in [47] suggest that among the halides the fluoride ligand is the most efficient electron-pair donor towards the metal. It must, however, be emphasized that the full explanation of this behavior might be more complex. An alternative interpretation based on Drago’s



$$\text{BDE}(\text{MX}^{++}) - \text{BDE}(\text{MX}) = F [E^\circ_{\text{ox}}(\text{M}^\cdot) - E^\circ_{\text{ox}}(\text{MX})] \quad (33)$$

Scheme 6. Thermochemical cycle for determination of oxidatively induced $\text{M}-\text{X}$ BDE changes in metal halides.

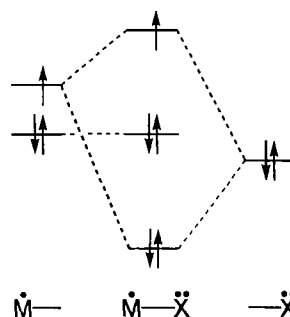


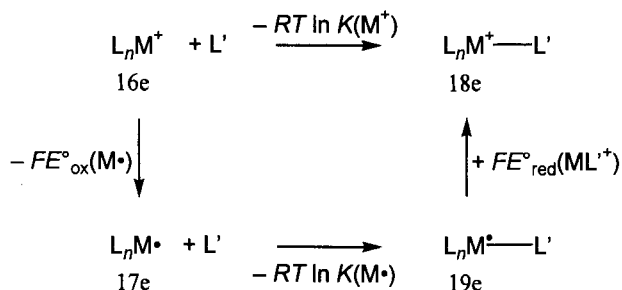
Figure 6. Simplified MO diagram to illustrate $p_{\pi}-d_{\pi}$ interaction in an M–X bond.

ECT model [50a–c] has also been proposed [50d–e] and theoretical studies have shown that covalent π -effects and σ -effects, and electrostatic effects and the ionicity of the M–X bond, might have a significant effect on trends in ν_{CO} and other observed parameters. The physical manifestations resemble those expected on the basis of π donation, but the explanation may be much more complex; it might more appropriate to discuss the halide effects in terms of an *apparent* π donor strength.

The presence of (apparent) halide-to-metal π bonding might be reflected in BDE changes when the repulsive $p_{\pi}-d_{\pi}$ interactions in saturated complexes change to attractive interactions through the generation of coordinative unsaturation by dissociation of a ligand L or by other means. 17-electron cation radicals might exhibit behavior reflecting *partial* unsaturation, and 16-electron di-cations *full* unsaturation. The bond to the better π donor should then be most strengthened, alternatively least weakened, when coordinative unsaturation is generated. This appears to be the case for the $\text{Cp}^*\text{Fe}(\text{dppe})\text{X}$ series, with F being the best ‘apparent π donor’. The presence of apparent π donation even in the 17-electron species is reminiscent of the 17/19-electron equilibria in organometallic radical chemistry: the halide, by virtue of a suitable p_{π} orbital, acts as an ‘intramolecular two-electron donor’ that interacts with the metal SOMO in much the same sense as an incoming two-electron donor interacts with a 17-electron radical (Figure 6). Preliminary results from DFT calculations (J.-Y. Saillard and K. Costuas, personal communication) indicate that reorganization energies are relatively constant in the halogen series, so the jump in the ΔBDE values from F to the other halogens appears to be associated with variations in the Fe–X bonds. Here, X-to-Fe π donation is one of several contributing factors.

3.7 Bonding of 2-Electron Donor Ligands in 18- and 19-Electron Complexes

The association and dissociation of ligands at metal centers is a key reaction type in organometallic chemistry, including organometallic radical chemistry. Typically,



$$\ln[K(\text{M}^+)/K(\text{M}\cdot)] = F/RT [E^\circ_{\text{ox}}(\text{M}\cdot) - E^\circ_{\text{red}}(\text{ML}'^+)] \quad (34)$$

Scheme 7. Thermochemical cycle for the determination of relative metal–ligand bond-dissociation energies in 18- and 19-electron complexes.

17-electron species undergo ligand substitution reactions many orders of magnitude faster than closely related 18-electron species. These rapid reactions are thought to occur by associative mechanisms that involve 19-electron intermediates [2c, e, h]. The 19th electron normally is considered to reside in a largely antibonding orbital, resulting in such species being rather labile with respect to ligand dissociation. Very little information is available concerning the relative M–L bond strengths in 18- and 19-electron species that only differ in the number of valence electrons and, consequently, charge. Scheme 7 shows a thermochemical cycle which may be useful in order to obtain such data. Eq. 34 requires knowledge about the reduction potential of the 18-electron species, taken to be a cationic complex $\text{L}_n\text{M} - \text{L}'^+$, and the oxidation potential for the 17-electron neutral species $\text{L}_n\text{M}\cdot$. The use of this method is unfortunately severely limited by the short lifetimes of most 17-electron radicals that are of interest in this context. Additionally, both redox processes will normally be irreversible due to rapid follow-up reactions (ligand loss from 19-electron $\text{L}_n\text{M} - \text{L}'^\cdot$, ligand or solvent association at 16-electron L_nM^+) but at least some semi-quantitative information may be obtained.

As seen in Figure 4 and discussed in Section 3.5, $\text{CpCr}(\text{CO})_3^+$ undergoes oxidation at 0.42 V whereas $\text{CpCr}(\text{CO})_3(\text{NCMe})^+$ is reduced at -0.92 V relative to the Fc. This translates to $K(\text{M}^+)/K(\text{M}\cdot) = 5 \times 10^{22}$ or $\Delta\text{BDE} = 130 \text{ kJ mol}^{-1}$. For acetonitrile coordination at $\text{CpCr}(\text{CO})_2[\text{P}(\text{OMe})_3]^{0/+}$, the corresponding values are -0.21 and -1.48 V relative to the Fc, resulting in $\Delta\text{BDE} = 123 \text{ kJ mol}^{-1}$. The *one-electron reductively induced* M–L bond activation for this heterolytic M–L cleavage in which the departing ligand retains both electrons is of the same magnitude as the *one-electron oxidatively induced* M–H bond activation for the heterolytic M–H cleavage (deprotonation) in which the metal retains both electrons (Section 3.4).

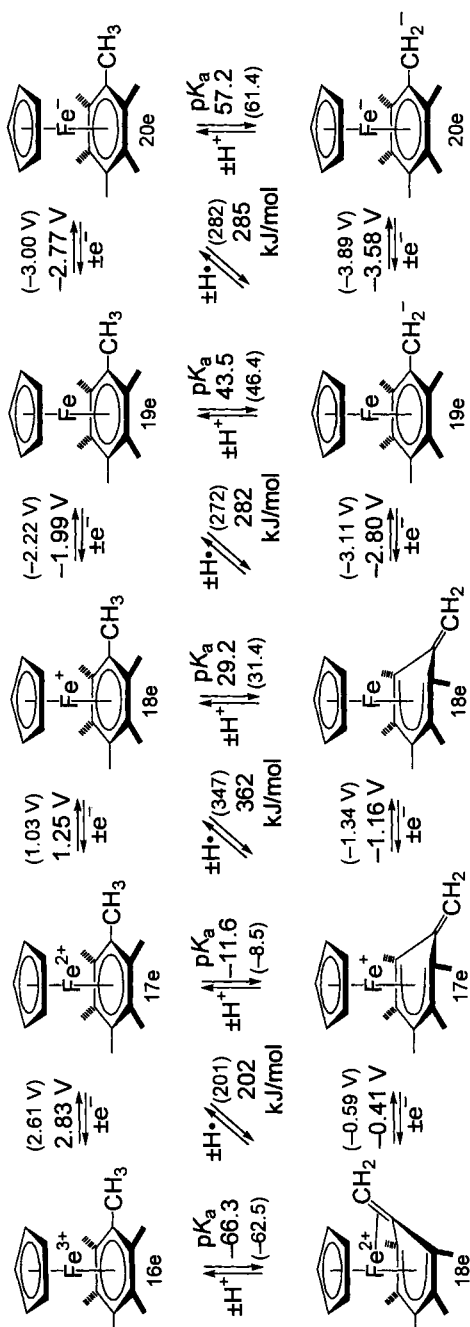
3.8 Changes in Ligand C–H Bond Strengths Induced by Electron Transfer

In Sections 3.5–3.7, one-electron changes in the oxidation state of a complex were shown to have profound effects on the energetics of metal–ligand bonding. Similarly, dramatic changes can occur for bonds within a coordinated ligand when a metal complex is subjected to electron-transfer processes. With the exception of a very recent contribution by Astruc and coworkers, which will be discussed first, very few studies have been performed in order to establish and to quantify such effects. Useful electrode-potential data that may be combined to yield such information are probably abundant, but scattered, in the literature. The discussion here will serve to show through selected examples how quantitative bond-energy data can be obtained, and is by no means intended to include all the pertinent data and reactions in the literature.

The H^+ and H^\bullet transfer reactions at the coordinated ligands that will be described in the following are frequently, but not always, accompanied by a metal–ligand hapticity change (for π -bonded ligands), a metal–ligand bond-order change (for σ -bonded ligands), or a C–C bond-order change (within a coordinated ligand). The thermodynamics of the reactions are often qualitatively understood when this is taken into account. The formation of new bonds, or more multiple character into existing ones, may significantly contribute to the observed changes in pK_a or BDE data when the oxidation state of a complex is changed. The influence of the hapticity and bond-order changes are extreme manifestations of the importance of reorganization energies that were discussed in Section 3.2.

3.8.1 Benzylic C–H Bonds of π -Coordinated Arenes

Astruc and coworkers [40a] recently reported a comprehensive investigation of the bonding energetics of benzylic C–H bonds in 16–20-electron complexes $Fe(C_5R_5)(\eta^6\text{-arene})^n$ ($n = -1$ to $+3$; $R = H, Me$; arene = C_6Me_6 , $C_6H_5CH_2Ph$, $C_6H_5CHPh_2$) where the entire analysis was based on variations on the thermochemical cycles in Schemes 2, 4, and 5. Acidity measurements were performed in DMSO. Electrode potential measurements were also conducted in DMSO, with a few exceptions. When electrode potentials were not accessible in DMSO, great care was taken to reliably convert data from other solvents. The most thorough investigation was done for compounds derived from the 18-electron species $CpFe^{II}(C_6Me_6)^+$ and $Cp^*Fe^{II}(C_6Me_6)^+$. The data that were obtained for these complexes are best summarized as in Scheme 8, where electrode potentials are referenced against Fc in DMSO. The relationship to Scheme 1 is obvious. Equilibrium pK_a measurements on the 18-electron cation $CpFe^{II}(C_6Me_6)^+$ (top center) serves as the anchoring point for the other pK_a and BDE data. The pK_a of the C_6Me_6 ligand is ca 14 pK_a units lower than for free C_6Me_6 . Factors that may contribute to this bond activation are distribution of charge onto the ligand, and stabilization of the



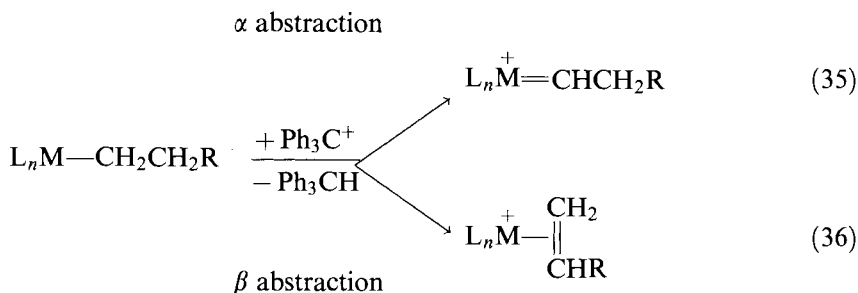
Scheme 8. Energetics of redox, proton transfer, and hydrogen atom transfer reactions of $\text{CpFe}(\text{C}_6\text{Me}_6)^n$ complexes in five different oxidation states. Numbers in parentheses are for the analogous $\text{Cp}^*\text{Fe}(\text{C}_6\text{Me}_6)^n$ complexes.

deprotonated ligand through the formation of a cyclohexadienyl ligand with an exocyclic C–C double bond. Reduction of $\text{CpFe}^{\text{II}}(\text{C}_6\text{Me}_6)^+$ gives the 19-electron ‘electron reservoir’ complex [1b, 2m, 51] $\text{CpFe}^{\text{II}}(\text{C}_6\text{Me}_6)^{\bullet}$ which at a $\text{p}K_{\text{a}}$ of 43.5 is ca 14 $\text{p}K_{\text{a}}$ units less acidic than the cation. In other words, the coordinated C_6Me_6 is approximately as poorly acidic as the free ligand—there is no charge stabilization upon complexation nor cyclohexadienyl formation in this case. For the $\text{Cp}^*\text{Fe}^{\text{II}}(\text{C}_6\text{Me}_6)^{\bullet}$ analog, the $\text{p}K_{\text{a}}$ was even somewhat *higher* than for the free ligand. The reduction of $\text{CpFe}^{\text{I}}(\text{C}_6\text{Me}_6)^{\bullet}$ is experimentally observable but the reduction of the conjugate base, 19-electron $\text{CpFe}^{\text{I}}(\text{C}_6\text{Me}_5\text{CH}_2^-)$, is not. Its reduction potential was approximated, based on the assumption that the added electron goes into an Fe-centered antibonding orbital of roughly known energy. The result is a further 14-unit $\text{p}K_{\text{a}}$ increase to 57.2 which was attributed to electrostatic effects. On the other side, oxidation of 18-electron $\text{CpFe}^{\text{II}}(\text{C}_6\text{Me}_6)^+$ to the 17-electron Fe^{III} dication leads to an acidity enhancement of about 40 units to a $\text{p}K_{\text{a}}$ of -11.6 . Interestingly, the SbCl_6^- salt of the analogous Cp^* complex, $\text{Cp}^*\text{Fe}^{\text{III}}(\text{C}_6\text{Me}_6)^{2+}$, with an estimated $\text{p}K_{\text{a}}$ in DMSO of -8.5 , can be isolated (!) and is the most strongly oxidizing thermally stable organometallic complex known. Estimates for the experimentally inaccessible electrode potentials for the further oxidation of $\text{CpFe}^{\text{III}}(\text{C}_6\text{Me}_6)^{2+}$ to the Fe^{IV} tri-cation, and for the oxidation of $\text{CpFe}^{\text{III}}(\text{C}_6\text{Me}_5\text{CH}_2)^+$ to the Fe^{IV} dication, were obtained through certain not unreasonable assumptions, and further decreased the $\text{p}K_{\text{a}}$ of the C_6Me_6 ligand to -66.3 .

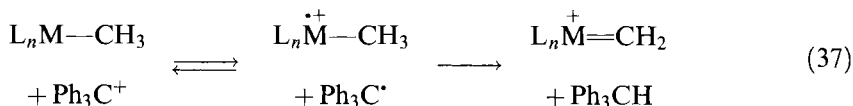
The benzylic C–H BDEs of the coordinated arenes were also highly dependent on the oxidation state of the complex. From Eq. 15, the benzylic C–H BDE of $\text{CpFe}^{\text{II}}(\text{C}_6\text{Me}_6)^+$ was determined as 362 kJ mol^{-1} , essentially unchanged from that in the free ligand. The BDE dropped to 292 kJ mol^{-1} for the neutral 19-electron $\text{CpFe}^{\text{I}}(\text{C}_6\text{Me}_6)^{\bullet}$, readily understood considering that an electron in the 19-electron complex resides in an antibonding orbital and that the H^{\bullet} abstraction product is a stable, closed-shell, 18-electron species. No further BDE change occurred for the 20-electron Fe^0 arene complex. However, the BDE of 202 kJ mol^{-1} in the 17-electron di-cation $\text{CpFe}^{\text{III}}(\text{C}_6\text{Me}_6)^{2+}$ makes the C–H bond 160 kJ mol^{-1} weaker than that of its 18-electron parent. The H^{\bullet} transfer generates a 16-electron cyclohexadienyl complex $\text{CpFe}^{\text{IV}}(\text{C}_6\text{Me}_5=\text{CH}_2)^{2+}$, and it is thought that coordination of the exocyclic double bond to give an 18-electron product contributes to the lowering of the BDE in this case.

3.8.2 α - and β -C–H Bonds in Metal Alkyls

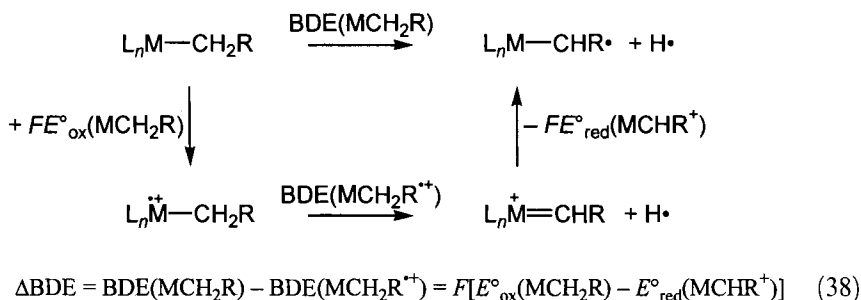
The trityl cation (Ph_3C^+) is a commonly used reagent to effect the abstraction of a hydride from coordinated ligands. For example, the preparation of metal alkylidene and alkene complexes by α - and β -hydride abstraction from metal alkyls using trityl salts is a well-established synthetic method, Eqs 35 and 36.



It has been proposed that hydride abstraction reactions with trityl reagents may in many cases be two-step reactions that occur via a one-electron oxidation followed by a hydrogen atom transfer from the incipient organometallic cation radical and trityl radical, as shown for a simple α abstraction from a methyl group in Eq. 37 [52]. It is difficult to distinguish between the two-step reaction and a direct, one-step hydride abstraction mechanism. If the second step in the two-step mechanism is rate limiting, then the two mechanisms may in principle pass through identical transition states for the rate-limiting step and will be kinetically indistinguishable. Trapping and/or observation of the trityl radical may be a good indication for an electron-transfer pathway, but it should still be demonstrated that the electron transfer reaction is not just a non-productive side equilibrium.



Bodner et al. [52a] presented strong evidence that α and β hydride abstractions from rhenium alkyls $\text{CpRe}(\text{NO})(\text{PPh}_3)\text{R}$ follow the two-step mechanism. Neutral Re alkyls that did not undergo reactions with $\text{Ph}_3\text{C}^\bullet$ were found to quickly react with Ph_3C^+ . The thermochemical cycle in Scheme 9 may be employed to estimate how a one-electron oxidation affects the C–H BDE of a metal alkyl to produce an alkylidene complex. Eq. 38 quantifies the BDE change; the assumption is again made that entropy contributions cancel so that the relationship provides enthalpy-based data. For the benzyl complex $\text{CpRe}(\text{NO})(\text{PPh}_3)\text{CH}_2\text{Ph}$, $E^\circ_{\text{ox}}(\text{MCH}_2\text{Ph}) = 0.17$ V relative to Ag/Ag^+ , and for $\text{CpRe}(\text{NO})(\text{PPh}_3)(=\text{CHPh})^+$, $E^\circ_{\text{red}}(\text{MCHPh}^+) = -1.30$ V. Both electrode processes were reversible [52a], and translates to an oxidatively induced bond weakening $\Delta\text{BDE} = 142$ kJ mol⁻¹. For $\text{CpRe}(\text{NO})(\text{PPh}_3)\text{CH}_3$, $E^\circ_{\text{ox}}(\text{MCH}_3) = 0.04$ V (reversible) relative to Ag/Ag^+ and $E^\circ_{\text{red}}(\text{MCH}_2^+) = -1.49$ V relative to Ag/Ag^+ (irreversible) [53]. Neglecting kinetic potential shifts on the latter this results in a bond weakening for the methyl C–H bond of 150 kJ mol⁻¹ as a result of the oxidation. These data establish beyond doubt that $\text{CpRe}(\text{NO})(\text{PPh}_3)\text{CH}_2\text{R}^{\bullet+}$ are much more prone to transfer H[•] to the trityl radical than are their neutral parents $\text{CpRe}(\text{NO})(\text{PPh}_3)\text{CH}_2\text{R}$. The stabilization gained by formation of a Re=C double bond following H[•] abstraction from the cation radical must significantly contribute to the bond weakening effect. The $\text{Re}-\text{CH}_2^\bullet$ radical would give a 19-



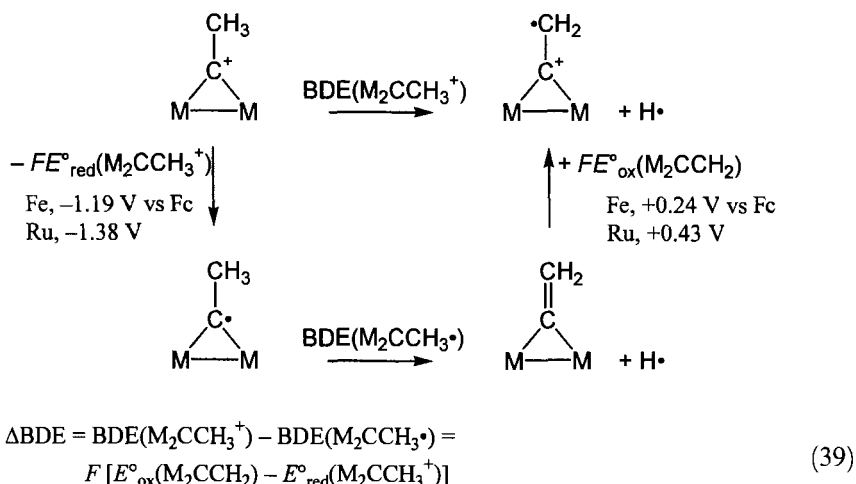
Scheme 9. Thermochemical cycle for determination of α -C–H BDE changes in coordinated alkyl groups caused by a one-electron oxidation.

electron metal center if a double bond were present, and therefore lacks this stabilization.

Similar considerations may be applied to β -hydride transfer processes. For example, $E^\circ_{\text{ox}}(\text{ReCH}_2\text{CHMe}_2) = +0.06$ V relative to Ag/Ag^+ (reversible) [52a] and $E_{\text{red}}(\text{Re}(\text{CH}_2=\text{CMe}_2)^+) = -1.34$ V (irreversible) which translates to a 135 kJ mol^{-1} bond weakening of the β C–H bond upon oxidation. In this case, H^\cdot loss from the Re-alkyl cation radical generates an alkene complex in which a new Re–C bond has been formed and this contributes substantially to the thermodynamic weakening of the C–H bond.

3.8.3 Bridging Alkylidyne Ligands in Dinuclear Complexes

Substantial effects of one-electron redox processes on BDEs of C–H bonds in coordinated ligands can also be seen in dinuclear complexes and probably in higher clusters. For example, the reduction of the μ_2 -ethyldiyne complexes $\text{Cp}_2\text{M}_2(\text{CO})_3(\mu\text{-CCH}_3)^+$ ($\text{M} = \text{Fe}, \text{Ru}$) led to disproportionation of the ethyldiyne groups to yield the vinylidene and ethylidene complexes $\text{Cp}_2\text{M}_2(\text{CO})_3(\mu\text{-C}=\text{CH}_2)$ and $\text{Cp}_2\text{M}_2(\text{CO})_3(\mu\text{-CHCH}_3)$ [54]. The reactions were proposed to take place via hydrogen atom transfer between two $\text{Cp}_2\text{M}_2(\text{CO})_3(\mu\text{-CCH}_3)^\cdot$ radicals in a fashion reminiscent of disproportionation of caged organic radicals. In this case, the thermochemical cycle in Scheme 10 can be used to demonstrate that the β -C–H bond in the ethyldiyne cations becomes substantially weakened following a one-electron reduction. Only irreversible electrode-potential data are available for the pertinent processes, but the semi-quantitative result is obtained that the reduction leads to an ethyldiyne C–H BDE decrease of ca 140 kJ mol^{-1} for Fe and ca 175 kJ mol^{-1} for Ru. In this case, the bond weakening is facilitated by the formation of a strong C=C bond and two closed-shell metal centers when C–H scission takes place from the radical; such is not the case when the reaction occurs from the cation.



Scheme 10. Thermochemical cycle for determination of reductively induced C–H bond activation in dinuclear ethynyl complexes.

3.9 Concluding Remarks

Thermochemical cycles that incorporate electrode potentials provide a means for obtaining reasonable estimates of bond energies and other thermodynamic quantities that are difficult or impossible to obtain directly. Absolute bond energies can be determined when suitable anchoring points are available. Otherwise, important and interesting information can be obtained from cycles that provide relative bond-energy data. The selected examples have focused mostly on M–H and C–H bonding, but the methodology can be applied to any X–Y bond where the suitable redox partners are available for electrochemical studies.

The effects of one-electron redox processes on various bond strengths is often substantial and can often be qualitatively understood by appropriate consideration of pertinent Lewis structures for each side of the redox couples. Significant $\text{p}K_{\text{a}}$ or BDE changes can be ascribed to changes in metal–ligand hapticities, metal–ligand bond orders, or C–C bond orders.

It is not uncommon that one-electron redox processes cause bond energy changes in the range 100–150 kJ mol^{−1}. Looking at these numbers as relative activation energies for chemical reactions, one obtains relative rates of ca 10¹⁷:1–10²⁶:1 for the pertinent bond-cleavage reactions at ambient temperature! From this, it becomes clear that electron transfer pathways can open new reaction pathways, and that in many cases initially uphill electron transfer equilibria can be productive due to extremely fast follow-up reactions. This is particularly important in the context of understanding and exploiting efficient electron transfer catalyzed chain reactions [1b, 2i].

Abbreviations

arphos	$\text{Ph}_2\text{PCH}_2\text{CH}_2\text{AsPh}_2$
BDE	Bond-dissociation energy (in enthalpy terms)
BDE_G	Bond-dissociation energy (in free energy terms)
COD	1,5-Cyclooctadiene
Cp	η^5 -Cyclopentadienyl, C_5H_5
Cp^*	η^5 -Pentamethylcyclopentadienyl, C_5Me_5
Cp'	Any substituted Cp
Cp^TMS	η^5 -Trimethylsilylcyclopentadienyl, $\text{C}_5\text{H}_4\text{SiMe}_3$
Cy	Cyclohexyl
DCE	1,2-Dichloroethane
dape	$(p\text{-MeOC}_6\text{H}_4)_2\text{PCH}_2\text{CH}_2\text{P}(p\text{-MeOC}_6\text{H}_4)_2$
depe	$\text{Et}_2\text{PCH}_2\text{CH}_2\text{PEt}_2$
dppe	$\text{Ph}_2\text{PCH}_2\text{CH}_2\text{PPh}_2$
dppf	$(\text{C}_5\text{H}_4\text{PPh}_2)_2\text{Fe}$, 1,1'-bis(diphenylphosphino)ferrocene
dppm	$\text{Ph}_2\text{PCH}_2\text{PPh}_2$
dppp	$\text{Ph}_2\text{PCH}_2\text{CH}_2\text{CH}_2\text{PPh}_2$
dtfpe	$(p\text{-CF}_3\text{C}_6\text{H}_4)_2\text{PCH}_2\text{CH}_2\text{P}(p\text{-CF}_3\text{C}_6\text{H}_4)_2$
EA	Electron affinity
Fc	Ferrocene, Cp_2Fe
IP	Ionization potential
Tp	Hydridotris(pyrazolyl)borate
Tp'	Hydridotris(3,5-dimethylpyrazolyl)borate
tripod	$\text{MeC}(\text{CH}_2\text{PPh}_2)_3$
triphos	$\text{PhP}(\text{CH}_2\text{CH}_2\text{PPh}_2)_2$

References

- (a) J. K. Kochi, *Organometallic Mechanisms and Catalysis*, Academic Press, New York, **1978**.
 (b) D. Astruc, *Electron Transfer and Radical Processes in Transition-Metal Chemistry*, VCH, Weinheim, **1995**.
- (a) N. G. Connelly, W. E. Geiger, *Chem. Rev.* **1996**, 96, 877–910. (b) D. Astruc, *Acc. Chem. Res.* **1991**, 24, 36–42. (c) D. R. Tyler, *Acc. Chem. Res.* **1991**, 24, 325–331. (d) *Organometallic Radical Processes* (Ed: W. C. Troglor), Elsevier, Amsterdam, **1990**. (e) D. R. Tyler, F. Mao, *Coord. Chem. Rev.* **1990**, 97, 119–140. (f) N. G. Connelly, *Chem. Soc. Rev.* **1989**, 18, 153–185. (g) *Paramagnetic Organometallic Species in Activation-/Selectivity, Catalysis* (Eds.: M. Chanon, M. Julliard, J. C. Poite), Kluwer Academic, Dordrecht, **1989**. (h) D. R. Tyler, *Progr. Inorg. Chem.* **1988**, 36, 125–194. (i) D. Astruc, *Angew. Chem., Int. Ed. Engl.* **1988**, 27, 643–660. (j) D. Astruc, *Chem. Rev.* **1988**, 88, 1189–1216. (k) M. C. Baird, *Chem. Rev.* **1988**, 88, 1217–1227. (l) J. C. Kotz in *Topics in Electrochemistry* (Eds.: A. J. Fry, W. E. Britton), Plenum, New York, **1986**, Chapter 3. (m) D. Astruc, *Acc. Chem. Res.* **1986**, 19, 377–383. (n) W. E. Geiger, *Progr. Inorg. Chem.* **1985**, 33, 275–351. (o) N. G. Connelly, W. E. Geiger, *Adv. Organomet. Chem.* **1984**, 23, 1–93.
- (a) J. A. M. Simões, J. L. Beauchamp, *Chem. Rev.* **1990**, 90, 629–688. (b) *Energetics of Organometallic Species* (Ed.: J. A. M. Simões), Kluwer Academic, Dordrecht, **1992**. (c) *Bonding Energetics in Organometallic Compounds*, ACS Symposium Series No. 428 (Ed.: T. J. Marks), American Chemical Society, Washington, DC, **1990**. (d) J. Halpern, *Inorg. Chim. Acta* **1985**, 100, 41–48. (e) J. A. Connor, *Top. Curr. Chem.* **1977**, 71, 71–110.

4. (a) D. T. Sawyer, A. Sobkowiak, J. L. Roberts, Jr., *Electrochemistry for Chemists*, 2nd ed., Wiley, New York, **1995**. (b) A. J. Bard, L. R. Faulkner, *Electrochemical Methods: Fundamentals and Applications*, 2nd ed., Wiley, New York, **1998**. (c) D. Pletcher, *A First Course in Electrode Processes*, The Electrochemical Consultancy, Romsey, UK, **1991**. (d) D. K. Gosser, Jr., *Cyclic Voltammetry. Simulation and Analysis of Reaction Mechanisms*, Verlag Chemie, Weinheim, **1993**.
5. (a) S. G. Lias, J. E. Bartmess, J. F. Liebman, J. L. Holmes, R. D. Levin, W. G. Mallard, *J. Phys. Chem. Ref. Data* **1988**, 17, Suppl. 1. (b) *NIST Chemistry WebBook, NIST Standard Reference Database Number 69* (Eds.: W. G. Mallard, P. J. Linstrom), National Institute of Standards and Technology, Gaithersburg, MD 20899, **1998** (<http://webbook.nist.gov/chemistry/>).
6. (a) A. S. Carson, in ref. [3b], p. 131–158. (b) J. A. M. Simões, in ref. [3b], p. 197–232.
7. (a) P. Hamon, L. Toupet, J.-R. Hamon, C. Lapinte, *Organometallics* **1992**, 11, 1429–1431. (b) P. Hamon, L. Toupet, J.-R. Hamon, C. Lapinte, *Organometallics* **1996**, 15, 10–12.
8. D. D. M. Wayner, V. D. Parker, *Acc. Chem. Res.* **1993**, 26, 287–294.
9. (a) R. Breslow, W. Chu, *J. Am. Chem. Soc.* **1973**, 95, 411–418. (b) R. Breslow, J. Grant, *J. Am. Chem. Soc.* **1977**, 99, 7745–7746. (c) B. Jaun, J. Schwarz, R. Breslow, *J. Am. Chem. Soc.* **1980**, 102, 5741–5748.
10. (a) A. M. de Nicholas, D. R. Arnold, *Can. J. Chem.* **1982**, 60, 2165–2179. (b) F. G. Bordwell, J.-P. Cheng, J. A. Harrelson, *J. Am. Chem. Soc.* **1988**, 110, 1229–1231. (c) F. G. Bordwell, J.-P. Cheng, *J. Am. Chem. Soc.* **1989**, 111, 1792–1795.
11. (a) E. M. Arnett, R. A. Flowers, R. T. Ludwig, A. Meckhof, S. Walek, *Pure Appl. Chem.* **1995**, 67, 729–734. (b) F. G. Bordwell, A. V. Satish, S. Zhang, X.-M. Zhang, *Pure Appl. Chem.* **1995**, 67, 735–740. (c) E. M. Arnett, R. A. Flowers, *Chem. Soc. Rev.* **1993**, 22, 9–15. (d) F. G. Bordwell, X.-M. Zhang, *Acc. Chem. Res.* **1993**, 26, 510–517.
12. S. S. Kristjánssdóttir, J. R. Norton in *Transition Metal Hydrides* (Ed.: A. Dedieu), VCH, Weinheim, **1992**, p. 309–359.
13. (a) M. Tilset, V. D. Parker, *J. Am. Chem. Soc.* **1989**, 111, 6711–6717; **1990**, 112, 2843 (corrigendum). (b) V. D. Parker, K. L. Handoo, F. Roness, M. Tilset, *J. Am. Chem. Soc.* **1991**, 113, 7493–7498.
14. (a) R. F. Jordan, J. R. Norton, *J. Am. Chem. Soc.* **1982**, 104, 1255–1263. (b) E. J. Moore, J. M. Sullivan, J. R. Norton, *J. Am. Chem. Soc.* **1986**, 108, 2257–2263. (c) S. S. Kristjánssdóttir, A. E. Moody, R. T. Weberg, J. R. Norton, *Organometallics* **1988**, 7, 1983–1987.
15. *Solubility Data Series: Hydrogen and Deuterium, Vol. 5/6* (Ed.: C. L. Young), Pergamon, Oxford, **1981**.
16. E. Brunner, *J. Chem. Eng. Data* **1985**, 30, 269–273.
17. *CRC Handbook of Chemistry and Physics* (Ed.: R. C. Weast), CRC Press, Boca Raton, 1987.
18. G. Gritzner, J. Kuta, *Pure Appl. Chem.* **1984**, 56, 461–466.
19. I. M. Kolthoff, M. K. Chantooni Jr., *J. Phys. Chem.* **1972**, 76, 2024–2034.
20. D. D. M. Wayner, D. J. McPhee, D. Griller, *J. Am. Chem. Soc.* **1988**, 110, 132–137.
21. G. Kiss, K. Zhang, S. L. Mukerjee, C. D. Hoff, *J. Am. Chem. Soc.* **1990**, 112, 5657–5658.
22. (a) M. Tilset, *J. Am. Chem. Soc.* **1992**, 114, 2740–2741. (b) V. Skagestad, M. Tilset, *J. Am. Chem. Soc.* **1993**, 115, 5077–5083. (c) A. Pedersen, V. Skagestad, M. Tilset, *Acta Chem. Scand.* **1995**, 49, 632–635.
23. Ref. [4b], Chapter 11.
24. L. Luo, C. Li, M. E. Cucullu, S. P. Nolan, *Organometallics* **1995**, 14, 1333–1338.
25. J. Ruiz, D. Astruc, *C. R. Acad. Sci., Ser. II: Chim.* **1998**, 1, 21–28.
26. R. J. Angelici, *Acc. Chem. Res.* **1995**, 28, 51–60.
27. D. Wang, R. J. Angelici, *J. Am. Chem. Soc.* **1996**, 118, 935–942.
28. P. G. Jessop, R. H. Morris, *Coord. Chem. Rev.* **1992**, 121, 155–284.
29. (a) G. Jia, R. H. Morris, *J. Am. Chem. Soc.* **1991**, 113, 875–883. (b) R. Morris, *Inorg. Chem.* **1992**, 31, 1471–1478. (c) G. Jia, A. J. Lough, R. H. Morris, *Organometallics* **1992**, 11, 161–171. (d) E. P. Cappellani, S. D. Drouin, G. Jia, P. A. Maltby, R. H. Morris, C. T. Schweitzer, *J. Am. Chem. Soc.* **1994**, 116, 3375–3388. (e) B. Chin, A. J. Lough, R. H. Morris, C. T. Schweitzer, C. D'Agostino, *Inorg. Chem.* **1994**, 33, 6278–6288. (f) M. Schlaf, A. J. Lough, P. A. Maltby, R. H. Morris, *Organometallics* **1996**, 15, 2270–2278.
30. K.-T. Smith, C. Rømming, M. Tilset, *J. Am. Chem. Soc.* **1993**, 115, 8681–8689.

31. W. S. Ng, G. Jia, M. Y. Hung, C. P. Lau, K. Y. Wong, L. Wen, *Organometallics* **1998**, *17*, 4556–4561.
32. (a) D. M. Heinekey, W. J. Oldham, Jr., *Chem. Rev.* **1993**, *93*, 913–926. (b) Crabtree, R. H. *Angew. Chem., Int. Ed. Engl.* **1993**, *32*, 789–805.
33. J. D. Protasiewicz, K. H. Theopold, *J. Am. Chem. Soc.* **1993**, *115*, 5559–5569.
34. S. Trofimenko, *Scorpionates*, Imperial College Press, London, 1999.
35. (a) M. D. Curtis, K.-B. Shiu, *Inorg. Chem.* **1985**, *24*, 1213–1218. (b) M. D. Curtis, K.-B. Shiu, W. M. Butler, J. C. Huffman, *J. Am. Chem. Soc.* **1986**, *108*, 3335–3343. (c) Y. Alvarado, O. Boutry, E. Gutiérrez, A. Monge, M. C. Nicasio, M. L. Poveda, P. J. Pérez, C. Ruiz, C. Bianchini, E. Carmona, *Chem. Eur. J.* **1997**, *3*, 860–873.
36. M. E. Kerr, X.-M. Zhang, J. W. Bruno, *Organometallics* **1997**, *16*, 3249–3251.
37. F. G. Bordwell, X.-M. Zhang, R. Filler, *J. Org. Chem.* **1993**, *58*, 6067–6071.
38. D. F. McMillen, D. M. Golden, *Annu. Rev. Phys. Chem.* **1982**, *33*, 493–532.
39. S. Zhang, F. G. Bordwell, *Organometallics* **1994**, *13*, 2920–2921.
40. (a) H. A. Trujillo, C. M. Casado, J. Ruiz, D. Astruc, *J. Am. Chem. Soc.* **1999**, *121*, 5674–5686. (b) H. A. Trujillo, C. M. Casado, D. Astruc, *J. Chem. Soc., Chem. Commun.* **1995**, 7–8.
41. J. R. Pugh, T. J. Meyer, *J. Am. Chem. Soc.* **1992**, *114*, 3784–3792.
42. O. B. Ryan, M. Tilset, V. D. Parker, *J. Am. Chem. Soc.* **1990**, *112*, 2618–2626.
43. F. Marken, A. M. Bond, R. Colton, *Inorg. Chem.* **1995**, *34*, 1705–1710.
44. (a) O. B. Ryan, M. Tilset, V. D. Parker, *Organometallics* **1991**, *10*, 298–304. (b) O. B. Ryan, M. Tilset, *J. Am. Chem. Soc.* **1991**, *113*, 9554–9561. (c) K.-T. Smith, M. Tilset, *J. Organomet. Chem.* **1992**, *431*, 55–64. (d) M. Tilset, A. Zlota, K. G. Caulton, *Inorg. Chem.* **1993**, *32*, 3816–3821. (e) K.-T. Smith, M. Tilset, R. Kuhlman, K. G. Caulton, *J. Am. Chem. Soc.* **1995**, *117*, 9473–9480. (f) K.-T. Smith, M. Tilset, S. S. Kristjánssdóttir, J. R. Norton, *Inorg. Chem.* **1995**, *34*, 6497–6504. (g) J. C. Fetting, H.-B. Kraatz, R. Poli, E. A. Quadrelli, R. C. Torralba, *Organometallics* **1998**, *17*, 5767–5775.
45. (a) M. Tilset, *Inorg. Chem.* **1994**, *33*, 3121–3126. (b) C. G. Zoski, D. A. Sweigart, N. J. Stone, P. H. Rieger, E. Mocellin, T. F. Mann, D. R. Mann, D. K. Gosser, M. M. Doeff, A. M. Bond, *J. Am. Chem. Soc.* **1998**, *110*, 2109–2116. (c) Y. Zhang, D. K. Gosser, P. H. Rieger, D. A. Sweigart, *J. Am. Chem. Soc.* **1991**, *113*, 4062–4068.
46. B. Pleune, D. Morales, R. Meunier-Prest, P. Richard, E. Collange, J. C. Fetting, R. Poli, *J. Am. Chem. Soc.* **1999**, *121*, 2209–2225.
47. M. Tilset, J.-R. Hamon, P. Hamon, *Chem. Commun.* **1998**, 765–766.
48. (a) C. Roger, P. Hamon, L. Toupet, H. Rabaâ, J.-Y. Saillard, J.-R. Hamon, C. Lapinte, *Organometallics* **1991**, *10*, 1045–1054. (b) P. Hamon, L. Toupet, J.-R. Hamon, C. Lapinte, *Organometallics* **1992**, *11*, 1429–1431. (c) P. Hamon, J.-R. Hamon, C. Lapinte, *J. Chem. Soc., Chem. Commun.* **1992**, 1602–1603. (d) P. Hamon, L. Toupet, J.-R. Hamon, C. Lapinte, *Organometallics* **1996**, *15*, 10–12.
49. (a) K. G. Caulton, *New J. Chem.* **1994**, *18*, 25–41. (b) N. M. Doherty, N. W. Hoffman, *Chem. Rev.* **1991**, *91*, 553–573.
50. (a) R. S. Drago, N. M. Wong, D. C. Ferris, *J. Am. Chem. Soc.* **1992**, *114*, 91–98. (b) R. S. Drago, *Inorg. Chem.* **1990**, *29*, 1379–1382. (c) R. S. Drago, *Inorg. Chem.* **1995**, *34*, 3543–3548. (d) P. L. Holland, R. A. Andersen, R. G. Bergman, J. Huang, S. P. Nolan, *J. Am. Chem. Soc.* **1997**, *119*, 12800–12814. (e) P. L. Holland, R. A. Andersen, R. G. Bergman, *Comments Inorg. Chem.* **1999**, *21*, 115–129.
51. D. Astruc, J.-R. Hamon, G. Althoff, E. Román, P. Batail, P. Michaud, J.-P. Mariot, F. Varret, D. Cozak, *J. Am. Chem. Soc.* **1979**, *101*, 5445–5447.
52. (a) G. S. Bodner, J. A. Gladysz, M. F. Nielsen, V. D. Parker, *J. Am. Chem. Soc.* **1987**, *109*, 1757–1764. (b) D. Mandon, D. Astruc, *Organometallics* **1989**, *8*, 2372–2377. (c) V. Guerschais, C. Lapinte, *J. Chem. Soc., Chem. Commun.* **1986**, 663–664. (d) D. Mandon, L. Toupet, D. Astruc, *J. Am. Chem. Soc.* **1986**, *108*, 1320–1322. (e) J. C. Hayes, N. J. Cooper, *J. Am. Chem. Soc.* **1982**, *104*, 5570–5572.
53. M. Tilset, G. S. Bodner, D. R. Senn, J. A. Gladysz, V. D. Parker, *J. Am. Chem. Soc.* **1987**, *109*, 7551–7553.
54. T. Aase, M. Tilset, V. D. Parker, *Organometallics* **1989**, *8*, 1558–1563.

4 Electron-transfer Reactions of Electron-reservoir Complexes and other Monoelectronic Redox Reagents in Transition-metal Chemistry

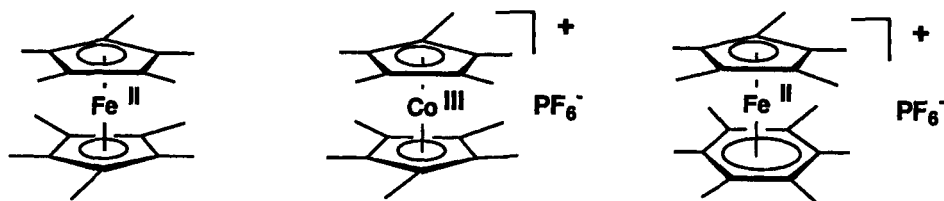
Didier Astruc

4.1 Introduction

Redox reactions are a characteristic of transition-metal complexes because transition metals can readily vary their number of valence electrons. Indeed, the large majority of redox reagents is based on transition metals [1, 2]. This feature is also encountered in biochemistry with ferredoxines and cytochromes [3–5], in catalysis which involves the well-known oxidative addition and reductive elimination reactions [6, 7], in photochemistry where the remarkably long life-times of the excited states of transition-metal complexes enable exergonic electron-transfer reactions from these excited states [8, 9], in various parts of supramolecular chemistry [10], especially molecular electronics [11], where devices almost systematically involve transition metal components, and in solid-state chemistry and physics (non-linear optics, conductors, and superconductors) [12]. This chapter concerns mono-electronic redox reagents with emphasis on organometallic electron-reservoir complexes which are so useful in this context both as oxidants and reductants. Although most redox reagents are inorganic or organometallic, a minority of organic reagents are sometimes used and will be included in the review. The subject of redox chemistry has already been extensively treated in the literature from various standpoints. We intend to give here only a subjective and personal view of this immense area. In organic chemistry, asymmetric catalysis of oxidation [13, 14] and reduction [15, 16] reactions is a broad, popular field which we are not treating here. Electrochemistry [17] and photochemistry [8, 9] are also sub-disciplines of chemistry systematically involving redox reactions which are not dealt with in this chapter, except for thermodynamic redox potentials and redox catalysis. Likewise, organometallic oxidative additions and reductive elimination [6, 7] will not be discussed except when induced or catalyzed by mono-electronic reagents. We will not include biochemical redox reactions [3–5] either despite their importance.

4.2 Standard Redox Potentials and Complementary References

We will mostly deal with non-aqueous solutions. The IUPAC has recommended the reporting of standard redox potential $E^{\circ'}$ relative to the ferrocene/ferrocenium ($\text{FeCp}_2^{0/+}$) redox couple rather than the aqueous saturated calomel electrode [18] which is only modestly stable in non-aqueous solutions [19, 20]. In early studies, redox potentials in non-aqueous solutions were reported relative to the SCE, but recent studies systematically report redox potentials relative to $\text{FeCp}_2^{0/+}$. Conversion of values reported relative to the SCE to values reported relative to $\text{FeCp}_2^{0/+}$ have been made [21]. Unfortunately, despite the IUPAC recommendation, the absolute redox potential value of the couple $\text{FeCp}_2^{0/+}$ is somewhat dependent on the nature of the solvent and the supporting electrolyte, because the iron center which is the subject of redox change is not too well protected by the ligand in ferrocenium [22–24]. Indeed, the nucleophiles can interact from the sides with the cationic iron center. The energy of this interaction shifts the redox potential and depends on the nature of the nucleophiles. Therefore, we have selected the permethylated transition-metal sandwich redox systems decamethylferrocene/decamethylferrocenium $[\text{FeCp}^*_2]^{0/+}$, decamethylcobaltocene/decamethylcobaltocenium $[\text{CoCp}^*_2]^{0/+}$ and $[\text{FeCp}(\eta^6\text{-C}_6\text{Me}_6)]^{0/+}$ as alternative and complementary reference systems. In these electron-reservoir complexes the transition-metal center is really shielded from external nucleophiles (solvent, counter-anion of the electrolyte) so that their nature does not interfere with the redox potential value.



The redox potential values of these redox couples are reported in Table 1 relative to the SCE in different solvents. The independence of the redox couples of the permethylated redox couples was verified by comparing the values of the redox potentials recorded relative to $[\text{FeCp}^*_2]^{0/+}$, taken as the reference, which are reported in Table 2 for a variety of solvents. Only the values of the $[\text{FeCp}_2]^{0/+}$ couple varies, not those of the permethylated redox couples. This result is consistent with the fact that the redox potentials of the permethylated redox couples are independent of the nature of the solvent and supporting electrolyte. That the $[\text{FeCp}_2]^{0/+}$ reference is not quite sufficiently accurate does not mean that the many results that have been reported in the recent literature relative to $[\text{FeCp}_2]^{0/+}$ have to be re-measured relative to the more accurate $[\text{FeCp}^*_2]^{0/+}$ reference. Indeed, it is possible to take advantage of all the results obtained relative to $[\text{FeCp}_2]^{0/+}$ using the conversion of

Table 1. $E_{1/2}$ values determined for the transition-metal sandwich complexes (V relative to the SCE).

Complex	$E_{1/2}$ in the solvents:					
	DMF	CH ₃ CN	THF	CH ₂ Cl ₂	DMSO	DME
FeCp ₂ ^{0/+}	0.470	0.382	0.547	0.475	0.435	0.580
FeCp* ₂ ^{0/+}	-0.125	-0.125	0.102	-0.070	-0.030	0.140
CoCp* ₂ ^{0/+}	-1.402	-1.525	-1.295	-1.497	-1.425	-1.260
FeCp*(C ₆ Me ₆) ^{0/+}	-1.762	-1.865	-1.645	-	-1.775	-1.605

Table 2. $E_{1/2}$ values determined for the transition-metal sandwich complexes (V relative to FeCp*₂).

Complex	$E_{1/2}$ in the solvents:					
	DMF	CH ₃ CN	THF	CH ₂ Cl ₂	DMSO	DME
FeCp* ₂ ^{0/+}	0	0	0	0	0	0
FeCp ₂ ^{0/+}	0.480	0.510	0.440	0.545	0.470	0.440
CoCp* ₂ ^{0/+}	1.390	1.390	1.400	1.390	1.395	1.400
FeCp*(C ₆ Me ₆) ^{0/+}	1.750	1.745	1.750	-	1.750	1.750

$E_{1/2}$ values were determined using the cationic form: $E^\circ \approx E_{1/2} = (E_{pa} + E_{pc})/2$. $n\text{-Bu}_4\text{N}^+\text{PF}_6^-$ (0.1 M); cationic complex: 10^{-3} M; $v = 400$ mV s⁻¹, 20 °C; working and counter electrodes: Pt; reference electrode: SCE; $\Delta E_p = E_{pa} - E_{pc} = 40\text{--}45$ mV (DMF), 45–50 mV (MeCN), 50–55 mV (THF), 50–60 mV (CH₂Cl₂), 50–60 mV (DMSO), 60–70 mV (DME). The shifts versus the theoretical value of 58 mV at 20 °C are due to variations in ohmic compensation. $E_{1/2}$ values were recorded with an accuracy of ± 0.005 V except the $E_{1/2}$ value of $[\text{FeCp}^*(\text{C}_6\text{Me}_6)]^{0/+}$ in CH₂Cl₂, which is not accurate because of the interference with the reduction of the solvent. In CH₂Cl₂, $n\text{-Bu}_4\text{N}^+$ salts with various counter-anions and concentrations (vide infra) were used, but the difference between the $E_{1/2}$ values of FeCp^*_{2+0} and CoCp^*_{2+0} remained constant (1.390 V). The difference between the $E_{1/2}$ values of FeCp_2^{+0} and FeCp^*_{2+0} varied, however, between 0.460 V and 0.545 V. The $E_{1/2}$ values relative to the SCE obtained for FeCp_2^{+0} and FeCp^*_{2+0} , respectively, are (V): $n\text{-Bu}_4\text{N}^+\text{PF}_6^-$ (0.1 M: 0.475 and -0.070; 0.4 M: 0.425 and -0.100); $n\text{-Bu}_4\text{N}^+\text{BF}_4^-$ (0.1 M: 0.585 and 0.045; 0.4 M: 0.555 and 0.035); $n\text{-Bu}_4\text{N}^+\text{Br}^-$ (0.1 M: 0.490 and -0.010; 0.4 M: 0.480 and 0.000); $n\text{-Bu}_4\text{N}^+\text{HSO}_4^-$ (0.1 M: 0.545 and 0.065; 0.4 M: 0.515 and 0.055); $n\text{-Bu}_4\text{N}^+\text{Cl}^-$ (0.1 M: 0.590 and 0.070; 0.4 M: 0.570 and 0.070).

values relative to $[\text{FeCp}_2]^{0/+}$ to values relative to $[\text{FeCp}^*_{2+0}]^{0/+}$ of Table 2 in various solvents. Likewise, it is possible to continue using ferrocene as the internal reference, and yet to have a solvent- and electrolyte-independent redox potential by conversion with Table 2. The standard redox potentials of the main reductants and oxidants E° relative to $[\text{FeCp}_2]^{0/+}$, $[\text{FeCp}_2]^{0/+}$, SCE and the normal hydrogen electrode (NHE) are given in Tables 3 and 4, respectively [23].

Table 3. Formal potentials (V) of the main reductants.

Reductant	Solvent	E° relative to:			
		FeCp* ₂	SCE	NHE	FeCp ₂
[C ₁₀ H ₈] ^{•-}	THF	-2.66	-2.76	-2.52	-3.10
—	DMF	-2.56	-2.68	-2.44	-3.05
Na	THF, DME	-2.60	-2.72	-2.58	-3.04
Li(Hg)	H ₂ O	-2.13	-2.16	-1.92	-2.60
[Anthracene] ^{•-}	THF	-2.08*	-1.98		
FeCp*(C ₆ Me ₆)	CH ₂ Cl ₂	-1.75*	-1.85	-1.61	-2.30
—	DMF	-1.75*	-1.76	-1.62	-2.24
[Perylene] ^{•-}	THF	-1.75*			
[Benzophenone] ^{•-}	THF	-1.75	-1.86	-1.62	-2.30
—	MeCN	1.68*	-1.69	-1.45	-2.17
FeCp(C ₆ Me ₆)	DMF	-1.54	-1.55	-1.31	-2.02
—	THF	-1.53*			
—	DMSO	-1.52*	-1.56	-1.32	-1.99
C ₆₀ ³⁻	MeCN-PhMe	-1.41*	-1.36	1.12	-1.87
CoCp* ₂	DMF	-1.39*	-1.40	-1.16	-1.87
FeCp(C ₆ H ₆)	THF	-1.34*			
C ₆₀ ²⁻	MeCN-PhMe	-0.915*	-0.91	-0.67	-1.37
CoCp ₂	DME	-0.74*	-0.86	-0.62	-1.33
C ₆₀ ⁻	MeCN-PhMe	-0.515*	-0.51	-0.27	-0.98
FeCp* ₂	DMF	0	-0.012	+0.23	-0.49
—	CH ₂ Cl ₂	0	-0.105	+0.13	-0.55
Hydrazine	DMSO	+0.06	-0.03	+0.21	-0.41

4.3 Reductants

4.3.1 Alkali- and other Metals; Amalgams and Alloys

Alkali metals

Alkali metals (Li, Na, K) have long been used as strong reductants, *but their use is dangerous* and should be limited to occasions when other reductants are not efficient. *These metals should be used only by very experimented chemists.* They are the strongest reductants, with standard potentials of ca 3 V relative to the SCE in aqueous systems:



Their reducing power increases and electropositivity increases from lithium to rubidium. For instance, lithium reacts slowly with water, sodium reacts vigorously, potassium ignites, and cesium and rubidium react explosively. It is difficult to de-

Table 4. Formal potentials (V) of the main oxidants.

Oxidant	Solvent	E^{of} relative to			
		FeCp* ₂	SCE	NHE	FeCp ₂
[N(C ₆ H ₂ Br ₃ -2,4,6) ₃] ⁺	MeCN	1.87	1.74	1.98	1.36
[N(C ₆ H ₃ Br ₂ -2,4) ₃] ⁺	MeCN	1.65	1.52	1.76	1.14
[NO] ⁺	CH ₂ Cl ₂	1.55	1.44	1.68	1.00
[RuL ₃] ₃ ⁺ , L = bpy or phen	MeCN	1.40*	1.25	1.49	0.87
[Thianthrene] ⁺	MeCN	1.32*	1.24	1.48	0.86
[N(C ₆ H ₄ Br-4) ₃] ⁺	MeCN	1.21*	1.05	1.29	0.70
[Fe(bipy) ₃] ³⁺	MeCN	1.17	1.04	1.28	0.66
Ag ⁺	CH ₂ Cl ₂	1.16	1.05	1.29	0.65
FeCp(η^5 -C ₅ H ₄ COMe) ⁺	MeCN	0.75*	0.71	0.95	0.27
Cl ₂	MeCN	0.69	0.56	0.80	0.18
DDQ	MeCN	0.635*	0.51	0.75	0.13
Br ₂	MeCN	0.58	0.45	0.69	0.07
FeCp ₂	MeCN	0.51*	0.38	0.62	0.
—	CH ₂ Cl ₂	0.55*	0.42	0.66	0.
[N ₂ C ₆ H ₄ F-4] ⁺	MeCN	0.44	0.31	0.55	−0.07
Fe[C ₅ (CH ₂ Ph) ₅] ₂	CH ₂ Cl ₂	0.49*	0.50	0.74	−0.06
—	THF, MeCN	0.41*			
—	DMF	0.34*	0.215	0.455	−0.14
I ₂	MeCN	0.37	0.24	0.48	−0.14
TCNE	MeCN	0.345*	0.11	0.35	−0.27
TCNQ	MeCN	0.32*	0.08	0.32	−0.30
FeCp* ₂	MeCN	0	−0.13	0.11	−0.51
—	CH ₂ Cl ₂	0	−0.105	0.13	−0.55

Footnote to Tables 3 and 4. Direct measurements relative to [FeCp*₂], are denoted *. The mono, di- and trianion of C₆₀ are accessible by reduction of C₆₀ using [FeCp(C₆Me₆)] [25]. The other values relative to [FeCp*₂] are: C₆₀^{3−/4−}: −1.895 V, C₆₀^{4−/5−}: −2.39 V and C₆₀^{5−/6−}: −2.39 V. The two later values are deduced from the values relative to [FeCp₂], reported in Ref. [25]. Other standard redox potentials E^{of} (V) of oxidants and reductants relative to various references extracted from Ref. [21] and corrected from the [FeCp₂] to the [FeCp*₂] reference using the ΔE^{of} values of Table 2.

termine their redox potentials precisely, however, because they vary considerably with the nature of the solvent. Differences of up to 1 V are encountered because of variations in the solvation of the cation, a notion already discussed in Section 4.2. For instance, with NH₃, the redox potential of Na/Na⁺ is ca 1 V less negative (approximately −2 V relative to the SCE) than in DMF (ca −3 V). Indeed, Na reacts with NH₃ to give solvated Na⁺ and the stable blue solution of solvated electrons which have frequently been used as reducing agents in organic chemistry (for instance to reduce aromatic compounds to cyclohexadienes). The influence of ion pairs on redox potentials has been reviewed [26].

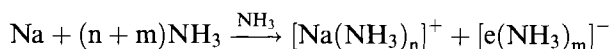
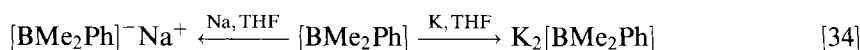
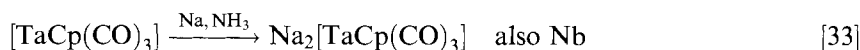
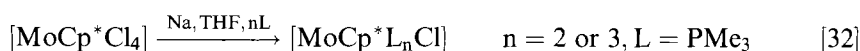
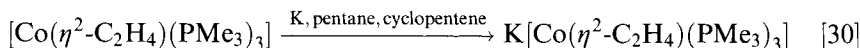
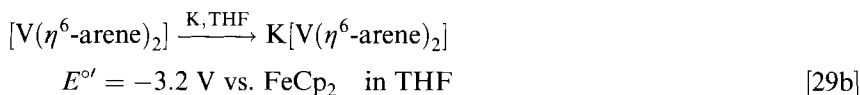
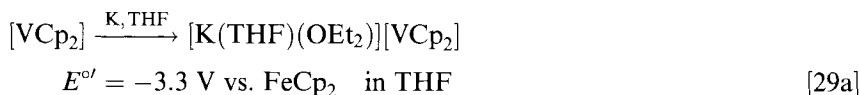
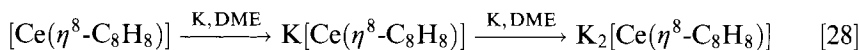


Table 5. Standard reduction potentials $E^{\circ'}$, relative to FeCp_2 , of metal ions in water.

Half reaction (acidic solution)	Standard reduction potential, $E^{\circ'}$ (V)
$\text{Li}^+(\text{aq}) + e^- \leftrightarrow \text{Li}(\text{s})$	-3.045
$\text{K}^+(\text{aq}) + e^- \leftrightarrow \text{K}(\text{s})$	-2.925
$\text{Na}^+(\text{aq}) + e^- \leftrightarrow \text{Na}(\text{s})$	-2.714
$\text{Al}^{3+}(\text{aq}) + 3e^- \leftrightarrow \text{Al}(\text{s})$	-1.66
$\text{Zn}^{2+}(\text{aq}) + 2e^- \leftrightarrow \text{Zn}(\text{s})$	-0.763
$\text{Fe}^{2+}(\text{aq}) + 2e^- \leftrightarrow \text{Fe}(\text{s})$	-0.44
$\text{Sn}^{2+}(\text{aq}) + 2e^- \leftrightarrow \text{Sn}(\text{s})$	-0.14

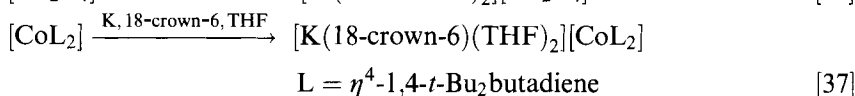
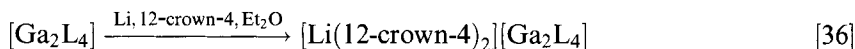
The redox potentials of the metals in water are given in Table 5 to provide an indication of the order of the reducing power of the main metals used as reductants [27].

Another major drawback is that metals must be used in excess of the necessary stoichiometric amount because it is impossible to know how much of the metal sample is contaminated with metal oxide and metal hydroxide covering the surface after contact with air. *Then excess metal must be destroyed very slowly by addition of absolute ethanol with the most extreme care, otherwise fire subsequent to reaction will occur almost systematically upon contact with air or water.* Metals freshly cut into pieces are particularly reactive. Even more reactive are the metallic sands obtained by heating pieces of the metal above its melting point in a suitable solvent, e.g. dry toluene, and the metallic mirrors formed by subliming a piece of metal (Na or more often K) from the bottom of a Schlenk flask on to its walls under vacuum. THF and DME are the solvents most often used for reductions with these metals, for example:

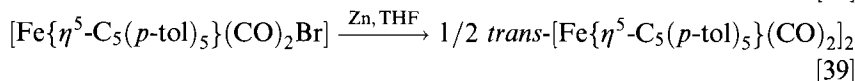
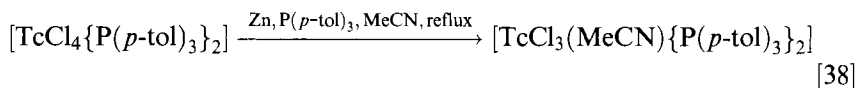


Alkali metals in the presence of a macrocycle or a cryptand

The presence of a polyether macrocycle or cryptand adapted to the size of the alkali cation [10] facilitates the reduction of molecules which are otherwise difficult to reduce by the alkali metal; it stabilizes and solubilizes the reduced molecules and induces the formation of crystals. Li^+ salts are stabilized by the presence of 12-crown-4 or 2,2,2-cryptand; Na^+ salts are stabilized by 12-crown-5 or 2,2,2 cryptand; and K^+ salts are stabilized by 18-crown-6 [10, 35], for example:

**Less reducing metals—Zn powder**

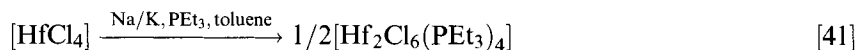
Zn powder is a useful reducing agent with a less negative redox potential than the alkali metals (Table 5), and it is not dangerous.



Transmetallation reactions are also known:

**Amalgams and alloys**

Amalgams and alloys, especially those of Na and K are very popular and have been extensively used for reductions. *Again, the potentials users of Na–K alloys (which are commercially available) should be warned that these reagents are extreme fire hazards when exposed to moist air, and should therefore be used and with extreme caution and carefully destroyed after the experiments, for example:*



Use of Na–Hg amalgams involves the handling of mercury, the vapor of which is toxic. Na–Hg amalgams are, on the other hand, milder reducing agents than Na metal. The redox potential of Na–Hg is probably ca 1 V less negative than that of sodium (despite a smaller difference in Table 6, see discussion below). It can even be stored in air without too much damage, its reaction with water being only slow and that with moist air extremely slow. This difference is because of its heat of formation from Na and Hg, a very exothermic reaction (preparation must take this into account and be conducted under a well-ventilated hood). If the amount of sodium is less than 1.25 %, the Na–Hg amalgam is in a liquid or semi-liquid (0.9 % is a good

Table 6. Standard redox potentials, E° , relative to FeCp_2 of alkali metals and amalgams in different solvents.

Reductant	Solvent	E° (V)
Na	THF, diglyme	-3.04
Li	NH_3	-2.64
Li-Hg	H_2O	-2.60
K	NH_3	-2.38
Na-Hg	Non-aqueous	-2.36
Na	NH_3	-2.25

amount for a convenient liquid state). The liquid state of the reductant is another significant advantage over pure sodium metal, because much better contact is obtained between the reductant with the substrate in solution. Na-Hg is most often used in THF or DME but diethyl ether, benzene, and toluene are also used. The redox potentials of the alkali metals and their main amalgams are compared in Table 6. The redox potentials of the alkali metals were measured by cathodic reduction of their cations and it is possible that adsorption of alkali-metal atoms on the metal cathode is also exothermic and results in some reduction of the absolute value of the redox potentials determined in this way. For instance, in Table 6, all the redox potentials of the metals are less negative than that of the naphthalene-naphthalene radical anion in the same solvent, even though the naphthalene radical anion is obtained by alkali-metal reduction of naphthalene in the same solvents! Ion pairing is stronger between alkali metals and nucleophiles (solvent, anion of the electrolyte) present in the electrochemical cell, which also contributes substantially to furnishing a less negative redox potential for the alkali metals. Thus the values of Table 6 should be regarded with caution in the light of the discussion above.

The di- and polynuclear metal-carbonyl complexes are readily reduced by Na-Hg to monometallic metal-carbonyl anions, their redox potentials usually being between -0.7 V and -1.7 V relative to FeCp_2 [42], i.e. well below the redox potential of Na/Hg (-2.36 V relative to FeCp_2 in non-aqueous solvents [43]). Redox potentials of a number of these complexes are listed in Table 7.

Binuclear complexes also containing Cp ligands are reduced at more negative potentials which are still accessible for Na-Hg, as are nitrosyl complexes, for example:

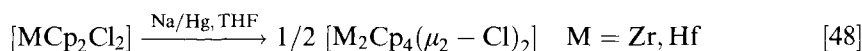
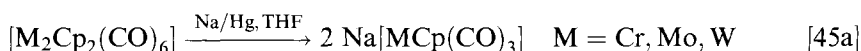
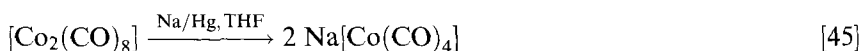


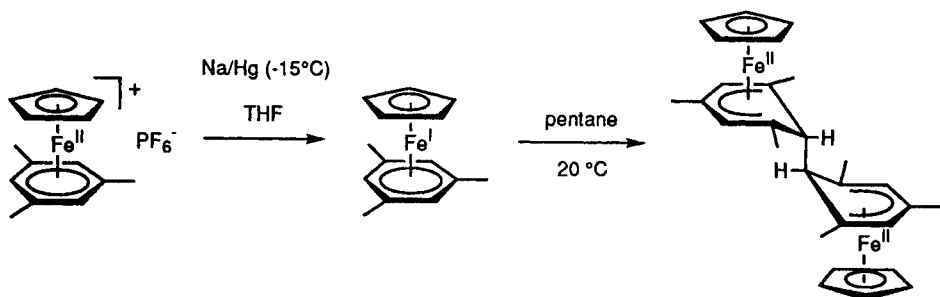
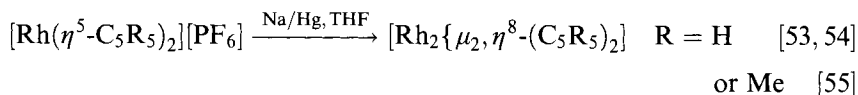
Table 7. Two-electron reduction potential for selected bi- and trinuclear metal-carbonyl complexes (V relative to the SCE; obtained from reactivity studies).

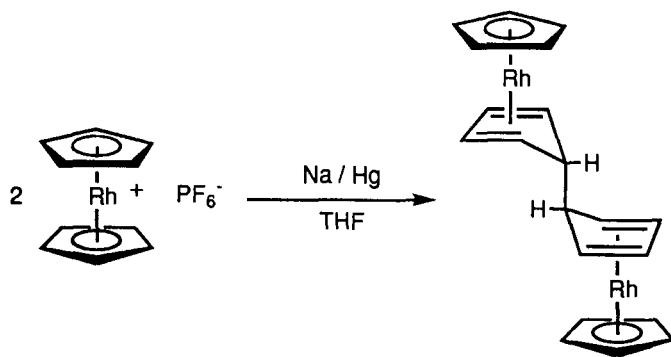
Compound	Product	Potential (V) ^a
[Co ₂ (CO) ₈]	2 [Co(CO) ₄] [−]	−0.15
[Cr ₂ Cp ₂ (CO) ₆]	2 [CrCp(CO) ₃] [−]	−0.70
[Mo ₂ Cp ₂ (CO) ₆]	2 [MoCp(CO) ₃] [−]	−0.79
[Fe ₃ (CO) ₁₂]	[Fe ₃ (CO) ₁₁] ^{2−}	−0.80
[W ₂ Cp ₂ (CO) ₆]	2 [WCp(CO) ₃] [−]	−0.80
[Ru ₃ (CO) ₁₂]	[Ru ₃ (CO) ₁₁] ^{2−}	−0.90
[Mn ₂ (CO) ₁₀]	2 [Mn(CO) ₅] [−]	−0.97
[Os ₃ (CO) ₁₂]	[Os ₃ (CO) ₁₁] ^{2−}	−1.10
[Re ₂ (CO) ₁₀]	2 [Re(CO) ₅] [−]	−1.20
[FeCp ₂ (CO) ₄]	[FeCp(CO) ₂] [−]	−1.70

^aThe 2e[−] oxidation of the metal-carbonyl anion to the dimer (2M[−] → M₂ + 2e[−]) is evaluated as a combination of the oxidation potential of the anion and the metal–metal bond strength [44].

These are only simple, classical examples, but many more studies are known. The monoelectronic reduction of inorganic or organometallic complexes leads to radicals which are usually unstable [10]. For instance, MCp(CO)_n radicals dimerize by formation of a metal–metal bond subsequent to the loss of a CO ligand as exemplified above [44, 45, 47]. The monoelectronic reduction of cationic complexes bearing a hydrocarbon ligand different from Cp often produces radicals whose SOMO has a strong ligand character. In these circumstances, ligand–ligand coupling occurs, leading to ligand-bridged dimers [49–52], for example (Scheme 1) [49, 50].

Coupling of Cp ligands also sometimes occurs with second- or third-row transition-metal complexes. For instance, reduction of the rhodocenium cation [53, 54] and even that of its Cp* [55] derivatives leads to rapid ligand–ligand coupling (equation and Scheme 2):

**Scheme 1.**

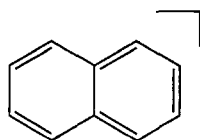


Scheme 2.

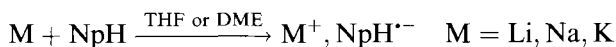
The other amalgams Mg–Hg [56] and Zn–Hg [57] and the commercially available alloy Na–Pb [21] have also occasionally been used.

4.3.2 Aromatic Radical Anions and Anions

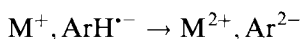
Naphthalene radical anion

NpH^{•-}

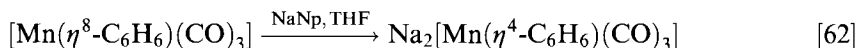
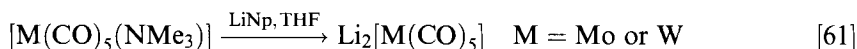
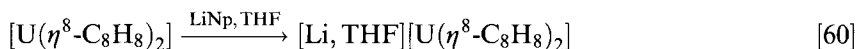
With a redox potential of -3.10 V relative to FeCp_2 in THF, the radical anion of naphthalene ($\text{NpH}^{\bullet-}$) is, in theory, the most powerful reducing agent used (see the discussion above, however):



The problem is that, because it is extremely electron rich, this species is also extremely air sensitive, and the real quantity which is being used is not known. In addition, it reacts to give neutral naphthalene which is difficult to separate from the desired product. Finally, another problem (encountered, for instance, in cluster chemistry [58]) is that it can over-reduce the substrate and lead to decomposition whereas less powerful reducing agents are not marred by this problem. Addition of pieces of Li, Na, or K to naphthalene in THF or DME under extremely dry reaction conditions gives a green solution of the naphthalene radical anion, and concentrations of 0.1 – 0.5 M are employed [59]. The formation of the dianion in this reaction has also been proposed, but its formation is uncertain. It is, in any case, presumably present at low levels only, if at all.

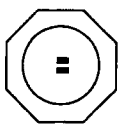


An advantage of naphthalene radical anion is that it is soluble in THF or DME, which facilitates the reduction, for example:

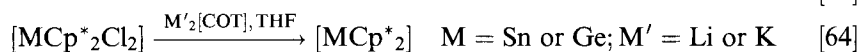
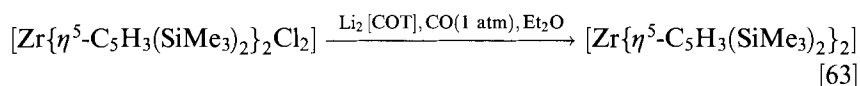


Finally, these reactions are sometimes marred by coordination of naphthalene on to the transition metal, as, for example, for the last reaction [62].

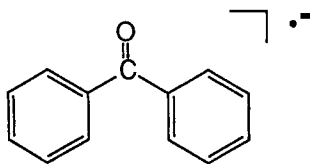
Cyclooctatetraene dianion



Aromatic salts M_2COT resulting from the two-electron reduction of cyclooctatetraene (COT) by alkali metals (Li, Na, K) have been used several times as reductants, although COT remains in solution which makes the separation difficult, for example:

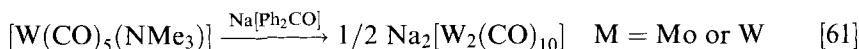


Benzophenone radical anion

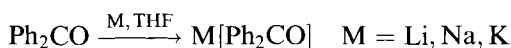


The blue benzophenone radical anion (the first recognized radical anion [65]) is well-known as a color test for the absence of water and oxygen from ether solvents over Na. In the presence of water, it forms the colorless pinacol by dimerization of the ketyl radical $Ph_2C(O)H^{\cdot-}$ (i.e. the protonated form of the radical anion) [66]. In the presence of dioxygen it is rapidly oxidized back to benzophenone, and thus removes traces of O_2 from N_2 [67]. It has been very little used as a stoichiometric

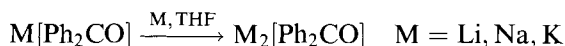
reductant, probably because it is not easy to separate and use in precise amounts, the benzophenone obtained after reduction would not be easy to separate from products, and its redox potential ($E^{\circ'} = -2.2$ V relative to FeCp_2) is very similar to that of Na in NH_3 and Na-Hg which are often used instead, for example:



For this latter reaction, it should be noted that the use of potassium naphthalide leads to further reduction to $\text{K}_2[\text{W}(\text{CO})_5]$; thus, the milder reductant $\text{Na}[\text{Ph}_2\text{CO}]$ selectively leads to a less reduced complex [61]. $\text{M}[\text{Ph}_2\text{CO}]$ salts have instead been used in catalytic amounts as mediators (see Section 4.4). They are prepared by reduction of benzophenone in THF, DME, or ammonia by pieces of alkali metals (Li, Na, K) [68]:



Their reducing power is in the order $\text{K}[\text{Ph}_2\text{CO}] > \text{Na}[\text{Ph}_2\text{CO}] > \text{Li}[\text{Ph}_2\text{CO}]$ because the strength of the ion pairing is in the opposite order [69]. This sequence is the opposite of that for polyaromatic anions such as naphthalide in ethers. These salts of $\text{Ph}_2\text{CO}^{\bullet-}$ can be reduced by excess metal to the purple salts of the dianion [70, 71], because the standard redox potential of the redox system $\text{Ph}_2\text{CO}^{\bullet-}/\text{Ph}_2\text{CO}^{2-}$ is less negative ($E^{\circ'} \approx -2.9$ V relative to FeCp_2 in THF [72, 73]) than those of the alkali metals in this solvent. The purple dianion is extremely sensitive to impurities, however, and is therefore not often seen:



Other polycyclic aromatic radical anions

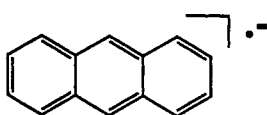
Given the degeneracy of the LUMO in polycyclic hydrocarbons, addition of an electron into these orbitals is more or less facile and leads to thermally stable radical anions; redox potentials for a number of polycyclic hydrocarbon-radical anions are listed in Table 8.

Table 8. Reduction potentials of polycyclic hydrocarbon-radical anions relative to FeCp_2 in DMF^a.

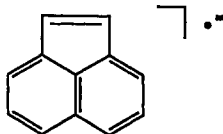
Compound	$E^{\circ'}$ (V relative to the SCE)	Compound	$E^{\circ'}$ (V)
Biphenyl	-3.16	Dibenz[<i>a, h</i>]anthracene	-2.47
Naphthalene	-3.07	Coronene	-2.46
Phenanthrene	-2.99	Perylene	-2.04
Chrysene	-2.78	Tetracene	-1.88
Pyrene	-2.56		

^aAdapted from Refs [74] (biphenyl/biphenyl^{•-} in DMF) and [75] (others relative to biphenyl/biphenyl^{•-}). Corrections into $E^{\circ'}$ values relative to FeCp_2 in DMF is made using Table 1.

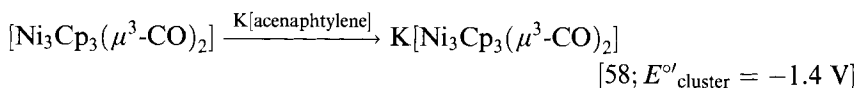
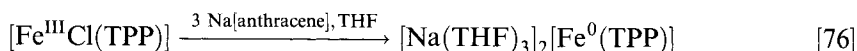
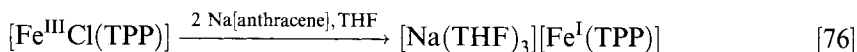
Sodium anthracenide and potassium acenaphthylenide have been used. They are much milder reducing agents than naphthalides, for example:



**anthracenide
radical anion**



**acenaphthylenide
radical anion**

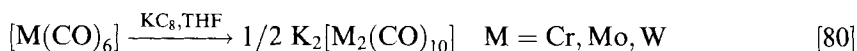


If the latter reaction is performed with the very strong reductant potassium naphthalide instead of potassium acenaphthylenide which is milder, it leads to decomposition as a result of over-reduction [58].

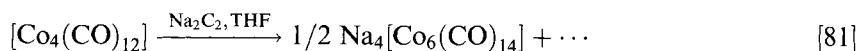
The radical anion of 2,2'-bipyridine is also a strong reductant which has been used as a mediator (see Section 4.3).

Alkali-metal carbides

Volpin has noted the similarity between potassium salts of polycyclic aromatics and potassium graphite KC_8 , an intercalation compound [75, 77, 78]. Table 7 shows that the reduction potentials of the radical anions become less negative as the number of fused rings increases. Graphite, which has an infinite number of fused rings, is thus easily reduced. The redox potential of KC_8 should thus be close to those of anthracene, pyrene, and coronene, i.e. ca -2.5 V relative to FeCp_2 in DMF, which also close to that of Na-Hg , for instance [75]. This compound is best described by the ionic form K^+C_8^- , because of the transfer of an electron from potassium to the conduction band of graphite. KC_8 is prepared from graphite powder and K at 350°C [79], which is certainly a limitation for the community of molecular chemists. It has been used as a reductant on a few occasions [79, 80]. The insoluble by-product, carbon, is eliminated by filtration, for example:



Sodium carbide, Na_2C_2 , has also been used as a mild reductant, especially to reduce mono- and polynuclear metal carbonyl complexes [81]. It is relatively stable toward moist air, for example:

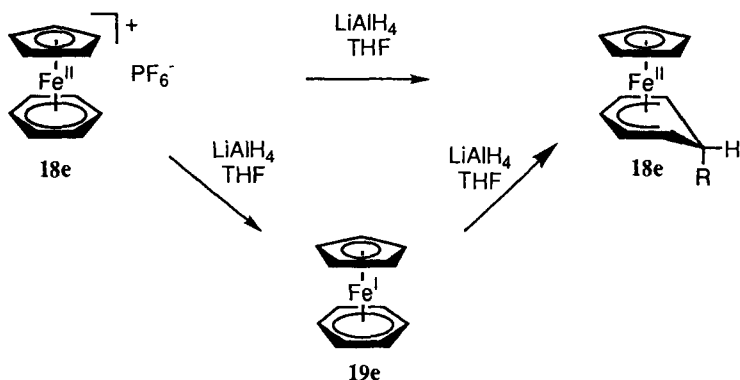


4.3.3 Hydrides, Grignard Reagents, Metal-alkyls and Metal-aryls, and Other Reductants

Hydrides

Commercial B and Al hydrides, e.g. NaH, LiAlH₄, NaBH₄, NH₄BH₄, and K[BH(CHMeEt)₃], are classic sources of hydride in organic, inorganic, and organometallic chemistry. The first example of their use as a monoelectronic reductant in transition-metal chemistry was disclosed with a variety of 18-electron cationic complexes [Fe^{II}Cp(arene)][PF₆]⁺ [82]. Although these complexes are reduced with overall hydride transfer onto the benzene ligand, it can be shown that this reduction comprises a first step, a single-electron transfer, then a second step, an H-atom transfer (Scheme 3). The 19-electron Fe^I intermediates resulting from the initial electron transfer were isolated or generated and characterized as intermediates by use of ESR, UV-Vis, and Mössbauer spectroscopy and by the observation of their characteristic forest-green color.

Very unstable Fe^I complexes such as [Fe^ICp(η⁶-C₆H₅F)] and [Fe^ICp(η⁵-C₄Me₄S)] could not be synthesized by Na-Hg reduction of their cationic precursor at -10 °C in THF, because decomposition was rapid. They could be rapidly generated by use of LiAlH₄ in THF at -95 °C and -50 °C respectively. The parent complex [Fe^ICp(η⁶-C₆H₆)] was generated at -60 °C under these conditions. Even the complexes [Fe^ICp(η⁶-C₆R₆)], R = Me or Et are generated rapidly by use of LiAlH₄. The electron-transfer reactions of LiAlH₄ are highly solvent-dependent. They were observed in THF and DME, but not in Et₂O. Although the standard redox potential has been estimated as $E^\circ = -0.7$ V [83], such a value does not give an idea of the reducing power of the hydride. Even if it is correct, the effective reduction potential of LiAlH₄ is more negative, because the electron-transfer reactions of LiAlH₄ are shifted towards the electron-transfer products by rapid decomposition of the radical AlH₄· to $\frac{1}{2}$ Al₂H₆ and H₂. Given the high rate and low temperatures above, one might conclude, however, that the effective reduction potential of LiAlH₄ is more negative than -1.2 V to -1.5 V relative to FeCp₂, the standard



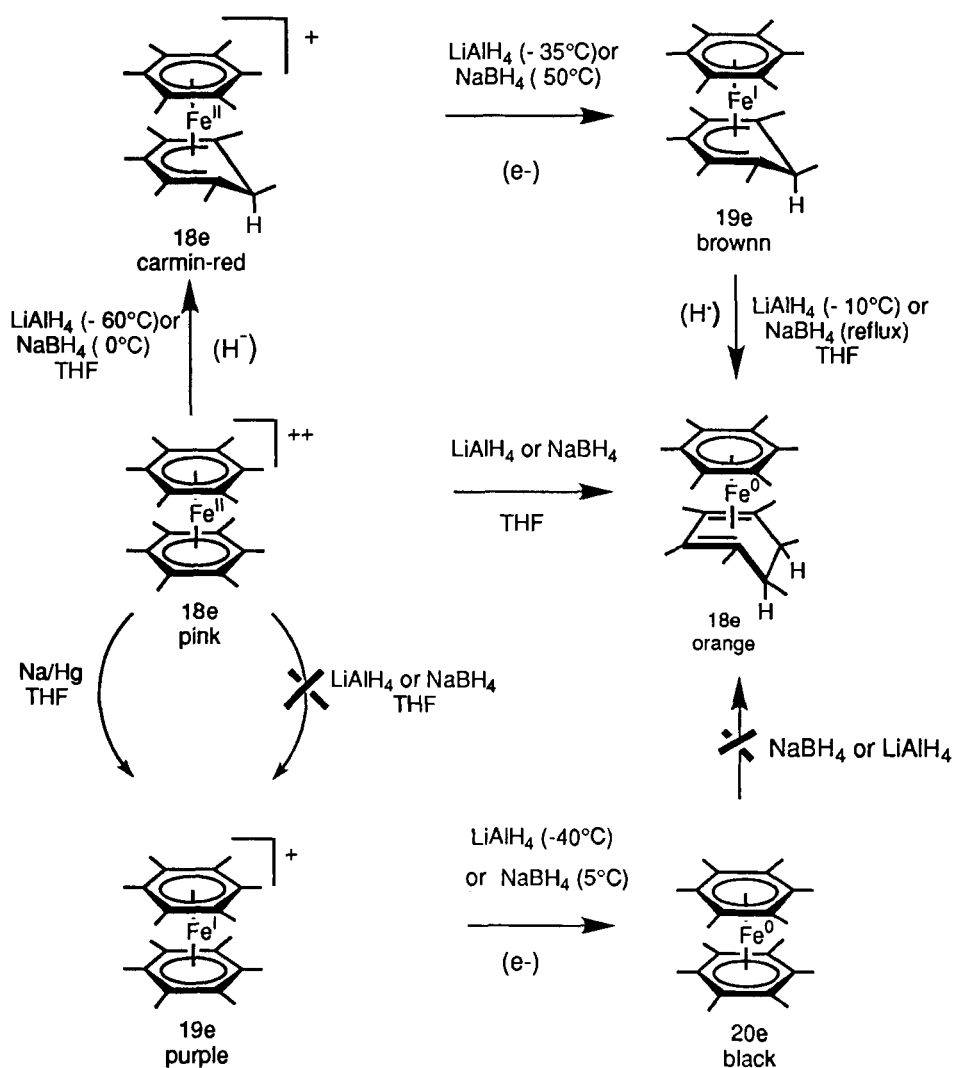
Scheme 3.

redox potentials of $[\text{Fe}^{\text{I/II}}\text{Cp}(\eta^6\text{-arene})]^{0/+}$ redox systems [84]. The hydrides LiAlH_4 and NaBH_4 also react with the complex $[\text{Fe}^{\text{II}}(\eta^5\text{-C}_6\text{Me}_5\text{H})(\eta^6\text{-C}_6\text{Me}_6)][\text{PF}_6]$ as monoelectronic reductants in THF at -35°C and 50°C respectively, this difference in reaction temperature illustrating that NaBH_4 is a much weaker reductant than LiAlH_4 . The relative tendencies of different hydrides to transfer an electron parallels those to transfer H^- , as both depend on the relative energy levels of the HOMOs of the hydrides. This different reactivity is not reflected by the differences between reported standard redox potentials, because that of NaBH_4 , $E^\circ = -0.6\text{ V}$ in diglyme [85], is almost the same as that of LiAlH_4 . Whether electron transfer or hydride transfer occurs from a hydride depends, of course, on the comparative electron acceptor and H^- acceptor properties of the substrate and on the solvent, concentrations, and reaction temperature. In the example above, the complexes $[\text{FeCp}(\eta^6\text{-arene})][\text{PF}_6]$ and $[\text{Fe}^{\text{II}}(\eta^5\text{-C}_6\text{Me}_5\text{H})(\eta^6\text{-C}_6\text{Me}_6)][\text{PF}_6]$ can accept either an electron (to give 19-electron complexes) or a hydride (to give mostly 18-electron cyclohexadienyl complexes), which makes the competition uncertain. Indeed, before the study, the organometallic community believed direct hydride transfer was occurring [86]. One might think in terms of a continuum of situations between the direct hydride transfer mechanism seemingly occurring with LiAlH_4 and the complexes $[\text{FeCp}(\eta^6\text{-arene})][\text{PF}_6]$ in ether and the clear stepwise electron transfer plus H-atom transfer mechanism occurring between the same substrates in THF and DME (suffices therefore to continuously vary the proportion of these two solvents). Experimental probes can be difficult to establish in such borderline situations, especially because the final products are the same with both mechanisms. There are instances, however, for which a clear-cut electron-transfer mechanism can be established even for potential hydride acceptors. For instance, two-hydride reduction of the complex $[\text{Fe}^{\text{II}}(\eta^6\text{-C}_6\text{Me}_6)_2][\text{PF}_6]_2$ gives $[\text{Fe}^0(\eta^4\text{-C}_6\text{Me}_6\text{H}_2)(\eta^6\text{-C}_6\text{Me}_6)]$.

It was possible to show that the mechanism proceeds by the transfer sequence: $\text{H}^- + e^- + \text{H}^+$. The monoelectronic reduction of the di-cation by use of Na-Hg in THF gives the 19-electron complex $[\text{Fe}^{\text{I}}(\eta^6\text{-C}_6\text{Me}_6)_2][\text{PF}_6]$ which reacts with either LiAlH_4 or NaBH_4 to give the 20-electron complex $[\text{Fe}^0(\eta^6\text{-C}_6\text{Me}_6)_2]$ [82, 87], but the reaction does not continue to give the di-hydrogenated complex obtained by hydride reduction starting from the di-cation. Thus, the direct hydride-transfer pathway and the electron-transfer pathways are clearly distinct when one starts from the di-cation. This shows that the electron-transfer pathway is no more like for a di-cation than for a mono-cation. The situation is, in fact, quite the opposite (Scheme 4) [82].

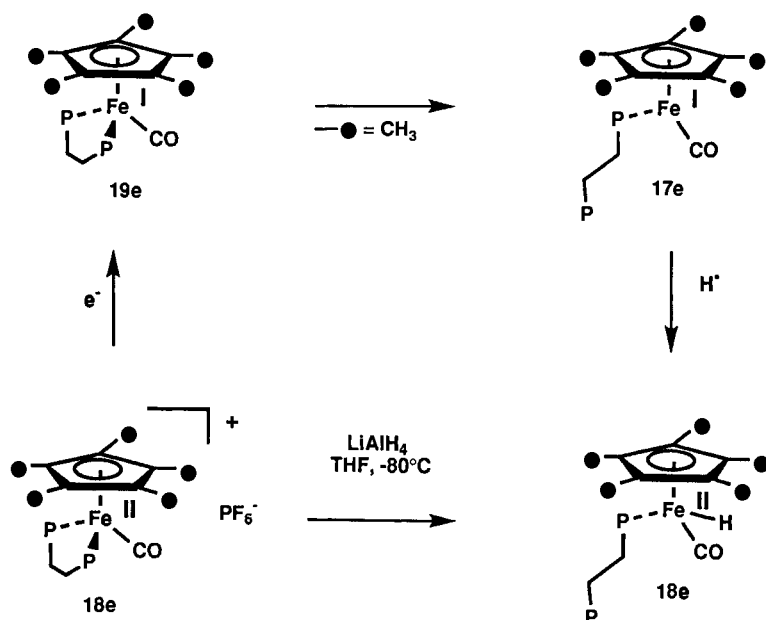
Similarly, the LiAlH_4 reduction of the piano-stool complex $[\text{FeCp}^*(\eta^2\text{-dppe})(\text{CO})][\text{PF}_6]$ in THF was also reported to proceed by single-electron transfer, leading to the isostructural 19-electron species $[\text{FeCp}^*(\eta^2\text{-dppe})(\text{CO})]$ which rapidly decoordinates to the 17-electron radical $[\text{FeCp}^*(\eta^1\text{-dppe})(\text{CO})]$ [88]. Finally, H-atom transfer onto the Fe^{I} center of this 17-electron species occurs to give the hydride $[\text{FeCp}^*(\eta^1\text{-dppe})(\text{CO})(\text{H})]$ (Scheme 5) [88, 89].

The LiAlH_4 reduction of the homologous complex $[\text{MoCp}^*(\text{CO})_3(\text{L})][\text{PF}_6]$ ($\text{L} = \text{phosphine}$) proceeded similarly to give a neutral radical resulting from electron transfer; this was followed by the formation of $[\text{MoCp}^*(\text{CO})(\text{L})_2(\text{H})]$ or $[\text{MoCp}^*(\text{CO})_2(\text{L})(\text{H})]$ [90]. LiAlH_4 also reduces polyaromatics and diarylketones



Scheme 4.

by a single-electron-transfer pathway [91, 92]. Other single-electron reduction of cationic transition-metal organometallic complexes to their neutral counterparts by NaBH_4 in THF–pentane [93] or by $[n\text{-Bu}_4][\text{BH}_4]$ in CH_2Cl_2 [94] are known. Electron-rich transition-metal hydrides such as, for instance, $[\text{VCp}(\text{CO})_3(\text{H})]^-$ can also behave as single-electron reductants towards electron-poor derivatives such as metal carbonyls [95]. Such hydrides are too sophisticated to be regarded as classic redox reagents, however. One might also expect that single-electron-transfer from transition-metal hydride complexes toward single-electron oxidants is a general trend. Such single-electron transfer steps generate 17-electron species which can

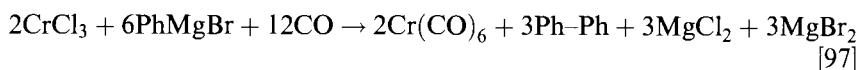


Scheme 5.

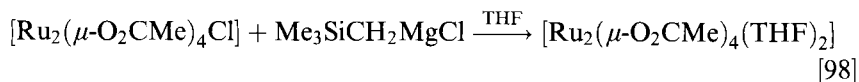
subsequently be subjected to fast ligand exchange and/or dimerization and/or reduction reactions [2, 96].

Grignard reagents and alkali-metal alkyls and aryls

Grignard reagents have long been known to be reductants of metal halides for the synthesis of metal carbonyls in the presence of carbon monoxide [97]:

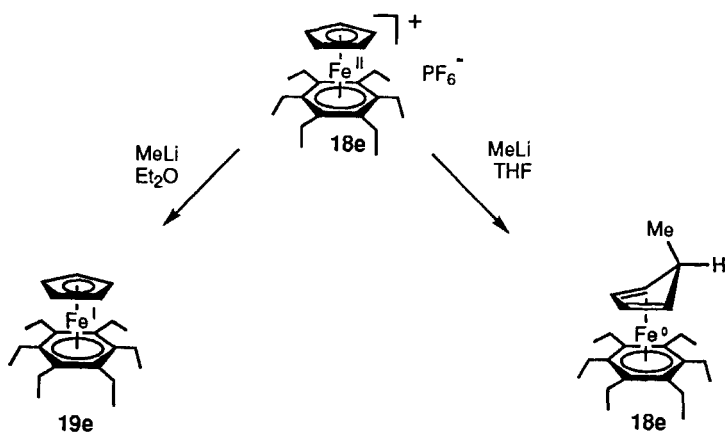


Wilkinson has also reported clear-cut examples of the use of RMgX as a single-electron reductant, although the oxidation products were not identified [98]:



There are many examples of the use of Grignard reagents or alkyllithium or aryllithium and other alkali-metal alkyls or aryls to alkylate, and also reduce, metal halides:





Scheme 6.

The solvent can have a dramatic effect on the electron transfer or alkylation properties of alkali-metal alkyls. Whereas MeLi reacts with $[\text{Fe}^{\text{II}}\text{Cp}(\eta^6\text{-C}_6\text{Et}_6)]\text{PF}_6^-$ in THF to afford methylation of the Cp ring with regioselectivity opposite to that expected from charge control, because of the steric effect, reaction in ether gives the single-electron transfer product only, i.e. the green 19-electron complex. This solvent effect is the opposite of that observed for reaction with NaBH_4 and LiAlH_4 , and noted above (Scheme 6) [100].

4.3.4 Miscellaneous Reductants

There are many reductants (CO, amines, phosphines, alcohols, sulfides, carboxylic acids, carboxylates, hydroquinones, electron-rich organometallics (low-oxidation state transition-metal complexes including those involved in oxidative addition), and organometallic anions) which are not single-electron reductants except towards single-electron oxidants, or are not commonly used as single-electron redox reagents (mostly inner-sphere reductants) and will, therefore, not be treated in detail here. We will only summarize these and give a few examples:

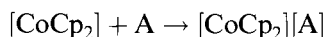
- When they are heated in the presence of CO under pressure, transition metal halides react to give metal carbonyls. For instance, RuCl_3 gives $[\text{Ru}_3(\text{CO})_{12}]$ under a 65-atmosphere pressure of CO [101].
- Ascorbic acid (vitamin C) is a well-known reductant in biochemistry, but it can also reduce transition-metal complexes (for instance Ru^{IV} to Ru^{II}) [102].
- Ethanol reduces, for example, $[\text{PtCl}_6]^{2-}$ to Zeise's salt $\text{K}[\text{PtCl}_3(\eta^2\text{-C}_2\text{H}_4)]$ [103].
- Reduction of Au^{III} to Au^{I} by sulfides has been known for a century [104] and is still useful [105].
- Sodium dithionite $\text{Na}_2\text{S}_2\text{O}_3$ reduces, inter alia, Fe^{III} [106] and Tc^{VII} [107].

- Derivatives of Sn^{II} , Ti^{III} , Cr^{II} , V^{II} , Cu^{I} , Sm^{II} are well-known as reductants [108, 109]. In particular, Kagan's reagent SmI_2 reduces acyl chlorides to diketones, aldehydes, and ketones to pinacols in aprotic media and to alcohols in protic media [110]. It has also been applied to many other organic reactions [110]. Cr^{II} salts have been extensively used to reduce alkyl- and aryl halides [109]. These reduced metal complexes have been known as reductants of transition metal ions since Taube's pioneering work [108, 109].
- Some reduced organometallic derivatives; e.g. $\text{Na}[\text{FeCp}(\text{CO})_2]$ ($E^{\circ'} = -1.74$ V relative to FeCp_2 [111]) and $[\text{Cp}^*\text{Cr}(\mu\text{-OPR}_2)_3\text{CoCp}]$ ($E^{\circ'} = -2.0$ V relative to FeCp_2 [112]), have been used in single occasions [112, 113] to reduce other organometallic complexes.
- Amines are weak reductants. For instance, triethylamine ($E_{\text{pa}} = +0.47$ V relative to FeCp_2 in MeCN [114]) has been used as sacrificial reductant in photocatalyzed water photosplitting [115]. Hydrazine $\text{NH}_2\text{-NH}_2$ is more common in aqueous systems than in non-aqueous ($E_{\text{pa}} = -0.4$ V relative to FeCp_2 in DMSO [116]). It has occasionally been used to reduce cationic organometallic complexes to their neutral counterparts, the oxidized product (N_2) being readily removed [117]. Tetrakis(dimethylamino)ethylene, $\text{C}_2(\text{NMe}_2)_4$, is a convenient, commercially available two-electron reducing agent, soluble in organic solvents, which reduces metal carbonyls such as $[\text{Co}_2(\text{CO})_8]$ to $[\text{C}_2(\text{NMe}_2)_4][\text{Co}(\text{CO})_4]_2$ [118].
- Phosphines are deoxygenating reagents which form phosphoranes, the driving force being the strong P=O bond in the latter. Thus, they deoxygenate various metal-oxo complexes and oxygen-containing ligands [119].

4.3.5 Metallocenes and bis-Arene Metal Sandwiches

Cobaltocene

Cobaltocene is the most frequently used single-electron reductant although its standard oxidation potential is not very negative ($E^{\circ'} = -1.31$ V relative to FeCp_2 in DME). Thus, it can only reduce organometallic compounds which are very easy to reduce. It is readily prepared under an inert atmosphere, but another drawback is that it is air-sensitive in both solution and the solid state and must be sublimed just before use [120]. Its properties as a reductant have been reviewed [21, 121, 122]. Noteworthy applications of cobaltocene are single-electron reductions of neutral complexes to their monoanions giving ion pairs with cobaltocenium as the counter-cation:



For instance, the $d^1\text{-}d^1$ dinuclear rhenium complex $\{[\text{Re}(\text{O})\text{Me}_2](\mu_2\text{-O})_2\}$ is reduced in this way to the mixed-valence $\text{Re}^{\text{V}}\text{-Re}^{\text{VI}}$ monoanion by cobaltocene [123]; several other examples are known [21]. Cobaltocene is not always an 'innocent' reductant. For instance, it undergoes ring coupling with the 19-electron complex $[\text{NiCp}(\eta^4\text{-C}_4\text{Ph}_4)]$ when used in excess to reduce the 18-electron cationic precursor $[\text{NiCp}(\eta^4\text{-C}_4\text{Ph}_4)][\text{PF}_6]$ [124]. It also reacts with alkyl halides to give ring-coupling

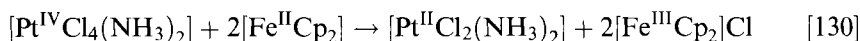
products and must therefore be used very rapidly in halogenated solvents such as chloroform and carbon tetrachloride [125]. Occasionally, the follow-up reaction of the reduced organometallic derivative can drive the endergonic electron-transfer reaction of cobaltocene [126].

Decamethylcobaltocene

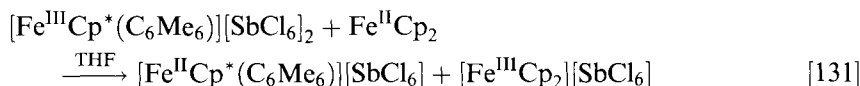
Decamethylcobaltocene [CoCp^*_2], [126], has a standard redox potential ca 0.6 V more negative than cobaltocene (-1.9 V relative to FeCp_2 in MeCN) and it has, therefore, been used when cobaltocene was not an efficient single-electron-transfer reductant [127–129]. The precipitation of the salt [CoCp^*_2][A] can be an additional driving force when the reduction of a neutral derivative A is slightly endergonic. For instance [$\text{W}(\eta^5\text{-C}_5\text{HPh}_4)(\text{CO})_2(\text{NO})$] ($E^\circ = -2.2$ V relative to FeCp_2) could be reduced by [CoCp^*_2] to such a salt, despite the endergonicity of 0.3 V [129].

Ferrocene

Ferrocene can be used as a weak reductant, but it is so weak that it has very rarely been used, for example:



It is useful for titration of strong oxidants, for example:

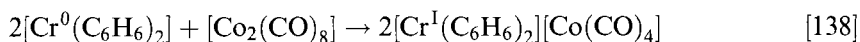


The reduction potential of ferrocene can be increased by introduction of methyl groups or electron-releasing substituents on the rings [132]. In particular, decamethylferrocene [FeCp^*_2], ($E^\circ = -0.59$ V relative to FeCp_2 in CH_2Cl_2), is a single-electron reductant which is used as a reductant much more frequently than is ferrocene. For instance, it can reduce TCNE to form [FeCp^*_2][TCNE], a ferromagnet [133]. The use of decamethylferrocene as a mild single-electron reductant is an especially practical means of reducing ferrocene derivatives. The many ferrocenium derivatives which have a redox potential close to that of ferrocene cannot be reduced efficiently by ferrocene because the redox reaction would be equilibrated rather than complete as hoped for. For instance, ferrocenium dendrimers containing theoretical numbers of ferrocenium units up to 243 were generated from ferrocenyl dendrimers by oxidation with $[\text{NO}][\text{PF}_6]$, and could be reduced back to ferrocenyl dendrimers by use of decamethylferrocene in THF. [FeCp^*_2][PF_6], which was generated in such reactions, precipitated and was easily removed by filtration of the THF solution in which the ferrocenyl dendrimers are soluble [134, 135].

Bis(arene) chromium complexes

The 18-electron sandwich complexes [$\text{Cr}(\eta^6\text{-arene})_2$] have a range of standard redox potentials from $E^\circ = -1.15$ V relative to FeCp_2 in CH_2Cl_2 (arene = C_6H_6) to $E^\circ = -1.45$ V (arene = C_6Me_6) [136] and even -1.5 V (arene = $\text{C}_6\text{H}_5\text{NMe}_2$) [137],

but have been very little used as reductants, for example:



**The d⁷ 19-electron organometallic electron-reservoir complexes
[Fe^I(η^5 -C₅R₅)(η^6 -C₆R'₆)]**

The d⁷ 19-electron sandwich complexes [Fe^I(η^5 -C₅R₅)(η^6 -C₆R'₆)] [139–143] (R = H or Me, R' = Me) are, on the basis of the values of their ionization potentials measured by He(I) photoelectron spectroscopy [143] the most electron-rich neutral molecules known. Accordingly, their redox potentials are very negative. For instance the standard oxidation potential of [Fe^ICp(η^6 -C₆Me₆)] ($E^\circ = -2.02$ in DMF) is 0.7 V more negative than that of cobaltocene, and that of [Fe^ICp*(η^6 -C₆Me₆)] ($E^\circ = -2.30$ V in DMF) is almost 1 V more negative than that of cobaltocene and as negative as that of the benzophenone radical anion. Other advantages of these Fe^I complexes as reductants are that they are crystalline and can be weighed accurately; they are also soluble in pentane, THF, and other organic solvents. They are thermally stable up to >100 °C and can be stored under an inert atmosphere; [Fe^ICp(η^6 -C₆Me₆)] sublimes at 70 °C (2×10^{-4} mmHg). A Mössbauer spectrum of this complex has even recently been recorded after storage for twenty years in a sealed tube.

They are Jahn–Teller active d⁷ complexes subject to rhombic distortion, as has been shown by the ESR and Mössbauer spectroscopy. For instance, the values of the *g* tensor recorded in the ESR spectra are *g* = 2.063, 2.000, 1.864 at 77 K (frozen DME) [144] and the temperature-dependent Mössbauer parameters in the solid state are I.S. = 0.74 mm s^{−1} and Q.S. = 1.6 mm s^{−1} at 4 K, 0.5 mm s^{−1} at 293 K for [Fe^ICp(η^6 -C₆Me₆)], indicative of a Boltzmann thermal population of the upper Kramers doublet [139, 145]. This indicates that the antibonding e*₁ orbital of the classic metallocene MO diagram is singly occupied, and has a high metal character (70 %) as confirmed by recent accurate DFT MO calculations [146]. These physical properties show that the redox center which undergoes the redox change is located on Fe at the center of the molecular framework. This ligand shell protects it from the classic breakdown processes encountered in molecular chemistry upon redox change such as radical-type reactions of the ligands known for the second- and third-row transition-metal sandwich complexes for which single-electron reduction has been attempted [147, 148]. At the same time, the SOMO is only slightly antibonding, so the destabilization provoked by its single occupancy is low enough for thermal stability of the hexamethylbenzene Fe^I complexes. These complexes were, therefore, denoted *electron-reservoir complexes* [139–141], which implies several properties [2]: strong single-electron stoichiometric reductants, redox catalysts, initiators of electron-transfer chain reactions, redox sensors and references for the determination of standard redox potentials by electrochemistry. Recently, these concepts were applied to the oxidation side with the isolation of the thermally stable d⁵ 17-electron complex [Fe^{III}Cp*(η^6 -C₆Me₆)] [SbX₆]₂ (X = Cl or F), and the finding that [Fe^{III}Cp(η^6 -C₆Me₆)]²⁺ is also a redox catalyst [131].

The Fe^I complexes are synthesized by Na–Hg reduction in THF or DME of their d⁶ 18-electron precursors [Fe^{II}Cp(η^6 -arene)][PF₆] and [Fe^{II}Cp*(η^6 -arene)][PF₆] at

Table 9. First ionization energy and E° of stable 19-electron complexes.

Complex	Ionization energy (eV)	(E° relative to FeCp_2) ^a	Ref.
$[\text{Cp}^*\text{Fe}(\eta^6\text{-C}_6\text{Me}_6)]$	4.21	−2.24 V	142a ^b
K metal	4.34	−2.38 V	142b
$[\text{CpFe}(\eta^6\text{-C}_6\text{Et}_6)]$	4.34	−2.14 V	142a ^b
$[\text{CpFe}(\eta^6\text{-C}_6\text{Me}_6)]$	4.68	−2.02 V	142a ^b
$[\text{CpFe}(\eta^6\text{-1,3,5-}i\text{-Bu}_3\text{C}_6\text{H}_3)]$	4.72	−1.87 V	142a ^b
$[\text{Cp}^*_2\text{Co}]$	4.8	−1.84 V	142c ^b
$[\text{Cp}_2\text{Co}]$	5.3	−1.20 V	144 ^c
$[\text{CpCo}(\eta^6\text{-C}_5\text{H}_5\text{BMe})]$	6.5	−0.80 V	144 ^c
$[\text{CpCo}(\eta^6\text{-C}_5\text{H}_5\text{BPh})]$	6.6	−0.78 V	144 ^c
$[\text{Co}(\eta^6\text{-C}_5\text{H}_5\text{BMe})_2]$	7.1	−0.36 V	144 ^c
$\text{Co}(\text{C}_5\text{H}_5\text{BPh})_2$	7.2		144 ^c

^a E° values are in DMF except K in NH_3 . Stable, neutral 19-electron complexes having an even more negative redox potential than $[\text{Cp}^*\text{Fe}(\text{C}_6\text{Me}_6)]$ are $[\text{Cp}^*\text{Fe}^{\text{I}}(\text{C}_6\text{Et}_5\text{H})]$ ($E^{\circ} = -2.27$ V) and $[\text{Fe}^{\text{I}}_2(\mu_2, \eta^{10}\text{-fulvalene})(\text{C}_6\text{Me}_6)_2]$ ($E^{\circ} = -2.30$ V).

^b Determined by $\text{He}(\text{I})$ photoelectron spectroscopy; see Green et al. [143a].

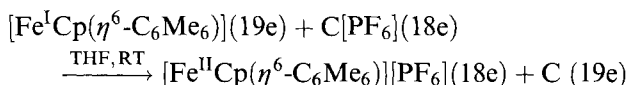
^c Determined by mass spectrometry; see Herberich et al. [144]; E° values are estimated in DMF from this reference.

ambient temperature for a few hours [139–142] (see Section 4.9, Experimental). The precursor salts $[\text{Fe}^{\text{II}}\text{Cp}(\eta^6\text{-arene})][\text{PF}_6]$ are easily synthesized by use of the ligand-exchange reaction of ferrocene with the appropriate arene in the presence of AlCl_3 , Al , H_2O (4:1:1) at 80°C , in the arene as solvent (or neat in the melt) or in an inert solvent such as heptane, cyclohexane, or decalin [100, 141, 149, 150] (Section 4.9). The precursor salts $[\text{Fe}^{\text{II}}\text{Cp}^*(\eta^6\text{-arene})][\text{PF}_6]$ are synthesized likewise from $[\text{FeCp}^*(\text{CO})_2\text{Br}]$, AlCl_3 and the arene under analogous conditions [141, 148] (Section 4.9). The presence of the arene ligand has opened access to a large variety of complexes with different substituents which can influence the redox potential and the ionization potential. Table 9 gathers the standard redox potentials and ionization potentials of stable 19-electron Fe^{I} and Co^{II} complexes.

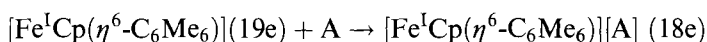
Many more $[\text{Fe}^{\text{I}}\text{Cp}(\text{arene})]$ complexes are known with numbers of methyl- or alkyl groups on the arene ring between one and six; this enables progressive variation of the redox potential. These Fe^{I} complexes are only stable at room temperature when the arene ring is bulky, i.e. C_6Me_6 , C_6Et_6 , $\text{C}_6\text{Et}_5\text{H}$, or $\text{C}_6\text{H}_3(t\text{-Bu})_3$. The parent complex $[\text{Fe}^{\text{I}}\text{Cp}(\eta^6\text{-C}_6\text{H}_6)]$ [154] and the complexes $[\text{Fe}^{\text{I}}\text{Cp}(\eta^6\text{-C}_6\text{H}_{6-n}\text{Me}_n)]$ [140] ($0 < n < 6$) are stable at -10°C and can be synthesized at -10°C by Na-Hg reduction of the PF_6^- precursor salts in DME or THF. They are best be used as single-electron reductants if the solution prepared in this way is used directly at this temperature without isolating the complex in the solid state (the solutions are easily titrated by the oxidant since the color of the iron complex color changes from forest-green (Fe^{I}) to colorless (Fe^{II} , yellow precipitate) [155]. These complexes are soluble in pentane and organic solvents and more or less progressively dimerize in these solvents by coupling of the benzene ligand to bicyclohexadienyl between 0°C and 25°C . This reaction is logically faster in the solid state. The complex $[\text{Fe}^{\text{I}}\text{Cp}^*(\eta^6\text{-C}_6\text{H}_6)]$ dimerizes much faster than the Cp analogs when the solvent is

removed even at low temperature, and cannot even be obtained in the solid state. It is believed that this trend is due to an equilibrium between the 19-electron and the 18-electron form of the species. Alternatively, if only one potential well accounts for the structure of these complexes, the weight of the 18-electron form among the mesomer forms could be more pronounced with the Cp* complex. The spin density on the benzene ligand is lower in the Cp* complex than in the Cp complex, however, which would favor the tautomerism view, at least in this case [100]. It is possible to introduce a carboxylate group on the Cp or on the C₆Me₆ ligand of the [FeCp(arene)] structure in order to solubilize these complexes in water under both the Fe^{II} and Fe^I forms. Indeed the Fe^I complex with a Cp-CO₂⁻ ligand has been isolated and characterized as a genuine 19-electron complex. It is purple and very reactive, although thermally stable. It is very useful as a strong single-electron reductant in water, especially if kinetic measurements are desired, since the aqueous solution containing the reductant is then homogeneous.

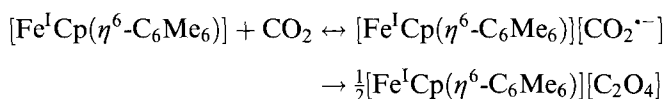
The most frequently used electron-reservoir complex for stoichiometric single-electron transfer reactions is [Fe^ICp(η⁶-C₆Me₆)], because of its stability and ease of preparation, and since it has one of the most negative redox potentials in the series. It can reduce most inorganic and organometallic cations [2]. For instance, it is very useful to synthesize neutral 19-electron complexes (C in the equation below) such as other [Fe^ICp(η⁶-arene)] complexes and [Fe^I(η⁵-C₆Me₆H)(η⁶-C₆Me₆)] from the 18-electron cationic precursors C[PF₆]:



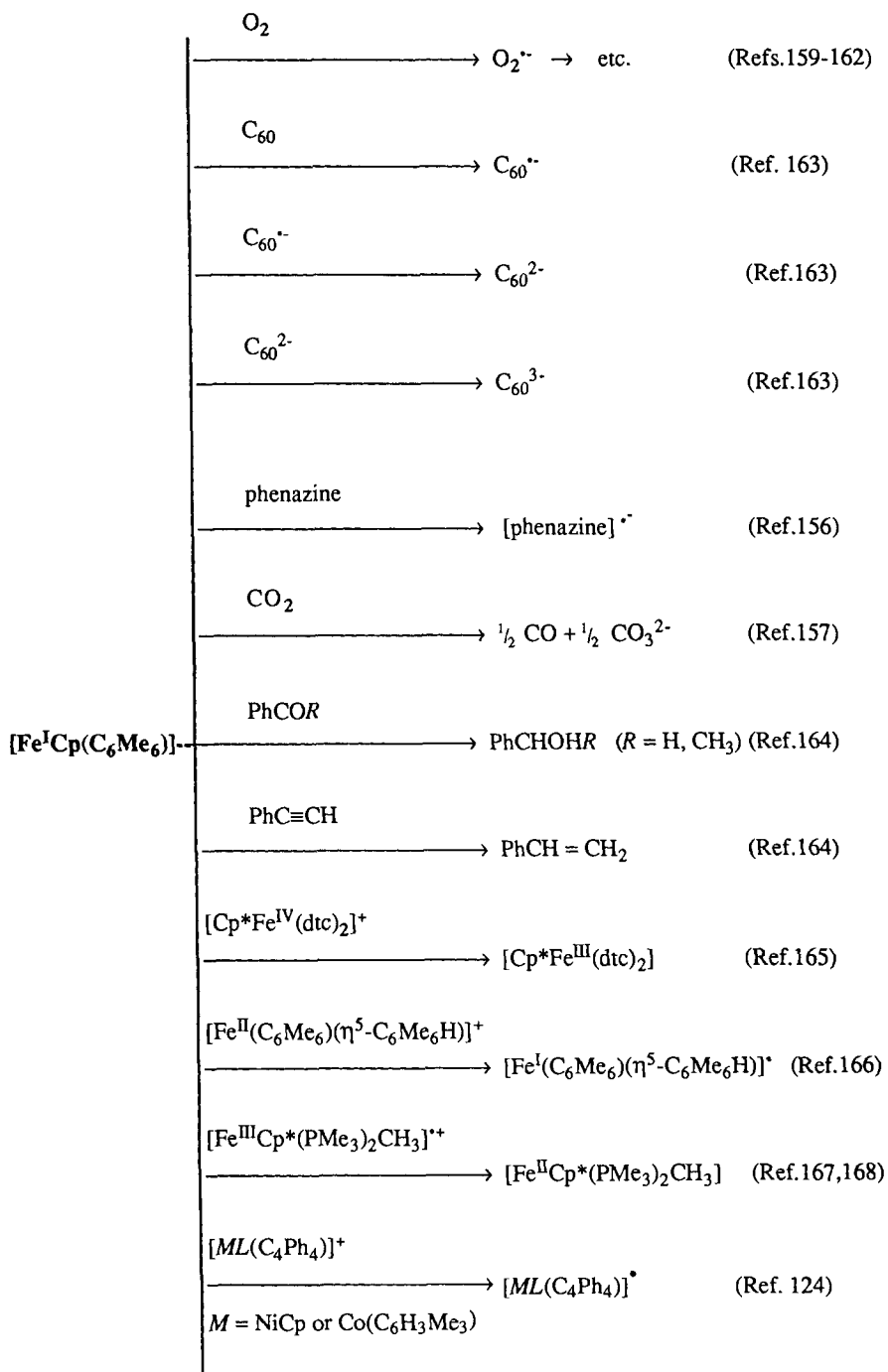
It can reduce a variety of neutral compounds A to their monoanion A⁻ in pentane, diethyl ether or THF; this has been shown with some polycyclic hetero-aromatics such as phenazine [156].



Compounds whose radical anions give follow-up reactions can be reduced, and the reaction medium (aqueous or non-aqueous) eventually governs the nature of the final products. A number of organic substrates such as aldehydes, ketones and alkynes have been reduced in this way. It is also possible to reduce substrates which have a potential much more negative than its standard redox potential. For instance, nitrate, nitrite and carbon dioxide are reduced [2]. In the latter case [157], the overpotential reaches 0.6 V and the reaction is still rapid because the rate of the follow-up reaction, i.e. the dimerization of CO₂^{•-}, is extremely high ($k = 10^9 \text{ M}^{-1} \text{ s}^{-1}$) [158].

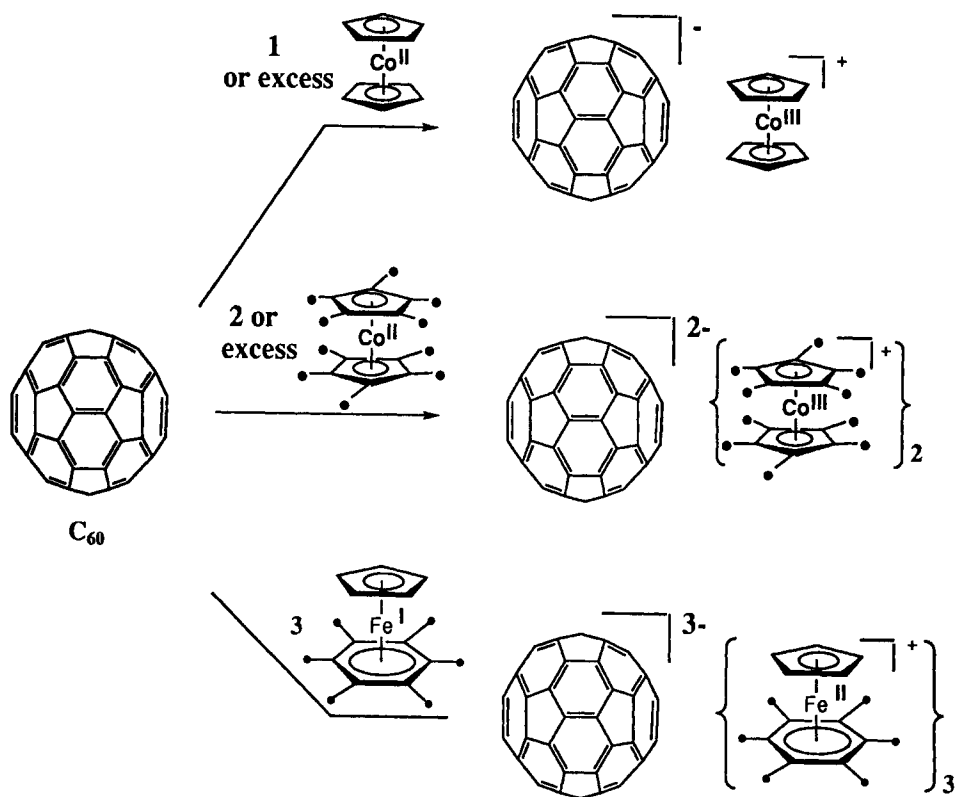


Scheme 7 shows representative examples of stoichiometric reductions using [Fe^ICp(η⁶-C₆Me₆)].



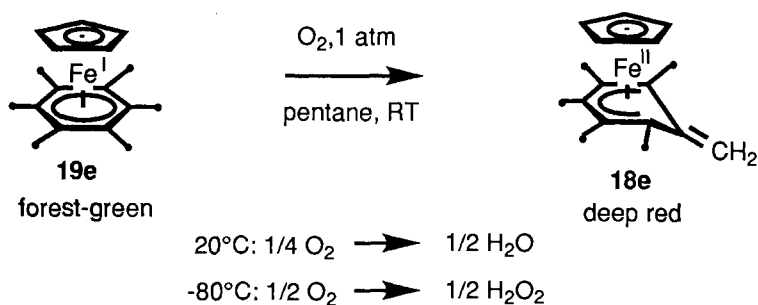
Scheme 7.

It is interesting to compare the relative reduction power of cobaltocene, decamethylcobaltocene and $[\text{Fe}^{\text{I}}\text{Cp}(\eta^6\text{-C}_6\text{Me}_6)]$ towards C_{60} . The first of these studies was carried out with $[\text{Fe}^{\text{I}}\text{Cp}(\eta^6\text{-C}_6\text{Me}_6)]$. It was shown that the mono-, di- and tri-anions of C_{60} were obtained as salts of $[\text{Fe}^{\text{II}}\text{Cp}(\eta^6\text{-C}_6\text{Me}_6)]^+$ depending on the stoichiometry of the reaction. The titration of C_{60} by $[\text{Fe}^{\text{I}}\text{Cp}(\eta^6\text{-C}_6\text{Me}_6)]$ is conveniently carried out since the solution remains deep forest-green when all the C_{60} is transformed into its trianion. The salt of the trianion $[\text{Fe}^{\text{II}}\text{Cp}(\eta^6\text{-C}_6\text{Me}_6)]_3 [\text{C}_{60}]$ is of special interest given the superconducting properties of the alkali-metal salts of this trianion [169]. In the present case, however, the lattice arrangement is governed by the organometallic cation which is larger than the anion, and the salt $[\text{Fe}^{\text{II}}\text{Cp}(\eta^6\text{-C}_6\text{Me}_6)]_3 [\text{C}_{60}]$ is paramagnetic [163]. In subsequent studies, it was shown that cobaltocene could only reduce C_{60} to its monoanion [170] whereas decamethylcobaltocene could lead to the dianion, but not the trianion (Scheme 8) [171].



Scheme 8.

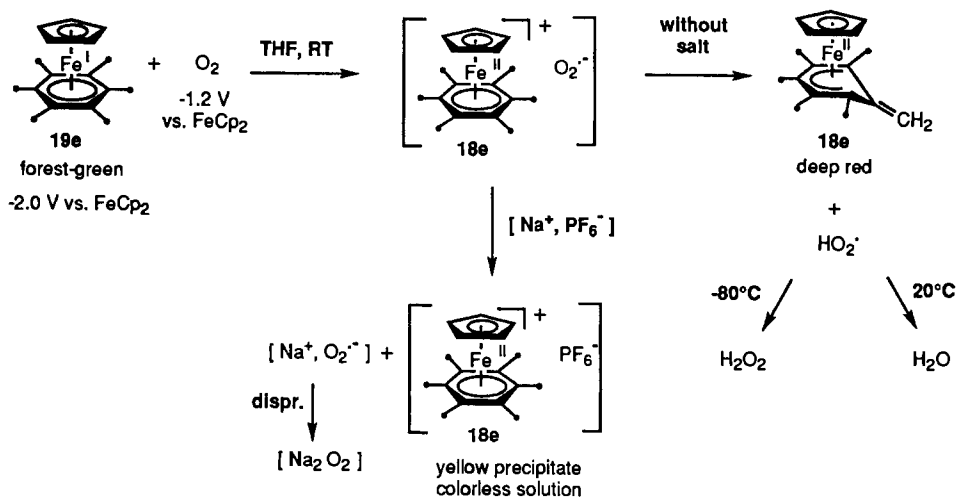
The reaction of $[\text{Fe}^{\text{I}}\text{Cp}(\eta^6\text{-C}_6\text{Me}_6)]$ with O_2 also proceed by a very favorable electron transfer to generate superoxide radical anion $\text{O}_2^{\bullet-}$ (the electron-transfer process is exergonic by about 0.85 V, i.e. 20 kcal mol⁻¹ or 83.6 kJ mol⁻¹), but it is very peculiar [159–162], and the follow-up reaction considerably depends on the presence of an inorganic salt, the salt effect being maximum with NaPF_6 [172]. In pentane or THF in the absence of a salt, the reaction is fast even at -80°C and yields the deep-red 18-electron complex $[\text{Fe}^{\text{II}}\text{Cp}(\eta^5\text{-C}_6\text{Me}_5\text{CH}_2)]$ resulting from an overall removal of a H atom from the 19-electron complex; $\frac{1}{2}$ equiv. H_2O is produced at 20°C whereas $\frac{1}{2} \text{H}_2\text{O}_2$ is formed at -80°C (Scheme 9):



Scheme 9.

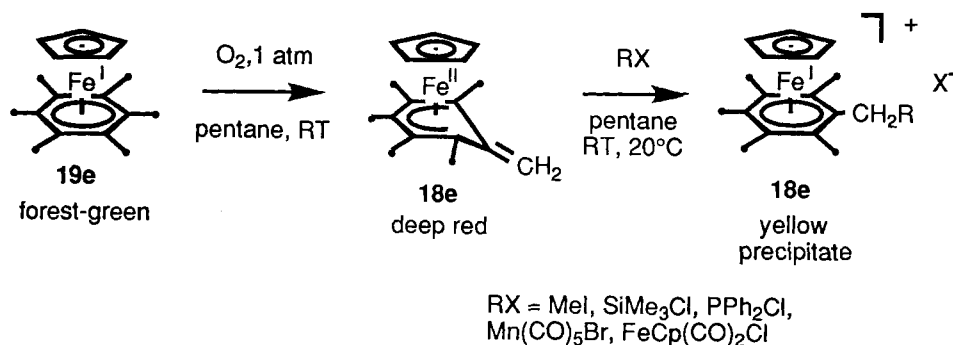
Superoxide radical anion can be characterized by ESR as an intermediate at low temperature. It is also possible to obtain the reaction product by reaction of KO_2 with $[\text{Fe}^{\text{II}}\text{Cp}(\eta^6\text{-C}_6\text{Me}_6)][\text{PF}_6]$ in DMSO in the presence of 18-crown-6. The overall H-atom abstraction in the above reaction of the 19e complex is thus decomposed into an electron transfer followed by benzylic deprotonation by $\text{O}_2^{\bullet-}$ in the ion pair $[\text{Fe}^{\text{II}}\text{Cp}(\eta^6\text{-C}_6\text{Me}_6)^+, \text{O}_2^{\bullet-}]$. This great reactivity of $\text{O}_2^{\bullet-}$ in the ion pair is due to the small size of this anion and to the fact that it is not strongly solvated in pentane or even in THF. It illustrates the dramatic reactivity of superoxide in a hydrophobic environment. When the reaction is carried out in THF, it is possible to do it in the presence of an inorganic salt such as NaPF_6 which completely changes its course: none of the deep-red complex $[\text{Fe}^{\text{II}}\text{Cp}(\eta^5\text{-C}_6\text{Me}_5\text{CH}_2)]$ is obtained (the resulting solution is colorless!) and a yellow precipitate of $[\text{Fe}^{\text{II}}\text{Cp}(\eta^6\text{-C}_6\text{Me}_6)][\text{PF}_6]$ together with Na_2O_2 (resulting from the disproportionation of $\text{O}_2^{\bullet-}$) are obtained (Scheme 10) [172].

The efficiency of the simple Na^+ salts to inhibit the reactivity of $\text{O}_2^{\bullet-}$ is very spectacular, and it matches the reactivity of superoxide dismutase enzymes in biological systems [173]. It is thus a unique property of the electron-reservoir complexes which lets us investigate the electron-transfer to O_2 in various media. The follow-up reactions of superoxide radical anion are reminiscent of its damage for cells in the aging processes which is well-known but little understood [173].



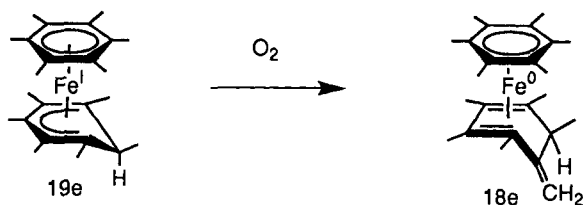
Scheme 10.

In the absence of benzylic proton, the reaction of Fe^{I} complexes with O_2 leads to peroxo-bridged dimers resulting from nucleophilic attack of superoxide radical anion with the 18-electron cationic sandwich in the ion pair. The mechanism is rather similar to the preceding one except for the reaction following the primary electron transfer. Superoxide was also characterized at low temperature, and a stoichiometric amount of NaPF_6 inhibits its reaction likewise, leading to $[\text{Fe}^{\text{II}}\text{Cp}(\eta^6\text{-C}_6\text{Me}_6)][\text{PF}_6]$ and Na_2O_2 . This thoroughly studied example illustrates the reactivity of the two partners of an ion cage in solvents such as pentane or THF in the absence of ions or solvating species, and indicates that a stoichiometric amount of NaPF_6 must be used in THF if this reactivity is not desired [162]. Thus, the reaction of the prototype electron-reservoir complex $[\text{Fe}^{\text{I}}\text{Cp}(\eta^6\text{-C}_6\text{Me}_6)]$ with neutral substrates were later carried out in the presence of NaPF_6 in stoichiometric amount when the aim was to reduce the substrate without being marred by the cage reactions. This can be easily done by using the THF solution used for the generation of the Fe^{I} complex from Na-Hg and the precursor PF_6 salt. Indeed, these 'quantitative' salt effects best provided by NaPF_6 are very useful in organometallic reactions [174, 175]. On the other hand, besides the interest in biomimetism, the useful product of the reaction of O_2 performed in the absence of a salt is not the reduced oxygen species, but the activated complex $[\text{Fe}^{\text{II}}\text{Cp}(\eta^5\text{-C}_6\text{Me}_5\text{CH}_2)]$. Indeed, this complex reacts smoothly with virtually all the electrophiles leading to the formation of carbon–element bonds. This has been shown with organic and inorganic halides (scheme below), CO_2 and CS_2 , metal carbonyls and organometallic complexes, which led for instance to the formation of bonds between the benzylic carbon and C, Si, P, Fe, Mn and Mo (Scheme 11) [161].



Scheme 11.

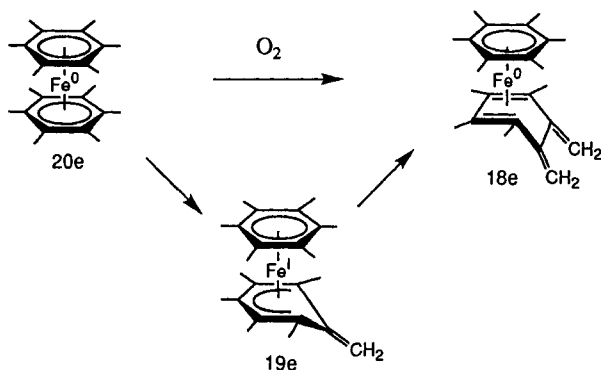
The reaction of O_2 with neutral 19-electron complexes bearing methyl groups on the rings is general and has been also found in other cases such as decamethylcobaltocene or others. Example (Scheme 12):



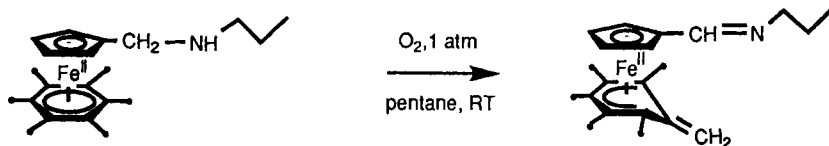
Scheme 12.

It is also possible to remove two H atoms using the 20-electron complex $[\text{Fe}^0(\eta^6\text{-C}_6\text{Me}_6)_2]$. The latter has a standard redox potential $E^\circ(\text{Fe}^{0/\text{I}}) = -1.85 \text{ V}$ relative to FeCp_2 in DMF, i.e. also much more negative than that of $\text{O}_2/\text{O}_2^{\cdot-}$ (-1.15 V relative to FeCp_2 in DMF). The intermediate $[\text{Fe}^{\text{I}}(\eta^5\text{-C}_6\text{Me}_5\text{CH}_2)(\eta^6\text{-C}_6\text{Me}_6)]$ resulting from removal of the first benzylic hydrogen has a structure very close that of $[\text{Fe}^{\text{I}}(\eta^5\text{-C}_6\text{Me}_6\text{H})(\eta^6\text{-C}_6\text{Me}_6)]$ (above) whose standard redox potential value is also very negative ($E^\circ(\text{Fe}^{\text{I}/\text{II}}) = -1.92 \text{ V}$ relative to FeCp_2 in DMF) [166]. The same sequence of electron transfer + deprotonation in the cage is thus occurring twice at this time, yielding the *ortho*-xylylene complex $[\text{Fe}^0\{\eta^4\text{-C}_6\text{Me}_4(\text{CH}_2)_2\}(\eta^6\text{-C}_6\text{Me}_6)]$, stable at -40°C and reactive towards electrophiles such as benzoyl chloride (Scheme 13) [166, 176].

The above examples shows that multiple H atoms may be removed from benzylic positions as long as the complexes resulting from overall H-atom abstraction have a standard redox potential more negative than that of $\text{O}_2/\text{O}_2^{\cdot-}$. During our attempt to extend this reaction to the functional complex $[\text{Fe}^{\text{I}}(\eta^5\text{-C}_5\text{H}_4\text{CH}_2\text{NH}n\text{-Pr})(\eta^6\text{-C}_6\text{Me}_6)]$ in order to carboxylate the hexamethylbenzene ligand, we found that the stoichiometry in dioxygen at 25°C was not 0.25 equiv. as expected, but 0.75



Scheme 13.



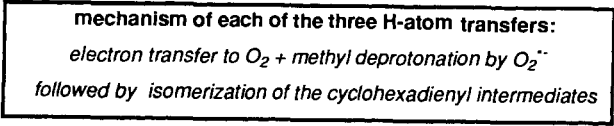
Scheme 14.

equiv., i.e. three times more. The resulting red product $[Fe^{II}(\eta^5-C_5H_4CH=Nn-Pr)(\eta^5-C_6Me_5CH_2)]$ which was obtained after a short contact with air under ambient conditions in pentane resulted in fact from the removal of three H atoms from this Fe^I complex (Scheme 14) [177].

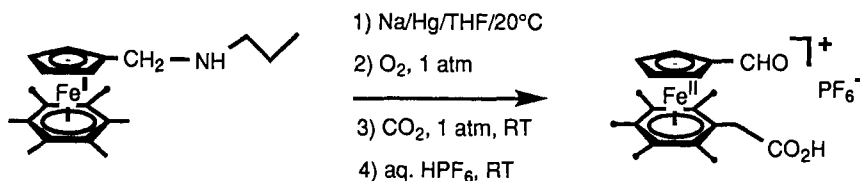
Intriguingly, the reaction proceeds with oscillatory color changes from green to red. When it is carried out by stepwise addition of $\frac{1}{4}$ equiv. dioxygen, the color indeed changes from green (Fe^I) to red (Fe^{II}), but the red complexes are not stable and turn green again except after the third addition of dioxygen. The final red complex is stable. Its formation can be taken into account according to H-atom transfer from the amine to the methylenecyclohexadienyl ligand to form again the hexamethylbenzene ligand which in turn reacts again with dioxygen (Scheme 15).

The complex resulting from triple C–H/N–H activation can be heterobifunctionalized by successive addition of CO_2 (carboxylation of the hexamethylbenzene ligand) and water (acidic hydrolysis of the imine to the aldehyde on the Cp substituent). This heterobifunctional complex is very useful for the branching to nanoscopic substrates and yet keep the solubility in aqueous media by means of the carboxylate group. Use of this functionalized electron-reservoir system in redox catalysis is promising. Thus, from the starting 18-electron complex, the overall heterobifunctionalization can be carried out in one pot as shown in Scheme 16 [177, 178].

The reactions of organic halides RX with the 19-electron complex $[Fe^I Cp(\eta^6-C_6Me_6)]$ itself lead to coupling of the R group onto the Cp ring, producing

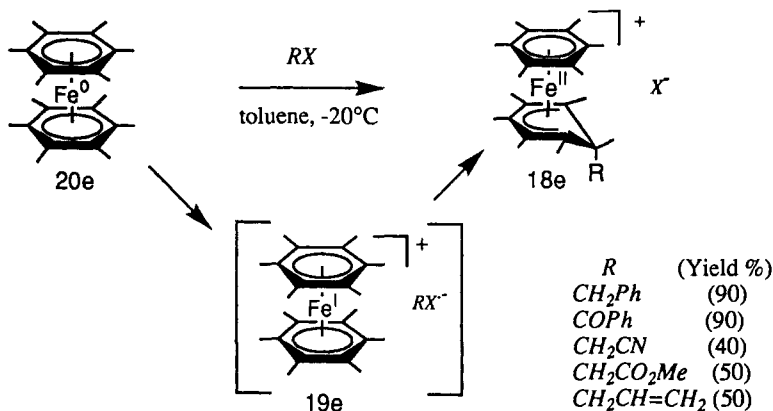


Scheme 15.



Scheme 16.

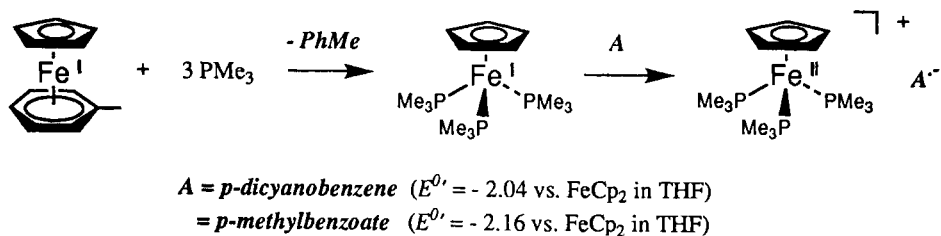
an equimolecular amount of $[\text{Fe}^{\text{I}}\text{Cp}(\eta^6\text{-C}_6\text{Me}_6)]\text{X}$ and $[\text{Fe}^0(\eta^4\text{-exo-RC}_5\text{H}_5)(\eta^6\text{-C}_6\text{Me}_6)]$, the latter adduct resulting from reaction between the starting Fe^{I} complex of the radical R^\bullet formed by reduction of RX by another Fe^{I} . This reaction resembles that known with cobaltocene, and is not very productive for a synthetic purpose. On the other hand, the 20-electron complex $[\text{Fe}^0(\eta^6\text{-C}_6\text{Me}_6)_2]$ becomes a radical cation after having transferred one electron to RX , and the radical generated radical R^\bullet can then couple to the 19-electron radical cation intermediate $[\text{Fe}^0(\eta^6\text{-C}_6\text{Me}_6)_2]^{+\bullet}$ to produce cationic 18-electron complexes with a functional cyclohexadienyl ligand. These reactions have been carried out with various functional halides (Scheme 17):



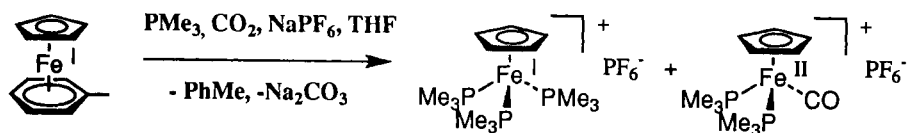
Scheme 17.

Such ligands can be deprotonated on a methyl substituent in α position with respect to the ring carbon bearing the functionalized group to give Fe^0 complexes and be subsequently removed by oxidation.

Starting from the parent 19-electron complex $[\text{Fe}^{\text{I}}\text{Cp}(\eta^6\text{-C}_6\text{H}_6)]$, it is possible to generate very strong single-electron reducing agents by reaction with phosphines such as PMe_3 . Indeed, this reaction leads to the exchange of the 6-electron ligand C_6H_6 with three 2-electron PMe_3 ligands. This provides the transient 19-electron species $[\text{Fe}^{\text{I}}\text{Cp}(\text{PMe}_3)_3]$, whose standard redox potential is close to -2.4 V relative to



Scheme 18.



Scheme 19.

FcCp_2 in THF. Aromatic substrates such as p -dicyanobenzene and p -methylbenzoate whose standard redox potentials are more negative than -2 V relative to FcCp_2 can be reduced (Scheme 18).

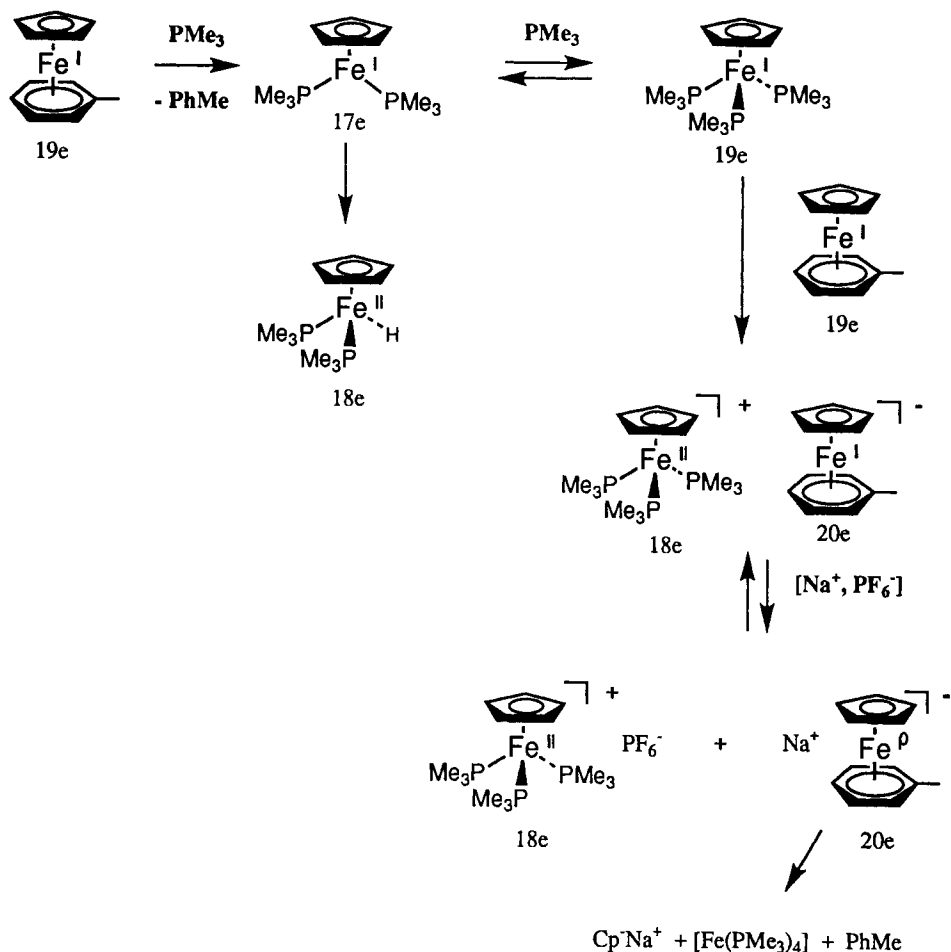
Even CO_2 can be rapidly reduced to CO and carbonate, and CO incorporates in the coordination sphere of the metal at the 19-electron level whose very favorable ligand substitution properties are well known (Scheme 19).

The reducing power of the 19-electron species $[\text{Fc}^{\text{I}}\text{Cp}(\text{PMe}_3)_3]$, is so great that, in the absence of substrate, the 19-electron complex $[\text{Fc}^{\text{I}}\text{Cp}(\eta^6\text{-C}_6\text{H}_6)]$, itself is reduced to the unstable 20-electron anionic species which undergoes fast decomplexation under the influence of the ion pair $[\text{Na}^+, \text{PF}_6^-]$. This process corresponds to the disproportionation of the Fc^{I} complex to Fc^0 and Fc^{II} (Scheme 20).

In the absence of PMe_3 $[\text{Na}^+, \text{PF}_6^-]$, catalyzes this same process, except that it is slower. In this case, the salt effect is catalytic simply because all the species remain in solution [179, 180]. Thus, the presence of $[\text{Na}^+, \text{PF}_6^-]$ is important to favor electron-transfer processes from the 19-electron complexes, whether they are stable ($[\text{Fc}^{\text{I}}\text{Cp}(\eta^6\text{-C}_6\text{Me}_6)]$) or not ($[\text{Fc}^{\text{I}}\text{Cp}(\eta^6\text{-C}_6\text{H}_6)]$ or $[\text{Fc}^{\text{I}}\text{Cp}(\text{PMe}_3)_3]$). Salt effects are important in chain reactions as well [180–185] (see Section 4.5).

4.4 Oxidants

In the preceding section, we have shown the electron-reservoir properties of the redox series $[\text{Fe}(\eta^5\text{-C}_5\text{R}_5)(\eta^6\text{-C}_6\text{Me}_6)]^{2+/+/0}$ on the reduction side with the neutral 19-electron Fe^{I} form. The 17-electron dicationic Fe^{III} form can be isolated as the SbX_6 salts ($\text{R} = \text{Me}$, $\text{X} = \text{F}$ or Cl) and used as very strong oxidants, with a stan-



Scheme 20.

standard redox potential $\text{Fe}^{\text{II/III}}$ about 1 V more positive than that ferrocenium to which it is isoelectronic. Mono-electronic oxidants have been reviewed [21]. We will only summarize them in this section, and give the most noteworthy recent findings.

4.4.1 Fe^{III} Sandwich Complexes: Ferrocenium Salts $[\text{FeCp}_2][\text{X}]$ and $[\text{FeCp}^*(\eta^6\text{-C}_6\text{Me}_6)][\text{SbX}_6]_2$

$[\text{FeCp}_2][\text{BF}_4]$ and $[\text{FeCp}_2][\text{PF}_6]$ are easily prepared by oxidation of ferrocene using a variety of oxidants (sulfuric acid [185], *p*-benzoquinone [21], NO^+ , iron trichloride, etc. [186–191].) and commonly used in organometallic chemistry as very useful, almost innocent single-electron oxidants. They are thermally stable and can

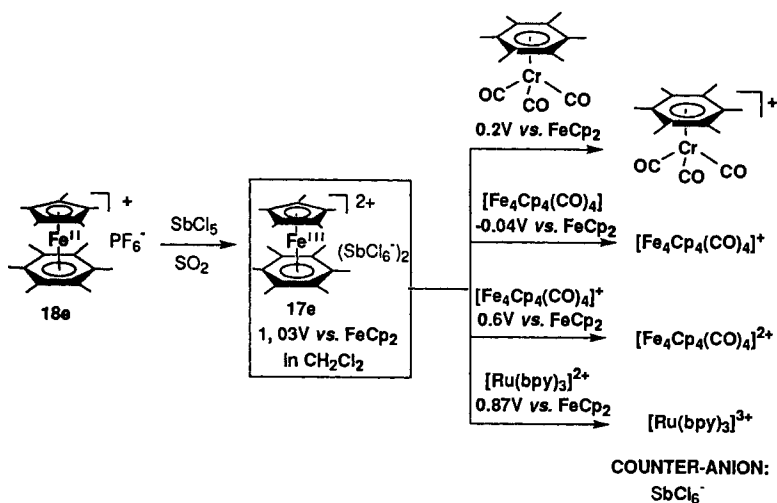
be handled in air in the solid state. They are more or less soluble in all the organic solvents, but must be used under an inert atmosphere in solution. They can also be used in the solid state (suspension) if the substrate is soluble in the solvent used. The reaction product, ferrocene, is soluble in non-polar solvents, which provides an easy means of separation. On the other hand, if excess ferrocenium salt is used, it is difficult to remove. These salts are non-innocent when the cation obtained upon ferrocenium oxidation is extremely reactive towards nucleophiles (for instance silicenium cation, early transition metal complexes). Fluorination of very reactive cations occurs indeed with the counter-anions BF_4^- or PF_6^- , and other counter-anions such as BPh_4^- , $\text{B}(\text{C}_6\text{F}_5)_4^-$, $\text{B}\{3,5\text{-C}_6\text{H}_3(\text{CF}_3)_2\}_4^-$, or even carborane or perfluorocarborane anions must then be used [192, 193].

Substituents on the ferrocene rings lead to variations of the redox potentials [194]. Monoacetylferrocenium $[\text{FeCp}(\eta^5\text{-C}_5\text{H}_4\text{COMe})]$, $[\text{BF}_4]$ ($E^\circ = 0.27$ V in CH_2Cl_2) is of particular interest because it is a stronger oxidant than parent ferrocenium salts. It can be prepared from $[\text{FeCp}(\eta^5\text{-C}_5\text{H}_4\text{COMe})]$ and AgBF_4 (or other oxidants) in CH_2Cl_2 followed by filtration of colloidal Ag and precipitation by addition of ether [21, 195]. It should be used as freshly prepared because it is moisture sensitive and slowly deteriorates. 1,1'-diacetylferrocenium $[\text{FeCp}(\eta^5\text{-C}_5\text{H}_4(\text{COMe})_2)]$, $[\text{BF}_4]$ ($E^\circ = 0.49$ V relative to FeCp_2 in CH_2Cl_2) is an even stronger oxidant which is prepared likewise and is more air-sensitive [195]. These salts are also presumably easily synthesized from $[\text{NO}][\text{BF}_4]$ in CH_2Cl_2 followed by precipitation using ether as other ferrocenium salts, and have already been used when ferrocenium salts were not strong enough oxidants [196].

$[\text{FeCp}^*(\eta^6\text{-C}_6\text{Me}_6)][\text{SbX}_6]_2$ is a very strong oxidant ($E^\circ = 1.03$ V relative to FeCp_2 in CH_2Cl_2). Its standard redox potential is much more positive than that of ferrocenium, although it is isoelectronic to it, simply because of the additional positive charge. It is obtained by single-electron oxidation of $[\text{FeCp}^*(\eta^6\text{-C}_6\text{Me}_6)][\text{PF}_6]$ using SbCl_5 in CH_2Cl_2 or SO_2 or SbF_5 in SO_2 and can be recrystallized from SO_2 . It can oxidize a wide range of compounds such as $[\text{Ru}(\text{bpy})_3]^{2+}$, $[\text{Cr}(\text{arene})(\text{CO})_3]$, and transition-metal clusters which cannot be oxidized by ferrocenium salts. It is a rare innocent, very strong oxidant (Scheme 21). It is soluble in acetone and insoluble in CH_2Cl_2 but, given its strong reducing power, it is best to use it in the solid state provided the substrate to oxidize is soluble in the solvent used [131].

4.4.2 Silver(I) Salts

Silver(I) salts are commercially available with a variety of counter-anions which made them popular oxidants in both organic [197] and inorganic chemistry [198]. They are typical non-innocent oxidants in transition-metal chemistry, hygroscopic and photosensitive, and their standard redox potential very much depends on the solvent [199]. Thus $\text{Ag}(\text{I})$ salts are strong oxidants in 'non-coordinating' solvents such as CH_2Cl_2 ($E^\circ = 0.65$ V relative to FeCp_2), but their standard redox potential is all the less positive as the solvent is a better ligand. In MeCN ($E^\circ = 0.04$ V relative to FeCp_2), its oxidizing power is apparently not superior to that of ferrocenium salt [199]. AgPF_6 can oxidize, in CH_2Cl_2 , substrates such as $[\text{N}(\text{C}_6\text{H}_4\text{Br-4})_3]$

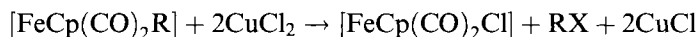


Scheme 21.

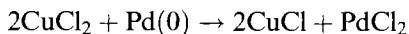
($E^{\circ'} = 0.70$ V relative to FeCp_2 in CH_2Cl_2), whose standard redox potential is slightly more positive than its own redox potential, because the redox equilibrium is shifted towards the products by the irreversible agglomeration and precipitation of silver particles. The silver ion Ag(I) has been used for almost a century as oxidant. For instance, in 1923, AgNO_3 was reported as an oxidant of metallic copper in acetonitrile to give the complex $[\text{Cu}(\text{MeCN})_6][\text{NO}_3]$ [200]. Although they are soluble in organic solvents, silver (I) salts are best used in the solid state (fresh samples) because of their sensitivity. Filtration of colloidal silver using Celite or Kieselguhr is advised after the reaction. Toluene is a practical solvent in order to remove excess reactant as well as silver metal. In CH_2Cl_2 and CHCl_3 , Ag(I) catalyzes the hydrolysis of the $[\text{PF}_6]^-$ counter-anion to $[\text{PO}_2\text{F}_2]^-$ in the presence of traces of water [201–203]. Side reactions of Ag(I) salts upon oxidation (non-innocent behavior) often involve the binding of reactive silver atoms with organometallic radicals generated by oxidation [21].

4.4.3 Copper(II) Salts

Copper(II) salts are familiar oxidants in organic chemistry [204, 205], but they have been little used by transition-metal chemists. They are commercially available with various counter-anions as anhydrous or hydrates (CuCl_2 is also simply obtained by heating $\text{CuCl}_2 \cdot 2\text{H}_2\text{O}$ in thionyl chloride) [206]. They have been used in CH_2Cl_2 and MeCN to cleave metal-carbon bonds in 18-electron iron (II) and ruthenium (II) complexes. The first step of this reaction is a single-electron oxidation [207].

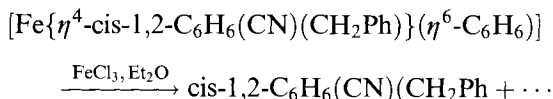


CuCl_2 is well-known as the oxidant of $\text{Pd}(0)$ in the catalytic Wacker process (aerobic oxidation of ethylene to acetaldehyde) [208].



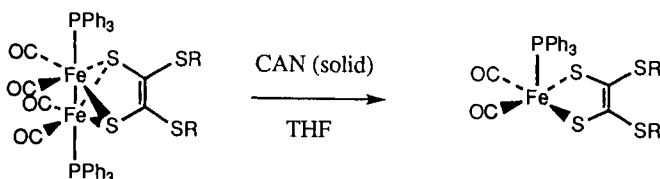
4.4.4 Iron(III) Chloride

Iron(III) trichloride is commercially available both as the anhydrous or hydrate form which can also be refluxed in thionyl chloride to generate the anhydrous form (purified by sublimation) most often used [209]. Anhydrous iron trichloride is about as strong as ferrocenium salts, but it is not necessarily innocent. It is sometimes used to recover functionalized metal-free hydrocarbon derivatives which have been transformed by temporary complexation and activation on a transition-metal center [210].



4.4.5 Cerium(IV) Ammonium Nitrate (CAN)

Cerium (IV) ammonium nitrate (CAN) $[\text{NH}_4]_2[\text{Ce}(\text{NO}_3)_6]$, is a water-soluble oxidant, classical in organic chemistry [197], which has sometimes been used in organometallic chemistry to disengage ligands from metal centers [211]. It can be used (i) in solution in an aqueous solvent such as ethanol, acetone and acetonitrile [212], (ii) with a phase-transfer catalyst such as $[\text{NBu}_4][\text{HSO}_4]$ [213] or (iii) in the solid state (suspension) in, for instance, THF [214], for example (Scheme 22):



Scheme 22.

4.4.6 Miscellaneous High-oxidation-state Inorganic Complexes

$\text{M}^{\text{III}}(\text{L-L})_3^{3+}$ ($\text{M} = \text{Cr}, \text{Fe}, \text{Ru}, \text{Os}, \text{Co}, \text{Ni}$; $\text{L-L} = \text{bipy}, \text{phen}, \text{etc.}$) have been widely used in inorganic chemistry as outer-sphere single-electron oxidants [215], unfortunately as the potentially very hazardous and explosive perchlorate

salts which should be replaced by PF_6^- or AsF_6^- salts. The tetracationic salt $[\text{Ni}^{\text{IV}}(\text{bipy})_3][\text{AsF}_6]_4$, with a standard redox potential $E^\circ = 2.06$ V, is a very strong oxidant which has been isolated [216]. $[\text{Fe}^{\text{III}}(\text{bipy})_3]^{3+}$ has been used as an oxidant to determine the number of hydride ligands in transition-metal hydride complexes [217].

The anionic complex $\text{M}_2[\text{IrCl}_6]$ ($\text{M} = \text{Na}$ and K) are commercially available and have been used as outer-sphere single-electron oxidants in mechanistic studies of the cleavage of metal-carbon bonds [218]. The isostructural oxidant $[\text{PtCl}_6]^{2-}$ is also known, especially its ability to oxidize saturated hydrocarbon by electrophilic C–H activation (inner-sphere two-electron oxidant) [219].

The neutral dithiolene complexes $[\text{Ni}(\text{S}_2\text{C}_2(\text{CF}_3)_2)]$ and $[\text{Mo}(\text{S}_2\text{C}_2(\text{CF}_3)_2)]$ are known as strong oxidants whose anions are stable, but their synthesis from the metal carbonyls [220] is tedious and dangerous in the case of the Ni complex because of the very high toxicity of $[\text{Ni}(\text{CO})_4]$. Therefore, they have been little used [221] for this reason and also because some other oxidants with analogous oxidizing properties are commercial or easily accessible.

The metal hexahalides MoF_6 , WF_6 , UF_6 and WCl_6 are strong oxidants which are commercially available and soluble in various organic solvents, but the hexafluorides are readily hydrolyzed to the extremely corrosive and dangerous HF, and have therefore been little used. The standard redox potential of WCl_6 is around 1.1 V relative to FeCp_2 [222, 223] and it oxidizes $[\text{N}(\text{C}_6\text{H}_4\text{Br}-4)_3]$ to $[\text{N}(\text{C}_6\text{H}_4\text{Br}-4)_3][\text{WCl}_6]$ [224].

4.4.7 Nitrosonium Salts, $[\text{NO}]\text{X}$

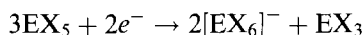
The nitrosonium salts, $[\text{NO}]\text{X}$, are strong oxidants whose oxidizing power is solvent dependent ($E^\circ = 0.56$ V in DMF, 0.87 V in MeCN and 1.00 V relative to FeCp_2 in CH_2Cl_2). They have been widely used in organic [225] and inorganic chemistry [12, 226, 227] and reviewed. They are commercially available ($\text{X} = \text{BF}_4$, PF_6 , SbF_6) and can be easily prepared and purified [226–231], for instance by recrystallization from MeCN at -20°C [229, 231]. They are very moisture sensitive, decomposing in air to higher oxides. They are stored in plastic containers under an inert atmosphere because the corrosive oxidation products attack glass. It has been reported that $[\text{NO}][\text{BF}_4]$ and $[\text{NO}][\text{PF}_6]$ can be rapidly weighed in air, however, and added as solids to substrates in a dry and deoxygenated solvent [21]. They are normally weighed in a dry-box for a more rigorous stoichiometry. In addition, a careful selection of solvents is necessary. Dichloromethane, alkanes, toluene, acetonitrile, nitromethane, ethyl acetate and carbon tetrachloride do not react, when they are carefully purified, with $[\text{NO}]\text{X}$ salts in an inert atmosphere. Acetone, pyridine, ethers, alcohols and water, even when they are carefully purified, react with $[\text{NO}]\text{X}$ salts whether the atmosphere is inert or not. Since the preparation of $\text{Na}[\text{SbCl}_6]$ from sodium and $[\text{NO}][\text{SbCl}_6]$ in liquid SO_2 in 1950 [232], the $[\text{NO}]\text{X}$ salts have been used in the oxidation of metals for the preparation of homoleptic solvento complexes $[\text{M}(\text{solvent})_n][\text{X}]_p$ ($\text{M} = \text{Cu}$, Ag , Au , Eu , Ni , Pd , etc.; solvent = MeCN, etc.; $n = 4$ or 6 ; $\text{X} = \text{BF}_4$ or ClO_4 ; $p = 1$ – 3) [233]. The hazardous, potentially ex-

plosive perchlorate salts must be avoided and obvious alternatives (BF_4 or PF_6) easily used instead. The $[\text{NO}]\text{X}$ salts have been used in organometallic chemistry, but they are non-innocent oxidants, the most frequent reaction subsequent to oxidation being coordination of NO which leads to the formation of nitrosyl complexes. As in organic chemistry [225, 234], it is likely that such reactions proceed by the inner-sphere pathways [21]. The $[\text{NO}]\text{X}$ salts are very useful for the oxidation, by an outer-sphere pathway, of ferrocene derivatives to the ferrocenium analogs, however, because nitrosyl complexes cannot coordinate in robust 18-electron complexes or in ferroceniums [134, 135]. NO derivatives have attracted a lot of interest recently since the discovery of the role of NO as a neurotransmitter.

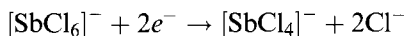
4.4.8 Phosphorus, Arsenic, and Antimony Pentahalides and Aluminum Trichloride

Phosphorus pentahalides PX_5 ($\text{X} = \text{Cl}$ and Br) are mild oxidants which were used already more than a century ago to oxidize platinum black to bridged dimers $[\text{Pt}_2(\mu_2\text{-X})_2\text{X}_2(\text{PX}_3)_2]$ [235a]. Oxidative chlorination of Pt^{II} to Pt^{IV} complexes by PCl_5 is classic, and compares favorably with use of Cl_2 which is common to carry out this reaction [235b].

The arsenic and antimony pentahalides EX_5 (E : group 15 element As or Sb; $\text{X} = \text{F}$ or Cl) are strong, irreversible oxidants; the gas AsF_5 has little been used, but SbCl_5 and SbF_5 are commercially available, very air-sensitive liquids which are used in dry and deoxygenated dichloromethane and liquid sulfur dioxide respectively. SbCl_5 is easier to handle than SbF_5 which gives the dangerous HF by reaction with moist air. Moreover, SbCl_5 is conveniently used in dichloromethane whereas SbF_5 is best used in liquid SO_2 . On the other hand, the side products (halogenation) are more frequently encountered with SbCl_5 than with SbF_5 . The redox process follows:



$[\text{EX}_6]^-$ can itself be an oxidant, for instance with ferrocene, iodides and aromatic amines [236]:



Although the standard redox potentials of SbX_5 ($\text{X} = \text{F}$ or Cl) are unknown because of the irreversibility of their redox reactions, it was possible to estimate rather accurately their oxidizing power by the investigation of their redox reactions with a series of 18-electron complexes $[\text{FeCp}^*(\eta^6\text{-arene})][\text{PF}_6]$ of known standard redox potentials. In these complexes, the arene ligands are polymethylaromatics in which the addition of each methyl group decreases the standard redox potential of the complex by 60 mV. For arene = hexamethylbenzene, pentamethylbenzene and tetramethyl-1,2,4,5-benzene (durene), the color change from yellow to purple observed upon reaction of SbX_5 ($\text{X} = \text{F}$ or Cl) with the complex $[\text{FeCp}^*(\eta^6\text{-arene})][\text{PF}_6]$ indicates that electron transfer occurs, and it is also possible to isolate the salts $[\text{FeCp}^*(\eta^6\text{-arene})][\text{SbX}_6]_2$. For mesitylene and less methylated aromatics, no color

change was observed, and the electron-transfer does not proceed. This is true for SbCl_5 in CH_2Cl_2 at 20°C and SbF_5 in SO_2 at -40° to -10°C . Although it is known that SbF_5 is a better oxidant than SbCl_5 , they have the same oxidizing power in the conditions used here, because the solvent, temperature and rate of the follow-up reactions also play roles. Thus, these pentahalides can oxidize substrates which have standard redox potentials up to 1.045 V relative to FeCp_2 , the standard redox potential of $[\text{FeCp}^*(\eta^6\text{-durene})][\text{PF}_6]$ in liquid SO_2 .

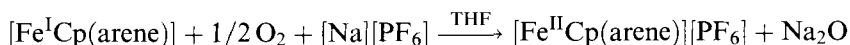
AlCl_3 is a strong oxidant whose oxidation potential has been estimated to be about 1.1 V, but the mechanism by which oxidation reactions proceed is mysterious. It has essentially been used (even without sublimation, the method of purification) for spectroscopic (ESR) studies to generate radical cations [237, 238].

4.4.9 Dioxygenyl cation, O_2^{++} , dioxygen O_2 , and superoxide anion $\text{O}_2^{\cdot-}$

The most oxidizing species ever isolated is Bartlett's dioxygenyl salt $[\text{O}_2][\text{PtF}_6]$ made from O_2 and PtF_6 and reported in 1962. Since dioxygen has a higher ionization energy (12.1 eV) than xenon (11.6 eV), this synthesis of $[\text{O}_2][\text{PtF}_6]$ led Bartlett to the idea that it would be possible to oxidize xenon using PtF_6 . It is in this way that Bartlett isolated the first rare-gas compound $[\text{Xe}][\text{PtF}_6]$ [239]. From this very high ionization potential, it could be calculated that $[\text{O}_2][\text{PtF}_6]$ has a standard redox potential of 4.9 V relative to FeCp_2 , although such high redox potentials cannot be reached in any solvent using electrochemistry. One may also imagine that considerable solvation energy of the dioxygenyl cation is released in any solvent, so the actual potential, still extremely high, is considerably less positive whenever a solvent is involved. The salts $[\text{O}_2][\text{EF}_6]$ ($\text{E} = \text{As}$ or Sb) are indeed air-sensitive, especially when the temperature is increased towards room temperature. Therefore, it has been used, especially in low-temperature Freon mixtures to oxidize several substrates which are difficult to oxidize [240–244] including organic compounds to their radical cations. Thus, for instance $[\text{O}_2]$, $[\text{AsF}_6]$ reacts with $\text{NMe}(\text{C}_6\text{H}_4\text{OMe-4})_2$ in CHF_2Cl at -130°C to give $[\text{NMe}(\text{C}_6\text{H}_4\text{OMe-4})_2][\text{AsF}_6]$ and O_2 which is released together with the solvent, leaving the salt [241].

Dioxygen O_2 is the most known and most common oxidant in combustion processes and in industry (Wacker process). It is not used in single-electron oxidation reactions, however, because the standard redox potential $\text{O}_2/\text{O}_2^{\cdot-}$ is relatively negative ($E^\circ = -1.2$ V relative to FeCp_2 in DMF), making O_2 a mediocre single-electron acceptor, and superoxide radical anion is very reactive (although thermodynamically very stable). Thus, O_2 is a non-innocent oxidant, giving coordination of O_2 or superoxide onto transition-metal centers (formation of dioxygen-, superoxo- and peroxo complexes MO_2 , oxo complexes $\text{M}=\text{O}$ and peroxide-bridged complexes MOM) and giving well-known radical reactions ($\text{R}^\cdot + \text{O}_2 \rightarrow \text{ROO}^\cdot$). In fact, it is a major concern for organometallic chemists to avoid contact of the reaction media with O_2 from air. Dioxygen can be used as a clean single-electron oxidant in reactions which are carried out in THF in the presence of one equiv. NaPF_6 in order to avoid the cage reactions of the intermediate ion pairs. This is a fairly general technique when the oxygen species cannot attack the metal center

which is coordinatively saturated.

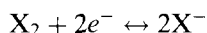


The interesting cage reactions of superoxide anion subsequent to the reaction of O_2 in the absence of a salt have been reviewed in the preceding section.

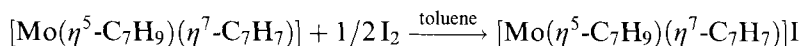
Superoxide radical anion, $\text{O}_2^{\bullet-}$, a weak reductant, is also an extremely weak oxidant as its standard redox potential of reduction to peroxide, O_2^{2-} , is about -2.4 V relative to FeCp_2 [245]. First made by Gay Lussac almost two centuries ago by reaction of K with O_2 , KO_2 is insoluble except in DMSO in the presence of 18-crown-6. Alternatively, soluble $\text{O}_2^{\bullet-}$ salts are generated cathodically in pyridine, DMF or DMSO in the presence of a solubilizing electrolyte of the type $[\text{R}_4\text{N}]\text{Cl}$ ($\text{R} = \text{Me}$ or $n\text{-Bu}$), which provides the superoxide salt $[\text{R}_4\text{N}][\text{O}_2]$ [245].

4.4.10 Halogens: Cl_2 , Br_2 , and I_2

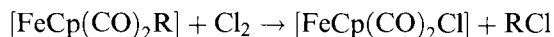
The halogens Cl_2 , Br_2 and I_2 are commercially available (cheap) common mild (but non-innocent) oxidants which are soluble in organic solvents including non-polar ones. The order of their oxidizing powers follows that of their standard oxidation potentials E° relative to FeCp_2 in MeCN: Cl_2 (0.18 V) $>$ Br_2 (0.07 V) $>$ I_2 (-0.14 V):



Oxidation of neutral organometallic complexes ML_n using I_2 often leads to the salts $[\text{ML}_n] \text{I}$ (which can be transformed into $[\text{ML}_n][\text{PF}_6]$ by addition of $[\text{NH}_4][\text{PF}_6]$ in water), but the triiodides I_3^- are also formed if excess I_2 is present in the reaction medium.



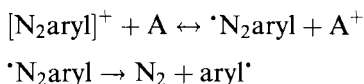
The use of Cl_2 or Br_2 and AlCl_3 together in a mixture of dichloromethane and carbon tetrachloride provides a very strong oxidant which can oxidize complexes whose oxidation potential is as high as 1.4 V relative to FeCp_2 such as $[\text{Pt}(\text{C}_6\text{Cl}_5)_4]^-$ [245]. Halogens cleave metal-carbon bonds of metal-alkyl complexes with halogenation of both the alkyl and the metal fragments (the first step is an outer-sphere electron transfer) [246].



4.4.11 Arenediazonium, $[\text{N}_2\text{aryl}]^+$

The arenediazonium salts $[\text{N}_2\text{aryl}]\text{X}$ ($\text{X} = \text{BF}_4$ or PF_6) have been very much used in organic synthesis [247]. They are known with a variety of *para* substituents R,

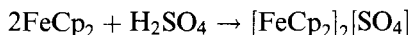
which allows variations of the standard redox potential E° relative to FeCp_2 : $\text{R} = \text{H}$ (-0.10 V), Me (-0.15 V), Cl (0.01 V), NO_2 (0.05 V) and NMe_2 (-0.50 V) [248, 249]. Except the latter, these values are almost the same as that of ferrocenium. The redox reaction of aryldiazonium cations are irreversible, however, which shift the redox equilibrium towards the products:



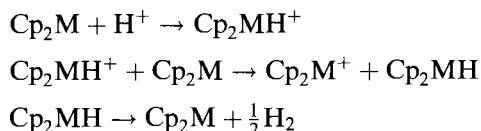
Therefore, they are better oxidants than ferrocenium salts. Indeed, they have been currently used in CH_2Cl_2 and THF to oxidize 18-electron complexes to their 17-electron counterparts [21], although the advantage of the irreversible oxidation has not been quantified. They are easily prepared [249, 250] and $[\text{N}_2\text{C}_6\text{H}_4\text{NEt}_2-4][\text{BF}_4]$ is commercially available. They are stable, can be handled in air, and are soluble in polar solvents (Me_2CO , MeCN) but not in CH_2Cl_2 , and decompose in THF and CHCl_3 [21]. They often behave as non-innocent oxidants in reactions of transition-metal complexes (H-atom abstraction, radical coupling, coordination and insertion in metal–ligand bonds are known) [21].

4.4.12 Acids

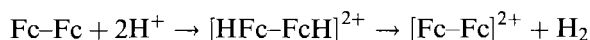
The reaction of concentrated sulfuric acid with neat ferrocene is a method of preparation of ferrocenium salts:



Cobaltocene $[\text{Cr}(\text{arene})_2]$, and $[\text{FeCp}^*_2]_2$ are also oxidized to the monocations by acids. It was shown in some cases that the first step consists in the protonation of the electron-rich metal center, and the likely follow-up reaction is oxidation of the neutral sandwich complex by the protonated complex [251].



A very interesting example is the oxidation of biferrocenylene Fc-Fc by protic acids, because dihydrogen readily evolves at the two-metal centers and the biferrocenylene di-cation is reduced to the neutral compound at low cathodic potential providing a catalyst for the reduction of protons [252, 253]:



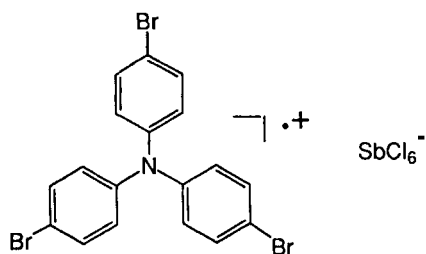
However, the reaction of a protic acid with transition-metal complexes bearing non-bonding valence electrons (Lewis bases) usually leads to transition-metal hy-

hydrides complexes resulting in a formal oxidation of the metal center by two units of oxidation states. Various strengths of acids are required since the range of basicity of transition-metal hydrides is extremely large. With d^0 complexes, protonation of a metal–ligand bond can be achieved since the metal cannot be oxidized. Thus, d^0 transition-metal-hydride complexes as well as electron-poor transition-metal hydrides are protonated at the M–H bond to give dihydrogen complexes [254, 255]. This type of reaction is in competition with the electron-transfer reaction, but is predominant most of the time.

The most currently chosen acids are HBF_4 and HPF_6 which can be used either in water or in ether, this second possibility having provided other cases of single-electron oxidation of electron-rich neutral organometallic complexes to their monocations as BF_4 or PF_6 salt [244]. Triflic acid, HO_3SCF_3 [256], and $[\text{NH}_4][\text{PF}_6]$ [257] can also be used in THF.

4.4.13 Triarylamminium Cations, $[\text{N}(\text{aryl})_3]^+$

The triarylamminium salts $[\text{N}(\text{aryl})_3][\text{X}]$ in which the *para* position is substituted (in order to inhibit nucleophilic reactions at that position) are among the most useful oxidants because they are strong, almost innocent oxidants known for a range of standard redox potentials from 0.16 V to -1.76 V relative to FeCp_2 depending of the nature and number of substituents (Table 10), and they are easily accessible by oxidation of the triarylamine in CH_2Cl_2 using $[\text{NO}]$ salts, silver salts in the presence



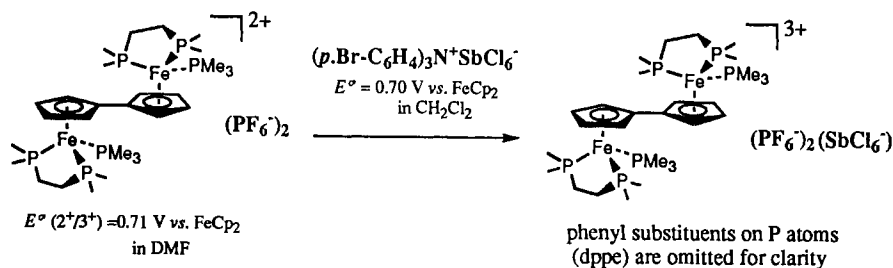
MAGIC BLUE

Table 10. Formal potentials (V, relative to Fc) of triarylamminium cations $[\text{N}(\text{aryl})_3]^+$ ^a.

Cation	E° (V)	Cation	E° (V)
$\text{C}_6\text{H}_4\text{OMe-4}$	0.16	$\text{C}_6\text{H}_4\text{NO}_2\text{-4}$	1.20
$\text{C}_6\text{H}_4\text{Me-4}$	0.40	$\text{C}_6\text{H}_4\text{Br}_2\text{-2,4}$	1.14
$\text{C}_6\text{H}_4(\text{COMe})\text{-4}$	0.90	$\text{C}_6\text{H}_4\text{Br}_3\text{-2,4,6}$	1.36
$\text{C}_6\text{H}_4\text{Br-4}$	0.70	C_6Cl_5	1.72 ^b
$\text{C}_6\text{H}_4\text{CN-4}$	1.08		

^a Standard redox potentials from Ref. [258] unless otherwise stated.

^b From Ref. [21].



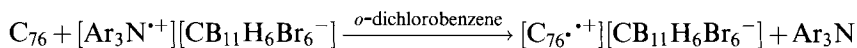
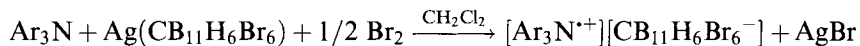
Scheme 23.

of iodine or SbCl_5 [258–260]. In addition, the most used one $[\text{N}(\text{C}_6\text{H}_4\text{Br}-4)_3]$, $[\text{SbCl}_6]$, named Magic Blue because of its intense royal blue color, is commercially available ($E^\circ = 0.70 \text{ V}$ relative to FeCp_2 in MeCN).

The most frequent counter-anions are BF_4^- (for the modest oxidants of this series), PF_6^- (almost no side reactions), SbCl_6^- (may give side nucleophilic reactions with the strongest oxidants of this series) and, for the strongest oxidants of this series, SbF_6^- . The BF_4^- salts are the most fragile of the group and should be used as freshly prepared. CH_2Cl_2 is a good solvent for their use (the SbCl_6 salts are only sparingly soluble) and MeOH must be avoided with, for instance, Magic Blue, because of *para*-methoxylation.

An example of the use of Magic Blue for the oxidation of a binuclear 36-electron complex to the 35-electron complex as shown in Scheme 23 (this complex is a delocalized mixed-valence compound on the Mössbauer time scale) [261].

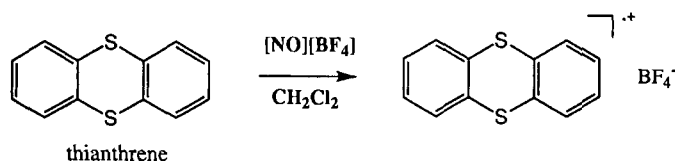
Since the oxidized species is sensitive to nucleophiles, even weakly nucleophilic counter-anions of strong oxidant can react with very sensitive species. This problem has been addressed for instance in the case of the oxidation of the fullerene C_{76} ($E^\circ = 0.81 \text{ V}$ relative to FeCp_2 for $\text{C}_{76}/\text{C}_{76}^+$) which is easier to oxidize than C_{60} ($E^\circ = 1.26 \text{ V}$ relative to FeCp_2 for $\text{C}_{60}/\text{C}_{60}^+$) and C_{70} ($E^\circ = 1.20 \text{ V}$ relative to FeCp_2 for $\text{C}_{70}/\text{C}_{70}^+$). The salt $[\text{Ar}_3\text{N}^+][\text{CB}_{11}\text{H}_6\text{Br}_6^-]$ (with $\text{Ar} = 2,4$ -dibromophenyl; $E^\circ = 1.16 \text{ V}$ relative to FeCp_2), a green solid, has been successfully used to synthesize the stable salt of the radical cation of C_{76} because the counter-anion was carefully designed as one of the weakest nucleophilic anions known [262]:



The strongest oxidants such as $[\text{N}(\text{C}_6\text{H}_4\text{Br}_{3-2,4,6})_3]^{++}$ ($E^\circ = 1.36 \text{ V}$ relative to FeCp_2 in MeCN) and $[\text{N}(\text{C}_6\text{Cl}_5)_3]^{++}$ ($E^\circ = 1.84 \text{ V}$ relative to FeCp_2 in MeCN [21]) can be generated using the appropriate amine and oxidant without the need to isolate them. These series of salts have been extensively used in organic chemistry and reviewed, and their use in transition-metal chemistry is spreading [21].

4.4.14 Thianthrene Radical Cation

Thianthrene can be oxidized by SbCl_5 or $[\text{NO}][\text{BF}_4]$ in CH_2Cl_2 to give the red-brown salts $[\text{thianthrene}][\text{SbCl}_6]$ and $[\text{thianthrene}][\text{BF}_4]$ (purple in solution) which are stable in dry air but react with water. They are also stable for two weeks in MeCN in the absence of excess $[\text{NO}]\text{X}$ salt [263, 264]. The E° value of 0.86 V relative to FeCp_2 in MeCN [265] makes them attractive relatively strong oxidants which have been little used.



$E^\circ = 0.86 \text{ V}$ vs. FeCp_2 in MeCN

4.4.15 Carbocations: Trityl, $[\text{C}(\text{aryl})_3]^+$, Salts and Salts of other Carbocations

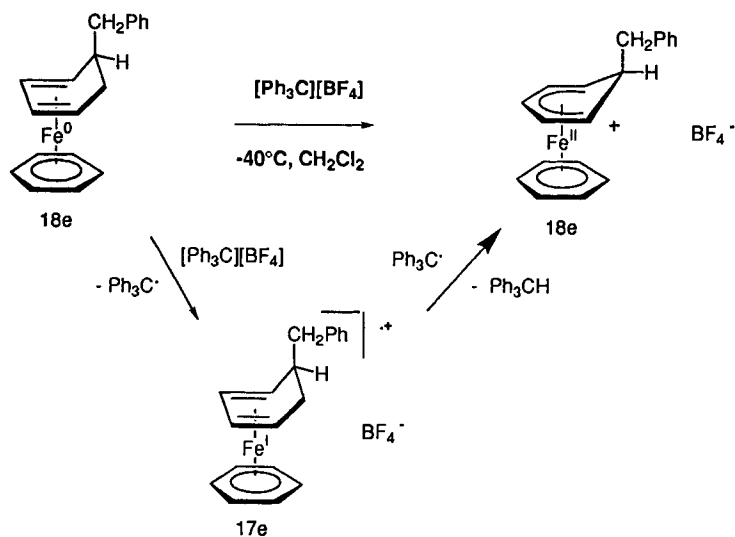
These carbocations can undergo three reactions: (i) single-electron oxidation, (ii) hydride abstraction and (iii) electrophilic addition. Thus, these compounds behave as mild single-electron oxidants towards reductants which do not react by other pathways. Actually, what is most interesting in these carbocations is the competition between electron-transfer and the other reactions. For instance, a hydride transfer can occur either directly or via the electron-transfer pathway using a trityl salt. From a synthetic standpoint, a hydride transfer which cannot be achieved directly for steric reasons may be attempted by means of the electron-transfer pathway.

The triphenylcarbenium ion (trityl cation) Ph_3C^+ ($E^\circ = -0.11 \text{ V}$ relative to FeCp_2 in MeCN [266]) is commercially available as the yellow-orange BF_4^- , PF_6^- , AsF_6^- , SbCl_6^- and CF_3SO_3^- salts which are also easily synthesized, as other substituted trityl salts, for instance from Ph_3COH (or Ar_3COH) and the acid in acetic or propionic anhydride [267]. They are moisture sensitive in the solid state and sometimes light sensitive, and can be purified by recrystallization from MeCN at low temperature or from CH_2Cl_2 -hexane or MeCN-ether mixtures. They can be used in CH_2Cl_2 , MeCN and liquid SO_2 (they are insoluble in alkane and arene solvents and slowly react with ether [267]). An excellent alternative to the Ph_3C^+ salts (and weaker oxidant) is $[\text{Ph}_2\text{C}(\text{C}_6\text{H}_4\text{OMe-4})][\text{BF}_4]$ ($E^\circ = -0.32 \text{ V}$ relative to FeCp_2 in MeCN) which is much more stable even in the presence of moist air, can be weighed and handled in air, and decompose in aqueous acetonitrile 100 times more slowly than $[\text{Ph}_3\text{C}][\text{BF}_4]$ [268].

In addition to its classic use as hydride abstractor in organic [267] and organometallic chemistry [21], $[\text{Ph}_3\text{C}][\text{BF}_4]$ has also been used as a single-electron oxidant [269] in a number of organometallic examples despite the side reactions. Indeed, the redox reaction of Ph_3C^+ salts produces the $\text{Ph}_3\text{C}^\cdot$ radical which dimerizes, but also

can couple to organometallic substrates or products or abstract a H atom from some solvents and substrates. The electron-transfer properties of Ph_3C^+ could be used in a strategy to remove a hydride for a synthetic purpose as follows. The trityl salt $[\text{Ph}_3\text{C}][\text{BF}_4]$ abstracts a hydride from the cyclohexadiene complex $[\text{Fe}(\eta^4\text{-C}_6\text{H}_8)(\text{CO})_3]$, giving the cyclohexadienyl complex $[\text{Fe}(\eta^5\text{-C}_6\text{H}_7)(\text{CO})_3][\text{BF}_4]$, which opens the route to the syntheses of *exo*-functional cyclohexadiene complexes by reaction with zinc or cadmium reagents. $[\text{Ph}_3\text{C}][\text{BF}_4]$ does not react with these functional complexes for steric reasons, however, so that reiteration of this process leading to heterobifunctional complexes is not possible [270]. With the more electron-rich isolobal analog $[\text{Fe}(\eta^5\text{-C}_6\text{H}_7)(\eta^6\text{-C}_6\text{H}_6)][\text{PF}_6]$, directly accessible by reaction of NaBH_4 with $[\text{Fe}(\eta^6\text{-C}_6\text{H}_6)_2][\text{PF}_6]_2$, reaction of a variety of carbanionic nucleophile RM as sodium or potassium reagents cleanly gives $[\text{Fe}(\eta^4\text{-exo-RC}_6\text{H}_7)(\eta^6\text{-C}_6\text{H}_6)]$. Reactions of these electron-rich organometallic compounds with $[\text{Ph}_3\text{C}][\text{BF}_4]$ at -40°C proceeds according to an exergonic electron transfer followed by an H-atom transfer between the two radicals $[\text{Fe}(\eta^4\text{-exo-RC}_6\text{H}_7)(\eta^6\text{-C}_6\text{H}_6)]^{\cdot+}$ and $\text{Ph}_3\text{C}^{\cdot}$. Although the direct hydride transfer was not possible for steric reasons, an overall hydride transfer of the *endo* hydride was achieved in this two-step way producing the functional complex $[\text{Fe}(\eta^5\text{-exo-RC}_6\text{H}_6)(\eta^6\text{-C}_6\text{H}_6)]$. Further reactions with functional carbanions produced *cis*-heterobifunctional complexes $[\text{Fe}(\eta^4\text{-exo, exo-RR}'\text{C}_6\text{H}_6)(\eta^6\text{-C}_6\text{H}_6)]$ which could be decomposed using the oxidant FeCl_3 (stronger than $[\text{Ph}_3\text{C}][\text{BF}_4]$) to the free *cis*-heterobifunctional cyclohexadienes (Scheme 24).

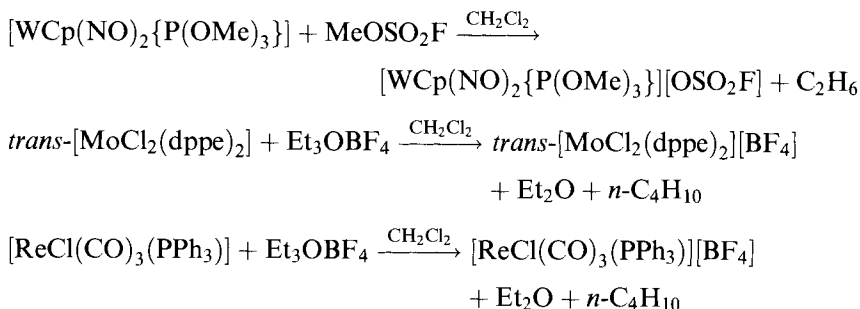
Other noteworthy examples of hydride transfer reactions of $[\text{Ph}_3\text{C}][\text{BF}_4]$ proceeding by an electron-transfer path in organo-transition metal chemistry are the formation of $[\text{WCp}_2(\text{H})(\eta^2\text{-C}_2\text{H}_4)]$ from $[\text{WCp}_2\text{Me}_2]$ [271] and of $[\text{ReCp}(\text{PPh}_3)\text{-}$



Scheme 24.

(NO)(=CHCH₂R)(PPh₃)(NO)] from [ReCp(PPh₃)(NO)(CH₂CH₂R)(PPh₃)(NO)] [272]. The early examples of the use of triphenylcarbonium salts in organometallic chemistry have been reviewed [273].

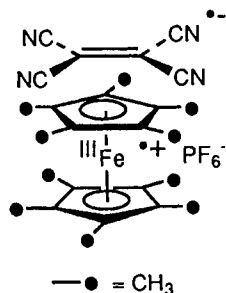
Other commercially available salts of carbocations such as MeOSO₂F [274] and Et₃OBf₄ [275, 276] have been used in one-electron oxidation reactions:



The tropylium cation, C₇H₇⁺, is a very mild oxidant ($E^\circ = -0.65$ V relative to FeCp₂ in MeCN [266]) as well as a mild hydride abstractor and a mild electrophile. The colorless BF₄ and PF₆ salts are commercially available and readily prepared, stable in air, non hygroscopic, soluble in Me₂CO, MeCN and liquid SO₂ and insoluble in CH₂Cl₂. There are several known examples of the use of these salts in CH₂Cl₂ or THF (suspension) for the one-electron oxidation of electron-rich (especially anionic) organometallic compounds, sometimes with coordination of the cycloheptatriene ligand.

4.4.16 TCNE, TCNQ, and other Cyanocarbons

TCNE ($E^\circ = -0.27$ and -1.27 V relative to FeCp₂ in MeCN) and TCNQ ($E^\circ = -0.30$ V and -0.88 V relative to FeCp₂ in MeCN) are commercially available mild one-electron acceptors which have attracted, as such, a considerable interest for the construction of low-dimensional organic and organometallic charge-transfer solids with magnetic [277] and conducting properties [278]. For instance, the salt

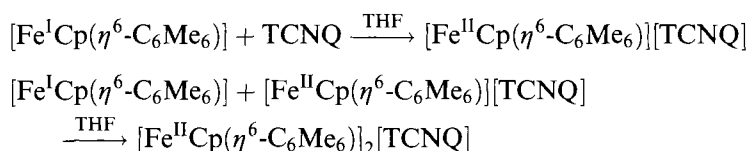


molecular ferromagnet

[TTF][TCNQ] was the first organic conductor [279] and the salt $[\text{FeCp}^*_2][\text{TCNE}]$ was one of the very first molecular ferromagnets [277, 280].

Thus, the interest of TCNE and TCNQ is more concentrated on their use as precursors of such materials than on their use as redox tools to obtain oxidized transition-metal compounds. Nevertheless, both aspects are somewhat connected, and transition-metal derivatives of TCNE and TCNQ have also been reviewed [281]. The most interesting aspect probably is the ability of TCNE to both oxidize and bind metal centers, but an important related problem is that TCNE is toxic.

TCNQ is reduced to the monoanion or dianion by the electron-reservoir complex $[\text{Fe}^{\text{I}}\text{Cp}(\eta^6\text{-C}_6\text{Me}_6)]$ depending on the stoichiometry and the respective redox potentials can let predict the same results with TCNE.



Another noteworthy example is the oxidation of the clusters $[\text{Co}_3(\text{CO})_9\text{E}]$ ($\text{E} = \text{S}$ or PPh) by TCNQ to the salts $[\text{Co}_3(\text{CO})_9\text{E}][\text{TCNQ}]$ in various solvents [282]. Other cyanocarbons behave as single-electron oxidants: *n*-hexacyanobutadiene, *n*- $\text{C}_4(\text{CN})_6$, the radical anion tris(dicyanomethylene) cyclopropane, $[\text{C}_6(\text{CN})_6]^{\cdot-}$ (better formulated as $[\text{C}_3\{\text{C}(\text{CN})_2\}_3]^{\cdot-}$) [283].

4.4.17 Miscellaneous Organic Oxidants

Commercially available 1,2 and 1,4 quinones are easily handled. The formal potential of the 1,4-benzoquinone/hydroquinone couple at pH 0 is ca 0.30 V relative to FeCp_2 . A variety of ferrocene derivatives including 1,1'-diacetylferrocene have been oxidized by 1,4-benzoquinone in the presence of HBF_4 , and the ferrocenium salts have been prepared using this reaction [284].

Diphenyliodonium salts $[\text{IPh}_2]\text{X}$ ($E^\circ = -0.9$ V relative to FeCp_2 [285]) are commercially available ($\text{X} = \text{Cl}, \text{Br}, \text{I}$) and the BF_4 , PF_6 , AsF_6 and SbF_6 can be made [286]. As aryldiazonium salts, they decompose, after electron transfer, to the phenyl radical which dimerizes to biphenyl and abstracts a H atom from the solvent.

Iodosobenzene PhIO is a yellow amorphous powder which explodes above 200 °C, and has been used to oxidize $[\text{FeCp}(\text{dppe})(\text{C}=\text{CHMe})]^+$ to $[\{\text{FeCp}(\text{dppe})\}_2-\{\mu_2\text{-C}=\text{C}(\text{Me})\text{C}(\text{Me})=\text{C}\}]^{2+}$ [287].

4-pyridinecarboxaldehyde, $\text{NC}_5\text{H}_4\text{CHO}$ -4, is a very weak oxidant ($E^\circ = \text{ca } -1.0$ V relative to FeCp_2 [288]) which is a commercially available liquid. It must be distilled before use and stored under inert atmosphere at -10°C . It may be useful to oxidize electron-rich organometallic complexes such as $[\text{Cr}(\eta^6\text{-arene})_2]$ which are good monoelectronic reductants, for instance for the purpose of ESR studies [289].

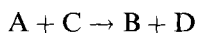
4.5 Electron-transfer-chain (ETC) Catalysis

4.5.1 Historical Background, Main Types of Reaction, and Principle

Electron-transfer-chain catalysis is the catalysis of reactions by electrons or electron holes. Most organic and transition-metal reactions catalyzed in this way do not involve an overall redox change. The ETC catalyzed reactions belong to the general group of chain reactions [181, 182] which started in the 1920s with the chain reaction between H_2 and Cl_2 initiated by sodium in the gas phase [183]. This latter reaction, as many others discovered since, is of the type of atom-transfer-chain (ATC) catalysis, which can be considered as the inner-sphere version of ETC catalysis [184]. In transition-metal chemistry, the first ETC- and ATC-catalyzed reactions were disclosed by Taube in 1952 who reported chlorine exchange in $[\text{AuCl}_4]^-$ initiated by the reductant $[\text{Fe}^{\text{II}}(\text{CN})_6]^{4-}$ [290]. Electrochemistry plays an important role in this field because electrodes are obvious sources of electrons and electron holes (although not the most practical ones for synthetic purpose). It is essential for the kinetic and thermodynamic investigations of the ETC systems, and this technique serves as an analytical tool for understanding the mechanism, thus improve the processes. This analytical approach of ETC mechanisms in molecular chemistry was first carried out by Feldberg who established the theoretical basis for the so called 'ECE' mechanism [291]. Once these features are determined, the ETC reactions are best carried out using redox reagents and especially electron-reservoir complexes as catalysts (initiators) given their very negative- and very positive redox potentials. ETC catalysis has spread over inorganic [292], organic [293] and organometallic chemistry [290, 294], although each sub-community seems to have developed very independently [292–294]. The first ETC catalyzed organic reactions were found by Russell [295], Kornblum [296] and Bunnett [297], and include the popular ETC catalyzed nucleophilic substitution in aromatic derivatives ($\text{S}_{\text{NAr}}1$) rationalized from an electrochemical standpoint by Savéant [298, 299]. The first ETC catalyzed reactions in organometallic chemistry are Feldberg's careful studies of the ligand exchange in the 15-electron species $[\text{Cr}^{\text{III}}(\text{CN})_6]^{3-}$ reported in 1972 [291] and Rieke's studies of the anodically catalyzed *trans* to *cis* isomerization of bis-carbene Mo^0 and W^0 complexes reported in 1976. Rieke's studies were also thorough kinetic and thermodynamic analyzes and involved electrochemistry as well as preparative aspects [300, 301]. In the early 80's, there was an explosion of the field [294]. For instance, the group of Bruce reported an impressive number of ligand-exchange reactions of carbonyls in clusters [302] and Kochi published several in-depth studies and thoroughly analyzed cases of ligand substitution in mono- and polynuclear organometallic complexes [303]. Not only ligand substitution and isomerization of inorganic–organometallic compounds can be catalyzed by ETC chain but also migratory insertion (for instance migratory insertion of CO into a Fe–C bond in $[\text{FeCp}(\text{CO})\text{L}(\text{Me})]$, $\text{L} = \text{CO}$ [304] or PPh_3 [305]) and extrusion (for instance extrusion of CO from a Mn–formyl bond in $[\text{Re}_2(\text{CO})_9(\text{CHO})]^-$) [306].

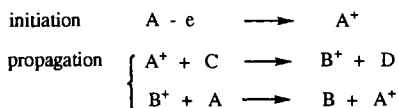
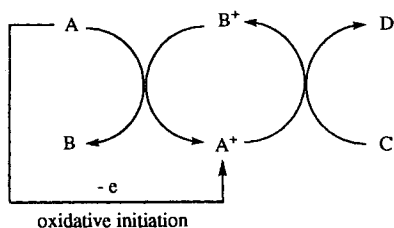
The principle of ETC catalysis consists in carrying out the reaction at a kinetically labile redox state of the reactant when the ground state is not enough reactive.

This can be achieved by addition or removal of one electron. However, this type of procedure can also be stoichiometric. Then, a stoichiometric amount of oxidant or reductant is required to bring the substrate into the reactive state. For instance, the oxidative decomplexation of organometallic compound for the purpose of organic synthesis often falls into this category. The reaction only becomes catalytic in redox reagent if the product reacts with the substrate in a redox (cross electron transfer) reaction, thus entering a chain process. For instance, in a ligand substitution reaction (the most frequent ETC catalyzed reaction), a complex A reacts with a ligand C to give the new complex B and the ligand D according to a chain process, the overall course of which is represented by:

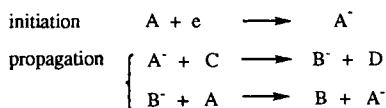
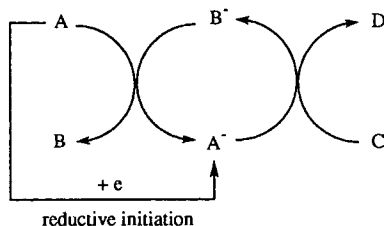


There are two ways to try to catalyze the reaction: oxidation or reduction. Most of the time, only one way is efficient catalytically for kinetic reasons. The propagation cycle contains two reactions: the cross redox (cross electron-transfer) reaction and the non-redox ('chemical') reaction. Since the non-redox reaction proceeds in the most reactive state of the substrate, it is usually difficult to obtain information on such species and the ergonicity of this step is thus usually obscure. On the other hand, it is very easy to obtain information on the redox step. One may just have a look at the relative standard redox potentials of the substrate and product, or even only to watch these two compounds and consider if the entering ligand is more or less electron-releasing than the leaving ligand for the metallic redox center. Since only one ligand is usually exchanged, the molecular orbital diagram is approximately the same for both complexes except that the set of orbitals of the more electron-rich compound is at a slightly higher energy level than the same set of orbitals of the other, less electron-rich complex. It is thus easy to forecast the ergonicity (exergonic or endergonic) of the cross redox step as a function of the fact that oxidation or reduction is used as indicated on Scheme 25:

B LESS ELECTRON-RICH THAN A
($E^\circ_{B/B^+} > E^\circ_{A/A^+}$)



B MORE ELECTRON-RICH THAN A
($E^\circ_{B/B^-} < E^\circ_{A/A^-}$)



Scheme 25.

The scheme shows that only one way provides an exergonic redox step: if the entering ligand is more electron-rich than the leaving ligand, reduction provides an exergonic redox step whereas oxidation provides an endergonic redox step. On the other hand, if the entering ligand is less electron-releasing than the leaving ligand, it is the opposite which is true. According to Marcus theory, an exergonic electron transfer is fast and an endergonic electron transfer is slow³. The radical intermediates are the subject of side reactions which favorably compete with an endergonic redox reaction. Thus, the redox propagation step should be exergonic in order to proceed, i.e. the wrong type of initiation should be most of the time avoided. All the very efficient (high coulombic efficiency), ETC catalyzed reactions proceed according to an exergonic redox propagation step. There are exceptions, however, because a slightly endergonic reaction can still be driven by an extremely fast follow-up 'chemical' propagation step. Usually, the redox initiator must be chosen in order to involve an exergonic redox step, and its strength should be such that the initiation step between the redox reagent and the substrate complex be exergonic, isoergonic or not more than very slightly endergonic (but this latter solution requires that the follow-up propagation reaction be fast).

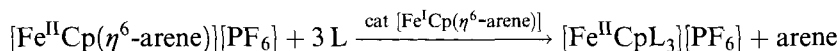
The redox initiators are easily chosen in the collection of oxidants and reductants described in the previous sections. In organic chemistry, very strong oxidants or reductants are required, because it is usually difficult to oxidize or reduce organic compounds, i.e. the organic compounds are oxidized or reduced at extreme potentials. Thus the triarylaminium salts on the oxidation side [258, 259] and the alkali metals (usually Na) on the reduction side are currently used. For instance, the nucleophilic aromatic substitution of halides by other nucleophiles is catalyzed by Na in NH₃ [297]. On the other hand, the redox potentials of inorganic and organometallic compounds are easily accessible, so that most oxidative initiations can be carried out using ferrocenium salts [Fe^{III}Cp₂][X], X = BF₄ or PF₆, on the oxidation side and the electron-reservoir complex [Fe^ICp(η^6 -C₆Me₆)] on the reduction side. Not only these initiators cover most of the redox scale, but substrates with oxidation potential more positive than that of ferrocenium salts or reduction potentials more negative than that of [Fe^ICp(η^6 -C₆Me₆)] can also react when their redox reaction is followed by a fast 'chemical' reaction, which is often the case.

4.5.2 The Electron-reservoir Complexes [Fe^ICp(η^6 -arene)] as ETC Catalysts

Substitution of the arene ligand by three two-electron donors in the complexes [Fe^{II}Cp(η^6 -arene)][PF₆]

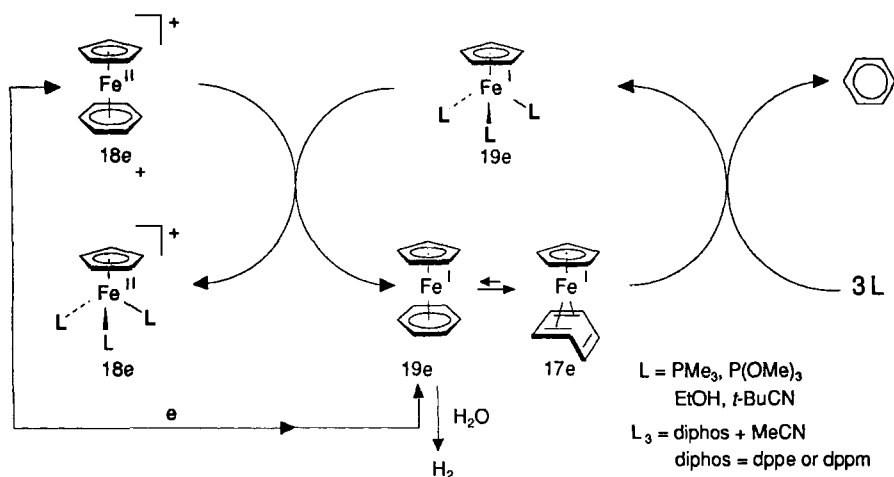
This type of reaction was first reported to be induced cathodically, the coulombic efficiency being variable as a function of the coordinating solvent or ligand [307, 308]. In all the cases, these ligands bind the metal via an heteroatom (O, N) which is not the subject of back-bonding. Thus, the overall electron-releasing character of three such ligand is larger than that of the arene ligand which receives back-bonding from the transition metal. Consequently, reduction is the appropriate mode of initiation in order to provide an exergonic redox reaction. J. Ruiz used the 19-electron complex [Fe^ICp(η^6 -arene)] as an initiator for the ETC catalyzed ligand substitution

reaction of the arene ligand with various phosphanes and diphosphanes in the isostructural complex $[\text{Fe}^{\text{II}}\text{Cp}(\eta^6\text{-arene})][\text{PF}_6]$, and the reaction is over in a few second at ambient temperature in THF (suspension) or MeCN (solution). Acetonitrile is also one of the three entering ligands L when the large PPh_3 , dppe or dppm is used, because only two coordination sites can be filled with such large ligands [180, 310]. In this case, the initiator and reduced form of the substrate have an identical structure, and this is a unique example of such a situation. The arene could be any of the methylated benzene derivatives $\text{C}_6\text{H}_6\text{Me}_{6-n}$ ($n = 0-6$) and the P donor could be PMe_3 , P(OMe)_3 , dpmm or dppe. With P(OPh)_3 , the donicity of this ligand is not good enough to provide an exergonic electron-transfer step. This catalysis is remarkably efficient since an amount of 1 % of Fe^{I} catalyst is sufficient to carry out the reaction quantitatively. The reaction of P donors with these 19-electron complexes was shown to be associative [180]. Indeed, these 19-electron Fe^{I} complexes are either in rapid equilibrium with the 17-electron form in which one double bond of the arene ligand is decoordinated or this 17-electron $[\text{Fe}^{\text{I}}\text{Cp}(\eta^4\text{-arene})]$ form simply is a mesomer of the 19-electron one (equation and Scheme 26) [146].



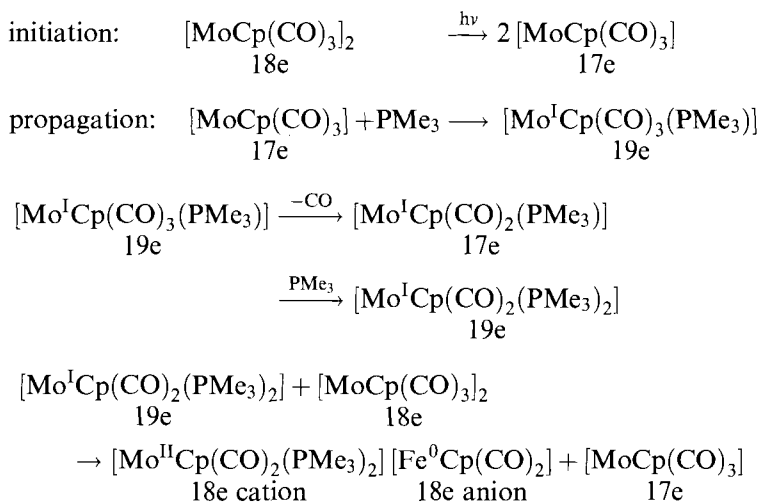
Disproportionation of bimetallic fulvalene carbonyl complexes to bimetallic zwitterions

A rare redox reaction carried out by ETC catalysis is the disproportionation of bimetallic metal carbonyl complexes such as $[\text{MoCp}(\text{CO})_3]_2$ containing a metal-metal bond, in the presence of a two-electron donor such as PMe_3 . In this typical example, the reaction leads to the ion pair $[\text{Mo}^{\text{II}}\text{Cp}(\text{CO})_2(\text{PMe}_3)_2][\text{Mo}^0\text{Cp}(\text{CO})_2]$. The photolysis of the dimer gives the 17-electron iron radical $[\text{Mo}^{\text{I}}\text{Cp}(\text{CO})_3]$ re-



Scheme 26.

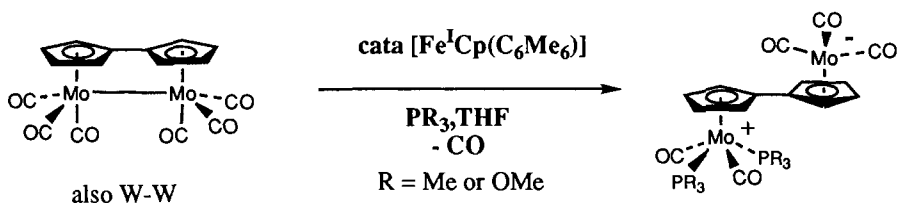
sulting from the cleavage of the Mo–Mo bond. In the presence of PMe_3 , rapid uptake of this ligand by the 17-electron iron radical leads to the 19-electron radical $[\text{Mo}^{\text{I}}\text{Cp}(\text{CO})_2(\text{PMe}_3)]$. These 17- and 19-electron radicals are in fast equilibrium resulting from ligand exchange until a side follow-up reaction shift the overall equilibrium. At the level of the 19-electron radical $[\text{Mo}^{\text{I}}\text{Cp}(\text{CO})_2(\text{PMe}_3)_2]$, reduction of the dimer by this electron-rich species is exergonic, thus fast, which generates the reaction product and the 17-electron radical $[\text{Mo}^{\text{I}}\text{Cp}(\text{CO})_3]$, and a new propagation cycle can start [311, 312]:



Analogous chain reactions proceed with the other dimers $[\text{Mn}(\text{CO})_5]_2$ and $[\text{FeCp}(\text{CO})_2]_2$ [311, 312].

When the dimers are held together by a fulvalene bridging ligand instead of two Cp ligands, the cationic and anionic parts of the product are not separated from each other, i.e. a zwitterion forms. The MoMo and WW fulvalene hexacarbonyl dimers are reduced at -1.22 V and -1.34 V relative to FeCp_2 in THF respectively [313], and these potentials are less negative than the oxidation potentials of the 19-electron complexes $[\text{Fe}^{\text{I}}\text{Cp}(\eta^6\text{-arene})]$. Thus the complexes $[\text{Fe}^{\text{I}}\text{Cp}(\eta^6\text{-C}_6\text{R}_6)]$, $\text{R} = \text{H}$ or Me are both efficient catalysts (0.1–0.2 equiv.) for the ETC disproportionation of the MoMo and WW fulvalene hexacarbonyl complexes in the presence of PR_3 ($\text{R} = \text{Me}$ or OMe) to the corresponding zwitterions $[\mu_2, \eta^{10}\text{-fulvalene}]\text{-}\{[\text{M}(\text{CO})_2(\text{PR}_3)_2] [\text{M}(\text{CO})_3]\}$. These reactions were also carried out thermally in the absence of catalyst, which gave lower reaction yields and required heating for days instead of a few minutes at ambient temperature in the presence of the catalyst. The mechanism is similar to the chain mechanism above, and the electron transfer between the two metal centers is now intramolecular and extremely fast, being facilitated through the delocalized bridging fulvalene ligand (Scheme 27) [314].

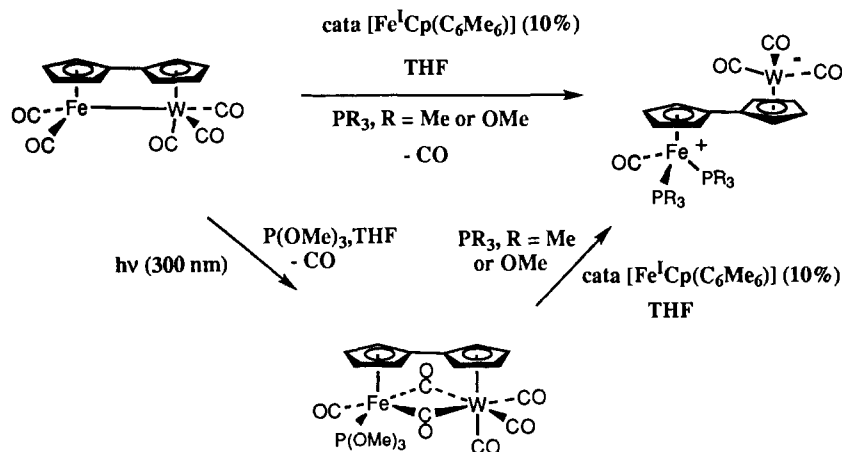
Similar reactions catalyzed by the 19-electron complexes $[\text{Fe}^{\text{I}}\text{Cp}(\eta^6\text{-C}_6\text{R}_6)]$ were carried out with heterobinuclear FeW, RuMo and RuW fulvalene pentacarbonyl complexes. Since the two metals are different, it was of interest to look at the re-



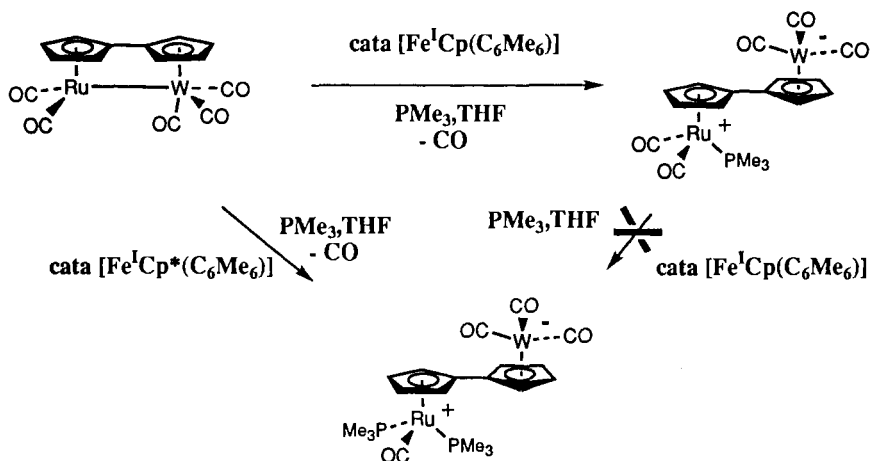
Scheme 27.

gioselectivity of the reaction. In the case of the FeW complex, the cathodic reduction of the Fe and W metal centers are separated, and the W center ($E_{\text{p1}} = -1.45$ V relative to FeCp_2) is more easily reduced than the Fe center ($E_{\text{p2}} = -2.0$ V relative to FeCp_2) [315, 316]. Both $[\text{Fe}^{\text{I}}\text{Cp}(\eta^6\text{-C}_6\text{H}_6)]$ and $[\text{Fe}^{\text{I}}\text{Cp}(\eta^6\text{-C}_6\text{Me}_6)]$ have oxidation potentials more negative than the first reduction wave, that of the W center, and indeed are good catalysts for the formation of the zwitterions in the presence of either PMe_3 or P(OMe)_3 . Since the reduction occurs first on the W center, cleavage of the metal-metal bond in the substrate which has accepted an electron leave an anionic W center and a neutral radical Fe center. The rapid ligand addition and substitution occurs on this latter center, finally leading to $[\mu_2, \eta^{10}\text{-fulvalene}]\{[\text{Fe}(\text{CO})(\text{PR}_3)_2][\text{W}(\text{CO})_3]\}$. Likewise, the tetracarbonyl mono-trimethylphosphite non-zwitterionic complex $[\mu_2, \eta^{10}\text{-fulvalene}][\mu_2\text{CO}]_2\{[\text{Fe}(\text{PR}_3)_2][\text{W}(\text{CO})_2]\}$ resulting from photolysis of the substrate in the presence of P(OMe)_3 leads to the same zwitterions upon ETC reactions catalyzed by $[\text{Fe}^{\text{I}}\text{Cp}(\eta^6\text{-C}_6\text{Me}_6)]$ as those yielded from the pentacarbonyl complex. This means that substitution of P(OMe)_3 is preferred to that of CO in this complex (Scheme 28) [317].

The RuMo and RuW complexes are reduced in a two-electron waves without differentiation of the two metals. This make the result of the regioselectivity of the



Scheme 28.

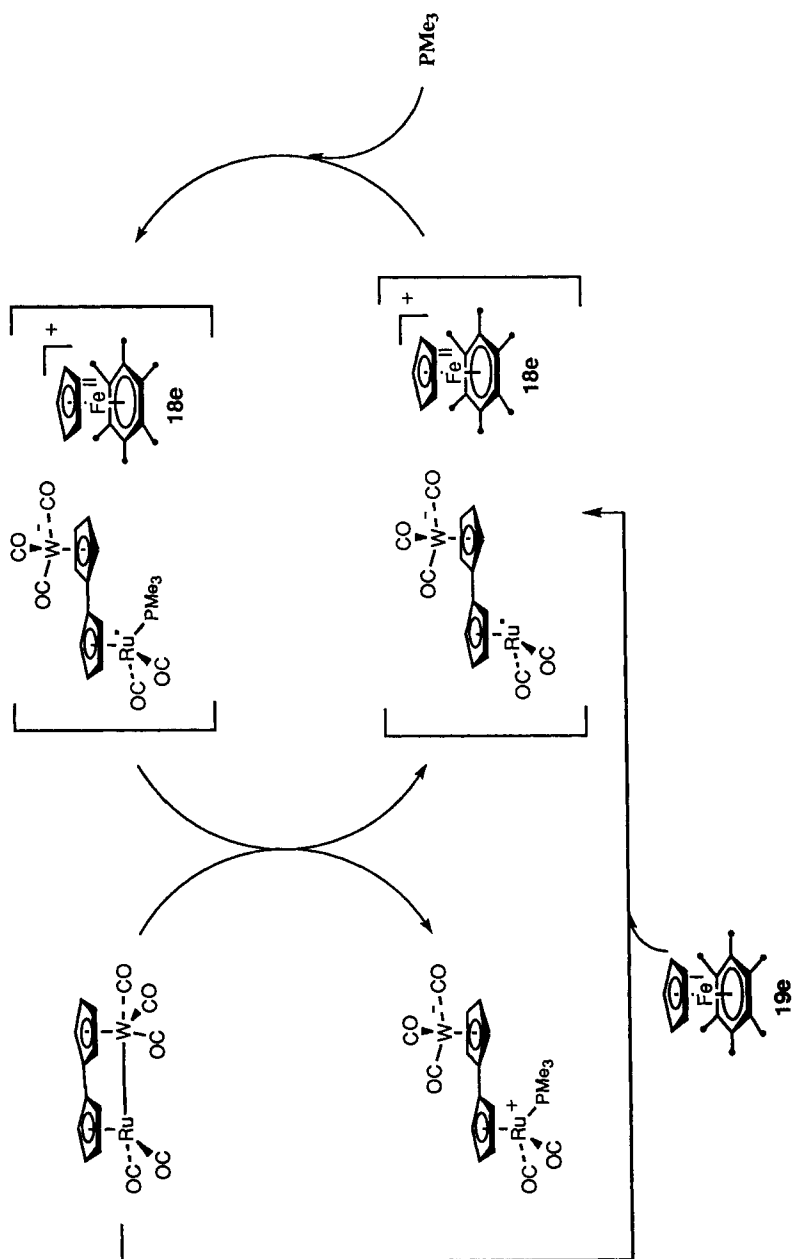


Scheme 29.

ETC catalyzed reaction of more interest. It is again the Ru center which undergoes the ligand substitution and become positive, which means that reduction again occurs first on Mo or W.

In the case of the RuW complex, the double ligand substitution occurs stepwise, indicating that the first ligand substitution is much easier than the second one. At this time, the driving force of the initiation redox reaction of the Fe^{I} complex is decisive concerning the number of COs which are substituted by PMe_3 . Thus, in THF, catalysis by $[\text{Fe}^{\text{I}}\text{Cp}(\eta^6\text{-C}_6\text{Me}_6)]$ of ligand substitution in $[\mu_2, \eta^{10}\text{-fulvalene}]\{\text{[Ru(CO)}_2\text{][W(CO)}_3]\}$ in the presence of PMe_3 leads to the monosubstituted zwitterion $[\mu_2, \eta^{10}\text{-fulvalene}]\{\text{[Ru}^{\text{II}}(\text{CO})_2(\text{PMe}_3)]\text{[W}^0(\text{CO})_3]\}$. On the other hand, the same reaction catalyzed by $[\text{Fe}^{\text{I}}(\eta^5\text{-C}_5\text{Me}_5)(\eta^6\text{-C}_6\text{Me}_6)]$ under the same conditions gives the disubstituted zwitterion $[\mu_2, \eta^{10}\text{-fulvalene}]\{\text{[Ru}^{\text{II}}(\text{CO})(\text{PMe}_3)_2]\text{[W}^0(\text{CO})_3]\}$. The 300 mV of additional driving force provided by the use of the Fe^{I} complex containing the permethylated Cp^* ligand appears to provoke the second ligand substitution. The monosubstituted complex cannot be reduced by $[\text{Fe}^{\text{I}}\text{Cp}(\eta^6\text{-C}_6\text{Me}_6)]$, but can be so by $[\text{Fe}^{\text{I}}(\eta^5\text{-C}_5\text{Me}_5)(\eta^6\text{-C}_6\text{Me}_6)]$ (Scheme 29).

The relative values of the oxidation potentials of the catalysts and of the reduction potentials of the starting and monosubstituted complexes are in accord with the observed selectivity. This also means that the second ligand substitution is slow compared to the cross redox reaction of the propagation step, and that the zwitterionic monosubstituted complex is thus an intermediate in the ETC catalyzed synthesis of the disubstituted zwitterion. The precipitation of the monosubstituted zwitterion also precludes the second substitution, since the latter occurs in MeCN even with $[\text{Fe}^{\text{I}}\text{Cp}(\eta^6\text{-C}_6\text{Me}_6)]$. Ion-pairing may play a substantial role in the balance between the various reaction pathways, and especially here in the competition between cross redox reaction, ligand substitution, side radical reactions and precipitation. In the present case, the counter-cation of the anionic species of the propagation cycle is the large 18-electron sandwich $[\text{Fe}^{\text{II}}\text{Cp}(\eta^6\text{-C}_6\text{Me}_6)]^+$ (Scheme 30).



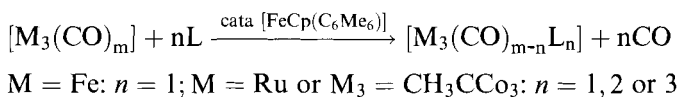
Scheme 30.

One of the conclusions of this study is that the first ligand substitution proceeds with a much higher coulombic efficiency than the second one, simply because of the increasing bulk at the metal center [317]. This trend was known from previous studies of carbonyl substitution by phosphanes in transition-metal carbonyl clusters catalyzed by benzophenone radical anion [318, 319]. In such a case, selective ETC catalysts may be designed as a function of the required exergonicity of the desired initiation step [317].

Substitution of carbonyls by phosphines in transition-metal clusters and ETC-catalyzed synthesis of dendrimers with cluster termini

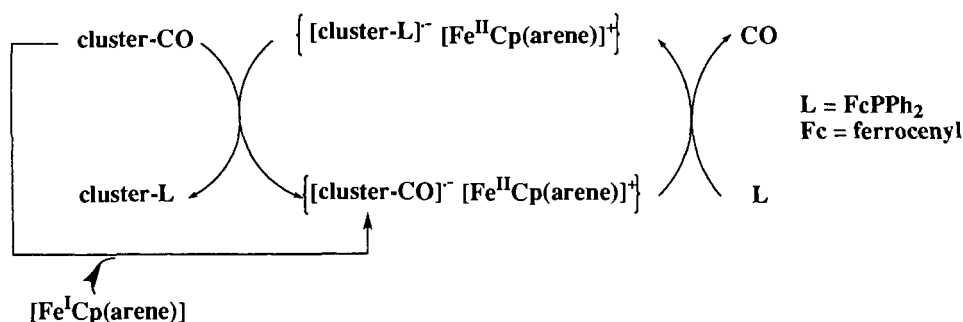
Many phosphane-substituted transition-metal clusters have been synthesized from late transition-metal carbonyl clusters and the appropriate phosphane using reductive ETC catalysis with reductive initiation [318–333]. Indeed such an initiation provides an exergonic cross electron-transfer propagation step. Most syntheses were carried out using a cathodic initiation or sodium benzophenone radical anion. The method was successful because it turned out that the first substitution of a carbonyl by a phosphane proceeds with high yield and coulombic efficiency in homoleptic metal carbonyl clusters and some others.

The family of 19-electron complexes $[\text{Fe}^{\text{I}}\text{Cp}(\eta^6\text{-arene})]$ has also been investigated as catalysts for the substitution of one, two and three carbonyls in metal-carbonyl clusters as shown below.

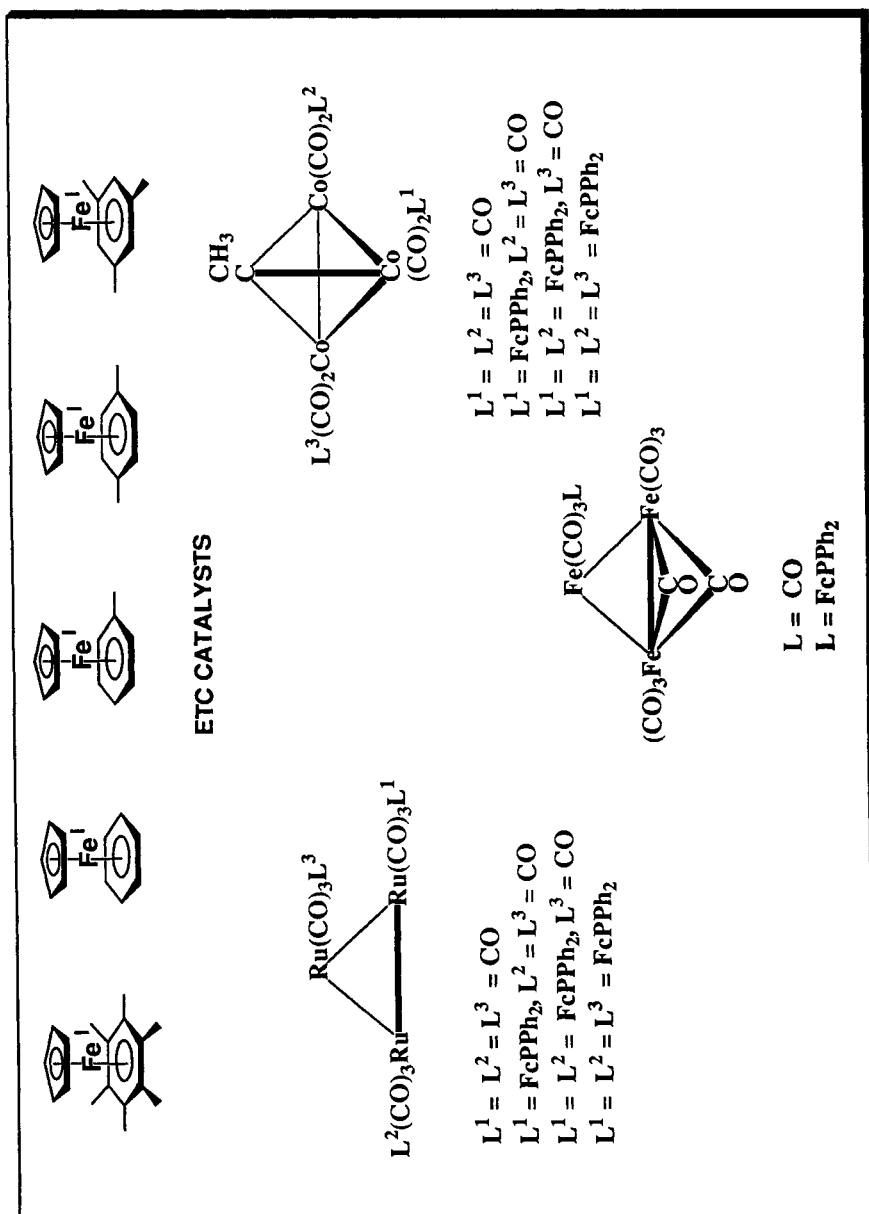


The standard mechanism is shown in Scheme 31 and the catalysts and products appear in Scheme 32.

The inconvenient of the sodium benzophenone catalyst is that it is not easy to determine the quantity of catalyst used since it is never isolated but simply generated from sodium and benzophenone in THF and the THF solution is used as it is. On the other hand, the quantities of Fe^{I} complexes are exactly known since they



Scheme 31.



Scheme 32.

can usually be weighted. In addition, they can be used in a variety of solvents and not only in THF. The goal was also partly synthetic and partly mechanistic, and the link between these two aspects is that mechanistic information leads to synthetic improvements. It was desirable to know if the Fe^{I} catalysts are as efficient as sodium benzophenone radical anion. First, the catalysis using $[\text{Fe}^{\text{I}}\text{Cp}(\eta^6\text{-C}_6\text{Me}_6)]$ was carried out. Then, the influence of the driving force of the initiator on the selectivity and efficiency of the catalytic process were also examined. Indeed, the change of driving force is easily reached with these 19-electron complexes by variation of the number of methyl groups on the ligands as we know from the preceding section. In particular, the progressive variation of the number of methyl group from 0 to 6 on the arene ligand is easily achieved. Each methyl group on the arene ligand makes the redox potential more negative by about 0.03 V to 0.04 V so that the standard redox potential of this series of initiators spreads from -1.75 V for $[\text{Fe}^{\text{I}}\text{Cp}(\eta^6\text{-C}_6\text{H}_6)]$ to -2.0 V relative to FeCp_2 for $[\text{Fe}^{\text{I}}\text{Cp}(\eta^6\text{-C}_6\text{Me}_6)]$ in THF. The results of the catalyzed ETC reactions are summarized below. Table 11 shows the data using only $[\text{Fe}^{\text{I}}\text{Cp}(\eta^6\text{-C}_6\text{Me}_6)]$, and the Table 12 compares the different $[\text{Fe}^{\text{I}}\text{Cp}(\eta^6\text{-arene})]$ catalysts.

The quantity of catalyst used was either 1 % or 10 %, and no reaction takes place under ambient condition in the absence of catalyst. When only one equiv. of phos-

Table 11. Amount (%) of substituted cluster in the mixture mono- + di- + trisubstituted products obtained using $[\text{Fe}^{\text{I}}\text{CpC}_6\text{Me}_6]$ as catalyst at 20°C (30 min) in THF on a one-millimolar scale (determined by ^1H NMR).

Starting cluster	Amount of L (no. of equiv.)	Amount of catalyst (%)	Number, <i>n</i> , of ligand(s) in the final product			Stability of products in solution
			<i>n</i> = 1	<i>n</i> = 2	<i>n</i> = 3	
$\text{Fe}_3(\text{CO})_{12}$ (Reaction at -40°C)	1	1	100	0	0	Mediocre
	1	10	100	0	0	Mediocre
	2	10	—	—	—	Decomposition
	2	10	—	—	—	Decomposition
$\text{Ru}_3(\text{CO})_{12}$	1	1	100	0	0	Stable
	1	10	80	20	—	Stable
	2	10	—	90	10	Stable
	3	1	10	60	30	Stable
	3	10	—	20	80	Stable
$\text{Ru}_3(\text{CO})_{10}\text{L}_2$	1	10	—	—	100	
$(\mu\text{-CCH}_3)\text{Co}_3(\text{CO})_9$	1	1	100	—	—	
	1	10	85	15	—	Stable
	2	10	15	80	trace	Mediocre
	3	1	70	25	0	Mediocre
	3	10	15	30	55	Mediocre

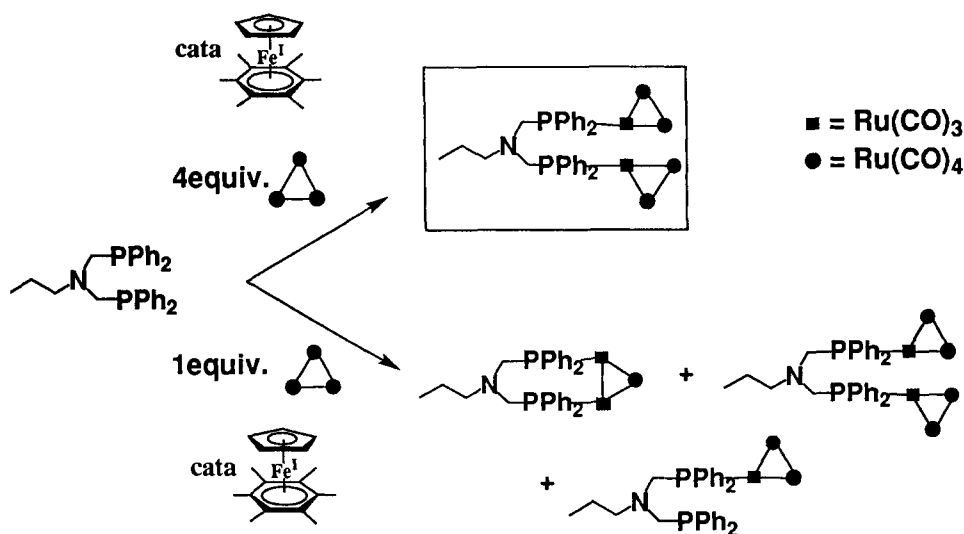
Table 12. Amount (%) of mono-, di- and trisubstituted ruthenium carbonyl clusters obtained by reaction of $[\text{Ru}_3(\text{CO})_{12}]$ with 3 equiv. FDPP and use of 10 % iron(I) electrocatalyst. The standard redox potentials of $[\text{Fe}^{\text{I}}\text{Cp}(\text{C}_6\text{H}_{6-n}\text{Me}_n)]$ in THF + $n\text{-Bu}_4\text{NPF}_6$, 0.1 M, are $E^{\circ'} = -(1.745 + 0.032n)$ V relative to $[\text{FeCp}_2]$ [84].

	Monosubstitution	Disubstituted	Trisubstituted
$[\text{FeCp}(\text{C}_6\text{Me}_6)]$	0	0	100
$[\text{FeCp}(\text{C}_6\text{H}_6)]$	10	70	20
$[\text{FeCp}(\text{toluene})]$	5	65	30
$[\text{FeCp}(p\text{-xylene})]$	0	60	40
$[\text{FeCp}(\text{mesitylene})]$	0	55	45

phine per cluster is used, the syntheses of monosubstituted clusters proceeds in high yield even with only 1 % catalyst except for the Fe_3 cluster which is slightly unstable in solution and partly decomposed on a chromatographic column. With two and three equiv. phosphine, the Ru_3 and Co_3 clusters could be obtained, but the reaction with 10 % catalyst gives much better yields of the desired products. This shows that side reactions are more competitive as substitution increases as expected because the bulk slows down the ligand exchange propagation step. The influence of the driving force of the catalyst is evident from the second table. The first substitution proceeds quantitatively even with the catalyst of weakest driving force $[\text{Fe}^{\text{I}}\text{Cp}(\eta^6\text{-C}_6\text{H}_6)]$. As the number of substitutions increases, however, the influence of the driving force of the catalyst becomes more dramatic. The largest influence is obtained for the third substitution as evidenced by the data in the table. The yield of trisubstituted cluster regularly increases, when 10 % catalyst is used, from 20 % with $[\text{Fe}^{\text{I}}\text{Cp}(\eta^6\text{-C}_6\text{H}_6)]$ to 100 %, obtained only with $[\text{Fe}^{\text{I}}\text{Cp}(\eta^6\text{-C}_6\text{Me}_6)]$. The conclusions of such a study are multiple. It confirms the crucial influence of the driving force of the initiator on the yield and efficiency in ETC catalyzed reactions. It indicates that a maximum efficiency requires a high driving force in the initiation when slow propagation steps are involved, which is the case in multiple substitution. It also indicates that, if a given number of substitutions is desired, the use of a catalyst of intermediate driving force is optimal in order to avoid the formation of more substituted compounds. Thus chemoselectivity is improved in this way. Another difference with sodium benzophenone radical anion is that the counter cation of the anionic cluster intermediates in the propagation ETC cycle is not Na^+ , but the large cation $[\text{Fe}^{\text{II}}\text{Cp}(\eta^6\text{-arene})]^+$. This makes the anion less strongly bound to the cation in the large organometallic ion pair than in the tight ion pair containing the sodium cation. Finally, the 19-electron complexes $[\text{Fe}^{\text{I}}\text{Cp}(\eta^6\text{-arene})]$ and especially $[\text{Fe}^{\text{I}}\text{Cp}(\eta^6\text{-C}_6\text{Me}_6)]$ are excellent catalysts for ETC reactions, and the variation of driving force by variation of the number of methyl groups offers an additional flexibility as a function of the requirements [334]. For instance, this study was very useful to determine the optimal conditions for more delicate substrates as follows.

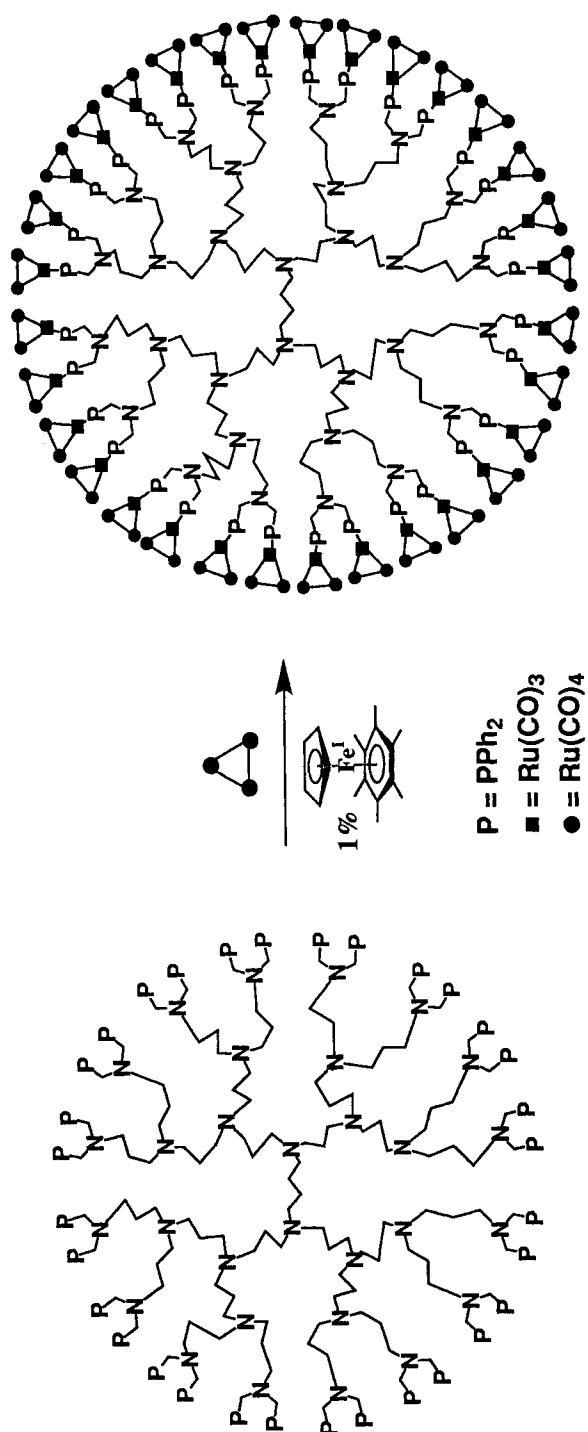
Introduction of the cluster fragment $\text{Ru}_3(\text{CO})_{11}$ at the termini of polyphosphine dendrimers

The clean introduction of clusters on to the termini of polyphosphine dendrimers is a real challenge because of the current interest of dendritic clusters in catalysis and the mixtures usually obtained in thermal reactions. The diphosphine $\text{CH}_3(\text{CH}_2)_2\text{N}(\text{CH}_2\text{PPh}_2)_2$ (abbreviated P-P below) was used as a simple, model ligand. The reaction between P-P and $[\text{Ru}_3(\text{CO})_{12}]$ [11] (molar ratio 1:1.05) in the presence of 0.1 equiv. $[\text{Fe}^1\text{Cp}(\eta^6\text{-C}_6\text{Me}_6)]$, in THF at 20°C led to the complete disappearance of $[\text{Ru}_3(\text{CO})_{12}]$ in a few minutes and the appearance of a mixture of chelate $[\text{P-P.Ru}_3(\text{CO})_{10}]$, monodentate $[\text{P-P.Ru}_3(\text{CO})_{11}]$ and bis-cluster $[\text{P-P}\cdot\{\text{Ru}_3(\text{CO})_{11}\}_2]$. This type of reaction was reported by Bruce with simple diphosphines [318, 319]. On the other hand, the reaction of P-P with $[\text{Ru}_3(\text{CO})_{12}]$ in excess (1:4) and only 0.01 equiv. $[\text{Fe}^1\text{Cp}(\eta^6\text{-C}_6\text{Me}_6)]$, in THF at 20°C led, in 20 min, to the formation of the air-stable, light-sensitive bis-cluster $[\text{P-P}\cdot\{\text{Ru}_3(\text{CO})_{11}\}_2]$ as the only reaction product (Scheme 33):

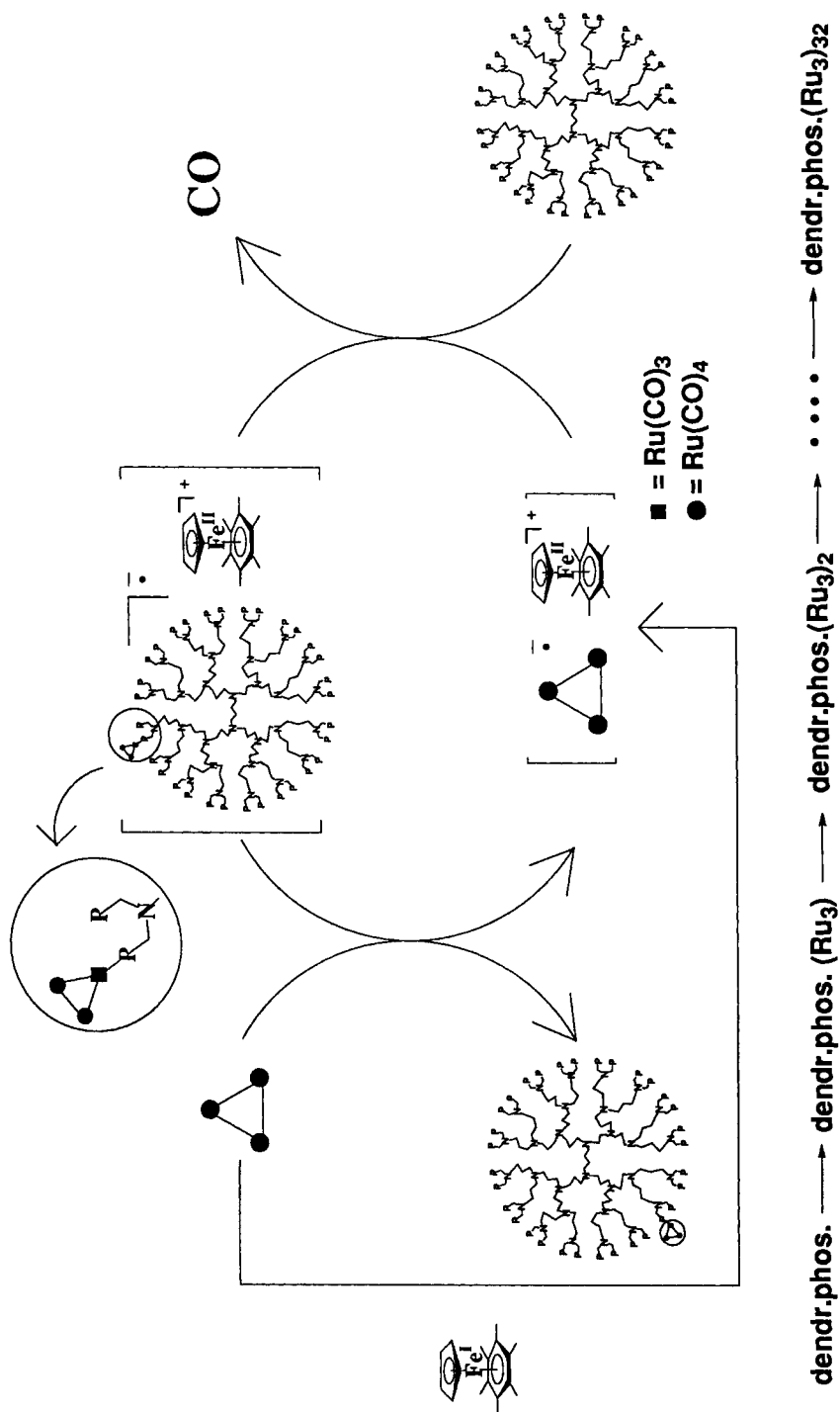


Scheme 33.

Given the simplicity of the above characterization of the reaction product by ^{31}P NMR [13] and the excellent selectivity of this model reaction when excess $[\text{Ru}_3(\text{CO})_{12}]$ was used, the same reaction between the phosphine dendrimers and $[\text{Ru}_3(\text{CO})_{12}]$ could be more confidently envisaged. This reaction, catalyzed by 1 % equiv. $[\text{Fe}^1\text{Cp}(\eta^6\text{-C}_6\text{Me}_6)]$ was carried out in THF at 20°C . The dendrimer-cluster assembly was obtained in 50 % yield. This shows the selectivity and completion of the coordination of each of the 32 phosphino ligands of P-P to a $\text{Ru}_3(\text{CO})_{11}$ cluster fragment (Scheme 34).



Scheme 34.



Scheme 35.

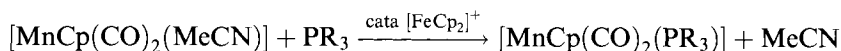
ETC mechanism proceeds for the introduction of the 32 cluster fragments in the dendrimer for ligation of the first $\text{Ru}_3(\text{CO})_{11}$ fragment to the dendritic phosphine. Then, this first complex [dendriphosphine. $\text{Ru}_3(\text{CO})_{11}$] would undergo the same ETC cycle as $[\text{Ru}_3(\text{CO})_{12}]$ initially does to generate the bis-cluster complex [dendriphosphine. $\{\text{Ru}_3(\text{CO})_{11}\}_2$], and so on (Scheme 35).

Finally, the 64-branch phosphine DAB-*dendr*-G4- $[\text{N}(\text{CH}_2\text{PPh}_2)_2]_{32}$ analogously reacts with $[\text{Ru}_3(\text{CO})_{12}]$ and 1 % $[\text{Fe}^{\text{I}}\text{Cp}(\eta^6\text{-C}_6\text{Me}_6)]$ (20 °C, THF, 20 min) to give the dark-red 192-Ru dendrimer. Characterization of the purity of these dendrimer-cluster assemblies is conveniently monitored by ^{31}P NMR. This application should find extension to other metal-carbonyl clusters and other families of phosphine dendrimers.

4.5.3 The Ferrocenium Salts as ETC Catalysts

The classical case of $[\text{MnCp}(\text{CO})_2(\text{MeCN})]$

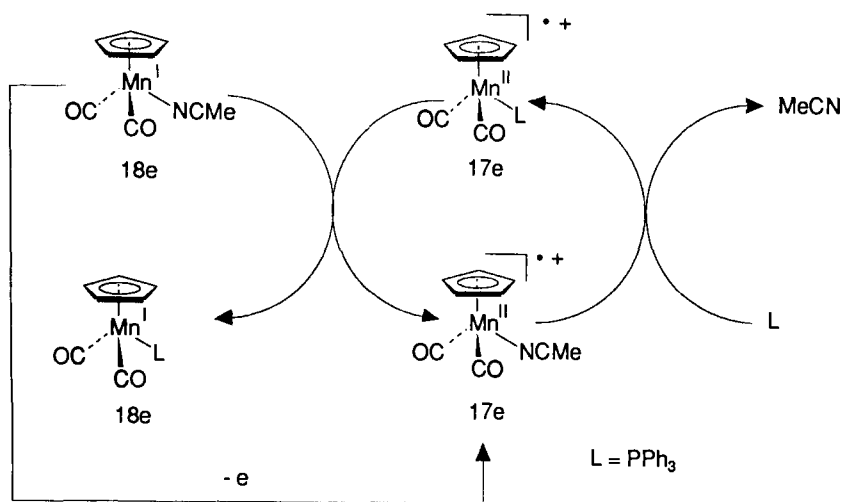
ETC-catalyzed reactions which required an oxidative initiation are often catalyzed by a ferrocenium salt in inorganic and organometallic chemistry despite the modest value of the reduction potential of ferrocenium cation. This is especially the case when the substrate is a neutral complex. Most ligand exchange reactions are those involving the substitution of CO. Thus, since CO is one of the less electron-donating ligand, substitution by other ligands systematically requires a cathodic initiation if an exergonic cross redox step is required. On the other hand, substitution of inorganic ligands such as nitriles, pyridine or ethers is favorably induced by an oxidizing initiation if it does require ETC catalysis at all to proceed. Indeed, these inorganic ligands are also very often easy to replace thermally. The classic case is that of $[\text{MnCp}(\text{CO})_2(\text{MeCN})]$ in which substitution by various phosphane ligands is favorably induced anodically or using ferrocenium salt as the ETC catalyst. The largest coulombic efficiencies (up to than 1000) ever found in ETC catalysis were indeed disclosed with this type of reaction (Scheme 36).



Since they are so clean, these reactions were the subject of in-depth mechanistic studies by electrochemistry [336–338], including by derivative cyclic voltammetry (DCV) [337, 338]. Acetonitrile and other solvento complexes are accessible by photolysis of transition-metal carbonyl complexes in the desired solvent. Such ETC catalyzed reactions are also of interest because they are practical and easily generalized, for instance to the series $\text{M}(\text{CO})_3\text{L}_3$ ($\text{M} = \text{Cr}, \text{Mo}, \text{W}$; $\text{L} = \text{MeCN}, \text{pyridine}$) [339].

Initiation by ferrocenium salts of an ETC-catalyzed chelation involving an endergonic cross propagation step

There are cases for which catalysis of an ETC reaction can proceed even if an endergonic cross electron transfer is involved. In such cases, the required conditions



Scheme 36.

are (i) that the endergonicity be weak and (ii) that the chemical propagation step be irreversible and fast in order to shift the unfavorable redox propagation step. Even if these conditions are fulfilled, the resulting coulombic efficiencies are weak (i.e. there are only small turnover numbers). The catalysis by ferrocenium salts of the chelation of the monodentate dithiocarbamate complexes $[\text{Fe}(\eta^5\text{-C}_5\text{R}_5)(\text{CO})_2(\eta^1\text{-S}_2\text{CNMe}_2)]$ ($\text{R} = \text{H}$ or Me) to $[\text{Fe}(\eta^5\text{-C}_5\text{R}_5)(\text{CO})(\eta^2\text{-S}_2\text{CNMe}_2)]$ disclosed in our group by Catheline [340] and Madonik [341] represents a typical example. The chelation of the Fe^{III} intermediate generated by single-electron oxidation of the substrate is so fast that this intermediate could not be detected using fast electrochemical techniques (cyclic voltammetry with sweep rates up to 5000 V s^{-1}) [341]. The yield could not overtake a certain limit even if the quantity of ferrocenium used was optimized (0.2 equiv. was the optimum as shown in Figure 1) because of the side reaction (CO exchange with a solvent molecule and precipitation of the generated 17-electron complex) [341]. The ferrocenium counter-anion influences the reaction because the ion pairing plays a crucial role in the competition between the cross redox propagation step and the side reactions of the 17-electron chelated cation intermediate (Scheme 37). Thus, the larger SbCl_6^- salt gave a better yield of chelated product $[\text{FeCp}(\text{CO})(\eta^2\text{-S}_2\text{CNMe}_2)]$ (63 %) than the PF_6^- (52 %) and BF_4^- (47 %) salts.

If the reaction is initiated by reduction, the very strong reductant naphthylsodium is required, and the cross redox step is now exergonic (thus all the starting material in consumed). The yields are not higher than with ferrocenium, however, because, reduction of the Fe^{II} substrate generates an inorganic anionic Fe^{I} intermediate. Such a low oxidation state is not favorable in inorganic chemistry. Thus, this Fe^{I} species rapidly decomposes to the dithiocarbamate anion $\text{S}_2\text{CNMe}_2^-$ and the radical $[\text{FeCp}(\text{CO})_2]$ which dimerizes to $[\text{FeCp}(\text{CO})_2]_2$ (Scheme 38). This efficient side reaction competes with the chemical propagation step, chelation. The driving force

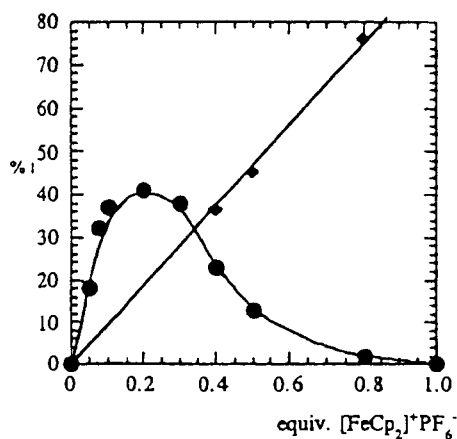
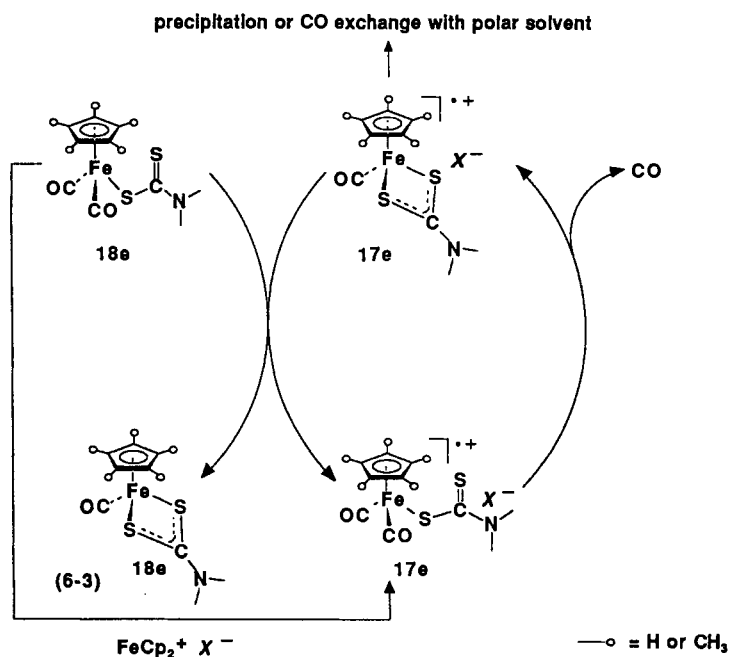
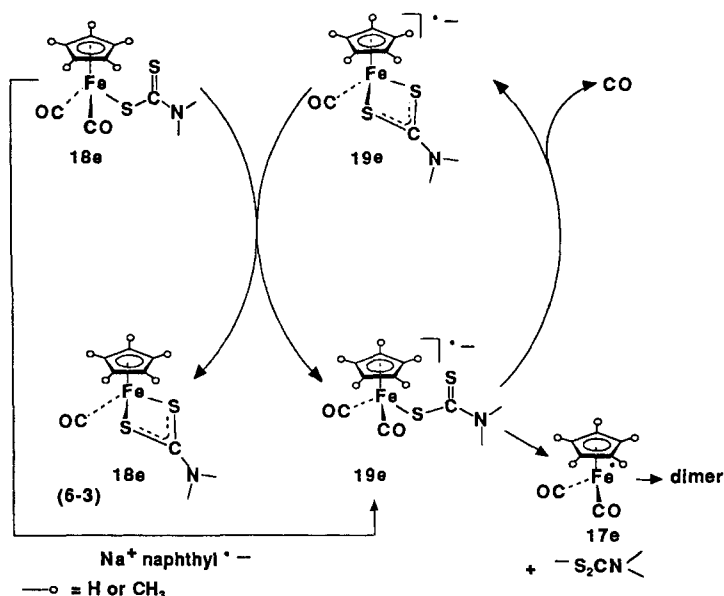


Figure 1. Yields of the ETC catalysis product $[\text{FeCp(CO)}(\eta^2\text{-dtc})]$ and stoichiometrically oxidized complex $[\text{FeCp(CO)}(\eta^2\text{-dtc})][\text{PF}_6^-]$ (circles) as a function of the amount (%) of $[\text{FeCp}_2][\text{PF}_6^-]$ added to the starting complex $[\text{FeCp(CO)}_2(\eta^1\text{-dtc})]$ (see Scheme 37).



Scheme 37.

of the initiator and the nature of the counter-cation also influence this competition, and thus the reaction yield, in a way similar to that detailed in Section 4.5.2. This case is probably a unique one for which both oxidative and reductive initiation could be used [342].



Scheme 38.

Coupling oxidative ETC catalysis using ferrocenium cation with organometallic catalysis: polymerization of terminal alkynes

A major drawback in homogeneous catalysis is sometimes the need to heat 18-electron transition-metal complexes, the catalyst precursors, so that they generate catalytically active species with vacant coordination sites. Since 18-electron complexes are most of the time inert to substitution reactions, they usually need to be heated to quite high temperature in order to generate efficient catalytically active species. Our concept consisted in generating catalytically active species in which the substrates are ligated to the transition-metal centers using the fast ETC catalyzed ligand substitution process under ambient conditions [185, 343]. Since 17- and 19-electron species react in ligand substitution reactions with rates in the range of 10^6 to 10^9 times higher than their 18-electron isostructural precursors [344, 345], the kinetic gain thereof could be used to perform homogeneous transition-metal catalysis under ambient conditions in cases where extensive heating was required. In short, the idea was to couple ETC catalyzed ligand substitution with homogeneous transition-metal catalysis. We choose the polymerization of terminal alkynes which was known to proceed at 100°C according to the Katz mechanism with the 18-electron catalyst $[\text{W}(\text{CO})_6]$ [346]. It was also known that $[\text{W}(\text{CO})_3(\text{MeCN})_3]$ could undergo oxidatively induced ETC catalyzed ligand substitution reaction with phosphanes [339]. We needed to bring two alkyne molecules on to the W center in order to achieve the catalytic alkyne polymerization according to the Katz mechanism [346]. We therefore envisaged that the substitution of two MeCN ligands by alkyne ligands would also be possible by oxidative ETC catalysis, since alkynes are

not as good donors as MeCN. What was needed was to use ferrocenium cation in catalytic amounts relative to the W catalyst itself, i.e. the amount of required ferrocenium salt was extremely minute. The use of ferrocenium in stoichiometric amount relative to the W catalyst would quantitatively generate catalytically inactive W^I . Also the reaction should be done in a solvent which would not be a good ligand to compete with alkynes. This catalytic engineering was successful and led to the rapid polymerization (10 min) of terminal alkynes under ambient conditions in toluene, THF, CH_2Cl_2 and neat but not in MeCN solvent. The optimum amount of $[FeCp_2][PF_6]$ was 20 % relative to the W catalyst in THF whereas this yield dropped continuously as this amount was increased, and reached only a few % when a stoichiometric amount of $[FeCp_2][PF_6]$ was used. The results were rather similar for different terminal alkynes, but the yield was only 6 % with the internal alkyne 2-hexyne. The yields, molecular weights and polydispersities with 10 % $[FeCp_2][PF_6]$ and without it are gathered in the Table 13.

The above data are consistent with a mechanism involving double ETC catalyzed substitution of two MeCN ligands by two terminal alkynes followed by isomerization of one alkyne ligand to a vinylidene ligand and Chauvin-type [347] square metathesis-like formation of a tungstacyclobutene, then continuation of the alkyne polymerization. It is assumed that the third MeCN ligand is only very slowly exchanged if at all, and probably not before polymerization (ancillary role, but no bulk interference). Indeed, the complex $[W(CO)_3(PPh_3)(MeCN)_2]$ is about ten times less active than $[W(CO)_3(MeCN)_3]$, presumably because of the large bulk of the PPh_3 ligand compared to MeCN [185] (Scheme 39). Obviously, this type of process combining ETC catalysis and homogeneous transition-metal catalysis has a future for other comparable applications.

Besides ETC catalysis, atom-transfer chain (ATC) catalysis has been reviewed [2]. The initiation involves radicals and the redox propagation step exchanges an

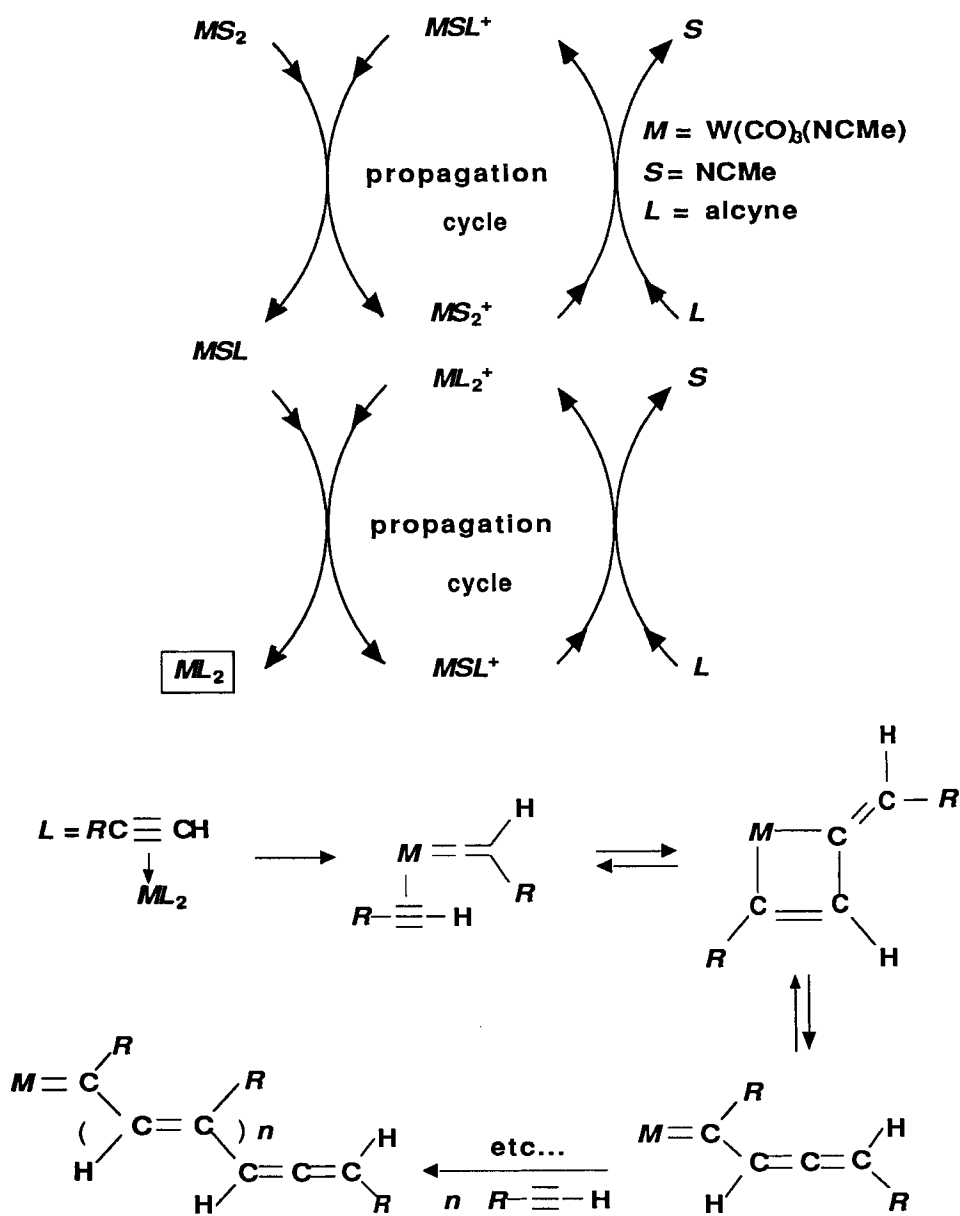
Table 13. Solvent effect on the polymerization of PhC_2H by $W(CO)_3(NCMe)_3$ and 0.1 equiv. $[FeCp_2]^+PF_6^-$ per W complex.

Solvent	THF	CH_2Cl_2	CH_3CN	Toluene	Bulk
Polymer yield (%) ^a	45 (15) ^b	42 (45) ^b	14 (12.6)	36 (13)	13 (7)
M_w^c	32000 (21350)	30200 (22250)	2070 (1530)	7000 (30600)	21400 (16800)
M_n^c	13200 (10650)	11600 (6250)	800 (600)	3400 (7000)	6400 (5600)
Polydispersity index ^c	2.42 (2.00)	2.61 (3.56)	2.57 (2.63)	2.06 (4.37)	3.34 (2.99)

^a Polymerized at RT, in the dark, under argon for 10 min; 50 equiv. alkyne per W complex was used.

^b As indication: numbers in brackets are the yields and characterizations obtained without addition of the cocatalyst $[FeCp_2]^+PF_6^-$ and after one week reaction time.

^c Determined by gel-permeation chromatography. The polydispersity index, close to 2, is indicative either of slow initiation or of random disruption of chain growth.



Scheme 39.

atom (H, halogen) or a group of atoms. There are many ways to generate radicals and single-electron reduction could be one of them [2].

4.6 Redox Catalysis

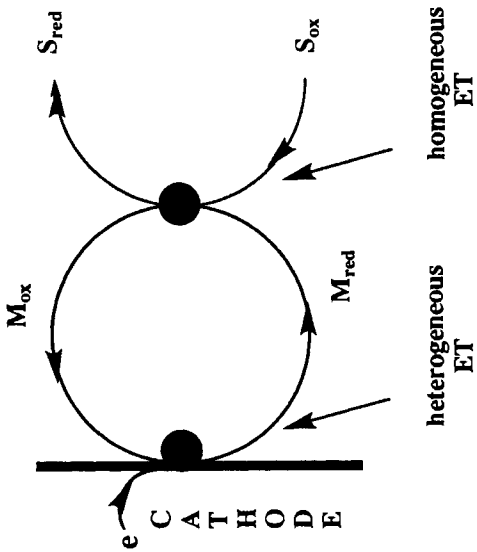
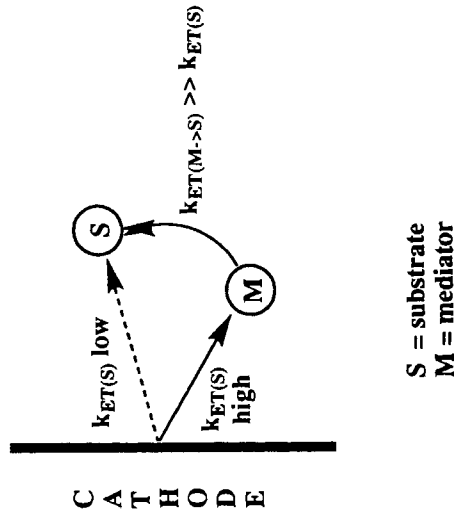
Redox catalysis is the catalysis of redox reactions and constitutes a broad area of chemistry embracing biochemistry (cytochromes, iron–sulfur proteins, copper proteins, flavodoxins and quinones), photochemical processes (energy conversion), electrochemistry (modified electrodes, organic synthesis) and ‘chemical’ processes (Wacker-type reactions). It has been reviewed altogether relatively recently [2]. We will essentially review here the redox catalysis by electron reservoir complexes and give a few examples of the use of ferrocenium derivatives.

4.6.1 Principle of Redox Catalysis of Electrochemical Reactions

The electrochemical redox reaction of a substrate resulting from the heterogeneous electron transfer from the electrode to this substrate (cathodic reduction) or the opposite (anodic oxidation) is said to be electrochemically reversible if it occurs at the Nernstian redox potential without surtension (overpotential). This is the case if the heterogeneous electron transfer is fast, i.e. there must not be a significant structural change in the substrate upon electron transfer. Any structural change slows down the electron transfer. When the rate of heterogeneous electron transfer is within the time scale of the electrochemical experiment, the electrochemical process is fast (reversible). In the opposite case, it appears to be slow (electrochemically irreversible). Structural transformations are accompanied by a slow electron transfer (slow E), except if this transformation occurs after electron transfer (EC mechanism).

Redox mediators or catalysts should facilitate the heterogeneous electron transfer from the electrode to the substrate (or the opposite) and partly cancel the required surtension observed in the absence of mediator or redox catalyst. Mediators or redox catalysts must undergo a redox change without significant structural change at a milder potential than the substrate. In this way, the heterogeneous electron transfer between the electrode and the mediator is Nernstian (fast i.e. electrochemically reversible). Electron transfer proceed more readily between the mediator or redox catalyst in solution than between the electrode and the substrate because the substrate and mediator or redox catalyst can move easily in the tridimensional bulk of the solution so that they find the right, optimal respective orientation of their orbitals for electron transfer. Such selective orientation of both partners of the electron transfer is much less easy with the electrode surface which is only two-dimensional. This is the reason for the kinetic advantage provided by the mediator or redox catalyst for a given driving force and is illustrated in Scheme 40.

The nomenclature [348] is such that a *mediator* exchanges electrons with substrates by an outer-sphere electron-transfer mechanism (for instance ferrocene/



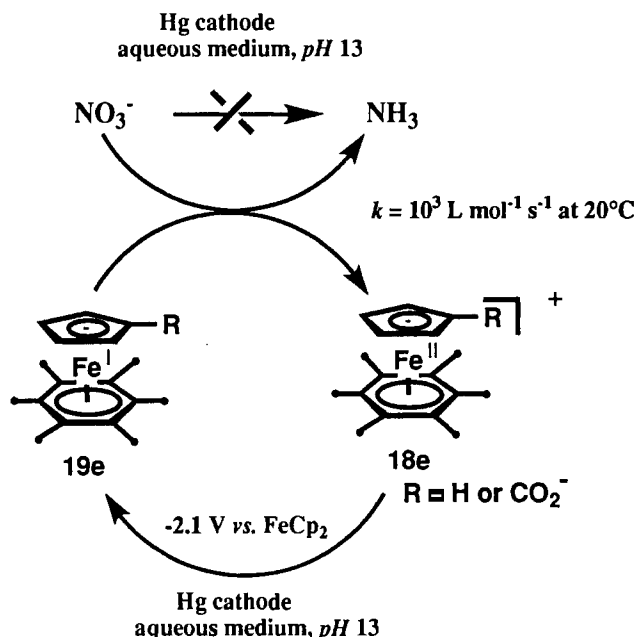
Scheme 40.

ferrocenium [349]) whereas a *redox catalyst* does so by an inner-sphere electron-transfer mechanism (for instance Ni^0 catalysts for the cathodic transformation of aryl halides [350, 351]). Redox catalysts provide a larger kinetic gain than redox mediators because inner-sphere electron transfers are much faster than outer-sphere ones.

4.6.2 Catalysis of Cathodic Reduction of Nitrates and Nitrites by the Electron-reservoir Complexes $[\text{Fe}^I(\eta^5\text{-C}_5\text{H}_4\text{R})(\eta^6\text{-arene})]$

The electroreduction of the complexes $[\text{Fe}^{\text{II}}\text{Cp}(\eta^6\text{-arene})][\text{PF}_6]$ was first studied in basic aqueous medium and ethanol. It was found that the complexes $[\text{Fe}^I(\eta^5\text{-C}_5\text{H}_4\text{R})(\eta^6\text{-C}_6\text{Me}_6)]$ ($\text{R} = \text{H}$ or CO_2^-) are both initiators for ETC catalyzed self-decomposition and redox catalysts for the reduction of water to dihydrogen on mercury cathode [352]. The reduction of water is a side reaction of the ETC catalytic process and limits its coulombic efficiency (Scheme 41). On such a cathode, the surtension of the reduction of water is very high, which makes this electrode especially suitable for the study of metal ions in such a medium. During this study, it was found that the most stable Fe^I complex $[\text{Fe}^I(\eta^5\text{-C}_5\text{H}_5)(\eta^6\text{-C}_6\text{Me}_6)]$, also catalyzes the cathodic reduction of nitrates to ammonia in the same basic aqueous medium (pH 13) [353, 354].

This result was all the more interesting as nitrate is not electroactive in these conditions in the absence of catalyst and the catalyst is stable after a large turnover number. The catalytic reduction of nitrate has been known for a long time [355], but this was the first example of organometallic catalyst for this reaction. Electro-



Scheme 41.

syntheses catalyzed by $[\text{Fe}^{\text{I}}(\eta^5\text{-C}_5\text{H}_4\text{CO}_2^-)(\eta^6\text{-C}_6\text{Me}_6)]$ under these conditions showed that NH_3 was produced in 63 % chemical yield and 57 % electrical yield with $\text{R} = \text{CO}_2^-$. Nitrite, hydroxylamine, hydrazine and dinitrogen (minute amounts) were intermediates towards the formation of ammonia. The cathodic reduction stopped at the level of hydroxylamine when the experiment was carried out at pH 7 instead of 13. Kinetic studies in homogeneous basic aqueous solution using a polarographic method were carried out with $[\text{Fe}^{\text{II}}(\eta^5\text{-C}_5\text{H}_4\text{R})(\eta^6\text{-arene})]$, $\text{R} = \text{CO}_2^-$, or when only the cationic Fe^{II} form was soluble in the medium ($\text{R} = \text{H}$; arene = benzene, *m*-xylene, hexamethylbenzene). These studies led to the conclusion that the rate of redox catalysis was independent of the nature of the catalyst within this series [353]. This study has recently been reconsidered, however, with the series of complexes $[\text{Fe}^{\text{II}}(\eta^5\text{-C}_5\text{H}_4\text{CO}_2^-)(\eta^6\text{-arene})][\text{PF}_6]$, arene = $\text{C}_6\text{Me}_{6-n}$, $n = 0$ to 6 [356]. The polarographic, cyclic voltammetry and chronoamperometry techniques were used to investigate the kinetics of the redox catalysis. The three techniques provided similar results. Thus, the rate constant of the redox catalysis can be calculated from the enhancement of the intensity of the cyclovoltammogram wave observed upon addition of the nitrate or nitrite salt into the electrochemical cell (Figure 2). A Marcus-type linear relationship was found between the logarithms of the rate constants and the standard redox potentials of the catalysts, indicating that the electron transfer in solution between the 19-electron Fe^{I} complex and nitrate or nitrite ion is rate limiting.

To investigate whether the mechanism proceeds by inner-sphere or outer-sphere electron transfer, other catalysts of the type $[\text{Fe}^{\text{II}}(\eta^5\text{-C}_5\text{H}_4\text{CO}_2^-)(\eta^6\text{-arene})][\text{PF}_6]$ were synthesized with bulky arenes such as 1,3,5-tris-*tert*-butylbenzene and $\text{C}_6(\text{CH}_2\text{CH}_2p\text{-C}_6\text{H}_4\text{OH})_6$. The rate constants were found to be one to two orders of

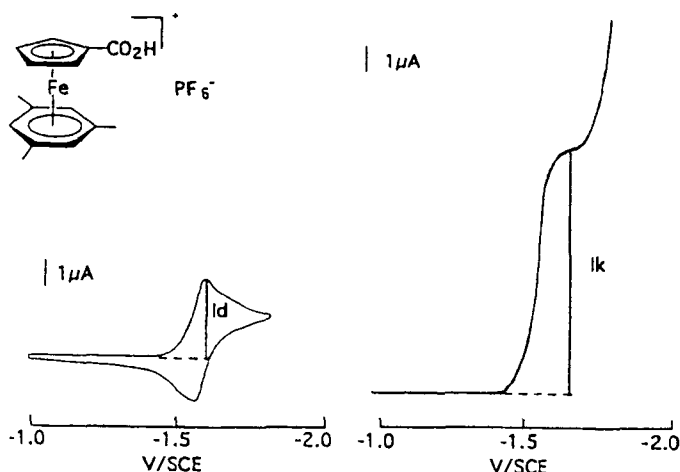


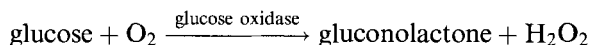
Figure 2. Redox catalysis of the reduction of nitrate on Hg cathode: cyclovoltammograms of $[\text{Fe}^{\text{II}}(\eta^5\text{-C}_5\text{H}_4\text{CO}_2^-)(\eta^6\text{-1,3,5-Me}_3\text{-C}_6\text{H}_3)]$ 1.27 M in aq. LiOH 0.1 M: a) in the absence of nitrate; b) in the presence of nitrate 1.18×10^{-2} M; scan rate: 0.1 V s^{-1} .

magnitude lower than what would be expected for the same driving force if the steric effect was not interfering, by comparison with the above series of catalysts with polymethylbenzene ligands. This showed a significant inner-sphere component to the electron-transfer process, although the kinetic drop would have been even more dramatic with a fully inner-sphere electron-transfer mechanism. It is likely that nitrate and nitrite ions coordinate to the 17-electron form of the Fe^{I} catalysts and that electron transfer proceeds in such intermediates rather than by outer sphere. However, the bond between an oxygen atom of nitrate or nitrite to such a low oxidation-state center must be very loose and long because π -back-bonding is impossible with these ligands [356].

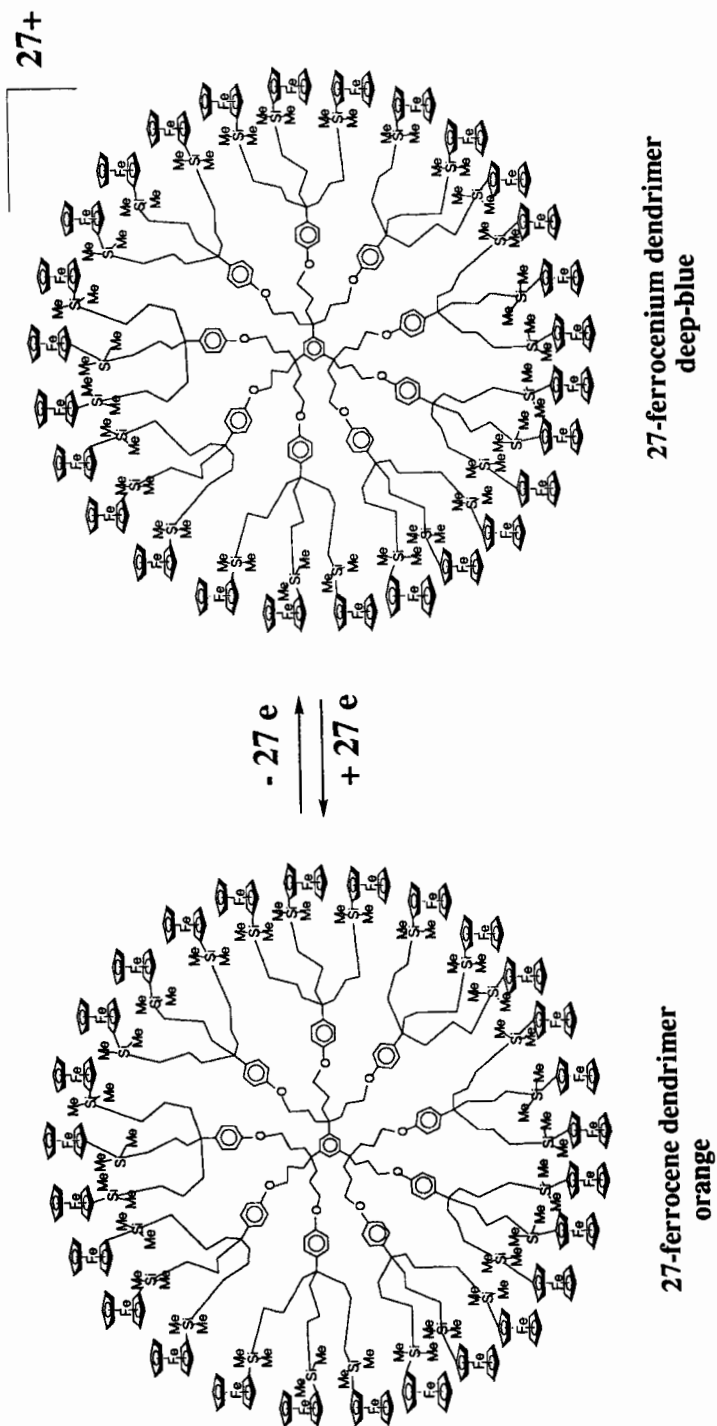
4.6.3 Mediation by Ferrocenium Cation: Derivatized Electrodes

We briefly mention here the use of the ferrocene/ferrocenium redox couple to mediate electron transfer on the oxidation (anodic) side, especially in derivatized electrode. This broad area has been reviewed [349]. For instance, polymers and dendrimers containing ferrocene units have been used to derivatize electrodes and mediate electron transfer between a substrate and the anode. Recently, ferrocene dendrimers up to a theoretical number of 243 ferrocene units were synthesized, reversibly oxidized, and shown to make stable derivatized electrodes. Thus, these polyferrocene dendrimers behave as molecular batteries (Scheme 42). These modified electrodes are characterized by the identical potential for the anodic and cathodic peak in cyclic voltammetry and by a linear relationship between the sweep rate and the intensity [134, 135]. Electrodes modified with ferrocene dendrimers were shown to be efficient mediators [357–359]. For the sake of convenience, the redox process of a smaller ferrocene dendrimer is represented below.

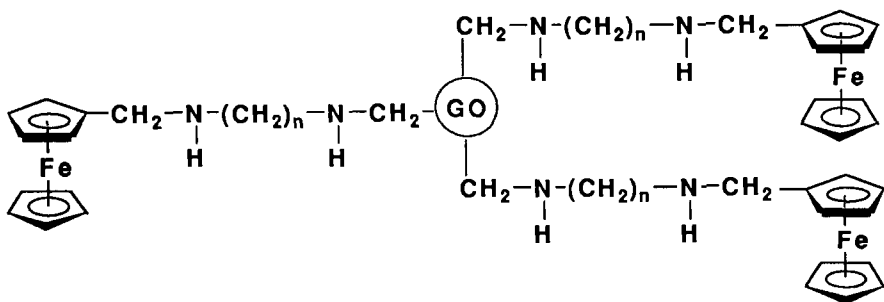
Electrical communication between redox centers of enzymes and electrodes is mediated by ferrocene links in amperometric redox biosensors. Direct communication with large enzymes is not possible because of the thick insulating protein layers around the redox centers of the proteins. This is the case, for instance, with the glycoprotein shell of glucose oxidase. Ferrocene units with low molecular weights can diffuse freely in and out the protein and mediate electron transfer. For instance, attachment of ferrocene units to amino groups of enzymes such as lysine, tyrosine and histidine led to increase of anodic current with glucose concentration when gold, platinum and carbon electrodes modified with such ferrocenylated enzymes [360–365].



An average of one mediator was bound per 12–75 kDa of enzyme. The mediators used have redox potentials 0.07 V to 0.55 V positive of the FAD/FADH enzyme's redox potential (-0.05 V relative to the NHE at pH 7), but those which have a redox potential more negative than glucose oxidase enzyme do not mediate electron transfer. Electrons can be relayed both by tunneling and by motion of the mediator in and out of the protein chains. For distances $>8 \text{ \AA}$, tunneling rates decrease ex-



Scheme 42.



Scheme 43.

ponentially with the electron transfer distance. Communication between glucose oxidase and a vitreous carbon electrode was effective when the chain between the enzyme and the ferrocene unit was long (>10 bonds), but not when the chain was short. A long flexible chain allows the ferrocene mediator unit to penetrate the enzyme to a sufficient depth to reduce the electron-transfer distance (Scheme 43) [364, 365]. Several variations are known [360–365].

4.7 Sensors

The binding of a redox system such as ferrocene to endoreceptors has been used to recognize particular guests. The first example concerned with the recognition of alkali-metal cations by a crown ether incorporating a ferrocenophane moiety [366] as shown on Figure 3.

The recognition of anions using amidometallocenes bound to endoreceptors such as crown ethers and calixarenes has been efficiently developed by Beer [368–371]. Our group has synthesized and examined dendrimers whose branches are terminated by amidoferrocene [372, 373] and amidocobalticinium [374, 375] units; they were shown to be very excellent exoreceptors for hydrogen sulfate and dihydrogen phosphate [373–375]. The variation of redox potential of the redox metallocene centers were much larger than that of monoamidometallocenes or tripodal amidometallocenes. The equivalence point determined by cyclic voltammetry was found to be one equiv. per dendritic branch in all the cases. Moreover, large dendritic effects were found, i.e. the variation of the redox potential obtained after addition of one equiv. anion per dendritic branch was all the larger as the dendritic generation increased ($3 \rightarrow 9 \rightarrow 18$ branches; Scheme 44).

These amidometallocenes do not significantly recognize halides, however, the redox potential shifts being very small [372]. Chloride and bromide were specifically recognized by 24-cationic dendrimers bearing iron sandwich units at the termini of the branches [376, 377]. The sandwich units was $[\text{FeCp}^*(\eta^6\text{-}N\text{-alkylaniline})]^+$.

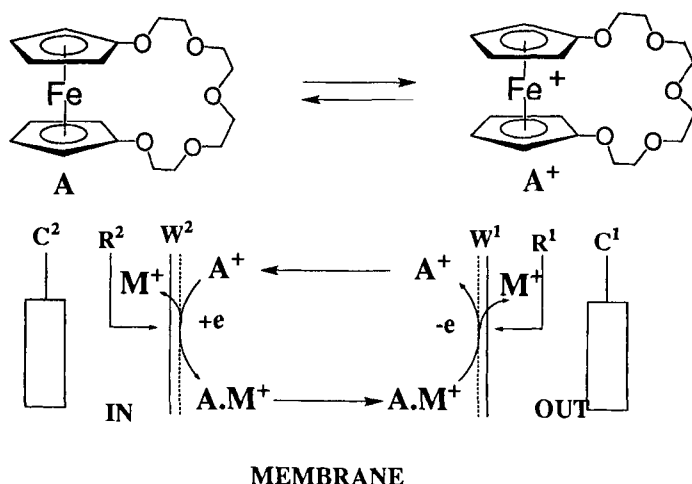


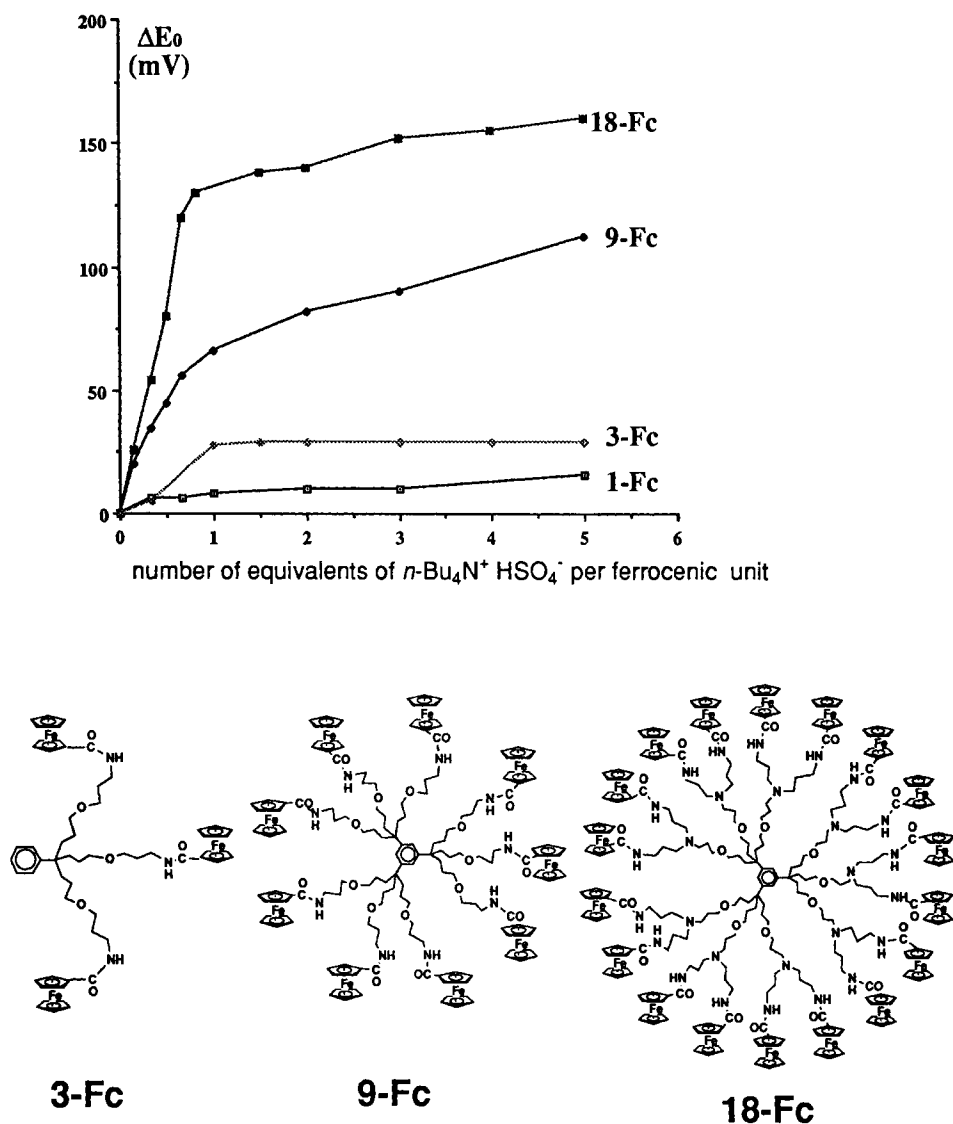
Figure 3. Amperometric sensory device: scheme of electrochemical ion transport with a redox-active crown ether. W^1 , W^2 : minigrad platinum working electrodes. C^1 , C^2 : platinum plate counter electrode. R^1 , R^2 : SCE reference.

Although these dendrimers have a different topology compared to the former, the corresponding 24-amidoferrocene dendrimers of the new type also recognize hydrogen sulfate and dihydrogen phosphate, but not the halides (Scheme 45).

Bromide and chloride were sensed by the variation of the chemical shift of the NH proton in ^1H NMR. The equivalence point for bromide was also one equiv. bromide per branch, but the recognition of chloride was sharper and different; the equivalence point for this anion was one equiv. chloride per dendritic tripod, i.e. eight equiv. chloride per dendrimer [376]. This complementarity between the two families of dendrimers shows that dendritic variation can be searched to recognize a given anion. Nevertheless, the recognition of oxoanions by amido- or amino-metallocene dendrimers is based on the synergy between three effects: (i) the electrostatic effect with the ferrocenium form, (ii) the H bonding (simple or double) and (iii) especially the topology effect. In the case of the 24-branch polycationic dendrimers, only one H bonding per branch is occurring.

4.8 Conclusion

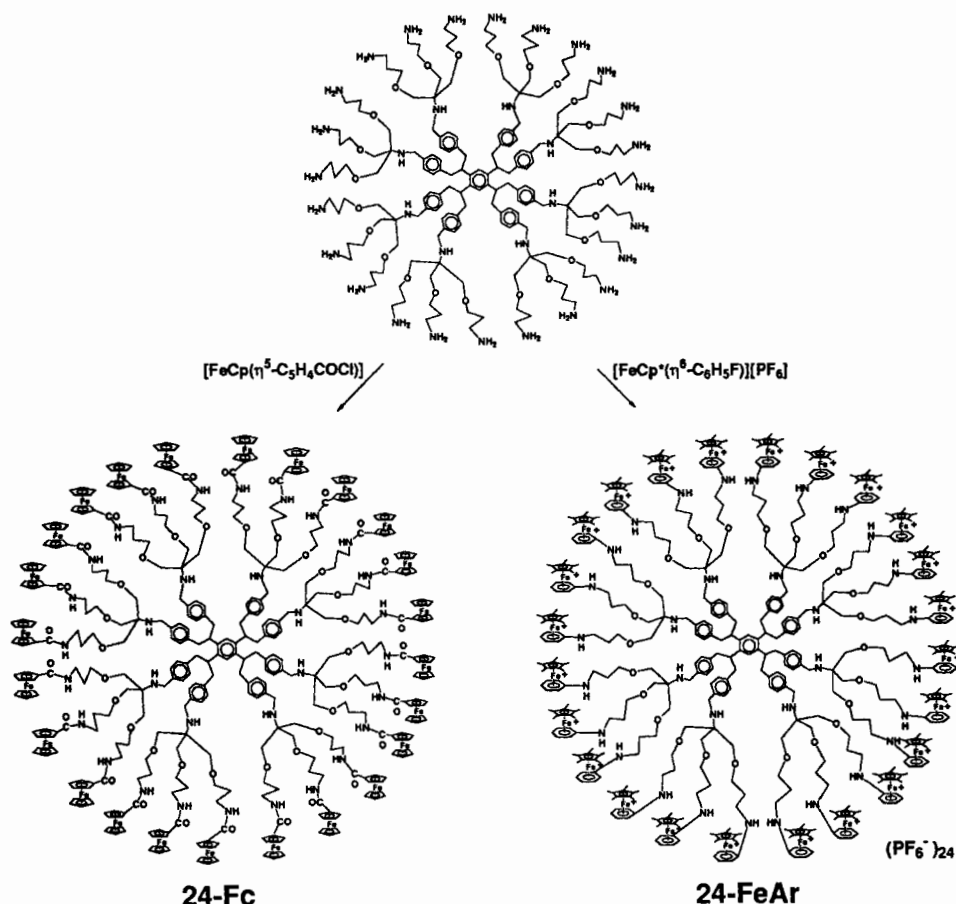
Redox reagents are useful for stoichiometric electron-transfer reactions, catalytic initiation of electron-transfer-chain (ETC) catalyzed reactions, as redox mediators (by outer-sphere electron transfer) or redox catalysts (by inner-sphere electron transfer) of redox reactions, as part of sensory devices when then are attached to



Scheme 44.

endo- or *exo*-receptors and as references for the determination of redox potentials by cyclic voltammetry.

Electron-reservoir complexes were so named because they have the ability to transfer electrons without breakdown at very negative or very positive redox potentials, can be synthesized in large quantities, are crystalline and thermally robust and can be used in various solvents. The 19-electron complexes $[\text{Fe}^I(\eta^5\text{-C}_5\text{R}_5)(\eta^6\text{-C}_6\text{Me}_6)]$ ($\text{R} = \text{H}$ or Me) are the most electron-rich neutral molecules known and the recently



Scheme 45.

disclosed 17-electron complex $[\text{Fe}^{\text{III}}(\eta^5\text{-C}_5\text{Me}_5)(\eta^6\text{-C}_6\text{Me}_6)][\text{SbX}_6]_2$, $\text{X} = \text{Cl}$ or F (isoelectronic to ferrocenium but with a redox potential $\text{Fe}^{\text{II/III}}$ one volt more positive), is the strongest known stable organometallic oxidant. Thus, they are ideal redox reagents in many respects, as largely exemplified in this review. Their driving force can be changed at will by variation of the number of methyl groups on the ligands, which leads to noteworthy selectivities in ETC chain reactions, for instance.

These electron-reservoir iron-sandwich complexes have been compared in this chapter on the reduction side with other redox reagents: alkali metals and their amalgams and alloys, radical anions of aromatic such as those of naphthalene (extremely strongly reducing) and benzophenone (strongly reducing), hydrides (electron-transfer rather than hydride transfer), cobaltocene and decamethylcobaltocene (good and strong reductants). On the oxidation side, ferrocenium salts (mild oxidants) have been most used and discussed together with the other one-electron oxidants: NO^+ , Ag^{I} , Cu^{II} , FeCl_3 , Ce^{IV} (CAN), halogens, aryl diazonium

salts, acids, the very useful triarylaminium radical cations, carbocations (trityl and derivatives), TCNE, TCNQ and quinones. Most of these redox reagents (except the metallocenes) are non innocent by contrast with the electron-reservoir complexes in which the permethylation of the ring(s) protects the metal center from external influences to a great extent.

The well-known metal polypyridine [378, 379] and metal-porphyrin [380–382] and phthalocyanine complexes also have extended redox series which make them good candidates as electron-reservoirs. They are thoroughly reviewed and discussed in other chapters of this volume.

4.9 Experimental: Syntheses of the Electron-reservoir Complexes

$[\text{Fe}^{\text{II}}(\eta^5\text{-C}_5\text{R}_5)(\eta^6\text{-C}_6\text{Me}_6)][\text{PF}_6]$, $[\text{Fe}^{\text{I}}(\eta^5\text{-C}_5\text{R}_5)(\eta^6\text{-C}_6\text{Me}_6)]$, and $[\text{Fe}^{\text{III}}(\eta^5\text{-C}_5\text{R}_5)(\eta^6\text{-C}_6\text{Me}_6)][\text{SbCl}_6]_2$ (R = H or Me)

4.9.1 $[\text{Fe}^{\text{II}}\text{Cp}(\eta^6\text{-C}_6\text{Me}_6)][\text{PF}_6]$

The reaction is conducted in a 500-mL three-necked, round-bottomed flask equipped with a nitrogen inlet and a reflux condenser topped with a gas outlet. Ferrocene (18.6 g, 100 mmol), aluminum powder (2.7 g, 100 mmol), and C_6Me_6 (16.2 g, 100 mmol) are added, together, to degassed decalin (200 mL) under nitrogen or argon. After stirring for 5 min, AlCl_3 (40 g, 300 mmol) is added to the solution. Finally, after another 5 min, H_2O (1.8 mL, 100 mmol) is introduced by syringe to the reaction medium. The mixture is heated to 190 °C with a oil bath for 12 h. The reaction mixture is hydrolyzed at 50 °C (to prevent solidification) very slowly under nitrogen or argon with degassed ice–water (100 mL). After filtration, the two layers are separated and the aqueous layer is washed with diethyl ether (3×50 mL). $\text{Al}(\text{OH})_3$ is precipitated by the addition of concentrated aqueous NH_4OH until pH 9. Filtration into aqueous HPF_6 solution (100 mmol) gives a yellow precipitate of $[\text{Fe}^{\text{II}}\text{Cp}(\eta^6\text{-C}_6\text{Me}_6)][\text{PF}_6]$. The latter is removed by filtration, dissolved in acetone (500 mL), and dried for 1 h over MgSO_4 . Addition of ethanol (400 mL) to the yellow filtered solution then slow evaporation of the acetone by rotary evaporation gives, after standing overnight at –25 °C, 27.8 g (65 %) of yellow microcrystals. The other complexes $[\text{FeCp}(\eta^6\text{-arene})][\text{PF}_6]$ are prepared similarly from the arene (neat) by reaction at 100 °C or under reflux overnight, then the above work-up $[\text{Fe}^{\text{III}}(\eta^5\text{-C}_5\text{Me}_5)(\eta^6\text{-C}_6\text{Me}_6)][\text{PF}_6]$ is analogously prepared from $[\text{Fe}^{\text{III}}(\eta^5\text{-C}_5\text{Me}_5)(\text{CO})_2\text{Br}]$ by reaction with C_6Me_6 and AlCl_3 overnight without water at 100 °C, then similar work-up [50].

4.9.2 $[\text{Fe}^{\text{I}}\text{Cp}(\eta^6\text{-C}_6\text{Me}_6)]$

A sample of the yellow crystalline salt $[\text{Fe}^{\text{II}}\text{Cp}(\eta^6\text{-C}_6\text{Me}_6)][\text{PF}_6] \cdot \text{PF}_6^{-1}$ (8.56 g, 20 mmol) in dimethoxyethane (30 mL) is stirred with Na–Hg (230 g, 0.9 %, 100 mmol)

for 1 h at ambient temperature under argon. The DME is then removed in vacuo, and the residue is extracted with pentane (3×50 mL) and filtered. The deep green solution is concentrated to 40 mL and cooled to -80°C . Filtration of this solution provides 4.53 g, 80 % yield, of $[\text{Fe}^{\text{I}}\text{Cp}(\eta^6\text{-C}_6\text{Me}_6)]$ as green microcrystals. Recrystallization can also be performed overnight in the freezer of the dry-lab (-40°C). Concentration and treatment of subsequent crops gives an overall 92 % yield of crystals.

4.9.3 $[\text{Fe}^{\text{I}}(\eta^5\text{-C}_5\text{Me}_5)(\eta^6\text{-C}_6\text{Me}_6)]$

A sample of $[\text{Fe}^{\text{I}}(\eta^5\text{-C}_5\text{Me}_5)(\eta^6\text{-C}_6\text{Me}_6)][\text{PF}_6]$ (0.498 g, 1 mmol) in THF (10 mL) was stirred on sodium amalgam (0.8 %, 10 g). The reduction was achieved in 1 h. THF was then removed in vacuo, and the residue was extracted with pentane (2×15 mL). Pentane was then removed in vacuo to leave a dark-green product. Recrystallization from pentane overnight in the freezer of the dry-lab (-40°C) gave dark-green crystals of $[\text{Fe}^{\text{I}}(\eta^5\text{-C}_5\text{Me}_5)(\eta^6\text{-C}_6\text{Me}_6)]$ (0.307 g, 87 % yield) [50].

4.9.4 $[\text{Fe}^{\text{III}}(\eta^5\text{-C}_5\text{Me}_5)(\eta^6\text{-C}_6\text{Me}_6)][\text{SbCl}_6]_2$

SbCl_5 (1 M solution in CH_2Cl_2 , 5 mmol) was added with magnetic stirring to $[\text{Fe}^{\text{III}}(\eta^5\text{-C}_5\text{Me}_5)(\eta^6\text{-C}_6\text{Me}_6)][\text{PF}_6]$ (0.498 g, 1 mmol) in CH_2Cl_2 (10 mL) under argon. Formation of a purple precipitate from the initially yellow solution was instantaneous. The purple solid was removed by filtration, washed with CH_2Cl_2 (4×15 mL) until the latter was colorless, then recrystallized from SO_2 at -40°C (0.624 g, 71 % yield). Analysis for $[\text{Fe}^{\text{III}}(\eta^5\text{-C}_5\text{Me}_5)(\eta^6\text{-C}_6\text{Me}_6)][\text{SbCl}_6]_2$: calc. for $\text{C}_{22}\text{H}_{33}\text{FeSb}_2\text{Cl}_{12}$: C 25.85, H 3.25. Found C 25.84, H 3.47.

Alternatively, $[\text{Fe}^{\text{III}}(\eta^5\text{-C}_5\text{Me}_5)(\eta^6\text{-C}_6\text{Me}_6)][\text{SbCl}_6]_2$ can also be synthesized from $[\text{Fe}^{\text{I}}(\eta^5\text{-C}_5\text{Me}_5)(\eta^6\text{-C}_6\text{Me}_6)]$. The complex $[\text{Fe}^{\text{I}}(\eta^5\text{-C}_5\text{Me}_5)(\eta^6\text{-C}_6\text{Me}_6)]$ (0.300 g, neat) was cooled to -80°C and SbCl_5 (1 M solution in CH_2Cl_2 , 5 mmol) at -80°C were added with magnetic stirring. The reaction mixture was then slowly warmed to room temperature and a brown solution and a purple precipitate appeared. The solution was then transferred by cannula, and the solid residue was washed with CH_2Cl_2 (4×15 mL) and recrystallized from SO_2 at -40°C to yield the complex $[\text{Fe}^{\text{III}}(\eta^5\text{-C}_5\text{Me}_5)(\eta^6\text{-C}_6\text{Me}_6)][\text{SbCl}_6]_2$ as a microcrystalline purple powder (0.694 g, 78 % yield). UV-Vis for 1 $[\text{SbF}_6]_2$: λ_{max} (MeCN) = 487 nm ($\epsilon = 228 \text{ L M}^{-1} \text{ cm}^{-1}$); λ_{max} (MeCN) = 525 nm ($\epsilon = 213 \text{ L M}^{-1} \text{ cm}^{-1}$).

References

1. H. Taube, *Electron Transfer Reactions of Complex Ions in Solution*, Academic Press, New York, 1970.
2. D. Astruc, *Electron Transfer and Radical Processes in Transition Metal Chemistry*, VCH, New York, 1995.

3. R. A. Marcus, N. Sutin, *Biophys. Biochem. Acta* **1985**, 811, 265.
4. I. Bertini, H. B. Gray, S. J. Lippard, J. S. Valentine, *Bioinorganic Chemistry*, University Science Books, Mill Valley, **1994**.
5. L. Stryer, *Biochemistry*, 2nd Ed., Freeman, New York, **1981**.
6. J. K. Kochi, *Organometallic Mechanisms and Catalysis*, Academic Press, New York, **1981**.
7. R. Crabtree, *The Organometallic Chemistry of the Transition Metals*, 2nd Ed., Wiley, New York, **1994**.
8. V. Balzani, F. Scandola, *Supramolecular Photochemistry*, Ellis Hordwood, New York, **1991**.
9. *Homogeneous and Heterogeneous Photocatalysis* (Ed.: V. Balzani, A. Juris, F. Scandola, E. Pelizzetti, N. Serpone), Reidel, Dordrecht, **1986**.
10. J.-M. Lehn, *Supramolecular Chemistry: Concepts and Perspectives*, VCH, Weinheim, **1995**.
11. *Molecular Electronics* (Guest Ed.: J.-P. Launay), Gauthier-Villars, Paris, *New J. Chem.* **1991**, 15, 97. See also Ref. [2] (Chapter 4), Ref. [8] (Chapter 12) and Ref. [10] (Chapter 8).
12. *Electron Transfer in Biology and in the Solid State* (Eds: M. K. Johnson et al.), *Adv. Chem. Ser.* No. 226, American Chemical Society, Washington, DC, **1990**.
13. R. A. Sheldon, J. K. Kochi, *Metal-Catalyzed Oxidations of Organic Compounds*, Academic Press, New York, **1981**.
14. M. Hudlicky, *Oxidations in Organic Chemistry*, A.C.S Monograph No. 186, American Chemical Society, Washington, DC, **1990**.
15. M. Hudlicky, *Reductions in Organic Chemistry*, Ellis Horwood, Chichester, **1984**.
16. J. Seyden-Penne, *Reductions by the Alumino- and Borohydrides in Organic Synthesis*, 2nd Ed.; Wiley, VCH, New York, **1997**.
17. A. J. Bard, L. R. Faulkner, *Electrochemical Methods*, Wiley, New York, **1980**.
18. G. J. Hills in *Reference Electrodes* (Eds: D. Ives, J. G. Janz), Academic Press, New York, **1961**, Chapter 10.
19. J. F. Coetzee, G. R. Padmanabhan, *J. Phys. Chem.* **1962**, 66, 7708.
20. V. D. Parker, *Adv. Phys. Org. Chem.* **1983**, 19, 131.
21. N. Connelly, W. E. Geiger, *Chem. Rev.* **1996**, 96, 877.
22. J. T. Hupp, *Inorg. Chem.* **1990**, 29, 5010.
23. J. Ruiz, D. Astruc, *C. R. Acad. Sci. Paris, Sér. IIC*, **1998**, 1, 27.
24. K. N. Brown, D. S. Fleming, P. T. Gulyas, P. A. Lay, A. F. Masters, *XVIIth Intern. Conf. Organomet. Chem.* Brisbane, Australia, **1996**, Abstr. OA12.
25. Q. Xie, E. Pérez-Cordero, L. Echegoyen, *J. Am. Chem. Soc.* **1992**, 114, 3978.
26. A. Loupy, B. Tchoubar, D. Astruc, *Chem. Rev.* **1992**, 92, 1141.
27. J. A. Davies, C. M. Hockensmith, V. Yu Kukushkin, Yu N. Kukushkin, *Synthetic Coordination Chemistry*, World Scientific, London, **1996**, Chapters 8 and 9.
28. K. Jonas, V. Z. Wiskamp, *Naturforsch.* **1983**, 38B, 1113.
29. (a) J. D. L. Holloway, W. E. Geiger, *J. Am. Chem. Soc.* **1979**, 101, 2038; (b) G. Fochi, X. Runjuan, A. Colligiani, *J. Chem. Soc. Dalton Trans.* **1990**, 2551.
30. H.-F. Klein, J. Gross, J. M. Bassett, U. Schubert, *Z. Naturforsch.* **1980**, 35B, 614.
31. D. Catheline, D. Astruc, *Organometallics* **1984**, 3, 1094.
32. F. Abugideiri, D. W. Keogh, R. Poli, *J. Chem. Soc., Chem. Commun.* **1994**, 2317.
33. K. M. Phahl, J. Ellis, *Organometallics* **1984**, 3, 230.
34. K. Okada, T. Kawata, M. Oda, *J. Chem. Soc. Chem. Commun.* **1995**, 233.
35. J. S. Bradshaw, K. E. Krakoviak, R. M. Izatt, *Aza-crown Macrocycles*, Wiley, New York, **1993**, Chapter 1.
36. M. M. Olmstead, P. P. Power, *J. Am. Chem. Soc.* **1986**, 108, 4235.
37. F. G. N. Cloke, P. B. Hitchcock, A. McCamley, *J. Chem. Soc. Chem. Commun.* **1993**, 248.
38. C. M. Archer, J. R. Dilworth, R. M. Thompson, M. McPartlin, D. C. Povey, J. D. Kelly, *Dalton Trans.* **1993**, 461.
39. L. D. Field, A. F. Masters, M. Gibson, D. R. Latimer, T. W. Hambley, I. E. Buys, *Inorg. Chem.* **1993**, 32, 211.
40. B. K. Coltrain, S. C. Jackels, *Inorg. Chem.* **1981**, 20, 2032.
41. M. E. Riehl, S. R. Wilson, G. S. Girolami, *Inorg. Chem.* **1993**, 32, 218.
42. M. S. Corraine, D. Atwood, *Organometallics* **10**, 2647.
43. J. Balej, *Electrochimica Acta* **1976**, 21, 953.

44. M. S. Corrairie, J. D. Atwood, *Organometallics* **1991**, *10*, 2985.
45. (a) M. Pfeffer, J. Fisher, A. Mitschler, *Organometallics* **1984**, *3*, 1531; (b) V. G. Syrkin, *Metal Carbonyls* (in Russian), Khimia, Moscow, **1984**.
46. W. P. Weiner, F. J. Hollander, R. G. Bergman, *J. Am. Chem. Soc.* **1984**, *106*, 7462.
47. J. Li, A. D. Hunter, R. McDonald, B. D. Santarsiero, S. G. Bott, J. L. Atwood, *Organometallics* **1992**, *11*, 3050.
48. T. Cuenca, P. Royo, *J. Organomet. Chem.* **1985**, *293*, 61.
49. C. Moinet, E. Román, D. Astruc, *J. Organomet. Chem.* **1977**, *128*, C45.
50. J.-R. Hamon, D. Astruc, P. Michaud, *J. Am. Chem. Soc.* **1981**, *103*, 758.
51. N. G. Connelly in *Paramagnetic Species in Activation, Selectivity, Catalysis* (Eds: M. Chanon, M. Juliard, J. C. Poite), Kluwer, Dordrecht, **1989**, p. 71.
52. N. G. Connelly, *Chem. Soc. Rev.* **1989**, *18*, 153.
53. E. O. Fischer, H. Waversik, *J. Organomet. Chem.* **1966**, *5*, 559.
54. H. J. Keller, H. Waversik, *J. Organomet. Chem.* **1967**, *8*, 185.
55. O.V. Gusev, L. I. Denisovich, M. G. Peterleitner, A. Z. Rubezhov, N. A. Ustynyuk, P. M. Maitlis, *J. Organomet. Chem.* **1993**, *452*, 219.
56. D. J. Cole-Hamilton, G. Wilkinson, *J. Chem. Soc. Dalton Trans.* **1979**, 1283.
57. M. Green, *Polyhedron* **1986**, *5*, 427.
58. J. J. Maj, A. D. Rae, L. F. Dahl, *J. Am. Chem. Soc.* **1982**, *104*, 3054.
59. *Radical Ions* (Ed.: E. T. Kaiser, L. Kevan), Interscience, New York, **1968**.
60. F. Billiau, G. Folcher, H. Marguet-Ellis, P. Rigny, E. Saito, *J. Am. Chem. Soc.* **1981**, *103*, 5603.
61. J. M. Maher, R. P. Beatty, N. J. Cooper, *Organometallics* **1982**, *1*, 215 and **1985**, *4*, 1354.
62. R. L. Thompson, S. J. Geib, N. J. Cooper, *J. Am. Chem. Soc.* **1991**, *113*, 8961.
63. A. Antinolo, M. F. Lappert, D. J. W. J. Winterborn, *J. Organomet. Chem.* **1985**, *272*, C37.
64. P. Jutzi, B. J. Heilscher, *Organomet. Chem.* **1985**, *291*, C25.
65. W. Schlenk, T. Weickel, *Chem. Ber.* **1911**, *44*, 1182.
66. *Electrochemistry of the Elements* (Eds: A. J. Bard, H. Lund), Marcel Dekker, New York, **1978**, Vol XII, p. 209.
67. L. F. Fieser, *Experiments in Organic Chemistry*, 3rd Ed., Heath & Co, Boston, p. 209.
68. M. I. Bruce, B. K. Nicholson, M. L. Williams, *Inorg. Synth.* **1989**, *26*, 273.
69. N. Hirota in *Radical Ions* (Eds: E.T. Kaiser, L. Kevan), Wiley, New York, **1968**, p. 65.
70. C. B. Wooster, *J. Am. Chem. Soc.* **1928**, *50*, 1388.
71. D. H. Geske, A. H. Maki, *J. Am. Chem. Soc.* **1960**, *82*, 2671.
72. B. S. Jensen, V. D. Parker, *J. Chem. Soc., Chem. Commun.* **1974**, 367.
73. J. Grimshaw, R. Hamilton, *Electroanal. Chem.* **1980**, *106*, 339.
74. M. Grezeszczuck, D. E. Smith, *J. Electroanal. Chem.* **1983**, *157*, 205.
75. N. Novikov, Yu., M. E. Volpin, *Upsekhii Khim.* **1971**, *40*, 1568.
76. T. Mashiko, C. A. Reed, K. J. Haller, W. R. Scheidt, *Inorg. Chem.* **1984**, *23*, 3192.
77. W. Rüdorff, *Adv. Inorg. Chem. Radiochem.* **1959**, *1*, 223.
78. A. Fürstner, *Advan. Organomet. Chem.* **1988**, *28*, 58.
79. K. A. Jensen, B. Nygaard, G. Elisson, P. H. Nielsen, *Acta Chem. Scand.* **1965**, *19*, 768.
80. C. Ungurenasu, M. Palie, *J. Chem. Soc., Chem. Commun.* **1975**, 388.
81. M. C. Manning, W. C. Troglor, *Inorg. Chim. Acta* **1981**, *50*, 247.
82. P. Michaud, D. Astruc, J. H. Ammeter, *J. Am. Chem. Soc.* **1982**, *104*, 3755.
83. L. Ebersson, *Acta Chem. Scand., Ser. B* **1984**, *38*, 439.
84. D. Astruc, *Chem. Rev.* **1988**, *88*, 1189.
85. P. Massur, Yu., I. S. Antonov, A. P. Tomilov, L. N. Ovsyannikov, *Soviet Electrochemistry* **1969**, *5*, 452.
86. S. G. Davies, M. L. H. Green, D. M. P. Mingos, *Tetrahedron* **1978**, *34*, 3047.
87. P. Michaud, J.-P. Mariot, F. Varret, D. Astruc, *J. Chem. Soc., Chem. Commun.* **1982**, 1383.
88. C. Lapinte, D. Catheline, D. Astruc, *Organometallics* **1984**, *3*, 817.
89. P. Michaud, C. Lapinte, D. Astruc, *Annals New York. Acad. Science* **1983**, *415*, 97.
90. M.-J. Tudoret, M.-L. Robo, C. Lapinte, *Organometallics* **1992**, *11*, 1419.
91. E. C. Ashby, A. B. Goel, R. N. de Priest, *J. Am. Chem. Soc.* **1980**, *102*, 7779.
92. E. C. Asby, A. B. Goel, R. N. de Priest, N. S. Prasad, *J. Am. Chem. Soc.* **1981**, *103*, 973.

93. N. G. Connelly, J. D. Payne, W. E. Geiger, *J. Chem. Soc., Dalton Trans.* **1983**, 295.
94. D. C. Boyd, N. G. Connelly, G. G. Herbosa, M. G. Hill, K. R. Mann, C. Mealli, A. G. Orpen, K. Richardson, P. H. Rieger, *Inorg. Chem.* **1994**, 33, 960.
95. W. D. Jones, J. M. Huggins, R. G. Bergman, *J. Am. Chem. Soc.* **1981**, 103, 4415.
96. D. R. Tyler in *Prog. Inorg. Chem.* (Ed.: S. J. Lippard), Wiley, New York, **1988**, 35, 125.
97. K. A. Kocheshkov, A. N. Nesmeyanov, M. M. Nad', *Dokl. Akad. Nauk. SSSR* **1940**, 26, 53.
98. A. J. Linsay, R. P. Tooze, M. Motevalli, M. B. Hurthouse, G. Wilkinson, *J. Chem. Soc., Chem. Commun.* 799 and 1383.
99. H. Lehmkuhl, H. Nehl, R. Benn, R. Mynott, *Angew. Chem.* **1986**, 98, 628.
100. D. Astruc, *Tetrahedron* **1983**, 39, 4027.
101. M. I. Bruce, C. M. Jensen, N. L. Jones, *Inorg. Syn.* **1989**, 26, 259.
102. C.-M. Che, M. Jamal, C.-K. Poon, W.-C. Chung, *Inorg. Chem.* **1985**, 24, 2868.
103. *Synthesis of Complex Compounds of the Platinum Metals* (Ed.: I. I. Cheryaev), (in Russian), Nauka, Moscow, **1964**, p. 24.
104. F. Herrmann, *Ber.* **1905**, 38, 2813.
105. R. Uson, A. Laguna, M. Laguna, *Inorg. Syn.* **1989**, 26, 85.
106. R. S. Wade, C. E. Castro, *Inorg. Chem.* **1985**, 24, 2862.
107. D. Brenner, A. Davison, J. Lister-James, A. G. Jones, *Inorg. Chem.* **1984**, 23, 3793.
108. H. Taube, *Chem. Rev.* **1951**, 50, 69.
109. Ref. [2], Chapter 5, p. 393.
110. H. Kagan, J.-L. Namy, *Tetrahedron* **1980**, 42, 6573.
111. J. R. Pugh, T. J. Meyer, *J. Am. Chem. Soc.* **1992**, 114, 3784.
112. M. Green, N. K. Jetha, R. J. Mercer, N. C. Norman, A. G. Orpen, *J. Chem. Soc., Dalton Trans.* **1988**, 1843.
112. U. Kölle, *Coord. Chem. Rev.* **1994**, 135, 623.
114. S. F. Nelsen, P. J. Hintz, *J. Am. Chem. Soc.* **1972**, 94, 7114.
115. J. Kiwi, K. Kalyanasundaram, M. Grätzel, *Struct. Bond.* **1981**, 49, 37.
116. F. A. Cotton, G. Wilkinson, *Advanced Inorganic Chemistry*, 5th Ed., Wiley, New York, **1988**, p. 316.
117. G. A. Carriedo, M. C. Crespo, V. Riera, M. G. Sanchez, M. L. Valin, D. Moreiras, X. Solans, *J. Organomet. Chem.* **1986**, 302, 47.
118. R. B. King, *Inorg. Chem.* **1965**, 4, 1518.
119. G. W. Parshall, *Inorg. Syn.* **1977**, 17, 110.
120. R. B. King, *Organometallic Syntheses* Academic Press, New York, **1965**, Vol. 1, p. 70.
121. J. E. Sheat, *J. Organomet. Chem. Library* **1977**, 7, 461.
122. R. D. Kemmit, D. R. Russell in *Comprehensive Organometallic Chemistry* (Eds: G. Wilkinson, F. G. A. Stone, E. W. Abel), Pergamon, Oxford, **1982**, Vol. 5, Chapter 34, p. 244.
123. R. W. Albach, U. Kürstardt, J. Behm, B. Ebert, M.-H. Delville, D. Astruc, *J. Organomet. Chem.* **1993**, 450, 165.
124. G. E. Herberich, W. Klein, U. Kölle, D. Spiliotis, *Chem. Ber.* **1992**, 125, 1589.
125. G. E. Herberich, E. Bauer, J. Schwarzer, *J. Organomet. Chem.* **1969**, 17, 445.
126. S. Nlate, V. Guerschais, C. Lapinte, *J. Organomet. Chem.* **1992**, 434, 89.
127. F. Calderazzo, G. Pampaloni, U. Englert, J. Strahle, *J. Organomet. Chem.* **1990**, 383, 45.
128. W. J. Bowyer, W. E. Geiger, *J. Am. Chem. Soc.* **1985**, 107, 5657.
129. P. Legzdins, R. Reina, M. J. Shaw, R. J. Batchelor, F. W. B. Einstein, *Organometallics* **1993**, 12, 1029.
130. A. Peloso, *J. Chem. Soc., Dalton Trans.* **1984**, 249.
131. J. Ruiz, F. Ogliaro, J.-Y. Saillard, J.-F. Halet, F. Varret, D. Astruc, *J. Am. Chem. Soc.* **1998**, 120, 11693.
132. K. N. Brown, P. T. Gulyas, P. A. Lay, N. S. McAlpine, A. F. Masters, L. Phillips, *J. Chem. Soc., Dalton Trans.* **1993**, 835.
133. J. S. Miller, A. J. Epstein, W. M. Reiff, *Chem. Rev.* **1988**, 88, 201.
134. S. Nlate, J. Ruiz, J.-C. Blais, D. Astruc, *Chem. Commun.* **2000**, 417.
135. S. Nlate, J. Ruiz, V. Sartor, R. Navarro, J.-C. Blais, D. Astruc, *Chem. Eur. J.* **2000**, 6, 2544.
136. R. Davis, L. A. P. Kane-Maguire in *Comprehensive Organometallic Chemistry* (Eds: G. Wilkinson, F. G. A. Stone, E. W. Abel), Pergamon, Oxford, **1982**, Vol. 3, Chapter 26.2, p. 975.

137. H. Brunner, H. Koch, *Chem. Ber.* **1982**, *115*, 65.
138. T. Bockman, J. K. Kochi, *J. Am. Chem. Soc.* **1989**, *111*, 4669.
139. D. Astruc, J.-R. Hamon, G. Althoff, E. Román, P. Batail, P. Michaud, J.-P. Mariot, F. Varret, D. Cozak, *J. Am. Chem. Soc.* **1979**, *101*, 5445.
140. (a) D. Astruc, *Acc. Chem. Res.* **1986**, *19*, 377; (b) D. Astruc, *Comments Inorg. Chem.* **1987**, *6*, 61.
141. D. Astruc, J.-R. Hamon, M. Lacoste, M.-H. Desbois, E. Román, *Organomet. Synthesis* (Ed.: R.B. King), *Vol. IV*, **1988**, p. 172–187.
142. (a) J. C. Green, M. R. Kelly, M. P. Payne, E. A. Seddon, D. Astruc, J.-R. Hamon, P. Michaud, *Organometallics* **1983**, *2*, 211; (b) D. Briggs Handbook of X-ray and Photoelectron Spectroscopy, Heyden, London, **1977**; (c) C. Cauletti, J. C. Green, M. R. Kelly, P. Powell, J. Van Tilborg, J. Robbin, J. Smart *Electron Spectrosc. Relat. Phenom.* **1980**, *19*, 327.
143. (a) G. E. Herberich, G. Greiss, H. F. Heil, J. Müller *J. Chem. Soc. Chem. Commun.* **1971**, 1328; (b) G. Herberich In *Comprehensive Organometallic Chemistry* (Eds.: G. Wilkinson, F. G. A. Stone, W. E. Abel), Pergamon, London, **1982**, Vol 5, p. 381.
144. M. V. Rajasekharan, S. Giezyński, J. H. Ammeter, J.-R. Hamon, P. Michaud, D. Astruc, *J. Am. Chem. Soc.*, **1982**, *104*, 2400.
145. J.-P. Mariot, P. Michaud, S. Lauer, D. Astruc, A. X. Trautwein, F. Varret, *J. Physique* **1983**, *44*, 1377.
146. F. Ogliaro, J.-Y. Saillard, J.-F. Halet, D. Astruc, *New J. Chem.* **2000**, *24*, 257.
147. E. O. Fisher, H. Waversik, *J. Organomet. Chem.* **1967**, *8*, 185.
148. E. O. Fischer, M. F. Schmidt, *Chem. Ber.* **1966**, *99*, 2206.
149. A. N. Nesmeyanov, A. N. Vol'kenau, I. N. Bolesova, *Tetrahedron Let.* **1963**, 1725.
150. I. U. Khand, P. L. Pauson, W. E. Watts, *J. Chem. Soc.* **1968**, C 2257.
151. D. Briggs, *Handbook of X-Ray and Photoelectron Spectroscopy*, Heyden, London, **1977**.
152. C. Cauletti, J. C. Green, M. R. Kelly, P. Powell, J. Van Tilborg, J. Robbins, J. Smart, *J. Electron Spectros. Relat. Phenom.* **1980**, *39*, 1.
153. J. E. Herberich, G. Greiss, H. F. Heil, J. Müller, *J. Chem. Soc. Chem. Commun.* **1971**, 1328.
154. A. N. Nesmeyanov, N. A. Vol'kenau, L. S. Shilovtseva, V. A. Petrakova, *J. Organomet. Chem.* **1973**, *61*, 329.
155. E. Alonso, J. Ruiz, D. Astruc, *J. Clust. Sci.* **1998**, *9*, 271.
156. M.-H. Desbois, P. Michaud, D. Astruc, *J. Chem. Soc., Chem. Commun.* **1985**, 450.
157. J. Ruiz, V. Guerschais, D. Astruc, *J. Chem. Soc., Chem. Commun.* **1989**, 812.
158. J.-C. Gressin, D. Michelet, L. Nadjo, J. M. Savéant, *Nouv. J. Chim.* **1979**, 545.
159. D. Astruc, E. Román, J.-R. Hamon, P. Batail, *J. Am. Chem. Soc.* **1979**, *101*, 2240.
160. J.-R. Hamon, D. Astruc, E. Román, P. Batail, J. J. Meyerle, *J. Am. Chem. Soc.* **1981**, *103*, 2431.
161. D. Astruc, J.-R. Hamon, E. Román, P. Michaud, *J. Am. Chem. Soc.* **1981**, *103*, 7502.
162. J.-R. Hamon, D. Astruc, *Organometallics* **1988**, *7*, 1036.
163. C. Bossard, S. Rigaut, D. Astruc, M.-H. Delville, G. Félix, A. Février-Bouvier, J. Amiel, S. Flandrois, P. Delhaès, *J. Chem. Soc., Chem. Commun.* **1993**, 333.
164. D. Astruc in *Mechanisms and Processes in Molecular Chemistry* (Ed.: D. Astruc), Gauthier-Villars, Paris, *New J. Chem.* **1992**, *16*, 305.
165. M.-H. Desbois, D. Astruc, *Angew. Chem. Int. Engl.* **1989**, *101*, 459.
166. D. Astruc, D. Mandon, A. M. Madonik, P. Michaud, N. Ardoin, F. Varret, *Organometallics* **1990**, *9*, 2155.
167. J. Morrow, D. Catheline, M.-H. Desbois, J. M. Manriquez, J. Ruiz, D. Astruc, *Organometallics* **1987**, *6*, 2605.
168. J. R. Morrow, D. Astruc, *Bull. Soc. Chim. Fr.* **1992**, *129*, 319.
169. A. F. Hebrard, M. J. Roseinsky, R. C. Hadden, D. W. Murphy, S. H. Glarum, T. T. M. Palbra, A. P. Ramirez, A. R. Kortan, *Nature* **1991**, *350*, 600.
170. J. Stinchcombe, A. Pénicaud, P. Bhyrappa, P. D. W. Boyd, C. A. Reed, *J. Am. Chem. Soc.* **1993**, *115*, 5212.
171. P. D. W. Boyd, P. Bhyrappa, P. Paul, J. Stinchcombe, R. D. Bolskar, Y. Sun, C. A. Reed, *J. Am. Chem. Soc.* **1995**, *117*, 2907.
172. J.-R. Hamon, D. Astruc, *J. Am. Chem. Soc.* **1983**, *105*, 5951.

173. I. Fridovitch in *Free Radicals in Biology* (Ed.: W. A. Pryor), Academic Press, New York, **1976**, pp. 239–277.
174. D. Astruc, M.-H. Delville, M. Lacoste, J. Ruiz, F. Moulines, J.-R. Hamon in *Recent Advances in the Chemistry of the Main-Group Elements* (Ed.: N. Hosmane), *Phosphorus, Sulfur, Silicon and the Related Elements*, **1994**, 87, 11.
175. A. Loupy, B. Tchoubar, *Salt Effects in Organic and Organometallic Chemistry*, VCH, Weinheim, **1992**.
176. A. M. Madonik, D. Astruc, *J. Am. Chem. Soc.* **1984**, 106, 2437.
177. S. Rigaut, M.-H. Delville, D. Astruc, *J. Am. Chem. Soc.* **1997**, 119, 11132.
178. D. Astruc, S. Rigaut, E. Alonso, M.-H. Delville, J. Ruiz, *Hung. Chim. Acta* **1998**, 135, 751.
179. J. Ruiz, M. Lacoste, D. Astruc, *J. Chem. Soc., Chem. Commun.* **1989**, 813.
180. J. Ruiz, M. Lacoste, D. Astruc, *J. Am. Chem. Soc.* **1990**, 112, 5471.
181. F. R. Mayo, *Acc. Chem. Res.* **1968**, 1.
182. A. G. Davies, *J. Organomet. Chem.* **1980**, 200, 87.
183. *Foundations of Chemical Kinetics*, E. N. Mir, Moscow, **1979** (English translation, p. 247).
184. Ref. [2], Chapter 6: Chain reactions.
185. M.-H. Desbois, D. Astruc, *New J. Chem.* **1989**, 13, 595.
186. M. J. Carney, J. S. Lesniak, M. D. Likar, J. R. Pladziewicz, *J. Am. Chem. Soc.* **1984**, 106, 2565.
187. J. C. Smart, B. L. Pinsky, *J. Am. Chem. Soc.* **1980**, 102, 1009.
188. D. N. Hendrickson, Y. S. Sohn, H. B. Gray, *Inorg. Chem.* **1971**, 10, 1559.
189. H. J. Schumann, *Organomet. Chem.* **1986**, 304, 341.
190. R. F. Jordan, R. E. Lapointe, C. S. Bajgur, S. F. Echols, R. Willett, *J. Am. Chem. Soc.* **1987**, 109, 4111.
191. a) R. P. Aggarwal, N. G. Connelly, M. C. Crespo, B. J. Dunne, P. M. Hopkins, A. G. Orpen, *J. Chem. Soc., Dalton Trans.* **1992**, 655; b) J. M. Forward, D. M. P. Mingos, A. V. Powell, *J. Organomet. Chem.* **1994**, 465, 251.
192. C. A. Reed, *Acc. Chem. Res.* **1998**, 31, 133.
193. B. T. King, Z. Janusek, B. Grüner, M. Trammel, B. C. Noll, J. Michl, *J. Am. Chem. Soc.* **1996**, 118, 3313; S. H. Strauss, *Chem. Rev.* **1993**, 93, 927.
194. W. E. Geiger in *Organometallic Radical Processes*, *J. Organomet. Chem. Library* 22 (Ed.: W. C. Trogler), Elsevier, Amsterdam, **1990**, pp. 142–172.
195. C. Guillon, P. Vierling, *J. Organomet. Chem.* **1994**, 464, C42.
196. A. Pedersen, M. Tilset, K. Følting, K. G. Caulton, *Organometallics* **1995**, 14, 875.
197. M. Hudlicky *Oxidation in Organic Chemistry*; ACS Monograph 186, American Chemical Society: Washington, DC, **1990**.
198. M. Bjorgvinsson, T. Heinze; H. W. Roesky, F. Pauer, D. Stalke, G. M. Sheldrick, *Angew. Chem., Int. Ed. Engl.* **1991**, 30, 1677.
199. a) L. Song, W. C. Trogler, *Angew. Chem., Int. Ed. Engl.* **1992**, 31, 770; b) F. A. Cotton, L. Falvello, T. Ren, K. Vidyasagar, *Inorg. Chim. Acta* **1992**, 194, 163.
200. H. H. Morgan, *J. Chem. Soc.* **1923**, 2901.
201. R. Fernandez-Galan, B. R. Manzano, A. Otero, M. Lanfranchi, M. A. Pellinghelli, *Inorg. Chem.* **1994**, 33, 2309.
202. C. White, S. J. Thompson, P. M. Maitlis, *J. Organomet. Chem.* **1977**, 134, 319.
203. N. G. Connelly, T. Einig, G. Garcia Herbosa, P. M. Hopkins, C. Mealli, A. G. Orpen, G. M. Rosair, F. Viguri, *J. Chem. Soc., Dalton Trans.* **1994**, 2025.
204. C. L. Jenkins, *Chem. Soc.* **1972**, 94, 843, 856.
205. A. Heumann, K.-J. Jens, M. Reglier, *Prog. Inorg. Chem.* **1994**, 42, 505.
206. A. R. Pray, *Inorg. Synth.* **1957**, 5, 153.
207. M. F. Joseph, J. A. Page, M. C. Baird, *Organometallics* **1984**, 3, 1749.
208. Ref. [13], Chapter 7.
209. S. P. Schmidt, F. Basolo, W. C. Trogler, *Inorg. Chim. Acta* **1987**, 131, 181.
210. D. Mandon, L. Toupet, D. Astruc, *J. Am. Chem. Soc.* **1986**, 108, 1320.
211. A. J. Pearson in *Comprehensive Organometallic Chemistry* (Eds: G. Wilkinson, F. G. A. Stone, E. W. Abel), Pergamon, Oxford, **1982**, Vol. 8, Chapter 58, p. 939.
212. M. W. Droege, W. D. Harman, H. Taube, *Inorg. Chem.* **1987**, 26, 1309.

213. W. Adam, M. A. Miranda, F. Mojjarrad, H. Sheikh, *Chem. Ber.* **1994**, *127*, 875.
214. D. Touchard, J.-L. Fillaut, D. U. Khasnis, P. H. Dixneuf, C. Meali, D. Massi, L. Toupet, *Organometallics* **1988**, *7*, 67.
215. K. L. Rollick, J. K. Kochi, *J. Am. Chem. Soc.* **1982**, *104*, 1319.
216. J. B. Chlistunoff, A. J. Bard, *Inorg. Chem.* **1992**, *31*, 4582.
217. T. H. Lemmen, E. G. Lundquist, L. F. Rhodes, B. R. Sutherland, D. E. Werterberg, K. G. Caulton *Inorg. Chem.* **1986**, *25*, 3915.
218. Ref. [6], Chapter 16.
219. A. E. Shilov *Metal Complexes in Biomimetic Chemical Reactions*, CRC Press, New York, **1997**.
220. A. Davison, R. H. Holm, *Inorg. Synth.* **1967**, *10*, 18; A. Davison, R. H. Holm, *Inorg. Synth.* **1967**, *10*, 22.
221. P. Baird, J. A. Bandy, M. L. H. Green, A. Hamnett, E. Marseglia, D. S. Obertelli, K. Prout, J. Qin, *J. Chem. Soc., Dalton Trans.* **1991**, 2377.
222. G. Olah, *Acc. Chem. Res.* **1980**, *13*, 330.
223. M. Gilet, A. Mortreux, J.-C. Folest, F. Petit, *J. Am. Chem. Soc.* **1983**, *105*, 3876.
224. L. Ebersson, L. Jonsson, O. Sanneskog, *Acta Chem. Scand., Ser. B.* **1985**, *39*, 113.
225. L. Ebersson, F. Radner, *Acc. Chem. Res.* **1987**, *20*, 53.
226. M. T. Mocella, M. S. Okamoto, E. K. Barefield, *Synth. React. Inorg. Met.-Org. Chem.* **1974**, *4*, 69.
227. K. G. Caulton, *Coord. Chem. Rev.* **1975**, *14*, 317.
228. N. G. Connelly, P. T. Draggett, M. Green, T. A. Kuc, *J. Chem. Soc., Dalton Trans.* **1977**, 70.
229. C. C. Addison, J. Lewis, *Quater. Rev.* **1955**, *9*, 115.
230. E. K. Kim, J. K. Kochi, *J. Am. Chem. Soc.* **1991**, *113*, 4962.
231. W. K. Musker, T. L. Wolford, P. B. Roush, *J. Am. Chem. Soc.* **1978**, *100*, 6416.
232. F. Seel, *Z. Anorg. Chem.* **1950**, *261*, 75.
233. R. R. Thomas, A. Sen, *Inorg. Synth.* **1990**, *28*, 63.
234. J. K. Kochi, *Acc. Chem. Res.* **1992**, *25*, 39.
235. a) A. E. Arbuzov, V. M. Zoroastrova, *Izv. Akad. Nauk SSSR, Ser. Khim.* **1952**, 818; b) V. Yu. Kukushin, N. P. Kiseleva *Koord. Khim.* **1988**, *14*, 334.
236. G. W. Cowell, A. Ledwith, A. C. White, H. J. Woods, *J. Chem. Soc. B* **1970**, 227.
237. W. Kaim, *Acc. Chem. Res.* **1985**, *18*, 160.
238. H. Bock, W. Kaim, *Acc. Chem. Res.* **1982**, *15*, 9.
239. N. Bartlett, D. H. Lohmann, *J. Chem. Soc.* **1962**, 5253.
240. a) T. J. Richardson, N. Bartlett, *J. Chem. Soc. Chem. Commun.* **1974**, 427; b) K. Zücher, T. J. Richardson, O. Glemser, N. Bartlett, *Angew. Chem. Int. Ed. Engl.* **1980**, *19*, 944.
241. a) J. P. Dinnocenzo, T. E. Banach, *J. Am. Chem. Soc.* **1986**, *108*, 6063; b) J. P. Dinnocenzo, T. E. Banach *J. Am. Chem. Soc.* **1988**, *110*, 911.
242. J. P. Dinnocenzo, T. E. Banach, *J. Am. Chem. Soc.* **1989**, *111*, 8646.
243. D. T. Sawyer, J. S. Valentine, *Acc. Chem. Res.* **1981**, *14*, 393.
244. M. L. H. Green, D. K. P. Ng, R. C. Tovey, A. N. Chernega, *J. Chem. Soc., Dalton Trans.* **1993**, 3203.
245. F. G. N. Cloke, P. J. Fyne, V. C. Gibson, M. L. H. Green, M. J. Ledoux, R. N. Perutz, A. Dix, A. Gourdon, K. Prout, *J. Organomet. Chem.* **1984**, *277*, 61.
246. D. A. Slack, M. C. Baird, *J. Am. Chem. Soc.* **1976**, *98*, 5539.
247. *The Chemistry of Diazonium and Diazo Groups* (Ed.: S. J. Patai), John Wiley & Sons, New York, **1978**.
248. R. M. Eloffson, F. F. Gadallah, *J. Org. Chem.* **1969**, *34*, 854.
249. M. P. Doyle, J. K. Guy, K. C. Brown, S. N. Mahapatro, C. M. van Zyl, J. R. Pladziewicz, *J. Am. Chem. Soc.* **1987**, *109*, 1536.
250. A. Roe, *Org. React.* **1949**, *5*, 193.
251. U. Kölle in *Mechanism and Processes in Molecular Chemistry* (Guest Ed.: D. Astruc), Gauthier-Villars, Paris, New. *J. Chem.* **1992**, *16*, 157.
252. T. E. Bitterwolf, A. C. Ling, *J. Organomet. Chem.* **1973**, *57*, C17.
253. U. T. Mueller-Westerhoff, *Angew. Chem. Int. Ed. Engl.* **1986**, *25*, 702.

254. R. H. Crabtree *The Organometallic Chemistry of Transition Metals*, 2nd Ed., Wiley, New York, **1994**, Chapters 3, 6 and 15.
255. J. Norton, *Acc. Chem. Res.* **1979**, *12*, 139.
256. J. R. Bleake, W.-J. Peng, *Organometallics* **1986**, *5*, 635.
257. D. O'Hare, V. J. Murphy, N. J. Kaltsoyannis, *J. Chem. Soc. Dalton Trans.* **1993**, 383.
258. E. Steckhan, *Top. Curr. Chem.* **1987**, *142*, 1.
259. E. Steckhan, *Angew. Chem., Int. Ed. Engl.* **1986**, *25*, 683.
260. L. Eberson, B. Larsson, *Acta Chem. Scand., Ser. B* **1986**, *40*, 210.
261. (a) M. Lacoste, D. Astruc, M.-T. Garland, F. Varret, *Organometallics*, **1988**, *7*, 2253; (b) M. Lacoste, M.-H. Delville, N. Ardoin, D. Astruc, *Organometallics* **1997**, *16*, 2343.
262. (a) R. D. Bolskar, R. S. Mathur, C. A. Reed, *J. Am. Chem. Soc.* **1996**, *118*, 13093; (b) C. Reed, R. D. Bolskar, *Chem. Rev.* **2000**, *100*, 1075.
263. B. Boduszek, H. J. Shine, *J. Org. Chem.* **1988**, *53*, 5142.
264. S. Lochynski, H. J. Shine, M. Siroka, T. K. Venkatachalam, *J. Org. Chem.* **1990**, *55*, 2702.
265. O. Hammerich, V. D. Parker, *Electrochim. Acta* **1973**, *18*, 537.
266. H. Volz, W. Lotsch, *Tetrahedron Lett.* **1969**, 2275.
267. H. J. Dauben Jr, L. R. Honnen, K. M. Harmon, *J. Org. Chem.* **1960**, *25*, 1442.
268. O. B. Ryan, M. Tilset, V. D. Parker, *J. Am. Chem. Soc.* **1990**, *112*, 2618.
269. L. R. Eberson, *Adv. Phys. Org. Chem.* **1982**, *18*, 79.
270. a) A. J. Birch, K. B. Chamberlain, M. A. Hass, D. J. Thompson, *J. Chem. Soc., Perkin Trans.* **1973**, *1*, 1882; b) A. J. Pearson, *Acc. Chem. Res.* **1980**, *13*, 463.
271. J. C. Hayes, G. D. N. Pearson, N. J. Cooper, *J. Am. Chem. Soc.* **1981**, *103*, 4648.
272. G. S. Bodner, J. A. Gladysz, M. F. Nielsen, V. D. Parker, *J. Am. Chem. Soc.* **1987**, *109*, 1757.
273. E. W. Abel, S. P. Tyfield, *Adv. Organomet. Chem.* **1970**, 126.
274. Y. S. Yu, R. A. Jacobson, R. J. Angelici, *Inorg. Chem.* **1982**, *21*, 3106.
275. C. Eaborn, N. Farrell, J. L. Murphy, A. Pidcock, *J. Chem. Soc., Dalton Trans.* **1976**, 58.
276. N. G. Connelly, P. M. Hopkins, A. G. Orpen, J. Slater, *J. Chem. Soc., Dalton Trans.* **1992**, 3303.
277. O. Kahn, *Molecular Magnetism*, VCH, New York, **1993**.
278. J. B. Torrance, *Acc. Chem. Res.* **1979**, *12*, 79.
279. L. R. Melby, R. J. Harder, W. R. Hertler, R. E. Mahler, R. E. Benson, W. E. Mochel, *J. Am. Chem. Soc.* **1962**, *84*, 3374.
280. J. S. Miller, A. J. Epstein, W. M. Reiff, *Chem. Rev.* **1988**, *88*, 201.
281. W. Kaim, M. Moscherosh, *Coord. Chem. Rev.* **1994**, *129*, 157.
282. U. Honrath, H. Vahrenkamp, *Z. Naturforsch.* **1984**, *39b*, 555.
283. J. S. Miller, D. T. Glatzhofer, D. M. O'Hare, W. M. Reiff, A. Chakraborty, A. J. Epstein, *Inorg. Chem.* **1989**, *28*, 2930.
284. C. Guillon, P. Vierling, *J. Organomet. Chem.* **1994**, 464, C42.
285. M. D. Haley in *Encyclopedia of Electrochemistry of the Elements* (Ed.: A. J. Bard), Marcel Dekker, New York, **1980**, Vol. IV, p. 283.
286. J. V. Crivello, J. H. W. Lam, *J. Org. Chem.* **1978**, *43*, 3055.
287. R. S. Iyer, J. P. Selegue, *J. Am. Chem. Soc.* **1987**, *109*, 910.
288. D. H. Evans in *Encyclopedia of Electrochemistry of the Elements* (Ed.: A. J. Bard), Marcel Dekker, New York, **1978**, Vol. XII, p. 563.
289. C. Elschenbroich, G. Heikenfeld, M. Wunsch, W. Massa, G. Baum, *Angew. Chem. Int. Ed. Engl.* **1988**, *27*, 414.
290. R. L. Rich, H. Taube, *J. Am. Chem. Soc.* **1954**, *76*, 2608.
291. S. W. Feldberg, L. Jetic, *J. Phys. Chem.* **1972**, *76*, 2439.
292. M. Chanon, *Acc. Chem. Res.* **1987**, *20*, 214.
293. L. Eberson "Electron Transfer in Organic Chemistry" Springer Verlag, Berlin, **1987**, Chapter X.
294. E. Román, D. Astruc, A. Darchen, *J. Chem. Soc., Chem. Commun.* **1976**, 512–513.
295. G. A. Russell, *Spec. Publ. Chem. Soc.* **1970**, *24*, 271.
296. N. Kornblum, *Angew. Chem.* **1975**, *87*, 797; *Angew. Chem. Int. Ed. Engl.* **1975**, *14*, 734.
297. J. F. Bunnett, *Acc. Chem. Res.* **1978**, *11*, 413; *Ibid* **1992**, *25*, 2.
298. J.-M. Savéant, *Acc. Chem. Res.* **1980**, *13*, 323

299. J.-M. Savéant in *Mechanisms and Processes in Molecular Chemistry* (Guest Ed.: D. Astruc), Gauthier-Villars, Paris, *New J. Chem.* **1992**, 16, 131.
300. R. D. Rieke, H. Kojima, K. Öfele, *J. Am. Chem. Soc.* **1976**, 98, 6735.
301. R. D. Rieke, H. Kojima, K. Öfele, *Angew. Chem. Int. Ed. Engl.* **1980**, 19, 538.
302. M. I. Bruce, *Coord. Chem. Rev.* **1987**, 76, 1.
303. J. K. Kochi, *J. Organomet. Chem.* **1986**, 300, 139.
304. R. H. Magnuson, R. Meirowitz, S. J. Zulu, W. P. Giering, *Organometallics* **1983**, 2, 460.
305. D. Miholová, A. A. Vlček, *J. Organomet. Chem.* **1982**, 240, 413.
306. B. A. Narayanan, C. Amatore, C. P. Casey, J. K. Kochi, *J. Am. Chem. Soc.* **1983**, 105, 6351.
307. C. Moinet, E. Román, D. Astruc, *J. Electroanal. Chem. Interfacial Electrochem.* **1981**, 241, 121.
308. A. Darchen, *J. Chem. Soc. Chem., Commun.* **1983**, 768; *J. Organomet.* **1986**, 302, 389.
309. P. Boudeville, A. Darchen, *Inorg. Chem.* **1991**, 30, 1663.
310. D. Astruc, M.-H. Delville, J. Ruiz in *Molecular Electrochemistry of Inorganic, Bioinorganic and Organometallic Compounds* (Eds: A. J. L. Pombeiro, J. A. Mc Cleverty), NATO ASI Series, Kluwer, Dordrecht, **1993**, 385, 277.
311. D. R. Tyler, *Coord. Chem. Rev.* **1985**, 63, 217.
312. D. R. Tyler, *Comments Inorg. Chem.* **1986**, 5, 215.
313. R. Moulton, T. W. Weidman, K. P. C. Vollhardt, A. J. Bard, *Inorg. Chem.* **1986**, 25, 1846.
314. D. S. Brown, M.-H. Delville, R. Boese, K. P. C. Vollhardt, D. Astruc, *Angew. Chem.* **1994**, 106, 715; *Angew. Chem. Int. Ed. Engl.* **1994**, 33, 661.
315. M.-H. Delville, D. S. Brown, K. P. C. Vollhardt, D. Astruc, *J. Chem. Soc., Chem. Commun.*, **1991**, 1355.
316. D. S. Brown, M.-H. Delville, K. P. C. Vollhardt, D. Astruc, *New J. Chem.* **1992**, 16, 899.
317. D. S. Brown, M.-H. Delville, K. P. C. Vollhardt, D. Astruc, *Organometallics* **1996**, 15, 2360.
318. M. I. Bruce, D. C. Kehoe, J. G. Matison, B. K. Nicholson, P. H. Rieger, M. L. J. Williams, *J. Chem. Soc. Chem. Commun.* **1982**, 442.
319. M. I. Bruce, J. G. Mattison, B. K. Nicholson, *J. Organomet. Chem.* **1983**, 247, 321.
320. M. G. Richmond, J. K. Kochi, *Inorg. Chem.* **1986**, 25, 656 and 1334; *Organometallics* **1987**, 6, 254.
321. H. H. Ohst, J. K. Kochi, *J. Chem. Soc. Chem. Commun.* **1986**, 121; *Inorg. Chem.* **1986**, 25, 2066.
322. M. Arewogoda, B. H. Robinson, J. Simpson, *J. Am. Chem. Soc.* **1983**, 105, 1893.
323. A. J. Downard, B. H. Robinson, J. Simpson, *Organometallics* **1986**, 5, 1122, 1132 and 1140.
324. S. Aime, M. Botta, R. Gobetto, D. Osella, *Organometallics* **1985**, 4, 1475; *Inorg. Chim. Acta* **1986**, 115, 129.
325. E. Cabrera, J. C. Daran, Y. Jeannin, *J. Chem. Soc. Chem. Commun.* **1988**, 607.
326. F. Richter, H. Varenkamp, *Angew. Chem. Int. Ed. Engl.* **1978**, 17, 864.
327. M. O. Albers, N. J. Coville, E. Singleton, *J. Organomet. Chem.* **1987**, 323, 37 and 326, 229.
328. N. G. Connelly, S. J. Raven, G. A. Carriedo, V. Riera, *J. Chem. Soc. Chem. Commun.* **1986**, 992.
329. T. Venäläinen, T. Pakkanen, *J. Organomet. Chem.* **1984**, 266, 269.
330. J. Pursiainen, T. A. Pakkanen, J. Jääskeläinen, *J. Organomet. Chem.* **1985**, 290, 85.
331. J. Rimmelin, P. Lemoine, M. Gross, A. A. Bahsoun, J. A. Osborn, *Nouv. J. Chim.* **1985**, 9, 181.
332. P. Lahuerta, J. Latorre, M. Sanau, H. Kisch, *J. Organomet. Chem.* **1985**, 286, C27.
333. E. K. Lahdi, C. Mahé, H. Patin, A. Darchen, *J. Organomet. Chem.* **1983**, 246, C61 and 259, 189.
334. E. K. Lahdi, C. Mahé, H. Patin, A. Darchen, *Nouv. J. Chim.* **1982**, 6, 539; *Organometallics* **1984**, 3, 1128.
335. E. Alonso, D. Astruc, *J. Am. Chem. Soc.* **2000**, 122, 3222.
336. J. W. Hersherberger, R. J. Klingler, J. K. Kochi, *J. Am. Chem. Soc.* **1983**, 105, 61.
337. M. Tilset in *Energetics of Organometallic Species* (Ed.: S. Martinho), Kluwer, Dordrecht, **1992**, p. 109.

338. M. Tilset in *Molecular Electrochemistry of Inorganic, Bioinorganic and Organometallic Compounds*, NATO ASI Series C385 (Eds.: A. J. L. Pombeiro, J. A. McCleverty), Kluwer, Dordrecht, **1993**, p. 269.
339. J. W. Herschberger, R. J. Klingler, J. K. Kochi, *J. Am. Chem. Soc.* **1982**, *104*, 3034.
340. D. Catheline, D. Astruc, Proceedings of the XXIIth Intern. Conf. Coord. Chem. Budapest, *Coord. Chem.* **1982**, *23*, F41.
341. J.-N. Verpeaux, M.-H. Desbois, A. Madonik, C. Amatore, D. Astruc, *Organometallics* **1990**, *9*, 630.
342. M.-H. Desbois, D. Astruc, *J. Chem. Soc., Chem. Commun.* **1990**, 943.
343. M.-H. Desbois, D. Astruc, *J. Chem. Soc., Chem. Commun.*, **1988**, 472.
344. W. C. Trogler in *Organometallic Radical Processes*, *J. Organomet. Chem. Library* 22 (Ed.: W. C. Trogler), Elsevier, Amsterdam, **1990**, p. 306.
345. H. Taube, *J. Chem. Ed.* **1986**, *45*, 452.
346. T. J. Katz, T. H. Ho, N. Y. Shih, V. Ying, Y. I. W. Stuart, *J. Am. Chem. Soc.* **1984**, *106*, 2659.
347. J. L. Hérisson, Y. Chauvin, *Makromol. Chem.* **1970**, *141*, 161.
348. J.-M. Savéant, *Acc. Chem. Res.* **1980**, *13*, 323.
349. R. W. Murray in *Electroanalytical Chemistry* (Ed.: A. J. Bard), Marcel Dekker, New York, **1984**, Vol. 13, pp. 191–357.
350. J.-F. Fauvarque, M. A. Petit, F. Pflüger, A. Jutand, C. Chevrot, M. Troupel, *Makromol. Chem. Commun.* **1983**, *4*, 455.
351. Y. Rollin, G. Meyer, M. Troupel, J.-F. Fauvarque, J. Périchon, *J. Chem. Soc., Chem. Commun.* **1983**, 793.
352. C. Moinet, E. Román, D. Astruc, *J. Am. Chem. Soc.* **1981**, *103*, 2431.
353. A. Buet, A. Darchen, C. Moinet, *J. Chem. Soc., Chem. Commun.* **1979**, 447.
354. E. Román, R. Dabard, C. Moinet, D. Astruc, *Tetrahedron Lett.* **1979**, *16*, 1433.
355. M. Tokuaka, *Collect. Czech. Chem. Commun.* **1932**, *4*, 444; **1934**, *6*, 339.
356. S. Rigaud, Ph. D. thesis, University Bordeaux I, **1997**.
357. J. Losada, I. Cuadrado, M. Morán, C. M. Casado, B. Alonso, M. Barranco, *Anal. Chim. Acta*, **1996**, *251*, 5.
358. I. Cuadrado, M. Morán, J. Losada, C. M. Casado, C. Pascual, B. Alonso, F. Lobete In *Advances in Dendritic Macromolecules* (Ed.: G. R. Newkome), JAI Press, Vol 3, Greenwich, Connecticut, **1996**, p. 151.
359. C. M. Casado, I. Cuadrado, M. Morán, B. Alonso, B. Garcia, B. Gonzales, J. Losada, *Coord. Chem. Rev.* **1999**, *185–186*, 53; I. Cuadrado, M. Morán, C. M. Casado, B. Alonso, J. Losada, *Coord. Chem. Rev.*, **1999**, *189*, 123.
360. A. Heller, *Acc. Chem. Res.* **1990**, *23*, 128.
361. Y. Degani, A. Heller, *J. Am. Chem. Soc.* **1988**, *110*, 2615.
362. I. Taniguchi, S. Miyamoto, S. Tomimura, F. M. Hawkrigide, *J. Electroanal. Chem.* **1988**, *240*, 33.
363. A. L. Crumbliss, H. A. O. Hill, D. Page, *J. Electroanal. Chem.* **1986**, *206*, 327.
364. Y. Degani, A. Heller, *J. Am. Chem. Soc.* **1989**, *111*, 2357, "Proceedings of the Third International Symposium on Redox Mechanism and Interfacial Properties of Molecules of Biological Importance" (Eds: G. Dryhurst, K. Niki, H. I. Honolulu), Plenum, New York, **1988**, p. 151.
365. C. Bourdillon, M. Majda, *J. Am. Chem. Soc.* **1990**, *112*, 1795.
366. T. E. Edmonds in *Chemical Sensors* (Ed.: T. E. Edmonds), Blackie, Glasgow, **1988**, Chapter 8, p. 193.
367. T. Saji, I. Kinoshita, *J. Chem. Soc., Chem. Commun.* **1986**, 716.
368. P. D. Beer, *Chem. Soc. Rev.* **1989**, *18*, 409.
369. P. D. Beer, *Advan. Inorg. Chem.* **1992**, *39*, 79.
370. P. D. Beer, *J. Chem. Soc., Chem. Commun.* **1996**, 689.
371. P. D. Beer, *Acc. Chem. Res.* **1998**, *31*, 71.
372. C. Valério, J.-L. Fillaut, J. Ruiz, J. Guittard, J.-C. Blais, D. Astruc, *J. Am. Chem. Soc.*, **1997**, *119*, 2588; D. Astruc, *Acc. Chem. Res.* **2000**, *33*, 287.
373. J. Guittard, J.-C. Blais, C. Valério, E. Alonso, J. Ruiz, J.-L. Fillaut, D. Astruc, *Pure Appl. Chem* **1998**, *70*, n° 4, 809; *Top. Curr. Chem.* **2000**, *210*, 229.
374. E. Alonso, C. Valério, J. Ruiz, D. Astruc, *New J. Chem.* **1997**, *21*, 1139–1141.

- 375. C. Valério, J. Ruiz, J.-L. Fillaut, D. Astruc, *C. R. Acad. Sci. Paris*, **1999**, 2, *Série II c*, 79.
- 376. C. Valério, E. Alonso, J. Ruiz, J.-C. Blais, D. Astruc, *Angew. Chem. Int. Ed. Engl.*, **1999**, 38, 1747.
- 377. C. Valério, F. Moulines, J. Ruiz, J.-C. Blais, D. Astruc, *J. Org. Chem.* **2000**, 65, 1996.
- 378. A. Vlček Jr., see this Section 2.2, Chapter 2.2.5.
- 379. W. Kaim, see this Section 2.2, Chapter 2.2.9.
- 380. S. Fukuzumi, see this Section 2.2, Chapter 2.2.8.
- 381. S. Fukuzumi, the *Phorphyrin Handbook*, Vol 8 (Eds.: K. M. Kadish, K. Smith, R. Guillard), Academic Press, San Diego, CA, 2000, pp. 115–152.
- 382. R. Guillard, K. M. Kadish, *Chem. Rev.* **1993**, **1988**, 88, 1121.

5 Electron-transfer Processes in Mononuclear Polypyridine Metal Complexes*

Antonín Vlček, Jr

5.1 Introduction

Transition metal complexes of 2,2'-bipyridine and other polypyridine ligands (N,N) show an exceptionally rich electron-transfer chemistry which makes them a clearly distinct class of coordination compounds. Detailed investigations of their electrochemistry, redox chemistry, and photochemistry have much strengthened our understanding of electron-transfer processes in general and enabled many interesting applications. Such important concepts as localization of a redox change [1–5], redox orbital [1, 3, 6], redox series [4, 7, 8], relations between electrochemistry and electronic spectroscopy [6, 9], or analogy between non-radiative decay of charge-transfer excited states and intramolecular electron transfer [10–14] were either discovered or deeply elaborated by use of metal–polypyridine complexes. In general, metal–polypyridines are known to exist in unusual oxidation states, to undergo sequential electron transfer, and/or to couple electron-transfer with bond activation. Consequently, they can act as redox catalysts [24, 30, 31], electron-transfer mediators [32], redox sensors [33–35], or electrochromic materials [36]. Moreover, their electron transfer reactivity is often retained upon electronic excitation, opening the field of photochemical excited-state electron transfer [37–39], with potential applications in light energy conversion [36, 40–43], photocatalysis [42, 44], fluorescence sensors [45], or in molecular electronic and photonic devices [38, 46].

The great structural variability of polypyridine complexes enable us to tune and control their redox properties over a very broad range. For example, variations in polypyridine ligand structure can shift the reduction or oxidation potential within a range almost 2 V wide. Further control can be achieved by changing the nature of the metal and, in mixed-ligand complexes, of ancillary ligands. Polypyridine com-

* This chapter is dedicated to the memory of my father, Professor Antonín A. Vlček (1927–1999), who has contributed much to the electrochemistry of metal–polypyridine complexes and to our understanding of underlying principles [1, 4–8, 15–29, 209].

plexes can be prepared stereochemically pure, with a predetermined chirality [47–50]. Moreover, it is relatively easy to connect metal–polypyridine units to form larger electro- and photo-active supermolecular assemblies, including dendrimers [38, 51–53]. The structural versatility and role of polypyridine complexes in processes and devices based on electron transfer are unique, paralleled perhaps only by metal porphyrins.

Transition metal polypyridine complexes have attracted much research interest for several decades. The first low-valent 2,2′-bipyridine (bpy) complexes, $[\text{Cr}(\text{bpy})_3]^+$ and $[\text{Cr}(\text{bpy})_3]^0$, were prepared by Herzog et al. as long ago as the fifties [54]. On the basis of magnetochemical data they were formulated as Cr^{I} and Cr^0 species, respectively. Soon after, facile electrochemical reduction of polypyridine complexes to their low-valent forms was observed by A. A. Vlcek. This was first demonstrated [22, 23] by reduction of $[\text{Co}^{\text{II}}(\text{bpy})_3]^{2+}$ to $[\text{Co}^{\text{I}}(\text{bpy})_3]^+$. Electrochemical reduction of Ni^{II} , Mn^{II} , and Cr^{III} complexes [25, 27] was described next. $[\text{Cr}(\text{bpy})_3]^{3+}$ is especially important [2, 25, 55] because this complex shows a six-step sequential reversible reduction, with a single electron being transferred in each step without a change in complex composition. A 7-membered redox series $[\text{Cr}(\text{bpy})_3]^z$; $z = 3+, 2+, 1+, 0, 1-, 2-, 3-$; was thus established and all its members isolated. The existence of such a redox series is a typical feature of metal–polypyridine chemistry. At about the same time, a redox-catalytic reactivity of polypyridine complexes was demonstrated by reduction of aromatic nitro compounds catalyzed by cobalt–bipyridine complexes [24]. These initial studies sparked a series of investigations of polypyridine (initially mostly bpy) complexes of other transition metals. Electrochemistry (polarography and, later, cyclic voltammetry) became the most important technique used to detect polypyridine complexes in unusual oxidation states and to assess their chemical stability. In parallel, many low-valent polypyridine complexes of almost all the first-row transition metals were prepared and isolated by chemical means, and their UV–Vis and IR absorption spectra determined, along with their magnetochemical properties [2]. The problem of redox change localization became soon apparent, because these studies revealed that it is often the polypyridine ligand which is reduced, instead of the metal atom. For example, $[\text{Cr}(\text{bpy})_3]^0$, originally believed to contain Cr^0 , was re-formulated as a Cr^{III} complex with three radical-anionic $\text{bpy}^{\cdot-}$ ligands, possibly with some electronic delocalization [2]. In the 80s, Bard et al. turned the attention to oxidation of bipyridine complexes at very positive potentials, finding that bpy and its analogs can also stabilize metal atoms in unusually high oxidation states [56–58].

A real explosion of research interest in metal polypyridines followed Adamson's and Gafney's discovery [59] that, upon irradiation with visible light, the long-lived excited state of $[\text{Ru}(\text{bpy})_3]^{2+}$ is oxidized in a bimolecular reaction with $[\text{Co}(\text{NH}_3)_5\text{Br}]^{2+}$ to $[\text{Ru}(\text{bpy})_3]^{3+}$. The great potential of bimolecular excited-state electron transfer for photochemical conversion and storage of light (solar) energy was immediately recognized [37]. The number of photo- and redox-active metal–polypyridine complexes was further extended by Wrighton's investigations [60–62] of the photochemistry of carbonyl complexes $[\text{Re}(\text{L})(\text{CO})_3(\text{N}, \text{N})]$. Photochemical research focused mostly on polypyridine complexes of heavy d^6 metals, especially Ru^{II} , Os^{II} , Re^{I} and, to a lesser extent, Rh^{III} and Ir^{III} . Many new polypyridine

ligands and their complexes were prepared. Their photochemical, photophysical, and electrochemical properties were investigated in much depth, especially by Balzani, Meyer, Elliott, DeArmond, Lever, Sutin, Creutz, Rillema, Scandola, and other research groups. The wealth of data available provided further insight into the molecular mechanism of metal–polypyridine electron-transfer reactions and revealed general structure–reactivity relationships and patterns. Sequential reduction by, at least, six one-electron steps have been observed [63–65] for tris-bipyridine complexes of Os^{II} and Ru^{II} , in addition to their metal-centered oxidation. On the basis of spectroscopic studies of reduction products it was soon realized that the electrons gained in the reduction of metal tris-bipyridine complexes are localized on individual ligands [66–69], instead of being delocalized over the whole complex molecule. The chemistry of redox series was deeply elaborated through the work of Aoyagui, DeArmond, Elliott, Roffia, A. A. Vlcek, and others. These observation led to detailed examination of the redox orbital concept [1, 6] by De Armond [3, 65, 69]. Redox potential patterns in metal–polypyridine redox series were analyzed and explained by A. A. Vlcek [4, 5, 7, 8]. In the early 80s much attention was attracted by an observation [70–72] of a close similarity between spectra of reduced forms and excited states of $[\text{Ru}(\text{bpy})_3]^{2+}$ and its analogs. This finding surprisingly implied that the excited electron is localized at a single bpy ligand, similarly to the localization of the extra electron in the respective reduced complexes.

In the 70s and 80s much was learned about the mechanism of excited-state electron transfer, control of excited-state lifetime, and on separation of products of photochemical redox reactions to prevent their recombination [32, 37, 39, 73, 74]. Although several schemes for light-energy conversion based on $[\text{Ru}(\text{bpy})_3]^{2+}$ have been proposed, none was practically applicable [40, 41, 75, 76]. Only in the late 80s was it found that Ru^{II} polypyridine complexes efficiently sensitize TiO_2 electrodes, leading to their use in a solar cell developed by Grätzel et al. [36, 43, 77–82]. The search for an optimum sensitizer of photoelectrochemical light energy conversion still continues and Ru^{II} polypyridines seem to be the most promising candidates [36].

Another important research area, linking metal–polypyridine and supramolecular chemistry, was opened in mid-eighties, initially by Balzani and Scandola. Metal–polypyridine units were recognized as excellent building blocks of oligonuclear complexes and supramolecular assemblies, because they can be linked together either through bridging ancillary ligands (e.g. CN^-) or polypyridine ligands themselves [38, 51, 52, 83], often with controlled stereochemistry [48–50]. For example, a dendrimer composed of twenty-two $\text{Ru}^{\text{II}}(\text{N},\text{N})_3^{2+}$ units has been made [53, 84]. In other types of supermolecular complexes, metal–polypyridine units are linked with other functionalities, for example receptor groups (crown ethers, calixarenes, etc.) or different electron- or energy-acceptors or -donors (porphyrins, C_{60} , etc.) [85–89]. Metal–polypyridine fragments are also used as redox- and/or photo-active components of catenanes and rotaxanes [90–92]. The supramolecular chemistry, electrochemistry, and photochemistry of metal–polypyridines is a very promising research area which is undergoing rapid expansion. Questions of electronic communication between individual active centers, and possible emergence of collective redox, photophysical or photochemical behavior, are very intriguing, as are possible applications in sensors and molecular electronic and photonic devices [38, 46].

Currently, metal–polypyridine units are the molecular building blocks of choice whenever a compound with special electro- and/or photo-activity is to be designed. The research emphasis has somewhat shifted from fundamental studies of electron transfer reactivity and excited state properties of individual complexes to the design of new functional molecules and supermolecules with predetermined properties.

The amount of research performed and literature published on electron-transfer reactions of metal–polypyridine complexes is enormous. Several excellent reviews [42, 74, 93–97] and books [38, 62, 98, 99] deal with polypyridine complexes, their redox chemistry, photochemistry, and applications. Hereinafter, the most prominent aspects of electron transfer reactivity of mononuclear metal–polypyridine complexes will be surveyed without attempting to cover exhaustively the vast original literature. Instead, the main purpose of this chapter is to single out the structural, thermodynamic, and kinetic factors which enable and control the special and diverse electron-transfer behavior of metal–polypyridine complexes in their electronic ground and excited states. Although supramolecular electron-transfer chemistry of metal–polypyridines is not discussed here in detail, because it is covered in Volume 3 of this monograph, links connecting the redox behavior of mononuclear polypyridine complexes and their supramolecular counterparts will be briefly outlined.

5.2 Electron-transfer Properties of Ground-state Polypyridine Complexes: A Survey

5.2.1 The 2,2'-Bipyridine and other Polypyridine Ligands

Formulas of selected polypyridine ligands and the abbreviations used are shown in the Appendix. 2,2'-Bipyridine (bpy) is the generic member of the polypyridine family and the most common polypyridine-type ligand. Many bpy ligands are derived from bpy merely by attaching different functional groups to its pyridine rings. These groups range from strong electron acceptors ($-\text{CF}_3$) or donors ($-\text{N}(\text{Et})_2$) to bulky aliphatic substituents ($-\text{Bu}^t$) or polyether chains. The choice of substituent enables us to control many of the properties of bpy complexes—their redox potentials, excited state energy and lifetime, chemical stability of reduction and oxidation products, and their solubility. Closing the central aromatic ring in 2,2'-bipyridine by connecting the 3,3' positions with a $-\text{CH}=\text{CH}-$ group leads to the 1,10-phenanthroline ligand, phen. Again, the properties of phenanthroline complexes can be controlled by use of functional groups. Linking three pyridine rings leads to 2,2':6',2''-terpyridine (tpy) which gives rise to another family of polypyridine complexes. Tpy complexes are especially important as building blocks of supermolecules [87].

Still more polypyridine-type ligands, better called polyazines, are derived from bpy and phen by replacing some of the CH groups of their aromatic rings with N

atoms. This strongly affects the redox properties of both the ligands and their complexes. A great variety of polyazine- and polypyridine-type bridging ligands [100] is, moreover, available for construction of polynuclear complexes.

α -Diimine ligands, e.g. 2-pyridine-*N*-carbaldehydes (PyCa) or 1,4-diazabutadienes (dab), should also be considered here, because the redox behavior of their complexes often resembles that of metal-polypyridines (polypyridines are, in fact, sometimes regarded as aromatic α -diimines).

Most of the interesting redox properties of metal-polypyridine complexes originate from the electron-transfer activity of polypyridine ligands themselves. The free bpy ligand and its analogs are sequentially reduced in two one-electron electrochemically reversible steps, producing the corresponding radical-anion and dianion, respectively:



The respective redox potentials of the first and second reduction step in THF [18, 21] are -2.68 and -3.31 V. The corresponding values in DMF [101] are -2.57 and -3.13 V. (*All redox potentials in this chapter are reported relative to the ferrocenelferricinium couple.*) Both reduced forms of bpy are intrinsically stable in strictly aprotic and anaerobic media. For bpy and some other polypyridines, the radical anions and/or dianions have been characterized by UV-Vis absorption, resonance Raman, and/or EPR spectroscopy [18, 21, 70, 71, 102, 103]. Bipyridine derivatives with strongly electron-accepting groups $-\text{C}(\text{O})\text{OEt}$ or $-\text{Ph}$ in 4,4' positions have a third reduction step at very negative potentials [18, 21]. Free phen [104] and tpy [101] are reduced by one electron at potentials similar to that of the first bpy reduction. The second reduction steps of phen and tpy are chemically irreversible.

Electrochemical oxidation of free bpy was observed as an irreversible process at ca $+1.8$ V in liquid SO_2 [105] and at ca $+2$ V in acetonitrile [106].

The strong dependence of the redox potentials of both reduction steps on substituents attached to aromatic rings of polypyridine ligands provides a very convenient means of tuning the redox properties, because the reduction potentials of polypyridine complexes reflect those of the free ligands. Generally, the first reduction of free bpy-type ligands occurs in the range from ca -2.8 to -2.20 V. This is significantly more negative than the reduction of most transition metals in common oxidation states. On the other hand, some polyazines and polypyridine derivatives such as abpy are reduced at much more positive potentials (e.g. -1.37 V for abpy [107]).

Polypyridines form stable complexes with most transition metals. Complexes with metals in oxidation states which correspond to the d^6 configuration seem to be most abundant. Polypyridines are bidentate ligands. Tpy is generally tridentate although it can coordinate as a bidentate ligand through two pyridine rings only. $\text{M}(\text{N},\text{N})$ chelate rings are rather stable, although a polypyridine ligand can dissociate from highly reduced complexes, especially of first-row transition metals.

Polypyridines are good σ -donors. Importantly, they also have low-lying, unoccupied π^* orbitals which can accept electrons on reduction. The extent of $d \rightarrow \pi^*$

back-donation is small for most metal–polypyridines, except for some complexes of first-row metals and some special ligands, e.g. abpy. Hence, most reduced polypyridine complexes are not complexes of metals in unusually low oxidation states, stabilized by π back-donation. Instead, they behave as complexes of metals in common oxidation states (usually with a d^6 configuration) with polypyridine radical-anions or dianions as ligands.

Important steric effects can be induced by attaching bulky substituents to positions adjacent to the nitrogen donor atoms, that is 6,6'-bpy and 2,9-phen. Resulting ligands strongly favor tetrahedral over octahedral or square-planar coordination. This effect was employed in the construction of entwined catenate ligands (catphen)₂ in which two phen ligands are connected by interlocked polyether rings attached to their 2,9 positions (see Appendix). Catphen-type ligands form complexes with most first-row transition metals [108]. They impose a pseudotetrahedral coordination geometry on the metal atoms.

An octahedral cage is obtained by connecting three bpy ligands together through their 5,5'-positions by amide links [109, 110].

5.2.2 Polypyridine Complexes

Titanium

Two successive, reversible one-electron reductions in the range from -2.0 to -3.1 V are observed for the $[\text{Ti}(\text{bpy})_3]$ complex [111]; these are attributed to the formation of $[\text{Ti}(\text{bpy})_3]^z$, $z = 1-, 2-$. These species seem to undergo partial bpy dissociation in solution. Oxidation-state assignment to Ti and the bpy ligands is not completely clear. Both reductions are assumed to be Ti-localized [111]. Indeed, the $z = 1-, 2-$ complexes have spectroscopic features [112, 113] of a $\text{bpy}^{\bullet-}$ ligand whereas $[\text{Ti}(\text{bpy})_3]^{2-}$ probably contains a bpy^{2-} ligand also [112].

Vanadium

$[\text{V}(\text{bpy})_3]^z$ complexes form [111, 114] a six-membered redox series $z = 2+, 1+, 0, 1-, 2-, 3-$. The corresponding one-electron redox steps are reversible. They occur in the range from -1.48 to -3.2 V. Correlation between spectroscopic and electrochemical data and dependence of redox potentials on methylation of bpy ligands indicate that the $[\text{V}(\text{bpy})_3]^{2+}/[\text{V}(\text{bpy})_3]^+$ and $[\text{V}(\text{bpy})_3]^+/[\text{V}(\text{bpy})_3]$ redox changes are metal-localized, whereas the steps $0/-1$, $-1/-2$, and $-2/-3$ seem to be ligand-localized. This suggests [111] the formulations $[\text{V}^{\text{II}}(\text{bpy})_3]^{2+}$, $[\text{V}^{\text{I}}(\text{bpy})_3]^+$, $[\text{V}^0(\text{bpy})_3]$, $[\text{V}^0(\text{bpy})_2(\text{bpy}^{\bullet-})]^-$, $[\text{V}^0(\text{bpy})(\text{bpy}^{\bullet-})_2]^{2-}$, and $[\text{V}^0(\text{bpy}^{\bullet-})_3]^{3-}$. A more recent EPR study [115] has indicated that $[\text{V}(\text{bpy})_3]$ has a highly delocalized structure, the unpaired electron occupying a delocalized orbital of ca 30 % metal 3d character. UV–Vis spectra of $[\text{V}^0(\text{bpy})_3]$ and $[\text{V}^0(\text{bpy})_2(\text{bpy}^{\bullet-})]^-$ have features arising from $\text{V} \rightarrow \text{bpy}$ metal-to-ligand charge transfer (MLCT) and $\text{bpy}^{\bullet-}$ intra-ligand transitions, respectively [114]. Nevertheless, it seems that the bonding in the first 3 or 4 members of the $[\text{V}(\text{bpy})_3]^z$ redox series is rather delocalized.

Chromium, molybdenum, and tungsten

Chromium forms [2, 25, 55, 111, 113, 116] a seven-membered redox series $[\text{Cr}(\text{bpy})_3]^z$; $z = 3+, 2+, 1+, 0, 1-, 2-, 3-$. All its members have been synthesized in the solid state. Corresponding one-electron redox steps are reversible, occurring in the range from -0.70 to -3.0 V. Some of the more reduced species ($z < 1+$) are partially labile in solution. A combination of electrochemical [25, 111] and spectroscopic (UV-Vis [2, 111, 117] and IR [113]) data indicates that the $3+/2+$ step is metal-localized $\text{Cr}^{\text{III}}/\text{Cr}^{\text{II}}$, although some electronic delocalization can occur at the $2+$ level. The $z = 1+$ and 0 members look rather delocalized. $[\text{Cr}(\text{bpy})_3]^0$ could be viewed as $[\text{Cr}^{\text{III}}(\text{bpy}^{\bullet-})_3]^0$ with a strong antiferromagnetic coupling between unpaired electrons of the Cr atoms and three $\text{bpy}^{\bullet-}$ ligands. Nevertheless, the use of integer metal and ligand oxidation states in the $z = 1+$ and 0 complexes seems inappropriate, owing to electron delocalization. Further reduction steps to $z = 1-, 2-, 3-$ are bpy -localized. Five members of an analogous $[\text{Mo}(\text{bpy})_3]^z$ redox series are known [111]: $z = 1+, 0, 1-, 2-, 3-$. The $1+/0$, $0/1-$, and $1-/2-$ reduction steps are reversible.

Complexes of the type $[\text{M}(\text{CO})_4(\text{N},\text{N})]$; $\text{M} = \text{Cr}, \text{Mo}, \text{W}$; have been prepared for many polypyridine ligands and α -diimines PyCa or dab. These compounds are very important spectroscopically and photochemically, because of their low-lying MLCT electronic transitions [96, 118]. Polypyridine complexes $[\text{M}(\text{CO})_4(\text{N},\text{N})]$ are reduced in two successive one-electron steps which are localized on the polypyridine ligand [20, 21, 119–122]. (Four reduction steps have been found [21] for $\text{N},\text{N} = 4,4'\text{-Ph}_2\text{-bpy}$.) A chemically partly reversible oxidation occurs at positive potentials [17].

Investigations of $[\text{M}(\text{CO})_4(\text{N},\text{N})]$ reduction were important for our understanding of the effects of metal coordination on the redox behavior of polypyridine ligands. Its simple molecular composition makes $[\text{M}(\text{CO})_4(\text{N},\text{N})]$ ideal for such studies, because the single $\text{M}(\text{N},\text{N})$ chelate ring is the only redox-active unit present. The most typical features of $[\text{M}(\text{CO})_4(\text{N},\text{N})]$ electrochemistry are: (i) The $\text{M}(\text{N},\text{N})$ chelate ring has the same reduction pattern (number of steps, number of electrons exchanged) as the free N,N ligand itself. Compared with the free ligands, reductions of the corresponding complexes are shifted positively by ca $0.5\text{--}0.8$ V. Hence even the most negative ligand-based reductions become observable upon coordination (e.g. the 3rd and 4th reduction of $4,4'\text{-Ph}_2\text{-bpy}$). The positive shift is even larger for a polyazine ligand bridging between two metal atoms [120] in complexes of the type $[\{\text{M}(\text{CO})_4\}_2(\mu\text{-N},\text{N})]$. (ii) Reduction potentials of the complexes correlate with reduction potentials of the free N,N ligand. (iii) Despite the first reduction being essentially N,N -localized, its potential is weakly dependent [20] on M : $\text{W} < \text{Mo} < \text{Cr}$. (iv) EPR [119–122] and IR [121, 122] spectra, and DFT calculations [122] confirm the predominant N,N -localization of the first reduction. Importantly, they show that reduction to $[\text{M}(\text{CO})_4(\text{N},\text{N}^{\bullet-})]$ affects also the electron density distribution within the $\text{M}(\text{CO})_4$ fragment by increasing the total electron density on all four CO ligands (on COs *trans* to N,N more than on *cis*) and by a spin-delocalization to axial (*cis*) CO ligands. (v) Reduction labilizes an axial $\text{M}\text{--}\text{CO}$ bond toward substitution [20, 21]. The rate of axial CO dissociation strongly increases on going from

$[\text{M}(\text{CO})_4(\text{N}, \text{N}^+)]$ to $[\text{M}(\text{CO})_4(\text{N}, \text{N}^{2-})]$. (vi) Potentials of both reduction steps of complexes $[\text{Mo}(\text{PBU}_3)_n(\text{CO})_{4-n}(\text{bpy})]$ or $[\text{Mo}(\text{PBU}_3)_n(\text{CO})_{4-n}(\text{tBu-dab})]$ shift slightly negatively when CO is replaced by a stronger electron donor PBU_3 : $n = 0 > 1 > 2$ [123] (vii) Oxidation labilizes a M–CO bond [17].

Manganese and rhenium: coordination compounds

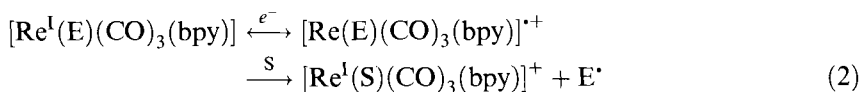
$[\text{Mn}^{\text{II}}(\text{bpy})_3]^{2+}$ is reduced in three one-electron steps to $[\text{Mn}^{\text{II}}(\text{bpy})_3]^z$; $z = 1+, 0, 1-$; which are accompanied by a partial loss of a bpy ligand [27, 116, 124]. Compared with other first-row metal bpy complexes the reductions occur rather negatively: $E_{1/2}(2+/1+) = -1.75$ V. Localization of the electrons added is uncertain. Magnetochemical data [125] suggest that the $z = 0$ and $1-$ species should be viewed as $[\text{Mn}^{\text{II}}(\text{bpy})(\text{bpy}^{\bullet-})_2]$ and $[\text{Mn}^{\text{II}}(\text{bpy}^{\bullet-})_3]^-$, essentially in agreement with IR spectra [113]. An irreversible oxidation of $[\text{Mn}^{\text{II}}(\text{bpy})_3]^{2+}$ and $[\text{Mn}^{\text{II}}(\text{phen})_3]^{2+}$ occurs at $+0.97$ V, producing, in the presence of traces of water, $[(\text{N}, \text{N})_2\text{Mn}(\mu\text{-O})_2\text{-Mn}(\text{N}, \text{N})_2]^{4+}$. These, formally $\text{Mn}^{\text{IV}}\text{Mn}^{\text{IV}}$ complexes, are strong oxidants, able to oxidize OH^- , Cl^- , and catechol [126]. $[(\text{phen})_2\text{Mn}(\mu\text{-O})_2\text{Mn}(\text{phen})_2]^{4+}$ oxidizes toluene by a unique hydride abstraction mechanism [127]. Manganese–polypyridine–oxo complexes have also been employed as models of the water-oxidation catalyst of plant photosynthesis [128].

The complex $[\text{Re}^{\text{II}}(\text{bpy})_3]^{2+}$ and its tpy and phen analogs undergo a Re-localized reduction to $[\text{Re}^{\text{I}}(\text{bpy})_3]^+$, followed by two, presumably bpy-localized, one-electron reductions. Oxidation of $[\text{Re}^{\text{II}}(\text{bpy})_3]^{2+}$ is irreversible, because of the formation of 7-coordinated $\text{Re}(\text{III})$ complexes [129].

Rhenium and manganese: organometallic compounds

$[\text{Re}^{\text{I}}(\text{E})(\text{CO})_3(\text{N}, \text{N})]^{n+}$ complexes form a special class of organometallic compounds with distinct electrochemical, photochemical, and photophysical properties [97]. Their electrochemical behavior epitomizes many general aspects of the redox chemistry of metal–diimine units. Neutral ($n = 0$) complexes exist with anionic axial ligands $\text{E} = \text{halides (X)}, \text{CN}^-, \text{CF}_3\text{SO}_3^-, \text{alkyl or aryl group, metal fragment like Mn}(\text{CO})_5, \text{Re}(\text{CO})_5, \text{Ph}_3\text{Sn, etc.}$ Cationic ($n = 1$) complexes are known for $\text{E} = \text{neutral Lewis base, e.g. pyridine derivatives, phosphines, phosphites, nitriles, isonitriles, CO, imidazole, histidine, etc.}$ The nature of the N,N ligand can also be varied broadly: bpy- or phen-type polypyridines, polyazines, and dab and PyCa-type ligands.

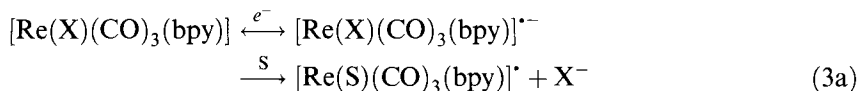
In principle, these complexes undergo a one-electron oxidation and two successive one-electron reductions. The potential and reversibility of the oxidation step depend very much on the axial ligand E. Oxidation of halide and cyanide complexes is followed by rapid loss of the oxidized axial ligand [130, 131]:



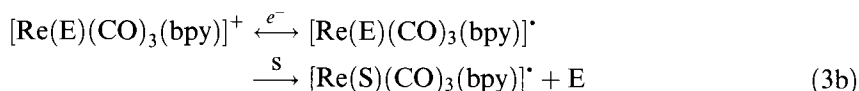
$E_{\text{ox}} = +1.00$ V and $+1.17$ V for $\text{E} = \text{Cl}$ and CN , respectively.

Oxidation of a metal-metal bonded complex $[\text{Re}^{\text{I}}(\text{Ph}_3\text{Sn})(\text{CO})_3(\text{bpy})]$ is also chemically irreversible. It occurs at less positive potential, +0.39 V [61]. On the other hand, cationic complexes $[\text{Re}^{\text{I}}(\text{CH}_3\text{CN})(\text{CO})_3(\text{bpy})]^+$ [130] and $[\text{Re}^{\text{I}}(\text{imidazole})-(\text{CO})_3(\text{bpy})]^+$ [132] are oxidized reversibly in CH_3CN at +1.40 and 1.46 V, respectively, producing the corresponding Re^{II} complexes. Oxidation is, however, irreversible in water. No oxidation was observed for $[\text{Re}(\text{CO})_4(\text{bpy})]^+$ and its bpym and phen analogs up to +1.6 V in acetonitrile [133].

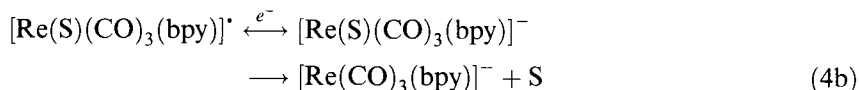
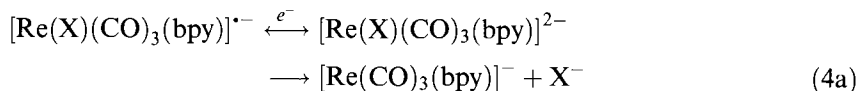
Reduction of $[\text{Re}^{\text{I}}(\text{E})(\text{CO})_3(\text{N},\text{N})]^{n+}$ occurs in two successive one-electron steps which are predominantly localized on the N,N ligand, with a partial, N,N-dependent, delocalization of the extra electron density over the $\text{Re}^{\text{I}}(\text{E})(\text{CO})_3^{n+}$ fragment [134]. The respective products, $[\text{Re}^{\text{I}}(\text{E})(\text{CO})_3(\text{N},\text{N}^{\cdot-})]^{(n-1)+}$ and $[\text{Re}(\text{E})(\text{CO})_3(\text{N},\text{N}^{2-})]^{(n-2)+}$, are amenable to dissociation of the axial ligand E, whose rate and extent depends on the N,N and E ligands, and on the temperature and the excess of free ligand E added:



X = Cl, Br



E = phosphines, phosphites, nitriles, THF, CO



For example, $[\text{Re}^{\text{I}}(\text{CN})(\text{CO})_3(\text{bpy})]$ in strictly aprotic solvents at low temperature is reduced in two chemically reversible one-electron steps at -1.77 and -2.42 V, which correspond to formation of $[\text{Re}^{\text{I}}(\text{CN})(\text{CO})_3(\text{bpy})]^z$; $z = 1-$ and $2-$, respectively [130]. The first reduction of $[\text{Re}(\text{CO})_4(\text{bpy})]^+$ or $[\text{Re}(\text{P}(\text{OEt}_3))(\text{CO})_3(\text{bpy})]^+$ is chemically reversible even at room temperature [133, 135]. Halide complexes $[\text{Re}^{\text{I}}(\text{X})(\text{CO})_3(\text{bpy})]$ (X = Cl, Br) have a complicated reduction pattern because of further reactions of the reduced products. Several reaction intermediates and products have been characterized spectroelectrochemically [131, 135-137] and rate constants of the main steps have been determined [130] by low-temperature cyclic voltammetry.

The rate and extent of dissociation of the axial ligand E upon uptake of the first electron (Eq. 3) depend on the nature of the axial ligand [134, 136], decreasing in the order $\text{Br}^- > \text{Cl}^- \gg \text{THF} > \text{PPh}_3$, $n\text{PrCN} > \text{P}(\text{OMe})_3$, CO. The structure of the polypyridine N,N ligand also has a profound effect. For series of complexes

$[\text{Re}(\text{Br})(\text{CO})_3(\text{N},\text{N})]^-$, $\text{X} = \text{Br}, \text{Cl}$, the reactivity orders are $t\text{Bu-dab} > \text{bpz} \approx \text{bpdz} > \text{bpym} \gg \text{bpm}, \text{abpy}$ and $\text{bpy} > i\text{Pr-PyCa} > 2,3\text{-dpp} > \text{abpy}$ [134, 136]. The reactivity decreases in the same order as the π^* -orbital coefficient at the N donor atoms [134].

For example, reduced bromo complexes are much more labile than their chloro counterparts [134]. In contrast, the solvento species $[\text{Re}(\text{S})(\text{CO})_3(\text{bpy})]^+$ are relatively stable in coordinating solvents S for $\text{S} = n\text{PrCN}$, but not for $\text{S} = \text{THF}$, in which they dimerize to $[\text{Re}(\text{CO})_3(\text{bpy})]_2$. Reduction of $[\text{Re}(\text{PPh}_3)(\text{CO})_3(\text{bpy})]^+$ generates $[\text{Re}^I(\text{PPh}_3)(\text{CO})_3(\text{bpy})]^*$, which is stable in $n\text{PrCN}$ even at room temperature. As an exception, $[\text{Re}^I(\text{P}(\text{OEt})_3)(\text{CO})_3(\text{bpy})]^*$ slowly reacts [135] with excess $\text{P}(\text{OEt})_3$ to give $[\text{Re}^I(\text{P}(\text{OEt})_3)_2(\text{CO})_2(\text{bpy})]^*$. The stabilizing effect of the abpy ligand is manifested by $[\text{Re}(\text{Br})(\text{CO})_3(\text{abpy})]^-$ which undergoes only a very slow Br^- substitution by a solvent molecule. The complexes $[\text{Re}(\text{L})(\text{CO})_3(\text{abpy})]^*$; and $[\text{Re}(\text{L})(\text{CO})_3(\text{bpym})]^*$ $\text{L} = \text{THF}, n\text{PrCN}$, or PPh_3 are stable in solution.

The rate of axial ligand dissociation increases dramatically with the number of electrons added, being much faster (Eq. 4) for $[\text{Re}(\text{X})(\text{CO})_3(\text{bpy})]^{2-}$ than $[\text{Re}(\text{X})(\text{CO})_3(\text{bpy})]^-$; $\text{X} = \text{Cl}$ or Br . Five-coordinated species $[\text{Re}(\text{CO})_3(\text{bpy})]^-$ are formed. The same reaction occurs for other polypyridine ligands. Only $[\text{Re}(\text{Br})(\text{CO})_3(\text{abpy}^{\cdot-})]^{2-}$ reacts via slow substitution of Br^- by a solvent (THF) molecule instead of dissociation, and full axial ligand labilization requires addition of one more (third) electron [136]. The complexes $[\text{Re}(\text{S})(\text{CO})_3(\text{bpym})]^-$; $\text{S} = n\text{PrCN}, \text{THF}$; are also stable in solvent S even at room temperature [137]. For other polypyridines, the two-electron reduced solvento species $[\text{Re}(\text{S})(\text{CO})_3(\text{N},\text{N})]^-$; $\text{S} = \text{CH}_3\text{CN}, n\text{PrCN}$; were observed [137] only at low temperature, in the solvent S, in equilibrium with $[\text{Re}(\text{CO})_3(\text{N},\text{N})]^-$.

The pentacoordinated complexes $[\text{Re}(\text{CO})_3(\text{N},\text{N})]^-$ have highly delocalized electronic structures and assignment of integer oxidation states to Re and N,N seems inappropriate. The complex $[\text{Re}(\text{CO})_3(\text{bpy})]^-$ undergoes two further reductions [130] at more negative potentials producing $[\text{Re}(\text{CO})_3(\text{bpy})]^{2-}$ and $[\text{Re}(\text{CO})_3(\text{bpy})]^{3-}$. Reoxidation of $[\text{Re}(\text{CO})_3(\text{bpy})]^-$ is rather complicated [130]; it reacts in with the parent complex $[\text{Re}(\text{Cl})(\text{CO})_3(\text{bpy})]$ to give $[\text{Re}(\text{S})(\text{CO})_3(\text{bpy})]^*$ and $[\text{Re}(\text{Cl})(\text{CO})_3(\text{bpy})]^-$. In a parallel reaction, $[\text{Re}(\text{CO})_3(\text{bpy})]^-$ dimerizes in the presence of Cl^- to give $[\{\text{Re}(\text{CO})_3(\text{bpy})\}_2(\mu\text{-Cl})]^{3-}$, which is electrochemically reoxidized to $[\text{Re}(\text{S})(\text{CO})_3(\text{bpy})]^*$.

Both $[\text{Re}(\text{S})(\text{CO})_3(\text{bpy})]^*$ (for weakly coordinating S) and $[\text{Re}(\text{CO})_3(\text{bpy})]^-$ react with CO_2 . Hence, $[\text{Re}(\text{Cl})(\text{CO})_3(\text{bpy})]$ and related complexes are catalysts of electrochemical CO_2 reduction to CO and/or formate [131, 135, 138–141].

The redox behavior of complexes of the type $[\text{Re}^I(\text{X})(\text{CO})_3(\text{R-dab})]$; $\text{X} = \text{halide}$; is similar to that of their polypyridine counterparts—one oxidation and two successive reductions which ultimately produce pentacoordinated $[\text{Re}^I(\text{CO})_3(\text{R-dab})]^-$ species [134, 136, 142]. There are, however, some remarkable differences between the redox chemistry of Re dab and polypyridine complexes: (i) Oxidation [134] to $[\text{Re}^{II}(\text{X})(\text{CO})_3(\text{R-dab})]^+$ is reversible and less positive (+0.58 V for $\text{X} = \text{Cl}$, $\text{R} = t\text{Bu}$), indicating the greater stability of Re^{II} -dab complexes and smaller involvement of E ligand orbitals in the HOMO of the Re^I complex. (ii) The rate of dissociation of the axial ligand after the first reduction to $[\text{Re}^I(\text{Br})(\text{CO})_3(\text{R-dab}^{\cdot-})]^-$

depends very much on the *N*-substituent R; dissociation of an axial Br[−] ligand is much faster for *i*Pr-dab than for aryl-dab ligands (aryl = *p*-tolyl or *p*-anisyl), which are strong π -acceptors [142].

Interestingly, the first reduction of Re-alkyl complexes [142] [Re(R)(CO)₃-(*i*Pr-dab)]; R = Me, Et, Bz; is reversible, occurring some 0.34 V more negatively than reduction of [Re(Br)(CO)₃(R-dab)]. This might be caused by a mixing between the Re-C σ and π^* (dab) orbitals. The second reduction of [Re(R)(CO)₃(*i*Pr-dab)] is irreversible. The same behavior was found for [Re(R)(CO)₃(bpy)].

Manganese complexes [Mn^I(E)(CO)₃(*i*Pr-dab)]^{*n*+}; E = Br (*n* = 0) or a donor solvent molecule (*n* = 1); are reduced [143] to a five-coordinated complex [Mn(CO)₃(*i*Pr-dab)][−] in a two-electron process by an ECE mechanism: The first reduction to [Mn(E)(CO)₃(*i*Pr-dab)]^{•(n−1)+} is followed by a very fast dissociation of the axial ligand E. The [Mn(CO)₃(*i*Pr-dab)][•] product is reduced to [Mn(CO)₃-(*i*Pr-dab)][−] at a more positive potential than that of the first reduction. Hence, an apparently two-electron reduction wave results. Reduction products are engaged in complicated coupling and reoxidation reactions. Only the complex [Mn^I(P(OEt)₃)-(CO)₃(*i*Pr-dab)]⁺ behaves differently [143], because its reduction produces the stable radical [Mn^I(P(OEt)₃)(CO)₃(*i*Pr-dab^{•−})].

Iron

[Fe(N,N)₃]^{*z*} complexes (N,N = bpy, phen, bpm) form [101, 144–147] a six-membered redox series *z* = 3+, 2+, 1+, 0, 1−, 2−. The 3+/2+ couple is metal-localized—Fe^{III}/Fe^{II}. For N,N = bpy, it occurs at +0.64 V. (Three more one-electron oxidations were found [57] at positive potentials in liquid SO₂.) Reduction steps are predominantly N,N-localized. They occur at rather negative potentials and are accompanied by partial ligand dissociation. For N,N = bpy, the 2+/1+ and 1+/0 couples were observed at −1.73 and −1.91 V, respectively. The presence of radical-anionic N,N^{•−} ligand(s) in the reduced Fe complexes (*z* = 1+, 0, 1−) was confirmed by UV–Vis spectroelectrochemistry [144], EPR [69], and resonance Raman [146] spectroscopy. Two more reduction steps were observed [148] for [Fe(4,7-Ph₂-phen)₃]²⁺, which is reduced in six one-electron steps to *z* = 4−. On the other hand, only three reductions up to *z* = 1− were found [144] for [Fe(tpy)₂]²⁺.

The catphen ligand forms tetracoordinated, encaged complex [Fe^{II}(catphen)₂]²⁺ which cannot be oxidized to Fe^{III}. In contrast, reversible reductions to [Fe(catphen)₂]⁺ and [Fe(catphen)₂]⁰ occur relatively positively, at −1.17 and −1.71 V, respectively [108]. The locations of these redox changes are unclear, although the positive potentials indicate Fe-reduction in the first step at least. The entwined geometry of the catphen ligand prevents low-valent Fe complexes from dissociation. The topological effect of catphen becomes even more obvious in comparison with sterically hindered, but not entwined, danphen ligand, which does not form complexes with Fe(II) [108].

Ruthenium and osmium

In aprotic solvents the complexes [Ru(bpy)₃]²⁺ and [Os(bpy)₃]²⁺ and their analogs form extensive redox series [4, 63–67, 101, 149, 150] comprising at least

eight members $[M(N,N)_3]^z$: $z = 3+, 2+, 1+, 0, 1-, 2-, 3-, 4-$. The oxidation to $[M^{III}(N,N)_3]^{3+}$ is metal-localized, occurring at $+0.85$ and $+0.42$ V for Ru and Os, respectively ($N,N = \text{bpy}$) [117]. Further oxidations of $[M^{III}(\text{bpy})_3]^{3+}$; $M = \text{Ru, Os}$; were found [56, 57] in liquid SO_2 solutions at very positive potentials, extending the redox series by three more members: $z = 6+, 5+, 4+$. They were described as complexes of Ru^{III} and Os^{IV} containing bpy and bpy^{++} ligands.

All six reductions of $[M(N,N)_3]^{2+}$ are invariably ligand-localized. They occur in two triplets, that is in two groups of three closely-spaced steps, the potential separation between the triplets (0.65 V for bpy) being much larger than that within the triplets, ca 0.2 V [4]. Characterization of reduction products by UV-Vis absorption [63, 66, 67, 150], resonance Raman [68], and EPR spectroscopy [69], and detailed analysis of the reduction pattern [4, 65] (Section 5.3.2) have shown that all reduction steps can be attributed to sequential reductions of individual ligands, which behave as (nearly) electronically isolated [3, 4, 65]. This implies the existence of complexes containing simultaneously N,N ligands in different oxidation states, for example $[\text{Ru}^{II}(\text{bpy})_2(\text{bpy}^{\bullet-})]^+$ or $[\text{Ru}^{II}(\text{bpy}^{\bullet-})_2(\text{bpy}^{2-})]^{2-}$, etc. Reduction potentials of $[M(N,N)_3]^{2+}$ complexes decrease linearly with decreasing reduction potential of free N,N ligands with a slope of 0.76–1.03, depending on the potential range examined [67, 74, 151]. Besides providing evidence of polypyridine-localization of the reduction steps, this dependence also enables us to tune the reduction potential of $[\text{Ru}(N,N)_3]^{2+}$ complexes over a very broad range, from ca -0.45 to -3.0 V for Ru (Section 5.3.3). Most Ru complexes show the first reduction between -1.0 and -2.0 V, however. The first reduction potential is, moreover, shifted positively by some 0.7–0.9 V relative to the free ligand values. This enables even the most negative ligand-localized steps to be observed for ligands like 4,4'- $\text{Ph}_2\text{-bpy}$ [149] or 4,4'-($\text{EtC}(\text{O})\text{O}$) $_2\text{-bpy}$ [65]. Thus, $[\text{Ru}(4,4'-(\text{EtC}(\text{O})\text{O})_2\text{-bpy})_3]^{2+}$ shows [65] ten reduction steps, all the way down to $[\text{Ru}(4,4'-(\text{EtC}(\text{O})\text{O})_2\text{-bpy})_3]^{8-}$! Surprisingly, even the oxidation potential of the $\text{Ru}^{II}/\text{Ru}^{III}$ couple is linearly dependent on the reduction potential of the ligand, albeit with a smaller slope than that found for the reduction-potential dependence [67]. Together, these two dependencies imply that the oxidation and reduction potentials in a series of $[\text{Ru}(N,N)_3]^{2+}$ complexes are linearly dependent on each other, and this has, indeed, been found [29] for many N,N ligands (Sections 5.3.2 and 5.3.3). Overall, the oxidation potential of $[\text{Ru}(N,N)_3]^{2+}$ can be tuned by the choice of the N,N ligand from ca $+0.15$ to $+1.8$ V, although most Ru complexes have oxidation between $+0.7$ and $+1.4$ V. Os complexes are oxidized ca 0.4 V more negatively than their Ru counterparts.

Reduction patterns of heteroleptic Ru^{II} polypyridine complexes $[\text{Ru}(\text{A})_n(\text{B})_{3-n}]^{2+}$ and $[\text{Ru}(\text{A})(\text{B})(\text{C})]^{2+}$, where A, B and C, are different polypyridine ligands, consist of separate reductions of individual ligands [5, 16, 149, 152, 153]. The localization problem, i.e. the order in which the ligands are reduced, is rather complicated. It depends on the energy of the redox orbitals of individual ligands (i.e. the reduction potentials of the free ligands), on electron–electron repulsion, on interligand interaction energy, and on solvation energy [5, 16]. For example, the strongly electron-accepting 5dcebpy = 5,5'-($\text{EtC}(\text{O})\text{O}$) $_2\text{-bpy}$ ligand in $[\text{Ru}(\text{bpy})_2(5\text{dcebpy})]^{2+}$ is reduced first. Hence, the first two reductions of this complex produce $[\text{Ru}(\text{bpy})_2(5\text{dcebpy}^{\bullet-})]^+$ and $[\text{Ru}(\text{bpy})_2(5\text{dcebpy}^{2-})]$, respectively, followed by a

more negative set of bpy-localized reductions [16]. A general theory of reduction patterns in heteroleptic complexes $[\text{Ru}(\text{A})_n(\text{B})_{3-n}]^{2+}$, which accounts well for experimental data, has been developed [5]. It is also applicable to dinuclear (and, possibly, polynuclear) complexes in which both the terminal and the bridging polypyridine ligands are reducible. The 8-step reduction of $[\{\text{Ru}(\text{bpym})_2\}_2(\mu\text{-bpym})]^{4+}$ is an example studied in much detail [19].

Substituted complexes of the type $[\text{M}^{\text{II}}(\text{N},\text{N})_2\text{XY}]^n$; $\text{M} = \text{Ru}, \text{Os}$, $\text{X}, \text{Y} = \text{halides}, \text{CN}^-, \text{C}_2\text{O}_4^{2-}, \text{py}, \text{en}, \text{NH}_3$, etc.; show, in general, two doublets of N,N-localized reductions [154–156]. The reduction behavior is complicated by loss of an ancillary ligand X upon the second and, more rapidly, the 3rd bpy-localized reduction. The reduction potentials are only slightly X-dependent. On the other hand, the $\text{M}^{\text{II}}/\text{M}^{\text{III}}$ oxidation potential is highly dependent on X . Extensive tables of oxidation and the first reduction potentials of these complexes are available [15, 28, 74, 157]. Their values can be predicted by use of electrochemical ligand parameters [15, 28, 157].

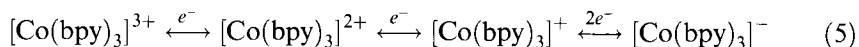
Labilization of an ancillary ligand X on reduction indicates the possibility of employing Ru and Os polypyridine complexes as redox catalysts (Section 5.3.5). Indeed, electrocatalysis of CO_2 reduction to CO or formate by $[\text{Ru}(\text{bpy})_2(\text{CO})_2]^{2+}$, $[\text{Ru}(\text{bpy})_2(\text{CO})\text{Cl}]^+$, or $[\text{Os}(\text{bpy})_2(\text{CO})\text{H}]^+$ has been reported [158, 159]. The electrocatalytically most active Ru -bpy species is, however, a film of a $-\text{Ru}-\text{Ru}-$ bonded polymer $[-\{\text{Ru}(\text{bpy})(\text{CO})_2\}_n-]$. It is formed on an electrode surface by reduction of various mono- or bis-bpy Ru^{II} carbonyl or carbonyl-chloro complexes [160–163]. Dissociation of a CO ligand from the polymer upon further bpy-localized reduction is the crucial step which enables CO_2 coordination and reduction.

Organometallic complexes $[\text{Ru}(\text{E})(\text{E}')(\text{CO})_2(\text{N},\text{N})]$ form another interesting class of redox-active complexes [164]. They undergo two one-electron reductions, usually accompanied by loss of an axial ligand E . Five-coordinated species $[\text{Ru}(\text{E})(\text{CO})_2(\text{N},\text{N})]^-$ are the ultimate products of the second reduction. The overall mechanism involves coupling reactions between intermediates and electron-transfer catalyzed reduction of the parent complex. This reactivity resembles reduction of $[\text{Re}(\text{Cl})(\text{CO})_3(\text{N},\text{N})]$, discussed above. $[\text{Ru}(\text{SnPh}_3)_2(\text{CO})_2(i\text{Pr-dab})]$ is rather exceptional, because it undergoes reversible reduction to a stable $[\text{Ru}(\text{SnPh}_3)_2(\text{CO})_2(i\text{Pr-dab}^{\bullet-})]^-$ complex [165]. Spectra and DFT calculations of this radical-anion imply significant delocalization of the spin density to axial SnPh_3 ligands.

Osmium and ruthenium in high oxidation states (III, IV, or V) form polypyridine (bpy, phen or tpy) hydroxo and oxo complexes, which have a rich redox chemistry [166, 167]. Redox changes are metal-localized and accompanied by reactions of $\text{M}=\text{O}$ or $\text{M}-\text{OH}$ bonds. These complexes are active as electrocatalysts of the oxidation of water to O_2 , or of Cl^- to Cl_2 , or they can transfer oxygen atoms and oxidize organic substrates like $(\text{CH}_3)_2\text{CHOH}$ or $\text{C}_6\text{H}_5-\text{CH}(\text{CH}_3)_2$.

Cobalt

Bipyridine forms a very stable $[\text{Co}(\text{bpy})_3]^{3+}$ complex with Co^{III} . Its sequential electrochemical reduction produces [22, 23, 147, 168] $[\text{Co}(\text{bpy})_3]^{2+}$, $[\text{Co}(\text{bpy})_3]^+$, and $[\text{Co}(\text{bpy})_3]^-$:



The corresponding redox potentials are: -0.15 , -1.38 , and -2.02 V in acetonitrile [147, 168]. Identical electrochemical behavior was found for cobalt complexes of phen, dmb, and 4,4'-Ph₂-bpy [147].

The complexes $[\text{Co}(\text{bpy})_3]^+$ and $[\text{Co}(\text{bpy})_3]^-$ undergo partial dissociation of a bpy ligand, so fully reversible reduction is observed only in the presence on an excess of free bpy. The two-electron reduction to the anion was observed only in CH₃CN, whereas the monocation is stable even in water. Interestingly, the neutral $[\text{Co}(\text{bpy})_3]^0$ complex was prepared [169] chemically in THF, although it was not detected electrochemically. $[\text{Co}(\text{bpy})_3]^+$ is a high-spin d^8 Co^I complex, stabilized by a Co \rightarrow bpy π -back-donation [170]. Besides electrochemical and chemical reduction, e.g. by BH₄⁻, $[\text{Co}(\text{bpy})_3]^+$ can be produced by pulse radiolysis [171] or flash photolysis [172, 173]. Release of a bpy ligand from reduced complexes makes cobalt-bipyridine complexes active redox catalysts. Substrates are activated by coordination to low-valent Co^I and undergo chemical transformation with concomitant regeneration of $[\text{Co}(\text{bpy})_3]^{2+}$. Besides the first reported [24] reduction of aromatic nitro compounds by BH₄⁻ catalyzed by $[\text{Co}(\text{bpy})_3]^{2+}$, it was found that cobalt-bipyridine complexes catalyze reduction of CO₂ to CO or of H⁺ to H₂ [30, 31, 44]. These reactions involve coordination of CO₂ or oxidative addition of H⁺ to the Co^I center, respectively [174]. $[\text{Co}(\text{bpy})_3]^+$ also mediates reduction of PhC \equiv CH to PhCH=CH₂ [175].

The mechanism and localization of reduction of the Co^I complex are subtly dependent on the character of diimine ligand [147]. Whereas a two-electron reduction to $[\text{Co}(\text{N},\text{N})_3]^-$ has been observed [147, 168] for N,N = bpy, phen, 4,4'-Me₂-bpy and 4,4'-Ph₂-bpy, for the $[\text{Co}(\text{tpy})_2]^+$ complex [176] a one-electron reduction to a formally Co⁰ complex, $[\text{Co}(\text{tpy})_2]$, is followed by another reduction to $[\text{Co}(\text{tpy})_2]^-$. The 1+/0 and 0/1- couples are separated by 0.36 V.

Sterically hindered danphen and entwined catphen ligands form [108] tetracoordinated, pseudotetrahedral complexes $[\text{Co}^{\text{II}}(\text{danphen})_2]^{2+}$ and $[\text{Co}^{\text{II}}(\text{catphen})_2]^{2+}$ which cannot be oxidized to Co^{III}. The reduction mechanism is different from that of $[\text{Co}(\text{bpy})_3]^{2+}$ or $[\text{Co}(\text{phen})_3]^{2+}$ (Eq. 5), because it consists [108] of two successive one-electron steps producing corresponding Co^I and Co⁰ complexes at -0.99 and -1.67 V for $[\text{Co}^{\text{II}}(\text{danphen})_2]^{2+}$ and at -0.99 and -1.71 V for $[\text{Co}^{\text{II}}(\text{catphen})_2]^{2+}$.

Rhodium

The stable $[\text{Rh}(\text{bpy})_3]^{3+}$ complex undergoes reduction to (formally) Rh^{II}, Rh^I and Rh⁰ species [177–180]. This redox chemistry is complicated by substitutional lability of the reduced species and their high reactivity, e.g. with H⁺ [181]. In general, $[\text{Rh}(\text{bpy})_3]^{3+}$ is reduced in a series of one-electron steps between -1.2 and -2.1 V. The complexes $[\text{Rh}(\text{bpy})_3]^{2+}$, $[\text{Rh}(\text{bpy})_2]^+$, $[\text{Rh}(\text{bpy})_2]$, and $[\text{Rh}(\text{bpy})_2]^-$ are produced. Reduction of $[\text{Rh}(\text{bpy})_2\text{Cl}_2]^+$ leads to the same species via Cl⁻ dissociation. The mechanism of reduction of Rh(III) phenanthroline complexes is similar, although the ligand-dissociation steps are slower. Reduction to $[\text{Rh}(\text{bpy})_3]^{2+}$ seems to be predominantly bpy-localized, although the possibility of relatively strong Rh-bpy π -delocalization cannot be excluded [180]. The possibility of a redox equilibrium between $[\text{Rh}^{\text{III}}(\text{bpy})_2(\text{bpy}^{\cdot-})]^{2+}$ and $[\text{Rh}^{\text{II}}(\text{bpy})_3]^{2+}$ has been proposed [180].

to account for the solution reactivity of $[\text{Rh}(\text{bpy})_3]^{2+}$. The complexes $[\text{Rh}(\text{bpy})_2]$ and $[\text{Rh}(\text{phen})_2]$ have been characterized by EPR as distorted-planar, electronically highly delocalized systems [179]. The substitutional lability of reduced Rh–polypyridine complexes [180] suggests that they can be active redox catalysts; although this role has been explored only very little, electrocatalytic reduction of CO_2 has been reported [30, 182].

An organometallic complex $[(\text{C}_5\text{Me}_5)\text{Rh}(\text{bpy})(\text{Cl})]^+$ is an efficient catalyst of electrochemical CO_2 and H^+ reduction [183–185]. Its redox behavior is similar to that of the analogous Ir complex (see below) and of $[(\text{C}_6\text{Me}_6)\text{M}(\text{bpy})(\text{Cl})]^+$; $\text{M} = \text{Ru}, \text{Os}$ [184].

Iridium

Similarly to polypyridine complexes of other d^6 metals, Ir(III)–bipyridine [106, 186] and phenanthroline [186, 187] complexes form extensive ligand-based redox series. The $[\text{Ir}(\text{bpy})_3]^z$ series comprises eight members related by one-electron steps [106]. $[\text{Ir}(\text{bpy})_3]^{3+}$ is reduced in six successive one-electron steps which occur in two groups of closely spaced three reductions spanning the range from -1.22 to -2.76 V. It also has an one-electron irreversible oxidation at ca $+1.7$ V, presumably to $[\text{Ir}(\text{bpy})_3]^{4+}$. The substituted complex $[\text{Ir}(\text{bpy})_2(\text{Cl})_2]^+$ has an irreversible oxidation and four one-electron reductions, presumably ligand-based. The reduction mechanism is complicated by dissociation of Cl^- ligand(s) on electron uptake [186].

The organometallic complex $[(\text{C}_5\text{Me}_5)\text{Ir}(\text{bpy})(\text{Cl})]^+$ undergoes an irreversible two-electron reduction with a concomitant loss of the Cl^- ligand [184, 185]. On the basis of spectroscopic data the resulting $[(\text{C}_5\text{Me}_5)\text{Ir}(\text{bpy})]$ was formulated [185] as an $\text{Ir}^{\text{II}}(\text{bpy}^{\cdot-})$ species. $[(\text{C}_5\text{Me}_5)\text{Ir}(\text{bpy})]$ can be protonated to yield photoactive $[(\text{C}_5\text{Me}_5)\text{Ir}(\text{bpy})(\text{H})]^+$. $[(\text{C}_5\text{Me}_5)\text{Ir}(\text{bpy})]$ is also further reduced at -3.29 V to $[(\text{C}_5\text{Me}_5)\text{Ir}^{\text{I}}(\text{bpy}^{2-})]^-$. The redox chemistry of $[(\text{C}_5\text{Me}_5)\text{Ir}(\text{bpy})(\text{Cl})]^+$ is relevant to electrocatalysis of CO_2 reduction [183] and photocatalysis of the water-gas-shift reaction [44, 188–190]. Further applications of this complex and of its Rh analog in electrocatalysis can be expected.

Nickel

Two redox series of Ni–bpy complexes are known [191]: $[\text{Ni}(\text{bpy})_3]^z$ and $[\text{Ni}(\text{bpy})_2]^z$. The complexes $[\text{Ni}(\text{bpy})_3]^{2+}$ and $[\text{Ni}(\text{bpy})_2]$ are the respective entries to the Ni–bpy chemistry, the latter complex having been prepared by a metal-vapor synthesis [191]. The electrochemical behavior (including redox potentials) is almost identical for both series. In CH_3CN both complexes form a four-membered redox series $z = 3+, 2+, 0, 1-$. $\text{Ni}^{\text{II}}/\text{Ni}^{\text{III}}$ oxidation is rather positive, $+1.3$ V. Further oxidations of $[\text{Ni}(\text{bpy})_3]^{3+}$ to $[\text{Ni}^{\text{IV}}(\text{bpy})_3]^{4+}$, $[\text{Ni}^{\text{IV}}(\text{bpy}^{\cdot+})(\text{bpy})_2]^{5+}$, and, finally, to the extremely unstable $[\text{Ni}^{\text{IV}}(\text{bpy}^{\cdot+})_2(\text{bpy})]^{6+}$ were observed [58] in liquid SO_2 . The $[\text{Ni}^{\text{IV}}(\text{bpy})_3]^{4+}$ complex seems to be in a temperature-dependent equilibrium with its electronic isomer $[\text{Ni}^{\text{III}}(\text{bpy}^{\cdot+})(\text{bpy})_2]^{4+}$.

Reduction of Ni^{II} complexes $[\text{Ni}(\text{bpy})_3]^{2+}$ and $[\text{Ni}(\text{bpy})_2]^{2+}$ occurs in a two-electron step [27, 191], at -1.64 V producing $[\text{Ni}(\text{bpy})_3]$ and $[\text{Ni}(\text{bpy})_2]$, respec-

tively. These complexes are further reduced at more negative potentials to the corresponding anions. $[\text{Ni}(\text{bpy})_3]$, $[\text{Ni}(\text{bpy})_3]^-$, and $[\text{Ni}(\text{bpy})_2]^-$ are prone to dissociation of a bpy ligand. $[\text{Ni}(\text{bpy})_2]^-$ is reduced by one electron to Ni metal and $2\text{bpy}^{\cdot-}$. In parallel, $[\text{Ni}(\text{bpy})(\text{CH}_3\text{CN})]^-$ is formed, which is further reduced to $[\text{Ni}(\text{bpy})(\text{CH}_3\text{CN})]^{2-}$. No direct information is available on the localization of these redox changes. Presumably, all anionic Ni complexes contain reduced bpy ligands [191]. Reduced Ni–bpy complexes undergo oxidative addition of organic halides RX . This reaction is the basis of coupling of R groups electrocatalyzed [192] by $[\text{Ni}(\text{X})_2(\text{bpy})]$.

The reduction mechanism changes for complexes containing sterically hindered danphen or catphen ligands. The 4-coordinated species $[\text{Ni}(\text{danphen})_2]^{2+}$ and $[\text{Ni}(\text{catphen})_2]^{2+}$ are reduced by one electron to the corresponding Ni^{I} complexes [108]. The distorted tetrahedral coordination required by these ligands stabilizes Ni^{I} complexes both thermodynamically (reduction occurs at ca -0.57 V) and kinetically towards ligand loss and, for $[\text{Ni}(\text{catphen})_2]^{2+}$, even towards reoxidation by O_2 [108]. $[\text{Ni}(\text{catphen})_2]^{2+}$, on the other hand, cannot be oxidized to a Ni^{III} complex.

Platinum

The $[\text{Pt}(\text{bpy})_2]^{2+}$ complex [193] is reduced in a sequence of three reversible one-electron steps in the range between -1.14 and -2.07 V, demonstrating the existence of a redox series $[\text{Pt}(\text{bpy})_2]^z$; $z = 2+, 1+, 0, 1-$. The first reduction product $[\text{Pt}(\text{bpy})_2]^+$ is very reactive. Depending on reaction conditions, it dimerizes to give $[\text{Pt}_2(\text{bpy})_3]^{2+}$ with a highly unusual structural unit: a Pt–Pt bond supported by a bridging bpy ligand [193]. Alternatively, electrically-conductive crystals of stacked Pt(I) complex $\{[\text{Pt}(\text{bpy})_2]_n\}_n$ can be grown electrolytically [194]. Complexes of the type $[\text{Pt}^{\text{II}}(\text{bpy})(\text{L})_2]^n$; $n = 2$, $\text{L} = \text{pyridine}$, NH_3 , PMe_3 , and $n = 0$, $\text{L} = \text{aryl}$, Me , Cl^- , CN^- , etc.; generally undergo two successive one-electron reductions [195–200]. The first step is localized on the bpy ligand, producing $[\text{Pt}^{\text{II}}(\text{bpy}^{\cdot-})(\text{L})_2]^{(n-1)}$. The redox potential of this step and the extent of Pt–bpy electronic delocalization depend on the ancillary ligand L, because of strong interaction between the ligands mediated by the Pt atom. The second reduction is Pt-localized. It leads to $[\text{Pt}^{\text{I}}(\text{bpy}^{\cdot-})(\text{L})_2]^{(z-1)}$, except for $\text{L} = \text{mesityl}$, for which the formula $[\text{Pt}^{\text{II}}(\text{bpy}^{2-})(\text{mes})_2]^{2-}$ has been suggested [197]. Oxidation of $[\text{Pt}^{\text{II}}(\text{bpy})(\text{L})_2]$ is generally irreversible, again with the exception of $[\text{Pt}^{\text{II}}(\text{bpy})(\text{mes})_2]$ for which the steric protection of the Pt atom enables reversible oxidation to Pt^{III} [197]. The influence of steric strain on redox behavior has been investigated for the series $[\text{Pt}^{\text{II}}(\text{R-phen})(\text{X})_2]$; $\text{X} = \text{halide}$, $\text{R-phen} = \text{phenanthroline derivatives}$ [201]. Reversible one-electron reduction was found only for complexes with undistorted planar geometry.

In another electrochemically and photochemically important group of Pt–polypyridine complexes [202, 203], an electron-accepting polypyridine ligand is combined with an electron-donating dithiolate dianion or dithiocarbamate anion: $[\text{Pt}^{\text{II}}(\text{S,S})(\text{N,N})]^n$; $n = 0$ or $1+$, respectively. These complexes are oxidized in an irreversible or partly reversible one-electron step and reduced in two successive, reversible one-electron steps between ca -1.5 and -2.4 V. Presumably, both reductions are N,N-localized.

Copper

The Cu^{I} complexes $[\text{Cu}(\text{bpy})_2]^+$ and $[\text{Cu}(\text{phen})_2]^+$ undergo electrochemically quasi-reversible or irreversible (phen) oxidation (-0.21 V, -0.35 V, respectively) to the corresponding Cu^{II} species. The reduction is accompanied by decomposition to Cu metal. This all changes when sterically hindered ligands 6,6'- Me_2 -bpy, 2,9- Me_2 -phen, 2,9- Ph_2 -phen, danphen, or catphen are used [108, 204]. These ligands favor the tetrahedral geometry of Cu^{I} but inhibit the octahedral or planar geometry of Cu^{II} . Hence, Cu^{I} complexes are strongly stabilized and the oxidation potential shifts positively to the range $+0.29$ to $+0.34$ V. Although reduction of $[\text{Cu}^{\text{I}}(6,6'\text{-Me}_2\text{-bpy})_2]^+$ is still irreversible, the more rigid, encaged geometry of $[\text{Cu}^{\text{I}}(\text{N},\text{N})_2]^+$; N,N = 2,9- Me_2 -phen, 2,9- Ph_2 -phen, danphen, or catphen; prevents the reduced complex from dissociation and $[\text{Cu}^{\text{I}}(\text{N},\text{N})(\text{N},\text{N}^{\cdot-})]$ species are formed by reversible reduction which occurs between -2.03 and -2.12 V. For danphen and catphen even the second reduction to $[\text{Cu}^{\text{I}}(\text{N},\text{N}^{\cdot-})_2]^-$ was observed ca 0.21 V more negatively [108, 204].

5.3 Electron-transfer Properties of Ground-state Polypyridine Complexes: Phenomena

The systematic survey given above enables us to single out general features of the redox chemistry of transition metal polypyridine complexes:

- multiple reductions and oxidations in sequences of reversible one-electron redox steps;
- the existence of redox series, that is of polypyridine complexes of the same composition but with different numbers of electrons (i.e. overall charge);
- for most polypyridine complexes, the redox steps are distinctly localized at the metal atom or a polypyridine ligand;
- for some complexes, reduction labilizes an ancillary ligand or a polypyridine ligand.

5.3.1 Localization of Redox Steps

In principle, redox changes of polypyridine complexes can be localized either on the metal atom, on a polypyridine ligand or delocalized over the whole complex molecule. Reduction steps of complexes containing more than one polypyridine ligand are localized on individual ligands instead of being delocalized over the ligand cluster. Hence, in heteroleptic complexes, it is necessary to determine the order in which the ligands are reduced. In this section metal and ligand localization will be discussed. Successive ligand-localized reductions will be treated in Section 5.3.2. The localization of a redox change is usually decided by use of the following experimental criteria:

- 1) Spectroelectrochemical (EPR, UV–Vis, res. Raman, and to a lesser extent IR) characterization of redox products often reveals features characteristic of reduced polypyridine ligands for ligand-localized reductions or of oxidized metal atoms for metal-centered oxidations. Stretching CO frequencies, obtained by IR spectroelectrochemistry, are an especially useful marker of a metal oxidation state in carbonyl–polypyridine complexes.
- 2) Potentials of polypyridine-localized redox couples depend linearly on the reduction potential of free polypyridines with a slope close to unity, when measured for homologous series of structurally related complexes [26, 67, 74, 101, 151, 205, 206]. This argument should be used with caution because even the potentials of metal-centered oxidation depends on the free polypyridine reduction potential, albeit with a significantly lower slope [29, 67] (Sections 5.3.2 and 5.3.3). Nevertheless, correlations of redox potentials in a series of $[M(N,N)_3]^z$ complexes, $N,N = \text{bpy}$, $4,4'\text{-Me}_2\text{-bpy}$, and $5,5'\text{-Me}_2\text{-bpy}$, with those of free ligands were often sufficient to identify N,N -localized reductions [101, 111, 117].
- 3) The energy of a spectroscopic metal-to-ligand charge-transfer (MLCT) electronic transition (if present) depends linearly on the difference between the oxidation and reduction potentials, if the oxidation and reduction are predominantly metal- and ligand-localized, respectively [6, 9, 74, 111, 117, 149, 152, 153, 205, 207–211]. This criterion can be used in various forms. The proper procedure uses the oxidation and reduction potential difference in series of complexes in which the polypyridine and/or ancillary ligands are varied. However, the oxidation potential alone can be correlated with spectroscopic energies in series of $[M(W)(X)(Y)(Z)(N,N)]$ or $[M(X)(Y)(N,N)_2]$ complexes, in which only the ancillary ligands are varied. If the reduction step is difficult to observe, or its localization is unclear, differences between the complex oxidation potential and the free ligand reduction potential can be correlated with the spectroscopic transition energy to decide on the localization of the oxidation step.
- 4) Experimentally observed redox patterns can be compared with those calculated by quantum-chemical techniques for a particular localization [5, 212]. This approach is especially useful for assignment of ligand-localized reductions in heteroleptic complexes.
- 5) The lack of correlations (2) or (3) and the appearance of spectroscopic features that do not resemble those of reduced polypyridine or an oxidized metal atom indicate a delocalized redox change.

Polypyridine complexes of second and third-row transition metals of a d^6 electron configuration are chemically stable and readily accessible, enabling the most convenient entry into metal–polypyridine redox chemistry and photochemistry. The corresponding metal atoms (Mo^0 , W^0 , Re^I , Ru^{II} , Os^{II} , Rh^{III} , Ir^{III} , and Cr^0 in tetracarbonyls) are much harder to reduce than polypyridine ligands and the π delocalization within the corresponding $M(N,N)$ chelate rings is, in most complexes, weak. At the same time, the first oxidation of second- and third-row transition d^6 metal atoms always occurs well before oxidation of polypyridine ligands. Consequently, the formal oxidation states of the metal atom and polypyridine ligands are well defined in the parent complexes and in their reduced forms and the first oxidation

product. Reductions are predominantly ligand-localized and reduced complexes can best be described as containing a d^6 metal atom and reduced polypyridine ligand(s). One-electron oxidized complexes are typical polypyridine complexes of d^5 metals (e.g. Ru^{III} , Re^{II} , etc.). Only the products of most positive oxidations in SO_2 possibly contain coordinated polypyridine cations.

Delocalized redox steps are rare among the polypyridine complexes of second- and third-row transition metals. Two-electron reduction of the organometallic species $[(\text{C}_5\text{Me}_5)\text{M}(\text{bpy})(\text{Cl})]^+$; $\text{M} = \text{Rh}, \text{Ir}$; and $[(\text{C}_6\text{Me}_6)\text{M}(\text{bpy})(\text{Cl})]^+$; $\text{M} = \text{Ru}, \text{Os}$; complexes [184, 185, 213, 214] is rather delocalized. Specifically, reduction of $[(\text{C}_5\text{Me}_5)\text{Ir}(\text{Ar-dab})(\text{Cl})]^+$ leads to $[(\text{C}_5\text{Me}_5)\text{Ir}(\text{Ar-dab})]$ which contains a delocalized, aromatic $\text{Ir}(\text{dab})$ chelate ring [214]. The second reduction (Eq. 4) of $[\text{Re}(\text{E})(\text{CO})_3(\text{N},\text{N})]^n$ to pentacoordinated species $[\text{Re}(\text{CO})_3(\text{N},\text{N})]^-$ is also largely delocalized. Few α -diimine and polypyridine-type ligands, especially abpy , bpm or Ar-dab favor metal–ligand delocalization, which arises from a relatively strong π -back-bonding. This is manifested, e.g., in the electrochemistry of $[\text{Ru}(\text{abpy})_3]^{2+}$ [107], see Section 5.3.3.

The localization problem (metal or ligand-centered) is more complicated in polypyridine complexes of first-row transition metals which are relatively easy to reduce and/or oxidize. Hence, potentials of metal-centered redox couples can occur in the range of polypyridine-localized reductions. Occupied d-orbitals of low-valent metal atoms can lie energetically close to the polypyridine π^* orbital, rising the possibility of delocalized redox changes. Because there is no simple rule enabling the prediction of the localization of redox steps in polypyridine complexes of first-row transition metals, their electron-transfer reactivity must be discussed individually (Section 5.2.2), with the aid of a general knowledge of the redox chemistry of the metal atoms and polypyridine ligands involved. Clear-cut metal-centered redox couples are known for polypyridine complexes of Cr, Fe, Co, and Cu: $\text{Cr}^{\text{II}}/\text{Cr}^{\text{III}}$, $\text{Fe}^{\text{II}}/\text{Fe}^{\text{III}}$, $\text{Co}^{\text{II}}/\text{Co}^{\text{III}}$, $\text{Co}^{\text{I}}/\text{Co}^{\text{II}}$, $\text{Cu}^{\text{I}}/\text{Cu}^{\text{II}}$. Well-defined polypyridine-localized reductions are known for $[\text{Fe}(\text{N},\text{N})_3]^{2+}$. Reduction of sterically confined $[\text{Cu}(\text{catphen})_2]^+$ and related $\text{Cu}(\text{I})$ complexes is also clearly catphen -localized, although reduction of sterically unhindered $[\text{Cu}(\text{N},\text{N})_2]^+$ species leads to decomposition and formation of metallic Cu. The most negative reductions of the first-row metal polypyridine complexes seem to be predominantly ligand-localized, producing formally N,N^{2-} complexes. This is, for example, observed for the last three reductions in the $[\text{Cr}(\text{bpy})_3]^z$ series, i.e. $z = 0/1-$, $1-/2-$, and $2-/3-$. The localization of redox couples occurring at intermediate potentials, which correspond to electron exchange between the species in the middle of the respective redox series, are hard to assign for first-row transition metals. Very often, these changes in the electron number are delocalized, affecting the metal atom and polypyridine ligands. The use of integer formal oxidation states is then inappropriate. This is, for example, observed for the $[\text{Cr}(\text{bpy})_3]^{2+}/[\text{Cr}(\text{bpy})_3]^+ / [\text{Cr}(\text{bpy})_3]^+$ couples, and for the reduction of Ti and V and, presumably, also Mn complexes. Delocalized redox changes are manifested by complicated UV–Vis and EPR spectra of the reduced forms which were, for Ti, V, Cr, and Fe, analyzed with the help of MO calculations [215]. Interesting experimental criteria for delocalized structures are also provided by IR spectra of the reduced bpy complexes measured in the range of bpy intraligand vibrations [113].

5.3.2 Redox Patterns

Typical polypyridine complexes of second- or third-row d^6 transition metals are characterized by metal-localized oxidation and a series of predominantly polypyridine-localized one-electron reductions. Their redox patterns are schematically shown in Figure 1.

Coordination to a metal atom shifts N,N-localized reductions positively by some 0.4–1 V, relative to the free ligand values. The magnitude of this shifts increases with the positive charge on the metal atom. For example, the first reduction of $[M^{III}(\text{bpy})_3]^{3+}$; $M = \text{Rh, Ir}$; occurs almost 0.5 V more positively than for their Ru and Os analogs $[M^{II}(\text{bpy})_3]^{2+}$ and the first reduction of $[\text{Re}(\text{CO})_4(\text{bpy})]^+$ is by 0.23 V more positive than that of isoelectronic $[\text{W}(\text{CO})_4(\text{bpy})]$. This positive potential shift is a result of stabilization of the reduced ligand by coordination [4]. Higher positive shifts can occur for polyazine ligands bridging between two metal atoms. The actual magnitude of this effect is a result of bonding and solvation effects [4, 212].

The number of reduction steps depends on the number and type of polypyridine ligands present. In principle, a complex with m polypyridine ligands, each of which carries k redox orbitals, will show a maximum of $2mk$ one-electron reductions, grouped in $2k$ separate sets each with m members [4, 212] (or, more simply, the maximum number of polypyridine-localized reduction steps equals the number of reduction steps of a free ligand multiplied by the number of ligands present). The bpy ligand and most polypyridines have only one low-lying, unoccupied π^* orbital, which acts as a redox orbital. Hence, usually $k = 1$ and the number of reduction steps is twice the number of polypyridine ligands, $2m$, see Figure 1. Polypyridines with electron-accepting substituents (e.g. 4,4'-Ph₂-bpy, or 4,4'-(COOEt)₂-bpy) have two low-lying π^* orbitals and, hence, their complexes have more than $2m$ reduction steps, although the full number of $2mk$ steps is usually not observed because the most negative lie outside the experimentally accessible potential range.

Figure 1 shows the origin of individual polypyridine-localized reduction steps of mono-, bis-, and tris-polypyridine complexes. It follows that a mono-polypyridine complex $[\text{M}(\text{W})(\text{X})(\text{Y})(\text{Z})(\text{N},\text{N})]$ will have the same number of reduction steps as the free N,N ligand itself. The potentials are shifted positively relative to those of the free ligand, as was discussed above. The first reduction leads to $[\text{M}(\text{W})(\text{X})(\text{Y})(\text{Z})(\text{N},\text{N}^{\bullet-})]^-$. The actual values of the corresponding reduction potential are a function of the N,N ligand and the metal fragment $\text{M}(\text{W})(\text{X})(\text{Y})(\text{Z})$. They can be calculated empirically, by use of electrochemical parameters, for the $\text{M}(\text{N},\text{N})$ fragment, ancillary ligands W, X, Y, Z, and the parameter S_L which describes the coupling between the ancillary ligands and the reducible N,N ligand [9, 15]. This coupling has been amply demonstrated experimentally, e.g. by the dependence of the first reduction potential of $[\text{Mo}(\text{CO})_{4-n}(\text{PBu}_3)_n(\text{bpy})]$ on the number of PBu_3 ligands ($n = 0, 2, 4$) [123] or by EPR spectra of $[\text{Re}(\text{E})(\text{CO})_3(\text{N},\text{N})]^{\bullet n}$ complexes; $\text{E} = \text{Cl}$ ($n = 1-$) or phosphine ($n = 0$) [134]. The effects of bpy-reduction on the $\text{Cr}(\text{CO})_4$ fragment in $[\text{Cr}(\text{CO})_4(\text{bpy})]$, analyzed by IR and EPR spectroelectrochemistry [121] and DFT calculations [122], also point to important interactions between bpy and CO ligands.

The second reduction of a mono-polypyridine complex corresponds to formation

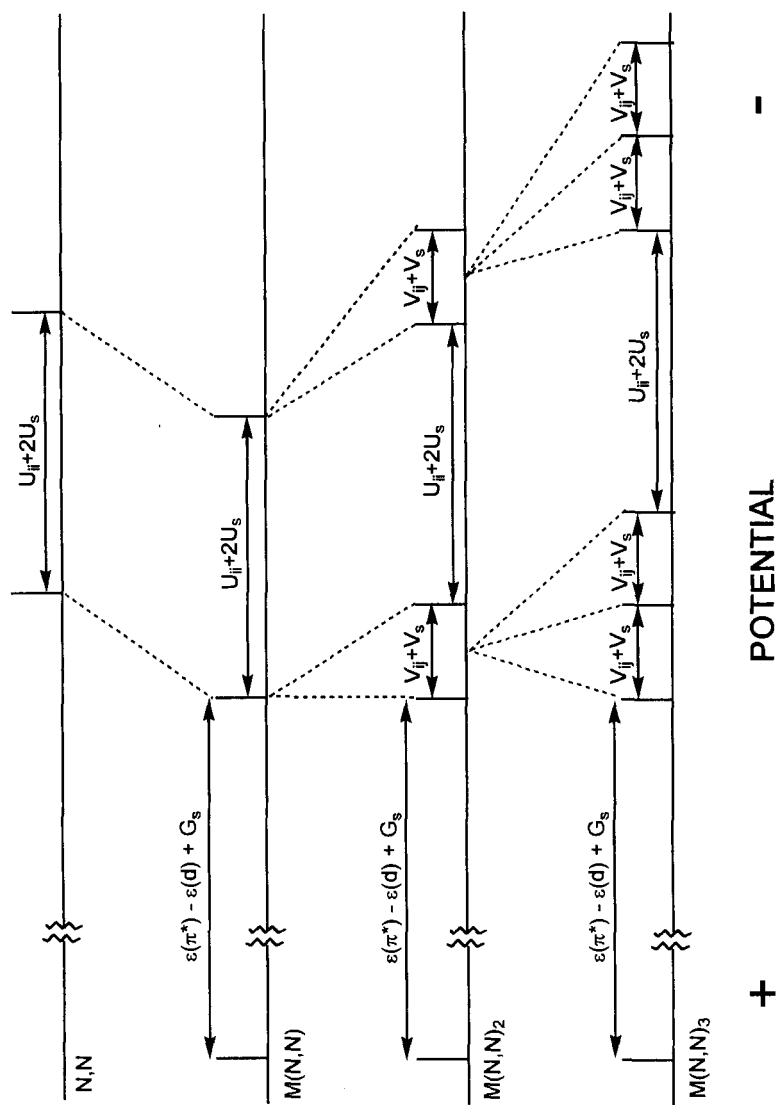


Figure 1. Redox patterns of a free polypyridine ligand and typical mono-, bis- and tris-polypyridine complexes [4, 8, 9, 212]. ε is the orbital energy, U_{ij} and V_{ij} are pair interaction energies between electrons placed on the same and different polypyridine ligands, respectively. U_s , V_s , and G_s are solvation energy terms. In the first approximation, interaction and solvation terms are assumed to be independent of the number of electrons, that is to be constant along the redox series. In reality, they show small changes. Interaction energies are positive and solvation terms are negative. Hence, solvation diminishes the redox potential differences. Dashed lines show the origin of reduction doublets and triplets in bis- and tris-polypyridine complexes, respectively.

of a dianion $[M(W)(X)(Y)(Z)(N,N^{2-})]^{2-}$. The difference between the first and second reduction potential is equal to the energy of a pair interaction between the two electrons placed on *the same* N,N ligand (i.e. between the two electrons in the π^* redox orbital), U_{ii} , plus a solvation term [4, 8, 212]. Experimental values of the potential difference (0.6–0.7 V for bpy complexes) are very close to those of the free ligands and almost independent on the metal fragment.

The two polypyridine ligands in bis-polypyridine complexes are reduced sequentially, one by one, at different potentials, instead of a single 2-electron step. Hence, the number of reduction steps doubles on going from mono- to bis-polypyridine complexes (Figure 1). Bis-polypyridine complexes are reduced in four one-electron reduction steps, grouped into two doublets [155]. The first two closely-spaced reductions (the first doublet) correspond to $M(N,N)(N,N)/M(N,N)(N,N^{\bullet-})/M(N,N^{\bullet-})(N,N^{\bullet-})$ couples while the reductions comprising the second doublet are due to $M(N,N^{\bullet-})(N,N^{\bullet-})/M(N,N^{\bullet-})(N,N^{2-})/M(N,N^{2-})(N,N^{2-})$ couples. The fact that the two N,N ligands are reduced separately is the consequence of an interligand electronic interaction, due to which the reduction of the second N,N ligand is more difficult if the first one was already reduced. The potential difference between the sequential reductions of the individual N,N ligands (i.e. within the doublet, ca 0.2 V) is then equal to the energy of a pair interaction between two electrons localized on *different* polypyridine ligands V_{ij} , plus a solvation term [4, 8, 212]. The potential difference between the doublets (0.6–0.7 V) corresponds to the energy of pair interaction between two electrons on *the same* N,N ligand, U_{ii} , plus a solvation term, as was discussed above for mono-polypyridine complexes. This description of the reduction pattern of metal bis-polypyridines is valid both for 6-coordinate species $[M(X)(Y)(N,N)_2]$ and for pseudotetrahedral complexes $[Cu(catphen)_2]$. The magnitude of the difference between the reduction potentials in $[Cu(catphen)_2]$, that is of the interaction energies between the extra electrons on the two phen moieties, is comparable with that in 6-coordinated bis-phen complexes, regardless of the different spatial orientation of the phen units. As for the mono-polypyridine complexes, potentials of ligand-localized reductions in 6-coordinate $[M(X)(Y)(N,N)_2]$ are slightly dependent on the nature of ancillary ligands X, Y and the metal atom M [216]. The magnitude of this effect can be estimated using Lever electrochemical parameters [9, 15].

The reduction pattern of tris-polypyridine complexes (Figure 1) can be easily deduced by considering interactions between the three N,N ligands [4, 5, 8, 149, 212]. They lead to sequential reduction of the individual N,N ligands which occurs in two triplets. The first triplet corresponds to reductions up to $[M(N,N^{\bullet-})_3]^z$ while the next three reduction steps, grouped in the second triplet, lead all the way down to $[M(N,N^{2-})_3]^{z-3}$. The potential difference between successive reductions within the triplets corresponds to the energy of interaction between electrons on different ligands V_{ij} , plus a solvation term. Corresponding values are typically between 0.13 and 0.25 V. Larger values (e.g. 0.36 found [107, 217] for $[Ru(abpy)_3]^{2+}$) indicate that the reductions can no longer be regarded as fully localized, most probably due to a metal-ligand π delocalization, which can mediate an interligand interaction. Even in well-behaved systems, the splitting between the most negative reductions within the second triplet is sometimes larger (ca. 0.3 V) than within the first triplet

[4, 5]. Apparently, this is caused by a change of the interligand interaction energy with the total number of electrons. The potential difference between the triplets is equal to the usual energy of interaction between the two electrons placed at *the same* N,N ligand, U_{ii} , plus a solvation term [4, 212]. Corresponding values are very similar for free polypyridines and their tris-complexes.

Heteroleptic complexes which contain chemically different polypyridine ligands give rise to complicated reduction patterns [5, 16, 149, 153]. The ligand with the most stable (lowest lying) π^* orbital gets reduced first. The following reduction sequence depends on the relative magnitude of the differences between the redox orbital energies (i.e. reduction potentials of the corresponding free ligands) and various pair interaction energies involved [5]. Hence, the ligands need not to be reduced in the order of the increasing energy of their redox orbital, that is in the order the decreasing reduction potentials of their free forms. It can even happen that several different electron configurations of the complex molecule, which differ in electron localization on different ligands, have very similar energies. Such complexes may exist as equilibrium mixtures of 'electronic isomers' [5].

The same approach to the interpretation and prediction of reduction patterns is valid also for polynuclear polypyridine complexes in which metal atoms are bridged by reducible polypyridine or polyazine ligand(s). Polyazines are generally reduced at more positive potentials than polypyridines and, moreover, reduction of a bridging ligand can be subjected to a larger positive shift than that of the terminal ligands. Therefore, bridging ligands are usually reduced first, before the terminal polypyridines. This is, for example, the case of the dinuclear complex $[(bpy)_2Ru(\mu-bpym)-Ru(bpy)_2]^{4+}$ in which the bpym ligand is reduced to $\mu-bpym^{\cdot-}$ and $\mu-bpym^{2-}$ before the first reduction of the bpy ligands [19]. Because of a very small interaction energy between the electrons on the two bpy ligands coordinated to different metal atoms, they are reduced at very similar or even identical potentials [19]. This type of redox pattern (viz. bridging ligands reduced first, terminal ligands bound to different metal atoms next, at similar potentials) was found [53, 84, 218] also for large supermolecular polypyridine complexes, including dendrimers (Section 5.3.6.).

An interpretation [4, 5, 8, 149, 212] of reduction sequences of $[M(N,N)_3]^z$ complexes requires to use redox orbitals localized on individual N,N ligands, instead of the $a_2 + e$ set of delocalized molecular orbitals of the $(N,N)_3$ ligand cluster, pertinent to the parent, unreduced complexes of a D_3 symmetry. The $[M(N,N)_3]^z$ complexes are then treated as a set of weakly interacting redox centers, that is individual N,N ligands. Qualitatively, this situation can be described using the redox orbital concept [1, 4, 6, 8] and assuming [3, 65, 69, 219] that the redox orbital is 'spatially isolated' at a single ligand. A quantum chemical model of sequential ligand-localized reductions, which includes solvation, has been developed for $[M(N,N)_3]^z$ as well as for heteroleptic complexes $[M(A)_{3-m}(B)_m]^z$, where A and B represent different reducible polypyridine ligands [5, 212]. It uses a unitary transformation of delocalized molecular orbitals into a set of localized redox orbitals and a specially developed form of the Hubbard Hamiltonian. This model allows us to express individual redox potentials and their differences in terms of redox orbital energies, inter- and intra-ligand electron pair interaction energies and solvation terms. A very good agreement between redox patterns predicted by this model and those observed ex-

perimentally has been found. It follows that the localization of redox changes on individual N,N ligands, as opposed to a delocalization over a (N,N)₃ ligand cluster, is driven by energetically favorable solvation and structural reorganization of the reduced ligand that accompany localization of an extra electron at a single ligand [212].

Most polypyridine complexes of second- and third-row transition metals also display a predominantly metal-localized oxidation at positive potentials which are chemically either reversible or partly reversible. Further one-electron oxidations often occur at more positive potentials in liquid SO₂ [57]. The first oxidation potential depends on the metal atom (for example, Ru > Os), the ancillary ligands in [M(W)(X)(Y)(Z)(N,N)] or [M(X)(Y)(N,N)₂] and, also, on the structure of the polypyridine ligand. Empirically, oxidation potentials can be calculated using additive Lever electrochemical parameters which quantify the influence of the metal atom and individual ligands on metal-centered redox couples [9, 157, 220].

The dependence of the first oxidation potential on the nature of the polypyridine ligand is intriguing. For example, a linear correlation between the potential of the Ru^{II}/Ru^{III} redox couple and the reduction potential of the free N,N ligand has been established for a series of [Ru(N,N)₃]²⁺ complexes [67]. The slope of this correlation is smaller than that of the correlation between the reduction potentials of the complex and the ligand. However, the very existence of these two correlations implies an existence of a linear correlation between the first reduction and oxidation potentials in a series of [Ru(N,N)₃]²⁺ complexes. Indeed, such a correlation has been found [29] for a large (52) set of these compounds with a slope of 1.16. It follows that the increase of the polypyridine π^* LUMO energy, which is responsible for the negative shift of the reduction potential, is accompanied by changes in other structural factors which stabilize the Ru^{III} oxidation state relative to Ru^{II} [29]. These include: (i) increase of σ -basicity [205, 210, 217], (ii) increase in the energy of occupied π polypyridine orbitals resulting in a π -donation to Ru^{III} [29], and, (iii) decrease of π -back donation from Ru^{II}.

Linear correlations between the first reduction and oxidation potentials were also found in series of [M^{II}(bpy)₂(X)(Y)]ⁿ; M = Ru, Os; where the ancillary ligands are varied [152, 216], and for heteroleptic tris-polypyridine complexes [210]. The existence of such correlation elegantly follows from the theory of electrochemical parameters [9]. Since the ancillary ligand nature affects the M^{II}/M^{III} potential much more than the bpy^{•-}/bpy potential, the slope of this correlation is only about 0.25, i.e. much smaller than that found for the [Ru(N,N)₃]²⁺ series, 1.16 [29].

The difference between the first reduction and oxidation potentials is an interesting parameter [6, 9, 207, 208]. Approximately, it corresponds to the difference between the energies of the metal-localized HOMO and polypyridine-localized π^* LUMO orbitals, plus a solvation term, Figure 1. This is the basis for the above-mentioned correlation with the spectroscopic MLCT transition energy (Section 5.4.3, Eqs 16 and 17) [6, 9, 207, 208]. The existence of a linear correlation between the oxidation and reduction potentials of [Ru(N,N)₃]²⁺ complexes with a near-unity slope implies, however, that their difference and, hence, the MLCT energy are only little dependent on the nature of the polypyridine ligand.

Redox patterns of first-row transition metal polypyridine complexes are very much

dependent on the metal atom, see Section 5.2.2. Redox behavior of $[\text{Fe}(\text{N},\text{N})_3]^{2+}$ complexes is similar to that of its Ru and Os counterparts. Tris-polypyridine complexes of Ti, V, Cr, Mn, and Fe show sequences of one-electron reductions and oxidations. However, there is no regular grouping of the redox steps into triplets because of delocalization of the redox changes whose extent, moreover, changes along redox series. Hence, delocalized redox orbitals, whose very nature changes with the number of electron added, have to be considered. Co^{I} and Ni^{I} polypyridine complexes are exceptional since they are reduced in two-electron steps.

5.3.3 Control of Redox Potentials by the Polypyridine Ligand Structure

Variations in the structure of a polypyridine ligand provide a means of control of the number of reduction steps of polypyridine complexes, of their reduction and oxidation potentials, and of the extent of π -delocalization between the metal atom and a polypyridine ligand. These aspects were discussed above in Sections 5.3.1 and 5.3.2. Here, the polypyridine influence on redox potentials will be discussed in more detail.

Potentials of ligand-localized reductions of polypyridine complexes depend on the ligand structure in the same way as free-ligand reduction potentials [26, 67, 74, 101, 151, 205]. Similar, but slightly less prominent correlation also exists between the potential of the first metal-localized oxidation and the free polypyridine reduction potential, see Section 5.3.2 [29, 67]. The first reduction steps of the generic bpy, phen and tpy ligands occur at similar potentials, between -2.4 and -2.6 V for the free ligands. The first reduction of the $[\text{Ru}(\text{bpy})_3]^{2+}$, $[\text{Ru}(\text{phen})_3]^{2+}$, and $[\text{Ru}(\text{tpy})_2]^{2+}$ complexes occur at -1.76 , -1.74 , and -1.74 V, respectively. The reduction potentials can be controlled either by introducing electron-accepting or donating substituents at pyridine rings of the generic polypyridine ligands or by introducing more N atoms, that is by going from polypyridines to polyazines. (Note that taphen and dppz complexes deviate from the correlations between ligand and complex reduction potentials [74].)

The first approach, substituting the H atoms on polypyridine ligands by electron-accepting or donating groups, affects reduction potentials without changing significantly the extent of a metal/polypyridine π -delocalization. A great variety of substituents were used to derivatize the bpy ligand, ranging from electron acceptors like CF_3 , $\text{C}(\text{O})\text{OEt}$, $\text{C}(\text{O})\text{Et}$, Ph, Cl, Br, to electron donors Me, OMe, NH_2 , or NR_2 . In most cases, the bpy ligand is substituted symmetrically, either at 4,4' or 5,5' positions. The effect of substituents at 5,5' positions is by 0.06 – 0.25 V larger than at the positions 4,4' [111, 221]. Redox potentials of bpy complexes can be tuned by substituents over a range of almost 1 V broad [74]. For example, $[\text{Ru}(5,5'-(\text{CF}_3)_2\text{-bpy})_3]^{2+}$ is reduced at -1.16 V while the reduction of $[\text{Ru}(4,4',5,5'-(\text{Me})_4\text{-bpy})_3]^{2+}$ occurs at -1.96 V. The same complexes are oxidized at $+1.30$ and $+0.67$ V, respectively [74, 222]. Oxidation of the complex $[\text{Ru}(4,4'-(\text{NMe}_2)_2\text{-bpy})_3]^{2+}$ is even more negative, -0.24 V [223]. Similar substituent-dependence occurs also for redox potentials of phen and tpy complexes [74, 224]. In general, the dependence of redox potentials on ligand substituents is well predictable. Both oxidation and reduction

potentials increase as the substituents become more electron accepting and decrease (become more negative) for electron-donating substituents. Linear correlations between redox potentials of polypyridine complexes and substituent Hammett parameters have been found [200, 206, 223–226].

Annealing two benzene rings to the bpy framework leads either to biquinoline or isomeric *iso*-biquinoline. Their respective complexes differ significantly in their redox behavior [74, 153, 227, 228]: The first reduction of $[\text{Ru}(\text{biq})_3]^{2+}$ is by 0.77 V more positive than that of $[\text{Ru}(i\text{-biq})_3]^{2+}$, in accordance with the trend in the reduction potentials of the free ligands. The difference between the oxidation and reduction potential for $[\text{Ru}(\text{biq})_3]^{2+}$ is unusually small, 2.20 V, relative to $[\text{Ru}(i\text{-biq})_3]^{2+}$, 2.63 V, and most other Ru-polypyridines.

Annealing one or two pyridine rings to the bpy framework forms the pynapy and dinapy ligands, respectively. They give rise to complexes that are relatively easy to oxidize and reduce [229]. The oxidation and the first reduction of $[\text{Ru}(\text{pynapy})_3]^{2+}$ occur at +0.69 and –1.38 V, respectively. The corresponding values for $[\text{Ru}(\text{dinapy})_3]^{2+}$ are +0.58 and –1.22 V. The differences between the oxidation and reduction potentials of these complexes are unusually low: 2.07 and 1.8 V, respectively. At the same time, differences between the first and second reduction potentials are rather high: about 0.24 V for both complexes. This behavior can be, as in the case of $[\text{Ru}(\text{biq})_3]^{2+}$ complexes, the result of a steric strain.

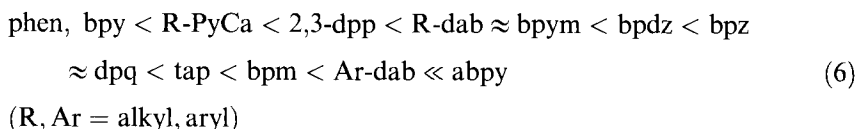
Introducing more N atoms into the framework of a bpy or phen ligand, that is on going from polypyridines to polyazines, changes not only redox potentials but also the localization of the π^* LUMO on N donor atoms and the σ -basicity [119, 217]. Generally, polyazine complexes are oxidized and reduced at more positive potentials than their polypyridine counterparts. This is demonstrated by the values for several representative complexes collected in Table 1. These data also demonstrate the parallel trend of the oxidation and reduction potential as a function of the ligand (see Section 5.3.2) which keeps the difference between them nearly constant, the only exceptions being bpm and taphen. The abpy ligand is clearly different: the

Table 1. The first oxidation ($E_{1/2}^{\text{ox}}$) and reduction ($E_{1/2}^{\text{red}}$) potentials of selected $[\text{Ru}(\text{N},\text{N})_3]^{2+}$ complexes. $\Delta E_{1/2}^{\text{red1,2}}$ denotes the difference between the first and second reduction potential. All values are relative to the Fc/Fc⁺ couple.

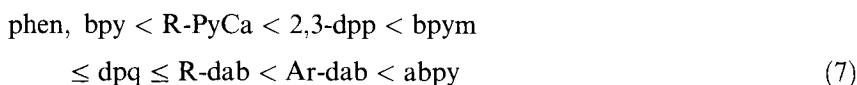
Complex	$E_{1/2}^{\text{ox}}$	$E_{1/2}^{\text{red}}$	$\Delta E_{1/2}^{\text{red1,2}}$	$E_{1/2}^{\text{ox}} - E_{1/2}^{\text{red}}$	Ref.
bpy	+0.85	–1.76	0.19	2.61	74
bpdz	+1.19	–1.39	0.25	2.58	217
bpym	+1.30	–1.30	0.17	2.60	217
bpz	+1.59	–1.07	0.19	2.66	217
bpm	+1.36	–0.97	0.15	2.33	217
phen	+0.88	–1.74	0.11	2.62	205
tap	+1.55	–1.14	0.13	2.69	211
taphen	+1.21	–1.09	–	2.30	288
abpy	–	–0.41	0.36	–	107, 217

reduction potential of $[\text{Ru}(\text{abpy})_3]^{2+}$ is very positive and the splitting between the first and second potential is rather large. These effects signal a much larger Ru-abpy π -delocalization as compared with other complexes. An exceptionally strong electron-acceptor ability of the abpy ligand was noted [136] also for $[\text{Re}(\text{L})(\text{CO})_3(\text{abpy})]^+$; L = THF or PPh_3 .

A comparison of electrochemistry of some of the free polypyridine ligands and their Ru^{II} , Re^{I} and Mo^0 complexes shows [97, 123, 134, 136, 137, 142, 230, 231] that, all other factors being constant, the potential of the first N,N-localized reduction increases in the order:



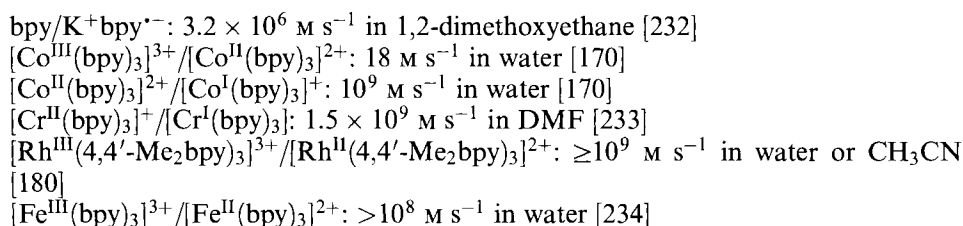
This implies that the π^* LUMO energy decreases in the same order, that is from bpy to Ar-dab and abpy. The $\text{Re} \rightarrow$ diimine π back bonding strengthens in a similar order:



R-dab ligands are somewhat stronger π -acceptors than aromatic diimines of comparable π^* orbital energy like dpp, bpym or dpq. This is caused by a larger contribution from the N-2p_z orbitals to the π^* orbital of the dab ligands, which, in turn, results in a larger $d\pi - \pi^*$ overlap. The very strong π acceptor ability of Ar-dab should be noted.

5.3.4 Electron-transfer Kinetics

Given the importance and great variety of electron-transfer reactions of polypyridine complexes, systematic kinetic studies are surprisingly scarce and only few kinetic data are available. Some representative rate constant values for homogeneous self-exchange redox reactions were reported:



The apparent slowness of the $\text{bpy}/\text{K}^+\text{bpy}^{\bullet-}$ rate could be caused by a strong ion-pairing with the K^+ ion upon reduction.

The spectacular 5×10^7 -fold acceleration on going from the $\text{Co}^{\text{III}}/\text{Co}^{\text{II}}$ to $\text{Co}^{\text{II}}/\text{Co}^{\text{I}}$ couple can easily be accounted for by different inner-sphere reorganization energies, according to the Marcus theory. Electron uptake by a $\text{t}_{2\text{g}}^6\text{Co}^{\text{III}}$ complex is accompanied by a large structural change, since two electrons are placed in a σ -antibonding e_g orbital of the $\text{t}_{2\text{g}}^5\text{e}_\text{g}^2\text{-Co}^{\text{II}}$ configuration. Accordingly, the average Co–N distance elongates [170] from 1.93 to 2.13 Å. On the other hand the extra electron in $[\text{Co}^{\text{I}}(\text{bpy})_3]^+$ is placed in a $\text{t}_{2\text{g}}$ orbital and its structural effects are largely compensated for by π -back bonding to bpy ligands. Consequently, the Co–N bond distance [170] is nearly the same (2.11 Å) as in the Co^{II} complex, reorganization energy is small and electron transfer fast. The solution kinetics of electron-transfer reaction involving $[\text{Co}^{\text{I}}(\text{bpy})_3]^+$ are complicated by concurrent bpy-dissociation equilibria [171, 172]. They give rise to various cross-reactions between $[\text{Co}^{\text{I}}(\text{bpy})_m]^+$ and $[\text{Co}^{\text{II}}(\text{bpy})_3]^{2+}$ complexes, which are all very fast $>10^8 \text{ M s}^{-1}$.

Notably, the self-exchange electron transfer $[\text{Co}^{\text{III}}(\text{bpy})_3]^{3+}/[\text{Co}^{\text{II}}(\text{bpy})_3]^{2+}$ is some 4–8 orders of magnitude faster than that between Co^{III} and Co^{II} amine complexes of a comparable size [235]. This demonstrates that bpy ligands are better able to compensate for redox-induced structural changes and to distribute the charge-change over a large molecular surface. Moreover, aromatic bpy ligands provide much better possibility for electronic coupling between the reactants. This can make the $[\text{Co}^{\text{III}}(\text{bpy})_3]^{3+}/[\text{Co}^{\text{II}}(\text{bpy})_3]^{2+}$ electron exchange partly adiabatic.

The much faster electron self-exchange rate observed for Rh than for Co reflects different localization of the corresponding redox couples, at the bpy ligand and the Co metal, respectively.

The heterogeneous rate constant [236] of electrochemical reduction of $[\text{Co}^{\text{III}}(\text{bpy})_3]^{3+}$ to $[\text{Co}^{\text{II}}(\text{bpy})_3]^{2+}$ is relatively slow, about 0.1 cm s^{-1} in CH_3CN or CH_2Cl_2 . Detailed studies of solvent and pressure effects [236, 237] have revealed that the rate of heterogeneous electron transfer is controlled by solvent dynamics. This implies that the electron transfer is adiabatic.

Electrochemical (heterogeneous) rate constants k° have been reported for a large set of $[\text{M}(\text{bpy})_3]^z/[\text{M}(\text{bpy})_3]^{z-1}$ redox couples [238], hereinafter denoted as $\text{M}^z/\text{M}^{z-1}$. According to the values obtained, the complexes fall into two categories:

- 1) Relatively fast reacting ($0.6 < k^\circ < 1.3 \text{ cm s}^{-1}$) complexes in which the redox change involves $\text{t}_{2\text{g}}$ orbitals and/or systems with a delocalized π bonding due to a strong $\text{t}_{2\text{g}}\text{-}\pi^*(\text{bpy})$ interaction: Ti/Ti^- , $(\text{V}^{2+}/\text{V}^+)$, V^+/V , V/V^- , $\text{Cr}^{2+}/\text{Cr}^+$, Cr^+/Cr , Mo^+/Mo , $\text{Fe}^{3+}/\text{Fe}^{2+}$, $\text{Os}^{3+}/\text{Os}^{2+}$. The V^{2+}/V^+ couple, although falling into this category, is rather slow, 0.35 cm s^{-1} . Interestingly, the rate of electrochemical reduction of $[\text{Fe}^{\text{III}}(\text{bpy})_{3-n}(\text{CN})_n]^z$ complexes gradually decreases as the bpy ligands are substituted by CN^- . The corresponding k° values (obtained in water) range [239] from 0.88 cm s^{-1} for $[\text{Fe}^{\text{III}}(\text{bpy})_3]^{3+}$ to 0.15 cm s^{-1} for $[\text{Fe}^{\text{III}}(\text{bpy})(\text{CN})_4]^-$. This could be caused by diminishing the size of the molecule and, hence, increasing outer-sphere reorganization energy.

- 2) Relatively slow reacting ($0.1 < k^\circ < 0.3 \text{ cm s}^{-1}$) complexes in which the redox change is localized on a single bpy ligand. These rate constants are comparable to that of the reduction of free bpy, i.e. of the $\text{bpy}/\text{bpy}^{\cdot-}$ redox couple, $0.13\text{--}0.21 \text{ cm s}^{-1}$, depending on the electrode material. This behavior is pertinent to following couples [238]: Cr^0/Cr^- , Mo^0/Mo^- , $\text{Fe}^{2+}/\text{Fe}^+$, $\text{Ru}^{2+}/\text{Ru}^+$, Ru^+/Ru^0 , Ru^0/Ru^- , $\text{Os}^{2+}/\text{Os}^+$, Os^+/Os^0 , Os^0/Os^- , and to the $[\text{Ir}(\text{bpy})_3]^{z+}$ series [106]: $\text{Ir}^{3+}/\text{Ir}^{2+}$, $\text{Ir}^{2+}/\text{Ir}^+$, Ir^+/Ir^0 , Ir^0/Ir^- , $\text{Ir}^-/\text{Ir}^{2-}$. Bpy-localized reductions of bis-bpy complexes $[\text{Ir}(\text{bpy})_2\text{Cl}_2]^+$, and $[\text{Fe}^{\text{II}}(\text{bpy})_2(\text{CN})_2]$ also belong to this class [106, 240]. It is interesting to note that the electron transfer rate constant is virtually independent of the oxidation state, that is of the number of electrons already present. The Ir series even shows [106] that the reduction steps in which a bpy ligand is reduced to $\text{bpy}^{\cdot-}$ (i.e. $\text{Ir}^{3+}/\text{Ir}^{2+}$, $\text{Ir}^{2+}/\text{Ir}^+$, Ir^+/Ir^0) have similar rate constants as the steps which correspond to $\text{bpy}^{\cdot-}/\text{bpy}^{2-}$ ligand-localized couples (i.e. Ir^0/Ir^- , $\text{Ir}^-/\text{Ir}^{2-}$).

The relatively slow rate of electrochemical bpy-localized reduction steps is rather puzzling. Possibly, it can be explained by large reorganization energy which arises from the fact that the redox change is localized on a single bpy ligand, instead of being delocalized over the whole complex ions. The internal reorganization energy would then consist of contributions from structural changes within the $\text{M}(\text{bpy})$ moiety affected. More importantly, localization of a redox change on a single ligand would lead to a significant dipole moment change, and, therefore, a large outer sphere reorganization energy.

Electrochemical rate constants are, generally, much lower than would correspond to the very fast homogeneous self-exchange rate constants observed for the $\text{Fe}^{3+}/\text{Fe}^{2+}$ or Cr^+/Cr^0 couples. (For example, the $1.5 \times 10^9 \text{ M s}^{-1}$ rate constant measured [233] for Cr^+/Cr^0 implies a heterogeneous rate constant of about 10^3 cm s^{-1} , in a sharp contrast to the experimental value of 1 cm s^{-1} .) Also, the slow electrochemical rates of bpy-localized redox couples do not agree with the ultrafast electron injection rates observed at semiconductor electrodes, see Section 5.4.6. To address these problems, it would be worthwhile to reexamine some of the electrochemical kinetic data using ultramicroelectrodes and to compare electrochemical and homogeneous electron transfer constants for a larger number of complexes. Moreover, the important questions of adiabaticity and possible kinetic solvent control were never addressed for bpy-localized redox couples.

A different type of electron transfer occurs in semi-reduced polypyridine complexes which contain bpy ligands in different oxidation states. Electron hopping between N,N and $\text{N},\text{N}^{\cdot-}$ ligands can take place in such species. This was indeed manifested [69, 241] by EPR line-broadening for several complexes $[\text{Fe}(\text{N},\text{N})_3]^+$ and $[\text{Ru}(\text{N},\text{N})_3]^z$; $z = 1+, 0$; $\text{N},\text{N} = \text{bpy}$, phen, and their Me_2 derivatives. Electron hopping occurs over an energy barrier [69] of $740\text{--}960 \text{ cm}^{-1}$ for $[\text{M}(\text{N},\text{N}^{\cdot-})(\text{N},\text{N})_2]^+$; $\text{M} = \text{Fe}, \text{Ru}$; and $300\text{--}440 \text{ cm}^{-1}$ for $[\text{Ru}(\text{N},\text{N}^{\cdot-})_2(\text{N},\text{N})]^0$. Electron hopping between $(\text{EtOOC})_2\text{-4,4'}$ -bpy and $(\text{EtOOC})_2\text{-4,4'}$ - $\text{bpy}^{\cdot-}$ ligands in $[\text{Ru}((\text{EtOOC})_2\text{-4,4'}$ -bpy) $_2(\text{X})_2]^{\cdot-}$ is manifested even electrochemically, by the redox potential temperature dependence [242]. In accordance with its formulation as $[\text{Fe}^{\text{II}}(\text{bpy}^{\cdot-})_3]^{\cdot-}$, no evidence for electron hopping was found for this complex [241].

5.3.5 Ligand Labilization

Polypyridine complexes are usually remarkably stable toward ligand dissociation upon reduction or oxidation. This is because polypyridines are very good ligands in their neutral, radical-anionic, as well as dianionic forms. However, in some cases (Section 5.2.2), a polypyridine ligand or, more often, an ancillary ligand gets labilized by reduction, with important chemical consequences and applications in catalysis.

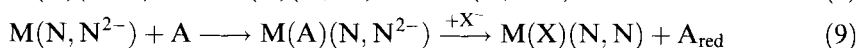
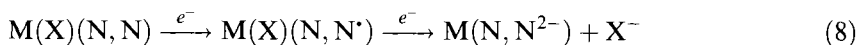
Tris-polypyridine complexes of first row transition metals undergo polypyridine dissociation upon reduction. Hence, their highly reduced forms has to be studied in the presence of an excess of free ligand, which complicates electrochemical investigations. For example, $[\text{Co}^{\text{III}}(\text{bpy})_3]^{3+}$, which has the d^6 electron configuration, is completely stable, while a bpy-dissociation from $[\text{Co}^{\text{II}}(\text{bpy})_3]^{2+}$ takes place with a rate constant of 3 s^{-1} . The Co^{I} complex $[\text{Co}^{\text{I}}(\text{bpy})_3]^+$ reacts faster [171] ($10\text{--}300 \text{ s}^{-1}$), giving rise to highly reactive coordinatively unsaturated Co^{I} species which activate organic substrates as well as CO_2 [30]. Similar reductively induced bpy dissociation was found [180] for $[\text{Rh}(\text{bpy})_3]^{3+}$ whose primary reduction product, $[\text{Rh}(\text{bpy})_3]^{2+}$ loses a bpy ligand with a rate constant of 1 s^{-1} . Further reduction to $[\text{Rh}(\text{bpy})_3]^+$ accelerates the bpy loss to $5 \times 10^4 \text{ s}^{-1}$. Moreover, $[\text{Rh}(\text{bpy})_3]^{2+}$ undergoes several redox-disproportionation equilibria whereby $[\text{Rh}(\text{bpy})_3]^{3+}$ and $[\text{Rh}(\text{bpy})_2]^+$ are produced. The reason for a bpy loss from $[\text{Rh}(\text{bpy})_3]^{2+}$ is not quite clear since, unlike its Co^{II} analog, it was formulated as a $d^6 \text{ Rh}^{\text{III}}$ complex $[\text{Rh}^{\text{III}}(\text{bpy})_2(\text{bpy}^{\cdot-})]^{2+}$. A close energetic proximity of the singly occupied $\pi^*(\text{bpy})$ orbital and the empty $e_g(\text{Rh})$ orbital could be the reason [180]. Except for Rh, even the most reduced complexes of second- and third-row transition metals are mostly stable, at least on the time scale of cyclic voltammetry at low-temperatures. A partial loss of a bpy ligand upon the fourth reduction has been noted [154] for $[\text{Os}(\text{bpy})_3]^{2+}$.

Ancillary ligands in substituted polypyridine complexes are often labilized upon reduction. This is, for example, the case of $[\text{M}(\text{CO})_4(\text{bpy})]$; $\text{M} = \text{Cr}, \text{Mo}, \text{W}$; which undergo electron transfer catalyzed substitution of an axial CO ligand [20]. Dissociation of a Cl^- ligand was observed [154, 155, 186, 216] on reduction of $[\text{M}(\text{bpy})_2(\text{L})(\text{Cl})]^{n+}$; $\text{M} = \text{Ru}, \text{Os}$; or on the second reduction of $[\text{Ir}(\text{bpy})_2(\text{Cl})_2]^{2+}$. For $[\text{Ru}(4,4'-(\text{EtOOC})_2\text{-bpy})_2(\text{X})_2]$, the following order of the rate of ligand dissociation upon the first reduction was found [242]: $\text{X} = \text{CN}^- < \text{NCS}^- < \text{Cl}^- < \text{I}^-$. Similarly, $[\text{Re}(\text{E})(\text{CO})_3(\text{N},\text{N})]^{n+}$ complexes undergo reductively-induced loss of the axial ligand $\text{E} = \text{halide}$ ($n = 0$) and, more slowly, of neutral ligands THF, PPh_3 , or RCN [130, 134–137, 243]. Dissociation of an electron accepting ligand $\text{E} = \text{P}(\text{OR})_3$ requires an addition of a second electron [135]. The organometallic complexes $[(\text{C}_5\text{Me}_5)\text{M}(\text{bpy})(\text{Cl})]^+$; $\text{M} = \text{Rh}, \text{Ir}$; and $[(\text{C}_6\text{Me}_6)\text{M}(\text{bpy})(\text{Cl})]^+$; $\text{M} = \text{Ru}, \text{Os}$; undergo a one-step, two-electron reduction, concerted with Cl^- dissociation [184, 185, 213].

Generally, the rate and extent of the reductively-induced ancillary ligand dissociation increase with the number of electrons added and decrease with increasing delocalization within the $\text{M}(\text{N},\text{N})$ chelate ring. Hence, reduced bpy or phen complexes are much more reactive than those of bpym, Ar-dab or, especially, abpy.

Labilization of the ancillary ligands in mono-reduced complexes appears to be linked with the extent of delocalization of unpaired electron density from the diimine π^* -orbital to the labilized ligand [121, 122, 134].

Reductively induced dissociation of an ancillary ligand from polypyridine complexes has a great importance for redox catalysis:



From this simplified scheme, it follows that the reductively-induced ligand labilization creates a vacant site to which a substrate A can coordinate. At the same time, the N,N ligand acts as an electron reservoir, accommodating electrons which are used to transform the coordinated substrate to A_{red} . A similar scheme can be drawn for one-electron substrate reduction following a ligand loss upon the first reduction. Indeed, both one- and two-electron catalytic reductions based on polypyridine complexes have been observed [135, 141].

An ancillary ligand in substituted polypyridine complexes can also be labilized by one-electron oxidation. The cases in which the oxidized radical of the ancillary ligand (e.g. CN^+ , Cl^+) dissociates are most interesting and need further mechanistic investigation. This is, for example, the case of [130, 131] $[Re^I(X)(CO)_3(bpy)]$; $X = Cl, CN$; Eq. 2, or [244] $[Ru(4,4'-(EtOC(O))_2-bpy)_2(X)_2]$; $X = CN, NCS^-, Cl^-, I^-$.

5.3.6 Redox Properties of Supramolecules Containing Metal–Polypyridine Units

Depending on the particular structure, the following supramolecular effects can be distinguished: (i) encapsulation of a metal–polypyridine unit, (ii) interaction between linked metal–polypyridine units, (iii) interactions between metal–polypyridine units and chemically different redox centers, and, (iv) host–guest interactions where a metal–polypyridine unit is the part of the host.

Encapsulation. The electrochemistry of a caged Ru^{II} complex in which all three bpy ligands are covalently linked together hardly differs from structurally similar tris-bpy complexes [109, 110]. A chemical stabilization of reduced first-row metal complexes by caged ligands can be expected. However, such species were not investigated. A spectacular encapsulation effect is shown by entwined catphen ligands which impose the coordination number four and a pseudotetrahedral geometry on first-row metal atoms, determining thus the redox behavior [108, 204] (Section 5.2.2). A strong enhancement of the stability of the reduced catenate complexes both toward decomposition (Cu) and reoxidation by O_2 (Ni) relative to their bis-danphen analogs should be noted.

A redox-induced translocation of an Fe atom occurs in complexes with tripodal, hemicaged ligands, each branch of which contains a bpy and hydroxamate [245] or a salicylate [246] binding sites. The Fe atom shuttles between the O-coordinating and bpy sites upon its oxidation to Fe^{3+} and reduction to Fe^{2+} , respectively.

Another type of redox-induced movement was found for $\text{Cu}^{2+/+}$ -catenates which contain both phen and tpy units in the catenate rings [247].

Dendrimers with a $[\text{Ru}(\text{bpy})_3]^{2+}$ core show the typical electrochemical behavior of the $[\text{Ru}(\text{bpy})_3]^{2+}$ unit, at least as the first reduction and oxidation are concerned [248]. Encapsulation by the dendrimer, which branches from the 4,4' positions of the bpy ligand(s) shifts the first oxidation and reduction potentials positively by ca 0.1 V, while the corresponding redox couples are no longer fully electrochemically reversible.

Metal atoms in polynuclear polypyridine complexes [51–53, 84, 87, 88] are usually bridged by another polypyridine or a polyazine ligand or by an ancillary ligand like CN^- . The use of a 2,3-dpp bridge leads to large dendrimers formed of interconnected $\text{Ru}^{\text{II}}(\text{dpp})_3$ moieties and terminal $\text{Ru}^{\text{II}}(\text{dpp})_2(\text{bpy})_2$ units. Dendrimers prepared so far contain up to 22 Ru centers [84]. Electronic interaction between metal atoms mediated by the bridge causes neighboring metal atoms to be oxidized at different potentials even if they are chemically identical. In large dendrimeric species, the peripheral metal atoms are oxidized first in a single multi-electron step, followed by an oxidation of the inner metal atoms at more positive potentials. Metal atoms of each layer are thus oxidized together and the number of electrons exchanged corresponds to the number of metal atoms present in the layer [249]. Polypyridine ligands are reduced sequentially as in mononuclear complexes, but the overall redox pattern is complicated by weak (few tens of mV) interactions between the dpp ligands at the neighboring centers, and by large positive shifts of reduction steps localized at the bridging ligands (Section 5.3.2). Generally, bridging polypyridine or polyazine ligands are reduced first: a group of closely spaced reductions converts all bridging ligands to anions, one by one. A stepwise reduction of all the bridging ligands to dianions comes next at more negative potentials. A group of very closely spaced reductions, in which one electron is added to each ligand of each terminal group, follows. In the next manifold of closely-spaced reductions, the second ligand of each terminal group is reduced. At the end of these reduction sequences, all bridging ligands are present as dianions and all terminal ligands as anions. Then, two sets of reductions of the terminal ligands to dianions occur. This type of redox pattern is quite general [53, 218, 250]. For example, 26 ligand-localized reduction steps have recently been distinguished and assigned for a hexanuclear Ru-polypyridine dendrimer [218]. The general reduction pattern described above may differ if the bridging ligands are difficult to reduce. Electrochemistry emerges as an important technique to characterize supramolecular species and to map electronic interactions between their components.

In other systems [51, 52, 87, 88], the tpy ligands of neighboring metal-containing units are connected through their 4' positions, either directly or by a spacer (e.g. 1,4-phenylene, or $-\text{C}\equiv\text{C}-$). Most of homometallic dinuclear complexes of this type show a single two-electron, metal-centered oxidation, indicating that the metal–metal interaction is negligible. The ligands are reduced sequentially. Localization of reduced steps was not studied in detail, but a perusal of trends in reported redox potentials [52] indicates that the interconnected ligands are reduced first.

Another type of supramolecular systems contain a metal–polypyridine unit (Ru^{II} or Os^{II} bis- or tris-polypyridines, $\text{Re}^{\text{I}}(\text{CO})_3(\text{N},\text{N})^+$, or $\text{Cu}^{\text{I}}(\text{catphen})_2^+$) linked co-

valently with chemically different redox- and/or photo-active groups: alkylviologens (MV^{2+} and derivatives) [91, 251], C_{60} [252], porphyrins [86, 253], phenothiazine (PTZ) [254, 255] etc. (See Appendix for MV^{2+} and PTZ.) These groups can be bound either as ancillary ligands, or covalently attached to the pyridine rings of N,N ligands, or inserted into catenate rings. Rotaxanes with a $Cu^I(-9,7-phen)_2^+$ central unit and $Ru(bpy)_3^{2+}$, C_{60} or porphyrin stoppers are also known [92]. Supramolecules of this type are designed and synthesized especially for photochemical applications. Their electrochemical behavior is, in most cases, a simple sum of that of their components. No electrochemically important synergetic effects or interactions between the components were observed. (Positive shifts of metal-centered oxidations observed in some dinuclear Cu-catenanes are due to a steric strain at the metal centers [256].) UV-Vis absorption spectra also show only sums of the features due to the components.

It is also possible to build metal-polypyridines into supramolecular hosts and receptors. For example, one of the bpy ligands may be a part of a crown ether ring [34], or it may be capped with a calixarene [33, 257] attached at the 4,4' positions. Electrochemical behavior of the metal-polypyridine unit is then affected by an interaction with a 'guest', e.g. an alkali metal cation.

5.3.7 Applications of Ground-state Electron Transfer

Most chemical applications of metal-polypyridine complexes are based on the high reactivity of their unusual oxidation states. Their use as stoichiometric reagents [258] seems to be largely limited to outer-sphere oxidations with tris-polypyridine complexes of Fe^{III} , Ru^{III} , and of the less oxidizing Co^{III} or Cr^{III} . Redox potentials of Fe and Ru complexes can be finely tuned, Section 5.3.3. By contrast, reduced polypyridine complexes are usually not employed as stoichiometric reductants, probably because of an abundance of other reducing agents which are more easily handled.

One of the most prominent feature of polypyridine complexes is that they can be easily oxidized and reduced both photochemically and electrochemically. This opens an enormous potential for applications in photocatalysis (Section 5.4.9) and electrocatalysis.

Most electrocatalytic processes studied so far are reductive, taking an advantage of a reductive ligand labilization, Section 5.3.5. They are essentially based on Eqs 8 and 9, but the real mechanisms are more complex. Electrocatalysis of CO_2 reduction is the most studied process [131, 135, 138, 139, 141, 158–163, 182, 183, 259] with $[Re^I(Cl)(CO)_3(N,N)]$, $[Ru^{II}(N,N)_3]^{2+}$, $[Ru^{II}(bpy)_2(CO)(Cl)]^+$, $[Ru^{II}(bpy)_2(CO)_2]^{2+}$, Os^{II} complexes, or $[(C_5Me_5)M(bpy)(Cl)]^+$; $M = Rh, Ir$; serving as catalysts. The catalyst is either homogeneous, in a solution phase, or deposited on the electrode surface as a polymer film [160–162, 259]. Depending on the catalyst and conditions, CO_2 reduction electrocatalyzed by $[Re(Cl)(CO)_3(bpy)]$ can follow either one- or two-electron mechanism [135, 141]. Electrogenenerated $[Re(CO)_3(bpy)]^{+*}$ and $[Re(CO)_3(bpy)]^{2-}$, are the respective active species.

Other examples of electrocatalysis include reduction of H^+ to H_2 catalyzed [185]

by $[(C_5Me_5)Ir(bpy)(Cl)]^+$, coupling of organic groups (with a C–C bond formation) catalyzed [192] by $[Ni(X)_2(bpy)]$, or coupling of alkynes and CO_2 catalyzed by $[Ni(bpy)_3]^{2+}$ in the presence of Mg^{2+} ions [260]. $[Co(bpy)_3]^{2+}$ is another useful reduction catalyst [24, 30, 31]. The active form, $[Co(bpy)_3]^+$, is usually generated chemically or photochemically [173].

An electrocatalytic oxidation of guanine in oligonucleotides and DNA using the $[Ru(bpy)_3]^{2+/3+}$ redox couple has been observed and its mechanism investigated [261]. Metal–polypyridine complexes with oxo ligands act as electrochemical catalysts of water, Cl^- , or hydrocarbon oxidations [128, 166, 167, 262].

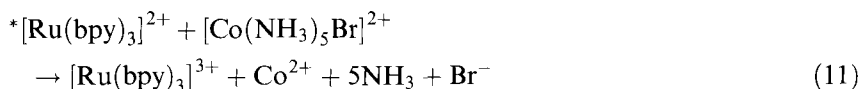
It is surprising that the great potential of metal–polypyridine complexes as reduction catalysts and electrocatalysts has not been investigated in more detail and extended to other types of substrates.

Supramolecules containing metal–polypyridine units, especially the $Ru(dpp)$ -based dendrimers, could be used as electron reservoirs or components of molecular-electronic devices. Supramolecules in which an electroactive $M(N,N)_n$ group is attached to a receptor capable of molecular recognition (crown ethers, calixarenes, cryptands etc.) can work as electrochemical sensors. Electrochemical recognition of cations as well as anions has been reported [33–35, 257, 263].

Redox series of metal–polypyridines still await their practical exploration. The existence of multistep, reversible, sequential reduction processes, each step occurring at a defined potential and being localized at a specific molecular site, is very promising for possible applications in molecular electronics. This would require to organize the active complexes in films, polymers or supermolecules. Up to now, only the electrochromic behavior of some $[Ru(N,N)_3]^{2+}$ complexes has been explored with potential applications in electrochromic glasses, displays and redox sensors [206, 262, 264].

5.4 Electron-transfer Properties of Electronically Excited Polypyridine Complexes

This area was opened [59] in 1972 by the observation of a bimolecular reaction between the long-lived MLCT excited state of $[Ru(bpy)_3]^{2+}$ and $[Co(NH_3)_5Br]^{2+}$:



Since then, excited state electron transfer of metal polypyridines has developed into a major research area which is covered by many excellent reviews and books [32, 37, 38, 42, 43, 62, 74, 83, 95, 98, 99, 265–270]. Herein, some general aspects and more recent developments will be discussed.

The prominent electron transfer photochemistry of polypyridine complexes stems from a unique combination of their ground state redox reactivity and excited state properties:

- 1) Fast one-electron oxidation and/or reduction of ground-state complexes at suitable potentials. (Out of all the multiple redox steps, it is only the first oxidation and the first reduction which are photochemically relevant.)
- 2) Chemical stability of oxidized and reduced complexes.
- 3) Presence of low-lying excited states which can be efficiently populated by optical excitation.
- 4) Excited state lifetimes are sufficiently long-lived to allow for an efficient bimolecular electron transfer.
- 5) Photochemical stability.

These conditions are met by excited states of many polypyridine complexes of d^6 metals and, in part, of d^3 Cr^{III} . Electron transfer reactivity is then retained upon electronic excitation, giving rise to important photochemistry and possible applications.

5.4.1 Basic Thermodynamic and Kinetic Aspects of Excited-state Electron Transfer

Optical excitation occurs as a vertical transition, without a change in molecular geometry or in the arrangement of the surrounding medium. It prepares a so-called Franck–Condon excited state. Since the molecular geometry and orientation of solvent molecules are not adapted to the changed electron density distribution, Franck–Condon excited states are not equilibrated. Hence, ultrafast relaxation to a thermally equilibrated excited state follows [118, 271]. For most polypyridine complexes, relaxation of a Franck–Condon state is a convoluted process that includes redistribution of electron density, change of a spin state (i.e. intersystem crossing), vibrational relaxation, and solvent relaxation. It is usually completed within a few hundreds of femtoseconds, although in some cases a full relaxation can take as long as few picoseconds [272, 273].

Relaxation of a Franck–Condon state produces an energetically low-lying, thermally equilibrated excited state [274–276]. In most cases, this is the lowest excited state. A molecule in a thermally equilibrated excited state is a distinct chemical species in its own right, which has defined equilibrium geometry, thermodynamic properties, and lifetime. It can be viewed as an energy-rich isomer of the respective ground state. Indeed, most of photochemical electron-transfer reactions of polypyridine complexes involve equilibrated states, whose lifetimes are long enough so that electron transfer can occur competitively with unproductive decay to the ground state. Direct electron transfer from Franck–Condon state is very rare, albeit possibly very important in photoelectrochemical light–energy conversion (Section 5.4.6).

Redox behavior of electronically excited molecules is derived from that of the

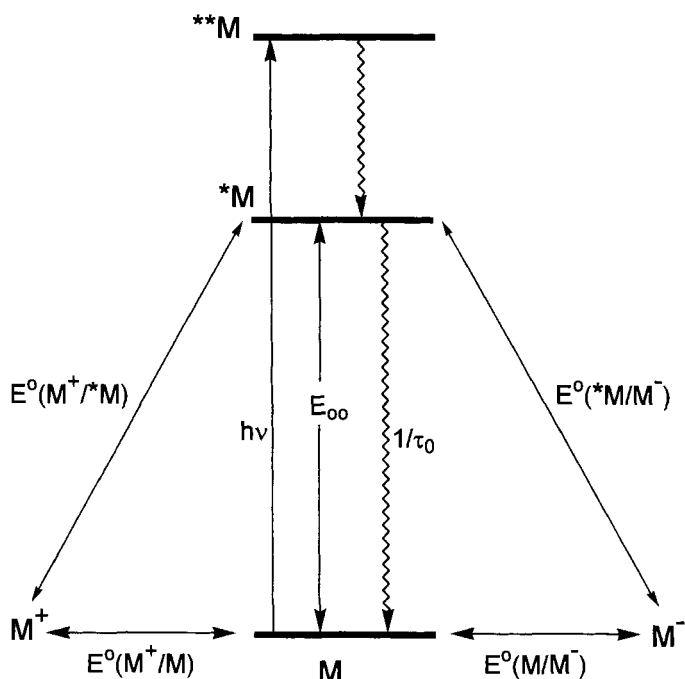


Figure 2. Generalized excited state diagram. M represents a ground-state molecule, $**M$ and $*M$ are the Franck–Condon and thermally equilibrated excited states, respectively. $h\nu$ is the excitation energy, E_{00} the excited state energy, and τ_0 is the inherent excited state lifetime. Relevant ground- and excited state redox couples are shown.

corresponding ground state species (Figures 2 and 5). Electronic excitation activates electron transfer reactivity in two ways: thermodynamically by shifting the redox potentials and kinetically by changing the electron distribution. Excited state redox potentials [37] are determined by the corresponding ground state potentials and the excited state energy, E_{00} :

$$E^\circ(M^+/*M) = E^\circ(M^+/M) - E_{00} \quad (12)$$

$$E^\circ(*M/M^-) = E^\circ(M/M^-) + E_{00} \quad (13)$$

where M and $*M$ represent the ground and excited state, respectively, see Figure 2. (The potentials $E^\circ(M^+/M)$ and $E^\circ(M/M^-)$ correspond to $E_{1/2}^{\text{ox}}$ and $E_{1/2}^{\text{red}}$, as used in Table 1.) Since redox potentials are thermodynamic quantities, they can be defined only for thermally equilibrated excited states. The excited state energy, E_{00} , is the energy difference between the minima of the ground and excited state potential energy surfaces. The entropy change between the ground and excited state is neglected. Eqs 12 and 13 show that, on excitation, the oxidation potential shifts

negatively and the reduction potential positively. This means that excited state of a molecule which, in its ground state, can be both reversibly oxidized and reduced (as many polypyridine complexes are) is simultaneously a very strong reductant and oxidant. This can be demonstrated using the best-known polypyridine photosensitizer, $[\text{Ru}(\text{bpy})_3]^{2+}$: In its ground state, it is neither an oxidant nor a reductant since its reduction and oxidation occurs at rather negative and positive potentials, -1.76 and $+0.85$ V, respectively. However, its MLCT excited state lies 2.12 eV above the ground state. This shifts the corresponding reduction and oxidation potentials to $+0.36$ and -1.27 V, making the MLCT-excited $[\text{Ru}(\text{bpy})_3]^{2+}$ a very strong oxidant *and* reductant.

The respective products of oxidation and reduction of an excited molecule, that is the species M^+ and M^- in their electronic ground states are themselves strong oxidants and reductants, respectively. They can return to the initial ground state molecule M by further electron-transfer reactions, as shown in Figure 3. Hence, photochemical electron transfer can operate as a catalytic cycle. (In the $[\text{Ru}(\text{bpy})_3]^{2+}$ example, M^+ and M^- represent $[\text{Ru}(\text{bpy})_3]^{3+}$ and $[\text{Ru}(\text{bpy})_3]^+$, respectively.)

5.4.2 Excited States of Polypyridine Complexes

Three basic types of excited states need to be considered here: (i) metal to ligand charge transfer excited states (MLCT) in which an electron is excited from a $d\pi$

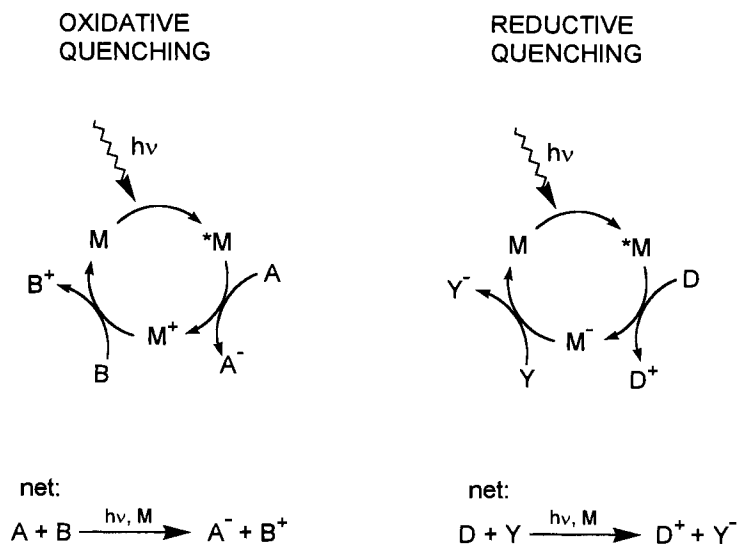


Figure 3. Photocatalytic cycles based on an oxidative (left) and reductive (right) quenching of an excited polypyridine complex M . (The photosensitizer M in these cycles has been called 'light absorption sensitizer' (LAS), since it enables a photochemical reactions between chemical species which do not absorb light [74, 266].)

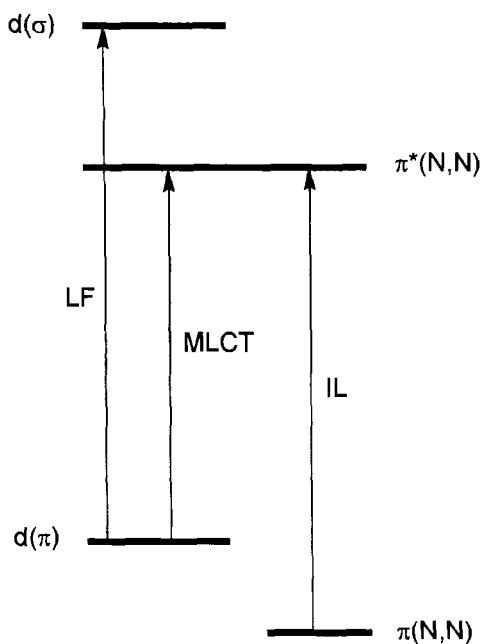


Figure 4. Typical electronic transitions of metal polypyridine complexes. LF = ligand field, MLCT = metal to ligand charge transfer, IL = intraligand, $d(\pi)$ and $d(\sigma)$ are metal d orbitals of a t_{2g} and e_g origin, respectively. $\pi(N,N)$ and $\pi^*(N,N)$ are the respective highest occupied and lowest unoccupied polypyridine π orbitals. LF states become the lowest-lying in complexes of first-row metals with a small d-orbital splitting. The IL state can lie below MLCT states for highly delocalized polypyridine ligands with a small $\pi^*-\pi$ gap, or if $d(\pi)$ orbitals lie low in energy due to high positive charge on the metal atom (Rh^{III} , Ir^{III}) or electron-accepting ancillary ligands (CO, RNC...).

(essentially t_{2g}) metal orbital to a π^* orbital localized predominantly on the polypyridine ligand, (ii) ligand-field, (LF) states which correspond to electron excitation within the predominantly metal-localized d-orbital manifold, and, (iii) intraligand excited states (IL) which originate in electron excitation from an occupied π polypyridine orbital to a corresponding π^* orbital. These three types of excitation are shown schematically in Figure 4.

The character of the lowest excited state depends on the nature of the metal atom, the polypyridine ligand and the ancillary ligands. MLCT excited states are the lowest excited states of those complexes which contain easily-oxidized low-valent metal atoms: Cr^0 , Mo^0 , W^0 , Mn^I , Re^I , Fe^{II} , Ru^{II} , Os^{II} , Pt^{II} , and Cu^I . These are the polypyridine complexes whose ground-state reduction and oxidation is predominantly localized on the metal atom and the polypyridine ligand, respectively (Section 5.3.1). MLCT electronic transitions are strongly allowed and usually occur in the visible spectral region. Hence, irradiation into MLCT absorption bands of poly-

pyridine complexes provides a very efficient way of collecting light energy. Many complexes which possess a lowest lying MLCT state also meet other practical conditions for a good photochemical sensitizer [277], namely those of convenient redox potentials of both oxidation and reduction and chemical stability of the excited, oxidized, and reduced forms.

Since the ligand-field splitting of the d-orbital manifold of low-valent d^6 metal atoms is relatively large, LF excited states of d^6 -metals occur at higher energy than MLCT states, with the only exception of Fe^{II} . Hence, LF states are not involved in electron transfer reactivity but they can provide a non-radiative deactivation pathway for the reactive MLCT state, shortening its lifetime. LF states do not exist for $d^{10} \text{Cu}^{\text{I}}$. The only polypyridine complexes with a redox-active LF state are $[\text{Cr}(\text{N},\text{N})_3]^{3+}$, whose ${}^2\text{T}/{}^2\text{E}$ LF states are strong oxidants [278, 279].

Intraligand excited states become the lowest in complexes of metal atoms which are difficult to oxidize, that is Rh^{III} and Ir^{III} . Moreover, IL excited states are relatively low-lying for those polypyridine ligands which have highly delocalized, extended π system, for example dppz or some phen derivatives. Hence, complexes of these ligands often have close-lying MLCT and IL states. This situation has interesting photophysical consequences [280–282]. The much stronger medium-dependence of the MLCT than IL excited state energy provides a way of controlling their relative energetic order. Generally, rigid or highly polar media shift MLCT states to higher energies. The order between MLCT and IL states also depends on the nature of the ancillary ligands, whereby the MLCT states are stabilized in energy by strong electron donors and destabilized by electron acceptors. This effect is, for example, demonstrated by $[\text{Re}(\text{Cl})(\text{CO})_3(\text{bpy})]$ and $[\text{Re}(\text{CO})_4(\text{bpy})]^+$, whose lowest-lying excited states are of a MLCT and IL origin, respectively [97, 133, 283]. Polypyridine complexes with lowest IL excited states are mostly poor excited state reductants. Moreover, their oxidized forms are often chemically unstable, precluding their use in photocatalytic cycles shown in the Figure 3, left. On the other hand, these species can be strong excited state oxidants. Photochemistry of complexes with lowest-lying IL excited states usually requires UV irradiation.

5.4.3 Control of the Electron-transfer Properties of MLCT Excited States of Polypyridine Complexes

It follows from the discussion in the Section 5.4.1 that excited state redox properties can be controlled through ground-state redox potentials (Sections 5.3.2. and 5.3.3.) and excited state energy E_{00} . The excited state energy is dependent on the molecular structure, but in a way that is interrelated with the structural dependence of the redox potentials. In Section 5.3.1 it was mentioned that the MLCT excitation energy, $h\nu$, (Figure 2) depends linearly on the difference between oxidation and reduction potentials. This dependence stems from the intramolecular charge separation that occurs in MLCT excited states:



where **B** represents ancillary ligands. For complexes containing two or three polypyridine ligands, the excited electron is localized [70–72, 219, 284] on a single N,N ligand:



in the same way as in reduced species. Indeed, the MLCT-excited and reduced polypyridine complexes show the same spectroscopic patterns (UV–Vis, res. Raman, IR), since they contain the same chromophore, viz. $N, N^{\bullet-}$. The localized formulation (Eq. 15) implies that electron hopping between N,N ligands ($N, N^{\bullet-} \leftrightarrow N, N$) should occur in MLCT-excited tris-polypyridine complexes. Indeed, such inter-ligand electron transfer was observed for $[\text{Os}(\text{bpy})_3]^{2+}$. It occurs in the picosecond time domain. The actual rate and mechanism depend on the solvent relaxation time [285, 286].

Energies of optical MLCT transitions ($h\nu$) and energy of a thermally equilibrated MLCT state (E_{00}) depend linearly on the difference between the reduction and oxidation potential [6, 9, 28, 149, 207, 208]:

$$h\nu = E^\circ(M^+/M) - E^\circ(M/M^-) + \chi_i + \chi_o + C \quad (16)$$

$$E_{00} = E^\circ(M^+/M) - E^\circ(M/M^-) - D \quad (17)$$

Reorganization energies χ_i and χ_o correspond to the inner-sphere (vibrational) and outer-sphere (solvent) reorganization that follows excitation into the Franck–Condon MLCT excited state (Figure 2). The parameters C and D include further electronic and solvation terms [9, 28]. Eqs 16 and 17 have been tested in numerous studies using absorption or emission energies (for example [9, 149, 152, 153, 205, 210, 287–290]) and, indeed, the predicted linear relationships between the transition or excited state energies and ($E^\circ(M^+/M) - E^\circ(M/M^-)$) were found. The experimentally determined slopes are usually slightly less than 1, due to a partial delocalization of redox changes and of MLCT excitation between the metal atom and the polypyridine ligand [9]. (*Note that E_{00} is defined here as an energy difference between fully equilibrated excited and ground state. Hence, it is different from the emission energy as used in ref. [9].)

Combining Eqs 12, 13, and 17 yields new expressions for excited state redox potentials [28]:

$$E^\circ(M^+/*M) = E^\circ(M/M^-) + D \quad (18)$$

$$E^\circ(*M/M^-) = E^\circ(M^+/M) - D \quad (19)$$

Now, the excited state oxidation potential is related to the potential of the ground-state ligand-localized redox couple and the excited state reduction potential is related to the potential of the ground-state metal-localized redox couple, see Figure 5. These relations are very logical since oxidation of an MLCT-excited polypyridine complex actually amounts to oxidation of the reduced polypyridine ligand $N, N^{\bullet-}$. Similarly, reduction of an MLCT-excited polypyridine complex corresponds to re-

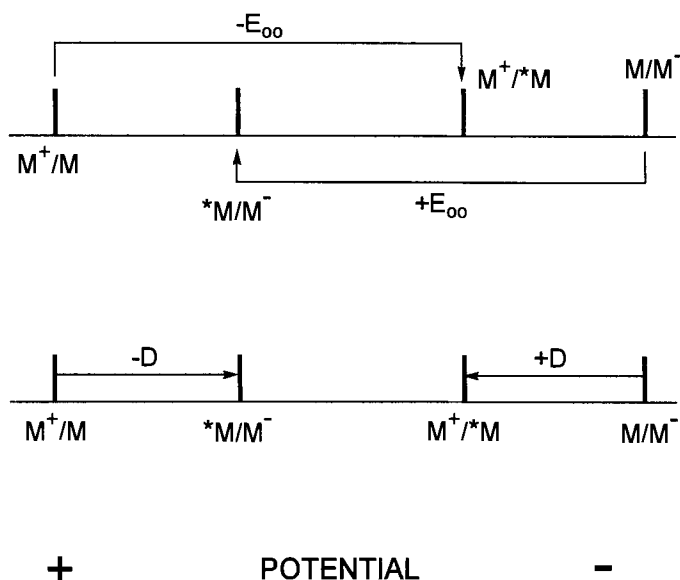


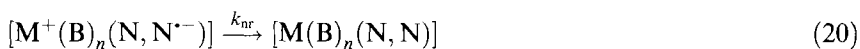
Figure 5. Relationship between ground- and excited state redox potentials. The upper diagram is valid generally, regardless of the excited state character. The lower diagram is applicable only to predominantly localized MLCT excited states of those complexes whose first oxidation and reduction are predominantly metal- and ligand-localized, respectively. See Figure 2 and Eqs 12, 13, 18, and 19.

duction of the oxidized central metal atom M^+ . (Note the formulation of a MLCT excited state as $[M^+(B)_n(N, N^{\bullet-})]$, Eqs 14 and 15) The parameter D is characteristic of a given homologous series of structurally related complexes. For example, an average value of 0.48 V (with a standard deviation of 0.09 V) was determined [28] for a group of 70 tris- and bis-polypyridine Ru^{II} complexes. Os^{II} complexes gave [28] a value of 0.54 V, with a standard deviation of 0.1 V. Importantly, Eqs 18 and 19 imply that excited state redox potentials are uniquely determined by ground state redox potentials, Figure 5. Hence, with the knowledge of D for the particular set of complexes, the excited state redox potential values can be estimated using electrochemical parameters [9, 15, 28, 157, 220]. Obviously, complexes with hard-to-reduce polypyridine ligands will be strong excited state reductants and complexes of hard-to-oxidize metals will be strong excited state oxidants.

It is often important to control the MLCT excitation energy, $h\nu$. Generally, it is advantageous if a photocatalytic reaction can be driven by light of as low energy as thermodynamically possible. Photosensitizers for solar energy conversion should ideally absorb throughout the whole visible spectral region. Hence, photoactive polypyridine complexes with rather low-lying MLCT states are needed. Eqs 16, 18, and 19 provide a clue how to tune MLCT excitation energy without losing valuable

redox properties. It has been shown in Sections 5.3.2. and 5.3.3. that the difference between the ground-state oxidation and reduction potentials changes only little in extended series of tris-polypyridine complexes, since the reduction and oxidation potentials are linearly dependent on each other with a slope close to one (1.16 for Ru^{II}) [29]. Hence, structural variations of a polypyridine ligand in tris-polypyridine complexes of the same metal atom have only limited effect on MLCT excitation energy, Eq. 16. In contrast, the redox-potential difference is strongly dependent on the nature of the ancillary ligands in mono- and bis-polypyridine complexes since the dependence between the reduction and oxidation potentials has a much smaller slope (ca 0.25 for $[\text{Ru}^{\text{II}}(\text{bpy})_2\text{XY}]$). Hence, varying the nature of ancillary ligands is a much more effective way to shift the MLCT excitation energy to the desired spectral range than varying the polypyridine ligand. Ancillary ligand variations are especially advantageous for designing complexes that should act as excited state reductants, since the corresponding excited state redox potential $E^\circ(\text{M}^+/\text{M}^*)$ is determined by the ground-state reduction potential $E^\circ(\text{M}/\text{M}^-)$, which, in turn, is only little dependent on the nature of the ancillary ligands. Therefore, changing the nature of ancillary ligands allows us to tune the MLCT excitation energy while keeping the excited state oxidation potential nearly constant, essentially determined by the polypyridine ligand chosen. Indeed, the most promising sensitizers for photoelectrochemical light energy conversions, $[\text{Ru}(4,4'-(\text{COOH})_2\text{-bpy})_2(\text{SCN})_2]$ and $[\text{Ru}(4,4',4''-(\text{COOH})_3\text{-tpy})(\text{NCS})_3]^-$ are mixed-ligand complexes [36]. Another way to control excitation energy is to change the metal atom. For example, MLCT transitions of Os^{II} complexes occur at lower energies than for their Ru^{II} counterparts, since the redox potential difference is smaller.

Excited state lifetime τ_0 is another important parameter to be controlled, especially if the photoactive complex is intended for bimolecular photochemical electron transfer. MLCT excited states of most polypyridine complexes decay both radiatively and non-radiatively, with the respective rate constants k_r and k_{nr} . The inherent excited state lifetime is defined as $\tau_0 = 1/(k_r + k_{nr})$. The non-radiative decay pathway in most cases prevails: $k_{nr} \gg k_r$. Hence: $\tau_0 \cong 1/k_{nr}$. Non-radiative decay of MLCT excited states can be treated as intramolecular electron transfer in the Marcus inverted region:



using the energy-gap law [10–12, 14, 291–295]. Generally, MLCT excited state lifetime is expected to increase with increasing excited state energy and decreasing structural distortion between the ground and excited state. Eqs 16 and 17 show that MLCT excited state energy E_{00} can be tuned by structural variations in the same way as the excitation energy, vide supra. For a given excited state energy, MLCT lifetime will increase with increasing structural rigidity and, namely, with increasing delocalization of the excited electron over the polypyridine ligand, which spreads the structural effects of excitation over a large number of bonds. The use of polypyridine ligands with extended delocalized π system can even compensate for a small energy gap, making it possible to design polypyridine complexes which

absorb light throughout much of the visible spectral region, while still possessing relatively long-lived MLCT excited states [293, 294].

The presence of a short-lived LF excited state that lies close above the MLCT state can seriously diminish MLCT excited state lifetimes of Ru^{II} complexes. Thermally activated population of such LF states from an MLCT state provides an efficient deactivation pathway and can lead to photochemical decomposition [152, 296, 297]. The energy gap between the MLCT and deactivating LF excited states can be increased by a judicious choice of the polypyridine and ancillary ligands, thereby increasing the MLCT lifetime and improving photostability [74, 152, 297, 298]. LF states do not intervene with a non-radiative decay of Os^{II}-polypyridine MLCT excited states since they are too high in energy. On the other hand, LF states lie below MLCT states in Fe^{II} complexes, providing an ultrafast deactivation pathway (e.g. $\tau_0 = 0.84$ ns for [Fe(bpy)₃]²⁺) [270].

Increasing the complex rigidity can prolong the MLCT lifetime and improve the complex photostability. This is the case of rigid caged [109, 110] or hemi-caged [299] derivatives of [Ru^{II}(bpy)₃]²⁺, in which all three bpy ligands are covalently linked together. The structural rigidity and electron delocalization have a profound effect on MLCT lifetimes of [Cu(N,N)₂]⁺ complexes [204, 268, 300–302]. Recently, it was found that MLCT excited state lifetime can be extended significantly by coupling with a long-lived IL state. For example, excited state lifetime of [Ru^{II}(bpy)₃]²⁺ derivatives in which a pyrene unit is covalently attached to one bpy ligand is 42 μ s long [282].

MLCT excited state lifetime decreases when polypyridine ligands are replaced by PyCa or dab-type ligands. This has been amply manifested by the photo-physical behavior of [Re(E)(CO)₃(N,N)]ⁿ⁺ complexes [97] and by the series [231] [Ru(bpy)_{3-n}(Me-PyCa)_n]²⁺; $n = 0, 1, 2, 3$. The MLCT lifetime decreases from 860 ns to 58 ns on going from the [Ru(bpy)₃]²⁺ to [Ru(bpy)₂(Me-PyCa)]²⁺, since the localization of the excited electron changes from bpy to PyCa. Replacement of further bpy ligands have almost no influence. Values of 62 and 67 ns were measured for [Ru(bpy)(Me-PyCa)₂]²⁺ and [Ru(Me-PyCa)₃]²⁺, respectively.

Finally, it should be noted that an enormous research effort have been spent on the development of photo-redox active polypyridine complexes and optimization of their excited state redox properties. The vast literature on this topic offers discussions and theories of the relations between molecular structure, medium and excited state redox properties and lifetimes, as well as a broad choice of polypyridine complexes suitable as photosensitizers, especially those based on Ru^{II} [9, 14, 28, 74, 95, 98, 151–153, 205, 217, 222, 224, 226, 287, 289, 290, 295, 297].

5.4.4 Properties of Some Common Photo-redox-active Metal–Polypyridine Chromophores

Chromium(III)

The lowest excited states of [Cr(N,N)₃]³⁺; N,N = bpy, phen and their derivatives; have a LF ²T₁/²E character [278, 279]. Excited state lifetimes are very long (63 μ s

for bpy, 270 μ s for phen). $[\text{Cr}(\text{N},\text{N})_3]^{3+}$ complexes are strong excited state oxidants [265, 278]: $E(^*\text{Cr}^{3+}/\text{Cr}^{2+}) \cong +1.3$ V. However, they did not find much use in photochemistry, perhaps due to poor absorption in the visible spectral region.

Rhenium(I)

The character and behavior of the lowest excited state of $[\text{Re}^{\text{I}}(\text{E})(\text{CO})_3(\text{N},\text{N})]^{n+}$ complexes is strongly dependent on the E and N,N ligands [97]. Complexes which have lowest $^3\text{MLCT}$ excited state are very useful in excited state electron-transfer reactions [61, 62, 303]. This situation occurs for E = Cl ($n = 0$), pyridine derivatives, nitriles or phosphines ($n = 1$), N,N = bpy or phen derivatives. Such species are photochemically stable and their excited state lifetimes range from tens to hundreds of nanoseconds, being controlled by the energy gap law [12]. Excited state redox properties can be broadly tuned by variations of the axial (E) and polypyridine ligands. Thermodynamically, $[\text{Re}^{\text{I}}(\text{E})(\text{CO})_3(\text{N},\text{N})]^{n+}$ complexes are both strong excited state oxidants and reductants. Their use in bimolecular excited state electron transfer is somewhat complicated by limited stability of their redox products, especially of oxidized Re^{II} species. Hence, they are mostly employed as excited state oxidants. The $\text{Re}^{\text{I}}(\text{CO})_3(\text{N},\text{N})^+$ unit can be linked with other metal-containing groups either through the axial ligand E (e.g. $\mu\text{-CN}^-$) or through a bridging polyaniline ligand ($\mu\text{-N},\text{N}$). The $\text{Re}^{\text{I}}(\text{CO})_3(\text{N},\text{N})^+$ moiety in polynuclear complexes often acts as an energy donor. It is also used to construct various chromophore-quencher complexes, in which the reducing or oxidizing unit is attached to the axial position. These species undergo intramolecular photochemical electron-transfer reactions, Section 5.4.7. Intraligand excited states become the lowest for those Re^{I} complexes in which the N,N ligand is highly delocalized (dppz, phenyl-substituted phen, etc.) and/or the axial ligand is a strong electron acceptor (CO, RNC). Such species are very powerful excited state oxidants.

Iron(II)

Polypyridine complexes of $\text{Fe}(\text{II})$ are strongly colored due to MLCT transitions. However, their MLCT excited states are very short-lived because of an efficient deactivation through lower-lying LF states. MLCT excited state lifetimes of $[\text{Fe}(\text{N},\text{N})_3]^{2+}$ range from 2.54 ns for tpy to 0.8 ns for bpy and phen [270]. Therefore, Fe^{II} complexes were deemed unsuitable for electron-transfer reactions. Recently, there is a renewed interest in excited state properties of Fe^{II} -polypyridines caused by the observation [304] of an ultrafast electron transfer from $[\text{Fe}(4,4'-(\text{COOH})_2\text{-bpy})_2(\text{CN})_2]$ ($\tau_0 = 330$ ps) to TiO_2 , see Section 5.4.6.

Ruthenium(II)

Bis- and tris-polypyridine complexes of Ru^{II} are the best known and most useful photo-redox active coordination compounds. The possibility to vary the structure and number of polypyridine ligands and of the ancillary ligands in mono- and bis-polypyridine complexes gives rise to a virtually endless number of photoactive species and provides many opportunities for controlling their properties. Photophysical,

photochemical and redox properties of Ru-polypyridines were collected in a very comprehensive review [74]. The lowest excited state of Ru^{II} complexes has a ³MLCT character. In most case, it is sufficiently long-lived for bimolecular excited state reactions (0.5–1.1 μs for [Ru(bpy)₃]²⁺ and [Ru(phen)₃]²⁺). MLCT lifetimes are strongly dependent on complex composition, the medium, and temperature. Their values are determined by the energy gap law [11, 74, 298] and by a thermally activated population of close-lying, upper LF states [74, 295]. A tuning of the LF—MLCT—ground state energy gaps is the key to control photophysical properties of Ru^{II} polypyridines [152, 297, 298]. Complexes in which the MLCT–LF gap is small have short MLCT lifetimes and are prone to slow photochemical substitution of a polypyridine ligand. As is discussed in the Section 5.4.3, the MLCT excitation and excited state energies are best controlled by variations of ancillary ligands in bis-polypyridine Ru^{II} complexes. Thermodynamically, Ru^{II}-polypyridines are both strong excited state oxidants and reductants. Their excited state redox potentials can be broadly tuned by structural variations in the same way as ground state redox potentials. Variations in the polypyridine ligand affect both the excited state reduction and oxidation potential while ancillary ligands have a much bigger effect on the excited state reduction potential E(*Ru²⁺/Ru⁺). Ru^{II}(N,N)₂²⁺ and Ru^{II}(N,N)₃²⁺ units are used as building blocks of photo-redox active polynuclear complexes [51, 83] and supermolecular assemblies, in which the Ru-polypyridine chromophore can act as an electron donor or acceptor and energy donor or acceptor. [Ru(tpy)₂]²⁺ is only a very weak light emitter and its MLCT excited state lifetime is extremely short (250 ps). Fortunately, photophysical and photo-redox properties of [Ru(tpy)₂]²⁺ can be much improved by placing electron-accepting or donating substituents at the 4' position of the tpy ligand [87, 224]. Groups which extend delocalization of the excited electron (Me₂SO₂, Ph, –C≡C–, etc.) are especially useful to prolong the MLCT lifetime. Depending on the substituents, [Ru(4'-X-tpy)₂]²⁺ and [Ru(4'-X-tpy)(4'-Y-tpy)]²⁺ are strong excited state reductants, oxidants, or energy donors [87, 224]. For geometric and synthetic reasons, [Ru(4'-X-tpy)(4'-Y-tpy)]²⁺ is an excellent building block for photo-redox active supramolecular systems [87]. Here, the (-tpy)Ru^{II}(tpy-) chromophores are linked with other molecular units through their 4' positions, either directly or by –C≡C– or 1,4-phenylene bridges [87, 305]. Besides connecting the components, the substitution at the 4' position also improves the photophysical properties of the Ru(tpy)₂ units [87, 305].

Osmium(II)

MLCT states are the lowest excited states for Os^{II} polypyridine complexes. Compared with the corresponding Ru^{II} species, the MLCT states of Os^{II}-polypyridines lie at lower energies (e.g. 1.66 eV for [Os(bpy)₃]²⁺). Thermodynamically, they are comparably strong excited state reductants as Ru^{II} complexes, but weaker oxidants. LF excited states are high in energy and do not provide a decay pathway for MLCT states, whose lifetime is thus governed by the energy gap law [10]. Due to a smaller energy gap and larger spin–orbit coupling, MLCT lifetimes of Os^{II} complexes are shorter than those of their Ru^{II} analogs of the same molecular composition. As members of polynuclear assemblies, Os^{II}-polypyridine units usually play the role of

an energy acceptor. Because of the absence of close-lying LF states, $[\text{Os}(\text{tpy})_2]^{2+}$ has a long MLCT excited state lifetime, 269 ns [87]. This chromophore finds much use as an energy acceptor in supramolecular systems.

Rhodium(III) and iridium(III)

The lowest-lying excited states of tris-polypyridine Rh^{III} and Ir^{III} complexes have intraligand $\pi\pi^*$ character [37, 269]. These states are populated by UV irradiation. They are long lived (μs range) and very strong oxidants (e.g. +1.42 V for $^*[\text{Ir}(\text{bpy})_3]^{3+}/[\text{Ir}(\text{bpy})_3]^{2+}$), but relatively weak reductants. In supramolecular systems, Ir^{III} and Rh^{III} usually function as excited-state energy donors or ground-state electron acceptors.

Platinum(II)

The $[\text{Pt}^{\text{II}}(\text{S,S})(\text{N,N})]^n$; complexes which combine an electron-accepting polypyridine ligand with an electron-donating dithiolate dianion ($n = 0$) or dithiocarbamate anion ($n = 1+$) are important chromophores and thermodynamically strong excited state oxidants and reductants, whose photochemistry still awaits deeper investigation [202, 203]. The much better chemical stability of their reduced than oxidized forms would favor their use as photochemical oxidants. The interesting photochemistry and emission of these species arise from low-lying ligand to ligand charge transfer excited states, in which an electron is excited from an occupied π orbital of the S,S ligand to a π^* polypyridine orbital.

Copper(I)

The properties of low-lying MLCT excited states of $[\text{Cu}^{\text{I}}(\text{N,N})_2]^+$ complexes are extremely dependent on the molecular geometry and the medium [300, 302, 306]. Unless protected by bulky ligands, the Cu^{II} atom in an MLCT excited state $[\text{Cu}^{\text{II}}(\text{N,N})(\text{N,N})^{\cdot-}]^+$ coordinates a donor solvent molecule. Resulting 5-coordinate exciplexes decay rapidly to the ground state [307]. Hence, long-lived MLCT excited states (tens to hundreds of nanoseconds), applicable in photochemical electron transfer, are found mostly for complexes of phen substituted at 2,9 positions with bulky substituents, especially aromatic ones, which force the excited molecule to maintain a pseudotetrahedral geometry and prevent solvent coordination. This is the case of N,N = 2,9- Ph_2 -phen, danphen, or, especially, catphen. Notably, these are the complexes which, in their respective ground states, show reversible one-electron reduction and rather positive oxidation. Resulting large redox-potential difference implies large MLCT excited state energy and, hence, longer lifetimes. $[\text{Cu}(\text{R}_2\text{-phen})_2]^+$ and related complexes are strong excited state reductants, able to reduce substrates in a homogeneous solution as well as inject electron into a semiconductor electrode [301, 306]. Their role as excited state oxidants, although thermodynamically possible, is hampered by slow electron transfer kinetics, caused by a high reorganization energy of the metal-localized $\text{Cu}^{\text{II}}/\text{Cu}^{\text{I}}$ couple. The $\text{Cu}(\text{catphen})_2^{2+}$ unit is used as the active part of various photo-redox active supramolecular assemblies.

5.4.5 Bimolecular Electron-transfer Reactions

The photocatalytic cycles shown in Figure 3 are based on oxidative (left) and reductive (right) quenching of electronically excited polypyridine complexes. Such cycles can operate in a homogeneous solution, provided that the excited state electron transfer is much faster than concurrent, unproductive decay to the ground state: $k_{\text{et}} \gg 1/\tau_0$, where τ_0 is the inherent excited state lifetime at given experimental conditions, but in the absence of the excited state chemical reaction: $1/\tau_0 = k_r + k_{\text{nr}}$, *vide supra*. Obviously, an electron-transfer reaction should be as fast as possible in order to utilize even short-lived excited states. However, diffusion restricts the maximum rate of bimolecular reactions: as the reaction rate increases, the kinetics become diffusion controlled. In practice, this means that only complexes with relatively long-lived excited states ($\tau_0 > 10$ ns) are useful in bimolecular excited state electron transfer. An occurrence of electron transfer shortens the actual excited state lifetime from τ_0 to τ . $\tau_0/\tau = 1 + k_q\tau_0 [Q]$, where Q is the species (quencher) reacting with the excited molecule and k_q is the reaction rate constant (not necessarily equal to k_{et}) [37].

Generally, electron-transfer reactions of MLCT excited states of polypyridine complexes occur with small reorganization energies on the side of the excited complex molecules. These reactions can be treated as non-adiabatic, using the Marcus theory. Reaction rates of bimolecular excited state electron transfer, as studied for many polypyridine complexes of d^6 metal atoms, are very fast, approaching the diffusion limit. When measured in series involving structurally related polypyridine complexes or quenchers, the logarithm of the rate constant ($\ln k_{\text{et}}$) usually increases with increasing driving force ($-\Delta G^\circ$) until it levels off between 10^9 and 10^{10} M s^{-1} . The decrease of the reaction rate at very high driving force values, predicted by the Marcus theory, was not seen in most of the reaction series examined. Therefore, kinetics of bimolecular electron transfer quenching of excited states of polypyridine complexes are often described by the Rehm–Weller formalism which replaces the Marcus-type quadratic dependence of the activation free energy on the driving force by empirical relationships. The Rehm–Weller kinetics and underlying mechanisms of bimolecular electron transfer quenching of excited polypyridine complexes were discussed in detail in several excellent articles [37, 38, 42, 265, 308].

The lack of observations of the predicted fall of electron transfer rate at very high driving force values is due to several factors: (i) examination of only limited driving force ranges, (ii) diffusion control of fast reaction rates, and, (iii) formation of redox products in electronically excited states that diminishes the actual driving force, are the most important reasons. However, despite of all these effects, the Marcus theory is perfectly valid for bimolecular electron-transfer reactions of excited polypyridine complexes. This has been demonstrated [309] by the observation of the full bell-shaped Marcus curve (that is the dependence of $\ln k_{\text{et}}$ on $-\Delta G^\circ$) for both oxidative and reductive quenching of a series of excited $[\text{Ru}(\text{N},\text{N})_3]^{2+}$ complexes by Fe^{III} cytochrome *c* and Fe^{II} cytochrome *c*, respectively. In this case, the maximum of the Marcus curve was shifted below the diffusion limit, because of a weak electronic coupling and, at the same time, to relatively low driving force values because of small reorganization energy. Moreover, very strong excited state oxidant $[\text{Ru}(4,4'-(\text{CF}_3)_2\text{-bpy})_3]^{2+}$ and reductant $[\text{Ru}(4,7-(\text{MeO})_2\text{-phen})_3]^{2+}$ were employed.

Oxidative and reducing quenching of excited polypyridine complexes produce strong ground state oxidants and reductants, respectively (Figure 2). For example, $[\text{Ru}(\text{bpy})_3]^{3+}$ ($E_{1/2}(3+/2+) = +0.85 \text{ V}$) and $[\text{Ru}(\text{bpy})_3]^+$ ($E_{1/2}(2+/+) = -1.76 \text{ V}$) are formed by oxidative and reductive quenching, respectively, of $^*[\text{Ru}(\text{bpy})_3]^{2+}$. Very often, these primary products of excited state electron transfer are the proper oxidants and reductants for the substrate, that is B or Y in Figure 3.

Inspection of the cycles shown in Figure 3 points to possible shortcut reactions which compete with the desired photocatalytic process. Besides the excited state decay, these are the back-reactions M^+/A^- or M^-/D^+ and product recombinations A^-/B^+ or D^+/Y^- . All these reactions regenerate the starting species without accomplishing any useful chemical transformation. They diminish the yield of the redox products and, hence, the efficiency of light energy utilization. One possible solution is to use sacrificial electron acceptors (A) or donors (D), which decompose on reduction or oxidation, respectively, preventing thus the back reaction. $[\text{Co}(\text{NH}_3)_5\text{Br}]^{2+}$ is an example of a sacrificial electron acceptor, widely used in oxidative quenching of excited polypyridine complexes, Eq. 11. Organic amines, whose cations undergo fragmentation, are typical sacrificial electron donors used in reductive quenching. Another strategy is to use reversible donors and acceptors (e.g. the very convenient methylviologen MV^{2+}), but to run photocatalytic reactions in organized or microheterogeneous systems (membranes, micelles, vesicles, etc.) which allow for a separation of redox products.

Since its first discovery [59] in 1972, bimolecular electron transfer reactivity of metal polypyridine complexes has been much developed and used in many photocatalytic processes, including, for example, water gas shift reaction, CO_2 reduction or transformation of organic substrates. However, the ultimate, but still elusive, goal is to use polypyridine complexes as molecular sensitizers of solar energy conversion, especially of photochemical water splitting. For example, $[\text{Ru}(\text{bpy})_3]^{2+}$ in its $^3\text{MLCT}$ excited state has enough energy and the right redox potentials to reduce and oxidize water to H_2 and O_2 , respectively [40, 41, 75, 76]. However, although many possible schemes based on a bimolecular excited state electron transfer have been developed, none of them shows the necessary efficiency and long-term stability, mostly due to short-cut reactions and chemical instability of the species involved. Nevertheless, much knowledge on tuning excited state properties and redox potentials of polypyridine complexes, and on handling electron-transfer reactions in homogeneous and microheterogeneous systems has been obtained in the course of this research. Bimolecular electron-transfer reactions of polypyridine complexes are amply covered by the original literature and many reviews [32, 37, 39, 42, 62, 74, 95, 98, 99, 265–268, 270, 301, 310].

5.4.6 Ultra-fast Electron Injection to Semiconductor Electrodes

At present, photoelectrochemistry on semiconductor (TiO_2) electrodes seems to be the most promising way forward towards light energy conversion by chemical means [36, 76–78]. Figure 6 shows schematically a photoelectrochemical cell. In principle, an electron can be excited directly from semiconductor's valence band into its conduction band, followed by the passage of current to a counter electrode.

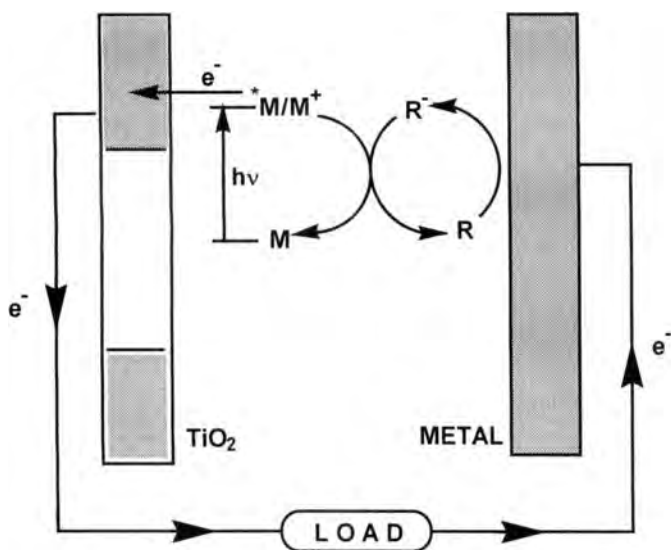


Figure 6. Schematic diagram of a photoelectrochemical cell based on a sensitized semiconductor electrode. M = metal-polypyridine sensitizer, R = reversible electron-relay system, e.g. I_2/I_3^- .

The circuit is closed with a suitable redox mediator R (e.g. I_3^-/I_2 couple) that transfers the electron back to the semiconductor. In this way, light energy is converted to electrical energy. However, TiO_2 does not absorb light in the visible spectral region, being thus unsuitable for applications in solar energy conversion. This drawback can be overcome (Figure 6) by using a sensitizer M, that is a photoactive compound which is excited by visible light and then transfers an electron directly from its excited state to the conduction band of the semiconductor electrode. Several polypyridine transition metal complexes proved to be good and efficient sensitizers. The best ones known [36] at the time of writing are $[Ru(4,4'-(COOH)_2-bpy)_2(NCS)_2]$ and $[Ru(4,4',4''-(COOH)_3-tpy)(NCS)_3]^-$. The $-COOH$ groups guarantee a strong adsorption to the surface of a TiO_2 electrode, while the NCS^- ligands shift light absorption to long wavelengths and provide good photochemical stability.

Importantly, it was found [80–82, 311] that interfacial electron transfer from MLCT-excited Ru^{II} polypyridine complexes to TiO_2 is an ultrafast process, completed in 25–150 fs! This groundbreaking discovery implies that the search for new sensitizers need not to be limited to complexes with long-lived excited states. Indeed, $[Fe(4,4'-(COOH)_2-bpy)_2(CN)_2]$, whose MLCT excited state lifetime is only ca 330 ps, was found [304] to act as a sensitizer in a TiO_2 -based solar cell. In fact, even the classical Grätzel cell [36, 77, 78] would not operate as well as it does, were the interfacial electron transfer not ultrafast, since the $[Ru(4,4'-(COOH)_2-bpy)_2(NCS)_2]$ sensitizer has an inherent excited state lifetime of only 50 ns.

In particular, it was found that electron transfer from an MLCT excited state of $[Ru(4,4'-(COOH)_2-bpy)(NCS)_2]$ into the conduction band of colloidal or thin-film

TiO₂ takes place with a time constant of about 50 fs in a colloidal solution [80–82], and less than 25 fs in high vacuum [311]. Some studies have indicated biphasic kinetics, with a minor component of about 1 ps. Similar ultrafast electron injection was found to occur also from an inherently short-lived MLCT excited state of [Fe(bpy-4,4'-(COOH)₂(CN)₂] [304], and [Fe(CN)₆]⁴⁻ [312], or from various organic dyes [313–317]. The rate is independent of temperature over a broad range (22–300 K, in vacuum [314]). Common to all these systems is a strong adsorption of the sensitizer molecule to the TiO₂ surface via various anchoring groups (–COOH, –P(O)(OH)₂, –CN, –OH, etc.) which also provides an electronic coupling by mixing between the bpy π^* orbital, into which the electron is excited, and the ultimate TiO₂ acceptor orbitals [82].

Typical electron injection times are faster than, or comparable with, relaxation of the optically prepared Franck–Condon ¹MLCT excited states. Hence, the electron injection can actually occur directly from the Franck–Condon state. This is the case of [Fe(4,4'-(COOH)₂-bpy)₂(CN)₂] which reacts from its optically prepared ¹MLCT state [304], before its deactivation through the lower-lying LF states can occur. The relaxation time of the ¹MLCT state of the actual [Ru(4,4'-(COOH)₂-bpy)₂(NCS)₂] sensitizer was determined as <75 fs [82], only a little slower than electron injection itself. Hence, it is possible that electron transfer occurs from both the optically prepared ¹MLCT and relaxed ³MLCT states.

The high degree of electronic coupling and ultrafast rates of electron injection imply that conventional electron transfer theories can hardly be used. It was suggested [311] that the electron injection rate is controlled “by the electron tunneling barrier, essentially determined by the anchor and spacer group, by the Franck–Condon overlap of the respective vibrational states of reactant and product, and by the escape time for the initially prepared wave packet describing the hot electron”. The high density of acceptor states in TiO₂ can also contribute to ultrafast injection rates [82]. More detailed quantitative theory is definitely needed.

Much attention has been devoted to the development of optimal photosensitizers of semiconductor electrodes [36, 43]. Ruthenium(II) polypyridine complexes are especially well suited for this purpose. They are strong light absorbers in the visible spectral region and bpy or tpy ligands can be easily derivatized with anchoring groups. Moreover, localization of the excited electron on the ligand which is attached to the semiconductor surface facilitates the electron injection.

5.4.7 Excited-state Electron-transfer in Supramolecules Containing Metal–polypyridine Chromophores

Several kinds of supramolecular effects on the redox behavior of metal–polypyridine units were mentioned in Section 5.3.6. Besides influencing photo-physical properties, incorporation of metal–bipyridine chromophores into supramolecular structures enables new electron-transfer reactions. Since these processes are dealt with in detail in other chapters, only basic principles and links between the behavior of isolated and supramolecular metal–polypyridine units will be mentioned here.

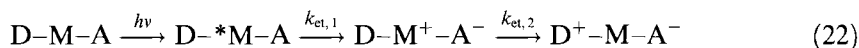
Encapsulation of a Ru^{II} atom into a caged [109, 110] or hemicaged [299] tris-bipyridine ligand extends the MLCT excited state lifetime and improves photostability relative to [Ru(bpy)₃]²⁺, while retaining the fast (diffusion controlled) bimolecular excited state electron transfer reactivity. In contrast, the [Ru(bpy)₃]²⁺ in the core of a dendrimer [248] has about the same inherent lifetime as the free complex but the rate of electron transfer quenching rapidly decreases with increasing the number and size of dendrimer branches.

Intramolecular excited state electron transfer in bi- and polynuclear metal polypyridine complex is a much studied process, especially in relation with the development of molecular wires [38, 51, 52, 83, 87, 88, 318]. The rates are dependent on the nature of the bridging groups linking the metal–polypyridine units. These process will be discussed in detail elsewhere in this book.

Multicomponent assemblies in which a photoredox-active metal–polypyridine unit is combined with electron acceptors and/or donors show very rich photo-induced electron transfer reactivity [38]. Such species are often called molecular dyads (triads, tetrads ...). Electron transfer usually occurs from an excited metal–polypyridine unit M to an attached acceptor:



The back reaction $M^+-A^- \rightarrow M-A$, which regenerates the initial state, often occurs in the inverted Marcus region, which makes it much slower than the forward electron transfer. In this situation, the charge-separated state can be utilized in follow-up reactions (energy conversion, catalysis) or as a bit of chemical information. A long-lived, long-distance charge separation can be produced in molecular triads in which an electron donor and acceptor are attached simultaneously to the photoactive center:



The electron injection from the MLCT-excited central metal–polypyridine unit M to an acceptor A seems to be kinetically preferred over an alternative $D-{}^*M-A \rightarrow D^+-M^--A$ step, even if the energetics are similar. This is because the excited electron resides at the complex periphery, that is at the polypyridine ligand to which the acceptor group is attached.

The maximum intramolecular electron transfer rates in dyads and triads are not diffusion-limited and very fast electron transfer rates can be expected. The rate constant k_{et} depends on the nature of the link between the active components, which not only hold them together but also provides an electronic coupling. In reality, most of the reactions studied occur on the time scale of a few tens of picoseconds and longer. The ultrafast rates known from metal–polypyridine/TiO₂ interfaces have not been attained in molecular systems. This can be caused by weaker electronic coupling and lower density of acceptor states. In some supramolecules, intramolecular electron transfer occurs concurrently with energy transfer. The overall photodynamics of molecular dyads and triads can thus be quite complicated, involving several excited and charge-separated states. Structural variations in

the bridging group can discriminate between electron- and energy-transfer [85, 88].

An occurrence of intramolecular electron transfer shortens the MLCT excited state lifetime: $1/\tau = 1/\tau_{\text{et}} + 1/\tau_0$ where $\tau_{\text{et}} = 1/k_{\text{et}}$. This is demonstrated by the $^3\text{MLCT}$ excited state of $[\text{Ru}(\text{bpy})_3]^{2+}$ [251], the ca 1 μs lifetime of which is shortened to a few tens of picoseconds when a methylviologen di-cation (MV^{2+}) is attached to the 4-position of the bpy ligand by a $-(\text{CH}_2)_n-$ chain; $n = 1-8$. This is caused by a $\text{bpy}^{\bullet-} \rightarrow \text{MV}^{2+}$ intramolecular electron transfer which occurs from the $^3\text{MLCT}$ excited state. The rate constant of $5.9 \times 10^{10} \text{ s}^{-1}$ ($\tau_{\text{et}} = 17 \text{ ps}$) has been determined for $n = 1$, decreasing with increasing n .

There is a great number of photo-redox active supramolecular systems which utilize metal-polypyridine moieties. A considerable knowledge about electron transfer mechanism was obtained by studying so-called chromophore-quencher complexes of the type $[\text{Re}(\text{Q})(\text{CO})_3(\text{bpy})]^{n+}$ in which Q is an electron acceptor, e.g. *N*-Me-4,4'-bipyridinium (MQ^+ , $n = 2$) [319–322], or an electron donor, for example phenothiazine-4-pyridine (py-PTZ, $n = 1$) [254, 255, 323–325], see Appendix for formulas. Thus, $\text{Re} \rightarrow \text{bpy}$ excitation of $[\text{Re}^{\text{I}}(\text{MQ}^+)(\text{CO})_3(\text{bpy})]^{2+}$ prepares a $[\text{Re}^{\text{II}}(\text{MQ}^+)(\text{CO})_3(\text{bpy}^{\bullet-})]^{2+}$ MLCT state which undergoes a $\text{bpy}^{\bullet-} \rightarrow \text{MQ}^+$ electron transfer in 8–15 ps, depending on the solvent relaxation time [322]. Excitation of $[\text{Re}(\text{py-PTZ})(\text{CO})_3(\text{bpy})]$ produces initially an MLCT state $[\text{Re}^{\text{II}}(\text{py-PTZ})(\text{CO})_3(\text{bpy}^{\bullet-})]^+$ which is rapidly ($4 \times 10^9 \text{ s}^{-1}$) converted to $[\text{Re}(\text{py-PTZ}^{\bullet+})(\text{CO})_3(\text{bpy}^{\bullet-})]^+$ by a $\text{PTZ} \rightarrow \text{Re}^{\text{II}}$ electron transfer. Following inter-ligand electron transfer $\text{bpy}^{\bullet-} \rightarrow \text{PTZ}^{\bullet+}$ regenerates the ground state. It is relatively slow ($4 \times 10^7 \text{ s}^{-1}$) because of a highly inverted character. Detailed investigation of its kinetics helped to understand the dynamical influence of structural and medium factors and to highlight similarities between inverted electron transfer and non-radiative decay of MLCT excited states. $[\text{Re}(\text{py-D})(\text{CO})_3(\text{bpy})]^+$ complexes in which D is an electron donor that undergoes fragmentation on oxidation (e.g. α -aminoalcohols or 1,2-diamines) show an irreversible photochemistry, whereby the $\text{D} \rightarrow \text{Re}^{\text{II}}$ intramolecular electron transfer, that follows $\text{Re} \rightarrow \text{bpy}$ MLCT excitation, causes bond breaking within the oxidized D group [326–329].

An interesting case of a charge separation across an oligopeptide chain has been found [330] for the triad $[\text{PTZ}-\text{Ru}^{2+}-\text{MV}^{2+}]$ shown in Figure 7. Excitation of the $\text{Ru}(\text{bpy})$ chromophore triggers a series of intramolecular electron-transfer reactions that eventually produce a charge separated state $[\text{PTZ}^{\bullet+}-\text{Ru}^{2+}-\text{MV}^{\bullet+}]$, which stores 1.17 eV and lives for 108 ns. Another interesting example of a charge separated state is provided by $[\text{Ru}(\text{bpy})_2(\text{bpy-C}_{60})]^{2+}$ where a rigid steroidal spacer links bpy and C_{60} [252]. A charge separated state $\text{Ru}^{3+}-\text{C}_{60}^{\bullet-}$ is formed after MLCT excitation of the $\text{Ru}(\text{bpy})$ center. In CH_3CN , the charge-separated state undergoes recombination to produce first a $\text{Ru}^{2+}-^3\text{C}_{60}$ excited state which then decays to the ground state. In contrast, a dynamic equilibrium between a $\text{Ru}^{3+}-\text{C}_{60}^{\bullet-}$ charge separated state and a $^*\text{Ru}-\text{C}_{60}$ excited state exists in CH_2Cl_2 . This is a very rare example of a reversible excited state transfer.

Intriguing excited state electron transfer dynamics are displayed by Cu^{I} -complexed rotaxanes which combine several photo-redox active units [92, 331, 332]. For example, a rotaxane $[\text{Cu}(\text{catphen})(\text{phen-9,7-(C}_{60})_2)]^+$ based on a $\text{Cu}^{\text{I}}(\text{phen})_2$

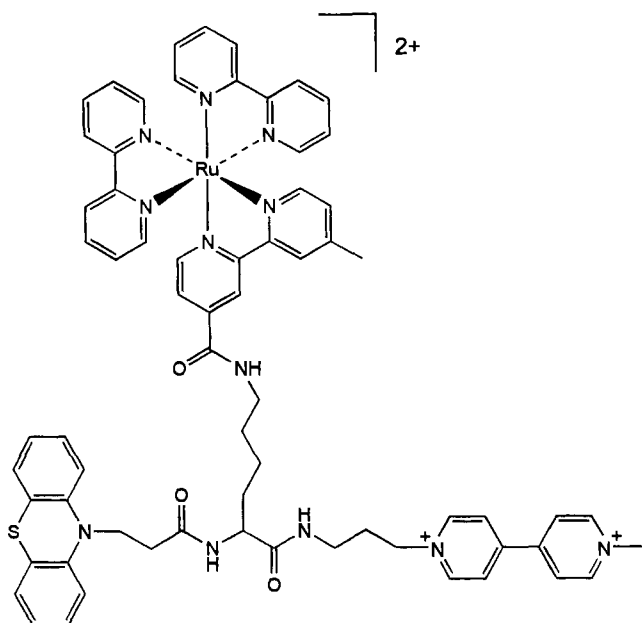
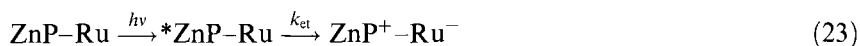


Figure 7. Structure of the triad [PTZ–Ru²⁺–MV²⁺]. A charge separated state [PTZ^{•+}–Ru²⁺–MV^{•+}] is formed upon excitation of the Ru(bpy)₃²⁺ unit [330].

central unit and two C₆₀ stoppers, shows quenching of both the ¹C₆₀ and ³MLCT Cu(phen)₂ excited states: the ¹C₆₀ state rapidly decays by an energy transfer ($k_{\text{et}} = 1.6 \times 10^9 \text{ s}^{-1}$) to the [Cu(phen)₂]⁺ unit while the ³MLCT excited state of Cu(phen)₂ undergoes an electron transfer ($k_{\text{et}} = 5.8 \times 10^9 \text{ s}^{-1}$) to C₆₀. In another example, fast electron transfer between *[Ru(bpy)₃]²⁺ and attached electron acceptor (–4,4′-bipyridinium or –2,7-diazapyrenium) is responsible for a light-driven threading and dethreading of a pseudorotaxane [332].

Dyads composed of a linked porphyrin and Ru(bpy)₃²⁺ show a very interesting photochemistry [85, 86, 89]. In assemblies with Zn-porphyrins (ZnP), the [Ru(bpy)₃]²⁺ unit plays the role of a ground state electron acceptor:



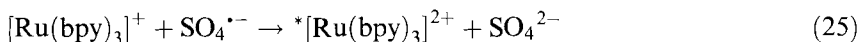
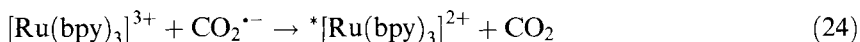
For a ZnP–[Ru(bpy)₃]²⁺ dyad where the linkage is provided by an amide group, intramolecular electron transfer is fast enough ($k_{\text{et}} = 6 \times 10^{11} \text{ s}^{-1}$; $\tau_{\text{et}} = 1.7 \text{ ps}$) to occur from the upper, S₂ excited state of ZnP ($\tau_0 = 1.6 \text{ ps}$) prior to its electronic relaxation to the long-lived S₁ state [253]. This is a very rare example of a capture of a high-lying excited state by a chemical reaction. The relaxed S₁-excited ZnP unit also reduces attached [Ru(bpy)₃]²⁺, but with a 100-times smaller rate [253]. In other systems, Zn and Au porphyrins were used as terminal groups of complexed rotaxanes based on a central [Cu(catpen)₂]⁺ unit [92, 333]. Excitation of these species triggers several intramolecular electron transfers between the porphyrin units, as well as those which change the Cu oxidation state. These reactions occur in the picosecond time domain. Intramolecular energy transfer is a common competing process in porphyrin–(metal–polypyridine assemblies) [86].

Finally, it is important to note (Section 5.3.6) that electrochemistry and UV–Vis absorption spectra of molecular dyads or triads based on metal polypyridines show that electronic interactions between the components of the systems discussed above are too small to influence ground-state behavior. Nevertheless, they are sufficient to allow for very fast intramolecular electron transfer when electronically excited. In fact electronic coupling of 0.002–0.005 eV would be quite enough, but hardly detectable electrochemically. Detailed studies of electrochemistry and spectroscopy of these supramolecular systems and their components are, nevertheless, essential for the understanding of the energetics of photoinduced intramolecular electron and energy transfer reactions.

5.4.8 Chemiluminescence

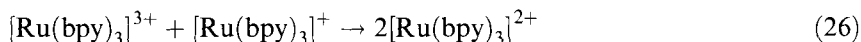
If an electron-transfer reaction occurs with a driving force that is higher than the excited state energy of its product, that species can be formed in an excited state, instead of the ground state. Formation of an excited state occurs with a smaller driving force ($-\Delta G^\circ - E_{00}$) than of the corresponding ground state ($-\Delta G^\circ$). For large $-\Delta G^\circ$ values, the ground state formation is slow because of the Marcus inverted effect. Reaction to the excited state then becomes kinetically competitive with the ground state formation. It is accompanied by light emission from the excited state formed. The chemiluminescence quantum yield increases with increasing ratio between the rate constants of the excited and ground state formation. Strong chemiluminescence can be expected for complexes which have high emission quantum yields and whose oxidized and/or reduced forms are chemically stable. This often is the case of polypyridine complexes of d⁶-metals (Re^I, Ru^{II}, Os^{II}) and of Cr^{III} whose excited state energies are in the range ca 1.5–2.3 eV, accessible by homogeneous or electrochemical redox reactions [32, 266, 277, 334–339].

For example, an intense orange chemiluminescence from the ³MLCT state of [Ru(bpy)₃]²⁺ has been observed during [Ru(bpy)₃]³⁺ reduction [334] by C₂O₄²⁻ or [Ru(bpy)₃]⁺ oxidation [340] by S₂O₈²⁻. These reactions follow complex multi-step mechanisms. The actual steps responsible for chemiluminescence are:



The [Ru(bpy)₃]³⁺ and [Ru(bpy)₃]⁺ complexes can be generated by another chemical reaction from [Ru(bpy)₃]²⁺, for example with PbO₂ or Mg, respectively. The whole chemiluminescent reaction can then be run cyclic, as a catalytic process, shown Figure 8. Alternatively, the oxidized or reduced Ru complex is generated electrochemically at an electrode inserted to the solution, giving rise to electrochemiluminescence.

MLCT excited states of metal–polypyridine complexes are also produced by recombination of their oxidized and reduced forms. For example, the reaction



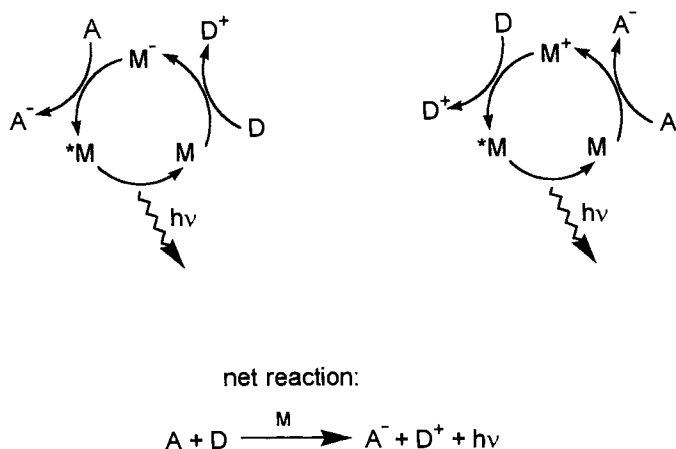
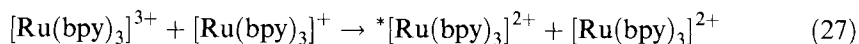


Figure 8. Chemiluminescence in redox-catalytic cycles. The metal–polypyridine complex M acts as light-emission sensitizer, LES [74, 266]. D and A can be either a chemical reductant and oxidant, respectively, or an electrode polarized at appropriate potential.

occurs with a driving force $-\Delta G^\circ = 2.61$ eV, well above the 2.12 eV energy of the emissive $^3\text{MLCT}$ state. Hence, a parallel reaction takes place:



with a nearly 100 % efficiency [341, 342]. Similar chemiluminescent reactions were observed for Os^{II} [336] and Re^{I} [60, 335] polypyridine complexes. Technically, they are performed at an electrode whose potential is rapidly switched between the values at which oxidation and reduction of the parent complex occurs.

Chemiluminescence quantum yields were studied as a function of the driving force for series of reactions between $[\text{Ru}(\text{N},\text{N})_3]^{3+}$ and $[\text{Co}(\text{N},\text{N})_3]^+$. The yield of $*[\text{Ru}(\text{N},\text{N})_3]^{2+}$ emission decreases from 0.31 to 0.07 with decreasing driving force [339].

5.4.9 Applications of Photochemical Electron Transfer

The strong oxidizing and reducing power of MLCT excited states of many metal (Ru^{II} , Os^{II} , Re^{I} , Cu^{I}) polypyridine complexes is employed in various photocatalytic processes, shown schematically in Figure 3. The excited polypyridine complex molecule can react directly with the substrate. More often, the excited state is first quenched by a fast reaction with a sacrificial electron acceptor or donor to form a powerful ground-state oxidant or reductant M^+ and M^- , respectively (Figure 3). These species then react with the substrate in a subsequent step. In this case, the photochemical step serves to invest an extra energy and to generate the reactive species in a sufficient concentration. General aspects of homogeneous photo-

catalytic reactions and the interference with detrimental short-cut reactions were discussed in the Section 5.4.5.

Many photocatalytic cycles were developed in relation to light energy conversion [40, 41], especially aiming at water photodecomposition to H_2 and O_2 . However, the low efficiency and poor long-term stability make most of homogeneous and microheterogeneous photocatalytic cycles unsuitable for practical energetic or synthetic applications. Sensitization of semiconductors (Section 5.4.6) is a much more promising way toward photochemical light energy conversion [36, 43, 76–78]. Photoelectrochemical cells operating on the principle shown in Figure 6 which, using the sensitizer $[\text{Ru}(4,4'-(\text{COOH})_2\text{-bpy})_2(\text{NCS})_2]$, achieve an efficiency of nearly 10 % and a reasonable long-term stability [36]. The ultrafast rate of electron injection from excited sensitizers to TiO_2 effectively prevents any photochemical decomposition and minimizes losses caused by excited state decay. Out of many different sensitizers examined, Ru polypyridine complexes show the biggest promise [36, 43]. The quest for more efficient and stable sensitizers still continues. The discovery of ultrafast rates of electron injection has directed researcher's attention also towards cheaper and more environmentally friendly Fe complexes [304].

Photochemical generation of strong reductants have been employed in photocatalytic reduction of CO_2 [30, 31, 44, 139, 343–346] to CO or formate, reduction of H^+ [30] to H_2 , or in photocatalyzed water-gas-shift reaction [44]. The mechanisms are very similar to those of the corresponding electrocatalyzed reactions (Section 5.3.7), only the active reductants are generated photochemically, instead of electrochemically. For example, $[\text{Re}(\text{Cl})(\text{CO})_3(\text{bpy})]$ is reduced photochemically by the sacrificial electron donor triethanolamine to $[\text{Re}(\text{Cl})(\text{CO})_3(\text{bpy})]^{+*}$ which loses Cl^- to give $[\text{Re}(\text{CO})_3(\text{bpy})]^+$. The latter species coordinates and reduces CO_2 , with an eventual photocatalyst regeneration. On the other hand, $[\text{Ru}(\text{bpy})_3]^+$, formed by photoreduction of $[\text{Ru}(\text{bpy})_3]^{2+}$, is substitutionally inert. Hence, CO_2 reduction photosensitized by $[\text{Ru}(\text{bpy})_3]^+$, involves two catalytic cycles, Figure 9. In the first cycle, the active catalyst of CO_2 reduction is photocatalytically reduced using $[\text{Ru}(\text{bpy})_3]^{2+}$ and CO_2 is then reduced in the second cycle, which involves ground-state reactions only.

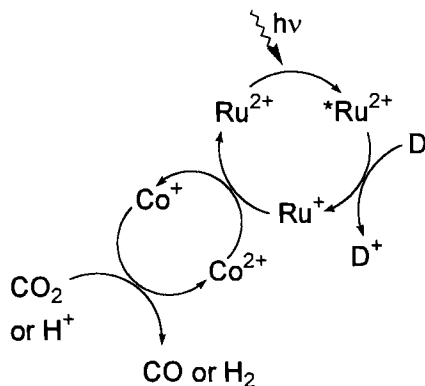


Figure 9. Photocatalytic reduction of CO_2 or H^+ using $[\text{Ru}(\text{bpy})_3]^{2+}$ photosensitizer and $[\text{Co}(\text{bpy})_3]^{2+}$ catalyst. The same scheme applies to photocatalytic reduction of CO_2 with different catalysts, e.g. $[\text{Ru}(\text{bpy})_2\text{XY}]^n$ ($\text{X}, \text{Y} = \text{CO}, \text{Cl}^-$), or $[\text{Ni}(\text{cyclam})]^{2+}$, instead of Co.

Electron-transfer reactions triggered by optical excitation of metal–polypyridines have very important applications in studying proteins and DNA. They are the basis of the flash-quench technique [347–351] used to investigate kinetics of electron-transfer reactions of metalloproteins, for example cytochromes, myoglobins or azurines: The complex $[\text{Ru}^{\text{II}}(\text{bpy})_2(\text{im})(\text{His-})]^{2+}$; im = imidazole is attached to a specific site at a protein surface through a histidine group (His-) and excited by a laser flash. The MLCT excited state created is then rapidly quenched by an electron-transfer reaction with a Fe or Cu center of the protein. The rate of this electron transfer and/or of the back reaction is then measured. Alternatively, the excited $*[\text{Ru}^{\text{II}}(\text{bpy})_2(\text{im})(\text{His-})]^{2+}$ unit at the protein surface is quenched by an oxidizing or reducing quencher presents in the solution. Again, various forward- and back electron-transfer reactions between the oxidized or reduced surface complex and the metalloprotein occur and their kinetics are measured. Since the Ru complex can be attached at different positions of the protein, it is possible to follow the electron-transfer kinetics as a function of the redox pathway through the protein. Derivatives of $[\text{Ru}^{\text{II}}(\text{bpy})_2(\text{im})(\text{His-})]^{2+}$ containing substituted bpy or phen ligands can be used to vary redox potentials and, hence, the electron transfer energetics [349]. Besides that, the strong excited-state oxidant $\text{Re}^{\text{I}}(\text{CO})_3(\text{phen})$ can be attached to surface histidine groups of metalloproteins, e.g. azurines [132]. Another strategy uses $[\text{Ru}(\text{bpy})_3]^{2+}$ attached covalently to an amino acid chain of cytochrome c through an -alanine-4-bpy link [352]. Electron injection from the MLCT excited state of $[\text{Ru}(\text{bpy})(\text{bpy-alanin-})]^{2+}$ to cyt-Fe^{3+} and the back reaction were found to proceed about ten times faster than those observed for histidine-bound $[\text{Ru}^{\text{III}}(\text{bpy})_2(\text{im})(\text{His-})]^{2+}$. This is because the electron transfer now occurs directly from/to the Ru(bpy) chelate ring, without the intervening imidazole group. The flash-quench and direct injection techniques are also used to induce protein folding [353].

In a very interesting extension of the flash-quench technique, electron transfer probes have been developed [354] (Figure 10) to oxidize or reduce an active site of cytochrome P450, which is deeply buried within the protein. Reaction between the probe and P450 forms a complex in which the alkyl chain penetrates through the protein and the end-group of the probe interacts with the active site. Laser excitation of this Ru^{II} -P450 complex in the presence of the quencher $[\text{Co}^{\text{III}}(\text{NH}_3)_5\text{Cl}]^{2+}$ oxidizes the $\text{Ru}(\text{bpy})_3^{2+}$ unit at the protein surface and triggers a rapid ($6 \times 10^3 \text{ s}^{-1}$) electron transfer $\text{P450} \rightarrow \text{Ru}^{\text{III}}$, which occurs along the alkyl chain. The structure and the chemistry of the oxidized cytochrome P450 active site is then studied spectroscopically. Similarly, chemistry of the reduced active site of cytochrome P450 can be explored if a reducing quencher (*para*-methoxy-*N,N*-dimethylaniline) is used. Electron injection $\text{Ru}^+ \rightarrow \text{P450}$ then occurs with a rate constant of $2 \times 10^4 \text{ s}^{-1}$.

Polypyridine complexes containing a phen ligand or its derivatives (4,7- Ph_2 -phen), dppz, tap, hat or other extended polypyridines or polyazines intercalate into DNA strands at specific sites. If the DNA-bound polypyridine complex is a sufficiently strong excited-state oxidant, a photoinduced guanine oxidation takes place with a concomitant DNA strand cleavage. This reaction has indeed been observed for $[\text{Ru}(\text{tap})_3]^{2+}$ or $[\text{Ru}(\text{hat})_3]^{2+}$ and some of their derivatives [355]. Photoexcited $[\text{Rh}(\text{phi})_2(\text{bpy})]^{3+}$ oxidizes DNA by an H-atom abstraction from a sugar moiety,

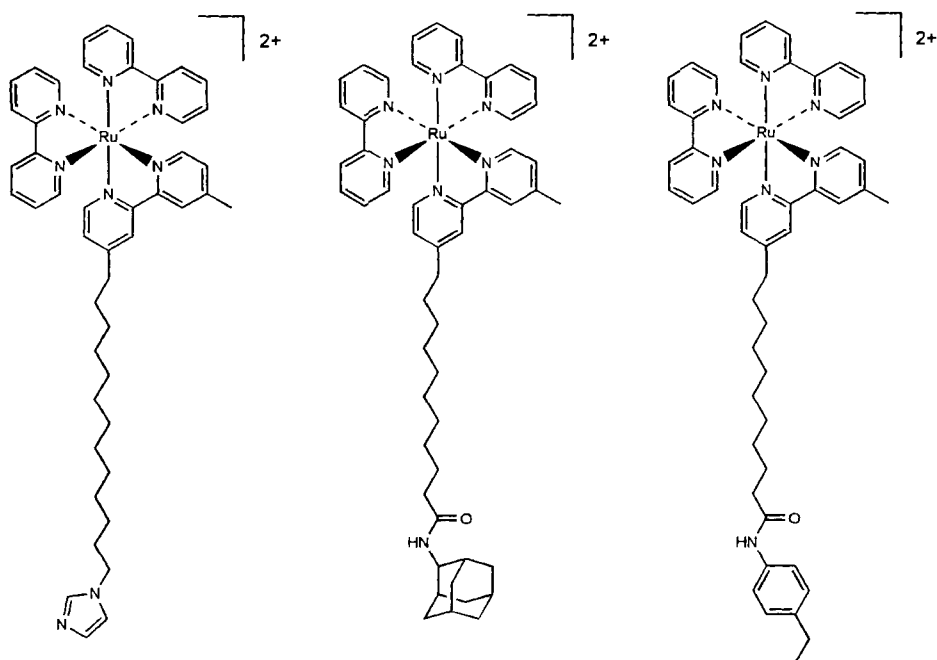


Figure 10. Structures of electron-transfer probes used to examine the chemistry of enzyme active sites which are deeply buried within the protein, in particular the cytochrome P450 [354].

again causing a strand cleavage [356]. However, in the latter case, the reaction occurs from the $\text{dpi} \rightarrow \text{Rh}$ ligand to metal charge transfer excited state, without a direct involvement of the bpy ligand. Interactions between DNA and metal-polypyridines can find application as medical diagnostic tools or light-activated anti-cancer drugs. For example, a photoinduced thymine repair in the DNA helix catalyzed by $[\text{Rh}(\text{phi})_2(4,4'\text{-Me}_2\text{-bpy})]^{3+}$ has been observed [357].

Electron injection from MLCT-excited Ru-polypyridine complexes are used to investigate electron transfer along DNA strands, that is to decide whether DNA can behave as a molecular wire [358–360]. In these studies, derivatives of $[\text{Ru}(\text{phen})_2(\text{dppz})]^{2+}$ act as excited-state electron donors and $[\text{Rh}^{\text{III}}(\text{phi})_2(\text{bpy})]^{3+}$ as a ground-state electron acceptor. Both complexes are anchored at different DNA sites and the rate of $^*\text{Ru} \rightarrow \text{Rh}$ photoinduced electron transfer is measured. In another study [361], a $[\text{Ru}^{\text{II}}(\text{bpy})_2(\text{im})(\text{NH}_2^-)]^{2+}$ unit attached to a terminal ribose of a DNA duplex acted as an excited-state oxidant toward a $[\text{Ru}^{\text{II}}(\text{NH}_3)_4(\text{py})(\text{NH}_2^-)]^{2+}$ unit attached at the other end.

A tremendous research effort is being devoted to intramolecular electron transfer in all kinds of supermolecules containing metal-polypyridine components, Section 5.4.7. At this moment, their applications in luminescence sensors is developed most.

It is based on quenching of the emission from a Ru^{II} or Re^{I} polypyridine part of the supermolecule by electron transfer with a redox-active species recognized and bound at the receptor site. Excited state electron transfer can be utilized even in pH-sensors, provided that pH affects the redox potential of the receptor group, e.g. a phenolate. Supermolecules in which a Ru-polypyridine chromophore is covalently linked with a redox-catalyst can utilize photoinduced excited state electron transfer to run energetically up-hill reactions. This is demonstrated, for example, by a $[\text{Ru}(\text{phen})_2(\text{phen-CH}_2\text{-cyclam-Ni}^{\text{II}})]^{4+}$ complex [362]. Upon excitation, the Ru(phen) center injects an electron into the Ni(cyclam) moiety, at which catalytic reduction of CO_2 proceeds. The Ru^{II} oxidation state is regenerated by reduction with ascorbate present in the solution. Hence, the overall reaction amounts to reduction of CO_2 to CO by ascorbate, photocatalyzed by $[\text{Ru}(\text{phen})_2(\text{phen-CH}_2\text{-cyclam-Ni}^{\text{II}})]^{4+}$. The CO yield is much larger than if isolated $[\text{Ru}(\text{phen})_3]^{2+}$ photosensitizer and $[\text{Ni}(\text{cyclam})]^{2+}$ catalysts are used in a mixture (Figure 9). The oxidizing power of MLCT-excited $\text{Ru}(\text{bpy})_3^{2+}$ unit has been explored in an assembly where a mono- or a tri-nuclear Mn-phenolate unit is linked to one of the bpy ligands [363]. This system is studied as a model of the photosystem II, since the Mn part is a potential water oxidation catalyst.

Polynuclear complexes, molecular dyads, triads, and other supermolecules composed of redox- and photo-active metal polypyridine units have a great promise as components of future molecular electronic or photonic devices as optical switches, relays, memories, etc. [38, 46].

5.5 Conclusions

Transition metal polypyridine complexes are highly redox-active, both in their electronic ground- and excited states. Their electron transfer reactivity and properties can be fine-tuned by variations in the molecular structure and composition. They are excellent candidates for applications in redox-catalysis and photocatalysis, conversion of light energy into chemical or electrical energy, as sensors, active components of functional supramolecular assemblies, and molecular electronic and photonic devices.

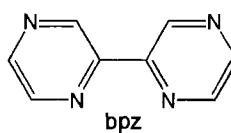
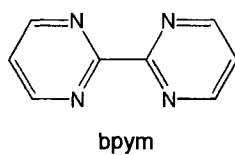
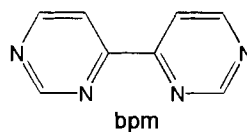
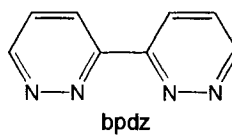
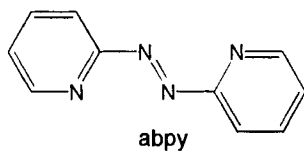
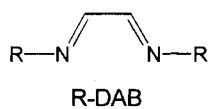
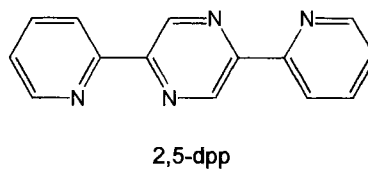
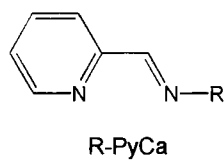
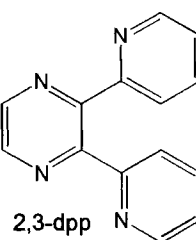
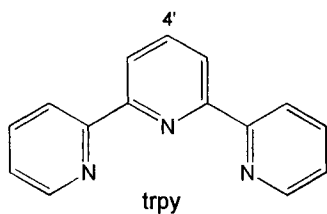
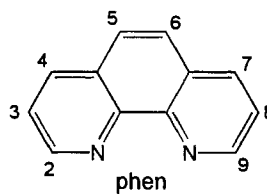
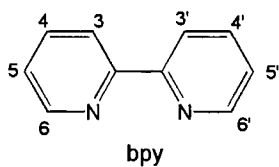
The rich electron-transfer behavior of transition metal polypyridine complexes originates in a unique combination of several factors:

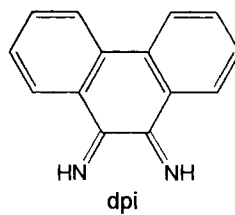
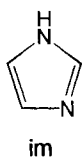
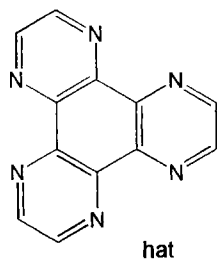
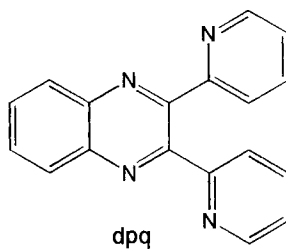
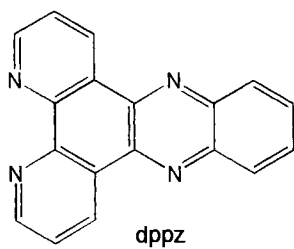
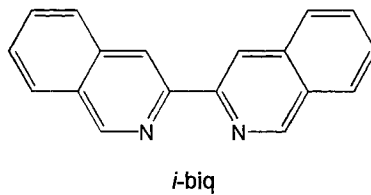
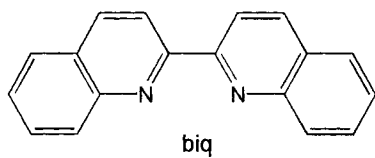
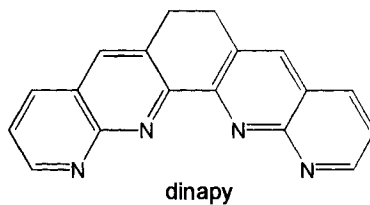
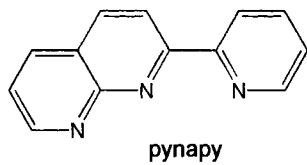
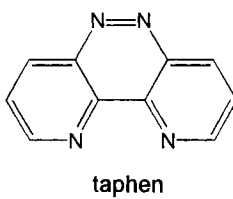
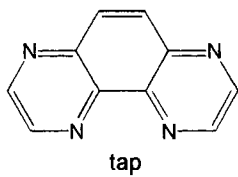
- Complexes of neutral polypyridine ligands with metals in ‘usual’ oxidation states (e.g. Cr^{III} , Mn^{II} , Fe^{II} , Co^{III} , Co^{II} , Ni^{II} , Cu^{I} , Ru^{II} , Rh^{III} , Re^{I} , Os^{II} , Ir^{III} , Pt^{II}) are stable and rather unreactive. This makes them convenient entries into the rich redox chemistry and photochemistry.
- Free polypyridine ligands are reduced in (at least) two successive one-electron steps.
- Redox activity of free polypyridines is retained upon coordination.

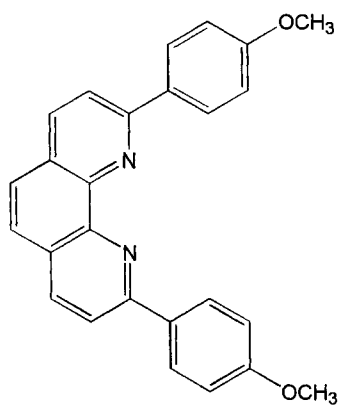
- Polypyridines are strongly coordinating ligands in all their oxidation states (i.e. as neutral species, radical anions or dianions.)
- Electron delocalization between the metal atom and a polypyridine ligand and between polypyridine ligands within the coordination sphere is weak. (Complexes of first-row transition metals in intermediate oxidation states and complexes of a few unusual polypyridines (abpy) are the only exceptions.)
- Oxidation of polypyridine complexes of d^6 -metal atoms is predominantly metal-localized while the reductions are polypyridine-localized. This defined localization, together with a small inter-ligand electronic interaction, gives rise to extensive redox series, that is series of polypyridine complexes of the same chemical composition, but different number and localization of electrons.
- Labilization of an ancillary ligand occurs upon reduction of some substituted polypyridine complexes, allowing for a substrate coordination and catalytic reduction.
- The predominant metal- and polypyridine-localization of ground-state oxidation and reduction, respectively, is paralleled by the localized character of metal \rightarrow polypyridine MLCT electronic excitation, whereby the excited electron resides on a single polypyridine ligand and the positive hole on the metal atom (more precisely, on the metal-ancillary ligands moiety).
- Excited state redox properties reflect those of the ground state. Excited states of polypyridine complexes are thermodynamically strong oxidants and reductants.
- The localized character of the first oxidation, reduction, and MLCT excitation allows the formulation of linear relationships between (i) the complex and free ligand reduction potentials, (ii) ground- and excited-state redox potentials, and, (iii) the difference between the ground-state first oxidation and first reduction potentials and MLCT excited-state energy. These relations are of a great importance in the design of polypyridine complexes for specific purposes.
- Electron-transfer reactions of polypyridine complexes occur with a small reorganization energy. They are very fast, depending on the reaction energetics and electronic coupling.
- In supramolecular systems, electronic interactions between metal–polypyridine and other redox-active or units are too small to perturb ground-state electrochemical and spectroscopic properties but are sufficient to enable very fast intramolecular electron-transfer reactions upon excitation.
- When connected to other components of a supramolecular assembly or to a semiconductor electrode through a polypyridine ligand, a metal–polypyridine unit is kinetically especially suited to inject an electron from its MLCT excited state, that is to act as an excited state reductant. Ultrafast rates can be reached.

Appendix

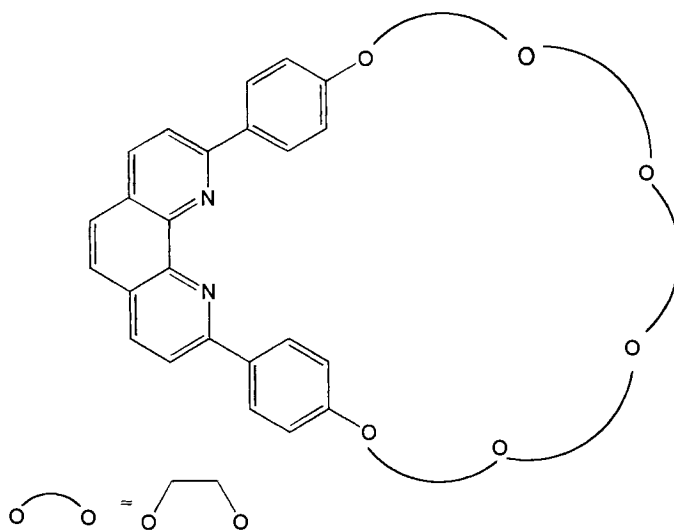
Formulas of selected polypyridine ligands and the abbreviations used.





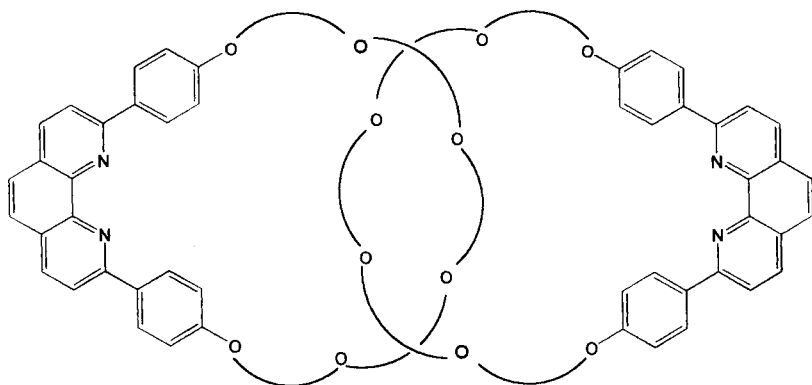


danphen

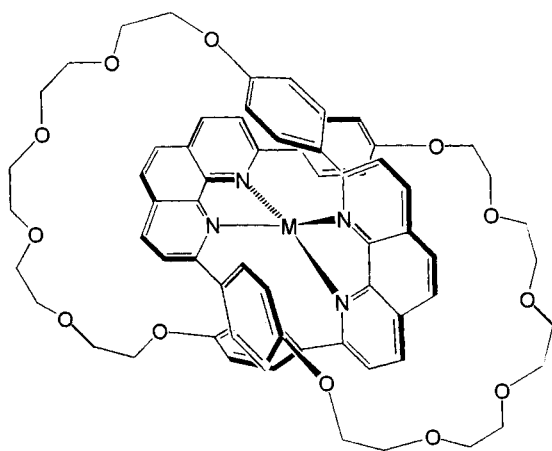


catphen

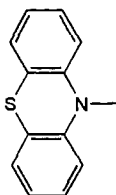
(The actual number of O-O units may differ.)



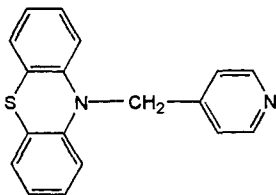
Two entwined catphen ligands



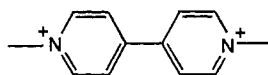
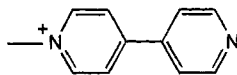
Pseudotetrahedral $[M(\text{catphen})_2]$ complex



PTZ



py-PTZ

MV²⁺MQ⁺

References

1. A. A. Vlček, *Rev. Chim. Minérale* **1968**, 5, 299–316.
2. E. König, S. Herzog, *J. Inorg. Nucl. Chem.* **1970**, 32, 585–599.
3. M. K. DeArmond, K. W. Hanck, D. W. Wertz, *Coord. Chem. Revs.* **1985**, 64, 65–81.
4. A. A. Vlček, *Coord. Chem. Rev.* **1982**, 43, 39–62.
5. S. Zálaiš, M. Krejčík, V. Drchal, A. A. Vlček, *Inorg. Chem.* **1995**, 34, 6008–6014.
6. A. A. Vlček, *Electrochim. Acta* **1968**, 13, 1063–1078.
7. A. A. Vlček, *IUPAC—Coord. Chem.* **1981**, 21, 99–112.
8. A. A. Vlček, *Rev. Chim. Minérale* **1983**, 20, 612–627.
9. A. B. P. Lever, E. S. Dodsworth, in E. I. Solomon, A. B. P. Lever (Eds.): *Inorganic Electronic Structure and Spectroscopy, Volume II: Applications and Case Studies*, J. Wiley & Sons, Inc. 1999, p. 227–289.
10. E. M. Kober, J. V. Caspar, R. S. Lumpkin, T. J. Meyer, *J. Phys. Chem.* **1986**, 90, 3722–3734.
11. J. V. Caspar, T. J. Meyer, *Inorg. Chem.* **1983**, 22, 2444–2453.
12. L. A. Worl, R. Duesing, P. Chen, L. Della Ciana, T. J. Meyer, *J. Chem. Soc. Dalton Trans.* **1991**, 849–858.
13. B. S. Brunschwig, S. Ehrenson, N. Sutin, *J. Phys. Chem.* **1986**, 90, 3657–3668.
14. P. Chen, T. J. Meyer, *Chem. Rev.* **1998**, 98, 1439–1477.
15. E. S. Dodsworth, A. A. Vlček, A. B. P. Lever, *Inorg. Chem.* **1994**, 33, 1045–1049.
16. B. Gaš, J. Klíma, S. Zálaiš, A. A. Vlček, *J. Electroanal. Chem.* **1987**, 222, 161–171.
17. J. Hanzlík, L. Pospíšil, A. A. Vlček, M. Krejčík, *J. Electroanal. Chem.* **1992**, 331, 831–844.
18. M. Krejčík, A. A. Vlček, *J. Electroanal. Chem.* **1991**, 313, 243–257.
19. M. Krejčík, A. A. Vlček, *Inorg. Chem.* **1992**, 31, 2390–2395.
20. D. Míhlová, A. A. Vlček, *J. Organomet. Chem.* **1985**, 279, 317–326.
21. D. Míhlová, B. Gaš, S. Zálaiš, J. Klíma, A. A. Vlček, *J. Organomet. Chem.* **1987**, 330, 75–84.
22. A. A. Vlček, *Nature* **1957**, 180, 753.
23. A. A. Vlček, *Z. Phys. Chem.* **1958**, 143–151.
24. A. A. Vlček, A. Rusina, *Proc. Chem. Soc.* **1961**, 161.
25. A. A. Vlček, *Nature* **1961**, 189, 393–394.
26. A. A. Vlček, *Progr. Inorg. Chem.* **1963**, 5, 211–384.

27. A. A. Vlček, *Pure and Appl. Chem.* **1965**, *10*, 61–70.
28. A. A. Vlček, E. S. Dodsworth, W. J. Pietro, A. B. P. Lever, *Inorg. Chem.* **1995**, *34*, 1906–1913.
29. A. A. Vlček, *Coord. Chem. Rev.* **2000**, *200–202*, 979–990.
30. N. Sutin, C. Creutz, E. Fujita, *Comments Inorg. Chem.* **1997**, *19*, 67–92.
31. F. R. Keene, C. Creutz, N. Sutin, *Coord. Chem. Rev.* **1985**, *64*, 247–260.
32. V. Balzani, F. Bolletta, *Comments Inorg. Chem.* **1983**, *2*, 211–226.
33. P. D. Beer, S. W. Dent, T. J. Wear, *J. Chem. Soc., Dalton Trans.* **1996**, 2341–2346.
34. V. W.-W. Yam, V. W.-M. Lee, F. Ke, K.-W. M. Siu, *Inorg. Chem.* **1997**, *36*, 2124–2129.
35. P. D. Beer, P. A. Gale, G. Z. Chen, *J. Chem. Soc., Dalton Trans.* **1999**, 1897–1909.
36. K. Kalyanasundaram, M. Grätzel, *Coord. Chem. Rev.* **1998**, *177*, 347–414.
37. V. Balzani, F. Bolletta, M. T. Gandolfi, M. Maestri, *Top. Curr. Chem.* **1978**, *75*, 1–64.
38. V. Balzani, F. Scandola, *Supramolecular Photochemistry*, Ellis Horwood, Chichester 1991.
39. V. Balzani, M. Maestri, in K. Kalyanasundaram, M. Grätzel (Eds.): *Photosensitization and Photocatalysis Using Inorganic and Organometallic Compounds*, Kluwer Academic Publishers, Dordrecht 1993, p. 15–50.
40. E. Amouyal, *Solar Energy Materials and Solar Cells* **1995**, *38*, 249–276.
41. A. J. Bard, M. A. Fox, *Acc. Chem. Res.* **1995**, *28*, 141–145.
42. K. Kalyanasundaram, in K. Kalyanasundaram, M. Grätzel (Eds.): *Photosensitization and Photocatalysis Using Inorganic and Organometallic Compounds*, Kluwer Academic Publishers, Dordrecht 1993, p. 113–160.
43. M. Grätzel, K. Kalyanasundaram, in K. Kalyanasundaram, M. Grätzel (Eds.): *Photosensitization and Photocatalysis Using Inorganic and Organometallic Compounds*, Kluwer Academic Publishers, Dordrecht 1993, p. 247–272.
44. R. Ziessel, in K. Kalyanasundaram, M. Grätzel (Eds.): *Photosensitization and Photocatalysis Using Inorganic and Organometallic Compounds*, Kluwer Academic Publishers, Dordrecht 1993, p. 217–245.
45. J. N. Demas, B. A. DeGraff, P. B. Coleman, *Anal. Chem.* **1999**, *71*, 793A–800A.
46. V. Balzani, F. Scandola, in D. N. Reinhoudt (Ed.): *Comprehensive Supramolecular Chemistry*, Vol. 10, Elsevier Science Ltd., Oxford 1996, p. 687.
47. A. von Zelewsky, *Coord. Chem. Rev.* **1999**, *190–192*, 811–825.
48. A. von Zelewsky, P. Belser, P. Hayoz, R. Dux, X. Hua, A. Suckling, H. Stoeckli-Evans, *Coord. Chem. Rev.* **1994**, *132*, 75–85.
49. P. Belser, S. Bernhard, E. Jandrasics, A. von Zelewsky, L. De Cola, V. Balzani, *Coord. Chem. Rev.* **1997**, *159*, 1–8.
50. U. Knof, A. von Zelewsky, *Angew. Chem. Int. Ed.* **1999**, *38*, 302–322.
51. V. Balzani, A. Juris, M. Venturi, S. Campagna, S. Serroni, *Chem. Rev.* **1996**, *96*, 759–833.
52. L. De Cola, P. Belser, *Coord. Chem. Rev.* **1998**, *177*, 301–346.
53. V. Balzani, S. Campagna, G. Denti, A. Juris, S. Serroni, M. Venturi, *Acc. Chem. Res.* **1998**, *31*, 26–34.
54. F. Hein, S. Herzog, *Z. anorg. allg. Chem.* **1952**, *267*, 337.
55. Y. Sato, N. Tanaka, *Bull. Chem. Soc. Jpn.* **1969**, *42*, 1021–1024.
56. J. G. Gaudiello, P. R. Sharp, A. J. Bard, *J. Am. Chem. Soc.* **1982**, *104*, 6373–6377.
57. E. Garcia, J. Kwak, A. J. Bard, *Inorg. Chem.* **1988**, *27*, 4377–4382.
58. J. B. Chlistunoff, A. J. Bard, *Inorg. Chem.* **1992**, *31*, 4582–4587.
59. H. D. Gafney, A. W. Adamson, *J. Am. Chem. Soc.* **1972**, *94*, 8238–8239.
60. J. C. Luong, L. Nadjo, M. S. Wrighton, *J. Am. Chem. Soc.* **1978**, *100*, 5790.
61. J. C. Luong, R. A. Faltynek, M. S. Wrighton, *J. Am. Chem. Soc.* **1980**, *102*, 7892.
62. G. L. Geoffroy, M. S. Wrighton, *Organometallic Photochemistry*, Academic Press, New York 1979.
63. C. M. Elliott, *J.C.S. Chem. Comm.* **1980**, 261–262.
64. S. Roffia, M. A. Raggi, M. Ciano, *J. Electroanal. Chem.* **1980**, *108*, 69–76.
65. Y. Ohsawa, M. K. DeArmond, K. W. Hanck, D. E. Morris, D. G. Whitten, P. E. Neveux, Jr., *J. Am. Chem. Soc.* **1983**, *105*, 6522–6524.
66. G. A. Heath, L. J. Yellowlees, P. S. Braterman, *J.C.S. Chem. Comm.* **1981**, 287–289.
67. C. M. Elliott, E. J. Hershenhart, *J. Am. Chem. Soc.* **1982**, *104*, 7519–7526.

68. S. M. Angel, M. K. DeArmond, R. J. Donohoe, K. W. Hanck, D. W. Wertz, *J. Am. Chem. Soc.* **1984**, *106*, 3688–3689.
69. D. E. Morris, K. W. Hanck, M. K. DeArmond, *J. Am. Chem. Soc.* **1983**, *105*, 3032–3038.
70. P. G. Bradley, N. Kress, B. A. Hornberger, R. F. Dallinger, W. H. Woodruff, *J. Am. Chem. Soc.* **1981**, *103*, 7441–7446.
71. M. Forster, R. E. Hester, *Chem. Phys. Lett.* **1981**, *81*, 42–47.
72. P. S. Braterman, A. Harriman, G. A. Heath, L. J. Yellowlees, *J. Chem. Soc. Dalton Trans.* **1983**, 1801–1803.
73. J. K. Nagle, D. M. Roundhill, *Chemtracts—Inorg. Chem.* **1992**, *4*, 141–155.
74. A. Juris, V. Balzani, F. Barigelletti, S. Campagna, P. Belser, A. von Zelewsky, *Coord. Chem. Rev.* **1988**, *84*, 85–277.
75. E. Borgarello, J. Kiwi, E. Pelizzetti, M. Visca, M. Grätzel, *Nature* **1981**, *289*, 158–160.
76. M. Grätzel, *Acc. Chem. Res.* **1981**, *14*, 376–384.
77. M. Grätzel, *Coord. Chem. Rev.* **1991**, *111*, 167–174.
78. B. O'Regan, M. Grätzel, *Nature* **1991**, *353*, 737.
79. M. K. Nazzeruddin, A. Kay, I. Rodicio, R. Humphry-Baker, E. Müller, P. Liska, N. Vlachopoulos, M. Grätzel, *J. Am. Chem. Soc.* **1993**, *115*, 6382–6390.
80. Y. Tachibana, J. E. Moser, M. Grätzel, D. R. Klug, J. R. Durrant, *J. Phys. Chem.* **1996**, *100*, 20056–20062.
81. R. J. Ellingson, J. B. Asbury, S. Ferrere, H. N. Ghosh, J. R. Sprague, T. Lian, A. J. Nozik, *J. Phys. Chem. B* **1998**, *102*, 6455–6458.
82. J. B. Asbury, R. J. Ellingson, H. N. Ghosh, S. Ferrere, A. J. Nozik, T. Lian, *J. Phys. Chem. B* **1999**, *103*, 3110–3119.
83. F. Scandola, C. A. Bignozzi, M. T. Indelli, in K. Kalyanasundaram, M. Grätzel (Eds.): *Photosensitization and Photocatalysis Using Inorganic and Organometallic Compounds*, Kluwer Academic Publishers, Dordrecht 1993, p. 161–216.
84. S. Campagna, G. Denti, S. Serroni, A. Juris, M. Venturi, V. Ricevuto, V. Balzani, *Chem. Eur. J.* **1995**, *1*, 211.
85. R. Ziessel, M. Hissler, A. El-ghayoury, A. Harriman, *Coord. Chem. Rev.* **1998**, *178–180*, 1251–1298.
86. L. Flamigni, F. Barigelletti, N. Armaroli, J.-P. Collin, I. M. Dixon, J.-P. Sauvage, J. A. Gareth Williams, *Coord. Chem. Rev.* **1999**, *190–192*, 671–682.
87. J.-P. Sauvage, J.-P. Collin, J.-C. Chambron, S. Guillerez, C. Coudret, V. Balzani, F. Barigelletti, L. De Cola, L. Flamigni, *Chem. Rev.* **1994**, *94*, 993–1019.
88. A. Harriman, R. Ziessel, *Chem. Commun.* **1996**, 1707–1716.
89. J.-P. Collin, P. Gaviña, V. Heitz, J.-P. Sauvage, *Eur. J. Inorg. Chem.* **1998**, 1–14.
90. J.-M. Kern, J.-P. Sauvage, J.-L. Weidmann, N. Armaroli, L. Flamigni, P. Ceroni, V. Balzani, *Inorg. Chem.* **1997**, *36*, 5329–5338.
91. P. R. Ashton, V. Balzani, A. Credi, O. Kocian, D. Pasini, L. Prodi, N. Spencer, J. F. Stoddart, M. S. Tolley, M. Venturi, A. J. P. White, D. J. Williams, *Chem. Eur. J.* **1998**, *4*, 590–607.
92. M.-J. Blanco, M. C. Jiménez, J.-C. Chambron, V. Heitz, M. Linke, J.-P. Sauvage, *Chem. Soc. Rev.* **1999**, *28*, 293–305.
93. W. R. McWhinnie, J. D. Miller, *Adv. Inorg. Chem. Radiochem.* **1969**, *12*, 135–215.
94. E. C. Constable, *Adv. Inorg. Chem.* **1989**, *34*, 1–63.
95. K. Kalyanasundaram, *Coord. Chem. Rev.* **1982**, *46*, 159–244.
96. D. J. Stufkens, *Coord. Chem. Rev.* **1990**, *104*, 39–112.
97. D. J. Stufkens, A. Vlček, Jr., *Coord. Chem. Rev.* **1998**, *177*, 127–179.
98. K. Kalyanasundaram, *Photochemistry of Polypyridine and Porphyrin Complexes*, Academic Press, London 1992.
99. D. M. Roundhill, *Photochemistry and Photophysics of Metal Complexes*, Plenum Press, New York 1994.
100. P. J. Steel, *Coord. Chem. Rev.* **1990**, *106*, 227–265.
101. T. Saji, S. Aoyagui, *J. Electroanal. Chem.* **1975**, *58*, 401–410.
102. P. S. Braterman, J.-I. Song, *J. Org. Chem.* **1991**, *56*, 4678–4682.
103. B. C. Noble, R. D. Peacock, *Spectrochimica Acta* **1990**, *46A*, 407–412.

104. A. Klein, W. Kaim, E. Waldhör, H.-D. Hausen, *J. Chem. Soc. Perkin Trans. 2* **1995**, 2121–2126.
105. J. B. Chlistunoff, A. J. Bard, *Inorg. Chem.* **1993**, 32, 3521–3527.
106. J. L. Kahl, K. Hanck, K. DeArmond, *J. Phys. Chem.* **1978**, 82, 540–545.
107. M. Krejčík, S. Zális, J. Klíma, D. Sýkora, W. Matheis, A. Klein, W. Kaim, *Inorg. Chem.* **1993**, 32, 3362–3368.
108. C. Dietrich-Buchecker, J.-P. Sauvage, J.-M. Kern, *J. Am. Chem. Soc.* **1989**, 111, 7791–7800.
109. L. De Cola, F. Barigelletti, V. Balzani, P. Belser, A. von Zelewsky, F. Vögtle, F. Ebmeyer, S. Grammenudi, *J. Am. Chem. Soc.* **1988**, 110, 7210–7212.
110. F. Barigelletti, L. De Cola, V. Balzani, P. Belser, A. von Zelewsky, F. Vögtle, F. Ebmeyer, S. Grammenudi, *J. Am. Chem. Soc.* **1989**, 111, 4662–4668.
111. T. Saji, S. Aoyagui, *J. Electroanal. Chem.* **1975**, 63, 405–419.
112. E. König, S. Herzog, *J. Inorg. Nucl. Chem.* **1970**, 32, 613–617.
113. Y. Saito, J. Takemoto, B. Hutchinson, K. Nakamoto, *Inorg. Chem.* **1972**, 11, 2003–2011.
114. E. König, S. Herzog, *J. Inorg. Nucl. Chem.* **1970**, 32, 601–611.
115. A. L. Rieger, J. L. Scott, P. H. Rieger, *Inorg. Chem.* **1994**, 33, 621–622.
116. M. C. Hughes, J. M. Rao, D. J. Macero, *Inorg. Chim. Acta* **1979**, 35, L321–324.
117. T. Saji, S. Aoyagui, *J. Electroanal. Chem.* **1975**, 60, 1–10.
118. A. Vlček, Jr., *Coord. Chem. Rev.* **1998**, 177, 219–256.
119. S. Ernst, W. Kaim, *J. Am. Chem. Soc.* **1986**, 108, 3578–3586.
120. W. Kaim, S. Kohlmann, *Inorg. Chem.* **1987**, 26, 68–77.
121. A. Vlček, Jr., F. Baumann, W. Kaim, F.-W. Grevels, F. Hartl, *J. Chem. Soc., Dalton Trans.* **1998**, 215–220.
122. S. Zális, C. Daniel, A. Vlček, Jr., *J. Chem. Soc., Dalton Trans.* **1999**, 3081–3086.
123. H. tom Dieck, K.-D. Franz, F. Hohmann, *Chem. Ber.* **1975**, 108, 163–173.
124. Y. Sato, N. Tanaka, *Bull. Chem. Soc. Jpn.* **1968**, 41, 2064–2066.
125. M. Inoue, K. Hara, T. Horiba, M. Kubo, *Bull. Chem. Soc. Jpn.* **1974**, 47, 2137–2140.
126. M. M. Morrison, D. T. Sawyer, *Inorg. Chem.* **1978**, 17, 333–337.
127. M. A. Lockwood, K. Wang, J. M. Mayer, *J. Am. Chem. Soc.* **1999**, 121, 11894–11895.
128. G. W. Brudvig, H. H. Thorp, R. H. Crabtree, *Acc. Chem. Res.* **1991**, 24, 311–316.
129. L. E. Helberg, S. D. Orth, M. Sabat, W. D. Harman, *Inorg. Chem.* **1996**, 35, 5584–5594.
130. F. Paolucci, M. Marcaccio, C. Paradisi, S. Roffia, C. A. Bignozzi, C. Amatore, *J. Phys. Chem. B* **1998**, 102, 4759–4769.
131. P. Christensen, A. Hamnett, A. V. G. Muir, J. A. Timney, *J. Chem. Soc. Dalton Trans.* **1992**, 1455–1463.
132. W. B. Connick, A. J. Di Bilio, M. G. Hill, J. R. Winkler, H. B. Gray, *Inorg. Chim. Acta* **1995**, 240, 169–173.
133. R. J. Shaver, D. P. Rillema, *Inorg. Chem.* **1992**, 31, 4101–4107.
134. A. Klein, C. Vogler, W. Kaim, *Organometallics* **1996**, 15, 236–244.
135. F. P. A. Johnson, M. W. George, F. Hartl, J. J. Turner, *Organometallics* **1996**, 15, 3374–3387.
136. G. J. Stor, F. Hartl, J. W. M. van Outersterp, D. J. Stufkens, *Organometallics* **1995**, 14, 1115–1131.
137. J. W. M. van Outersterp, F. Hartl, D. J. Stufkens, *Organometallics* **1995**, 14, 3303–3310.
138. J. Hawecker, J.-M. Lehn, R. Ziessel, *J. Chem. Soc., Chem. Commun.* **1984**, 328–330.
139. J. Hawecker, J.-M. Lehn, R. Ziessel, *Helv. Chim. Acta* **1986**, 69, 1990–2009.
140. K. Koike, H. Hori, M. Ishizuka, J. R. Westwell, K. Takeuchi, T. Ibusuki, K. Enjouji, H. Konno, K. Sakamoto, O. Ishitani, *Organometallics* **1997**, 16, 5724–5729.
141. B. P. Sullivan, C. M. Bolinger, D. Conrad, W. J. Vining, T. J. Meyer, *J. Chem. Soc., Chem. Commun.* **1985**, 1414–1416.
142. B. D. Rossenaar, F. Hartl, D. J. Stufkens, *Inorg. Chem.* **1996**, 35, 6194–6203.
143. B. D. Rossenaar, F. Hartl, D. J. Stufkens, C. Amatore, E. Maisonhaute, J.-N. Verpeaux, *Organometallics* **1997**, 16, 4675–4685.
144. P. S. Braterman, J.-I. Song, R. D. Peacock, *Inorg. Chem.* **1992**, 31, 555–559.
145. N. Tanaka, T. Ogata, S. Niizuma, *Bull. Chem. Soc. Jpn.* **1973**, 46, 3299–3301.
146. S. M. Angel, M. K. DeArmond, R. J. Donohoe, D. W. Wertz, *J. Phys. Chem.* **1985**, 89, 282–285.

147. J. M. Rao, M. C. Hughes, D. J. Macero, *Inorg. Chim. Acta* **1979**, 35, L369–L373.
148. T. Saji, S. Aoyagui, *J. Electroanal. Chem.* **1980**, 110, 329–334.
149. Y. Ohsawa, K. W. Hanck, M. K. DeArmond, *J. Electroanal. Chem.* **1984**, 175, 229–240.
150. C. D. Tait, D. B. MacQueen, R. J. Donohoe, M. K. De Armond, K. W. Hanck, D. W. Wertz, *J. Phys. Chem.* **1986**, 90, 1766–1771.
151. F. Barigelletti, A. Juris, V. Balzani, P. Belser, A. von Zelewsky, *Inorg. Chem.* **1987**, 26, 4115–4119.
152. H. B. Ross, M. Boldaji, D. P. Rillema, C. B. Blanton, R. P. White, *Inorg. Chem.* **1989**, 28, 1013–1021.
153. A. Juris, S. Campagna, V. Balzani, G. Gremaud, A. von Zelewsky, *Inorg. Chem.* **1988**, 27, 3652–3655.
154. S. Roffia, M. Ciano, *J. Electroanal. Chem.* **1979**, 100, 809–817.
155. S. L. Tan, M. K. De Armond, K. W. Hanck, *J. Electroanal. Chem.* **1984**, 181, 187–197.
156. T. Matsumura-Inoue, T. Tominaga-Morimoto, *J. Electroanal. Chem.* **1978**, 93, 127–139.
157. A. B. P. Lever, *Inorg. Chem.* **1990**, 29, 1271–1285.
158. H. Ishida, K. Tanaka, T. Tanaka, *Organometallics* **1987**, 6, 181–186.
159. M. R. M. Bruce, E. Megehee, B. P. Sullivan, H. H. Thorp, T. R. O'Toole, A. Downard, J. R. Pugh, T. J. Meyer, *Inorg. Chem.* **1992**, 31, 4864–4873.
160. M. N. Collomb-Dunand-Sauthier, A. Deronzier, R. Ziessel, *J. Chem. Soc., Chem. Comm.* **1994**, 189–191.
161. S. Chardon-Noblat, M. N. Collomb-Dunand-Sauthier, A. Deronzier, R. Ziessel, D. Zsoldos, *Inorg. Chem.* **1994**, 33, 4410–4412.
162. M. N. Collomb-Dunand-Sauthier, A. Deronzier, R. Ziessel, *Inorg. Chem.* **1994**, 33, 2961–2967.
163. S. Chardon-Noblat, A. Deronzier, R. Ziessel, D. Zsoldos, *Inorg. Chem.* **1997**, 36, 5384–5389.
164. M. P. Aarnts, F. Hartl, K. Peelen, D. J. Stufkens, C. Amatore, J.-N. Verpeaux, *Organometallics* **1997**, 16, 4686–4695.
165. M. P. Aarnts, M. P. Wilms, K. Peelen, J. Fraanje, K. Goubitz, F. Hartl, D. J. Stufkens, E. J. Baerends, A. Vlček, Jr., *Inorg. Chem.* **1996**, 35, 5468–5477.
166. T. J. Meyer, *J. Electrochem. Soc.* **1984**, 131, 221C–228C.
167. J. A. Gilbert, D. S. Eggleston, W. R. Murphy, Jr., D. A. Geselowitz, S. W. Gersten, D. J. Hodgson, T. J. Meyer, *J. Am. Chem. Soc.* **1985**, 107, 3855–3864.
168. N. Tanaka, Y. Sato, *Bull. Chem. Soc. Jpn.* **1968**, 41, 2059–2064.
169. S. Herzog, R. Klausch, J. Lantos, *Z. Chem.* **1964**, 4, 150.
170. D. J. Szalda, C. Creutz, D. Mahajan, N. Sutin, *Inorg. Chem.* **1983**, 22, 2372–2379.
171. H. A. Schwarz, C. Creutz, N. Sutin, *Inorg. Chem.* **1985**, 24, 433–439.
172. P. Biagini, T. Funaioli, A. Juris, G. Fachinetti, *J. Organomet. Chem.* **1990**, 390, C61–C63.
173. C. Creutz, N. Sutin, *Coord. Chem. Rev.* **1985**, 64, 321–341.
174. C. Creutz, H. A. Schwarz, N. Sutin, *J. Am. Chem. Soc.* **1984**, 106, 3036–3037.
175. D. A. Reitsma, F. R. Keene, *Organometallics* **1994**, 13, 1351–1354.
176. J. M. Rao, M. C. Hughes, D. J. Macero, *Inorg. Chim. Acta* **1976**, 16, 231–236.
177. G. Kew, K. DeArmond, K. Hanck, *J. Phys. Chem.* **1974**, 78, 727–734.
178. G. Kew, K. Hanck, K. DeArmond, *J. Phys. Chem.* **1975**, 79, 1828–1835.
179. H. Căldărăru, M. K. De Armond, K. W. Hanck, V. E. Sahini, *J. Am. Chem. Soc.* **1976**, 98, 4455–4457.
180. C. Creutz, A. D. Keller, H. A. Schwarz, N. Sutin, A. P. Zipp, in D. B. Rorabacher, J. F. Endicott (Eds.): *Mechanistic Aspects of Inorganic Reactions*. ACS Symposium Series 198, ACS, Washington, D.C. 1982, p. 385–402.
181. Q. G. Mulazzani, S. Emmi, M. Z. Hoffman, M. Venturi, *J. Am. Chem. Soc.* **1981**, 103, 3362–3370.
182. C. M. Bolinger, B. P. Sullivan, D. Conrad, J. A. Gilbert, N. Story, T. J. Meyer, *J. Chem. Soc., Chem. Commun.* **1985**, 796–797.
183. C. Caix, S. Chardon-Noblat, A. Deronzier, *J. Electroanal. Chem.* **1997**, 434, 163–170.
184. W. Kaim, R. Reinhardt, M. Sieger, *Inorg. Chem.* **1994**, 33, 4453–4459.
185. M. Ladwig, W. Kaim, *J. Organomet. Chem.* **1992**, 439, 79–90.
186. S. Roffia, M. Ciano, *J. Electroanal. Chem.* **1978**, 87, 267–274.

187. J. L. Kahl, K. Hanck, K. DeArmond, *J. Phys. Chem.* **1979**, *83*, 2606–2611.
188. R. Ziessel, *J. Chem. Soc., Chem. Commun.* **1988**, 16–17.
189. R. Ziessel, *Angew. Chem. Int. Ed. Engl.* **1991**, *30*, 844–847.
190. R. Ziessel, *J. Am. Chem. Soc.* **1993**, *115*, 118–127.
191. B. J. Henne, D. E. Bartak, *Inorg. Chem.* **1984**, *23*, 369–373.
192. Y. Rollin, M. Troupel, D. G. Tuck, J. Perichon, *J. Organomet. Chem.* **1986**, *303*, 131–137.
193. A. R. Brown, Z. Guo, F. W. J. Mosselmans, S. Parsons, M. Schröder, L. J. Yellowlees, *J. Am. Chem. Soc.* **1998**, *120*, 8805–8811.
194. R. Palmans, D. B. MacQueen, C. G. Pierpont, A. J. Frank, *J. Am. Chem. Soc.* **1996**, *118*, 12647–12653.
195. P. S. Braterman, J.-I. Song, C. Vogler, W. Kaim, *Inorg. Chem.* **1992**, *31*, 222–224.
196. P. S. Braterman, J.-I. Song, F. M. Wimmer, S. Wimmer, W. Kaim, A. Klein, R. D. Peacock, *Inorg. Chem.* **1992**, *31*, 5084–5088.
197. A. Klein, W. Kaim, *Organometallics* **1995**, *14*, 1176–1186.
198. L. Yang, F. L. Wimmer, S. Wimmer, J. Zhao, P. S. Braterman, *J. Organomet. Chem.* **1996**, *525*, 1–8.
199. D. Collison, F. E. Mabbs, E. J. L. McInnes, K. J. Taylor, A. J. Welch, L. J. Yellowlees, *J. Chem. Soc., Dalton. Trans.* **1996**, 329–334.
200. E. J. L. McInnes, R. D. Farley, C. C. Rowlands, A. J. Welch, L. Rovatti, L. J. Yellowlees, *J. Chem. Soc., Dalton Trans.* **1999**, 4203–4208.
201. F. P. Fanizzi, G. Natile, M. Lanfranchi, A. Tiripicchio, F. Laschi, P. Zanello, *Inorg. Chem.* **1996**, *35*, 3173–3182.
202. W. Paw, S. D. Cummings, M. A. Mansour, W. B. Connick, D. K. Geiger, R. Eisenberg, *Coord. Chem. Rev.* **1998**, *171*, 125–150.
203. J. A. Zuleta, M. S. Burberry, R. Eisenberg, *Coord. Chem. Rev.* **1990**, *97*, 47–64.
204. P. Federlin, J.-M. Kern, A. Rastegar, C. Dietrich-Buchecker, P. A. Marnot, J.-P. Sauvage, *New. J. Chem.* **1990**, *14*, 9–12.
205. Y. Kawanishi, N. Kitamura, S. Tazuke, *Inorg. Chem.* **1989**, *28*, 2968–2975.
206. F. Pichot, J. H. Beck, C. M. Elliott, *J. Phys. Chem. A* **1999**, *103*, 6263–6267.
207. E. S. Dodsworth, A. B. P. Lever, *Chem. Phys. Lett.* **1985**, *119*, 61–66.
208. E. S. Dodsworth, A. B. P. Lever, *Chem. Phys. Lett.* **1986**, *124*, 152–158.
209. S. I. Gorelsky, E. S. Dodsworth, A. B. P. Lever, A. A. Vlček, *Coord. Chem. Rev.* **1998**, *174*, 469–494.
210. D. P. Rillema, G. Allen, T. J. Meyer, D. Conrad, *Inorg. Chem.* **1983**, *22*, 1617–1622.
211. A. Masschelein, L. Jacquet, A. Kirsch-De Mesmaeker, J. Nasielski, *Inorg. Chem.* **1990**, *29*, 855–860.
212. S. Zális, V. Drchal, *Chem. Phys.* **1987**, *118*, 313–323.
213. W. Kaim, R. Reinhardt, E. Waldhör, J. Fiedler, *J. Organomet. Chem.* **1996**, *524*, 195–202.
214. S. Greulich, W. Kaim, A. F. Stange, H. Stoll, J. Fiedler, S. Zális, *Inorg. Chem.* **1996**, *35*, 3998–4002.
215. I. Hanazaki, S. Nagakura, *Bull. Chem. Soc. Jpn.* **1971**, *44*, 2312–2321.
216. B. P. Sullivan, D. Conrad, T. J. Meyer, *Inorg. Chem.* **1985**, *24*, 3640–3645.
217. S. D. Ernst, W. Kaim, *Inorg. Chem.* **1989**, *28*, 1520–1528.
218. M. Marcaccio, F. Paolucci, C. Paradisi, S. Roffia, C. Fontanesi, L. J. Yellowlees, S. Serroni, S. Campagna, G. Denti, V. Balzani, *J. Am. Chem. Soc.* **1999**, *121*, 10081–10091.
219. M. K. De Armond, M. L. Myrick, *Acc. Chem. Res.* **1989**, *22*, 364–370.
220. A. B. P. Lever, *Inorg. Chem.* **1991**, *30*, 1980–1985.
221. Y. Ohsawa, M.-H. Whangbo, K. W. Hanck, M. K. DeArmond, *Inorg. Chem.* **1984**, *23*, 3426–3428.
222. M. Furue, K. Maruyama, T. Oguni, M. Naiki, M. Kamachi, *Inorg. Chem.* **1992**, *31*, 3792–3795.
223. M. K. Nazeeruddin, S. M. Zakeeruddin, K. Kalyanasundaram, *J. Phys. Chem.* **1993**, *97*, 9607–9612.
224. M. Maestri, N. Armaroli, V. Balzani, E. C. Constable, A. M. W. Cargill Thompson, *Inorg. Chem.* **1995**, *34*, 2759–2767.
225. J. K. Hino, L. Della Ciana, W. J. Dressick, B. P. Sullivan, *Inorg. Chem.* **1992**, *31*, 1072–1080.

226. V. Skarda, M. J. Cook, A. P. Lewis, G. S. G. McAuliffe, A. J. Thomson, D. J. Robbins, *J. Chem. Soc. Perkin Trans. II* **1984**, 1309–1311.
227. P. Bugnon, R. E. Hester, *Chem. Phys. Lett.* **1983**, 102, 537–543.
228. P. Belser, A. von Zelewsky, A. Juris, F. Barigelletti, A. Tucci, V. Balzani, *Chem. Phys. Lett.* **1982**, 89, 101–104.
229. E. Binamira-Soriaga, S. D. Sprouse, R. J. Watts, W. C. Kaska, *Inorg. Chim. Acta* **1984**, 84, 135–139.
230. J. A. Baiano, R. J. Kessler, R. S. Lumpkin, M. J. Munley, W. R. Murphy, Jr., *J. Phys. Chem.* **1995**, 99, 17680–17690.
231. M. Maruyama, Y. Kaizu, *Inorg. Chim. Acta* **1996**, 247, 155–159.
232. W. L. Reynolds, *J. Phys. Chem.* **1963**, 67, 2866–2868.
233. T. Saji, S. Aoyagui, *Bull. Chem. Soc. Jpn.* **1973**, 46, 2101–2105.
234. R. Stasiw, R. G. Wilkins, *Inorg. Chem.* **1969**, 8, 156–157.
235. P. Hendry, A. Ludi, *Adv. Inorg. Chem.* **1990**, 35, 117–198.
236. R. Pyati, R. W. Murray, *J. Am. Chem. Soc.* **1996**, 118, 1743–1749.
237. Y. Fu, A. S. Cole, T. W. Swaddle, *J. Am. Chem. Soc.* **1999**, 121, 10410–10415.
238. T. Saji, S. Aoyagui, *J. Electroanal. Chem.* **1975**, 63, 31–37.
239. T. Saji, T. Yamada, S. Aoyagui, *J. Electroanal. Chem.* **1975**, 61, 147–153.
240. T. Saji, T. Yamada, S. Aoyagui, *Bull. Chem. Soc. Jpn.* **1975**, 48, 1641–1642.
241. A. G. Motten, K. Hanck, M. K. DeArmond, *Chem. Phys. Lett.* **1981**, 79, 541–546.
242. G. Wolfbauer, A. M. Bond, D. R. MacFarlane, *J. Chem. Soc., Dalton Trans.* **1999**, 4363–4372.
243. W. Kaim, S. Kohlmann, *Inorg. Chem.* **1990**, 29, 2909–2914.
244. G. Wolfbauer, A. M. Bond, D. R. MacFarlane, *Inorg. Chem.* **1999**, 38, 3836–3846.
245. L. Zelikovich, J. Libman, A. Shanzer, *Nature* **1995**, 374, 790.
246. T. R. Ward, A. Lutz, S. P. Parel, J. Ensling, P. Gütllich, P. Buglyó, C. Orvig, *Inorg. Chem.* **1999**, 38, 5007–5017.
247. D. J. Cárdenas, A. Livoreil, J.-P. Sauvage, *J. Am. Chem. Soc.* **1996**, 118, 11980–11981.
248. F. Vögtle, M. Plevcoets, M. Nieger, G. C. Azzellini, A. Credi, L. De Cola, V. De Marchis, M. Venturi, V. Balzani, *J. Am. Chem. Soc.* **1999**, 121, 6290–6298.
249. P. Ceroni, F. Paolucci, C. Paradisi, A. Juris, S. Roffia, S. Serroni, S. Campagna, A. J. Bard, *J. Am. Chem. Soc.* **1998**, 120, 5480–5487.
250. M. Venturi, A. Credi, V. Balzani, *Coord. Chem. Rev.* **1999**, 185–186, 233–256.
251. E. H. Yonemoto, G. B. Saupe, R. H. Schmehl, S. M. Hubig, R. L. Riley, B. L. Iverson, T. E. Mallouk, *J. Am. Chem. Soc.* **1994**, 116, 4786–4795.
252. M. Maggini, D. M. Guldi, S. Mondini, G. Scorrano, F. Paolucci, P. Ceroni, S. Roffia, *Chem. Eur. J.* **1998**, 4, 1992–2000.
253. D. LeGourriérec, M. Andersson, J. Davidsson, E. Mukhtar, L. Sun, L. Hammarström, *J. Phys. Chem. A* **1999**, 103, 557–559.
254. P. Chen, T. D. Westmoreland, E. Danielson, K. S. Schanze, D. Anthon, P. E. Neveux, Jr., T. J. Meyer, *Inorg. Chem.* **1987**, 26, 1116–1126.
255. P. Chen, R. Duesing, D. K. Graff, T. J. Meyer, *J. Phys. Chem.* **1991**, 95, 5850–5858.
256. C. O. Dietrich-Buchecker, J.-F. Nierengarten, J.-P. Sauvage, N. Armaroli, V. Balzani, L. De Cola, *J. Am. Chem. Soc.* **1993**, 115, 11237–11244.
257. P. D. Beer, Z. Chen, A. J. Goulden, A. Grieve, D. Hesek, F. Szemes, T. Wear, *J. Chem. Soc., Chem. Commun.* **1994**, 1269.
258. N. G. Connelly, W. E. Geiger, *Chem. Rev.* **1996**, 96, 877–910.
259. T. R. O'Toole, L. D. Margerum, T. D. Westmoreland, W. J. Vining, R. W. Murray, *J. Chem. Soc., Chem. Commun.* **1985**, 1416–1417.
260. S. Dérien, E. Duñach, J. Périchon, *J. Am. Chem. Soc.* **1991**, 113, 8447–8454.
261. M. F. Sístare, R. C. Holmberg, H. H. Thorp, *J. Phys. Chem. B* **1999**, 103, 10718–10728.
262. S. Gould, R. M. Leasure, T. J. Meyer, *Chem. Brit.* **1995**, 31, 891–893.
263. P. D. Beer, P. A. Gale, G. Z. Chen, *Coord. Chem. Rev.* **1999**, 185–186, 3–36.
264. C. M. Elliott, J. G. Redepenning, *J. Electroanal. Chem.* **1986**, 197, 219–232.
265. V. Balzani, F. Bolletta, F. Scandola, R. Ballardini, *Pure & Appl. Chem.* **1979**, 51, 299–311.
266. V. Balzani, F. Barigelletti, L. De Cola, *Top. Curr. Chem.* **1990**, 158, 31–71.

267. N. Serpone, in M. A. Fox, M. Chanon (Eds.): *Photoinduced Electron Transfer. Part D. Photoinduced Electron-transfer reactions: Inorganic Substrates and Applications*, Elsevier, Amsterdam 1988, p. 47.
268. M. Ruthkosky, F. N. Castellano, G. J. Meyer, *Inorg. Chem.* **1996**, *35*, 6406–6412.
269. V. Balzani, F. Scandola, in J. S. Connolly (Ed.): *Photochemical Conversion and Storage of Solar Energy*, Academic Press, New York 1981, p. 97–129.
270. C. Creutz, M. Chou, T. L. Netzel, M. Okumura, N. Sutin, *J. Am. Chem. Soc.* **1980**, *102*, 1309–1319.
271. A. Vlček, *Coord. Chem. Rev.* **2000**, *200–202*, 933–977.
272. N. H. Damrauer, G. Cerullo, A. Yeh, T. R. Bousie, C. V. Shank, J. K. McCusker, *Science* **1997**, *275*, 54–57.
273. N. H. Damrauer, J. K. McCusker, *J. Phys. Chem. A* **1999**, *103*, 8440–8446.
274. A. W. Adamson, *Pure & Appl. Chem.* **1979**, *51*, 313–329.
275. P. D. Fleischauer, A. W. Adamson, G. Sartori, *Progr. Inorg. Chem.* **1972**, *17*, 1.
276. A. W. Adamson, in K. Kalyanasundaram, M. Grätzel (Eds.): *Photosensitization and Photocatalysis Using Inorganic and Organometallic Compounds*, Kluwer Academic Publishers, Dordrecht 1993, p. 1–14.
277. V. Balzani, A. Juris, F. Scandola, in E. Pelizzetti, N. Serpone (Eds.): *Homogeneous and Heterogeneous Photocatalysis*, D. Reidel Publishing Company 1986, p. 1–27.
278. N. Serpone, M. A. Jamieson, M. S. Henry, M. Z. Hoffman, F. Bolletta, M. Maestri, *J. Am. Chem. Soc.* **1979**, *101*, 2907–2916.
279. N. Serpone, M. A. Jamieson, R. Sriram, M. Z. Hoffman, *Inorg. Chem.* **1981**, *20*, 3983–3988.
280. A. I. Baba, J. R. Shaw, J. A. Simon, R. P. Thummel, R. H. Schmehl, *Coord. Chem. Rev.* **1998**, *171*, 43–59.
281. W. E. Ford, M. A. J. Rodgers, *J. Phys. Chem.* **1992**, *96*, 2917–2920.
282. A. Harriman, M. Hissler, A. Khatyr, R. Ziessel, *Chem. Commun.* **1999**, 735–736.
283. G. F. Strouse, H. U. Gudel, *Inorg. Chim. Acta* **1995**, *240*, 453–464.
284. H. Riesen, E. Krausz, *Comments Inorg. Chem.* **1995**, *18*, 27–63.
285. J. L. Pogge, D. F. Kelley, *Chem. Phys. Letters* **1995**, *238*, 16–24.
286. J. P. Cushing, C. Butoi, D. F. Kelley, *J. Phys. Chem. A* **1997**, *101*, 7222–7230.
287. D. P. Rillema, D. G. Taghdiri, D. S. Jones, C. D. Keller, L. A. Worl, T. J. Meyer, H. A. Levy, *Inorg. Chem.* **1987**, *26*, 578–585.
288. A. Juris, P. Belser, F. Barigelletti, A. von Zelewsky, V. Balzani, *Inorg. Chem.* **1986**, *25*, 256–259.
289. S. R. Johnson, T. D. Westmoreland, J. V. Caspar, K. R. Barqawi, T. J. Meyer, *Inorg. Chem.* **1988**, *27*, 3195–3200.
290. E. M. Kober, J. L. Marshall, W. J. Dressick, B. P. Sullivan, J. V. Caspar, T. J. Meyer, *Inorg. Chem.* **1985**, *24*, 2755–2763.
291. J. V. Caspar, T. J. Meyer, *J. Phys. Chem.* **1983**, *87*, 952–957.
292. J. V. Caspar, E. M. Kober, B. P. Sullivan, T. J. Meyer, *J. Am. Chem. Soc.* **1982**, *104*, 630–632.
293. G. F. Strouse, J. R. Schoonover, R. Duesing, S. Boyde, W. E. Jones, T. J. Meyer, *Inorg. Chem.* **1995**, *34*, 473–487.
294. J. A. Treadway, B. Loeb, R. Lopez, P. A. Anderson, F. R. Keene, T. J. Meyer, *Inorg. Chem.* **1996**, *35*, 2242–2246.
295. T. J. Meyer, *Pure & Appl. Chem.* **1986**, *58*, 1193–1206.
296. B. Durham, J. V. Caspar, J. K. Nagle, T. J. Meyer, *J. Am. Chem. Soc.* **1982**, *104*, 4803–4810.
297. D. P. Rillema, C. B. Blanton, R. J. Shaver, D. C. Jackman, M. Boldaji, S. Bundy, L. A. Worl, T. J. Meyer, *Inorg. Chem.* **1992**, *31*, 1600–1606.
298. G. H. Allen, R. P. White, D. P. Rillema, T. J. Meyer, *J. Am. Chem. Soc.* **1984**, *106*, 2613–2620.
299. R. F. Beeston, W. S. Aldridge, J. A. Treadway, M. C. Fitzgerald, B. A. DeGraff, S. E. Stitzel, *Inorg. Chem.* **1998**, *37*, 4368–4379.
300. M. T. Miller, P. K. Gantzel, T. B. Karpishin, *Inorg. Chem.* **1999**, *38*, 3414–3422.
301. M. Ruthkosky, C. A. Kelly, F. N. Castellano, G. J. Meyer, *Coord. Chem. Rev.* **1998**, *171*, 309–322.

302. M. T. Miller, T. B. Karpishin, *Inorg. Chem.* **1999**, *38*, 5246–5249.
303. K. Kalyanasundaram, *J. Chem. Soc. Faraday Trans. 2* **1986**, *82*, 2401–2415.
304. S. Ferrere, B. A. Gregg, *J. Am. Chem. Soc.* **1998**, *120*, 843–844.
305. L. Hammarström, F. Barigelletti, L. Flamigni, M. T. Indelli, N. Armaroli, G. Calogero, M. Guardigli, A. Sour, J.-P. Collin, J.-P. Sauvage, *J. Phys. Chem. A* **1997**, *101*, 9061–9069.
306. C. Kutal, *Coord. Chem. Revs.* **1990**, *99*, 213–252.
307. D. R. McMillin, J. R. Kirchhoff, K. V. Goodwin, *Coord. Chem. Rev.* **1985**, *64*, 83–92.
308. F. Scandola, V. Balzani, G. B. Schuster, *J. Am. Chem. Soc.* **1981**, *103*, 2519–2523.
309. C. Turró, J. M. Zaleski, Y. M. Karabatsos, D. G. Nocera, *J. Am. Chem. Soc.* **1996**, *118*, 6060–6067.
310. D. G. Whitten, *Acc. Chem. Res.* **1980**, *13*, 83–90.
311. T. Hannappel, B. Burfeindt, W. Storck, F. Willig, *J. Phys. Chem. B* **1997**, *101*, 6799–6802.
312. H. N. Ghosh, J. B. Asbury, Y. Weng, T. Lian, *J. Phys. Chem. B* **1998**, *102*, 10208–10215.
313. J. M. Rehm, G. L. McLendon, Y. Nagasawa, K. Yoshihara, J. Moser, M. Grätzel, *J. Phys. Chem.* **1996**, *100*, 9577–9578.
314. B. Burfeindt, T. Hannappel, W. Storck, F. Willig, *J. Phys. Chem.* **1996**, *100*, 16463–16465.
315. N. J. Cherepy, G. P. Smestad, M. Grätzel, J. Z. Zhang, *J. Phys. Chem. B* **1997**, *101*, 9342–9351.
316. M. Hilgendorff, V. Sundström, *J. Phys. Chem. B* **1998**, *102*, 10505–10514.
317. H. N. Ghosh, J. B. Asbury, T. Lian, *J. Phys. Chem. B* **1998**, *102*, 6482–6486.
318. P. Belser, S. Bernhard, C. Blum, A. Beyeler, L. De Cola, V. Balzani, *Coord. Chem. Rev.* **1999**, *190–192*, 155–169.
319. P. Chen, M. Curry, T. J. Meyer, *Inorg. Chem.* **1989**, *28*, 2271–2280.
320. P. Chen, E. Danielson, T. J. Meyer, *J. Phys. Chem.* **1988**, *92*, 3708–3711.
321. J. R. Schoonover, P. Chen, W. D. Bates, R. B. Dyer, T. J. Meyer, *Inorg. Chem.* **1994**, *33*, 793–797.
322. D. J. Liard, A. Vlček, Jr., *Inorg. Chem.* **2000**, *39*, 485–490.
323. N. E. Katz, S. L. Mecklenburg, D. K. Graff, P. Chen, T. J. Meyer, *J. Phys. Chem.* **1994**, *98*, 8959–8961.
324. P. Chen, S. L. Mecklenburg, T. J. Meyer, *J. Phys. Chem.* **1993**, *97*, 13126–13131.
325. J. R. Schoonover, G. F. Strouse, P. Chen, W. D. Bates, T. J. Meyer, *Inorg. Chem.* **1993**, *32*, 2618–2619.
326. Y. Wang, B. T. Hauser, M. M. Rooney, R. D. Burton, K. S. Schanze, *J. Am. Chem. Soc.* **1993**, *115*, 5675–5683.
327. L. A. Lucia, Y. Wang, K. Nafisi, T. L. Netzel, K. S. Schanze, *J. Phys. Chem.* **1995**, *99*, 11801–11804.
328. Y. Wang, L. A. Lucia, K. S. Schanze, *J. Phys. Chem.* **1995**, *99*, 1961–1968.
329. Y. Wang, K. S. Schanze, *J. Phys. Chem.* **1996**, *100*, 5408–5419.
330. S. L. Mecklenburg, B. M. Peek, J. R. Schoonover, D. G. McCafferty, C. G. Wall, B. W. Erickson, T. J. Meyer, *J. Am. Chem. Soc.* **1993**, *115*, 5479–5495.
331. N. Armaroli, F. Diederich, C. O. Dietrich-Buchecker, L. Flamigni, J.-F. Nierengarten, J.-P. Sauvage, *Chem. Eur. J.* **1998**, *4*, 406–416.
332. P. R. Ashton, R. Ballardini, V. Balzani, E. C. Constable, A. Credi, O. Kocian, S. J. Langford, J. A. Preece, L. Prodi, E. R. Schofield, N. Spencer, J. F. Stoddart, S. Wenger, *Chem. Eur. J.* **1998**, *4*, 2413–2422.
333. J.-C. Chambron, A. Harriman, V. Heitz, J.-P. Sauvage, *J. Am. Chem. Soc.* **1993**, *115*, 6109–6114.
334. I. Rubinstein, A. J. Bard, *J. Am. Chem. Soc.* **1981**, *103*, 512–516.
335. M. M. Richter, J. D. Debad, D. R. Striplin, G. A. Crosby, A. J. Bard, *Anal. Chem.* **1996**, *68*, 4370–4376.
336. H. D. Abruña, *J. Electroanal. Chem.* **1984**, *175*, 321–326.
337. A. Vogler, L. El-Sayed, R. G. Jones, J. Namnath, A. W. Adamson, *Inorg. Chim. Acta* **1981**, *53*, L35–L37.
338. V. Balzani, F. Bolletta, *J. Photochem.* **1981**, *17*, 479–485.
339. D. K. Liu, B. S. Brunshwig, C. Creutz, N. Sutin, *J. Am. Chem. Soc.* **1986**, *108*, 1749–1755.
340. F. Bolletta, M. Ciano, V. Balzani, N. Serpone, *Inorg. Chim. Acta* **1982**, *62*, 207–213.

341. N. E. Tokel-Takvoryan, R. E. Hemingway, A. J. Bard, *J. Am. Chem. Soc.* **1973**, *95*, 6582–6589.
342. W. L. Wallace, A. J. Bard, *J. Phys. Chem.* **1979**, *83*, 1350–1357.
343. J.-M. Lehn, R. Ziessel, *J. Organomet. Chem.* **1990**, *382*, 157–173.
344. C. Kutal, A. J. Corbin, G. Ferraudi, *Organometallics* **1987**, *6*, 553–557.
345. C. Kutal, M. A. Weber, G. Ferraudi, D. Geiger, *Organometallics* **1985**, *4*, 2161–2166.
346. J. Hawecker, J.-M. Lehn, R. Ziessel, *J. Chem. Soc., Chem. Commun.* **1983**, 536–538.
347. J. R. Winkler, H. B. Gray, *Chem. Rev.* **1992**, *92*, 369–379.
348. D. S. Wuttke, M. J. Bjerrum, J. R. Winkler, H. B. Gray, *Science* **1992**, *256*, 1007–1009.
349. G. A. Mines, M. J. Bjerrum, M. G. Hill, D. R. Casimiro, I.-J. Chang, J. R. Winkler, H. B. Gray, *J. Am. Chem. Soc.* **1996**, *118*, 1961–1965.
350. L. K. Skov, T. Pascher, J. R. Winkler, H. B. Gray, *J. Am. Chem. Soc.* **1998**, *120*, 1102–1103.
351. D. R. Casimiro, J. H. Richards, J. R. Winkler, H. B. Gray, *J. Phys. Chem.* **1993**, *97*, 13073–13077.
352. D. S. Wuttke, H. B. Gray, S. L. Fisher, B. Imperiali, *J. Am. Chem. Soc.* **1993**, *115*, 8455–8456.
353. J. R. Telford, P. Wittung-Stafshede, H. B. Gray, J. R. Winkler, *Acc. Chem. Res.* **1998**, *31*, 755–763.
354. J. J. Wilker, I. J. Dmochowski, J. H. Dawson, J. R. Winkler, H. B. Gray, *Angew. Chem. Int. Ed.* **1999**, *38*, 90–92.
355. I. Ortmans, C. Moucheron, A. Kirsch-De Mesmaeker, *Coord. Chem. Rev.* **1998**, *168*, 233–271.
356. J. K. Barton, in I. Bertini, H. B. Gray, S. J. Lippard, J. S. Valentine (Eds.): *Bioinorganic Chemistry*, University Science Books, Mill Valley, CA 1994, p. 455–503.
357. P. J. Dandliker, R. E. Holmlin, J. K. Barton, *Science* **1997**, *275*, 1465–1467.
358. C. J. Murphy, M. R. Arkin, Y. Jenkins, N. D. Ghatlia, S. H. Bossmann, N. J. Turro, J. K. Barton, *Science* **1993**, *262*, 1025–1029.
359. M. R. Arkin, E. D. A. Stemp, R. E. Holmlin, J. K. Barton, A. Hörmann, E. J. C. Olson, P. F. Babara, *Science* **1996**, *273*, 475–480.
360. E. D. A. Stemp, R. E. Holmlin, J. K. Barton, *Inorg. Chim. Acta* **2000**, *297*, 88–97.
361. T. J. Meade, J. F. Kayyem, *Angew. Chem. Int. Ed. Engl.* **1995**, *34*, 352–354.
362. E. Kimura, X. Bu, M. Shionoya, S. Wada, S. Maruyama, *Inorg. Chem.* **1992**, *31*, 4542–4546.
363. D. Burdinski, K. Wieghardt, S. Steenken, *J. Am. Chem. Soc.* **1999**, *121*, 10781–10787.

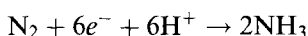
6 Electron Transfer in Catalytic Dinitrogen Reduction

Alexander E. Shilov

6.1 Introduction

Dinitrogen, N₂, is chemically very inert, yet its hydrogenation to ammonia is exothermic, i.e. thermodynamically favored at low temperatures. In practice, however, the hydrogenation requires high temperatures and pressures because of kinetic obstacles to consecutive cleavage of the N≡N triple bond.

Hydrogenation is closely related to N₂ reduction, because the same result is achieved when N₂ receives six electrons from an electron donor and six protons from the medium:



The reduction of dinitrogen to ammonia constitutes the first observed step in biological nitrogen fixation. Because nature might have chosen and developed an optimum means of reducing N₂ by use of comparatively mild electron donors in protic surroundings at ambient temperature and pressure, it has long seemed very attractive to try to understand the mechanism of biological N₂ fixation and to use the knowledge of this mechanism for construction of synthetic systems capable of performing a similar process in a chemistry laboratory.

Progress in both understanding biological dinitrogen reduction and in the search for purely chemical systems which reduce N₂ at low temperatures was initially very slow, but in recent decades there have been very important developments in investigations of enzymatic N₂ reduction and at the same time in low-temperature dinitrogen chemistry including N₂ reduction in solution. We now know both stoichiometric and catalytic systems reducing N₂ to hydrazine and ammonia in solution, and we understand how to make N₂ unusually chemically active under mild conditions. Polynuclear metal complexes have been found to be catalysts for chemical reduction of N₂ in protic media when bound to the surface of such donors as titanium(III) hydroxides, metals amalgams, or mercury cathodes in electrochemical

reduction. Recently the FeMo cofactor of nitrogenase, which was isolated for the first time in 1977 and which is also a polynuclear complex of composition Fe₇MoS₉ (homocitrate), was found to be an active catalyst of acetylene reduction and of reduction of other nitrogenase substrates; it also coordinates dinitrogen in non-protein surroundings. For the first time, we can now compare catalytic functions of FeMoco in natural and non-protein surrounding on the one hand and also on the other hand FeMoco and synthetic complexes active to dinitrogen and other nitrogenase substrates when bound to the surface of the same artificial electron donor.

Peculiarities of the N₂ molecule make it necessary to use special means of electron transfer to and inside the active center containing the substrate. The mechanism of the catalysis in protic surroundings, at least for dinitrogen reduction, presumably necessarily includes coupled one-electron transfer from an external electron donor and multi-electron transfer to the substrate coordinated in the polynuclear complex. The coupled electron transfer helps to activate and reduce the 'difficult' substrate dinitrogen at ambient temperatures.

In this article, the reasons for this mechanism in catalytic reduction of N₂ will be considered, and results for electron transfer in biological N₂ reduction and model synthetic systems will be compared. Hopefully, this consideration will lead to understanding how inert dinitrogen can be turned into a very active substrate readily reacting in solution in the presence of comparatively mild reducing agents.

6.2 Peculiarities of the N₂ Molecule

The inertness of dinitrogen is very well known and reflected in its properties (Table 1). Dinitrogen has very high bond-dissociation energy, high ionization potential, and a negative electron affinity. Proton affinity, though positive, is comparatively small, smaller than, for example, that of methane (5.3 ± 0.3 eV). Dinitrogen is a very weak base, and does not interact even with strong acids. It should be noted, however, that the bond-dissociation energy does not by itself explain the inertness of dinitrogen. The triple-bond-dissociation energy of acetylene (230 kcal mol⁻¹)

Table 1. Some physical constants and characteristics of dinitrogen.

Interatomic distance	1.095 Å
Ionization potential	15.58 eV
N≡N dissociation energy	225 kcal mol ⁻¹
Vibration frequency (gas)	2231 cm ⁻¹
Electron affinity	-1.8 eV
Proton affinity	5.12 eV
Singlet-triplet energy	6.17 eV
Solubility in water	1.7×10^{-3} cm ³ /cm ³
Solubility in benzene	1.11×10^{-1} cm ³ /cm ³

is approximately the same as for dinitrogen, and for carbon monoxide it is even higher (256 kcal mol⁻¹), but both C₂H₂ and CO are usually chemically much more reactive than dinitrogen.

The electronic configuration of dinitrogen can be represented as $(1\sigma_s)^2(1\sigma_u)^2(2\sigma_g)^2(2\sigma_u)^2(1\pi_u)^4(3\sigma_g)^2$. The highest occupied orbital $3\sigma_g$ is higher than $1\pi_u$ because of the mixing of s and p orbitals. Both occupied orbitals $3\sigma_g$ and $1\pi_u$ are strongly bonding; the energy level of $3\sigma_g$ is -15.6 eV; for $1\pi_u$ it is -17.1 eV. The lowest unoccupied orbital $1\pi_g^*$ is strongly antibonding: +7.3 eV.

Important conclusions about the reasons for the inertness of dinitrogen can be drawn by considering the energies required for consecutive cleavage of the triple bonds in the N₂ molecule. Dissociation of the first of the three bonds requires more than 100 kcal mol⁻¹, almost half the total triple bond energy. For acetylene, the first bond of the three to be broken is, in contrast, the weakest (53 kcal mol⁻¹). This sharp difference is the main reason for their different reactivity. The strength of this first bond in N₂ (compared with acetylene) is evidently largely a consequence of high energy level of diazene; this is because of the repulsion of the two unshared electron pairs and the electron pair of the remaining π -bond in N₂H₂ after cleavage of one of the π -bonds of N₂; in acetylene, the electron pairs of two σ -bonds with H atoms (as distinct from the two unshared pairs on N₂) are less strongly repelled by electrons of the π -bond.

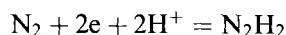
This feature of dinitrogen is an intrinsic characteristic of the molecule, rather than a reflection of the nature of species reacting with it. Thus, the energy of the N₂ triplet state (which can be regarded as a N₂ molecule with one of π -bonds cleaved) is much higher (6.17 eV) than the corresponding triplet state of acetylene (ca 3.7 eV).

This difference results in different thermodynamics of one- and two-electron reactions of acetylene and dinitrogen—often these reactions are thermodynamically favorable for acetylene but forbidden for dinitrogen.

For example, the hydrogenation of acetylene (and ethylene) by one molecule of H₂ is strongly exothermic (ΔH° for the reaction C₂H₂ + H₂ → C₂H₄ is -42 kcal mol⁻¹) whereas the corresponding reaction for dinitrogen, N₂ + H₂ → N₂H₂, is strongly endothermic (ΔH° is +51 and +56 kcal mol⁻¹ for *trans*- and *cis*-diazene respectively). Even addition of a hydrogen atom, which for acetylene is 41 kcal mol⁻¹ exothermic, for dinitrogen (the reaction N₂ + H• → •N₂H) is ca 9 kcal mol⁻¹ endothermic. A radical chain reaction of dihydrogen with dinitrogen initiated by addition of H atom to N₂ is, therefore impossible, as is catalytic hydrogenation via diazene as an intermediate (and this is probably the main reason for the absence of activity of typical hydrogenation catalysts towards dinitrogen).

Consecutive electron transfer to the N₂ molecule with simultaneous addition of protons reflects these thermodynamics peculiarities of dinitrogen (Figure 1).

One- and two-electron transfer with simultaneous addition of protons



corresponds to negative redox potentials and requires much stronger reducing

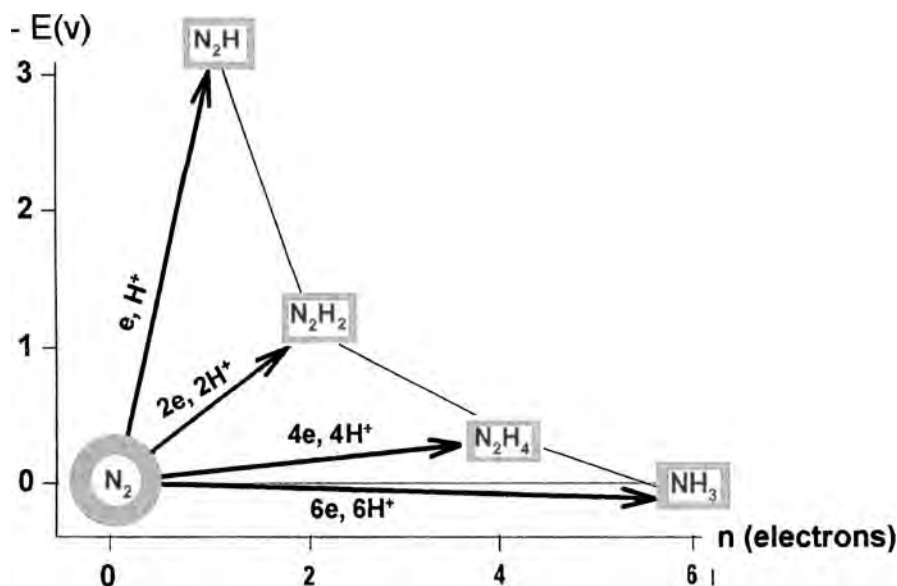
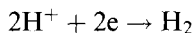


Figure 1. Redox potentials of one-, two-, four-, and six-electron reductions of dinitrogen.

agents than dihydrogen. Strong reducing agents such as lithium metal can react with N_2 to form nitrides, but such reactions are very unlikely in protic media because the conditions favor a simpler reaction with protons to form H_2 :



At the same time consideration of Figure 1 reveals the possibility of using milder reducing agents which are perhaps sufficiently stable in protic media.

The second and the third bonds cleaved in N_2 are, in contrast, very weak—ca 60 kcal mol^{-1} each. Four- and six-electron reductions to hydrazine and ammonia in aqueous solution thus correspond to redox potentials of -0.36 and $+0.55 \text{ V}$, respectively, and require considerably weaker reductants than for one- and two-electron reductions.

If, therefore, we have a metal cluster capable of accepting, e.g., four electrons one by one and then of reacting with N_2 to form a hydrazine derivative, further protonation might lead to the formation of hydrazine without intermediate formation of not only the N_2H radical but also the N_2H_2 molecule. Such a cluster can then function as a catalyst for N_2 reduction to hydrazine or ammonia by comparatively weak one-electron reducing agent sufficiently stable in protic media. The mechanism of four-electron reduction of dinitrogen was proposed ca 30 years ago [1] and helped the discovery of catalysts of N_2 reduction in protic media. The first step in such a four-electron or even six-electron mechanism of dinitrogen reduction must always be formation of an intermediate complex with a transition metal compound.

The properties of dinitrogen and systems reducing N_2 are considered in more detail in the author's recent book (Ref. [2] and references therein).

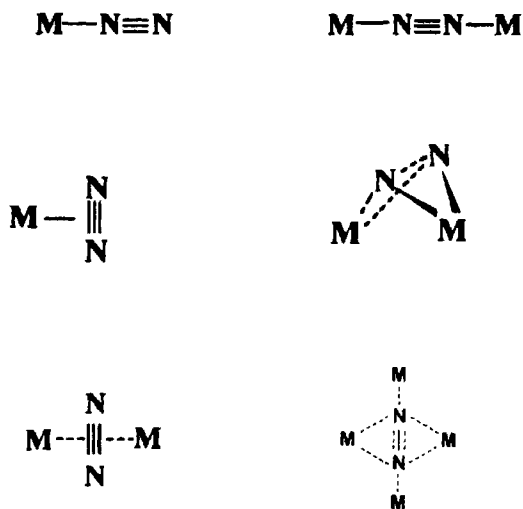


Figure 2. Typical structures of dinitrogen complexes with transition metal compounds (M = metal + other ligands).

6.3 Dinitrogen Complexes with Transition Metals: Possible Catalysts for N_2 Reduction

Since 1965, when the first dinitrogen complex with ruthenium(II) was discovered [3a] N_2 complexes with several transition metal compounds have been prepared. As with other unsaturated molecules, in these complexes dinitrogen acts both as electron donor and electron acceptor, the latter properties being more pronounced. Different kinds of complex are obtained experimentally and considered theoretically (e.g. see review [3b]).

Examples of the structures of N_2 complexes are shown in Figure 2.

It is important for further reduction of the complexes that the dinitrogen ligand is a much stronger base than free dinitrogen and can be protonated. Addition of protons strongly increases the electron-accepting properties of coordinated dinitrogen and facilitates electron transfer from metals M to N_2 , leading eventually to reduction of dinitrogen to N_2H_4 or NH_3 . (Below 'M' denotes a metal atom with corresponding ligands.)

Linear complexes of the types $M-N\equiv N$ and $M-N\equiv N-M$ were discovered first, and are generally more stable and more thoroughly studied than other types of complex. Their relative stability is, apparently, because the highest occupied molecular orbital ($3\sigma_g$) is a σ -orbital. Also, in mononuclear $M-N\equiv N$ complexes as

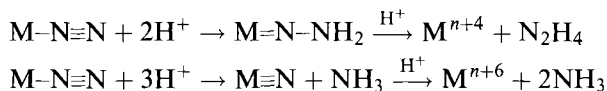
distinct from edge-on $M-\begin{array}{c} N \\ ||| \\ N \end{array}$ complexes both π -bonds of dinitrogen are

involved in binding with M. Other types of complex might, however, be important as intermediates in a reduction process.

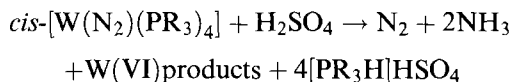
Let us now consider the participation of metal–dinitrogen complexes in N_2 reduction. We may safely postulate that the stronger the $M-N$ bonds in the complex the weaker is the NN bond, i.e. the more activated is dinitrogen. If we want to avoid thermodynamically unfavorable diazene, N_2H_2 , we must have at least four available d-electrons entering both π^* -orbitals of coordinated dinitrogen. From consideration of experimental and theoretical results obtained for protonation and reduction of dinitrogen in stable dinitrogen complexes with transition metal compounds the following general conclusions can be made.

6.4 Mononuclear Complexes $M-N\equiv N$

In such complexes dinitrogen usually remains chemically inert, although it can occasionally be reduced to hydrazine or ammonia by protonation by acids:



It is apparent that four or even six electrons should be available on M and on reduction its oxidation state should be changed by four or six units. Initially, therefore, M must be in a very low oxidation state, and it is difficult to imagine mononuclear dinitrogen complexes as *intermediates* not only in catalytic N_2 reduction but even in stoichiometric reduction of dinitrogen if these complexes have to be formed from low-valent M and N_2 in the presence of an acid. Actually specially prepared mononuclear complexes containing dinitrogen can occasionally be protonated, as was found by Chatt et al. [3b], and this can be coupled with the reduction of N_2 , e.g. tungsten(0) dinitrogen complex reacts with sulfuric acid in methanol, forming tungsten(VI):



With the similar molybdenum complex the yield of ammonia reaches only ca 0.7 mol per metal atom, the remainder being evolved as free dinitrogen, with molybdenum being oxidized to molybdenum(III). Apparently, however, no such complexes have been observed as intermediates in dinitrogen reduction in protic media.

6.5 Linear Dinuclear Complexes $M-N\equiv N-M$

Protonation of dinitrogen with N_2 reduction is, in principle, more favorable thermodynamically in dinuclear complexes than as described in Section 6.4, because the

oxidation state of metals increase by two units only in the formation of hydrazine and by three units in the formation of ammonia. Consideration of the molecular orbitals of such complexes leads to the conclusion that in linear dinuclear complexes only d^2 – d^4 electronic configurations correspond to sufficient activation of N_2 , d^3 being the optimum (e.g. see Ref. [2]).

Increasing the number of electrons reduces the activation of N_2 , because the electrons occupy the orbitals which are bonding with respect to the NN bond, and actually stabilize it. In agreement with this prediction dinitrogen is sufficiently activated to be reduced by protonation by dinuclear complexes of titanium(II), zirconium(II), niobium(III), tantalum(III), molybdenum(IV), and tungsten(IV), whereas it is not reduced by protonation by certain d^6 – d^{10} complexes, such as those of molybdenum(0), ruthenium(II), or rhodium(I). Apparently dinuclear complexes $M-N\equiv N-M$ in which M has the d^3 electronic configuration can be intermediates in dinitrogen reduction in protic media, particularly if they represent part of polynuclear complexes (*vide infra*).

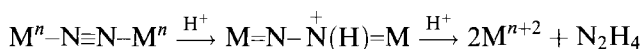
In di- and polynuclear complexes with N_2 perpendicular orientation of NN in a complex $M-\begin{array}{c} N \\ ||| \\ N \end{array}-M$ seems to correspond to more activated N_2 molecules than the linear coordination $M \cdots N\equiv N \cdots M$

6.6 Polynuclear Dinitrogen Complexes

As the number of metal atoms in a polynuclear dinitrogen complex is increased, weaker reducing agents can be used to achieve the same level of the substrate activation, because with sufficient metal atoms surrounding dinitrogen the oxidation state of metal atoms can increase by one unit only and the complexes can have sufficient electron capacity to afford four- or even six-electron reduction with comparatively small energy requirements. Few polynuclear complexes have yet been isolated and generalizations can be made only with care. Nevertheless, up to six metal atoms can be bound to dinitrogen, each with an M–N bond, for example the complex with gold [3c]. Presumably in non-linear dinitrogen complexes there is no definite limitation to the number of d-electrons present on the metal atoms for the activation of bound dinitrogen; it must, however, also be taken into account that there might be an optimum value of this number for N_2 activation.

It should be mentioned that consecutive two-electron reduction of dinitrogen is still usually considered likely in the literature, with diazene, N_2H_2 , as an intermediate but stabilized by complexation with transition metals. At the same time there is no doubt that both π -bonds of N_2 can be used simultaneously for four d-electrons (entering two degenerate π_g^* -orbitals) from one, two, or several metal atoms forming a complex with dinitrogen, and separate cleavage of each π -bond seems to be unnecessary, more so because it is thermodynamically unfavorable. Therefore, for-

mation of, for example, a hydrazine derivative and subsequently hydrazine itself:



can be regarded as a genuine four-electron reduction.

6.7 Polynuclear Complex as Optimum Catalyst for N₂ Reduction

In principle protic media favor *catalytic* dinitrogen reduction more than aprotic media, because solvent molecules can protonate the intermediate product forming N₂H₄ or NH₃ and liberating the catalyst for new cycles of dinitrogen activation and reduction. There is, however, an obstacle in protic media which has already been mentioned: strong reducing agents can react with the solvent to form H₂ instead of reacting with N₂.

We can try to visualize an optimum catalyst for dinitrogen reduction in protic media taking into account the considerations presented earlier. An optimum catalyst might be defined as that functioning with the weakest, yet thermodynamically permitted, reducing agent. The catalyst is expected to be a polynuclear cluster capable to coordinate dinitrogen. At least four electrons of the cluster should be available to enter both antibonding π_g^* orbitals of dinitrogen. Metal atoms should be bound by flexible bridges to enable adjustment to changes of distances in the process of dinitrogen reduction. The simplest proposal for catalytic mechanism of dinitrogen reduction would be the formation of a polynuclear complex able to reduce N₂ to N₂H₄ or NH₃. The formation of such a complex will, presumably, involve several steps of intermolecular one-electron transfer from the external electron donor to the oxidized state of the complex, after that the complex will reduce N₂ independently in multi-electron manner, while transforming itself again into its initial oxidized state.

This mechanism looks simple and reasonable, but it is *not* optimum, at least for such a 'difficult' substrate as dinitrogen. Indeed, to reduce the catalyst to the state which then is able to reduce N₂ we need a reducing agent which is a stronger one-electron reductant than the cluster catalyst in each step of its reduction including, for example, the final difficult one-electron step to form the highly reduced state of the catalyst capable of coordinating and reducing N₂. The reducing agent might be less strong and the catalytic complex more suitable for dinitrogen activation if intermolecular electron transfer from the external reducing agent and intramolecular electron transfer from the catalytic complex to the coordinated dinitrogen occur simultaneously with 'reductive coaction' of the external electron donor. It might be expected that if the catalyst and the external reducing agent function in such a coupled manner in the most difficult steps of substrate reduction we shall have more optimum catalytic system. Electrons from the external reducing agent should be transferred to the catalyst coordinating N₂ together with protons

simultaneously or immediately one after the other to avoid accumulation of negative or positive charges which would destabilize the catalyst.

Protons can go directly to the dinitrogen ligand if it is sufficiently basic to accept H^+ from the proton donor; alternatively it might temporarily form a hydride, by addition to metal, or protonate another ligand (as S or O atoms) bound to metal in the vicinity of dinitrogen.

Each electron transferred to the cluster will shift electrons from the cluster to coordinated N_2 , which is mainly an electron-accepting ligand. Therefore, coordination of dinitrogen will increase the positive charge on the metal atoms and facilitate further electron transfer from the external donor. Protonation of dinitrogen will increase the positive charge further and in this its turn will facilitate electron transfer from the external reducing agent. At some stage the protonated dinitrogen ligand will be transformed to a hydrazine or ammonia derivative. This step might be rate-controlling, because the oxidation state of several, perhaps three, metal atoms will be increased by one unit each. It might require further electron transfer from the external reductant (to make the total number of electrons equal to at least four) and this reductant must, therefore, be situated at sufficiently short distance from the catalyst during the entire process of substrate reduction.

This mechanism with *coupled* one-electron intermolecular electron transfer from the external donor and intramolecular multi-electron transfer from the catalyst to coordinated N_2 is, presumably, more efficient than the simpler mechanism considered above with one-electron and multi-electron transfers separated in time. In this mechanism the strongest reductant, which is of necessity the external reducing agent, is used for *direct* reduction of the substrate, whereas for consecutive one-electron and multi-electron processes its reducing power is used only to prepare the reduced form of the catalyst.

6.8 Electron Transfer in Biological Nitrogen Fixation

Biological nitrogen fixation involves reduction of dinitrogen catalyzed by a metalloenzyme nitrogenase. As has already been mentioned, there has recently been considerable progress in the study of biological nitrogen fixation, and the mechanism of electron transfer in the process of N_2 reduction is becoming ever more clear. Several excellent reviews describing the structure and functions of nitrogenase and the mechanism of biological dinitrogen reduction have recently been published [4–6]. Here only main features of this process will be described. The first observed product of the reduction is ammonia; this is subsequently used in amino acid synthesis. Nitrogenase comprises two separable proteins: Fe protein and MoFe protein. Fe protein is a dimer of identical subunits with a molecular mass of 60 kDa. It contains one $[Fe_4S_4]$ cluster and is a specific one-electron donor for MoFe protein. MoFe protein is a tetramer of two types of subunit, $\alpha_2\beta_2$, with a

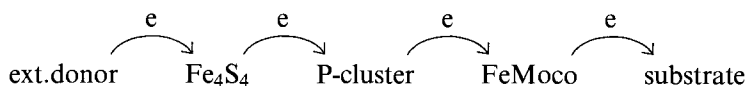
total molecular mass of 240 kDa. It contains two atoms of Mo, 32 atoms of Fe, and the same number of S^{2-} ions per molecule. These atoms are grouped together in two types of cluster—so called P-clusters and iron-molybdenum cofactors (FeMoco). In the presence of the two proteins (Fe protein and MoFe protein) dinitrogen is reduced to ammonia, the stoichiometry under optimum conditions is:



Thus N_2 reduction is coupled with ATP hydrolysis; it is apparent that two ATP molecules are hydrolyzed on transfer of each electron. One mole of dihydrogen is produced per mole of fixed dinitrogen even at saturating N_2 pressures. These results are obtained with molybdenum nitrogenase [4], containing iron molybdenum cofactor as the active site for dinitrogen and other nitrogenase substrates. As well as molybdenum nitrogenase two other 'alternative' nitrogenases are known [5]; these do not contain molybdenum. One contains vanadium instead of molybdenum, the other contains only iron as a transition metal and is called 'iron-only' nitrogenase. (A new nitrogenase functioning at elevated temperature was recently described in a series of articles [7]. This nitrogenase is very different from the traditional ones and it is too early to make any conclusions concerning the mechanism of its action.)

All three nitrogenases have much in common in their structures and functioning, although there are also some differences in detail. Molybdenum nitrogenase seems to be more stable and more efficient than the vanadium-containing enzyme and, particularly, iron-only nitrogenase. With the Mo-containing nitrogenase only one H_2 is produced at saturating dinitrogen pressures, according to the stoichiometry presented above, whereas the two others produce several dihydrogen molecules. Other molecules containing triple bonds can be reduced in the presence of nitrogenase, e.g. acetylene produces ethylene, HCN gives CH_3NH_2 , nitriles (RCN) afford $RCH_3 + NH_3$ etc. Thus even for simple reactions at least two electrons are necessary for the reduction. Important results were obtained recently by Rees et al. [8] (see also review [6]) who determined the molecular structure of Fe protein and MoFe protein by X-ray analysis. The molecular structure of metal-containing clusters was also elucidated. These results contributed much to the understanding of the electron-transfer mechanism in nitrogenase function, although some details of this mechanism are still not quite clear. There are two locking sites for Fe protein at MoFe protein and two pairs of P-clusters and FeMo cofactors. Each set of clusters functions separately (the distance between two FeMoco is 50 Å).

The first electron acceptor from the external donor is the Fe_4S_4 cluster situated between two subunits of Fe protein. From Fe_4S_4 an electron travels first to a P-cluster, then to FeMo cofactor, and finally to an activated substrate molecule. According to the X-ray data the shortest distance from the Fe_4S_4 cluster of the Fe protein to the P cluster of the MoFe protein is ca 18 Å, that from P cluster to FeMo cofactor is ca 14 Å, and the distance from Fe_4S_4 to FeMoco is ca 32 Å. The P-cluster lies between Fe_4S_4 and FeMoco. Thus, electron transfer in nitrogenase can be presented as:



The distances 18 Å and 14 Å inside the protein complex are typical of electron transfer in biological systems. The reduced Fe protein with two bound MgATP binds to the MoFe protein and a single electron is transferred from the Fe protein to the MoFe protein. This process is coupled to the hydrolysis of two ATP.

For the process *in vivo* flavodoxin is the external electron donor. For isolated nitrogenase, dithionite $\text{S}_2\text{O}_4^{2-}$ is traditionally used as electron donor. If dithionite is the external donor, the oxidized iron protein with 2MgADP (after the electron is transferred) then dissociates from the MoFe protein. This dissociation, which initially seemed necessary for enzyme function, is, however, apparently a result of the salt effect of dithionite, the concentration of which for effective electron transfer must be sufficiently large.

When photo-electron transfer is used with a dye, such as eosin or dibromofluorescein in combination with NADH (and the dithionite concentration is low, ca 4×10^{-4} M), no dissociation of proteins is detected. Kinetic laser spectroscopy helped Syrtsova et al. [9] to follow electron transfer from the Fe protein to the MoFe protein and it was shown that, unlike the situation with dithionite, Fe protein in the complex with MoFe protein could undergo reduction by the photodonor as efficiently as in the free state in solution and electron transfer proceeds in the complex of two proteins without dissociation.

According to X-ray analysis the P-cluster which functions as intermediate electron acceptor from Fe_4S_4 cluster of the Fe protein contains eight iron atoms and seven inorganic sulfur atoms (Figure 3). The P-cluster can be considered as two bridged Fe_4S_4 and Fe_4S_3 clusters and therefore presumably it can be a donor of at least two electrons transferred to FeMo cofactor. When both Fe_4S_n parts of the P-cluster are fully reduced the P-cluster must be a comparatively strong electron donor. Moreover spectroscopic studies indicate that all eight iron atoms can be in ferrous state with a full charge of -4 [10]. Presumably the state of the most reduced form of the P-cluster is still unknown, but this result confirms its strong electron donor properties even if no more electrons are accepted by P-cluster in the process of substrate reduction until it gives up one electron to the FeMo cofactor.

Iron molybdenum cofactor, FeMoco was isolated from MoFe protein for the first time in 1977 by Shah and Brill [11]. Since then the cofactor, which naturally attracted much interest as the probable active site of the enzyme, has been thoroughly studied. Although the structure of isolated cofactor remains unknown X-ray studies by Rees et al. have enabled construction of the internal structure of the protein.

It is a polynuclear complex and consists of two cubane fragments Fe_4S_3 and Fe_3MoS_3 connected by three S^{2-} bridges (Figure 3). The 1:7:9 ratio for Mo:Fe:S in the proposed structure is in agreement with analytical data for FeMoco for the isolated cofactor (Mo:Fe:S = 1:6–8:8–9)

The cluster is connected with the protein matrix through cysteine side groups (Cys 275), a ligand of Fe1 and histidine (His 442) which is a ligand of Mo. These Fe

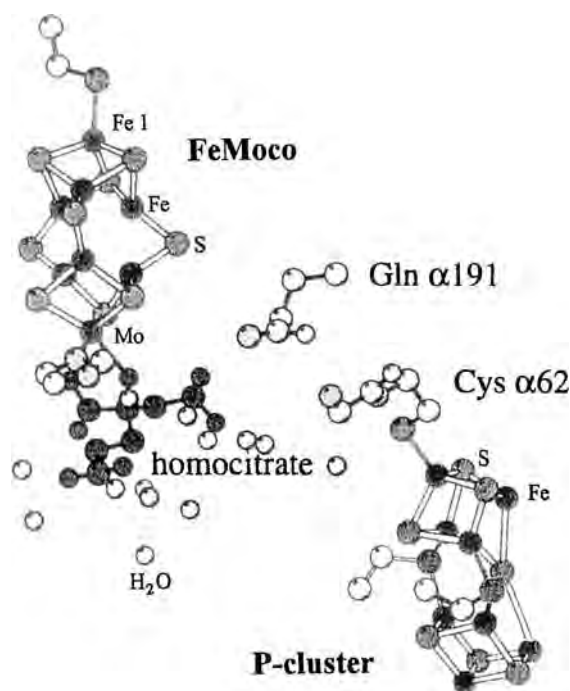


Figure 3. FeMo cofactor, P-cluster and their environment of the MoFe protein from *Azotobacter vinelandii* [6]. This is corrected to take into account that the P-cluster is of the 8Fe–7S type, and not of the 8Fe–8S type as previously believed).

and Mo atoms are on the third-order axis a distance of 7.5 Å from each other. In the structure Mo has octahedral coordination and is connected, in addition to three sulfur atoms, to an N atom of histidine and two O atoms of hydroxyl and carboxyl groups of a homocitrate molecule which was also found to be present in FeMo cofactor when it is isolated from the protein. The tetrahedral coordination found for Fe1 and octahedral for Mo are typical of coordination of these atoms both in model compounds and iron–sulfur proteins. The main peculiarity of the model is that six of the seven iron atoms in the cofactor have a triangular-pyramidal coordination, and are thus coordinatively unsaturated.

The Fe–Fe distances in the cluster were found to be 2.4–2.6 Å, which indicates the existence of some bonding between them. This bonding, evidently stabilizing the cluster, would not, however, prevent coordination of a substrate molecule; therefore, although there is no direct evidence, the substrates, including dinitrogen, are coordinated by several, possibly four or even all six iron atoms when they are activated by FeMoco.

The absence of a large number of bridges binding FeMoco and protein explains why the cofactor can be easily extracted from the protein without loss of its catalytic activity when it is reset again on apoprotein (protein matrix deprived of the cofactor).

The role of molybdenum (if there is no direct Mo–N bonding in the complex with the substrate) is not quite clear, but it can be speculated that Mo^{IV} with d² electronic configuration present in the cofactor reduces the number of electrons (compared

with Fe^{II}) without much changing its redox potential, and this might help activate dinitrogen (if there is certain optimum number of electrons for N_2 activation). Presumably it also changes the polarity of the complex and this might strengthen the activation of bound dinitrogen.

EPR studies of the isolated cofactor in the state reduced by dithionite, FeMoco (s-r) (i.e. semi-reduced) show that it retains the characteristic signal with spin 3/2 observed for the so-called 'M center' (which is in fact FeMoco inside MoFe protein). The broadening of the signal of the isolated FeMoco , compared with the signal of the M center, is attributed to a small change in the ligand sphere of the cofactor upon isolation. In the presence of added thiophenol the EPR signal returns to its form inside the protein apparently because S group of the thiophenol becomes the ligand of the Fe1 atom (instead of cysteine 275 SH group). The cyclic voltammogram of the cofactor on the glass carbon electrode in DMF shows that in addition to the process $\text{FeMoco}(\text{ox}) \rightarrow \text{FeMoco}(\text{s-r})$ at -0.32 V there is the reduction at -1.1 V with the corresponding oxidation at -0.9 V. These waves are ascribed by the authors [12] to the pair $\text{FeMoco}(\text{s-r})/\text{FeMoco}(\text{red})$.

When the Marcus theory of electron transfer was applied to electron transfer in nitrogenase, it was found that non-adiabatic theory is not applicable. It was therefore concluded that an event associated with either MgATP binding or hydrolysis acts to gate electron transfer between Fe protein and MoFe protein [13a]. The role of MgATP might be explained by the necessity to transfer electrons against the thermodynamic potential in the process of electron transfer from the Fe_4S_4 cluster of the Fe protein to the P-cluster of the MoFe protein to create particularly strong electron donor for FeMoco , although the mechanism of its action is not quite clear.

Recent investigations of electron transfer in the tight complex combining the Fe protein isolated from the bacterium *Clostridium pasteurianum* (Cp2) with the MoFe protein isolated from another bacterium *Azotobacter vinelandii* (Av1) demonstrated that primary electron transfer occurs within this complex even in the absence of MgATP and that the latter accelerates electron transfer more than 10 000-fold [13b]. Analysis of this effect shows that MgATP apparently shifts the redox potential of Fe protein (E_0) to a more negative value, therefore changing ΔE (difference in redox potentials of the electron donor and acceptor); this change alone is not, however, likely to be sufficient for the observed nucleotide-dependent rate acceleration. The important observation of this work is that Cp2Av1 is unable to transfer more than one electron to MoFe protein even when MgATP is present. This explains why Cp2Av1 complex is inactive towards any substrates of nitrogenase (even H_2 is not formed) because at least two electrons are required, even for such substrates as acetylene to produce ethylene, and protons to produce dihydrogen.

This supports the view that two electrons are transferred to P-cluster and the second electron requires probably very precise complementarity of the two proteins unattainable in the complex Cp2Av1. Perhaps the transfer of this second electron corresponds to particularly strongly negative value of redox potential.

In conclusion, it can be said that enzymatic reduction of dinitrogen requires substrate coordination on the polynuclear FeMo cofactor. To ensure catalytic reduction of the substrate the reduced cofactor is situated at a distance typical of

electron transfer (14 Å) from the P-cluster, which contains at least two electrons capable of being transferred to FeMoco. MgATP hydrolysis helps to increase the rate of electron transfer to the P-cluster and at least one electron is transferred from the Fe_4S_4 cluster against the thermodynamic potential presumably increasing the electron-donor properties of the P-cluster for subsequent transfer of electrons to MoFe cofactor. In their reduced states both are sufficiently strong reducing agents with redox potentials presumably more negative than -1 V. Using electrochemical terminology the P-cluster can be regarded as a 'nano-electrode' with the catalyst, FeMoco bound to it. It might be thought that the mechanism of catalysis for dinitrogen reduction is close to that for the 'optimum catalyst' considered above. The P-cluster and FeMoco might function in the coupled way in the most difficult stages of dinitrogen reduction in the coordination sphere of FeMoco. Accordingly it was shown that P-clusters are oxidized in a certain step when dinitrogen is reduced by nitrogenase [13a].

6.9 N_2 Reduction in Aprotic Media

Enzymatic dinitrogen reduction involves an electron donor, e.g. flavodoxin in vivo or dithionite in vitro (which we now know can be replaced by photoelectron donor), a system of electron transfer, and a site of dinitrogen activation, where the N_2 molecule is bound and subsequently reduced to ammonia with participation of protons. As we have seen, this site, evidently FeMoco, is itself a well organized molecular system which, in combination with the P-cluster, reduces N_2 by a mechanism of coupled one-electron and multi-electron transfer. If we can use a stronger reducing agent then the system for N_2 activation and reduction presumably need not be so well organized. In aprotic media we can use very strong reducing agents, although the reaction naturally cannot produce hydrazine or ammonia because of the lack of protons. At least stoichiometric reaction can be expected to break the NN bond and to form nitrides from intermediate N_2 complexes and then to produce ammonia upon subsequent addition of an acid.

Until the 1960s, however, dinitrogen was considered so chemically inert that no attempts had been made by investigators working with transition metal compounds in the presence of strong reducing agents to verify the possibility of N_2 reduction—dinitrogen gas was used as an inert atmosphere for conducting various reactions.

In 1964 Vol'pin and Shur published their paper [14] describing the results of dinitrogen reduction in aprotic media. The reaction turned out to be quite general. In the presence of different transition metal compounds, for example $CrCl_3$, $MoCl_5$, WCl_6 , $FeCl_3$, and $TiCl_4$, when N_2 under high pressure (100–150 atm) was reacted with strong reducing agents, for example $LiAlH_4$, $EtMgBr$, or $i-Bu_3Al$, ammonia was produced on acid decomposition of the products formed. The system $Cp_2TiCl_2 + EtMgBr$ ($Cp = \pi-C_5H_5$) in ether was found to be even more active towards N_2 —the yield of NH_3 (after hydrolysis) was 67 mol % with respect to Ti

compound even at atmospheric pressure and nearly quantitative at elevated N_2 pressures. The number of transition metal compounds and possible reductants was later greatly increased by Vol'pin et al. and also by other groups of investigators.

Apart from the compounds already mentioned, vanadium, manganese, and cobalt chlorides, tetra-alkoxy derivatives of titanium, acetylacetonates of V, Cr, Mo, Mn, and Ni, Cp derivatives of Zr and Nb, and triphenyl phosphine complexes of Ti and Fe were found to be active. Later lanthanide complexes were included in the list of dinitrogen-reducing systems, the most effective being compounds of samarium and yttrium.

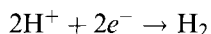
The transition metals of groups IV, V and VI, particularly Ti, V, Cr, Mo, and W, have the strongest N_2 -reducing capacity. Ti compounds are particularly active. In the first row of transition metals, the ammonia yields decrease generally from left to right, in line with the decreasing stability of the metal nitrides. Co and Ni compounds are usually of low or no activity. Palladium, copper and platinum complexes have no activity in any system tested.

Yields of NH_3 (after hydrolysis) depend on the reducing agents. They include such strong reductants as organometallic compounds ($RMgX$, RLi , and R_3Al), metal hydrides ($LiAlH_4$ and LiH), free metals, and aromatic radical ions. Catalytic hydrogenation was not observed, but occasionally H_2 increased the yield of NH_3 (after hydrolysis) in combination with other reducing agents.

Catalytic reduction was, however, occasionally observed. $TiCl_4$ can catalyze the reduction of N_2 by aluminum metal in the presence of $AlBr_3$ at $130^\circ C$ and N_2 pressure of 100 atm. Yields of ammonia (after hydrolysis) usually vary from 0.01 to 1 mol mol $^{-1}$ transition metal compound, indicating that two transition metal atoms participate in the reduction of one N_2 molecule, although in some systems (particularly with very strong reductants) up to 2 mol NH_3 are produced per mol transition metal.

6.10 Dinitrogen Reduction in Protic Media

As has already been mentioned protic media are attractive for N_2 reduction, in particular because hydrazine or ammonia can be directly produced and the search for catalytic reduction is more promising. There is, however, an important obstacle—the strong reducing agent can be unstable in protic surroundings, readily producing dihydrogen:



The choice of the systems active to N_2 in protic solutions must, therefore, naturally be more limited than in aprotic media.

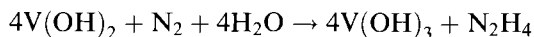
The first reproducible results demonstrating efficient dinitrogen reduction with participation of protons were reported in 1970 [15]. Table 2 lists systems reducing N_2 in the presence of water or methyl alcohol. They are mainly based on V^{II} and

Table 2. Systems reducing N₂ in protic media ($p_{\text{N}_2} \approx 100$ atm).

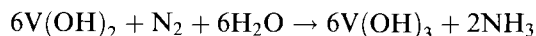
M	Reductant	$T(^{\circ}\text{C})$	Products	Yield (mol mol ⁻¹ M ⁻¹)
Ti ^{II} (d ²)	Na(Hg)	20	N ₂ H ₄ , NH ₃	0.01
V ^{III} (d ³)	V(OH) ₂ + Mg(OH) ₂			
	pH 14.3	20	N ₂ H ₄ , NH ₃	0.65
	pH 12	20	NH ₃	0.35
	V ^{II} + catechol, pH 10.5	20	NH ₃	0.75
Mo ^{III} (d ³)	Ti(OH) ₃	60	N ₂ H ₄ , NH ₃	1
	Ti(OH) ₃ + Mg(OH) ₂	110	N ₂ H ₄ , NH ₃	170
	Cr(OH) ₂	90	N ₂ H ₄ , NH ₃	0.80
	without Mo	90		0.015
	Na(Hg) ($p = 1$ atm)	20	N ₂ H ₄ , NH ₃	1700
	Eu(Hg) ($p = 1$ atm)	20	N ₂ H ₄ , NH ₃	26
Nb ^{III} (d ²)	Nb(OH) ₃	35	N ₂ H ₄ , NH ₃	0.09
Ta ^{III} (d ²)	Ta(OH) ₃	35	N ₂ H ₄	0.02

Mo^{III} compounds, although later Nb^{III}, Ta^{III} and Ti^{II} compounds were also included. It is clear that all the systems found so far are based on d² and d³ electronic configurations. They are active in alkaline solution and include mainly hydroxides, i.e. the systems are heterogeneous. There is also a unique family of homogeneous systems based on solutions of vanadium(II) complexes with catechols. One of the simplest and most effective heterogeneous systems is mixed V^{II}–Mg^{II} hydroxide. The reduction of N₂ occurs in aqueous or alcohol suspensions of freshly prepared hydroxide formed by adding excess alkali to the solution of a mixture of VCl₂ and MgCl₂. The reaction produces hydrazine and ammonia at high rates at room and lower temperatures and atmospheric N₂ pressure.

At high concentrations of alkali (pH 13–14) and high N₂ pressures hydrazine is mainly produced according to the stoichiometry:



At low alkali concentrations (pH 8–12) ammonia is produced directly from dinitrogen without intermediate formation of free hydrazine:



Freshly prepared mixed hydroxide contains vanadium(II) clusters reactive towards dinitrogen. Some indirect evidence indicates that the number of vanadium ions in the clusters activating dinitrogen approaches four or six. For example, introduction of other ions, such as V³⁺ inhibits N₂ reduction and quantitative analysis of the V³⁺ inhibition effect leads to the conclusion that tetramers are the likely species; tetramers are also suggested by analysis of ethane and ethylene formation in the reduction of acetylene.

Kinetic analysis of N_2 reduction shows that the reaction can be regarded as pseudo-homogeneous. Analysis reveals Michaelis–Menten dependence of the reaction rate on dinitrogen pressure. This enables estimation of the enthalpy of dinitrogen complex formation and the activation energy— $\Delta H = -4 \text{ kcal mol}^{-1}$ and $E = 8.4 \text{ kcal mol}^{-1}$. These values indicate that the intermediate complex is very unstable and highly reactive. Mixed V^{II} – Mg^{II} hydroxide is one system that disproves generally accepted views of dinitrogen as very inert molecule. N_2 can be very active in systems that are neither strong bases or acids nor very strong reductants or oxidants. The important condition for high chemical reactivity of N_2 is the possibility of accepting simultaneously at least four electrons by intramolecular electron transfer in an intermediate polynuclear complex including at least four atoms that are electron donors.

6.11 Soluble Complexes of Vanadium (II)

The exact structure of the intermediate vanadium(II) cluster in the mixed V^{II} – Mg^{II} hydroxide and in other hydroxides active towards N_2 is, of course, difficult to elucidate, and it was important to find a homogeneous system reducing N_2 in protic media. This was realized in 1972 with complexes of V^{II} with catechols or substituted aromatic diols and triols which were found to reduce N_2 efficiently in homogeneous water and alcohol solutions [16].

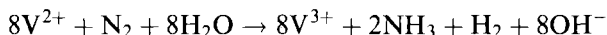
With unsubstituted catechol complexes in water the reaction proceeds in the pH range 8.5 to 13.5 with maximum yields at ca pH 10.5. For substituted catechols the pH range corresponding to the most active complexes reacting with N_2 differs noticeably (Table 3). Later the number of catecholate V^{II} complexes active towards dinitrogen was greatly increased but the family of the V^{II} complexes with aromatic diols and their relationship towards N_2 remain quite unique—no other complexes have yet been found that reduce dinitrogen in protic media, homogeneously, with reasonably high yields of products.

The reaction of N_2 with V^{II} catechol complexes in methanol occurs at room temperature and atmospheric N_2 pressure. The yield of NH_3 , which is the only reaction product, reaches ca 50 % relative to $V^{II} \rightarrow V^{III}$ oxidation. In aqueous so-

Table 3. Dinitrogen reduction by vanadium(II) complexes with aromatic ligands (L) (room temperature, $[V^{II}] = 0.05 \text{ M}$, $[L] = 0.5 \text{ M}$).

L	Solvent	p_{N_2} (atm)	Time (h)	Yield NH_3 (%)	$[NaOH]/[L]^a$ or pH ^b
Catechol	CH_3OH	1	0.03	47	1.14 ^a
Catechol	CH_3OH	15	0.17	75	1.14 ^a
Catechol	H_2O	100	1.5	60	10.5 ^b
Gallic acid	H_2O	100	4.0	48	12.9 ^b
Pyrogallol	H_2O	100	4.0	60	13.5 ^b

lutions such yields are observed only at elevated dinitrogen pressures. In the absence of N_2 a parallel reaction of V^{II} oxidation by the solvent protons proceeds with H_2 evolution. As N_2 pressure increases the yields of NH_3 increase and those of H_2 decrease. But even at the elevated pressure the yield of NH_3 does not exceed 75 % and does not increase when the N_2 pressure is increased further; 25 % of the electrons are used for H_2 formation. Thus, analogous to enzymatic reduction with Mo nitrogenase, the stoichiometry of the reaction at saturating N_2 pressure corresponds to the equation:



This equation including H_2 evolution *coupled* with the reduction of N_2 reflects the polynuclear character of the intermediate complex.

Acetylene is quantitatively reduced by V^{II} catecholate to ethylene with *cis*-deuteroethylene formed selectively from C_2D_2 , also similarly to enzymatic reduction of C_2D_2 by nitrogenase. Distinct from N_2 reduction, the pH range for the reduction of acetylene is much broader than for dinitrogen (from ca pH 5 to concentrated alkali solution). Kinetic studies of the oxidation of vanadium(II) catecholate complex by dinitrogen have led to the reaction equation:

$$-d[V^{II}]/dt = k_1[V^{II}]^2[N_2] + k_2[V^{II}]^{0.5}$$

The first term of the equation corresponds to the reduction of N_2 to NH_3 and the second to the parallel and *independent* evolution of H_2 formed from the solvent protons.

N_2H_4 which could be the intermediate in the reaction is easily and quantitatively reduced to NH_3 in V^{II} -catechol solutions. When N_2 reduction is stopped at its initial stages by addition of an acid or an oxidant (VO_2SO_4) a small quantity of N_2H_4 is found. A kinetic study of the reduction of specially added hydrazine revealed, however, that the rate constant is at least two orders of magnitude smaller than necessary for free hydrazine to be the intermediate producing ammonia. The results show that N_2H_4 is formed by decomposition of an intermediate by acid or oxidant; the intermediate, not being free hydrazine, seems similar to a vanadium hydrazine derivative. Similar results indicating intermediate N_2^{4-} derivative formation were obtained in enzymatic dinitrogen reduction. The second order of vanadium concentration in the rate equation for N_2 reduction, and at the same time the one-half order for H_2 formation, are indicative of the complex polynuclear structure. It is possible, for example, to assume that the active complex contains four vanadium atoms and two complexes are needed to reduce N_2 to NH_3 , whereas a dinuclear complex produced H_2 , and this dinuclear complex is formed in equilibrium dissociation of the tetramer into two dimers. In this case H_2 formation coupled with N_2 reduction could be explained assuming that after ammonia formation by the octamer, for which six vanadium atoms are required, a dimer of V^{II} is formed and this readily produces dihydrogen.

EPR spectra observed for the active complex at a pH of ca 10.5 led to the conclusion that the complex is trinuclear and that ammonia is formed when the trinuclear

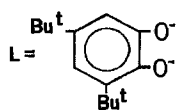
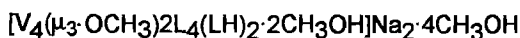
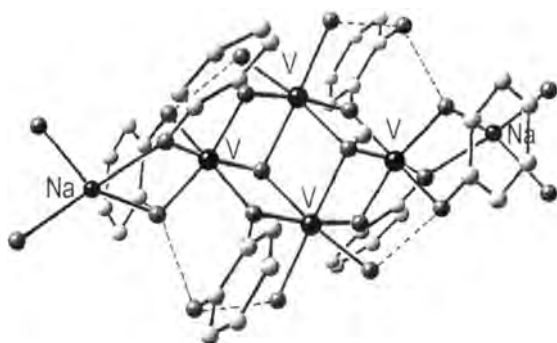


Figure 4. The X-ray structure of vanadium di-*tert*-butyl catecholate complex [18].

clear complex coordinating N_2 reacts with another trinuclear complex, not containing N_2 , to produce two molecules of NH_3 by use of six vanadium electrons [17]. Although this mechanism did not explain the one-half order for (independent) formation of H_2 it was accepted in the paper [17] and in later reviews (e.g. Ref. [2]).

New important information about the structure of the intermediate complex was obtained from the X-ray studies of V^{II} complex with di-*tert*-butylcatecholate [18]. The complex, the structure of which is presented in Figure 4, contains four vanadium ions; two are divalent and two trivalent, but they are indistinguishable, thus their oxidation state is 2.5 and the complex can be regarded as existing in a *semi-reduced* state, similar to the s-r state of FeMoco in the presence of dithionite, which is not sufficiently reduced to activate dinitrogen.

The tetrameric vanadium complex contains also two sodium ions. Each is coordinated by two oxygen atoms of methanol molecules and by two oxygen atoms of different catechol molecules. Because of this coordination, oxygen atoms are μ_2 -bridging Na and V atoms. One of the three independent catechol molecules participates in the coordination of the vanadium atoms by one O only whereas the second atom is protonated and does not participate in the metal coordination. It is apparent that the complex

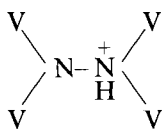


contains the core with two μ_3 -bridges formed by methanol OR groups. When all vanadium ions are in the V^{II} state in the form of the complex active to N_2 this

μ_3 -bridging OR group is probably loosely bound to three V^{2+} ions, and this core containing four V^{2+} ions most probably becomes the site activating N_2 in a complex of the type:



Ultimate intramolecular electron transfer from $4V^{2+}$ to N_2 will produce the hydrazido derivative, particularly on protonation of one of the four nitrogen atoms:



These findings prompted us to reconsider the results of EPR spectra and to make more profound analysis of kinetic data for N_2 reduction by catecholate vanadium(II) complexes. The conclusion was that a tetra-vanadium structure for the complexes is in a better agreement with the EPR spectra than a trinuclear structure; kinetic results also confirmed the tetranuclear structure of the complex [19]. We therefore regard the tetranuclear structure as confirmed for unsubstituted and substituted catecholate V^{II} complexes, at least for those so far investigated.

Thus the conclusion is that tetranuclear complexes are likely to be the active species in the reduction of N_2 to hydrazido derivatives, and then to hydrazine, by reaction with solvent in protic media, whereas octanuclear complexes (or transition states) are needed to transform N_2^{4-} species into two ammonia molecules.

6.12 Catalytic Dinitrogen Reduction

A catalytic system for dinitrogen requires the presence of a sufficiently strong reducing agent that would reduce the oxidized form of the catalytic complex (after reaction with N_2) to the initial reduced state. For example if we could reduce vanadium(III) complexes formed in N_2 reduction by vanadium(II) we would be able to create a catalytic system functioning with the chosen reductant. Finding such a strong reducing agent which is able to reduce V^{III} to V^{II} in *alkaline solutions* is, however, apparently difficult and H_2 is formed instead.

More likely candidates as catalysts from the data of Table 2 are molybdenum(III) complexes which activate N_2 to reduction only in the presence of a stronger reducing agent, such as $Ti(OH)_3$, $Cr(OH)_2$, or $Ta(OH)_3$. Presumably these strong reductants take part in the process, transferring electrons to molybdenum atoms

coordinating dinitrogen. Molybdenum(III) activates N_2 in a di- or polynuclear complex forming an intermediate of the type $Mo \equiv N \equiv N \equiv Mo$ which is unable to produce hydrazine or ammonia readily at the expense of Mo^{III} oxidation to Mo^V or Mo^{VI} . The reaction might become thermodynamically more favorable if a stronger reducing agent situated nearby simultaneously transfers electrons, reducing molybdenum to its initial Mo^{III} state. Therefore to reduce dinitrogen catalytically we might try to construct a system containing a bulk reducing agent which adsorbs the catalytic Mo^{III} complex at the surface and is an electroconductive material, in order to use the electrons from remotely situated atoms. For electrochemical reduction electrons from the cathode can be used if the catalytic complex is adsorbed at the surface of the electrode.

The first catalytic system based on this approach for N_2 reduction in protic media was realized with Mo^{III} as the catalyst and Ti^{III} hydroxide as the reductant [15]. With pure $Ti(OH)_3$ the yields of products of N_2 reduction in the presence of Mo^{III} formed in the process of co-precipitation of both metal hydroxides (or hydroxo complexes) by addition of alkali reaches only equimolar amounts with respect to molybdenum even at elevated temperatures and N_2 pressures. In the presence of salts of some other metals, e.g. Mg^{2+} , Ca^{2+} , or Sr^{2+} , in solution before the addition of alkali, the yields increase and the system becomes catalytic. The effect of magnesium salts was particularly pronounced. Yields of hydrazine and ammonia are increased and at sufficiently high temperatures and pressures reach several hundred turnovers per molybdenum. The highest yields are obtained when the ratio of Mg^{2+} to Ti^{3+} is 1:2. At this ratio a compound of formula $MgTi_2O_4$ is produced and forms fine crystals, as was revealed by X-ray analysis and electron microscopy. The catalytic effect of Mo^{III} is observed when the complexes of molybdenum(III) are adsorbed on the surface of $MgTi_2O_4$. Accordingly, whereas for stoichiometric reduction with mixed hydroxides it is essential to have both metals present in homogeneous solution before addition of alkali, for catalytic reduction $MgTi_2O_4$ can be formed initially without molybdenum. After subsequent addition of the molybdenum compound catalytic activity towards N_2 is observed.

The magnesium–titanium compound $MgTi_2O_4$ has semiconducting properties, and evidently the molybdenum complex with coordinated dinitrogen forms an electron trap on the surface. Dihydrogen is rapidly evolved in the absence of N_2 , particularly at high temperatures. Introduction of molybdenum even in very small amounts compared with titanium strongly inhibits H_2 evolution in the presence of N_2 . Evidently Mo complexes are adsorbed at the active sites of $MgTiO_4$, preventing electron flow to the H_2 evolution centers. The dependence of the reaction rate on N_2 pressure is Michaelis in form, which enables estimation of the equilibrium constant for dinitrogen complex formation and the rate constant for N_2 reduction in the complex. The temperature dependence of the constants gives a value of -7 kcal mol^{-1} and -17 e.u. for the enthalpy and entropy of complex formation; the activation energy, E , for N_2 reduction in the complex is 20 kcal mol^{-1} [20].

It can be mentioned that a titanium(III) compound was recently found [21] to be an efficient electron donor for the Fe_4S_4 cluster in Fe protein of nitrogenase and can therefore be used in N_2 enzymatic reduction.

6.13 Catalytic Dinitrogen Reduction by Amalgams

The mechanism proposed for the catalytic reduction of N_2 by an electroconductive reductant has prompted the use of amalgams as reducing agents. Amalgams such as those formed by sodium and europium are sufficiently strong reductants (redox potentials -1.84 and -1.4 V, respectively) and at the same time they are reasonably stable in contact with water or alcohol. The amalgams can be prepared electrochemically by use of a mercury cathode and passing electron current through the solution containing metal ions; they can, therefore, be used for the electrochemical reduction of dinitrogen.

Introduction of the sodium amalgam has increased the yield of the reduction products, N_2H_4 and NH_3 , in the catalytic system based on Mo^{III} and $MgTi_2O_4$ described above. Obviously the amalgam transfers electrons through $MgTi_2O_4$ to the Mo^{III} catalytic complex and prevents titanium(III) oxidation. It is clear that if conditions could be found under which the catalytic complex were bound directly to the surface of the amalgam, an electron-conducting material such as $MgTi_2O_4$ would be unnecessary.

We found these conditions by introducing surface-active materials to a solution of a specially prepared catalytic complex containing molybdenum and stabilized by magnesium ions [22]. The structure of the complex which was isolated from the solution in its oxidized form is presented on Figure 5 [23]. When it is reduced to the Mo^{III} state the complex becomes an active catalyst of dinitrogen reduction to hydrazine and ammonia by sodium amalgam. Phospholipid (phosphatidylcholine)

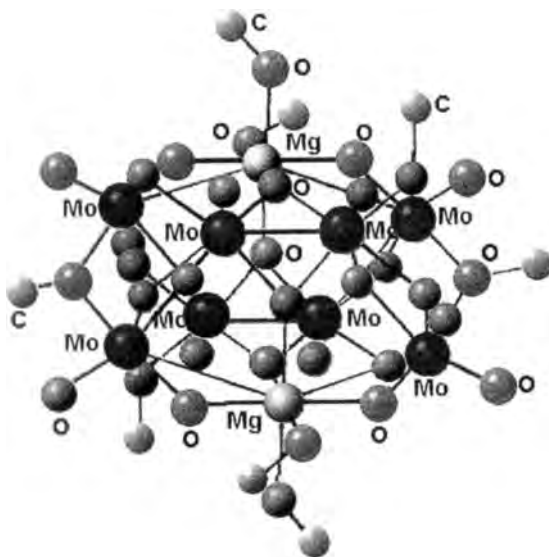


Figure 5. The X-ray structure of the anionic part of the octamolybdenum complex [23].

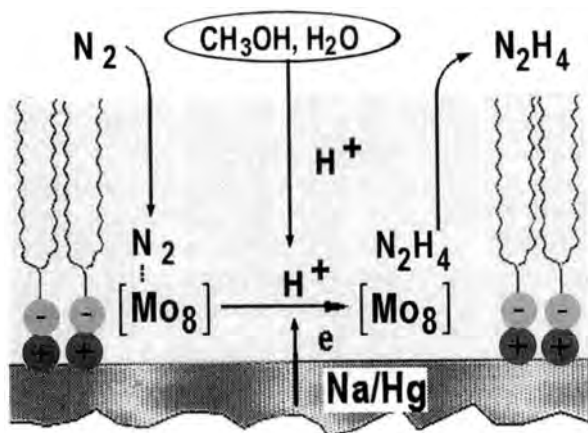


Figure 6. Proposed mechanism of dinitrogen reduction catalyzed by octamolybdenum(III) complex incorporated in the phospholipid film on the amalgam surface.

and also polyvinyl alcohol, both surface-active materials, were found to strongly increase the reaction rates and the products yields.

The yields were found also to increase in the presence of phosphines, particularly trimethyl or tributyl phosphine. After all the improvements of the catalyst and reaction conditions the system became by far the most active of known non-biological catalytic systems for the reduction of dinitrogen at ambient temperature and pressure. The specific activity (the rate of N_2 reduction per mole of the complex) reached and even exceeded that of nitrogenase. Up to 1000 turnovers relative to the molybdenum complex can be observed at atmospheric pressure and more than 10 000 turnovers at elevated N_2 pressures.

The role of the surface-active materials, e.g. phosphatidylcholine, is to form a thin film on the surface of the amalgam, with the catalyst incorporated and thus bound to the surface of the electron donor (Figure 6). With phosphatidylcholine the film is kept at the surface because of attachment of the positive phospholipid heads to the negatively charged surface. Electrons are transferred from the amalgam to the catalytic complex in the process of catalytic reduction. Similarly to the function of the P-cluster in nitrogenase the electron donor participates not only in the initial reduction of molybdenum in the catalytic complex to the Mo^{III} state but also during subsequent steps of substrate reduction. We can therefore speak of 'reductive coaction' of the donor in the process of N_2 reduction, according to the mechanism described in previous sections.

If the complex is reduced to the Mo^{III} state and there is no external electron donor in the system (the amalgam is removed) there is no reduction of dinitrogen, even stoichiometric, confirming the mechanism in which the reducing agent participates directly, in a coupled manner, in the reduction of the substrate which is co-ordinated by the catalytic complex.

More evidence for the participation of the reductant in the catalytic process is the dependence of the rate on the redox potential of the reductant. The reduction rate for the europium amalgam (redox potential -1.4 V compared with -1.84 V for sodium amalgam) is approximately two orders of magnitude smaller than for

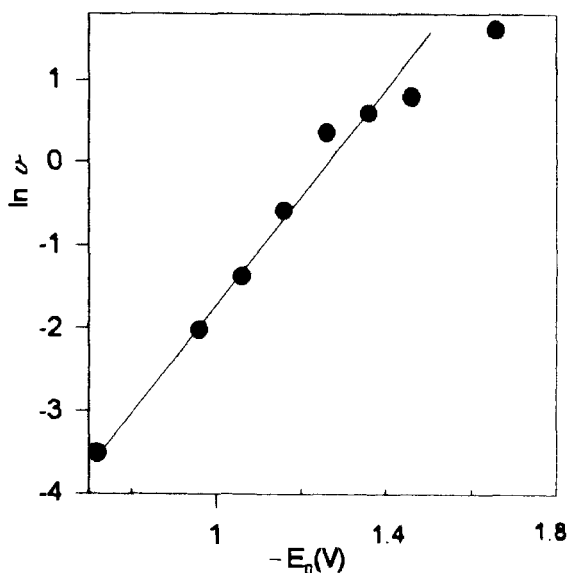


Figure 7. Dependence on induced potential of the rate of formation of ethylene by reduction of acetylene [25]. The catalyst: octamolybdenum cluster (8.5×10^{-6} M); the reductant: Zn amalgam (2 %, w/w); the cocatalyst: thiophenol (4.7×10^{-3} M); $T = 20^\circ\text{C}$; $p_{(\text{C}_2\text{H}_2)} = 100$ mm Hg.

Na(Hg). The dependence of the rate of reaction for acetylene reduction by the Zn amalgam on the induced potential is shown in Figure 7. It is apparent that the dependence follows the Tafel law: $\ln v = A + \alpha E$ (here v is the rate and E is the induced potential).

This dependence was also found for electrochemical reduction of dinitrogen. As has been mentioned, the structure of the catalytic complex presented in Figure 4 corresponds to its oxidized form (Mo^{V} and Mo^{VI}). Unfortunately no crystals suitable for X-ray analysis were obtained for the Mo^{III} state of the complex, but there is evidence that in the reduced state the complex still contains 8Mo and 2Mg. It is possible that on reduction of the complex to the Mo^{III} state the structure becomes less rigid and some coordination sites become open to coordinate N_2 .

6.14 FeMoco as Catalyst for the Reduction of Nitrogenase Substrates at Amalgam Surfaces

As we have already seen, FeMo cofactor of nitrogenase is a polynuclear complex of composition Fe_7MoS_9 (homocitrate), and all the available evidence implies it is the active site at which dinitrogen and other nitrogenase substrates are activated and reduced. Yet despite its first isolation in 1977 the catalytic activity of FeMoco was detected only in 1997, i.e. 20 years later.

One possible reason for this is that, according to the mechanism described above, the cofactor must function in a coupled manner with electron transfer from the

P-cluster which is situated close to FeMoco. Presumably attempts to use it as a catalyst outside the MoFe protein had been made earlier with such reductants as NaBH_4 which functions as a separate entity only during collisions, i.e. comparatively rarely. As has already been mentioned, in FeMoco iron atoms probably co-ordinate dinitrogen activating it to further reduction. No iron complexes have yet been synthesized which function as catalysts for N_2 reduction in protic media, although several iron complexes reducing dinitrogen in *aprotic* media are known (e.g. Ref. [2]). Presumably such complexes will be prepared in the future, but meanwhile in the light of the catalytic mechanism described above it was natural to investigate the catalytic activity of the FeMo cofactor itself on the surface of multi-electron donors such as amalgams.

It was, indeed, found that FeMo cofactor in solution in DMF and NMF is an active catalyst for reduction of acetylene and other nitrogenase substrates by zinc, europium, and sodium amalgams [24, 25]. The reaction proceeds on the surface of the electron donor, thiophenol functions as a cocatalyst, not only as the proton donor but evidently also the cofactor ligand connecting it, in particular, with the surface of the amalgam. Some of the properties of the isolated cofactor, for example formation of ethylene and ethane from acetylene, inhibiting action of carbon monoxide, dihydrogen evolution, etc. are similar to those of the cofactor inside the protein, in particular, when the cofactor is bound to proteins of N_2 -fixing organisms different from that from which FeMoco was isolated. Dinitrogen was found to inhibit acetylene reduction by europium amalgam in the presence of FeMoco, the inhibitive effect being *quantitatively identical* with that observed in the reduction catalyzed by nitrogenase (Figure 8) [26]. The conclusion can therefore be drawn that the catalytic action of FeMoco is similar to that of synthetic molybdenum(III) complexes bound to the surface of the amalgam. To be catalytically active FeMoco

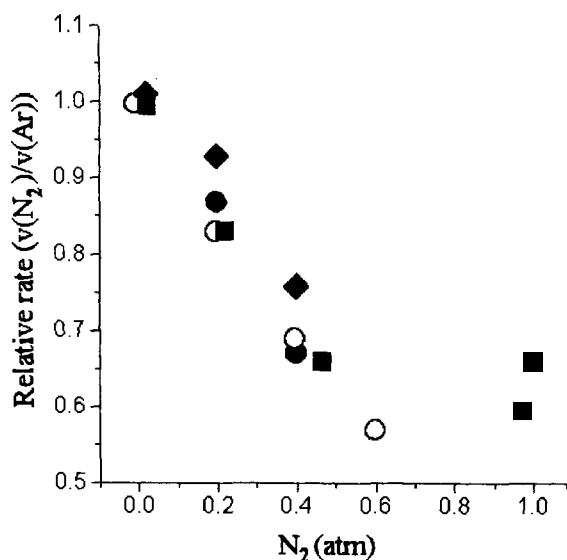


Figure 8. Inhibition of acetylene reduction by dinitrogen in protein and non-protein systems with FeMoco as catalyst, $p_{(\text{C}_2\text{H}_2)} = 10$ mm Hg. ■, isolated FeMoco with Eu amalgam as a reductant [26]; ●, nitrogenase from *A. vinelandii* (wild type) [27]; ◆, mutant DJ540 [28]; ○, wild-type MoFe protein [28].

must be bound to a multi-electron donor (such as amalgam or cathode in electrochemical reduction) and to be open to an acid with a certain pK which ensures synchronous protonation and electron transfer. To reduce dinitrogen it seems to be necessary to have a sufficiently strong acid to protonate the substrate but not to destroy the catalyst, which is less stable than synthetic catalysts in the presence of acids.

If both conditions are fulfilled (the presence of a reducing agent in close vicinity to FeMoco and a proton-donating substance of an appropriate pK) FeMoco can be catalytically active outside the MoFe protein.

In conclusion, it may be said that to achieve catalytic reduction of dinitrogen in both enzymatic and purely chemical systems in protic media it is essential to unite a one-electron reductant and a polynuclear catalyst activating dinitrogen in a single system such that they function in a coupled manner—one-electron transfer from the external reducing agent must be coupled with poly-electron transfer inside the polynuclear catalyst containing the substrate. Hopefully further development of this field along the lines of this mechanism will lead to new active catalytic systems reducing dinitrogen.

References

1. Likhtenshtein, G. I. and Shilov, A. E., *Zh. Fiz. Khim.*, 44, 849, **1970**.
2. Shilov, A. E., *Metal Complexes in Biomimetic Chemical Reactions*, CRC Press, Boca Raton, New York, **1997**.
3. (a) Allen, A. D. and Senoff, C. V., *Chem. Commun.*, 621, **1965**; (b) Hidai, M. and Mizobe, Y., *Chem. Rev.*, 95, 1115, **1995**; (c) Chatt, J., Dilworth, J. R., and Richards, R. L., *Chem. Rev.*, 78, 589, **1978**; (d) Shan, H., Yang, Y., James, A. J. and Sharp P. R., *Science*, 275, 1460, **1997**.
4. Burgess, B. K. and Lowe, D. J., *Chem. Rev.*, 96, 2983, **1996**.
5. Eady, R. R., *Chem. Rev.*, 96, 3013, **1996**.
6. Howard, J. B., and Rees, D. C., *Chem. Rev.*, 96, 2965, **1996**.
7. Gadkari, D., Mörsdorf, G. and Meyer, O., *J. Bacteriol.*, 174, 6840, **1992**.
8. Kim, J. and Rees, D. C., *Nature*, 360, 553, **1992**.
9. Druzhinin, S. Yu., Syrtsova, L. A., Khramov, A. V., Moravsky, A. P. and Shkodina, N. I., *Biochemistry* (Moscow), 61, 480, **1996**.
10. Surerus, K. K., Hendrich, M. P., Christie, P. D., Rottgardt, D., Orme-Johnson, W. H. and Münk, E., *J. Am. Chem. Soc.*, 114, 8579, **1992**.
11. Shah, V. K. and Brill, W. J., *Proc. Natl. Acad. Sci USA*, 74, 3249, **1977**.
12. Schultz, F. A., Greller, S. F., Burgess, B. K., Lough, S. and Newton, W. E., *J. Am. Chem. Soc.*, 107, 5364, **1985**.
13. (a) Lanzilotta, W. N., Parker, V. D. and Seefeldt, *Biochemistry*, 37, 399, **1998**; (b) Chan, J. M., Ryle, M. J. and Seefeldt, *J. Biol. Chem.*, 274, 17593, **1999**.
14. Vol'pin and Shur, V. B., *Dokl. Akad. Nauk SSSR*, 156, 1102, **1964**.
15. (a) Denisov, N. T., Shuvalov, V. F., Shuvalova, N. I., Shilova, A. K. and Shilov, A. E., *Kinet. Katal.*, 11, 813, **1970**; (b) Shilov, A. E., Denisov, N. T., Efimov, O. N., Shuvalov, V. F., Shuvalova, N. I. and Shilova, A. K., *Nature*, 231, 469, **1971**.
16. Nikonova, L. A., Ovcharenko, A. G., Efimov, O. N., Avilov, V. A. and Shilov, A. E., *Kinet. Katal.*, 13, 1602, **1972**.
17. Luneva, N. P., Moravsky, A. P. and Shilov, A. E., *Nouv. J. Chim.*, 5, 21, **1981**.
18. Luneva, N. P., Mironova, S. A., Shilov, A. E., Antipin, M. Yu., Struchkov, Yu. T., *Angew. Chem. Intl. Ed. Engl.*, 32, 1178, **1993**.
19. Dzhabiev, T. S., Mironova, S. A. and Shilov, A. E., *Kinet. Katal.*, 40, 844, **1999**.

20. Denisov, N. T. and Shuvalova, N. I., *React. Kinet. Catal. Lett.*, 4, 431, **1976**.
21. Angove, H. C., Yoo, S. J., Burgess, B. K. and Münck, E., *J. Am. Chem. Soc.*, 119, 8730, **1997**.
22. Didenko, L. P., Gavrilov, A. B., Shilova, A. K., Strelets, V. V., Tsarev, V. N., Shilov, A. E., Machaev, V. D., Banerjee, A. K. and Pospíšil, L., *Nouv. J. Chim.*, 10, 584, **1986**.
23. Antipin, M. Yu., Struchkov, Yu. T., Shilov, A. E. and Shilova, A. K., *Gazz. Chim. Ital.*, 123, 265, **1993**.
24. Bazhenova, T. A., Bazhenova, M. A., Petrova, G. N. and Shilov, A. E., *Kinet. Katal.*, 38, 319, **1997**.
25. Bazhenova, T. A., Bazhenova, M. A., Mironova, S. A., Petrova, G. N., Shilova, A. K., Shuvalova, N. I. and Shilov, A. E., *Inorg. Chim. Acta*, 270, 221, **1998**.
26. Bazhenova, T. A., Bazhenova, M. A., Petrova, G. N. and Shilov, A. E., *Kinet. Katal.*, #6, **1999** (in print).
27. Rivera-Ortiz, J. M., and Burris, R. M., *J. Bacteriol.*, 123, 537, **1975**.
28. Kim, C.-H., Newton, W. E. and Dean, D. R., *Biochemistry*, 34, 2798, **1995**.

7 Transition-metal Complexes as Models of the Active Sites of Hydrogenases*

Cameron E. Forde and Robert H. Morris

7.1 Hydrogen Chemistry

7.1.1 Introduction

Controlling the movement of electrons and protons is vital to life and a variety of biologic systems have evolved with this purpose. Certain enzymes have the ability to separate the protons and electrons of dihydrogen and to harness the energy of this molecule to the synthesis of more complex molecules. Dihydrogen is the simplest molecule and yet the enzymes used to activate it (or to produce it) are amazingly complex. Part of the complexity of hydrogenase enzymes extends from the wealth of oxidation and protonation states of the active site metal cluster. This is due in part to the variety of interactions between dihydrogen and transition metals. While the ability of certain metals to evolve dihydrogen when exposed to acid or even water has been known for a long time, the ability of metals to form hydrides and subsequently the existence of 'non-classical' hydrides or dihydrogen complexes of the metals are more recent discoveries. Long before chemists proposed that dihydrogen forms complexes with transition metals, enzymes had been making use of transition metals to activate dihydrogen.

The chemistry of model systems of hydrogenase enzymes has developed along with the study of the enzymes. Developments in the characterization of the enzyme have spurred the development of model systems that provide a better understanding of the function of the enzyme. Ultimately, a complete understanding of the chemistry of the hydrogenase enzymes will require the synthesis of both areas of study. In this review we consider the work that has been done to characterize the enzyme, focussing on the areas that are amenable for study using model systems. We then

* Portions of this work appeared in the Ph. D. thesis of Cameron E. Forde, University of Toronto, 1997.

consider the model systems that shed light on the spectroscopic properties, the function and the structure of the hydrogenase enzymes. The work on theoretical models is then presented with a view toward a fuller understanding of the enzymes and the development of better models. In order to place the chemistry of hydrogenase enzymes and model systems in the context of known metal hydride and dihydrogen chemistry, we present a brief summary of these fields first.

7.1.2 Metal Hydride Chemistry

The properties of metal hydrides vary a great deal and depend to a large extent upon the metal. For example, the interactions between hydrides and alkali or alkaline earth elements tend to be ionic in nature while more covalent interactions are observed between hydride ligands of later elements (e.g. tin). For the transition metals the M–H bond strength increases going from 3d to 4d to 5d metals. The M–H bond strength is also influenced by the *trans* ligand. That is, the M–H bond is destabilized by high *trans*-influence ligands such as hydride or alkyl. The reactivity of metal hydrides can be described in terms of their ability to transfer a hydride (hydricity) [1] or their ability to transfer a proton (acidity) [2]. The hydricity is higher for the early transition elements with electron-donating ligands.

Transition metal hydride complexes are often highly fluxional. This feature is often reported for polyhydride complexes. An example of this is the report of the solid state and solution structures of the series of the iron group metals $[\text{MH}_3\text{L}_4]^+$ where L is either PMe_3 or PEt_3 [3]. These complexes can adopt a six-coordinate dihydrogen hydride or a seven coordinate trihydride conformation. The dihydrogen hydride conformation can exist in *cis* or *trans* configurations while the trihydride conformation can adopt a tricapped tetrahedral or a classical *cis*-trihydride arrangement. Variable temperature NMR spectra were used to determine the activation parameters for the fluxional processes. The relative stabilities of these different geometries for iron and ruthenium have been determined using *ab initio* calculations [4, 5].

Protonation of a metal hydride is one of the routes by which metal dihydrogen complexes can be formed. Addition of a proton to a hydride is a more facile process than the addition of a proton to a metal. This is due to the greater electronic rearrangement required to protonate a metal center than that required to protonate a hydride ligand. This feature of metal hydrides is a kinetic effect: the ultimate fate of the nascent dihydrogen complex is determined by thermodynamics. Depending upon the relative stabilities, the dihydrogen ligand can oxidize the metal center forming a dihydride, remain coordinated to the metal, or detach from the metal as $\text{H}_2(\text{g})$.

7.1.3 Metal Dihydrogen Chemistry

The physical properties of dihydrogen are well understood. Free hydrogen gas has a bond length of 0.74 Å, with a bond strength of 103 kcal mol^{−1}. The potential of proton reduction is set at 0 V for the normal hydrogen electrode (NHE) under

standard conditions (pH 0, 25 °C). This potential is pH dependent and a potential of -414 mV is calculated for pH 7 according to the Nernst equation. This equation also reveals that as the concentration of dihydrogen decreases from saturation the potential will rise. There is thus a range of potentials over which dihydrogen can be formed depending upon the conditions.

The first stable dihydrogen complex reported was $\text{W}(\text{H}_2)(\text{CO})_3(\text{PPr}^i_3)_2$ [6]. Several hundred stable dihydrogen complexes have been reported since this initial report and several reviews have appeared covering the synthesis, properties and reactivity of dihydrogen complexes [7–9]. The majority of the transition metals form stable dihydrogen complexes. Of interest with respect to the chemistry of hydrogenase enzymes are the dihydrogen complexes of nickel and of iron. There are numerous iron dihydrogen complexes but only one nickel complex has been reported. The nickel(0) complex $\text{Ni}(\text{H}_2)(\text{CO})_3$ is formed by photolysis of $\text{Ni}(\text{CO})_4$ in a hydrogen matrix at low temperature [10]. If the hydrogenase enzymes make use of nickel dihydrogen interactions then much of the chemistry of these enzymes has no precedence in the current literature. We attribute the lack of stable nickel dihydrogen complexes to the reduced ability of nickel to participate in stabilizing π -back donation with the dihydrogen ligand. Iron is better able to form stable dihydrogen complexes as its d-orbitals are higher in energy and able to stabilize the interaction with dihydrogen. More iron dihydrogen chemistry is discussed later in the section on modeling.

There are two components of the bonding interaction between a dihydrogen ligand and a transition metal. The interaction between dihydrogen and a transition metal is described as having $\sigma(\text{H}_2)$ -to- $\sigma(\text{metal})$ and $\pi(\text{metal})$ -to- $\sigma^*(\text{H}_2)$ components. The extent of the σ -donation is controlled by a variety of factors including the metal and the oxidation state as well as the ancillary ligands, especially the ligand *trans* to the H_2 ligand. The π -back-donation contribution confers stability, though homolytic cleavage results from too much back bonding. A positive charge on the metal enhances the σ -interaction with dicationic complexes with dihydrogen *trans* to a π -acid ligand being particularly strongly bonded [11].

The H–H bond length increases upon coordination to a metal center. The H–H separation in a dihydrogen complex can be determined by a number of techniques. Neutron diffraction yields this value directly, though there is a need to correct for the vibrational motion of the ligand [12]. X-ray crystallography is a less useful technique because of the poor X-ray scattering characteristics of the dihydrogen ligand. An NMR method is commonly used to correlate the spin–lattice relaxation time with the H–H bond length [13, 14]. The motion of the dihydrogen ligand has an effect on the relaxation time and two H–H separations are calculated for each of the two regimes depending upon whether the rotation of the dihydrogen moiety is greater or less than the spectrometer frequency. It is not uncommon for the rotational frequency of the dihydrogen ligand to be greater than 500 MHz! Another NMR technique to probe the H–H separation relies on the determination of the coupling constant between hydrogen and deuterium observed in the analogous HD complex. The H–D coupling constant decreases with a linear correlation from that of the free HD gas (43.2 Hz [15]) as the separation between the nuclei increases. These methods are quite useful for characterizing diamagnetic model complexes but

have limited applicability to the characterization of any H_2 ligands that might be present in an enzyme containing paramagnetic centers.

The acidity of a dihydrogen molecule increases upon coordination. The pK_a decreases from 35 for free H_2 gas (we find that in THF it is greater than 46 with pK_a $HPCy_3^+$ at 9.7) as a function of the metal and its oxidation state as well as the ancillary ligands. A very wide range of pK_a values has been reported for transition-metal dihydrogen complexes. There are now several examples of dihydrogen complexes with pK_a values below zero. The acidity of dihydrogen complexes of the d^6 transition metals can be estimated [16]. This method is applicable to the dihydrogen complexes of iron(II). The predictive powers of this method demonstrate that the properties of a dihydrogen ligand are influenced by the ancillary ligands. This is a direct result of the ability of ancillary ligands to influence the electrochemistry of the metal center.

The effect of the metal center on the properties of the dihydrogen ligand has been probed for the series of complexes $trans-[M(H_2)H(R_2PCH_2CH_2PR_2)_2]^+$ ($M = Fe, Ru, Os$; $R = Ph, Et$) [17]. These dihydrogen complexes are formed by protonation of the dihydride precursor compounds. The stretching frequency of the terminal hydride (ν_{M-H}) is found to increase down the period while the H–H separation in the dihydrogen ligand is approximately the same for iron and ruthenium but is greater for osmium. The lability of the dihydrogen ligand as judged by the H/D exchange properties increases from Os to Fe to Ru.

The ligand *trans* to the dihydrogen ligand is found to have a profound effect on the properties of the dihydrogen ligand. An early report compared the effect of chloride versus hydride in the series $trans-[Ru(H_2)X(R_2PCH_2CH_2PR_2)_2]^+$ ($R = Ph, Et$) [18]. The H–H separation in the dihydrogen ligand is longer when the *trans* ligand is chloride than hydride. This is attributed to the fact that chloride has a weak ligand field. Therefore the t_{2g} π -bonding d-electrons are higher in energy and back-donate more strongly into the σ^* orbital of the dihydrogen ligand.

An experimental report of the effect of the ligand *trans* to dihydrogen confirmed these theoretical results. The acidity of a series of ruthenium and osmium complexes, $trans-[M(H_2)XL_2]^{n+}$ ($L = Ph_2P(CH_2)_3PPh_2$; $X = CO, Cl, H$) has been determined [19]. The complex $[Ru(H_2)(CO)(dppp)_2]^{2+}$ is highly acidic with an estimated pK_a of -6 .

The effects of the *trans* ligand on the acidity of some dihydrogen complexes of ruthenium and osmium with the general formula $trans-[M(H_2)L(H_2PCH_2CH_2PH_2)_2]^{n+}$ have been quantified using density functional theory [20]. The ligand, L , affects the stability of the dihydrogen ligand as well as the stability of the conjugate base hydride, both of which influence the acidity of the dihydrogen complex. Ligands which destabilize the dihydrogen ligand while stabilizing the conjugate base hydride complex will lead to the most acidic dihydrogen complexes. The effect can be broken down in terms of the role of the ligand as a sigma donor and either a π -acceptor or π -donor. Strong sigma donor ligands (like hydride or alkyl) destabilize the conjugate base hydride and result in less acidic dihydrogen complexes. Strong π -donating ligands stabilize the dihydrogen ligand and destabilize the conjugate base hydride resulting in a less acidic dihydrogen complex. The most acidic dihydrogen com-

plexes result when the *trans* ligand is a strong π -acceptor ligand. Such a ligand stabilizes the conjugate base hydride and destabilizes the dihydrogen ligand. This result is of importance to the chemistry of hydrogenases as the strong π -acceptor ligands CN and CO are implicated as discussed later.

The effects of the ancillary ligand, L, on the M–H₂ bond dissociation energy in the chromium, molybdenum and tungsten complexes, ML(CO)₄(H₂), have been determined using ab initio calculations [21]. In this report it was found that the stability of the dihydrogen ligand increases when L is a strong σ -donor ligand while strong π -accepting ligands weaken the metal–dihydrogen bond. Conversely, the degree of activation of the dihydrogen ligand increases when the number of π -accepting ligands is reduced.

The dihydrogen ligand is often considered to be a highly labile ligand that interacts only transiently with metals. This perception is due in part to the properties of the Kubas complex that is only stable in an atmosphere of dihydrogen. Indeed, there are many other examples of highly labile dihydrogen ligands. However, this is not to say that all dihydrogen ligands are readily displaced from metal centers. The substitution of dihydrogen from *trans*-[Fe(H₂)H(dppe)₂]⁺ by a neutral ligand (MeCN, PhCN, or DMSO) is an example of a dihydrogen ligand which is difficult to displace [22]. In this case the kinetic and activation parameters support a mechanism in which one arm of one of a chelating diphosphine ligand opens up a coordination site for attack of the neutral ligand.

7.2 Hydrogenase Enzymes

7.2.1 Introduction to Hydrogenase Enzymes

Hydrogenases (EC 1.12.2.1) are enzymes that catalyze the two-electron oxidation of dihydrogen as well as the reduction of protons to form H₂. A given hydrogenase enzyme is optimized either for H₂ uptake or H₂ production, though there is also an example of a bidirectional hydrogenase (*Clostridium pasteurianum* hydrogenase I). The function of a given hydrogenase enzyme (H₂ uptake as opposed to H₂ forming) is determined by the physiological conditions like pH and factors inherent to the enzyme such as the co-factors that are present. These enzymes are found in lower life forms (archaebacteria, bacteria, and algae) and exist in both soluble and membrane-bound (both periplasmic and cytosolic) forms. With the exception of the H₂-producing methylenetetrahydromethanopterin dehydrogenase [23], all hydrogenases are metalloenzymes with redox-active iron–sulfur clusters and an active site metal cluster where H₂ is either consumed or formed. The metal content is used to subdivide the hydrogenase enzymes into three categories: iron-only [Fe], iron–nickel [FeNi] and iron–nickel–selenium [FeNiSe]-hydrogenases. These three categories of hydrogenase enzymes are distinct, though the [FeNiSe]-hydrogenase enzymes exhibit more resemblance to the [FeNi]-hydrogenases than they do to the [Fe]-hydrogenase

enzymes. The majority of hydrogenase enzymes are of the [FeNi] variety and these have also been the most studied. The hydrogenase enzymes have a number of interesting properties that have been modeled in a number of ways. In order to put the model chemistry into context we will present the properties of these enzymes in this section before considering the model systems in the following section.

Several recent reviews cover the model chemistry of [FeNi]-hydrogenases. The role of nickel in the active site of [FeNi]-hydrogenases has been reviewed [24]. This report concludes that a redox active role for the nickel ion in [FeNi]-hydrogenase enzymes is not supported by the current model chemistry. The involvement of cysteine ligands and/or the iron center is proposed to account for the redox activity of [FeNi]-hydrogenase enzymes. The nickel thiolate model chemistry is the subject of another review that raises the possibility of the involvement of nickel(I) hydrido complexes in the catalytic cycle of [FeNi]-hydrogenase [25]. The chemistry of nickel thiolate model complexes has been reviewed in order to elucidate the preferred oxidation state and coordination chemistry of nickel with relevance to the active site of [FeNi]-hydrogenases [26]. Nickel is known to take on a variety of roles in biology and these roles have also been reviewed [27–29].

The hydrogenase enzymes are very complex and a number of techniques have been used to probe the properties of these enzymes. Part of the complexity of hydrogenase enzymes is due to the different redox and protonation states in which the enzymes can exist. The presence of a variety of protonation and redox states is to be expected from enzymes whose function is to turn protons into dihydrogen (or vice versa). The existence of multiple redox and protonation states greatly complicates studies of the enzyme. The different redox states of the enzyme were first identified in relation to the different EPR signals that are observed. In the next section we consider the EPR evidence about the active sites of [Fe]-, [FeNi]- and [FeNiSe]-hydrogenase enzymes. A system of nomenclature to describe these various redox states will be developed in this section. We then present results of the oxidative and reductive titrations that have been reported to characterize the different redox states. Another useful technique used to characterize hydrogenase enzymes is infrared spectroscopy. A number of signals are observed for these enzymes that are not normally associated with protein samples. This section is rounded out with a description of some of the other techniques that have been used to explore the properties of the active sites of hydrogenases. After having presented the spectroscopic characterization we present the experiments that have been reported on the characterization of the function of these enzymes. We end our discussion of hydrogenase enzymes with the solid state structural characterization of the [FeNi]-, [FeNiSe]- and [Fe]-hydrogenase enzymes.

7.2.2 Spectroscopic Characterization of Hydrogenase Enzymes

Electron paramagnetic resonance

One of the techniques that have been used extensively to characterize hydrogenase enzymes is electron paramagnetic resonance. There are several paramagnetic

Table 1. Some examples of the EPR parameters observed for the various states of [FeNi]-hydrogenase enzymes from different sources.

Organism	State	<i>g</i> Values	Refs
<i>D. gigas</i>	A	2.31, 2.23, 2.02	31, 32
	B	2.33, 2.16, 2.02	
	C	2.19, 2.16, 2.02	
<i>C. vinosum</i>	A	2.34, 2.16, 2.01	33
	B	2.32, 2.24, 2.01	
<i>D. vulgaris</i> (Hildenborough)	A	2.31, 2.23, 2.02	31
	B	2.33, 2.16, 2.02	
	C	2.19, 2.16, 2.02	
<i>D. vulgaris</i> (Hildenborough) cytoplasmic	A	2.32, 2.23, 2.0	34
	B	2.33, 2.16, 2.0	
	C	2.19, 2.14, 2.01	
<i>T. roseopersicina</i>	A	2.32, 2.23, 2.01	35
	B	2.33, 2.17, 2.01	
	C	2.19, 2.14, 2.01	

centers in the various metal-containing hydrogenases. Of interest to this work are the EPR signals associated with the active site. The active sites of the hydrogenase enzymes exist in different redox and protonation states, some of which give rise to EPR signals. Different EPR signals are observed for the [FeNi]-, [FeNiSe]-, and [Fe]-hydrogenases. There are also other states that are not redox active and in the case of the [FeNi]-hydrogenases, we will present these states in the discussion of the infrared properties below.

The active sites of [FeNi]-hydrogenases give rise to a number of interesting EPR spectra. There are three EPR active states labeled **A**, **B** and **C**. Each of these states produces a rhombic EPR spectrum. Data for a variety of different [FeNi]-hydrogenases are collected in Table 1. These signals have been assigned to the Ni ion on the basis of ⁶¹Ni-labeling studies [30].

The [FeNi]-hydrogenase from *Desulfovibrio gigas* was studied by electron spin echo envelope modulation (ESEEM) spectroscopy in the **A** and **C** states [36]. The two states differ in their solvent accessibility as determined by exchange with solvent deuterons. The **A** state is solvent inaccessible while the **C** state is solvent accessible. Coupling to a ¹⁴N nucleus is observed in both states. The solvent accessibility of these two states has been confirmed by ENDOR spectroscopy. This study reveals two types of exchangeable proton species in the **C** state [37]. One of these protons interacts less strongly with the paramagnetic center and is consistent with a bound water or hydroxide ligand. The second proton species interacts more strongly and is not consistent with assignment as a hydride. This ligand is possibly a dihydrogen ligand or an agostic interaction. Oxidation of the **C** state produces the **B** state which retains only one exchangeable proton species. This species has a smaller coupling consistent with a water or hydroxide ligand. A comparison of these three states using Q-band pulsed ENDOR on ⁵⁷Fe and natural-abundance Fe [FeNi]-hydrogenases

from both *D. gigas* and *D. desulfuricans* reveals that the non-protein bridge present in the A state is broken in the other two states [38]. This work also assigns the oxidation states of the active site metal ions in the A state as [Fe(II)Ni(III)] where the iron ion is low spin, $S = 0$.

The active sites of [Fe]-hydrogenases exhibit different EPR spectra than the [FeNi]-hydrogenases. An early study of [Fe]-hydrogenase enzymes from *Desulfovibrio vulgaris* (Hildenborough), *Megasphaera elsdenii*, and two from *Clostridium pasteurianum* revealed that these enzymes exhibit signals due to $[4\text{Fe-4S}]^+$ clusters in their reduced state and more complex signals when oxidized [39]. These authors conclude that the active site of all four have S greater than 0 and integer, which in the oxidized state is exchange-coupled to an $S = 1/2$ species, most likely a low spin Fe(III) center.

The active sites of the [Fe]-hydrogenases from *Megasphaera elsdenii* and *Desulfovibrio vulgaris* (Hildenborough) have been investigated with one- and two-dimensional pulsed EPR spectroscopy [40]. The presence of a nitrogen-containing ligand was detected in the active sites of both enzymes. Unusual quadrupole values suggest a non-protein source for these nitrogen-containing ligands, consistent with cyanide ligands. The presence of an imidazole ring from a histidine residue is also suggested based on these EPR measurements, and this residue is likely part of a proton shuttle.

Infra-red absorption spectroscopy

The infrared spectra of hydrogenase enzymes exhibit absorbances in a region that is not normally associated with protein samples. This region, $1900\text{--}2100\text{ cm}^{-1}$ is more commonly associated with molecules with triple bonds. As we will see later this absorption can be attributed to carbonyl and cyanide ligands at the active site. In this section we consider the evidence from infra-red absorption spectroscopy as it pertains to the active sites of hydrogenase enzymes. Once again, we present the work on [FeNi]-hydrogenases and then the [Fe]-hydrogenases.

Studies of the infrared spectra carbon monoxide inhibited forms of [FeNi]-hydrogenase revealed that the native protein exhibits absorbances at energies not normally associated with protein samples. These absorbances in the $1900\text{--}2100\text{ cm}^{-1}$ region are also observed in [Fe]-hydrogenase samples. This absorption is attributed to the cyanide and carbonyl ligands at the active site metal centers. Cyanide and carbon monoxide are not commonly found as ligands to metal centers in metalloproteins. The different redox states of the enzymes give rise to different absorption spectra.

Exposure of the [FeNi]-hydrogenase from *Chromatium vinosum* to carbon monoxide produces a band in the infrared spectrum at 2060 cm^{-1} [41]. A shift to 2017 cm^{-1} is observed when ^{13}CO is employed. This band is in addition to the three bands at 2082, 2069 and 1929 cm^{-1} that are attributed to the native cyanide and carbonyl ligands. The two weak bands in the region $2040\text{--}2100\text{ cm}^{-1}$ are separated by $12\text{--}16\text{ cm}^{-1}$ and the separation of the average of these weak bands from the strong band shifts according to the state of the enzyme [42]. Labeling studies, using

Table 2. Infrared absorption wavenumbers in the range of 1900–2100 cm^{-1} associated with various states of the active site of the [FeNi]-hydrogenase enzymes from *C. vinosum* and *D. gigas*.

State	$\nu_{\text{CN}}(\text{sym})$	$\nu_{\text{CN}}(\text{asym})$	ν_{CO}	Ref.
<i>Chromatium vinosum</i>				
A/B	2093	2081	1944	41, 42
C	2088	2076	1950	
R	2075	2060	1936	
<i>Desulfovibrio gigas</i>				
A	2093	2083	1947	44, 45
SU	2099	2089	1950	
B	2090	2079	1946	
SI'	2069	2055	1914	
SI''	2085	2075	1934	
C	2086	2073	1952	
R	2073	2060	1940	

^{15}N or ^{13}C , and chemical analyzes have implicated one carbon monoxide molecule and two cyanide groups [43].

In the case of the [FeNi]-hydrogenase of *Desulfovibrio gigas* IR absorption in the 1900–2100 cm^{-1} region has been assigned for each of the redox-active states [44]. These data are collected in Table 2. This study revealed the presence of an EPR silent state labeled SU that exists as a mixture of two protonation states. The changes in IR properties have been used to determine the electrochemical potentials required for the changes in redox state. These data are presented in the following section.

The unusual IR properties of [FeNi]-hydrogenases are shared by the [Fe]-hydrogenases [46]. Analysis of the spectra of the [Fe]-hydrogenase of *D. vulgaris* obtained under a variety of redox conditions strongly indicate that [Fe]-hydrogenases contain a low-spin Fe ion in the active site with one CN group and one CO molecule as intrinsic, non-protein ligands [47].

Electrochemical titrations

Reductive titrations of the [FeNi]-hydrogenase from *Chromatium vinosum* were performed by variation of the H_2 -partial pressure [48]. Changes in the redox state of the active site were monitored by loss of the EPR signal. The reduction potential of the active site exhibits a pH dependence of $-60 \text{ mV (pH unit)}^{-1}$. This dependence suggests that the reduction of the active site is coupled with protonation.

The electrochemical potentials of different states of the [FeNi]-hydrogenase enzyme from *D. gigas* have been probed using oxidative titrations at pH 8.0 [49, 50]. In addition to the redox events of the iron-sulfur clusters the data are best fit to a model involving four different active site redox states between 0 and -400 mV . The potentials of these four redox states are collected in Table 3.

Table 3. Mid-point reduction potentials (mV relative to the NHE) reported for [FeNi]-hydrogenase enzymes under the given conditions.

Organism	A-SU	B-SI	SI-C	C-R	pH/T	Ref.
<i>C. vinosum</i>	-115	-115	nr	nr	8.0/30	48
<i>D. gigas</i>	nr	-150	-330	-370	8.0/nr	50
<i>D. gigas</i>	-210	-135	-365	-430	7.7/40	44

nr = not reported

The periplasmic [Fe]-hydrogenase from *Desulfovibrio vulgaris* (Hildenborough) exists in two different catalytic forms: as isolated the protein is O₂-insensitive; upon reduction the protein becomes active and O₂-sensitive [51]. EPR-monitored redox titrations reveal a single reduction of the active site at a potential of -307 mV, just above the onset potential of H₂ production.

Other techniques

Two techniques that are particularly useful in the characterization of hydrogenase enzymes are Mössbauer and X-ray absorption spectroscopies. At low temperature (4.2 K), the [3Fe-xS] cluster exhibits a paramagnetic Mössbauer spectrum typical for oxidized [3Fe-xS] clusters. At higher temperatures (greater than 20 K), the paramagnetic spectrum collapses into a quadrupole doublet with parameters magnitude of δ EQ magnitude of -0.7 ± 0.06 mm s⁻¹ and δ = 0.36 ± 0.06 mm s⁻¹, typical of high-spin Fe(III). The observed isomer shift is slightly larger than those observed for the three-iron clusters in *D. gigas* ferredoxin II [52] and in *Azotobacter vinelandii* ferredoxin I [53] and may indicate a different iron coordination environment. When *D. gigas* hydrogenase is poised at potentials lower than -80 mV (relative to the normal hydrogen electrode), the [3Fe-xS] cluster is reduced and becomes EPR-silent. The Mössbauer data indicate that the reduced [3Fe-xS] cluster remains intact, i.e. it does not interconvert into a [4Fe-4S] cluster. Also, the electronic properties of the reduced [3Fe-xS] cluster suggest that it is magnetically isolated from the other paramagnetic centers [54].

X-ray absorption spectroscopy is a useful technique to probe the ligand environment of the nickel ion at the active site. Early EXAFS experiments using the NiK-edge on the [FeNi]-hydrogenase from *Thiobacillus roseopersicina* in the C state suggested the involvement of an unusual nickel-iron cluster [55]. When these studies were extended to compare the three EPR active states (A, B and C) and two EPR silent states (SI and R) no significant change in the edge energy is observed [56]. The data are best fit to a model involving six-coordinate nickel with a mixture of N/O- and S-donor ligands. Similar results are obtained for the [FeNi]-hydrogenase from *Alcaligenes eutrophus* in the as-isolated A state [57]. Upon reduction a model with four S-donor ligands with a Ni-S distance of 2.19 Å is appropriate. The incorporation of an iron atom in accordance with the crystallographic results (vide infra) improves the fit of the model to the data. However, the EXAFS technique is limited

in that it is difficult to distinguish between S and Fe scattering atoms at distances greater than 2.4 Å.

7.2.3 Hydrogenase Function

The function of a hydrogenase enzyme is either to produce H_2 or to oxidize H_2 . The [FeNi]-hydrogenases, in general, function as H_2 -uptake enzymes, though there are examples of [FeNi]-hydrogenases that evolve H_2 (e.g. *Pyrococcus furiosus*). Another generalization that can be made is that [Fe]-hydrogenase enzymes are 10 to 100 times as active as the [FeNi]-hydrogenase enzymes. However this greater activity comes at the price of greater oxygen sensitivity. While [FeNi]-hydrogenases are deactivated to varying extents by exposure to oxygen, [Fe]-hydrogenases are irreversibly deactivated by oxygen. The [FeNiSe]-hydrogenases are much less sensitive to exposure to oxygen.

Different patterns in the pH dependence of hydrogenase activity have been observed with enzymes purified from different species of *Desulfovibrio*. With the cytoplasmic hydrogenase from *Desulfovibrio baculatus* strain 9974, the pH optima in H_2 production and uptake were respectively 4.0 and 7.5 with a higher activity in production than in uptake. This contrasts with the periplasmic hydrogenase from *Desulfovibrio vulgaris* (Hildenborough). In this case the highest exchange activity was near pH 5.5. The periplasmic hydrogenase from *Desulfovibrio gigas* has the same pH optimum in the exchange (7.5–8.0) as in the H_2 uptake. The ratio of H_2 to HD production is greater than one for the first of these enzymes and below one for the latter two enzymes [58]. The absolute activities cannot be compared due to the effect of enzyme concentration on both the H_2 -uptake and H_2 -evolution assays [59].

7.2.4 Structural Characterization of Hydrogenase Enzymes

The structural characterization of hydrogenase enzymes has clarified much of the mystery that had surrounded the active sites of these enzymes. The report of the crystal structure of the [FeNi]-hydrogenase from *D. gigas* [60] revealed that the active site of this enzyme contained nickel and a second metal later identified as iron (PDB 1frv and 2frv) [45]. The nickel ion is coordinated by four cysteine residues. Two of these residues form a bridge to the iron ion. The second reported structure also contains a third bridging ligand that these authors suggest is most likely hydroxide. No other protein-based ligands coordinate these metals, though the iron ion has three other ligands that were modeled as water in the original structure. The later structure model used two cyanide ligands and one carbon monoxide ligand.

A second [FeNi]-hydrogenase structure, from *Desulfovibrio vulgaris* (Miyazaki F), revealed a similar active site cluster (PDB 1h2a) [61]. Like the structure of the *D. gigas* enzyme, the active site cluster consists of a nickel ion coordinated by four cysteine residues, two of which form a bridge to the iron ion. The iron ion has three nonprotein ligands that are proposed to be the diatomics S=O, CO and CN mole-

cules. In this case the third bridging atom is proposed to be sulfide as hydrogen sulfide (0.37 equiv.) is released on incubation under H_2 in the presence of cytochrome c3 or methylviologen [62]. The X-ray crystal structure of the reduced form of *D. vulgaris* (Miyazaki F) [FeNi]-hydrogenase reveals an overall structure that is very similar to that of the oxidized form, with the exception that the third monatomic bridge is absent, leaving this site unoccupied [63]. The coordinates of one other structure, the [FeNi]-hydrogenase enzyme from *D. fructosovorans*, have been deposited (PDB 1frf).

The single crystal X-ray diffraction structure of the [FeNiSe]-hydrogenase from *Desulfomicrobium baculatum* in the reduced, active form has also been reported [64]. The active site metal cluster is similar to those of the [FeNi]-hydrogenases reported with some interesting differences. The most obvious difference is the presence of a selenocysteine residue in place of one of the terminal cysteine residues. The reduced active site of *D. baculatum* has a nickel-iron distance that is 0.4 Å shorter than in the oxidized *D. gigas* enzyme. Like the reduced *D. vulgaris* enzyme, the bridging ligand is absent in the reduced *D. baculatum* hydrogenase.

The structures of two [Fe]-hydrogenase enzymes have also been reported. The structure of the [Fe]-hydrogenases from *Clostridium pasteurianum* reveals that the active site H-cluster of the enzyme is composed of a typical [4Fe-4S] cubane bridged via a cysteine thiolate to a binuclear Fe center (PDB 1feh) [65]. The structure of the [Fe]-hydrogenase from *Desulfovibrio desulfuricans* reveals this same arrangement (PDB 1hfc) [66]. These two crystal structure reports differ in their assignment of the bridging ligands of the two iron atoms of the binuclear cluster. The structure of the binuclear cluster from *C. pasteurianum* is reported to have two sulfides and one carbon monoxide as bridging ligands. In place of the sulfide bridges the binuclear cluster from *D. desulfuricans* is modeled with a bridging 1,3-propanedithiol molecule. The iron atoms are modeled as having octahedral coordination geometries with carbonyl or cyanide molecules. The presence of an iron moiety with CO and CN ligands in all types of hydrogenases suggests that this functional unit is incorporated for its ability to activate dihydrogen [66].

The structure of the CO inhibited form of the [Fe]-hydrogenase from *Clostridium pasteurianum* has also been reported (PDB 1c4c) [67]. The structural characterization indicates the addition of a single molecule of carbon monoxide. Carbon monoxide binds to an iron atom of the binuclear iron center at the site of a terminally bound water molecule in the native state (PDB 1c4a).

7.3 Modeling with Transition-metal Complexes

7.3.1 Introduction

We have shown in the previous section that there are a number of unusual properties of hydrogenase enzymes. In this section we present the work that has appeared in the literature toward modeling these unusual properties. As we will see there are a number of cases where the development of model systems has led to a greater

understanding of the enzyme. That is, after all, the goal of making model complexes. In the following presentation of model systems we will focus on the ways in which the model chemistry provides an improved understanding of the hydrogenase enzymes.

The presentation of the modeling of the hydrogenase enzymes is divided into four sections based on the aspect of the hydrogenase enzyme that is being modeled; spectroscopic, structural, functional and theoretical modeling. Spectroscopic models attempt to reproduce the unusual spectroscopic features that characterize the hydrogenase enzymes. These include EPR, IR and electrochemical properties. The structural aspects of the enzyme active site have been modeled through attempts to synthesize a complex or cluster with similar coordination environments as the enzyme active site. This type of modeling is usually assessed based upon the ability to reproduce metrical parameters such bond lengths or angles. The abilities of the enzymes to convert protons to dihydrogen (or vice versa) and to catalyze the exchange of H^+/H_2 comprise the functional aspects of the enzyme system that have been modeled with transition metal complexes. Theoretical techniques have also been employed to better understand the chemistry of hydrogenase enzymes. In the following sections we present the work on each of these types of modeling systems.

7.3.2 Spectroscopic Modeling

Many spectroscopic models have focussed on reproducing the unusual EPR properties of the different paramagnetic states of the active sites of the hydrogenase enzymes. Model chemistry should be instrumental in determining the coordination geometry and oxidation state of the paramagnetic center. As we mentioned above, the nickel ion has been implicated as the source of the EPR signals of the active site and model chemistry has focussed on monomeric nickel complexes.

The Ni(III) complexes of *N*-mercaptoacetylglucyl-L-histidine and *N*-mercaptoacetylglucylglycylglycine clearly show the rhombic EPR pattern and *g* values similar to the Ni(III) chromophore of hydrogenases [68]. These results suggested that the Ni(III) center of hydrogenases contains one cysteine sulfur coordination as equatorial ligand in a tetragonal geometry. In addition, an axial nitrogen ligand and a sulfur-rich Ni(III) site, as in an S4 donor set, were thought to be ruled out.

A number of model systems have attempted to reproduce the anomalous IR spectra of [FeNi]-hydrogenases. Initial efforts focussed on cyanide, carbon monoxide and nitric oxide complexes as these ligands are known to absorb in this portion of the infrared spectrum [69].

Some iron and nickel cyanide and carbonyl complexes have been reported as models of the [FeNi]-hydrogenase enzymes. The preparation and structures of the trigonal bipyramidal nickel and iron complexes with the tetradentate ligands tris(2-phenylthiol)phosphine (PS3) and tris(3-phenyl-2-thiophenyl)phosphine (PS3*) have been reported [70, 71]. The nickel carbonyl complex $[\text{Ni}(\text{PS3}^*)(\text{CO})]^{2-}$ exhibits ν_{CO} at 2029 cm^{-1} compared with the value of 1940 cm^{-1} for the iron carbonyl complex $[\text{Fe}(\text{PS3}^*)(\text{CO})]^{2-}$. Both of these complexes lose CO upon oxidation. The use of cyanide in place of carbon monoxide allows for the preparation of both $[\text{Fe}^{\text{II}}(\text{PS3})(\text{CN})]^{2-}$ and $[\text{Fe}^{\text{III}}(\text{PS3}^*)(\text{CN})]^-$ complexes. The IR properties of

Table 4. Selected IR properties of some carbonyl and cyanide complexes of nickel and iron with the PS3 and PS3* ligands [70, 71].

Complex	ν_{CN}	ν_{CO}
$[\text{Ni}^{\text{II}}(\text{PS3}^*)(\text{CO})]^{2-}$	na	2029
$[\text{Fe}^{\text{II}}(\text{PS3}^*)(\text{CO})]^{2-}$	na	1940
$[\text{Fe}^{\text{II}}(\text{PS3})(\text{CN})]^{2-}$	2070	na
$[\text{Fe}^{\text{III}}(\text{PS3}^*)(\text{CN})]^{-}$	2094	na
$[\text{Fe}^{\text{II}}(\text{PS3})(\text{CN})(\text{CO})]^{2-}$	2079	1904
$[\text{Fe}^{\text{III}}(\text{PS3})(\text{CN})(\text{CO})]^{-}$	2108	2006

these complexes are collected in Table 4. Addition of carbon monoxide to $[\text{Fe}^{\text{II}}(\text{PS3})(\text{CN})]^{2-}$ produces the six-coordinate complex $[\text{Fe}^{\text{II}}(\text{PS3})(\text{CN})(\text{CO})]^{2-}$ where the cyanide ligand remains *trans* to the phosphine. This latter complex can be oxidized electrochemically and increases in both ν_{CN} and ν_{CO} are observed.

The work of Darensbourg et al. has superseded these early model systems. A series of model compounds with the core unit $\text{Fe}(\text{CO})_2(\text{CN})$ or $\text{Fe}(\text{CO})(\text{CN})_2$ were found to reproduce the unique IR absorption spectra of [FeNi]-hydrogenases very well. The IR spectrum of the [FeNi]-hydrogenase enzyme from *D. gigas* in the A state exhibits bands at 1947, 2093, and 2083 cm^{-1} . The IR spectrum of the iron(II) model complex K $[\text{CpFe}(\text{CO})(\text{CN})_2]$ in acetonitrile exhibits absorption bands at 1949, 2094, and 2088 cm^{-1} which are assigned to the ν_{CO} , the symmetric ν_{CN} and the asymmetric ν_{CN} , respectively. The energies and peak-widths at half-maximum of this absorption are sensitive to the oxidation state of the iron center, to the medium and to the counter-ion. Polar media produce broad bands with peak width at half-maximum of the ν_{CO} band of 17 cm^{-1} in water. The use of non-polar solvents is required to achieve the narrow (4 cm^{-1}) peak width at half-maximum observed for the enzyme.

In spite of their structural and amino acid sequence differences, Fe-only and Ni-containing hydrogenases achieve the same catalytic reactions. A chemical modification of histidine residues using a highly specific reagent (pentaammineruthenium II) has been carried out on *Desulfovibrio vulgaris* Hildenborough Fe-hydrogenase and *Desulfovibrio desulfuricans* Norway Ni-Fe-Se-hydrogenase. The preliminary results suggest the existence of a general mechanism involving histidine residues in the two groups of hydrogenases. These residues may be part of the histidine-containing motive shown to be present in both Fe- and Ni-Fe-hydrogenase sequences by Hydrophobic Cluster Analysis. This analysis suggests a functional role for the small subunit of *Desulfovibrio vulgaris* Hildenborough [Fe]-hydrogenase [72].

7.3.3 Functional Modeling

As mentioned in the introduction, the addition of acid, or in some cases even water (e.g. the alkali metals), to metals can result in the evolution of hydrogen. The

potential role of nickel dihydrogen complexes in metal-containing hydrogenases was proposed early in the history of hydrogenase literature [73]. The report of a nickel(II) complex that produces dihydrogen electrochemically was later reported [74]. This was followed by a report of the production of dihydrogen by protonation of a nickel(I) complex [75]. However, the key to modeling the active sites of hydrogenase enzymes requires the ability to do more than evolve dihydrogen. Ideally what is needed in a successful model is the ability to not only evolve dihydrogen but also to activate dihydrogen. In this section we present the work on the model systems that mimic the function of hydrogenase enzymes.

One interesting model system incorporates nickel(II) into the rubredoxin protein scaffold [76]. Rubredoxins are electron-transport proteins with a redox-active mononuclear iron center coordinated by four cysteine residues. The nickel-substituted rubredoxin evolves H_2 and HD when exposed to D_2 . This system is much less active than the native enzymes with activities less than an order-of-magnitude below [FeNi]- and [FeNiSe]-hydrogenases. The ratio of H_2 to $H_2 + HD$ initially produced is used as an indicator of the mechanism. The Ni-rubredoxin model system has ratios in the range 0.45–0.60. Values of this ratio around 0.3 are indicative of heterolytic cleavage of the D_2 unit while values closer to 1 support a homolytic activation mechanism. Like the hydrogenase enzymes, the model system is inhibited by carbon monoxide. The concentration of CO required for 50 % inhibition is similar to that required for [Fe]-hydrogenase from *D. vulgaris* but much lower than that required for 50 % inhibition of the [FeNi]-hydrogenase enzymes.

Model systems that couple H_2 oxidation with the reduction of a cofactor have been reported. The complex Cp^*L_2RuH catalyzes the reduction of NAD [77] or methyl viologen [78] under dihydrogen. This system demonstrates that a ruthenium model system can catalyze the activation of hydrogen without the benefit of the protein scaffold.

An iron(II) hydride model system presents the possibility that protonation can occur at the cyanide ligand [79]. The site of protonation in the complexes $trans\text{-}FeH(CN)(R_2PCH_2CH_2PR_2)_2$ is controlled by the nature of the substituents R of the chelating diphosphine ligands. When the substituents are ethyl groups the site of protonation is the hydride ligand and the stable dihydrogen complex $trans\text{-}[Fe(H_2)(CN)(Et_2PCH_2CH_2PEt_2)_2]^+$ is formed. When the substituents are phenyl groups the site of protonation is at cyanide forming the hydrogen isocyanide ligand in the complex $trans\text{-}[Fe(H)(CNH)(Ph_2PCH_2CH_2PPh_2)_2]^+$. This variation in reactivity is attributed to the greater electron-donating ability of the alkyl-substituted phosphine ligands. The presence of more electron-donating ethyl groups results in a more basic hydride and thus a less acidic dihydrogen complex. Presumably the less electron-donating phenyl groups result in a dihydrogen complex that is more acidic than the corresponding hydrogen isocyanide ligand.

Two very acidic iron(II) dihydrogen complexes have been reported that have either carbonyl or hydrogen isocyanide ligands [11]. The complexes $trans\text{-}[Fe(H_2)(L)(Ph_2PCH_2CH_2PPh_2)_2]^{2+}$ ($L = CO, CNH$) are prepared by addition of triflic acid to the hydrido complexes $trans\text{-}[FeH(CO)(Ph_2PCH_2CH_2PPh_2)_2]^+$ or $trans\text{-}FeH(CN)(Ph_2PCH_2CH_2PPh_2)_2$. The short H–H separations in these dihydrogen complexes, as determined by NMR methods, suggest that there is very little back donation from the metal to the H_2 unit. Some degree of back-donation

has been thought to be necessary for the stabilization of the metal–dihydrogen interaction.

The analogous ruthenium and osmium complexes [80, 81] demonstrate similar reactivity. The series of complexes $\text{trans-[M(H}_2\text{)(CN)L}_2\text{]}^+$ and $\text{trans-[M(H}_2\text{)(CNH)L}_2\text{]}^{2+}$, where M = Fe, Ru, Os and L = bidentate phosphine, are prepared by protonation of the hydrido precursor complexes using triflic acid. The ruthenium complexes are the least stable and the dihydrogen ligand dissociates and is replaced by the triflate anion. The exposure of $\text{trans-[Ru(OTf)(CNH)L}_2\text{](OTf)}$ to 1 atm H_2 results in the elimination of triflic acid and produces a mixture of $\text{trans-[Ru(H}_2\text{)(CN)L}_2\text{]}^+$ and $\text{trans-[Ru(H)(CNH)L}_2\text{]}^+$ with the ratio of these two complexes being controlled by the electronic nature of the bidentate phosphine ligands. As mentioned above for the analogous iron complexes, the more electron-donating phosphine donor ligands stabilize the formation of the dihydrogen complex while the hydrido analog is favored by less electron-donating phosphine ligands.

One of the intriguing features of hydrogenase enzymes is their ability both to activate and to produce dihydrogen at neutral pH. This feature suggests that there is a hydrido species that can be protonated at neutral pH, or in other words a dihydrogen species with a $\text{p}K_{\text{a}}$ near 7. The ability of metals to lower the $\text{p}K_{\text{a}}$ of dihydrogen from 35 in the gas was discussed in the section on dihydrogen chemistry. There are other sites of potential protonation that must be considered. Two examples of such sites are the cysteine thiolates and the cyanide ligands at the active site. Protonation of ligands in the coordination sphere alters the properties of the active site. For example the protonation of thiolato donors results in an increase in the lability of this ligand [82].

7.3.4 Structural Modeling

Several reports have been published of complexes that model the binuclear active sites of [FeNi]-, [FeNiSe]- and [Fe]-hydrogenases. Most of these efforts have focussed on reproducing the metrical parameters that have been reported for the corresponding enzyme. Initially efforts centered on modeling a tetrathiolato nickel center thought to be the active site of [FeNi]-hydrogenases. The revelation that the active site is an iron–nickel heterodimer has prompted revision of the models. Much of the nickel thiolate model chemistry through 1995 has been reviewed [24–26] and in the following section we will focus on recent results that model the known binuclear active sites. Efforts to model the heterodimeric nickel–iron center will be presented first followed by the di-iron model complexes.

A nickel–iron complex is formed from the reaction of the nickel(II) complex of the tetradentate ligand *N,N'*-diethyl-3,7-diazaanonane-1,9-dithiolate with $\text{Fe(CO)}_2(\text{NO})_2$ [83]. The carbonyl ligands on the iron are displaced and the thiolato donors assume a bridging mode leaving two terminal nitrosyl ligands about the four-coordinate iron center. X-ray crystallography revealed that the dimer has a short Fe–Ni separation of 2.797(1) Å and Fe–N–O angles of 167.0(5) and 174.6(5)°. The infrared spectrum exhibits two intense bands attributed to the symmetric and asymmetric stretching modes of the nitrosyl ligands at 1663 and 1624 cm^{-1} .

A binuclear nickel-iron complex is formed by the reaction of $[\text{Fe}(\text{CO})\text{N}(\text{CH}_2\text{CH}_2\text{S})_3]^-$ with $\text{NiCl}_2(\text{dppe})$ under an atmosphere of carbon monoxide [84]. One of the chloride ligands is displaced from nickel and two of the thiolato donors adopt bridging modes while the iron becomes six-coordinate by addition of one CO ligand. The dimer is characterized by a long Fe–Ni separation of 3.308 Å, much longer than that found reported for the hydrogenase enzyme of *D. gigas* [60]. The IR spectrum exhibits intense absorptions at 1944 and 2000 cm^{-1} which is assigned to the axial and equatorial CO ligands, respectively.

Two recent reports present the displacement of carbon monoxide ligands by addition of cyanide to iron carbonyl dimers. In the first report [85] the addition of cyanide to the known complexes $[\text{Fe}(\text{CO})_3]_2(\mu\text{-SMe})_2$ (see Ref. [86].) or $[\text{Fe}(\text{CO})_3]_2(\mu^2\text{-SCH}_2\text{CH}_2\text{CH}_2\text{S})$ (see Ref. [87].) results in the formation of $[\text{Fe}(\text{CN})(\text{CO})_2]_2(\mu\text{-SMe})_2^{2-}$ or $[\text{Fe}(\text{CN})(\text{CO})_2]_2(\mu^2\text{-SCH}_2\text{CH}_2\text{CH}_2\text{S})^{2-}$, respectively. The synthesis and structure of the latter complex is also the subject of the second report [88]. Attempts to prepare a monocyano-substituted complex were unsuccessful and the use of excess cyanide lead to the formation of the same dicyano complex. X-ray crystallographic studies of $(\text{Ph}_4\text{P})_2[\text{Fe}(\text{CN})(\text{CO})_2]_2(\mu\text{-SMe})_2$ were foiled by the co-crystallization of isomers where the methyl thiolate ligands are disposed to create a mixture of diequatorial and equatorial, axial isomers. These isomers are in equilibrium and the latter isomer is favored four to one. X-ray crystallographic studies of $(\text{Et}_4\text{N})_2[\text{Fe}(\text{CN})(\text{CO})_2]_2(\mu^2\text{-SCH}_2\text{CH}_2\text{CH}_2\text{S})$ reveal a short Fe–Fe separation 2.517 Å. This distance is within bonding range and shorter than the 2.6 Å separation observed in the two protein structures.

7.3.5 Theoretical Modeling

The crystallographic studies have provided the theoretical studies with the fodder to make models to better understand the chemistry of the active sites of $[\text{FeNi}]$ - and $[\text{Fe}]$ -hydrogenases. The theoretical models start with the coordinates from the X-ray crystal structures and use density functional theory (DFT) to handle the complexity of these transition-metal systems. The geometries are optimized and the energies calculated using some level of theory. The catalytic cycle is then explored by preparing a number of models using assumptions about what species are involved in the catalytic cycle. In the presentation of the theoretical models that follows we will present the assumptions of each model system and the implications about the chemistry of the active site that are gleaned.

In one model system, that uses DFT and the B3LYP level of theory, the dinuclear cluster is assumed to be neutral in all states [89]. The active site coordinates are taken from the crystal structure of the $[\text{FeNi}]$ -hydrogenase from *D. gigas* [60] and two cyanide ligands and one carbonyl ligand are added. The cysteine residues are modeled as either HS^- or H_2S . The bridging ligands are modeled as HS^- since H_2S results in dissociation of these ligands. This model has reasonable metal thiolate distances (2.8–3.0 Å) and a bent structure with a Fe–S–Ni angle close to 90°. The terminal cysteine residues are modeled in the same manner: as two thiolates, two thiols, or one of each. Taken together with the assumption of cluster neutrality,

each of these states requires a different set of oxidation states for the two metals. The model with two terminal HS ligands uses Ni(III) and Fe(III) oxidation states to maintain overall neutrality. This model is ruled out as the reaction with H₂ is calculated to be far too exothermic. The other two models more faithfully reproduce the experimental results. The model with two terminal H₂S ligands requires Ni(II)–Fe(II) oxidation states for the cluster while the mixed H₂S/HS-model needs Ni(III)–Fe(II) or Ni(II)–Fe(III) oxidation states. Of these two models, the mixed ligand system reproduces the experimental energetics. In this model only the iron is found as a site for H₂ binding. The catalytic cycle suggested by these calculations involves transfer of a proton from the iron-bound dihydrogen to a bridging HS-ligand. This newly formed H₂S bridge dissociates from the nickel center and one of the cyanide ligands forms a Fe–CN–Ni bridge. A mechanism where this proton is transferred to a protein residue cannot be ruled out. Throughout this mechanism of H₂ oxidation the formal oxidation states of the metals do not change. This apparent contradiction is due to the formal assignment of hydride ligands as H whereas thiol hydrogens are treated as H⁺. Thus the two electrons from H₂ oxidation are allotted to the hydride ligand without changing the oxidation state of the metals. One of the merits of this model is the low energy barrier for the H₂ activation step that is in good agreement with the experimental value. The catalytic cycle proceeds with a hydride transfer from iron to nickel.

A second model of [FeNi]-hydrogenase, that also uses DFT with the B3LYP level of theory, uses the infrared spectroscopy results as a check of the quality of the model in a given state [90]. This test makes use of the observation that the C–O stretching frequencies correlate well with the C–O bond length [91]. Since the C–O stretching frequency is sensitive to changes in the electron density of the iron center, it reflects the electronic distribution. In this manner the ability of the model to reproduce the electronic state is assessed. In this model system the cysteine residues are modeled as methyl thiolate ligands and the charge on the metal cluster is not restricted to neutrality. One of the main features of this model is the ability of the thiolate bridges to fold when one of the terminal thiolates is protonated. The mechanism starts with one of these bent structures. The **SI** state exists as a mixture of protonation states which in this model are [(MeS)₂Ni(μ-MeS)₂Fe(CN)₂(CO)]²⁻ and [(MeS)(MeSH)Ni(μ-MeS)₂Fe(CN)₂(CO)]⁻. The latter complex reacts with H₂ and again the iron is found to be the site of H₂ activation. The mechanism proceeds by oxidation of the nickel(II) ion. The dihydrogen unit is split heterolytically to form (MeSH)₂Ni(μ-H)(μ-MeS)₂Fe(CN)₂(CO). This cluster loses a proton from a terminal methane thiol ligand followed by a rearrangement where the hydride ligand is transferred as a proton to regenerate the methane thiol ligand and form nickel(I). The oxidation of the nickel(I) center and loss of a proton from one of the methane thiol ligands recreates the initial species of the catalytic cycle.

In a third theoretical model the [FeNi]-hydrogenase from *D. gigas* is modeled using a hybrid density functional theory–molecular mechanics (DFT/MM) method [92]. In this model approximately 30 atoms of the active site (including the four cysteine residues) are modeled with DFT while molecular mechanics is used for the rest of the atoms within a 7 Å radius (about 300 atoms). The next shell includes about 10 000 protein and solvent atoms within 27 Å of the active site whose posi-

tions are not optimized. A 45 Å radius shell of water molecules rounds out the model. The inclusion of the protein and water matrix provides an improvement over the previous models that use a vacuum medium. This is reflected by the observation that the calculated C–O stretching frequencies are consistently lower when the protein and solvent matrix are excluded. The active states of the enzyme are modeled with a bridging hydride ligand replacing the bridging oxide of the inactive form. Thus the model of the active site in the **SI** state can be represented as $[(\text{Cys})_2\text{Ni}(\mu\text{-H})(\mu\text{-Cys})_2\text{Fe}(\text{CN})_2(\text{CO})]^{3-}$. Unlike the previous two models, nickel is invoked as the site of dihydrogen attack in this model, though an exhaustive search for alternative binding sites was not performed. The attack of dihydrogen on the nickel ion results in heterolytic activation with the formation of a nickel hydride and a protonated cysteine residue.

A DFT model of the [Fe]-hydrogenase from *C. pasteurianum* has also appeared [93]. This model uses $[(\text{MeS})(\text{CO})(\text{CN})\text{Fe}(\mu\text{-S})_2(\mu\text{-CO})\text{Fe}(\text{CO})(\text{CN})]^{z-}$, where z is the overall charge on the cluster. One of the unique features of this model is that the two bridging sulfides are redox active, being represented as either two sulfide, S^{2-} , ions or as one persulfide, S_2^{2-} , ion, a difference of two electrons. A similar property has not been proposed for the bridging cysteines in the [FeNi]-hydrogenase models. The bridging carbonyl ligand is found to have a low energy barrier to shifting to coordination to the distal iron. This distal iron atom is also a site of dihydrogen coordination, though the binding is weak. There is a low energy path to transfer of a proton to one of the bridging sulfides.

7.4 Conclusions

Much information on the nature of the active sites of hydrogenase enzymes has been gleaned from studies on the enzymes as well as from studies of model systems. The information we have presented here demonstrates how each of these areas of study has contributed towards illuminating the chemistry of the hydrogenase enzymes. While the enzyme studies reveal much about the possible mechanisms by which hydrogenase enzymes might operate, it is the modeling studies that will provide the information required for a full understanding of these complex enzymatic systems. Modeling studies reveal much of the hidden workings of the enzymes. The techniques are complementary. Studies of the hydrogenase enzymes provide the scaffold around which modeling studies can build a viable mechanism of dihydrogen activation or production.

A number of generalities can be drawn from the similarities that are observed between the three classes of enzymes, [Fe]-, [FeNi]-, and [FeNiSe]-hydrogenases. The similarities in the structure of the active sites are the most pertinent for the purposes of modeling experiments. The three classes of enzymes share a common iron center with two cyanide ligands and one carbon monoxide ligand. This moiety was first proposed from experiments on the enzyme and confirmed by model studies. This $[\text{Fe}(\text{CN})_2(\text{CO})]$ moiety is connected to a second metal ion which is either

nickel or iron, depending on the class of hydrogenase enzyme. This second metal is potentially redox active and is bridged to the dicyano carbonyl iron center via two cysteine residues. This second metal center has two terminal ligands that are either cysteine or selenocysteine. These similarities suggest a common mechanism of H_2 activation for all three classes of hydrogenase enzyme. Given that no model nickel compound has been reported to activate dihydrogen we are left to conclude that it is the $Fe(CN)_2(CO)$ unit which is responsible for H_2 -activation. The Ni-61 EPR studies would then suggest that the second metal site could act as a hydride reservoir. For now this is merely speculation though it does account for some of the interesting properties of the enzymes.

In addition to the common features of the three classes of hydrogenase it is instructive to examine the differences that exist between them. One of the most obvious differences is the function of the different classes of hydrogenase. The [Fe]-hydrogenase enzymes are primarily H_2 -activating while the [FeNi]- and [FeNiSe]-hydrogenase enzymes are H_2 -producing. This is an over-simplification as there are hydrogenase enzymes that are able both to form H_2 as well as to activate H_2 . It does, however, suggest that the enzymes have evolved with a preference for the metal which better enables it to perform the task of either activating or producing dihydrogen.

References

1. T. Y. Cheng, B. S. Brunschwig, R. M. Bullock, *J. Am. Chem. Soc.* **120** (1998) 13121–13137.
2. S. S. Kristj  nsd  ttir, J. R. Norton, in A. Dedieu (Ed.): *Transition Metal Hydrides: Recent Advances in Theory and Experiment*, VCH, New York 1992.
3. D. G. Gusev, R. H  bener, P. Burger, O. Orama, H. Berke, *J. Am. Chem. Soc.* **119** (1997) 3716–3731.
4. F. Maseras, N. Koga, K. Morokuma, *Organometallics* **13** (1994) 4008–4016.
5. F. Maseras, M. Duran, A. Lled  s, J. Bertr  n, *J. Am. Chem. Soc.* **113** (1991) 2879–2884.
6. G. J. Kubas, R. R. Ryan, B. I. Swanson, P. J. Vergamini, H. J. Wasserman, *J. Am. Chem. Soc.* **106** (1984) 451–452.
7. G. J. Kubas, *Acc. Chem. Res.* **21** (1988) 120–128.
8. P. G. Jessop, R. H. Morris, *Coord. Chem. Rev.* **121** (1992) 155–284.
9. D. M. Heinekey, W. J. J. Oldham, *Chem. Rev.* **93** (1993) 913–926.
10. R. L. Sweany, M. A. Polito, A. Moroz, *Organometallics* **8** (1989) 2305–2308.
11. C. E. Forde, S. E. Landau, R. H. Morris, *J. Chem. Soc., Dalton Trans.* (1997) 1663–1664.
12. P. A. Maltby, M. Schlaf, M. Steinbeck, A. J. Lough, R. H. Morris, W. T. Klooster, T. F. Koetzle, R. C. Srivastava, *J. Am. Chem. Soc.* **118** (1996) 5396–5407.
13. D. G. Hamilton, R. H. Crabtree, *J. Am. Chem. Soc.* **110** (1988) 4126–4133.
14. M. T. Bautista, K. A. Earl, P. A. Maltby, R. H. Morris, C. T. Schweitzer, A. Sella, *J. Am. Chem. Soc.* **110** (1988) 7031–7036.
15. P. E. Bloyce, A. J. Rest, I. Whitwell, W. A. G. Graham, R. Holmes-Smith, *J. Chem. Soc., Chem. Commun.* (1988) 846–848.
16. R. H. Morris, *Inorg. Chem.* **31** (1992) 1471–1478.
17. M. T. Bautista, E. P. Cappellani, S. D. Drouin, R. H. Morris, C. T. Schweitzer, A. Sella, J. Zubkowski, *J. Am. Chem. Soc.* **113** (1991) 4876–4887.
18. B. Chin, A. J. Lough, R. H. Morris, C. T. Schweitzer, C. D'Agostino, *Inorg. Chem.* **33** (1994) 6278–6288.
19. E. Rocchini, A. Mezzetti, H. R  gger, U. Burckhardt, V. Gramlich, A. Del Zotto, P. Martinuzzi, P. Rigo, *Inorg. Chem.* **36** (1997) 711–720.

20. Z. Xu, I. Bytheway, G. Jia, Z. Lin, *Organometallics* 18 (1999) 1761–1766.
21. S. Dapprich, G. Frenking, *Organometallics* 15 (1996) 4547–4551.
22. M. G. Basallote, J. Durán, M. J. Fernandez-Trujillo, G. González, M. A. Máñez, M. Martí-nez, *Inorg. Chem.* 37 (1998) 1623–1628.
23. C. Zirngibl, W. Van Dongen, B. Schworer, R. Von Bunau, M. Richter, A. Klein, R. K. Thauer, *Eur. J. Biochem.* 208 (1992) 511–520.
24. M. J. Maroney, *Comments Inorg. Chem.* 17 (1995) 347–375.
25. C. M. Goldman, P. K. Mascharak, *Comments Inorg. Chem.* 18 (1995) 1–25.
26. J. C. Fontecilla-Camps, *J. Biol. Inorg. Chem.* 1 (1996) 91–98.
27. J. R. J. Lancaster, *The Bioinorganic Chemistry of Nickel*, VCH, New York 1988.
28. S. W. Ragsdale, *Curr. Opin. Chem. Biol.* 2 (1998) 208–215.
29. M. J. Maroney, *Curr. Opin. Chem. Biol.* 3 (1999) 188–199.
30. J. J. Moura, I. Moura, B. H. Huynh, H. J. Kruger, M. Teixeira, R. C. DuVarney, D. V. Der-Vartanian, A. V. Xavier, H. D. Peck, Jr., J. LeGall, *Biochem. Biophys. Res. Commun.* 108 (1982) 1388–1393.
31. M. Teixeira, I. Moura, A. V. Xavier, B. H. Huynh, D. V. DerVartanian, H. D. Peck, Jr., J. LeGall, J. J. Moura, *J. Biol. Chem.* 260 (1985) 8942–8950.
32. R. Cammack, D. S. Patil, V. M. Fernandez, *Biochem. Soc. Trans.* 13 (1985) 572–578.
33. J. W. van der Zwaan, S. P. Albracht, R. D. Fontijn, E. C. Slater, *FEBS Lett* 179 (1985) 271–7.
34. C. V. Romao, I. A. Pereira, A. V. Xavier, J. LeGall, M. Teixeira, *Biochem. Biophys. Res. Commun.* 240 (1997) 75–79.
35. R. Cammack, C. Bagyinka, K. L. Kovacs, *Eur. J. Biochem.* 182 (1989) 357–362.
36. A. Chapman, R. Cammack, C. E. Hatchikian, J. McCracken, J. Peisach, *FEBS Lett.* 242 (1988) 134–138.
37. C. Fan, M. Teixeira, J. J. G. Moura, I. Moura, B.-H. Huynh, J. Le Gall, H. D. J. Peck, B. M. Hoffman, *J. Am. Chem. Soc.* 113 (1991) 20–24.
38. J. E. Huyett, M. Carepo, A. Pamplona, R. Franco, I. Moura, J. J. G. Moura, B. M. Hoffman, *J. Am. Chem. Soc.* 119 (1997) 9291–9292.
39. M. W. Adams, M. K. Johnson, I. C. Zambrano, L. E. Mortenson, *Biochimie* 68 (1986) 35–42.
40. P. J. van Dam, E. J. Reijerse, W. R. Hagen, *Eur. J. Biochem.* 248 (1997) 355–361.
41. K. A. Bagley, C. J. Van Garderen, M. Chen, E. C. Duin, S. P. Albracht, W. H. Woodruff, *Biochemistry* 33 (1994) 9229–9236.
42. K. A. Bagley, E. C. Duin, W. Roseboom, S. P. Albracht, W. H. Woodruff, *Biochemistry* 34 (1995) 5527–5535.
43. A. J. Pierik, W. Roseboom, R. P. Happe, K. A. Bagley, S. P. Albracht, *J. Biol. Chem.* 274 (1999) 3331–3337.
44. A. L. de Lacey, E. C. Hatchikian, A. Volbeda, M. Frey, J. C. Fontecilla-Camps, V. M. Fernandez, *J. Am. Chem. Soc.* 119 (1997) 7181–7189.
45. A. Volbeda, E. Garcia, C. Piras, A. L. Delacey, V. M. Fernandez, E. C. Hatchikian, M. Frey, J. C. Fontecilla-Camps, *J. Am. Chem. Soc.* 118 (1996) 12989–12996.
46. T. M. van der Spek, A. F. Arendsen, R. P. Happe, S. Yun, K. A. Bagley, D. J. Stufkens, W. R. Hagen, S. P. Albracht, *Eur. J. Biochem.* 237 (1996) 629–634.
47. A. J. Pierik, M. Hulstein, W. R. Hagen, S. P. Albracht, *Eur. J. Biochem.* 258 (1998) 572–578.
48. J. M. Coremans, C. J. van Garderen, S. P. Albracht, *Biochim. Biophys. Acta* 1119 (1992) 148–156.
49. D. P. Barondeau, L. M. Roberts, P. A. Lindahl, *J. Am. Chem. Soc.* 116 (1994) 3442–3448.
50. L. M. Roberts, P. A. Lindahl, *Biochemistry* 33 (1994) 14339–14350.
51. A. J. Pierik, W. R. Hagen, J. S. Redeker, R. B. Wolbert, M. Boersma, M. F. Verhagen, H. J. Grande, C. Veeger, P. H. Mutsaers, R. H. Sands, et al., *Eur. J. Biochem.* 209 (1992) 63–72.
52. B. H. Huynh, J. J. G. Moura, I. Moura, T. A. Kent, J. LeGall, A. V. Xavier, E. Munck, *J. Biol. Chem.* 255 (1980) 3242–3244.
53. M. H. Emptage, T. A. Kent, B. H. Huynh, J. Rawlings, W. H. Orme-Johnson, E. Munck, *J. Biol. Chem.* 255 (1980) 1793–1796.
54. B. H. Huynh, D. S. Patil, I. Moura, M. Teixeira, J. J. Moura, D. V. DerVartanian, M. H. Czechowski, B. C. Prickril, H. D. Peck, Jr., J. LeGall, *J. Biol. Chem.* 262 (1987) 795–800.
55. M. J. Maroney, G. J. Colpas, C. Bagyinka, N. Baidya, P. K. Mascharak, *J. Am. Chem. Soc.* 113 (1991) 3962–3972.

56. C. Bagyinka, J. P. Whitehead, M. J. Maroney, *J. Am. Chem. Soc.* **115** (1993) 3576–3585.
57. Z. Gu, J. Dong, C. B. Allan, S. B. Choudhury, R. Franco, J. J. G. Moura, I. Moura, J. LeGall, A. E. Przybyla, W. Roseboom, S. P. J. Albracht, M. J. Axley, R. A. Scott, M. J. Maroney, *J. Am. Chem. Soc.* **118** (1996) 11155–11165.
58. P. A. Lespinat, Y. Berlier, G. Fauque, M. Czechowski, B. Dimon, J. Le Gall, *Biochimie* **68** (1986) 55–61.
59. A. Der, C. Bagyinka, T. Pali, K. L. Kovacs, *Anal. Biochem.* **150** (1985) 481–486.
60. A. Volbeda, M. H. Charon, C. Piras, E. C. Hatchikian, M. Frey, J. C. Fontecilla-Camps, *Nature* **373** (1995) 580–587.
61. Y. Higuchi, T. Yagi, N. Yasuoka, *Structure* **5** (1997) 1671–1680.
62. Y. Higuchi, T. Yagi, *Biochem. Biophys. Res. Commun.* **255** (1999) 295–259.
63. Y. Higuchi, H. Ogata, K. Miki, N. Yasuoka, T. Yagi, *Structure Fold Des.* **7** (1999) 549–556.
64. E. Garcin, X. Vernede, E. C. Hatchikian, A. Volbeda, M. Frey, J. C. Fontecilla-Camps, *Structure Fold Des.* **7** (1999) 557–566.
65. J. W. Peters, W. N. Lanzilotta, B. J. Lemon, L. C. Seefeldt, *Science* **282** (1998) 1853–1858.
66. Y. Nicolet, C. Piras, P. Legrand, C. E. Hatchikian, J. C. Fontecilla-Camps, *Structure Fold Des.* **7** (1999) 13–23.
67. B. J. Lemon, J. W. Peters, *Biochemistry* **38** (1999) 12969–12973.
68. Y. Sugiura, J. Kuwahara, T. Suzuki, *Biochem. Biophys. Res. Commun.* **115** (1983) 878–881.
69. K. Nakamoto, *Infrared and Raman Spectra of Inorganic and Coordination Compounds*, Wiley, New York 1997.
70. D. H. Nguyen, H. F. Hsu, M. Millar, S. A. Koch, C. Achim, E. L. Bominaar, E. Munck, *J. Am. Chem. Soc.* **118** (1996) 8963–8964.
71. H. F. Hsu, S. A. Koch, C. V. Popescu, E. Munck, *J. Am. Chem. Soc.* **119** (1997) 8371–8372.
72. I. Mus-Veteau, F. Guerlesquin, *Biochem. Biophys. Res. Commun.* **201** (1994) 128–134.
73. R. H. Crabtree, *Inorg. Chim. Acta* **125** (1986) L7–L8.
74. L. L. Efron, H. H. Thorp, G. W. Brudvig, R. H. Crabtree, *Inorg. Chem.* **31** (1992) 1722–1724.
75. T. L. James, L. Cai, M. C. Muetterties, R. H. Holm, *Inorg. Chem.* **35** (1996) 4148–4161.
76. P. Saint-Martin, P. A. Lespinat, G. Fauque, Y. Berlier, J. LeGall, I. Moura, M. Teixeira, A. V. Xavier, J. J. G. Moura, *Proc. Natl. Acad. Sci. (USA)* **85** (1988) 9378–9380.
77. R. T. Hembre, S. McQueen, *J. Am. Chem. Soc.* **116** (1994) 2141–2142.
78. R. T. Hembre, J. S. McQueen, V. W. Day, *J. Am. Chem. Soc.* **118** (1996) 798–803.
79. P. I. Amrhein, S. D. Drouin, C. E. Forde, A. J. Lough, R. H. Morris, *J. Chem. Soc., Chem. Commun.* (1996) 1665–1666.
80. T. P. Fong, A. J. Lough, R. H. Morris, A. Mezzetti, E. Rocchini, P. Rigo, *J. Chem. Soc., Dalton Trans.* (1998) 211–213.
81. T. P. Fong, C. E. Forde, A. J. Lough, R. H. Morris, P. Rigo, E. Rocchini, T. Stephan, *J. Chem. Soc., Dalton Trans.* (1999) 4475–4486.
82. T. Y. Bartucz, A. Golombek, A. J. Lough, P. A. Maltby, R. H. Morris, R. Ramachandran, M. Schlaf, *Inorg. Chem.* **37** (1998) 1555–1562.
83. F. Osterloh, W. Saak, D. Haase, S. Pohl, *Chem. Commun.* (1997) 979–980.
84. S. C. Davies, D. J. Evans, D. L. Hughes, S. Longhurst, J. R. Sanders, *Chem. Commun.* (1999) 1935–1936.
85. M. Schmidt, S. M. Contakes, T. B. Rauchfuss, *J. Am. Chem. Soc.* **121** (1999) 9736–9737.
86. R. B. King, *J. Am. Chem. Soc.* **84** (1962) 2460.
87. A. Winter, L. Zsolnai, G. Huttner, *Z. Naturforsch.* **37b** (1982) 1430–1436.
88. A. Le Cloirec, S. P. Best, S. Borg, S. C. Davies, D. J. Evans, D. L. Hughes, C. J. Pickett, *Chem. Commun.* (1999) 2285–2286.
89. M. Pavlov, P. E. M. Siegbahn, M. R. A. Blomberg, R. H. Crabtree, *J. Am. Chem. Soc.* **120** (1998) 548–555.
90. S. Niu, L. M. Thomson, M. B. Hall, *J. Am. Chem. Soc.* **121** (1999) 4000–4007.
91. S. L. Morrison, J. J. Turner, *J. Mol. Struct.* **317** (1994) 39–47.
92. P. Amara, A. Volbeda, J. C. Fontecilla-Camps, M. J. Field, *J. Am. Chem. Soc.* **121** (1999) 4468–4477.
93. I. Dance, *Chem. Commun.* (1999) 1655–1656.

8 Biomimetic Electron-transfer Chemistry of Porphyrins and Metalloporphyrins

Shunichi Fukuzumi and Hiroshi Imahori

8.1 Introduction

Porphyrins contain an extensively conjugated π system and a highly delocalized π system such as this is suitable for efficient electron-transfer reactions, because the uptake or release of electrons results in minimal changes of structure and solvation on electron transfer [1]. Numerous metal ions can tightly bind with porphyrin macrocyclic ligands to afford metalloporphyrins which can undergo metal-centered electron-transfer reactions and porphyrin ligand-centered reactions [1]. Therefore, a variety of redox states can be achieved for metalloporphyrins through multi-electron oxidation or reduction processes [1]. Metalloporphyrins can form a metal-carbon σ -bond to afford organometallic porphyrins [2]. The strength of such binding is significantly altered, depending on the redox state of metalloporphyrins [2]. Consequently, cleavage or formation of the metal-carbon bond can be finely tuned by changing the redox state. Thus, the electron transfer oxidation or reduction of metalloporphyrins and organometallic porphyrins is often accompanied by the subsequent formation or cleavage of the bond, leading to a rich chemistry for metalloporphyrins and organometallic porphyrins [1, 2]. Such formation of reactive intermediates associated with electron-transfer reactions of metalloporphyrins has played an important role in the catalytic function of metalloporphyrins not only in chemical but also in biological processes [3–5]. Axial ligands can also bind or coordinate to the metal to attenuate the electron-transfer reactions of metalloporphyrins including the site of electron transfer, i.e. metal-centered or the porphyrin ligand-centered electron transfer [1]. The use of photoexcited states of porphyrins and metalloporphyrins (i.e., in the singlet or triplet excited state) further widens the scope of electron-transfer reactions, because photoexcitation significantly enhances both the electron-acceptor or -donor properties of photoexcited porphyrins and metalloporphyrins. The rich redox properties of porphyrins and metalloporphyrins both in the ground and excited states have rendered them es-

sential components of biological electron transport systems including photosynthesis and respiration [6–15].

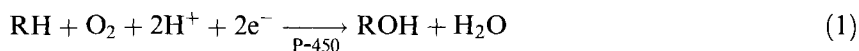
Because the electron-transfer processes of porphyrins and metalloporphyrins have been reviewed elsewhere [1, 16, 17], this chapter focuses on mechanistic aspects of chemical processes associated with the electron-transfer reactions of metalloporphyrins and organometallic porphyrins. When an electron-transfer process is followed by subsequent bond-breaking and bond-forming, the overall reaction often becomes the same as electrophile–nucleophile reactions in which electron shift and bond formation occur in a concerted manner via a polar mechanism. Such electron transfer or alternative polar (concerted) processes have been among the most central propositions in reaction mechanisms [18–26]. Because both processes involve the formation of a significant amount of charge in the transition state, it has been difficult to differentiate between electron transfer and polar mechanisms on the basis of the classical approach of electronic and substitution effects. Advances in time-resolved spectroscopy, including laser flash photolysis and a low-temperature stopped-flow technique, have, however, provided the means of monitoring fast electron-transfer reactions and subsequent chemical reactions, by enabling detection of unstable reactive intermediates produced in electron-transfer reactions.

In the first part of this review, recent advances in the mechanistic aspects of reactions of high-valent metalloporphyrin intermediates produced by the oxidation of metalloporphyrins and organometallic porphyrins are highlighted in relation to the enzymatic reaction mechanisms of biological oxidation of substrates including water. This section is followed by an overview of the reverse process, i.e. the four-electron reduction of O₂ to water catalyzed by cytochrome c oxidases and model complexes. Finally biomimetic electron-transfer systems of porphyrins and metalloporphyrins in organized media are presented in relation to practical endeavors such as the design of molecular-scale photonic devices and solar-energy conversion systems.

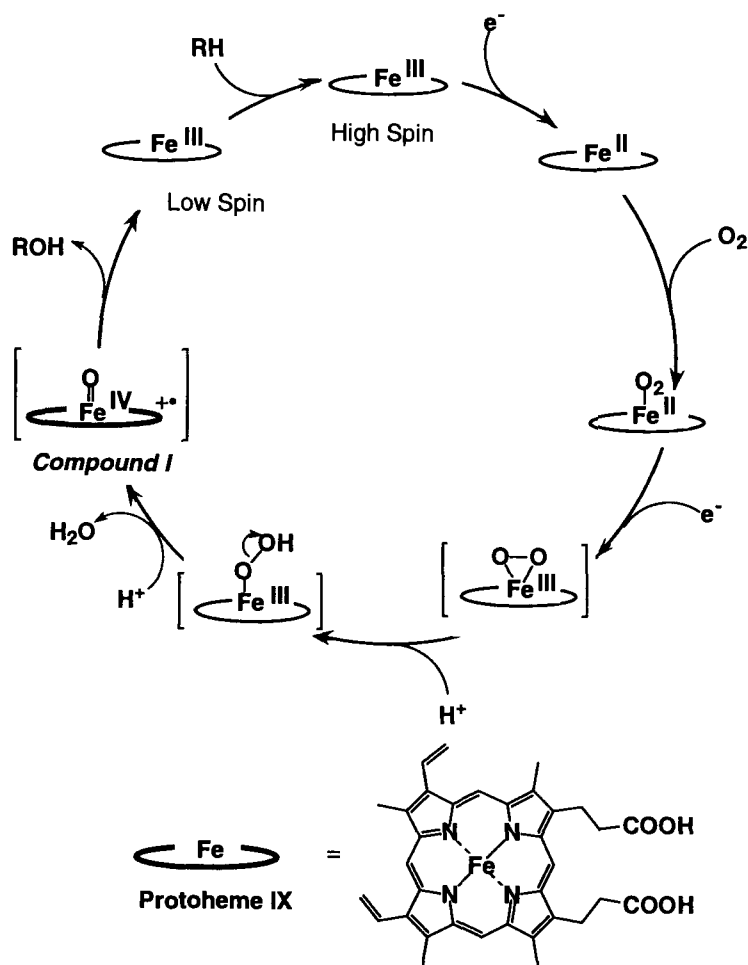
8.2 High-valent Intermediates of Heme Enzymes

8.2.1 P-450 Catalytic Mechanisms

Cytochromes P-450, the CO complexes of which have a characteristic absorption maximum at 450 nm, use molecular oxygen to catalyze monooxygenation of versatile organic compounds such as hydrocarbons, sulfides, and amines with reducing agents (Eq. 1) [27–33].



For decades extensive efforts have been devoted to the elucidation of the molecular mechanisms of oxygen activation and oxidation reactions. The following mechanism is generally assumed for dioxygen activation and monooxygenation (Scheme 1) [27–33].



Scheme 1.

Starting from the low-spin Fe^{III} state of a six-coordinate metalloporphyrin complex with cysteinate and water, the binding of an organic substrate (RH) occurs to give the high-spin Fe^{III} state. This step is followed by a one-electron reduction via 5,10-dihydroflavin adenine dinucleotide (FADH₂) to give a high-spin Fe^{II} complex which can bind oxygen. After a second one-electron reduction to a high-spin Fe^{II} complex, a low-spin peroxo Fe^{III} complex is formed. Two protons are then added to produce a high-valent iron-oxo porphyrin π radical cation, [(P)Fe^{IV}=O]^{•+} (or a formally pentavalent iron-oxo complex [(P)Fe^V=O]) by release of one water molecule, thereby cleaving the O–O bond. Formal oxygen transfer from [(P)Fe^{IV}=O]^{•+} to RH occurs to yield the monooxygenated product, accompanied by regeneration of the starting low-spin Fe^{III} state (Scheme 1). The high-valent iron-oxo porphyrin

$[(P)Fe^{IV}=O]^{*+}$ or $(P)Fe^V=O$) is the reactive intermediate in the monooxygenation step.

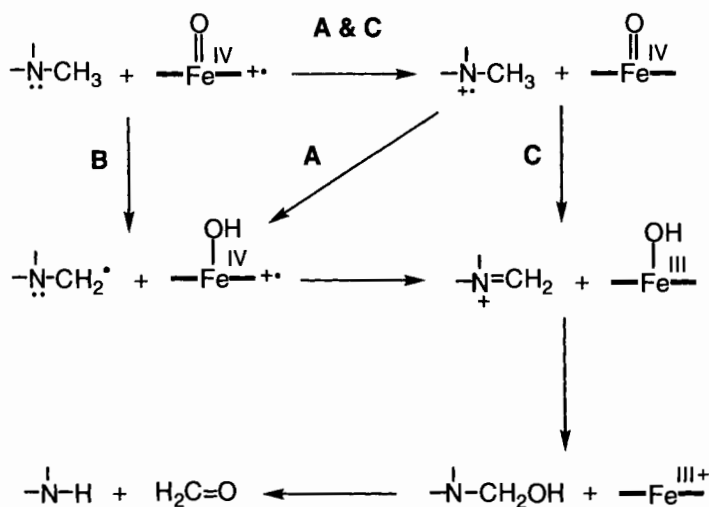
The use of a synthetic model system has provided valuable mechanistic insights into the molecular catalytic mechanism of P-450. Groves et al. [34], were the first to report cytochrome P-450-type activity in a model system comprising iron *meso*-tetraphenylporphyrin chloride $[(TPP)FeCl]$ and iodosylbenzene (PhIO) as an oxidant which can oxidize the Fe^{III} porphyrin directly to $[(TPP)Fe^{IV}=O]^{*+}$ in a 'shunt' pathway. Thus, $(TPP)FeCl$ and other metalloporphyrins can catalyze the monooxygenation of a variety of substrates by PhIO [35–40], hypochlorite salts [41, 42], *p*-cyano-*N,N*-dimethylaniline *N*-oxide [43–46], percarboxylic acids [47–50] and hydroperoxides [51, 52]. Catalytic activity was, however, rapidly reduced because of the destruction of the metalloporphyrin during the catalytic cycle [34–52]. When $(TPP)FeCl$ was immobilized on the surface of silica or silica–alumina, catalytic reactivity and catalytic lifetime both increased significantly [53]. There have been several reports of supported catalysts based on such metalloporphyrins adsorbed or covalently bound to polymers [54–56]. Catalyst lifetime was also significantly improved by use of iron porphyrins such as *meso*-tetramesitylporphyrin chloride $[(TMP)FeCl]$ and iron *meso*-tetrakis(2,3,4,5,6-pentafluorophenyl)porphyrin chloride $[(TPFPP)FeCl]$, which resist oxidative destruction, because of steric and electronic effects and thereby act as efficient catalysts of P-450 type reactions [57–65].

8.2.2 Reaction Pathways of $[(P)Fe^{IV}=O]^{*+}$

In the catalytic cycle in Scheme 1, details of the reaction between the high-valent iron–oxo porphyrin π radical cation $[(P)Fe^{IV}=O]^{*+}$ and a substrate have yet to be clarified [66]. Three possibilities have survived after extensive studies of the mechanisms of the reactions of high-valent iron–oxo porphyrins, in particular the dealkylation of amines by cytochrome P-450: (A) a sequential electron–proton–electron transfer; (B) direct hydrogen transfer then electron transfer; and (C) electron transfer followed by hydrogen transfer (Scheme 2) [67–74].

It was believed that a sequential electron–proton–electron transfer mechanism would result in small isotope effects and that a hydrogen transfer mechanism would result in large isotope effects. Because small isotope effects were observed for amine dealkylation by cytochrome P-450, a sequential electron–proton–electron transfer mechanism was proposed for the reaction [67, 75–77]. The magnitude of a single isotope effect provides only limited information about a reaction mechanism, however, and isotope effects might be logically consistent with any type of C–H cleavage reaction.

To distinguish between paths A and B in Scheme 2, Dinnocenzo and coworkers [78–80] determined intramolecular isotope effects for deprotonation from the radical cations (path A) and for hydrogen-atom abstraction from a series of substituted *N,N*-dimethylanilines (path B); these were compared with isotope effects for *N*-demethylation of the same series of *N,N*-dimethylanilines. The deprotonation isotope-effect profile for the radical cations of *N,N*-dimethylanilines were determined by monitoring electron-transfer reactions from *N,N*-dimethylanilines to $[Fe(phen)_3]^{3+}$

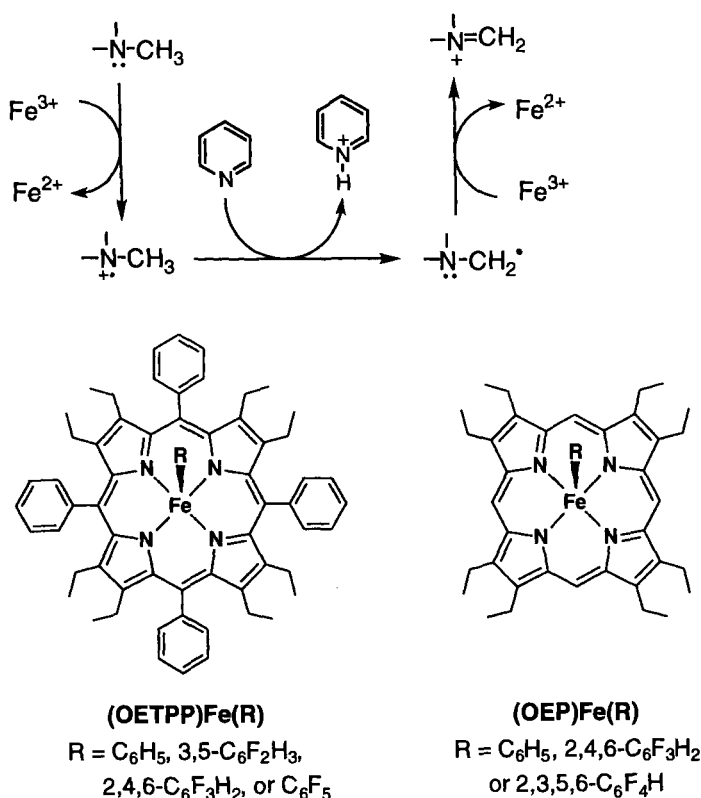


Scheme 2.

(phen = 1,10-phenanthroline), a well-known outer-sphere one-electron oxidant [81], in the presence of pyridine as base. The mechanism of such electron-transfer reactions has been well established in electron-transfer reactions of NADH analogs with $[\text{Fe}(\text{phen})_3]^{3+}$ in the presence of pyridine [82–84], and can be applied to the reaction of *N,N*-dimethylanilines as shown in Scheme 3.

The rate of initial electron transfer from *N,N*-dimethylaniline to $[\text{Fe}(\text{phen})_3]^{3+}$ is diffusion-limited. This is followed by the rate-determining proton transfer from the radical cation to pyridine to give the deprotonated α -amino radical which is rapidly oxidized by a second equivalent of $[\text{Fe}(\text{phen})_3]^{3+}$ to yield the product iminium ion. Kinetic isotope effects ($k_{\text{H}}/k_{\text{D}}$) for the proton transfer were determined from the d_3/d_0 ratios of the products derived from *p*-substituted *N*-methyl-*N*-trideuteromethylanilines. The $k_{\text{H}}/k_{\text{D}}$ value first increases and then decreases with increasing $\text{p}K_{\text{a}}$ of *p*-substituted *N,N*-dimethylaniline. Such a bell-shaped isotope effect profile is typical of proton-transfer reactions [82, 85]. The maximum $k_{\text{H}}/k_{\text{D}}$ value is determined as 8.8 which is much larger than the corresponding value for the demethylation of the same substrate by cytochrome P-450 (2.6) [79].

The isotope effect profile for hydrogen atom abstraction from the same series of *p*-substituted *N,N*-dimethylanilines was determined by using the *tert*-butoxyl radical (*t*-BuO $^\bullet$) as the hydrogen-atom abstracting agent; this species is known to abstract hydrogen atoms from the α -carbon atoms of amines [86]. The *tert*-butoxyl radical was generated by the coumarin-sensitized photoreduction of the *N-tert*-butoxy-4-phenylpyridinium ion [87, 88]. A small, steady decrease in the $k_{\text{H}}/k_{\text{D}}$ value for hydrogen-atom abstraction from *p*-substituted *N,N*-dimethylanilines is observed when the $\text{p}K_{\text{a}}$ of the radical cations is increased. This is quite different from the bell-shaped isotope-effect profile for the proton-transfer reactions. Such differences demonstrate that isotope profiles can serve as sensitive probes for distinguishing



Scheme 3

P-450 amine dealkylation mechanisms. Because $k_{\text{H}}/k_{\text{D}}$ values for *N*-demethylation of *p*-substituted *N,N*-dimethylanilines by cytochrome P-450 are nearly identical with those for the hydrogen abstraction reactions of *t*-BuO \cdot , it was proposed that P-450 reacted by a direct hydrogen-atom-abstraction mechanism (**B**) rather than a sequential electron-proton-electron-transfer mechanism (**A**) [78, 80]. Identical relationships between $k_{\text{H}}/k_{\text{D}}$ values for reactions of *t*-BuO \cdot and P-450 has been expanded for other substrates including *p*-xylene, toluene, benzyl alcohol, and tertiary trialkylamine [78]. It has thus been suggested that all these P-450 reactions proceed by a common hydrogen-atom transfer mechanism [78].

For a synthetic P-450 model system, however, an opposite conclusion was drawn from similar analysis of kinetic isotope effects for *N*-demethylation of *p*-substituted *N,N*-dimethylanilines by PhIO, catalyzed by iron *meso*-tetrakis(2,3,4,5,6-pentafluorophenyl)porphyrin chloride, (TPFPP)FeCl [89]. Intramolecular $k_{\text{H}}/k_{\text{D}}$ values obtained from the d_3/d_0 ratios of the products derived from 4-*X-N*-methyl-*N*-tri-deuteriomethylanilines [2.0 ($\text{X} = \text{NO}_2$), 2.0 ($\text{X} = \text{CN}$), 2.6 ($\text{X} = \text{Br}$), 3.1 ($\text{X} = \text{H}$), 3.2 ($\text{X} = \text{Me}$), and 3.3 ($\text{X} = \text{OMe}$)], decreased regularly on going from electron-donating to electron-withdrawing substituents. Such a trend is the complete oppo-

site to that found for the hydrogen-atom-abstraction reactions of some of these substrates with *t*-BuO[•], but also different from the bell-shaped isotope-effect profile obtained for proton-transfer reactions (vide supra) [89]. The intermolecular $k_{\text{H}}/k_{\text{D}}$ values were also determined by competitive experiments with 4-X-substituted *N,N*-dimethyl- and *N,N*-bis(trideuteromethyl)anilines, with X = H, Br, and OMe, as 1.6, 1.5 and 1.9, respectively. These values are quite different from the corresponding intramolecular $k_{\text{H}}/k_{\text{D}}$ values. Such a difference between intramolecular and intermolecular kinetic isotope effects implies a multi-step rather than single-step reaction. An electron transfer pathway followed by hydrogen transfer (C in Scheme 2) is consistent with these results.

8.2.3 Reorganization Energies for Electron-transfer Reactions of High-valent Iron Porphyrins

The electron transfer pathway has been examined by analyzing relative reactivities of 4-X-substituted *N,N*-dimethylanilines, determined by competitive kinetics; the reactivities span a wide reactivity range of 25 (from X = NO₂ to X = MeO) and can be fitted to the Rehm–Welter equation [90] for electron-transfer reactions (Eq. 2):

$$\Delta G^\ddagger = (\Delta G^\circ_{\text{et}}/2) + [(\Delta G^\circ_{\text{et}}/2)^2 + (\Delta G^\ddagger_0)^2]^{1/2} \quad (2)$$

where $\Delta G^\circ_{\text{et}}$ is the free energy change for electron transfer and ΔG^\ddagger_0 is the intrinsic barrier that represents the activation free energy when the driving force of electron transfer is zero, i.e., $\Delta G^\ddagger = \Delta G^\ddagger_0$ at $\Delta G^\circ_{\text{et}} = 0$ [90]. The ΔG^\ddagger values are related to the rate constant of electron transfer (k_{et}) as given by Eq. 3, where Z is the collision frequency (i.e., $1 \times 10^{11} \text{ M}^{-1} \text{ s}^{-1}$).

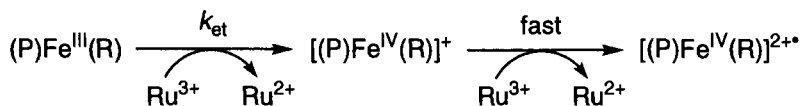
$$\Delta G^\ddagger = 2.3RT \log(Z/k_{\text{et}}) \quad (3)$$

The k_{et} values can be calculated from the $\Delta G^\circ_{\text{et}}$ and ΔG^\ddagger_0 values by use of Eqs 2 and 3. The $\Delta G^\circ_{\text{et}}$ value is obtained from the one-electron oxidation potential of an electron donor (E°_{ox}) and the one-electron reduction potential of an acceptor (E°_{red}), because $\Delta G^\circ_{\text{et}} = F(E^\circ_{\text{ox}} - E^\circ_{\text{red}})$.

The reorganization energy of electron transfer (λ) is defined as $4\Delta G^\ddagger_0$. The λ value was evaluated as 47 kcal mol^{−1} for the postulated electron transfer from *N,N*-dimethylanilines to [(TPFPP)Fe^{IV}=O]^{•+} by fitting the data to Eqs 2 and 3. Essentially the same λ value can be obtained by fitting the data to the Marcus equation (Eq. 4) [91] except for the region where the rate becomes close to a diffusion-limited value [81, 92].

$$\Delta G^\ddagger = (\lambda/4)[1 + (\Delta G^\circ_{\text{et}}/\lambda)]^2 \quad (4)$$

Although such a large λ value is rather unusual in electron-transfer reactions of metalloporphyrins [1], the electron transfer kinetics for generation of iron(IV) por-



Scheme 4.

phyrins or iron(IV) porphyrin π radical cations indicated a large reorganization energy was required for electron-transfer reactions involving high-valent metalloporphyrins [93]. The investigated compounds are represented as (P)Fe(R) where P^{2-} = the dianion of 2,3,7,8,12,13,17,18-octaethyl-5,10,15,20-tetraphenylporphyrin (OETPP) and $\text{R} = \text{C}_6\text{H}_5$, 3,5- $\text{C}_6\text{F}_2\text{H}_3$, 2,4,6- $\text{C}_6\text{F}_3\text{H}_2$, or C_6F_5 , or P^{2-} = the dianion of 2,3,7,8,12,13,17,18-octaethylporphyrin (OEP) and $\text{R} = \text{C}_6\text{H}_5$, 2,4,6- $\text{C}_6\text{F}_3\text{H}_2$, or 2,3,5,6- $\text{C}_6\text{F}_4\text{H}$.

The first one-electron transfer from (P)Fe(R) to $[\text{Ru}(\text{bpy})_3]^{3+}$ (bpy = 2,2'-bipyridine) leads to an Fe(IV) σ -bonded complex, $[(\text{P)Fe}^{\text{IV}}(\text{R})]^+$ [94], and occurs at a rate which is much lower than that of the second one-electron transfer from $[(\text{P)Fe}^{\text{IV}}(\text{R})]^+$ to $[\text{Ru}(\text{bpy})_3]^{3+}$ to give $[(\text{P)Fe}^{\text{IV}}(\text{R})]^{2+}$ (Scheme 4).

Metal-centered oxidation is therefore kinetically more difficult than the porphyrin macrocycle oxidation. The reorganization energies (λ in kcal mol^{-1}) for the metal-centered oxidation of (OETPP)Fe^{III}(R) to [(OETPP)Fe^{IV}(R)]⁺ ($\text{R} = \text{C}_6\text{H}_5$, 3,5- $\text{C}_6\text{F}_2\text{H}_3$, and 2,4,6- $\text{C}_6\text{F}_3\text{H}_2$), (OETPP)Fe^{III}(C_6F_5) to [(OETPP)Fe^{IV}(C_6F_5)]⁺, and (OEP)Fe^{III}(R) to [(OEP)Fe^{IV}(R)]⁺ are 54, 49, and 42 kcal mol^{-1} , respectively [93]. Each is significantly larger than reorganization energies for the porphyrin-centered oxidations involving the same series of compounds, i.e. the second electron transfer of (P)Fe(R) for the ligand-centered oxidation, ca 24 kcal mol^{-1} , which is comparable with the λ value for free base porphyrins [95]. Thus, a large reorganization energy is required for the electron-transfer oxidation of (P)Fe^{III}(R) to [(P)Fe^{IV}(R)]⁺. It is interesting to note that the λ value (49 kcal mol^{-1}) for the electron transfer oxidation of (OETPP)Fe^{III}(C_6F_5) to [(OETPP)Fe^{IV}(C_6F_5)]⁺ is approximately the same as the λ value (47 kcal mol^{-1}) for the postulated electron-transfer reduction of $[(\text{TPFPP)Fe}^{\text{IV}}=\text{O}]^{+}$ by *N,N*-dimethylanilines (vide infra) [89].

8.2.4 Electron-transfer Pathway of $[(\text{P)Fe}^{\text{IV}}=\text{O}]^{+}$

To clarify the mechanism of reaction of P-450, it is crucial to characterize the reactive intermediates in the rate-determining step. Definitive evidence for an electron-transfer mechanism (C in Scheme 2) for the *N*-demethylation of *N,N*-dimethylanilines has been obtained by direct observation of the reduction of the high-valent species responsible for P-450 catalysis [96]. For peroxidase, an oxoferryl porphyrin π -radical cation, compound I $[(\text{P)Fe}^{\text{IV}}=\text{O}]^{+}$, has been well characterized as the species equivalent to the proposed active intermediate of P-450 [97–103]. Compound I of horseradish peroxidase (HRP) can be readily generated by chemical oxidation of HRP [100–103]. The involvement of the electron-transfer process of compound I in the oxidation of several amines catalyzed by HRP was

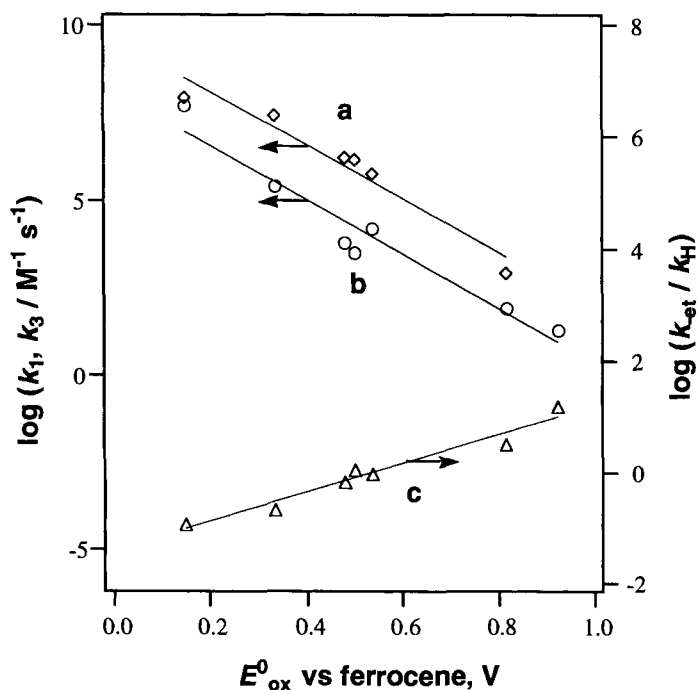


Figure 1. Dependence of kinetic values on the oxidation potential of DMA (E°_{ox}). (a) (\diamond): bimolecular rate constant of HRP compound **I** with DMA, k_1 . (b) (\circ): bimolecular rate constant of $[(\text{TMP})\text{Fe}^{\text{IV}}=\text{O}]^{*+}$ with DMA, k_3 . (c) (Δ): $k_{\text{et}}/k_{\text{H}}$ determined by use of Eq. 6 [96].

demonstrated by the ESR detection of the corresponding aminium radicals [97–99]. Reactions of compound **I** with 4-X-substituted *N,N*-dimethyl- and *N,N*-bis(trideuteriomethyl)anilines (DMA) were monitored spectroscopically by use of a double-mixing stopped-flow technique [96]. When HRP compound **I** and the amines were mixed under stopped-flow conditions in a buffer solution (pH 7.0) at 273 K, rapid formation of compound **II** $[(\text{P})\text{Fe}^{\text{IV}}=\text{O}]$ (k_1) and the subsequent relatively slow conversion (k_2) to the resting ferric state were observed directly. Both $\log k_1$ and $\log k_2$ increase with decreasing E°_{ox} as the electron-transfer process becomes thermodynamically more favorable. A linear correlation between $\log k_1$ and E°_{ox} is shown in Figure 1a. No kinetic isotope effects are observed. Thus, the rate-determining step is clearly electron transfer from DMA to HRP compound **I** and compound **II**.

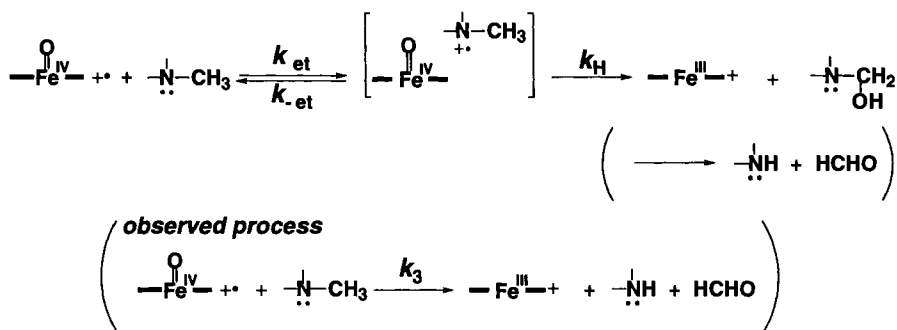
According the Marcus theory of outer-sphere electron-transfer (Eq. 4), the slope of a linear correlation between $\log k_1$ and E°_{ox} can be derived as given by Eq. 5.

$$\partial(\log k_1)/\partial(E^\circ_{\text{ox}}) = -\frac{1}{2}(1/2.3RT)(1 + \Delta G^\circ_{\text{et}}/\lambda) \quad (5)$$

The slope of the linear correlation between $\log k_1$ and E°_{ox} (-7.65) is slightly less negative than the value (-9.2) expected from Eq. 5 at $\Delta G^\circ_{\text{et}} = 0$

$[\partial(\log k_1)/\partial(E^\circ_{\text{ox}})] = -(1/2)(1/2.3RT) = -9.2$ at 273 K]. This means that electron transfer from DMA to HRP compound **I** is slightly exergonic, because $\partial(\log k_1)/\partial(E^\circ_{\text{ox}}) > -(1/2)(1/2.3RT) = -9.2$ at 273 K when $\Delta G^\circ_{\text{et}} < 0$. This is consistent with the highly positive one-electron reduction potential of HRP compound **I** ($E^\circ_{\text{red}} = 0.898$ V relative to the NHE, or 0.662 V relative to the SCE) [104]. The unknown value of the reorganization energy (λ) for electron-transfer reactions from *N,N*-dimethylanilines to HRP compound **I** and the experimental errors involved in estimating the redox potentials in water have precluded complete fit of the rate constants to values calculated from Eqs 3 and 4, although a linear correlation between $\log k_1$ and E°_{ox} for a wide range of E°_{ox} indicates that a large reorganization energy is required for the electron-transfer reduction of compound **I**, i.e. $|\Delta G^\circ_{\text{et}}/\lambda| \ll 1$ in Eq. 5 as postulated for electron transfer from *N,N*-dimethylanilines to $[(\text{TPFPP})\text{Fe}^{\text{IV}}=\text{O}]^{*+}$ (vide supra) [89]. A large reorganization energy ($\lambda = 61.9$ kcal mol⁻¹) [104] has, in fact, been derived from the electron self-exchange rate between HRP compound **I** and compound **II** (4.4×10^{-1} M⁻¹ s⁻¹) by applying the Marcus theory of electron transfer (Eq. 4) [91] to the rate of electron transfer from ferrocyanide to HRP compound **I** (8×10^5 M⁻¹ s⁻¹) [105]. An even larger reorganization energy ($\lambda = 78.0$ kcal mol⁻¹) [104] was derived from the electron self-exchange rate between HRP compound **II** and ferric HRP (4.9×10^{-4} M⁻¹ s⁻¹) [104]. The extremely large λ value (78.0 kcal mol⁻¹) for the metal-centered electron-exchange between HRP compound **II** (Fe^{IV}) and ferric HRP (Fe^{III}) is consistent with the large λ value (83 kcal mol⁻¹) derived from the reaction between $[(\text{OEP})\text{Fe}^{\text{IV}}(\text{R})]^{*+}$ and $(\text{OEP})\text{Fe}^{\text{III}}(\text{R})$ [93]. The large λ value for electron self-exchange between HRP compound **I** and compound **II** ($\lambda = 78.0$ kcal mol⁻¹) [104] suggests a significant contribution of the metal-centered reduction of $[(\text{P})\text{Fe}^{\text{IV}}=\text{O}]^{*+}$ to give compound **II**, which should have $(\text{P})\text{Fe}^{\text{III}}-\text{O}^\bullet$ character as another resonance form of $(\text{P})\text{Fe}^{\text{IV}}=\text{O}$. This system can be used as an authentic case for the electron-transfer reactivity of compound **I** with *N,N*-dimethylanilines which can be compared with the reactivities of compound **I** of P-450 and of synthetic analogs with the same substrates.

Although characterization of compound **I** of P-450 has remained poor [106], compound **I** of a synthetic model, i.e., $[(\text{TMP})\text{Fe}^{\text{IV}}=\text{O}]^{*+}$ has been well characterized spectrophotometrically [107]. $[(\text{TMP})\text{Fe}^{\text{IV}}=\text{O}]^{*+}$ was prepared by reaction of $(\text{TMP})\text{Fe}^{\text{III}}(\text{OH})$ with *m*-chloroperoxybenzoic acid (*m*CPBA) in CH₂Cl₂ at 223 K [193]. The reactions of $[(\text{TMP})\text{Fe}^{\text{IV}}=\text{O}]^{*+}$ with 4-X-substituted *N,N*-dimethylanilines (DMA) in CH₂Cl₂ at 223 K were monitored by UV-Vis spectral changes of $[(\text{TMP})\text{Fe}^{\text{IV}}=\text{O}]^{*+}$ and found to afford $(\text{TMP})\text{Fe}^{\text{III}}$ without observation of any intermediates [96]. There is linear correlation between the rate constants (k_3) and E°_{ox} (Figure 1b), similar to the correlation observed for $\log k_1$ and E°_{ox} (Figure 1a). The parallel relationship between these two plots indicates that electron transfer from DMA to $[(\text{TMP})\text{Fe}^{\text{IV}}=\text{O}]^{*+}$ plays an important role in the rate-determining step for the reaction of the P-450 model complex with DMA. Kinetic isotope effects are, however, clearly observed for reactions of $[(\text{TMP})\text{Fe}^{\text{IV}}=\text{O}]^{*+}$ with 4-X-substituted *N,N*-dimethyl- and *N,N*-bis(trideuteromethyl)anilines. The $k_{3\text{H}}/k_{3\text{D}}$ value increases with increasing E°_{ox} from a value close to unity (1.3 for X = OMe) to a large value of 5.9 for X = NO₂ [96]. More importantly, there is a large difference between the intermolecular kinetic isotope effects ($k_{3\text{H}}/k_{3\text{D}}$) and intramolecular isotope effects



Scheme 5.

$(k_{\text{H}}/k_{\text{D}})$ derived from product analysis (e.g., $k_{3\text{H}}/k_{3\text{D}} = 1.3$, $k_{\text{H}}/k_{\text{D}} = 3.9$ for $\text{X} = \text{OMe}$) [96]. The small $k_{\text{H}}/k_{\text{D}}$ values compared with those for proton-transfer reactions of $\text{DMA}^{\cdot+}$ [79] indicate that a proton-transfer step is unlikely to be involved. Thus, the rate-determining step might involve a hydrogen atom-transfer step after the initial electron transfer, as shown in Scheme 5 (mechanism C in Scheme 2).

If this is so, the product isotope effect reflects the hydrogen-transfer step (k_{H}) from the radical cation of *N,N*-dimethylaniline ($\text{DMA}^{\cdot+}$) to $(\text{TMP})\text{Fe}^{\text{IV}}=\text{O}$ in competition with the back-electron-transfer step ($k_{\text{-et}}$). With decreasing one-electron oxidation potential (E°_{ox}) of DMA, equivalent to the one-electron reduction potential (E°_{red}) of $\text{DMA}^{\cdot+}$, the rate of back-electron-transfer from $(\text{TMP})\text{Fe}^{\text{IV}}=\text{O}$ to $\text{DMA}^{\cdot+}$ decreases, becoming slower than the hydrogen-transfer step, at which point the electron-transfer step from DMA to $[(\text{TMP})\text{Fe}^{\text{IV}}=\text{O}]^{\cdot+}$ becomes the rate-determining step. This might be the reason why the kinetic isotope effect is close to unity for $\text{X} = \text{OMe}$ ($k_{3\text{H}}/k_{3\text{D}} = 1.3$) whereas the product isotope effect directly reflects the hydrogen-transfer step ($k_{\text{H}}/k_{\text{D}} = 3.9$ for $\text{X} = \text{OMe}$). For $\text{X} = \text{NO}_2$ the hydrogen-transfer step might be the rate-determining step, because of the fast back-electron-transfer whereby the $k_{3\text{H}}/k_{3\text{D}}$ value (5.9) becomes nearly the same as the $k_{\text{H}}/k_{\text{D}}$ value (6.2). According to Scheme 5, a quantitative relationship can be derived between the kinetic isotope effects ($k_{3\text{H}}/k_{3\text{D}}$) and the product isotope effects ($k_{\text{H}}/k_{\text{D}}$); this is given by Eq. 6 [96].

$$k_{3\text{H}}/k_{3\text{D}} = (k_{\text{H}}/k_{\text{D}}) \{ (k_{\text{D}}/k_{\text{H}}) + (k_{\text{-et}}/k_{\text{H}}) \} / \{ 1 + (k_{\text{-et}}/k_{\text{H}}) \} \quad (6)$$

When forward electron transfer is the rate-determining step, $k_{\text{-et}}/k_{\text{H}} \ll 1$, Eq. 6 is reduced to $k_{3\text{H}}/k_{3\text{D}} = 1$. On the other hand, when $k_{\text{-et}}/k_{\text{H}} \gg 1$, Eq. 6 is reduced to $k_{3\text{H}}/k_{3\text{D}} = k_{\text{H}}/k_{\text{D}}$. Thus, the difference between $k_{\text{H}}/k_{\text{D}}$ and $k_{3\text{H}}/k_{3\text{D}}$ should decrease with increasing $k_{\text{-et}}/k_{\text{H}}$. The $k_{\text{-et}}/k_{\text{H}}$ value can be obtained from the $k_{3\text{H}}/k_{3\text{D}}$ and $k_{\text{H}}/k_{\text{D}}$ values by use of Eq. 7, which is derived from Eq. 7 [96]. The $k_{\text{-et}}$ value for back-electron-transfer from $(\text{TMP})\text{Fe}^{\text{IV}}=\text{O}$ to $\text{DMA}^{\cdot+}$:

$$k_{\text{-et}}/k_{\text{H}} = \{ (k_{3\text{H}}/k_{3\text{D}}) - 1 \} / \{ (k_{\text{H}}/k_{\text{D}}) - (k_{3\text{H}}/k_{3\text{D}}) \} \quad (7)$$

is expected to increase with increasing E°_{ox} for DMA, which corresponds to E°_{red} of $\text{DMA}^{\bullet+}$, as the free energy change of back-electron-transfer decreases. The hydrogen atom-transfer rate constant (k_{H}) might be rather insensitive to E°_{ox} compared with the back-electron-transfer rate constant ($k_{\text{-et}}$). In fact, the $k_{\text{-et}}/k_{\text{H}}$ value increases with increasing E°_{ox} , as shown in Figure 1c [96]. Thus comparison of the rate constants for reactions of $[(\text{TMP})\text{Fe}^{\text{IV}}=\text{O}]^{\bullet+}$ and HRP compound **I** with DMA and analyses of kinetic and product isotope effects clearly indicates that *N*-demethylation of DMA by $[(\text{TMP})\text{Fe}^{\text{IV}}=\text{O}]^{\bullet+}$ proceeds via electron transfer from DMA to $[(\text{TMP})\text{Fe}^{\text{IV}}=\text{O}]^{\bullet+}$ followed by hydrogen-atom transfer from $\text{DMA}^{\bullet+}$ to $(\text{TMP})\text{Fe}^{\text{IV}}=\text{O}$ in competition with back-electron-transfer (**C** in Scheme 2). This competition is responsible for the difference between the kinetic and product isotope effects which vary depending on the ratio of the rate constant for back-electron-transfer to that for the hydrogen transfer. The contribution of metal-centered reduction of $[(\text{TMP})\text{Fe}^{\text{IV}}=\text{O}]^{\bullet+}$ by DMA would give an iron(III)-oxyl radical character $[(\text{TMP})\text{Fe}^{\text{III}}-\text{O}^\bullet]$ (vide supra), which would facilitate hydrogen atom-abstraction from $\text{DMA}^{\bullet+}$.

8.2.5 Electron Transfer Compared with Direct Oxygen Transfer

Comparison of the rate constants of $[(\text{TMP})\text{Fe}^{\text{IV}}=\text{O}]^{\bullet+}$ and HRP compound **I** was further extended to reactions with a series of sulfides [108]. HRP is known to convert thioanisole to the corresponding sulfoxide [109], although peroxidases typically catalyze two sequential one-electron oxidations such as one-electron oxidation of phenol derivatives to phenoxy radicals [110]. The yield of the sulfoxide from the stoichiometric reaction of HRP compound **I** with thioanisole is only $25 \pm 5\%$. The sulfoxidation involves oxygen-transfer from an oxoferryl species to sulfide, because ^{18}O in $\text{H}_2^{18}\text{O}_2$ has been shown to be incorporated into the product sulfoxide [108, 111]. The initial rapid conversion of compound **I** to compound **II** (k_1) by thioanisole is followed by further reduction to the ferric resting state, as is found for reactions with DMA [108, 112, 113]. A linear correlation between $\log k_1$ and E°_{ox} for the reactions of HRP compound **I** with thioanisoles (Figure 2) is readily combined with the relationship for DMA (Figure 1a) into a single, common relationship (Eq. 8) [108].

$$\log k_1 = -10.5E^\circ_{\text{ox}} + 14.6 \quad (8)$$

Such a unified correlation strongly indicates that the reduction of HRP compound **I** by thioanisoles proceeds via electron transfer rather than direct oxygen transfer. Electron transfer from the sulfide to HRP compound **I** in the protein cage might be followed by two competitive processes: (i) oxygen rebound to afford the sulfoxide; and (ii) diffusion of a sulfenium radical from the protein cage to enable the observation of HRP compound **II** as shown in Scheme 6 [108].

In contrast with the reactions of HRP compound **I** in Figure 2, there is no unified correlation for the reactions of a synthetic model $[(\text{TMP})\text{Fe}^{\text{IV}}=\text{O}]^{\bullet+}$ with DMA and thioanisoles in plots of $\log k_{\text{obs}}$ against E°_{ox} (Figure 3) [108].

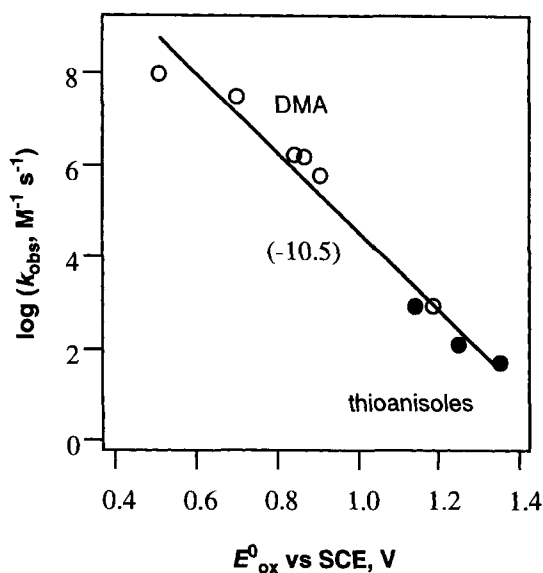
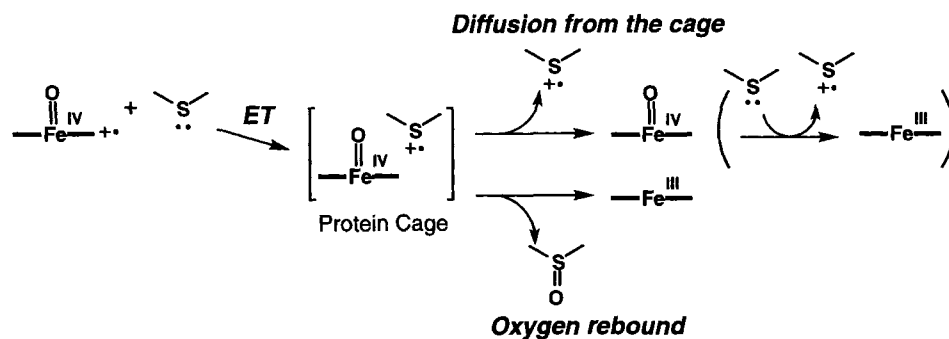


Figure 2. Plots of bimolecular rate constants for the reaction of HRP compound I with DMAs (○) and thioanisoles (●) against the oxidation potentials of DMAs and thioanisoles (E°_{ox}). The slope of the line is shown in parentheses [108].



Scheme 6.

Values of k_{obs} for reactions of $[(\text{TMP})\text{Fe}^{\text{IV}}=\text{O}]^{++}$ with thioanisoles are at least by two-orders of magnitude larger than those for electron transfer from DMA to $[(\text{TMP})\text{Fe}^{\text{IV}}=\text{O}]^{++}$. In addition, k_{obs} values of thioanisoles are much less sensitive to E°_{ox} values of thioanisoles compared to the large slope observed for the linear correlation between $\log k_1$ and E°_{ox} for electron transfer from DMA to $[(\text{TMP})\text{Fe}^{\text{IV}}=\text{O}]^{++}$. This indicates that the reduction of $[(\text{TMP})\text{Fe}^{\text{IV}}=\text{O}]^{++}$ by thioanisoles proceeds via direct oxygen transfer as shown in Scheme 7 rather than the electron-transfer/oxygen-rebound pathway in Scheme 6 [108].

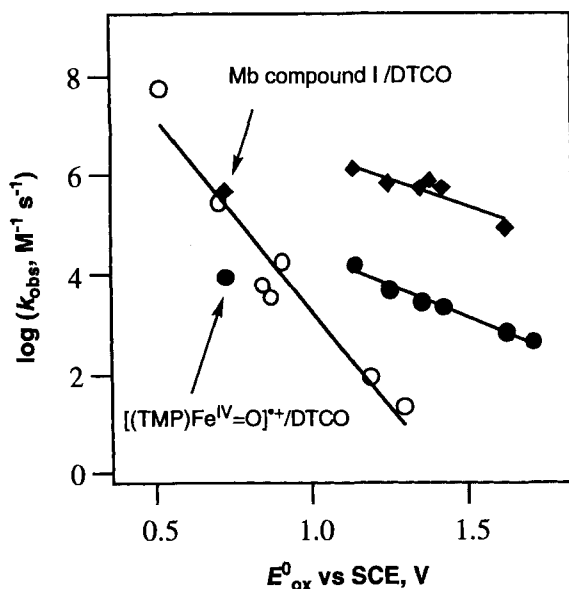
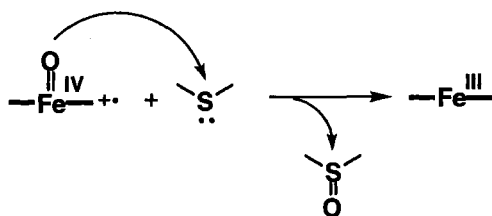


Figure 3. Plots of bimolecular rate constants for the reaction of compound **I** against the oxidation potentials, E°_{ox} , of DMA and sulfides: $[(\text{TMP})\text{Fe}^{\text{IV}}=\text{O}]^{*+}$ with DMAs (\circ) and sulfides (\bullet), His64Ser Mb compound **I** with sulfides (\blacklozenge) [108].

Direct Oxygen Transfer



Scheme 7.

The reactions of compound **I** of a sperm whale myoglobin His64Ser mutant (His64Ser Mb) [114] were also examined to compare the reactivity of His64Ser Mb compound **I** toward thioanisoles with that of the synthetic model $[(\text{TMP})\text{Fe}^{\text{IV}}=\text{O}]^{*+}$ [108]. His64Ser Mb compound **I** is readily produced by reaction with *m*CPBA. There is a parallel relationship between the plots for $[(\text{TMP})\text{Fe}^{\text{IV}}=\text{O}]^{*+}$ and His64Ser Mb compound **I**, both of which are far above the electron transfer correlation for the reduction of HRP compound **I** by DMA and thioanisoles [108]. This indicates that the reduction of His64Ser Mb compound **I** also proceeds via direct oxygen transfer in Scheme 7 rather than the electron-transfer/oxygen-rebound pathway (Scheme 6) [108].

Comparison of the linear correlation between $\log k_{\text{obs}}$ and E°_{ox} for direct oxygen transfer from $[(\text{TMP})\text{Fe}^{\text{IV}}=\text{O}]^{*+}$ to sulfides with that for the electron transfer from DMA to $[(\text{TMP})\text{Fe}^{\text{IV}}=\text{O}]^{*+}$ in Figure 3 suggests that the relationship for direct oxygen transfer might be included in the relationship for electron transfer when a

sulfide with a lower E°_{ox} value is employed for the reaction with $[(\text{TMP})\text{Fe}^{\text{IV}}=\text{O}]^{*+}$. In such a reaction electron transfer from the sulfide to $[(\text{TMP})\text{Fe}^{\text{IV}}=\text{O}]^{*+}$ could become preferable to direct oxygen-transfer and an alternation of the reaction mechanism from direct oxygen transfer to electron transfer would occur, depending on the E°_{ox} value. This supposition was demonstrated by use of 1,5-dithiacyclooctane (DTCO), the E°_{ox} value of which is much lower than those of thioanisoles [108]. The k_1 value for the reduction of $[(\text{TMP})\text{Fe}^{\text{IV}}=\text{O}]^{*+}$ by DTCO becomes even smaller than the value expected from the electron-transfer correlation between $\log k_1$ and E°_{ox} in Figure 3 [108]. Such a small k_{obs} value for DTCO compared with the k_{obs} value for DMA at the same E°_{ox} value is consistent with the larger reorganization energy (λ) expected for electron transfer oxidation producing a σ radical cation (DTCO^{*+}) than the λ values of π radical cations (DMA^{*+}) [18]. Thus reduction of $[(\text{TMP})\text{Fe}^{\text{IV}}=\text{O}]^{*+}$ by DTCO might proceed via electron transfer from DTCO to $[(\text{TMP})\text{Fe}^{\text{IV}}=\text{O}]^{*+}$ rather than direct oxygen transfer.

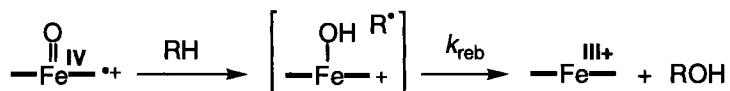
Alteration of the reaction mechanism from direct oxygen transfer to electron transfer becomes more evident in the reduction of His64Ser Mb compound **I** by DTCO, because rapid formation of compound **II** was clearly observed; this was followed by the slow conversion of compound **II** to the ferric state [108]. The k_{obs} value for electron transfer from DTCO to His64Ser Mb compound **I** agrees with a linear correlation for reactions of $[(\text{TMP})\text{Fe}^{\text{IV}}=\text{O}]^{*+}$ with DMA via electron transfer (see Figure 3) [108].

In summary, the reduction of HRP compound **I** and $[(\text{TMP})\text{Fe}^{\text{IV}}=\text{O}]^{*+}$ by thioanisoles proceeds via electron transfer whereas the sulfoxidation of thioanisoles with $[(\text{TMP})\text{Fe}^{\text{IV}}=\text{O}]^{*+}$ and His64Ser Mb compound **I** occurs via direct oxygen transfer. When thioanisoles are replaced by a much stronger reductant (DTCO), however, the reactions of both $[(\text{TMP})\text{Fe}^{\text{IV}}=\text{O}]^{*+}$ and His64Ser Mb compound **I** proceed via electron transfer. The heme group of Mb has been shown to be located close to the protein surface [29, 115–117]; it is therefore more accessible for substrates than the heme group of HRP. Thus reactions of His64Ser Mb compound **I** and synthetic model $[(\text{TMP})\text{Fe}^{\text{IV}}=\text{O}]^{*+}$ can proceed via direct oxygen transfer which requires strong interaction between compound **I** and the substrates rather than electron transfer which can occur at a longer distance for the reactions of HRP compound **I**. When a strong electron donor such as DTCO is employed, the electron-transfer pathway can become energetically preferable to direct oxygen transfer; it can proceed at a long separation distance before interacting strongly with the reaction center.

8.2.6 ‘Agostic’ Interaction

In the hydroxylation of unactivated C–H bonds in hydrocarbons by cytochromes P-450, a hydrogen atom is thought to be abstracted from the substrate C–H bond by a high-valent iron–oxo intermediate, forming a carbon radical which captures an hydroxyl radical from iron (Scheme 8) [27, 118, 119].

This is called an oxygen-rebound mechanism. Large intramolecular isotope effects ($k_{\text{H}}/k_{\text{D}} = 11$) for substrates with CHD groups [120, 121], C–H bond selectivi-

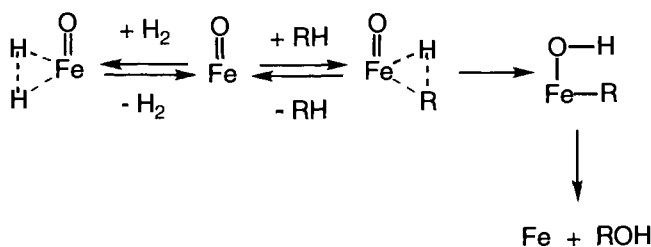


Scheme 8.

ties consistent with those for radical reactions [122] (tertiary > secondary > primary) [123, 124], and loss of stereochemistry in the hydroxylations of norbornane [121, 125] suggest the hydrogen transfer mechanism (Scheme 8). This mechanism was further supported by the detection of rearranged products from carbon radicals in several P-450 oxidations [126]. When, however, the rate constant for the oxygen-rebound step in hydroxylations (k_{reb} in Scheme 8) by a rat liver P-450 isozyme was determined by use of a radical clock substrate [127] widely varying results were obtained (1.4×10^{10} – $1.3 \times 10^{13} \text{ s}^{-1}$) [128–130]. When a hypersensitive radical clock (*trans,trans*-2-*tert*-butoxy-3-phenylcyclopropylmethane) was used to determine the rate constant more accurately it was found that most of the rearranged products were derived from a cationic intermediate produced during the course of the hydroxylation reaction; it was suggested that this process is the origin of the wide variation in the rate constant [131]. The radical species in the hydroxylation reaction was found to have a very short lifetime (70 fs) and it cannot, therefore, be a true intermediate but is part of a reacting ensemble [131]. The small amount of the radical rearrangement product indicates that the rebound step is non-synchronous but concerted with C–H bond cleavage leading to C–O bond formation [131]. The extremely short lifetime of the carbon radical also indicates that the oxygen atom is within bonding distance of carbon at the instant of hydrogen abstraction. This means that a ‘side-on’ approach of oxygen to the C–H bond is favored over the linear C–H–O arrangement of conventional hydrogen-atom abstraction. In addition, the regioselectivity in the reaction of methylcubane with *t*-BuO \cdot has been shown to be quite different from that with cytochrome P-450 enzymes [132]. This is consistent with a concerted mechanism involving ‘side-on’ approach to the C–H bond of the substrate.

Such a ‘side-on’ approach is reminiscent of a three-center two-electron bond, referred to as an agostic interaction [133–136]. An ‘agostic’ substrate–catalyst complex has recently been proposed as a key intermediate before the oxygen-transfer step in the hydroxylation of cyclohexane by PhIO with (TPFPP)FeCl, as shown in Scheme 9 [137].

Substrates such as H₂ which can form strong agostic complexes are expected to inhibit the oxidation of more weakly bound substrates by sequestering the active oxidant (Scheme 9). In fact, the oxidation of cyclohexane was inhibited by the presence of H₂ [137]. On removal of the H₂ from the reaction system, the rate of cyclohexanol production returns to its original value in the absence of H₂, demonstrating that the inhibition is reversible. The pressure at which the rate was half that of the uninhibited reaction ($P_{1/2}$) was 1.4 atm at 0 °C [137]. When H₂ was replaced by D₂, the $P_{1/2}$ value became smaller (1.0 atm) [137]. Such an inverse isotope effect can be compared with the value (0.78) reported for H₂/D₂ binding to a tungsten



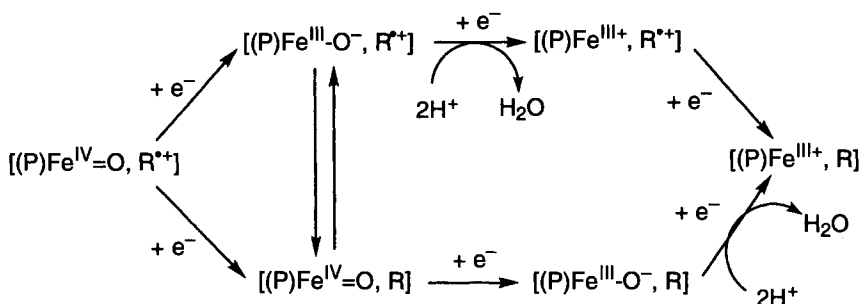
Scheme 9.

complex [138]. Methane also inhibits the oxygenation of cyclohexane, possibly because of formation of a complex with $[(\text{TPFP})\text{Fe}^{\text{IV}}=\text{O}]^+$. It has been shown that even heptane can coordinate to iron(II) with a double A-frame porphyrin and that the metal-to-carbon distances determined by X-ray analysis are 2.5–2.8 Å, typical of moderate to weak agostic interaction [139]. Results from density-functional calculations on iron porphyrin complexes of methane and ethane are indicative of significant charge-transfer character of the complexes (e.g. 0.23 e for ethane) in which the alkane acts as an electron donor [139]. Thus, a charge-transfer-type interaction might play an important role in the ‘agostic’ substrate-catalyst complex in Scheme 9. Although the importance of charge-transfer complexes as intermediates in a variety of redox reactions has been well documented [83, 140–145], the ‘agostic’ substrate–catalyst complex proposed in Scheme 9 has yet to be characterized [137].

8.2.7 Site of Electron Transfer in Compound I

Electron-transfer reactions between cytochrome *c* and cytochrome *c* peroxidase have been studied extensively because of the well-characterized structures and biophysical properties of the reactants [146–150]. It is well known that the resting ferric form of cytochrome *c* peroxidase is oxidized by hydrogen peroxide to compound **I**, which contains an oxyferryl heme moiety in which the iron atom has a formal oxidation state of 4+ [146–150]. The other is a porphyrin π radical cation or organic radical (R^+) localized on an amino acid residue of Trp-191 [151–154]; this is formed by transfer of the oxidized equivalent to the amino acid side chain [150]. The site of electron transfer in the reduction of compound **I** has been controversial and two forms of compound **II** have been identified, $(\text{P})\text{Fe}^{\text{IV}}=\text{O}$ containing the oxyferryl heme $\text{Fe}(\text{IV})$ [155–158] and $[(\text{P})\text{Fe}^{\text{III}}]^{\cdot 2+}$ containing $\text{Fe}(\text{III})$ and the porphyrin π radical cation which oxidizes the amino acid side-chain to produce an organic radical $[(\text{P})\text{Fe}^{\text{III}}]^+, \text{R}^+$ [159–165] as shown in Scheme 10.

These two pathways have been shown to be affected by ionic strength (μ) [166]. At low ionic strength (below $\mu = 50$ mM) the $\text{Fe}(\text{IV})$ site of compound **I** is preferentially reduced, followed by reduction of the radical site in the slow phase of the reaction [166]. At high ionic strength (e.g. $\mu = 200$ mM), the radical site is preferentially reduced, giving a compound **II** that retains the $\text{Fe}(\text{IV})$ site [166]. The switch of the site of electron transfer between the $\text{Fe}(\text{IV})$ site and the radical site seems to



Scheme 10.

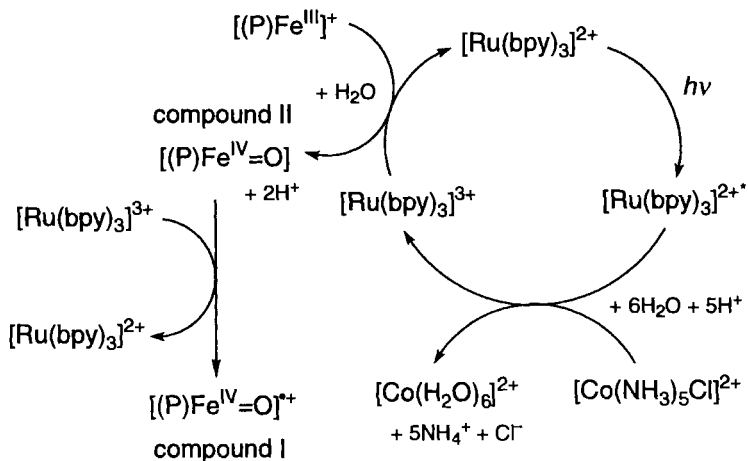
be controlled by the orientation of the two proteins in the complex, which depends on ionic strength [147]. In yeast cytochrome c-peroxidase complex crystallized at high ionic strength, a short electron transfer pathway from heme to Trp-191 becomes available; there is more intimate contact between cytochrome c and the peroxidase for the complex crystallized at low ionic strength [147]. It was suggested that at low ionic strength the orientation was dominated by electrostatic forces and that at high ionic strength the orientation was dominated by the hydrophobic interaction [166].

8.2.8 Photoinduced Electron-transfer Oxidation

The fast oxidation processes of HRP and its functional model peptides [microperoxidase-8 (MP8)] generating the corresponding compound I ($[(\text{P})\text{Fe}^{\text{IV}}\text{=O}]^{\bullet+}$) and compound II ($[(\text{P})\text{Fe}^{\text{IV}}\text{=O}]$) have been successfully monitored by use of laser-flash photolysis [167, 168]. The photocatalytic system for generation of HRP compound I and compound II is shown in Scheme 11 [168].

The MLCT (metal to ligand charge transfer) excited state of $[\text{Ru}(\text{bpy})_3]^{2+*}$ ($[\text{Ru}(\text{bpy})_3]^{2+*}$) is produced by irradiation with visible light; electron transfer from $[\text{Ru}(\text{bpy})_3]^{2+*}$ to the Co^{III} complex gives $[\text{Ru}(\text{bpy})_3]^{3+}$ [168]. The oxidizing power of $[\text{Ru}(\text{bpy})_3]^{3+}$ is sufficient to oxidize the ferric resting state of HRP ($[(\text{P})\text{Fe}^{\text{III}}]^+$) at the ligand center to give the porphyrin π radical cation ($[(\text{P})\text{Fe}^{\text{III}}]^{\bullet+}$). This step is followed by the slower step of conversion of $[(\text{P})\text{Fe}^{\text{III}}]^{\bullet+}$ to compound II, $(\text{P})\text{Fe}^{\text{IV}}\text{=O}$, accompanied by deprotonation of the coordinated water [168].

The kinetics at 430 nm after a laser flash of the photocatalytic system (pH 8.5) in Scheme 11 are biphasic—a fast reaction on a millisecond time-scale because of formation of $[(\text{P})\text{Fe}^{\text{III}}]^{\bullet+}$ was followed by a much slower reaction on a second time-scale because of the conversion of $[(\text{P})\text{Fe}^{\text{III}}]^{\bullet+}$ to compound II, $(\text{P})\text{Fe}^{\text{IV}}\text{=O}$ [168]. In general, ferric porphyrins have ligand-centered one-electron oxidation potentials at which ferric porphyrins are oxidized to ferric porphyrin π radical cations; these are higher than oxidation potentials for metal-centered one-electron oxidation to ferryl porphyrins [102, 170]. Despite the smaller (by ca 0.3 eV) driving force for ligand-centered oxidation than for metal-centered oxidation [102, 170], ligand-centered oxidation of HRP occurs before metal-centered oxidation (Scheme 11). This is be-



Scheme 11.

cause ligand-centered oxidation requires a much smaller reorganization energy for electron transfer and it is, therefore, kinetically favored—as seen in the electron-transfer oxidation of (P)Fe(R) [93]. Only the first process requires [Ru(bpy)₃]³⁺, which was reduced to [Ru(bpy)₃]²⁺. The formation of [Ru(bpy)₃]²⁺ was readily monitored at 450 nm. The rate of formation of [(P)Fe^{III}]^{•2+} shows first-order dependence on the [Ru(bpy)₃]³⁺ concentration (Eq. 9), whereas conversion to compound **II** is first-order with respect to [(P)Fe^{III}]^{•2+} concentration (Eq. 10). The rate constant (*k*_{et1}) for electron transfer from [(P)Fe^{III}]^{•+} to [Ru(bpy)₃]³⁺ was determined as $2.5 \times 10^7 \text{ M}^{-1} \text{ s}^{-1}$ at pH 10.3 [168]. The rate constant (*k*_{et2}) for generation of (P)Fe^{IV}=O at pH 10.8 ($95 \pm 7 \text{ s}^{-1}$) is over 20 times larger than that at lower pH ($4.1 \pm 0.9 \text{ s}^{-1}$) [168].

$$d[(P)Fe^{III} \cdot 2+]/dt = k_1[(P)Fe^{III} +][Ru(bpy)_3]^{3+} \quad (9)$$

$$d[(P)Fe^{IV}=O]/dt = k_2[(P)Fe^{III}]^{2+} \quad (10)$$

In acidic solutions ferric MP8 is also rapidly oxidized by $[\text{Ru}(\text{bpy})_3]^{3+}$ to a ferric porphyrin π radical cation; the rate constant $k_{\text{etI}} = 5.6 \times 10^9 \text{ M}^{-1} \text{ s}^{-1}$ which is much larger than the value for HRP [167]. In alkaline solutions, the oxidation product is ferryl MP8 which is represented as a generalized form, $(\text{P})\text{Fe}^{\text{IV}}=\text{O}$. In this instance, however, transformation of $[(\text{P})\text{Fe}^{\text{III}}]^{2+}$ to $(\text{P})\text{Fe}^{\text{IV}}=\text{O}$ was too fast to be detected [167].

In contrast with HRP, P-450 cannot be oxidized efficiently by external redox agents such as $[\text{Ru}(\text{bpy})_3]^{3+}$, because heme is deeply buried in P-450 [169]. By tethering a $[\text{Ru}(\text{bpy})_3]^{2+}$ photosensitizer to a protein substrate through a hydrocarbon chain, however, the heme porphyrin π radical cation or the Fe^{IV} species which corresponds to compound **II** has been detected successfully upon laser photolysis of the $[\text{Ru}(\text{bpy})_3]^{2+}$ -tethered P-450 in the presence of $[\text{Co}(\text{NH}_3)_5\text{Cl}]^{2+}$ [169].

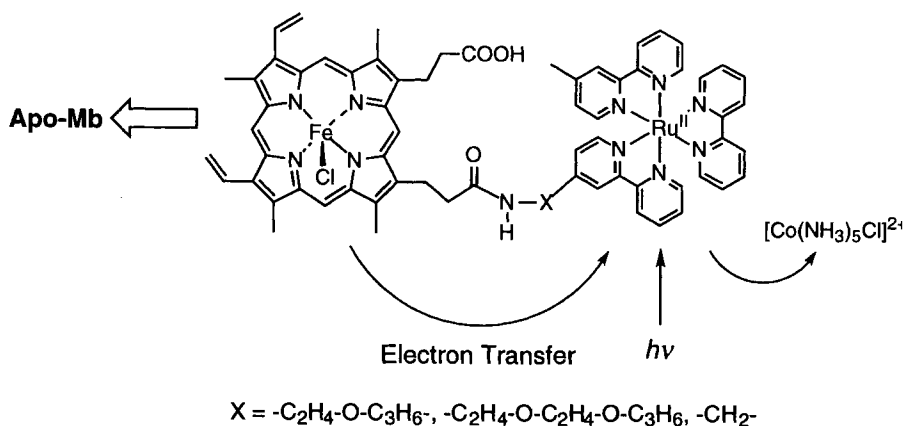
HRP compound **II** is further oxidized by electron transfer with $[\text{Ru}(\text{bpy})_3]^{3+}$ to afford compound **I** (Scheme 11) [168]. Compound **II** was generated spontaneously after photolysis of the HRP- $[\text{Ru}(\text{bpy})_3]^{2+}$ - $[\text{Co}(\text{NH}_3)_5\text{Cl}]^{2+}$ system [168]. The rate of formation of compound **I** obeys second-order kinetics, being first order in each reactant, as given by Eq. 11 [168].

$$d[(\text{P})\text{Fe}^{\text{IV}}=\text{O}]^{\bullet+}/dt = k_{\text{et}}[(\text{P})\text{Fe}^{\text{IV}}=\text{O}][[\text{Ru}(\text{bpy})_3]^{3+}] \quad (11)$$

The rate constant for electron transfer from HRP compound **II** to $[\text{Ru}(\text{bpy})_3]^{3+}$ is nearly independent of pH. Although the k_{et} value ($1.1 \times 10^8 \text{ M}^{-1} \text{ s}^{-1}$) is slightly larger than the value for formation of $[(\text{P})\text{Fe}^{\text{III}}]^{\bullet+}$ ($2.5 \times 10^7 \text{ M}^{-1} \text{ s}^{-1}$) at pH 10.3, the k_{et} value ($1.1 \times 10^8 \text{ M}^{-1} \text{ s}^{-1}$) is significantly smaller than the value ($5.6 \times 10^9 \text{ M}^{-1} \text{ s}^{-1}$) for the porphyrin ligand-centered oxidation of ferric MP8 by $[\text{Ru}(\text{bpy})_3]^{3+}$, despite the higher driving force for electron transfer from HRP compound **II** to $[\text{Ru}(\text{bpy})_3]^{3+}$ ($\Delta G^\circ_{\text{et}} = -8.1 \text{ kcal mol}^{-1}$ obtained from the E°_{ox} value of HRP compound **I**, which is equal to E°_{red} of HRP compound **II** [104], and the E°_{red} value of $[\text{Ru}(\text{bpy})_3]^{3+}$) [171]. When the Marcus theory (Eq. 4) [91] is applied to the k_{et} value ($1.1 \times 10^8 \text{ M}^{-1} \text{ s}^{-1}$), the λ value is evaluated as $\lambda = 30.2 \text{ kcal mol}^{-1}$. If the reorganization energy for electron self-exchange between $[\text{Ru}(\text{bpy})_3]^{3+}$ and $[\text{Ru}(\text{bpy})_3]^{2+}$ is neglected [93], a large λ value ($60.4 \text{ kcal mol}^{-1}$) is obtained for the electron self-exchange between HRP compound **I** and compound **II**, because the λ value for the cross reaction is equal to the average of the λ value for electron self-exchange for each reactant. This value is quite consistent with a large reorganization energy ($\lambda = 61.9 \text{ kcal mol}^{-1}$) [104] derived from the electron-transfer rate from ferrocyanide to HRP compound **I** (vide supra). Such a large λ value for electron self-exchange between HRP compound **I** and compound **II** and the slower rate than that for the purely ligand-centered oxidation of ferric MP8, despite the larger driving force, is indicative of a significant contribution from the metal-centered oxidation of HRP compound **II** rather than the porphyrin ligand-centered oxidation. This means that HRP compound **II**, formally $(\text{P})\text{Fe}^{\text{IV}}=\text{O}$ should contain a significant amount of $(\text{P})\text{Fe}^{\text{III}}-\text{O}^\bullet$ character, as discussed in the section on P-450 reaction mechanisms (vide supra).

Stepwise conversion of $[(\text{P})\text{Fe}^{\text{III}}]^{\bullet+}$ to $(\text{P})\text{Fe}^{\text{IV}}=\text{O}$ has been clearly shown by cofactor reconstitution and use of myoglobin (Mb) bearing a ruthenium complex $[\text{Ru}(\text{bpy})_3-\text{Mb}]$ (see Scheme 12) [172].

The reconstitution of chemically modified heme with apo-Mb has been well established [173–176]. The one-electron reduction potential of ferryl-Mb (Fe^{IV} -heme) was reported as 0.896 V relative to the NHE [177] which is less positive than the one-electron oxidation potential of $[\text{Ru}(\text{bpy})_3]^{2+}$ (1.25 V). Thus, generation of ferryl-Mb by electron transfer from the met-Mb (ferric state) moiety to the Ru^{3+} moiety might be thermodynamically favorable. An appropriate amount of a sacrificial electron acceptor such as $[\text{Co}(\text{NH}_3)_3\text{Cl}]^{2+}$ which can quench the Ru^{2+} excited state oxidatively was, however, required to produce the Ru^{3+} state in competition with the reductive quenching of the Ru^{2+} excited state by the met-Mb [178, 179]. No direct electron transfer from the met-Mb (ferric state) moiety to the Ru^{2+} excited state occurs, because this process is thermodynamically disfavored [178, 179].

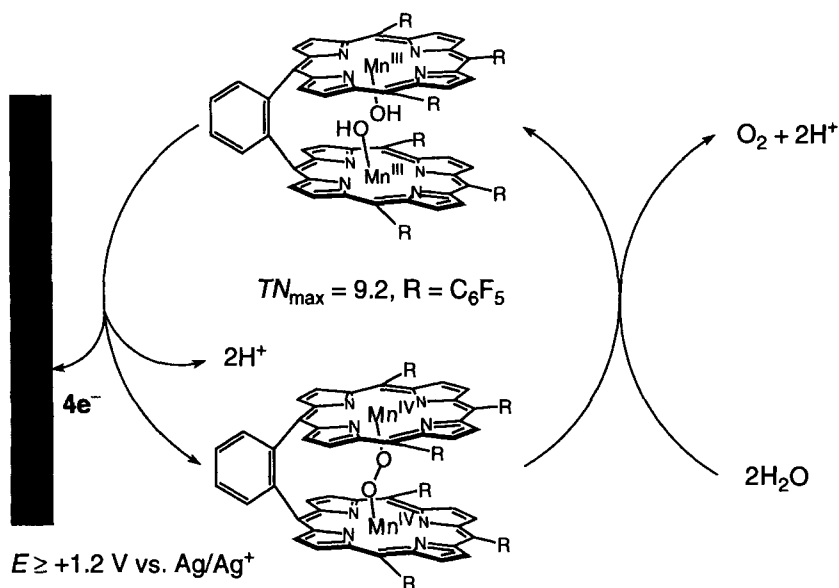


Scheme 12.

Steady-state irradiation with visible light of a deaerated aqueous solution containing Ru(bpy)₃-met-Mb in the presence of [Co(NH₃)₅Cl]²⁺ at pH = 7.5 results in the formation of ferric-Mb [172] which has a strong absorption maximum at 408 nm with weak peaks at 505 and 630 nm [180]. No reaction occurred at pH < 6. Laser-flash photolysis study has revealed that the Ru²⁺ excited state is oxidatively quenched by [Co(NH₃)₅Cl]²⁺ (3 mM) within 0.04 μs in competition with the reductive quenching by met-Mb. Simple bleaching of a Soret band region as a result of formation of the ferric porphyrin π radical cation [181] was detected 1 μs after the laser pulse; this rapid reaction was followed by the appearance of a new peak, from ferryl-Mb, at 426 nm. The rate constants for the first and second stages were determined as 7.1 × 10⁵ s⁻¹, and 4.0 × 10⁴ s⁻¹, respectively [172]. The rate constant for electron transfer from the met-Mb to the Ru³⁺ state (first stage) is independent of pH whereas that for transformation from the ferric porphyrin π radical cation to the ferryl-Mb (second stage) is dependent on pH and the value increased from 4.0 × 10⁴ s⁻¹ at pH 7.5 to 2.0 × 10⁵ at pH 9.0, as expected from the concomitant deprotonation of coordinated water to generate the ferryl-Mb [172].

8.2.9 Oxygen-evolving Complex

Four-electron oxidation of water to oxygen in photosystem II (PSII) is catalyzed by the oxygen-evolving complex (OEC) which contains a tetranuclear manganese cluster as the active site of water oxidation in photosynthetic organisms [182–184]. Extensive efforts have been devoted to developing synthetic models of OEC [185–189], but only rarely have the model complexes actually catalyzed water oxidation [190–195]. The first example of a manganese-based homogeneous catalyst for the oxidation of water is the dimanganese complex of cofacial dimers of triphenylporphyrin linked by an *o*-phenylene bridge, as shown in Scheme 13 [190].



Scheme 13.

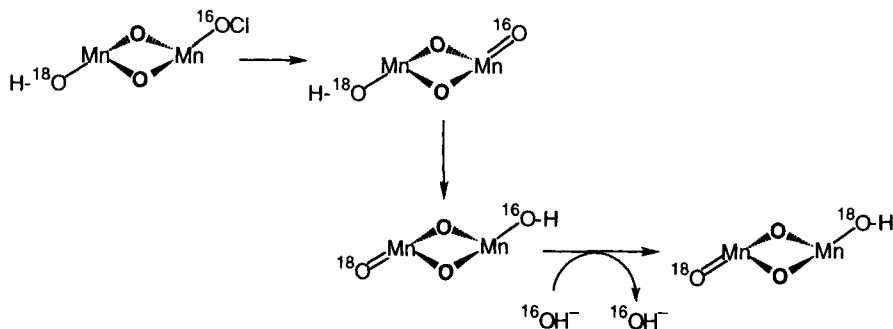
Anodic oxidation of an aqueous acetonitrile solution in the absence of the manganese porphyrin dimers did not result in evolution of oxygen at potentials up to +2.3 V (relative to Ag/Ag^+), whereas electrochemical oxidation in the presence of the dimer resulted in oxygen evolution at potentials between +1.2 and +2.0 V with a faradaic efficiency of 5–17 % [190]. The maximum turnover number (mol O_2 /mol catalyst) was 9.2 when a manganese porphyrin dimer with $R = \text{C}_6\text{F}_5$ in Scheme 13 was employed as a catalyst at 2.0 V in the presence of $n\text{-Bu}_4\text{NOH}$ [190]. It was confirmed that the rate of oxygen evolution was proportional to catalyst concentration and, on the basis of a labeling experiment using H_2^{18}O , that the O_2 evolved came from H_2O [190]. Although the catalytic mechanism remains to be clarified, it is proposed that OH^- might coordinate to each Mn ion of the dimer inside the cavity and that four-electron oxidation at the electrode gives $\text{Mn}^{\text{IV}}=\text{O}$ dimer in which the O–O bond is formed efficiently to afford an $\text{Mn}^{\text{IV}}\text{--O--O--Mn}^{\text{IV}}$ complex because of the proximity of two Mn ions. The peroxy bridge could then be replaced by an OH^- ion, evolving O_2 and accompanied by regeneration of the Mn^{III} dimer (Scheme 13) [190].

Similar manganese porphyrin dimers linked by different spacer molecules had catalase activity [196]. The activity was highest when the Mn–Mn separation was ca 4 Å, in agreement with the Mn–Mn separation in the hypothetical $\text{Mn}^{\text{IV}}\text{--O--O--Mn}^{\text{IV}}$ complex [196]. The high-valent Mn porphyrin dimer has been prepared by the oxidation of the Mn^{III} dimer with *m*CPBA. The Mn^{IV} dimer thus formed was stable for hours at temperatures ranging from -78 to -20°C and it was detected by ESI MS (electrospray ionization mass spectroscopy) [197]. Cyclooctene was oxidized by *m*CPBA (1.1 equivalent for each Mn ion) with the Mn^{III} dimer to

yield the epoxide in 41 % yield on the basis of the amount of *m*CPBA [197]. After the reaction, the Mn complex was recovered in the Mn^{IV} state [197]. This indicates that only one $\text{Mn}^{\text{IV}}=\text{O}$ in the dimer was effective in the epoxidation and that another equivalent of the oxidant was consumed in conversion of the Mn^{III} to the Mn^{IV} dimer [197].

The first clear example of an O–O bond-forming reaction involving a di- μ -oxo dimanganese complex has recently been reported for the $\text{Mn}(\text{III})$ – $\text{Mn}(\text{IV})$ complex, $[\text{H}_2\text{O}(\text{terpy})\text{Mn}(\text{O})_2\text{Mn}(\text{terpy})\text{OH}_2](\text{NO}_3)_3$ (terpy is 2,2':6',2''-terpyridine) [194]. The X-ray structure was well-characterized and revealed a di- μ -oxo core with dimensions typical of such complexes (2.7 Å for the Mn–Mn distance) [194]. An ESR spectrum of the di- μ -oxo dimanganese complex contained 16 lines characteristic of $\text{Mn}(\text{III})$ – $\text{Mn}(\text{IV})$ mixed valence dimers [198]. Water is oxidized to O_2 by NaClO in the presence of the di- μ -oxo dimanganese complex. An ^{18}O -labeling experiment indicated the participation of $\text{Mn}^{\text{IV}}=\text{O}$ species in the water oxidation, as shown in Scheme 14. The first step is the formation of a $\text{Mn}^{\text{V}}=\text{O}$, in which the O atom originates from $^{16}\text{OCl}^-$. The terminal oxo ligand can rapidly exchange with an ^{18}O -labeled hydroxide or aqua ligand on the other Mn ion of the di- μ -oxo dimanganese complex. The ^{16}O -hydroxide/aqua ligand can then exchange rapidly with the solvent, to produce a complex in which where both Mn sites are ^{18}O labeled, to yield $^{18}\text{O}_2$ (Scheme 14) [194].

Unfortunately, however, the catalytic reactions end with the complete conversion of the Mn to permanganate after ca 6 h [194]. The detailed mechanism for the catalytic oxidation of water remains to be clarified.



Scheme 14.

8.3 Catalytic Reduction of Oxygen

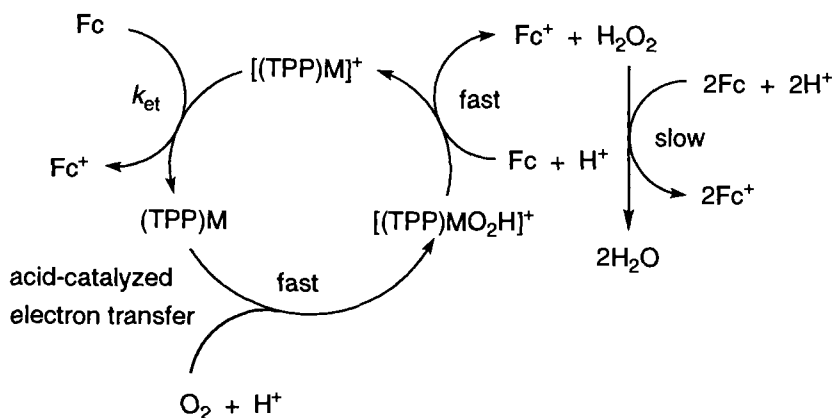
The reverse reaction of the oxidation of water to oxygen described above is four-electron reduction of O_2 to H_2O by cytochrome c oxidases; this is the key step in the

respiratory storage of metabolic energy as ATP (adenosine triphosphate) [199–203]. The most important feature of cytochrome c oxidases is that they do not release one-electron or two-electron reduced products (O_2^- and H_2O_2 , respectively) both of which would be toxic and devastating to the cell [199–203]. To understand the catalytic mechanism of the four-electron reduction of O_2 considerable efforts have long been made to prepare synthetic analogs of the active center of cytochrome c oxidases [204–207]. Studies on cytochrome c oxidases and the model complexes have recently been stimulated by the publication of X-ray structures of cytochrome c oxidases [208–212]. Cytochrome c oxidase has a heteronuclear heme $\text{a}_3/\text{Cu}_\text{B}$ metal center in which a myoglobin-type iron center and a copper atom (Cu_B) coordinate to three imidazoles from histidine residues on the distal side [208–212]. A Cu(II) binding site has recently been constructed successfully by use of cytochrome c peroxidase mutant (Arg48His, Trp51His, His52Ala, Ser81His) from yeast mitochondria [213]. Two other metal sites, a coordinately saturated heme and a dinuclear Cu_2 center are involved in storing and transferring the electrons during the four-electron reduction of O_2 [208–212]. Although many issues still remain to be resolved, particularly the exact role of Cu in the catalytic cycle, ongoing research on cytochrome c oxidase model systems has provided valuable mechanistic insight into the catalytic mechanism of the four-electron reduction of O_2 as described below.

8.3.1 Two-electron Reduction

Even simple metalloporphyrins such as $[(\text{TPP})\text{M}]^+$ where $\text{M} = \text{Co}$, Fe and Mn can enable reduction of O_2 to H_2O by ferrocene derivatives (Fc) used as an electron donor in the presence of HClO_4 in acetonitrile [214, 215]. However, the rate-determining step is the two-electron reduction of O_2 to H_2O_2 (Scheme 15) [214, 125]. Nonetheless, the catalytic effect of $[(\text{TPP})\text{M}]^+$ for the reduction of O_2 by Fc is remarkable, because the oxidation of ferrocene by O_2 hardly occurred in the presence of HClO_4 without $[(\text{TPP})\text{M}]^+$ [216]. The rate-determining step for the $[(\text{TPP})\text{M}]^+$ -catalyzed two-electron reduction of O_2 to H_2O_2 has been shown to be the initial electron transfer from Fc to $[(\text{TPP})\text{M}]^+$ as shown in Scheme 15 [215]. The reduced metalloporphyrin, $(\text{TPP})\text{M}$, is rapidly oxidized by acid-catalyzed electron-transfer reduction of O_2 by Fc, regenerating $[(\text{TPP})\text{M}]^+$ via formation of the putative hydroperoxo complex (Scheme 15) [215].

The rate constants (k_et) of electron transfer from Fc to $[(\text{TPP})\text{M}]^+$ agree well with those evaluated in light of the Marcus equations [91] for outer-sphere electron transfer (Eq. 4) [215]. Such agreement clearly demonstrates that electron transfer from Fc to $[(\text{TPP})\text{M}]^+$ in Scheme 15 proceeds via an outer-sphere pathway. In contrast to this, the k_et value of the acid-catalyzed electron transfer from $(\text{TPP})\text{Co}$ to O_2 is 10^9 -fold larger than that expected from an outer-sphere electron transfer [215]. Such huge enhancement of the observed rate relative to that calculated for outer-sphere electron transfer indicates the strong inner-sphere nature of acid-catalyzed electron transfer from $(\text{TPP})\text{Co}$ to O_2 ; this should result in formation of the hydroperoxo complex, $[(\text{TPP})\text{CoO}_2\text{H}]^+$ (Scheme 15, $\text{M} = \text{Co}$). Other metalloporphyrins ($\text{M} = \text{Fe}$ and Mn) can also act as efficient catalysts of the reduction of



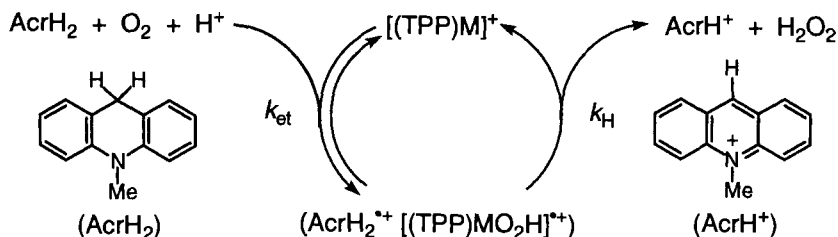
Scheme 15.

O_2 by Fc in the presence of HClO_4 in acetonitrile. The inner-sphere nature of the acid-catalyzed electron transfer from $(\text{TPP})\text{M}$ to O_2 is essential to the catalytic cycle. Otherwise $[(\text{TPP})\text{M}]^+$ would act solely as an electron mediator and no acceleration of the overall electron transfer from Fc to O_2 would be achieved.

An NADH analog, 10-methyl-9,10-dihydroacridine (AcrH_2) can also reduce O_2 to H_2O in the presence of a catalytic amount of $[(\text{TPP})\text{M}]^+$ ($\text{M} = \text{Co}, \text{Fe}$) in the presence of HClO_4 in MeCN [217, 218]. In this instance also the two-electron reduction of O_2 to H_2O_2 is the rate-determining step. The catalytic two-electron reduction of O_2 by AcrH_2 also proceeds via electron transfer from AcrH_2 to $[(\text{TPP})\text{M}]^+$ in the presence of O_2 and HClO_4 to produce a radical pair ($\text{AcrH}_2^{\cdot+} [(\text{TPP})\text{CoO}_2\text{H}]^{\cdot+}$) followed by hydrogen transfer from $\text{AcrH}_2^{\cdot+}$ to $[(\text{TPP})\text{MO}_2\text{H}]^{\cdot+}$ to yield 10-methylacridinium ion (AcrH^+) and H_2O_2 , accompanied by regeneration of $[(\text{TPP})\text{M}]^+$ (Scheme 16) [218].

The kinetic isotope effect ($k_{\text{H}}/k_{\text{D}} = 7.1$) observed when AcrH_2 is replaced by AcrD_2 is ascribed to this hydrogen-transfer step [218].

To achieve the four-electron reduction of O_2 to H_2O without releasing H_2O_2 another metal ion such as Cu ion in cytochrome c oxidase is required to stabilize the two-electron reduced peroxy species by forming a bimetallic peroxo complex. This



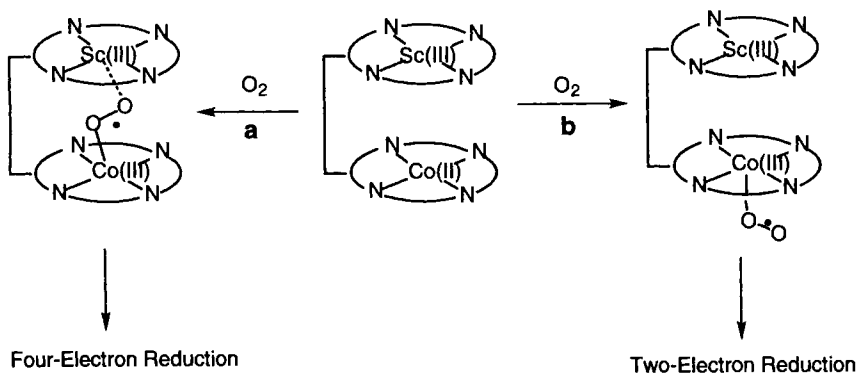
Scheme 16.

would make the release of peroxide unfavorable, resulting in the direct four-electron reduction of O_2 to H_2O . The initial electron transfer to O_2 is also accelerated by the interaction of O_2^- with a metal ion which can act as a Lewis acid. Such catalysis of metal ions to accelerate the electron-transfer reduction of a variety of substrates, including oxygen, has been well documented [219, 220]. The existence of a strong interaction between O_2^- and Sc^{3+} has been demonstrated by observation of the ESR spectrum of the $\text{O}_2^- - \text{Sc}^{3+}$ complex [221]. The $\text{O}_2^- - \text{Sc}^{3+}$ complex is generated by photoinduced electron transfer from the dimeric 1-benzyl-1,4-dihydronicotinamide $[(\text{BNA})_2]$, which can act as a unique two-electron donor [222, 223], to O_2 [221]. The clear eight-line isotropic spectrum at the center is ascribed to the superhyperfine coupling of O_2^- with the 7/2 nuclear spin of the scandium nucleus ($a_{\text{Sc}} = 3.82 \text{ G}$) [221]. The isotropic g value (2.0165) is appreciably smaller than the average value (2.030) [224] of the principal three g components of O_2^- at 77 K, being consistent with spin delocalization to the scandium nucleus, as demonstrated by observation of the superhyperfine coupling. The two inequivalent $a(^{17}\text{O})$ values (21 and 14 G) observed for the $\text{O}_2^- - \text{Sc}^{3+}$ complex containing ^{17}O are fully consistent with 'end-on' coordination form of $^{\cdot}\text{O}-\text{O}^- - \text{Sc}^{3+}$ in which the electron spin is more localized at the terminal oxygen [221].

8.3.2 Four-electron Reduction

Several dimeric metalloporphyrins [225–230] have been used to achieve four-electron reduction of O_2 to H_2O . The binding of O_2 to the metal center inside the cavity of two porphyrins seems to be essential for the four-electron reduction of O_2 to H_2O as shown in Scheme 17 [230].

When O_2 binds the Co(II) center of the bisporphyrin inside the cavity to produce the *endo* complex (path a), the superoxo complex interacts strongly with the Sc(III) ion, leading to the further reduction to H_2O via the corresponding peroxo complex in which the interaction with Sc(III) becomes much stronger. Heterolytic cleavage

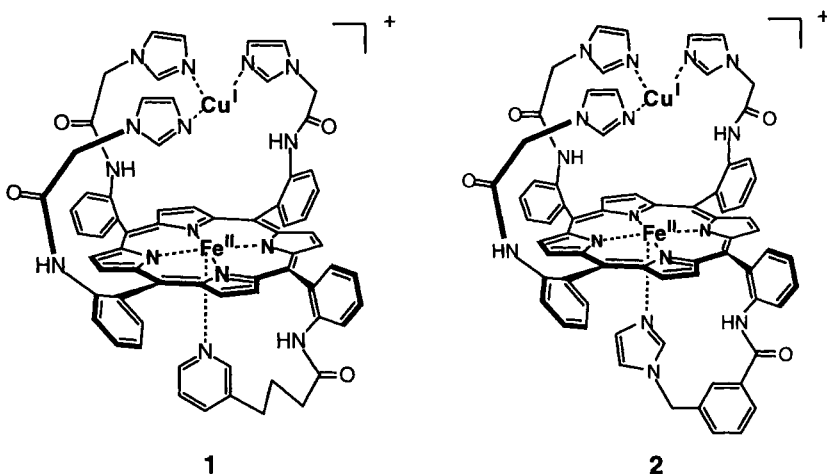


Scheme 17.

of the O–O bond can then occur, followed by a further two-reduction to yield H_2O . When the Co(II) center binds O_2 outside the cavity, however, there is no interaction of the superoxo complex with the Sc(III) ion (path **b**). Then protonation predominates, followed by the further one-electron reduction to yield H_2O_2 .

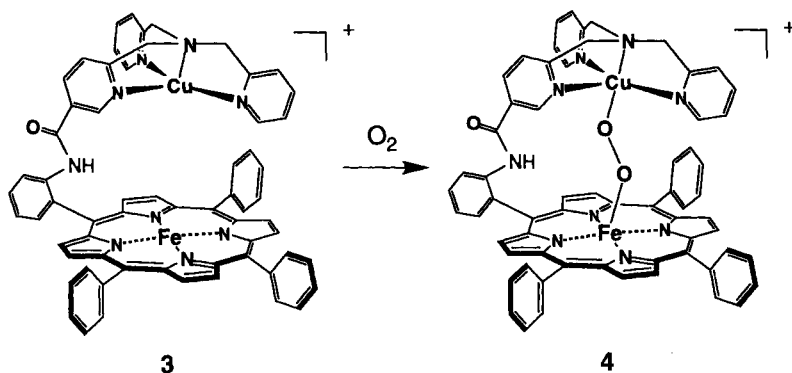
Several heterodinuclear Fe–Cu or Co–Cu complexes that closely resemble the native enzyme active sites have recently been prepared to elucidate the catalytic mechanism of cytochrome c oxidases [231–245]. The use of a covalently attached axial ligand seems essential to achieve efficient electroreduction of O_2 to H_2O [235, 238, 241–243]. The closest structural analogs of the heme a_3/Cu_B active site of cytochrome c oxidases reported so far are Fe–Cu complexes (**1** and **2**) in which the Cu coordination site is provided by three imidazole ligands [242]. These biomimetic model complexes afford clean electroreduction of O_2 to H_2O over a wide range of pH with no leakage of H_2O_2 [243].

The acetamide linkages in **1** and **2** provide enough flexibility to the distal imidazole ligands, and they are short enough to keep Cu–Fe distance within the 4.5–5.5 Å range, but not to coordinate to the iron atom [242]. Oxygen binds irreversibly with **1** or **2** to form a putative peroxo- $\text{Fe}^{\text{III}}(\text{O}^{2-})\text{Cu}^{\text{II}}$ intermediate, which is too unstable to be characterized [243].



Extensive efforts have been made to identify the active oxygen intermediates during the catalytic reduction of O_2 to H_2O by cytochrome c oxidases, although the characterization of the active oxygen intermediates remains to be fully understood [246–248]. A stable peroxo $\text{Fe}^{\text{III}}\text{–Cu}^{\text{II}}$ complex (**4**) has been reported to be formed by the reaction of a $\text{Fe}^{\text{II}}\text{–Cu}^{\text{I}}$ complex (**3**) with O_2 (Scheme 18); this complex was characterized spectroscopically [237].

The ESI mass spectrum in MeCN gives a peak at $m/z = 1094$ and the isotope pattern expected from a monocation **4** [237]. The observed Raman band indicates a peroxo O–O stretching vibration at 803 cm^{-1} which is shifted to 759 cm^{-1} on use of $^{18}\text{O}_2$ ($\Delta^{16}\text{O}_2/^{18}\text{O}_2 = 44\text{ cm}^{-1}$) [237, 247]. The peroxo complex **4** is ESR silent,



Scheme 18.

which is indicative of strong magnetic coupling between the two metals [237]. These results suggest that the peroxo ligand in **4** is bridging in end-on fashion, as shown in Scheme 18, rather than side-on fashion [237]. However, a side-on coordination mode is also possible for other Cu-Fe bimetallic peroxide complexes with different ligands [241, 244]. The magnetic properties and reactivities of Cu-Fe bimetallic peroxide complexes have been shown to be altered drastically by subtle changes of ligand architecture [244]. The electron-transfer properties of this new type of O₂ adduct remain to be clarified.

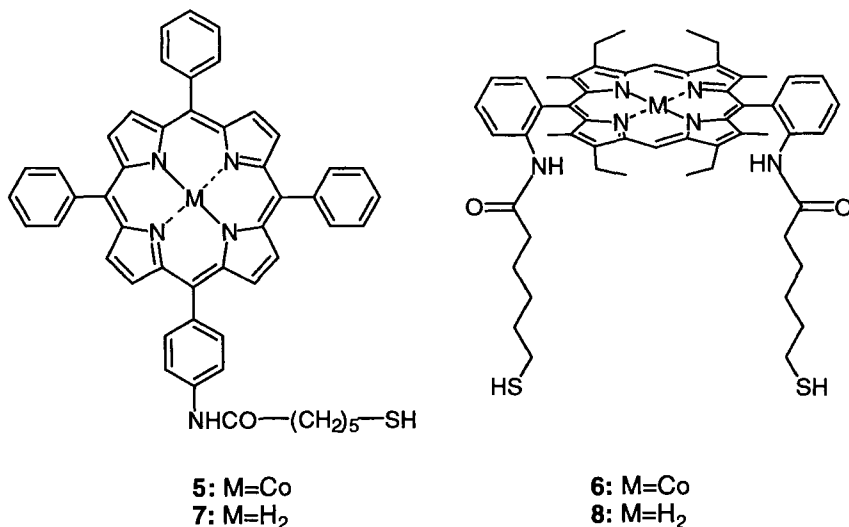
8.4 Electron Transfer in Organized Media

When porphyrins and metalloporphyrins are placed with suitable redox couples in organized media, biomimetic electron-transfer systems involving the redox-active porphyrins can be constructed to achieve catalytic redox reaction and vectorial electron transport [249–254]. The biomimetic examples include Langmuir–Blodgett films [255–265], lipid bilayer membranes [266–284], micelles [285–292], vesicles [293–298], self-assembled monolayers [299–339], and others [340, 341]. The covalent attachment of a porphyrin to a donor and/or an acceptor enhances the electronic coupling between the porphyrin and the redox couples through the bridge, with the result that intramolecular electron transfer predominates over an intermolecular electron transfer. Thus, incorporation of the porphyrin-containing dyads and the more sophisticated systems into the organized media seems to be promising for the realization of molecule-based catalysis and artificial photosynthetic materials in which the occurrence of efficient electron transfer is the heart of the strategy. This section focuses on self-assembled monolayers of porphyrin-containing systems, which have been developed intensively during the recent years, although a variety of important studies from other areas is also reported.

8.4.1 Electrocatalysis of Self-assembled Monolayers of Porphyrins

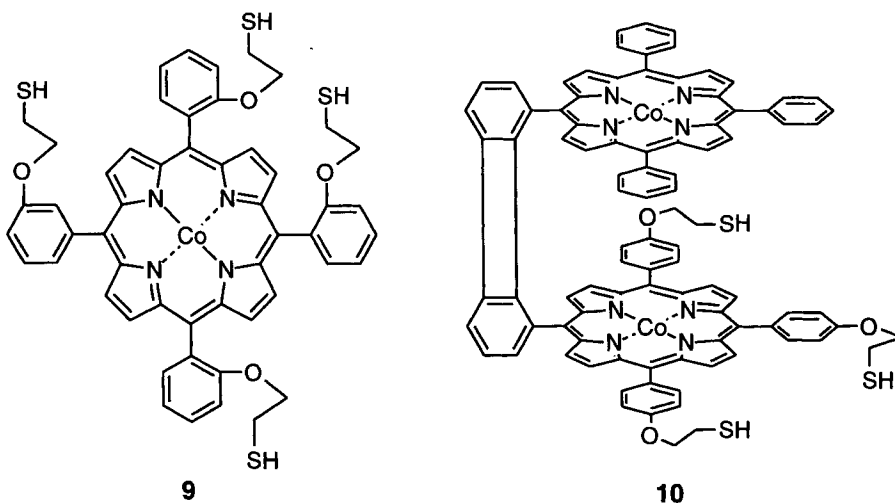
Self-assembled monolayers have recently attracted much attention as a new methodology for molecular assembly [249, 342]. They enable highly organized chemical binding of molecules of interest to the surfaces of, e.g., metals, semiconductors, and insulators. The well-ordered structure of self-assembled monolayers is in sharp contrast with conventional Langmuir–Blodgett films and lipid bilayer membranes in terms of stability, uniformity, and manipulation. Functional molecules can be arranged unidirectionally at the molecular level on substrates when substituents which will self-assemble on the substrates are attached to a terminal of the molecules. The wide variety of examples reported to date include porphyrins and metalloporphyrins in self-assembled monolayers [299–339].

One of the first reported self-assembled monolayers of porphyrins is cobalt(II)-porphyrins **5** and **6** and the analog free-base porphyrins **7** and **8**, in which the number and location of the thiol-containing tails are varied systematically [300, 314].



Electrochemical data indicate that self-assembled monolayers of **5** and **6** catalyze the two-electron reduction of O₂ to H₂O₂. The monolayer from **6** is a more effective electrocatalyst for the reduction of O₂ than that from **5** [300]. The different reactivity results from different interfacial architecture; this is confirmed by infrared, X-ray photoelectron, and visible spectroscopic measurements [300] which revealed coplanar, inclined π – π stacking of the porphyrin ring in the monolayer of **5** and head-to-tail orientation of the porphyrin ring in the monolayer of **6**. Treatment of the monolayer of **8** with Co(OAc)₂ in methanol resulted in electrocatalytic activity in the reduction of O₂ [300]. In contrast, a monolayer of **7** treated similarly failed to catalyze dioxygen reduction [300], although treatment of a mixed monolayer of **7** and CH₃(CH₂)₃SH with Co(OAc)₂ results in electrocatalytic activity similar to that of **6**.

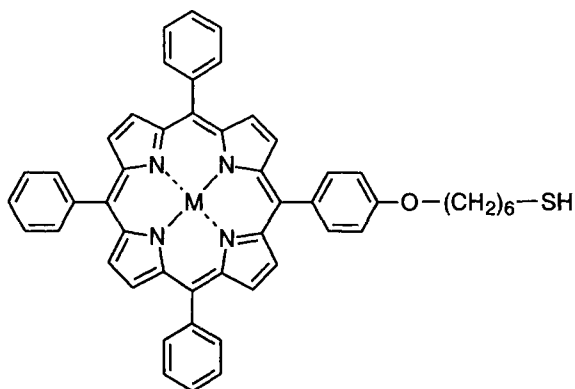
A tetraphenylporphyrin derivative with four thiol moieties **9** and a similar bis(cobalt) cofacial diporphyrin with three thiol moieties **10**, prepared independently at the same time, electrocatalytically reduce O_2 on a variety of gold surfaces [301, 316].



Cyclic voltammetric and X-ray photoelectron spectroscopic measurements showed the formation of nearly one monolayer where the porphyrin rings with thiol groups are coplanar to the electrode surface through two or three S–Au linkages per porphyrin [301, 316]. The value (Γ) of surface coverage for **9** was determined to be $7.2\text{--}8.6 \times 10^{-11} \text{ mol cm}^{-2}$ ($190\text{--}230 \text{ \AA}^2 \text{ molecule}^{-1}$). This value is quite consistent with a preference for orientation of the porphyrin ring coplanar with the gold surface ($262 \text{ \AA}^2 \text{ molecule}^{-1}$). Self-assembled monolayers of **9** and **10** afforded two-electron reduction of O_2 to H_2O_2 . This is in sharp contrast with the electrocatalytic activity of **10** chemisorbed on an edge-plane pyrolytic graphite electrode in which the four-electron reduction of O_2 was achieved [225–227, 343–346]. These results indicate that the edge-plane graphite surface plays a crucial role in biomimetic catalysis of the four-electron reduction of O_2 .

Self-assembled monolayers of metalloporphyrins **11–16**, similar to **5** and **7**, have also been constructed on gold surfaces [307, 335]. The Γ value of surface coverage was estimated to be $3.8 \times 10^{-10} \text{ mol cm}^{-2}$ ($44 \text{ \AA}^2 \text{ molecule}^{-1}$), suggesting closely packed structures of the porphyrin with perpendicular orientation to the gold surface [335]. The insertion of the metal ion into a self-assembled monolayer of free base porphyrin **17** on the gold surface has been performed by refluxing the metal ion solution in which the modified gold electrode was immersed [335].

The extent of metal insertion is strongly dependent on the type of metal ion. Cobalt (II), nickel (II), and zinc (II) are readily incorporated into the porphyrin ring, whereas manganese (II), iron (II), and copper (II) are difficult to insert under the same experimental conditions [335]. Self-assembled monolayers of **12** and **13** have electro-catalytic activity in the reduction of O_2 to H_2O and H_2O_2 , respectively.



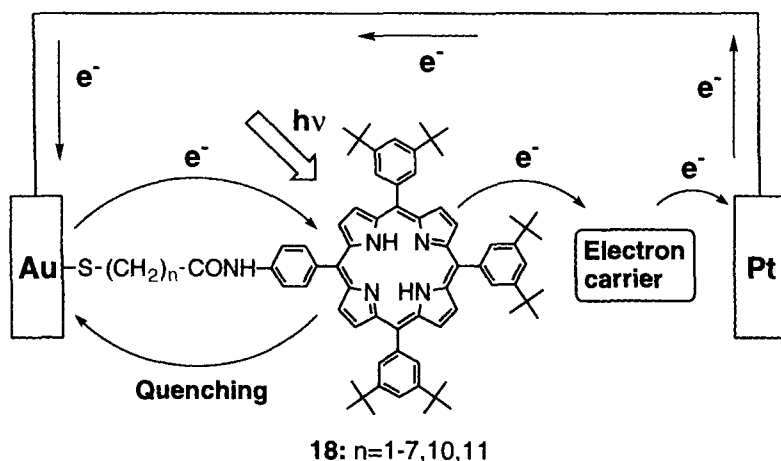
11: M=Mn(II); **12:** M=Fe(II); **13:** M=Co(II); **14:** M=Ni(II);
15: M=Cu(II); **16:** M=Zn(II); **17:** M=H₂

Although mechanistic aspects of electron transfer in these systems remains ambiguous, catalysts self-assembled on the gold surface are amenable to the surface analysis as compared with those immobilized on conventional electrodes. More detailed studies including elaborate molecular design are required to elucidate the relationship between the interfacial structure and the electrocatalytic function.

8.4.3 Photoinduced Electron Transfer of Metalloporphyrins in Self-assembled Monolayers

Photoinduced electron-transfer reactions on gold electrodes modified with porphyrins and metalloporphyrins have been extensively studied to enable the development of molecular devices for solar-energy conversion and of photonic sensors [302, 305, 309–312, 318–320, 323, 325, 327–329, 331–334, 336, 338, 339]. Systematic studies on the structure and photoelectrochemical properties of the self-assembled monolayer of porphyrins **18** on a gold electrode have been reported to clarify the effects of the spacer length [302, 325, 338]. In the molecular design of **18**, six *t*-butyl groups were introduced into *meso*-phenyl rings of the porphyrin moiety to increase solubility in organic solvents and to suppress the quenching of the excited states of the porphyrins in the monolayers because of the porphyrin aggregation (Scheme 19) [347].

The structure of the self-assembled monolayers was investigated by use of ultraviolet–visible absorption spectroscopy in transmission mode, cyclic voltammetry, ultraviolet–visible ellipsometry, and fluorescence spectroscopy [338]. These experiments showed that as the length of the spacing methylene chain was increased the self-assembled monolayers tended to form highly ordered structures on the gold electrode, with surface coverage reaching 1.5×10^{-10} mol cm⁻² (110 Å² molecule⁻¹) [338]. Adjacent porphyrin rings take J-aggregate-like partially stacked struc-



Scheme 19.

tures in the monolayer [338]. The porphyrin ring plane in the monolayer with an even number ($n = 2, 4, 6, 10$) of methylene spacers ($-(\text{CH}_2)_n-$) is tilted significantly to the gold surface, whereas porphyrins with odd numbers ($n = 1, 3, 5, 7, 11$) of methylene spacers adopt nearly perpendicular orientation to the gold surface [338].

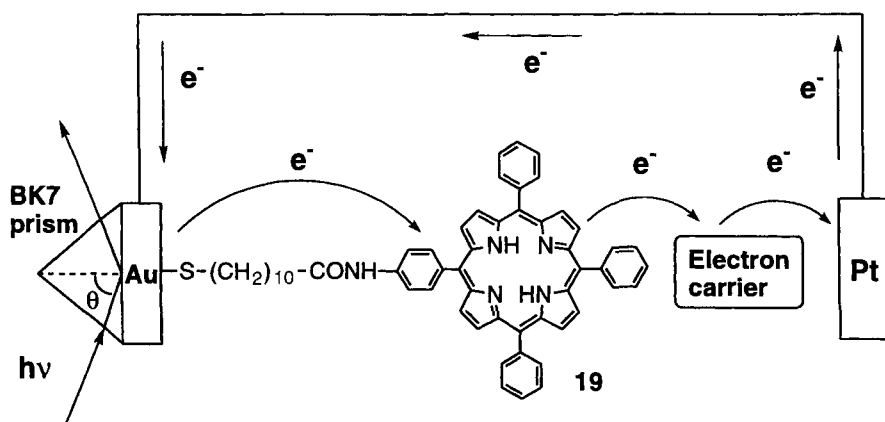
Photoelectrochemical studies of gold electrodes modified with **18** were performed in an argon-saturated Na_2SO_4 aqueous solution containing methyl viologen as an electron carrier and using a platinum wire counter electrode and a Ag/AgCl reference electrode [338]. An increase in the cathodic photocurrent was observed on increasing the negative bias (from 700 mV to -200 mV) relative to the gold electrode [338]. This indicates that the vectorial photocurrent flows from the gold electrode to the counter electrode through the monolayer and the electrolyte. The quantum yield for photocurrent generation increases in a zigzag fashion with increasing spacer length up to $n = 6$ (ca 0.3 %) and then starts decreasing with a further increase in the spacer length. Such dependence of the quantum yield on spacer length can be explained by competition between electron transfer and energy transfer of the singlet excited state of the porphyrin as shown in Scheme 19.

Photoirradiation of the modified electrode results in electron transfer from the singlet excited state of the porphyrin ($E^\circ_{\text{ox}} = -0.80$ V ($n = 11$) relative to Ag/AgCl) to the methyl viologen ($E^\circ_{\text{red}} = -0.62$ V relative to Ag/AgCl) or O_2 ($E^\circ_{\text{red}} = -0.48$ V relative to Ag/AgCl). The reduced electron carrier diffuses to release an electron to the platinum electrode, whereas the resultant porphyrin radical cation ($+1.10$ V relative to Ag/AgCl) captures an electron from the gold electrode, generating the cathodic current flow. There is, however, a competitive deactivation pathway in the excited porphyrin, via energy transfer quenching by the gold electrode, judging from the extremely short fluorescence lifetimes of the porphyrins (ca 10–40 ps) on the gold surface compared with those (ca 1–10 ns) on quartz or semiconductor surfaces [347–351]. Electronic coupling between the porphyrin and

the electrode would decrease as the number of methylene spacers was increased, leading to the less quenching of the excited porphyrin by the electrode via energy transfer through the spacer [352–356]. The rate of electron transfer from the gold electrode to the resulting porphyrin radical cation should, on the other hand, decrease with increasing spacer length. Thus, the offset effect of suppression of quenching by the gold electrode and reduced electron-transfer between the porphyrin and the electrode with increasing methylene spacer length is responsible for the nonlinear dependence of the quantum yield on the spacer length (*vide supra*). These results clearly show that optimization of each process is vital to achieving highly efficient sequential electron transfer by organized molecular systems used to mimic vectorial electron flow in photosynthesis.

The surface plasmon resonance technique has been applied to the characterization of the monolayer thickness of a self-assembled monolayer and to measurement of protein interactions with a self-assembled monolayer on the metal surface [357, 358]. Surface plasmon excitation has also been used as an effective excitation source to cause photoinduced electron transfer from the singlet excited state of the porphyrin in a self-assembled monolayer to electron carriers such as methyl viologen and O_2 in the electrolyte solution, leading to photocurrent generation [309, 327, 328, 336]. The surface plasmon was generated with p-polarized 632.8 nm light at an incident angle of 73° on a porphyrin (**19**)-modified gold surface of BK-7 right-angle prism by an attenuated total reflection method and by use of a Kretschmann–Raether configuration as shown in Scheme 20 [327, 328, 336].

The photoelectrochemical measurements were conducted in an oxygen-saturated 0.1 M aqueous solution of Na_2SO_4 using the **19**-modified gold working electrode, a platinum counter electrode, and an Ag/AgCl reference electrode [328]. The intensity of the cathodic photocurrent under the surface plasmon excitation is enhanced by a factor of ca 6 compared with direct photoirradiation [325, 338]. Such an enhancement of the photocurrent indicates that it is produced via the generation of surface plasmon and excitation of the porphyrin immobilized on the gold surface. These



Scheme 20.

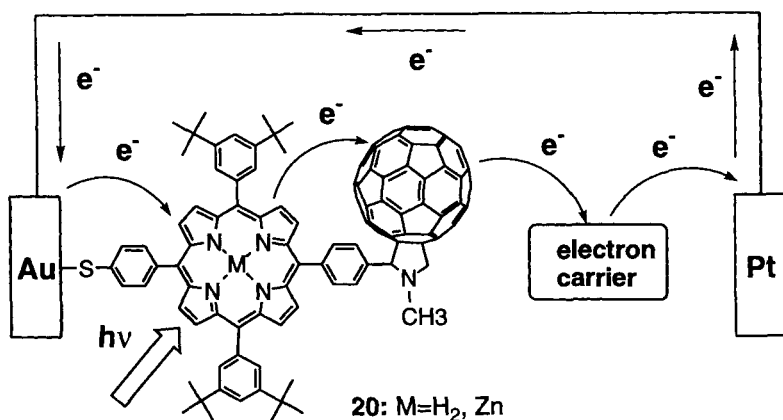
results demonstrate that the surface plasmon resonance can be used to develop molecule-based photonic materials.

8.4.4 Self-assembled Monolayers of Porphyrin-containing Dyads

The importance and complexity of electron-transfer reactions in photosynthesis have inspired many synthetic chemists to design and prepare donor–acceptor linked systems that mimic the highly efficient multistep electron-transfer process [17, 334]. Because porphyrins and metalloporphyrins are essential components in photosynthetic electron transfer, they have been frequently employed in donor–acceptor linked molecules [17, 334]. Some covalently linked porphyrin-containing arrays, e.g. triads, tetrads, and pentads, produce a long-lived, charge-separated state with a high quantum yield, demonstrating that a sequential electron transfer is a pivotal strategy for the construction of artificial photosynthetic systems [17, 334]. Efficient conversion of light to photocurrents or chemical energies via the charge-separated state has, however, often been hampered by the poor unidirectional electron flow in covalently linked molecules incorporated into artificial membranes such as lipid bilayers and Langmuir–Blodgett membranes and/or organized at electrodes [258, 259, 261–265, 268, 271, 294, 295].

The spherical shape of buckminsterfullerene (C_{60}) containing a large number of π -electrons makes this carbon allotrope an ideal component for construction of efficient electron-transfer systems. Recent advances in synthetic methodology have made it possible to link C_{60} with porphyrins [17, 323, 334]. The first porphyrin–fullerene dyad (**20**) in a self-assembled monolayer was reported in 1996 [309, 318, 332]. Because sulfides are relatively stable compared with thiols and disulfides, a methylthio group is attached to the end of a porphyrin ring whereas the opposite end is a C_{60} moiety in **20**. The structures of the self-assembled monolayer formed on a gold electrode were studied by spectroscopic methods including X-ray photoelectron spectroscopy, ultraviolet–visible spectroscopic ellipsometry, ultraviolet–visible absorption spectroscopy, and Fourier transform infrared spectroscopy, as well as electrochemical methods [309, 318, 332]. The experimental data revealed that the porphyrin- C_{60} molecules were tilted and nearly parallel to the gold surface, leading to the formation of loosely packed structures ($\Gamma = 1.6\text{--}3.7 \times 10^{-11}$ mol cm $^{-2}$). Photoelectrochemical measurements were conducted in an argon-saturated aqueous solution of Na_2SO_4 , containing methyl viologen as an electron carrier, and using the modified gold electrode as a working electrode and a platinum counter electrode, as shown in Scheme 21 [309, 318, 332].

Under short-circuit conditions the cathodic photocurrent was observed for the photoelectrochemical cell; the quantum yield was ca 0.5 % [309, 318, 332]. The photocurrent intensity in the free-base porphyrin- C_{60} system was enhanced fivefold compared with that in the corresponding free-base porphyrin monomer system. Such enhancement of the photocurrent demonstrates that C_{60} acts as an effective mediator in a sequential electron-transfer process. The photocurrent intensity in the free-base porphyrin- C_{60} cell was ca one order of magnitude larger than that in the zinc porphyrin- C_{60} cell [309, 318, 332]. Two different electron-transport mecha-

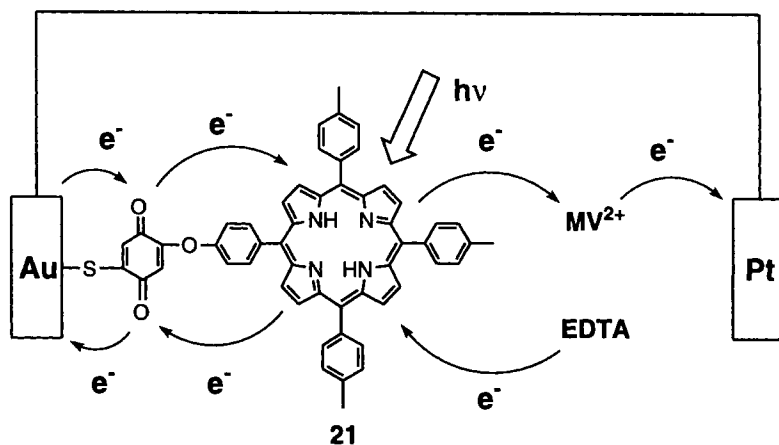


Scheme 21.

nisms were proposed for photocurrent generation in self-assembled monolayers of porphyrin-C₆₀ systems—ion-pair formation for the zinc porphyrin-C₆₀ cell and exciplex formation for the free-base porphyrin-C₆₀ cell. The shorter lifetime in the charge-separated state of the former leads to a poor generation of the photocurrent, whereas the longer lifetime in the exciplex of the latter results in a pronounced increase of the photocurrent [309, 318, 332].

The dyad **21** consisting of a porphyrin linked to a thiol-appended benzoquinone as an acceptor was also prepared to construct a self-assembled monolayer system [310, 320]. The amount of **21** adsorbed, (Γ), was evaluated as 6.2×10^{-11} mol cm⁻² (270 Å² molecule⁻¹) from the amount of charge of the cyclic voltammogram. This occupied area of **21** doesn't agree with that expected for orientation of the porphyrin ring vertical to the electrode (90 Å² molecule⁻¹), indicating the rather poor packing of the molecule at the gold electrode. Photoelectrochemical measurements were performed in a nitrogen-saturated aqueous solution of Na₂SO₄ (pH 4.5), containing 50 mM EDTA as electron donor and 5 mM methyl viologen as electron acceptor, and using the modified gold working electrode, a platinum wire counter electrode, and an Ag/AgCl reference electrode as shown in Scheme 22.

Anodic and cathodic photocurrents were observed when the applied potential was more positive and negative than +200 mV which corresponds to the first reduction potential of the quinone moiety in the monolayer, respectively [359]. The potential dependence of the photocurrents as a function of pH in the electrolyte solution correlates well with the shift of the redox potential of the quinone as a function of pH [359]. When the applied potential is more positive than the redox potential of the quinone, photoinduced electron transfer occurs from the singlet excited state of the porphyrin to the gold electrode through the quinone, followed by a hole shift from the resultant porphyrin radical cation to EDTA, leading to the generation of anodic electron flow [359]. On the other hand, when the applied potential is more negative than the redox potential of the quinone moiety, photoinduced electron transfer takes place from the singlet excited state of the porphyrin



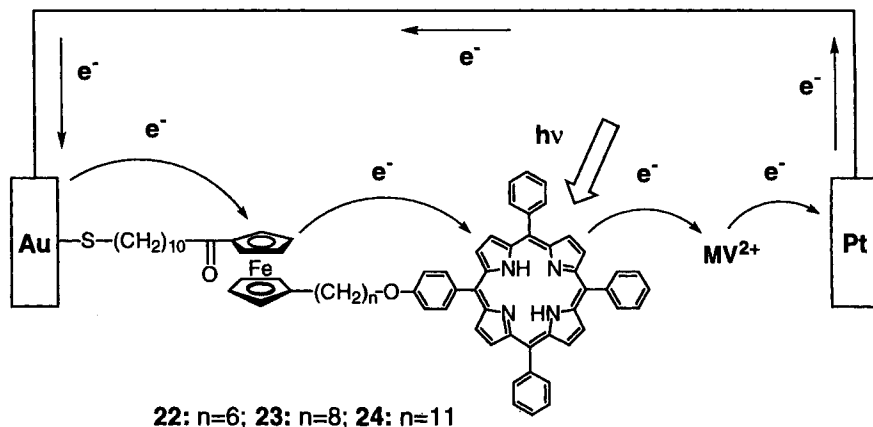
MV^{2+} : methylviologen; EDTA: ethylenediaminetetraacetic acid

Scheme 22.

to the methyl viologen, followed by a successive hole shift from the porphyrin radical cation to the gold electrode through the quinone moiety, producing the anodic electron flow [359].

Ferrocene acting as an efficient electron donor has also been linked with a porphyrin ring to construct the highly ordered structure of self-assembled monolayers of ferrocene-porphyrin dyad with an alkanethiol tail **22–24**, as shown in Scheme 23 [319, 329, 331].

The amounts of **22–24** adsorbed were estimated as $2.3 \times 10^{-10} \text{ mol cm}^{-2}$ ($71 \text{ \AA}^2 \text{ molecule}^{-1}$) for all the monolayers of **22–24** from the amount of charge in anodic peaks of the ferrocene moieties. The occupied area is close to that expected for ori-



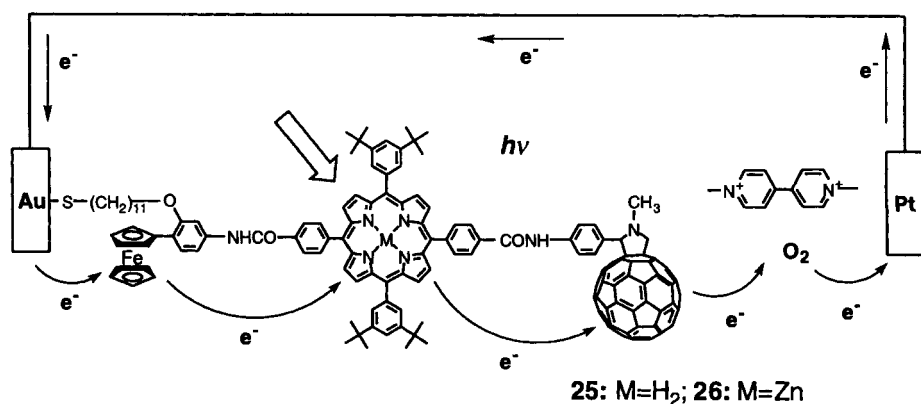
Scheme 23.

entation of the porphyrin ring perpendicular to the electrode ($50 \text{ \AA}^2 \text{ molecule}^{-1}$) rather than that for vertical orientation ($250 \text{ \AA}^2 \text{ molecule}^{-1}$). Angle-resolved X-ray photoelectron spectroscopic studies on the monolayer of **23** confirmed that alkyl chains both between the porphyrin and the ferrocene and between the ferrocene and the thiol group were aligned with a tilt angle of 30° to the gold surface, with perpendicular orientation of the porphyrin plane [329]. The cathodic photocurrent was observed when the gold electrode modified with monolayers of **22–24** was irradiated with monochromatic light of 430 nm at an applied potential of -200 mV in a 0.1 M aqueous NaClO_4 solution containing 5 mM methyl viologen as an acceptor [331]. Quantum yields based on the absorbed photons were determined as 4.0, 11, and 12 % for photoelectrochemical cells of monolayers of **22**, **23** and **24**, respectively [331]. The photocurrent is generated via photoinduced electron transfer from the singlet excited state of the porphyrin to methyl viologen, then by successive hole transfer from the porphyrin to the gold electrode through the ferrocene moiety (Scheme 23) [331]. Photocurrent generation is limited by the efficiency of intermolecular electron-transfer quenching of the singlet excited state of the porphyrin by methyl viologen in competition with facile energy transfer quenching by the gold electrode, as described for the **18** monolayer system (*vide supra*). In addition, strong aggregation of the porphyrins without bulky substituents around the porphyrin moiety (**22–24**) in the monolayer might accelerate the non-radiative decay of the singlet excited state of the porphyrin. The flexible methylene spacer between the porphyrin and the ferrocene moieties does not enable comparison of the photo-dynamics in solutions with those in the monolayer on the gold surface; this is in sharp contrast with photoelectrochemical cells of the monolayers prepared from porphyrin- C_{60} dyad [309, 318, 332] and triad systems (*vide infra*) [333, 334, 339].

8.4.5 Self-assembled Monolayers of Porphyrin-containing Triads

A highly ordered self-assembled monolayer system of porphyrin-containing dyads has been extended to accommodate porphyrin-containing triads (**25** and **26**) [333, 334, 339]. The alkanethiol-attached triads **25** and **26** involve a linear array of ferrocene (Fc), porphyrin (P), and C_{60} as shown in Scheme 24. The energy gradient of each redox state in the triad is in the order: $\text{Fc}-^1\text{P}^*-\text{C}_{60} > \text{Fc}-\text{P}^{+\bullet}-\text{C}_{60}^{\bullet-} > \text{Fc}^+-\text{P}-\text{C}_{60}^{\bullet-}$. This makes it possible to achieve sequential electron transfer within the triad. The use of C_{60} as an electron acceptor in the triad has enabled the attainment of a long lifetime of the charge separated state and high quantum efficiency, as a consequence of the small reorganization energy of C_{60} [323, 334, 360–373]. Alkanethiols with long methylene chains ($n \geq 10$) are known to form densely packed self-assembled monolayers at a gold surface by use of the S–Au linkage [249, 342]. Thus, when a thiol group with a long alkyl chain is introduced at the end of donor–acceptor linked molecules, it would be arranged unidirectionally at the end of the gold electrodes, leading to formation of a uniform self-assembled monolayer with a thickness of ca 50 \AA (Scheme 24).

The fluorescence lifetime measurements of **25** and **26** in solution suggest that the quenching of the singlet excited porphyrin by the attached C_{60} is a major deactiva-



Scheme 24.

tion pathway in both triads [339]. The time-resolved transient spectra of the triads in different solvents revealed that initial photoinduced electron transfer or partial charge-transfer from $^1\text{P}^*$ to C_{60} occurred in the triads, followed by rapid charge shift from the ferrocene to P^{*+} to produce $\text{Fc}^+-\text{P}-\text{C}_{60}^{*-}$ [369]. The zinc complex affords a lifetime of 40 ns and 15.6 μs in benzene and DMF, respectively [369]. The overall quantum yield for formation of $\text{Fc}^+-\text{P}-\text{C}_{60}^{*-}$ depends on the solvent used. The quantum yield of the zinc complex is 65 % in benzonitrile, based on the absorption of both the porphyrin and C_{60} [369]. Given the relative absorption ratio of the porphyrin and the C_{60} , the quantum yield relative to $^1\text{ZnP}^*$ exceeds 80 %. The amount of **25** adsorbed at the gold electrode was estimated as $1.9 \times 10^{-10} \text{ mol cm}^{-2}$ ($= 86 \text{ \AA}^2 \text{ molecule}^{-1}$), which is comparable with those for well-ordered self-assembled monolayers of porphyrins [319, 325, 331, 338] and C_{60} [374–376] at gold electrodes. This indicates that the triad molecules are well-packed with nearly perpendicular orientation to the gold surface.

Photoelectrochemical experiments using the triad-modified gold electrode, a platinum wire, and an Ag/AgCl electrode were conducted in the presence of electron carriers such as oxygen and/or methyl viologen [333, 334, 339]. The cathodic photocurrent was detected under irradiation of the modified gold electrode with monochromatic light of 438.5 nm. Increasing cathodic photocurrent was observed with increasing negative bias on the gold electrode. This indicates that the direction of the electron flow is from the gold electrode to the counter electrode through the electrolyte. When the applied potential was more negative than +500 mV, which corresponds to the oxidation potential of the ferrocene, the photocurrent intensity increased drastically. Thus, the photocurrent efficiency is controlled by the rate of electron-transfer between the gold electrode and the ferrocene [319, 331]. The action spectra of the cells agree with the absorption spectra of **25** and **26** on the gold electrode. Such agreement indicates clearly that the porphyrin is a major photoactive species in photocurrent generation. The quantum yields for photoelectrochemical cells of **25** and **26** under the optimum conditions using an oxygen-

saturated solution in the presence of methyl viologen were found to be 25 % and 20 %, respectively. This is the highest value (25 %) among donor–acceptor linked molecules on monolayer-modified metal electrodes and in artificial membranes [258, 259, 268, 271, 294, 295, 309, 310, 318, 319, 325, 331, 332, 377].

The high quantum yield may be achieved via photoinduced electron transfer from the singlet excited state of the porphyrin to the C_{60} , then hole-shift from the resulting porphyrin radical cation to the ferrocene to produce the charge-separated state, $Fc^+-P-C_{60}^{\bullet-}$ in the monolayer (Scheme 24). The fast electron transfer to C_{60} , because of the small reorganization energy can compete well with deactivation as a result of the gold electrode [325, 338]. Electron carriers such as oxygen ($E^\circ_{red} = -0.48$ V for $O_2/O_2^{\bullet-}$) [378] and/or methyl viologen ($E^\circ_{red} = -0.62$ V for $MV^{+2}/MV^{\bullet+}$) are reduced by the $C_{60}^{\bullet-}$ moiety of $Fc^+-P-C_{60}^{\bullet-}$ to produce the radical anions which eventually give an electron to the counter electrode. The electron-transfer rate from the gold electrode to Fc^+ in $Fc^+-P-C_{60}^{\bullet-}$ is, on the other hand, affected by the potential applied to the gold electrode. Thus the rate of electron-transfer from the gold electrode to Fc^+ increases as the applied potential is reduced, leading to an increase in the photocurrent.

8.5 Summary

This review has focused on recent advances in the electron-transfer chemistry of porphyrins and metalloporphyrins, which is relevant to their biological role. Electron-transfer reactions of porphyrins and metalloporphyrins have been studied for long time and they are now relatively well understood on the basis of fundamental redox properties such as reorganization energies and the one-electron redox potentials in the light of the Marcus theory of electron transfer [1]. However, reaction mechanisms involving reactive intermediates such as high-valent metalloporphyrins produced in electron-transfer reactions of metalloporphyrins have remained incompletely understood, as discussed in this review. Axial coordination sites available in metalloporphyrins play an essential role in the construction of useful catalytic systems for biomimetic reactions and energy conversion, because simple combination of outer-sphere electron-transfer reactions would not increase overall electron-transfer rates. Strong inner-sphere interaction between substrates and metalloporphyrins results in the formation of a variety of substrate-bound intermediates; in particular new types of bimetallic active oxygen porphyrin complexes acting as reactive intermediates during the four-electron reduction of oxygen have been explored rapidly. Recent advances in self-assembled monolayer systems of porphyrins and metalloporphyrins have provided a promising means of developing biomimetic electron-transfer systems (in which highly ordered, well-designed architectures act as efficient catalysts) and organic solar cells. In each the search for new and better catalytic systems involving porphyrins and metalloporphyrins continues to be guided by beautifully constructed natural enzymatic systems.

Acknowledgment

The authors are deeply indebted to the work of all collaborators and coworkers whose names are listed in the references of this chapter (in particular, Prof. K. M. Kadish, Prof. Y. Watanabe and Prof. Y. Sakata). S.F. acknowledges continuous support of his study on electron-transfer chemistry by a Grant-in-Aid from the Ministry of Education, Science, Culture and Sports, Japan.

References

1. S. Fukuzumi, *The Porphyrin Handbook*, Vol. 8 (Eds.: K. M. Kadish, K. Smith, R. Guilard), Academic Press, San Diego, CA, **2000**, pp. 115–152.
2. R. Guilard, K. M. Kadish, *Chem. Rev.* **1988**, *88*, 1121.
3. D. Mansuy, P. Battioni, in *Metalloporphyrins in Catalytic Oxidations* (Ed.: R. A. Sheldon), Marcel Dekker, New York, **1994**, pp. 99–132.
4. D. Mansuy, *Pure Appl. Chem.* **1987**, *59*, 759.
5. D. Mansuy, *Coord. Chem. Rev.* **1993**, *125*, 129.
6. A. R. Battersby, *Science* **1994**, *264*, 1551.
7. J. Deisenhofer, H. Michel, *Angew. Chem. Int. Ed. Engl.* **1989**, *28*, 829.
8. G. von Jagow, W. D. Engel, *Angew. Chem. Int. Ed. Engl.* **1980**, *19*, 659.
9. W. Kaim, B. Schwederski, *Bioinorganic Chemistry: Inorganic Elements in the Chemistry of Life*, Wiley, New York, **1994**.
10. R. E. Dickerson, R. Timkovich, *Enzymes* (3rd Ed.), **1975**, *11*, 397.
11. M. A. Cusanovich, in *Bioorganic Chemistry*, Vol. 4 (Ed.: E. E. van Tamelen), Academic Press, New York, **1978**.
12. E. Margoliash, in *Electron Transport and Oxygen Utilization* (Ed.: C. Ho), Elsevier, New York, **1982**.
13. H. Sigel, A. Sigel, Eds., *Electron-transfer reactions in Metalloproteins, in Metal Ions in Biological Systems*, Vol. 27, Marcel Dekker, New York, **1991**.
14. S. S. Isied, *Prog. Inorg. Chem.* **1984**, *32*, 443.
15. T. E. Meyer, M. D. Kamen, *Adv. Protein Chem.* **1982**, *35*, 105.
16. K. M. Kadish, E. van Caemelbecke, G. Royal, *The Porphyrin Handbook*, Vol. 8 (Eds.: K. M. Kadish, K. Smith, R. Guilard), Academic Press, San Diego, CA, **2000**, pp. 1–114.
17. D. Gust, T. A. Moore, *The Porphyrin Handbook*, Vol. 8 (Eds.: K. M. Kadish, K. Smith, R. Guilard), Academic Press, San Diego, CA, **2000**, pp. 153–190.
18. L. Eberson, *Electron-transfer reactions in Organic Chemistry*, Springer, Tokyo, **1987**.
19. D. Astruc, *Electron-Transfer and Radical Processes in Transition-Metal Chemistry*, VCH, New York, **1995**.
20. J. F. Bunnett, *Acc. Chem. Res.* **1992**, *25*, 2.
21. M. Chanon, M. L. Tobe, *Angew. Chem. Int. Ed. Engl.* **1982**, *21*, 1.
22. S. Fukuzumi, in *Advances in Electron-transfer chemistry*, Vol. 2 (Ed.: P. S. Mariano), JAI Press, Greenwich, CT, **1992**, pp. 65–175.
23. M. Patz, S. Fukuzumi, *J. Phys. Org. Chem.* **1997**, *10*, 129.
24. J. K. Kochi, *Angew. Chem. Int. Ed. Engl.* **1988**, *27*, 1227.
25. E. C. Ashby, *Acc. Chem. Res.* **1988**, *21*, 414.
26. M. Chanon, M. Rajzmann, F. Chanon, *Tetrahedron* **1990**, *46*, 6193.
27. P. R. Ortiz de Montellano, *Cytochrome P450. Structure, Mechanism, and Biochemistry* (2nd Ed.), Plenum Publishing Corporation, New York, **1995**.
28. F. P. Guengerich, T. L. Macdonald, *Acc. Chem. Res.* **1984**, *17*, 9.
29. P. R. Ortiz de Montellano, *Acc. Chem. Res.* **1987**, *20*, 289.
30. F. P. Guengerich, *J. Biol. Chem.* **1991**, *266*, 10019.
31. D. Dolphin, T. G. Traylor, L. Y. Xie, *Acc. Chem. Res.* **1997**, *30*, 251.

32. D. Ostovic, T. C. Bruice, *Acc. Chem. Res.* **1992**, 25, 314.
33. D. Mansuy, *Comp. Biochem. Phys. C* **1998**, 121, 5.
34. J. T. Groves, T. E. Nemo, R. S. Myers, *J. Am. Chem. Soc.* **1979**, 101, 1032.
35. J. T. Groves, T. E. Nemo, *J. Am. Chem. Soc.* **1983**, 105, 5786.
36. J. T. Groves, R. S. Myers, *J. Am. Chem. Soc.* **1983**, 105, 5791.
37. J. T. Groves, D. V. Subramanian, *J. Am. Chem. Soc.* **1984**, 106, 2177.
38. J. P. Collman, T. Kodadek, S. A. Raybuck, J. I. Brauman, L. M. Papazian, *J. Am. Chem. Soc.* **1985**, 107, 4343.
39. C. M. Dicken, F.-L. Lu, M. W. Nee, T. C. Bruice, *J. Am. Chem. Soc.* **1985**, 107, 5776.
40. T. Mori, T. Santa, T. Higuchi, T. Mashino, M. Hirobe, *Chem. Pharm. Bull.* **1993**, 41, 292.
41. J. P. Collman, J. I. Brauman, B. Meunier, T. Hayashi, T. Kodadek, S. A. Raybuck, *J. Am. Chem. Soc.* **1985**, 107, 2000.
42. B. Meunier, E. Guilmet, M.-E. De Carvalho, R. Poilblanc, *J. Am. Chem. Soc.* **1984**, 106, 6668.
43. M. W. Nee, T. C. Bruice, *J. Am. Chem. Soc.* **1982**, 104, 6123.
44. M. F. Powell, E. F. Pai, T. C. Bruice, *J. Am. Chem. Soc.* **1984**, 106, 3277.
45. D. C. Heimbrook, R. I. Murray, K. D. Egeberg, S. G. Sligar, M. W. Nee, T. C. Bruice, *J. Am. Chem. Soc.* **1984**, 106, 1514.
46. C. M. Dicken, T. C. Woon, T. C. Bruice, *J. Am. Chem. Soc.* **1986**, 108, 1636.
47. J. T. Groves, Y. Watanabe, T. J. McMurphy, *J. Am. Chem. Soc.* **1983**, 105, 4489.
48. L.-C. Yuan, T. C. Bruice, *J. Am. Chem. Soc.* **1985**, 107, 512.
49. W. A. Lee, T. C. Bruice, *J. Am. Chem. Soc.* **1985**, 107, 513.
50. L.-C. Yuan, T. C. Bruice, *J. Am. Chem. Soc.* **1986**, 108, 1643.
51. H. J. Ledon, P. Durbut, F. Varescon, *J. Am. Chem. Soc.* **1981**, 103, 3601.
52. D. Mansuy, P. Battioni, J.-P. Renaud, *J. Chem. Soc. Chem. Commun.* **1984**, 1255.
53. S. Fukuzumi, S. Mochizuki, T. Tanaka, *Isr. J. Chem.* **1987/1988**, 28, 29.
54. J. R. Lindsay-Smith, in *Metalloporphyrins in Catalytic Oxidations* (Ed.: R. A. Sheldon), Marcel Dekker, New York, **1994**, pp. 325–361.
55. F. Bedioui, *Coord. Chem. Rev.* **1995**, 144, 39.
56. P. Battioni, E. Cardin, M. Louloudi, B. Schöllhorn, G. A. Spyroulias, D. Mansuy, T. G. Traylor, *Chem. Commun.* **1996**, 2037.
57. B. Meunier, *Chem. Rev.* **1992**, 92, 1411.
58. P. E. Ellis, Jr., J. E. Lyons, *Coord. Chem. Rev.* **1990**, 105, 181.
59. G.-X. He, R. D. Arasasingham, G.-H. Zhang, T. C. Bruice, *J. Am. Chem. Soc.* **1991**, 113, 9828.
60. P. Battioni, J. P. Renaud, J. F. Bartoli, M. Reina- Artiles, M. Fort, D. Mansuy, *J. Am. Chem. Soc.* **1988**, 110, 8462.
61. A. Thellend, P. Battioni, D. Mansuy, *J. Chem. Soc. Chem. Commun.* **1994**, 1035.
62. O. Brigaud, P. Battioni, D. Mansuy, C. Giessner- Prettre, *New J. Chem.* **1992**, 16, 1031.
63. C. K. Chang, F. Ebina, *J. Chem. Soc. Chem. Commun.* **1981**, 778.
64. J. F. Bartoli, O. Brigaud, P. Battioni, D. Mansuy, *J. Chem. Soc. Chem. Commun.* **1991**, 440.
65. M. W. Grinstaff, M. G. Hill, J. A. Labinger, H. B. Gray, *Science* **1994**, 264, 1311.
66. W.-D. Woggon, H. Fretz, in *Advances in Detailed Reaction Mechanism*, Vol. 2 (Ed.: J. M. Coxon), JAI Press, Greenwich, CT, **1992**, pp. 111–147.
67. G. T. Miwa, J. S. Walsh, G. L. Kedderis, P. F. Hollenberg, *J. Biol. Chem.* **1983**, 258, 14445.
68. P. G. Wislocki, G. T. Miwa, A. Y. H. Lu, in *Enzymatic Basis of Detoxification*, Vol. 1 (Ed.: W. B. Jakoby), Academic Press, New York, **1980**, p 135.
69. R. E. White, M. J. Coon, *Ann. Rev. Biochem.* **1980**, 49, 315.
70. F. P. Guengerich, T. L. Macdonald, *Acc. Chem. Res.* **1984**, 17, 9.
71. J. H. Dawson, M. Sono, *Chem. Rev.* **1987**, 87, 1255.
72. T. D. Porter, M. J. Coon, *J. Biol. Chem.* **1991**, 266, 13469.
73. P. F. Hollenberg, *FASEB J.* **1992**, 6, 686.
74. F. P. Guengerich, T. L. Macdonald, in *Advances in Electron-transfer chemistry*, Vol. 3 (Ed.: P. S. Mariano), JAI press, Greenwich, CT, **1993**, p. 191.
75. F. P. Guengerich, C.-H. Yun, T. L. MacDonald, *J. Biol. Chem.* **1996**, 271, 27321.
76. J. R. L. Smith, D. N. Mortimer, *J. Chem. Soc. Chem. Commun.* **1985**, 64.

77. J. R. L. Smith, D. N. Mortimer, *J. Chem. Soc. Perkin Trans. 2* **1986**, 1743.
78. J. I. Manchester, J. P. Dinnocenzo, L. Higgins, J. P. Jones, *J. Am. Chem. Soc.* **1997**, *119*, 5069.
79. S. B. Karki, J. P. Dinnocenzo, J. P. Jones, K. R. Korzekwa, *J. Am. Chem. Soc.* **1995**, *117*, 3657.
80. J. P. Dinnocenzo, S. B. Karki, J. P. Jones, *J. Am. Chem. Soc.* **1993**, *115*, 7111.
81. S. Fukuzumi, C. L. Wong, J. K. Kochi, *J. Am. Chem. Soc.* **1980**, *102*, 2928.
82. S. Fukuzumi, Y. Kondo, T. Tanaka, *J. Chem. Soc. Perkin Trans. 2* **1984**, 673.
83. S. Fukuzumi, K. Koumitsu, K. Hironaka, T. Tanaka, *J. Am. Chem. Soc.* **1987**, *109*, 305.
84. S. Fukuzumi, Y. Tokuda, T. Kitano, T. Okamoto, J. Otera, *J. Am. Chem. Soc.* **1993**, *115*, 8960.
85. R. P. Bell, *The Proton in Chemistry* (2nd Ed.), Cornell University Press, Ithaca, NY, **1973**, Chapter 12.
86. D. Griller, J. A. Howard, P. R. Marriott, J. C. Scaiano, *J. Am. Chem. Soc.* **1981**, *103*, 619.
87. I. Wölfe, J. Lodaya, B. Sauerwein, G. B. Schuster, *J. Am. Chem. Soc.* **1992**, *114*, 9304.
88. T. M. Bockman, K. Y. Lee, J. K. Kochi, *J. Chem. Soc. Perkin Trans. 2* **1992**, 1581.
89. E. Baciocchi, O. Lanzalunga, A. Lapi, L. Manduchi, *J. Am. Chem. Soc.* **1998**, *120*, 5783.
90. A. Rehm, A. Weller, *Isr. J. Chem.* **1970**, *8*, 259.
91. R. A. Marcus, *Annu. Rev. Phys. Chem.* **1964**, *15*, 155.
92. F. Scandola, V. Balzani, *J. Am. Chem. Soc.* **1979**, *101*, 6142.
93. S. Fukuzumi, I. Nakanishi, K. Tanaka, T. Suenobu, A. Tabard, R. Guillard, E. Van Caemelbecke, K. M. Kadish, *J. Am. Chem. Soc.* **1999**, *121*, 785.
94. K. M. Kadish, E. Van Caemelbecke, E. Gueletii, S. Fukuzumi, K. Miyamoto, T. Suenobu, A. Tabard, R. Guillard, *Inorg. Chem.* **1998**, *37*, 1759.
95. S. Marguet, P. Hapiot, P. Neta, *J. Phys. Chem.* **1994**, *98*, 7136.
96. Y. Goto, Y. Watanabe, S. Fukuzumi, J. P. Jones, J. P. Dinnocenzo, *J. Am. Chem. Soc.* **1998**, *120*, 10762.
97. B. W. Griffin, P. L. Ting, *Biochemistry* **1978**, *17*, 2206.
98. J. Van der Zee, D. R. Duling, R. P. Mason, T. E. Eling, *J. Biol. Chem.* **1989**, *264*, 19828.
99. H. B. Dunford, J. S. Stillman, *Coord. Chem. Rev.* **1987**, *19*, 187.
100. P. George, *Science* **1953**, *117*, 220.
101. R. R. Fergusson, *J. Am. Chem. Soc.* **1956**, *78*, 741.
102. Y. Hayashi, I. Yamazaki, *J. Biol. Chem.* **1979**, *254*, 9101.
103. Z. S. Farhangrazi, B. R. Copeland, T. Nakayama, T. Amachi, I. Yamazaki, L. S. Powers, *Biochemistry* **1994**, *33*, 5647.
104. Z. S. Farhangrazi, M. E. Fossett, L. S. Powers, W. R. Ellis, Jr. *Biochemistry* **1995**, *34*, 2866.
105. B. B. Hasinoff, H. B. Dunford, *Biochemistry* **1970**, *9*, 4930.
106. T. Egawa, H. Shimada, Y. Ishimura, *Biochem. Biophys. Res. Commun.* **1994**, *201*, 1464.
107. J. T. Groves, Y. Watanabe, *J. Am. Chem. Soc.* **1988**, *110*, 8443.
108. Y. Goto, T. Matsui, S. Ozaki, Y. Watanabe, S. Fukuzumi, *J. Am. Chem. Soc.* **1999**, *121*, 9497.
109. S. Kobayashi, M. Nakano, T. Goto, T. Kimura, A. P. Schaap, *Biochem. Biophys. Res. Commun.* **1986**, *135*, 166.
110. L. P. Candeias, L. K. Folkes, P. Wardman, *Biochemistry* **1997**, *36*, 7081.
111. D. R. Doerge, N. M. Cooray, M. E. Brewster, *Biochemistry* **1991**, *30*, 8960.
112. U. Perez, H. B. Dunford, *Biochim. Biophys. Acta* **1990**, *1038*, 98.
113. U. Perez, H. B. Dunford, *Biochemistry* **1990**, *29*, 2757.
114. T. Matsui, S. Ozaki, Y. Watanabe, *J. Biol. Chem.* **1997**, *272*, 32735.
115. M. Gajhede, D. J. Schuller, A. Henriksen, A. T. Smith, T. L. Poulos, *Nat. Struct. Biol.* **1997**, *4*, 1932.
116. M. L. Quillin, R. M. Arduini, J. S. Olson, G. N. Phillips, Jr. *J. Mol. Biol.* **1993**, *234*, 140.
117. P. R. Ortiz de Montellano, D. E. Kerr, *Biochemistry* **1985**, *24*, 1147.
118. E.-D. Wogon, H. Fretz, in *Advances in Detailed Reaction Mechanisms*, Vol. 2 (Ed., J. M. Coxon), JAI Press, Greenwich, CT, pp. 111–147.
119. F. P. Guengerich, T. L. Macdonald, *FASEB J.* **1990**, *4*, 2453.
120. L. M. Hjelmeland, L. Aronow, J. R. Trudell, *Biochem. Biophys. Res. Commun.* **1977**, *76*, 541.

121. J. T. Groves, G. A. McClusky, R. E. White, M. J. Coon, *Biochem. Biophys. Res. Commun.* **1978**, *81*, 154.
122. J. Fossey, D. Lefort, M. Massoudi, J.-Y. Nedelec, J. Sorba, *Can. J. Chem.* **1985**, *63*, 678.
123. J. T. Groves, T. E. Nemo, *J. Am. Chem. Soc.* **1983**, *105*, 6243.
124. D. Bouy-Debec, O. Brigaud, P. Leduc, P. Battioni, D. Mansy, *Gazz. Chim. Ital.* **1996**, *126*, 233.
125. M. H. Gelb, D. C. Heimbrook, P. Malkonen, S. G. Sligar, *Biochemistry* **1982**, *21*, 370.
126. P. R. Ortiz de Montellano, R. A. Stearns, *J. Am. Chem. Soc.* **1987**, *109*, 3415.
127. D. Griller, K. U. Ingold, *Acc. Chem. Res.* **1980**, *13*, 317.
128. J. K. Atkinson, K. U. Ingold, *Biochemistry* **1993**, *32*, 9209.
129. J. K. Atkinson, P. F. Hollenberg, K. U. Ingold, C. C. Johnson, M.-H. Le Tadic, M. Newcomb, D. A. Putt, *Biochemistry* **1994**, *33*, 10630.
130. M. Newcomb, M.-H. Le Tadic, D. A. Putt, P. F. Hollenberg, *J. Am. Chem. Soc.* **1995**, *117*, 3312.
131. M. Newcomb, M.-H. Le Tadic, D. L. Chestney, E. S. Roberts, P. F. Hollenberg, *J. Am. Chem. Soc.* **1995**, *117*, 12085.
132. S.-Y. Choi, P. E. Eaton, P. F. Hollenberg, K. E. Liu, S. J. Lippard, M. Newcomb, D. A. Putt, S. P. Upadhyaya, Y. Xiong, *J. Am. Chem. Soc.* **1996**, *118*, 6547.
133. M. Brookhart, M. L. H. Green, L. L. Wong, *Prog. Inorg. Chem.* **1988**, *36*, 1.
134. D. H. R. Barton, D. Doller, *Acc. Chem. Res.* **1992**, *25*, 504.
135. R. H. Crabtree, *Angew. Chem. Int. Ed. Engl.* **1993**, *32*, 789.
136. C. Hall, R. N. Perutz, *Chem. Rev.* **1996**, *96*, 3125.
137. J. P. Collman, A. S. Chien, T. A. Eberspacher, J. I. Brauman, *J. Am. Chem. Soc.* **1998**, *120*, 425.
138. B. R. Bender, G. J. Kubas, L. H. Jones, B. I. Swanson, J. Eckert, K. B. Capps, C. D. Hoff, *J. Am. Chem. Soc.* **1997**, *119*, 9179.
139. D. R. Evans, T. Drovetskaya, R. Bau, C. A. Reed, P. D. W. Boyd, *J. Am. Chem. Soc.* **1997**, *119*, 3633.
140. S. Fukuzumi, K. Mochida, J. K. Kochi, *J. Am. Chem. Soc.* **1979**, *101*, 5961.
141. S. Fukuzumi, J. K. Kochi, *J. Am. Chem. Soc.* **1980**, *102*, 2141.
142. S. Fukuzumi, J. K. Kochi, *J. Am. Chem. Soc.* **1980**, *102*, 7290.
143. S. Fukuzumi, J. K. Kochi, *J. Am. Chem. Soc.* **1981**, *103*, 7240.
144. S. Fukuzumi, N. Nishizawa, T. Tanaka, *J. Org. Chem.* **1984**, *49*, 3571.
145. K. M. Zaman, S. Yamamoto, N. Nishimura, J. Maruta, S. Fukuzumi, *J. Am. Chem. Soc.* **1994**, *116*, 12099.
146. H. R. Bosshard, H. Anni, T. Yonetani, in *Peroxidases in Chemistry and Biology*, Vol. II (Eds.: J. Everse, K. E. Everse, M. B. Grisham), CRC Press, Boca Raton, FL, **1990**, pp. 51–84.
147. H. Pelletier, J. Kraut, *Science* **1992**, *258*, 1748.
148. A. F. W. Coulson, J. E. Erman, T. Yonetani, *J. Biol. Chem.* **1971**, *246*, 917.
149. P. S. Ho, B. M. Hoffman, C. H. Kang, E. Margoliash, *J. Biol. Chem.* **1983**, *258*, 4356.
150. J. E. Erman, L. B. Vitello, J. M. Mauro, J. Kraut, *Biochemistry* **1989**, *28*, 7992.
151. M. Sivaraja, D. B. Goodin, M. Smith, B. M. Hoffman, *Science* **1989**, *245*, 738.
152. L. A. Fishel, M. F. Farnum, J. M. Mauro, M. A. Miller, J. Kraut, Y. Liu, X.-L. Tan, C. P. Scholes, *Biochemistry* **1991**, *30*, 1986.
153. J. M. Mauro, L. A. Fishel, J. T. Hazzard, T. E. Meyer, G. Tollin, M. A. Cusanovich, J. Kraut, *Biochemistry* **1988**, *27*, 6243.
154. C. P. Scholes, Y. Liu, L. A. Fishel, M. F. Farnum, J. M. Mauro, J. Kraut, *Isr. J. Chem.* **1989**, *29*, 85.
155. L. Geren, S. Hahm, B. Durham, F. Millett, *Biochemistry* **1991**, *30*, 9450.
156. S. Hahm, B. Durham, F. Millett, *Biochemistry* **1992**, *31*, 3472.
157. K. Wang, H. Mei, L. Geren, M. A. Miller, A. Saunders, X. Wang, J. L. Waldner, G. J. Pielak, B. Durham, F. Millett, *Biochemistry* **1996**, *35*, 15107.
158. S. Hahm, L. Geren, B. Durham, F. Millett, *J. Am. Chem. Soc.* **1993**, *115*, 3372.
159. J. T. Hazzard, T. L. Poulos, G. Tollin, *Biochemistry* **1987**, *26*, 2836.
160. J. T. Hazzard, S. J. Moench, J. E. Erman, J. D. Satterlee, G. Tollin, *Biochemistry* **1988**, *27*, 2002.

161. M. A. Miller, J. T. Hazzard, J. M. Mauro, S. L. Edwards, P. C. Simons, G. Tollin, J. Kraut, *Biochemistry* **1988**, 27, 9081.
162. G. Tollin, J. T. Hazzard, *Arch. Biochem. Biophys.* **1991**, 287, 1.
163. J. T. Hazzard, G. Tollin, *J. Am. Chem. Soc.* **1991**, 113, 8956.
164. F. E. Summers, J. E. Erman, *J. Biol. Chem.* **1988**, 263, 14267.
165. J. E. Erman, D. S. Kang, K. L. Kim, F. E. Summers, A. L. Matthis, L. B. Vitello, *Mol. Cryst. Liq. Cryst.* **1991**, 194, 253.
166. M. R. Nuevo, H.-H. Chu, L. B. Vitello, J. E. Erman, *J. Am. Chem. Soc.* **1993**, 115, 5873.
167. D. W. Low, J. R. Winkler, H. B. Gray, *J. Am. Chem. Soc.* **1996**, 118, 117.
168. J. Berglund, T. Pascher, J. R. Winkler, H. B. Gray, *J. Am. Chem. Soc.* **1997**, 119, 2464.
169. J. J. Wilker, I. J. Dmochowski, J. H. Dawson, J. R. Winkler, H. B. Gray, *Angew. Chem. Int. Ed. Engl.* **1999**, 38, 90.
170. T. C. Bruice, *Acc. Chem. Res.* **1991**, 24, 243.
171. M. Z. Hoffman, F. Bolleta, L. Moggi, G. L. Hug, *J. Phys. Chem. Ref. Data* **1989**, 18, 219.
172. I. Hamachi, S. Tsukiji, S. Shinkai, S. Oishi, *J. Am. Chem. Soc.* **1999**, 121, 5500.
173. Y.-Z. Hu, S. Tsukiji, S. Shinkai, S. Oishi, I. Hamachi, *J. Am. Chem. Soc.* **2000**, 122, 241.
174. I. Hamachi, S. Tanaka, S. Shinkai, *J. Am. Chem. Soc.* **1993**, 115, 10458.
175. I. Hamachi, Y. Tajiri, S. Shinkai, *J. Am. Chem. Soc.* **1994**, 116, 7437.
176. I. Hamachi, Y. Tajiri, T. Nagase, S. Shinkai, *Chem. Eur. J.* **1997**, 3, 1025.
177. B. He, R. Sinclair, B. R. Copeland, R. Makino, L. S. Powers, I. Yamazaki, *Biochemistry* **1996**, 35, 2413.
178. I. Hamachi, S. Tanaka, S. Shinkai, *J. Am. Chem. Soc.* **1993**, 115, 10458.
179. I. Hamachi, S. Tanaka, S. Tsukiji, S. Shinkai, S. Oishi, *Inorg. Chem.* **1998**, 37, 4380.
180. T. Yonetani, H. Schleyer, *J. Biol. Chem.* **1967**, 242, 1974.
181. P. Gans, G. Buisson, E. Duée, J.-C. Marchon, B. S. Erler, W. F. Scholz, C. A. Reed, *J. Am. Chem. Soc.* **1986**, 108, 1223.
182. V. K. Yachandra, K. Sauer, M. P. Klein, *Chem. Rev.* **1996**, 96, 2927.
183. R. J. Debus, *Biochim. Biophys. Acta* **1992**, 1102, 269.
184. B. A. Diner, G. T. Babcock, in *Oxygenic Photosynthesis: The Light Reactions* (Eds.: D. R. Ort, C. F. Yocum), Kluwer Academic Publishers, Dordrecht, The Netherlands, **1996**, p 213.
185. K. Wieghardt, *Angew. Chem. Int. Ed. Engl.* **1994**, 33, 725.
186. G. Christou, *Acc. Chem. Res.* **1989**, 22, 328.
187. J. Limburg, V. A. Szalai, G. W. Brudvig, *J. Chem. Soc. Dalton Trans.* **1999**, 1353.
188. W. Rüttinger, G. C. Dismukes, *Chem. Rev.* **1997**, 97, 1.
189. R. Manchanda, G. W. Brudvig, R. H. Crabtree, *Coord. Chem. Rev.* **1995**, 144, 1.
190. S. W. Gersten, G. J. Samuels, T. J. Meyer, *J. Am. Chem. Soc.* **1982**, 104, 4029.
191. Y. Naruta, M. Sasayama, T. Sasaki, *Angew. Chem. Int. Ed. Engl.* **1994**, 33, 1839.
192. D. Geselowitz, T. J. Meyer, *Inorg. Chem.* **1990**, 29, 3894.
193. J. A. Halfen, S. Mahapatra, E. C. Wilkinson, S. Kaderli, V. G. Young, Jr., L. Que, Jr., A. D. Zuberbuhler, W. B. Tolman, *Science* **1996**, 271, 1397.
194. J. Limburg, J. S. Vrettos, L. M. Liable-Sands, A. L. Rheingold, R. H. Crabtree, G. W. Brudvig, *Science* **1999**, 283, 1524.
195. J. Limburg, G. W. Brudvig, R. H. Crabtree, *J. Am. Chem. Soc.* **1997**, 119, 2761.
196. Y. Naruta, M. Sasayama, *J. Chem. Soc. Chem. Commun.* **1994**, 2667.
197. K. Ichihara, Y. Naruta, *Chem. Lett.* **1998**, 185.
198. H. H. Thorp, G. W. Brudvig, *New J. Chem.* **1991**, 15, 479.
199. L. Stryer, *Biochemistry* (4th Ed.), Freeman, New York, **1995**.
200. G. Palmer, *J. Bioenerg. Biomembr.* **1993**, 25, 145.
201. B. G. Malmström, *Chem. Rev.* **1990**, 90, 1247.
202. G. T. Babcock, M. Wikström, *Nature* **1992**, 356, 301.
203. S. Ferguson-Miller, G. T. Babcock, *Chem. Rev.* **1996**, 96, 2889.
204. J. P. Collman, F. C. Anson, S. Bencosme, A. Chong, T. Collins, P. Denisevich, E. Exitt, T. Geiger, J. A. Ibers, G. Jameson, C. Konai, K. Meier, R. Oakley, R. Pettman, E. Schmitou, J. Sessler, in *Molecular Engineering: The Design and Synthesis of Catalysis for the Rapid 4-Electron Reduction of Molecular Oxygen to Water* (Eds.: J. P. Collman et al.), Pergamon, U. K., **1981**, pp. 29–45.

205. J. P. Collman, P. S. Wagenknecht, J. E. Hutchison, *Angew. Chem. Int. Ed. Engl.* **1994**, *33*, 1537.
206. S. J. Lippard, *Science* **1993**, *261*, 699.
207. K. D. Karlin, *Science* **1993**, *261*, 701.
208. S. Iwata, C. Ostermeier, B. Ludwig, H. Michel, *Nature* **1995**, *376*, 660.
209. T. Tsukihara, H. Aoyama, E. Yamashita, T. Tomizaki, H. Yamaguchi, K. Shinzawa-Itoh, R. Nakashima, R. Yaono, S. Yoshikawa, *Science* **1995**, *269*, 1069.
210. T. Tsukihara, H. Aoyama, E. Yamashita, T. Tomizaki, H. Yamaguchi, K. Shinzawa-Itoh, R. Nakashima, R. Yaono, S. Yoshikawa, *Science* **1996**, *272*, 1136.
211. S. Yoshikawa, K. Shinzawa-Itoh, R. Nakashima, R. Yaono, E. Yamashita, N. Inoue, M. Yao, M. J. Fei, C. P. Libeu, T. Mizushima, H. Yamaguchi, T. Tomizaki, T. Tsukihara, *Science* **1998**, *280*, 1723.
212. C. Ostermeier, A. Harrenga, U. Ermler, H. Michel, *Proc. Natl. Acad. Sci. U.S.A.* **1997**, *94*, 10547.
213. J. A. Sigman, B. C. Kwok, A. Gengenbach, Y. Lu, *J. Am. Chem. Soc.* **1999**, *121*, 8949.
214. S. Fukuzumi, S. Mochizuki, T. Tanaka, *Chem. Lett.* **1989**, 27.
215. S. Fukuzumi, S. Mochizuki, T. Tanaka, *Inorg. Chem.* **1989**, *28*, 2459.
216. S. Fukuzumi, K. Ishikawa, T. Tanaka, *Chem. Lett.* **1986**, 1.
217. S. Fukuzumi, S. Mochizuki, T. Tanaka, *J. Chem. Soc. Chem. Commun.* **1989**, 391.
218. S. Fukuzumi, S. Mochizuki, T. Tanaka, *T. Inorg. Chem.* **1990**, *29*, 653.
219. S. Fukuzumi, *Bull. Chem. Soc. Jpn.* **1997**, *70*, 1.
220. S. Fukuzumi and S. Itoh, in *Advances in Photochemistry*, Vol. 25 (Eds. D. C. Neckers, D. H. Volman, G. von Büna), Wiley, New York, **1999**, pp. 107–172.
221. S. Fukuzumi, M. Patz, T. Suenobu, Y. Kuwahara, S. Itoh, *J. Am. Chem. Soc.* **1999**, *121*, 1605.
222. S. Fukuzumi, T. Suenobu, M. Patz, T. Hirasaka, S. Itoh, M. Fujitsuka, O. Ito, *J. Am. Chem. Soc.* **1998**, *120*, 8060.
223. M. Patz, Y. Kuwahara, T. Suenobu, S. Fukuzumi, *Chem. Lett.* **1997**, 567.
224. R. N. Bagchi, A. M. Bond, F. Scholz, R. Stösser, *J. Am. Chem. Soc.* **1989**, *111*, 8270.
225. R. R. Durand, Jr., C. S. Bencosme, J. P. Collman, F. C. Anson, *J. Am. Chem. Soc.* **1983**, *105*, 2710.
226. J. P. Collman, P. Denisevich, Y. Konai, M. Marrocco, K. Koval, F. C. Anson, *J. Am. Chem. Soc.* **1980**, *102*, 6027.
227. C. K. Chang, H.-Y. Liu, I. Abdalmuhdi, *J. Am. Chem. Soc.* **1984**, *106*, 2725.
228. J. P. Collman, C. S. Bencosme, R. R. Durand, Jr., R. P. Kreh, F. C. Anson, *J. Am. Chem. Soc.* **1983**, *105*, 2699.
229. Y. Le Mest, M. L'Her, J. P. Collman, N. H. Hendricks, L. McElwee-White, *J. Am. Chem. Soc.* **1986**, *108*, 533.
230. R. Guilard, S. Brandes, C. Tardieux, A. Tabard, M. L'Her, C. Miry, P. Gouerec, Y. Knop, J. P. Collman, *J. Am. Chem. Soc.* **1995**, *117*, 11721.
231. A. Nanthakumar, M. S. Nasir, K. D. Karlin, N. Ravi, B. H. Huynh, *J. Am. Chem. Soc.* **1992**, *114*, 6564.
232. S. C. Lee, R. H. Holm, *J. Am. Chem. Soc.* **1993**, *115*, 5833.
233. J. P. Collman, P. C. Herrmann, B. Boitrel, X. Zhang, T. A. Eberspacher, L. Fu, J. Wang, D. L. Rousseau, E. R. Williams, *J. Am. Chem. Soc.* **1994**, *116*, 9783.
234. T. Sasaki, Y. Naruta, *Chem. Lett.* **1995**, 663.
235. J. P. Collman, L. Fu, P. C. Herrmann, X. Zhang, *Science* **1997**, *275*, 949.
236. A. Nanthakumar, S. Fox, N. N. Murthy, K. D. Karlin, *J. Am. Chem. Soc.* **1997**, *119*, 3898.
237. T. Sasaki, N. Nakamura, Y. Naruta, *Chem. Lett.* **1998**, 351.
238. J. P. Collman, L. Fu, P. C. Herrmann, Z. Wang, M. Bröring, R. Schwenninger, B. Boitrel, *Angew. Chem. Int. Ed. Engl.* **1998**, *37*, 3397.
239. F. Tani, Y. Matsumoto, Y. Tachi, T. Sasaki, Y. Naruta, *Chem. Commun.* **1998**, 1731.
240. B. S. Lim, R. H. Holm, *Inorg. Chem.* **1998**, *37*, 4898.
241. J. P. Collman, *Inorg. Chem.* **1997**, *36*, 5145.
242. J. P. Collman, R. Schwenninger, M. Rapta, M. Bröring, L. Fu, *Chem. Commun.* **1999**, 137.

243. J. P. Collman, M. Rapta, M. Bröring, L. Aptova, R. Schwenninger, B. Boitrel, L. Fu, M. L'Her, *J. Am. Chem. Soc.* **1999**, *121*, 1387.
244. M.-A. Kopf, Y.-M. Neuhold, A. D. Zuberbühler, K. D. Karlin, *Inorg. Chem.* **1999**, *38*, 3093.
245. R. A. Ghiladi, T. D. Ju, D.-H. Lee, P. Moënné-Loccoz, S. Kaderli, Y.-M. Neuhold, A. D. Zuberbühler, A. S. Woods, R. J. Cotter, K. D. Karlin, *J. Am. Chem. Soc.* **1999**, *121*, 9885.
246. R. B. Gennis, *Proc. Natl. Acad. Sc. U.S.A.* **1998**, *95*, 12747.
247. T. Kitagawa, T. Ogura, *Prog. Inorg. Chem.* **1997**, *45*, 431.
248. R. B. Gennis, *Biochim. Biophys. Acta* **1998**, *1365*, 241.
249. A. Ulman, *An Introduction to Ultrathin Organic Films*, Academic Press, San Diego, **1991**.
250. S. V. Lymar, V. N. Parmon, K. I. Zamarev, In *Photoinduced Electron Transfer III*, (Ed.: J. Mattay), Springer, Berlin, **1991**, pp. 1–66.
251. M. A. Fox, In *Photoinduced Electron Transfer III*, (Ed.: J. Mattay), Springer, Berlin, **1991**, pp. 67–102.
252. I. Willner, B. Willner, In *Photoinduced Electron Transfer III*, (Ed.: J. Mattay), Springer, Berlin, **1991**, pp. 153–218.
253. J. K. Hurst, In *Kinetics and Catalysis in Microheterogeneous Systems*, (Eds.: M. Grätzel, K. Kalyanasunderam), Marcel Dekker, New York, **1991**, pp. 183–226.
254. J. N. Robin, D. J. Cole-Hamilton, *Chem. Soc. Rev.* **1991**, *20*, 49.
255. K. Naito, A. Miura, M. Azuma, *Thin Solid Films* **1992**, *210–211*, 268.
256. S. Isoda, S. Nishikawa, S. Ueyama, Y. Hanazato, H. Kawakubo, M. Maeda, *Thin Solid Films* **1992**, *210–211*, 290.
257. Y. Nishikawa, S.-i. Fukui, M.-a. Kakimoto, Y. Imai, K. Nishiyama, M. Fujihira, *Thin Solid Films* **1992**, *210–211*, 296.
258. X. D. Wang, B. W. Zhang, J. W. Bai, Y. Cao, X. R. Xiao, J. M. Xu, *J. Phys. Chem.* **1992**, *96*, 2886.
259. Y. Cao, B. W. Zhang, W. Y. Qian, X. D. Wang, J. W. Bai, X. R. Xiao, J. G. Jia, J. W. Xu, *Sol. Energy Mater. Solar Cells* **1995**, *38*, 139.
260. T.-H. Tran-Thi, T. Fournier, A. Y. Sharonov, N. Tkachenko, H. Lemmetyinen, P. Grenier, K.-D. Truong, D. Houde, *Thin Solid Films* **1996**, *273*, 8.
261. H. Yonemura, K. Ohishi, T. Matsuo, *Chem. Lett.* **1996**, 661.
262. H. Hosono, T. Tani, I. Uemura, *Chem. Commun.* **1996**, 1893.
263. K. Liang, K.-Y. Law, D. G. Whitten, *J. Phys. Chem. B* **1997**, *101*, 540.
264. H. Hosono, M. Kaneko, *J. Chem. Soc., Faraday Trans.* **1997**, *97*, 1313.
265. N. V. Tkachenko, A. Y. Tauber, P. H. Hynninen, A. Y. Sharonov, H. Lemmetyinen, *J. Phys. Chem. A* **1999**, *103*, 3657.
266. S. W. Feldberg, G. H. Armen, J. A. Bell, C. K. Chang, C.-B. Wang, *Biophys. J.* **1981**, *34*, 149.
267. E. Bienvenue, P. Seta, A. Hofmanová, C. Gavach, M. Momenteau, *J. Electroanal. Chem.* **1984**, *162*, 275.
268. P. Seta, E. Bienvenue, A. L. Moore, P. Mathis, R. V. Bensasson, P. A. Liddell, P. J. Pessiki, A. Joy, T. A. Moore, D. Gust, *Nature* **1985**, *316*, 653.
269. T. J. Dannhauser, M. Nango, N. Oku, K. Anzai, P. A. Loach, *J. Am. Chem. Soc.* **1986**, *108*, 5865.
270. M. Woodle, J. W. Zhang, D. Mauzerall, *Biophys. J.* **1987**, *52*, 577.
271. Y. Sakata, H. Tatemitsu, E. Bienvenue, P. Seta, *Chem. Lett.* **1988**, 1625.
272. P. Seta, E. Bienvenue, P. Maillard, M. Momenteau, *Photochem. Photobiol.* **1989**, *49*, 537.
273. M. Nango, A. Mizusawa, T. Miyake, J. Yoshinaga, *J. Am. Chem. Soc.* **1990**, *112*, 1640.
274. K. C. Hwang, D. Mauzerall, *J. Am. Chem. Soc.* **1992**, *114*, 9705.
275. M. Nango, H. Kryu, P. A. Loach, *J. Chem. Soc., Chem. Commun.* **1988**, 697.
276. J. T. Groves, S. B. Ungashe, *J. Am. Chem. Soc.* **1990**, *112*, 7796.
277. P. J. Clapp, B. Armitage, P. Roosa, D. F. O'Brien, *J. Am. Chem. Soc.* **1994**, *116*, 9166.
278. J. T. Groves, G. D. Fate, J. Lahiri, *J. Am. Chem. Soc.* **1994**, *116*, 5477.
279. J. Lahiri, G. D. Fate, S. B. Ungashe, J. T. Groves, *J. Am. Chem. Soc.* **1996**, *118*, 2347.
280. K. Iida, M. Nango, M. Matsutaka, M. Yamaguchi, K. Sato, Kazumasa, Tanaka, K. Akimoto, K. Yamashita, K. Tsuda, Y. Kuroono, *Langmuir* **1996**, *12*, 450.
281. M. Nango, K. Iida, M. Yamaguchi, K. Yamashita, K. Tsuda, A. Mizusawa, T. Miyake, A. Masuda, J. Yoshinaga, *Langmuir* **1996**, *12*, 1981.

282. T. Komatsu, K. Yamada, E. Tsuchida, U. Siggel, C. Böttcher, J.-H. Fuhrhop, *Langmuir* **1996**, *12*, 6242.
283. M. Nango, T. Hikita, T. Nakano, T. Yamada, M. Nagata, Y. Kurono, T. Ohtsuka, *Langmuir* **1998**, *14*, 407.
284. K. Sun, D. Mauzerall, *J. Phys. Chem. B* **1998**, *102*, 6440.
285. M. P. Pileni, A. M. Braun, M. Grätzel, *J. Photochem. Photobiol.* **1979**, *31*, 423.
286. M. P. Pileni, *Chem. Phys. Lett.* **1980**, *75*, 540.
287. M.-P. Pileni, M. Grätzel, *J. Phys. Chem.* **1980**, *84*, 1822.
288. P.-A. Brugger, P. P. Infelta, A. M. Braun, M. Grätzel, *J. Am. Chem. Soc.* **1981**, *103*, 320.
289. R. H. Schmehl, D. G. Whitten, *J. Phys. Chem.* **1981**, *85*, 3473.
290. P. Brochette, M. P. Pileni, *Nouv. J. Chim.* **1985**, *9*, 551.
291. S. M. B. Costa, J. M. F. M. Lopes, M. J. T. Martins, *J. Chem. Soc., Faraday Trans. 2* **1986**, *82*, 2371.
292. P. Brochette, T. Zemb, P. Mathis, M.-P. Pileni, *J. Phys. Chem.* **1987**, *91*, 1444.
293. J. K. Hurst, D. H. P. Thompson, J. S. Connolly, *J. Am. Chem. Soc.* **1987**, *109*, 507.
294. G. Steinberg-Yfrach, P. A. Liddell, S.-C. Hung, A. L. Moore, D. Gust, T. A. Moore, *Nature* **1997**, *385*, 239.
295. G. Steinberg-Yfrach, J.-L. Rigaud, E. N. Durantini, A. L. Moore, D. Gust, T. A. Moore, *Nature* **1998**, *392*, 479.
296. S. V. Lymar, R. F. Khairutdinov, V. A. Soldatenkova, J. K. Hurst, *J. Phys. Chem. B* **1998**, *102*, 2811.
297. R. F. Khairutdinov, J. K. Hurst, *J. Phys. Chem. B* **1998**, *102*, 6663.
298. R. F. Khairutdinov, J. K. Hurst, *Nature* **1999**, *402*, 509.
299. D. K. Luttrull, J. Graham, J. A. DeRose, D. Gust, T. A. Moore, S. Lindsay, *Langmuir* **1992**, *8*, 765.
300. J. Zak, H. Yuan, M. Ho, L. K. Woo, M. D. Porter, *Langmuir* **1993**, *9*, 2772.
301. J. E. Hutchison, T. A. Postlethwaite, R. W. Murray, *Langmuir* **1993**, *9*, 3277.
302. T. Akiyama, H. Imahori, Y. Sakata, *Chem. Lett.* **1994**, 1447.
303. D. Li, L. W. Moore, B. I. Swanson, *Langmuir* **1994**, *10*, 1177.
304. G. A. Schick, Z. Sun, *Thin Solid Films*, **1994**, *248*, 86.
305. T. R. E. Simpson, D. A. Russell, I. Chambrier, M. J. Cook, A. B. Horn, S. C. Thorpe, *Sens. Actuators, B* **1995**, *29*, 353.
306. I. Chambrier, M. J. Cook, D. A. Russell, *Synthesis* **1995**, 1283.
307. K. Shimazu, M. Takechi, H. Fujii, M. Suzuki, H. Saiki, T. Yoshimura, K. Uosaki, *Thin Solid Films* **1996**, *273*, 250.
308. W. Han, S. Li, S. M. Lindsay, D. Gust, T. A. Moore, A. L. Moore, *Langmuir* **1996**, *12*, 5742.
309. T. Akiyama, H. Imahori, A. Ajavakom, Y. Sakata, *Chem. Lett.* **1996**, 907.
310. T. Kondo, T. Ito, S. Nomura, K. Uosaki, *Thin Solid Films* **1996**, *284–285*, 652.
311. T. R. E. Simpson, M. J. Cook, M. C. Petty, S. C. Thorpe, D. A. Russell, *Analyst* **1996**, *121*, 1501.
312. M. J. Cook, R. Hersans, J. McMurdo, D. A. Russell, *J. Mater. Chem.* **1996**, *6*, 149.
313. L.-H. Guo, G. McLendon, H. Razafitrimo, Y. Gao, *J. Mater. Chem.* **1996**, *6*, 369.
314. H. Yuan, L. K. Woo, *J. Porphyrin Phthalocyanine* **1997**, *1*, 189.
315. T. R. E. Simpson, D. J. Revell, M. J. Cook, D. A. Russell, *Langmuir* **1997**, *13*, 460.
316. J. E. Hutchison, T. A. Postlethwaite, C.-h. Chen, K. W. Hathcock, R. S. Ingram, W. Ou, R. W. Linton, R. W. Murray, *Langmuir* **1997**, *13*, 2143.
317. E. Katz, I. Willner, *Langmuir* **1997**, *13*, 3364.
318. H. Imahori, T. Azuma, K. Ushida, M. Takahashi, T. Akiyama, M. Hasegawa, T. Okada, Y. Sakata, *SPIE* **1997**, *3142*, 104.
319. K. Uosaki, T. Kondo, X.-Q. Zhang, M. Yanagida, *J. Am. Chem. Soc.* **1997**, *119*, 8367.
320. T. Kondo, M. Yanagida, S.-i. Nomura, T. Ito, K. Uosaki, *J. Electroanal. Chem.* **1997**, *438*, 121.
321. D. W. J. McCallien, P. L. Burn, H. L. Anderson, *J. Chem. Soc., Perkin Trans. 1* **1997**, 2581.
322. M. J. Crossley, J. K. Prashar, *Tetrahedron Lett.* **1997**, *38*, 6751.
323. H. Imahori and Y. Sakata, *Adv. Mater.* **1997**, *9*, 537.
324. D. L. Pillound, C. C. Moser, K. S. Reddy, P. L. Dutton, *Langmuir* **1998**, *14*, 4809.

325. H. Imahori, H. Norieda, S. Ozawa, K. Ushida, H. Yamada, T. Azuma, K. Tamaki, Y. Sakata, *Langmuir*, **1998**, *14*, 5335.
326. D. A. Offord, S. B. Sachs, M. S. Ennis, T. A. Eberspacher, J. H. Griffin, C. E. D. Chidsey, J. P. Collman, *J. Am. Chem. Soc.* **1998**, *120*, 4478.
327. A. Ishida, Y. Sakata, T. Majima, *Chem. Commun.* **1998**, 57.
328. A. Ishida, Y. Sakata, T. Majima, *Chem. Lett.* **1998**, 267.
329. M. Yanagida, T. Kanai, X.-Q. Zhang, T. Kondo, K. Uosaki, *Bull. Chem. Soc. Jpn.* **1998**, *71*, 2555.
330. F. D. Cruz, K. Driaf, C. Berthier, J.-M. Lameille, F. Armand, *Thin Solid Films* **1999**, *349*, 155.
331. T. Kondo, T. Kanai, K. Iso-o, K. Uosaki, *Z. Phys. Chem.* **1999**, *212*, 23.
332. H. Imahori, S. Ozawa, K. Ushida, M. Takahashi, T. Azuma, A. Ajavakom, T. Akiyama, M. Hasegawa, S. Taniguchi, T. Okada, Y. Sakata, *Bull. Chem. Soc. Jpn.* **1999**, *72*, 485.
333. H. Imahori, H. Yamada, S. Ozawa, K. Ushida, Y. Sakata, *Chem. Commun.* **1999**, 1165.
334. H. Imahori, Y. Sakata, *Eur. J. Org. Chem.* **1999**, 2445.
335. N. Nishimura, M. Ooi, K. Shimazu, H. Fujii, K. Uosaki, *J. Electroanal. Chem.* **1999**, *473*, 75.
336. A. Ishida, T. Majima, *Chem. Commun.* **1999**, 1299.
337. D. T. Gryko, C. Clausen, J. S. Lindsey, *J. Org. Chem.* **1999**, *64*, 8635.
338. H. Imahori, H. Norieda, Y. Nishimura, I. Yamazaki, K. Higuchi, N. Kato, T. Motohiro, H. Yamada, T. Tamaki, M. Arimura, Y. Sakata, *J. Phys. Chem. B*, **2000**, *104*, 1253.
339. H. Imahori, H. Yamada, Y. Nishimura, I. Yamazaki, Y. Sakata, *J. Phys. Chem. B*, **2000**, *104*, 2099.
340. J. Kiwi, M. Grätzel, *J. Phys. Chem.* **1980**, *84*, 1503.
341. U. Resch, S. M. Hubig, M. A. Fox, *Langmuir* **1991**, *7*, 2923.
342. A. Ulman, *Chem. Rev.* **1996**, *96*, 1533.
343. H. Y. Liu, M. J. Weaver, C.-B. Wang, C. K. Chang, *J. Electroanal. Chem.* **1983**, *145*, 439.
344. H. Y. Liu, I. Abdalmuhdi, C. K. Chang, F. C. Anson, *J. Phys. Chem.* **1985**, *89*, 665.
345. J. P. Collman, K. Kim, *J. Am. Chem. Soc.* **1986**, *108*, 7847.
346. J. P. Collman, L. L. Chang, D. A. Tyvoll, *Inorg. Chem.* **1995**, *34*, 1311.
347. M. Anikin, N. V. Tkachenko, H. Lemmetyinen, *Langmuir* **1997**, *13*, 3002.
348. H. A. Dick, J. R. Bolton, G. Picard, G. Munger, R. M. Leblanc, *Langmuir* **1988**, *4*, 133.
349. D. Gust, T. A. Moore, A. L. Moore, D. K. Luttrull, J. M. DeGraziano, N. J. Boldt, M. V. Auweraer, F. C. De Schryver, *Langmuir* **1991**, *7*, 1483.
350. B. Choudhury, A. C. Weedon, J. R. Bolton, *Langmuir* **1998**, *14*, 6192.
351. B. Choudhury, A. C. Weedon, J. R. Bolton, *Langmuir* **1998**, *14*, 6199.
352. R. R. Chance, A. Prock, R. Silbey, *Adv. Chem. Phys.* **1978**, *37*, 1.
353. D. H. Waldeck, A. P. Alivisatos, C. B. Harris, *Surface Sci.* **1985**, *158*, 103.
354. X.-L. Zhou, X.-Y. Zhu, J. M. White, *Acc. Chem. Res.* **1990**, *23*, 327.
355. G. Cnosse, K. E. Drabe, D. A. Wiersma, *J. Chem. Phys.* **1993**, *98*, 5276.
356. W. L. Barnes, *J. Mod. Opt.* **1998**, *45*, 661.
357. D. G. Hanken, R. M. Corn, *Anal. Chem.* **1995**, *67*, 3767.
358. G. B. Sigal, C. Bamdad, A. Barberis, J. Strominger, Jr., G. M. Whitesides, *Anal. Chem.* **1996**, *68*, 490.
359. Y. Sato, M. Fujita, F. Mizutani, K. Uosaki, *J. Electroanal. Chem.* **1996**, *409*, 145.
360. H. Imahori, K. Hagiwara, T. Akiyama, S. Taniguchi, T. Okada, Y. Sakata, *Chem. Lett.* **1995**, 265.
361. H. Imahori, Y. Sakata, *Chem. Lett.* **1996**, 199.
362. H. Imahori, K. Hagiwara, T. Akiyama, M. Aoki, S. Taniguchi, T. Okada, M. Shirakawa, Y. Sakata, *J. Am. Chem. Soc.* **1996**, *118*, 11771.
363. H. Imahori, K. Hagiwara, T. Akiyama, M. Aoki, S. Taniguchi, T. Okada, M. Shirakawa, Y. Sakata, *Chem. Phys. Lett.* **1996**, *263*, 545.
364. Y. Sakata, H. Imahori, H. Tsue, S. Higashida, T. Akiyama, E. Yoshizawa, M. Aoki, K. Yamada, K. Hagiwara, S. Taniguchi, T. Okada, *Pure Appl. Chem.* **1997**, *69*, 1951.
365. H. Imahori, K. Yamada, M. Hasegawa, S. Taniguchi, T. Okada, Y. Sakata, *Angew. Chem. Int. Ed. Engl.* **1997**, *36*, 2626.
366. S. Higashida, H. Imahori, T. Kaneda, Y. Sakata, *Chem. Lett.* **1998**, 605.

- 367. K. Tamaki, H. Imahori, Y. Nishimura, I. Yamazaki, A. Shimomura, T. Okada, Y. Sakata, *Chem. Lett.* **1999**, 227.
- 368. K. Tamaki, H. Imahori, Y. Nishimura, I. Yamazaki, Y. Sakata, *Chem. Commun.* **1999**, 625.
- 369. M. Fujitsuka, O. Ito, H. Imahori, K. Yamada, H. Yamada, Y. Sakata, *Chem. Lett.* **1999**, 721.
- 370. K. Yamada, H. Imahori, Y. Nishimura, I. Yamazaki, Y. Sakata, *Chem. Lett.* **1999**, 895.
- 371. H. Imahori, K. Tamaki, H. Yamada, K. Yamada, Y. Sakata, Y. Nishimura, I. Yamazaki, M. Fujitsuka, O. Ito, *Carbon*, **2000**, 38, 1599.
- 372. C. Luo, D. M. Guldi, H. Imahori, K. Tamaki, Y. Sakata, *J. Am. Chem. Soc.* **2000**, 122, 6535.
- 373. N. V. Tkachenko, C. Guenther, H. Imahori, K. Tamaki, Y. Sakata, S. Fukuzumi, H. Lemmetyinen, *Chem. Phys. Lett.* **2000**, 326, 344.
- 374. C. A. Mirkin, W. B. Caldwell, *Tetrahedron* **1996**, 52, 5113.
- 375. H. Imahori, T. Azuma, S. Ozawa, H. Yamada, K. Ushida, A. Ajavakom, H. Norieda, Y. Sakata, *Chem. Commun.* **1999**, 557.
- 376. H. Imahori, T. Azuma, A. Ajavakom, H. Norieda, H. Yamada, Y. Sakata, *J. Phys. Chem. B* **1999**, 103, 7233.
- 377. M. Fujihira, *Mol. Cryst. Liq. Cryst.* **1990**, 183, 59.
- 378. *In Standard Potentials in Aqueous Solution* (Eds.: A. J. Bard, R. Rarsons, J. Jordan), Marcel Dekker, New York, **1985**.

9 ESR Spectroscopy of Inorganic and Organometallic Radicals

Wolfgang Kaim

9.1 Introduction: The Information Accessible from ESR

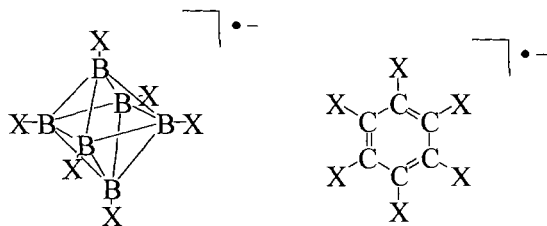
Electron spin resonance (ESR) or, more generally, electron paramagnetic resonance (EPR) [1], is a physical method of analysis which, although restricted to paramagnetic species, is a powerful tool not only for the identification of such systems but also for kinetic investigations and, above all, for the study of their electronic structures. Information can come from the often temperature-dependent line-widths of the ESR signals (which are related to mobility and relaxation behavior), from the g factors (the equivalents of NMR 'chemical shifts'), from electron–nuclear hyperfine coupling (which might require electron–nuclear double resonance, ENDOR, as a more sophisticated method of analysis), and from zero-field splitting parameters, D , or exchange coupling values, J , for two-spin (triplet) or multi-spin systems.

It is assumed that the interested reader of this chapter has a basic knowledge of the theory and instrumentation associated with this particular variety of magnetic resonance, including perhaps a general introduction to the field of organic radicals. In keeping with the handbook character of this series, the following discussion will focus on special aspects of this method in inorganic and organometallic chemistry with emphasis on practical guidelines and references for the experimentalist, as suggested by own experience and illustrated by selected recent examples; a complementary excellent monograph on radical processes specifically in transition metal chemistry has recently appeared [2].

9.2 Inorganic and Organometallic Radicals: Definition, Generation and Peculiarities

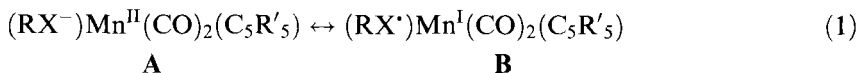
The ESR spectroscopy of inorganic and organometallic systems with main group or transition element [2, 3] paramagnetic centers is distinguished from the study of organic radicals [4] by this method:

- 1) by the large number of isotopes available from the periodic table for electron–nuclear hyperfine interaction [5];
- 2) by the large spin–orbit coupling effects from the heavier elements (which affect both line-widths and g factors) [6];
- 3) by the possible use of s, p, d or f orbitals for the primary accommodation of spin; and
- 4) by possible occurrence of spin-delocalized spatial arrangements ('clusters') like, e.g., near-octahedral $[\text{B}_6\text{X}_6]^{*-}$ [7], which are quite different from the familiar planar π systems in organic radical compounds such as the formally analogous ions $[\text{C}_6\text{X}_6]^{*-}$ (X = halogen) [8].



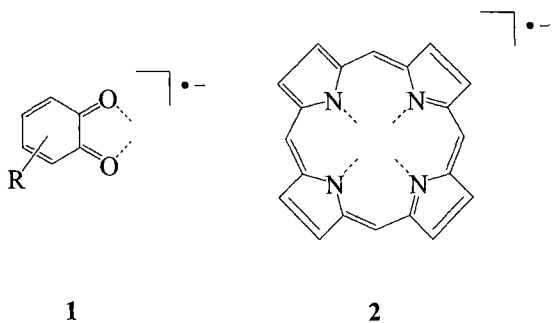
Although inorganic or organometallic radical species may well consist of a single paramagnetic center with at least one unpaired s, p, d or f electron, there are also oligonuclear compounds with the ESR-detectable spin distributed over more than one 'inorganic' atom. Such phenomena are quite familiar in the field of oligomers (e.g. the 'platinum blues' $[\text{Pt}^{2-x}\text{L}_n]_4$) or paramagnetic clusters of transition metals such as $(\text{CoCp})_3(\mu_3\text{-CPh})_2$ [9]; they also occur, however, in the area of main-group elements as exemplified by ESR-characterized species such as $[\text{R}_2\text{Al-AlR}]^*$ [10], $[\text{R}_4\text{Ga}_4]^{*-}$ [11], $[\text{B}_6\text{X}_6]^{*-}$ [7], or $[\text{B}_9\text{X}_9]^{*-}$ [12] (R = alkyl, X = halogen), all with Group 13 element-centered spins.

In the context of inorganic and organometallic chemistry the term 'radical' needs a qualifying statement. Whereas paramagnetic main-group element compounds and most paramagnetic d block organometallic complexes with significant covalent bonding are usually referred to as radicals, the classical, i.e. non-organometallic transition metal coordination compounds [2, 3] e.g. of copper(II) or manganese(II) are usually not labeled correspondingly. Thus, the compounds $(\text{RX})\text{Mn}(\text{CO})_2(\text{C}_5\text{R}'_5)$ have been regarded as 'radical' species [13] although the spin resides mainly on the metal (low-spin Mn^{II} configuration **A** instead of the radical alternative **B** in Eq. 1), depending to some extent on the electronic effect of R [14]. In contrast, more conventional low-spin manganese(II) complexes such as $[(\text{ON})\text{Mn}(\text{CN})_5]^{2-}$ are not generally referred to as radicals [15]. The main reason for this practice lies in the often analogous reactivity (e.g. H-abstraction [16]) of organometallic 'radicals' in comparison with typical organic radicals such as $\cdot\text{CH}_3$.



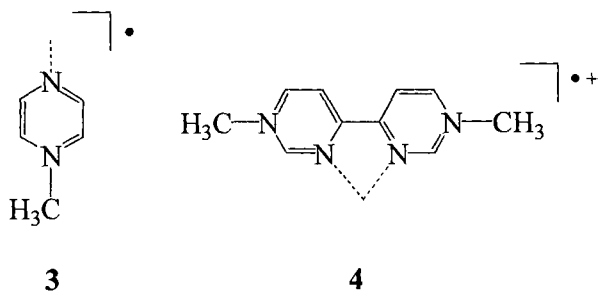
X = NH, S, Se; R' = H, CH₃; R = aryl, alkyl

Paramagnetic coordination compounds where the spin resides *predominantly* on one or more of the organic (or inorganic) ligands are quite common, especially complexes of radical anions [17] such as *o*-semiquinones **1** or other negatively charged chelates such as tetrapyrrole macrocycles **2** [18].



(..... : potential coordinative bond)

Neutral radicals (e.g. NO[•] [19] or *N*-methylpyrazinium **3** [20]) and even cation radicals such as **4** [21] can also bind metal complex fragments to form ESR-detectable species.



Inorganic and organometallic radicals can be deliberately generated for ESR measurements in solution by irradiation (radiolysis, photolysis) [22] or by use of electrode processes ('ESR spectroelectrochemistry') [23] inside the microwave cavity of an ESR spectrometer ('in situ' or 'intra muros' generation), and they can occur as intermediates (transients) [2] or final 'escape' products of thermally or light-induced electron transfer reactions [24, 25]. The use of suitable oxidants or reductants for chemical radical generation in the organometallic field has been excellently reviewed by Connelly and Geiger [26].

The following discussion summarizes important criteria and parameters for the application of ESR in inorganic and organometallic chemistry, illustrated by selected examples.

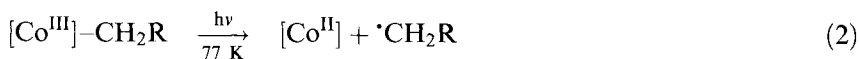
9.3 Selected ESR Parameters

9.3.1 Concentration and Lifetime of Radicals

Many of the frequently invoked radicals in inorganic or organometallic chemistry, e.g. the thermally or photochemically generated species $\cdot\text{M}(\text{CO})_5$, $\text{M} = \text{Mn}$ or Re [27], are too short-lived to be observed in the necessary useful concentrations of about $c > 10^{-7} \text{ M}$ by conventional ESR methods under standard conditions. Although continuous wave (CW) ESR is a well-established detection method for kinetic techniques such as stopped or continuous flow [28], this method is limited to lifetimes of ca $\tau > 10^{-4} \text{ s}$ for the paramagnetic intermediates. To detect and study species which would be shorter-lived under standard conditions the following techniques have been developed; they are illustrated by examples involving an important elementary process in organometallic chemistry, viz. homolytic $\text{M}-\text{C}_{\text{sp}^3}$ bond dissociation.

Irradiation of immobilized species in matrices by use of electrons, UV-Vis, X- or γ -rays and direct observation of thus stabilized radicals under static conditions [22]

Many short-lived small inorganic radicals and unusual transition metal centers have been generated by photolysis or radiolysis methods in matrices [22]. (The matrix can be a glassy frozen solvent or a solid, e.g. zeolite or other oxide). This method is, however, also suitable for investigation of rather complex systems such as alkyl cobalamins and related ' B_{12} ' species [29, 30]. Irradiation with visible light is even sufficient to cleave the crucial $\text{Co}-\text{C}_{\text{alkyl}}$ bond in these macrocyclic compounds to yield Co^{II} products and the less persistent alkyl radical intermediates; both can be detected by ESR in low-temperature matrices (Eq. 2) [30].

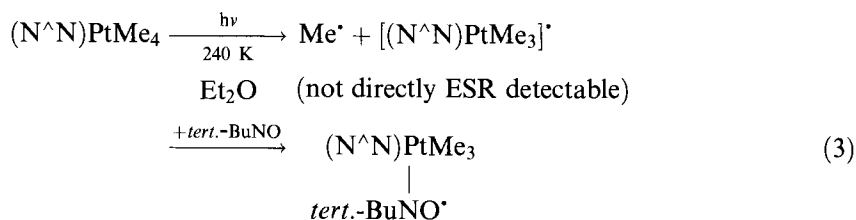


CD_3OD

$[\text{Co}] = \text{cobalt corrin complex}$

Trapping of short-lived radical intermediates as generated by photolytic, thermal or chemical processes with the help of NO-containing 'spin traps' such as alkyl nitrones or nitroso compounds [31]

This popular approach, illustrated by Eq. 3 [32] for an organometallic example, must be carefully checked with respect to the question whether the resulting stable and thus ESR-observable species (e.g. a nitroxide radical complex) is perhaps just a product from a preformed 'charge-transfer' complex between the substrate and the spin trap.



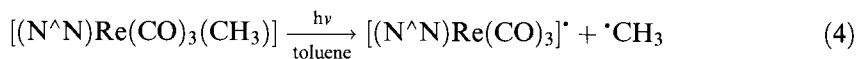
$\text{N}^{\wedge}\text{N} = \alpha$ -diimine

$$a(^{14}\text{N}) = 1.58\text{ mT}$$

$$a(^{195}\text{Pt}) = 4.0\text{ mT}$$

Pulsed ESR methods

Pulsed ESR methods (FT-ESR) have been increasingly developed during the last decade for use in direct time-resolved studies [33] of transient species. Although this technique is excellently suited to the investigation of typical inorganic and organometallic reactivity such as the light-induced metal/ sp^3 -carbon bond homolysis (Eq. 4) [34], the corresponding metal-containing radical products such as $[(\text{N}^{\wedge}\text{N})\text{Re}(\text{CO})_3]^{\bullet}$ ($\text{N}^{\wedge}\text{N} = \alpha$ -diimine ligand) may not be directly detectable owing to unfavorable relaxation properties (cf. Section 9.3.2).



$\text{N}^{\wedge}\text{N} = 4,4'$ -dimethyl-2,2'-bipyridine

This organometallic radical product could, however, be detected by irradiation in glassy frozen matrices [34]. The alkyl radicals, as very short-lived metal-free products, could be observed and analyzed by FT-ESR with respect to CIDEP (chemically induced dynamic electron polarization) effects [34].

9.3.2 Line-width and Temperature

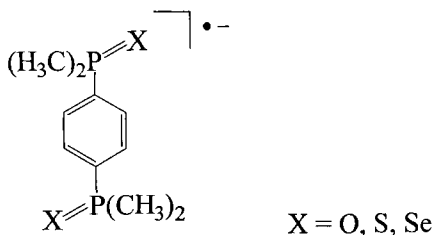
Whereas almost all organic radicals give rather narrow ESR signals in solution, with widths of individual hyperfine lines well below 1 Gauss (0.1 mT) [4], signals in the spectra of inorganic and organometallic radicals can be severely broadened, sometimes beyond ESR detectability even at very low temperatures. In the absence of special (e.g. dynamic) effects, this phenomenon is usually a result of strongly shortened relaxation times after excitation by microwave radiation. The enhanced relaxation of inorganic or organometallic radicals is generally favored by the presence of heavy atoms with their large spin-orbit coupling constants [6] and the numerous available states, often close-lying, involving contributions from s, p, d or f atomic orbitals of one or more of the 'inorganic' atoms. Di- and polynuclear radical

compounds (clusters) and high symmetry species (T_d , O_h) with degenerate spin-bearing orbitals can have particularly pronounced effects for the very same reason—close-lying excited states from which rapid relaxation to the ground state can occur.

To detect such radicals by ESR, low temperatures must be routinely employed, and even then otherwise (e.g. structurally or magnetically) well-characterized species can remain 'ESR-silent' at 77 K ($[B_6I_6]^{*-}$ [8], $[Fe(C_5H_5)_2]^+$ [35a], $[(bpy)_2Ru(\mu-OC(R)NNC(R)O)Ru(bpy)_2]^{3+}$ [35b]) or 4 K ($Re^{VI}S_4^{2-}$ [36a], $[(N^{\wedge}N)Pt^{III}R_2]^+$ ($N^{\wedge}N = \alpha$ -diimine) [36b], $[In_4R_4]^{*-}$ [11], $[(bpy)_2Os(\mu-OC(R)NNC(R)O)Os(bpy)_2]^{3+}$ [35c]). Obviously, such effects can occur with main-group element-, transition metal- and even ligand-centered spins [37]. NMR of paramagnetic substances can then sometimes be employed as a complementary technique [38]; lowering the symmetry, e.g. by coordination of metal complex fragments to ReS_4^{2-} is another alternative [36a, c].

In contrast, disappearance of ESR signals when the temperature is *lowered* is usually a sign of intermolecular association, e.g. to form a spin-spin coupled dimer with a singlet ground state. Triplet states might, however, then be thermally accessible, or the triplet may even become the ground state of the system (cf. Section 9.3.5).

Decreasing ESR line-width and improved spectral resolution at higher temperatures is usually a sign of enhanced mobility in solution resulting in better averaged anisotropic contributions from hyperfine and g tensors; ESR spectroscopy at X-band frequency is distinguished by a characteristic time-scale of ca 10^{-8} s (cf. Section 9.3.6). Inorganic and organometallic radicals are often severely affected by selective 'anisotropic line-broadening' [4] because of large A or g anisotropy and/or slow tumbling (long rotational correlation times) in solution; the higher masses of inorganic elements and the resulting larger moments of inertia often contribute to increased ESR line-widths as exemplified by the series of compounds $[R_2M-MR]^{\bullet}$, $M = Al, Ga$ [10, 39b, c], or **6** [39a].

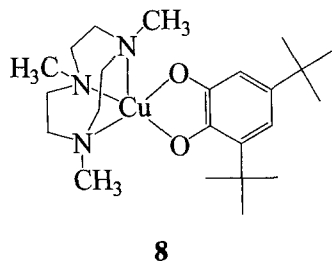
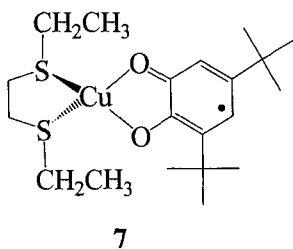


6

9.3.3 The g Factor

According to the ESR resonance condition, $h\nu_r = g\beta H_r$, the g value is the proportionality factor between the resonance frequency ν_r and the resonance field H_r .

The g factor thus has the same role as the absolute chemical shift in NMR spectroscopy. In a purely electron spin-governed ('spin only') situation, the g factor would have the value $g_e = 2.0023$ as calculated and measured for the free electron [1], although even small contributions from excited states with non-zero orbital angular momentum through spin-orbit coupling will affect this value, especially if nuclei with high spin-orbit coupling constants [6] contribute significantly. Thus easily detectable deviations, Δg , of the isotropic g factor from the free electron value are observed for inorganic and organometallic radicals, even if the spin is still largely (>95 %) ligand-centered; a deviation such as $g_{iso} = 2.0093$ for the Cu^{I} -semiquinone complex **7** [40] translates to $\Delta g = 0.0070$, a relative shift of about 3500 ppm.



For metal-centered spin, this deviation can be substantially higher. Thus, for the Cu^{II} /catecholate compound **8** $g_{iso} = 2.113$, which corresponds to a shift of ca 5.5×10^4 ppm [40].

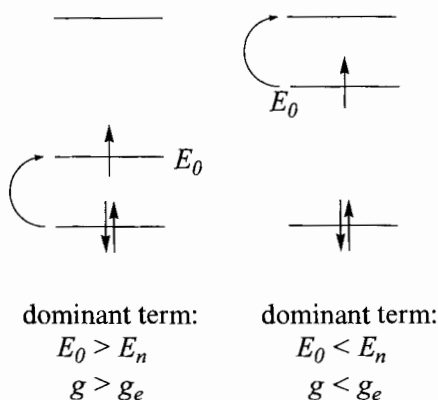
The sign of the deviation is indicative of the frontier orbital situation—according to Stone's approximation (Eq. 5) [41]:

$$g = g_e - \frac{2}{3} \sum_i \sum_n \sum_{kj} \frac{\langle \psi_0 | \xi_k \mathbf{L}_{ik} \delta_k | \psi_n \rangle \langle \psi_n | \mathbf{L}_{ij} \delta_j | \psi_0 \rangle}{E_n - E_0} = g_e + \Delta g \quad (5)$$

ξ : spin orbit coupling constant

\mathbf{L} : angular momentum operator

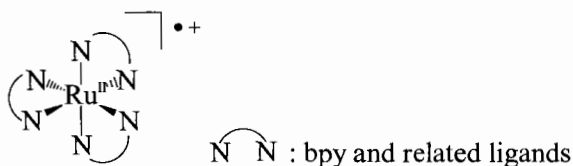
E_0 : energy of singly occupied molecular orbital (SOMO)



Scheme 1.

A deviation to higher values than g_e is to be expected if $E_0 > E_n$, i.e. if the highest lying fully occupied MO lies closer to the SOMO than the lowest empty MO. Such is the case for almost all low-spin d^5 and d^9 systems [2] (cf. **8**) or for the radical complex **7** [40].

The other alternative, $E_0 < E_n$, with the lowest empty MO lying closer to the SOMO than the highest occupied MO leads to lower g factors than g_e as is typical for d^1 systems [2] and, e.g., for **9** [42].

**9**

The effect of increasing spin-orbit coupling constants on the deviation Δg of g from g_e is evident, e.g., for Group-6 carbonylmethyl(0) complexes $[(OC)_nM](A^{\bullet-})$ of heterocyclic anion radical ligands where the greatest such deviation—positive or negative—is invariably observed for the tungsten homolog [43]. Such correlations are, however, only valid for paramagnetic systems with the inorganic nuclei in chemically comparable environments. An example where the $4d^5$ compound has less g anisotropy g_1-g_3 than a $3d^5$ analog is described below [44a].

In efforts to mimic the function of heterobimetallic hydrogenases and provide potential molecular catalysts for fuel cell technology the Fe,Ru-heterobimetallic hydride complex $[Cp^*RuH(dppf)]$, $dppf = 1,1'$ -bis(diphenylphosphino)ferrocene, has been reported [44b] to catalyze the elementary reaction $H_2 \rightarrow 2H^+ + 2e^-$. It was suggested [44b] that the crucial oxidation involves the ruthenium center and not

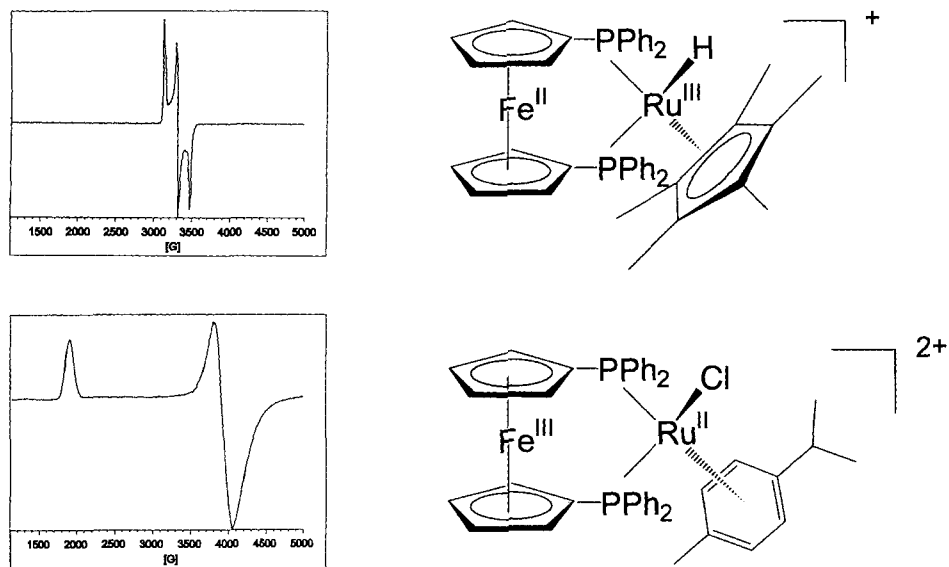


Figure 1. Comparison of iron and ruthenium oxidation in 1,1'-bis(diphenylphosphino)ferrocene-ruthenium(II) complexes (ESR spectra [44a] from electrolytically oxidized solutions of precursors [44b, c] in THF at 4 K): Oxidation of $[\text{Cp}^*\text{RuH}(\text{dppf})]$, $\text{dppf} = 1,1'$ -bis(diphenylphosphino)ferrocene, and $[(\text{Cym})\text{RuCl}(\text{dppf})](\text{PF}_6)$, $\text{Cym} = p$ -cymene, occurs at ruthenium for the former compound but yields a ferrocenium species for the latter.

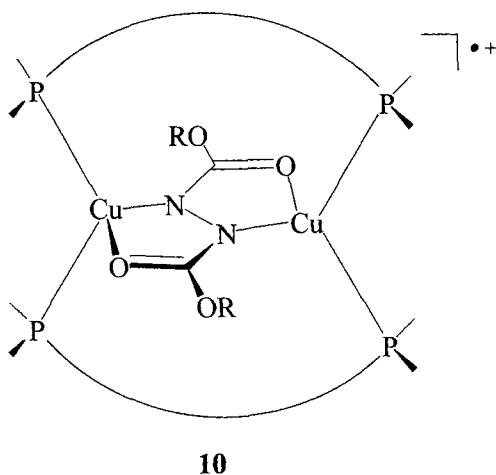
the iron of the ferrocene ligand. Figure 1 illustrates the EPR evidence that there is a viable alternative $\text{Fe}^{\text{II}}\text{Ru}^{\text{III}}$ rather than $\text{Fe}^{\text{III}}\text{Ru}^{\text{II}}$ by describing a similar species, the recently structurally characterized [44c] complex $[(\text{Cym})\text{RuCl}(\text{dppf})](\text{PF}_6)$ with a neutral arene (p -cymene) instead of a cyclopentadienide and a chloride instead of a hydride co-ligand at ruthenium.

Both complexes are reversibly oxidized but the resulting ESR signals in glassy frozen solution differ significantly (Figure 1). Whereas the organometallic low-symmetry low-spin ruthenium(III) center in $[\text{Cp}^*\text{RuH}(\text{dppf})]^+$ has relatively small g anisotropy with $g_1 = 2.187$, $g_2 = 2.088$ and $g_3 = 1.991$ ($g_1 - g_3 = 0.196$), the ferrocenium systems with their special symmetry and d orbital splitting are typically distinguished by broad ESR signals, often observable only at 4 K [35a], with large g anisotropy. Complex $[(\text{Cym})\text{RuCl}(\text{dppf})]^{2+}$ is thus properly formulated as a ferrocenium/ Ru^{II} system with $g_1 = 3.612$ and $g_{2,3} = 1.765$ ($g_1 - g_3 = 1.847$) [44a].

In just the same way as the hyperfine coupling, the g factor has tensor structure [1] which can be studied in detail by examining single crystals of radicals [3b, 45]. In many instances, however, the intermediate character of such species allows for investigation in the powder state only or in glassy frozen solutions which then yield up to three separated g factor components, according to the symmetry of the SOMO [3]. The splitting of these g components, including the total g anisotropy, symmetry, and positions of the individual components is valuable ESR information

for the identification of the SOMO as has long been known for classical paramagnetic transition metal complexes, e.g. in metal d [3] or f [46] orbital analysis. The influence of increasing spin-orbit coupling constants from heavier elements on the g anisotropy $g_1 - g_3$ is nicely illustrated by the series of chalcogen-based 19-electron triatomic bent radicals [47a] $\text{O}_3^{\cdot-}$ ($g_1 - g_3 = 0.0161$), $\text{SeO}_2^{\cdot-}$ ($g_1 - g_3 = 0.0342$), and the new $\text{TeS}_2^{\cdot-}$ ($g_1 - g_3 = 0.0719$) [47b].

Large line-widths, sometimes in conjunction with insufficiently resolved hyperfine structure, can preclude the determination of individual g factor components close to $g = 2$ under conventional ESR conditions (X band, 9.5 GHz, 330 mT). As in NMR spectroscopy, an increase in the field and frequency is then appropriate via the Q band (35 GHz) to the W band (95 GHz) or even higher frequencies and magnetic fields [48]. An application of such high-field ESR for the inorganic radical **10** with sizeable metal participation has been reported [49a].



10

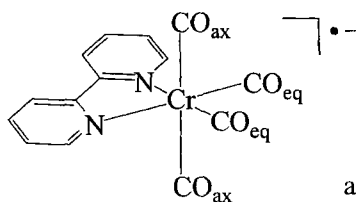
The rather large $^{63,65}\text{Cu}$ hyperfine coupling of about 1.7 mT [49b] from two copper nuclei in the stable, crystalline [49c] blue complex **10** has raised the question whether these centers are still correctly described as Cu^{I} or whether they have some Cu^{II} character. Unfortunately, the extensive hyperfine coupling [49b] from two $^{63,65}\text{Cu}$, two ^{14}N and four ^{31}P nuclei caused complete broadening of the X band ESR signal in glassy frozen solution. Increasing the frequency by a factor of 25 to 245 GHz, however, revealed three well-separated g components [49a] the values of which ruled out any significant contribution from copper(II) states.

9.3.4 Electron–Nuclear Hyperfine Coupling

In principle, ESR hyperfine coupling between the unpaired electron and the various nuclei (isotopes) of the radical species is the most informative data from ESR, both

for identification of the species and for elucidation of the electronic structure. Although, ideally, all nuclei with non-zero nuclear spins couple to a certain extent with the unpaired electron in a molecule and thus reveal the nature of the singly occupied molecular orbital (SOMO), there might be severe limitations affecting this kind of information.

- 1) To begin with, the intrinsic line-width might be too large for the resolution of the hyperfine structure for the reasons given in Section 9.3.2 or because of dynamic phenomena (e.g. electron hopping [42, 50]; Section 9.3.6). Graphical analysis of only partially resolved ESR hyperfine structure may be facilitated by mathematical derivatization, e.g. of the usually recorded first derivative to the second derivative spectrum [45] (whereby mere turning points become maxima or minima), or by computer-assisted simulation (spectrum synthesis) with estimated line-widths and line-shapes. Computer simulation is not only necessary when very many lines (see point 4, below) from several different coupling nuclei overlap, it may also be appropriate when large line-widths and unusual nuclear spin situations combine to yield ESR spectra of unfamiliar appearance. One such example are the various manifestations of 'two-line' patterns as observed [51, 86], e.g., for the dominant coupling of one rhenium atom with the unpaired electron. It arises through the cancellation (by overlap) of the innermost lines of the sextet expected for the hyperfine interaction with $^{185,187}\text{Re}$ (100 % total natural abundance, $I = 5/2$ and very similar nuclear magnetic moments for both isotopes). Increasing the line-width by lowering the temperature illustrates this effect experimentally (Figure 2).
- 2) Secondly, the isotopic properties [5] of the nuclei of interest might not be suitable because of absent nuclear spin ($I = 0$; e.g. ^{12}C , ^{18}O , ^{32}S , ^{56}Fe) or the low natural abundance of isotopes with $I \neq 0$ (^{13}C : 1.1 %, $I = 1/2$; ^{17}O : 0.038 %, $I = 5/2$; ^{33}S : 0.75 %, $I = 3/2$; ^{57}Fe : 2.15 %, $I = 1/2$). Manipulation of the natural isotopic composition, e.g. by selective enrichment, is then appropriate. The enrichment may involve metal isotopes such as ^{95}Mo (15.9 %, $I = 5/2$) or ^{61}Ni (1.1 %, $I = 3/2$) in biological probes [52] (where this method might even analytically establish the presence of corresponding trace elements), or, e.g., ^{13}C nuclei in radical ligands, as illustrated by compound **11** with its very different participation of axial and equatorial carbonyl ligands in the spin distribution [53, 64b].

**11**

$$a(^{13}\text{C}_{\text{eq}}) < 0.01 \text{ mT}$$

$$a(^{13}\text{C}_{\text{ax}}) = 0.601 \text{ mT}$$

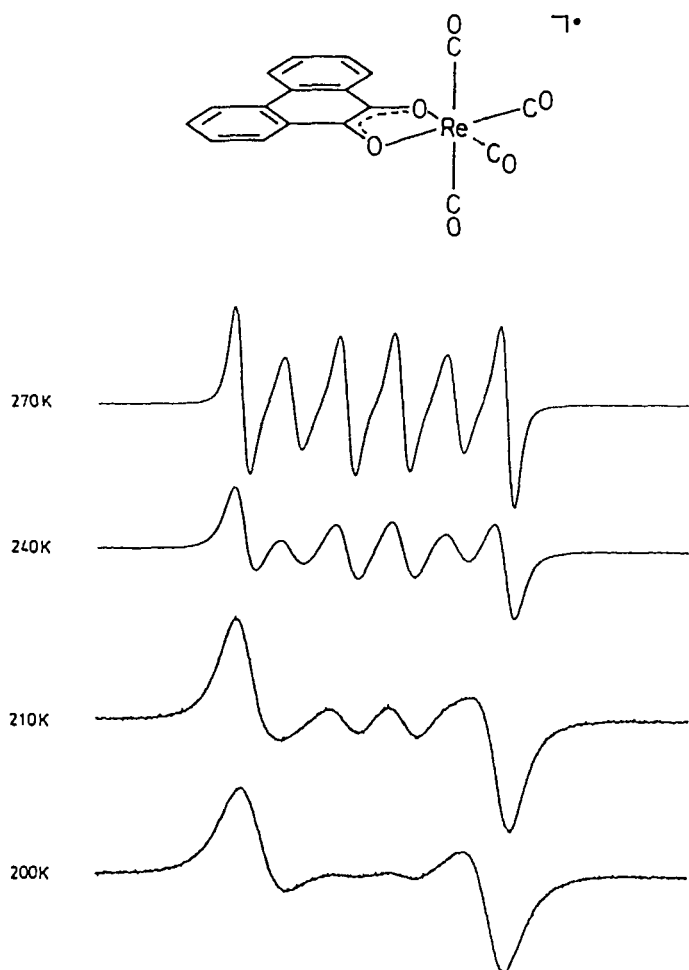
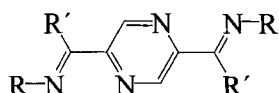


Figure 2. Temperature dependence of the ESR spectrum of tetracarbonyl(phenanthrenesemiquinone)rhenium(I) complex $[(pq)Re(CO)_4]^+$ in toluene (cf. K. A. M. Creber, T. I. Ho, C. Depew, D. Weir, J. K. S. Wan, *Can. J. Chem.* **1982**, 60, 1504). The $^{185,187}Re$ sextet hyperfine coupling dominates, yet increasing line-width at lower temperatures causes significant distortion of the sextet coupling as a result of overlapping of the innermost lines.

Similarly, de-enrichment or isotope exchange may also improve the detectability of ESR hyperfine structure and permit the assignment of coupling constants. Isotopically pure ^{65}Cu instead of the naturally occurring $^{63,65}Cu$ isotope mixture has been used in bioinorganic studies and H/D exchange (2D : $I = 1$, $\mu_H/\mu_D = 6.5$) is frequently employed in, e.g., transition metal hydride chemistry [54].

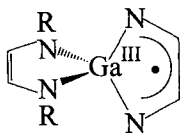
3) A further limitation even in otherwise favorable circumstances is the very low

nuclear magnetic moment μ of certain isotopes such as ^{101}Rh (100 %, $I = 1/2$) [55a] or $^{191,193}\text{Ir}$ (100 %, $I = 3/2$) which then results in small and frequently undetectable hyperfine coupling, even with high spin density on the nucleus. As an example, distinctly increased g anisotropy and relaxation rates are observed for electrogenerated $\text{M}^{\text{I}}/\text{M}^{\text{II}}$ mixed-valent systems $[(\text{Cp}^*\text{M}(\mu\text{-dip})\text{MCp}^*)^+]^+$ ($\text{M} = \text{Rh}, \text{Ir}$; dip = 2,5-diiminopyrazine ligand) in comparison with the related radicals $[\text{Cp}^*\text{ClM}(\mu\text{-dip})\text{MClCp}^*]^{\cdot+}$; hyperfine information (which would settle the question of localized or delocalized valences) could not, however, be obtained because of the unfavorable isotopic situation [55b, c].



dip

Conversely, a fairly large inorganic isotope coupling constant such as 1.8 mT for $^{69,71}\text{Ga}$ may suggest an unusual oxidation state (here mononuclear Ga^{II}) [56] in a compound **12** where in fact a regular diamagnetic Ga^{III} center binds one radical anion and one dianionic α -diimine ligand [57].

**12**

In a similar manner, the platinum(I) oxidation state has sometimes been invoked [58] in complexes $[(\text{N}^{\wedge}\text{N})\text{PtL}_n]^k$ ($\text{N}^{\wedge}\text{N} = \alpha$ -diimine ligand) because of large ^{195}Pt isotope coupling where in fact the Pt^{II} center is bound to a one-electron reduced $\text{N}^{\wedge}\text{N}$ ligand [36b, 59]. True Pt^{I} species with $5d^9$ configuration are quite rare and reactive and have very large coupling constants and g anisotropies [60].

- 4) The multiplicative connection in Eq. 6 for the total number of hyperfine lines can rapidly lead to so many overlapping individual lines that analysis from the ESR experiment alone becomes impossible and an unresolved, inhomogeneously broadened signal results.

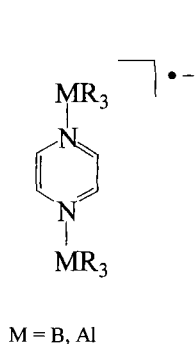
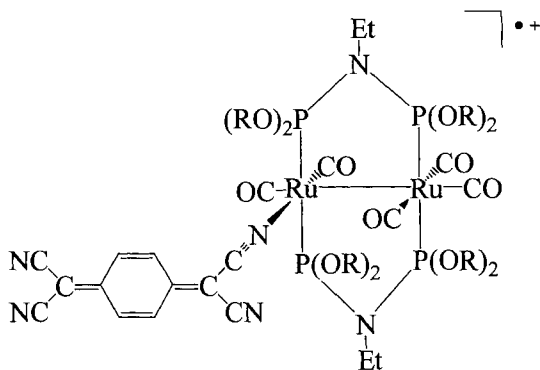
$$N = \prod_i (2n_i I_i + 1) \quad (6)$$

N : number of hyperfine lines

n_i : number of equivalent nuclei in set i

I_i : nuclear spin of the isotopes in set i

Fortunately, many nuclei do not contribute to hyperfine splitting in any given radical because of absent nuclear spin, low magnetic moment, or marginal spin density; there are, however, exceptions. For instance, the symmetrical delocalization of spin over all boron and halogen atoms in the stable, near-octahedral cluster radical anion $B_6I_6^{\bullet-}$ [7] results in a total number of 25 606 theoretical lines involving the nuclei ^{10}B (19.8 %, $I = 3$), ^{11}B (80.2, $I = 3/2$), ^{127}I (100 %, $I = 5/2$), according to a statistical treatment for the seven isotopic combinations of the chemically symmetrical species $[^{10}B_n^{11}B_{6-n}^{127}I_6]^{\bullet-}$, $n = 0-6$. In such cases, or for low-symmetry systems with many *different* coupling constants [21b], use of the electron-nuclear double resonance (ENDOR) technique reduces the number of lines, because each coupling constant is represented by only two lines on the radiofrequency scale [61]. Because of the required saturation of the ESR transition and rather specific requirements for the relaxation rates [61], which are different for each nucleus, the ENDOR method is not always straightforward with inorganic or organometallic radicals in solution; examples are, however, known for main group element radicals such as **13** (^{10}B , ^{11}B , ^{27}Al heteronuclear ENDOR) [62] and transition metal containing species [21b, 31b, 63] such as **14** [63b].

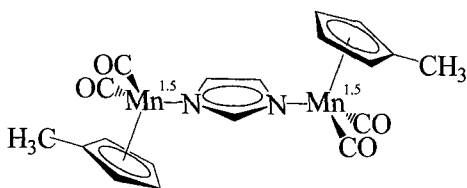
**13****14**

Pulsed ENDOR methods have been developed to obtain maximum hyperfine information [33a, 55a].

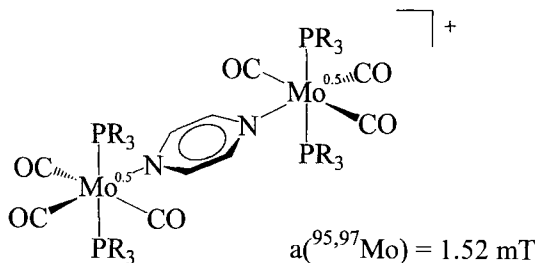
The occurrence of hyperfine coupling for a particular isotope indicates non-zero spin density at that nucleus in accordance with the Fermi contact term (which includes the electron wave function evaluated at the nucleus) [1]. The analysis in terms of spin density then requires at least a comparison with the (calculated [5]) isotropic hyperfine splitting constant a_0 ; ideally, results from increasingly available open-shell quantum-chemical calculation procedures [64] are employed.

The hyperfine structure may also indicate, in a rather elementary way, the symmetry and thus intramolecular electron exchange situation of radicals. For instance,

organometallic mixed-valent species $(R_5C_5)(OC)_2Mn^{1.5}(\mu-L^-)Mn^{1.5}(CO)_2(C_5R_5)$, $L = RO^-$ or imidazolate (**15**), exhibit their delocalized ground state (involving rapid intramolecular electron exchange) through the coupling of one unpaired electron with two *equivalent* nuclei ^{55}Mn (100 %, $I = 5/2$) [65]. The resulting eleven lines are spaced with a coupling constant roughly one half of that for corresponding mononuclear species $(R_5C_5)(OC)_2Mn^{II}(L^-)$ [65]. In contrast, dinuclear $Mn^{III}Mn^{IV}$ model complexes for the oxygen-evolving manganese clusters in photosystem II clearly show 16 lines with an intensity distribution that indicates two different coupling constants for the two Mn centers, signifying slow intramolecular electron exchange and a localized mixed-valent situation [66].

**15**

Similar metal-metal spin delocalization could be established directly by ESR for dimolybdenum systems **16** [67] or $[(Tp^*)(X)ClMo(\mu-L)MoCl(X)(Tp^*)]^x$,

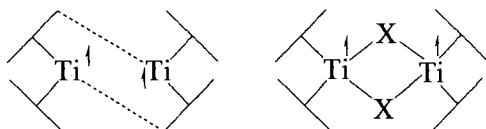
**16**

Tp^* = tris(pyrazolyl)borate derivative, L = bipyridine ($X = NO$) or bisphenolate ($X = O$) bridging ligands [68]. Because of the presence of only 25.5 % as hyperfine coupling-active nuclei *Mo (^{95}Mo with 15.9 % and ^{97}Mo with 9.6 %, both with $I = 5/2$), the delocalization is evident from the approximately halved hyperfine coupling constants (as compared with mononuclear Mo^I species) and from the relative ESR intensities of lines corresponding to molecules with $^*Mo-^*Mo$, $^*Mo-Mo$ and $Mo-Mo$ isotope combinations [67, 68].

9.3.5 Zero-field Splitting and Exchange Coupling

The presence of two spins in a triplet [70, 71] or biradical [72] species results in additional ESR features, viz. fine structure effects as a result of electron spin–electron spin interactions [69]. The phenomena observed and results derived therefrom are best discussed for simple examples, viz., the interaction of two equivalent centers in structurally well-characterized molecules.

A particularly simple situation exists in titanium(III) or vanadium(IV) dimers with d^1 configured centers. Titanium(III) dimers with sandwich structures have been studied in respect of ESR and magnetic effects of d^1 – d^1 interaction [70]. As an example, neutral and ionic titanacarborane dimers with Ti^{III} – Ti^{III} distances of ca 3.7 Å afforded well-resolved triplet ESR spectra [70], especially, with the support of a commercial ‘dual mode’ ESR cavity which, in the parallel polarization ESR mode, $B_2 \parallel B_1$, enhances the observability of otherwise forbidden $\Delta M_S = \pm 2$ transitions over the regular $\Delta M_S = \pm 1$ transitions. Analysis of both features provides zero-field splitting parameters D (axial) and E (rhombic), g factor components, and spin–spin distances which agree with the crystallographically determined features and permit a discussion of through-bond and through-space interaction [70].



Inspection of the half-field region, especially with the dual mode cavity, may reveal triplet ESR features and thus spin–spin interaction in coordination chemistry even when such effects are not necessarily expected. The tendency of inorganic and organometallic compounds to associate via coordinate or other bonds can be detected through corresponding triplet ESR signals, as illustrated by the crystallographically characterized copper(II) complex **8** [79] which seems to form a dimer with ESR half-field features on cooling in a frozen glassy solution of THF [79].

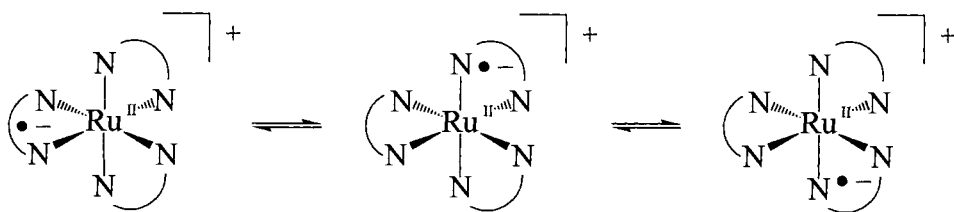
Weak coupling of organometallic biradicals such as the hydrogen-bridged dimer of $(\eta^7\text{-C}_7\text{H}_7)\text{V}(\eta^5\text{-C}_5\text{H}_4\text{COOH})$ can be detected in solution via simulation of ESR spectra [72]. Rather small exchange coupling constants $|J| < 1 \text{ cm}^{-1}$ may thus be established, providing a complementary technique to NMR and susceptibility measurements.

9.3.6 Dynamic Effects

In common with all spectroscopic methods, ESR is characterized by a certain ‘characteristic time-scale’ as determined by the typical energy involved in the transition. For ESR at X band frequency, this window lies between ca 10^{-7} and 10^{-10} s,

i.e. in the range of intermediate-to-slow molecular rotations and vibrations. The processes resulting in dynamic ESR effects might thus involve, e.g., conformational changes, as frequently encountered in the ESR spectroscopy of organic radicals [4]. Such structural changes also play an important role in inorganic and organometallic chemistry [73]; the changes in electron and atom location (i.e. coordination) are, however, more typical and will be illustrated here by examples.

The exchange of one unpaired electron between two or more equivalent or nearly equivalent sites can be monitored by ESR spectroscopy. A classical example is the 'hopping' of an added or charge transfer-generated electron between the three α -diimine chelate ligands of $[\text{Ru}(\text{bpy})_3]^{n+}$ (**9**) and related complexes.



Scheme 2

In contrast with the short-lived MLCT-excited states $^*[\text{Ru}(\text{bpy})_3]^{2+}$ [74], the electrogenerated $[\text{Ru}(\text{bpy})_3]^{+}$ can be conveniently studied by temperature-dependent ESR [42, 50a, b]. Analysis of the broad unresolved lines of this and related species reveals electron hopping between the three equivalent ligand sites with activation energies of approximately 10 kJ mol^{-1} . Similar slow vs. fast exchange phenomena were reported for the 'extended atom' [75] species **17** which contains an encapsulated Na^+ ion and mobile spins in the bpy-containing periphery.

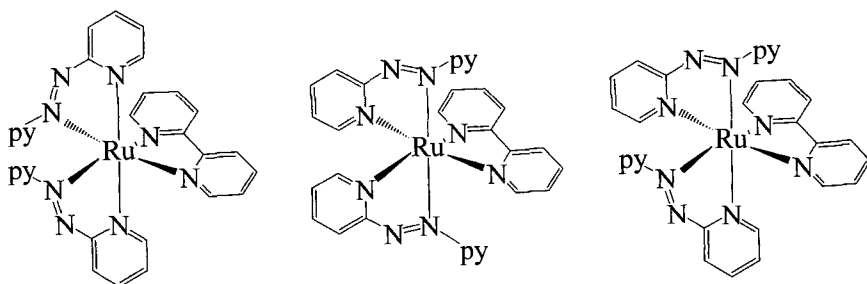
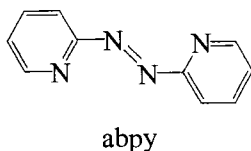
Characteristically, more unsymmetrical analogs $[\text{Ru}(\text{L})(\text{bpy})_2]^{+}$ with one better accepting ligand L give much narrower, often resolved, ESR signal lines, because of the localization of spin on L [42].

For the remaining alternative $[\text{Ru}(\text{L})_2(\text{bpy})]^{+}$ in that series, e.g. with $\text{L} = 2,2'$ -azobispyridine (abpy), the hopping behavior between the two L sites was found

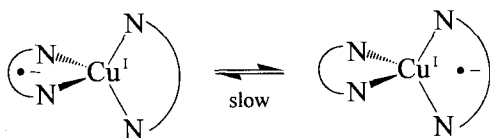


17

[50c] to depend characteristically on the stereochemistry of the complex which can exist in three different configurations [50c].



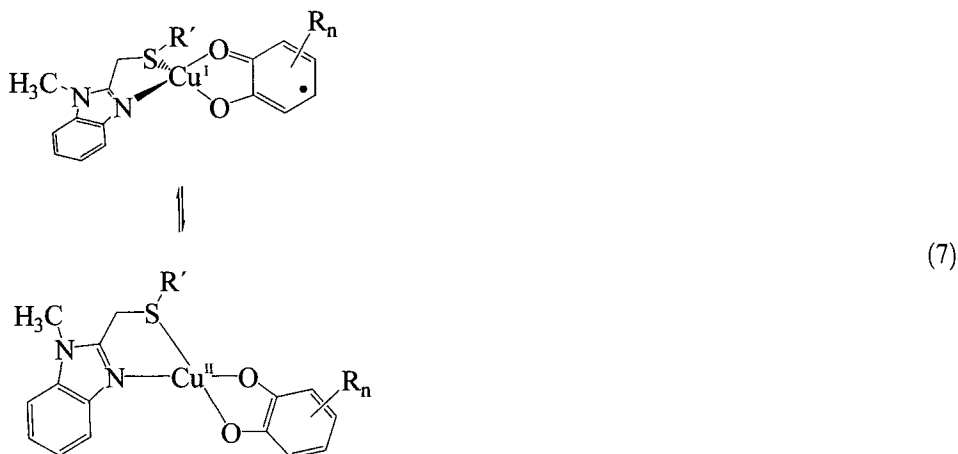
In contrast, the complex $[\text{Cu}^{\text{I}}(\text{N}^{\wedge}\text{N})_2]^{\bullet}$ gave no ESR signals for rapid electron hopping between the two $\text{N}^{\wedge}\text{N} = 2,9\text{-diphenyl-1,10-phenanthroline}$ ligands—probably as a result of the nearly orthogonal arrangement of the ligand π systems [77].



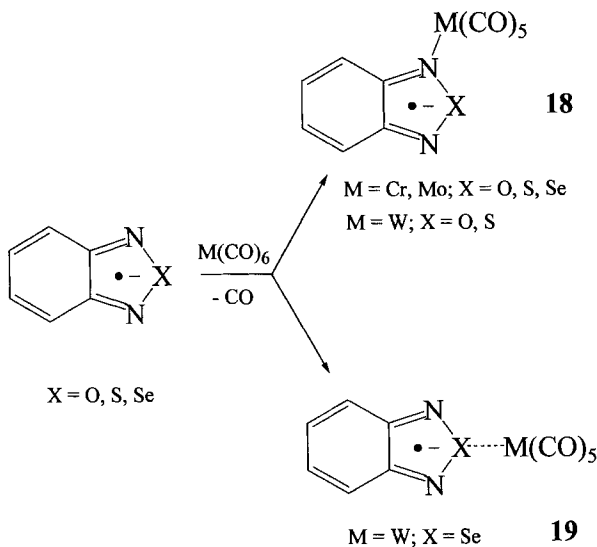
In special circumstances the metal and a ligand can compete for the spin in a paramagnetic complex. As this alternative involves oxidation-state changes, it is referred to as valence tautomerization or redox isomerization [78]. Such behavior is observed for *o*-semiquinone complexes of cobalt and manganese [78]; recently, a copper(I)-semiquinone–copper(II)-catecholate equilibrium system (7) of biochemical interest has been analyzed by temperature-dependent ESR [79].

An equilibrium such as (7) between two paramagnetic species with sufficiently different ESR signals can be analyzed quantitatively [79] by double integration, i.e. from the conventionally recorded first derivative signal to the zeroth derivative spectrum and then further to the first integrated form. The procedure requires a careful definition of the baseline, especially for broader spectra.

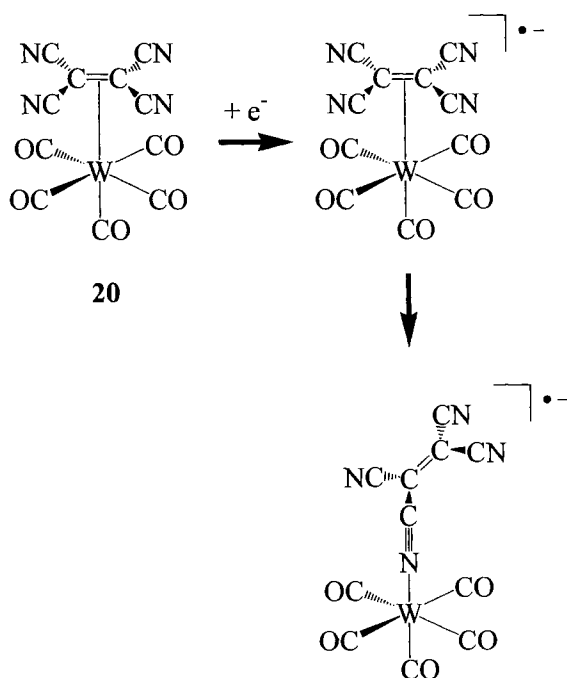
Changes in the coordination mode of paramagnetic complexes can sometimes be easily followed by ESR spectroscopy. For instance, the alternative binding (18, 19) of the Group-6 metal fragments $(\text{OC})_5\text{M}$ to either the N or the chalcogen atom of



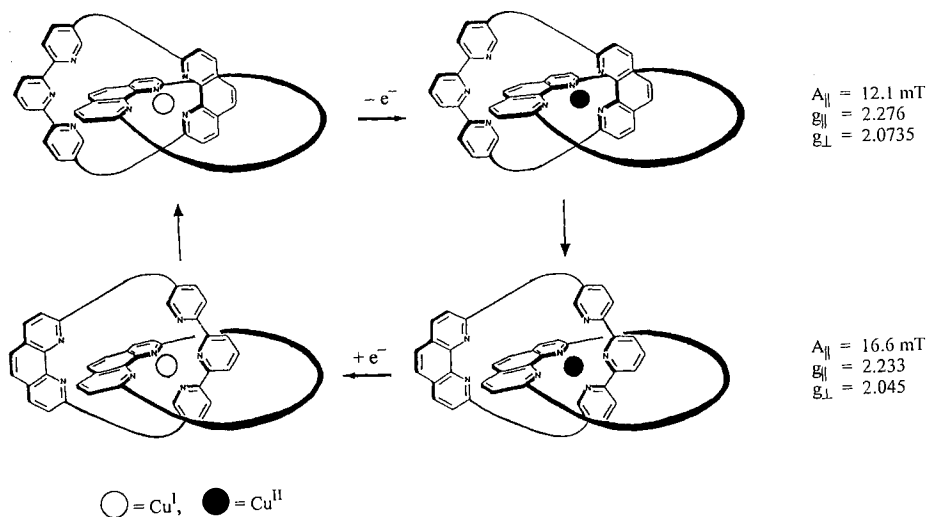
reduced 2,1,3-benzochalcogenodiazoles can be evident from the symmetry of the ESR hyperfine splitting in the radical anion ligand [80].



An electron transfer-sensitive σ/π coordination alternative of substituted olefins to metal centers has been demonstrated [81] in the system $[(\text{NC})_2\text{C}=\text{C}(\text{CN})_2\text{W}(\text{CO})_5]^n$ (**20**) where the π complex with $n = 0$ (olefin coordination) changes reversibly to an ESR detectable σ complex (nitrile coordination) after one-electron reduction ($n = -1$). Even in the absence of a detailed spin population analysis the low symmetry of the anionic complex is evident from at least three distinctly different ^{14}N coupling constants in the ESR spectrum [81].

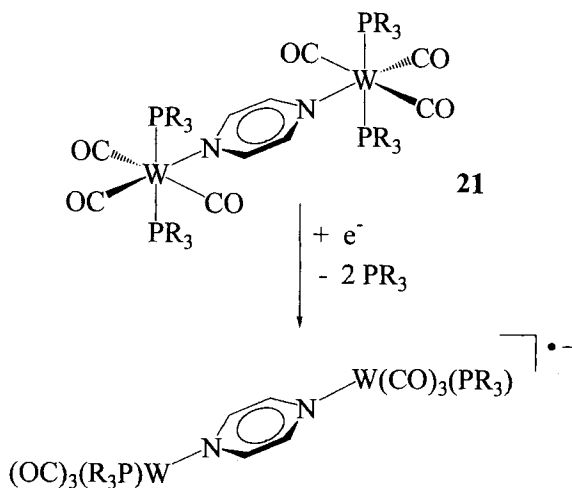


Examples of ESR-detected coordination changes do not have to involve organic radical ligands. For instance, the relatively slow changeover in a multimodal copper(II) catenate could be conveniently monitored by ESR spectroscopy [82].



The electrochemically triggered molecular rearrangement involves oxidation from a four-coordinate Cu^{I} to an intermediate four-coordinate Cu^{II} species which has a distinctly different ESR spectrum (higher g , lower $a(^{63,65}\text{Cu})$; measured in frozen solution) than the more stable five-coordinate Cu^{II} alternative. The latter is formed by fairly slow rotation of interlocking macrocyclic rings; it reverts to the four-coordinate arrangement on re-reduction [82].

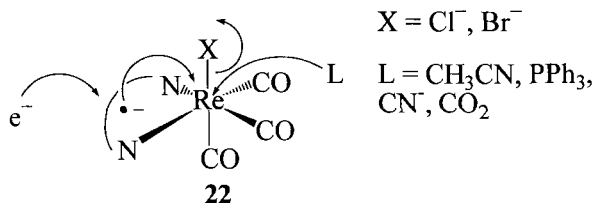
In favorable circumstances, ESR spectroscopy is also capable of detecting coordination changes which might have otherwise gone unnoticed. As an example, the reduction of the complex **21** produces a well-resolved ESR spectrum which shows only two equivalent ^{31}P nuclei (100 %, $I = 1/2$) interacting with the unpaired electron [83]. Apparently, two triorganophosphane ligands are lost after the reduction because of the high electron density created at the d^6 -configured metal centers [83] (pentacoordination [84]).



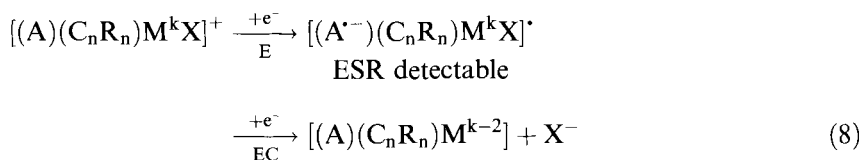
9.3.7 ESR Information and Chemical Reactivity

ESR Spectroscopy is not only superbly suited to the analysis of metal centered [3], metal/ligand mixed [35b] or ligand centered [85] singly occupied molecular orbitals; in favorable circumstances some ESR parameters can even be directly correlated with chemical reactivity. Although such correlations are obvious if ESR-monitored metal oxidation-state changes are involved, even small but variable amounts, δ , of unpaired electron density transmitted from radical ligands to potentially reactive metal centers can cause significant reactivity variations which are mirrored by ESR data. As an example, the rhenium halide bond labilization in reduced complexes $[(\text{N}^{\wedge}\text{N})\text{Re}(\text{CO})_3\text{X}]^{\cdot-}$ (**22**; $\text{N}^{\wedge}\text{N} = \alpha$ -diimine ligand, $\text{X} = \text{halogen}$) correlates with the $^{185,187}\text{Re}$ (and, if detectable, ^{14}N) hyperfine splittings [86]. Both kinds of ESR data quantify the ligand-to-metal spin transfer δ at the ligand-metal interface in

such $18+\delta$ valence electron compounds [86–88]; this, in turn, determines the substitutional labilization of the axial and partially [51, 86] charge-accepting ligand.



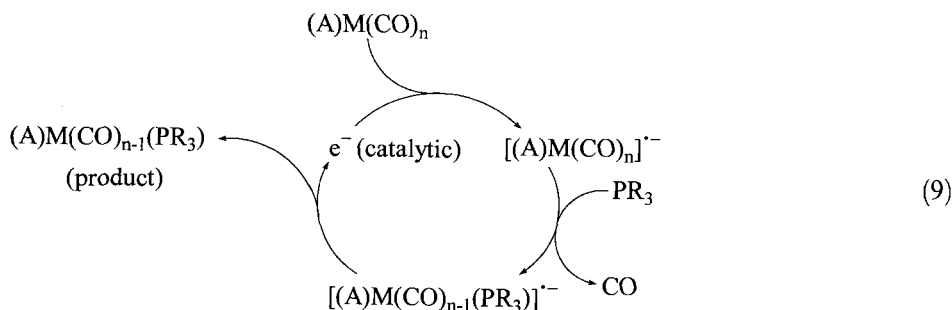
A related interesting phenomenon is the electron reservoir behavior of coordination compounds [89]. For instance, compounds $[(A)(C_nR_n)M^kX]^+$ with acceptor-bound organometallic reaction centers can accommodate one first added electron in the acceptor ligand A before a second added electron combines with the stored one to effect a chemically productive two-electron process at the metal (Eq. 8) [90].



$M = \text{Rh}, \text{Ir}, k = +\text{III}, n = 5; M = \text{Os}, k = +\text{II}, n = 6; X = \text{halogen};$

$A = \text{acceptor, e.g. } \alpha\text{-diimine}$

In the synthetically attractive field of electron transfer catalysis (ETC) [2, 91], ESR data of radical intermediates can correlate with the variable efficiency of processes such as the ETC-catalyzed substitution (9) by substantiating the amount of ligand-to-metal electron transfer in the ground state [87].



requirement for ETC:

$E_{\text{red}} [(A)M(CO)_{n-1}(PR_3)]$

$< E_{\text{red}} [(A)M(CO)_n];$

$A = \text{pyridine derivative, } \alpha\text{-diimine}$

9.3.8 Concluding Remarks

The previous chapters and examples were meant to familiarize the reader with current conventional ESR methodology and remove any barriers to the application of this kind of spectroscopy in electron-transfer studies. Unavoidably, not all aspects of inorganic ESR could be treated properly; for instance, both the ESR spectroscopy of bioinorganic systems (e.g. heme species or iron–sulfur clusters) or materials chemistry (e.g. defect centers, radicals in zeolites) are vast and entirely independent research areas. Nevertheless, the molecular species presented here might serve as introductory examples to illustrate the versatility of this particular kind of magnetic resonance.

Acknowledgments

Support for the author's ESR research has been continuously provided by the Deutsche Forschungsgemeinschaft (DFG) and Volkswagenstiftung. In particular, support for the recent graduate college 'Magnetic Resonance' at the University of Stuttgart is gratefully acknowledged. For assistance with the processing of the manuscript my special thanks are due to Mrs Angela Winkelmann and Dr. Brigitte Schwederski.

References

1. J. A. Weil, J. R. Bolton, J. E. Wertz, *Electron Paramagnetic Resonance*, Wiley, New York, **1994**.
2. D. Astruc, *Electron Transfer and Radical Processes in Transition-Metal Chemistry*, VCH, New York, **1995**.
3. (a) B. A. Goodman, J. B. Raynor, *Adv. Inorg. Chem. Radiochem.* **1970**, *13*, 135; (b) F. E. Mabbs, D. Collison, *Electron Paramagnetic Resonance of d Transition Metal Compounds*, Elsevier, Amsterdam, **1992**; (c) J. R. Pilbrow, *Transition Ion Electron Paramagnetic Resonance*, Clarendon Press, Oxford, **1990**; (d) P. H. Rieger in *Organometallic Radical Processes* (W. C. Trogler, Ed.), Elsevier, Amsterdam, **1990**, p. 270.
4. F. Gerson, *High Resolution E.S.R. Spectroscopy*, VCH, Weinheim, **1970**.
5. J. A. Weil, J. R. Bolton, J. E. Wertz, *Electron Paramagnetic Resonance*, Wiley, New York, **1994**, pp. 534.
6. J. A. Weil, J. R. Bolton, J. E. Wertz, *Electron Paramagnetic Resonance*, Wiley, New York, **1994**, pp. 532.
7. (a) V. Lorenzen, W. Preetz, F. Baumann, W. Kaim, *Inorg. Chem.* **1998**, *37*, 4011; (b) M. Wanner, W. Kaim, V. Lorenzen, W. Preetz, *Z. Naturforsch.* **1999**, *54b*, 1103.
8. M. Ballester, J. Castaner, J. Riera, J. Pujadas, O. Armet, C. Onrubia, J.A. Rio, *J. Org. Chem.* **1984**, *49*, 770.
9. (a) O. Renn, A. Albinati, B. Lippert, *Angew. Chem.* **1990**, *102*, 71; *Angew. Chem. Int. Ed. Engl.* **1990**, *29*, 84; (b) W. E. Geiger, N. G. Connelly, *Adv. Organomet. Chem.* **1985**, *24*, 87; (c) D. Astruc, *Electron Transfer and Radical Processes in Transition-Metal Chemistry*, VCH, New York, **1995**, p. 250.
10. N. Wiberg, T. Blank, W. Kaim, B. Schwederski, G. Linti, *Eur. J. Inorg. Chem.* **2000**, 1475.
11. A. Haaland, K.-G. Martinsen, H. V. Volden, W. Kaim, E. Waldhör, W. Uhl, U. Schütz, *Organometallics* **1996**, *15*, 1146.

12. H. Binder, R. Kellner, K. Vaas, M. Hein, F. Baumann, M. Wanner, R. Winter, W. Kaim, W. Hönlle, Y. Grin, U. Wedig, M. Schultheiss, R.K. Kremer, H.G. von Schnering, O. Groeger, G. Engelhardt, *Z. Anorg. Allg. Chem.* **1999**, 625, 1059.
13. (a) D. Sellmann, J. Müller, P. Hofmann, *Angew. Chem.* **1982**, 94, 708; *Angew. Chem. Int. Ed. Engl.* **1982**, 21, 691; (b) D. Sellmann, J. Müller, *J. Organomet. Chem.* **1985**, 281, 249; (c) A. Winter, G. Huttner, L. Zsolnai, P. Kroneck, M. Gottlieb, *Angew. Chem.* **1984**, 96, 986; *Angew. Chem. Int. Ed. Engl.* **1984**, 23, 975; (d) A. Winter, G. Huttner, M. Gottlieb, I. Jibril, *J. Organomet. Chem.* **1985**, 286, 317.
14. (a) R. Gross, W. Kaim, *Angew. Chem.* **1985**, 97, 869; *Angew. Chem. Int. Ed. Engl.* **1985**, 24, 856; (b) R. Gross and W. Kaim, *Inorg. Chem.* **1987**, 26, 3596.
15. Cf. p. 283 in ref. 3a).
16. D. Astruc, *Electron Transfer and Radical Processes in Transition-Metal Chemistry*, VCH, New York, **1995**, p. 358.
17. (a) W. Kaim, *Coord. Chem. Rev.* **1987**, 76, 187; (b) W. Kaim, M. Moscherosch, *Coord. Chem. Rev.* **1994**, 129, 157; (c) D. Astruc, *Electron Transfer and Radical Processes in Transition-Metal Chemistry*, VCH, New York, **1995**, p. 234.
18. (a) D. Astruc, *Electron Transfer and Radical Processes in Transition-Metal Chemistry*, VCH, New York, **1995**, p. 216.
19. F. Baumann, W. Kaim, L. M. Baraldo, L. D. Slep, J. A. Olabe, J. Fiedler, *Inorg. Chim. Acta* **1999**, 285, 129.
20. E. Waldhör, W. Kaim, J. A. Olabe, L. D. Slep, J. Fiedler, *Inorg. Chem.* **1997**, 36, 2969.
21. (a) W. Matheis, W. Kaim, *J. Chem. Soc., Faraday Trans.* **1990**, 86, 3337; (b) W. Matheis, J. Poppe, W. Kaim, S. Zalis, *J. Chem. Soc., Perkin Trans. 2* **1994**, 1923.
22. P. W. Atkins, M. C. R. Symons, *The Structure of Inorganic Radicals*, Elsevier, Amsterdam, **1967**, p. 36.
23. (a) P. T. Kissinger, W. R. Heineman, *Laboratory Techniques in Electroanalytical Chemistry*, 2nd. Ed., Marcel Dekker, New York, **1996**, p. 930; (b) A. J. Bard, L. R. Faulkner, *Electrochemical Methods*, Wiley, New York, **1980**, p. 618.
24. (a) W. Kaim, *Top. Curr. Chem.* **1994**, 169, 231; (b) S. Hasenzahl, W. Kaim, T. Stahl, *Inorg. Chim. Acta* **1994**, 225, 23; (c) M. Kaupp, H. Stoll, H. Preuss, W. Kaim, T. Stahl, G. van Koten, E. Wissing, W. J. J. Smeets, A. L. Spek, *J. Am. Chem. Soc.* **1991**, 113, 5606.
25. (a) W. Kaim, in *Electron and Proton Transfer in Chemistry and Biology*, (Eds.: A. Müller, E. Diemann, W. Junge, H. Ratajczak), Elsevier, Amsterdam, **1992**, p. 45; (b) W. Kaim, B. Olbrich-Deussner, in *Organometallic Radical Processes*, (Ed.: W. C. Trogler), Elsevier, Amsterdam, **1990**, p. 173.
26. N. G. Connelly, W. E. Geiger, *Chem. Rev.* **1996**, 96, 877.
27. (a) T. Kobayashi, K. Yasufuku, J. Iwai, H. Yesaka, H. Noda, H. Ohtani, *Coord. Chem. Rev.* **1985**, 64, 1; (b) M. C. R. Symons, R. L. Sweany, *Organometallics* **1982**, 1, 834.
28. P. W. Atkins, M. C. R. Symons, *The Structure of Inorganic Radicals*, Elsevier, Amsterdam, **1967**, p. 41.
29. C. D. Garr, R.G. Finke, *Inorg. Chem.* **1993**, 32, 4414.
30. (a) D. N. R. Rao, M. C. R. Symons, *J. Chem. Soc. Chem. Commun.* **1982**, 954; (b) M. C. R. Symons, *NATO ASI Ser., Ser. C* **1989**, 257; (c) K. Warncke, J. C. Schmidt, S.-C. Ke, *J. Am. Chem. Soc.* **1999**, 121, 10522.
31. (a) D. Rehorek, *Chem. Soc. Rev.* **1991**, 20, 341; (b) E. Samuel, D. Caurant, C. Gourier, Ch. Elschenbroich, K. Agbaria, *J. Am. Chem. Soc.* **1998**, 120, 8088.
32. A. Klein, S. Hasenzahl, W. Kaim, *J. Chem. Soc., Perkin Trans. 2* **1997**, 2573.
33. (a) A. Schweiger, *Angew. Chem.* **1991**, 103, 223; *Angew. Chem. Int. Ed. Engl.* **1991**, 30, 265; (b) H. van Willigen, P. R. Levstein, M. H. Ebersole, *Chem. Rev.* **1993**, 93, 173.
34. C. J. Kleverlaan, D. J. Stufkens, I. P. Clark, M. W. George, J. J. Turner, D. M. Martino, H. van Willigen, A. Vlcek, Jr., *J. Am. Chem. Soc.* **1998**, 120, 10871.
35. (a) Ch. Elschenbroich, E. Bilger, R. D. Ernst, D. R. Wilson, M. S. Kralik, *Organometallics* **1985**, 4, 2068; (b) V. Kasack, W. Kaim, H. Binder, J. Jordanov, E. Roth, *Inorg. Chem.* **1995**, 34, 1924; (c) W. Kaim, V. Kasack, *Inorg. Chem.* **1990**, 29, 4696.
36. (a) R. Schäfer, W. Kaim, M. Moscherosch, M. Krejcik, *J. Chem. Soc., Chem. Commun.* **1992**, 834; (b) W. Kaim, A. Klein, *Organometallics* **1995**, 14, 1176; (c) W. Kaim, R. Schäfer,

- F. Hornung, M. Krejčík, J. Fiedler, S. Zalis in *Transition Metal Sulphides—Chemistry and Catalysis*, NATO ASI Series, (T. Weber, Ed.) Kluwer Academic Publishers, Dordrecht, **1998**, p. 37.
37. J. Poppe, M. Moscherosch, W. Kaim, *Inorg. Chem.* **1993**, 32, 2640.
 38. (a) Y. Ohsawa, M. K. DeArmond, K. W. Hanck, C. G. Moreland, *J. Am. Chem. Soc.* **1985**, 107, 5383; (b) G. N. La Mar, Horrocks, Jr., W. DeWitt, R. H. Holm (Eds.), *NMR of Paramagnetic Molecules*, Academic Press, New York, **1973**; (c) N. Juranic, *Coord. Chem. Rev.* **1989**, 96, 253.
 39. (a) W. Kaim, *Z. Naturforsch.* **1981**, 36b, 150; (b) W. Uhl, U. Schütz, W. Kaim, E. Waldhör, *J. Organomet. Chem.* **1995**, 501, 79; (c) N. Wiberg, K. Amelunxen, H. Nöth, H. Schwenk, W. Kaim, A. Klein, T. Scheiring, *Angew. Chem.* **1997**, 109, 1258; *Angew. Chem. Int. Ed. Engl.* **1997**, 36, 1213.
 40. J. Rall, W. Kaim, *J. Chem. Soc., Faraday Trans.* **1994**, 90, 2905.
 41. A. J. Stone, *Mol. Phys.* **1964**, 7, 311; (b) H. Fischer in *Free Radicals*, Vol. II (Ed.: J. K. Kochi), Wiley, New York, **1973**, p. 452.
 42. W. Kaim, S. Ernst, V. Kasack, *J. Am. Chem. Soc.* **1990**, 112, 173.
 43. W. Kaim, *Inorg. Chem.* **1984**, 23, 3365.
 44. (a) T. Sixt, J. Fiedler, W. Kaim, *Inorg. Chem. Commun.* **2000**, 3, 80; (b) R. T. Hembre, J. S. McQueen, V. W. Day, *J. Am. Chem. Soc.* **1996**, 118, 798; (c) S. B. Jensen, S. J. Rodger, M. D. Spicer, *J. Organomet. Chem.* **1998**, 556, 151.
 45. J. H. MacNeil, A. C. Chiverton, S. Fortier, M. C. Baird, R. C. Hynes, A. J. Williams, K. F. Preston, T. Ziegler, *J. Am. Chem. Soc.* **1991**, 115, 9834.
 46. (a) M. Yamaga, N. Kodama, T. Yosida, B. Henderson, K. Kindo, *J. Phys. Condens. Matter* **1997**, 9, 9639; (b) E. D. Thoma, H. Shields, Y. Zhang, B. C. McCollum, R. T. Williams, *J. Luminescence* **1997**, 71, 93.
 47. (a) P. W. Atkins, M. C. R. Symons, *The Structure of Inorganic Radicals*, Elsevier, Amsterdam, **1967**, pp. 119 and 142; (b) A. Pfitzner, F. Baumann, W. Kaim, *Angew. Chem.* **1998**, 110, 2057; *Angew. Chem. Int. Ed. Engl.* **1998**, 37, 1955.
 48. A.-L. Barra, L.-C. Brunel, D. Gatteschi, L. Pardi, R. Sessoli, *Acc. Chem. Res.* **1998**, 31, 460.
 49. (a) A.-L. Barra, L.-C. Brunel, F. Baumann, M. Schwach, M. Moscherosch, W. Kaim, *J. Chem. Soc., Dalton Trans.* **1999**, 3855; (b) W. Kaim, M. Moscherosch, *J. Chem. Soc., Faraday Trans.* **1991**, 87, 3185; (c) M. Moscherosch, J. S. Field, W. Kaim, S. Kohlmann, M. Krejčík, *J. Chem. Soc. Dalton Trans.* **1993**, 211.
 50. (a) D. E. Morris, K. W. Hanck, M. K. De Armond, *Inorg. Chem.* **1983**, 105, 3032; (b) D. E. Morris, K. W. Hanck, M. K. De Armond, *J. Electroanal. Chem.* **1983**, 149, 115; (c) M. Heilmann, F. Baumann, W. Kaim, J. Fiedler, *J. Chem. Soc., Faraday Trans.* **1996**, 92, 4227.
 51. (a) W. Kaim, S. Kohlmann, *Chem. Phys. Lett.* **1987**, 139, 365; (b) W. Kaim, S. Kohlmann, *Inorg. Chem.* **1990**, 29, 2909.
 52. (a) R. C. Bray, L. S. Meriwether, *Nature (London)* **1966**, 212, 467; (b) S. P. J. Albracht, *Biochim. Biophys. Acta* **1994**, 1188, 167.
 53. A. Vlcek, F. Baumann, W. Kaim, F.-W. Grevels, F. Hartl, *J. Chem. Soc., Dalton Trans.* **1998**, 215.
 54. D. Astruc, *Electron Transfer and Radical Processes in Transition-Metal Chemistry*, VCH, New York, **1995**, p. 217.
 55. (a) H. Schönberg, S. Boulmaâz, M. Wörle, L. Liesum, A. Schweiger, H. Grützmacher, *Angew. Chem.* **1998**, 110, 1492; *Angew. Chem. Int. Ed. Engl.* **1998**, 37, 1423; (b) S. Berger, A. Klein, M. Wanner, J. Fiedler, W. Kaim, *Inorg. Chem.* **2000**, 39, 2516; (c) W. Kaim, S. Berger, S. Greulich, R. Reinhardt, J. Fiedler, *J. Organomet. Chem.* **1999**, 582, 153.
 56. (a) F. G. N. Cloke, G. R. Hanson, M. J. Henderson, P. B. Hitchcock, C. L. Raston, *J. Chem. Soc. Chem. Commun.* **1989**, 1002; (b) F. G. N. Cloke, C. I. Dalby, M. J. Henderson, P. B. Hitchcock, C. H. L. Kennard, R. M. Lamb, C. L. Raston, *J. Chem. Soc. Chem. Commun.* **1990**, 1394.
 57. W. Kaim, W. Matheis, *J. Chem. Soc., Chem. Commun.* **1991**, 597.
 58. F. P. Fanizzi, G. Natile, M. Lanfranchi, A. Tiripicchio, F. Laschi, P. Zanello, *Inorg. Chem.* **1996**, 35, 3173.

59. (a) P.S. Braterman, J.-I. Song, F.M. Wimmer, S. Wimmer, W. Kaim, A. Klein, R.D. Peacock, *Inorg. Chem.* **1992**, *31*, 5084; (b) A. Klein, W. Kaim, E. Waldhör, H.-D. Hausen, *J. Chem. Soc., Perkin Trans. 2* **1995**, 2121; (c) A. Klein, E. J. L. McInnes, T. Scheiring, S. Zalis, *J. Chem. Soc. Faraday Trans.* **1998**, *94*, 2979; (d) E. J. L. McInnes, R. D. Farley, S. A. Macgregor, K. J. Taylor, L. J. Yellowlees, C. C. Rowlands, *J. Chem. Soc. Faraday Trans.* **1998**, *94*, 2985.
60. T. Schmauke, E. Möller, E. Roduner, *J. Chem. Soc. Chem. Commun.* **1998**, 2589 and references cited.
61. H. Kurreck, B. Kirste, W. Lubitz, *Electron Nuclear Double Resonance Spectroscopy of Radicals in Solution*, VCH, New York, **1988**.
62. (a) W. Kaim, W. Lubitz, *Angew. Chem.* **1983**, *95*, 915; *Angew. Chem. Int. Ed. Engl.* **1983**, *22*, 892; *Angew. Chem. Suppl.* **1983**, 1209; (b) H. Kurreck, B. Kirste, W. Lubitz, *Electron Nuclear Double Resonance Spectroscopy of Radicals in Solution*, VCH, New York, **1988**, p. 103.
63. (a) W. Kaim, S. Ernst, *J. Phys. Chem.* **1986**, *90*, 5010; (b) S.E. Bell, J.S. Field, R.I. Haines, M. Moscherosch, W. Matheis, W. Kaim, *Inorg. Chem.* **1992**, *31*, 3269.
64. (a) V. Barone, in *Recent Advances in Density Functional Methods, Part I* (D. O. Chong, Ed.), World Scientific Publ. Co., Singapore, **1996**; (b) S. Zalis, C. Daniel, A. Vlcek, Jr., *J. Chem. Soc. Dalton Trans.* **1999**, 3081.
65. R. Gross, W. Kaim, *Inorg. Chem.* **1986**, *25*, 4865.
66. (a) K. Wieghardt, *Angew. Chem.* **1989**, *101*, 1179; *Angew. Chem. Int. Ed. Engl.* **1989**, *28*, 1153; (b) G. C. Dismukes, in *Mixed Valency Systems: Applications in Chemistry, Physics and Biology*, NATO ASI Ser., Ser. C, Vol. 343 (K. Prassides, Ed.), Kluwer Academic Publishers, Dordrecht, **1991**, p. 137.
67. W. Bruns, W. Kaim, E. Waldhör, M. Krejci, *J. Chem. Soc., Chem. Commun.* **1993**, 1868.
68. J. A. McCleverty, M. D. Ward, *Acc. Chem. Res.* **1998**, *31*, 842.
69. J. A. Weil, J. R. Bolton, J. E. Wertz, *Electron Paramagnetic Resonance*, Wiley, New York, **1994**, p. 151.
70. N. S. Hosmane, Y. Wang, H. Zhang, K.-J. Lu, J. A. Maguire, T. G. Gray, K. A. Brooks, E. Waldhör, W. Kaim, R. K. Kremer, *Organometallics* **1997**, *16*, 1365 and references cited.
71. (a) Ch. Elschenbroich, J. Heck, *J. Am. Chem. Soc.* **1979**, *101*, 6773; (b) Ch. Elschenbroich, J. Heck, *Angew. Chem.* **1981**, *93*, 278; *Angew. Chem. Int. Ed. Engl.* **1981**, *20*, 267; (c) Ch. Elschenbroich, A. Bretschneider-Hurley, J. Hurley, A. Behrendt, W. Massa, S. Wocadlo, E. Reijerse, *Inorg. Chem.* **1995**, *34*, 743.
72. Ch. Elschenbroich, O. Schiemann, O. Burghaus, K. Harms, *J. Am. Chem. Soc.* **1997**, *119*, 7452.
73. W. E. Geiger, *Prog. Inorg. Chem.* **1985**, *33*, 275.
74. H. Yersin, W. Humbs, J. Strasser, *Coord. Chem. Rev.* **1997**, *159*, 325.
75. (a) L. Echegoyen, A. DeCian, J. Fischer, J.-M. Lehn, *Angew. Chem.* **1991**, *103*, 884; *Angew. Chem. Int. Ed. Engl.* **1991**, *30*, 838; (b) L. Echegoyen, E. Perez-Cordero in *Transition Metals in Supramolecular Chemistry* (L. Fabbri, A. Poggi, Eds.), Kluwer Academic Publishers, Dordrecht, **1994**, p. 115.
76. J. Fees, H.-D. Hausen, W. Kaim, *Z. Naturforsch.* **1995**, *50b*, 15.
77. A.F. Stange, E. Waldhör, M. Moscherosch, W. Kaim, *Z. Naturforsch.* **1995**, *50b*, 115.
78. (a) O.-S. Jung, D. H. Jo, Y.-A. Lee, Y. S. Sohn, C. G. Pierpont, *Angew. Chem.* **1996**, *108*, 1796; *Angew. Chem. Int. Ed. Engl.* **1996**, *35*, 1694; (b) D. M. Adams, B. Li, J. D. Simon, D. N. Hendrickson, *Angew. Chem.* **1995**, *107*, 1580; *Angew. Chem. Int. Ed. Engl.* **1995**, *34*, 1481; (c) A. S. Attia, C. G. Pierpont, *Inorg. Chem.* **1995**, *34*, 1172.
79. J. Rall, M. Wanner, M. Albrecht, F. M. Hornung, W. Kaim, *Chem. Eur. J.* **1999**, *5*, 2802.
80. W. Kaim, V. Kasack, *Angew. Chem.* **1982**, *94*, 712; *Angew. Chem. Int. Ed. Engl.* **1982**, *21*, 700.
81. T. Roth, W. Kaim, *Inorg. Chem.* **1992**, *31*, 1930.
82. F. Baumann, A. Livoreil, W. Kaim, J.-P. Sauvage, *J. Chem. Soc., Chem. Commun.* **1997**, 35.
83. W. Bruns, W. Kaim, E. Waldhör, M. Krejci, *Inorg. Chem.* **1995**, *34*, 663.
84. (a) D. J. Darensbourg, K. K. Klausmeyer, J. H. Reibenspies, *Inorg. Chem.* **1995**, *34*, 4676; (b) F. Hartl, A. Vlcek, Jr., L. A. deLearie, C. G. Pierpont, *Inorg. Chem.* **1990**, *29*, 1073.
85. (a) J. Fees, W. Kaim, M. Moscherosch, W. Matheis, J. Klima, M. Krejci, S. Zalis, *Inorg. Chem.* **1993**, *32*, 166; (b) S. Ernst, C. Vogler, A. Klein, W. Kaim, S. Zalis, *Inorg. Chem.* **1996**, *35*, 1295; (c) E. Waldhör, M. M. Zulu, S. Zalis, W. Kaim, *J. Chem. Soc., Perkin Trans. 2* **1996**, 1197.

86. A. Klein, C. Vogler, W. Kaim, *Organometallics* **1996**, 15, 236.
87. (a) B. Olbrich-Deussner, W. Kaim, *J. Organomet. Chem.* **1988**, 340, 71; (b) B. Olbrich-Deussner, W. Kaim, *J. Organomet. Chem.* **1989**, 361, 335.
88. (a) D. M. Schut, K. J. Keana, D. R. Tyler, P. H. Rieger, *J. Am. Chem. Soc.* **1995**, 117, 8939; (b) D. Astruc, *Electron Transfer and Radical Processes in Transition-Metal Chemistry*, VCH, New York, **1995**, p. 207.
89. (a) M.-H. Desbois, D. Astruc, J. Guillin, J.-P. Mariot, F. Varret, *J. Am. Chem. Soc.* **1985**, 107, 52; (b) D. Astruc, *Electron Transfer and Radical Processes in Transition-Metal Chemistry*, VCH, New York, **1995**, p. 337.
90. W. Kaim, R. Reinhardt, J. Fiedler, *Angew. Chem.* **1997**, 109, 2600; *Angew. Chem. Int. Ed. Engl.* **1997**, 36, 2493. See also F. Baumann, A. Stange, W. Kaim, *Inorg. Chem. Commun.* **1998**, 1, 305.
91. D. Miholova, A. A. Vlcek, *J. Organomet. Chem.* **1985**, 279, 317.

Volume III

Part 1

Biological Systems

1 Electron Transfer in Metalloproteins

Harry B. Gray and Jay R. Winkler

1.1 Introduction

Electron transfer (ET) reactions are key steps in a great many biological processes [1]. The urgent demands of life impose stringent requirements on the speed and specificity of these transformations. A vast array of redox enzymes, often containing transition metal cofactors, has evolved to meet the narrow tolerances associated with biological electron flow. In these proteins, electrons transfer rapidly (<ms) over distances as great as 20 Å, with little release of free energy [2]. It is reasonable to question whether these elaborate structures are necessary to sustain electron flow and, if so, how do folded polypeptides accomplish this task?

1.2 The Semiclassical Model of Electron Transfer

Theoretical efforts beginning in the late 1950s and continuing to the present day have provided a remarkably detailed description of ET reactions [3]. The semiclassical model (Eq. 1) describes the first-order rate constant for electron transfer from a donor

$$k_{\text{ET}} = \sqrt{\frac{4\pi^3}{h^2 \lambda k_B T}} H_{\text{AB}}^2 \exp \left\{ -\frac{(\Delta G^\circ + \lambda)^2}{4\lambda k_B T} \right\} \quad (1)$$

(**D**) to an acceptor (**A**) held at fixed distance and orientation as a function of temperature (*T*), reaction driving force ($-\Delta G^\circ$), a nuclear reorganization parameter (λ), and electronic coupling matrix element (H_{AB}). The reorganization parameter reflects the changes in structure and solvation that result when an electron moves from **D** to **A**. A balance between nuclear reorganization and reaction driving force

determines both the transition-state configuration and the height of the barrier to the ET process. At the optimum driving force ($-\Delta G^\circ = \lambda$), rates become activationless (k_{ET}°), limited only by the strength of the **D/A** interaction. When **D** and **A** are in van der Waals contact, the coupling strength is usually so large that ET occurs every time the transition-state configuration is formed. In this adiabatic limit, the ET rate is independent of H_{AB} and the prefactor depends only on the frequency of motion along the reaction coordinate. The nonadiabatic limit (Eq. 1) obtains when the **D/A** interaction is weak and the transition state must be reached many times before an electron is transferred. The electronic coupling element measures the frequency of crossing from reactants (**D** + **A**) to products (**D**⁺ + **A**[−]) in the region of the transition state.

The barriers to electron exchange between hydrated transition metal ions are readily interpreted in terms of the semiclassical theory [3]. The 0.67-eV activation energy for electron exchange between aquo ferrous and ferric complexes, for example, implies a 2.7-eV reorganization energy. The major contribution (1.5 eV) is attributed to the 0.14-Å difference in Fe–O bond lengths in the ferric and ferrous ions. The remainder (1.2 eV) arises from repolarization of the aqueous solvent upon electron transfer. When the ferrous and ferric ions are in contact, this large reorganization energy leads to a 30-ms time constant for electron exchange. Even at short range, then, the barriers to ET between hydrated metal ions are too great for the demands of biological electron flow. To reduce the reorganization energy, proteins must sequester the redox-active metals in hydrophobic cavities, away from the polar aqueous solvent. In this way, a three-fold decrease in reorganization energy can be achieved, decreasing the time constant for electron exchange by over seven orders of magnitude (Figure 1).

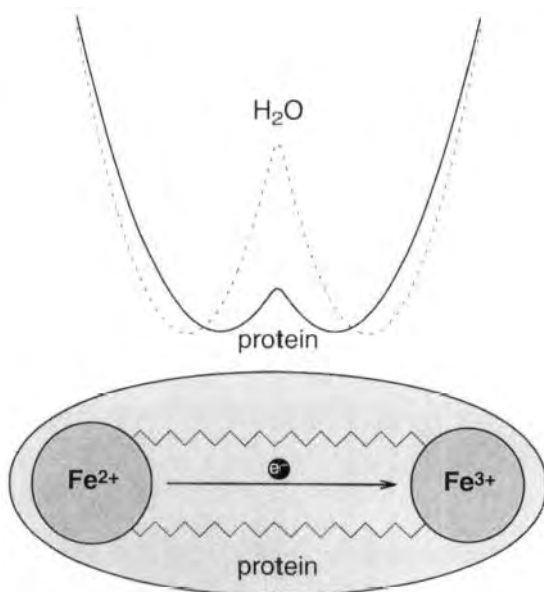


Figure 1. Schematic representation of the free-energy surfaces for electron exchange between hydrated ferrous and ferric ions in aqueous solution and between the ions complexed in a protein.

The singular feature of electron transfer is that reactions can proceed at very high rates when **D** and **A** are separated by long distances. The electron tunnels through a potential barrier between **D** and **A**; for a square barrier, H_{AB} displays an exponential dependence on the distance between the reactants (**R**) [4]. The medium between redox centers is vitally important for long-range ET. Owing to an estimated $3.5\text{-}\text{\AA}^{-1}$ distance decay constant (β), the time required for electron exchange between hydrated ferrous and ferric ions balloons to almost 10^{17} years if the complexes are separated by $20\text{ }\text{\AA}$ in a vacuum [5]. Superexchange coupling via hole and electron states of the intervening medium enhances the **D/A** electronic interaction and produces a more gradual decrease in rate with distance [6–8]. Fill the void between hydrated ferrous and ferric ions with water ($\beta = 1.68\text{ }\text{\AA}^{-1}$) [9] and the time constant for $20\text{-}\text{\AA}$ electron exchange decreases dramatically (2×10^3 years), but is still far too slow to support biological activity. It is clear, then, that in addition to lowering reorganization barriers, the protein must play a pivotal electronic coupling role. The question is the following: how does a heterogeneous array of covalent and non-covalent contacts in a folded polypeptide mediate long-range electronic coupling?

1.3 Ru-Modified Proteins

Investigations of protein–protein ET reactions have provided important insights into biological electron flow [10–14]. Natural systems, however, often are not amenable to the systematic studies that are required for evaluation of the key ET parameters λ and H_{AB} . A successful alternative approach involves measurements of ET in metalloproteins that have been labeled with redox-active molecules [15–19]. By varying the binding site and chemical composition of the probe molecule, it has been possible to elucidate the factors that control the rates of long-range ET reactions in proteins.

Ruthenium complexes are excellent reagents for protein modification and electron-transfer studies. Ru^{2+} -aquo complexes readily react with surface His residues on proteins to form stable derivatives [20, 21]. Low-spin pseudo-octahedral Ru-complexes exhibit small structural changes upon redox cycling between the Ru^{2+} and Ru^{3+} formal oxidation states [3, 22]. Hence, the inner-sphere barriers to electron transfer (λ_1) are small. With the appropriate choice of ligand, the $\text{Ru}^{3+/2+}$ reduction potential can be varied from <0.0 to >1.5 V versus NHE [23]. Ru-bpy complexes bound to Lys and Cys residues have been employed to great advantage in studies of protein–protein ET reactions. The kinetics of electron transfer in cytochrome *b*₅/cytochrome *c* [24], cytochrome *c*/cytochrome *c* peroxidase [12], and cytochrome *c*/cytochrome *c* oxidase [25] complexes have been measured with the aid of laser-initiated ET from a Ru-bpy label.

A great deal of work on Ru-modified proteins has employed the $\text{Ru}(\text{bpy})_2(\text{im})$ (HisX)²⁺ (bpy = 2,2'-bipyridine; im = imidazole) label [16, 21, 26] (Figure 2). In addition to favorable ET properties, these Ru-bpy complexes have long-lived, luminescent metal-to-ligand charge-transfer excited states that can be prepared with



Figure 2. Ribbon structure representation of the crystal structure of $\text{Ru}(\text{bpy})_2(\text{im})(\text{His83})^{2+}$ -labeled *Pseudomonas aeruginosa* azurin [26].

short laser pulses. These excited states enable a wider range of ET measurements than is possible with nonluminescent complexes. Furthermore, the bpy ligands raise the $\text{Ru}^{3+/2+}$ reduction potential (>1 V versus NHE) so that observed ET rates are close to k_{ET}° , improving the reliability of H_{AB} and λ determinations.

1.4 Reorganization Energy

The semiclassical ET model predicts that rates will depend on reaction driving force and temperature [3]. Investigations of the dependences of ET rates on either of these two parameters can be used to obtain reorganization energies. Although conceptually straightforward, both methods have difficulties. In order to vary the reaction driving force, changes in one or both redox sites are required. These chemical modifications must be chosen with care to ensure that λ does not change along with ΔG° . Studies of the temperature dependence of k_{ET} are easier in principle, but will not provide accurate λ values unless the temperature dependence of ΔG° is determined as well [3, 27].

1.4.1 Cytochrome *c*

ET in a Ru-modified protein was first measured in $\text{Ru}(\text{NH}_3)_5(\text{His33})^{3+}$ -ferricytochrome *c* [28]. The rate of Ru^{2+} to Fe^{3+} electron transfer over a distance of 18 \AA at

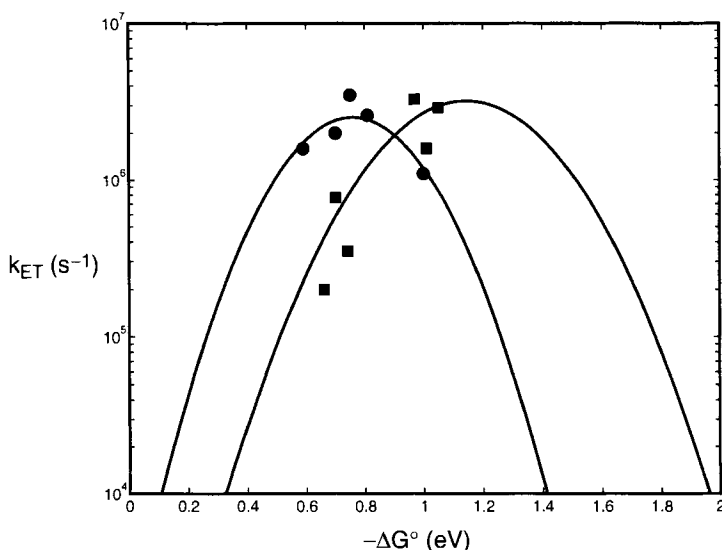


Figure 3. Driving force-dependence of intramolecular electron transfer rates in Ru-ammine-His33 modified Zn-substituted cytochrome *c* (■), and Ru-bpy-His33 modified Fe-cytochrome *c* (●). Solid lines were generated using Eq. 1 and the following parameters: Ru-ammine, $\lambda = 1.15$ eV, $H_{AB} = 0.10$ cm⁻¹; Ru-bpy, $\lambda = 0.74$ eV, $H_{AB} = 0.095$ cm⁻¹.

a driving force of 0.2 eV is 30 s⁻¹. Replacement of the native Fe center in the heme with Zn paved the way for ET measurements at higher driving forces [15, 29, 30]. Indeed, replacement of a heme center with a Zn-porphyrin has provided many opportunities for investigations of *interprotein* ET reactions. Hoffman and co-workers have used this technique in their work on ET in hybrid hemoglobins and cytochrome *c*/cytochrome *c* peroxidase complexes [10], and Zn-substituted cytochrome *c* has been exploited in studies of conformationally regulated ET in cytochrome *c*/plastocyanin complexes [14]. The driving-force dependence of *intraprotein* ET rates in Ru(NH₃)₄L(His33)-Zn-cytochrome *c* (L = NH₃, pyridine, isonicotinamide) yielded the parameters $\lambda = 1.15$ eV and $H_{AB} = 0.1$ cm⁻¹ [15, 30] (Figure 3). The Marcus cross-relation ($\lambda_{12} = \frac{1}{2}[\lambda_{11} + \lambda_{22}]$) describes the reorganization energy for the reaction between **D** and **A** (λ_{12}) as the mean of the reorganization energies for electron exchange between **D** and **D**⁺ (λ_{11}) and exchange between **A** and **A**⁻ (λ_{22}) [3]. The Fe-cytochrome *c* self-exchange reorganization energy has been estimated to be 0.7 eV [31]. If the Zn-cytochrome *c* reorganization energy is comparable to that of the Fe protein, then it is apparent that the hydrophilic Ru-ammine complex is responsible for about two-thirds of the total reorganization energy in Ru-ammine-modified cytochrome *c* ET reactions ($\lambda(\text{Ru}^{3+/2+}) = 1.7$ eV). This result is in good agreement with estimates of the self-exchange reorganization energy in Ru(NH₃)₆^{3+/2+} [3, 22].

Studies of self-exchange reactions have demonstrated that replacing ammonia

ligands with diimine ligands substantially reduces the reorganization energy associated with $\text{Ru}^{3+/2+}$ ET [3, 22]. The difference can be attributed to a decrease in solvent polarization by the larger Ru-diimine ions, and to somewhat smaller inner-sphere barriers as well. It was expected, then, that the reorganization energy for ET in $\text{Ru}(\text{bpy})_2(\text{im})(\text{His33})\text{-Fe-cytochrome } c$ would be less than 1.15 eV. Indeed, a study of the driving-force dependence of $\text{Fe}^{2+} \rightarrow \text{Ru}^{3+}$ ET rates in $\text{Ru}(\text{LL})_2(\text{im})(\text{His33})\text{-Fe-cytochrome } c$ (LL = bpy, 4,4'-(CH_3)₂-bpy, 4,4',5,5'-(CH_3)₄-bpy, 4,4'-(CONH(C_2H_5))₂-bpy) gave $\lambda = 0.74$ eV and $H_{\text{AB}} = 0.095$ cm⁻¹ [32, 33]. The 0.4-eV decrease in reorganization energy resulting from replacement of the Ru-ammine complex with a Ru-bpy label is in excellent agreement with estimates from cross-reactions of model complexes [3, 22].

The large difference in reorganization energy between Ru-ammine and Ru-bpy modified cytochromes highlights the important role of water in protein electron transfer. The bulky bpy ligands shield the charged metal center from the polar aqueous solution, reducing the solvent reorganization energy. In the same manner, the medium surrounding a metalloprotein active site will affect the reorganization energy associated with its ET reactions. A hydrophilic active site will lead to larger reorganization energies than a hydrophobic site. Consequently, the kinetics of protein ET reactions will be very sensitive to the active-site environment.

The exponential factor in Eq. 1 reflects the interplay between driving force and reorganization energy that regulates ET rates. The remarkable prediction of the semiclassical ET model is that rates reach a maximum value as a function of driving force ($-\Delta G^\circ = \lambda$). At low driving forces, rates increase with $-\Delta G^\circ$ but, at very high driving forces ($-\Delta G^\circ > \lambda$), ET rates are expected to decrease (inverted effect). Experimental studies of ET rates in synthetic model complexes [34–36] and in biological systems [19, 33, 37] have provided convincing evidence for inverted driving-force effects. Importantly, a reaction in the inverted region can be accelerated if a pathway is available that releases less free energy in the actual ET step [38]. This can be accomplished by the formation of electronically excited products ($^*\text{D}^+$, $^*\text{A}^-$), because the ET driving force will be lower by an amount equal to the energy of the excited electronic state. An ET process that forms excited products will be the preferred pathway if its driving force is closer to λ than that of a reaction forming ground-state products. Chemiluminescent ET reactions are a familiar example of such processes and are a clear demonstration of the inverted effect [3].

The rates of heme reduction by $^*\text{Ru}^{2+}$ and Ru^+ in $\text{Ru}(\text{His33})\text{cytochrome } c$ have been examined at very high driving forces ($1.3 \text{ eV} \leq -\Delta G^\circ \leq 1.9 \text{ eV}$) [33]. The semiclassical model predicts significant inverted effects in this region, but at driving forces above 1.3 eV rates leveled at a value eight-fold below the maximum ET rate. Rate/energy leveling is a common phenomenon, particularly in excited-state ET reactions; formation of electronically excited products is a likely explanation for the absence of inverted effects [38]. In the case of cytochrome *c* heme reduction by Ru^+ , reactions that form low-lying metal-to-ligand charge transfer excited states of the ferroheme ($\text{Fe}(d\pi) \rightarrow \text{porphyrin}(\pi^*)$; 1.05–1.3 eV) should be faster than reactions forming ground-state products. The low-lying excited states of ferro- and ferrihemes are likely to mask inverted driving-force effects in the ET reactions of heme proteins.

1.4.2 Azurin

The remarkable properties of the blue copper active site in azurin and related proteins have been studied for nearly five decades [39, 40]. Hydrated copper ions and synthetic Cu complexes tend to be rather sluggish redox reagents because of large structural changes that accompany electron transfer [40–42]. The structure of the active site in blue copper proteins, by contrast, is the same in both oxidation states of the protein [40, 43]. Whether this structural invariance is an intrinsic property of the ligand set or is enforced by the protein fold has been a hotly debated topic [40, 44–47]. Regardless of its origin, this active-site property enables copper to transfer electrons rapidly owing to a low ($\text{Cu}^{2+}/\text{Cu}^+$) reorganization energy [48].

Measurements of the temperature dependence of the rate of $\text{Cu}^+ \rightarrow \text{Ru}^{3+}$ ET in $\text{Ru}(\text{bpy})_2(\text{im})(\text{His83})\text{azurin}$ between 170 and 308 K have been used to determine the reorganization energy for electron exchange in the protein. Between 276 and 308 K, ET rates are temperature-invariant [49]. More remarkable was the observation that the $\text{Cu}^+ \rightarrow \text{Ru}^{3+}$ ET rate at 170 K is slightly greater than that measured at room temperature [50] (Figure 4). Data over this wide temperature range, along with determinations of the temperature dependence of ΔG° , constrain λ to a value of 0.7 ± 0.1 eV. The reorganization energy for $\text{Cu}^+ \rightarrow \text{Ru}(\text{LL})_2(\text{im})(\text{His83})^{3+}$ ET in azurin is the same, within error, as that for $\text{Fe}^{2+} \rightarrow \text{Ru}(\text{LL})_2(\text{im})(\text{His33})^{3+}$ ET in cytochrome *c*, indicating that the two redox proteins have comparable self-exchange reorganization energies (0.7 ± 0.1 eV). The fact that the reorganization energy for electron exchange in $\text{Cu}(\text{phen})_2^{2+/+}$ [42] is almost 2 eV greater than that for azurin illustrates the important role played by the folded polypeptide in lowering barriers to ET reactions [48].

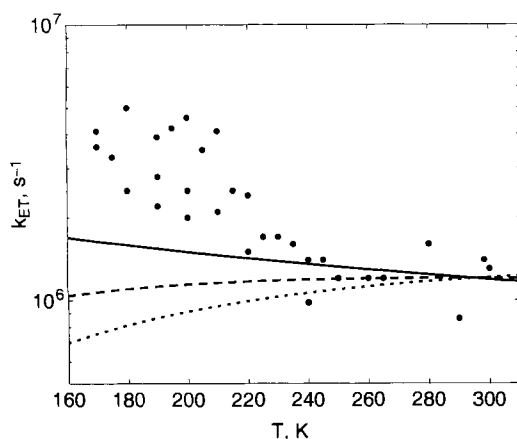


Figure 4. Temperature dependence of Cu^+ to Ru^{3+} ET rates in $\text{Ru}(\text{bpy})_2(\text{im})(\text{His83})^{2+}$ -azurin. Lines were calculated using Eq. 1 with $H_{\text{AB}} = 0.07 \text{ cm}^{-1}$ and $\lambda = 0.7$ eV (solid line); 0.5 eV (dashed line); and 1.0 eV (dotted line).

1.5 Electronic Coupling

1.5.1 Theoretical Models

Nonadiabatic ET reactions are characterized by weak electronic interaction between the reactants and products at the transition-state nuclear configuration ($H_{AB} \ll k_B T$). This coupling is directly related to the strength of the electronic interaction between the donor and acceptor [51]. When donors and acceptors are separated by long distances ($>10 \text{ \AA}$), direct overlap of their wavefunctions will be vanishingly small; the material between the two redox sites must mediate the coupling.

Uniform-barrier models

In 1974, Hopfield described biological ET in terms of electron tunneling through a square potential barrier [4]. In this model, H_{AB}^2 (and, hence, k_{ET}) drops off exponentially with increasing D/A separation. The height of the tunneling barrier relative to the energies of the D/A states determines the distance decay constant (β). Hopfield estimated $\beta \sim 1.4 \text{ \AA}^{-1}$ for biological ET reactions on the basis of measurements of the temperature dependence of ET from a cytochrome to the oxidized special pair in the photosynthetic reaction center of *Chromatium vinosum*. This calculation was performed before the reaction center structure had been determined. The analysis suggested an 8- \AA edge-edge separation; later structural studies revealed that the actual distance was somewhat greater (12.3 \AA) [52].

Superexchange-coupling models

Superexchange models are often employed to describe long-range electronic couplings; electronic states of the intervening bridge mediate the D/A interaction. If oxidized states of the bridge mediate the coupling, the process is referred to as “hole transfer”; mediation by reduced bridge states is known as “electron transfer”. In 1961, McConnell developed a nearest-neighbor superexchange coupling model to describe charge-transfer interactions between donors and acceptors separated by spacers comprised of identical repeat units [53]. The total coupling (H_{AB}) is given as the product of the coupling decays for each bridge site (ϵ). For a bridge built from identical repeat units separated by m bonds, H_{AB} will be proportional to ϵ^m . In this model, the ET rate constant will exhibit an exponential dependence on the number of bonds separating D and A; experimental studies on synthetic D-br-A complexes support this prediction.

Ab initio calculations of H_{AB} for bridges composed of saturated alkane spacers suggest that the simple superexchange model is not quantitatively accurate [54–56]. Nonnearest-neighbor interactions were found to dominate the couplings and, except in a few cases, nearest-neighbor interactions were relatively unimportant. A particularly significant finding is that the nonnearest neighbor interactions make the coupling along a saturated alkane bridge quite sensitive to its conformation.

The medium separating redox sites in proteins is comprised of a complex array of

bonded and nonbonded contacts, and an *ab initio* calculation of coupling strengths is a formidable challenge. The homologous-bridge (McConnell) superexchange model is not suitable because of the diverse interactions in proteins. Beratan, Onuchic, and coworkers developed a generalized tunneling pathway (TP) superexchange coupling model that accommodates the structural complexity of a protein matrix [57–60]. The TP model reduces the diverse interactions between the atoms in a folded polypeptide to a set of three types of contacts: covalent bonds, hydrogen bonds, and through space contacts. Each type of contact is assigned a coupling decay value (ε_C , ε_H , and ε_S) which permits implementation of a search algorithm for finding optimal coupling pathways through proteins. The total coupling of a single pathway is given as a product of the couplings for the individual links (Eq. 2) [5].

$$H_{AB} \propto \prod \varepsilon_C \prod \varepsilon_H \prod \varepsilon_S \quad (2)$$

A tunneling pathway can be described in terms of an effective covalent tunneling path comprised of n (nonintegral) covalent bonds, with a total length equal to σ_1 (Eq. 3). The relationship between σ_1 and the direct **D**–**A** distance (**R**) reflects

$$H_{AB} \propto (\varepsilon_C)^n \quad (3a)$$

$$\sigma_1 = n \times 1.4 \text{ \AA/bond} \quad (3b)$$

the coupling efficiency of a pathway. The variation of ET rates with **R** is expected to depend upon the coupling decay for a single covalent bond (ε_C); the magnitude of ε_C depends critically upon the energy of the tunneling electron relative to the energies of the bridge hole and electron states.

Distance dependences of ET rates

The **D**–**A** distance decay of protein ET rate constants depends on the capacity of the polypeptide matrix to mediate distant electronic couplings. If dominant coupling pathways mediate long-range electron transfer in proteins, then single-site mutations could have profound effects on enzyme function. In addition, if single pathways operate in biological ET reactions, then they have presumably been optimized through natural selection. These consequences of tunneling pathways impart a certain lack of robustness into the protein structure–function relationship. Concerns about this issue led Dutton and coworkers to propose that a folded polypeptide matrix behaves like a glassy solvent, imposing a uniform barrier (UB) to electron tunneling [52, 61]. Analysis of a variety of ET rates—especially those from the photosynthetic reaction center—produced a universal distance decay constant for protein electron transfer that was in remarkable agreement with Hopfield’s 1974 estimate (1.4 \AA^{-1}) [52]. Disagreements over the appropriate **D/A** distance measure (edge-to-edge, center-to-center) fueled disputes about whether the large body of protein ET data supports a homogeneous barrier model, or whether a structure-dependent model is necessary. Recently, the UB model has been amended to include the packing density of the protein matrix [62]. Although this model ignores

bond connectivity, it does embody many of the same elements as the TP model by accounting for, in a rudimentary fashion, the protein structure dependence of long-range couplings.

The great strength of the TP model is that a straightforward analysis of a protein structure identifies residues that are important for mediating long-range coupling. Employing this model, Beratan, Betts, and Onuchic predicted in 1991 that proteins comprised largely of β -sheet structures would be more effective at mediating long-range couplings than those built from α helices [58]. This analysis can be taken a step further by comparing the coupling efficiencies of individual protein secondary structural elements (β sheets, α helices). The coupling efficiency can be determined from the variation of σ_1 as a function of \mathbf{R} . A linear σ_1/\mathbf{R} relationship implies that k_{ET}° will be an exponential function of \mathbf{R} ; the distance decay constant is determined by the slope of the σ_1/\mathbf{R} plot and the value of ϵ_C [16].

A β sheet is comprised of extended polypeptide chains interconnected by hydrogen bonds; the individual strands of β sheets define nearly linear coupling pathways along the peptide backbone spanning 3.4 Å per residue. The tunneling length for a β strand exhibits an excellent linear correlation with β -carbon separation (R_β); the best linear fit with zero intercept yields a slope of 1.37 σ_1/R_β (distance decay constant = 1.0 Å⁻¹) (Figure 5). Couplings across a β sheet depend upon the ability of hydrogen bonds to mediate the D/A interaction. The standard parameterization of the TP model defines the coupling decay across a hydrogen bond in terms of the

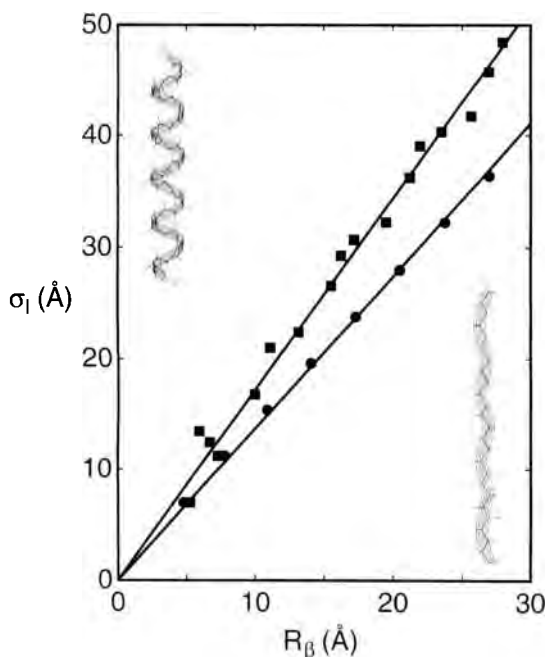


Figure 5. Plot of calculated tunneling path length (σ_1) versus β -carbon separation (R_β) for ET along an idealized α helix (■, using the standard H-bond coupling parameters in the TP model) and a β strand (●).

heteroatom separation. If the two heteroatoms are separated by twice the 1.4-Å covalent-bond distance, then the hydrogen-bond decay is assigned a value equal to that of a covalent bond. Longer heteroatom separations lead to weaker predicted couplings but, as yet, there is no experimental confirmation of this relationship.

In the coiled α -helix structure a linear distance of just 1.5 Å is spanned per residue. In the absence of mediation by hydrogen bonds, σ_1 is a very steep function of R_β , implying that an α helix is a poor conductor of electronic coupling ($2.7 \sigma_1/R_\beta$, distance decay constant = 1.97 Å^{-1}). If the hydrogen-bond networks in α helices mediate coupling, then the Beratan–Onuchic parameterization of hydrogen-bond couplings suggests a σ_1/R_β ratio of 1.72 (distance decay constant = 1.26 Å^{-1}) (Figure 5). Treating hydrogen bonds as covalent bonds further reduces this ratio ($1.29 \sigma_1/R_\beta$, distance decay constant = 0.94 Å^{-1}). Hydrogen-bond interactions, then, will determine whether α helices are vastly inferior to or are slightly better than β sheets in mediating long-range electronic couplings. It is important to note that the coiled helical structure leads to poorer σ_1/R_β correlations, especially for values of R_β under 10 Å. In this distance region, the TP model predicts little variation in coupling efficiencies for the different secondary structures.

Analyses of ET rate/distance relationships require a consistent definition of the D/A distance [63–65]. When comparing rates from systems with different donors and/or acceptors, it can be difficult to identify a proper distance measure. All maximum ET rates should extrapolate to a common adiabatic rate as R approaches van der Waals contact. So-called edge-to-edge distances are often employed but there are many ambiguities, not the least of which is defining the set of atoms that constitute the edges of **D** and **A**. For planar aromatic molecules (e.g., chlorophylls, pheophytins, quinones), edge–edge separations are usually defined on the basis of the shortest distance between aromatic carbon atoms of **D** and **A**. In transition-metal complexes (e.g., Fe-heme, Ru-ammine, Ru-bpy), however, atoms on the periphery are not always well coupled to the central metal, and empirical evidence suggests that metal–metal distances are more appropriate.

1.5.2 Blue Copper Proteins

Azurin

In azurin, a prototypal blue protein with a β -barrel tertiary structure, the central Cu atom is coordinated to Cys112 (S), His117 (N), and His46 (N) donor atoms in a trigonal planar structure, with weakly interacting Met121 (S) and Gly45 (carbonyl O atom) ligands above and below the plane [66, 67]. Individual β strands extend from these ligands, forming a β sheet. Coupling-limited rates (k_{ET}^0) have been obtained for Ru-modified azurin mutants with His residues at different sites on the β strands extending from Met121 (His122, His124, His126) and Cys112 (His109, His107) [49, 50, 68–70]. The variation of tunneling time with the Cu–Ru separation (distance decay constant of 1.1 Å^{-1}) is in remarkably good agreement with the predicted value of 1.0 Å^{-1} for a strand of an ideal β sheet (Figure 6). Detailed electronic structure calculations indicate that the S atom of Cys112 has by far the

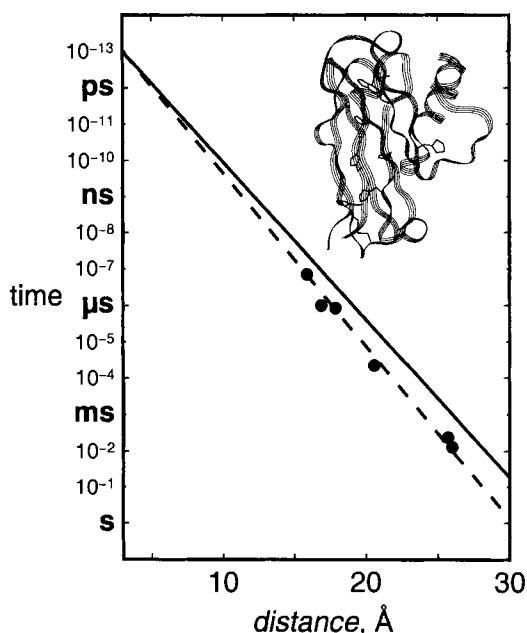


Figure 6. Tunneling timetable for ET in Ru-modified azurin. The solid line is the TP prediction for coupling along a β strand ($\beta = 1.0 \text{ \AA}^{-1}$); the dashed line illustrates a 1.1 \AA^{-1} distance decay.

strongest coupling to the Cu center; the His (imidazole) couplings are only one-third that of the Cys ligand, and the Met121 (S) and Gly45 (O) couplings are just one-tenth of the Cys coupling [71, 72]. These highly anisotropic ligand interactions strongly favor pathways that couple to the Cu through Cys112. Couplings along different β strands would be expected to have the same distance-decay constants, but different intercepts at close contact. Relatively strong Cu/Ru couplings also have been found for ET reactions involving Ru-modified His83 [49, 50, 69]. Given the variations in structure and composition of intervening media, it is somewhat surprising that the distance dependence of ET in Ru-modified azurin can be described by a single straight line.

One explanation for uniform distance dependence of couplings along the Met121 and Cys112 strands is that strong interstrand hydrogen bonds serve to direct all of the distant couplings through the Cys112 ligand [69, 73, 74]. A hydrogen bond between Met121(O) and Cys112(NH) could mediate coupling from the Ru complex bound to His122. A second hydrogen bond (Gly123(O)–Phe110(NH)) would provide a coupling link for His124 and His126 ET reactions. The importance of the pathways that cross from the Met121 strand to the Cys112 strand depends upon the coupling efficiencies of the hydrogen bonds. Model-complex studies have demonstrated efficient electron transfer across hydrogen-bonded interfaces [75, 76]. In the standard Beratan–Onuchic pathway model, hydrogen-bond couplings are distance-scaled and generally afford weaker couplings than covalent bonds [5]. This procedure for calculating hydrogen-bond couplings cannot explain the similar distance dependences of ET along the Met121 and Cys112 strands in Ru-modified azurins.

Treating the hydrogen bonds as covalent bonds in the TP model ($\epsilon_H = \epsilon_C^2$), however, does lead to better agreement with experiment [69].

Long-range ET from the Cys3–Cys26 disulfide radical anion to the copper in azurin has been studied extensively by Farver and Pecht [77]. Estimates based on experimental rate data indicate that the S_2/Cu coupling is unusually strong for a donor/acceptor pair separated by 26 Å. Interestingly, both the Cys3–Cys26 and His83 tunneling times fit on the 1.1 Å^{-1} distance decay defined by the couplings along the Met121 and Cys112 strands. Similar methods have been employed to study the ET properties of a Cu_A site constructed in azurin [78].

Plastocyanin

Rates of Cu^+ to Ru^{3+} electron transfer also have been measured in modified mutants of spinach plastocyanin, a blue copper protein from the photosynthetic ET chain [79]. Ru–bipyridine complexes were introduced at surface sites, with Cu–Ru distances ranging from 13 to 24 Å. ET rate constants, measured using laser flash-quench techniques, vary from 10^4 to 10^7 s^{-1} . ET in Ru-modified plastocyanin is not activationless as it is in Ru-modified azurin, suggesting a slightly greater reorganization energy for the photosynthetic protein. The distance dependence of ET in Ru-modified plastocyanin is exponential with a distance decay factor identical with that reported for Ru-modified azurin (1.1 Å^{-1}).

The reduced forms of several blue copper proteins are known to undergo a pH-dependent change in Cu-ligation; the pK_a values for these transformations lie in the 5–7 range. In the low-pH forms of these proteins an imidazole ligand dissociates from the Cu center and is protonated [80]. The reduction potential of the Cu site in the low-pH form of the protein, owing to the trigonal coordination geometry composed of S(Cys), N(His) and S(Met) ligands, is substantially greater than that of the neutral-pH form. The pH dependence of Cu^+ to Ru^{3+} ET has been examined in *Scenedesmus obliquus* plastocyanin labeled with a Ru complex at His59 ($Ru(tpy)(bpy)(His59)^{2+}$) [81]. The pK_a for His87 dissociation in the reduced form of this protein is 5.5 [82]. At pH 7, the Cu^+ to Ru^{3+} ET rate is $2.9(2) \times 10^7 \text{ s}^{-1}$. Biphasic ET kinetics are observed in acidic solutions (pH 5.6–4.1). The rate for the faster phase agrees well with that measured at pH 7, and has been attributed to oxidation of a population of protein in the high-pH form. The slower phase corresponds to oxidation of the low-pH, trigonal Cu sites. The strong temperature and pH dependences of the slower reaction suggest that Cu^+ rearranges to the high-pH tetrahedral geometry prior to electron transfer to Ru^{3+} [80].

1.5.3 Heme Proteins

Cytochrome *c*

ET rates have been measured in eight different $Ru(bpy)_2(im)(HisX)^{2+}$ derivatives of wild-type and mutant cytochromes *c* [16, 32, 68, 83]. Maximum ET rates do not correlate well with a simple exponential distance dependence (Figure 7). Two modified proteins, for example, have comparable ET rates ($Ru(His72)$, $9.0 \times 10^5 \text{ s}^{-1}$;

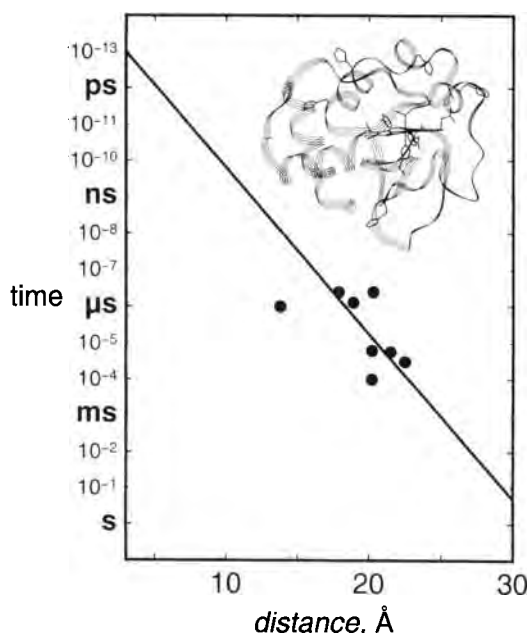


Figure 7. Tunneling timetable for ET in Ru-modified cytochrome *c*. The solid line illustrates a 1.05 Å^{-1} distance decay.

Ru(His39), $3.2 \times 10^6 \text{ s}^{-1}$), yet the Ru-Fe distances differ by 6.5 Å (His72, 13.8 Å ; His39, 20.3 Å). Moreover, the D/A distances in the Ru(His39) and Ru(His62) derivatives are nearly identical (20.3 and 20.2 Å , respectively), yet their maximum ET rates differ by a factor of 300 (3.2×10^6 and $1.0 \times 10^4 \text{ s}^{-1}$, respectively). The scatter in the data illustrates conclusively that the UB model does not adequately describe long-range couplings in proteins; a model that takes into account the structure of the bridging medium is required to explain the data.

Myoglobin

Donor–acceptor pairs separated by α helices include the heme-Ru redox sites in two Ru-modified myoglobins, Ru(bpy)₂(im)(HisX)-Mb (X = 83, 95) [70]. The tunneling pathway from His95 to the Mb-heme is comprised of a short section of α helix terminating at His93, the heme axial ligand. The coupling for the $[\text{Fe}^{2+} \rightarrow \text{Ru}^{3+}(\text{His95})]\text{-Mb}$ ET reaction [70] is of the same magnitude as that found in Ru-modified azurins with comparable D–A spacings. This result is consistent with the TP model, which predicts very little difference in the coupling efficiencies of α helices and β sheets at small D–A separations. The $[\text{Fe}^{2+} \rightarrow \text{Ru}^{3+}(\text{His83})]\text{-Mb}$ [70] tunneling time, however, is substantially longer than those found in β -sheet structures at similar separations, in accord with the predicted distance decay constant for an α helix (Figure 8).

Cytochrome *b*₅₆₂

ET rate data are available for nine Ru-modified derivatives of cytochrome *b*₅₆₂, a four-helix-bundle protein [84]. The tunneling times for Ru-modified *b*₅₆₂ exhibit far

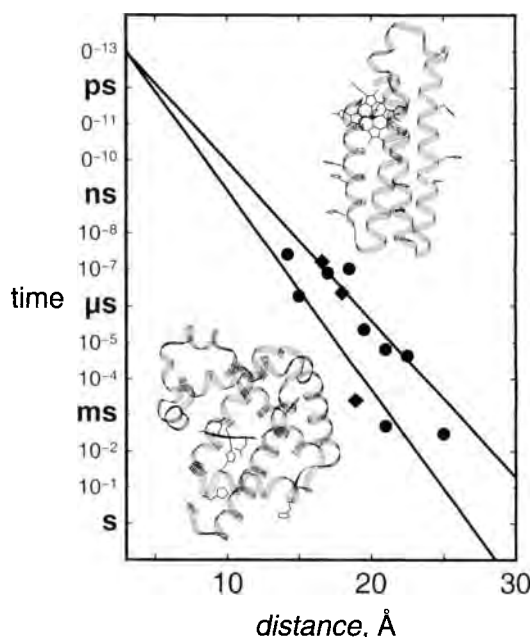


Figure 8. Tunneling timetable for ET in Ru-modified myoglobin (◆) and cytochrome b_{562} (●). The solid lines illustrate the TP predictions for coupling along β strands ($\beta = 1.0 \text{ Å}^{-1}$) and α helices ($\beta = 1.3 \text{ Å}^{-1}$).

more scatter than was found for Ru-modified azurin. Two derivatives exhibit ET rates close to those predicted for coupling along a simple α helix, and several others lie close to the β -strand decay (Figure 8). In these proteins, as in Ru(His70)Mb, the intervening medium is not a simple section of α helix. Coupling across helices, perhaps on multiple interfering pathways, is likely to produce a complex distance dependence. Interpretation of the relative ET rates in cytochrome b_{562} will require a more detailed analysis of the medium separating the redox sites [85].

1.5.4 High-Potential Iron-Sulfur Protein (HiPIP)

Results with Ru-modified HiPIP provide additional evidence for structure-dependent couplings [86]. The Ru(His42) and Ru(His50) derivatives of this protein have metal–metal separations of 12 Å , yet the rate of ET from the reduced $[\text{Fe}_4\text{S}_4]$ cluster to Ru^{3+} is 300 times slower in the Ru(His50) derivative. The poor coupling in Ru(His50) has been attributed to a 3.8 Å through-space gap in the optimum Fe–Ru pathway.

1.6 Electron Tunneling through Water

Very little consideration has been given to the involvement of solvent hole and electron states [87–89] in the mediation of distant couplings in proteins. In fluid

solution, when the positions of **D** and **A** are not constrained by a covalent bridge, diffusion places an upper limit on the time scale ($<10^{-9}$ s) and, therefore, the distance range (<9 Å for $\beta = 1.0$ Å $^{-1}$) for electron tunneling. Nevertheless, analyses of non-exponential fluorescence-quenching kinetics are consistent with $\beta = 1.2 \pm 0.2$ Å $^{-1}$ for tunneling through fluid organic solvents [90]. Longer tunneling distances can be examined if **D** and **A** are immobilized. Pulse radiolysis and photochemical investigations of intermolecular electron transfer in aqueous and organic glasses have produced β values in the 0.75–1.4 Å $^{-1}$ range [91, 92].

Although immobilizing **D** and **A** eliminates the problem of diffusion, it introduces complications into the analysis of the kinetics data. In a typical experiment, a small concentration of electron or hole donors is embedded in a glassed solvent amid a higher concentration of randomly distributed acceptors. The donor is a photo-excited chromophore or a radiolytically generated radical. The time-dependent survival probability of the donor depends on the concentration of acceptors, the rate constant for electron/hole transfer when **D** and **A** are in van der Waals contact (k_0), and the distance decay factor β . Extracting reliable values for k_0 and β from time-resolved spectroscopic measurements, however, can be rather difficult because the two parameters are highly correlated [90, 93]. For the case of photoinitiated ET in glasses, measurements of luminescence decay kinetics *and* luminescence quantum yields at several different quencher concentrations provide enough information to decouple k_0 and β , permitting reliable values to be determined for each parameter [90].

The relevant solvent for protein electron transfer is water. Indeed, aqueous-solution redox processes pervade chemistry and biology and ET reactions in water have been among the most intensively studied [1, 3, 94]. The high dielectric constant of water has long been recognized to impose large reorganization barriers to ET [3], but little is known about its ability to mediate long-range couplings [88, 89, 95]. In 1984, Larsson suggested that long-range ET in water would be inefficient ($\beta = 2.4$ Å $^{-1}$) because of the large energy gap between the hole states of water and those of **D** and **A** [96]. More recent theoretical treatments, however, have produced β values in the 1.0 to 1.8 Å $^{-1}$ range [88, 97, 98].

An experimental investigation of $\text{Ru}(\text{tpy})_2^{2+}$ (tpy = 2,2':6,2''-terpyridine) luminescence quenching by $\text{Fe}(\text{OH}_2)_6^{3+}$ in aqueous acidic glasses has placed rigorous limits on the distance decay constant for tunneling through water [9]. In the absence of quenchers, the luminescence lifetime of $\text{Ru}(\text{tpy})_2^{2+}$ is 8.0 μs in $\text{H}_2\text{SO}_4/\text{H}_2\text{O}$ and $\text{HSO}_3\text{F}/\text{H}_2\text{O}$ glasses (25 %, v/v) at 77 K, and 10.2 μs in $\text{D}_2\text{SO}_4/\text{D}_2\text{O}$ (25 %, v/v). Addition of moderate concentrations of the powerfully oxidizing $\text{Fe}(\text{OH}_2)_6^{3+}$ ion (0.01–0.5 M, $E^\circ = 0.77$ V versus NHE[99]) to the glasses leads to accelerated and highly nonexponential $^*\text{Ru}(\text{tpy})_2^{2+}$ decay kinetics. Distance decay constants for $\text{Fe}(\text{OH}_2)_6^{3+}$ quenching of $^*\text{Ru}(\text{tpy})_2^{2+}$ in aqueous glasses were extracted from measurements of luminescence decay kinetics as functions of quencher concentration. The luminescence lifetime of $^*\text{Ru}(\text{tpy})_2^{2+}$ in aqueous glasses is long enough to allow a significant distance range (~ 25 Å) to be probed. Quantum-yield data were used to scale the intensities of the decay kinetics so that just two parameters were required to fit the data. A distance decay constant of 1.68 ± 0.07 Å $^{-1}$ adequately describes ET in the three different glasses, and the rate constants for ET at van der

Waals contact are approximately 10^{13} s^{-1} . Although large concentrations of acid (25 %, v/v) are required for vitrification, water is still the dominant component in these matrices. On a molar basis, the acidic glasses are greater than 90 % $\text{H}_2\text{O}/\text{H}_3\text{O}^+$. The fact that the distance decay parameter in the HSO_3F glass is virtually identical with that obtained in the H_2SO_4 glass provides additional evidence that the oxo anions are not playing an important coupling role.

The distance decay factor for tunneling through water provides an interesting comparison to results from **D-br-A** complexes. ET across saturated alkane spacers is best described by an exponential distance decay constant of 0.9 \AA^{-1} [6]. The $1.2\text{-}\text{\AA}^{-1}$ β value reported for tunneling in 2-methyl tetrahydrofuran glasses can be explained by weaker coupling between solvent molecules than between adjacent carbon atoms in the covalently bonded alkane chain. The average distance decay constant found for tunneling through proteins is 1.1 \AA^{-1} , although there is significant deviation from a simple exponential distance dependence because proteins do not provide a homogeneous tunneling barrier. The region representing the distance decay for coupling through water ($\beta = 1.61\text{--}1.75 \text{ \AA}^{-1}$) demonstrates that, although better than a vacuum ($\beta = 3\text{--}4 \text{ \AA}^{-1}$), tunneling 20 \AA through water is at least 100 times slower than tunneling through protein or hydrocarbon bridges. Exclusion of water from the space between redox centers is a key factor in maximizing the efficiency of long-range electron transfer in biological molecules and assemblies.

1.7 Tunneling Timetables

The master tunneling timetable for Ru-modified proteins demonstrates that virtually all observed ET rates fall in a zone defined by the predicted distance decays for α helices (1.3 \AA^{-1}) and β strands (1.0 \AA^{-1}) (Figure 9). This large set of kinetics data provides compelling support for tunneling mediated by the sigma-bond framework of the protein. Measured protein ET rates that lie outside of this zone should be examined carefully for possible alternative mechanisms. The relatively large β value for water indicates that, in addition to large reorganization barriers, this ubiquitous biological solvent also imposes a large tunneling barrier to long-range ET. The poor coupling efficiency of water suggests that pathways involving interstitial water molecules in proteins may not be as effective as all-peptide pathways.

Simple theoretical models (e.g., uniform barrier, tunneling pathway) do not capture all of the critical factors that control the rates of protein ET reactions [85]. Refined pathway models are being developed that, in most cases, aim to identify the atoms most responsible for mediating **D/A** electronic couplings [59, 60, 73, 100]. With increasing levels of sophistication in both theory and experiment, new questions are emerging from the study of protein ET. The TP model was based on the static structure of a protein, but it is clear that protein structures are dynamic. How protein dynamics affect long-range couplings is an issue of great current interest [101–103]. Very long-range reactions proceed too slowly to sustain many biological transformations. Multistep tunneling processes, even with endergonic intermediate

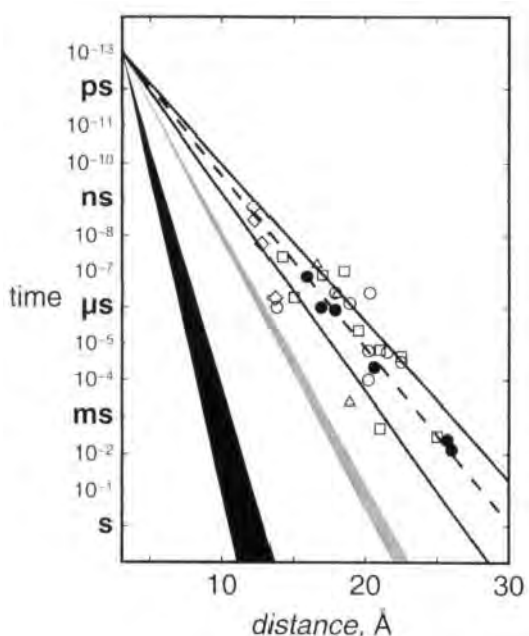


Figure 9. Tunneling timetable for ET in Ru-modified proteins: azurin (●); cytochrome *c* (○); myoglobin (△); cytochrome *b*₅₆₂ (□); and HiPIP (◆). The solid lines illustrate the TP predictions for coupling along β strands ($\beta = 1.0 \text{ \AA}^{-1}$) and α helices ($\beta = 1.3 \text{ \AA}^{-1}$); the dashed line illustrates a 1.1 \AA^{-1} distance decay. Distance decay for electron tunneling through water is shown as a gray wedge. Estimated distance dependence for tunneling through vacuum is shown as the black wedge.

steps, can compete effectively with single-step long-range reactions [62, 84]. Long-range ET reactions via a series of real intermediates, rather than the virtual intermediates implicated in pathway models, may play important roles in many biochemical transformations [104].

Acknowledgment

Our research on the electron transfer reactions of metalloproteins is supported by the National Science Foundation, the National Institutes of Health, and the Arnold and Mabel Beckman Foundation.

References

1. H. B. Gray, W. R. Ellis, Jr., in I. Bertini, H. B. Gray, S. J. Lippard, J. S. Valentine (Eds.): *Bioinorganic Chemistry*, University Science Books, Mill Valley, CA 1994, p. 315–363.
2. B. E. Ramirez, B. G. Malmström, J. R. Winkler, H. B. Gray, *Proc. Natl. Acad. Sci. USA* 92 (1995) 11949–11951.
3. R. A. Marcus, N. Sutin, *Biochim. Biophys. Acta* 811 (1985) 265–322.
4. J. J. Hopfield, *Proc. Natl. Acad. Sci. USA* 71 (1974) 3640–3644.
5. J. N. Onuchic, D. N. Beratan, J. R. Winkler, H. B. Gray, *Annu. Rev. Biophys. Biomol. Struct.* 21 (1992) 349–377.
6. J. F. Smalley, S. W. Feldberg, C. E. D. Chidsey, M. R. Linford, M. D. Newton, Y.-P. Liu, *J. Phys. Chem.* 99 (1995) 13141–13149.

7. J. W. Verhoeven, *Adv. Chem. Phys.* 106 (1999) 603–644.
8. M. R. Wasielewski, in M. A. Fox, M. Chanon (Eds.): *Photoinduced Electron Transfer. Part A: Conceptual Basis for Electron Transfer*, Elsevier, Amsterdam 1988.
9. A. Ponce, H. B. Gray, J. R. Winkler, *J. Am. Chem. Soc.* 122 (2000) 8187–8191.
10. J. M. Nocek, J. S. Zhou, S. DeForest, S. Priyadarshy, D. N. Beratan, J. N. Onuchic, B. M. Hoffman, *Chem. Rev.* 96 (1996) 2459–2489.
11. G. McLendon, R. Hake, *Chem. Rev.* 92 (1992) 481–490.
12. F. Millett, M. A. Miller, L. Geren, B. Durham, *J. Bioenerg. Biomembr.* 27 (1995) 341–351.
13. V. L. Davidson, *Acc. Chem. Res.* 33 (2000) 87–93.
14. M. M. Ivkovic-Jensen, G. M. Ullmann, S. Young, O. Hansson, M. M. Crnogorac, M. Ejdeback, N. M. Kostic, *Biochemistry* 37 (1998) 9557–9569.
15. J. R. Winkler, H. B. Gray, *Chem. Rev.* 92 (1992) 369–379.
16. H. B. Gray, J. R. Winkler, *Annu. Rev. Biochem.* 65 (1996) 537–561.
17. D. W. Conrad, H. Zhang, D. E. Stewart, R. A. Scott, *J. Am. Chem. Soc.* 114 (1992) 9909–9915.
18. J. Sun, J. F. Wishart, S. S. Isied, *Inorg. Chem.* 34 (1995) 3998–4000.
19. J. R. Scott, A. Willie, M. Mark, P. S. Stayton, S. G. Sligar, B. Durham, F. Millett, *J. Am. Chem. Soc.* 115 (1993) 6820–6824.
20. K. M. Yocom, J. B. Shelton, J. R. Shelton, W. E. Schroeder, G. Worosila, S. S. Isied, E. Bordignon, H. B. Gray, *Proc. Natl. Acad. Sci. USA* 79 (1982) 7052–7055.
21. I.-J. Chang, H. B. Gray, J. R. Winkler, *J. Am. Chem. Soc.* 113 (1991) 7056–7057.
22. G. M. Brown, N. Sutin, *J. Am. Chem. Soc.* 101 (1979) 883–892.
23. A. B. P. Lever, *Inorg. Chem.* 29 (1990) 1271–1285.
24. B. Durham, J. L. Fairris, M. McLean, F. Millett, J. R. Scott, S. G. Sligar, A. Willie, *J. Bioenerg. Biomembr.* 27 (1995) 331–340.
25. L. P. Pan, S. Hibdon, R.-Q. Liu, B. Durham, F. Millett, *Biochemistry* 32 (1993) 8492–8498.
26. S. Faham, M. W. Day, W. B. Connick, B. R. Crane, A. J. Di Bilio, W. P. Schaefer, D. C. Rees, H. B. Gray, *Acta Crystallogr. D* 55 (1999) 379–385.
27. R. A. Marcus, N. Sutin, *Inorg. Chem.* 14 (1975) 213–216.
28. J. R. Winkler, D. G. Nocera, K. M. Yocom, E. Bordignon, H. B. Gray, *J. Am. Chem. Soc.* 104 (1982) 5798–5800.
29. H. Elias, M. H. Chou, J. R. Winkler, *J. Am. Chem. Soc.* 110 (1988) 429–434.
30. T. J. Meade, H. B. Gray, J. R. Winkler, *J. Am. Chem. Soc.* 111 (1989) 4353–4356.
31. S. M. Andrew, K. A. Thomasson, S. H. Northrup, *J. Am. Chem. Soc.* 115 (1993) 5516–5521.
32. M. J. Bjerrum, D. R. Casimiro, I.-J. Chang, A. J. Di Bilio, H. B. Gray, M. G. Hill, R. Langen, G. A. Mines, L. K. Skov, J. R. Winkler, D. S. Wuttke, *J. Bioenerg. Biomembr.* 27 (1995) 295–302.
33. G. A. Mines, M. J. Bjerrum, M. G. Hill, D. R. Casimiro, I.-J. Chang, J. R. Winkler, H. B. Gray, *J. Am. Chem. Soc.* 118 (1996) 1961–1965.
34. G. L. Closs, J. R. Miller, *Science* 240 (1988) 440–447.
35. L. S. Fox, M. Kozik, J. R. Winkler, H. B. Gray, *Science* 247 (1990) 1069–1071.
36. H. B. Gray, J. R. Winkler, D. J. Wiedenfeld, *Coord. Chem. Rev.* (2000) in press.
37. G. McLendon, J. R. Miller, *J. Am. Chem. Soc.* 107 (1985) 7811–7816.
38. T. M. McCleskey, J. R. Winkler, H. B. Gray, *J. Am. Chem. Soc.* 114 (1992) 6935–6937.
39. B. G. Malmström, J. Leckner, *Curr. Opin. Chem. Biol.* 2 (1998) 286–292.
40. H. B. Gray, B. G. Malmström, R. J. P. Williams, *JBIC* (2000) in press.
41. G. B. Jameson, J. A. Ibers, in I. Bertini, H. B. Gray, S. J. Lippard, J. S. Valentine (Eds.): *Bioinorganic Chemistry*, University Science Books, Mill Valley, CA 1994, p. 167–252.
42. M. A. Augustin, J. K. Yandell, *Inorg. Chem.* 18 (1979) 577–583.
43. W. E. B. Shepard, B. F. Anderson, D. A. Lewandoski, G. E. Norris, E. N. Baker, *J. Am. Chem. Soc.* 112 (1990) 7817–7819.
44. D. W. Randall, D. R. Gamelin, L. B. LaCroix, E. I. Solomon, *JBIC* 5 (2000) 16–29.
45. U. Ryde, M. H. M. Olsson, B. O. Roos, J. O. A. De Kerpel, K. Pierloot, *JBIC* (1999) in press.
46. M. H. M. Olsson, U. Ryde, B. O. Roos, K. Pierloot, *JBIC* 3 (1998) 109–125.
47. U. Ryde, M. H. M. Olsson, K. Pierloot, B. O. Roos, *J. Mol. Biol.* 261 (1996) 586–596.
48. J. R. Winkler, P. Wittung-Stafshede, J. Leckner, B. G. Malmström, H. B. Gray, *Proc. Natl. Acad. Sci. USA* 94 (1997) 4246–4249.

49. A. J. Di Bilio, M. G. Hill, N. Bonander, B. G. Karlsson, R. M. Villahermosa, B. G. Malmström, J. R. Winkler, H. B. Gray, *J. Am. Chem. Soc.* **119** (1997) 9921–9922.
50. L. K. Skov, T. Pascher, J. R. Winkler, H. B. Gray, *J. Am. Chem. Soc.* **120** (1998) 1102–1103.
51. M. D. Newton, *J. Phys. Chem.* **92** (1988) 3049–3056.
52. C. C. Moser, J. M. Keske, K. Warncke, R. S. Farid, P. L. Dutton, *Nature* **355** (1992) 796–802.
53. H. M. McConnell, *J. Chem. Phys.* **35** (1961) 508–515.
54. C. Liang, M. D. Newton, *J. Phys. Chem.* **96** (1992) 2855–2866.
55. C. Liang, M. D. Newton, *J. Phys. Chem.* **97** (1993) 3199–3211.
56. L. A. Curtiss, C. A. Naleway, J. R. Miller, *Chem. Phys.* **176** (1993) 387–405.
57. D. N. Beratan, J. N. Onuchic, J. J. Hopfield, *J. Chem. Phys.* **86** (1987) 4488–4498.
58. D. N. Beratan, J. N. Betts, J. N. Onuchic, *Science* **252** (1991) 1285–1288.
59. S. S. Skourtis, D. N. Beratan, *Adv. Chem. Phys.* **106** (1999) 377–452.
60. J. J. Regan, J. N. Onuchic, *Adv. Chem. Phys.* **107** (1999) 497–553.
61. R. S. Farid, C. C. Moser, P. L. Dutton, *Curr. Opin. Struct. Biol.* **3** (1993) 225–233.
62. C. C. Page, C. C. Moser, X. Chen, P. L. Dutton, *Nature* **402** (1999) 47–52.
63. J. R. Winkler, H. B. Gray, *JBIC* **2** (1997) 399–404.
64. C. C. Moser, C. C. Page, X. Chen, P. L. Dutton, *JBIC* **2** (1997) 393–398.
65. R. J. P. Williams, *JBIC* **2** (1997) 373–377.
66. H. Nar, A. Messerschmidt, R. Huber, M. van de Kamp, G. W. Canters, *J. Mol. Biol.* **221** (1991) 765–772.
67. E. T. Adman, *Adv. Protein Chem.* **42** (1991) 145–197.
68. R. Langen, I.-J. Chang, J. P. Germanas, J. H. Richards, J. R. Winkler, H. B. Gray, *Science* **268** (1995) 1733–1735.
69. J. J. Regan, A. J. Di Bilio, R. Langen, L. K. Skov, J. R. Winkler, H. B. Gray, J. N. Onuchic, *Chem. Biol.* **2** (1995) 489–496.
70. R. Langen, J. L. Colón, D. R. Casimiro, T. B. Karpishin, J. R. Winkler, H. B. Gray, *JBIC* **1** (1996) 221–225.
71. M. D. Lowery, E. I. Solomon, *Inorg. Chim. Acta* **200** (1992) 233–243.
72. J. A. Guckert, M. D. Lowery, E. I. Solomon, *J. Am. Chem. Soc.* **117** (1995) 2817–2844.
73. J. N. Gehlen, I. Daizadeh, A. A. Stuchebrukhov, R. A. Marcus, *Inorg. Chim. Acta* **243** (1996) 271–282.
74. I. Daizadeh, J. N. Gehlen, A. A. Stuchebrukhov, *J. Chem. Phys.* **106** (1997) 5658–5666.
75. C. Turro, C. K. Chang, G. E. Leroi, R. I. Cukier, D. G. Nocera, *J. Am. Chem. Soc.* **114** (1992) 4013–4015.
76. P. J. F. de Rege, S. A. Williams, M. J. Therien, *Science* **269** (1995) 1409–1413.
77. O. Farver, I. Pecht, *Adv. Chem. Phys.* **107** (1999) 555–589.
78. O. Farver, Y. Lu, M. C. Ang, I. Pecht, *Proc. Natl. Acad. Sci. USA* **96** (1999) 899–902.
79. K. Sigfridsson, M. Ejdeback, M. Sundahl, O. Hansson, *Arch. Biochem. Biophys.* **351** (1998) 197–206.
80. J. M. Guss, P. R. Harrowell, M. Murata, V. A. Norris, H. C. Freeman, *J. Mol. Biol.* **192** (1986) 361–387.
81. A. J. Di Bilio, C. Dennison, H. B. Gray, B. E. Ramirez, A. G. Sykes, J. R. Winkler, *J. Am. Chem. Soc.* **120** (1998) 7551–7556.
82. A. G. Sykes, *Chem. Soc. Rev.* **14** (1985) 283–315.
83. D. S. Wuttke, M. J. Bjerrum, J. R. Winkler, H. B. Gray, *Science* **256** (1992) 1007–1009.
84. J. R. Winkler, A. Di Bilio, N. A. Farrow, J. H. Richards, H. B. Gray, *Pure Appl. Chem.* **71** (1999) 1753–1764.
85. J. R. Winkler, *Curr. Opin. Chem. Biol.* **4** (2000) 192–198.
86. E. Babini, I. Bertini, M. Borsari, F. Capozzi, C. Luchinat, X. Zhang, G. L. C. Moura, I. V. Kurnikov, D. N. Beratan, A. Ponce, A. J. Di Bilio, J. R. Winkler, H. B. Gray, *J. Am. Chem. Soc.* **122** (2000) 4532–4533.
87. Y. Sakata, H. Tsue, M. P. O’Neil, G. P. Wiederrecht, M. R. Wasielewski, *J. Am. Chem. Soc.* **116** (1994) 6904–6909.
88. M. D. Newton, *J. Electroanal. Chem.* **438** (1997) 3–10.
89. S. Hayashi, S. Kato, *J. Phys. Chem. A* **102** (1998) 3333–3342.

90. K. Weidemaier, H. L. Tavernier, S. F. Swallen, M. D. Fayer, *J. Phys. Chem. A* 1997 (1997) 1887–1902.
91. J. R. Miller, *J. Phys. Chem.* 79 (1975) 1070–1078.
92. J. R. Miller, J. V. Beitz, R. K. Huddleston, *J. Am. Chem. Soc.* 106 (1984) 5057–5068.
93. S. W. Swallen, K. Weidemaier, H. L. Tavernier, M. D. Fayer, *J. Phys. Chem.* 100 (1996) 8106–8117.
94. A. J. Bard, L. R. Faulkner, *Electrochemical Methods*, John Wiley & Sons, Inc., New York, 1980.
95. K. Kumar, I. V. Kurnikov, D. N. Beratan, D. H. Waldeck, M. B. Zimmt, *J. Phys. Chem. A* 102 (1998) 5529–5541.
96. S. Larsson, *J. Phys. Chem.* 88 (1984) 1321–1323.
97. N. E. Miller, M. C. Wander, R. J. Cave, *J. Phys. Chem. A* 103 (1999) 1084–1093.
98. I. Benjamin, D. Evans, A. Nitzan, *J. Chem. Phys.* 106 (1997) 6647–6654.
99. C.-T. Lin, W. Böttcher, M. Chou, C. Creutz, N. Sutin, *J. Am. Chem. Soc.* 98 (1976) 6536–6544.
100. I. Daizadeh, J.-X. Guo, A. A. Stuchebrukhov, *J. Chem. Phys.* 110 (1999) 8865–8868.
101. I. Daizadeh, E. S. Medvedev, A. A. Stuchebrukhov, *Proc. Natl. Acad. Sci. USA* 94 (1997) 3703–3708.
102. V. R. Vogel, A. V. Pastukhov, B. L. Psikha, A. I. Kotelnikov, *Biofizika* 45 (1997) 1008–1014.
103. H. Mei, K. Wang, N. Peffer, G. Weatherly, D. S. Cohen, M. Miller, G. Pielak, B. Durham, F. Millett, *Biochemistry* 38 (1999) 6846–6854.
104. J. Jortner, M. Bixon, T. L. Langenbacher, M. E. Michel-Beyerle, *Proc. Natl. Acad. Sci. USA* 95 (1998) 12759–12765.

2 Photosynthesis: Bacterial Reaction Center

Christopher C. Moser, Christopher C. Page, and P. Leslie Dutton

2.1 The Bioenergetic Context of Bacterial Reaction Centers

At a time when the electron transfer proteins of photosynthesis and respiration were first being teased apart, and well before any clear structural pictures of the proteins were available, Mitchell proposed a unifying chemiosmotic model of biological energy transduction for all bioenergetic membranes [1]. In this view, individual electron transfer proteins were embedded in an electrically insulating lipid membrane and designed to couple the energetically favorable transfer of electrons to the vectorial movement of protons across this membrane. It is now well established that the transmembrane electric field and proton concentration gradient generate a delocalized energy source which power other membrane proteins, such as the ATPase, which couples the movement of protons back across the membrane to the phosphorylation of ADP to ATP. The development of a relatively high concentration of ATP over ADP provides the principal soluble energy source for coupled chemistry in all parts of the cell.

Figure 1 shows a modern realization of Mitchell's picture in which the various electron transfer proteins and their redox centers are drawn schematically, but informed by the considerable structural information that has become available through X-ray crystallography. At the top, the reaction center proteins of bacteria represented by *Rhodobacter sphaeroides* and *Rhodospseudomonas viridis* for which high-resolution structures are available, and the reaction centers of the chloroplast membranes Photosystem I and II, all absorb light and separate charge across the membrane while generating oxidants and reductants. At the bottom, respiratory proteins represented by those found in mitochondrial membranes (similar to a range of counterparts in many bacterial membranes), guide electrons from reductant sources to oxidant sinks. The basic design links NADH to O₂ by chains of electron transfer centers within the protein complexes which are in turn inter-connected by the diffusible redox carriers cytochrome *c* and ubiquinone (Q).

Because Q is membrane-soluble and couples protons to electrons upon oxidation and reduction, it has a dominant role in chemiosmotic energy conversion. The re-

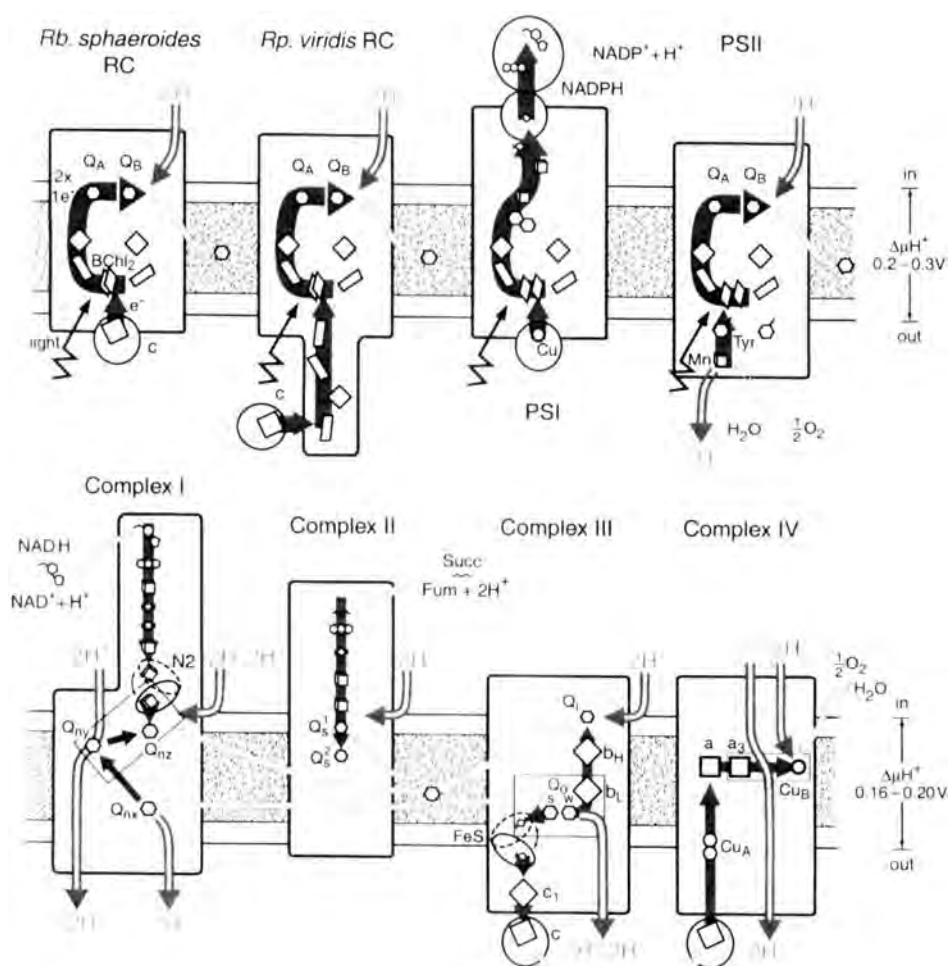


Figure 1. The major transmembrane photosynthetic reaction centers (RC) (top) and respiratory complexes (bottom) are composed of light (zigzag) activated chains (dark gray) of redox centers (open polygons) that create a transmembrane electric field and move protons (double arrows) to create a transmembrane proton gradient, fulfilling the requirements of Mitchell's chemiosmotic hypothesis. Diffusing substrates include ubiquinone (hexagon) and other sources of oxidants and reductants. PSI and PSII, photosystems I and II, respectively.

duction of Q with proton binding on one side of the membrane, followed by oxidation of QH_2 with proton release on the other side of the membrane, and the return of the neutral Q provides the basic and simplest chemiosmotic mechanism. Indeed, much of the form of the respiratory system can be understood in the simple terms of providing chains of redox centers to bring electrons to and from sites of quinone binding and oxidation/reduction. Nature has derived a means to wring extra efficiency out of Q oxidation and reduction by bifurcating electron transfer at

certain quinone binding sites, which leads to circulating eddies in the overall flow of electrons. Thus, at the Q_o binding site of Complex III (cytochrome bc_1 complex), one electron of the pair carried by QH_2 is delivered via a high potential chain to cytochrome c , while the other is carried by a low potential chain back across the membrane to Q_i . This eddy was first observed by Chance [2] (at about the same time as Mitchell was formulating his hypothesis), when introduction of an oxidant (via cytochrome c) induced a puzzling reduction of cytochrome b . We believe an analogous reductant-induced oxidation is also part of the design of the still unclear mechanism of Complex I [3].

Photosynthetic reaction centers plug into the chemiosmotic scheme by using light-excited states to create both an oxidant and a reductant. For the purple bacterial reaction centers, these oxidants and reductants are the redox carriers already described, oxidized cytochrome c and reduced ubiquinone QH_2 . Thus, in combination with Complex III, light drives a relatively straightforward cyclic electron transfer that generates a transmembrane electric field and proton gradient.

The photosystems of cyanobacteria and plants are more complicated. Photosystem I (PSI) reduces the soluble redox carrier protein ferredoxin that in turn generates NAD(P)H by ferredoxin/NAD(P) oxidoreductase. PSI also generates oxidized plastocyanin, a functional analogue of cytochrome c . Light activation of Photosystem II (PSII) leads to reduction of Q , as in the purple photosynthetic bacteria, but also to the oxidation of water to O_2 , which accumulates as a waste product in the atmosphere in what is essentially noncyclic electron flow. This waste product, of course, is what allows the essentially linear mitochondrial respiratory system in our own cells to continue to operate. The oxidized plastocyanin and QH_2 are substrate to a plant version of the mitochondrial complex III, the cytochrome b_6f complex. Thus, like the mitochondrial complexes, PSII, cytochrome b_6f and PSI are linked in a linear electron transfer chain to generate an electrochemical protein gradient. In a less clearly understood sequence PSI can apparently also participate in cyclic electron transfer via ferredoxin, which through a series of intermediate proteins leads to the reduction of membrane Q . Electrons from Q then apparently complete the cycle by oxidizing plastocyanin through the cytochrome b_6f complex.

The most basic design requirements of the bacterial photosynthetic reaction centers then, are a light energy absorbing center and two chains of redox centers that connect this light-activatable center to cytochrome c and quinone on opposite sides of the membrane. The physical process by which electrons are transferred between members of the chains in reaction centers, and indeed in the vast majority of electron transfer proteins, was also revealed by Chance, together with Devault, in these same years [4].

2.2 Tunneling Revealed in Photosynthesis

Devault and Chance [4] found that the light activation of chlorophyll in the membranes of the photosynthetic bacterium *Chromatium vinosum* which led to oxidation

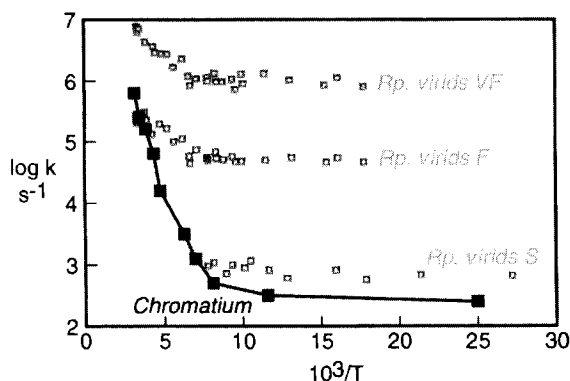


Figure 2. Electron transfer kinetics of cytochrome *c* oxidation in *Chromatium vinosum* [4] and *Rhodospseudomonas viridis* [16] display temperature independence at low temperature, a herald of tunneling. The early *Chromatium* data were analyzed as a single phase, while the *Rp. viridis* data were analyzed into three phases, dominated by very fast (VF) and fast (F) phases at high temperatures, and dominated by slow (S) phase at low temperatures.

of a heme, would continue when the membranes were frozen and chilled even down to liquid helium temperatures (Figure 2). Near room temperature there was a strong Arrhenius-like dependence of the rate on temperature, but below 100 K, the rate maintained a nearly temperature-independent value. They recognized that this non-Arrhenius temperature independence meant that the slow electron transfer was not proceeding over a thermally activated barrier, but directly through the barrier—the hallmark of electron tunneling.

In tunneling, the wavefunction of the electron on a heme donor can penetrate the insulating barrier and overlap to a small but finite extent with the wavefunction of the electron on the acceptor. The greater the overlap (the lower the barrier or the closer the centers), the greater the speed that the electron tunnels from donor to acceptor. Making a host of reasonable assumptions, Devault and Chance estimated an electron transfer distance of about 30 Å. A great many theories have been applied to this single experiment, which continues to be a useful way to examine all the factors which can control the rate of electron tunneling in proteins [5].

2.3 Basic Electron Tunneling Theory

Traditionally, analysis of biological tunneling between independent redox centers that are well separated in space begins with nonadiabatic electron tunneling theory [5] and Fermi's Golden Rule in which the electron tunneling rate, k_{et} , is the product of two terms: and electronic coupling term, V_R^2 , and a nuclear term, here represented by FC for Franck–Condon weighted density of states.

$$k_{et} = \frac{2\pi}{\hbar} V_R^2 FC \quad (1)$$

2.3.1 The V_R^2 Term

The simplest view of electron tunneling begins with a uniform barrier in which the tunneling rate is expected to depend approximately exponentially on distance.

$$k_{et} \propto e^{-\beta R} \quad (2)$$

The coefficient in the exponent, β , is a reflection of the barrier height. We naturally expect that the barrier will be lower and tunneling faster if the donor and acceptor are relatively directly connected by a covalent bridge. The tunneling electron will find the regions near these atomic nuclei and bonded regions between nuclei a more energetically favorable place to be relative to the more vacuum-like regions away from these atoms. Indeed, tunneling rates do appear to fall off approximately exponentially with distance for a variety of rigidly bridged covalently linked donors and acceptors. The β value for such bridges is around 0.9 \AA^{-1} [6, 7]. This would correspond, in this simple view, to a barrier height of about 0.8 eV.

The value of β in a vacuum will depend on how much energy is required to pull an electron off the redox center. For many typical biological redox centers in isolation, this will be around 8 eV, leading to an expected β around 2.8 \AA^{-1} . β in a protein falls in between, with a value of about 1.4 \AA^{-1} [6], corresponding to an effective barrier height of about 2 eV. This β value is found to correspond to an average of the bonded and vacuum β weighted according to the average volume of a protein structure within and without the van der Waals radius of atoms [8]. Protein regions that are better packed than average appear to have a β smaller than 1.4 \AA^{-1} , while those more loosely packed appear to have a larger β . Nevertheless, a survey of electron transfer proteins with available structures shows that the standard deviation for the packing is relatively small, leading to a β range in protein of about $1.4 \pm 0.2 \text{ \AA}^{-1}$.

Furthermore, there is no statistically significant correlation of β with the productivity or wastefulness of a biological electron transfer reaction (Figure 3) [6]. Nature does not select the structure of the intervening protein medium to guide productive electron transfer and hinder unproductive electron transfer. Part of the reason can be seen in Figure 3. Although changes in β can have a profound effect on rates at long distances, changes in the biologically relevant range of 4 to 14 \AA will tend to be an order of magnitude or less. Apparently, making adjustments in the protein medium to enhance packing between redox centers is harder, given all the other roles that the protein medium must play, than maintaining proximity between redox partners. Moving redox centers closer by just 1.7 \AA leads to an order of magnitude increase in the tunneling rate.

2.3.2 The FC Term

In Fermi's Golden Rule, FC represents the Franck–Condon weighted density of states. A Franck–Condon formulation is used because the more massive atomic nuclei remain in the same position as the relatively light electron tunnels from the

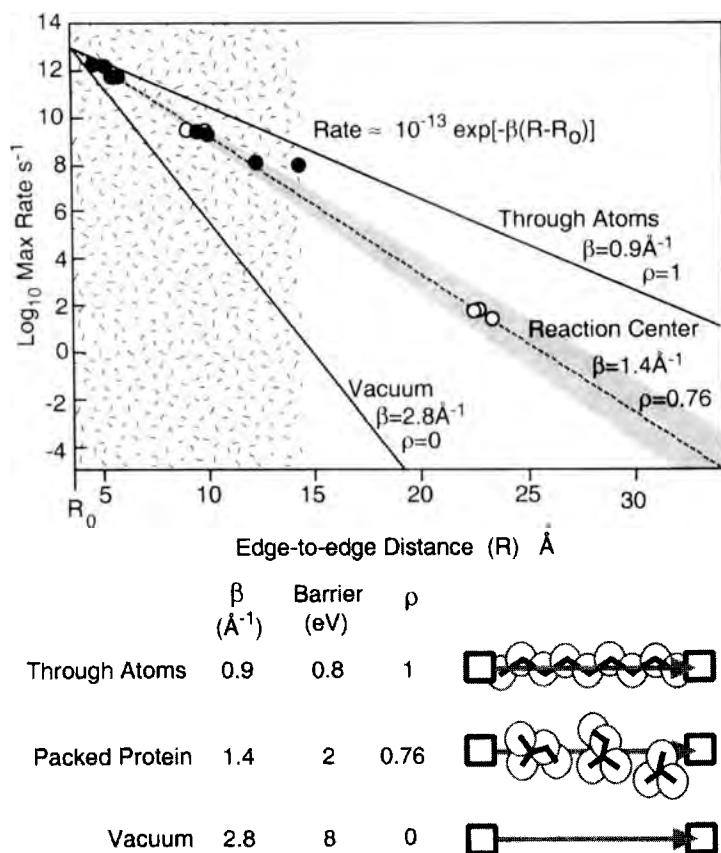


Figure 3. Electron tunneling falls off exponentially with the edge-to-edge distance between redox centers with a slope (β) that depends on the barrier height. The free energy optimized tunneling rate for productive (\bullet) and unproductive (\circ) electron transfers in photosynthetic reaction centers both lie near a $\beta = 1.4 \text{ \AA}^{-1}$, suggesting an effective barrier height near 2 eV. The barrier height for covalently bridged centers is smaller ($\beta \sim 0.9 \text{ \AA}^{-1}$ or 0.8 eV), while that expected for vacuum is larger ($\beta \sim 2.8 \text{ \AA}^{-1}$ or 8 eV). The β in protein can be viewed as an average of the β for atoms and vacuum reflecting the packing density (ρ) of atoms between the redox centers. The distance range for physiologically productive reactions is 4 to 14 \AA (vertical shading).

donor to acceptor. In addition, the electron must move from a donor state to an acceptor state of the same energy.

There are a number of ways to describe this FC term. An early way of describing the nuclear position and free energy-dependent FC term was proposed in Nobel prize-winning work by Marcus [9, 10]. Marcus approximated the reactant and product, before and after electron transfer, as simple harmonic oscillators with intersecting parabolic potential surfaces. As the driving force of the reaction increases and the product potential surface drops further down in energy, the barrier that must be crossed in going from the bottom of the reactant parabola to the bottom of

the product parabola initially gets smaller and smaller. Eventually, the two parabolas intersect at the bottom of the reactant parabola and there is no barrier. The electron transfer rate in this Marcus view has a Gaussian dependence on the free energy, with a maximum rate at the mean free energy, where the optimal driving force defines the reorganization energy λ . Counter-intuitively, after increasing the driving force to where the electron transfer rate reaches a maximum ($\lambda = -\Delta G$), overdriving the reaction actually slows the rate of electron transfer down (the Marcus inverted region).

Despite its utility at room temperature, simple Marcus theory cannot explain the DeVault and Chance experiment. All Marcus reactions have a conspicuous temperature dependence except in the region close to where $\Delta G = -\lambda$. Marcus theory does not predict that a temperature-dependent reaction will shift to a temperature-independent reaction as the temperature is lowered. Hopfield proposed a quantum enhancement of Marcus theory that would permit the behavior seen in the experiment [11]. He introduced a characteristic frequency of vibration ($\hbar\omega$) that is coupled to electron transfer, in other words, a vibration that distorts the nuclei of the reactant to resemble the product state. This quantum expression includes a hyperbolic cotangent (Coth) term that resembles the Marcus expression at higher temperatures, but becomes essentially temperature independent at lower temperatures. Other quantized expressions, such as a full quantum mechanical simple harmonic oscillator behavior [12] and that of Jortner [13], give analogous temperature behavior.

2.3.3 An Empirical Tunneling Expression with Quantized FC

The electron transfer reactions in the *Rb. sphaeroides* and *Rp. viridis* bacterial reaction centers have been extensively manipulated and measured. The structure, and hence distances between redox cofactors, are known. The free energy of many reactions have been modified systematically by either cofactor substitution or amino acid replacement, so that the free energy optimized rate can be estimated with some accuracy. Furthermore, a number of these reactions have also been studied as a function of temperature, revealing a more gentle temperature dependence than that predicted by simple Marcus theory. Thus, independent of the DeVault and Chance observations, we have a reason to use a quantized FC expression. To adopt a Hopfield-like FC expression, we need to choose an $\hbar\omega$, which is a difficult parameter to define experimentally. Nevertheless, a value somewhere around 0.05 to 0.07 eV seems appropriate for several biological reactions to give to following biological tunneling rate estimate [14]:

$$\log k_{et}^{exer} = 15 - 0.6R - 3.1(\Delta G + \lambda)^2/\lambda \quad (3)$$

In this expression, the rate is in units of s^{-1} , the edge-to-edge distance in Å, and the free energy ΔG and reorganization energy λ in units of eV. This room temperature expression is simple enough that it allows quick mental order of magnitude estimates of tunneling rates and often allows a prediction of the electron tunneling rate

for an unknown reaction, or an assessment of whether an observed rate is a tunneling rate or rate limited by some other, nontunneling reaction.

If the packing density (ρ) between redox cofactors is known (i.e., the fractional volume of the medium between the cofactors that is within the van der Waals radius of protein atoms), the value of β can be adjusted to reflect a higher or lower effective barrier to electron tunneling to improve the rate estimate [8]:

$$\log k_{et}^{exer} = 13 - (1.2 - 0.8\rho)(R - 3.6) - 3.1(\Delta G + \lambda)^2/\lambda \quad (4)$$

To extend this expression to any temperature means that we have to include an explicit $\hbar\omega$, the Boltzman constant k_B and absolute temperature (T) in the final Gaussian term for the Franck–Condon factor. The resulting expression is harder to solve in one's head, but can be useful.

$$\begin{aligned} \log k_{et}^{exer} = 13 - (1.2 - 0.8\rho)(R - 3.6) \\ - 0.22(\Delta G + \lambda)^2/(\lambda\hbar\omega\text{Coth}[\hbar\omega/2k_BT]) \end{aligned} \quad (5)$$

2.4 Devault and Chance's Prediction

Devault and Chance made rough estimates of some of the basic theoretical parameters and arrived at a predicted tunneling distance of about 30 Å. Subsequent resolution of the analogous RC structure in *Rp. viridis* [15] showed the heme to bacteriochlorophyll dimer (BChl₂) distance to be substantially correct, but in an unexpected way. The RC contained not one heme but four arranged in a near line extending away from the BChl₂ (Figure 4). We label these hemes Heme1, Heme2, etc. in order of distance from the BChl₂, although they are often known by their reduced alpha-band absorption maxima. As Devault and Chance lowered the temperature, the dominant heme that was oxidized by BChl₂⁺ shifted from the nearby Heme1 (*c*₅₅₉) to the low potential Heme2 (*c*₅₅₂). Even the more distant Heme3 (*c*₅₅₆) can be seen to participate in electron transfer in *Rp. viridis*.

The low-temperature kinetics data of these early difficult experiments did not have the time or spectral resolution to consider these possibilities. However, there is now an excellent set of temperature-dependent kinetics data for the similar bacterium *Rp. viridis* [16, 17]. These data clearly show multiphasic kinetics that can be resolved into very fast, fast and slow phases, most of which slow with temperature roughly an order of magnitude before reaching a temperature-independent plateau. What does change dramatically with temperature is the contribution of each of these phases, with the fast phases falling away dramatically at a temperature around 210 K for the wild-type *Rp. viridis*. Thus, the overall result is a dramatic decrease in half-time of the reaction with temperature, as Devault and Chance observed.

Several obvious questions are presented by this reinterpretation of the pioneering Devault and Chance experiments. First, why does Heme1 stop functioning as the

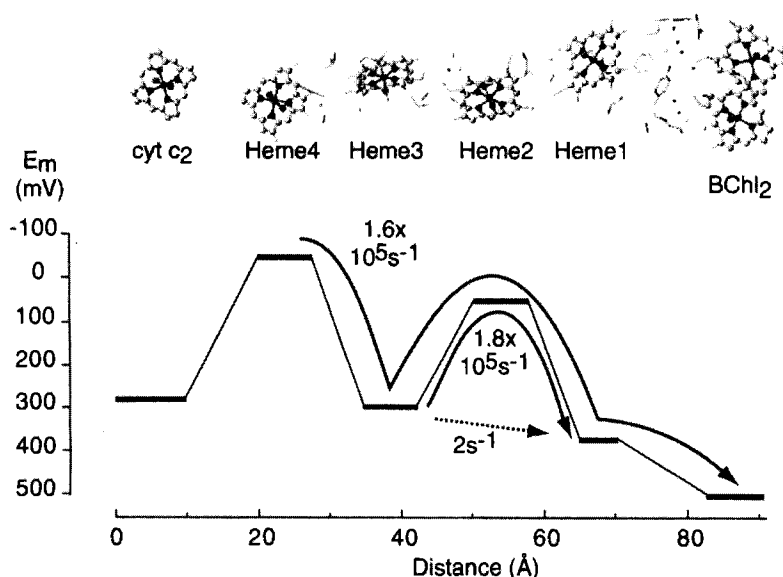


Figure 4. Electron transfer along the chain of *c* hemes in *Rhodospseudomonas viridis* is physiologically rapid, despite the more than 80 Å traversed through a series of endergonic and exergonic tunneling reactions. Rates from Heme4 to BChl_2^+ (solid curve) and rates from Heme3 directly to Heme1 (dashed line) or through Heme2 (solid curve) are calculated using the equations in the text.

temperature is lowered? It appears that the midpoint potential of Heme1 and BChl_2 are quite close. In the analogous *Rp. viridis*, the functional redox midpoint potentials (E_m) are even closer than the redox titration equilibrium values [17, 18] as the charges on the various hemes exert an electrostatic influence on one another. In whole cells, the transmembrane electric field seems to make the acting potential difference between BChl_2 and Heme1 even smaller [19]. The driving force for the reaction is apparently so small that changes in the environment (such as rearrangement of nearby water molecules) can make the driving force unfavorable on freezing, and eliminate the fast phase of the reaction.

What would happen if Heme1 did not freeze out? Mutants have been created in which the relatively fast ~ 200 -ns Heme1 oxidation does not freeze out and remains relatively temperature-insensitive down to cryogenic helium temperatures [20]. Thus, Hopfield's original reason for proposing a quantized Marcus expression in order to get a smooth transition over three orders of magnitudes between the temperature-dependent and temperature-independent regions appears to have been removed. Incidentally, these same mutants, together with their crystal structures and midpoint potential measurements [21], clearly show that numerous changes of an amino acid directly between Heme1 and BChl_2 (and presumably on any electron transfer "pathway" that might be drawn between them) have little effect on the electron tunneling rate. The changes that are observed can be easily understood in terms of small changes in distance, free energy, and packing. The wild-type amino

acid is not even the fastest and by no means “optimized” as a naïve view of natural selection might suggest.

If the dominant electron transfer at low temperature is from the considerably more distant Heme2 (24.6 Å), why is the rate as fast as a millisecond and not the 10- to 100-ms timescale typical for these distances, packing densities and driving forces (Eq. 3)? Furthermore, at moderate potentials when Heme1 and Heme3 are reduced but the much lower potential Heme2 in between is oxidized, how can Heme3 reduce photo-oxidized Heme1? To address these questions we need to look into the role of electron transfer chains in biological systems.

2.5 The Design of Natural Electron Transfer Chains

Chains of redox cofactors are commonly used to guide electron transfer through protein complexes and to and from catalytic sites. Many examples can be seen in Figure 1. The natural robust design of electron transfer proteins places redox centers close enough that the tunneling rates through the chains are rapid compared to the timescale of the catalytic turnover of the enzyme [8]. Thus, there is little selective pressure to have the redox potentials of members in a chain step evenly from low potential to high potential along the chain. Indeed, redox potentials can vary rather wildly up and down, as long as the overall electron transfer through the chain is modestly favorable. There are many examples from photosynthetic and respiratory redox chains and from enzymes [8].

To extend the empirical tunneling expressions above to consider endergonic reactions, we can assume for simplicity that the forward and reverse electron transfers can be related by a temperature and Boltzman constant-dependent equilibrium constant.

$$\log k_{et}^{ender} = \log k_{et}^{exer} - (\Delta G/RT) \log e \quad (6)$$

At room temperature, the $-(\Delta G/RT) \log e$ term slows the reaction by an order of magnitude for every approximately 60 mV. Although this equation may be conveniently used to provide a rate estimate for endergonic electron transfer, the equation may not always be a good approximation for reactions in which both the forward and reverse reactions are rate-limited by tunneling. Instead, the ratio of the forward and reverse reaction rates may be temperature-independent, as has been demonstrated in Tutton salts [22]. In this case it may be best simply to extend the exergonic equation into the endergonic region.

2.5.1 The High Potential Redox Cofactor Chain in *Rp. viridis*

The use of electron transfer chains enables living systems to transfer electrons rapidly between widely separated components, when transfer would be impossibly

slow by direct electron tunneling. Using the above equations, electron transfer from cytochrome c_2 interfacing with Heme4 of the *Rp. viridis* chain can reduce $\text{BChl}_2^+ \sim 60 \text{ \AA}$ away at the other end of the chain at $\sim 10^4 \text{ s}^{-1}$, compared to the direct tunneling rate which would take longer than the age of the universe. This is achieved despite the fact that the midpoint potentials of the intervening hemes are highly nonoptimized for this reaction: the electron has to scale two endergonic steps that are each more than 300 mV uphill. Nevertheless, the proximity of the redox centers in the chains allows this to be achieved robustly. Indeed, simulations indicate that long-distance electron transfer through the c heme chain would proceed at physiologically appropriate rates even after relatively dramatic changes in the zigzag potential profile found in the natural chain (Figure 5).

The situation is different at nonbiological cryogenic temperatures however. Consider the reaction from Heme3 to Heme1 and BChl_2^+ , which takes place in about 2 μs and represents up to one-third of the total heme oxidation after a single flash at room temperature in whole cells [19]. The reorganization energies for these reactions are not well measured, but we can make rate estimates using typical reorganization energies of around 0.7 to 0.8 eV. At room temperature, using Eq. 3, direct electron tunneling from Heme3 to Heme1 over 21.5 \AA is far too slow at 2 s^{-1} . Endergonic electron transfer from Heme3 to Heme2 over 8.1 \AA would be 40 μs , while the reverse exergonic reaction would be about 0.4 ns. Electron tunneling from Heme2 to Heme1 over 7.0 \AA would be about 50 ps. The overall solution of these coupled rates gives a room temperature characteristic time of Heme3 to Heme1 electron transfer of about 6 μs ; close to the observed value of 1.7 μs [17, 23–25]. Indeed, if the reported electrostatic coupling between oxidized Heme1 and Heme3 were to raise the nonequilibrium E_m of Heme2 by only 30 mV, the calculated and observed rates would be the same. At 245 K the exergonic rate from Heme2 to Heme1 will slow slightly (assuming a characteristic frequency of about 0.05 eV and a Gaussian FC expression akin to Hopfield [11]). But the endergonic rate from Heme3 to Heme2 will slow by a factor of 2.6 just because of the Boltzman term alone. Ortega and Mathis report a slowing from 1.7 μs to 6.3 μs , a factor of 3.7, entirely in line with the calculated value [17]. However, at cryogenic helium temperatures the endergonic rate penalty predicted from Eq. 6 would be too severe to allow rapid endergonic Heme3 to Heme2 to Heme1 electron tunneling. Now the direct Heme3 to Heme1 rate would dominate, with a calculated rate around 1 s^{-1} . This is difficult to observe experimentally in wild-type, however, because the low-temperature rise in Heme1 E_m removes it from participation at these temperatures.

On the other hand, the low-temperature tunneling from Heme2 to BChl_2 can be observed. At an edge-to-edge distance of about 24.6 \AA , even with a slightly better than average packing of 78 %, the half-time of tunneling at low temperature will be about 10 to 100 ms, depending on the choice of reorganization energy and the characteristic frequency $\hbar\omega$. This is significantly slower than the 1–2 ms observed rate (Figure 2). This suggests that when the Heme1 cofactor is prevented from its natural thermally activated participation, it falls back to the role of lowering the barrier for electron tunneling. A rise in the average packing from 78 % to 88 % would accelerate the tunneling rate to observed low-temperature values. Since Heme1 occupies roughly one-third of the distance span between Heme2 and BChl_2 ,

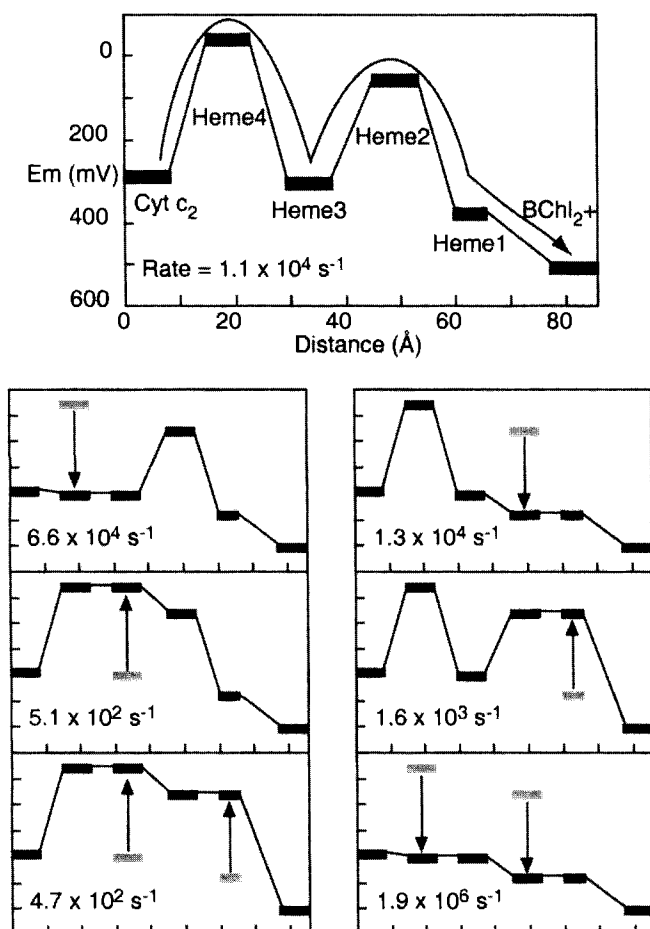


Figure 5. The robustness of long-distance electron transfer through the cytochrome *c* heme chain in *Rhodospseudomonas viridis* is apparent from the relative insensitivity to extensive changes in the redox midpoint potentials of the individual hemes along the chain. Using the equations described in the text, most cytochrome *c*₂ to BChl₂⁺ rates remain physiologically rapid as the zigzag potential profile is changed.

a β for the reduced Heme1 atoms of about $0.5\text{--}0.6 \text{ \AA}^{-1}$ (as opposed 0.9 \AA^{-1} for amino acid atoms) for an effective barrier height of about 0.3 eV would accomplish the appropriate rate acceleration.

While intervening but electrochemically incompetent hemes may lower the tunneling barrier compared to protein at cryogenic temperatures, we do not support a view in which heme-to-heme electron transfer is generally considered to be from iron center to center (13.9 \AA between Heme2 to Heme1 and 16.1 \AA between Heme1 and BChl₂) with a special β for electron transfer through the heme of 0.6 \AA^{-1} . Indeed, our preference for using macrocycle edge-to-edge distances in our tunneling

calculations comes from the success of this method in the majority of rate predictions in multiheme systems, including the *Rp. viridis* heme chain.

By distinguishing the intervening heme cofactor from the amino acid tunneling medium, we have a picture that resembles superexchange. Some apparently prefer to introduce a superexchange reaction rather than contemplate a significantly endergonic intermediate reaction, even at room temperature [26, 27]. In superexchange, electron transfer from donor to acceptor occurs in a single-step coherent mechanism that uses the intermediate redox center only as a virtual intermediate (although in this case the virtual intermediate would correspond to putting an extra electron on a heme that was already reduced). The rate of this tunneling mechanism is dependent on the electronic coupling of the donor and acceptor with this virtual intermediate and the energy gap between the real donor and acceptor states and the virtual intermediate state. Generally, superexchange through an intermediate protein redox center requires an unusually strong electronic coupling between redox centers. This is hard to achieve for redox centers separated by several angstroms. However, when the redox centers are within 5 Å, then endergonic electron transfer becomes a competing mechanism. There is no clear evidence of cofactor superexchange as a tunneling mechanism at physiological temperatures (although superexchange can become reasonable at cryogenic temperatures), and hence no clear evidence that natural selection exploits cofactor superexchange in the design of electron transfer systems.

2.5.2 The Low-Potential Chain in *Rp. viridis* and *Rb. sphaeroides*

By focusing on the DeVault and Chance observations, we have concentrated on describing the engineering of the donor side of the photosynthetic reaction centers. A redox chain is also responsible for the transfer of an electron from the excited BChl₂ to the ubiquinone acceptor on the low-potential side of the reaction center. While the overall engineering time constraint on the donor side is the typical micro- to millisecond time scale of most enzymatic k_{cat} values and intraprotein electron transfers in Mitchell's chemiosmotic system, the acceptor side faces the much more severe time constraint of the typically nanosecond decay rate of excited states. Thus, the initial photosynthetic charge separation after light excitation of the BChl₂ relies on even more closely spaced redox components and avoids large endergonic electron transfer reactions as the electron is guided to monomer BChl and bacteriopheophytin (BPh) on a timescale of 3 ps.

Reaction center design hits a relatively weak link at this point. The electron on BPh has several possible acceptors: the physiologically productive Q_A (10.0 Å distant and 0.6 eV in driving force in *Rb. sphaeroides*), and several physiologically unproductive reactions, including unproductive charge recombination by direct electron transfer between BPh⁻ and ground-state BChl₂⁺, which takes place over nearly the same distance as BPh⁻ to Q_A; equally unproductive back electron transfer through nearby BChl to BChl₂^{*} followed by radiative decay; as well as electron transfer to other redox centers such as the "inactive" BPh on the M side of the reaction center protein (16.5 Å and probably slightly endergonic). Of the 1.4 eV

of overall driving force delivered by the photon to BChl₂, relatively little (~ 0.2 eV) is consumed upon reducing BPh; however, reduction of Q_A by BPh expends about half of this energy. This assures that the FC factor for this reaction will be nearly optimal at about 200 ps. The similar distance BPh⁻ to ground state BChl₂⁺ has nearly 1.2 eV of driving force, and therefore should be within an inverted region of the Marcus relationship with a suboptimal FC factor. Under these conditions physiologically productive electron transfer takes place with 99 % efficiency.

However, if the distance between BPh and Q_A were just a few angstroms longer, or if the driving force of this reaction was several tenths of an eV larger or smaller, then the quantum efficiency of the reaction center would suffer as charge recombination became more common. On the other hand, if the driving force for the BPh⁻ to BChl₂⁺ ground-state reaction were *decreased*, then this inverted region reaction would accelerate and also lower the efficiency of productive charge separation. Experiments with reaction centers oriented in an external electric field provide some evidence that this is the case [28]. Moreover, shortening the distance between redox centers—usually a method of increasing robustness in electron transfer protein design—does not improve the robustness of this step in photosynthesis. Shortening this distance would indeed make BPh to Q_A electron transfer faster than BPh to BChl₂⁺ electron transfer, but at the cost of speeding up the reverse, Q_A⁻ to BChl₂⁺ electron transfer. The relatively long time that the electron resides on Q_A (microseconds) before electron transfer to Q_B means that this reverse endergonic reaction can become significant.

The near mirror symmetry of the low-potential chain components places BChl and BPh redox components on the M or “B” side of the reaction center, where they could interfere with normal charge separation. Using the tunneling equations described, the electron transfer rates between any and all of the redox centers in the reaction center can be simulated. The excited BChl₂^{*} is presented with two BChl monomers to accept the electron. Simply by lowering the M-side BChl monomer redox potential more than 100 meV below the BChl₂^{*} (see [29]) or significantly raising the reorganization energy of this M-side reaction to a more typical 0.5 to 0.7 eV, slows the wrong side rate sufficiently to avoid these unproductive reactions. If the wrong side BPh were to become reduced, it is always possible to have BPh to BPh electron transfer across the symmetry axis of the reaction center. However, at a distance of 16.5 Å, this low driving force reaction at about 0.3 ms will compete unfavorably with charge recombination to BChl₂⁺ unless it has been previously reduced by the *c* heme chain.

It appears that the blunt tool of natural selection has encouraged the proliferation of natural electron transfer proteins that are robust and can suffer the insults of mutation and genetic changes while still preserving significant function, and has removed designs that may be highly optimized but fragile. For the reaction center, dimerization has duplicated the low-potential chain of redox cofactors, but productive directional electron transfer down one branch appears to be relatively easily accomplished by mutations that break the symmetry and impose unfavorable Franck–Condon factors on the disfavored side. Electron transfer from the chlorins to the quinones seems to be a relatively clumsy reaction that maintains the high quantum efficiency of the reaction center at the price of consuming a large driving

force, which robs charge separation of some of its overall redox engineering efficiency. It may be that the robust function in *C. vinosum*—and especially in *Rp. viridis* where the long-wavelength-absorbing chlorophylls b make the chlorin to quinone energy gap relatively small—is assured by a counterbalancing highly robust high-potential heme chain, which fills the hole on BChl_2^+ to prevent wasteful back-reactions. This robustness, of course is one of the reasons that DeVault and Chance were able to make their ground-breaking observations more than three decades ago.

References

1. P. Mitchell, *Nature* 191 (1961) 144–148.
2. B. Chance, 2nd Int'l. Conf. Biochem. Abs. Paris (1952) 32.
3. P. L. Dutton, C. C. Moser, V. D. Sled, F. Daldal, T. Ohnishi, *Biochim. Biophys. Acta* 1364 (1998) 245–257.
4. D. DeVault, B. Chance, *Biophys. J.* 6 (1966) 825–847.
5. D. DeVault, *Q. Rev. Biophys.* 13 (1980) 387–564.
6. C. C. Moser, J. M. Keske, K. Warncke, R. S. Farid, P. L. Dutton, *Nature* 355 (1992) 796–802.
7. J. F. Smalley, S. W. Feldberg, C. E. D. Chidsey, M. R. Linford, M. D. Newton, Y. P. Liu, *J. Phys. Chem.* 99 (1995) 13141–13149.
8. C. C. Page, C. C. Moser, X. Chen, P. L. Dutton, *Nature* 402 (1999) 47–52.
9. R. A. Marcus, *J. Chem. Phys.* 24 (1956) 966–978.
10. R. A. Marcus, N. Sutin, *Biochim. Biophys. Acta* 811 (1985) 265–322.
11. J. J. Hopfield, *Proc. Natl. Acad. Sci. USA* 71 (1974) 3640–3644.
12. V. G. Levich, R. R. Dogonadze, *Doklady Akad. Nauk. SSSR* 124 (1959) 123–126.
13. J. Jortner, *J. Chem. Phys.* 64 (1976) 4860–4867.
14. C. C. Moser, P. L. Dutton, *Biochim. Biophys. Acta* 1101 (1992) 171–176.
15. H. Michel, J. Deisenhofer, O. Epp, *EMBO J.* 5 (1986) 2445–2451.
16. J. M. Ortega, P. Mathis, *FEBS Lett.* 301 (1992) 45–48.
17. J. M. Ortega, P. Mathis, *Biochemistry* 32 (1993) 1141–1151.
18. M. R. Gunner, B. Honig, *Proc. Natl. Acad. Sci. USA* 88 (1991) 9151–9155.
19. F. Baymann, F. Rappaport, *Biochemistry* 37 (1998) 15320–15326.
20. J. M. Ortega, B. Dohse, D. Oesterhelt, P. Mathis, *Biophys. J.* 74 (1998) 1135–1148.
21. B. Dohse, P. Mathis, J. Wachtveitl, E. Laussermair, S. Iwata, H. Michel, D. Oesterhelt, *Biochemistry* 34 (1995) 11335–11343.
22. A. P. Trapani, H. L. Strauss, *J. Am. Chem. Soc.* 111 (1989) 910–917.
23. R. J. Shopes, D. Holten, L. M. A. Levine, C. A. Wraight, *Photosynth. Res.* 12 (1987) 165–180.
24. D. Holten, M. W. Windsor, W. W. Parson, J. P. Thornber, *Biochim. Biophys. Acta* 501 (1978) 112–126.
25. S. M. Dracheva, L. A. Drachev, A. A. Konstantinov, A. Y. Semenov, V. P. Skulachev, A. M. Arutjunjan, V. A. Shuvalov, S. M. Zaberezhnaya, *Eur. J. Biochem.* 171 (1988) 253–264.
26. M. Bixon, J. Jortner, *J. Chem. Phys.* 89 (1988) 3392–3393.
27. M. Bixon, J. Jortner, M. E. Michelbeyerle, *Chem. Phys.* 197 (1995) 389–404.
28. C. C. Moser, R. J. Sension, A. Z. Szarka, S. T. Repinec, R. M. Hochstrasser, P. L. Dutton, *J. Chem. Phys.* 197 (1995) 343–354.
29. W. W. Parson, Z. T. Chu, A. Warshel, *Biochim. Biophys. Acta* 1017 (1990) 251–272.

3 Respiration: Cytochrome Oxidase

Bo G. Malmström

3.1 Introduction

Living organisms are chemical machines and, like all machines, are driven by energy. Ultimately, this energy is derived from the sun, the solar energy being captured in the processes of photosynthesis (see Volume III, Part 1, Chapters 1, 2). The immediate energy demand of all living cells is, however, satisfied by the breakdown of foodstuffs, which is coupled to the synthesis of ATP, the universal energy-storage molecule in living cells. In anaerobic organisms a limited amount of ATP is formed in the reactions of glycolysis, with the concomitant formation of NADH, the reduced form of the coenzyme of the oxidative enzymes of the glycolytic system. In aerobic organisms, from bacteria to humans, on the other hand, much more energy is derived from the oxidation of this NADH by molecular oxygen. This occurs in the respiratory chain, a series of electron transfer (ET) complexes firmly bound to the inner mitochondrial membrane in eukaryotes, or to the plasma membrane in bacteria. The ET complexes of the respiratory chain are shown in Figure 1, together with the ATP synthase. The ET reactions in these complexes—the names of which are given in the figure—are coupled to the translocation of protons from one side of the membrane to the other, and the electrochemical potential thus created is used to drive the synthesis of ATP in the ATP synthase complex, according to the chemiosmotic principle of Mitchell [1].

The terminal component of the respiratory chain is cytochrome *c* oxidase, which reduces dioxygen to two molecules of water. This cytochrome was discovered as the *Atmungsferment* by Warburg already in the 1920s and shown by him to be a heme protein in 1929 [2], an achievement for which he was awarded the Nobel Prize for Physiology or Medicine in 1931. The electron donor of the oxidase, cytochrome *c*, had been found earlier by Keilin (see [3]), as had one of the oxidase heme components, cytochrome *a*, whereas Keilin did not observe the dioxygen-reacting cytochrome *a*₃ until 1939. Keilin had before this discovery maintained that the oxidase is not a heme but a copper enzyme, and we now know that it also contains two

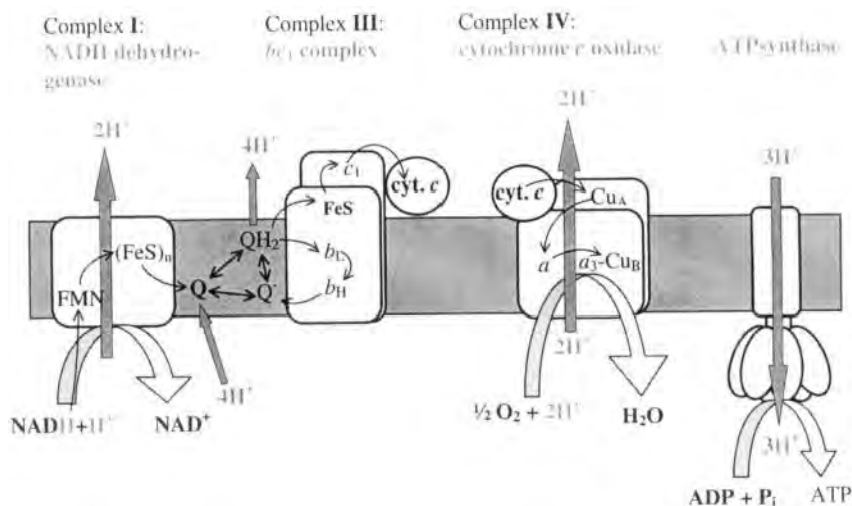


Figure 1. The respiratory chain of mitochondria.

copper sites, Cu_A and Cu_B (see [4] for recent reviews on cytochrome oxidase structure and function). The redox centers of the oxidase are $>10 \text{ \AA}$ apart, except for cytochrome *a*₃ and Cu_B, which form a bimetallic unit, and the focus of this chapter will be the intramolecular ET reactions between these centers and their coupling to proton transfer.

3.2 Structure of Cytochrome Oxidase

For a long time, research on long-range ET in the respiratory chain and other membrane-bound systems was severely hampered by the lack of detailed structural information. The first such system for which a high-resolution X-ray structure became available was a bacterial photosynthetic reaction center, determined by Deisenhofer et al. in 1985 [5], and this resulted in these investigators receiving a Nobel Prize for Chemistry in 1988. Michel and collaborators then attempted to obtain crystals of a bacterial cytochrome oxidase, and they published the structure of *Paracoccus* oxidase in *Nature* on 24 August 1995 [6]. A day later, the structure of bovine heart cytochrome oxidase was described in *Science* by the Yoshikawa group in Japan [7]. The structures of the three heaviest subunits of the bovine oxidase, which are remarkably similar to their bacterial counterparts, as well as the location of the cytochrome *c* binding site, are illustrated in Figure 2 (left). As can be seen, the redox centers are bound to the two heaviest of the three subunits, Cu_A in subunit II and cytochrome *a* as well as cytochrome *a*₃-Cu_B in subunit I. The spatial relationship between the redox centers is highlighted in Figure 2 (right). The two

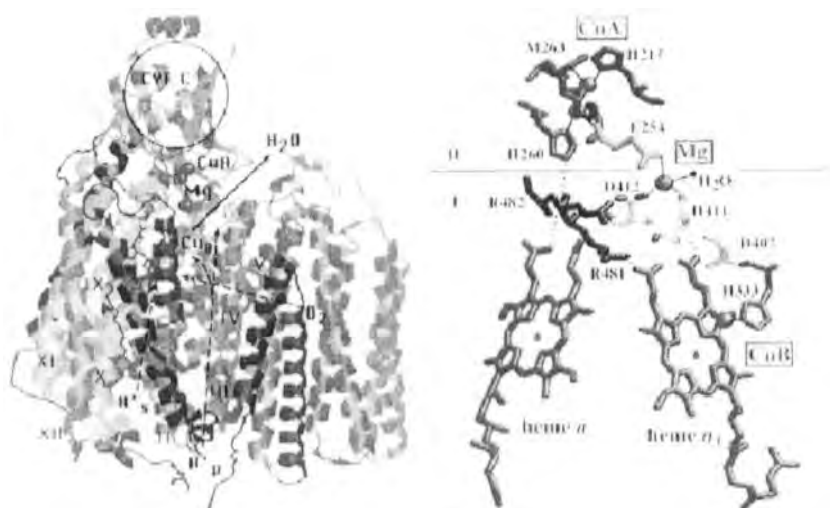


Figure 2. The crystal structure of the three heaviest subunits of cytochrome oxidase, with the binding site for cytochrome *c* indicated (left), and of the redox centers (right). From Ref. [4a], with permission.

hemes are almost equidistant from Cu_A (22.1 Å to cytochrome *a* and 19.5 Å to cytochrome *a*₃), and the heme–heme distance is 13.2 Å.

As can be seen in Figure 2, Cu_A is a binuclear unit, a point which for a long time was a controversial issue (see [8] for reviews). This unit has a single unpaired electron, which is completely delocalized over the two Cu ions and the bridging S atoms [9]. As will be discussed later (Section 3.4.1), the binuclear, delocalized nature of this site is important for its ET properties. Cytochrome *a* is a low-spin heme with two axial His ligands from separate transmembrane helices in subunit I. Cytochrome *a*₃ has one axial His from the same helix that provides one of the cytochrome *a* ligands, whereas the other axial site is free to interact, in its reduced form, with the dioxygen molecule. In the oxidized enzyme, cytochrome *a*₃ is anti-ferromagnetically coupled to Cu_B. In the structures it was, in addition, possible to discern putative proton pathways, which will be introduced later (Sections 3.3.2 and 3.4.4).

3.3 Methods for Studying Electron Transfer in Cytochrome Oxidase

The rates of the internal ET reactions between the redox sites, as well as that in the subunit II–cytochrome *c* ET complex, are all higher than the time resolution of the stopped-flow method ($\sim 10^3$ s⁻¹), so that more rapid techniques must be used to study these reactions. Generally, photochemical techniques involving a laser flash

have been employed (see [10] for reviews). The ET kinetics has usually been followed by changes in optical absorption of the redox centers in the visible (the cytochromes) or near-infrared (Cu_A) regions, but the dioxygen-reduction sequence has also been monitored by low-temperature electron paramagnetic resonance (EPR) [11] and resonance Raman [12].

3.3.1 Electron Injection into Cytochrome Oxidase

Even if pulse radiolysis has been used [13], most studies of the initial electron entry into cytochrome oxidase are based on the finding that at low ionic strength cytochrome *c* forms a strong electrostatic complex with the oxidase [14]. Cytochrome *c* itself cannot be photoactivated, but in the complex with the enzyme it can be reduced by photochemically generated radicals, such as that of 5-diazariboflavin [15]. Another approach has been to employ a photoinduced uroporphyrin/NADH reduction system [16].

More direct ET into the oxidase has been initiated photochemically with an artificial electron donor, tris(2,2'-bipyridyl)ruthenium [17], electrostatically bound to the enzyme, and with Ru-labeled cytochrome *c* [18]. An objection to these types of experiments is, of course, that they involve unnatural electron donors, whose site of interaction with the oxidase may be different from that of cytochrome *c* itself. This objection does not apply to experiments in which the strongly reducing triplet state of bound Zn-cytochrome *c* is generated photochemically to inject an electron into the oxidase [19], since this derivative of cytochrome *c* has the same structure and has been shown to bind to the same site as the native protein [20].

The electron exchange between cytochrome *c* and the oxidase can also be studied in experiments in which the fully reduced electrostatic complex is oxidized by O_2 in a flow-flash (see Section 3.3.3) experiment [21].

3.3.2 Flash Photolysis of Mixed-Valence Carboxycytochrome Oxidase

Incubation of oxidized cytochrome oxidase under an atmosphere of CO results in the formation of the so-called mixed-valence state, a form in which the cytochrome $a_3\text{-Cu}_B$ site is reduced and has bound CO, whereas cytochrome *a* and Cu_A remain oxidized [22]. The dissociation of the bound CO by flash photolysis in the absence of O_2 induces an electron backflow from the reduced cytochrome $a_3\text{-Cu}_B$ site to the oxidized redox centers, as first discovered by Boelens et al. [23] and later confirmed by Brzezinski and Malmström [24]. These authors thought that the electron acceptor is Cu_A , but later it has been shown [25] that both cytochrome *a* and Cu_A are sequentially reduced (see Section 3.4.2). In addition, it was found that oxidation of cytochrome a_3 causes deprotonation of an acid-base group in its vicinity [26], as will be discussed further in Section 3.4.4.

One basis for the technique described is the fact that the internal ET and the proton reactions are faster than CO recombination with reduced cytochrome a_3

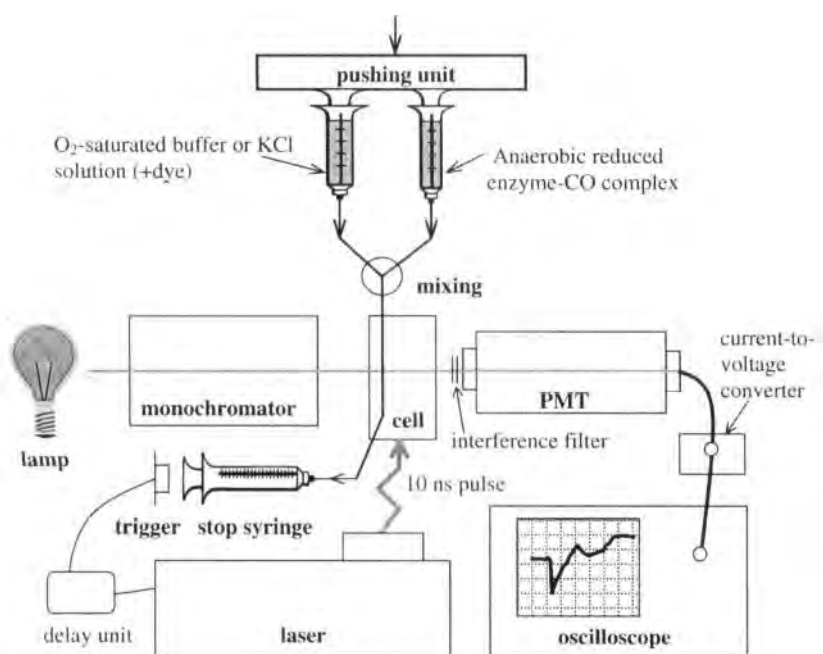


Figure 3. A flow-flash apparatus. PMT, photomultiplier tube.

[27]. The rebinding of CO shifts the ET and proton equilibria back to their original positions, which makes it possible to initiate the reactions repeatedly with a new laser flash. In this way, several kinetic traces can be averaged, which considerably improves the signal-to-noise ratio.

3.3.3 The Flow-Flash Technique: The Reduced Cytochrome Oxidase–Dioxygen Reaction

The method generally used for studying the reaction of reduced cytochrome oxidase with dioxygen is the flow-flash technique developed by Gibson and Greenwood [27a]. The experimental set-up used in the Göteborg laboratory is shown in Figure 3, and most modern flow-flash apparatus have this general design. In a flow-flash experiment, the mixed-valence enzyme or the fully reduced oxidase–CO complex is mixed with an O₂ solution in a stopped-flow apparatus. The mixing device fires a light flash after a short delay (50–200 ms), and this dissociates the bound CO and initiates the reaction with O₂, as illustrated for the fully reduced enzyme in Figure 4. The basis of the technique is the fact that O₂ binding is faster than CO recombination [27a]. The results from flow-flash experiments on ET and proton-transfer reactions involved in the reoxidation of reduced cytochrome oxidase by O₂ will be discussed in Sections 3.4.3 and 3.4.4.

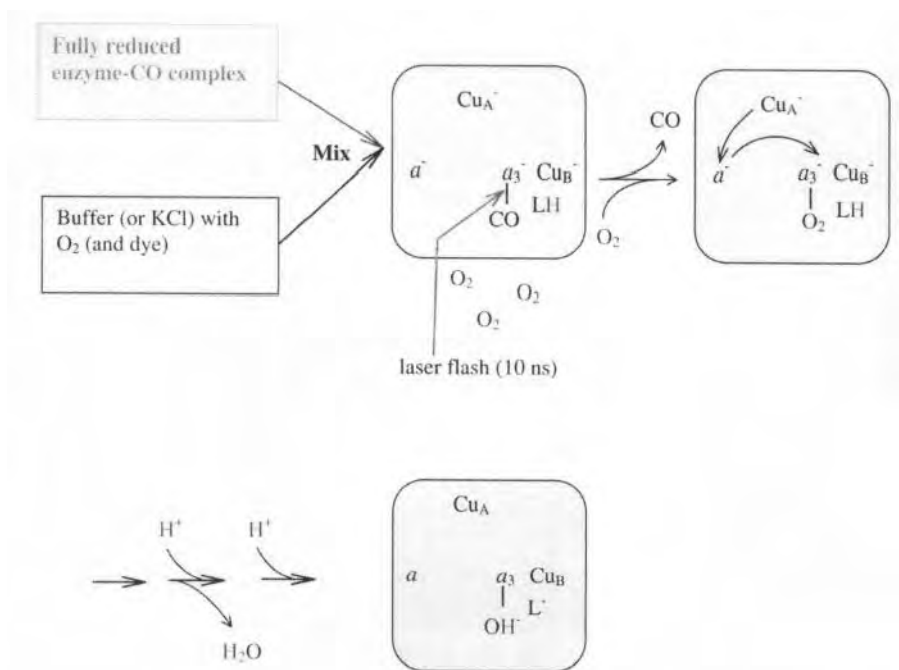


Figure 4. A flow-flash experiment with the fully reduced enzyme.

3.4 Electron Transfer Reactions in Cytochrome Oxidase

3.4.1 Reduction of the Initial Electron Acceptor

On the basis of stopped-flow experiments, it was long considered that the primary acceptor of an electron from cytochrome *c* is cytochrome *a* [27b, 28], but it was recognized early on that Cu_A is also rapidly reduced [29]. In a study of the reaction of the reduced cytochrome *c*-cytochrome oxidase complex with dioxygen, Hill concluded that Cu_A is actually the primary electron acceptor [21], and this conclusion was supported by experiments with external electron donors [15, 16a, 17], with Ru-modified cytochrome *c* [18] and with Zn-cytochrome *c* [19]. Cu_A as the primary electron acceptor could be reconciled with the earlier stopped-flow results implicating cytochrome *a*, because there was found to be a rapid redox equilibrium between Cu_A and cytochrome *a* [13, 25, 30] ($\sim 10^4$ s⁻¹; see Section 3.4.2). In addition, cytochrome *a* in the oxidized enzyme has a higher reduction potential than Cu_A [31], so that the addition of a single electron in a stopped-flow experiment results in a larger degree of reduction of cytochrome *a* compared to Cu_A.

The conclusion that Cu_A is the primary acceptor of electrons from cytochrome *c* is supported by work with small, soluble Cu_A domains, consisting of only the C-terminal, solvent-exposed portion of subunit II [32]. The Cu_A sites in these domains

can be rapidly reduced by external electron donors [33] as well as by cytochrome *c* itself [32a, 33] or by Zn-cytochrome *c* [19].

The rate of electron entry into the Cu_A site in electrostatic complexes with cytochrome oxidase has been found to be $\sim 10^5 \text{ s}^{-1}$ with an artificial electron donor [17] as well as with Ru-modified cytochrome *c* [18] or with Zn-cytochrome *c* [19]. An equally high rate was also observed with native cytochrome *c* in the experiments with the oxidation by dioxygen of the complex with the reduced oxidase [21]. Such a high rate could only be obtained at the low driving force involved ($\sim 30 \text{ meV}$), if the reorganization energy (λ) for ET is very small [34]. The fact that the rate is not even higher with Zn-cytochrome *c*, despite a 1-eV higher driving force, was attributed [19] to the reaction being in the Marcus inverted region [34]. It has been shown [35] that a small λ is a result of the mixed-valence, delocalized nature of the binuclear Cu_A site. Mutagenesis work producing a localized binuclear [36] or a mononuclear Cu site [37] has demonstrated that the unique structure of the native site is, in fact, essential for rapid reduction by cytochrome *c*.

Electron entry from cytochrome *c* into the oxidase undoubtedly involves its exposed heme edge. This is surrounded by four lysyl residues [38], which are involved in electrostatic binding to a negative patch of aspartate and glutamate residues on the extramembranous domain of subunit II, as has been demonstrated by site-directed mutagenesis [39]. One of the acidic residues (Asp178) in this negative patch is located in a loop just above one of the Cu_A ligand histidines (His181) in the structure of the *Paracoccus* oxidase [6], as can be seen in the detailed structure of the Cu_A site shown in Figure 5, and a corresponding Asp residue is also found in a number of engineered Cu_A domains [32], including two with their X-ray structures determined [40]. This suggests an obvious ET pathway from the heme of cytochrome *c* to the binuclear Cu_A site.

3.4.2 Internal Electron Transfer Reactions

Flash photolysis of the mixed-valence cytochrome oxidase–CO compound leads to a drop in the apparent reduction potential of cytochrome *a*₃, and this results in a backflow of electrons from cytochrome *a*₃ to the other redox sites. Three kinetic phases can be observed [26, 41], with relaxation rate constants (i.e., the sum of the rate constants for the forward and reverse reactions of the equilibria involved) of 3×10^5 , 2×10^4 , and $\sim 10^3 \text{ s}^{-1}$. The first two phases involve ET $a_3 \rightarrow a$ and $a \rightarrow \text{Cu}_A$, respectively; the third phase is strongly pH-dependent and represents further electron re-equilibration between *a*₃ and *a*, following the dissociation of a proton caused by the initial oxidation of *a*₃ [26, 41a], as will be further discussed in Section 3.4.4. Direct electron equilibration between *a*₃ and Cu_A is not observed.

The normal forward ET reactions in the turnover of cytochrome oxidase, $\text{Cu}_A \rightarrow a$ and $a \rightarrow a_3$, can be calculated to have rate constants of 1.2×10^4 and $2 \times 10^5 \text{ s}^{-1}$. Thus, the electron transfer steps per se may not provide any limitation on the turnover rate but rather their coupling to other reactions, such as proton transfers (Section 3.4.4) or conformational changes. The λ values associated with the two internal ET reactions have been estimated to be 0.3 and 0.76 eV, respec-

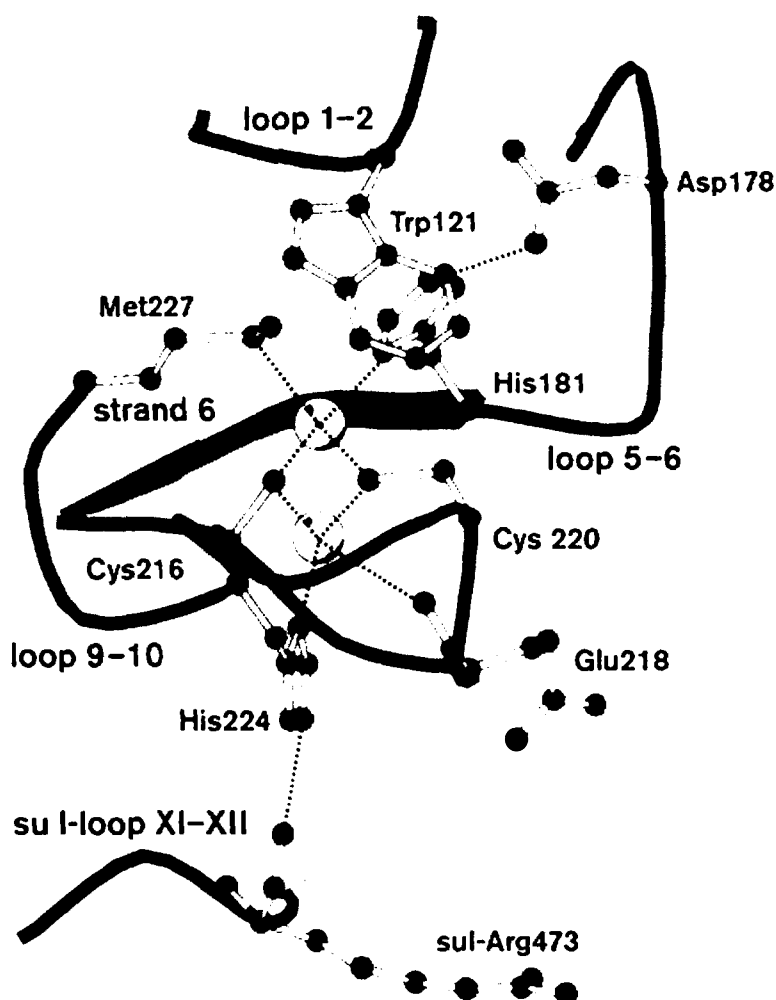


Figure 5. The Cu_A site of subunit II with the loop providing the ligands and the connection to subunit I. From Ref. [4b], with permission.

tively [41a, 42]. The first value emphasizes again (cf. Section 3.4.1) that the inner λ associated with the reduction of Cu_A must be very small; it can be noted that extended x-ray absorption fine structure (EXAFS) spectroscopic measurements have shown that the structural changes on reduction are minimal [43]. The major part of the higher value of λ for the $a \rightarrow a_3$ ET must be associated with a_3 , which may be related to the fact that the dioxygen-reducing site is available to the solvent via proton pathways (see Section 3.4.4).

The crystal structures clearly suggest pathways for electron tunneling between the redox centers of cytochrome oxidase, as illustrated in Figure 6 [44]. It may first be noted that an electron from cytochrome *c* must enter the Cu_A site from a binding

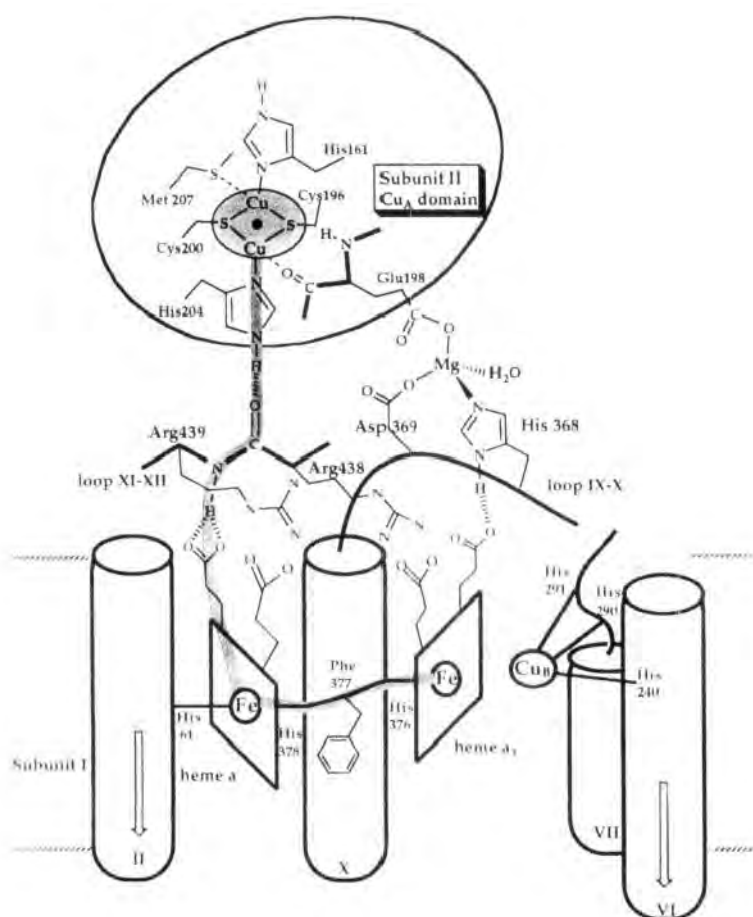


Figure 6. Part of the structure of subunits I and II showing the ET pathways. From Ref. [44], with permission.

site above the ligand His161 (see Section 3.4.1), whereas it will leave it via a pathway starting with the ligand His204 (the numbering is here that for the bovine enzyme). The necessity of different pathways for entering and leaving the initial electron acceptor may be one additional reason, besides the lowered reorganization energy (Section 3.4.1), for this being a binuclear Cu site rather than a blue copper, to which it is otherwise related; the electronic delocalization over the entire site effectively reduces the tunneling distance.

The internal ET reactions in cytochrome oxidase have recently been subjected to a detailed pathway analysis [45]. The pathway for the Cu_A → *a* ET starts with a hydrogen bond between His204 and a carbonyl group in a loop of subunit I (Figure 6). The total pathway comprises 14 covalent bonds and two H bonds, corresponding to an effective tunneling length of 25.2 Å, and an activationless rate of

$9 \times 10^5 \text{ s}^{-1}$ was estimated. As the driving force for the reaction is only 90 meV, λ must be small to achieve the experimentally observed rate of $1.2 \times 10^4 \text{ s}^{-1}$, and a value as low as 0.3 eV has been estimated, as already discussed. All potential $\text{Cu}_A \rightarrow a_3$ tunneling pathways are so long (tunneling lengths of 30.8–33.6 Å) that they would give rates several orders of magnitude lower than the rate for the $\text{Cu}_A \rightarrow a$ ET. This explains, why $\text{Cu}_A \rightarrow a_3$ ET is not observed, despite the fact that the distances from Cu_A to the two hemes differ only slightly (22.1 and 19.5 Å, respectively).

There are three almost equivalent pathways for the $a \rightarrow a_3$ ET reaction [45], all going through the ligand histidines of the two hemes (His378 and His376). The one shown in Figure 6 utilizes the single residue (Phe377) between these histidines, and it comprises 16 covalent bonds, corresponding to a tunneling length of 22.4 Å. The estimated activationless rate is $7 \times 10^6 \text{ s}^{-1}$, and a λ of 0.44 eV would give the experimentally observed relaxation rate of $3 \times 10^5 \text{ s}^{-1}$; this λ value is somewhat lower than the value estimated from the temperature dependence of the rate [42] (see above).

3.4.3 The Reduction of Dioxygen

The sequence of reactions in which dioxygen is reduced to two molecules of water by four electrons, entering cytochrome oxidase one at a time from cytochrome c , must necessarily involve a number of partially reduced oxygen intermediates. Information about such species has mainly been derived from flow-flash experiments with the fully or partially reduced oxidase (Section 3.3.3), but some of these oxygen species have also been generated artificially by the addition of H_2O_2 to the oxidized enzyme [46]. Early evidence for oxygen intermediates was obtained by Wikström [47] in experiments in which the electron flow in mitochondria was reversed by an electrochemical potential across the membrane. Detailed reviews on the oxygen chemistry in cytochrome oxidase are available [4a,b, 48], and an outline of the reactions involved is given in Figure 7.

When O_2 reacts with the fully reduced cytochrome oxidase (R in Figure 7), a ferrous-oxy intermediate at cytochrome a_3 forms in a second-order reaction with a rate constant of $10^8 \text{ M}^{-1} \text{ s}^{-1}$ [49]. The rate saturates, however, at high concentrations of O_2 [50], indicating initial binding to another site prior to heme binding, and there is evidence that this site is reduced Cu_B [49b, 51]. The ferrous-oxy species was first observed at low temperatures by Chance et al. [11a] and named compound A (see Figure 7). It has also been observed by resonance-Raman spectroscopy [12b–d].

Compound A is converted to the P intermediate concomitantly with the oxidation of cytochromes a and a_3 (Figure 7) at a rate of $3.5 \times 10^4 \text{ s}^{-1}$ [49a, 52]. Even if P is shown as a peroxide (hence its name), the actual structure of this species is still a matter of debate. It has been suggested to be ferryl ($\text{Fe}^{4+}=\text{O}^{2-}$) cytochrome a_3 [53], but the fact that P is formed also in the reaction of the two-electron reduced enzyme with O_2 [52c, 54] speaks against this. As alternatives Fe^{5+} [55], Cu_B^{3+} [46a] or even a protein radical [46c,d, 56] have been proposed. It has been reported [46a,d] that no correlation exists between the radical EPR signal and the concentration of any intermediate, including P, but it should be noted that a radical was first observed in

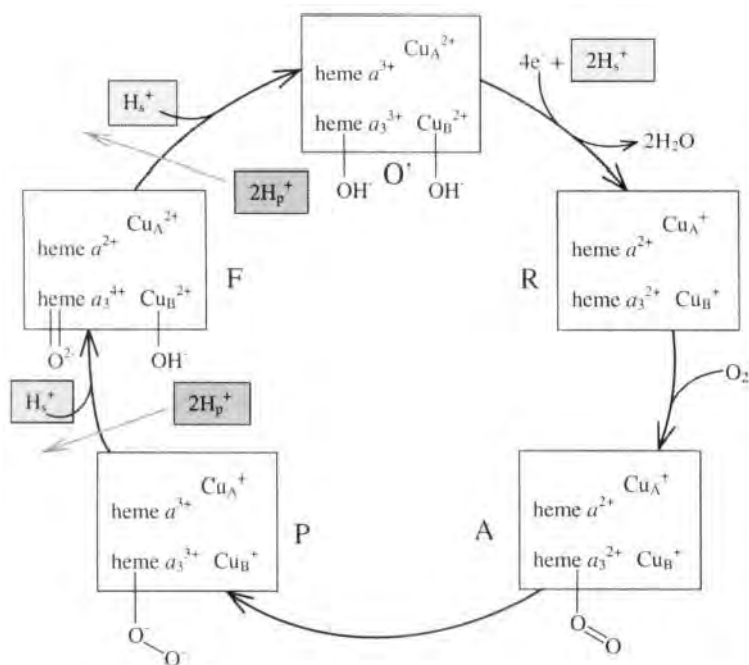


Figure 7. The catalytic cycle of cytochrome oxidase.

experiments, in which intermediates were trapped during turnover by rapid-freeze techniques [57]. In addition, a protein radical is also formed, when the mixed-valence oxidase reacts with O_2 [56]. Isotope-labeling experiments have clearly shown that the observed EPR signal is associated with a tyrosine radical [46d], most likely Tyr244 (bovine numbering), which is covalently linked to the Cu_B ligand His240 [58].

As just discussed, reactions with H_2O_2 can be used to generate P [46], but recently it has been shown that a species ($\text{Fe}^{4+}=\text{O}^{2-}$, Cu_B^+) is formed, when the mixed-valence enzyme reacts with H_2O_2 [59], and this species is not an intermediate in the reaction of the fully or partially reduced oxidase with O_2 . It may, however, become useful for investigations of the role of Cu_B in the proton-pump mechanism, since it has this ion reduced.

The conversion $\text{P} \rightarrow \text{F}$ (Figure 7) is accompanied by an electron equilibration between Cu_A and cytochrome a , and its rate is pH-dependent [60] and displays a kinetic isotope effect in D_2O [60b]. Consequently, it has been suggested [51, 60a,c] that the formation of F is controlled by the protonation of the binuclear site. The conclusion that F really is a ferryl ion intermediate is supported by resonance-Raman measurements [61].

In the final phase of the dioxygen reaction, cytochrome a donates an electron to F with the concomitant uptake of a proton [60] (Figure 7), and the fully oxidized enzyme is formed [52b, 60b,d]. This has at least one OH^- bound at the binuclear center [61, 62]. Like the previous step ($\text{P} \rightarrow \text{F}$), the rate of formation of O is sug-

gested to be limited by proton transfer [60b]. It has been reported [47b, 63] that the $P \rightarrow F$ and $F \rightarrow O$ transitions are the only steps in the entire catalytic cycle that are coupled to proton translocation, but this has been questioned [64]. In addition, recent work by the Wikström group [65] also gives a more complex picture. The energy for proton translocation is harnessed during the O_2 -reduction phase, but only half of it is utilized for proton pumping during the oxidation of the reduced enzyme; the other half is released, when the O_2 -oxidized enzyme is re-reduced.

3.4.4 Coupling between Electron and Proton Transfer

A revelation in the crystal structure of the *Paracoccus* cytochrome oxidase [6] was the identification of two possible proton pathways, now commonly called the K- and the D-pathways, leading from the proton uptake side of the membrane to the binuclear center, as illustrated in Figure 8; there were also indications, although less clear, of a proton-exit pathway (Figure 8). Putative proton pathways were also identified in the bovine oxidase [66], with some similarities to the proposed pathways in the bacterial oxidase. Originally, the D-pathway was assigned to translocated protons and the K-pathway to substrate protons (protons consumed in dioxygen reduction) [6], but later site-directed mutagenesis experiments of the residues shown

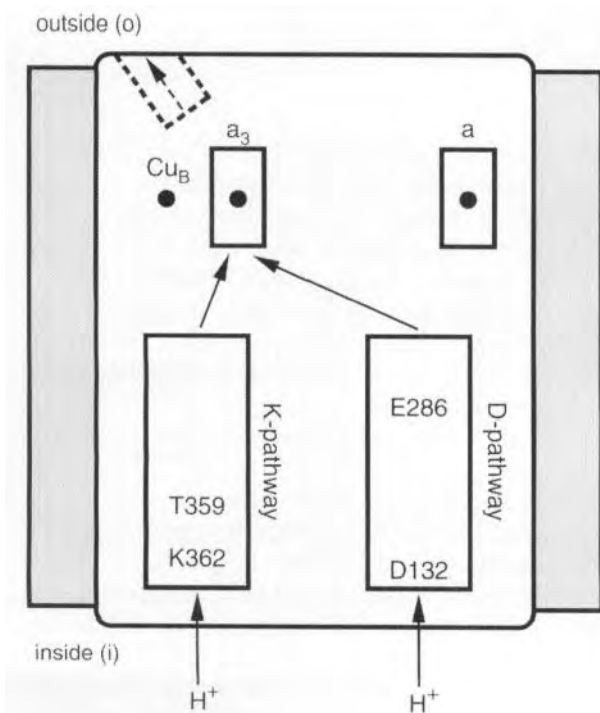


Figure 8. Schematic view of possible proton transfer pathways in subunit I.

in Figure 8 (K362, T359, D132 and E286) [67] forced a revision of this assignment. The present picture is one in which the two channels are used for different parts of the catalytic cycle (see [4b]). Thus, the K-pathway is used solely for proton uptake coupled to the initial reduction of cytochrome a_3 -Cu_B, whereas the D-pathway is used for the proton uptake in the $P \rightarrow F$ and $F \rightarrow O$ transitions. However, substrate protons also use the D-pathway during these steps.

The identity of the group in the vicinity of cytochrome a_3 , which releases a proton on oxidation of this heme (see Figure 4), as concluded from electron-backflow experiments with the mixed-valence oxidase [26, 41a] (see Section 3.4.2), is not known, but it has been suggested to be OH⁻ coordinated to the metal [26]. This could also be the group which, when protonated, was found to stabilize the reduced form of cytochrome a_3 in the normal, forward reaction [68]. The redox state of this center is, however, not always controlled in such a direct manner. For example, ET $a \rightarrow a_3$ in the $P \rightarrow F$ transition is prevented before a proton is taken up, because this is necessary for the Cu_A $\rightarrow a$ ET (60b, 69).

The uptake of protons via the D-pathway has been proposed to be facilitated by a hydrogen-bonded network of H₂O molecules, forming a proton wire [70]. However, even at high resolution, only one ordered H₂O molecule is seen [58, 71]. The proton-exit pathway has not been definitely identified, but recent experiments with mutations in arginine residues (R438 and R439; bovine enzyme numbering) with the related cytochrome bo_3 [72] suggest that it starts with the propionate side chain of the cytochrome a_3 heme group. This, in its anionic form, is proposed to accept a proton from E242 in a continuation of the D-pathway and then donate it to the arginine residues in the exit pathway.

3.5 Concluding Remarks

The reason for the great interest in the ET processes in cytochrome oxidase is ultimately to understand how these are coupled to proton pumping. Even if a good deal is known about the coupling between ET and proton transfer in the enzyme (Section 3.4.4), mechanisms for the proton pump remain largely hypothetical. In principle, two types of pump mechanisms can be envisaged: 1) Indirect-coupling mechanisms, in which the proton binding occurs at a site separate from the redox change and is mediated by redox-coupled conformational changes; and 2) direct-coupling mechanisms, in which the proton-binding group is directly associated with a redox center. Redox-linked conformational changes have been found in a crystal-structure study with the bovine enzyme [58], and subtle structural changes have also been observed in the bacterial oxidase by Fourier transform-infra-red (FT-IR) spectroscopy [73]. Most investigators favor direct-coupling mechanisms, however. One such mechanism, named the histidine cycle [74], involves dissociation and protonation of one of the histidine ligands to Cu_B. Recent crystallographic data show, however, that Cu_B does not change ligation on reduction [75]. Michel [64] has

proposed a radically different type of mechanism, largely based on considerations of electrostatic interactions [76], but continued exchanges in the literature [77] demonstrate that a consensus on pump mechanism has not been achieved. A challenging task for future research will be to move pump mechanisms from the realm of hypotheses to concrete reality.

Acknowledgments

I would like to thank Dr. Pia Ädelroth for useful discussions and for providing Figure 1, 3, 4 and 7; I am also indebted to Mr. Johan Leckner for preparing Figure 8. My own work has been supported by the Nobel Institute for Chemistry.

References

1. P. Mitchell, *Nature* **1961**, *191*, 144–148.
2. O. Warburg, E. Negelein, *Biochem. Z.* **1929**, *214*, 64–100.
3. D. Keilin, *The History of Cell Respiration and Cytochrome*, The University Press, Cambridge, 1966.
4. (a) S. Ferguson-Miller, G.T. Babcock, *Chem. Rev.* **1996**, *96*, 2889–2907; (b) H. Michel, J. Behr, A. Harrenga, A. Kannt, *Annu. Rev. Biophys. Biomol. Struct.* **1998**, *27*, 329–356; (c) C. Ostermeier, S. Iwata, H. Michel, *Curr. Opin. Struct. Biol.* **1996**, *6*, 460–466.
5. J. Deisenhofer, O. Epp, K. Miki, R. Huber, H. Michel, *Nature* **1985**, *318*, 618–624.
6. S. Iwata, C. Ostermeier, B. Ludwig, H. Michel, *Nature* **1995**, *376*, 660–669.
7. T. Tsukihara, H. Aoyama, E. Yarnashita, T. Tornizaki, H. Yarnaguchi, K. Shinzawa-Itoh, R. Nakashima, R. Yaono, S. Yoshikawa, *Science* **1995**, *269*, 1069–1074.
8. (a) H. Beinert, *Eur. J. Biochem.* **1997**, *245*, 521–532; (b) P. Lappalainen, M. Saraste, *Biochim. Biophys. Acta* **1994**, *1187*, 222–225; (c) B.G. Malmström, R. Aasa, *FEBS Lett.* **1993**, *325*, 49–52.
9. (a) J.A. Farrar, F. Neese, P. Lappalainen, P.M.H. Kroneck, M. Saraste, W.G. Zumft, A.J. Thomson, *J. Am. Chem. Soc.* **1996**, *118*, 11501–11514; (b) M. Karpefors, C.E. Slutter, J.A. Fee, R. Aasa, B. Källebring, S. Larsson, T. Vännegård, *Biophys. J.* **1996**, *71*, 2823–2829; (c) C. Luchinat, A. Soriano, K. Djinnovic-Carugo, M. Saraste, B.G. Malmström, I. Bertini, *J. Am. Chem. Soc.* **1997**, *119*, 11023–11027.
10. (a) J.R. Winkler, B.G. Malmström, H.B. Gray, *Biophys. Chem.* **1995**, *54*, 199–209; (b) R.E. Sharp, S.K. Chapman, *Biochim. Biophys. Acta* **1999**, *1432*, 143–158.
11. (a) B. Chance, C. Saronio, J.S. Leigh, Jr., *J. Biol. Chem.* **1975**, *250*, 9226–9237; (b) G.M. Clore, L.-E. Andréasson, B. Karlsson, R. Aasa, B.G. Malmström, *Biochem. J.* **1980**, *185*, 155–167.
12. (a) G.T. Babcock, J.M. Jean, L.N. Johnston, G. Palmer, W.H. Woodruff, *J. Am. Chem. Soc.* **1984**, *106*, 8305–8306; (b) S. Han, Y.-C. Ching, D.L. Rousseau, *Proc. Natl. Acad. Sci. USA* **1990**, *87*, 2491–2495; (c) T. Ogura, S. Takahashi, K. Shinzawa-Itoh, S. Yoshikawa, T. Kitagawa, *J. Am. Chem. Soc.* **1990**, *112*, 5630–5631; (d) C. Varotsis, W.H. Woodruff, G.T. Babcock, *ibid.* **1989**, *111*, 6439–6440.
13. K. Kobayashi, H. Une, K. Hayashi, *J. Biol. Chem.* **1989**, *264*, 7976–7980.
14. B. Michel, H.R. Bosshard, *J. Biol. Chem.* **1984**, *259*, 10085–10091.
15. L.-P. Pan, J.T. Hazzard, J. Lin, G. Tollin, S.I. Chan, *J. Am. Chem. Soc.* **1991**, *113*, 5908–5910.
16. (a) R.W. Larsen, J. R. Winkler, S.I. Chan, *J. Phys. Chem.* **1992**, *96*, 8023–8027; (b) M.H.B. Stowell, R.W. Larsen, J. R. Winkler, D.C. Rees, S.I. Chan, *J. Am. Chem. Soc.* **1993**, *97*, 3054–3057.
17. T. Nilsson, *Proc. Natl. Acad. Sci. USA* **1992**, *89*, 6497–6501.

18. L.P. Pan, S. Hibdon, R.-Q. Liu, B. Durham, F. Millett, *Biochemistry* **1993**, 32, 8492–8498.
19. P. Brzezinski, M. Sundahl, P. Ädelroth, M.T. Wilson, B. El-Agez, P. Wittung, B.G. Malmström, *Biophys. Chem.* **1995**, 54, 191–197.
20. J.M. Vanderkooi, M. Erecinska, *Eur. J. Biochem.* **1975**, 60, 199–207.
21. B.C. Hill, *J. Biol. Chem.* **1991**, 266, 2219–2226.
22. (a) P. Brzezinski, B.G. Malmström, *FEBS Lett.* **1985**, 187, 111–114; (b) C. Greenwood, M.T. Wilson, M. Brunori, *Biochem. J.* **1974**, 137, 205–215.
23. R. Boelens, R. Wever, B.F. van Gelder, *Biochim. Biophys. Acta* **1982**, 682, 264–272.
24. P. Brzezinski, B.G. Malmström, *Biochim. Biophys. Acta* **1987**, 894, 29–38.
25. M. Oliveberg, B.G. Malmström, *Biochemistry* **1991**, 30, 7053–7057.
26. S. Hallén, P. Brzezinski, B.G. Malmström, *Biochemistry* **1994**, 33, 1467–1472.
27. (a) Q.H. Gibson, C. Greenwood, *Biochem. J.* **1963**, 86, 541–554; (b) Q.H. Gibson, C. Greenwood, D.C. Wharton, G. Palmer, *J. Biol. Chem.* **1965**, 240, 888–894.
28. (a) L.-E. Andréasson, *Eur. J. Biochem.* **1975**, 53, 591–597; (b) L.-E. Andréasson, B.G. Malmström, C. Strömberg, T. Vännegård, *FEBS Lett.* **1972**, 28, 297–301.
29. (a) T.M. Antalís, G. Palmer, *J. Biol. Chem.* **1982**, 257, 6194–6206; (b) C. Greenwood, T. Brittain, M.T. Wilson, M. Brunori, *Biochem. J.* **1976**, 157, 591–598; (c) M.T. Wilson, C. Greenwood, M. Brunori, E. Antonini, *ibid.* **1975**, 147, 145–153.
30. J.E. Morgan, P.M. Li, D.-J. Jang, M.A. El-Sayed, S.I. Chan, *Biochemistry* **1989**, 28, 6975–6983.
31. D.F. Blair, W.R. Ellis, Jr., H. Wang, H.B. Gray, S.I. Chan, *J. Biol. Chem.* **1986**, 261, 11524–11537.
32. (a) P. Lappalainen, R. Aasa, B.G. Malmström, M. Saraste, *J. Biol. Chem.* **1993**, 268, 26416–26421; (b) C.E. Slutter, D. Sanders, P. Wittung, B.G. Malmström, R. Aasa, J.H. Richards, H.B. Gray, J.A. Fee, *Biochemistry* **1996**, 35, 3387–3395; (c) C. von Wachenfeldt, S. de Vries, J. van der Oost, *FEBS Lett.* **1994**, 340, 109–113.
33. C.E. Slutter, R. Langen, D. Sanders, S.M. Lawrence, P. Wittung, A.J. Di Bilio, M.G. Hill, J.A. Fee, J.H. Richards, J.R. Winkler, B.G. Malmström, *Inorg. Chim. Acta* **1996**, 243, 141–145.
34. R.A. Marcus, N. Sutin, *Biochim. Biophys. Acta* **1985**, 811, 265–322.
35. S. Larsson, B. Källebring, P. Wittung, B.G. Malmström, *Proc. Natl. Acad. Sci. USA* **1995**, 92, 7167–7171.
36. V. Zickermann, M. Verkhovsky, J. Morgan, M. Wikström, S. Anemüller, E. Bill, G.C.M. Steffens, B. Ludwig, *Eur. J. Biochem.* **1995**, 234, 686–693.
37. F. Malatesta, N. Flavia, V. Zickermann, B. Ludwig, M. Brunori, *FEBS Lett.* **1998**, 434, 322–324.
38. W.H. Koppenol, E. Margoliash, *J. Biol. Chem.* **1982**, 257, 4426–4437.
39. (a) P. Lappalainen, N.J. Watmough, C. Greenwood, M. Saraste, *Biochemistry* **1995**, 34, 5824–5830; (b) H. Witt, V. Zickermann, B. Ludwig, *Biochim. Biophys. Acta* **1995**, 1230, 74–76.
40. (a) M. Wilmanns, P. Lappalainen, M. Kelly, E. Sauer-Eriksson, M. Saraste, *Proc. Natl. Acad. Sci. USA* **1995**, 92, 11955–11959; (b) P.A. Williams, N.J. Blackburn, D.A. Sanders, H. Bellamy, E.A. Stura, J.A. Fee, D.E. McRee, *Nature Struct. Biol.* **1999**, 6, 509–516.
41. (a) P. Ädelroth, P. Brzezinski, B.G. Malmström, *Biochemistry* **1995**, 34, 2844–2849; (b) M. Verkhovsky, J. E. Morgan, M. Wikström, *ibid.* **1992**, 31, 11860–11863.
42. P. Brzezinski, *Biochemistry* **1996**, 35, 5611–5615.
43. N.J. Blackburn, S. de Vries, M.E. Barr, R.P. Houser, W.B. Tolman, D. Sanders, J.A. Fee, *J. Am. Chem. Soc.* **1997**, 119, 6135–6143.
44. B.E. Ramirez, B.G. Malmström, J.R. Winkler, H.B. Gray, *Proc. Natl. Acad. Sci. USA* **1995**, 92, 11949–11951.
45. J.J. Regan, B.E. Ramirez, J.R. Winkler, H.B. Gray, B.G. Malmström, *J. Bioenerg. Biomembr.* **1998**, 30, 35–39.
46. (a) M. Fabian, G. Palmer, *Biochemistry* **1995**, 34, 13802–13810; (b) J.M. Wrigglesworth, *Biochem. J.* **1984**, 217, 715–719; (c) M. Fabian, G. Palmer, *Biochemistry* **1999**, 38, 6270–6275; (d) F. MacMillan, A. Kannt, J. Behr, T. Prisner, H. Michel, *Biochemistry* **1999**, 38, 9179–9184; (e) S. Jünemann, P. Heathcote, P.R. Rich, *Biochim. Biophys. Acta* **2000**, 1456, 56–66.
47. (a) M. Wikström, *Proc. Natl. Acad. Sci. USA* **1981**, 78, 4051–4054; (b) M. Wikström, *Nature* **1989**, 338, 776–778.

48. G.T. Babcock, M. Wikström, *Nature* **1992**, 356, 301–309.
49. (a) M. Oliveberg, P. Brzezinski, B.G. Malmström, *Biochim. Biophys. Acta* **1989**, 977, 322–328; (b) M. Verkhovsky, J. E. Morgan, A. Puustinen, M. Wikström, *Biochemistry* **1996**, 35, 16241–16246.
50. (a) J.A. Bailey, C.A. James, W.H. Woodruff, *Biochem. Biophys. Res. Commun.* **1996**, 220, 1055–1060; (b) C. Greenwood, Q.H. Gibson, *J. Biol. Chem.* **1967**, 242, 1782–1787; (c) B. Ludwig, Q.H. Gibson, *ibid.* **1981**, 256, 10092–10098.
51. M. Oliveberg, B.G. Malmström, *Biochemistry* **1992**, 31, 3560–3563.
52. (a) S. Han, Y.C. Ching, D.L. Rousseau, *Proc. Natl. Acad. Sci. USA* **1990**, 87, 8408–8412; (b) B.C. Hill, C. Greenwood, *Biochem. J.* **1984**, 218, 913–921; (c) A. Sucheta, K.E. Georgiades, Ö. Einarssdóttir, *Biochemistry* **1997**, 36, 554–565.
53. D.A. Proshlyakov, T. Ogura, K. Shinzawa-Itoh, S. Yoshikawa, E.H. Appelman, T. Kitagawa, *J. Biol. Chem.* **1994**, 269, 29385–29388.
54. M. Verkhovsky, J. E. Morgan, M. Wikström, *Biochemistry* **1996**, 35, 12235–12240.
55. T. Ogura, S. Hirota, D.A. Proshlyakov, K. Shinzawa-Itoh, S. Yoshikawa, T. Kitagawa, *J. Am. Chem. Soc.* **1996**, 118, 5443–5449.
56. D.A. Proshlyakov, M.A. Pressler, G.T. Babcock, *Proc. Natl. Acad. Sci. USA* **1998**, 95, 8020–8025.
57. M.T. Wilson, P. Jensen, R. Aasa, B.G. Malmström, T. Vänngård, *Biochem. J.* **1982**, 203, 483–492.
58. S. Yoshikawa, K. Shinzawa-Itoh, R. Nakashima, R. Yaono, E. Yamashita, N. Inoue, M. Yao, M.J. Fei, C.P. Libeu, T. Mizushima, H. Yamaguchi, T. Tomizaki, T. Tsukihara, *Science* **1998**, 280, 1723–1729.
59. D. Zaslavsky, I.A. Smirnova, P. Ädelroth, P. Brzezinski, R.B. Gennis, *Biochemistry* **1999**, 38, 2307–2311.
60. (a) P. Ädelroth, M. Ek, P. Brzezinski, *Biochim. Biophys. Acta* **1998**, 1367, 107–117; (b) S. Hallén, T. Nilsson, *Biochemistry* **1992**, 31, 11853–11859; (c) M. Oliveberg, S. Hallén, T. Nilsson, *ibid.* **1991**, 30, 436–440; (d) S. Paula, A. Sucheta, I. Szundi, Ö. Elnarsdóttir, *ibid.* **1999**, 38, 3025–3033.
61. S. Han, Y.-C. Ching, D.L. Rousseau, *Nature* **1990**, 348, 89–90.
62. (a) Y.C. Fann, I. Ahmed, N.J. Blackburn, J.S. Boswell, M.L. Verkhovskaya, B.M. Hoffman, M. Wikström, *Biochemistry* **1995**, 34, 10245–10255; (b) C. Varotsis, Y. Zhang, E.H. Appelman, G.T. Babcock, *Proc. Natl. Acad. Sci. USA* **1993**, 90, 237–241.
63. A. Jasaitis, M.I. Verkhovsky, J. E. Morgan, M.L. Verkhovskaya, M. Wikström, *Biochemistry*, **1999**, 38, 2697–2706.
64. H. Michel, *Proc. Natl. Acad. Sci. USA* **1998**, 95, 12819–12824.
65. M.I. Verkhovsky, A. Jasaitis, M.L. Verkhovskaya, J. E. Morgan, M. Wikström, *Nature*, **1999**, 400, 480–483.
66. T. Tsukihara, H. Aoyama, E. Yamashita, T. Tomizaki, H. Yamaguchi, K. Shinzawa-Itoh, R. Nakashima, R. Yaono, S. Yoshikawa, *Science* **1996**, 272, 1136–1144.
67. (a) P. Ädelroth, R.B. Gennis, P. Brzezinski, *Biochemistry* **1998**, 37, 2470–2476; (b) P. Ädelroth, M. Svensson Ek, D.M. Mitchell, R.B. Gennis, P. Brzezinski, *ibid.* **1997**, 36, 13824–13829; (c) J.P. Hosler, J.P. Shapleigh, D.M. Mitchell, Y. Kim, M.A. Pressler, C. Georgiou, G.T. Babcock, J.O. Alben, S. Ferguson-Miller, R.B. Gennis, *ibid.* **1996**, 35, 10776–10783; (d) A.A. Konstantinov, S. Siletsky, D. Mitchell, A. Kaulen, R.B. Gennis, *Proc. Natl. Acad. Sci. USA* **1997**, 94, 9085–9090; (e) T.V. Vygodina, C. Pecoraro, D. Mitchell, R.B. Gennis, A.A. Konstantinov, *Biochemistry* **1998**, 37, 3053–3061; (f) D. Zaslavsky, R.B. Gennis, *ibid.* **1998**, 37, 3062–3067.
68. M. Verkhovsky, J. E. Morgan, M. Wikström, *Biochemistry* **1995**, 34, 7483–7491.
69. M. Karpefors, P. Ädelroth, Y. Zhen, S. Ferguson-Miller, P. Brzezinski, *Proc. Natl. Acad. Sci. USA* **1998**, 95, 13606–13611.
70. (a) R. Pomès, G. Hummer, M. Wikström, *Biochim. Biophys. Acta* **1998**, 1365, 255–260; (b) S. Riistama, G. Hummer, A. Puustinen, R.B. Dyer, W.H. Woodruff, M. Wikström, *FEBS Lett.* **1997**, 414, 275–280.
71. C. Ostermeier, A. Harrenga, U. Ermler, H. Michel, *Proc. Natl. Acad. Sci. USA* **1997**, 94, 10547–10553.

- 72. A. Puustinen, M. Wikström, *Proc. Natl. Acad. Sci. USA* **1999**, 96, 35–37.
- 73. P. Hellwig, C. Ostermeier, H. Michel, B. Ludwig, W. Mäntele, *Biochim. Biophys. Acta* **1998**, 1409, 107–112.
- 74. J. E. Morgan, M. Verkhovsky, M. Wikström, *J. Bioenerg. Biomembr.* **1994**, 26, 599–608.
- 75. A. Harrenga, H. Michel, *J. Biol. Chem.* **1999**, 274, 33296–33299.
- 76. A. Kannt, C.R.D. Lancaster, H. Michel, *Biophys. J.* **1998**, 74, 708–721.
- 77. (a) H. Michel, *Nature*, **1999**, 402, 602–603; (b) M.I. Verkhovsky, A. Jasaitis, M.L. Verkhovskaya, J. E. Morgan, M. Wikström, *ibid.* **1999**, 402, 603.

4 Redox Enzymes: Correlation of Three-Dimensional Structure and Mechanism for Heme-Containing Oxygenases and Peroxidases

Alycen E. Pond, Amy P. Ledbetter, Masanori Sono, David B. Goodin, and John H. Dawson

4.1 Introduction

Heme proteins are arguably the most versatile class of proteins in biology. This group of metalloproteins contains a common heme prosthetic group, yet performs a wide variety of chemical reactions including electron transfer (cytochromes) [1, 2], oxygen activation and insertion (cytochrome P450s) [3–6], oxygen transport (hemoglobin and myoglobin) [3, 7, 8], substrate oxidation (peroxidases and catalases) [9–11], and nitric oxide biosynthesis (nitric oxide synthase) [12, 13]. The heme prosthetic group consists of a highly symmetrical and conjugated protoporphyrin IX macrocycle coordinated to an iron atom [2]. As shown in Figure 1, this group, also termed heme *b*, has two propionate groups, two vinyl groups, and four methyl groups as substituents on the porphyrin ring system. A unique property of the heme prosthetic group is the significant electron and spin delocalization possible among the porphyrin macrocycle, the centrally ligated iron, and the two axial ligands [14–18]. The ability of the porphyrin macrocycle to efficiently redistribute the net atomic charges and unpaired spin density plays a key role in the formation and stabilization of the various heme species required for function [14–18]. Modifications in either the level of conjugation or the substituents on the ring structure influence the electronic properties of the system, and thus result in distinct reactivity and spectroscopic properties [19].

The utilization of heme *b* in the coupling of substrate oxidation to dioxygen or peroxide reduction is seen for three types of heme-containing proteins: oxygenases (Reaction 1A/1B), oxidases (Reaction 2), and peroxidases (Reaction 3). There are two classes of oxygenases where either one oxygen atom from molecular oxygen (or hydrogen peroxide, Reaction 1B) is incorporated into the substrate and the second atom is reduced to water (monooxygenases) or both oxygen atoms are incorporated to give a doubly oxygenated product (dioxygenases). Oxidases and peroxidases do not produce an oxygenated product, rather substrates are oxidized as molecular

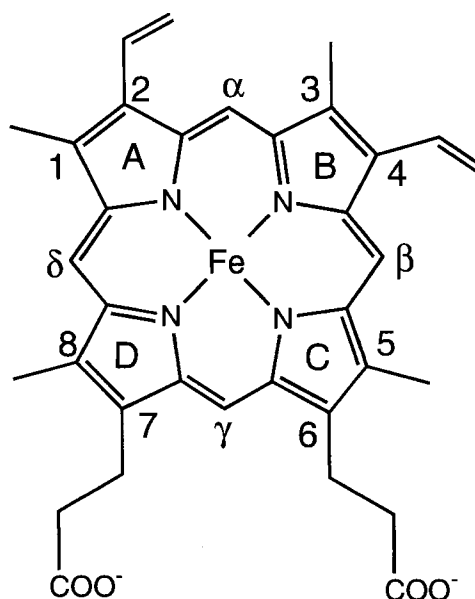
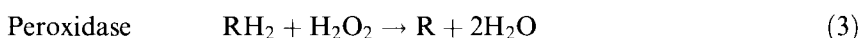
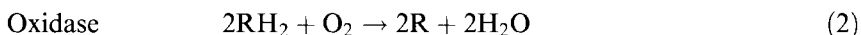
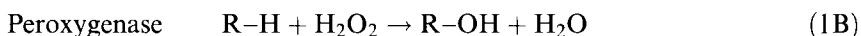
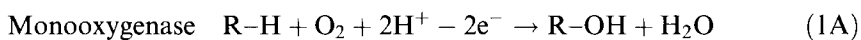


Figure 1. Structure of protoheme IX (iron protoporphyrin IX, heme *b*).



oxygen or hydrogen peroxide are reduced to water, respectively. While all three classes of enzymes possess the same heme core, their catalytic function varies greatly. The basis for this variance stems from the three factors that control the properties of metals in biological systems: (i) the coordination state of the metal complex; (ii) the nature of the axial ligands in the fifth and sixth coordination sites; and (iii) the protein environment enclosing the metal complex including the polarity of the surroundings and the accessibility of substrates and solvent to the metal [3]. Monooxygenases have various structural features that are not shared by the peroxidases, and vice versa [3]. An understanding of how these differences correlate to enzyme function is essential in defining the relationships between oxygenases and oxidases. In this review we provide updated accounts of the mechanisms of heme-containing monooxygenases and peroxidases, with particular emphasis on the relation of their respective mechanisms to their high-resolution X-ray crystal structures.

4.2 Cytochrome P450

4.2.1 Introduction

The monooxygenase family has the catalytic ability to incorporate an oxygen atom from molecular oxygen to yield a singly oxygenated product while reducing the second oxygen to water. In the years before 1955, the sole role of oxygen in biological systems was believed to be as an electron acceptor in dioxygen-utilizing oxidases or dehydrogenases. In that year, Mason et al. [20] and Hayaishi et al. [21] independently demonstrated through $^{18}\text{O}_2$ labeling experiments that one or both oxygen atoms from molecular oxygen can be incorporated into organic molecules following enzymatic oxidation. The enzymes that incorporate oxygen atoms from dioxygen were termed “oxygenases” by Hayaishi [22]. Shortly after the discovery of oxygenases and their enzymatic activity, Garfinkel [23] and Klingenberg [24] independently described the presence of a carbon monoxide (CO)-binding pigment in liver microsomes, which exhibited unusual absorbance maxima near 450 nm in the ferrous-CO minus ferrous difference spectrum. Omura and Sato [25] later identified this pigment (“P”) as a heme protein containing a protoporphyrin IX (Figure 1) prosthetic group and assigned it the name “cytochrome P450”.

Enzymes of the P450 superfamily are by far the best characterized of all heme-containing monooxygenases, and are extensively distributed throughout the plant, animal, and microorganism kingdoms. To date, more than 500 isozymes have been cloned and sequenced with enzymatic activities covering a vast variety of reactivities including hydroxylation of inactivated alkanes, conversion of alkenes to epoxides, arenes to phenols, and sulfides to sulfoxides to sulfones (Figure 2). The hydroxylation of various harmful organic molecules by P450 enzymes greatly increases the solubility of the organic substrate, thereby facilitating their excretion from biological systems. In contrast to their beneficial roles, P450 enzymes can also transform certain otherwise nonreactive molecules such as benzo(a)pyrene into highly reactive carcinogens [3], making P450 enzymes attractive targets for cancer-related drug design and development.

With the exception of microbial P450 enzymes, the majority of P450 proteins are membrane-bound, being associated with either the inner mitochondrial or endoplasmic reticulum (microsomal) membrane. Initial efforts to release the membrane-bound P450s from the membrane by detergent solubilization led to a loss of monooxygenase reactivity, as well as a shift the characteristic 450 nm absorbance peak to 420 nm in the difference spectrum [25]. Subsequently, successful solubilization and purification of the active form of the P450 proteins and associated electron transport proteins were achieved for the mitochondrial and microsomal P450s by Estabrook and Coon and their respective coworkers [26, 27]. Gunsalas and coworkers [28] discovered a soluble camphor-inducible bacterial monooxygenase P450 (P450CAM) system in *Pseudomonas putida*. The solubility of P450CAM allows large quantities to be purified for detailed mechanistic and spectroscopic studies, as well as successful crystallographic analysis. The crystal structure determined by Poulos and coworkers [29–33] provides researchers with a model to study

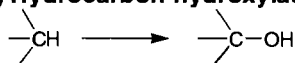
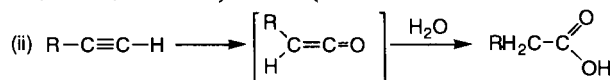
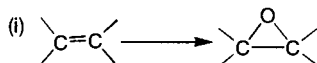
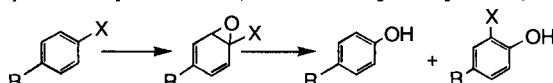
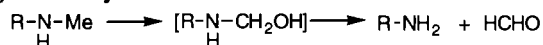
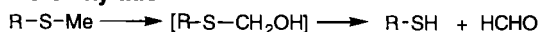
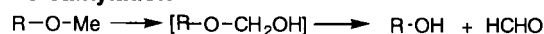
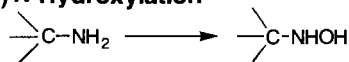
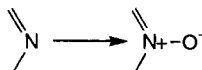
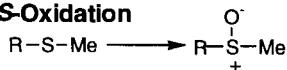
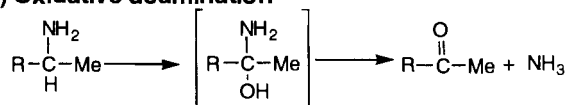
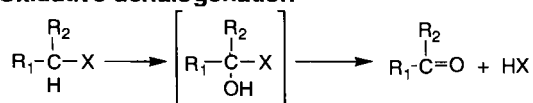
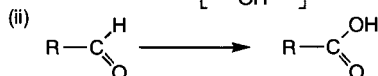
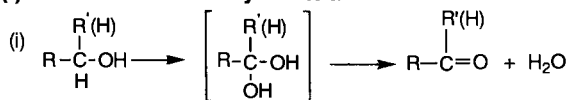
(a) Hydrocarbon hydroxylation**(b) Alkene epoxidation / Alkyne oxygenation****(c) Arene epoxidation, aromatic hydroxylation, NIH shift****(d) N-Dealkylation****(e) S-Dealkylation****(f) O-Dealkylation****(g) N-Hydroxylation****(h) N-Oxidation****(i) S-Oxidation****(j) Oxidative deamination****(k) Oxidative dehalogenation****(l) Alcohol and Aldehyde oxidations**

Figure 2. Schematic summary of some of the diverse P450-catalyzed reactions. (Adapted from Ref. [6].)

the relationship between the P450s and their substrates, making P450CAM the preferred vehicle for studying the relationship between structure and function of the P450 family.

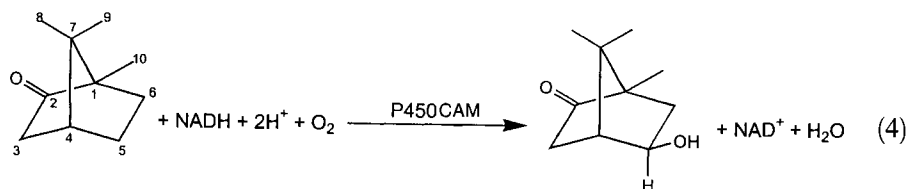
4.2.2 Reaction Cycle of P450

Electron transport systems

In catalyzing its monooxygenase reaction, P450 can utilize either NADH or NADPH as an electron source. The electron transport system varies among the P450 proteins, and thus allows for an organization of the superfamily into smaller classes. Most bacterial and mitochondrial P450 systems are termed Class I P450s, utilizing flavin and iron–sulfur prosthetic groups for electron transfer from NAD(P)H [34]. Figure 3A illustrates such a system where reducing equivalents flow from NAD(P)H to a FAD-containing protein to an iron–sulfur protein to the P450. Microsomal systems are termed Class II P450s and employ a single flavoprotein, NADPH-cytochrome P450 reductase, containing both FAD and FMN components to shuttle electrons from NADH to the P450 (Figure 3B) [34]. P450BM-3 is an unusual bacterial P450 from *Bacillus megaterium* that is a natural fusion protein consisting of a P450 domain and a NADPH-cytochrome P450 reductase domain that enables the protein to be self-sufficient (Figure 3C) [34, 35]. Finally, P450nor from *Fusarium oxysporum* is a Class IV P450 that appears to accept electrons directly from reduced pyridine nucleosides without intervening electron carriers (Figure 3D) [36].

The reaction cycle and intermediates

The common feature of P450 enzymes is their utilization of a cysteine-ligated heme active site to catalyze their respective monooxygenase chemistry. The monooxygenation reaction catalyzed by P450CAM in the hydroxylation of (1*R*)-camphor is shown in Reaction 4. The reaction cycle determined for P450CAM (Figure 4) is likely shared by most members of the P450 family [37], and involves four well-characterized and isolatable complexes, 1–4, [4, 37]. The substrate-free resting state, 1, is six-coordinate low-spin with a proximal cysteine residue from the protein and a distal water molecule from the solvent serving as the axial ligands (Figure 5B). Addition of camphor displaces the solvent molecule, yielding a five-coordinate high-spin complex, 2, with a vacant coordination site on the distal side of the heme that will ultimately be available for dioxygen binding. The shift of the iron spin



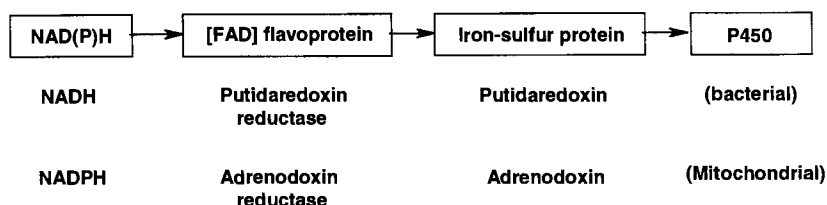
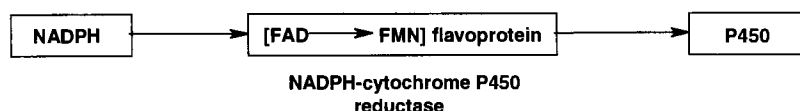
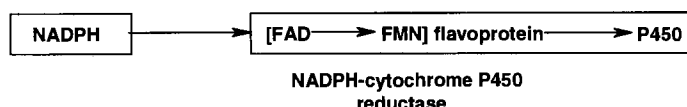
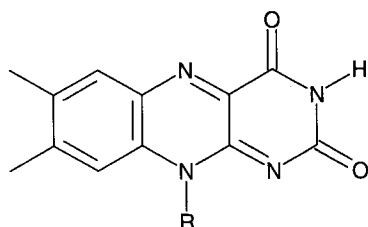
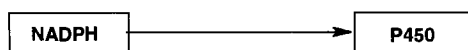
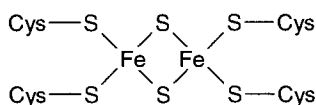
A) Mitochondrial and Bacterial Systems**B) Microsomal Systems****C) *Bacillus megaterium* (P450-BM3)****D) *Fusarium oxysporum* (P450_{nor})****Flavin moiety of FAD and FMN****Fe₂S₄Cys₄ Iron-sulfur Cluster**

Figure 3. Electron donors and transport pathways for A) mitochondrial and bacterial; B) microsomal; C) *Bacillus megaterium*; and D) *Fusarium oxysporum* P450 systems. The structures of the flavin moiety of FAD and FMN (bottom left) and the Fe₂S₄Cys₄ cluster (bottom right).

state from low- to high-spin upon substrate binding results in a significant increase in the redox potential (E°) of the heme iron (-330 to -173 mV versus NHE). As seen in Reaction 1A, the activation of molecular oxygen for monooxygenase chemistry requires the input of two electrons. For P450CAM, these electrons are provided by NADH via two electron transport proteins (Figure 3A): putidaredoxin reductase (a FAD-containing protein) and putidaredoxin (an iron-sulfur protein). Substrate binding facilitates electron donation from the reduced putidaredoxin

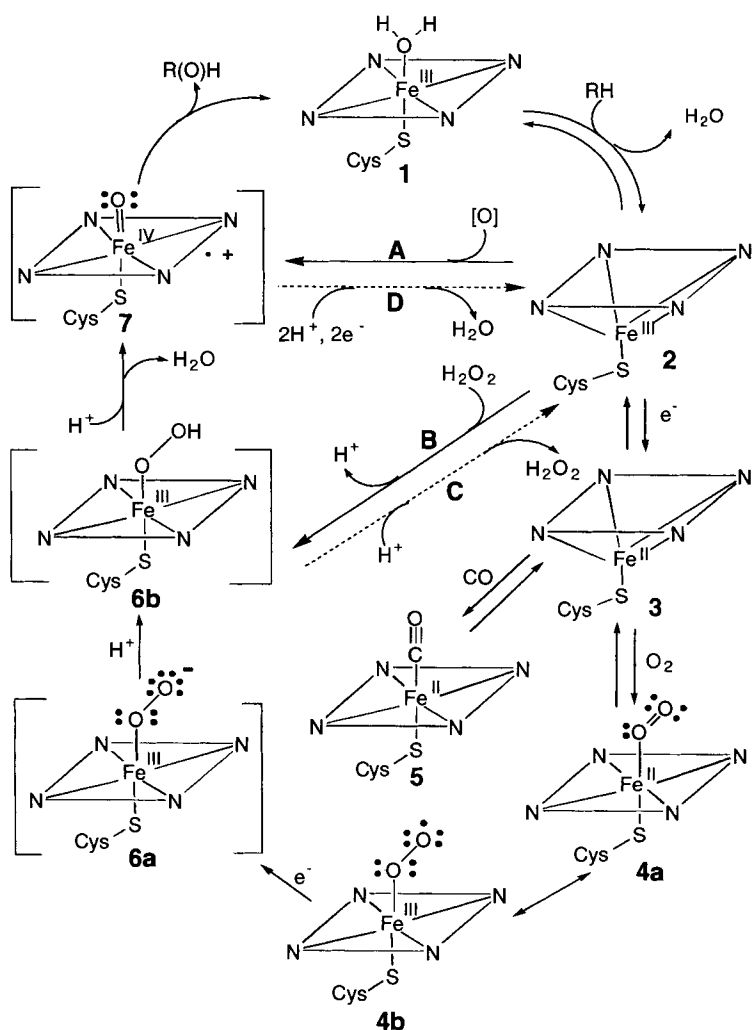


Figure 4. Catalytic cycle of cytochrome P450 including the postulated structures of the putative intermediates. RH represents the substrate and R(O)H represents the product. The porphyrin macrocycle is abbreviated as a parallelogram with nitrogens at the corners. See text for details. (Adapted from Ref. [6].)

($E^{\text{of}} = -196 \text{ mV}$) to the ferric P450CAM heme iron to produce the ferrous state of the protein, **3**. Dioxygen binds to the ferrous heme iron to form the ferrous oxy complex, **4a/4b**, whose valence structure can be presented either as the ferrous-O₂, **4a**, or as the ferric superoxide, **4b**, complex. Addition of carbon monoxide to **3** yields a ferrous carbon monoxide adduct, **5**, with its characteristic absorbance peak at 450 nm [37].

Addition of a second electron from NADH, **4a/4b**, the rate-limiting step of the

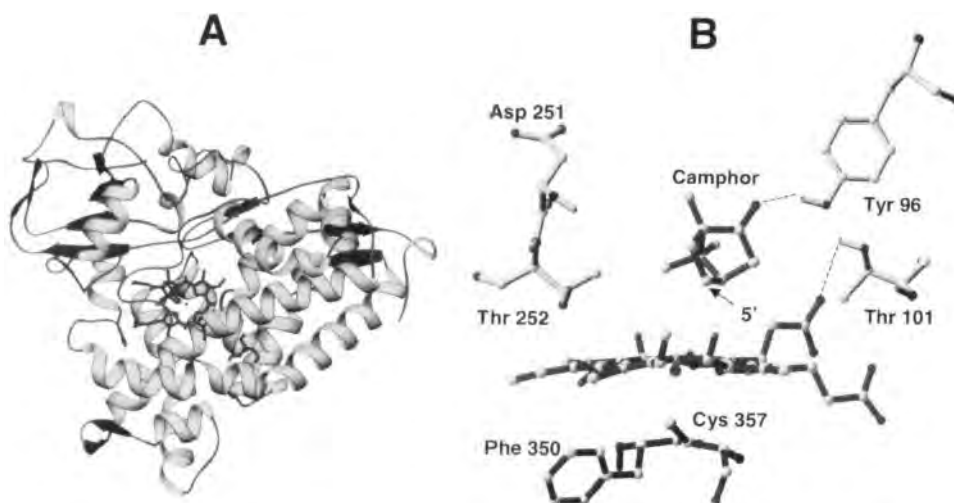


Figure 5. (A) Schematic representation of the crystal structure of P450CAM generated from the X-ray coordinates [58]. Helical regions, β -sheet regions, and the heme group are shown. (B) Key catalytic residues and the location of camphor in the heme active site [58]. The heme is ligated to a cysteine residue with the sixth position vacant. Dashed lines represent hydrogen bonding interactions between the C2 carbonyl of camphor and Tyr96, and the heme propionate and Thr101. The site of hydroxylation on the camphor molecule is denoted with an arrow.

catalytic cycle [38, 39], is proposed to give a ferric peroxide complex, **6a**, which can then be protonated to yield a ferric hydroperoxide species, **6b**. Addition of a second proton to this outer oxygen leads to heterolytic cleavage of the O–O bond, releasing water and generating the proposed oxo-ferryl ($\text{O}=\text{Fe}^{\text{IV}}$) porphyrin radical intermediate, **7**. Intermediate **7** is equivalent to the high-valent iron-oxo species of the peroxidases called Compound I. Compound I is the most likely candidate for the “reactive oxygen” form of P450 that hydroxylates inactivated hydrocarbon substrates. Abstraction of a hydrogen atom from the substrate by **7** forms a substrate-based carbon radical and an iron-bound hydroxyl radical. Radical rebound then yields the hydroxylated product and regenerates **1** [3, 4, 6, 40].

The short circuit or peroxide shunt

The cycle can also be turned over by two shunt pathways (pathway **A** and **B** in Figure 4). First, oxygen atom donors ($[\text{O}]$) such as iodosobenzene and peracids can replace the two electrons and dioxygen required for the normal catalytic cycle and react directly with **2** to generate oxygenated products likely through intermediate **7** (Pathway **A**) [4, 27, 41]. Similarly, some P450 proteins are able to replace molecular oxygen and NADH with hydrogen peroxide in a manner similar to the peroxidases. Pathway **B** illustrates the utilization of hydrogen peroxide to form **7** from substrate-bound ferric P450CAM (**2**) via the ferric hydroperoxide species, **6b** (4). Conversely,

pathways **C** and **D** illustrate the uncoupling of NADH oxidation and oxygen transfer. Protonation of the iron bound oxygen in **6b** releases hydrogen peroxide generating the five-coordinate ferric state, **2**, with no oxygen transfer to substrate (pathway **C**), a two-electron uncoupling reaction. Also, two-electron reduction and diprotonation of the oxo group in **7** gives a second molecule of water, regenerates complex **2**, and no oxygenated product yielding a four-electron uncoupling reaction (pathway **D**) [42–44].

Poulos has discussed the most likely causes of these latter two uncoupling reactions based on examination of the crystal structures of complexes of P450CAM with various camphor analogues and of site-directed mutants of P450CAM with modified substrate-binding sites [45]. The presence of excess solvent molecules near the heme, as well as an increase in substrate mobility, have been suggested as possible explanations for the uncoupling of electron transfer to oxygen transfer. Despite being the ultimate source of the protons needed for catalytic turnover, the presence of excess solvent within the active site could promote various uncoupling reactions. In related work, Sligar and coworkers have demonstrated that steric factors on the distal side of the heme strongly influence the coupling of oxygen and electron transfer in P450CAM and the partitioning between two- and four-electron uncoupling [42].

4.2.3 Molecular Structure of P450

In 1985, P450CAM was the first P450 protein to be successfully crystallized and have its structure determined [29]. The protein has an asymmetrical triangular shape consisting of 12 α helices and five anti-parallel β sheets (Figure 5A). The heme prosthetic group is deeply embedded into the hydrophobic interior of the protein, sandwiched between two long α helices, with no significant exposure to the surface of the protein. Previous spectroscopic investigations of P450CAM established that a cysteine residue serves as the endogenous ligand donated by the protein [4]. This finding was substantiated by the crystal structure identifying Cys357 as the proximal ligand to the heme (Figure 5B). Several years later, the structure of the P450 domain of P450BM-3 was determined [46], giving researchers models for a class I (P450CAM) and a class II (P450BM-3) P450. A side-by-side comparison of these two proteins can be seen in Figure 6. Subsequently, the successful crystallization and crystallographic analysis of two other class I P450s, P450TERP [47] and P450eryF [48, 49], a class IV P450, P450nor [50, 51], and P450csa [52] have been achieved. Additional structures of P450CAM and P450BM-3 in various coordination states and oxidation states [53–55] and several mutant forms of P450CAM [56–58] are also available.

Comparison of the amino acid sequences of members of the P450 family has revealed two areas of sequence similarity [59]. One region contains the proximal cysteine ligand along with the residues comprising its binding pocket. The second area of conservation corresponds to Thr252 of P450CAM located on helix I, which interacts directly with the bound dioxygen molecule of the P450–O₂ complex (Figure 5B). Both these areas are vital for efficient catalytic turnover, and will be discussed in later sections. With the availability of the structural data of the above

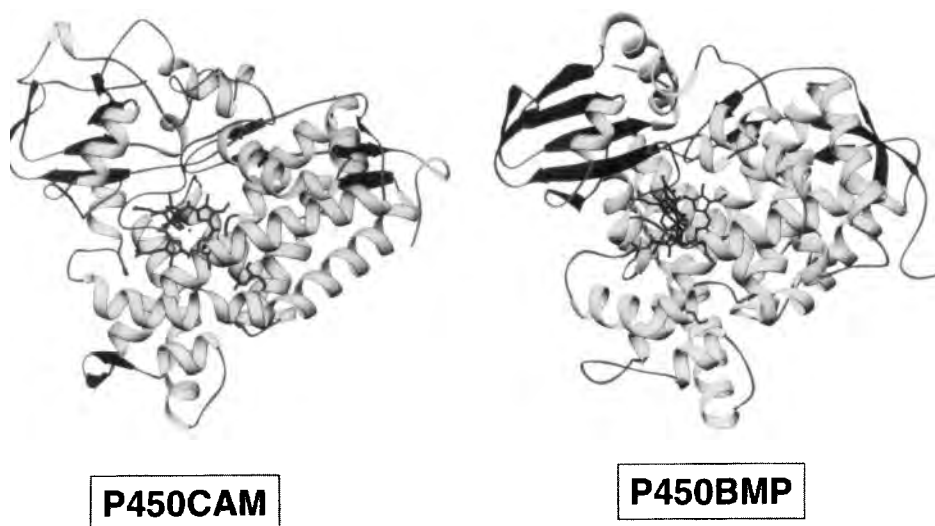


Figure 6. A side-by-side comparison of the secondary structures of P450CAM (left) and P450BM-3 (right) generated from their respective X-ray coordinates [58, 210]. Helical regions, β -sheet regions, and the heme group are shown.

P450s, it appears that the overall structural protein fold and the spatial organization of the heme-binding site are highly conserved, despite a less than 20% sequence identity among the proteins. Closer examination of these structures shows that there is ample diversity in the primary, secondary, and tertiary structures of the proteins to accommodate their wide variety of substrates, redox partners, and cellular locations. Detailed structural comparisons of these P450 proteins by Poulos et al. [33] and Peterson and colleagues [34, 59] can be found in the P450 literature.

In this new millennium, significant advancements have already been made in the crystallographic study of P450 proteins. First, McRee and coworkers produced the first X-ray crystal structure of a microsomal P450, P450 2C5 [60]. Comparison of this structure with those of microbial P450s indicates that the overall fold of the two types of P450 proteins is similar, as is the structural core surrounding the heme-binding site. However, significant structural differences exist between the substrate binding sites, and the modes of interaction with both electron donors and the membrane. Close analysis of the P450 2C5 structure provides a basis for the study of the interaction of a microsomal P450 with the endoplasmic reticulum, its substrate, and its redox partner. McRee and coworkers suggest a monofacial attachment of P450 2C5 to the membrane via a broad, hydrophobic surface that is adjacent to the anchor provided by a transmembrane helix at the N terminus [60]. The orientation of P450 2C5 relative to the membrane positions the electrostatic dipole of the P450 in such a manner to maximize the attraction between the protein and its reductase [60]. The entrance to the substrate access channel is located in the membrane attachment surface, suggesting that lipophilic substrates and products can enter or exit the P450 directly from the bilayer. An alternative substrate access

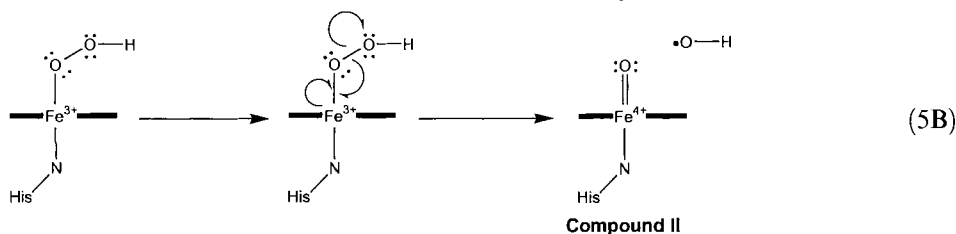
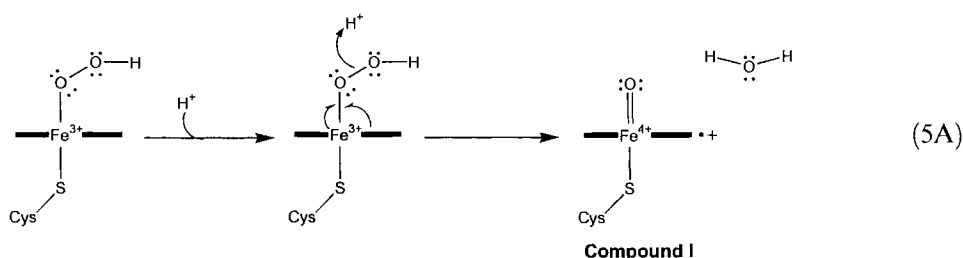
channel is also present, which would allow more water-soluble metabolites to exit directly into the cytoplasm [60]. As there is high sequence similarity between P450 2C5 and 91 other members of family 2 P450 enzymes [60], this structure and its analysis will provide researchers with a template by which to model the interactions of other microsomal P450s.

In a second crystallographic stride forward, Schlichting et al. have obtained structures for previously nonisolatable intermediates in the hydroxylation reaction of camphor by P450CAM utilizing trapping techniques and cryocrystallography [61]. The structure of the oxyferrous complex (**6a**) has been determined to a 0.91 Å resolution, showing a dioxygen molecule which binds end-on to the heme iron with the outer oxygen atom pointing towards Thr252. The bond distance between the heme iron and the inner oxygen is 1.8 Å with a Fe–O–O tilt angle of 132° [61], in agreement with previous extended X-ray absorption fine structure (EXAFS) [62] and resonance Raman [63] studies. In addition to altering the electron density surrounding the heme group, the binding of dioxygen also affects the distal binding pocket in two crucial ways. First, a new ordered solvent molecule (WAT 901) is now present near both the outer oxygen atom and the hydroxyl group of Thr252. Secondly, the backbone atoms of the highly conserved Asp251 and Thr252 have undergone a conformational change in which the carbonyl of Asp251 has flipped 90° towards Asn255, and the amide nitrogen of Thr252 has rotated towards the heme pocket [61]. These alternations result in new hydrogen-bonding interactions among the distal protein residues that appear to stabilize the new solvent molecule, WAT 901.

The addition of a second electron through irradiation of crystals of the oxyferrous complex with long-wavelength X-rays alters the electron density at and around the P450 active site [61]. Difference maps suggest that cleavage of the dioxygen bond has occurred, leaving a single oxygen atom bound to the heme iron. The electron density above the heme is too small to accommodate two oxygen atoms, and is best fit with a single oxygen atom bound to the heme at a distance of 1.65 Å [61]. This distance is much shorter than the 1.8 Å distance of an iron–oxygen single bond, and is in close agreement with computational (1.66 Å) [64] and EXAFS measurements for an oxo ferryl complex in a peroxidase [65]. This potential glimpse of compound I gives credence to the proposed catalytic mechanism of P450CAM and may translate to other P450 systems.

4.2.4 Mechanism of Oxygen Activation

A distinguishing characteristic of monooxygenases and peroxidases from the globins is the ability of the former two proteins to heterolytically cleave the O–O bond (Reaction 5A), while the latter utilize homolytic cleavage (Reaction 5B). This subtle difference in mechanism allows monooxygenases and peroxidases to perform their wide variety of catalytic activities, while globins serve as oxygen carriers. As can be seen in Reactions 5A and 5B, the high-valent Compound I species is formed only when both electrons in the O–O bond go with the leaving group, i.e., heterolytic cleavage. When the bond is cleaved homolytically, as seen for the globins, the



electrons in the bond are split between the two oxygen atoms, forming Compound II, a less reactive oxo intermediate. The ability of monooxygenases and peroxidases to cleave the O–O bond heterolytically is a direct result of their respective active site protein environments, particularly the proximal ligand and catalytically active protein residues on the distal side of the heme.

The “push–pull” mechanism of the peroxidases

Heme-containing peroxidases carry out heterolytic O–O bond cleavage starting from the ferric state and binding hydrogen peroxide to form the high-valent iron-oxo intermediate, Compound I. The crystal structure of cytochrome *c* peroxidase, a prototypical heme-containing peroxidase, led Poulos to propose a “push–pull” mechanism for the formation of Compound I [66]. In this system, it is proposed that heterolytic cleavage is achieved by a combination of electron density “push” from the anionic proximal histidine, and “pull” by the distal histidine and arginine couple (Figure 7) [66, 67]. The “push” is provided by the proximal histidine ligand whose electron donor capabilities are enhanced due to a strong hydrogen-bonding interaction (partial deprotonation) with a neighboring carboxylate group, thereby increasing its imidazolate character relative to the corresponding histidine ligand of hemoglobin or myoglobin. This anionic character may also serve to stabilize the higher oxidation states of the heme iron during catalysis. Simultaneously, the distal histidine accepts a proton from the inner oxygen of the bound hydrogen peroxide and transfers it to the outer oxygen to generate a good leaving group. The distal histidine works in concert with a strategically positioned cationic arginine residue that serves to stabilize the developing anionic charge on the outer oxygen during bond cleavage. The combination of the distal histidine and arginine provide the “pull” effect. Recent site-directed mutation of residues on both the proximal and distal side supports the push–pull effects on the formation of Compound I of CCP

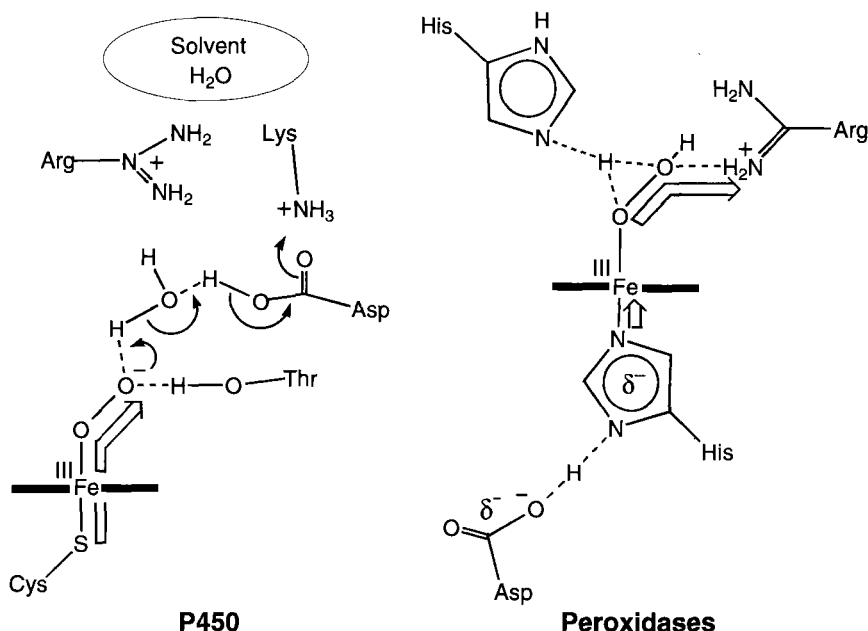


Figure 7. Schematic view of the “push-pull” mechanism for O–O bond cleavage of an iron-bound peroxide in thiolate-ligated (left) and histidine-ligated (right) systems such as P450 and HRP, respectively. (Adapted from Ref. [6].)

[66–71], especially the replacement of the distal histidine with a leucine residue which suppressed the rate of Compound I formation 10⁵-fold [67, 69, 70].

The “push” effect of the proximal cysteine ligand for P450

Nearly 25 years ago, Dawson proposed that the P450 proximal thiolate ligand serves as a strong internal electron donor to facilitate O–O bond cleavage to generate Compound I (Figure 7) [72]. Three lines of evidence for the “push” of the cysteinate ligand have been reported. First, bound distal thiolates show enhanced basicity *trans* to the endogenous cysteinate of P450CAM relative to parallel myoglobin adducts [73]. Second, significant differences have been reported for the affinities of anionic ligands to ferric P450 and myoglobin, with anionic ligands having much lower affinity for ferric P450CAM than ferric myoglobin, presumably due to the anionic character of the proximal thiolate ligand [74]. Finally, Dawson and coworkers have observed shifts in the in the X-ray absorption energies for thiolate-ligated heme iron derivatives relative to those lacking a thiolate ligand to provide a direct measure of the strong electron-releasing nature of the thiolate axial ligand [75]. More recently, studies using a His → Cys myoglobin mutant [76] or a thiolate-ligated porphyrin model system [77] demonstrate that the thiolate-ligated systems favor the heterolytic cleavage of the O–O bond compared to wild-type myoglobin

and neutral histidine-ligated porphyrin models that predominantly cleave the O–O bond homolytically. Once the O–O bond is cleaved heterolytically, the anionic character of the thiolate ligand helps to stabilize the high-valent nature of Compound I.

In 1999, Hager and coworkers provided the first evidence that the strong anionic character of the thiolate ligand may not be the only determining factor in the differentiation between homo- and heterolytic cleavage of the O–O bond. Replacement of the proximal thiolate ligand in the related peroxidase enzyme of chloroperoxidase (CPO), a versatile heme enzyme from *Caldariomyces fumageo*, with a histidine resulted in a recombinant mutant that retains most of its chlorination, peroxidation, epoxidation, and catalase activities [78]. This retention of activity despite the loss of thiolate ligation indicates that the environment of the distal pocket may play as important a role as the proximal ligand in differentiating between homo- and heterolytic cleavage of the O–O bond. CPO has a very polar distal environment that is typical of peroxidases. As evidenced by the high activity levels of the Cys → His mutants, this polar environment likely plays a major role in maintaining the diverse catalytic activities of this enzyme.

The proton shuttle in P450

The “push” of the thiolate ligand cannot, by itself, accomplish heterolytic cleavage of the O–O bond (Figure 7). In addition, there must be a source of protons to enable the outer oxygen atom of the bound peroxide (Figure 4, species **6a**) to leave as water. Theoretical studies by Loew and Harris [64] indicate that the protonation of the outer oxygen leads to significant weakening of the O–O bond. This weakening is manifested in both an increase in O–O bond length from 1.33 to 1.46 Å, and a decrease in the bond order from 0.87 to 0.48 [64]. However, only the addition of the second proton results in the cleavage of the dioxygen bond, resulting in the formation of Compound I [64]. These results provide strong support for consecutive or simultaneous double protonation of the outer oxygen atom of the ferrous dioxygen complex being the ultimate cause of O–O bond breakage.

Extensive study of the P450CAM active site has identified two potential routes for proton transfer (Figure 8). The first involves two highly conserved residues, Thr252 and Asp251 [58, 79–83]. The second possibility is via a water chain and the highly conserved Glu366 [84]. Sligar and coworkers have proposed that Thr252 and Asp251 form a proton relay network that works in conjunction with two other charged amino acids to reach the surface solvent and provide a conduit for protons [58, 80–83]. Replacement of Thr252 with alanine (T252A) results in a drastic drop in hydroxylation activity (~95 %) without a simultaneous decrease in NADPH and O₂ consumption (i.e., increased uncoupling) [82, 85]. Similarly, replacement of the corresponding Thr268 with alanine (T268A) in P450BM-3 results in a decrease in substrate (laurate) hydroxylation (~85 %) and an increase in uncoupling [86]. However, in P450CAM substituting Thr252 with either a serine or an O-Me-Thr residue produces an enzyme that retains high activity [79, 87]. The mechanistic results obtained with these mutants indicate that the role of Thr252 in the hydroxylation mechanism is to provide a hydrogen bond rather than a proton during

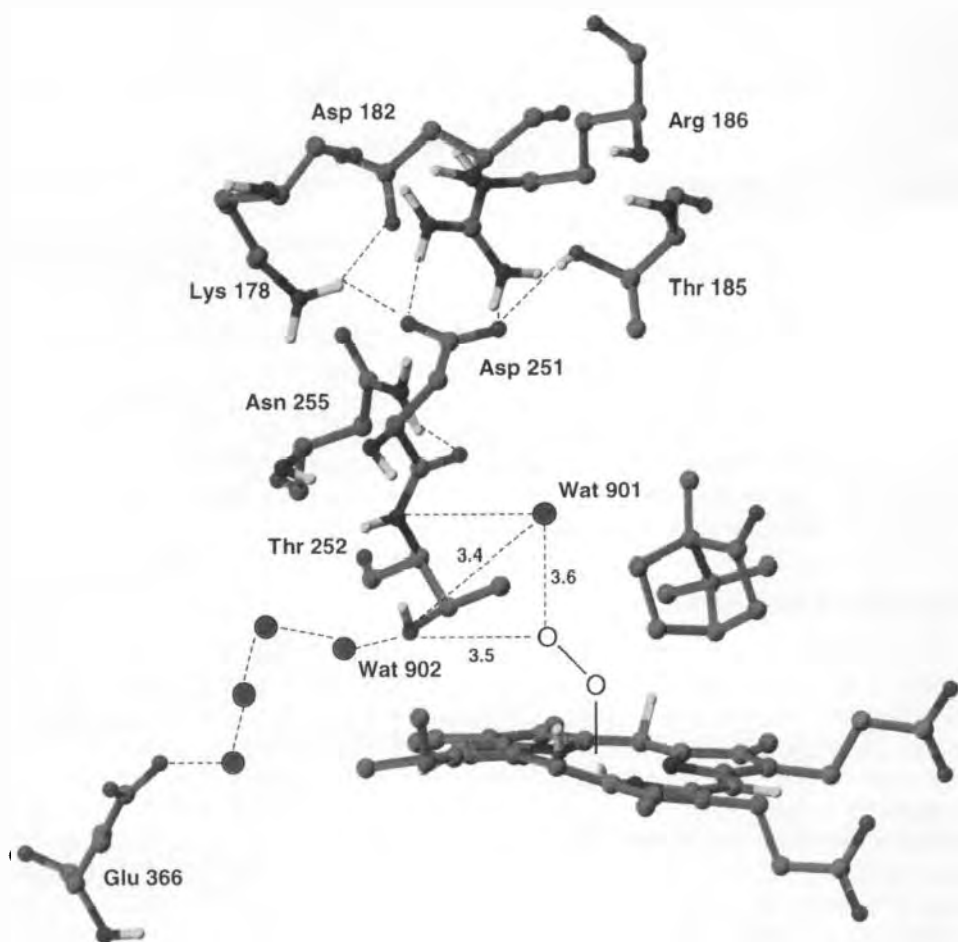


Figure 8. A schematic view of the proposed proton shuttle in the distal pocket of P450CAM. Distal residues and the heme were generated using the X-ray coordinates [58]. Dashed lines represent hydrogen-bonding interactions as determined in Ref. [61]. Water molecules are represented by isolated spheres, with WAT 901 and WAT 902 in positions determined in Ref. [61].

turnover (Figure 8). The recent crystal structure of the oxyferrous complex of P450CAM confirms this assignment, showing Thr252 within hydrogen bonding distance to the bound dioxygen molecule as well as a potentially catalytic solvent molecule, WAT 901 [61].

Replacement of Asp251 with asparagine (D251N) decreases the rate of hydroxylation by two orders of magnitude, with relatively little uncoupling and shifts the rate limiting in the catalytic cycle [58, 80, 88]. Based on isotopic and crystallographic studies of wild-type and D251N P450CAM, *Sligar and coworkers proposed* a proton shuttle involving two new solvent molecules in the active site, with Asp251 serving as a “carboxylate switch” between solvent-accessible residues and the cata-

lytic water molecules (Figure 8) [79]. However, the availability of recent structural data has altered this proposal somewhat, with Asp251 now serving as a “carbonyl switch” that stabilizes WAT 901 instead [61].

The intrinsic diversity of the family must be kept in mind when trying to apply results for P450CAM to the P450 superfamily. In P450eryF, a P450 that catalyzes the hydroxylation of 6-deoxyerythronolide, there is an alanine (Ala245) in the position corresponding to Thr252 in P450CAM. Mutation of this residue in P450eryF to a threonine (A245T) results in a dysfunctional protein, similar to the opposite mutation in P450CAM (T252A). Therefore, P450eryF must utilize a varied source of protons in its catalytic cycle. Molecular dynamic simulations by Harris and Loew [64, 84] have identified a stable hydrogen-bonding network leading from the outer oxygen of the iron-bound dioxygen to the carboxylic oxygen of Glu360, a highly conserved residue in the P450 family. This residue is located in a solvent-accessible channel, and is likely the ultimate source of protons in P450eryF [64, 84]. The corresponding residue in P450CAM, Glu366, does not appear to serve the same purpose in the catalytic cycle as its mutation to a methionine shows little effect on catalytic activity [89]. Instead, structural data suggest that this residue may “anchor” a solvent chain that extends between Thr252 and Glu366 (Figure 8) [61]. Therefore, neither the role of a specific amino acid nor the consequence of a mutation can be inferred for one P450 enzyme based on the results for another isozyme.

4.3 Nitric Oxide Synthase

4.3.1 Introduction

Nitric oxide ($\bullet\text{NO}$) is a diatomic, reactive radical that has become the focus of intense scientific investigation during the past two decades. Its role as a biological messenger places this small molecule at the heart of a number of complex regulatory mechanisms in diverse biological systems. The ability of $\bullet\text{NO}$ to diffuse freely from its point of origin rather than using classical biological trafficking routes (i.e., specific transporters or channels) makes regulation dependent on its actual biosynthesis, and not its movement through the body. Before 1981, $\bullet\text{NO}$ biosynthesis was believed to be restricted to bacteria that engaged in nitrification and denitrification reactions [90]. For the first time in 1981, nitrogen oxides were conclusively demonstrated as significant products in mammalian metabolism [90]. Building on this discovery, numerous research groups have focused on the role of $\bullet\text{NO}$ in mammalian systems. Stemming from this research, $\bullet\text{NO}$ has been implicated as a neurotransmitter in the brain, a vasodilator in smooth muscles, and an immunocytotoxic reagent in macrophages [90]. As the potential functions of $\bullet\text{NO}$ become more established, scientific attention has shifted towards its regulation and therefore to the enzyme responsible for its biosynthesis, nitric oxide synthase (NOS). Following initial sequencing and development of a recombinant system in 1991, the amount of knowledge accumulated about NOS is astounding.

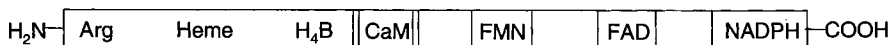
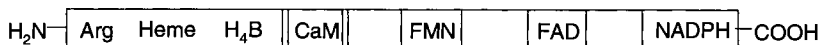
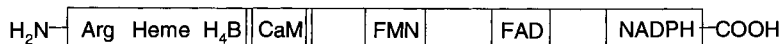
Neuronal NOS 160 kDa**Endothelial NOS 133 kDa****Inducible NOS 130 kDa****Oxygenase Domain****Reductase Domain**

Figure 9. Map of the primary amino acid sequence of nNOS, eNOS, and iNOS. A calcium-calmodulin binding region separates the oxygenase and reductase domains. The reductase domain contains binding sites for two flavin cofactors (FAD and FMN) as well as a binding site for the electron donor, NADPH. The oxygenase domain contains binding sites for the heme, the substrate (L-arginine), and tetrahydrobiopterin (H₄B). (Adapted from Ref. [90].)

4.3.2 The Isoforms

To date, three isoforms of NOS have been identified: neuronal NOS (nNOS, NOS-I, brain), inducible NOS (iNOS, NOS-II, immune system), and endothelial NOS (eNOS, NOS-III, cardiovascular system). These isoforms have been purified from different sources, and many have been cloned and functionally expressed [91]. Each isoform of NOS is comprised of a N-terminal oxygenase domain and a C-terminal reductase domain connected by a 30-amino acid recognition sequence for the binding of the calcium/calmodulin (Ca²⁺/CaM) complex (Figure 9) [12, 90, 92–95]. The oxygenase domain contains binding sites for the heme, the cofactor tetrahydrobiopterin (H₄B), and the substrate, L-arginine (L-Arg). The reductase domain contains binding sites for NADPH, flavin mononucleotide (FMN), and flavin-adenine dinucleotide (FAD) that shuttle electrons to the heme center to couple product formation. The Ca²⁺/CaM complex acts as a hinge between the oxygenase and reductase domains, allowing communication between domains [96, 97]. In nNOS and eNOS, the electron flavin-to-heme transfer must be initiated by the binding of the Ca²⁺/CaM complex, whereas iNOS is active at all times because Ca²⁺/CaM is always bound. Recently, work with iNOS indicates that the electrons flow between the oxygenase and reductase domains on adjacent subunits (Figure 10) [98]. This “domain swapping” provides a means for NOS to prevent uncoupling of NADPH oxidation and may provide a way for H₄B function or Ca²⁺/CaM control of heme iron reduction [98].

Dimerization of the oxygenase domains is essential for catalytic activity and for binding of the pterin cofactor [99]. Recent structural data for the dimeric oxygenase domains of NOS [100–102] reveal an extensive dimer interface that creates binding sites for the two pterins, sequesters the heme from the solvent, and helps to structure the substrate binding site (Figure 11). Upon dimerization, all three isoforms pro-

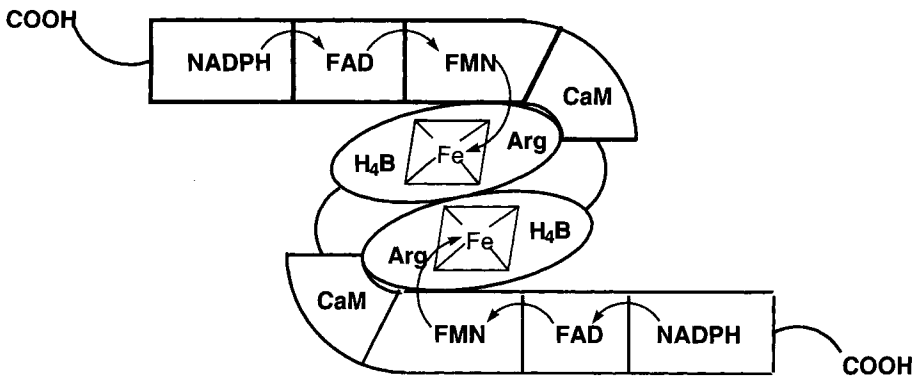


Figure 10. Proposed model for the iNOS dimer indicating domain swapping and electron transfer pathway. (Adapted from Ref. [98].)

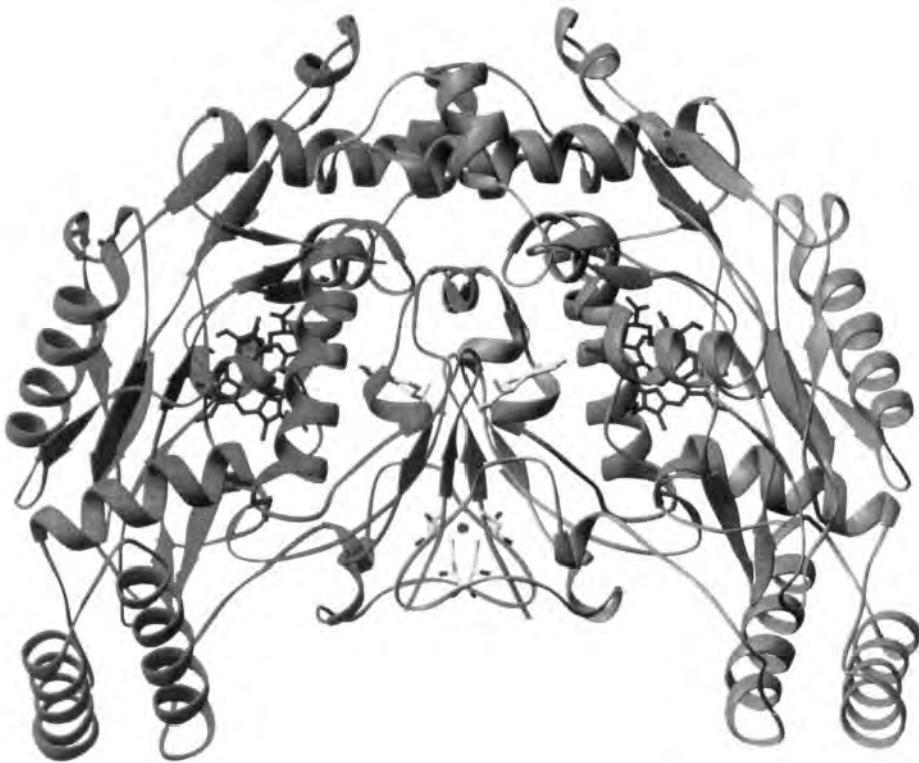
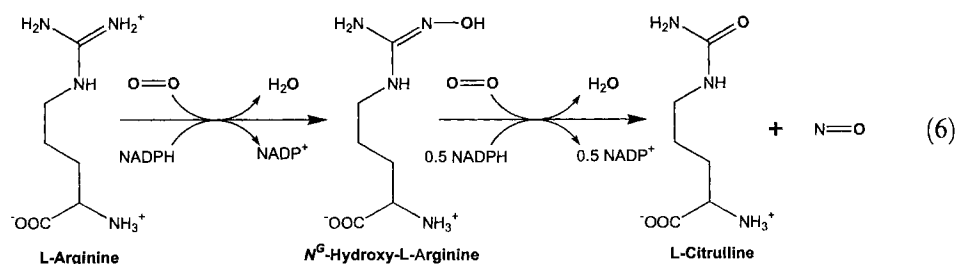


Figure 11. Schematic ribbon drawing of the iNOS oxygenase dimer generated from the X-ray coordinates [107] illustrating the locations of heme, L-arginine, tetrahydrobiopterin, and the zinc ion. The zinc ion is tetrahedrally coordinated to its protein ligands.



duce $\bullet\text{NO}$ by catalyzing the oxidation of L-arginine to L-citrulline and $\bullet\text{NO}$, via the intermediate, N^ω -hydroxy-L-arginine (NHA) (Reaction 6) [12, 92, 95]. The reaction is a variation on the hydroxylation reaction catalyzed by P450 enzymes; thus, it is not surprising that NOS and P450 are very similar biological machines. Both have a thiolate-ligated heme prosthetic group at their respective active sites, and utilize a FMN/FAD reductase system for electron transport from NADPH. With an exception of P450 BM-3, NOS is distinct from P450s in that NOS is a “self-sufficient” monooxygenase in which both the oxygenase and reductase domains are part of a single peptide. Unlike P450 BM-3 that is also self-sufficient by having a fused oxygenase and reductase domains in a single peptide [103], NOS employs a H_4B group, the function of which is poorly understood. However, it is required for efficient catalysis, and essential for $\bullet\text{NO}$ production [104].

Neuronal production of $\bullet\text{NO}$ is triggered when an activated neuron releases a chemical messenger (glutamate) from the presynaptic neuron to bind to receptor sites (N -methyl-D-aspartate) on the postsynaptic neuron. The transmission of this nerve impulse opens a channel in the receptor allowing the influx of calcium ions. These ions can then bind to calmodulin already present in the cell, forming a $\text{Ca}^{2+}/\text{CaM}$ complex that binds to and activates nNOS [90]. The $\bullet\text{NO}$ radical that is produced in turn activates soluble guanylate cyclase in the postsynaptic neuron and potentially in the presynaptic neuron.

Similar to the activation mechanism found in the neuronal cells, chemical messengers (e.g., hormones or acetylcholine) bind to their corresponding receptors on endothelial cell membrane. This binding triggers the opening on a membrane channel, resulting in a flow of calcium into the cell. Once in the cell, the calcium binds to a calmodulin molecule, forming the $\text{Ca}^{2+}/\text{CaM}$ complex that in turn activates eNOS through binding. As eNOS is bound to the inner surface of plasma membrane of the cell, the $\bullet\text{NO}$ produced diffuses freely into both the blood vessel and into the underlying vascular smooth muscles cells. In the blood vessel, $\bullet\text{NO}$ enters blood platelets and decreases their aggregation with each other and their adhesion to endothelial cells [90]. Within the muscle cells, $\bullet\text{NO}$ activates sGC, producing an increase in cyclic guanine monophosphate (cGMP) levels. cGMP decreases the amount of free calcium levels in the muscle cell, allowing the blood vessels to vasodilate [90].

Unlike nNOS and eNOS, inducible NOS does not require calcium for activation. Instead, the enzyme is synthesized in macrophages in response to cytokines. Once

synthesized, iNOS immediately begins production of $\bullet\text{NO}$ that diffuses at least partially into the nearby tumor cell. Once inside the cell, $\bullet\text{NO}$ can disrupt a number of cellular processes, including electron transport needed for adenosine triphosphate synthesis, and the tricarboxylic acid cycle. In addition, $\bullet\text{NO}$ can also inhibit the ribonucleotide reductase necessary for DNA synthesis and cell division [90].

4.3.3 The Molecular Structure of NOS

The recent advances in NOS structure analysis have shed light on the roles of the pterin, the substrate, and the newly discovered zinc ion in dimer formation and stabilization as well as catalytic activity. Work by numerous groups on iNOS (murine and human) [100, 101, 105–107], and eNOS (human and bovine) [101, 102] provides an intimate view of the various interactions between cofactors and protein–protein interplay in dimer formation. Structural work on the neuronal isoform of NOS is presently ongoing, with preliminary results indicating high structural similarity to published structures of the other NOS isoforms (T.L. Poulos, personal communication).

Prior to the elucidation of these structures, it was known that NOS must dimerize through the oxygenase domain for catalytic function [99]. Structures of the oxygenase dimer of both iNOS and eNOS reveal that dimer formation reinforces the substrate binding channel and sequesters two pterin molecules within two symmetry-related lariats (see Figure 11) [100–102]. The dimer interface is extensive with between 1200 and 2800 Å² of buried surface [100–102]. Additionally, conformational changes upon dimerization of iNOS expose the heme edge opposite of the center channel, and provide a possible interaction surface for the complementarily shaped reductase domain [100].

Similar to the P450s, the substrate (L-Arg) is held in place by hydrogen-bonding interactions that position the atom to be hydroxylated within 4 to 5 Å from the heme iron (Figure 12) [100–102]. Interactions of the L-Arg guanidinium group at the bottom of the heme pocket suggest a mechanism for $\bullet\text{NO}$ synthesis where the proton donation from the substrate to the iron-bound dioxygen facilitates heterolytic cleavage of the O–O bond, yielding Compound I [100]. This interaction serves to neutralize the guanidinium group, and discriminates between Compound I and the ferric superoxy species in the two steps of $\bullet\text{NO}$ synthesis. The only major difference between the binding modes of L-Arg and NHA in the active site results from the addition of the NHA hydroxyl group. The structure of this complex shows the oxime nitrogen (N^{ω}) of NHA projecting towards the center of the porphyrin macrocycle ~ 4 Å away from the iron [106]. This positioning leaves no proton readily available for the breakdown of the ferric superoxy complex to Compound I, thereby allowing the dioxygen species to serve as the active oxygen intermediate in the reaction of NOS with NHA. However, direct interaction between the ferric superoxy complex and NHA is unlikely. Modeling studies with the structure of NHA-bound iNOS indicate that the terminal oxygen of the ferric superoxy species is distant from the NHA hydroxyl group and therefore does not appear able to interact with this substrate moiety [106]. Instead, free radical addition of the ferric superoxy to the

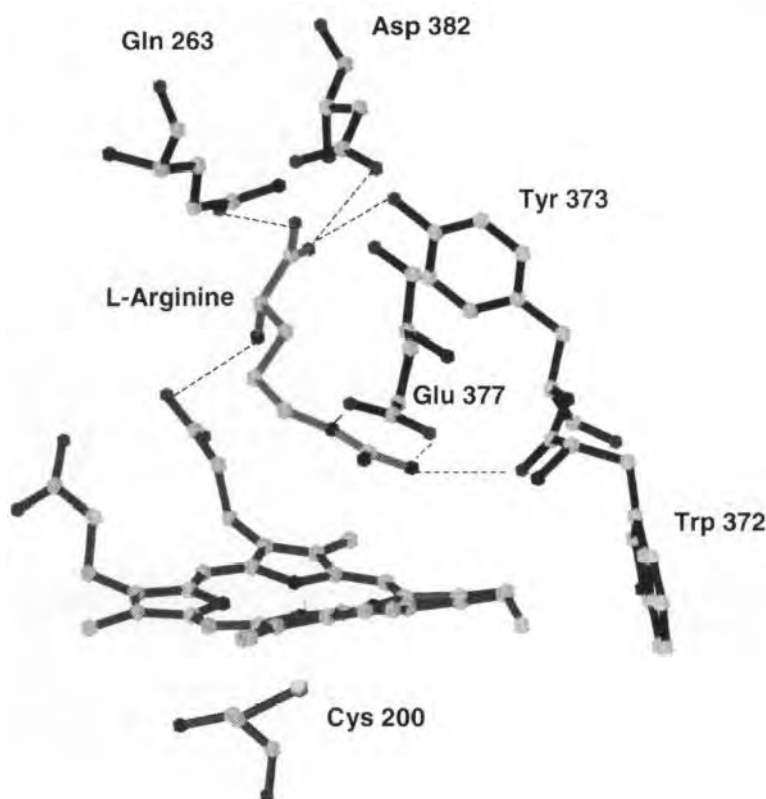


Figure 12. Key catalytic residues and the location of L-arginine in the heme active site [100]. The heme is ligated to a cysteine residue with the sixth position vacant. Dashed lines represent hydrogen-bonding interactions between the substrate and the distal heme environment as depicted in Ref. [100].

NHA oxime or proton donation from protonated N^{ω} to the heme species are suggested as likely mechanistic pathways [106]. Regardless of the final mechanism, the L-Arg and NHA-bound structures of NOS imply that NOS catalysis selects between two different reductive activations of dioxygen.

The essential pterin cofactors of the NOS bind at the dimer interface ~ 13 Å apart and $\sim 40^\circ$ from coplanarity (Figure 11) [100–102, 106, 107]. The H_4B heteroatoms participate in a number of hydrogen-bonding interactions—most importantly with a tryptophan residue from the same subunit, and a phenylalanine residue from the adjacent subunit (Figure 13). These two residues maintain π -stacking interactions with the H_4B pteridine ring increasing both pterin affinity and $\bullet NO$ synthesis activity [100–102, 106, 107]. Additionally, the pterin interacts with the same heme propionate group as L-Arg and NHA (Figure 13), allowing allosteric interaction between the pterin and the substrate via the propionate group. Recent structural

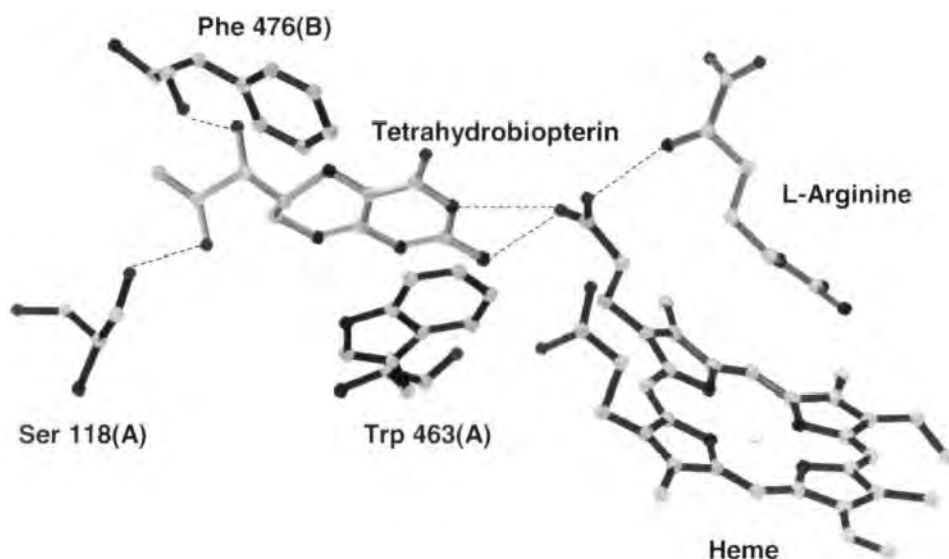


Figure 13. The H₄B binding-site in iNOS generated from the X-ray coordinates [100]. The amino acids involved in hydrogen-bonding interaction with the pterin are shown. (A) or (B) denote the subunit of the residue.

data of NOS with H₄B bound, as well as other substituted and oxidized pterins, indicates that H₄B likely binds in its neutral form and fulfills roles ranging from dimer stabilization to acting as a redox cofactor or modifier of heme reactivity [106].

The most recent discovery revealed by structural NOS data is the positioning of a tetrahedrally coordinated zinc ion at the base of the dimer interface (see Figure 11). Seen first for eNOS [102], this divalent metal site has since been observed in iNOS [100, 101, 106] and nNOS (T.L. Poulos, personal communication). The zinc ion is coordinated to pairs of symmetry-related cysteine residues, and is equidistant from both pterin cofactors (~ 12 Å) and heme groups (~ 20 Å). This remote location from the catalytic heme iron, as well as its complete coordination by four cysteines (Figure 14A), is consistent with a structural rather than enzymatic role for the zinc ion. Structures of zinc-free iNOS show the formation of a self-symmetric disulfide bond (Figure 14B) across the dimer interface that adversely effects subunit association, formation of the pterin-binding site, and catalytic activity [107, 108], supporting the structural role proposed for the zinc site. In addition, the surface of the area closest to the zinc site in eNOS is the most electropositive region of the molecular surface, and provides an excellent docking site for the strongly electronegative reductase domain [102]. Similar calculations for iNOS reveal no such surface near the zinc site, and point instead to the surface surrounding the exposed heme edge as the potential site for reductase binding [108].

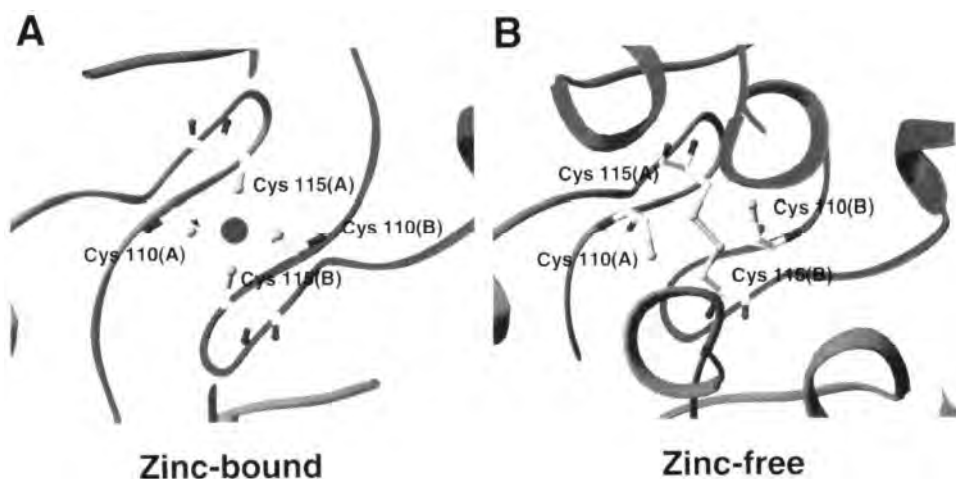


Figure 14. Ribbon drawing of the (A) zinc-bound and (B) zinc-free states of the iNOS oxygenase domain as determined by X-ray coordinates [107].

4.3.4 The Mechanism of NOS

Proposals regarding the NOS catalytic mechanism of the conversion of L-Arg to L-citrulline and •NO have ranged from sole participation of the heme cofactor (a P450-type mechanism) to interactions between the substrate, heme, and the H₄B cofactor. The conversion of L-Arg to NHA is a two-electron oxidation of one of the guanidino nitrogens of L-Arg. This step is believed to parallel a P450 hydroxylation reaction with direct involvement of the heme in oxygen activation [4, 6, 109]. In the second half of the overall reaction, the conversion of NHA to L-citrulline and •NO is a three-electron oxidation of the substrate involving electron removal, oxygen insertion, and carbon–nitrogen bond scission to form product [12, 90, 110]. NADPH stoichiometry for all three isoforms under multiple turnover conditions suggests that 1.5 mol of NADPH is consumed to generate 1 mol of •NO and L-citrulline [111–113]. Of these three electrons, the conversion of L-Arg to NHA utilizes two electrons, while the formation of •NO and L-citrulline from NHA requires the remaining 0.5 mol of NADPH. Related ¹⁸O₂ experiments demonstrated that the oxygen atoms incorporated into •NO and L-citrulline originate from different molecules of molecular oxygen [114, 115]. The interesting aspect of NOS chemistry is that the enzyme converts substrates (L-Arg, O₂ and NADPH) with an even number of electrons into products that also contain an even number of electrons (L-citrulline, water, and NADP⁺) plus the free-radical species, •NO [90].

Conversion of L-Arg to *N*^ω-hydroxy-L-arginine

The first half of the working mechanism shown in Figure 15 originates from proposals in the NOS literature [116, 117] involving the formation of a high-valent oxo

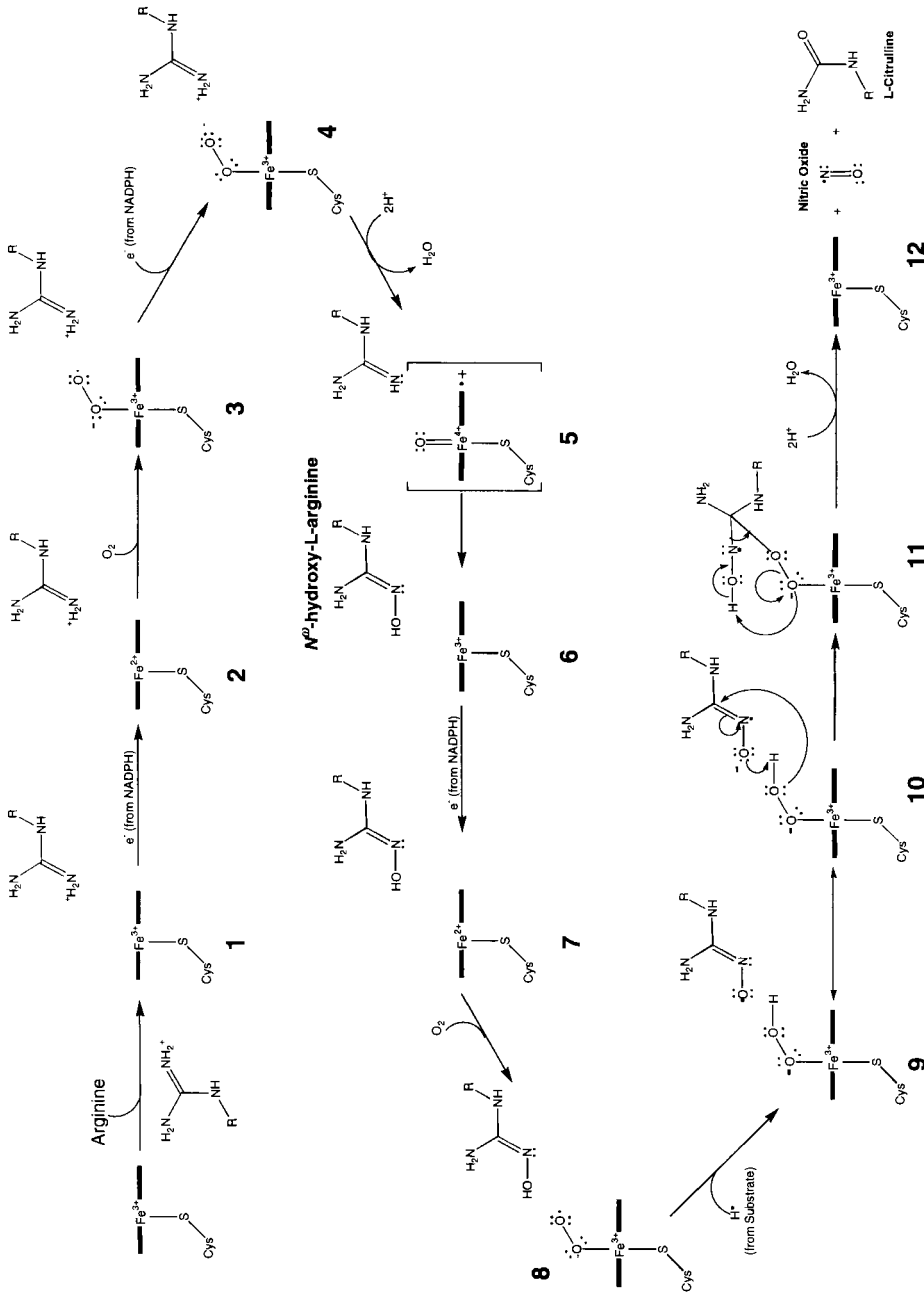


Figure 15. Proposed mechanism for the biosynthesis of nitric oxide from L-arginine. See text for details. (Adapted from Ref. [90].)

heme complex analogous to Compound I in P450 and peroxidase chemistry. Initially, the ferric five-coordinate largely high-spin resting state binds L-Arg to form the totally high-spin substrate bound complex (1). Upon addition of an electron from NADPH, the ferric-iron is reduced to the deoxyferrous complex (2). One equivalent of dioxygen binds to the ferrous heme iron to form the oxyferrous complex, shown in Figure 15 as the ferric superoxide resonance form (3). Addition of a second electron to 3 from NADPH is proposed to give a ferric peroxide complex (4) that can then be doubly protonated to lose water and yield the oxo-ferryl ($\text{O}=\text{Fe}^{\text{IV}}$) porphyrin radical intermediate (5). Unlike P450s where protons are shuttled in from the surface of the protein via a distal charge relay, structural data implicate the proton-rich guanidinium group of L-Arg as the proton source (Figure 16) [100]. The position of the terminal nitrogen 3.8 Å from the heme iron permits the donation of protons to the peroxo-iron, facilitating O–O bond cleavage and reduction of the guanidinium charge [100]. Following O–O bond cleavage, the substrate can then react with the remaining electrophilic oxo-iron species to form the hydroxylated product, NHA.

Similarities between NOS and P450 (e.g., thiolate-ligation to the heme, close proximity of the substrate to the active oxygen intermediate, and O_2 and NADPH requirements) provide a powerful argument for a P450-type reaction mechanism. However, other mechanistic proposals have been offered which liken NOS to an amino acid hydroxylase rather than to a P450. The reasoning behind an alternative catalytic pathway for NOS is two-pronged. First, hydrogen peroxide is unable to catalyze the formation of NHA from L-Arg. This reaction—also known as the peroxide shunt—allows hydrogen peroxide to replace O_2 and the two electrons from NADPH, and is well established for P450 enzymes. Second, experiments by Perry and Marletta determined that addition of exogenous nonheme iron increased nNOS activity [118]. This stimulation led to the proposal that the pterin and the nonheme iron are in close proximity such that both participate in oxygen activation and hydroxylation [118]. This catalytic mechanism would account for the inability of hydrogen peroxide to substitute for oxygen and NADPH. Recent crystallographic analysis of tyrosine hydroxylase [119] and NOS [100–102, 106] refute these proposed roles for mononuclear iron and the pterin by revealing little similarity between the two enzymes. In fact, no mononuclear metal binding site could be found in NOS [100–102, 106]. In light of this evidence, the monooxygenation of L-Arg by NOS likely follows a P450-type mechanism, despite the ineffectiveness of hydrogen peroxide in catalytic turnover.

Conversion of N^ω -hydroxy-L-arginine to L-citrulline and •NO

Single turnover experiments by Stuehr and coworkers have determined that only one exogenous electron is necessary for conversion of NHA to products [120]. These results argue against participation of the P450-like oxo-ferryl intermediate and instead favor a ferric-superoxide complex as the reactive oxygen intermediate in the catalytic mechanism. In the first half of the NOS reaction, the ferric superoxy complex is thought to be only an intermediate that leads to a “reactive oxygen species” capable of hydroxylating L-Arg, whereas in the second half it may react

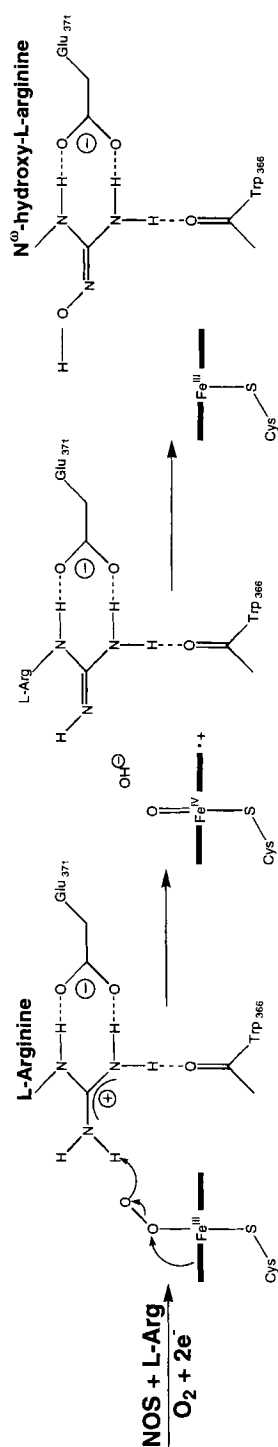


Figure 16. Proposed L-arginine-assisted NOS oxygen activation. First, substrate L-arginine (only guanidinium shown) donates a proton to the peroxo-iron, facilitating O-O bond cleavage and conversion to a proposed oxo-ferryl π -cation radical species. The radical species then rapidly hydroxylates the neutral guanidinium to N^{ω} -hydroxy-L-arginine. (Adapted from Ref. [100].)

directly with the substrate, NHA. Following the formation of NHA (Figure 15), reduction of the regenerated ferric five-coordinate species (6) by an electron from NADPH yields a five-coordinate ferrous adduct (7). Dioxygen binds in the sixth coordination site to form the ferric-superoxide complex (8). A hydrogen atom from the NHA reduces the ferric-superoxide adduct to form the ferric-hydroperoxide complex (9) and a cation radical on the guanidino carbon of the substrate. The ferric-hydroperoxide species nucleophilically attacks the guanidino carbon ($^-\text{O}-\text{N}^+=\text{C}(\text{NH}_2)-\text{NHR}$) of the substrate (10), which undergoes electron arrangement (11) to produce L-citrulline, $\bullet\text{NO}$, and the ferric resting state (12) [12, 110].

The exact identity of the reactive oxygen intermediate in the conversion of NHA to products is the focus of much experimental investigation. Structures of NHA-bound iNOS [106] impose mechanistic constraints due to steric clash between NHA and the iron-bound dioxygen ligand. This negative interaction favors either free radical addition of the ferric superoxy to the NHA oxime or proton donation from protonated N^ω to the heme species [106]. Furthermore, positioning of the NHA hydroxyl group may direct NOS towards a ferric-peroxo-NHA radical intermediate prior to breakdown into products [106]. However, these structures do not discount participation of a high-valent iron-oxo species in the second half of the reaction. In fact, an iron-oxo would be well situated relative to the NHA oxime to form an oxaziridine (which has a triangular ring with C, N, and O atoms) that could ring-open to produce L-citrulline and $\bullet\text{NO}$ [106]. This type of intermediate has also been proposed to explain the additional products, cyanoornithine and NO^- , observed when the NOS reaction is shunted with peroxide [121]. However, L-citrulline formation in the hydrogen peroxide-dependent oxidation of NHA can be accounted by either mechanism involving a ferric peroxo or an iron-oxo intermediate. Thus, the reaction with hydrogen peroxide cannot be considered to occur exclusively via an iron-oxo intermediate. The lack of cyanoornithine and NO^- under natural turnover conditions favors ferric superoxy over Compound I as the reactive oxygen intermediate when NADPH and O_2 serve as reactants. Recent spectral evidence obtained by Stuehr and coworkers [114] demonstrates that the ferrous oxygenase domain of nNOS can catalyze a quantitative conversion of NHA and dioxygen to citrulline and $\bullet\text{NO}$ in a single turnover reaction. Stopped-flow spectral analysis indicates formation of a ferrous-oxy (or ferric superoxy) species ($\lambda_{\text{max}} = 427 \text{ nm}$) prior to NHA oxidation [116]. Two other groups, using full-length NOS with bound L-Arg [122] or nNOS oxygenase domain with bound N^ω -methyl-L-Arg [123], have observed a ferrous-oxy species that exhibits a considerably more blue-shifted Soret absorption band ($\lambda_{\text{max}} = 415\text{--}419 \text{ nm}$) at -30°C in 50 % ethylene glycol. Examination of the formation and reactivity of the ferric superoxy complex with NHA shows a build-up of the ferric NO species prior to regeneration of the ferric resting state [116]. The accumulation of this intermediate establishes the $\bullet\text{NO}$ radical as the primary product rather than other N-oxides such as nitroxyl, which would generate a ferrous NO complex with the heme. The sum of these studies, while not completely dismissing Compound I as an active participant in catalytic turnover, supports the proposed mechanism shown in Figure 15, indicating that the O–O bond is intact during the NHA oxidation in NADPH-dependent catalysis.

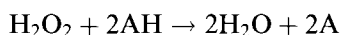
The role of tetrahydrobiopterin

Initially, the role of H₄B in the NOS system appeared to one of dimer stabilization, as indicated by its tight binding at the dimer interface [100–102]. Recent structural and mechanistic investigations have helped to clarify and expand this role, arguing that the cofactor may also participate directly in the NOS catalytic mechanism. Comparison of a series of dihydro- (H₂B) and tetrahydropterins (H₄B) in supporting electron transfer, •NO formation, and dimer formation demonstrates the absolute requirement for reduced pterin for formation of products but not for stable dimer formation [124]. In addition, H₄B decreases the stability of the NOS oxyferrous complex [125], which clearly implies communication between the pterin and heme sites. Studies of dimerization and catalytic competency of H₄B-free iNOS indicate that the pterin is essential for conversion of L-Arg to NHA, but not for conversion of NHA to products [104]. The inability of pterin-free NOS to convert L-Arg to NHA implies a direct catalytic role for H₄B in this portion of the reaction mechanism. Low-temperature, rapid-reaction experiments investigating the effect of H₄B on the decay of the oxyferrous complex of nNOS indicate that the pterin donates an electron to the heme dioxy complex in the presence of L-Arg [122]. Furthermore, recent EPR experiments show the formation of an apparently stable H₃B• radical under single turnover conditions when L-Arg is the substrate [117]. These results, coupled with the known location of the pterin within the crystal structure, are most consistent with H₄B being involved in electron transfer to the heme group in NOS rather than direct interaction with the substrate. The role of H₄B in the conversion of NHA to products is more ambiguous. Pterin-free NOS is still able to convert NHA to L-citrulline and •NO; however, cyanoornithine and NO[−] are also formed [104]. The variation of the product profile in the absence of H₄B implies a role for the pterin in the NHA reaction. A direct redox role is unlikely, as some L-citrulline and •NO are formed. However, the formation of the cyanoornithine and NO[−] products is similar to the effect of shunting NOS with peroxide, indicating that the pterin may play a role in the modulation of the reductive pathway of the ferric superoxy heme complex.

4.4 Heme-Containing Plant Peroxidases

4.4.1 Introduction

Heme peroxidases are found extensively throughout the plant, animal, and bacterial kingdoms. These enzymes catalyze the oxidation of a wide variety of organic and inorganic substrates, with the concomitant reduction of hydrogen peroxide or other hydroperoxides (ROOH) to water to alcohols (ROH), respectively:



Peroxidases fall into two superfamilies (plant and mammalian) and a third, indistinct group that includes chloroperoxidase (a P450-like hybrid) and di-heme cytochrome *c* peroxidase from *Pseudomonas aeruginosa*. The plant peroxidase superfamily contains enzymes of plant, fungal, and bacterial origin [126]. Mammalian peroxidases make up the second superfamily, and include lactoperoxidase, myeloperoxidase, and prostaglandin H synthase. Both families have been the focus of numerous excellent reviews, several of which have discussed the differences between the plant and mammalian peroxidases [126–130]. Here, recent experimental investigations focused on the plant peroxidases will be discussed.

The plant peroxidase superfamily can be further divided into three classes based on sequence and structural similarities [126]. Class I constitutes intracellular peroxidases of prokaryotic origin, such as yeast cytochrome *c* peroxidase (CCP) and pea cytosolic ascorbate peroxidase (APX). The main role of this class of peroxidases appears to be the removal of hydrogen peroxide. Secretory fungal peroxidases such as lignin peroxidase (LIP) and manganese peroxidase (MnP) from *Phanerochate chrysosporium* and *Corpinus* peroxidase (CIP) make up Class II. These enzymes are monomeric glycoproteins, with four conserved disulfide bridges and two conserved calcium sites. The secretory plant peroxidases form Class III. These enzymes are also monomeric glycoproteins, with four conserved disulfide bridges and two conserved calcium sites; however, the location of the disulfide bridges varies from those in Class II enzymes. Enzymes in Class III include peanut peroxidase (PNP), barley grain peroxidase (BP 1), and horseradish peroxidase (HRP), the most thoroughly investigated heme-containing peroxidase.

4.4.2 The Molecular Structure of Heme Peroxidases

In 1980, CCP became the first heme peroxidase to be structurally characterized. Reaction mechanisms, substrate binding sites and ligand interactions were proposed based on the various structures of CCP and carefully applied to the entire plant peroxidase family. During the past decade, a vast number of X-ray crystal structures have been reported for other members of the plant peroxidase superfamily. Presently, structural data are available for members of Class I: CCP [131–137] and APX [138–140]; Class II: MnP [141, 142], LIP [143, 144] and CIP [145]; and Class III: HRP [146–148], PNP [149] and BP 1 [150]. Of the numerous plant peroxidases, Class III members are the most readily available and have been the most extensively studied. The solution of crystal structures of three Class III peroxidases is a recent and exciting development. These structures provide researchers with the structural framework for addressing several mechanistic questions, such as how and where substrates bind to the enzyme, and how the protein controls the location of oxidizing equivalents derived from peroxide. In addition, the availability of structural information for the members of each class gives researchers the first opportunity to compare closely the tertiary environment among members of the same and different classes. This comparative power provides great insight into the relationship between structure and function within the plant peroxidase superfamily.

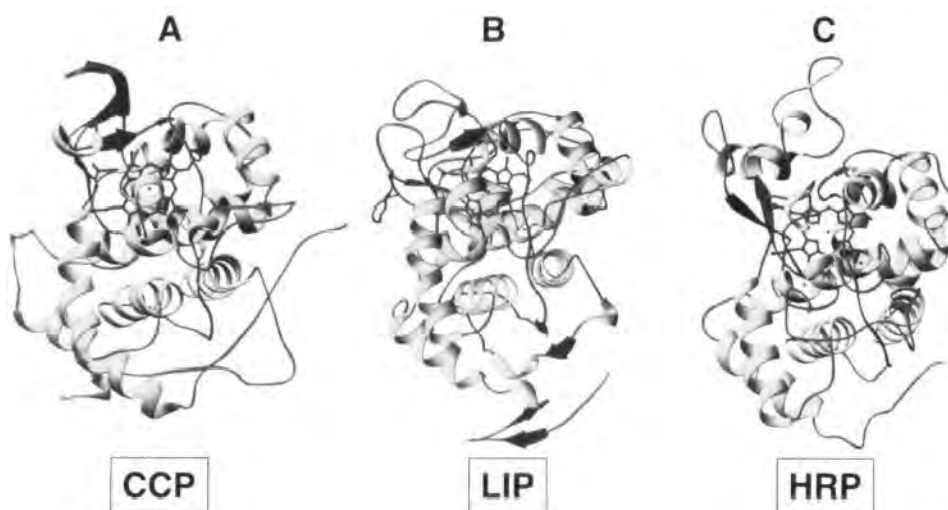


Figure 17. Schematic representation of the secondary structure of (A) CCP; (B) LIP; and (C) HRP determined from X-ray coordinates [137, 143, 211]. Helical regions, β -sheet regions, and the heme group are shown.

Although there is little sequence homology (often <20 %) within the plant superfamily, the overall folding and organization of the secondary structure is conserved. Figure 17 shows a side-by-side comparison of the secondary and tertiary structure of a representative member of each plant superfamily class. The enzymes are divided into N- and C-terminal domains, with the heme positioned in a cavity at the domain interface. The secondary structure is dominated by α helices (10 to 11 helices) connected by loops and turns of varying lengths. β -sheet structure is minimal. There are nine invariant residues in the plant peroxidase superfamily, five of which are involved in catalysis [128]. The other conserved residues play important structural roles, such as a buried salt bridge between an aspartate and arginine and several glycine and proline residues that direct the orientation of the peptide backbone [126, 129]. Figure 18 shows the active site environment of CCP, LIP, and HRP and the nonvariant residues. The proximal ligand to the heme is a histidine residue that is anionic in nature due to a conserved hydrogen bond to a proximal aspartate residue [128]. On the distal side of the heme, a polar histidine and arginine couple form a hydrophobic cavity above the heme that is important in the stabilization of the bound peroxide and the heterolytic cleavage of the O–O bond [128]. Additionally, an aromatic tryptophan (Class I) or phenylalanine (Class II and III) on the distal side of the heme helps to stabilize the high-valent oxygen intermediates as well as to exclude substrates from the active site. Similarly, a tryptophan (Class I) or phenylalanine (Class II and III) can be found in the proximal cavity and is believed to direct the location of the second oxidizing equivalent of Compound I [128].

In addition to these similarities, there are several distinctions among the plant peroxidases that help to differentiate between catalytic mechanism and substrate

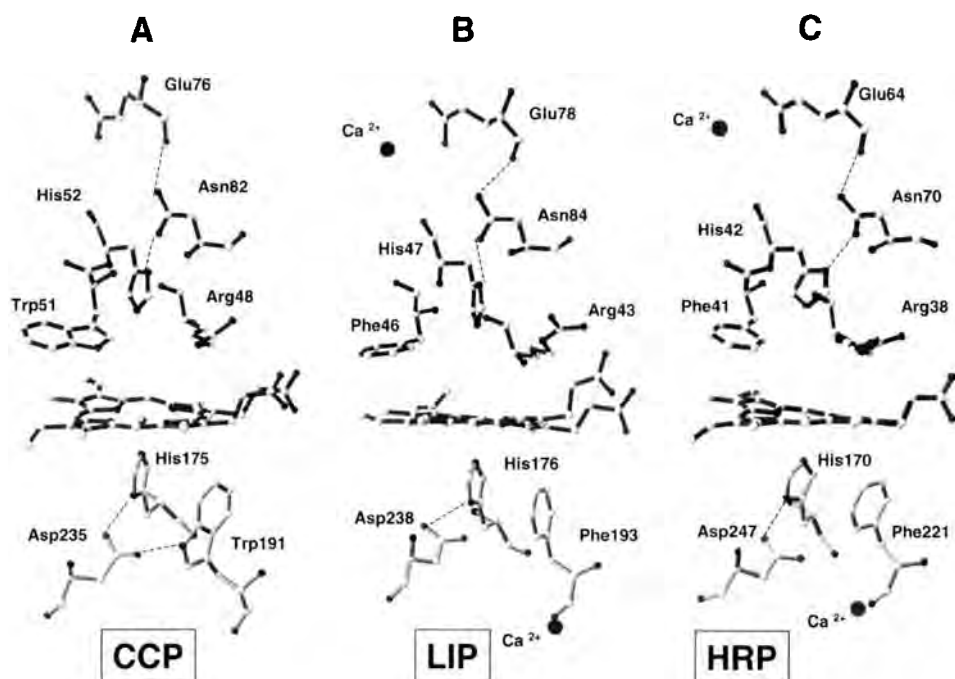


Figure 18. Key catalytic residues for (A) CCP; (B) LIP; and (C) HRP determined from X-ray coordinates [137, 143, 211]. The heme group is coordinated by a histidine and the sixth position is vacant. Calcium-binding sites for LIP and HRP are shown as spheres. Dashed lines represent hydrogen-bonding interactions.

affinity of the class members. In Class II and III peroxidases, all the cysteine residues in the protein (8 to 10 residues) form disulfide bridges that impart a high degree of rigidity to the protein [129]. Glycosylation sites for the Class II and III peroxidases point away from the molecule and are evenly distributed over the surface of the protein. This scattering suggests that the purpose of the carbohydrates is to increase the solubility of the enzyme in water, and perhaps to increase resistance to free radical-induced protein cross-linking [146].

With the exception of CCP, it is widely accepted that substrates interact with peroxidases at the heme edge rather than above the heme, as seen for the oxygenases. This postulation has been supported by structural and chemical modification data. Chemical modification studies with HRP have shown that the area directly above the heme is inaccessible to exogenous substrates [151–153]. Instead, suicide inhibitors bind at the δ -meso heme carbon (see Figure 1). The structure of HRP in the presence of benzhyroxamic acid (BHA), a model for oxidizing substrates, demonstrates that the aromatic portion of BHA does in fact interact with the proposed aromatic binding region of HRP located at the heme edge [147]. However, BHA is an atypical reducing substrate with unique hydrogen bonding potential for the

active site residues of the distal heme pocket, and therefore may not be an accurate structural model of the peroxidase–substrate complex. Recently, a structure of the HRP–ferulic acid (FA) complex in the presence and absence of cyanide has been published [148]. As FA is known to act as an *in vivo* substrate for peroxidases [148], these structures may provide a more precise model for the oxidation of small phenolic complexes by a plant peroxidase. Similar to BHA, FA binds in the aromatic binding pocket, but its exact orientation is ambiguous due to a flexibility of the aromatic donor binding region. This flexibility allows for the fast exchange of solvent molecules and small phenolic compounds, thereby protecting the heme group from autooxidative damage by the radical product of catalytic turnover [148]. Addition of cyanide to the system yields a six-coordinate low-spin heme complex that is thought structurally to model the transient intermediate ($\text{Fe}^{3+}\text{--OOH}^-$) prior to Compound I formation. Comparison of the structures of this ternary complex (HRP–FA–CN) with those of native HRP, the HRP–BHA and the HRP–FA species illustrates movement of the distal histidine 0.5 Å towards the cyanide nitrogen, thus supplying a short hydrogen bond to stabilize the binding of the ligand. The distal arginine does not move in any of the structures, but does help to stabilize cyanide by forming a hydrogen bond to the cyanide nitrogen [148]. This stabilization role for the distal arginine may imply that the residue assists in heterolytic bond cleavage by acting as a hydrogen bond donor to the transient $\text{Fe}^{3+}\text{--OOH}^-$ complex [148]. Similar to HRP, both APX and MnP have been shown to interact with their respective substrates at the heme edge rather than above the prosthetic group [139, 141, 142].

As the peroxidases interact with their substrates via the heme edge, it is important that the oxidizing equivalents of the high-valent active oxygen intermediates are accessible to the substrates. To this end, two calcium-binding sites—one distal and one proximal to the heme—serve dual structural and catalytic roles for the Class II and III proteins [127–129]. The distal site is important in the ordering of the distal active site residues, particularly the catalytically active histidine [127]. The proximal cation is responsible for structural stability, as well as promoting the location of the second oxidizing equivalent on the porphyrin macrocycle rather than a protein residue [127]. APX, a Class I peroxidase, contains a single cation binding site on the proximal side of the heme occupied by a potassium ion [138]. The cation destabilizes the electrostatic environment surrounding the proximal tryptophan involved in hydrogen bonding interactions with the proximal histidine ligand and the nearby aspartate (Figure 19). This long-range electrostatic effect forces the second oxidizing equivalent of Compound I to remain on the heme macrocycle, ideally positioned for reactions at the heme edge [154]. CCP, also a Class I peroxidase, interacts with its natural substrate, cytochrome *c*, not at the heme edge but via an electron transfer pathway that begins at Trp191 and terminates at the protein surface (Figure 20). As a result, CCP has no bound cations and maintains a stable cation radical on the indole ring of Trp191 rather than the porphyrin during catalytic turnover [137]. The continuing accumulation of structural information for plant peroxidases will allow the key similarities and differences to be exploited through mutagenesis to explore the physiochemical differences between members of the plant superfamily.

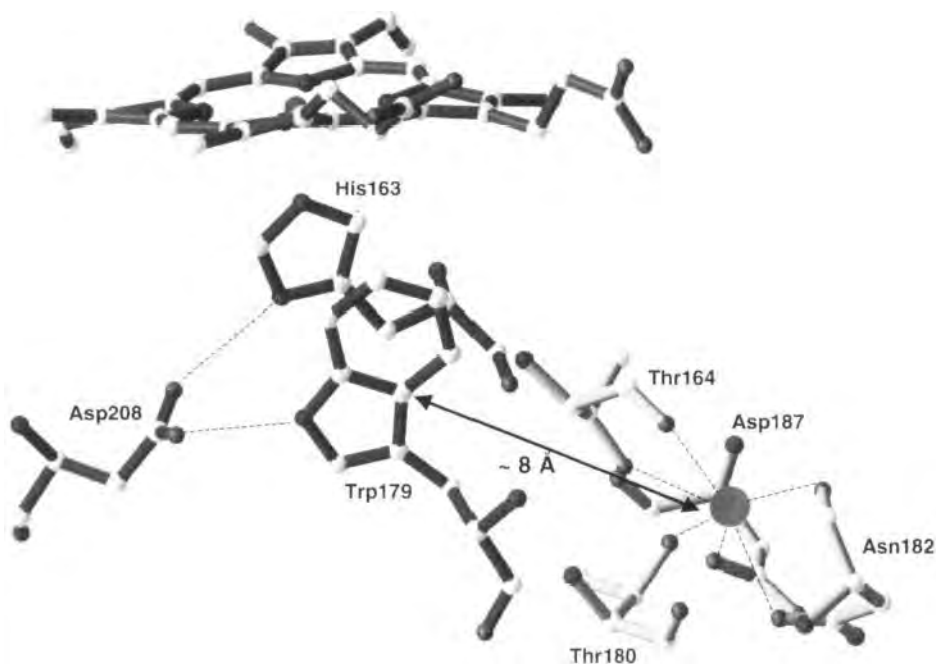


Figure 19. The APX proximal residues and cation-binding pocket generated from the X-ray coordinates [139]. The cation is shown as a sphere, with its protein interactions represented by dashed lines.

4.4.3 The Catalytic Mechanism of Heme Peroxidases

The general peroxidase mechanism

Following the determination of the crystal structure of CCP, a catalytic mechanism for its reaction with hydrogen peroxide was proposed [131, 136]. Due to the conservation of the active site residues in the plant peroxidase superfamily, similar mechanisms of Compound I formation are also thought to hold for other plant and fungal peroxidases. Of the structures shown schematically in Figure 21, three have been spectroscopically, and structurally characterized while two are proposed intermediates. The pathway is initiated by the direct reaction of neutral hydroperoxides (ROOH) or hydrogen peroxide with the ferric five-coordinate high-spin resting state complex (**1**) to generate a transient hydroperoxide adduct termed Compound 0 (**2**). Formation of this intermediate species is postulated by theoretical molecular dynamic simulations [155] and density functional studies [156], as well as being observed for HRP at low temperature [157]. This intermediate species then undergoes a protein-assisted conversion to an oxywater complex (**3**) [155, 156]. Facile heterolytic O–O bond cleavage of this oxywater complex yields the high-valent active oxygen intermediate, Compound I (**4**). For the majority of peroxidases

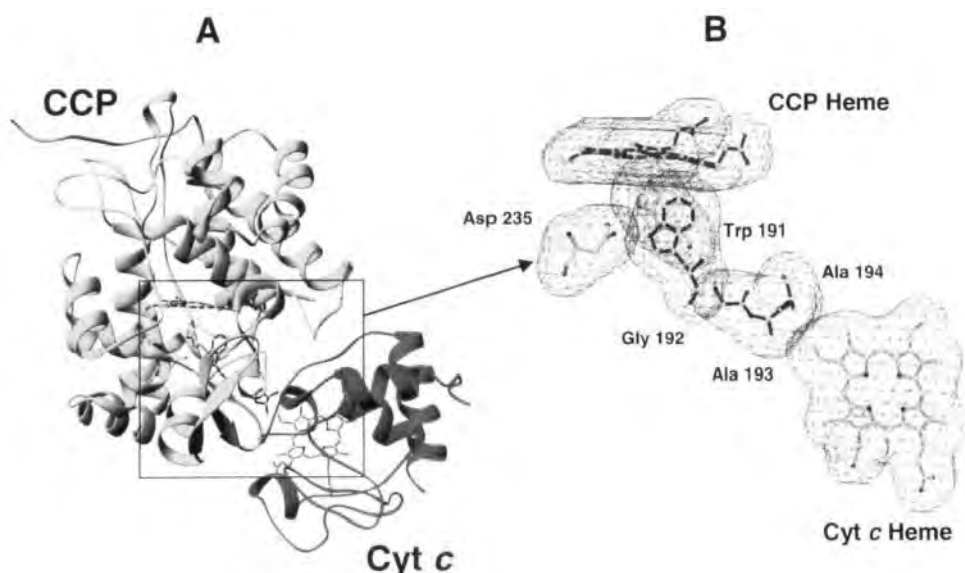


Figure 20. (A) Ribbon drawing of the interaction between CCP and its redox substrate, cytochrome *c* determined from X-ray coordinates [137]. The hemes are shown for CCP and cytochrome *c* along with the proximal residues involved in electron transport between the proteins. (B) A close-up of the electron transport chain and their overlapping electron density.

this complex is an oxo-ferryl species with a porphyrin cation radical similar to the Compound I seen in the P450 catalytic cycle (see Figure 4, complex 7). In CCP, the second oxidizing equivalent is intramolecularly transferred from the porphyrin to proximal Trp191 residue (Figure 18A), yielding a stable complex with a protein cation radical coupled with an oxo-ferryl heme [158, 159]. Reduction of Compound I to Compound II (5), an oxo-ferryl complex, and then to the ferric resting state, occurs with concomitant one-electron substrate oxidation forming reactive transient radical species that may dimerize, disproportionate, or attack another species causing cooxidation. Alternatively, oxygen atom donors can be added to the ferric resting state to generate Compound I, via a shunt pathway similar to that seen for P450 enzymes.

Influence of the active site environment on heme coordination and reactivity

The distal cavity

Extensive crystallographic and mutagenic studies have identified the key catalytic residues important in the formation and stabilization of the active oxygen intermediates. On the distal side of the heme, the conserved distal arginine/histidine couple is vital to efficient catalytic turnover by stabilizing and heterolytically cleaving bound peroxide to form the high-valent intermediate, Compound I (see Figure 7) [128]. The distal histidine acts as a general acid–base catalyst in the reaction of a

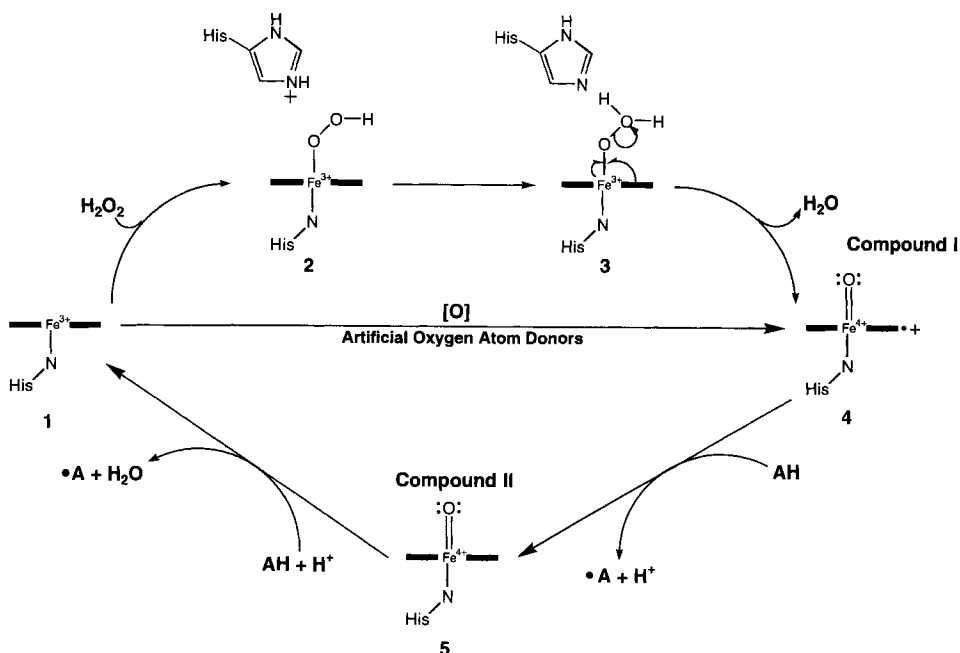


Figure 21. Peroxidase reaction cycle. AH represents the oxidizable substrate, and •A is the product. See text for details.

peroxidase with hydrogen peroxide by first deprotonating the iron-bound oxygen of peroxide (Figure 21, 2) then transferring the proton to the outer oxygen (Figure 21, 3) [128]. Deletion of this residue in both CCP (H52L) and HRP (H42A and H42V) results in the drastic reduction of the rate of Compound I formation by five orders of magnitude [160, 161]. This decrease in activity is presumably due to the elimination of a critical acid–base catalyst from the active site. Interestingly, activity of the H42A HRP mutant is restored by the addition of exogenous 2-substituted imidazoles (H42A + imidazole) [162]. Bronstead analysis predicts that ~60 % of a positive charge develops on the imidazole in the transition state of Compound I formation [162], confirming the acid–base role of the distal histidine.

Surprisingly, conversion of His42 of HRP to a glutamate [163], a residue shown to participate in general acid–base chemistry in chloroperoxidase (CPO) [164], yields an enzyme with lowered rates of Compound I formation and lowered levels of peroxidase activity [163]. In CPO, Compound I is formed at a rate ($2.3 \times 10^6 \text{ M}^{-1} \text{ s}^{-1}$) [165] much higher than H42E HRP ($4.9 \times 10^3 \text{ M}^{-1} \text{ s}^{-1}$) and comparable to wild-type HRP ($1.4 \times 10^7 \text{ M}^{-1} \text{ s}^{-1}$) [163]. The inefficient formation of Compound I is likely due to a decrease in the basicity of the glutamate residue and its improper orientation in H42E HRP compared to that of the native histidine. These alterations in the distal pocket destabilize the heme-peroxide-Glu42 ternary intermediate of the peroxide reaction [163]. The crystal structure of CPO shows that the distal

Glu is fixed in position by a hydrogen bond with an adjacent histidine [164]. Similarly, the orientation and basicity of the distal histidine in the plant peroxidases appears to be maintained by conserved hydrogen bonding interactions between the catalytic histidine and a highly conserved asparagine residue (see Figure 18). In HRP, mutation of this asparagine (Asn70) to valine (N70V) abolishes its hydrogen-bonding capabilities, causing a decrease in the rate of Compound I formation [166, 167]. Further studies reveal that its replacement with an aspartate (N70D) yields a mutant that should maintain the hydrogen bond with His42 but is still inactive [168]. Inactivation of HRP is likely due to the loss of a second hydrogen bonding interaction between Asp70 and the backbone carbonyl of a conserved glutamate residue (Glu64; Figure 18C). The disruption of this secondary interaction alters the orientation of the aspartate with regard to His42, resulting in the breakage of the Asp70–His42 hydrogen bond [168]. These findings demonstrate the manner by which the active site environment of the plant peroxidases has evolved to stabilize and promote the distal histidine as an active participant in the formation and stabilization of Compound I.

In contrast, the distal arginine residue does not appear to be absolutely essential in the formation of Compound I. In the mechanism proposed by Poulos et al. [131], the positively charged distal arginine is responsible for the promotion of O–O bond heterolysis by stabilizing the precursor enzyme–peroxide complex. Consistent with this proposed role, mutation of this polar residue to a neutral leucine in HRP (R38L) and CCP (R48L) causes a decrease in the rate of Compound I formation, particularly in the HRP mutants [169–173]. The reasoning for this variation of mutagenic effect stems from the increased polarity of the CCP distal pocket compared to that of HRP. As a result, the deletion of the distal arginine in CCP does not cause as drastic an effect on the ability of the enzyme to form Compound I [170, 171]. Moreover, the recently demonstrated crystal structure of HRP with ferulic acid and cyanide bound indicates that the distal arginine does indeed stabilize the bound ligand through hydrogen-bonding interactions [148].

Additional experiments with R38L HRP indicate that Arg38 may also play an important role in the binding of peroxide to the heme iron [171]. Researchers propose that the polar character of Arg38 in HRP facilitates the access of hydrogen peroxide to the heme and/or provides an electrostatic interaction with the incoming peroxide, which may induce the deprotonation of hydrogen peroxide at neutral pH [171]. Additionally, the reaction of H38L HRP with hydrogen peroxide results in the accumulation of a previously unseen intermediate formed prior to Compound I formation [171]. The spectroscopic properties of this complex are dissimilar from those of the proposed ferric peroxy intermediate (Figure 21, 2) isolated at low temperature for the reaction of wild-type HRP with peroxide [157]. Theoretical molecular modeling studies assign the new spectral intermediate to a neutral peroxide-bound ferric heme species [174].

In both peroxidases, the decay of Compound I is drastically increased by the deletion of the distal arginine, emphasizing its role as a stabilizer of the high-valent intermediate [169–171, 173, 175]. Crystallographic and resonance Raman data have shown that the distal arginine is very flexible, and can move towards or away from the ligand in the sixth position as needed [135, 176]. This flexibility allows the gua-

nitidinium groups to move inside the cavity and form a stabilizing hydrogen bond with the ferryl oxygen atom of Compound I and II [134].

The proximal cavity

Crystal structure data from representatives of each of the three classes of the plant peroxidase superfamily confirm that the side chain of an aspartate residue is involved in a key hydrogen bond to the N δ 1H of the proximal histidine residue (see Figure 18) [128, 146]. The purpose of this residue has been most investigated for CCP where the carboxylate side chain of Asp235 is involved in hydrogen bonds with both Trp191 and the proximal His175 ligand (Figure 18A). Using the wild-type enzyme and three CCP mutants (D235A, D235E, and D235N), three main roles have been proposed for this residue based on extensive spectroscopic characterization [71, 177]. First, the strong hydrogen bond from the proximal His to the adjacent Asp is believed to increase the electron density on the histidine imidazole ring, which in turn allows the imidazole group to stabilize the heme iron as it cycles through ferric and ferryl states during the catalytic cycle [71, 177]. Second, the strong hydrogen bond is believed to hold the iron below the heme plane, helping to maintain a vacant sixth coordination site [178]. Finally, the formation of a second hydrogen bond with the catalytically important Trp191 optimizes the orientation of the Trp side chain with respect to the heme and His175. Interestingly, the D235N CCP only showed a five-fold decrease in the rate of formation of Compound I [71] while the D235A CCP mutant rapidly forms Compound I [177]. These results demonstrate that the electronic donation to the heme iron via His175 does not significantly increase Compound I formation, indicating that Asp235 is not especially important for the reaction of the peroxidase with hydrogen peroxide. Recent mutagenic studies on CIP (D245N) and MnP (D242S and D242E) (two Class II peroxidases) confirm that changes in the axial ligand hydrogen-bonding network alter the occupancy of the sixth coordination site for the ferric protein as well as the reactivity of Compound II but not Compound I [179–181]. Similarly, mutation of the proximal ligand itself (His175) to Gln, Glu, or Cys results in CCP mutants that react with hydrogen peroxide as fast as wild-type CCP with the H175E mutant being hyperactive [182, 183]. Taken together, these data emphasize the importance of the distal rather than the proximal residues in the formation of Compound I. However, the proximal environment serves the equally significant roles of maintaining a free sixth coordination site for hydrogen peroxide binding and stabilizing Compound I once formed.

The role of the divalent cations in Class II and III peroxidases

All Class II and III plant peroxidases have two calcium binding sites, one proximal and one distal to the heme plane (see Figure 18B and C). These divalent cations appear to be vital for efficient peroxide catalysis by maintaining the structural integrity of the heme active site and directing the location of the second oxidizing equivalent derived from peroxide. A series of mutagenic studies with LIP and MnP ascertain that the calcium ions for these two peroxidases are released upon thermal inactivation [184–186]. The loss of these ions results in perturbations of the coordi-

nation sphere of the heme iron. LIP converts from an active five-coordinate high-spin complex to a mixture of active five-coordinate high-spin and inactive six-coordinate low-spin species [184]. The heme environment of MnP is particularly altered, resulting in an inactive six-coordinate low-spin complex with spectroscopic characteristics consistent with bis-histidyl ligation [185, 186]. In HRP, mutation of Glu64—a residue involved in both calcium binding and a hydrogen-bonding network with His42—gives an enzyme with significantly decreased oxidation activities [187]. This decrease in activity is attributed to the loss of the distal calcium ion, which causes the reorientation of both His42 and Arg38 [187].

APX contains a single cation binding site occupied by a potassium ion (see Figure 20) [138, 140]. This site is not seen for CCP, implicating the cation in the catalytic mechanism or regulation of APX. Similar to CCP, APX has an aromatic tryptophan on the proximal side of the heme that forms hydrogen bonds with both the proximal histidine ligand and the nearby aspartate (Figure 19) [138, 140]. In CCP, the analogous tryptophan is the location of the second oxidizing equivalent of Compound I. However, in APX, this equivalent is located on the porphyrin, similar to the Class II and III peroxidases [128, 154, 188]. Incorporation of a cation binding site into CCP results in an enzyme that is unable to form a stable cation radical on the proximal tryptophan. These results suggest that long-range electrostatic effects can control the reactivity of a redox amino acid side chain [189–191]. A similar result is seen for a mutant of HRP where the redox inactive proximal phenylalanine is replaced with a tryptophan (F221W). In this case, an unstable tryptophan cation radical is formed upon reaction with peroxide, but quickly dissipates into the protein matrix due to the improper orientation of the indole ring and its proximity to the proximal calcium ion [192]. Deletion of the cation site in APX results in an inactive six-coordinate low-spin species with spectroscopic similarity to a bis-histidyl complex [193]. Despite being located ~ 8 Å from the peroxide binding site, mutation of residues involved in binding of the potassium ion results in long-range conformational alterations [193]. Taken together, these studies emphasize the role the proximal cation plays in the both location of the oxidizing equivalents of Compound I, as well as in the preservation of the structural integrity of the heme active site.

4.4.4 Can Peroxidases Catalyze Peroxygenase Chemistry?

With resemblance of the active intermediates of their respective mechanistic cycles, it is somewhat surprising that peroxidase and monooxygenases do not catalyze similar reactions. Investigations by Ortiz de Montellano and coworkers have shown that the extent of protein surface exposure of the heme macrocycle for peroxidases and P450s plays an important role in the discretion of function of the enzyme [152, 153, 194]. Examination of reactions of HRP and P450CAM with alkyl- and phenylhydrazines shows that the hydrazine interacts with the iron of the monooxygenase, but is limited to the heme edge of the peroxidase [151–153]. Various distal side mutations in HRP have been made in an effort to maintain catalytic efficiency while opening up the distal cavity [162, 195]. Enhanced oxygenase activity

of HRP mutants such as F41A [161], H42A [161], H42E [163], and the two double mutants, F41H/H42A [195] and H42A/R38H [127] is the direct result of increasing substrate accessibility to the oxo-iron of Compound I. These results support the current hypothesis that the reactivity of the heme prosthetic group depends not only on the coordination of the heme iron itself but also on the topology of the protein surrounding it.

4.4.5 Development of CCP as a Protein Model System for Heme-Containing Enzymes

Complementary to the studies of native proteins and synthetic model systems, site-directed mutagenesis allows researchers rationally to design structural and catalytic mimics for different heme proteins from basic protein scaffolding such as CCP. This technique enables the researcher to alter the axial ligation of the protein in order to test principles obtained from earlier studies on the native protein, and to determine key structural features governing the discretion among protein functions. In the area of P450 models, this technique has been utilized to replace the histidine proximal ligand of CCP with a cysteine in order to engineer a P450-like protein in a peroxidase protein environment [183, 196]. Peroxidase and P450 enzymes have similar proposed reaction intermediates (e.g., Compounds I and II), though the lifetime and reactivity of those intermediates vary. As the main difference between a peroxidase and a P450 protein is the ratio of electron transfer to oxygenation, or the branching ratio, the catalytic differences between CCP and P450 are quite subtle. Initial attempts to place a cysteine ligand into a peroxidase environment were not successful [181]. Poulos and coworkers mutated the proximal His175 of CCP to Cys, but this did not result in thiolate ligation to the heme [183]. Instead, they determined by X-ray crystallography that the proximal Cys had been oxidized to cysteic acid [183]. It was suggested that this had occurred due to the smaller size of Cys relative to His, presumably leaving the Cys too far from the heme iron to bind properly, and thus susceptible to oxidation. Recent work by Lu, Dawson and co-workers indicates that the negative charge of the proximal Asp235 residue of CCP conflicts with the negative charge of the mutated thiolate ligand [196]. Replacement of Asp235 with a leucine residue resulted in a double mutant of CCP (H175C/D235L) which has UV-visible, magnetic circular dichroism and EPR spectral characteristics that are similar to those of camphor-bound P450 [196], indicating the potential of this system as a model for P450 enzymes.

Rational design has also been utilized to engineer artificial metal binding sites into CCP in an effort to mimic the active sites of MnP (a heme and manganese ion center), cytochrome *c* oxidase (COX, a heme and Cu_B center) and the potassium-binding site of APX. In the case of the MnP mimic, creation of a manganese binding site near the heme of CCP results in a model system which binds a single manganese ion, reacts with hydrogen peroxidase to form Compound I, and catalyzes the steady state oxidation of Mn²⁺ at enhanced rates compared to wild-type CCP [197–199]. In an effort to improve the MnP model, the two active site tryptophan residues (Trp191 and Trp51) of CCP have been mutated to their MnP-analogous phenyl-

alanine residues [200]. The results of this study demonstrate that, while the W191F and W51F mutations both play important roles in stabilizing Compound I, only the W51F mutation contributes significantly to increasing the MnP activity [200]. This effect is attributed to the ability of this mutation to increase the reactivity of Compound II, whose oxidation of Mn^{2+} is the rate-determining step in the reaction mechanism [200]. Preliminary results for the COX mimic indicate the successful binding of a copper ion above the heme plane of CCP upon mutation of three distal residues to histidines (R48H, W51H, and S81H) [201]. EPR studies of this CCP mutant strongly suggest that the heme Fe(III) is antiferromagnetically coupled to the added Cu(II) similar to the case in the Cu_B -heme center in all terminal oxidases [201]. Design of a proximal cation binding site similar to that seen for APX and the Class II and III plant peroxidases has also been accomplished for CCP [190, 191]. As expected, insertion of a potassium ion on the proximal side of CCP heme increases the electrostatic potential surrounding Trp191, and the proximal environment is no longer able to effectively stabilize a cationic Trp radical [190, 191]. In an extension of this work, slight alteration of the CCP template that binds potassium results in a CCP mutant that can bind a calcium ion [189]. Similar to the potassium-bound CCP, the cation decreases the stability of the Trp191 cation radical during hydrogen peroxide turnover [189]. The engineering of these varied metal-binding sites yields a deeper understanding for the structural factors that control metal-binding site selectivity.

In a departure from designing artificial metal-binding sites within CCP, recent attention has focused on replacing bulky amino acids with smaller residues such as glycine or alanine to form artificial cavities within the protein environment. Termed cavity mutants, these proteins have the unique ability to bind exogenous ligands either to reconstitute their wild-type activity or to catalyze an unnatural reaction. Initially, this approach focused on the deletion of the proximal ligand and the titration of different exogenous ligands into the proximal cavity in an effort to rescue the catalytic activity of the protein (Figure 22). Pioneered by Barrick for sperm whale myoglobin [202], this method has since been accomplished for CCP [203], heme oxygenase [204], and HRP [205]. For H175G CCP, studies to date have focused on the dynamics of binding unnatural ligands and the resulting effects on catalytic activity. Crystallographic analysis of H175G CCP in the presence of exogenous imidazole shows that the imidazole ligand occupies the same position as the natural histidine, and that there is little deviation in the protein structure [203]. Surprisingly, the imidazole-reconstituted system is devoid of activity despite the binding of the imidazole to the heme in the proximal pocket [203]. An oxo-ferryl species has been generated, although more slowly than for the wild-type [203]. Solid-state deuterium NMR studies investigated whether the unfettering of the proximal ligand from the protein enables it to adopt varied conformations or energetics that alter the pathway or interaction with hydrogen peroxide [206]. No evidence for intermediate ring flipping exchange dynamics or for large angular librations of the ring is observed [206]. Thus, the absence of enzymatic activity is not due to a disordered state for the untethered imidazole.

In an effort to introduce novel substrate oxidation into CCP, the catalytically important Trp191 is replaced with a glycine residue, forming a cavity on the prox-

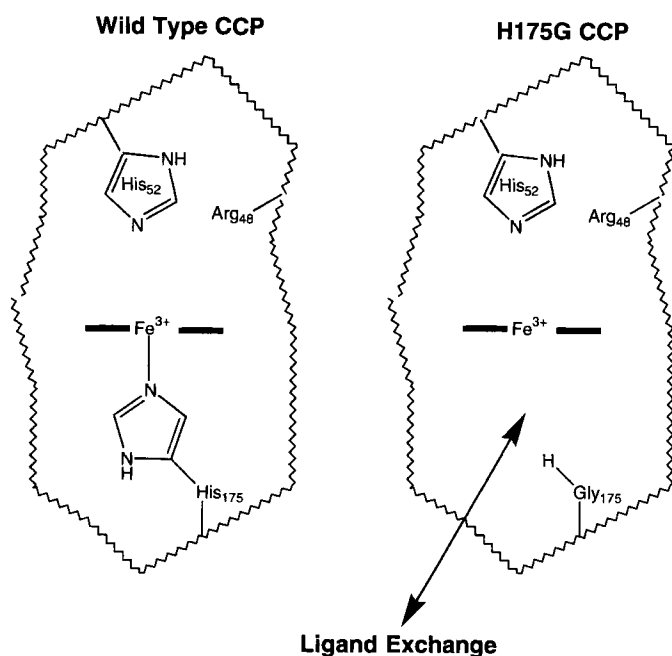


Figure 22. Schematic representation of the active sites of wild-type CCP and the CCP cavity mutant (H175G). Exogenous ligands can be titrated in, or dialyzed out of, the cavity.

imal side of the heme. This buried cavity is able to bind a range of small cationic imidazoles [207], illustrating its ability to stabilize molecules with positive charge. Similar to the imidazoles, 2-aminothiazole (2AT) will also bind within the cavity, as evidenced by calorimetric and crystallographic results [208]. Two separate reactions are observed between 2AT and the oxidized centers of W191G CCP. First, EPR and optical spectra show that 2AT acts as an electron donor to the ferryl center of W191G CCP to reduce it back to the ferric resting state [208]. Second, a less efficient reaction between 2AT and W191G CCP results in the specific covalent modification of Tyr236 [208]. This unexpected result provides the specific assignment of Tyr236 as the site of the alternate radical center when Trp191 is unavailable [208].

Recently, a cavity has been engineered into the distal cavity in an attempt to mimic the oxygenase activity of NOS. Crystallographic and optical studies show that the mutation of Arg48 to an alanine yields a cavity capable of binding *N*^ω-hydroxy-L-arginine (NHA) and *N*-hydroxyguanidine (NHG) [209]. Compound I formation is retained, with as many as three products being observed from the R48A/peroxide-catalyzed oxidation of NHA and NHG [209]. Characterization by mass-spectrometry of the derivatized products of NHA oxidation identified a yellow species as *N*-nitrosoarginine, thus implicating *N*-nitrosoguanidine as the product of NHG oxidation [209]. Therefore, while the hydrogen peroxide-dependent chemistry

catalyzed by R48A CCP has some features in common with that of NOS, namely the ability to oxidize *N*-hydroxyguanidines but not guanidines, the reaction products are clearly distinct from those previously reported for NOS (i.e., cyanamide or N^δ -cyanoornithine) [209].

4.5 Conclusions

The relationship between protein structure and function is an area of continuously growing knowledge, as well as problems. The various mechanisms by which oxygenases and peroxidases accomplish their respective reactions are a testament to the reactive versatility of the heme prosthetic group. For P450 enzymes, emerging crystallographic and mechanistic information is moving this field of biochemical research in new and exciting directions. With the growing understanding of how these enzymes interact with their respective substrates, redox partners and—in some cases—the membrane, the rational engineering of P450s may not be far away. Such a stride will enable researchers to tailor this versatile monooxygenase toward specific, biologically active compounds involved in both positive and negative physiological process. In the newer field of NOS research, the recent availability of structural data for two of the three NOS isoforms has helped to create a clearer picture of how this monooxygenase discriminates between active oxygen intermediates in its catalytic mechanism. Presently, mechanistic and mutagenic studies designed to test structure-based proposals are clarifying the role of the heme prosthetic group and the tetrahydrobiopterin in the efficient biosynthesis of nitric oxide. Finally, the recent addition of the crystal structure of HRP to the growing body of structural information on the plant peroxidase superfamily has enabled researchers to compare and contrast the secondary make-up of these versatile oxidases. The roles of many of the catalytic residues conserved across the three classes are now well understood—the result of exhaustive mutagenic and crystallographic studies. The exploitation of CCP as a protein scaffold for the engineering of novel activities and metal binding sites into a peroxidase environment now offers a biological alternative to inorganic model chemistry. The investigation and expansion of this application of rational protein design provides researchers with an opportunity to investigate the structure–function relationships in heme-containing enzymes that differentiate their catalytic activities.

Acknowledgments

We thank Professor Thomas L. Poulos for conveying results from his laboratory prior to publication. Additionally, we thank Drs. Anna-Maria Hays, Mark P. Roach, and Pamela A. Williams for helpful discussions and assistance in the preparation of this review.

Abbreviations

P450	cytochrome P450
P450CAM	camphor-hydroxylating P450 from <i>Pseudomonas putida</i>
NADH	nicotinamide adenine dinucleotide
NADPH	nicotinamide adenine dinucleotide phosphate
FAD	flavin adenine dinucleotide
FMN	flavin mononucleotide
P450BM-3	fatty acid-hydroxylating P450 from <i>Bacillus magisterium</i>
P450nor	nitric oxide-reducing P450 from <i>Fusarium oxysporum</i>
P450TERP	α -terpineol-oxidizing P450 from <i>Pseudomonas spheroids</i>
P450eryF	macrolide-hydroxylating P450 from <i>Saccaropolyspora erythraea</i>
P4502C5	microsomal P450 from rabbit
EXAFS	extended X-ray absorption fine structure
CCP	cytochrome <i>c</i> peroxidase
CPO	chloroperoxidase
•NO	nitric oxide
NOS	nitric oxide synthase
iNOS	inducible NOS
nNOS	neuronal NOS
eNOS	endothelial NOS
Ca ²⁺ /CaM	calcium–calmodulin complex
H ₄ B	tetrahydrobiopterin
H ₂ B	dihydrobiopterin
L-Arg	L-arginine
NHA	<i>N</i> ^ω -hydroxy-L-arginine
cGMP	cyclic guanine monophosphate
H ₃ B•	one-electron oxidized H ₄ B
APX	ascorbate peroxidase
LIP	lignin peroxidase
MnP	manganese peroxidase
CIP	peroxidase from <i>Coprinus cinereus</i>
PNP	peanut peroxidase
BP 1	barley grain peroxidase
HRP	horseradish peroxidase, isozyme C
BHA	benzhydroxamic acid
FA	C-ferulic acid
CN	cyanide
COX	cytochrome <i>c</i> oxidase
2AT	2-aminothiazole
NHG	<i>N</i> -hydroxyguanidine

References

1. Durham, B. and Millet, F.S. (1994) in *Encyclopedia of Inorganic Chemistry* (King, R.B.), pp. 1642, Wiley and Sons, Ltd., New York.
2. Walker, F.A. and Simons, U. (1994) in *Encyclopedia of Inorganic Chemistry* (King, R.B.), pp. 1785, Wiley and Sons, Ltd., New York.
3. Dawson, J.H. (1988) *Science* 240, 433–439.
4. Ortiz de Montellano, P.R. (Ed.) (1995) *Cytochrome P450: Structure, Function, and Biochemistry*, 2, Plenum, New York.
5. Dawson, J.H. and Eble, K.S. (1986) in *Advances in Inorganic and Bioinorganic Mechanisms* pp. 1–64, Academic Press, Ltd., London.
6. Sono, M., Roach, M.P., Coulter, E.D. and Dawson, J.H. (1996) *Chem. Rev.* 96, 2841–2887.
7. Antonini, E. and Brunori, M. (1971) *Hemoglobin and Myoglobin in their Reactions with Ligands* (Neuberger, A. and Tatum, E.L.), North-Holland Publishing Co., Amsterdam.
8. Goff, H.M. (1994) in *Encyclopedia of Inorganic Chemistry* (King, R.B.), pp. 1635, Wiley and Sons Ltd., New York.
9. Perutz, M. (1990) in *Mechanisms of Cooperativity and Allosteric Regulation in Proteins* pp. Cambridge University Press, New York.
10. English, A.M. (1994) in *Encyclopedia of Inorganic Chemistry* (King, R.B.), pp. 1682, Wiley and Sons Ltd., New York.
11. Dunford, H.B. (1991) in *Peroxidases in Chemistry and Biology* (Everse, J., Everse, K.E. and Grisham, M.B.), pp. 1, CRC Press, Boca Raton.
12. Marletta, M.A. (1993) *J. Biol. Chem.* 268, 12231–12234.
13. Stuehr, D.J. (1997) *Annu. Rev. Pharmacol. Toxicol.* 37, 339–359.
14. Reynolds, C.H. (1988) *J. Org. Chem.* 53, 6061.
15. Yamamoto, U., Noro, T. and Ohno, K. (1992) *Int. J. Quantum Chem.* 42, 1563.
16. Ghosh, A. (1997) *J. Phys. Chem. B* 101, 3290–3297.
17. Lamoen, D. and Parrinello, M. (1996) *Chem. Phys. Lett.* 248, 309.
18. Matsuzawa, N., Masafumi, A. and Dixon, D. (1995) *J. Phys. Chem.* 99, 7698.
19. Timkovich, R. and Bondoc, L.L. (1990) *Adv. Biophys. Chem.* 1, 203.
20. Mason, H.S., Fawlk, W. and Peterson, J. (1955) *J. Am. Chem. Soc.* 77, 2914.
21. Hayaishi, O., Katagiri, M. and Rothberg, S. (1955) *J. Am. Chem. Soc.* 77, 5450.
22. Hayaishi, O. (1974) in *Molecular Mechanisms of Oxygen Activation* (Hayaishi, O.), pp. 1–28, Academic Press, New York.
23. Garfinkel, D. (1958) *Arch. Biochem. Biophys.* 77, 493.
24. Klingenberg, A. (1958) *Arch. Biochem. Biophys.* 75, 376.
25. Omura, T. and Sato, R. (1964) *J. Biol. Chem.* 239, 2370.
26. Estabrook, R.W., Cooper, D.Y. and Rosenthal, O. (1963) *Biochem. Z.* 338, 741.
27. White, R.E. and Coon, M.J. (1980) *Annu. Rev. Biochem.* 49, 315–356.
28. Gunsalus, I.C., Meeks, J.R., Lipscomb, J.D., Debrunner, P. and Munck, E. (1974) in *Molecular Mechanisms of Oxygen Activation* (Hayaishi, O.), pp. 559–613, Academic Press, New York.
29. Poulos, T.L., Finzel, B.C., Gunsalus, I.C., Wagner, G.C. and Kraut, J. (1985) *J. Biol. Chem.* 260, 16122–16130.
30. Poulos, T.L., Finzel, B.C. and Howard, A.J. (1987) *J. Mol. Biol.* 195, 687–700.
31. Poulos, T.L. (1988) *Pharm. Res.* 5, 67–75.
32. Poulos, T.L. (1995) *Curr. Opin. Struct. Biol.* 5, 767–774.
33. Poulos, T.L., Cupp-Vickery, J.R. and Li, H. (1995) in *Cytochrome P450: Structure, Mechanism, and Biochemistry* (Ortiz de Montellano, P.R.), pp. 125–150, Plenum, New York.
34. Graham, S.E. and Peterson, J.A. (1999) *Arch. Biochem. Biophys.* 369, 24–29.
35. Fulco, A.J. (1991) *Annu. Rev. Pharmacol. Toxicol.* 31, 177–203.
36. Shiro, Y., Fujii, M., Isogai, Y., Adachi, S.-i., Iizuka, T., Obayashi, E., Makino, R., Nakahara, K. and Shoun, H. (1995) *Biochemistry* 34, 9052–9058.
37. Dawson, J.H. and Sono, M. (1987) *Chem. Rev.* 87, 1255–1276.
38. Brewer, C.B. and Peterson, J.A. (1988) *J. Biol. Chem.* 263, 791–798.

39. Pederson, T.C., Austin, R.H. and Gunsalus, I.C. (1977) in *Microsomes and Drug Oxidations* (Ullrich, V., Roots, I., Hildebrandt, A., Estabrook, R.W. and Conney, A.H.), pp. 275–283, Pergamon Press, Oxford, England.
40. Hawkins, B.K. and Dawson, J.H. (1992) *Front. Biotransform.* 7, 216.
41. Porter, T.D. and Coon, M.J. (1991) *J. Biol. Chem.* 266, 13469–13472.
42. Mueller, E.J., Loida, P.J. and Sligar, S.G. (1995) in *Cytochrome P450: Structure, Mechanism and Biochemistry* (Ortiz de Montellano, P.R.), pp. 83–124, Plenum, New York.
43. Loida, P.J. and Sligar, S.G. (1993) *Biochemistry* 32, 11530–11538.
44. Kadkhodayan, S., Coulter, E.D., Maryniak, D.M., Bryson, T.A. and Dawson, J.H. (1995) *J. Biol. Chem.* 270, 28042–28048.
45. Raag, R. and Poulos, T.L. (1992) *Front. Biotransform.* 7, 1–43.
46. Ravichandran, K.G., Boddupalli, S.S., Hasemann, C.A., Peterson, J.A. and Deisenhofer, J. (1993) *Science* 261, 731–736.
47. Hasemann, C.A., Ravichandran, K.G., Peterson, J.A. and Deisenhofer, J. (1994) *J. Mol. Biol.* 236, 1169–1185.
48. Cupp-Vickery, J.R., Li, H. and Poulos, T.L. (1994) *Proteins: Struct. Funct. Genet.* 20, 197–201.
49. Cupp-Vickery, J.R. and Poulos, T.L. (1995) *Nat. Struct. Biol.* 2, 144–153.
50. Park, S.-Y., Shimizu, H., Adachi, S.-I., Nakagawa, A., Tanaka, I., Nakahara, K., Shoun, H., Obayashi, E., Nakamura, H., Iizuka, T. and Shiro, Y. (1997) *Nat. Struct. Biol.* 4, 827–832.
51. Nakahara, K., Shoun, H., Adachi, S., Iizuka, T. and Shiro, Y. (1994) *J. Mol. Biol.* 239, 158–159.
52. Palma, P.N., Moura, I., LeGall, J., Van Beeumen, J., Wampler, J.E. and Moura, J.J.G. (1994) *Biochemistry* 33, 6394–6407.
53. Poulos, T.L., Finzel, B.C. and Howard, A.J. (1986) *Biochemistry* 25, 5314–5322.
54. Poulos, T.L. and Howard, A.J. (1987) *Biochemistry* 26, 8165–8174.
55. Li, H. and Poulos, T.L. (1997) *Nat. Struct. Biol.* 4, 140–146.
56. Raag, R. and Poulos, T.L. (1989) *Biochemistry* 28, 917–922.
57. Raag, R., Martinis, S.A., Sligar, S.G. and Poulos (1991) *Biochemistry* 30, 11420–11429.
58. Vidakovic, M., Sligar, S.G., Li, H. and Poulos, T.L. (1998) *Biochemistry* 37, 9211–9219.
59. Hasemann, C.A., Kurumbail, R.G., Boddupalli, S.S., Peterson, J.A. and Deisenhofer, J. (1995) *Structure* 3, 41–62.
60. Williams, P.A., Cosme, J., Sridhar, V., Johnson, E.F. and McRee, D.E. (2000) *Mol. Cell* 5, 121–131.
61. Schlichting, I., Berendzen, J., Chu, K., Stock, A.M., Maves, S.A., Benson, D.E., Sweet, R.M., Ringe, D., Petsko, G.A. and Sligar, S.G. (2000) *Science* 287, 1615–1622.
62. Dawson, J.H., Kau, L.S., Penner-Hahn, J.E., Sono, M., Eble, K.S., Bruce, G.S., Hager, L.P. and Hodgson, K.O. (1986) *J. Am. Chem. Soc.* 108, 8114–8116.
63. Macdonald, I.D.G., Sligar, S.G., Christian, J.F., Unno, M. and Champion, P.M. (1999) *J. Am. Chem. Soc.* 121, 376–380.
64. Loew, G.H. and Harris, D.L. (2000) *Chem. Rev.* 100, 407–419.
65. Penner-Hahn, J.E., Smith Eble, K., McMurry, T.J., Renner, M., Balch, A.L., Groves, J.T., Dawson, J.H. and Hodgson, K.O. (1986) *J. Am. Chem. Soc.* 108, 7819–7825.
66. Poulos, T.L. (1988) *Adv. Inorg. Biochem* 7, 1–36.
67. Poulos, T.L. and Finzel, B.C. (1984) *Peptide Protein Rev.* 4, 115–171.
68. Sundaramoorthy, M., Choudhury, K., Edwards, S.L. and Poulos, T.L. (1991) *J. Am. Chem. Soc.* 113, 7755–7757.
69. Erman, J.E., Vitello, L.B., Miller, M.A. and Kraut, J. (1992) *J. Am. Chem. Soc.* 114, 6592–6593.
70. Erman, J.E., Vitello, L.B., Miller, M.A., Shaw, A., Brown, K.A. and Kraut, J. (1993) *Biochemistry* 32, 9798–9806.
71. Vitello, L.B., Erman, J.E., Miller, M.A., Mauro, J.M. and Kraut, J. (1992) *Biochemistry* 31, 11524–11535.
72. Dawson, J.H., Holm, R.H., Trudell, J.R., Barth, G., Linder, R.E., Bunnenberg, E., Djerassi, C. and Tang, S.C. (1976) *J. Am. Chem. Soc.* 98, 3707–3708.
73. Sono, M., Andersson, L.A. and Dawson, J.H. (1982) *J. Biol. Chem.* 257, 8308–8320.

74. Sono, M. and Dawson, J.H. (1982) *J. Biol. Chem.* 257, 5496–5502.
75. Liu, H.I., Sono, M., Kadkhodayan, S., Hager, L.P., Hedman, B., Hodgson, K.O. and Dawson, J.H. (1995) *J. Biol. Chem.* 270, 10544–10550.
76. Adachi, S., Nagano, S., Ishimori, K., Watanabe, Y., Morishima, I., Egawa, T., Kitagawa, T. and Makino, R. (1993) *Biochemistry* 32, 241–252.
77. Urano, Y., Higuchi, T., Hirobe, M. and Nagano, T. (1997) *J. Am. Chem. Soc.* 119, 12008–12009.
78. Yi, X., Mroczko, M., Manoj, K.M., Wang, X. and Hager, L.P. (1999) *Proc. Natl. Acad. Sci. USA* 96, 12412–12417.
79. Shimada, H., Kimata, Y., Hirose, T., Kanamori, Y., Toba, Y. and Ishimura, Y. (1995) in *9th International Conference on Cytochrome P450 Biochemistry, Biophysics, and Molecular Biology* (eds.), pp. 16, Zurich, Switzerland.
80. Gerber, N.C. and Sligar, S.G. (1994) *J. Biol. Chem.* 269, 4260–4266.
81. Aikens, J. and Sligar, S.G. (1994) *J. Am. Chem. Soc.* 116, 1143–1144.
82. Martinis, S.A., Atkins, W.M., Stayton, P.S. and Sligar, S.G. (1989) *J. Am. Chem. Soc.* 111, 9252–9253.
83. Loida, P.J. and Sligar, S.G. (1993) *Protein Eng.* 6, 207–212.
84. Harris, D.L. and Loew, G.H. (1996) *J. Am. Chem. Soc.* 118, 6377–6387.
85. Imai, M. and Ishimura, Y. (1989) *Proc. Natl. Acad. Sci. USA* 86, 7823.
86. Yeom, H., Sligar, S.G., Li, H. and Poulos, T. (1995) *Biochemistry* 34, 14733–14740.
87. Kimata, Y., Shimada, H., Hirose, T. and Ishimura, Y. (1995) *Biochem. Biophys. Res. Commun.* 208, 96–102.
88. Gerber, N.C. and Sligar, S.G. (1992) *J. Am. Chem. Soc.* 114, 8742–8743.
89. Shimada, H., Makino, R., Unno, M., Horiuchi, T. and Ishimura, Y. (1994) in *Cytochrome P450 8th International Conference* (Lechner, M.C. and Libbey, J., eds.), pp. 299–306, Paris, France.
90. Feldman, P.L., Griffith, O.W. and Stuehr, D.J. (1993) *Chem. Engineer. News December*, 26–38.
91. Marletta, M.A. (1994) *Cell* 78, 927–930.
92. Stuehr, D.J. and Griffith, O.W. (1992) *Adv. Enzymol. Relat. Areas Mol. Biol.* 65, 287–346.
93. Nathan, C. (1992) *FASEB J.* 6, 3051–3064.
94. Masters, B.S.S., McMillan, K., Sheta, E.A., Nishimura, J.S., Roman, L.J. and Martasek, P. (1996) *FASEB J.* 10, 1107.
95. Bredt, D.S. and Snyder, S.H. (1994) *Annu. Rev. Biochem.* 63, 175–195.
96. Bredt, D.S., Hwang, P.M., Glatt, C.E., Lowenstein, C., Reed, R.R. and Snyder, S.H. (1991) *Nature* 351, 714–718.
97. Abusoud, H.M. and Stuehr, D.J. (1993) *Proc. Natl. Acad. Sci. USA* 90, 10769–10772.
98. Siddhanta, U., Presta, A., Fan, B., Wolan, D., Rousseau, D.L. and Stuehr, D.J. (1998) *J. Biol. Chem.* 273, 18950–18958.
99. Ghosh, K. and Stuehr, D.J. (1995) *Biochemistry* 34, 801–807.
100. Crane, B.R., Arvai, A.S., Ghosh, D.K., Wu, C., Getzoff, E.D., Stuehr, D.J. and Tainer, J.A. (1998) *Science* 279, 2121–2126.
101. Fischmann, T.O., Hruza, A., Da Niu, X., Fossetta, J.D., Lunn, C.A., Dolphin, E., Prongay, A.J., Reichert, P., Lundell, D.J., Narula, S.K. and Weber, P.C. (1999) *Nat. Struct. Biol.* 6, 233–242.
102. Raman, C.S., Li, H., Martasek, P., Kral, V., Masters, B.S.S. and Poulos, T.L. (1998) *Cell* 95, 939–950.
103. Narhi, L.O. and Fulco, A.J. (1987) *J. Biol. Chem.* 262, 6683–6690.
104. Rusche, K.M., Spiering, M.M. and Marletta, M.A. (1998) *Biochemistry* 37, 15503–15512.
105. Crane, B.R., Arvai, A.S., Gachhui, R., Wu, C., Ghosh, D.K., Getzoff, E.D., Stuehr, D.J. and Tainer, J.A. (1997) *Science* 278, 425–431.
106. Crane, B.R., Arvai, A.S., Ghosh, S., Getzoff, E.D., Stuehr, D.J. and Tainer, J.A. (2000) *Biochemistry* 39, 4608–4621.
107. Li, H., Raman, C.S., Glaser, C.B., Blasko, E., Young, T.A., Parkinson, J.F., Whitlow, M. and Poulos, T.L. (1999) *J. Biol. Chem.* 274, 21276–21284.
108. Crane, B.R., Rosenfeld, R.J., Arvai, A.S., Ghosh, D.K., Ghosh, A., Tainer, J.A., Stuehr, D.J. and Getzoff, E.D. (1999) *EMBO J.* 18, 6271–6281.

109. Guengerich, F.P. and Macdonald, T.L. (1990) *FASEB J.* 4, 2453–2459.
110. Griffith, O.W. and Stuehr, D.J. (1995) *Annu. Rev. Physiol.* 57, 707–736.
111. Klatt, P., Schmidt, K., Uray, G. and Mayer, B. (1993) *J. Biol. Chem.* 268, 14781–14787.
112. Stuehr, D.J., Kwon, N.S., Nathan, C.F., Griffith, O.W., Feldman, P.L. and Wiseman, J. (1991) *J. Biol. Chem.* 266, 6259–6263.
113. Presta, A., Liu, J., Sessa, W.C. and Stuehr, D.J. (1997) *Nitric Oxide* 1, 74–87.
114. Kwon, N.S., Nathan, C.F., Gilker, C., Griffith, O.W., Matthews, D.E. and Stuehr, D.J. (1990) *J. Biol. Chem.* 265, 13442–13445.
115. Leone, A.M., Palmer, R.M.J., Knowles, R.G., Francis, P.L., Ashton, D.S. and Moncada, S. (1991) *J. Biol. Chem.* 266, 23790–23795.
116. Boggs, S., Huang, L. and Stuehr, D.J. (2000) *Biochemistry* 39, 2332–2339.
117. Hurshman, A.R., Krebs, C., Edmondson, D.E., Huynh, B.H. and Marletta, M.A. (1999) *Biochemistry* 38, 15689–15696.
118. Perry, J. and Marletta, M.A. (1998) *Proc. Natl. Acad. Sci. USA* 95, 1101–1106.
119. Goodwill, K., Sabatier, C., Marks, C., Raag, R., Fitzpatrick, P. and Stevens, R. (1997) *Nat. Struct. Biol.* 4, 578–585.
120. Abu-Soud, H.M., Presta, A., Mayer, B. and Stuehr, D.J. (1997) *Biochemistry* 36, 10811–10816.
121. Clague, M.J., Wishnok, J.S. and Marletta, M.A. (1997) *Biochemistry* 36, 14465–14473.
122. Bec, N., Gorren, A.C.F., Voelker, C., Mayer, B. and Lange, R. (1998) *J. Biol. Chem.* 273, 13502–13508.
123. Ledbetter, A.P., McMillan, K., Roman, L.J., Siler Masters, B.S., Dawson, J.H. and Sono, M. (1999) *Biochemistry* 38, 8014–8021.
124. Presta, A., Siddhanta, U., Wu, C., Sennequier, N., Huang, L., Abu-Soud, H.M., Erzurum, S. and Stuehr, D.J. (1998) *Biochemistry* 37, 298–310.
125. Abu-Soud, H.M., Gachhui, R., Raushel, F. and Stuehr, D.J. (1997) *J. Biol. Chem.* 272, 17349–17353.
126. Welinder, K.G. (1992) *Curr. Opin. Struct. Biol.* 2, 388–393.
127. Smith, A.T. and Veitch, N.C. (1998) *Curr. Opin. Chem. Biol.* 2, 269–278.
128. English, A.M. and Tsapraillis, G. (1995) *Adv. Inorg. Chem.* 43, 79–125.
129. Banci, L. (1997) *J. Biotechnol.* 53, 253–263.
130. Poulos, T.L. (1993) *Curr. Opin. Biotechnol.* 4, 484–489.
131. Poulos, T.L., Freer, S.T., Alden, R.A., Edwards, S.L., Skogland, U., Takio, K., Eriksson, B., Xuong, N.H., Yonetani, T. and Kraut, J. (1980) *J. Biol. Chem.* 255, 575–580.
132. Poulos, T.E. and Kraut, J. (1980) *J. Biol. Chem.* 255, 10322–10330.
133. Edwards, S.L., Poulos, T.L. and Kraut, J. (1984) *J. Biol. Chem.* 259, 12984.
134. Edwards, S.L., Xuong, N.H., Hamlin, R.C. and Kraut, J. (1987) *Biochemistry* 26, 1503–1511.
135. Edwards, S.L. and Poulos, T.L. (1990) *J. Biol. Chem.* 265, 2588–2595.
136. Miller, M.A., Shaw, A. and Kraut, J. (1994) *Nat. Struct. Biol.* 1, 524–531.
137. Pelletier, H. and Kraut, J. (1992) *Science* 258, 1748–1755.
138. Patterson, W.R. and Poulos, T.L. (1994) *J. Biol. Chem.* 269, 17020–17024.
139. Patterson, W.R. and Poulos, T.L. (1995) *Biochemistry* 34, 4331–4341.
140. Mandelman, D., Jamal, J. and Poulos, T.L. (1998) *Biochemistry* 37, 17610–17617.
141. Sundaramoorthy, M., Kishi, K., Gold, M.H. and Poulos, T.L. (1994) *J. Biol. Chem.* 269, 32759–32767.
142. Sundaramoorthy, M., Kishi, K., Gold, M.H. and Poulos, T.L. (1997) *J. Biol. Chem.* 272, 17574–17580.
143. Poulos, T.L., Edwards, S.L., Wariishi, H. and Gold, M.H. (1993) *J. Biol. Chem.* 268, 4429–4440.
144. Piontek, K., Glumoff, T. and Winterhalter, K. (1993) *FEBS Lett.* 315, 119–124.
145. Petersen, J.F.W., Kadziola, A. and Larsen, S. (1994) *FEBS Lett.* 339, 291–296.
146. Gajhede, M., Schuller, D.J., Henriksen, A., Smith, A.T. and Poulos, T.L. (1997) *Nat. Struct. Biol.* 4, 1032–1038.
147. Henriksen, A., Schuller, D.J., Meno, K., Welinder, K.G., Smith, A.T. and Gajhede, M. (1998) *Biochemistry* 37, 8054–8060.
148. Henriksen, A., Smith, A.T. and Gajhede, M. (1999) *J. Biol. Chem.* 274, 35005–35011.

149. Schuller, D.J., Ban, N., van Huystee, R.B., McPherson, A. and Poulos, T.L. (1996) *Structure* 4(3), 311–321.
150. Henriksen, A., Welinder, K.G. and Gajhede, M. (1998) *J. Biol. Chem.* 273, 2241–2248.
151. Ortiz de Montellano, P.R. (1987) *Acc. Chem. Res.* 20, 289–294.
152. Ator, M.A. and Ortiz de Montellano, P.R. (1987) *J. Biol. Chem.* 262, 1542–1551.
153. Ator, M.A., David, S.K. and Ortiz de Montellano, P.R. (1987) *J. Biol. Chem.* 262, 14954–14960.
154. Patterson, W.R., Poulos, T.L. and Goodin, D.B. (1995) *Biochemistry* 34, 4342–4345.
155. Filizola, M. and Loew, G.H. (2000) *J. Am. Chem. Soc.* 122, 18–25.
156. Wirstam, M., Blomberg, M.R.A. and Siegbahn, P.E.M. (1999) *J. Am. Chem. Soc.* 121, 10178–10185.
157. Baek, H.K. and Vanwart, H.E. (1992) *J. Am. Chem. Soc.* 114, 718–725.
158. Sivaraja, M., Goodin, D.B., Smith, M. and Hoffman, B.M. (1989) *Science* 245, 738–740.
159. Scholes, C.P., Liu, Y., Fishel, L.A., Farnum, M.F., Mauro, J.M. and Kraut, J. (1989) *Isr. J. Chem.* 29, 85–92.
160. Miller, M.G., Coletta, M., Mauro, J.M., Putnam, L.D., Farnum, M.F., Kraut, J. and Traylor, T.G. (1990) *Biochemistry* 29, 1777–1791.
161. Newmyer, S.L. and Ortiz de Montellano, P.R. (1995) *J. Biol. Chem.* 270, 19430–19438.
162. Newmyer, S.L. and Demontellano, P.R.O. (1996) *J. Biol. Chem.* 271, 14891–14896.
163. Tanaka, M., Ishimori, K., Mukai, M., Kitagawa, T. and Morishima, I. (1997) *Biochemistry* 36, 9889–9898.
164. Sundaramoorthy, M., Turner, J. and Poulos, T.L. (1995) *Structure* 3, 1367–1377.
165. Sun, W., Kadima, T.A., Pickard, M.A. and Dunford, H.B. (1994) *Biochem. Cell Biol.* 72, 321–331.
166. Nagano, S., Tanaka, M., Ishimori, K., Watanabe, Y. and Morishima, I. (1996) *Biochemistry* 35, 14251–14258.
167. Mukai, M., Nagano, S., Tanaka, M., Ishimori, K., Morishima, I., Ogura, T., Watanabe, Y. and Kitagawa, T. (1997) *J. Am. Chem. Soc.* 119, 1758–1766.
168. Tanaka, M., Nagano, S., Ishimori, K. and Morishima, I. (1997) *Biochemistry* 36, 9791–9798.
169. Smith, A.T., Sanders, S.A., Sampson, C., Bray, R.C., Burke, J.F. and Thorneley, R.N.F. (1993) in *Plant Peroxidases Biochemistry and Physiology, Third International Symposium Proceedings* (Welinder, K.G., Rasmussen, S.K., Penel, C. and Greppin, H.), pp. 159–168, University of Geneva, Geneva.
170. Smulevich, G., Paoli, M., Burke, J.F., Sanders, S.A., Thorneley, R.N. and Smith, A.T. (1994) *Biochemistry* 33, 7398–7407.
171. Rodriguezlopez, J.N., Smith, A.T. and Thorneley, R.N.F. (1996) *J. Biol. Chem.* 271, 4023–4030.
172. Rodriguez-Lopez, J.N., Smith, A.T. and Thorneley, R.N.F. (1996) *J. Inorg Biochem.* 1, 136–142.
173. Vitello, L.B., Erman, J.E., Miller, M.A., Wang, J. and Kraut, J. (1993) *Biochemistry* 32, 9807–9818.
174. Harris, D.L. and Loew, G.H. (1996) *J. Am. Chem. Soc.* 118, 10588–10594.
175. Miller, M.A., Mauro, J.M., Smulevich, G., Coletta, M., Kraut, J. and Traylor, T.G. (1990) *Biochemistry* 29, 9978–9988.
176. Neri, F., Kok, D., Miller, M.A. and Smulevich, G. (1997) *Biochemistry* 36, 8947–8953.
177. Ferrer, J.C., Turano, P., Banci, L., Bertini, I., Morris, I.K., Smith, K.M., Smith, M. and Mauk, A.G. (1994) *Biochemistry* 33, 7819–7829.
178. Sinclair, R., Hallam, S., Chen, M., Chance, B. and Powers, L. (1996) *Biochemistry* 35, 15120–15128.
179. Veitch, N.C., Gao, Y. and Welinder, K.G. (1996) *Biochemistry* 35, 14370–14380.
180. Smulevich, G., Neri, F., Marzocchi, M.P. and Welinder, K.G. (1996) *Biochemistry* 35, 10576–10585.
181. Whitwam, R.E., Koduri, R.S., Natan, M. and Tien, M. (1999) *Biochemistry* 38, 9608–9616.
182. Smulevich, G., Neri, F., Willemsen, O., Choudhury, K., Marzocchi, M.P. and Poulos, T.L. (1995) *Biochemistry* 34, 13485–13490.

183. Choudhury, K., Sundaramoorthy, M., Hickman, A., Yonetani, T., Woehl, E., Dunn, M.F. and Poulos, T.L. (1994) *J. Biol. Chem.* 269, 20239–20249.
184. Nie, G. and Aust, S.D. (1997) *Biochemistry* 36, 5113–5119.
185. Sutherland, G.R., Zapanta, L.S., Tien, M. and Aust, S.D. (1997) *Biochemistry* 36, 3654–3662.
186. Sutherland, G.R.J. and Aust, S.D. (1997) *Biochemistry* 36, 8567–8573.
187. Tanaka, M., Ishimori, K. and Morishima, I. (1998) *Biochemistry* 37, 2629–2638.
188. Pappa, H., Patterson, W.R. and Poulos, T.L. (1996) *J. Inorg. Biochem.* 1, 61–66.
189. Bonagura, C.A., Bhaskar, B., Sundaramoorthy, M. and Poulos, T.L. (1999) *J. Biol. Chem.* 274, 37827–37833.
190. Bonagura, C.A., Sundaramoorthy, M., Bhaskar, B. and Poulos, T.L. (1999) *Biochemistry* 38, 5538–5545.
191. Bonagura, C.A., Sundaramoorthy, M., Pappa, H.S., Patterson, W.R. and Poulos, T.L. (1996) *Biochemistry* 35, 6107–6115.
192. Morimoto, A., Tanaka, M., Takahashi, S., Ishimori, K., Hori, H. and Morishima, I. (1998) *J. Biol. Chem.* 273, 14753–14760.
193. Cheek, J., Mandelman, D., Poulos, T.L. and Dawson, J.H. (1999) *J. Biol. Inorg. Chem.* 4, 64–72.
194. Ortiz de Montellano, P.R., Choe, Y.S., DePillis, G. and Catalano, C.E. (1987) *J. Biol. Chem.* 262, 11641–11646.
195. Savenkova, M.I., Newmyer, S.L. and Ortiz de Montellano, P.R. (1996) *J. Biol. Chem.* 271, 24598–24603.
196. Sigman, J.A., Pond, A.E., Dawson, J.H. and Lu, Y. (1999) *Biochemistry* 38, 11122–11129.
197. Yeung, B.K.S., Wang, X., Sigman, J.A., Petillo, P.A. and Lu, Y. (1997) *Chem. Biol.* 4, 215–221.
198. Wilcox, S.K., Putnam, C.D., Sastry, M., Blankenship, J., Chazin, W.J., McRee, D.E. and Goodin, D.B. (1998) *Biochemistry* 37, 16853–16862.
199. Wang, X. and Lu, Y. (1999) *Biochemistry* 38, 9146–9157.
200. Gengenbach, A., Syn, S., Wang, X. and Lu, Y. (1999) *Biochemistry* 38, 11122–11129.
201. Sigman, J.A., Kwok, B.C., Gengenbach, A. and Lu, Y. (1999) *J. Am. Chem. Soc.* 121, 8949–8950.
202. Barrick, D. (1994) *Biochemistry* 33, 6546–6554.
203. McRee, D.E., Jensen, G.M., Fitzgerald, M.M., Siegel, H.A. and Goodin, D.B. (1994) *Proc. Natl. Acad. Sci. USA* 91, 12847–12851.
204. Wilks, A., Sun, J., Loehr, T.M. and Ortiz de Montellano, P.R. (1995) *J. Am. Chem. Soc.* 117, 2925–2926.
205. Newmyer, S.L., Sun, J., Loehr, T.M. and Ortiz de Montellano, P.R. (1996) *Biochemistry* 35, 12788–12795.
206. Liu, K., Williams, J., Lee, H., Fitzgerald, M.M., Jensen, G.M., Goodin, D.B. and McDermott, A.E. (1998) *J. Am. Chem. Soc.* 120, 10199–10202.
207. Fitzgerald, M.M., Churchill, M.J., McRee, D.E. and Goodin, D.B. (1994) *Biochemistry* 33, 3807–3818.
208. Musah, R.A. and Goodin, D.B. (1997) *Biochemistry* 36, 11665–11674.
209. Hirst, J. and Goodin, D.B. (2000) *J. Biol. Chem.* 275, 8582–8591.
210. Sevrionkova, I.F., Li, H., Zhang, H., Peterson, J.A. and Poulos, T.L. (1999) *Proc. Natl. Acad. Sci. USA* 96, 1863–1868.
211. Gajhede, M., Schuller, D.J., Henriksen, A., Smith, A.T. and Poulos, T.L. (1997) *Nat. Struct. Biol.* 4, 1032–1038.

5 Electron Transfer and Charge Transport Processes in DNA

Frederick D. Lewis

5.1 Introduction

5.1.1 Background

The nucleic acids DNA and RNA are biopolymers with several essential biological functions, including the storage and transport of genetic information [1, 2]. They are constructed from relatively simple building blocks consisting of a pendant heterocycle (nucleobase) covalently attached to a backbone consisting of an alternating sugar-phosphate copolymer. Single-strand DNA and RNA can exist in a variety of secondary and tertiary structures. Cellular DNA exists predominantly as a duplex in which hydrogen-bonded base pairs form extended one-dimensional π -stacked arrays (see Section 5.1.2). This highly ordered structure is found nowhere else in nature, and thus has a special fascination for both biologist and chemists. Materials chemists have recently exploited the unique structural properties of the nucleic acids to prepare an amazing variety of two- and three-dimensional nanostructures [3]. The advent of molecular electronics has stimulated interest in molecular technologies based on DNA [4]. The use of DNA as a data carrier also provides the conceptual basis for DNA-based computing [5].

The nucleic acids can be oxidized by chemical and photochemical oxidants and by ionizing radiation [6–9]. Oxidation can result in strand cleavage, leading to loss or mutation of the genetic information carried by DNA or RNA and can lead in turn to cell death. Damage to duplex DNA is the most important effect of ionizing radiation upon the living cell, and thus has been the subject of extensive investigation by radiation biologists [9]. Oxidative cleavage of duplex DNA is observed to be site-selective, occurring predominantly at guanine-containing sites, particularly those with two or three adjacent guanines in the same strand. Since radiation can ionize all of the nucleobases, charge migration from the initial site of oxidation to the site of cleavage must occur. Understanding the nature of the charge migration process is thus essential to understand oxidative damage to DNA. The possibility

that the π -stacked nucleobases of duplex DNA might serve as a conduit or “ π -way” for electron transport was suggested by Eley and Spivey [10] in 1962, based on their studies of conductivity in dry samples of DNA and RNA.

During the past decade, photochemical methods have been widely used to investigate electron transfer processes in DNA [11–15]. Three distinct types of photo-induced electron transfer processes have been identified:

- 1) The direct electron transfer process between an excited molecule and nucleobase which occur either upon collision or excitation of a ground-state complex. Studies of this processes have helped define the energetic and geometric requirements for nucleobase oxidation and reduction.
- 2) A single-step electron transfer process between an excited molecule and ground-state molecule separated by a variable number of base pairs, DNA-mediated electron transfer. The possible occurrence of wire-like behavior in DNA has generated considerable controversy and the attention of the popular science press [16].
- 3) Charge transport, a process in which a cation radical (hole) generated at a specific site can migrate over long distances in DNA to a trap site where strand cleavage may occur [17].

Several recent reviews have dealt with specific aspects of the photoinduced electron-transfer process in DNA, including photoinduced cleavage and the distance dependence of electron transfer processes [6, 11–15]. Most of these have dealt mainly with a specific class of photooxidizing agents, transition metal complexes. Numerous shorter polemics either defending or attacking the “molecular wire” paradigm have also appeared [18]. The objective of this review is to present the current status of experimental and theoretical work on photoinduced electron transfer and charge transport processes in DNA. Emphasis will be placed on experiments which provide information about the dynamics of these processes either by direct spectroscopic measurements or indirect measurements of strand cleavage efficiency. The introduction is intended to provide a background for the nonexpert in the structure and properties of DNA and studies of its direct ionization. The following sections treat the three classes of photoinduced electron transfer described in the preceding paragraph and studies of DNA conductivity.

5.1.2 Structure and Properties of DNA

DNA structure

The primary structure of an oligonucleotide containing the four common deoxyribonucleotides found in DNA is shown in Figure 1a [19]. Each deoxyribonucleotide consists of three parts; a negatively charged phosphate, the sugar 2'-deoxyribose, and the heterocyclic nucleobase. The bases cytosine (C) and thymine (T) are derivatives of pyrimidine which has a single aromatic ring, whereas the bases adenine (A) and guanine (G) are derivatives of purine which has two fused aromatic rings.

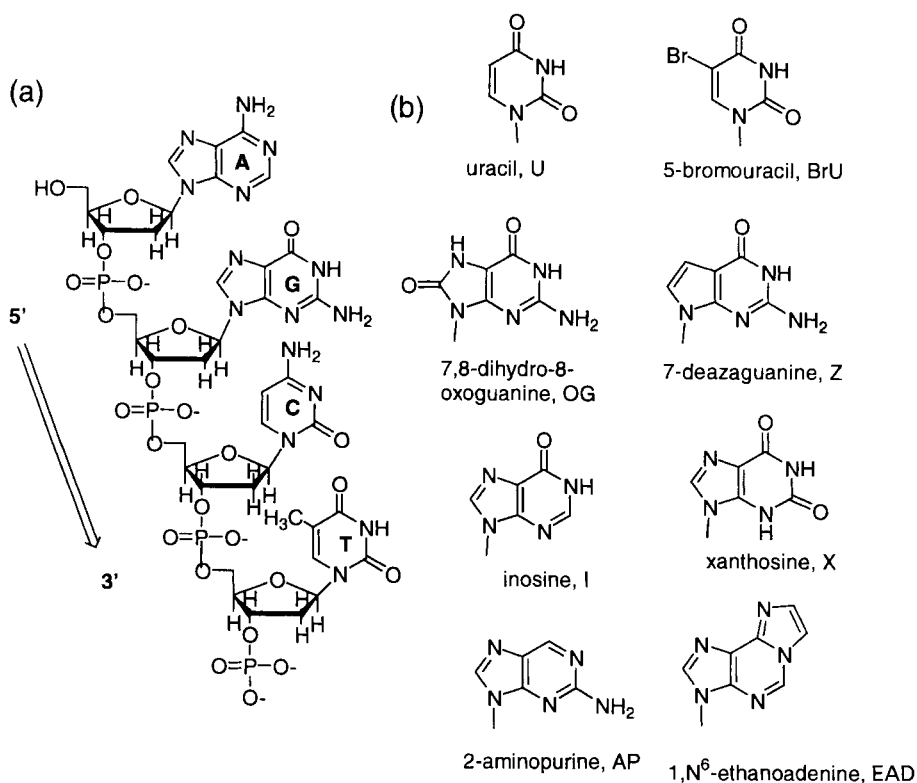


Figure 1. (a) The structure of an oligonucleotide composed of the four naturally occurring nucleobases adenine (A), guanine (G), cytosine (C), and thymine (T). (b) The structures of nucleobase analogues employed in electron transfer studies, and abbreviations used in this chapter.

A nucleotide lacking its phosphate is called a nucleoside, and a nucleoside lacking a sugar is called a nucleobase or base. The primary structure of RNA differs from that of DNA in that the sugar is ribose rather than 2'-deoxyribose and the pyrimidine thymine is replaced by uracil (U). In both DNA and RNA the phosphate group connects the 5' position of one ribose with the 3' position of the next. Thus, the oligonucleotide has a 5' → 3' polarity. Chemical modifications of the five common nucleobases are frequently encountered, particularly in RNA. The structures of several modified bases which have been employed in investigations of electron transfer process are shown in Figure 1b.

Under physiological conditions DNA exists predominantly as a duplex formed between complementary anti-parallel strands of DNA in which the purines of one strand are hydrogen bonded to the pyrimidines of the complementary strand and vice versa to form G:C and A:T base pairs. The Watson-Crick G:C base pairs (Figure 2) possess three hydrogen bonds and the A:T base pairs two hydrogen bonds, each hydrogen bond contributing approximately 2 kcal mol^{-1} to the stabil-

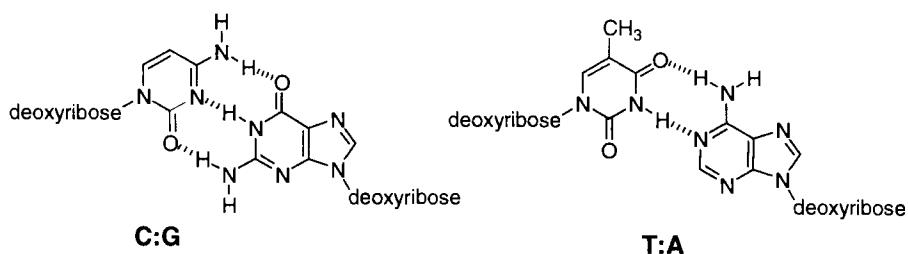


Figure 2. Base pairing in Watson–Crick C:G and T:A base pairs.

ity of the duplex. Duplex DNA can adopt one of several secondary structures, the most common of which is termed B-form DNA. B-form DNA adopts a right-hand helical structure (Figure 3) in which the hydrophobic base pairs form a π -stacked array perpendicular to the helical axis, with a stacking distance of 3.4 Å [20]. Base stacking is energetically favorable, making a substantial contribution to the thermodynamic stability of B-form DNA. The two hydrophilic sugar-phosphate backbones lie on the outside of the helix, creating two grooves of similar depth but different widths, known as the major and minor grooves. A complete helical turn occurs every ten base pairs, and thus each base pair is rotated by approximately 36° with respect to its neighbor.

Most studies of DNA-mediated electron transfer and charge transport have employed B-form DNA. However, duplex or double-strand (ds) DNA can adopt other

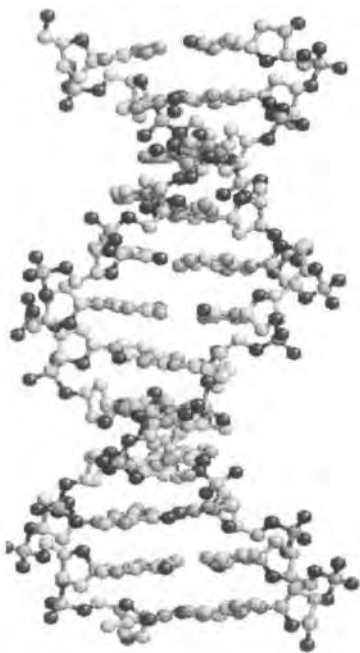


Figure 3. Structure of a B-form DNA 12-base pair duplex [20].

structures including A-form and Z-form DNA. In addition, higher-order triplex and quadruplex structures are stable under certain conditions. Local structures are dependent upon the base sequence. For example, poly-A:poly-T regions favor B-form local structures, whereas poly-G:poly-C regions favor A-form local structures. The B-form structure can also be distorted by base-pair mismatches (e.g., a G:T base pair), a missing base (abasic site), or one or more “extra” bases, which result in formation of a bulge in one strand of the duplex. For the purposes of this discussion, it will be assumed that duplex DNA adopts an idealized B-form structure except when otherwise noted.

Crystal structures of B-form DNA can give a misleading impression of structural rigidity. A recent report of the crystal structure of a 6-mer complex of daunomycin with 1.1 Å resolution at 100 K revealed that the phosphates and ribose can adopt two or more distinct conformations, even at low temperature in the solid state [21]. Experimental and theoretical studies indicate that the duplex sugar-phosphate backbone undergoes conformational changes on a time-scale of 20–200 ps, but that base pair hydrogen bonds remain intact on this time scale [22]. A recent investigation of the dynamic Stokes shift of a duplex containing a fluorescent base-pair analogue found the interior of DNA undergoes geometry changes on slower time scales (300 ps and 13 ns) [22d].

RNA exists predominantly as a single strand possessing highly varied and complex secondary structures [1–3, 19]. These include regions of intra-strand base pairs connected by loops and junctions. Single-strand (ss) DNA also has a complex secondary structure with regions of local base stacking and loop regions formed by intra-strand base-pairing. While this structural diversity is in some ways analogous to that present in proteins, the availability of crystal structures for proteins has made possible the investigation of the distance and pathway dependence of long-range electron transfer. However, studies of bridge-mediated electron transfer in RNA or single-strand DNA are complicated by the lack of structural information.

Investigations of electron transfer and charge transport processes in ds DNA have involved a variety of organic and inorganic probe molecules which can interact with the duplex structure in different ways. For example, metal ions can form inner- and outer sphere complexes with one or more nucleobase lone pairs in the major or minor groove. Planar aromatic molecules can intercalate between two adjacent base pairs. Intercalation results in perturbation of the duplex structure to accommodate the intercalated molecule, most notably an unwinding of the double-helical structure. A crystal structure of the self-complementary duplex d(CGTAACG) with two intercalated anthraquinone derivatives is shown in Figure 4 [23]. The anthraquinone is fully intercalated with its pendant aminoalkyl groups located in the major groove. Intercalation leads to unwinding and stiffening of the helix, which can result in decreased rates of base dynamic motion [24]. Planar aromatic molecules can also form π -stacked complexes with the external base-pair, a so-called end-stacked geometry [25]. The author's laboratory has employed hairpin-forming *bis*-oligonucleotide conjugates with aromatic linkers in their studies of electron transfer dynamics. The structure of a stilbenediether-linked hairpin is shown in Figure 5 [26]. The six base pairs adopt a normal B-form duplex structure with the stilbene π -stacked with the adjacent base pair. Metallointercalators have been ex-

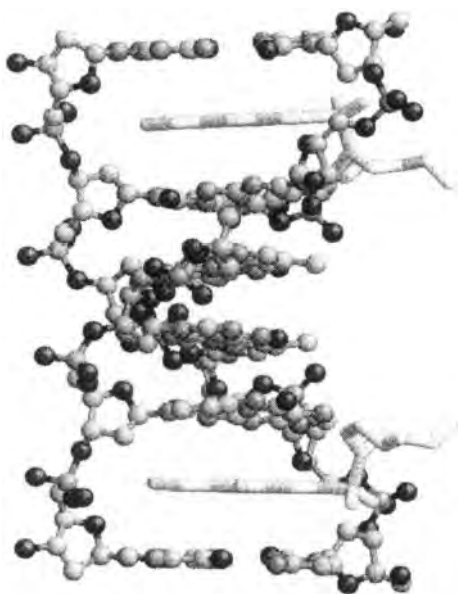


Figure 4. Structure of a 6-mer duplex with two intercalated anthraquinone derivatives shown with cylindrical bonds [23].

tensively employed in studies of DNA electron transfer processes [11–15]. The crystal structure of a rhodium complex intercalated into DNA has recently been published [see Addendum].

Electronic spectra

The individual nucleobases, nucleosides, and nucleotides all have broad absorption bands with maxima near 260 nm [8]. These bands result from overlapping $n \rightarrow \pi^*$

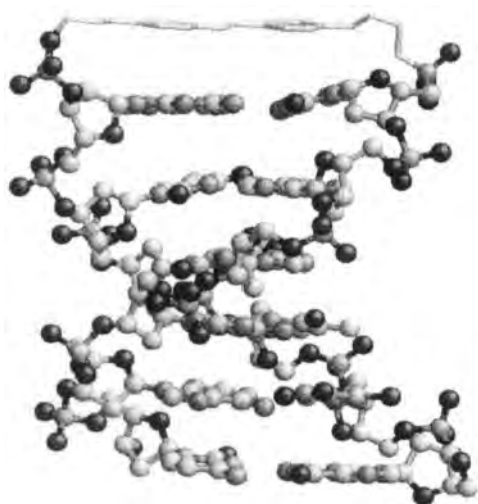


Figure 5. Structure of a stilbene diether-linked hairpin. The linker is shown at top of structure with cylindrical bonds [26].

and $\pi \rightarrow \pi^*$ transitions. An indication of the complexity of the nucleobase electronic spectra is provided by a recent study of the electronic transitions in the adenine derivatives 7-methyl and 9-methyladenine for which the near-UV spectrum was resolved into five moderately strong $\pi \rightarrow \pi^*$ transitions and a single weak $n \rightarrow \pi^*$ transition [27]. Stacking of the nucleobases in B-form duplex DNA results in a c. 20–25 % decrease in the 260-nm absorbance compared to that of the single-strand DNA, a phenomenon known as hypochromism [28]. The observation of hypochromism provides a simple diagnostic for the duplex formation upon hybridization of complementary strands. B-form DNA also has a characteristic circular dichroism spectrum, with a positive band near 280 nm and a negative band near 250 nm, which is distinct from those for A-form and Z-form DNA [27]. Neither the natural nucleobases nor oligonucleotides absorb at wavelengths longer than 300 nm. Thus, selective excitation of probe chromophores in the presence of a large excess of DNA is possible using wavelengths >300 nm.

The naturally occurring nucleobases, nucleosides, and nucleotides are all very weakly fluorescent, with singlet lifetimes <20 ps and fluorescence quantum yields $<5 \times 10^{-4}$ [8]. Even weaker fluorescence is observed for duplex DNA. The nucleobase singlet energies, as determined from the $0,0'$ singlet state transitions, all lie between 285 and 300 nm, guanine having the lowest singlet energy and adenine the highest [8]. Intersystem crossing quantum yields for the nucleobases, nucleosides, and nucleotides are also low ($<10^{-2}$). Thus, the singlet states decay predominantly by nonradiative processes which occur with rate constants of approximately 10^{12} s^{-1} . Rapid nonradiative decay may help minimize photochemical damage to cellular DNA by ultraviolet radiation. The short singlet lifetimes and low intersystem crossing yields also preclude the use of the singlet nucleobases as excited state donors or acceptors in studies of photoinduced electron transfer.

Fluorescent nucleobase analogues have been employed as probes of DNA structure and dynamics. Among these are 2-aminopurine (AP) [29, 30] and 1, N^6 -ethanoadenine (EAD) [30, 31] (see Figure 1b). AP and EAD have absorption maxima at 305 and 294 nm, respectively, and absorb at wavelengths longer than 300 nm where the natural nucleobases do not absorb. AP and EAD have been incorporated into synthetic oligonucleotides. When base-paired with T, AP adopts a normal π -stacked B-form DNA structure. Due to its large size, EA stacks poorly in the duplex. Unlike A which is very weakly fluorescent, both AP and EAD are strongly fluorescent with quantum yields of 0.68 and 0.56, respectively, for the nucleoside in aqueous solution at pH 7.0. The fluorescence decay times for the nucleosides in water are 10.4 ns for AP and 23.8 ns for EAD, respectively. The fluorescence of EAD is partially quenched upon incorporation into DNA [30, 31]. The fluorescence of AP is strongly quenched upon incorporation of AP into DNA, and its fluorescence decay becomes a complex multi-exponential function [29, 30].

Ionization potentials and electron affinities

The gas phase ionization potentials (IP) of the nucleobases have been determined by means of photoelectron spectroscopy and photoionization mass spectrometry [32]. Values for the first vertical and adiabatic ionization potentials are summarized

Table 1. Experimental and calculated ionization potentials (IP) and electron affinities (EA) of the nucleobases^a.

Base	IP _{ad} ^b	IP _{vert} ^c	IP _{calcd} ^d	EA _{ad} ^e	EA _{vert} ^f
Guanine, G	7.77	8.24	8.04	−1.23	−0.7
Adenine, A	8.26	8.44	8.48	−0.74	−0.3
Cytosine, C	8.68	8.94	9.00	−0.40	0.2
Thymine, T	8.87	9.14	9.45	−0.32	0.3
Uracil, U				−0.19	0.4

^aData from Ref. [33]. Values in electron volts (1 eV = 23.045 kcal mol^{−1}). See Figure 1(b) for base structures.

^bExperimental adiabatic ionization potential.

^cExperimental vertical ionization potential.

^dCalculated vertical ionization potential.

^eCalculated adiabatic electron affinity (EA).

^fCalculated vertical electron affinity.

in Table 1. The order of both vertical and adiabatic IP values is $G < A < C < T$. Values of the Koopmans' IP (HOMO energy) obtained by Sevilla and coworkers [33] from *ab initio* calculations at the 3-21G level are in good agreement with the measured vertical IPs [32]. The vertical IPs are larger than the adiabatic values by an amount equal to the cation radical reorganization energy. The large difference in vertical and adiabatic IP values for G are attributed to more extensive geometric relaxation than is the case for the other nucleobases [34].

The effect of solvation on the IPs of nucleotides has been investigated by LeBreton and coworkers using a combination of photoelectron spectroscopy and computational methods. They conclude that the first and second ionization potentials of the nucleotides deoxycytidine 5'-phosphate (CMP) and deoxythymidine 5'-phosphate (TMP) arise from ionization of the negatively charged phosphate group and nucleobase, respectively, both in the gas phase and in solution. The difference in the calculated first and second ionization potentials is smaller for the hydrated versus gas phase nucleosides as a consequence of the larger solvation energy for the zwitterion formed upon ionization of the nucleobase versus the neutral radical formed upon ionization of the phosphate. The calculated adiabatic ionization potentials for the hydrated nucleobases CMP and TMP are 5.8 and 6.0 eV, respectively, considerably lower than the gas phase nucleobase ionization potentials (Table 1).

The electron affinities (EA) of the nucleobases have not been determined experimentally. Calculated values for the vertical and adiabatic EA obtained by scaling experimental and calculated values for other aromatic molecules are summarized in Table 1 [33a]. The vertical values follow the order $U > T > C > A > G$, with U having the largest (most positive) EA. The calculated adiabatic EA for C is less positive than the values for T or U. Chen and Chen [36] have asserted that the electron affinities of the purines are larger than those of the pyrimidines. However, this claim appears to be based upon questionable reduction potential measurements (see p. 114). The nucleobase anion radicals are estimated to be stabilized by c. 3 eV in aqueous solution.

Table 2. Calculated ionization potentials (IP) of single and stacked bases^a.

Base	IP (eV)	Bases	IP (eV)
Guanine, G	7.75	5'-GG	7.28
Adenine, A	8.24	5'-GA	7.51
Cytosine, C	8.87	5'-GC	7.68
Thymine, T	9.14	5'-GT	7.69
8-Oxoguanine (OG) ^b	7.54	5'-G _o G	7.06

^a Ionization potentials estimated from Koopmans' theorem from Ref. [38a] except as noted. See Figure 1(b) for base structures.

^b Data for OG from Ref. [39].

Base pairing of the nucleobases in duplex DNA can affect their calculated ionization potentials and electron affinities. Colson et al. [33b] reported that base pairing lowers the IP of guanine, but has little effect on the ionization of adenine in the A:T base pair. The effects of base pairing on ionization potentials has been investigated by Hunter and Clark [34] using *ab initio* and density functional calculations. The isodesmic relations in Eqs. 1 and 2 show that A⁺⁺ and G⁺⁺ are stabilized by 10.2 and 17.4 kcal mol⁻¹, respectively, upon base pairing.



Thus the difference in G versus A ionization potentials is larger for the base pair than for the individual base. The extra stabilization of the G:C⁺⁺ base pair is attributed to the strong hydrogen-bonding interaction in the central hydrogen bond of the G:C base pair. Base pairing is also reported to affect the calculated nucleobase EA, resulting in C having a higher (more positive) EA than T [33c].

The π -stacking of nucleobases in single-strand and duplex DNA also lowers their ionization potentials. Kim et al. [37] have recently reported that the experimental ionization potentials of the dinucleotide 5'pGpA is 2.0 eV lower than that of 5'dGMP. Calculations by Sugaiyama and Saito [38] indicate that the IP of G is lower when π -stacked with any of the four nucleobases, but that the effect is largest for adjacent guanines, a GG step (Table 2). Similar computational results have been obtained by Kim et al. [37] and Prat et al. [39]. This trend follows directly from simple perturbation theory, the largest splitting between interacting orbitals being expected when they have the same energy. The formation of stable dimer cation radicals is also observed for simple aromatics such as benzene in the gas phase [38]. An even larger stabilization energy is calculated for the cation radical formed from three versus two adjacent guanines [37, 38]. Schuster and colleagues [41] have suggested that cation radicals or electron holes in duplex DNA are delocalized over several adjacent stacked bases, a situation analogous to that of polarons in single crystals. Formation of dimer cation radicals or more highly delocalized polarons

should be accompanied by a decrease in the π -stacking distance as a consequence of decreased electron–electron repulsion between the stacked aromatic molecules.

The nucleobase analogue 7,8-dihydro-8-oxoguanine (OG; Figure 1b) is of particular interest as a likely intermediate in the oxidation of guanine [6, 7]. Calculations by Prat et al. [39] indicate that the IP of OG is c. 0.4 eV lower than that of G. Stacking of OG with guanine (either 3' or 5') results in a further decrease in the IP of OG.

Unlike the cation radicals of aromatic molecules, the anion radicals do not form stable dimer anion radicals, presumably due to an increase in electron–electron repulsion [42]. To our knowledge, there is no experimental or computational evidence for stabilization of nucleobase anion radicals upon π -stacking in duplex DNA.

Electrochemical oxidation and reduction

Solution-phase oxidation and reduction potentials of the nucleobases, nucleosides, and nucleotides have been determined using both electrochemical and radical ion equilibration measurements [42–47]. Table 3 summarizes the redox potentials of the nucleosides in the polar aprotic solvent acetonitrile determined by Seidel et al. [43] by means of cyclic voltammetry and the redox potentials in aqueous solution determined by Steenken and coworkers [42] by means of pulse radiolysis equilibrium analysis using time-resolved spectrophotometric detection. Also reported by Enescu and Linqvist [44] are the standard oxidation potentials of the nucleotides in water. The reduction potential of guanine is reported by Seidel et al. [43] to be too large to be measured in dimethylformamide (DMF) solution. A report that guanine was more easily reduced than the other nucleobases [36] is inconsistent with more recent data. Nucleobase analogues (Figure 1b) with altered redox potentials have been

Table 3. Nucleoside oxidation and reduction potentials in aprotic solvents and water^a.

Base	E _{ox} , CH ₃ CN ^b	E _{ox} , H ₂ O ^c	E _{rdn} , CH ₃ CN ^b	E _{rdn} , H ₂ O ^d
Guanine, G	1.49	1.29	<−2.76	
Adenine, A	1.96	1.42, 1.69 ^f	−2.52	
Cytosine, C	2.14	~1.6	−2.35	−1.12
Thymine, T	2.11	~1.6	−2.18	−1.11
Uracil, U	≥2.39	~1.6	−2.07	−1.11
8-Oxoguanine (OG)	1.05 ^e			
Xanthosine, X		1.25 ^f		
7-Deazaguanine, Z		1.0 ^g		
Inosine, I		1.39 ^f , 1.4 ^g		

^a All values in V versus NHE. See Figure 1(b) for base structures.

^b Data in acetonitrile solution from Ref. [43] except as noted.

^c Data from Ref. [42] at pH = 7.0.

^d Data from Ref. [42] at pH = 7.0.

^e Value in dimethylformamide solution (relative to 1.49 V for G) from Ref. [46].

^f Values for the nucleotides (relative to 1.29 for G) from Ref. [44].

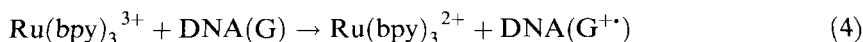
^g Value (relative to 1.29 for G) from Ref. [47].

widely used in studies of DNA electron transfer. Electrochemical potentials for several of these analogues are included in Table 3.

The nucleoside redox potentials measured in acetonitrile solution (Table 3) approximately parallel the gas phase adiabatic IP and calculated adiabatic EA of the nucleobases (Table 1). Namely, guanosine is more readily oxidized than adenosine by c. 0.4 eV, and thymidine is more readily reduced than cytidine by c. 0.1 eV. The difference between the guanosine and adenosine oxidation potentials in water reported by Steenken et al. [42a,b] is much smaller than the value reported by Enescu and Linqvist [44] ($\Delta E_{\text{ox}} = 0.13$ and 0.40, respectively; Table 3). A larger difference appears to be more consistent with observations of selective oxidation of guanine in DNA [6, 7]. The absolute value of the redox potentials determined in aqueous solution are much smaller than those measured in nonaqueous solution (Table 3). The large differences in experimental oxidation potentials in acetonitrile versus water are attributed by Seidel et al. [43] to a combination of the increased solvation energy in water (c. 0.1 eV) and coupled electron transfer and proton transfer (c. 0.3 eV). Oxidation and reduction of the nucleosides results in a large increase in their acidities and basicities, respectively, leading to significant differences in their aqueous potentials measure under acidic, neutral, and basic conditions [42]. Seidel et al. [43] note that there is no satisfactory explanation for the large discrepancy between the electrochemical reduction potentials determined in nonaqueous solution and the values obtained by pulse radiolysis in aqueous solution.

Both base pairing and π -stacking are expected to affect the magnitude and possibly the relative order of the nucleoside redox potentials. Steenken et al. [42a] have used thermodynamic cycles to predict the equilibrium constant for proton transfer in oxidized or reduced base pairs. The calculated equilibrium constant for proton transfer in the $\text{C}^{\cdot-}:\text{G}$ base pair is large ($K \geq 10^3$) compared to that for the $\text{A}:\text{T}^{\cdot-}$ base pair ($K \leq 10^{-7}$). This difference could account for the localization of electrons on G:C base pairs, in spite of the larger EA and nonaqueous reduction potential of T versus C. The calculated equilibrium constant for proton transfer in the $\text{C}:\text{G}^{+\cdot}$ base pair ($K \sim 2.5$) is also much larger than for the $\text{A}^{+\cdot}:\text{T}$ base pair ($K \geq 10^{-6}$). This would reinforce the preference of an electron hole for a G:C versus A:T base pair. Steenken [18a] has suggested that rapid proton transfer in oxidized or reduced base pairs would effectively trap the electron or hole, and thus preclude long-range electron transfer in DNA. Recent experimental evidence (Section 5.4) indicates that this need not be the case.

There have been several reports of the complex electrochemical behavior of single-strand and duplex DNA absorbed on electrode surfaces [48]. However, there have been no reports to date of the measurement of nucleotide oxidation or reduction potentials in duplex DNA. Johnston and coworkers [49] have used electrochemical methods to study the dynamics of the selective oxidation of guanine in single-strand and duplex DNA by $\text{Ru}(\text{bpy})_3^{3+}$ which is generated by oxidation of $\text{Ru}(\text{bpy})_3^{2+}$ (Eqs. 3 and 4).



The reduction potential of $\text{Ru}(\text{bpy})_3^{3+}$ is sufficiently large to oxidize guanine, but not the other nucleobases. When the guanine density is low, its oxidation requires binding of $\text{Ru}(\text{bpy})_3^{3+}$ in a 2.5–5-bp region containing a guanine [49e]. DNA sites containing GG or GGG steps are more readily oxidized than those containing a single guanine. $\text{Os}(\text{bpy})_3^{3+}$ is found to oxidize OG, but not guanine [49e]. The rate constants for guanine and OG oxidation by $\text{Ru}(\text{bpy})_3^{3+}$ and $\text{Os}(\text{bpy})_3^{3+}$, respectively, are substantially slower for duplex versus single-strand DNA, but increase with the introduction of base mismatches. The dependence of rate on structure is attributed to distance dependence of the electron transfer process, with closer approach of the reactants being possible for single-strand versus duplex DNA and for mismatched versus base-paired duplexes. Alternatively, the higher effective oxidation potential of guanine in duplex versus single-strand DNA or mismatched duplexes may result from a difference in effective solvent polarity (Section 5.2).

5.1.3 Direct Ionization of DNA

Radical anion formation via radiolysis

Exposure of living cells to ionizing radiation can have lethal consequences which result from RNA and DNA single- and double-strand breaks [9]. Strand breaks result from a combination of free radical and electron transfer processes, the latter being known to result from the formation of nucleobase anion and cation radicals. Thus, the formation and migration of electrons and holes has been a topic of active investigation by radiation biologists and chemists for over four decades [50, 51]. A comprehensive review of these investigations is beyond the scope of this chapter, and thus only selected information is presented.

Radiolysis of aqueous solution results predominantly in the ionization of water to produce a hydrated electron, e_{aq}^- , and H_2O^+ [9]. The former species can be captured by any of the four DNA nucleotides, leading to the formation of their anion radicals [52]. The latter species transfers a proton to water, resulting in the formation of H_3O^+ and the hydroxyl radical, HO^\bullet . Abstraction of hydrogen atoms from DNA by HO^\bullet accounts for the majority of the strand cleavage which occurs upon radiolysis of DNA in aqueous solution [9]. Free radical reactions can be suppressed by the addition of radical scavengers or by irradiation in frozen glasses in which HO^\bullet radical migration is inhibited. Radiation of DNA in water can also result in its direct ionization, leading to the formation of nucleobase cation radicals and either anion radicals or solvated electrons.

The identity of the radical ions formed upon steady-state radiation of DNA in low-temperature glasses has been established by means of electron paramagnetic resonance (EPR) spectroscopy [53]. EPR analysis indicates that electrons and holes are localized on a single nucleobase rather than being delocalized over several stacked bases at low temperatures. Radical ion formation is presumed to occur randomly at all four nucleosides. However, EPR studies establish that the electron holes are localized predominately on guanine, which has the lowest gas phase ionization potential and solution oxidation potential (Tables 1 and 3). Yan et al. [54]

report that hole transfer from adenine to guanine in duplex DNA is nearly complete within several minutes at 100 K. Electrons can be localized on either cytosine or thymine, the two nucleobases with the highest EA and lowest solution reduction potentials. There has been some controversy over which anion radical is favored, the results appearing to depend upon experimental conditions. Yan et al. [54] report that both $T^{\cdot-}$ and $C^{\cdot-}$ are formed initially, but that $C^{\cdot-}$ is converted to $T^{\cdot-}$, which undergoes protonation upon annealing. Replacement of thymine by bromodeoxyuridine (BrU; Figure 1b), an isostere with lower reduction potential, results in trapping of electrons on BrU [55–57].

The reaction of hydrated electrons formed by radiolysis with peroxydisulfate yields the sulfate radical anion $SO_4^{\cdot-}$ which is a strong chemical oxidant ($E_{ox} = 2.4$ V/NHE) [50, 58]. The oxidation of both purine and pyrimidine nucleotides by $SO_4^{\cdot-}$ occurs with rate constants near the diffusion-controlled limit ($2.1\text{--}4.1 \times 10^9$ M⁻¹ s⁻¹). Candeias and Steenken [58a] employed absorption spectroscopy to investigate acid–base properties of the guanosine cation radical formed by this technique. The cation radical has a pK_a of 3.9, and is rapidly deprotonated at neutral pH to yield the neutral $G(-H)^{\cdot}$. Both $G^{+\cdot}$ and $G(-H)^{\cdot}$ have broad featureless absorption spectra with extinction coefficients <2000 at wavelengths longer than 350 nm. This has hampered the use of transient absorption spectra to study their formation and decay. Candeias and Steenken [58b] have also studied the oxidation of di(deoxy)nucleoside phosphates which contain guanine and one of the other three nucleobases by $SO_4^{\cdot-}$, and observe only the formation of $G^{+\cdot}$ under acidic conditions and $G(-H)^{\cdot}$ under neutral conditions.

The observation of electron and hole localization on the bases of highest EA and lowest IP, respectively, indicates that both electrons and holes can migrate via the stacked bases in duplex DNA, both in solution and in low-temperature glasses [53]. Using a statistical model, Yan et al. [54] concluded that the distribution of DNA radical ions observed at 77 K could be explained by the migration of cold (thermalized) holes and electrons over as few as two or three bp.

The distance over which electrons can migrate in aqueous solutions and glasses containing DNA has been investigated using added electron scavengers. Reduction of the nucleobase analogue BrU (Figure 1b), an isostere of thymine, results in loss of bromide ion [59]. Fielden et al. [55] employed fluorescence-detected pulse radiolysis to investigate the effect of increasing the BrU content upon the luminescence from dried fibers of native DNA from murine lymphoma cells. Assuming that luminescence results from radical ion pair annihilation, their results indicate that the electrons and holes can migrate over as many as 100 bp at 93 K. Recently, Razskazovskii et al. [57] used EPR spectroscopy to investigate the temperature dependence of electron migration in γ -irradiated samples of randomly brominated DNA, and concluded that electron migration can occur via an activationless process over distances of c. 11 bp at 77 K. At higher temperatures a second, activated migration process was observed and attributed to a hopping mechanism. Beach et al. [56] employed DNA from *E. coli* which was grown on cultures with variable BrU-content to study electron migration both in solution and in cells at room temperature; they concluded that electron migration occurred over 6–10 bp in solution, but only 5–6 bp in *E. coli*.

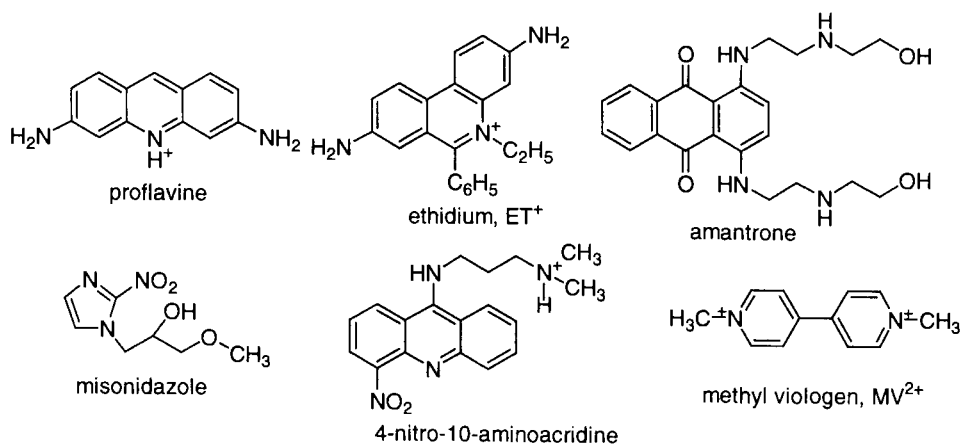


Figure 6. Intercalating dyes used in studies of charge migration in DNA.

The use of cationic intercalating dyes (Figure 6) as electron scavengers has been investigated by several groups [60–64]. Whillans [60] used pulse radiolysis with transient absorption detection to study trapping of electrons by the dyes proflavine and ethidium bromide. An upper limit of 5 bp was estimated for electron migration at room temperature in aqueous solution, and no evidence was found for free electron migration. Cullis and coworkers [61] used anthraquinone derivatives such as amantrene as electron-scavenging intercalators in their study of electron migration in DNA at 77 K in an aqueous glass. They concluded that the mean distance traveled by the ejected electrons prior to capture was c. 31 bp. O’Neil and coworkers [62a,b] have investigated electron migration to the intercalated dye misonidazole in solid freeze-dried DNA. Their initial conclusion was that mean distance of electron migration is 25 bp [62a]; however, re-analysis of their data provided shorter distances or 17 ± 2 [62b] and 5 to 10 bp [63].

Anderson and Wright [64] have recently investigated electron migration from reduced cytosine bases in DNA to several nitroacridine and nitroquinoline intercalators (e.g., 4-nitro-10-aminoacridine; Figure 6) at room temperature in aqueous solution by means of pulse radiolysis. The time scale for their measurements is 10^{-6} to 10^{-3} s, and is limited by the time required for capture of e_{aq}^- by DNA (c. 5 μ s) and by the decay time of C^{--} in the absence of intercalators (c. 230 μ s). Electron migration was found to be an activated process, the rate of which is dependent upon both the average separation between the C^{--} donor and the intercalator and the driving force for electron transfer. The average migration distances for several different acceptors were in the range 3–7 bp, somewhat shorter than those obtained in previous experiments. The observation of longer electron migration distances at 77 K versus room temperature in studies with both intercalators and BrU as electron scavengers is consistent with the occurrence at room temperature of an activated trapping process such as proton transfer, which competes with electron migration. The results of Anderson and Wright [64] suggest that the rates of proton

transfer processes occur on the μs time scale, rather than the much faster rates recently suggested by Steenken [18a].

The use of pulse radiolysis to study charge migration in DNA has clearly established that electron migration from base radical anions to electron scavengers can occur over distances of c. 3–10 bp at room temperature, and longer distances at low temperatures. These processes are initiated by random scavenging of the hydrated electrons by all four DNA nucleobases, and terminated by electron transfer to randomly positioned BrU or intercalated scavengers. Thus only average electron migration distances can be estimated. To date, no information is available from pulse radiolysis studies concerning the migration of cation radicals (hole migration). Furthermore, the μs time scale of initiation is too slow to permit direct measurement of the dynamics of rapid charge transfer processes.

Radical cation formation via photoionization

Low-intensity 254 nm ultraviolet irradiation of DNA results in pyrimidine photohydration and photodimerization [8]. Photoionization of nucleobases can be effected by the absorption of a single 193-nm photon or two photons of lower energy (typically 248 or 266 nm) [65]. The availability of ArF excimer lasers has facilitated the investigation of 193-nm single photon excitation. Quantum yields for cation radical formation from nucleobases and single-strand and duplex DNA are typically 0.02–0.05, and are not highly nucleobase-dependent [66]. Quantum yields for two-photon 246-nm excitation are power-dependent, and are typically much lower than for 193-nm single-photon excitation. The nucleobases absorb most of the incident ultraviolet light, and thus are photoionized in preference to the phosphate groups.

The migration of electron holes formed by means of photoionization has been investigated in a di(deoxy)nucleoside phosphate, single-strand, and double-strand DNA. Candeias and Steenken [58b] found that in the case of adenylylguanonsine hole transfer from $A^{+\bullet}$ to guanine is complete within 50 ns, the time resolution of their 193-nm laser flash photolysis apparatus. Similarly, the electron holes in ss DNA are localized on guanine within 50 ns of laser excitation [66b]. O'Neill co-workers [67] have investigated hole migration in RNA and several ss oligo(deoxy)nucleotides. They find that in RNA hole migration to guanine is complete within the μs time resolution of their laser flash photolysis experiment. Hole transfer from $A^{+\bullet}$ or $C^{+\bullet}$ to guanine in the oligonucleotides is >80 % complete on this time scale, from which they concluded that the distance of hole migration in single-strand oligonucleotides is limited to two or three bases.

The photoionization of ds DNA has been investigated using both single-photon 193-nm and two-photon 248- or 266-nm excitation [65–69]. As is the case for ss DNA and RNA, transient absorption spectra recorded on a μs time scale indicate that the holes are located predominantly on guanine. Photoionization results in both single- and double-strand breaks in duplex DNA, with initial studies establishing that strand breaks occur preferentially at guanine [65]. Recently, Sies et al. [68] have reported that strand breaks occur preferentially at sites where there are two adjacent guanines (GG step) or, less often, where a guanine is adjacent to adenine. These results are indicative of hole migration from the locus of photo-

ionization to GG or GA sites which function as hole traps due to their low ionization potentials (Table 2). The selectivity of strand cleavage at GG sites is more pronounced for 193-nm versus 248-nm excitation. Angelov et al. [69] have studied the photoproducts formed upon 266-nm, two-photon excitation of DNA and find that both 8-oxo-7,8-dihydro-2'-dedoxyguanosine (OG; Figure 1b) and 7,8-dihydro-2'-dedoxyadenosine are formed. Thus, they conclude that adenine may serve as a secondary site for hole trapping in DNA.

Shafirovich et al. [70] have recently employed two-photon excitation of the nucleobase 2-aminopurine (AP; Figure 1b) to site-selectively generate cation radicals in both single-strand and duplex DNA. Since AP absorbs at wavelengths longer than 300 nm, the use of high-intensity 308-nm excitation results in photoionization of AP, but not the natural nucleobases. The efficiency of photoionization follows the order: free AP > ss > ds, with estimated quantum yields of 0.1 and 0.002 for ss and ds photoionization, respectively. These low quantum yields are attributed to rapid quenching of singlet AP by neighboring nucleobases, a process which is more efficient in ds versus ss DNA (Section 5.3.3, p. 151). Quenching shortens the AP singlet lifetime and decreases the probability of two-photon absorption. Using nanosecond transient absorption spectroscopy, electron transfer from GG steps to AP⁺⁺ could be detected in single-strand but not in duplex DNA. The efficiency of strand cleavage in both ss and ds DNA was found to decrease rapidly with increasing separation between the photoionized AP and the GG step.

Shafirovich et al. [71] have also investigated the migration of electrons photo-injected into DNA by two-photon excitation (335 nm) of pyrene derivatives covalently bound to ss and ds DNA. They find that in ds DNA the photoinjected electrons migrate to the acceptor methyl viologen (MV²⁺; Figure 6) which is bound to the DNA within the c. 7-ns time resolution of the laser apparatus. From the dependence of the MV⁺ yield upon the MV²⁺ concentration, and the assumption of a random distribution of the pyrene donor and MV²⁺ acceptor, they conclude that the photoinjected electrons have an average migration distance of 12 bp. No fast electron migration is observed in ss DNA, indicating the necessity of base stacking for electron transport and for binding of MV²⁺.

5.2 Collisional and Static Contact Electron Transfer in DNA

5.2.1 Energetics and Dynamics of Direct Electron Transfer Processes

Nucleobases can serve as either electron donors or electron acceptors in photo-induced electron transfer reactions with electronically excited acceptors (Ac) or donors (D), respectively. The free energy of photoinduced electron transfer reaction in which the nucleobase (N) serves as a donor or acceptor can be estimated using the Rehm–Weller equations (Eqs. 5 and 6), respectively,

$$\Delta G_{\text{et}} = E^0(\text{N}^{+\bullet}/\text{N}) - E^0(\text{Ac}/\text{Ac}^{-\bullet}) - E^*(\text{Ac}) + \Delta G^\circ(\varepsilon) \quad (5)$$

$$\Delta G_{\text{et}} = E^0(\text{D}^{+\bullet}/\text{D}) - E^0(\text{N}/\text{N}^{-\bullet}) - E^*(\text{D}) + \Delta G^\circ(\varepsilon) \quad (6)$$

where E^* is the singlet or triplet 0,0 energy of the excited state and $\Delta G^\circ(\epsilon)$ is a solvent-dependent correction term that is small (c. -0.1 V) in water and polar organic solvents [72]. The ion pair formed in the charge separation process can return to the ground state by means of return electron transfer (charge recombination). The free energy for this process is simply the sum of the redox potentials.

The oxidation and reduction potentials of the nucleosides in water or organic solvents (Table 3) can be employed to calculate the free energies of electron transfer processes involving a single nucleoside in the corresponding solvent. The potentials of the π -stacked nucleobases in ds DNA have not been measured, and thus calculation of the free energy of electron transfer processes involving ds DNA require assumption of the appropriate potentials. In view of the hydrophobic character of the π -stacked base array we have proposed that the values for polar organic solvents are more appropriate than those for water, particularly in the case of rapid electron transfer processes that are not coupled to proton transfer [73].

The rate constants for collisional (dynamic) quenching can be determined experimentally from the dependence of excited state lifetime or luminescence intensity using the Stern–Volmer equation (Eq. 7),

$$\tau^0/\tau = I^0/I = 1 + k_q\tau^0[Q] \quad (7)$$

where τ^0 and τ are the lifetimes and I^0 and I are the intensities in the absence and presence of the quencher Q [74]. The observed rate is dependent upon the diffusion controlled formation and dissociation of an encounter complex (k_{diff} and $k_{-\text{diff}}$) and the activation-controlled rate constant for electron transfer (k_{et}) (Eq. 8). According to basic Marcus theory, the free enthalpy of activation and rate constant for an outer-sphere electron transfer process can be described by Eqs. 9 and 10, respectively,

$$k_q = k_{\text{diff}}(1 + k_{\text{et}}/k_{-\text{diff}}) \quad (8)$$

$$\Delta G^\ddagger = \lambda/(1 + \Delta G/\lambda)^2/4 \quad (9)$$

$$k_{\text{et}} \sim \exp(-\Delta G^\ddagger/RT) \quad (10)$$

where ΔG is the free energy of reaction (Eq. 5 or 6) and λ is the reorganization energy. One quantum mechanical version of Eq. 10 is provided by the single-mode Marcus–Levich–Jortner equation (Eq. 11) [75],

$$k_{\text{et}} = \frac{2\pi}{\hbar} \cdot \frac{H_{\text{DA}}^2}{\sqrt{4\pi\lambda_s k_B T}} \cdot e^{-S_c} \sum_{n=0}^{\infty} \frac{S_c^n}{n!} \cdot e^{-(\Delta G + \lambda_s + n \cdot \hbar \cdot \langle \omega_c \rangle)^2 / 4\lambda_s k_B T} \quad (11)$$

$$S_c = \frac{\lambda_i}{\hbar \cdot \langle \omega_c \rangle}$$

where \hbar is Planck's constant, k_B is the Boltzmann constant, T is the temperature, H_{DA} is the electronic coupling matrix element, S_c is the dimensionless nuclear coupling constant, ΔG is the free energy change (Eq. 5 or 6), λ_i is the nuclear reorganization energy, λ_s is the solvent reorganization energy, and $\langle \omega_c \rangle$ is average

vibrational frequency. Application to photoinduced electron transfer requires the assumptions that the initial (excited) state is vibrationally relaxed, that $\hbar\langle\omega_c\rangle \gg k_B T$, and that the donor and acceptor exist in a single minimized geometry.

Both Eqs. 10 and 11 predict that k_{et} should first increase as ΔG becomes more exergonic (normal region), reach a maximum, and then become smaller when ΔG becomes highly exergonic (inverted region). Rate constants for collisional electron transfer quenching increase with increasing exergonicity in the normal region, as predicted by Marcus theory, and become diffusion controlled when $\Delta G \leq -10$ kcal mol⁻¹ [72]. The rate constants remain diffusion controlled even for highly exergonic electron transfer, rather than decreasing in inverted region. Under these conditions quenching may occur by formation of a charge transfer-stabilized exciplex rather than by outer-sphere electron transfer [76].

Investigations of bimolecular quenching of excited-state donors and acceptors by nucleosides, nucleotides, and oligonucleotides are frequently complicated by the formation of ground-state complexes. Equilibrium constants for ground-state complexation are typically larger in water than in organic solvents due to hydrophobic association. Coulombic attraction may also favor complexation between positively charged acceptors and negatively charged nucleotides or oligonucleotides. Exceptionally large association constants are observed for ds DNA with positively charged species than can bind to multiple nucleobase donor sites in the major or minor groove, or can be intercalated between adjacent π -stacked base pairs. In cases where static quenching is exergonic, the rate constant for electron transfer can be significantly larger than the rate constant for luminescence, resulting in essentially complete luminescence quenching. The rate constants for such ultrafast electron transfer processes can be measured by transient absorption spectroscopy.

Ground-state association of the donor and acceptor results in static quenching. Since no diffusion is required, the rate constant for static quenching is described by Eq. 12,

$$I^0/I = 1 + K_S[Q] \quad (12)$$

where K_S is the equilibrium constant for 1:1 complex formation [74]. The occurrence of bimolecular quenching by both static and dynamic mechanisms can complicate the interpretation of electron transfer quenching rate constants obtained from Stern–Volmer plots. In the case where the ground-state complex is non-fluorescent, the expression for lifetime quenching (Eq. 7) remains unchanged. However, the expression for intensity quenching is replaced by Eq. 13,

$$I^0/I = (1 + K_D[Q])(1 + K_S[Q]) \quad (13)$$

where K_D is the Stern–Volmer constant for dynamic quenching, $k_q\tau^0$ [74]. This form of the Stern–Volmer equation is second order in $[Q]$, resulting in upward curvature for plots of I^0/I versus $[Q]$. Thus, measurement of k_{et} from fluorescence data requires either lifetime measurements or graphical separation of K_D and K_S . Alternatively, transient absorption spectroscopy can be employed to determine either the decay time of the singlet state or the rise time of the radical ions.

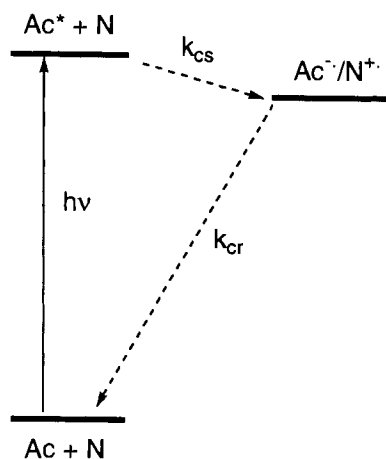


Figure 7. Energy level diagram for photochemical charge separation and charge recombination for an excited state acceptor (Ac) and donor nucleobase (N).

Both dynamic and static electron transfer quenching of a neutral donor or acceptor by a nucleoside or nucleotide result in formation of a radical ion pair. The radical ion pair can decay by charge recombination to yield the ground state molecules (Figure 7), undergo chemical reactions, or diffuse apart [77]. The charge recombination of singlet radical ion pairs is a highly exergonic process. Thus, according to Eqs. 10 or 11 the rate constant for charge recombination should increase as the energy gap between the ion pair and ground state becomes smaller (inverted region). In the case of triplet radical ion pairs, charge recombination is spin forbidden, and thus a spin flip must occur prior to charge recombination. Intersystem crossing in strongly coupled triplet radical ion pairs is generally slow, and thus the triplet radical ion pair has a much higher probability of undergoing chemical reactions in competition with charge recombination than does the singlet radical ion pair.

5.2.2 Bimolecular Electron Transfer Processes of Nucleosides, Nucleotides, and Oligonucleotides

Neutral organic acceptors and donors

The fluorescence of the nucleobase analogues 2-aminopurine (AP) and 1,*N*⁶-ethanoadenine (EAD) is quenched by added nucleotides in aqueous solution [30]. The slopes of Stern–Volmer plots for quenching of fluorescence intensity follows the order $Z > G > I \sim A \sim C \sim T$; however, rate constants for static and dynamic electron transfer have not been reported. The singlet energy and ground- and excited-state reduction potentials are reported in Table 4, and are consistent with the oxidation of Z and G by an electron transfer mechanism in which the singlet state serves as an electron acceptor and the nucleotide as a ground-state donor (Eq. 5). Based on the results obtained with other singlet aromatic molecules (*vide infra*), it is

possible that the less efficient quenching observed for the pyrimidines involves oxidation of the singlet state (Eq. 6).

Pyrene has been widely employed as a fluorescent probe for biopolymers due to its strong and characteristic monomer and excimer fluorescence [78]. Lianos and Georghiou [79] investigated the ground- and excited-state interactions of pyrene with the nucleotides GMP, AMP, CMP, and TMP in aqueous buffer, and observed complex formation in both the ground and excited singlet states. The values of the ground-state association constants are larger for the purines than for the pyrimidines; however, this situation is reversed in the excited state. Quenching of singlet pyrene by the nucleotides occurs via both static and dynamic processes, except in the case of AMP for which little quenching is observed. The rate constants for dynamic quenching by GMP, CMP, and TMP are all near the rate of diffusion in water.

Geacintov et al. [80] reported similar results for quenching of the fluorescence of the benzo[a]pyrene tetraol metabolite BPT (Table 4) by nucleosides. An electron transfer mechanism for quenching was established using nanosecond transient absorption measurements. Quenching of singlet BPT by dG in the polar aprotic solvent dimethylsulfoxide (DMSO) results in formation of the BPT anion radical; however none of the other nucleosides is an effective quencher in DMSO. This result is consistent with an electron transfer mechanism in which BPT serves as the electron acceptor and dG as the electron donor (Eq. 5). Using the nucleoside oxidation potentials in acetonitrile solution from Table 3, photooxidation of dG is expected to be approximately isoergonic (Eq. 5), whereas oxidation of the other nucleosides is endergonic in polar aprotic solvents. Quenching of BPT by dG is also highly efficient in water, though the BPT anion radical is not observed, presumably due to rapid charge recombination. Quenching of singlet BPT by dT or dC in aqueous solution results in formation of the BPT cation radical. The observation of electron transfer quenching in water, but not in DMSO, is consistent with the much lower (less negative) nucleoside reduction potentials in aqueous solution (see Table 3).

The most detailed investigation to date of electron transfer quenching by nucleosides and nucleotides is that of Seidel et al. [43], who investigated the static and dynamic quenching of eight fluorescent coumarin derivatives in water. Depending on the redox properties of the singlet excited coumarin and nucleoside, the coumarin can function as either the electron donor or electron acceptor. For example, the coumarin C120 (Table 4) is reduced by guanosine and oxidized by thymidine or cytidine. The fluorescence of C120 is slightly enhanced upon complexation with adenosine. Similar results are observed for quenching by nucleotides. Correlations of the rate constants for dynamic quenching in water with the standard free energy for photoinduced electron transfer obtained using nonaqueous redox potentials are qualitatively similar in appearance to that observed by Rehm and Weller for aromatic donors and acceptors in organic solvents [72a]. However, the calculated values of ΔG_{et} underestimate the apparent values in aqueous solution by 0.5 to 0.9 eV! The solvation energy in water accounts for only a small part of this difference (c. 0.1 eV) and the remainder is attributed to a combination of proton-coupled electron transfer and hydrophobic interactions. No quenching of the coumarin singlets is observed in either hydroxylic (methanol, ethanol) or nonhydroxylic (aceto-

nitrile, dimethyl formamide (DMF)) solvents, in accord with the higher nucleoside oxidation potentials in nonaqueous solvent (see Table 3).

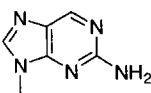
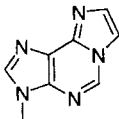
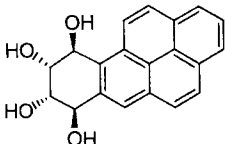
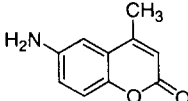
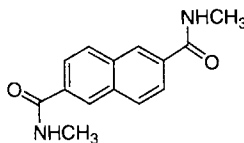
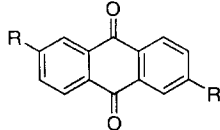
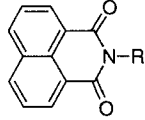
Lewis et al. [73] have reported the occurrence of static and dynamic quenching of the singlet acceptor 2,6-naphthalenedicarboxamide (NA; Table 4) by nucleosides in both aqueous and an organic solvent, DMF. Static quenching was observed for all four nucleosides with similar efficiencies in both water and DMF. The rate constants for dynamic quenching by the purines and pyrimidines are similar in water ($k_{\text{qd}} = 1.2\text{--}2.8 \times 10^9 \text{ M}^{-1} \text{ s}^{-1}$); however, the purines display larger rate constants than the pyrimidines for dynamic quenching in DMF. This result is consistent with exergonic quenching of singlet NA by all four nucleotides in water, but only by the purines in DMF.

Triplet acceptors have received less attention than their singlet counterparts. The longer lifetimes of triplet versus singlet acceptors provides a kinetic advantage in studies of dynamic quenching, but not in studies of static quenching. The triplet state of pyrene is not quenched by nucleosides in either aqueous or organic solvents [80]. The lower excitation energy of the pyrene triplet versus singlet (see Table 4) renders electron transfer quenching of the triplet endergonic. Anthraquinone derivatives have been used by Armitage and coworkers [81] in their studies of charge transport in DNA (Section 4.4). Due to their rapid intersystem crossing rate constants and high reduction potentials, anthraquinones are expected to be excellent triplet acceptors. The anthraquinone derivative AQC(2) (Table 4) forms a ground-state complex with GMP. Excitation of this complex results in the formation of the anthraquinone anion radical, which has been detected by transient absorption spectroscopy. The growth of $\text{AQC}^{\cdot -}$ is biphasic, the faster component occurring within 50 ps and the slower component extending to 5 ns. The $\text{AQC}^{\cdot -}$ formed upon reaction of the triplet with DNA decays slowly via spin-forbidden charge recombination in the absence of oxygen (c. 5 ms is required for complete decay). The decay of $\text{AQC}^{\cdot -}$ is more rapid in the presence of oxygen (10 μs in aerated solution), presumably due to electron transfer to oxygen.

Bernstein et al. [82] have recently investigated the dynamics of collisional quenching of triplet C_{60} by silyl derivatives of guanine and 8-oxoguanine in benzonitrile solution. The observed rates are $3.3 \times 10^6 \text{ M}^{-1} \text{ s}^{-1}$ and $1.1 \times 10^8 \text{ M}^{-1} \text{ s}^{-1}$, respectively, in accord with an electron transfer mechanism in which the silylated nucleobase of lower oxidation potential (Table 3) is the better electron donor.

Saito et al. [83] have reported that bimolecular quenching of the triplet state of the naphthalene imide NIa (Table 4) by the oligonucleotide 5'TTGGTA results in the formation of the anion radical $\text{NIa}^{\cdot -}$. The triplet decay time of the triplet transient absorption is the same as the rise time of the anion radical, providing a bimolecular rate constant of $5.3 \times 10^7 \text{ M}^{-1} \text{ s}^{-1}$. Rogers and Kelley [84] have recently studied the quenching of several triplet imide and diimide derivatives by the four nucleotides. Quenching of the naphthalene imide NIb and diimide derivatives (Table 4) is more rapid in the case of GMP than the other three nucleotides. Lower kinetic selectivity is displayed by a triplet benzophenone diimide, which is a more powerful triplet-state oxidant. Bimolecular quenching of the triplet naphthalene imides and diimides by calf-thymus DNA also results in formation of the acceptor anion radicals. However, no anion radical formation is observed when the naphthalene imide acceptors

Table 4. Structures, singlet or triplet energies (E^S or E^T), reduction or oxidation potentials (E_{rdn} or E_{ox}), and excited state reduction or oxidation potentials (E^*_{rdn} or E^*_{ox}) of neutral organic acceptors and donors^a.

Structure	Energetics
	2-aminopurine, AP [30] $E^S = 3.65$ $E_{\text{rdn}} = -2.15$ $E^S_{\text{rdn}} = 1.5$
	ethanoadenine, EAD [30] $E^S = 3.55$ $E_{\text{rdn}} = -2.15$ $E^S_{\text{rdn}} = 1.4$
	(+)- <i>trans</i> -BPT [80] $E^S = 3.28$, $E^T = 2.1$ $E_{\text{rdn}} = -1.84$ $E_{\text{ox}} = 1.23$ $E^S_{\text{rdn}} = 1.44$ $E^S_{\text{ox}} = 2.05$
	coumarin-120, C120 [43] $E^S = 3.22$ $E_{\text{rdn}} = -1.90$ $E_{\text{ox}} = 1.38$ $E^S_{\text{rdn}} = 1.23$ $E^S_{\text{ox}} = 1.84$
	naphthalenedicarboximide, NA [73] $E^S = 3.55$ $E_{\text{rdn}} = -1.81$ $E^S_{\text{rdn}} = 1.74$
	anthraquinone, AQC(2) [81] $E^T = 2.73$ $E_{\text{rdn}} = -0.82$ $E^T_{\text{rdn}} = 1.91$ $R = \text{CONH}(\text{CH}_2)_4\text{NH}_3^+$
	naphthalene imide, NI [83, 84] $E^S = 3.40$, $E^T = 2.29$ $E_{\text{rdn}} = -1.01$ $E^S_{\text{rdn}} = 2.39$ $E^T_{\text{rdn}} = 1.28$ $R_a = -(\text{CH}_2)_4\text{CH}(\text{NH}_2)\text{CO}_2\text{CH}_3$ $R_b = -(\text{CH}_2)_3\text{OH}$

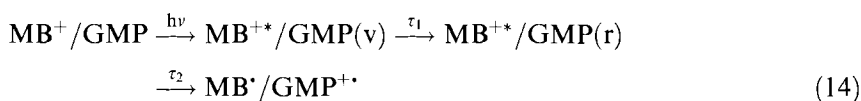
^a Excited state energies in eV, redox potentials in V, versus NHE.

are associated with DNA. Presumably electron transfer from DNA nucleobases to the associated imide singlets is more rapid than imide intersystem crossing, and singlet-state charge recombination is faster than the 0.1 μ s time scale of the transient absorption measurements.

Cationic organic acceptors

The photophysical and photochemical behavior of the phototoxic cationic acridinium and phenothiazinium dyes (Table 5) with nucleic acids have been widely investigated [85–87]. Both classes of dyes form ground-state complexes with nucleotides and oligonucleotides and are quenched by static and dynamic mechanisms. Ground-state equilibrium constants for *N*-methylacridinium (MA^+) are larger for GMP and AMP than for CMP or TMP; however, the dynamic quenching constants are diffusion controlled for all four nucleotides [85]. The short-lived fluorescence of methylene blue (MB^+) is quenched by the purines xanthosine (XMP; Table 3) and GMP but not by AMP (which slightly enhances the MB^+ fluorescence) or the pyrimidine nucleosides [87]. The fluorescence of thionine (TH^+) is quenched by AMP as well as GMP in accord with its larger singlet-state oxidation potential (Table 5) [86]. The singlet-state lifetimes of MB^+ and TH^+ are reduced from c. 400 ps in the absence of nucleotides to 6 ps and 1 ps, respectively, in the presence of GMP. Quenching of triplet MB^+ is observed with XMP but not GMP, in accord with the lower oxidation potential of the former.

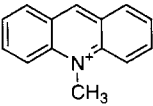
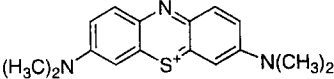
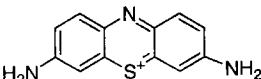
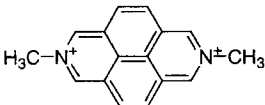
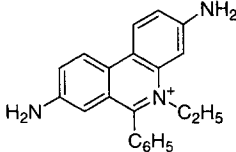
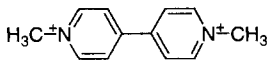
Enescu and Lindqvist [44] have investigated the deactivation pathways for the complexes of several purine nucleotides with MB^+ by means of picosecond transient absorption spectroscopy. They observe rapid biexponential decay of complexes of singlet MB^+ with GMP and XMP. The fast decay components ($\tau_1 < 10$ ps) were attributed to solvent relaxation and the slower decay components ($\tau_2 \sim 50$ ps for GMP and 10 ps for XMP) to charge transfer (Eq. 14),



where v and r are the vibrationally excited and relaxed states, respectively. Only slow decay attributed to charge transfer was observed for AMP (400 ps) and IMP (150 ps), in accord with their higher oxidation potentials (see Table 3). The absence of any intermediate detectable by transient spectroscopy was attributed to rapid charge recombination. In the case of the TH^+ -GMP system, >95 % recovery of ground-state bleaching occurs within 5 ps [86].

The dynamics of both static and dynamic quenching of the fluorescent singlet states of diazapyrenium salts by nucleotides has been investigated by Brun and Harriman using sub-nanosecond time-resolved transient absorption spectroscopy [88]. Observation of the reduced acceptor $\text{DAP}^{+\bullet}$ (Table 5) supports an electron transfer mechanism for fluorescence quenching. Diffusion-controlled rate constants were observed for quenching of DAP^{2+} by all four deoxynucleotides. Excitation of

Table 5. Structures, singlet energies (E^S), reduction potentials (E_{rdn}), and excited state reduction potentials (E^S_{rdn}) of cationic organic acceptors^a.

Structure	Energetics
	methylacridinium, MA ⁺ [85] $E^S = 2.75$ $E_{\text{rdn}} = -0.24$ $E^S_{\text{rdn}} = 2.51$
	methylene blue, MB ⁺ [86] $E^S = 1.83$ $E_{\text{rdn}} = 0.04$ $E^S_{\text{rdn}} = 1.87$
	thionine, TH ⁺ [86] $E^S = 2.03$ $E_{\text{rdn}} = 0.05$ $E^S_{\text{rdn}} = 2.08$
	diazapyrene, DAP ²⁺ [88] $E^S = 2.95$ $E_{\text{rdn}} = -0.26$ $E^S_{\text{rdn}} = 2.69$
	ethidium, ET ⁺ [47] $E^S = 2.39$ $E_{\text{rdn}} = -1.2$ $E^S_{\text{rdn}} = 1.2$ $E_{\text{ox}} = 1.68$ $E^S_{\text{ox}} = 0.52$
	methyl viologen, MV ²⁺ $E_{\text{rdn}} = -0.44$

^a Excited state energies in eV, redox potentials in V, versus NHE.

the ground-state complexes formed between DAP²⁺ and the nucleotides resulted in rate constants of $c. 5 \times 10^8 \text{ s}^{-1}$ for charge separation, much slower than normally observed for contact charge-transfer complexes in organic solvents [89]. Brun and Harriman [88] suggest that these slow rates may reflect a large D–A separation and unfavorable D–A geometry for electron transfer in the ground-state complex. Charge recombination of the geminate ion pairs is even slower than charge separation, in accord with the large change in free energy accompanying this process (Figure 7). Rate constants for charge separation increase as the calculated ΔG_{et} becomes more exergonic, reaching a maximum value when $\Delta G_{\text{et}} \approx 10 \text{ kcal mol}^{-1}$,

and rate constants for charge recombination decrease as this process becomes more exergonic, in accord with the predictions of Marcus theory (Eqs. 10 and 11).

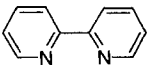
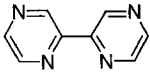
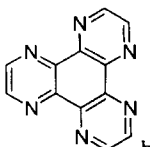
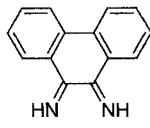
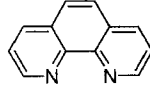
The dynamics of electron transfer from purine nucleotides to singlet excited ethidium cation (ET^+ ; Table 5) has been recently investigated by Barton and Zewail and colleagues [90]. They find that the fluorescence decay time of ground-state complex formed between ET^+ and G is somewhat longer than that of ET^+ in water (1.6 ns). However, the complex formed between ET^+ and the stronger donor Z (Table 3) has a fluorescence decay time of 70 ps. Analysis of the fluorescence anisotropy provided a longer decay time, leading to the proposal that the excited complex decays by a two-stage process similar to that proposed by Enescu and Lindqvist [45] (Eq. 14). As is the case for the MB^+ -nucleotide complexes, no transients assigned to the products of electron transfer are observed.

Transition metal complex acceptors

Luminescent polypyridyl Ru(II) complexes have been employed in numerous studies of DNA photooxidation [13, 14]. The dynamics of electron transfer quenching of the $^3\text{MLCT}$ states of Ru(II) complexes have been investigated by Krisch-De Mesmaeker and co-workers [14, 91]. The prototypical Ru(II) complex Ru(bpy)_3^{2+} is not a sufficiently strong oxidant or reductant to effect electron transfer from nucleotides or DNA. Ru(II) complexes with polyazaaromatic ligands (Table 6) are much stronger excited state oxidants than is Ru(bpy)_3^{2+} , and their luminescence is quenched by purine nucleotides in water [91]. A plot of $\log(k_{\text{et}})$ versus E^*_{red} for quenching of the $^3\text{MLCT}$ states by GMP and AMP has the appearance of a typical Rehm–Weller plot [72a]. Fitting of these data to the Marcus equation provides a value of $\Delta G^\ddagger = 7.5 \text{ kcal mol}^{-1}$ and values of 1.16 V and 1.56 V versus NHE for the oxidation potentials of GMP and AMP, respectively, in aqueous solution. The 0.4 V difference in GMP versus AMP potentials is larger than that reported by Steenken and Jovanovic [42b], but similar to that reported by Enescu and Lindqvist [44]. Laser flash photolysis of strongly oxidizing Ru(II) complexes with GMP yields transients which decay on the millisecond time scale and are assigned to the cage escaped Ru(I) complex and deprotonated GMP^+ .

Quenching of the excited states of several Rh(III) complexes possessing the ligands phi and phen (Table 6) by nucleosides and nucleotides has been investigated by Turro et al. [92]. The lowest excited states of the phi complexes are assigned to ligand-centered $\text{phi } n, \pi^*$ states which have decay times of c. 200–300 ns. Both static and dynamic quenching are observed for the negatively charged purine nucleotides, but only dynamic quenching for the neutral purine nucleosides. Rate constants for dynamic quenching by the both guanine and adenine bases, nucleosides, and nucleotides are all near the rate of diffusion in water. No quenching is observed for the pyrimidines. Laser flash photolysis of several complexes with GMP results in the formation of transients which are assigned to the reduced complex and oxidized GMP and which decay on the microsecond time scale. These may be cage-escaped products as in the above-mentioned study [91].

Table 6. Structures, excited state energies (E^*), reduction potentials (E_{rdn}), and excited state reduction potentials (E^*_{rdn}) of some Ru(II) and Rh(III) acceptors^a.

Ligand	Energetics
 bpy	$\text{Ru}(\text{bpy})_3^{2+}$ [91] $E^* = 2.01$ $E_{\text{rdn}} = -1.35$ $E^*_{\text{rdn}} = 0.66$
 tpz	$\text{Ru}(\text{tpz})_3^{2+}$ [91] $E^* = 2.13$ $E_{\text{rdn}} = -0.86$ $E^*_{\text{rdn}} = 1.27$
 hat	$\text{Ru}(\text{hat})_3^{2+}$ [91] $E^* = 2.08$ $E_{\text{rdn}} = -0.62$ $E^*_{\text{rdn}} = 1.46$
 phen	$\text{Rh}(\text{phen})_2(\text{phen})^{3+}$ [92] $E^* = 2.0$ $E_{\text{rdn}} = -0.05$ $E^*_{\text{rdn}} = 1.95$
 phen	$\text{Rh}(\text{phen})_2(\text{phen})^{3+}$ [92] $E^* = 2.0$ $E_{\text{rdn}} = -0.05$ $E^*_{\text{rdn}} = 1.95$

^a Excited state energies in eV, redox potentials in V, versus NHE.

5.2.3 Electron Transfer Process Involving Covalently Attached Nearest-Neighbor Nucleobases

Electron transfer in mononucleoside and dinucleoside conjugates

The fluorescence decay of dinucleoside monophosphates containing the modified base ethanoadenine (EAD) (see Table 4) and the natural bases guanine and uracil have been investigated by Kubota et al. [31c]. The fluorescence quantum yields are lower for the conjugates than for the nucleotide of EAD (<0.1 versus 0.52). The observation of multiple exponential fluorescence decay was attributed to multiple conformations. A small component with a decay time similar to that of unmodified EAD was attributed to an extended conformation and two shorter components to loosely stacked folded conformations. While the mechanism of fluorescence quenching was not addressed, an electron transfer mechanism in which singlet EAD can serve as an electron acceptor (with guanine) or electron donor (with uracil) is

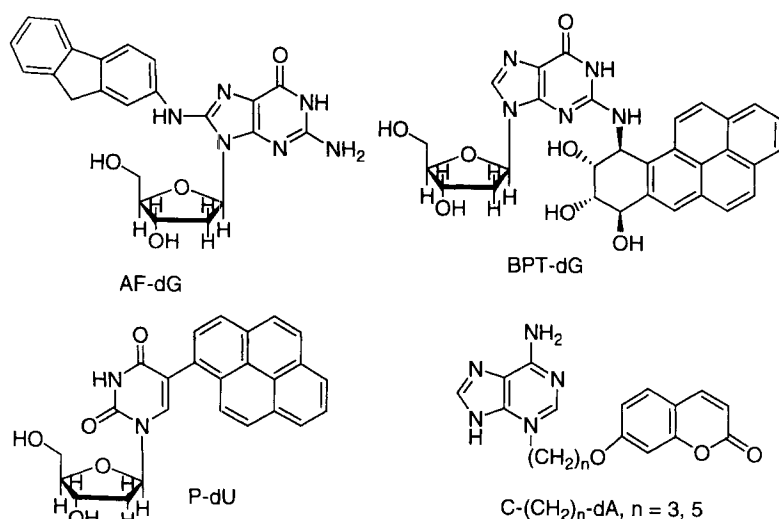


Figure 8. Structures of several arene-mononucleoside conjugates.

consistent with the results of Kelley and Barton for bimolecular quenching of EAD by nucleotides [30].

The behavior of purine nucleobases modified by covalent attachment of an aromatic hydrocarbon to the purine ring has been investigated by Geacintov and co-workers [80b, 93–95]. Extensive quenching of the fluorescence of the aminofluorene [93] and benzo[a]pyrene [94, 95] chromophores is observed in the conjugates AF-dG and BPT-dG (Figure 8). In the case of the BPT-dG conjugate, the formation and decay of BPT^{••} was observed by laser flash photolysis in DMF solution. The rate constants for charge separation and recombination are $9 \times 10^9 \text{ s}^{-1}$ and $2 \times 10^9 \text{ s}^{-1}$, respectively. These relatively slow rates for an intramolecular electron transfer process may reflect an unfavorable donor–acceptor geometry, as in the case of static quenching of DAP²⁺ by nucleotides studied by Brun and Harriman [88]. Formation of BPT^{••} is not detected in aqueous solution, presumably due to more rapid charge recombination [94]. Somewhat faster rate constants were observed for the *cis* versus *trans* stereoisomer of BPT, indicative of conformationally dependent quenching dynamics.

Relatively little fluorescence quenching is observed for the analogous conjugate of BPT with dA. However, when a second dG, dT, or dA nucleotide is attached to dA, fluorescence quenching is observed. Presumably, dT and dA serve as electron acceptors and singlet BPT as the electron donor. The extent of quenching is greater when the second nucleotide is attached to the 5' rather than the 3' position of the BPT-dA conjugate, providing further evidence for the dependence of quenching dynamics upon conformation.

The photophysics of several pyrene-dU conjugates have been investigated by Netzel and coworkers [96, 97]. Singlet pyrene serves as an electron donor, and uracil as an electron acceptor, in these conjugates. The conjugate P-dU (Figure 8) and an analogue with a carbonyl group separating the pyrene and uracil display charge-transfer fluorescence in organic solvents [96]. The observation of multiple exponential pyrene fluorescence decay was attributed to the presence of multiple ground-state conformers. The use of longer linkers containing amide groups also results in multiple exponential kinetics for quenching of singlet pyrene by dU [97].

The ground- and excited-state interactions between 7-alkoxycoumarin and nucleobases attached by a flexible trimethylene or pentamethylene linker ($\text{C}-(\text{CH}_2)_n\text{-dA}$, Figure 8) have been investigated by Wenska and Paszyc [98]. The equilibrium between folded and extended conformations favors the former in water and the latter in organic solvents. Dynamic quenching is observed in aqueous solution with rate constants that decrease in the order $\text{dA} > \text{dT} > \text{dU}$ ($k_q = 8.1 \times 10^8 \text{ s}^{-1}$ for dA connected via a trimethylene linker) in accord with an electron transfer mechanism in which the singlet coumarin serves as an electron acceptor and the nucleobase as electron donor. Dynamic quenching is more rapid for trimethylene versus pentamethylene linkers, as is generally observed for flexibly linked donor-acceptor systems. Dynamic quenching is also more rapid in aqueous versus organic solvent in accord with the lower base oxidation potentials in water (Table 3).

Seidel and coworkers [43, 99] have studied intramolecular quenching of the aminocoumarin C120 (Table 4) attached to mononucleotides by a flexible linker. They observe relatively slow quenching in water, with rates that decrease in the order $\text{dG} > \text{dT} > \text{dC} > \text{dA}$ ($k_q = 2.5 \times 10^8 \text{ s}^{-1}$ for dG and $0.2 \times 10^8 \text{ s}^{-1}$ for dA). This order is consistent with an electron transfer mechanism in which the coumarin serves as a weak acceptor in its reactions with purines, and as a weak donor in its reactions with pyrimidines. The observation of quenching in water but not in organic solvents is consistent with the observed effect of solvent upon nucleobase redox potentials (see Table 3). The behavior of C120 covalently attached to dinucleotides via a phosphorothiolate linkage adjacent to the 3'-terminus has also been investigated [99]. Variation of the 5' base with dA as the 3' base provides lifetime data for the dinucleotide conjugates indicative of quenching reactivity similar to that observed for the mononucleotide conjugates, $\text{dT} \sim \text{dG} > \text{dC} > \text{dA}$.

The intramolecular interaction of the 9-aminoacridine dye quinacrine with the nucleobases attached via a flexible polymethylene linker has been studied by Constant et al. [100]. The dye and nucleobase form π -stacked intramolecular complexes in water and, to a lesser extent, in organic solvents. Complex formation with adenine or thymine results in an increase in the acridine fluorescence intensity, presumably due to decreased solvation by water. In contrast, complexation with guanine results in quenching of the acridine fluorescence, presumably due to electron transfer.

Contact electron transfer in oligonucleotide conjugates

The fluorescence properties of oligonucleotides containing 2-aminopurine (AP; Table 4) have been investigated in several laboratories [29, 31]. Ward and Reich [29a] observed that the fluorescence intensity of the duplexes formed from the

alternating copolymers AP-U and AP-T is c. 0.1 to 1.5 % of that for the free AP monomer. Melting of the duplex results in an increase in fluorescence intensity. Law et al. [29b] also observed a c. 10-fold increase in fluorescence intensity upon melting of several 11-mers containing AP at the middle of one strand and each of the four nucleobases in the opposing position of the complementary strand. Nordlund et al. [29c] investigated the fluorescence of a 10-mer containing AP near the middle of one strand. The AP fluorescence decay was found to be multi-exponential. The longest decay time was assigned to an unstacked AP and three shorter decay times to AP with varying degrees of stacking with neighboring nucleobases. Hochstrassar et al. [29d] obtained similar results for ds DNA in which one strand has a 3'AP, and interpreted them in terms of multiple conformations ranging from fully stacked to unstacked. Kelley and Barton [30] also report low fluorescence quantum yields ($\Phi_f \leq 0.06$) and multiple exponential decays for duplexes containing AP, but do not address the possibility of quenching by neighboring nucleobases.

The photophysics of pyrene-oligonucleotide conjugates has been investigated in several laboratories [95, 101–103]. Quenching of singlet pyrene is more efficient when the conjugate BPT-dA (Figure 8) is incorporated into an 11-mer than in the simple mononucleotide conjugate [95]. Enhanced quenching was attributed to electron transfer involving neighboring nucleobases in either the ss or ds conjugate. When a P-dU conjugate (Figure 8) with a flexible linker is incorporated into an oligonucleotide, quenching by flanking nucleotides is observed to follow the order $C > T > G > A$ [101]. The greater reactivity for pyrimidines versus purines is consistent with an electron transfer mechanism in which singlet pyrene serves as the electron donor and the pyrimidine base as an electron acceptor. Duplex formation results in an increase in the pyrene singlet lifetime, presumably due to restricted access of the tethered pyrene to the acceptor nucleobases. Similar results were obtained for oligonucleotide conjugates in which a bispyrene with a flexible tether is attached to the 5'-end of the oligonucleotide [102]. The pyrene excimer fluorescence is more effectively quenched by neighboring T versus G in the ss conjugate. However, duplex formation eliminates this preference.

Electron transfer quenching in end-labeled pyrene-oligonucleotide conjugates with flexible linkers has been investigated by Zahavy and Fox [103]. The labeled strand is a purine 10-mer possessing one guanine and its complement a pyrimidine 10-mer. The presence of multiple ground-state conformations and the occurrence of quenching both by guanine and the pyrimidines complicates the kinetic analysis.

Nucleoside analogues in which an aromatic hydrocarbon replaces the natural base have been prepared by Ren et al. [25a]. Self-complementary oligonucleotides possessing a 5' terminal analogue (5'-dXCGCGCG, where X = pyrene, phenanthrene, or naphthalene deoxynucleosides) are thermodynamically more stable than the corresponding duplexes lacking the aromatic base. The thermal stability was taken as evidence for a duplex geometry in which the aromatic residue is π -stacked with the adjacent base pair. The fluorescence of both naphthalene and pyrene are reported to be strongly quenched in these duplexes. Fluorescence was observed for phenanthrene; however, neither quantum yields nor lifetimes have been reported for these duplexes.

The dynamics of quenching of the fluorescence of oligonucleotides labeled on the

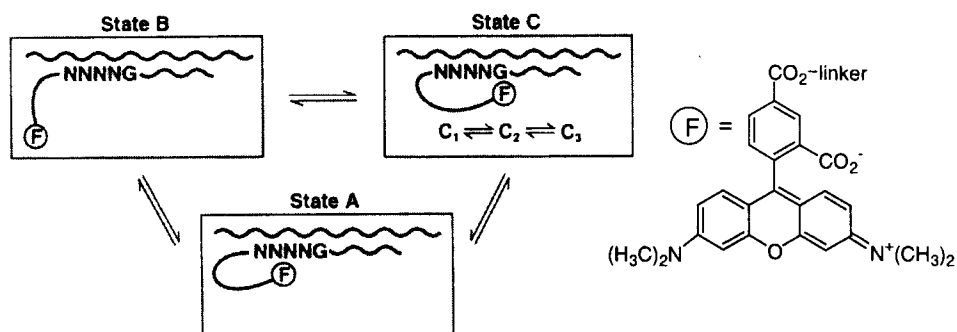
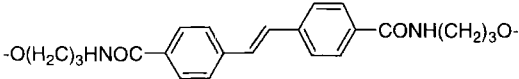
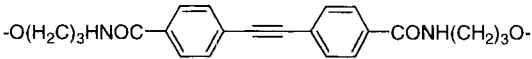
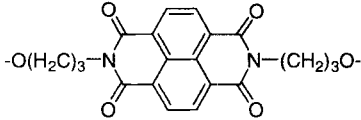
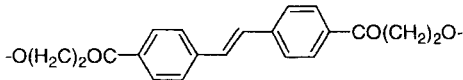


Figure 9. Three-state model for quenching of a rhodamine (F) end-labeled conjugate (G = guanine, N = other nucleobase) [105b]. Copyright 1998 National Academy of Sciences, U.S.A.

5' end by a 5-carboxytetramethylrhodamine dye (F; Figure 9) has been investigated by several research groups [104, 105]. Vámosi et al. [104] proposed a three-state model on the basis of their detailed analysis of steady-state fluorescence intensity and fluorescence decay data. According to this model, the tethered dye can exist in one of three ground-state conformations which do not interconvert on the time scale of fluorescence decay. One is a “dark state” in which the dye forms a ground-state complex with a quenching nucleobase, presumably guanine. The other two are both fluorescent but with different decay times in the range 0.5–1 ns and 2.5–3 ns. All three states are observed for both ss and ds DNA; however, the population of the dark state is higher for ds versus ss DNA. Subsequent investigations of rhodamine-oligonucleotide conjugates by single molecule fluorescence confirmed the presence of one dark and two fluorescent states. The three-state model proposed by Eggeling et al. [105b] is shown in Figure 9. According to this model, states A and B are the long-lived and short-lived fluorescent states whose decay times depend mainly on the local polarity, which is higher for rhodamine in water than when associated with the ss or ds oligonucleotide. The dark state C is assigned to ground-state complexation of rhodamine with guanine.

Oligonucleotide conjugates in which a Ru(II) complex is covalently attached to a modified pyrimidine nucleoside have been investigated by the groups of Netzel [106] and Kirsch-De Mesmaeker [107]. The former workers appended a modified $\text{Ru}(\text{bpy})_3^{2+}$ complex to a cytosine or thymine located near the middle of an 8-mer. The Ru(II) luminescence is not quenched in either the labeled ss or the duplex formed with its unlabeled complement, in accord with the low reduction potential of the $\text{Ru}(\text{bpy})_3^{2+}$ excited state (Table 6). The latter group has employed a photo-reactive $\text{Ru}(\text{TAP})_2\text{dip}^{2+}$ complex (TAP = 1,4,5,8-tetraazaphenanthrene and dip = 4,7-diphenyl-1,10-phenanthroline) tethered to a thymine located near the middle of a 17-mer. The relatively short tether forces the complex to remain inside the major groove of the duplex. The extent of luminescence quenching for several duplexes with different base sequences could be correlated with the proximity of the label to the nearest guanine.

Table 7. Structures, singlet energies (E^S), reduction or oxidation potentials (E_{rdn} or E_{ox}), and excited state reduction or oxidation potentials (E^S_{rdn} or E^S_{ox}) of DNA hairpin linkers.

Linker	Energetics
 <p>SA</p>	stilbenediamide [110] $E^S = 3.35$ $E_{\text{rdn}} = -1.67$ $E^S_{\text{rdn}} = 1.68$
 <p>DPA</p>	diphenylacetylenediamide [111] $E^S = 3.76$ $E_{\text{rdn}} = -1.74$ $E^S_{\text{rdn}} = 2.02$
 <p>NDI</p>	naphthalenediimide [112] $E^S = 3.24$ $E_{\text{rdn}} = -0.59$ $E^S_{\text{rdn}} = 2.65$
 <p>SE</p>	stilbenediether [26] $E^S = 3.45$ $E_{\text{ox}} = 1.16$ $E^S_{\text{ox}} = 2.29$

^a Excited state energies in eV, redox potentials in V, versus NHE.

Contact electron transfer in bis(oligonucleotide) conjugates

The synthesis of bis(oligonucleotide) conjugates in which an arene-dicarboxamide (Table 7) serves as a linker connecting two oligonucleotides has been reported by Letsinger and co-workers [108]. The fluorescence intensities for conjugates possessing stilbene-4,4'-dicarboxamide linkers with mixed base sequence 5-mer arms are lower (Figure 10a) than that of the unmodified linker and are dependent upon the base sequence, conjugates in which a guanine is located adjacent to the stilbene being the least strongly fluorescent ($\Phi_f < 10^{-3}$). Conjugates such as the 10-mers A and B in Figure 10a display double or triple exponential decay, with one decay component longer and one or two components shorter than that of the linker with no attached nucleotides [109]. The decrease in fluorescence quantum yield is more pronounced than the decrease in the average lifetime.

These observations are consistent with the three-state model proposed by Vámosi et al. [104] for ss rhodamine-oligonucleotide conjugates. Similar results have been obtained for conjugates possessing naphthalenedicarboxamide linkers (NA; Table 4) [73]. In this case, dark states account for >90 % of the single-strand conjugates. Duplex formation between complementary bis(oligonucleotide) conjugates such as A and B (Figure 10a), both of which possess SA or NA linkers, results in the formation of duplexes which display strong excimer fluorescence from the stilbene or naphthalene excimer [73, 109].

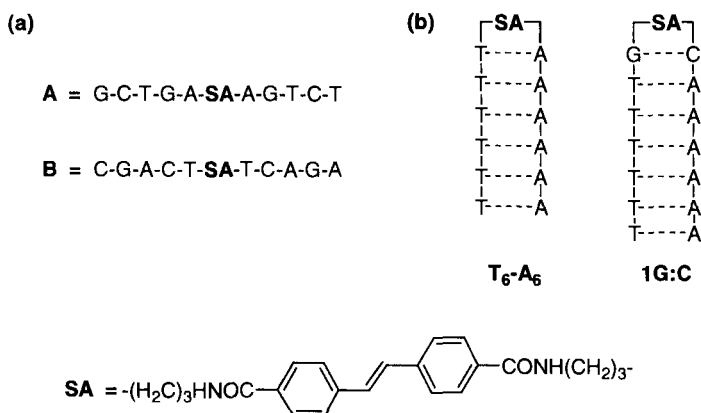


Figure 10. Structures of (a) complementary bis(oligonucleotides) conjugates [109] and (b) hairpin-forming bis(oligonucleotides) conjugates [110].

Letsinger and Wu [108c] observed that conjugates containing stilbene-4,4'-dicarboxamide linkers and complementary arms form exceptionally stable hairpin structures (see Figure 5) [26]. Hairpins possessing polyA-polyT stems (e.g., T₆-A₆; Figure 10b) are strongly fluorescent; however, hairpins with polyG-polyC stems are essentially nonfluorescent. Subsequent investigations by Lewis and coworkers [110] established that a hairpin containing a single adjacent G:C base pair (1G:C; Figure 10b) undergoes charge separation to yield the stilbene anion radical and guanine cation radical with a rate constant of $1 \times 10^{12} \text{ s}^{-1}$. The radical ion pair decays to the ground state with a rate constant of $4.3 \times 10^{10} \text{ s}^{-1}$. The slower rate constant for charge recombination versus charge separation is consistent with the large energy gap for the latter process (Figure 7), which places it in the “inverted region” (Eq. 11). In contrast, the singlet stilbene in the hairpin T₆-A₆ does not undergo electron transfer quenching and has a singlet decay time of 2.0 ns, which is exceptionally long for a singlet stilbene. The oxidation of guanine but not adenine is consistent with the free energies of electron transfer calculated using Eq. 5 and the data in Tables 3 and 7 ($\Delta G_{\text{et}} = -0.3 \text{ eV}$ for G and $+0.2 \text{ eV}$ for A).

The observation of single exponential fluorescence decay for T₆-A₆ and charge separation and charge recombination rates for 1G:C indicates that these hairpins are conformationally homogeneous, unlike the other oligonucleotide conjugates and duplex-intercalator systems investigated to date. The high melting temperatures of the stilbene-linked hairpins suggests that their conformational homogeneity is a consequence of the thermodynamic stability of their B-form duplex structure (see Figure 5).

The free energy for photoinduced electron transfer in hairpin-forming bis(oligonucleotide) conjugates can be modified by changing either the nucleobase or the linker (Eqs. 5 or 6) [110–112]. Rate constants for charge separation and re-

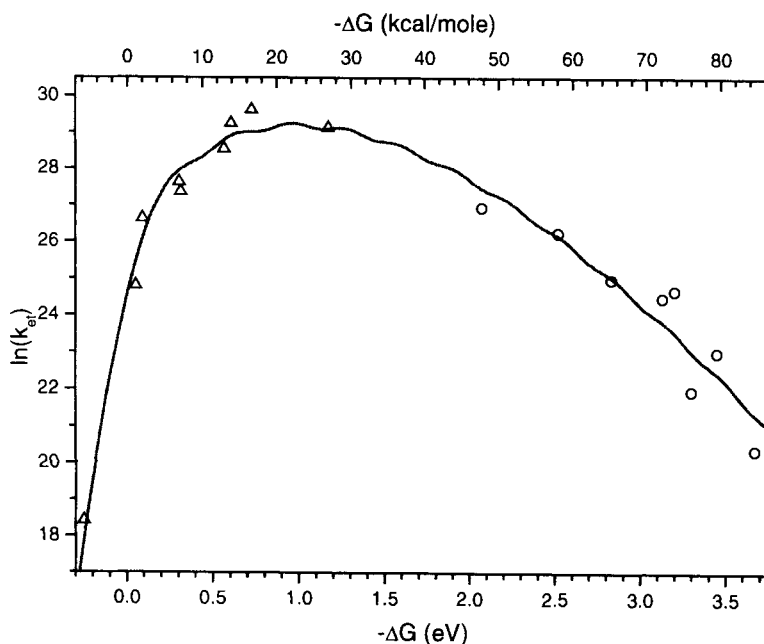


Figure 11. Rate constants for charge separation (Δ) and charge recombination (O) in DNA hairpins with acceptor linkers (Table 7) and nearest-neighbor nucleobase donors [112].

combination in SA-linked hairpins are more rapid when guanine is replaced by 7-deazaguanine (Z), but are slower when the G:C base pair is replaced by an inosine-thymine (I:T) base pair, in accord with the reported oxidation potentials for Z and I (see Table 3) [112]. The 4,4'-diphenylacetylenedicarboxamide (DAP) [111] and naphthalenediimide (NDI) [112, 113] linkers are stronger singlet-state acceptors (Table 7) which can oxidize adenine as well as guanine. The stilbenediether linker (SE; Table 7) is a strong electron donor which can reduce either T or C [26].

A plot of the rate constants for charge separation and charge recombination obtained with SA, DAP, and NI acceptors and nucleobase donors versus exothermicity (ΔG_{et}) is shown in Figure 11. Rate constants for charge separation reach their optimum value of c. 10^{13} s^{-1} when $\Delta G_{et} \sim -0.5 \text{ eV}$. Rate constants for charge recombination decrease only slowly with increasing exothermicity. Both data sets can be fitted to Eq. 11 by making the simplifying assumption that the electronic coupling for charge separation and charge recombination is the same. This fit provides values of the solvent reorganization energy, $\lambda_s = 0.23 \text{ eV}$, the nuclear reorganization energy, $\lambda_i = 0.99 \text{ eV}$, and the electronic matrix coupling element, $H_{DA} = 347 \text{ cm}^{-1}$. The solvent reorganization energy is significantly smaller than values reported for aromatic contact radical ion pairs in polar solvents such as acetonitrile [77, 79], suggesting that the effective polarity of the duplex interior is similar to that of a moderately polar ether solvent [114]. The value of H_{DA} is con-

siderably smaller than that reported by Gould and Farid [77] for the contact radical ion pairs with cyanoanthracene acceptors and alkylbenzene donors (750 cm^{-1}). The smaller value may result from a rigid hairpin geometry which prevents optimal donor–acceptor overlap. A rigid geometry could also account for a value of λ_i which is lower than that observed by Hubig et al. [89] for charge recombination of olefin/TCNE charge transfer complexes. It is interesting to note that analysis of the data of Brun and Harriman [88] for charge separation and recombination of DAP^{2+} -nucleotide complexes provides a much smaller value of $H_{\text{DA}} = 1.2\text{ cm}^{-1}$, similar to the value reported by Gould and Farid [77] for a solvent-separated radical ion pair.

5.2.4 Electron Transfer Quenching of Intercalated Acceptors by Nearest-Neighbor Nucleobases

Intercalation of dyes into ds DNA can result in shifts in their fluorescence spectra and either increased or decreased fluorescence intensity [115]. Ethidium bromide (ET^+ ; Table 5) has been widely used as a fluorescent probe for DNA due to its marked increase in fluorescence quantum yield and lifetime upon intercalation ($\tau_s = 1.8\text{ ns}$ and 22.5 ns in water and DNA, respectively) [116]. The short lifetime of ET^+ in water is attributed to proton transfer quenching. The long lifetime of ET^+ when randomly intercalated in native DNA is consistent with its low singlet-state reduction potential ($E_{\text{rdn}}^{\text{S}} = 1.2\text{ V}$; Table 5) which renders quenching by guanine endergonic by c. 0.3 eV , using the oxidation potential of guanine in acetonitrile solution (see Table 3). Hall et al. [117] have observed that short-wavelength (310-nm) excitation of ET^+ covalently tethered to one end of a DNA duplex results in covalent bonding between ET^+ and an adjacent guanine. Since this reaction does not occur upon long-wavelength excitation of ET^+ , it is attributed to the reaction of an upper singlet state. The ultrafast dynamics of contact charge transfer processes make it possible for upper singlet state reactions to compete with internal conversion.

In contrast to the enhanced fluorescence of ET^+ upon intercalation, the fluorescence of many positively charged dyes is strongly quenched upon association with DNA [115]. Among these are the diazapyrenium dication (DAP^{2+}) and the methylene blue cation (MB^+). In view of the low singlet-state reduction potentials of these dyes (Table 5), photooxidation of neighboring purine nucleobases was suggested as the likely mechanism of quenching by Hélène and colleagues [118]. Brun and Harriman [88] have investigated the interaction of DAP^{2+} with ds DNA by means of time-resolved fluorescence and transient absorption spectroscopy. Their observation of multiple exponential fluorescence and transient decay was explained by the presence of dye molecules that are either fully and partially intercalated, loosely bound to the DNA exterior, or free in solution. Both charge separation and charge recombination for the fully intercalated dye were concluded to occur with rate constants $>10^{10}\text{ s}^{-1}$. These rates are much faster than those observed for the ground-state complex of DAP^{2+} with single nucleotides (see Section 5.2.2, p. 127), suggesting a more favorable geometry for electron transfer in the intercalated complexes. More efficient quenching and faster quenching rates were observed for

poly[dGdC] versus poly[dAdT], in accord with the lower oxidation potential of G versus A.

The dynamics of electron transfer quenching of intercalated MB^+ by neighboring base pairs have been investigated by Atherton and Harriman [119]. Intercalation of MB^+ is more favorable in poly[dGdC] than in poly[dAdT], surface binding competing with intercalation in the latter polymer. Intercalation results in a dramatic reduction in the MB^+ fluorescence quantum yield and decay time. Rate constants for the forward and return quenching processes in poly[dGdC] determined by transient absorption spectroscopy are $2.5 \times 10^{11} \text{ s}^{-1}$ and $3.3 \times 10^{10} \text{ s}^{-1}$, respectively. For MB^+ intercalated in poly[dAdT] the forward rate constant is $1.4 \times 10^{10} \text{ s}^{-1}$, and the return process was assumed to be even faster since the transient products of electron transfer were not observed. The quenching rates for surface-bound MB^+ are much slower. The authors suggested that the quenching process involved hydrogen atom transfer since the rate constants appeared to be too rapid for a non-adiabatic electron transfer process. However, recent studies have shown that even faster forward and return electron transfer processes can occur for π -stacked donor–acceptor contact complexes [110, 111].

Fast singlet-state contact electron transfer between intercalated acceptors and adjacent nucleobases can readily compete with intersystem crossing of the singlet acceptor. As previously described (Section 5.2.1), Kelly and colleagues [84a,b] observed that bimolecular electron transfer quenching of a naphthalene imide (NI; Table 4) by nucleotides occurs via a triplet-state mechanism. However, when intercalated in native DNA, quenching of the singlet state ($\tau_S = 2.4 \text{ ns}$) is more rapid than intersystem crossing [84b].

5.3 Single-Step Electron Transfer Process in Acceptor–DNA–Donor Systems

5.3.1 Background

As discussed in Section 5.2.1, the rate constant for a single-step superexchange electron transfer process between a donor and acceptor within a collision complex can be described by the Marcus–Levich–Jortner equation (Eq. 11). This equation also can be applied to bridge-mediated A–B–D systems under well-defined conditions in addition to those described in Section 5.2. First, the bridge states should lie well above the initial $\text{A}^*-\text{B}-\text{D}$ and final $\text{A}^--\text{B}-\text{D}^+$ states, as shown in Figure 12. Second, the A–B–D system must exist in a single conformation (or distribution of “kinetically equivalent” conformations) both prior to excitation and during the electron transfer process. Assuming that the energetics (ΔG_{et} and λ_i) for bridge-mediated electron transfer are independent of distance, the only term in Eq. 11 which is distance-dependent is H_{DA} , the electronic coupling matrix element. The distance dependence of H_{DA} is related to the donor acceptor distance (R) by Eq. 15 [75],

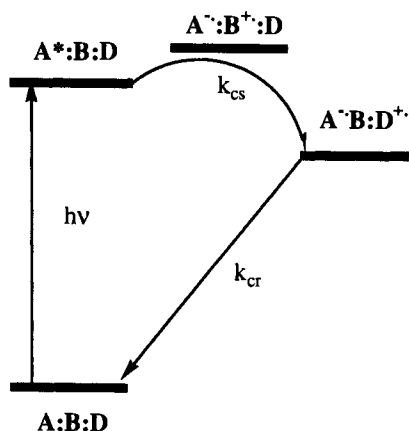


Figure 12. Energy level diagram for photochemical charge separation and charge recombination for an acceptor-bridge-donor (A-B-D) system.

$$H_{DA} = H_{DA}^0 \exp(-\beta(R - R_0/2)) \quad (15)$$

$$k_{et} = k_0 e^{-\beta R} \quad (16)$$

$$\beta = 2/R_0 \ln(\Delta E/t_{nm}) \quad (17)$$

where R_0 is a reference geometry and β is a characteristic of the specific donor-bridge-acceptor system. Combination of Eqs. 10 and 15 provides Eq. 16, the dependence of electron transfer rate upon β , where the pre-exponential factor k_0 is largely determined by the Franck-Condon factors for the electron transfer process. Finally, β is dependent upon ΔE , the energy gap between the initial and bridge states, and t_{nm} the electronic mixing matrix element between adjacent bridge sites. When $(\Delta E/t_{nm}) \gg 1$ this dependence can be approximated by Eq. 17.

Two types of A-B-D superexchange systems have been investigated experimentally, those in which an “unnatural” acceptor and donor are separated by a variable number of base pairs (Section 5.3.2) and those in which an “unnatural” acceptor is separated from the “natural” donor guanine (or a more readily oxidized base analogue or GG step) by a variable number of A:T base pairs (Section 5.3.3). The operation of a superexchange mechanism in either system requires that the excited acceptor not be quenched by the base pairs constituting the bridge. For the latter systems, this requires that the oxidation potential of adenine lies well above that of guanine. Based on the evidence presented in Section 5.1.2 (pp. 114–115), we conclude that this difference is ≈ 0.5 V. Both systems are also subject to complications arising from conformational disorder. Disorder in the A-B-D ground state (static disorder) may be reflected in multiple exponential decay of the A-B system in the absence of a donor. Dynamic disorder due to motion of the π -stacked base pairs forming the bridge could result in gating of the electron transfer process. Either type of disorder would result in an ensemble of values for k_{cs} . As is the case for contact electron transfer, the charge separation process is expected to lie in the normal region and charge recombination in the inverted region.

Equation 16 has been found to describe successfully the distance dependence of the electron transfer dynamics in a large number of systems in which there is a large energy difference between the oxidized or reduced states of the bridge and the initial and final donor–acceptor states [120]. In the case of proteins, the exponential dependence of electron transfer rate constant upon distance is observed for as much as a 10^{10} -fold decrease in rate constant [121]. Values of β for electron transfer in proteins and in D–B–A systems with hydrocarbon bridges typically fall in the range $0.9\text{--}1.6\text{ \AA}^{-1}$ [121, 122]. Electronic structure calculations by Beratan and colleagues [123] for stacks of benzene or naphthalene molecules separated by the 3.4 \AA π -stacking distance in DNA provide values of $\beta \sim 1.4\text{ \AA}^{-1}$. Similar values of β were calculated for several of the experimental systems discussed in the following sections. However, smaller values of β are observed for bridges with conjugated π -orbitals and an example of wire-like behavior in a D–B–A system with a *p*-phenylenevinylene bridge has recently been reported by Davis et al. [124].

Several alternatives to a superexchange mechanism for long-distance electron transfer in D–B–A systems have been advanced. Felts et al. [125] predicted on the basis of their solution to the Redfield equation for the density matrix of the full D–B–A system that an activated adiabatic mechanism which is only weakly distance-dependent might become significant under highly specific conditions. Davis et al. [126a] developed a similar model using a phenomenological treatment of the interaction of a quantum mechanical system with an external bath. This treatment has recently been extended to a full correlation–function treatment with both temperature and length dependence [126b]. Similar results have been reported by Mukamel and colleagues [127]. According to Felts et al. [125], the adiabatic pathway can result in rate constants faster than those for the distance-dependent superexchange mechanism under certain well-defined conditions. Among these is the requirement of thermal population of the bridge states which can occur only when the D–B gap is very small and the temperature is moderately high. Even under these conditions, the adiabatic mechanism may be slower than superexchange when the bridge contains only a small number of sites. Electron transport in DNA via a hole-hopping mechanism is discussed in Section 5.4 of this chapter.

The π -stacked bases of ds DNA might be expected to provide a better medium for bridge-mediated electron transfer than the sigma bonds of proteins or hydrocarbons. It has in fact been proposed by Turro and Barton [18d] that ultrafast photoinduced electron transfer processes involving intercalated donors and acceptors can occur with little or no distance dependence. According to this paradigm, duplex DNA can function as a “molecular wire” or “ π -way”.

5.3.2 Electron Transfer in Donor–DNA–Acceptor Systems

Nontethered intercalators

There have been numerous investigations of the fluorescence quenching of intercalated ethidium (ET^+ ; Table 5) by intercalated or groove bound quenchers [128–

134]. In the initial studies of Baguley and coworkers [128], ET^+ served as the electron acceptor and a series of 9-anilinoacridines as the electron donors. The efficiency of quenching was observed to be dependent upon the acridine oxidation potential, in accord with an electron transfer mechanism for quenching of the ET^+ fluorescence intensity and lifetime. Their fluorescence quantum yield and decay data has recently been re-analyzed by Tuite [11], who suggests that nearest neighbor binding of donor and acceptor results in total quenching and that quenching over longer distances results in a reduction in fluorescence intensity and lifetime. The efficiency of quenching was also found to depend upon the host nucleic acid, decreasing in the order poly(dAdT) > native DNA > poly(dGdC). This trend may reflect the dependence of electron transfer upon the average D–A separation, DNA structure, or the dynamics of the electron transfer quenching process.

Quenching of ET^+ fluorescence by diazpyrenium dichloride (DAP^{2+} ; Table 5) has been investigated by Brun and Harriman [129, 130]. Singlet ET^+ serves as the electron donor and DAP^{2+} as the electron acceptor in this system. Based on the data in Table 5, electron transfer should be exergonic by c. 0.26 eV. The decay of the ET^+ transient absorption and the formation and decay of the electron transfer products were directly observed by picosecond transient absorption spectroscopy. Time-resolved fluorescence studies reveal the presence of either three or four decay components, one of which has a decay time similar to that of unquenched intercalated ET^+ (21.1 ns). The several decay components both for charge separation and charge recombination are assigned to donor–acceptor separations of three, four, and five base pairs, in order of increasing decay time. It is asserted that no D–A pairs are separated by a smaller number of base pairs due to the mutual exclusion of intercalated molecules. However, it is unlikely that fluorescence would be observed for shorter D–A separations, as suggested by Tuite [11] in analyzing Baguley's results [128]. The slopes of plots of $\ln k_{\text{cs}}$ or k_{cr} versus R (Eq. 16) provide values of k_0 and β for electron transfer in calf-thymus DNA which are summarized in Table 8.

Table 8. Values of k_0 and β for superexchange DNA-mediated electron transfer^a.

System	k_0 (s^{-1})	β (\AA^{-1})
$\text{ET}^+/\text{DAP}^{2+}$ in calf-thymus DNA: charge separation	1.1×10^{13}	0.91
charge recombination [129]	1.3×10^{14}	1.49
$\text{ET}^+/\text{DAP}^{2+}$ in poly(dAdT)	2.5×10^{14}	1.0
$\text{ET}^+/\text{DAP}^{2+}$ in poly(dGdC) [130]	5.8×10^{13}	1.0
SA/G, (T:A) _n spacer, hairpin poly(dT) arm		
charge separation	7.8×10^{12}	0.66
charge recombination [110b]	1.6×10^{12}	0.90
SA/G, (T:A) _n spacer, in hairpin poly(dA) arm		
charge separation	3.2×10^{13}	0.71
charge recombination [110b]	6.2×10^{12}	0.94
Acridinium/G, (T:A) _n spacer [148b]	1.9×10^{12}	1.47
EA/G, (T:A) _n spacer [30]		1.0

^aData for systems in which kinetics based on kinetic spectroscopic data at several D–A distances is available.

Similar values of β are obtained when acridine orange is used in place of ethidium as the acceptor.

Harriman [130] has recently investigated the dynamics of electron transfer quenching of ET^+ fluorescence by DAP^{2+} in poly(dAdT) and poly(dGdC). Similar values of $\beta = 1.0 \text{ \AA}^{-1}$ are observed for both polymers; however, the rate constants for poly(dAdT) are c. four-fold faster at any fixed distance, in accord with the earlier observations of Baguley and coworkers [128]. The temperature dependence of the fluorescence decay data for quenching of ET^+ by DAP^{2+} has also been investigated by Harriman. Analysis of these data according to simple Marcus theory (Eqs. 9 and 10) provides a reorganization energy which approaches a value of $\lambda = 0.4 \text{ eV}$ as the D–A separation increases. Harriman points out that the small value of λ is indicative of a “rigid matrix that is not readily polarized”. The values of λ at shorter D–A separations (c. 0.48 eV) are somewhat larger than those that we observe for contact electron transfer in hairpin-forming bis(oligonucleotide) conjugates (0.23 eV ; Section 5.2.3). This difference may reflect the greater rigidity of hairpin versus normal duplex structures. Values for the electronic coupling matrix element H_{DA} decrease from c. 4 cm^{-1} at a D–A separation of 10 \AA to 0.1 at 17 \AA . These values are significantly smaller than our value for contact electron transfer (347 cm^{-1}) that is indicative of weak coupling across several base pairs.

Quenching of the luminescence of intercalated ET^+ by the intercalating complex $[\text{Rh}(\phi)_2\text{phen}]^{3+}$ (see Table 6 for ligand structures) was investigated by Kelley et al. [131]. Multiple exponential fluorescence decay is observed for ET^+ in the presence of the Rh(III) complex, as is the case in Hariman’s study of quenching by DAP^{2+} [130]. In fact, the 2 ns decay times reported by Barton are very similar to those assigned by Harriman to electron transfer between intercalated donor and acceptor separated by four and five base pairs in poly[dAdT]. Quenching of fluorescence intensity was also investigated and found to be more extensive than would have been expected on the basis of the fluorescence lifetime quenching. This result is consistent with static quenching at short donor–acceptor distances as suggested by Tuite [11].

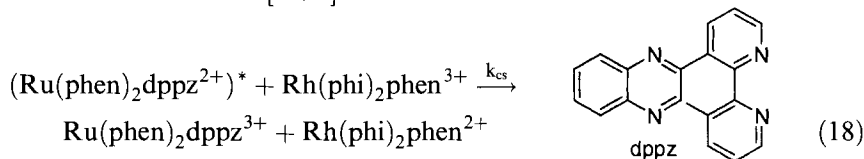
The fluorescence of intercalated ET^+ is also quenched by methylviologen (Table 5; MV^{2+}), a surface-bound acceptor—a process which is exergonic by c. 0.08 V (Table 5). Quenching of the steady-state fluorescence of ET^+ by MV^{2+} was investigated by Fromherz and Rieger [132]. A large increase in the Stern–Volmer quenching constant upon addition of DNA was attributed to both the enhanced lifetime of intercalated versus free ethidium and the enhanced local concentration of MV^{2+} due to binding to DNA. Atherton and Beaumont [133] observed by means of transient absorption spectroscopy that both formation and decay of reduced MV^+ occurs within c. 1 ns. Harriman [130] has recently determined a rate constant of $6.3 \times 10^8 \text{ s}^{-1}$ for quenching of intercalated ethidium by nearest neighbor MV^{+2} under saturation conditions. From the temperature dependence of the rate constant, the activation energy for electron transfer ($\Delta G^\ddagger = 3.0 \text{ kcal mol}^{-1}$), reorganization energy ($\lambda = 0.66 \text{ eV}$), and electronic coupling matrix element ($H_{\text{DA}} = 18 \text{ cm}^{-1}$) were obtained. Similar values of λ were obtained for the quenching of several other intercalated dyes by MV^{2+} .

The quenching of intercalated ET^+ by metal ions has been investigated by Atherton and Beaumont [134a,b]. Both static quenching by metal ions associated

with the phosphate ions and diffusional quenching are proposed to occur. In the case of quenching by Cu^{2+} , most of the initially formed oxidized ethidium decays via geminate recombination with Cu^+ . The remaining oxidized ethidium undergoes multiexponential decay on a millisecond time scale. This decay was analyzed using a kinetic model that assumes reduction occurs via charge recombination with Cu^+ ions located at increasing fixed distances relative to the oxidized ethidium [134b]. This analysis provides a value of $\beta = 0.73 \text{ \AA}^{-1}$, though in view of the multiple assumptions made in arriving at this value, it should be viewed with circumspection.

The quenching of transition metal complexes bound to DNA has been extensively studied by Barton and coworkers [13]. In the initial studies of Barton, Turro and colleagues [135], marked enhancement of the efficiency of quenching of the electron donor $\text{Ru}(\text{phen})_3^{2+}$ by the acceptors $\text{Co}(\text{phen})_3^{3+}$ and $\text{Co}(\text{bpy})_3^{3+}$ (see Table 6 for ligand structures) was observed in the presence of DNA. Whereas it was initially suggested that DNA might be mediating efficient long-range electron transfer between intercalated complexes, later investigations showed that these complexes do not intercalate and that the primary effect of groove binding to DNA is to increase the local donor and acceptor concentrations and decrease their mobility [136], as proposed by Fromherz and Rieger [132] in their study of quenching of intercalated ET^+ by groove-bound MV^{2+} .

Metal complexes which possess one or more large planar aromatic ligand can intercalate strongly between the base pairs of DNA. The complex $[\text{Ru}(\text{phen})_2\text{dppz}]^{2+}$ has a binding constant of $>10^6$, and its luminescence intensity increases by $>10^3$ upon intercalation. This "light switch" behavior facilitates the distinction between electron transfer quenching of the free versus bound complex [137]. In 1994, Barton, Turro and coworkers [138] reported the remarkable enhancement of quenching of the luminescence intensity of this intercalated complex by an intercalated complex $\text{Rh}(\text{phi})_2\text{phen}^{3+}$ (Eq. 18) when compared to the nonintercalated complex $\text{Ru}(\text{N-H}_3)_6^{3+}$. Moreover, no quenching of the lifetime of $\text{Ru}(\text{phen})_2\text{dppz}^{2+}$ was observed on the nanosecond time scale. Based on the assumption that the donor and acceptor are bound randomly to DNA, the authors concluded that a quenching efficiency of $>80\%$ was obtained with an average D–A separation $\geq 35 \text{ \AA}$ (10 bp). No quenching of the $\text{Ru}(\text{phen})_2\text{dppz}^{2+}$ decay time was observed on a nanosecond time scale, from which it was concluded that the rate constant for charge separation is $>10^9 \text{ s}^{-1}$. A series of studies by these investigators using different metal complexes and oligonucleotides led to the conclusion that wire-like behavior required strong coupling between the donor and acceptor π ligands and the intervening aromatic base pairs [139]. Much less efficient electron transfer is observed when the quencher is groove-bound rather than intercalated [139d].



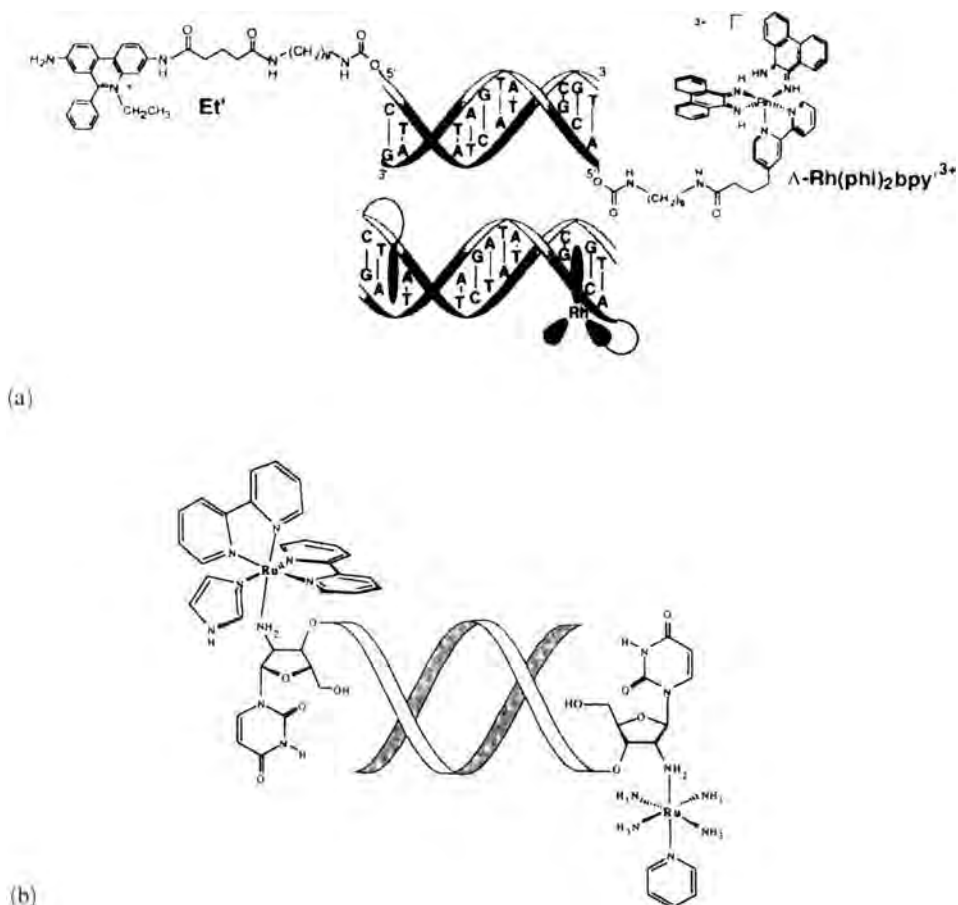
Subsequent investigation of this and related systems by Barton, Barbara and colleagues [140] using picosecond time-resolved fluorescence and transient absorp-

tion spectroscopy again failed to detect lifetime quenching, leading to a revised estimate $>3 \times 10^{10} \text{ s}^{-1}$ for the charge separation process. Charge recombination was also concluded to occur with rate constants $\sim 10^{10} \text{ s}^{-1}$ based on the absence of transient absorption by the products of charge separation. Two models for ultrafast charge separation and recombination were considered. A cooperative binding model with quenching over short D–A distances was rejected in favor of a random binding model with quenching over long distances. However, soon thereafter Olson et al. [141], independently of Barton, reported that the cooperative binding model was consistent with quantitative modeling of the available dynamic data. Kinetic modeling provided a value of $\beta = 1.0 \text{ \AA}^{-1}$ for the distance-dependent electron transfer in DNA. Concurrently, Lincoln et al. [142] reported that the intercalated donor and acceptor employed by Barton and Turro are bound cooperatively with only two base pairs separating nearest-neighbor donor–acceptor pairs. Barton has questioned the experimental evidence for cooperative binding, and presented evidence for anticooperativity in binding of $\text{Rh}(\text{phen})_2(\text{phen})^{3+}$ and $\text{Ru}(\text{phen})_2\text{dppz}^{2+}$ to a 10-mer duplex [139d, 144]. Further details of this controversy are provided in reviews by Barton [13], Barbara [15], and Tuite [11].

Tethered intercalators

The use of donors and acceptors that are covalently attached to an oligonucleotide reduces the uncertainty concerning location encountered with nontethered donors and acceptors. Barton and coworkers have used long, flexible tethers to attach chromophores to the 5' end of oligonucleotides [131, 144]. In 1993, they reported the remarkable observation that the intense fluorescence of the duplex formed between a 15-mer oligonucleotide with a tethered $[\text{Ru}(\text{phen})_2\text{dppz}]^{2+}$ chromophore and a nonlabeled complementary strand is completely quenched when the $\text{Ru}(\text{II})$ -labeled 15-mer is hybridized with a complementary strand possessing a 5'-tethered $[\text{Rh}(\text{phen})_2\text{phen}]^{3+}$ [144]. Photochemical studies of duplexes containing either the tethered $\text{Ru}(\text{II})$ or $\text{Rh}(\text{III})$ complex indicated that intercalation occurs with equal probability 1 or 2 bp from the 5' terminus [117]. On the assumption that this is also the case for the doubly labeled duplex, totally efficient luminescence quenching was concluded to result from ultrafast electron transfer over a distance of $\geq 41 \text{ \AA}$ (11 bp).

Kelley et al. [131] have also investigated the distance-dependent fluorescence quenching in duplexes containing a 5'-tethered ethidium on one strand and a 5'-tethered $[\text{Rh}(\text{phen})_2\text{bpy}]^{3+}$ on the complementary strand (Figure 13a). In the absence of $\text{Rh}(\text{III})$, a ET^+ -modified 10-mer duplex displays triple exponential decay with decay times of 7.6, 2.4, and 1.2 ns, presumably corresponding to three different duplex–intercalator geometries. In the presence of $\text{Rh}(\text{III})$ only modest changes in the decay times and preexponentials occur. When the length of the doubly tethered duplex was increased from 10 bp to 14 bp, the fraction of ET^+ fluorescence quenching by the $\text{Rh}(\text{III})$ complex decreased from 29 % to 8 %. The fluorescence intensity quenching was attributed to a long-range electron transfer process which is weakly distance-dependent. In support of this explanation, a single C:A base pair mismatch near the middle of a doubly labeled 10-mer reduces the extent of quenching from 21 % to 4 %.



tethered $\text{Rh}(\text{phi})_2\text{bpy}^{3+}$ acceptor on the complementary strand in extended and intercalated conformations. Reprinted with permission from ref. 131. Copyright 1997 American Chemical Society.

(b) Diagram of a duplex containing a 5'- $\text{Ru}(\text{bpy})_2\text{im}^{3+}$ acceptor on one strand and a 5'- $\text{Ru}(\text{NH}_3)_4\text{py}^{2+}$ donor on the complementary strand [146].

The observation of intensity but not lifetime quenching in the $\text{ET}^+-\text{Rh}(\text{III})$ doubly tethered system was attributed to “gated” electron transfer [131, 145]. According to this explanation, ultrafast long-distance electron transfer can occur only when the donor–acceptor and intervening base pairs are perfectly aligned. This would require that the excited states of the residual fluorescent duplexes adopt this optimal geometry no faster than the nanosecond time scale of the longest decay component—much longer than the picosecond time scales reported for many DNA relaxation processes (Section 5.1.2). The proposal of gated electron transfer also poses the question as to why this phenomenon was not observed for the $\text{Ru}(\text{II})$ - $\text{Rh}(\text{III})$ doubly tethered system? The observation of partial luminescence upon

mixing of two duplexes which possess a single tethered Ru(II) or Rh(III) complex [144] and self-quenching of the ET^+ -Rh system at concentrations $>20 \mu\text{M}$ [131] provide a possible explanation. End-to-end aggregation [19] of the Ru(II)-Rh(III) doubly tethered system would be favored by cooperative ligand interactions, and would result in a short distance between the Ru(II) in one duplex and the Rh(III) in the next.

DNA-mediated electron transfer between two nonintercalated tethered metal complexes has been investigated by Meade and Kayyem [146]. They prepared complementary 8-mer oligonucleotide conjugates in which two different Ru complexes are directly attached to the 2-amine of a 5' terminal aminosugar (Figure 13b). The reported distance between the two metal centers is 21 \AA ; however, the precise location of the metal complexes with respect to the duplex base pairs is not known. The rate constant for electron transfer between the acceptor Ru(III) and donor Ru(II) complexes was determined by the flash-quench technique to be $1.6 \times 10^6 \text{ s}^{-1}$. This single measurement is similar to that observed in proteins with similar D–A distances, and has been frequently cited as evidence against unusually facile electron transfer in DNA. However, in view of the importance attached to this study, it is unfortunate that additional experimental details have not been forthcoming.

Recently Aich et al. [147] have reported intriguing results for electron transfer in 20-mer and 54-mer duplex possessing a fluorescein electron donor at the 5' position of one strand and a rhodamine acceptor the 5' position of the complementary strand. No quenching of the fluorescein is observed in the normal B-form duplexes; however, upon addition of Zn^{2+} the duplex adopts a M-form geometry for which highly efficient quenching is observed in both the 20-mer and 54-mer (95 % and 76 % quenching, respectively). M-form DNA is proposed to adopt a double-helical structure similar to that of B-form DNA, with a metal ion replacing a proton in each base pair and a metal–metal distance of c. 4.0 \AA . Fluorescence decay measurements of the B-form and M-form 20-mer duplex show that the former has biexponential decay with components of 4.0 and 2.1 ns, and the latter triexponential decay dominated by a 10 ps component. The quenching process was concluded to occur via rapid, long-distance electron transfer. However, no definitive structural data is available for M-DNA and the radical ion products of electron transfer have not been detected. Thus, the claim of wire-like behavior must be viewed at this time with appropriate reservations.

5.3.3 DNA-Mediated Oxidation of Nucleobases

Stilbenedicarboxamide-linked DNA hairpins

As described in Section 5.2.3 (p. 136), the hairpin $\text{T}_6\text{-A}_6$ (Figure 10) which possesses a polyA-polyT stem and a stilbeneamide linker is strongly fluorescent. However, the adjacent G:C base pair in 1G:C results in totally efficient fluorescence quenching via an electron transfer mechanism [110]. Incorporation of a single G:C base pair at different positions relative to the stilbene linker permitted investigation

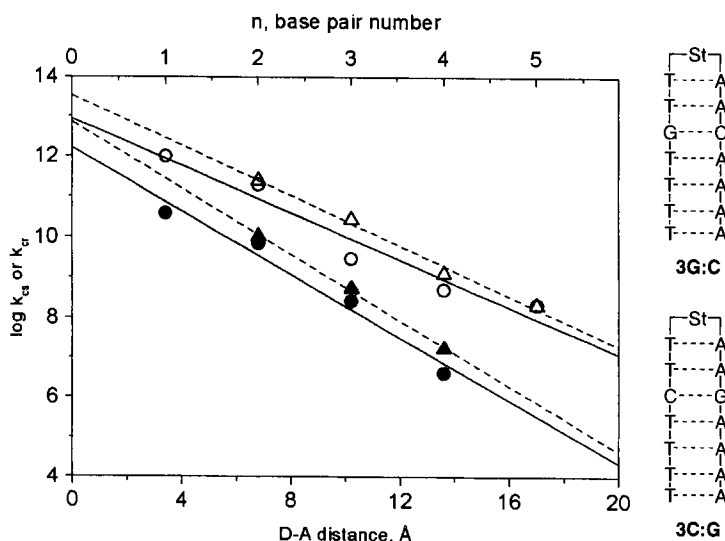


Figure 14. Distance-dependence of the rate constants for charge separation (open symbols) and charge recombination (filled symbols) for hairpin families in which guanine is either in the polyT arm (e.g., 3G:C, \circ , \bullet , solid lines) or in the polyA arm (e.g., 3C:G, Δ , \blacktriangle , dashed lines) [110b].

of the distance-dependent formation and decay of the stilbene anion radical by means of femtosecond time-resolved transient absorption spectroscopy. Rate constants for charge separation and charge recombination for two families of hairpins in which the guanine donor is located in either the poly[dT] or poly[dA] strand can be obtained from analysis of the transient decay data.

Plots of the log of the rate constants for charge separation and charge recombination versus the distance between the stilbene acceptor and guanine donor (calculated assuming a constant 3.4 Å π -stacking distance) are shown in Figure 14. The linear nature of these plots is consistent with a superexchange mechanism for bridge-mediated electron transfer (Section 5.3.1). According to Eq. 16, the slopes and intercepts from Figure 14 provide the values of β and k_0 summarized in Table 8. DNA-mediated electron transfer should be more favorable via a poly[dA] versus poly[dT] spacer due to the lower bridge energies for A versus T [120]. However, the experimentally determined values of β for both charge separation and charge recombination are only slightly larger when guanine is in the poly[dA] versus poly[dT] hairpin arm (Figure 14). This is a consequence of larger rate constants for short D–A separations ($n < 5$) for guanine in the poly[dA] arm but similar rates at long D–A separations ($n = 5$). Thus, the kinetic advantage for electron transfer via a polypurine versus polypyrimidine strand appears to be rather small, and to operate only over short distances.

The effects of donor oxidation potential upon the dynamics of charge separation and recombination has been determined for several donors (guanine, deazaguanine, oxoguanine, deazaguanine, and inosine; Table 3) separated from the stilbenedimethylcarboxamide linker by two T:A base pairs. Analysis of the kinetic data for charge separation and recombination according to Eq. 11 provides values of the solvent and internal reorganization energies, λ_s and λ_i , similar to those for nearest neighbor quenching (Figure 11). However, the electronic coupling matrix element $H_{DA} = 25 \text{ cm}^{-1}$, substantially smaller than the value of 347 cm^{-1} for nearest-neighbor quenching. The smaller value of H_{DA} is consistent with weak coupling of the donor and acceptor with the base pairs of the bridge, as observed by Harriman [130].

The dynamics of charge separation and recombination have also been determined for hairpins containing a GG step separated from the stilbene linker by two T:A base pairs [110b]. Cleavage of native and synthetic DNA by photonucleases occurs selectively at GG steps [6, 7] which have been proposed to function as hole traps as a consequence of their low oxidation potentials (see Table 2). The value of k_{cs} for a GG step is two to three times faster than that for an isolated guanine—a rate enhancement similar to that for the nucleobase Z. However, the value of k_{cr} is two to three times slower than that for an isolated guanine, whereas k_{cr} for Z is faster than that for guanine. Delocalization of the hole over the two guanines in the GG steps may be accompanied by contraction of the GG π -stacking distance, which would result in a larger reorganization energy for the charge recombination process. As a consequence of the larger value of k_{cs} and smaller value of k_{cr} for the GG step versus an isolated guanine, the GG step can function as a shallow hole trap.

Intercalated acceptors

Tanaka and coworkers [148a,b] have investigated DNA-mediated electron transfer in a series of synthetic duplexes which possess the acridinium salt AC^+ attached to an L-threoninol residue with a tetramethylene tether at a defined site in an oligonucleotide conjugate. Duplex formation with a complementary strand possessing an adenine opposite the modified residue is proposed to result in AC^+ intercalation with expulsion of adenine from the duplex to an extrahelical location (Figure 15a,b). In the absence of nearby G:C base pairs, the intercalated AC^+ has a fluorescence quantum yield of 0.66 and a decay time of 22.8 ns. In view of the high calculated singlet-state reduction potential of AC^+ ($E^S = 2.69 \text{ eV}$, $E_{rdn} = -0.73 \text{ V}$, $E^S_{rdn} = 1.96 \text{ eV}$) it is surprising that isoergonic oxidation of adenine (see Table 3) is not observed. Both the quantum yield and decay time are reduced by c. 98 % by the presence of a G:C base pair on either side of the acridine. The extent of quenching of AC^+ by guanine decreases rapidly with the number of A:T base pairs intervening between acridine and guanine, c. 60 % quenching being observed for one A:T base pair and <5 % quenching for two A:T base pairs. The quantum yield and lifetime data provide values of $\beta = 1.5 \text{ \AA}^{-1}$ and $k_o = 1.9 \times 10^{12} \text{ s}^{-1}$.

Barton and coworkers [47, 149] have recently investigated fluorescence quenching

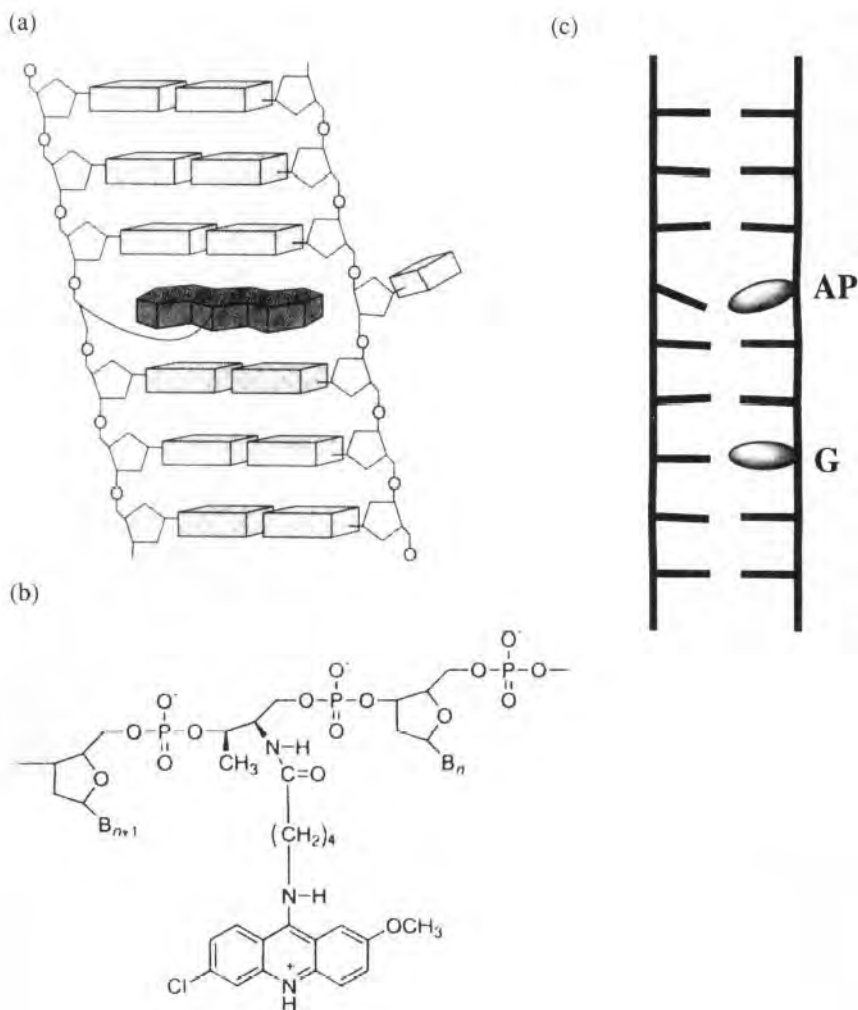


Figure 15. (a) Diagram of a duplex containing an intercalated acridine dye with an extrahelical adenine and (b) structure of the acridine conjugate [148]. Copyright 1999, with permission from Elsevier Science. (c) Diagram of a duplex containing an aminopurine (AP) and single guanine (G) [30].

in duplexes formed between an oligonucleotide containing ethidium (ET^+) tethered to the 5'-end with a complementary oligonucleotide containing the readily oxidized base deazaguanine (Z) located at a variable distance from the 3'-end. Very long tethers (consisting of chains of 14–16 atoms) are necessary to provide strong intercalation which is proposed to occur near the point of attachment. The extent of ET^+ fluorescence quenching by Z is found to decrease as the number of base pairs between Z and the most probable location for ET^+ is increased, c. 70 % quenching being observed for two intervening base pairs and <5 % quenching for six inter-

vening base pairs. There is no corresponding decrease in the fluorescence decay times, dual exponential decay with decay times of c. 9 ns and 2–3 ns being observed both in the absence and presence of Z.

The observation of intensity but not lifetime quenching was attributed to a component of ultrafast (static) electron transfer. In order to distinguish between the distance dependence of static electron transfer and the results of dynamic measurements, Barton has used the term γ to define the distance dependence of the fluorescence quantum yield data. Values of $\gamma = 0.33$ and 0.20 \AA^{-1} were obtained for two duplexes having different bases adjacent to Z [47]. A substantial decrease in the quenching efficiency was observed when the base-paired partner for Z was changed from C to T, A, or G. These observations establish that the fluorescence intensity of ET^+ in these duplexes is sensitive to the location of Z, the neighboring base pairs, and the presence of mismatches.

The dynamics of ethidium singlet-state decay have been studied by Wan et al. [149] using femtosecond transient absorption and fluorescence up-conversion for duplexes in which the donor Z is located at the 5th, 6th or 7th base pair. A 1–10-ps decay component is observed both for systems containing Z and those in which it is absent (and thus presumably do not undergo electron transfer). A second 75–100-ps component is also observed for the duplexes containing Z. In addition, significant nanosecond decay components are observed both in the absence and presence of Z, in accord with the results of Barton's previous study [47]. The two picosecond components of the singlet-state decay for the $\text{ET}^+\text{-B-Z}$ systems are assigned to distance-independent ultrafast electron transfer. However, transient absorption spectra of the products of electron transfer have not been reported, and thus these assignments should be viewed as tentative.

Modified nucleotide acceptors

Kelley and Barton [30] have recently investigated the fluorescence quenching of the adenine analogues EAD and AP (Table 4) by G and Z (Table 3) in ds DNA. The results of bimolecular quenching of EAD and AP by mononucleotides are discussed in Section 5.2.3 (p. 123). Fluorescence quantum yields and decay times were determined for duplexes containing EAD or AP as the electron acceptor and a single G or Z base as the electron donor (Figure 15c). The fluorescence quantum yield for an EAD-containing duplex in the absence of G or Z is smaller than that for the EAD nucleoside in water ($\Phi_f \sim 0.3$ versus 0.56) and the fluorescence decay times are shorter (dual exponential decay with decay times of 0.77 and 7.3 ns versus 23.8 ns for the EAD nucleoside). Thus relatively slow quenching of singlet EAD by neighboring A:T base pairs may occur. The presence of a G adjacent to EAD in the same strand results in a substantial decrease both the fluorescence intensity and decay times. An adjacent AG sequence results in partial quenching, and an AAG sequence in only slight quenching. These results are qualitatively similar to those reported by Tanaka and colleagues [148a,b] for intercalated acridine; however, the value of β calculated by Kelley and Barton from their quantum yield data is somewhat smaller than that reported by Tanaka (1.0 versus 1.4 \AA^{-1}).

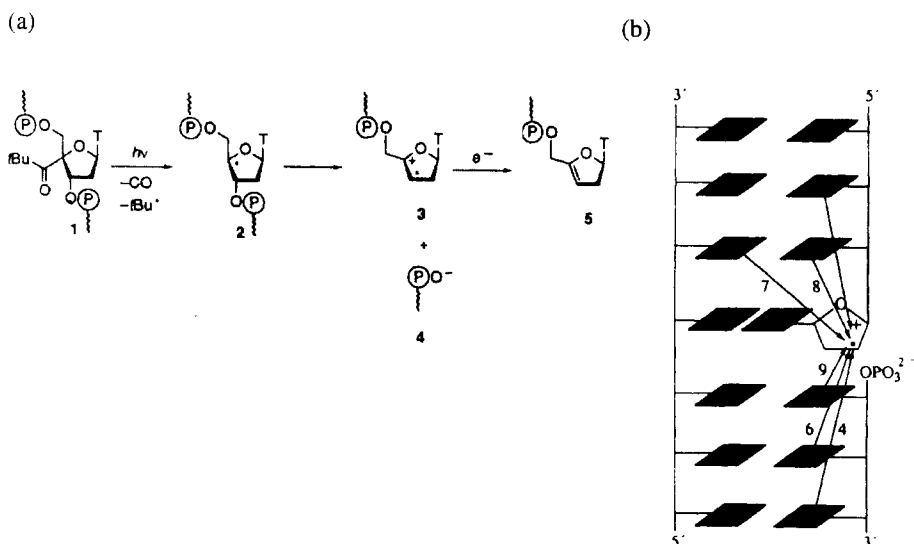
Kelley and Barton [30] have also investigated quenching of the fluorescence

intensity of AP by G and Z by duplex DNA. In the absence of a neighboring G or Z, they observe low fluorescence quantum yields ($\Phi_f < 0.07$), indicative of extensive quenching by neighboring A:T base pairs. As noted in Section 5.2.3, the fluorescence of AP is extensively quenched in alternating AP-T and AP-U copolymers which lack strong donor bases [29a], and the fluorescence decay of AP in duplex DNA is multiexponential with decay times ranging from 50 ps to 9 ns [29d,e]. Kelley and Barton [30] report that introduction of a G or Z base near AP in the same strand of a synthetic duplex results in a decrease in AP fluorescence intensity, but little change in the dual exponential fluorescence decay times measured with a time resolution of c. 0.1 ns. This could result from quenching of the shortest-lived fully stacked ground-state conformations, but no quenching of the less-well stacked conformations [29d,e]. Analysis of the distance dependence of the fluorescence intensity quenching provides γ (p. 151) values of 0.4 and 0.6 Å⁻¹ for quenching of AP by G and Z, respectively.

Kelley and Barton [30] have also investigated quenching of the fluorescence of EAD and AP by G and Z when the donor and acceptor are located in different strands. In the case of EAD, little quenching is observed; in the case of AP, quenching of both the fluorescence intensity and the shorter-lived decay component is observed. Analysis of the quantum yield data provides values of $\gamma = 0.1$ and 0.4 Å⁻¹ for quenching of AP by G and Z, respectively. It is interesting to note that strand-selective quenching is observed for these nucleobase analogues which are located in a specific strand, but not for Tanaka's acridinium intercalator [148] or our stilbene-linked hairpins [110] in which the acceptor overlaps with both strands.

An ingenious indirect method of investigating the distance dependence of electron transfer in DNA based on the relative yields of competing chemical processes has been developed by Giese and coworkers [150]. As outlined in Scheme 1a, irradiation of a 4-acylated thymidine (T*) incorporated into an oligonucleotide **1** results in α -cleavage to yield the radical **2** which undergoes spontaneous cleavage to yield the cation radical **3** and the phosphorylated oligonucleotide **4**. The cation radical can be reduced to yield **5** via electron transfer from a GGG hole trap located at varying distances from the labeled T* (Scheme 1b), leading to further cleavage of the oligonucleotide or reaction with water to form products derived from the cation radical **3**. The relative rates for the electron transfer and trapping processes can be obtained from yields of strand cleavage products using the expression: $k_{et}/k_{water} = [5]/([4] - [5])$. Assuming that the pseudo first-order rate constant k_{water} is independent of base sequence, this ratio provides the relative rates of electron transfer from GGG to the cation radical **3**. Analysis of the data obtained for six different duplexes provides a value of $\beta = 1.0 \pm 0.15$ Å⁻¹.

Meggers et al. have modified the approach outlined in Scheme 1 by placing a guanine adjacent to the acetylated thymine [150b]. This results in rapid primary hole transfer from the deoxyribose to the adjacent guanine. The efficiency of secondary hole transfer processes from G⁺⁺ to a GGG hole trap can then be determined as a function of the number of base pairs separating the G⁺⁺ and GGG sites. The efficiency of strand scission at the GGG site is found to decrease as the number of AT base pairs separating the G⁺⁺ and GGG sites increases. A plot of the relative rate of hole transfer versus the distance provides a value of $\beta = 0.7$ Å⁻¹.



Scheme 1. (a) Mechanism for photochemical formation of cation radical 3 and (b) electron transfer from neighboring guanines to the radical cation [150a].

There are several advantages of the approach outlined in Scheme 1. First, the presence of the acetylated base should not perturb duplex base stacking. Second, the cation radical 3 is formed irreversibly, which precludes competition of charge recombination with charge migration. Third, the cation radical 3 is a putative intermediate in the oxidative cleavage of DNA under biological conditions. An obvious limitation of this approach is its failure to provide direct kinetic information for the charge migration processes.

5.3.4 Summary of Results for Single-Step Electron Transfer

Values of k_0 and β for DNA-mediated electron transfer in systems where distance-dependent kinetic data is available are summarized in Table 8. Somewhat higher values of k_0 were obtained in Harriman's [129, 130] studies of randomly intercalated donors and acceptors than in the studies of (T:A)_n-mediated oxidation of guanine by Lewis [110a,b] and Tanaka and colleagues [148]. This might result from errors in data extrapolation to zero distance, difference in bridge base pair sequence, or differences in acceptor–bridge interactions. The values of β are in the range 0.66 to 1.49 Å⁻¹. A value near the low end of this range ($\beta = 0.70$ Å⁻¹) has also been obtained by Meggers et al. [150b] from analysis of strand cleavage efficiencies. Values near the high end of this range are typical of proteins [121], whereas values near the low end are more typical of conjugated polyenes [124].

According to Eq. 17, the value of β should depend upon ΔE , the energy gap between the initial and bridge states (see Figure 12, p. 140), and t_{nm} the electronic

coupling matrix element between bridge states. Grozema et al. [153] have reported that the calculated value of β for an AT bridge increases from c. 0.5 to 1 \AA^{-1} as ΔE increases from 0.4 to 0.7 eV . In the case of Meggers' data [150b], ΔE should equal the difference in oxidation potentials for G versus A, which we estimate to be $\sim 0.5 \text{ eV}$. Based on the singlet-state reduction potentials of ET^+ and SA, values of $\Delta E = 0.7$ and 0.2 eV , respectively, can be estimated for these systems, in accord with the smaller value of β for the SA hairpin system [110, 129]. Small values of ΔE ($< 0.2 \text{ eV}$) are also expected for the acridinium acceptor used by Fukui et al. [148b] and the EAD acceptor used by Kelley and Barton [30] in their studies of electron transfer mediated by $(\text{T:A})_n$ base pairs. Kelley and Barton [30] suggest that a large value of β for the EAD/G system might reflect poor orbital overlap between EAD which cannot adopt a normal π -stacked geometry and the adjacent base pairs. Information about the geometry of the acridinium/G system studied by Fukui et al. [148a,b] is not available.

The reader may desire an explanation of the low values of γ derived by Barton and coworkers [30, 131, 137–140] from fluorescence quenching data for systems in which the dynamics of electron transfer have not been directly measured. In most cases, the absolute efficiency (quantum yield) of the quenching processes studied in these systems is rather low, and thus they may represent long-range electron transfer by mechanisms other than superexchange, such as to those described by Felts et al. [125], Davis and colleagues [126], and Okada et al. [127]. However, the author considers that it is highly unlikely that such processes occur with rate constants $> 10^9 \text{ s}^{-1}$. In view of the complex nature of these systems, the author is loath to offer a detailed interpretation, and refers the reader to commentaries by others who have been directly involved in this research [13, 15].

5.4 Photoinitiated Charge Transport in DNA

5.4.1 Background

As described in Section 5.3, photoinduced electron transfer in DNA via a single-step superexchange mechanism is strongly distance-dependent (Eq. 16). The available kinetic data suggest that electron transfer can compete effectively with excited-state decay pathways of singlet acceptors over no more than four or five base pairs. However, data from pulse radiolysis investigations (Section 5.1.3) and studies of photoinitiated DNA strand cleavage (Section 5.4.2) indicate that electrons can migrate over distances substantially longer than several base pairs. Based on strand cleavage studies, Breslin, Schuster and colleagues [151a,b] suggested in 1996 that electron transfer over long distances in DNA might occur by an alternative hole-hopping mechanism.

An energy level scheme for photoinitiated hole hopping in DNA is shown in Figure 16. Photoinduced electron transfer between the singlet acceptor and the nearest guanine, creates the initial hole on guanine, which can then undergo

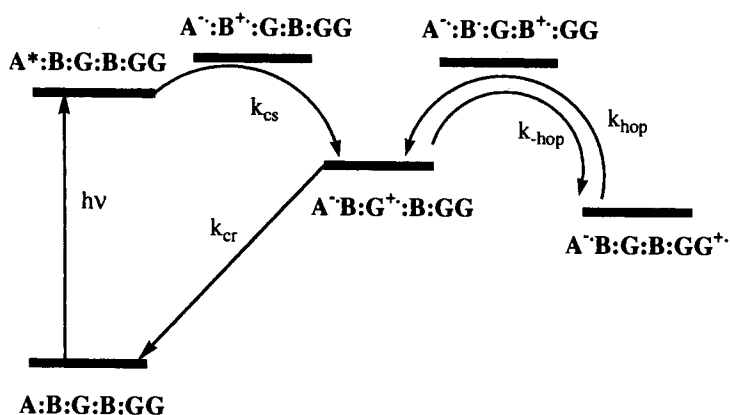


Figure 16. Energy level diagram for photochemical charge separation and charge recombination via a hole-hopping mechanism for an acceptor–bridge–donor system.

reversible hopping steps until the hole trap consisting of a GG or GGG step is reached. In this scheme, hopping must compete with charge recombination. However, Meggers' method of irreversible photogeneration of a guanine cation radical (Scheme 1) avoids this competition [150]. The use of triplet acceptors in combination with oxygen as an anion radical scavenger can also circumvent competing charge recombination [151]. Since GG is a shallow hole trap (Section 5.3.3), hole hopping between multiple GG steps can also occur.

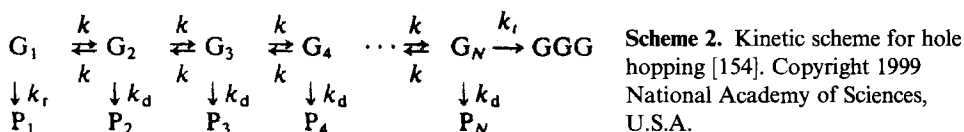
The theoretical basis for hole hopping and electron transport in DNA was investigated as early as 1974 by Dee and Baur [152]. Recently, Jortner and colleagues [120, 154] have proposed that hole hopping could be treated as a series of hops between guanines, with each hop treated as a superexchange process. According to this theory, the efficiency of a process involving N equal hopping steps can be described by Eq. 19,

$$\Phi \propto \exp[-N(k_d/k_{\text{hop}})^{1/2}] \quad (19)$$

where k_{hop} is the hole-hopping rate constant for each hopping step, and k_d is the rate constant for chemical processes of the guanine cation radicals which compete with hole hopping (Scheme 2, $k = k_{\text{hop}}$). This equation can be written in the form of Eq. 16 for superexchange electron transfer to provide Eq. 20,

$$\Phi \propto \exp(-\beta'R) \quad (20)$$

where β' is a characteristic of the system, and R is the donor–acceptor distance. In view of the longer distances over which hole hopping take place, static and dynamic disorder are likely to be even more important than they are for shorter distance



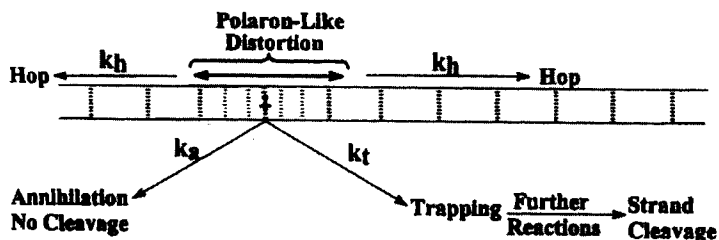
electron transfer processes. Quantum mechanical hopping models have been used successfully by several groups to correlate theory with experiment, and will be discussed in Section 5.4.4 [153–155].

Henderson et al. [41] have proposed a modified version of the hole-hopping mechanism which accounts for the conformational flexibility of DNA and for changes in geometry which most likely accompany introduction of a cation radical into the π -stacked duplex structure. This mechanism, described as “phonon-assisted polaron-like hopping”, is shown schematically in Scheme 3. According to this proposal, polaron formation is the consequence of a local structural distortion that delocalizes the cation radical over several adjacent bases. The polaron migrates by a thermally activated hopping process with hop lengths that are dependent upon the base sequence. The distance dependence of the charge migration process is thus determined by the relative rates of hopping (k_h), charge annihilation (k_a), and chemical trapping processes (k_t) which ultimately lead to strand cleavage.

5.4.2 DNA Cleavage and Thymine Dimer Repair over Long Distances

DNA cleavage

Single-strand cleavage of duplex DNA has been observed in the presence of a variety of photochemical oxidants [6, 7]. Cleavage occurs selectively at the 5'G of GG steps, with lower reactivity observed for isolated guanines. This pattern of cleavage is different from that for photonucleases which operate by a free radical or singlet oxygen mechanism. Transient absorption spectroscopy has provided evidence for electron transfer from a nucleobase to the excited oxidant as the initial step in the strand cleavage process. Treatment of the irradiated duplex with hot piperidine is, in most cases, necessary in order to observe strand cleavage. The chemical reactions leading to strand cleavage are complex and not fully elucidated. Reaction of the



Scheme 3. Phonon-assisted polaron-like hole hopping. Reprinted with permission from ref. 161c. Copyright 1999 American Chemical Society.

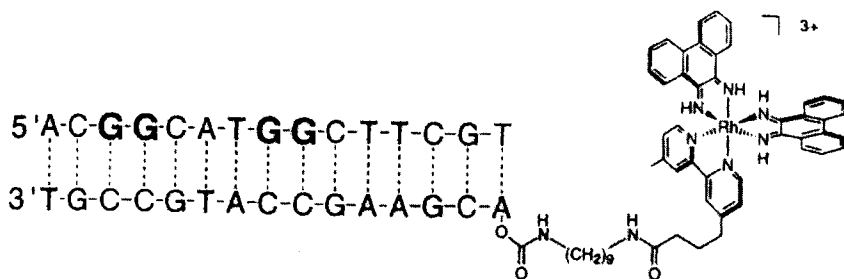
guanine cation radical with either water or oxygen is proposed to be the initial chemical reaction, leading to the formation of 8-oxo-G. However, 8-oxoG must undergo further chemical processes in order for strand scission to be observed. Quantum yields for the overall process have been reported in only a few cases. The low values ($<10^{-3}$) could result from inefficiencies in: (a) the initial electron transfer processes leading to formation of the reactive guanine cation radical; (b) chemical reactions of the guanine cation radical; and (c) the piperidine-promoted strand cleavage process.

Photoinduced cleavage at the GG step of a 6-mer by a nontethered triplet naphthalimide was proposed by Saito et al. [83] to be initiated by a contact electron transfer process (Section 5.2.4). Schuster's initial studies of oxidative cleavage by nontethered triplet anthraquinone (AQ) led to the suggestion that GG oxidation might occur indirectly, via oxidation of any of the nucleobases followed by hole migration from the primary electron donor to a GG hole trap [151]. This suggestion was supported by the observation of efficient cleavage at all seven GG steps of a 248-bp restriction fragment by a randomly intercalated anthraquinone acceptor. The observation of cleavage in these reactions requires the presence of oxygen. Electron transfer from AQ^- to oxygen presumably prevents charge recombination with guanine cation radicals.

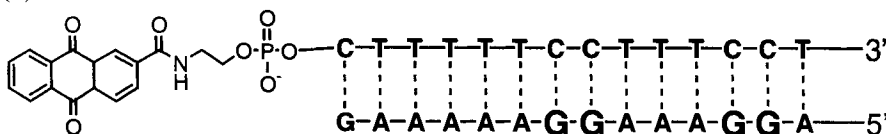
In a benchmark 1996 letter to *Nature*, Barton and colleagues [156] reported that 365-nm irradiation of a duplex which possesses an end-tethered intercalating $Rh(\phi)_2bpy^{+3}$ complex in one strand and two GG steps in the complementary strand (Figure 17a) results in cleavage at both the proximal and distal GG steps. Since the distal 5'G is located 10 bp from the locus of intercalation, long-range electron transfer clearly occurs in this duplex. Two possible mechanism for this process were discussed: concerted long-range electron transfer; and oxidation of a base near the intercalated acceptor followed by hole migration to the two GG steps. Subsequent investigations of duplexes possessing a tethered $Rh(\phi)_2bpy^{+3}$ photo-oxidant showed the ratio of distal/proximal cleavage decreased only slightly from c. 1.2 to 1.0 as the separation between the proximal and distal GG steps increased from 6 to 15 bp [157a]. This ratio is also relatively insensitive to the base pair sequence between the GG steps. However, the distal/proximal ratio decreases when a base bulge is present between the GG steps, from 1.2 in the absence of a bulge to c. 0.5 in the presence of a TTT bulge [157b]. The distal/proximal ratio was also observed to decrease upon complex formation with a protein that binds to the base sequence separating the two GG steps [157d]. This decrease was attributed to a protein-induced distortion of DNA base stacking.

Barton and coworkers [158] have also employed the flash-quench technique to study to oxidative cleavage of duplexes in which one strand contains a tethered 5'- $Ru(phen)_2dppz^{2+}$ complex and the complementary strand contains one or more GG step. Strand cleavage occurs selectively at the 5'G of a GG step located 11 bp from the locus of $Ru(II)$ intercalation in the presence of an electron acceptor such as $Ru(NH_3)_6^{3+}$ or methyl viologen (MV^+ ; Table 5). Excitation of the intercalated $Ru(II)$ complex followed by diffusional or static quenching by the added acceptor generates the powerful oxidant $Ru(III)$. In the absence of a GG step, oxidation occurs at all single guanines with comparable efficiency. The presence of a mis-

(a)



(b)



(c)

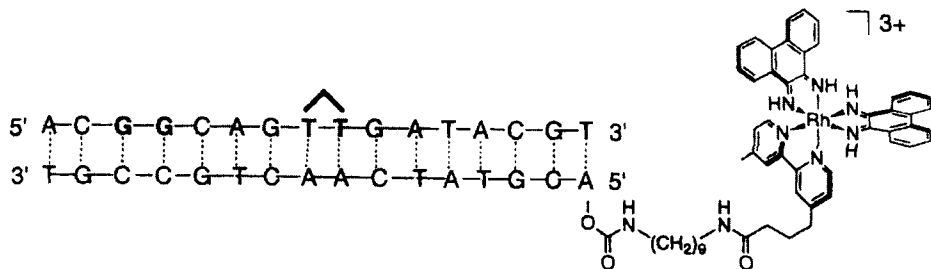


Figure 17. (a) Diagram of a duplex possessing a 5'-tethered Rh(III) acceptor on one strand and two GG steps in the complementary strand [156]. Reprinted by permission from Nature, copyright 1996 Macmillan Magazines Ltd. (b) Diagram of a duplex possessing a 5'-tethered anthraquinone acceptor on one strand and two GG steps in the complementary strand. Reprinted with permission from ref. 159. Copyright 1997 American Chemical Society. (c) Diagram of a duplex possessing a 5'-tethered Rh(III) acceptor on one strand a thymine photodimer in the complementary strand [163]. Reprinted with permission from ref. 163b. Copyright 1998 American Chemical Society.

matched GA or GT base pair between the locus of intercalation and the GG step results in a pronounced decrease in the efficiency of strand cleavage. Photoinduced cleavage at both proximal and distal GG steps has also been observed for a duplex which possesses a 5'-tethered ethidium in one strand, and two GG steps in the complementary strand [117].

Gasper and Schuster [159] have investigated photoinduced strand cleavage in

duplexes which incorporate an end-stacked anthraquinone linked covalently to the 5'-terminus on one strand and possess two or more GG steps in the complementary strand (Figure 17b). They observe cleavage with comparable efficiency at GG steps located 7 and 12 bp from the anthraquinone. Neither the proximal GG step nor an abasic site between the two steps inhibits cleavage at the distal GG site; however, an 8-oxoguanine (OG; Figure 1) in the proximal site does inhibit cleavage at the distal GG site. Evidently, OG functions as a more effective hole trap than the proximal GG. This could result from either slow hole transport from OG^+ to the distal GG or rapid chemical reactions of OG^+ . Similar results have recently been reported for duplexes in which an intercalated anthraquinone is tethered at mid-strand with two GG steps on either side [160]. In this case, more cleavage is observed at the proximal versus distal GG steps; however, there is little preference for cleavage on the 3' versus 5' side of the anthraquinone. Replacement of one of the proximal GG steps by OG inhibits distal cleavage, but has no effect on cleavage on the other side of the intercalator. Experiments in which the GG steps and OG were placed in complementary strands provided evidence that strand-to-strand hopping occurs, but is less efficient than migration along a single strand.

End-stacked tethered anthraquinones have also been employed to investigate long-distance cleavage at GG steps in structures other than standard B-form DNA [161]. Cleavage in single-stranded overhangs has been studied using complementary strands which contain GG steps both in the duplex and single-strand regions [161a]. Comparable efficiency is observed in both regions, leading to the proposal that coiling in the single-strand region brings the GG steps into close contact. In a study of DNA structures with GG steps in both triplex and duplex regions it was found that charge migration occurs through the triplex region, but that strand cleavage is less efficient in triplex versus duplex regions [161b]. Diminished reactivity in the triplex region was attributed to a structure which inhibits reactions of the GG cation radicals with water. Similarly, charge migration is observed to occur in the A-form helices of RNA/DNA hybrids, but strand cleavage is much less efficient than in B-form DNA [161c]. Long-range hole migration is also observed in PNA/DNA duplexes [161d].

Thymine dimer repair

Model studies of photochemical repair of the thymine [2 + 2] photodimer have shown that both oxidation and reduction can result in cycloreversion via a radical ion mechanism [162]. Barton and coworkers [163a,b] have investigated the photo-initiated repair of duplexes containing thymine dimer sites using both nontethered and tethered Rh(III) complexes as photooxidizing agents (Figure 17c). The quantum yield for photorepair of a Rh(III)-tethered duplex is 2×10^{-6} , approximately 30 times lower than for photorepair using nontethered Rh^{3+} . It is possible that the exceptionally low quantum yield reflects a hole-hopping mechanism in which charge recombination of an oxidized base with Rh(II) is much more efficient than hopping to the thymine dimer site and dimer cleavage.

The repair efficiency in this system increases as the distance between thymine dimer and intercalated Rh(III) complex is increased from 4 bp to 6 bp, but decreases in the presence of base bulges between the dimer and intercalator. Subse-

quent investigation of duplexes containing a tethered Rh(III) intercalator in one strand and both a thymine dimer and GG step in the complementary strand showed that dimer repair and GG cleavage both occur. The yield of dimer repair is >10 times that of GG damage. Since the GG site has a lower oxidation potential than a thymine dimer, selective dimer repair presumably reflects a faster rate for dimer cycloreversion than for the reactions of $\text{GG}^{+\bullet}$ that lead to strand cleavage.

5.4.3 Distance-Dependent Hole Migration in DNA

Strand cleavage studies

In their studies of distance-dependent strand cleavage in DNA, Giese and colleagues [150a,b] found that three or four AT base pairs separating the photochemically generated deoxyribose or guanine oxidant and a GGG trap site were sufficient to totally inhibit oxidative cleavage at the trap site (Section 5.3.3, p. 152; see also, Scheme 1). In addition, they made the remarkable observation that oxidative cleavage could be observed over much longer distances when a combination of AT and GC base pairs separated the $\text{G}^{+\bullet}$ and GGG sites. Thus more efficient cleavage at GGG was observed for a four-base pair sequence containing a single GC base pair than for a three-base pair sequence containing only AT base pairs. Relative yields for a series of duplexes containing one, two or four repeating TTG sequences between the $\text{G}^{+\bullet}$ and GGG are reported and shown in Figure 18 [150c]. A plot of $\ln(\Phi_{\text{rel}})$ versus R according to Eq. 20 provides a slope $\beta' = 0.07 \text{ \AA}^{-1}$, significantly smaller than those for DNA-mediated superexchange electron transfer (Table 8). Also shown in Figure 18 is the relative efficiency of GGG cleavage for a duplex possessing a 15-bp sequence containing alternating AT and GC base pairs with guanines located in both strands. Cleavage is seen to be more efficient for this duplex than for shorter duplexes having the TTG repeat sequence. Thus, it appears that hole hopping is not constrained to occur in a single strand, and is more efficient when the distance between hops is shorter.

Núñez et al. [157a] have recently reported the results of photoinduced cleavage of 63-mer duplexes which contain a 5'-tethered Rh(III) or Ru(II) complex in one strand and six GG base pairs in the complementary strand (Figure 19a). Direct irradiation of the Rh^{3+} duplex or irradiation of the Ru^{2+} duplex in the presence of methyl viologen followed by piperidine treatment results in cleavage at all six GG steps. Unlike earlier studies where distal/proximal cleavage ratios greater than 1.0 were observed [156–158], proximal cleavage is more efficient than distal cleavage in these systems. The relative efficiency of cleavage at longer distances was observed to be greater for the Rh(III) versus Ru(II) system, and to increase with increasing temperature. These results were interpreted in terms of a hole-hopping mechanism in which the GG steps serve as electronically coupled “stepping stones.” It was further suggested that hopping might occur between “delocalized base domains,” rather than between discrete base positions.”

Similar results have been reported by Schuster and coworkers [41, 160] for a 60-mer duplex possessing a tethered 5'-anthraquinone in one strand and four GG steps

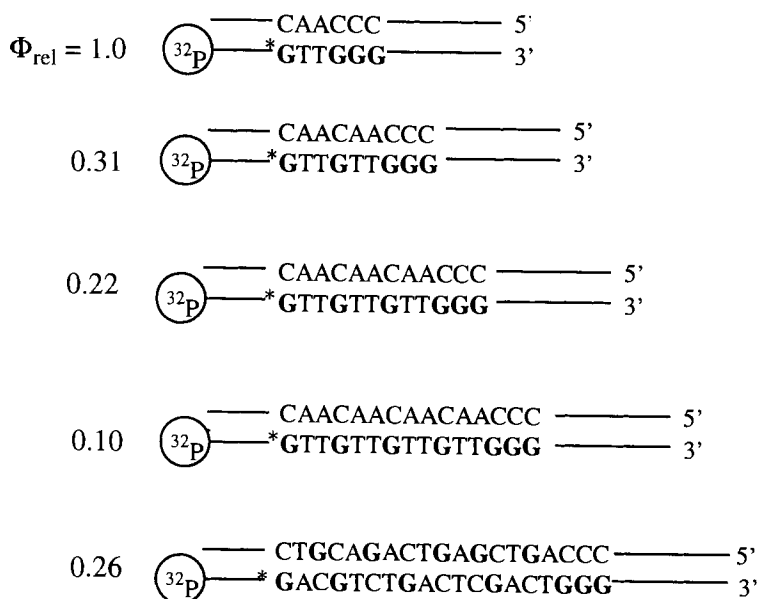


Figure 18. Relative efficiencies of strand cleavage at a GGG site following charge migration via hole hopping from *G [150].

in the complementary strand and for a 71-mer possessing seven GG steps in the complementary strand (Figure 19b). In both cases the efficiency of strand cleavage was found to decrease with increasing distance between the GG and the end-stacked anthraquinone. A plot of $\ln(\Phi_{\text{rel}})$ versus distance has a slope $\beta' = 0.02 \text{ \AA}^{-1}$ for both duplexes, even smaller than the value obtained by Giese et al. [150c].

A closely related approach to the study of hole hopping in DNA was recently reported by Nakatani et al. [164] using a modified nucleobase in which a strong electron acceptor, cyanobenzophenone, is covalently attached to 2'-deoxyuridine (BP-U) by means of a rigid acetylene linker (Figure 19c). The efficiency of strand cleavage at a GG trap site was determined as a function of the base sequence between BP-U and the GG trap. It was found that a single guanine primary electron donor located in the base pair immediately adjacent to the BP-U was necessary in order to observe cleavage at a remote GG trap site. The presence of a single AT base pair between the BP-U and primary G donor results in a marked decrease in remote GG cleavage. The efficiency of GG cleavage is also dependent upon the base sequence separating the primary G donor and the GG site. A 5'TGTGTA3' sequence is able to mediate hole transfer, but a 5'TATATA3' sequence is not, in accord with Giese's observation that three or more AT base pairs effectively block hole transfer [150]. When two GG steps are present in the same strand separated by two AT base pairs, cleavage is observed at both the sites with a distal/proximal ratio of 0.83, similar to the value observed by Barton and coworkers [156–158].

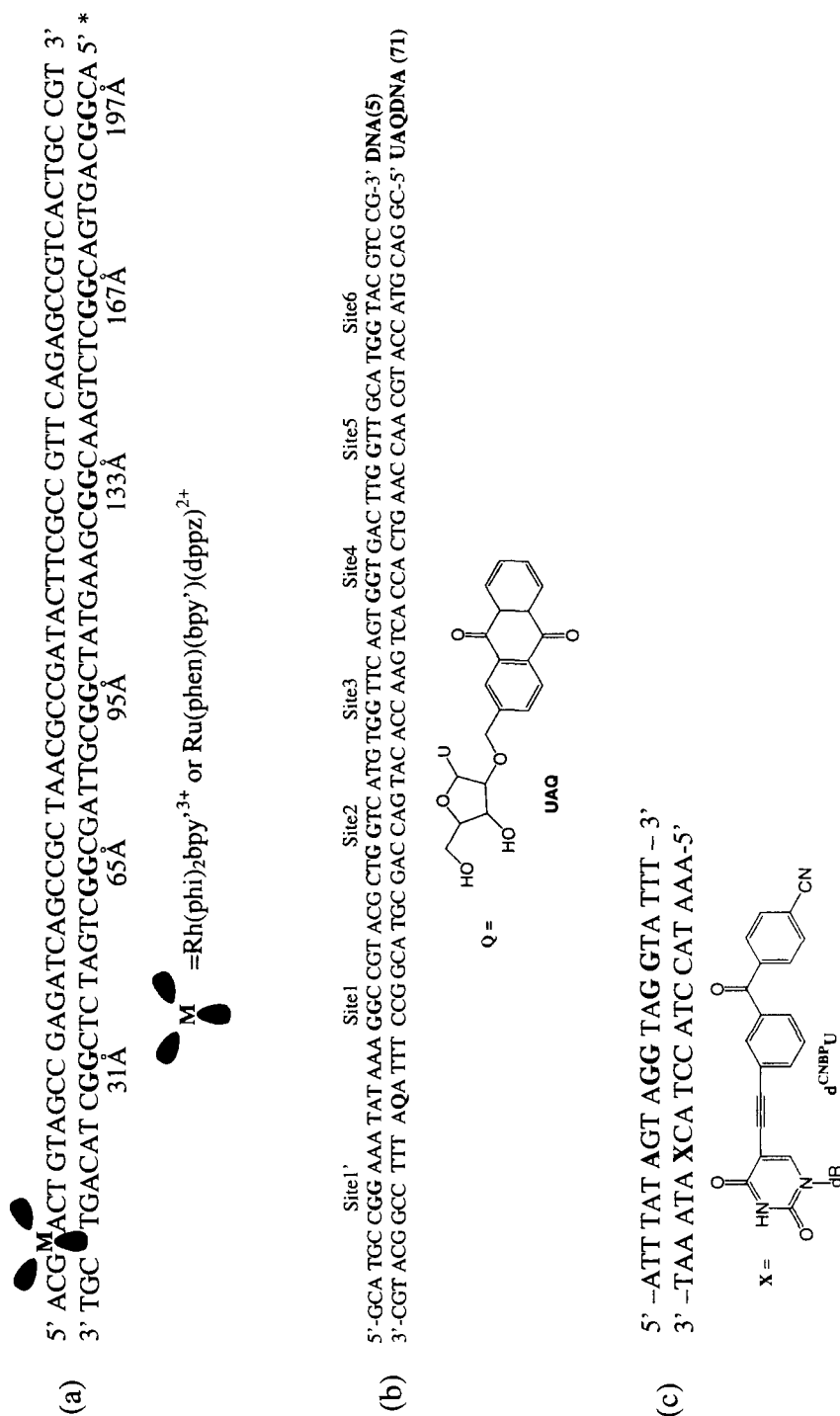


Figure 19. (a) Diagram of a duplex possessing a 5'-tethered Rh(III) or Ru(II) acceptor on one strand and six GG steps in the complementary strand [157a]. Copyright 1999, with permission from Elsevier Science. (b) Diagram of a duplex possessing a uridine-anthraquinone conjugate (Q) in one strand and six GG steps in the complementary strand. Reprinted with permission from ref. 160. Copyright 1999 American Chemical Society. (c) Diagram of a duplex possessing a uridine-cyanobenzophenone conjugate (X) in one strand and two GG steps in the complementary strand. Reprinted with permission from ref. 164. Copyright 1999 American Chemical Society.

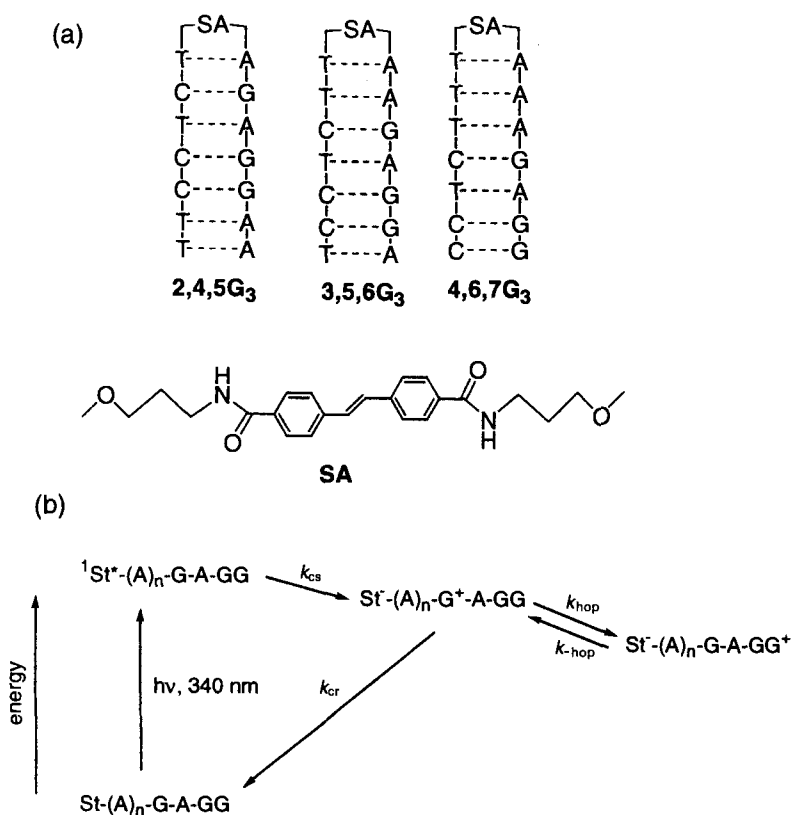


Figure 20. (a) Structures of hairpins containing an GAGG sequence separated from the SA acceptor by 1–3 A:T base pairs. (b) Kinetic model for the hole-hopping process.

Dynamics of hole hopping

The stilbene-linked hairpins used by Lewis and coworkers to investigate the dynamics of charge transfer and recombination in DNA (Section 4.3.3) contain a single G:C base pair (see Figure 10). These structures can be modified by the introduction of an AGG sequence adjacent to the G:C base pair (Figure 20a) [165]. The occurrence of hole hopping from the initially oxidized G to the GG step should not affect the dynamics of charge separation. However, a new long-lived component should be observed for the decay of the stilbene anion radical ($\text{St}^{\cdot-}$) if hole hopping competes successfully with charge recombination. In the case of the hairpins 3,5,6G₃ and 4,6,7G₃, but not 2,4,5G₃, new long-lived decay components are observed in accord with the occurrence of hole hopping.

Analysis of the transient decay data using the kinetic model shown in Figure 20b provides a rate constant of $k_{\text{hop}} = 1.0 \pm 0.5 \times 10^8 \text{ s}^{-1}$ for the hole-hopping processes in the hairpins 3,5,6G₃ and 4,6,7G₃. This rate is consistent with the failure of hole hopping to compete with charge recombination in 2,4,5G₃ ($k_{\text{cr}} = 1.0 \times 10^{10} \text{ s}^{-1}$). It

is also much too slow to compete with charge recombination in contact singlet ion pairs (Section 5.2.3). However, it is consistent with the ability of hole-hopping processes to compete with slower chemical reactions of G^+ . The kinetic analysis also provides the rate constant for the return process of $k_{-\text{hop}} = 5 \pm 1 \times 10^6 \text{ s}^{-1}$. The ratio $k_{\text{hop}}/k_{-\text{hop}} \sim 15$ is consistent with the observation that oxidative cleavage of DNA occurs predominantly at GG (or GGG) steps, but that GG steps do not inhibit further hole migration. When the AGG sequence in the hairpin 3,5,6G₃ is replaced with either a TGG or a AAGG sequence, no long-lived decay components are observed. Evidently hole hopping across T or AA is much slower than charge recombination in these hairpins ($k_{\text{cr}} \sim 5 \times 10^8 \text{ s}^{-1}$).

Theoretical analysis of hole hopping

The data of Giese and coworkers [150] for the distance and sequence dependence of strand cleavage has been analyzed by three groups. Grozema et al. [153] investigated two theoretical models: a quantum mechanical charge migration model based on the tight binding approach; and the Miller–Abrahams model of incoherent hopping. The former, but not the latter, was found to be consistent with Giese’s data.

Bixon et al. [154] analyzed Giese’s data for the sequence $G^+(\text{TTG})_N\text{GGG}$ using the kinetic model of Scheme 2 and obtained the parameters $k_r/k \sim k_d/k = 0.08$ and $k_t/k \sim 1$. An estimate of $k \sim 10^9 \text{ s}^{-1}$ for hole hopping mediated by two TA base pairs was calculated using superexchange theory (Eq. 11). This value is higher than the experimental value of $k \sim 10^8 \text{ s}^{-1}$ for hole hopping mediated by a single AT base pair. Estimates of k_r based on experimental data are in the microsecond time domain [64, 150a], much slower than the value of $k_r \sim 10^8 \text{ s}^{-1}$ calculated by Bixon et al. [154]. The reasons for these discrepancies remain to be clarified.

The analysis of Giese’s data by Berlin et al. [155] provides a similar value of $k_d/k = 0.11$ and a value of the distance dependence of hole transport $\beta' \sim 0.1 \text{ \AA}^{-1}$. This value is c. 10-fold smaller than the values of $0.6 < \beta < 1.4$ obtained for superexchange electron transfer in accord with the dominance of the hole-hopping mechanism at large D–A distances. By using a combination of hole hopping over several guanines and superexchange between neighboring guanines, both Bixon et al. [154] and Berlin et al. [155] have obtained excellent agreement between calculated and observed relative rate constants.

5.5 Conductivity of Ionized DNA Assemblies

5.5.1 Background

The idea that a “ π -electron ... can traverse the entire length of a polynucleotide helix along its axis” was advanced by Eley and Spivy in 1962 [10]. While this suggestion has been much quoted, it seems based on questionable d.c. conductivity data. Similar conductivities were observed for several samples of “dry” DNA,

RNA, and proteins when compressed between platinum electrodes. Subsequent studies have established that proteins and ss DNA or RNA do not function as molecular wires; however, the conductivity of ds DNA remains the subject of debate. Recently there have been several studies of DNA conductivity in fibers, single crystals, aligned films, and monolayer assemblies. Far from resolving the controversy, they seem to have intensified it.

An early attempt to calculate the mobility of electrons and holes in ds DNA using SCF LCAO molecular orbital methods was reported by Dee and Bauer [152]. They assumed that charge migration occurred via site-to-site interaction between neighboring base pairs rather than via long-range quantum mechanical tunneling. Their calculated value of the electronic conductivity along the helix axis is c. $10^{-4} \Omega^{-1} \text{ cm}^{-1}$, “more nearly like that of a weak inorganic semiconductor than that of an organic molecular crystal.”

5.5.2 DNA Fibers and Single Molecules

The radiation-induced conductivity in hydrated samples of aligned versus non-aligned solid DNA fibers was compared by Warman et al. [166]. The dry fibers were found to be essentially nonconducting, as a water content of 10–15 waters per base pair is necessary to observe conductivity. Under these conditions, the conductivity of the aligned and nonaligned films was found to be similar. It was concluded that conductivity in solid B-DNA “is due to highly mobile charge carriers within the outer mantle of the biopolymer chains rather than within the base-pair cores.”

Bernhard and colleagues [167] have investigated the generation of radical ions in crystalline DNA by means of X-radiation with EPR detection at 4 K. A radical ion density corresponding to one radical ion per 57 bp was observed for single crystals of both A-form and B-form DNA. Similar results were observed for DNA films and powders and a crystalline protein. From this they concluded that holes and electrons are trapped on guanine and cytosine, respectively at 4 K and that, above 80 K, migration of electrons and holes is propagated by hopping between shallow traps. The decrease in conductivity at low temperatures is characteristic of an insulator rather than a conductor.

Fink and Schönenberger [168] have studied the electrical conduction of small DNA ropes consisting of a few molecules under high vacuum conditions by employing a modified low-energy electron point source microscope. A single rope which spans a 2- μm hole in a gold-plated carbon foil is broken with a manipulation tip, and its conductivity probed by applying an electrical potential between the tip and carbon foil. DNA ropes that are 600 nm long display no charging, and a single molecule of DNA is found to have a low estimated resistance. From these studies, it is concluded that the electronic transport mechanism must be of an electronic nature rather than ionic conduction, as proposed by Warman et al. [166]. However, the mechanism of charge transport remains unclear. The authors point out that any molecule attached to the DNA by an ionic or covalent bond (including the π -stacked nucleobases) could affect the conductivity.

Recently, the current generated when voltage is applied to one (or several) 30-mer

polyG-polyC duplex suspended between two metal nanoelectrodes has been measured by Porath et al. [169]. The current is essentially zero below a threshold voltage of several volts, consistent with the behavior of a Y-gap semiconductor. At higher voltages the current rises sharply showing that DNA can transport charge carriers. The observed voltage gap is concluded to be incompatible with either a single-step electron transfer process or with hopping models, and it is concluded that electronic interactions between the bases lead to a molecular band in which the electronic states are delocalized over the entire length of the molecule. It would be interesting to determine if duplexes with alternating purine and pyrimidine bases displayed similar behavior.

Duplex DNA has been used as a template for the fabrication of a nanometer-scale wire by Braun et al. [170]. Using molecular assembly methods, they attached a single 12 μm -long duplex to two gold electrodes by means of gold-sulfur bonding. Exchange of Ag^+ ions for Na^+ followed by solution chemical “developing” provided a 100 nm-wide conductive wire consisting of metallic silver aggregates bound to the DNA skeleton. The current was found to be carried solely by the silver deposited on the DNA template.

5.5.3 Thin Films and Monolayer Assemblies

The electric conductivity of cast films prepared from a precipitated ds DNA-lipid complex which has a 1:1 ratio of phosphate groups to cationic amphiphile has been studied by Okahata et al. [171]. The conductivity in stretched films put on a comb-shaped electrode is highly anisotropic, having a substantially larger value when the DNA strand axis is perpendicular to the gold electrodes than when it is parallel. Little or no conductivity is observed for an unstretched film or for a DNA-lipid cast film prepared from ss poly(dA). Photoinduced conductivity was observed after soaking the aligned films of the ds, but not the ss film, in a solution of acridine orange. Based on the conductivity of the films prepared from ds, but not ss DNA, these authors conclude that the photocurrents pass through the stacked base pairs of the aligned DNA strands in the films. However, ionic transport by a mechanism similar to that proposed by Warman et al. [166] would also require the more rigid structure of ds DNA, and evidently was not considered.

Both ss and ds oligonucleotides have been attached to electrode surfaces using a variety of covalent linkages [172–174]. Napier et al. [172] have developed sensors for specific base sequences by attaching a complementary ss oligonucleotide to a polymer-coated electrode surface via amide linkages. Upon hybridization, the duplex will bind electroactive small molecules which associate with the duplex and can be detected by electrochemical measurements or electrogenerated chemiluminescence.

Barton and coworkers [173a–c] have attached ds oligonucleotides to gold surfaces by means of thiol-terminated tethers. The surface-attached ds DNA is proposed to form a densely packed monolayer in which the DNA helical axes are at an average 45° angle to the surface. The electroactive dye methylene blue intercalates in the surface-attached duplexes to form a 1:1 complex in which the dye is located at G:C-rich sites remote from the electrode surface [173a]. Cyclic voltametry of the

DNA–dye assemblies provided a nearly reversible response at scan rates up to 500 mV s^{-1} . Thus, electron transfer through the ds DNA and hexamethylenethiol linker was concluded to be fast on the electrochemical time scale. Similar conclusions were drawn from the cyclic voltametry of the electroactive intercalator daunomycin selectively bound to G:C sites at varying locations within a duplex attached to the electrode surface with a 13-atom alkylamide tether [173c].

Hartwich et al. [174] have investigated electron transport through self-assembled monolayers of ss and ds oligonucleotides attached to a gold surface by means of a short alkanethiol linker. To the opposite end of the oligonucleotide the quinone PQQ (pyrrolo-quinoline-quinone) was attached by condensation after formation of the monolayer. The functionalized ds helices are proposed to be tilted at an angle of $30 \pm 10^\circ$ with respect to the gold surface. Voltametric waves for the diffusing $\text{Fe}(\text{CN})_6^{3-/4-}$ couple were observed for the ds, but not for the ss, monolayers. In addition, two mismatches in the 12-mer duplex are sufficient to significantly reduce the rate of electron transport through the ds monolayer. Anisotropic conduction is attributed to the concerted movement of cations in the direction of the ds helical axis when an electric field is applied. These workers conclude that their results, like those of Okahata et al. [171] and Fink and Schönenberger [168] are consistent with a doped ionic semiconductor model and speculate that oxidation of guanine may create a n-type dopant in ds DNA.

5.6 Conclusions and Prospects

Investigations of the dynamics of photoinduced electron transfer processes in DNA have revealed many of the important features of these processes. The excitation of a π -stacked singlet electron acceptor–nucleobase electron donor complex can result in ultrafast charge separation and charge recombination when charge separation is exergonic (Section 4.2). Rate constants for charge separation increase as ΔG_{et} becomes more exergonic (normal region), whereas rate constants for charge recombination decrease as ΔG_{et} becomes more exergonic (inverted region) [110–112], in accord with a superexchange mechanism (Eqs. 10 and 11). When the acceptor and nucleobase are not π -stacked, the rates of both charge separation and recombination are much slower due to the lower electronic coupling between the donor and acceptor, behavior characteristic of a solvent-separated radical ion pair [88].

Electron transfer processes can occur over longer distances when the π -stacked singlet acceptor is not quenched by the neighboring nucleobase (Section 4.3). Both exogenous donors and guanine (or more readily oxidized nucleobase analogue) have been used as the electron donors. In cases where dynamic information is available from time-resolved spectroscopy the rate constants for both charge separation and recombination are strongly distance-dependent [110, 130]. Values of the exponential distance-dependence parameter β lie in the range $0.6\text{--}1.4 \text{ \AA}^{-1}$ (Table 8), and depend upon both the acceptor–DNA electronic coupling and reorganization energy, in accord with a single-step superexchange mechanism (Eq. 16).

Evidence for long-distance electron transfer processes which are not strongly distance-dependent have been obtained from studies of fluorescence intensity quenching and photoinduced strand cleavage and thymine dimer repair (Section 4.4). Recent studies of the distance-dependence of DNA strand cleavage have provided evidence for a hole-hopping mechanism in which a photochemically generated hole can migrate from the locus of its generation to a remote GG or GGG step where strand cleavage occurs [41, 150, 157, 160]. Hole hopping is believed to involve guanine bases due to their low oxidation potentials, though other bases or ensembles of neighboring bases may be involved. Analysis of the relative strand cleavage efficiencies provides values of the distance-dependence $\beta' < 0.1$ (Eq. 20), in accord with a hole-hopping mechanism.

The efficiency of the hopping process is determined by the number of hops and the relative rates of hopping versus competing processes, which include charge recombination and chemical reactions of the guanine cation radicals. The first measurements of the dynamics of a hopping process provide a value of c. 10^8 s^{-1} for hopping from a guanine cation radical to a GG step across a single adenine [165]. Rapid charge recombination in radical ion pairs limits the efficiency of photo-initiated hole hopping using singlet acceptors. This limitation can be avoided by the use of triplet acceptors if intersystem crossing of the singlet precursor is more rapid than singlet charge separation [84]. Irreversible photogeneration of a cation radical has been used creatively in studies of hole transport in DNA [150], but cannot be used directly to provide information about dynamics.

Investigations of photoinitiated charge transport processes in DNA have thus far been limited to hole transport. Electron transport in DNA following reduction by solvated electrons (Section 4.1.3) has been observed to occur over multiple base pairs, although the dynamics of this process has not been investigated. Bixon et al. [154] have suggested that electron transport in DNA might be highly efficient if there is significant electronic coupling between thymine and cytosine bases, which have similar reduction potentials. A preliminary study of base pair photoreduction by a π -stacked singlet donor showed that both charge separation and recombination with neighboring base pairs is very rapid [26], as is the case for photooxidation of DNA [110]. No studies of long-distance photoinjection of electrons into DNA have been reported to date.

Investigations of electrical conductivity in single molecules and ensembles of DNA (Section 4.5) have led to divergent interpretations. Sample preparation and characterization in these studies is far more challenging than it is in the study of single DNA molecules in dilute solution. Similarly, the measurement of conductivity for single molecules presents formidable technical difficulties.

The studies summarized in this chapter provide an overview of our rapidly evolving knowledge of electron transfer and charge transport processes in DNA. The biological implications are clear. Both oxidative damage and repair of DNA can involve electron transport processes in which an electron or hole migrates over distances of up to 100 base pairs (several hundred Å). However, much remains to be learned about the efficiency and dynamics of these processes, both in single DNA molecules and DNA-based materials. Reducing the energy gap between a singlet acceptor and a DNA bridge could lead to increased rates and efficiencies of single-

step electron transfer processes at long distances. Improved methods for photo-injection of holes and electrons into DNA could result in more efficient long-distance transport processes. These and other advances could ultimately lead to the development of effective single molecule and nanostructured devices for molecular electronics.

Acknowledgments

The author wishes to express his gratitude to his colleagues and students. First, to Robert L. Letsinger for revealing the beauty of nucleic acid chemistry. Next, to Michael R. Wasielewski and his students for unraveling the complexities of electron transfer dynamics, to Mark Ratner for explaining the relationship of experiment and theory, and to Martin Egli and his students for solving the first hairpin structure—our “Rosetta Stone”. Finally to my students, especially to Taifeng Wu who got us off to a running start, to Yifan Zhang, Xiaoyang Liu, Yansheng Wu, and Jianqin Liu who have carried the torch, and to the indispensable Rajdeep Kalgutar. The author’s research on DNA electron transfer is supported by the Division of Chemical Sciences, Office of Basic Energy Sciences, U.S. Department of Energy.

References

1. (a) G. M. Blackburn, M. J. Gait, *Nucleic Acids in Chemistry and Biology*, 2nd ed., Oxford University Press, Oxford, **1996**; (b) Z. Shabarova, A. Bogdanov, *Advanced Organic Chemistry of Nucleic Acids*, VCH, Weinheim, **1994**.
2. S. M. Hecht, Ed. *Bioorganic Chemistry: Nucleic Acids*, Oxford University Press, Oxford, **1996**.
3. (a) L. M. Adleman, *Science* **1994**, 266, 1021–1023; (b) D. Faulhammer, A. R. Cukras, R. J. Lipton, L. F. Landweber, *Proc. Natl. Acad. Sci. USA* **2000**, 97, 1385–1389; (c) E. Winfree, F. Liu, L. A. Wenzler, N. C. Seeman, *Nature* **1998**, 394, 539–544; (d) J. J. Storhoff, C. A. Mirkin, *Chem. Rev.* **1999**, 99, 1849–1862.
4. (a) C. A. Mirkin, M. A. Ratner, *Annu. Rev. Phys. Chem.* **1992**, 43, 719–754; (b) J. M. Tour, *Chem. Rev.* **1996**, 96, 537–553; (c) A. P. de Silva, H. Q. N. Gunaratne, T. Gunnlaugsson, A. J. M. Huxley, C. P. McCoy, J. T. Rademacher, T. E. Rice, *Chem. Rev.* **1997**, 97, 1515–1566; (d) I. Willner, *Acc. Chem. Res.* **1997**, 30, 347–356; (e) Fox, M. A. *Acc. Chem. Res.* **1999**, 32, 201–207.
5. (a) L. M. Adleman, *Science* **1994**, 266, 1021–1023; (b) D. Faulhammer, A. R. Cukras, R. J. Lipton, L. F. Landweber, *Proc. Natl. Acad. Sci. USA* **2000**, 97, 1385–1389.
6. C. J. Burrows, J. G. Muller, *Chem. Rev.* **1998**, 98, 1109–1151.
7. B. Armitage, *Chem. Rev.* **1998**, 98, 1171–1200.
8. J. Cadet, P. Vigny in *Bioorganic Photochemistry*, Vol. 1 (Ed.: H. Morrison), John Wiley & Sons, New York, **1990**, pp. 1–272.
9. (a) G. Kraft, M. Kramer *Adv. Radiation Biol.* **1993**, 17, 1–52; (b) P. O’Neill, E. M. Fieldew, *ibid.* **1993**, 17, 53–120.
10. D. D. Eley, D. I. Spivey, *Trans. Faraday Soc.* **1962**, 58, 411–415.
11. E. Tuite, in *Organic and Inorganic Photochemistry*, Vol. 2 (Eds.: V. Ramamurthy, K. S. Schanze), Marcel Dekker, New York, **1998**, pp. 55–74.
12. (a) T. L. Netzel, *J. Chem. Ed.* **1997**, 74, 646–651; (b) T. L. Netzel in *Organic and Inorganic Photochemistry*, Vol. 2 (Eds.: V. Ramamurthy, K. S. Schanze), M. Dekker, New York, **1998**, pp. 1–54; (c) T. L. Netzel, *J. Biol. Inorg. Chem.* **1998**, 3, 210–214.

13. (a) E. D. A. Stemp, J. K. Barton, in *Metal Ions in Biological Systems*, Vol. 33 (Eds.: A. Sigel, H. Sigel), Marcel Dekker, New York, **1996**, pp. 325–365; (b) R. E. Holmlin, P. J. Dandliker, J. K. Barton, *Angew. Chem. Int. Ed. Engl.* **1997**, *36*, 2714–2730; (c) K. E. Erkkila, D. T. Odom, J. K. Barton, *Chem. Rev.* **1999**, *99*, 2777–2795.
14. A. Kirsch-De Mesmaeker, J.-P. Lecomte, J. M. Kelly, *Topics Curr. Chem.* **1996**, *177*, 25–76.
15. P. F. Barbara, E. J. C. Olson, *Adv. Chem. Phys.* **1999**, *107*, 647–676.
16. (a) G. Taubes, *Science* **1997**, *275*, 1420–1421; (b) K. E. Wilson, *Chem. Eng. News* **1997**, *75*, 33–38; (c) K. E. Wilson, *ibid.* **1998**, *76*, 51–54.
17. (a) K. E. Wilson, *Chem. Eng. News* **1999**, *77* (34), 43–48; (b) C. Wu, *Science News* **1999**, *156*, 104–106; (c) M. A. Ratner, *Nature* **1999**, *397*, 480–481.
18. (a) S. Steenken, *Biol. Chem.* **1997**, *378*, 1293–1297; (b) D. N. Beratan, S. Priyadarshy, S. M. Risser, *Chem. & Biol.* **1997**, *4*, 3–8; (c) S. Priyadarshy, S. M. Risser, D. N. Beratan, *J. Biol. Inorg. Chem.* **1998**, *3*, 196–200; (d) N. J. Turro, J. K. Barton, *ibid.* **1998**, *3*, 201–209; (e) F. D. Lewis, R. L. Letsinger, *ibid.* **1998**, *3*, 215–221; (f) E. S. Krider, T. J. Meade, *ibid.* **1998**, *3*, 222–225.
19. (a) R.H. Sarma, *Nucleic Acid Geometry and Dynamics*, Pergamon, N. Y., **1980**; (b) W. Saenger in *Principles of Nucleic Acid Structure*, (Ed.: C. R. Cantor), Springer-Verlag, New York, **1984**.
20. H. Rozenberg, D. Rabinovich, F. Frolow, R. S. Hegde, Z. Shakked, *Proc. Natl. Acad. Sci. USA* **1998**, *95*, 15194–15199.
21. G. S. Schuerman, L. Van Meervelt, *J. Am. Chem. Soc.* **2000**, *122*, 232–240.
22. (a) P. N. Borer, S. R. LaPlante, A. Kumar, N. Zanatta, A. Martin, A. Hakkinen, G. C. Levy, *Biochemistry* **1994**, *33*, 2441–2450; (b) S. Georghiou, T. D. Bradrick, A. Philippetis, J. M. Beecham, *Biophys. J.* **1996**, *70*, 1909–1922; (c) C. Kojima, A. Ono, M. Kainosho, T. L. James, *J. Magn. Reson.* **1998**, *135*, 310–333; (d) E. B. Brauns, M. L. Madaras, R. S. Coleman, C. J. Murphy, M. A. Berg, *J. Am. Chem. Soc.* **1999**, *121*, 11644–11649.
23. S. M. Gasper, B. Armitage, X. Shui, G. G. Hu, C. Yu, G. B. Schuster, L. D. Williams, *J. Am. Chem. Soc.* **1998**, *120*, 12402–12409.
24. H. P. Spielmann, *Biochemistry* **1998**, *37*, 16863–16876.
25. (a) R. X.-F. Ren, N. C. Chaudhuri, P. L. Paris, S. Rumney IV, E. T. Kool, *J. Am. Chem. Soc.* **1996**, *118*, 7671–7678; (b) E. T. Kool, *Chem. Rev.* **1997**, *97*, 1473–1487.
26. F. D. Lewis, X. Liu, Y. Wu, S. E. Miller, M. R. Wasielewski, R. L. Letsinger, R. Sanishvili, A. Joachimiak, V. Tereshko, M. Egli, *J. Am. Chem. Soc.* **1999**, *121*, 9905–9906.
27. A. Holmén, A. Broo, B. Albinsson, B. Nordén, *J. Am. Chem. Soc.* **1997**, *119*, 12240–12250.
28. C. R. Cantor, R. R. Schimmel, *Biophysical Chemistry*, W. H. Freeman, San Francisco, **1980**, 399–404.
29. (a) D. C. Ward, E. Reich, *J. Biol. Chem.* **1969**, *244*, 1228–1237; (b) S. M. Law, R. Eritja, M. F. Goodman, K. J. Breslauer, *Biochemistry* **1996**, *35*, 12329–12337; (c) T. M. Nordlund, S. Andersson, L. Nilsson, R. Rigler, *Biochemistry* **1989**, *28*, 9095–9103; (d) R. A. Hochstrasser, T. E. Carver, L. C. Sowers, D. P. Millar, *ibid.* **1994**, *33*, 11971–11979; (e) J. T. Stivers, *Nucleic Acids Res.* **1998**, *26*, 3837–3844.
30. S. O. Kelley, J. K. Barton, *Science* **1999**, *283*, 375–381.
31. (a) J. A. Secrist III, J. R. Barrio, N. J. Leonard, G. Weber, *Biochemistry* **1972**, *11*, 3499–3506; (b) R. D. Spencer, G. Weber, G. L. Tolman, J. R. Barrio, N. J. Leonard, *Eur. J. Biochem.* **1974**, *45*, 425–429; (c) Y. Kubota, Y. Motoda, Y. Fujisaki, R. F. Steiner, *Biophys. Chem.* **1983**, *18*, 225–232.
32. (a) N. S. Hush, A. S. Cheung, *Chem. Phys. Lett.* **1975**, *34*, 11–13; (b) V. M. Orlov, A. N. Smirnov, Ya. M. Varshavsky, *Tetrahedron Lett.* **1976**, 4377–4378.
33. (a) M. D. Sevilla, B. Besler, A.-O. Colson, *J. Phys. Chem.* **1995**, *99*, 1060–1063; (b) A.-O. Colson, B. Besler, M. D. Sevilla, *ibid.* **1992**, *96*, 9787–9794; (c) A.-O. Colson, B. Besler, D. M. Close, M. D. Sevilla, *ibid.* **1992**, *96*, 661–668.
34. M. Hutter, T. Clark, *J. Am. Chem. Soc.* **1996**, *118*, 7574–7577.
35. (a) N. S. Kim, P. R. LeBreton, *J. Am. Chem. Soc.* **1996**, *118*, 3694–3707; (b) H. Fernando, G. A. Papadantonakis, N. S. Kim, P. R. LeBreton, *Proc. Natl. Acad. Sci. USA* **1998**, *95*, 5550–5555.
36. E. S. Chen, E. C. M. Chen, *Bioelectrochem. Bioenerg.* **1998**, *46*, 15–19.

37. N. S. Kim, Q. Zhu, P. R. LeBreton, *J. Am. Chem. Soc.* **1999**, *121*, 11516–11530.
38. (a) H. Sugiyama, I. Saito, *J. Am. Chem. Soc.* **1996**, *118*, 7063–7068; (b) Y. Yoshioka, Y. Kitagawa, Y. Takano, K. Yamaguchi, T. Nakamura, I. Saito, *ibid.* **1999**, *121*, 8712–8719.
39. F. Prat, K. N. Houk, C. S. Foote, *J. Am. Chem. Soc.* **1998**, *120*, 845–846.
40. T. Majima, S. Tojo, S. Takamuku, *J. Phys. Chem.* **1997**, *101*, 1048–1055.
41. P. T. Henderson, D. Jones, G. Hampikian, Y. Kan, G. B. Schuster, *Proc. Natl. Acad. Sci. USA* **1999**, *96*, 8353–8358.
42. (a) S. Steenken, J. P. Telo, H. M. Novais, L. P. Candeias, *J. Am. Chem. Soc.* **1992**, *114*, 4701–4709; (b) Steenken, S. V. Jovanovic, *J. Am. Chem. Soc.* **1997**, *119*, 617–618.
43. C. A. M. Seidel, A. Schulz, M. H. M. Sauer, *J. Phys. Chem.* **1996**, *100*, 5541–5553.
44. M. Enescu, L. Lindqvist, *J. Phys. Chem.* **1995**, *99*, 8405–8411.
45. J. R. Wiley, J. M. Robinson, S. Ehdiaie, E. C. M. Chen, E. S. D. Chen, W. E. Wentworth, *Biochem. Biophys. Res. Commun.* **1991**, *180*, 841–844.
46. C. Sheu, C. S. Foote, *J. Am. Chem. Soc.* **1995**, *117*, 6439–6442.
47. S. O. Kelley, J. K. Barton, *Chem. Biol.* **1998**, *5*, 413–425.
48. (a) E. Palecek, V. Kolar, F. Jelen, U. Heinemann, *Bioelectrochem. Bioenerg.* **1990**, *23*, 285–298; (b) C. M. A. Brett, A. M. O. Brett, S. H. P. Serrano, *J. Electroanal. Chem.* **1994**, *366*, 225–231.
49. (a) D. H. Johnston, K. C. Glasgow, H. H. Thorp, *J. Am. Chem. Soc.* **1995**, *117*, 8933–8938; (b) D. H. Johnston, H. H. Thorp, *J. Phys. Chem.* **1996**, *100*, 13837–13843; (c) J. Kim, M. F. Sistare, P. J. Carter, H. H. Thorp, *Coord. Chem. Rev.* **1998**, *171*, 341–349; (d) M. F. Sistare, R. C. Holmberg, H. H. Thorp, *J. Phys. Chem. B* **1999**, *103*, 10718–10728; (e) P. A. Ropp, H. H. Thorp, *Chem. Biol.* **1999**, *6*, 599–605.
50. S. Steenken, *Chem. Rev.* **1989**, *89*, 503–520.
51. M. Faraggi, C. Ferradini, J.-P. Jay-Gerin, *New J. Chem.* **1995**, *19*, 1203–1215.
52. J. P. Barnes, W. A. Bernhard, *J. Phys. Chem.* **1995**, *99*, 11248–11254.
53. S. Gregoli, M. Olast, A. Bertinchamps, *Radiation Res.* **1982**, *89*, 238–254.
54. M. Yan, D. Becker, S. Summerfield, P. Renke, M. D. Sevilla, *J. Phys. Chem.* **1992**, *96*, 1983–1989.
55. E. M. Fielden, S. C. Lillicrap, A. B. Robins, *Radiation Res.* **1971**, *48*, 421–431.
56. C. Beach, A. F. Fuciarelli, J. D. Zimbrick, *Radiation Res.* **1994**, *137*, 385–393.
57. Y. Razskazovskii, S. G. Swarts, J. M. Falcone, C. Taylor, M. D. Sevilla, *J. Phys. Chem. B* **1997**, *101*, 1460–1467.
58. (a) L. P. Candeias, S. Steenken, *J. Am. Chem. Soc.* **1989**, *111*, 1094–1099; (b) L. P. Candeias, S. Steenken, *ibid.* **1993**, *115*, 2437–2440.
59. T. M. Dietz, T. H. Koch, *Photochem. Photobiol.* **1989**, *49*, 121–129.
60. D. H. Whillans, *Biochim. Biophys. Acta* **1975**, *414*, 193–205.
61. (a) P. M. Cullis, J. D. McClymont, M. C. R. Symons, *J. Chem. Soc. Faraday Trans.* **1990**, *86*, 591–592; (b) A. Pezeshk, M. C. R. Symons, J. D. McClymont, *J. Phys. Chem.* **1996**, *100*, 18562–18566.
62. (a) A. T. Al-Kazwini, P. O'Neill, G. E. Adams, E. M. Fielden, *Radiation Res.* **1990**, *121*, 149–153; (b) A. T. Al-Kazwini, P. O'Neill, D. Papworth, G. E. Adams, E. M. Fielden, *ibid.* **1991**, *125*, 348–349.
63. D. E. Charlton, *Radiation Res.* **1991**, *125*, 346–347.
64. R. F. Anderson, G. A. Wright, *Phys. Chem. Chem. Phys.* **1999**, *1*, 4827–4831.
65. H. Görner, *J. Photochem. Photobiol. B* **1994**, *26*, 117–139.
66. (a) L. P. Candeias, S. Steenken, *J. Am. Chem. Soc.* **1992**, *114*, 699–704; (b) L. P. Candeias, P. O'Neill, G. D. D. Jones, S. Steenken, *Int. J. Radiat. Biol.* **1992**, *61*, 15–20.
67. (a) T. Melvin, M. A. Plumb, S. W. Botchway, P. O'Neill, A. W. Parker, *Photochem. Photobiol.* **1995**, *61*, 584–591; (b) T. Melvin, S. Botchway, A. W. Parker, P. O'Neill, *J. Chem. Soc. Chem. Commun.* **1995**, 653–654; (c) T. Melvin, S. W. Botchway, A. W. Parker, P. O'Neill, *J. Am. Chem. Soc.* **1996**, *118*, 10031–10036.
68. H. Sies, W. A. Schulz, S. Steenken, *J. Photochem. Photobiol. B* **1996**, *32*, 97–102.
69. D. Angelov, A. Spassky, M. Berger, J. Cadet, *J. Am. Chem. Soc.* **1997**, *119*, 11373–11380.
70. V. Shafirovich, A. Dourandin, W. Huang, N. P. Luneva, N. E. Geacintov, *J. Phys. Chem. B* **1999**, *103*, 10924–10933.

71. V. Y. Shafirovich, A. Dourandin, N. P. Luneva, N. E. Geacintov, *J. Phys. Chem. B* **1997**, *101*, 5863–5868.
72. (a) D. Rehm, A. Weller, *Israel J. Chem.* **1970**, *8*, 259–271; (b) A. Weller, *Zeit. Phys. Chem. Neu. Folg.* **1982**, *133*, 93–98.
73. F. D. Lewis, Y. Zhang, X. Liu, N. Xu, R. L. Letsinger, *J. Phys. Chem. B* **1999**, *103*, 2570–2578.
74. J. R. Lakowicz, *Principles of Fluorescence Spectroscopy*, 2nd ed., Kluwer Academic, Plenum **1999**, 239–243.
75. M. Bixon, J. Jortner, *Adv. Chem. Phys.* **1999**, *106*, 35–202.
76. K. Kikuchi, Y. Takahashi, T. Katagiri, T. Niwa, M. Hoshi, T. Miyashi, *Chem. Phys. Lett.* **1991**, *180*, 403–408.
77. I. R. Gould, S. Farid, *Acc. Chem. Res.* **1996**, *29*, 522–528.
78. F. M. Winnik, *Chem. Rev.* **1993**, *93*, 587–614.
79. P. Lianos, S. Georghiou, *Photochem. Photobiol.* **1979**, *29*, 13–21.
80. (a) N. E. Geacintov, R. Zhao, V. A. Kuzmin, S. K. Kim, L. J. Pecora, *Photochem. Photobiol.* **1993**, *58*, 185–194; (b) V. Y. Shafirovich, P. P. Levin, V. A. Kuzmin, T. E. Thorgeirsson, D. S. Kliger, N. E. Geacintov, *J. Am. Chem. Soc.* **1994**, *116*, 63–72; (c) V. Y. Shafirovich, S. H. Courtney, N. Ya, N. E. Geacintov, *ibid.* **1995**, *117*, 4920–4929.
81. B. Armitage, C. Yu, C. Devadoss, G. B. Schuster, *J. Am. Chem. Soc.* **1994**, *116*, 9847–9859.
82. R. Bernstein, F. Prat, C. S. Foote, *J. Am. Chem. Soc.* **1999**, *121*, 464–465.
83. I. Saito, M. Takayama, H. Sugiyama, K. Nakatani, *J. Am. Chem. Soc.* **1995**, *117*, 6406–6407.
84. (a) J. E. Rogers, L. A. Kelly, *J. Am. Chem. Soc.* **1999**, *121*, 3854–3861; (b) J. E. Rogers, S. J. Weiss, L. A. Kelly, *ibid.* **2000**, *122*, 427–436.
85. Y. Kubota, Y. Motoda, Y. Shigemune, Y. Fujisaki, *Photochem. Photobiol.* **1979**, *29*, 1099–1106.
86. E. M. Tuite, J. M. Kelly, *J. Photochem. Photobiol. B: Biol.* **1993**, *21*, 103–124.
87. D. A. Dunn, V. H. Lin, I. E. Kochevar, *Photochem. Photobiol.* **1991**, *53*, 47–56.
88. A. M. Brun, A. Harriman, *J. Am. Chem. Soc.* **1991**, *113*, 8153–8159.
89. S. M. Hubig, T. M. Bockman, J. K. Kochi, *J. Am. Chem. Soc.* **1996**, *118*, 3842–3851.
90. T. Fiebig, C. Wan, S. O. Kelley, J. K. Barton, A. H. Zewail, *Proc. Natl. Acad. Sci. USA* **1999**, *96*, 1187–1192.
91. (a) J.-P. Lecomte, A. Kirsch-De Mesmaeker, M. M. Feeney, J. M. Kelly, *Inorg. Chem.* **1995**, *34*, 6481–6491; (b) C. Moucheron, A. Kirsch-De Mesmaeker, J. M. Kelly, *J. Photochem. Photobiol. B: Biol.* **1997**, *40*, 91–106; (c) I. Ortman, C. Moucheron, A. Kirsch-De Mesmaeker, *Coord. Chem. Rev.* **1998**, *168*, 233–271.
92. C. Turro, D. B. Hall, W. Chen, H. Zuilhof, J. K. Barton, N. J. Turro, *J. Phys. Chem. A* **1998**, *102*, 5708–5715.
93. L. P. A. van Houte, R. van Grondelle, J. Retèl, J. G. Westra, D. Zinger, J. C. Sutherland, S. K. Kim, N. E. Geacintov, *Photochem. Photobiol.* **1989**, *49*, 387–394.
94. (a) L. Margulis, P. F. Pluzhnikov, B. Mao, V. A. Kuzmin, Y. J. Chang, T. W. Scott, N. E. Geacintov, *Chem. Phys. Lett.* **1991**, *187*, 597–603; (b) D. O'Connor, V. Y. Shafirovich, N. E. Geacintov, *J. Phys. Chem.* **1994**, *98*, 9831–9839.
95. (a) N. E. Geacintov, K. Solntsev, L. W. Johnson, J. Chen, A. D. Kolbanovskiy, T. Liu, V. Y. Shafirovich, *J. Phys. Org. Chem.* **1998**, *11*, 561–565; (b) N. E. Geacintov, V. Y. Shafirovich, B. Li, B. Mao, N. Ya, *Spectrum* **1997**, *10*(2), 1–16.
96. (a) T. L. Netzel, M. Zhao, K. Nafisi, J. Headrick, M. S. Sigman, B. E. Eaton, *J. Am. Chem. Soc.* **1995**, *117*, 9119–9128; (b) T. L. Netzel, K. Nafisi, J. Headrick, B. E. Eaton, *J. Phys. Chem.* **1995**, *99*, 17948–17955.
97. (a) C. E. Kerr, C. D. Mitchell, J. Headrick, B. E. Eaton, T. L. Netzel, *J. Phys. Chem. B* **2000**, *104*, 1637–1650; (b) C. E. Kerr, C. D. Mitchell, Y. M. Ying, T. L. Netzel, *J. Phys. Chem. B* **2000**, *104*, 2166–2175.
98. G. Wenska, S. Paszyc, *Can. J. Chem.* **1988**, *66*, 513–516.
99. C. Seidel, K. Rittinger, J. Cortés, R. S. Goody, M. Köllner, J. Wolfrum, K. O. Greulich, *Proc. SPIE Int. Soc. Opt. Eng.* **1991**, *1432*, 105–116.
100. J. F. Constant, P. Laûgaa, B. P. Roques, J. Lhomme, *Biochemistry* **1988**, *27*, 3997–4003.

101. (a) J. Telser, K. A. Cruickshank, L. E. Morrison, T. L. Netzel, *J. Am. Chem. Soc.* **1989**, *111*, 6966–6976; (b) M. Manoharan, K. L. Tivel, M. Zhao, K. Nafisi, T. L. Netzel, *J. Phys. Chem.* **1995**, *99*, 17461–17472.
102. F. D. Lewis, Y. Zhang, R. L. Letsinger, *J. Am. Chem. Soc.* **1997**, *119*, 5451–5452.
103. E. Zahavy, M. A. Fox, *J. Phys. Chem. B* **1999**, *103*, 9321–9327.
104. G. Vámosi, C. Gohlke, R. M. Clegg, *Biophys. J.* **1996**, *71*, 972–994.
105. (a) L. Edman, Ü. Mets, R. Rigler, *Proc. Natl. Acad. Sci. USA* **1996**, *93*, 6710–6715; (b) C. Eggeling, J. R. Fries, L. Brand, R. Günther, C. A. M. Seidel, *Proc. Natl. Acad. Sci. USA* **1998**, *95*, 1556–1561.
106. J. Telser, K. A. Cruickshank, K. S. Schanze, T. L. Netzel, *J. Am. Chem. Soc.* **1989**, *111*, 7221–7226.
107. A. Kirsch-De Mesmaeker, C. Moucheron, N. Boutonnet, *J. Phys. Org. Chem.* **1988**, *11*, 566–576.
108. (a) M. Salunkhe, T. Wu, R. L. Letsinger, *J. Am. Chem. Soc.* **1992**, *114*, 8768–8772; (b) R. L. Letsinger, T. Wu, *J. Am. Chem. Soc.* **1994**, *116*, 811–812; (c) R. L. Letsinger, T. Wu, *J. Am. Chem. Soc.* **1995**, *117*, 7323–7328.
109. F. D. Lewis, T. Wu, E. L. Burch, D. M. Bassani, J.-S. Yang, S. Schneider, W. Jäger, R. L. Letsinger, *J. Am. Chem. Soc.* **1995**, *117*, 8785–8792.
110. (a) F. D. Lewis, T. Wu, Y. Zhang, R. L. Letsinger, S. R. Greenfield, M. R. Wasielewski, *Science* **1997**, *277*, 673–676; (b) F. D. Lewis, T. Wu, X. Liu, R. L. Letsinger, S. R. Greenfield, S. E. Miller, M. R. Wasielewski, *J. Am. Chem. Soc.* **2000**, *122*, 2889–2902.
111. F. D. Lewis, X. Liu, S. E. Miller, M. R. Wasielewski, *J. Am. Chem. Soc.* **1999**, *121*, 9746–9747.
112. F. D. Lewis, R. S. Kalgutkar, X. Liu, Y. Wu, J. Liu, R. T. Hayes, M. R. Wasielewski, *J. Am. Chem. Soc.* in press.
113. S. Bevers, T. P. O'Dea, L. W. McLaughlin, *J. Am. Chem. Soc.* **1998**, *120*, 11004–11005.
114. G. L. Closs, J. R. Miller, *Science* **1988**, *240*, 440–447.
115. (a) G. Löber, L. Kittler, *Photochem. Photobiol.* **1977**, *25*, 215–233; (b) L. Kittler, G. Löber, F. A. Gollmick, H. Berg, *J. Electroanal. Chem.* **1980**, *116*, 503–511; (c) S. Georghiou, *Photochem. Photobiol.* **1977**, *26*, 59–68.
116. J. Olmsted III, D. R. Kearns, *Biochemistry* **1977**, *16*, 3647–3654.
117. D. B. Hall, S. O. Kelley, J. K. Barton, *Biochemistry* **1998**, *37*, 15933–15940.
118. (a) A. Slama-Schwok, J. Jazwinski, A. Béré, T. Montenay-Garestier, M. Rougée, C. Hélène, J.-M. Lehn, *Biochemistry* **1989**, *28*, 3227–3234; (b) A. Slama-Schwok, M. Rougée, V. Ibanez, N. E. Geacintov, T. Montenay-Garestier, J.-M. Lehn, C. Hélène, *ibid.* **1989**, *28*, 3234–3242.
119. S. J. Atherton, A. Harriman, *J. Am. Chem. Soc.* **1993**, *115*, 1816–1822.
120. J. Jortner, M. Bixon, T. Langenbacher, M. E. Michel-Beyerle, *Proc. Natl. Acad. Sci. USA*, **1998**, *95*, 12759–12765.
121. J. R. Winkler, H. B. Gray, *Chem. Rev.* **1992**, *92*, 369–379.
122. K. P. Ghiggino, A. H. A. Clayton, J. M. Lawson, M. N. Paddon-Row, *New J. Chem.* **1996**, *20*, 853–859.
123. (a) S. M. Risser, D. N. Beratan, T. J. Meade, *J. Am. Chem. Soc.* **1993**, *115*, 2508–2510; (b) S. Priyadarshy, S. M. Risser, D. N. Beratan, *J. Phys. Chem.* **1996**, *100*, 17678–17682.
124. W. B. Davis, W. A. Svec, M. A. Ratner, M. R. Wasielewski, *Nature* **1998**, *396*, 60–63.
125. A. K. Felts, W. T. Pollard, R. A. Friesner, *J. Phys. Chem.* **1995**, *99*, 2929–2940.
126. (a) W. B. Davis, M. R. Wasielewski, M. A. Ratner, V. Mujica, A. Nitzan, *J. Phys. Chem. A* **1997**, *101*, 6158–6164; (b) D. Segal, A. Nitzan, W. B. Davis, M. R. Wasielewski, M. A. Ratner, *J. Phys. Chem. B* **2000**, *104*, 3817–3829.
127. A. Okada, V. Chernyak, S. Mukamel, *J. Phys. Chem. A* **1998**, *102*, 1241–1251.
128. (a) B. C. Baguley, W. A. Denny, G. J. Atwell, B. F. Cain, *J. Med. Chem.* **1981**, *24*, 170–177; (b) B. C. Baguley, B. F. Cain, *Mol. Pharmacol.* **1982**, *22*, 486–492.
129. A. M. Brun, A. Harriman, *J. Am. Chem. Soc.* **1992**, *114*, 3656–3660.
130. A. Harriman, *Angew. Chem. Int. Ed.* **1999**, *38*, 945–949.
131. S. O. Kelley, R. E. Holmlin, E. D. A. Stemp, J. K. Barton, *J. Am. Chem. Soc.* **1997**, *119*, 9861–9870.
132. P. Fromherz, B. Rieger, *J. Am. Chem. Soc.* **1986**, *108*, 5361–5362.

133. S. J. Atherton, P. C. Beaumont, *J. Phys. Chem.* **1987**, *91*, 3993–3997.
134. (a) S. J. Atherton, P. C. Beaumont, *J. Phys. Chem.* **1986**, *90*, 2252–2259; (b) S. J. Atherton, P. C. Beaumont, *ibid.* **1995**, *99*, 13025–13029.
135. M. D. Purugganan, C. V. Kumar, N. J. Turro, J. K. Barton, *Science* **1988**, *241*, 1645–1649.
136. G. Orellana, A. Kirsch-De Mesmaeker, J. K. Barton, N. J. Turro, *Photochem. Photobiol.* **1991**, *54*, 499–509.
137. A. E. Friedman, J.-C. Chambron, J.-P. Sauvage, N. J. Turro, J. K. Barton, *J. Am. Chem. Soc.* **1990**, *112*, 4960–4962.
138. C. J. Murphy, M. R. Arkin, N. D. Ghatlia, S. Bossmann, N. J. Turro, J. K. Barton, *Proc. Natl. Acad. Sci. USA*, **1994**, *91*, 5315–5319.
139. (a) E. D. A. Stemp, M. R. Arkin, J. K. Barton, *J. Am. Chem. Soc.* **1995**, *117*, 2375–2376; (b) R. E. Holmlin, E. D. A. Stemp, J. K. Barton, *ibid.* **1996**, *118*, 5236–5244; (c) M. R. Arkin, E. D. A. Stemp, C. Turro, N. J. Turro, J. K. Barton, *ibid.* **1996**, *118*, 2267–2274; (d) E. D. A. Stemp, R. E. Holmlin, J. K. Barton, *Inorg. Chim. Acta*, **2000**, *297*, 88–97.
140. M. R. Arkin, E. D. A. Stemp, R. E. Holmlin, J. K. Barton, A. Hörmann, E. J. C. Olson, P. F. Barbara, *Science* **1996**, *273*, 475–479.
141. E. J. C. Olson, D. Hu, A. Hörmann, P. F. Barbara, *J. Phys. Chem. B* **1997**, *101*, 299–303.
142. P. Lincoln, E. Tuite, B. Nordén, *J. Am. Chem. Soc.* **1997**, *119*, 1454–1455.
143. S. J. Franklin, C. R. Treadway, J. K. Barton, *Inorg. Chem.* **1998**, 5198–5210.
144. C. J. Murphy, M. R. Arkin, Y. Jenkins, N. D. Ghatlia, S. H. Bossmann, N. J. Turro, J. K. Barton, *Science*, **1993**, *262*, 1025–1029.
145. B. M. Hoffman, M. A. Ratner, *Inorg. Chim. Acta*, **1996**, *243*, 233–238.
146. T. J. Meade, J. F. Kayyem, *Angew. Chem. Int. Ed. Engl* **1995**, *34*, 352–354.
147. P. Aich, S. L. Labiuk, L. W. Tari, L. J. T. Delbaere, W. J. Roesler, K. J. Falk, R. P. Steer, J. S. Lee, *J. Mol. Biol.* **1999**, *294*, 477–485.
148. (a) K. Fukui, K. Tanaka, *Angew. Chem. Int. Ed.* **1998**, *37*, 158–161; (b) K. Fukui, K. Tanaka, M. Fujitsuka, A. Watanabe, O. Ito, *J. Photochem. Photobiol. B: Biol.* **1999**, *50*, 18–27.
149. C. Wan, T. Fiebig, S. O. Kelley, C. R. Treadway, J. K. Barton, A. H. Zewail, *Proc. Natl. Acad. Sci. USA* **1999**, *96*, 6014–6019.
150. (a) E. Meggers, D. Kusch, M. Spichty, U. Wille, B. Giese, *Angew. Chem. Int. Ed.* **1998**, *37*, 460–462; (b) E. Meggers, M. E. Michel-Beyerle, B. Giese, *J. Am. Chem. Soc.* **1998**, *120*, 12950–12955; (c) B. Giese, S. Wessely, M. Spormann, U. Lindemann, E. Meggers, M. E. Michel-Beyerle, *Angew. Chem. Int. Ed.*, **1999**, *38*, 996–998.
151. (a) D. T. Breslin, G. B. Schuster, *J. Am. Chem. Soc.* **1996**, *118*, 2311–2319; (b) D. Ly, Y. Kan, B. Armitage, G. B. Schuster, *J. Am. Chem. Soc.* **1996**, *118*, 8747–8748.
152. D. Dee, M. E. Baur, *J. Chem. Phys.* **1974**, *60*, 541–556.
153. F. C. Grozema, Y. A. Berlin, L. D. A. Siebbeles, *Int. J. Quant. Chem.* **1999**, *75*, 1009–1016.
154. M. Bixon, B. Giese, S. Wessely, T. Langenbacher, M. E. Michel-Beyerle, J. Jortner, *Proc. Natl. Acad. Sci. USA* **1999**, *96*, 11713–11716.
155. Y. A. Berlin, A. L. Burin, M. A. Ratner, *J. Phys. Chem. A* **2000**, *104*, 443–445.
156. D. B. Hall, R. E. Holmlin, J. K. Barton, *Nature* **1996**, *382*, 731–735.
157. (a) M. E. Núñez, D. B. Hall, J. K. Barton, *Chem. & Biol.* **1999**, *6*, 85–97; (b) D. B. Hall, J. K. Barton, *J. Am. Chem. Soc.* **1997**, *119*, 5045–5046; (c) S. R. Rajski, S. Kumar, R. J. Roberts, J. K. Barton, *J. Am. Chem. Soc.* **1999**, *121*, 5615–5616.
158. M. R. Arkin, E. D. A. Stemp, S. C. Pulver, J. K. Barton, *Chem. & Biol.* **1997**, *4*, 389–400.
159. S. M. Gasper, G. B. Schuster, *J. Am. Chem. Soc.* **1997**, *119*, 12762–12771.
160. D. Ly, L. Sanii, G. B. Schuster, *J. Am. Chem. Soc.* **1999**, *121*, 9400–9410.
161. (a) Y. Kan, G. B. Schuster, *J. Am. Chem. Soc.* **1999**, *121*, 10858–10864; (b) Y. Kan, G. B. Schuster, *ibid.* **1999**, *121*, 11607–11614; (c) V. Sartor, P. T. Henderson, G. B. Schuster, *ibid.* **1999**, *121*, 11027–11033; (d) B. Armitage, D. Ly, T. Koch, H. Frydenlund, H. Ørum, H. G. Batz, G. B. Schuster, *Proc. Natl. Acad. Sci. USA* **1997**, *94*, 12320–12325.
162. A. Sancar, *Annu. Rev. Biochem.* **1996**, *65*, 43–81.
163. (a) P. J. Dandliker, R. E. Holmlin, J. K. Barton, *Science* **1997**, *275*, 1465–1467; (b) P. J. Dandliker, M. E. Núñez, J. K. Barton, *Biochemistry* **1998**, *37*, 6491–6502.
164. K. Nakatani, C. Dohno, I. Saito, *J. Am. Chem. Soc.* **1999**, *121*, 10854–10855.

165. F. D. Lewis, X. Liu, J. Liu, S. E. Miller, R. T. Hayes, M. R. Wasielewski, *Nature* **2000**, 406, 51–53.
166. J. M. Warman, M. P. de Haas, A. Rupperecht, *Chem. Phys. Lett.* **1996**, 249, 319–322.
167. M. G. Debije, M. T. Milano, W. A. Bernhard, *Angew. Chem. Int. Ed.* **1999**, 38, 2752–2756.
168. H.-W. Fink, C. Schönenberger, *Nature* **1999**, 398, 407–410.
169. D. Porath, A. Bezryadin, S. de Vries, C. Dekker, *Nature* **2000**, 403, 635–638.
170. E. Braun, Y. Eichen, U. Sivan, G. Ben-Yoseph, *Nature* **1998**, 391, 775–778.
171. Y. Okahata, T. Kobayashi, K. Tanaka, M. Shimomura, *J. Am. Chem. Soc.* **1998**, 120, 6165–6166.
172. M. E. Napier, C. R. Loomis, M. F. Sistare, J. Kim, A. E. Eckhardt, H. H. Thorp, *Bioconjugate Chem.* **1997**, 8, 906–913.
173. (a) S. O. Kelley, J. K. Barton, N. M. Jackson, M. G. Hill, *Bioconjugate Chem.* **1997**, 8, 31–37; (b) S. O. Kelley, J. K. Barton, N. M. Jackson, L. D. McPherson, A. B. Potter, E. M. Spain, M. J. Allen, M. G. Hill, *Langmuir* **1998**, 14, 6781–6784; (c) S. O. Kelley, N. M. Jackson, M. G. Hill, J. K. Barton, *Angew. Chem. Int. Ed.* **1999**, 38, 941–945.
174. G. Hartwich, D. J. Caruana, T. de Lumley-Woodyear, Y. Wu, C. N. Campbell, A. Heller, *J. Am. Chem. Soc.* **1999**, 121, 10803–10812.

Addendum

Since the preparation of this manuscript a number of significant papers related to the topic of this chapter have been published. Several of these merit special mention, including a concise overview of the topic by Grinstaff [1] and reviews of long distance charge transport by Schuster [2] and Giese [3] that summarize the seminal contributions of their laboratories. The crystal structure of a sequence-specific rhodium intercalator bound to an eight-base pair duplex has been determined with 1.2 Å resolution [4]. The occurrence of oxidative repair of thymine dimers in DNA via a long-distance hole-transport mechanism has been challenged by Dotse et al. [5]. However, further evidence in support of dimer repair has been advanced by McLaughlin, Barton and colleagues [6]. The effects of distance and base sequence upon hole transport between GGG and GG sequences has been investigated by Nakatani et al. [7] and Williams et al. [8], respectively, and the dynamics and equilibria for oxidation of G, GG, and GGG sequences have been studied in the author's laboratory [9].

1. M. W. Grinstaff, *Angew. Chem. Int. Ed.* **1999**, 38, 3629–3635.
2. G. B. Schuster, *Acc. Chem. Res.* **2000**, 33, 253–260.
3. B. Giese, *Acc. Chem. Res.* **2000**, 33, 631–636.
4. C. L. Kielkopf, K. E. Erkkila, B. P. Hudson, J. K. Barton, D. C. Rees, *Nature Struct. Biol.* **2000**, 7, 117–121.
5. A. K. Dotse, E. K. Boone, G. B. Schuster, *J. Am. Chem. Soc.* **2000**, 122, 6825–6833.
6. D. A. Vicic, D. T. Odom, M. E. Nunez, D. A. Gianolio, L. W. McLaughlin, J. K. Barton, *J. Am. Chem. Soc.* **2000**, 122, 8603–8611.
7. K. Nakatani, C. Dohno, I. Saito, *J. Am. Chem. Soc.* **2000**, 122, 5893–5894.
8. T. T. Williams, D. T. Odom, J. K. Barton, *J. Am. Chem. Soc.* **2000**, 122, 9048.
9. F. D. Lewis, X. Liu, J. Liu, R. T. Hayes, M. R. Wasielewski, *J. Am. Chem. Soc.* **2000**, 122, in press.

Volume III

Part 2

Artificial Supramolecular Systems

1 Covalently Linked Systems Based on Organic Components

Michael N. Paddon-Row

1.1 Introduction

Electron transfer (ET) is the most elementary and ubiquitous of all chemical reactions, playing a key role in many essential biological processes. There are three principal modes of energetically activating ET, namely thermal, optical, and photoinduced ET (Figure 1). Optical ET differs from photoinduced ET in that, for the former process, ET occurs during electronic excitation into a charge transfer (CT) or intervalence band, whereas for the latter process ET takes place after electronic excitation, from a locally excited state intermediate. Three important types of ET are charge separation, charge recombination, and charge shift (Figure 1), and these may be promoted either thermally, photochemically or optically.

A particularly significant type of ET is photoinduced charge separation between two bichromophores (or redox centres), as illustrated in Figure 2. The first step involves local excitation of either the Donor (**D**) or Acceptor (**A**) chromophore to generate the locally excited state, e.g., $^*\mathbf{D}-\mathbf{A}$. Exergonic charge separation (k_{cs}) competes with decay modes (k_d) leading to the ground state, to generate the charge-separated (CS) state, $^+\mathbf{D}-\mathbf{A}^-$. The importance of the photoinduced charge separation process lies in its transduction of light energy into useful chemical potential, measured by the free energy change, ΔG_{cr} , for charge recombination. Such CS states may therefore be regarded as molecular photovoltaic devices. A classic example of the usefulness of photoinduced charge separation in biology is the vital role it plays in the primary events of photosynthesis.

The successful design of both natural and artificial molecular photovoltaic devices rests on meeting three fundamental requirements, namely [1]:

- 1) The quantum yield for the charge separation process should be as high as possible. That is, $k_{cs} \gg k_d$ (Figure 2).
- 2) The lifetime, τ_{cr} ($= 1/k_{cr}$), of the CS state must be sufficiently long to enable it to carry out “useful” chemical work. In practice, it would be useful to aim for τ_{cr}

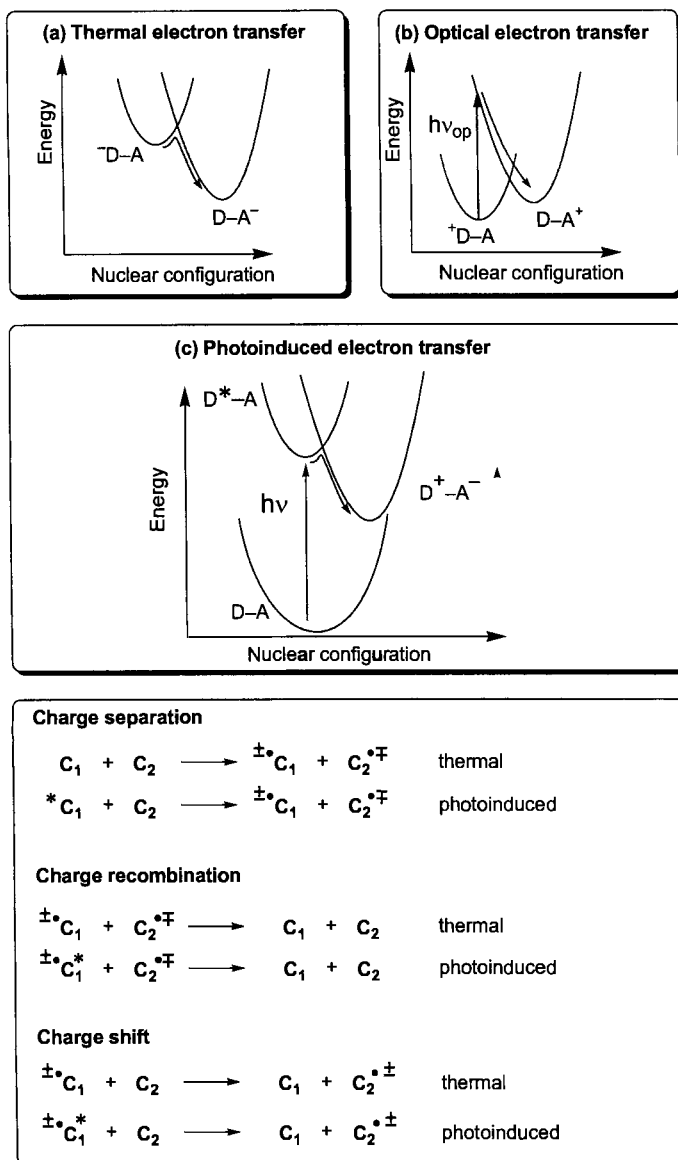
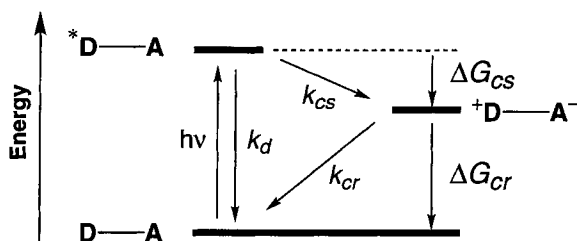


Figure 1. Three different types of electron transfer processes. Bottom box: Those chromophores bearing an asterisk (e.g., *C_1) indicate that they are in an electronically excited state, generated by absorption of light.

Figure 2. Energy diagram illustrating the possible pathways available in a photoinduced charge separation process between a donor (D) and an acceptor (A).



values lying in the microsecond domain, since this would allow diffusion controlled reactions involving the CS state to occur with 100 % efficiency, even in viscous solvents.

- 3) The energy content of the CS state should be as high as possible, thereby ensuring maximum conversion of photonic energy into chemical potential. Thus, $|\Delta G_{cs}|$ should be as small as practicable while ensuring that requirement (1) is met.

Meeting these design criteria requires a sound knowledge of the fundamental mechanisms of electron transfer processes. The theoretical framework for most ET reactions is based on a simple two-state model (Figure 3). The energy surface for an ET process, conveniently represented by a one-dimension reaction coordinate which is supposed to describe changes in both geometry of the D-A system and solvent orientation, may be regarded in terms of two diabatic surfaces, one representing the electronic configuration of the reactant, D-A, and the other representing the electronic configuration of the product, $^+D-A^-$. In the region where the diabatic surfaces intersect, the two configurations mix, symmetry permitting, and this results in an avoided crossing. The magnitude of the avoided crossing is given by $2V_{el}$, where V_{el} is the electronic coupling matrix element and may be regarded as a rough measure of the strength of orbital interactions between D and A.

In the case of long-range ET, where the donor and acceptor chromophores are separated by distances which exceed the sum of their van der Waals radii, V_{el} is

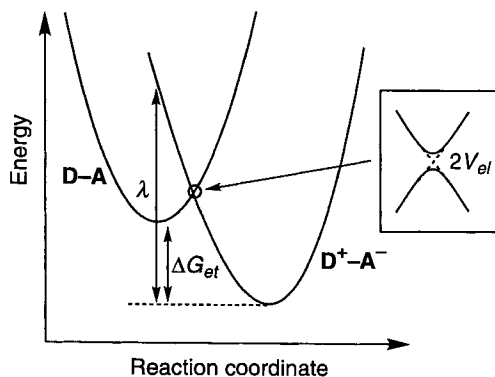


Figure 3. Energy diagram for charge separation resolved into reactant-like and product-like diabatic surfaces. The two diabatic curves do not intersect, but interact, to give an avoided crossing, whose energy gap is twice the electronic coupling, V_{el} , for the interaction.

generally very small ($<150\text{ cm}^{-1}$). ET then occurs nonadiabatically and the Fermi Golden Rule formalism of Eq. 1 may be used to express the ET rate constant, k_{et} :

$$k_{et} = \frac{4\pi^2}{h} |V_{el}|^2 FCWD \quad (1)$$

In this equation, *FCWD* is the Franck–Condon weighted density of states, and it contains information concerning overlap between the vibrational wavefunctions of the reactant and product states.

In the Marcus–Hush semiclassical treatment, Eq. 1 is simplified to Eq. 2 [2, 3]. In this expression, ΔG_{et} is the free energy change associated with the ET process and λ is the reorganization energy (Figure 3), and is approximately given by the sum of vibrational contributions from the donor and acceptor chromophores (internal reorganization energy, λ_i) and low-frequency contributions from the solvent (solvent reorganization energy, λ_s); \hbar and k_B are Planck’s constant and Boltzmann’s constant, respectively, and T is the temperature.

$$k_{et} = \frac{4\pi^2}{\hbar} |V_{el}|^2 \frac{1}{\sqrt{4\pi\lambda k_B T}} \exp\left(\frac{-\{\Delta G_{et} + \lambda\}^2}{4\lambda k_B T}\right) \quad (2)$$

Thus, within the context of Marcus–Hush theory, the three important variables that determine the ET rate constant are V_{el} , λ , and ΔG_{et} . It therefore follows that an understanding of ET processes entails an understanding of how these three variables are determined by factors such as the electronic properties of the donor and acceptor chromophores, the nature of the intervening medium, and interchromophore separation and orientation. The distance dependence of ET dynamics is a particularly important problem and, in order to investigate it experimentally, it is obviously advisable to employ donor–acceptor systems that are “rigid” in the sense that the donor and acceptor groups are held in well-defined distances and orientations with respect to each other.

It is possible to investigate the distance dependence of ET dynamics *intermolecularly* by dissolving the donor and acceptor chromophores in glasses. In these systems, the donor and acceptor groups are statistically distributed over a wide range of orientations and distances; nevertheless reasonable ET rate–distance profiles have been obtained from statistical analysis of the rate data [4, 5]. A more tractable method is to use systems in which the donor and acceptor groups are connected to each other, either by covalent linkages or by noncovalent interactions, such as H-bonds. The purpose of this chapter is to provide a brief overview of the important mechanistic insights into intramolecular ET processes using covalently linked multichromophoric systems. These systems will be denoted by **D–B–A** for a bichromophoric system (or dyad) in which the donor (**D**) and acceptor (**A**) groups are covalently attached to a bridge (**B**). This review will be restricted to organic chromophores, as opposed to transition metal complexes which are reviewed in Chapter 3 of this section of the handbook. Porphyrin-based chromophores will only be briefly mentioned, as they are treated in detail in Chapter 2 of this section.

Bridges that will be surveyed include saturated hydrocarbon bridges, unsaturated conjugated hydrocarbon bridges, and DNA. This review is not intended to be exhaustive, because many extensive reviews have already been published in this area [6–14].

1.2 The Superexchange Mechanism

There is another, compelling reason for studying intramolecular ET in covalently linked multichromophoric systems, and this involves the question of the influence of the intervening medium on ET dynamics. Clearly, the medium will influence ET dynamics by its effect on the driving force ($-\Delta G_{et}$) and the solvent reorganization energy terms in the Marcus–Hush expression. More subtly, the medium may even participate in the ET process by electronic coupling with the donor and acceptor chromophores. This interaction is manifested by a strengthening of the electronic coupling term, V_{el} .

Before considering more deeply, the question of the involvement of the medium on the electronic coupling between the donor and acceptor groups, it is instructive to examine the situation of ET taking place in vacuo. In the absence of any intervening medium between the redox couple, the electronic coupling depends on the direct, through-space (TS) overlap between the orbitals of the donor and acceptor groups that are primarily involved in the electron transfer process. Because orbital overlap decays exponentially with increasing interorbital separation, it is expected that the magnitude of TS electronic coupling should display similar decay characteristics [15]. Thus, both V_{el} and the associated ET rate constant, k_{et} , decay approximately exponentially with increasing interchromophore separation, r , according to Eqs. 3 and 4:

$$V_{el} \propto \exp(-0.5\beta_{el}r) \quad (3)$$

$$k_{et} \propto \exp(-\beta r) \quad (4)$$

where β_{el} and β are damping factors. It is often assumed that β_{el} and β have identical magnitudes, but this is not strictly correct because β , being a phenomenological quantity, incorporates distance dependence contributions, not only from V_{el} , but also from Franck–Condon factors, such as the solvent reorganization energy, λ_s . Thus, β is expected to be slightly larger than β_{el} , although it is often assumed that β_{el} and β have similar magnitudes.

The analysis of TS coupling may be quantified by calculating the coupling between two degenerate π -type orbitals placed in a vacuum as a function of interorbital separation (Figure 4). The orbital degeneracy is lifted by TS orbital overlap and gives rise to a splitting energy, $\Delta E(\pi)$. It is readily shown that $\Delta E(\pi)$ is twice the electronic coupling V_{el} for ET in the system (Figure 4) and a simple *ab initio* MO calculation predicts that $\beta_{el} \approx 3.0 \text{ \AA}^{-1}$ for TS coupling [15]. This is a very large

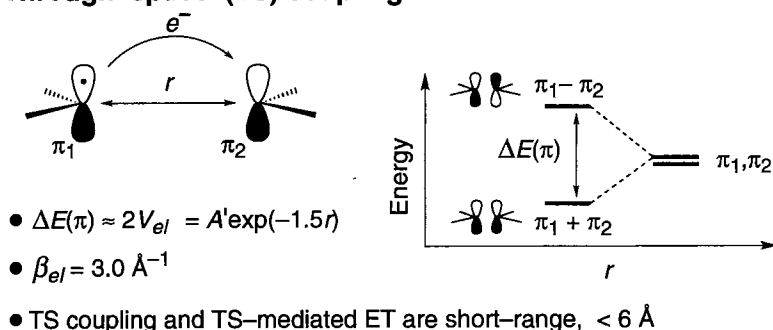
Through-space (TS) coupling:

Figure 4. Distance dependence of through-space interactions between two equivalent π -type orbitals. The value of β_{el} was obtained using the HF/3-21G theoretical model.

value for the damping factor, and it suggests that the ET rate is attenuated by a factor of 20 per angstrom increase in the interorbital separation. Consequently, long-range ET occurring through-space (i.e., in a vacuum) should be very slow for donor–acceptor separations exceeding 6 Å.

We now return to the question of whether an intervening nonconjugated medium could facilitate ET. Such a medium, which may comprise a saturated hydrocarbon bridge, a protein or oligopeptide, π -stacks, or even solvent molecules, could facilitate ET by what is known as a superexchange mechanism [16, 17]; to put it crudely, the medium provides “orbitals” ($\pi, \pi^*, \sigma, \sigma^*$, etc.) which the migrating electron can use to tunnel between the chromophores (Figure 5). In those situations where the medium is saturated and only σ and σ^* orbitals are available for coupling with the chromophores, the superexchange mechanism is then often referred to as a through-bond (TB) coupling mechanism [15, 18, 19].

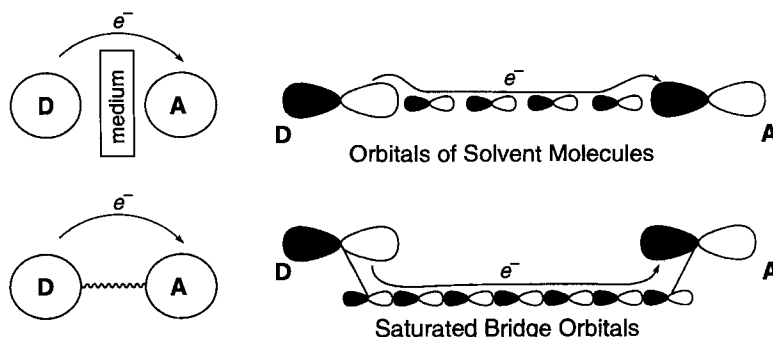
Long-range ET mediated by the intervening medium

Figure 5. Long-range ET. Direct overlap between the donor and acceptor orbitals is negligible, and ET occurs by an indirect mechanism involving electron tunneling through the orbitals of the intervening medium, e.g., solvent molecules (upper) or a covalently linked saturated bridge (lower).

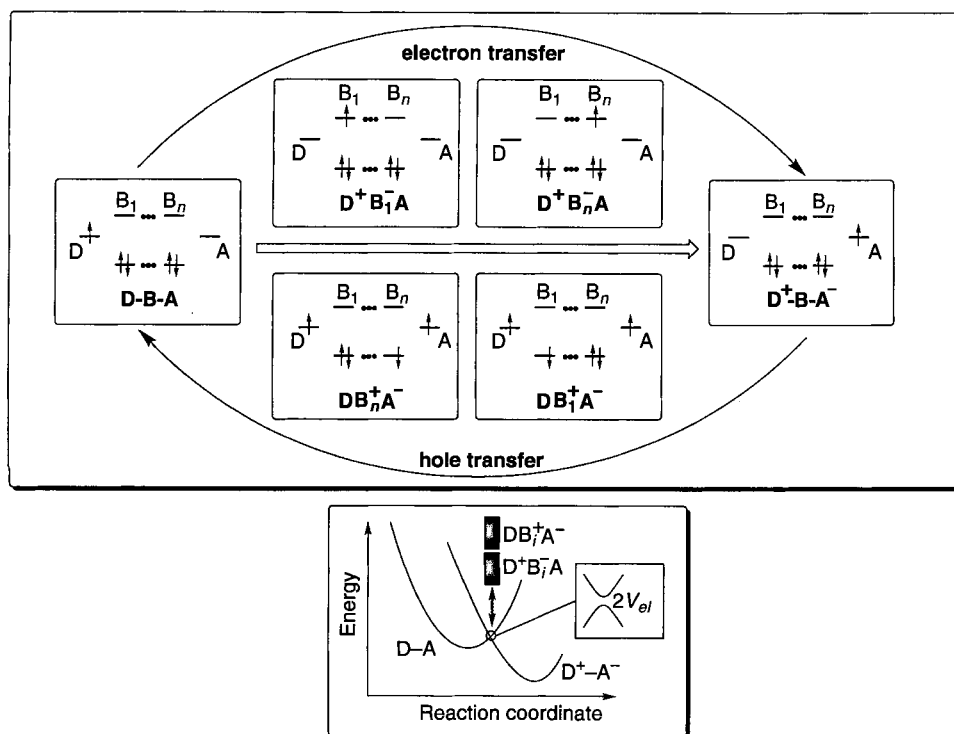


Figure 6. Schematic of the superexchange mechanism. In the region of the avoided crossing, virtual states resulting from ionization of the bridge are constructed, and these configurations are mixed into the reactant and product diabatic configurations to give the coupling, V_{el} . If virtual anionic bridge states, $^+D-B-A^-$, are more important than cationic bridge states, $D-B^+-A^-$, in the mixing scheme the process is often termed electron transfer. If the reverse holds, then it is termed hole transfer.

A more accurate representation of the superexchange mechanism is depicted in Figure 6 for the case of charge separation occurring in a $D-B-A$ dyad in which the bridge, B , consists of n subunits, B_i . Each subunit might, for example, be a two-center bond such as a C-C bond, or a larger entity, such as a benzene ring. The charge separation process may now be viewed as coupling of the reactant $D-B-A$ and product $^+D-B-A^-$ states with the two sets of virtual ionic bridge configurations $^+D-B_i^-A^-$ and $D-B_i^+-A^-$ ($i = 1, 2, \dots, n$). The first set of virtual configurations is generated by transferring the active electron from D into the various virtual orbitals of the bridge, whereas the second set of configurations is generated by transferring an electron from the various filled orbitals of the bridge to A .

It is important to note that, in the superexchange mechanism, these virtual ionic bridge configurations have no physical existence; they are not intermediates in the charge separation process since their energies are much higher than those of the reactant and product states. These virtual configurations generally only become significant in the region of the avoided crossing of the reactant and product diabatic

configurations on the potential energy surface for charge separation, whereupon they mix with the reactant and product configurations (Figure 6, lower section). This mixing results in an increase in the magnitude of the electronic coupling, V_{el} , over that resulting merely from direct, TS mixing of the reactant and product configurations alone. If the ${}^+\mathbf{D}-\mathbf{B}_i^--\mathbf{A}$ configurations mix more strongly with the reactant and product configurations at the avoided crossing than the $\mathbf{D}-\mathbf{B}_i^+-\mathbf{A}^-$ configurations, then the charge separation is said to occur by an electron transfer mechanism. This is because the mixing may be viewed in terms of an electron being propagated through the bridge. If, on the other hand, the $\mathbf{D}-\mathbf{B}_i^+-\mathbf{A}^-$ configurations mix more strongly with the reactant and product configurations than the ${}^+\mathbf{D}-\mathbf{B}_i^--\mathbf{A}$ configurations, then the charge separation is said to occur by a hole transfer (HT) mechanism, since the mixing may be loosely viewed as the propagation of a hole through the bridge.

A simple orbital description of the McConnell version of the superexchange, or TB mechanism [17] is given in Figure 7a for a system comprising two identical chromophores, \mathbf{C} , which are coupled through n identical bridge subunits, \mathbf{B}_i , each subunit contributing a single orbital to the coupling scheme. Within the McConnell treatment, only nearest-neighbor interactions are included and these are denoted by T , for the interaction between the chromophore \mathbf{C} and its nearest bridge subunit and by t , for the interaction between two adjacent bridge subunits.

The McConnell model may be exemplified by considering superexchange-mediated HT in a covalently linked dyad possessing a saturated hydrocarbon bridge (Figure 7b) [14]. In this case, the predominant coupling involves the bridge σ orbitals, rather than the σ^* orbitals, because the former are closer in energy to the donor

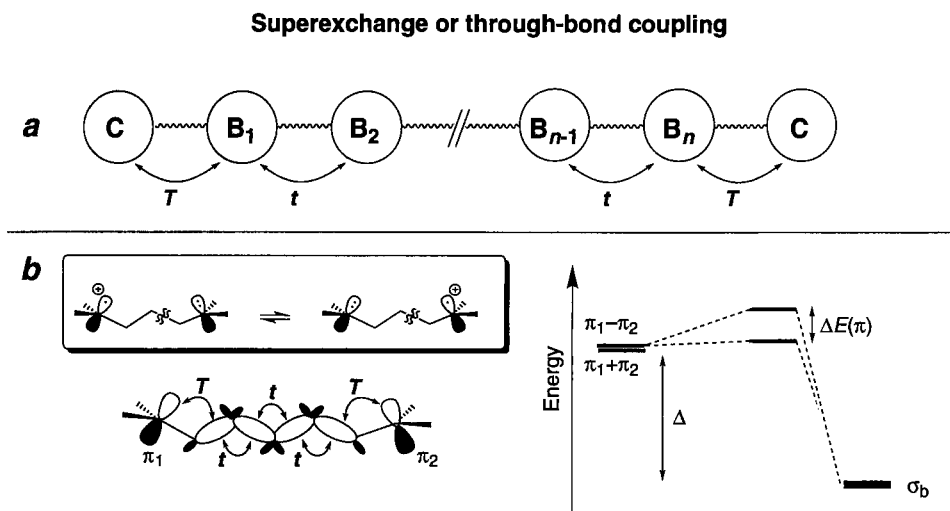


Figure 7. Orbital description of the superexchange (through-bond) mechanism. T is the interaction matrix element between the π orbital and the C–C σ orbital and t is the interaction matrix element between two *geminal* C–C σ orbitals.

level than are the latter [20]. Mixing of the (nearly) degenerate symmetry-adapted pair of π orbitals of the chromophores with the σ manifold of the bridge results in the lifting of the π orbital degeneracy by an amount $\Delta E(\pi)$ which, to second order, is given by [17]

$$\Delta E(\pi) = -2 \left(\frac{T^2}{\Delta} \right) \left(\frac{t}{\Delta} \right)^{n-1} \quad (5)$$

where Δ is the energy gap between the chromophore π orbitals and the bridge σ orbitals prior to their interaction with each other, and n is the number of σ orbitals (= number of bonds in the bridge). This is an intuitive result in that there is a T interaction for the coupling of each chromophore to the bridge and a t/Δ factor for each hop between adjacent bridge sites.

There are two important predictions of the McConnell model. Firstly, the splitting due to TB coupling falls off exponentially with the number of bonds in the relay. Equating Eq. 5 with Eq. 3 (bearing in mind that $\Delta E(\pi) = 2V_{el}$) gives:

$$\beta = 2 \ln \left| \frac{\Delta}{t} \right| \quad (6)$$

Secondly, the net splitting is given by a product of two terms, one giving the coupling of the chromophore to the bridge (T^2/Δ) and the other term, $(t/\Delta)^{n-1}$, giving the propagation of the interaction along the bridge.

It should be noted that there are a number of assumptions and approximations in the derivation of the McConnell equation. These include:

- 1) Restriction to nearest-neighbor interactions only.
- 2) Restriction to a single relay between the chromophores.
- 3) Restriction to only a single orbital on each site.
- 4) The assumption that all bridge sites are identical.
- 5) The assumption that the weak-coupling limit is valid (i.e., $|t/\Delta| \ll 1$ and $|T/\Delta| \ll 1$).

The assumption regarding the equivalence of the various bridge sites is readily relaxed, giving [21–23]

$$\Delta E(\pi) = \frac{-2T_{D,1}T_{n,A}}{\Delta_1} \prod_{i=1}^{n-1} \frac{t_{i,i+1}}{\Delta_{i+1}} \quad (7)$$

where $t_{i,i+1}$ is the coupling between the bridge sites i and $i+1$, $T_{D,1}$ and $T_{n,A}$ are the matrix elements giving the coupling of the chromophores to the ends of the bridge and $\Delta_i = \varepsilon - \varepsilon_i$ is the energy difference between the chromophore levels and the bridge level i . (The “D” and “A” denote “donor” and “acceptor” chromophores, respectively.)

In summary, both through-space and superexchange (or TB) mechanisms predict an exponential diminution of ET rate with distance, but that TB-mediated ET

should display a weaker distance dependence. The important question is, what is the distance dependence (i.e., β) of TB-mediated electron transfer dynamics, and how does the value of β depend on the nature, i.e., the electronic properties, of the bridge? This question may be profitably investigated experimentally using covalently linked **D–B–A** systems. The bridges in these systems, therefore, often serve the dual function of providing both a molecular scaffolding to which the chromophores are affixed at well-defined separations and orientations, and a medium which modulates the ET dynamics by the superexchange mechanism.

1.3 Experimental Investigations of the Superexchange Mechanism for ET Processes

Early studies of the distance dependence of ET dynamics focused on intramolecular electron-spin transfer in radical anions containing two equivalent π -moieties separated by a hydrocarbon bridge (Figure 8). One of these moieties, which houses the unpaired electron, functions as the donor, while the other (neutral) is an acceptor. ESR studies of the radical anions of α,ω -diarylethanes, **Ar**-(CH₂)_{*n*}-**Ar** **1**(*n*) and re-

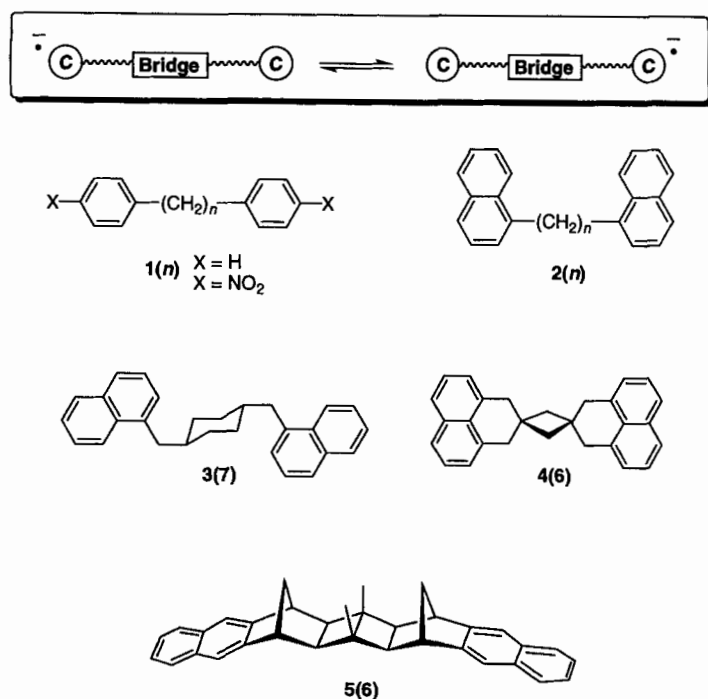


Figure 8. Some covalently linked dyads for investigating thermal charge shift reactions in the radical anions.

lated systems, showed that electron transfer or, more accurately, spin transfer, was rapid on the hyperfine time-scale ($>10^7 \text{ s}^{-1}$) for $n = 1, 2$ but that it is slow for longer chains [24–27]. At the time, these results suggested that for the first two members of the series, **1(1)** and **1(2)**, the chains are short enough to permit ET to occur directly, through space, whereas for the higher members of the series, the chains, although flexible, permit only occasional “contact” between the two terminal aromatic moieties to take place. The possibility that ET in **1(1)** and **1(2)** was occurring through the alkane chain was investigated theoretically by McConnell [17]. Indeed, it was this study which led to the development of his famous superexchange equation, Eq. 5.

McConnell’s calculations led to the conclusion that TB-mediated electron transfer is fast for **1(1)** and **1(2)** but that it falls off exponentially with increasing chain length, by a factor of at least 10 for each additional CH_2 unit. This conclusion was based on the assumption that the ratio $|t/\Delta|$ for **1(*n*)** is about 0.25 (see Eq. 5). Interestingly, this estimate for $|t/\Delta|$ gives a β value of 2.8 \AA^{-1} (Eq. 6) which is comparable to that calculated recently for the TS mechanism [15]. McConnell’s calculations supported the experimental data at the time and they also suggested that the rate of TB-mediated ET should display a strong exponential decay with increasing donor–acceptor separation, becoming insignificant for alkane bridges containing more than two methylene groups. Thus, the observation of intramolecular ET in the series of dinaphthyl radical anions **2(*n*)** for values of n ranging from 3 to 20 was attributed to short-range, through-space ET, permitted by the flexible alkyl chain occasionally adopting appropriate conformations [28].

The belief (based on the McConnell 1961 paper [17]) that TB-mediated ET should be strongly damped with distance prevailed for quite some time, notwithstanding the clearly stated caveat in that paper that the numerical details should not be taken too seriously. It was this widespread belief which caused the conundrum over the observation of extremely rapid (10^7 s^{-1}) intramolecular ET in the radical anion of the semiflexible *trans*-dinaphthyl-cyclohexane system **3(7)** [29]. In the case of **3(7)** and the majority of other structure numbers, the number contained within parentheses refers to the number of C–C sigma bonds in the shortest chain (or relay or bridge) connecting the donor and acceptor chromophores. Thus, for **3(7)** the two naphthalene chromophores are connected by two relays, each of which contains seven C–C bonds. In a few other cases, e.g., **1(*n*)**, the number in parentheses refers to the number of repeating units in the chain (e.g., the number of CH_2 groups in the hydrocarbon chain of **1(*n*)**). The context within which the parenthetical number, corresponding to a particular molecular structure, is used, i.e., number of bonds versus number of repeating units, should become apparent upon inspection of the structural formula. For steric reasons, the cyclohexane ring in **3(7)** is forced to adopt the conformation as depicted; consequently, the two naphthalene rings are about 7 \AA apart (edge-to-edge). In spite of this very large interchromophore distance, the rapid ET rate was tacitly attributed to a TS mechanism, rather than to a TB mechanism occurring through two relays, each comprising seven saturated C–C bonds. A similar TS mechanism was advanced to account for the observation of rapid intramolecular ET in the anion radical of **4(6)** [27].

In contrast, kinetic studies of the dissolving metal reduction (Birch reduction) of

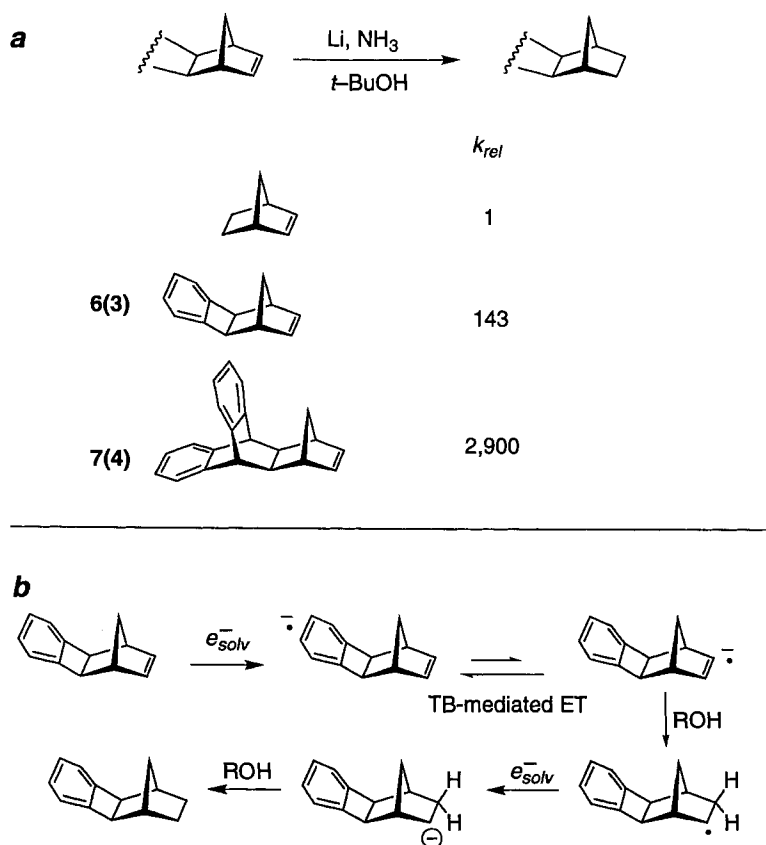


Figure 9. Metal–ammonia reductions of double bonds aided by a through-bond(TB)-mediated ET process from benzene radical anions.

the benzo-bridge-alkene systems, such as **6(3)** and **7(4)** were being interpreted in terms of a TB-mediated ET mechanism (Figure 9). It was found that the alkene double bonds in these systems were undergoing unusually rapid Birch reduction, which is quite out of character because nonconjugated double bonds are practically inert under Birch reduction conditions [30, 31]. For example, the double bond in **7(4)** is reduced some 2900 times more rapidly than the double bond in norbornene. The proposed mechanism involves electron capture by the benzene group followed by intramolecular endergonic ET to the double bond and subsequent protonation of the resulting radical anion of the alkene (Figure 9b). The total rigidity of the norbornylogous bridges prevented the two chromophores from making close contact. Consequently, a TB-mediated ET mechanism, occurring through three bonds in **6(3)** and through four bonds in **7(4)** was proposed [30, 31].

The advantages offered by the rigidity of the norbornylogous bridge was exploited in the ESR and ENDOR studies of ET in the radical anion of the 6-bond

dinaphtho system **5(6)** [32]. In solvents of high-cation-solvating power (e.g., HMPA) rapid ($>10^7 \text{ s}^{-1}$) intramolecular ET was observed. Considering that the two naphthalene groups in **5(6)** are held 7.4 Å apart, it seems inescapable that the rapid ET rate observed in the derived radical anion is due to a TB mechanism. Consequently, the results observed for the radical anions of **3(7)** and **4(6)** were re-interpreted in terms of a TB-mediated ET mechanism [32].

It is quite amazing that the ET rates are so rapid ($>10^7 \text{ s}^{-1}$) in the radical anions of **3–5**, considering that the free energy change, ΔG_{et} , for ET in these systems is zero; consequently, the free energy of activation for the reaction is at its maximum value (this follows from Eq. 2; the nominator in the exponent is equal to λ^2 for a self-exchange process and it is not reduced by the presence of an exergonic ΔG_{et} term).

Calcaterra, Closs and Miller observed rapid intramolecular ET in the radical anions **8–10** in which the chromophores are attached to a rigid steroid bridge (Figure 10) [33]. The edge-to-edge distance between the two chromophores in these molecules is about 11 Å, and they are separated by nine C–C bonds. The radical anions of **7–10** in 2-methyltetrahydrofuran at room temperature were generated by reaction with solvated electrons formed by pulse radiolysis. These studies differ from those discussed above in that the ET processes in **7–10** are exergonic, rather

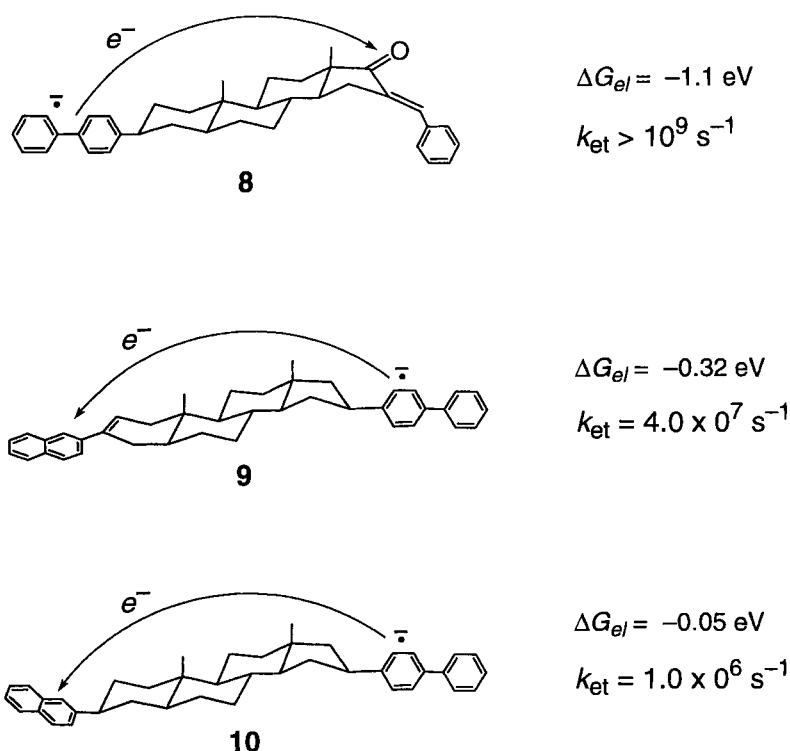
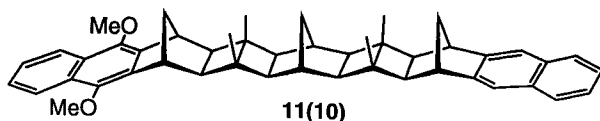


Figure 10. Charge shift reactions instigated by pulse radiolysis [33].

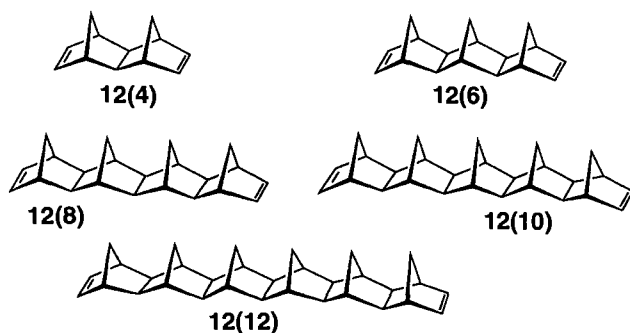
than self-exchange (the direction of ET is shown in Figure 10). The ET rate increases dramatically as the ET reaction becomes more exergonic. Considering the large “through-space” separation between the chromophores in these systems, it is extremely unlikely that the rapid ET is occurring by a TS mechanism. Thus, the steroid bridge must be mediating the ET by a TB coupling mechanism.

Intramolecular hole transfer has also been investigated [34, 35], a spectacular example being that observed using the 10-bond dyad **11(10)** [35]. In this system, the naphthalene (**Np**) and dimethoxynaphthalene (**DMN**) chromophores are rigidly separated, approximately 12 Å apart. Pulse radiolysis of a cyclohexane solution of **11(10)** at room temperature generated a statistical mixture of the two radical cations, $^+\text{Np-B-DMN}$ and Np-B-DMN^+ . Exergonic hole transfer from the **Np** radical cation to **DMN** in this mixture was found to occur on a subnanosecond time scale, thereby confirming that TB-mediated HT is extremely rapid, even over 10 bonds!



The anionic and cationic charge shift reactions discussed above all point to the conclusion that, contrary to earlier belief, superexchange-mediated ET reactions appear to be quite long-range processes, taking place on a (sub)nanosecond time scale over distances exceeding 10 Å. What is the distance dependence of the charge shift rates for these processes? Clearly, the β value must be much smaller than the earlier estimate [17] of c. 2.8 Å^{-1} , otherwise HT in the 4-bond analogue of **11(10)** would be predicted to occur within the unrealistically short time of 10^{-15} s , which is shorter than the period of a molecular vibration.

The first reliable determination of the distance dependence of the magnitude of the electronic coupling for charge shift reactions came from photoelectron spectroscopic (PES) and electron transmission spectroscopic (ETS) studies on the series of polynorbornane dienes **12(n)** (Figure 11) in conjunction with *ab initio* MO calculations. The dienes, **12(n)**, where n represents the number of C–C σ bonds along the side of the bridge, have played a pivotal role in the development of a detailed understanding of the role of TB interactions [14, 15, 18, 20, 36]. Figure 11 summarizes theoretical π -splittings and π^* -splittings ($\Delta E(\pi)$ and $\Delta E(\pi^*)$, respectively) for six molecules in the **12(n)** series, as well as experimentally determined π -ionization potential splittings, $\Delta IP(\pi)$, and π^* -electron affinity splittings, $\Delta EA(\pi^*)$ (from PES and ETS measurements, respectively) for the first two members of the series. The theoretical splittings were obtained from Hartree–Fock/3-21G calculations on the neutral molecules. Overall, excellent agreement is found between the calculated and measured splittings. This is remarkable since the calculations make use of the Koopmans’ theorem approximation [37] (i.e., they neglect orbital relaxation and electron correlation changes accompanying ionization or electron attachment) and employed the relatively modest 3-21G split-valence basis set [38]. Studies of other bichromophoric systems have revealed that splittings calculated using Koopmans’



Molecule	π Splittings (eV)		π^* Splittings (eV)	
	$\Delta IP(\pi)$	$\Delta E(\pi)$	$\Delta EA(\pi^*)$	$\Delta E(\pi^*)$
12(4)	0.87	1.02	0.80	0.91
12(6)	0.32	0.34	0.25	0.18
12(8)	—	0.15	—	0.088
12(10)	—	0.078	—	0.031
12(12)	—	0.04	—	0.010

Figure 11. Splittings for **12(*n*)** from ionization potentials, $\Delta IP(\pi)$, and electron affinities, $\Delta EA(\pi^*)$, together with HF/3-21G Koopmans' theorem splittings, $\Delta E(\pi)$, and $\Delta E(\pi^*)$.

theorem and using the 3-21G basis set are generally in good agreement with those obtained from calculations including relaxation and correlation effects and employing more flexible basis sets [36, 39]. The 3-21G basis set is insufficiently flexible for describing TS interactions occurring over distances exceeding 4 Å, and its success in calculating the net splittings in chromophore–bridge–chromophore systems with the chromophores separated by more than 4 Å is due to the domination of TB interactions.

The splittings in the **12(*n*)** series decay exponentially with increasing number of bridge σ -bonds:

$$\Delta E(\pi) = 5.89 \exp(-0.44n); \quad \beta_{el} = 0.88 \text{ bond}^{-1} \quad (8)$$

and

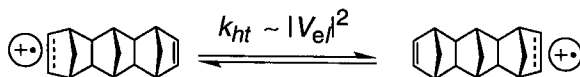
$$\Delta E(\pi^*) = 8.22 \exp(-0.60n); \quad \beta_{el} = 1.2 \text{ bond}^{-1} \quad (9)$$

where the β_{el} values were calculated using Eq. 3. The distance used in these equations is expressed using the number, n , of bonds which connect the two chromophores, rather than angstroms, since this number better represents the TB character of the interaction in these dienes.

The relevance of the PES and ETS studies to HT and ET processes is that the experimental $\Delta IP(\pi)$ splittings obtained for **12(4)** and **12(6)** are, to a good approximation, equal to twice the respective electronic coupling terms, V_{el} , for hole transfer in their radical cations (Figure 12). Likewise, the $\Delta EA(\pi^*)$ values obtained from the ETS measurements on these molecules are approximately equal to twice the respective electronic coupling terms, V_{el} , for electron transfer in their radical anions.

The origin of these relationships may be understood by considering, as an example, the potential energy surface for hole transfer in a diene radical cation, shown in

The vertical $\Delta IP(\pi)$ value for a symmetrical diene is proportional to V_{el} for hole transfer in the cation radical:



- $\Delta IP(\pi) = 2V_{el}$
- $\Delta E(\pi) = 2V_{el}$ (from Koopmans' theorem)

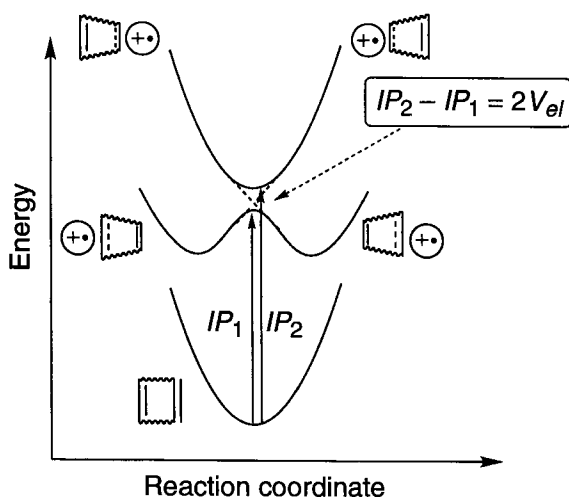


Figure 12. The relationship between the π ionization potential splitting energy in a diene and the electronic coupling element for hole transfer in the corresponding radical cation.

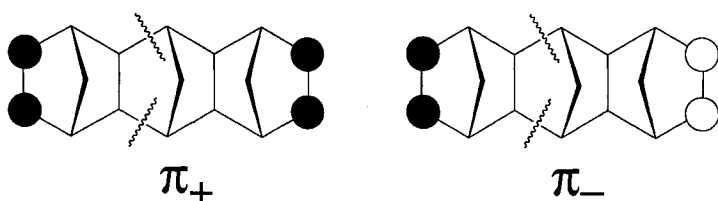


Figure 13. The two symmetry-adapted (through-space) combinations of π orbitals.

Figure 12. It is assumed that the neutral diene has C_{2v} symmetry. The diene radical cation has three π electrons and four π MOs, from which the two lowest energy configurations, namely $\pi_+^2\pi_-$ and $\pi_+\pi_-^2$, may be constructed, where the meaning of π_+ and π_- is explained in Figure 13. These two configurations may be represented simply by specifying the singly occupied π orbital in them, i.e., π_+ or π_- . Which of these two configurations is the ground state depends on the structure of the diene radical cation [15, 18, 40], and is not germane to this discussion.

The upper pair of potential energy curves in Figure 12 represents the adiabatic surfaces for the two π radical cations, e.g. π_+ and π_- . In the case of weak coupling between the two double bonds, the lower adiabatic surface has two minima, each of which corresponds to a distinct charge localized radical cation as indicated. In this case, the ground-state radical cation is nonsymmetrical, having the positive charge localized on one of the double bonds. Interconversion between the degenerate charge localized states takes place via the avoided crossing region which, presumably, has C_{2v} symmetry. In contrast, the higher electronically excited state surface (which would correspond, say to π_+) has a single energy minimum of C_{2v} symmetry. Thus, the charge is completely delocalized in this state, the three π electrons being evenly distributed over both double bonds.

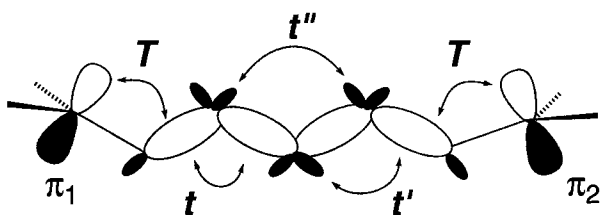
The minimum of the ground-state potential energy hypersurface of the neutral diene lies directly below a point on the avoided crossing seam of the energy hypersurfaces of the two radical cation states that connects all points associated with C_{2v} symmetry. The transitions shown in Figure 12 represent the (Franck–Condon) vertical $IP(\pi)$ values for the formation of the π_+ and π_- radical cation states. The observed splitting energy, $\Delta IP(\pi)$, therefore provides a direct measure of $2V_{el}$ for hole transfer between the two radical cations. Similar reasoning may be used to demonstrate the connection between the experimental $\Delta EA(\pi^*)$ splits and V_{el} for electron transfer in the radical anions of the dienes.

It should be pointed out, however, that the true magnitude of V_{el} for hole transfer is not exactly equal to that determined by PE spectroscopy because the latter value corresponds to the energy difference between the cation states with geometries identical to that of the neutral diene, whereas the actual path for hole transfer will almost certainly traverse a different (and lower energy) region of the avoided crossing seam that is associated with a structure which is slightly different from that of the relaxed neutral species.

The good agreement between the experimental splits and the Koopmans' theorem calculated values suggests that the latter method offers a simple, yet approximate, way of calculating V_{el} for ET and HT processes in a variety of dyads. This proposal has been amply verified [23, 41–46].

Two important conclusions arise from the experimental and computational studies on **12**(*n*). Firstly, the $\Delta E(\pi)$ and $\Delta E(\pi^*)$ splittings for these dienes are large; even for the 12-bond diene, **12**(**12**), $\Delta E(\pi)$ and $\Delta E(\pi^*)$ are 0.04 and 0.01 eV, respectively, notwithstanding the 13.5 Å edge-to-edge distance between the two double bonds in this molecule [47]. Noting that a value of about 3 meV (24 cm⁻¹) for the electronic coupling element V_{el} is sufficient to promote rapid ET [2], the calculated V_{el} values of 20 and 5 meV for HT and ET, respectively, in **12**(**12**) suggest that TB-mediated ET and HT should be extremely rapid over very large distances indeed. These results are entirely in accord with the large experimental ET rates in **8**–**10** and for HT in the radical cation of **11**(**10**).

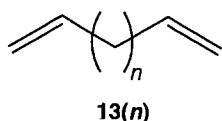
The second conclusion is the weak distance dependence of TB-mediated electronic coupling found for **12**(*n*), compared to that predicted on the basis of a TS mechanism. Thus, $\beta_{el} = 0.8$ and 1.2 bond⁻¹, for π and π^* coupling, respectively, in **12**(*n*), whereas $\beta_{el} = 3.0$ Å⁻¹ for a TS coupling mechanism. Why does the McConnell model predict a much stronger distance dependence behavior for TB-mediated electronic coupling ($\beta_{el} \approx 2.8$ Å⁻¹)? The main reason is the complete neglect of non-nearest-neighbor interactions in the McConnell model which, in fact, are quite large. This may be seen from the HF/3-21G calculated matrix elements for interactions between localized natural bond orbitals (NBOs) [48] in an alkane bridge (Figure 14) [45]. Although the matrix element between two adjacent C–C NBOs, t , is dominant, those which skip over one bond (t') and two bonds (t'') are by no means negligible. Indeed, inclusion of the t' matrix elements in a nonperturbative McConnell treatment of alkane dienes **13**(*n*) leads to a β_{el} value (0.88 bond⁻¹) which is much smaller than that obtained using the standard “nearest-neighbor” McConnell model (1.64 bond⁻¹), but which is still larger than the full Hartree–Fock value of 0.54 bond⁻¹. Upon inclusion of the t'' interactions, the β_{el} value becomes 0.58 bond⁻¹, very close to the Hartree–Fock result [45].



$$T = -1.13 \text{ eV} \quad t = -4.11 \text{ eV}$$

$$t' = 0.80 \text{ eV} \quad t'' = -0.29 \text{ eV}$$

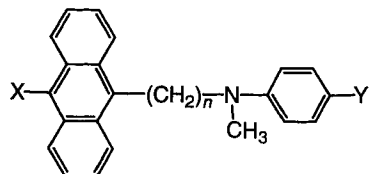
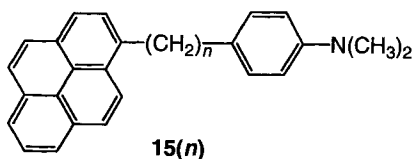
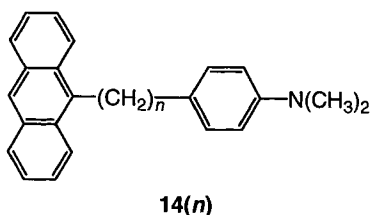
Figure 14. HF/3-21G computed matrix elements for interactions between various natural bond orbitals (NBOs).



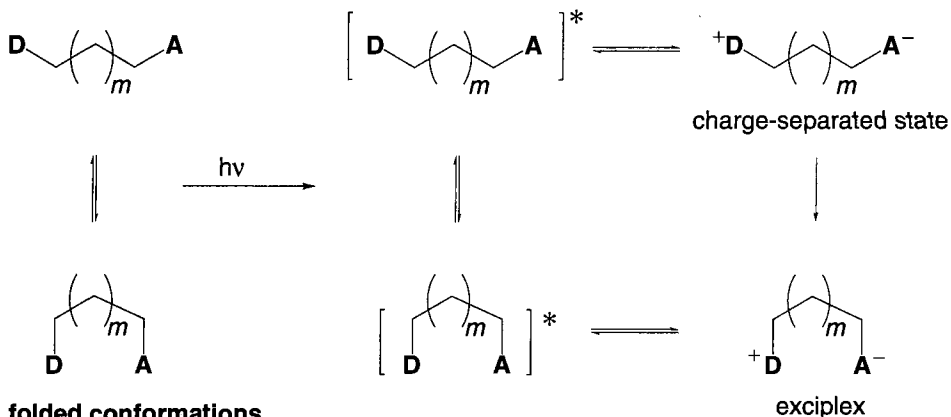
1.4 Examples of TS- and TB-Mediated Photoinduced ET Reactions

Investigations of photoinduced ET reactions in a wide range of covalently linked organic dyads are uncovering important mechanistic insights into charge separation processes. In particular, the photophysics of the dyads **14(n)** [49, 50], **15(n)** [51, 52], and **16(n)** [53–56] have been extensively studied. These systems, on account of the conformational flexibility of the polymethylene chains provide valuable information on the interplay between the dependence of photoinduced ET rates on chain conformation and the dynamics of the interconversion between various conformations of the chain. In these dyads, the aniline group (**An**) is the donor and the locally excited 9-anthracene group (**Anth**) in **14(n)** and **16(n)** and the locally excited 1-pyrenyl moiety (**Pyr**) in **15(n)** are the acceptor groups.

The overall photophysical processes which occur in these types of dyads are shown in Figure 15. Two sets of conformations may be identified in a dyad pos-



- 16(n)** a X = CN, Y = OMe, $n = 1 - 4$
 b X = CN, Y = H, $n = 1 - 4$

extended conformations

$$m = n - 2; \quad (n = \text{number of CH}_2 \text{ groups in the tether})$$

Figure 15. Schematic of photoinduced charge separation in a flexible tethered dyad. The extended and folded conformations are each intended to represent several similar conformations.

sessing a polymethylene chain comprising n CH_2 groups ($m = n - 2$), namely the extended set, in which the donor and acceptor groups are spatially well separated from each other by at least 4 \AA , and the folded set of conformations, in which the donor and acceptor groups may approach more closely to each other and are also able to adopt a face-to-face, sandwich-like disposition. The extended and folded sets are in dynamic equilibrium, although the population of the folded set of conformations diminishes with increasing chain length, on account of entropy factors.

Electronic excitation of either the donor or acceptor of the dyad generates two sets of locally excited states. In principle, the population of the folded set of excited states may be increased but in practice, this likelihood becomes negligible for long chain lengths ($n > 6$) since competing ET and decay processes occur more rapidly than the rate of production of a sandwich conformation from an extended one, which would require rotation about several C–C bonds to achieve.

The extended set of locally excited conformations will produce the charge-separated (CS) set of states, whereas the folded set will generate the exciplex state. Finally, Coulombic-induced molecular folding (harpooning [57]) in the extended set of CS states will lead to increased production of the exciplex state. The dynamic competition between the various processes outlined in Figure 15 depends not only on the chain length and the redox properties of the donor and acceptor groups, but also on solvent polarity.

Thus, for the three-carbon chain dyad **14(3)**, formation of both CS and exciplex states, ${}^-\text{Anth-B-An}^+$, was observed in the polar solvent acetonitrile. In contrast, in the nonpolar solvent 2-methylbutane, only formation of the exciplex state was observed [49, 50]. Presumably, in acetonitrile the CS state is stabilized by solvation

and so the driving force ($-\Delta G_{et}$; Figure 3) for its production is sufficiently high to permit its rapid formation (see Eq. 2). In 2-methylbutane, the driving force for production of the CS state is much weaker, and its rate of formation now becomes too slow to compete effectively with decay of the locally excited states of the extended set of conformations to the ground state.

The photophysics of the **Pyr-B-An** dyads **15**(*n*) also displayed interesting solvent-dependent behavior. In the case of **15**(1), photoinduced ET takes place readily in acetonitrile, to give the CS state, but it does not occur in nonpolar solvents—presumably because the driving force for formation of the CS is not very exergonic. Nevertheless, photoinduced ET is observed to take place for the three-atom chain dyad **15**(3) in polar and nonpolar solvents. In acetonitrile, the extended CS state is formed, whereas the exciplex is formed in *n*-hexane. In contrast to the shorter analogue **15**(1), the ideal, face-to-face sandwich-like orientation between the chromophores is attainable in the exciplex formed from **15**(3). Using the more viscous 2-propanol solvent allowed observation of the CS state, followed by slow formation of the exciplex. Apparently, the viscous solvent “slows” down the bond rotations that convert the CS state into the exciplex [51, 52].

Extensive photophysical studies have been carried out on the 9-anthryl-bridge-aniline dyad series **16**(*n*; X = CN; Y = H or OMe) [53–56]. For shorter members of these series (*n* < 5), rather predictable photoinduced ET behavior is assumed to occur; that is, following local excitation of the **Anth** acceptor, conformational changes in the bridge bring the two chromophores close enough for direct, through-space ET to take place. However, novel photophysical behavior was observed for the two-atom chain systems **16**(2a) and **16**(2b). In these dyads, TB coupling between the **Anth** acceptor LUMO and the **An** HOMO is believed to be strong enough to endow significant charge transfer to the ground state. This belief is supported by X-ray crystal structure data which reveal the conformation of **16**(2a) to possess near-optimal alignment of the **Anth** and **An** π -type orbitals for TB overlap with the central C–C bond of the ethane bridge, as depicted in Figure 16. These molecules may, therefore, be directly excited into the CS state. These experimental results provide additional support for photoinduced ET occurring by a TB-mediated mechanism [56].

There is ample evidence that the formation of excimers and exciplexes in covalently linked, α,ω -diarylalkanes is optimum for a chain length comprising three methylene groups, since this configuration allows a face-to-face sandwich-type structure to be achieved without imposing severe entropic penalties [58, 59]. A two-carbon atom chain is rather too short for optimal exciplex formation, but it facilitates TB mediated ET from an all-*trans* conformation, as shown in Figure 16b.

Investigations of charge transfer absorption bands in the series **17**(*n*) also reveal the importance of the TB coupling mechanism for a two-carbon atom bridge. A charge transfer absorption band, resulting from electron transfer from the dimethoxybenzene donor to the *N*-alkylpyridinium acceptor, was observed for the first two members of the series, **17**(*n*), *n* = 1, 2, but not for higher members, *n* = 3, 4. The comparatively intense CT band observed for **17**(2) was attributed to efficient TB-mediated charge transfer resulting from the molecule adopting the all-*trans* conformation, similar to that depicted for **16**(2a) in Figure 16b [60].

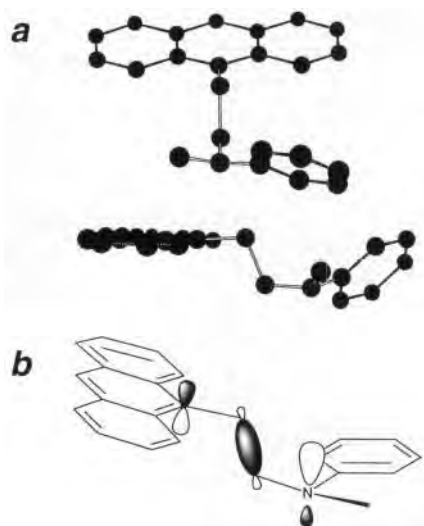
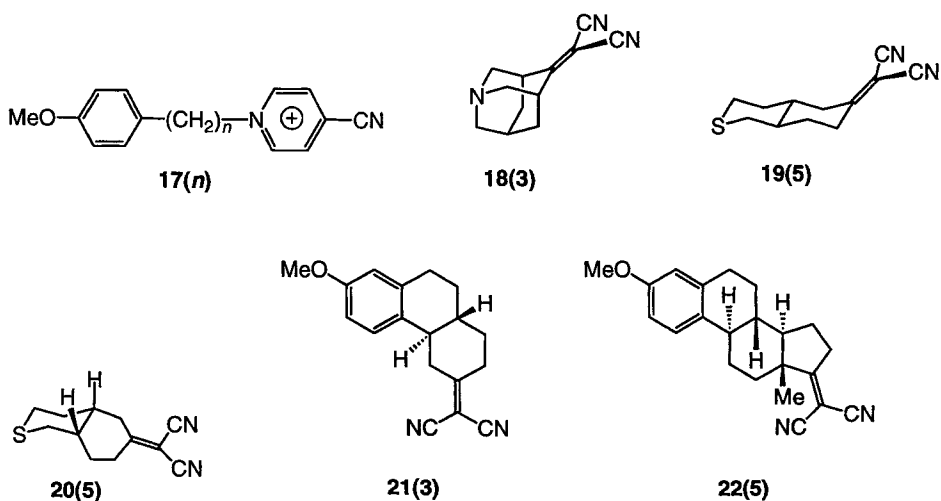


Figure 16. (a) Schematic of the X-ray structure of **16(2a)**, minus the CN and OMe substituents [56]. (b) Schematic showing the all-*trans* orbital overlap between the two chromophores and the central C–C bond of the bridge.

Charge transfer absorption and fluorescence bands were observed in **18(3)** and **19(5)** and related systems, the cause of which was explained in terms of TB interactions extending through three bonds, in the case of the former and through five bonds in the case of the latter [61, 62]. Confirmation of the operation of the TB mechanism in **19(5)** was obtained by the finding that the intensity of the CT absorption band for the *cis*-fused isomer, **20(5)** was more than five times weaker than that for the *trans*-fused isomer **19(5)** [62, 63]. Such behavior is to be expected of a TB mechanism whose strength is known to become progressively weaker with increasing numbers of *cis*-conformations in the chain [18, 19].



1.5 Distance Dependence of TB-Mediated ET in Saturated Hydrocarbon Bridges

The investigation of the distance dependence of ET dynamics using covalently linked dyads possessing flexible polymethylene chains has one advantage, but two potential serious disadvantages. The main advantage is ease of synthesis. The two disadvantages stem from the dynamic flexibility of the polymethylene chain. Firstly, for medium-length bridges there exist at any time conformations in which the donor and acceptor groups lie close enough to interact directly, through-space. The TB mechanism for ET in these systems will therefore compete unfavorably with the TS mechanism. Consequently, one might observe complicated distance dependence behavior for ET rates in such systems, changing from TB to TS for medium chain lengths and back to TB for long chain lengths. Nevertheless, clever strategies have been developed to circumvent this problem, and they will be discussed below. Secondly, it is known that the strength of TB coupling depends sensitively on the conformation of the sigma bonds in the bridge (*vide infra*) [18, 19]. Since polymethylene chains display a myriad of different conformations in solution, it follows that the ET rate obtained for any particular flexible-chain dyad will be averaged over all the possible conformations, making any interpretation in terms of TB coupling difficult.

Because of these considerations, most investigations of distance and orientation dependence of ET dynamics have been carried out using rigid bridges. It is also helpful if the **D–B–A** dyads possess symmetry. This facilitates the analysis of the electronic coupling between the chromophores and the bridge, as well as enabling one to explore the effect of orbital symmetry on ET dynamics.

As discussed above, the first study of the distance dependence of electronic coupling associated with ET and HT applied PES, ETS and Koopmans' theorem calculations to the rigid, symmetrical polynorbornane dienes **12(n)**, from which β_{el} values of 0.88 and 1.2 bond^{-1} were found for HT in the radical cations and ET in the radical anions, respectively. Although the electronic coupling could be calculated for a broad range of bridge lengths (up to 16 bonds), only the first two members of the series could be studied experimentally. It was clearly imperative to obtain an experimental determination of the distance dependence of ET rates based on more than two distances!

The breakthrough came with the design and successful synthesis of the dyads **23(n)** (Figure 17) [64]. These dyads, like the series **12(n)**, are based on the rigid norbornylogous bridge whose length ranges from four bonds (4.6 Å, edge-to-edge) to 13 bonds (14.2 Å). The **DMN** donor and dicyanovinyl (**DCV**) acceptor are well-suited for studying both photoinduced charge separation in the neutral systems and thermal charge shift ET in the derived anion radicals.

There are two points that should be borne in mind in the following discussion. Firstly, β values will generally be given in units of bond^{-1} , rather than in \AA^{-1} , because it seems more logical to do so when addressing the distance dependence of electronic coupling through bonds, rather than through space. The two units are simply related, however, by dividing the number of bonds in a particular bridge by

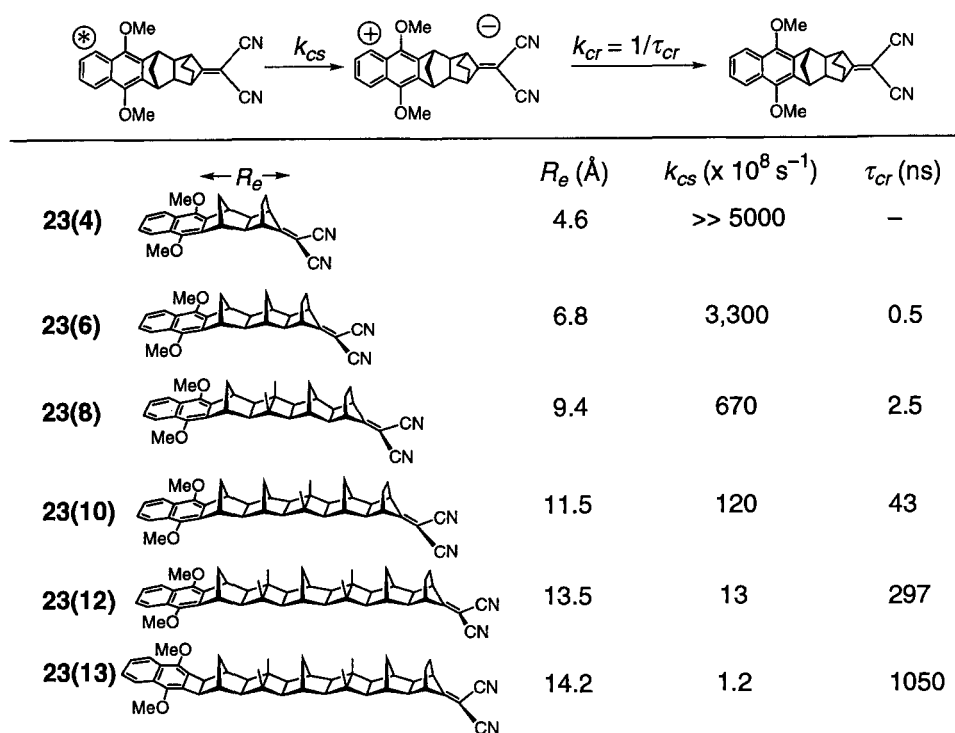


Figure 17. Rate data for photoinduced charge separation in the dyads **23(n)**. Charge separation rates, k_{cs} , were measured in THF and charge recombination lifetimes, τ_{cr} , in 1,4-dioxane [8, 66].

the edge-to-edge distance between the points of attachment of the chromophores to the bridge [47]. Secondly, as mentioned earlier, experimentally determined damping factors which have been derived from distance dependence behavior of ET rates and which have not been corrected for the distance dependence of Franck–Condon factors are denoted by β , whereas those damping factors which have been so corrected and refer, therefore, to the distance dependence of the electronic coupling element, V_{el} , are denoted by β_{el} .

Photoinduced charge separation in **23(n)** involves initial formation of the locally excited DMN chromophore and subsequent charge separation to form the CS state $^+\text{DMN-DCV}^-$ (Figure 18). The photoinduced charge separation rates, k_{cs} , for **23(n)** in THF were found to be extremely rapid, even for the 13-bond system (Figure 17), and they were fairly insensitive to solvent polarity, provided the charge separation process remained exergonic [65, 66]. For example, the photoinduced charge separation rate for **23(8)** increased by a factor of only 1.5, upon changing the solvent from cyclohexane (dielectric constant, $\epsilon_s = 2.02$) to acetonitrile ($\epsilon_s = 37.5$) [67].

That charge separation to form $^+\text{DMN-B-DCV}^-$ had actually occurred, following flash photolysis of the dyads **23(n)**, was unequivocally demonstrated using

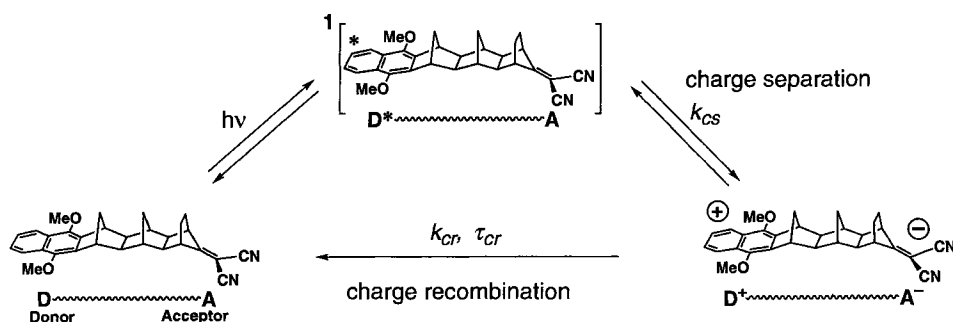


Figure 18. A reaction schematic of the processes occurring following photon absorption by a dyad.

time-resolved microwave conductivity which provides a good estimate of the dipole moment, μ^* , of the product state [68]. The very large experimental values of μ^* for **22(n)** and their near-perfect agreement with the predicted values, μ , based on a point charge model (Figure 19) are entirely consistent with the formation of the giant dipolar states $^+\text{DMN-B-DCV}^-$ [8, 69, 70].

Having thereby established that we were indeed measuring rates of charge separation, the distance dependence of the ET dynamics in **23(n)** could be determined. Reasonable exponential fits were obtained for the charge separation rates as a function of the number of bridge bonds in various solvents. The phenomenological damping factor β was found to lie in the range [66]

$$\beta = 0.92 - 1.25 \text{ bond}^{-1}, \text{ or } 0.82 - 1.11 \text{ \AA}^{-1} \quad (10)$$

depending on the solvent. Presumably, the slight solvent dependence of β is due to the variation of the distance dependence of solvent reorganization energy with solvent.

This study, together with other experiments on **23(n)** (vide infra) provided the first definitive experimental evidence for the exponential distance dependence of long-range ET processes which was predicted on the basis of an exponential decay behavior of the electronic coupling element, V_{el} , with increasing donor–acceptor separation (Eq. 3).

The β values for photoinduced charge separation in **23(n)** (Eq. 10) are gratifyingly similar in magnitude to those predicted for hole transfer ($\beta_{el} = 0.88 \text{ bond}^{-1}$) and electron transfer ($\beta_{el} = 1.2 \text{ bond}^{-1}$) in the respective radical cations and anions of the dienes **12(n)** (vide supra), and lends strong support to the assertion that the extremely rapid rates of photoinduced ET observed in **23(n)** are the result of a superexchange mechanism mediated by the norbornylogous bridge.

An additional, elegant method of confirming the operation of TB-mediated ET in **23(n)** is to utilize one of the most important properties of TB interactions, namely the all-*trans* rule. This rule states that the magnitude of TB coupling depends on the configuration of the sigma-bridge and is maximized for an all-*trans* configuration

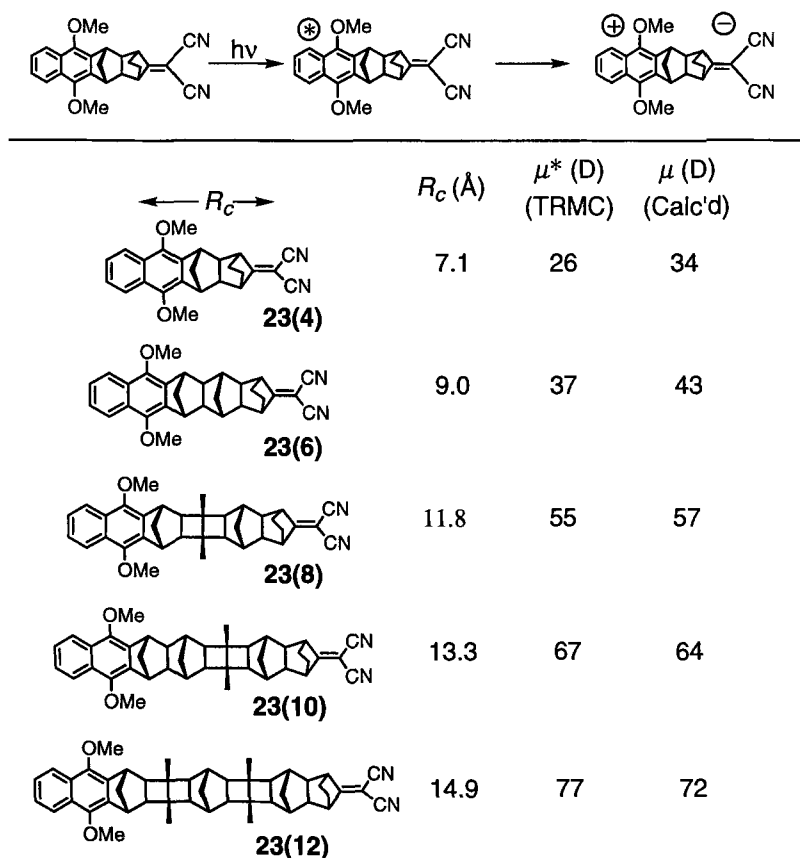


Figure 19. Dipole moments, μ^* , of the CS states of **23(n)** measured in benzene by time-resolved microwave conductivity (that for **23(4)** was measured in cyclohexane). The calculated values, μ , are based on a point charge model [8].

and becomes progressively weaker with an increasing number of *cis* or *gauche* “kinks” in the bridge (Figure 20a) [18, 19].

If the TB coupling mechanism were mediating the photoinduced ET processes observed for **23(n)**, then the rates of these processes should be modulated by changes in the configuration of the norbornylogous bridge, in accordance with the all-*trans* rule. This was tested using “kinked” systems, such as **24(8)** which possesses two *cisoid* arrangements of bridge bonds (Figure 20b). The photoinduced ET rate for the all-*trans* system **23(8)** was found to be faster than the “kinked” molecule **24(8)** by as much as an order of magnitude (Figure 20b), thereby confirming the operation of TB-mediated ET in the **23(n)**–**24(n)** series [71]. The modulation of ET dynamics by TB-mediated coupling in accordance with the all-*trans* rule has subsequently been used to interpret ET rate data for rigid, covalently linked systems containing porphyrin and quinone chromophores [72].

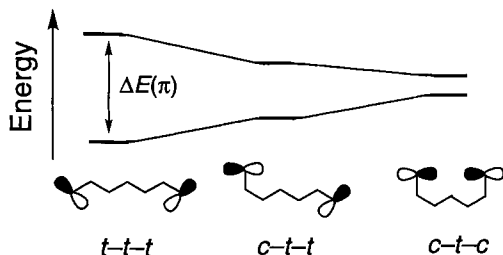
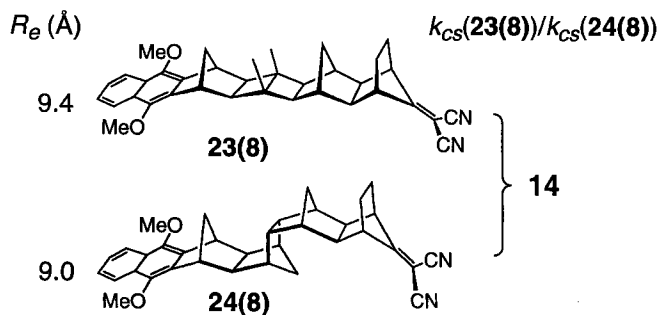
a The *all-trans* rule of TB coupling:**b** Experimental verification

Figure 20. (a) The *all-trans* rule of through-bond coupling; the magnitude of $\Delta E(\pi)$ decreases with increasing number of *cisoid* conformations in the bridge. (b) Ratio of the rates of photoinduced ET for **23(8)** and **24(8)** measured in acetonitrile [71].

It is amazing just how efficacious the TB mechanism can be in promoting ET. Thus, even for the 12-bond system, in which the DMN and DCV chromophores are 13.5 Å apart, photoinduced ET takes place on a nanosecond time scale with an efficiency approaching that found in the photosynthetic reaction center. Given the remarkable ability of the norbornylogous bridge and other saturated bridges [9] to promote ET over large distances, it is tempting to regard such bridges as molecular wires. However, it would be erroneous to do so, for reasons that will be given later.

The lifetimes, τ_{cr} , of the CS states, ${}^+\text{DMN-B-DCV}^-$ for direct charge recombination to the corresponding ground states markedly increase with increasing bridge length as, for example, revealed by the lifetime data for dioxane solvent (Figure 17). For a given bridge, τ_{cr} is significantly greater than the lifetime, τ_{cs} ($= 1/k_{cs}$) for charge separation, and this is mainly a consequence of the charge recombination reaction lying well into the Marcus inverted region [3, 73]. The driving force, $-\Delta G_{cs}$ for photoinduced charge separation in **23(n)** is about 1.0 eV in polar solvents, and is

almost as large as the estimated total reorganization energy for the process [66]. The charge separation reaction therefore occurs under near barrierless conditions (Eq. 2). In contrast, the driving force for the charge recombination process is substantially larger than the associated reorganization energy. Consequently, within the context of classical theory (Eq. 2), charge recombination in **23**(*n*) is associated with an activation barrier and this will slow it down, compared to the charge separation reaction.

The charge recombination rates for **23**(*n*) followed exponential decays with β values lying in the range [8, 35, 70]

$$\beta = 0.86 - 1.11 \text{ bond}^{-1}, \text{ or } 0.77 - 0.99 \text{ \AA}^{-1} \quad (11)$$

These values are similar, but slightly smaller than those observed for the charge separation reaction (Eq. 10). Clearly, the charge recombination process is also taking place by a TB-mediated mechanism in these dyads.

This study of charge recombination in the CS states of **23**(*n*) represented the first systematic measurement of the distance dependence of ET rates in the Marcus inverted region. The key conclusion from this study was the finding that the distance dependence of ET rates in the Marcus inverted region is similar to that in the normal region; that is, the β values are similar (cf. Eqs. 10 and 11).

The distance dependence behavior of the charge recombination (CR) rates for **23**(*n*) was found to be somewhat idiosyncratic in low-polarity solvents. Whereas a good exponential decay was found for the CR rates for all members of the series **23**(*n*) in dioxane (Figures 17 and 21), the CR rate reached a plateau and actually decreased for $n > 6$ in alkanes and for $n > 10$ in benzene (Figure 21).

The explanation for this phenomenon is the establishment of an extra decay channel for charge recombination; in addition to the normal CR process, k_{cr} , (upper right box of Figure 21) leading directly to the ground state, competing back electron transfer (BET) occurs to give the locally excited state, $^*\text{D-B-DCV}^-$ (k_{bet}) for the longer systems in nonpolar solvents. The locally excited state either decays to the ground state (k_d) or returns to the CS state (k_{cs}). The observation of delayed fluorescence for the $n > 6$ compounds in alkane solvents confirmed this mechanism [74]. This BET dominates the overall normal decay kinetics of the CS state for longer members of the series **23**(*n*) in nonpolar solvents because of the gradual increase in the level of the CS states resulting from the diminishing energy of Coulombic attraction between the charged centers, as shown for benzene solvent in Figure 22. The lifetimes of the CS states of **23**(*n*) for $n = 4$ –10, increase exponentially with increasing n , and no BET occurs because these states lie energetically too far below that of the locally excited state to be of importance. However, the CS state of **23**(12) is almost isoenergetic with $^*\text{DMN-B-DCV}$, and the dominant decay mode is BET followed by delayed fluorescence [70, 74]. Incidentally, the observation of the onset of delayed fluorescence in a system by altering the solvent polarity reveals the energy of the CS state since it must be very close to the energy of the locally excited state which may be easily and accurately determined.

Fluorescence spectra of the dyads **23**(*n*) revealed the presence of discrete charge transfer emission bands for bridge lengths up to 10 sigma bonds [75]. These bands

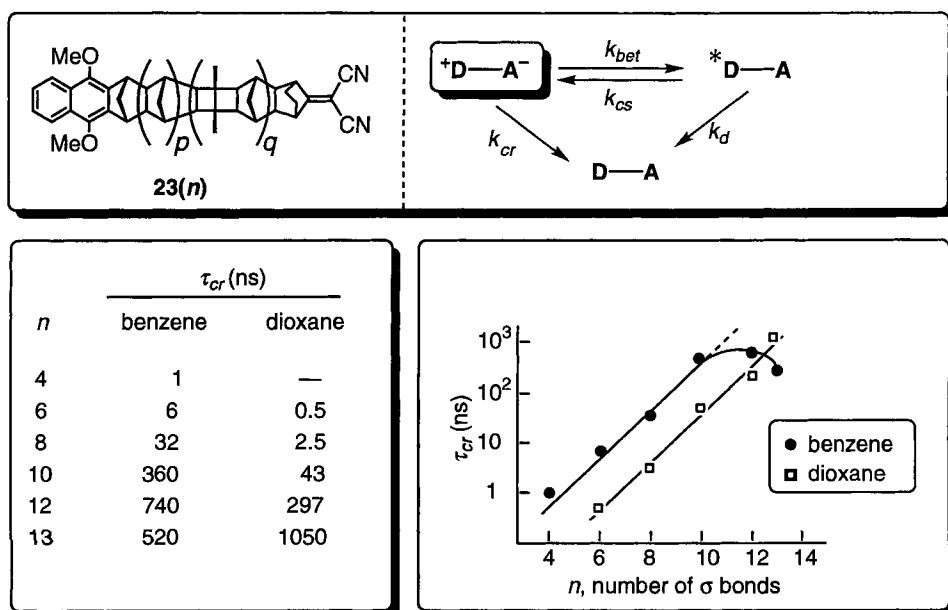


Figure 21. Dependence of the lifetime of the CS state of **23(n)** on the number of intervening σ bonds for benzene and dioxane solvents. The straight lines drawn through the data (extended as a dashed line for benzene) correspond to an exponential dependence of the charge recombination lifetime, τ_{cr} on n [74]. Note that the experimentally determined charge recombination lifetime, τ_{cr} , is *not* necessarily equal to $1/k_{cr}$, because it also includes a contribution from the lifetime of the BET process ($1/k_{bet}$).

enable the calculation of the electronic coupling element, V_{el} for charge recombination from the CS state to the ground state, since the radiative transition probability is related to V_{el} . The magnitude of V_{el} for the CR process in *n*-butylether (Figure 23) was found to decrease exponentially with increasing number of intervening bonds, from 370 cm^{-1} for **23(4)** to 17.6 cm^{-1} for **23(10)**. The damping factor, β_{el} for the decay of the electronic coupling element is

$$\beta_{el} = 1.02 \text{ bond}^{-1}, \text{ or } 0.91 \text{ \AA}^{-1} \quad (12)$$

which is remarkably similar to the β values found for charge separation and charge recombination, viz. Eqs. 10 and 11. Furthermore, the CR rate for **23(n)** was found to be proportional to $|V_{el}|^2$, thus providing experimental verification of the golden rule relationship, Eq. 1 [75].

Thermal charge shift intramolecular ET in the radical anions of **23(n)** (Figure 24a) using pulse radiolysis was found to be very rapid, $>10^9 \text{ s}^{-1}$ for all molecules [76]. Although direct measurements of the ET rate constants could not be obtained, optical electron transfer bands were observed in the visible–near–infrared absorp-

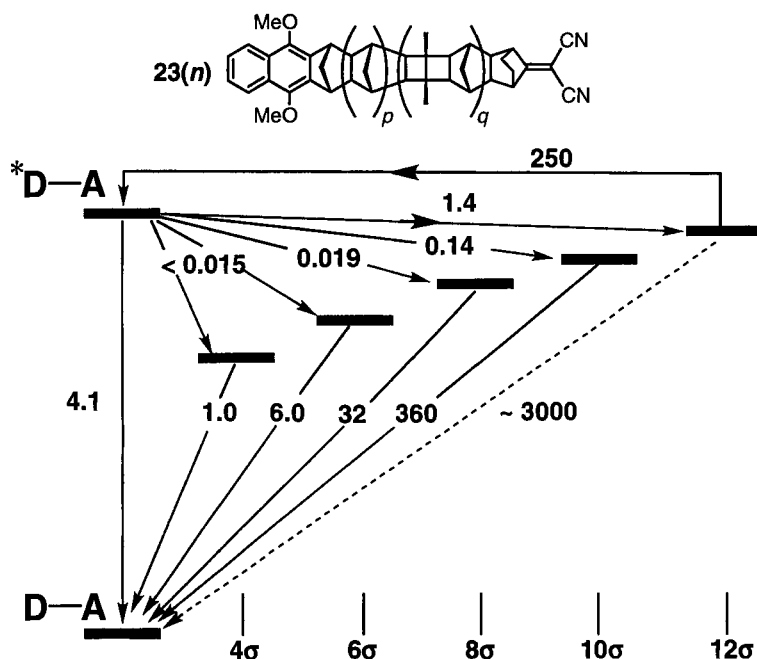


Figure 22. An ergodynamic representation of the changes occurring in the energy level of the CS states of **23(n)** as the number, n , of intervening σ bonds increases in a nonpolar solvent, together with the resulting changes in the ET kinetics between the CS state and the locally excited donor and ground states shown on the extreme left. The diagram shows how indirect charge recombination, by back ET, to regenerate the locally excited donor can eventually dominate the overall decay kinetics for long distances due to diminishing energy of Coulombic attraction between the charged centers. The lifetimes shown were measured in benzene solvent and are given in ns [74].

tion spectra of the radical anions of **23(4)**, **23(8)**, and **3(8)** (Figure 24b). These bands corresponded to optically induced ET from the DCV^- radical anion to **DMN** (Figure 24a). Analysis of these bands using Hush theory [77, 78] led to estimates of the magnitude of the electronic coupling V_{el} for the charge shift reaction (Figure 24c). These limited data give a β_{el} value of:

$$\beta_{el} = 0.84 \text{ bond}^{-1}, \text{ or } 0.75 \text{ \AA}^{-1} \quad (13)$$

The large values of V_{el} imply that the thermal charge shift ET reactions in the radical anions of **23(n)** are actually occurring adiabatically rather than non-adiabatically.

It is interesting to note that the electronic coupling elements, V_{el} are much larger for the charge shift ET reactions in the anion radicals of **23(n)** (Figure 24c) than for CR in the CS states in the respective systems (Figure 23), notwithstanding the comparable β_{el} values for the two reactions. For example, for **23(8)**, V_{el} is six times

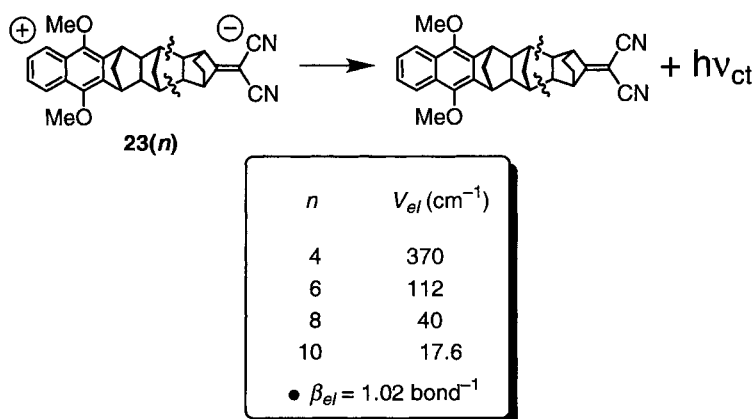


Figure 23. Values of the electronic coupling elements, V_{el} , calculated from charge transfer fluorescence data for **23**(n) in *n*-butylether [75].

larger for charge shift ET than for CR. This difference in the V_{el} values is not surprising, considering that different active orbitals are involved in the two reactions.

The final investigation of the distance dependence of ET dynamics in norbornyl-ogous bridged systems involved photoinduced charge shift ET in **25**(4) and **25**(6) which possess the *N*-methylpyridinium acceptor (Figure 25) [79]. Local excitation of the DMN donor results in charge shift to form the distonic radical cation, e.g., **26**(4) from **25**(4). From the ET rates for the two dyads, an approximate damping factor of

$$\beta = 0.88 \text{ bond}^{-1}, \text{ or } 0.77 \text{ \AA}^{-1} \quad (14)$$

was obtained.

Summarizing the results for **23**(n)–**25**(n), the experimentally determined β values for different types of ET reactions (e.g., photoinduced charge separation, thermal charge shift ET, optical ET, etc.) having different driving forces, and occurring in both the Marcus normal and inverted regions, all lie within the rather narrow range of

$$\beta \approx 0.84 - 1.2 \text{ bond}^{-1} \quad (15)$$

(Eqs. 10–14) with the majority lying within 0.85 – 0.95 bond^{-1} . The near-constancy of β in these studies strongly indicates that its value reflects the distance dependence of the magnitude of TB coupling in the norbornyl-ogous bridge, a conclusion which receives support from the PES, ETS, and computational studies on **12**(n) (Eqs. 8 and 9). Thus, these results point to the overwhelming conclusion that TB-mediated ET occurs in **23**(n)–**25**(n) with a β value of c. 0.9 bond^{-1} .

Does the magnitude of β depend on the type of hydrocarbon bridge? Several important studies have provided an answer to this question. Through-bond coupling

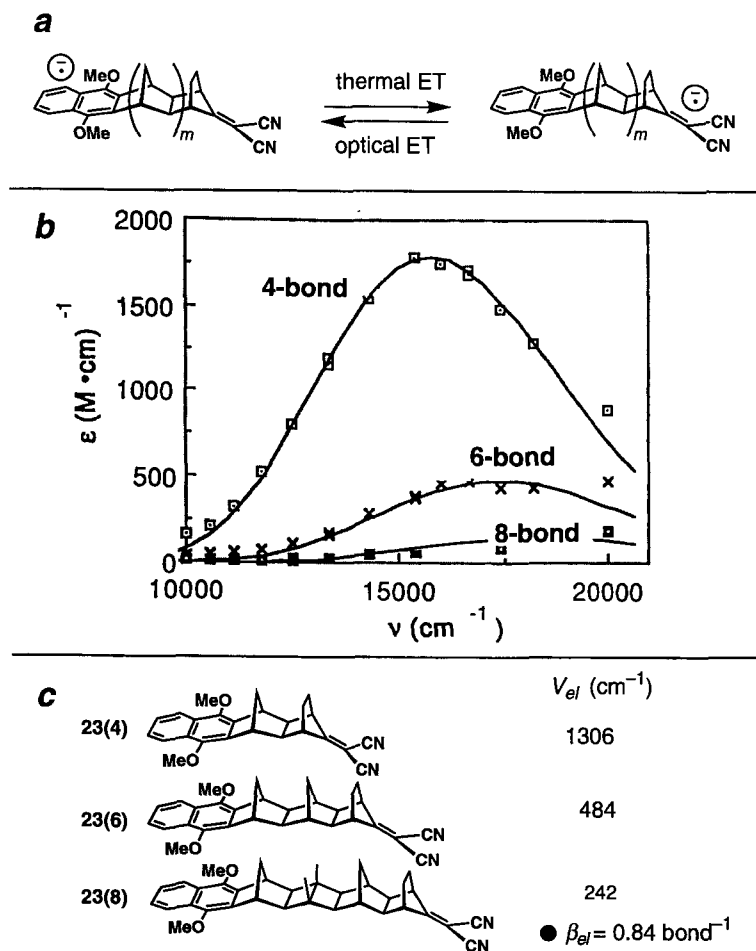



Figure 24. (a) Thermal ET occurs exergonically from DMN to DCV. Optical ET occurs in the opposite direction. (b) Optical electron transfer bands for the radical anions of **23**(*n*) in THF. (c) Values of the electronic coupling elements, V_{el} , were calculated from these bands using the following estimates of the reorganization energies: internal reorganization energy $\lambda_i = 0.55$ eV for all three dyads, and solvent reorganization energy $\lambda_s = 0.47$, 0.66 and 0.79 eV for **23**(4), **23**(6) and **23**(8), respectively [76].

in fused cyclohexane bridges has been investigated by Closs, Miller and colleagues [9, 34, 80]. This group measured thermal intramolecular charge shift ET rates in radical anions generated by pulse radiolysis, representative of which are **27**–**30** and **10**(**10**), in which the naphthalene acceptor and biphenyl radical anion donor are separated by 4–7 and 10 bonds, respectively (Figure 26; the through-bond count (in parentheses) is determined using the shortest path connecting the two chromophores). The distance dependence of the measured ET rates gave a poor fit to an



26(4)

25(6)

Naph  Biph
27(4)



29(6)

30(7)

10(10)

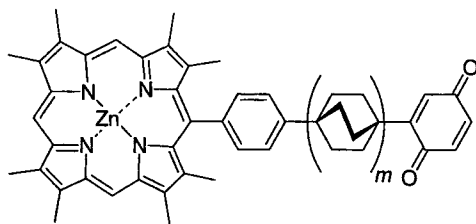
$$\beta = 0.90 \text{ bond}^{-1}, \text{ or } 0.80 \text{ \AA}^{-1} \quad (16)$$

Photoinduced ET in the dyads **31**(*n*), possessing porphyrin and quinone chromophores covalently linked to an oligo-bicyclo[2.2.2]octane bridge was investigated on the grounds that these systems were useful mimics of the photosynthetic reaction centre and that, therefore, the distance dependence of ET rates in **31**(*n*) should provide useful mechanistic information for interpreting the ET dynamics taking place in the photosynthetic reaction center [81–83]. The distance dependence of the ET rate, from the locally excited porphyrin donor to the quinone acceptor, gave a β value of:

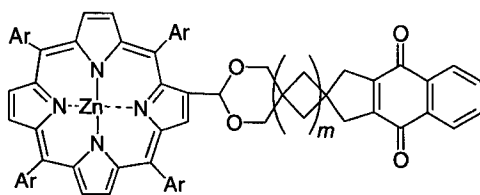
$$\beta = 1.4 \text{ bond}^{-1}, \text{ or } 1.2 \text{ \AA}^{-1} \quad (17)$$

This is a larger value than those reported from other studies (Eqs. 10–16), and may reflect a significant contribution from the distance dependence of the Franck–Condon factor in the form of the solvent reorganization energy term. This is certainly plausible since the rate data were determined in a polar solvent (butyronitrile) and the solvent reorganization energy increases with increasing solvent polarity.

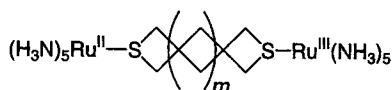
Electron transfer mediated by an oligo-spirocyclobutane bridge has been studied in two systems, **32**(*n*) and **33**(*n*). Photoinduced charge separation in **32**(*n*) is asso-



31(*n*) $n = 4m + 1$ ($m = 0, 1, 2$)



32(*n*) $n = 2m + 6$ ($m = 0, 1, 2, 3$)



33(*n*) $n = 2m + 4$ ($m = 0, 1, 2$)

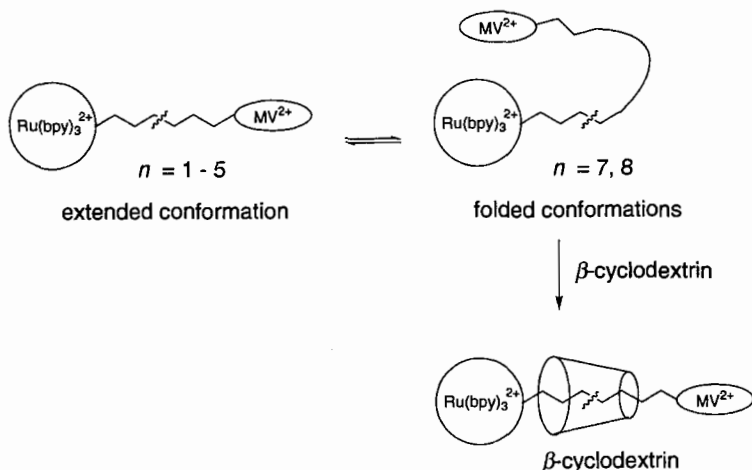
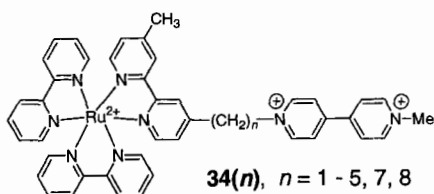


Figure 27. Polymethylene-linked dyads. For longer members of the series, β -cyclodextrin was added to ensure the chain was kept in the extended conformation [86].

ciated with a β value of [84]:

$$\beta = 1.03 \text{ bond}^{-1}, \text{ or } 0.92 \text{ \AA}^{-1} \quad (18)$$

The mixed-valence complexes **33(n)** displayed intervalence absorption bands from which the electronic coupling elements, V_{el} were calculated using Hush theory [77, 78]. The distance dependence of V_{el} was found to be [85]:

$$\beta = 0.88 \text{ bond}^{-1}, \text{ or } 0.78 \text{ \AA}^{-1} \quad (19)$$

Recent studies have shed light on the distance dependence of the rates of ET reactions proceeding through polymethylene chains. The rates of photoinduced forward and thermal charge recombination ET in the series of dyads **34(n)** (Figure 27) have been measured for various chain lengths, $n = 1-5, 7$, and 8 [86].

The rate of photoinduced ET, from the locally excited MLCT state of the Ru(bpy)_3^{2+} donor to the viologen acceptor in acetonitrile was found to decay exponentially with increasing chain length, from $n = 1-5$ and becomes roughly constant for $n = 5, 7$, and 8 . These results were interpreted in terms of TB-mediated ET

for dyads with short chain lengths ($n < 6$), for which the dyads exist predominantly in the extended conformation.

For longer chain lengths ($n > 6$), a through-solvent mechanism for ET was proposed and was assumed to occur in the various folded conformations of the dyads which are present in the longer chain systems (Figure 27). Support for this conjecture was obtained by encapsulation of the polymethylene chain by β -cyclodextrin which has the effect of “straightening” out the folded conformations (Figure 27). The photoinduced ET rates for the $n = 7, 8$ dyads determined in the presence of β -cyclodextrin now obeyed the same exponential decay with increasing chain length as the shorter chain members. Approximate values for the electronic coupling element were calculated from the rate data and estimates of the solvent reorganization energy. The distance dependence of V_{el} was found to be:

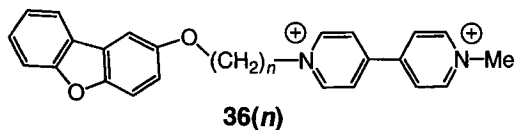
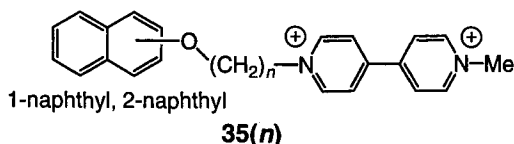
$$\beta_{el} = 1.32 \text{ bond}^{-1}, \text{ or } 1.18 \text{ \AA}^{-1} \quad (20)$$

The distance dependence for the reverse process, thermal charge recombination back to the ground state of **34**(n), which occurs in the Marcus inverted region, was also determined and was found to be similar to that for the forward photoinduced ET reaction:

$$\beta_{el} = 1.18 \text{ bond}^{-1}, \text{ or } 1.06 \text{ \AA}^{-1} \quad (21)$$

A similar study has been carried out on the series of polymethylene dyads **35**(n) and **36**(n) in which $n = 3\text{--}12$ [87]. The rate data fitted an exponential decay with increasing values of n , provided that the experiments were carried out in the presence of β -cyclodextrin for dyads with $n > 7$ (vide supra). The damping factor was calculated to be:

$$\beta_{el} = 1.09 \text{ bond}^{-1}, \text{ or } 0.97 \text{ \AA}^{-1} \quad (22)$$



In summary, the experimentally determined β values listed above in Eqs. 10–22 are, with two exceptions (Eqs. 17 and 20), reasonably constant, which is remark-

able, considering they have been measured for several different kinds of saturated hydrocarbon bridges, using various ET and HT processes occurring in both the Marcus normal and inverted regions. From these data, the average value of β for superexchange-mediated ET in saturated hydrocarbon bridges is:

$$\beta_{av} = 0.95 \pm 0.10 \text{ bond}^{-1} \quad (23)$$

This value, which contains a contribution from the distance dependence of the Franck–Condon factor, as well as that from electronic coupling, is only a rough indicator of the effectiveness of electronic coupling through saturated hydrocarbon bridges.

The approximate constancy of β for saturated hydrocarbon bridges does not imply similar magnitudes for V_{el} for different bridges of the same length, however. Consider, for example, the V_{el} values for charge recombination in the CS states of **23(n)** (Figure 23) and the charge shift reaction in the radical anions of the same series of dyads (Figure 24). For a given bridge length, the magnitude of V_{el} is between three and six times larger for the charge shift process than for the CR reaction. This difference is qualitatively understandable from a consideration of the simple McConnell model (Eq. 5); the magnitude of the electronic coupling depends on the ratio (T/Δ) and the magnitude of this ratio depends on the electronic properties of the donor and the type of active orbital involved in the ET or HT process (i.e., HOMO (highest occupied molecular orbital) or LUMO (lowest unoccupied molecular orbital)). For the CR process (Figure 23), the DMN HOMO is the active donor orbital, whereas for the charge shift reaction the DMN LUMO is the active donor orbital. Since the DMN HOMO and LUMO have different magnitudes of atomic orbital coefficients and they are also associated with different values of Δ , it follows that (T/Δ) will have different values for the two ET processes.

The McConnell expression (Eq. 5) also explains the relative insensitivity of β to the type of ET or HT process and to variation in redox properties of the chromophores. The distance dependence, β , of the electronic coupling is, within the weak coupling approximation implied by Eq. 5, governed by the ratio $|\Delta/t|$ in Eq. 6. The sensitivity of β to variation in the magnitude of Δ is given by Eq. 24:

$$\frac{\partial \beta}{\partial \Delta} = \frac{2}{\Delta} \quad (24)$$

For saturated hydrocarbon bridges, the energy gap, Δ between the π and π^* manifolds of the chromophores and the respective σ and σ^* manifolds of the bridge is large, of the order of several eV. Consequently, the term given on the right-hand side of Eq. 24 is small and so, therefore, will be the variation of β with Δ . However, this analysis is crude because of the neglect of non-nearest-neighbor interactions in the McConnell model. In the following two sections, it will be seen that the magnitudes of both β_{el} and V_{el} may, in fact, be modulated by the structure of the saturated hydrocarbon bridge as a result of interference effects.

1.6 A Simple Model for Dissecting TB Coupling in Bridges

The excellent agreement between the HF/3-21G Koopmans' theorem calculations of the $\Delta E(\pi)$ and $\Delta E(\pi^*)$ splitting energies with those determined experimentally (see Figure 11) offers a simple computational method for estimating the magnitude of the electronic coupling element for HT and ET in a variety of systems [14]. Notwithstanding this success, there is a need for gaining insight into which specific interactions are responsible for the couplings, and how they depend on the structure of the bridge. Several elegant treatments are available which provide such insight [14, 21–23, 36, 39, 42–45, 88–101]. Herein, a method, originally developed by Heilbronner and Schmelzer [40] is described which relies on the adoption of a localized orbital representation.

The groups of Paddon-Row, Jordan and coworkers [14, 36, 45, 96–101], Newton and coworkers [23, 43, 44] and Miller and coworkers [42, 92–94] have made use of the natural bond orbitals (NBOs) of Weinhold and coworkers [48]. These are a set of orthogonalized localized orbitals that conform closely to chemists' intuitive orbitals (core, two-center bonding and antibonding, lone pair, and Rydberg orbitals).

In general, Hartree–Fock calculations on molecules give molecular orbitals (MOs) that extend (i.e., are delocalized) over the entire molecular framework. These so-called canonical MOs (CMOs) may be transformed into localized orbitals, such as NBOs. Technically, the Fock matrix in the basis of CMOs (F^{CMO}) is converted into a Fock matrix in the basis of NBOs (F^{NBO}). The diagonal elements of F^{NBO} correspond to self-energies of the localized orbitals, and the off-diagonal matrix elements give the interactions between localized orbitals. Diagonalization of the full F^{NBO} matrix gives back the canonical MOs and eigenvalues. The major advantage of localized orbital approaches comes from the ability to construct Fock matrices retaining only a subset of the interactions. In essence, this allows one to construct a series of model one-electron Hamiltonians, with all matrix elements being derived from *ab initio* calculations. Examination of the splittings obtained from diagonalization of these modified Fock matrices provides information on the importance of specific interactions for the electronic couplings.

Figure 28 illustrates the application of the NBO analysis method to a simple four-orbital model, consisting of two *p* orbitals (p_1 and p_4) and the σ (σ_2) and σ^* (σ_3^*) of the intervening C–C bond. The diagonal entries of the NBO Fock matrix give the energies of the p_1, p_4, σ_2 , and σ_3^* localized orbitals in the absence of mixing with other localized orbitals. Firstly, the $\langle p_1 | F | p_4 \rangle$ off-diagonal matrix element is “switched on”. Diagonalization of the resulting 2×2 sub-matrix gives the delocalized orbitals $p_+ = (p_1 + p_2)$ and $p_- = (p_1 - p_2)$, and the resulting splitting provides a measure of the TS interaction. In the next step, mixing with σ_2 is included and this causes p_+ to be “pushed above” p_- , leading to the so-called inverted sequence of orbital ordering [40]. (By symmetry, p_- cannot mix with σ_2 .) Finally, switching on the interaction with σ_3^* results in a small stabilization of p_- . This analysis shows how NBOs can be used to separate the TS and TB interactions, and also how they can be used to estimate the relative importance of different TB coupling pathways.

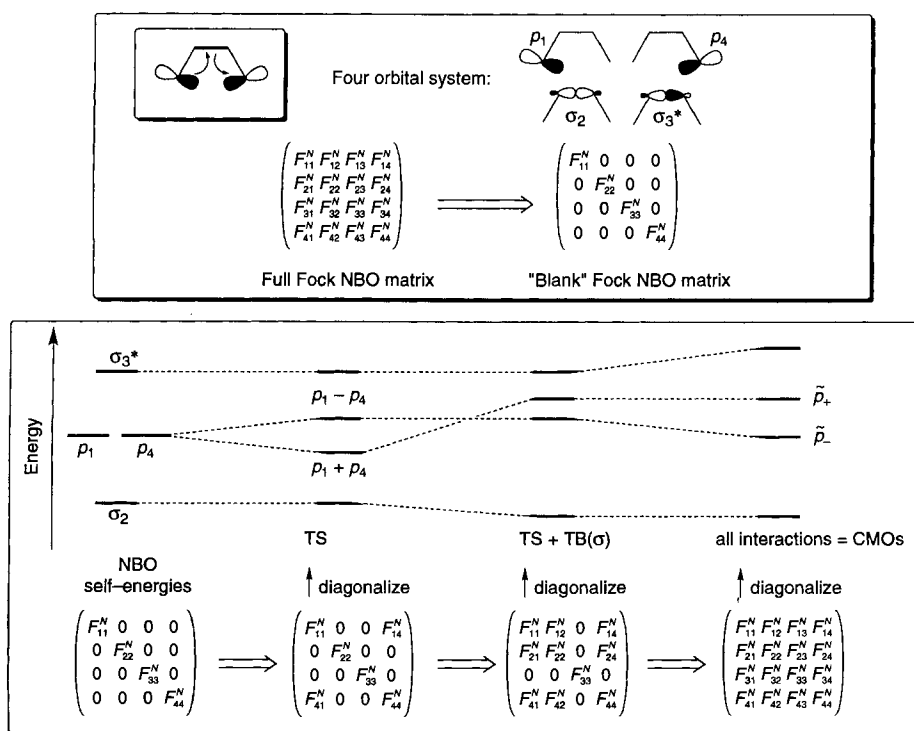


Figure 28. Illustration of the use of the NBO procedure for analyzing TB and TS interactions. The model includes two chromophore p orbitals and the σ and σ^* orbitals of the central C–C σ bond of the bridge. In the bottom part of the figure, the Fock matrix is built up, starting with the matrix of self-energies by adding, in succession, the TS coupling between p_1 and p_4 , the TB mixing with σ_2 , and, finally, the TB mixing with σ_2^* .

1.7 Interference Effects in TB Coupling

Figure 29 summarizes the β_{el} values obtained from the π_+ , π_- splittings for six ethylene–bridge–ethylene systems, **37**(n)–**41**(n) and **12**(n), differing in the type of hydrocarbon bridge. The π_+ , π_- splittings calculated for these molecules range from 0.017 to 0.058 eV, and the β_{el} values range from 0.50 to 2.48 bond^{−1}. The largest splitting and the smallest β_{el} value occur for the simple all-*trans* alkane bridge diene, **41**(n), and the smallest splittings and largest β_{el} value are for the molecules **37**(n) and **38**(n) with the fused cyclobutane bridge units. These results are surprising, since one would have expected bridges with multiple linkages between the π orbitals to be more effective at TB coupling than the “single strand” all-*trans*-(CH₂) _{n} bridge. This suggests that in the systems with bridges comprising hydrocarbon ring units, there must be considerable destructive interference between different TB coupling pathways, with the importance of destructive interference depending on the structure of the bridge units [91, 102].

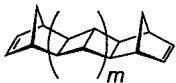
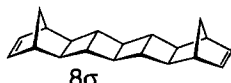
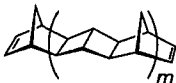
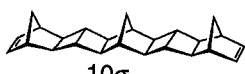

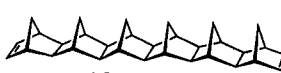

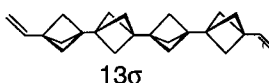

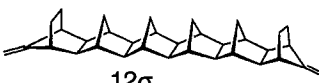
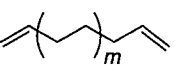
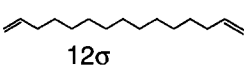
	β_{el} (bond ⁻¹)	Example	$\Delta E(\pi)$ (eV)
37(<i>n</i>) 	2.48	 8σ	0.017
38(<i>n</i>) 	1.22	 10σ	0.025
12(<i>n</i>) 	0.68	 12σ	0.043
39(<i>n</i>) 	0.60	 13σ	0.038
40(<i>n</i>) 	0.58	 12σ	0.035
41(<i>n</i>) 	0.50	 12σ	0.058

Figure 29. Limiting β_{el} values for the π_+, π_- splittings in six ethylene-bridge-ethylene systems. These are obtained by fitting the HF/3-21G π_+, π_- splittings for consecutive members of the series to $\Delta E(\pi) = A \exp(-\beta_{el}n)$, where n equals the number of bonds along one side of the bridge.

The NBO procedure may be used to construct models that allow one to identify the major sources of destructive interference, and this is illustrated using the polynorbornane **12**(*n*) series. Each model retains the localized π orbitals on the ethylenic groups as well as a subset of the NBOs associated with the bridge. HF/3-21G calculations are carried out on the **12**(*n*), $n = 4, 6, 8, 10$, and 12 , molecules, and the canonical MOs are transformed to NBOs, which are used to construct a series of models shown in Figure 30. In terms of increasing sophistication these models are:

- A:** Only a single relay of C–C σ bonds is retained.
- B:** The two main relays of C–C σ bonds are retained, but no interactions between the relays are permitted.
- C:** Same as **B**, except that interactions between the two main relays (cross-talk) are permitted. The cross-talk interactions are symbolized by wavy lines.

These three models ignore interactions involving the C–H bonds, the bridging methylene groups, and the C–C bonds shared by fused rings. This approximation is justified since more complete NBO calculations in which such interactions are included lead to the same qualitative conclusions. The π_+, π_- splittings for the $n = 8, 10$, and 12 members of these models as well as the associated β_{el} values are sum-

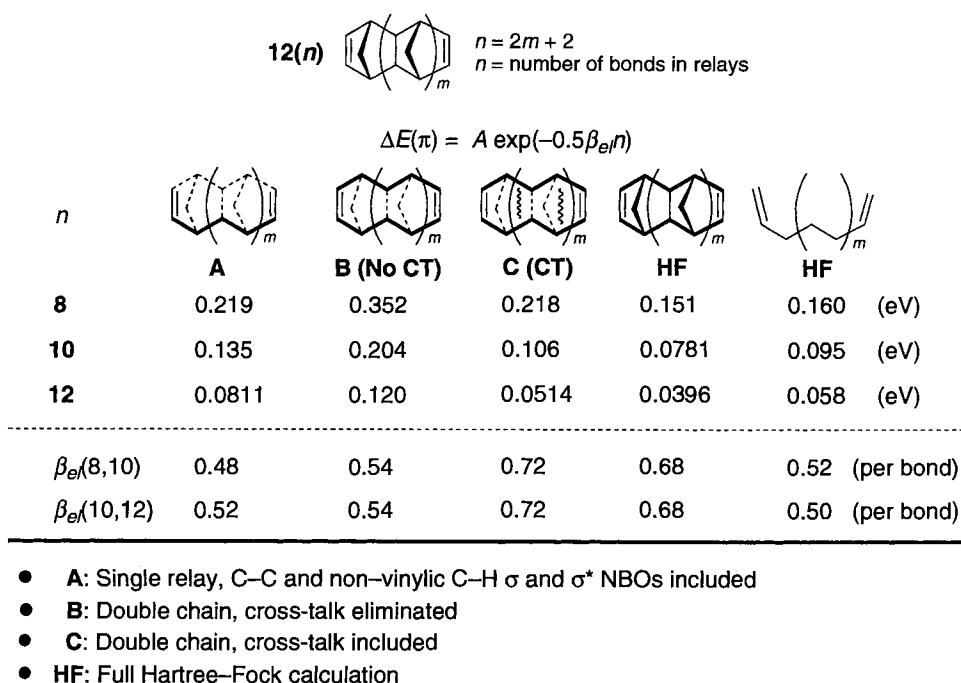


Figure 30. Analysis of cross-talk interactions in **12(*n*)**. Splitting energies are in eV. Three models, constructed from NBO/3-21G matrix elements for **12(8)**, **12(10)**, and **12(12)** are considered: model **A** allows for coupling through a single relay; model **B** through two relays, but with no cross-talk; and model **C** through two relays with cross-talk (represented by wavy lines). Results from Hartree–Fock calculations on the **12(*n*)** series as well as for the corresponding molecules with all-*trans* alkane bridges **41(*n*)** are also included.

marized in Figure 30. Also included are the Hartree–Fock results for the full molecules (**12(8)**, **12(10)**, and **12(12)**) and for the corresponding series of dienes **41(*n*)** with a single all-*trans* alkane bridge. (In the latter reference compounds, the ethylenic groups are oriented as in the polynorbornane dienes **12(*n*)**.) Due to the enhanced coupling of the chromophore to the bridge made possible by the inclusion of the second relay, the splittings are larger for model **B** than for **A**. On the other hand, the β_{el} values are nearly the same for these two models, showing that the enhancement of the coupling of the chromophores to the bridge does not modify the ability of the bridge to relay the coupling. Not surprisingly, the β_{el} values for models **A** and **B** are nearly the same as those obtained from the HF calculations on the reference dienes with the single all-*trans* alkyl bridge.

The π_+ , π_- splittings decrease appreciably and the β_{el} values increase by about 30 % on going from model **B** to model **C**. The smaller splittings and their more rapid attenuation with increasing bridge length in model **C** are the result of the cross-talk interactions between the two relays. The splittings and β_{el} values for model **C** are close to those obtained from the HF calculations on the poly-

norbornane dienes, i.e., the $12(n)$ series. This shows that the destructive interference in the $12(n)$ series also results from cross-talk between the two parallel relays.

In order to understand the origin of the destructive interference, it is instructive to consider the McConnell model [17] for coupling in symmetrical chromophore–(trans-alkane bridge)–chromophore systems. In the simplest version of this model, each chromophore and each bridge site has a single active orbital, all bridge sites are assumed to be identical, and only nearest-neighbor interactions are retained. In the limit of weak coupling (Δ large, t/Δ small), the splitting arising from coupling through n bonds is given by Eq. 5.

If the NBO basis set is chosen such that adjacent orbitals overlap in-phase, as depicted in Figure 7, then the t matrix element is negative (as, for that matter, is T). The sign of Δ is taken to be positive. As a result of these conventions, for chains with an even number of bridge sites, the splitting energy $\Delta E(\pi)$ is positive (i.e., the $\pi_+ (= \pi_1 + \pi_2)$ level lies below the π_- level), whereas for chains with an odd number of bridge sites it is negative (i.e., the $\pi_- (= \pi_1 - \pi_2)$ level lies below the π_+ level). This dependence of the level ordering on the parity of the number of bridge sites is often referred to as the parity rule, which states that the level ordering follows the natural sequence (i.e., π_- above π_+) for even values of n , and the inverted sequence (i.e., π_+ above π_-) for odd values of n (Figure 31) [15, 18].

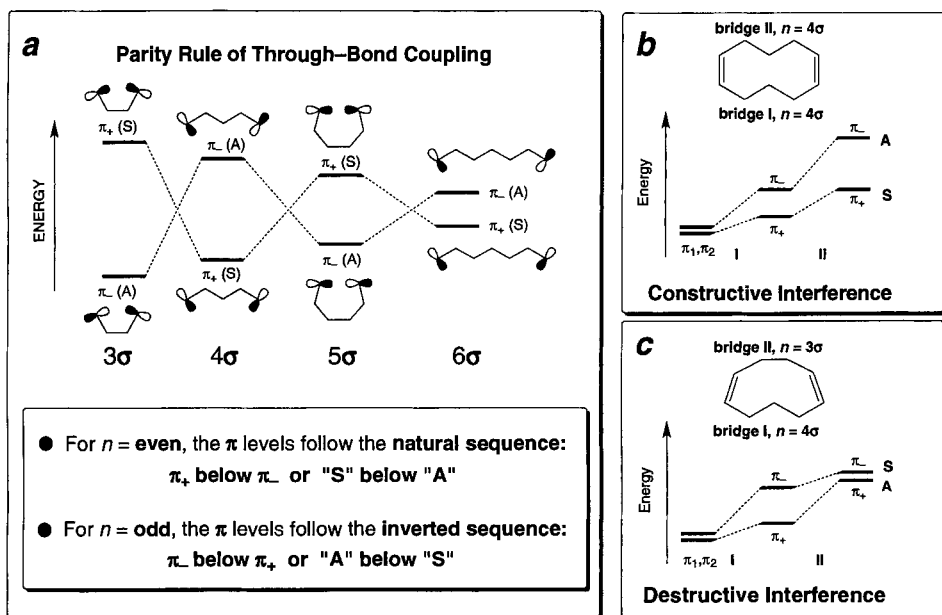


Figure 31. (a) The parity rule of through-bond coupling. The level sequence alternates with the parity of the number of σ bonds in the bridge. The labels S and A denote the symmetries of the orbitals. (b) Constructive interference resulting from two relays having the same (even) parity. (c) Destructive interference resulting from two relays having opposite parity.

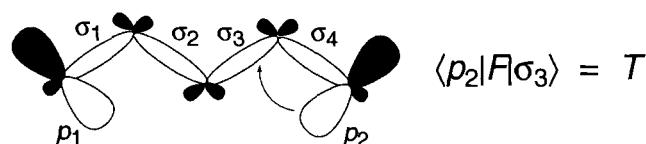
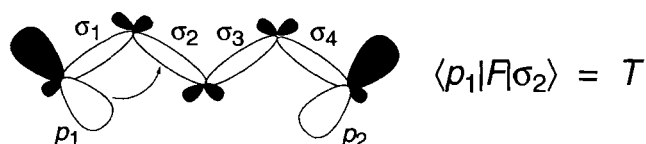
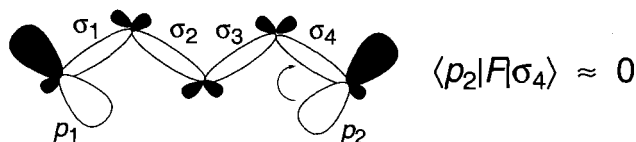
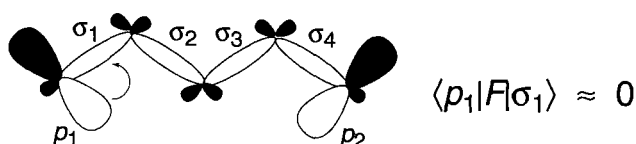
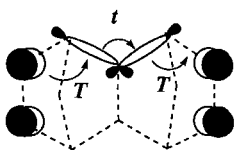


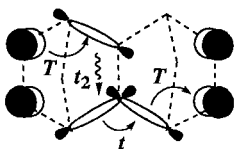
Figure 32. Matrix elements describing the coupling of a p (or π) orbital of the chromophore to an all-*trans* alkane bridge. The dominant chromophore–bridge coupling is represented by T .

Within the context of the McConnell model, model **B** gives splittings precisely two times larger than those for model **A**: the presence of two noninteracting bridges coupling the chromophores leads to a doubling of the splittings. However, for both models **A** and **B**, the McConnell treatment gives $\beta_{el} = 2 \ln(|\Delta/t|)$ (see Eq. 6), and there is no change in the distance dependence of the coupling brought about by the introduction of the second, independent relay.

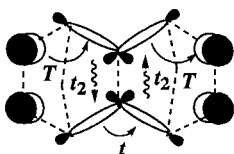
Consider now model **C**, focusing initially on the molecule with four σ bonds ($n = 4$) along each relay. Because the π orbitals are nearly orthogonal to the σ orbitals, the major coupling of the chromophores to the bridges is via the allylic C–C σ bonds, i.e., via bonds 2 and 3 (see Figure 32). For the purpose of delineating the origin of the destructive interference, the terminal C–C bonds of the bridges can be ignored. For this “reduced” model, the possible coupling pathways are shown in Figure 33. Pathway (a) is of the conventional McConnell-type. The extra factor of two (compared to Eq. 5) is due to the presence of the two bridges. Pathway (b) allows for one “hop” between the two relays. In the expression for the energy, this introduces an extra factor of t_2/Δ , where t_2 represents the interaction between the C–C σ bonds of the two relays (cf. Eq. 7). Because t_2/Δ is negative, the energy contribution of pathway (b) has the opposite sign from the associated with pathway



$$(a) \quad \Delta E(\pi) = -2 \frac{2T^2}{\Delta} \left(\frac{t}{\Delta} \right) \quad (\text{positive})$$



$$(b) \quad \Delta E(\pi) = -4 \frac{2T^2}{\Delta} \left(\frac{t}{\Delta} \right) \left(\frac{t_2}{\Delta} \right) \quad (\text{negative})$$



$$(c) \quad \Delta E(\pi) = -2 \frac{2T^2}{\Delta} \left(\frac{t}{\Delta} \right) \left(\frac{t_2}{\Delta} \right)^2 \quad (\text{positive})$$

Figure 33. Through-bond coupling pathways in model **C** for **12(4)**. The t_2 matrix element is responsible for the cross-talk interactions (represented by wavy lines). The energy contribution of each pathway is given as are the signs of the interactions.

(a). The multiplicative factor of four allows for the existence of four independent pathways that involve a single t_2 interaction between the two relays. Pathway (c) permits two hops between the two relays, and as a result its energy contribution acquires a factor of $(t_2/\Delta)^2$ and has the same sign as pathway (a). There are two such pathways.

For values of t/Δ and t_2/Δ appropriate for the polynorbornane dienes (-0.41 and -0.11 , respectively), the net contribution of pathways (a), (b), and (c) to the coupling is about 20 % smaller than were only pathway (a) operative. Moreover, because of the growing number of locations at which a single hop between the two relays may occur, the relative contribution of the cross-talk terms grows with increasing bridge length, leading to an increase in the β_{el} values describing the distance dependence of the electron coupling between the chromophores.

The above analysis also readily identifies why the coupling is so poor in the molecules **37(n)** and **38(n)** containing fused cyclobutane bridges. For these, the quantity t_2/Δ , which gives the contribution of a hop from one side of the cyclobutane bridge to the other, is -0.24 , over twice as large in magnitude as that in the

polynorbornane bridges. As a result, the destructive interference is considerably greater in the molecules with the cyclobutane bridge units [103, 104].

The origin of the destructive cross-talk interference occurring in the polynorbornane bridges may be recast into a very simple model based on the parity rule. Thus, the net coupling through two relays having the same parity is given by the sum of the absolute magnitude of the coupling associated with each relay and is therefore strengthened by what may be called *constructed interference* (Figure 31b). In contrast, the net coupling through relays having opposite parities is given by the difference in the absolute magnitude of the coupling associated with each relay and is therefore diminished by *destructive interference* (Figure 31c).

From Figure 33, it is easily seen that coupling pathways that make either zero or an even number of jumps from one main relay to the other, such as pathways (a) and (c), have opposite parity to those that make an odd number of jumps, such as pathway (b). Thus, pathways (a) and (c) involve coupling along two and four bonds, respectively, whereas pathway (b) involves coupling along three bonds. Consequently, the coupling in these dienes is degraded by destructive interference effects [103, 104].

Can this simple and intuitive analysis of interference effects on coupling through bridges, based on the parity rule, be used advantageously to design systems in which destructive interference is minimized or, better yet, in which the interaction between the different pathways is predominantly *constructive*?

The answer to this is affirmative, and several such systems have been devised, two examples of which are **42(n)** and **43(n)** (Figure 34). In contrast to the “standard” polynorbornane diene series **12(n)**, in which the existence of pathways of different parity destructively interfere (Figure 35a), all reasonable TB coupling pathways in **42(n)** and **43(n)** have the same parity, namely even, in the case of the former (Figure 35b) and odd, in the case of the latter (Figure 35c). Consequently, it is predicted that the net TB coupling in both **42(n)** and **43(n)** should be superior to that in **38(n)**, even though all three systems possess the same basic type of bridge. Gratifyingly, HF/3-21G calculations confirm this expectation. The calculated β_{el} values of **42(n)** and **43(n)** are *ten times smaller* than that for **38(n)** and the strength of the coupling for a given bridge length is greater for the former (Figure 34). For example, $V_{el}(= 0.5 \cdot \Delta E(\pi))$ for both **42(10)** and **43(10)** is ten times larger than that for **38(10)**, and this translates into a predicted two orders of magnitude rate enhancement for HT in the radical cations of **42(n)** and **43(n)**, relative to **38(10)** (remember that rate depends on the *square* of V_{el}). Bridges such as **42(n)** and **43(n)** deserve the epithet *superbridges*! [104].

The weak distance dependence data for π -TB interactions in **42(n)** and **43(n)** are intriguing, since they suggest that TB coupling through a single hydrocarbon chain may be greatly amplified by a proximate alkane chain which is only weakly coupled, if at all, to the chromophores (e.g., Figure 36a). In the upper part of Figure 36a, the two double bonds are connected to the same alkane bridge which is located close to an alkane chain. All inter-relay jumps begin and end on the diene bridge, and they all have the same parity. Placing two long-chain terminal alkenes in a head-to-tail arrangement (lower part of Figure 36a) will likewise result in only constructive interference effects since only an odd number of inter-relay jumps contribute sig-

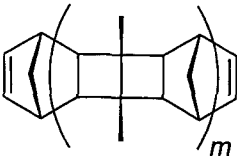
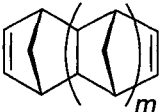
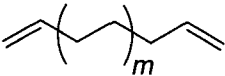
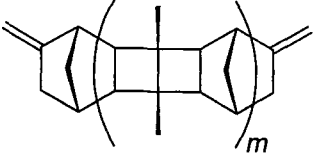
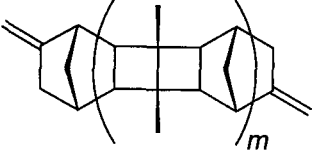
		β_{el} (per bond)	$\Delta E(\pi)$ (eV) (10-bond)
38(n)		1.22	0.025
12(n)		0.68	0.078
41(n)		0.50	0.096
42(n)		0.11	0.263
43(n)		0.10	0.259

Figure 34. HF/3-21G β_{el} and $\Delta E(\pi)$ values (for $n = 10$) for various dienes.

nificantly to the overall coupling [104]. (A different type of interference between alkane chains and chromophores has been reported [105].

Indeed, such amplification may be responsible for some very small β values that have allegedly been obtained from various experimental electron transfer studies on self-assembled monolayers containing long-chain alkanes [106–109]. For example, a β value of only 0.007 bond^{-1} has been reported for electron transfer in self-assembled monolayers of viologen-terminated alkanecystamines that had been chemisorbed onto gold electrodes [109]. In such instances, amplification of TB coupling within a redox-active-terminated alkanethiol molecule may arise from cooperative through-space interactions (i.e., constructive interference) with alkane chains from neighboring adsorbed molecules, either diluent nonredox-active alkanethiols or other redox-active-terminated alkanethiol molecules (e.g., Figure 36b). Admittedly, these chains are not as close to each other as are the two main relays in

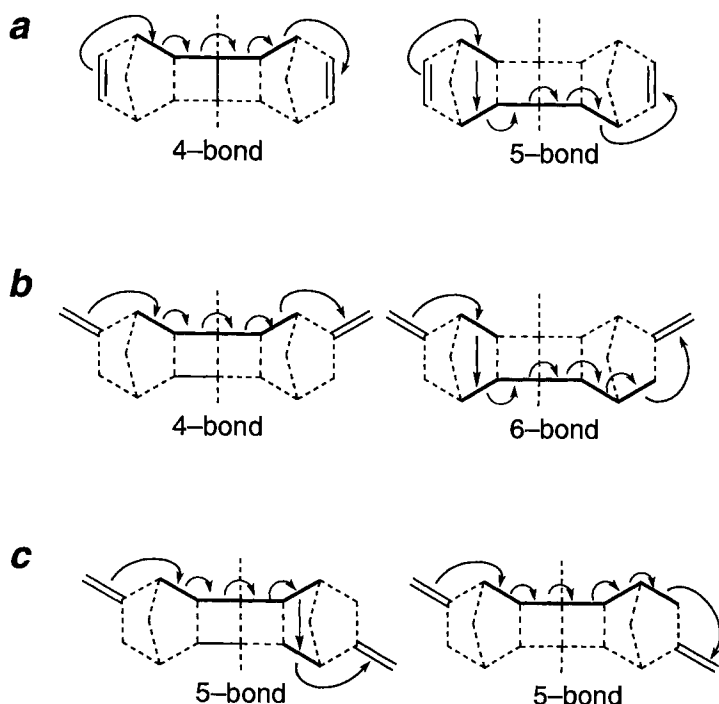
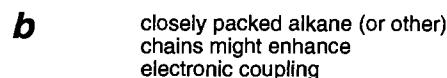


Figure 35. Schematic showing some nearest-neighbor coupling pathways for (a) **38(6)**, (b) **42(6)**, and (c) **43(6)**. All reasonable pathways have the same parity in **42(*n*)** (even parity) and in **43(*n*)** (odd parity).

42(*n*) and **43(*n*)**, but this disadvantage is possibly compensated by the presence of many more alkane chains surrounding each redox system in the monolayer. It should also be pointed out that other studies of interfacial electron transfer in long-chain alkane monolayers have reported normal β values of c. 0.95 bond^{-1} , suggesting that the distance dependence of electronic coupling through an alkane chain in self-assembled monolayer is not influenced by neighboring alkane chains [110–115]. Hopefully, the conundrum surrounding the widely disparate β values from various experimental studies on ET through self-assembled monolayers will soon be resolved.

1.8 Porphyrin and C₆₀ Chromophores

The bulk of studies of ET processes in norbornylogous systems has used the DMN and DCV chromophores. The reason for this is that, in fairly polar solvents, the magnitude of the free energy change, ΔG_{cs} , for photoinduced charge separation



in **23(n)** happens to be nearly equal in magnitude but opposite in sign to the total reorganization energy, λ [66, 67]. The exponential term in the Marcus–Hush rate expression (Eq. 2), is therefore nearly unity, making the photoinduced charge separation process for **23(n)** almost barrierless. This situation simplifies the analysis and interpretation of the ET rate data.

Nevertheless, other chromophores have been investigated and they have provided interesting insights, particularly porphyrin and C_{60} groups, since these serve as useful mimics of the cofactors present in the photosynthetic reaction center (Figure 37). Electron transfer involving porphyrins and fullerenes will be presented in more detail elsewhere in this Handbook Volume III, Part 2, Chapter 2 and Volume II, Part 1, Chapter 5 respectively), and so only a brief discussion is presented here. An excellent overview of photoinduced ET processes in C_{60} -based multichromophoric systems has been produced previously [116].

Photoinduced electron transfer reactions have been studied in the dyads **44(6)**, **45(9)**, and **46(11)**. The 6-bond porphyrin–quinone dyad **44(6)** serves as a model for aspects of ET in the photosynthetic reaction center, since congeners of these chromophores are present in the center as cofactors (Figure 37). Photoinduced ET in

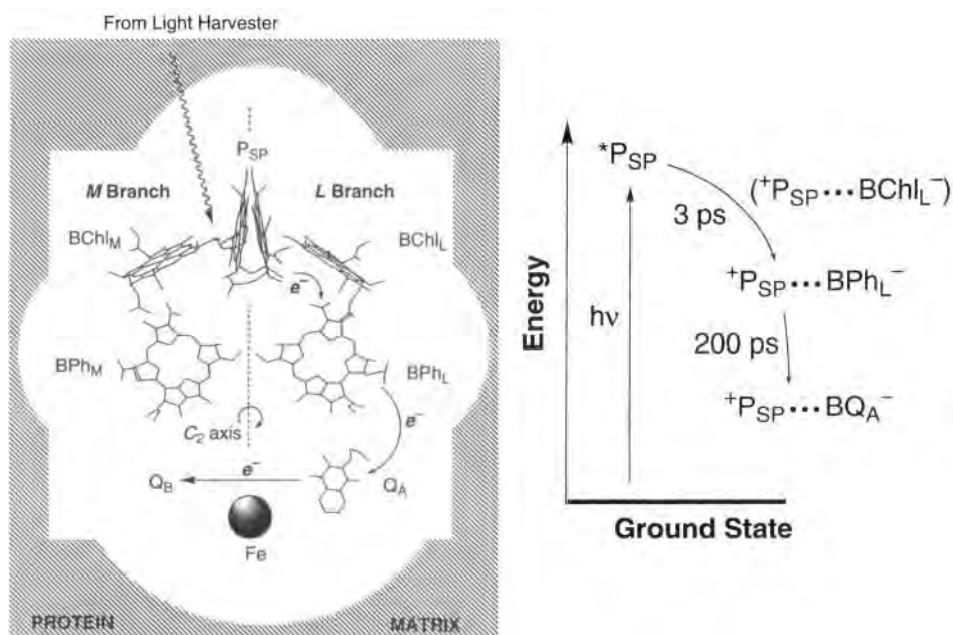


Figure 37. Schematics of the photosynthetic reaction center and the energetics of the charge separation steps, together with the individual ET rates along the *L* branch.

44(6) takes place on a nanosecond time scale (Figure 38) with high efficiency, even though the charge separation process for this system is far from barrierless [117]. The charge separation rate is comparable to that found in the photosynthetic reaction center. As with the **23(n)** series, the rapid charge separation rate observed for **44(6)** testifies to the extraordinary ability of rigid hydrocarbon bridges to mediate long-range ET processes. The charge recombination rate from the CS state of **44(6)** is about one order of magnitude slower than the charge separation rate (Figure 38).

The two C_{60} -based dyads, **45(9)** and **46(11)**, display interesting photophysical features. Rapid (subnanosecond time scale) photoinduced charge separation, from locally excited porphyrin to the C_{60} acceptor, in **45(9)** takes place in benzonitrile (Figure 38). The amazing feature of this system is not so much the rapid rate of charge separation (which is quite unusual!), but the extremely long lifetime of $0.4 \mu\text{s}$ for the CS state [118]. It is instructive to compare the rate data for this system with those for **47** (Figure 38) in which the same chromophores are connected by a single-strand *flexible* tether [119]. Whereas the charge separation rates for the two systems are similar, the charge recombination rates are dramatically different, that for **45(9)** being *three* orders of magnitude smaller than that for **47**! This huge difference in the CR rates is attributed to orbital symmetry effects. The rigidity of **45(9)** ensures that the molecule has C_s point group symmetry. Because the singlet CS state of **45(9)** has A'' symmetry, but the ground state has A' symmetry, the CR process is formally

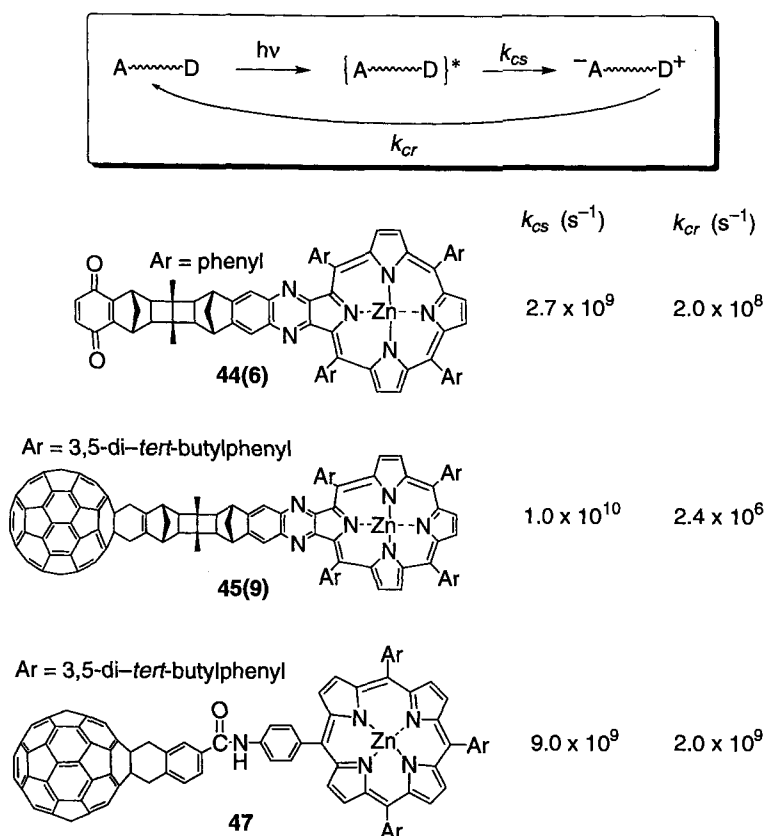
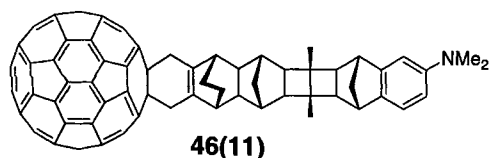
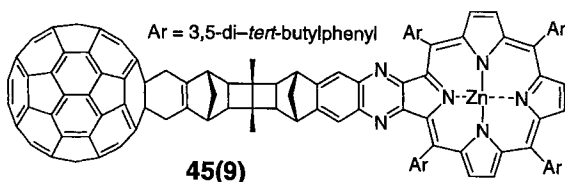
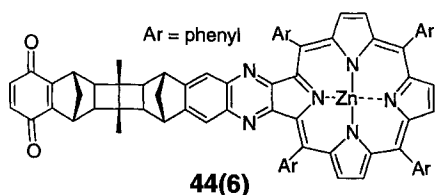


Figure 38. Rates of photoinduced charge separation and subsequent charge recombination processes in some dyads (in benzonitrile).

symmetry forbidden and this slows down the CR rate. The flexible nature of the tether in **47** removes this symmetry restriction and the CR rate is, therefore, more rapid in this system.

The aniline- C_{60} dyad **46(11)** was no less spectacular than **45(9)**, considering the greater interchromophore separation that exists in this system (11 bonds), compared to **45(9)** (9 bonds). The photoinduced charge separation rate for **46(11)** is about $6 \times 10^9 \text{ s}^{-1}$ and the CR lifetime is 250 ns (both in benzonitrile) [120]. Why are charge separation processes involving the C_{60} acceptor so rapid in **45(9)** and **46(11)**? Intuitively, one would have predicted the opposite behavior; because of its large size, the MOs of the C_{60} chromophore have small atomic coefficients compared to those of most other chromophores in use, such as DMN. Thus, the magnitude of the coupling of the C_{60} group to the bridge would be expected to be small. However, unlike the normal chromophores, which are generally planar, the curved nature of the C_{60} surface enables it to couple to the bridge using many more atoms



than, say the DMN group, as illustrated in Figure 39a. There are 12 interactions between the orbitals of the C_{60} chromophore and the bridge, but only four interactions between the orbitals of a planar aromatic chromophore and the bridge. The result is strong coupling between the C_{60} group and the bridge, and this is manifested by the extensive delocalization of the C_{60} HOMO into the bridge (Figure 39b) [120].

Another factor which generally facilitates photoinduced charge separation in *all* dyads containing the C_{60} acceptor is the smaller internal reorganization energy, λ_i for C_{60} , compared to most acceptor groups [121]. This is probably due to the large size of the C_{60} unit; its conversion to the radical mono-anion does not produce large structural distortions. From Eq. 2, it may be seen that, for ET taking place within the normal region, the activation barrier decreases and the corresponding ET rate *increases* with *decreasing* λ_i . Since most photoinduced CS processes take place within the Marcus normal region, replacing an acceptor having a higher λ_i than C_{60} (e.g., a quinone) with C_{60} will therefore lead to an acceleration of the photoinduced charge separation process.

In contrast, charge recombination processes from CS states produced by photo-initiation normally take place within the inverted region. Thus, the small reorganization energy of C_{60} will *slow* down CR processes, relative to other acceptors having higher λ_i values.

In summary, the comparatively small internal reorganization energy of C_{60} , together with its excellent redox properties, should make the C_{60} chromophore a valuable electron acceptor component in molecular photovoltaic devices.

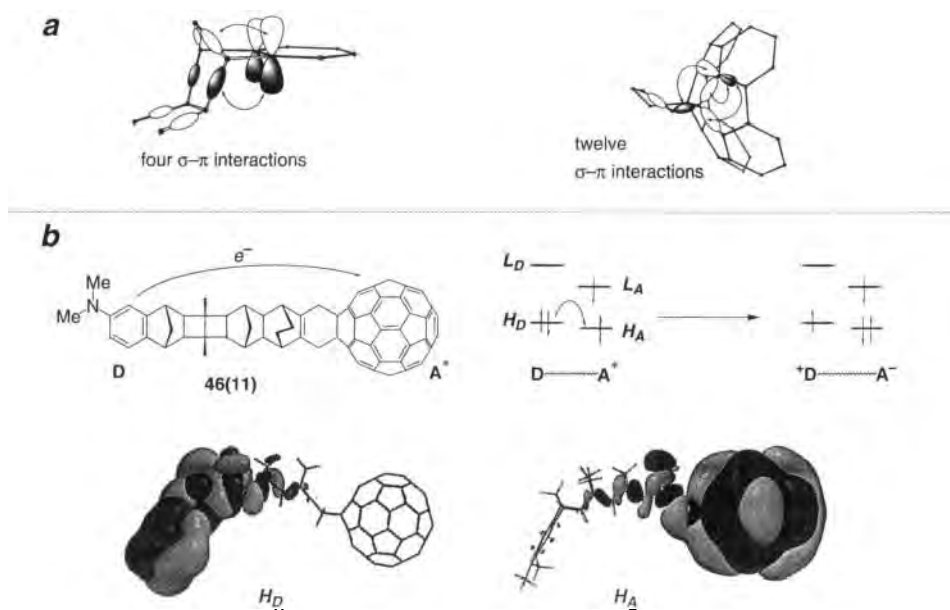


Figure 39. (a) Interactions between the orbitals of the bridge and those of a planar aromatic molecule and C_{60} . In the former, there are four interactions, two of which are shown, the other two involve the corresponding orbitals in the background. In the case of C_{60} , three interactions are shown and there are three more similar groups of three interactions involving symmetry-related orbitals, making a total of 12 interactions. (b) The active orbitals involved in photoinduced charge separation. H_D is the HOMO of the aniline donor and H_A is the HOMO of the C_{60} acceptor; the orbital plots were obtained from AM1 calculations.

1.9 Superexchange versus Molecular Wire Behavior

The rather astonishing revelation that ET can take place rapidly ($>10^9 \text{ s}^{-1}$) over inter-chromophore separations exceeding 10 \AA through saturated hydrocarbon bridges has led to the oft-asked question: If hydrocarbon bridges are able to strongly mediate ET, may they be considered to possess molecular wire (or electrical-conducting) behavior? The answer is an unequivocal no, they may not be regarded as wires. Electrical conduction through a bridge requires that the electron from the donor becomes thermally injected into the conduction band of the bridge and that it actually becomes localized within the bridge and is transported through the bridge, from donor to acceptor, by an incoherent scattering mechanism, such as a polaron. The distance dependence of the ET rate in such a molecular wire is determined by Ohmic scattering, and therefore varies inversely with bridge length [122–124]. The molecular wire mechanism is summarized in Figure 40. It is expected to operate only when the energy gap, Δ , between the donor level and the bridge conduction

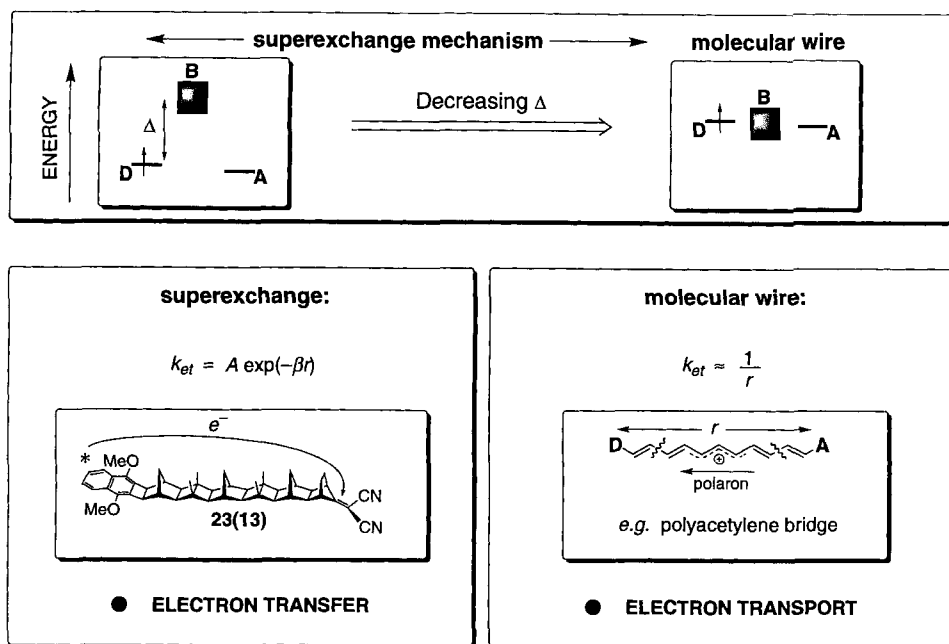


Figure 40. A schematic illustrating the difference between the superexchange mechanism and molecular wire behavior in a D–B–A dyad. Superexchange: the virtual bridge states lie well above the donor level (Δ is large) and, consequently, the electron is never localized within the bridge; instead, the electron is transferred from donor to acceptor in one coherent jump. The distance dependence behavior is exponential decay. Molecular wire behavior: The virtual bridge states are energetically comparable to the donor level (Δ is very small). In this case, the electron may be thermally injected into the bridge and becomes localized within the bridge, whereupon it moves from the donor to the acceptor incoherently as a defect, such as a polaron. The distance dependence behavior is Ohmic (varies inversely with distance).

band is very small, of the order $k_B T$. This condition is satisfied for long, conjugated bridges, such as graphite and doped polyacetylenes (Figure 40; right-hand inset).

Conjugated bridges, such as polyacetylenes, may be considered as giant chromophores whose MOs are essentially delocalized over the whole bridge. A variant of wire behavior is a bridge comprising a set of weakly coupling units (B_i), each of which is able to capture the migrating charge for a short period of time before passing it on to one of its neighboring units (Figure 41). For example, the bridge might consist of a series of small aromatic rings as units which are connected to each other by short alkane chains. Assuming that all of the bridge units are energetically nearly degenerate (Figure 41a), the migrating charge (electron or hole) randomly hops, from bridge unit to bridge unit, up and down the chain, until it is eventually irreversibly trapped by the acceptor which acts as a thermodynamic sink. Hopping between adjacent bridge units takes place through the intervening medium

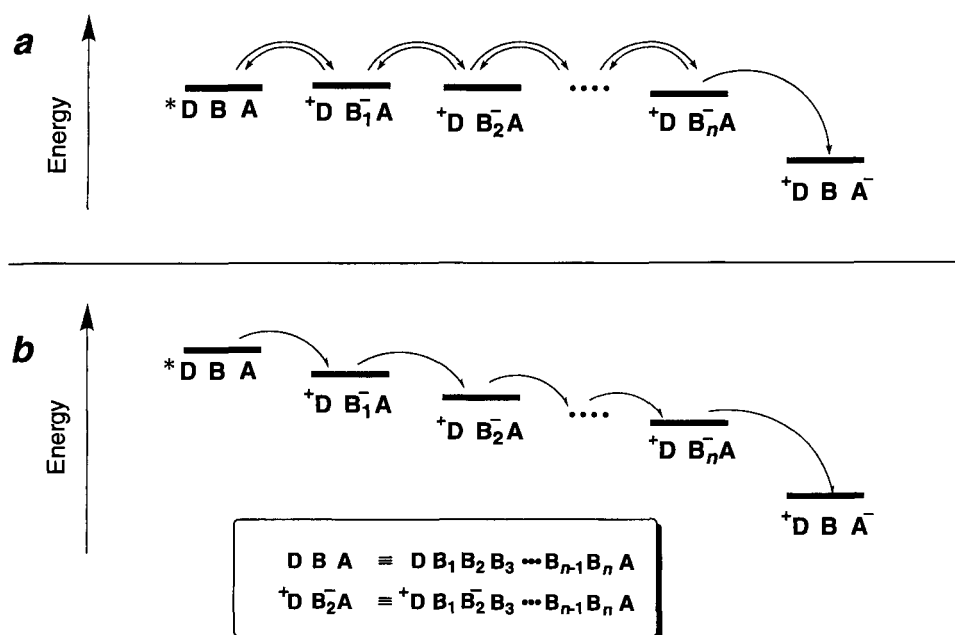


Figure 41. Two charge-hopping mechanisms. The donor injects an electron (or hole) into the bridge which consists of discrete redox units. (a) The bridge units are nearly degenerate. Consequently, the injected electron (or hole) moves randomly and reversibly up and down the bridge, finally becoming irreversibly trapped by the acceptor. (b) The bridge units constitute an ordered redox cascade; the electron or hole moves essentially irreversibly along the bridge towards the acceptor.

(e.g., saturated C–C bonds, solvent molecules) by a superexchange mechanism, or even through-space, if the units are in van der Waals contact with each other.

If each single hopping step occurs over the same distance, then the hopping dynamics will display a weak distance dependence, varying inversely with respect to a small power of the number, N , of hopping steps, viz. Eq. 25 [125–127]:

$$k_{et} = N^{-\eta} \quad \eta \approx 1-2 \quad (25)$$

The electron or hole hopping mechanism may be made to take place only in one direction along the bridge by ensuring that the bridge units constitute a redox gradient (Figure 41b). Again, this mechanism avoids the exponential decay of ET or HT dynamics with distance, following a more gentle curve instead.

In contrast, in the superexchange (or TB) mechanism, Δ is very large—at least 2 eV—and so the electron cannot be thermally injected into the bridge. Instead, the electron moves coherently, in one sudden “jump”, from donor to acceptor and it never becomes localized within the bridge. The distance dependence of the ET rate for this mechanism is exponential decay (Figure 40). The conduction band for saturated hydrocarbon bridges corresponds roughly to the empty σ^* orbital levels.

Since these levels are several eV higher in energy than the π and π^* levels of most unsaturated donor systems, ET mediated by such bridges can normally occur only by the superexchange mechanism.

It is useful to introduce a nomenclature for distinguishing between ET occurring by the conduction and superexchange mechanisms. The term electron *transport* is used in the context of molecular wire behavior, while electron *transfer* is used in the context of the superexchange mechanism.

There is a simple way of visualizing the superexchange mechanism. Consider ET taking place from the dimethylaniline donor to the locally excited singlet state of C_{60} in **46(11)** (Figure 39b) [120]. The active orbitals which are primarily involved in the ET process are the aniline HOMO (H_D) and the half-filled C_{60} HOMO (H_A). Because of TB (superexchange) coupling of the bridge to the chromophores, the HOMOs of the chromophores are no longer localized to their respective chromophores, but are extended into the bridge. This is evident from the AM1 plots for H_A and H_D (Figure 39b). These orbital extensions into the bridge result in favorable overlap between H_A and H_D , and this enables ET to take place.

In principle, it should be possible to design a series of **D–B–A** dyads with a bridge, **B** possessing suitable electronic characteristics such that the superexchange mechanism prevails for short bridge lengths, but switches over to molecular wire behavior for bridge lengths exceeding a certain critical value. In order to achieve this possibility, the bridge must meet the requirement that its conduction band level falls sufficiently steeply with increasing bridge length so that it approaches the highest filled level of the donor, at which point electron transport could be the dominant mechanism (Figure 40).

A suitably constituted conjugated bridge should meet this requirement and Wasielewski's group has recently used this stratagem to demonstrate that the mechanism does, indeed, switch from electron transfer to electron transport for a critical bridge length [128]. The systems, **48(n)**, shown in Figure 42, comprise a tetracene (TET) donor and pyromellitimide (PI) acceptor, both covalently linked to *p*-phenylenevinylene oligomers of increasing length, ranging from one aromatic ring, in **48(1)**, to five, in **48(5)**. Rates of photoinduced charge separation, from locally excited TET to PI, were measured for this series in methyltetrahydrofuran. Two distinct ET behaviors were observed (Figure 42, inset). For the two shortest bridges, the charge separation rate falls quite strongly with a β value of about 0.4 \AA^{-1} . This distance dependence behavior is consistent with the operation of the superexchange mechanism for charge separation in **48(1)** and **48(2)**. Indeed, this β value is similar in magnitude to the value of $\beta = 0.57 \text{ \AA}^{-1}$, measured for interfacial electron transfer between a gold electrode and a ferrocene group covalently connected to gold by π -conjugated mercapto-oligo(phenylene-ethynylene) bridges, $\text{HS}(p\text{-C}_6\text{H}_4\text{-C}\equiv\text{C-})_m(\eta^5\text{C}_5\text{H}_5)$ ($m = 2$ or 3) [113].

In contrast, there is an abrupt change in mechanism beginning with **48(3)** for which the charge separation rate is greater than that for **48(1)**, even though the bridge in the former system is 13 \AA longer than in the latter. Moreover, extremely weak distance dependence of the charge separation rates is observed for the longer members of the series **48(3)–48(5)**, for which β is only 0.04 \AA^{-1} . The distance decay characteristics for the charge separation rates for **48(3)–48(5)** were interpreted in

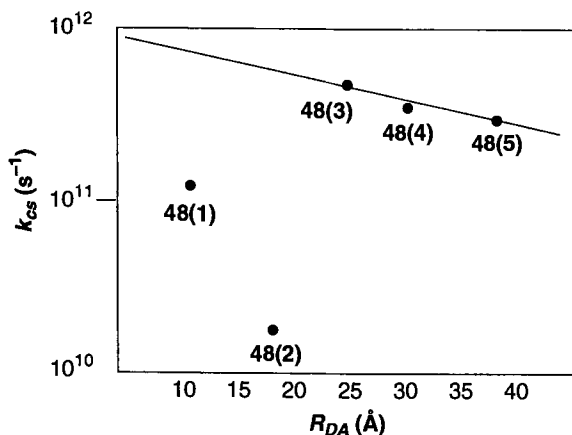
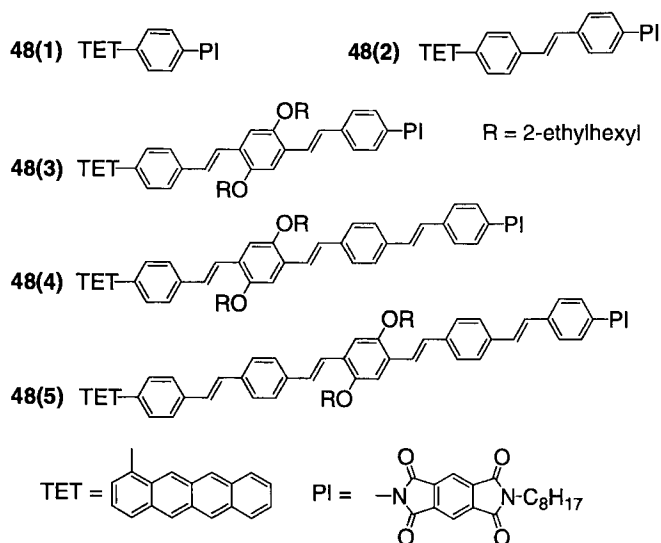


Figure 42. The series of dyads used for investigating the switchover from superexchange characteristics to molecular wire behavior. Also shown is a schematic of the photoinduced charge separation rate versus donor–acceptor distance [128].

terms of molecular wire behavior: in these systems, the LUMO of the bridge approaches that for the locally excited TET chromophore and thermal injection of a TET electron into the bridge becomes energetically plausible [128].

Finally, it is instructive to compare the β value of about 0.4 Å^{-1} for photoinduced ET through the unsaturated bridges of **48(1)** and **48(3)** with the value of about 0.85 Å^{-1} (0.95 bond^{-1}) for ET through saturated hydrocarbon bridges (Eq. 23). From this comparison, one is led to conclude that the distance dependence of the superexchange mechanism for ET is about two times weaker through unsaturated

hydrocarbon bridges than through saturated hydrocarbon bridges. Perusal of Eq. 6, which is based on the McConnell model, explains why this conclusion is reasonable: the virtual ionic states of an unsaturated bridge, which are derived from π -ionizations or π -electron capture, lie closer in energy to the donor level than do the virtual ionic states of a saturated hydrocarbon bridge, which are derived from σ -ionizations or σ -electron capture (i.e., the energy gap, Δ , of Eq. 6 is smaller for the unsaturated bridge than for the saturated bridge).

1.10 Superexchange through Aromatic Bridges

With the exception of **48(1)** and **48(2)**, we have focussed only on the superexchange-mediated ET and HT processes through saturated hydrocarbon bridges. A brief survey of the participation of aromatic groups in the superexchange mechanism will now be given. A particularly clear-cut demonstration of ET occurring through aromatic bridges came from investigations of photoinduced charge separation in **49(n)** and **50(n)**, $n = 1, 2$ (Figure 43) [129]. The ET reaction occurs from the dimethylaniline donor to the locally excited singlet state of either pyrene, in the case of **49(n)**, or anthracene, in the case of **50(n)**. It was found that the ET rate decreased by a factor of 22 to 27, upon going from $n = 1$ to $n = 2$ or, equivalently, by increasing the bridge length by four bonds. This leads to a β value of:

$$\beta = 0.77 \text{ bond}^{-1} \quad (26)$$

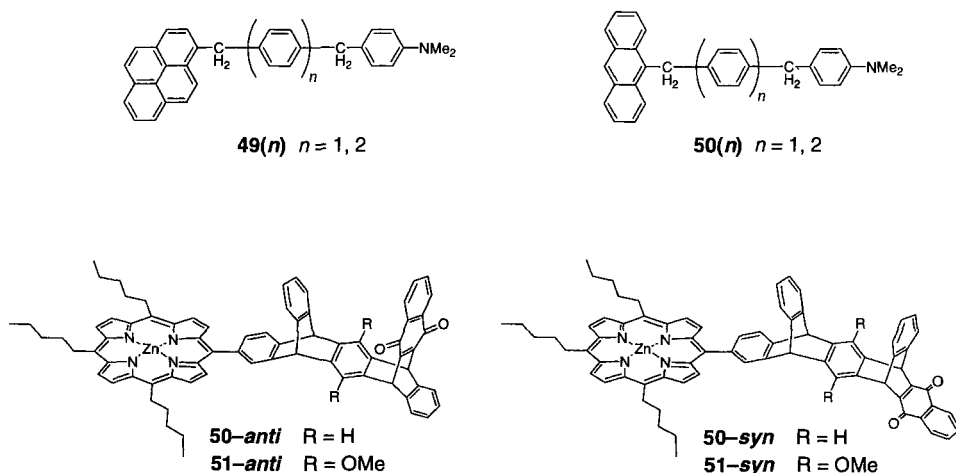


Figure 43. Some multichromophoric systems for investigating superexchange through aromatic groups.

This value is significantly smaller than the β value of 0.95 bond^{-1} for saturated hydrocarbon bridges (Eq. 23), and it reflects the lower energies of the virtual ionic states of aromatic molecules compared to saturated hydrocarbon molecules (vide supra and Eq. 6). The value of β for these systems is, however, noticeably larger than that measured for photoinduced ET in **48(1)** and **48(2)**. These elegant studies have been extended to cover other aromatic-bridge systems [130].

The rates of photoinduced charge separation, from the locally excited porphyrin donor to the naphthoquinone acceptor, were measured for the *syn* and *anti* stereoisomers of **50** and **51** (Figure 43). The charge separation rates for **50** and **51** were nearly identical for both sets of isomers. Interestingly, the charge recombination rates for **51-anti** and **51-syn** are about 3.5 times larger than those of **50-anti** and **50-syn**, respectively. This observation was explained in terms of a superexchange mechanism involving an electronic configuration of the bridge in which the virtual cationic state of dimethoxybenzene contributes (e.g., Figure 6) [72].

A spectacular example of superexchange is believed to occur during photoinduced ET in the C-H₂P-Im carotenoid-porphyrin-pyromellitimide trichromophore (triad) **52** (Figure 44) [131]. Selective photoexcitation of the carotenoid chromophore led to the formation of the giant charge-separated state $^+\text{C-H}_2\text{P-Im}^-$ within a few picoseconds. This rapid formation of the giant CS state was

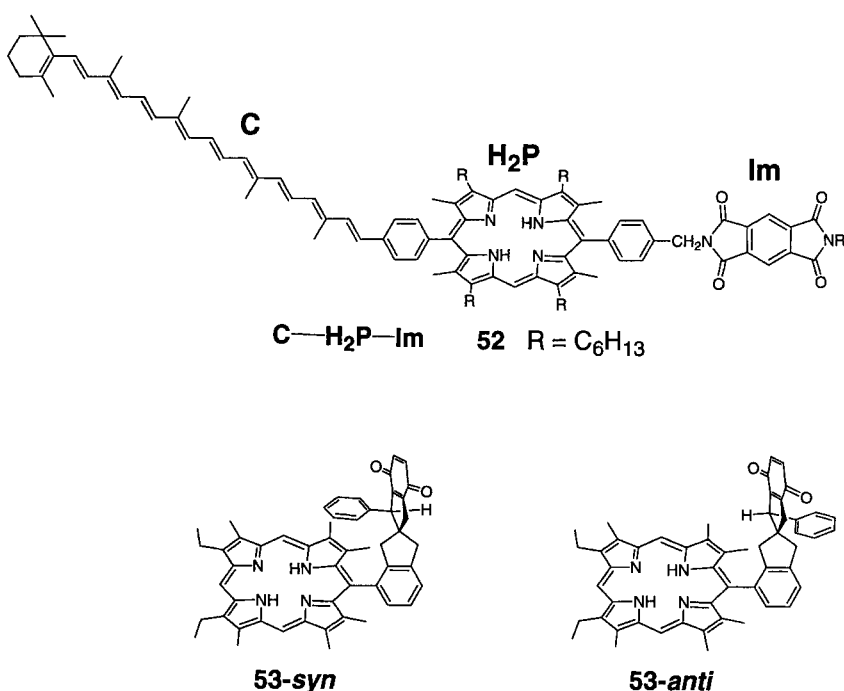


Figure 44. Further examples of multichromophoric systems for investigating superexchange through aromatic groups.

interpreted in terms of direct, long-range ET from the singlet excited state of the carotenoid, *C , to **Im** mediated by a superexchange interaction involving the π -MOs of the H_2P group. An alternative mechanism to the superexchange-mediated long-range electron transfer process is (reversible) singlet–singlet excitation energy transfer from *C to H_2P , to form $C-H_2P^*-Im$, followed by ET from the porphyrin to **Im**, which generates the intermediate CS state $C-H_2P^+-Im^-$. Thermal hole transfer from H_2P^+ to **C** produces the product giant CS state. The correctness of the superexchange mechanism received support from experiments which selectively excited the H_2P chromophore where it was found that the rate of formation of $^+C-H_2P-Im^-$ from $C-H_2P^*-Im$ is considerably slower, compared with that starting from $^*C-H_2P-Im$ [131].

Photoinduced ET from the locally excited porphyrin to the naphthoquinone in the *syn* and *anti* stereoisomers of **53** was studied in order to ascertain the consequence of placing a phenyl group in the space between the redox couple in **53-syn** (Figure 44) [132]. The edge-to-edge distances between the phenyl and the porphyrin or quinone rings in the *syn* isomer are in the range of 2.5–4.2 Å. Therefore, it is possible for ET to take place from porphyrin to quinone in the *syn* isomer by a superexchange process involving the phenyl group's orbitals. However, the rate of charge separation for **53-syn** is almost the same as that for a reference compound in which the phenyl group is absent. It was concluded that superexchange involving the phenyl ring does not occur in either isomer of **53**, and that charge separation in these molecules takes place by superexchange through the C–C σ bonds of the bridge.

The failure to observe superexchange-mediated ET through the phenyl group in **53-syn** may be due to the need for the aromatic ring to adopt a more favorable orientation with respect to the donor and acceptor chromophores, or it might be due to the fact that the virtual anionic states of the phenyl group are not low enough in energy to mix strongly enough with the excited donor state. An interesting case in which, perhaps, a more favorable orientation of the aromatic group does result in superexchange-mediated ET has recently been reported using a supramolecular assembly consisting of the clip-shaped receptor molecule **55** and the aromatic guest molecule hexyl 3,5-dihydroxybenzoate **56** (Figure 45) [133, 134].

Steady-state fluorescence studies of **55** in carbon tetrachloride gave a fluorescence quantum yield identical with that observed for the model system **54** in which the quinone acceptor has been replaced by a dimethoxybenzene group. This result shows that no photoinduced ET, from the locally excited porphyrin donor to the benzoquinone acceptor, is taking place in **55** in CCl_4 solvent. Addition of the guest hexyl 3,5-dihydroxybenzoate **56** to a solution of **55** in CCl_4 results in >75 % quenching of the porphyrin fluorescence. In contrast, the fluorescence for the model system **54** in CCl_4 did not diminish in intensity upon addition of the guest **56**. The fluorescence quenching observed for **55** in the presence of the guest **56** was therefore attributed to the occurrence of rapid photoinduced electron transfer taking place in the host–guest complex **57**. Hydrogen bonding between the two hydroxy groups of **56** and the pair of imide carbonyl oxygen atoms of **55** place **56** in face-to-face orientation with respect to the porphyrin and quinone chromophores, an ideal orientation for promoting superexchange coupling between the three π -systems.

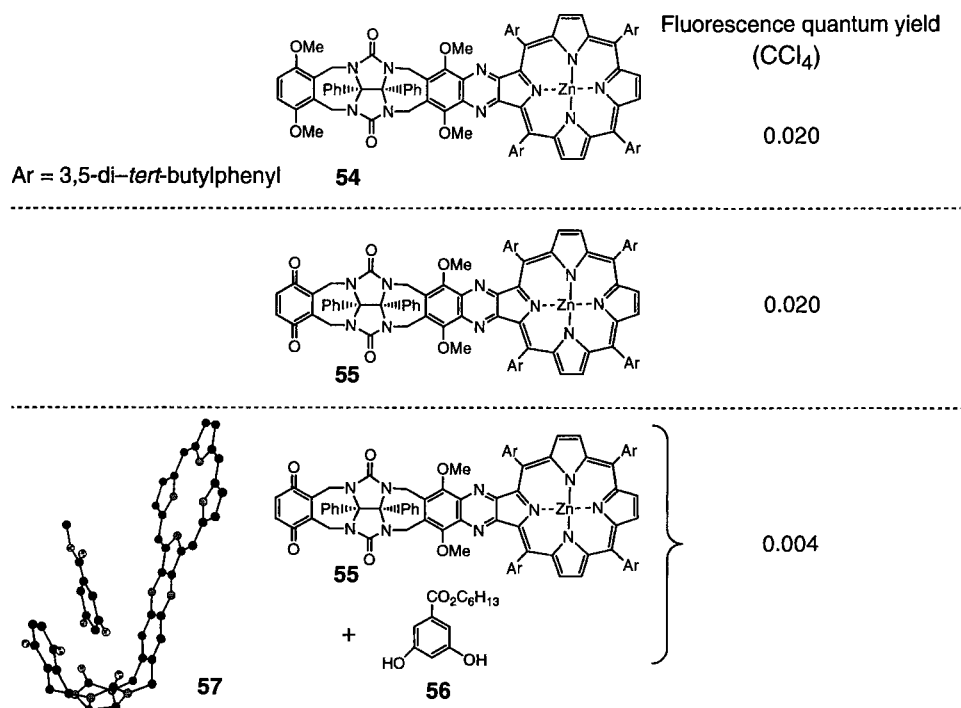


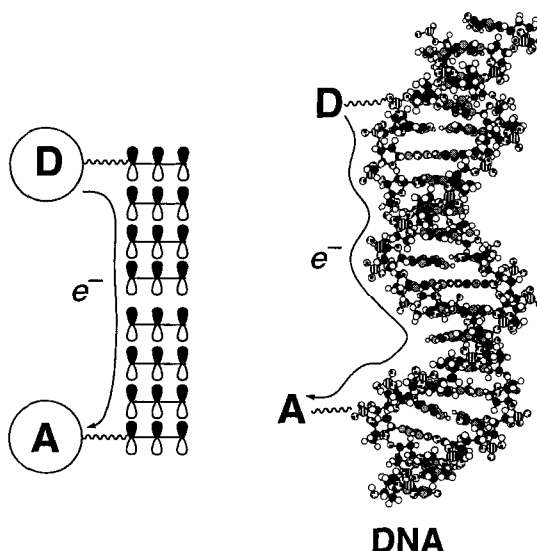
Figure 45. A clip-shaped dyad **55** for investigating superexchange through aromatic systems. The resorcinol **56** becomes complexed to **55** by H-bonding interactions, shown schematically by **57**. Fluorescence quantum yields (CCl₄) reveal that the porphyrin donor fluorescence is strongly quenched in **57**, indicating that ET from the porphyrin to the quinone is occurring through the complexed resorcinol by a superexchange mechanism [134].

1.11 Electron Transfer Mediated by π -Stacks in DNA

Imagine a columnar stack of aromatic rings placed about 3.4 Å apart in parallel planes (Figure 46). How well would such an array mediate ET and HT processes, and by what mechanism would the charge transfer take place, superexchange or by a conduction-like mechanism with the electron or hole “hopping” between aromatic rings?

This problem is receiving intense scrutiny because of its relevance to ET and HT processes in duplex DNA in which the base pairs are approximately stacked in the manner described above [135]. Although the main biological function of DNA is not the transfer of electrons or holes, there is mounting evidence that it may suffer long-range oxidative damage by the migration of holes through the π -stack over extremely large distances (>50 Å) [135–139].

Figure 46. Schematic of the mediation of ET by a π -stack of aromatic rings, such as the base pairs of duplex DNA. The D and A groups associated with the DNA molecule may be covalently linked to the helix, they may be intercalators, or they may be DNA base pairs.



Because duplex DNA may be regarded as a covalently linked multichromophoric system comprising organic chromophores (DNA base pairs), it is appropriate to present a brief discussion of the mechanism of ET and HT in this biopolymer, even though it is treated in greater depth in Volume III, Part 1, Chapter 5 of this Handbook. The discussion will be restricted to the distance dependence of ET and HT dynamics and the question of whether the mechanism of ET and HT reactions is superexchange or charge “hopping”.

Whether ET or HT in DNA occurs by charge hopping or superexchange will largely depend on the relative energy levels of the bridge states (i.e., the DNA bases) and the initial state (donor state). If the bridge states are energetically higher than the initial state, then the electron or hole cannot reside in the bridge, and the charge transfer must occur by a superexchange mechanism i.e., by a single coherent “jump”, from donor to acceptor. The charge transfer dynamics will then follow an exponential decay with distance according to Eq. 4. If, on the other hand, the bridge and donor levels are similar, then thermal injection of an electron or hole into the bridge may take place, and the transport will occur by a hopping mechanism. The hopping dynamics will display weak distance dependence, varying inversely with respect to a small power of the distance according to Eq. 25.

Thus, because of its exponential distance dependence, superexchange-mediated ET and HT in DNA should not be significant for donor–acceptor separations exceeding 15 Å, whereas ET and HT occurring by a hopping mechanism are expected to be much longer range processes, extending beyond 50 Å.

The composition and sequence of the base pairs in DNA should have an important effect on the ET and HT mechanisms. With regard to HT, guanine (*G*) is much more easily oxidized than adenine (*A*) or thymine (*T*); consequently, hole injection into the DNA helix will generate a $G^{+\bullet}$ radical cation. The hole may now randomly

walk over large distances along the DNA helix by hopping between adjacent **G** bases, which have similar redox properties. The hole, however, will never reside on either **A** or **T** bases since their oxidation potentials are higher than that of **G**. The **A–T** base pairs serve, instead, as a superexchange medium through which the charge tunnels between two adjacent **G** bases. The rate of hopping between a pair of adjacent **G** bases is therefore governed by the number of intervening **A–T** base pairs according to the superexchange mechanism. The overall HT hopping rate between donor and acceptor is therefore determined by the largest number of **A–T** base pairs between a pair of adjacent **G** bases in the charge transfer pathway. If each hopping step in an HT pathway involves the same number of intervening **A–T** base pairs, then the hopping mechanism obeys the distance dependence relationship given by Eq. 25 [140].

A number of distance dependence studies have been carried out using synthetic DNA duplexes. In most of these investigations, the data were found to be consistent with the superexchange mechanism since the ET and HT rates followed exponential decays with increasing distance.

An example of the types of distance dependence experiments that are being carried out on DNA is shown in Figure 47 [141]. The DNA strand is a synthetic 6-mer duplex comprising five **A–T** base pairs and a single **G–C** base pair located at various positions along the helix. The duplex is capped by a stilbene hairpin which serves as a photooxidant. Photoexcitation of the stilbene group initiates electron transfer from the **G** donor to the locally excited stilbene acceptor (or equivalently, HT from stilbene to **G**). Importantly, neither **A** nor **T** is able to transfer an electron to the locally excited stilbene since their oxidation potentials are too high. By varying the stilbene–**G** separation it was possible to obtain a distance dependence for the HT rate, which turned out to be exponential with $\beta = 0.64 \text{ \AA}^{-1}$ [141].

A variety of distance dependence studies of ET through DNA, involving different base-pair sequences and different redox couples, have produced β values ranging from $<0.2 \text{ \AA}^{-1}$ to 1.4 \AA^{-1} , i.e., (in units of \AA^{-1}) <0.2 [142–144], 0.64 [141], 0.73

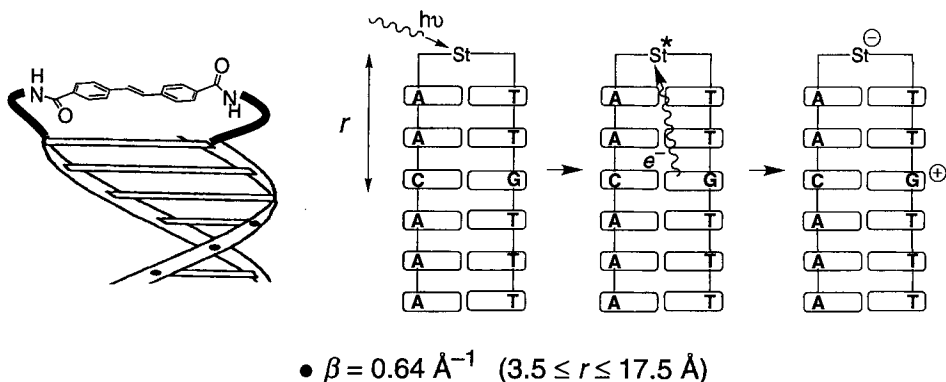


Figure 47. Schematic of photoinduced ET process in a synthetic 6-mer comprising five **A–T** base pairs and one **G–C** base pair located at various distances from the stilbene acceptor [141]. The locally excited stilbene is a potent enough acceptor to effect an ET from **G**, but not from **A** or **T**.

[145], 0.88 [146], 1.0 [147, 148], and 1.42 [149]. With the exception of the very low β value of $<0.2 \text{ \AA}^{-1}$ by Barton and colleagues [142–144], the remaining studies give β ranging from 0.64 – 1.42 \AA^{-1} , suggesting that electron transfer in DNA is protein-like (β for ET in proteins ranges from 0.9 – 1.6 \AA^{-1} [150, 151]; see also Chapter 1 in Section 3.1 of this Handbook).

The large spread in experimentally determined β values for electron transfer in DNA contrasts markedly with the rather narrow range of β values measured for ET occurring through saturated hydrocarbon bridges by the superexchange mechanism (vide supra). Application of simple McConnell theory shows that this large spread is still consistent with the operation of a superexchange mechanism for ET in DNA. From Eq. 24, the sensitivity of β varies inversely with the donor–bridge energy gap Δ . For saturated hydrocarbon bridges, this gap is large and so β will be less sensitive to variation in the energy of the donor. For DNA, however, the virtual ionic states of the base pairs are π -type; consequently, Δ is much smaller and changes in the donor energy should markedly affect the magnitude of β .

Although the β values listed above are consistent with the operation of a superexchange mechanism, the very low values reported by Barton et al. could be interpreted in terms of a hopping or molecular wire mechanism. Indeed, although one theoretical treatment predicts DNA to behave like a protein [150], another predicts that, under certain conditions, a distance-independent ET mechanism term arises which eventually dominates the exponentially distance-dependent superexchange mechanism [122]. Recent femtosecond photoinduced ET studies by Zewail and Barton on DNA possessing an intercalated, covalently tethered ethidium (acceptor) and a 7-deazaguanidine donor revealed the presence of an ultrarapid ET component whose rate was distance-independent for donor-acceptor separations less than 17 \AA [152]. This study lends support to the conjecture that DNA might display wire behavior.

Recent experiments have demonstrated the operation of the hole-hopping mechanism between **G** bases in DNA [125, 140]. In these experiments, Norrish I photocleavage of an acylated nucleoside in a synthetic duplex DNA leads to the formation of a sugar radical (Figure 48a) which then suffers heterolysis to give the radical cation. This sugar radical cation initiates the HT process by transferring the positive charge to a nearby **G** base (Figure 48a). The hole is then free to leave the initial site, $\text{G}_{23}^{+\bullet}$, and wander through the DNA molecule, hopping between adjacent **G** bases; this meandering is only terminated when the hole encounters a **GGG** unit and is irreversibly trapped (**GGG** has a lower oxidation potential than **G**). By varying the length, composition and sequence of the π -stack spanning $\text{G}_{23}^{+\bullet}$ and **GGG**, the distance dependence of the HT dynamics could be measured (Figure 48b).

For **58(1)**–**58(4)**, in which one to four **A–T** base pairs are inserted between $\text{G}_{23}^{+\bullet}$ and **GGG**, the relative HT rate from $\text{G}_{23}^{+\bullet}$ to **GGG** follows an exponential decay with increasing **G**₂₃–**GGG** separation, with an associated β value of 0.7 \AA^{-1} . The operation of the superexchange mechanism for HT in this series of DNA molecules is to be expected since the **A–T** radical cation states are significantly higher in energy than $\text{G}^{+\bullet}$.

Replacement of one of the four **A–T** base pairs in **58(4)** with a **G–C** base pair, to give **59(4)** and **60(4)**, led to a two orders of magnitude increase in the HT rate

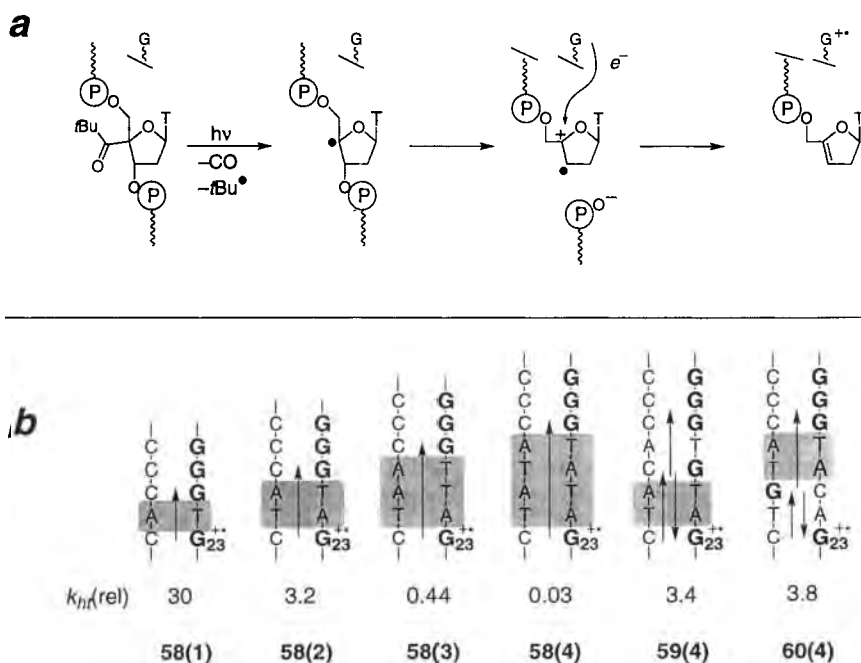


Figure 48. Exploring hole transfer propagation through DNA [125]. (a) The hole is generated by photocleavage, followed by heterolysis and subsequent hole generation at a nearby *G* base. (b) Relative rates of HT, from $G_{23}^{\bullet+}$ to *GGG*, through various DNA duplexes. The shaded areas highlight the longest path between adjacent *G* bases.

relative to **58(4)**. This rate enhancement was attributed to reversible hole hopping between G_{23} and the inserted *G* unit [125]. The longest superexchange pathway in both **59(4)** and **60(4)** has been reduced to only two *A–T* base pairs, compared to four in **58(4)**. It is not surprising, therefore, that the HT rates for **59(4)** and **60(4)** are larger than that for **58(4)** and almost the same as that for **58(2)**, which also has a superexchange pathway comprising two *A–T* base pairs.

By using synthetic duplex DNA molecules in which every hopping step between adjacent *G–C* pairs involves the same number (two) of intervening *A–T* pairs, the validity of Eq. 25, with $\eta = 1.7$ was demonstrated [140].

In summary, these experiments suggest that the hole (or electron) is able to hop incoherently among the *G* bases in a random walk which gives rise to a weak algebraic decay of the HT rate with distance (Eq. 25, $\eta = 1.7$). Moving the electron from one *G* unit to the next requires the operation of the superexchange mechanism, because of the unfavorable redox properties of the intervening *A* and *T* bases. Because of the strong distance dependence of the superexchange mechanism, HT dynamics will be sensitive to the base sequence; the higher the density of *G* bases along the HT pathway, the faster will be the HT rate and the further the hole will be able to travel. Indeed, by judicious placement of *G* units, charge transfer has been observed to occur rapidly over distances exceeding 54 Å [140].

With regard to electron transfer in DNA radical anions (as opposed to HT in the radical cations), the hopping mechanism involves the intermediacy of radical anions of the *C* and *T* bases which have similar reduction potentials. Since one of these bases is present in each base pair, it is predicted that ET proceeding by the hopping mechanism would not be sequence-dependent [127, 140]. Indeed, it has been predicted that measurable hole hopping through DNA could occur over distances as large as 300 Å [127].

1.12 Electron Transfer Mediated through Hydrogen Bonds

Given that ET through proteins is fundamental to many biological processes, and that H-bonds are prevalent in proteins, it is important to determine how efficiently ET can be mediated by H-bonds. The subject of ET in H-bonded and ion-paired systems is presented in Volume III, Part 2, Chapter 4 of this Handbook. Of the numerous studies which have been reported [153–161], that by Therien is of particular relevance to this chapter because it provides a comparative study of ET mediated by saturated bonds and by H-bonds [161]. Therefore, the Therien study will be briefly described here.

The Zn(II)porphyrin–bridge–Fe(III)porphyrin systems, together with their photoinduced ET rate constants, are shown in Figure 49. The ET rate constant for the H-bonded system **61** is comparable to that for **62**, which possesses a partially unsaturated hydrocarbon bridge, whereas the rate for **63**, which contains a fully saturated bridge, is notably slower than the ET rate for **61**. These data suggest that electronic coupling mediated by H-bonds is significant and that, therefore, H-bonded networks may provide dominant pathways for ET in proteins [161].

The observation that ET through a hydrogen-bonded complex is faster than that through a saturated bridge of equivalent length is somewhat surprising, since the strength of the electronic coupling through an H-bond is probably less than that through two geminal C–C bonds [162]. However, it is possible that the diminished ET rate in **63**, compared to **61**, is due to destructive interference in **63**, produced by the TB coupling pathway proceeding through the central ring-fusion bond in the bicyclo[3.3.0]octane unit.

1.13 The Effect of Orbital Symmetry on ET Dynamics

Orbital symmetry can influence ET dynamics through the electronic coupling term, V_{el} , and it is of considerable interest to ascertain the degree of this influence. Covalently linked dyads provide the best way of achieving this experimentally.

The rigid, symmetric norbornylogous systems are well-suited for investigating orbital symmetry effects, two examples of which are shown in Figure 50. Charge

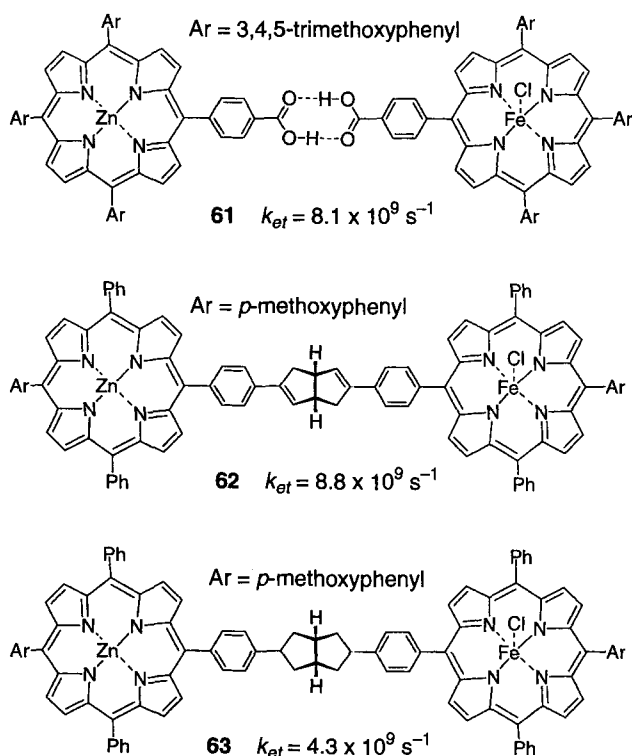


Figure 49. Three dyads possessing Zn(II) porphyrin donor and Fe(III) porphyrin acceptor linked by (from top to bottom) H-bonded bridge, a partially unsaturated bridge and a saturated bridge [161].

recombination from the CS state of **23(8)** is symmetry forbidden since the ground and CS states have opposite state symmetries. This arises because the DMN HOMO and the DCV LUMO in the CS state are each singly occupied but have different symmetries with respect to the molecular plane of symmetry, i.e., a'' and a' , respectively. Consequently, the overall symmetry of the CS state is A'' , whereas that for the ground state is A' .

That charge recombination in the CS states of the series **23(n)** is symmetry forbidden is partly responsible for the unusually long lifetimes observed for the CS states (see Figure 17). The extent to which this orbital symmetry forbiddenness influences the CR process in **23(n)** was gauged by comparing the magnitude of the electronic coupling element, V_{el} for CR in **23(8)** with that for **64(8)**. In the latter system the CR process is symmetry allowed because the maleonitrile LUMO has a'' symmetry, thereby endowing both the CS and ground states of **64(8)** with A' symmetry. From the analysis of charge transfer fluorescence bands that accompanied CR in both **23(8)** and **64(8)**, the V_{el} values for CR in these molecules were calculated to be 36 and 129 cm^{-1} , respectively (in benzene). This result implies that orbital

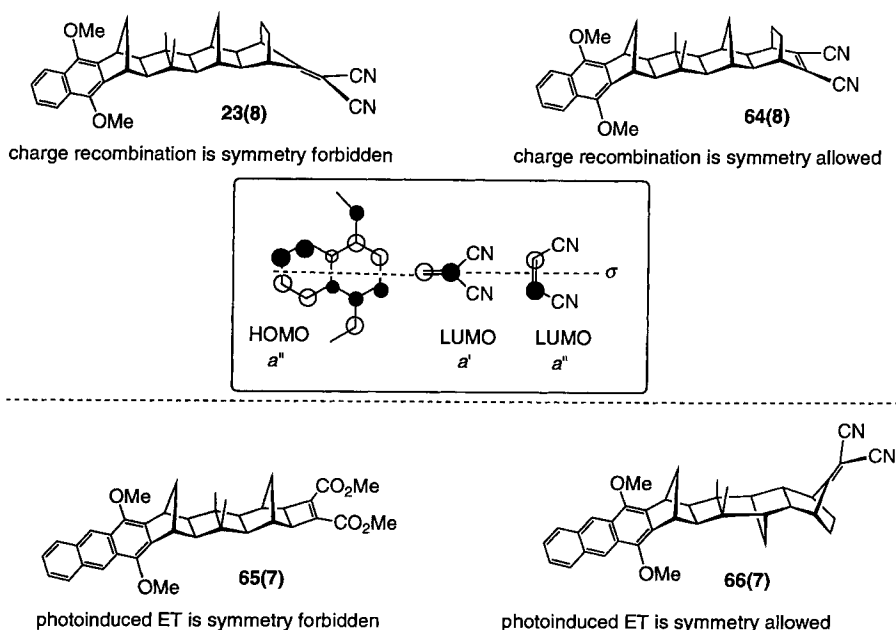


Figure 50. Dyads used for investigating orbital symmetry effects on ET rates. Center: Orbital symmetries of the active MOs involved in the ET processes for **23(8)** and **64(8)**.

symmetry influences electronic coupling by a factor of 3.6 and the charge recombination rates by a factor of 13 (i.e., the CR rate varies with the square of the electronic coupling; see Eq. 2) [163].

The second example of orbital symmetry effects concerns photoinduced charge separation in the norbornylidene dyads, **65(7)** and **66(7)**, which is symmetry-forbidden in the former system but symmetry allowed in the latter. In these systems, orbital symmetry effects are more pronounced than in **23(8)** and **64(8)**, amounting to a 28-fold modulation in the magnitude of V_{el} [164].

A final example of orbital symmetry-forbidden ET is photoinduced ET in **67** (Figure 51). The electronic coupling for photoinduced ET in this molecule should be zero, if this system retains local D_{2d} symmetry within the bismethyleneadamantane unit. However, the experimental photoinduced intramolecular ET rate in this system is extremely rapid, $>10^8 \text{ s}^{-1}$ [165].

Although the data for **23(8)** and **65(7)** (Figure 50) reveal that orbital symmetry does have an effect on ET rates, the rates can still be rapid, nevertheless. For example, the orbital symmetry-forbidden rate of photoinduced ET in **23(13)** is a massive 10^8 s^{-1} .

Clearly, certain vibrational motions (vibronic coupling) in these systems remove the offending symmetry constraint, and lead to a substantial magnitude of V_{el} [166, 167]. Intriguing questions then arise from these experimental data, such as: Is there more than one vibrational mode responsible for generating strong electronic cou-

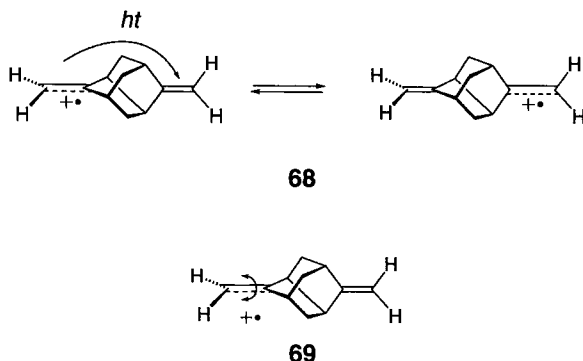
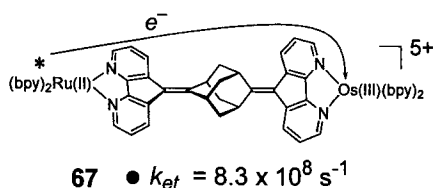


Figure 51. Photoinduced ET in **67** occurs rapidly [165], even though the process is formally forbidden by orbital symmetry. The dynamics of the ET process for **67** is modeled by molecular dynamics calculations of hole transfer in the bis-methyleneadamantane radical cation **69**.

pling? Which modes are primarily responsible for producing the coupling? Answers to these questions are amenable to experimental verification through judicious use of isotopic labeling.

Recently, Jones et al. have described a molecular dynamics (MD) model, which incorporates the trajectory surface hopping (TSH) method (MD-TSH), that shows promise in answering a number of important questions in ET, including those mentioned above [168]. For example, this method has been applied to the dynamics of thermal hole transfer in the bismethyleneadamantane radical cation **68** which serves as a model for **67**. It was found that, instead of V_{el} being zero at the avoided crossing for HT in **68**, it possessed an average value of 0.01 eV. This large value for V_{el} is achieved mainly through the symmetry-breaking torsional vibration about the terminal methylene group of the one-electron π -bond, e.g., **69** [169].

1.14 Effect of Donor–Acceptor Orientation on ET Rates

It is fair to say from the above discussions that the distance dependence of ET dynamics has been extensively measured and explained in terms of the super-exchange (TB) mechanism. These investigations, involving covalently linked multi-chromophoric systems, have also shed light on aspects of the mechanism of the

early ET events occurring in the photosynthetic reaction centres (PRCs) of certain photosynthetic bacteria (see Figure 37).

These ET events are observed to take place on a picosecond time scale, with near unit efficiency, over interchromophore separations exceeding 10 Å. Moreover, ET in the PRC takes place with exquisitely controlled directionality: The primary ET cascade, emanating from the P_{SP} “special pair”, and terminating at the quinone groups, Q_A and Q_B , takes place exclusively along the so-called *L* branch, rather than along the *M* branch, even though both branches are apparently related by near-perfect C_2 symmetry (Figure 37). Since the chlorophyll-like and quinone co-factors are clearly not connected to each other by bonds, conjugated or otherwise, how does the ET process take place so rapidly and how does it “know” which path, the *L* or *M* branch, to take? Although the precise mechanism of ET in the PRC remains unknown, the finding that superexchange-mediated ET through saturated bonds and proteins [151] is a long-range and efficient process lends strong support to the conjecture that the dynamics and directionality of ET in the PRC are controlled by the protein matrix surrounding the center.

Another factor which might be important in modulating ET dynamics is the donor–acceptor orientation. Again, rigid covalently linked dyads are playing a key role in this type of investigation.

Sakata and colleagues have synthesized and studied the photophysics of the dyads **70–73** (Figure 52) [170, 171]. Two types of rigid hydrocarbon bridges were employed to maintain the benzoquinone acceptor at a fixed distance and orientation relative to the porphyrin ring. The orientation of the bridge in each molecule is fixed owing to severe steric congestion between the two neighboring porphyrin

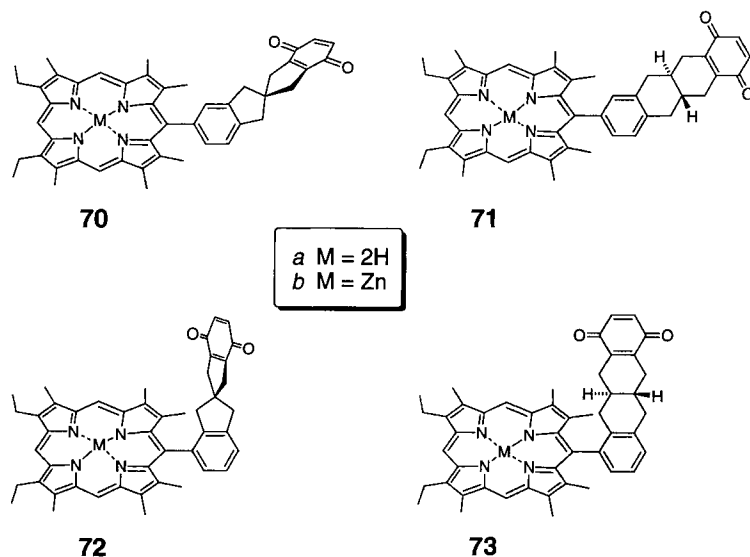


Figure 52. Some porphyrin–quinone dyads used for investigating orientation effects on ET dynamics.

methyl groups and the intervening *meso*-phenyl group which forces the latter into a near-90° orientation with respect to the plane of the porphyrin ring. The spiro[4.4]nonane (SP) and *trans*-decalin (TD) bridges provide very similar donor–acceptor distances, and each has the same number of C–C bonds (four) connecting the two chromophores to the *meso*-phenyl group; however, the SP and TD bridges provide porphyrin–quinone orientations which differ by 90°.

For the free base porphyrin-systems **70a–73a**, it was found that the rate of photoinduced charge separation was greater for the SP systems than for the corresponding TD system: $k_{cs}(\mathbf{70a}):k_{cs}(\mathbf{71a}) \approx 5$ and $k_{cs}(\mathbf{72a}):k_{cs}(\mathbf{73a}) \approx 9$ [171]. Similarly, for the zinc porphyrin molecules, **70b–73b**, the rates of both photoinduced charge separation and subsequent dark charge recombination were greater for the SP molecules than for the corresponding TD molecules.

Because of the near-identical driving forces for, and donor–acceptor distances in, the SP and TD molecules, the rate differences were attributed to differences in the electronic coupling term, V_{el} , rather than to any differences in the Franck–Condon factor. The coupling may be partitioned into a through-bond (through-bridge) component, a direct through-space interaction between the porphyrin and quinone and a superexchange interaction occurring through the intervening solvent molecules between the porphyrin and quinone moieties (*vide infra*). Calculations indicated that TB coupling is approximately the same magnitude through both SP and TD bridges. Consequently, it was concluded that the orientation dependence of the ET rates was due to a combination of through-solvent and through-space effects [170, 171].

It is noteworthy that orientation effects do not seem to be manifested in the series of dyads **32(n)**, even though the quinone–porphyrin orientation for even values of n differs from that for odd values of n by 90°. This deduction was made on the basis that the rate of photoinduced charge separation for **32(n)** followed a good exponential decay with increasing n , with all points associated with both even and odd values of n falling on the same straight line [84].

The dependence of ET rates on the dihedral angle between the two rings of the free base porphyrin donor and the Fe(III) porphyrin acceptor in **74** has been investigated (Figure 53) [172]. The dihedral angle was varied by using the biphenyl bridges shown in the lower part of Figure 53; each of these biphenyl bridges has a definite dihedral angle between the two aromatic rigs, determined by either structural or steric factors. It was found that the rate of photoinduced ET, from locally excited free base porphyrin to Fe(III) porphyrin followed a $\cos 2\theta$ dependence (θ is the dihedral angle about the biphenyl moiety) and was a minimum for $\theta = 45^\circ$ and a maximum for $\theta = 0^\circ$ and 90° . This $\cos 2\theta$ dependency of ET rate is a result of symmetry arguments applied to the nodal structures of the porphyrins and holds, no matter what the mechanism of ET in **74** happens to be, through-space or through-bond (although it is almost certainly the latter which prevails) [173]. These rate data show that changing the dihedral angle from 45° to 0° and 90° results in rate enhancement factors of about 15 and 12, respectively [172].

In summary, orientation effects on ET rates are important, amounting to modulation of rates by factors as large as 20. They are certainly as important as bridge configuration effects (*i.e.*, the all-*trans* rule) and orbital symmetry effects in influ-

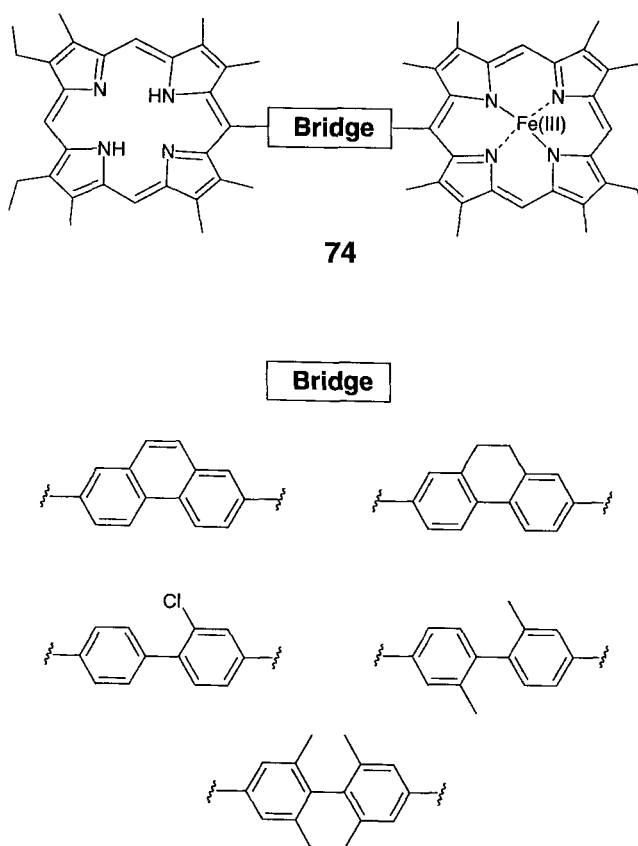


Figure 53. A bisporphyrin dyad for investigating orientation effects on ET dynamics. The dihedral angle between the two porphyrin rings is adjusted by varying the biphenyl bridge [172].

encing ET dynamics. However, a clearer understanding of the origin of orientation effects on ET dynamics is needed.

1.15 Modulation of Electron Transfer Dynamics by Electric Fields

We now turn to another important influence on ET dynamics, electric fields. It is reasonable that the presence of a strong electric field should influence the dynamics of charge separation processes because the dipole moment associated with the newly formed CS state will interact with the field. This interaction will modify the barrier height for the charge separation process. Indeed, it has been postulated that electric field effects might be the cause of the observed directionality of electron transfer in the photosynthetic reaction centre (see Figure 37).

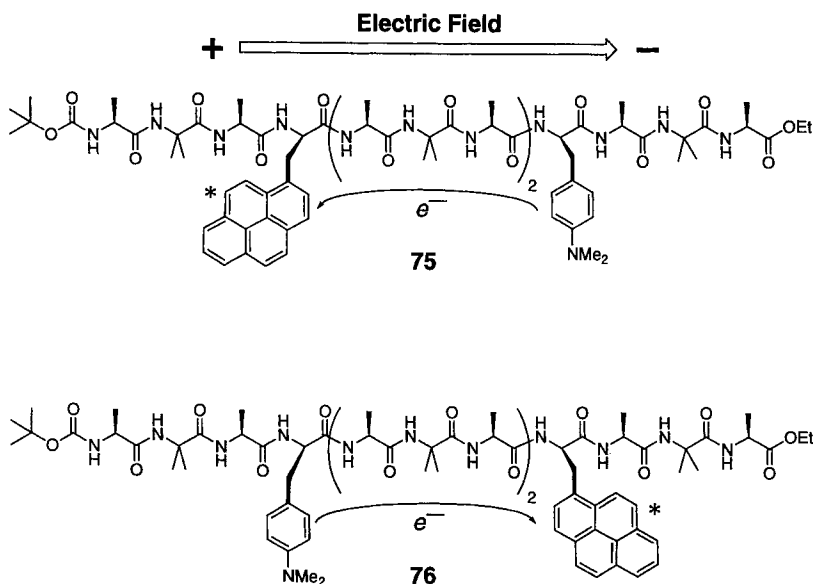
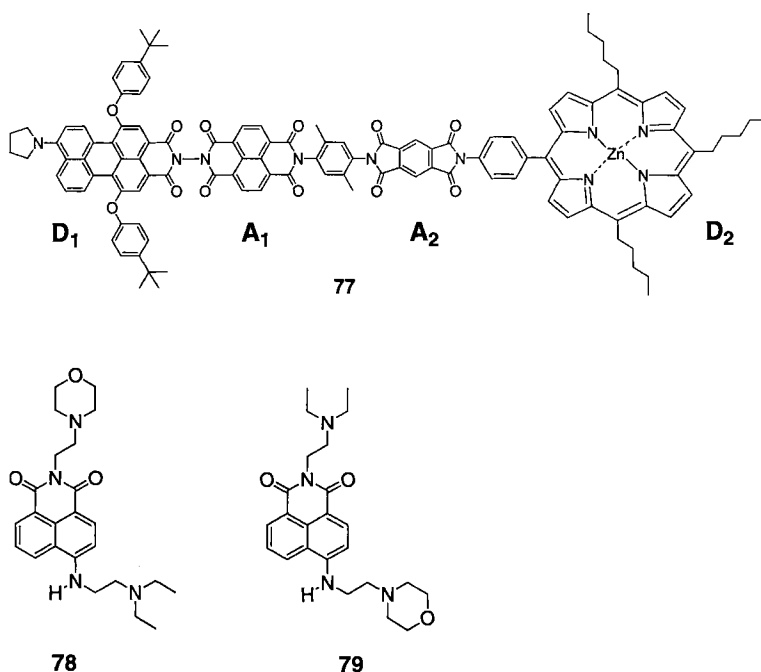


Figure 54. The helical oligopeptide-based dyads used for investigating electric field effects on ET dynamics [174].

The dependence of ET rates on the strength and direction of the electric field has been investigated using the rigid synthetic helical peptides **75** and **76** (Figure 54) possessing covalently linked dimethylaniline (**An**) donor and pyrene (**Pyr**) acceptor [174]. The photoinduced charge separation process involves transfer of an electron from the aniline to the locally excited singlet state of the pyrene (**Pyr***) to give the CS state, $^+\text{An-peptide-Pyr}^-$. In **75**, the dipole of the resulting CS state is aligned antiparallel to the electric field vector generated by the peptide backbone. The CS state of **75** is therefore stabilized by the presence of the electric field (the positive and negative ends of which are located at the nitrogen and carboxylate termini, respectively). In **76**, the positions of the two chromophores are switched, everything else remaining unchanged; in this case, the CS state is now destabilized (relative to **75**) by interaction with the electric field.

Consequently, it is predicted that the charge separation rate should be greater for **75** than for **76**, since the former is associated with a more negative free energy change and therefore, from Eq. 2, with a lower activation barrier. In agreement with qualitative prediction, it was found that the ratio of the photoinduced charge separation rates $k_{cs}(\text{75}):k_{cs}(\text{76})$ is 27 in tetrahydrofuran (THF), a low-polarity solvent, but fell to only 5 in the more polar methanol solvent [174]. The attenuation of the ET rate ratio with increasing solvent polarity is also consistent with the electric field mechanism since the interaction between the electric field of the protein and the dipole of the CS state will be weakened in more polar solvents.



Confirmation that electric field effects were responsible for the enhanced ET rate in **75** relative to **76** was obtained by repeating the ET measurements in THF containing various quantities of water—a solvent which is known to cause protein unfolding and hence to a loss of electric field. Indeed, the $k_{cs}(\mathbf{75}):k_{cs}(\mathbf{76})$ ratio fell from 27 in neat THF to only about 1.8–2.4 in THF–water mixtures [175].

Electric field effects are finding uses in molecular switches. Thus, Wasielewski et al. have synthesized a covalently linked tetrachromophoric system **77**, D_1 – A_1 – A_2 – D_2 . Selective photoinduced ET can be made to take place to give either of the two radical mono-ion pairs, $^+D_1$ – A_1^- – A_2 – D_2 or D_1 – A_1 – A_2^- – D_2^+ . However, formation of the bis-ion pair $^+D_1$ – A_1^- – A_2^- – D_2^+ is completely prevented by the electric field of the neighboring ion pair in the mono-ion pair precursor [176]. That is, the neighboring field causes the second photoinduced charge separation step to become endergonic.

A small covalently linked triad which exhibits unidirectional, path-selective photoinduced ET has been described [177]. The singlet excited state of the 4-aminonaphthalimide fluorophore in **78** and **79** acts as an acceptor and the diethylamino and morpholino groups as donors, although the former is a more potent donor than the latter. It was found that in each molecule, photoinduced ET always took place from the dialkylamine that is attached to the 4-amino position, irrespective of the difference in driving force for the two dialkylamino groups. This observation was attributed to the presence of the large excited state dipole of the 4-aminonaphthalimide whose magnitude and direction only favors ET taking place in the direction from the donor which is attached to the 4-amino position [177].

1.16 Design of Dyads with Rapid Solvent-Independent Charge Separation

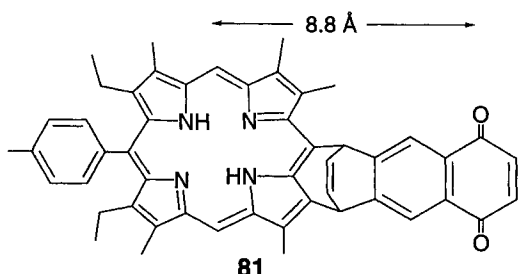
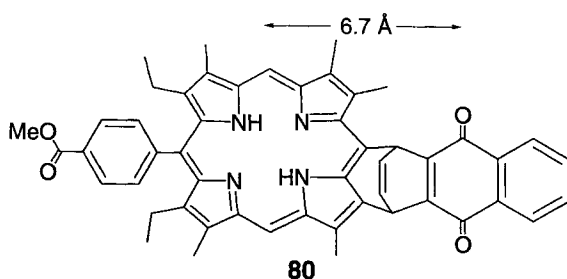
An interesting challenge with obvious applications is the following: Is it possible to design, from first principles, a dyad for which the rate of photoinduced charge separation is virtually solvent- and temperature-independent? It has, indeed, been shown that it is possible to do so, at least within the context of simple Marcus–Hush theory [67]. Recalling from the Marcus–Hush equation (Eq. 2) that a barrierless ET process means that $-\Delta G_{et} = \lambda$ ($\lambda = \lambda_i + \lambda_s$), it was shown that those factors which render a charge separation process optimally rapid and barrierless also make the rate virtually solvent-independent. This result implies that, for a given system, there is a unique value for a quantity called the polar free energy change, P_{opt} , that will make the reaction rate-optimal and solvent-independent. P_{opt} for a particular system represents the limiting value of ΔG_{et} for charge separation across an infinite distance in polar media and is readily accessible from the independently determined redox potentials and excitation energies of the individual donor and acceptor chromophores. From Marcus–Hush theory, together with the condition that the ET process is barrierless, the expression (Eq. 27) may be derived [67]:

$$P_{opt} \approx -\lambda_i - \frac{e^2}{n^2} \left(\frac{1}{r} - \frac{1}{R_c} \right) \quad (27)$$

where λ_i is the internal reorganization energy of the dyad, e is the charge of the electron, n is the refractive index of the solvent (normally taken to be equal to 2.0), r is the average ionic radius of the chromophores, and R_c is the center-to-center interchromophore separation. The weak temperature dependence of ET dynamics for systems which satisfy Eq. 27 follows from the fact that such ET processes are barrierless and, therefore, from Eq. 2, the ET rates depend only on $T^{-1/2}$.

The importance of Eq. 27 is that it relates P_{opt} , which can be experimentally determined from the redox and photophysical properties of the donor and acceptor chromophores, to R_c ; that is for a preset interchromophore separation, R_c , the redox and photophysical properties of the chromophores must be chosen so that they give a value of P_{opt} which is identical to that calculated from Eq. 28. Conversely, for a given pair of chromophores, there is a unique value of R_c for which the free energy of activation for photoinduced charge separation in the dyad is largely solvent-independent.

This model was used successfully to explain the different solvent dependencies of the rates of photoinduced charge for the dyad **23(8)** and the naphthalene analogue (i.e., the methoxy groups are replaced by hydrogens) [67]. Equation 27 has recently been used to explain the interesting contrasting photoinduced electron transfer properties of the two closely related covalently linked porphyrin–naphthoquinone dyads **80** and **81** [178]. It was found that dyad **80**, whose quinone carbonyl groups are 6.7 Å from the center of the porphyrin donor, exhibits photoinduced ET whose



rates are practically solvent- and temperature-independent. In contrast, the rates of photoinduced ET in the dyad **81**, whose carbonyl groups are further removed from the porphyrin center (8.8 Å) display much stronger temperature and solvent dependence. It was found that the R_c value for **80** (6.7 Å) more closely satisfies Eq. 27 than did that for **81**—the former proceeded under barrierless conditions, whereas the latter gives a P value which differs from P_{opt} by 0.17 eV [178].

1.17 Verification of the Marcus Inverted Region

From Eq. 2, the activation free energy for an ET process is given by:

$$\Delta G_{et}^\ddagger = \frac{(\Delta G_{et} + \lambda)^2}{4\lambda} \quad (28)$$

Electron transfer reactions for which $-\Delta G_{et} < \lambda$ are said to take place in the Marcus normal region and their rates increase with increasing exergonicity, becoming optimal (barrierless) when $-\Delta G_{et} = \lambda$. When the reaction becomes even more exergonic, then $-\Delta G_{et} > \lambda$ and an activation barrier reappears; the reaction is now in the Marcus inverted region, and the ET rate is predicted to decrease with increasing exergonicity. This prediction was elegantly verified for thermal charge

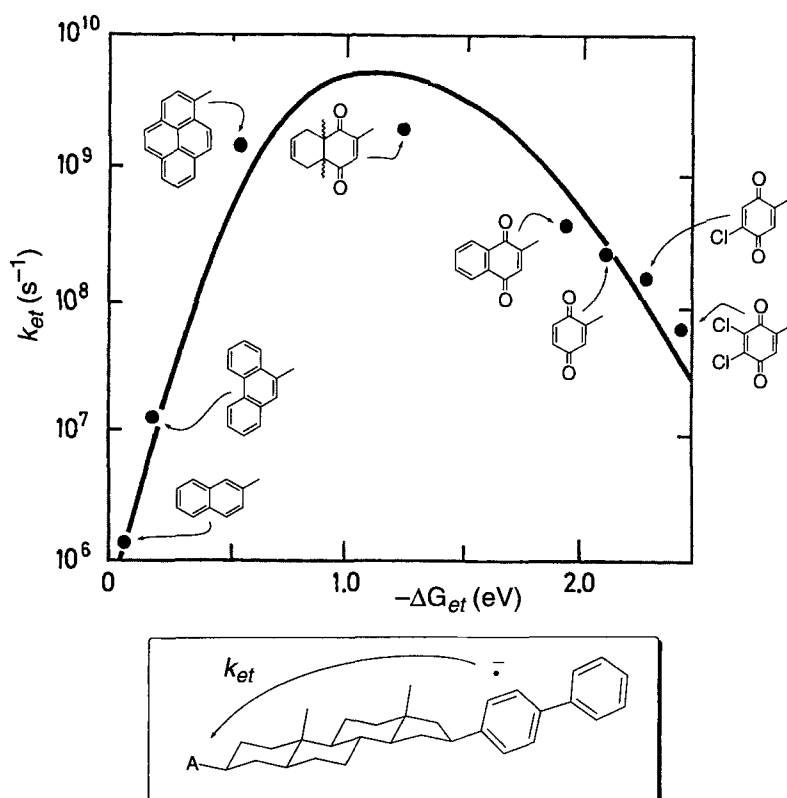


Figure 55. Schematic of the plot of the rate of ET from a biphenyl radical anion to an acceptor **A**, as a function of driving force [179].

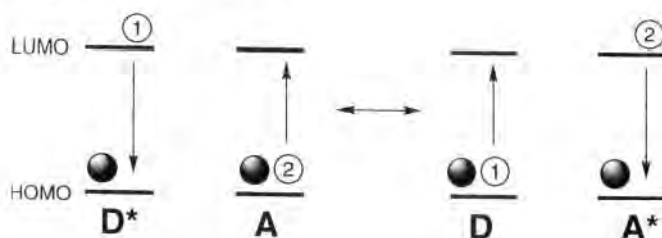
shift reactions in the radical anions of the rigid **D-steroid-A** dyads, shown in Figure 55, which were generated by pulse radiolysis [179]. The driving force ($-\Delta G_{et}$) for the reaction was adjusted by changing the acceptor. It was found that, in qualitative agreement with classical Marcus theory, the ET rate increased with increasing exergonicity, peaked and then fell off. This work nicely illustrates another use for rigid covalently linked dyads: the main purpose of the bridge in this series of experiments was to hold the donor and acceptor groups at a constant distance from each other.

1.17.1 Through-Bond-Mediated Electronic Energy Transfer

The transfer of excitation energy from a locally excited donor chromophore to an acceptor, resulting in the formation of the electronically excited acceptor state, is known as electronic energy transfer (EET). There are two basic EET mechanisms,



a Förster Mechanism



b Exchange Mechanism (Dexter)

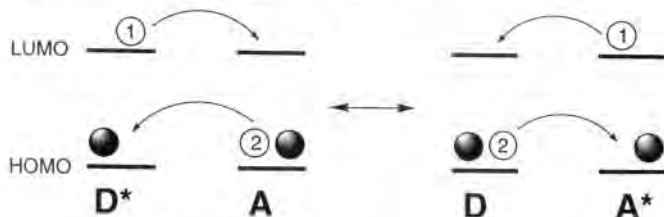


Figure 56. Two principal mechanisms of excitation energy transfer (EET). (a) The Förster dipole–dipole mechanism, in which the active electrons, ① and ②, remain, respectively, on **D** and **A** throughout the process. (b) In the (Dexter) exchange mechanism, electrons ① and ② exchange locations.

namely the Förster and the Dexter (exchange) mechanisms. In the Förster mechanism (Figure 56a), EET takes place through the interaction of the oscillating dipole of the excited donor with that of the acceptor. This dipole–dipole interaction is long-range, and the rates of EET by the Förster mechanism decay inversely with the sixth power of the interchromophore separation. Note that because electrons one and two (Figure 56a) do not exchange their locations during the EET process, there is no dependence of EET dynamics on the donor–acceptor orbital overlap in the Förster mechanism.

In the exchange mechanism (Figure 56b), the two electrons exchange orbitals and so the EET dynamics now depend on inter-orbital overlap and therefore should display an exponential decay with distance. In fact, the exchange mechanism may

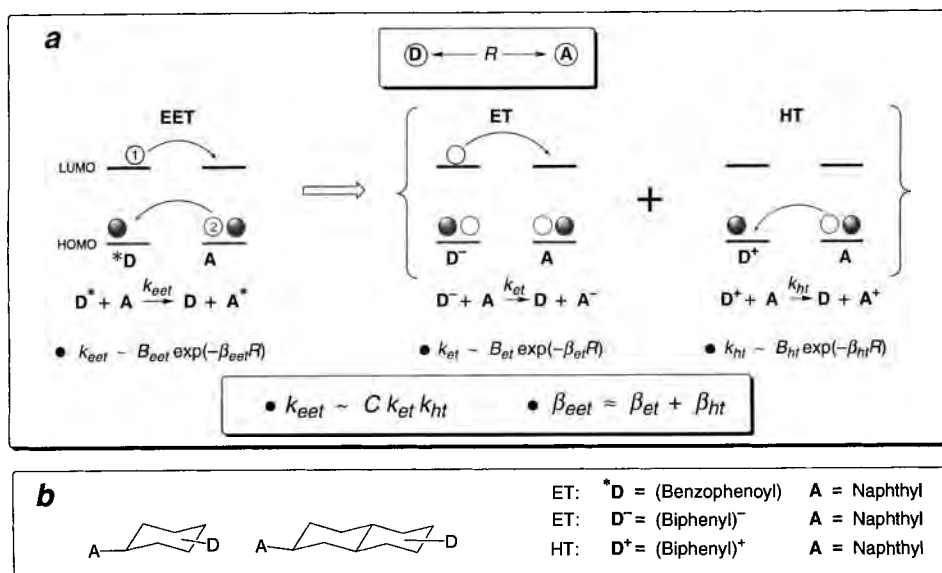


Figure 57. (a) Analysis of the exchange mechanism for EET in terms of two-electron transfer processes, one involving ET in the corresponding anion (center) and the other involving hole transfer (HT) in the corresponding cation (right-hand side). (b) The dyads that were used to test experimentally the relationship $k_{eet} \sim k_{et}k_{ht}$ for a triplet-triplet EET process [180]. *D is the triplet-excited state of benzophenoyl.

be regarded as a double ET process, one electron moving from the donor LUMO to the acceptor LUMO and the other from the acceptor HOMO to the donor HOMO. This important insight is illustrated in Figure 57a, from which it should be clear that the damping factor, β_{eet} , for EET occurring by an exchange mechanism is approximately equal to the sum of the damping factors for two separate ET processes, β_{et} for electron transfer in the radical anion, and β_{ht} for hole transfer in the radical cation. This prediction has been confirmed by correlating the rates of triplet-triplet EET with those for ET and HT for the systems shown in Figure 57b [180].

Although the exchange mechanism was originally formulated in terms of direct orbital overlap between the donor and acceptor chromophores, it is clear that it can be extended to cover the case of TB-mediated EET. This is because TB coupling provides a mechanism for spatially extending the active orbitals of the two chromophores into the intervening medium, thereby facilitating interchromophore orbital overlap. TB-mediated EET has been explored using the rigid norbornylogous systems **82(n)**–**84(n)** (Figure 58) [181, 182].

The experiments involved measuring the rates of singlet-singlet EET from the first excited singlet state of DMN to the ketone or dione chromophore. The distance dependence of the EET rates in **82(n)** follows an exponential decay, rather than an inverse sixth-power law, thereby confirming that an exchange mechanism and not a

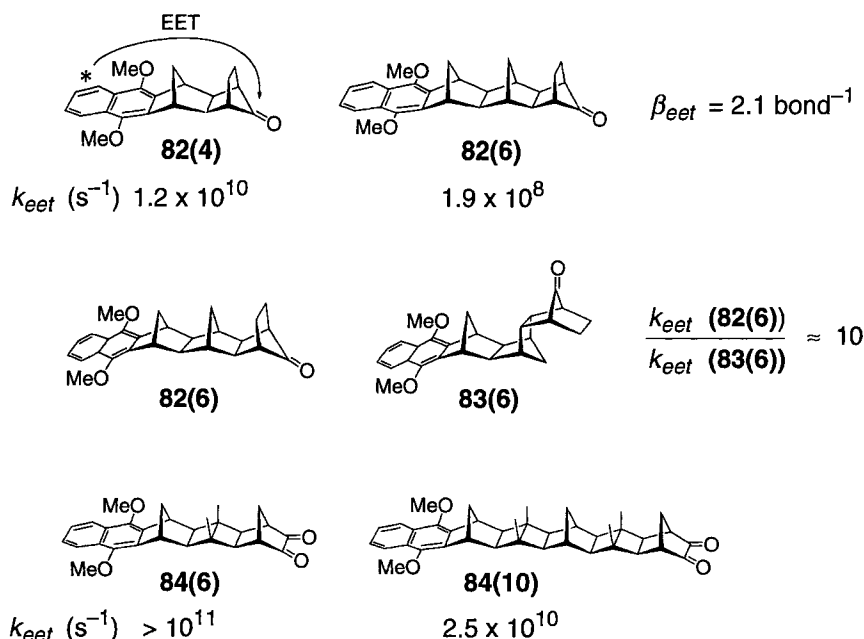


Figure 58. Rate data for singlet–singlet EET between locally excited DMN donor and carbonyl or dione acceptor in various norbornylogous systems [181].

Förster mechanism is operating in these systems [181]. The magnitude of β_{eet} was found to be about 2.1 per bond and is about double that found for photoinduced charge separation in the structurally related **DMN–B–DCV** systems **23(n)** (vide supra). This relationship agrees with the postulate that β_{eet} is the sum of damping factors for two separate ET processes. Consistent with the TB-mediated EET mechanism was the finding that singlet–singlet EET occurs about 10 times more rapidly in the all-*trans* system **82(6)** than in the “kinked” system **83(6)** [181].

How rapidly can TB-mediated EET be propagated? Considering that the rate of TB-mediated EET falls off much more rapidly than that for a single ET process, it is not surprising that most TB-mediated EET processes are insignificant for interchromophore separations exceeding 10 Å. However, there are exceptions, the most dramatic of which are provided by the series **84(n)**. Thus, the rate of singlet–singlet EET for the 10-bond system **84(10)** is an enormous $2.5 \times 10^{10} \text{ s}^{-1}$ and that for **84(6)** is too fast to be measured on a picosecond time scale [182]. The EET rate for **84(10)** is two orders of magnitude larger than that measured for the 6-bond system, **82(6)**, and six orders of magnitude faster than that predicted for the 10-bond system **82(10)**.

Just why TB-mediated EET takes place so rapidly in **84(10)** is currently a mystery, but this example certainly underscores the importance of the through-bond mechanism in mediating not only ET, but also EET processes.

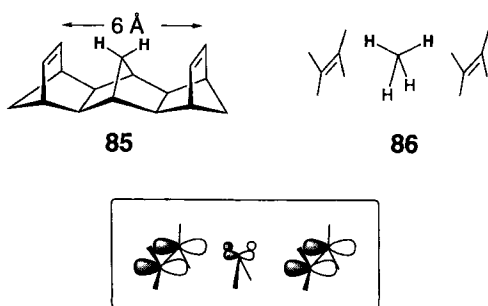


Figure 59. Interactions between the π MOs of the two double bonds and the pseudo- π orbitals of the methano group in **85** and the methane molecule in **86**.

1.18 Electron Transfer Mediated by Solvent Molecules

That electron transfer may be facilitated by a TB or superexchange mechanism raises the possibility that solvent molecules may also mediate ET. Presumably, the electronic coupling through solvent will not be as strong as that through a covalently linked bridge because the solvent molecules are further apart, both from each other and from the chromophores. In addition, the solvent molecules are tumbling about, and this will lead to an electronic coupling whose magnitude is less than that resulting from freezing the solvent molecules in the optimal configuration. An indication that ET could be effectively mediated by saturated hydrocarbon solvents came from early photoelectron spectroscopic and ESR studies on U-shaped dienes such as **85** (Figure 59) [15, 183, 184]. These studies revealed a remarkably large π -splitting energy of 0.52 eV for **85** which could only be explained in terms of substantial interactions between the π MOs of the double bonds and the pseudo- π orbitals of the central methano bridge (Figure 59, inset). Calculations predicted a large π -splitting of 0.32 eV for the molecular sandwich **86** which models electronic coupling between the double bonds and a methane “solvent” molecule. Given that a coupling of only 0.003 eV is sufficient to accelerate long-range ET [2], a predicted split of 0.32 eV for **86** is amazing and suggests that solvent-mediated ET should be an important process, although not as dramatic as that suggested by the idealized solvent-substrate configuration shown by **86**.

Efforts have been made to determine the importance of solvent-mediated ET in intermolecular electron transfer processes in rigid matrices [4, 5] and also in liquid solution [185, 186]. For example, the distance dependence of intermolecular ET dynamics in glassy matrices indicate that solvent-mediated ET is significant. The value of $\beta = 1.2 \text{ \AA}^{-1}$ was established for electron transfer occurring in a methyl-tetrahydrofuran matrix at 77 K under optimal driving force conditions [4]. This value is substantially smaller than that predicted for a through-space mechanism ($\beta \approx 3.0 \text{ \AA}^{-1}$), and is not much larger than that measured for ET mediated by a through-saturated-bonds mechanism ($\beta \approx 0.85 \text{ \AA}^{-1}$). Although important, the kinetic data for ET in glasses are averaged over a broad range of solute–solvent ori-

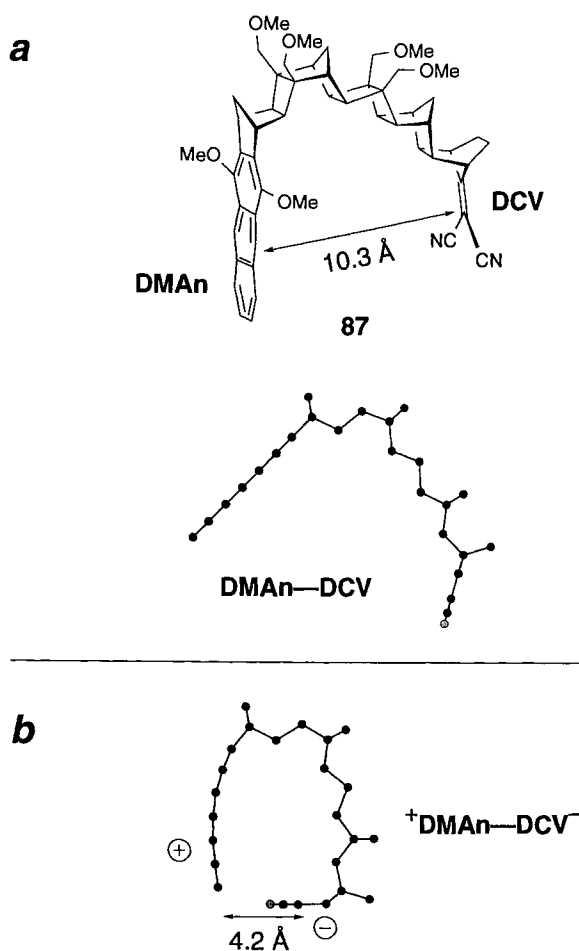


Figure 60. (a) A U-shaped dyad **87** [187]. The distance between the **DMAn** and **DCV** chromophores is 10.3 Å (HF/3-21G). (b) UHF/3-21G Gas-phase-optimized geometry of the CS state of **87** [202].

entations, and it would be desirable to investigate solvent-mediated ET under more controlled conditions where solute–solvent orientation and distance are more precisely known.

Experimental progress is being made in this direction through the synthesis of rigid U-shaped systems based on the norbornylogous bridge, representative of which are **87–91** (Figures 60–63). In these systems, the terminal chromophores face each other across a “rigid” cavity created by a norbornylogous bridge. The length and configuration of the connecting bridge are designed to minimize TB-mediated ET through the bridge, while encouraging solvent-mediated ET to occur by providing a cavity within which a certain number of solvent molecules are present (in a dynamic sense).

The dyad **87** possesses a cavity c. 10 Å wide which is sufficiently large to accommodate a solvent molecule, such as benzonitrile (Figure 60) [187]. Such a molecule

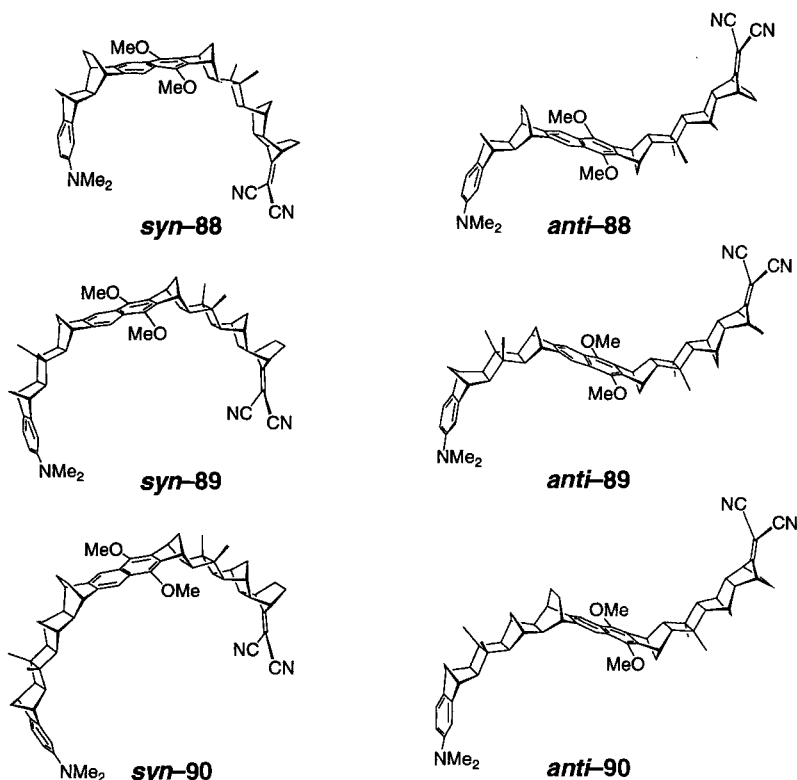


Figure 61. The *syn*- and *anti*-triads **88–90**. Geometries were optimized at the HF/3-21G level [192, 193].

would be able to provide a coupling pathway for mediating photoinduced charge separation between the locally excited singlet state of the dimethoxyanthracene (**DMA**) donor and the **DCV** acceptor. Estimated values of the electronic coupling, V_{el} , for photoinduced charge separation in **87** in various solvents were extracted from the rate data. For benzonitrile solvent, $V_{el} = 14 \text{ cm}^{-1}$, whereas for acetonitrile, $V_{el} < 2 \text{ cm}^{-1}$. These data were interpreted in terms of solvent-mediated ET using the following argument. Because photoinduced charge separation in **87** involves the LUMOs of the two chromophores, the strongest coupling with the solvent molecule will occur with the latter's LUMO rather than the HOMO. Consequently, the magnitude of V_{el} for solvent-mediated charge separation in **87** should increase with increasing electron affinity of the solvent molecule, and this is in accord with observation since the electron affinity of benzonitrile is greater than that of acetonitrile [187]. Photoinduced charge separation studies on a 9-bond **DMA**-**9-DCV** analogue of the 11-bond dyad **87**, which possesses a smaller cavity size of 7.1 \AA , likewise revealed evidence of significant through-solvent-mediated ET in electronegative solvents [188–191].

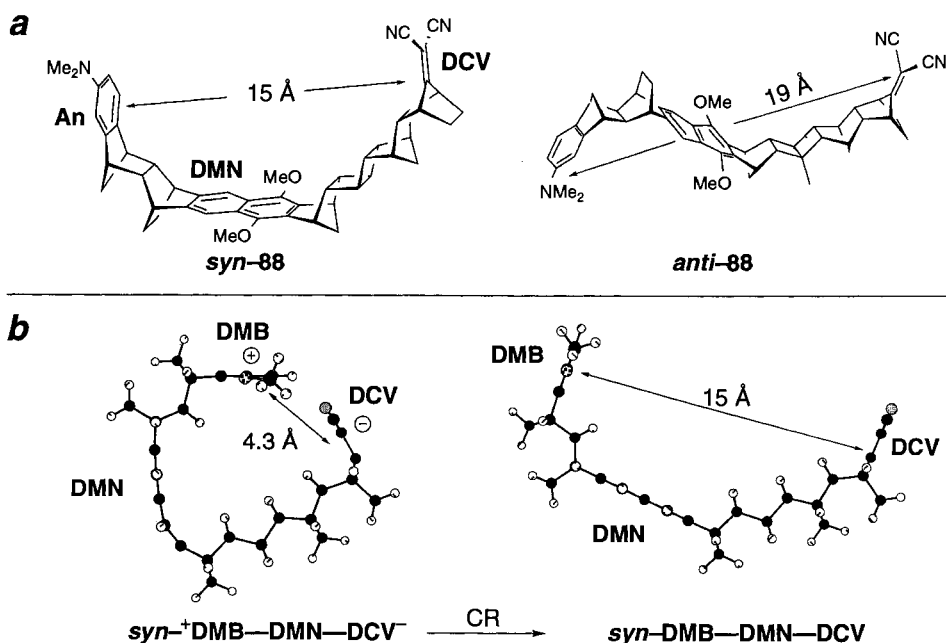


Figure 62. (a) Two trichromophoric systems used for investigating through-solvent-mediated charge recombination processes. (b) Profiles of the (U)HF/3-21G gas-phase structures of the CS state (left) and ground state (right) of an analogue of *syn*-88 in which the dimethylaniline donor is replaced by 1,4-dimethoxybenzene (DMB).

The series of rigid *syn* and *anti* triads **88–90** (Figure 61) provide useful models for investigating aspects of long-range photoinduced charge separation and subsequent dark charge recombination processes [192, 193]. These systems possess a **DMN** primary donor covalently linked to a **DCV** acceptor by an 8-bond norbornylogous bridge and to a dimethylaniline (**An**) secondary donor by a 4-, 6-, or 8-bond bridge. The *syn* isomers possess a U-shaped cavity, across which the **An** and **DCV** chromophores face each other, which is absent in the *anti* isomers.

The primary motive behind the synthesis of this series was to produce giant CS states $^+\text{An-DMN-DCV}^-$, in which the charge separation occurs over large distances, comparable to than for **23(8)**, but with much greater quantum yield than for the latter (which is $\approx 30\%$). Giant CS states are useful because increasing the distance between the charges in the CS state leads to greater longevity of that state to unwanted charge recombination. It was anticipated that the overall ET process would take place in two consecutive steps, i.e., ET from locally excited **DMN** to **DCV**, to give $\text{An-}^+\text{DMN-DCV}^-$, followed by hole transfer from **DMN** to **An** to give the final giant CS state $^+\text{An-DMN-DCV}^-$. There are many examples of the successful use of covalently linked multichromophoric systems for effecting photoinduced charge separation over large distances with high quantum yields [11, 12,

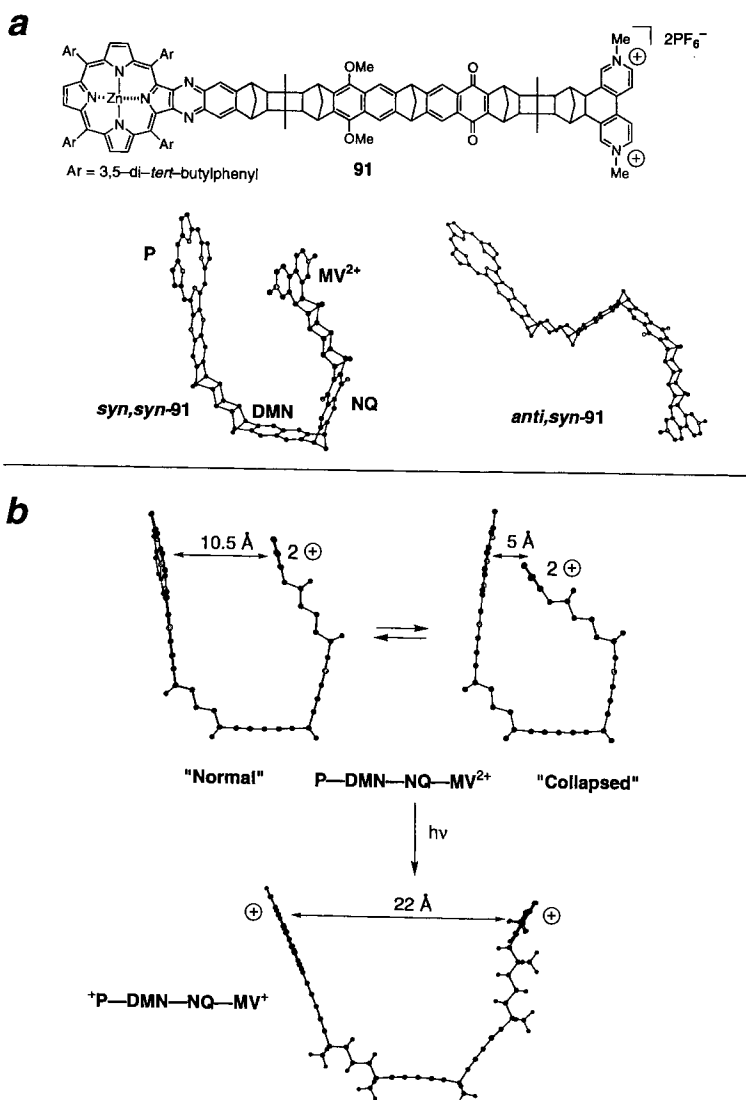


Figure 63. (a) Two tetrachromophoric systems **91**. (b) Profiles of the (U)HF/3-21G gas-phase structures for the "collapsed" ground state and giant CS state of *syn,syn*-**91**. The "normal" ground-state structure was located using the AM1 semi-empirical method.

178, 194–197], and they will be discussed in more detail Volume III, Part 2, in Chapter 2 of this Handbook. The multichromophore strategy obviously drew its inspiration from the ET cascade which takes place in the photosynthetic reaction center (see Figure 37).

Efficient photoinduced charge separation, to generate the giant CS state, was found to occur in all systems **88–90** in solvents that were sufficiently polar to stabilize the giant CS state over the “shorter” CS state $\text{An}^+\text{DMN-DCV}^-$ [198–200]. For the *syn* isomers, this process occurred even in nonpolar alkane solvents, whereas the *anti* isomers required more polar solvents because of the greater separation between the **An** and **DCV** chromophores in the latter isomers, compared to the corresponding *syn* isomers (cf. *syn-88* and *anti-88*; Figure 62a).

Although the formation of the giant CS states from **88–90** could be achieved, the lifetimes of the CS states for the *syn* isomers were amazingly short, compared to those for the respective *anti* isomers. For example, the lifetime of the giant CS state of *syn-88* is only 0.1 ns, compared to 73 ns for the *anti* isomer (in butyl ether) [201].

Solvent-mediated charge recombination taking place within the U-shaped cavity of *syn-88* could explain this result, but there is a problem with this explanation in that the CR rates are rapid, even in saturated solvents such as decalin, which have very high-lying LUMOs. Electronic coupling of the donor and acceptor LUMOs to this type of solvent molecule should, therefore, be weak and it will be further weakened by the large cavity size in *syn-88* (15 Å) which would require coupling through at least two solvent molecules.

A plausible solution to this dilemma has been found. Gas-phase ab initio MO calculations were carried out on the ground and CS states of an analogue of *syn-88*, in which 1,4-dimethoxybenzene (**DMB**) replaces the **An** chromophore (Figure 62b). Whereas the terminal chromophores in the optimized ground state structure of *syn-88* are about 15 Å apart, this separation is predicted to be only about 4.3 Å in the giant CS state $^+\text{DMB-DMN-DCV}^-$ [202]!. This large contraction in the inter-terminal separation, upon creation of the CS state is the result of electrostatic attractions between the oppositely charged terminal chromophores. The contraction is achieved by out-of-plane bending of the aromatic rings and the **DCV** radical anion and energetically is not very costly. Although these calculations refer to the gas phase, such geometric distortions should also occur in solvents of low dielectric constant, such as decalin. It is noteworthy that the small inter-terminal separation in the CS state of *syn-88* might actually enable *direct* through-space-mediated charge recombination to occur, thereby nicely explaining why CR in this molecule is so fast in weakly polar solvents of low electron affinity.

The photophysical results for the giant porphyrin–dimethoxynaphthalene–naphthoquinone–viologen tetrad, **P-DMN-NQ-MV²⁺**, **91** (Figure 63), complement those obtained for **88** [203]. Photoinduced charge separation, to form the giant CS state, $^+\text{P-DMN-NQ-MV}^+$, readily occurs in the *syn,syn* isomer, but not in the *anti,syn* isomer. This result immediately informs one that the charge separation process is not occurring through the bridge in *syn,syn-91* because if it did, then photoinduced charge separation should also be observed in the *anti,syn* isomer, since the bridges in the two systems are identical in terms of length and constitution. As observed for the charge recombination behavior for *syn-88*, the rate of photoinduced charge separation in *syn,syn-91* appears to be insensitive to solvent electron affinity. Another puzzle was the finding that the giant CS state is quite long-lived,

500 ns, which stands in marked contrast to the very short lifetime of c. 0.1 ns for the CS state of **syn-88** [203].

The conundrum may be explained by the operation of electrostatically induced geometric distortion in *both* ground and giant CS states of **syn, syn-91**. Gas-phase *ab initio* MO calculations indicate that there is an electrostatic attraction between the zinc porphyrin and the viologen dication in the ground state of **syn, syn-91** and that this results in a “collapsed” conformer, in which the porphyrin and viologen groups are only about 5 Å apart [204]. This “collapsed” structure is largely brought about by out-of-plane bending of the central pair of naphthalene rings. AM1 calculations suggest the presence of another, higher-energy conformation in which the termini are at the “normal” separation of c. 10 Å, corresponding to a fully relaxed bridge. Perhaps the “collapsed” and “normal” conformations are in rapid equilibrium. Photoinduced charge separation in the “collapsed” conformation could take place by a direct through-space mechanism without requiring electronic participation of the solvent. This would explain the solvent independence of the rate of photoinduced charge-separation observed for **syn, syn-91**. Because of the large inter-terminal separation of 10.5 Å in the “normal” conformer of **syn, syn-91**, charge separation in this conformer may be too slow to compete with unproductive decay of the locally excited porphyrin moiety.

Gas-phase geometry optimization of the giant CS state $^+P\text{-DMN-NQ-MV}^+$ offers an explanation for its very long lifetime. In this species, the terminal chromophores, both being positively charged, repel each other. As a result, the inter-terminal separation increases markedly, to about 22 Å (Figure 63b). Both through-space- and through-solvent-mediated charge recombination in $^+P\text{-DMN-NQ-MV}^+$ possessing this geometry would be unfavorable, and this would explain its long lifetime (TB-mediated CR is likewise unfavorable considering that the electronic coupling between the porphyrin and viologen chromophores must extend over 23 bonds of the bridge).

Gas-phase calculations on the CS state of **87** also predict a large change in the cavity size, from 10 Å in the ground state, to only about 4.2 Å in the CS state (Figure 60b), and that this is mainly caused by out-of-plane bending of both **DCV** and **DMA**n groups [202]. Similar geometric distortions are predicted for other U-shaped dyads in their CS states.

The predicted geometry changes that accompany charge separation in **87-91** are further examples of the harpooning mechanism [205] which is known to occur in semiflexible systems in nonpolar solvents [206, 207] and in the gas phase [57]. A typical harpooning reaction is exemplified by piperidine-based dyads such as **92** (Figure 64): Long-range photoinduced ET, from the aniline donor to the locally excited cyanonaphthalene acceptor, takes place in the chair conformation, to generate the extended CS state **93** which then undergoes an electrostatically driven conformational change (“harpooning”) into a compact (boat) exciplex-like species **94**.

In summary, solvent-mediated ET studies are proving a challenge. The prediction that “rigid” U-shaped systems undergo large structural distortions in their CS states, particularly in low-dielectric solvents, raises issues of interpretation of the data that are yet to be resolved satisfactorily.

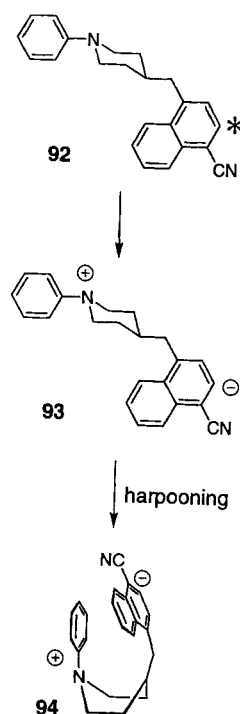


Figure 64. An example of electrostatically driven folding ("harpooning") involving ring inversion [206].

1.19 Epilogue

The past 15 years have witnessed remarkable progress in the understanding of the character of long-range ET processes, and this has been achieved—in no small part—by the study of ET in covalently linked multichromophoric systems. Through the elegant combination of synthesis, photophysical measurements and computational quantum chemical calculations, the scope and significance of superexchange-mediated ET have been delineated. For example, it is now known that ET mediated by saturated hydrocarbon bridges can take place rapidly over distances exceeding 12 Å, and that the ET dynamics may be modulated in a predictable manner, for example by changing the bridge configuration, by orbital symmetry constraints and by the presence of strong electric fields.

These significant findings form the basis of a set of design principles for the construction of molecular photovoltaic cells and other nanoscale electronic devices in which the control of both the rate and directionality of ET processes is an essential requirement. The successful construction of an artificial light-driven proton pump, based on principles of long-range ET processes illustrates the promise of this approach [197].

Of course, it is impracticable to synthesize nanoscale devices based solely on covalently linked bridged systems, and it is reassuring to learn that ET is also strongly

mediated by H-bonded networks and by solvent molecules, thereby opening the way for the construction of photovoltaic supramolecular assemblies.

The conditions which favor the incoherent *electron transport* mechanism, associated with molecular wire behavior, over the coherent superexchange *electron transfer* mechanism are being elucidated, mainly through studies of systems possessing covalently linked *conjugated* bridges and DNA molecules. This is an exciting, emerging area of research which lies at the heart of molecular electronics.

Recent HT studies on DNA suggest that the double helix is able to act as a hole conductor, and that its conducting ability may be fine-tuned by altering the location and density of *G* sites in the helix. These findings offer the possibility of using DNA as a charge transport device in nanoscale architecture. This is an important challenge to be met in the near future! Hopefully, this review will inspire chemists from various areas to pursue not only applications of ET processes but also those fundamental issues of ET theory that still need to be resolved [208].

Acknowledgments

Support from the Australian Research Council is gratefully acknowledged, as is the award of an ARC Senior Research Fellowship.

References

1. K. A. Jolliffe, S. J. Langford, M. G. Ranasinghe, M. J. Shephard, M. N. Paddon-Row, *J. Org. Chem.* **1999**, *64*, 1238.
2. N. S. Hush, *Coord. Chem. Rev.* **1985**, *64*, 135.
3. R. A. Marcus, N. Sutin, *Biochim. Biophys. Acta* **1985**, *811*, 265.
4. J. R. Miller, J. V. Beitz, R. K. Huddleston, *J. Am. Chem. Soc.* **1984**, *106*, 5057.
5. J. R. Miller, *New J. Chem.* **1987**, *11*, 83.
6. M. Bixon, J. Jortner, *Adv. Chem. Phys.* **1999**, *106*, 35.
7. M. N. Paddon-Row, *Acc. Chem. Res.* **1994**, *27*, 18.
8. M. N. Paddon-Row, A. M. Oliver, J. M. Warman, K. J. Smit, M. P. de Haas, H. Oevering, J. W. Verhoeven, *J. Phys. Chem.* **1988**, *92*, 6958.
9. G. L. Closs, J. R. Miller, *Science* **1988**, *240*, 440.
10. M. R. Wasielewski, in M. A. Fox, M. Chanon (Eds.): *Photoinduced Electron Transfer*, Part A, Elsevier, Amsterdam 1988, p. 161.
11. D. Gust, T. A. Moore, A. L. Moore, *Acc. Chem. Res.* **1993**, *26*, 198.
12. M. R. Wasielewski, *Chem. Rev.* **1992**, *92*, 435.
13. M. N. Paddon-Row, J. W. Verhoeven, *New J. Chem.* **1991**, *15*, 107.
14. K. D. Jordan, M. N. Paddon-Row, *Chem. Rev.* **1992**, *92*, 395.
15. M. N. Paddon-Row, K. D. Jordan, in J. F. Liebman, A. Greenberg (Eds.): *Modern Models of Bonding and Delocalization*, Vol. 6, VCH Publishers, New York 1988, p. 115.
16. P. W. Anderson, *Phys. Rev.* **1950**, *79*, 350.
17. H. M. McConnell, *J. Chem. Phys.* **1961**, *35*, 508.
18. M. N. Paddon-Row, *Acc. Chem. Res.* **1982**, *15*, 245.
19. R. Hoffmann, *Acc. Chem. Res.* **1971**, *4*, 1.
20. V. Balaji, L. Ng, K. D. Jordan, M. N. Paddon-Row, H. K. Patney, *J. Am. Chem. Soc.* **1987**, *109*, 6957.
21. S. Larsson, *J. Chem. Soc., Faraday Trans. 2* **1983**, 1375.

22. S. Larsson, *J. Am. Chem. Soc.* **1981**, *103*, 4034.
23. M. D. Newton, *Chem. Rev.* **1991**, *91*, 767.
24. V. V. Voevodskii, S. P. Solodovnikov, V. N. Chibrikov, *Doklady Akad. Nauk S.S.S.R.* **1959**, *129*, 1082.
25. S. I. Weissman, *J. Am. Chem. Soc.* **1958**, *80*, 6462.
26. J. E. Harriman, A. H. Maki, *J. Chem. Phys.* **1963**, *39*, 778.
27. F. Gerson, W. Huber, W. B. Martin, J. P. Caluwe, T. Pepper, M. Szwarc, *Helv. Chim. Acta* **1984**, *67*, 416.
28. K. Shimada, G. Moshuk, H. D. Connor, P. Caluwe, M. Szwarc, *Chem. Phys. Lett.* **1972**, *14*, 396.
29. K. Shimada, M. Szwarc, *Chem. Phys. Lett.* **1974**, *28*, 540.
30. M. N. Paddon-Row, R. Hartcher, *J. Am. Chem. Soc.* **1980**, *102*, 662.
31. M. N. Paddon-Row, R. Hartcher, *J. Am. Chem. Soc.* **1980**, *102*, 671.
32. F. Gerson, T. Wellauer, A. M. Oliver, M. N. Paddon-Row, *Helv. Chim. Acta* **1990**, *73*, 1586.
33. L. T. Calcaterra, G. L. Closs, J. R. Miller, *J. Am. Chem. Soc.* **1983**, *105*, 670.
34. M. D. Johnson, J. R. Miller, N. S. Green, G. L. Closs, *J. Phys. Chem.* **1989**, *93*, 1173.
35. J. M. Warman, M. Hom, M. N. Paddon-Row, A. M. Oliver, J. Kroon, *Chem. Phys. Lett.* **1990**, *172*, 114.
36. M. J. Shephard, M. N. Paddon-Row, K. D. Jordan, *Chem. Phys.* **1993**, *176*, 289.
37. T. Koopmans, *Physica* **1934**, *1*, 104.
38. J. S. Binkley, J. A. Pople, W. J. Hehre, *J. Am. Chem. Soc.* **1980**, *102*, 939.
39. S. Larsson, M. Braga, *Chem. Phys.* **1993**, *176*, 367.
40. E. Heilbronner, A. Schmelzer, *Helv. Chim. Acta* **1975**, *58*, 936.
41. M. N. Paddon-Row, S. S. Wong, *Chem. Phys. Lett.* **1990**, *167*, 432.
42. C. A. Naleway, L. A. Curtiss, J. R. Miller, *J. Phys. Chem.* **1991**, *95*, 8434.
43. C. Liang, M. D. Newton, *J. Phys. Chem.* **1992**, *96*, 2855.
44. C. Liang, M. D. Newton, *J. Phys. Chem.* **1993**, *97*, 3199.
45. K. D. Jordan, D. Nachtigallova, M. N. Paddon-Row, in E. R. Davidson (Ed.): *Modern Electronic Structure Theory and Applications in Organic Chemistry*, World Scientific Publishing Co., Singapore 1997, p. 257.
46. K. D. Jordan, M. N. Paddon-Row, in P. v. R. Schleyer (Ed.): *Encyclopedia of Computational Chemistry*, Wiley, New York 1998, p. 826.
47. D. C. Craig, M. N. Paddon-Row, *Aust. J. Chem.* **1987**, *40*, 1951.
48. A. E. Reed, L. A. Curtiss, F. Weinhold, *Chem. Rev.* **1988**, *88*, 899.
49. M. K. Crawford, Y. Wang, K. B. Eiseenthal, *Chem. Phys. Lett.* **1981**, *79*, 529.
50. Y. Wang, M. K. Crawford, K. B. Eiseenthal, *J. Am. Chem. Soc.* **1982**, *104*, 529.
51. N. Mataga, *Pure Appl. Chem.* **1984**, *56*, 1255.
52. N. Mataga, *Pure Appl. Chem.* **1993**, *65*, 1605.
53. N. C. Yang, S. B. Neoh, T. Naito, L. K. Ng, D. A. Chernoff, D. B. McDouals, *J. Am. Chem. Soc.* **1980**, *102*, 2806.
54. N. A. van Dantzig, H. S. Shou, J. C. Alfano, N. C. Yang, D. H. Levy, *J. Chem. Phys.* **1994**, *100*, 7068.
55. S. L. Zhang, M. J. Lang, S. Goodman, C. Durnell, V. Fidler, G. R. Fleming, N. C. Yang, *J. Am. Chem. Soc.* **1996**, *118*, 9042.
56. N. C. Yang, S. L. Zhang, M. J. Lang, S. Goodman, C. Durnell, G. R. Fleming, H. L. Carrell, R. M. Garavito, *Adv. Chem. Phys.* **1999**, *106*, 645.
57. B. Wegewijs, J. W. Verhoeven, *Adv. Chem. Phys.* **1999**, *106*, 221.
58. F. Hirayama, *J. Chem. Phys.* **1965**, *42*, 3163.
59. T. Förster, in M. Gordon, W. R. Ware (Eds.): *The Exciplex*, Academic Press, New York 1975, p. 1.
60. J. W. Verhoeven, *Adv. Chem. Phys.* **1999**, *106*, 603.
61. A. W. J. D. Dekkers, J. W. Verhoeven, W. N. Speckamp, *Tetrahedron* **1973**, *29*, 1691.
62. P. Pasman, F. Rob, J. W. Verhoeven, *J. Am. Chem. Soc.* **1982**, *104*, 5127.
63. P. Pasman, J. W. Verhoeven, T. J. de Boer, *Tetrahedron Lett.* **1977**, *17*, 207.
64. M. N. Paddon-Row, E. Cotsaris, H. K. Patney, *Tetrahedron* **1986**, *42*, 1779.

65. N. S. Hush, M. N. Paddon-Row, E. Cotsaris, H. Oevering, J. W. Verhoeven, M. Heppener, *Chem. Phys. Lett.* **1985**, *117*, 8.
66. H. Oevering, M. N. Paddon-Row, H. Heppener, A. M. Oliver, E. Cotsaris, J. W. Verhoeven, N. S. Hush, *J. Am. Chem. Soc.* **1987**, *109*, 3258.
67. J. Kroon, J. W. Verhoeven, M. N. Paddon-Row, A. M. Oliver, *Angew. Chem., Int. Ed. Engl.* **1991**, *30*, 1358.
68. M. P. de Haas, J. M. Warman, *Chem. Phys.* **1982**, *73*, 35.
69. J. M. Warman, M. P. de Haas, M. N. Paddon-Row, E. Cotsaris, N. S. Hush, H. Oevering, J. W. Verhoeven, *Nature* **1986**, *320*, 615.
70. J. M. Warman, M. P. de Haas, J. W. Verhoeven, M. N. Paddon-Row, *Adv. Chem. Phys.* **1999**, *106*, 571.
71. A. M. Oliver, D. C. Craig, M. N. Paddon-Row, J. Kroon, J. W. Verhoeven, *Chem. Phys. Lett.* **1988**, *150*, 366.
72. M. R. Wasielewski, M. P. Niemczyk, D. G. Johnson, W. A. Svec, D. W. Minsek, *Tetrahedron* **1989**, *45*, 4785.
73. R. A. Marcus, *Angew. Chem., Int. Ed. Engl.* **1993**, *32*, 1111.
74. J. M. Warman, K. J. Smit, M. P. de Haas, S. A. Jonker, M. N. Paddon-Row, A. M. Oliver, J. Kroon, H. Oevering, J. W. Verhoeven, *J. Phys. Chem.* **1991**, *95*, 1979.
75. H. Oevering, J. W. Verhoeven, M. N. Paddon-Row, J. M. Warman, *Tetrahedron* **1989**, *45*, 4751.
76. K. W. Penfield, J. R. Miller, M. N. Paddon-Row, E. Cotsaris, A. M. Oliver, N. S. Hush, *J. Am. Chem. Soc.* **1987**, *109*, 5061.
77. N. S. Hush, *Prog. Inorg. Chem.* **1967**, *8*, 391.
78. N. S. Hush, *Electrochim. Acta* **1968**, *13*, 1005.
79. A. H. A. Clayton, K. P. Ghiggino, G. J. Wilson, P. J. Keyte, M. N. Paddon-Row, *Chem. Phys. Lett.* **1992**, *195*, 249.
80. G. L. Closs, L. T. Calcaterra, N. J. Green, K. W. Penfield, J. R. Miller, *J. Phys. Chem.* **1986**, *90*, 3673.
81. A. D. Joran, B. A. Leland, G. G. Geller, J. J. Hopfield, P. B. Dervan, *J. Am. Chem. Soc.* **1984**, *106*, 6090.
82. B. A. Leland, A. D. Joran, P. M. Felker, J. J. Hopfield, A. H. Zewail, P. B. Dervan, *J. Phys. Chem.* **1985**, *89*, 5571.
83. A. D. Joran, B. A. Leland, P. M. Felker, A. H. Zewail, J. J. Hopfield, P. B. Dervan, *Nature* **1987**, *327*, 508.
84. S. Knapp, T. G. M. Dhar, J. Albaneze, S. Gentemann, J. A. Potenza, D. Holten, H. J. Schugar, *J. Am. Chem. Soc.* **1991**, *113*, 4010.
85. Stein, C. A., N. A. Lewis, G. Seitz, *J. Am. Chem. Soc.* **1982**, *104*, 2596.
86. E. H. Yonemoto, G. B. Saupe, R. H. Schmehl, S. M. Hubig, R. L. Riley, B. L. Iverson, T. E. Mallouk, *J. Am. Chem. Soc.* **1994**, *116*, 4786.
87. J. W. Park, B. A. Lee, S. Y. Lee, *J. Phys. Chem. B* **1998**, *102*, 8209.
88. D. N. Beratan, J. J. Hopfield, *J. Am. Chem. Soc.* **1984**, *106*, 1584.
89. D. N. Beratan, J. N. Onuchic, J. J. Hopfield, *J. Chem. Phys.* **1985**, *83*, 5326.
90. D. N. Beratan, *J. Am. Chem. Soc.* **1986**, *108*, 4321.
91. J. N. Onuchic, D. N. Beratan, *J. Am. Chem. Soc.* **1987**, *109*, 6771.
92. L. A. Curtiss, C. A. Naleway, J. R. Miller, *J. Phys. Chem.* **1993**, *97*, 4050.
93. L. A. Curtiss, C. A. Naleway, J. R. Miller, *Chem. Phys.* **1993**, *176*, 387.
94. L. A. Curtiss, C. A. Naleway, J. R. Miller, *J. Phys. Chem.* **1995**, *99*, 1182.
95. N. Koga, K. Sameshima, K. Morokuma, *J. Phys. Chem.* **1993**, *97*, 13117.
96. M. N. Paddon-Row, S. S. Wong, K. D. Jordan, *J. Am. Chem. Soc.* **1990**, *112*, 1710.
97. M. N. Paddon-Row, S. S. Wong, K. D. Jordan, *J. Chem. Soc., Perkin Trans. 2* **1990**, 417.
98. M. N. Paddon-Row, S. S. Wong, K. D. Jordan, *J. Chem. Soc., Perkin Trans. 2* **1990**, 425.
99. M. N. Paddon-Row, K. D. Jordan, *J. Am. Chem. Soc.* **1993**, *115*, 2952.
100. M. N. Paddon-Row, M. J. Shephard, K. D. Jordan, *J. Am. Chem. Soc.* **1993**, *115*, 3312.
101. M. N. Paddon-Row, M. J. Shephard, K. D. Jordan, *J. Phys. Chem.* **1993**, *97*, 1743.
102. M. J. Shephard, M. N. Paddon-Row, K. D. Jordan, *J. Am. Chem. Soc.* **1994**, *116*, 5328.
103. M. J. Shephard, M. N. Paddon-Row, *J. Phys. Chem.* **1995**, *99*, 17497.

104. M. N. Paddon-Row, M. J. Shephard, *J. Am. Chem. Soc.* **1997**, *119*, 5355.
105. J. Cheng, C. J. Miller, *J. Phys. Chem. B* **1997**, *101*, 1058.
106. D. Möbius, *Ber. Bunsenges. Phys. Chem.* **1978**, *82*, 848.
107. H. J. Kuhn, *Photochemistry* **1979**, *10*, 111.
108. H. J. Kuhn, *Pure Appl. Chem.* **1979**, *51*, 341.
109. E. Katz, N. Itzhak, I. Willner, *Langmuir* **1993**, *9*, 1392.
110. H. O. Finklea, D. D. Hanshaw, *J. Am. Chem. Soc.* **1992**, *114*, 3173.
111. L. H. Guo, J. S. Facci, G. McLendon, *J. Phys. Chem.* **1995**, *99*, 8458.
112. M. T. Carter, G. K. Rowe, J. N. Richardson, L. M. Tender, R. H. Terrill, R. W. Murray, *J. Am. Chem. Soc.* **1995**, *117*, 2896.
113. S. B. Sachs, S. P. Dudek, R. P. Hsung, L. R. Sita, J. F. Smalley, M. D. Newton, S. W. Feldberg, C. E. D. Chidsey, *J. Am. Chem. Soc.* **1997**, *119*, 10563.
114. K. Weber, L. Hockett, S. Creager, *J. Phys. Chem. B* **1997**, *101*, 8286.
115. K. Slowinski, R. V. Chamberlain, C. J. Miller, M. Majda, *J. Am. Chem. Soc.* **1997**, *119*, 11910.
116. H. Imahori, Y. Sakata, *Adv. Mater.* **1997**, *9*, 537.
117. M. Antolovich, P. J. Keyte, A. M. Oliver, M. N. Paddon-Row, J. Kroon, J. W. Verhoeven, S. A. Jonker, J. M. Warman, *J. Phys. Chem.* **1991**, *95*, 1933.
118. T. D. M. Bell, T. A. Smith, K. P. Ghiggino, M. G. Ranasinghe, M. J. Shephard, M. N. Paddon-Row, *Chem. Phys. Lett.* **1997**, *268*, 223.
119. H. Imahori, K. Hagiwara, M. Aoki, T. Akiyama, S. Taniguchi, T. Okada, M. Shirakawa, Y. Sakata, *J. Am. Chem. Soc.* **1996**, *118*, 11771.
120. R. M. Williams, M. Koeberg, J. M. Lawson, Y. Z. An, Y. Rubin, M. N. Paddon-Row, J. W. Verhoeven, *J. Org. Chem.* **1996**, *61*, 5055.
121. H. Imahori, K. Hagiwara, T. Akiyama, M. Aoki, S. Taniguchi, T. Okada, M. Shirakawa, Y. Sakata, *Chem. Phys. Lett.* **1996**, *263*, 545.
122. A. K. Felts, W. T. Pollard, R. A. Friesner, *J. Phys. Chem.* **1995**, *99*, 2929.
123. W. B. Davis, M. R. Wasielewski, M. A. Ratner, V. Mujica, A. Nitzan, *J. Phys. Chem.* **1997**, *101*, 6158.
124. A. Okada, V. Chernyak, S. Mukamel, *J. Phys. Chem.* **1998**, *102*, 1241.
125. E. Meggers, M. E. Michel-Beyerle, B. Giese, *J. Am. Chem. Soc.* **1998**, *120*, 12950.
126. J. Jortner, M. Bixon, T. Langenbacher, M. E. Michel-Beyerle, *Proc. Natl. Acad. Sci. USA* **1998**, *95*, 12759.
127. M. Bixon, B. Giese, S. Wessely, T. Langenbacher, M. E. Michel-Beyerle, J. Jortner, *Proc. Natl. Acad. Sci. USA* **1999**, *96*, 11713.
128. W. B. Davis, W. A. Svec, M. A. Ratner, M. R. Wasielewski, *Nature* **1998**, *396*, 60.
129. H. Heitele, M. E. Michel-Beyerle, *J. Am. Chem. Soc.* **1985**, *107*, 8286.
130. P. Finckh, H. Heitele, M. Volk, M. E. Michel-Beyerle, *J. Phys. Chem.* **1988**, *92*, 6584.
131. A. Osuka, H. Yamada, K. Maruyama, N. Mataga, T. Asahi, M. Ohkouchi, T. Okada, I. Yamazaki, Y. Nishimura, *J. Am. Chem. Soc.* **1993**, *115*, 9439.
132. S. Higashida, H. Tsue, K. Sugiura, T. Kaneda, Y. Sakata, Y. Tanaka, S. Taniguchi, T. Okada, *Bull. Chem. Soc. Jpn.* **1996**, *69*, 1329.
133. J. N. H. Reek, A. E. Rowan, R. Degelder, P. T. Beurskens, M. J. Crossley, S. Defeyter, F. Deschryver, R. J. M. Nolte, *Angew. Chem., Int. Ed. Engl.* **1997**, *36*, 361.
134. J. N. H. Reek, A. E. Rowan, M. J. Crossley, R. J. M. Nolte, *J. Org. Chem.* **1999**, *64*, 6653.
135. R. E. Holmlin, P. J. Dandliker, J. K. Barton, *Angew. Chem., Int. Ed.* **1998**, *36*, 2715.
136. D. B. Hall, R. E. Holmlin, J. K. Barton, *Nature* **1996**, *382*, 731.
137. S. M. Gasper, G. B. Schuster, *J. Am. Chem. Soc.* **1997**, *119*, 12762.
138. D. B. Hall, J. K. Barton, *J. Am. Chem. Soc.* **1997**, *119*, 5045.
139. P. J. Dandliker, R. E. Holmlin, J. K. Barton, *Science* **1997**, *275*, 1465.
140. B. Giese, S. Wessely, M. Spormann, U. Lindemann, E. Meggers, M. E. Michel-Beyerle, *Angew. Chem., Int. Ed.* **1999**, *38*, 996.
141. F. D. Lewis, T. F. Wu, Y. F. Zhang, R. L. Letsinger, S. R. Greenfield, M. R. Wasielewski, *Science* **1997**, *277*, 673.
142. C. J. Murphy, M. R. Arkin, Y. Jenkins, N. D. Ghatlia, S. H. Bossmann, N. J. Turro, J. K. Barton, *Science* **1993**, *262*, 1025.

143. M. R. Arkin, E. D. A. Stemp, R. E. Holmlin, J. K. Barton, A. Hormann, E. J. C. Olson, P. F. Barbara, *Science* **1996**, 273, 475.
144. S. O. Kelley, R. E. Holmlin, E. D. A. Stemp, J. K. Barton, *J. Am. Chem. Soc.* **1997**, 119, 9861.
145. S. J. Atherton, P. C. Beaumont, *J. Phys. Chem.* **1995**, 99, 12025.
146. A. M. Brun, A. Harriman, *J. Am. Chem. Soc.* **1992**, 114, 3656.
147. E. Meggers, D. Kusch, M. Spichly, U. Wille, B. Giese, *Angew. Chem., Int. Ed.* **1998**, 37, 460.
148. A. Harriman, *Angew. Chem., Int. Ed.* **1999**, 38, 945.
149. K. Fukui, K. Tanaka, *Angew. Chem., Int. Ed.* **1998**, 37, 158.
150. S. Priyadarshy, S. M. Risser, D. N. Beratan, *J. Phys. Chem.* **1996**, 100, 17678.
151. R. Langen, J. L. Colon, D. R. Casimiro, T. B. Karpishin, J. R. Winkler, H. B. Gray, *J. Biol. Inorg. Chem.* **1996**, 1, 221.
152. C. Z. Wan, T. Fiebig, S. O. Kelley, C. R. Treadway, J. K. Barton, A. H. Zewail, *Proc. Natl. Acad. Sci. USA* **1999**, 96, 6014.
153. J. M. Zaleski, C. K. Chang, G. E. Leroi, R. I. Cukier, D. G. Nocera, *J. Am. Chem. Soc.* **1992**, 114, 3564.
154. C. Turro, C. K. Chang, G. E. Leroi, R. I. Cukier, D. G. Nocera, *J. Am. Chem. Soc.* **1992**, 114, 4013.
155. J. A. Roberts, J. P. Kirby, D. G. Nocera, *J. Am. Chem. Soc.* **1995**, 117, 8051.
156. A. Berman, E. S. Izraeli, H. Levanon, B. Wang, J. L. Sessler, *J. Am. Chem. Soc.* **1995**, 117, 8252.
157. T. Hayashi, H. Ogoshi, *Chem. Soc. Rev.* **1997**, 26, 355.
158. M. D. Ward, *Chem. Soc. Rev.* **1997**, 26, 365.
159. J. P. Kirby, J. A. Roberts, D. G. Nocera, *J. Am. Chem. Soc.* **1997**, 119, 9230.
160. A. Berg, Z. Shuali, M. Asano-Someda, H. Levanon, M. Fuhs, K. Mobius, *J. Am. Chem. Soc.* **1999**, 121, 7433.
161. P. J. F. de Rege, S. A. Williams, M. J. Therien, *Science* **1995**, 269, 1409.
162. J. N. Betts, D. N. Beratan, J. N. Onuchic, *J. Am. Chem. Soc.* **1992**, 114, 4043.
163. A. M. Oliver, M. N. Paddon-Row, J. Kroon, J. W. Verhoeven, *Chem. Phys. Lett.* **1992**, 191, 371.
164. Y. Zeng, M. B. Zimmt, *J. Am. Chem. Soc.* **1991**, 113, 5107.
165. L. De Cola, V. Balzani, F. Barigelletti, L. Flamigni, P. Belser, S. Bernhard, *Recl. Trav. Chim. Pays-Bas* **1995**, 114, 534.
166. J. R. Reimers, N. S. Hush, *Chem. Phys.* **1990**, 146, 105.
167. J. R. Reimers, N. S. Hush, D. M. Sammeth, P. R. Callis, *Chem. Phys. Lett.* **1990**, 169, 622.
168. G. A. Jones, B. K. Carpenter, M. N. Paddon-Row, *J. Am. Chem. Soc.* **1998**, 120, 5499.
169. G. A. Jones, B. K. Carpenter, M. N. Paddon-Row, *J. Am. Chem. Soc.* **1999**, 121, 11171.
170. Y. Sakata, H. Tsue, M. P. O'Neil, G. P. Wiederrecht, M. R. Wasielewski, *J. Am. Chem. Soc.* **1994**, 116, 6904.
171. H. Tsue, S. Nakashima, Y. Goto, H. Tatemitsu, S. Misumi, R. J. Abraham, T. Asahi, Y. Tanaka, T. Okada, N. Mataga, Y. Sakata, *Bull. Chem. Soc. Jpn.* **1994**, 67, 3067.
172. A. Helms, D. Heiler, G. McLendon, *J. Am. Chem. Soc.* **1991**, 113, 4325.
173. R. J. Cave, R. A. Marcus, P. Siders, *J. Phys. Chem.* **1986**, 90, 1436.
174. E. Galoppini, M. A. Fox, *J. Am. Chem. Soc.* **1996**, 118, 2299.
175. M. A. Fox, E. Galoppini, *J. Am. Chem. Soc.* **1997**, 119, 5277.
176. D. Gosztola, M. P. Niemczyk, M. R. Wasielewski, *J. Am. Chem. Soc.* **1998**, 120, 5118.
177. A. P. de Silva, T. E. Rice, *Chem. Commun.* **1999**, 163.
178. J. P. Sumida, P. A. Liddell, S. Lin, A. N. Macpherson, G. R. Seely, A. L. Moore, T. A. Moore, D. Gust, *J. Phys. Chem.* **1998**, 102, 5512.
179. J. R. Miller, L. T. Calcaterra, G. L. Closs, *J. Am. Chem. Soc.* **1984**, 106, 3047.
180. G. L. Closs, M. D. Johnson, J. R. Miller, P. Piotrowiak, *J. Am. Chem. Soc.* **1989**, 111, 3751.
181. J. Kroon, A. M. Oliver, M. N. Paddon-Row, J. W. Verhoeven, *J. Am. Chem. Soc.* **1990**, 112, 4868.
182. N. Lokan, M. N. Paddon-Row, T. A. Smith, M. La Rosa, K. P. Ghiggino, S. Speiser, *J. Am. Chem. Soc.* **1999**, 121, 2917.
183. A. M. Oliver, M. N. Paddon-Row, M. C. R. Symons, *J. Am. Chem. Soc.* **1989**, 111, 7259.

184. M. N. Paddon-Row, L. M. Englehardt, B. W. Skelton, A. H. White, F. Jørgensen, S., H. K. Patney, *J. Chem. Soc., Perkin Trans. 2* **1987**, 1835.
185. I. R. Gould, R. H. Young, L. J. Mueller, S. Farid, *J. Am. Chem. Soc.* **1994**, *116*, 8176.
186. I. R. Gould, S. Farid, *Acc. Chem. Res.* **1996**, *29*, 522.
187. H. Han, M. B. Zimmt, *J. Am. Chem. Soc.* **1998**, *120*, 8001.
188. R. J. Cave, M. D. Newton, K. Kumar, M. B. Zimmt, *J. Phys. Chem.* **1995**, *99*, 17501.
189. K. Kumar, Z. Lin, D. H. Waldeck, M. B. Zimmt, *J. Am. Chem. Soc.* **1996**, *118*, 243.
190. Y. Gu, K. Kumar, Z. Lin, I. Read, M. B. Zimmt, D. H. Waldeck, *J. Photochem. Photobiol. A: Chem.* **1997**, *105*, 189.
191. M. B. Zimmt, *Chimia* **1997**, *51*, 82.
192. J. M. Lawson, M. N. Paddon-Row, *J. Chem. Soc., Chem. Commun.* **1993**, 1641.
193. J. M. Lawson, D. C. Craig, A. M. Oliver, M. N. Paddon-Row, *Tetrahedron* **1995**, *51*, 3841.
194. K. Maruyama, A. Osuka, N. Mataga, *Pure & Appl. Chem.* **1994**, *66*, 867.
195. A. Harriman, F. Odobel, J. P. Sauvage, *J. Am. Chem. Soc.* **1995**, *117*, 9461.
196. G. P. Wiederrecht, M. P. Niemczyk, W. A. Svec, M. R. Wasielewski, *J. Am. Chem. Soc.* **1996**, *118*, 81.
197. G. Steinberg-Yfrach, P. A. Liddell, S. C. Hung, A. L. Moore, D. Gust, T. A. Moore, *Nature* **1997**, *385*, 239.
198. J. M. Lawson, M. N. Paddon-Row, W. Schuddeboom, J. M. Warman, A. H. A. Clayton, K. P. Ghiggino, *J. Phys. Chem.* **1993**, *97*, 13099.
199. M. R. Roest, J. M. Lawson, M. N. Paddon-Row, J. W. Verhoeven, *Chem. Phys. Lett.* **1994**, *230*, 536.
200. M. R. Roest, J. W. Verhoeven, W. Schuddeboom, J. M. Warman, J. M. Lawson, M. N. Paddon-Row, *J. Am. Chem. Soc.* **1996**, *118*, 1762.
201. M. R. Roest, Ph. D. Thesis, University of Amsterdam, Amsterdam, 1996.
202. M. J. Shephard, M. N. Paddon-Row, *J. Phys. Chem. A* **1999**, *103*, 3347.
203. K. A. Jolliffe, T. D. M. Bell, K. P. Ghiggino, S. J. Langford, M. N. Paddon-Row, *Angew. Chem., Int. Ed.* **1998**, *37*, 916.
204. K. A. Jolliffe, S. J. Langford, A. M. Oliver, M. J. Shephard, M. N. Paddon-Row, *Chem. Eur. J.* **1999**, *5*, 2518..
205. J. W. Verhoeven, *Pure & Appl. Chem.* **1990**, *62*, 1585.
206. B. Wegewijs, R. M. Hermant, J. W. Verhoeven, M. P. de Haas, J. M. Warman, *Chem. Phys. Lett.* **1987**, *140*, 587.
207. X. Y. Lauteslager, I. H. M. van Stokkum, H. J. van Ramesdonk, A. M. Brouwer, J. W. Verhoeven, *J. Phys. Chem. A* **1999**, *103*, 653.
208. P. F. Barbara, T. J. Meyer, M. A. Ratner, *J. Phys. Chem.* **1996**, *100*, 13148.

2 Covalently Linked Systems Containing Porphyrin Units

Devens Gust, Thomas A. Moore and Ana L. Moore

2.1 Introduction

Much of the work on energy and electron transfer in porphyrin-based covalently linked supramolecular structures falls under the general rubric of artificial photosynthesis. Mimicking the natural photosynthetic conversion of sunlight into more useful forms of energy by artificial means has been a goal of photochemistry for nearly 100 years [1]. This chapter will emphasize supramolecular structures consisting of porphyrin linked to other chromophores, electron donors, and electron acceptors. These structures demonstrate a wide variety of intramolecular electron and energy transfer processes that take place among the different components. Similar processes lie at the core of the energy conversion in photosynthesis.

Artificial photosynthesis, broadly defined, is any attempt to mimic aspects of photosynthetic energy conversion by photochemical processes in laboratory-made systems. Artificial photosynthetic constructs must include a chromophore capable of absorbing light in the visible range that at the same time can act as an energy or electron donor or acceptor. Although a variety of organic and inorganic chromophores have been investigated in this respect, porphyrins and related molecules have been used extensively. Synthetic porphyrins have been especially appealing because of their similarity to the natural chromophores, their light absorption and redox properties, their stability, their relatively easy synthetic accessibility, and the large number of structural variations that are available. The great variety of structural modifications makes it possible to engineer the chromophore in order to obtain properties such as light absorption, energy transfer ability, redox potential, electronic coupling, and photoprotection.

Artificial photosynthetic systems may be designed in order to study any aspect of the natural process, including singlet energy transfer (antenna function), photo-induced electron transfer, triplet energy transfer (photoprotection), light-driven proton transfer, the coupling of light-initiated events to the synthesis of ATP, or

other biologically relevant energy-requiring processes. In this review, we will concentrate only on systems that mimic photosynthetic photoinduced electron transfer.

This chapter will begin with a simple introduction to the basic principles underlying photoinduced electron transfer and subsequently, representative examples of molecules that display interesting electron transfer phenomena will be discussed. The work reported in the 1990s will be emphasized. However, a large body of important work has appeared previous to this time, especially during the latter half of the 1970s and the 1980s. The highlights of this early work will be presented, and the reader will be referred to earlier comprehensive reviews. The present chapter is illustrative of the many types of research currently taking place in this area, but does not intend to be comprehensive.

2.2 Basic Principles Underlying Photoinduced Electron Transfer

In this section, some basic theoretical approaches to understanding electron transfer will be reviewed. Although more complex and more quantitatively accurate theories exist (see Volume I of this handbook), a discussion of these is beyond the scope of this review. The simple theories discussed below are intended only to provide a useful framework for thinking about the photophysics and photochemistry of the porphyrin based donor–acceptor systems reviewed in this chapter.

Absorption of light by an organic chromophore results in rapid formation of the lowest excited singlet state, S_1 . As shown in Figure 1, promoting an electron from the highest occupied molecular orbital (HOMO) to the lowest unoccupied molecular orbital (LUMO) gives a simple, illustrative description of an electronic configuration that makes up this state. Even if the excitation process produces an excited singlet state of higher energy, S_n , relaxation to the lowest-energy excited state is generally (but not always) faster than other photophysical or photochemical processes. The first excited singlet state of a porphyrin (1P) or other chromophore may relax back to the ground state either radiatively (fluorescence), or nonradiatively (internal conversion and vibrational relaxation). It may also undergo intersystem crossing to yield the triplet state (3P), which in turn can relax by radiative (phosphorescence) or nonradiative courses.

When a suitable donor or acceptor is available, interchromophore energy or electron transfer can compete with these unimolecular processes. For example, as is evident from Figure 1, 1P has a vacancy in its HOMO, and may consequently accept an electron from a nearby donor moiety. Alternatively, 1P also has a high-energy electron in its LUMO, and may readily donate this electron to an appropriate acceptor species. In general, a molecule in its excited state is both more easily oxidized and more easily reduced than in its ground state.

Because, the lifetimes of the excited singlet states of free base porphyrins are seldom longer than ~ 10 ns, and the lifetimes of metalated porphyrin singlet states

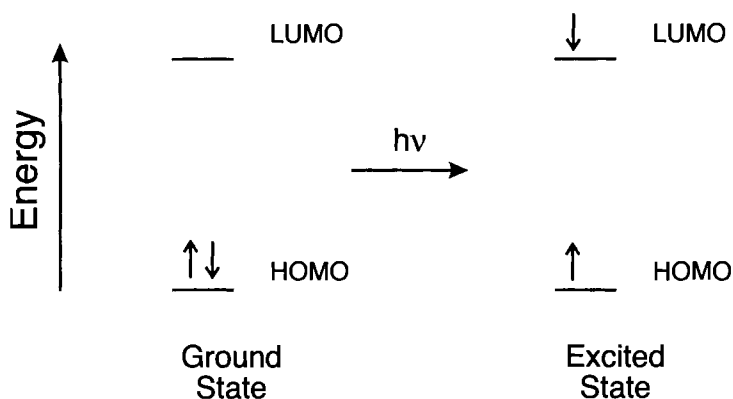


Figure 1. Schematic diagram showing occupation of the frontier orbitals of a chromophore in the ground and first excited singlet states.

are typically even shorter, a high quantum yield for photoinduced electron transfer requires that the electron transfer process occur with a time constant of at least 1 to 0.1 ns. In most of the reactions discussed in this review, the electron transfer occurs in the nonadiabatic regime. Equation 1 has been developed to describe electron transfer rate constants (k_{et}) under these conditions [2–4].

$$k_{et} = \sqrt{(\pi/\hbar^2 \lambda k_B T)} |V|^2 \exp[-(\Delta G^\circ + \lambda)^2 / 4\lambda k_B T] \quad (1)$$

Rapid electron transfer requires optimizing the parameters in Eq. 1 that are a function of the molecular design. The pre-exponential factor includes the electronic matrix element V that describes the coupling of the reactant state with that of the product. Element V is a function of the overlap of the donor and acceptor orbitals. In addition to Planck's constant \hbar , Boltzmann's constant k_B , and the absolute temperature T , the pre-exponential factor also includes the reorganization energy for the reaction, λ . The reorganization energy is associated with the nuclear motions involved in transforming the molecule from the initial to the final state. Frequently λ is expressed as the sum of a solvent-independent term λ_i , which originates from internal molecular structural differences between the reactant and product, and λ_s , the solvent reorganization energy, which is due to differences in the orientation and polarization of solvent molecules around the (usually neutral) ground state and the (usually zwitterionic) charge-separated state. The exponential term is the Franck–Condon factor that includes the standard free energy change for the reaction, ΔG° , as well as λ .

Electron transfer as described by Eq. 1 may occur in three regimes. In the “normal” region, increasing thermodynamic driving force for electron transfer (as ΔG° becomes more negative) leads to more rapid electron transfer, as would be expected

for most chemical reactions. When $-\Delta G^\circ$ equals λ , the rate of electron transfer is maximized as a function of driving force, and electron transfer becomes activationless. Finally, when $-\Delta G^\circ > \lambda$, increasing driving force leads to a decrease in the electron transfer rate constant. This is the “inverted” region of Eq. 1. Semiclassical refinements of Eq. 1 have been found to be more appropriate for describing electron transfer rates in the “inverted” region [5, 6].

2.2.1 Electronic Coupling

The electronic coupling of the reactant state with the product state, V , is a function of the overlap of the donor and acceptor orbitals. This in turn depends on energetic, spatial, geometric, and symmetry factors. At relatively large donor–acceptor separations, it can be assumed that the relevant orbitals decay exponentially with distance. In these cases, the electron transfer rate constant will depend on this separation as per Eq. 2, where R_{DA} is the donor–acceptor separation and β is a constant that expresses the sensitivity of the

$$k_{et} = v \exp(-\beta R_{DA}) \quad (2)$$

electron transfer rate constant to distance. In most of the covalently linked electron donor–acceptor systems discussed below, electronic coupling occurs via a superexchange interaction involving the bonds of the bridge between the two moieties (see Volume III, Part 2, Chapter 1). In such cases, the dependence of the electron transfer rate constant on the number of covalent bonds joining the donor and acceptor π -electron systems is also usually well described by an exponential function.

2.2.2 Solvent Effects

Electron transfer reactions involve changes in the overall charges on the donor and acceptor moieties. The stability of charged species depends strongly on the environment. An ion is stabilized by solvent molecules that can arrange themselves so as to partially cancel its charge. Both the free energy change, ΔG° , and the reorganization energy, λ , in Eq. 1 are generally strong functions of the solvent, and therefore electron transfer rate constants are also solvent-dependent.

A simple way to model this effect is to treat the solvent as a dielectric continuum. This treatment often fails quantitatively, but is a useful qualitative framework in which to consider solvent effects. For example, the effect of solvent on the driving force for electron transfer, ΔG° , is given by Eq. 3, which is taken from the work of Weller [7]. This treatment assumes electron transfer from the first excited singlet state of a donor D to an acceptor A and

$$\Delta G^\circ = e(E_D - E_A)_r + \frac{e^2}{4\pi\epsilon_0\epsilon_s} \left[\frac{1}{2R_D} + \frac{1}{2R_A} - \frac{1}{R_{DA}} \right] - \frac{e^2}{4\pi\epsilon_0\epsilon_s^r} \left[\frac{1}{2R_D} + \frac{1}{2R_A} \right] - E_{1D} \quad (3)$$

treats the charge-separated state as two spherical ions with radii R_D and R_A separated by a distance R_{DA} and immersed in a solvent of static dielectric constant ϵ_s . The quantities E_D and E_A represent the first oxidation and reduction potentials of the donor and acceptor as measured electrochemically in a reference solvent of dielectric constant ϵ_s^r , ϵ_0 is the permittivity of free space, e is the electronic charge, and E_{1D} is the energy of the donor first excited singlet state above the ground state. This equation includes two opposing effects. As the solvent dielectric constant increases, the individual ions in the charge-separated state are stabilized by the solvent dipoles. At the same time, Coulombic stabilization of each charge by the other is decreased as the dielectric constant increases due to screening effects.

The solvent also has an effect on the reorganization energy, λ , in Eq. 1. As mentioned above, the total reorganization energy is conveniently expressed as the sum of a solvent-independent term, λ_i , which originates from internal molecular structural differences between the initial and final states, and λ_s , the solvent reorganization energy. Marcus has proposed that λ_s depends on the static (ϵ_s) and high frequency ($\epsilon_{op} = n^2$, where n is the index of refraction) dielectric constants of the solvent as shown in Eq. 4 [8, 9].

$$\lambda_s = \frac{e^2}{4\pi\epsilon_0} \left(\frac{1}{2R_D} + \frac{1}{2R_A} - \frac{1}{R_{DA}} \right) \left(\frac{1}{\epsilon_{op}} - \frac{1}{\epsilon_s} \right) \quad (4)$$

2.3 Intramolecular Photoinduced Electron Transfer in Porphyrin-Based Systems: Dyads

The reaction center of photosynthetic organisms converts excitation energy to chemical energy in the form of transmembrane charge separation. It is a molecular-sized photovoltaic device, consisting mainly of protein but also containing redox-active cofactors. The bacterial reaction center uses excitation energy to transfer an electron from an excited bacteriochlorophyll special pair across the thickness of the membrane to a quinone labeled Q_B . In the resulting charge-separated state, the electron and positively charged "hole" are spatially (and electronically) well separated, which disfavors rapid charge recombination to the ground state. The slow charge recombination process allows the organism ample time to harvest the stored energy by subsequent reactions.

The majority of the research on the photochemistry of porphyrins linked to other moieties has been in the area of photoinduced electron transfer, and the systems studied are all in some sense mimics of the photosynthetic process described above. The simplest way to prepare a system in which porphyrin excited states can act as electron donors or acceptors is to mix a porphyrin with an electron acceptor or donor in a suitable solvent. Experiments of this type have been done for years, and a good deal about porphyrin photophysics and photochemistry has been learned from them. Although these systems are easy to construct, they have serious problems for the study of photoinduced electron transfer. In solution, donor–acceptor separation and relative orientation cannot be controlled. As indicated above, electron transfer is a sensitive function of these variables. In addition, because electron transfer requires electronic orbital overlap, the donor and acceptor must collide in order for transfer to occur. As this happens via diffusion, electron transfer rates and yields are often affected or controlled by diffusion. As mentioned above, porphyrin excited singlet states typically have lifetimes of a few nanoseconds. Therefore, efficient photoinduced electron transfer must occur on a time scale shorter than this. This is difficult or impossible to achieve via diffusion. Thus, photoinduced electron transfer between freely diffusing partners is confined mainly to electron transfer from excited triplet states, which have the required long lifetimes (on the micro to the millisecond time scale).

Photoinduced electron transfer on a shorter time scale, and therefore transfer to or from excited singlet states, requires an organizational principle that constrains the donor–acceptor separation. Various approaches to such organization exist. In natural photosynthesis, for example, the protein component holds the various donor and acceptor species at precise separations and angles, and also provides the appropriate environment which assists the electron transfer. One widely used approach in synthetic systems is to employ covalent bonding networks to constrain separations and orientations. The bonds can also provide a mechanism for orbital overlap through the phenomenon of superexchange, wherein the orbitals of the intervening bonds can mix with those of the donor and acceptor, thereby increasing net donor–acceptor electronic coupling and facilitating electron transfer. This chapter focuses on porphyrin-containing species of this type.

Porphyrin-containing donor–acceptor systems have been an active area of research for over 20 years, and there is an extremely large body of literature in the area [10]. In this chapter, we exemplify the major approaches to this research, but the main focus areas are illustrated with one or two examples, and references to additional work are provided. In many cases, we illustrate concepts with molecules studied in our own laboratories simply for reasons of convenience, although a number of other studies may have been reported.

The simplest covalently linked system for studying photoinduced electron transfer consists of a porphyrin bonded to an electron acceptor or donor moiety with appropriate redox properties. Most of these studies have employed free-base, zinc, or magnesium porphyrins because the first excited singlet states of these molecules are relatively long-lived (typically 1–10 ns), so that electron transfer can compete with other decay pathways. In addition, they have relatively high fluorescence

quantum yields, and fluorescence measurements are convenient for determination of the lifetimes of the excited states. Because the majority of such porphyrins are readily oxidized, they are often linked to organic electron acceptors such as other porphyrins, quinones, aromatic imides, and fullerenes. Although, as we shall see, such two-part—or dyad—systems are not ideal for the observation of long-lived photoinduced charge separation, they are relatively easy to prepare, and their study has revealed a wide variety of interesting photochemistry.

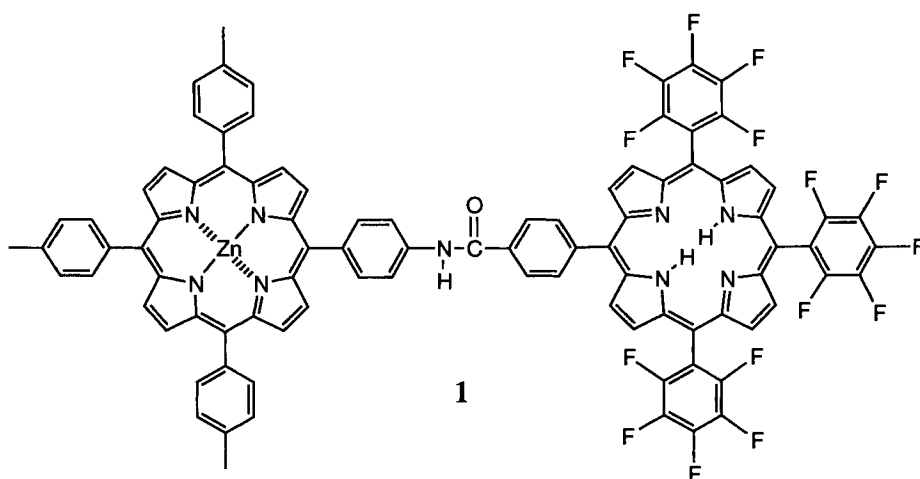
2.3.1 Porphyrins Covalently Linked to Other Porphyrins

The first photoinduced electron transfer step of bacterial photosynthesis involves electron donation from a bacteriochlorophyll-pair excited singlet state to a nearby bacteriochlorophyll derivative. This suggests that interporphyrin photoinduced electron transfer would be a commonly observed phenomenon in synthetic systems. Surprisingly, this is not the case, in spite of the huge number of covalently linked porphyrin dyads and more complex systems that have been prepared and studied. The reason is that porphyrins and their relatives have relatively low energy excited singlet states, and the redox potentials of the most commonly prepared and studied free base porphyrins are such that photoinduced electron transfer to produce porphyrin radical anions and cations is thermodynamically unfavorable. By introducing transition metals that can undergo redox reactions, a wide range of redox potentials is made available. However, such metalation also tends to produce porphyrins with very short-lived excited states, and photoinduced electron transfer cannot compete readily with other deactivation pathways.

Still it is possible to engineer covalently linked systems in order to observe interporphyrin photoinduced electron transfer by tuning redox potentials through peripheral substitution, metalation, and change in the structure of the porphyrin core, and such transfer has been observed in many systems [11–38]. Representative examples of some of these strategies will be described below.

Adjusting redox potentials by peripheral substitution

Porphyrin dyad **1** includes a zinc porphyrin moiety, which is a good electron donor by virtue of the metal, linked to a free base porphyrin bearing three pentafluorophenyl groups, which is a good electron acceptor due to the electron-withdrawing properties of these substituents [13, 29]. Based on these factors, photoinduced electron transfer involving the first excited singlet state of either porphyrin to produce a charge-separated state is thermodynamically favorable. The absorption spectrum of **1** in dichloromethane is essentially a linear combination of the spectra of model porphyrins, indicating that the linkage does not perturb the chromophores significantly. If a solution of **1** is excited at 560 nm, where most of the light is absorbed by the zinc porphyrin moiety, and the fluorescence emission spectrum is measured, it is found that nearly all the emission is due to the free base porphyrin; the zinc



porphyrin emission is strongly quenched. The weakness of this emission is due in part to quenching of the zinc porphyrin first excited singlet state $^1\text{P}_{\text{Zn}}\text{-P}_{\text{F}}$ through singlet–singlet energy transfer to the attached free base porphyrin, yielding $\text{P}_{\text{Zn}}\text{-}^1\text{P}_{\text{F}}$. Fluorescence excitation studies show that this transfer occurs with a quantum yield of 0.77. This singlet–singlet transfer is indicated as step 1 in Figure 2.

Time-resolved fluorescence studies of **1** yield information concerning the rates of the energy transfer and other pathways for decay of the porphyrin excited singlet states. Model zinc and free base porphyrins have fluorescence lifetimes of 1.6 ns and 8.5 ns in dichloromethane, respectively. The decay of the fluorescence of **1**, however, shows two components with time constants (τ_f) of 0.082 and 2.7 ns. Decay-associated spectra show that the shorter component represents the lifetime of the zinc porphyrin first excited singlet state, whereas the longer lifetime is that of the free base porphyrin moiety. Thus, both porphyrin first excited singlet states are quenched, and an intramolecular process in addition to singlet energy transfer must be taking place. The quenching is assigned to electron transfer to form $\text{P}_{\text{Zn}}^{\bullet+}\text{-P}_{\text{F}}^{\bullet-}$. This conclusion is supported by the spectroscopic observation of a long-lived charge-separated state formed via photoinduced electron transfer in a closely related carotene–diporphyrin triad molecule (see below), and of a photogenerated charge-separated state in a related diporphyrin using transient absorption techniques on the picosecond time scale [13]. Steady-state and time-resolved fluorescence results allow calculation of the rate constants for the various pathways shown in Figure 2. As indicated above, the quantum yield of singlet–singlet energy transfer from $^1\text{P}_{\text{Zn}}\text{-P}_{\text{F}}$ to give $\text{P}_{\text{Zn}}\text{-}^1\text{P}_{\text{F}}$ is 0.77 from fluorescence steady-state measurements. This value for the quantum yield and the fluorescence lifetime of the zinc porphyrin (0.082 ns) allow the calculation of the rate constant for the energy transfer from $^1\text{P}_{\text{Zn}}\text{-P}_{\text{F}}$ to give $\text{P}_{\text{Zn}}\text{-}^1\text{P}_{\text{F}}$, k_1 , as $9.4 \times 10^9 \text{ s}^{-1}$, from the relationship $\Phi_1 = k_1 \tau_f$. As-

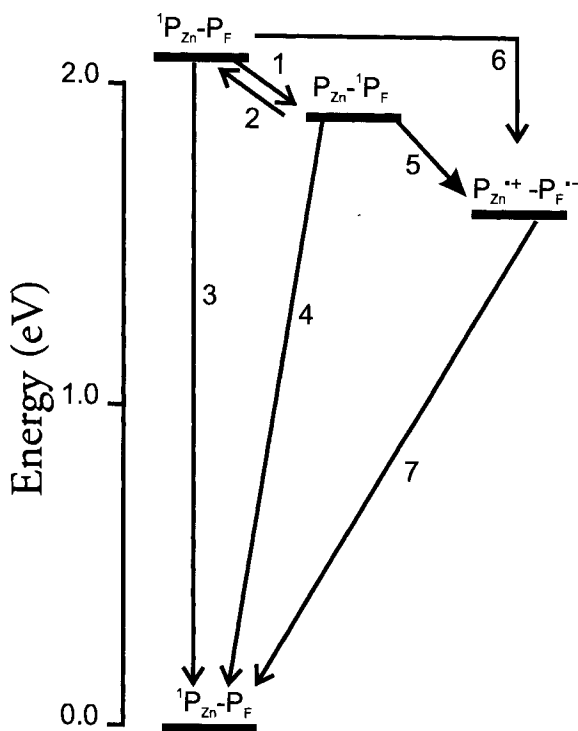


Figure 2. Transient states and interconversion pathways for porphyrin dyad **1**. Steps 3 and 4 include intersystem crossing to the triplet, internal conversion to the ground state, and fluorescence.

suming that the repopulation of ${}^1P_{Zn}-P_F$ via step 2 is negligible (endergonic), the rate constant for photoinduced electron transfer from the zinc porphyrin first excited singlet state to the free base porphyrin (k_6) can be obtained from Eq. 5.

$$1/\tau_f = k_1 + k_3 + k_6 \quad (5)$$

The value of k_3 may be estimated as $6.3 \times 10^8 \text{ s}^{-1}$ from the 1.6-ns fluorescence lifetime of a model zinc porphyrin which cannot undergo energy or electron transfer. Thus, by Eq. 5, k_6 is $2.2 \times 10^9 \text{ s}^{-1}$. Because the 2.7-ns component has the spectrum of the free base porphyrin, it represents the decay of $P_{Zn}-{}^1P_F$. This decay should include step 4 and the electron transfer step 5. The value of the rate constant for step 4 may be estimated as $1.2 \times 10^8 \text{ s}^{-1}$ from the 8.5-ns the singlet excited state lifetime (τ_0) measured for a model porphyrin for P_F . The electron transfer rate constant from the free base porphyrin to yield $P_{Zn}^{*+}-P_F^{*-}$, k_5 , is $2.5 \times 10^8 \text{ s}^{-1}$ from:

$$k_5 = 1/\tau_f - 1/\tau_0 \quad (6)$$

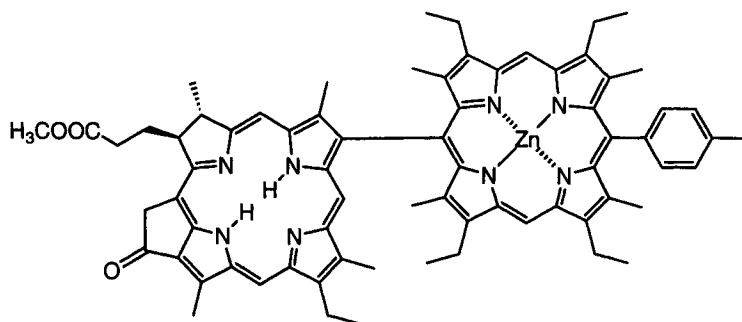
The effect of thermodynamic driving force on the rate constants for interporphyrin photoinduced electron transfer was investigated by synthesizing a series of porphyrin dyads in which the substitution pattern, and therefore the driving force, was varied, and studying photoinduced electron transfer using time-resolved fluorescence techniques [12]. In the series of dyads the thermodynamic driving force for interporphyrin photoinduced charge separation spans a range of 1.13 eV. Time-resolved fluorescence studies yielded 22 rate constants for photoinduced electron transfer in dichloromethane solution ranging from $4.1 \times 10^7 \text{ s}^{-1}$ to $5.0 \times 10^{11} \text{ s}^{-1}$. The data are consistent with the theoretical treatments of Marcus and Levich (Eq. 1), although there is no evidence for inverted behavior. In the normal region, electron transfer between free base porphyrin moieties is about four times faster than transfer involving a zinc porphyrin having the same thermodynamic driving force, based on electrochemical measurements. Photoinduced electron transfer to an excited singlet state and electron transfer from an excited singlet state have the same dependence upon free energy change. In a separate study, it was found that coordination of pyridine or related ligands to the metal atom of a zinc porphyrin-free base porphyrin dyad increases the rate of photoinduced electron transfer by increasing the driving force [29].

As noted above in the discussion of Eqs. 3 and 4, solvent can have a large effect on the rates of photoinduced electron transfer reactions through alterations of driving force and reorganization energy. Photoinduced electron transfer in four dyads consisting of electron-donating porphyrins covalently linked to electron-accepting porphyrins (P_D - P_A) has been studied in 17 solvents [24]. As with dyad **1**, excitation of either porphyrin moiety is followed by singlet-singlet energy transfer to the attached porphyrin and/or photoinduced electron transfer to yield the P_D^{*+} - $P_A^{\bullet-}$ charge-separated state. Electron transfer rate constants were determined as described above for **1**. Reasonable correlation of the electron transfer rate constants with the solvent static dielectric constant was observed using the Marcus theory of electron transfer (Eq. 1) and the Weller dielectric continuum model for the variation of thermodynamic driving force with dielectric constant (Eq. 3). Little or no improvement in the correlation was introduced by inclusion of a solvent dependence of the total reorganization energy using Eq. 4. These results differ significantly from those reported for porphyrin-quinone dyads (see below) [39–42]. The differences may be due to a reduced sensitivity to specific solvent interactions by the large, diffuse porphyrin ions, as was observed for the fullerene-based systems described below. Comparisons among the dyads suggest that inclusion of a *meso*-aryl group in the linkage joining the donor and acceptor porphyrins attenuates electron transfer rates only weakly.

Adjusting redox potentials by alteration of the π -electron system of the macrocycle

By changing the π -electron distribution in the porphyrin ring, substantial changes in redox potential may be achieved. Chlorins, for example, are used as electron donors

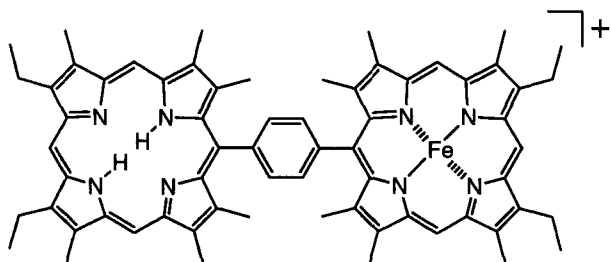
and acceptors in photosynthesis, and have also been incorporated into multiporphyrin units capable of displaying photoinduced electron transfer. Dyad **2**, for example, consists of a free base chlorin (CH, a reasonably good electron acceptor) linked to an octaalkyl-substituted zinc porphyrin (a good donor by virtue of zinc substitution and the peripheral substitution) [21]. The short linkage between the macrocycles forces their planes to be nearly perpendicular. In polar solvents such as butyronitrile, the energy of the $P_{Zn}^{*+}-CH^{*-}$ charge-separated state is estimated as 1.8 eV on the basis of electrochemical measurements, which is below the energies of the first excited singlet state of either cyclic tetrapyrrole. Excitation of a butyronitrile solution of **2** at 610 nm, where the chlorin absorbs most of the light, leads to formation of the $P_{Zn}^{*+}-CH^{*-}$ charge-separated state with a time constant of 4 ps. Charge recombination occurs in 43 ps. In toluene, on the other hand, the excited states are not appreciably quenched, and no charge separation is observed. Probably this is because in nonpolar solvents, the energy of $P_{Zn}^{*+}-CH^{*-}$ is pushed higher than the energy of the relevant excited states, as per Eq. 3. A modification of **2** in which both centers are metalated with zinc also demonstrates fluorescence quenching in polar solvents, but no charge-separated states were detected by transient absorption measurements. This quenching has been attributed to some degree of mixing of high-energy charge-separated states with the excited states [21].

**2**

Adjusting redox potentials by changing the central metal

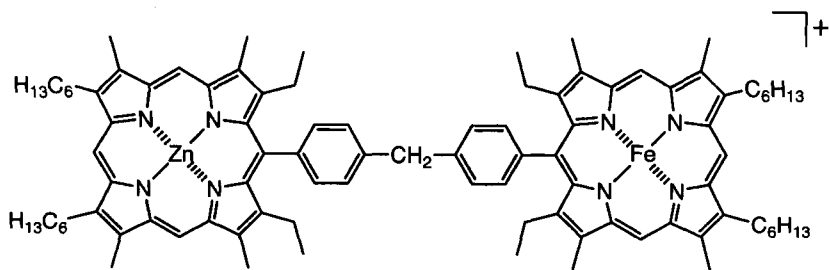
The insertion into porphyrins of central metals capable of easy oxidation or reduction can shift the site of redox chemistry from the macrocycle π -electron system to the metal. While this substitution allows large changes in the redox properties of a porphyrin, it may introduce changes in the photophysics if a transition metal is employed. For example, iron (III) porphyrins are particularly good electron acceptor moieties, and have been used as components of porphyrin dyad and more complex systems that show photoinduced electron transfer behavior [11, 18, 19, 26, 31, 32, 34, 43, 44]. McLendon and coworkers used this strategy with dyad **3**, in

which a free base porphyrin is linked to an Fe(III) porphyrin via a *meso* phenyl group, and related molecules [31]. Excitation of the free base porphyrin in methanol allowed detection of photoinduced electron transfer with a rate constant of $2 \times 10^{11} \text{ s}^{-1}$ to yield a $\text{P}^{*+}\text{-P}_{\text{Fe(II)}}$ charge-shifted state.

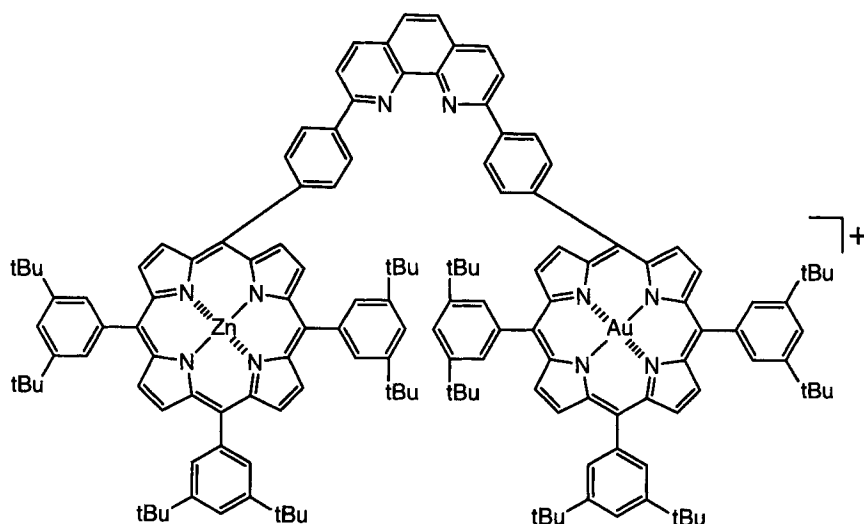
**3**

In 1992, McLendon and coworkers reported results of a study of another series of porphyrin dyads with zinc in one porphyrin and iron in the second. These were related in structure to dyad **3**, but the number of phenyl linkers varied from one to three. These workers found an apparent value for β in Eq. 2 of 0.4 \AA^{-1} . They explained this result by a theory that attributes the drop in rate constant not to increased distance, but rather to the decrease in conjugation between the porphyrins that occurs at each phenyl ring junction due to the biphenyl twist angle of $\sim 50^\circ$. Each phenyl ring results in a drop in rate of approximately six-fold [32].

In 1990, Osuka, Maruyama, Mataga, and coworkers examined porphyrin dyad **4** and other molecules closely related to dyad **3** with different aromatic linkers joining the macrocycles [19]. When the zinc porphyrin of **4** was excited in dimethylformamide solution, $^1\text{P}_{\text{Zn}}\text{-P}_{\text{Fe(III)}}$ was produced. It decayed with a time constant of 52 ps, and the $\text{P}_{\text{Zn}}^{*+}\text{-P}_{\text{Fe(II)}}$ state was observed by transient absorption techniques. The charge-shifted state decayed in 1.6 ns. By studying photoinduced electron transfer in the entire series of molecules with different linkages, the dependence of rate constant on the separation of the porphyrins was determined. A value for β in Eq. 2 of 0.4 \AA^{-1} was obtained.

**4**

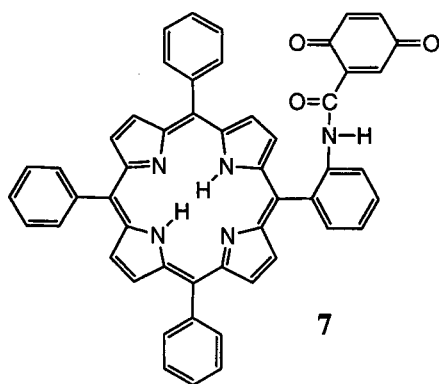
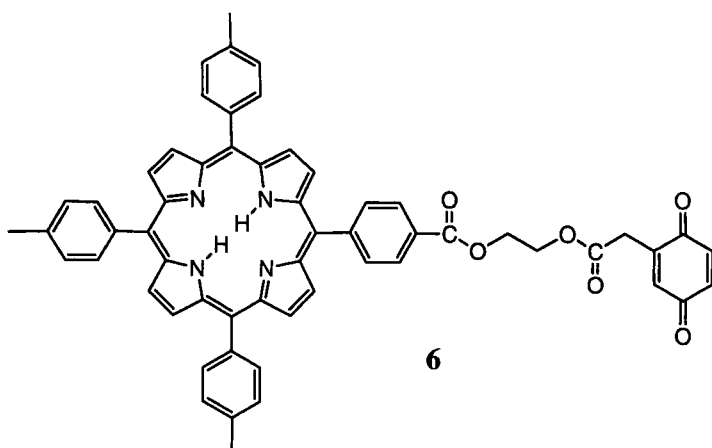
Gold porphyrins have also been exploited as electron acceptors. Dyad **5**, for example, is a V-shaped molecule consisting of a zinc tetraarylporphyrin linked to an Au(III) tetraarylporphyrin through a phenanthroline spacer [30]. Excitation of the zinc porphyrin yields $^1\text{P}_{\text{Zn}}\text{-P}_{\text{Au}}^+$, which by electron transfer decays to yield the $\text{P}_{\text{Zn}}^{\bullet+}\text{-P}_{\text{Au}}^{\bullet}$ state. This charge shift reaction has a time constant of 55 ps in butyronitrile solution. The state $\text{P}_{\text{Zn}}^{\bullet+}\text{-P}_{\text{Au}}^{\bullet}$ decays back to the ground state with a lifetime of 600 ps. Excitation of the gold porphyrin moiety yields the excited triplet state, $\text{P}_{\text{Zn}}\text{-}^3\text{P}_{\text{Au}}^+$, which decays by a combination of electron transfer from the zinc porphyrin to give $\text{P}_{\text{Zn}}^{\bullet+}\text{-P}_{\text{Au}}^{\bullet}$ and triplet energy transfer to yield $^3\text{P}_{\text{Zn}}\text{-P}_{\text{Au}}^+$. The lifetime of $\text{P}_{\text{Zn}}\text{-}^3\text{P}_{\text{Au}}^+$ is 120 ps, and that of $\text{P}_{\text{Zn}}^{\bullet+}\text{-P}_{\text{Au}}^{\bullet}$ is again 600 ps. Electron transfer occurs through the bonds of the linker joining the two porphyrin moieties, as is generally the case in covalently linked systems. It was concluded that electron transfer from the zinc porphyrin excited singlet state is mediated by the LUMO of the spacer, whereas transfer to the gold porphyrin triplet state involves the HOMO of the spacer. Charge recombination shows no preferred pathway, and may involve through-space transfer between the porphyrins, which are in relatively close proximity.



5

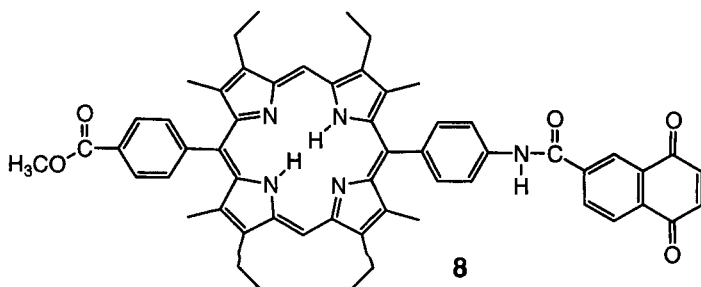
2.3.2 Porphyrins Covalently Linked to Quinones

The first covalently linked porphyrin-based systems for mimicry of photosynthetic electron transfer were reported in the late 1970s. These were porphyrin–quinone dyad molecules **6** and **7** [45–47]. Subsequent to these reports, a very large number of porphyrin–quinone dyads have been studied, and still work in this field continues. Connolly and Bolton reviewed the work in the 1970s and 1980s [48]. Since that



time, a number of other reviews of these and related systems have appeared [10, 43, 49–60], and the material in them complements that in this chapter.

The basic photophysical behavior of porphyrin–quinone systems is illustrated by dyad **8**, in which a naphthoquinone derivative is linked to a porphyrin via an amide bond [61]. The photophysics of this molecule has been investigated using techniques



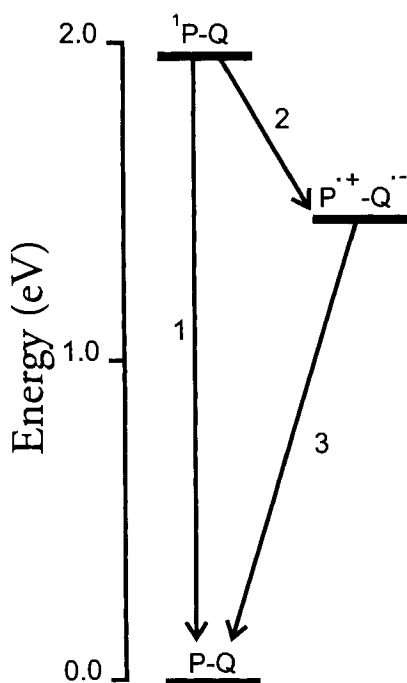


Figure 3. Transient states and interconversion pathways for a porphyrin–quinone dyad such as **8**.

such as time-resolved fluorescence spectroscopy and time-resolved absorption spectroscopy.

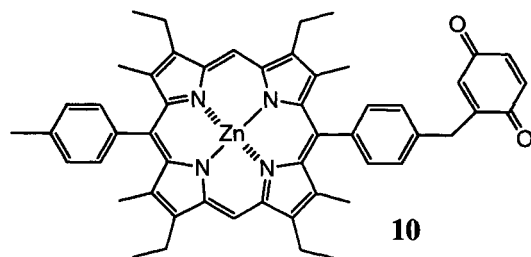
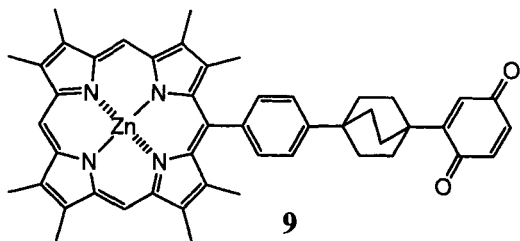
The states of interest are shown in Figure 3. In **8** and most other porphyrin–quinone dyads, the electronic interaction between the porphyrin and quinone moieties is relatively weak, and the absorption spectrum is essentially the sum of the spectra of the individual chromophores, as measured for model compounds. The energy of the first excited singlet state (Figure 3) is estimated as the wavenumber average of the longest-wavelength absorption maximum and the shortest-wavelength fluorescence maximum. In the case of **8**, this is 1.97 eV. The energy above the ground state of the $P^{\bullet+}-Q^{\bullet-}$ charge-separated state resulting from photoinduced electron transfer may be estimated from the first oxidation potential of the porphyrin and first reduction potential of the quinone, measured electrochemically on the dyad itself or suitable model compounds. For **8**, this value is 1.45 eV, and ΔG° for the photoinduced electron transfer is -0.52 eV. Such estimates are most valid in polar solvents similar to those used for the electrochemical measurements. In other solvents, Eq. 3 or more sophisticated treatments may be used to correct for solvent effects.

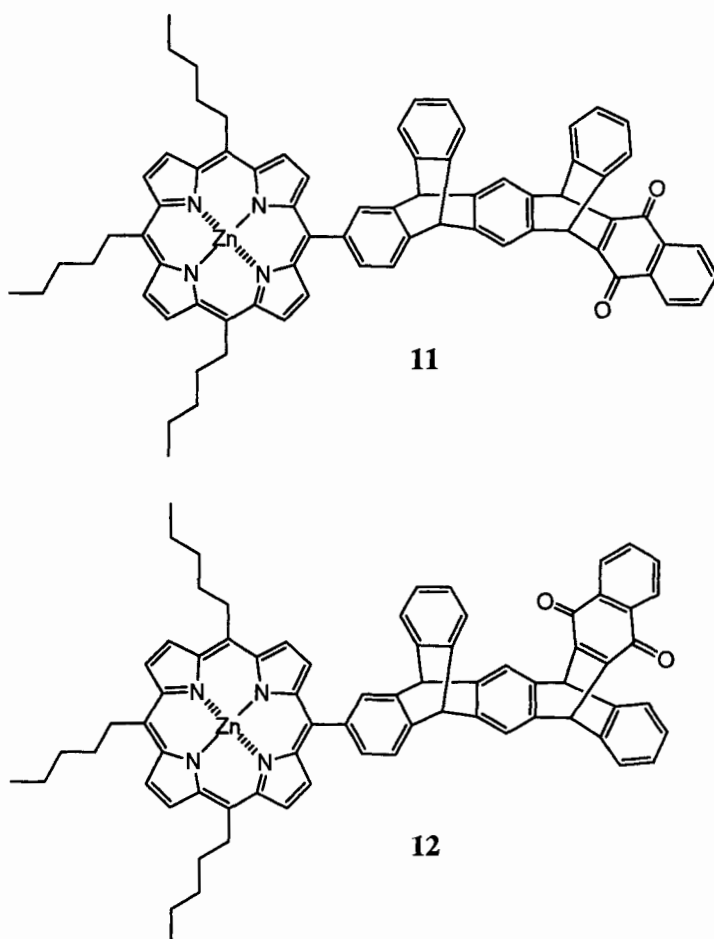
Excitation of the porphyrin moiety of **8** in benzonitrile solution with a 9-ps pulse

of laser light at 590 nm yields the first excited singlet state, $^1\text{P-Q}$. Time-resolved fluorescence measurements report the decay of this state by an exponential process with a lifetime (τ_f) of 102 ps. As the lifetime of a model porphyrin lacking the quinone moiety is 9.3 ns, this represents a strong quenching of the porphyrin excited state. The attachment of the quinone opens up a new pathway for decay—photoinduced electron transfer to generate $\text{P}^{+\bullet}\text{-Q}^{\bullet-}$ (step 2 in Figure 3). The rate constant for step 2 can be calculated by the expression of Eq. 6, where $1/\tau_0$ corresponds to k_1 , the reciprocal of the 9.3-ns lifetime of the model porphyrin, which is the sum of the rate constants for decay of the porphyrin first excited singlet state by internal conversion, intersystem crossing, and fluorescence. Thus, $k_2 = 9.7 \times 10^9 \text{ s}^{-1}$. The quantum yield of photoinduced electron transfer is given by $\Phi_2 = k_2\tau_f$ and equals 0.99.

The $\text{P}^{+\bullet}\text{-Q}^{\bullet-}$ state can be observed by transient absorption spectroscopy because the absorption spectrum of the charge-separated state differs from that of the porphyrin first excited singlet state. Measurement of the transient absorption spectrum of a benzonitrile solution of **8** as a function of time following excitation with a 150 to 200-fs laser pulse at 590 nm allowed determination of the rate constant for decay of $\text{P}^{+\bullet}\text{-Q}^{\bullet-}$ back to the ground state (step 3 in Figure 3). The value obtained for k_3 is $5.3 \times 10^{11} \text{ s}^{-1}$ [61].

Structures **9** to **22** illustrate a few of the many porphyrin–quinone dyads in the literature. Most of these demonstrate photoinduced electron transfer behavior similar to that described for **8** [48]. A large number of such dyads have been reported since 1990 [11, 39, 40, 52, 55, 56, 62–105]. As will be illustrated below, some classes of these molecules have proven to be very useful in the study and application of photoinduced electron transfer phenomena.





Effect of electronic coupling on porphyrin–quinone electron transfer rates

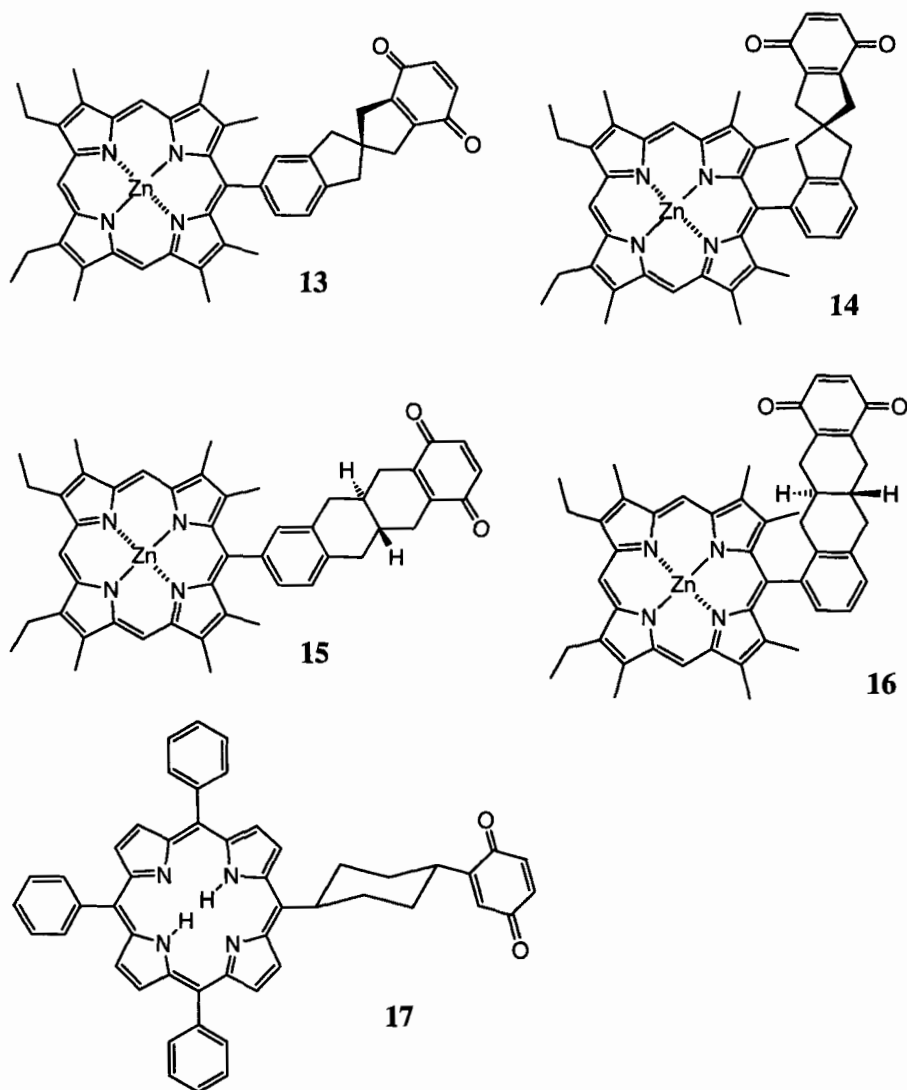
By changing the nature of the donor–acceptor linkage while keeping driving force essentially constant, the effect of the electronic coupling V in Eq. 1 can be investigated [103]. Compound **9** is an example where by inserting one or two additional bicyclooctyl groups the coupling between the porphyrin and quinone, V was varied [107]. A value for β in Eq. 2 of ≥ 1.4 was determined for the bicyclooctyl group, whose insertion or removal gives rise to a 4 Å change in donor–acceptor separation. Values for β of ~ 1 are commonly observed in organic linked donor–acceptor systems where large-scale intramolecular motions are precluded [108–112].

Dyads **11** and **12** differ only in the *syn* or *anti* relationship of the phenyl groups in the porphyrin–quinone linkage. Photoinduced electron transfer in **12** is approximately twice as rapid as in the stereoisomeric **11**, and this is attributed to better orbital overlap in the spacer of **12**, giving rise to a larger coupling [113].

Another interesting example is provided by dyads **13–16** [59, 74, 91]. The simi-

larity in structures among these four molecules suggests that the Franck–Condon factors for electron transfer are similar for all four, and that differences in rates must be due to differences in coupling. However, photoinduced electron transfer in tetrahydrofuran solution is 3.4 times faster in **13** than in **15**, and 8.1 times faster in **14** than in **16**. In principle, these differences could be due to differences in the bonding patterns in the bridges (superexchange), or simply differences in direct donor–acceptor interactions through the solvent medium. The authors argue on the basis of AM1 calculations that the direct interactions are most important.

Photoinduced electron transfer in dyad **17** and related compounds has been extensively studied using optical and electron paramagnetic resonance (EPR) tech-



niques [55, 63, 75, 85, 100, 101, 104]. These results have been compared with those of theoretical calculations of V , and good agreement for variations of dihedral angle and donor-acceptor separation has been obtained.

Effect of driving force on porphyrin-quinone electron transfer rates

Dyad **9** and related molecules prepared by Dervan and coworkers are good examples for these types of studies [87, 107, 114, 115]. The phenyl and bicyclo[2.2.2]octyl linkers joining the zinc porphyrin and the quinone effectively constrain the center-to-center distance between the donor and acceptor, although rotation about the single bonds in the linkage is facile. By varying the substituents on the quinone moiety, the reduction potential of this species was altered, and consequently the thermodynamic driving force for photoinduced electron transfer was varied over a range of values from about 0.5 to 1.4 eV (depending upon the solvent). This system was used to investigate the dependence of the photoinduced electron transfer rate constant on ΔG° , and the results are interpretable in terms of Eqs. 1, 3, 4 and similar treatments. In accord with Eq. 1, when the driving force is relatively small, the photoinduced electron transfer rate constant increases with increasing driving force. At higher driving force values, when $-\Delta G^\circ$ approaches the reorganization energy λ , the rate constant tends to become relatively independent of ΔG° . Interestingly, it was not possible to confirm the existence of the inverted region for photoinduced electron transfer (Eq. 1) in these molecules. This may be because it was not possible to synthesize a dyad with sufficient thermodynamic driving force. This is a common limitation in porphyrin-based systems, in part because the excitation energy of absorbing chromophore is relatively low, and this in turn requires electron donors and acceptors that are easily oxidized or reduced.

A similar result was obtained by Osuka and coworkers with dyad **10** and related molecules in which the driving force for electron transfer was altered by quinone substitution [79, 80]. No evidence for inverted behavior in photoinduced charge separation was observed up to a driving force of ~ 1.54 eV. In the charge recombination reaction of $P_{Zn}^{++}-Q^{*-}$, a decrease in rate with increasing driving force was observed, in accord with inverted behavior in Eq. 1.

Effect of solvent and temperature on porphyrin-quinone electron transfer rates

As mentioned before, electron transfer rate constants are in general strongly dependent upon solvent, as increasing the solvent polarity increases both the driving force (Eq. 3) and the reorganization energy (Eq. 4). Some of the most extensive investigations of solvent dependence have been reported by Bolton and coworkers, who have investigated photoinduced electron transfer in a porphyrin-quinone dyad in 16 different solvents [39-42]. Photoinduced electron transfer rate constants vary from $2.0 \times 10^7 \text{ s}^{-1}$ in 1,2-dimethoxyethane to $2.3 \times 10^9 \text{ s}^{-1}$ in chloroform. The results were found to correlate reasonably well with Eq. 1 when the effects of solvent on both ΔG° and λ were taken into account. The reorganization energy was estimated using Eq. 4. Agreement with theory was rather poor using Eq. 3 to estimate ΔG° , and better agreement was achieved by measuring the redox properties of the donor and acceptor moieties in each solvent, and using these to estimate ΔG° directly. Correcting ΔG° by taking into account Coulombic stabilization of the ions

in the charge-separated state also gave good correlations. This work points out the pitfalls of using equations such as Eqs. 3 and 4. These equations are easy to apply and can yield qualitative insights, but they oversimplify solvent effects by treating the solvent as a dielectric continuum. Electron transfer reactions in general are very sensitive to solvent properties and specific solvent–solute interactions are bound to be important.

Other investigations of the effect of solvent on electron transfer rate constants in porphyrin–quinone dyads have been reported [68, 80, 115, 116]. In general, the results are in qualitative agreement with expectations based on Eqs. 1, 3, and 4 or related expressions, but there are usually quantitative deviations due, at least in part, to the specific interactions mentioned above.

It is clear from Eq. 1 that in general, temperature will affect the rate of electron transfer reactions. However, lowering the temperature of a reaction mixture often has another effect that has a very large influence on transfer rate constants. As the temperature is decreased, a regime is eventually reached in which solvent molecular translational and rotational motions are slow as the solvent becomes glassy or crystalline. In this regime, the solvent molecules are no longer free to effectively solvate and stabilize the ions in a charge-separated state, or transition state leading to a charge-separated product. In Eqs. 3 and 4, this effect could be interpreted as a decrease in the solvent dielectric constant, which lowers the solvent reorganization energy, and increases the energy of a charge-separated state. In many cases, the energetics of the donor–acceptor system have been designed to maximize the fraction of photon energy stored in the charge-separated species in relatively polar solvents. Thus, when the molecule is studied in, for example, a frozen organic glass, the energy of the charge-separated state is raised. However, the energy of the photoexcited state is basically unaffected by the medium properties, and the result is that the driving force for photoinduced electron transfer is reduced to the point that formation of the charge-separated state is too slow to compete with other pathways for decay of the excited state. The process could even become endergonic. For example, as mentioned above, photoinduced electron transfer is rapid in dyad **8** in most organic solvents at ambient temperatures. However, when the molecule is dissolved in a 2-methyltetrahydrofuran glass at 77 K, no porphyrin fluorescence quenching is observed and electron transfer does not occur.

Wasielewski and coworkers have studied a series of molecules in which porphyrins are linked to quinones and similar electron acceptors, and determined that when a solvent such as 2-methyltetrahydrofuran freezes, about 0.8 eV of driving force is lost [116]. These researchers have prepared dyads with a driving force for photoinduced electron transfer greater than this value in polar solvents, and found that they are capable of displaying photoinduced electron transfer even in frozen organic glasses. This, in turn, has opened the door to low-temperature EPR studies of the charge-separated states in various donor–acceptor systems and their decay pathways [66, 99, 117].

Rigid porphyrin–quinone systems

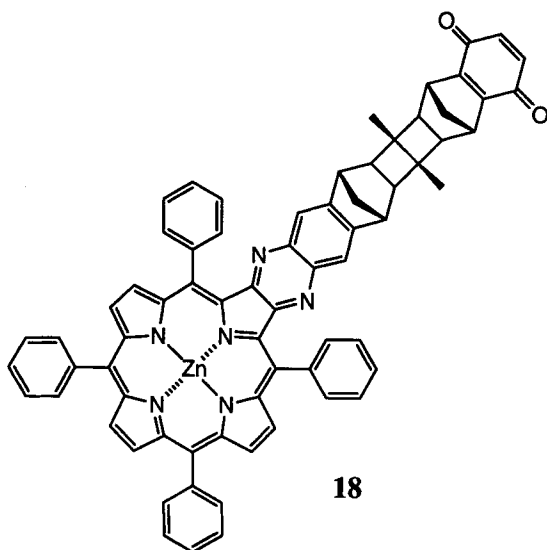
Porphyrin-containing donor–acceptor systems have been employed to test various theoretical descriptions of electron transfer. Such studies require not only accurate

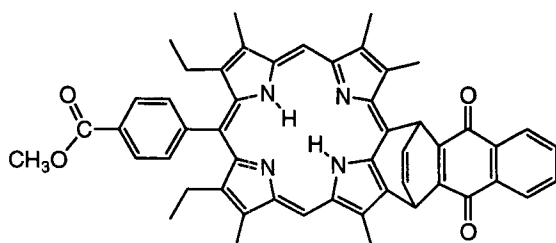
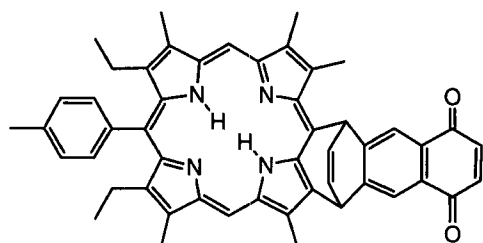
spectroscopic and electrochemical data, but also a precise knowledge of molecular structure, because electron transfer rates depend on electronic coupling interactions (Eq. 1). Interpretation of the results of these studies is simpler if the system possess a high degree of structural "rigidity," that is low conformational mobility. Some systems have come close to achieving this objective.

All of the dyads discussed above—and certainly most of those that have been prepared—feature at least one single bond in the donor–acceptor linkage about which some degree of rotation can occur. This can complicate interpretation of electron transfer rate data in several ways. It may be difficult to determine which of several likely conformations is of lowest energy, or whether several conformations may be populated under the conditions of the experiment. If interconversion of various conformers on the time scale of electron transfer is slow, multiple rate constants may be observed. If interconversion is rapid, the measured rate constants will be relevant only for the average population.

Such considerations have led to the design and synthesis of dyads with a very high degree of structural rigidity. Dyad **18** is an example where the bicyclic linkages severely restrict large-scale intramolecular motions [67, 118, 119]. Fluorescence decay studies in chloroform yield a rate constant for photoinduced electron transfer of $1.5 \times 10^{10} \text{ s}^{-1}$, which is remarkably rapid, given the large donor–acceptor separation. Clearly, the bonding network in the linkage provides the electronic coupling, via superexchange. Rapid electron transfer through rigid linkages of this general type have been observed with other donor–acceptor systems and analyzed in detail [67, 118, 120, 121] (see Volume III, Part 2, Chapter 1).

Dyads **19** and **20** also feature a very rigid bicyclic scaffold between donor and acceptor, and show some unusual properties [98, 105]. The two molecules differ significantly only in the location of the naphthoquinone carbonyl groups relative to the porphyrin macrocycle. Dyad **19**, whose quinone carbonyl groups are rela-



**19****20**

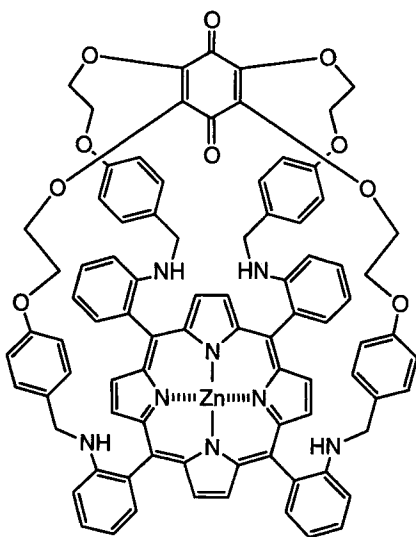
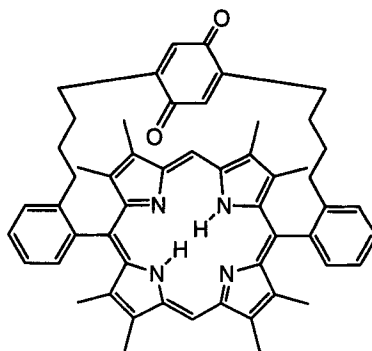
tively close to the porphyrin macrocycle, exhibits photoinduced electron transfer rate constants of $\sim 1 \times 10^{12} \text{ s}^{-1}$. The transfer rate is virtually independent of solvent dielectric constant and temperature within the range 77–295 K, which spans the glass transition of the 2-methyltetrahydrofuran solvent. Dyad **20**, which has a similar donor–acceptor linkage but whose quinone carbonyl groups are $\sim 2 \text{ \AA}$ farther from the porphyrin, features photoinduced electron transfer rate constants that decrease with decreasing solvent dielectric constant. Moreover, electron transfer in this molecule ceases at low temperatures. Photoinduced electron transfer in dyad **20** exhibits the usual dependence on free energy change and solvent reorganization observed in most porphyrin–quinone systems and interpretable in terms of Eqs. 1–4, as discussed above. The unusual behavior of **19** is reminiscent of that observed in photosynthetic reaction centers, and may be attributed at least in part to the smaller separation of the porphyrin radical cation and the quinone radical anion. Equations 3 and 4 predict that a small separation can lead to nearly barrierless electron transfer and make transfer less susceptible to effects due to changes in solvent dielectric properties and temperature. Charge recombination rates in dyads **19** and **20** are substantially slower than charge separation rates, unlike those observed with many porphyrin–quinone systems.

The ionic separation may not be the only factor giving rise to the behavior of **19**, as the photoinduced electron transfer rate constant does not change appreciably, even when the driving force is increased by $\sim 0.4 \text{ eV}$ through introduction of zinc into the porphyrin macrocycle. In this connection, very rapid photoinduced electron transfer has been observed in other zinc-containing porphyrin–quinone systems [80, 86], and photoinduced electron transfer in zinc-containing porphyrin dyads has

been found to lie on a somewhat different rate versus free energy change curve than that of their free base analogues [12]. The lack of sensitivity to environmental factors suggests that photoinduced electron transfer in **19** is controlled mainly by intramolecular vibrations. Vibrational overlap terms may play a role either in the context of radiationless transition theory, or as limiting factors in the conversion of reactant to product on a quasi-adiabatic potential surface [98, 122].

An interesting class of porphyrin–quinone systems that show photochemical behavior related to that of **19** comprises cyclophanes, where the quinone is “tethered” across the face of the porphyrin by two or more linkages containing single bonds [62, 76, 77, 86, 92–95, 123–132]. Dyads **21** and **22** are representative examples. These molecules can in principle achieve strong electronic coupling through a face-to-face arrangement of the porphyrin and quinone. Some of these systems demonstrate a very weak dependence of the rate of photoinduced electron transfer on solvent and temperature, much as is observed for **19**. For example, dyad **21**, a cyclophane system examined by Lindsey, Mauzerall and coworkers undergoes photoinduced electron transfer with rate constants about 1000 times smaller than observed for **19** [62, 125]. However, the dependence on solvent and temperature is weak. Analysis of the results is somewhat complex because the flexible linkages allow two conformers with significant populations.

A group of researchers from Heidelberg and Munich have studied an extensive series of cyclophane systems related to **22** [77, 86, 92, 94, 95, 123, 129–133]. Dyads with relatively low driving force for electron transfer in polar solvents (comparable to **19**) show relatively slow photoinduced electron transfer in nonpolar solvents, and significantly faster transfer in polar solvents. For a few molecules with large negative ΔG° values, photoinduced electron transfer occurs in about 1 ps in all solvents

**21****22**

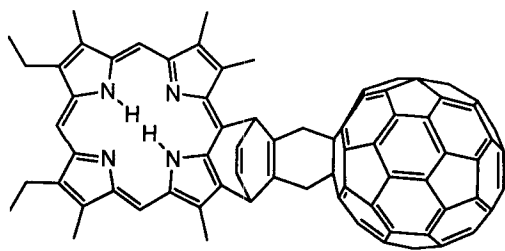
investigated, and at low temperatures. Exact transfer rate constants are unavailable because of instrumental limitations, but it is clear that the behavior of these cyclophanes is similar in many respects to that of dyad **19**. In these cases as well, electron transfer rate constants appear to be influenced mainly by internal molecular vibrations, rather than external factors, and may be approaching the “theoretical limit” [86, 122]. Charge recombination rates in these molecules also appear to be insensitive to solvent, unlike those observed for **19** and **20**. However, this interpretation may be complicated by conformational heterogeneity arising from flexibility in the porphyrin–quinone linkage. More rigid analogues of these cyclophanes may help to resolve these questions.

2.3.3 Porphyrins Covalently Linked to Fullerenes

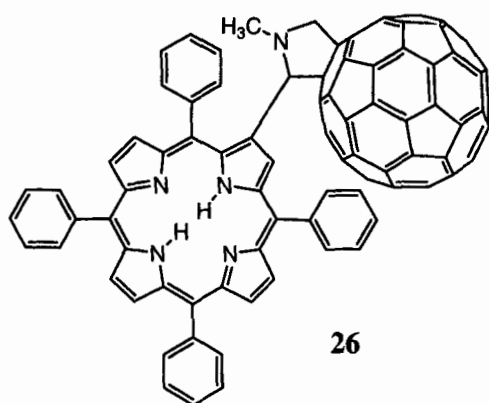
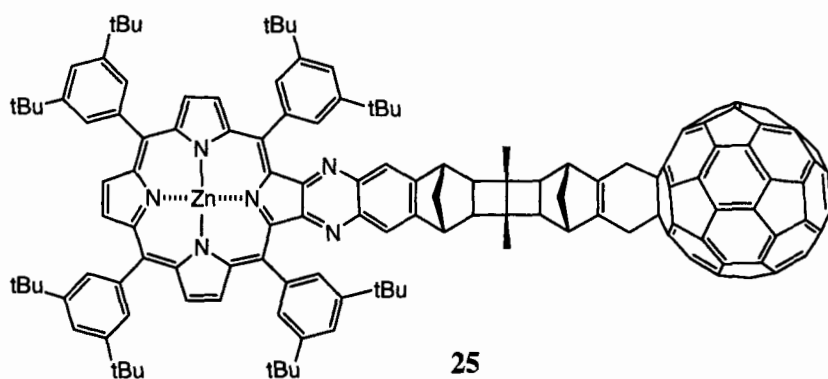
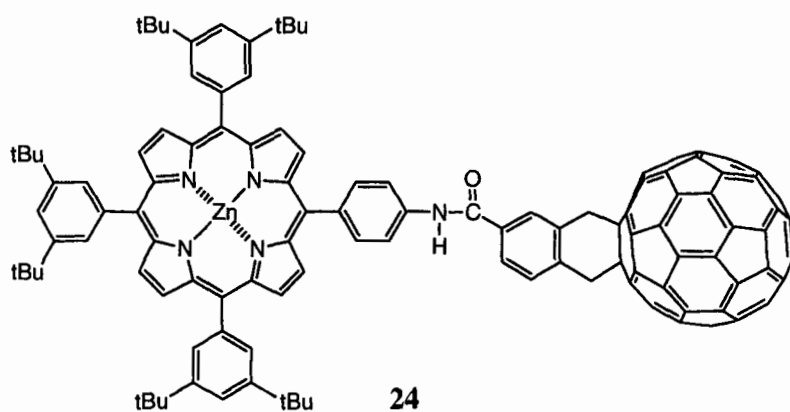
The dark color of C_{60} in solution in organic solvents is indicative of light absorption in the visible spectrum, and the potential for interesting photochemistry. In addition, the well-known ability of fullerenes to undergo up to six electrochemical reductions at relatively accessible potentials suggests that they might serve as electron acceptors or relays in multicomponent donor–acceptor systems. Recent advances in synthetic methodology have allowed the functionalization of fullerenes, and this in turn has opened the door to linking fullerenes to other pigments and electron donor–acceptor moieties.

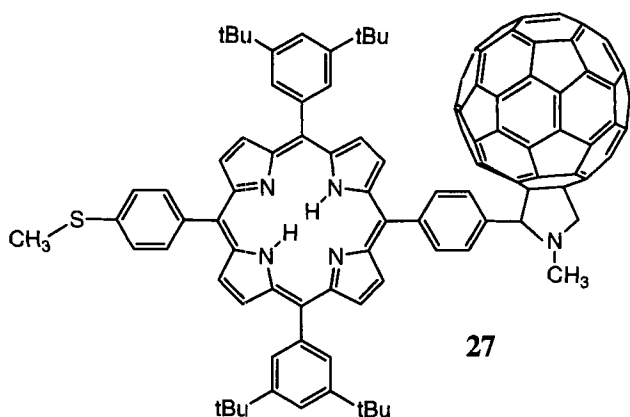
We reported the first example of such a compound, porphyrin–fullerene dyad **23**, in 1994 [134, 135]. Since that paper, a number of examples of dyads consisting of fullerenes linked to porphyrins or phthalocyanines have been prepared [136, 137–159]. Some of these, such as **24**, use amide linkages related to those employed in some porphyrin–quinone systems [137, 149, 152]. In dyad **25**, the moieties are linked by an extended, rigid bridge, of the type that has been shown to facilitate rapid long-range electron transfer in other systems [146, 147]. A number of dyads feature pyrrolidine-functionalized fullerenes, as in **26** and **27** [90, 139, 145, 148].

The general photochemical behavior of such dyads will be illustrated by dyad **26** and its zinc analogue [141, 153]. The photochemical behavior of these two dyads can be discussed with reference to Figure 4, which shows the relevant states and interconversion pathways. The energies of the excited singlet states in the figure



23





were estimated from absorption and emission properties. The fullerene absorbs throughout the visible until ~ 710 nm, but the extinction coefficients are much lower than those of the porphyrin. As with the other dyads discussed above, the absorption spectra are essentially linear combinations of those of the component chromophores, and the spectra show no evidence of strong electronic interaction of the chromophores. Cyclic voltammetric studies on **26**, its zinc analogue and model compounds allow estimation of the energies of $P^{+\bullet}-C_{60}^{\bullet-}$ and $P_{Zn}^{+\bullet}-C_{60}^{\bullet-}$ as 1.58 and 1.38 eV, respectively, above the ground states in polar solvents.

Analysis of time-resolved fluorescence and absorption data for the dyads and appropriate model compounds allows calculation of rate constants for various photochemical processes. In toluene, $^1P-C_{60}$ of **26** decays by singlet–singlet energy transfer (step 1 in Figure 4, $k_1 = 4.5 \times 10^{10} \text{ s}^{-1}$) to yield $P-^1C_{60}$, which undergoes intersystem crossing to the triplet state. No photoinduced electron transfer is observed. In benzonitrile, $^1P-C_{60}$ decays by a combination of photoinduced electron transfer by step 2 ($k_2 = 1.8 \times 10^{11} \text{ s}^{-1}$) to give $P^{+\bullet}-C_{60}^{\bullet-}$ and singlet energy transfer by step 1 ($k_1 = 7.1 \times 10^{10} \text{ s}^{-1}$). The $P-^1C_{60}$ formed in this manner or by direct absorption of light decays by photoinduced electron transfer step 3 to also yield the $P^{+\bullet}-C_{60}^{\bullet-}$ state ($k_3 = 1.3 \times 10^{10} \text{ s}^{-1}$). The charge-separated state may be readily identified using transient absorption spectroscopy through the absorption of the porphyrin radical cation in the 600–700 nm region and the fullerene radical anion at about 1000 nm. The overall quantum yield of charge separation via both pathways is 0.99. The $P^{+\bullet}-C_{60}^{\bullet-}$ state decays by charge recombination to the ground state with $k_6 = 3.4 \times 10^9 \text{ s}^{-1}$.

Qualitatively, the excited singlet states of the zinc dyad decay by similar pathways. However, the rate constants are different due mostly to differences in energetics. The first excited singlet state of the zinc porphyrin moiety is higher in energy than the corresponding state of the free base dyad, and the energy of the charge-separated state is lower due to stabilization of the positive charge in the zinc porphyrin. In toluene, $^1P_{Zn}-C_{60}$ decays by singlet energy transfer to the fullerene giving $P_{Zn}-^1C_{60}$ with a quantum yield of essentially unity. The fullerene singlet state

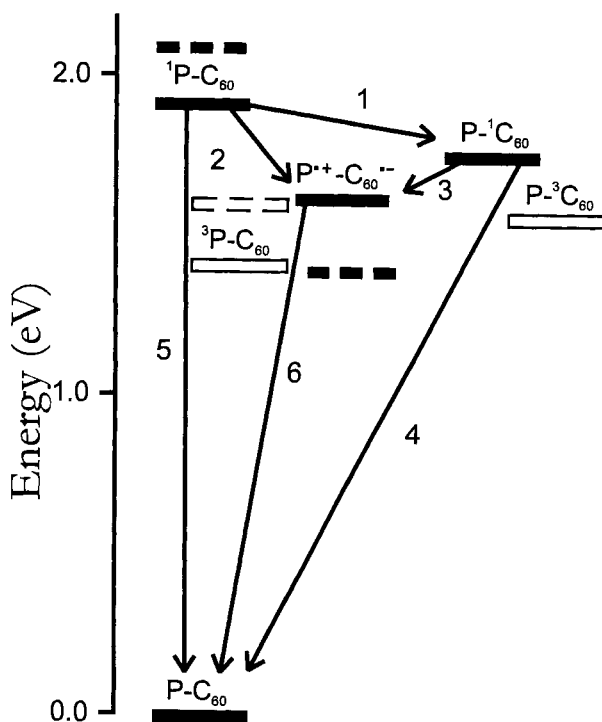


Figure 4. Transient states and interconversion pathways for porphyrin–fullerene dyads. The solid bars represent energies for free-base porphyrin–fullerene dyad **26**, and the dashed bars represent energies for the zinc-porphyrin–fullerene dyad. Solid bars represent singlet or charge-separated states, and hollow bars stand for triplet states. The energies of the charge-separated states refer to polar solvents.

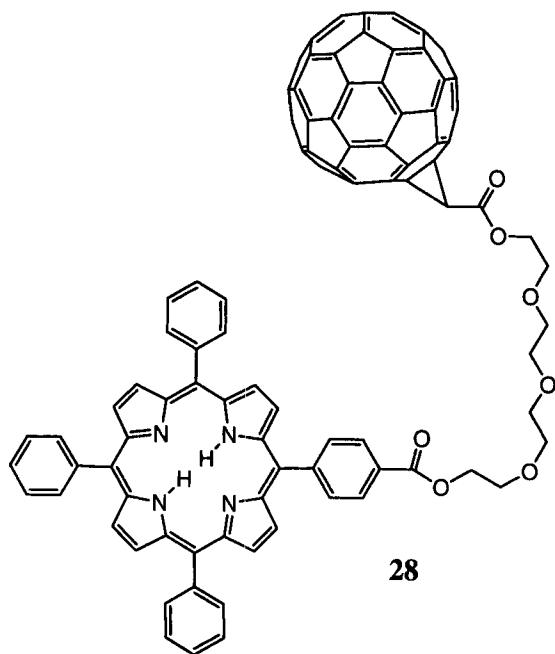
decays with a rate constant of $7.0 \times 10^8 \text{ s}^{-1}$. This rate constant is similar to that for decay of $^1\text{C}_{60}$ in model compounds, and presumably involves mainly intersystem crossing to the triplet.

In benzonitrile, $^1\text{P}_{\text{Zn}}\text{-C}_{60}$ decays in 1.9 ps by a combination of electron transfer and singlet energy transfer. If we assume that the rate constant for energy transfer step 1 in Figure 4 is approximately the same in toluene and benzonitrile ($4.9 \times 10^{10} \text{ s}^{-1}$), then the rate constant for photoinduced electron transfer step 2 is $4.8 \times 10^{11} \text{ s}^{-1}$, the quantum yield of charge separation from this state is 0.91, and the quantum yield of singlet energy transfer is 0.09. As no fluorescence emission with a lifetime longer than 1.9 ps was detected from $\text{P}_{\text{Zn}}\text{-C}_{60}$ in benzonitrile, photoinduced electron transfer from $\text{P}_{\text{Zn}}\text{-}^1\text{C}_{60}$ to give $\text{P}_{\text{Zn}}^{*\text{+}}\text{-C}_{60}^{*\text{-}}$ (step 3) must also occur with a rate constant of $\sim 5 \times 10^{11} \text{ s}^{-1}$. The $\text{P}_{\text{Zn}}^{*\text{+}}\text{-C}_{60}^{*\text{-}}$ state formed from the two pathways is produced with an overall quantum yield of essentially unity, and decays with $k_6 = 2.0 \times 10^{10} \text{ s}^{-1}$.

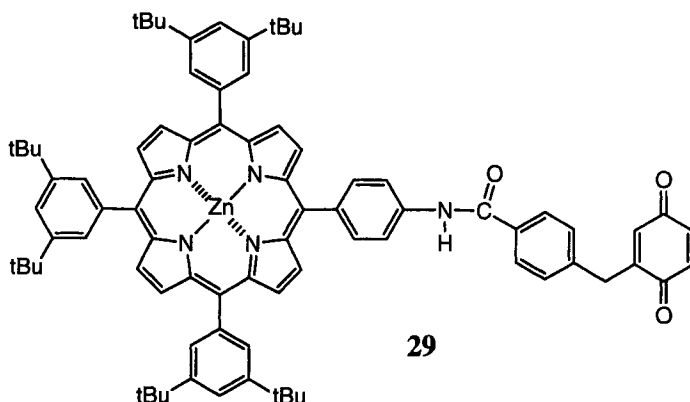
Imahori, Sakata and coworkers have bound porphyrin–fullerene dyad **27** to a

gold surface using the sulfide moiety, and observed photocurrents from this construct when it makes up part of a photoelectrochemical cell [148].

Porphyrin–fullerene dyad **28** and related molecules are cleverly designed ion-selective switches [143, 144]. In the absence of metal ions, the molecule exists in a relatively extended conformation, but in the presence of potassium ion, the molecule forms a crown-ether-like complex with the metal ion in which the porphyrin and fullerene interact more strongly. This increased interaction results in spectral perturbations and an enhanced quenching of the porphyrin fluorescence, which is likely due to enhanced electron or energy transfer to the fullerene.



In general, the studies of photoinduced electron transfer in porphyrin–fullerene dyads have shown that charge-separated states are produced in high yield, and have long lifetimes, relative to those of similar porphyrin–quinone systems [135, 141, 152, 153, 158]. For example, a comparison of the photochemistry of porphyrin–fullerene dyad **24** with that of the structurally related porphyrin–quinone dyad **29** shows that redox potentials and electronic coupling interactions are similar in the two compounds [152]. In tetrahydrofuran solution, photoinduced electron transfer in **24** occurs with a rate constant of $9 \times 10^9 \text{ s}^{-1}$. In **29**, the corresponding rate is $1.5 \times 10^9 \text{ s}^{-1}$, even though the driving force is larger by 0.28 eV. The most remarkable difference is in the charge recombination reaction. In **24** occurs with a rate constant of $2 \times 10^9 \text{ s}^{-1}$, whereas in porphyrin–quinone dyad **29**, the rate constant is greater than $5 \times 10^{10} \text{ s}^{-1}$. The differences in rate constants have been ascribed to a significantly smaller λ_i and λ_s for the large, diffuse fullerene radical ion

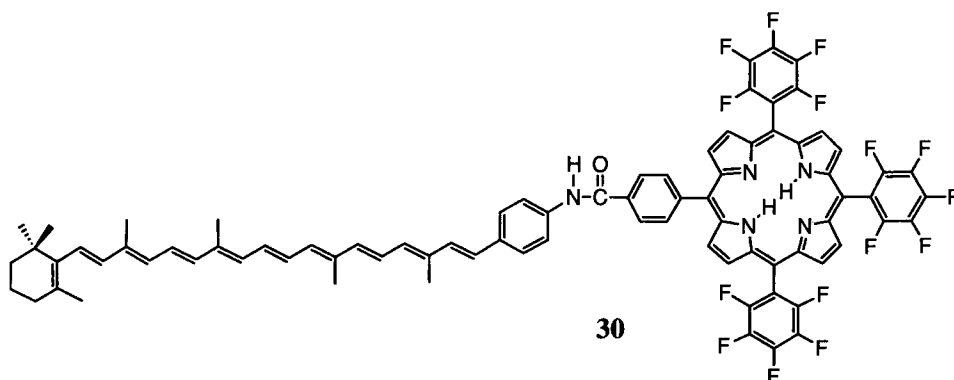


than for the quinone radical anion, where the negative charge is concentrated in the region of the oxygen atoms [152].

2.3.4 Porphyrins Covalently Linked to Carotenoid Polyenes

Carotenoid polyenes such as β -carotene and related compounds are easily oxidized, and in principle could serve as electron donors to porphyrin excited singlet states. It has been known for more than 20 years that in concentrated solutions, β -carotene quenches the fluorescence of chlorophylls, and photoinduced electron transfer has been suggested as a possible mechanism [160]. Similar quenching has been observed in porphyrin-carotene dyads [112, 161–167]. Although photoinduced electron transfer is a possible mechanism for such quenching, other possibilities such as singlet-singlet energy transfer from the porphyrin to a lower-lying carotenoid excited singlet state (which is a formally forbidden transition, not observed in absorption), and alteration of the porphyrin rate constants for fluorescence, internal conversion or intersystem crossing [165]. The dominant mechanism will depend upon the particular molecular structure.

There is one experimentally verified example of the quenching of a porphyrin first excited singlet state by photoinduced electron transfer from an attached carotenoid [166]. Carotenoporphyrin **30** features a synthetic carotenoid polyene linked to a porphyrin bearing three pentafluorophenyl groups. The electron-withdrawing nature of these fluorinated groups increases the reduction potential of the porphyrin so that there is a relatively large driving force for photoinduced electron transfer. Excitation of the porphyrin moiety of **30** in butyronitrile solution with a ~ 200 -ps laser pulse gives the porphyrin first excited singlet state, $C^{-1}P_F$, which decays with a rate constant of $1.8 \times 10^{10} \text{ s}^{-1}$ to yield the $C^{+\bullet}-P_F^{-\bullet}$ charge-separated state with a quantum yield of essentially unity. The state was identified via the strong transient absorption of the carotenoid radical cation, with a maximum at 960 nm. It decays with a lifetime of 2.9 ps. It is possible that a similar electron transfer process is responsible for the porphyrin fluorescence quenching observed in other carotenoporphyrins.



porphyrin systems, but that charge recombination is much more rapid than charge separation, making spectroscopic observation of the carotenoid radical cation difficult.

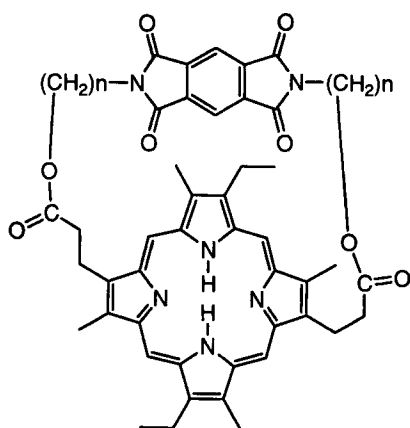
A novel noncovalent system featuring porphyrin excited singlet state quenching by carotenoids has been reported [168]. It consists of a *meso*-tetraarylporphyrin bearing cyclodextrin units on the 5- and 15-aryl groups. The two cyclodextrin units work cooperatively to bind a single β -carotene molecule, which is held so that its center is very close to the porphyrin π -electron system. Porphyrin fluorescence quenching was observed, and used to determine a binding constant for the complex.

A study of a *meso*-tetraphenylporphyrin bearing four negatively charged, bixin-based carotenoid substituents has shown that in water at pH 9, unilamellar vesicles made up of monolayer membranes are formed [169]. In the presence of guanidinium porphyrin counter ions, excitation at wavelengths absorbed by porphyrins leads to photoinduced electron transfer. Spectroscopic evidence for the bixin radical cations and porphyrin radical anions was obtained. Presumably, photoinduced electron transfer from the bixin to porphyrin first excited singlet states is involved in the formation of the radical ions.

Electron donation from a carotenoid excited singlet state to a porphyrin is energetically possible in some cases, but has not been observed. Carotenoid excited singlet states in general are not photochemically active because of their short lifetimes. The electric-dipole-allowed S_2 state, which is observed spectroscopically in absorption, has a lifetime of ~ 200 fs, and the forbidden S_1 state, which is populated by relaxation from S_2 , decays in ~ 10 ps. Thus, any electron transfer process would have to be extremely rapid, requiring a large thermodynamic driving force and relatively strong donor–acceptor electronic interactions.

2.3.5 Porphyrins Covalently Linked to Aromatic Imides

Most of the early studies of photoinduced electron transfer in porphyrin-containing supermolecules used quinones as electron acceptors. However, other electron-accepting moieties offer significant advantages in some cases. In 1985, Cowan and



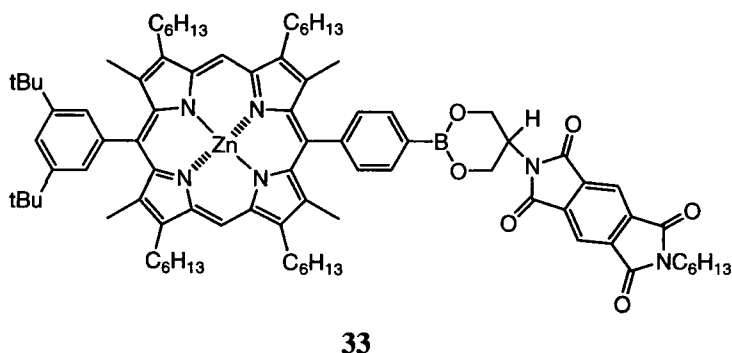
31 $n = 2$

32 $n = 3$

coworkers [170, 171] reported the use of an aromatic imide as an electron acceptor in cyclophane dyads **31**, **32** and related dyads. Since that time, a number of other researchers have employed such acceptors, and they have proven useful in dyad, triad, and more complex devices [14, 15, 56, 173–185]. Imide acceptors can be more chemically robust than quinones, and can be linked to other molecules in ways that limit conformational mobility. In some cases, their radical anions have characteristic absorption spectra that allow relatively easy spectroscopic detection.

Beddard, Cowan, Sanders and coworkers have used porphyrin–imide (P-Im) dyads **31**, **32** and related molecules to make an extensive study of the effect of driving force, solvent, electronic coupling, metalation state, coordination state, conformation, and temperature on electron transfer rate constants [171]. Rate constant data were obtained using transient fluorescence and absorption techniques. As one might expect, based on the chemistry of the porphyrin–quinone systems discussed above, excitation of the porphyrin moiety yields $^1\text{P-Im}$, which decays by electron transfer to give the $\text{P}^{+\bullet}\text{-Im}^{\bullet-}$ charge-separated state which ultimately recombines to the ground state. The results are in general agreement with the predictions of theoretical expectations as outlined at the beginning of this chapter. For example, electron transfer rate constants as a function of thermodynamic driving force are in accord with quantum mechanical extensions of Eq. 1, and inverted behavior is observed for charge recombination reactions. With long bridging groups in these cyclophanes, it was found that the pyromellitimide acceptor was bound to the central metal in the case of metalated porphyrins. This binding was disrupted upon addition of pyridine, which binds strongly to the metal, and the result is a reduction in the electron transfer rate constant. Thus, the pyridine may be used to switch electron transfer off.

An interesting phenomenon has been observed in porphyrin–imide dyad **33** and

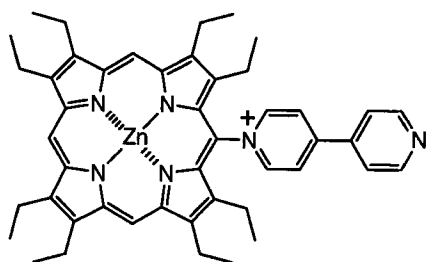


related compounds [186]. Excitation of the porphyrin moiety of **33** in benzene leads to moderately rapid photoinduced electron transfer to the imide, and a resultant shortening of the fluorescence lifetime of $^1\text{P}_{\text{Zn}}\text{-Im}$ from 1.56 ns to 1.18 ns. The charge-separated state was detected by transient absorption spectroscopy, and has a lifetime of 40 ns. Addition of five equivalents of tetra-*n*-butylammonium fluoride resulted in coordination of fluoride ion to the boronate ester in the bridge between the porphyrin and imide, and this in turn led to a return of the fluorescence lifetime of $^1\text{P}_{\text{Zn}}\text{-Im}$ to 1.56 ns. Thus, coordination of fluoride evidently prevents electron transfer quenching of the porphyrin first excited singlet state. The reasons for this effect are not known, but may involve either the presence of the negative charge (which increases the energy of $\text{Im}^{\bullet-}$ via an electrostatic effect), or changes in electronic coupling due to hybridization changes at boron. The effect might be useful in a switch or sensor application.

2.3.6 Porphyrins Covalently Linked to Viologens

Viologen derivatives are attractive as electron-accepting units for porphyrin-containing dyads and more complex donor–acceptor systems because they are easily reduced, easily linked to other molecules through alkylation of the nitrogen atoms of precursors, and can impart a degree of solubility in polar solvents due to their charged nature. In addition, the viologen radical monocation absorbs in the visible spectrum, and can be used as a convenient way to monitor charge separation. As a result, a number of covalently linked porphyrin–viologen systems have been reported [126, 187–205]. In general, excitation of a porphyrin–viologen dyad yields the porphyrin first excited singlet state, which can either donate an electron to the viologen to form a charge-transfer state, or undergo intersystem crossing to yield the porphyrin triplet state. Because the viologen moiety is easily reduced, the porphyrin triplet state may also act as an electron donor.

An example of such a system is dyad **34**, consisting of a zinc porphyrin (P_{Zn}) linked to a viologen-like moiety, pyridylpyridinium (V^+), which is also a reasonably good electron acceptor (−0.71 V versus SCE) [189]. Excitation of the porphyrin yields $^1\text{P}_{\text{Zn}}\text{-V}^+$, which decays by photoinduced electron transfer to give $\text{P}_{\text{Zn}}^{\bullet+}\text{-V}^{\bullet}$.

**34**

with a rate constant of $3.8 \times 10^9 \text{ s}^{-1}$, as derived from time-resolved fluorescence studies. In the free base analogue, the corresponding rate constant is $7.7 \times 10^9 \text{ s}^{-1}$.

Magnetic field effects on charge recombination reactions in porphyrin–viologen systems have been observed in solution and in Langmuir–Blodgett monolayers [190, 201, 202]. Photovoltaic effects have also been observed in such films, and these have been used to initiate hydrogen evolution from platinized films [193, 195].

2.4 Intramolecular Photoinduced Electron Transfer in Porphyrin-Based Systems: Triads

As illustrated above, studies of porphyrin–acceptor dyads have allowed investigation of the basic parameters influencing the rates and yields of electron transfer reactions in covalently linked systems with relatively low-energy chromophores that absorb visible light. Although most of these studies have been carried out in solution, the results are still useful for helping understand electron transfer in photosynthetic reaction centers. Indeed, several of the systems discussed above are able to mimic well some of the key features of photosynthesis, such as absorption of visible light, and photoinduced electron transfer reactions that occur in high yield to give energetic charge-separated states. Like natural reaction centers, some of the porphyrin–quinone systems even function at low temperatures. However, all of these dyads also demonstrate rapid charge recombination to the ground state. The $\text{P}^{+\bullet}\text{Q}^{-\bullet}$ state of **8** in benzonitrile, for example, decays in less than 2 ps. This rapid decay, which is not observed in photosynthetic reaction centers, severely limits any possibility of exploiting the chemical potential energy of the charge-separated state in order to carry out redox chemical reactions, charge injection into electrical circuits, etc.

The source of the problem lies in the requirement that photoinduced electron transfer be very rapid in order to compete with decay of excited states by the usual photophysical processes. Rapid transfer requires significant electronic coupling between the initial and final states (Eq. 1), and such coupling nearly always results in

a degree of coupling for the charge-recombination reaction that leads to very rapid collapse of the charge-separated state. In principle, charge recombination can be slowed by energetic considerations. If the thermodynamic driving force for charge separation from the porphyrin first excited singlet state is relatively small, then the driving force for recombination to the ground state will be relatively large, and Eq. 1 predicts that this will slow down the reaction (inverted region). This phenomenon is evident in some of the porphyrin–quinone systems discussed above. However, the effect is relatively small, and $P^{*+}\text{-}Q^{\bullet-}$ states typically recombine in picoseconds to hundreds of picoseconds.

A much more successful solution to this problem is employed by reaction centers. Secondary electron acceptors are employed so that the initially formed radical ions are rapidly separated spatially and electronically by subsequent electron transfer reactions. Each step in this sequence of electron transfers is short-range, rapid and efficient, but the net result is a weakly coupled biradical with a long lifetime. Using this strategy, reaction centers can produce a very long-lived, highly energetic charge-separated states with a quantum yield approaching unity. There is some energetic price paid for this result, as each step in the electron-transfer cascade must be sufficiently exergonic to both occur rapidly and retard the reverse reaction, which could lead to charge recombination.

2.4.1 Triads with Porphyrin–Quinone Components

In the early 1980s this biomimetic strategy was first employed in photosynthetic model systems. Carotenoid–porphyrin–quinone triad **35**, which was reported in 1983, includes a typical porphyrin–quinone and incorporates a carotenoid polyene as a secondary electron donor [206, 207]. The photochemistry of this molecule, as determined using a variety of spectroscopic techniques, is illustrated in Figure 5. Excitation of the porphyrin moiety of this triad in benzonitrile solution is followed by photoinduced electron transfer to the porphyrin to yield $C\text{-}P^{*+}\text{-}Q^{\bullet-}$ (step 2 in Figure 5) with a rate constant k_2 of $2 \times 10^9 \text{ s}^{-1}$ [208]. The quantum yield of this state is essentially unity, as photoinduced electron transfer is much more rapid than decay of $C\text{-}^1P\text{-}Q$ by other pathways (step 1). As with other porphyrin–quinone dyads, for example **8**, this state recombines rapidly to the ground state by step 3 ($k_3 = 6 \times 10^{11} \text{ s}^{-1}$). However, competing with charge recombination is electron donation from the carotenoid (which is more easily oxidized than the porphyrin by $\sim 0.30 \text{ V}$). This process (step 4 in Figure 5), yields $C^{*+}\text{-}P\text{-}Q^{\bullet-}$ with $k_4 = 1 \times 10^{11} \text{ s}^{-1}$. The final $C^{*+}\text{-}P\text{-}Q^{\bullet-}$ state is formed with an overall quantum yield of 0.13, and has a lifetime of 340 ns in benzonitrile. The multistep electron transfer pathway in **35** increases the lifetime of the charge separation by a factor of $\sim 10^5$. This is accomplished by greatly reducing the electronic coupling between the radical ions that now are separated by the neutral porphyrin moiety. The two-step sequence still demonstrates a respectable yield of the final charge-separated state because the photoinduced electron transfer step is much more rapid than decay of the excited state by other pathways, and the rate of the second electron transfer step is comparable to that of charge recombination of $C\text{-}P^{*+}\text{-}Q^{\bullet-}$.

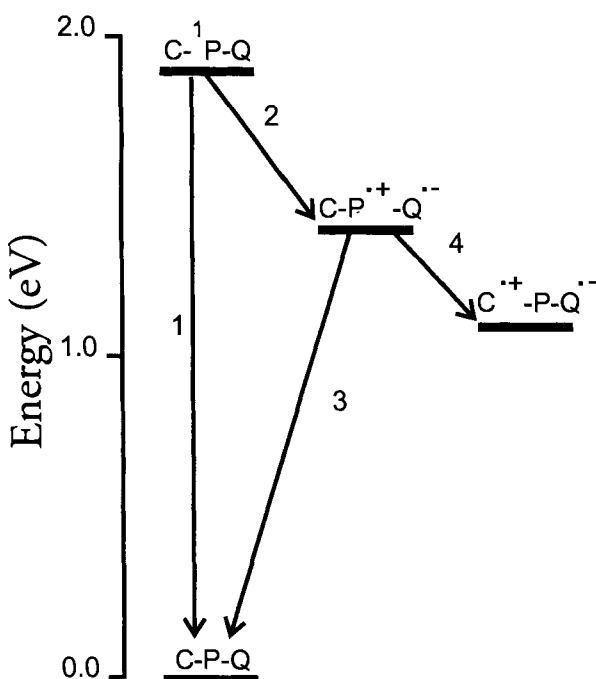
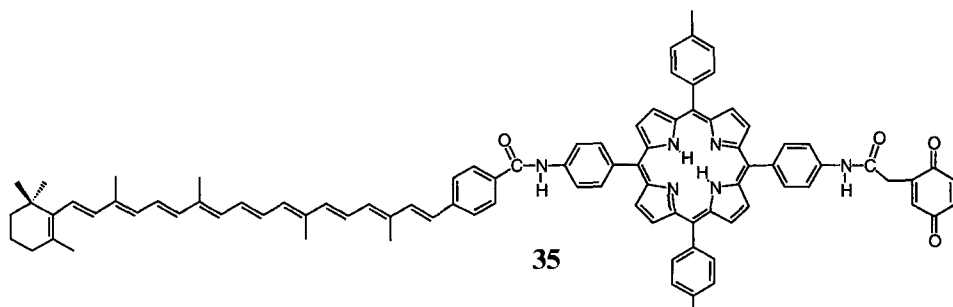


Figure 5. Transient states and interconversion pathways for carotenoporphyrin-quinone triad **35**.

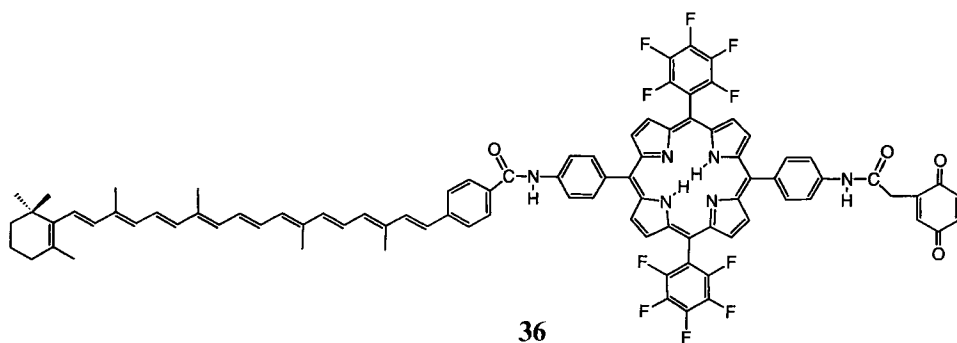


The $C^{\cdot+}\text{-P-Q}^{\cdot-}$ state in triads such as **35** eventually recombines to the ground state, unless it is harvested by subsequent reactions. The simplest possible recombination pathway involves electron transfer from the quinone radical anion directly to the carotenoid radical cation. However, this pathway can be very slow, even if thermodynamics are very favorable, because of the weak electronic coupling between the radical ions. In some cases, charge recombination has been found to fol-

low a two-step mechanism. Slow, endergonic electron transfer from the porphyrin back to the carotenoid is followed by rapid recombination of the resulting $C-P^{++}-Q^{\bullet-}$ intermediate [209]. In other systems, both direct and two-step recombination are seen, whereas other triads recombine only by the direct mechanism [172].

In triad **35**, the initial $C-P^{++}-Q^{\bullet-}$ species is formed with a quantum yield of essentially unity. However, the final $C^{++}-P-Q^{\bullet-}$ state is generated with a quantum yield of only 0.13 in benzonitrile and 0.04 in dichloromethane. The decrease in quantum yield for the final state is due to electron transfer from the carotenoid to the porphyrin radical cation (step 4 in Figure 5) that is not rapid enough to compete successfully with charge recombination to the ground state (step 3). Equation 1 suggests that one way to improve the quantum yield is to fine-tune the thermodynamics of the system in order to enhance the rate of step 4, and ideally reduce the rate of step 3. Triad **36** was designed to investigate this strategy [210]. Replacing the tolyl substituents on the porphyrin macrocycle of **35** with pentafluorophenyl substituents increases the oxidation potential of the porphyrin by ~ 200 mV. Excitation of the porphyrin moiety of **36** in dichloromethane solution is followed by photoinduced electron transfer to the quinone to yield an intermediate $C-P^{++}-Q^{\bullet-}$ state which evolves into a final $C^{++}-P-Q^{\bullet-}$ species with an overall quantum yield of 0.30 and a lifetime of 455 ns. This significant increase over the quantum yield of 0.04 observed for **35** in the same solvent is attributed for the most part to the 200 meV increase in energy of the intermediate $C-P^{++}-Q^{\bullet-}$ state. This increase in energy decreases the driving force for the photoinduced electron transfer step 2 (see Figure 5), and thus reduces the quantum yield of this first step from 0.97 in **35** to 0.41 in **36**, according to Eq. 1. However, it also increases the rate of carotenoid-to-porphyrin electron transfer step 4, and this enhances competition of this step with charge recombination. Additionally, charge recombination by step 3 is strongly exergonic, and lies in the inverted region of Eq. 1. Thus, raising the energy of $C-P^{++}-Q^{\bullet-}$ increases the driving force for this step, and this leads to a decrease in the rate constant for charge recombination. The result is a substantially increased overall yield of the final $C^{++}-P-Q^{\bullet-}$ state.

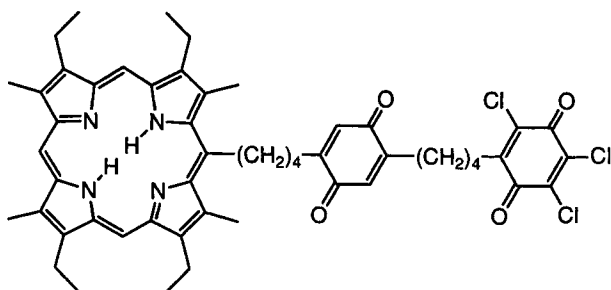
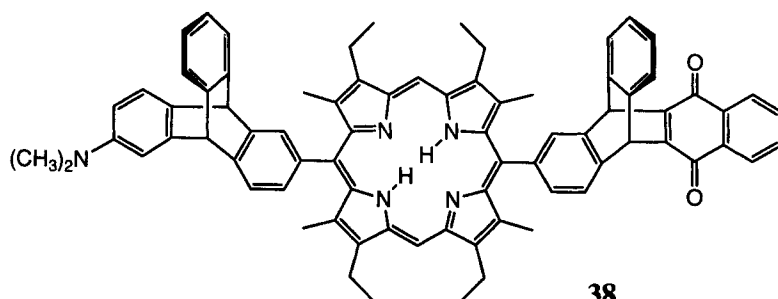
A second example of multistep electron transfer in a model photosynthetic system also appeared in 1983 [211]. Triad **37** consists of an etioporphyrin electron photo-



donor linked to a diquinone ensemble. The distal quinone is the most easily reduced. Thus, this molecule has an engineered gradient of redox potential. Excitation of the porphyrin leads to the formation of a $P^{*+}-Q-Q^{\bullet-}$ charge-separated state, which most likely is formed by a two-step electron transfer sequence involving an intermediate $P^{*+}-Q^{\bullet-}-Q$ species. This electron transfer sequence is similar to that of photosynthetic reaction centers, where the primary donor chlorophyll initiates a chain of transfers to acceptors of increasing reduction potential. The lifetime of $P^{*+}-Q-Q^{\bullet-}$ is ~ 300 ps in benzene, which is only moderately longer than that of a related $P^{*+}-Q^{\bullet-}$ model dyad (130 ps) [211]. It has been proposed that this short lifetime is a consequence of the relatively flexible linkages joining the donor and acceptor species [212]. Internal rotations about these linkages permit the radical ions to approach one another, and this leads to sufficient electronic coupling so that charge recombination is relatively rapid. This is precluded in triad **35** because of the relatively rigid, short linkages between the various moieties, which feature amide bonds with partial double bond character.

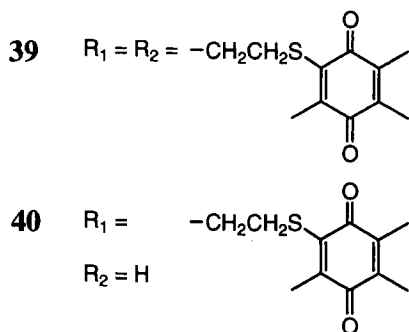
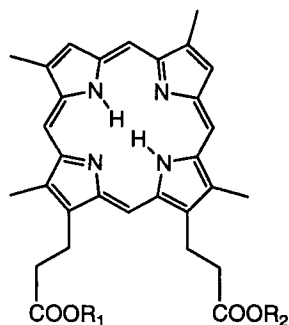
Another early triad system is **38**, which was reported in 1985 [213]. The triad is similar to **35**, but the secondary electron donor is a dimethylaniline species. The bicyclic linkages joining the components preclude large-scale folding of the molecule, and subsequent "short circuiting" as was observed in **37**. The photochemistry of triad **38** is similar to that observed for **35**, and the lifetime of the final state in butyronitrile solution at ambient temperatures is $2.45 \mu\text{s}$.

Compounds related to **38** have been used to study the dependence of electron

**37****38**

transfer rate constants on parameters such as solvent and temperature [60, 116]. A system featuring a zinc porphyrin and a more easily oxidized secondary electron donor (D) carries out photoinduced electron transfer at 5 K, and the resulting spin-polarized $D^{\bullet+}$ - P_{Zn} - $Q^{\bullet-}$ biradical was observed by EPR spectroscopy [66]. Although EPR spectroscopy has been used effectively in the study of radical pair states in photosynthetic reaction centers, relatively few examples exist of similar studies in model compounds [99, 136, 214, 215]. This is partly due to the fact that relatively few synthetic systems yield long-lived charge-separated biradical states at the low temperatures that are ideal for EPR experiments.

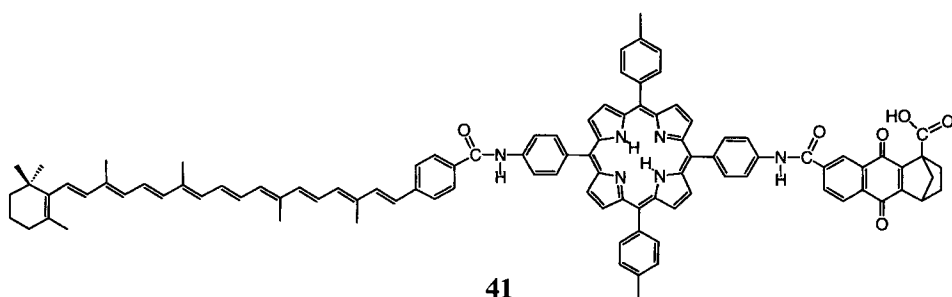
Triad **39** was reported by Borovkov and coworkers [82]. Although a model for the porphyrin moiety of these compounds has an excited singlet state lifetime of 17.4 ns in acetone solution, the corresponding lifetimes for triad **39** and dyad **40** are 0.41 and 0.77 ns, respectively. The quenching is attributed to photoinduced electron transfer to form a porphyrin–quinone charge-separated state. From these data and Eq. 6, quenching rate constants of $2.4 \times 10^9 \text{ s}^{-1}$ and $1.2 \times 10^9 \text{ s}^{-1}$ may be calculated for **39** and **40**, respectively. The similarity of structures suggests that the increase in electron transfer quenching of the porphyrin in triad **39** relative to dyad **40** may be attributed to the fact that in **39**, two photoinduced electron transfer pathways operate in parallel to compete with decay of the excited state by other pathways (see below, Section 2.5.2). Of course, the increase in quantum yield of electron transfer is relatively small in **39** because the quenching of the porphyrin singlet state by a single quinone is relatively efficient. However, it is easy to see that if this was



not the case, the quantum yield of the charge-separated state could be increased considerably by the availability of the second pathway.

One of the advantages of quinone-based acceptors is that they are capable not only of participating in electron transfer, but also of carrying on proton transfer processes [216, 217]. For example, triad **41** illustrates a strategy for slowing charge recombination based on coupling photoinduced electron transfer to a proton transfer process [217]. Triad **41** features a quinone internally hydrogen bonded to a carboxylic acid group; no such hydrogen bonding is possible in related model triads. The photochemical properties of these molecules were studied using steady-state and transient absorption and emission spectroscopies in three solvents: benzonitrile, dichloromethane and chloroform. Each of the triads undergoes photoinduced electron transfer from the porphyrin singlet state (C^1P-Q) to yield the charge-separated state $C-P^{+}-Q^{\bullet-}$. In all of these triads electron transfer from C competes with fast electron-hole recombination ($k \sim 10^{12} \text{ s}^{-1}$) to yield a final $C^{+}-P-Q^{\bullet-}$ state. Triad **41** produces the final state with a quantum yield of 0.22 in benzonitrile, which is a factor of ~ 2 higher than for reference triads. It is postulated that following the initial photoinduced electron transfer in **41**, a fast ($k \sim 10^{12} \text{ s}^{-1}$) proton shift from the carboxylic acid to the quinone anion radical competes with the recombination reaction to produce a proton-shifted state ($C-P^{+}-Q^{\bullet-}H \cdots ^-OOC$). Such a fast proton shift is expected due to the marked increase in pK_a at the quinone site (the pK_a of a model protonated naphthoquinone is ~ -6 while the pK_a of the semiquinone is ~ 5). The new proton-shifted state has an increased lifetime, and this augments the yield of electron donation by C. The increased lifetime of the proton-shifted state is attributed to the lower driving force for electron-hole recombination to the high-energy ground state ($C-P-Q^{\bullet+}H \cdots ^-OOC$) in which the quinone is protonated. Assuming a reorganization energy of $\sim 1 \text{ eV}$, the proton transfer step changes the recombination step from a faster rate in the Marcus inverted region ($\sim 1.5 \text{ eV}$ driving force) to a slower rate in the normal region ($\sim 0.5 \text{ eV}$).

The fact that the pK_a of the various oxidation states of quinones differ dramatically has been exploited in a recent design of artificial systems that mimic the light-driven transmembrane proton transport characteristic of natural photosynthesis [218]. Triad artificial reaction centers structurally related to **41** were vectorially inserted into the phospholipid bilayer of a liposome (vesicle) such that the majority of the quinone moieties are near the external surface of the membrane, and the majority of the carotenoids extend inward, toward the interior surface. The membrane

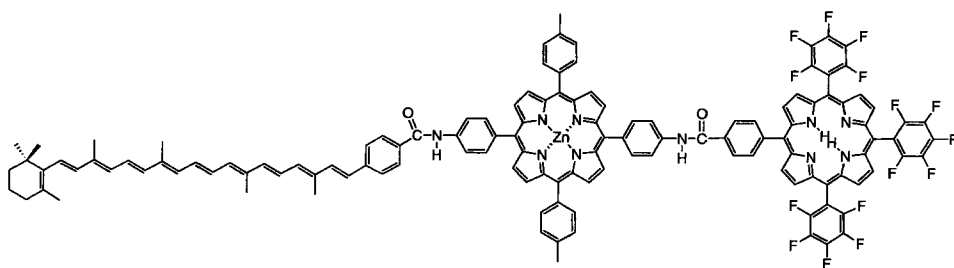


also contains a lipophilic quinone, Q_s , that can readily diffuse in the membrane. Excitation of the porphyrin of the triad generates $C^{*+}-P-Q^{-}$, which donates an electron to Q_s . The resulting semiquinone radical anion is protonated near the exterior surface of the liposome, diffuses through the bilayer, and is oxidized near the interior liposome surface by the carotenoid radical cation. The result is a protonated quinone, Q_sH^+ , which is a strong acid ($pK_a \sim -5$) and releases its proton into the interior volume of the liposome. Thus, the system is a proton pump that uses light energy to build up proton motive force inside the liposome. A transmembrane proton motive force of about 4 kcal mol^{-1} may be established in this way. In later work, an ATP synthase enzyme from spinach chloroplasts has been inserted into the liposomal membrane. The enzyme uses the light-generated proton motive force to synthesize ATP from ADP and inorganic phosphate [219]. Thus, the final step of the bacterial photosynthetic process outlined above has been mimicked using porphyrin-based systems.

2.4.2 Triads with Diporphyrin Components

Interporphyrin photoinduced electron transfer can of course be the basis of light-driven charge separation in more complex systems. For example, triad **42** is similar in structure to dyad **1**, with the addition of a carotenoid moiety, which can serve as a secondary donor as in **35** [13]. Excitation of **42** in dichloromethane with a laser pulse at 590 nm creates two porphyrin first excited singlet states, $C-^1P_{Zn}-P_F$ and $C-P_{Zn}-^1P_F$. As with **1**, both states decay at least in part by photoinduced electron transfer to give an initial $C-P_{Zn}^{*+}-P_F^{-}$ charge-separated state. This state can recombine to the ground state, but as with the other triads discussed above, electron donation from the carotene competes with this to yield a final $C^{*+}-P_{Zn}-P_F^{-}$ state with an overall quantum yield of 0.32 with 590-nm excitation. The lifetime of this final state is 240 ns.

A study by Sessler and coworkers of $P-P_{Zn}-Q$ triads with structures closely related to that of tetrad **53** (see below) has shown remarkably rapid photoinduced electron transfer from the distal free base porphyrin to the quinone. Singlet energy transfer from the free base to the proximal zinc porphyrin on such a time scale is deemed unlikely for thermodynamic reasons, since the first excited singlet state of the zinc



42

moiety is at higher energy than that of the free base. Thus, charge separation is envisioned to occur by long-range electron transfer from the free base porphyrin, where the proximal zinc porphyrin mediates electron transfer via a superexchange mechanism [73, 220].

2.4.3 Triads with Fullerene Components

As described above, photoinduced electron transfer studies in porphyrin–fullerene dyads demonstrated that charge-separated states can be produced in high yield, and that they have long lifetimes relative to quinone-containing dyads. These properties of fullerene systems suggest that they might be ideal components of more complex systems, where slow charge recombination would favor evolution of a charge-separated state into a longer-lived species via multistep electron transfers. This is indeed the case, as illustrated by carotene–porphyrin–fullerene triad **43** [136, 154, 156]. The photochemistry of this triad may be discussed with reference to Figure 6, which shows the relevant high-energy states and decay pathways. Time-resolved spectroscopic studies have shown that at ambient temperatures in 2-methyltetrahydrofuran solution, excitation of the porphyrin moiety yields C^1P-C_{60} , which decays in 10 ps by electron transfer to the fullerene to generate $C^{+}P^{+}-C_{60}^{--}$ (step 3 in Figure 6, $k_3 = 1.0 \times 10^{11} \text{ s}^{-1}$). Also, the fullerene excited singlet state accepts an electron from the porphyrin to yield $C^{+}P^{+}-C_{60}^{--}$ ($k_2 = 3.1 \times 10^{10} \text{ s}^{-1}$). The overall quantum yield of $C^{+}P^{+}-C_{60}^{--}$ by these two pathways is essentially unity. Secondary electron transfer from the carotenoid (step 4) competes with charge recombination by step 7 to give the final $C^{+}-P-C_{60}^{--}$ charge-separated state. The rise time of this state is 80 ps, and the overall yield is ~ 0.14 , as determined by the comparative method. The $C^{+}-P-C_{60}^{--}$ state decays in 170 ns exclusively by charge recombination to produce the carotenoid triplet state ($\Phi_t = 0.13$). Decay of $^3C-P-C_{60}$ occurs in 4.9 μs ($k_{10} = 2.0 \times 10^5 \text{ s}^{-1}$).

Unlike the situation with the quinone- and imide-based acceptors, photoinduced electron transfer is also observed in frozen organic glasses down to at least 8 K. For example, excitation of the porphyrin moiety of **43** in a 2-methyltetrahydrofuran glass at 77 K is followed by appearance of the $C^{+}-P-C_{60}^{--}$ charge-separated state, which is formed with a quantum yield of ~ 0.10 . The rise time for $C^{+}-P-C_{60}^{--}$ is 770 ps, which is presumably the reciprocal of $(k_4 + k_7)$ at this temperature.

The decay of the carotenoid radical cation absorption of $C^{+}-P-C_{60}^{--}$ occurs on the micro second time scale in the frozen glass. It is accompanied by the rise of $^3C-P-C_{60}$ generated by charge recombination of the $C^{+}-P-C_{60}^{--}$ biradical, which is formed with a quantum yield of ~ 0.07 . The major component of the decay of the $^3C-P-C_{60}$ transient has a time constant of 10 μs , which is a typical lifetime for a carotenoid triplet state. The absorption of $C^{+}-P-C_{60}^{--}$ at 77 K does not decay exponentially, but an “average” decay rate of $7.5 \times 10^5 \text{ s}^{-1}$ may be calculated from the data [155]. Time-resolved experiments have allowed detection of the EPR resonances of the $C^{+}-P-C_{60}^{--}$ biradical and $^3C-P-C_{60}$. The spin-polarization of the carotenoid triplet spectrum verifies formation of this state by the radical pair

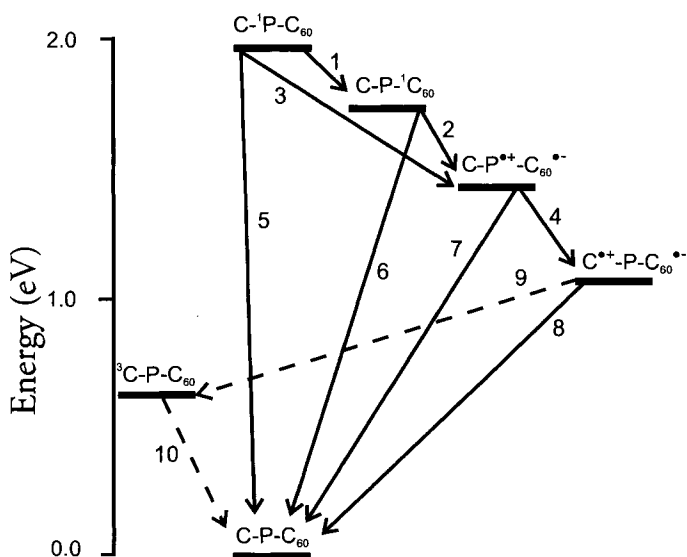
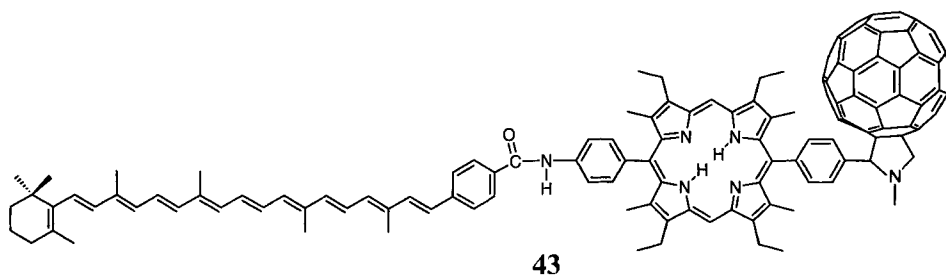


Figure 6. Transient states and interconversion pathways for carotenoporphyrin–fullerene triad **43**.

mechanism, wherein the initially formed singlet biradical of $C^+-P-C_{60}^{\bullet-}$ interconverts with the corresponding triplet biradical, which recombines to give the carotenoid triplet state [136].

The low-temperature formation of $C^+-P-C_{60}^{\bullet-}$ and its recombination to a triplet state allow some interesting and potentially useful magnetic field effects. In the presence of a small (20 mT) static magnetic field, the lifetime of the $C^+-P-C_{60}^{\bullet-}$ charge-separated state in **43** is increased by 50 % [155]. This is ascribed to the effect of the magnetic field on interconversion of the singlet and triplet biradicals. At zero field, the initially formed singlet biradical state is in equilibrium with the three triplet biradical sublevels, and all four states have comparable populations. Decay to the carotenoid triplet only occurs from the three triplet sublevels. In the presence



of the field, the S and T_0 states are still rapidly interconverting, but the T_+ and T_- states are isolated from the other two due to the electronic Zeeman interaction, and are not significantly populated. Under these conditions, recombination to the triplet occurs only from T_0 , and the lifetime of the charge-separated state increases. This effect can be used as the basis for a magnetically controlled optical or optoelectronic switch (AND gate).

The photochemistry of triad **43** has a number of unusual features. For example, it has been mentioned that two-step photoinduced electron transfer to generate long-lived charge separation occurs even at 8 K in a glass. As discussed above, the vast majority of systems based on other electron acceptors fail to undergo charge separation under these conditions [48, 54, 60]. It is generally thought that this failure is due mainly to the fact that upon freezing, the effective solvent dielectric constant decreases dramatically because the solvent dipoles cannot reorient to stabilize the newly formed ions. As mentioned above, studies of porphyrins linked to quinones and related acceptors have shown that the loss of stabilization in going from liquid butyronitrile to a 2-methyltetrahydrofuran glass at low temperatures is ~ 0.8 eV, and that only dyads with a greater driving force for electron transfer can still function at these temperatures [116]. The free energy change for formation of $C-P^{+\bullet}-C_{60}^{\bullet-}$ from $C-^1P-C_{60}$ is only 0.54 eV, based on cyclic voltammetry in benzonitrile. Thus, the fullerene anion radical in **43** must be substantially less susceptible to destabilization in nonpolar solvents than other organic ions such as quinone anion radicals. This is likely due to the fact that the negative charge is spread over a large, delocalized carbon framework. In quinone radical anions, on the other hand, the charge is concentrated on the oxygen atoms, and thus may be more susceptible to specific solvation effects [156]. The low total reorganization energy of fullerenes can also contribute to the differences in electron transfer rates, as discussed above.

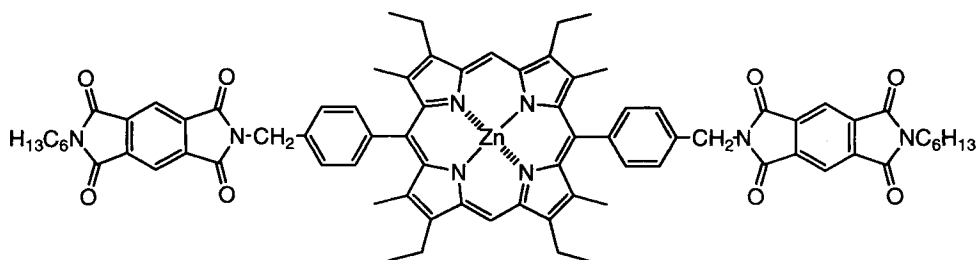
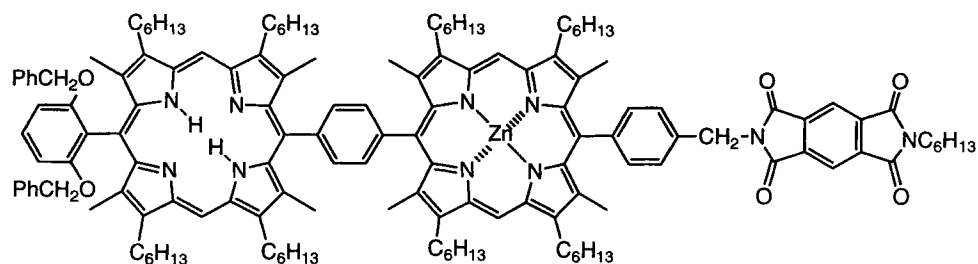
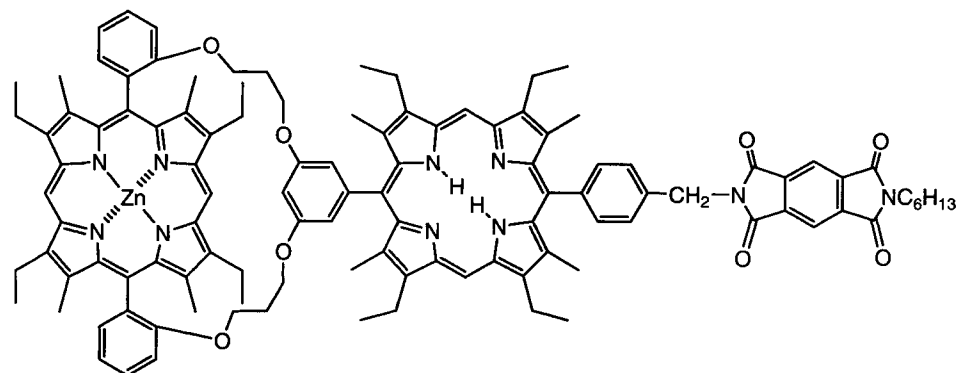
A few other triads and more complex systems consisting of a porphyrin linked to two or more fullerene moieties have been reported [150, 159, 221]. The most complex to date is a tetraarylporphyrin linked to four fullerene moieties through double ester-containing bridges to the porphyrin *meso* aryl groups [151]. This molecule is rendered soluble in organic solvents via 16 twelve-carbon aliphatic chains. The porphyrin fluorescence is strongly quenched by the attached C_{60} moieties.

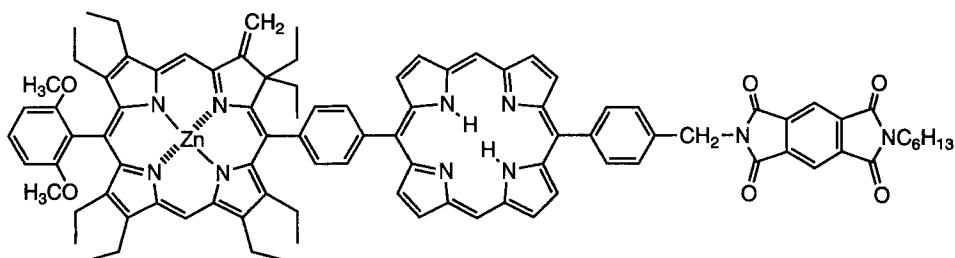
Both simple porphyrin–fullerene dyads and more complex systems may be very useful in artificial photosynthetic or molecular-scale electronic applications, due especially to the low reorganization energy of fullerenes and their low sensitivity to solvent parameters.

2.4.4 Triads with Aromatic Imide Components

Osuka, Mataga, Maruyama and coworkers have synthesized and studied a large variety of molecules that employ imides as acceptors [14–16, 56, 172–179, 182, 186, 222–226]. Representative molecules are triads **44** [179], **45** [174], **46** [175], and **47** [16]. The general photochemistry of these molecules is similar to that observed for

31 and **32**. For example, excitation of zinc porphyrin–pyromellitimide triad **44** in tetrahydrofuran at 532 nm gives the first excited singlet state of the porphyrin, $\text{Im-}^1\text{P}_{\text{Zn}}\text{-Im}$. Picosecond transient absorption studies show that this state decays into the $\text{Im-P}_{\text{Zn}}^{+\cdot}\text{-Im}^{\cdot-}$ charge-separated state in 60 ps. The charge-separated state recombines to give the ground state with a time constant of 100 ps [227]. The charge-separated state is particularly easy to detect in this molecule because of the sharp absorption band of the pyromellitimide radical anion at 715 nm.

**44****45****46**

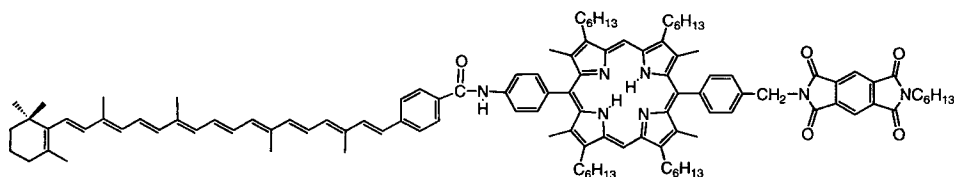


47

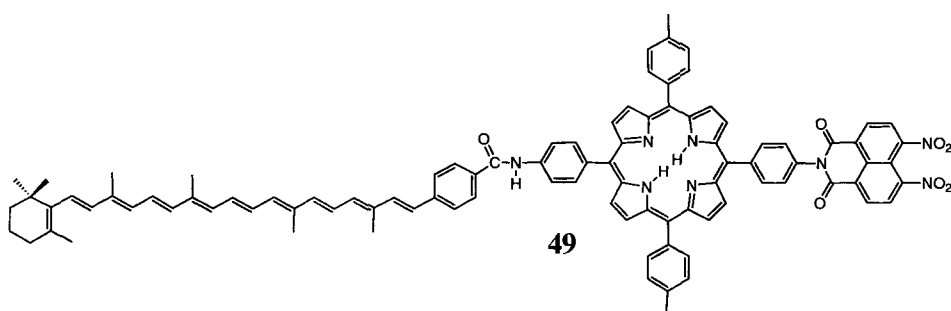
Zinc chlorins are more easily oxidized than their free base counterparts, and this fact has been used in the design of some chlorin-porphyrin-imide triads that demonstrate multistep electron transfer [16]. For example, triad **47** consists of a zinc chlorin linked to a free base porphyrin that also bears a pyromellitimide acceptor moiety. Phenyl linkers join all active constituents. Excitation of the zinc chlorin moiety of **47** in tetrahydrofuran gives $^1\text{CZ-P-Im}$, which decays with a 20-ps time constant to yield $\text{CZ}^{++}\text{-P}^{--}\text{-Im}$. This initial charge-separated state evolves into $\text{CZ}^{++}\text{-P-Im}^{--}$ with a lifetime of 120 ps. The $\text{CZ}^{++}\text{-P-Im}^{--}$ state is formed with an overall quantum yield of 0.90 and decays biphasically with time constants of 110 ns and 400 ns.

Osuka, Maruyama and Mataga have also reported the energy- and electron-transfer properties of a series of carotene-porphyrin-imide triads, such as **48** [172, 173, 178, 228]. They report that excitation of the carotenoid moiety of **48** in tetrahydrofuran solution leads to the formation of a $\text{C}^{++}\text{-P-Im}^{--}$ charge-separated state within 40–50 ps. The state has a lifetime of 15 ns. The $\text{C}^{++}\text{-P-Im}^{--}$ state is also formed upon excitation of the porphyrin, presumably via a route similar to that shown in Figure 5, but with a much slower time constant. The authors suggested that with carotenoid excitation, the $\text{C}^{++}\text{-P-Im}^{--}$ species is formed via direct, long-range electron transfer from the carotene to the imide, involving superexchange coupling through the porphyrin. No porphyrin anionic intermediate was implicated in the process.

C-P-Im triad **49** was prepared in order to further investigate this phenomenon [184]. An electron acceptor moiety based on the 4,5-dinitro-1,8-naphthalenedicarboximide system was used in this triad, as this imide is more easily reduced than pyromellitimide (-0.88 V versus ferrocene/ferrocenium as an internal reference, compared to -1.24 V for the imide moiety of **48**), and can therefore serve as an acceptor for a wider variety of donors. Excitation of the porphyrin moiety of **49**



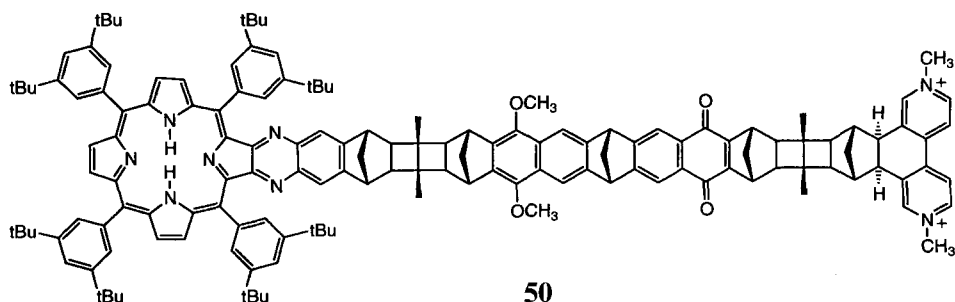
48



with visible light in benzonitrile solution leads to rapid ($k = 1.0 \times 10^{10} \text{ s}^{-1}$) photo-induced electron transfer to generate in 96 % yield a charge-separated state consisting of the porphyrin radical cation and imide radical anion. As with other triads, the intermediate $\text{C-P}^{+\bullet}\text{-Im}^{\bullet-}$ state decays by two routes: charge recombination to the ground state (analogous to step 3 in Figure 5) and electron transfer from the carotenoid to give the final $\text{C}^{+\bullet}\text{-P-Im}^{\bullet-}$ species (step 4). This final state is formed with a quantum yield of 0.33 and has a lifetime of 430 ns. In contrast to the results reported for **48** and related triads, triad **49** shows no evidence for photoinduced electron transfer from the carotenoid first excited singlet state. For example, with excitation at 556 nm, where the carotenoid moiety absorbs 43 % of the light, the carotenoid radical cation absorption was found to rise with the time constant of the decay of $\text{C-}^1\text{P-Im}$ (99 ps), and no rise time corresponding to the 7.7-ps lifetime of $^1\text{C-P-Im}$ was observed. A variety of other evidence bolstered this conclusion. The reasons for the difference in behavior of these two triads is not clear, although it is possible that a combination of structural differences between the two systems might conspire to favor transfer from the carotenoid in **48** [184].

2.4.5 Triad with a Viologen Component

An interesting and much more complex system is **50**, which consists of a rigid array containing a porphyrin donor and two electron acceptors; a quinone and a methyl



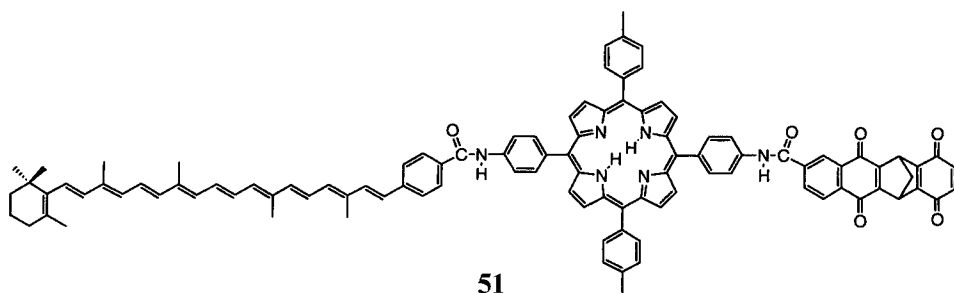
viologen derivative [188]. This molecule has a U-shaped conformation in which the bridge curves back toward the porphyrin, bringing the viologen unit to about 10 Å from the center of the porphyrin. Excitation of the porphyrin yields the porphyrin–viologen charge-separated state with a time constant of 330 ps. Charge recombination is biphasic, with lifetimes of 500 ns (~70 %) and tens of μ s (~30 %). There are three possible mechanisms for charge separation. Direct electron donation from the porphyrin to the viologen may occur. Alternatively, an electron may be donated from the porphyrin through the bridge to the naphthoquinone, which may then transfer an electron to the viologen. In principle, electron transfer through the bridge to the viologen, without intermediate reduction of the naphthoquinone could occur as well. However, the experimental data so far do not allow assignment of the mechanism.

2.5 Intramolecular Photoinduced Electron Transfer in Complex Porphyrin-Based Systems: Tetrads, Pentads, and Hexads

The early triad biomimetic systems proved beyond argument the value of the multistep electron transfer strategy for temporal stabilization of photochemically generated charge-separated states. They have been followed by a large number of other triad and more complex systems that demonstrate new principles and approaches to electron transfer that may only be realized in systems including multiple donors and acceptors. Some of these will be illustrated below.

2.5.1 Sequential Multistep Electron Transfer Process: Tetrads

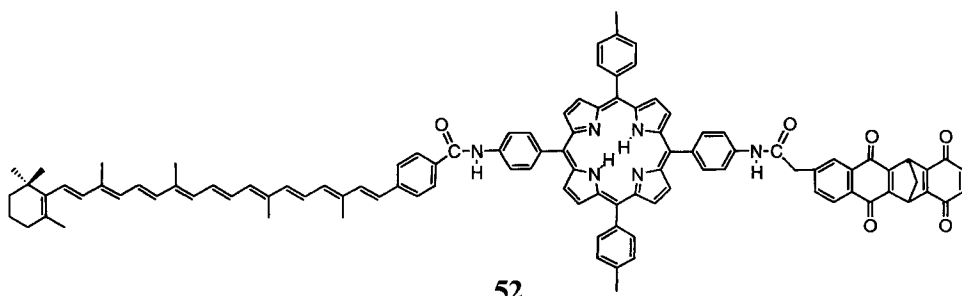
We have reported the preparation and photochemistry of C-P-Q_A-Q_B tetrad **51** [229, 230]. Excitation of the porphyrin moiety of this molecule in dichloromethane solution yields C-¹P-Q_A-Q_B, which decays by electron transfer to the attached naphthoquinone ($k = 6.6 \times 10^{10} \text{ s}^{-1}$) to yield C-P^{•+}-Q_A^{•-}-Q_B. Subsequent electron transfers from carotene to porphyrin and Q_A to Q_B compete with charge recombination to the ground state, and form a sequence of transfers that move the positive

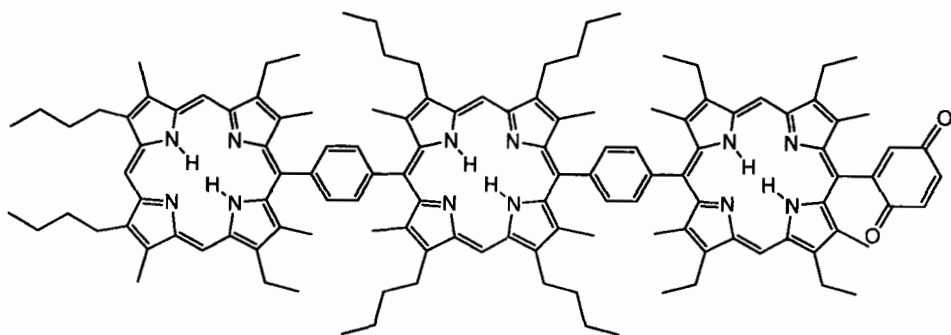


charge to the carotenoid and the negative charge to the benzoquinone to yield a final $C^{*+}\text{-P-Q}_A\text{-Q}_B^{\cdot-}$ charge-separated state. The initial $C\text{-P}^{*+}\text{-Q}_A^{\cdot-}\text{-Q}_B$ species is formed with a quantum yield of 1.0, whereas the $C^{*+}\text{-P-Q}_A\text{-Q}_B^{\cdot-}$ final state is produced with a quantum yield of 0.23 at 298 K and has a lifetime of 460 ns.

A closely related tetrad featuring two porphyrin moieties and a single naphthoquinone acceptor has also been reported [13]. Excitation of either porphyrin moiety of C-P-P-Q in anisole solution is followed by rapid ($>10^8\text{ s}^{-1}$) singlet-singlet energy transfer between the two porphyrins, whose absorption and emission spectra are essentially identical. C-P- 1 P-Q decays by photoinduced electron transfer to the quinone with a rate constant of $2.4 \times 10^8\text{ s}^{-1}$. Sequential transfer of the radical cation "hole" to the second porphyrin, and then to the carotenoid yields a final $C^{*+}\text{-P-P-Q}^{\cdot-}$ state with a quantum yield of 0.25 and a lifetime of 2.9 μs .

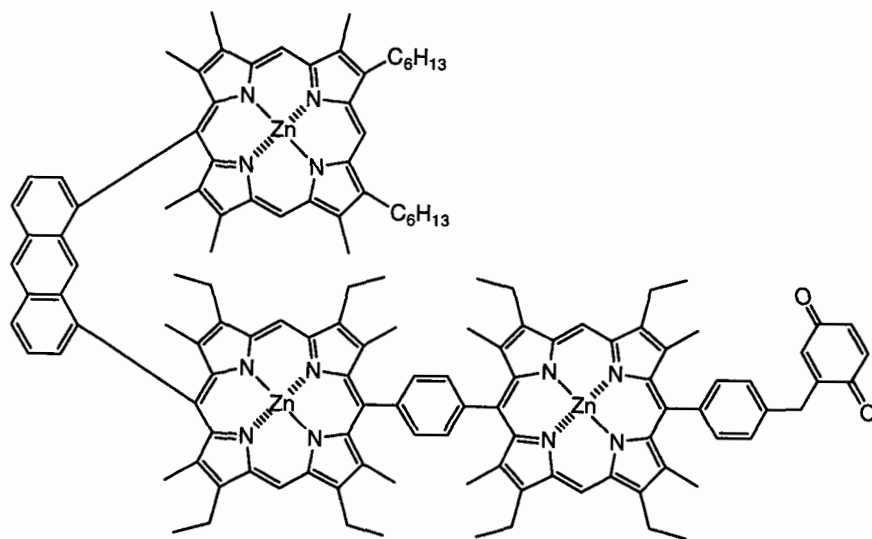
Based on the results for **51**, a second C-P- $\text{Q}_A\text{-Q}_B$ molecular tetrad **52** was prepared in an attempt to increase the quantum yield of long-lived charge separation [231]. This tetrad was engineered so that the electronic coupling between the porphyrin and adjacent naphthoquinone moiety is reduced, relative to **51**, by insertion of a methylene group in the linkage. Time-resolved fluorescence studies showed that excitation of the porphyrin moiety of **52** in dichloromethane solution is followed by photoinduced electron transfer to yield an initial $C\text{-P}^{*+}\text{-Q}_A^{\cdot-}\text{-Q}_B$ state, which is formed with a rate constant of $2.3 \times 10^9\text{ s}^{-1}$ and a quantum yield of 0.87. In chloroform, the rate is $4.1 \times 10^9\text{ s}^{-1}$ and the quantum yield is 0.94. Transient absorption studies revealed that this state evolves by subsequent electron transfer pathways similar to those for **51** to a final $C^{*+}\text{-P-Q}_A\text{-Q}_B^{\cdot-}$ charge-separated state whose lifetime is 7.4 μs in dichloromethane and 740 ns in chloroform. The quantum yield of the final state is 0.49 in dichloromethane and 0.57 in chloroform. The yield of the final state is substantially higher than that in tetrad **51** in spite of the fact that the quantum yield of the initial $C\text{-P}^{*+}\text{-Q}_A^{\cdot-}\text{-Q}_B$ species is lower. This is because the weaker electronic coupling interaction between the porphyrin and Q_A in **52** slows down charge recombination of $C\text{-P}^{*+}\text{-Q}_A^{\cdot-}\text{-Q}_B$, but has little effect on the rate constants of the electron transfer pathways that allow evolution of $C\text{-P}^{*+}\text{-Q}_A^{\cdot-}\text{-Q}_B$ into the final $C^{*+}\text{-P-Q}_A\text{-Q}_B^{\cdot-}$ state, since these do not involve the porphyrin-quinone interaction. This reduction in electronic coupling also decreases both the rate of the initial photoinduced electron transfer reaction and the charge recombination of the final $C^{*+}\text{-P-Q}_A\text{-Q}_B^{\cdot-}$ state, relative to **51**.



**53**

A variety of other porphyrin–quinone-based multicomponent systems bearing four or more donor and acceptor moieties have been reported. For example, P-P-P-Q tetrad **53** and related compounds have been reported by Sessler and coworkers [64, 65, 73, 220, 232–236]. Fluorescence and time-resolved absorption experiments with **53** were interpreted in terms of rapid (~ 10 -ps) singlet–singlet energy transfer between the porphyrin units in the linear array and extremely fast (< 350 -fs) photo-induced electron transfer to the quinone from the proximal porphyrin excited singlet state to give a charge-separated species.

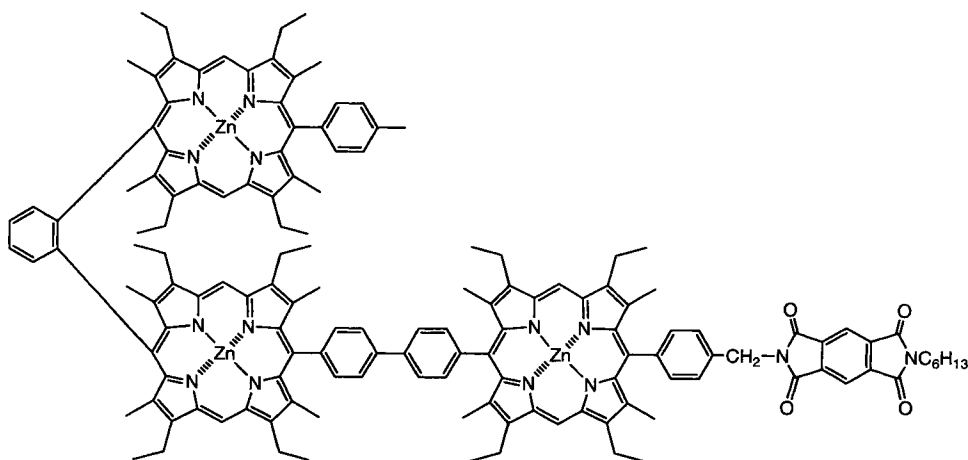
Osuka, Maruyama, Mataga and coworkers have reported a variety of closely related supramolecular systems such as **54**, in which a stacked, cofacial zinc dipor-

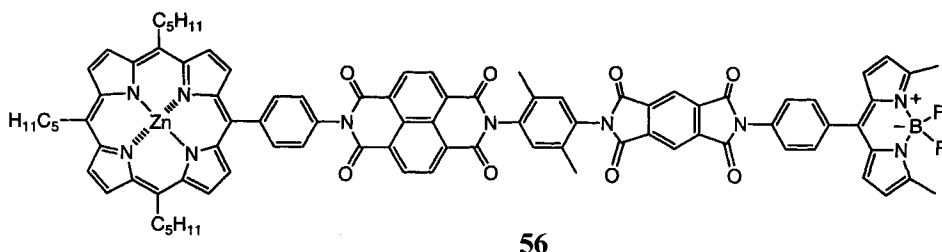
**54**

phyrin unit is linked to a monomeric zinc porphyrin, which in turn bears a benzoquinone moiety ($P_{Zn2}-P_{Zn}-Q$) [11, 72, 237]. Excitation of the monomeric porphyrin moiety of **54** yields $P_{Zn2}-^1P_{Zn}-Q$, which decays by photoinduced electron transfer to give $P_{Zn2}-P_{Zn}^{++}-Q^{--}$. Detection of a long-lived (nanosecond) charge-separated state suggests that electron transfer from the diporphyrin unit to the monomeric porphyrin radical cation competes with charge recombination to yield $P_{Zn2}^{++}-P_{Zn}-Q^{--}$. Excitation of the diporphyrin unit also yields a charge-separated state; via either singlet-singlet energy transfer to the monomeric porphyrin followed by electron transfer as described above, or direct electron transfer to the quinone moiety.

In $P_{Zn2}-P_{Zn}-Im$ tetrad **55**, the photochemistry in tetrahydrofuran is more complex [179]. The porphyrins in the P_{Zn2} unit are stacked, and interact so as to lower the energy of the first excited singlet state by 0.16 eV and the oxidation potential by 0.24 V, relative to a monomeric porphyrin model. Thus, the P_{Zn2} unit is both an excitation and a hole sink, relative to P_{Zn} . Excitation of P_{Zn} yields $P_{Zn2}-^1P_{Zn}-Im$, which decays with a time constant of 35 ps by two competing pathways. One of these is energy transfer to the stacked porphyrins, yielding $^1P_{Zn2}-P_{Zn}-Im$, which does not undergo photoinduced electron transfer, and decays to the ground state. The second is electron transfer to the pyromellitimide, giving $P_{Zn2}-P_{Zn}^{++}-Im^{--}$. Competing with the decay of this species by charge recombination is electron transfer from P_{Zn2} ($k = 4.3 \times 10^9 \text{ s}^{-1}$) to give $P_{Zn2}^{++}-P_{Zn}-Im^{--}$. This final state has a lifetime of 2.5 μs . The quantum yield of the final state would depend upon the excitation wavelength, but is limited by two factors: the competition for the excited state of P_{Zn} by both energy transfer to P_{Zn2} and electron transfer to Im , and the relatively slow electron transfer from P_{Zn2} to P_{Zn}^{++} , which leads to a considerable loss of the intermediate $P_{Zn2}-P_{Zn}^{++}-Im^{--}$ species to charge recombination.

Supramolecular species with imide acceptors have been designed as sophisticated optical switches [183, 238, 239], tetrad **56** being one example [238]. These function via sequential two-photon absorptions that result in photoinduced electron transfer



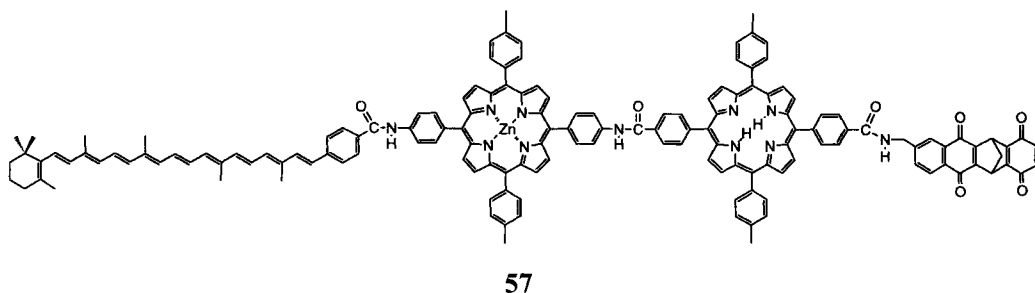


phenomena leading to new charge-separated species, or changes in rate constants for electron transfer processes.

2.5.2 Sequential and Parallel Multistep Electron Transfer Process: Pentads

In pentad **57** and related pentads, the sequential electron transfer is extended to five donor–acceptor moieties [240–242]. This molecule also conveniently illustrates a second electron transfer strategy that is useful in multicomponent systems—parallel multistep electron transfer.

Spectroscopic studies of this molecule reveal the photochemistry illustrated in Figure 7, which shows the relevant transient species and their possible inter-conversion routes. The pentad is designed so that photoinduced electron transfer from the free base porphyrin to the attached naphthoquinone can be followed by a cascade of electron transfer pathways which converge upon a final $C^{+}\text{-P}_{\text{Zn}}\text{-P-Q-Q}^{-}$ charge-separated state. The process begins with excitation of the free base porphyrin moiety. This can occur via direct absorption of light, or by singlet–singlet energy transfer from the attached zinc porphyrin. The rate constant for the energy transfer process (step 1 in Figure 7) is $2.3 \times 10^{10} \text{ s}^{-1}$ in chloroform solution, as determined from global analysis of the time-resolved fluorescence of the molecule at 14 wavelengths. The energy transfer quantum yield is about 90 %.



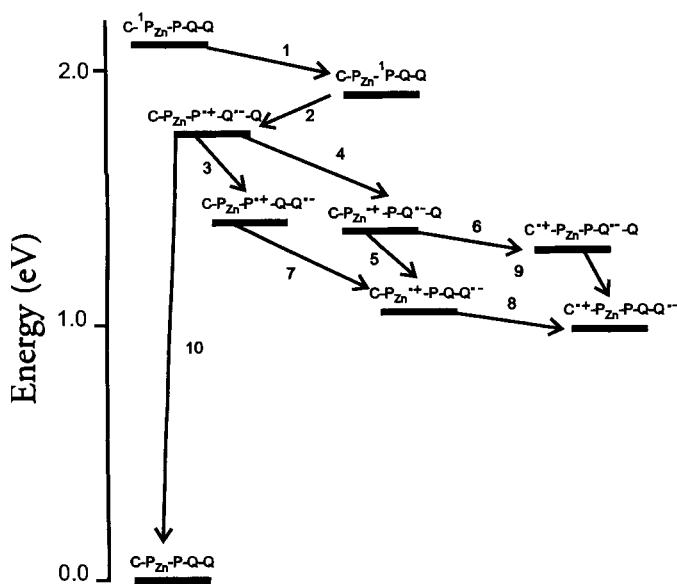


Figure 7. Transient states and interconversion pathways for carotenodiporphyrin-diquinone pentad **57**.

The free base porphyrin first excited singlet state decays in part by electron transfer to the attached naphthoquinone (step 2 in Figure 7) to produce $\text{C-P}_{\text{Zn}}\text{-P}^+\text{-Q}^{\bullet-}\text{-Q}$. The rate constant is $7.1 \times 10^8 \text{ s}^{-1}$, and the quantum yield is 0.85. This initial charge-separated state can in principle decay to the ground state through charge recombination (step 10). However, two electron transfer steps operating in parallel compete with recombination. One of these, step 3, involves electron migration from the naphthoquinone radical anion to the attached benzoquinone, which is a better electron acceptor. The other, step 4, is electron donation from the zinc porphyrin to the free base porphyrin radical cation. This reaction has a reasonable driving force, as the zinc stabilizes the positive charge on the macrocycle. Although the two new intermediates can decay by charge recombination, these reactions are expected to be slow compared to step 10 because the charges are farther apart (less electronic coupling). The two intermediates can in turn undergo electron transfer by steps 5, 6, and 7 to yield yet another two intermediates that both decay to $\text{C}^+\text{-P}_{\text{Zn}}\text{-P-Q-Q}^{\bullet-}$. This ultimate state may be readily detected spectroscopically by observation of the carotenoid radical cation absorption in the 950-nm region. In chloroform at ambient temperatures, 650-nm excitation yields the final state with an overall quantum yield of 0.83. As this yield is essentially the same as that of the initially formed $\text{C-P}_{\text{Zn}}\text{-P}^+\text{-Q}^{\bullet-}\text{-Q}$ species, the parallel electron transfer pathways compete very efficiently with step 10. The lifetime of $\text{C}^+\text{-P}_{\text{Zn}}\text{-P-Q-Q}^{\bullet-}$ is 55 μs in chloroform solu-

tion. In dichloromethane solution, the lifetime of $C^{*+}\text{-P}_{Zn}\text{-P-Q-Q}^{\bullet-}$ is increased to about 200 μs , and the quantum yield drops to 0.6.

The use of sequential and parallel multistep electron transfer pathways in the pentad has increased the lifetime of charge separation from picoseconds in porphyrin–quinone dyads to hundreds of microseconds, a factor of 10^8 . By successful molecular engineering, this has been achieved while maintaining a quantum yield near unity and preserving a significant fraction of the photon energy as chemical potential in the final charge-separated state. Such molecules show that biomimetic systems can perform essentially as well as natural photosynthesis in these respects.

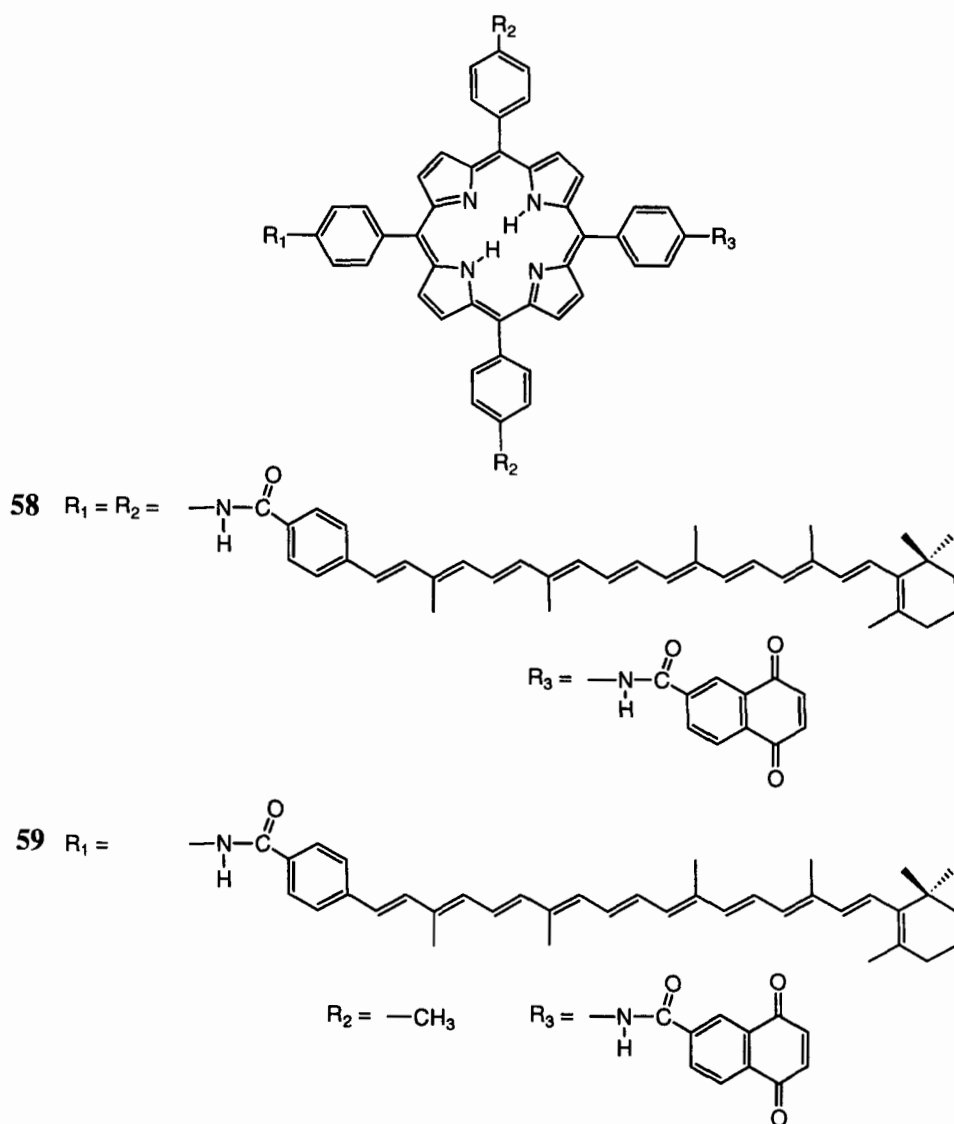
Achieving a high quantum yield in pentad **57** may be ascribed in large part to the use of parallel electron transfer to compete with charge recombination steps. The use of this strategy is also illustrated by tetrads **51** and **52** (see above).

Another example of the parallel multistep strategy is given by pentad **58**, which features a porphyrin–quinone system bearing three carotenoid secondary donors [243]. Excitation of the porphyrin moiety of model C-P-Q triad **59** leads to the formation of a charge-separated state $C^{*+}\text{-P-Q}^{\bullet-}$ with an overall quantum yield of 0.044 in benzonitrile solution. Electron transfer from the porphyrin first excited singlet state gives $C\text{-P}^{*+}\text{-Q}^{\bullet-}$ with a quantum yield of ~ 1.0 . However, electron transfer from the carotenoid to the porphyrin radical cation to form the final state does not compete well with charge recombination of $C\text{-P}^{*+}\text{-Q}^{\bullet-}$, reducing the yield. Pentad **58**, $C_3\text{-P-Q}$, features carotenoid, porphyrin and quinone moieties closely related to those in the triad. Excitation of this molecule gives a $C^{*+}\text{-P}(C_2)\text{-Q}^{\bullet-}$ state with higher quantum yield than in the triad (0.073). The enhanced yield is ascribed to the fact that three carotenoid-to-porphyrin electron donation pathways operating in parallel compete with charge recombination of $C_3\text{-P}^{*+}\text{-Q}^{\bullet-}$. The yield does not increase by the statistically predicted factor of three because there is a small difference in the stability of the porphyrin radical cation in the triad **59** and the pentad **58**. This difference slightly increases the rate of charge recombination of $C_3\text{-P}^{*+}\text{-Q}^{\bullet-}$ while slightly decreasing the rate of forward electron transfer leading to the final $C^{*+}\text{-P}(C_2)\text{-Q}^{\bullet-}$ species.

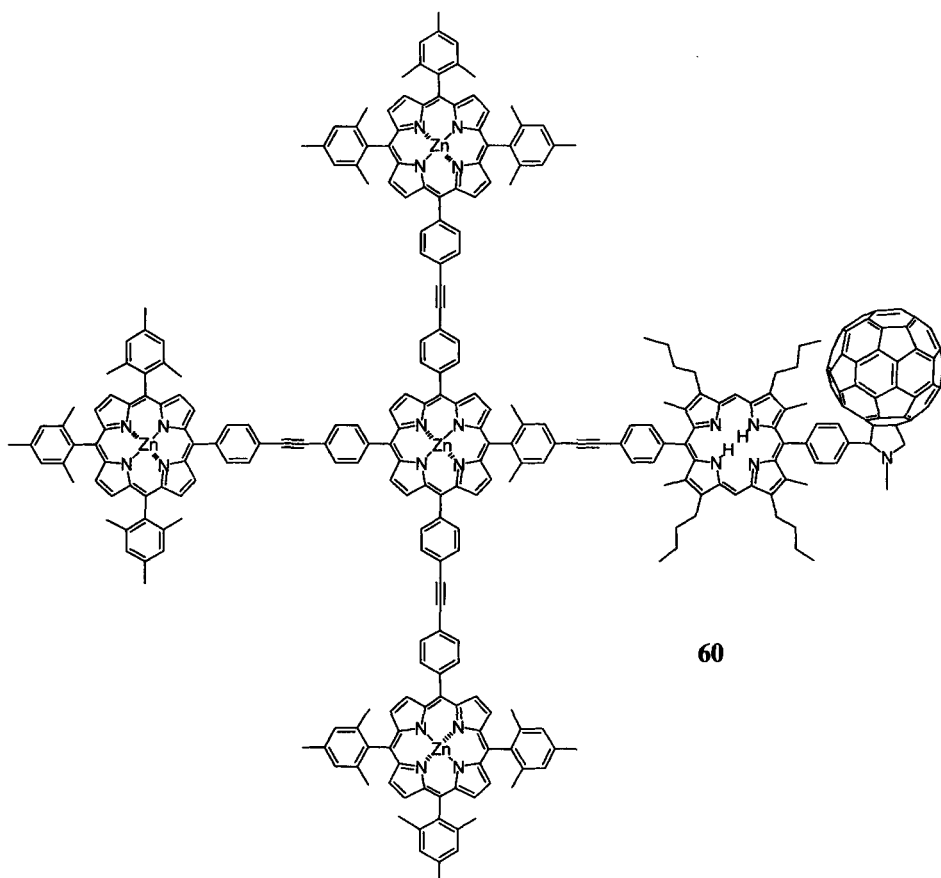
2.5.3 An Artificial Photosynthetic Antenna–Reaction Center System

Photosynthetic antenna function is based on singlet–singlet energy transfer among chromophores. This process has been mimicked in artificial, covalently linked arrays. For example, metalated and free base porphyrins have been linked with alkyne units to form dimers, trimers, tetramers, pentamers and more complex supermolecules that absorb light and rapidly and efficiently transfer singlet excitation to energy sinks such as a free base porphyrin moiety [244–250]. Some molecules of these types have been designed to act as photonic “wires” [251] and gates [252]. Other porphyrin arrays with demonstrated or potential antenna function have been reported [253].

Given the progress made in the mimicry of both photosynthetic antennas and



reaction centers, a next step would be to link an artificial light-harvesting array with a synthetic reaction center to produce a functional energy conversion assembly. Indeed, a model photosynthetic antenna consisting of four covalently linked zinc tetraarylporphyrins, $(P_{ZP})_3-P_{ZC}$, covalently joined to a free base porphyrin-fullerene artificial photosynthetic reaction center, $P-C_{60}$, to form $(P_{ZP})_3-P_{ZC}-P-C_{60}$, hexad **60**, has been recently reported [254].



In order to evaluate the performance of hexad **60**, rate constants were extracted from the steady-state and time-resolved spectroscopic data. The time-resolved fluorescence and absorption data yield a time constant of 700 ps that is associated with the zinc porphyrin moieties. The shortening of the zinc porphyrin singlet lifetime from 2.4 ns in tetrad $(P_{ZP})_3-P_{ZC}$ to give a 700-ps component in a model pentad, $(P_{ZP})_3-P_{ZC}-P$, and **60** is a result of singlet-singlet energy transfer from the zinc porphyrins to the free base porphyrin. In **60**, fluorescence from the free base porphyrin is quenched from its usual lifetime of ~ 10 ns to such a degree that fluorescence is no longer observable. The picosecond transient absorbance results yield additional time constants of 3 ps, 12 ps, and 1330 ps.

The model chosen for interpretation of the kinetic and spectroscopic data dealing with singlet energy and electron transfer in hexad **60** is shown in Figure 8. The energies of the various spectroscopic states were determined from the wavenumber average of the longest-wavelength absorption and shortest-wavelength emission maxima of **60** and appropriate model compounds. The zinc porphyrin first excited

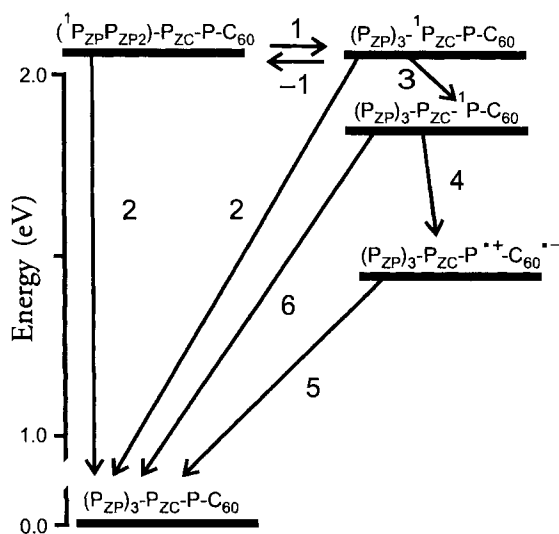


Figure 8. Transient states and interconversion pathways for antenna–reaction center complex–hexad 60.

singlet states lie at 2.06 eV, whereas the energy of $(P_{ZP})_3-P_{ZC}-^1P-C_{60}$ is 1.96 eV above the ground state. The fullerene excited singlet state is not shown in the diagram, as the results show that this state was not significantly populated by either direct excitation or energy transfer in these experiments. The energy of the $(P_{ZP})_3-P_{ZC}-P^{*+}-C_{60}^{*-}$ charge-separated state was estimated as 1.43 eV, based on the electrochemically determined oxidation potential of a model porphyrin (0.84 V versus SCE) [61] and reduction potential of a model fullerene (−0.59 V versus SCE) [255].

The rate constant for photoinduced electron transfer k_4 and the charge recombination rate constant k_5 are directly observed experimentally. The reciprocal of the 3-ps time constant detected in the transient absorption experiments, equals k_4 , $3 \times 10^{11} \text{ s}^{-1}$. This assignment is verified by the results for a model P- C_{60} dyad, where the same value was obtained for the rate constant for photoinduced electron transfer. The charge recombination of $(P_{ZP})_3-P_{ZC}-P^{*+}-C_{60}^{*-}$ is associated with the 1330-ps decay component observed in transient absorption, as demonstrated by the spectral signature of the fullerene radical anion with absorption in the 1000-nm region. This lifetime is within a factor of 2.5 of the lifetime observed for the $P^{*+}-C_{60}^{*-}$ in a model dyad (480 ps).

The values for the singlet energy transfer rate constants k_1 and k_3 do not appear directly in the experimental decays. Solution of a set of rate differential equations using the experimentally measured lifetimes of 12 ps and 700 ps as constants yields values of $2.0 \times 10^{10} \text{ s}^{-1}$ for k_1 and $4.1 \times 10^9 \text{ s}^{-1}$ for k_3 . The value thus obtained for k_1 is in excellent agreement with the results of Hsiao and coworkers [245], who

measured a rate constant of $1.9 \times 10^{10} \text{ s}^{-1}$ for singlet energy transfer between two zinc porphyrins in a linear trimeric array of zinc porphyrins with diphenylethyne linkages very similar to those in **60**.

The singlet–singlet energy transfer between the central zinc porphyrin in the antenna of **60** and the free base porphyrin (k_3) is slow (240 ps) compared with that among the zinc porphyrins (k_1) (50 ps). Thus, the rate constant k_3 is a bottleneck that limits the quantum yield of the final charge-separated state $(\text{P}_{\text{ZP}})_3\text{-P}_{\text{ZC}}\text{-P}^{++}\text{-C}_{60}^{*-}$. Structural modifications are envisioned to improve the performance of this antenna–reaction center device.

The quantum yield of $(\text{P}_{\text{ZP}})_3\text{-P}_{\text{ZC}}\text{-P}^{++}\text{-C}_{60}^{*-}$ is wavelength-dependent. Based on light absorbed by the free base porphyrin the yield is unity, due to the very large rate constant for photoinduced electron transfer, k_4 . The quantum yield based on excitation of the zinc porphyrins in the antennas is 0.70. In this process, the light-gathering power of the system is increased tremendously at many wavelengths, as four zinc porphyrin moieties feed excitation energy to the reaction center.

2.6 Conclusions

Even though a considerable number of electron donor–acceptor systems involving porphyrins have been illustrated or outlined above, this review only serves as a preface to this dynamic field of research. All of the multicomponent constructs presented herein depend upon strong covalent bonds to maintain structural integrity and control the degree of interchromophore interactions. The covalent approach is an excellent way to precisely tune and control electronic coupling and other interactions. The examples given demonstrate that porphyrins are remarkable building blocks for the molecular engineer. They feature strong absorption in the visible region of the spectrum and tunable redox properties. A well-developed synthetic chemistry provides ready access to modifications of the porphyrin periphery, central metal, metal ligands and π -electron system in order to tune their redox and photophysical properties. Moreover, related chemistry can be used for the covalent attachment of the required electron or energy donors and acceptors. These properties suggest that porphyrin donor–acceptor systems will continue to be useful as simple systems in which to study the basic principles of energy and photoinduced electron transfer, and as model systems for understanding biological energy and electron transfer processes such as photosynthesis. Also, it is likely that porphyrin-based systems will be important in more applied efforts such as the design of molecular-scale photonic or optoelectronic devices, solar energy-harvesting systems, sensors, and as components of membrane-linked constructs that mimic the complex processes of biological systems.

References

1. Ciamician, G. *Science* **1912**, 36, 385.
2. Marcus, R. A. *J. Chem. Phys.* **1956**, 24, 966.
3. Marcus, R. A.; Sutin, N. *Biochim. Biophys. Acta* **1985**, 811, 265.
4. Levich, V. *Adv. Electrochem. Electrochem. Eng.* **1966**, 4, 249.
5. Jortner, J. *J. Chem. Phys.* **1976**, 64, 4860.
6. Jortner, J. *J. Am. Chem. Soc.* **1980**, 102, 6676.
7. Weller, A. *Z. Physik. Chem. NF* **1982**, 133, 93.
8. Marcus, R. A. *Can. J. Chem.* **1959**, 37, 155.
9. Marcus, R. A. *J. Chem. Phys.* **1965**, 43, 2654.
10. Gust, D.; Moore, T. A. In *The Porphyrin Handbook, Volume 8, Electron Transfer*; Kadish, K.M., Smith, K.M. Guillard, R., Eds.; Academic Press: San Diego, 2000; p. 153.
11. Maruyama, K.; Osuka, A. *Pure & Appl. Chem.* **1990**, 62, 1511.
12. DeGraziano, J. M.; Liddell, P. A.; Leggett, L.; Moore, A. L.; Moore, T. A.; Gust, D. *J. Phys. Chem.* **1994**, 98, 1758.
13. Gust, D.; Moore, T. A.; Moore, A. L.; Gao, F.; Luttrull, D. K.; DeGraziano, J. M.; Ma, X. C.; Makings, L. R.; Lee, S.-J.; Trier, T. T.; Bittersmann, E.; Seely, G. R.; Woodward, S.; Bensasson, R. V.; Rougée, M.; de Schryver, F. C.; Van der Auweraer, M. *J. Am. Chem. Soc.* **1991**, 113, 3638.
14. Osuka, A.; Zhang, R. P.; Maruyama, K.; Mataga, N.; Tanaka, Y.; Okada, T. *Chem. Phys. Lett.* **1993**, 215, 179.
15. Osuka, A.; Marumo, S.; Maruyama, K.; Mataga, N.; Tanaka, Y.; Taniguchi, S.; Okada, T.; Yamazaki, I.; Nishimura, Y. *Bull. Chem. Soc. Jpn.* **1995**, 68, 262.
16. Osuka, A.; Marumo, S.; Mataga, N.; Taniguchi, S.; Okada, T.; Yamazaki, I.; Nishimura, Y.; Ohno, T.; Nozaki, K. *J. Am. Chem. Soc.* **1996**, 118, 155.
17. Shinoda; Tsukube, H.; Nishimura, Y.; Yamazaki, I.; Osuka, A. *Tetrahedron Lett.* **1997**, 53, 13657.
18. Osuka, A.; Tanabe, N.; Kawabata, S.; Yamazaki, I.; Nishimura, Y. *J. Org. Chem.* **1995**, 60, 7177.
19. Osuka, A.; Maruyama, K.; Mataga, N.; Asahi, T.; Yamazaki, I.; Tamai, N. *J. Am. Chem. Soc.* **1990**, 112, 4958.
20. Osuka, A.; Kobayashi, F.; Maruyama, K.; Mataga, N.; Asahi, T.; Okada, T.; Yamazaki, I.; Nishimura, Y. *Chem. Phys. Lett.* **1993**, 201, 223.
21. Wasielewski, M. R.; Johnson, D. G.; Niemczyk, M. P.; Gaines, G. L. I.; O'Neil, M. P.; Svec, W. A. *J. Am. Chem. Soc.* **1990**, 112, 6482.
22. Susumu, K.; Kunitomo, K.; Segawa, H.; Shimidzu, T. *J. Photochem. Photobiol. A: Chem.* **1995**, 92, 39.
23. Anderson, S. E.; Anderson, H. L.; Bashall, A.; McPartlin, M.; Sanders, J. K. M. *Angew. Chem. Int. Ed. Engl.* **1995**, 34, 1096.
24. DeGraziano, J. M.; Macpherson, A. N.; Liddell, P. A.; Noss, L.; Sumida, J. P.; Seely, G. R.; Lewis, J. E.; Moore, A. L.; Moore, T. A.; Gust, D. *New J. Chem.* **1996**, 20, 839.
25. Dubowchik, G. M.; Hamilton, A. D. *J. Chem. Soc., Chem. Commun.* **1986**, 1391.
26. Fujita, I.; Netzel, T. L.; Chang, C.; Wang, C.-B. *Proc. Natl. Acad. Sci. USA* **1982**, 79, 413.
27. Fujita, I.; Fajer, J.; Chang, C. K.; Wang, C.-B.; Bergkamp, M. A.; Netzel, T. L. *J. Phys. Chem.* **1982**, 86, 3754.
28. Gust, D.; Moore, T. A.; Moore, A. L.; Leggett, L.; Lin, S.; DeGraziano, J. M.; Hermant, R. M.; Nicodem, D.; Craig, P.; Seely, G. R.; Nieman, R. A. *J. Phys. Chem.* **1993**, 97, 7926.
29. Gust, D.; Moore, T. A.; Moore, A. L.; Kang, H.-K.; DeGraziano, J. M.; Liddell, P. A.; Seely, G. R. *J. Phys. Chem.* **1993**, 97, 13637.
30. Harriman, A.; Heitz, V.; Sauvage, J.-P. *J. Phys. Chem.* **1993**, 97, 5940.
31. Heiler, D.; McLendon, G. L.; Rogalskyj, P. *J. Am. Chem. Soc.* **1987**, 109, 604.
32. Helms, A.; Heiler, D.; McLendon, G. L. *J. Am. Chem. Soc.* **1992**, 114, 6227.
33. Lambrabte, A.; Janot, J. M.; Bienvenue, E.; Miquel, G.; Seta, P. *Bioelectrochem. Bioenerg.* **1992**, 27, 449.

34. Mataga, N.; Yao, H.; Okada, T.; Kanda, Y. *Chem. Phys.* **1989**, *131*, 473.
35. Netzel, T. L.; Kroger, P.; Chang, C.; Fujita, I.; Fajer, J. *Chem. Phys. Lett.* **1979**, *67*, 223.
36. Overfield, R. E.; Scherz, A.; Kaufmann, K. J.; Wasielewski, M. R. *J. Am. Chem. Soc.* **1983**, *105*, 4256.
37. Wang, X. D.; Zhang, B. W.; Bai, J. W.; Cao, Y.; Xiao, X. R.; Xu, J. M. *J. Phys. Chem.* **1992**, *96*, 2886.
38. Zaleski, J. M.; Chang, C. K.; Leroi, G. E.; Cukier, R. I.; Nocera, D. G. *J. Am. Chem. Soc.* **1992**, *114*, 3564.
39. Liu, J.-Y.; Schmidt, J. A.; Bolton, J. R. *J. Phys. Chem.* **1991**, *95*, 6924.
40. Liu, J.-Y.; Bolton, J. R. *J. Phys. Chem.* **1992**, *96*, 1718.
41. Schmidt, J. A.; Siemiarz, A.; Weedon, A. C.; Bolton, J. R. *J. Am. Chem. Soc.* **1985**, *107*, 6112.
42. Schmidt, J. A.; Liu, J.-Y.; Bolton, J. R.; Archer, M. D.; Gadzekpo, V. P. Y. *J. Chem. Soc., Faraday Trans. 1* **1989**, *85*, 1027.
43. McLendon, G. L. *Acc. Chem. Res.* **1988**, *21*, 160.
44. Brookfield, R. L.; Ellul, H.; Harriman, A. *J. Chem. Soc., Faraday Trans. 2* **1985**, *81*, 1837.
45. Kong, J. L.; Loach, P. A. In *Frontiers of Biological Energetics: From Electrons to Tissues*; Dutton, P. L., Scarpa, H., Eds.; Academic Press: New York, 1978; p 73.
46. Kong, J. L.; Loach, P. A. *J. Heterocyclic Chem.* **1980**, *17*, 737.
47. Tabushi, I.; Koga, N.; Yanagita, M. *Tetrahedron Lett.* **1979**, 257.
48. Connolly, J. S.; Bolton, J. R. In *Photoinduced Electron Transfer, Part D*; Fox, M. A., Chanon, M., Eds.; Elsevier: Amsterdam, 1988; p 303.
49. Bard, A. J.; Fox, M. A. *Acc. Chem. Res.* **1995**, *28*, 141.
50. Bixon, M.; Fajer, J.; Feher, G.; Freed, J. H.; Gamliel, D.; Hoff, A. J.; Levanon, H.; Möbius, K.; Nechushtai, R.; Norris, J. R.; Scherz, A.; Sessler, J. L.; Stehlik, D. *Israel J. Chem.* **1992**, *32*, 449.
51. Gust, D.; Moore, T. A. *Science* **1989**, *244*, 35.
52. Gust, D.; Moore, T. A. *Top. Curr. Chem.* **1991**, *159*, 103.
53. Gust, D.; Moore, T. A. *Adv. Photochem.* **1991**, *16*, 1.
54. Gust, D.; Moore, T. A.; Moore, A. L. *Acc. Chem. Res.* **1993**, *26*, 198.
55. Kurreck, H.; Huber, M. *Angew. Chem. Int. Ed. Engl.* **1995**, *34*, 849.
56. Maruyama, K.; Osuka, A.; Mataga, N. *Pure Appl. Chem.* **1994**, *66*, 867.
57. Meyer, T. J. *Acc. Chem. Res.* **1989**, *22*, 163.
58. Sakata, Y. *Yuki Gosei Kagaku Kyokai Shi* **1981**, 39.
59. Sakata, Y.; Imahori, H.; Tsue, H.; Higashida, S.; Akiyama, T.; Yoshizawa, E.; Aoki, M.; Yamada, K.; Hagiwara, K.; Taniguchi, S.; Okada, T. *Pure & Appl. Chem.* **1997**, *69*, 1951.
60. Wasielewski, M. R. *Chem. Rev.* **1992**, *92*, 435.
61. Kuciauskas, D.; Liddell, P. A.; Hung, S.-C.; Lin, S.; Stone, S.; Seely, G. R.; Moore, A. L.; Moore, T. A.; Gust, D. *J. Phys. Chem.* **1997**, *101*, 429.
62. Delaney, J. K.; Mauzerall, D. C.; Lindsey, J. S. *J. Am. Chem. Soc.* **1990**, *112*, 957.
63. Gersdorff, J.; Huber, M.; Schubert, H.; Niethammer, D.; Kirste, B.; Plato, M.; Möbius, K.; Kurreck, H.; Eichberger, R.; Keitzmann, R.; Willig, F. *Angew. Chem. Int. Ed. Engl.* **1990**, *29*, 670.
64. Sessler, J. L.; Johnson, M. R.; Creager, S. E.; Fettingner, J. C.; Ibers, J. A. *J. Am. Chem. Soc.* **1990**, *112*, 9310.
65. Sessler, J. L.; Capuano, V. L. *Angew. Chem. Int. Ed. Engl.* **1990**, *29*, 1134.
66. Wasielewski, M. R.; Gaines, G. L. I.; O'Neil, M. P.; Svec, W. A.; Niemczyk, M. P. *J. Am. Chem. Soc.* **1990**, *112*, 4559.
67. Antolovich, M.; Keyte, P. J.; Oliver, A. M.; Paddon-Row, M. N.; Kroon, J.; Verhoeven, J. W.; Jonker, S. A.; Warman, J. M. *J. Phys. Chem.* **1991**, *95*, 1933.
68. Gaines, G. L. I.; O'Neil, M. P.; Svec, W. A.; Niemczyk, M. P.; Wasielewski, M. R. *J. Am. Chem. Soc.* **1991**, *113*, 719.
69. Gust, D.; Moore, T. A.; Moore, A. L.; Ma, X. C.; Nieman, R. A.; Seely, G. R.; Belford, R. E.; Lewis, J. E. *J. Phys. Chem.* **1991**, *95*, 4442.
70. Kolling, O. W. *J. Phys. Chem.* **1991**, *95*, 192.
71. Lin, Z.-M.; Feng, W.-Z.; Leung, H.-K. *J. Chem. Soc., Chem. Commun.* **1991**, 209.

72. Osuka, A.; Nagata, T.; Maruyama, K. *Chem. Lett.* **1991**, 481.
73. Rodriguez, J.; Kirmaier, C.; Johnson, M. R.; Friesner, R. A.; Holten, D.; Sessler, J. L. *J. Am. Chem. Soc.* **1991**, *113*, 1652.
74. Sakata, Y.; Tsue, H.; Goto, Y.; Misumi, S.; Asahi, T.; Nishikawa, S.; Okada, T.; Mataga, N. *Chem. Lett., Chem. Soc. Jpn.* **1991**, 1307.
75. Dieks, H.; Sobek, J.; Tian, P.; Kurreck, H. *Tetrahedron Lett.* **1992**, *33*, 5951.
76. Frey, W.; Klann, R.; Laerner, F.; Elsaesser, T.; Baumann, E.; Futscher, M.; Staab, H. A. *Chem. Phys. Lett.* **1992**, *190*, 567.
77. Heitele, H.; Pollinger, F.; Kremer, K.; Michel-Beyerle, M. E.; Futscher, M.; Voit, G.; Weiser, J.; Staab, H. A. *Chem. Phys. Lett.* **1992**, *188*, 270.
78. Kamioka, K.; Cormier, R. A.; Lutton, T. W.; Connolly, J. S. *J. Am. Chem. Soc.* **1992**, *114*, 4414.
79. Osuka, A.; Zhang, R. P.; Maruyama, K.; Yamazaki, I.; Nishimura, Y. *Bull. Chem. Soc. Jpn.* **1992**, *65*, 2807.
80. Asahi, T.; Ohkouchi, M.; Matsusaka, R.; Mataga, N.; Zhang, R. P.; Osuka, A.; Maruyama, K. *J. Am. Chem. Soc.* **1993**, *115*, 5665.
81. Borovkov, V. V.; Ishida, A.; Takamuku, S.; Sakata, Y. *Chem. Lett.* **1993**, 737.
82. Borovkov, V. V.; Ishida, A.; Takamuku, S.; Sakata, Y. *Chem. Lett.* **1993**, 145.
83. Krieger, C.; Dernbach, M.; Voit, G.; Carell, T.; Staab, H. A. *Chem. Ber.* **1993**, *126*, 811.
84. Schlüpmann, J.; Lenzian, F.; Plato, M.; Möbius, K. *J. Chem. Soc., Faraday Trans.* **1993**, *89*, 2853.
85. Vongersdorff, J.; Kirste, B.; Kurreck, H. *Liebigs Ann. Chem.* **1993**, 897.
86. Heitele, H.; Pollinger, F.; Haberle, T.; Michel-Beyerle, M. E.; Staab, H. A. *J. Phys. Chem.* **1994**, *98*, 7402.
87. Khundkar, L. R.; Perry, J. W.; Hanson, J. E.; Dervan, P. B. *J. Am. Chem. Soc.* **1994**, *116*, 9700.
88. Liddell, P. A.; Lin, S.; Macpherson, A. N.; DeGraziano, J. M.; Seely, G. R.; Moore, A. L.; Moore, T. A.; Gust, D. *Photochem. Photobiol.* **1994**, *59S*, 19S.
89. Maruyama, K.; Osuka, A.; Mataga, N. *Pure & Appl. Chem.* **1994**, *66*, 867.
90. Paddon-Row, M. N. *Acc. Chem. Res.* **1994**, *27*, 18.
91. Sakata, Y.; Tsue, H.; O'Neil, M. P.; Wiederrecht, G. P.; Wasielewski, M. R. *J. Am. Chem. Soc.* **1994**, *116*, 6904.
92. Staab, H. A.; Döhling, A.; Voit, P.; Dernbach, M. *Tetrahedron Lett.* **1994**, *35*, 7617.
93. Staab, H. A.; Feurer, A.; Hauck, R. *Angew. Chem. Int. Ed. Engl.* **1994**, *33*, 2428.
94. Staab, H. A.; Krieger, C.; Anders, C.; Rückemann, A. *Chem. Ber.* **1994**, *127*, 231.
95. Staab, H. A.; Carell, T.; Döhling, A. *Chem. Ber.* **1994**, *127*, 223.
96. Tsue, H.; Nakashima, S.; Goto, Y.; Tatemitsu, H.; Misumi, S.; Abraham, R. J.; Asahi, T.; Tanaka, Y.; Okada, T.; Mataga, N.; Sakata, Y. *Bull. Chem. Soc. Jpn.* **1994**, *67*, 3067.
97. Kurreck, H.; Aguirre, S.; Batchelor, S. N.; Dieks, H.; Gersdorff, J.; Kay, C. W. M.; Mössler, H.; Newman, H.; Niethammer, D.; Schlüpmann, J.; Sobek, J.; Speck, M.; Stabingis, T.; Sun, L.; Tian, P.; Wieche, A.; Möbius, K. *Solar Energy Materials and Solar Cells* **1995**, *38*, 91.
98. Macpherson, A. N.; Liddell, P. A.; Lin, S.; Noss, L.; Seely, G. R.; DeGraziano, J. M.; Moore, A. L.; Moore, T. A.; Gust, D. *J. Am. Chem. Soc.* **1995**, *117*, 7202.
99. Wasielewski, M. R.; Wiederrecht, G. P.; Svec, W. A.; Niemczyk, M. P. *Solar Energy Materials and Solar Cells* **1995**, *38*, 127.
100. Dieks, H.; Senge, M. O.; Kriste, B.; Kurreck, H. *J. Org. Chem.* **1997**, *62*, 8666.
101. Elger, G.; Kurreck, H.; Wiehe, A.; Johnen, E.; Fuhs, M.; Prisner, T.; Vrieze, J. *Acta Chem. Scand.* **1997**, *51*, 593.
102. Mehta, G.; Muthusamy, S.; Maiya, B. G.; Arounaguir, S. *Tetrahedron Lett.* **1997**, *38*, 7125.
103. Tauber, A. Y.; Heleja, J.; Kilpelainen, I.; Hynninen, P. H. *Acta Chem. Scand.* **1997**, *51*, 88.
104. Zimmermann, J.; von Gersdorff, J.; Kurreck, H.; Röder, B. *J. Photochem. Photobiol. B* **1997**, *40*, 209.
105. Sumida, J. P.; Liddell, P. A.; Macpherson, A. N.; Seely, G. R.; Moore, A. L.; Moore, T. A.; Gust, D. *J. Phys. Chem. A* **1998**, *102*, 5512.
106. Wasielewski, M. R. In *Photoinduced Electron Transfer, Part A*; Fox, M.A., Chanon, M., Eds.; Elsevier: Amsterdam, 1988; p 161.

107. Leland, B. A.; Joran, A. D.; Felker, P. M.; Hopfield, J. J.; Zewail, A. H.; Dervan, P. B. *J. Phys. Chem.* **1985**, 89, 5571.
108. Hush, N. S.; Paddon-Row, M. N.; Cotsaris, E.; Oevering, H.; Verhoeven, J. W.; Heppener, M. *Chem. Phys. Lett.* **1985**, 117, 8.
109. Warman, J. M.; de Haas, M. P.; Paddon-Row, M. N.; Cotsaris, E.; Hush, N. S.; Oevering, H.; Verhoeven, J. W. *Nature (London)* **1986**, 320, 615.
110. Warman, J. M.; Smit, K. J.; Jonker, S. A.; Verhoeven, J. W.; Oevering, H.; Kroon, J.; Paddon-Row, M. N.; Oliver, A. M. *Chem. Phys.* **1993**, 170, 359.
111. Closs, G. L.; Miller, J. R. *Science* **1988**, 240, 440.
112. Gust, D.; Moore, T. A.; Liddell, P. A.; Nemeth, G. A.; Makings, L. R.; Moore, A. L.; Barrett, D.; Pessiki, P. J.; Bensasson, R. V.; Roug  , M.; Chachaty, C.; de Schryver, F. C.; Van der Auweraer, M.; Holzwarth, A. R.; Connolly, J. S. *J. Am. Chem. Soc.* **1987**, 109, 846.
113. Wasielewski, M. R.; Niemczyk, M. P.; Johnson, D. G.; Svec, W. A.; Minsek, D. W. *Tetrahedron* **1989**, 45, 4785.
114. Joran, A. D.; Leland, B. A.; Geller, G. G.; Hopfield, J. J.; Dervan, P. B. *J. Am. Chem. Soc.* **1984**, 106, 6090.
115. Joran, A. D.; Leland, B. A.; Felker, P. M.; Zewail, A. H.; Hopfield, J. J.; Dervan, P. B. *Nature (London)* **1987**, 327, 508.
116. Wasielewski, M. R.; Gaines, G. L. I.; O'Neil, M. P.; Svec, W. A.; Niemczyk, M. P.; Prodi, L.; Gosztola, D. J. In *Dynamics and Mechanisms of Photoinduced Transfer and Related Phenomena*; Mataga, N.; Okada, T.; Masuhara, H., Eds.; Elsevier Science Publishers: 1992; p 87.
117. Hasharoni, K.; Levanon, H.; Greenfield, S. R.; Gosztola, D. J.; Svec, W. A.; Wasielewski, M. R. *J. Am. Chem. Soc.* **1996**, 118, 10228.
118. Antolovich, M.; Oliver, A. M.; Paddon-Row, M. N. *J. Chem. Soc., Perkin Trans. 2* **1989**, 783.
119. Gulyas, P. T.; Langford, S. J.; Lokan, N. R.; Ranasinghe, M. G.; Paddon-Row, M. N. *J. Org. Chem.* **1997**, 62, 3038.
120. Oevering, H.; Paddon-Row, M. N.; Heppener, M.; Oliver, A. M.; Cotsaris, E.; Verhoeven, J. W.; Hush, N. S. *J. Am. Chem. Soc.* **1987**, 109, 3258.
121. Oliver, A. M.; Paddon-Row, M. N.; Kroon, J.; Verhoeven, J. W. *Chem. Phys. Lett.* **1992**, 191, 371.
122. Jortner, J.; Bixon, M.; Heitele, H.; Michel-Beyerle, M. E. *Chem. Phys. Lett.* **1992**, 197, 131.
123. Heitele, H. *Angew. Chem. Int. Ed. Engl.* **1993**, 32, 359.
124. Lindsey, J. S.; Mauzerall, D. C.; Linschitz, H. *J. Am. Chem. Soc.* **1983**, 105, 6528.
125. Lindsey, J. S.; Delaney, J. K.; Mauzerall, D. C.; Linschitz, H. *J. Am. Chem. Soc.* **1988**, 110, 3610.
126. Irvine, M.; Harrison, R. J.; Beddard, G. S.; Leighton, P.; Sanders, J. K. M. *Chem. Phys.* **1986**, 104, 315.
127. Leighton, P.; Sanders, J. K. M. *J. Chem. Soc. Chem. Commun.* **1985**, 24.
128. Osuka, A.; Furuta, H.; Maruyama, K. *Chem. Lett.* **1986**, 479.
129. Pollinger, F.; Heitele, H.; Michel-Beyerle, M. E. *Chem. Phys. Lett.* **1992**, 198, 645.
130. Staab, H. A.; Voit, G.; Weiser, J.; Futscher, M. *Chem. Ber.* **1992**, 125, 2303.
131. Staab, H. A.; Weiser, J.; Futscher, M.; Voit, G.; R  ckemann, A.; Anders, C. *Chem. Ber.* **1992**, 125, 2285.
132. Staab, H. A.; Weiser, J.; Baumann, E. *Chem. Ber.* **1992**, 125, 2275.
133. Pollinger, F.; Heitele, H.; Michel-Beyerle, M. E.; Tercel, M.; Staab, H. A. *Chem. Phys. Lett.* **1993**, 209, 251.
134. Liddell, P. A.; Macpherson, A. N.; Sumida, J. P.; Demanche, L. J.; Moore, A. L.; Moore, T. A.; Gust, D. *Photochem. Photobiol.* **1994**, 59S, 36S.
135. Liddell, P. A.; Sumida, J. P.; Macpherson, A. N.; Noss, L.; Seely, G. R.; Clark, K. N.; Moore, A. L.; Moore, T. A.; Gust, D. *Photochem. Photobiol.* **1994**, 60, 537.
136. Carbonera, D.; Di Valentini, M.; Corvaja, C.; Agostini, G.; Giacometti, G.; Liddell, P. A.; Kuciauskas, D.; Moore, A. L.; Moore, T. A.; Gust, D. *J. Am. Chem. Soc.* **1998**, 120, 4398.
137. Imahori, H.; Hagiwara, K.; Akiyama, T.; Taniguchi, S.; Okada, T.; Sakata, Y. *Chem. Lett.* **1995**, 265.
138. Linssen, T. G.; D  rr, K.; Hanack, M.; Hirsch, Q. *J. Chem. Soc., Chem. Commun.* **1995**, 103.
139. Drovetskaya, T.; Reed, C. A.; Boyd, P. D. W. *Tetrahedron Lett.* **1995**, 36, 7971.

140. Imahori, H.; Cardoso, S. L.; Tatman, D.; Lin, S.; Macpherson, A. N.; Noss, L.; Seely, G. R.; Sereno, L.; Chessa de Silber, J.; Moore, T. A.; Moore, A. L.; Gust, D. *Photochem. Photobiol.* **1995**, 62, 1009.
141. Kuciauskas, D.; Lin, S.; Seely, G. R.; Moore, A. L.; Moore, T. A.; Gust, D.; Drovetskaya, T.; Reed, C. A.; Boyd, P. D. W. *J. Phys. Chem.* **1996**, 100, 15926.
142. Imahori, H.; Sakata, Y. *Chem. Lett.* **1996**, 199.
143. Safonov, I. G.; Baran, P. S.; Schuster, D. I. *Tetrahedron Lett.* **1997**, 38, 8133.
144. Baran, P. S.; Monaco, R. R.; Kahn, A. U.; Schuster, D. I.; Wilson, S. R. *J. Am. Chem. Soc.* **1997**, 119, 8363.
145. Sun, Y.; Drovetskaya, T.; Bolskar, R. D.; Bau, R.; Boyd, P. D. W.; Reed, C. A. *J. Org. Chem.* **1997**, 62, 3642.
146. Bell, T. D. M.; Smith, T. A.; Ghiggino, K. P.; Ranasinghe, M. G.; Shepard, M. J.; Paddon-Row, M. N. *Chem. Phys. Lett.* **1997**, 268, 223.
147. Ranasinghe, M. G.; Oliver, A. M.; Rothenfluh, D. F.; Salek, A.; Paddon-Row, M. N. *Tetrahedron Lett.* **1996**, 37, 4797.
148. Akiyama, T.; Imahori, H.; Ajawakom, A.; Sakata, Y. *Chem. Lett.* **1996**, 1996, 907.
149. Imahori, H.; Hagiwara, K.; Aoki, M.; Akiyama, T.; Taniguchi, S.; Okada, T.; Shirakawa, M.; Sakata, Y. *J. Am. Chem. Soc.* **1996**, 118, 11771.
150. Nierengarten, J.-F.; Oswald, L.; Nicoud, J.-F. *Chem. Commun.* **1998**, 1545.
151. Nierengarten, J.-F.; Schall, C.; Nicoud, J.-F. *Angew. Chem. Int. Ed. Engl.* **1998**, 37, 1934.
152. Imahori, H.; Hagiwara, K.; Akiyama, T.; Aoki, M.; Taniguchi, S.; Okada, T.; Shirakawa, M.; Sakata, Y. *Chem. Phys. Lett.* **1996**, 263, 545.
153. Gust, D.; Moore, T. A.; Moore, A. L. *Res. Chem. Inter.* **1997**, 23, 621.
154. Gust, D.; Moore, T. A.; Moore, A. L.; Liddell, P. A.; Kuciauskas, D.; Sumida, J. P.; Nash, B.; Nguyen, D. In *Recent Advances in the Chemistry and Physics of Fullerenes and Related Materials*, Vol. 4; Kadish, K.M., Rutherford, A.W., Eds.; The Electrochemical Society: Pennington, NJ, 1997; p 9.
155. Kuciauskas, D.; Liddell, P. A.; Moore, A. L.; Moore, T. A.; Gust, D. *J. Am. Chem. Soc.* **1998**, 120, 10880.
156. Liddell, P. A.; Kuciauskas, D.; Sumida, J. P.; Nash, B.; Nguyen, D.; Moore, A. L.; Moore, T. A.; Gust, D. *J. Am. Chem. Soc.* **1997**, 119, 1400.
157. Martín, N.; Sánchez, L.; Illescas, B.; Pérez, I. *Chem. Rev.* **1998**, 98, 2527.
158. Imahori, H.; Sakata, Y. *Adv. Mater.* **1997**, 9, 537.
159. Bourgeois, J. P.; Diederich, F. N.; Echegoyen, L.; Nierengarten, J.-F. *Helv. Chim. Acta* **1998**, 81, 1835.
160. Beddard, G. S.; Davidson, R. S.; Trethewey, K. R. *Nature (London)* **1977**, 267, 373.
161. Moore, A. L.; Joy, A. M.; Tom, R.; Gust, D.; Moore, T. A.; Bensasson, R. V.; Land, E. J. *Science* **1982**, 216, 982.
162. Cardoso, S. L.; Moore, T. A.; Moore, A. L.; Gust, D. *Photochem. Photobiol.* **1994**, 59S, 92S.
163. Cardoso, S. L.; Nicodem, D.; Moore, A. L.; Moore, T. A.; Gust, D. *J. Braz. Chem. Soc.* **1996**, 7, 19.
164. Dedreczeny, M. P.; Wasielewski, M. R.; Shinoda, S.; Osuka, A. *J. Am. Chem. Soc.* **1997**, 119, 6407.
165. Gust, D.; Moore, T. A.; Moore, A. L.; Devadoss, C.; Liddell, P. A.; Hermant, R. M.; Nieman, R. A.; Demanche, L. J.; DeGraziano, J. M.; Gouni, I. *J. Am. Chem. Soc.* **1992**, 114, 3590.
166. Hermant, R. M.; Liddell, P. A.; Lin, S.; Alden, R. G.; Kang, H.-K.; Moore, A. L.; Moore, T. A.; Gust, D. *J. Am. Chem. Soc.* **1993**, 115, 2080.
167. Moore, T. A.; Gust, D.; Moore, A. L. In *Carotenoids: Chemistry and Biology*; Krinsky, N.I., Mathews-Roth M.M., Taylor R.F., Eds.; Plenum Press: New York, 1989; p 223.
168. French, R. R.; Wirz, J.; Woggon, W.-D. *Helv. Chim. Acta* **1998**, 81, 1521.
169. Komatsu, T.; Tsuchida, E.; Böttcher, C.; Donner, D.; Messerschmidt, C.; Siggel, U.; Stocker, W.; Rabe, J. P.; Fuhrhop, J.-H. *J. Am. Chem. Soc.* **1997**, 119, 11660.
170. Cowan, J. A.; Sanders, J. K. M. *J. Chem. Soc., Perkin Trans. I* **1985**, 1985, 2435.
171. Harrison, R. J.; Pearce, B.; Beddard, G. S.; Cowan, J. A.; Sanders, J. K. M. *Chem. Phys.* **1987**, 116, 429.

172. Osuka, A.; Yamada, H.; Shinoda, T.; Nozaki, K.; Ohno, O. *Chem. Phys. Lett.* **1995**, 238, 37.
173. Osuka, A.; Yamada, H.; Maruyama, K.; Mataga, N.; Asahi, T.; Yamazaki, I.; Nishimura, Y. *Chem. Phys. Lett.* **1991**, 181, 419.
174. Osuka, A.; Nagata, T.; Maruyama, K.; Mataga, N.; Asahi, T.; Yamazaki, I.; Nishimura, Y. *Chem. Phys. Lett.* **1991**, 185, 88.
175. Osuka, A.; Nagata, T.; Kobayashi, F.; Zhang, R. P.; Maruyama, K.; Mataga, N.; Asahi, T.; Ohno, T.; Nozaki, K. *Chem. Phys. Lett.* **1992**, 199, 302.
176. Ohkouchi, M.; Takahashi, A.; Mataga, N.; Okada, T.; Osuka, A.; Yamada, H.; Maruyama, K. *J. Am. Chem. Soc.* **1993**, 115, 12137.
177. Osuka, A.; Zhang, R. P.; Maruyama, K.; Ohno, T.; Nozaki, K. *Chem. Lett.* **1993**, 1727.
178. Osuka, A.; Yamada, H.; Maruyama, K.; Mataga, N.; Asahi, T.; Ohkouchi, M.; Okada, T.; Yamazaki, I.; Nishimura, Y. *J. Am. Chem. Soc.* **1993**, 115, 9439.
179. Osuka, A.; Nakajima, S.; Maruyama, K.; Mataga, N.; Asahi, T.; Yamazaki, I.; Nishimura, Y.; Ohno, T.; Nozaki, K. *J. Am. Chem. Soc.* **1993**, 115, 4577.
180. Smirnov, S. N.; Braun, C. L.; Greenfield, S. R.; Svec, W. A.; Wasielewski, M. R. *J. Phys. Chem.* **1996**, 100, 12329.
181. Greenfield, S. R.; Svec, W. A.; Gosztola, D. J.; Wasielewski, M. R. *J. Am. Chem. Soc.* **1996**, 118, 6767.
182. Osuka, A.; Marumo, S.; Wada, Y.; Yamazaki, I.; Yamazaki, T.; Shirakawa, Y.; Nishimura, Y. *Bull. Chem. Soc. Jpn.* **1995**, 68, 2909.
183. Wasielewski, M. R.; O'Neil, M. P.; Gosztola, D. J.; Niemczyk, M. P.; Svec, W. A. *Pure & Appl. Chem.* **1992**, 64, 1319.
184. Tan, Q.; Kuciauskas, D.; Lin, S.; Stone, S.; Moore, A. L.; Moore, T. A.; Gust, D. *J. Phys. Chem. B* **1997**, 101, 5214.
185. Gosztola, D. J.; Yamada, H.; Wasielewski, M. R. *J. Am. Chem. Soc.* **1995**, 117, 2041.
186. Shiratori, H.; Ohno, T.; Nozaki, K.; Yamazaki, I.; Nishimura, Y.; Osuka, A. *Chem. Commun.* **1998**, 1539.
187. Liu, J. X.; Zhou, Q. F.; Xu, H. J. *Chin. Chem. Lett.* **1993**, 4, 339.
188. Jolliffe, K. A.; Bell, T. D. M.; Ghiggino, K. P.; Langford, S. J.; Paddon-Row, M. N. *Angew. Chem. Int. Ed. Engl.* **1998**, 37, 916.
189. Baraka, M. E.; Janot, J. M.; Ruhlmann, L.; Giraudeau, A.; Deumié, M.; Seta, P. *J. Photochem. Photobiol. A: Chem.* **1998**, 113, 163.
190. Yonemura, H.; Ohishi, K.; Matsuo, T. *Chem. Lett.* **1996**, 661.
191. Okura, I.; Hosono, H. *Inorg. Chim. Acta* **1991**, 189, 145.
192. Amao, Y.; Kamachi, T.; Okura, I. *J. Photochem. Photobiol. A: Chem.* **1996**, 98, 59.
193. Cao, Y.; Zhang, B. W.; Qian, W. Y.; Wang, X. D.; Bai, J. W.; Ziao, X. R.; Jia, J. G.; Xu, J. W. *Solar Energy Materials and Solar Cells* **1995**, 38, 139.
194. Hosono, H.; Tani, T.; Uemura, I. *Chem. Commun.* **1996**, 1893.
195. Hosono, H.; Kaneko, M. *J. Photochem. Photobiol. A* **1997**, 107, 63.
196. Ashton, P. R.; Johnston, M. R.; Stoddart, J. F.; Tolley, M. S.; Wheeler, J. W. *J. Chem. Soc., Chem. Commun.* **1992**, 1128.
197. Hirota, J.; Okura, I. *J. Phys. Chem.* **1993**, 97, 6867.
198. Kanda, Y.; Sato, H.; Okada, T.; Mataga, N. *Chem. Phys. Lett.* **1986**, 129, 306.
199. McMahon, R. J.; Force, R. K.; Patterson, H. H.; Wrighton, M. S. *J. Am. Chem. Soc.* **1988**, 110, 2670.
200. Nakamura, H.; Motonaga, A.; Ogata, T.; Nakao, S.; Nagamura, T.; Matsuo, T. *Chem. Lett.* **1986**, 1615.
201. Nakamura, H.; Uehata, A.; Motonaga, A.; Ogata, T.; Matsuo, T. *Chem. Lett.* **1987**, 543.
202. Saito, T.; Hirata, Y.; Sato, H.; Yoshida, T.; Mataga, N. *Bull. Chem. Soc. Jpn.* **1988**, 61, 1925.
203. Blondeel, G.; Keukeleire, D. D.; Harriman, A.; Milgrom, L. R. *Chem. Phys. Lett.* **1985**, 118, 77.
204. Batteas, J. D.; Harriman, A.; Kanda, Y.; Mataga, N.; Nowak, A. K. *J. Am. Chem. Soc.* **1990**, 112, 126.
205. Noda, S.; Hosono, H.; Okura, I.; Yamamoto, Y.; Inoue, Y. *J. Chem. Soc., Faraday Trans.* **1990**, 86, 811.

206. Gust, D.; Mathis, P.; Moore, A. L.; Liddell, P. A.; Nemeth, G. A.; Lehman, W. R.; Moore, T. A.; Bensasson, R. V.; Land, E. J.; Chachaty, C. *Photochem. Photobiol.* **1983**, 37S, S46–S46.
207. Moore, T. A.; Gust, D.; Mathis, P.; Mialocq, J.-C.; Chachaty, C.; Bensasson, R. V.; Land, E. J.; Doizi, D.; Liddell, P. A.; Lehman, W. R.; Nemeth, G. A.; Moore, A. L. *Nature (London)* **1984**, 307, 630.
208. Hung, S.-C.; Lin, S.; Macpherson, A. N.; DeGraziano, J. M.; Kerrigan, P. K.; Liddell, P. A.; Moore, A. L.; Moore, T. A.; Gust, D. *J. Photochem. Photobiol. A: Chem.* **1994**, 77, 207.
209. Gust, D.; Moore, T. A.; Makings, L. R.; Liddell, P. A.; Nemeth, G. A.; Moore, A. L. *J. Am. Chem. Soc.* **1986**, 108, 8028.
210. Moore, T. A.; Gust, D.; Hatlevig, S.; Moore, A. L.; Makings, L. R.; Pessiki, P. J.; de Schryver, F. C.; Van der Auweraer, M.; Lexa, D.; Bensasson, R. V.; Rougée, M. *Israel J. Chem.* **1988**, 28, 87.
211. Nishitani, S.; Kurata, N.; Sakata, Y.; Misumi, S.; Karen, A.; Okada, T.; Mataga, N. *J. Am. Chem. Soc.* **1983**, 105, 7771.
212. Sakata, Y.; Kishimoto, M.; Nishitani, S.; Tatemitsu, H.; Misumi, S.; Karen, A.; Okada, T.; Mataga, N.; Moore, T. A.; Gust, D. *Studies in Organic Chemistry* **1987**, 31, 427.
213. Wasielewski, M. R.; Niemczyk, M. P.; Svec, W. A.; Pewitt, E. B. *J. Am. Chem. Soc.* **1985**, 107, 5562.
214. Hasharoni, K.; Levanon, H.; Bowman, M. K.; Norris, J. R.; Gust, D.; Moore, T. A.; Moore, A. L. *Appl. Magn. Res.* **1990**, 1, 357.
215. Hasharoni, K.; Levanon, H.; Tang, J.; Bowman, M. K.; Norris, J. R.; Gust, D.; Moore, T. A.; Moore, A. L. *J. Am. Chem. Soc.* **1990**, 112, 6477.
216. Hung, S.-C.; Macpherson, A. N.; Lin, S.; Liddell, P. A.; Seely, G. R.; Moore, A. L.; Moore, T. A.; Gust, D. In *Photochemistry and Radiation Chemistry: Complementary Methods for the Study of Electron Transfer* 1998; p 177.
217. Hung, S.-C.; Macpherson, A. N.; Lin, S.; Liddell, P. A.; Seely, G. R.; Moore, A. L.; Moore, T. A.; Gust, D. *J. Am. Chem. Soc.* **1995**, 117, 1657.
218. Steinberg-Yfrach, G.; Liddell, P. A.; Hung, S.-C.; Moore, A. L.; Gust, D.; Moore, T. A. *Nature (London)* **1997**, 385, 239.
219. Steinberg-Yfrach, G.; Rigaud, J.-L.; Durantini, E. N.; Moore, A. L.; Gust, D.; Moore, T. A. *Nature (London)* **1998**, 392, 479.
220. Sessler, J. L.; Johnson, M. R.; Lin, T.-Y.; Creager, S. E. *J. Am. Chem. Soc.* **1988**, 110, 3659.
221. Higashida, S.; Imahori, H.; Kaneda, T.; Sakata, Y. *Chem. Lett.* **1998**, 605.
222. Osuka, A.; Kobayashi, F.; Nakajima, S.; Maruyama, K.; Yamazaki, I.; Nishimura, Y. *Chem. Lett.* **1993**, 161.
223. Osuka, A.; Marumo, S.; Taniguchi, S.; Okada, T.; Mataga, N. *Chem. Phys. Lett.* **1994**, 230, 144.
224. Osuka, A.; Marumo, S.; Maruyama, K.; Mataga, N.; Ohkouchi, M.; Taniguchi, S.; Okada, T.; Yamazaki, I.; Nishimura, Y. *Chem. Phys. Lett.* **1994**, 225, 140.
225. Osuka, A.; Yamada, H.; Maruyama, K.; Ohno, T.; Nozaki, K.; Okada, T.; Tanaka, Y.; Mataga, N. *Chem. Lett.* **1995**, 591.
226. Osuka, A.; Nakajima, S.; Okada, T.; Taniguchi, S.; Nozaki, K.; Ohno, T.; Yamazaki, I.; Nishimura, Y.; Mataga, N. *Angew. Chem. Int. Ed. Engl.* **1996**, 35, 92.
227. Osuka, A.; Nakajima, S.; Maruyama, K.; Mataga, N.; Asahi, T.; Yamazaki, I.; Nishimura, Y.; Ohno, T.; Nozaki, K. *J. Am. Chem. Soc.* **1993**, 115, 4577.
228. Osuka, A.; Yamada, H.; Maruyama, K.; Mataga, N.; Asahi, T.; Ohkouchi, M.; Okada, T.; Yamazaki, I.; Nishimura, Y. *J. Am. Chem. Soc.* **1993**, 115, 9439.
229. Gust, D.; Moore, T. A.; Moore, A. L.; Barrett, D.; Harding, L. O.; Makings, L. R.; Liddell, P. A.; de Schryver, F. C.; Van der Auweraer, M.; Bensasson, R. V.; Rougée, M. *J. Am. Chem. Soc.* **1988**, 110, 321.
230. Gust, D.; Moore, T. A.; Moore, A. L.; Seely, G. R.; Liddell, P. A.; Barrett, D.; Harding, L. O.; Ma, X. C.; Lee, S.-J.; Gao, F. *Tetrahedron* **1989**, 45, 4867.
231. Lee, S.-J.; DeGraziano, J. M.; Macpherson, A. N.; Shin, E.-J.; Seely, G. R.; Kerrigan, P. K.; Moore, A. L.; Moore, T. A.; Gust, D. *Chem. Phys.* **1993**, 176, 321.
232. Sessler, J. L.; Piering, S. *Tetrahedron Lett.* **1987**, 28, 6569.
233. Sessler, J. L.; Johnson, M. R. *Angew. Chem.* **1987**, 99, 679.

234. Sessler, J. L.; Johnson, M. R.; Lin, T.-Y. *Tetrahedron* **1989**, *45*, 4767.
235. Sessler, J. L.; Capuano, V. L.; Harriman, A. *J. Am. Chem. Soc.* **1993**, *115*, 4618.
236. Sessler, J. L.; Capuano, V. L. *Tetrahedron Lett.* **1993**, *34*, 2287.
237. Osuka, A.; Maruyama, K.; Mataga, N.; Asahi, T.; Yamazaki, I.; Tamai, N.; Nishimura, Y. *Chem. Phys. Lett.* **1991**, *181*, 413.
238. Debreczeny, M. P.; Svec, W. A.; Wasielewski, M. R. *Science* **1996**, *274*, 584.
239. O'Neil, M. P.; Niemczyk, M. P.; Svec, W. A.; Gosztola, D. J.; Gaines, G. L. I.; Wasielewski, M. R. *Science* **1992**, *257*, 63.
240. Gust, D.; Moore, T. A.; Moore, A. L.; Lee, S.-J.; Bittersmann, E.; Luttrull, D. K.; Rehms, A. A.; DeGraziano, J. M.; Ma, X. C.; Gao, F.; Belford, R. E.; Trier, T. T. *Science* **1990**, *248*, 199.
241. Gust, D.; Moore, T. A.; Moore, A. L. In *Biological Materials Processing*; Calvert P., Frankel R., Rieke P., Eds.; Materials Research Society: Pittsburgh, 1991; p 141.
242. Gust, D.; Moore, T. A.; Moore, A. L.; Macpherson, A. N.; Lopez, A.; DeGraziano, J. M.; Gouni, I.; Bittersmann, E.; Seely, G. R.; Gao, F.; Nieman, R. A.; Ma, X. C.; Demanche, L. J.; Luttrull, D. K.; Lee, S.-J.; Kerrigan, P. K. *J. Am. Chem. Soc.* **1993**, *115*, 11141.
243. Maniga, N. I.; Sumida, J. P.; Stone, S.; Moore, A. L.; Moore, T. A.; Gust, D. *J. Porphyrins Phthalocyanines* **1999**, *3*, 32.
244. Bothner-By, A. A.; Dadok, J.; Johnson, T. E.; Lindsey, J. S. *J. Phys. Chem.* **1996**, *100*, 17,551.
245. Hsiao, J.-S.; Krueger, B. P.; Wagner, R. W.; Johnson, T. E.; Delaney, J. K.; Mauzerall, D. C.; Fleming, G. R.; Lindsey, J. S.; Bocian, D. F.; Donohoe, R. J. *J. Am. Chem. Soc.* **1996**, *118*, 11181.
246. Li, F.; Gentemann, S.; Kalsbeck, W. A.; Seth, J.; Lindsey, J. S.; Holten, D.; Bocian, D. F. *J. Mater. Chem.* **1997**, *7*, 1245.
247. Seth, J.; Palaniappan, V.; Johnson, T. E.; Prathapan, S.; Lindsey, J. S.; Bocian, D. F. *J. Am. Chem. Soc.* **1994**, *116*, 10578.
248. Seth, J.; Palaniappan, V.; Wagner, R. W.; Johnson, T. E.; Lindsey, J. S.; Bocian, D. F. *J. Am. Chem. Soc.* **1996**, *118*, 11194.
249. Strachan, J. P.; Gentemann, S.; Seth, J.; Kalsbeck, W. A.; Lindsey, J. S.; Holten, D.; Bocian, D. F. *J. Am. Chem. Soc.* **1997**, *119*, 11191.
250. Wagner, R. W.; Johnson, T. E.; Lindsey, J. S. *J. Am. Chem. Soc.* **1996**, *118*, 11166.
251. Wagner, R. W.; Lindsey, J. S. *J. Am. Chem. Soc.* **1994**, *116*, 9759.
252. Wagner, R. W.; Lindsey, J. S.; Seth, J.; Palaniappan, V.; Bocian, D. F. *J. Am. Chem. Soc.* **1996**, *118*, 3996.
253. Van Patten, P.; Shreve, A. P.; Lindsey, J. S.; Donohoe, R. J. *J. Phys. Chem. B* **1998**, *102*, 4209.
254. Kuciauskas, D.; Liddell, P. A.; Lin, S.; Johnson, T. E.; Weghorn, S. J.; Lindsey, J. S.; Moore, A. L.; Moore, T. A.; Gust, D. *J. Am. Chem. Soc.* **1999**, *121*, 8604.
255. Maggini, M.; Karlsson, A.; Scorrano, G.; Sandona, G.; Farina, G.; Prato, M. *J. Chem. Soc., Chem. Commun.* **1994**, 589–590.

3 Covalently Linked Systems Containing Metal Complexes

Franco Scandola, Claudio Chiorboli, Maria Teresa Indelli, and Maria Anita Rampi

3.1 Introduction

3.1.1 Scope and Limitations

Electron transfer (ET) is the single most important chemical reaction. Indeed, it is: (i) an elementary process amenable to very detailed theoretical description and experimental investigation; (ii) the key step of a number of biological processes of enormous relevance to life; and (iii) a fundamental feature of many processes of great technological impact. This handbook emphasizes the central role of ET in chemistry, its volumes, sections, and chapters reflecting the wide spectrum of ET aspects currently being of interest from both fundamental and practical viewpoints. The aim of this chapter is to provide an overview of ET in covalently linked systems containing metal complexes.

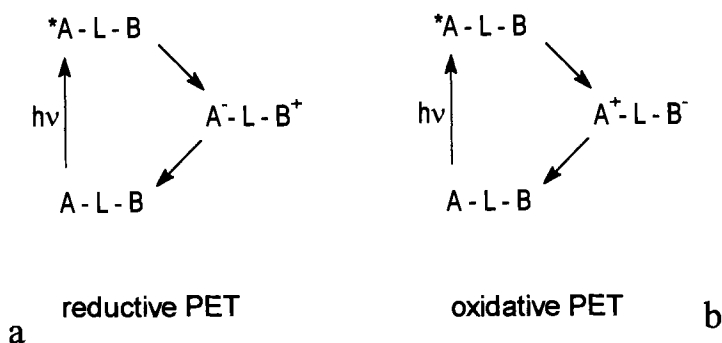
The minimal set for any ET process includes two redox active molecular units, an electron donor A, and an electron acceptor B. When A and B are free species in solution, the ET process is bimolecular.



Bimolecular ET processes are far from ideal from a mechanistic standpoint, as the experimental kinetics is complicated by diffusion effects and the spatial relationship between A and B is completely undefined. If, on the other hand, A and B are pre-assembled in a *supramolecular* structure, the ET process becomes unimolecular, the kinetics is expected to be free from diffusional artifacts, and the spatial relationship between A and B may be to some extent defined. Although *supramolecular* systems based on “weak” interactions are interesting as well (see Volume III, Part 2, Chapters 4–8), the present review is specifically concerned with systems where the A and B units are *covalently linked* via a suitable bridging group, L.

A fundamental aspect of unimolecular ET processes must be pointed out. In difference to bimolecular reactions—where exergonic ET processes can be simply triggered by mixing the reactants—for a supramolecular species in its ground state any intercomponent ET process is, by definition, energetically uphill. Thus, inter-component ET in a supramolecular system must always be induced “externally”. The most obvious, though not unique, way to induce unimolecular ET is to excite electronically one of the molecular components. The sudden increase in oxidizing and reducing power of the unit that undergoes photoexcitation can make inter-component ET thermodynamically allowed. Two possible schemes for photo-induced electron transfer (PET) are shown in Figure 1, these differing in whether

Photoinduced Electron Transfer (PET)



Photoinduced Charge Shift (PCS)

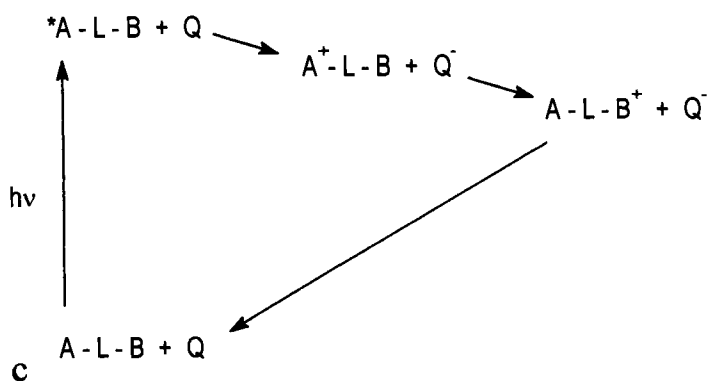


Figure 1. Different types of photoinduced electron transfer processes (PET) within a covalently linked system: (a) reductive PET; (b) oxidative PET; (c) charge shift.

the photoexcited molecular component plays the role of donor (oxidative PET, Figure 1b) or acceptor (reductive PET, Figure 1a). For obvious reasons, in the absence of chemical complications (i.e., if A^+-L-B^- or A^--L-B^+ are not intrinsically labile or are not scavenged by external species), a PET system is always reversible, that is, the primary products of the forward ET process spontaneously undergo back ET to regenerate the starting ground-state system. In the literature, the photoinduced forward process and the back reaction are often called “charge separation” and “charge recombination”. This notation is strictly appropriate only for neutral systems (e.g., organic donor–acceptor systems), but can be used in a conventional sense also for charged species (as for inorganic donor–acceptor systems). An additional, though more complex, scheme for triggering intramolecular electron transfer with light is photoinduced charge shift (PCS). In this case, oxidative or reductive bimolecular electron transfer quenching is used to generate a thermodynamically unstable redox isomer of the covalently linked system, that relaxes by intramolecular electron transfer to the thermodynamically favored species (before undergoing the final bimolecular recombination step). The process is depicted in Figure 1c for the case of oxidative bimolecular quenching.

A large number of covalently linked systems are currently being synthesized and investigated, differing in the nature of A, B, and L, as well as in the number of functional units in the supramolecular system (nuclearity). It is common to call simple two-component donor–acceptor systems such as that of Eq. 2 “dyads”, and progressively more complex systems “triads”, “tetrads”, “pentads”, etc.. Systems where all the A and B units are organic molecules are dealt with in Chapter 1 of this section. The present chapter deals with systems where at least one of the A/B functional units is a transition metal coordination compound. From this definition, however, are excluded: (a) systems where A and/or B are porphyrins or related species (dealt with in Chapter 2); and (b) systems of high nuclearity with dendritic structures (dealt with in Chapter 9).

As outlined below (Section 3.1.3), electronic energy transfer (EnT) between a donor and an acceptor (Figure 2) is a process that shares with electron transfer a number of formal and substantial similarities. In bimetallic dyads, energy transfer and PET are often strongly intertwined, either as competitive or as mechanistically related processes. Therefore, the discussion will not be strictly limited to ET processes, but will include, when required, EnT results as well.

Electronic Energy Transfer (EnT)

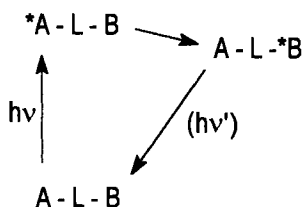


Figure 2. Electronic energy transfer within a covalently linked system.

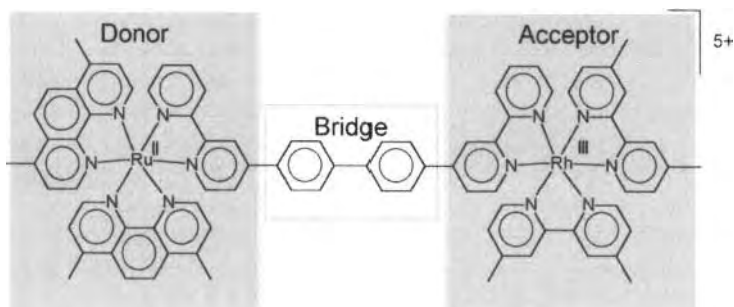


Figure 3. An example of a covalently linked supramolecular species, dissected into its molecular components.

3.1.2 Covalently Linked Systems as Supramolecular Species

As represented in Figures 1 and 2, a covalently linked system undergoing PET (or EnT) is a supramolecular species containing three types of subunits: an electron (energy) donor; an electron (energy) acceptor; and a bridge. In this schematic picture, the donor and the acceptor are “active” components directly involved in the transfer process, whereas the bridge is assumed to have a predominantly structural role (see, however, the discussion in Section 3.1.3). For real supramolecular systems, the identification of molecular components may not always be as straightforward as indicated in Figure 1.

For classical supramolecular systems [1–3], made of individually existing molecular species assembled together by weak interactions (electrostatic, hydrogen bonding, or host–guest), the dissection into molecular components is obvious. The situation becomes more complicated when the definition of supramolecular systems is broadened to include covalently linked systems [4, 5]. Consider, for example, the binuclear complex in Figure 3. On the basis of simple bonding arguments, this species could be considered as a large, single molecule. It can usefully be viewed as a supramolecular species, however, to the extent to which some of its fragments (molecular components) possess intrinsic (i.e., context-independent, or at best slightly perturbed) properties. Properties relevant to PET are the redox properties and, for the components that undergo excitation, the chromophoric properties. From this standpoint, the system in Figure 3 includes two easily identifiable molecular components, the ruthenium polypyridine donor and the rhodium polypyridine acceptor, whose intrinsic chromophoric and redox properties closely resemble those of $\text{Ru}(\text{Me}_2\text{phen})_2(\text{bpy})^{2+}$ and the $\text{Rh}(\text{Me}_2\text{bpy})_2(\text{bpy})^{3+}$ model compounds. These two active components are separated by a biphenylene fragment, which can be considered as a bridge. This distinction is justified if one looks at PET in terms of the frontier orbitals of the various fragments (Figure 4) where the bridge is characterized by HOMO and LUMO levels lying far away in energy from those of the active components. This is true for the system of Figure 3, where conjugation is prevented by ring-to-ring twisting (not shown in this schematic picture), both within

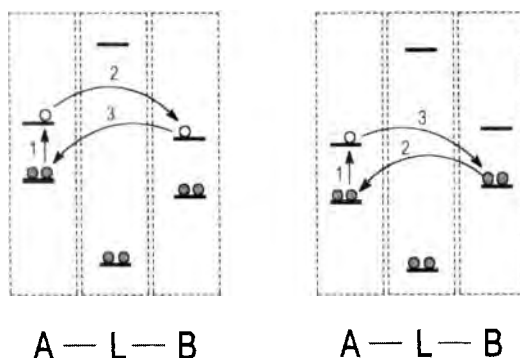


Figure 4. A schematic representation of photoinduced electron transfer in terms of frontier orbitals of donor (A), acceptor (B), and bridge (L) fragments.

the biphenylene bridge and between the bridge and the bipyridine fragments. This condition is met by most of the bridges dealt with in this review. Some exceptions will be discussed later.

3.1.3 Intercomponent Processes: A Short Summary

In covalently linked systems, the most important intercomponent processes are PET and EnT (Figures 1 and 2). The theoretical aspects of such processes are dealt with in detail in Volume I, Part 1, Chapter 1. For the sake of convenience, this section summarizes some the basic concepts that will be used in the following discussion.

Electron transfer

For a supramolecular system, A-L-B, the driving force of an excited-state electron transfer process can be easily calculated (Eq. 3) on the basis of electrochemical and spectroscopic data on the isolated molecular components (with, in case, small corrections for electrostatic work terms) [6]. For the case of oxidative PET (Figure 1b; Eq. 2), the relevant expression is given in Eq. 3.



$$\begin{aligned} \Delta G(^*A-L-B/A^+-L-B^-) &= E^0(A^+/A) - E^0(B/B^-) \\ &\quad + E_{coul}(A-L-B) - E_{coul}(A^+-L-B^-) \\ &\approx -E(A)^{0-0} + E^0(A^+/A) - E^0(B/B^-) \\ &\quad + E_{coul}(A-L-B) - E_{coul}(A^+-L-B^-) \end{aligned} \quad (3)$$

In Eq. 3, $\Delta G(^*A-L-B/A^+-L-B^-)$ is the free energy change, $E(A)^{0-0}$ is the excitation energy, $E^0(A^+/A)$ and $E^0(B/B^-)$ are the oxidation and reduction potentials of the molecular components (expressed as one-electron energies, in eV), and $E_{coul}(A-L-B)$ and $E_{coul}(A^+-L-B^-)$ are the Coulombic stabilization energies of reactants and products.

As far as kinetics is concerned, electron transfer processes can be described in terms of quantum mechanical [7–9] or classical [10–14] models. From a quantum mechanical viewpoint, both photoinduced electron transfer (Eq. 2) and charge recombination (Eq. 4) can be viewed as examples of radiationless transitions between



different, weakly interacting electronic states of the supermolecule A-L-B. The probability of such processes is given by a “golden rule” expression of the type [10–13]

$$k_{el} = \frac{4\pi}{\hbar} H_{if}^{el2} FCWD^{el} \quad (5)$$

where H_{if}^{el} is the electronic coupling between the two states interconverted by the electron transfer process and $FCWD^{el}$ is a thermally averaged vibrational Franck–Condon factor (“Franck–Condon-weighted density of states”).

The electronic factor

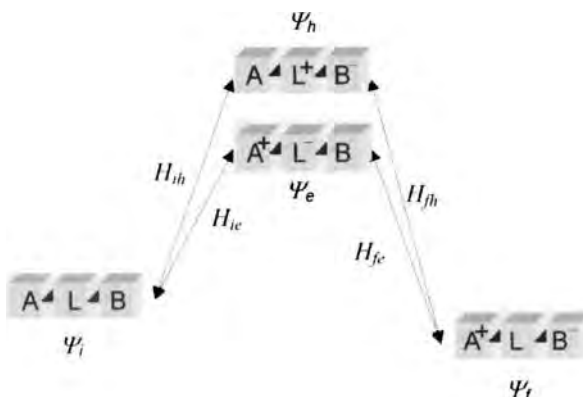
For a donor–acceptor pair in the absence of any intervening medium (through-space mechanism), the exponential fall-off of the orbital tails leads to an expected exponential decrease of H_{if}^{el} with distance (Eq. 6)

$$H_{if}^{el} = H_{if}^{el}(0) \exp \left[-\frac{\beta}{2} (r_{AB} - r_0) \right] \quad (6)$$

where r_{AB} is the donor–acceptor distance, $H_{if}^{el}(0)$ is the interaction at “contact” distance r_0 , and β is an appropriate attenuation parameter (the $\frac{1}{2}$ factor arises as β was originally defined as the exponential attenuation parameter for rate constant rather than for electronic coupling). For donor–acceptor sites in vacuum, estimated values of β are in the range $2\text{--}5 \text{ \AA}^{-1}$ [14]. Thus, at the donor–acceptor distances usually found in dyads, through-space coupling is expected to be negligible. In dyads, however, the bridging group does not act simply as a passive spacer, but rather as an active connector mediating the donor–acceptor electronic coupling (through-bond mechanism) [14, 15]. A convenient way to account for through-bond electronic coupling is in terms of “superexchange” [14, 16–21]. The essential point is that, although direct interaction between the initial and final states of the electron transfer process is negligible, indirect coupling takes place by mixing with high-energy states of charge transfer character involving the bridge (often called “virtual states”). Two superexchange coupling pathways can be generally envisioned, electron-transfer or hole-transfer involving donor-to-bridge or bridge-to-acceptor charge transfer virtual states (Figure 5). The second-order perturbation expression describing the superexchange coupling is

$$H_{if}^{el} = \frac{H_{ie}H_{fe}}{\Delta E_e} + \frac{H_{ih}H_{fh}}{\Delta E_h} \quad (7)$$

Figure 5. State diagram illustrating superexchange interaction between a donor (A) and an acceptor (B) through a simple bridging group (L). Ψ_h and Ψ_e are the hole- and electron-transfer “virtual” states. For the others symbols, see text.



where H_{ie} , H_{fe} , H_{ih} , H_{fh} , are the appropriate donor–bridge and bridge–acceptor coupling elements (Figure 5) and ΔE_e and ΔE_h are the energy differences between the virtual states and the initial or final state (these energy differences are taken at the transition-state nuclear geometry, where the initial and final state have the same energy). In this expression, the key parameters determining the electron-mediating properties of a bridge are the energy denominators: (i) easily reducible bridges, i.e., bridges with relatively low-energy LUMOs, are good electron-transfer superexchange mediators; (ii) easily oxidizable bridges, i.e., bridges with relatively high-energy HOMOs, are good hole-transfer superexchange mediators.

The above picture involving a single virtual state (of electron- or hole-transfer type) is strictly appropriate for few very simple bridges (e.g., ambidentate ligands such as cyanide, pyrazine) [18, 20]. In dyads, however, bridges have often a modular structure, being made of a sequence of individual weakly interacting units (see, e.g., the dyad of Figure 3). In such a case, not only the chemical nature, but also the length of the bridge will be relevant to its “conducting” properties. This can be seen by extending the superexchange model to involve virtual charge transfer states localized on each single modular unit, as shown schematically in Figure 6, where a three-module bridge is considered and, for the sake of simplicity, only the electron-transfer pathway is shown. In such a case, the appropriate perturbation expression is

$$H_{if}^{el} = \frac{H_{i1}}{\Delta E_{i1}} \frac{H_{12}}{\Delta E_{i2}} \frac{H_{23}}{\Delta E_{i3}} H_{3f} \quad (8)$$

For a bridge involving n identical modular units, the donor–acceptor superexchange coupling is summarized by Eq. 9 (for each pathway).

$$H_{if}^{el} = \frac{H_{i1}H_{nf}}{\Delta E} \left(\frac{H_{12}}{\Delta E} \right)^{n-1} \quad (9)$$

It is seen that for through-bond superexchange interaction, an exponential dependence on number of modular units in the bridge is obtained. For linear bridges,

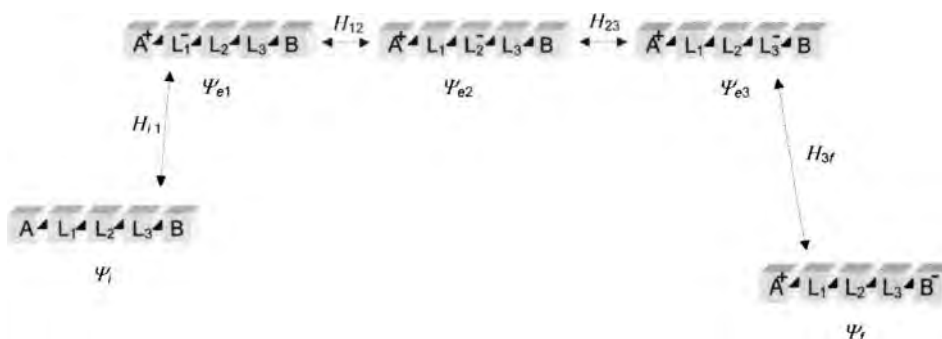


Figure 6. State diagram illustrating superexchange interaction between a donor (A) and an acceptor (B) through a modular bridge. Ψ_{e1} , Ψ_{e2} and Ψ_{e3} are local electron-transfer “virtual” states.

this translates into an exponential dependence on donor–acceptor distance (the same is true for bent bridges, if an effective through-bridge distance is considered rather than the straight through-space one. Thus, Eq. 6 can also be used, in a phenomenological sense, to describe the distance dependence of donor–acceptor coupling through a modular bridge. The meaning of the various terms of Eq. 6 is seen by comparison with Eq. 9. In this case, r_0 is the length increment associated to the individual module, and $H_{if}^{el}(0) = (H_{i1}H_{nf})/\Delta E$ represents the donor–acceptor coupling for a one-module bridge. The attenuation factor $\beta = 2\ln(H_{12}/\Delta E)$ is a bridge-specific parameter depending on (i) the magnitude of the coupling between adjacent modules, and (ii) the energy of the electron- (or hole-) transfer states localized on each module. As described in detail in Chapter 1, the predicted exponential decay of the electronic coupling and the effects of (i) and (ii) have been verified in several homogeneous series of dyads containing modular organic bridges of variable length.

The above paragraphs underline the importance of the bridge in mediating donor–acceptor coupling. As a colloquial way to emphasize this role, it has become customary to consider bridges as “molecular wires”, to refer to their coupling ability as “conducting” properties, etc. It should be clear that these expressions, however used, are devoid of any real meaning. In the superexchange picture the bridge levels are always much higher in energy than those of donor and acceptor. In this mechanism, the electron tunnels in a single step from donor to acceptor, without being at any time localized on the bridge (in contrast to what happens for conduction along a wire). Real wire-like behavior, i.e., sequential donor-to-bridge and bridge-to-acceptor ET, can only be achieved when one of the electron transfer states involving the bridge is sufficiently low in energy as to become intermediate between the initial and final states (Figure 7). This is a rather uncommon situation, although it can be reached in special cases, using potent electron donors (e.g., singlet excited states of aromatic hydrocarbons) and highly conjugated bridges (e.g., *p*-phenylenevinylene oligomers) [22]. When wire-like conditions are reached, very small distance dependence of electron transfer rates is expected.



Figure 7. State diagram for a sequential donor-to-bridge-to-acceptor electron transfer (wire-like behavior).

The nuclear factor

The $FCWD^{el}$ term of Eq. 5 (often referred to as the “nuclear factor” of the rate constant) is a thermally averaged Franck–Condon factor connecting the initial and final states. It contains a sum of overlap integrals between the nuclear wavefunctions of reactant and product of the same energy. The nuclear wavefunctions include both (inner) vibrational modes and (outer) solvent reorganizational modes. The summation is made over the initial levels of the reactant, suitably weighted for their Boltzmann population. The expression of $FCWD^{el}$, which is quite complicated in a general case [10], becomes relatively simple in idealized situations. For example, in a simple approximation in which the solvent modes (average frequency, ν_o) are thermally excited and treated classically ($h\nu_o \ll k_B T$), and the internal vibrations (average frequency, ν_i) are frozen and treated quantum mechanically ($k_B T \ll h\nu_i$), and a single internal mode is assumed to be involved, the $FCWD^{el}$ term is given by Eq. 10 [10, 12].

$$FCWD^{el} = \left(\frac{1}{4\pi\lambda_o k_B T} \right)^{1/2} \sum_m S^m \frac{e^{-S}}{m!} \exp \left[-\frac{(\Delta G^\circ + \lambda_o + m h \nu_i)^2}{4\lambda_o k_B T} \right] \quad (10)$$

$$S = \frac{\lambda_i}{h \nu_i} \quad (11)$$

In Eq. 10, the summation extends over m , the number of quanta of the inner vibrational mode in the product state, ΔG° is the thermodynamic driving force of the process, S is the defined by Eq. 11, and λ_o is the outer-sphere (solvent) reorganizational energy, given in its simplest form [7–9] by

$$\lambda_o = e^2 \left(\frac{1}{2r_A} + \frac{1}{2r_B} - \frac{1}{r_{AB}} \right) \left(\frac{1}{D_{op}} - \frac{1}{D_s} \right) \quad (12)$$

where e is the electron charge, D_{op} and D_s are the optical and static dielectric constants of the solvent, r_A and r_B are the radii of the two molecular components, and r_{AB} is the intercomponent distance. In Eq. 11, λ_i is the inner-sphere (vibrational) reorganizational energy given, in the single mode approximation, by

$$\lambda_i = \frac{1}{2} k \Delta Q^2 \quad (13)$$

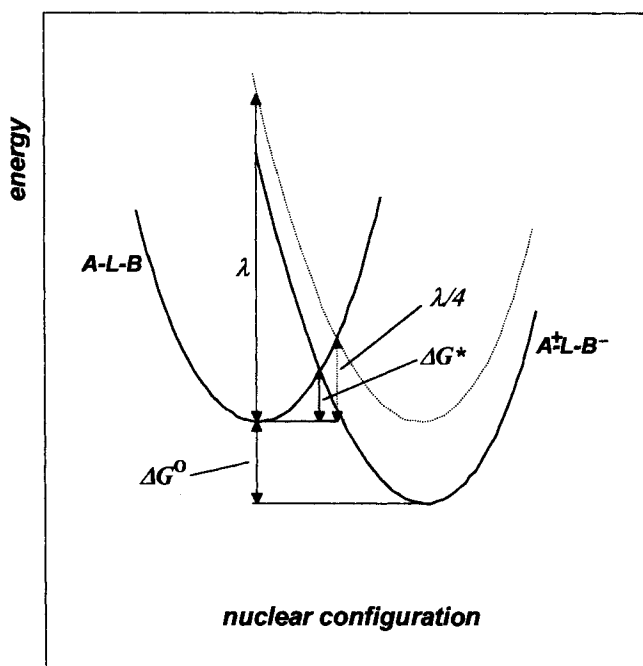


Figure 8. Energy profiles and kinetic parameters for an electron transfer reaction.

where k is an average force constant and ΔQ is the change in equilibrium geometry along the vibrational mode considered.

It can be shown [8] that in the high temperature limit (i.e., when $h\nu < k_B T$ for all relevant nuclear modes, an approximation not too inaccurate for many practical cases at room temperature), the nuclear factor takes the simple form

$$FCWD^{el} = \left(\frac{1}{4\pi\lambda k_B T} \right)^{1/2} \exp \left[-\frac{(\Delta G^\circ + \lambda)^2}{4\lambda k_B T} \right] \quad (14)$$

where $\lambda = \lambda_i + \lambda_o$. The exponential term of Eq. 14 is the same as that predicted by the classical Marcus model [7–9], based on parabolic energy curves for reactants and products such as those of Figure 8, where the activation free energy is that required to go from the equilibrium geometry of the reactants to the crossing point. Both classical (Eq. 14) and quantum mechanical (Eq. 10) models contain an important prediction, namely, that three typical kinetic regimes exist, depending on the driving force of the electron transfer reaction: (i) a “normal” regime for small driving forces ($-\lambda < \Delta G^\circ < 0$) where the ET process is thermally activated and is favored by an increase in driving force; (ii) an “activationless” situation ($-\lambda \approx \Delta G^\circ$) where very small changes in rate are obtained by changing the driving force; (iii) an “inverted” regime for strongly exergonic reactions ($-\lambda > \Delta G^\circ$) where the ET process *slows down* with increasing driving force. Increasing λ slows down the process in the normal regime, but accelerates it in the inverted regime. The three

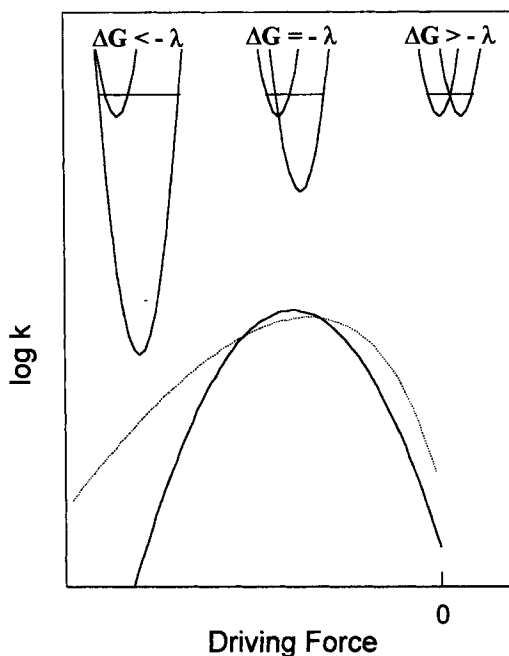


Figure 9. Free energy dependence of electron transfer rate (continuous line: classical treatment, Eq. 14; dotted line: quantum treatment, Eq. 10). The three kinetic regimes, “normal”, “activationless”, “inverted”, are shown schematically in terms of classical Marcus’ parabolae.

kinetic regimes are schematically shown, in terms of classical Marcus’ parabolae, in Figure 9. The main difference between the high-temperature limit expression (Eq. 14) and the quantum mechanical expression of $FCWD^{el}$ (Eq. 10) lies in the type of quantitative free-energy dependence predicted in the inverted region (Figure 9). The classical limit predicts a parabolic decrease of $\ln k_{el}$ with increasing driving force [7], as compared with a linear decrease (the so-called “energy-gap-law” of radiationless transitions) predicted for very negative ΔG values by the quantum mechanical models [10]. Definite proof for the existence of the inverted region has been reached in systematic studies of homogeneous series of reactions [23, 24].

Energy transfer

In a supramolecular system, electronic energy transfer (Figure 2) can be viewed as a radiationless transition between two “local” electronically excited states of the system (Eq. 15).



The rate constant for the energy transfer process is thus given by a “golden rule” expression similar to that seen above (Eq. 5) for electron transfer.

$$k_{en} = \frac{4\pi}{h} (H_{if}^{en})^2 FCWD^{en} \quad (16)$$

In Eq. 16, H_{if}^{en} is the electronic coupling between the two excited states interconverted by the energy transfer process, and $FCWD^{en}$ is an appropriate Franck–Condon factor.

As for ET, the Franck–Condon factor can be cast either in quantum mechanical [25–27] or in classical [28] terms. In quantum mechanical terms, this factor is a thermally-averaged sum of vibrational overlap integrals, representing the distribution of the transition probability over several isoenergetic “virtual transitions” (from *A to A , and from B to *B) in the two molecular components. Classically, it accounts for the combined effects of energy gradient and nuclear reorganization on the rate constant. In both cases, “normal” and “inverted” regions analogous to those found for ET transfer processes are predicted. In spite of some specific difficulties (e.g., highly exergonic processes are difficult to achieve, due to the presence of higher excited states of the products) experimental studies of Franck–Condon effects in energy transfer processes have been successfully carried out [29, 30].

The electronic factor H_{if}^{en} is a two-electron matrix element involving the HOMOs and LUMOs of the energy-donor and energy-acceptor centers. Following standard arguments [31], this factor can be split into additive *Coulombic* and *exchange* terms. The two terms depend differently on various parameters of the system (spin of ground and excited states, donor–acceptor distance, etc.). This leads to the identification of two main energy transfer mechanisms, as represented pictorially in Figure 10.

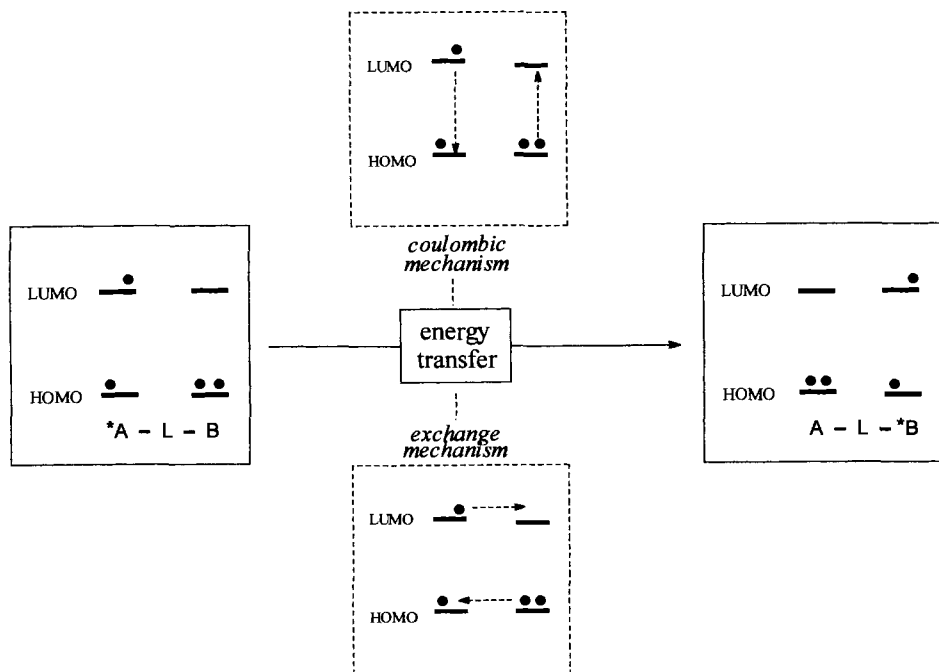


Figure 10. Pictorial representation of the Coulombic and exchange energy transfer mechanisms.

The Coulombic (also called “resonance”, “dipole–dipole”, or “Förster-type”) mechanism [32] is a long-range mechanism that does not require physical contact between donor and acceptor. The most important term within the Coulombic interaction is the dipole–dipole term, that obeys the same selection rules as the corresponding electric dipole transitions of the two partners (Figure 10). Therefore, Coulombic energy transfer is expected to be efficient in systems in which the radiative transitions connecting the ground and the excited state of each partner have high oscillator strength. The relationship between the rate constant for Coulombic energy transfer and the spectroscopic and photophysical properties of the two molecular components is given by the classical Förster formula (Eq. 17)

$$k_{en}^{coul} = 1.25 \times 10^{17} \frac{\Phi_A}{n^4 \tau_A r_{AB}^6} \int_0^\infty F_A(\bar{\nu}) \varepsilon_B \frac{d\bar{\nu}}{\bar{\nu}^4} \quad (17)$$

where Φ_A is the quantum yield of donor emission, n is the solvent refractive index, τ_A is the lifetime of the donor emission, and r_{AB} is the distance (in nm) between donor and acceptor. F_A is the emission spectrum of the donor (in wavenumbers and normalized to unity), and ε_B is the decadic molar extinction coefficient of the acceptor. With a good spectral overlap integral and appropriate photophysical parameters, the $(1/r_{AB}^6)$ distance dependence allows energy transfer to occur efficiently over distances (e.g., 50 Å), largely exceeding the molecular diameters. Coulombic energy transfer is therefore also called “long-range energy transfer”. The typical example of efficient coulombic mechanism is that of singlet–singlet energy transfer (Eq. 18)



In metal complexes, the only excited state of appreciable lifetime is generally the lowest, spin-forbidden excited state [33], so that Coulombic energy transfer is only expected to take place in then presence of very strong spin-orbit coupling (e.g., when 5d metal complexes are involved).

The *exchange* (also called “Dexter-type”) mechanism [32] is a short-range mechanism that requires orbital overlap, and therefore physical contact, between donor and acceptor. The exchange interaction can be visualized as the simultaneous exchange of two electrons between the donor and the acceptor (Figure 10). The spin selection rules for this type of mechanism reflect the need to obey spin conservation in the reacting pair as a whole. This allows the exchange mechanism to be operative in many cases in which the excited states involved are spin-forbidden in the spectroscopic sense. Thus, the typical example of efficient exchange mechanism is that of triplet–triplet energy transfer (Eq. 19).



Exchange energy transfer from the lowest spin forbidden excited state is expected to be the rule for metal complexes [34].

For reasons similar to those discussed above for ET processes, the rate constant of exchange energy transfer is expected to be sensitive to the nature of the bridge.

Using arguments similar to those of superexchange, mixing with electronically excited states localized on the bridge is expected to effectively mediate the donor–acceptor exchange interaction. Again, bridges with low-energy excited states will be particularly efficient. And again, if the electronically excited states localized on the bridge become lower in energy than that of the donor, a switch from direct one-step energy transfer to stepwise donor-to-bridge and bridge-to-acceptor energy migration could take place. With long, modular bridges, the exchange interaction is expected to fall off exponentially with through-bond distance, or with number of intervening units in the bridge [35–37]. Interestingly, in a homogeneous series of dyads where triplet energy transfer (Eq. 19), electron transfer (Eq. 20), and hole transfer (Eq. 21)



processes could be studied as a function of distance across the same saturated organic bridges, the value of the attenuation factor β (see Eq. 6) for energy transfer was found to be the sum of those for electron and hole transfer [38]. This supports the simple picture of exchange energy transfer as a “simultaneous double electron transfer”, with an electronic matrix element being proportional to the product of those for the corresponding electron and hole transfer processes.

3.1.4 Coordination Compounds as Molecular Components

As molecular components of a supramolecular system, coordination compounds display some peculiar features. A coordination compound is by definition a “complex” species, made by combination of metal and ligands. Although the ligands and (to some extent) the metal may exist separately as individual chemical species, they come into strong electronic interaction upon complex formation, leading to completely new characteristic properties. In other words, coordination compounds are not real supramolecular systems. Nevertheless, their complex nature is at the origin of some peculiar features, that may be relevant to their behavior as molecular components of dyads and larger covalently linked supramolecular systems. Some of these features can be discussed, taking the dyad of Figure 3 as an example.

The Ru(II)-based molecular component of the dyad in Figure 3 can be adequately modeled by $\text{Ru}(\text{bpy})_3^{2+}$, the archetypal chromophore of inorganic photochemistry [39, 40]. In $\text{Ru}(\text{bpy})_3^{2+}$, the HOMO is largely metal t_{2g} in character, while the LUMO is largely $\text{bpy } \pi^*$ in character. This predominant localization of the frontier orbitals has several interesting consequences. First, oxidation [$E^0(3+/2+) = 1.26$ V versus SCE] and reduction [$E^0(2+/+) = -1.28$ V versus SCE] of the unit involve different sites: $\text{Ru}(\text{bpy})_3^{3+}$ is a true Ru(III) complex, whereas the $\text{Ru}(\text{bpy})_3^{+}$ is not a Ru(I) species, but rather a Ru(II) complex with two neutral ligands and one ligand radical anion [41]. Second, the lowest excited states of $\text{Ru}(\text{bpy})_3^{2+}$ are of metal-to-ligand charge transfer (MLCT) character, with an electron distribution

resembling a Ru(III) complex with two neutral ligands and one ligand radical anion. Despite the presence of appreciable spin-orbit coupling, the MLCT states can be considered as having singlet or triplet spin multiplicity. The lowest singlet is responsible for the intense visible absorption (λ_{max} , 450 nm), while the lowest triplet is responsible for the characteristic phosphorescence emission (λ_{max} = 600 nm, E^{0-0} = 2.12 eV, Φ = 4×10^{-2} , τ = 0.6 μ s in room-temperature fluid solution). The relatively small singlet–triplet energy difference (c. 0.4 eV) is a consequence of the charge transfer nature of the transition. Within the triplet lifetime, fast equilibration between the three MLCT states localized on different ligands can be usually assumed [42]. The fractional population of such localized states (33 % in symmetric complexes such as Ru(bpy)₃²⁺) can be substantially unbalanced in less symmetric cases. In ligand-bridged bimetallic systems, a relevant question may be whether the predominant population is on the bridging ligand or on the ancillary ones. This depends on the relative LUMO energies (or redox potentials) of the three ligands. In the Ru(II) polypyridine unit of the dyad in Figure 3, because of the appreciable (albeit small) conjugation with the polyphenylene chain, the lowest energy site for the excited electron is definitely the bridging bipyridine.

For typical organic donor–acceptor systems, simple HOMO–LUMO pictures such as those of Figure 4 and 10 are often used to describe photoinduced electron or energy transfer. When coordination compounds are used as A and/or B molecular components, this type of picture might be overly simplistic given the peculiar localization of HOMOs and LUMOs. Figure 11a shows schematically the redox sites involved in MLCT excitation (process 1), photoinduced electron transfer (process 2) and charge recombination (process 3) for a typical Ru(II)–Rh(III) dyad. These localization aspects are likely to be important in the analysis of intramolecular electron transfer rates, where intercomponent distance and electronic coupling play a crucial role.

Similar arguments apply to the case of intercomponent energy transfer involving coordination compounds. In a Ru(II)–Os(II) dyad such as that of Figure 11b, exchange energy transfer following MLCT absorption the Ru(II) component (process 1) and leading to MLCT emission from the Os(II) component (process 3) can be visualized as two simultaneous cross-electron-transfer processes (processes 2): between the two bpy ends of the bridging ligand, and between the two metal centers. It should be noticed that, with short bridges such as that of the Ru(II)–Os(II) dyad of Figure 11c, what is formally (by analogy to the previous case) an intercomponent energy transfer phenomenon in fact amounts to a simple metal-to-metal electron transfer (process 2).

3.2 Bimetallic and Polymetallic Systems

A large number of covalently linked bi- and polymetallic systems have been synthesized and studied during the past 20 years. Early work has been reviewed, and a number of review articles are available [43–51]. The exhaustive review by Balzani

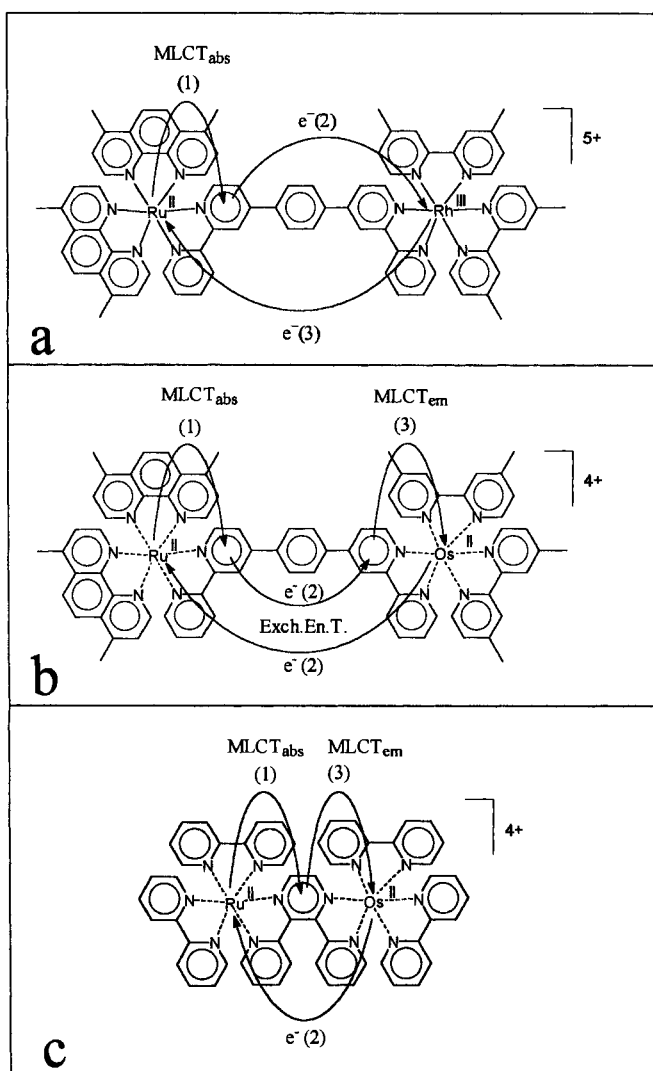


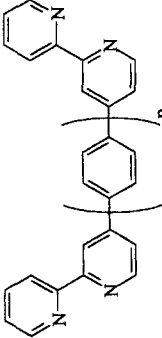
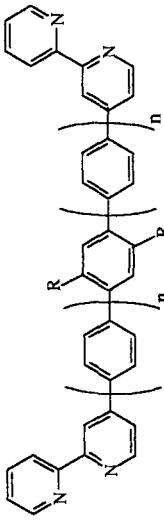
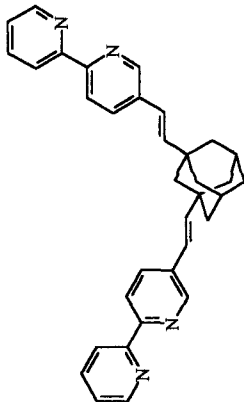
Figure 11. Schematic representation of the redox sites involved in photoinduced electron and energy transfer processes within dyads based on metal complexes.

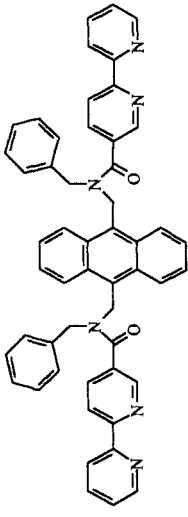
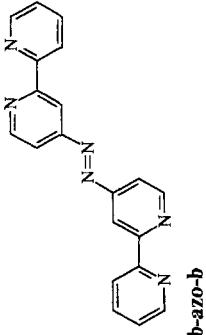
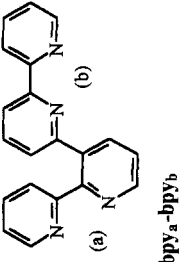
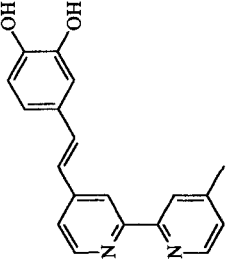
and coworkers provides complete literature coverage up to 1996 [47]. Some recent overview articles focus on specific classes of systems [48–51]. The field continues to grow at an impressive rate, and a representative selection of the bi- and polymetallic systems reported during the past four years (1996–1999) is summarized in Table 1. Since the emphasis of this chapter is on photoinduced energy and electron transfer processes, only unsymmetric systems (heterometallic complexes, homometallic complexes with the metals in different coordination environments) are included in Table 1. Two classes of bi- and polymetallic systems are deliberately excluded from the table. Cyano-bridged complexes [45, 48] are characterized by a strong metal–

Table 1. Bimetallic and polymetallic complexes

[illegible]

Table 1 (continued)

Bridging ligand	No. Complex	Process	Reference
 bpy-(ph) _n -bpy	5 $[(\text{Me}_2\text{phen})_2\text{Ru}(\text{bpy}-(\text{ph})_n-\text{bpy})\text{Rh}(\text{Me}_2\text{bpy})_2]^{5+}$ $n = 1, 2, 3$ $\{(\text{bpy})_2\text{Ru}(\text{bpy}-(\text{ph})_n-\text{bpy})\text{Ru}(\text{tpy})(\text{CN})\}^{3+}$	PETox EnT	[63] [64]
 $R = \text{nhexyl}$ bpy-(ph) _n -ph'-(ph) _n -bpy	6 $[(\text{Me}_2\text{phen})_2\text{Ru}(\text{bpy}-(\text{ph})_n-\text{ph}'-(\text{ph})_n-\text{bpy})\text{Rh}(\text{Me}_2\text{bpy})_2]^{5+}$ $\{(\text{bpy})_2\text{Ru}(\text{bpy}-(\text{ph})_n-\text{ph}'-(\text{ph})_n-\text{bpy})\text{Os}(\text{bpy})_2\}^{4+}$ $\{(\text{bpy})_2\text{Ru}(\text{bpy}-(\text{ph})_n-\text{ph}'-(\text{ph})_n-\text{bpy})\text{Os}(\text{bpy})_2\}^{4+}$ $\{(\text{bpy})_2\text{Ru}(\text{bpy}-(\text{ph})_n-\text{ph}'-(\text{ph})_n-\text{bpy})\text{Os}(\text{bpy})_2\}^{4+}$	PETox EnT EnT EnT	[63] [65] [65] [65]
 bpy-a-bpy	7 $\{(\text{bpy})_2\text{Ru}(\text{bpy}-a-\text{bpy})\text{Os}(\text{bpy})_2\}^{4+}$ $\{(\text{bpy})_2\text{Ru}(\text{bpy}-a-\text{bpy})\text{Os}(\text{bpy})_2\}^{5+}$	EnT PETox	[66] [66]

 <p>bpy-An-bpy</p>	8	[(bpy) ₂ Ru(bpy-An-bpy)Os(bpy) ₂] ⁴⁺	EnT	[67]
 <p>b-azo-b</p>	9	[(bpy) ₂ Ru(b-azo-b)Os(bpy) ₂] ⁴⁺	EnT ^c	[68]
 <p>bpy_a-bpy_b</p>	10	[(Cl) ₂ (CO ₃)Re(bpy _a -bpy _b)Ru(bpy) ₂] ²⁺ [(Cl) ₂ (CO ₃)Re(bpy _b -bpy _a)Ru(bpy) ₂] ²⁺ [{(Cl) ₂ (CO ₃)Re(bpy _b -bpy _a)} ₂ Ru(bpy)] ²⁺ [{(Cl) ₂ (CO ₃)Re(bpy _b -bpy _a)} ₃ Ru] ²⁺ [(bpy) ₂ Ru(bpy _a -bpy _b)Os(bpy) ₂] ⁴⁺ [(bpy) ₂ Ru(bpy _b -bpy _a)Os(bpy) ₂] ⁴⁺ [(bpy) ₂ Ru(bpy _a -bpy _b)Pt(Cl) ₂] ²⁺ [(bpy) ₂ Ru(bpy _b -bpy _a)Pt(Cl) ₂] ²⁺	EnT EnT EnT EnT EnT EnT	[69, 70] [69, 70] [71] [71] [72] [72] [73] [73]
 <p>bpy-(CH)₂-catH₂</p>	11	[(bpy) ₂ Ru(bpy-(CH) ₂ -cat)Ru(bpy) ₂] ³⁺ [(bpy) ₂ Ru(bpy-(CH) ₂ -cat)Pd(bpy)] ²⁺ [(bpy) ₂ Ru(bpy-(CH) ₂ -cat)Pt(PPh ₃) ₂] ²⁺ [(bpy) ₂ Ru(bpy-(CH) ₂ -cat)Ru(NO)(Cp)] ¹²⁺	d d d d	[74] [74] [74] [74]

16	$[(bpy)_2Ru(2,5-dpp)Os(bpy)_2]^{4+}$	EnT	[82]
17	$[(bpy)_2Ru(dpq)\{Ir(Cl)_2\}^{5+}]^{5+}$ $[(bpy)_2Ru(dpq)Os(bpy)_2]^{4+}$ $[(bpy)_2Ru(dpq)Pt(Cl)_2]^{2+}$ $[(bpy)_2Os(dpq)Pt(Cl)_2]^{2+}$	PET _{ox}	[83] [84] [85] [85]
18	$[(bpy)_2Ru(dpb)\{Ir(Cl)_2\}^{5+}]^{5+}$ $[(bpy)_2Ru(dpb)Os(bpy)_2]^{4+}$ $[(bpy)_2Ru(dpb)Pt(Cl)_2]^{2+}$ $[(bpy)_2Os(dpb)Pt(Cl)_2]^{2+}$	PET _{ox}	[83] [84] [85] [85]
19	$[(bpy)_2Ru(HAT)Ir(ppy)_2]^{3+}$ $[(bpy)_2Ru(HAT)Rh(ppy)_2]^{3+}$	EnT EnT	[86] [86]
20	$[(bpy)_2Ru(bpbimH_2)Co(bpy)_2]^{5+}$ $[(bpy)_2Ru(bpbimH_2)Ru(decb)_2]^{4+}$	PET _{ox} EnT	[87] [88]

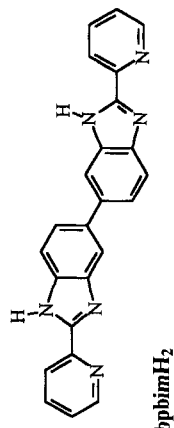
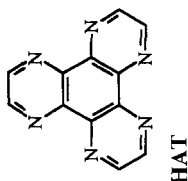
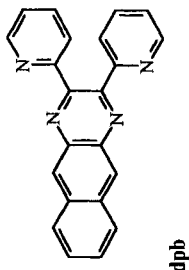
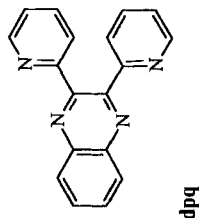
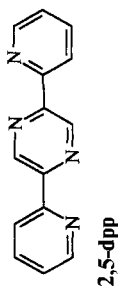
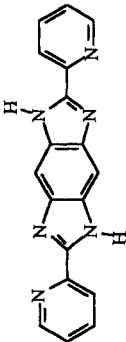
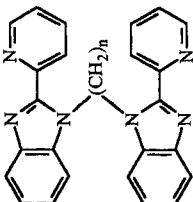


Table 1 (continued)

Bridging ligand	No. Complex	Process	Reference
 dpimbH ₂	21	PET _{ox}	[87]
	$[(bpy)_2Ru(dpimbH_2)Co(bpy)_2]^{5+}$		
 pbim-S _n -pbim	22	PET _{ox} PET ^e	[87] [89]
	$[(bpy)_2Ru(pbim-S_5-pbim)Co(bpy)_2]^{5+}$		
	$[(bpy)_2Ru(pbim-S_n-pbim)Ru(bpy)_2]^{4+}$ n = 5, 6	PET ^e	[89]
	$[(Me_2bpy)_2Ru(pbim-S_5-pbim)Ru(Me_2bpy)_2]^{4+}$	PET ^e	[89]
	$[(decb)_2Ru(pbim-S_5-pbim)Ru(Me_2bpy)_2]^{4+}$	PET ^e	[89]
	$[(decb)_2Ru(pbim-S_n-pbim)Ru(bpy)_2]^{4+}$ n = 2-6, 10	EnT	[88, 90]
	$[(decb)_2Ru(pbim-S_n-pbim)Ru(bpy)_2]^{4+}$ n = 2-6, 10	EnT	[90]
	$[(Me_2bpy)_2Ru(pbim-S_n-pbim)Os(bpy)_2]^{4+}$ n = 3, 4, 5	PET _{ox}	[90]
	$[(Me_2bpy)_2Ru(pbim-S_n-pbim)Os(bpy)_2]^{5+}$ n = 3, 4, 5	EnT	[90]
	$[(Me_2bpy)_2Ru(pbim-S_n-pbim)Os(Me_2bpy)_2]^{4+}$ n = 4, 5	PET _{ox}	[90]
	$[(Me_2bpy)_2Ru(pbim-S_n-pbim)Os(Me_2bpy)_2]^{5+}$ n = 4, 5		

23	$[(\text{decb})_2\text{Ru}(\text{pbim-S}_B\text{-pbim})\text{Ru}(\text{bpy})_2]^{4+}$	EnT	[88]
24	$[(\text{bpy})_2\text{Ru}(\text{mpzt})\text{Ru}(\text{bpy})_2(\text{Cl})]^{3+}$ $[(\text{bpy})_2\text{Ru}(\text{mpzt})\text{Os}(\text{bpy})_2(\text{Cl})]^{3+}$ $[\text{Cl}(\text{bpy})_2\text{Ru}(\text{mpzt})\text{Os}(\text{bpy})_2(\text{Cl})]^{3+}$ $[(\text{bpy})_2\text{Os}(\text{mpzt})\text{Os}(\text{bpy})_2(\text{Cl})]^{3+}$	EnT EnT EnT EnT	[91] [91] [91] [91]
25	$[(\text{bpy})_2\text{Ru}(\text{a-bpt-b})\text{Os}(\text{bpy})_2]^{3+}$ $[(\text{bpy})_2\text{Ru}(\text{b-bpt-a})\text{Os}(\text{bpy})_2]^{3+}$ $[(\text{bpy})_2\text{Ru}(\text{a-bpt-b})\text{Ru}(\{2,3\text{-dpp}\})\text{Ru}(\text{bpy})_2]^{7+}$	EnT EnT EnT	[92, 93] [92, 93] [92]
26	$[(\text{bpy})_2\text{Ru}(\text{bpzt})\text{Ru}(\text{bpy})_2]^{3+}$		[94, 95]
27	$[(\text{bpy})_2\text{Ru}(\text{HQ})\text{Os}(\text{bpy})_2]^{3+}$		[96]

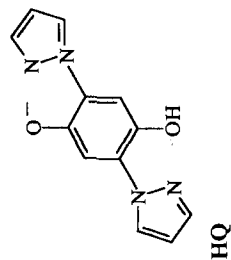
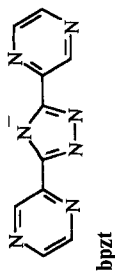
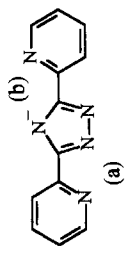
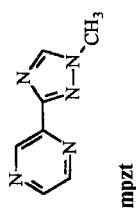
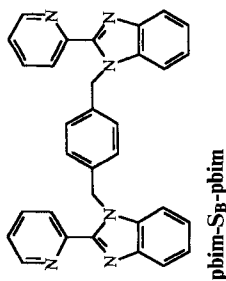
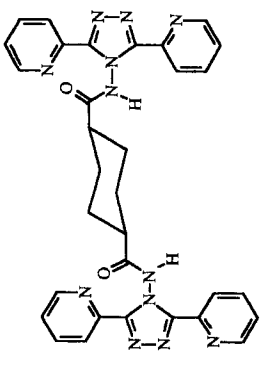
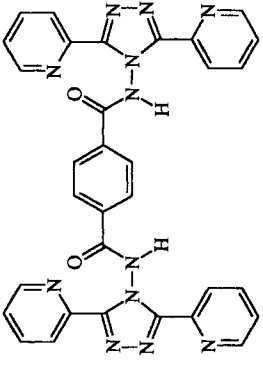
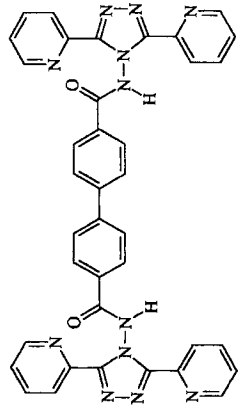
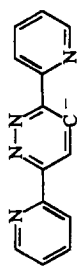


Table 1 (continued)

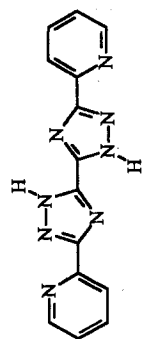
Bridging ligand	No. Complex	Process	Reference
 <p style="text-align: center;">dpt-cy-dpt</p>	<p>28</p> <p>$[(\text{bpy})_2\text{Ru}(\text{dpt-cy-dpt})\text{Os}(\text{bpy})_2]^{4+}$ $[(\text{bpy})_2\text{Ru}(\text{dpt-cy-dpt})\text{Ru}(\text{biq})_2]^{4+}$</p>	<p>EnT EnT</p>	<p>[97] [98]</p>
 <p style="text-align: center;">dpt-ph-dpt</p>	<p>29</p> <p>$[(\text{bpy})_2\text{Ru}(\text{dpt-ph-dpt})\text{Ru}(\text{biq})_2]^{4+}$</p>	<p>EnT</p>	<p>[98]</p>
 <p style="text-align: center;">dpt-bph-dpt</p>	<p>30</p> <p>$[(\text{bpy})_2\text{Ru}(\text{dpt-bph-dpt})\text{Ru}(\text{biq})_2]^{4+}$</p>	<p>EnT</p>	<p>[98]</p>

[99]

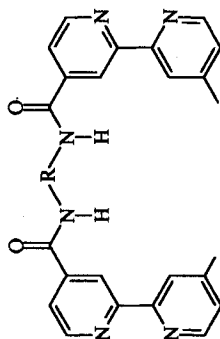
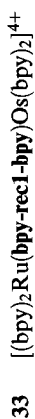


dppm

[100]

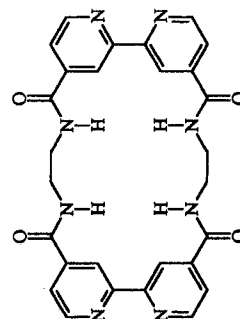
bpbH₂

[101]



bpy-rec1-bpy

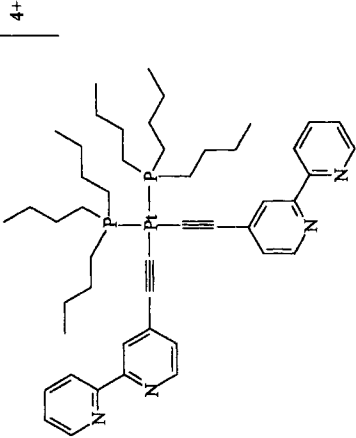
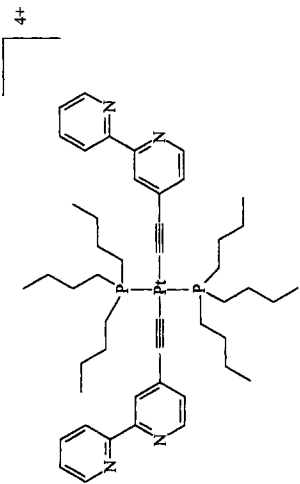
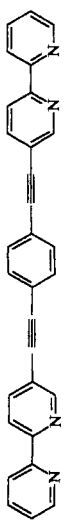
[102]



bpy-rec2-bpy

EnT

Table 1 (continued)

Bridging ligand	No. Complex	Process	Reference
	35	EnT	[49, 103]
bpy-cPt-bpy			
	36	EnT	[49, 103]
bpy-tPt-bpy			
	37	EnT	[49]

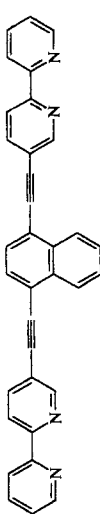
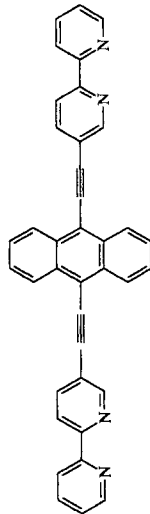
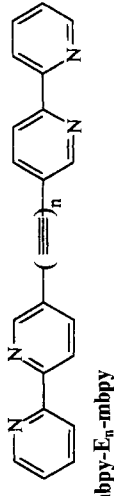
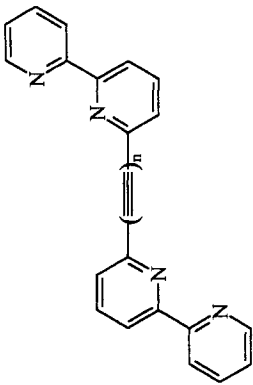
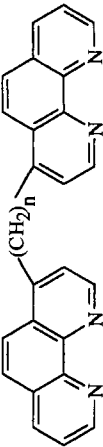

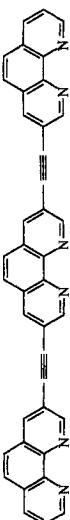
38	 <p>bpy-E-naph-E-bpy</p>	$[(bpy)_2Ru(bpy-E-naph-E-bpy)Os(bpy)_2]^{4+}$	EnT	[49]
39	 <p>bpy-E-A-E-bpy</p>	$[(bpy)_2Ru(bpy-E-A-E-bpy)Os(bpy)_2]^{4+}$	EnT ^f	[49]
40	 <p>pbpy-E_n-pbpy</p>	$[(bpy)_2Ru(pbpy-E_n-pbpy)Os(bpy)_2]^{4+}$ n = 1, 2	EnT	[105–107]
41	 <p>mbpy-E_n-mbpy</p>	$[(bpy)_2Ru(mbpy-E_n-mbpy)Os(bpy)_2]^{4+}$ n = 1, 2	EnT	[105–107]

Table 1 (continued)

Bridging ligand	No. Complex	Process	Reference
 obpy-E _n -obpy	42	EnT	[105–107]
 p-(CH ₂) _n -p	43	PET _{ox} PET _{ox} PET _{ox}	[108] [108] [108]
 phen-E-phen	44		[109]
 phen-phen-phen	45		[109]

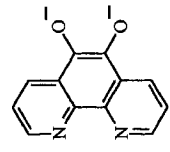
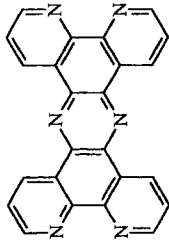
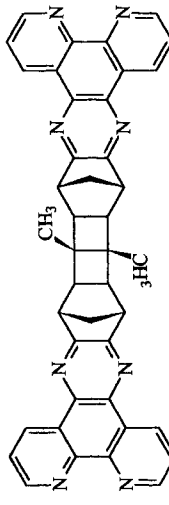
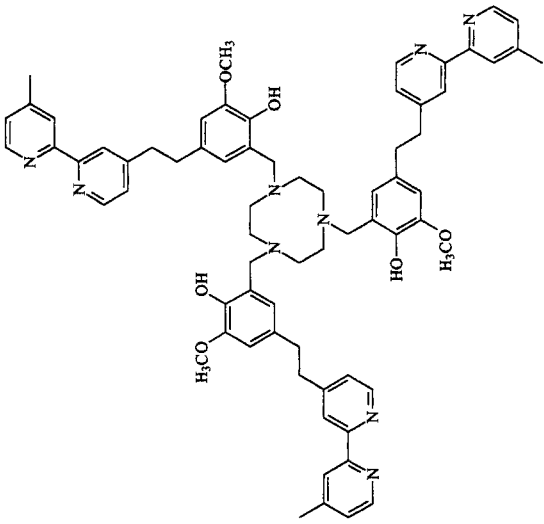
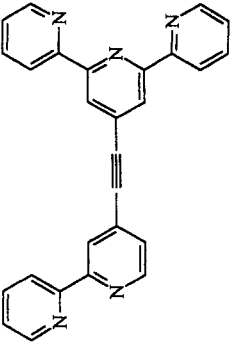
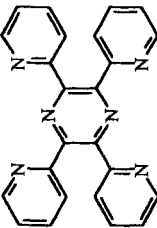
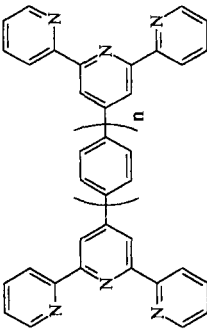
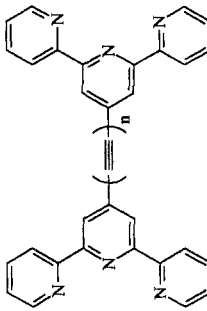
 <p>dpcat</p>	46 $[(\text{Me}_2\text{bpy})_2\text{Ru}(\text{dpcat})\text{Pt}(\text{Me}_2\text{bpy})]^{2+}$	EnT	[110]
 <p>tpphz</p>	47 $[(\text{Me}_2\text{bpy})_2\text{Ru}(\text{tpphz})\text{Pt}(\text{Me}_2\text{bpy})]^{2+}$ $[(\text{bpy})_2\text{Ru}(\text{tpphz})\text{Os}(\text{bpy})_2]^{4+}$ $[(\text{phen})_2\text{Ru}(\text{tpphz})\text{Os}(\text{phen})_2]^{4+}$ $[\text{Ru}\{(\text{tpphz})\text{Ru}(\text{bpy})_2\}_3]^{8+}$ $[\text{Ru}\{(\text{tpphz})\text{Ru}(\text{phen})_2\}_3]^{8+}$	EnT EnT EnT EnT EnT	[110] [111] [112] [113] [112]
 <p>dpq-6-dpq</p>	48 $[(\text{bpy})_2\text{Ru}(\text{dpq-6-dpq})\text{Os}(\text{bpy})_2]^{4+}$	EnT	[114]

Table 1 (continued)

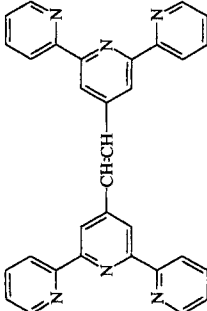
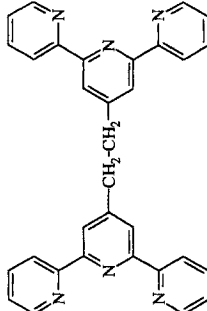
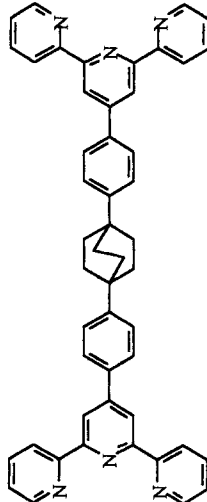
Bridging ligand	No.	Complex	Process	Reference
 <p>P3</p>	49	$\{ \{ (\text{bpy})\text{Ru} \}_3 (\text{P3}) \text{Mn} \}^{7+}$	PCS	[115]
 <p>bpy-E-tpy</p>	50	$\{ \{ (\text{bpy})_2\text{Ru}(\text{bpy-E-tpy}) \}_2 \text{Fe} \}^{6+}$ $\{ (\text{bpy})_2\text{Ru}(\text{bpy-E-tpy})\text{Ru}(\text{tpy}) \}^{4+}$		[116] [49]

51		$[(\text{tpy})\text{Ru}(\text{tpp})\text{Ru}(\text{Cl})_3]^{2+}$	$[(\text{tpy})\text{Ru}(\text{tpp})\text{Ru}(\text{Cl})_3]^+$	$[(\text{tpy})\text{Os}(\text{tpp})\text{Ru}(\text{Cl})_3]^+$	$[(\text{tpy})\text{Ru}(\text{tpp})\text{Ru}(\text{tpp})]^{4+}$	$[(\text{tpp})\text{Ru}(\text{tpp})\text{Os}(\text{tpy})]^{4+}$	$[\text{Ru}\{\text{tpp}\}\text{Ru}(\text{tpy})]_2]^{6+}$	PET_{ox}	[117] [118] [118] [118, 119] [118, 119] [120]
								EnT	
52		$[(\text{tpy})\text{Ru}(\text{tpy-tpy})\text{Rh}(\text{tpy})]^{5+}$	$[(\text{tpy})\text{Ru}(\text{tpy-ph-tpy})\text{Rh}(\text{tpy})]^{5+}$	$[(\text{tpy})\text{Ru}(\text{tpy-(ph)}_2\text{-tpy})\text{Rh}(\text{tpy})]^{5+}$	$[(\text{tpy})\text{Ru}(\text{tpy-tpy})\text{Os}(\text{tpy})]^{4+}$	$[(\text{tpy})\text{Ru}(\text{tpy-ph-tpy})\text{Os}(\text{tpy})]^{4+}$	$[(\text{tpy})\text{Ru}(\text{tpy-(ph)}_2\text{-tpy})\text{Os}(\text{tpy})]^{4+}$	PET_{ox}	[121–123] [121–123] [121–123] [123, 124] [123, 124] [123, 124]
								EnT	
								EnT	
								EnT	
53		$[\{\text{tpy}\}\text{Ru}(\text{tpy-E}_1\text{-tpy})\}_2\text{Fe}]^{6+}$	$[\{\text{tpy}\}\text{Ru}(\text{tpy-E}_2\text{-tpy})\}_2\text{Fe}]^{6+}$	$[\{\text{tpy}\}\text{Ru}(\text{tpy-E}_1\text{-tpy})\}_2\text{Co}]^{6+}$	$[\{\text{tpy}\}\text{Ru}(\text{tpy-E}_2\text{-tpy})\}_2\text{Co}]^{6+}$	$[(\text{tpy})\text{Ru}(\text{tpy-E}_1\text{-tpy})\text{Os}(\text{tpy})]^{4+}$	$[(\text{tpy})\text{Ru}(\text{tpy-E}_2\text{-tpy})\text{Os}(\text{tpy})]^{4+}$	EnT	[125, 126] [125, 126] [125] [125]
								PET_{ox}	
								PET_{ox}	
								EnT	[106, 127] [106, 127]
								EnT	

tpp

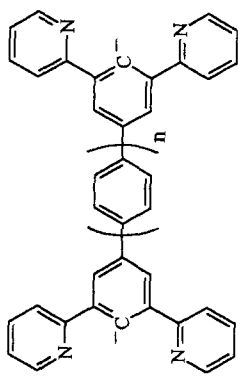
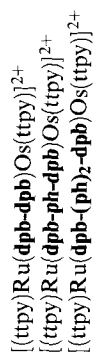
tpy-(ph)_n-tpytpy-E_n-tpy

Table 1 (continued)

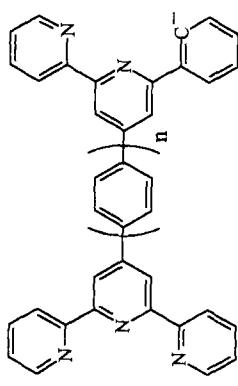
Bridging ligand	No.	Complex	Process	Reference
 $\text{tpy}-(\text{CH})_2\text{-tpy}$	54	$[\{(\text{tpy})\text{Ru}(\text{tpy}-(\text{CH})_2\text{-tpy})\}_2\text{Fe}]^{6+}$	EnT	[126]
 $\text{tpy}-(\text{CH}_2)_2\text{-tpy}$	55	$[\text{Fe}\{(\text{tpy}-(\text{CH}_2)_2\text{-tpy})\text{Ru}(\text{tpy})\}_2]^{6+}$	EnT	[126]
 tpy-Ph-bco-Ph-tpy	56	$[(\text{ttpy})\text{Ru}(\text{tpy-Ph-bco-Ph-tpy})\text{Os}(\text{ttpy})]^{4+}$ $[(\text{ttpy})\text{Ru}(\text{tpy-Ph-bco-Ph-tpy})\text{Os}(\text{ttpy})]^{5+}$	EnT PETox	[124, 128, 129] [129]

[124, 130]
[124, 130]
[124, 130]

EnT
EnT
EnT



[131]
[131]
[131]
[131]



[132]

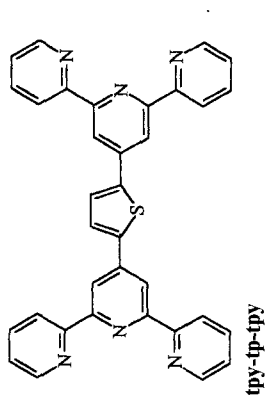
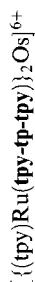
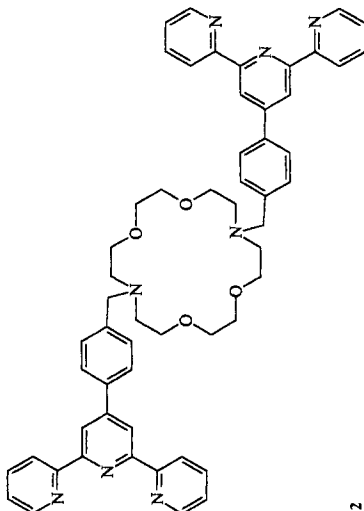
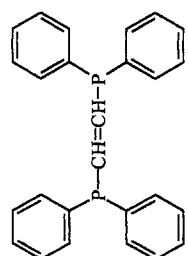
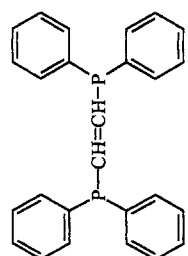
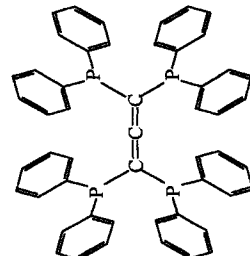
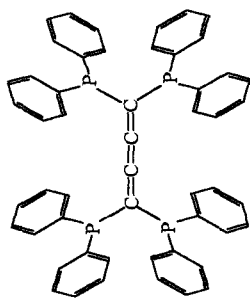
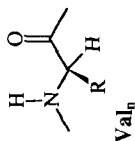
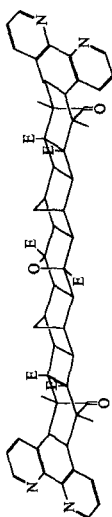


Table 1 (continued)

Bridging ligand	No.	Complex	Process	Reference
	60	$[\{(tpy)RuL^2\}_2Fe]^{6+}$ $[\{(tpy)RuL^2\}_2Ni]^{6+}$		[133] [133]
 L^2	61	$[(bpy)(CO)_2Re\{(dppene)Re(bpy)(CO)_3\}_2]^{3+}$	EnT	[134]
 $dppene$	62	$[(bpy)_2Ru(C_3P_4)Os(bpy)_2]^{4+}$	EnT	[135, 136]
 C_3P_4				

63	$[(bpy)_2Ru(C_4P_4)Os(bpy)_2]^{4+}$	EnT	[136]
64	$[(bpy)_2Ru(embpy)-(Val)_n-Co(NH_3)_5]^{4+}$ $n = 1, 2, 3$	PET _{ox}	[137]
65	$[(bpy)_2Ru(nor)Os(bpy)_2]^{4+}$	EnT	[138]

**C₄P₄****Val_n****nor**

^a PET: $Re(I)-Ru(III)-Fe(III) \rightarrow Re(II)-Ru(II)-Fe(III)$.

^b PET: $Fe(II)-*Ru(II)-Rh(III) \rightarrow Fe(II)-Ru(III)-Rh(II)$.

^c The bridge is the energy-acceptor. When it is reduced, EnT from the Ru-center to Os-center takes place.

^d The emission of the $Ru(bpy)_3^{2+}$ core is quenched. The nature of the intramolecular process is unknown.

^e Two-photon excitation, intramolecular disproportionation.

^f EnT process from both the Ru-based and Os-based components to antryl unit.

^g The emission of $M(tpy)(tpp)^{2+}$ ($M = Ru(II), Os(II)$) unit is quenched. The nature of the intramolecular process is unknown.

metal electronic coupling; as a consequence, their behavior differs from that of the other ligand-bridged species in Table 1 in peculiar features such as intense intervalence transfer spectra [21, 52], and ultrafast energy [53] and electron transfer [54] processes. On the other hand, polymetallic systems of high nuclearity (≥ 4) and dendrimeric structure [55] are dealt with specifically in other chapters of this book.

In Table 1, the bi- and polymetallic complexes are grouped according to the bridging ligand, indicated by a structural formula, an appropriate abbreviation, and a reference number. Abbreviations for the ancillary (nonbridging) ligands can be found in Appendix I. The type of process observed for each system (when clearly identified by the authors) is included in Table 1. The acronyms are PET_{OX} and PET_{RED} for oxidative or reductive photoinduced electron transfer (Figure 1a,b), PCS for photoinduced charge shift (Figure 1c), and EnT for electronic energy transfer (Figure 2). The bimetallic dyads are always written so that the left-hand side metal identifies the initially excited chromophore (molecular component A in Figures 1 and 2). When necessary, footnotes are included to add further specifications.

Selected examples of bi- and polymetallic systems will be discussed in detail in subsequent sections.

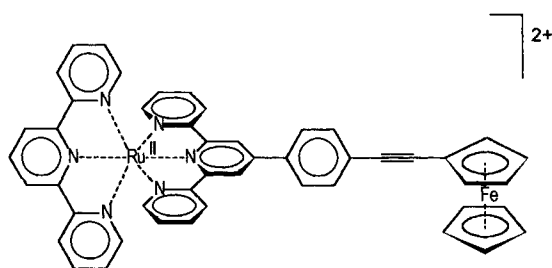
3.3 Chromophore–Quencher Systems

Many interesting hybrid systems involve covalently linked inorganic and organic molecular components. The inorganic moiety usually plays the role of the light-absorbing chromophore (component A in Figures 1 and 2), while the organic component acts as the electron- or energy-transfer quencher (component B in Figures 1 and 2). Therefore, such systems are generally indicated as “chromophore–quencher” complexes. Early work has been reviewed [44], and recent work has been covered by Schanze in his extensive monograph [139].

In this section, representative examples of the chromophore–quencher systems that have appeared during the past few years (1996–1999) are referred to. The chromophoric units are almost invariably of the MLCT type, with Ru(II) and Re(I) polypyridine complexes being by far the most frequent cases. On the other hand, a great variety of organic quencher units have been used, and the same is true for the covalent linkage between the two types of unit. The chromophore–quencher systems, in contrast to the bi- and polymetallic ones, cannot be easily summarized in a tabular format. Rather, references will be briefly listed below, grouping the various chromophore–quencher systems according to the type of organic quencher unit. Selected examples will be described in more detail in subsequent sections.

3.3.1 Ferrocenes

Ferrocene is easily oxidized (E^0 , +0.49 V versus SCE) and has a relatively low-lying (c. 1.8 eV) very short-lived triplet state. Therefore, with many common chromo-



(1)

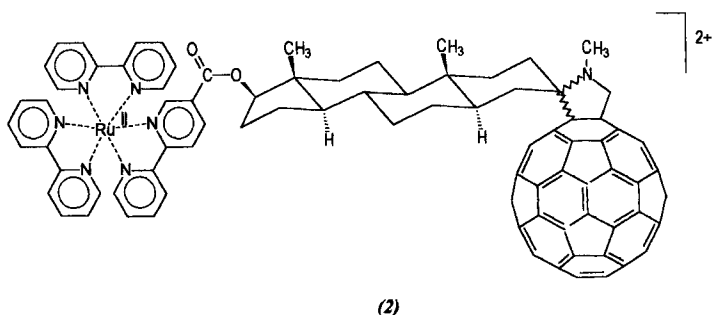
phores, ferrocenyl groups are good potential quencher units, with two mechanisms available: reductive PET (Figure 1a) and EnT (Figure 2). As a benchmark, for $\text{Ru}(\text{bpy})_3^{2+}$ and ferrocene, PET and EnT have comparable driving forces, being exergonic by c. 0.35 eV and c. 0.32 eV, respectively. In bimolecular quenching of $\text{Ru}(\text{bpy})_3^{2+}$ by ferrocene, the main process is EnT [140]. The preference for EnT over PET is probably related to the smaller reorganizational energy of the former process, as shown by the increasing amount of PET found when the driving force of this process is increased by using ferrocene derivatives of lower redox potential [140].

In the chromophore–quencher system (1) a ferrocenyl unit is connected to a $\text{Ru}(\text{tpy})_2^{2+}$ unit via a p -phenylene-acetylene spacer [141]. The weak emission of the $\text{Ru}(\text{tpy})_2^{2+}$ chromophore is completely quenched in the dyad [142]. For this system, an EnT mechanism could be inferred by analogy with the behavior of related bimolecular systems [140], but PET followed by fast back electron transfer cannot be ruled out. This mechanistic ambiguity is common to most studies on related chromophore–ferrocene dyads [143–146].

While for most chromophore–ferrocene dyads the photophysical behavior can be interpreted in terms of competing EnT and PET, additional complexities arise when the two units are connected by fully conjugated bridges (e.g., polyene chains). In fact, in such systems the lowest excited state may eventually become a Fe-to-bridge MLCT state [143].

3.3.2 Fullerenes

Fullerene (C_{60}) has low-lying excited states (S_1 , 1.94 eV; T_1 , 1.58 eV) [147], and is a good electron acceptor (first reduction at -0.35 V versus SCE, further reduction steps cathodically shifted by c. 0.53 V each) [148]. It is therefore a good candidate to act as a quencher, by both EnT (Figure 2) and oxidative PET (Figure 1b) mechanisms. A convenient feature from the viewpoint of experimental PET studies is the facile spectroscopic detection of fullerene radical anions. In fullerenes the reorganizational energy λ (Section 3.1.3) is small, as a consequence of the large molecular dimensions (λ_o) and the high degree of electron delocalization (λ_i). This is a positive kinetic feature towards the achievement of efficient and long-lived charge separa-



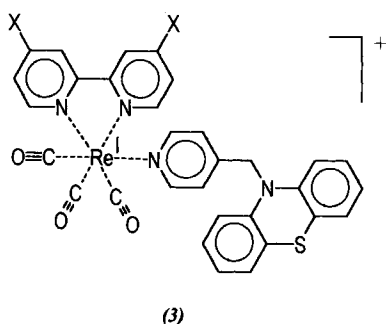
tion, as it is expected to accelerate the forward process (in the Marcus normal region) and to slow down charge recombination (in the Marcus inverted region). Because of these many interesting features, fullerenes have been recently used as molecular components in several kinds of supramolecular systems [149, 150]. Systems where fullerenes are covalently linked to porphyrins and other organic chromophores are dealt with in Volume III, Part 2, Chapters 1 and 2.

A number of dyads have recently been synthesized and studied, where a $\text{Ru}(\text{bpy})_3^{2+}$ chromophore is covalently linked to a fullerene derivative by bridges of various degrees of flexibility [151–154]. System (2) involves a rigid steroid-type spacer [153]. In acetonitrile, PET is exergonic by 0.24 eV and EnT by 0.47 eV. Despite its smaller driving force, PET is the primary process observed, with the charge separated state being formed in 0.2 ns. Interestingly, the charge recombination does not lead directly to the ground state (as, e.g., in Figure 1b), but rather the fullerene triplet is formed (in 100 ns) as an intermediate species.

3.3.3 Amines

Various types of amines have been used in chromophore–quencher systems for reductive PET (Figure 1a). Chromophore–quencher systems with aliphatic amines have often been used as potential luminescent chemosensors, for their pH-dependent quenching ability [155–157]. In some cases, the reductive PET can take advantage of irreversible (e.g., bond fragmentation) [158] or reversible (e.g., ring opening) [159] chemical reactions following formation of the amine radical cation. Dimethylaniline derivatives, with reduction potentials of c. 0.85 V versus SCE, have been used as attached groups to reductively quench $\text{Re}(\text{I})$ [160] and $\text{Ru}(\text{II})$ [161] polypyridine chromophores.

By far the most popular electron donor used in inorganic chromophore–quencher systems has been phenothiazine (PTZ). The pioneering studies of Meyer and co-workers [162, 163] on the chromophore–quencher complex (3) showed rapid (<10 ns) quenching of the MLCT excited state of the chromophore, with formation of a charge-separated state containing a reduced $\text{Re}(\text{I})$ complex (i.e., a $\text{Re}(\text{I})\text{-bpy}^{\bullet-}$ species) and the PTZ^+ radical cation. Charge recombination takes place in several tens of nanoseconds, with rates depending on the X-substituents. More recent work

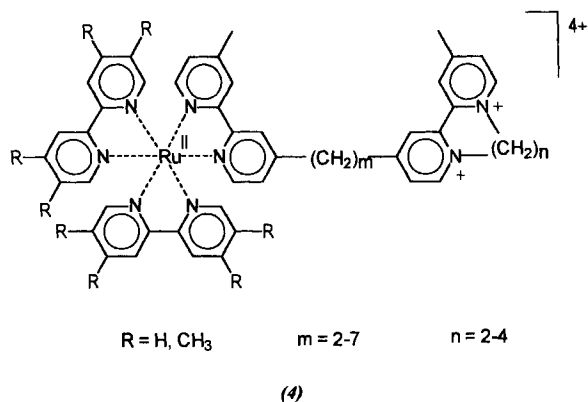


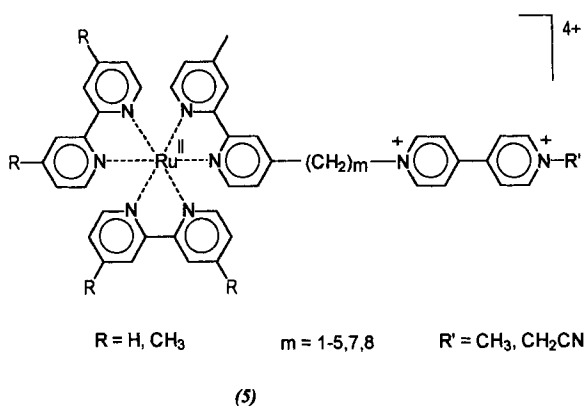
on PTZ-containing dyads involves these systems with slightly different chromophores (e.g., bipyrimidine Re(I) systems) [164] or in heterogeneous environments (e.g., chemisorbed on SnO_2 [165], TiO_2 [166], SiO_2 [167]).

The PTZ unit has been widely used as the electron donor component in triad systems for photoinduced charge separation (see Section 3.4.5).

3.3.4 Pyridinium Ions

The most widely used electron acceptors in inorganic chromophore–quencher systems have been bipyridinium dications, often called “viologens” (quaternarized derivatives of 4,4′-bipyridine) or “diquat” (cyclic quaternarized derivatives of 2,2′-bipyridine). The classical studies of Elliott, Schmehl, and Mallouk have been concentrated on dyads of types (4) and (5). For dyads (4) [168, 169], oxidative PET takes place, with forward processes in the 80 to 1700-ps time scale and very fast (<30 ps) charge recombination. The main observations are that: (i) electron transfer to the diquat quencher occurs from the directly linked bipyridine ligand; (ii) fast equilibration between the MLCT excited states on the three bipyridine ligands precedes electron transfer; (iii) the electron transfer rates are in the “normal” Marcus





free-energy region and correlate accordingly with the driving force (depending on R and n); and (iv) the rates decrease exponentially with the number of methylene spacers, consistent with a through-bond ET mechanism. For dyads (5) [170, 171], both forward and back electron transfer rates could be measured. The back reaction depends on driving force as predicted for the Marcus inverted region. The rates of both processes decrease exponentially with the number of carbon atoms in the chain up to $m = 5$. After correction for the distance dependence of solvent reorganizational energy, the attenuation factor β is very similar for the two processes (1.0 – 1.2 \AA^{-1}). Dyads similar to (5), except for the presence of an amide linkage between the chromophore and the alkyl chain, have been studied by Kelly and Rodgers, with similar mechanistic conclusions [172]. A number of covalently linked systems containing various Ru(II) polypyridine complexes and various viologen-type quenchers (including the interesting 2,7-diazapyrenium unit) have been designed and studied by Balzani, Stoddart, and coworkers [173] in the context of their efforts towards light-driven pseudorataxane-type molecular machines (see Volume III, Part 2, Chapter 6).

Viologens have been used as covalently linked quenchers for Cu(I) bipyridine chromophores, leading to fast ($<10 \text{ ns}$) charge separation and remarkably slow (30 ns to $2 \text{ }\mu\text{s}$, depending on solvent) charge recombination [174]. More complex systems, similar to (5) but with two viologens on the same bipyridine of the Ru(II) chromophore, have been designed to mimic the presence of two ET in the reaction center of natural photosynthesis [175].

3.3.5 Other Systems

A variety of other quencher units have been recently used in inorganic chromophore–quencher systems. Electron acceptors include diimides [176, 177], quinones [178, 179], and nitroaromatics [180].

A number of interesting inorganic–organic dyads have been recently investigated that, rather than chromophore–quencher, could be called “chromophore–sensitizer”

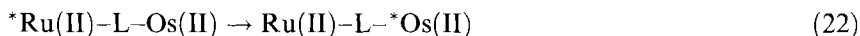
systems. In fact, the appended units are high-energy dyes (coumarins) that transfer energy at the singlet level to Ru(II) polypyridine chromophore [181, 182].

3.4 Selected Topics

3.4.1 Electronic Energy Transfer in Bimetallic Systems: Ru(II)–Os(II) Dyads

Binuclear systems containing ruthenium(II) and osmium(II) complexes as active metal units represent by far the most extensively investigated class of compounds for the study of electronic energy transfer processes [50, 51]. An interesting series of Ru(II)–Os(II) polynuclear species of larger nuclearity containing 2,3-dpp and/or 2,5-dpp as bridging ligands, synthesized toward the development of artificial antenna systems [55], are dealt with in Volume 5, Part 1, Chapter 7.

In most of the dinuclear systems studied, the Ru-based and Os-based chromophoric components are tris-bipyridine or bis-terpyridine complexes connected by a large variety of bridging ligands (Table 1). For both metal components, the lowest excited states are triplet states of metal-to-ligand charge transfer (MLCT) nature. The Os(II) unit is easier to oxidize than Ru(II) unit, and thus the MLCT levels lie at higher energy in the Ru-based component than in the Os-based component. Therefore the Ru(II) units play the role of donor and the Os(II) units of acceptor in an intercomponent energy transfer process (Eq. 22). In a large number of cases both components are luminescent, so that the evidence for the occurrence of energy transfer has been generally obtained observing the quenching of the Ru-based luminescence and the sensitization of the Os-based luminescence.



In these systems the energy transfer process can occur by two mechanisms: the Förster-type mechanism (through-space); and the Dexter-type mechanism (through-bond). Very often these mechanisms occur competitively, and in some cases their relative contribution is difficult to evaluate. The method generally used to decide the type of mechanism is that of evaluating the rate constants (k_{en}^{F}) according to Förster treatment and compare the calculated values with the experimental ones [51]. It is important to note that, in this type of calculation, the values obtained are affected by large uncertainties in the input parameters. In particular, the choice of the appropriate value of the donor–acceptor distance is crucial. Uncertainties on this value can arise from: (i) flexibility of some of the bridges used; (ii) the MLCT nature of the excitation; and (iii) uncertainty on the localization of the MLCT excited state (in terms of the specific ligand involved). In Figure 12 the values of k_{en}^{F} for the couple $\text{Ru}(\text{bpy})_3^{2+}/\text{Os}(\text{bpy})_3^{2+}$ calculated according to Eq. 17 by using the spectroscopic quantities taken from Ref. [51] are plotted (continuous line) as a function of the separation distance between donor and acceptor (r_{AB}). The values calculated for the analogous couple $\text{Ru}(\text{tppy})_2^{2+}/\text{Os}(\text{tppy})_2^{2+}$ are practically identical. The values of the rate constants measured for some of Ru(II)–Os(II) dinuclear com-

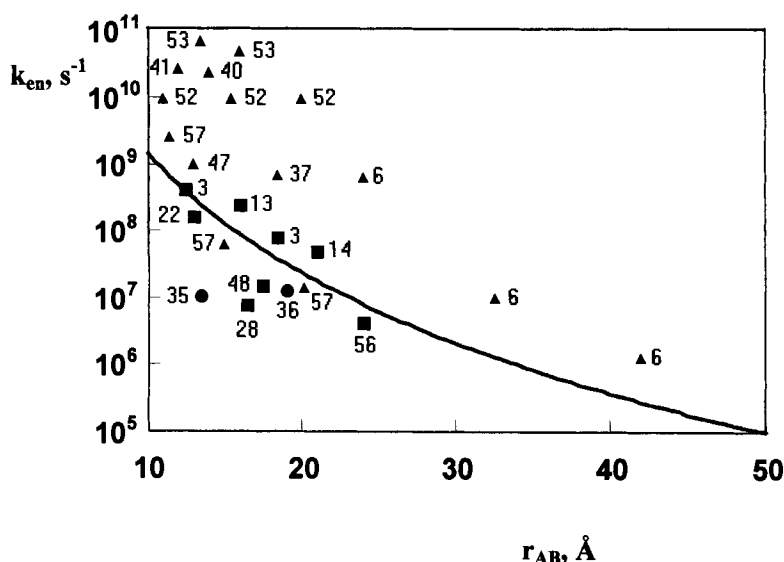
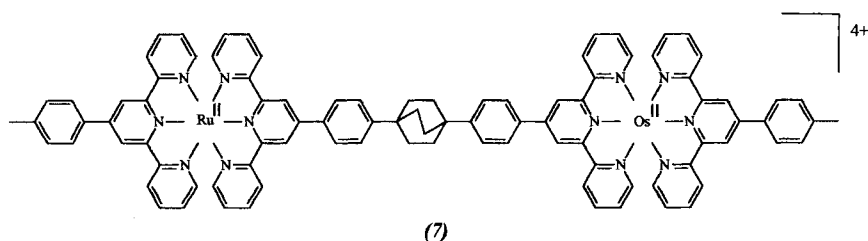
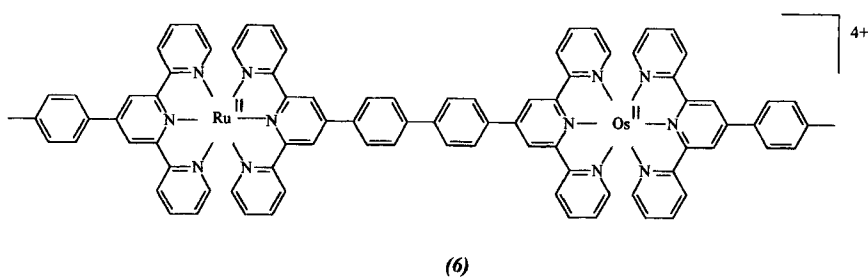


Figure 12. Calculated k_{en} values (continuous line) according to Förster (Eq. 17), as a function of the metal–metal distance for the $\text{Ru}(\text{bpy})_3^{2+}/\text{Os}(\text{bpy})_3^{2+}$ couple. The parameters used are taken from Ref. [51]. Data points are experimental values for $\text{Ru}(\text{II})$ – $\text{Os}(\text{II})$ dyads, labeled according to the type of bridge (see Table 1): unsaturated bridges (\blacktriangle), aliphatic bridges (\blacksquare), bridges containing metal complex spacers (\bullet). The experimental values for the dyads labeled 3 are taken from M. Furue, T. Yoshidzumi, S. Kinoshita, T. Kushida, S. Nozakura, M. Kamachi, *Bull. Chem. Soc. Jpn.*, **1991**, 64, 1632.

plexes, designated by the labels of the bridging ligands used in Table 1, are collected in Figure 12.

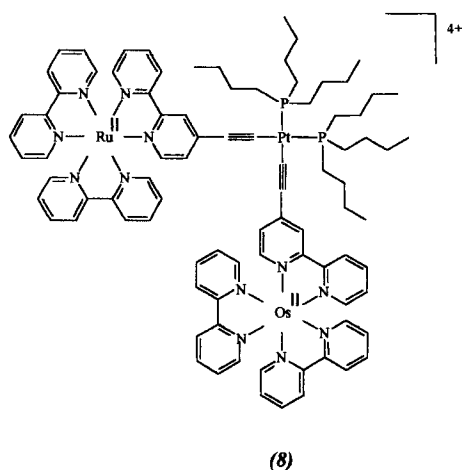
The important observation is that the experimental values obtained for the systems with aliphatic bridging ligands (\blacksquare in Figure 12) are similar within one order of magnitude to the calculated k_{en}^F values. On the other hand, in the case of unsaturated bridges (containing aromatic and/or polyynes spacers; \blacktriangle in Figure 12), the energy transfer process was generally found to be relatively fast, with rate constants that are by far higher than the calculated k_{en}^F values (for the exception represented by the points 57; see below). This suggests that the Förster mechanism accounts for the observed energy transfer process in the case of aliphatic bridge, while the large electronic coupling between the donor and acceptor units provided by unsaturated spacers favors the Dexter mechanism. For some systems it seems reasonable to admit, however, that both mechanisms can play an important role. A significant example of substantial shift between the two types of mechanism is represented by the comparison between dinuclear complexes (6) and (7) (labeled 52 and 56 in Figure 12) investigated by Barigelletti and coworkers [124].

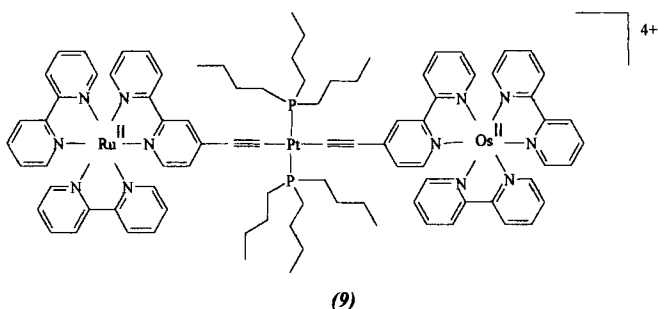
In the species containing two phenyl units as spacer (6) the high energy transfer rate constant is indicative of a Dexter through-bond mechanism. The interposition of a saturated group like bicyclo[2.2.2]octane (bco) between the two phenyls (7)



causes a dramatic decrease in the energy transfer rate. The authors conclude that this effect cannot be simply accounted for by the increased intermetal distance ($d = 20 \text{ \AA}$ and 24 \AA for the complexes (6) and (7) respectively), but a major role must be ascribed to the electronically insulating properties of the bco saturated group. Actually, in system (7) the energy transfer rate constant has dropped to a value close to the calculated Förster value.

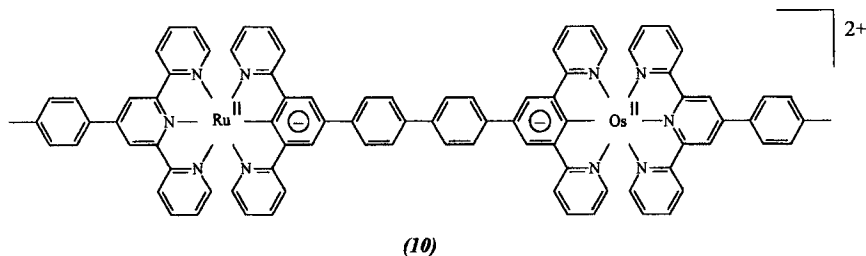
In some cases structural effects could give indications about the type of mechanism. Ziessel et al. [49, 103] have used the Pt^{II} bis- σ -acetylide spacer to construct two isomeric binuclear complexes, *cis* (8) and *trans* (9) forms, with different metal-to-

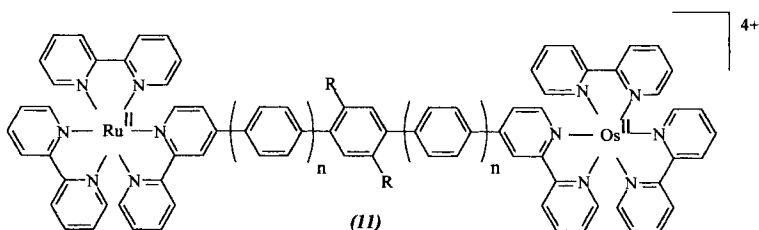




metal distance between the Ru-based and Os-based chromophoric units ($d_{M-M} = 13.7 \text{ \AA}$ and 19.2 \AA for *cis* and *trans* isomers, respectively). In the *cis* complex, because of shorter metal-to-metal distance, faster energy transfer via Förster mechanism is expected, while similar energy transfer rate constants for the two isomers could be expected for a Dexter mechanism given the same through-bond length. Experimentally, the energy transfer process was found to occur slightly slower for the *cis* isomer than for the *trans* analogue. This result is interpreted by the authors as due to the fact that both mechanisms are operative and their relative contribution to the overall energy transfer process is different for the two isomers: the energy transfer in the *cis* isomer is dominated by Coulombic interactions, while the electron exchange is the preferred mechanism for the *trans* complex where the stereochemistry of the bridge increases the orbital overlapping and therefore favors the electronic coupling between the donor and acceptor units.

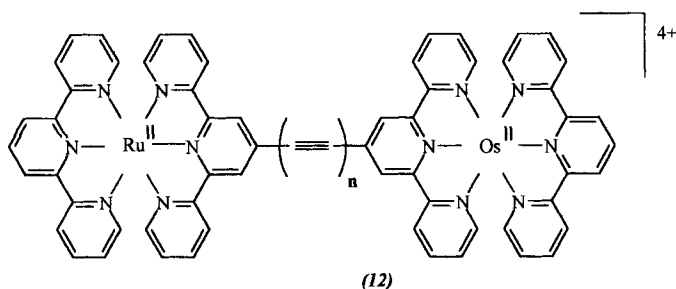
From a close inspection of Figure 12, the data points labeled 57 appear to be anomalous with respect to the other triangle data points, i.e., if compared with the values obtained for the other dyads containing unsaturated bridges. These points correspond to systems where the two metal units are connected by cyclometalated bridging ligand [124, 130], e.g., dyad (10). In such a system, the Ru \rightarrow Os energy transfer process is much slower ($k < 2 \times 10^7 \text{ s}^{-1}$) with respect to the case of system (6) (labeled 52 in Figure 12; $k = 5 \times 10^{10} \text{ s}^{-1}$), despite the fact that the two systems contain the same diphenylene spacer. The reason for this behavior is the different localization of MLCT states involved in the transfer process: in (6) the MLCT excited states involve the bridge, while in (10) the MLCT states are localized on the terminal ligands and therefore in the latter case, the energy transfer pathway is longer. This result highlights the crucial role of localization aspects in determining the energy transfer rate.





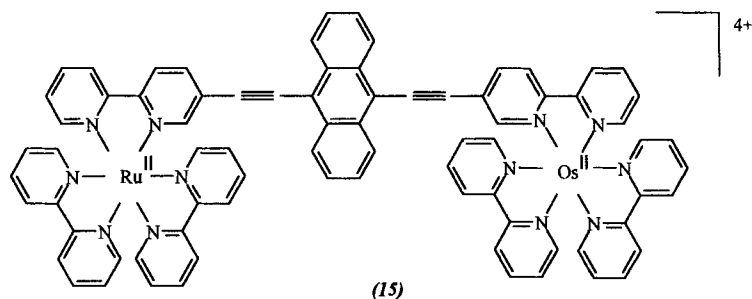
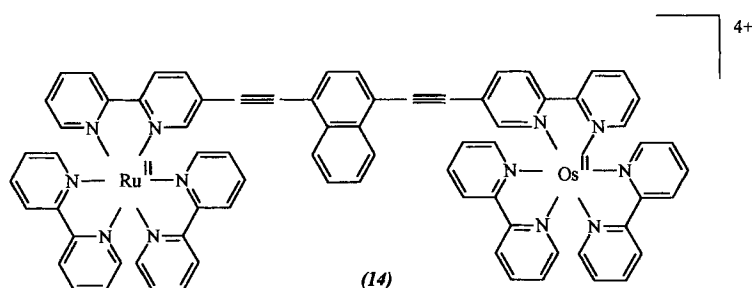
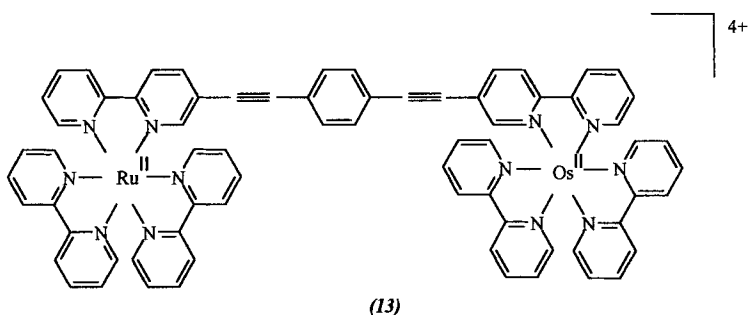
In energy as well as in electron transfer processes, an important issue is the distance dependence of the rate constant. It is important to note that in the case of energy transfer in polynuclear complexes systematic studies are performed only in very few cases. The series of the binuclear complexes (11) ($n = 1, 2, 3$) investigated by Balzani and coworkers [65], represent an excellent example of systems particularly suited for this type of study because the modular composition of oligophenylene spacer allows changing the metal-to-metal distance in a systematic way. The important result is that in these systems the energy transfer process is highly efficient, even for a distance of 42 Å, indicating that the oligophenylene bridge behaves as a good energy transducer. The rate constant has been found to decrease exponentially with increasing the metal-metal distance and an attenuation coefficient (β) of 0.32 Å^{-1} has been obtained.

For the series of complexes (12) ($n = 1, 2$) containing alkyne spacers, Harriman and Ziessel have estimated an attenuation factor of the order of 0.17 Å^{-1} [106, 127]. This relatively small value indicates that through alkyne bridges the “electronic conduction” for energy transfer is more efficient with respect to the polyphenylene counterparts.



Ziessel et al. have explored extensively the possibility of controlling and modulating the electronic properties of a bridge by incorporating additional unit into the unsaturated polyacetylenic backbone [49]. An elegant example that illustrates this point is represented by a series of Ru-Os binuclear complexes where the polyacetylenic bridge contain a phenyl (13), a naphthyl (14), and an anthryl (15) group, respectively.

Along this series, the energy of both HOMOs and LUMOs resident on the bridge decreases with the increasing size and conjugation of the polycycle. The power of



this approach is demonstrated by the results of the photophysical investigation, which clearly indicate that the energy of the polycyclic unit causes a profound effect on both rate and pathway of the energy transfer process (Figure 13). For the phenyl-bridged complex (13), where the triplet of the bridge is higher in energy than that of the donor, an exchange energy transfer process takes place directly from the Ru-based to Os-based metal units. In the naphthyl-bridged Ru-Os system (14), where the triplet of the bridge is between the triplet of the Ru-based and Os-based units, the energy transfer occurs in a stepwise manner: first to the central naphthalene unit of the bridge and then to the terminal Os-based fragment. In the anthryl-bridged system (15), the triplet of the bridge is lower than those of both metal components and rapid energy transfer processes from both metal units to the bridging anthryl group were observed. Decreasing the energy of the triplet of the

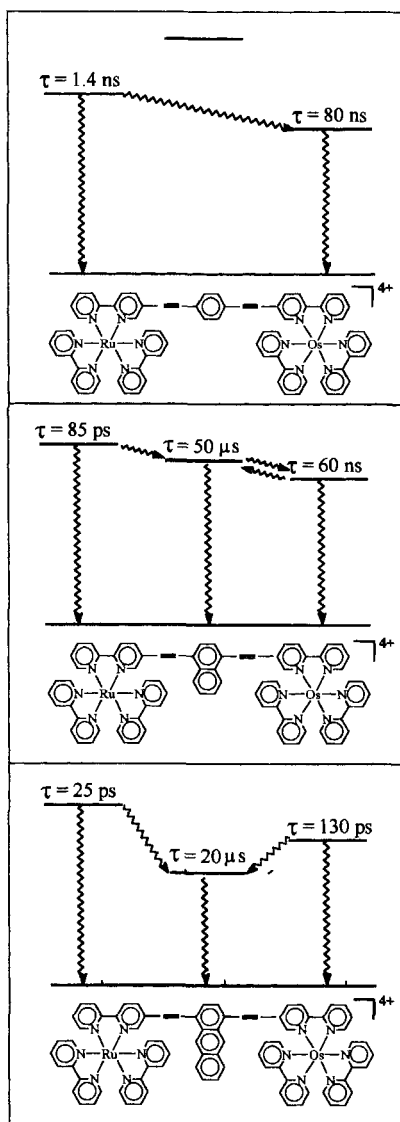
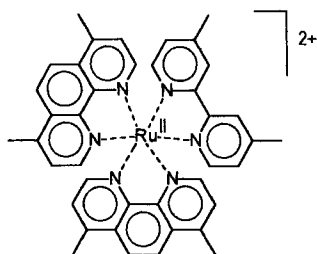


Figure 13. Schematic energy-level diagram for aryl-bridged Ru(II)-Os(II) dyads.

polycyclic unit causes its direct participation in the energy-transfer sequence until, as in the case of anthracene, the bridge becomes a trap.

3.4.2 Photoinduced Electron Transfer in Bimetallic Systems: Ru(II)-Rh(III) dyads

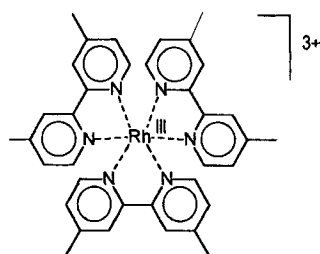
A dyad for oxidative PET (Figure 1b) contains a photoexcitable donor (A) and an electron acceptor (B) that, for ideal performance, should fulfil a rather stringent set of conditions.



(16)

For practical purposes (using visible light, achieving selective excitation), A should feature low-energy intense absorption (i.e., be a visible chromophore). Also intrinsic to the function of A is that it have a strong excited-state reducing character. These two conditions automatically limit the magnitude of the ground-state oxidation potential, as E^{0-0} , $E^0(\text{A}^+/\text{*A})$, and $E^0(\text{A}^+/\text{A})$ are mutually related (Eq. 3). Additional useful features include a relatively long excited state lifetime (to support relatively slow ET processes), and that it have easily detectable emission (for facile excited-state monitoring). A good compromise between all these requisites is achieved by complexes of the Ru(II) polypyridine family (although other d^6 systems such as Re(I) and Os(II) also have interesting properties). Using $\text{Ru}(\text{Me}_2\text{phen})_2(\text{Me}_2\text{bpy})^{2+}$ (**16**) as a paradigmatic case, the relevant properties are $E^{0-0} = 2.16$ eV, $E^0(\text{A}^+/\text{*A}) = -1.02$ V, $E^0(\text{A}^+/\text{A}) = 1.14$ V versus SCE, $\lambda_{\text{max}}^{\text{em}} = 610$ nm, $\Phi = 0.11$, $\tau = 1.8$ μs [183].

The B component must also meet a set of specific requirements. First, it must be practically nonchromophoric (so as to avoid interference with excitation light absorption by A), and second, it should be a good ground-state electron acceptor [$E^0(\text{B}/\text{B}^-) > E^0(\text{A}^+/\text{*A})$]. It should also have a lack of low-energy excited states [$E^{0-0}(\text{*B}) > E^{0-0}(\text{*A})$, in order to avoid EnT quenching], and also be kinetically stable in the reduced B^- form (at least in the time scale of the charge recombination process). Among metal polypyridine complexes, the choice for good electron acceptors is practically limited to a number of trivalent metal systems. Few of these systems, however, are actually suitable. In 3d metals, e.g., Co(III), Cr(III), low-energy ligand-field states are present. Moreover, in some cases, e.g., Co(III), the reduced forms are highly labile. Most of the above requirements are met, on the other hand, by d^5 systems such as, e.g., Os(III). Oxidative PET has indeed been studied in a number of Ru(II)–Os(III) polypyridine dyads [66, 76–78, 90, 129]. In all these systems, however, the reduction of the acceptor unit is so facile (e.g., for $\text{Os}(\text{bpy})_3^{3+}$, $E^0(\text{III}/\text{II}) = 0.78$ V versus SCE) that almost all of the excited-state energy is wasted in the forward process, and very little is stored transiently in the charge-separated products. A more attractive situation is found using Rh(III) polypyridine complexes as acceptor units. Taking $\text{Rh}(\text{Me}_2\text{bpy})_3^{3+}$ (**17**) as a paradigmatic case for this class of molecular components, relevant properties are: $E^{0-0} = 2.77$ eV, $E^0(\text{B}/\text{B}^-) = -0.89$ V versus SCE, $\tau = 3$ ns [183]. The kinetic lability of the Rh(II) species—which could be a drawback for long time scale experiments



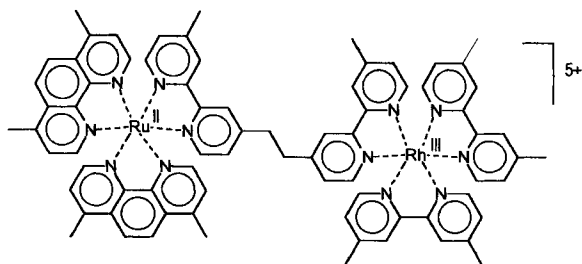
(17)

(milliseconds)—is irrelevant to the fast, reversible PET processes taking place within the dyads.

A number of Ru(II)–Rh(III) polypyridine dyads have been synthesized and studied during the past few years [60, 63, 117, 121, 122, 183]. The mechanistic aspects of such studies are discussed in some detail in this section.

Energetics and general behavior

The general properties of Ru(II)–Rh(III) polypyridine dyads can be discussed taking dyad (18) as an example [183]. The absorption spectrum of dyad (18), as compared with those of suitable models of the molecular components, (16) and (17), is shown in Figure 14. This shows that the spectra of the molecular components are strictly additive, as expected for weak intercomponent interaction. It also shows that selective (100 %) excitation of the Ru(II) chromophore can be easily performed in the visible region, whereas partial excitation of the Rh(III) component (c. 70 % at 300 nm) can be achieved in the ultraviolet (where overlapping ligand-centered (LC) bands of both molecular components are observed). The energy level diagram for this dyad is shown in Figure 15. Indicated are the common photophysical processes taking place within each molecular components, i.e., prompt intersystem crossing to form the long-lived triplet states. Also indicated are a number of thermodynamically allowed intercomponent processes, including:



(18)

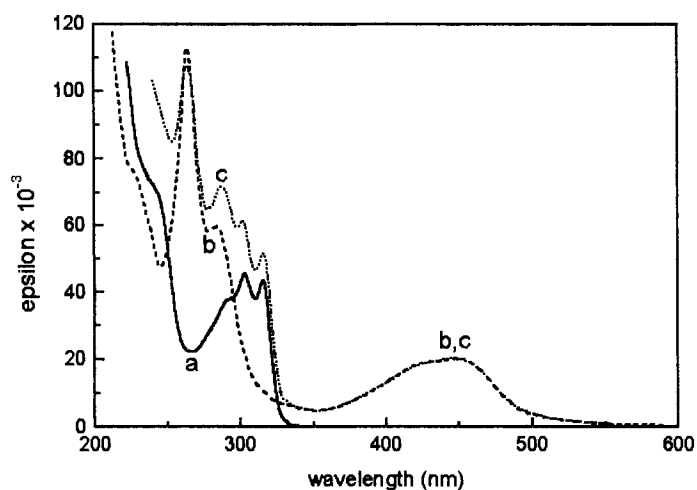


Figure 14. Absorption spectra of Ru(II)–Rh(III) dyad (dotted line, c), Ru(II) model (dashed line, b), and Rh(III) model (continuous line, a).

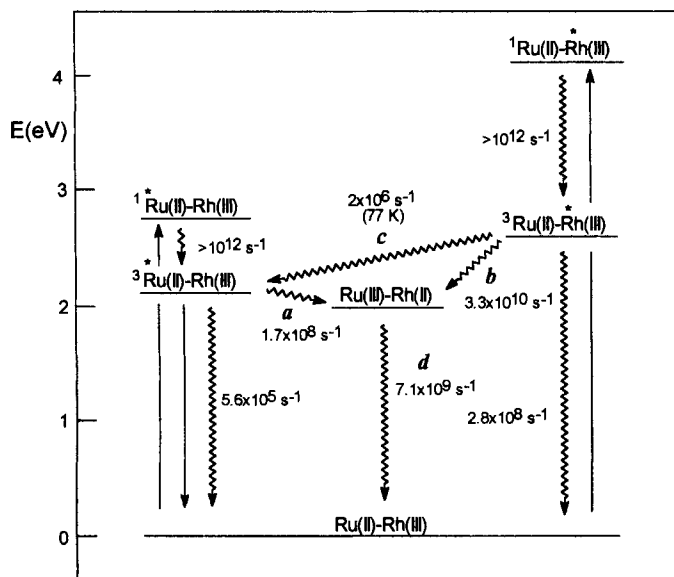


Figure 15. Energy level diagram of the Ru(II)–Rh(III) dyad (18).

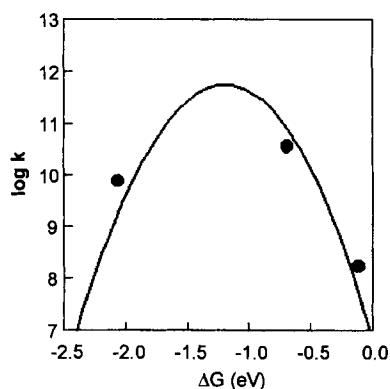


Figure 16. Plot of $\log k$ versus ΔG° for the three electron transfer processes of dyad (**18**).

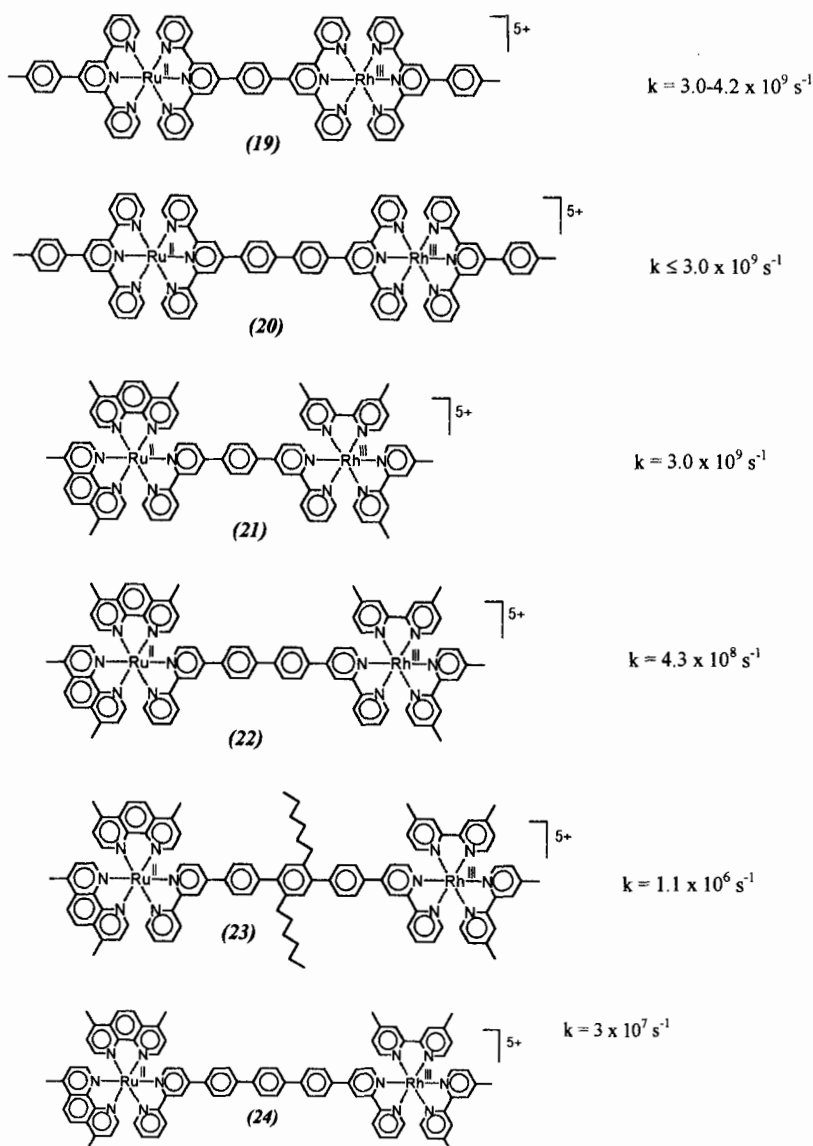
- | | |
|---|--|
| (a) $^*\text{Ru(II)}-\text{Rh(III)} \rightarrow \text{Ru(III)}-\text{Rh(II)}$ | oxidative quenching of the excited Ru(II) |
| (b) $\text{Ru(II)}-^*\text{Rh(III)} \rightarrow \text{Ru(III)}-\text{Rh(II)}$ | reductive quenching of the excited Rh(III) |
| (c) $\text{Ru(II)}-^*\text{Rh(III)} \rightarrow ^*\text{Ru(II)}-\text{Rh(III)}$ | EnT from Rh(III) to Ru(II) |
| (d) $\text{Ru(III)}-\text{Rh(II)} \rightarrow \text{Ru(II)}-\text{Rh(III)}$ | charge recombination |

For dyad (**18**), all these processes could be time-resolved under the appropriate experimental conditions (visible excitation for *a*, UV excitation for *b* and *d*, rigid matrix for *c*), leading to the detailed kinetic picture of Figure 15 [183]. The widely different rates of the three ET processes (*a*, *b*, *d*) can be rationalized in terms of predominant driving force effects, as shown schematically in Figure 16 (although more subtle effects of electronic factors cannot be ruled out; see Section 3.1.4 and Figure 11a).

Bridge and distance effects

In subsequent studies of Ru(II)–Rh(III) polypyridine dyads, the chromophoric and acceptor units were of the tris-bipyridine (or phenanthroline) type [63] or of the bis-terpyridine type [121, 122], whereas the bridges were based on *p*-phenylene spacers (Scheme I). With these rod-like, longitudinally rigid dyads, attention was focused on the slightly exergonic oxidative quenching following Ru(II) excitation (process *a* in Figure 15), and the emphasis was placed on the study of bridge and distance effects. In analyzing the results of these studies, it should be borne in mind that the energetics of PET (see, e.g., Figure 15) is practically the same for the bpy (or phen) complexes and for the tpy ones. The rate constants reported in Scheme I indicate, as expected, a general decrease of electron transfer rates with increasing bridge length. The following observations are worth of comment.

A comparison between dyad (**18**) and dyad (**21**) demonstrates that the phenylene group is a better “conducting” spacer (see Section 3.1.3 for a caveat on this colloquial terminology, however) as compared to methylene: despite the longer metal–metal distance, the reaction is faster across the phenylene spacer ($k = 3.0 \times 10^9 \text{ s}^{-1}$)



Scheme I

than across the methylene one ($k = 1.7 \times 10^8 \text{ s}^{-1}$). This is no doubt related to the lower energy of the LUMO of the phenylene group, facilitating superexchange interaction (Eq. 7).

Dyads (19) and (21), despite the vast difference (three orders of magnitude) in lifetimes of the chromophores involved, give identical PET rates. This is experimentally gratifying and confirms that the energetics of PET (see, e.g., Figure 15) is practically the same for dyads of the bpy (or phen) and tpy families.

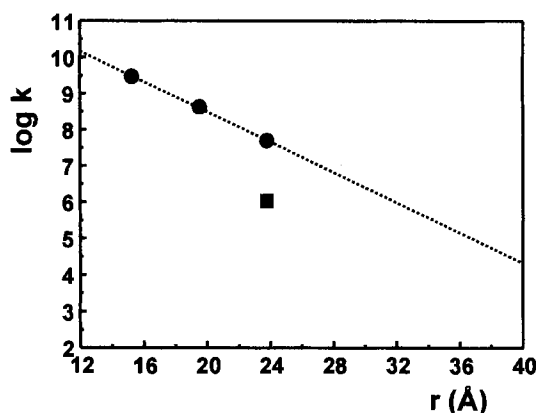
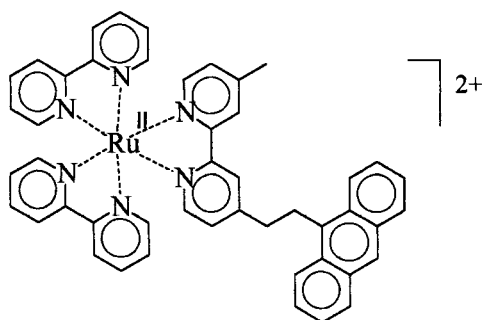


Figure 17. Distance dependence of forward electron transfer rates in dyads (21), (22), (24) (circles) and (23) (squares).

The rate constants for PET of dyads (21)–(24) are displayed on a logarithmic plot as a function of the metal–metal distance in Figure 17. It can be seen that the three systems with unsubstituted polyphenylene spacers exhibit a nice exponential dependence of rates on distance. This is the behavior predicted by Eqs. 5 and 6 on the basis of the exponential decay of the electronic factor H_{AB} , if the distance dependence of the FCWD term can be neglected. From this viewpoint, a nice feature of the Ru(II)–Rh(III) dyads is the charge-shift nature of the process (PET leads from a $2+/3+$ to a $3+/2+$ species). Thus, in contrast to typical organic dyads (where a pair of opposite charges is created in the PET process), the two Coulombic terms in Eq. 3 exactly cancel out, and the driving force is independent on the donor–acceptor distance. This eliminates one of the two possible causes of distance dependence of the FCWD term. The remaining one is λ_o , expected to increase slightly with distance (Eq. 12). Its contribution to the observed rate decrease is presumably relatively small, but is difficult to evaluate exactly as it depends on the assumed partitioning of λ into λ_i and λ_o . Therefore, the β value obtained from the slope of the line in Figure 17 (0.5 \AA^{-1}) should be regarded as an upper limiting value for the attenuation factor of the intercomponent electronic coupling (Eq. 6). This value is much lower than those observed for rigid saturated bridges ($0.8\text{--}1.2 \text{ \AA}^{-1}$) [15, 184–186], and similar to that obtained for electron transfer between porphyrins across oligophenylene spacers [187].

Of particular interest is the fact that dyad (23), which is identical to dyad (24) except for the presence of two solubilizing hexyl groups on the central phenylene ring, undergoes PET c. 50 times slower than its unsubstituted analogue. This is most likely related to the notion that electronic coupling through a polyphenylene spacer is a sensitive function of the twist angle between adjacent spacers [188, 189]. Such twist angle is presumably c. 45° for unsubstituted adjacent phenylene rings (as in biphenyl). It is expected to increase, however, in the presence of alkyl substituents. Assuming a cosine angle dependence for adjacent coupling terms (e.g., H_{12} and H_{23} in Eq. 8 and Figure 6), an increase in twist angle upon substitution from c. 45° to c. 75° would be sufficient to account for the observed rate decrease.

The study of the Ru(II)–Rh(III) dyads in Scheme I has shown that rigid polyphenylene bridges are efficient mediators of long-distance PET. Coupled with the



(25)

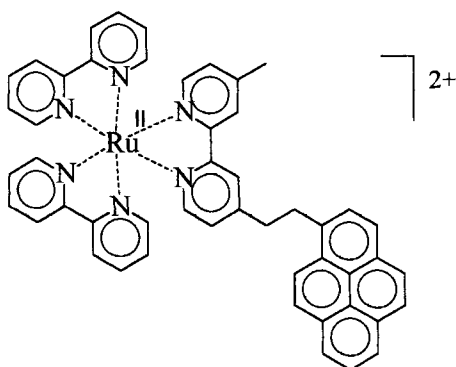
long lifetime of the excited Ru(II) chromophore, such bridges could (in principle) sustain PET over very long distances (e.g., extrapolating from Figure 17, ≥ 40 Å). In principle, the dependence of the electronic coupling on the inter-spacer twist angle could be used for tuning or switching purposes.

3.4.3 Reversible Energy Transfer in Systems with Aromatic Hydrocarbon Units

Chromophore–quencher systems where the organic molecular components are aryl hydrocarbons are under intense study [67, 190–205]. In these systems an inorganic moiety (based on polypyridine complexes of Ru(II), Os(II), Re(I)) and an aryl hydrocarbon (naphthalene, anthracene, pyrene) are covalently linked by flexible aliphatic [187–201] or rigid conjugated bridges [49, 190, 191, 193].

In dyads formed by the Ru(bpy)₃²⁺ complex and an anthracene moiety (**25**), a strong quenching of the MLCT luminescence of the Ru-based unit is observed [195]. This quenching is attributed to exergonic triplet–triplet energy transfer from the metal complex to anthracene. The process, in which anthracene acts as an EnT quencher, is represented in Figure 18. A similar behavior has been observed in a dyad formed by a Re(bpy)(CO)₃ unit and an anthracene moiety [202].

When the aryl linked to the Ru(bpy)₃²⁺ unit is a pyrene (**26**), an enhancement (from about 1 μs to 11.2 μs) of the MLCT lifetime is observed [204]. This result is interpreted on the basis of a reversible energy transfer mechanism implying equilibrium between the MLCT and aromatic triplet states which are very close in energy (Figure 18). This effect is confirmed by Wilson et al. [196] in an elegant study of a family of dyads formed by the Ru(bpy)₃²⁺ unit and pendant naphthalene, pyrene, or anthracene. The photophysical properties of each dyad are determined by intramolecular energy transfer processes that are governed by the relative position of the various triplet energy levels: the initial excitation energy is localized respectively on the MLCT state for Ru-naphthalene and on the anthracene triplet for the Ru-anthracene. Since the Ru-based MLCT and the lowest pyrene triplet state are almost isoenergetic, an equilibrium is established resulting in a long-lived lifetime for the Ru-pyrene (5.3 μs) [196].



(26)

The reversible triplet energy transfer between MLCT and a long-lived, almost isoenergetic triplet state of aryl moieties suggests an interesting strategy for extending the triplet lifetime of the metal complex fragment. This new approach seems to be more effective in improving the photophysical properties of these chromophores than the traditional ones based on using rigid matrices or on rising the triplet energy (energy gap law).

A dramatic effect of the reversible energy transfer mechanism has been obtained by Harriman, Zissel and coworkers [49, 190, 191, 193] in a family of dyads where the metal complexes (Ru(II) or Os(II)-based) are connected to the aryl unit by an alkyne connector, which is known to promote strong, directional electronic coupling. In particular, the results show that in a dyad formed by a $\text{Ru}(\text{bpy})_3^{2+}$ [190, 191] fragment linked by the ethynyl bridge to pyrene, the lifetime of the MLCT triplet state increases 40-fold with respect to that of the parent complex (i.e., from 1.4 μs to 40 μs) [191]. The prolongation of the triplet lifetime is consistent with MLCT being in equilibrium with the triplet associated to the pyrene unit which is situated at slightly lower energy and reflects both the low percentage of the MLCT triplet present in the equilibrium mixture and the relatively long inherent lifetime of the pyrene units [191].

The same study [191] shows that the extremely short lifetime ($\tau < 1$ ns) of the chromophore $\text{Ru}(\text{tpy})_2^{2+}$ can be effectively enhanced by attaching an ethynylated pyrene. In the related dyad containing pyrene and $\text{Ru}(\text{tpy})_2^{2+}$, the lifetime of the $\text{Ru}(\text{tpy})$ fragment ($\tau = 570$ ns) greatly exceeds that recorded for any other ethynylated mononuclear $\text{Ru}(\text{tpy})$ fragment ($\tau = 50$ ns) [49]. In this case, prolongation of the MLCT triplet lifetime cannot be explained only in terms of reversible triplet energy transfer, since the pyrene triplet state energy is slightly higher than the MLCT of the metal complex. The authors attribute the extra stabilization of the MLCT to mixing between the MLCT triplet and the pyrene like $\pi-\pi^*$ triplet [191].

An analogous mechanism of reversible energy transfer is operative in a dyad where an $\text{Os}(\text{bpy})_3^{2+}$ unit is connected to an anthracene system by an ethynyl bridge: the lifetime of the $\text{Os}(\text{II})(\text{bpy})$ fragment ($\tau = 420$ ns) is almost ten times longer than that of the parent complex ($\tau = 60$ ns) [193].

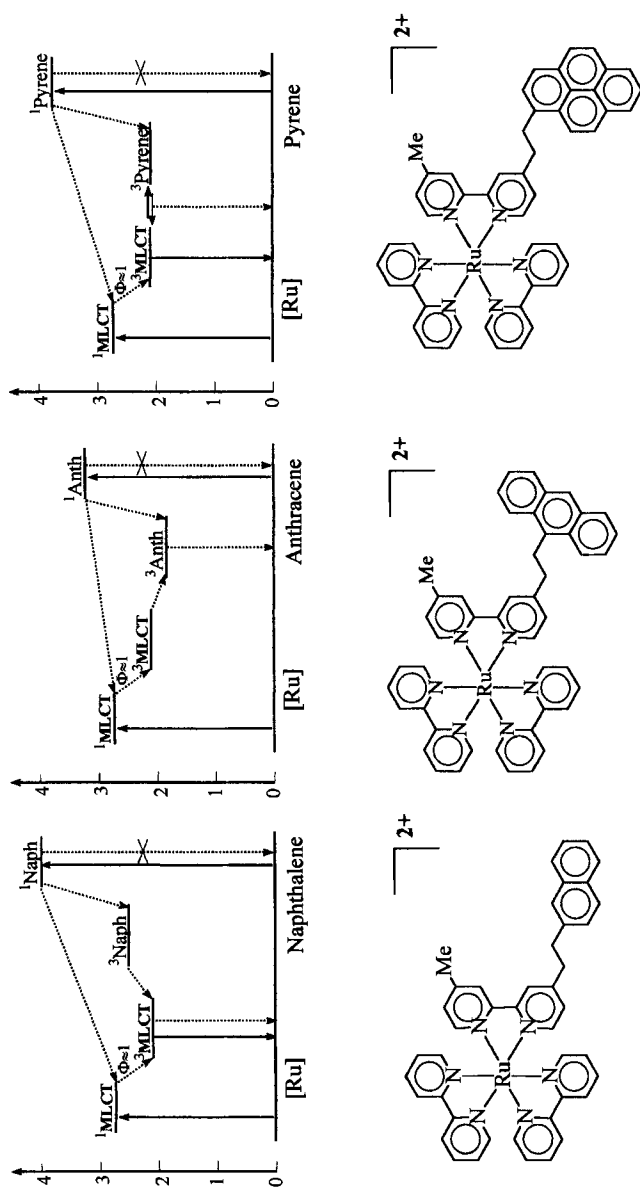
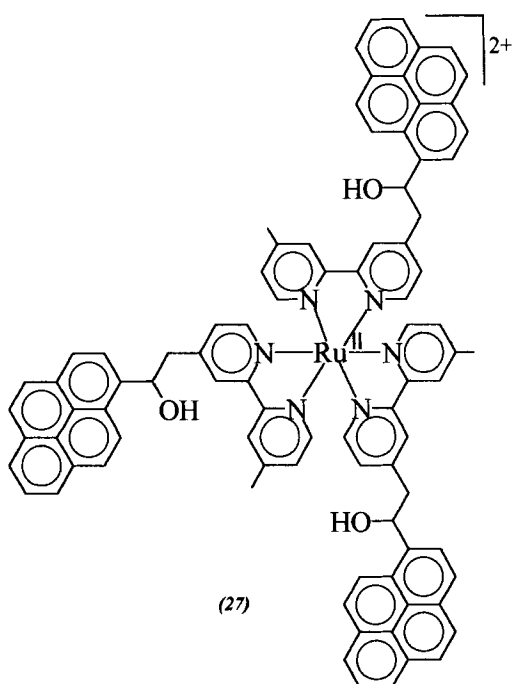


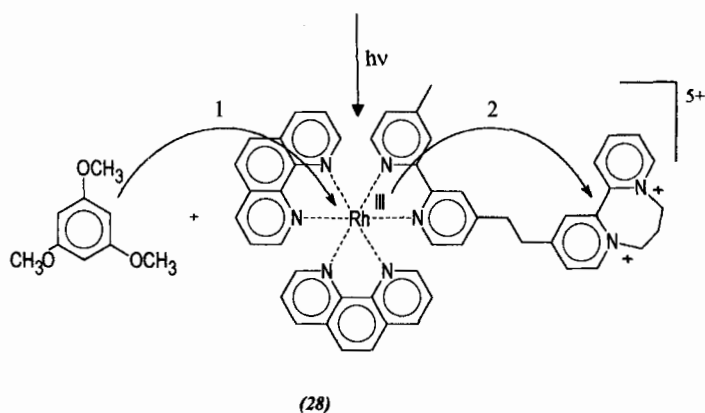
Figure 18. Schematic energy-level diagrams and photophysical processes for Ru(bpy)₃²⁺-aryl dyads.



The mechanism of reversible triplet–triplet energy transfer is used in a light-harvesting array constructed around a the $\text{Ru}(\text{bpy})_3^{2+}$ core and bearing one or three pyrenyl units in the periphery (27) [192]. UV excitation of these systems yields a strong visible MLCT-based emission, with a lifetime of 2.9 and 9.0 μs respectively for the mono- and the tris-pyrene system. The equilibrium constant between the MLCT and the pyrene triplet, and therefore the triplet lifetimes, are modulated by the fractional contribution of each individual triplet molecule involved in the equilibrium. This approach allows for a synthetic control of the luminescence lifetime by simply changing the number of pyrenyl units.

3.4.4 Photoinduced Charge Shift in Chromophore–Quencher Systems

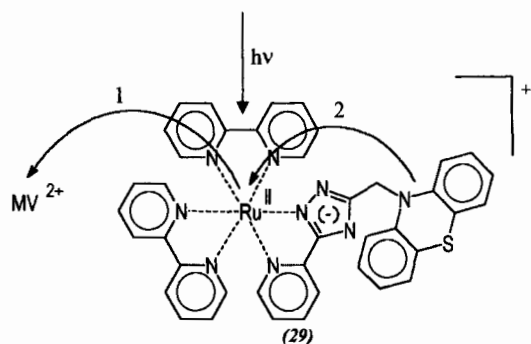
One of the available ways for investigating intramolecular electron transfer is that of inducing a charge shift by bimolecular PET (Figure 1c). The feasibility of this relies on the fact that the bimolecular event producing the thermodynamically unfavored electronic isomer of the dyad is faster than the intramolecular electron transfer process to be observed. When this requirement is met, since the back recombination reaction is a bimolecular process, relatively slow intramolecular electron transfer processes can be studied. This type of process has been extensively used for studying electron transfer in proteins [206], but has not been frequently applied to dyads. In an early study [207], the $\text{Rh}(\text{III})$ –diquat dyad (28) was

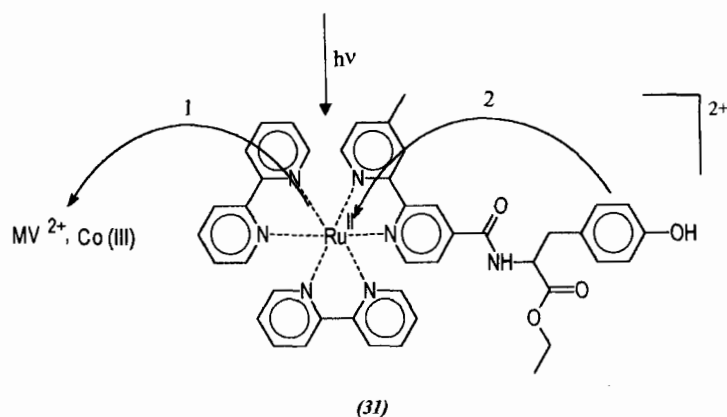
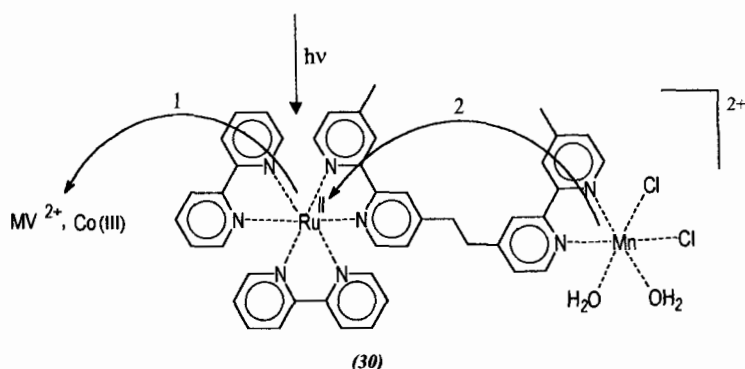


quenched reductively by trimethoxybenzene. The primary product, Rh(II)-diquat, was shown to undergo intramolecular ET to Rh(III)-diquat^{•-} with a rate constant of $3 \times 10^7 \text{ s}^{-1}$. This figure is consistent with PET rates obtained with similar bridges and driving forces, e.g., in (18).

An example of intramolecular charge shift initiated by oxidative bimolecular quenching is that of the Ru(II)-phenothiazine dyad (29) [208]. Quenching of the excited Ru(II) chromophore by methylviologen gives Ru(III)-phenothiazine as primary product. In this primary product, intramolecular ET takes place in 170 ns to yield Ru(II)-phenothiazine^{•+}.

In a series of papers [61, 209], photoinduced charge shift has been used by Hammarström and coworkers to mimic some aspects of the oxygen-evolving part of photosystem II, where the photo-oxidized chlorophyll dimer, P_{680}^+ , is reduced by electron transfer from a nearby manganese cluster, mediated by a tyrosyl group. The dyads used were of type (30) and (31), including a Ru(II) complex as photo-excitable chromophore and a Mn(II) complex or a tyrosine group as electron donors. The acceptors in the bimolecular PET step were methyl viologen or Co(III). Charge shift from the Mn(II) complex [61] or from the tyrosine [209] to the photo-oxidized



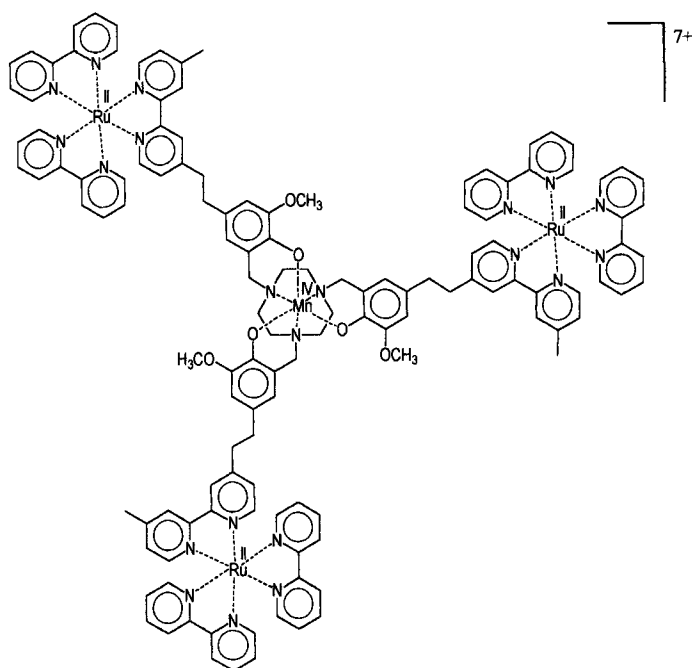


Ru(III) center was observed, with rate constants of the order of 10^5 s^{-1} . Related model systems, mimicking the interactions between the tyrosine and other residues, have also been studied [209].

Some complex model systems, incorporating a Ru(II) photoexcitable unit and both phenolate and manganese complexes, have recently been produced by Wiegardt and coworkers [115, 210]. One such model, involving a mononuclear Mn(IV) species, is the tetranuclear species (32) [115]. In the presence of methylviologen, the usual charge shift from the phenolate to the photo-oxidized Ru(III) center takes place, although the mechanism is complicated by the possibility of direct oxidative intramolecular PET. Even more complex models based on similar design, but containing a trinuclear Mn(II) species acting as the electron source for intramolecular oxidative PET, have been developed [115].

3.4.5 Multi-Step Charge Separation in Triads

In principle, the photoinduced charge separation obtained in dyads offers a potential route for the conversion of light energy into chemical energy. To that purpose,



(32)

the charge-separated products of PET should react with appropriate substrates to yield high-energy, kinetically stable products (fuels). From this viewpoint, however, dyads are of little practical use because of the occurrence of the back electron transfer reaction (Figure 1a,b). This charge recombination process is usually quite fast, whereas the reactions to be performed on the substrate are inevitably multi-electron, and thus intrinsically slow processes. The reactions involved in water splitting are given, as an example, in Eqs. 23 and 24.



A strategy to overcome this problem—largely inspired by the architecture of natural photosynthetic reaction centers—is that of going from dyads to more complex supramolecular systems in which a sequence of electron transfer steps is used to achieve charge separation. In such systems, charge recombination must take place between spatially remote sites and is thus expected to be substantially slowed down. The simplest of such system is a *triad*, as illustrated schematically in Figure 19 for two possible schemes. In Figure 19a, the two consecutive ET steps are (1) from the excited chromophore, P, to an acceptor molecular component, A, and (2) from a donor unit, D, to the oxidized chromophore. In Figure 19b, the two consecutive electron transfer steps are (1) from the excited chromophore, P, to a primary ac-

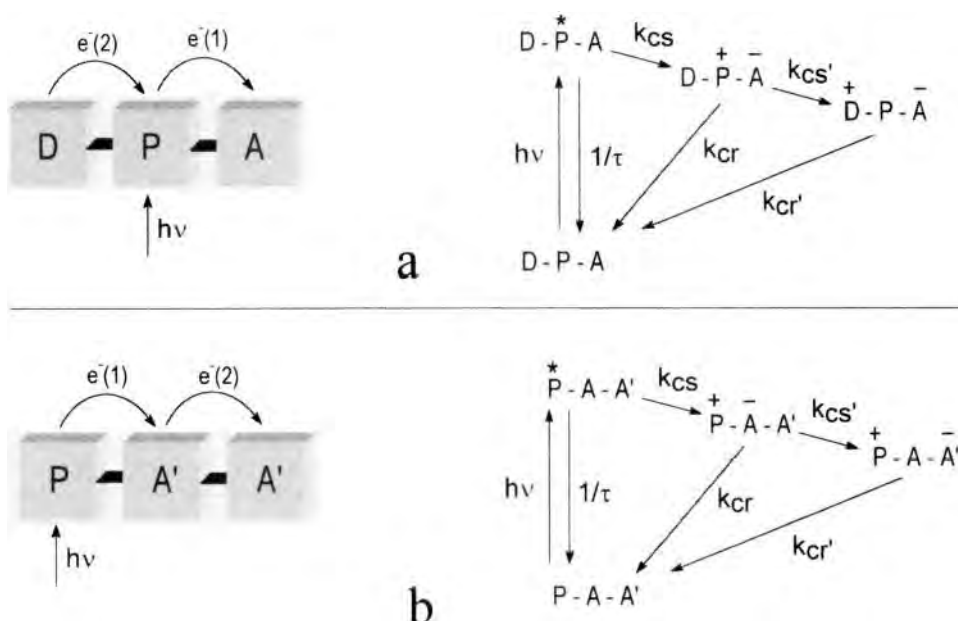


Figure 19. Two types of triads for photoinduced charge separation. Molecular components are designated as: P (chromophore); D (donor); A (acceptor); A' (secondary acceptor). Electron transfer processes are designated as: *cs* (primary PET); *cr* (primary charge recombination); *cs'* (secondary charge separation); *cr'* (final charge recombination).

ceptor, A, and (2) from the primary to a secondary acceptor unit, A'. In both cases, the yield of charge separation is given by

$$\Phi_{cs} = \frac{k_{cs}}{k_{cs} + (1/\tau)k_{cs'} + k_{cr}} \quad (25)$$

while the lifetime of the charge separated state is simply $1/k_{cr'}$. Of the two terms in Eq. 25, the first one (efficiency of quenching of the excited chromophore) is easily maximized, especially with intrinsically long-lived chromophores such as e.g., Ru(II) polypyridine complexes. In fact, the key to efficient stepwise charge separation lies in the second term of Eq. 25, i.e., in the competition between primary charge recombination, k_{cr} , and secondary ET process, $k_{cs'}$.

Several triads (as well as more complex systems, tetrads, pentads, etc.) have been successfully developed making use of organic molecular components [211–213], some of which (porphyrins, quinones, carotenoids) are reminiscent of those found in the natural systems (for detailed accounts, see Volume III, Part 2, Chapters 1 and 2). Remarkable efficiencies and lifetimes of charge separation have been reached with such systems. Their potential has been impressively demonstrated by incorporation into liposomal membranes performing the photo-driven synthesis of ATP [214].

A number of triads have also been designed and studied in which at least one of the molecular components—usually the light-absorbing chromophore—is a transition metal coordination compound. Acceptor molecular components are often viologens or quinones, while donor molecular components are most often phenothiazine units or amine units. Some representative examples are given in Figures 20 and 21. As a prototype system, let us consider that of Figure 20a, extensively studied by Meyer and coworkers [215, 216] (related systems containing cyclic 2,2'-bipyridinium units (diquat) were studied by Elliott and coworkers [217, 218]). With $X = X' = \text{CH}_3$, the system behaves as in Figure 19a, where *cs* and *cs'* are faster than 5 ns, whereas the charge-separated state recombines (*cr'*) in a time scale of 100–200 ns. A detailed study, in which all the four positional isomers (donor and acceptor groups in one *trans* and three *cis* positions) were separately investigated, yielded slightly different rates for different isomers. The yield of formation of the charge-separated $\text{PTZ}^{\bullet+}\text{-Ru(II)-MV}^{\bullet+}$ was 0.20–0.25 [215]. With $X = \text{COOH}$ and $X' = \text{CH}_3$, the slightly different energetics improves the charge separation yield by making both *cr* and *cs'* (Figure 19a) more exergonic than in the previous case. Since *cr* is in the inverted region and *cs'* in the normal one, the former process is slowed down, while the latter is accelerated [216].

The triad of Figure 20b, based on the Ru(II) bis terpyridine chromophore with intrinsic *trans* geometry, has been developed by Sauvage and coworkers [219]. The system in Figure 20c is an example of triads containing an anthraquinone group as acceptor [220, 221]. The system of Figure 20d is actually a tetrad, including two identical chromophores connected by an ethylenic bridge, one carrying a donor (PTZ) and one carrying an acceptor (of the monoquat type) [222]. The two triads of Figure 21a,b involve similar molecular components as some of the previously considered ones, but the connecting scheme is different [223, 224]. Here, the chromophore, the donor, and the acceptor units are all covalently connected to a central lysine unit. The strategy of using amide linkages for connecting molecular components to amino acids has been recently extended by Meyer to the construction of triad systems on helical proline oligomers used as a scaffold [225].

Relatively different molecular components have been used by Ziessel et al. [226] in the construction of triad (33), where the donor is the *p*-(diethylamino)-styryl group, and the acceptor is the 4-pyridyl-3,8-dimethyl-1,3,5,7,9-decapentaenyl group. A remarkably long-lived transient (4 μs) is attributed to the charge separated state.

3.5 Concluding Remarks

This review is not intended to provide an exhaustive picture of photoinduced electron (and energy) transfer in covalently linked inorganic systems. It should demonstrate, however, that this is an active and attractive field of research. Coordination compounds, because of their intrinsic combinatorial nature, offer wide possibilities in terms of tailoring spectroscopic, redox, and photophysical properties of molecular components. The continuing progress in chemical synthesis provides a variety of

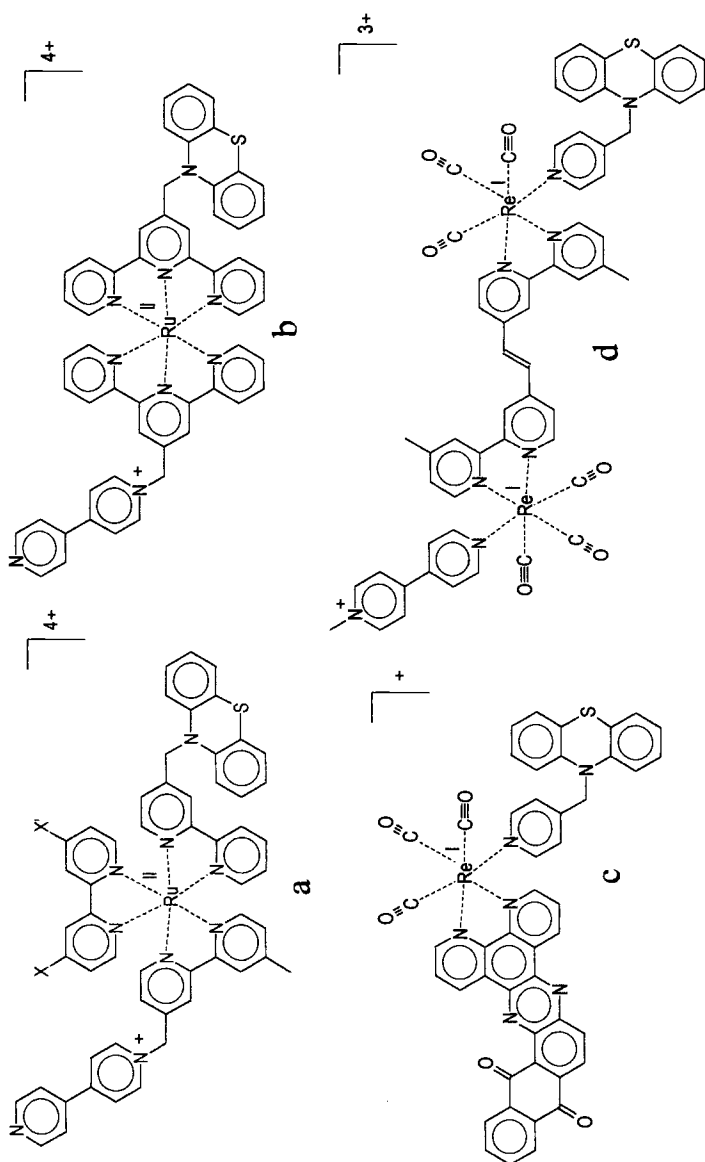


Figure 20. Various types of systems for stepwise charge separation containing inorganic chromophores and organic donor-acceptor units.

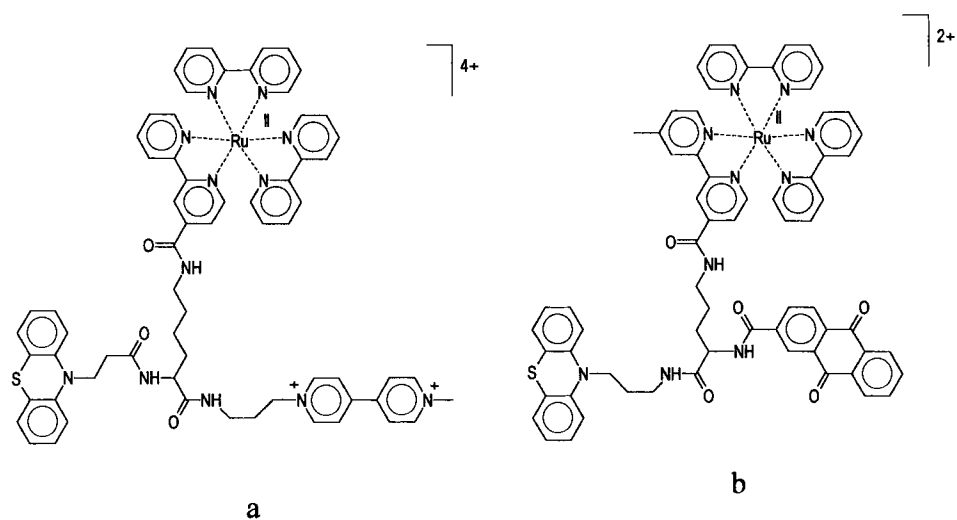
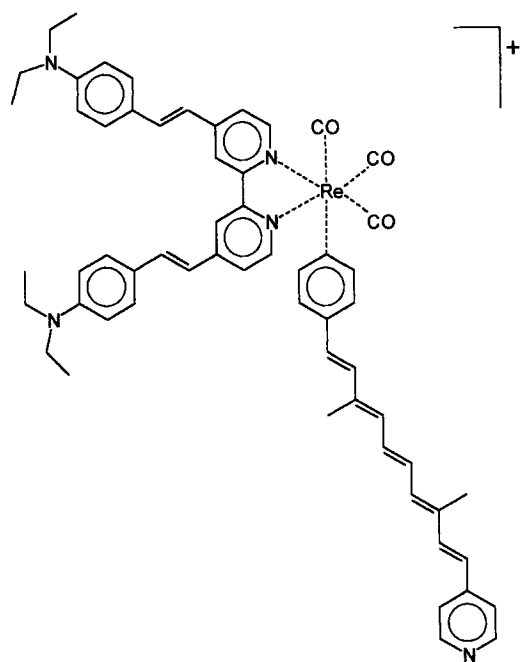


Figure 21. Two triads with inorganic chromophore and organic donor-acceptor units built around a central lysine core.



intercomponent connecting motifs and permits the rational design of supramolecular structures with the desired organization of molecular components in the dimensions of space and energy. For basic studies of electron (and energy) transfer kinetics and mechanisms, covalently linked inorganic systems may offer some advantages with respect to their organic analogues, especially in terms of easily tunable redox properties and long excited state lifetimes. In a more perspective view of supramolecular chemistry, covalently linked inorganic systems can be considered as useful tools towards the construction of devices for energy conversion, sensing, signaling, and information processing and storage at the molecular level.

Appendix

Abbreviations	Ligands	Bridges (see Table 1)
2,3-dpp		15
2,5-dpp		16
4,4'-bpy		1
5,5'-Me ₂ bpy	5,5'-dimethyl-2,2'-bipyridine	
a-bpt-b		25
AN	Acetonitrile	
b-azo-b		9
biq	2,2'-biquinoline	
bpbH ₂		32
bpbmH ₂		20
bpm		2
bpy	2,2'-bipyridine	
bpy-(CH) ₂ -catH ₂		11
bpy-(ph)n-bpy		5
bpy-(ph)n-ph'-(ph)n-bpy		6
bpy-a-bpy		7
bpy _a -bpy _b		10
bpy-An-bpy		8
bpy-cPt-bpy		35
bpy-E-A-E-bpy		39
bpy-E-naph-E-bpy		38
bpy-E-ph-E-bpy		37
bpy-etphet-bpy		4
bpy-E-tpy		50
bpym	2,2'-bipyrimidine	
bpy-rec1-bpy		33
bpy-rec2-bpy		34
bpy-tPt-bpy		36
bpzt		26
C ₃ P ₄		62
C ₄ P ₄		63

Abbreviations	Ligands	Bridges (see Table 1)
cmbpy	4-carboxy-4'-methyl-2,2'-bipyridine	
Cp	cyclopentadienyl anion	
dcb	4,4'-dicarboxy-2,2'-bipyridine	
decb	4,4'-bis(ethoxycarbonyl)-2,2'-bipyridine	
dpb		18
dpcat		46
dpb-(ph) _n -dpb		57
dpimbH ₂		21
dppene		61
dppn		31
dpq		17
dpq-6-dpq		48
dpt-bph-dpt		30
dpt-cy-dpt		28
dpt-ph-dpt		29
ecpq	4-carboxyethyl-2-(2-pyridyl)quinoline	
en	ethanediamine	
FAF		13
HAT		19
HQ		27
L ²		60
L ⁵		12
mbpy-E _n -mbpy		41
Mebpy-(CH ₂) ₂ -bpyMe		3
Me ₂ bpy	4,4'-dimethyl-2,2'-bipyridine	
Me ₂ phen	4,7-dimethyl-1,10phenanthroline	
mpzt		24
MQ	N-methyl-4,4'-bipyridinium	
nor		65
obpy-E _n -obpy		42
P3		49
p-(CH ₂) _n -p		43
PAP		14
pbim-SB-pbim		23
pbim-S _n -pbim		22
pbpy-E _n -pbpy		40
phen	1,10-phenanthroline	
phen-E-phen		44
phen-phen-phen		45
PPh ₃	triphenylphosphine	
ppy	2-phenylpyridine	
tpy		51
tpphz		47
tpy	2,2',6',2''-terpyridine	
tpy-(CH) ₂ -tpy		54
tpy-(CH ₂) ₂ -tpy		55
tpy-(ph) _n -bpyb ⁻		58
tpy-(ph) _n -tpy		52

Abbreviations	Ligands	Bridges (see Table 1)
tpy-E _n -tpy		53
tpy-ph-bco-ph-tpy		56
tpy-tp-tpy		59
ttpy	4'-p-tolyl-2,2',6',2''-terpyridine	
Val _n		64

References

1. J.-M. Lehn, *Angew. Chem. Int. Ed. Engl.* **1988**, 27, 89.
2. D. J. Cram, *Angew. Chem. Int. Ed. Engl.* **1988**, 27, 1009.
3. C. J. Pedersen, *Angew. Chem. Int. Ed. Engl.* **1988**, 27, 1021.
4. V. Balzani, F. Scandola, *Supramolecular Photochemistry*, Horwood, Chichester, UK, **1991**.
5. J.-M. Lehn, *Supramolecular Chemistry: Concepts and Perspectives*, WCH, Weinheim, **1995**.
6. D. Rehm, A. Weller, *Isr. J. Chem.* **1970**, 8, 259.
7. R. A. Marcus, *Annu. Rev. Phys. Chem.* **1964**, 15, 155.
8. N. Sutin, *Prog. Inorg. Chem.* **1983**, 30, 441.
9. R. A. Marcus, N. Sutin, *Biochim. Biophys. Acta* **1985**, 811, 265.
10. J. Jortner, *J. Chem. Phys.* **1976**, 64, 4860.
11. J. Ulstrup, *Charge Transfer Processes in Condensed Media*, Springer Verlag, Berlin, **1979**.
12. J. R. Miller, J. V. Beitz, R. K. Huddleston *J. Am. Chem. Soc.* **1984**, 106, 5057.
13. T. J. Meyer, H. Taube, in *Comprehensive Coordination Chemistry* (Eds.: S. J. Wilkinson, R. D. Gillard, and J. A. McCleverty), Pergamon Press, Oxford, **1987**, Vol. 1, p 331.
14. M. D. Newton, *Chem. Rev.* **1991**, 91, 767.
15. H. Oevering, J. W. Verhoeven, M. N. Paddon-Row, J. M. Warman, *Tetrahedron*, **1989**, 45, 4751.
16. J. Halpern, L. E. Orgel, *Disc. Faraday Soc.* **1960**, 29, 32.
17. H. M. McConnell, *J. Chem. Phys.* **1961**, 35, 508.
18. B. Mayoh, P. Day, *J. Chem. Soc. Dalton* **1974**, 846
19. J. R. Miller, J. V. Beitz, *J. Chem. Phys.* **1981**, 74, 6746.
20. D. E. Richardson, H. Taube, *J. Am. Chem. Soc.* **1983**, 105, 40.
21. F. Scandola, R. Argazzi, C. A. Bignozzi, C. Chiorboli, M. T. Indelli, M. A. Rampi, *Coord. Chem. Rev.* **1993**, 125, 283.
22. W. B. Davis, W. A. Svec, M. A. Ratner, M. R. Wasielewski, *Nature* **1998**, 396, 60.
23. G. L. Closs, J. R. Miller *Science* **1988**, 240, 440.
24. I. R. Gould, J. E. Moser, B. Armitage, S. Farid, *J. Am. Chem. Soc.* **1989**, 111, 1917.
25. G. Orlandi, S. Monti, F. Barigelletti, V. Balzani, *Chem. Phys.* **1980**, 52, 313.
26. Z. Murtaza, A. P. Zipp, L.A. World, D. Graff, W. E. Jr. Jones, W. D. Bates, T. J. Meyer, *J. Am. Chem. Soc.* **1991**, 113, 5113.
27. K. R. Naqvi, C. Steel, *Spectrosc. Lett.* **1993**, 26, 1761.
28. V. Balzani, F. Bolletta, F. Scandola, *J. Am. Chem. Soc.* **1980**, 102, 2152.
29. M. E. Sigman, G. L. Closs, *J. Phys. Chem.* **1991**, 95, 5012.
30. D. B. MacQueen, J. R. Eyler, K. S. Schanze, *J. Am. Chem. Soc.* **1992**, 114, 1897.
31. A. A. Lamola, in *Energy Transfer and Organic Photochemistry* (Eds: A. A. Lamola, N. J. Turro), Interscience, **1969**.
32. N. J. Turro, *Modern Molecular Photochemistry*, Benjamin, **1978**.
33. G. A. Crosby, *J. Chem. Educ.* **1983**, 60, 791.
34. F. Scandola, V. Balzani, *J. Chem. Educ.* **1983**, 60, 814.
35. G. D. Scholes, K. P. Ghiggino, A. M. Oliver, M. N. Paddon-Row, *J. Phys. Chem.* **1993**, 97, 11871.
36. H. Oevering, J. W. Verhoeven, M. N. Paddon-Row, E. Cotsaris, N.S. Hush, *Chem. Phys. Lett.* **1988**, 143, 488.

37. G. L. Closs, P. Piotrowiak, J. M. McInnis, G. R. Fleming, *J. Am. Chem. Soc.* **1988**, *110*, 2652.
38. G. L. Closs, M. D. Johnson, J. R. Miller, P. Piotrowiak, *J. Am. Chem. Soc.* **1989**, *111*, 3751.
39. A. Juris, V. Balzani, F. Barigelletti, S. Campagna, P. Belser, A. Von Zelewsky, *Coord. Chem. Rev.* **1988**, *84*, 85.
40. K. Kalyanasundaram, *Photochemistry of Polypyridine and Porphyrin Complexes*, Academic: New York, **1992**.
41. G. A. Heath, L. J. Yellowlees, P. S. Braterman, *Chem. Phys. Lett.* **1982**, *92*, 646.
42. Y. J. Chang, X. Xu, T. Yabe, S. C. Yu, D. R. Anderson, L. K. Orman, J. B. Hopkins, *J. Phys. Chem.* **1990**, *94*, 729.
43. F. Scandola, M. T. Indelli, C. Chiorboli, C. A. Bignozzi, *Top. Curr. Chem.* **1990**, *158*, 73.
44. V. Balzani, F. Scandola, *Supramolecular Photochemistry*, Horwood, Chichester, UK, **1991**, Chapters 5 and 6.
45. F. Scandola, C. A. Bignozzi, M. T. Indelli, in *Photosensitization and Photocatalysis Using Inorganic and Organometallic Compounds*, (Eds.: K. Kalyanasundaram, M. Grätzel) Kluwer, Dordrecht, **1993**, p 161.
46. J.-P. Sauvage, J.-P. Collin, J.-C. Chambron, S. Guillerez, C. Coudret, V. Balzani, F. Barigelletti, L. De Cola, L. Flamigni, *Chem. Rev.* **1994**, *94*, 993.
47. V. Balzani, A. Juris, M. Venturi, S. Campagna, S. Serroni, *Chem. Rev.* **1996**, *96*, 759.
48. J. F. Endicott, M. A. Watzky, X. Song, T. Buranda, *Coord. Chem. Rev.* **1997**, *159*, 295.
49. R. Ziessel, M. Hissler, A. El-ghayoury, A. Harriman, *Coord. Chem. Rev.* **1998**, *177*, 1251.
50. L. De Cola, P. Belser, *Coord. Chem. Rev.* **1998**, *177*, 301.
51. F. Barigelletti, L. Flamigni, *Chem. Soc. Rev.* **2000**, *29*, 0000.
52. C. Wang, B. K. Mohney, R. D. Williams, V. Petrov, J. T. Hupp, G. C. Walker, *J. Am. Chem. Soc.* **1998**, *120*, 5848.
53. J. R. Schoonover, K. C. Gordon, R. Argazzi, H. H. Woodruff, K. A. Peterson, C. A. Bignozzi, R. B. Dyer, T. J. Meyer, *J. Am. Chem. Soc.* **1993**, *115*, 10996.
54. D. A. V. Kliner, K. Tominaga, G. C. Walker P. F. Barbara, *J. Am. Chem. Soc.* **1992**, *114*, 8323.
55. V. Balzani, S. Campagna, G. Denti, A. Juris, S. Serroni, M. Venturi, *Acc. Chem. Res.* **1998**, *31*, 26.
56. B. W. Pfennig, J. K. Goertz, D. W. Wolff, J. L. Cohen, *Inorg. Chem.* **1998**, *37*, 2608.
57. S. E. Ronco, D. W. Thompson, S. L. Gahan, J. D. Petersen, *Inorg. Chem.* **1998**, *37*, 2020.
58. G. N. A. Nallas, S. W. Jones, K. J. Brewer, *Inorg. Chem.* **1996**, *35*, 6974.
59. V. W. W. Yam, V. W. M. Lee, K. K. Cheung, *Organometallics* **1997**, *16*, 2833.
60. C. J. Kleverlaan, M. T. Indelli, C. A. Bignozzi, L. Pavanin, F. Scandola, G. Hasselman, G. J. Meyer, *J. Am. Chem. Soc.* **2000**, *122*, 2840.
61. L. Sun, H. Berglund, R. Davydov, T. Norrby, L. Hammarstrom, P. Korall, A. Borje, C. Philouze, K. Berg, A. Tran, M. Andersson, G. Stenhagen, J. Martensson, M. Almgren, S. Styring, B. Akermark, *J. Am. Chem. Soc.* **1997**, *119*, 6996.
62. J. R. Shaw, G. S. Sadler, W. F. Wacholtz, C. K. Ryu, R. H. Schmehl, *New J. Chem.* **1996**, *20*, 749.
63. M. T. Indelli, R. H. Schmehl, L. De Cola, F. Scandola, unpublished results.
64. Y. Y. Liang, A. I. Baba, W. Y. Kim, S. J. Atherton, R. H. Schmehl, *J. Phys. Chem.* **1996**, *100*, 18408.
65. B. Schlicke, P. Belser, L. DeCola, E. Sabbioni, V. Balzani, *J. Am. Chem. Soc.* **1999**, *121*, 4207.
66. M. Frank, M. Nieger, F. Vvgtle, P. Belser, A. vonZelewsky, L. DeCola, V. Balzani, F. Barigelletti, L. Flamigni, *Inorg. Chim. Acta* **1996**, *242*, 281.
67. P. Belser, R. Dux, M. Baak, L. DeCola, V. Balzani, *Angew. Chem., Int. Ed. Engl.* **1995**, *34*, 595.
68. J. Otsuki, M. Tsujino, T. Iizaki, K. Araki, M. Seno, K. Takatera, T. Watanabe, *J. Am. Chem. Soc.* **1997**, *119*, 7895.
69. D. A. Bardwell, F. Barigelletti, R. L. Cleary, L. Flamigni, M. Guardigli, J. C. Jeffery, M. D. Ward, *Inorg. Chem.* **1995**, *34*, 2438.
70. J. R. Schoonover, A. P. Shreve, R. B. Dyer, R. L. Cleary, M. D. Ward, C. A. Bignozzi, *Inorg. Chem.* **1998**, *37*, 2598.
71. R. L. Cleary, K. J. Byrom, D. A. Bardwell, M. D. Ward, G. Calogero, N. Armaroli, L. Flamigni, F. Barigelletti, *Inorg. Chem.* **1997**, *36*, 2601.
72. V. Balzani, D. A. Bardwell, F. Barigelletti, R. L. Cleary, M. Guardigli, J. C. Jeffery, T. Sovrani, M. D. Ward, *J. Chem. Soc. Dalton Trans.* **1995**, 3601.

73. A. M. Barthram, M. D. Ward, A. Gessi, N. Armaroli, L. Flamigni, F. Barigelletti, *New J. Chem.* **1998**, 22, 913.
74. A. D. Shukla, B. Whittle, H. C. Bajaj, A. Das, M. D. Ward, *Inorg. Chim. Acta* **1999**, 285, 89.
75. N. C. Fletcher, M. D. Ward, S. Encinas, N. Armaroli, L. Flamigni, F. Barigelletti, *Chem. Commun.* **1999**, 2089.
76. L. DeCola, V. Balzani, F. Barigelletti, L. Flamigni, P. Belser, S. Bernhard, *Rec. Trav. Chim. Pays-Bas* **1995**, 114, 534.
77. V. Balzani, F. Barigelletti, P. Belser, S. Bernhard, L. DeCola, L. Flamigni, *J. Phys. Chem.* **1996**, 100, 16786.
78. P. Belser, S. Bernhard, C. Blum, A. Beyeler, L. DeCola, V. Balzani, *Coord. Chem. Rev.* **1999**, 192, 155.
79. D. W. Thompson, A. W. Wallace, V. Swayambunathan, J. F. Endicott, J. D. Petersen, S. E. Ronco, J.-S. Hsiao, J. R. Schoonover, *J. Phys. Chem. A* **1997**, 101, 8152.
80. Y.-Y. Ng, S.-M. Peng, C. M. Che, *New J. Chem.* **1996**, 20, 781.
81. E. Brauns, S. W. Jones, J. A. Clark, S. M. Molnar, Y. Kawanishi, K.Y. Brewer, *Inorg. Chem.* **1997**, 36, 2861.
82. S. Serroni, A. Juris, M. Venturi, S. Campagna, I. Resino Resino, G. Denti, A. Credi, V. Balzani, *J. Mater. Chem.* **1997**, 7, 1227.
83. G. N. A. Nallas, K. J. Brewer, *Inorg. Chim. Acta* **1996**, 253, 7.
84. M. M. Richter, G. E. Jensen, K. J. Brewer, *Inorg. Chim. Acta* **1995**, 230, 35.
85. M. Milkevitch, E. Brauns, K. J. Brewer, *Chem.* **1996**, 35, 1737.
86. I. Ortmans, P. Didier, A. Kirsch-De Mesmaeker, *Inorg. Chem.* **1995**, 34, 3695.
87. A. Yoshimura, K. Nozaki, N. Ikeda, T. Ohno, *J. Phys. Chem.* **1996**, 100, 1630.
88. A. Yoshimura, K. Nozaki, N. Ikeda, T. Ohno, *Bull. Chem. Soc. Jpn.* **1996**, 69, 2791.
89. R. Nozaki, N. Ikeda, T. Ohno, *New J. Chem.* **1996**, 20, 739.
90. B. Gholamkhash, K. Nozaki, T. Ohno, *J. Phys. Chem. B* **1997**, 101, 9010.
91. R. Hage, H. E. B. Lempers, J. G. Haasnoot, J. Reedijk, F. M. Weldon, J. G. Vos, *Inorg. Chem.* **1997**, 36, 3139.
92. S. Serroni, S. Campagna, G. Denti, T. E. Keyes, J.G. Vos, *Inorg. Chem.* **1996**, 35, 4513.
93. L. DeCola, F. Barigelletti, V. Balzani, R. Hage, J. G. Haasnoot, J. Reedijk, J. G. Vos, *Chem. Phys. Lett.* **1991**, 178, 491.
94. H. P. Hughes, J. G. Vos, *Inorg. Chem.* **1995**, 34, 4001.
95. C. G. Coates, T. E. Keyes, H. P. Hughes, P. M. Jajaweera, J. J. McGarvey, J. G. Vos, *J. Phys. Chem. A* **1998**, 102, 5013.
96. T. E. Keyes, R. J. Foster, P. M. Jayaweera, C. G. Coates, J. J. McGarvey, J. G. Vos, *Inorg. Chem.* **1998**, 37, 5925.
97. G. Giuffrida, G. Calogero, V. Ricevuto, S. Campagna, *Inorg. Chem.* **1995**, 34, 1957.
98. G. Giuffrida, G. Calogero, G. Guglielmo, V. Ricevuto, S. Campagna, *Inorg. Chim. Acta* **1996**, 251, 255.
99. S. Campagna, S. Serroni, A. Juris, M. Venturi, V. Balzani, *New J. Chem.* **1996**, 20, 773.
100. E. Muller, Md.K. Nazeeruddin, M. Gratzel, K. Kalyanasundaram, J. C. Promé, *New J. Chem.* **1996**, 20, 759.
101. P. D. Beer, S. W. Dent, G. S. Hobbs, T. J. Wear, *Chem. Commun.* **1997**, 99.
102. P. D. Beer, F. Szemes, V. Balzani, C. M. Salà, M. G. B. Drew, S. W. Dent, M. Maestri, *J. Am. Chem. Soc.* **1997**, 119, 11864.
103. V. Grosshenny, A. Harriman, M. Hissler, R. Ziessel, *J. Chem. Soc. Faraday Trans.* **1996**, 92, 2223.
104. A. Harriman, M. Hissler, R. Ziessel, A. DeCian, J. Fisher, *J. Chem. Soc., Dalton Trans.* **1995**, 4067.
105. V. Grosshenny, A. Harriman, M. Hissler, R. Ziessel, *Platinum Met. Rev.* **1996**, 40, 26.
106. A. Harriman, R. Ziessel, *Chem. Commun.* **1996**, 1707.
107. A. Harriman, F. Romero, R. Ziessel, A.C. Benniston, *J. Phys. Chem. A* **1999**, 103, 5399.
108. N. Komatsuzaki, Y. Himeda, T. Hirose, H. Sugihara, K. Kasuga, *Bull. Chem. Soc. Jpn.* **1999**, 72, 725.
109. P. J. Connors Jr, D. Tzalis, A. L. Dunnick, Y. Tor, *Inorg. Chem.* **1998**, 37, 1121.
110. W. Paw, W. B. Connick, R. Eisenberg, *Inorg. Chem.* **1998**, 37, 3919.

111. C. Chiorboli, C. A. Bignozzi, F. Scandola, E. Ishow, A. Gourdon, J-P. Launay, *Inorg. Chem.* **1999**, 38, 2402.
112. S. Campagna, S. Serroni, S. Bodige, F. M. MacDonnell, *Inorg. Chem.* **1999**, 38, 692.
113. E. Ishow, A. Gourdon, J-P. Launay, P. Lecante, M. Verelst, C. Chiorboli, F. Scandola, C. A. Bignozzi, *Inorg. Chem.* **1998**, 37, 3603.
114. P. T. Gulyas, T. A. Smith, M. N. Paddon-Row, *J. Chem. Soc. Dalton Trans.* **1999**, 1325.
115. D. Burdinski, K. Wieghardt, S. Steenken, *J. Am. Chem. Soc.* **1999**, 121, 10781.
116. V. Grossshenny, A. Harriman, J-P. Gisselbrecht, R. Ziessel, *J. Am. Chem. Soc.* **1996**, 118, 10315.
117. J-D. Lee, L. M. Vrana, E. R. Bullock, K. J. Brewer, *Inorg. Chem.* **1998**, 37, 3575.
118. L. M. Vogler, K. J. Brewer, *Inorg. Chem.* **1996**, 35, 818.
119. L. M. Vogler, S. W. Jones, G. E. Jensen, R.G. Brewer, K.J. Brewer, *Inorg. Chim. Acta* **1996**, 250, 155.
120. P. Bonhote, A. Lecas, E. Amouyal, *Chem. Commun.* **1998**, 885.
121. M. T. Indelli, F. Scandola, J-P. Collin, J-P.; Sauvage, A. Sour, *Inorg. Chem.* **1996**, 35, 303.
122. M. T. Indelli, F. Scandola, L. Flamigni, J-P. Collin, J-P.; Sauvage, A. Sour, *Inorg. Chem.* **1997**, 36, 4247.
123. J-P. Collin, P. Gavina, V. Hietz, J-P. Sauvage, *Eur. J. Inorg. Chem.* **1998**, 1.
124. F. Barigelletti, L. Flamigni, J-P. Collin, J-P.; Sauvage, *Chem. Commun.* **1997**, 333.
125. V. Grossshenny, A. Harriman, R. Ziessel, *Angew. Chem. Int. Ed. Engl.* **1995**, 34, 2705.
126. A. Benniston, A. Harriman, R. Ziessel, *New J. Chem.* **1997**, 21, 405.
127. V. Grossshenny, A. Harriman, R. Ziessel, *Angew. Chem. Int. Ed. Engl.* **1995**, 34, 1100.
128. L. Hammarstrom, F. Barigelletti, L. Flamigni, N. Armaroli, A. Sour, J-P. Collin, J-P. Sauvage, *J. Am. Chem. Soc.* **1996**, 118, 11972.
129. F. Barigelletti, L. Flamigni, V. Balzani, J-P. Collin, J-P. Sauvage, A. Sour, *New J. Chem.* **1995**, 19, 255.
130. F. Barigelletti, L. Flamigni, M. Guardigli, A. Juris, M. Beley, S. Chodorowski-Kimmes, J-P. Collin, J-P. Sauvage, *Inorg. Chem.* **1996**, 35, 136.
131. E. C. Constable, A. M. W. Cargill Thompson, *New J. Chem.* **1996**, 20, 65.
132. E. C. Constable, C. E. Hosecroft, E. S. Schofield, S. Encinas, N. Armaroli, F. Barigelletti, L. Flamigni, E. Figgermeier, J. G. Vos, *Chem. Commun.* **1999**, 869.
133. K. L. Bushell, S. M. Couchman, J. C. Jeffery, L. H. Rees, M. D. Ward, *J. Chem. Soc. Dalton Trans.* **1998**, 3397.
134. S. M. Woessner, J. B. Helms, K. M. Lantzky, B. P. Sullivan, *Inorg. Chem.* **1999**, 38, 4378.
135. B. Hong, S. R. Woodcock, S. K. Saito, J. V. Ortega, *J. Chem. Soc. Dalton Trans.* **1998**, 2615.
136. J. V. Ortega, B. Hong, S. Ghosal, J. C. Hemminger, B. Breedlove, C. P. Kubiak, *Inorg. Chem.* **1999**, 38, 5102.
137. S. R. L. Fernando, G. V. Kozlov, M. Y. Ogawa, *Inorg. Chem.* **1998**, 37, 1900.
138. A. C. Schultz, L. S. Kelso, M. R. Johnston, R. N. Warrenner, F. R. Keene, *Inorg. Chem.* **1999**, 38, 4906.
139. K. S. Schanze, K. A. Walters, in *Organic and Inorganic Photochemistry*, (Eds.: V. Ramamurthy, K. S. Schanze) Marcel Dekker, New York, **1998**, p 75.
140. E. J. Lee, M. S. Wrighton, *J. Am. Chem. Soc.* **1991**, 113, 8562.
141. U. Siemeling, U. Vorfeld, B. Neumann, H.-G. Stammer, P. Zanello, F. Fabrizi de Biani, *Eur. J. Inorg. Chem.* **1999**, 1.
142. A. Kettner, U. Siemeling, M. A. Rampi, F. Scandola, unpublished results.
143. A. C. Benniston, V. Goulle, A. Harriman, J.-M. Lehn, B. Marczinke, *J. Phys. Chem.* **1994**, 98, 7798.
144. S. Choua, A. Kirsch-De Mesmaeker, L. Jacquet, C. Marzin, N. Chabert, *J. Photochem. Photobiol. A: Chemistry*, **1996**, 99, 127.
145. G. Y. Zheng, D. P. Rillema, J. H. Reibenspies, *Inorg. Chem.* **1999**, 38, 794.
146. K. Hutchinson, J. C. Morris, T. A. Nile, J. L. Walsh, D. W. Thompson, J. Petersen, J. R. Schoonover, *Inorg. Chem.* **1999**, 38, 2516.
147. W. C. Hung, C. D. Ho, C. P. Liu, Y. P. Lee, *J. Phys. Chem.* **1996**, 100, 3927.
148. F. Paolucci, M. Maccaccio, S. Roffia, G. Orlandi, F. Zerbetto, M. Prato, M. Maggini, G. Scorrano, *J. Am. Chem. Soc.* **1995**, 117, 6572.
149. N. Martin, L. Sanchez, B. Illescas, I. Pérez, *Chem. Rev.* **1998**, 98, 2527.

150. F. Diederich, M. Gómez-López, *Chem. Soc. Rev.* **1999**, 29, 263.
151. M. Maggini, A. Donò, G. Scorrano, M. Prato, *J. Chem. Soc. Chem. Commun.* **1995**, 845.
152. N. S. Sariciftci, F. Wudl, A. J. Heeger, M. Maggini, G. Scorrano, M. Prato, J. Bourassa, P. C. Ford, *Chem. Phys. Lett.* **1995**, 247, 210.
153. M. Maggini, D. M. Guldi, S. Mondini, G. Scorrano, F. Paolucci, P. Ceroni, S. Roffia, *Chem. Eur. J.* **1998**, 4, 1992.
154. A. Polese, S. Mondini, A. Bianco, C. Toniolo, G. Scorrano, D. M. Guldi, M. Maggini, *J. Am. Chem. Soc.* **1999**, 121, 3446.
155. R. Grigg, J. M. Holmes, S. K. Jones, W. D. J. A. Norbert, *J. Chem. Soc. Chem. Commun.* **1994**, 185.
156. A. P. de Silva, H. Q. N. Guaratne, T. Gunnlaugsson, A. J. M. Huxley, C. P. McCoy, J. T. Rademacher, T. E. Rice, *Chem. Rev.* **1997**, 97, 1515.
157. K.-H. Wong, M. C.-W. Chan, C.-M. Che, *Chem. Eur. J.* **1999**, 5, 2845.
158. Y. Wang, K. S. Schanze, *J. Phys. Chem.* **1996**, 100, 5408.
159. L. A. Lucia, D. G. Whitten, K. S. Schanze, *J. Am. Chem. Soc.* **1996**, 118, 3057.
160. C. M. Partigianoni, S. Chodorowski-Kimmes, J. A. Treadway, D. Striplin, S. A. Trammell, T. J. Meyer, *Inorg. Chem.* **1999**, 38, 1193.
161. C.-Y. Duan, Z.-L. Lu, X.-Z. You, Z.-Y. Zhou, T. C. K. Mak, Q. Luo, J.-Y. Zhou, *Polyhedron*, **1998**, 17, 4131.
162. P. Chen, T. D. Westmoreland, E. Danielson, K. S. Schanze, D. Anthon, P. E. Neveux, T. J. Meyer, *Inorg. Chem.* **1987**, 26, 1116.
163. P. Chen, R. Duesing, G. Tapolsky, T. J. Meyer, *J. Am. Chem. Soc.* **1989**, 111, 8305.
164. R. J. Shaver, M. W. Perkovic, D. P. Rillema, C. Woods, *Inorg. Chem.* **1995**, 34, 5449.
165. C. S. Christ Jr., J. Yu, X. Zhao, G. T. R. Palmore, M. S. Wrighton, *Inorg. Chem.* **1992**, 31, 4439.
166. R. Argazzi, C. A. Bignozzi, T. A. Heimer, F. N. Castellano, G. J. Meyer, *J. Am. Chem. Soc.* **1995**, 117, 11815.
167. B. W. Pfenning, P. Chen, T. J. Meyer, *Inorg. Chem.* **1996**, 35, 2898.
168. L. F. Cooley, C. E. L. Headford, C. M. Elliott, D. F. Kelley, *J. Am. Chem. Soc.* **1988**, 112, 6673.
169. C. K. Ryu, R. Wang, R. H. Schmehl, S. Ferrere, M. Ludwikow, J. W. Merkert, C. E. L. Headford, C. M. Elliott, *J. Am. Chem. Soc.* **1992**, 114, 430.
170. E. H. Yonemoto, G. B. Saupe, R. H. Schmehl, S. H. Hubig, R. H. Riley, B. L. Iverson, T. E. Mallouk, *J. Am. Chem. Soc.* **1994**, 116, 4786.
171. E. H. Yonemoto, R. H. Riley, Y. I. Kim, S. J. Atherton, R. H. Schmehl, T. E. Mallouk, *J. Am. Chem. Soc.* **1992**, 114, 8081.
172. L. A. Kelly, M. A. J. Rodgers, *J. Phys. Chem.* **1995**, 99, 13132.
173. P. R. Ashton, R. Ballardini, V. Balzani, E. C. Constable, A. Credi, O. Kocian, S. J. Langford, J. A. Preece, L. Prodi, E. R. Schofield, N. Spencer, J. F. Stoddardt, S. Wenger, *Chem. Eur. J.* **1998**, 4, 2413.
174. M. Ruthkosky, C. A. Kelly, M. C. Zaros, G. J. Meyer, *J. Am. Chem. Soc.* **1997**, 119, 12004.
175. S. H. Bossmann, M. F. Ottaviani, D. van Loyen, H. Dürr, C. Turro, *Chem. Commun.* **1999**, 2487.
176. M. D. Hossain, M. Haga, H. Monjushiro, B. Gholamkhash, K. Nozaki, T. Ohno, *Chem. Lett.* **1997**, 537.
177. D. W. Dixon, N. B. Thornton, V. Steullet, T. Netzel, *Inorg. Chem.* **1999**, 38, 5526.
178. V. Goulle, A. Harriman, J.-M. Lehn, *J. Chem. Soc. Chem. Commun.* **1993**, 1034.
179. S. Arounaguirri, B. G. Maiya, *Inorg. Chem.* **1999**, 38, 842.
180. C. A. Berg-Brennan, D. I. Yoon, R. V. Slone, A. P. Kazala, J. T. Hupp, *Inorg. Chem.* **1996**, 35, 2032.
181. D. S. Tyson, F. N. Castellano, *Inorg. Chem.* **1999**, 38, 4382.
182. D. S. Tyson, I. Gryczynski, F. N. Castellano, *J. Phys. Chem. A* **2000**, 104, 0000.
183. M. T. Indelli, C. A. Bignozzi, A. Harriman, J. R. Schoonover, F. Scandola, *J. Am. Chem. Soc.* **1994**, 116, 3768.
184. M. D. Johnson, J. R. Miller, N. S. Green, G. L. Closs, *J. Phys. Chem.* **1989**, 93, 1173.
185. A. D. Joran, B. A. Leland, P. M. Felker, A. H. Zewail, J. J. Hopfield, P. D. Dervan, *Nature* **1987**, 327, 508.
186. A. H. Clayton, K. P. Ghiggino, G. J. Wilson, P. J. Keyte, M. N. Paddon-Row, *Chem. Phys. Lett.* **1992**, 195, 249.

187. A. Helms, D. Heiler, G. McLendon, *J. Am. Chem. Soc.* **1992**, *114*, 6227.
188. A. Helms, D. Heiler, G. McLendon, *J. Am. Chem. Soc.* **1991**, *113*, 4325.
189. J. N. Onuchic, D. N. Beratan, *J. Am. Chem. Soc.* **1987**, *109*, 6771.
190. A. Harriman, M. Hissler, A. Khatyr, R. Ziessel, *Chem. Commun.* **1999**, 735.
191. A. Harriman, M. Hissler, A. Khatyr, R. Ziessel, *Chem. Eur. J.* **1999**, *11*, 336.
192. D. S. Tyson, F. N. Castellano, *J. Phys. Chem. A* **1999**, *103*, 10955.
193. A. El-ghayoury, A. Harriman, R. Ziessel, *Chem. Commun.* **1999**, 2027.
194. S. Serroni, S. Campagna, R. P. Nascone, G. S. Hanan, J. E. Davidson, J. M. Lehn, *Chem. Eur. J.* **1999**, *5*, 3523.
195. G. J. Wilson, A. Laukinokis, W. H. F. Sasse, W. H. Mau, *J. Phys. Chem.* **1998**, *102*, 5150.
196. G. J. Wilson, A. Laukinokis, W. H. F. Sasse, W. H. Mau, *J. Phys. Chem.* **1997**, *101*, 4860.
197. A. Beyeler, P. Belsler, L. De Cola, *Angew. Chem. Int. Engl.* **1997**, *36*, 2779.
198. G. J. Wilson, W. H. F. Sasse, W. H. Mau, *Chem. Phys. Lett.* **1996**, *250*, 583.
199. C. Weinheimer, Y. Choi, T. Caldwell, P. Gresham, J. Olmsted III, *J. Photochem. Photobiol. A* **1994**, *78*, 119.
200. S. Boyde, G. P. Strouse, W. E. Jones Jr, T. J. Meyer, *J. Am. Chem. Soc.* **1989**, *111*, 7448.
201. J. A. Simon, S. L. Curry, R. H. Schmehl, T. R. Schatz, P. Piotrowiak, X. Jin, R. P. Thummel, *J. Am. Chem. Soc.* **1997**, *119*, 11012.
202. N. B. Thornton, K. S. Schanze, *New J. Chem.* **1996**, *20*, 791.
203. Z. Murtaza, D. K. Graff, A. P. Zipp, L. A. Worl, W. E. Jones Jr, W. D. Bates, T. J. Meyer, *J. Phys. Chem.* **1994**, *98*, 10504.
204. W. E. Ford, M. A. J. Rodgers, *J. Phys. Chem.* **1992**, *96*, 2917.
205. Z. Murtaza, A. P. Zipp, L. A. Worl, D. K. Graff, W. E. Jones Jr., W. D. Bates, T. J. Meyer *J. Am. Chem. Soc.* **1991**, *113*, 5113.
206. H. B. Gray, J. R. Winkler, *Annu. Rev. Biochem.* **1996**, *65*, 537.
207. M. T. Indelli, E. Polo, C. A. Bignozzi, F. Scandola, *J. Phys. Chem.* **1991**, *95*, 3889.
208. S. Fanni, T. E. Keyes, S. Compagna, J. G. Vos, *Inorg. Chem.* **1998**, *37*, 5933.
209. L. Sun, M. Burkitt, M. Tamm, M. K. Raymond, M. Abrahamson, D. LeGourri  rec, Y. Frapart, A. Magnuson, P. H. K  nez, P. Brandt, A. Tran, L. Hammarstr  m, S. Styring, B.   kermark, *J. Am. Chem. Soc.* **1999**, *121*, 6834, and references therein.
210. D. Burdinski, E. Bothe, K. Wieghardt, *Inorg. Chem.* **2000**, *39*, 105.
211. M. R. Wasielewski, *Chem. Rev.* **1992**, *92*, 435.
212. D. Gust, T. A. Moore, A. Moore, *Acc. Chem. Res.* **1993**, *26*, 198.
213. D. Kuciauskas, P. A. Liddell, S. Lin, T. E. Johnson, S. J. Weghorn, J. S. Lindsey, A. Moore, T. A. Moore, D. Gust, *J. Am. Chem. Soc.* **1999**, *121*, 8604.
214. G. Steinbergfrach, J. L. Rigaud, E. N. Durantini, A. L. Moore, D. Gust, T. A. Moore, *Nature* **1998**, *392*, 479.
215. J. A. Treadway, P. Chen, T. J. Rutherford, F. R. Keene, T. J. Meyer, *J. Phys. Chem. A* **1997**, *101*, 6824.
216. K. A. Maxwell, M. Sykora, J. M. DeSimone, T. J. Meyer, *Inorg. Chem.* **2000**, *39*, 71.
217. S. L. Larson, C. M. Elliott, D. F. Kelley, *J. Phys. Chem.* **1995**, *99*, 6530, and references therein.
218. T. Klumpp, M. Linsenmann, S. L. Larson, B. R. Limoges, D. B  r  sner, E. B. Krissinel, C. M. Elliott, U. E. Steiner, *J. Am. Chem. Soc.* **1999**, *121*, 1076.
219. J.-P. Collin, S. Guillerez, J.-P. Sauvage, F. Barigelletti, L. De Cola, L. Flamigni, V. Balzani, *Inorg. Chem.* **1991**, *30*, 4230.
220. K. A. Opperman, S. L. Mcklenburg, T. J. Meyer, *Inorg. Chem.* **1994**, *33*, 5292.
221. R. L  pez, A. M. Leiva, F. Zuloaga, B. Loeb, E. Norambuena, K. M. Omberg, J. R. Schoonover, D. Striplin, M. Devenney, T. J. Meyer, *Inorg. Chem.* **1999**, *38*, 2924.
222. G. F. Strouse, J. R. Schoonover, R. Duesing, T. J. Meyer, *Inorg. Chem.* **1995**, *34*, 2725.
223. S. L. Mecklenburg, B. M. Peek, J. R. Schoonover, D. J. McCafferty, C. J. Wall, B. W. Erickson, T. J. Meyer, *J. Am. Chem. Soc.* **1993**, *115*, 5479.
224. S. L. Mecklenburg, D. J. McCafferty, J. R. Schoonover, B. M. Peek, B. W. Erickson, T. J. Meyer, *Inorg. Chem.* **1994**, *33*, 2974.
225. C. A. Slate, D. R. Striplin, J. A. Moss, P. Chen, B. W. Erickson, T. J. Meyer, *J. Am. Chem. Soc.* **1998**, *120*, 4885.
226. R. Ziessel, A. Juris, M. Venturi, *Inorg. Chem.* **1998**, *37*, 5061.

4 Electron Transfer in Hydrogen-Bonded Donor–Acceptor Supramolecules

Christopher J. Chang, Joshua D. K. Brown, Michelle C. Y. Chang, Erin A. Baker and Daniel G. Nocera

4.1 Introduction

Electron transfer in hydrogen-bonded systems represents a new and unique area of research, arising from the disparate fields of electron transfer and noncovalent self-assembly. To date, synthetic model systems feature electron donors (D) and acceptors (A) juxtaposed by hydrogen bond interfaces ($-\text{[H]}-$); a schematic of the basic system architecture is shown in Figure 1. Photon absorption initiates the transfer of an electron which, in its journey from donor to acceptor, must negotiate the proton and its motion within the interface. Accordingly, supramolecular systems of the type depicted in Figure 1 provide an opportunity to disentangle the various physical phenomena that govern how protons influence the rates of electron transfer.

The interplay between proton and electron transfers has far-ranging implications in biology, chemistry, and physics. For instance, proton motion coupled to electron transfer is the basic mechanism of bioenergetic conversion. Oxidases and reductases have structures optimized to gather energy along charge-separating networks to drive proton translocation. The resultant proton gradient gives rise to a trans-membrane chemical potential that provides energy for the activation of small molecules and the synthesis of complex biomolecules [1–3]. At the other end of the scientific spectrum, the coupling between proton and electron lies at the heart of the quintessential issues in electrochemistry such as hydrogen ion discharge at a platinum electrode [4, 5]. Recently, efforts in supramolecular solid-state chemistry have been directed toward the rational design of coupled electron–proton transfer systems with novel electronic or photonic properties [6–9]. From a more fundamental standpoint, electron transfer in hydrogen-bonded systems steps beyond the outer-sphere reactions treated by Marcus theory. The making and breaking of chemical bonds, occurrences not originally considered in Marcus theory, typically attend electron transfer in many oxidation-reduction reactions [10–15]. The systems depicted in Figure 1 display reactions of this type, as the overall oxidation-reduction

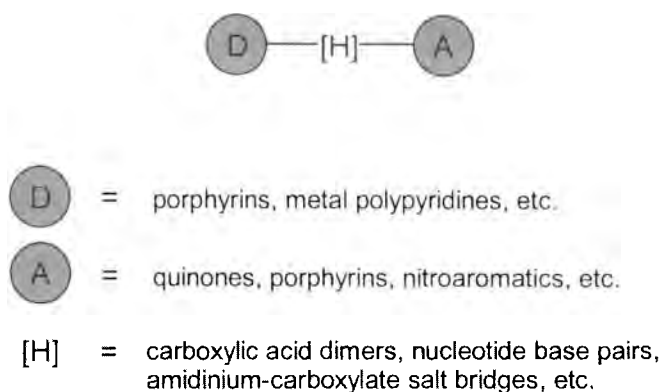
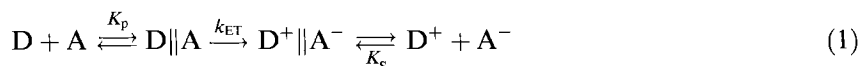


Figure 1. Schematic representation of hydrogen-bonded donor–acceptor supramolecules.

transformation may involve both electron transfer and bond-making/-breaking processes that accompany proton motion within the hydrogen bond interface.

4.2 Background

The hydrogen-bonded electron transfer construct depicted in Figure 1 finds its genesis in the original experimental systems by which electron transfer theory was validated. Through the 1970s, bimolecular electron transfers between donor (D) and acceptor (A) represented in Eq. 1, first in the form of self-exchange, and later as cross-reactions, created the basis for our understanding of electron transfer [16–18].



In these systems, the donor and acceptor diffuse together to give a precursor complex, $D\|A$, whose formation is described by the equilibrium constant K_p . Electron transfer, characterized by rate constant k_{ET} , occurs within the associated donor–acceptor pair, converting the precursor complex to successor complex $D^+\|A^-$. Subsequent separation of the oxidized donor (D^+) and reduced acceptor (A^-) from the successor complex is described by K_s . The rate of *intermolecular* electron transfer depends not only on the factors that influence k_{ET} but also on factors affecting the formation of the precursor complex [19]. More quantitatively, as described by Eq. 2, the expression for intermolecular electron transfer has the form of a consecutive reaction mechanism described by an observed rate constant (k_{obs}) consisting of rate constants for diffusion (k_d) and the activated electron transfer.

$$k_{obs} = \frac{k_{ET}k_d}{(k_{ET} + k_d)} \quad (2)$$

The diffusion limit will obscure very fast rates of electron transfer ($k_{\text{obs}} = k_{\text{d}}$ for $k_{\text{ET}} \gg k_{\text{d}}$) [16]. Even if electron transfer is slow with respect to diffusion ($k_{\text{obs}} = k_{\text{ET}}$), work accompanies the formation of the precursor complex and/or separation of the successor complex (this is especially prevalent when the reactants and/or products are charged). Work term contributions to the observed rate of reaction can overwhelm the intrinsic factors that govern the electron transfer event [19]. For this reason, excluding special circumstances [20–26], intermolecular reactions are not ideal systems for examining the mechanistic details of electron transfer.

Problems associated with precursor formation and successor dissociation are circumvented when the nonspecific interaction between donor and acceptor in Eq. 1, represented by \parallel , is replaced by a *covalent* linker. As the many chapters of this Series attest, the restriction of electron transfer to an *intramolecular* process, where the distance between donor and acceptor is fixed, has led, in the past two decades, to an explosion in our knowledge of electron transfer processes and the factors that control them. These include: the donor–acceptor separation distance; the nature of the intervening medium and the relative orientation between the donor and acceptor sites (all of which influence electronic coupling); the driving force of the reaction (ΔG°); and the nuclear reorganization of reactants and solvent (λ).

In the context of the foregoing discussion, the hydrogen-bonded donor–acceptor supramolecules of Figure 1 meld the constructs of both inter- and intramolecular electron transfer. From the standpoint of intermolecular electron transfer, these systems represent a preformed precursor complex held together by noncovalent interactions; from the standpoint of intramolecular electron transfer, these systems provide a fixed-distance donor–acceptor pair in which charge transport occurs along a noncovalent pathway.

The formation of the donor–acceptor complexes of Figure 1 occurs by “self-assembly”, which is defined as the noncovalent interaction of two or more molecular subunits to form an aggregate whose novel structure and properties are determined by the natures and positioning of the components [27–32]. The construction of complex, multicomponent aggregates requires intermolecular interactions that are directional and/or selective. The selectivity, particularly in asymmetric and multiply-bonded systems, allows for considerable influence over the association process by careful use of complementary components. With directionality, it is possible to control the separation and, in some cases, the relative orientation between donor–acceptor subunits.

Of the various noncovalent intermolecular interactions that have been exploited in supramolecule design, the hydrogen bond [29–31] has emerged as the paramount synthon for self-assembly. Following the definition put forth by Pimentel and McClellan in their classic 1960 text, *The Hydrogen Bond* [33], hydrogen bonds are noncovalent forces that arise when the proton of an acid is brought into intimate contact (i.e., a separation less than the sum of the van der Waals radii) with the nonbonding lone pair of a base. Despite this simple concept, a precise description of the electronic nature of the hydrogen bond continues to elude both theorists and experimentalists. This is due to the fact that hydrogen bonds form a more diverse range of interactions than do either covalent/ionic bonds or van der Waals forces; strong hydrogen bonds resemble the former and weak hydrogen bonds resemble the

latter. The reader is referred to Jeffrey's *An Introduction to Hydrogen Bonding* for structural and statistical studies on the strength and geometry of hydrogen bonds [34]. In the absence of unequivocal metrics for hydrogen bonding, Etter has used graph-set analysis based on X-ray diffraction data to propose a number of phenomenological rules for the assembly of complex aggregates arising from the formation of hydrogen bonds [35]. Although many additional factors outside the heuristics may influence the nature of the final superstructure, supramolecular chemists are now capable of exerting exquisite control of hydrogen-bonding networks towards the assembly of a variety of novel and structurally complex donor–acceptor systems. Against this backdrop of expertise, the D—[H]—A systems of Section 4.4 emerge.

4.3 Scope of the Chapter

In this chapter, we review electron transfer model systems where the hydrogen-bonded bridge provides a structural scaffold that is chemically and spatially unique from the donors and acceptors to which it is attached. The chapter is devoted to two basic classes of hydrogen bond networks: those that do not contain a permanent charge dipole (e.g., $-(\text{COOH})_2-$, guanine–cytosine, etc.) and those that do (e.g., amidinium–carboxylate). The first class of network is selective and directional, but the association strength varies greatly from case to case. The second class of network, succinctly denoted as a salt bridge, offers a combination of the selectivity and directionality of hydrogen bonds with the strength of a permanent electrostatic dipole. We focus on the particular salt bridge formed between amidinium and carboxylate, as this interface is of central importance to research efforts aimed at addressing the mechanistic details of the coupling between proton and electron. We designate the resulting dynamic process proton-coupled electron transfer (PCET).

Systems not covered in this chapter, but falling under the purview of non-covalently associated donor–acceptor pairs, include those in which the electrostatic scaffold directly comprises the donor and acceptor or in which the hydrogen bond interface is nonspecific. In the former case, the donor and acceptor carry opposite charges, and there is no unique scaffold providing the electrostatic interaction. Here, optical electron transfer is often observed in the form of an ion-pair charge transfer (IPCT). IPCT complexes were first identified by Linhard [36, 37] in the 1940s, and seminal work on such systems has since been carried out by Kochi [38–40], Billing [41, 42], Vogler [42, 43] and others [44]. This research has been extensively reviewed, most recently by Kochi in Volume II, Part 2, Chapter 2 of this handbook. Perhaps of more relevance to the present chapter, but not reviewed herein, are systems assembled from noncovalent electrostatic scaffolds that are unique from the donor–acceptor centers. These include “face-to-face” dimers and higher aggregates (represented schematically in Figure 2) formed by associated cationic and anionic macrocycles (e.g., porphyrins, phthalocyanines, porphyrazines) [45–63]. Photoinitiated electron transfer in these systems, which bear relevance to

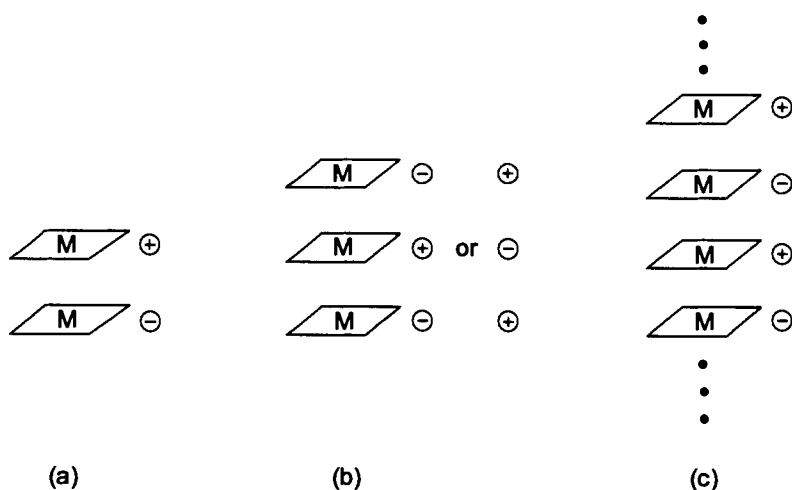


Figure 2. Cofacial macrocycles associated via electrostatic interactions to give (a) dimers, (b) trimers and (c) higher aggregates. Typical cationic groups are pyridinium or trimethylanilinium; typical anionic groups are sulfonate or carboxylate. Boxes represent porphyrin, phthalocyanine or porphyrazine; $M = 2H, Zn, Cu, MnCl$, etc.

the special pair of the photosynthetic reaction center, has been monitored using transient absorption, emission and EPR techniques. An interesting application of electrostatically associated porphyrin systems for the activation of small molecules has been carried out by D'Souza and coworkers [64, 65]. Using self-assembled dimers of cationic and anionic cobalt porphyrins adsorbed on graphite electrodes, the efficient and selective catalytic four-electron reduction of oxygen to water is observed near physiological pH.

Lastly, biological or modified biological aggregates, such as protein-protein complexes [66, 67] and semi-synthetic cofactor assemblies [68], are not reviewed in the present chapter. Ill-defined electron transfer pathways as found in the one-point hydrogen bonding of simple organic solvent-solute interactions also will not be discussed. Mataga's noteworthy achievements in this latter area have been recently reviewed [69].

4.4 Electron Transfer Reactivity of $D-[H]-A$ Supramolecule Systems

Before discussing specific $D-[H]-A$ systems, it is appropriate to identify common experimental properties and modalities that are pertinent to their assembly and electron transfer reactivity. Because of the dynamic nature of noncovalent interactions, the supramolecular assemblies of this section have, for the most part, been characterized by spectroscopic techniques. Association constants for adduct for-

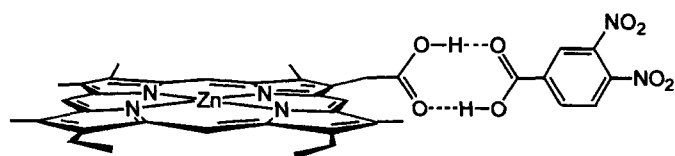
mation are usually determined using ^1H NMR, absorption or fluorescence spectroscopy. In extremely rare cases, assemblies have been characterized by X-ray crystallography; examples discussed later are a cofacial porphyrin–quinone complex, a protonated sapphyrin–benzoate adduct, and an amidinium porphyrin complexed with benzoate.

For virtually all of the supramolecular systems reviewed here, electron transfer is initiated by photoexciting the donor or acceptor; accordingly, either the donor or the acceptor must have a sufficiently long-lived excited state to support electron transfer. By using a photon to initiate the electron transfer event, a number of issues that may complicate the study of these self-assembled aggregates are readily resolved. For example, associated and unassociated donors and acceptors are present in solution owing to the equilibrium for the self-assembly of the hydrogen-bonded interface. For most systems, the pertinent excited-state lifetime is too short for diffusional electron transfer to come into play. Hence, photoinitiation of electron transfer from a donor to an acceptor selectively targets the associated pair, allowing one to view the intramolecular reaction in a “snapshot”. For systems with longer-lived excited states, concentration-dependent measurements allow intramolecular electron transfer through the hydrogen bond interface to be isolated from the non-specific bimolecular electron transfer reaction of unassociated and freely diffusing reactants. Another potential complication is the spontaneous mismatching of donor and acceptor subunits. Some interfaces are selective for donor–acceptor formation because they involve complementary interactions (e.g., Watson–Crick base pairs, amidinium–carboxylate salt bridges). For those interfaces that are not complementary, such as dicarboxylic acid scaffolds, donor–donor and acceptor–acceptor pairs will be present in addition to the desired donor–acceptor pair. However, formation of homodimers is inconsequential to the electron transfer kinetics because the charge separation reaction in homodimers is usually endothermic. Electron transfer will not be photoinitiated in these pairs.

We now present a selection of electron donor–acceptor supramolecules assembled via hydrogen bonding, organized according to the type of hydrogen bond interface employed.

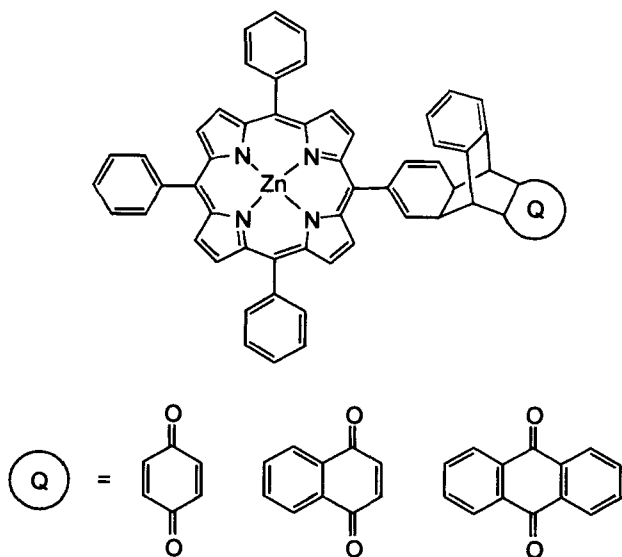
4.4.1 Carboxylic Acid Dimers

The propensity of carboxylic acids to form cyclic dimers in low-polarity, non-hydrogen bonding solvents offers a facile, if not selective, method for assembling electron donor–acceptor pairs via a hydrogen-bonding interface. Indeed, the first systematic kinetics study of a hydrogen-bonded donor–acceptor pair employed a $-(\text{COOH})_2-$ motif in the construction of **1**, comprised of a carboxylic acid-modified zinc(II) porphyrin donor associated with a 3,4-dinitrobenzoic acid acceptor [70]. Assembly **1a** has an association constant of 552 M^{-1} in dichloromethane as determined by monitoring changes in the infrared CO and OH stretching vibrations. In good agreement with this result are association constants measured using static fluorescence quenching of the zinc(II) porphyrin excited state ($K_A = 698\text{ M}^{-1}$ for protio **1a** in *o*-dichlorobenzene and $K_A = 316\text{ M}^{-1}$ for deuterio **1b** in dichloromethane).

**1** (a, ^1H ; b, ^2H)

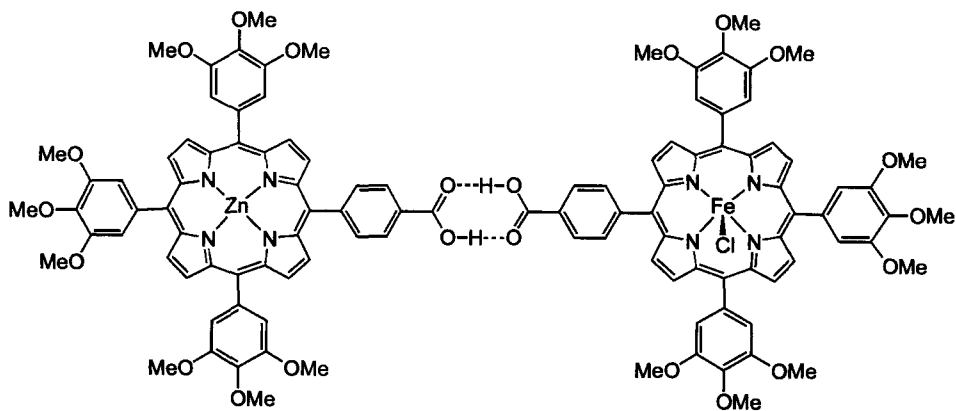
The zinc(II) porphyrin of **1** is particularly suitable for electron transfer studies because it is a photoactivated electron donor with easily monitored spectral properties. Forward and back electron transfer rate constants for **1a** ($k_F = 5.0 \times 10^{10} \text{ s}^{-1}$, $k_B = 1.0 \times 10^{10} \text{ s}^{-1}$) and **1b** ($k_F = 3.0 \times 10^{10} \text{ s}^{-1}$, $k_B = 6.2 \times 10^9 \text{ s}^{-1}$) were determined using picosecond transient absorption spectroscopy. Importantly, the static quenching of **1a** in CH_2Cl_2 is not observed when the carboxylic acid network is disrupted by the addition of hydrogen-bonding solvents or when the carboxylic acid functionalities of the donor–acceptor pair are esterified. Moreover, analysis of the transient absorption profiles of esterified control systems (where association of a donor–acceptor pair is obviated by esterification) provides no indication of porphyrin radical cation formation on the picosecond time scale.

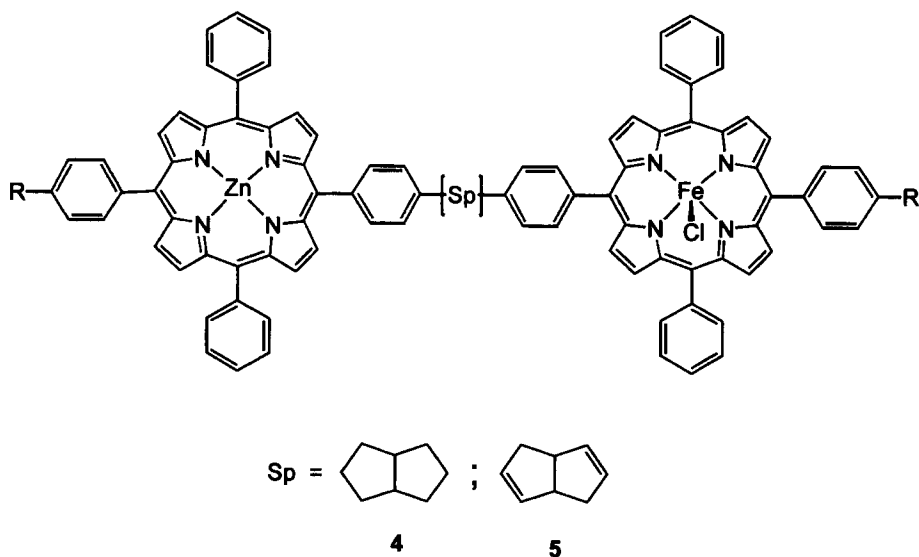
System **1** is a benchmark in D—[H]—A electron-transfer studies because it provides the first direct experimental validation to the hypothesis that donor–acceptor coupling is affected by the presence and nature of the noncovalent interaction. Comparison of **1** with Wasielewski's covalently linked model system **2** [71], which

**2**

possesses a comparable donor–acceptor separation and driving force, reveals that the rates of electron transfer for these systems are of a similar order of magnitude. These results confirmed previous theoretical predictions [72–74] that hydrogen bond pathways for electron transfer can be competitive with covalent bond routes. More notably, the charge separation and recombination rate constants for **1** exhibit pronounced deuterium isotope effects ($k_{\text{H}}/k_{\text{D}} = 1.7$ and 1.6, respectively). As theoretically elaborated [75], it is this observed deuterium isotope effect that reveals coupling between electron and proton. Since charge redistribution within this interface is negligible, the only mechanism available to couple electron and proton arises from the dependence of electronic coupling on the position of the protons within the interface.

Following this same approach, Therien and coworkers studied model **3** [76]. This assembly represents an advance in the construction of D—[(COOH)₂—A systems inasmuch as the hydrogen bond scaffold is rigid. In an attempt to quantify the coupling between a donor–acceptor pair through a hydrogen bond interface, the electron transfer kinetics of **3** were compared to those of similar donor–acceptor pairs linked by interfaces composed of covalent carbon σ (**4**) and π (**5**) networks featuring the same number of bonds as **3**. However, an intervening phenyl ring may electronically isolate the hydrogen bond interface from the porphyrin excited state [77, 78]. Such electronic insulation of the electron transfer donor–acceptor centers from the interface will obviate coupling between the electron and proton. This is born out by the forward electron transfer rate constants of **3–5** (**3**, $k_{\text{ET}} = 8.1 \times 10^9 \text{ s}^{-1}$; **4**, $k_{\text{ET}} = 4.3 \times 10^9 \text{ s}^{-1}$; **5**, $k_{\text{ET}} = 8.8 \times 10^9 \text{ s}^{-1}$), which were measured by using time-resolved fluorescence spectroscopy to monitor the disappearance of the zinc(II) porphyrin singlet excited state in the presence of acceptor. The electron transfer rate constant is doubled when the donor–acceptor pair is bridged by the dicarboxylic acid interface **3** instead of the saturated bicyclic carbon bridge **4**; this result was attributed to greater electronic coupling mediated by the former type of scaffold. However, the conclusion is clouded by assumptions made in the determination of



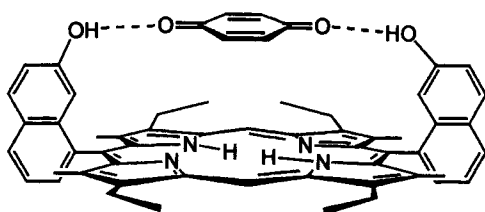


redox potentials, which were deduced from porphyrin precursors rather than the electron transfer reactants themselves. The possibility of energy transfer, which is typically significant for donor–acceptor systems composed of zinc(II)–iron(III) porphyrin pairs [77, 79–82], was also not considered. Indeed, *ab initio* analysis of **3**–**5** [83] predicts that the hydrogen-bonded pathway of **3** exhibits weaker electronic coupling than the covalent bond pathways of **4** and **5**. This calculation is consistent with experimental results obtained for **1**, numerous other experimental systems (*vide infra*) and theoretical treatments of electron transfer along hydrogen-bonded pathways [72–74, 84].

4.4.2 Cofacial Porphyrin–Quinone Systems

The organization of porphyrins and quinones in a cofacial manner offers the opportunity to probe the effect of geometric factors on the electron transfer chemistry of this biologically important cofactor pair. When combined with hydrogen bond molecular recognition, a powerful, modular approach for examining a systematic series of molecular adducts is obtained. The cofacial presentation of quinones to porphyrins via hydrogen-bonding interactions is facilitated by the planarity of the porphyrin macrocycle and the ability to readily functionalize it to afford a shape-selective cleft for guest recognition. In addition, the aromaticity of the porphyrin ring provides a stabilizing force for guest quinones via π – π stacking and/or charge-transfer interactions.

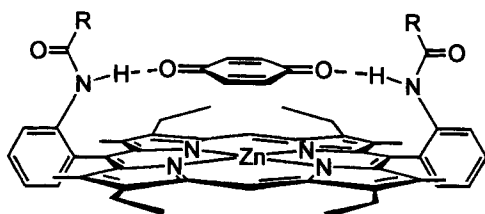
Ogoshi, Aoyama and coworkers have exploited these properties of the porphyrin architecture to cofacially associate *cis*-bis(2-hydroxy-1-naphthyl) porphyrin **6** with a variety of *para*-quinones via two-point hydrogen-bonding and charge-transfer



6

interactions [85]. Association constants for these face-to-face host–guest adducts, measured using ^1H NMR and IR spectroscopy, range from $K_A = 7.8 \text{ M}^{-1}$ for tetramethoxy-1,4-benzoquinone to $K_A = 2.3 \times 10^2 \text{ M}^{-1}$ for anthraquinone. It was suggested that steric inhibition arising from the methoxy substituents is the reason for the lower binding affinity of the guest; however, it is not clear if the strength of hydrogen bonding and/or magnitude of π -stacking interactions can also play a role in stabilizing the porphyrin–quinone aggregates. The porphyrin–quinone complexes are completely nonfluorescent, consistent with an efficient intramolecular electron transfer from the photoexcited porphyrin to the bound quinone. Control experiments with a bis(naphthyl) porphyrin, possessing no recognition site, and *p*-benzoquinone show electron transfer to proceed only by a diffusion-limited quenching mechanism. Similar hosts for the recognition of *para*-quinones comprised of *cis*-bisamide-functionalized porphyrins **7–12** have been recently reported [86]. Studies of the binding of *p*-benzoquinone with **9** and **11** show that host–guest association of the bisamide clefts of **7–12** and the hydroxy-naphthyl cleft of **6** are comparable.

Ogoshi, Hayashi, and coworkers have elaborated their approach further by focusing on the recognition of ubiquinone (coenzyme Q_{10}) and its analogues. An important electron and proton carrier in the mitochondrial respiratory chain, ubiquinone contains a long isoprenoid tail and is able to move freely through the lipid bilayer to deliver electron/proton equivalents to oxidoreductases [87, 88]. Consequently, the noncovalent molecular recognition of ubiquinone at redox reaction receptor sites may regulate the rate of electron/proton transfer in the respiratory chain. Dynamic molecular recognition of the ubiquinone analog tetramethoxy-*p*-benzoquinone is achieved by *meso*-tetrakis(2-hydroxy-4-nonylphenyl)-porphyrin



7: $\text{R} = \text{C}_7\text{F}_{15}$

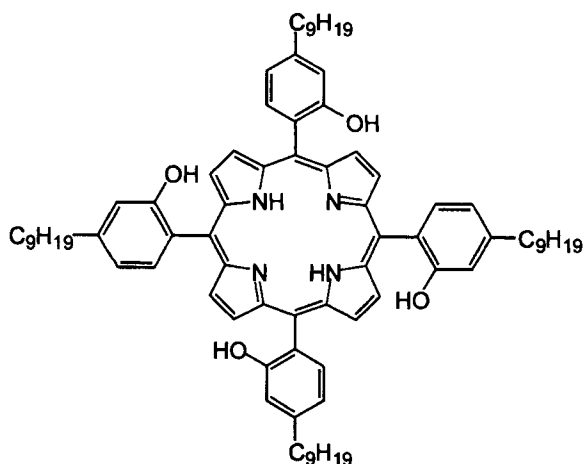
8: $\text{R} = \text{C}_7\text{H}_{15}$

9: $\text{R} = \text{CF}_3$

10: $\text{R} = \text{CH}_3$

11: $\text{R} = \text{C}_6\text{F}_5$

12: $\text{R} = \text{C}_6\text{H}_5$

**13**

13 [89]. As depicted in Figure 3, the guest acts as a trigger for the atropisomerization of **13** to enrich the particular $\alpha,\alpha,\alpha,\alpha$ -isomer by the induced interaction. The fluxional nature of the host–guest assembly can be thought of as a first step toward modeling the intricate structural docking interactions necessary for function in many biological systems.

Porphyrins **14** and **15**, containing four convergent hydroxy groups, form molecular clefts that bind tetramethoxy-*p*-benzoquinone to give 1:1 adducts [68, 90–94]. Association constants of the quinone guest with **14** and **15**, determined from absorption and fluorescence titration experiments, are $K_A = 7.9 \times 10^2 \text{ M}^{-1}$ and

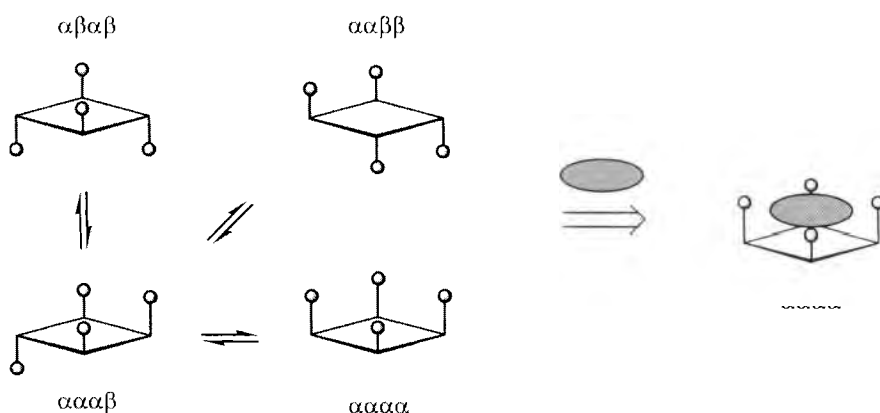
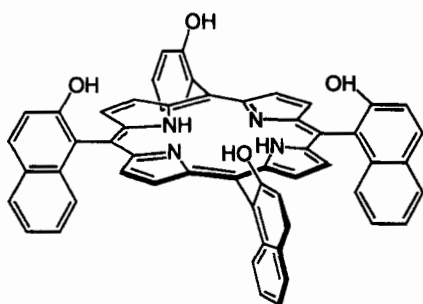
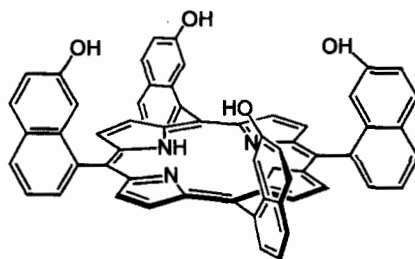


Figure 3. Induced atropisomerization of **13** by quinone guest to enrich the particular $\alpha,\alpha,\alpha,\alpha$ -isomer.

**14****15**

$6.1 \times 10^5 \text{ M}^{-1}$, respectively. The single crystal X-ray structure of **14**-tetramethoxy-*p*-benzoquinone has been obtained (Figure 4). The separation distance of 3.35 \AA between the bound quinone and porphyrin agrees well with the van der Waals distance between aromatic rings (3.4 \AA). The four OH groups of the porphyrin host form the expected hydrogen bonds with the two carbonyl and four methoxy oxygens of the tetramethoxy-*p*-benzoquinone guest. Stern–Volmer plots indicate efficient fluorescence quenching of **14** and **15** in the low concentration range of quinone ($< 5 \times 10^{-3} \text{ M}$); in contrast, no fluorescence quenching of zinc(II) meso- $\alpha,\alpha,\alpha,\alpha$ -tetra(2-methoxy-1-naphthyl)porphyrin is detected in the same concentration range of quinone. Upon excitation at $\lambda = 570 \text{ nm}$, transient difference spectra of the **14**- and **15**-quinone adducts show a significant time-dependent absorption at 640 nm , which is characteristic of a zinc porphyrin cation radical. Estimates of the forward electron transfer rate constants are $k_{\text{ET}} \geq 4 \times 10^{11} \text{ s}^{-1}$ for both systems. Charge recombination rates for the quinone complexes of **14** and **15** are $k_{\text{ET}} = (1.1 \pm 0.4) \times 10^{11} \text{ s}^{-1}$ and $(6.8 \pm 0.3) \times 10^{11} \text{ s}^{-1}$, respectively. Both charge separation and recombination rate constants in these assemblies are comparable to those reported in covalently linked porphyrin–quinone systems.

D'Souza has studied assemblies of type **16** [95], which take advantage of the two-point hydrogen bonds formed by hydroquinone–quinone pairing to afford the quinhydrone acceptor. Lifetime measurements using single photon counting point

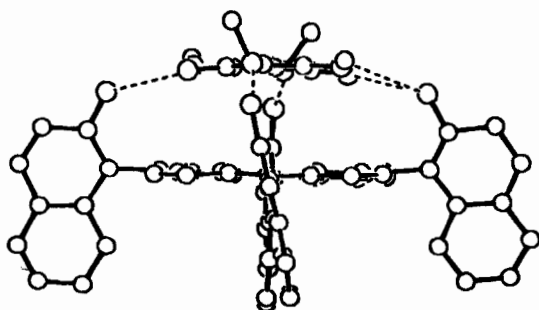
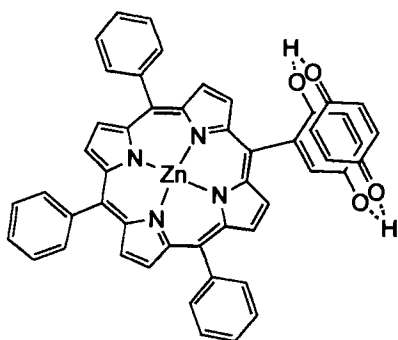


Figure 4. Thermal ellipsoid representation of **14**-tetramethoxy-*p*-benzoquinone. (Reprinted with permission from the American Chemical Society.)



16

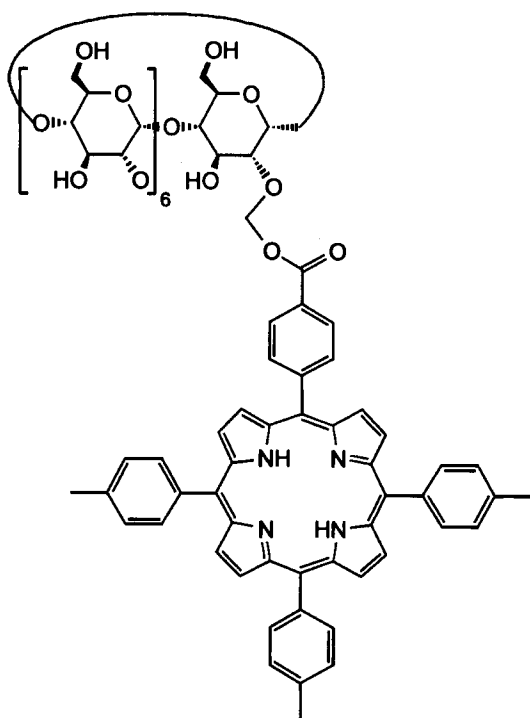
toward enhanced electron transfer quenching of the electronically excited zinc(II) porphyrin by association of the second quinone. A comparison of these results with the measured reduction potentials indicates that the efficiency of fluorescence quenching scales logically with the oxidizing abilities of quinone and quinhydrone.

4.4.3 Quinone Recognition by Cyclophanes

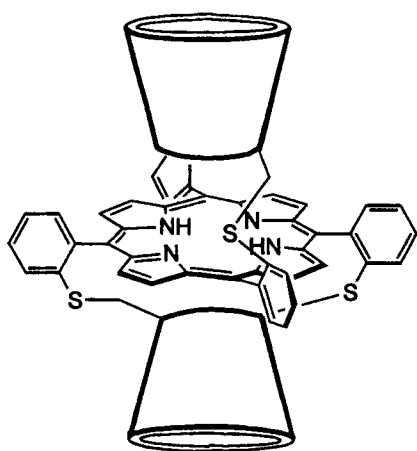
In the systems of the previous section, direct recognition of the quinone by the porphyrin donor affords the noncovalent assembly. An alternative method for the construction of noncovalent assemblies is to append the porphyrin with remote cyclophanes that have the ability to recognize quinone acceptors via hydrogen bonding. Weedon and coworkers studied the EPR spectra of broad-band irradiated ($\lambda = 500$ nm) frozen solutions of β -cyclodextrin functionalized porphyrin **17** in the presence of various *p*-benzoquinones [96, 97]. Electron transfer was inferred from EPR signals assigned to the porphyrin cation and quinone anion radicals. Comparison of **17** with analogous bimolecular control systems points toward binding of the quinone in the hydrophobic pocket of the cyclodextrin to afford an efficient intramolecular electron transfer pathway.

The cyclodextrin-sandwiched porphyrin **18** of Kuroda [98] effectively recognizes hydrophobic quinones in water, with association constants ranging from $K_A = 7.4 \times 10^3 \text{ M}^{-1}$ for 1,4-naphthoquinone to $K_A > 5 \times 10^5 \text{ M}^{-1}$ for an adamantyl-functionalized benzoquinone. In contrast, the association of *p*-benzoquinone is negligible. Molecular modeling predicts that the quinone approaches the porphyrin from an out-of-plane direction. Time-resolved fluorescence measurements give an estimate of the intramolecular electron transfer rate constant on the order of 10^9 s^{-1} for all quinones studied.

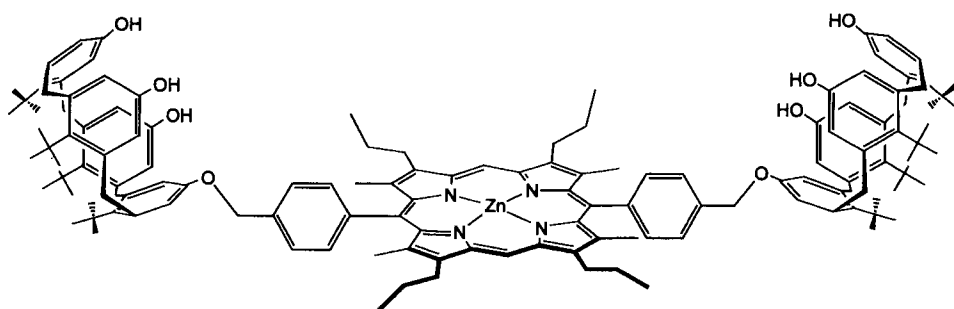
Calixarenes have also been used as cyclophane hosts for the binding of quinone acceptors via hydrogen bonding. Arimura and Sessler have appended bis-hydroxy-containing calix[4]arenes to zinc(II) porphyrins. Two phenolic OH groups on the calix[4]arene serve as tweezers to complex a quinone via two-point hydrogen



17

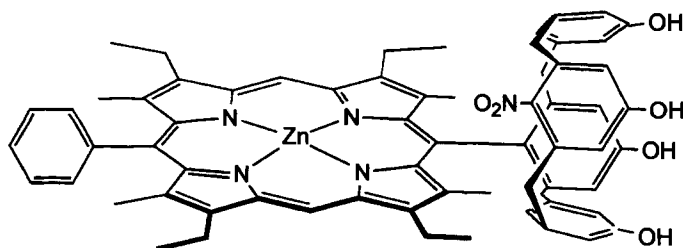


18



19

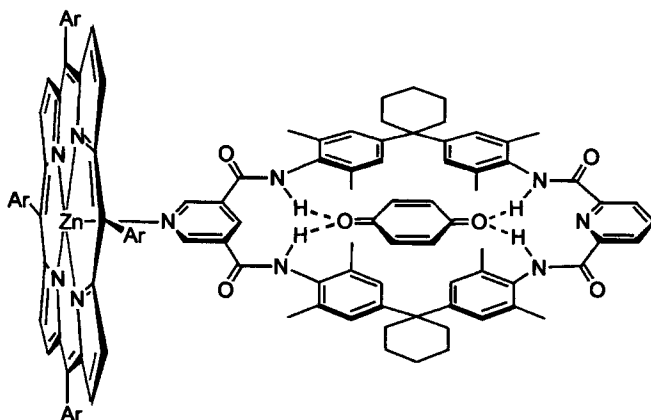
bonding. The symmetric assembly **19** consists of a zinc(II) porphyrin containing two calix[4]arene functional groups [99]. Weiss and coworkers have reported a similar system for the multisite binding of transition metals, alkali or alkaline-earth metals and organic fragments [100]. Surprisingly, a Job's plot of the bis-functionalized porphyrin **19** with *p*-benzoquinone establishes the formation of the 1:1 host:guest complex, instead of the expected 2:1 adduct. A binding constant of $K_A = 40 \pm 10 \text{ M}^{-1}$, determined from ^1H NMR measurements, is considerably less than that observed for typical hydrogen-bonded complexes. This weak association of quinone to **19** may result from strong intramolecular hydrogen-bonding interactions between two adjacent hydroxy groups present in the calix[4]arene. Time-resolved fluorescence studies of the porphyrin in the presence of varying amounts of *p*-benzoquinone give a fluorescence decay profile with two components. A concentration-independent decay component is attributed to a quenching process involving unidirectional electron transfer from the calix[4]arene-Zn(II) porphyrin to bound *p*-benzoquinone. The photoinduced electron transfer rate constant is $k_{\text{ET}} = (8.0 \pm 0.2) \times 10^8 \text{ s}^{-1}$, with a quantum yield of $\Phi = 0.56$. The authors state that it is not clear whether electron transfer occurs through bond, solvent or both pathways. Ensemble **20**, containing a zinc(II) porphyrin with a calix[4]arene directly attached to one of the *meso* positions of the porphyrin ring, forms a 1:1 adduct with *p*-benzoquinone [101]. As for **19**, the formation constant for **20** is small ($K_A = 70 \pm 10 \text{ M}^{-1}$) and time-resolved



20

fluorescence measurements exhibit a fast (30-ps), concentration-independent decay component.

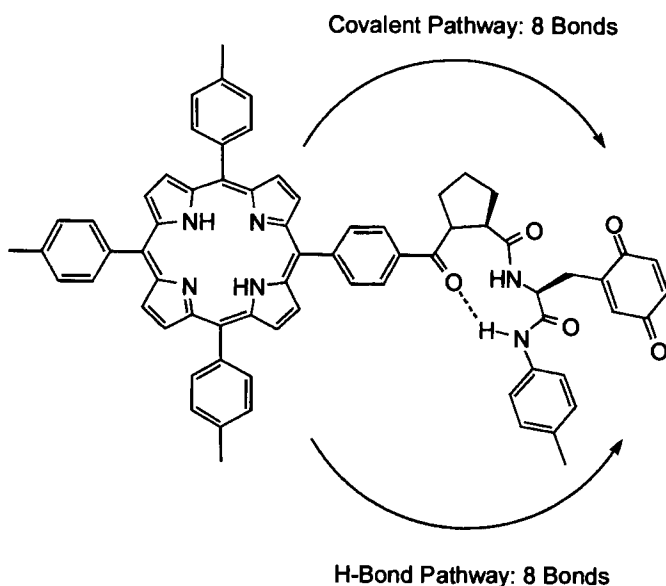
Amide-containing macrocycles have been examined by Hunter and coworkers as hosts for the recognition of a range of structurally related dicarbonyl compounds in nonpolar media [102, 103]. The dicarbonyl compounds are held in this type of receptor by a combination of two-point hydrogen bonding to the amide protons and π -stacking with the phenyl rings of the cyclic framework ($K_A > 10^3 \text{ M}^{-1}$). A pyridine-functionalized scaffold, equipped with convergent and divergent recognition sites, binds two cofactors, a zinc(II) porphyrin and *p*-benzoquinone, to form the termolecular electron donor–acceptor assembly **21**. The ternary complex is the predominant species (65 %) in a 1:1:1 mixture of the porphyrin, macrocycle and quinone at a concentration of $5 \times 10^{-3} \text{ M}$. The presence of the macrocycle greatly enhances the steady-state quenching of the porphyrin fluorescence by quinone. Control experiments show only a small decrease in porphyrin fluorescence on addition of quinone in the absence of macrocycle, attesting to intramolecular electron transfer within the 1:1:1 complex of **21**.



21

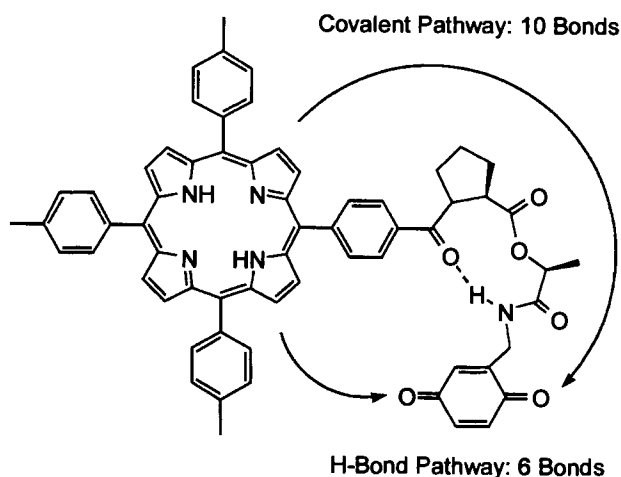
4.4.4 Peptide-Based Motifs

The search for protein or peptide-based “pathways” for electron transfer is an area of intense research. The most common secondary structures of proteins are the α -helix and β -sheet, with the latter most frequently employed in the construction of D—[H]—A systems. β -sheets consist of a two-dimensional array of fully extended polypeptide chains (β -strands) stabilized by a pattern of interchain hydrogen bonds. It has been suggested that the hydrogen bonding in β -sheets provides an efficient medium for long-range electronic coupling [104]. In order to assess the conduction efficiency of an electron through a β -sheet motif, a number of peptide-containing conjugates have been prepared.

**22**

Maruyama and Tamiaki have synthesized the elegant peptide-bridged porphyrin–quinone conjugate **22**, which mimics the β -turn structure found in proteins by forming a hydrogen-bonded loop [105]. Two eight-bond pathways are available for electron transfer: a through-backbone pathway and a through-hydrogen bond pathway. Photoexcitation of the free-base or zinc(II) porphyrin in **22** initiates electron transfer to the quinone acceptor. Electron transfer rate constants, determined from time-resolved fluorescence quenching measurements, are $k_{\text{ET}} = 2.1 \times 10^8 \text{ s}^{-1}$ and $4.0 \times 10^9 \text{ s}^{-1}$ for free-base-**22** and zinc(II)-**22**, respectively. These data suggest that electron transfer through the hydrogen bond pathway is slightly attenuated with respect to the corresponding covalent pathway.

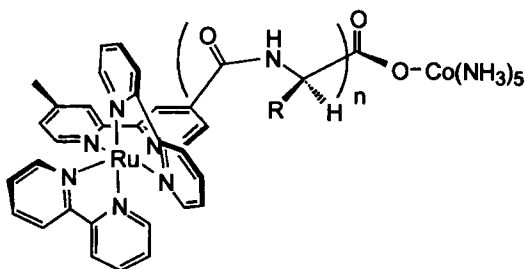
Bowler and Williamson developed a similar donor–acceptor compound, **23**, with a β -turn-forming depsipeptide bridge [106], to study hydrogen-bond-mediated electron transfer through a single amide NH to CO bond. The placement of donor and acceptor is chosen to favor electron transfer through the hydrogen-bond interface of the β -turn. An advantage of **23** over **22** is the replacement of the central amide linkage with an ester, which ensures β -turn folding (eliminating the possibility of γ -turn folding). Infrared spectroscopy indicates that the β -turn conformation in **23** is approximately 85 % populated in nonpolar solvents such as CH_2Cl_2 , and completely disrupted in polar solvents like DMSO. Using time-resolved fluorescence spectroscopy, very fast electron transfer ($k_{\text{ET}} = 1.1 \times 10^9 \text{ s}^{-1}$) is observed in the presence of the β -turn. When the β -turn is disrupted (using DMSO), electron transfer is no longer competitive with the intrinsic fluorescence emission of the



23

porphyrin donor, indicating that the β -turn is an efficient coupling medium for electron transfer.

Ogawa and coworkers have examined peptide β -strand mimics of the general type **24** ($R = \text{CH}(\text{CH}_3)_2$, $n = 1-3$), consisting of a ruthenium(II) polypyridyl electron donor tethered to a cobalt(III) pentammine electron acceptor by an polyvaline peptide chain [107]. A related parallel β -sheet mimic has also been studied [108]. These compounds adopt the conformational properties found within the individual strands of a β -pleated sheet in both aqueous and methanol solutions. Emission lifetime measurements and HPLC product analyses suggest that the binuclear donor–acceptor compounds undergo photoinduced electron transfer. The values of k_{ET} decrease with increasing donor–acceptor distance according to $\beta = 1.1 \text{ \AA}^{-1}$, which is observed for electron transfers both in water at 298 K and in ethanol–

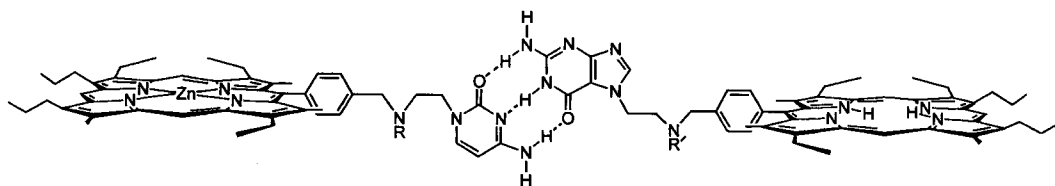


24

methanol glasses at 77 K. Notably, this value falls within the range for electron transfers occurring along the β -strands of ruthenium-modified azurin [109], and concurs with Gray and coworkers' [104] predictions for the rate of electron transfer along an individual strand of a β -sheet.

4.4.5 Watson–Crick Base-Pairing

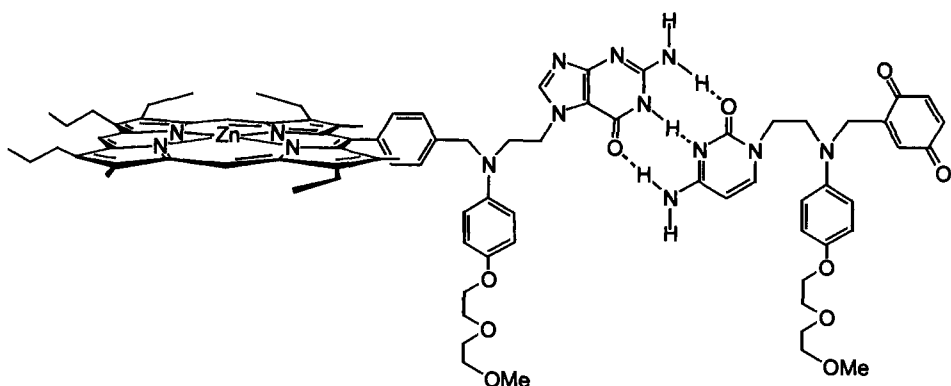
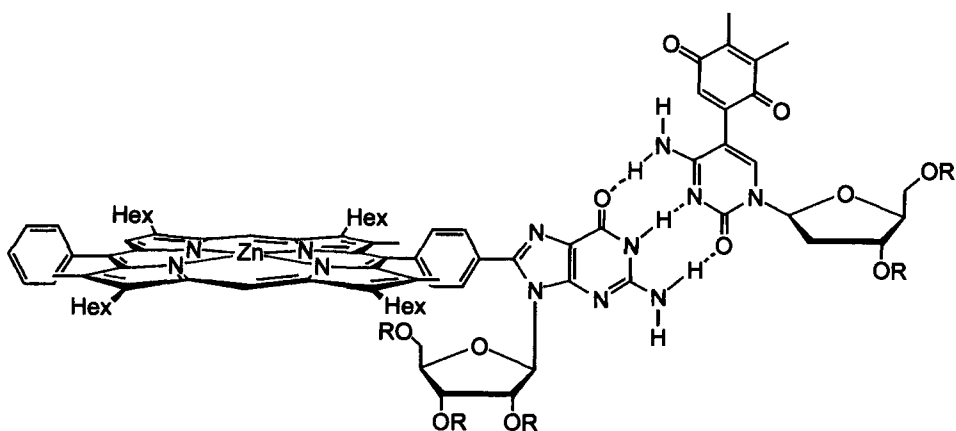
The Watson–Crick base-pairing of DNA is perhaps the most ubiquitous example of how hydrogen bonding can shape and stabilize large, organized supramolecular assemblies. Sessler and coworkers have extensively exploited the two-point hydrogen bonding between adenine and thymine bases and the three-point hydrogen bonding between guanine and cytosine bases to construct a series of well-defined aggregates to study photoinduced electron transfer. Although **25** (R, R' = porphyrin, alkyl ether) was not designed for electron transfer investigations, ^1H NMR studies confirm the association of donor–acceptor pairs via guanine–cytosine subunits in non-polar solvents such as chloroform. Photophysical studies of this ensemble show efficient singlet and triplet energy transfer over 10 to 30 Å from the zinc(II) porphyrin donor to the free-base porphyrin acceptor [110, 111]. Control experiments verify that hydrogen bonding is essential for the observed photoprocesses. Fluorescence experiments using analogous donors and acceptors that lack the appended recognition units show no evidence of energy transfer at similar concentrations. Furthermore, the fluorescence of the photo-donor can be restored by the addition of ethanol, which causes a disruption of the hydrogen-bonding scaffold.



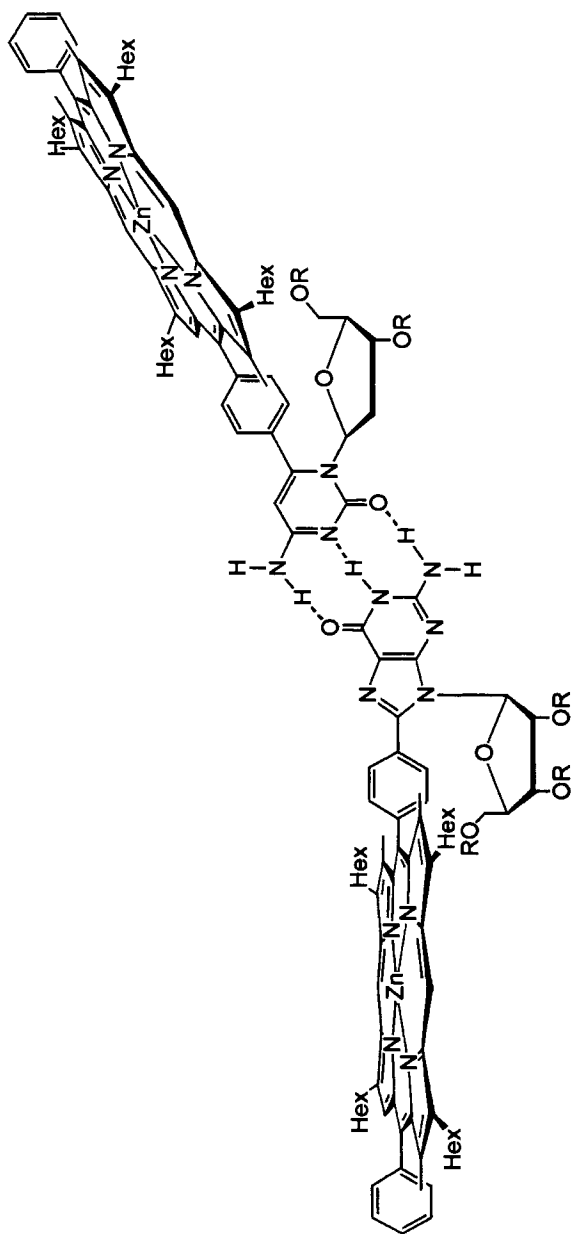
25

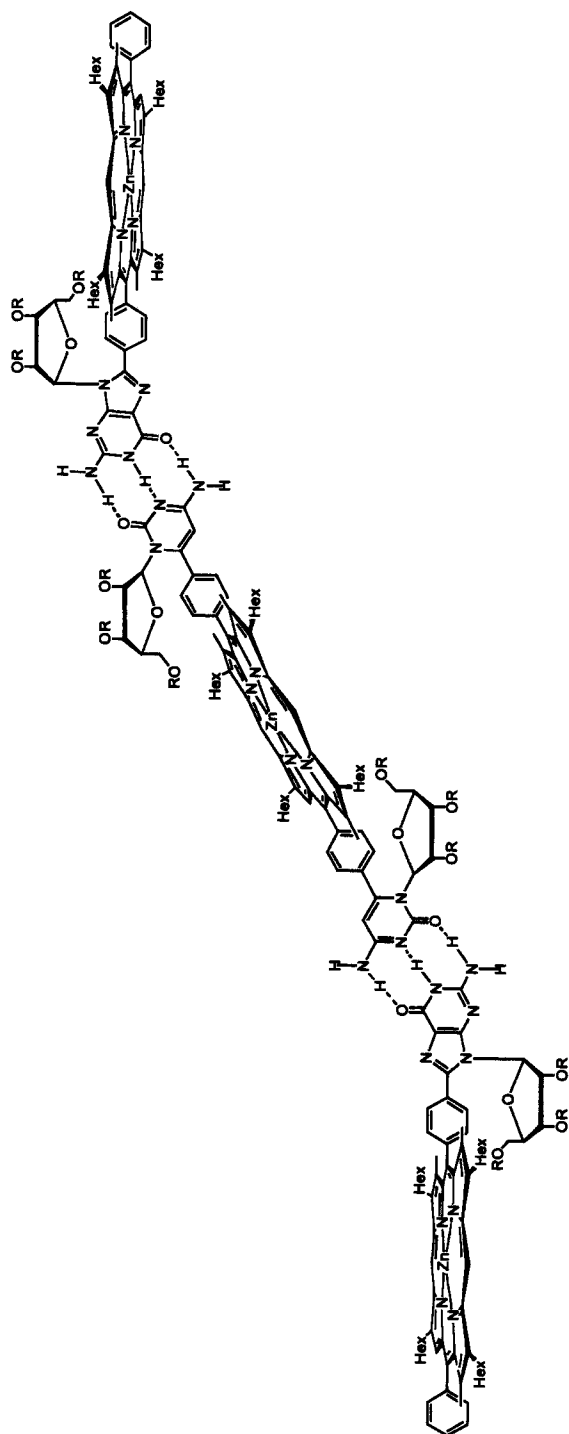
This same general approach can be used to promote electron transfer. Compound **26** poises a guanine-functionalized zinc(II) porphyrin donor at ~ 20 Å from a 2-cytosine-*p*-benzoquinone acceptor [112]. The aggregate, however, is quite flexible with many possible conformations. Analysis of the biphasic fluorescence decay curves of the guanine–zinc(II) porphyrin in the presence of its cytosine–quinone conjugate yields an electron–transfer rate constant of $k_{\text{ET}} = 4.2 \times 10^8 \text{ s}^{-1}$. Again, hydrogen bonding is necessary for function, as analogues without the appended nucleobases show no evidence of electron transfer at concentrations similar to those used for kinetics studies of **26**.

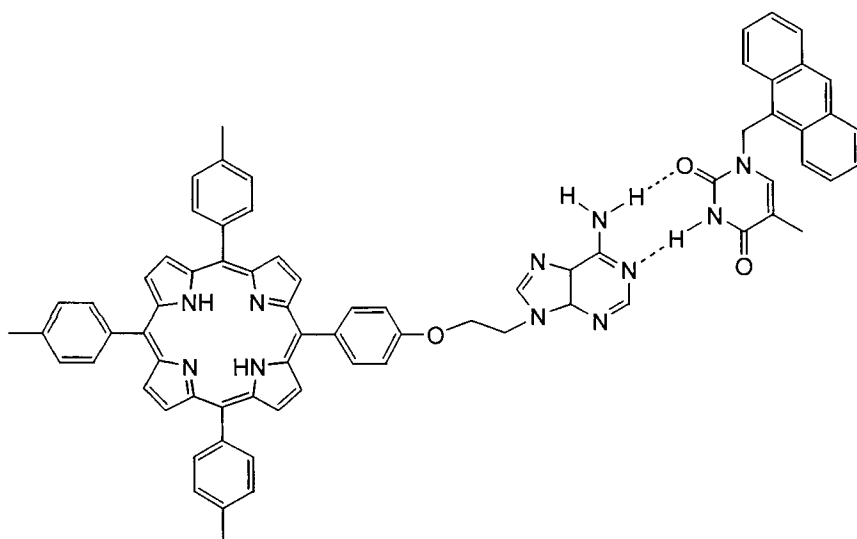
Due to concerns of through-space and through-solvent pathway contributions to the electron-transfer kinetics of **26**, a more rigid system, **27** (R = SiMe₂^tBu)

**26****27**

[113], was developed to better define the electron transfer reactivity of this class of ensembles. The association constant for **27**, derived from ^1H NMR titration measurements ($K_A = 1.6 \times 10^4 \text{ M}^{-1}$), is significantly higher than that observed for the flexible aggregate, thus pointing to the superior pre-organization of **27**. Time-resolved fluorescence measurements of **27** under conditions identical to those used to study **26** reveal that electron transfer in the former is notably faster ($k_{\text{ET}} \sim 8 \times 10^8 \text{ s}^{-1}$ for **27**) despite substantially less driving force ($\Delta G^\circ \sim -43 \text{ kJ mol}^{-1}$ for **27**, $\Delta G^\circ \sim -96 \text{ kJ mol}^{-1}$ for **26**). Related supramolecules **28** and **29** ($\text{R} = \text{SiMe}_2^t\text{Bu}$) have been prepared and their photoinduced energy-transfer processes have been studied [114]. Here, the rigid Watson–Crick hydrogen-bonding





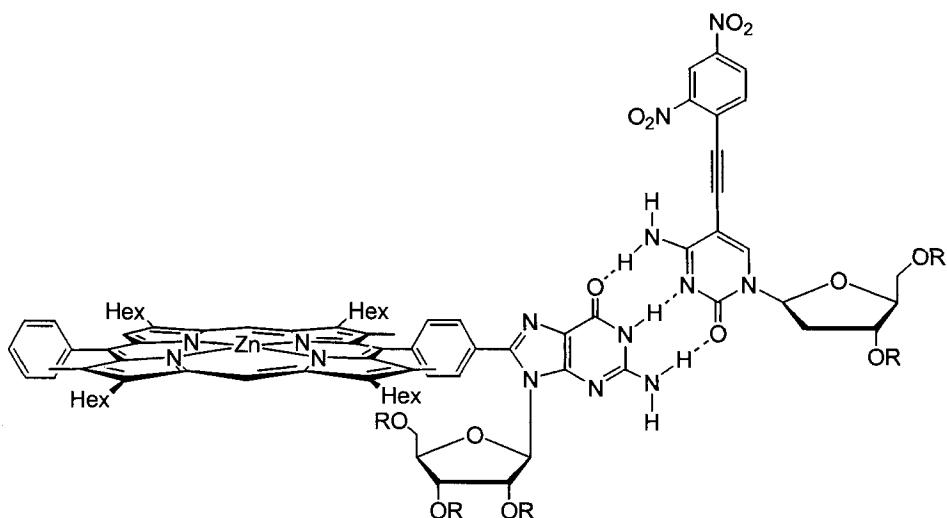


30

motif allows for the association of either one or two guanosine-functionalized zinc(II) porphyrins with a mono- or dicytidine-free base porphyrin. The energy transfers occur with high quantum efficiencies ($\Phi = 0.62$ for the singlet–singlet transfer, $\Phi = 0.93$ for the triplet–triplet transfer).

The flexible porphyrin–anthracene system of Sirish and Maiya assembles via complementary adenine–thymine base pairing [115]. Ensemble **30** associates with a binding constant of $K_A = 47 \pm 5 \text{ M}^{-1}$. ^1H NMR data suggest that both Hoogsteen and Watson–Crick adenine–thymine associations exist in solution. Time-resolved fluorescence data are consistent with the possibility of energy and electron transfer from the singlet excited state of the anthracene to the porphyrin.

In order to determine more precisely and directly the parentage of the excited state donor in D(porphyrin)—[H]—A systems, Sessler, Levanon, and coworkers have undertaken time-resolved EPR spectroscopy of base-paired systems **27** and **31** ($\text{R} = \text{SiMe}_2^t\text{Bu}$) embedded in nematic liquid crystals [116, 117]. Selective pulsed laser excitation of the zinc(II) porphyrin at $\lambda = 532 \text{ nm}$ results in long-range electron transfer to the quinone or dinitrobenzene acceptor. Recently, a set of W-band time-resolved EPR experiments on **31** was carried out to observe directly the radical pair [118]. Electron transfer appears to originate from the triplet excited state of the porphyrin. This result has important ramifications for future investigations, because it challenges the assumption that electron transfer in D(porphyrin)—[H]—A systems occurs from the singlet excited state, which is too short-lived to support bimolecular reactivity. Conversely, electron transfer from porphyrin triplet excited states should encompass both intra- and intermolecular reaction kinetics. The results

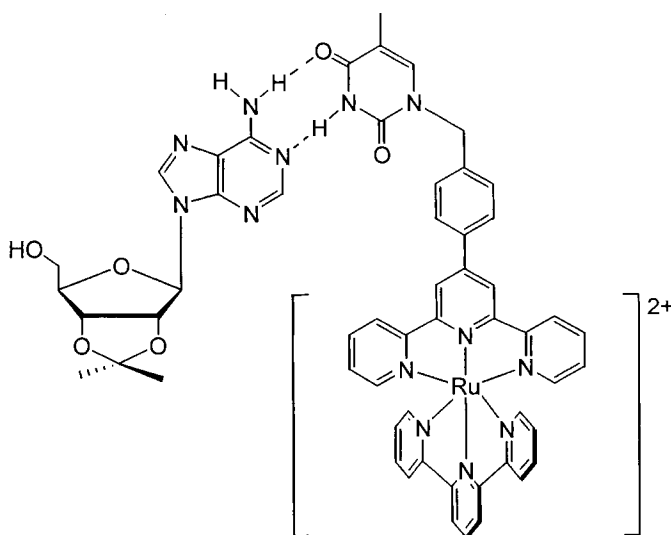


31

of these studies therefore highlight the importance of determining the concentration dependence of electron transfer kinetics for all D(porphyrin)—[H]—A systems.

Electron transfer from long-lived triplet excited states is the rule rather than the exception when metal polypyridyl complexes, and not porphyrins, are the photoexcitable donors or acceptors. Constable and Fallahpour have described the preparation and recognition properties of a thymine-functionalized terpyridine and its bis-homoleptic iron(II) and ruthenium(II) complexes [119]. The ruthenium(II) complex forms specific two-point hydrogen bonds with an organic-soluble adenosine analogue. ^1H NMR studies of adduct **32** in CD_3CN over a temperature range of 248–298 K give the thermodynamic quantities $\Delta H = -1.60 \text{ kJ mol}^{-1}$ and $\Delta S = 22.33 \text{ J mol}^{-1} \text{ K}^{-1}$ with an extracted stability constant of $\log K_A = 1.44$ at 298 K.

Ward and coworkers have synthesized complexes **33–36** ($\text{R} = {}^t\text{Bu}$, $\text{M} = \text{Ru, Os}$), in which luminescent ruthenium(II) or osmium(II) tris-bipyridyl cores are functionalized with adenine, thymine, guanine, and cytosine, respectively [120, 121]. Mixing components **33** and **34** results in 1:1 adduct formation but with a rather small stability constant ($K_A \sim 100 \text{ M}^{-1}$); thus, the photophysical properties of the associated pair are difficult to study in the presence of large excesses of the free component parts. However, use of **35** and **36**, with the guanine–cytosine three-point hydrogen bond replacing the weaker adenine–thymine two-point hydrogen bond, circumvents this issue [122]. The association constant for ruthenium-**35** and osmium-**36** is $K_A \sim 6000 \text{ M}^{-1}$ in CH_2Cl_2 , and efficient quenching of the ruthenium energy donor by the osmium acceptor is observed. Along similar lines, Sessler and coworkers have prepared complex **37** ($\text{R} = \text{SiMe}_2{}^t\text{Bu}$) for possible hydrogen-bonding attachment to porphyrin chromophores [123].

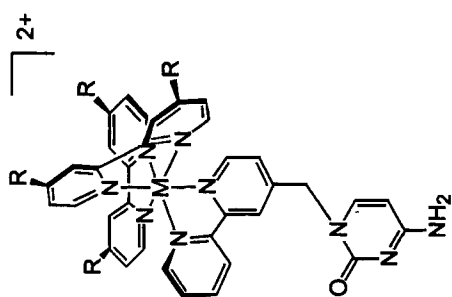


32

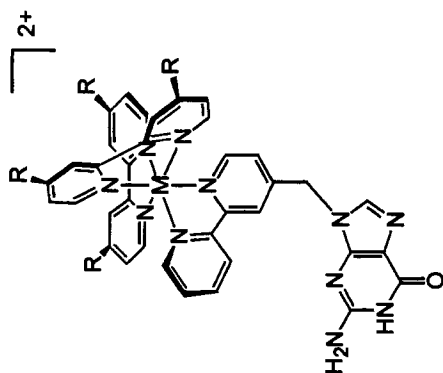
Lastly, electron transfer in $D-[H]-A$ assemblies is not a prerogative of the excited states of metal complexes. Organic ensembles **38** and **39** ($R = \text{SiMe}_2^t\text{Bu}$), containing a dimethylaniline–anthracene redox pair, have been synthesized recently [124]. Preliminary time-resolved and steady-state fluorescence experiments indicate the occurrence of photoinduced electron transfer. In work related to Watson–Crick base-paired systems, the excited state of the fluorescent pyrene derivative **40** is efficiently quenched (94–99 %) by 2'-deoxyguanosine (dG), 2'-deoxycytidine (dC), or 2'-deoxythymidine (dT) in aqueous solution [125]. A PCET mechanism is thought to be responsible for this process, as the thermodynamics of electron transfer are unfavorable unless coupled to a rapid proton-transfer step. The quenched lifetime of **40** in the presence of dC and dT in H_2O is significantly extended by a factor of 1.5–2.0 in D_2O ; this isotope effect is similar to that observed in the kinetics studies of **1** [70]. The invoked PCET reaction mechanism also accounts for the inability of dC and dT to quench the fluorescence of **40** in the aprotic organic solvent DMSO.

4.4.6 Diimide-Based Assemblies

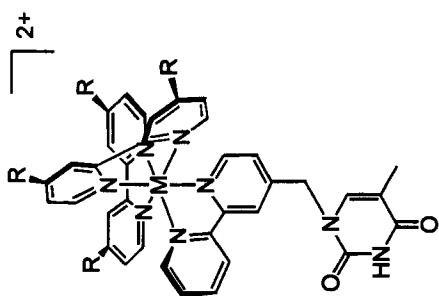
Diimide functionalities provide an attractive hydrogen-bonding scaffold for the association of donor–acceptor pairs. In all the examples surveyed here, the electron acceptors are derivatized naphthalene- or benzene-tetracarboxamides; these acceptors have proved particularly useful for analysis of electron transfer reactions owing to the characteristic absorptions of their anion radicals. Osuka, Okada,



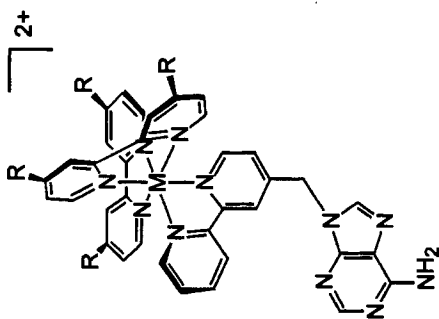
36



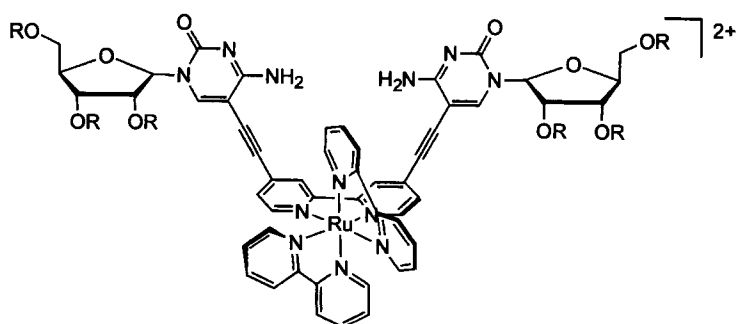
35



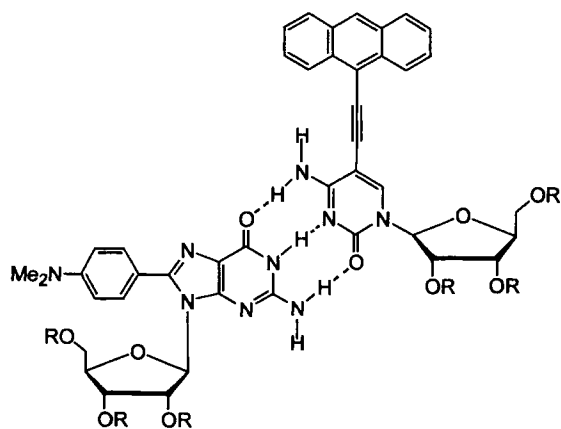
34



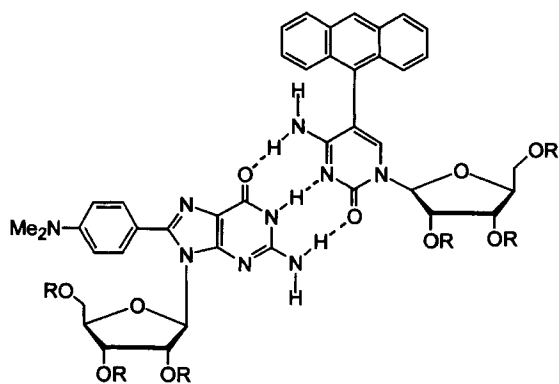
33



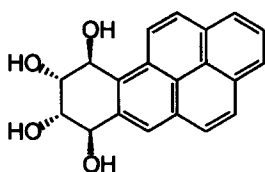
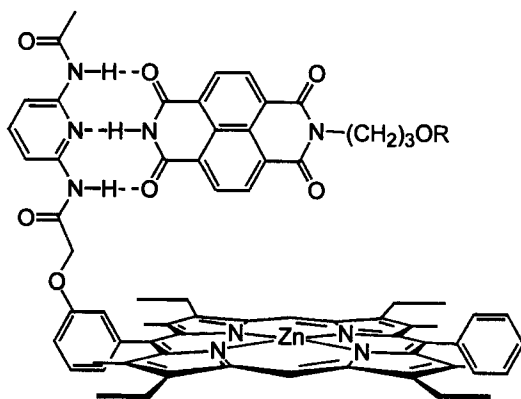
37



38

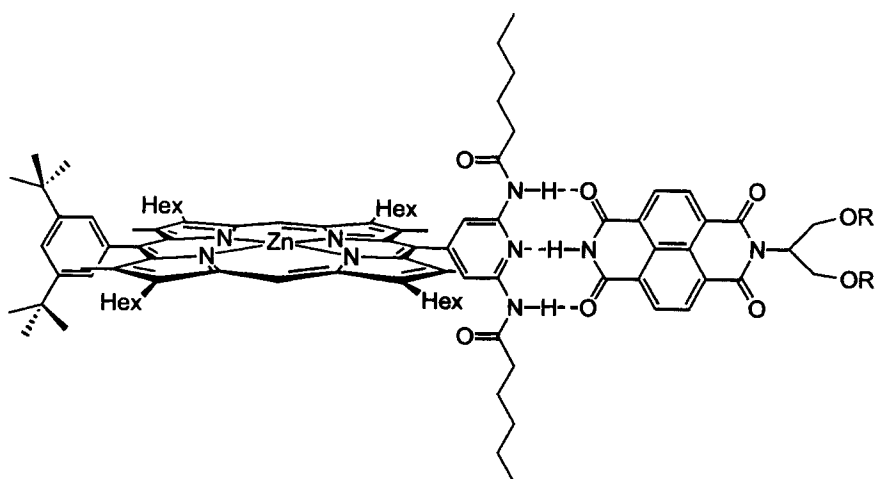


39

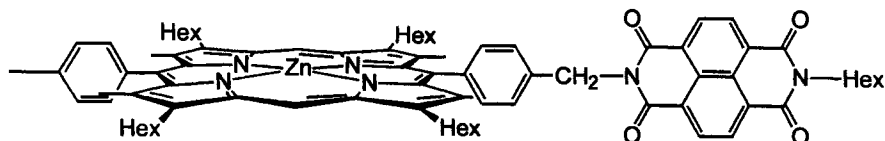
**40****41**

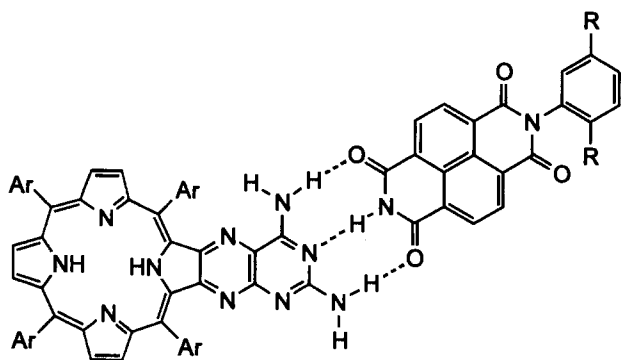
Mataga and coworkers have synthesized a zinc(II) porphyrin functionalized with a 2,6-diacylaminopyridine moiety; this porphyrin recognizes a siloxyl-modified naphthalene-tetracarboxamide through a three-point hydrogen-bonding interaction to form donor–acceptor adduct **41** ($R = \text{SiMe}_2^t\text{Bu}$) [126]. The benzene-tetracarboxamide analogue has also been prepared. The high association between naphthalene-tetracarboxamide and porphyrin to produce **41** ($K_A = 1.6 \times 10^4$ and $1.3 \times 10^5 \text{ M}^{-1}$ in CDCl_3 and C_6D_6 , respectively) is attributed to a geometrically matched interaction, as the benzene-tetracarboxamide analogue, which contains a five-membered cyclic diimide ring, binds much less tightly ($K_A = 2.9 \times 10^2 \text{ M}^{-1}$ in C_6D_6). The efficient quenching of porphyrin fluorescence by the naphthalene-tetracarboxamide in C_6D_6 is inhibited in polar solvents such as THF, which suppresses the association of the donor–acceptor pair. Absorption bands corresponding to the reduced tetracarboxamide acceptor decay within 20 ps of photoexciting benzene solutions of **41**, suggesting that charge separation and recombination are very rapid.

More tractable electron transfer kinetics are observed for assembly **42** ($R = \text{SiMe}_2^t\text{Bu}$), which consists of a donor–acceptor pair similar to that of **41** but oriented in a side-on manner [127]. The association constants for the matched three-

**42**

point hydrogen bonding in this system are $K_A = 280$, 100, and 79 M^{-1} in benzene, CDCl_3 , and CD_2Cl_2 , respectively. A Job's plot is consistent with a 1:1 complexation stoichiometry. As **41**, efficient quenching of the porphyrin excited state pair is not observed in polar solvents such as THF or DMF, indicating that complexation via hydrogen bonding is crucial for efficient fluorescence quenching. Upon photoexcitation of supramolecule **42** at $\lambda = 532 \text{ nm}$ in benzene, the time-resolved transient absorption spectrum shows the unequivocal formation of a charge-separated state. Formation of both the diimide anion (474 nm) and zinc porphyrin cation (655 nm) radicals were observed at 20 ps; each radical subsequently decayed with a time constant of 270 ps, giving a rate constant for charge recombination of $k_{\text{ET}} = 3.7 \times 10^9 \text{ s}^{-1}$. Time profile analysis of the absorption band maximum (458 nm) of the S_1 state of the zinc porphyrin yields a rate constant for charge separation of $k_{\text{ET}} = 4.1 \times 10^{10} \text{ s}^{-1}$. A pronounced deuterium isotope effect for **42** is found for both charge separation ($k_{\text{H}}/k_{\text{D}} = 1.4$) and recombination ($k_{\text{H}}/k_{\text{D}} = 1.5$), similar to what was observed for the electron transfer kinetics of **1** [70]. For comparison, transient absorption studies of covalently linked model **43**, with similar

**43**



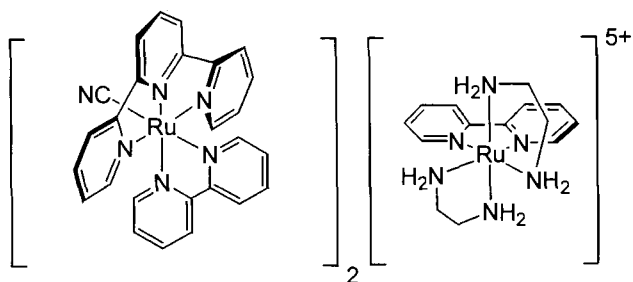
44

driving force and a slightly shorter estimated center-to-center distance (14.7 Å for **42**, 12.8 Å for **43**), give rates of $k_{\text{ET}} = 9.9 \times 10^{10} \text{ s}^{-1}$ and $6.7 \times 10^8 \text{ s}^{-1}$ for charge separation and recombination, respectively. Taken together, the results from kinetics studies of **42** and **43** provide additional experimental support to the notion that hydrogen bonds can provide an efficient bridge for mediating electron transfer.

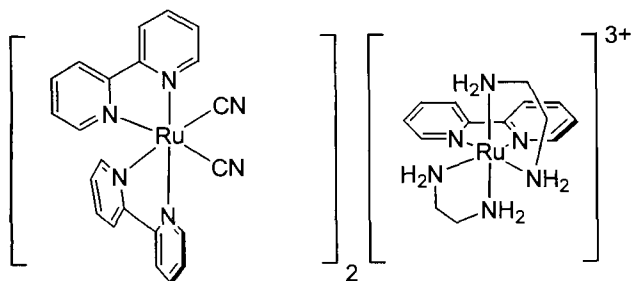
A naphthalene-tetracarboxamide acceptor has also been employed by Sessler and coworkers in the rigid framework of **44** (Ar = 3,5-(^tBu)₂-phenyl, R = ^tBu) which features a chlorin as the singlet-excited state electron donor [128]. A three-point hydrogen bond stabilizes a coplanar supramolecular complex with a ~ 7 Å edge-to-edge distance between the redox sites. Association constants for the assembly are $K_{\text{A}} = 663 \text{ M}^{-1}$ and 364 M^{-1} in toluene and CDCl₃, respectively. Steady-state fluorescence and single-photon counting studies of **44** suggest electron transfer. However, the picosecond transient absorption spectrum shows no evidence for the formation of the diimide anion radical upon irradiation of **44** at $\lambda = 532 \text{ nm}$. In light of these results, Sessler and coworkers propose that the rate of charge recombination is greater than the rate of charge separation to such an extent that the concentration of the ion-pair species cannot build to an observable level.

4.4.7 Mixed-Valence Metal Complexes

Within the Hush formalism of electron transfer [129], the electronic coupling through hydrogen bond interfaces may be deduced from the intensity of a mixed-valence transition between juxtaposed donor–acceptor pairs. We highlight the only such detailed study in this section. Curtis and coworkers have studied a collection of hydrogen-bonded mixed-valence adducts formed between ruthenium(II) electron-donor and ruthenium(III) electron-acceptor complexes in solution [130]. Using acetonitrile or nitromethane as a solvent, hydrogen-bonded assemblies of the type $\{[(\text{tpy})(\text{bpy})\text{Ru}^{\text{II}}(\text{CN})_2]_2, (\text{en})_2\text{Ru}^{\text{III}}(\text{bpy})\}^{5+}$ **45** (bpy = 2,2'-bipyridine, tpy = 2',6'', 2'-terpyridine, en = ethylenediamine) and $\{[(\text{bpy})_2\text{Ru}^{\text{II}}(\text{CN})_2]_2, (\text{en})_2\text{Ru}^{\text{III}}(\text{bpy})\}^{3+}$



45



46

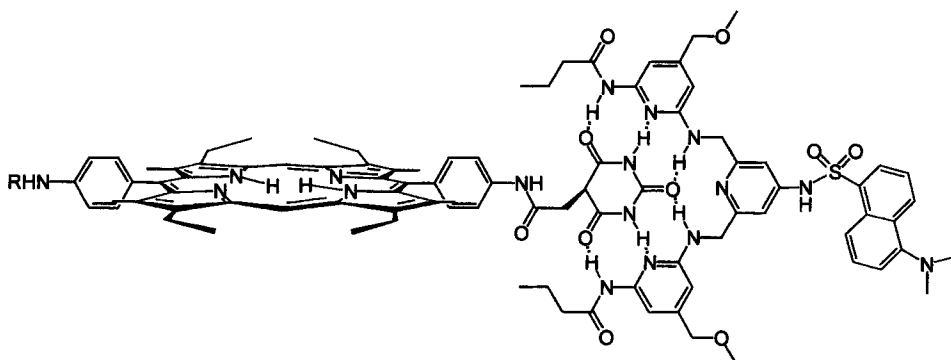
46 are produced. The 2:1 stoichiometry of the ternary aggregates is verified according to Job's method. The self-assembly of the systems is thought to proceed through hydrogen bond interactions between the protons of the en ligands (acid donors) and the nitrogens of the cyanide ligands (base acceptors). The electrochemical waves for the one-electron redox reactions of the individual metal centers separate when measurements are performed in low-donor solvents. The magnitude of this separation suggests that two hydrogen bonds are approximately twice as effective as one for establishing electronic communication between metal redox centers. Direct evaluation of the electronic coupling energies from absorption spectra [129] shows that electronic coupling through the hydrogen bonds of both the mono and dicyano adducts is approximately 65–75 % as efficient as through σ -covalent bonds of the known dithiaspiroalkane-bridged systems [131–133]. Compared to π -conjugated bridging pathways, the coupling through the hydrogen bonds of **45** and **46** is approximately 30–40 % as strong. These interesting results clearly merit further research in the area of mixed-valence metal complexes containing hydrogen bond bridges.

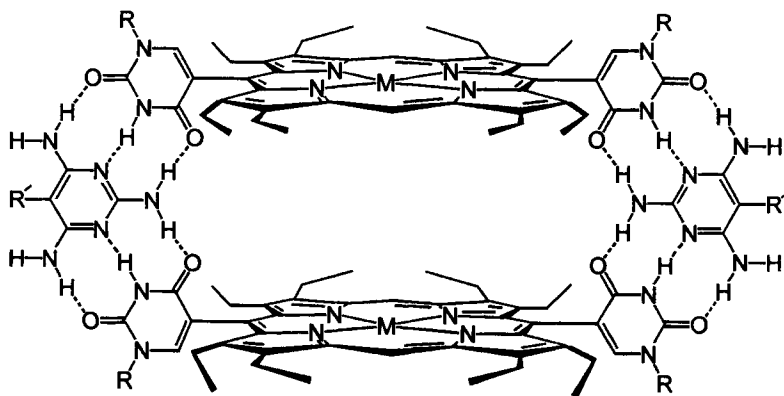
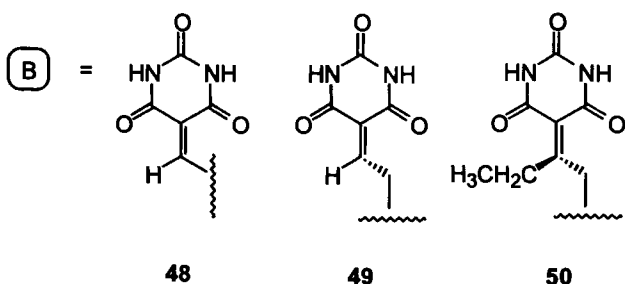
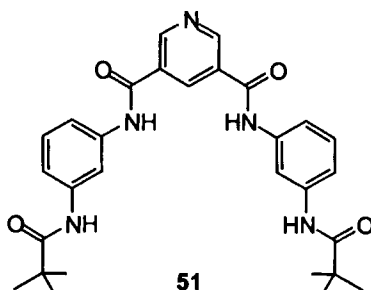
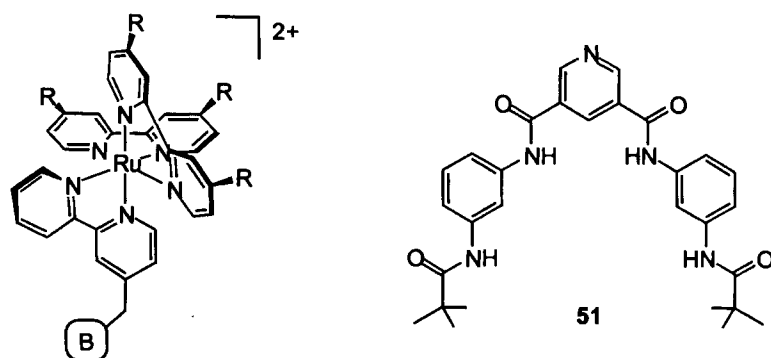
4.4.8 Barbituric Acid-Containing Complementary Pairs

Hamilton and coworkers have prepared well-organized assemblies of type **47** ($R =$ benzyloxycarbonyl), which associate in CH_2Cl_2 via six hydrogen bonds between a porphyrin–barbiturate conjugate and a bis(2,6-diaminopyridine)-derivatized receptor [134]. The estimated distance between the self-assembled centers is $\sim 23 \text{ \AA}$. Efficient energy transfer from a dansyl-functionalized receptor to the porphyrin–barbiturate guest is observed by emission quenching. Control experiments with a dansyl derivative incapable of hydrogen bonding show no fluorescence quenching. Knapp, Isied and coworkers have elaborated this general approach in the preparation of a series of ruthenium(II) tris-bipyridine complexes, **48–50** ($R = \text{'Bu}$), appended with barbituric acid or barbital groups [135, 136]. Complexes **48–50** associate with a multifunctionalized amidopyridine host **51** to form 1:1 adducts in chlorinated solvents. Significant binding ($K_A \sim 10^2 \text{ M}^{-1}$) is observed only for guest **49** in its enolate form, which is promoted over the keto form by the cationic ruthenium(II) center. Studies of electron transfer between osmium and ruthenium polypyridines bridged by this motif have recently been undertaken [137]. Comparison of the electron transfer rate constants observed to those obtained for analogous covalently bonded complexes [138] shows that charge transport is only modestly slower in the hydrogen-bonded systems.

4.4.9 Miscellaneous Hydrogen-Bonded Ensembles

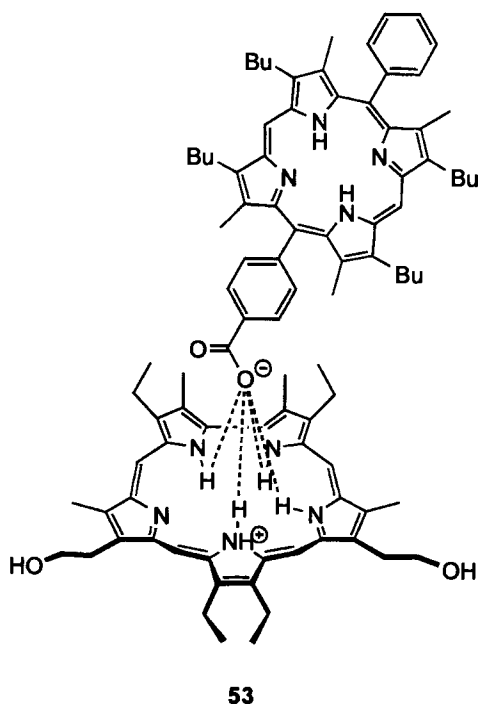
A number of other hydrogen-bonded assemblies containing photoactive groups warrant mention here. Lehn and coworkers have described the self-assembly of a supramolecular cofacial bisporphyrin cage **52** ($R, R' =$ decyl, octyl) via 12 hydrogen bonds [139]. Unlike the porphyrin monomer, whose fluorescence is highly concentration-dependent due to self-quenching via π -stacking aggregation, the fluorescence intensity of bisporphyrin cage **52** is remarkably constant over the con-



**52**

centration range of 1 to 10 mM. When ethanol containing 0.1 % HCl is added to a dichloromethane solution of **52**, the emission reverts to that of the unassembled protonated porphyrin at that same concentration.

Sessler and coworkers have investigated the photophysical properties of systems based on anion chelation by monoprotonated sapphyrins. Archetypal ensemble **53**



[140, 141], consisting of a monocarboxyporphyrin and a protonated pentapyrrolic saphyrin, forms in CH_2Cl_2 with an association constant of $K_A \sim 10^3 \text{ M}^{-1}$. The proclivity of the saphyrin to bind carboxy guests was established using high-resolution FAB mass spectrometry; in the case of the benzoate adduct, an X-ray crystal structure was also obtained (Figure 5). Upon irradiation of **53** at $\lambda = 417 \text{ nm}$, singlet–singlet energy transfer from the porphyrin to the saphyrin occurs; spectral data are consistent with a Förster-type mechanism. Porphyrin dicarboxylates bind inside the cleft of an amide-linked cofacial saphyrin to form aggregates of the type represented by **54** [142]. Affinity constants are on the order of $K_A \sim 10^5 \text{ M}^{-1}$ in nonpolar solvents such as dichloromethane. Steady-state fluorescence

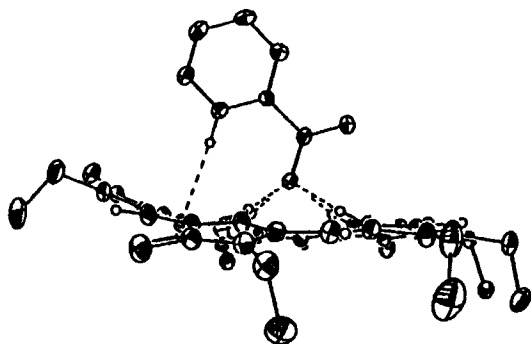
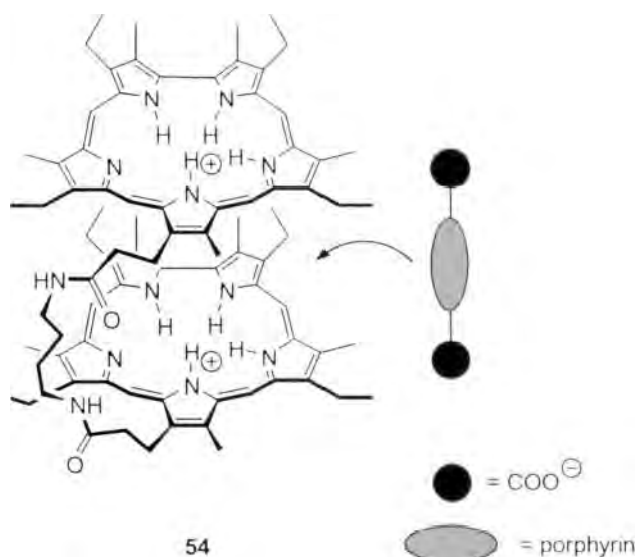


Figure 5. Thermal ellipsoid representation of the protonated saphyrin of **53** complexed with benzoate. (Reprinted with permission from the American Chemical Society.)



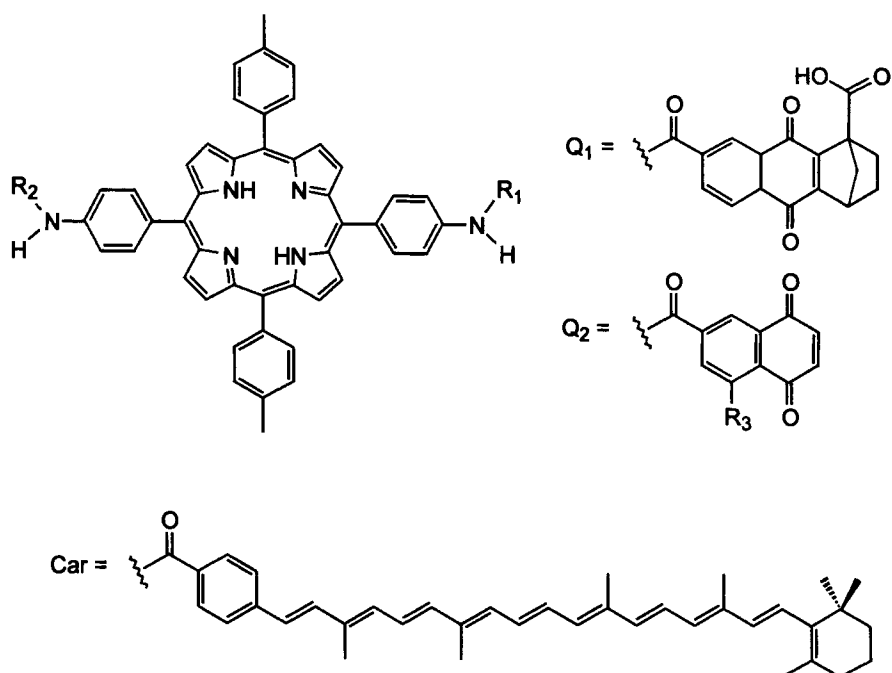
measurements support the conclusion that photoinduced energy transfer occurs between the porphyrin subunit and the sapphyrin dimer.

Gust, Moore, Moore and coworkers' covalent cartenoid–porphyrin–quinone molecular triads **55**–**60** contain a cyclized hydrogen bond within the quinone acceptor framework [143]. The naphthaquinone moiety of **55** is fused to a norbornene system whose bridgehead position bears a carboxylic acid, which can hydrogen bond to an adjacent quinone. Photoinduced electron transfer from the porphyrin to the quinone leads to a marked pK_a increase of the latter, resulting in a fast proton transfer ($k_{PT} \sim 10^{12} \text{ s}^{-1}$) to form the semiquinone. Back electron transfer from the semiquinone is attenuated as a consequence of the proton-stabilized charge-separated species. This leads to a two-fold increase in the quantum yield of the charge-separated state of **55**, as compared to those of the reference triads **56** and **57** (see Volume III, Part 2, Chapter 2).

Self-assembly of monopyrazolylporphyrins by hydrogen bonding has been examined by Ikeda and coworkers [144]. IR spectral measurements of the pyrazole NH stretches indicate that self-aggregates hydrogen bond at concentrations above $\sim 10^{-2} \text{ M}$. The identities of cyclic dimer **61** and tetramer **62** are confirmed by electrospray ionization mass spectrometry (ESI). ^1H NMR titrations in CDCl_3 give association constants of $K_A \sim 39 \text{ M}^{-1}$ and $\sim 9.3 \times 10^{-3} \text{ M}^{-1}$ for **61** and **62**, respectively. No electron transfer studies on these systems have yet been undertaken.

4.4.10 Salt Bridge Systems

In the D—[H]—A systems of Sections 4.4.1 to 4.4.9, little charge redistribution occurs within the interface upon electron transfer. For instance, in the symmetric dicarboxylic acid interfaces of Section 4.4.1, proton displacement from one side of



55: R₁ = Q₁; R₂ = Car

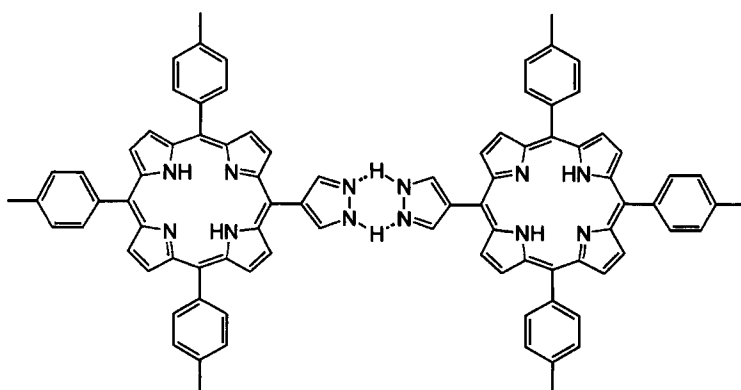
56: R₁ = Q₂; R₂ = Car; R₃ = Cl

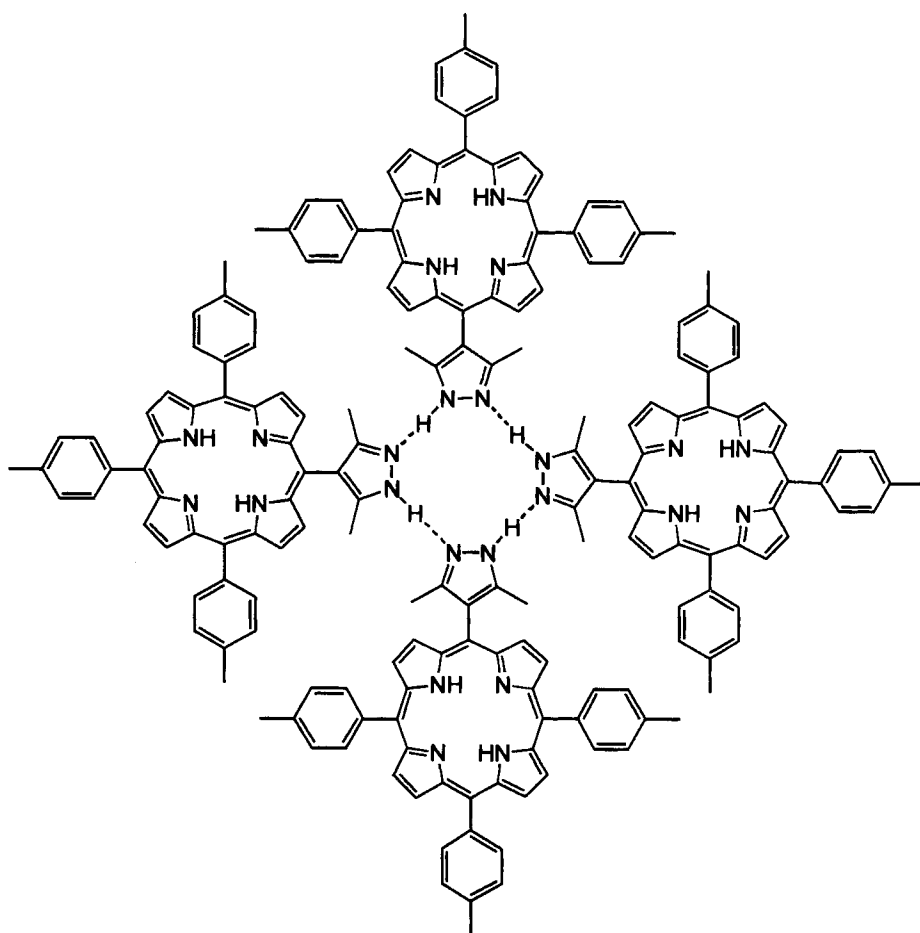
57: R₁ = Q₂; R₂ = Car; R₃ = H

58: R₁ = Q₁; R₂ = H

59: R₁ = Q₂; R₂ = H; R₃ = Cl

60: R₁ = Q₂; R₂ = H; R₃ = H





62

the dicarboxylic acid interface is compensated by the concomitant displacement of a proton from the other side. Because charge redistribution within this interface is negligible, the effect of the proton on electron transfer kinetics is small. As noted in Section 4.4.1, the only mechanism available to couple proton and electron in this type of system arises from dependence of the electronic coupling on the position of the protons within the interface. As demonstrated by many systems presented in Section 4.4, coupling through a hydrogen bond interface is only slightly inferior to that through a covalent pathway. In both cases, electron transfer is fast. Similar results are obtained for donor-acceptor centers separated by base pairs [145], which cannot be ionized. These cases, however, are unusual in biology, where uncompensated proton displacement typically accompanies the redox process. The charge shift resulting from electron *and* proton motion couples to the polarization of the

surrounding environment [146–152], thus providing a unique mechanism for PCET [22, 148]. In this case, changes in polarity, charge and energetics resulting from electron transfer are affected by proton displacement within the interface. To explore the importance of these issues, we have begun exploring PCET reactions that are mediated by a salt bridge, which combines the dipole of an electrostatic ion-pair interaction with a hydrogen-bonding scaffold.

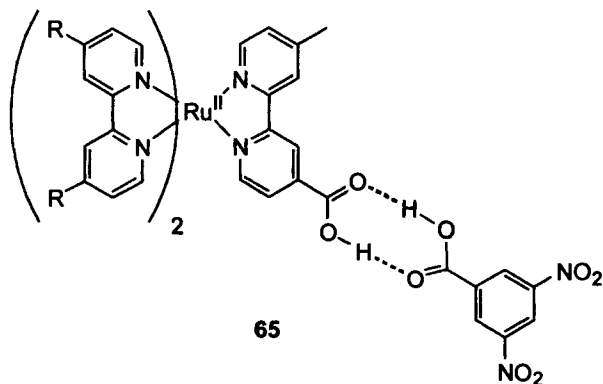
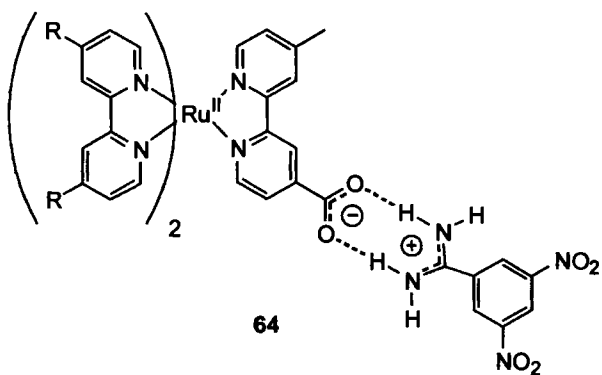
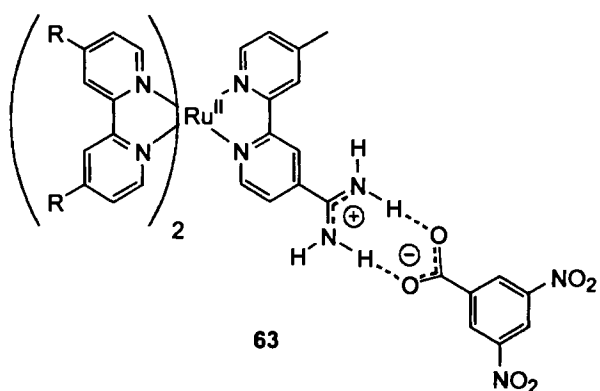
Our initial work is based on the amidinium-carboxylate salt bridge, with flanking electron donors and acceptors. This interaction models the arginine–aspartate (Arg–Asp) salt bridge, an important stabilizing structural element in many biological systems including the active sites of dihydrofolate reductase [153], cytochrome *c* oxidase [154–158] and siroheme reductase [159]. Unlike Arg–Asp, which has multiple guanidinium-carboxylate interactions, amidinium presents two N–H bonds to carboxylate in one specific binding mode, thereby simplifying PCET studies. The two-point hydrogen bond of the amidinium-carboxylate interface features two favorable secondary interactions [160, 161] supported by the electrostatic stabilization of proximal opposing charges within the salt bridge. Accordingly, the amidinium-carboxylate salt bridge readily forms and association persists in solution, even when the dielectric constant of the solvent is high. Counterions are not required to stabilize this interface since the salt bridge may be formed directly from free amidine and carboxylic acid.

Ruthenium polypyridyl systems

The effect of the salt bridge on electron transfer can be determined directly by a comparative kinetics study of a D–[amidinium-carboxylate]–A complex and its switched interface D–[carboxylate-amidinium]–A congener. We have reported such a study for a supramolecular series of complexes where the donor is a ruthenium(II) polypyridyl with one bipyridine (bpy) ligand modified by either amidinium or carboxylate and the acceptor is the complementarily modified 3,5-dinitrobenzene (DNB) [162, 163]. The same donor–acceptor pair bridged by a symmetrical dicarboxylic acid interface has also been examined.

The assembly of supramolecules **63–65** (R = H, Me) was characterized by ^1H NMR, and absorption and infrared spectroscopy. Job's plots confirm the 1:1 adduct formation between the modified-ruthenium polypyridyl and its appropriate 3,5-DNB partner. In low-polarity solvents, association constants for **63** and **64** are large (in CH_2Cl_2 , $K_A = 5.6 \times 10^5 \text{ M}^{-1}$ and $K_A > 10^7 \text{ M}^{-1}$, respectively). The smaller association of **63** is consistent with the electron-withdrawing nitro groups conferring a decreased basicity on the carboxylate group of the 3,5-DNB acceptor, thus resulting in a weaker hydrogen-bonding interaction.

Supramolecules **63–65** were designed to exploit the well-known redox chemistry of electronically excited $[\text{Ru}(\text{bpy})_3]^{2+}$ -type complexes with nitroaromatics [164]. For both systems (R = H and Me), the excited-state lifetime of the Ru(II) polypyridyl donor is sufficiently long that concentration-dependent and -independent kinetics were observed. The concentration-dependent rate arises from the bimolecular electron transfer reaction between uncomplexed Ru(II) polypyridyl donor and the 3,5-DNB acceptor. The measured bimolecular rate constants were in ac-



cordance with that measured by Meyer and coworkers for the reaction between $[\text{Ru}(\text{bpy})_3]^{2+}$ and dinitrobenzene [164]. Moreover, the rate constants were similar to those observed when the carboxylate was esterified, preventing association between the amidinium and nitro functionalities (confirmed by NMR). The concentration-

Table 1. Rates for unimolecular and bimolecular electron transfer for donor–acceptor complexes with amidinium–carboxylate and dicarboxylic acid dimer bridges in dichloromethane at 22 °C

Salt bridge complex	$\Delta G^\circ/\text{eV}$	$k_{\text{ET}}/10^9 \text{ M}^{-1} \text{ s}^{-1\text{a}}$	$k_{\text{PCET}}/10^6 \text{ s}^{-1\text{b}}$
63	−0.14	1.2	8.4
64	−0.34	3.3	310
65	−0.23	3.2	43

^aThe bimolecular reaction of the respective constituents (non-hydrogen bonded) as determined by Stern–Volmer quenching kinetics.

^bUnimolecular electron transfer of the salt bridge associated donor–acceptor pair.

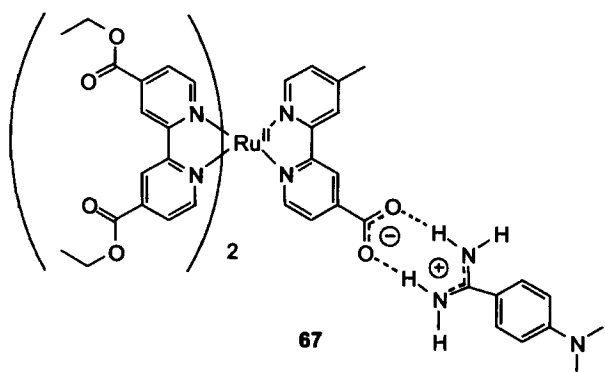
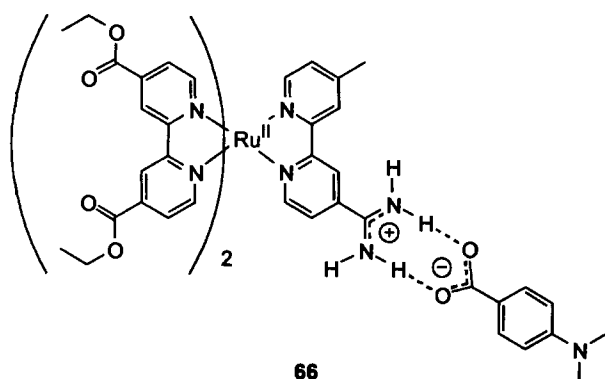
independent lifetime decay component was attributed to the intramolecular PCET rate process of **63–65**.

A reliable kinetics study of the electron transfer reactions of **63–65** demands that the excited-state structure of the ruthenium(II) polypyridyl complexes be properly designed. Electron transfer in these assemblies is initiated by laser excitation of the metal-to-ligand charge transfer (MLCT) transition of the ruthenium(II) polypyridyl complex. Depending on the energetics of the MLCT excited state, two potential reaction pathways arise for the oxidative quenching reaction. For the case where the lowest energy MLCT excited state is localized on the bpy ligand modified with the salt bridge, the excited electron will be placed directly on the PCET pathway. Conversely, a lowest-energy MLCT excited state involving the ancillary bpy ligand will send the excited electron away from the PCET reaction pathway. In the absence of methyl substitution of the bpy rings, the MLCT excited states involving the ancillary bpy and the amidinium- or carboxylate-modified bpy are close in energy, thereby obscuring a comparative PCET study [163]. By tetramethylating the ancillary bpy ligands (tmbpy), the resulting tmbpy MLCT excited state is energetically destabilized by approximately 0.4 eV with respect to the MLCT excited states of either the amidinium- or carboxylate-modified bpy. Accordingly, photoexcitation of **63–65** (R = Me) cleanly promotes the transferring electron onto the salt bridge-functionalized ligand, from where it can smoothly advance to the DNB acceptor.

As shown by the data in Table 1, the unimolecular electron transfer rate constant within the D—[carboxylate-amidinium]—A assembly **64** is a factor of ~ 100 faster than that for assembly **63**, in which the interface is oriented in the opposite direction. This rate disparity may have several origins. For **63**, the permanent dipole of the salt bridge is in the direction of electron transfer. In contrast, the electron transfer pathway in **64** opposes the salt bridge dipole. Internal electrostatic fields affect the rates of electron transfer by altering the driving force of reaction relative to the isolated constituents. This results in an unfavorable energetic contribution in the case of **63** and a favorable one in the case of **64**. The thermodynamics may be further modified by reorganization energies associated with the salt bridge. In **63**, a proton shift from the ruthenium(II) amidinium donor to the carboxylate acceptor can stabilize the developing charge of the electron on the acceptor. Since the proton charge is strongly coupled to the solvent dipoles, charge shift within the salt bridge will be accompanied by significant solvent polarization, thereby giving rise to ad-

ditional Franck–Condon factors. For D—[carboxylate-amidinium]—A, the proton already resides on the acceptor, and there it is likely to remain upon the arrival of the electron. Franck–Condon factors are thus minimized for **64**. It should be emphasized that complete proton transfer in **63** is not necessary for the PCET to be strongly perturbed; any shift of the proton from its initial state will affect the Franck–Condon factors for PCET [146–152]. Finally, differences in hydrogen bond strengths in these asymmetric interfaces may play a role in the efficiencies of electronic coupling. The electron-withdrawing nitro groups on the acceptor will stabilize the negative charge on the carboxylate, resulting in a weaker hydrogen bond for **63** than for **64** and, hence, a correspondingly weaker electronic-coupling pathway.

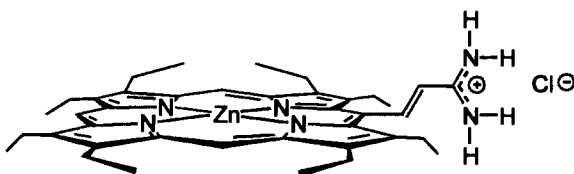
With the electronic framework established for the PCET reactions of ruthenium(II) polypyridyl complexes, we wondered whether the influence of the salt bridge on electron transfer rates was specific to an oxidative quenching pathway. Thus, we also investigated the electron transfer reactions of ruthenium(II) polypyridyls bound to electron donors. In the case of the reductive quenching pathway, the PCET reaction effectively amounts to hole transfer through the amidinium-carboxylate bridge. Accordingly, the excited electron must be removed from the PCET pathway upon MLCT excitation—an effect that is achieved by modifying the ancillary bpy ligands with electron-withdrawing diethylcarboxy groups. Assemblies **66** and **67** are formed by mixing the ruthenium(II) polypyridyl acceptor with its



appropriate amidinium or carboxylate-modified dimethylaniline (DMA) partner [165]. As determined by a Benesi–Hildebrand fit of the change in absorption of the ruthenium complex MLCT band as a function of added DMA derivative, association constants for **66** and **67** are $K_A = 2.8 \times 10^4 \text{ M}^{-1}$ and $5.5 \times 10^3 \text{ M}^{-1}$, respectively. A unimolecular electron transfer rate of $k_{\text{PCET}} = 1.7 \times 10^9 \text{ s}^{-1}$ is found for **66**, for which proton motion is minimized. As expected on the basis of the above PCET considerations, this behavior of the reductive quenching pathway is in contradistinction to the oxidative quenching results for **63** and **64**. Unfortunately, a more explicit analysis of the effect of the salt bridge on the electron transfer pathway is obviated by the large differences in driving force between **66** and **67**. Nonetheless, the overall electron transfer kinetics of **63–67** clearly show that PCET kinetics in salt bridge assemblies are dominated by the orientation of the salt bridge relative to the direction of electron transport. The fastest rates of electron transfer for both oxidative and reductive quenching pathways are observed when the electron is transferred to the site already carrying the positive charge of the interface.

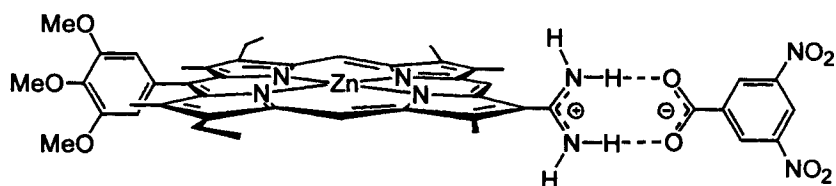
Porphyrin supramolecules

The large changes in optical density for electron and proton transfer products of porphyrin-based systems make them ideal candidates for studying PCET by transient spectroscopy. We have adapted Garigipati's strategy [166] to prepare porphyrin amidines for the first time by reacting nitriles with Weinrub's amide transfer reagent [167], methylaluminum(III) chloramide. The complex of zinc(II) vinyl amidine porphyrin **68** with acceptor 3,4-DNB exhibits a unimolecular electron transfer rate constant of $k_{\text{PCET}} = 7.5 \times 10^8 \text{ s}^{-1}$ as determined by time-resolved fluorescence spectroscopy [168].



68

With the objective of introducing a more rigid linking scaffold than the one provided by **68**, an elaborate synthetic strategy has been developed to introduce amidinium functionalities directly onto the porphyrin ring at the β position; **69**, which is exemplary of our efforts, affords a detailed characterization of the PCET network [169]. Though the proclivity for salt bridge formation was firmly established previous to **69**, we had not characterized by X-ray structural analysis an electron donor–acceptor complex assembled by an amidinium–carboxylate interface. With its absence of counterions, the X-ray crystal structure shown in Figure 6 highlights the simplicity of **69** for PCET studies. NMR studies unequivocally show that the assembly is preserved in solution. The concentration-dependent downfield shift of



zinc(II)-69-3,5-DNB

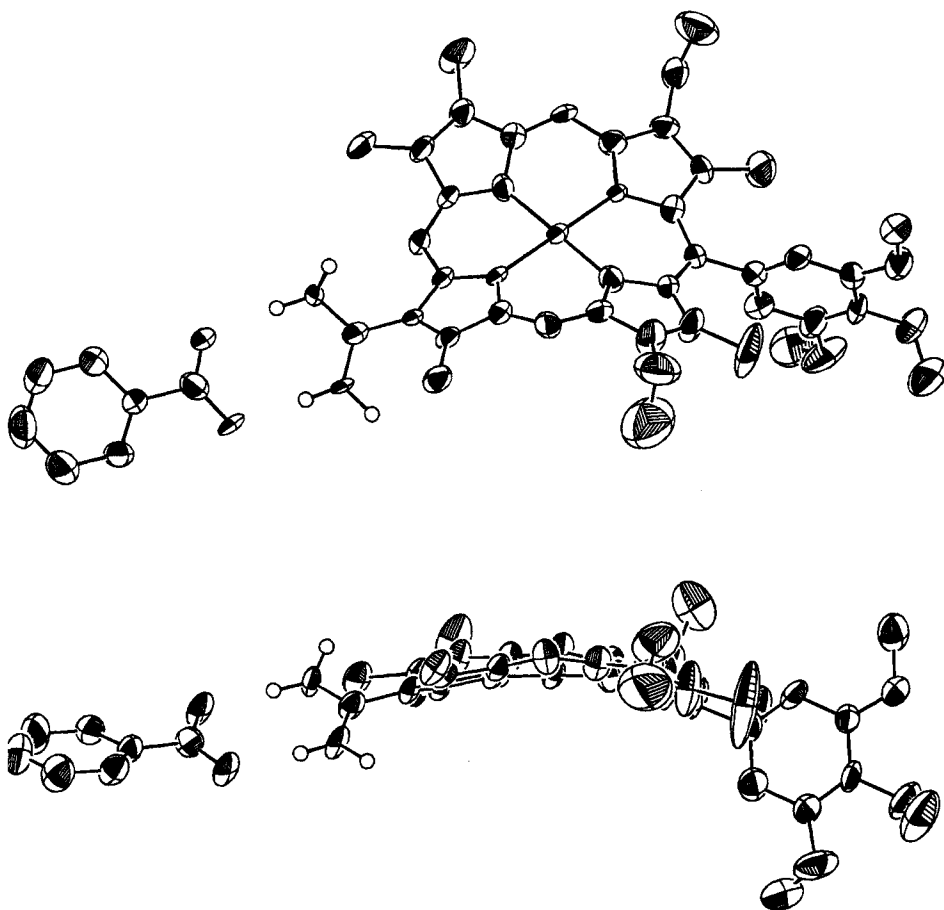


Figure 6. Thermal ellipsoid representation of nickel(II)-69 complexed with benzoate.

amidinium protons involved in hydrogen bonding (NH_{ax} varying by >2 ppm) to the carboxylate is contrasted by an insensitivity of the chemical shift (<0.5 ppm) for the amidinium protons external to the salt bridge (NH_{eq}). Such behavior has emerged as a signature of salt bridge formation. Additionally, *meso* protons are a sensitive measure of π -stacking in porphyrin systems [170, 171]; in **69** they do not shift, indicating that π -stacking is not an important mechanism of association. This is also expected on the basis of thermodynamic considerations; π -stacking is a much weaker interaction than the two-point hydrogen bond of the salt bridge. Association constants of nickel(II)-**69** with the carboxylate are exceptionally large ($K_{\text{A}} = 7.7 \times 10^5 \text{ M}^{-1}$ in CH_2Cl_2), even when the dielectric constant of the solvent is high ($K_{\text{A}} = 280 \text{ M}^{-1}$ in DMSO).

The Soret and Q-bands of the porphyrin undergo a blue shift immediately upon association of zinc(II)-**69** to the carboxylate ion. The perturbation of the absorption profile upon salt bridge formation suggests that the interface is strongly coupled to the porphyrinic chromophore and correspondingly to the electron transfer pathway. Upon excitation of the salt bridge complex of zinc(II)-**69** and acceptor 3,5-DNB, photoinitiated electron transfer occurs; a unimolecular rate constant of $k_{\text{PCET}} = 6.4 \times 10^7 \text{ s}^{-1}$ is calculated from the fluorescence decay kinetics. The electron transfer rate constant for the associated salt bridge complex is considerably smaller than that of covalently linked zinc(II) porphyrin donor–acceptor systems. For example, an electron transfer rate constant of $k_{\text{ET}} = 3 \times 10^{10} \text{ s}^{-1}$ is found for Wasielewski's zinc(II) porphyrin–[Sp]–quinone (Sp = rigid polycyclic bridge) system **2** at equivalent driving forces ($\Delta G^\circ = -0.30 \text{ eV}$) [71]; this faster rate is even more striking considering the longer electron transfer distance in **2** (edge-to-edge distance: zinc(II) porphyrin–[Sp]–quinone = 10.5 \AA ; **69**-DNB = 7.0 \AA). Undoubtedly, the pronounced effect of the interface protons on the kinetics of **69**-DNB arises from their strong coupling to the electron transfer pathway, engendered by the direct attachment of the salt bridge network to the porphyrin donor macrocycle.

4.5 Concluding Remarks

With the field of hydrogen-bonded electron transfer in its infancy, new frontiers await exploration and numerous issues remain to be addressed. The D—[H]—A supramolecules of the preceding sections define two basic PCET reaction mechanisms:

- 1) Electron transfer occurs through a hydrogen bond interface in which the interface proton(s) is(are) effectively stationary; here, the hydrogen bond mediates the efficiency of electron conduction.
- 2) Proton motion within the interface accompanies the electron transfer event; hence, charge rearrangement results from the motion of both the electron *and* the proton.

Placing these two cases in context, simple electron transfer (ET) is generally defined within the Marcus–Levich framework,

$$k_{\text{ET}} = V_{\text{el}}^2 \cdot FC_{\text{ET}} \quad (3)$$

where V_{el} is the electronic coupling and FC_{ET} is the Franck–Condon weighted density of states. Electron transfers described by 1) and 2) step beyond this basic model because both the electron *and* the proton may affect V_{el} *and* FC (for this case we define a FC_{PCET}). V_{el} will depend parametrically on the position of the proton in the interface; extensive charge redistribution (e.g., salt bridge systems of Section 4.4.10) will lead to FC_{PCET} contributions. The FC_{PCET} effect is specific to case 2). To understand the origins of the FC_{PCET} factor, consider again a simple electron transfer reaction. The electron tunnels through the potential barrier from donor to acceptor when the solvent fluctuates to a configuration where the energies of the reactants and products are essentially equal. For case 2), the electron *and* proton tunnel and now both events are induced by solvent fluctuations; coupling arises because the electron and proton influence each other thermodynamically and kinetically [146–152]. As the electron moves, the $\text{p}K_{\text{a}}$ s of the donor and acceptor will change; but to predict kinetics, the driving force (ΔG°) of the reaction is not sufficient. The FC_{PCET} factors will also be affected by changes in ΔG° and by the charge redistribution resulting from electron *and* proton motion. Thus, any motion of the proton from its initial position will perturb V_{el} and FC_{ET} , thereby affecting the kinetics for electron transfer.

The many systems described in Section 4.4, as well as the D—[H]—A supramolecules that continue to emerge, provide ample opportunity to investigate and assess quantitatively the role of hydrogen bonding and protons on electronic coupling (i.e., the problem defined by 1)). It is already clear from the large body of work performed to date that electronic coupling through a hydrogen bond is smaller, but only slightly so, than that through a covalent bond. The richer problem defined by 2) is just beginning to be examined on an intimate mechanistic level, and there are a number of fundamental questions that warrant investigation. What is the timing between the electron and the proton, and what factors distinguish synchronous and asynchronous transfer of the electron and proton? What are the structural/electronic features of the PCET network by which the proton and electron communicate with each other? With the additional charge redistribution resulting from proton motion, how do the energetics (e.g., reorganization, free energy) of charge transfer in a PCET reaction differ from those in an ET reaction?

Answers to these questions are predicated on the ingenious design of new supramolecular systems. First and foremost, well-defined model systems that allow the independent timing of proton and electron are needed; some systems—notably those described in Section 4.4.10—are poised to attack this issue because they display unique spectroscopic signatures for the transfer of the electron and the proton. In addition to directly probing the sequence and rates of the two events, kinetic isotope effects for the proton and the electron transfers may be ascertained. Isotope effects have been used to infer PCET mechanisms in oxygen activation by model

compounds and enzyme catalysis. Meyer's measurements of the kinetic isotope effects of hydroxo to oxo conversion in ruthenium polypyridyl compounds [172–174], and Mayer's studies on hydrogen atom abstraction by various metal-oxo compounds [175] have led to the conclusion that such reaction mechanisms involve concerted PCET. Similarly, Klinman has pioneered the use of isotope effect measurements on a variety of enzyme processes involving proton/hydrogen atom/hydride transfers to construe mechanistic details of the PCET pathways in a variety of enzymatic transformations [176, 177]. In these biocatalysis and catalysis studies, the isotope effects are determined from substrate disappearance and/or product appearance kinetics, which can encompass a mechanistic complexity extending beyond PCET. As Klinman notes, the interpretation of results is highly dependent on theoretical models. For systems in which the independent timing of the proton and the electron can be achieved, the isotope effects for the kinetically resolved electron and proton events may be measured directly. We anticipate that the data provided from such measurements and the accompanying theories will comprise a powerfully predictive framework, which will be useful in future interpretations of isotope effects in catalytic reactions in enzymes and model systems.

On a second front, in all of the systems described here, the hydrogen bond interface is required to maintain assembly of the supramolecular complex. This construct makes it difficult to assess the effect of pK_a on the coupled electron- and proton-transfer reactions. By placing a network proximal to, yet distinct from, the electron transfer pathway while maintaining independent spectroscopic signatures for electron and proton transfer, the kinetics for the isolated events can be examined as the pK_a of the environment is systematically varied.

New methods for the measurement of electron transfer in hydrogen-bonded systems also loom on the horizon. The study of electron transfer in hydrogen-bonded assemblies has been restricted primarily to photoinitiated reactions. Yet these systems lend themselves to examination by other experimental methodologies as well. For instance, radiolysis, the experimental brethren of photolysis [178], has yet to be applied to the study of electron transfer through hydrogen-bonded interfaces. Electron transfer through hydrogen bonds can also be studied using electrochemical methods. Recently, Whitesides and Rampi have measured the current across junctions formed from juxtaposing two self-assembled monolayers [179]. Comparative measurements of junctions comprised of covalent, ionic, hydrogen bond or van der Waals connections give insight into the relative abilities of these interfaces to mediate electron conductivity and transport.

Finally, with experimental methodologies for PCET measurements in place, and with the knowledge acquired from model studies and accompanying theoretical treatments, future research directions will invariably turn toward defining the mechanisms of coupled electron–proton processes, at a rigorous level, in the complex machinery of biology. Issue 1), of how hydrogen bonds conduct electrons along the pathways of proteins and enzymes, has already been extensively explored [104, 109, 180, 181]. However, other processes, especially those encompassed by case 2), largely have been ignored for a several reasons. Paramount among these are the difficulties of clearly identifying the electron- and proton-transfer pathways in complex biological structures and of isolating the kinetics of the PCET event from

the multitude of other events that accompany biological function, such as conformational dynamics, allosteric regulation, and substrate transport to the active site. Such issues have long been recognized as roadblocks to further advancement in understanding the precise details of PCET in many protein and enzyme mechanisms. For instance, Malmström states in his review of cytochrome *c* oxidase [182], ‘In many ways the situation is disappointing, however. The mechanism deals only with the formal kinetics and the chemical nature of the catalytic intermediates, but it provides no information on the molecular mechanism’. In the area of photosynthesis, the disconnect between intimate mechanistic detail and protein/enzyme function is even more striking. Some 30 years after Mitchell’s initial proposal of proton translocation driven by electron transfer [183], Feher and Okamura succinctly state in their review of bacterial RCs [184] that ‘we do not know from experimental measurements whether electron transfer precedes or follows proton transfer, since these individual steps have not been kinetically resolved’.

Of the impressive PCET systems in biology, ribonucleotide reductase (RNR) provides an attractive “laboratory” for mechanistic study. RNR enzymes catalyze the reduction of the four common ribonucleotides to their corresponding deoxyribonucleotides via a thiyl radical hydrogen-abstraction mechanism [185–187]. The redox pathway for the Class I enzymes has been deduced from docked crystal structures of the R2 [188] and R1 subunits from *E. coli* [189]. The oxidizing equivalent of a tyrosyl radical, Y122, generated at the dinuclear iron center of the R2 subunit, is conveyed to the catalytic cysteine residue C439 in the R1 active site where ribonucleotide reduction occurs [190, 191]. Hole transfer between the R1/R2 subunits is proposed to proceed along the 35 Å, tightly coupled PCET pathway shown in Figure 7, as determined from mutagenesis [192, 193], sequence conservation [194], and docking studies of the individual subunits [189]. As has been discussed [191], the oxidation potential of tyrosyl radical (0.94 V) is insufficient to generate a thiyl radical from cysteine thiol (−1.33 V); thus, only oxidation of a deprotonated cysteine thiolate (−0.77 V) is favored, implicating a PCET mechanism. Recent theoretical studies support this contention by predicting proton and electron synchronization (i.e., hydrogen atom transfer) to be highly favored over electron transfer [195]. These extensive discussions notwithstanding, the PCET pathway shown in Figure 7 has escaped direct experimental investigation. In the context of the thematic focus of this chapter, the pathway is formed from the self-assembly of subunits R1 and R2. Consequently, RNR may be viewed as an extremely complex hydrogen-bonded “supramolecule”. The quantitative measurement of electron and proton transport in supramolecules such as these is one of the formidable challenges confronting PCET studies in the near future.

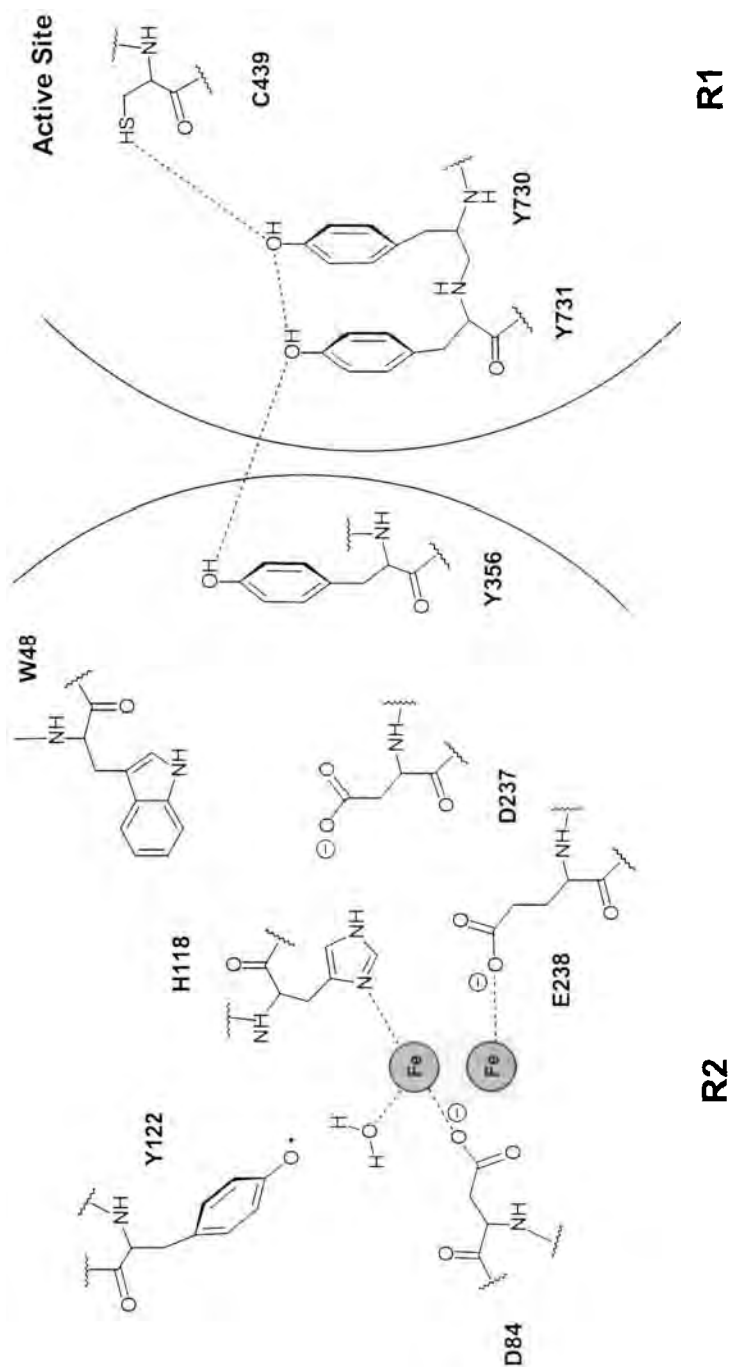


Figure 7. Proposed proton-coupled electron transfer (PCET) pathway between the R2 and R1 subunits of the *E. coli* ribonucleotide reductase (RNR) complex. The conserved amino acids are shown schematically (*E. coli* numbering).

Acknowledgments

We dedicate this chapter to the memory of Bo Malmström. The National Institutes of Health (GM47274) supported the research presented in this review from our group.

References

1. R. H. Holm, E. I. Solomon (Eds.): *Chem. Rev.* (Special Issue: Bioinorganic Enzymology) 96 (1996) 2237.
2. A. Muller, H. Ratajczaks, W. Junge, E. Diemann, *Electron and Proton Transfer in Chemistry and Biology*, Elsevier, Amsterdam 1992.
3. G. T. Babcock, M. Wikström, *Nature* 356 (1992) 301.
4. A. M. Kuznetsov, J. Ulstrup, *Electrochim. Acta* 45 (2000) 2339.
5. J. Ulstrup, *Charge Transfer Processes in Condensed Media*, Springer-Verlag, Berlin 1979.
6. R. R. Birge, *Annu. Rev. Phys. Chem.* 41 (1990) 683.
7. H. Durr, H. Bouas-Laurent, *Photochromism: Molecules and System*, Elsevier, Amsterdam 1990.
8. M. Scherl, D. Haarer, J. Fischer, A. DeCian, J.-M. Lehn, Y. Eichen, *J. Phys. Chem.* 100 (1996) 16175.
9. T. J. Marks, M. A. Ratner, *Angew. Chem. Int. Ed.* 34 (1995) 155.
10. H. Taube, *Angew. Chem. Int. Ed.* 23 (1984) 329.
11. S. Shaik, A. Shurki, *Angew. Chem. Int. Ed.* 38 (1999) 587.
12. R. Bianco, J. T. Hynes, *J. Phys. Chem. A* 103 (1999) 3797.
13. B. J. Gertner, J. T. Hynes, *Science* 271 (1996) 1563.
14. J.-M. Savéant, *Acc. Chem. Res.* 26 (1993) 455.
15. M. Robert, J.-M. Savéant, *J. Am. Chem. Soc.* 122 (2000) 514.
16. R. A. Marcus, N. Sutin, *Biochim. Biophys. Acta* 811 (1985) 265.
17. N. Sutin, *Acc. Chem. Res.* 15 (1982) 275.
18. R. A. Scott, A. G. Mauk, H. B. Gray, *J. Chem. Ed.* 62 (1985) 932.
19. R. A. Marcus, N. Sutin, *Inorg. Chem.* 14 (1975) 213.
20. R. D. Mussell, D. G. Nocera, *J. Am. Chem. Soc.* 110 (1988) 2764.
21. R. D. Mussell, D. G. Nocera, *Inorg. Chem.* 29 (1990) 3711.
22. R. D. Newsham, R. I. Cukier, D. G. Nocera, *J. Phys. Chem.* 95 (1991) 9660.
23. C. Turró, J. M. Zaleski, Y. M. Karabatsos, D. G. Nocera, *J. Am. Chem. Soc.* 118 (1996) 6060.
24. Z. Murtaza, D. K. Graff, A. P. Zipp, L. A. Worl, W. E. Jones, W. D. Bates, T. J. Meyer, *J. Phys. Chem.* 98 (1994) 10504.
25. T. M. McCleskey, J. R. Winkler, H. B. Gray, *Inorg. Chim. Acta* 225 (1994) 319.
26. T. M. McCleskey, J. R. Winkler, H. B. Gray, *J. Am. Chem. Soc.* 114 (1992) 6935.
27. J.-M. Lehn, *Supramolecular Chemistry: Concepts and Perspectives*, VCH, Weinheim, Germany 1995.
28. F. Vögtle, *Supramolecular Chemistry: An Introduction*, Marutzen, Tokyo 1995.
29. D. Philp, J. F. Stoddart, *Angew. Chem. Int. Ed.* 35 (1996) 1154.
30. J. R. Fredericks, A. D. Hamilton, in Y. Murakami (Ed.): *Comprehensive Supramolecular Chemistry*, Vol. 3, Pergamon, Oxford, UK 1996, p. 565.
31. G. M. Whitesides, J. P. Mathias, C. T. Seto, *Science* 254 (1991) 1312.
32. M. M. Conn, J. Rebek, Jr., *Chem. Rev.* 97 (1997) 1647.
33. G. C. Pimentel, A. L. McClellan, *The Hydrogen Bond*, W. H. Freeman, San Francisco 1960.
34. G. A. Jeffrey, *An Introduction to Hydrogen Bonding*, Oxford University Press, New York 1997.
35. M. C. Etter, *Acc. Chem. Res.* 23 (1990) 120.
36. M. Linhard, *Z. Elektrochem.* 50 (1944) 224.

37. M. Linhard, M. Weigel, *Z. Anorg. Allg. Chem.* 266 (1951) 49.
38. S. M. Hubig, J. K. Kochi, *J. Am. Chem. Soc.* 121 (1999) 1688.
39. S. M. Hubig, R. Rathore, J. K. Kochi, *J. Am. Chem. Soc.* 121 (1999) 617.
40. R. Rathore, S. M. Hubig, J. K. Kochi, *J. Am. Chem. Soc.* 119 (1997) 11468.
41. R. Billing, *Coord. Chem. Rev.* 159 (1997) 257.
42. R. Billing, A. Vogler, *J. Photochem. Photobiol. A* 103 (1997) 239.
43. A. Vogler, H. Kunkely, *Comments Inorg. Chem.* 19 (1997) 283.
44. For example, see H. Kisch, *Coord. Chem. Rev.* 159 (1997) 385 and references therein.
45. T.-H. Tran-Thi, *Coord. Chem. Rev.* 160 (1997) 53.
46. T. Shimidzu, T. Iyoda, *Chem. Lett.* (1981) 853.
47. E. Ojadi, R. Selzer, H. Linschitz, *J. Am. Chem. Soc.* 107 (1985) 7783.
48. H. van Willigen, U. Das, E. Ojadi, H. Linschitz, *J. Am. Chem. Soc.* 107 (1985) 7784.
49. U. Hofstra, R. B. M. Koehorts, T. J. Schaafsma, *Chem. Phys. Lett.* 130 (1986) 555.
50. S. Gaspard, *C. R. Acad. Sci. Paris* 298 (1984) 379.
51. J. A. Goodwin, W. R. Scheidt, *J. Phys. Chem.* 94 (1990) 4432.
52. M. Hugerat, H. Levanon, E. Ojadi, L. Biczok, H. Linschitz, *Chem. Phys. Lett.* 181 (1991) 400.
53. F. J. Vergeldt, R. B. M. Koehorts, T. J. Schaafsma, J.-C. Lambry, J.-L. Martin, D. G. Johnson, M. R. Wasielewski, *Chem. Phys. Lett.* 182 (1991) 107.
54. H. Segawa, C. Takehara, K. Honda, T. Shimidzu, T. Asahi, N. Mataga, *J. Phys. Chem.* 96 (1992) 503.
55. K. Kemnitz, T. Sakahuchi, *Chem. Phys. Lett.* 196 (1992) 497.
56. M. Hugerat, A. van der Est, E. Ojadi, L. Biczok, H. Linschitz, H. Levanon, D. Stehlik, *J. Phys. Chem.* 100 (1996) 495.
57. A. Berg, M. Rachamim, T. Galili, H. Levanon, *J. Phys. Chem.* 100 (1996) 8791.
58. S. S. Serdem, *J. Porphyrins Phthalocyanines* 2 (1998) 61.
59. D. J. Fermin, H. D. Duong, Z. Ding, P.-F. Brevet, H. H. Girault, *J. Am. Chem. Soc.* 121 (1999) 10203.
60. D. K. Geiger, C. A. Kelly, *Inorg. Chim. Acta* 154 (1988) 137.
61. T.-H. Tran-Thi, *Chem. Phys. Lett.* 148 (1988) 327.
62. T.-H. Tran-Thi, J. F. Lipskier, D. Houde, C. Pepin, E. Keszei, J. P. Jay-Gerin, *J. Chem. Soc. Faraday Trans.* 88 (1992) 2129.
63. J. F. Lipskier, T.-H. Tran-Thi, *Inorg. Chem.* 32 (1993) 722.
64. F. D'Souza, Y.-Y. Hsieh, G. R. Deviprasad, *Chem. Commun.* (1998) 1027.
65. F. D'Souza, Y.-Y. Hsieh, G. R. Deviprasad, *J. Porphyrins Phthalocyanines* 2 (1998) 429.
66. G. McLendon, R. Hake, *Chem. Rev.* 92 (1992) 481.
67. V. L. Davidson, *Acc. Chem. Res.* 33 (2000) 87.
68. T. Hayashi, H. Ogoshi, *Chem. Soc. Rev.* 26 (1997) 355.
69. N. Mataga, H. Miyasaka, in J. Jortner, M. Bixon (Eds.): *Electron Transfer-From Isolated Molecules to Biomolecules*, vol. 107 of *Adv. Chem. Phys.*, Wiley, New York 1999, p. 431.
70. C. Turró, C. K. Chang, G. E. Leroi, R. I. Cukier, D. G. Nocera, *J. Am. Chem. Soc.* 114 (1992) 4013.
71. M. R. Wasielewski, M. P. Niemczyk, W. A. Svec, E. B. Pewitt, *J. Am. Chem. Soc.* 107 (1985) 1080.
72. D. N. Beratan, J. N. Onuchic, J. J. Hopfield, *J. Chem. Phys.* 86 (1987) 4488.
73. D. N. Beratan, J. N. Betts, J. N. Onuchic, *Science* 252 (1991) 1285.
74. J. N. Onuchic, D. N. Beratan, *J. Chem. Phys.* 92 (1990) 722.
75. X. G. Zhao, R. I. Cukier, *J. Phys. Chem.* 99 (1995) 945.
76. P. J. F. de Rege, S. A. Williams, M. J. Therien, *Science* 269 (1995) 1409.
77. A. Helms, D. Heiler, G. L. McLendon, *J. Am. Chem. Soc.* 113 (1991) 4325.
78. Y. Deng, S. D. Carpenter, D. G. Nocera, unpublished results.
79. A. Helms, D. Heiler, G. McLendon, *J. Am. Chem. Soc.* 114 (1992) 6227.
80. D. Heiler, G. McLendon, P. Rogalskyj, *J. Am. Chem. Soc.* 109 (1987) 604.
81. H. Tamiaki, K. Nomura, K. Maruyama, *Bull. Chem. Soc. Jpn.* 67 (1994) 1863.
82. C. F. Portela, J. Brunckova, J. L. Richards, B. Schoellhorn, Y. Iamamoto, D. Madge, T. G. Traylor, C. L. Perrin, *J. Phys. Chem. A* 103 (1999) 10540.
83. M. D. Newton, *J. Electroanal. Chem.* 438 (1997) 3.

84. L. D. Zusman, D. N. Beratan, in J. Jortner, M. Bixon (Eds.): *Electron Transfer-From Isolated Molecules to Biomolecules*, vol. 106 of *Adv. Chem. Phys.*, Wiley, New York 1999, p. 377.
85. Y. Aoyama, M. Asakawa, Y. Matsui, H. Ogoshi, *J. Am. Chem. Soc.* **113** (1991) 6233.
86. K. Tanaka, Y. Yamamoto, I. Machida, S. Iwata, *J. Chem. Soc. Perkin Trans. II* (1999) 285.
87. R. B. Gennis, *Biomembranes*, Springer-Verlag, New York 1989.
88. F. L. Crane, *Annu. Rev. Biochem.* **46** (1977) 439.
89. T. Hayashi, T. Asai, H. Hokazono, H. Ogoshi, *J. Am. Chem. Soc.* **115** (1993) 12210.
90. T. Hayashi, T. Miyahara, N. Hashizume, H. Ogoshi, *J. Am. Chem. Soc.* **115** (1993) 2049.
91. T. Hayashi, T. Miyahara, Y. Aoyama, M. Nonoguchi, H. Ogoshi, *Chem. Lett.* (1994) 1749.
92. T. Hayashi, T. Miyahara, Y. Aoyama, M. Kobayashi, H. Ogoshi, *Pure Appl. Chem.* **66** (1994) 797.
93. T. Hayashi, T. Miyahara, S. Kumazaki, H. Ogoshi, K. Yoshihara, *Angew. Chem. Int. Ed.* **35** (1996) 1964.
94. T. Hayashi, T. Miyahara, N. Koide, Y. Kato, H. Masuda, H. Ogoshi, *J. Am. Chem. Soc.* **119** (1997) 7281.
95. F. D'Souza, *J. Am. Chem. Soc.* **118** (1996) 923.
96. M. C. Gonzalez, A. R. McIntosh, J. R. Bolton, A. C. Weedon, *Chem. Commun.* (1984) 1138.
97. M. C. Gonzalez, A. C. Weedon, *Can. J. Chem.* **63** (1985) 602.
98. Y. Kuroda, M. Ito, T. Sera, H. Ogoshi, *J. Am. Chem. Soc.* **115** (1993) 7003.
99. T. Arimura, C. T. Brown, S. L. Springs, J. L. Sessler, *Chem. Commun.* (1996) 2293.
100. R. Milbradt, J. Weiss, *Tetrahedron Lett.* **36** (1995) 2999.
101. T. Arimura, S. Ide, H. Sugihara, S. Murata, J. L. Sessler, *New J. Chem.* **23** (1999) 977.
102. H. Adams, F. J. Carver, C. A. Hunter, N. J. Osborne, *Chem. Commun.* (1996) 2529.
103. C. A. Hunter, R. J. Shannon, *Chem. Commun.* (1996) 1361.
104. H. B. Gray, J. R. Winkler, *Annu. Rev. Biochem.* **65** (1996) 537.
105. H. Tamiaki, K. Maruyama, *Chem. Lett.* (1993) 1499.
106. D. A. Williamson, B. E. Bowler, *J. Am. Chem. Soc.* **120** (1998) 10902.
107. A. B. Gretchikhine, M. Y. Ogawa, *J. Am. Chem. Soc.* **118** (1996) 1543.
108. S. R. L. Fernando, G. V. Kozlov, M. Y. Ogawa, *Inorg. Chem.* **37** (1998) 1900.
109. R. Langen, I.-J. Chang, J. P. Germanas, J. H. Richards, J. R. Winkler, H. B. Gray, *Science* **268** (1995) 1733.
110. A. Harriman, D. J. Magda, J. L. Sessler, *Chem. Commun.* (1991) 345.
111. A. Harriman, D. J. Magda, J. L. Sessler, *J. Phys. Chem.* **95** (1991) 1530.
112. A. Harriman, Y. Kubo, J. L. Sessler, *J. Am. Chem. Soc.* **114** (1992) 388.
113. J. L. Sessler, B. Wang, A. Harriman, *J. Am. Chem. Soc.* **115** (1993) 10418.
114. J. L. Sessler, B. Wang, A. Harriman, *J. Am. Chem. Soc.* **117** (1995) 704.
115. M. Sirish, B. G. Maiya, *J. Porphyrins Phthalocyanines* **2** (1998) 327.
116. A. Berman, E. S. Izraeli, H. Levanon, B. Wang, J. L. Sessler, *J. Am. Chem. Soc.* **117** (1995) 8252.
117. M. Asano-Someda, H. Levanon, J. L. Sessler, R. Wang, *Mol. Phys.* **95** (1998) 935.
118. A. Berg, Z. Shuali, M. Asano-Someda, H. Levanon, M. Fuhs, K. Möbius, R. Wang, C. Brown, J. L. Sessler, *J. Am. Chem. Soc.* **121** (1999) 7433.
119. E. C. Constable, R.-A. Fallahpour, *J. Chem. Soc. Dalton Trans.* (1996) 2389.
120. C. M. White, M. F. Gonzalez, D. A. Bardwell, L. H. Rees, J. C. Jeffery, M. D. Ward, N. Armaroli, G. Calogero, F. Barigelletti, *J. Chem. Soc. Dalton Trans.* (1997) 727.
121. M. D. Ward, *Chem. Soc. Rev.* **26** (1997) 365.
122. N. Armaroli, F. Barigelletti, G. Calogero, L. Flamigni, C. M. White, M. D. Ward, *Chem. Commun.* (1997) 2181.
123. J. L. Sessler, C. T. Brown, R. Wang, T. Hirose, *Inorg. Chim. Acta* **251** (1996) 135.
124. J. L. Sessler, personal communication.
125. V. Y. Shafirovich, S. H. Courtney, N. Ya, N. E. Geacintov, *J. Am. Chem. Soc.* **117** (1995) 4920.
126. A. Osuka, E. Shiratori, R. Yoneshima, T. Okada, S. Taniguchi, N. Mataga, *Chem. Lett.* (1995) 913.
127. A. Osuka, R. Yoneshima, H. Shiratori, T. Okada, S. Taniguchi, N. Mataga, *Chem. Commun.* (1998) 1567.

128. J. L. Sessler, C. T. Brown, D. O'Connor, S. L. Springs, R. Wang, M. Sathisatham, T. Hirose, *J. Org. Chem.* **63** (1998) 7370.
129. N. S. Hush, *Prog. Inorg. Chem.* **8** (1967) 391.
130. J. Yang, D. Seneviratne, G. Arbatin, A. M. Andersson, J. C. Curtis, *J. Am. Chem. Soc.* **119** (1997) 5329.
131. C. A. Stein, N. A. Lewis, G. Seitz, *J. Am. Chem. Soc.* **104** (1982) 2596.
132. C. A. Stein, N. L. Lewis, G. Seitz, A. D. Baker, *Inorg. Chem.* **22** (1986) 1124.
133. A. P. L. Rendell, G. B. Bacskey, N. S. Hush, *J. Am. Chem. Soc.* (1988) 8343.
134. P. Tecilla, R. P. Dixon, G. Slobodkin, D. S. Alavi, D. H. Waldeck, A. D. Hamilton, *J. Am. Chem. Soc.* **112** (1990) 9408.
135. T. Chin, Z. Gao, I. Lelouche, Y.-g. Shin, A. Purandare, S. Knapp, S. S. Isied, *J. Am. Chem. Soc.* **119** (1997) 12849.
136. A. S. Salameh, T. Ghaddar, S. S. Isied, *J. Phys. Org. Chem.* **12** (1999) 247.
137. T. H. Ghaddar, E. W. Castner, S. S. Isied, *J. Am. Chem. Soc.* **122** (2000) 1233.
138. L. De Cola, V. Balzani, F. Barigelletti, L. Flamigni, P. Belser, A. von Zelewsky, M. Frank, F. Vögtle, *Inorg. Chem.* **32** (1993) 5228.
139. C. M. Drain, R. Fischer, E. G. Nolen, J.-M. Lehn, *Chem. Commun.* (1993) 243.
140. V. Král, S. L. Springs, J. L. Sessler, *J. Am. Chem. Soc.* **117** (1995) 8881.
141. S. L. Springs, D. Gosztola, M. R. Wasielewski, V. Král, A. Andrievsky, J. L. Sessler, *J. Am. Chem. Soc.* **121** (1999) 2281.
142. S. L. Springs, A. Andrievsky, V. Král, J. L. Sessler, *J. Porphyrins Phthalocyanines* **2** (1998) 315.
143. S.-C. Hung, A. N. Macpherson, S. Lin, P. A. Liddell, G. R. Seely, A. L. Moore, T. A. Moore, D. Gust, *J. Am. Chem. Soc.* **117** (1995) 1657.
144. C. Ikeda, N. Nagahar, E. Moetgi, N. Yoshioka, H. Inoue, *Chem. Commun.* (1999) 1759.
145. J. L. Sessler, B. Wang, S. L. Springs, C. T. Brown, in Y. Murakami (Ed.): *Comprehensive Supramolecular Chemistry*, Vol. 4, Pergamon, Oxford 1997, p. 311.
146. R. I. Cukier, *J. Phys. Chem.* **99** (1995) 16101.
147. R. I. Cukier, *J. Phys. Chem.* **100** (1996) 15428.
148. R. I. Cukier, D. G. Nocera, *Annu. Rev. Phys. Chem.* **49** (1998) 337.
149. J.-Y. Fang, S. Hammes-Schiffer, *J. Chem. Phys.* **107** (1997) 5727.
150. J.-Y. Fang, S. Hammes-Schiffer, *J. Chem. Phys.* **107** (1997) 8442.
151. A. V. Soudackov, S. Hammes-Schiffer, *Chem. Phys. Lett.* **299** (1999) 503.
152. A. Soudackov, S. Hammes-Schiffer, *J. Am. Chem. Soc.* **121** (1999) 10598.
153. E. H. Howell, J. E. Villafranca, M. S. Warren, S. J. Oatley, J. Kraut, *Science* **231** (1986) 1123.
154. C. Ostermeier, A. Harrenga, U. Ermler, H. Michel, *Proc. Natl. Acad. Sci. USA* **94** (1997) 10547.
155. S. Iwata, C. Ostermeier, B. Ludwig, H. Michel, *Nature* **376** (1995) 660.
156. S. Yoshikawa, K. Shinzawa-Itoh, R. Nakashima, R. Yaono, E. Yamashita, N. Inoue, M. Yao, M. J. Fei, C. P. Libeu, T. Mizushima, H. Yamaguchi, T. Tomizaki, T. Tsukihara, *Science* **280** (1998) 1723.
157. T. Tsukihara, H. Aoyama, E. Yamashita, T. Tomizaki, H. Yamaguchi, K. Shinzawa-Itoh, R. Nakashima, R. Yaono, S. Yoshikawa, *Science* **272** (1996) 1136.
158. T. Tsukihara, H. Aoyama, E. Yamashita, T. Tomizaki, H. Yamaguchi, K. Shinzawa-Itoh, R. Nakashima, R. Yaono, S. Yoshikawa, *Science* **269** (1995) 1069.
159. B. R. Crane, L. M. Siegel, E. D. Getzoff, *Science* **270** (1995) 59.
160. W. L. Jorgensen, J. Pranata, *J. Am. Chem. Soc.* **112** (1990) 2008.
161. J. Pranata, S. G. Wierschke, W. L. Jorgensen, *J. Am. Chem. Soc.* **113** (1991) 2810.
162. J. P. Kirby, J. A. Roberts, D. G. Nocera, *J. Am. Chem. Soc.* **119** (1997) 9230.
163. J. A. Roberts, J. P. Kirby, D. G. Nocera, *J. Am. Chem. Soc.* **117** (1995) 8051.
164. C. R. Bock, J. A. Connor, A. R. Gutierrez, T. J. Meyer, D. G. Whitten, B. P. Sullivan, J. K. Nagle, *J. Am. Chem. Soc.* **101** (1979) 4815.
165. J. A. Roberts, J. P. Kirby, S. T. Wall, D. G. Nocera, *Inorg. Chim. Acta* **263** (1997) 395.
166. R. A. Garigipati, *Tetrahedron Lett.* **31** (1990) 1969.
167. J. I. Levin, E. Turos, S. M. Weinreb, *Synth. Comm.* **12** (1982) 989.
168. J. P. Kirby, N. A. van Dantzig, C. K. Chang, D. G. Nocera, *Tetrahedron Lett.* **36** (1995) 3477.

169. Y. Deng, J. A. Roberts, S.-M. Peng, C. K. Chang, D. G. Nocera, *Angew. Chem. Int. Ed.* **36** (1997) 2124.
170. R. J. Abraham, F. Eivazi, H. Pearson, K. M. Smith, *Chem. Commun.* (1976) 698.
171. C. K. Chang, *J. Heterocycl. Chem.* **14** (1977) 1285.
172. R. A. Binstead, B. A. Moyer, G. J. Samuels, T. J. Meyer, *J. Am. Chem. Soc.* **103** (1981) 2897.
173. S. W. Gersten, G. J. Samuels, T. J. Meyer, *J. Am. Chem. Soc.* **104** (1982) 4029.
174. E. L. Lebeau, S. A. Adeyemi, T. J. Meyer, *Inorg. Chem.* **37** (1998) 6476.
175. J. M. Mayer, *Acc. Chem. Res.* **31** (1998) 441.
176. A. Kohen, J. P. Klinman, *Chem. Biol.* **6** (1999) R191.
177. A. Kohen, J. P. Klinman, *Acc. Chem. Res.* **31** (1998) 397.
178. J. F. Wishart, D. G. Nocera, *Advances in Chemistry Series, Vol. 254*, Oxford University Press, Washington, D.C. 1998.
179. R. E. Holmlin, R. Haag, R. F. Ismagilov, M. A. Rampi, G. M. Whitesides, submitted for publication.
180. O. Farver, L. K. Skov, G. Gilardi, G. van Pouderoyen, G. W. Canters, S. Wherland, I. Pecht, *Chem. Phys.* **204** (1996) 271.
181. M. W. Mutz, M. A. Case, J. F. Wishart, R. Ghadiri, G. L. McLendon, *J. Am. Chem. Soc.* **121** (1999) 858.
182. B. G. Malmström, *Acc. Chem. Res.* **26** (1993) 332.
183. P. Mitchell, *Nature* **191** (1961) 144.
184. M. Y. Okamura, G. Feher, *Annu. Rev. Biochem.* **61** (1992) 861.
185. J. Stubbe, *J. Biol. Chem.* **265** (1990) 5329.
186. J. Stubbe, W. A. van der Donk, *Chem. Biol.* **2** (1995) 793.
187. S. Licht, G. J. Gerfen, J. Stubbe, *Science* **271** (1996) 477.
188. P. Nordlund, B.-M. Sjöberg, H. Eklund, *Nature* **370** (1990) 593.
189. U. Uhlin, H. Eklund, *Nature* **370** (1994) 533.
190. B.-M. Sjöberg, P. Reichard, A. Gråslund, A. Ehrenberg, *J. Biol. Chem.* **252** (1977) 536.
191. J. Stubbe, P. Riggs-Gelasco, *Trends Biochem. Sci.* **23** (1998) 438.
192. M. Ekberg, M. Sahlin, M. Eriksson, B.-M. Sjöberg, *J. Biol. Chem.* **271** (1996) 20655.
193. I. Climent, B.-M. Sjöberg, C. Y. Huang, *Biochemistry* **31** (1992) 4801.
194. B. Kauppi, B. B. Nielsen, S. Ramaswamy, I. K. Larsen, M. Thelander, L. Thelander, H. Eklund, *J. Mol. Biol.* **262** (1996) 706.
195. P. E. M. Seigbahn, L. Eriksson, F. Himo, M. Pavlov, *J. Phys. Chem. B* **102** (1998) 10622.

5 Host–Guest and Cage-Type Systems

Luigi Fabbrizzi, Maurizio Licchelli and Angelo Taglietti

5.1 Metal Ions Inside Aza-Crowns

Transition metal ions have a natural tendency to exchange electrons, giving rise to a variety of oxidation states, the relative stability of which can be modified at will by changing the ligand's features. A special versatility can be achieved when the metal is coordinated by a multidentate cyclic ligand, for two main reasons: (i) the coordinating tendencies and the affinity towards a given oxidation state can be modulated by modifying the geometrical features of the molecular framework; and (ii) trapping by the closed and often sterically constrained structure provides kinetical stability to otherwise elusive oxidation states, extending their lifetime in solution [1, 2]. A clear example is provided by the nickel(II) cation which, as a solvated ion, does not show any tendency to release/uptake electrons. However, when coordinated by a cyclic polyamine, Ni^{II} can be oxidized to Ni^{III} —a state which, under particular conditions, can be indefinitely stable. The number of amine donor atoms contained in the multidentate framework has a profound effect on the stabilization on the Ni^{III} state, as expressed by the potential associated with the $\text{Ni}^{\text{III}}/\text{Ni}^{\text{II}}$ couple. More surprisingly, even if the number of donor atoms remains the same, the $E_{1/2}(\text{Ni}^{\text{III}}/\text{Ni}^{\text{II}})$ value can vary significantly with ligand's structural parameters, e.g., ring size [1]. In this connection, Figure 1 displays the values of $E_{1/2}(\text{Ni}^{\text{III}}/\text{Ni}^{\text{II}})$, measured in an MeCN solution, at 25 °C, through cyclic voltammetry studies, for 1:1 complexes with tetramine and pentamine macrocycles and with 1:2 complexes with triamine macrocycles, whose formulae are shown in Chart 1.

As far as quadridentate ligands are concerned, the easiest attainment of the Ni^{III} state, denoted by the less positive redox potential, is observed with the 14-membered macrocycle, **5**, known as cyclam. Both contraction and expansion of tetramine ring atomicity, to 12 and to 16, respectively, makes the potential more positive, thus destabilizing Ni^{III} with respect to Ni^{II} . Moreover, the isomeric 14-membered macrocycle, **6** (isocyclam) stabilizes the Ni^{III} state to a much lesser extent than cyclam. Notice that the two macrocyclic complexes simply differ in the sequence of the five-

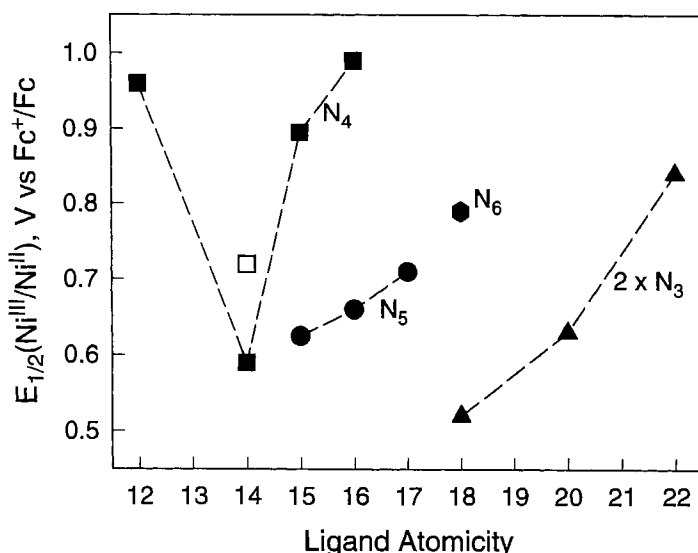


Figure 1. Ring size effect on the potential of the $\text{Ni}^{\text{III}}/\text{Ni}^{\text{II}}$ redox change of *n*-dentate poly-aza macrocycles. Points N_4 , N_5 , and N_6 refer to 1:1 complexes with tetra-aza (systems 4, 5, 7, 8; ■), penta-aza (systems 9–11; ●) and hexa-aza (system 12; ◆) macrocycles respectively. Points $2 \times \text{N}_3$ refer to 1:2 metal complexes with tri-aza macrocycles (systems 1–3; ▲). The open square refers to the isocyclam system, 6. $E_{1/2}$ values measured in acetonitrile (0.1 M Et_4NBF_4) at 25 °C.

and six-membered chelate rings: alternating for the cyclam complex (5,6,5,6) and grouped for isocyclam (5,5,6,6). This state of affairs can be qualitatively explained by considering that cyclam has the right size and possesses the correct geometric features to place its donor atoms in the coordination positions required by the Ni^{II} center, thus establishing especially strong coordinative interactions. This raises the energy of the metal-centered HOMO level, and makes the electron release particularly easy. A small modification of ligand's geometric features, as observed with the isocyclam system, seriously alters the intensity of the metal–ligand interactions, thus disfavoring Ni^{III} attainment [3]. Addition of a further donor atom (pentamine macrocycles) does not favor the formation of the trivalent complex [4], nor is stabilization observed with six-coordination in bis-triamine complexes [5]. This behavior may seem contradictory, if one considers that Ni^{III} , d^7 , low-spin, likes octahedral coordination and should therefore prefer ligands providing a number of amine donor atoms larger than four. In tetramine macrocyclic complex (e.g., cyclam and isocyclam), the ligand encompasses the equatorial plane, while axial positions are occupied by solvent (MeCN) molecules. In pentamine complexes, the macrocycle folds in order to put a nitrogen atom in one of the apical sites: this probably induces serious steric constraints and reduces the overall intensity of metal–ligand interactions. On the other hand, in bis-triamine complexes, six amine nitrogen atoms are available for the Ni^{III} beloved six-coordination, but the cyclic nature of the ligand sterically prevents regular octahedral coordination for rings of varying size. In par-

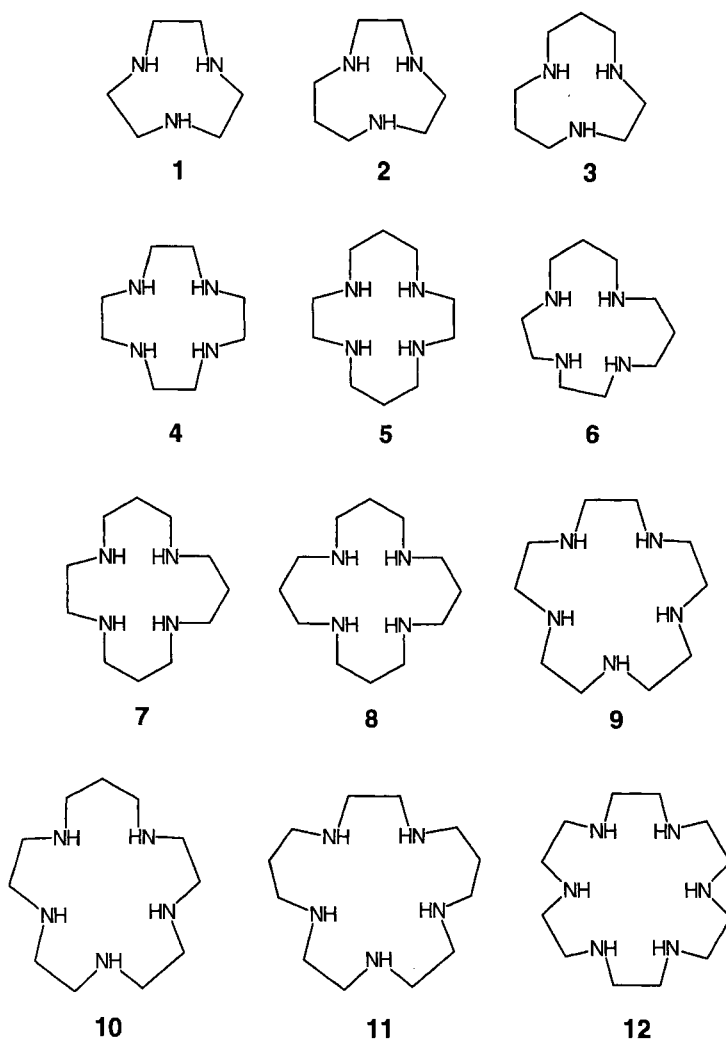


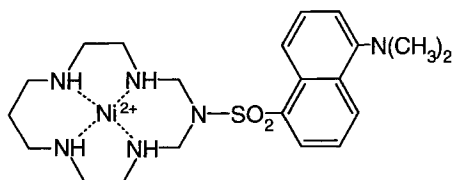
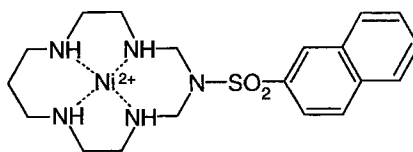
Chart 1. Poly-aza macrocycles of varying size and denticity used in the investigation of the $\text{Ni}^{\text{III}}/\text{Ni}^{\text{II}}$ redox change.

ticular, in 1:2 complexes with a series of triamine macrocycles of varying atomicity (1, 2, 3), the attainment of the trivalent state takes place at a more positive potential than for the 1:1 complex of cyclam (5). In contrast, progressive expansion of the triaza-macrocyclic ring induces only a moderate increase of the $\text{Ni}^{\text{III}}/\text{Ni}^{\text{II}}$ potential (see \blacktriangle in Figure 1). Steric effects associated with six-coordination are emphasized with the hexamine macrocycle 12, whose 1:1 Ni^{III} complex is formed at a particularly high potential [4].

In conclusion, the $\text{Ni}^{\text{II}}(\text{cyclam})^{2+}$ moiety seems the appropriate redox active plat-

form for carrying out electron transfer processes, both inter- and intra-molecular, and to manage two metal oxidation states of comparable stability. This property has been effectively exploited to control intramolecular photoinduced electron transfer in functionalized tetra-aza-macrocyclic complexes which behave as redox switches of fluorescence or luminescent sensors.

A fluorescent fragment can be appended to the Ni^{II} -14-membered tetramine platform, through a convenient metal-template synthesis [6, 7], to give systems **13** and **14**. The fluorescent subunits, a dansyl group (in system **13**) and a 2-naphthalene fragment (in system **14**), have been appended to the cyclam-like framework, through a sulphonamide nitrogen atom inserted in the ring: this atom does not show any coordinating tendencies, and the 14-membered macrocycle exhibits the same coordinating behavior as cyclam. In particular, it allows an easy attainment of the Ni^{III} state.

**13****14**

Let us consider first the behavior of the dansyl derivative. When the metal center is in the divalent state, the dansyl group (*dns*) displays its typical emission properties (band centered at 510 nm in MeCN). However, on oxidation to Ni^{III} , through controlled potential exhaustive electrolysis in an MeCN solution, the emission is fully quenched. Quenching has been ascribed to an electron transfer process from the excited fluorogenic fragment dns^* to the Ni^{III} ion. The occurrence of this process can be accounted for on a thermodynamic basis. In particular, the ΔG° value associated with the dns^* -to- Ni^{III} electron transfer, which can be calculated through the cycle illustrated in Figure 2, is distinctly negative: -1.93 eV. On the other hand, for the Ni^{II} -to- dns^* electron transfer process, a positive value of ΔG° is calculated through the pertinent thermodynamic cycle ($\Delta G^\circ \geq 0.7$ eV; see Figure 2), which accounts for the regular *dns* emission in the Ni^{II} derivative. As a consequence, the light emission by the dansyl fragment can be switched ON/OFF at will, by carrying out consecutive controlled electrolysis experiments on a MeCN solution of **13**: when the potential of the platinum gauze used as a working electrode is set at 0.23 V versus Fc^+/Fc , Ni^{II} is oxidized to Ni^{III} and the fluorescent emission is quenched; when the working potential is set back at -0.07 V versus Fc^+/Fc , Ni^{III} is reduced to Ni^{II} and fluorescence is revived.

A similar behavior has been observed with system **14**, in which the emission of the naphthalene fragment is turned ON/OFF through electrochemical oxidation and reduction processes [7]. Fluorescence quenching/revival of dansyl and naphthalene subunits of systems **13** and **14** can be driven chemically in a MeOH solution through sequential addition of an oxidizing agent ($\text{S}_2\text{O}_8^{2-}$) and of a reducing agent (NO_2^-).

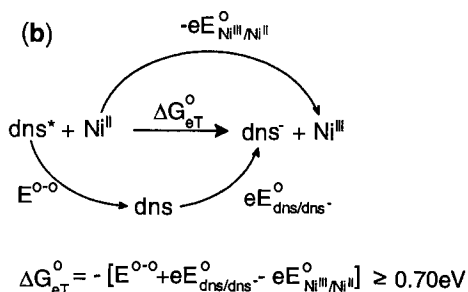
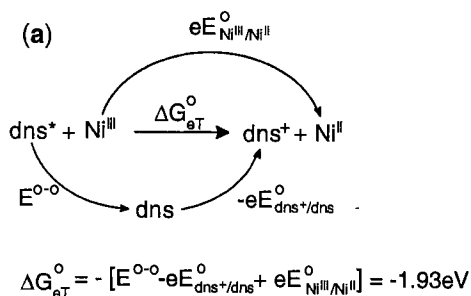
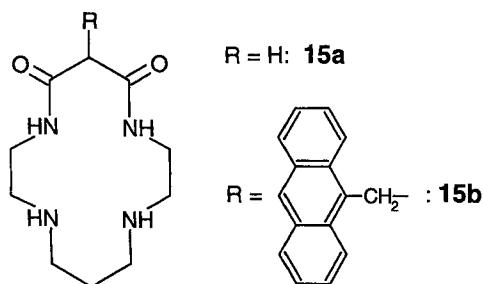
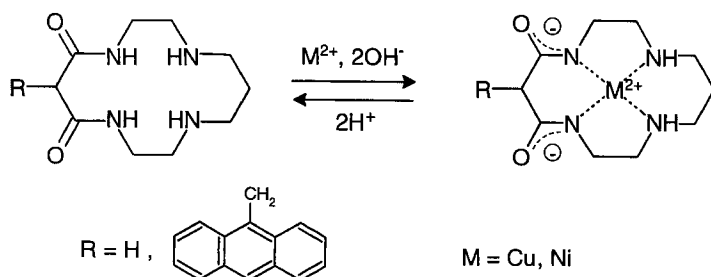


Figure 2. Thermodynamic cycles for evaluating the free energy changes ΔG_{eT}° associated with the intramolecular photoinduced electron transfer processes in system **13** in its oxidized (a) and reduced (b) form. The E^{0-0} quantity, the spectroscopic energy, is obtained from the emission spectrum; the E° values, electrode potentials associated with the given redox change, can be determined through voltammetry experiments. The Coulombic term ($e^2/\epsilon r$) has been considered negligible under the present circumstances.

Systems **13** and **14** represent prototypes of molecular switches of luminescence which are operated through a redox input: the system consists of a luminescent unit (the light bulb of the everyday life) and of a metal-containing redox unit (the true switch) [8]. The ON/OFF situation is achieved when one of the two stable oxidation states of the metal quenches the nearby excited fluorophore and the other does not. In principle, redox switches of luminescence based on an electron transfer mechanism can be obtained by properly assembling a photoactive fragment and a metal-centered redox couple, possibly hosted by a cyclic framework. A further example based on the $\text{Cu}^{\text{II}}/\text{Cu}^{\text{I}}$ redox couple will be discussed in Section 5.4.

Luminescence quenching in functionalized macrocycles forms the basis of a class of efficient molecular sensors for transition metals. A recent example is given by system **15b**, in which an anthracene fragment has been appended to the carbon

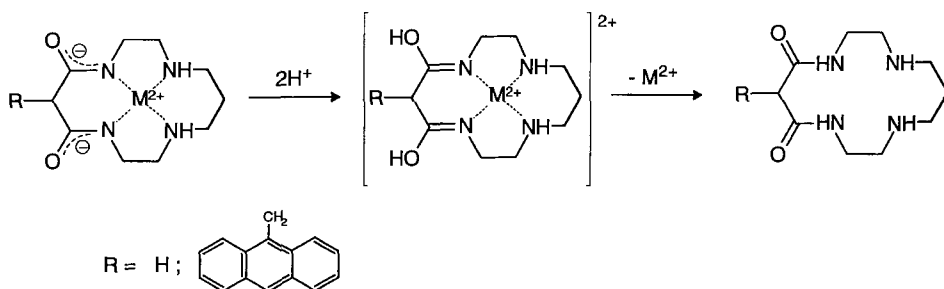




Scheme 1. The coordinating behavior of diamine–diamide macrocyclic ligands. The coordination of a divalent transition metal M^{II} ($M = Cu, Ni$) involves the simultaneous deprotonation of the two amide groups, with formation of a neutral species.

framework of the 14-membered macrocycle dioxocyclam (**15a**) [9]. Dioxocyclam contains two amine nitrogen atoms and two amide groups and, in its neutral form, displays poorly coordinating tendencies towards transition metal ions. However, in presence of an equimolar amount of a divalent 3d cation (e.g., Cu^{II} , Ni^{II}), at the appropriate pH value, the macrocycle, indicated in the following as H_2L , extrudes two hydrogen ions from the amide groups and simultaneously incorporates the metal, according to equilibrium: $M^{2+} + H_2L \rightleftharpoons [M^{II}(L^{2-})] + 2H^+$ [10]. The structural aspects of the complexation equilibrium are sketched in Scheme 1. In the $[M^{II}(L^{2-})]$ complex, the metal feels the coordination of two amine nitrogen atoms and of two nitrogen atoms belonging to deprotonated amide groups. In each deprotonated fragment, the electrical charge, due to a π -delocalization mechanism, is distributed on nitrogen and oxygen atoms.

The complexation equilibrium is fast and reversible. In particular on addition of acid, each deprotonated amide group uptakes an H^+ , thus losing its coordinating tendencies: as a consequence the metal center is instantaneously extruded from the tetra-aza ring. In this aspect, the behavior of dioxocyclam is totally different from that of the tetramine analogue cyclam, whose complexes display an extreme inertness towards demetallation. In fact, the mechanical resistance to the detachment of the coordinated donor atoms prevents amine protonation, which makes Cu^{II} and Ni^{II} cyclam complexes persist almost indefinitely in strong acidic solutions: for instance, in the case of the $[Ni^{II}(\text{cyclam})]^{2+}$ complex in 1 M $HClO_4$ at 25 °C, a half-life of 32 years has been evaluated [11]. In contrast, decomplexation of a $[M^{II}(\text{dioxocyclamato}(2-))]$ complex in acidic solution does not involve any sterically demanding ligand rearrangement, but simply proceeds through the electron redistribution onto the amide donor groups. In particular, two H^+ ions go to protonate the partially negatively charged oxygen atoms of the deprotonated amide groups, withdrawing any negative charge from the nitrogen atoms and drastically reducing the coordinating tendencies of the macrocycle. As a consequence, the metal ion is released to the solution, while the typical dioxocyclam unit is formed again, through a fast keto-enolic equilibrium, as illustrated in Scheme 2 [12].



Scheme 2. Fast demetallation in acidic solution of $[\text{M}^{\text{II}}(\text{dioxocyclamato}(2-))]$ complexes ($\text{M} = \text{Cu}, \text{Ni}$). The partially negatively charged oxygen atoms of the carbonyl groups are quickly protonated, and the consequent drastic reduction of the coordinating tendencies of the adjacent nitrogen atoms promotes metal extrusion.

The process of fast and reversible pH-driven metal inclusion–extrusion can be easily followed, in the case of **15b** derivative, through the emission of the anthracene fragment covalently linked to the macrocycle. Figure 3 shows the fluorescence intensity, I_F , versus pH profile obtained in the course of spectrofluorimetric titration experiments. First, when an aqueous MeCN solution of **15b** (H_2L), containing excess acid is titrated with standard base, the typical anthracene emission spectrum is not modified over the pH range 3 to 10.5. If the titration experiment is carried out in presence of 1 equivalent of Cu^{II} , at $\text{pH} = 3.6$, I_F begins to decrease sigmoidally,

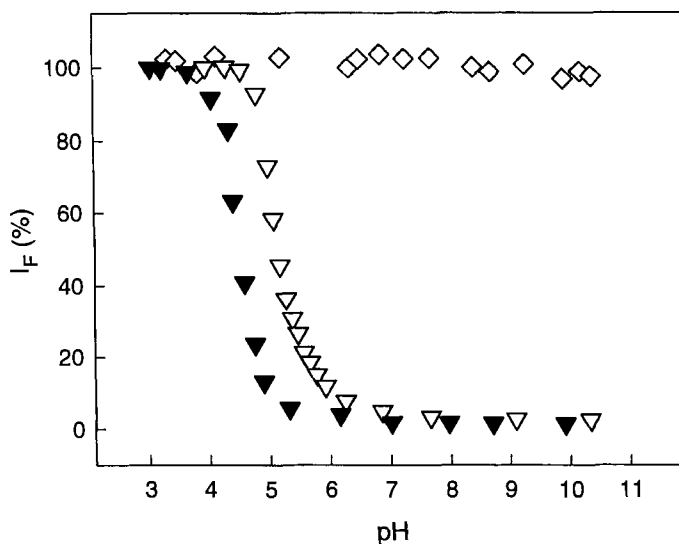


Figure 3. Spectrofluorimetric titration by standard base of the two-component system **15b**, in aqueous MeCN. (◇), **15b** plus excess acid; (▼), **15b**, plus 1 equiv. of Cu^{II} and excess acid; (▽), **15b**, plus 1 equiv. of Ni^{II} and excess acid.

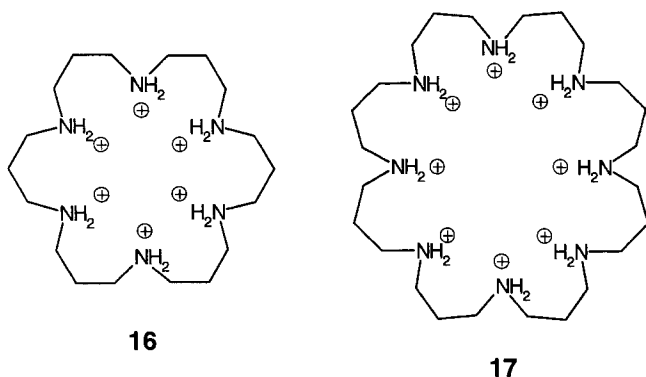
to be completely quenched at pH = 5.3. Quenching reflects Cu^{II} complexation, and is intrinsically due to the occurrence of an electron transfer process from the divalent metal center to the excited fluorophore, *An**. The *An**-to-Cu^{II} electron transfer is characterized by a distinctly negative ΔG° value: -0.50 eV. If Cu^{II} is replaced by Ni^{II}, an analogous sigmoidal decay of I_F is observed, displaced to the right of about 1 pH unit. The higher pH corresponds to the formation of a less stable complex of Ni^{II} with the dioxocyclamato(2-) subunit with respect to Cu^{II}. Also for Ni^{II}, quenching is due to a fluorophore-to-metal electron transfer, a process fully justified on a thermodynamic basis: $\Delta G^\circ_{ET} = -0.35$ eV.

Interestingly, if the same titration experiment is performed in presence of any other 3d divalent cation (Mn^{II}, Fe^{II}, Co^{II}, Zn^{II}), no fluorescence quenching is observed over the entire 2–12 pH interval. In this connection, it must be noted that deprotonation of the amide groups of the dioxocyclam subunit is an especially endothermic process, which can take place only if the unfavorable heat effect is compensated by the exothermic formation of strong metal–ligand bonds. This situation occurs only with metal ions late in the 3d series, e.g., Ni^{II} and Cu^{II}, but not with cations earlier in the same series. Thus, the anthracene functionalized dioxocyclam system represents a selective fluorescent sensor for Cu^{II} and Ni^{II}, whose signal transduction mechanism is an electron transfer process [13].

5.2 Anions Inside Aza-Crowns

Polyaza macrocycles in their protonated form, either full or partial, are able to interact with anionic species, by establishing noncovalent interactions (both electrostatic and hydrogen bonding). Complexation of anions by synthetic polyammonium molecules has been explored over the past two decades, and several examples of selective recognition of different anionic substrates have been reported [14–22].

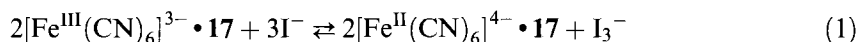
Some polyammonium macrocycles such as [24]aneN₆H₆⁶⁺, **16**, and [32]aneN₈H₈⁸⁺, **17**, have the right structural features to include negatively charged



metal complexes such as metal cyanides of the general formula $[M(CN)_6]^{n-}$ ($M = Fe^{II}, Ru^{II}$ with $n = 4$; $M = Fe^{III}, Co^{III}, Cr^{III}$ with $n = 3$) and $[M(bipy)(CN)_4]^{n-}$ ($M = Ru^{II}$, $n = 4$) [14, 23–26]. In the resulting adducts, which have been defined *supercomplexes* [27, 28], the macrocyclic receptor can be viewed as a pre-organized second coordination sphere ligand [29]. The inclusion into the fully protonated polyazamacrocyclic receptors significantly modifies the properties of the anionic complexes and, in particular, their ability to take part in electron transfer processes.

In this connection, metal cyanides included in the polyammonium host are generally characterized by more positive reduction potential values for the M^{III}/M^{II} redox couple. This behavior reflects the higher thermodynamic stabilization of the adduct, with the anion possessing the higher negative charge, $[M^{II}(CN)_6]^{4-}$, in which the metal is present in its lower oxidation state. For example, electrochemical studies showed that $[Fe^{II}(CN)_6]^{4-}$ and $[Ru^{II}(CN)_6]^{4-}$ both form 1:1 adducts with **16** and **17**, and are oxidized more difficultly in the presence of the polyammonium macrocycles than in their absence [30, 31]. The self electron exchange process is reversible and takes place without any dissociation of the supercomplex. The higher stability of adducts of the more negatively charged species accounts for a host–guest interaction that is mainly electrostatic in nature. However, hydrogen bonds between the protonated nitrogens and the nitrogens of the cyanide ligands play an important structural role [26].

$[Fe^{III}(CN)_6]^{3-}$, when included in **17**, is involved in an electron transfer reaction with iodide which cannot take place in the absence of the macrocyclic species. In fact, the $E^\circ(Fe^{III}/Fe^{II})$ value for the hexacyano complex is considerably lower than $E^\circ(I_2/I^-)$, so that the electron transfer from I^- to Fe^{III} center is thermodynamically disfavored. However, in the presence of **17**, in an acidic aqueous solution (e.g., pH = 4.4), the redox potential of Fe^{III}/Fe^{II} couple inside the supercomplex is increased to such an extent that the reaction (see Eq. 1), which is essentially isoergonic, proceeds to an equilibrium situation ($K = 7\ M^{-2}$, at 25 °C).



The kinetics of Eq. 1 corresponds to a first-order process, characterized by a rather low rate constant ($k_{obs} = 8.9 \times 10^{-4}\ s^{-1}$ at 25 °C), whose value increases with increasing temperature. As the inclusion complex forms only when the macrocyclic ligand is fully protonated, on addition of base the adduct dissociates and the exoergonic reaction reverse of Eq. 1 takes place. The thermal reaction provides an example of an electron transfer process which can be switched ON/OFF by a pH change [32].

Flash irradiation with visible light ($\lambda > 400\ nm$) of a thermally equilibrated solution gives rise to an instantaneous increase of the I_3^- concentration, followed by a slow decrease in the dark. Although the extremely short lifetime of the $[Fe(CN)_6]^{3-}$ excited state prevents any type of bimolecular process, a photoinduced electron transfer process is responsible for the increased I_3^- concentration upon irradiation. The positively charged supercomplex forms an ion pair with the iodide anion, so that a very fast electron transfer process can take place following a unimolecular kinetics.

Supercoordination by the polyammonium macrocycle has a thermodynamic effect, as it induces an anodic shift of the $\text{Fe}^{\text{III}}/\text{Fe}^{\text{II}}$ potential; it has also a kinetic effect on the photoinduced process, through the formation of the ion-pair with iodide.

5.3 Metals Inside Aza-Cages

The template reaction involving $[\text{Co}^{\text{III}}(\text{en})_3]^{3+}$ ($\text{en} = 1,2\text{-diaminoethane}$), formaldehyde and ammonia in an aqueous basic solution affords one of the most celebrated metal-cage compounds, the $[\text{Co}^{\text{III}}(\text{sepulchrates})]^{3+}$, **18**, currently indicated as $[\text{Co}^{\text{III}}(\text{sep})]^{3+}$ [33–35]. After sepulchrates synthesis, which remains as one of the most powerful methodologies of preparation of macropolycyclic systems, many different cage complexes have been synthesized by still following a template approach. For example the cobalt–dinitrosarcophagine system, **20**, also known as $[\text{Co}(\text{diNOsar})]^{3+}$, can be obtained by employing the formally triprotic acid nitromethane instead of ammonia (still a formally triprotic acid) [36].

The use of different triprotic acids or more sophisticated bidentate amino-ligands as well as the functionalization of preformed cages has increasingly lengthened the list of metal–azacage complexes available today [37].

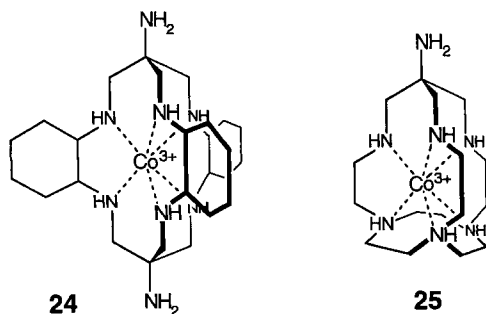
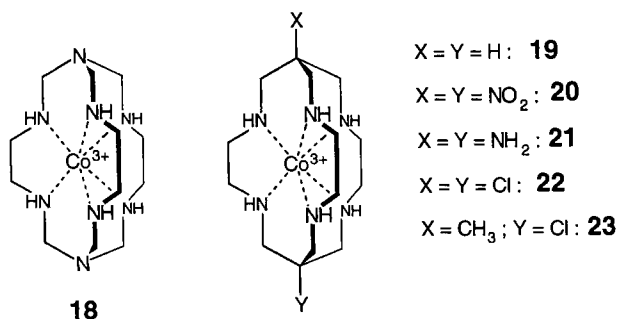
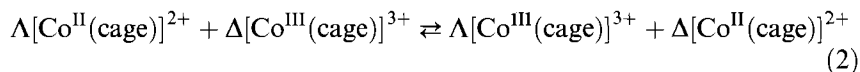


Table 1. Rate constants for electron self-exchange rates determined for different Co^{III}/Co^{II} systems in water at 25 °C.

Complex	<i>k</i> (M ⁻¹ s ⁻¹)
[Co(NH ₃) ₆] ^{2+/3+}	10 ^{-7a}
[Co(en) ₃] ^{2+/3+}	3.4 × 10 ^{-5b}
[Co(sep) ₃] ^{2+/3+} , 18	5.1 ^c
[Co(sar)] ^{2+/3+} , 19	2.1 ^d
[Co(diamsar) ₃] ^{2+/3+} , 21	0.5 ^d
[Co(diClasar)] ^{2+/3+} , 22	3.0 ^e
[Co(ClMesar) ₃] ^{2+/3+} , 23	2.4 ^e
[Co(diamchar) ₃] ^{2+/3+} , 24	1.0 ^e

^aFrom Ref. [39]; ^bfrom Ref. [40]; ^cfrom Ref. [38]; ^dfrom Ref. [41]; ^efrom Ref. [42].

Owing to the resistance of the macropolycyclic ligand to detach its donor atoms from the metal, the aza-cage complexes are extremely inert (a feature which accounts for the fanciful, yet funereal names given to the early aza-cages **18** and **20**). As a result, not only the intrinsically substitutionally inert Co^{III} complexes, but also the corresponding substitutionally labile Co^{II} derivatives, display an uncommon sluggishness. Co^{II}–amine complexes usually exchange their ligands on a millisecond time scale, while [Co^{II}(sep)]²⁺ is stable for hours in solution at room temperature, as shown by exchange experiments with ⁶⁰Co²⁺ [33, 38]. The extreme inertness of Co–cage complexes of both oxidation states recommended their use in the study of electron self-exchange processes. The rates of Co^{III}/Co^{II} self-exchange reaction for different cage complexes have been determined polarometrically by observing the change in optical rotation, when mixing the chiral form of one oxidation state, e.g., Λ[Co^{II}(cage)]²⁺, with the enantiomeric form of the other, Δ[Co^{III}(cage)]³⁺, according to Eq. 2.



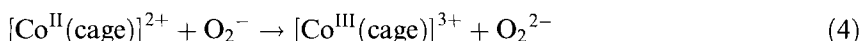
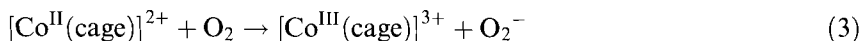
The values of rate constants measured for complexes **18–24** are reported in Table 1. Noticeably, the self-exchange processes in the cage systems are 10⁷ and 10⁵-fold faster than those determined for [Co(NH₃)₆]^{2+/3+} and [Co(en)₃]^{2+/3+}, respectively. This behavior may be surprising, considering the electronic similarity of hexamine and cage complexes. In addition, one might expect that the insulating aliphatic backbone of the cage could make the electron transfer process even more unfavorable. A proposed explanation of the unusually high self-exchange rate of the [Co(sep)]^{2+/3+} system was referred to the presence of unshared electron pairs on the nitrogen atoms of the caps, which could allow a more direct communication between the metal centers. However, a similar rate value was determined also for the [Co(sar)]^{2+/3+}, which does not contain any capping tertiary nitrogen atom [41]. A further explanation was related to the different hydration of the complex and of the

activated complex. Cage complexes are less hydrated than $[\text{Co(en)}_3]^{2+/3+}$ and $[\text{Co}(\text{NH}_3)_6]^{2+/3+}$ reference systems: thus, the cage complex in the course of the electron transfer process should experience a smaller solvational reorganization, which should favor the self-exchange process. This hypothesis was not confirmed by the studies carried on the bulkier complex **24** for which the rate of the self-exchange process is similar to those determined for other cage systems (see Table 1) [43].

Molecular mechanics calculations have demonstrated that the metal ion encapsulation induces a strain in the ligand (i.e., distortion of the expected bond angles and torsion angles). In contrast, crystallographic investigations have shown that the Co–N bond lengths in $[\text{Co}^{\text{III}}(\text{sep})]^{3+}$ and $[\text{Co}^{\text{II}}(\text{sep})]^{2+}$ do not differ greatly from those measured for the corresponding $[\text{Co}^{\text{III}}(\text{NH}_3)_6]^{3+}$ and $[\text{Co}^{\text{II}}(\text{NH}_3)_6]^{2+}$ [38]. In any case, the cage hole appears a little too large for Co^{III} , and a little too small for Co^{II} : the resulting strain in both oxidation states induces a stretching of the Co^{III} –N bonds and a compression of the Co^{II} –N bonds. In this way the $[\text{Co}^{\text{III}}(\text{sep})]^{3+}$ – $[\text{Co}^{\text{II}}(\text{sep})]^{2+}$ assembly could be helped towards the transition state, even if no evidence of such a strain effect can be obtained by the ground-state metal–ligand bond lengths [42].

Configurational and conformational effects on the rates of electron exchange process have been determined for some stereo- and dia-stereoisomers of *N*-methyl derivatives of **21** [44].

A further intriguing electron transfer process involving Co–cage complexes refers to the quantitative reaction with O_2 to give H_2O_2 . Usually, the Co^{II} –amine complexes react with O_2 to give Co^{III} –peroxy dimers such as $[(\text{NH}_3)_5\text{Co}–\text{O}–\text{O}–\text{Co}(\text{NH}_3)_5]^{4+}$. However, the tightness and bulkiness of the cage ligand structures prevents O_2 from accessing the encapsulated Co^{II} center, and this precludes formation of the peroxo dimer. This would imply the occurrence of an outer-sphere electron transfer process involving the Co^{II} –cage complex and dioxygen. The rate-determining step of this reaction has been established as the formation of the superoxide intermediate, which subsequently and rapidly reacts with another $[\text{Co}^{\text{II}}(\text{cage})]^{2+}$, to give peroxide (see Eqs. 3 and 4).



Alternatively, superoxide can disproportionate in acidic medium to give H_2O_2 and O_2 . For $[\text{Co}^{\text{II}}(\text{sep})]^{2+}$ the global reaction is very fast and the second-order rate constant is $43 \pm 5 \text{ M}^{-1} \text{ s}^{-1}$ [38, 45]. For other cage systems such as $[\text{Co}^{\text{II}}(\text{amsartacn})]^{2+}$, **25**, the reaction is considerably slower ($k = 0.14 \text{ M}^{-1} \text{ s}^{-1}$). The strikingly different behavior can be accounted for on the basis of the reduction potential value, which is less negative in the case of **25** [45].

Other outer-sphere electron transfer rate constants were measured for reactions between different caged complexes in the Co^{II} and Co^{III} oxidation states, and between some caged complexes and different reducing or oxidizing species such as Cr^{2+} , Eu^{2+} , V^{2+} , U^{3+} , $[\text{Co}(\text{NH}_3)_6]^{3+}$, $[\text{Co}(\text{en})_3]^{3+}$, and $[\text{Co}(\text{bipy})_3]^{3+}$. The spectrophotometrically determined values agree with those calculated by using the

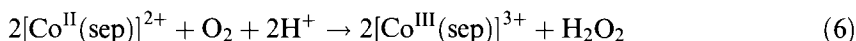
Marcus–Hush model. Agreement is especially tight for the reactions involving the cages, $[\text{Co}(\text{NH}_3)_6]^{3+}$ and $[\text{Co}(\text{en})_3]^{3+}$ [41].

The special features of Co–cage complexes can be exploited in reactions which involve photoinduced electron transfer processes [46–54]. Photoexcitation of Co^{III} complexes in their LMCT band usually leads to an excited state that formally is a Co^{II} species. The subsequent efficient decomposition can be interpreted in terms of lability of Co^{II} complexes. In contrast, in the case of $[\text{Co}^{\text{III}}(\text{cage})]^{3+}$ complexes such as **18**, a radiationless conversion to the ground state (i.e., back electron transfer) strongly predominates over ligand dissociation. In view of the photoinertness of their Co^{II} derivatives, Co^{III} -cage complexes can be used as photosensitizers in electron transfer reactions involving ion-pair systems such as **18**-iodide and **18**-oxalate. As observed for other Co^{III} complexes, **18** forms ion pairs with most anions. The interaction with anionic reducing species such as iodide give rise to an IPCT (Ion-Pair Charge Transfer) adduct, which displays a typical band in the near-UV spectral region. Light excitation into IPCT band causes the promotion of an electron from the I^- in the outer coordination sphere to the Co^{III} ion (see Eq. 5).



In degassed solutions, the first step can be followed either by a back electron transfer which restores the starting ion-pair, or by the separation of the primary photoproducts. In the latter case, **I** is scavenged by I^- ion to yield I_2^- which is able to reoxidize $[\text{Co}^{\text{II}}(\text{sep})]^{2+}$. I_2^- can also undergo a disproportionation reaction affording I_3^- and I^- . As I_3^- can reoxidize $[\text{Co}^{\text{II}}(\text{sep})]^{2+}$, no net reaction takes place.

In the presence of oxygen, the reoxidation of Co^{II} species can follow different routes such as those reported in Eqs. 6 and 7.



In this way, while $[\text{Co}^{\text{III}}(\text{sep})]^{3+}$ is regenerated, I_3^- accumulates and the net photoreaction can be described as the oxidation of I^- to I_3^- by dioxygen, photo-assisted by the $[\text{Co}^{\text{III}}(\text{sep})]^{3+}$ complex [46].

The ion-pair approach to the design of photosensitizers for electron transfer processes has been followed also in the case of $[\text{Co}^{\text{III}}(\text{sep})]^{3+}$ –oxalate system. In a deoxygenated solution, the excitation in the IPCT band of $[\text{Co}^{\text{III}}(\text{sep})]^{3+}$ – HC_2O_4^- causes the reduction of $[\text{Co}^{\text{III}}(\text{sep})]^{3+}$ to $[\text{Co}^{\text{II}}(\text{sep})]^{2+}$ and the oxidation of oxalate to carbon dioxide. The $[\text{Co}^{\text{II}}(\text{sep})]^{2+}$ complex is a sufficiently strong reductant to reduce H^+ to H_2 at moderately acidic pH values. Thus, when the photoreaction is carried out in the presence of colloidal platinum catalyst, such a reaction indeed occurs, and H_2 evolves from the solution in addition to carbon dioxide. Under such conditions, the overall reaction is the oxidation of oxalate, which plays the role of sacrificial agent, combined with the reduction of water to yield carbon dioxide and dihydrogen, according to Eq. 8.

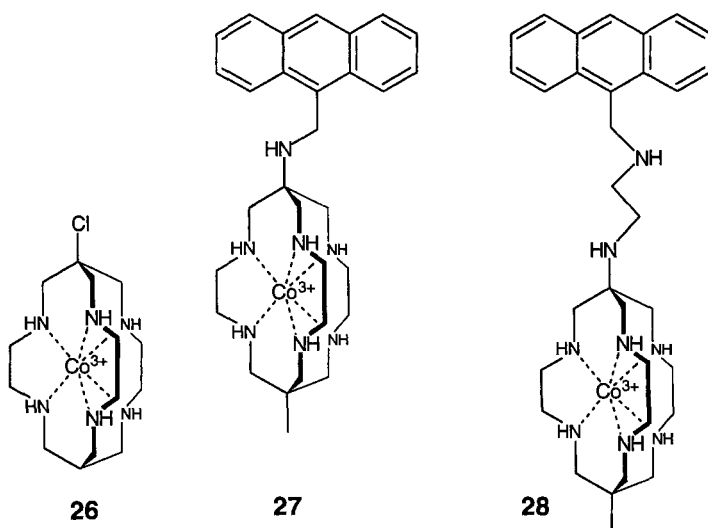


The turnover of $[\text{Co}^{\text{III}}(\text{sep})]^{3+}$, which plays the role of photosensitizer, is higher than 700 at pH 3.0 [47].

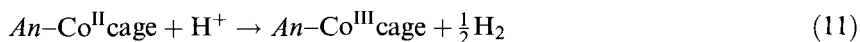
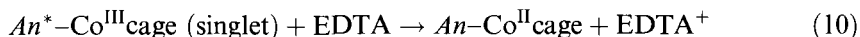
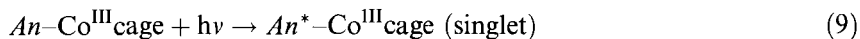
Cage complexes can be also employed as electron relays in the catalyzed photochemical splitting of water. The role of a relay, or electron mediator, is to accept an electron from an excited sensitizer, usually $[\text{Ru}(\text{bipy})_3]^{2+}$, and to use it in the catalyzed reduction of water to H_2 . Actually, the features displayed by $[\text{Co}^{\text{III}}(\text{sep})]^{3+}$ and its analogues seem to match well with the properties requested for an ideal relay in such a process: (i) a reversible reduction behavior at a reasonable negative potential ($-0.8 < E^\circ < -0.2$); (ii) good thermal and photochemical inertness; (iii) good kinetic factors for outer-sphere electron transfer reactions (i.e., high self-exchange rate); and (iv) stability under hydrogenation conditions. $[\text{Co}^{\text{III}}(\text{sep})]^{3+}$ has been firstly used as a relay in a catalytic cycle involving $[\text{Ru}(\text{bipy})_3]^{2+}$ as a photosensitizer and EDTA as a sacrificial donor, in the presence of colloidal platinum. $[\text{Co}^{\text{III}}(\text{sep})]^{3+}$ quenches the excited state of $[\text{Ru}(\text{bipy})_3]^{2+}$ by an oxidative electron transfer to yield $[\text{Ru}(\text{bipy})_3]^{3+}$ and $[\text{Co}^{\text{II}}(\text{sep})]^{2+}$. The Co^{II} derivative reduces water (or better H^+) to H_2 , while the Ru^{II} sensitizer is restored through reaction with EDTA [48, 49]. Although the rate of H_2 production is lower than that determined for the commonly used methylviologen relay, the turnover in the case of $[\text{Co}^{\text{III}}(\text{sep})]^{3+}$ is much higher, thanks to its high stability under the reaction conditions [50].

Owing to the great interest in photoreduction reactions, electron transfer processes involving $[\text{Co}^{\text{III}}(\text{cage})]^{3+}$ and polypyridine–ruthenium(II) complexes have been extensively investigated. The rate constants for the quenching process range from 2×10^8 to $1 \times 10^9 \text{ M}^{-1} \text{ s}^{-1}$ at 25°C . The yields of electron transfer products range from 0.3 to 1.0. These results are in agreement with the relatively low magnitude of the back electron transfer rate constants (8×10^6 to $8 \times 10^8 \text{ M}^{-1} \text{ s}^{-1}$), which can be explained in terms of poor coupling of $[\text{Ru}^{\text{III}}(\text{bipy})_3]^{3+}$ and $[\text{Co}^{\text{II}}(\text{cage})]^{2+}$ orbitals. An energy transfer mechanism operating beside the electron transfer has also been postulated to explain the overall quenching process [51]. However, an electron transfer contribution $\geq 95\%$ has been estimated for $[\text{Ru}^{\text{II}}(\text{bipy})_3]^{2+}$ quenching involving $[\text{Co}^{\text{III}}(\text{cage})]^{3+}$ complexes with standard reduction potentials less negative than -0.34 V versus NHE. At more negative potentials, the competition of the energy transfer lowers the efficiency of cobalt–cage system in the water photoreduction cycle. On the other hand, at potential higher than -0.25 V versus NHE, the lack of a thermodynamic driving force makes the rate of H_2 production too low. As a result, only a few $[\text{Co}^{\text{III}}(\text{cage})]^{3+}$ complexes display a good efficiency as electron transfer agents in photoreduction of water by systems containing: (i) $[\text{Ru}^{\text{II}}(\text{bipy})_3]^{2+}$ as a photosensitizer; (ii) EDTA as a sacrificial donor; and (iii) colloidal Pt (dispersed on polyvinylalcohol) as a catalyst. The most effective electron mediator of the series is $[\text{Co}^{\text{III}}(\text{ClSar})]^{3+}$, **26**, which, when compared with the reference system methylviologen, displays an equivalent ability to produce dihydrogen, but higher long-term stability in the photochemical cycles [52].

A two-component system containing both the photosensitizer and the electron relay has been obtained by covalently linking a cobalt–cage subunit to an anthracene moiety, *An*. The system **27** is not fluorescent ($\Phi < 2 \times 10^{-4}$), owing to the occurrence of an intramolecular quenching of the excited anthracene by the Co^{III} complex. Investigations on the photophysical features of **27** (i.e., transient absorp-



tion spectroscopy) have shown that the quenching process can be mainly ascribed to an energy transfer mechanism, and that electron transfer accounts for less than 5 % of total quenching. The contribution of the electron transfer process is very low, but when the system **27** is used under the above-mentioned conditions (EDTA as electron donor and Pt in polyvinylalcohol as catalyst), it is important enough to give rise to a detectable photoreduction and to induce dihydrogen production ($\Phi(\frac{1}{2}\text{H}_2) = 0.01$ at pH = 6.5) [53]. Moreover, the efficiency of the $[\text{Co}^{\text{III}}(\text{sep})]^{3+}$ –anthracene conjugate can be improved by introducing a longer spacer between the aromatic photosensitizer and the metal-containing electron relay [54]. System **28**, unlike **27**, emits the blue fluorescence characteristic of anthracene ($\Phi = 0.003$). This shows that, as expected, the rates of the radiationless deactivation processes (energy and electron transfer) decrease on increasing the length of the spacer. Apparently, the distance dependence effect is more severe for the energy transfer contributing process than for electron transfer process, since for **28** the yield of dihydrogen formation, under the standard conditions of water photoreduction, is higher ($\Phi(\frac{1}{2}\text{H}_2) = 0.14$ at pH = 6.5) than for **27**. A singlet excited state has been invoked as the effective intermediate in the photoreduction process: the state is involved in an intramolecular electron transfer to form a Co^{II} species which quantitatively generates H_2 in the presence of the Pt catalyst, according to Eqs. 9–11.



The study performed on systems **27** and **28** has demonstrated the advantage of the two-component approach to improve the efficiency of photoinduced electron

transfer processes. In fact, whereas an anthracene subunit is an efficient photosensitizer when covalently linked to the molecular relay, it does not work when used as a separate molecule.

5.4 Metals Inside Thia-Crowns

Macrocyclic polythioethers form coordination compounds with many transition metal ions [55] and, owing to their moderate π -acidity (intermediate between that of amines and phosphines), can exert a stabilizing effect on lower oxidation states of the encircled metal [56]. Copper complexes of thiacrowns have been widely investigated, even in view of the fact that they can be considered convenient models in the study of redox properties of cuproproteins (systems whose active site is a copper center bound to the thioether groups of methionine residues [57]).

The coordination of copper ion by macrocyclic quadri- and quinque-dentate thioethers makes the $\text{Cu}^{\text{II}}/\text{Cu}^{\text{I}}$ reduction process easier, and also increases the rate of the redox self-exchange electron transfer process [55]. For example, $[\text{Cu}(\text{13-aneS}_4)]^{2+}$ undergoes a one-electron reduction at 0.52 V versus NHE [58] (cf. $E^\circ(\text{Cu}^{\text{II}}/\text{Cu}^{\text{I}}) = 0.15$ V versus NHE for the aquated ion in water) and the rate constant for the corresponding self-exchange electron transfer is $3 \times 10^5 \text{ M}^{-1} \text{ s}^{-1}$ [59] (to be compared to $k = 5 \times 10^{-7} \text{ M}^{-1} \text{ s}^{-1}$ for the aquated ion [60]). In this connection, it is interesting to note that blue copper proteins are characterized by relatively high potential values and rate constants for the $\text{Cu}^{\text{II}}/\text{Cu}^{\text{I}}$ self-exchange ranging between 10^5 – $10^6 \text{ M}^{-1} \text{ s}^{-1}$ [61].

For $\text{Cu}^{\text{II}}/\text{Cu}^{\text{I}}$ systems, the electron transfer takes place with a large rearrangement of the inner coordination sphere, as Cu^{II} generally prefers distorted octahedral or square pyramidal environments whereas Cu^{I} likes better a tetrahedral geometry. This consideration implies that, in unconstrained systems, one or two Cu–S bonds must be broken and bond angles must be drastically modified upon Cu^{II} reduction. Therefore, any steric constraint imposed by the coordinated ligand could strongly affect the kinetics of the $\text{Cu}^{\text{II}}/\text{Cu}^{\text{I}}$ electron transfer process.

Owing to the above-mentioned similarities (redox potential values and rate constants) displayed by blue copper proteins and copper–thiacrown complexes, a systematic study has been performed on these low-molecular weight models in order to establish relationships between structural features and redox properties (in particular the kinetics of the $\text{Cu}^{\text{II}}/\text{Cu}^{\text{I}}$ redox change). In this respect, thiacrowns present definite advantages compared to other ligands: (i) the presence of a single type of donor atom (other than possible solvent molecules) in the inner coordination sphere; (ii) no protonation phenomena (which in the case of polyamino ligands makes the study in protic media difficult); (iii) highly positive potentials for the $\text{Cu}^{\text{II}}/\text{Cu}^{\text{I}}$ couple in aqueous media; and (iv) high stability constants with respect to nonmacrocyclic polythiaethers (about 100-fold higher in water) [58].

A thorough study has been performed on the complexes of macrocyclic polythiaethers (such as **29–34** reported in Chart 2) by using electrochemical techniques

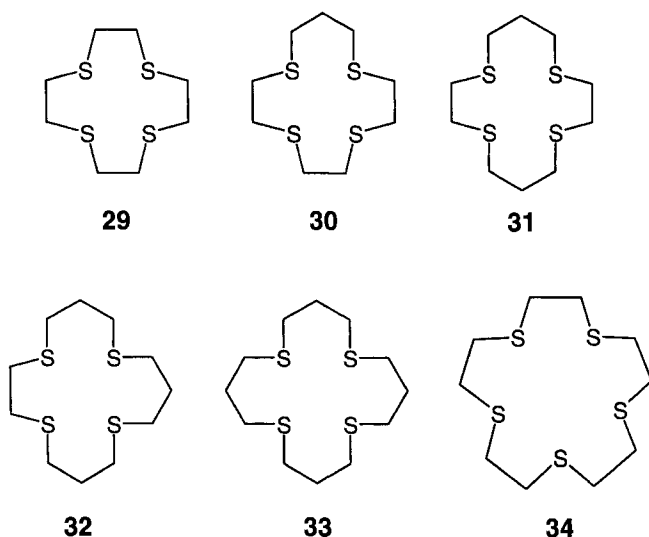


Chart 2. Poly-thia macrocycles of varying size and denticity used in the investigation of the $\text{Cu}^{\text{II}}/\text{Cu}^{\text{I}}$ redox change.

(voltammetric and potentiostatic measurements), in order to determine the formal reduction potentials, and by kinetic investigations (stopped-flow spectrophotometric and NMR techniques) on different cross-reactions involving Cu^{II} reduction or Cu^{I} oxidation, in order to measure the rate constants related to the electron transfer processes. The redox potentials determined for copper complexes of **29–34** range from 0.67 to 0.85 V versus SCE (in 4:1 methanol/water mixture; see Table 2) [62]. Cyclic voltammetric studies show that several systems (e.g., [15]aneS₅, **34**) display a reversible behavior both in water and in aqueous solvents, in which a single reduction and a single oxidation peak are observed at different sweep rates and temperature. In other cases (e.g., [14]aneS₄, **31**), the emergence of a second irreversible oxidation peak is observed at a higher potential. The relative intensity of the oxidation peak increases with increasing potential sweep rate and/or with decreasing temperature. This behavior is consistent with the existence of two alternate conformers of the Cu^{I} complex which are reoxidized to the corresponding Cu^{II} species at different potential values. The irreversible process observed at a more

Table 2. Potential values for the $\text{Cu}^{\text{II}}/\text{Cu}^{\text{I}}$ redox change determined for poly-thia macrocyclic complexes in 80 % MeOH–20 % water (by weight) at 25 °C. (From Ref. [62])

Ligand	$E_{1/2}(\text{Cu}^{\text{II}}/\text{Cu}^{\text{I}})$ V versus SCE
[12]aneS ₄ , 29	0.72
[13]aneS ₄ , 30	0.67
[14]aneS ₄ , 31	0.69
[15]aneS ₄ , 32	0.78
[16]aneS ₄ , 33	0.80
[15]aneS ₅ , 34	0.85

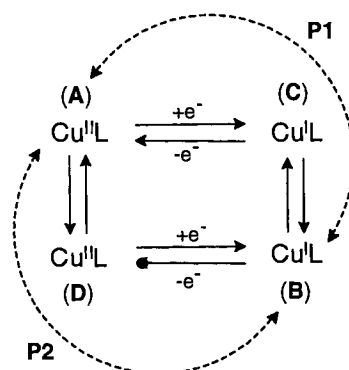


Figure 4. Proposed dual-pathway square scheme mechanism for the $\text{Cu}^{\text{II}}/\text{Cu}^{\text{I}}$ electron transfer process. (A) and (B) represent the stable forms of Cu^{II} and Cu^{I} complexes, respectively, while the species (C) and (D) represent metastable conformers.

positive potential value corresponds to the oxidation of the less stable conformer. In particular, this process takes place in the time scale of the cyclic voltammetry experiment and is observed only at high potential sweep rate or at low temperature. The redox process can be described with a dual-path, square-scheme mechanism in which the electron transfer step (from or to the copper center) takes place sequentially, rather than concertedly, with a conformational change.

As depicted in Figure 4, **A** and **B** represent the stable conformers of Cu^{II} and Cu^{I} respectively, in the coordination environment closest to their preferred geometry. **C** represents the less stable conformer of Cu^{I} , in an environment close to that of the stable conformer of Cu^{II} , **A**, while **D** represents the less stable conformer of Cu^{II} , whose geometric arrangement is close to that of **B**. According to this scheme, the $\text{Cu}^{\text{II}}/\text{Cu}^{\text{I}}$ redox process may take place by either of two pathways (**P1** or **P2**). It derives that the conformational rearrangement could precede or succeed the electron transfer step.

The mechanism depicted in Figure 4 is in accordance with the results obtained by kinetic studies. The rate constants calculated for different reduction reactions involving Cu^{II} -thiacrown complexes are often some orders of magnitude higher than the rate constants determined for the corresponding oxidation process involving Cu^{I} -thiacrown complexes [58]. This discrepancy may result from the different re-organizational barriers experienced by the metal centers in the two oxidation states. It is suggested that the two opposite processes (reduction of Cu^{II} and oxidation of Cu^{I}) proceed through different pathway (**P1** or **P2** in Figure 4). Low-temperature voltammetric measurements (down to -77°C) account for a higher stability of the intermediate species **C** with respect to the intermediate **D** [59]. Therefore, under conditions of low driving force, where all the conformational species are present at the equilibrium, pathway **P1** may be more favored. Such a hypothesis is in accordance with the results of NMR line-broadening studies carried out under equilibrium conditions [63].

On the basis of the above-mentioned experimental evidence, the $\text{Cu}^{\text{II}}/\text{Cu}^{\text{I}}$ redox exchange in thiacycrown complexes can be considered as an example of *gated* or *directional* electron transfer [64], as the rate of the conformational change can limit the reaction in one direction only.

X-ray crystallographic studies confirm that severe structural changes accompany the electron transfer process (in particular, at least one Cu–S bond is expected to be broken upon the Cu^{II}/Cu^I reduction), and support the hypothesis that conformational rearrangements influence the rate of overall redox process. For example, reduction of the [Cu^{II}(**31**)]²⁺ complex, in which the metal center and the four sulfur atoms are coplanar in a tetragonal arrangement, requires the inversion of two donor atoms (or a rupture of a Cu–S bond followed by the formation of a Cu–Solvent bond) and a dramatic change in the bond angles to produce the stable tetrahedral conformation preferred by the Cu^I center [65]. In the case of **34**, the Cu^{II} complex displays a distorted square pyramidal stereochemistry and, upon reduction, one of the equatorial Cu–S bond is broken to generate a distorted tetrahedral Cu^I complex with a relative small change in bond angles [66]. As a consequence of the lower conformational barrier, the rate constant for the Cu^{II}/Cu^I self-exchange process is higher in the case of **34** ($k = 2 \times 10^5 \text{ M}^{-1} \text{ s}^{-1}$ [67]) than in the case of **31** ($k \cong 10^4 \text{ M}^{-1} \text{ s}^{-1}$ [68]). Further studies performed on the copper complexes of more rigid thiacycrows such as **35–39** (see Chart 3) have confirmed the importance of

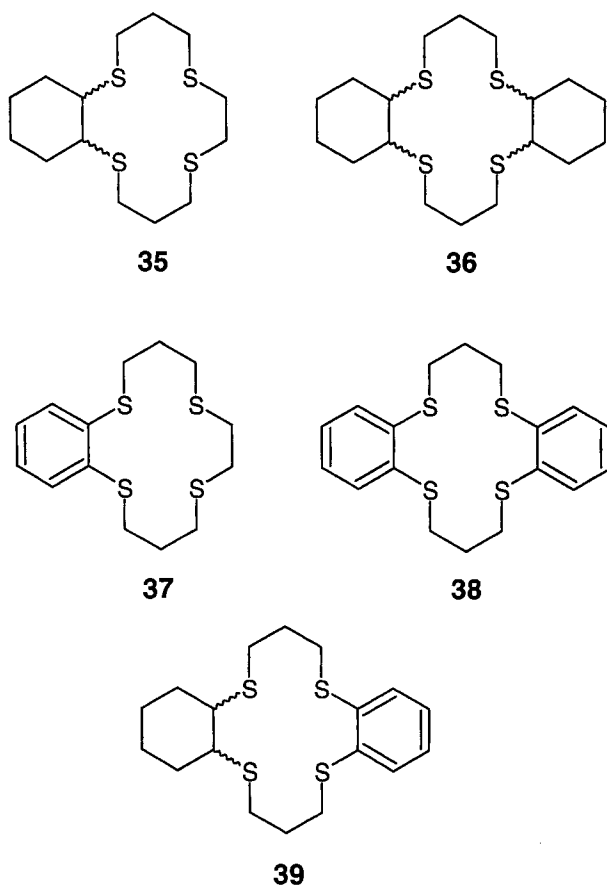
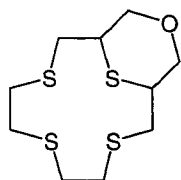


Chart 3. Rigid macrocyclic tetra-thiaethers used in the investigation of the Cu^{II}/Cu^I redox change. All the stereoisomers deriving from different configurations of cyclohexyl rings have been studied.

conformational rearrangements in determining the rate of the $\text{Cu}^{\text{II}}/\text{Cu}^{\text{I}}$ electron transfer process [69–71]. For the complex containing the system **36**, a three-rung ladder scheme has been proposed instead of the above-mentioned square scheme, in order to consider all the possible conformers (and the corresponding conformational changes) for both Cu^{II} and Cu^{I} species [71].

Recently, it has been hypothesized that the rate for the $\text{Cu}^{\text{II}}/\text{Cu}^{\text{I}}$ electron transfer could be improved by introducing in the macrocyclic backbone a particular constraint which forces the Cu^{II} ion to a square-pyramidal arrangement. In such a way, the metal ion would be out of the plane formed by sulfur atoms, and the strained S–Cu–S bond angles would nearly approximate the angles of the tetrahedral Cu^{I} species. Among tetra-thia-crowns, the best candidate to verify this hypothesis is [12]ane S_4 , **29**. As its Cu^{I} complex salts is poorly soluble, ligand framework has been properly modified to give **40**.

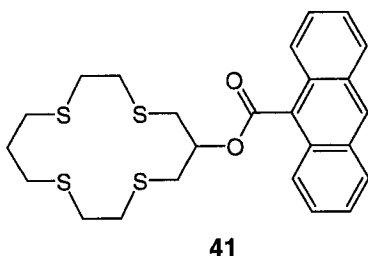


40

X-ray crystallographic studies have shown that the Cu^{II} complex of **40** exhibits a square-pyramidal geometry (with a water molecule occupying the fifth coordination position), whereas the corresponding Cu^{I} complex displays a tetrahedral geometry with one of the sulfur atoms (the one belonging to the thioxane ring) coordinated to the copper center of another complex molecule. Very significantly, the rate constant for the $\text{Cu}^{\text{II}}/\text{Cu}^{\text{I}}$ self-exchange process is especially high: $7 \times 10^5 \text{ M}^{-1} \text{ s}^{-1}$, which represents (at present) the highest value ever observed for a $\text{Cu}^{\text{II}}/\text{Cu}^{\text{I}}$ self-exchange process [72]. This example shows that tailor-made ligands can be designed specifically in order to modify at will the kinetics of the electron transfer process involving the $\text{Cu}^{\text{II}}/\text{Cu}^{\text{I}}$ redox change.

The $\text{Cu}^{\text{II}}/\text{Cu}^{\text{I}}$ couple inside a tetra-thia-crown coordinating environment has been also employed to build up a photoactive system which displays a switching behavior similar to that already discussed for systems **13** and **14**.

In the two-component system **41** an anthracene moiety has been appended to the [14]ane S_4 framework through an estereal bridge. In a MeCN solution, **41** displays a fluorescence spectrum that is less intense, and much less structured and shifted towards higher wavelengths than that typically observed for anthracene. The spectrum is similar to that of the alkyl esters of 9-anthracenoic acid, and can be ascribed to a charge transfer excited state (An^*_{CT}) [73]. On addition of 1 equiv. of $[\text{Cu}^{\text{I}}(\text{MeCN})_4]^+$ to the solution of **41**, the monovalent cation is incorporated by the tetra-thia ring, but the emission spectrum is not altered. The subsequent addition of an excess of the mild oxidizing agent $[\text{NO}]\text{BF}_4$ makes the solution turn bright blue, due to the formation of the Cu^{II} derivative, and the fluorescence to be completely quenched. Emission measurements at 77 K. allow the fluorescence quenching to be



assigned to a photoinduced electron transfer process from the An^*_{CT} state to the Cu^{II} center—a process that is highly favored from a thermodynamic point of view ($\Delta G^\circ_{ET} = -1.86$ eV). In the case of copper(I) complex, the Cu^I -to- An^*_{CT} electron transfer is not thermodynamically favored ($\Delta G^\circ_{ET} = 0.01$ eV), and no fluorescence quenching is observed [74].

The effect of the metal oxidation state on the emission intensity has been also investigated by performing controlled potential exhaustive electrolysis experiments. When an MeCN, poorly emissive solution of the Cu^{II} complex is reduced cathodically to the corresponding colorless Cu^I species, a strong fluorescence enhancement is observed. As the redox process is fully reversible, fluorescence can be switched ON/OFF at will, by setting the potential of the working electrode at the proper potentials for Cu^{II} -to- Cu^I (ON) and Cu^I -to- Cu^{II} (OFF) changes to take place.

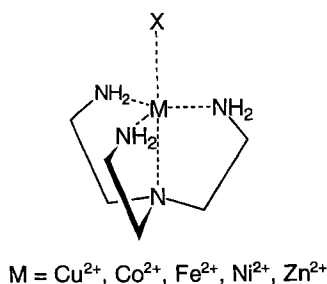
5.5 Anions Inside Zn^{II} –Polyamine-Based Systems

The growing interest for the design of supramolecular systems behaving as sensors for anionic species has prompted the study of multicomponent assemblies in which the anionic guest is recognized by a metal-containing host taking profit of coordinative interactions rather than of electrostatic interactions (which include hydrogen bonding).

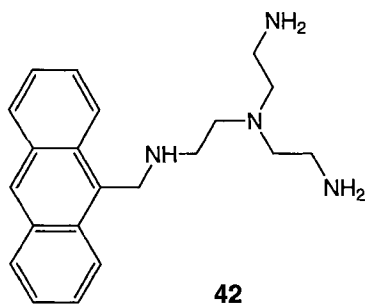
In recent years, some examples of fluorescent sensors for anions based on the metal–ligand interaction and operating through a photoinduced electron transfer process have been reported. Following the typical two-component approach, molecular-level fluorescent sensors are designed by covalently linking a light-emitting fragment to the receptor suitable for the envisaged analyte [75]. As a receptor, a coordinatively unsaturated metal center is chosen, which leaves one or more vacant coordination sites available for anion binding. A representative example is provided by the $[M^{II}(\text{tren})]^{2+}$ platform (tren = tris(2-aminoethyl)amine).

The branched tetramine tren is a typical ligand for divalent transition metal cations, and forms fairly stable complexes in aqueous solution [76] ($M^{2+} + \text{tren} = [M(\text{tren})]^{2+}$, $\log K$: Cu^{II} , 18.5; Ni^{II} , 14.6; Zn^{II} , 14.5; Co^{II} , 12.7; Fe^{II} , 8.8), which usually exhibit a trigonal bipyramidal geometry, the fifth vacant coordination site being occupied by a solvent molecule or by a coordinating anion (Figure 5).

Figure 5. The tetra-dentate ligand tren coordinates metal ions according to a trigonal-bipyramidal geometry. The fifth coordination site is available for a solvent molecule or for a coordinating anion.



System **42**, trenAn, which is obtained by appending an anthracene fragment (chosen as fluorophore) to the tetramine framework, is reacted with a metal ion M^{II} to give the $[\text{M}^{\text{II}}(\text{trenAn})]^{2+}$ system, which leaves a position available for anion binding.



Genuine transition metal ions (e.g., Cu^{II}) cannot be used as metal centers for building up a fluorescent sensor based on the trenAn system. In fact, d block metal ions tend to quench any proximate excited fluorophore through either an electron transfer or an electronic energy transfer process [13]. The post-transition cation Zn^{II} could be an acceptable surrogate of 3d metal ions for the following reasons: (i) it forms fairly stable complexes with tren in aqueous solution; and (ii) it cannot be involved in any photoinduced electron transfer process (owing to its absolute redox inactivity) or energy transfer process (due to its closed shell electronic configuration, d^{10}).

Since coordinatively unsaturated Zn^{II} polyamine complexes display a good affinity towards the COO^- group, the $[\text{Zn}^{\text{II}}(\text{42})]^{2+}$ platform was first tested for fluorescent sensing of carboxylate anions. For instance, there is evidence from spectrophotometric titration experiments that $[\text{Zn}^{\text{II}}(\text{42})]^{2+}$ forms a stable adduct with benzoate, in ethanolic solution at 25 °C. However, even after the addition of a large excess of benzoate to an ethanolic solution of $[\text{Zn}^{\text{II}}(\text{42})]^{2+}$, the typical fluorescent emission of the anthracene fragment is not altered at all. Quite interestingly, when a solution of $[\text{Zn}^{\text{II}}(\text{42})]^{2+}$ is titrated with the 4-*N,N*-dimethylamine-benzoate anion, the anthracene emission is progressively quenched: the fluorescence intensity, I_{F} , versus anion equivalents profile corresponds to the formation of a 1:1 adduct, and

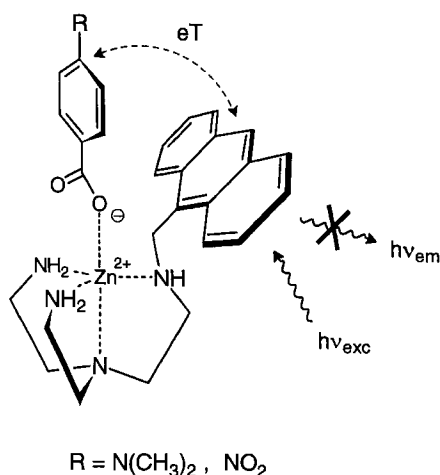
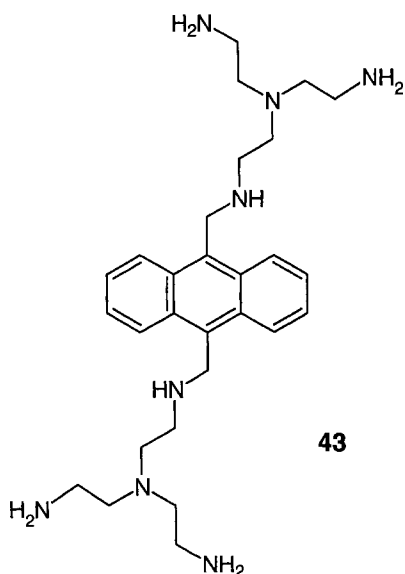


Figure 6. An electron transfer process to or from the redox active carboxylate anion coordinated to the metal center is responsible for the quenching of the emission of the photoexcited anthracene moiety in the [Zn(42)]²⁺ system.

the log K value for the $[\text{Zn}^{\text{II}}(42)]^{2+} + \text{RCOO}^- \rightleftharpoons [\text{Zn}^{\text{II}}(42)(\text{RCOO})]^+$ equilibrium is 5.45 (Figure 6). Quenching has to be ascribed to the occurrence of an electron transfer process from the *N,N*-dimethylaniline donor fragment, DMA, to the excited anthracene subunit, An^* . The DMA-to- An^* electron transfer (eT) process is characterized by a negative value of the free energy change ($\Delta G^\circ_{\text{ET}} = -0.4$ eV); on the other hand, molecular modeling indicates that coordination to the Zn^{II} center brings the 4-*N,N*-dimethylamine-benzoate donating fragment close enough to the anthracene subunit to ensure the occurrence of a fast and efficient electron transfer mechanism. Fluorescence quenching is observed also for the titration of $[\text{Zn}^{\text{II}}(42)]^{2+}$ with 4-nitro-benzoate and the log K value for the 1:1 adduct formation is 4.73. In this case, quenching is guaranteed by a thermodynamically favored An^* -to-nitrobenzoate electron transfer process ($\Delta G^\circ_{\text{ET}} = -1.0$ eV). In conclusion, the $[\text{Zn}^{\text{II}}(42)]^{2+}$ coordinatively unsaturated complex barely represents a proper example of host for anionic guests, but it is a good starting point towards the realization of metal-based host systems, in which the recognition event of the envisaged guest is signaled via an electron transfer process favored by the proximity of the redox active anion [77].

Along this line, a receptor system containing two $[\text{Zn}^{\text{II}}(\text{tren})]^{2+}$ subunits, linked together by an anthracene fragment, was designed.

The dimetallic receptor $[\text{Zn}^{\text{II}}_2(43)]^{4+}$ is expected to act as a good and selective host for imidazole-containing substrates. Imidazole (imH) is a protic acid but, owing to its very high $\text{p}K_{\text{A}}$ value (14.4), does not deprotonate in water. However, in the presence of two appropriately positioned metal ions, imH may deprotonate and form the imidazolate ion, im^- , which simultaneously bridges the two metal centers. An aqueous solution containing the dimetallic host $[\text{Zn}^{\text{II}}_2(43)]^{4+}$ and adjusted to $\text{pH} = 9.6$ exhibits the typical anthracene fluorescent emission. On addition of imH, fluorescence is quenched substantially, and the I_{F} versus equivalents of imH profile points towards the formation of a 1:1 adduct ($[\text{Zn}^{\text{II}}_2(43)(\text{im})]^{3+}$, log $K = 3.65$),



whose hypothesized structural arrangement is illustrated in Figure 7. In particular, bridging of the two Zn^{II} centers brings imidazolate close to the anthracene subunit, with a distance of about 3 Å between the two aromatic fragments lying in a coparallel fashion. It is probable that π -stacking interactions are present and contribute to the surprisingly high stability in water of the host-guest adduct. This arrangement favors the occurrence of an electron transfer process from the electron-rich im^- anion to the facing excited fluorophore An^* . Histidine shows a similar behavior, with a $\log K$ value for the 1:1 adduct ($[\text{Zn}^{\text{II}}_2(\mathbf{43})(\text{his})]^{3+}$, $\log K = 2.92$) lower than observed for plain imidazole, probably due to the electrostatic repulsive interactions between the charged metal centers and the ammonium group of histidine [78].

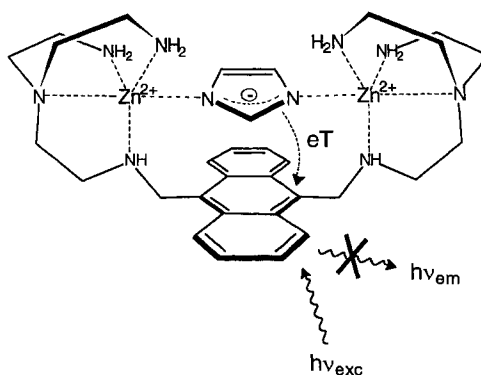
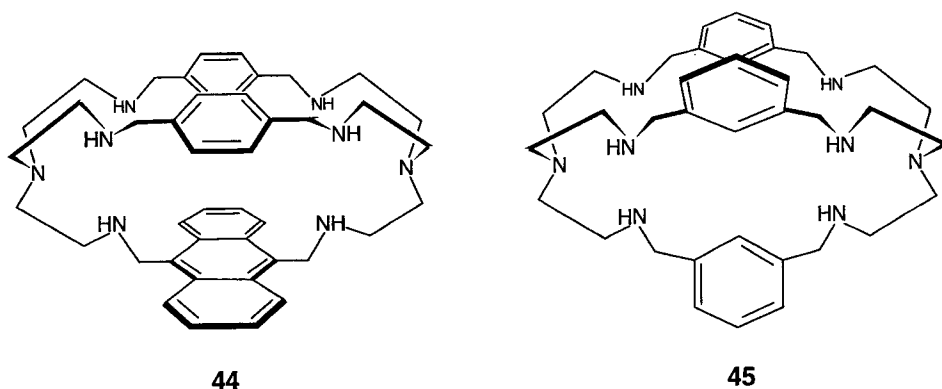


Figure 7. The imidazolate ion bridges the two metal centers of $[\text{Zn}_2(\mathbf{43})]^{4+}$, and an electron is transferred to the facing photo-excited anthracene subunit, causing emission quenching.



A further step in the development of fluorescent sensors based on $[\text{Zn}^{\text{II}}(\text{tren})]^{2+}$ and anthracene fragments is the construction of a cage-shaped host. For example, **44** can be obtained by reacting the ligand **43** with two equivalents of terephthalaldehyde and subsequent reduction of the four imine bonds of the Schiff base.

As previously reported for dicopper complex of cage compound **45** [79], the steric constraints imposed by the polycyclic framework induce clear selectivity effects in the recognition of ambidentate anions. In particular, spectrophotometric titration studies have shown that the $[\text{Cu}^{\text{II}}_2(\text{45})]^{4+}$ receptor gives 1:1 complexes of varying stability with ambidentate anions in aqueous solution. Also the $[\text{Zn}^{\text{II}}_2(\text{44})]^{4+}$ complex, which is stable in aqueous solution over a substantial range of pH, can encapsulate ambidentate anions, to give stable 1:1 inclusion complexes. In particular, by titrating with a standard N_3^- solution an aqueous solution 10^{-4} M in $[\text{Zn}^{\text{II}}_2(\text{44})]^{4+}$ complex buffered at pH 8, a linear decrease of fluorescence is observed until the addition of 1 equiv. of azide. From the titration profile, a value of $\log K$ of 5.8 can be calculated for the inclusion equilibrium.

Fluorescence quenching is ascribed to the occurrence of an electron transfer process from the electron-rich N_3^- ion to the nearby An^* fragment (Figure 8).

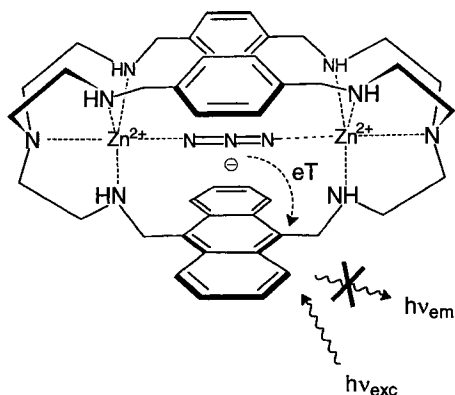


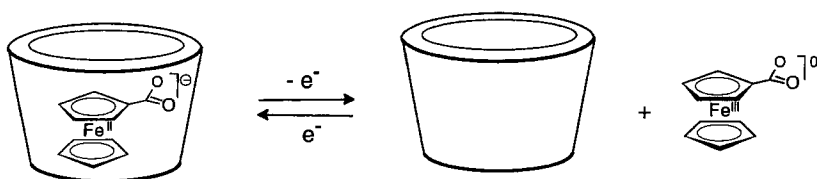
Figure 8. The azide anion, when enclosed in the zinc(II) cryptate $[\text{Zn}_2(\text{44})]^{4+}$, causes the quenching of the facing anthracene fragment: an electron is transferred from the electron rich anion to the photoexcited spacer. Inclusion of cyanate anion does not alter fluorescence emission, due to lack of the suitable redox potential allowing electron transfer.

Through molecular modeling, a distance of ca 3 Å can be estimated between the closest nitrogen atoms of N_3^- and carbon atoms of the anthracene fragment, which allows the occurrence of a fast and efficient through-space electron transfer process. When titrating a solution of the $[\text{Zn}^{\text{II}}_2(\mathbf{44})]^{4+}$ complex with a series of inorganic anions (NO_3^- , HCO_3^- , SO_4^{2-} , Cl^- , Br^-), no decrease of fluorescence intensity was observed, even after the addition of a large excess of anion. Moreover, the spectrofluorimetric titration profile of N_3^- was not modified in presence of a 10-fold excess of the anion, indicating a much poorer affinity. The case of NCO^- is different: on addition of NCO^- to the receptor solution, no decrease in I_F was observed. However, the titration profile of N_3^- was remarkably affected by the presence of NCO^- : the greater NCO^- concentration, the less steep the I_F decrease, which indicates the presence of a competitive equilibrium for anion inclusion within the cage. In particular, a $\log K$ of 6.5 can be calculated through competition studies for the NCO^- inclusion equilibrium. Thus, NCO^- has a slightly greater affinity for $[\text{Zn}^{\text{II}}_2(\mathbf{44})]^{4+}$ than N_3^- , but, when included in the cage, due to its lower oxidation potential, it is unable to transfer an electron to the nearby An^* fragment. N_3^- and NCO^- anions have the same shape and similar dimensions ("bite length" of 2.34 and 2.42 Å, respectively): the rather high values of the host–guest formation constants reflect the favorable dimensional complementarity between the host cavity (the Zn–Zn distance) and the anion bite length. The other linear triatomic anion, NCS^- , quenches fluorescence, but a much lower value of $\log K$ for the inclusion is observed, 2.45. In this connection, it must be noted that NCS^- is a one-electron reducing agent of strength comparable to that of N_3^- ($\text{NCS}^{\cdot}/\text{NCS}^-$ potential: 1.62 V versus NHE; $\text{N}_3^{\cdot}/\text{N}_3^-$: 1.33), which accounts for the occurrence of an intra-complex photo-induced electron transfer process and fluorescence quenching. However, the much greater bite length of NCS^- (2.75 Å) should induce an endothermic rearrangement of the cage framework, making inclusion 2200 times much less favorable than for N_3^- [80].

5.6 Cyclodextrins

The attention towards electron transfer processes involving host–guest adducts of cyclodextrins (CDs) has become important with regard to their use as modifiers of organic electrode reactions. CDs, when added to solution or to electrode surfaces, can improve the selectivity of electrochemical synthesis. To elucidate the details of electron transfer reactions of guest molecules complexed inside CDs, the redox behavior of ferrocenecarboxylic acid in presence of β -CD was studied, and this showed that the oxidation of the complexed ferrocenecarboxylic anion, FCA^- , must proceed via the dissociation of the host–guest adduct to form free FCA^- which then transfers an electron to the electrode [81].

The work of Kaifer and colleagues [82a–c] and other researchers [83a,b] on different ferrocene derivatives complexed with β -CD illustrates a similar behavior: the monoelectronic oxidation drastically lowers the host–guest affinity (see Scheme 3).



Scheme 3. Redox control on the β -CD complexation of a ferrocene-carboxylate, Fc-COO^- . β -CD displays a higher affinity for the negatively charged FcCOO^- than for the overall neutral ferrocenium carboxylate, Fc^+COO^- . One-electron oxidation favors the release of the guest to the solution, whereas one-electron reduction induces re-complexation by β -CD.

From a different point of view, oxidation in presence of the β -CD host takes place only on the free ferrocene guest, and no direct oxidation of the complexed guest takes place, suggesting that the electron transfer from the complexed ferrocene guest is in some way disfavored because of some thermodynamic or kinetic effect exerted by the host framework.

Following the same approach, CD complexation of cobaltocenium derivatives was investigated [84]. In this case, the positively charged guest (cobaltocenium) is not bound with a significant stability constant, as the neutral cavity of CD is a good receptor only for neutral substrates. However, monoelectronic reduction to neutral cobaltocene increases the affinity between CD and the neutral guest which forms. The same situation is found using viologens as guests. The one-electron reduction of the dicationic, weakly interacting guest leads to a radical cationic species which is not still strongly bound, whereas two-electron reduction gives a neutral guest which forms a very stable adducts with the β -CD host [85].

A particular emphasis is to be made on these systems: the recognition of ferrocene-based substrates can be switched off by monoelectronic oxidation of the substrate itself, whereas in the case of positively charged guests the binding interaction can be electrochemically activated by either a mono- (for cobaltocenium) or bi-electronic (for viologen) reduction process [86].

Several examples of CDs bearing a photo- or redox-active fragment displaying either electron donor or electron acceptor properties have been prepared during the past decade. In all these systems, the two-component approach was followed, by covalently linking a redox active fragment and a receptor subunit: when a guest with the proper redox potential is complexed, an electron is transferred to or from the redox active moiety appended to the CD.

In 1993, Kuroda and colleagues [87] reported the cyclodextrin-sandwiched porphyrin **46**. This receptor is able to bind quinonic substrates as function of their hydrophilicity (Figure 9). Addition of redox active quinones to an aqueous solution of the host **46** results in fluorescence quenching of the porphyrin moiety, due to the occurrence of a photoinduced electron transfer from the excited fragment of the host to the complexed acceptor guest. ESR studies on irradiated frozen solutions showed the presence of the porphyrin radical cation and of the quinone radical anion. Electron transfer reactions were also studied by means of time-resolved fluorescence spectroscopy, obtaining a clean single exponential decay of the receptor

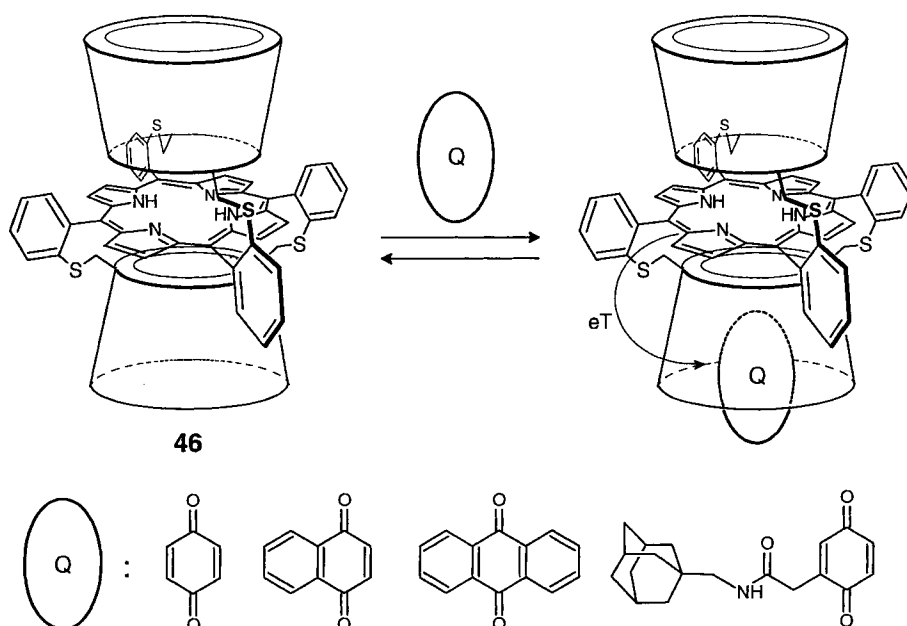


Figure 9. Inclusion of quinone substrates into the cyclodextrin moiety promotes the occurrence of an electron transfer process from the photoexcited porphyrin fragment to the quinone.

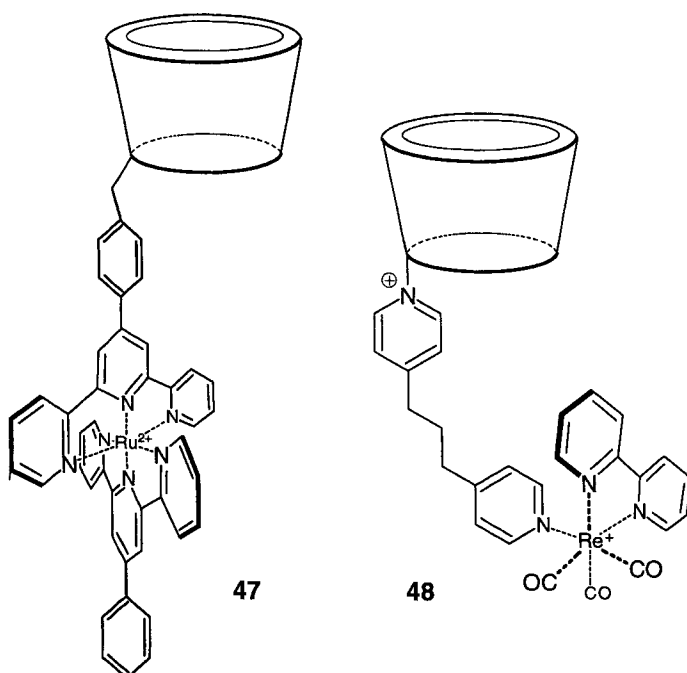
with a τ_s of 3.2 ns, and a biexponential decay for the host–guest adduct. For every complexed guest, the lifetime for the long-lived component is identical to that of the uncomplexed host (3.2 ns), while the second short-lived component is much lower (ranging between 0.5–0.7 ns). From these data, the rate constants of intramolecular electron transfer reactions were calculated to be around 10^9 s^{-1} , a value which was found reasonable for this type of process [87].

In another recent example, a terpyridine fragment has been appended to the lower rim of a β -CD, and a subsequent reaction with $\text{Ru}(\text{ttp})\text{Cl}_3$ yielded the complex **47**, $[(\beta\text{-CD-ttp})\text{Ru}(\text{ttp})][\text{PF}_6]_2$.

When the redox active guest anthraquinone-2-carboxylic acid is added to compound **47**, a partial quenching of about 20 % of the MLCT emission of the ruthenium center of the complex is observed, while no quenching is observed when the same substrate is added to the metal complex in absence of the cyclodextrin receptor. The partial quenching can be then ascribed to the occurrence of an electron transfer process between the guest complexed into the CD cavity and the appended metal center [88].

The same approach was used by Nakamura and coworkers: compound **48** profits from a polypyridyltricarboxylrhenium(I) luminophore, whose luminescence is quenched by addition of *N,N*-diethylaniline (DEA) [89].

The luminescence decay in presence of DEA is fitted by a two-exponential model, with a long-lived component, which is present also on the guest free receptor, and



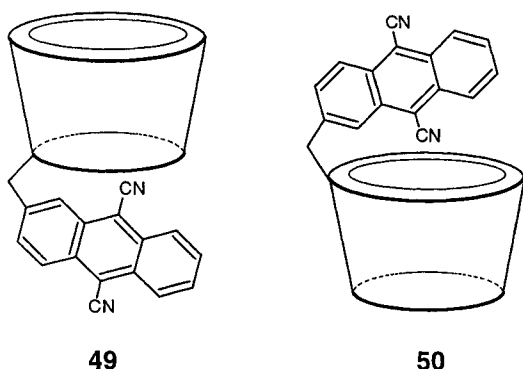
a short-lived one, which is observed only in the host–guest adduct. The observed luminescence quenching results from the sum of two different mechanisms: (i) a dynamic quenching contribution arising from a diffusional collision between the luminophore and the free substrate in solution, which mainly affects the longer-living component; and (ii) a static quenching contribution which derives from an electron transfer from the donor guest trapped into the CD cavity to the Re complex fixed outside the host cavity. The rate of electron transfer k_{eT} is estimated to be $3.7 \times 10^7 \text{ s}^{-1}$.

A very similar behavior is shown by compounds **49** and **50**: the addition of several sulfonated aromatic guests produces both static and dynamic fluorescence quenching of the dicyanoanthracene moiety appended in different arrangements to the CD host.

Also in this case, the photoinduced electron transfer from the complexed redox active guests to the organic fluorophore appended to the receptor subunit of the host is responsible for the static component of the observed quenching process [90].

5.7 Calixarenes and Related Compounds

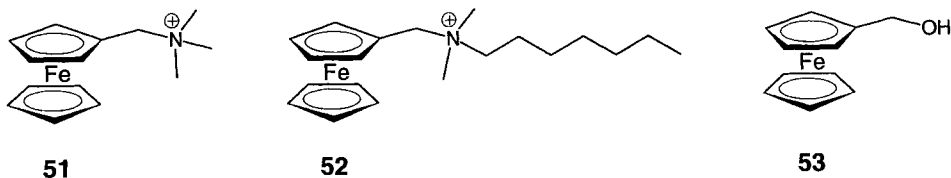
Calixarenes, just like CDs, are electroinactive hosts, but the electrochemical properties of redox active substrates can undergo sensible changes when host–guest in-



teractions take place. A representative example is provided by ferrocene inclusion in sulfonatocalixarenes, whose behavior is in some way specular to that of cyclodextrins. Voltammetric experiments have shown that the host interacts more strongly with the oxidized, neutral ferroceniumcarboxylate, $\text{Fc}^+ \text{-COO}^-$, than with the reduced, anionic form of the guest, Fc-COO^- , for which electrostatic repulsions with the negatively charged host should operate. The effect of calixarene addition on peak currents is much smaller than that observed with β -CD, which indicates that the reduced ferrocene guest is not significantly bound to the host [86].

Using neutral or positively charged ferrocene substrates does not change the observed trend. When sulfonatocalixarene is added to ferrocenic substrates such as **51**, **52** and **53**, the half-wave potential associated with oxidation processes is shifted towards more negative values (shifts range between 50 and 120 mV); complexation by the anionic host stabilizes the oxidized, positively charged ferrocenium species, and once again the oxidized species are more strongly bound than the reduced forms. Calixarene complexation also causes a decrease in the apparent diffusion coefficient of the electroactive substrate, due to the greater bulk of host-guest adducts with respect to the corresponding uncomplexed ferrocene derivatives. A current decrease is observed, compared to uncomplexed ferrocene, indicating that complexation of the ferrocenic guests takes place before their oxidation [91].

As far as functionalized calixarenes are concerned, two very close examples of electron transfer reaction between a complexed substrate and a redox active fragment bound to the calixarenic receptor were provided by Sessler's group [92] and by Weiss and Mildbradt [93]. Two calix[4]arenes moieties are linked together by a Zn^{II} porphyrin (Figure 10). When benzoquinone is added to a CH_2Cl_2 solution of compound **54**, quenching of the metalloporphyrin fluorescence is observed. More-



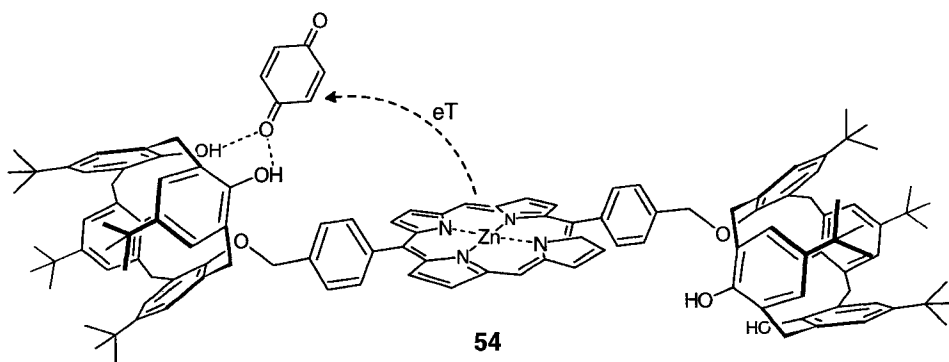
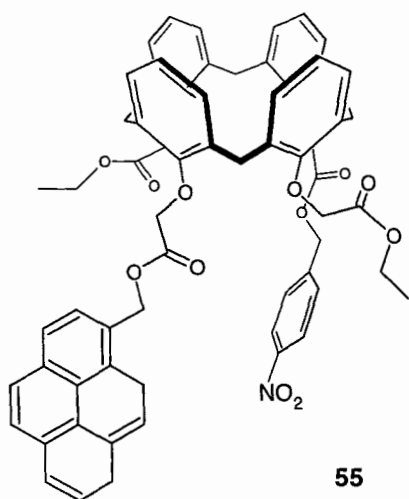


Figure 10. Binding of a quinone to the calixarene compartment of system **54** promotes the occurrence of a Zn^{II} (porphyrin)-to-quinone photoinduced electron transfer process.

over, the Stern–Volmer plot obtained from the steady-state measurements gave a curved line, in contrast with that found with the control compound without the guest units, for which a linear plot was observed. As in the case of cyclodextrins, this behavior is consistent with the excited state of the guest molecule being quenched by both static and dynamic processes. Time-resolved measurements on the empty guest (i.e., in absence of benzoquinone) and on the control compound showed the presence of a monoexponential decay with a lifetime of 1.6 and 1.7 ns, respectively. When benzoquinone is added to the control compound, a monoexponential decay is still observed, displaying a distinctly lower dynamic lifetime, as one might expect for an intermolecular quenching process. Addition of benzoquinone to host **54** results in a decay profile which was fitted with two exponential components: a long-lived component with variable lifetime depending upon substrate concentration, and a short-lived component with a constant lifetime of 700 ps, which is attributed to a quenching process due to an electron transfer from the calixarene- Zn^{II} porphyrin system to the benzoquinone guest. Weiss's compound, which slightly differs in the bridge linking the calixarene receptor and the Zn^{II} porphyrin, showed a similar behavior in a 19:1 THF/water solution.

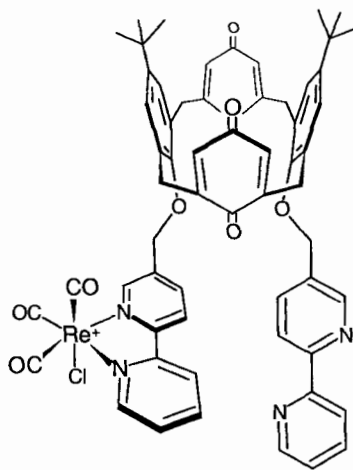
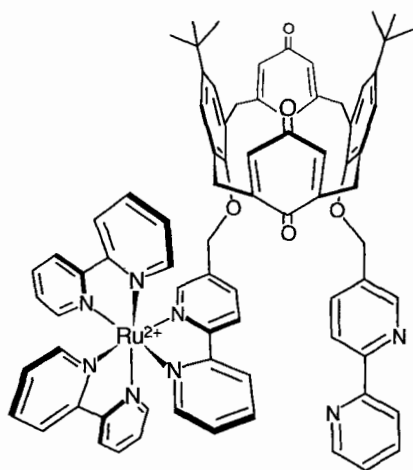
Following a different approach, both the redox active fragments (the donor and the acceptor) can be placed within a host molecule, thus making an electron transfer possible inside the host cavity. In these circumstances, one might attempt to perturb the electron transfer process through the inclusion of an appropriate guest.

One of the smartest examples of this approach involving a calixarene platform has been provided by Shinkai and colleagues [94]. In this system (**55**), a calix[4]arene brings a pyrene fragment as a fluorophore and a nitrobenzene fragment as an acceptor of electrons, bound via ester groups. System **55** displays a very low fluorescence quantum yield—a feature which can be accounted for considering that the ester groups can rotate freely, thus occasionally bringing the excited fluorophore and the nitrobenzene acceptor moiety very close, and favoring the occurrence of an electron transfer process. Upon addition of alkaline metal salts, fluorescence emission sensibly increases, in correspondence of the formation of a 1:1 host–guest



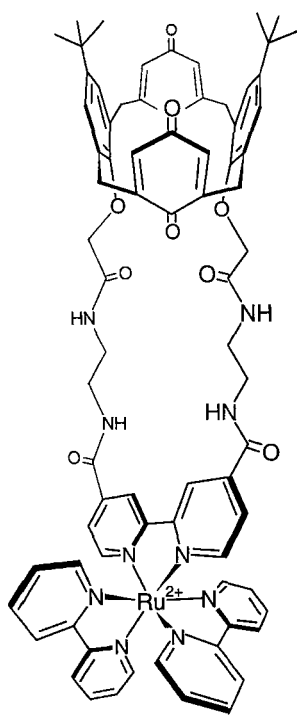
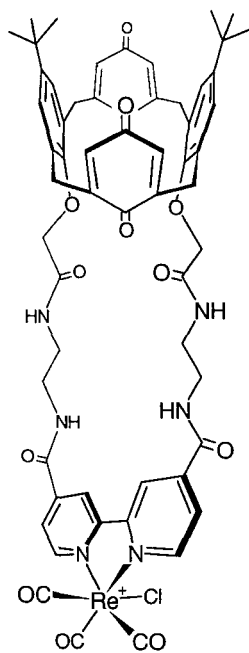
adduct between **55** and the metal cation. Fluorescence revival is to be ascribed to the ester carbonyl's reorientation towards the inside of the host, to ensure metal binding into the ionophoric compartment. This reorientation drastically reduces the freedom of movement of the electroactive fragments, thus decreasing the efficiency of the electron transfer process from the excited fluorophore to the nitrobenzene acceptor.

A further example of steric control on electron transfer processes involving calixarene hosts has been provided by Ziessel and coworkers who appended one (**56**) or two [$\text{Ru}^{\text{II}}(\text{bpy})_3$] moieties and a *fac*-[$\text{Re}^{\text{I}}\text{Cl}(\text{CO})_3(\text{bpy})$] (**57**) to a calix[4]diquinone [95]. For all the complexes the luminescence quantum yield is very low because of



photoinduced electron transfer occurring from the metal center to the close quinone fragment of the host. This explanation is supported by molecular dynamic simulations showing that when the calixarene moiety exists in a noncone conformation, the redox active fragments can become arranged in a coparallel fashion, which brings them in orbital contact, and makes the electron transfer process very favorable. The addition of Ba^{2+} cations to the rhenium complex **57** induces complete quenching of the residual luminescence: the cation stabilizes by ion pairing the emergent negative charge generated by the electron transfer process, which is therefore made easier. Quite interestingly, addition of Ba^{2+} (but also of many others mono-, di- and tri-valent cations) to **56** leads to a strong restoration of the Ru^{II} complexes luminescence. In this case, the moderately favorable effect exerted by the metal on the electron transfer process is more than compensated by the guest-forced adoption of the cone conformation, which precludes any orbital overlap between the redox active subunits of the host, the quinones and the metal complex, thus reducing the intramolecular electron transfer rate in host **56** from $1.7 \times 10^8 \text{ s}^{-1}$ down to $0.44 \times 10^6 \text{ s}^{-1}$.

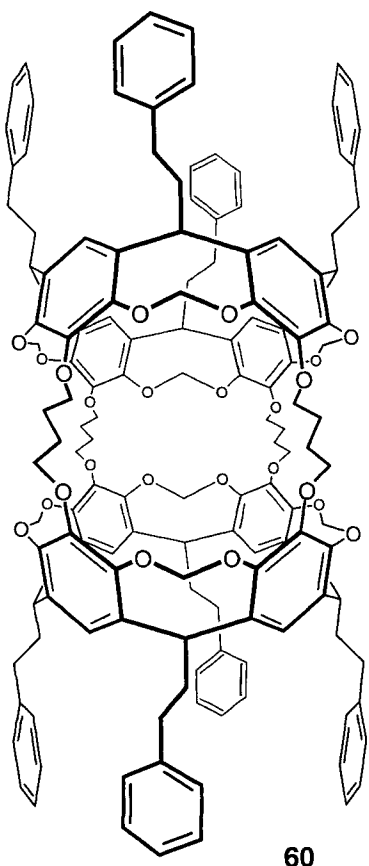
Beer, Balzani and coworkers [96] have recently realized an anion sensor based on the same subunits, which operates through an intramolecular electron transfer between an appended luminescent metal complex and a quinone fragment, both included within a calixarene framework. Systems **58** and **59** display a remarkable

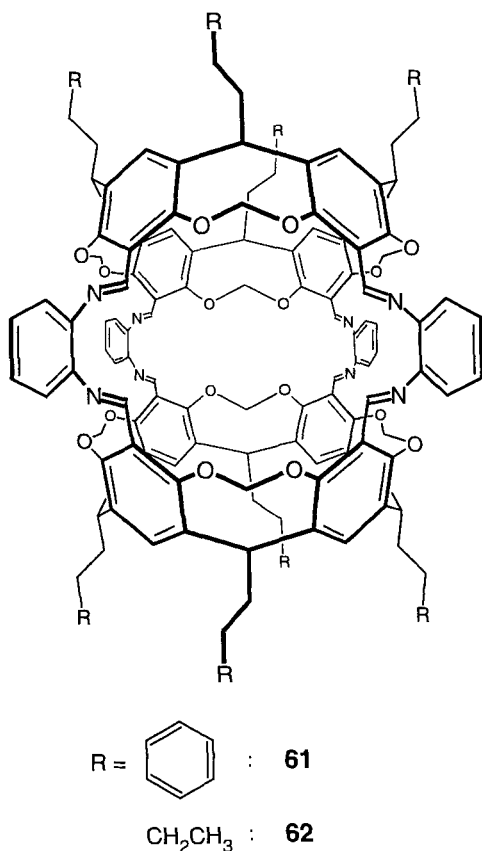
**58****59**

emission retrieval effect upon addition of acetate, chloride, and hydrogenphosphate in DMSO solution. The anionic guest complexation within the host cavity once again induces a perturbation of the intramolecular photoinduced electron transfer from the MLCT excited state of the Ru^{II} (**58**) and Re^{I} (**59**) complex to the quinone acceptors of the calixarene.

5.8 Carcerands and Hemicarcerands

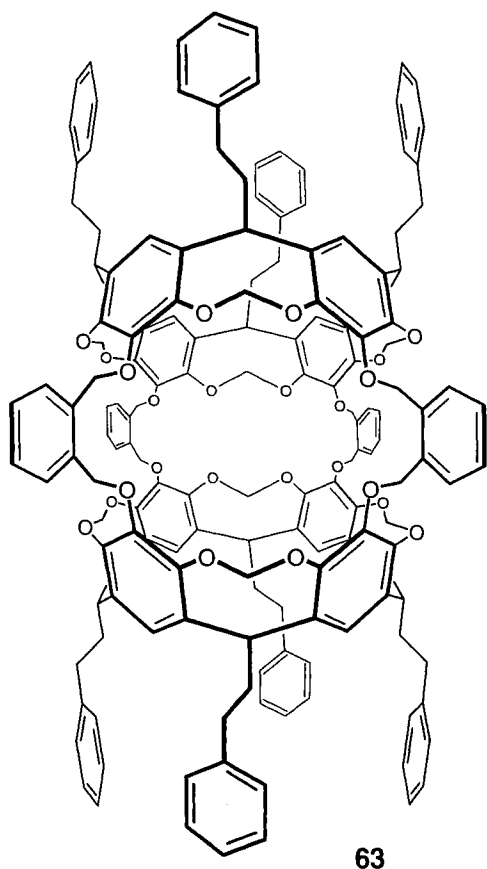
The first attempt to perform redox reactions on guest molecules inside hemicarcerand cages was carried out by Robbins and Cram in 1993 [97]. Chemical oxidation with either ceric ammonium nitrate–silica gel in CCl_4 at room temperature or thallic trifluoroacetate in refluxing CCl_4 was performed on hydroquinone guests trapped inside hemicarcerand **60**, thus obtaining the corresponding quinone hemicarceplexes. When the incarcerated quinones are reduced with samarium iodide in





refluxing THF, the corresponding original hydroquinones are obtained without any side reaction, and without hemicarceplex destruction. Under the same conditions, the corresponding hemicarceplex containing nitrobenzene was reduced to the corresponding hydroxylamine in high yield. These reactions demonstrate that electrons can be transferred into and out the interior phase of the host, and that the redox reactions can take place without a direct contact of the guest and the reagent.

Studies on the electrochemical behavior of ferrocene encapsulated in the hemicarcerands **61** and **62**, indicated that encapsulation induces substantial changes in the oxidation behavior of the ferrocene subunit [98]. In particular, encapsulated ferrocene exhibits a positive shift of the oxidation potential of c. 120 mV, probably because of the poor solvation of ferrocenium inside the apolar guest cavity. Lower apparent standard rate constants were found for the heterogeneous electron transfer reactions, compared to those found in the uncomplexed ferrocene under identical experimental conditions. This effect may be due to two main contributions: (i) the increased effective molecular mass of the electroactive species; and (ii) the increased distance of maximum approach of the redox active center to the electrode surface.

**63**

One of the best known examples of electron transfer reactions involving hemicarceplexes is the one investigated independently by Pina, Balzani and colleagues [99] and by Deshayes and coworkers [100]. The latter study is focused mainly on triplet energy transfer, a process which can be mechanistically related to electron transfer [101].

In Pina's work, 2,3-butanedione is trapped inside hemicarcerand **63** to give the corresponding hemicarceplex, and the reactions with several electron donors are investigated in order to elucidate the effect of the encapsulation on the rates of the electron transfer to the triplet excited state of the guest. The determination of phosphorescence quenching lifetimes of free and incarcerated 2,3-butanedione reveals that quenching for uncomplexed 2,3-butanedione occurs at the diffusion-controlled limits for any donor quencher (e.g., amines), whereas in the case of the encapsulated substrate the rate constants are lower (ranging between 3.5×10^4 and $4 \times 10^8 \text{ s}^{-1}$) and display an approximately linear dependence upon the oxidation potential of the external quencher. In particular, rate constants decrease with the

increasing amine resistance to the oxidation. These results indicate that the electronic interaction between external quenchers and the incarcerated biacetyl is very small, due to the shielding effect exerted by the walls of the hemicarcerand.

References

1. L. Fabbrizzi, *Comments Inorg. Chem.*, **1985**, 4, 33.
2. A. G. Lappin, A. McAuley, *Adv. Inorg. Chem.*, **1988**, 32, 241.
3. L. Sabatini, L. Fabbrizzi, *Inorg. Chem.*, **1979**, 18, 438.
4. A. Bencini, L. Fabbrizzi, A. Poggi, *Inorg. Chem.*, **1981**, 20, 2544.
5. A. Buttafava, L. Fabbrizzi, A. Perotti, A. Poggi, G. Poli, B. Seghi, *Inorg. Chem.*, **1986**, 25, 1456.
6. A. De Blas, G. De Santis, L. Fabbrizzi, M. Licchelli, P. Pallavicini, *Pure Appl. Chem.*, **1993**, 65, 455.
7. G. De Santis, L. Fabbrizzi, M. Licchelli, N. Sardone, A. H. Velders, *Chem. Eur. J.*, **1996**, 2, 1243.
8. L. Fabbrizzi, M. Licchelli, P. Pallavicini, *Acc. Chem. Res.*, **1999**, 32, 846.
9. L. Fabbrizzi, A. Poggi, B. Seghi, *Inorg. Synth.*, **1985**, 23, 82.
10. L. Fabbrizzi, F. Forlini, A. Perotti, B. Seghi, *Inorg. Chem.*, **1984**, 23, 807.
11. E. Billo, *Inorg. Chem.*, **1984**, 23, 236.
12. L. C. Siegfried, T. A. Kaden, *J. Phys. Org. Chem.*, **1992**, 5, 549.
13. L. Fabbrizzi, M. Licchelli, P. Pallavicini, A. Perotti, A. Taglietti, D. Sacchi, *Chem. Eur. J.*, **1996**, 2, 75.
14. B. Dietrich, M. W. Hosseini, J.-M. Lehn, R. B. Session, *J. Am. Chem. Soc.*, **1981**, 103, 1282.
15. M. W. Hosseini, J.-M. Lehn, *J. Am. Chem. Soc.*, **1982**, 104, 3525.
16. E. Kimura, *Top. Curr. Chem.*, **1985**, 128, 113.
17. M. W. Hosseini, J.-M. Lehn, *Helv. Chim. Acta*, **1986**, 69, 587.
18. H. M. Colquhoun, J. F. Stoddart, D. J. Williams, *Angew. Chem., Int. Ed. Engl.*, **1986**, 25, 487.
19. A. Bianchi, M. Micheloni, P. Paoletti, *Coord. Chem. Rev.*, **1991**, 110, 17.
20. M. A. Santos, M. G. B. Drew, *J. Chem. Soc., Faraday Trans.*, **1991**, 87, 1321.
21. M. Mitewa, P. R. Bontchev, *Coord. Chem. Rev.*, **1994**, 135–136, 129.
22. F. P. Schmidtchen, M. Berger, *Chem. Rev.*, **1997**, 97, 1609.
23. M. F. Manfrin, L. Moggi, V. Castelvetro, V. Balzani, M. W. Hosseini, J.-M. Lehn, *J. Am. Chem. Soc.*, **1985**, 107, 6888.
24. M. W. Hosseini in *Perspective in Coordination Chemistry* (Eds.: A. F. Williams, C. Floriani, A. F. Merbach), VCH, Weinheim, **1992**, p. 333.
25. J. Sotomayor, A. J. Parola, F. Pina, E. Zinato, P. Ricciari, M. F. Manfrin, L. Moggi, *Inorg. Chem.*, **1995**, 34, 6532.
26. M. A. Rampi, M. T. Indelli, F. Scandola, F. Pina, A. J. Parola, *Inorg. Chem.*, **1996**, 35, 3355.
27. J.-M. Lehn, *Acc. Chem. Res.*, **1978**, 11, 49.
28. J.-M. Lehn, *Pure Appl. Chem.*, **1980**, 52, 2441.
29. V. Balzani, N. Sabbatini, F. Scandola, *Chem. Rev.*, **1986**, 86, 319.
30. F. Peter, M. Gross, M. W. Hosseini, J.-M. Lehn, R. B. Session, *J. Chem. Soc., Chem. Commun.*, **1981**, 1067.
31. F. Peter, M. Gross, M. W. Hosseini, J.-M. Lehn, *J. Electroanal. Chem.*, **1983**, 144, 279.
32. F. Pina, A. J. Parola, A. Saint-Maurice, M. F. Manfrin, L. Moggi, M. T. Indelli, F. Scandola, *J. Chem. Soc., Dalton Trans.*, **1997**, 2327.
33. I. I. Creaser, J. M. Harrowfield, A. J. Herlt, A. M. Sargeson, J. Springborg, R. J. Geue, M. R. Snow, *J. Am. Chem. Soc.*, **1977**, 99, 3181.
34. A. M. Sargeson, *Chemistry Britain*, **1979**, 15, 23.
35. J. M. Harrowfield, A. J. Herlt, A. M. Sargeson, *Inorg. Synth.*, **1980**, 20, 85.
36. R. J. Geue, T. W. Hambley, J. M. Harrowfield, A. M. Sargeson, M. R. Snow, *J. Am. Chem. Soc.*, **1984**, 106, 5488.

37. G. A. Bottomley, I. J. Clark, I. I. Creaser, L. M. Engelhardt, R. J. Geue, K. S. Hagen, J. M. Harrowfield, G. A. Lawrance, P. A. Lay, A. M. Sargeson, A. J. See, B. W. Skelton, A. H. White, F. R. Wilner, *Aust. J. Chem.*, **1994**, *47*, 143, and references therein.
38. I. I. Creaser, R. J. Geue, J. M. Harrowfield, A. J. Herlt, A. M. Sargeson, M. R. Snow, J. Springborg, *J. Am. Chem. Soc.*, **1982**, *104*, 6016.
39. A. Hammershøi, G. Geselowitz, H. Taube, *Inorg. Chem.*, **1984**, *23*, 979.
40. F. P. Dwyer, A. M. Sargeson, *J. Phys. Chem.*, **1961**, *65*, 1892.
41. I. I. Creaser, A. M. Sargeson, A. W. Zanella, *Inorg. Chem.*, **1983**, *22*, 4022.
42. A. M. Sargeson, *Pure Appl. Chem.*, **1984**, *56*, 1603.
43. R. J. Geue, M. G. McCarthy, A. M. Sargeson, *J. Am. Chem. Soc.*, **1984**, *106*, 8282.
44. R. J. Geue, A. J. Hendry, A. M. Sargeson, *J. Chem. Soc., Chem. Commun.*, **1989**, 1646.
45. A. Hammershøi, A. M. Sargeson, *Inorg. Chem.*, **1983**, *22*, 3554.
46. F. Pina, M. Ciano, L. Moggi, V. Balzani, *Inorg. Chem.*, **1985**, *24*, 844.
47. F. Pina, Q. G. Mulazzani, M. Venturi, M. Ciano, V. Balzani, *Inorg. Chem.*, **1985**, *24*, 848.
48. V. Houlding, T. Geiger, U. Kölle, M. Grätzel, *J. Chem. Soc., Chem. Commun.*, **1982**, 681.
49. M. A. Rampi Scandola, F. Scandola, A. Indelli, V. Balzani, *Inorg. Chim. Acta*, **1983**, *76*, L67.
50. P. A. Lay, A. W. H. Mau, W. H. F. Sasse, I. I. Creaser, L. R. Gahan, A. M. Sargeson, *Inorg. Chem.*, **1983**, *22*, 2347.
51. C.-Y. Mok, A. W. Zanella, C. Creutz, N. Sutin, *Inorg. Chem.*, **1984**, *23*, 2891.
52. I. I. Creaser, L. R. Gahan, R. J. Geue, A. Launikonis, P. A. Lay, J. D. Lydon, M. G. McCarthy, A. W. H. Mau, A. M. Sargeson, W. H. F. Sasse, *Inorg. Chem.*, **1985**, *24*, 2671.
53. A. W. H. Mau, W. H. F. Sasse, I. I. Creaser, A. M. Sargeson, *New J. Chem.*, **1986**, *10*, 589.
54. I. I. Creaser, A. Hammershøi, A. Launikonis, A. W. H. Mau, A. M. Sargeson, W. H. F. Sasse, *Photochem. Photobiol.*, **1989**, *49*, 19.
55. S. R. Cooper, *Acc. Chem. Res.*, **1988**, *21*, 141.
56. S. G. Murray, F. R. Hartley, *Chem. Rev.*, **1981**, *81*, 365.
57. O. Farver, I. Pecht, *Coord. Chem. Rev.*, **1989**, *94*, 17.
58. D. B. Rorabecher, M. M. Bernardo, A. M. C. Vande Linde, G. H. Leggett, B. C. Westerby, M. J. Martin, L. A. Ochrymowicz, *Pure Appl. Chem.*, **1988**, *60*, 501.
59. G. H. Leggett, B. C. Dunn, A. M. C. Vande Linde, L. A. Ochrymowicz, D. B. Rorabecher, *Inorg. Chem.*, **1993**, *32*, 5911.
60. M. J. Sisley, R. B. Jordan, *Inorg. Chem.*, **1992**, *31*, 2880.
61. (a) C. M. Groeneveld, S. Dahlin, B. Reinhammar, G. W. Canters., *J. Am. Chem. Soc.*, **1987**, *109*, 3247; (b) G. W. Canters, H. A. O. Hill, N. A. Kitchen, E. T. Adman, *J. Magn. Res.*, **1984**, *57*, 1-23; (c) S. Dahlin, B. Reinhammar, M. T. Wilson, *Biochem. J.*, **1984**, *218*, 609; (d) A. Lommen, G. W. Canters, *J. Biol. Chem.*, **1990**, *265*, 2768.
62. E. R. Dockal, T. E. Jones, W. F. Sokol, R. J. Engerer, D. B. Rorabecher, L. A. Ochrymowicz, *J. Am. Chem. Soc.*, **1976**, *98*, 4322.
63. D. B. Rorabecher, N. E. Meagher, K. L. Juntunen, P. V. Robandt, G. H. Leggett, C. A. Salhi, B. C. Dunn, R. R. Schroeder, L. A. Ochrymowicz, *Pure Appl. Chem.*, **1993**, *65*, 573.
64. (a) B. M. Hoffman, M. A. Ratner, *J. Am. Chem. Soc.*, **1987**, *109*, 6237; (b) B. S. Brunswick, N. Sutin, *J. Am. Chem. Soc.*, **1989**, *111*, 7454.
65. L. L. Diaddario, E. R. Dockal, M. D. Glick, L. A. Ochrymowicz, D. B. Rorabacher, *Inorg. Chem.*, **1985**, *24*, 356.
66. P. V. R. Corfield, C. Ceccarelli, M. D. Glick, I. N.-Y. Moi, L. A. Ochrymowicz, D. B. Rorabacher, *J. Am. Chem. Soc.*, **1985**, *107*, 2399.
67. A. M. Q. Vande Linde, K. L. Juntunen, O. Mols, M. B. Ksebati, L. A. Ochrymowicz, D. B. Rorabacher, *Inorg. Chem.*, **1991**, *30*, 5037.
68. N. E. Meagher, K. L. Juntunen, C. A. Salhi, L. A. Ochrymowicz, D. B. Rorabacher, *J. Am. Chem. Soc.*, **1992**, *114*, 10411.
69. C. A. Salhi, Q. Yu, M. J. Heeg, N. M. Villeneuve, K. L. Juntunen, R. R. Schoeder, L. A. Ochrymowicz, D. B. Rorabacher, *Inorg. Chem.*, **1995**, *34*, 6053.
70. B. C. Dunn, L. A. Ochrymowicz, D. B. Rorabacher, *Inorg. Chem.*, **1997**, *36*, 3253.
71. N. M. Villeneuve, R. R. Schoeder, L. A. Ochrymowicz, D. B. Rorabacher, *Inorg. Chem.*, **1997**, *34*, 4475.

72. K. Krylova, C. P. Kulatilleke, M. J. Heeg, C. A. Salhi, L. A. Ochrymowicz, D. B. Rorabacher, *Inorg. Chem.*, **1999**, 38, 4322–4328.
73. R. S.-L. Shon, D. O. Cowan, W. W. Schmlegel, *J. Phys. Chem.*, **1975**, 79, 2087.
74. G. De Santis, L. Fabbrizzi, M. Licchelli, C. Mangano, D. Sacchi, *Inorg. Chem.*, **1995**, 34, 3581.
75. (a) A. P. de Silva, H. Q. N. Gunaratne, T. Gunnlaugsson, A. J. M. Huxley, C. P. McCoy, J. T. Rademacher, T. E. Rice, *Chem. Rev.*, **1997**, 97, 1515; (b) L. Fabbrizzi, A. Poggi, *Chem. Soc. Rev.*, **1995**, 24, 197.
76. (a) R. J. Mocketakis, A. E. Martell, J. M. Lehn, E. I. Watanabe, *Inorg. Chem.*, **1982**, 21, 4253; (b) J. Prue, G. Schwarzenbach, *Helv. Chim. Acta*, **1950**, 33, 963.
77. G. De Santis, L. Fabbrizzi, M. Licchelli, A. Poggi, A. Taglietti, *Angew. Chem., Int. Ed. Engl.*, **1996**, 35, 202.
78. L. Fabbrizzi, G. Francese, M. Licchelli, A. Perotti, A. Taglietti, *Chem. Commun.*, **1997**, 581.
79. L. Fabbrizzi, P. Pallavicini, A. Perotti, L. Parodi, A. Taglietti, *Inorg. Chim. Acta*, **1995**, 238, 5.
80. L. Fabbrizzi, I. Faravelli, G. Francese, M. Licchelli, A. Perotti, A. Taglietti, *Chem. Commun.*, **1998**, 971.
81. T. Matsue, D. H. Evans, T. Osa, N. Kobayashi, *J. Am. Chem. Soc.*, **1985**, 107, 3411.
82. (a) R. Isnin, C. Salam, A. E. Kaifer, *J. Org. Chem.*, **1991**, 56, 35; (b) R. Isnin, A. E. Kaifer, *J. Am. Chem. Soc.*, **1991**, 113, 8188; (c) L. A. Godinez, S. Patel, C. M. Criss, A. E. Kaifer, *J. Phys. Chem.*, **1995**, 99, 17499.
83. (a) A. Harada, S. Takahashi, *J. Chem. Soc., Chem. Commun.*, **1984**, 645; (b) H.-J. Thiem, M. Brandl, R. Breslow, *J. Am. Chem. Soc.*, **1988**, 110, 8612.
84. Y. Wang, S. Mendoza, A. E. Kaifer, *Inorg. Chem.*, **1998**, 37, 317.
85. A. Mirzorian, A. E. Kaifer, *Chem. Eur. J.*, **1997**, 3, 1052.
86. A. E. Kaifer, *Acc. Chem. Res.*, **1999**, 32, 62.
87. Y. Kuroda, M. Ito, T. Sera, H. Ogoshi, *J. Am. Chem. Soc.*, **1993**, 115, 7003.
88. S. Weidner, Z. Pikramenou, *Chem. Commun.*, **1998**, 1473.
89. A. Nakamura, S. Okutsu, Y. Oda, A. Ueno, F. Toda, *Tetrahedron Lett.*, **1994**, 35, 7241.
90. B. K. Hubbard, L. A. Beilstein, C. E. Heath, C. J. Abelt, *J. Chem. Soc., Perkin Trans. 2*, **1996**, 1005.
91. L. Zhang, A. Macias, T. Lu, J. I. Gordon, G. W. Gokel, A. E. Kaifer, *J. Chem. Soc., Chem. Commun.*, **1993**, 1017.
92. T. Arimura, C. T. Brown, S. L. Springs, J. L. Sessler, *Chem. Commun.*, **1996**, 2293.
93. R. Milbradt, J. Weiss, *Tetrahedron Lett.*, **1995**, 36, 2999.
94. I. Aoki, T. Sakaki, S. Shinkai, *J. Chem. Soc., Chem. Commun.*, **1992**, 730.
95. (a) M. Hissler, A. Harriman, P. Jost, G. Wipff, R. Ziessel, *Angew. Chem. Int. Ed.*, **1998**, 37, 3249; (b) A. Harriman, M. Hissler, P. Jost, G. Wipff, R. Ziessel, *J. Am. Chem. Soc.*, **1999**, 121, 14.
96. P. D. Beer, V. Timoshenko, M. Maestri, P. Passaniti, V. Balzani, *Chem. Commun.*, **1999**, 1755.
97. T. A. Robbins, D. J. Cram, *J. Am. Chem. Soc.*, **1993**, 115, 12199.
98. S. Mendoza, P. D. Davidov, A. E. Kaifer, *Chem. Eur. J.*, **1998**, 4, 864.
99. A. J. Parola, F. Pina, E. Ferreira, M. Maestri, V. Balzani, *J. Am. Chem. Soc.*, **1996**, 118, 11616.
100. (a) A. Farran, K. Deshayes, C. Matthews, I. Balanescu, *J. Am. Chem. Soc.*, **1995**, 117, 9614; (b) A. Farran, K. Deshayes, *J. Phys. Chem.*, **1996**, 100, 3305.
101. P. Piotrowiak, *Chem. Soc. Rev.*, **1999**, 28, 143.

6 Electron Transfer Processes in Pseudorotaxanes

Margherita Venturi, Alberto Credi, and Vincenzo Balzani

6.1 Introduction

A particularly interesting family of host–guest systems [1] is that in which a linear guest is threaded through the cavity of a macrocyclic host (Figure 1). A compound which exhibits such a supramolecular structure is usually called pseudorotaxane [2], with reference to the name rotaxane (see Volume III, Part 2, Chapter 7) used to indicate the species in which the ring is prevented to dethread by the presence of bulky stoppers at the ends of the linear guest.

As for any host–guest complex, the formation of a pseudorotaxane occurs via a molecular recognition process between two “instructed” [1a] components. It is a thermodynamically controlled self-assembly process, resulting from the spontaneous interaction of stereoelectronically complementary units contained in the thread and macrocyclic components.

Pseudorotaxanes may be involved in electron transfer processes from three different viewpoints: (i) the recognition process between the thread and the macrocycle may result from a charge-transfer interaction, which implies the appearance of characteristic spectroscopic and electrochemical properties; (ii) the pseudorotaxane structure can be dethreaded/rethreaded by chemically, electrochemically, and photochemically induced electron transfer processes, which leads to the concept of molecular machines; and (iii) dethreading/rethreading of pseudorotaxanes can control the occurrence of charge transfer and electron transfer processes, which offers a route to information processing at the molecular level.

6.2 Main Types of Pseudorotaxanes

The formation of host–guest systems may occur as a result of a variety of interactions deriving from the size, shape, and electronic properties of the two partners.

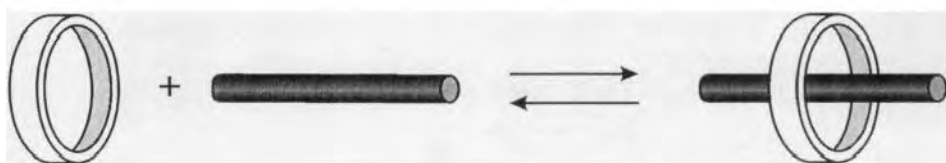


Figure 1. Schematic representation of a pseudorotaxane structure formed from a macrocyclic host and a linear guest.

The most important types of interactions are those involving hydrogen bonding, electron donor/acceptor ability, hydrophobic/hydrophylic character, π - π stacking, ion-ion, ion-dipole, and dipole-dipole forces and, on the side of the strong interaction limit, metal-ligand bond. Usually it is not difficult to understand which is the most important interaction in a given system. It should be noted, however, that in some cases the strongest interaction as far as association is concerned is not that causing the most relevant changes in the properties of the system (e.g., UV-visible absorption, fluorescence and NMR spectra, electrochemical behavior) ongoing from the separated components to the supramolecular structure. This is particularly true for a peculiar host-guest structure like that of pseudorotaxanes.

A number of pseudorotaxanes have been obtained by threading (i) a wire-type component containing electron-acceptor units into a macrocycle which comprises electron-donor units, or, vice versa, (ii) a wire-type component containing electron-donor units into a macrocycle which comprises electron-acceptor units. Some examples are shown in Figure 2: (a) the 1,1'-dibenzyl-4,4'-bipyridinium electron-acceptor dication 1^{2+} threaded into the 1,5-dinaphtho-38-crown-10 **2** [3]; (b) the electron-acceptor aromatic diimide **3** threaded into macrocycle **2** [4]; (c) the acyclic polyether **5** containing a dioxybenzene electron-donor unit threaded into the electron-acceptor cyclobis(paraquat-*p*-phenylene) tetracationic cyclophane 4^{4+} [5]; and (d) the acyclic polyether **6** containing a tetrathiafulvalene electron-donor unit threaded into the electron-acceptor cyclophane 4^{4+} [6]. Although in all these cases a large contribution to the association driving force comes from the electron donor/acceptor interaction, other kinds of interactions—particularly hydrogen bonding—can play an important role, as clearly shown in the cases of pseudorotaxanes constituted by 4,4'-bipyridinium [7a] or 1,2-bis(pyridinium)ethane [7b] threads and crown ether macrocycles.

Several pseudorotaxanes have been obtained by threading wire-type and macrocyclic components carrying complementary hydrogen-bonding functions. For example: (i) a wire-type component containing a secondary ammonium function, such as the *N,N*-dibenzylammonium ion 7^+ , threaded into a suitable crown ether like dibenzo[24]crown-8, **8** (Figure 3a) [8]; and (ii) a wire-type component containing amide functions threaded into a cyclic isophthalamide [2a]. Besides hydrogen bonding, other types of interactions (e.g., ion-dipole, π -stacking) can contribute to stabilize the pseudorotaxane structure.

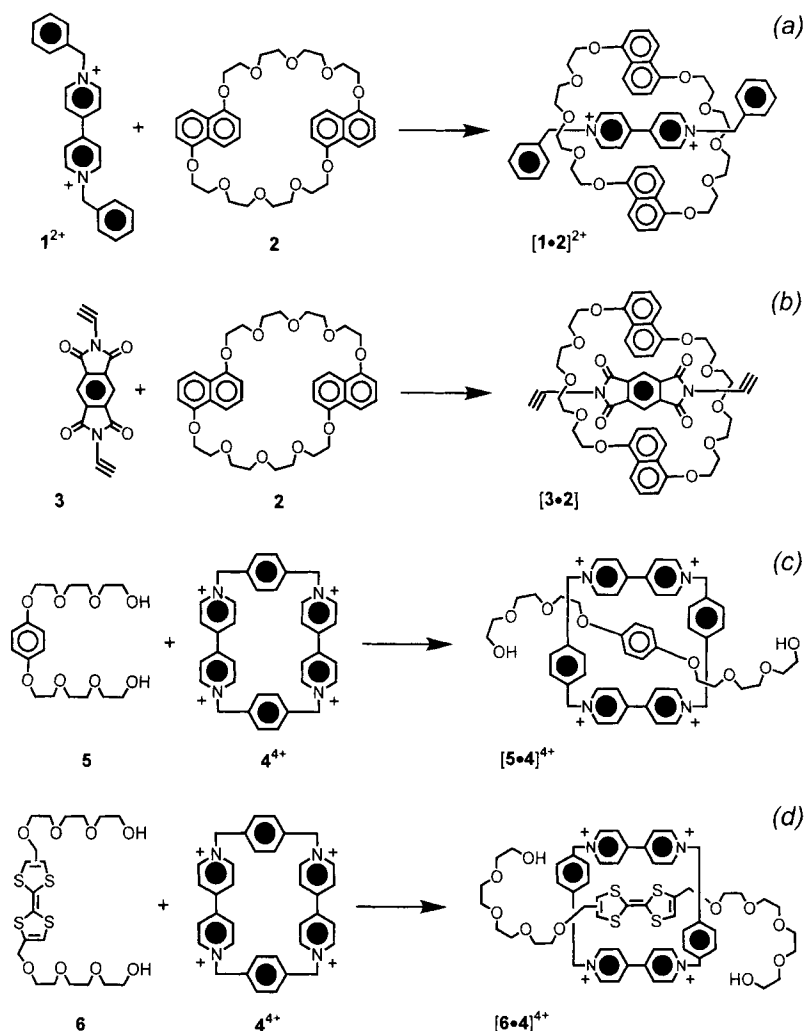


Figure 2. Some examples of pseudorotaxanes based on charge-transfer interactions: (a) from Ref. [3]; (b) from Ref. [4]; (c) from Ref. [5]; (d) from Ref. [6].

Pseudorotaxanes can also be obtained as a consequence of simple hydrophobic/hydrophilic interactions. This is the case for the since long known species in which a wire-type component (9^{2+}) threads the cavity of α -cyclodextrin **10** (Figure 3b) [9].

A different approach is the metal-based template method [2c], for example starting from a wire (**11**) and a macrocycle (**12**), both containing a phenanthroline unit, and using Cu^+ as a template (Figure 3c) [2c]. Species of this kind are essentially metal complexes, and may have very large formation constants.

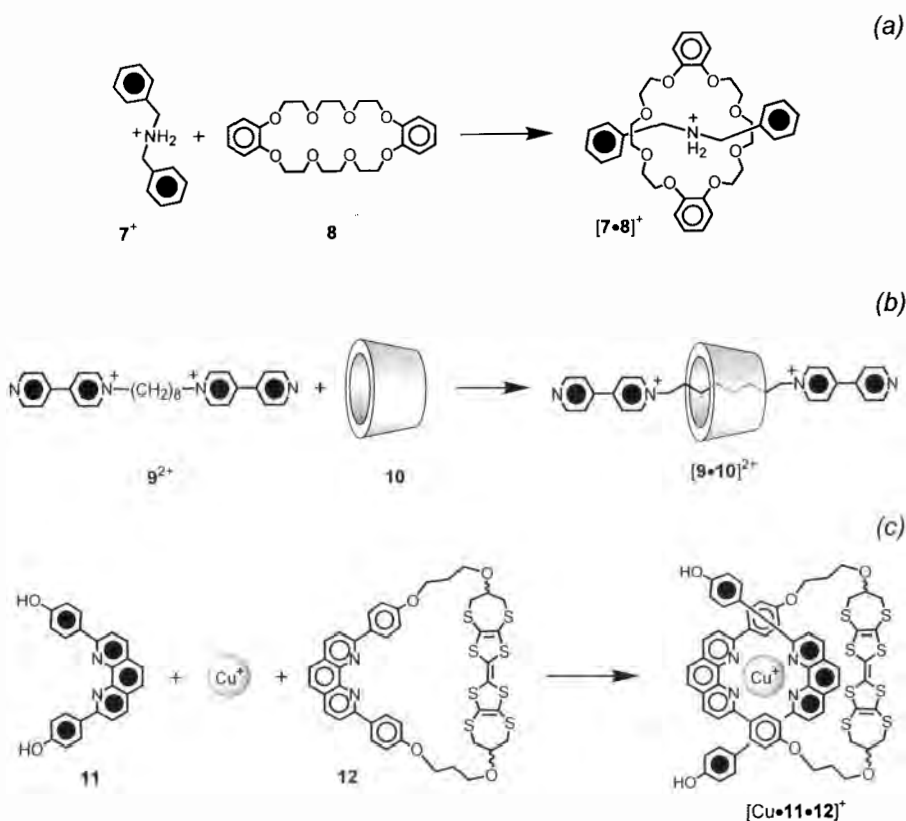


Figure 3. Three examples of templated synthesis of pseudorotaxanes. (a) Via hydrogen-bonding interactions [8]; (b) hydrophobic/hydrophylic interactions [9]; (c) metal-ligand interactions [2c].

6.3 Some General and Particular Aspects of Pseudorotaxane Chemistry

The examples reported above refer to pseudorotaxane species with a 1:1 thread/macrocycle ratio ($[2]$ pseudorotaxanes). It is also possible to obtain species exhibiting different stoichiometric ratios, as illustrated by the $[5]$ pseudorotaxane formed from four cyclophane 4^{4+} components and a $Zn(II)$ -phthalocyanine with appended four polyether substituents carrying π -electron-rich hydroquinone units [11]. Examples of pseudorotaxanes in which a macrocycle (13) is threaded by two linear components (7^+) [12] and a linear component (14) threads two macrocycles (4^{4+}) [13] are shown in Figure 4. Long linear arrays can be obtained by using homoditopic threads and macrocycles (e.g., 15^{2+} and 16 in Figure 5, respectively) [14]. Homogeneous or heterogeneous pseudopolyrotaxanes (Figure 6a) [2a] have also been prepared, as well dendritic ones (Figure 6b) [15]. It should also be noted that

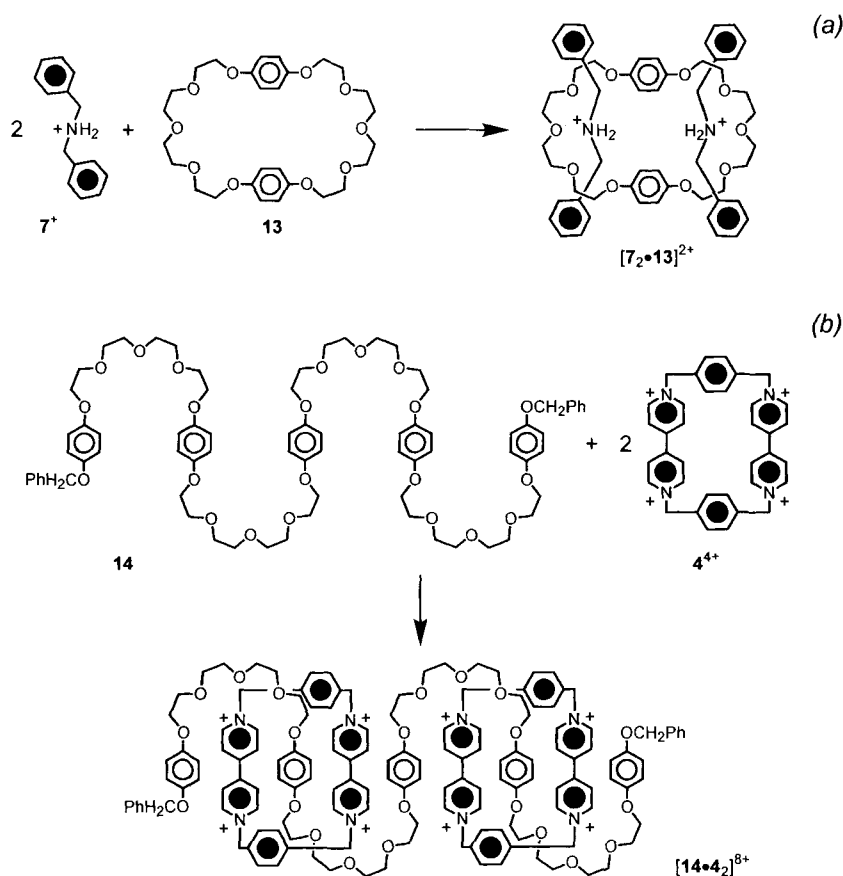


Figure 4. Examples of pseudorotaxanes with (a) 2:1 and (b) 1:2 stoichiometric ratio between thread and macrocycle [12, 13].

in some cases self-assembly between a wire-type species and a macrocyclic ring takes place, but does not lead to the expected pseudorotaxane structure (see, for example the host–guest system formed by **17**⁴⁺ and **18**; Figure 7) [16]. For particular purposes, it is interesting to incorporate in the pseudorotaxane components units capable of exhibiting specific (photochemical, electrochemical, etc.) properties; for example (Figure 8), a thread (**19H**⁺) with an ammonium function and a photoactive anthracene as a stopper [17], a bipyridinium-type wire (**20**⁴⁺) with a photo- and redox-active Ru(bpy)₃²⁺ moiety [18], a crown ether (**21**) incorporating a binaphthyl unit [19], and a cyclophane (**22**⁴⁺) containing a Re complex and two bipyridinium units [20].

Particularly interesting pseudorotaxane species can be constructed by using components which incorporate different recognition functions, such as a thread (**23**⁴⁺) containing ammonium and bipyridinium functions (Figure 9a) [12], or species

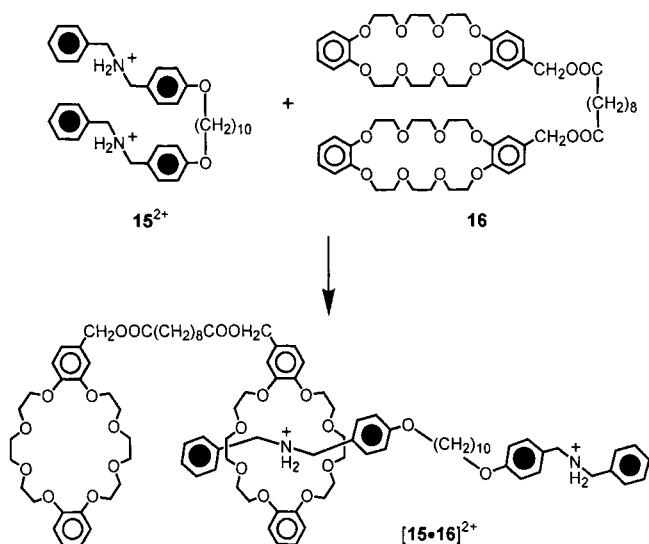


Figure 5. An example of a pseudorotaxane formed by complementary homoditopic components [14].

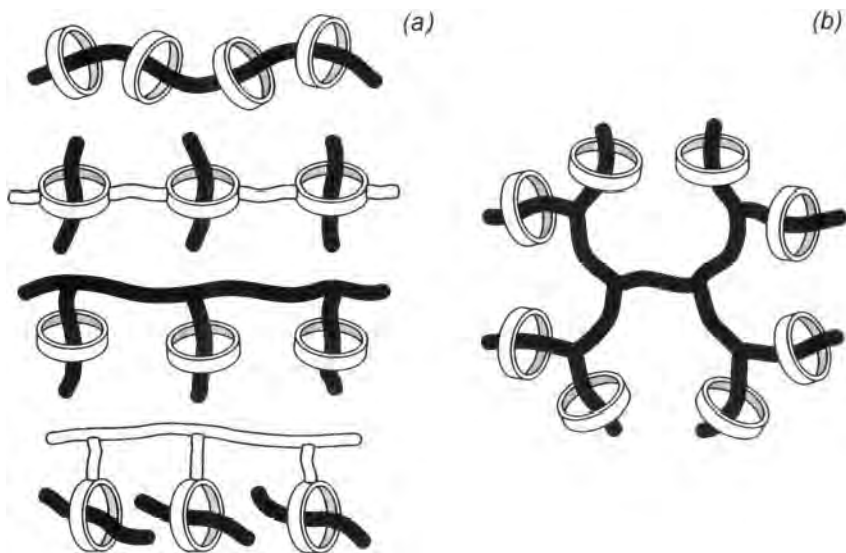


Figure 6. Schematic representation of (a) pseudopolyrotaxanes [2a] and (b) a dendritic pseudopolyrotaxane [15].

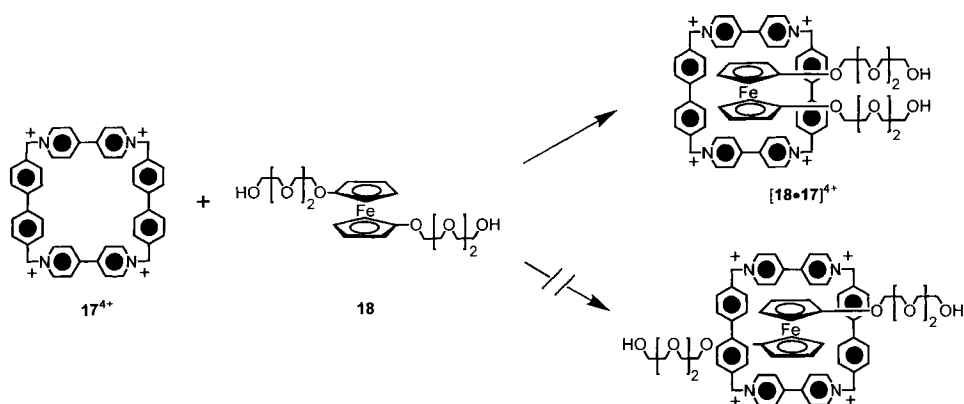


Figure 7. Self-assembly between a wire-type compound and a macrocyclic ring leading to an inclusion complex not showing the expected pseudorotaxane structure [16].

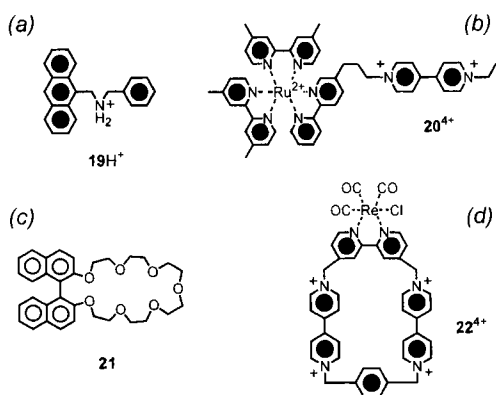


Figure 8. Examples of pseudorotaxane components containing units capable of exhibiting specific properties. (a) A wire with an ammonium function and a photoactive anthracene as a stopper [17b]; (b) a bipyridinium-type wire with a photo- and redox-active Ru(bpy)₃²⁺ moiety [18]; (c) a crown ether incorporating a binaphthyl unit [19]; (d) a cyclophane containing a Re complex and two bipyridinium units [20].

[21, 22] (e.g., 24²⁺) consisting of a macrocyclic head and a tail that bring complementary recognition sites (Figure 9b) [21].

If two bulky substituents (stoppers) are placed at the ends of the thread (Figure 10a), a pseudorotaxane is transformed into a rotaxane, a structure that does not allow dethreading because of the presence of the two stoppers. If the thread has relatively bulky substituents since the beginning, the ring can slip through them—a process that requires overcoming of a more or less high activation barrier (Figure 10b) [23]. For such systems, dethreading of the ring is not impossible, but requires overcoming of an even higher activation barrier (Figure 10b), so that under ap-

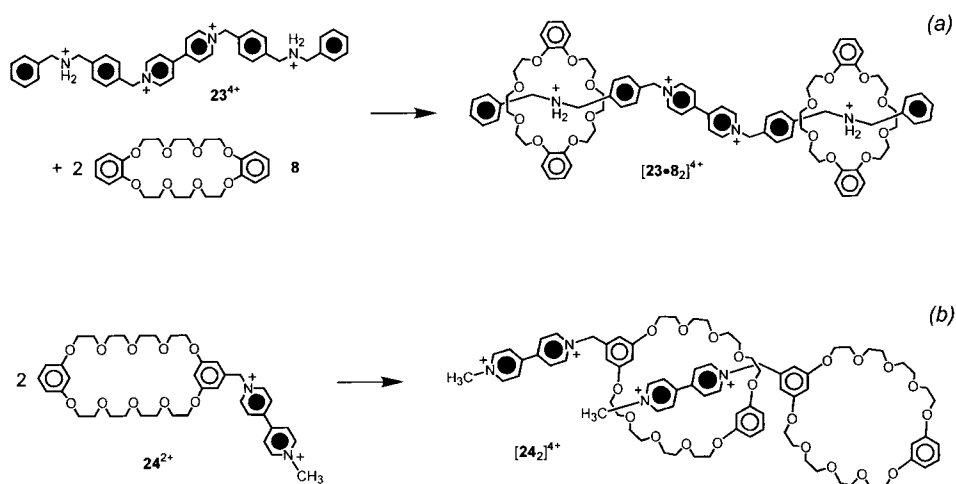


Figure 9. Examples of pseudorotaxanes formed from components incorporating different recognition functions. (a) A pseudorotaxane with a wire containing a bipyridinium and two ammonium functions [12]; (b) a pseudorotaxane formed by a component containing two complementary recognition sites [21].

appropriate condition (e.g., low temperature) they behave as rotaxanes. This shows that pseudorotaxanes may possess some rotaxane-like character. From another viewpoint, we can say that pseudorotaxanes belong to the fuzzy domain between two sets of extremes (Figure 10c), corresponding to either (i) the two isolated components, or (ii) the assembled rotaxane structure [24]. This is indeed a nice example of fuzzy logic in chemistry—a concept that it is now proving its value for a great variety of industrial chemical processes [25].

6.4 Spectroscopic and Electrochemical Consequences of Charge–Transfer Interactions

The charge–transfer (CT) interaction between electron-donor and electron-acceptor units has several important consequences from the spectroscopic and electrochemical viewpoints [5], and plays a fundamental role as far as the machine-like behavior of these supramolecular species is concerned [26–28].

6.4.1 Absorption and Emission Spectra

The donor/acceptor interaction introduces low-energy CT excited states which are responsible not only for the color of these supramolecular species (due to the presence of broad and weak absorption bands in the visible region), but also for the

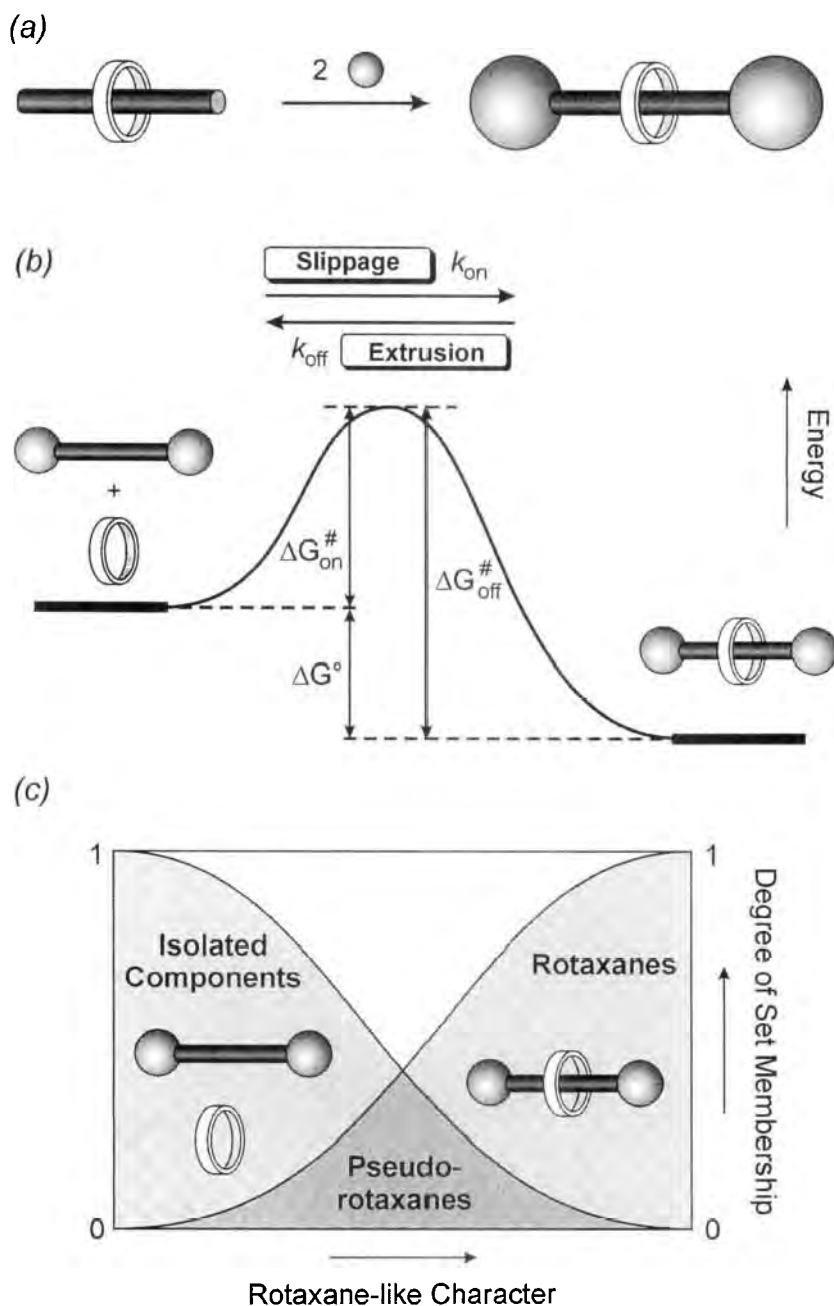


Figure 10. (a) A true rotaxane formed by placing very bulky stoppers at the ends of a pseudo-rotaxane thread. (b) Schematic energy diagram for the self-assembly of rotaxane-like entities via slippage of a macrocycle through relatively bulky stoppers [23]. (c) Schematic illustration showing that pseudorotaxanes belong to the fuzzy domain between isolated components and rotaxane structures [24].

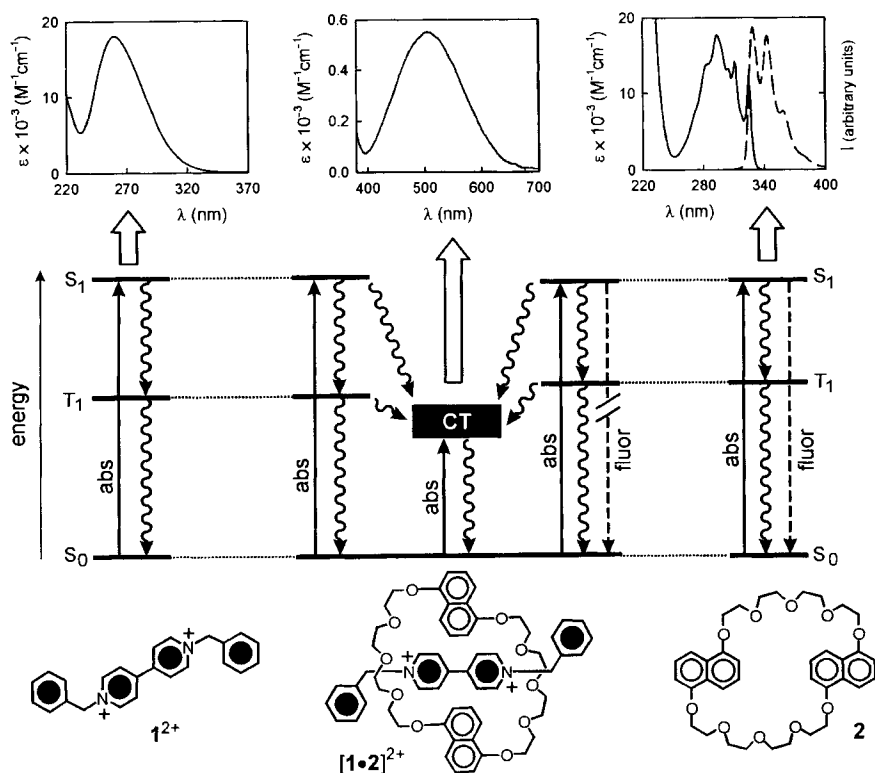


Figure 11. The CT absorption band of pseudorotaxane $[1\cdot 2]^{2+}$ and the absorption and emission bands of its components 1^{2+} and 2 (MeCN, 298 K) [29]. For more detail, see text.

quenching of the potentially luminescent excited states localized on the molecular components (Figure 11). For example [29], both macrocycle 2 and thread 1^{2+} exhibit UV absorption bands, and 2 shows an emission band with $\lambda_{\text{max}} = 330 \text{ nm}$; when the two components are threaded, a new absorption band is present in the visible region ($\lambda_{\text{max}} = 505 \text{ nm}$, $\epsilon = 550 \text{ M}^{-1} \text{ cm}^{-1}$ in acetonitrile solution), and no emission can be seen [29b].

6.4.2 Electrochemical Properties

As far as the electrochemical behavior is concerned, it should be noted that, when engaged in CT interactions, the electron-donor and electron-acceptor units become more difficult to oxidize and to reduce, respectively.

For example, consider again thread 1^{2+} [29], macrocycle 2 [30], and their pseudorotaxane $[1\cdot 2]^{2+}$ (Figure 12). 1^{2+} exhibits two reversible one-electron reduction processes, and macrocycle 2 , which contains two dioxynaphthalene electron-donor

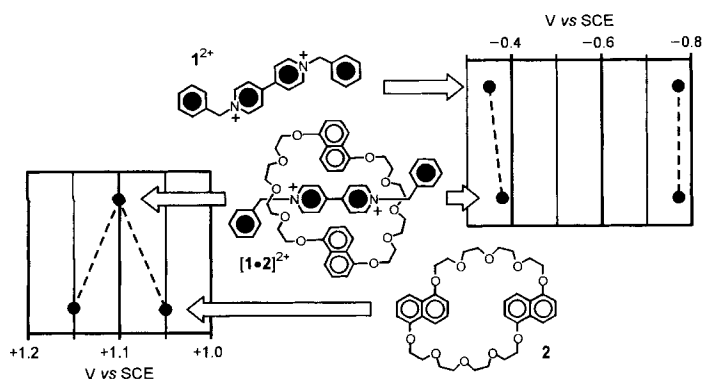


Figure 12. Comparison between the electrochemical behavior of pseudorotaxane $[1\cdot 2]^{2+}$ and its components 1^{2+} and **2** (MeCN, 298 K).

units, shows two (not fully reversible) oxidation processes. When the two components are engaged in the pseudorotaxane structure, the first reduction process of 1^{2+} is displaced by 30 mV towards more negative potentials, whereas the second reduction process is not affected. As far as macrocycle **2** is concerned, in the pseudorotaxane structure its two oxidation processes merge into a two-electron process that occurs at a potential 50 mV more positive than the first oxidation process of the free macrocycle. These results are consistent with: (i) the presence of a CT interaction between the electron-acceptor and electron-donor units; (ii) the occurrence of dethreading upon first reduction of 1^{2+} ; and (iii) the lack of interaction of the two electron-donor units of macrocycle **2** when threaded by 1^{2+} . Dethreading after the first 1^{2+} reduction is confirmed by comparison with the behavior of the analogous rotaxane [23], where also the second reduction process is displaced towards more negative potentials. The fact that the first reduction process of pseudorotaxane $[1\cdot 2]^{2+}$ is reversible indicates that the dethreading/rethreading movement is fast on the electrochemical time scale.

6.5 Electron Transfer Controlling Dethreading/Rethreading Processes

6.5.1 Pseudorotaxanes as Simple Molecular Machines

Dethreading/rethreading of the wire and ring components of a pseudorotaxane is reminiscent of the movement of a piston in a cylinder (see Figure 1), and therefore such a system may be considered as a very simple molecular-level machine. While *natural* molecular-level machines have long been known (our own body can be viewed as a complex ensemble of molecular-level machines) [31], the problem of the construction of *artificial* molecular-level machines was posed for the first time by

Feynman [32] in his famous address *There is Plenty of Room at the Bottom* to the American Physical Society in 1959. In his address, he raised a number of interesting issues (including the need to use cold chemical reactions as energy inputs to make such machines work), and he concluded with the following reflection:

“What would be the utility of such machines? Who knows? I cannot see exactly what would happen, but I can hardly doubt that when we have some control of the re-arrangement of things on a molecular scale we will get an enormously greater range of possible properties that substances can have, and of different things we can do”.

Much better than physicists, chemists are in an ideal position to develop bottom-up strategies towards the design of molecular-level machines, since they are able to manipulate molecules, i.e., the smallest entities of matter that have distinct shapes and properties. Forty years ago, however, the chemical community was not ready to receive Feynman’s stimulation. Only recently, after the development of supramolecular chemistry [1], has the study of artificial molecular-level machines become an important research topic in chemistry [15, 26–28, 33].

Recent investigations in this field have demonstrated, in agreement with Feynman’s suggestions [32], that the input of external energy needed to make such machines work can be provided by different types of chemical reactions. It has also been realized that electrochemical and photochemical processes are the most convenient ones to be used for this purpose.

As we have seen above, several pseudorotaxane structures are stabilized—at least in part—by CT interactions. In these systems, if the CT interactions are destroyed or weakened, dethreading can occur. This can be done by reduction of an electron-acceptor unit or by oxidation of an electron-donor unit contained in the thread or in the macrocycle. In most cases, the CT interactions can be restored by an opposite redox process, which thus promotes a reverse mechanical movement leading to the original structure.

Since the electron transfer processes can be induced photochemically, electrochemically, or chemically, the reported examples have been divided, for the sake of convenience, according to the nature of the redox input.

6.5.2 Photochemically Induced Processes

As we have seen above, CT interactions introduce low-energy excited states responsible for the absorption bands in the visible region (Figure 11). Light excitation in these CT absorption bands formally leads to the transfer of an electron from the donor to the acceptor component (optical electron transfer). As a consequence—particularly when this process leads to formation of charges of the same sign in the two components—one can expect destabilization of the pseudorotaxane structure followed by dethreading. In practice, however, this simple approach does not work because the back electron transfer process is much faster than the separation of the molecular components—a process which requires extended nuclear motions and

solvent rearrangement. In some particular cases [34], laser flash photolysis experiments have suggested that a small fraction of the irradiated pseudorotaxane may undergo dissociation.

In order really to achieve photoinduced dethreading, a different approach has been devised [35, 36], based on the use of an external electron transfer photosensitizer (P) and a sacrificial reductant (Red), as illustrated in Figure 13 in the case of the pseudorotaxane formed by thread **25** and macrocycle **4**⁴⁺. The photosensitizer must be able first, to absorb light efficiently, and second, to have a sufficiently long-lived and reductant excited state, so that its excitation (Process ①) in the presence of the pseudorotaxane will lead (Process ②) to the transfer of an electron to a bipyridinium unit of the cyclophane. The relatively fast back electron transfer from the reduced cyclophane component to the oxidized photosensitizer is prevented by the sacrificial reductant which, if present in a sufficient amount, intercepts the oxidized photosensitizer and regenerates (Process ③) the original photosensitizer. Good candidates for the role of photosensitizer are 9-anthracenecarboxylic acid [37] and metal complexes [38] such as [Ru(bpy)₃]²⁺, while efficient reductant scavengers are triethanolamine and polycarboxylate (e.g., oxalate) anions [39]. Under these conditions, the persistent reduction of a bipyridinium unit of **4**⁴⁺ is achieved and the pseudorotaxane dethreads (Process ④), as evidenced by absorption spectral changes and, more importantly, by the increase in the intensity of the dioxynaphthalene fluorescence, that can only originate from free **25**. Oxygenation of the solution, from which O₂ was initially removed, reoxidizes the cyclophane back (Process ⑤) to the tetracationic form, thereby promoting rethreading (Process ⑥) with **25**, as also shown by the absorption and luminescence spectra.

This strategy has been extended recently to second-generation pseudorotaxanes [**20•2**]⁴⁺ and [**25•22**]⁴⁺ in which the metal-complex photosensitizer (the “light-fueled” motor) has been incorporated (Figure 14) either into the thread [18] or into the ring [20] component. The successful operation of these pseudorotaxanes as molecular machines is the result of first, the appropriate choice of the functional units, and second, their covalent linking into the thread and ring components in order to achieve the correct integration of the needed functions (e.g., receptor ability, redox features, photophysical properties, etc.), the right sequence of processes, and the lack of interference between the active units. As in the case of the molecular machine shown in Figure 13, the dethreading and rethreading motions of the pseudorotaxanes represented in Figure 14 can be triggered by visible light irradiation and oxygenation of the solution, respectively: also, the motions can be easily monitored by means of UV-visible absorption and luminescence spectroscopy. The most important readout signal is the intensity of the dioxynaphthalene fluorescence associated with the free ring **2** (Figure 14a) or free thread **25** (Figure 14b) components. It is worth noting that many deoxygenation–irradiation(dethreading)/oxygenation(rethreading) cycles can be performed on the same solution without any appreciable loss of signal until most of the reductant scavenger is consumed. It should also be stressed that systems which rely on this photosensitizer–scavenger strategy utilize, in addition to light energy, the irreversible decomposition of a reductant scavenger that produces “waste” species. In this regard, the search for efficient molecular machines exploiting “clean”, reversible photochemical reactions (in

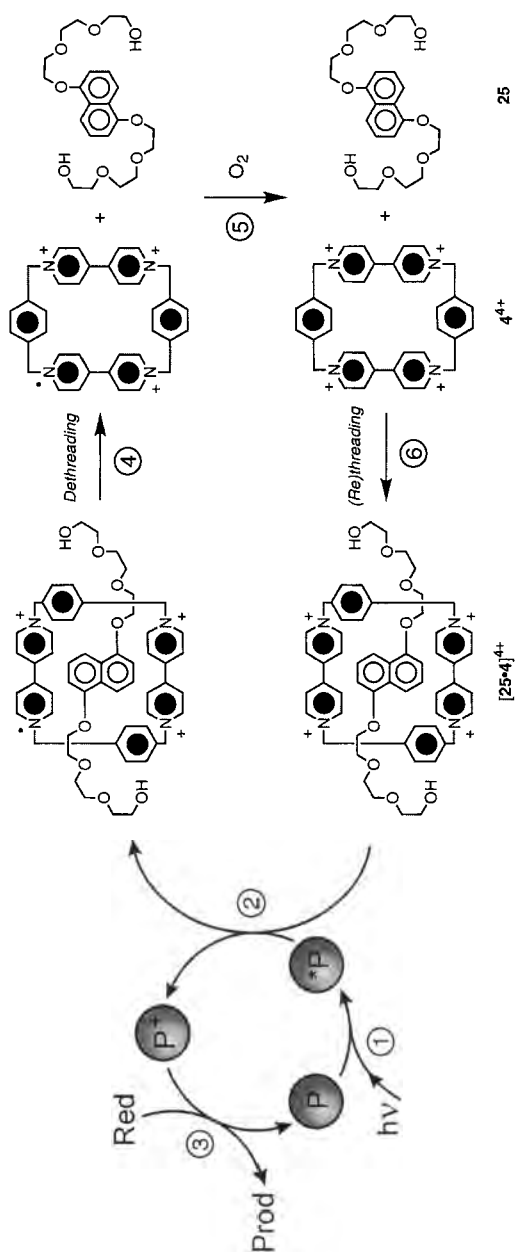


Figure 13. The photochemically induced dethreading (MeCN or H_2O , 298 K) of pseudorotaxane $[25\cdot 4]^{4+}$ based on the use of the external photosensitizer P (e.g., 9-anthracenecarboxylic acid) and the reductant scavenger Red (triethanolamine). Rethreading occurs upon oxygenation of the solution [35, 36].

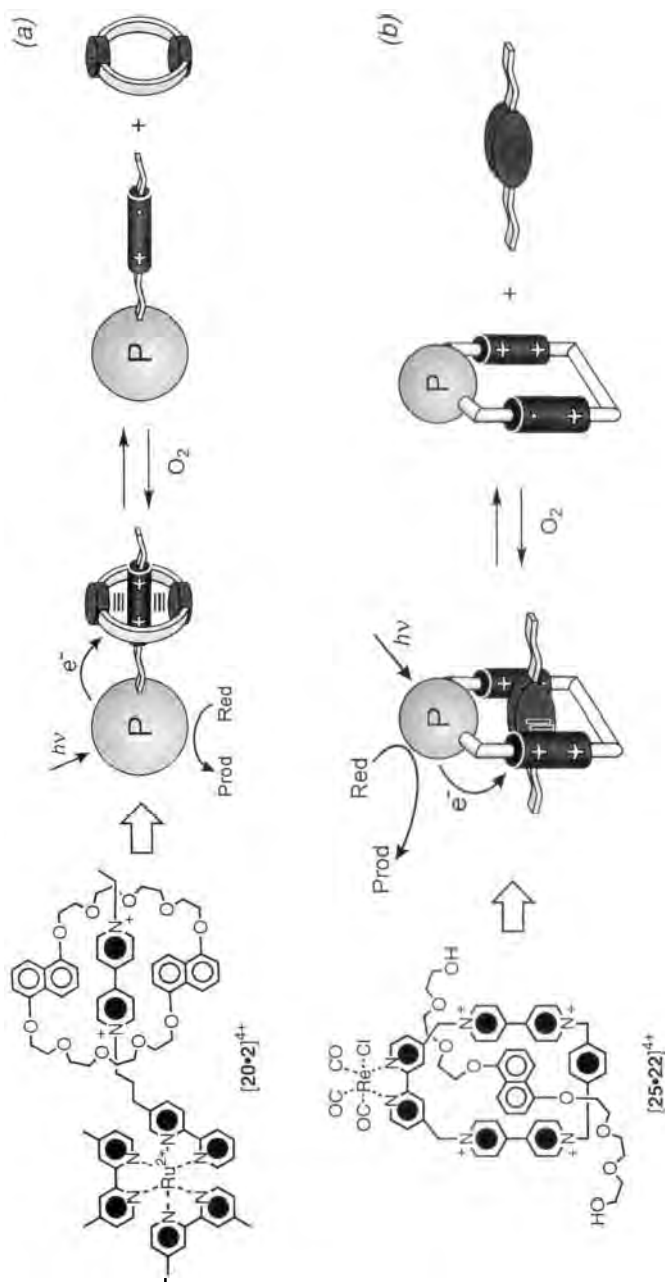


Figure 14. Photocyclable molecular machines based on pseudorotaxanes. In these second-generation systems the “light-fueled” motor (i.e., the photosensitizer, P) is part of the (a) wire-like [18] or (b) macrocyclic component [20]. Red (triethanolamine) is a reductant scavenger. Conditions: (a) EtOH, 298 K; (b) H₂O, 298 K.

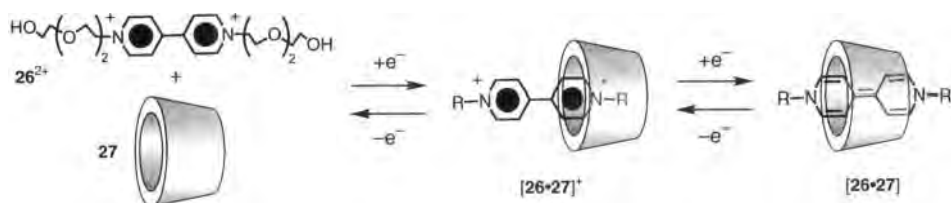


Figure 15. The electrochemically induced threading/dethreading processes associated with pseudorotaxane $[26 \cdot 27]^{2+}$ (H_2O , pH 7, 298 K) [44].

other words, machines which use only light as an energy supply) is of fundamental importance.

6.5.3 Electrochemically Induced Processes

Electrochemistry provides a handle on both the input stimuli and the readout signals that are necessary for the operation of molecular machines [33], [40]. A large number of inclusion complexes, in which the association/dissociation of the components can be triggered by changing the oxidation state of the guest or the host, have been investigated [15, 33], [40–42]. Some of the key features of such systems are: (i) the presence of an electroactive unit in one component which exhibits reversible redox processes; and (ii) the effect of the other component(s) on the electrochemical behavior of the component containing the electroactive unit, a property which allows the investigation of the complexation/decomplexation process by, for example, voltammetric techniques.

Cyclodextrins are a class of hosts that are inactive electrochemically, yet can form stable inclusion complexes with a variety of electroactive guests [43]. For instance (Figure 15), it has been found [44] that, while bipyridinium-containing compounds in the dicationic forms (e.g., 26^{2+}) are not bound by β -cyclodextrin (**27**), they interact weakly with the cavity of this host when reduced to their monocationic forms, and give fairly stable pseudorotaxane complexes with **27** when they are finally reduced to their uncharged forms. Similar results have been found [45] for cobaltocenium derivatives; these do not interact with cyclodextrins, yet become good guests for inclusion in **27** upon one-electron reduction to yield the neutral cobaltocene. Ferrocene and its derivatives exhibit [46] the opposite behavior, that is, they are strongly bound in their most stable oxidation state, which corresponds to uncharged species, whereas they are not bound in the oxidized state. These features have been exploited recently to construct dendrimers (see Volume III, Part 2, Chapter 9) that display redox-controllable multisite complexation of **27**, on account of the fact that the dendrimers contain up to 16 ferrocene units [47] or up to 32 cobaltocenium units [48] on their peripheries. Such dendrimers form very large supramolecular architectures that can be either broken apart or assembled by redox inputs. Similar investigations have been carried out on calixarenes, another important class of redox-

inactive receptors [49–51]. However, in contrast with cyclodextrins, the binding to calixarenes becomes stronger on increasing the charge on the guest. This result has been exploited [50] to design a three-component supramolecular system, in which an electroactive guest can choose reversibly between two macrocyclic hosts, depending on its oxidation state [52].

One of the most extensively studied receptors in recent years has been the cyclophane 4^{4+} . It constitutes a very efficient host for a wide variety of electron-donating guests [2b,d,e,i]. Since it is redox-active [5, 53], its binding ability can be subjected to electrochemical control. The tetracationic cyclophane 4^{4+} shows two bielectronic reduction processes, the first one corresponding to the uptake of the first electron by each of the equivalent bipyridinium units, and the second one to the subsequent reduction of radical cations to neutral units. When 4^{4+} is threaded by a component containing an electron-donor unit, as a consequence of the CT interaction (see above), the half-wave potential associated with the first reduction process is shifted to more negative values. The fact that this cyclophane exhibits another reduction process at more negative potentials is very important, as has been pointed out in the case of 1^{2+} , since it can be used to monitor the occurrence of decomplexation induced by the first two-electron reduction [15, 33/]. For instance, in the presence of an excess of a thread-like compound containing a dioxybenzene unit (**5**), the potential value for the first bielectronic reduction of 4^{4+} is shifted cathodically, while the second reduction process is practically unaffected [5]. This observation is consistent with formation of a pseudorotaxane between the cyclophane and the thread (Figure 2c), and also dethreading of the pseudorotaxane upon two-electron reduction of the 4^{4+} host, so that the second two-electron reduction process reflects that of the free host. The occurrence of the dethreading process is not surprising, because reduction of the electron-acceptor component weakens the CT interaction that helps to hold together the components of the supramolecular architecture. Since all these processes are reversible, oxidation of the reduced cyclophane back to 4^{4+} affords the original pseudorotaxane. In principle, it is also possible to obtain useful information on the occurrence of dethreading/rethreading processes from the electrochemical behavior of the electron-donor guest, which is not exactly the case for dioxybenzene unit [23].

More interesting are pseudorotaxanes wherein both the cyclophane and thread components exhibit chemically reversible redox processes, as in the case of the complex of 4^{4+} with tetrathiafulvalene (TTF) [6, 54] and related threads like **6** (see Figure 2d) [6, 55]. With such an improvement in design it is possible not only to monitor the formation of the supramolecular species by studying both the reduction of the electron-acceptor component and the oxidation of the electron-donor one, but also to control the dethreading/rethreading process in a dual-mode (reductive and oxidative fashion). The molecular thread **6**, obtained by linking a TTF unit with two polyether chains (Figure 16), forms a very stable ($K = 5 \times 10^5 \text{ M}^{-1}$ in MeCN) pseudorotaxane with 4^{4+} [55b]. Although the TTF unit in **6** retains the same electron-donor power of plain TTF, as revealed by comparing their voltammograms, the K value for the $[6 \cdot 4]^{4+}$ pseudorotaxane is 50 times higher than that for the TTF complex. This result indicates that the presence of the polyether chains strengthens the association because of the hydrogen bonding between the oxygen

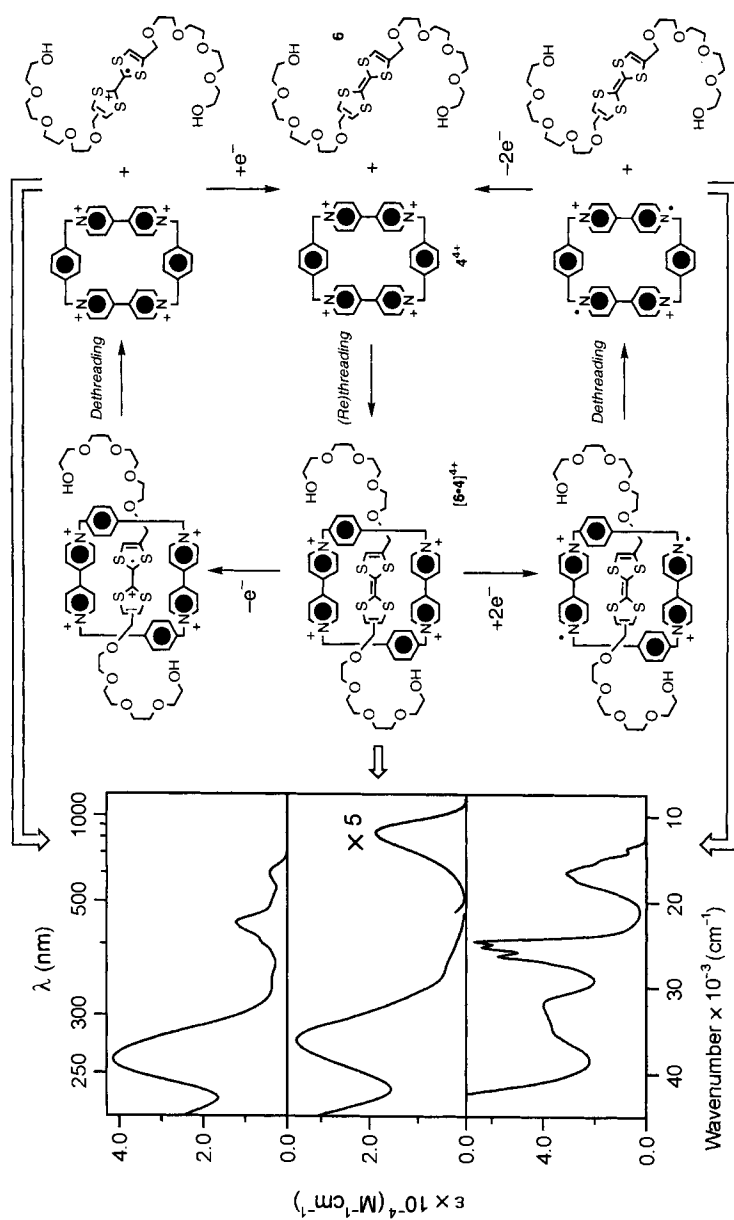


Figure 16. The electrochemically induced dethreading/rethreading processes associated with pseudorotaxane [6•4]⁴⁺ and the absorption spectra recorded (MeCN, 298 K) before oxidation (top) and after oxidation (center) or reduction (bottom) [6].

atoms in the chain and the hydrogen atoms in the α -positions with respect to the nitrogen atoms of the bipyridinium units. This cooperative interaction is extremely important in improving the on/off switching. It has been shown [6] that reversible dethreading/rethreading cycles of the $[6\bullet 4]^{4+}$ pseudorotaxane (as well as of the analogous complex with TTF) can be performed either by oxidation and successive reduction of the electron-donating thread, or by reduction and successive oxidation of the electron-accepting cyclophane. Such processes are accompanied by pronounced spectral differences (Figure 16) that can be followed easily by the naked eye, since the solution changes color from the emerald green typical of the pseudorotaxane to either brown or deep blue upon oxidative or reductive dethreading, respectively. This unique behavior makes such a system appealing for the construction of electrochromic display devices and, since its input(electrochemical)/output(color) characteristics correspond to those of the XNOR (eXclusive NOR) logic operation [6], for the design of molecular-level logic gates [56, 57]. Moreover, the voltammetric behavior on oxidation of this system is scan-rate dependent [58], indicating that the dethreading/rethreading processes (Figure 16), associated with the redox steps of the TTF unit, take place on the time scale of the electrochemical experiment.

The supramolecular complex composed (Figure 17) of the enlarged tetracationic cyclophane 17^{4+} and the ferrocene-based thread **18** has been studied recently with the aim of developing new dual-mode switchable systems [16]. This tetracation is an electron-acceptor cyclophane related to 4^{4+} ; however, while the cavity of 4^{4+} is ideal for accommodating aromatic rings, that of 17^{4+} is perfect for hosting ferrocene [59]. By means of absorption and electrochemical experiments, it has been found [16] that the $[18\bullet 17]^{4+}$ complex, which interestingly does not adopt a pseudorotaxane geometry, can be dethreaded reversibly (Figure 17) either by oxidation/reduction of the ferrocene unit of **18**, or by reduction/oxidation of the bipyridinium units of 17^{4+} .

A three-component supramolecular system, composed (Figure 18) of TTF (which can exist in three stable forms, namely, TTF, TTF^+ , and TTF^{2+}) and two hosts, specifically the electron-accepting cyclophane (4^{4+}) and the electron-donating crown ether **2**, has also been investigated [30]. In its role of an electron donor, TTF forms, with 4^{4+} , a 1:1 inclusion complex [60] which can be dissociated/reassociated reversibly by cyclic oxidation/reduction of TTF [6, 54], while TTF^{2+} acts [30] as an electron acceptor, giving a 1:1 inclusion complex ($K = 4 \times 10^3 \text{ M}^{-1}$ in MeCN at 298 K) with **2**. By contrast, TTF^+ is not bound by either of the two hosts. When the electrochemical potential applied to the solution becomes more positive than +0.4 V versus SCE, TTF is oxidized to the radical cation and the $[TTF\bullet 4]^{4+}$ complex disassembles, giving three essentially noninteracting species. Further one-electron oxidation of TTF^+ to TTF^{2+} at potentials more positive than +0.7 V versus SCE leads to the insertion of the dication into the cavity of **2**. Since both oxidized forms of TTF are stable, the initial state can be restored by subsequent reduction. This system (Figure 18) can therefore be switched reversibly between three distinct states by exercising electrochemical control upon the guest behavior of TTF [61]. The fact that the three states have different colors, coupled with the ease of their electrochemical interconversion, renders this supramolecular system suitable for electrochromic applications. Moreover, as discussed below (Section 6.6.4), this sys-

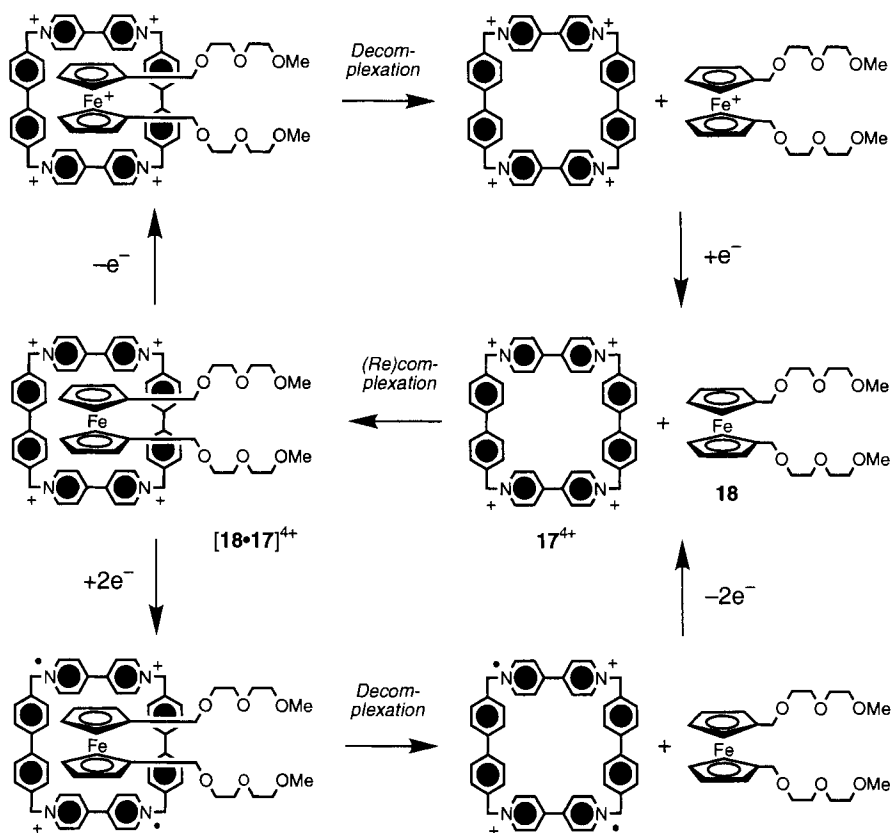


Figure 17. The decomplexation/recomplexation of the inclusion complex $[18 \cdot 17]^{4+}$ upon electrochemical reduction or oxidation (MeCN, 298 K) [16].

tem could form the basis for the construction of molecular devices in which energy transfer or electron transfer processes between selected components can be controlled [30].

In suitably designed compounds, an intramolecular pseudorotaxane structure can be obtained. An example is given by compound 28^{4+} , which contains a 4^{4+} -type cyclophane covalently linked to a dioxynaphthalene group by a polyether chain [36, 62]. In solution, the tail threads through the cavity of its own head, positioning the dioxynaphthalene group between the two bipyridinium units of the cyclophane (Figure 19). Consistently, the absorption spectrum recorded in MeCN at 298 K of *in-28* $^{4+}$ shows a band at 515 nm in the visible region, arising from CT interactions between the dioxynaphthalene group and the sandwiching bipyridinium units. Such an absorption band is also shown by a model self-complexed system [36] bearing a bulky stopper at the end of the tail. The stopper prevents dethreading of the tail, and so this model compound can exist only in a self-complexed conformation. The similarities between the absorption spectra of *in-28* $^{4+}$ and of this model compound

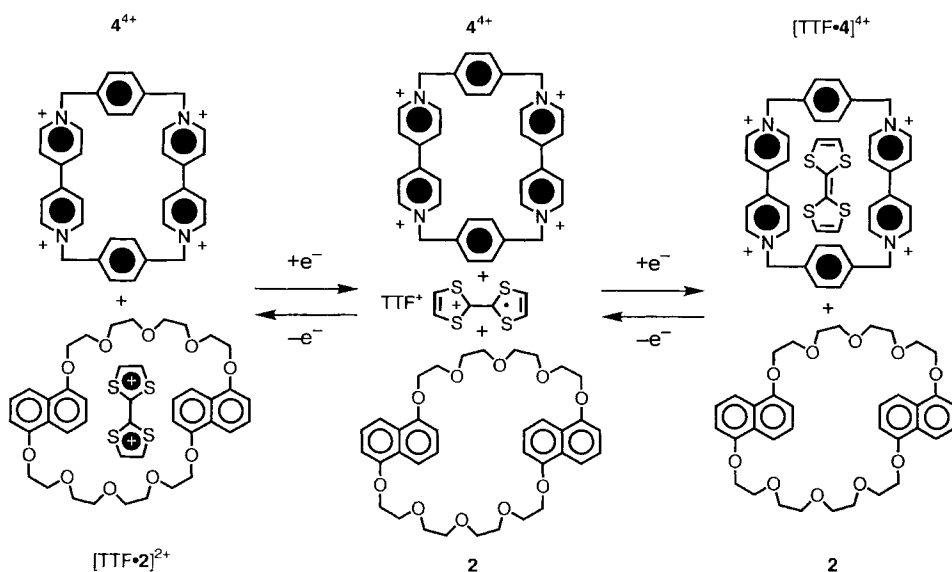


Figure 18. Redox switching between the complexes $[TTF \cdot 2]^{2+}$, incorporating the macrocyclic polyether **2** and the dication TTF^{2+} , and $[TTF \cdot 4]^{4+}$, composed of the tetracationic cyclophane 4^{4+} and TTF (MeCN, 298 K) [30].

indicate that *in-28* $^{4+}$ also exists completely in its self-complexed conformation in solution. The cyclic voltammogram of *in-28* $^{4+}$ shows two reversible two-electron reduction waves. The first one (-0.35 V versus SCE) corresponds to the simultaneous addition of one electron to each of the two bipyridinium units, and the second one (-0.71 V) corresponds to the simultaneous addition of a second electron to each of the two bipyridinium units. A model tetracationic cyclophane that does not incorporate the dioxynaphthalene tail undergoes two consecutive two-electron reduction processes at -0.29 and -0.70 V, respectively. Thus, the first reduction process occurs at a more negative potential in the case of *in-28* $^{4+}$, while the second reduction process occurs at the same potential in both compounds. These observations indicate that the dioxynaphthalene group of *in-28* $^{4+}$ is sandwiched (Figure 19) initially between the two bipyridinium units, making their first reduction more difficult. However, after the addition of one electron to each of the two bipyridinium units, the dioxynaphthalene unit is expelled from the cavity of the tetracationic cyclophane and the second reduction process is not affected by the presence of the electron-rich unit [36].

6.5.4 Chemically Induced Processes

The assembly of complexes based on electron donor/acceptor interactions can also be controlled by means of redox stimuli provided by the addition of oxidants and

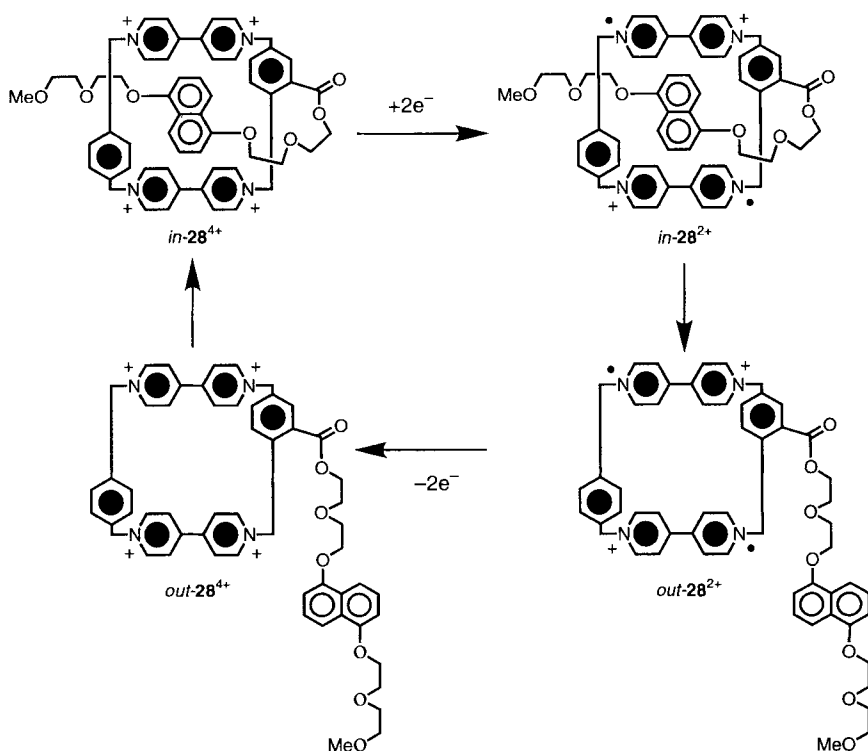


Figure 19. Electrochemically induced dethreading/rethreading of the self-complexing compound **28**⁴⁺ (MeCN, 298 K) [36].

reductants. The inclusion complex [TTF•**4**]⁴⁺ discussed above [6, 54], formed between the electron-acceptor cyclophane **4**⁴⁺ and TTF, as well as pseudorotaxanes [6, 55] composed of **4**⁴⁺ and thread-like species containing a tetrathiafulvalene unit like **6**, can be disassembled [3, 6, 55] into their free components by oxidation of the TTF unit to its radical cation with one equivalent of Fe(ClO₄)₃ in MeCN or aqueous solution. The one-electron oxidized form of the TTF unit is stable in such conditions, and can be reduced back to its neutral form by adding a stoichiometric amount of ascorbic acid. The reduction results in the insertion of the TTF unit into the tetracationic cyclophane. Dethreading can also be achieved by adding *o*-chloroanil, which forms an adduct with the TTF unit; upon addition of Na₂S₂O₅ in the presence of water, *o*-chloroanil is reduced, affording the original complex or pseudorotaxane [55b]. Such dethreading/rethreading processes can be easily monitored by UV-visible absorption spectroscopy since first, the system shows a broad absorption band with a maximum around 850 nm, ascribed to the CT interaction between the electron-rich TTF unit and the electron-poor bipyridinium units of **4**⁴⁺, and second, the neutral and cationic forms of the TTF unit exhibit very different absorption features.

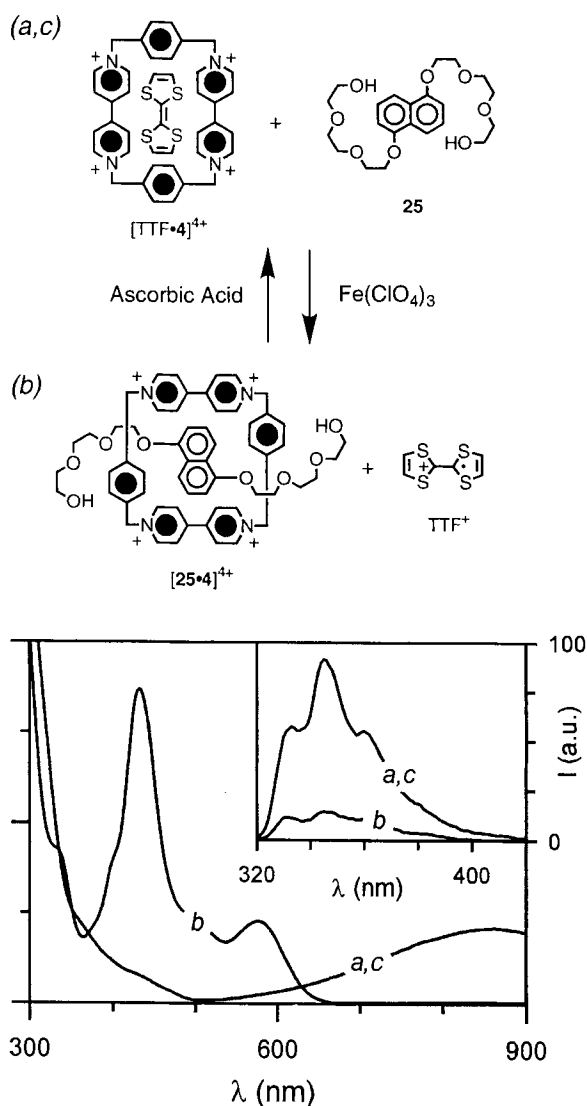


Figure 20. Top: the chemically induced interchange of guests **25** and TTF into the cavity of cyclophane **4**⁴⁺. Bottom: absorption and (inset) fluorescence ($\lambda_{\text{exc}} = 295 \text{ nm}$) spectra of: (a) a $5 \times 10^{-5} \text{ M}$ aqueous solution (298 K) of [TTF•4]⁴⁺ and **25**; (b) the same solution after addition of 1 equiv. of Fe(ClO₄)₃; (c) solution (b) after addition of 1 equiv. of ascorbic acid [3].

A supramolecular system has also been devised in which it is possible, by means of chemical stimuli, to select which one of two guests enters a macrocycle's cavity and to interchange reversibly the two guests (Figure 20) [3]. Addition of the thread-like compound **25**, which contains a electron-rich dioxynaphthalene unit, to an aqueous solution of the [TTF•4]⁴⁺ complex affects neither the CT absorption band characteristic of the complex nor the strong fluorescence band of the dioxynaphthalene-based thread (curves *a* in Figure 20), indicating that this thread does not displace TTF from inside the macrocyclic host. On addition of a stoichiometric

amount of $\text{Fe}(\text{ClO}_4)_3$ (with respect to TTF), the absorption bands of the radical cation TTF^+ are formed, and the CT band of $[\text{TTF} \cdot \mathbf{4}]^{4+}$ disappears, while the fluorescence band of the dioxynaphthalene-based species is substantially quenched (curves *b* in Figure 20). These results show that oxidation causes expulsion of TTF^+ from $\mathbf{4}^{4+}$ and its replacement by the dioxynaphthalene-based thread. On subsequent addition of ascorbic acid, the system returns to its initial state (curves *c* in Figure 20).

The 2,7-dibenzylidiazapyrenium dication $\mathbf{29}^{2+}$ has a strong affinity for aliphatic amines, giving rise to charge-transfer complexes. This property can be exploited to dethread the pseudorotaxane formed by $\mathbf{29}^{2+}$ with the 1,5-dinaphtho-38-crown-10 macrocycle $\mathbf{2}$ (Figure 21) [63]. Macrocycle $\mathbf{2}$ also forms a pseudorotaxane with the 1,1'-dibenzyl-4,4'-bipyridinium thread $\mathbf{1}^{2+}$ [3]. On mixing macrocycle $\mathbf{2}$ with threads $\mathbf{29}^{2+}$ and $\mathbf{1}^{2+}$ in $\text{CH}_2\text{Cl}_2/\text{MeCN}$ 9:1 (v/v) solution, the cavity of the macrocycle is occupied by the $\mathbf{29}^{2+}$ thread, since the stability constant of pseudorotaxane $[\mathbf{29} \cdot \mathbf{2}]^{2+}$ is about two orders of magnitude larger than that of $[\mathbf{1} \cdot \mathbf{2}]^{2+}$. Upon addition of excess hexylamine, strong spectral changes are observed, indicating quantitative formation of the adduct between $\mathbf{29}^{2+}$ and the amine, whereas luminescence measurements show that the pseudorotaxane $[\mathbf{1} \cdot \mathbf{2}]^{2+}$ is formed in amount corresponding to its stability constant (Figure 21) [3]. The process can be fully reversed by addition of acid. This interchange process is similar to the redox-driven [3] or metal ion-driven [64] interchange between two electron-donors guests into the cavity of the electron-acceptor cyclophane $\mathbf{4}^{4+}$ and to the exchange of two macrocycles on changing the redox properties of the guest species [30] (see Section 6.5.3).

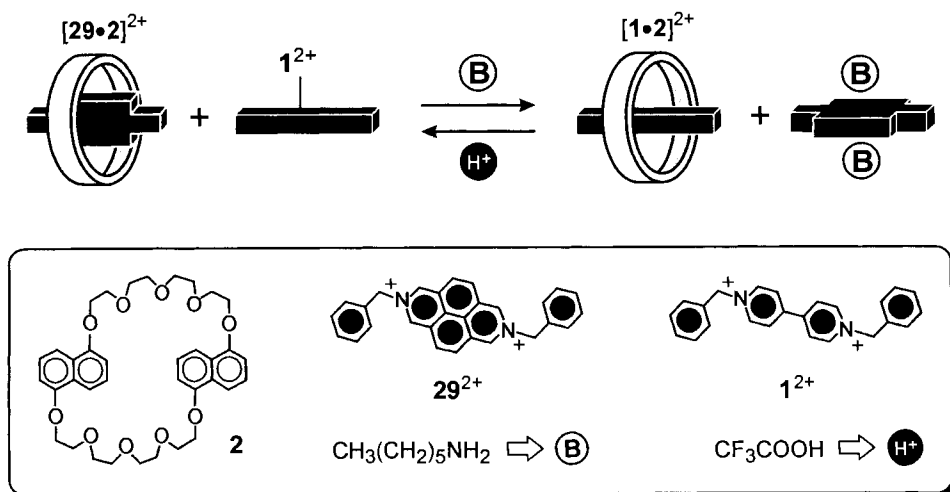


Figure 21. Schematic representation of the reversible interchange between two threads in a pseudorotaxane structure upon amine/acid stimulation ($\text{CH}_2\text{Cl}_2/\text{MeCN}$ 9:1 (v/v), 298 K) [3].

6.6 Electron Transfer Controlled by Dethreading/Rethreading Processes

6.6.1 Pseudorotaxanes and Information Processing

In the previous section we have described pseudorotaxane systems in which electron transfer inputs govern dethreading/threading processes, opening the way to the control of nuclear movements (molecular machines). In this section, we will see that, in their turn, nuclear movements induced by an appropriate stimulation (e.g., an acid/base reaction) can govern the occurrence of electron transfer processes or CT interactions. This aspect of pseudorotaxane chemistry can be exploited for the construction of electronic devices for information processing at the molecular level.

6.6.2 Plug–Socket Systems

Crown ethers and ammonium ions can give rise to pseudorotaxanes under acid/base control [8]. Recently, luminescent units such as dioxybenzene [12, 17], dioxynaphthalene [12, 17b], binaphthyl [19, 65], and anthracene [17], have been incorporated into crown ethers or ammonium ions, in order to study the photoinduced processes that take place within pseudorotaxanes that can be threaded/detreaded by acid/base inputs. An example dealing with energy transfer, but that can be easily extended to electron transfer, is shown in Figure 22 [19]. The absorption and fluorescence spectra of a CH_2Cl_2 solution containing amine **30** and the crown ether **21** indicate the absence of any interaction between the two compounds. Addition of a stoichiometric amount of $\text{CF}_3\text{SO}_3\text{H}$ with respect to the amine causes profound changes in the fluorescence spectrum of the solution, particularly as a result of the quenching of the luminescence of **21**, and also the sensitization of the luminescence of **30** upon excitation with light absorbed exclusively by the crown ether. These observations are consistent with the formation of a pseudorotaxane-type adduct wherein very efficient energy transfer takes place from the binaphthyl unit of the crown ether to the anthracenyl group incorporated within the dialkylammonium ion. Such a pseudorotaxane can be disassembled by the subsequent addition of a stoichiometric amount of base, thereby interrupting the photoinduced energy flow, as indicated by the fact that the initial absorption and fluorescence spectra are restored. Such systems can be viewed (Figure 22) as molecular-level plug–socket devices, since they are characterized by chemically controlled, reversible *plug in/plug out* behavior, and photoinduced energy transfer in the *plug in* state. Interestingly, the *plug in* process does not take place when a plug component incompatible with the size of the socket, such as the benzyl-substituted amine **19**, is employed [19]. As mentioned above, extension to photoinduced electron transfer processes is straightforward. Furthermore, since the enantiomeric recognition of ammonium ions by crown ethers containing binaphthyl is a well-known property [65], stereoselective *plug in/plug out* systems can also be designed.

Interestingly, a similar system, where the chemical stimuli provided by counterions are employed to achieve switching, has also been reported [66].

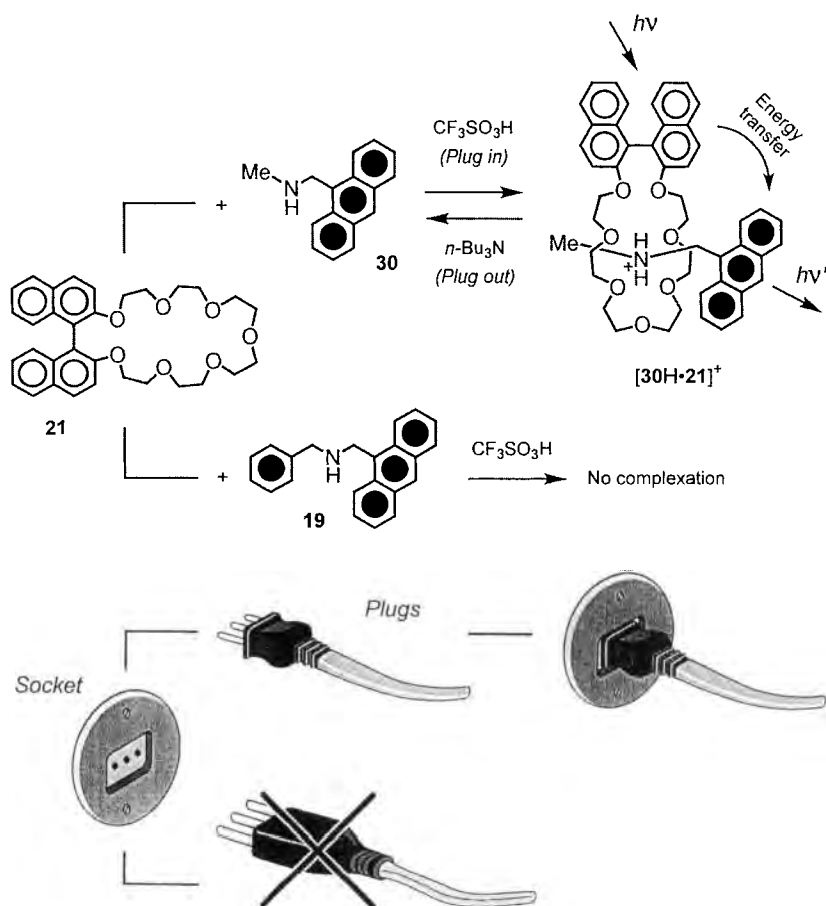


Figure 22. The reversible acid/base-driven threading/dethreading motions of pseudorotaxane $[30H \cdot 21]^+$ (CH_2Cl_2 , 298 K) [19]. In the threaded structure, energy transfer can take place from the binaphthyl unit of the crown ether to the anthracenyl group of the dialkylammonium ion. The acid-driven threading of compound **19**, incorporating a bulky benzene group, through the macrocyclic cavity of **21** does not occur. Such systems can be viewed as molecular-level plug–socket devices.

6.6.3 Extensions

The plug–socket concept has been developed to design a molecular-level extension. The investigated [67] system (Figure 23) consists of macrocycles **2** and 32^{2+} , the latter carrying a $Ru(bpy)_3^{2+}$ moiety, and thread $31H^{3+}$ which contains two different recognition sites, namely an ammonium and a bipyridinium function. Thread $31H^{3+}$ can undergo hydrogen-bonding interactions with macrocycle 32^{2+} and acceptor–donor interactions with macrocycle **2**. Once the two connections have been established, light excitation of the $Ru(bpy)_3^{2+}$ moiety of macrocycle 32^{2+} causes the

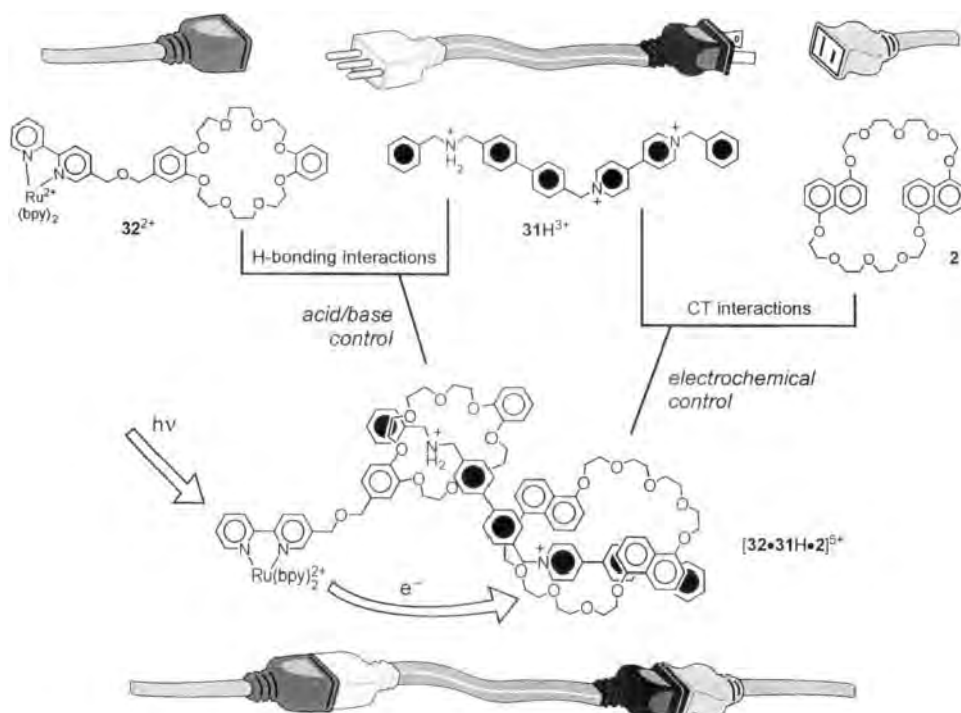


Figure 23. A molecular-level extension. Thread 31H^{3+} can undergo a hydrogen-bonding interaction with macrocycle 32^{2+} and an acceptor–donor interaction with macrocycle **2** (MeCN, 298 K). Once the two connections have been established, photoinduced electron transfer occurs from the excited state of the $\text{Ru}(\text{bpy})_3^{2+}$ moiety of macrocycle 32^{2+} to the bipyridinium unit hosted in macrocycle **2** [67].

transfer of an electron to the bipyridinium unit hosted in macrocycle **2**. Extensions containing a plug and a socket instead of two plugs, in which an electron is transferred from a socket to a remote plug, have also been designed.

6.6.4 Logic Gates and Switches

Machine-like movements induced by external stimuli in pseudorotaxanes correspond to a binary logic behavior. As mentioned above, this can result in systems that perform as molecular-level logic gates. An interesting example of a pseudorotaxane system behaving as an XOR logic gate is illustrated in Figure 24 [56]. Pseudorotaxane $[29 \cdot 33]^{2+}$, composed by the diazapyrenium thread 29^{2+} and the 2,3-dinaphtho-30-crown-10 macrocycle **33**, can be disassembled by aliphatic amines because of the previously discussed formation of an adduct between the diazapyrenium thread and amines [63]. This process can be coupled with the possibility

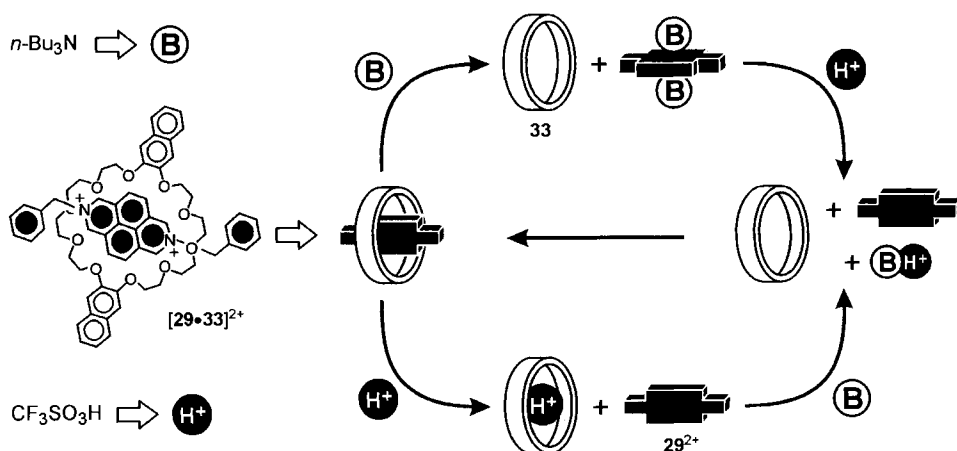


Figure 24. Schematic representation of the dethreading/rethreading pattern of pseudorotaxane $[29\cdot 33]^{2+}$ ($\text{CH}_2\text{Cl}_2/\text{MeCN}$ 9:1 (v/v), 298 K) which corresponds to an XOR logic function [56].

of dethreading the same system by protonation of the crown ether in nonpolar solvents. It has been shown [56] that $[29\cdot 33]^{2+}$ in $\text{CH}_2\text{Cl}_2/\text{MeCN}$ 9:1 (v/v) can be dethreaded upon addition of $n\text{-Bu}_3\text{N}$ and assembled again by adding protons. The same result can be obtained by reversing the order of the two chemical inputs; that is, dethreading can be achieved by protonation of the crown ether's cavity, and rethreading can be obtained by the addition of $n\text{-Bu}_3\text{N}$. All these processes are accompanied by on/off switching of easily monitorable changes in the absorption and luminescence spectra, particularly of an intense fluorescence band, characteristic of the aromatic crown ether, with a maximum at 343 nm. It is worth emphasizing that these results contrast with the usual behavior of chemical systems that either remain unchanged or undergo very different changes upon addition of reactants of opposite chemical nature such as amines and acids. An important consequence of this behavior is that the input/output relationships of the system correspond to those of the XOR (eXclusive OR) logic operation [56]. This development shows [26] that carefully designed dual-mode chemically driven molecular machines are potentially useful for information processing.

A somewhat related system is based on the electrochemically driven exchange of a guest between two hosts (see Section 6.5.3 and Figure 18). The mechanical movements taking place in such a system open the way to second-generation devices in which the electrochemically driven movements can control the selection of the partner in energy transfer or electron transfer processes [30]. Consider, for example a system (Figure 25) where a chromophoric group **A** is appended to the potential guest and chromophoric groups **B** and **C**, whose lowest excited states are lower than that of **A**, are appended to the potential hosts 4^{4+} and **2**, respectively. In such a system, light excitation of **A** could lead to no energy transfer (OFF), energy transfer to **B** (ON 1), or energy transfer to **C** (ON 2), depending on the potential value selected by the operator. Clearly, if energy transfer has to proceed through the

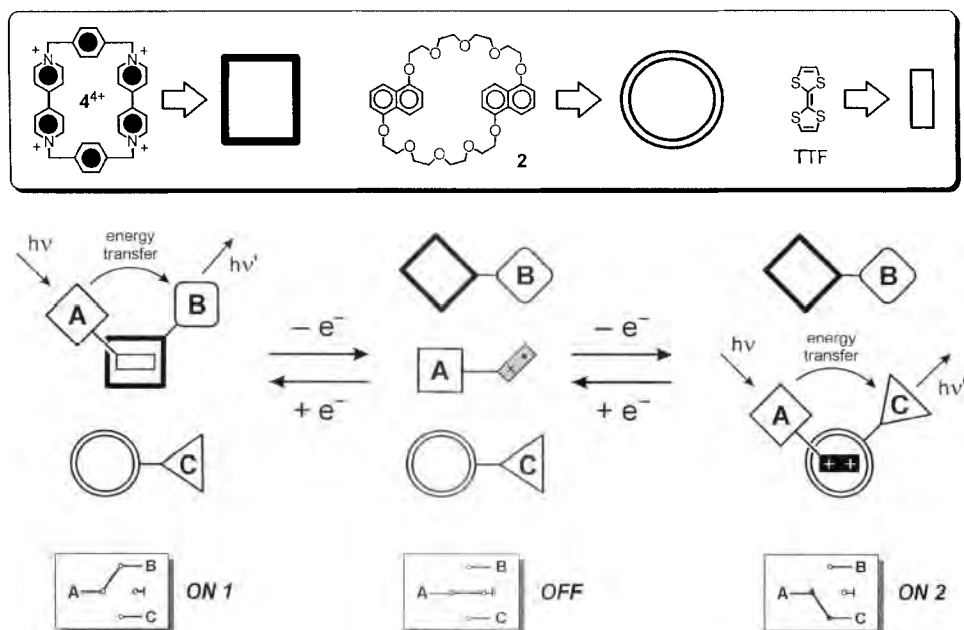


Figure 25. Schematic representation of the concept of a three-pole supramolecular switching of energy transfer. The association/dissociation processes are those shown in Figure 18; A, B, and C are suitably chosen photoactive groups. For more details, see text [30].

charge-transfer connections, there are severe limitations as to the choice of the chromophoric groups to be used. However, it does not seem unlikely that systems can be designed where molecular association either relies on a different kind of interaction (e.g., hydrogen bonding), or simply plays the role of bringing the two chromophoric groups at a suitable distance for through-space energy transfer. Similar switching of electron transfer processes could also be performed and more complex energy transfer and/or electron transfer patterns are conceivable. The strategy described above can also be used, in principle, to catalyze chemical reactions.

6.6.5 Sensors

As we have seen above, the formation of pseudorotaxanes in most cases is accompanied by noticeable changes in the spectroscopic and electrochemical properties. This feature can be exploited for sensory purposes [15, 68]. Changes in fluorescence are particularly useful in this regard because fluorescence spectroscopy is a simple and sensitive technique. Interestingly, an amplification of the fluorescence change signal can be obtained in appropriately designed systems. For example [68b,c], in a conjugated polymer with many appended fluorescent electron-donor macrocycles, the threading of an electron acceptor into one of the macrocycles can cause the

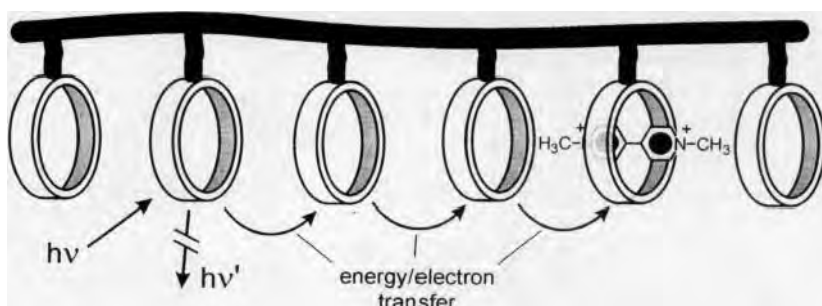


Figure 26. Schematic representation of a sensory signal amplification upon formation of a poly-pseudorotaxane from a conjugated polymer with appended many fluorescent electron-donor macrocycles. Threading only one macrocycle by an electron acceptor can cause the quenching, by energy or electron transfer, of the fluorescent excited state of remote macrocycles [68b].

quenching of several of them because of an intrastrand energy or electron migration (Figure 26).

6.6.6 Other Systems

An interesting case of a CT interaction triggered by a chemical input is exhibited by compound **34**⁺, which is made of a macrocycle containing electron-donor units, with appended a 4-pyridyl(4-pyridinium) tail [69]. In CH₂Cl₂ solution, **34**⁺ shows the well-known absorption bands of the component chromophoric groups, as well as the fluorescence band of the dioxynaphthalene unit. Addition of trifluoroacetic acid causes the appearance of the characteristic broad and weak CT band in the visible region ($\lambda_{\text{max}} = 510 \text{ nm}$, $\epsilon = 270 \text{ M}^{-1} \text{ cm}^{-1}$) and the disappearance of the dioxynaphthalene fluorescence band. This shows that, upon protonation of the pyridine unit, the tail becomes a strong electron acceptor which, therefore, threads the electron-donor macrocycle (Figure 27). Subsequent addition of tributylamine causes the disappearance of the CT absorption and the revival of the fluorescence, showing

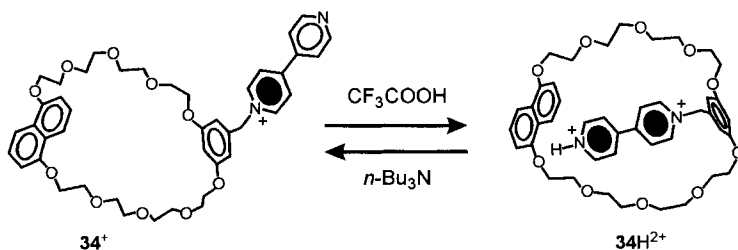


Figure 27. Reversible threading/dethreading of compound **34**⁺ upon acid/base stimulation (CH₂Cl₂, 298 K) [69].

that the process is fully reversible. In MeCN, addition of acid does not cause the threading process since the protonated (dicationic) tail is strongly stabilized in polar solvents.

Compound 34^+ can be used in another interesting cyclic processes, as shown schematically in Figure 28 [69]. In CH_2Cl_2 solution, addition of the electron-acceptor wire-type *trans*-1,2-bis(1-benzyl-4-pyridinium)ethylene compound 35^{2+} causes a threading process with formation of the $[35 \cdot 34]^{3+}$ pseudorotaxane (Figure 28). Subsequent addition of trifluoroacetic acid causes the protonation of the pyridine unit of the tail of 34^+ . Since the protonated tail is a stronger electron acceptor than thread 35^{2+} , the latter is pushed out of the macrocycle, as indicated by changes in the absorption and emission spectra. The process is fully reversible by addition of tributylamine. In such a system, proton can close and amine can re-open the “door” of the macrocyclic cavity of 34^+ , thus preventing or allowing encapsulation of an external guest.

6.7 Heterogeneous Systems

The systems discussed above have been studied in solution, where each molecule behaves independently. Incoherence, therefore, remains a major impediment to designing and realizing systems capable of performing useful functions. The problem of obtaining ordered arrays of molecular devices that can communicate with the macroscopic world can be addressed by their aggregation on surfaces [70] or organization at liquid–gas or liquid–liquid interfaces [71].

For example, one can design systems like those illustrated in Figure 29 in which either the thread or the macrocycle is immobilized on an appropriate solid surface [72]. If the surface is an electrode [73], it may be possible to induce a coherent dethreading/rethreading movement under electrochemical control. By using a semiconductor surface, it may be possible to cause light-induced processes. An interesting approach is provided by the emerging field of heterosupramolecular chemistry, where molecular or supramolecular species are linked to nanoparticles [74].

6.8 Conclusions

Pseudorotaxanes represent a particular class of *complexes*—a term first used to describe Werner-type [75] metal complexes, also called coordination compounds. Complexes formed by organic molecules began to attract the attention of chemists around 1950, Mulliken in particular, in a landmark series of papers [76], formulated a theoretical treatment to explain the bonding characteristics and spectral properties of organic complexes based on charge-transfer interactions. During the past 20

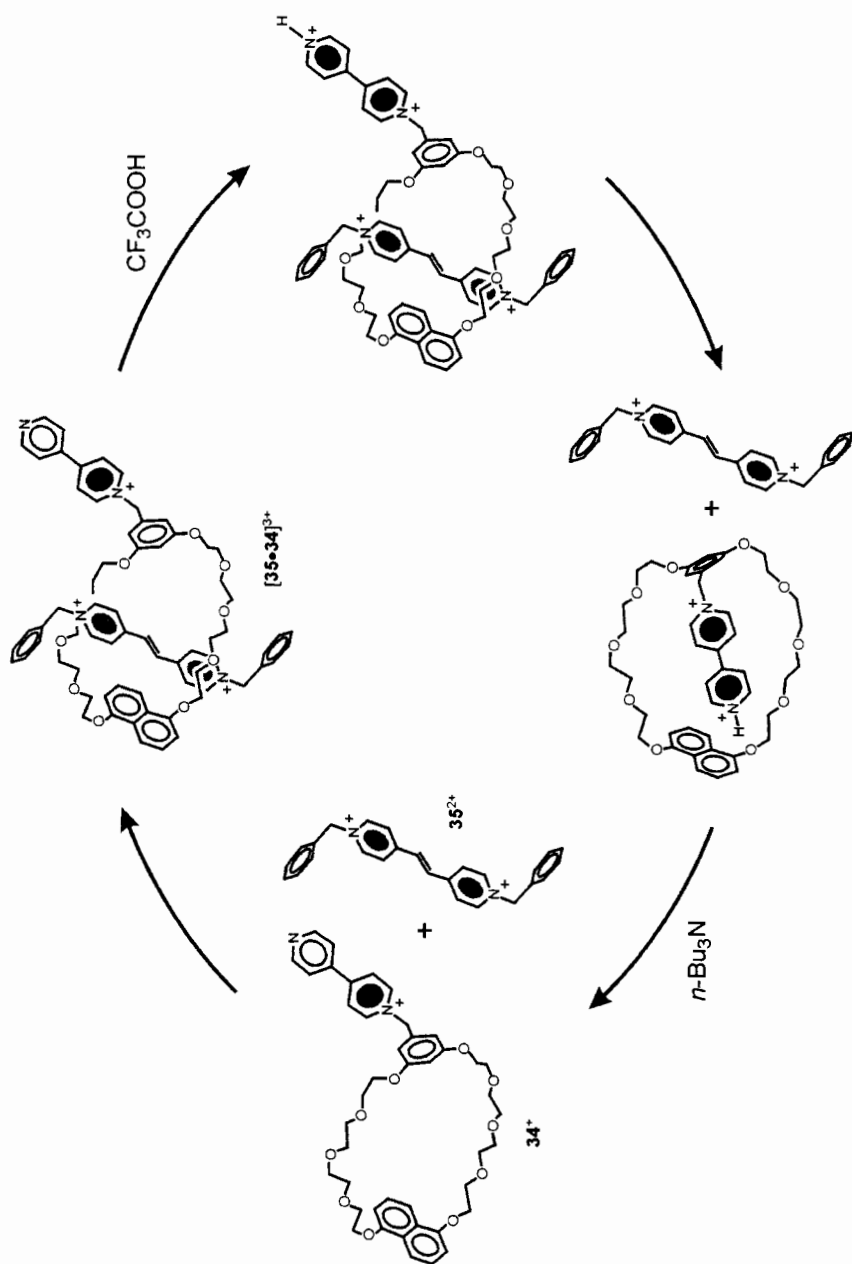


Figure 28. The chemically driven processes occurring for the $34^+/35^{2+}$ system (CH_2Cl_2 , 298 K) [69].

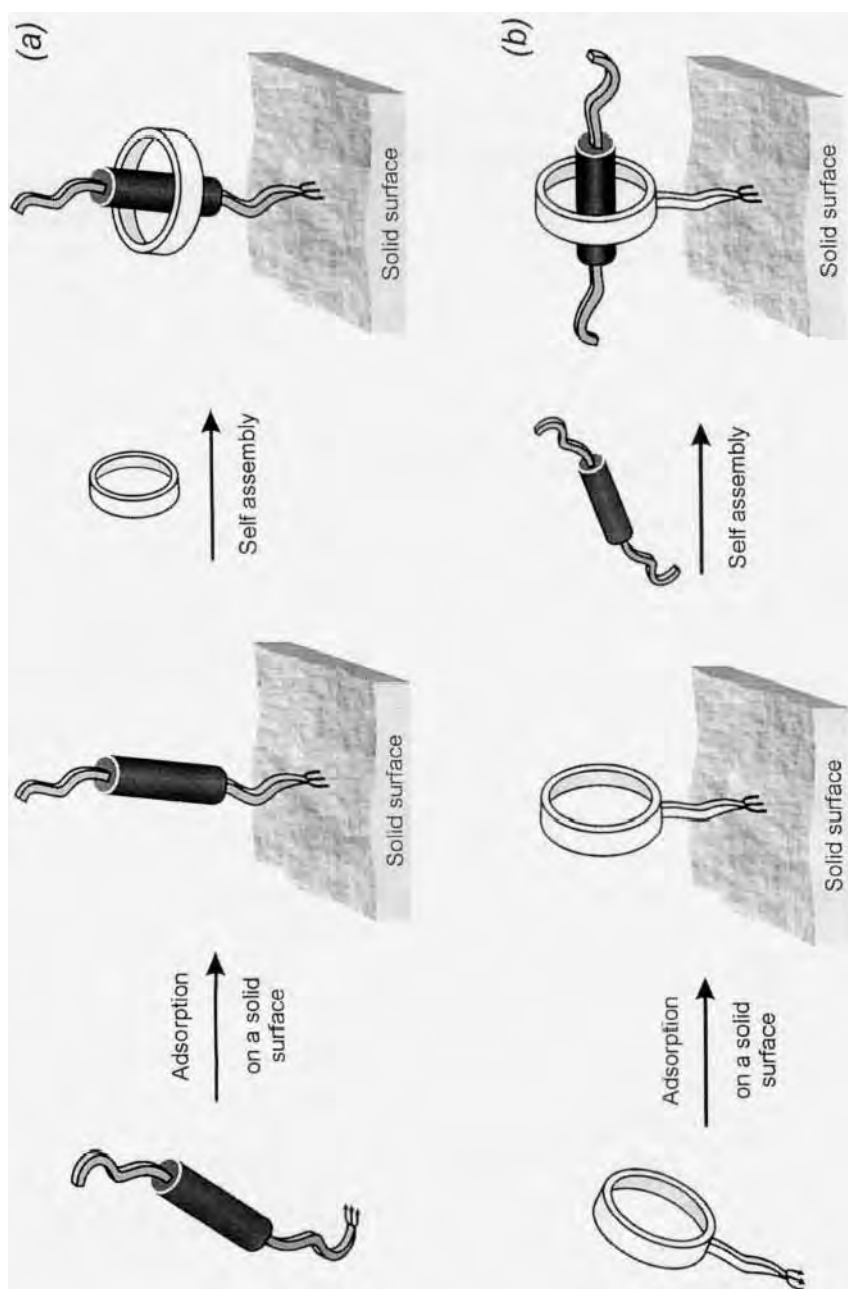


Figure 29. Pseudorotaxanes formed by grafting (a) a thread or (b) a macrocycle on a surface.

years, it has become clear that both metal-based coordination compounds and organic charge-transfer complexes belong to the broader field of supramolecular chemistry, which includes any kind of species formed from the associations of cationic, anionic, and neutral molecular compounds [77].

Pseudorotaxanes based on charge-transfer interactions belong to the Mulliken-type complexes. Furthermore, they exhibit an organized structure somewhat similar to that of metal-based coordination compounds [33], [78]. Because of this combination of properties, pseudorotaxanes offer the opportunity to make use of electron transfer concepts and techniques along new directions. As we have seen above, electron transfer processes (performed by chemical, photochemical, or electrochemical stimulations) can be exploited to control threading/dethreading mechanical-like movements while, in their turn, mechanical-like movements (performed by chemical, photochemical, or electrochemical stimulations) can govern the occurrence of electron transfer processes or charge-transfer interactions. These concepts may be useful for the design of devices for information processing at the molecular level.

Acknowledgments

We thank the University of Bologna (Funds for Selected Research Topics), MURST (Supramolecular Devices Project), and the EU (TMR project FMRX-CT96-0076) for financial support.

References

1. (a) J.-M. Lehn, *Supramolecular Chemistry*, VCH, Weinheim, **1995**. (b) *Comprehensive Supramolecular Chemistry* (Eds. J.L. Atwood, J.E.D. Davies, D.D. Macnicol, F. Vögtle), Pergamon Press, Oxford, **1996**, Vol. 2.
2. (a) H.W. Gibson, M.C. Bheda, P.T. Engen, *Progr. Polym. Sci.* **1994**, *19*, 843. (b) D.B. Amabilino, J.F. Stoddart, *Chem. Rev.* **1995**, *95*, 2725. (c) J.-C. Chambron, C. Dietrich-Buchecker, J.-P. Sauvage, in *Comprehensive Supramolecular Chemistry* (Eds. J.L. Atwood, J.E.D. Davies, D.D. Macnicol, F. Vögtle), Pergamon Press, Oxford, **1996**, Vol. 9, p. 43. (d) D.B. Amabilino, F.M. Raymo, J.F. Stoddart, in *Comprehensive Supramolecular Chemistry* (Eds. J.L. Atwood, J.E.D. Davies, D.D. Macnicol, F. Vögtle), Pergamon Press, Oxford, **1996**, Vol. 9, p. 85. (e) D. Philp, J.F. Stoddart, *Angew. Chem. Int. Ed. Engl.* **1996**, *35*, 1154. (f) R. Jäger, F. Vögtle, *Angew. Chem. Int. Ed. Engl.* **1997**, *36*, 931. (g) S.A. Nepogodiev, J.F. Stoddart, *Chem. Rev.* **1998**, *98*, 1959. (h) D.H. Busch, A.L. Vance, A.G. Kolchinski, in *Comprehensive Supramolecular Chemistry* (Eds. J.L. Atwood, J.E.D. Davies, D.D. Macnicol, F. Vögtle), Pergamon Press, Oxford, **1996**, Vol. 9, p. 1. (i) F.M. Raymo, J.F. Stoddart, *Chem. Rev.* **1999**, *99*, 1643. (j) *Molecular Catenanes, Rotaxanes and Knots* (Eds.: J.-P. Sauvage, C.O. Dietrich-Buchecker), Wiley-VCH, Weinheim, **1999**.
3. A. Credi, M. Montalti, V. Balzani, S.J. Langford, F.M. Raymo, J.F. Stoddart, *New J. Chem.* **1998**, 1061.
4. D.G. Hamilton, J.E. Davies, L. Prodi, J.K.M. Sanders *Chem. Eur. J.* **1998**, *4*, 608.
5. P.L. Anelli, P.R. Ashton, R. Ballardini, V. Balzani, M. Delgado, M.T. Gandolfi, T.T. Goodnow, A.E. Kaifer, D. Philp, M. Pietraszkiewicz, L. Prodi, M.V. Reddington, A.M.Z. Slawin, N. Spencer, J.F. Stoddart, C. Vicent, D.J. Williams, *J. Am. Chem. Soc.* **1992**, *114*, 193.

6. M. Asakawa, P. Ashton, V. Balzani, A. Credi, G. Mattersteig, O.A. Matthews, M. Montalti, N. Spencer, J.F. Stoddart, M. Venturi, *Chem. Eur. J.* **1997**, *3*, 1992.
7. (a) K.N. Houk, S. Menzer, S.P. Newton, F.M. Raymo, J.F. Stoddart, D.J. Williams, *J. Am. Chem. Soc.* **1999**, *121*, 1479. (b) S.J. Loeb, J.A. Wisner, *Angew. Chem. Int. Ed.* **1998**, *37*, 2838.
8. P.R. Ashton, P.J. Campbell, E.J.T. Chrystal, P.T. Glink, S. Menzer, D. Philp, N. Spencer, J.F. Stoddart, P.A. Tasker, D.J. Williams, *Angew. Chem. Int. Ed. Engl.* **1995**, *34*, 1865.
9. R.S. Wylie, D.H. Macartney, *J. Am. Chem. Soc.* **1992**, *114*, 3136.
10. C. Wu, P.R. Lecavalier, Y.X. Shen, H.W. Gibson, *Chem. Mater.* **1991**, *3*, 569.
11. M. Kimura, Y. Misawa, Y. Yamaguchi, K. Hanabusa, H. Shirai, *Chem. Commun.* **1996**, 2785.
12. P.R. Ashton, R. Ballardini, V. Balzani, M.C.T. Fyfe, M.T. Gandolfi, M.V. Martínez-Díaz, M. Morosini, C. Schiavo, K. Shibata, J.F. Stoddart, A.J.P. White, D.J. Williams, *Chem. Eur. J.* **1998**, *4*, 2332.
13. P.R. Ashton, D. Philp, N. Spencer, J.F. Stoddart, *J. Chem. Soc. Chem. Commun.* **1991**, 1677.
14. N. Yamaguchi, H.W. Gibson, *Angew. Chem. Int. Ed.* **1999**, *38*, 143.
15. A.E. Kaifer, *Acc. Chem. Res.* **1999**, *32*, 62.
16. V. Balzani, J. Becher, A. Credi, M.B. Nielsen, F.M. Raymo, J.F. Stoddart, A.M. Talarico, M. Venturi, *J. Org. Chem.* **2000**, *65*, 1947.
17. (a) M. Montalti, R. Ballardini, L. Prodi, V. Balzani *J. Chem. Soc. Chem. Commun.* **1996**, 2011. (b) P.R. Ashton, R. Ballardini, V. Balzani, M. Gómez-López, S.E. Lawrence, M.V. Martínez-Díaz, M. Montalti, A. Piersanti, L. Prodi, J.F. Stoddart, D.J. Williams, *J. Am. Chem. Soc.* **1997**, *119*, 10641.
18. P.R. Ashton, R. Ballardini, V. Balzani, E.C. Constable, A. Credi, O. Kocian, S.J. Langford, J.A. Preece, L. Prodi, E.R. Schofield, N. Spencer, J.F. Stoddart, S. Wenger, *Chem. Eur. J.* **1998**, *4*, 2411.
19. E. Ishow, A. Credi, V. Balzani, F. Spadola, L. Mandolini, *Chem. Eur. J.* **1999**, *5*, 984.
20. P.R. Ashton, V. Balzani, O. Kocian, L. Prodi, N. Spencer, J.F. Stoddart, *J. Am. Chem. Soc.* **1998**, *120*, 11190.
21. N. Yamaguchi, D. Nagvekar, H.W. Gibson, *Angew. Chem. Int. Ed.* **1998**, *37*, 2361.
22. (a) R. Wolf, M. Asakawa, P.R. Ashton, M. Gómez-López, C. Hamers, S. Menzer, I.W. Parsons, N. Spencer, J.F. Stoddart, M.J. Tolley, D.J. Williams, *Angew. Chem. Int. Ed.* **1998**, *37*, 975. (b) P.R. Ashton, I. Baxter, S.J. Cantrill, M.C.T. Fyfe, P.T. Glink, J.F. Stoddart, A.J.P. White, D.J. Williams, *Angew. Chem. Int. Ed.* **1998**, *37*, 1294. (c) M.B. Nielsen, S.B. Nielsen, J. Becher, *Chem. Commun.* **1998**, 475. (d) A. Mirzoian, A.E. Kaifer, *Chem. Commun.* **1999**, 1603.
23. M. Asakawa, P.R. Ashton, R. Ballardini, V. Balzani, M. Belohradsky, M.T. Gandolfi, O. Kocian, L. Prodi, F.M. Raymo, J.F. Stoddart, M. Venturi, *J. Am. Chem. Soc.* **1997**, *119*, 302.
24. P.R. Ashton, I. Baxter, M.C.T. Fyfe, F.M. Raymo, N. Spencer, J.F. Stoddart, A.J.P. White, D.J. Williams, *J. Am. Chem. Soc.* **1998**, *120*, 2297.
25. (a) D.H. Rouvray, *Chem. Br.* **1995**, *31*, 554. (b) D.H. Rouvray, *Chem. Ind.* **1997**, January 20, 60. (c) D.H. Rouvray, *Fuzzy Logic in Chemistry*, Academic Press, London, **1997**.
26. V. Balzani, A. Credi, M. Venturi, in *Supramolecular Science: Where It Is and Where It Is Going* (Eds. R. Ungaro, E. Dalcanele), Kluwer, Dordrecht, **1999**, p. 1.
27. V. Balzani, M. Gómez-López, J.F. Stoddart, *Acc. Chem. Res.* **1998**, *31*, 405.
28. V. Balzani, A. Credi, F.M. Raymo, J.F. Stoddart, *Angew. Chem. Int. Ed.* **2000**, *39*, 3349.
29. (a) P.R. Ashton, R. Ballardini, V. Balzani, A. Credi, M.T. Gandolfi, D.J.-F. Marquis, S. Menzer, L. Pérez-García, L. Prodi, J.F. Stoddart, M. Venturi, A.J.P. White, D.J. Williams, *J. Am. Chem. Soc.* **1995**, *117*, 11171. (b) Unpublished results of our laboratories.
30. P.R. Ashton, V. Balzani, J. Becher, A. Credi, M.C.T. Fyfe, G. Mattersteig, S. Menzer, M. Nielsen, F.M. Raymo, J.F. Stoddart, M. Venturi, D.J. Williams, *J. Am. Chem. Soc.* **1999**, *121*, 3951.
31. (a) D.S. Goodsell, *Our Molecular Nature: The Body's Motors, Machines, and Messages*, Copernicus, New York, **1996**. (b) P.D. Boyer, *Annu. Rev. Biochem.* **1997**, *66*, 717. (c) P.R. Cook, *Science* **1999**, *284*, 1790.
32. (a) R.P. Feynman, *Eng. Sci.* **1960**, *23*(5), 22. (b) R.P. Feynman, *Sat. Rev.* **1960**, *43*, 45.
33. (a) V. Balzani, F. Scandola, *Supramolecular Photochemistry*, Horwood, New York, **1991**. (b) V. Balzani, *Tetrahedron*, **1992**, *48*, 10443. (c) R.A. Bissell, A.P. de Silva, H.Q.N. Gunaratne,

- P.L.M. Lynch, G.E.M. Maguire, C.P. McCoy, K.R.A.S. Sandanayake, *Top. Curr. Chem.* **1993**, 168, 223. (d) L. Fabbrizzi, A. Poggi, *Chem. Soc. Rev.* **1995**, 24, 197. (e) A.C. Benniston, *Chem. Soc. Rev.* **1996**, 25, 427. (f) M. Gómez-López, J.A. Preece, J.F. Stoddart, *Nanotechnology*, **1996**, 7, 183. (g) M.D. Ward, *Chem. Ind.* **1997**, 640. (h) V. Balzani, A. Credi, F. Scandola, *Chim. Ind. (Rome)*, **1997**, 79, 751. (i) T.M. Swager, *Acc. Chem. Res.* **1998**, 31, 201. (j) J.-P. Sauvage, *Acc. Chem. Res.* **1998**, 31, 611. (k) J.-C. Chambron, J.-P. Sauvage, *Chem. Eur. J.* **1998**, 4, 1362. (l) M. Venturi, A. Credi, V. Balzani, *Coord. Chem. Rev.* **1999**, 185/186, 233.
34. (a) A.C. Benniston, A. Harriman, D. Philp, J. F. Stoddart, *J. Am. Chem. Soc.* **1993**, 115, 5298. (b) A.C. Benniston, A. Harriman, in *Physical Supramolecular Chemistry* (Eds. L. Echegoyen, A.E. Kaifer), Kluwer, Dordrecht, **1996**, 179. (c) A.C. Benniston, A. Harriman, D.S. Yufit, *Angew. Chem. Int. Ed. Engl.* **1997**, 36, 2356.
35. R. Ballardini, V. Balzani, M.T. Gandolfi, L. Prodi, M. Venturi, D. Philp, H.G. Ricketts, J.F. Stoddart, *Angew. Chem. Int. Ed. Engl.* **1993**, 32, 1301.
36. P. R. Ashton, R. Ballardini, V. Balzani, S.E. Boyd, A. Credi, M.T. Gandolfi, M. Gómez-López, S. Iqbal, D. Philp, J.A. Preece, L. Prodi, H.G. Ricketts, J.F. Stoddart, M.S. Tolley, M. Venturi, A.J.P. White, D.J. Williams, *Chem. Eur. J.* **1997**, 3, 152.
37. O. Johansen, A.W.H. Mau, W.H.F. Sasse, *Chem. Phys. Lett.* **1983**, 94, 107.
38. A. Juris, V. Balzani, F. Barigelli, S. Campagna, P. Belser, A. von Zelewsky, *Coord. Chem. Rev.* **1988**, 84, 85.
39. E. Amouyal, *Sol. Energy Mater. Sol. Cells* **1995**, 38, 249.
40. P.L. Boulas, M. Gómez-Kaifer, L. Echegoyen, *Angew. Chem. Int. Ed.* **1998**, 37, 216.
41. A. Niemz, V.M. Rotello, *Acc. Chem. Res.* **1999**, 32, 42.
42. A.E. Kaifer, *Supramolecular Electrochemistry*, Wiley-VCH, Weinheim, **1999**.
43. K.A. Connors, *Chem. Rev.* **1997**, 97, 1325.
44. A. Mirzoian, A.E. Kaifer, *Chem. Eur. J.* **1997**, 3, 1052.
45. Y. Wang, S. Mendoza, A.E. Kaifer, *Inorg. Chem.* **1998**, 37, 317.
46. See, e.g.: (a) B. Siegel, R. Breslow, *J. Am. Chem. Soc.* **1975**, 97, 6869. (b) F.M. Menger, M.J. Sherrod, *J. Am. Chem. Soc.* **1988**, 110, 8606. (c) R. Isnin, A.E. Kaifer, *J. Am. Chem. Soc.* **1991**, 113, 8188. (d) L.A. Godínez, S. Patel, C.M. Criss, A.E. Kaifer, *J. Phys. Chem.* **1995**, 99, 17449.
47. R. Castro, I. Cuadrado, B. Alonso, C.M. Casado, M. Mórán, A.E. Kaifer, *J. Am. Chem. Soc.* **1997**, 119, 5760.
48. B. Gonzáles, C.M. Casado, B. Alonso, I. Cuadrado, M. Mórán, Y. Wang, A.E. Kaifer, *Chem. Commun.* **1998**, 2569.
49. L. Zhang, A. Macías, T. Lu, J.I. Gordon, G.W. Gokel, A.E. Kaifer, *J. Chem. Soc. Chem. Commun.* **1993**, 1017.
50. Y. Wang, J. Alvarez, A.E. Kaifer, *Chem. Commun.* **1998**, 1457.
51. A.R. Bernardo, T. Lu, E. Córdova, L. Zhang, G.W. Gokel, A.E. Kaifer, *J. Chem. Soc. Chem. Commun.* **1994**, 529.
52. For a related redox-switchable three-component system, see: R. Deans, A. Niemz, E.C. Breinlinger, V.M. Rotello, *J. Am. Chem. Soc.* **1997**, 119, 10863.
53. E.A. Smith, R.R. Lilienthal, R.J. Fonseca, D.K. Smith, *Anal. Chem.* **1994**, 66, 3013.
54. W. Devonport, M.A. Blower, M.R. Bryce, L.M. Goldenberg, *J. Org. Chem.* **1997**, 62, 885.
55. (a) M. Asakawa, P.R. Ashton, V. Balzani, S.E. Boyd, A. Credi, G. Mattersteig, S. Menzer, M. Montalti, F.M. Raymo, C. Ruffilli, J.F. Stoddart, M. Venturi, D.J. Williams, *Eur. J. Org. Chem.* **1999**, 985. (b) V. Balzani, A. Credi, G. Mattersteig, O.A. Matthews, F.M. Raymo, J.F. Stoddart, M. Venturi, A.J.P. White, D.J. Williams, *J. Org. Chem.* **2000**, 65, 1924.
56. A. Credi, V. Balzani, S.J. Langford, J.F. Stoddart, *J. Am. Chem. Soc.* **1997**, 119, 2679.
57. For other recent examples of the implementation of logic functions with molecular systems, see: (a) A.P. de Silva, H.Q.N. Gunaratne, C.P. McCoy, *J. Am. Chem. Soc.* **1997**, 119, 7891. (b) A.P. de Silva, I.M. Dixon, H.Q.N. Gunaratne, T. Gunnlaugsson, P.R.S. Maxwell, T.E. Rice, *J. Am. Chem. Soc.* **1999**, 121, 1393. (c) F. Pina, M. Maestri, V. Balzani, *Chem. Commun.* **1999**, 107. (d) T. Gunnlaugsson, D.A. Mac Dónail, D. Parker, *Chem. Commun.* **2000**, 93.

58. D.H. Evans, *Chem. Rev.* **1990**, *90*, 739.
59. (a) P.R. Ashton, S. Menzer, F.M. Raymo, G.K.H. Shimizu, J.F. Stoddart, D.J. Williams, *Chem. Commun.* **1996**, 487. (b) M. Asakawa, P.R. Ashton, S. Menzer, F.M. Raymo, J.F. Stoddart, A.J.P. White, D.J. Williams, *Chem. Eur. J.* **1996**, *2*, 877.
60. E. Cordova, R.A. Bissel, N. Spencer, P.R. Ashton, J.F. Stoddart, A.E. Kaifer, *J. Org. Chem.* **1993**, *58*, 6550.
61. The three-pole nature of this system is clearly apparent if compared to the two-pole nature of other three-component systems; see, e.g., Refs. [3], [50], and [52].
62. For related self-complexing compounds, see: (a) P.R. Ashton, M. Gómez-López, S. Iqbal, J.A. Preece, J.F. Stoddart, *Tetrahedron Lett.* **1997**, *38*, 3635. (b) M.B. Nielsen, J.G. Hansen, J. Becher, *Eur. J. Org. Chem.* **1999**, 2807.
63. R. Ballardini, V. Balzani, A. Credi, M.T. Gandolfi, S.J. Langford, S. Menzer, L. Prodi, J.F. Stoddart, M. Venturi, D.J. Williams, *Angew. Chem. Int. Ed. Engl.* **1996**, *35*, 978.
64. M. Asakawa, S. Iqbal, J.F. Stoddart, N.D. Tinker, *Angew. Chem. Int. Ed. Engl.* **1996**, *35*, 976–978.
65. (a) E.B. Kyba, K. Koga, L.R. Sousa, M.G. Siegel, D.J. Cram, *J. Am. Chem. Soc.* **1973**, *95*, 2692. (b) X.X. Zhang, J.S. Bradshaw, R.M. Izatt, *Chem. Rev.* **1997**, *97*, 3313.
66. M. Montalti, L. Prodi, *Chem. Commun.* **1998**, 1461.
67. Work in progress in our laboratories.
68. (a) M.J. Marsella, P.J. Carroll, T.M. Swager, *J. Am. Chem. Soc.* **1995**, *117*, 9832. (b) Q. Zhou, T.M. Swager, *J. Am. Chem. Soc.* **1995**, *117*, 12593. (c) T.M. Swager, *Acc. Chem. Res.* **1998**, *31*, 201. (d) K.S. Bang, M.B. Nielsen, R. Zubarev, J. Becher, *Chem. Commun.* **2000**, 215.
69. A. Credi, “Molecular-level machines and logic gates”, Ph. D. Dissertation, University of Bologna, **1998**.
70. For recent examples of supramolecular systems deposited on surfaces, see: (a) P. Laitenberger, C.G. Claessens, L. Kuipers, F.M. Raymo, R.E. Palmer, J.F. Stoddart, *Chem. Phys. Lett.* **1997**, *279*, 209. (b) G. Ashkenasy, G. Kalyuzhny, J. Libman, I. Rubinstein, A. Shanzer, *Angew. Chem. Int. Ed.* **1999**, *38*, 1257. (c) M. Lahav, L. Leiserowitz, *Angew. Chem. Int. Ed.* **1999**, *38*, 2533. (d) Semenov, J.P. Spatz, M. Möller, J.-M. Lehn, B. Sell, D. Schubert, C.H. Weidl, U.S. Schubert, *Angew. Chem. Int. Ed.* **1999**, *38*, 2547. (e) N. Bampos, C.N. Woodburn, M.E. Welland, J.K.M. Sanders, *Angew. Chem. Int. Ed.* **1999**, *38*, 2780. (f) H. Imahori, H. Yamada, S. Ozawa, K. Ushida, Y. Sakata, *Chem. Commun.* **1999**, 1165.
71. For recent examples of Langmuir films composed of molecular and supramolecular systems incorporating interlocked components, see: (a) R.C. Ahuja, P.-L. Caruso, D. Möbius, G. Wildburg, H. Ringsdorf, D. Philp, J.A. Preece, J.F. Stoddart, *Langmuir* **1993**, *9*, 1534. (b) R.C. Ahuja, P.-L. Caruso, D. Möbius, D. Philp, J.A. Preece, H. Ringsdorf, J.F. Stoddart, G. Wildburg, *Thin Solid Films*, **1996**, *284/285*, 671. (c) D.B. Amabilino, M. Asakawa, P.R. Ashton, R. Ballardini, V. Balzani, M. Belohradsky, A. Credi, M. Higuchi, F.M. Raymo, T. Shimizu, J.F. Stoddart, M. Venturi, K. Yase, *New J. Chem.* **1998**, 959. (d) D.E. Lynch, D.G. Hamilton, N.J. Calos, B. Wood, J.K.M. Sanders, *Langmuir* **1999**, *15*, 5600.
72. Another problem related to movements in supramolecular systems like pseudorotaxanes in solution is that of establishing which component is moving and which is not—a question that cannot even be addressed because of the lack of a fixed reference system. The problem, however, becomes addressable when in a [2]pseudorotaxane either the thread or the macrocycle is immobilized on a fixed frame such as a surface.
73. For examples of electrodes modified with species related to the supramolecular structures described in this chapter, see: (a) T. Lu, L. Zhang, G.W. Gokel, A.E. Kaifer, *J. Am. Chem. Soc.* **1993**, *115*, 2542. (b) M.T. Rojas, R. Königer, J.F. Stoddart, A.E. Kaifer, *J. Am. Chem. Soc.* **1995**, *117*, 336. (c) M.T. Rojas, A.E. Kaifer, *J. Am. Chem. Soc.* **1995**, *117*, 5883. (d) G. Bidan, M. Billon, B. Divisia-Blohorn, J.-M. Kern, L. Raehm, J.-P. Sauvage, *New J. Chem.* **1998**, 1139. (e) J.-M. Kern, L. Raehm, J.-P. Sauvage, *C. R. Acad. Sci. Paris* **1999**, *2*, 41. (f) M. Lahav, A.N. Shipway, I. Willner, *J. Chem. Soc. Perkin Trans. 2* **1999**, 1925. (g) C. P. Collier, E.W. Wong, M. Belohradsky, F.M. Raymo, J.F. Stoddart, J.R. Heath, *Science* **1999**, *285*, 391. (h) J. Buey, T.M. Swager, *Angew. Chem. Int. Ed.* **2000**, *39*, 608.
74. (a) X. Marguerettaz, G. Redmond, S.N. Rao, D. Fitzmaurice, *Chem. Eur. J.* **1996**, *2*, 420. (b)

- L. Cusack, S.N. Rao, D. Fitzmaurice, *Chem. Eur. J.* **1997**, 3, 202. (c) G. Will, G. Boschloo, R. Hoyle, S.N. Rao, D. Fitzmaurice, *J. Phys. Chem. B* **1998**, 102, 10272. (d) S. Conolly, S.N. Rao, R. Rizza, N. Zaccheroni, D. Fitzmaurice, *Coord. Chem. Rev.* **1999**, 185/186, 277.
75. (a) A. Werner, *Zeits. Anorg. Chem.* **1893**, 3, 267. (b) F.A. Cotton, G. Wilkinson, *Advanced Inorganic Chemistry*, Wiley, New York, **1980**.
76. (a) R.S. Mulliken, *J. Am. Chem. Soc.* **1950**, 62, 600. (b) R.S. Mulliken, *J. Am. Chem. Soc.* **1952**, 64, 811. (c) R.S. Mulliken, W.B. Person, *Molecular Complexes*, Wiley, New York, **1969**.
77. (a) J.-M. Lehn, *Angew. Chem. Int. Ed. Engl.* **1988**, 27, 89. (b) D.J. Cram, *Angew. Chem. Int. Ed. Engl.* **1988**, 27, 1009. (c) C.J. Pedersen, *Angew. Chem. Int. Ed. Engl.* **1988**, 27, 1021.
78. V. Balzani, A. Credi, M. Venturi, *Coord. Chem. Rev.* **1998**, 171, 3.

7 Electron Transfer Processes in Rotaxanes and Catenanes

Roberto Ballardini, Maria Teresa Gandolfi, and Vincenzo Balzani

7.1 Introduction

Rotaxanes [a name derived from the Latin words *rota* (wheel) and *axis* (axle)] [1] and *catenanes* [from the Latin word *catena* (chain)] [1] are supramolecular (multi-component) species [1–10] strictly related (Figure 1) to pseudorotaxanes, which were described in Volume III, Part 2, Chapter 6. Whereas pseudorotaxanes can undergo dissociation into their wire-like and macrocyclic components, rotaxanes and catenanes are interlocked species, whose dissociation requires breaking of a covalent bond. It should be pointed out, however, that, as discussed in detail in the previous chapter 6, the boundary between rotaxanes and pseudorotaxanes is somewhat “fuzzy” because, for example, when the stoppers are not extremely bulky compared to the hole of the macrocyclic component, a rotaxane at low temperature might well be a pseudorotaxane at elevated temperature [11].

Research on rotaxanes and catenanes has developed exponentially during the past few years [1–10]. Before discussing the electron transfer processes taking place in rotaxanes and catenanes, we will briefly recall the synthetic approaches to these fascinating compounds. The general way to indicate a rotaxane or a catenane is [n]rotaxane and [n]catenane, where n is the number of interlocked components.

7.2 Synthesis

Early attempts at the synthesis of catenanes were based on the so-called statistical approach. For example, according to this approach, a molecular thread X–Y, functionalized on both ends, may enter into a macrocycle of adequate size; subsequent cyclization of X–Y leads to two interlocked rings. Since the probability that cyclization occurs while X–Y is threaded through the macrocycle is very small, only poor yields can be expected.

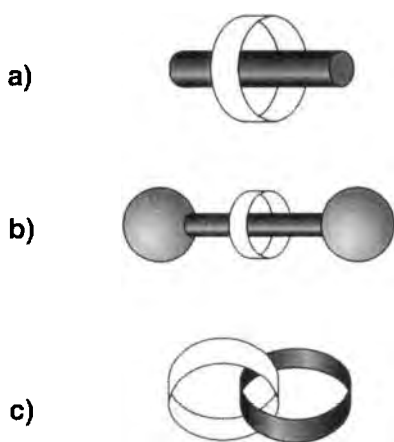


Figure 1. Schematic representation of (a) [2]pseudo-rotaxanes, (b) [2]rotaxanes, and (c) [2]catenanes.

The first evidence for formation of a catenane following this approach was reported in 1960 [12], whereas the first synthesis of a rotaxane was reported in 1967 [13]. In the same year it was discovered that catenanes are also formed in nature by DNA [14, 15]. From a preparative viewpoint, statistical threading became significant in 1976, when a threading process that probably involves a weak molecular recognition between the thread and the macrocycle was used [16]. Alternative methods used to obtain catenanes were the Möbius strip approach [17], which is again statistical in nature, and the direct synthesis about a central core [18, 19], which is successful but requires a great deal of technical expertise and manipulation. With the development of the host–guest chemistry in the late 1970s [20, 21], several research groups began to develop new methods for synthesizing rotaxanes and catenanes.

The general strategy to prepare rotaxanes and catenanes with high yields is based on the template effect [22], which relies on the presence of molecular recognition sites between the components to be assembled. The most common templated syntheses involve the use of metal ions [4], donor–acceptor components [3, 5, 8], and the formation of hydrogen bonds [5, 6]. However, other properties, such as hydrophobic–hydrophylic character, π – π stacking, ion–ion, ion–dipole, and dipole–dipole forces can also play a role. In several cases, in fact, more than one type of interaction is operative. It should also be noted that in some cases the strongest interaction, as far as association is concerned, is not that causing the most relevant changes (compared to the separated components) in properties such as electrochemical behavior and absorption, fluorescence, and NMR spectra.

Figure 2 shows the routes by which components bearing suitable recognition sites lead to the formation of rotaxanes: (i) *threading* a molecule through a preformed ring followed by capping the end of the thread; (ii) *slipping* a preformed ring over the stoppers of a preformed dumbbell-shaped into a thermodynamically favorable site on the rod part of the dumbbell; and (iii) *clipping* a macrocycle onto a preformed dumbbell.

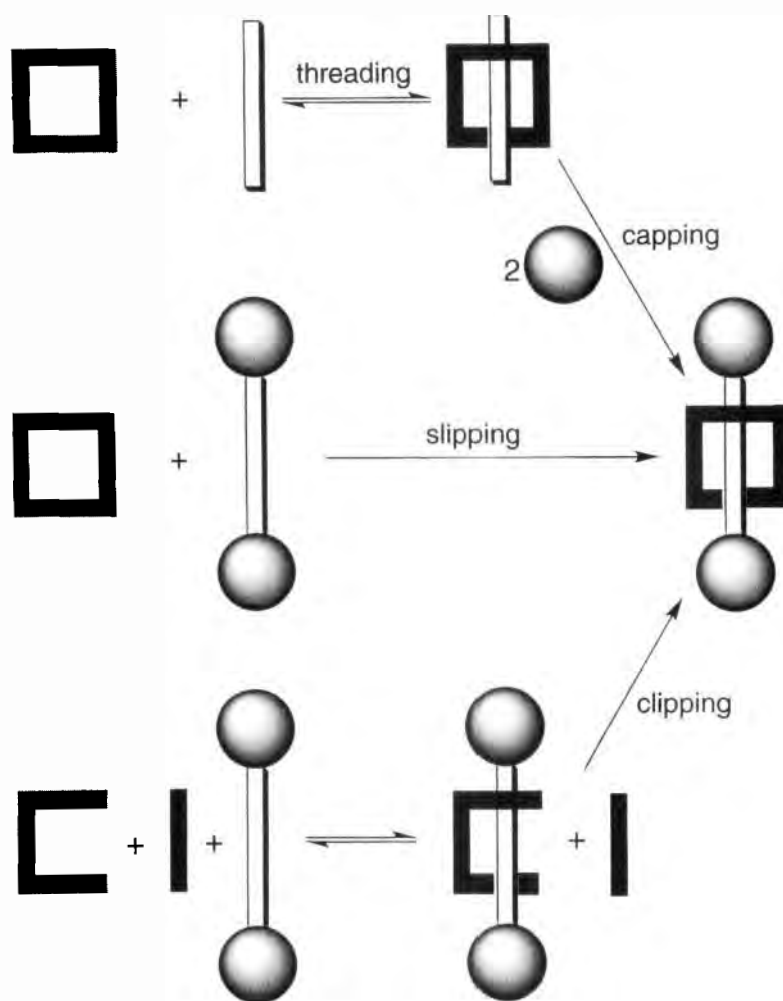


Figure 2. Routes for the synthesis of [2]rotaxanes.

Figure 3 shows the synthesis of the [2]rotaxane 3^{4+} by the threading or the clipping approach [23]. In the first case (Figure 3a), threading of the electron-acceptor tetracationic cyclophane 1^{4+} by the thread **2**, which contains a hydroquinone electron-donating unit, yields a pseudorotaxane; then, reaction of the terminal hydroxy groups of the thread with triisopropylsilyl triflate leads to the [2]rotaxane 3^{4+} . In the clipping approach (Figure 3b), the [2]rotaxane is obtained from the reaction of the dication 4^{2+} with dibromide **5** in the presence of the preformed dumbbell-shaped component **6**. Figure 4 shows the preparation of a [3]rotaxane by riveting two rings together, taking advantage from the hydrogen-bond driven preformation of a pseudorotaxane structure [24].

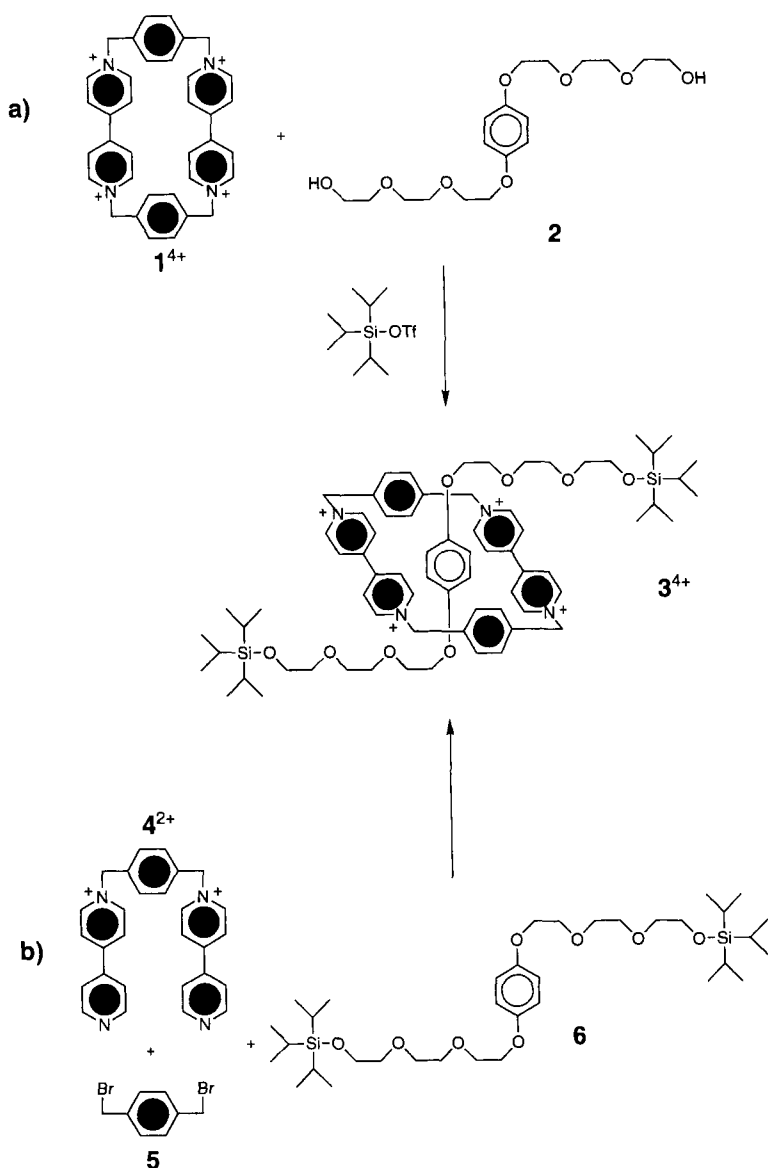


Figure 3. Synthesis of a [2]rotaxane by the (a) threading and (b) clipping approaches [23].

In the case of catenanes, the most rationale preparation strategy is clipping of a preformed macrocycle with a suitable U-type component that is subsequently cyclized. A double clipping procedure can also be used (Figure 5) [5].

Figure 6 shows the synthesis, templated by donor–acceptor and hydrogen-bonding interactions, of [2]catenane **8**⁴⁺ [23]. Reaction of the dication **4**²⁺ with the

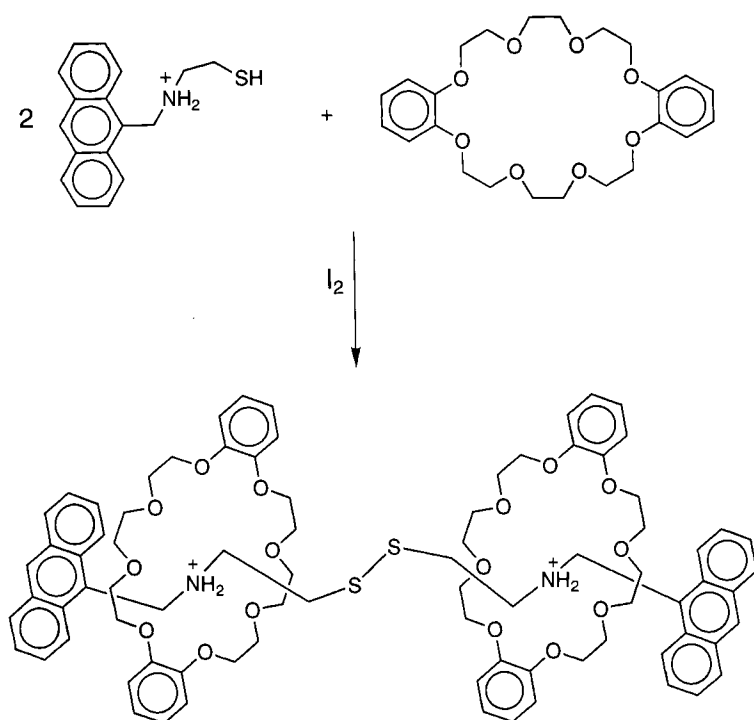


Figure 4. Synthesis of a [3]rotaxane by riveting two rings together [24].

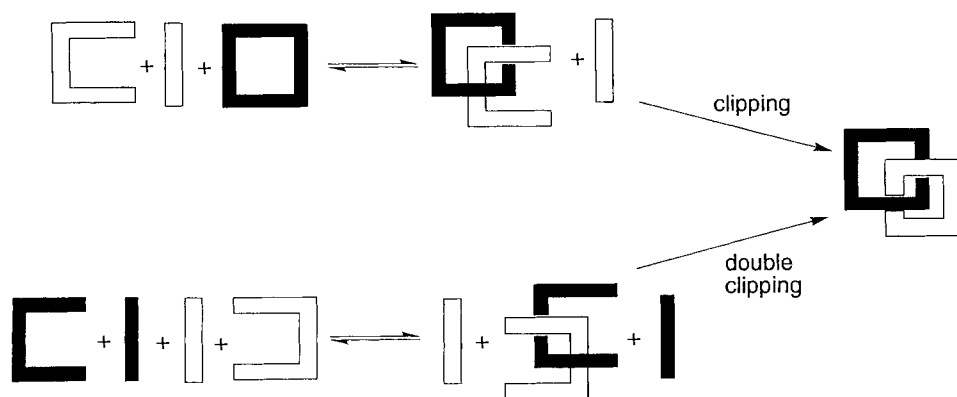


Figure 5. Routes for the synthesis of [2]catenanes.

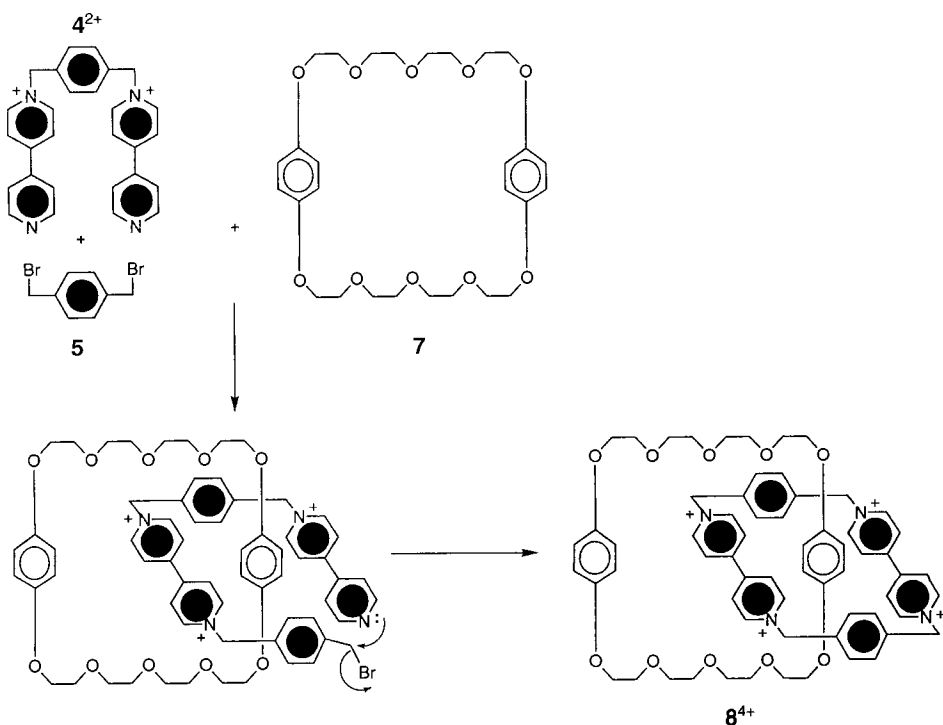


Figure 6. Synthesis of a [2]catenane templated by donor–acceptor and hydrogen bond interactions [23].

dibromide **5** gives a tricationic intermediate which interacts with bis(*p*-phenylene)-34-crown-10 (**7**) to afford a pseudorotaxane-like, or precatenane, structure. The subsequent macrocyclization, as a result of nucleophilic displacement of bromide ion, gives the corresponding [2]catenane 8^{4+} .

In some cases, catenanes are formed from relatively small molecules by one-pot synthesis in a more or less serendipitous manner [25]. Figure 7 shows the one-pot synthesis of the amide-based [2]catenane **9** from very simple compounds [25c]; this synthesis is thought to involve the perpendicular preorganization of the components caused by three templating effects: (i) steric complementarity; (ii) hydrogen bonding between carbonyl oxygen atoms and amide protons; and (iii) π - π interactions between the benzene rings of host and guest units.

Besides simple rotaxanes and catenanes, a great variety of more complex systems have been synthesized, including: branched [n]rotaxanes [26a], [n]rotaxanes bearing dendritic stoppers [26b], catenanes composed by two, three, five, or seven interlocked macrocycles [26c,e], polyrotaxanes and polycatenanes [2–6, 8], catenanes with very special shapes [27], rotocatenanes [28], pretzelanes [29], and knots [4]. Some of these compounds are shown in Figure 8.

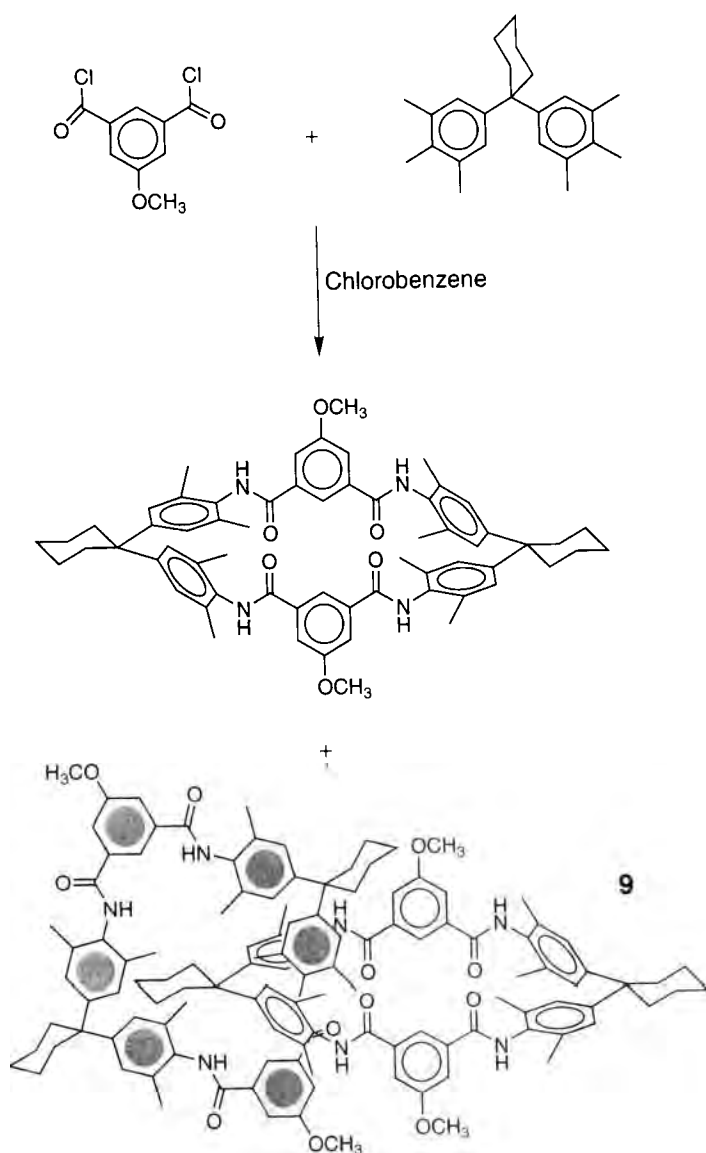


Figure 7. One-pot synthesis of an amide-based [2]catenane. Besides the catenane, macrocycles are also formed [25c].

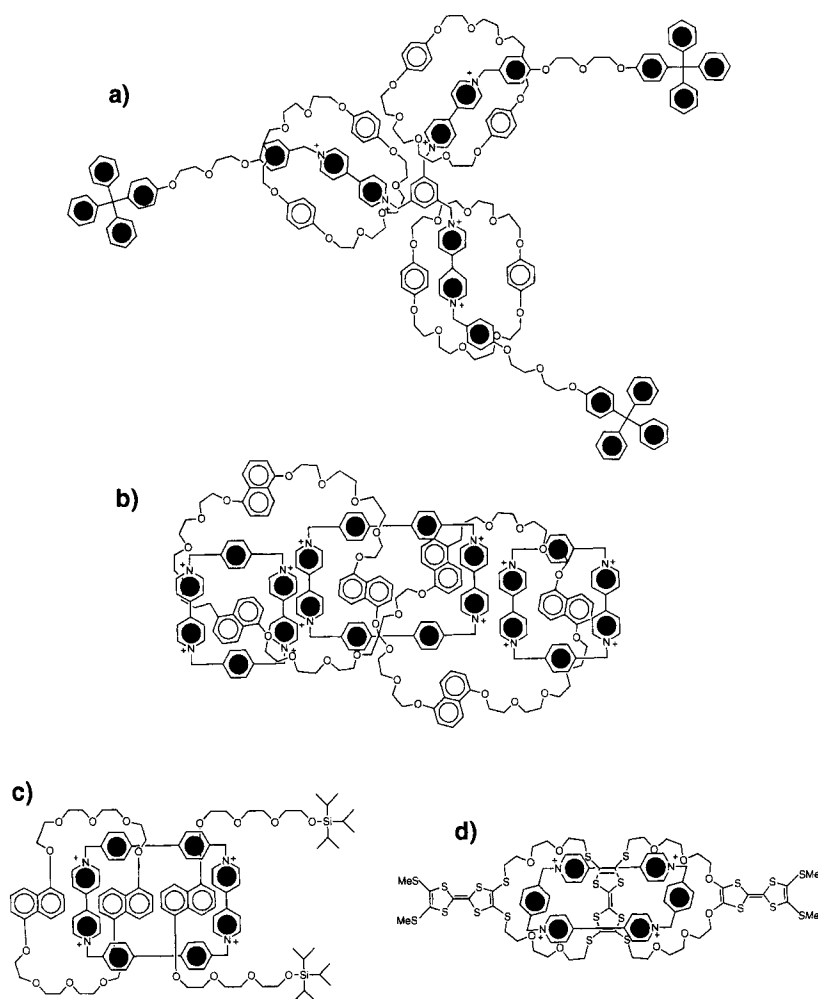


Figure 8. Examples of rotaxanes and catenanes with peculiar structures. (a) A branched [4]rotaxane [26a]; (b) a [5]catenane (olympiadane) [26c]; (c) a rotocatenane [28]; (d) a [2]catenane with three rings [27d].

7.3 Spectroscopic and Electrochemical Consequences of Charge–Transfer Interactions

As in the case of pseudorotaxanes (see Volume III, Part 2, Chapter 6), charge–transfer (CT) interactions between electron-donor and electron-acceptor units in rotaxanes and catenanes have several important consequences from the spectro-

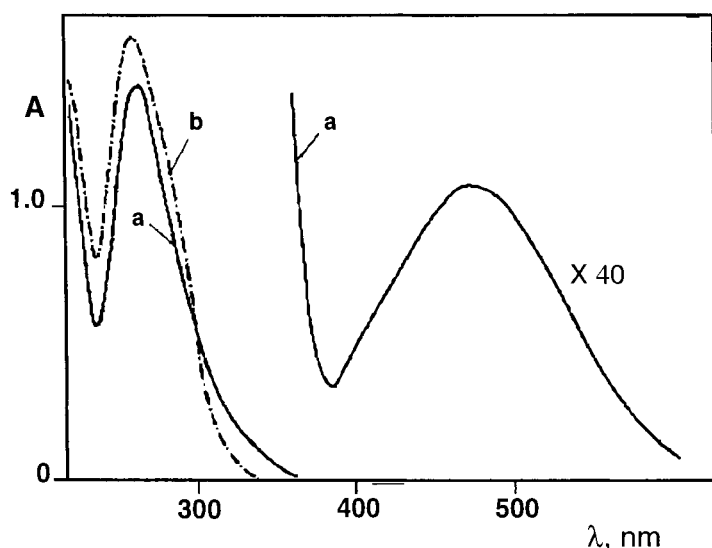


Figure 9. Absorption spectrum in MeCN at 25 °C of (a) a 4.0×10^{-5} M solution of catenane 8^{4+} and (b) equimolar amounts of its separated components (cyclophane 1^{4+} and macrocycle **7**) [23].

scopic and electrochemical viewpoints [23] and play a fundamental role as far as the machine-like behavior of these compounds is concerned [30–33].

7.3.1 Absorption and Emission Spectra

The donor–acceptor interaction introduces low-energy CT excited states which are responsible for the presence of broad and relatively weak (ϵ of the order of 10^2 – 10^3 $\text{M}^{-1} \text{cm}^{-1}$) bands in the visible spectral region. For example, [2]catenane 8^{4+} shows a broad absorption band, with maximum at 470 nm ($\epsilon = 700 \text{ M}^{-1} \text{cm}^{-1}$), which is not present in the spectra of the separated components (Figure 9) [23]. As expected, the position of the CT bands moves towards higher energies with increasing ionization potential of the donor and decreasing electronic affinity of the acceptor. When different electron-donor and/or electron-acceptor units are present in the same compound, the CT absorption region is very broad because of the contribution of CT transitions at different energies [34]. This is also the case of catenanes made of symmetric rings, like 8^{4+} , because the two identical electron-donor (or -acceptor) units present in the separated components occupy topologically different (“alongside” and “inside”) positions in the catenane and, therefore, they are no longer equivalent. Besides the absorption bands arising from CT interactions, bands due to transitions substantially localized in the component species are of course present in the absorption spectra of rotaxanes and catenanes. These bands are more or less perturbed (particularly in intensity) compared to the bands exhibited by the separated components (see, e.g., Figure 9).

The CT excited states usually are not emissive because the low energy gap and the strong distortion with respect to the ground state favor the occurrence of radiationless deactivation. Furthermore, the presence of the low-energy CT excited states causes rapid radiationless decay of the upper lying, potentially luminescent excited states localized on the molecular components. Therefore, rotaxanes and catenanes based on CT interactions usually do not exhibit any luminescence. For example, the intense emission band with maximum at 320 nm ($\tau = 2.5$ ns) exhibited by macrocycle **7** [11a] is no longer present in catenane **8**⁴⁺ [23].

7.3.2 Electrochemical Behavior

As far as the electrochemical behavior is concerned, it should be recalled that, when engaged in CT interactions, the electron-donor and electron-acceptor units become more difficult to oxidize and to reduce, respectively (see Volume III, Part 2, Chapter 6). Furthermore, as mentioned above, units which are topologically equivalent in an isolated component become nonequivalent when the component is engaged in nonsymmetric interactions with another component. Consider, for example, the case of [2]rotaxane **3**⁴⁺ and [2]catenane **8**⁴⁺, in which one of the two components is cyclophane **1**⁴⁺ (Figure 10) [23]. Such a cyclophane, which comprises two equivalent, noninteracting, bipyridinium electron-acceptor units, shows two bielectronic reduction processes, the first one corresponding to the uptake of the first electron by each of the equivalent bipyridinium units, and the second one to the subsequent reduction of the monoreduced units to give neutral species [23, 35]. In rotaxane **3**⁴⁺, cyclophane **1**⁴⁺ is threaded by the dumbbell component **6**, which contains an electron-donor unit. As a consequence of the CT interaction, the half-wave potentials associated with the first and second reduction processes of the bipyridinium units are shifted to more negative values. In the rotaxane structure, the two bipyridinium units are still equivalent because they experience an equal amount of electron donation and therefore are reduced at the same potential. A CT interaction is present also in catenane **8**⁴⁺, since the macrocycle **7** contains electron-donor units. Therefore, the reduction potentials of the bipyridinium units of the cyclophane move again towards more negative potentials (Figure 10). In the catenane structure, however, the two bipyridinium units occupy topologically different (“alongside” and “inside”) positions. The unit which is inside the macrocycle **7** experiences a stronger CT interaction than the unit which is alongside. Therefore, the first two-electron reduction process splits into two distinct one-electron processes. When both the bipyridinium units have been monoreduced, the CT interaction with the electron-donor units of macrocycle **7** becomes very weak, so that the second reduction process does not split. In some cases, splitting of the second two-electron reduction process can also be observed [36]. The above discussion, which refers to the reduction of the electron-acceptor components, can be extended to the oxidation of the electron-donor components [23, 26e, 36, 37].

As an example of more complex systems, we now consider the electrochemical behavior of macrocycle **10**, which contains three electron-donor dioxynaphthalene units, and [2]catenane **11**⁴⁺ and [3]catenane **12**⁸⁺ in which macrocycle **10** is inter-

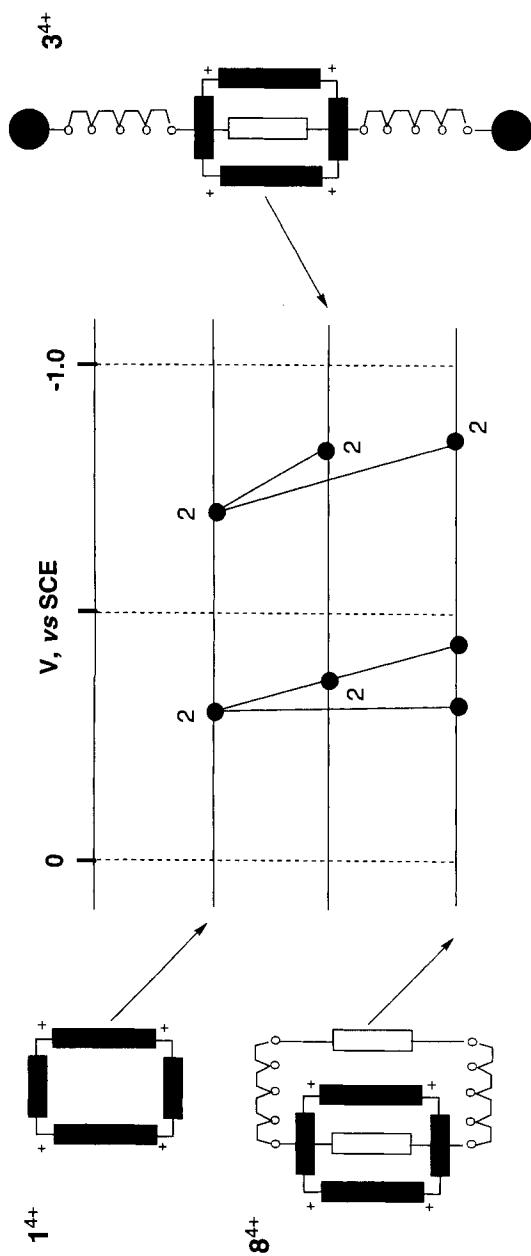


Figure 10. Correlation diagram for the electrochemical reduction of cyclophane 1^{4+} , [2]rotaxane 3^{4+} , and [2]catenane 8^{4+} (MeCN, 25 °C, potentials versus SCE); bielectronic processes are indicated [23].

locked with cyclophane **1**⁴⁺ as an electron acceptor component [26c]. Figure 11 shows the correlation diagram for the redox processes observed in these compounds. In the catenanes, the two bipyridinium units of cyclophane **1**⁴⁺ are engaged in donor–acceptor interactions and occupy spatially different sites, as discussed above. Therefore, it can again be expected that their reduction takes place in separated processes at more negative potentials compared to free **1**⁴⁺. This is clearly the case for the first reduction of the two bipyridinium units in the [2]catenane **11**⁴⁺: the alongside unit is reduced at –0.36 V, and the inside one at –0.47 V versus SCE. Comparison with the [2]catenane composed of **1**⁴⁺ and 1,5-dinaphtho-38-crown10 (a macrocycle like **10**, but containing only two donor units) [36a] shows that in **11**⁴⁺ the first reduction process is practically unaffected by changing the macrocycle, whereas the second one is considerably displaced towards less negative potentials. This difference could result from the greater size and flexibility of macrocycle **10** which allow one of the donor units to interact with the alongside bipyridinium unit of the cyclophane and, at the same time do not force two donor units to sandwich the inside bipyridinium unit. After the first reduction, the electron donor–acceptor interaction becomes weaker, and the flexible nature of the **10** could facilitate a rapid interchange between monoreduced inside and alongside units, with a consequent lack of splitting of the second process. For [3]catenane **12**⁸⁺, composed of **10** and two equivalent **1**⁴⁺ cyclophanes, simultaneous reduction of the alongside units of the two cyclophanes is followed by simultaneous reduction of the inside units. Both processes are displaced to less negative potentials compared to **11**⁴⁺ because the ratio between electron-donor and electron-acceptor units decreases from 3/2 to 3/4, and the positive charge increases. The splitting of the second reduction process of the bipyridinium units is consistent with the crowded structure of the catenane which presumably prevents rapid interchange between inside and alongside units.

In macrocycle **10**, the three donor units undergo distinct oxidation processes, indicating that there are electronic interactions between oxidized and nonoxidized units. As a consequence of the CT interaction with the electron-acceptor cyclophane, in the catenane **11**⁴⁺ all these processes move to more positive potential values with respect to the free macrocycle. A detailed comparison between the two oxidation patterns is made difficult because, in the catenane structure, the donor–acceptor interactions between nonoxidized and oxidized donor units are partially or completely prevented. In the [3]catenane **12**⁸⁺, only two oxidation processes are observed, a feature which is consistent with the presence of an outside and two equivalent inside donor units.

7.4 Rotaxanes

7.4.1 Rotaxane Chemistry

Because of their *wheel* and *axle* structure, much of the interest in rotaxane chemistry is focused on the mechanical movements of the ring around and along the dumbbell-shaped component. Of particularly interest is the possibility to control

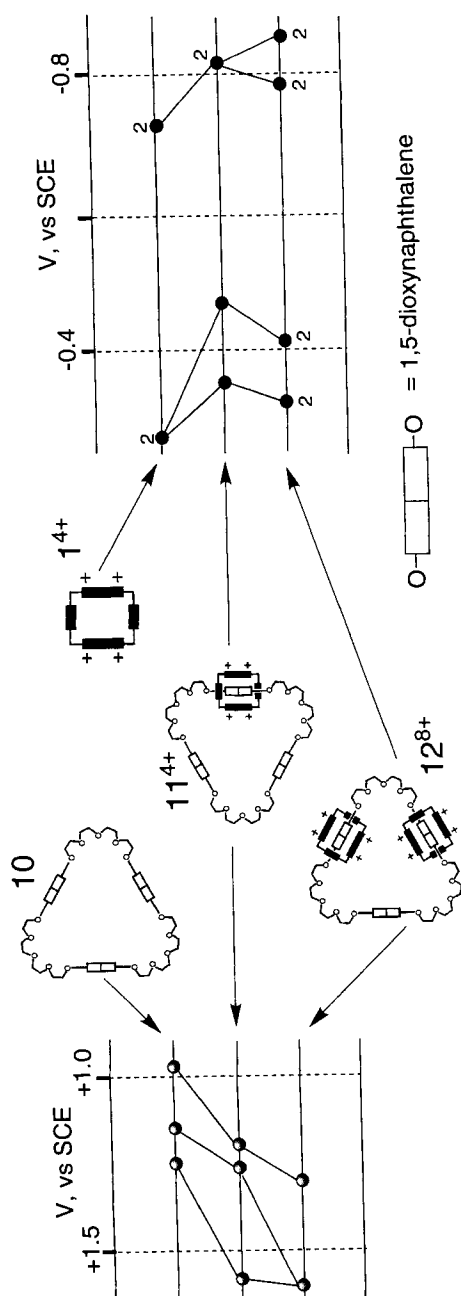


Figure 11. Correlation diagram for the electrochemical behavior of [2]catenane **11**⁴⁺, [3]catenane **12**⁸⁺, and their **1**⁴⁺ and **10** components (MeCN solution, 25 °C, potentials versus SCE); bielectronic processes are indicated [26c].

such movements by external stimuli which modify the electronic interactions between the wheel and axle components. This topic will be discussed in detail below. There are, however, other interesting aspects of rotaxane chemistry. For example, it has been shown that the wheels can be used as noncovalent protecting groups towards functional groups contained in the axle [38].

7.4.2 Shuttling Processes

It is possible to synthesize [2]rotaxanes containing two identical recognition sites within their dumbbell component. The result is a degenerate equilibrium state in which the macrocyclic component can shuttle back and forth along the linear portion of the dumbbell. Such a system constitutes a *molecular shuttle*. Two examples [11a,b, 39] of [2]rotaxanes that behave as degenerate molecular shuttles are shown in Figure 12.

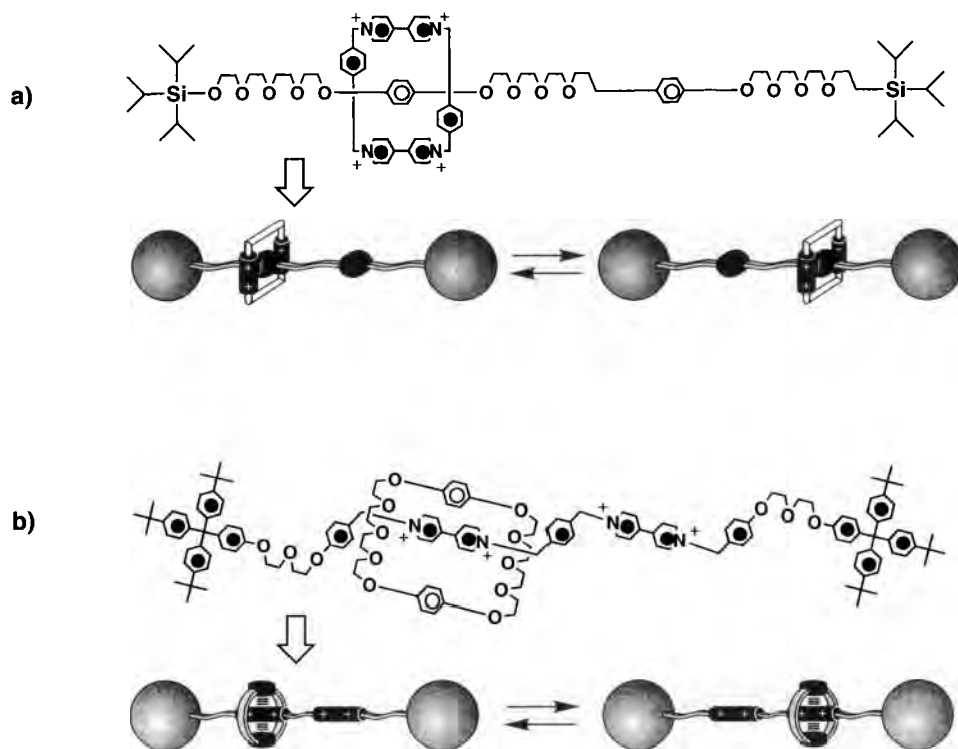


Figure 12. Shuttling of a ring between two equivalent stations in a [2]rotaxane. (a) The bipyridinium-based cyclophane shuttles from one 1,4-dioxymethylene recognition site to the other at a rate of c. 2000 s^{-1} in $(\text{CD}_3)_2\text{CO}$ at ambient temperature [39a,b]. (b) The 1,4-dioxymethylene-based macrocyclic polyether shuttles from one bipyridinium recognition site to the other one at a rate of c. $3 \times 10^5\text{ s}^{-1}$ under the same conditions [39c].

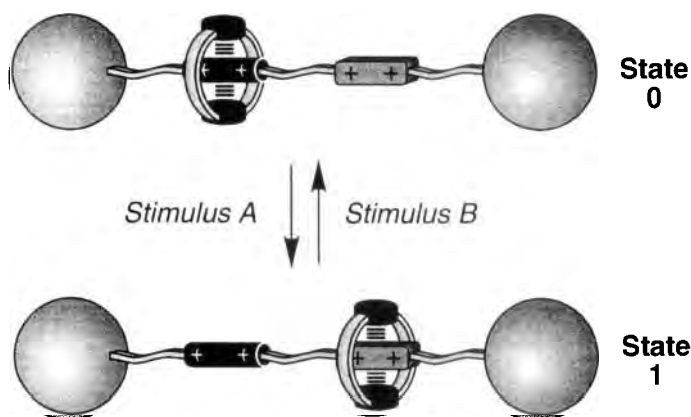


Figure 13. The two spatial arrangements (co-conformations) associated with a [2]rotaxane, incorporating two different recognition sites within its dumbbell-shaped component, can be interchanged by appropriate stimuli.

When the two recognition sites in the dumbbell-shaped component differ in their constitutions, the [2]rotaxane can exist as two different, equilibrating, three-dimensional spatial arrangements (co-conformations [40]) whose populations reflect their relative free energies as determined primarily by the strengths of the two different sets of noncovalent bonding interactions. In the schematic representation shown in Figure 13, it has been assumed that the molecular shuttle resides preferentially in 'state 0' until a stimulus is applied that switches off the stronger of the two recognition sites, thus inducing the macrocycle to move to the second weaker recognition site ('state 1'). In appropriately designed [2]rotaxanes, this nondegenerate process can be controlled reversibly using stimuli that are either chemical, electrochemical, or photochemical [30–33, 41]. The most common useful processes to alter reversibly the stereoelectronic properties of one of the two recognition sites are protonation/deprotonation and oxidation/reduction processes, but solvent-induced co-conformational changes have also been extensively investigated [42]. By switching off and on the recognition properties of one of the two recognition sites, the relative proportions of the two species can be controlled reversibly. Such compounds exhibit an abacus-like geometry and behave according to binary logic. Therefore, they could be used, in principle, for information processing at the molecular level.

7.4.3 Electrochemically Controlled Shuttling Processes

Figure 14 shows [2]rotaxane **13**⁴⁺ which contains two recognition sites in its dumbbell-shaped component. In this compound, the stable structure is that with the macrocyclic component surrounding the benzidine recognition site, but shuttling of the macrocycle between the two sites can be controlled electrochemically [43]. The

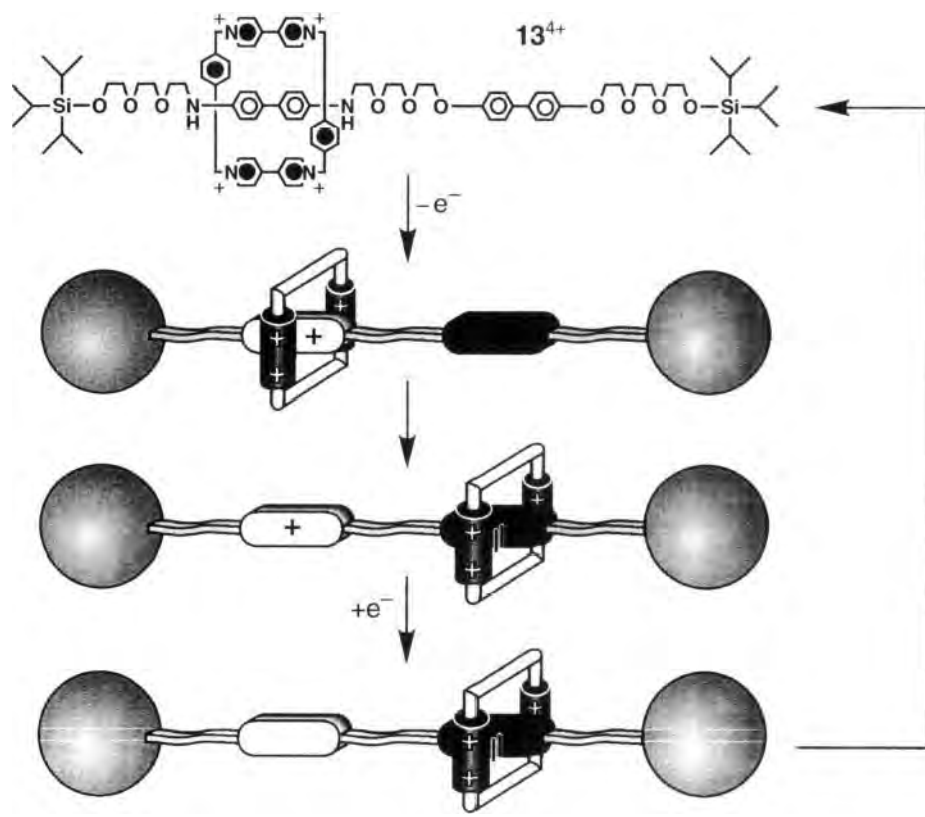


Figure 14. Shuttling of the macrocyclic component of [2]rotaxane 13^{4+} along its dumbbell-shaped component can be controlled electrochemically by oxidizing/reducing the benzidine unit [43]. Shuttling of the macrocycle component can also be controlled by protonating/deprotonating the benzidine unit (see text).

benzidine site undergoes two consecutive one-electron oxidations. Comparison of the half-wave potentials of the [2]rotaxane with those of a model compound incorporating a benzidine unit not encircled by the tetracationic cyclophane shows that the potential for the first oxidation is more positive in the [2]rotaxane, while that for the second oxidation is the same in both compounds. These observations indicate that the tetracationic cyclophane 1^{4+} makes the first one-electron oxidation of the encircled benzidine unit more difficult. However, once this unit is oxidized to the corresponding radical cation, the tetracationic cyclophane moves away from it to encircle the biphenol unit, and so does not influence the second one-electron oxidation. Upon reduction of the benzidine unit back to its neutral state, the original equilibrium between the two co-conformations associated with the [2]rotaxane is restored. The shuttling of the macrocycle component in 13^{4+} can also be controlled by protonation/deprotonation [43].

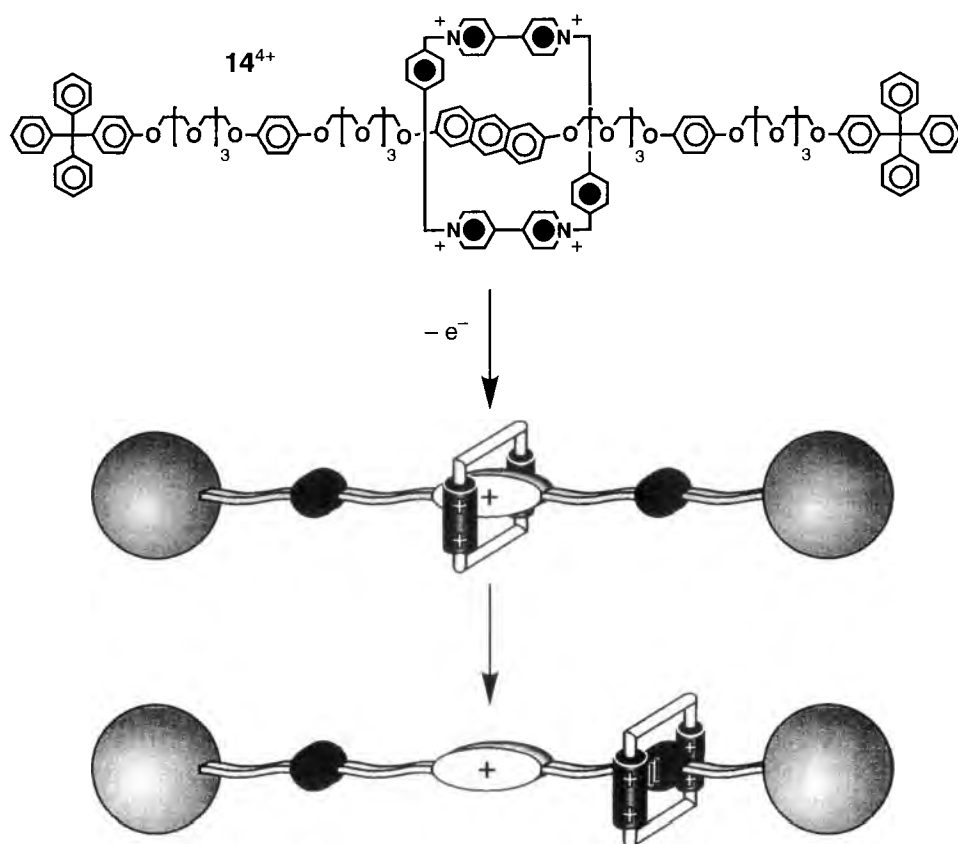


Figure 15. Shuttling of the macrocyclic component of 14^{4+} along its dumbbell-shaped component can be induced by oxidizing electrochemically the anthracene unit system [44].

The [2]rotaxane 14^{4+} incorporates a π -electron-deficient macrocycle and a π -electron-rich dumbbell (Figure 15) [44]. ^1H NMR studies demonstrated that, in solution, the macrocycle resides around the 2,6-dioxyanthracene recognition site. This arrangement is stabilized by π - π stacking interactions between the bipyridium units of the macrocycle and the sandwiched 2,6-dioxyanthracene recognition site of the dumbbell, as well as by $[\text{C}-\text{H}\cdots\text{O}]$ interactions between the α -bipyridinium hydrogen atoms and the polyether oxygen atoms. The cyclic voltammogram of a MeCN solution of this [2]rotaxane shows a first oxidation wave (+1.03 V versus SCE) that corresponds to the oxidation of the 2,6-dioxyanthracene recognition site. This oxidation occurs at a potential that is more positive than that of a model compound incorporating this unit. As far as the oxidation of the two 1,4-dioxybenzene units is concerned, two waves (+1.29 and +1.59 V versus SCE) are observed. The oxidation of the first 1,4-dioxybenzene unit of the [2]rotaxane occurs at a potential that is almost identical to that of a model compound incorporating this unit. The

oxidation of the second 1,4-dioxybenzene unit occurs at a potential that is almost identical to that of a model [2]rotaxane incorporating this unit encircled by the tetracationic cyclophane. These observations suggest that the tetracationic cyclophane resides initially around the 2,6-dioxyanthracene recognition site (Figure 15), making its oxidation more difficult. However, once this recognition site is oxidized, the tetracationic cyclophane moves away from it and encircles one of the two 1,4-dioxybenzene units.

Electrochemically induced shuttling has also been obtained [45] in [2]rotaxanes based on Cu^+ , as described in detail in Volume III, Part 2, Chapter 8.

7.4.4 Photochemically Controlled Shuttling Processes

In the rotaxanes based on electron donor–acceptor interactions there are low-energy CT excited states which are responsible for the absorption bands observed in the visible region (see, e.g., Figure 9). Light excitation in these CT absorption bands formally leads to the transfer of an electron from an electron-donor to an electron-acceptor unit (optical electron transfer). As a consequence, one can expect destabilization of the original rotaxane structure, followed by a displacement of the ring along the wire (in pseudorotaxanes, such a destabilization is expected to lead to dethreading; see Volume III, Part 2, Chapter 6). In practice, however, this simple approach to obtain a photoinduced motion of the ring is not likely to be successful, because the back electron transfer process is much faster than the extended nuclear motions and solvent rearrangement needed for moving the ring. An attempt along this direction has been performed on the rotaxane $\mathbf{15}^{4+}$ shown in Figure 16 [46]. Direct excitation into the CT absorption band results in the transfer of an electron from the central dioxybenzene donor to the cyclophane acceptor. Rapid ($\tau = 30$ ps) back electron transfer occurs, in competition with a minor process involving hole transfer to a ferrocene stopper. The latter process creates a longer-lived ($\tau = 555$ ns) excited state, but back electron transfer to form the initial ground state is still much faster than the motion of the ring.

In order to achieve photoinduced shuttling, the carefully designed [2]rotaxane $\mathbf{16}^{6+}$ shown in Figure 17 has been recently synthesized [47]. This compound is made of the electron-donor macrocycle **R**, and a dumbbell-shaped component which contains: (i) a photoactive Ru(II) polypyridine complex (**P**) as one of its stoppers; (ii) a 4,4'-bipyridinium unit (**A**₁) and a 3,3'-dimethyl-4,4'-bipyridinium unit (**A**₂) as electron accepting stations; (iii) a *p*-terphenyl-type ring system as a rigid spacer (**S**); and (iv) a tetraarylmethane group as the second stopper (**T**). The structure of [2]rotaxane $\mathbf{16}^{6+}$ was characterized by mass spectrometry and NMR spectroscopy, which also established, along with cyclic voltammetry, that the stable translational isomer is the one in which the **R** component encircles the **A**₁ unit, in keeping with the fact that this station is a better electron acceptor than the other one. The electrochemical, photophysical, and photochemical (under continuous and pulsed excitation) properties of the [2]rotaxane, its dumbbell-shaped component, and some model compounds containing electro- and photoactive units (Figure 17), have been investigated. In an attempt to obtain the photoinduced abacus-like movement of the

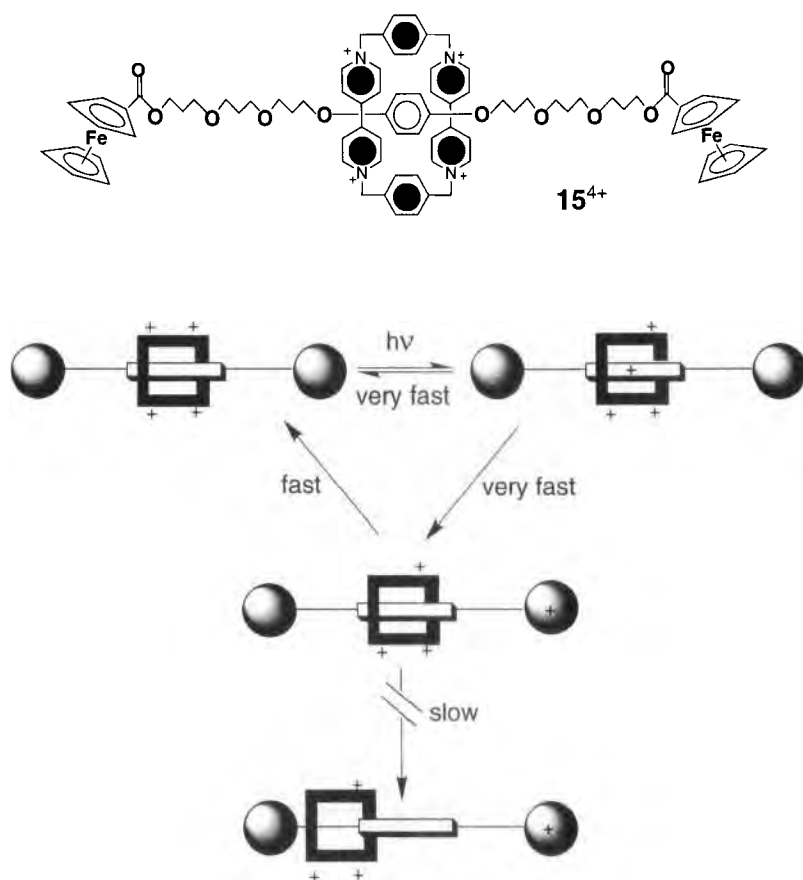


Figure 16. Optical electron transfer excitation of [2]rotaxane 15^{4+} [46]. Shuttling does not take place because the direct and ferrocene-mediated back electron transfer reactions are much faster than the motion of the ring.

R macrocycle between the two stations A_1 and A_2 , two strategies have been devised: one was fully based on processes involving only the rotaxane components (intramolecular mechanism), while the other one required the help of external reactants (sacrificial mechanism).

The intramolecular mechanism, illustrated in Figure 18, is based on the following four operations [47]:

- (a) *Destabilization of the stable translational isomer.* Light excitation of the photo-active unit **P** (Step ①) should be followed by the transfer of an electron from the excited state to the A_1 station, which is encircled by the ring **R** (Step ②), in order to “deactivate” this station: such a photoinduced electron transfer process has to compete with the intrinsic excited-state decay (Step ③).
- (b) *Ring displacement.* The ring should move from the reduced station A_1^- to A_2

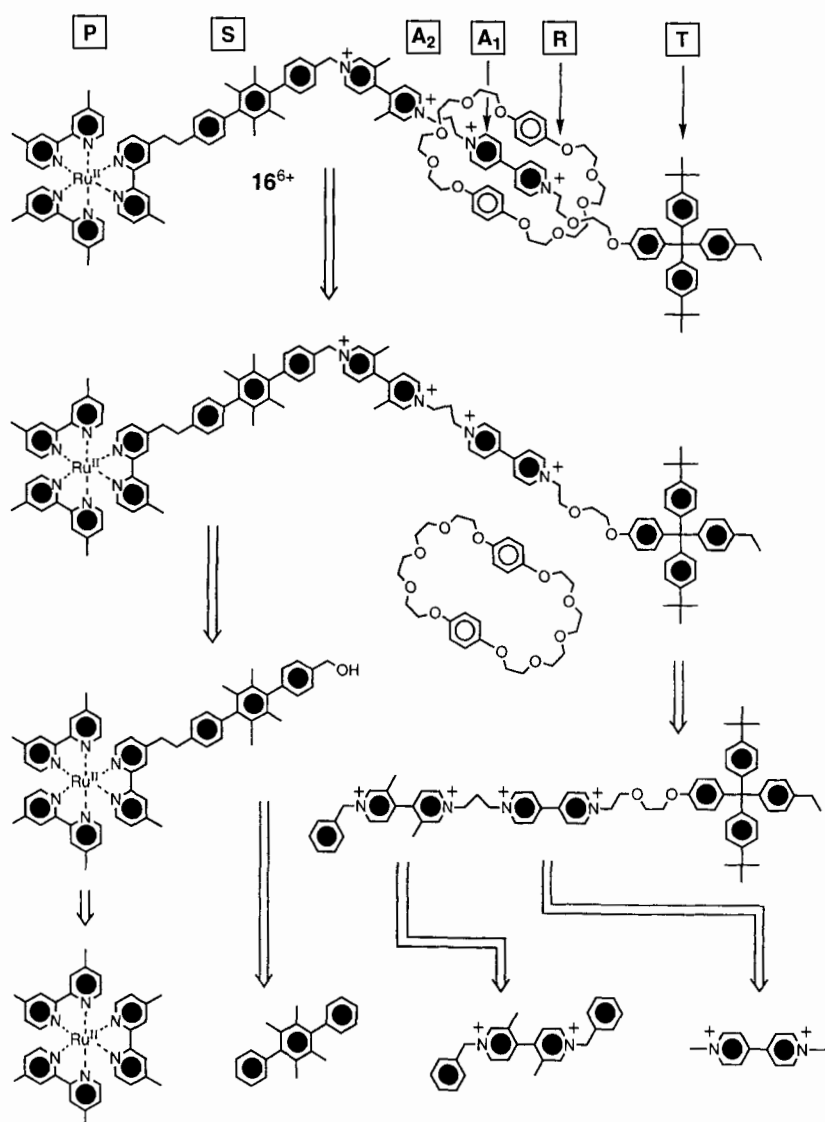


Figure 17. The [2]rotaxane 16^{6+} designed to achieve an abacus-type behavior under light excitation [47].

(Step 4), a step that has to compete with the back electron transfer process from A_1^- (still encircled by **R**) to the oxidized photoactive unit P^+ (Step 5). This is the most difficult requirement to meet in the intramolecular mechanism.

- (c) *Electronic reset.* A back electron transfer process from the “free” reduced station A_1^- to P^+ should take place (Step 6), with consequent restoration of the electron-acceptor power to the A_1 station.

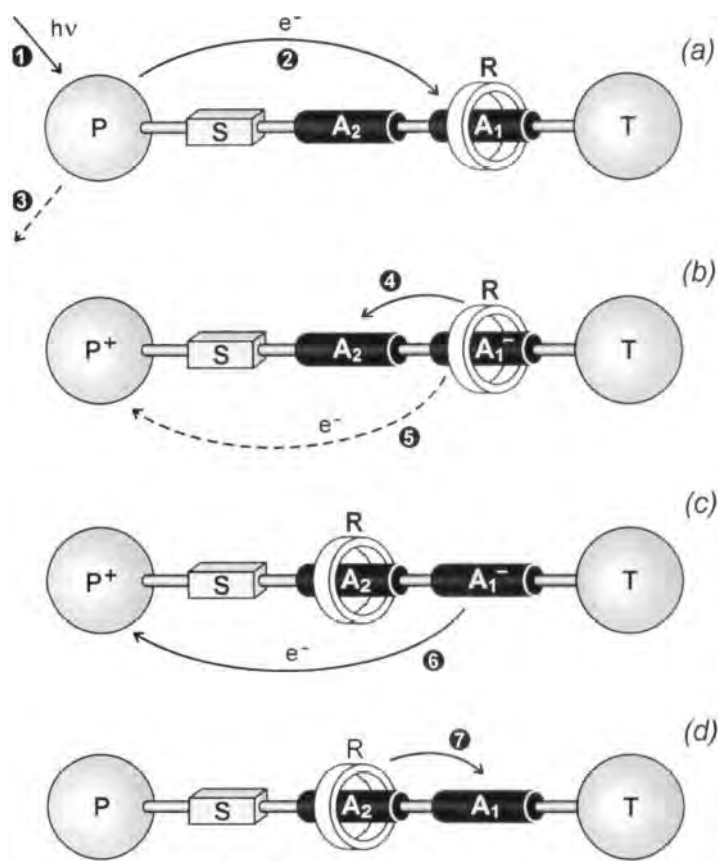


Figure 18. Intramolecular mechanism for the light-driven switching of the ring **R** between the two stations **A₁** and **A₂**. The dashed lines indicate processes that compete with those needed to perform shuttling [47].

(d) *Nuclear reset.* As a consequence of the electronic reset, back movement of the ring from **A₂** to **A₁** should occur (Step ⑦).

The most important requirement to meet in the intramolecular mechanism is the successful competition of Step ④ (which involves complex nuclear movements) with Step ⑤ (which only involves the transfer of an electron).

The alternative, less-demanding, sacrificial mechanism is based on the use of external redox reactants that operate after the photoinduced deactivation of the **A₁** station, as illustrated in Figure 19. This involves [47]:

- (a) *Destabilization of the stable translational isomer*, as in the previous mechanism.
- (b') *Ring displacement after scavenging of the oxidized photoactive unit.* If the solution contains a suitable reductant **Red**, a fast reaction of **Red** with **P⁺** (Step ⑧)

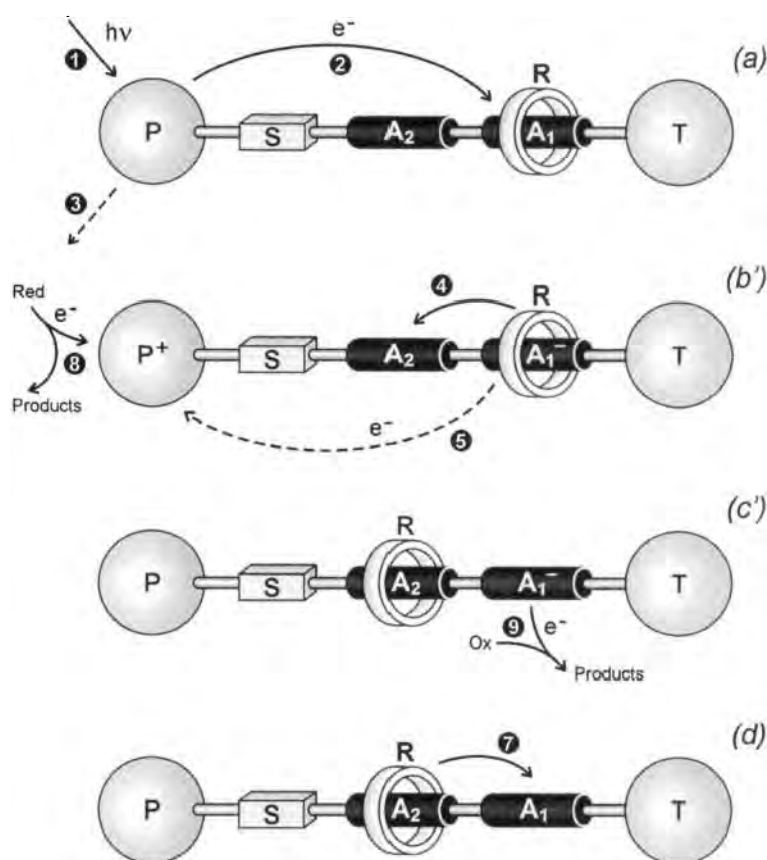


Figure 19. Sacrificial mechanism for the light-driven switching of the ring **R** between the two stations **A₁** and **A₂**. The dashed lines indicate processes that compete with those needed to perform shuttling [47].

may compete successfully with the back electron transfer reaction (Step ⑤); in such a case, the displacement of the ring to **A₂** (Step ④), even if it is slow, can take place because the originally occupied station remains in its reduced state **A₁⁻**.

(c') *Electronic reset.* After an appropriate time, restoration of the electron-acceptor power of the **A₁** station can be obtained by oxidizing **A₁⁻** with a suitable oxidant **Ox** (Step ⑨).

(d) *Nuclear reset*, as in the previous mechanism (Step ⑦).

The results obtained have shown that electronic reset of the system after light excitation (Step ⑤ in Figure 18) occurs with rate constant $8.3 \times 10^5 \text{ s}^{-1}$, which is likely comparable to that of the ring displacement (Step ④) [39c]. While clear evi-

dence for the intramolecular mechanism could not be obtained, the photochemically driven switching was successfully performed by the sacrificial mechanism (Figure 19) with triethanolamine as **Red** and dioxygen as **Ox** [47]. Of course, the intramolecular switching mechanism (Figure 18) is much more appealing than the sacrificial one, principally because the former mechanism implies the conversion of light energy into mechanical energy without using other chemicals and without generation of waste products.

A photochemically induced ring movement has been obtained in a [2]rotaxane based on Cu^+ [45], as described in detail in Volume III, Part 2, Chapter 8. Shuttling of a α -cyclodextrin torus along an azobiphenoxy-containing dumbbell has also been obtained by exploiting the *trans/cis* photoisomerization of the azobiphenoxy unit [48].

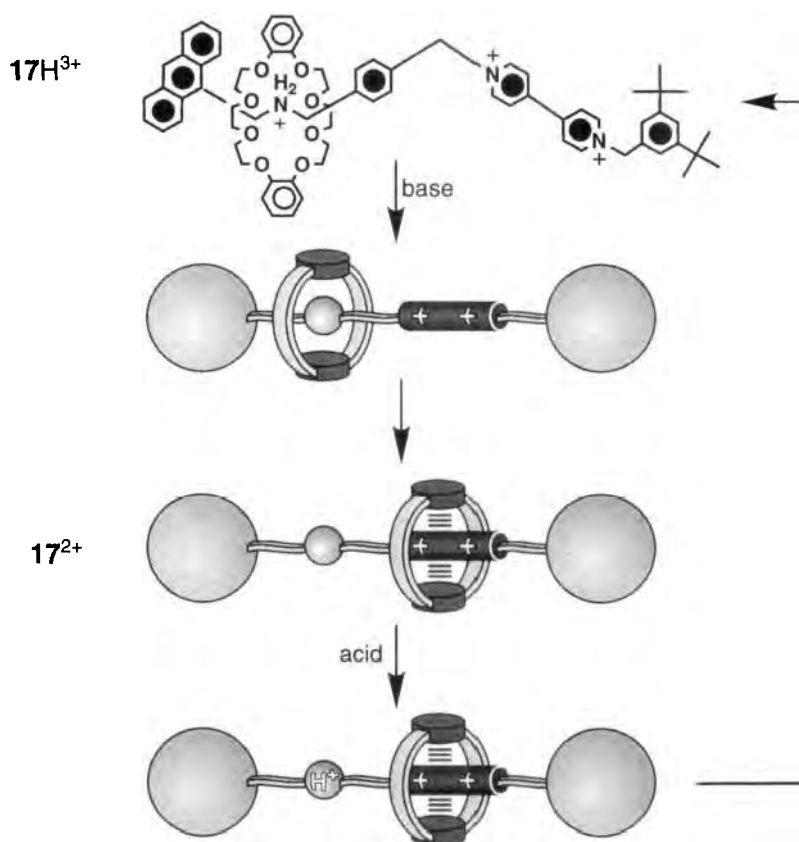


Figure 20. Ring motions in [2]rotaxane 17H^{3+} upon deprotonation/protonation [49].

7.4.5 Chemically Controlled Shuttling Processes

No example has so far been reported of a shuttling process controlled by electron transfer chemical reactions. There are, however, very interesting examples of shuttling processes controlled by acid/base reactions. One case is that of the previously discussed compound **13**⁴⁺ (see Figure 14), in which the shuttling of the macrocycle component can be controlled not only electrochemically, but also by protonation/deprotonation of the benzidine unit [43].

Another very interesting case of shuttling controlled by acid/base reactions is that of [2]rotaxane **17H**³⁺, which incorporates a dialkylammonium and a bipyridinium recognition site in its dumbbell-shaped component (Figure 20) [49]. The macrocycle resides exclusively around the ammonium recognition site as a result of a combination of [⁺N–H···O] and [C–H···O] interactions between the [CH₂NH₂⁺] hydrogen atoms of the dumbbell and the oxygen atoms of the macrocycle. Upon addition of an excess of a suitable amine to a solution of this [2]rotaxane, deprotonation of the ammonium recognition site occurs. As a result, the intercomponent hydrogen bonds are destroyed and the macrocycle moves to the bipyridinium recognition site. However, the original structure is restored after the addition of a suitable acid, since the protonation of the ammonium recognition site is followed by the return of the macrocycle back to encircle the [NH₂⁺] center. The shuttling process can be followed by ¹H NMR spectroscopy (in (CD₃)₂CO) and by electrochemical techniques (in MeCN) [49].

Rotaxanes changing shape through switchable thread–macrocycle interactions have also been reported [50].

7.5 Catenanes

7.5.1 Functional Catenanes

Since the synthetic methods to obtain catenanes have been well established, increasing attention is devoted to the incorporation of novel functions in these structures. Of particular interest are the catenanes in which either the electron-acceptor cyclophane ring or the electron-donor macrocycle contain a 2,2'-bipyridine ligand. Starting from the **L**₁⁴⁺ cyclophane ligand (Figure 21), the mononuclear [Re(CO)₃Cl**L**₁]⁴⁺, [Ru(bpy)₂**L**₁]⁶⁺, [Ag(**L**₁)₂]⁹⁺, and [Cu(**L**₁)₂]⁹⁺ complexes have been prepared [51]. From the bis-chelating cyclophane ligand **L**₂⁴⁺, the dinuclear complexes [{Re(CO)₃Cl}₂**L**₂]⁴⁺ and [{Ru(bpy)₂}₂**L**₂]⁸⁺ have also been obtained (Figure 22) [51].

In the case of **L**₂⁴⁺ it was not possible to synthesize [2]catenanes because the cavity of this cyclophane is too large to give stable complexes with aromatic crown ethers in the templated synthetic approach. Starting from **L**₁⁴⁺, however, it was possible to prepare the [2]catenane ligands **L**₃⁴⁺ and **L**₄⁴⁺ which were then used to prepare several mononuclear [2]catenane complexes (Figure 23). These compounds were characterized by NMR spectroscopy, mass spectrometry and, in some cases, X-ray crystallography.

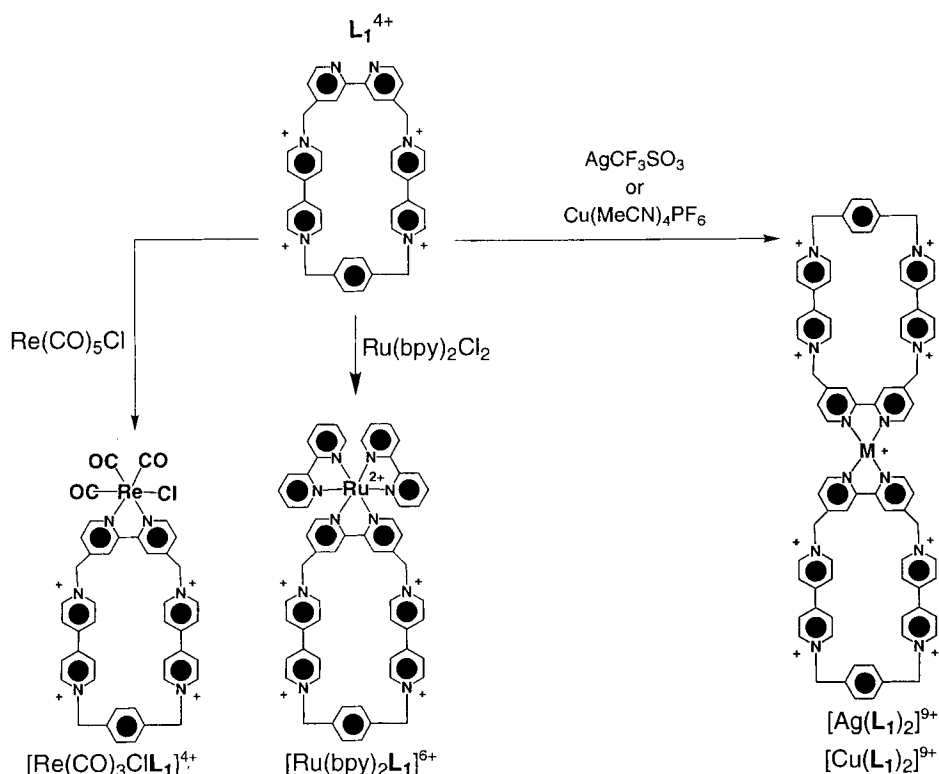


Figure 21. Preparation of mononuclear complexes of the cyclophane ligand L_1^{4+} [51].

The absorption spectra, luminescence properties, and electrochemical behavior of the L_1^{4+} , L_2^{4+} , and L_4^{4+} ligands, and of the $[\text{Re}(\text{CO})_3\text{Cl}L_1]^{4+}$, $[\text{Re}(\text{CO})_3\text{Cl}L_4]^{4+}$, $[\{\text{Re}(\text{CO})_3\text{Cl}\}_2L_2]^{4+}$, $[\text{Ru}(\text{bpy})_2L_1]^{6+}$, $[\text{Ru}(\text{bpy})_2L_4]^{6+}$, and $[\{\text{Ru}(\text{bpy})_2\}_2L_2]^{8+}$ complexes have then been investigated [51]. Besides the ligand-centered bands, the Re(I) and Ru(II) complexes display metal-to-ligand charge-transfer (MLCT) bands in the visible region similar to those of the $\text{Re}(\text{CO})_3(\text{Cl})(\text{bpy})$ and $[\text{Ru}(\text{bpy})_3]^{2+}$ model compounds. None of the examined complexes exhibits emission at room temperature because the potentially luminescent MLCT excited state undergoes electron transfer quenching by the bipyridinium-type units contained in the L_1^{4+} , L_2^{4+} , and L_4^{4+} ligands. In rigid matrix at 77 K, where electron transfer cannot occur, emission can be observed from the complexes containing the tetracationic cyclophane ligands L_1^{4+} and L_2^{4+} , but not from those containing the catenane ligand L_4^{4+} , in which quenching can still take place by energy transfer to a low-energy CT excited state of the catenane moiety [51].

In the potential window examined ($-2.2/+2.1$ V versus SCE), L_1^{4+} and L_2^{4+} can reversibly accept five and, respectively, six electrons, with processes localized on their bipyridinium- and bpy-type units. The catenane ligand L_4^{4+} , besides the re-

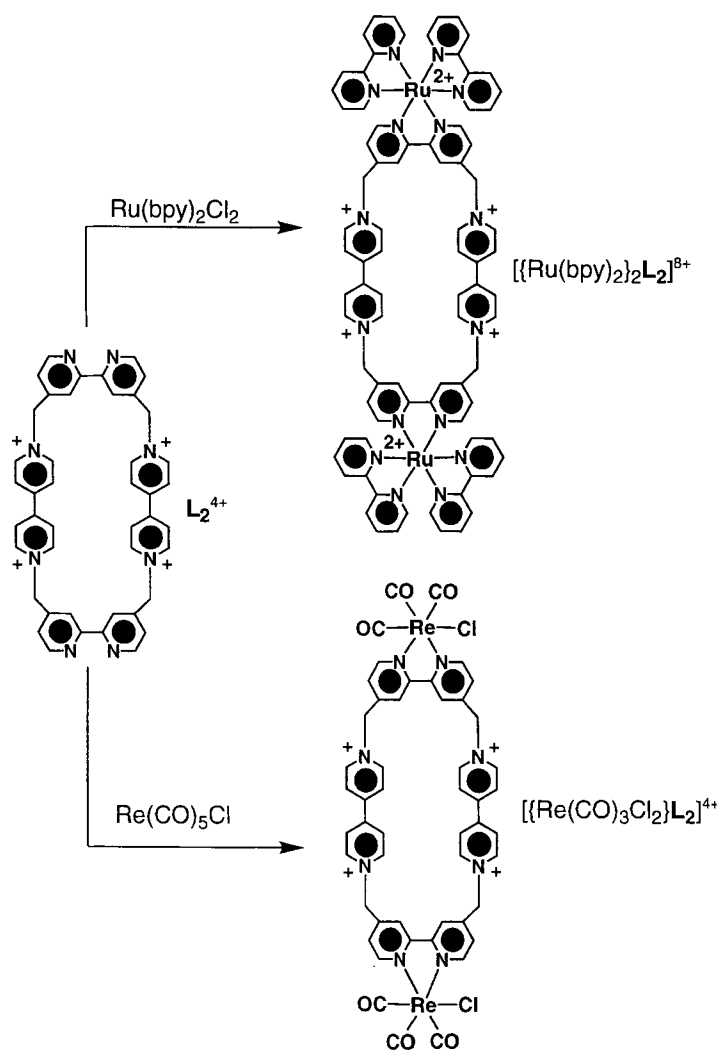


Figure 22. Preparation of binuclear complexes of the cyclophane ligand L_2^{4+} [51].

duction processes concerning the L_1^{4+} cyclophane, displays two oxidation processes involving the dioxynaphthalene moieties of the 1,5-dinaphtho-38-crown-10. The $[Re(CO)_3L_1Cl]^{4+}$, $[Re(CO)_3L_4Cl]^{4+}$, $[\{Re(CO)_3Cl\}_2L_2]^{4+}$, $[Ru(bpy)_2L_1]^{6+}$, $[Ru(bpy)_2L_4]^{6+}$, and $[\{Ru(bpy)_2\}_2L_2]^{8+}$ complexes display several redox processes (up to a total of 10 exchanged electrons in the case of $[Ru(bpy)_2L_4]^{6+}$ and $[\{Ru(bpy)_2\}_2L_2]^{8+}$) that can be assigned to: (i) reduction of the bipyridinium- and bpy-type moieties of the catenane ligands; (ii) reduction of the bpy ligands (in the Ru complexes); (iii) oxidation of the metals; and (iv) oxidation of the dioxynaphthalene moieties of the 1,5-dinaphtho-38-crown-10 (in the complexes containing the

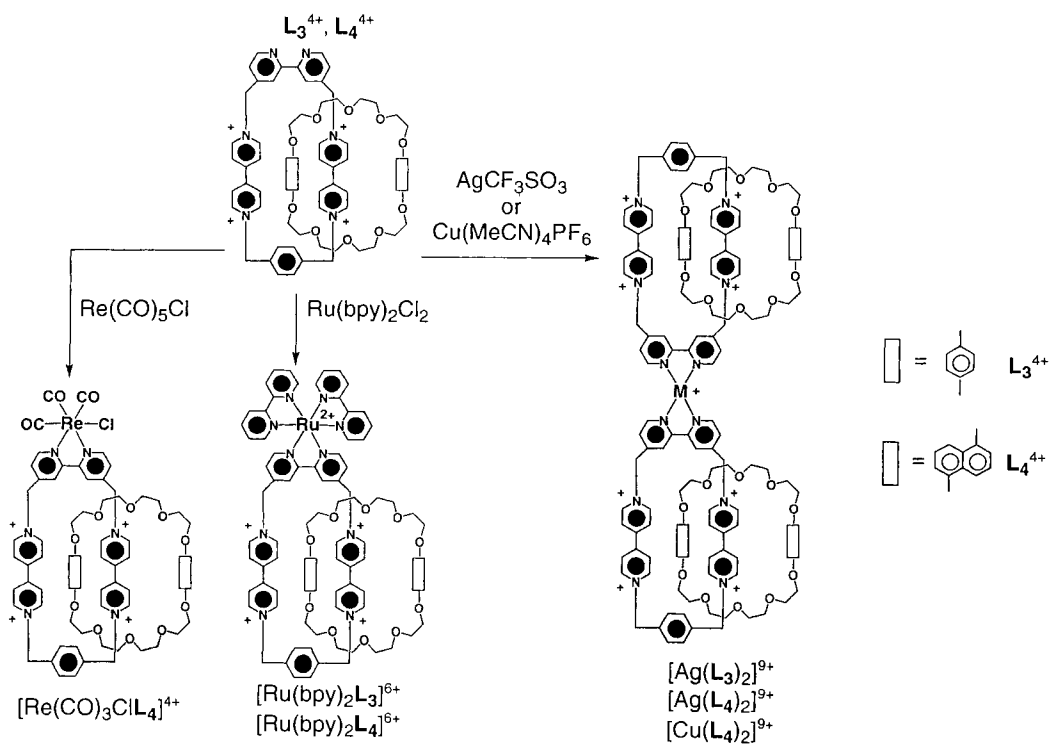


Figure 23. Preparation of mononuclear complexes of the catenane ligands L_3^{4+} and L_4^{4+} [51].

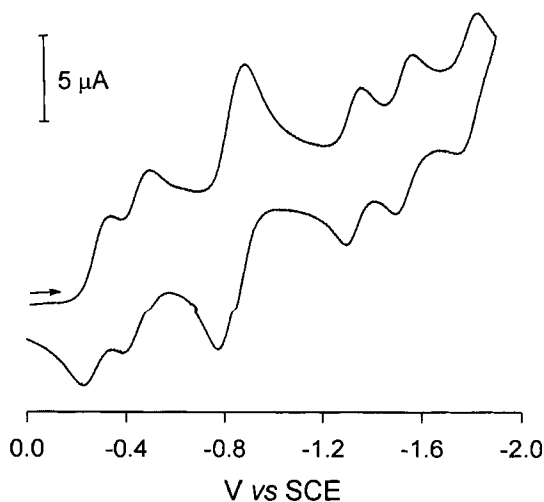


Figure 24. Cyclic voltammetric behavior on reduction of $5 \times 10^{-4} \text{ M } [Ru(bpy)_2L_4]^{6+}$ (MeCN, 25°C) [51].

L_4^{4+} catenane ligand). The cyclic voltammetric behavior on reduction of $[\text{Ru}(\text{bpy})_2\text{L}_4]^{6+}$ is shown in Figure 24: two monoelectronic waves and a bielectronic wave, assigned to the first and second reductions of the bipyridinium units, are followed by three monoelectronic waves involving reduction of the bipyridine moieties [51].

An interesting aspect of the above-described metal catenanes is the topologically different (“alongside” and “inside”) positions of the two bipyridinium units with respect to the crown ether (Figure 23) and, as a consequence, their redox asymmetry (Figure 24). Such a situation is reminiscent of the redox asymmetry present in the two branches of the reaction center of bacterial photosynthesis [52]. The photochemical behavior of [2]catenane $[\text{Ru}(\text{bpy})_2\text{L}_3]^{6+}$ has therefore been investigated by picosecond laser spectroscopy [53]. The excited state of the Ru moiety transfers an electron to the tetracationic cyclophane with rate constant $5.9 \times 10^{10} \text{ s}^{-1}$, and the back electron transfer restoring the ground state occurs with rate constant $2.4 \times 10^{10} \text{ s}^{-1}$. Unfortunately, no conclusion could be drawn as to the electron transfer path, since the two bipyridinium units cannot be distinguished by spectroscopic means.

As mentioned above, a coordinating bipyridine unit can also be incorporated in the electron-donor macrocycle of a catenane. This strategy has been followed to prepare the L_5^{4+} ligand and its $[\text{Ru}(\text{Me}_2\text{bpy})_2\text{L}_5]^{6+}$ complex (Figure 25) [54]. Electrochemical and dynamic ^1H NMR experiments, as well as molecular modeling, suggested that there are two conformers. Luminescence quenching data indicated that the rate of the electron transfer reaction from the excited state of the Ru moiety to the bipyridinium units of the cyclophane is $\geq 1 \times 10^8 \text{ s}^{-1}$ in water and that, apparently, there are two different back electron transfer processes of rate constants 4.1×10^6 and $1.9 \times 10^6 \text{ s}^{-1}$, assigned to two different conformers [54]. The $[\text{Ru}(\text{Me}_2\text{bpy})_2\text{L}_5]^{6+}$ catenane has recently been used as a component of a triad and incorporated into a protein scaffold [55].

Other interesting units that have been incorporated in the electron-donor macrocyclic component of catenanes are porphyrins (Figure 26) [56]. The compounds containing a free-base porphyrins can be protonated in strongly acidic solutions, causing electrostatic repulsions which result in conformational reorientations and changes in rotation rates [57].

Several [2]catenanes incorporating a calix[4]arene unit in their electron-acceptor cyclophane components have also been prepared (see, e.g., Figure 27) [58]. In these compounds, the characteristic charge-transfer bands arising from the donor-acceptor interaction are present, but no luminescence can be observed.

7.5.2 Ring Motions

When the synthesis of a [2]catenane leads to the interlocking of two different macrocycles each containing two identical recognition sites, then circumrotation of a macrocycle through the cavity of the other leads to degenerate equilibrium states. An example of a degenerate [2]catenane is shown in Figure 28, wherein the dynamic processes in solution are illustrated [23].

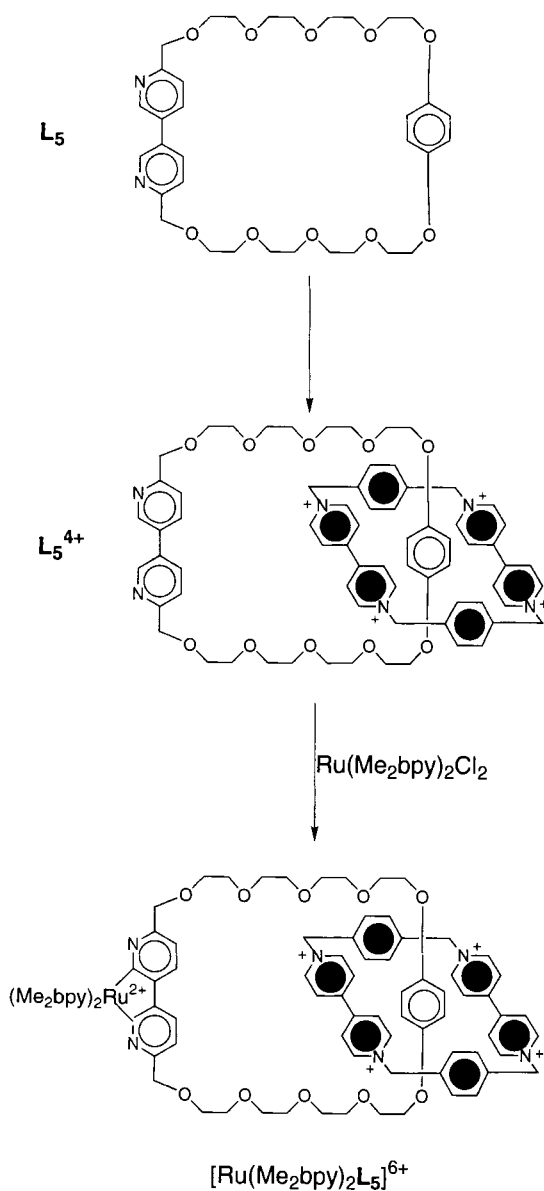


Figure 25. Macrocyclic ligand L_5 , its [2]catenane derivative L_5^{4+} , and the $[\text{Ru}(\text{Me}_2\text{bpy})_2\text{L}_5]^{6+}$ [2]catenane complex [54].

When one of the two macrocycles carries two different recognition sites, then the opportunity exists to control the dynamic processes in these switchable [2]catenanes in a manner reminiscent of the controllable molecular shuttles (Figure 29) [30–34, 41]. In essence, the requirement for being able to switch between ‘state 0’ and ‘state 1’ in such a [2]catenane is that the symmetric macrocyclic component resides preferentially around one of the two different recognition sites incorporated within the non-

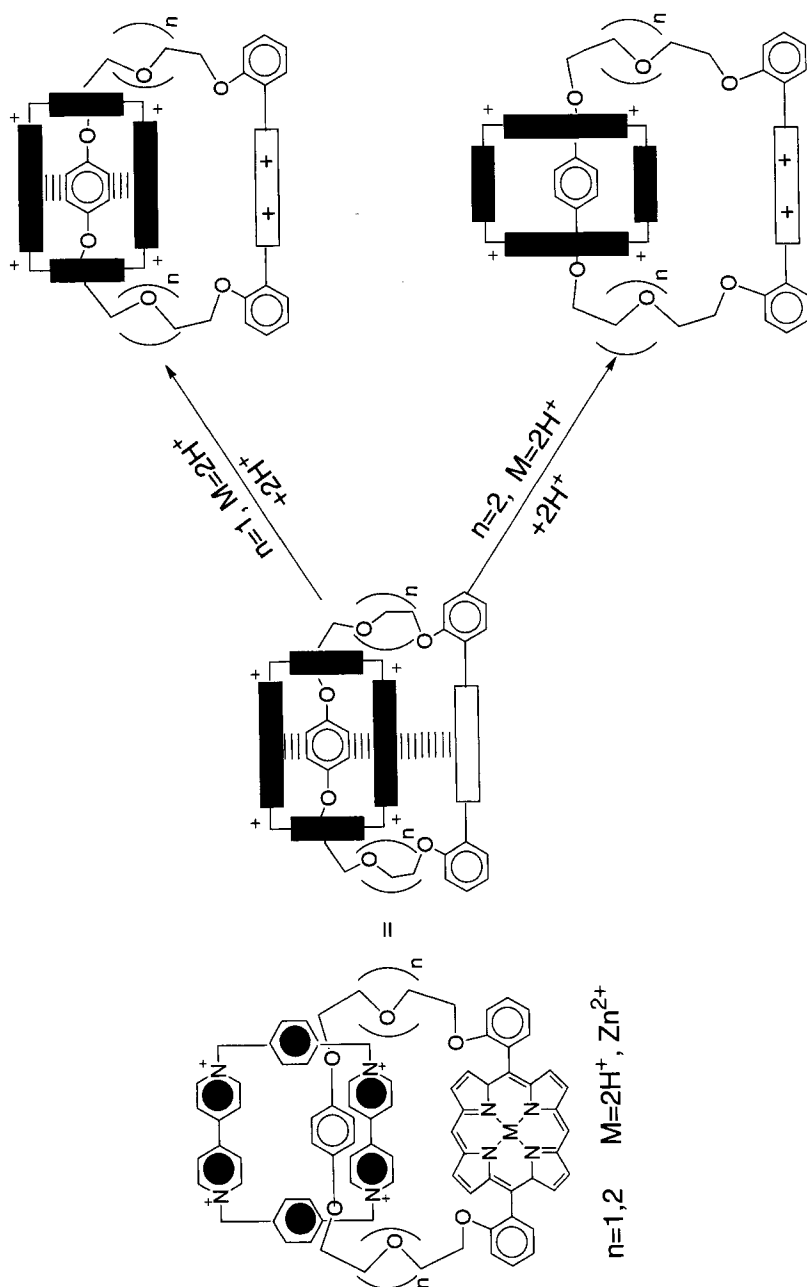


Figure 26. Porphyrin [2]catenanes and possible structural changes accompanying diprotonation of the porphyrin ring [57].

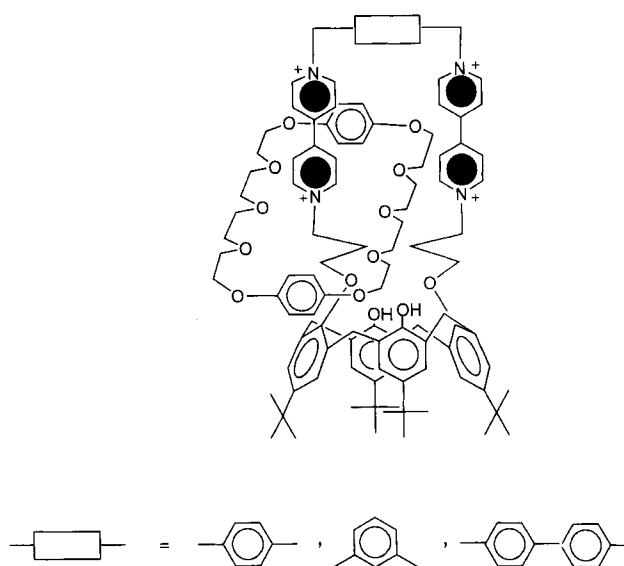


Figure 27. Calix[4]arene-[2]catenanes [58].

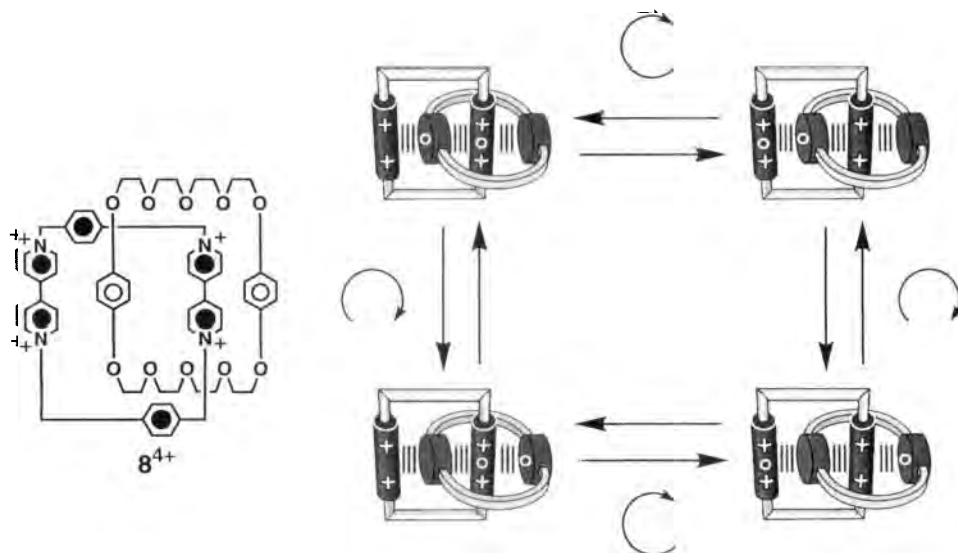


Figure 28. Dynamic processes associated with [2]catenane 8^{4+} in solution, which involve the circumrotations of the macrocyclic components through each other's cavities [23].

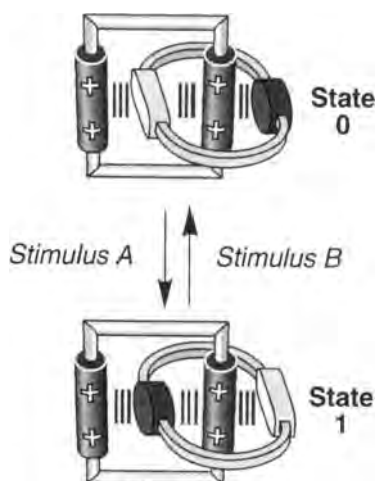


Figure 29. The two spatial arrangements associated with a [2]catenane, incorporating two different recognition sites within one of its two macrocyclic components, can be interchanged by appropriate stimuli.

symmetric macrocycle. The two associated spatial arrangements (co-conformations) [40] are stabilized by intercomponent noncovalent bonding interactions, and their interconversion requires the circumrotation of the nonsymmetric macrocycle through the cavity of the symmetric one. In solution, the equilibrium between the two spatial arrangements is governed by the relative magnitudes of the intercomponent noncovalent bonding interactions. By switching off and on again the recognition properties of one of the two recognition sites of the nonsymmetric macrocycle, the relative populations of the two spatial arrangements can be controlled reversibly.

Complexation/decomplexation of metal ions or of neutral organic molecules, protonation/deprotonation reactions, and oxidation/reduction processes can all be exploited to alter reversibly the stereoelectronic properties of one of the two recognition sites, thus affecting its ability to sustain noncovalent bonds [30–34, 41]. These kinds of switchable [2]catenanes can be prepared following the template-directed synthetic strategy illustrated in Figure 5, wherein one of the two macrocyclic components is preformed and then the other one is clipped around it with the help of noncovalent bonding interactions.

7.5.3 Electrochemically Controlled Ring Motions

In the [2]catenane **18**⁴⁺ (Figure 30) the ring motion can be controlled electrochemically by oxidizing/reducing reversibly the tetrathiafulvalene unit [59]. The cyclic voltammogram of the ‘free’ macrocyclic polyether shows a reversible wave (c. +0.3 V versus SCE, MeCN) for the monoelectronic oxidation of the tetrathiafulvalene (TTF) unit. In the [2]catenane, the TTF unit is located inside the cavity of the tetracationic cyclophane, and its monoelectronic oxidation occurs at more positive potentials. Furthermore, a large separation between the anodic and cathodic peaks associated with this process is observed. This separation varies as the scan rate is changed. Upon increasing the scan rate, the anodic peak moves to more positive

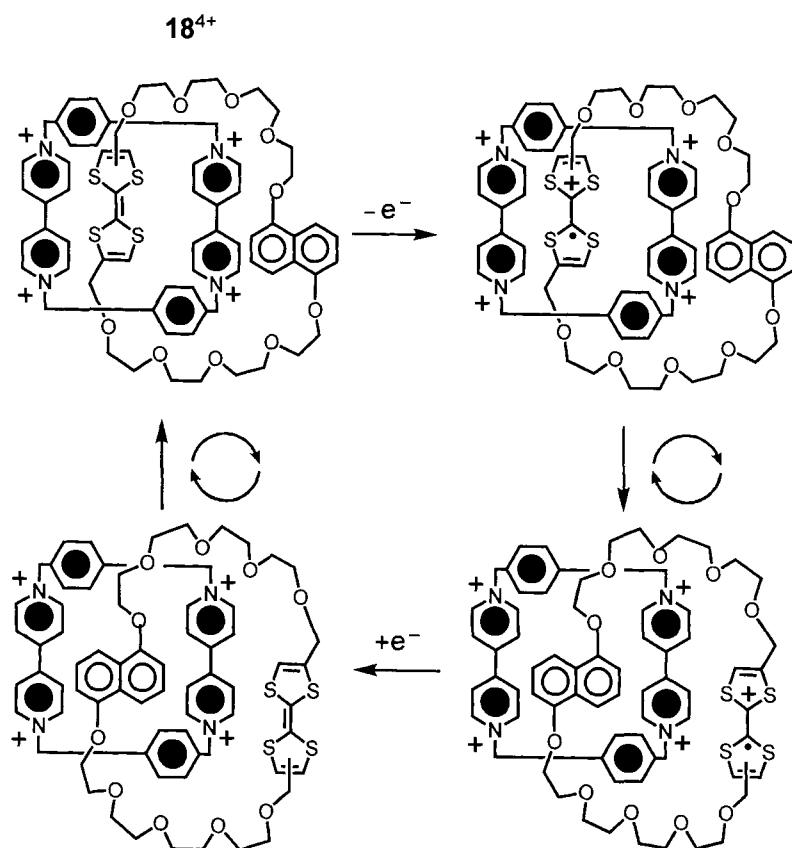


Figure 30. Circumrotation of the macrocyclic polyether component of the [2]catenane 18^{4+} can be controlled oxidizing/reducing reversibly the tetrathiafulvalene unit [59].

potentials, while the cathodic one shifts to less-positive values. These observations indicate that the oxidation/reduction of the TTF unit is accompanied by the circumrotation of the macrocyclic polyether through the cavity of the tetracationic cyclophane and that this co-conformational change is occurring on the time scale of the electrochemical experiment. Indeed, after monooxidation, the newly formed monocationic TTF unit is expelled from the cavity of the tetracationic cyclophane, and is replaced by the neutral dioxynaphthalene unit. After reduction, the original co-conformation is restored as the neutral TTF unit replaces the dioxynaphthalene unit inside the cavity of the tetracationic cyclophane [60, 61].

The [2]catenane 19^{4+} incorporates (Figure 31) a macrocyclic polyether containing two dioxybenzene units, and a tetracationic cyclophane comprising a bipyridinium and a *trans*-bis(pyridinium)ethylene unit [36a, 62]. The ^1H NMR spectrum $[(\text{CD}_3)_2\text{CO}, 213 \text{ K}]$ of 19^{4+} shows the signals for two distinct co-conformations in a ratio of 92:8. In the major isomer, the bipyridinium unit is located inside the cavity of the macrocyclic polyether and the *trans*-bis(pyridinium)ethylene unit is posi-

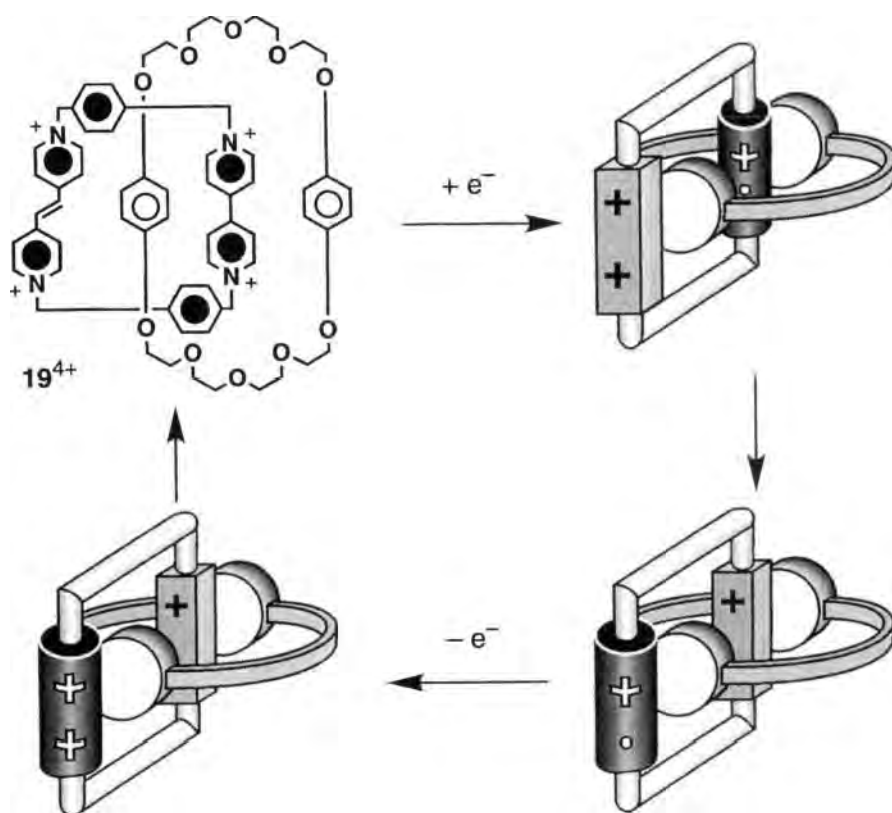


Figure 31. Circumrotation of the tetracationic cyclophane component of the [2]catenane 19^{4+} can be controlled reversibly by reducing/oxidizing electrochemically its bipyridinium unit [36a].

tioned alongside. The first two reduction waves in the cyclic voltammogram of the 'free' tetracationic cyclophane occur at -0.31 and -0.43 V versus SCE. They correspond to the first monoelectronic reductions of the bipyridinium and of the *trans*-bis(pyridinium)ethylene unit, respectively. In case of the [2]catenane, these two waves are shifted to more negative potentials and occur at -0.39 and -0.49 V versus SCE. These observations indicate that the bipyridinium unit is preferentially located inside the cavity of the macrocyclic polyether (Figure 31), and its reduction is more difficult than in the case of the 'free' tetracationic cyclophane. However, once this unit is reduced, the tetracationic cyclophane circumrotates through the cavity of the macrocyclic polyether moving the *trans*-bis(pyridinium)ethylene unit inside, as shown by comparison of its reduction potential with that of a catenane model compound [36a]. Upon back oxidation of the reduced bipyridinium unit, the original equilibrium between the two co-conformations associated with the [2]catenane 19^{4+} is restored.

As described in detail in Volume III, Part 2, Chapter 8, electrochemically induced movements can also be obtained in the [2]catenate containing Cu^+ ions [63, 64].

7.5.4 Photochemically Controlled Ring Motions

The only example presently available of photochemically controllable ring motion through an electron transfer reaction in a catenane structure concerns a Cu^+ -based [2]catenane, which is discussed in Volume III, Part 2, Chapter 8 [64]. Examples of catenanes containing *cis-trans* photoisomerizable units and where ring motions can be photochemically controlled are also known [65].

7.5.5 Chemically Controlled Ring Motions

Some examples of chemically controlled ring motions in catenanes through electron transfer or charge transfer processes have been reported.

In the case of the previously discussed [2]catenane **18**⁴⁺ shown in Figure 30, switching from the more stable translational isomer (which contains a TTF unit inside the tetracationic cyclophane) to a less stable one can be obtained not only by oxidation of the TTF unit, but also by addition of *o*-chloroanil. ¹H NMR spectroscopy shows that *o*-chloroanil gives an adduct, presumably CT in nature, with the TTF unit which locks this unit alongside the cavity of the cyclophane. On addition of $\text{Na}_2\text{S}_2\text{O}_5$ the adduct is destroyed and the original isomer with the TTF unit inside the cavity of the cyclophane is restored [59, 66].

The [2]catenane **20**⁴⁺ incorporates (Figure 32) a macrocyclic polyether containing two dioxybenzene units and a tetracationic cyclophane comprising a bipyridinium and a diazapyrenium unit [67]. X-ray crystallographic analysis of this compound revealed that the macrocyclic polyether encircles exclusively the diazapyrenium ring system in the solid state. The ¹H NMR spectrum [$(\text{CD}_3)_2\text{CO}$, 193 K] of **20**⁴⁺ shows the signals for two distinct co-conformations in a ratio of 96:4. In the major isomer, the diazapyrenium ring system is located inside the cavity of the macrocyclic polyether, and the bipyridinium unit is positioned alongside. The ability of *n*-hexylamine to form adducts (most likely of CT nature) with the diazapyrenium moiety can be exploited to displace the equilibrium between the two co-conformations in favor of the isomer having the diazapyrenium unit alongside the cavity of the macrocyclic polyether [68]. The differential pulse voltammogram (MeCN, 298 K) of **20**⁴⁺ shows two peaks at -0.31 and -0.57 V versus SCE for the monoelectronic reduction of the alongside bipyridinium unit and of the inside diazapyrenium unit, respectively. After the addition of *n*-hexylamine, the first peak shifts by -60 mV to a potential that corresponds to the monoelectronic reduction of a bipyridinium unit encircled by the dioxybenzene-based macrocyclic polyether [36a]. Similarly, the second peak shifts by -20 mV to a potential that is associated with the monoelectronic reduction of a diazapyrenium unit interacting with *n*-hexylamine. On addition of $\text{CF}_3\text{SO}_2\text{H}$, protonation of *n*-hexylamine occurs. As a result, the adduct formed between *n*-hexylamine and the diazapyrenium unit of the [2]catenane is destroyed and the original equilibrium between the two co-conformations associated with **20**⁴⁺ is restored. The differential pulse voltammogram recorded after the addition of $\text{CF}_3\text{SO}_2\text{H}$ is identical with that recorded before the addition of *n*-hexylamine [68].

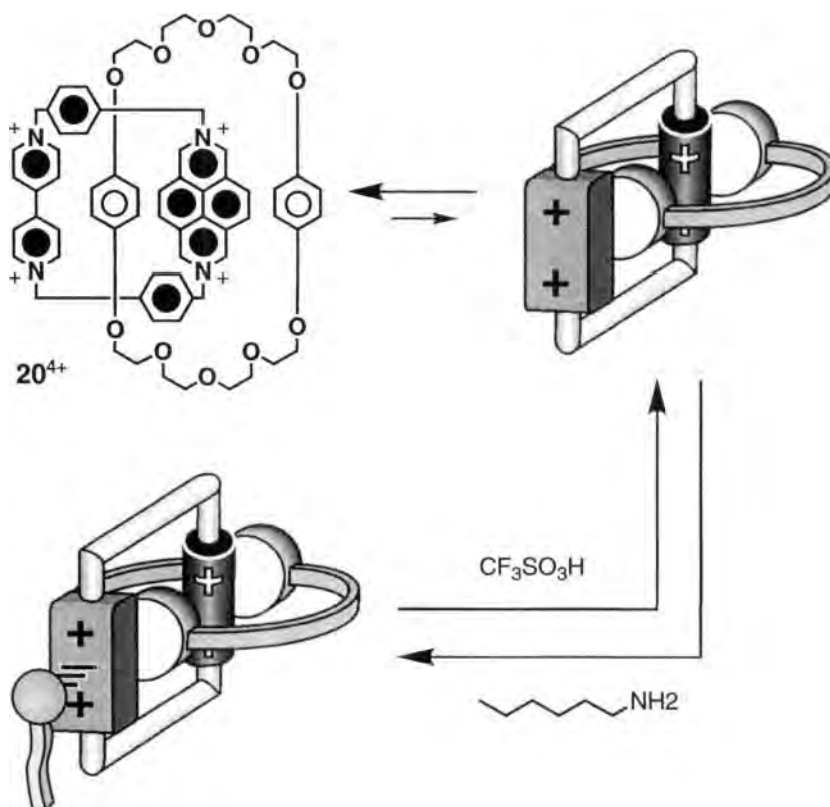


Figure 32. Circumrotation of the tetracationic cyclophane component of the [2]catenane 20^{4+} can be controlled reversibly by adding/protonating *n*-hexylamine which forms a charge-transfer adduct with the diazapyrenium unit of this [2]catenane [68].

7.6 Molecular-Level Machines

The unique architecture of rotaxanes and catenanes (as well as pseudorotaxanes; see Volume III, Part 2, Chapter 6) lend themselves to the occurrence of large-amplitude motions by their component parts—a property reminiscent of the movements displayed by the working parts of machines in the macroscopic world. The concept of machine at the molecular level is not a new one. Our body can be looked upon as an extremely complex ensemble of molecular-level machines that power our movements, repair damage, and orchestrate our inner worlds of thought, sense, and emotion [69]. The challenge of constructing artificial molecular machines was posed for the first time by Feynman [70] in his famous address, *There is Plenty of Room at the Bottom*, to the American Physical Society in 1959. In his address, he raised a number of interesting issues, such as:

“... What are the possibilities of small but movable machines?... An internal combustion engine of molecular size is impossible ... Other chemical reactions, liberating energy when cold, can be used instead ... What would be the utility of such machines?...”

Although some intriguing examples of simple molecular-level machines (e.g., a phototweezer) [71] were reported during the 1980s, it has only been during the past few years that, thanks to the rapid growth of supramolecular chemistry [20], the issues raised by Feynman have become hot topics in contemporary scientific research [30–33, 41]. Catenanes and rotaxanes are indeed providing cogent answers to the first of Feynman’s questions: when the motions of their component parts can be induced and controlled by external inputs of energy, such exotic chemical systems can certainly be viewed as simple molecular machines. As Feynman [70] predicted, the input of external energy to make such machines work has to be a cold chemical reaction. What apparently he did not predict, somewhat amazingly, is the possibility that the required chemical energy can be provided by electrochemical reactions and, most importantly, by light excitation.

Reversible structural rearrangements governed by external inputs are interesting not only from the viewpoint of mechanical movements, but also for information processing at the molecular level. Reversible switching between two “states” (see Figures 13 and 29) corresponds to a binary logic behavior. Indeed, molecular-level information processing [72] seems to be a possible answer to Feynman’s question [70] about the utility of such “*small but movable machines*”. Although the term “molecular computer” is still an emotive one among chemists, the continuous advances in the field of molecular electronics [73] and the fact that today’s silicon-based technology is rapidly approaching the upper limits of its physical capabilities [74] leads to the prediction that the chemical (molecular-level) computer is likely to replace our present technology by the year 2025 [75].

We would also like to point out that, similar to their macroscopic counterparts, molecular-level machines have to be organized structurally and work as functionally integrated, multicomponent systems [32, 41a]. The first step is to produce an accurate design of the working mechanism of the machine, followed by a search for those components that exhibit the required properties, and then finally to find the means to assemble them in the required order. A clear example of the level reached by this kind of research is given by the [2]rotaxane **16**⁴⁺ shown in Figures 17–19, which was obtained by assembling in a predetermined sequence as many as six different components, each one exhibiting suitable spectroscopic and redox properties [47].

7.7 Modified Electrodes and Heterosupramolecular Systems

The investigation of rotaxanes and catenanes in solution is not only of fundamental importance to understand their complex behavior, but it also represents a starting

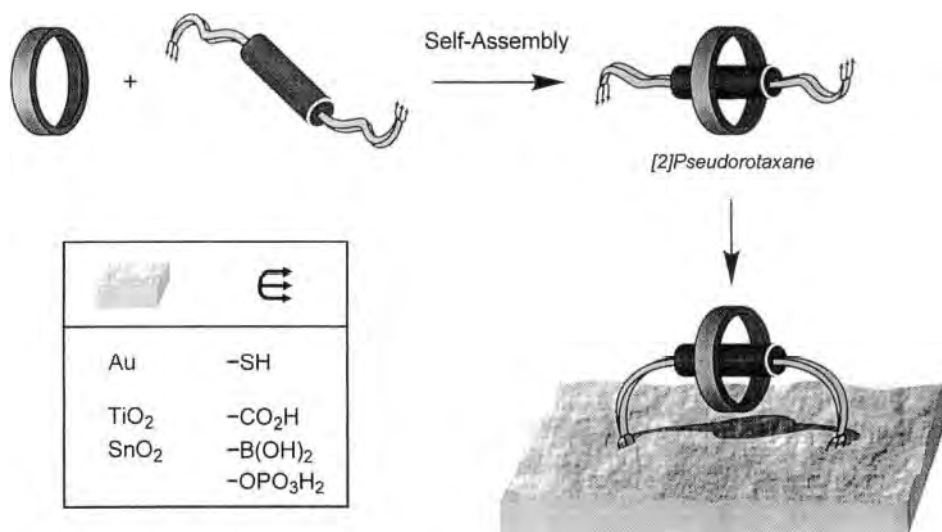


Figure 33. Pictorial representation of the preparation of a surface-attached catenane by coupling self-assembly in solution with chemisorption onto a solid support [83].

point for the construction of molecular-level machines. A solution, however, contains a huge number of molecules which behave incoherently since they cannot be addressed individually, and hence controlled [76]. It seems reasonable therefore that, before functional supramolecular assemblies can be employed in a machine-like manner, they have to be interfaced with the macroscopic world by ordering them in some way. The next generation of molecular machines will need to be organized at interfaces [77] or deposited on surfaces [78] so that they can behave coherently, either in parallel or in series, and can also be addressed on the nanometer scale [79].

The self-assembly of molecular components in solution can be coupled (Figure 33) to deposition techniques for obtaining surface-attached supramolecular and interlocked molecular systems. Among the most interesting examples are a monolayer constituted of the tetracationic cyclophane **1**⁴⁺ catenated onto a gold surface by means of a molecular thread bearing thiol groups at both ends [80], and a polyrotaxane deposited as a film onto an electrode by electropolymerization [81]. In the latter case, rotation of the ring component around the polymer-derivatized thread, confined to the film, can be electrochemically triggered.

Another interesting approach is provided by the emerging field of heterosupramolecular chemistry [82]. Heterosupramolecules, that is supramolecular systems in which one or more components are in the condensed phase (e.g., nanocrystals), are expected to offer considerable advantages from the viewpoints of molecular organization and addressability. Following the strategy outlined in Figure 33, hetero[2]catenanes in which TiO₂ or SnO₂ nanosized particles are incorporated as a part of one of the ring components have been prepared, and are presently the subject of photochemical and electrochemical investigations [83].

7.8 Conclusions

CT interactions and electron transfer processes play a fundamental role in the chemistry of rotaxanes and catenanes. CT interactions are often responsible for the driving forces that lead to the syntheses of these compounds; such interactions “live on” when the components have been interlocked, and therefore contribute to determine the actual structure of the resulting compound. Because of the presence of CT interactions, the electronic absorption and emission spectra, as well as the electrochemical behavior, of many rotaxanes and catenanes exhibit characteristic features, quite different from those exhibited by the separated components.

In interlocked compounds such as rotaxanes and catenanes, electron-donor and -acceptor units not only cause the presence of CT interactions, but are also responsible for the occurrence of intercomponent and intermolecular oxidation and reduction processes. Such processes weaken or even destroy the CT interactions that stabilize the structure of the compound, with a consequent change in its conformation. External inputs, like electrons or photons, can be used to cause the redox processes and the structural rearrangements that follow. Suitably designed rotaxanes and catenanes can therefore exhibit machine-like movements that correspond to a binary logic behavior.

Since reliable and efficient strategies for the synthesis of rotaxanes and catenanes have been established, current research is focused on functionalization of the component parts of these interlocked species and on the construction of increasingly complex compounds in the search for new and valuable properties.

Acknowledgments

We thank the University of Bologna (Funds for Selected Research Topics) and MURST (Supramolecular Devices Project), and the EU (TMR Project FMRX-CT96-0076) for financial support.

References

1. G. Schill, *Catenanes, Rotaxanes and Knots*, Academic Press, New York, **1971**.
2. H.W. Gibson, M.C. Bheda, P.T. Engen, *Progr. Polym. Sci.*, **1994**, *19*, 843.
3. D.B. Amabilino, J.F. Stoddart, *Chem. Rev.*, **1995**, *95*, 2725.
4. J.-C. Chambron, C.O. Dietrich-Buchecker, J.-P. Sauvage, in *Comprehensive Supramolecular Chemistry* (Eds. J.L. Atwood, J.E.D. Davies, D.D. MacNicol, F. Vögtle), Pergamon Press, Oxford, **1996**, Vol. 9, p. 43.
5. (a) D.B. Amabilino, F.M. Raymo, J.F. Stoddart, in *Comprehensive Supramolecular Chemistry* (Eds. J.L. Atwood, J.E.D. Davies, D.D. MacNicol, F. Vögtle), Pergamon Press, Oxford, **1996**, Vol. 9, p. 85. (b) D. Philp, J.F. Stoddart, *Angew. Chem. Int. Ed. Engl.*, **1996**, *35*, 1154.
6. R. Jäger, F. Vögtle, *Angew. Chem. Int. Ed. Engl.*, **1997**, *36*, 931.
7. D.G. Hamilton, J.E. Davies, L. Prodi, J.K.M. Sanders, *Chem. Eur. J.*, **1998**, *4*, 608.
8. F.M. Raymo, J.F. Stoddart, *Chem. Rev.*, **1999**, *99*, 1643.

9. *Catenanes, Rotaxanes and Knots* (Eds.: J.-P. Sauvage, C.O. Dietrich-Buchecker), Wiley-VCH, Weinheim, **1999**.
10. G.A. Breault, C.A. Hunter, P.C. Mayers, *Tetrahedron*, **1999**, 55, 5265.
11. (a) P.R. Ashton, R. Ballardini, V. Balzani, M. Belohradsky, M.T. Gandolfi, D. Philp, L. Prodi, F.M. Raymo, M.V. Reddington, N. Spencer, J.F. Stoddart, M. Venturi, D.J. Williams, *J. Am. Chem. Soc.*, **1996**, 118, 4931. (b) M. Asakawa, P.R. Ashton, R. Ballardini, V. Balzani, M. Belohradsky, M.T. Gandolfi, O. Kocian, L. Prodi, F.M. Raymo, J.F. Stoddart, M. Venturi, *J. Am. Chem. Soc.*, **1997**, 119, 302. (c) P.R. Ashton, I. Baxter, M.C.T. Fyfe, F.M. Raymo, N. Spencer, J.F. Stoddart, A.J.P. White, D.J. Williams, *J. Am. Chem. Soc.*, **1998**, 120, 2297.
12. E. Wasserman, *J. Am. Chem. Soc.*, **1960**, 82, 443.
13. I.T. Harrison, S.J. Harrison, *J. Am. Chem. Soc.*, **1967**, 89, 5732.
14. B. Hudson, A.J. Vinograd, *Nature*, **1967**, 216, 647.
15. S.A. Wasserman, N.R. Cozzarelli, *Science*, **1986**, 232, 951.
16. (a) G. Agam, D. Graiver, A. Zilkha, *J. Am. Chem. Soc.*, **1976**, 98, 5206. (b) G. Agam, A. Zilkha, *J. Am. Chem. Soc.*, **1976**, 98, 5214.
17. D.M. Walba, R.M. Richards, R.C. Haltiwanger, *J. Am. Chem. Soc.*, **1982**, 104, 3219.
18. G. Schill, A. Lüttringhaus, *Angew. Chem. Int. Ed. Engl.*, **1964**, 3, 546.
19. G. Schill, W. Beckmann, W. Vetter, *Chem. Ber.*, **1980**, 113, 941.
20. (a) J.-M. Lehn, *Angew. Chem. Int. Ed. Engl.*, **1988**, 27, 89. (b) D.J. Cram, *Angew. Chem. Int. Ed. Engl.*, **1988**, 27, 1009. (c) C.J. Pedersen, *Angew. Chem. Int. Ed. Engl.*, **1988**, 27, 1021.
21. *Comprehensive Supramolecular Chemistry* (Eds. J.L. Atwood, J.E.D. Davies, D.D. MacNicol, F. Vögtle), Pergamon Press, Oxford, **1996**, Vol. 2.
22. D.H. Busch, A.L. Vance, A.G. Kolchinski, in *Comprehensive Supramolecular Chemistry* (Eds. J.L. Atwood, J.E.D. Davies, D.D. MacNicol, F. Vögtle), Pergamon Press, Oxford, **1996**, Vol. 9, p. 1.
23. P.L. Anelli, P.R. Ashton, R. Ballardini, V. Balzani, M. Delgado, M.T. Gandolfi, T.T. Goodnow, A.E. Kaifer, D. Philp, M. Pietraszkiewicz, L. Prodi, M.V. Reddington, A.M.Z. Slawin, N. Spencer, J.F. Stoddart, C. Vicent, D.J. Williams, *J. Am. Chem. Soc.*, **1992**, 114, 193.
24. A.G. Kolchinski, N.W. Alcock, R.A. Roesner, D.H. Busch, *Chem. Commun.*, **1998**, 1437.
25. (a) C.A. Hunter, *J. Am. Chem. Soc.*, **1992**, 114, 5003. (b) A.G. Johnston, D.A. Leigh, R.J. Pritchard, M.D. Degan, *Angew. Chem. Int. Ed. Engl.*, **1995**, 34, 1209. (c) F. Vögtle, T. Dunnwald, T. Schmidt, *Acc. Chem. Res.*, **1996**, 29, 451.
26. (a) D.B. Amabilino, M. Asakawa, P.R. Ashton, R. Ballardini, V. Balzani, M. Belohradsky, A. Credi, M. Highuci, F.M. Raymo, T. Shimizu, J.F. Stoddart, M. Venturi, K. Yae, *New J. Chem.*, **1998**, 22, 959. (b) D. B. Amabilino, P.R. Ashton, V. Balzani, C.L. Brown, A. Credi, J.M.J. Fréchet, J.W. Leon, F.M. Raymo, N. Spencer, J.F. Stoddart, M. Venturi, *J. Am. Chem. Soc.*, **1996**, 118, 12012. (c) D. Amabilino, P.R. Ashton, V. Balzani, S.E. Boyd, A. Credi, J.Y. Lee, S. Menzer, J.F. Stoddart, M. Venturi, D.J. Williams, *J. Am. Chem. Soc.*, **1998**, 120, 4295. (d) D.B. Amabilino, P.R. Ashton, J.A. Bravo, F.M. Raymo, J.F. Stoddart, A.J.P. White, D.J. Williams, *Eur. J. Org. Chem.*, **1999**, 1295. (e) P.R. Ashton, V. Baldoni, V. Balzani, C.G. Claessens, A. Credi, H.D.A. Hoffmann, F.M. Raymo, J.F. Stoddart, M. Venturi, A.J.P. White, D.J. Williams, *Eur. J. Org. Chem.*, **2000**, 1121.
27. (a) Z.-T. Li, P.C. Stein, N. Svenstrup, K.H. Lund, J. Becher, *Angew. Chem. Int. Ed. Engl.*, **1995**, 34, 2524. (b) Z.-T. Li, P.C. Stein, J. Becher, D. Jensen, P. Mørk, N. Svenstrup, *Chem. Eur. J.*, **1996**, 2, 624. (c) M.B. Nielsen, Z.-T. Li, J. Becher, *J. Mater. Chem.*, **1997**, 7, 1175. (d) M.B. Nielsen, J. Becher, *Liebigs Ann./Recueil*, **1997**, 2177.
28. M.B. Nielsen, N. Thorup, J. Becher, *J. Chem. Soc. Perkin Trans. 1*, **1998**, 1305.
29. (a) C. Yamamoto, Y. Okamoto, T. Schmidt, R. Jager, F. Vögtle, *J. Am. Chem. Soc.*, **1997**, 119, 10547. (b) A. Mohry, H. Schwier, F. Vögtle, *Synthesis*, **1999**, 1753.
30. V. Balzani, M. Gómez-López, J. F. Stoddart, *Acc. Chem. Res.*, **1998**, 31, 405.
31. D.A. Leigh, A. Murphy, *Chem. Ind.*, **1999**, March 1, 179.
32. V. Balzani, A. Credi, M. Venturi, in *Supramolecular Science: Where It Is and Where It Is Going* (Eds. R. Ungaro, E. Dalcanele), Kluwer, Dordrecht, **1999**, p. 1.
33. V. Balzani, A. Credi, F.M. Raymo, J.F. Stoddart, *Angew. Chem. Int. Ed.*, **2000**, 33, 3349.
34. R. Ballardini, V. Balzani, M.T. Gandolfi, R.E. Gillard, J.F. Stoddart, E. Tabellini, *Chem. Eur. J.*, **1998**, 4, 449.

35. E.A. Smith, R.R. Lillenthal, R.J. Fonseca, D.K. Smith, *Anal. Chem.*, **1994**, 66, 3013.
36. (a) P.R. Ashton, R. Ballardini, V. Balzani, A. Credi, M.T. Gandolfi, S. Menzer, L. Pérez-García, L. Prodi, J.F. Stoddart, M. Venturi, A.J.P. White, D.J. Williams, *J. Am. Chem. Soc.*, **1995**, 117, 11171. (b) R. Ballardini, V. Balzani, C.L. Brown, A. Credi, R.E. Gillard, M. Montalti, D. Philp, J.F. Stoddart, M. Venturi, A.J.P. White, B.J. Williams, D.J. Williams, *J. Am. Chem. Soc.*, **1997**, 119, 12503.
37. E. Cordova, R.A. Bissell, A.E. Kaifer, *J. Org. Chem.*, **1995**, 60, 1033.
38. A.H. Parham, B. Windsch, F. Vögtle, *Eur. J. Org. Chem.*, **1999**, 1233.
39. (a) P.L. Anelli, N. Spencer, J.F. Stoddart, *J. Am. Chem. Soc.*, **1991**, 113, 5131. (b) P.L. Anelli, M. Asakawa, P.R. Ashton, R.A. Bissell, G. Clavier, R. Górski, A.E. Kaifer, S.J. Langford, G. Mattersteig, S. Menzer, D. Philp, A.M.Z. Slawin, N. Spencer, J.F. Stoddart, M.S. Tolley, D.J. Williams, *Chem. Eur. J.*, **1997**, 3, 1113. (c) P.R. Ashton, D. Philp, N. Spencer, J.F. Stoddart, *J. Chem. Soc. Chem. Commun.*, **1992**, 1124.
40. M.C.T. Fyfe, P.T. Glink, S. Menzer, J.F. Stoddart, A.J.P. White, D.J. Williams, *Angew. Chem. Int. Ed. Engl.*, **1997**, 36, 2068.
41. (a) V. Balzani, F. Scandola, *Supramolecular Photochemistry*, Horwood, New York, **1991**. (b) V. Balzani, *Tetrahedron*, **1992**, 48, 10443. (c) R.A. Bissell, A.P. de Silva, H.Q.N. Gunaratne, P.L.M. Lynch, G.E.M. Maguire, C.P. McCoy, K.R.A.S. Sandanayake, *Top. Curr. Chem.*, **1993**, 168, 223. (d) L. Fabbrizzi, A. Poggi, *Chem. Soc. Rev.*, **1995**, 24, 197. (e) A.C. Benniston, *Chem. Soc. Rev.*, **1996**, 25, 427. (f) M. Gómez-López, J.A. Preece, J.F. Stoddart, *Nanotechnology*, **1996**, 7, 183. (g) M.D. Ward, *Chem. Ind.*, **1997**, 640. (h) V. Balzani, A. Credi, F. Scandola, *Chim. Ind. (Rome)*, **1997**, 79, 751. (i) M. Venturi, A. Credi, V. Balzani, *Coord. Chem. Rev.*, **1999**, 185/186, 233. (j) T.M. Swager, *Acc. Chem. Res.*, **1998**, 31, 201. (k) J.-P. Sauvage, *Acc. Chem. Res.*, **1998**, 31, 611. (l) J.-C. Chambron, J.-P. Sauvage, *Chem. Eur. J.*, **1998**, 4, 1362. (m) A.E. Kaifer, *Acc. Chem. Res.*, **1999**, 32, 62.
42. For examples of solvent-induced co-conformational changes in [2]rotaxanes, see: (a) C. Gong, H.W. Gibson, *Angew. Chem. Int. Ed. Engl.*, **1997**, 36, 2331; (b) A.X. Lane, D.A. Leigh, A. Murphy, *J. Am. Chem. Soc.*, **1997**, 119, 11092; (c) W. Clegg, C. Gimenez-Saiz, D.A. Leigh, A. Murphy, A.M.Z. Slawin, S.J. Teat, *J. Am. Chem. Soc.*, **1999**, 121, 4124. For examples of solvent-induced co-conformational changes in [2]catenanes, see Ref. [34] and: (d) P.R. Ashton, M. Blower, D. Philp, N. Spencer, J.F. Stoddart, M.S. Tolley, *New J. Chem.*, **1993**, 17, 689. (e) D.A. Leigh, K. Moody, J.P. Smart, K.J. Watson, A.M.Z. Slawin, *Angew. Chem. Int. Ed. Engl.*, **1996**, 35, 306. (f) M. Asakawa, P.R. Ashton, W. Dehaen, G. L'abbé, S. Menzer, J. Nouwen, F.M. Raymo, J.F. Stoddart, M.S. Tolley, S. Toppet, A.J.P. White, D.J. Williams, *Chem. Eur. J.*, **1997**, 3, 772.
43. (a) R.A. Bissell, E. Córdova, A.E. Kaifer, J.F. Stoddart, *Nature*, **1994**, 369, 133. (b) E. Córdova, R.A. Bissell, N. Spencer, P.R. Ashton, J.F. Stoddart, A.E. Kaifer, *J. Org. Chem.*, **1993**, 58, 6550.
44. R. Ballardini, V. Balzani, W. Dehaen, A.E. Dell'Erba, F.M. Raymo, J.F. Stoddart, M. Venturi, *Eur. J. Org. Chem.*, **1999**, 591.
45. (a) N. Armadori, V. Balzani, J.-P. Collin, P. Gaviña, J.-P. Sauvage, B. Ventura, *J. Am. Chem. Soc.*, **1999**, 121, 4397. (b) L. Raehm, J.-M. Kern, J.-P. Sauvage, *Chem. Eur. J.*, **1999**, 5, 3310.
46. (a) A.C. Benniston, A. Harriman, *Angew. Chem. Int. Ed. Engl.*, **1993**, 32, 1459. (b) A.C. Benniston, A. Harriman, V.M. Lynch, *Tetrahedron Lett.*, **1994**, 35, 1473. (c) A.C. Benniston, A. Harriman, V.M. Lynch, *J. Am. Chem. Soc.*, **1995**, 117, 5275.
47. P.R. Ashton, R. Ballardini, V. Balzani, A. Credi, R. Dress, E. Ishow, C.J. Kleverlaan, O. Kocian, J.A. Preece, N. Spencer, J.F. Stoddart, M. Venturi, S. Wagner, *Chem. Eur. J.*, **2000**, 6, 3558.
48. H. Murakami, A. Kawabuchi, K. Kotoo, M. Kunitake, N. Nakashima, *J. Am. Chem. Soc.*, **1997**, 119, 7605.
49. P.R. Ashton, R. Ballardini, V. Balzani, I. Baxter, A. Credi, M.C.T. Fyfe, M.T. Gandolfi, M. Gómez-López, M.-V. Martínez-Díaz, A. Piersanti, N. Spencer, J.F. Stoddart, M. Venturi, A.J.P. White, D.J. Williams, *J. Am. Chem. Soc.*, **1998**, 120, 11932.
50. W. Clegg, C. Gimenez-Saiz, D.A. Leigh, A. Murphy, A.M.Z. Slawin, S.J. Teat, *J. Am. Chem. Soc.*, **1999**, 121, 4124.
51. P.R. Ashton, V. Balzani, A. Credi, O. Kocian, D. Pasini, L. Prodi, N. Spencer, J.F. Stoddart, M.S. Tolley, M. Venturi, A.J.P. White, D.J. Williams, *Chem. Eur. J.*, **1998**, 4, 590.

52. (a) J. Deisenhofer, H. Michel, *Angew. Chem. Int. Ed. Engl.*, **1989**, 28, 829. (b) R. Huber, *Angew. Chem. Int. Ed. Engl.*, **1989**, 28, 848.
53. A. Benniston, P.R. Mackie, A. Harriman, *Angew. Chem. Int. Ed.*, **1998**, 37, 354.
54. (a) Y.-Z. Hu, D. van Loyen, O. Schwarz, S. Bossmann, H. Dürr, V. Huch, M. Veith, *J. Am. Chem. Soc.*, **1998**, 120, 5822. (b) Y.-Z. Hu, S. Bossmann, D. van Loyen, O. Schwarz, H. Dürr, *Chem. Eur. J.*, **1999**, 5, 1261.
55. Y.-Z. Hu, S. Tsukiji, S. Shinkai, I. Hamachi, *Chem. Lett.*, **1999**, 517.
56. M.J. Gunter, D.C.R. Hockless, M.R. Johnston, B.W. Skelton, A.H. White, *J. Am. Chem. Soc.*, **1994**, 116, 4810.
57. M.J. Gunter, M.R. Johnston, *J. Chem. Soc. Chem. Commun.*, **1994**, 829.
58. Z.-T. Li, G.-Z. Ji, C.-X. Zhao, S.-D. Yuan, H. Ding, C. Huang, A.-L. Du, M. Wei, *J. Org. Chem.*, **1999**, 64, 3572.
59. M. Asakawa, P.R. Ashton, V. Balzani, A. Credi, C. Hamers, G. Mattersteig, M. Montalti, A.N. Shipway, N. Spencer, J.F. Stoddart, M.S. Tolley, M. Venturi, A.J.P. White, D.J. Williams, *Angew. Chem. Int. Ed.*, **1998**, 37, 333.
60. For the electrochemically controlled suppression of the circumrotation of the macrocyclic components of a [2]catenane, see: P. Ceroni, D.A. Leigh, L. Mottier, F. Paolucci, S. Roffia, D. Tetard, F. Zerbetto, *J. Phys. Chem. B*, **1999**, 103, 10171.
61. For the electrochemical characterization of a neutral [2]catenane incorporating π -electron-rich and π -electron-deficient components, see: D.G. Hamilton, M. Montalti, L. Prodi, M. Fontani, P. Zanello, J.K.M. Sanders, *Chem. Eur. J.*, **2000**, 6, 608.
62. P.R. Ashton, R. Ballardini, V. Balzani, M.T. Gandolfi, D.J.-F. Marquis, L. Pérez-García, L. Prodi, J.F. Stoddart, M. Venturi, *J. Chem. Soc. Chem. Commun.*, **1994**, 177.
63. D.J. Cárdenas, A. Livoreil, J.-P. Sauvage, *J. Am. Chem. Soc.*, **1996**, 118, 11980.
64. A. Livoreil, J.-P. Sauvage, N. Armaroli, V. Balzani, L. Flamigni, B. Ventura, *J. Am. Chem. Soc.*, **1997**, 119, 12114.
65. (a) F. Vögtle, W.M. Müller, U. Müller, M. Bauer, K. Rissanen, *Angew. Chem. Int. Ed. Engl.*, **1993**, 32, 1295. (b) M. Bauer, W.M. Müller, U. Müller, K. Rissanen, F. Vögtle, *Liebigs Ann.*, **1995**, 649. (c) M. Asakawa, P.R. Ashton, V. Balzani, C.L. Brown, A. Credi, O.A. Matthews, S.P. Newton, F.M. Raymo, A.N. Shipway, N. Spencer, A. Quick, J.F. Stoddart, J.P. White, D.J. Williams, *Chem. Eur. J.*, **1999**, 5, 860.
66. V. Balzani, A. Credi, G. Mattersteig, O.A. Matthews, F.M. Raymo, J.F. Stoddart, M. Venturi, A.J.P. White, D.J. Williams, *J. Org. Chem.*, **2000**, 65, 1924.
67. P.R. Ashton, S.E. Boyd, A. Brindle, S.J. Langford, S. Menzer, L. Pérez-García, J.A. Preece, F.M. Raymo, N. Spencer, J.F. Stoddart, A.J.P. White, D.J. Williams, *New J. Chem.*, **1999**, 23, 587.
68. V. Balzani, A. Credi, S.J. Langford, F.M. Raymo, J.F. Stoddart, M. Venturi, *J. Am. Chem. Soc.*, **2000**, 122, 3542.
69. (a) D.S. Goodsell, *Our Molecular Nature: The Body's Motors, Machines, and Messages*, Copernicus, New York, **1996**. (b) P.D. Boyer, *Annu. Rev. Biochem.*, **1997**, 66, 717. (c) P.R. Cook, *Science*, **1999**, 284, 1790.
70. (a) R.P. Feynman, *Eng. Sci.*, **1960**, 23(5), 22. (b) R.P. Feynman, *Sat. Rev.*, **1960**, 43, 45.
71. S. Shinkai, O. Manabe, *Top. Curr. Chem.*, **1984**, 121, 67.
72. (a) A.P. de Silva, H.Q.N. Gunaratne, C.P. McCoy, *Nature*, **1993**, 364, 42. (b) A.P. de Silva, H.Q.N. Gunaratne, T. Gunnlaugsson, A.J.M. Huxley, C.P. McCoy, J.T. Rademacher, T.E. Rice, *Chem. Rev.*, **1997**, 97, 1515. (c) A. Credi, V. Balzani, S.J. Langford, J.F. Stoddart, *J. Am. Chem. Soc.*, **1997**, 119, 2679. (d) F. Pina, A. Roque, M.J. Melo, M. Maestri, L. Belladelli, V. Balzani, *Chem. Eur. J.*, **1998**, 4, 1184. (e) A.P. de Silva, H.Q.N. Gunaratne, C.P. McCoy, *J. Am. Chem. Soc.*, **1999**, 121, 1393. (f) T. Gunnlaugsson, D. A. MacDónail, D. Parker, *Chem. Commun.*, **2000**, 93.
73. (a) *Molecular Electronic Devices* (Ed.: F.L. Carter), Dekker, New York, **1982**. (b) *Molecular Electronic Devices* (Ed.: F.L. Carter), Dekker, New York, **1987**. (c) *Molecular Electronic Devices* (Eds.: F.L. Carter, R.E. Siatkowski, H. Wohltjen), Elsevier, Amsterdam, **1988**. (d) *Molecular Electronics. Science and Technology* (Ed.: A. Aviram), Engineering Foundation, New York, **1989**. (e) *Molecular Electronics: Materials and Methods* (Ed.: P.I. Lazarev), Kluwer Academic Publishers, Dordrecht, **1991**. (f) *Molecular Electronics* (Ed.: G.J. Ashwell), Wiley,

- New York, **1992**. (g) *Introduction to Molecular Electronic Devices* (Eds.: M.C. Petty, M.R. Bryce, D. Bloor), Oxford University Press, New York, **1995**. (h) *Molecular Electronics* (Eds.: J. Jortner, M. Ratner), Blackwell Science, Oxford, **1997**. (i) *Molecular Electronics: Science and Technology* (Eds.: A. Aviram, M. Ratner), New York Academy of Sciences, New York, **1998**. (j) *Chem. Rev.*, **1999**, 99, 1641–1990 (Special Issue on Nanostructures).
74. D.A. Muller, T. Sorsch, S. Moccio, F.H. Baumann, K. Evans-Lutterodt, G. Timp, *Nature*, **1999**, 399, 758.
 75. D.H. Rouvray, *Chem. Br.*, **1998**, 34(2), 26.
 76. An intriguing question about molecular machines is to establish which components are moving and which are not. Since, in solution, the motions of the molecular components cannot be referred to a fixed reference point, the question cannot even be addressed. One answer to this question is the immobilization of one or more components to a fixed frame such as a surface.
 77. For recent examples of Langmuir films composed of molecular and supramolecular systems incorporating interlocked components, see: (a) R.C. Ahuja, P.-L. Caruso, D. Möbius, G. Wildburg, H. Ringsdorf, D. Philp, J.A. Preece, J.F. Stoddart, *Langmuir*, **1993**, 9, 1534. (b) R.C. Ahuja, P.-L. Caruso, D. Möbius, D. Philp, J.A. Preece, H. Ringsdorf, J.F. Stoddart, G. Wildburg, *Thin Solid Films*, **1996**, 284/285, 671. (c) D.B. Amabilino, M. Asakawa, P.R. Ashton, R. Ballardini, V. Balzani, M. Belohradsky, A. Credi, M. Higuchi, F.M. Raymo, T. Shimizu, J.F. Stoddart, M. Venturi, K. Yase, *New J. Chem.*, **1998**, 959. (d) D.E. Lynch, D.G. Hamilton, N.J. Calos, B. Wood, J.K.M. Sanders, *Langmuir*, **1999**, 15, 5600.
 78. For recent examples of supramolecular systems deposited on surfaces, see: (a) P. Laitenberger, C.G. Claessens, L. Kuipers, F.M. Raymo, R.E. Palmer, J.F. Stoddart, *Chem. Phys. Lett.*, **1997**, 279, 209. (b) G. Ashkenasy, G. Kalyuzhny, J. Libman, I. Rubinstein, A. Shanzer, *Angew. Chem. Int. Ed.*, **1999**, 38, 1257. (c) M. Lahav, L. Leiserowitz, *Angew. Chem. Int. Ed.*, **1999**, 38, 2533. (d) A. Semenov, J.P. Spatz, M. Möller, J.-M. Lehn, B. Sell, D. Schubert, C.H. Weidl, U.S. Schubert, *Angew. Chem. Int. Ed.*, **1999**, 38, 2547. (e) N. Bampos, C.N. Woodburn, M.E. Welland, J.K.M. Sanders, *Angew. Chem. Int. Ed.*, **1999**, 38, 2780. (f) H. Imahori, H. Yamada, S. Ozawa, K. Ushida, Y. Sakata, *Chem. Commun.*, **1999**, 1165.
 79. For an example of fabrication of logic gates from an array of Langmuir-type monolayer of rotaxanes sandwiched between two electrodes, see: (a) C.P. Collier, E.W. Wong, M. Belohradsky, F.M. Raymo, J.F. Stoddart, P.J. Kuekes, R.S. Williams, J.R. Heath, *Science*, **1999**, 285, 391. (b) E.W. Wong, C.P. Collier, M. Belohradsky, F.M. Raymo, J.F. Stoddart, J.R. Heath, *J. Am. Chem. Soc.*, submitted.
 80. T. Lu, L. Zhang, G.W. Gokel, A.E. Kaifer, *J. Am. Chem. Soc.*, **1993**, 115, 2542. For a related system based on a “Cu-precateenate”, see: J.-M. Kern, L. Raehm, J.-P. Sauvage, *C. R. Acad. Sci. Paris*, **1999**, 2, 41.
 81. G. Bidan, M. Billon, B. Divisia-Blohorn, J.-M. Kern, L. Raehm, J.-P. Sauvage, *New J. Chem.*, **1998**, 1139. For related recent examples, see: J. Buey, T.M. Swager, *Angew. Chem. Int. Ed.*, **2000**, 39, 608; C.P. Collier, E.W. Wong, M. Belohradsky, F.M. Raymo, J.F. Stoddart, P.J. Kuekes, R.S. Williams, J.R. Heath, *Science*, **1999**, 285, 391.
 82. (a) X. Marguerettaz, G. Redmond, S.N. Rao, D. Fitzmaurice, *Chem. Eur. J.*, **1996**, 2, 420. (b) L. Cusack, S.N. Rao, D. Fitzmaurice, *Chem. Eur. J.*, **1997**, 3, 202. (c) G. Will, G. Boschloo, R. Hoyle, S.N. Rao, D. Fitzmaurice, *J. Phys. Chem. B*, **1998**, 102, 10272. (d) S. Conolly, S.N. Rao, R. Rizza, N. Zaccheroni, D. Fitzmaurice, *Coord. Chem. Rev.*, **1999**, 185/186, 277.
 83. R. Argazzi, C. A. Bignozzi, V. Balzani, J. Cao, A. Credi, G. Mattersteig, F.M. Raymo, J.F. Stoddart, M. Venturi, in preparation.

8 Metal-Assembled Catenanes, Rotaxanes, and Knots

*Nicola Armaroli, Jean-Claude Chambron, Jean-Paul Collin,
Christiane Dietrich-Buchecker, Lucia Flamigni, Jean-Marc Kern, and
Jean-Pierre Sauvage*

8.1 Introduction

Twenty years ago, the only interlocking ring systems (catenanes) that had been made and convincingly characterized were those prepared by Schill and his coworkers [1]. In biology, DNA had also been shown to form simple to complex catenanes during certain processes or under the action of topoisomerases [2]. It was difficult to imagine that synthetic or natural interlocking rings would display any kind of interesting property related to electron transfer. Today, catenanes are almost common molecules, and they have been the subject of numerous studies dealing with electrochemistry, photoinduced electron transfer, and controlled molecular motions. This change of situation reflects the rapid evolution of the field of catenanes, rotaxanes, and knots [3]—part of the general area called *chemical topology* [4].

The synthesis of these chemical objects has been made possible thanks to the introduction of template reactions, either using transition metal complexes or organic functions as templating cores. The concept of templated synthesis itself was introduced several decades ago, in particular by Busch and his coworkers [5], simultaneously to the accidental preparation of a macrocyclic nickel(II) complex from very simple organic precursors [6]. The recognition that a transition metal can be used to gather various organic fragments in its coordination sphere, maintain and orient them in a given geometry so as to allow the preparation of well-defined and relatively sophisticated multifunctional ligands after the appropriate covalent bonds have been formed, is indeed conceptually very important. It has opened the door to many multicomponent compounds incorporating one or several transition metal centers. More importantly, in the present context, it has provided the precursor ideas which allowed to make the first [2]catenane (consisting of two interlocking rings) complexed to a transition metal center more than 15 years ago [7].

Catenanes have a nonplanar molecular graph, which means that it will be impossible to draw their backbone on a sheet of paper without introducing crossing

points (two for a [2]catenane), regardless of the deformation that the chemical bonds can undergo (bond angles and lengths). In this respect, catenanes are really three-dimensional species. They are thus very well adapted to the complexation of transition metals which, in most cases, interact with ligands disposed in a three-dimensional space and not only in a plane. As will be discussed in this chapter, this property of controlling the coordination polyhedron of the metal is one of the characteristics of the present molecules. By imposing a given arrangement, and in particular a tetrahedral geometry, the electrochemical properties of the corresponding complexes are of special interest. A striking example is that of stable nickel(I) complexes, whose relatively easy isolation relies on the special stabilization of low oxidation states (Co^{I} , Ni^{I} , or Cu^{I}) provided by a tetrahedral arrangement.

Interlocking structure provides to the corresponding multicomponent assemblies the ability to move and rearrange by gliding one given ring within another ring with which it is interlocked, or by translating a wheel along an axle which threads it. This unique feature allows reversible rearrangements of the coordination sphere (from tetrahedral to 5-coordinate or more, and vice versa). Electron transfer, in this case, is followed by motion: a redox process triggers a controlled rearrangement of the metal ligands set, this large amplitude motion being facilitated by the interlocking nature of the compounds.

Another specificity of catenanes and rotaxanes relates to the marked flexibility of the molecules once demetallated, and to the very large geometric differences between the complexes and free ligands. Such a property can be utilized to test electron transfer theories if the molecules incorporate donor and acceptor groups (porphyrins, in general), whose distance and mutual orientation can be dramatically modified at will by metallating or demetallating the appropriate coordination sites. Interestingly, most—if not all—of the compounds described in the present chapter display novel photophysical and photochemical properties, leading to intramolecular energy or electron transfer between given components of the system.

8.2 Electrochemical Properties of Metallocatenates and Knots

8.2.1 Introduction

A catenane consists of two or several interlocked macrocycles, whereas a trefoil molecular knot is formed by a single closed molecular thread displaying three crossing points. The particular class of catenanes and molecular knots that has been synthesized and studied, combines the topological properties of systems having a nonplanar graph [1a, 4a, 8] with the complexing ability of 1,10-phenanthroline-type chelates or terpyridine-type chelates [9, 10]. Therefore, they can behave as ligands, and the resulting complexes are called catenates.

In most of the metallocatenates described here, the coordinating rings include 2,9-di-*p*-phenyl-1,10-phenanthroline (dpp) derivatives as complexing subunit. The special arrangement of the coordinating fragments that form the complexing core is

due to the nature of these fragments. By complexation to a metal, two dpp subunits lock together, while binding the metal, and adopt an entwined topography. The highly rigid and encaging system thus obtained favors distorted tetrahedral geometries. The aromatic character of the ligands and their strong π - π accepting ability, together with the preferred shape of catenates, are expected to highly stabilize low oxidation states, for two different reasons. The first factor, π - π donor-acceptor character of the coordinating subunits, is really stabilizing, whereas the second factor corresponds to a strong destabilization of high oxidation states, due to the poor ligand field of tetrahedral geometry and to steric factors that disfavor 5-coordinate complexes. The topography of the system [10] is thus such that low oxidation states will be preferred to high valence states. The topographic properties of a complex are related to the shape of the molecule and to the bond lengths and angles within the coordination site. The stability of the complexes (kinetic and thermodynamic) will now be measured by the topology of the ligand: the interlocking of the rings prevents the dpp subunits from dissociating, and thus greatly contributes to inhibiting dissociation of the complexes. Thus, complexes of unusually low valence states may be made and isolated with interlocked ligands, whereas the corresponding acyclic dpp complexes are too labile to be studied.

Electrochemical and photophysical properties of metallocatenates are strongly dependent on the geometry of the coordinating sphere of the central metal(s). In this section, which is devoted to the electrochemical properties of metallocatenates, we will first describe the particular properties of various [2]catenates in which the metal is tetracoordinated, that is the constitutive macrocycles of the [2]catenates contain a dpp moiety each. The interaction of metal centers in homodinuclear [3]catenates and in molecular knots will be developed in Sections 8.2.5 and 8.2.6. In Section 8.2.7, the electrochemical properties of a ruthenium [2]catenate will be discussed. In that case, each ring includes a tris-chelating moiety, a terpyridine (tpy), providing an octahedral environment to the templating metal. Catenates formed with homo- and/or heterobischelating macrocycles will deal with the field of molecular machines, and their particular properties are described in Section 8.5.

8.2.2 Metallo[2]catenates in which the Metal is in a Tetrahedral Environment: Stabilization of Low Oxidation States

The basic framework of the catenanes (Cat) described in this section (free ligand and metal complexes) is presented in Figure 1.

For comparison, 2,9-di-*p*-anisyl-1,10-phenanthroline **1** (dap), which can be considered as the acyclic analogue of the various investigated catenanes, has also been examined (Figure 2). In particular, the ability of dap to stabilize low oxidation states has been tested in parallel to that of Cat. The propensity of aromatic polyimine chelates to stabilize the low oxidation states was recognized long ago. The most studied cases are probably those of Fe^{II} and Cu^{I} . For the former, the stability of the tris-bipyridine (bpy) complex was demonstrated in particular by the high redox potential of the $\text{Fe}^{3+}/\text{Fe}^{2+}$ couple (+1.026 V versus NHE in 1 M H_2SO_4 [11] and +1.012 V versus SCE in CH_3CN [12].

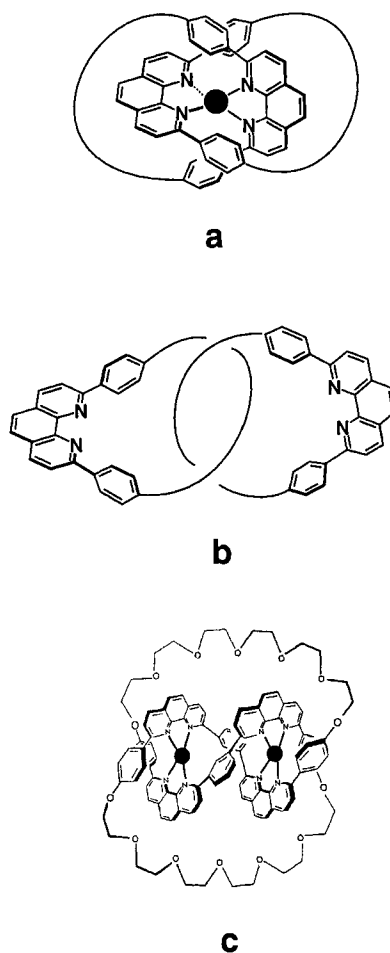


Figure 1. Schematic framework of a dpp-containing metallocatenate (a), of the related free ligand (b) and of a metallated molecular knot (c).

The question related to the oxidation number of the transition metal in certain highly reduced compounds was also addressed a long time ago [13–15]. It was noticed that, in particular, the 18-electron rule was no longer valid for a variety of complexes [16]. Clearly, complexes of metals in formally negative or zero oxidation states are in some cases best regarded as complexes of the ligand anion. Catenanes and their acyclic analogue dap contain strong π -acceptor ligands of the phenanthroline (phen) type, and are thus expected to behave as discussed above. In addition, a very important characteristic of catenanes and, to a lesser extent, of dap is of geometric origin. The presence of bulky substituents α to the nitrogen atoms of the constitutive chelates inhibits the formation of octahedral complexes, but favors tetrahedral geometries. Due to the presence of two aromatic substituents α to the chelates, the metallocatenate (noted $[\text{M.Cat}]^{n+}$, M being the metal and Cat the catenane ligand) and $[\text{M}(\text{dap})_2]^{n+}$, adopt “an entwined topography”, which leads to

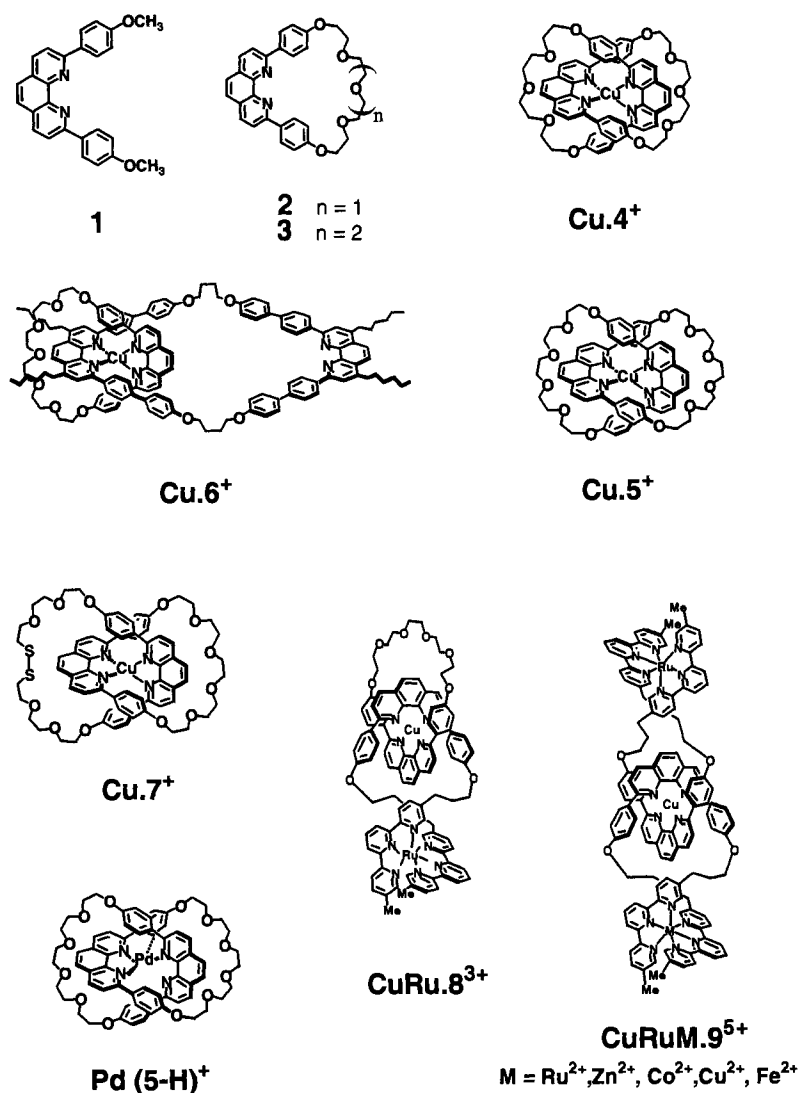


Figure 2. Representation of macrocycles, of the corresponding acyclic ligand **dap** (1), and of the different metallated [2]catenanes.

highly encaged and rigid systems. This particular geometry was evidenced by X-ray crystal analysis of the molecular structure of various catenanes [17]. In addition, the topological link of catenanes (interlocked ligands) inhibits separation in two coordinating subunits when they are complexed to a given cationic species. These characteristics enable Cat to bind strongly to transition metals, even in their lowest oxidation states. Comparison of Cat and dap complexes will evidence these topological factors, since the geometry around the complexed species M^{n+} is likely to

Table 1. ^a Cu^{2+/+} redox potentials^b of various copper [2]catenates

Compound	E ⁰ (V)	Compound	E ⁰ (V)
Cu^{2+/+}	1.05 ^c	Cu.Ru.8³⁺	0.58
Cu.4⁺	0.685	CuRuRu.9⁵⁺	0.64
Cu.5⁺	0.565	CuRuZn.9⁵⁺	0.68
Cu.6⁺	0.575	CuRuCo. 9⁵⁺	0.66
Cu.7⁺	0.70 ^d	CuRuCu.9⁵⁺	0.61
		CuRuFe.9⁵⁺	0.63

^a See text for references.^b Unless otherwise stated, all potentials refer to SCE in acetonitrile.^c E_{1/2}, see Ref. [23].^d Potential versus Ag quasi-reference, in dichloromethane.

be virtually identical for [M.Cat]ⁿ⁺ and [M(dap)₂]ⁿ⁺. Furthermore, Cat is able to complex transition metals even after having accepted one or two electrons, whereas dap complexes dissociate much more readily upon exhaustive reduction. Here again, this is related to the different topological properties of the two coordinating systems.

8.2.3 Copper [2]catenates

Copper [2]catenates were the most widely studied metallocatenates. Some are shown in Figure 2 in which the complexing core is formed by two dpp subunits. **Cu.5⁺** is a [2]catenate formed with two interlocked identical 30-membered macrocycles **3**. A copper [2]catenate made from a smaller homologue of **3**, the 27-membered ring **2**, has also been synthesized and studied [7a]. **Cu.5⁺** and the corresponding free ligand **5** [7b], are the archetypes of this wide family [10] of topologically nontrivial molecules formed by the catenanes. **2** [7a] and **3** [7b] differ only by the length of the polyoxoethylene chains which connect the para positions of the dpp moieties. The design of **6** [18] is noticeably different, the 56-membered ring including two 2,9-bis (*p*-biphenyl)-1,10-phenanthroline units. In **Cu.6⁺** only one chelating moiety is used for metal complexation, the other one being available for the coordination of another metal ion, and opening the way to the iterative construction of polycatenanes. In **Cu.7⁺**, the 34-membered macrocycle includes a disulfide bridge, allowing the chemisorption of this species onto a gold surface [19, 20]. **CuRu.8³⁺** [21] and **CuRuM.9⁵⁺** [22] (M = Ru²⁺, Zn²⁺, Co²⁺, Fe²⁺, Cu²⁺) are dimetallic or trimetallic complexes respectively, containing interlocking rings.

In CH₃CN or CH₂Cl₂, all copper(I) [2]catenates are reversibly oxidized to the divalent complexes (Figure 3). The oxidation potentials are high (~0.6 V versus SCE), making the Cu^{II} species relatively strong oxidants.

The present systems are noticeably different from [Cu(*bpy*)₂]⁺ for which the Cu^{2+/+} couple has a redox potential value of 0.19 V versus SCE [23]. The relatively high Cu²⁺/Cu⁺ redox potentials of the presently studied compounds are in good agreement with earlier systems: 6,6'-dimethyl-2,2'-bipyridine [24] (dmbp) or 2,9-

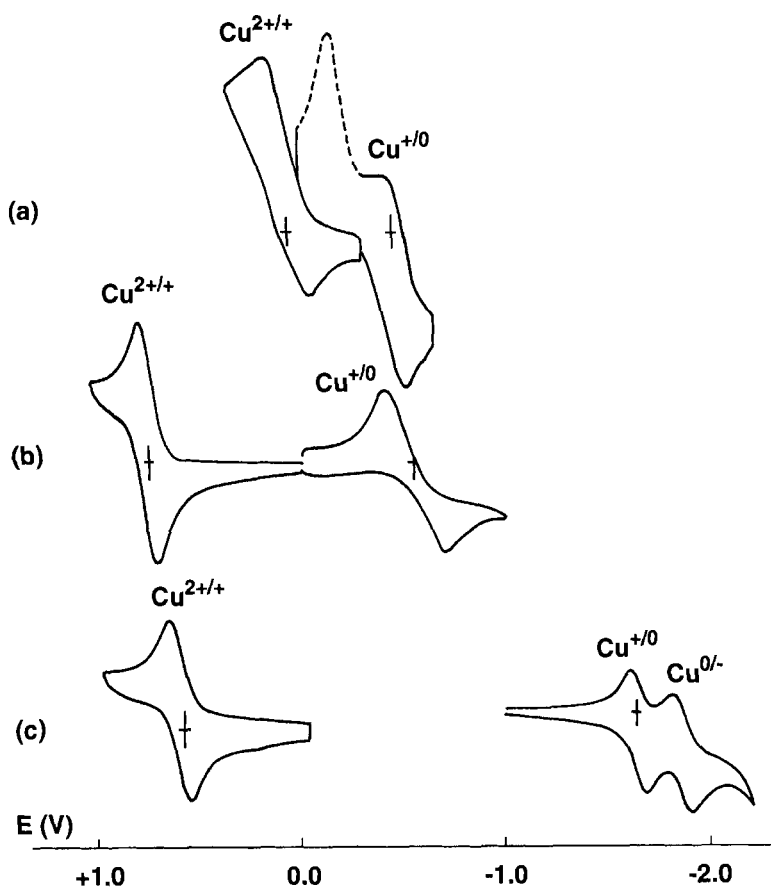


Figure 3. Cyclic voltammograms of bis-chelate copper complexes (a) $[\text{Cu}(\text{phen})_2]^+$ and (b) $[\text{Cu}(\text{dmbp})_2]^+$ in $\text{CH}_3\text{CN}-(n\text{-C}_4\text{H}_9)_4\text{NClO}_4$ (0.1 M), and (c) of copper-catenate Cu.5^+ in CH_3CN for oxidation, in DMF for reduction. Oxidation on Pt, reduction on the hanging mercury electrode.

dimethyl-1,10-phenanthroline complexes [24–26]. The particular redox properties of all those $\text{Cu}^{2+}/\text{Cu}^+$ couples can be assigned to geometric factors [27]. Cu.5^{2+} was readily and quantitatively electrogenerated from the copper(I) precursor [28]. The deep green catenate is stable in solution and can be crystallized. The low-energy band at 666 nm ($\epsilon = 820 \text{ M}^{-1} \text{ cm}^{-1}$) is ligand field in nature, this also being observed in related Cu^{II} complex $[\text{Cu}(\text{dpp})_2](\text{ClO}_4)_2$ [29], the structure of which showed a pseudotetrahedral geometry of the Cu^{II} center. Despite the closeness of the structures of Cu.4^+ and Cu.5^+ (they differ only by the length of the polyoxoethylene chains which connect the *para* positions of the dpp units) the oxidation potential of Cu.4^+ is noticeably more positive (124 mV) compared to that of the Cu.5^+ homologue [23]. This anodic shift of the redox potential can be explained by the more pronounced steric constraints in the Cu.4^+ homologue, preventing re-

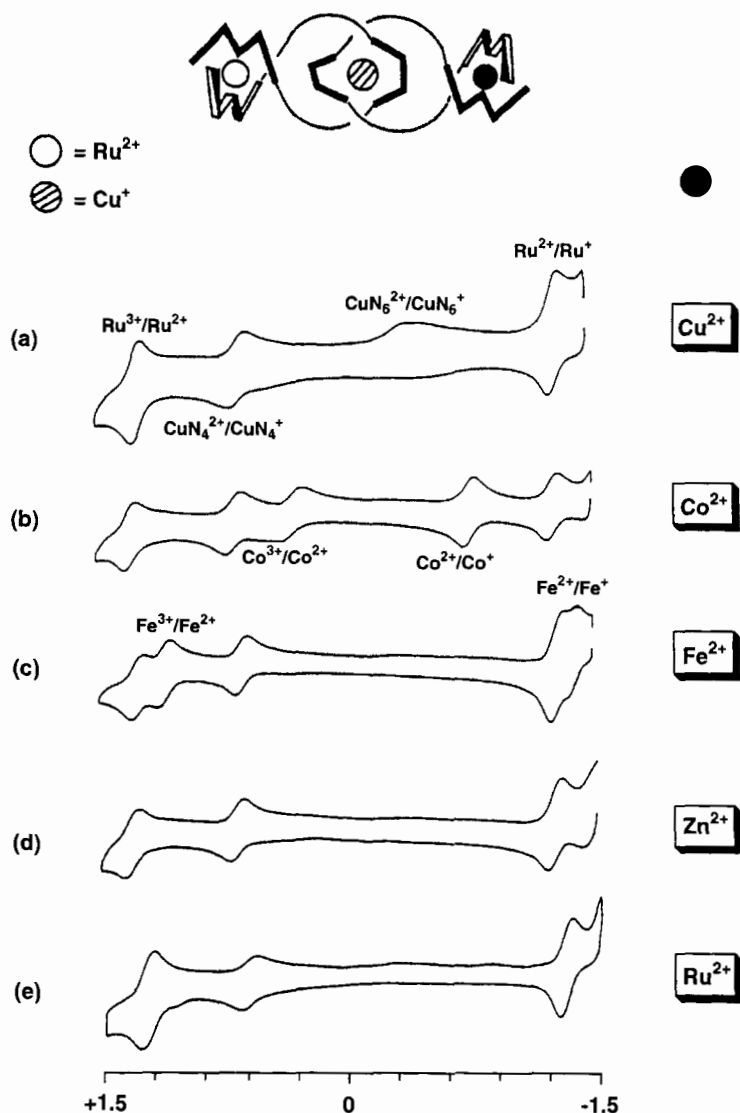


Figure 4. Cyclic voltammetry studies of the CuRuM.9^{5+} catenates containing two (a, e) or three (b, c, d) different metals, and clearly showing the distinct electrochemical response of each unit. The formal $\text{Ru}^{2+}/\text{Ru}^+$ couple corresponds to a ligand-localized process.

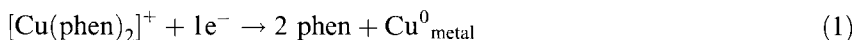
arrangement of the coordination geometry after oxidation. For the heterodimetallic and heterotrimetallic copper-catenates [21, 22], $\text{Cu}^{2+}/\text{Cu}^+$ redox potential values collected in Table 1 show minimal dependence (if any) on the various clipping metals (Figure 4). Reduction of copper(I) [2]catenates was only studied in detail [7b, 23, 28] for Cu.5^+ (Table 2).

Table 2. Electrochemical properties of **Cu.5**⁺ versus free Cu⁺ ion [23]^a

Cu.5 ⁺	E _{1/2} (V)	Free metal	E _{1/2} (V)
+2/+1	0.565 (CH ₃ CN)	+1/0	−0.31 ^{b,c} (CH ₃ CN)
+1/0	−1.650 (DMF)	+1/0	−0.53 ^{c,d} (CH ₃ CN)
0/−1	−1.860 (DMF)		

^a All potentials refer to SCE; the systems are reversible.^b Pt electrode.^c See Ref. [30].^d Polarography at the dropping mercury electrode.

Comparison of the reduction process with that of the acyclic analogue [Cu(1)₂]⁺ allowed to discriminate topographical and topological contributions to the overall electrochemical behavior of **Cu.5**⁺. For **Cu.5**⁺ (as for [Cu(1)₂]⁺), two reversible one-electron transfers are observed at very negative potentials (−1.650 and −1.860 V versus SCE for **Cu.5**⁺). This behavior is distinctly different from that of other complexes containing unsubstituted chelates, like *bpy* and *phen* (Figure 3). For instance, the following reductive dissociation takes place at −0.262 V [23]:



In the case of the *phen* complex, reduction of the monovalent state leads to copper metal, the initial electron transfer occurring either in the Cu 4s orbital or via a *phen* π^* orbital. Fast dissociation follows this monoelectronic reduction step. The redox orbitals involved during the reduction process of the copper catenate are likely to be ligand-localized. This is also supported by the small difference between the redox potentials of the Cu^{+1/0} and Cu^{0/−1} couples ($\Delta E_{1/2} \sim 200$ mV). Electrolysis of **Cu.5**⁺ in the cavity of an EPR spectrometer confirms the radical anion nature of the formally copper(0) complex obtained by one-electron reduction of the catenate: $g = 2.000 \pm 0.002$, $\Delta H = 39$ G.

The reduction potentials of **Cu.5**⁺ and [Cu(1)₂]⁺ are almost identical for both of the formally Cu^{+1/0} and Cu^{0/−1} couples, but the kinetic stability of the reduced catenate is dramatically more pronounced than that of its acyclic analogue. At low scan rates (<10 mV s^{−1}), even the first reduction of [Cu(1)₂]⁺ becomes irreversible, whereas the corresponding process for **Cu.5**⁺ remains completely reversible [7b, 28]. Furthermore, the electrochemical reduction of **Cu.5**⁺ allows the build-up of the formally zero-valent complex indicated by a deep-blue solution ($\lambda_{\text{max}} = 603$ nm, $\epsilon = 5300$ M^{−1} cm^{−1}; $\lambda_{\text{max}} = 840$ nm, $\epsilon = 4300$ M^{−1} cm^{−1}) (Figure 5).

It is noteworthy that, due to the topologically different properties of the copper-catenate and the copper-entwined complex [Cu(dap)₂]⁺, electrolysis of the second leads only to copper metal and free dap.

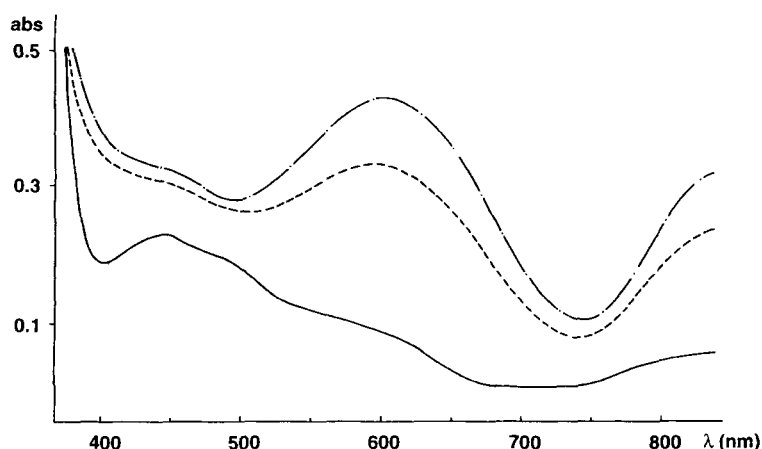


Figure 5. Reduction of Cu.5^+ : successive electronic spectra during electrolysis (DMF, -1.73 V, Au grid). $t = 0$ (—), 25 min (---), 90 min (— · —).

8.2.4 Electrochemical Study of Various Monometallated Catenanes in which the Metal is Tetracoordinated

Catenane **5** was here again mainly used for this study, and comparison of the electrochemical behavior of the catenate complexes and the analogous complexes of the acyclic ligand **1** will be particularly emphasized in this section. The cations include Li^+ , H^+ , Co^{2+} , Ni^{2+} , Zn^{2+} , Ag^+ , Cd^{2+} , and Pd^{2+} . The electrochemical data are collected in Table 3.

The redox processes observed might involve either metal-centered reactions (d or s orbitals) or electron transfer to the organic ligand (π^* orbitals of the dpp subunits). In some cases, the assignment can be made via EPR measurements and redox potential values. If the $\text{Cu}^{2+}/\text{Cu}^+$ couple always involves a metal-centered redox process, the electron transfer to Li.5^+ clearly occurs on the ligand moiety. No distinction can be made between both pathways for many of the complexes studied.

Lithium-catenate and free ligands [28]

Catenane **5** is insoluble in CH_3CN . Ligand **1** is fairly soluble in this medium, and is expected to display electronic properties similar to those of catenate **5**:



Li.5^+ is stable in CH_3CN , and shows two reduction waves, but only the first (-1.80 V) is reversible. These electron transfers were observed on both Hg and Pt at

Table 3. Electrochemical properties of various M_5^{n+} catenates: $E_{1/2}$ values (V) determined by cyclic voltammetry or by polarography^a

Redox process	Li	H	Co	Ni	Zn	Ag	Cd	Pd
+2/0	/	/	/	/	/	/	-0.91 ^{b,c} irr (CH ₃ CN)	/
+2/+1	/	/	-0.600 (CH ₃ CN)	-0.180 (CH ₃ CN)	-0.960 (CH ₂ Cl ₂)	/	~1.15 ^c qrev (CH ₂ Cl ₂)	+0.55 ^b (CH ₃ CN)
+1/0	-1.80 (CH ₃ CN)	-1.075 ^c irr (CH ₂ Cl ₂)	-1.315 (CH ₃ CN)	-1.325 (CH ₃ CN)	-1.260 qrev (CH ₂ Cl ₂)	-0.70 ^d (CH ₃ CN)	-1.35 ^c qrev (CH ₂ Cl ₂)	-1.95 (CH ₃ CN)
0/-1	1.93 qrev (CH ₃ CN)	/	/	/	/	/	/	-2.23 (CH ₃ CN)

^a All potentials refer to SCE, except for Pd(5-H⁺) for which the potential refers to Fc⁺/Fc. The systems are reversible except in few cases indicated by qrev (quasi-reversible) or irr (irreversible). The potentials have been determined by cyclic voltammetry on both Pt and Hg electrodes, leading to identical values, unless otherwise noted.

^b Only Hg electrode.

^c Peak potential.

^d Polarography at the dropping mercury electrode.

^e Only Pt electrode.

the same potential values, and correspond to reduction of the catenate moiety, free Li^+ being reversibly reduced to Li-Hg at -1.96 V under identical conditions.



Electrolysis of Li.5^+ at -1.90 V leads to the build-up of a red species which subsequently decomposes in solution. This compound is likely to be the lithium-stabilized radical anion $[\text{Li}^+.\text{5}^{\bullet-}]^0$. The interlocking nature of **5** allows complexation of Li^+ , whereas **1** is unable to form any stable complex.

Cobalt-catenate [28]

Two perfectly reversible one-electron reduction steps are observed for Co.5^{2+} , at -0.53 V ($\text{Co}^{2+/+}$) and -1.205 V ($\text{Co}^{+/0}$). Comparison of the electrochemical properties of the cobalt catenate with the previously reported data for cobalt *bpy* or phen complexes [31, 32] shows here again a strong stabilization of the reduced states, Co^{I} and Co^{II} . Other sterically constrained polyimine ligands also lead to stabilized monovalent cobalt complexes [33–37]. Remarkable also is the drastic structural effect of the catenate on the $\text{Co}^{3+/2+}$ redox potential: whereas *bpy* or phen complexes of cobalt(II) can easily be oxidized to octahedral cobalt(III) [36, 38], the redox potential value of the $\text{Co}^{3+/2+}$ couple being close to 0 V, no oxidation peak is observed for Co.5^{2+} prior to ligand oxidation ($E_p > 1.6$ V). The destabilization effect of Co^{III} due to tetrahedral environment provided by the entwined and interlocked structure of **5** is thus very large (>1.5 V).

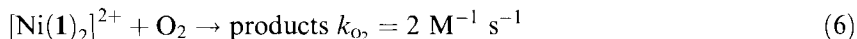
Nickel-catenate [28, 39]

A surprising stabilization of monovalent nickel occurs by coordination to **5**. In CH_3CN , the redox potential of the $\text{Ni}^{2+/+}$ couple is -0.18 V. The same explanation as that put forward for Co complexes applies here to account for the stabilization of Ni^{I} complex of **5**. The potential stability range of the Ni^{I} -catenate (-1.32 to -0.18 V) is remarkably broad. The behavior of Ni.5^{2+} is strikingly different from that of *bpy* nickel(II) complexes [40–42]. In the case of unsubstituted *bipy* ligands, electrochemical reduction of $[\text{Ni}(\text{bpy})_3]^{2+}$ leads directly to $[\text{Ni}(\text{bpy})_3]^0$ in a two-electron process ($E_{1/2} = -1.3$ V) [40], and monovalent nickel is not observed.

Monovalent nickel-catenate Ni.5^+ can be prepared by electrolysis of the divalent precursor. An EPR study clearly shows that this compound is a true d^9 nickel(I) complex [39] ($g_1 = 2.388$, $g_2 = 2.143$, and $g_3 = 2.071$, CH_2Cl_2 , frozen solution). X-ray studies of $(\text{Ni}^{\text{I}}.\text{5})(\text{ClO}_4)$ and $(\text{Ni}^{\text{II}}.\text{5})(\text{BF}_4)_2$ [43] revealed a pronounced difference for the environment of the metal centers in these two structures. Whereas the ligand system is perfectly well adapted to a tetrahedral geometry for monovalent nickel, the divalent state leads to a strongly distorted structure, in accordance with a d^8 configuration which is not likely easily to accommodate a tetrahedral environment. Accordingly, the two chelate planes of the nickel(I) catenate being perpendicular to one another, no intramolecular stacking interactions between aromatic groups are

observed, whereas in the Ni^{II} case strong π - π interactions between phenyl rings and phenanthroline nuclei take place. Due to almost identical topographical properties of $[\text{Ni}(\text{1})_2]^{2+}$ and Ni.5^{2+} , the redox potential values of the corresponding $\text{Ni}^{2+}/+$ couples are equal. However, the behavior of both compounds with respect to re-oxidation by O_2 is drastically different.

The reactivity of $[\text{Ni}(\text{1})_2]^{2+}$ is much more pronounced than that of nickel(I) catenate. In CH_2Cl_2 , the bimolecular rate constants corresponding to the reaction of the monovalent nickel complex with O_2 are as follows:



The topological properties of Ni.5^+ (interlocked ligands) thus have a dramatic influence on its kinetic inertness.

Silver-catenate [28]

The silver(I) catenate Ag.5^+ is certainly one of the most difficult silver(I) complexes to reduce. The reduction potential of free Ag^+/Ag^0 at the dropping mercury electrode determined in CH_3CN is +0.420 V. A noticeable ligand effect is observed for $[\text{Ag}(\text{1})_2]^+$, since a significant shift of its reduction potential (235 mV) to less positive values is observed. More remarkable is the behavior of the silver catenate. Its reduction occurs at -0.70 V in CH_3CN , and is thus 1.12 V more cathodic than that of free Ag^+ . Thus, the topological effect estimated by comparing the reduction potentials of $[\text{Ag}(\text{1})_2]^+$ and Ag.5^+ is 0.885 V. This particular property of the silver(I) catenate was used for the evaluation of the topological characteristics of different polypyrrole matrices built around dpp moieties [44].

Zinc-catenate [28]

The reduction processes of both $[\text{Zn}(\text{1})_2]^{2+}$ and Zn.5^{2+} occur in two one-electron steps in CH_3CN or in CH_2Cl_2 , with a relatively broad (300-mV) stability range of the formally monovalent zinc complexes (Figure 6).

Exhaustive electrolysis of the zinc(II) catenate at the first reduction wave plateau (-1.1 V) leads to the formation of a pink-red solution ($\lambda_{\text{max}} = 530 \text{ nm}$, $\epsilon \sim 1000 \text{ M}^{-1} \text{ cm}^{-1}$) of the corresponding monovalent complex. EPR measurements performed on a frozen solution of the electrochemically generated monovalent zinc catenate show the presence of a paramagnetic radical species ($g = 2.00246$, $\Delta H = 11.46 \text{ G}$). The reduced states Zn.5^+ and Zn.5^0 , containing formally monovalent and zerovalent zinc, respectively, are better described as zinc(II)-stabilized anion radicals.

Cadmium-catenate [28]

In CH_3CN , free Cd^{2+} , $[\text{Cd}(\text{1})_2]^{2+}$ and Cd.5^{2+} are reduced in a two-electron process at -0.285, -0.400 and -0.850 V, respectively. In each case, the divalent cationic species is reduced to cadmium amalgam. In CH_2Cl_2 and on Pt, the electrochemical

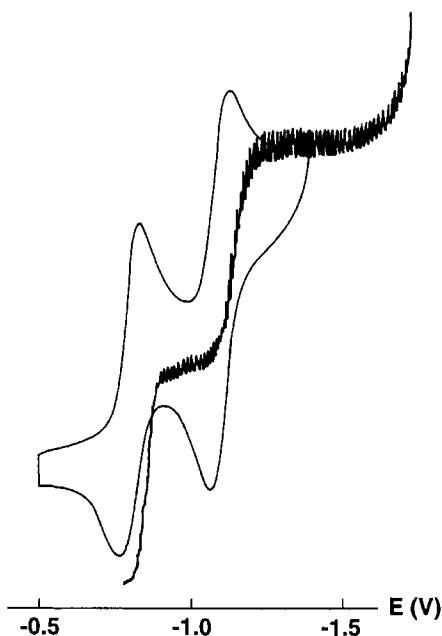


Figure 6. Cyclic voltammetry (CV) on platinum and polarography at the dropping mercury electrode (DME) of $[\text{Zn}(\mathbf{1})_2]^{2+}$ in 0.1 M CH_2Cl_2 - $(n\text{-C}_4\text{H}_9)_4\text{NClO}_4$ (0.1 M) (scan rate for CV, 40 mV s^{-1} ; E versus $\text{Ag}/\text{Ag}_3\text{I}_4^-$).

behavior of $\text{Cd}(\mathbf{5})^{2+}$ is different. The corresponding cyclic voltammetry indicates that reduction occurs in two steps at -1.15 V and -1.36 V. The monovalent and zerovalent complexes could not be built-up in solution. However, it is remarkable that the mono- and direduced cadmium catenates could be observed as transient species when the dissociation reaction is not favored by amalgam formation. Here again, this particular property mainly originates from the interlocking of the ligand, since reduction of $[\text{Cd}(\mathbf{1})_2]^{2+}$ leads only to complete dissociation with no observable transient species.

Palladium-catenate [45]

In the case of all of the catenate complexes discussed above, the ligand imposes a more or less distorted tetrahedral geometry to the metal center. However, complexation of Pd^{2+} with **5** follows a different route. Insertion of Pd^{2+} into **5** yields the monocation $[\text{Pd}^{\text{II}}(\mathbf{5}\text{-H})]^+$ via *ortho*-metallation of one of the phenyl rings to give planar coordination by an N_3C donor set. The structure of $[\text{Pd}^{\text{II}}(\mathbf{5}\text{-H})]^+$ is a compromise between the stereochemical and conformational preferences of metal and ligand where the disparity between the requirements of square planar Pd^{II} and tetrahedral **5** is resolved by *ortho*-metallation. $[\text{Pd}^{\text{II}}(\mathbf{5}\text{-H})]^+$ shows a reversible oxidation at $+0.55$ V versus Fc^+/Fc (Fc = ferrocene) assigned to a $\text{Pd}^{3+/2+}$ couple. Two reversible reductions are observed for the palladium complex at extreme cathodic potentials, $E_{1/2} = -1.95$ and -2.23 V) versus Fc^+/Fc .

In conclusion, from this electrochemical study, one can conclude that the most

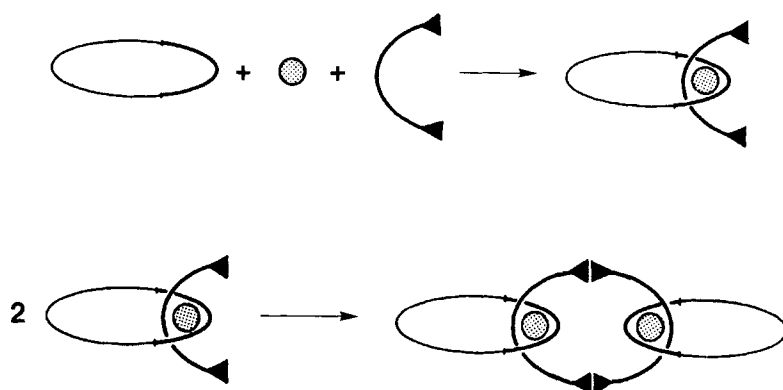


Figure 7. Synthetic strategy to obtain a [3]catenane by cyclodimerization of a difunctional precursor. The circles represent the templating transition metal, and the triangles the terminal diynes.

striking property of this family of catenane-type ligands is their ability to stabilize low oxidation states of several transition metals. Comparison of the catenanes with their acyclic analogues shows in several cases a strong contribution of the topological factor of the catenane to such stabilization effect. Whereas the reduction potential values of $[M.Cat]^{n+}$ and $[M(dap)_2]^{n+}$ are in several instances very close, the kinetic stability of the reduced catenane with respect to dissociation or reoxidation is always noticeably more pronounced than that of the corresponding open-chain complex.

8.2.5 Dimetallic [3]Catenates

Synthesis

[3]Catenates have been prepared in good yield by double acetylenic oxidative coupling from a terminal diyne threaded into a preformed chelating ring according to Figure 7 [46]. The precursor used, the reaction conditions, and the [3]catenane thus obtained are represented in Figure 8.

The dicopper complex $CuCu.10^{2+}$ made of two peripheral 30-membered rings separately interlocked to a bis-diacetylenic 44-membered central cycle could be fully characterized by extensive NMR and crystallographic studies [47]. These studies provided clear evidence that the molecular shape of $CuCu.10^{2+}$ was approximately the same in the CH_2Cl_2 solution and in the solid state. Indeed, the molecule does not present an extended geometry (as the diagram in Figure 8 would suggest), but rather it is completely curled up so as to allow close contact between various parts of the two copper(I) complex subunits (Figure 9).

The [3]catenane $CuCu.10^{2+}$ could be fully demetalated with excess potassium cyanide, affording the free ligand **10** which could be later easily remetalated giving thus access to the following homodinuclear [3]catenates: $AgAg.10^{2+}$, $ZnZn.10^{4+}$, $CoCo.10^{4+}$, and $NiNi.10^{4+}$.

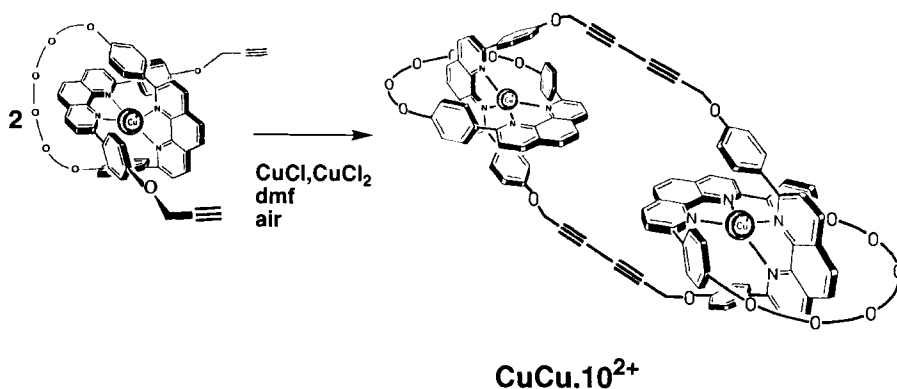


Figure 8. Synthesis of the [3]catenate **CuCu.10²⁺**.

Homodinuclear [3]catenates

The strong electronic interactions between the two metal centers were not expected, since the 8.5 Å Cu...Cu distance, found in the X-ray structure of **CuCu.10²⁺**, is rather long. Nevertheless, since the space between the metal centers is filled up with stacking aromatic nuclei in the folded conformation, some interesting effects (of one complex subunit on the properties of the other) could be observed. The electronic properties of the various symmetrical dimetallic [3]catenates were studied and

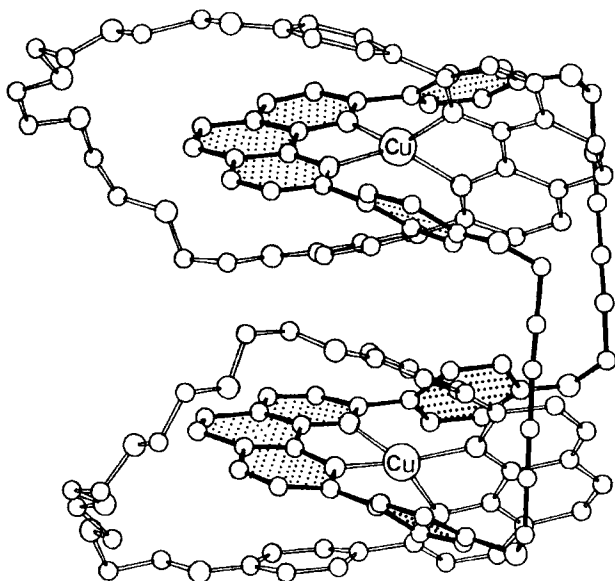


Figure 9. Crystal structure of the [3]catenate **CuCu.10²⁺**.

Table 4. Electrochemical properties of homodimetallic [3]catenates and comparison to the corresponding monometallic [2]catenates.^a $\Delta E_{[3]-[2]}$ is the difference between the potentials of the wave observed, respectively, for a given [3]catenate and the analogous [2]catenate

Complex	Oxidation	Reduction		$\Delta E_{[3]-[2]}$
	1st wave	1st wave	2nd wave	
CuCu.10²⁺	+0.670	−1.610 irr	−1.830 irr	+0.03
Cu.5⁺^b	+0.565	−1.650 ^g	−1.860 ^g	
AgAg.10²⁺	^c	−0.540 ^d		+0.16
Ag.5⁺^b	^c	−0.700 ^e		
ZnZn.10⁴⁺	^c	−0.970 irr ^f	−1.340 irr ^f	−0.01
Zn.5²⁺	^c	−0.960 qrev	−1.260 qrev	
CoCo.10⁴⁺	^c	−0.450	−1.243	+0.15
Co.5²⁺	^c	−0.600	−1.315	
NiNi.10⁴⁺	^c	−0.080	−1.295	+0.10
Ni.5²⁺	^c	−0.180	−1.325	

^aRedox potential (V) measured in CH₃CN versus the saturated calomel electrode (SCE), determined by cyclic voltammetry at the platinum electrode, 0.1 M (nC₄H₉)₄N⁺.BF₄[−]; room temperature under argon; scan rate, 100 mV s^{−1}; the systems are reversible except in a few cases indicated by qrev (quasi reversible) and irr (irreversible).

^bTaken from Ref. [28].

^cNo oxidation wave is detected before irreversible oxidation of the ligand.

^dPolarography measurement at the dropping mercury electrode (DME) in CH₂Cl₂.

^eSame as ^d, but in CH₃CN.

^fIn CH₂Cl₂.

^gIn DMF; Hg electrode.

compared to those previously obtained for the corresponding [2]catenates [28] designed by **M.5ⁿ⁺**.

The electrochemical data collected in Table 4 show at first that most of the [3]catenates studied undergo highly reversible electroreductive processes. A typical example is that of **CoCo.10⁴⁺**, for which the cyclic voltammogram is represented in Figure 10.

The $\Delta E_{[3]-[2]}$ values given in Table 4 reflect the greater tendency of the [3]catenates to be reduced as compared to their monometallic analogues, although the electronic properties (σ and π electron-donating and -accepting character) of the individual coordinating species are identical for both systems. A possible explanation is that in [3]catenates the reduced species is slightly stabilized by electrostatic interaction with the positively charged second subcomplex. This stabilizing charge effect may occur by direct metal-to-metal or through-space interactions. Given the large metal-to-metal distance (8.5 Å) found in the structure of **CuCu.10²⁺**, and assuming that the metals cannot be much closer in the other complexes due to steric repulsion within the organic skeleton of the ligand, it is reasonable to assume that this stabilizing charge effect occurs predominantly via the π system of the ligands.

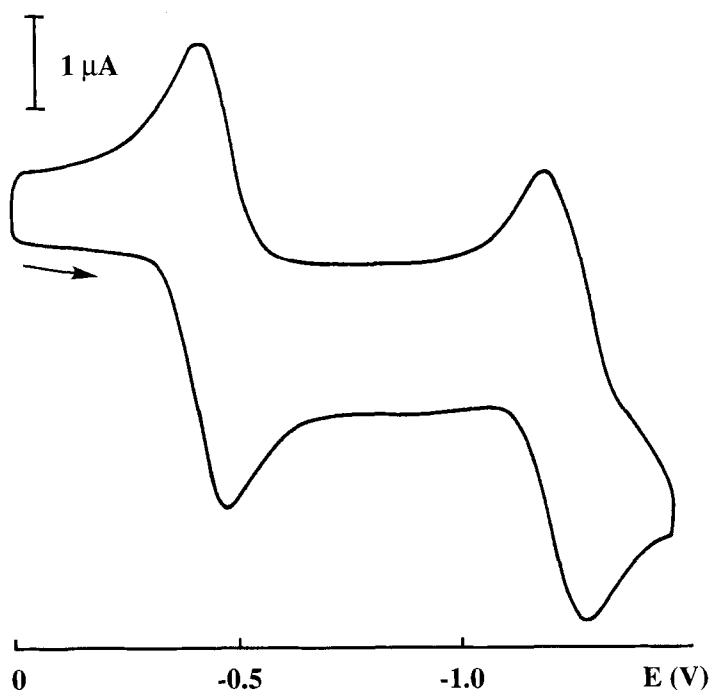


Figure 10. Cyclic voltammogram of **CoCo.10⁴⁺** (4.2×10^{-4} M) in $\text{CH}_3\text{CN}-(\text{nC}_4\text{H}_9)_4\text{N}^+.\text{BF}_4^-$ 0.1 M (Pt, scan rate 100 mV s^{-1} , E versus SCE).

Interestingly, **ZnZn.10⁴⁺** and **Zn.5²⁺** are reduced at almost the same potential. This indicates that the [3]catenate is less curled up in this case due to strong electrostatic repulsion between the two hard dicationic Zn^{II} centers. ^1H NMR data fully corroborate this hypothetical more extended conformation of **ZnZn.10⁴⁺**.

Heterodinuclear [3]catenates

The controlled demetallation of **CuCu.10²⁺** by potassium cyanide at room temperature afforded the mononuclear complex **Cu.10¹⁺** containing a vacant site ready for coordination. Addition of the appropriate salt (AgBF_4 or $\text{Co}(\text{BF}_4)_2$) to **Cu.10¹⁺** leads to the heterodinuclear [3]catenates **CuAg.10²⁺** and **CuCo.10³⁺** for which the specific electrochemical properties [48] were studied and compared to those of their monometallic analogues, namely **M.5ⁿ⁺** (Table 5).

As expected, the redox potential of the $\text{Cu}^{2+}/\text{Cu}^+$ couple is slightly shifted towards anodic values in **CuAg.10²⁺** as compared to **Cu.5⁺**. This effect is even more pronounced in **CuCo.10³⁺**: the copper(II) state is significantly more difficult to electro-generate than for the mono-nuclear species **Cu.5⁺**. The positive shift of the $\text{Cu}^{2+}/\text{Cu}^+$ redox potential in di-metallic species as compared to **Cu.5⁺** shows that the two metal complex subunits of the [3]catenates do interact. This may reflect an

Table 5. Electrochemical properties of the heterodinuclear complexes **CuM.10ⁿ⁺**

Compound	Redox couple	E _{red} (V) ^a
CuAg.10²⁺	Cu ^{II} /Cu ^I	+0.668 ^b
	Ag ^I /Ag ⁰	−0.480 ^c
CuCo.10³⁺	Cu ^{II} /Cu ^I	+0.785 ^b
	Co ^{II} /Co ^I	−0.360 ^b
	Co ^I /Co ⁰	−1.180 ^b
Cu.5⁺	Cu ^{II} /Cu ^I	+0.565
Ag.5⁺	Ag ^I /Ag ⁰	−0.700 ^d
Co.5²⁺	Co ^{II} /Co ^I	−0.600
	Co ^I /Co ⁰	−1.315

^aReduction potential (V) in CH₃CN, versus the saturated calomel electrode (SCE) determined by cyclic voltammetry at the platinum electrode, scan rate: 100 mV s^{−1}.

^bSame as ^a, but in CH₂Cl₂.

^cPolarography measurement at the dropping mercury electrode (DME) in CH₂Cl₂.

^dPolarography measurement at the DME in CH₃CN.

electrostatic interaction between the cationic metal centers (through-space or via the stacking π -system). As in **CuCu.10²⁺** the oxidation reaction of copper(I) to the di-valent state is made more difficult by the vicinity of an additional positive charge. The rise in copper(I) oxidation potential ($\Delta E_{\text{Cu}^{2+}/\text{Cu}^+}$) from **Cu.5⁺** to **CuM.10ⁿ⁺** represents the extent of electrochemical stabilization of the low valence state Cu^I by the second metal. As foreseen, it increases with the positive charge of M (Table 6).

The large value found for Co²⁺ (+0.22 V) is a good indication for a folded up conformation of **CuCo.10³⁺** which allows a strong electrostatic repulsion between Cu²⁺ and Co²⁺. In an extended geometry, the two metal centers would be too far away to interact, as was the case in the less-folded tetracationic species **ZnZn.10⁴⁺**. The electrostatic interaction between the two positively charged metals of the [3]catenates **CuM.10ⁿ⁺** is also reflected by the reduction potentials of the M-containing parts. The M-containing subunit is easier to reduce as compared to **M.5^{(n−1)+}** due to the proximity of the Cu⁺ center in the curled up [3]catenates **CuAg.10²⁺** and **CuCo.10³⁺**. Table 5 shows that this Cu⁺ effect is roughly the same on Ag⁺ or Co²⁺ (+0.22 and 0.24 V for $\Delta E_{\text{Ag}^+/\text{Ag}^0}$, and $\Delta E_{\text{Co}^{2+}/\text{Co}^+}$, respectively).

Table 6. Increase of the copper(I) oxidation potential in **CuM.10ⁿ⁺** complexes, upon variation of the **M^{m+}** ion (ΔE in V)

M^{m+}	Cu⁺	Ag⁺	Co²⁺
$\Delta E_{\text{Cu}^{2+}/\text{Cu}^+}$	+0.10	+0.10	+0.22

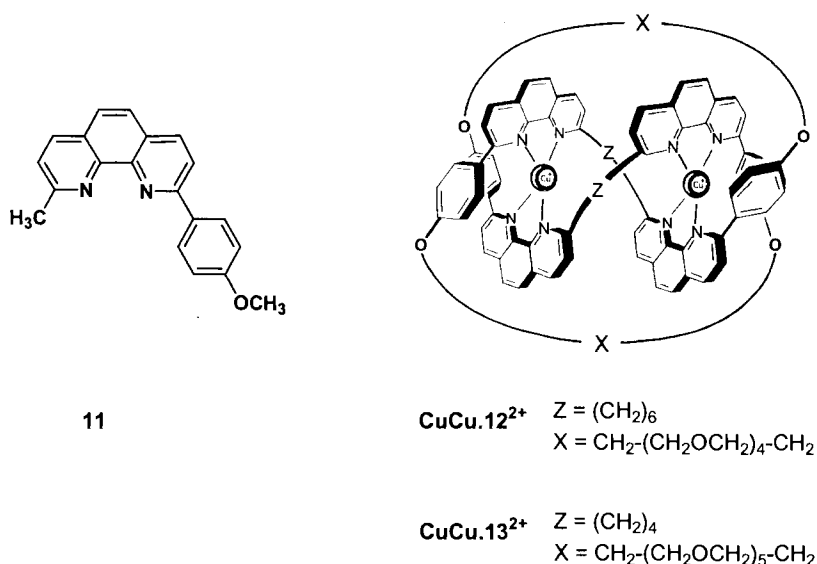


Figure 11. Dicopper(I) trefoil knots and related acyclic monocopper(I) complex.

8.2.6 Dimetallic Molecular Trefoil Knots

The early “methylenic” bridged symmetrical dicopper knots

The electrochemical properties of the dicopper knots represented in Figure 11 were compared to that of the simply entwined copper complex **Cu.(11)₂⁺**, which should have identical electronic properties so that any difference between the latter mono-copper complex and the dicopper knotted ones can be attributed both to structural (i.e., geometric) and topological factors and, in particular, to the geometry of the copper(I) coordination polyhedra and the accessibility to the metal centers [49].

Cyclic voltammetry measurements (Table 7) showed clearly that the acyclic complex **Cu.(11)₂⁺** was the easiest one to oxidize, and that in the dinuclear knots **CuCu.12²⁺** and **CuCu.13²⁺**, the two copper(I) centers behave independently of one another. The redox potential of **CuCu.12²⁺** appears surprisingly high (140 mV higher than the redox potential of **CuCu.13²⁺**), which indicates that the 84-

Table 7. Oxidation potentials of copper(I) mono- and dinuclear knots complexes^a

	Cu(11)₂⁺	CuCu.12²⁺	CuCu.13²⁺
E^0 (V)	0.42	0.75	0.61

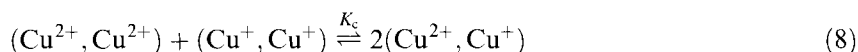
^aCyclic voltammetry in CH₃CN versus SCE, LiClO₄ (0.1 M) as supporting electrolyte, oxidation on Pt, scan rate 100 mV/s.

membered knotted cycle is highly constraining and allows only limited freedom for the copper(I) centers to change their geometry. This observation is in good accordance with the structure of the complex [50]: the $-(\text{CH}_2)_6-$ linker is sufficiently long to form a well-twisted central double helix, thus ensuring efficient shielding of the metal centers. On the other hand, the pentaethylene glycol link is too short for the molecule to easily distort. The rigidity thus obtained “freezes” the copper centers in a pseudotetrahedral geometry, making any deformation of their coordination polyhedra towards a square planar geometry extremely difficult.

These results strongly suggest that the electrochemical properties of the knots are not governed by the topological factors alone. They are obviously also very sensitive to structural parameters which become prevailing when switching from the aliphatic flexible spacers between two phenanthroline units to the more rigid 1,3-phenylene spacer in knot **CuCu.14**²⁺.

The *meta*-phenylene bridged knots

Knot **CuCu.14**²⁺ in which the two phenanthrolines are connected by a 1,3-phenylene bridge could be characterized both by ¹H NMR and crystallographic studies as being a highly rigid and compact edifice with a much shorter Cu...Cu distance than in the previously synthesized knots (4.76 Å, cf. 6.3 or 7.0 Å) [51]. Due to this very short Cu...Cu distance, knot **CuCu.14**²⁺ undergoes two very distinct oxidation processes. The redox potentials of the Cu²⁺/Cu⁺ couples measured in CH₃CN against the saturated calomel electrode (SCE), all reversible ($\Delta E_p = 60$ mV), appear at $E^\circ = +0.68$ V for **CuCu.14**^{3+/2+} and at $E^\circ = +0.92$ V for **CuCu.14**^{4+/3+}. The surprisingly high value found for **CuCu.14**^{4+/3+} indicates a strong electronic interaction between the two copper centers. The presence of divalent copper(II) located close to the copper(I) undergoing the redox reaction renders the oxidation of this second metal difficult, and thus shifts the Cu²⁺/Cu⁺ redox potential substantially towards anodic values. Furthermore, the large difference of redox potential values for the two couples Cu²⁺Cu²⁺/Cu²⁺Cu⁺ (+0.92 V) and Cu²⁺Cu⁺/Cu⁺Cu⁺ (+0.68 V), $\Delta E = 0.24$ V, is remarkable. It corresponds to a large comproportionation constant K_c , for the following reaction:



K_c being larger than 10^4 , it should be possible to isolate and study the mixed-valence state **CuCu.14**³⁺.

Another feature also strongly related to the compactness of the *m*-phenylene bridged knot is its extreme kinetic inertness in the cyanide demetalation process, which could be shown to imply two rate-limiting steps that are well resolved in time (Figure 12) [52].

If the removal of both copper(I) ions requires heating for 24 h under reflux in acetonitrile and a 1000-fold excess of potassium cyanide, by contrast, less drastic conditions afford quantitatively the stable, isolable, singly demetalated species **Cu.14**¹⁺ which, because of its free coordination site, seemed an ideal precursor for the synthesis of nonsymmetrical knotted complexes. Indeed, simple addition of the

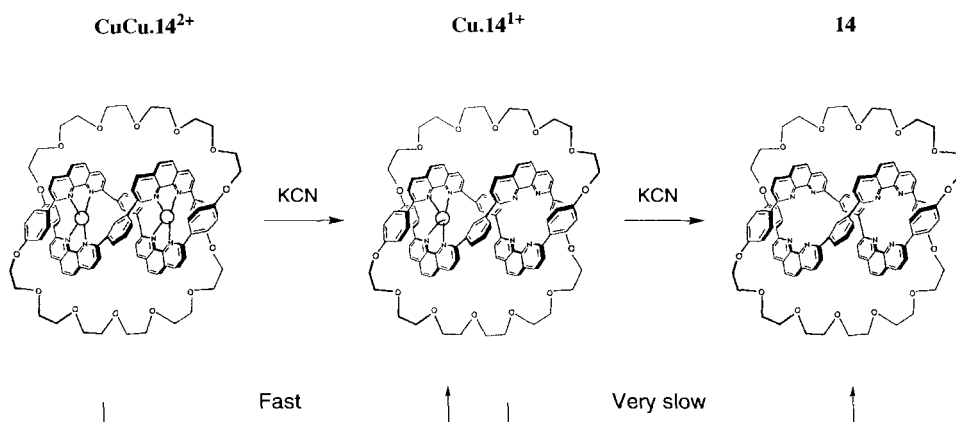


Figure 12. Representation of the two steps in the demetalation of the dicopper(I) knot CuCu.14^{2+} .

appropriate metal salt to Cu.14^{1+} afforded in quantitative yield the heterodinuclear complexes CuZn.14^{3+} and CuAg.14^{2+} . Both of these heterodinuclear complexes undergo only one oxidation process: $E^\circ = +0.69$ V for $\text{CuAg.14}^{3+/2+}$ and $E^\circ = +0.90$ V for $\text{CuZn.14}^{4+/3+}$.

The $\text{CuCu.14}^{3+/2+}$ and $\text{CuAg.14}^{3+/2+}$ reduction potentials are very similar to those found for the other copper complexes containing entwined or interlocked ligands [28]. By contrast, the $\text{CuZn.14}^{4+/3+}$ reduction potential is very high and comparable to the value found for the $\text{CuCu.14}^{4+/3+}$ complex. Here again, this value reflects the strong electron-withdrawing influence of a divalent metal atom located close to the copper center undergoing the redox reaction. As expected, the presence of a positively charged species substantially destabilizes the divalent state of the copper center.

All the electrochemical data obtained for the phenylene bridged knots clearly show that the presence of a “conducting” spacer inside a narrow rigid central helical core leads to electrochemical properties that are noticeably different from those of knotted complexes in which the two metal-based components are linked by nonconducting $-(\text{CH}_2)_n-$ spacers [49].

8.2.7 A Mononuclear Hexacoordinated Ruthenium Bis-Terpyridine [2]Catenate

The catenanes and knots described so far, originating from the use of 2,9-diaryl-1,10-phenanthroline in combination with copper(I) as assembling and templating centre, contain all tetrahedral coordination sites that are particularly well suited to low oxidation states with various transition metals. In order to prepare interlocking ring ligands able to complex metals in high oxidation states, 6-coordinate systems are preferable. This requirement led to the synthesis of a bis(terpyridine)ruthenium(II) catenate following the three-dimensional template route described in Figure 13 [53].

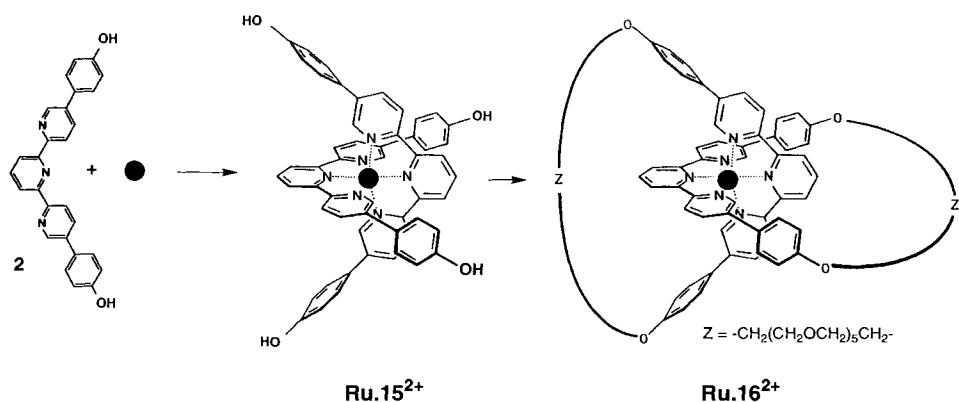


Figure 13. Template synthesis of the ruthenium bis-terpyridine catenate **Ru.16²⁺**.

Such multistep synthesis, the key step of which involved the reaction of the ruthenium(II) complex of 5,5''-bis(4-hydroxyphenyl)terpyridine (**Ru.15²⁺**) with two equivalents of the diiodo derivative of hexaethylene glycol afforded the target catenate **Ru.16²⁺**. The electrochemical data obtained for **Ru.16²⁺** and its open-chain precursor **Ru.15²⁺** are summarized in Table 8, along with those of $[\text{Ru}(\text{tpy})_2]^{2+}$ ($\text{tpy} = 2,2':6',2''\text{-terpyridine}$) given for comparison.

The oxidation potentials of the Ru^{II} ions in the catenate complex and in **Ru.15²⁺** are both slightly higher than in $[\text{Ru}(\text{tpy})_2]^{2+}$, which is simply an effect of substituting the terpyridine. More important is the fact that the oxidation potentials of **Ru.16²⁺** and **Ru.15²⁺** are the same, which indicates that closure of the two rings to form the catenate does not have a large effect on the geometry around the ruthenium ion. The two ligand-based reductions of **Ru.16²⁺** and **Ru.15²⁺** appear significantly easier than for $[\text{Ru}(\text{tpy})_2]^{2+}$. This was expected due to the more highly conjugated nature of the ligands; again, however, they are approximately the same. These results suggest that the Ru-N_6 coordination environment is very similar for all three complexes, and hence that no significant change in the geometry at the metal ion has arisen as a result of closing the macrocyclic rings. It might be expected that if the linker chain were shorter, closure of the rings could pinch the terpyridyl moieties enough to promote a noticeable change in the coordination environment of the ruthenium ion.

Table 8. Summary of electrochemical results for $[\text{Ru}(\text{tpy})_2]^{2+}$ -type complexes and catenate^a

Compound	$E_{1/2}^{[2+/3+]}$	$E_{1/2}^{[2+/1+]}$	$E_{1/2}^{[1+/0]}$
Ru.16²⁺^b	+1.32	−1.23	−1.45
Ru.15²⁺^b	+1.32	−1.25	−1.46
$[\text{Ru}(\text{tpy})_2]^{2+}$	+1.25	−1.40	−1.65

^a All potentials in V versus SCE in acetonitrile.

^b Measured at a scan rate of 200 mV/s.

8.3 Photophysical Properties of Catenates and Knots

8.3.1 Introduction

The pioneering work of McMillin and colleagues [54] has shown that the $[\text{Cu}(\text{phen})_2]^+$ -type motif (phen = 1,10-phenanthroline) is very interesting from the photophysical point of view, provided that the phenanthroline chelating units bear substituents, typically in the 2,9 and/or 4,7 positions [54e–f]. Only in these cases, in fact, a relatively long-lived, luminescent metal-to-ligand-charge-transfer (MLCT) excited state is made available, whereas for plain $[\text{Cu}(\text{phen})_2]^+$ such an excited state is short-lived and not luminescent under any condition. This behavior is a consequence of the structure of the excited complex, where a formally Cu^{II} ion is formed following the excitation in the MLCT manifold, thus favoring a strong flattening towards a square planar geometry in place of the starting pseudotetrahedral arrangement, preferred by Cu^{I} . The strongly distorted excited molecule tends to form pentacoordinated exciplexes with the counteranion and/or the solvent molecules [54d,g], which are deactivated to the ground state via nonradiative paths. As a consequence, any factor which can limit such deactivation process is able to increase the luminescence quantum yield and excited state lifetime of $[\text{Cu}(\text{phen})_2]^+$ -type complexes. Practically, one can act on three factors: (i) solvent nature; (ii) chemical nature, size, and number of the substituents; and (iii) type of counteranion. In order to maximize the luminescence performances, poor donor solvents, numerous [54n] and/or cumbersome substituents (which physically prevent the undesired nucleophilic attack), and poor donor counteranions must be utilized. As a matter of fact, most of the photophysical investigations on copper phenanthrolines are reported in CH_2CH_2 , phenyl substituents are usually placed on the chelating unit, and BF_4^- or PF_6^- counteranions are employed.

Importantly, the MLCT nature of the lowest excited state of $[\text{Cu}(\text{phen})_2]^+$ -type complexes has been unambiguously demonstrated by several techniques, including resonance Raman [55] and transient absorption [56] spectroscopy.

Finally, it must be pointed out that a great deal of work was published on related metal assembled compounds such as linear or circular helicates [57], cages [58], and rack-type complexes [59]. However, since little or no discussion related to charge-transfer spectroscopy or photoinduced electron transfer was reported, they will not be presented here.

8.3.2 Metallo-[2]catenates

The first report on the photophysical properties of metal catenates dates back to 1989 [54h], when a comparison between a 27- (**Cu.4**⁺; Figure 2) and 30-membered (**Cu.5**⁺; Figure 14) ring catenates was reported.

The absorption spectra of the two complexes are significantly different both at 298 and 90 K, and the emission band of the smaller size catenate is blue-shifted relative to **Cu.5**⁺ (715 versus 730 nm). Interestingly, the lifetime of **Cu.4**⁺ in

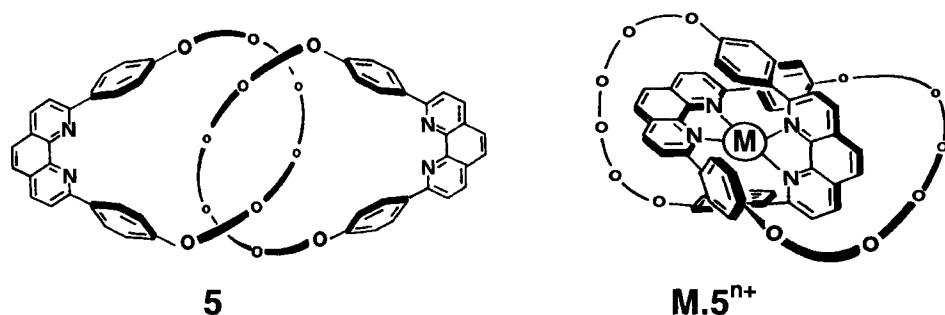


Figure 14. The [2]catenand **5** and its catenates **M.5ⁿ⁺** ($M = \text{Li}^+, \text{H}^+, \text{Ag}^+, \text{Co}^{2+}, \text{Ni}^{2+}, \text{Zn}^{2+}, \text{Cd}^{2+}, \text{Pd}^{2+}$). The line connecting the oxygen atoms of the closing chains represent $-(\text{CH}_2)_2-$ groups. The Pd^{II} catenate shows a cyclometallate structure, as represented in Figure 2 (**Pd(5-H)⁺**).

CH_2Cl_2 deaerated solution (280 ns) is longer than that of **Cu.5⁺** (190 ns). This is a consequence of the more rigid structure of the smaller-size complex that disfavors excited state distortions, and has been well correlated with electrochemical data that show a remarkable 124-mV anodic shift in passing from the 30- to the 27-membered ring (see Section 8.2.3).

Some years later, the investigation on **Cu.5⁺** was extended to the corresponding **M.Catⁿ⁺** catenates ($M = \text{Li}^+, \text{H}^+, \text{Ag}^+, \text{Co}^{2+}, \text{Ni}^{2+}, \text{Zn}^{2+}, \text{Pd}^{2+}, \text{Cd}^{2+}$) [60] (Figure 14). The absorption spectra of all these compounds in CH_2Cl_2 solution are reported in Ref. [60]. The ligand-centered (LC) $\pi\pi^*$ transitions in the UV spectral region (220–400 nm, ϵ_{max} of the order of $10^4 \text{ M}^{-1} \text{ cm}^{-1}$), are strongly affected by metal complexation, and a certain similarity is found for catenates bearing ions with the same electrical charge. The low-energy absorption bands above 400 nm are strongly dependent on the electronic configuration of the complexing ion; as a consequence, a remarkably different spectral shape is observed from case to case. Closed shell (d^{10}) divalent ions such as Zn^{2+} and Cd^{2+} bring about a broadening of the ligand-centered bands toward the visible spectral region. This is due to the sizeable charge transfer character of the ligand-centered transitions in the di-*n*isylphenanthroline-type (dap) ligands [61], that are thus lowered in energy by the electrostatic effect of the divalent complexing ion. Such an effect is not found for monovalent ions like Ag^+ (d^{10}) and Li^+ ; the spectra of **Ag.5⁺** and **Li.5⁺** do not exhibit any broadening above 400 nm. By contrast, the complexation with H^+ causes a spectral widening towards the red spectral region, even more dramatic than in the case of Zn^{2+} and Cd^{2+} , probably due to the very high charge density of the proton.

For Cu^+ (d^{10}) and open-shell metal ions, the absorption spectra in the visible spectral range are totally different, and weak bands (ϵ of the order of $10^3 \text{ M}^{-1} \text{ cm}^{-1}$) are found up to 600–700 nm. **Cu.5⁺** exhibits the expected wide MLCT absorption (see above), whereas the bands observed for Ni^{2+} (d^8) and Co^{2+} (d^7) are assigned to metal-centered (MC) or ligand-to-metal-charge-transfer (LMCT) transitions. Finally, the Pd^{2+} (d^8) catenate has to be considered a special case since it is actually a

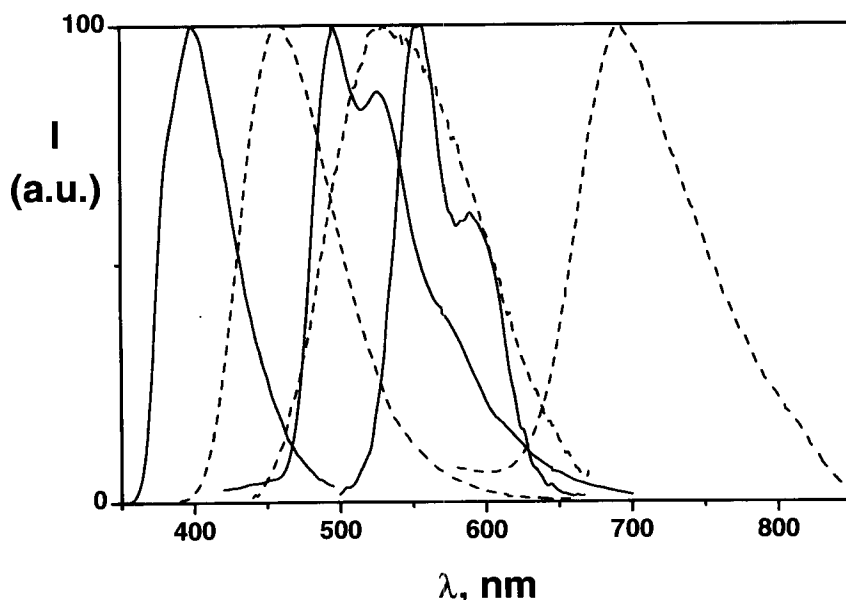


Figure 15. Luminescence spectra of some $M.5^+$ catenates in CH_2Cl_2 . From left- to right-hand-side, maxima correspond to $M = Li^+, Zn^{2+}, Ag^+, H^+, Pd^{2+}, Cu^+$ (alternate full and dashed line, for the sake of clarity). The spectra of the silver(I) and palladium(II) catenates are recorded at 77 K, all the others at 298 K.

cyclometallate [62], and for such Pd^{2+} complexes MC and MLCT excited configurations may lie very close in energy, and contribute to the observed spectra [62]. However, it must be pointed out that a localized molecular orbital approach for cyclometallated compounds can only be used as a first approximation, since a large degree of covalency in the metal–ligand bond is expected.

The wide tuning of the electronic properties of [2]catenates, as observed from electrochemistry and UV-visible absorption, causes a nice modulation of the luminescence properties in CH_2Cl_2 solution. On changing the metal ion, the luminescence bands of this catenate family are tuned throughout the whole visible spectral region [60] (Figure 15). The luminescence data at 298 and 77 K in CH_2Cl_2 are reported in Table 9.

In detail, the luminescence bands of the $Li^+, Cd^{2+}, Zn^{2+}, H^+$ catenates $M.5^+$ are of LC ($\pi\pi^*$) character (fluorescence and phosphorescence); for $Ag.5^+$ only the 77 K LC phosphorescence is observed due to the rapid singlet–triplet intersystem crossing induced by the heavy metal ion; the luminescence band shown (only) at 77 K by $Pd.5^+$ is difficult to attribute (see above), but a substantial MLCT character is indicated by the spectral red-shift and shorter lifetime compared to, for instance, $Ag.5^+$; finally, the $Cu.5^+$ shows the typical MLCT band (see above). No luminescence is observed for $Ni.5^+$ and $Co.5^+$ owing to the presence of low-lying non-

Table 9. Luminescence data of **5** and its **M.5ⁿ⁺** complexes in CH₂Cl₂

	298 K			77 K			
	$\lambda_{\text{max}}^{\text{a,b}}$ (nm)	τ (ns)	Φ_{cm}	$\lambda_{\text{max}}^{\text{a,c}}$ (nm)	τ (ns)	$\lambda_{\text{max}}^{\text{a,d}}$ (nm)	τ (s)
5	400	2.0	0.42	382	2.2	524	0.79
H.5⁺	555	11.0	0.022	460	13.0	515	0.87
(H₂).5²⁺	590	4.5	0.015	485	6.4	515	0.74
Li.5⁺	400	2.5	0.35	378	2.5	532	2.1
Cu.5⁺	730 ^e	175 ^f	0.0011	/	/	685 ^e	1.1×10^{-6}
Ag.5⁺	/	/	/	/	/	498	0.012
Co.5²⁺	/	/	/	/	/	/	/
Ni.5²⁺	/	/	/	/	/	/	/
Zn.5²⁺	463	2.0	0.082	433	5.0	495	0.78
Pd.(5-H)⁺	/	/	/	/	/	555 ^g	3.0×10^{-4}
Cd.5²⁺	443	<1	0.015	420	7.5	498	0.35

^aValues corrected for the photomultiplier response.^bLigand-centered (LC) fluorescence, unless otherwise noted.^cLC fluorescence.^dLC phosphorescence, unless otherwise noted.^eMetal-to-ligand-charge-transfer (MLCT) luminescence band.^f125 ns in air-equilibrated solution.^gMost likely MLCT emission with some LC contribution; see text for more details.

emissive MC excited states which offer a rapid, radiationless decay path to the ligand-centered $\pi\pi^*$ levels.

8.3.3 Multicomponent Metallo-[3]catenates

The wide tunability in the redox and electronic properties of [2]catenates by varying the complexing ion suggests that intercomponent photoinduced energy or electron transfer processes could occur in thoroughly designed polynuclear catenates containing such chromophoric units [63–64] (Figure 16).

The absorption spectra of the free ligand **10** and its mono- and dinuclear complexes **Cu.10⁺**, **CuCu.10²⁺**, **CuAg.10²⁺**, **CuZn.10³⁺**, **CuZn.10³⁺**, are reported in Ref. [64]; these spectra are well-matched with the sum of the spectra of the two chromophoric (**M.5ⁿ⁺**-type) component units. The luminescence properties of all [3]catenates at 298 and 77 K in CH₂Cl₂ are reported in Table 10.

The emission behavior of the free ligand **10** and of the homodinuclear **CuCu.10²⁺** catenate is quite comparable to that of the simpler corresponding [2]catenand **2** and [2]catenate **Cu.5ⁿ⁺**. By contrast, a dramatic luminescence quenching of one of the two moieties is observed in all the heterodinuclear compounds.

Cu.10⁺ is made of a catenand (metal-free) and a catenate (metal-complexed) moiety. Selective excitation of the Cu^I-complexed moiety in the visible spectral re-

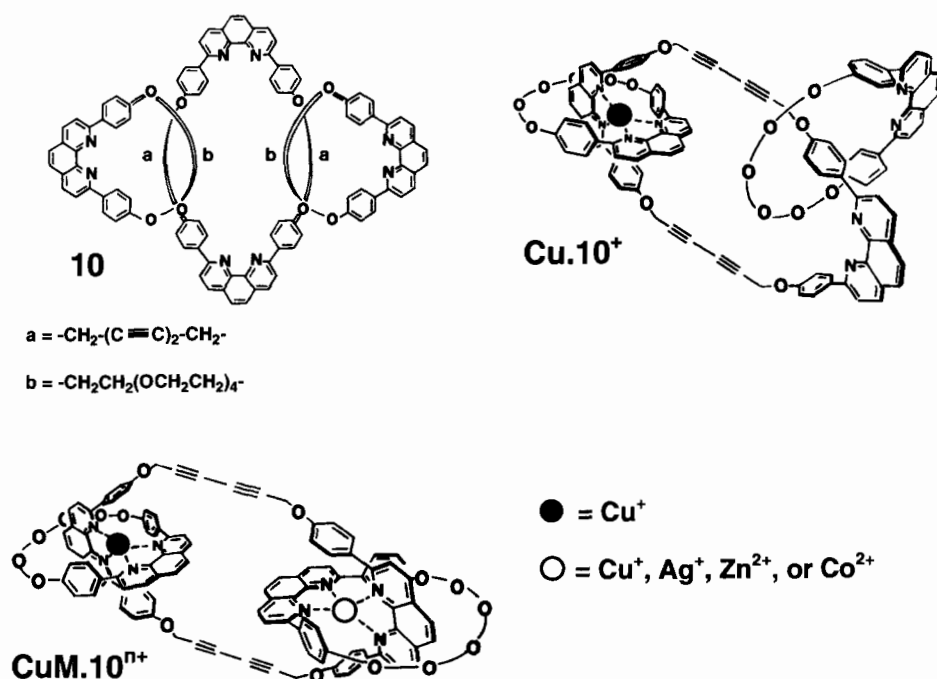


Figure 16. The [3]catenand **10** and its mononuclear (**Cu.10⁺**), and dinuclear (**CuM.10ⁿ⁺**) metal-locatenates ($M = \text{Cu}^+, \text{Ag}^+, \text{Co}^{2+}, \text{Zn}^{2+}$).

gion gives rise to a MLCT emission band, whose quantum yield is identical to that of the parent **Cu.5⁺** and twice that of **CuCu.10²⁺**. This shows clearly that in the dinuclear complex the coordination geometry is modified relative to the mononuclear species, due to the reciprocal steric interactions of the two moieties which are quite close to each other as observed in the solid state [47]. Excitation in the 320-nm LC band gives a blue-shifted, dramatically quenched fluorescence band. The corresponding lifetime, which is 2.4 ns in the reference compound, is shortened to 40 ps. In principle, such quenching can occur by either energy or electron transfer, but excitation spectra clearly show that energy transfer is not the predominant process. Indeed, electron transfer from the Cu^+ ion of the catenand moiety to the LC state of the dap fragment of the catenand moiety is thermodynamically allowed ($\Delta G = -0.43$ eV). A similar behavior was more recently observed [18] for the [2]catenand **Cu.6⁺** made of two moieties, i.e., a Cu.Cat-type and a free phen-type fragment; also in this case a very rapid luminescence quenching of the uncomplexed subunit is observed ($k_q = 1.6 \times 10^{10} \text{ s}^{-1}$).

CuAg.10²⁺ exhibits only the MLCT emission of the Cu-based moiety both at 298 and at 77 K, at any excitation wavelength. This shows that population of the excited LC levels of the Ag-based moiety, is followed by energy transfer to the Cu^I-complexed moiety, as confirmed by excitation spectra.

Table 10. Luminescence data for the [3]catenane **10** and its complexes in CH₂Cl₂

	298 K			77 K	
	$\lambda_{\text{max}}^{\text{a}}$ (nm)	τ (ns)	Φ_{em}	$\lambda_{\text{max}}^{\text{a}}$ (nm)	τ (ns)
10	404 ^b	2.4	0.33	382 ^b	2.6
Cu.10⁺	399 ^b	0.040	$\sim 0.01^{\text{d}}$	519 ^c	8.0×10^8
				378 ^b	^e
CuCu.10²⁺	735 ^f	168	5.9×10^{-4}	715 ^f	1.9×10^3
CuAg.10²⁺	735 ^f	162	6.1×10^{-4}	750 ^f	1.4×10^3
CuZn.10³⁺	457 ^b	0.090	0.0068	735 ^f	1.8×10^3
	725 ^f	163	^g	/	/
CuCo.10³⁺	/	/	/	730 ^f	1.7×10^3
	/	/	/	/	/

^aValues corrected for the photomultiplier response.^bLigand-centered (LC) fluorescence.^cLC phosphorescence.^dIncluding some contribution from impurities of **10**.^eNot available value under these conditions; no LC phosphorescence was detected.^fLuminescence from the lowest metal-to-ligand-charge-transfer (MLCT) excited state of the Cu(I)-complexed moiety.^gImpossible to evaluate because the MLCT emission overlaps with a higher energy luminescence band (see text).

A similar behavior is found for **CuZn.10³⁺**, where the Cu-based moiety shows luminescence properties quite similar to those of **CuAg.10²⁺** and **CuCu.10²⁺**; instead, the Zn-based moiety is quenched, with $k_{\text{q}} = 1.1 \times 10^{10} \text{ s}^{-1}$ at 298 K. Quite peculiarly, for this [3]catenate a broad emission band with maximum at 560 nm is detected, that can hardly be assigned to an impurity of some sort [64]. Tentatively, it was attributed to an intercomponent CT interaction which could play a role in the quenching of the LC fluorescence in **CuZn.10³⁺**.

Finally, the **CuCo.10³⁺** catenate does not luminesce under any condition, showing that the potentially luminescent MLCT level of the Cu-complexed moiety is quenched by the Co-based one. A possible quenching mechanism is energy transfer, since the d⁷ Co²⁺ metal ion has low-energy d-d levels ($< 10\,000 \text{ cm}^{-1}$) [65], but also electron transfer is thermodynamically allowed ($\Delta G = -0.54 \text{ eV}$).

A comprehensive view of the intercomponent processes taking place in this family of [3]catenates is illustrated schematically in Figure 17.

8.3.4 Proton [2]- and [3]Catenates

In CH₂Cl₂ solution, 1,10-phenanthroline and its derivatives can be protonated on the nitrogen atoms, and the reaction can be followed by absorption and luminescence spectroscopy [61].

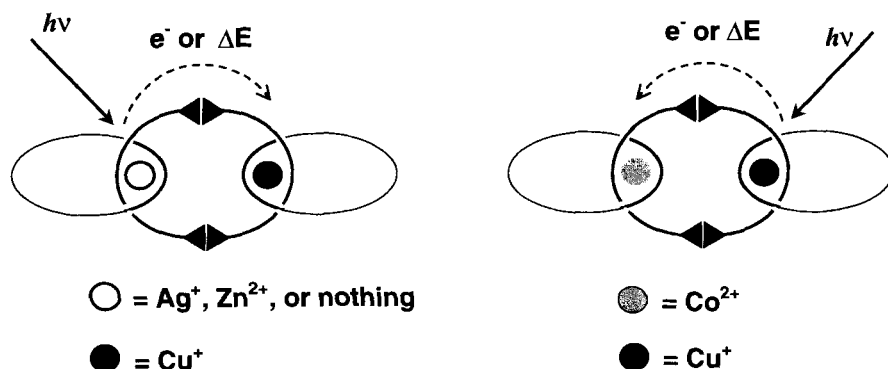


Figure 17. Direction of photoinduced processes observed in the [3]catenates CuM.10^{n+} .

On addition of increasing amounts of acid, the absorption spectra of phenanthrolines undergo strong changes and a single family of isosbestic points is found; in parallel, the intensity of the starting emission band decreases and a new, red-shifted band emerges [61]. These results clearly demonstrate that a single protonation reaction takes place and prompted us to investigate by UV-visible spectroscopy the protonation of the catenands and catenates having one or more protonable sites, i.e., **5** [60], **10** [66], and Cu.10^+ [66].

For the [2]catenand **5**, two clearly distinct protonation reactions are found, and it was demonstrated unambiguously that both protonated forms have a catenate structure [60, 67], i.e., the two dap fragments are arranged in an entwined structure identical to that involved for metal catenates. The driving force for this unexpected behavior is likely to be the $\pi\pi^*$ electronic donor–acceptor interactions between phenanthroline and anisyl fragments that can be established only in the catenate-type arrangement, and not in a open form. The luminescence properties of **5** and its protonated forms H.5^+ and $(\text{H}_2)\text{.5}^+$ are reported in Table 9.

Also in the case of Cu.10^+ , where a [2]catenand-type moiety is present, a two-step protonation reaction occurs, but in this case the luminescence of such moiety is quenched by the Cu-based one [66]. Unfortunately, it is not possible to determine the quenching rate and mechanism for a variety of reasons, including: (i) the instability of the protonated forms under laser irradiation in CH_2Cl_2 [56]; (ii) the lack of electrochemical potentials of the protonated forms; and (iii) the weakness of the MLCT emission band of the Cu-based moiety, which is partially masked by the tail of the emission of the protonated subunit, albeit quenched. However, the energy transfer mechanism is thermodynamically allowed and probably active.

For the [3]catenand **10**, four successive protonation reactions are observed via absorption and luminescence spectroscopy [66]. Interestingly, after the first protonation step a nonsymmetrical proton catenate is formed, where one moiety is protonated and the other is free. In this case, luminescence quenching of the unprotonated subunit by the protonated one is found, most likely by energy transfer.

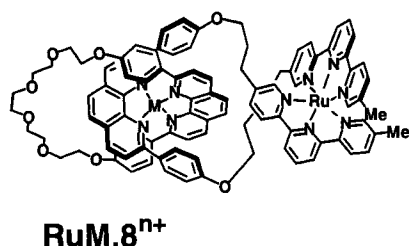


Figure 18. The [2]catenates **RuM.8ⁿ⁺** ($M = \text{Ag}^+$, Cu^+ , Zn^{2+} , or nothing).

8.3.5 Multicomponent Metallo-[2]catenanes

The complexes **RuCu.8³⁺** (Figure 18) represent a special case of [2]catenates where one of the two interlocked rings is closed via coordinative bonds. From the photophysical point of view, such compounds offer the possibility of studying dinuclear complexes where the two subunits have different coordination geometry, i.e., octahedral ($[\text{Ru}(\text{tpy})_2]^{2+}$ -type) and tetrahedral ($[\text{M}(\text{phen})_2]^+$ -type) [68]. The $[\text{Ru}(\text{tpy})_2]^{2+}$ -type unit has been extensively investigated [69] and also largely employed in the construction of rod-like polynuclear complexes [70]. The absorption spectra of such Ru^{II} -complexes exhibit intense LC $\pi\pi^*$ absorption bands in the UV and weaker MLCT features in the visible spectral region. The lowest MLCT excited state of $[\text{Ru}(\text{tpy})_2]^{2+}$ is short-lived ($\tau < 1$ ns) and not luminescent at room temperature (unlike the $[\text{Ru}(\text{bpy})_3]^{2+}$ -type compounds), whereas at 77 K a strong luminescence band ($\tau = 10.6 \mu\text{s}$) [69] is observed.

The absorption spectra of the **RuM.8ⁿ⁺** catenates [68] correspond to the sum of the spectra of the pertinent model compounds, as observed for the [3]catenates described in Section 8.3.3. This indicates that ground-state intercomponent interactions are weak, and is consistent with the fact that the two moieties are linked by aliphatic chains. The luminescence properties are reported in Table 11 and compared to those of the proper model compounds; they show that in all cases there is always luminescence quenching of one of the two moieties, suggesting that strong intercomponent excited state interactions occur.

For **Ru.8²⁺** and **RuZn.8³⁺**, at 298 K, the fluorescence of the lowest ligand-centered singlet excited state (^1LC) of the uncomplexed (**5**-type) and complexed (**Zn.5²⁺**-type) moieties is strongly quenched by the $[\text{Ru}(\text{tpy})_2]^{2+}$ -based unit (Table 11); the quenching rate constants result to be $> 5 \times 10^{10} \text{ s}^{-1}$. From the electrochemical results [68] one can argue that for **Ru.8²⁺**, both oxidative and reductive electron transfer processes are not thermodynamically allowed upon excitation of the lowest ligand-centered level of the free moiety. Instead, energy transfer to the lowest MLCT level of the other subunit is energetically allowed, and can account for the observed quenching process. In the case of **RuZn.8⁴⁺**, oxidative electron transfer quenching of the Ru^{II} center is thermodynamically allowed, but only upon excitation of the **Zn.5²⁺**-type moiety, so this could perhaps contribute to the quenching process of ^1LC at 298 K. At 77 K, for both **Ru.8²⁺** and **RuZn.8⁴⁺**, complete quenching of the ^1LC and ^3LC (lowest ligand-centered triplet excited state) levels of the “phen-type” moieties is observed and it can be accounted for by

Table 11. Luminescence data for the **RuM.8ⁿ⁺** compounds in CH₂Cl₂.^a Data for the model **M.5^{m+}** compounds are also reported for comparison purposes (see Ref. [60])

	298 K			77 K	
	λ_{\max}^b (nm)	τ (ns)	Φ_{em}	λ_{\max}^b (nm)	τ (ns)
Ru.8²⁺	398 ^c	$\leq 0.040^d$	< 0.004	395 ^{c,d}	0.080 ^d
	615 ^e	0.190	$\sim 10^{-5}$	602	9.0×10^3
5	400 ^e	2.0	0.42	382 ^e	2.2
				524 ^f	7.9×10^8
RuZn.8⁴⁺	438 ^c	$\leq 0.040^d$	< 0.001	418 ^{c,d}	0.100 ^d
	615 ^e	0.130	$\sim 10^{-5}$	600 ^e	8.9×10^3
Zn.5²⁺	463 ^c	2.0	0.082	433 ^e	1.0
				495 ^f	7.8×10^8
RuAg.8³⁺	605 ^e	0.130	$\sim 10^{-5}$	602 ^e	9.2×10^3
Ag.5⁺	/	/	/	498 ^f	1.2×10^7
RuCu.8³⁺	605 ^e	0.110	$\sim 10^{-5}$	600 ^e	3.0 ^g
	750 ^h	97 ⁱ	7×10^{-4}	685 ^h	1.1×10^3
Cu.5⁺	730 ^h	125 ^j	9×10^{-4}	685 ^h	1.1×10^3

^a Air-equilibrated solutions.^b Values corrected for the photomultiplier response.^c Ligand-centered (LC) fluorescence of the bisphenanthroline-type moiety.^d In butyronitrile. CH₂Cl₂ solutions undergo photodegradation under UV laser irradiation.^e Metal-to-ligand-charge-transfer (MLCT) luminescence from the Ru^{II}-complexed moiety.^f LC phosphorescence of the bisphenanthroline-type moiety.^g Glassy butyronitrile matrix.^h MLCT luminescence from the Cu(I)-complexed moiety.ⁱ 120 ns in oxygen-free solution.^j 175 ns in oxygen-free solution.

an energy transfer to the MLCT levels of the [Ru(tpy)₂]²⁺ fragment, which turns out to be sensitized in the excitation spectra.

For **RuAg.8³⁺**, at 298 K oxidative electron transfer quenching of the Ru^{II} center is thermodynamically allowed (regardless of the excited component) so that a contribution of such mechanism to the observed complete fluorescence quenching of the Ag^I-complexed moiety cannot be excluded, probably in competition with a fast ¹LC → ³LC intersystem crossing, in analogy with what was observed for the mononuclear **Ag.5⁺**. In rigid matrix at 77 K, sensitization of the MLCT Ru^{II}-based emission is observed; therefore, the lack of fluorescence and phosphorescence is clearly related to an energy transfer process to the MLCT level of the [Ru(tpy)₂]²⁺ moiety.

In the case of **RuCu.8³⁺**, the picture is different because the lowest excited state is no longer the MLCT level of the [Ru(tpy)₂]²⁺ moiety, but that of the [Cu(phen)₂]²⁺-type. The excitation spectra (taken at 720 nm) show that there is no appreciable contribution from the [Ru(tpy)₂]²⁺-based absorption bands in the visi-

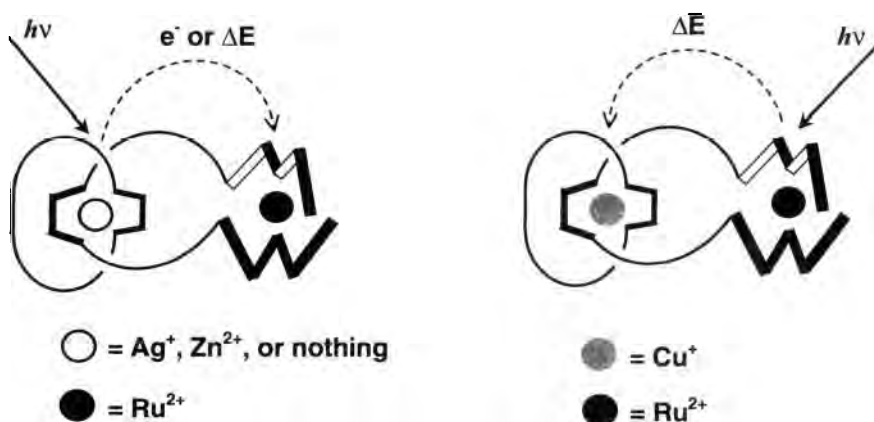


Figure 19. Direction of photoinduced processes observed in the [2]catenates **RuM.8ⁿ⁺**.

ble spectral region, because the very fast internal deactivation cannot compete with energy transfer. In contrast, at 77 K, the [Ru(tpy)₂]²⁺-based emission is dramatically quenched, with a rate constant of $3 \times 10^8 \text{ s}^{-1}$; unfortunately the excitation spectrum read on the Cu^I-based emission could not be recorded, due to the signal weakness. Nevertheless, the observed quenching can be assigned to an energy transfer mechanism. In fact, at 298 K, the electron transfer (corresponding to the reduction and oxidation of the Ru^{II} and of the Cu^I metal center, respectively) is exergonic by only 0.17 eV—a value most likely not sufficient to allow for electron transfer in a 77 K rigid matrix.

In conclusion, for the **RuM.8ⁿ⁺** [2]catenates family, photoinduced intercomponent energy and/or electron transfer processes are evidenced. The direction of such processes can be tuned upon a suitable choice of the metal ion complexing the [M(phen)₂]ⁿ⁺-type coordination center, according to the schematic representation of Figure 19.

8.3.6 Homo- and Heterodinuclear Knots

The dicopper(I) trefoil knots **CuCu.12²⁺**, **CuCu.13²⁺**, **CuCu.17²⁺**, and **CuCu.18²⁺**, are shown in Figure 20. From the structural point of view they have the same coordinating ligands, but along the series the two coordination cores are linked by fragments of different length, i.e., the internal polymethylene chain (Z) and the external polyethyleneoxy unit (X) used in the final cyclization synthetic step. Therefore such complexes provide a unique opportunity to study whether slight structural modification of the coordination environment, as those induced by different Z or X chains, can lead to some changes in the UV-visible spectroscopic properties [49]. Some selected photophysical properties are reported in Table 12.

The absorption bands of the knots in the UV region are, as for the catenanes, mainly due to ligand-centered $\pi\pi^*$ transitions, and are only slightly affected by the

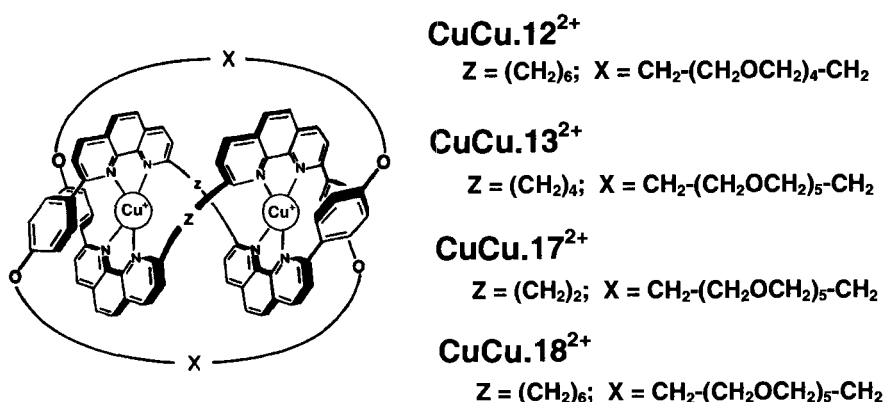


Figure 20. The dicopper(I) knots made of two identical chromophoric centers linked by two threads (X and Z), each of which can be of different length.

actual structure of each knot. More pronounced variations are found for the MLCT transitions in the visible spectral region, where the molar absorption coefficients at the absorption maxima are identical for all the knots, but the spectral shapes have remarkable differences [49]. This shows that the three groups of MLCT absorption bands evidenced for the $[\text{Cu}(\text{phen})_2]^{n+}$ -type complexes (and denominated I, II, and III) [54i] are, to a different extent, affected by the length of the Z and X bridges. For instance **CuCu.17²⁺**, where the Z connection is the shortest, exhibits a peculiar broadening on the red side of the lower energy bands I and II.

Table 12. Selected photophysical properties for the dicopper(I) knots with the interchromophoric polymethylene spacer^a

	Z^b	X^c	298 K					77 K	
			λ_{max}^d (nm)	τ^e (ns)	Φ_{em}^e ($\times 10^4$)	$10^{-3} k_r^f$ (s^{-1})	$10^{-6} k_{\text{nr}}^g$ (s^{-1})	λ_{max}^d (nm)	τ^h (μs)
CuCu.12²⁺	6	16	742	208	7.2	3.5	4.8	750	0.9
CuCu.13²⁺	4	19	750	154	4.1	2.7	6.5	750	0.9
CuCu.17²⁺	2	19	750	149	3.7	2.5	6.7	770	1.2
CuCu.18²⁺	6	19	742	174	5.5	3.2	5.7	755	1.2

^a In CH_2Cl_2 , unless otherwise specified.

^b Number of atoms of the aliphatic chain Z.

^c Number of atoms of the ether chain X.

^d Values corrected for the photomultiplier response.

^e Deaerated solutions.

^f Radiative decay rate constants.

^g Nonradiative decay rate constants.

^h $\text{CH}_2\text{Cl}_2/\text{MeOH}$ (1:1) glassy matrix.

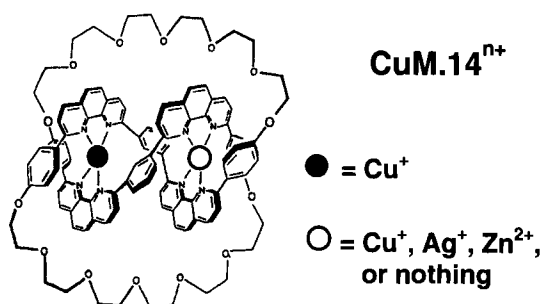


Figure 21. The homo- and hetero-dinuclear knots **CuM.14ⁿ⁺** with the phenylene interchromophoric spacer.

All the knots exhibit MLCT luminescence bands at 298 and 77 K, but the luminescence properties are not identical along the series. The most interesting result is that the luminescence bands of **CuCu.12²⁺** and **CuCu.18²⁺** are blue-shifted, more intense, and longer-lived compared to those of the other knots and also of the proper mononuclear model compound [49]. They also display larger radiative (k_r) and smaller nonradiative (k_{nr}) rate constants compared to those of the other knots. This suggests that they possess a more symmetric and rigid structure than the other knots, which tends to disfavor the nonradiative deactivation of the lowest excited state via pentacoordinated exciplexes (see above). Importantly, this fits well with electrochemical results, which show that **CuCu.12²⁺** has a surprisingly high oxidation potential (+0.75 V versus SCE) 140 mV higher, for instance, than that of **CuCu.13²⁺** (see Section 8.2.6).

In summary, for this family of dicopper(I) dinuclear knots the photophysical and electrochemical properties allow them to be ordered in a series where the two extremes are **CuCu.12²⁺** and **CuCu.17²⁺**, the former being the most rigid and the one in which Cu^I is best shielded. This shows that the length of the shorter Z connection plays an important role in determining the fine structure of the geometric arrangement.

The possibility of observing photoinduced intercomponent processes in hetero-dinuclear knotted complexes was made possible with the knots bearing a phenylene unit, as interchromophoric spacer [52b] (Figure 21). In fact, in this case the synthetic yield of the parent dicopper complex is high enough to allow further decomplexation–recomplexation steps, as required.

The photophysical properties of the complexes thus obtained (**Cu.14⁺**, **CuCu.14²⁺**, **CuAg.14²⁺**, **CuZn.14³⁺**) are reported in Ref. [52b]. The absorption spectra exhibit the usual LC $\pi\pi^*$ bands in the UV, and the weaker MLCT bands in the visible spectral region. The spectra are rather different from those of the above homodinuclear series, and this is a consequence of the fact that two phenyl substituents are placed on the phenanthroline rings, whereas in the previous case there is one phenyl and one alkyl residue. This is expected to strongly affect the electronic MLCT transitions, also as a consequence of a slightly different coordination geometry.

Some luminescence data are reported in Table 13. Only one emission band is observed above 700 nm, assigned to the lowest MLCT excited state, irrespective of the excitation wavelength. The good matching between absorption and excitation

Table 13. Luminescence data for the **CuM.14ⁿ⁺** knots in CH₂Cl₂^a

	λ_{\max}^b (nm)	τ (ns)	Φ_{em} ($\times 10^4$)
Cu.14⁺	740	120	6
CuCu.14²⁺	730	200	9
CuAg.14²⁺	725	240	13
CuZn.14³⁺	950	11	~0.5

^a Deaerated solutions.^b Values corrected for the photomultiplier response, except for **CuZn.14³⁺**.

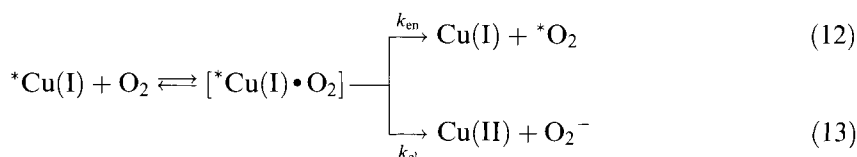
spectra throughout the UV/visible spectral region shows that, for any knot, complete conversion occurs of all the upper lying excited states to the lowest emitting MLCT level. This implies that in the heterodinuclear compounds intercomponent energy transfer towards the Cu-based moiety takes place from the other chromophoric center. In the case of **CuZn.14³⁺**, an emission band at 950 nm (attributed to the lowest MLCT excited state of the Cu-based unit) is detected. Such dramatic shift is attributed to a strong electrostatic effect of the nearby divalent Zn²⁺ ion on the MLCT transitions. Such an effect is not observed for the monovalent Ag⁺ ion in **CuAg.14²⁺**, and also in the previously described [3]catenate **CuZn.10³⁺**, where the two moieties were electronically insulated and further apart. In other words, the phenylene spacer leads to spectroscopic (and electrochemical) properties quite different from those of homonuclear knotted complexes in which the two chromophoric units are linked by insulating polymethylene chains. The comparison with heterodinuclear [3]catenates shows the strong conducting electronic character of such an aromatic spacer.

8.3.7 Quenching by Dioxygen

For all the above-reported Cu^I catenates and knots, on excitation of the MLCT absorption bands in air-equilibrated CH₂Cl₂ solution, sensitized singlet oxygen luminescence at 1270 nm is recorded [18, 49, 64, 68]. Indeed, this can provide a good clue for photoinduced energy transfer to the molecular oxygen dissolved in the solvent. However, it has been shown that the intimate nature of excited state quenching by dioxygen is often quite difficult to elucidate [71]. For instance, the occurrence of singlet oxygen luminescence at 1270 nm is necessary (but not sufficient) to demonstrate that energy transfer occurs. In fact, upon encounter of an excited molecule (M) with dioxygen (O₂), electron transfer can be followed by a back electron transfer reaction, yielding singlet oxygen [72]:



Moreover, specific donor–acceptor interactions (e.g., exciplex formation), often related to the oxidation potential of the quencher, can play an important role [71b,c]. Therefore, the actual mechanism for the quenching of the MLCT lowest excited state in $[\text{Cu}(\text{phen})_2]^+$ -type complexes in CH_2Cl_2 solution has not been elucidated, also because the reduction potential of O_2 in dichloromethane solution is not known. However, since such potential has been reported in several organic solvents (e.g., DMF, pyridine, CH_3CN) to be -0.85 V , we can tentatively attribute a potential around 1 V in the less-polar CH_2Cl_2 . Hence, taking the (average) MLCT excited state energy as 1.7 eV and the average oxidation potential for $\text{Cu}^+/\text{Cu}^{2+}$ as 0.6 V , one can argue that electron transfer cannot be excluded. The situation can be schematized as follows:



The Stern–Volmer quenching rate constants were determined for all our knots and catenates [18, 49, 52b, 64, 68], and are in the range $1.1\text{--}2.5 \times 10^6\text{ s}^{-1}\text{ M}^{-1}$. These values, especially when compared to those of mononuclear complexes such as $[\text{Cu}(\text{dmp})_2]^+$ ($\text{dmp} = 2,9\text{-di-}p\text{-methyl-1,10-phenanthroline}$), show a clear trend where the rate constants decrease upon increasing the rigidity of the systems and the protection of the Cu^{I} ion, thus reflecting the increasing steric hindrance toward orbital overlap between the $[\text{Cu}(\text{phen})_2]^+$ -type chromophoric unit and O_2 . Such steric constraints are also evidenced by quenching experiments with acetone [64], although in this case neither energy nor electron transfer are responsible for the observed quenching. This is in fact simply due to the formation of pentacoordinated exciplexes which deactivate via nonradiative paths (see above); however, the rates of such process are also strongly dependent on steric hindrance, and somehow parallel the trend observed for quenching rates by O_2 .

8.4 Porphyrinic Rotaxanes: Control of the Photoinduced Electron Transfer Rate between PZn and PAu^+ by the Assembler Metal

8.4.1 Introduction

The publication in 1984 of the resolution of the X-ray crystal structure of the reaction center (RC) of the photosynthetic bacterium *Rhodospseudomonas viridis* [73] inspired many research groups, and thus initiated the design and synthesis of multifarious multicomponent systems expected both to display structural analogy with the RC and to fulfill some of its photochemical and electron transfer functions [74].

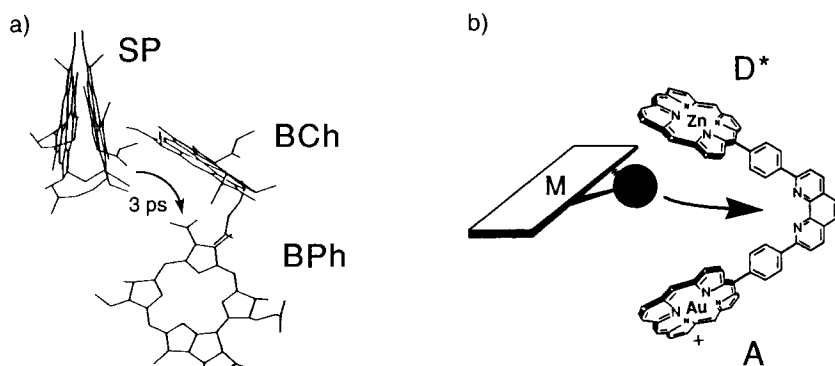


Figure 22. (a) A fragment of the photosynthetic reaction center with the three components: Special Pair (SP), “Accessory” Bacteriochlorophyll (BCh), and Bacteriopheophytin (BPh). Photoinduced electron transfer from SP to BPh takes place at a *global* rate of $(3 \text{ ps})^{-1}$. (b) Principle of the modular mimetic approach. D and A are the donor and acceptor porphyrins, respectively. M is an electron transfer mediator whose introduction between D and A can be realized via coordination of a metal center (solid circle) which will also bind the chelating part of the bisporphyrin spacer.

Mimicking the electron transfer processes occurring within the Special Pair (SP)/Accessory Bacteriochlorophyll (BCh)/Bacteriopheophytin (BPh) trichromophoric fragment, where SP is the excited state electron donor, and BPh the terminal electron acceptor of this triad (Figure 22a) seemed particularly attractive. An oblique bisporphyrin looked appealing since these porphyrin-like nuclei are mostly organized in an oblique fashion to one another. The required electronic properties can be controlled by the nature of the metal centers of each porphyrin. Surprisingly, the number of (M^I , M^2) metal couples fulfilling these requirements is quite limited. Zinc(II) and gold(III) were selected as metals for the donor component and the acceptor subunit respectively, because both metal centers are electroinactive once complexed by a porphyrin, and all the expected properties are in agreement with the objective. Noteworthy, the (Zn^{II} , Au^{III}) strategy is reminiscent of the photosynthetic RC. In nature, energy transfer has been avoided by decreasing the energy level of the donor, using a bacteriochlorophyll dimer (the SP), whereas in the present approach the same effect is obtained by raising the excited state level of the electron acceptor (Au^{III} porphyrin). Finally, a *modular approach* was particularly attractive in order to introduce chemical groups, supposed to control the electron transfer rate between D and A. The use of a chelate as spacer between both porphyrin components allowed for the insertion of an aromatic group via coordination to a transition metal whose function was both to serve as structural element (gathering center) and to tune the electronic properties of the third component interspersed between D and A. The principle is indicated in Figure 22b. The most thoroughly studied bisporphyrin **19** and Cu^I -complexed [2]rotaxane **Cu.20⁺** of Figure 23 were selected among the systems that were designed and synthesized for this purpose [75, 76].

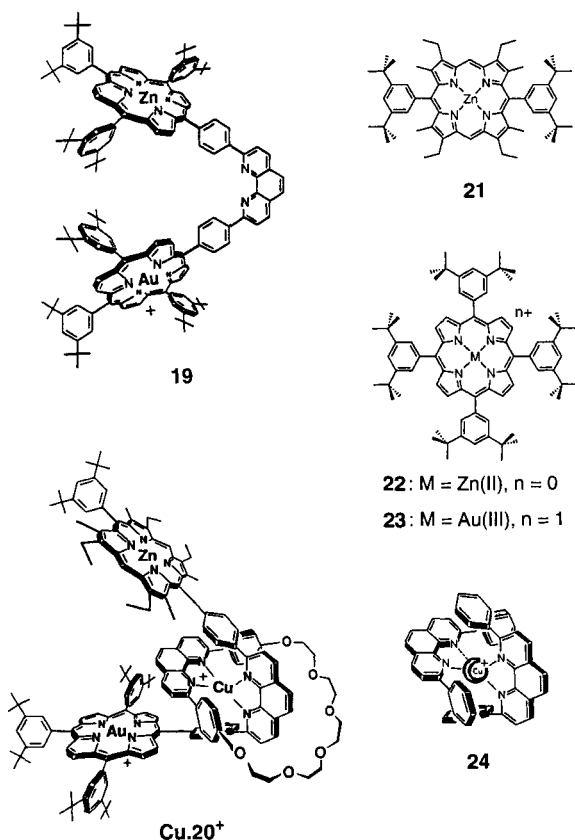


Figure 23. Chemical structures of Zn/Au bisporphyrin **19**, Cu^I-complexed [2]rotaxane **Cu.20⁺**, and the model compounds **21–24**.

8.4.2 Properties of the Reference Compounds

Photophysical and electrochemical data recorded for the reference compounds **21–24** of Figure 23 are collected in Table 14. Additional data corresponding to bisporphyrins **19** and **Cu.20⁺** are given in Table 15, and were used to calculate the exothermicities of the electron transfer reactions occurring in these compounds. The Zn porphyrins **21** and **22** fluoresce in DMF at room temperature but, as expected, Au porphyrin **23** is non fluorescent. Phosphorescence from **22** and **23** was observed in methanol glasses at 77 K.

Transient differential absorption spectra were recorded for **22** and **23** after excitation with a 30-ps laser pulse at 532 nm. For **22**, the transient spectrum is assigned to the first excited singlet state. This species decays on the nanosecond time scale to produce a long-lived triplet excited state. The spectrum observed for **23** decays via first-order kinetics with a lifetime of 1.4 ns to reform the ground state, which is assigned to the first excited triplet state.

[Cu(dpp)₂]⁺ (**24**) has a long-lived MLCT excited state, which is luminescent at room temperature. Stabilization of Cu^I by the dpp ligand is evident from the unusually high oxidation potential of [Cu(dpp)₂]⁺.

Table 14. Photophysical and electrochemical data for the reference compounds **21–24**

Property ^a	21	22	23	24^b
E_s (eV)	2.18 ^b	2.06	2.21	
Φ_f		0.045	<0.0001	
τ_s (ns)	2.2 ^c	2.3		
E_t (eV)		1.64	1.82	
Φ_t		0.72	1.0	0.00107 ^e
τ_t (μ s)	20 ^d	820	0.0014	0.250 ^e
E_{red}° (V)	−1.60 ^c	−1.63	−0.59	−1.65 ^f
E_{ox}° (V)	+0.64 ^c	+0.62	+1.62	+0.58 ^g
$^sE_{red}^\circ$ (V)	+0.58	+0.43	+1.62	
$^tE_{red}^\circ$ (V)		+0.01	+1.23	
$^sE_{red}^\circ$ (V)	−1.54	−1.44	−0.59	
$^tE_{red}^\circ$ (V)		−1.02	−0.20	

^a Unless otherwise noted, in DMF solution and from Ref. [75a]; redox potentials in V versus SCE. s and t super- or subscripts refer to the singlet and triplet excited states, respectively.

^b Ref. [76b].

^c Ref. [77a].

^d Ref. [77b].

^e Ref. [54h], in CH₂Cl₂ solution.

^f Free dpp ligand: −2.00 V.

^g Metal-centered process. There is a second oxidation step at +1.90 V, which is ligand-centered (+1.95 V for free dpp).

Table 15. Absorption and electrochemical data for the bis-porphyrin compounds **19** and **Cu.20⁺**

Property ^a	19^b	Cu.20⁺
Absorption λ_{max} , nm, (ϵ), M ^{−1} cm ^{−1}	418 (239 000)	413 (678 000)
	431 (257 000)	538 (32 000)
	528 (12 300)	573 (9600) ^c
	563 (11 700)	
	604 (7000)	
E_{red}° (V)	−0.49 (Au) ^d	−0.49 (Au)
E_{ox}° (V)	+0.82 (Zn)	+0.68 (Zn)
		+0.54 (Cu)

^a Unless otherwise noted, in DMF solution and from Ref. [76b]; redox potentials in V versus SCE.

^b Ref. [75a].

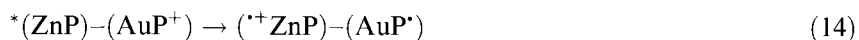
^c In CH₃CN solution and from Ref. [76a].

^d Refers to the fragment of the molecule undergoing the redox process.

8.4.3 Photochemistry of the Zinc/Gold Bisporphyrin

Upon selective excitation at 598 nm of the Zn^{II} porphyrin component of **19**, a weak fluorescence, with a quantum yield of 0.0012 and a lifetime of 55 ps, is observed, which corresponds to ca. 97 % fluorescence quenching. Excitation of **19** with a 30-ps

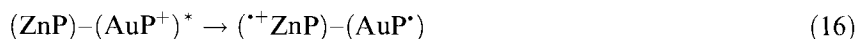
laser pulse at 598 nm, forms the excited singlet state of the Zn porphyrin (Figure 24a, trace 0 ps) as identified by comparison with the spectrum obtained for **22**. This excited state decays rapidly to form a transient exhibiting absorptions at 440 nm and between 640 and 750 nm (trace 100 ps) and which decays itself with a lifetime of 600 ps (Figure 24b). This transient can be assigned to a charge-transfer (CT) state in which the Zn porphyrin is a π -radical cation and the Au^{III} porphyrin a neutral radical:



Decay of the CT state regenerates cleanly the ground-state bisporphyrin:



Immediately after excitation of **19** with a 30-ps laser pulse at 532 nm, where the Au porphyrin subunit absorbs ca. 85 % of incident photons, the Au porphyrin excited triplet state can be identified (Figure 24c) by comparison with the spectrum obtained for **23**. This species (trace 0 ps) decays with a lifetime of 120 ps to form a mixture of two products. The shorter-lived product (trace 0.8 ns), which accounts for 77 % of the decay of the Au porphyrin excited triplet state, corresponds to the CT state, as described for 598 nm excitation:



It decays with a lifetime of 570 ps due to reverse electron transfer (Figure 24d). The longer-lived product (trace 1.5 ns) is the triplet excited state of the Zn porphyrin subunit, obtained in ca. 15 % yield by energy transfer from the Au porphyrin triplet. It decays with a lifetime of 1.3 ns, possibly by intramolecular electron transfer to the appended Au porphyrin.

In summary, excitation of either porphyrin subunit in **19** results in electron transfer from Zn to Au porphyrins to form the CT state. For the Zn porphyrin, both singlet and triplet excited states function as electron donors, whereas for the Au porphyrin, intersystem crossing to the triplet manifold is quantitative and the triplet acts as an electron acceptor. The rate constants and reaction exoergonicities for the ET steps described above are compiled in Table 16.

8.4.4 Photochemistry of the Copper(I)-complexed Zinc/Gold Bisporphyrin-Stoppered [2]Rotaxane

The sequence of events following excitation of either porphyrin of the **Cu.20**⁺ [2]rotaxane is depicted in Figure 25.

Excitation into the Zn^{II} porphyrin component

Upon selective excitation of **Cu.20**⁺ at 586 nm, extremely weak fluorescence could be observed, corresponding to >99 % quenching. Immediately after excitation with

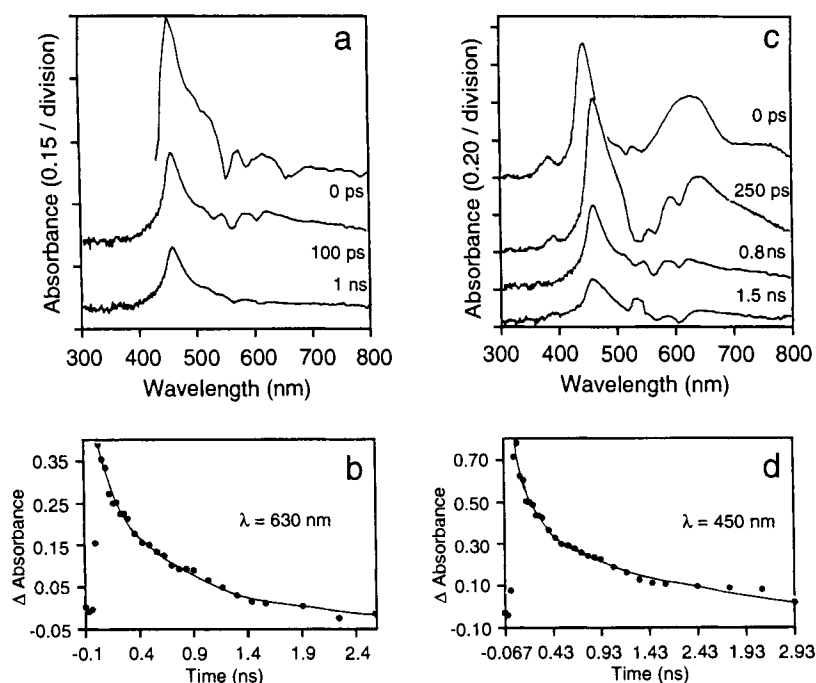
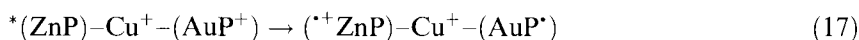


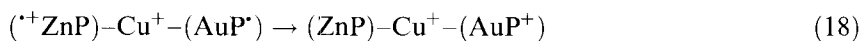
Figure 24. (a) Transient absorption spectra recorded after excitation of **19** in DMF with a 30-ps laser pulse at 598 nm; delay times are given on the traces. (b) Typical kinetic trace observed for the conditions as in (a). (c) Transient absorption spectra recorded after excitation of **19** in DMF with a 30-ps laser pulse at 532 nm. (d) Typical kinetic trace observed for the conditions as in (c).

a 0.5-ps laser pulse at 586 nm, the characteristic differential absorption spectral features of the CT state were observed (Figure 26a and b):



The Zn porphyrin excited singlet state could not be resolved, and formation of the CT state followed the laser pulse profile (Figure 26c). Therefore, the lifetime of the Zn porphyrin excited singlet state was <1 ps.

Absorbance attributed to the CT state decayed with a lifetime of 20 ps (Figure 26d) to leave a residual species having the characteristic differential absorption spectrum of the Au porphyrin neutral radical (Figure 26a and b). Deactivation of the CT state may involve direct reverse electron transfer between porphyrinic species:



or ET from the central copper(I) complex to the Zn porphyrin π -radical cation:

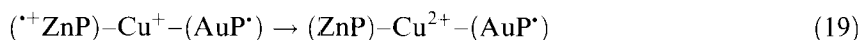
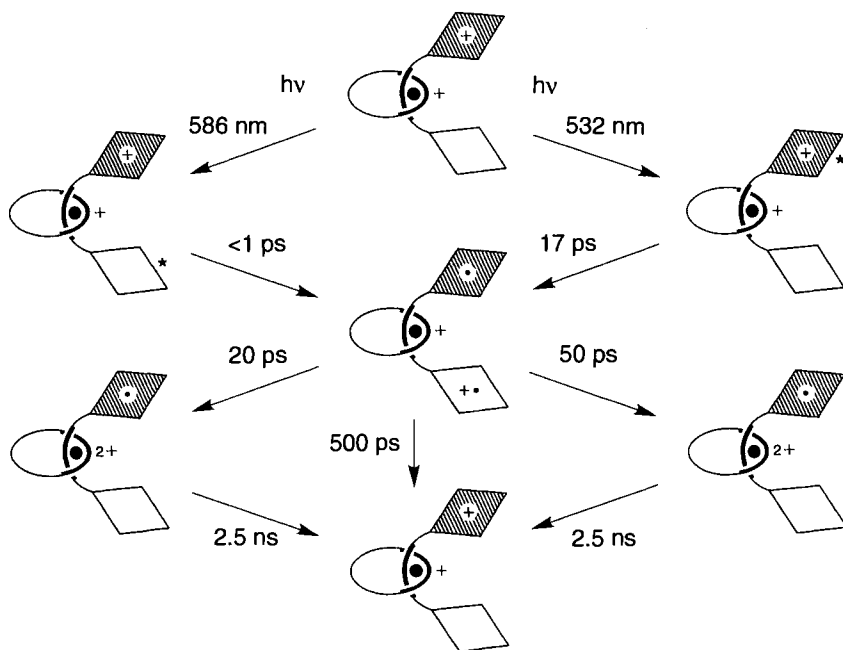


Table 16. Rate constants and reaction exoergonicities for the various electron transfer steps occurring within **19** and **Cu.20**⁺^a

	Reaction	n ^b	k/10 ⁸ (s ⁻¹)	ΔG ^o ^c (eV)
19	$^*(\text{ZnP})-(\text{AuP}^+) \rightarrow (^+\text{ZnP})-(\text{AuP}^*)$	14	178	-0.75
19 ^d	$(^+\text{ZnP})-(\text{AuP}^*) \rightarrow (\text{ZnP})-(\text{AuP}^+)$	15	17	-1.31
19 ^e	$(^+\text{ZnP})-(\text{AuP}^*) \rightarrow (\text{ZnP})-(\text{AuP}^+)$	15	18	-1.31
19	$(\text{ZnP})-(\text{AuP}^+)^* \rightarrow (^+\text{ZnP})-(\text{AuP}^*)$	16	76	-0.51
Cu.20 ⁺	$^*(\text{ZnP})-\text{Cu}^+-(\text{AuP}^+) \rightarrow (^+\text{ZnP})-\text{Cu}^+-(\text{AuP}^*)$	17	>10 000	-1.01
Cu.20 ⁺ ^d	$(^+\text{ZnP})-\text{Cu}^+-(\text{AuP}^*) \rightarrow (\text{ZnP})-\text{Cu}^{2+}-(\text{AuP}^*)$	19	480	-0.14
Cu.20 ⁺ ^e	$(^+\text{ZnP})-\text{Cu}^+-(\text{AuP}^*) \rightarrow (\text{ZnP})-\text{Cu}^{2+}-(\text{AuP}^*)$	19	180	-0.14
Cu.20 ⁺	$(^+\text{ZnP})-\text{Cu}^+-(\text{AuP}^*) \rightarrow (\text{ZnP})-\text{Cu}^+-(\text{AuP}^+)$	18	20	-1.17
Cu.20 ⁺	$(\text{ZnP})-\text{Cu}^{2+}-(\text{AuP}^*) \rightarrow (\text{ZnP})-\text{Cu}^+-(\text{AuP}^+)$	20	4	-1.03
Cu.20 ⁺	$(\text{ZnP})-\text{Cu}^+-(\text{AuP}^+)^* \rightarrow (^+\text{ZnP})-\text{Cu}^+-(\text{AuP}^*)$	21	530	-0.65

^aFrom Ref. [76b].^bReaction number as reported in the text.^cCalculated using the data obtained for **19** and **Cu.20**⁺ (Table 15), and the excited state energies of Table 14.^dSinglet charge-transfer state.^eTriplet charge-transfer state.**Figure 25.** Pictorial representation of the reaction sequence initiated by the excitation of the rotaxane **Cu.20**⁺ into either porphyrin subunit. The thick lines represent phenanthroline chelates, and the black disk, Cu⁺. The empty and hatched diamonds are the Zn and Au porphyrins, respectively.

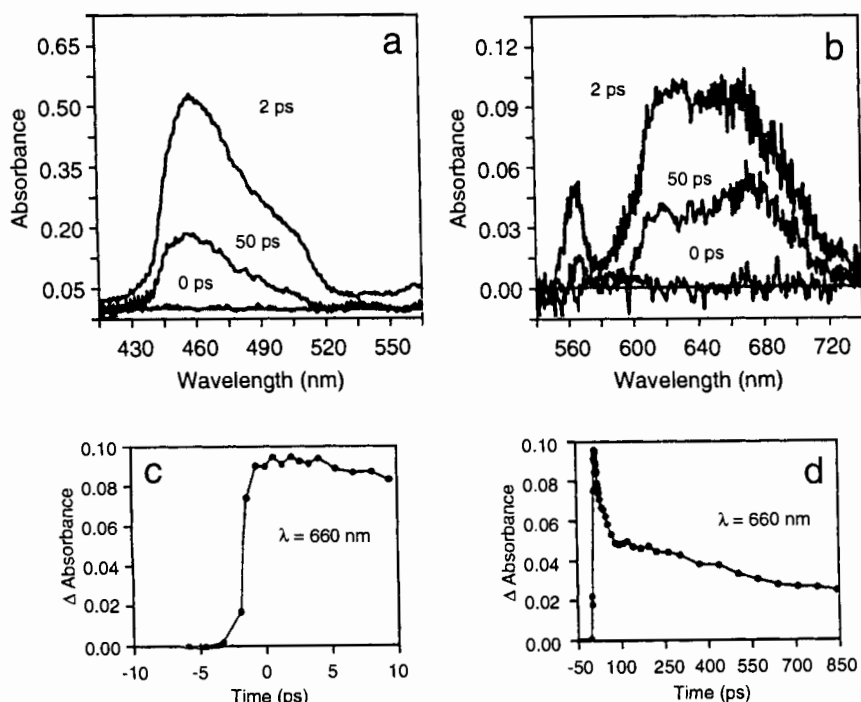
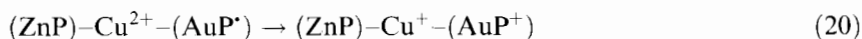


Figure 26. (a, b) Transient differential absorption spectra recorded after excitation of **Cu.20⁺** in DMF with a 0.5-ps laser pulse at 586 nm; delay times are given on the traces. (c) Growth of the transient absorbance at 660 nm attributed to the charge-transfer state. (d) Decay profile recorded for the above experiment at 660 nm. Note its clear biphasic nature.

On the basis of differential molar absorption coefficients, the latter process appears to be quantitative. Indeed, using the rate constant for direct reverse electron transfer (Eq. 18) derived following excitation into the Au porphyrin subunit ($k_{18} = 2.0 \times 10^9 \text{ s}^{-1}$), oxidation of the central **Cu^I** complex ($k_{19} = 4.8 \times 10^{10} \text{ s}^{-1}$) should account for ca. 95 % of the total decay of the intermediate CT state. The residual Au porphyrin neutral radical decayed on a much longer time scale (Figure 26d) due to electron donation to the **Cu²⁺** complex:



The most reliable estimate of the rate constant for Eq. 20 ($k_{20} = 4.0 \times 10^8 \text{ s}^{-1}$) was obtained following excitation of **Cu.20⁺** with a 30-ps laser pulse at 559 nm.

Excitation into the **Au^{III}** porphyrin component

Excitation of **Cu.20⁺** with a 30-ps laser pulse at 532 nm, where the Au porphyrin subunit absorbs about 80 % of the total incident photons, resulted in formation of the Au porphyrin triplet excited state. This species decayed within the laser pulse to

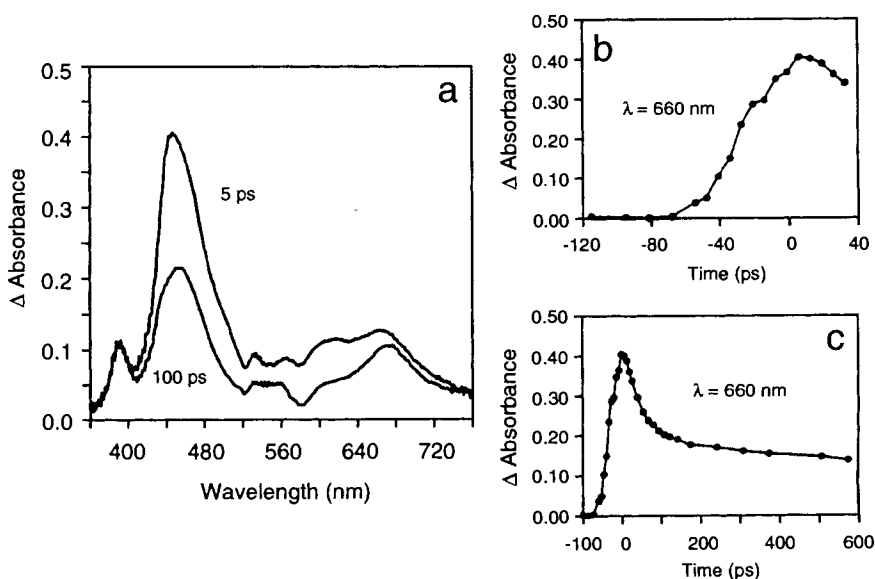
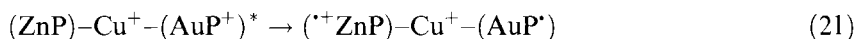


Figure 27. (a) Transient differential absorption spectra recorded after excitation of **Cu.20⁺** in DMF with a 30-ps laser pulse at 532 nm; delay times are given on the traces. (b) Growth of the transient absorption at 660 nm attributed to the charge-transfer state. (c) Decay profile recorded for the above experiment at 660 nm.

form the CT state (Figure 27b), as detected by its transient differential absorption spectrum (Figure 27a).



The lifetime of the Au porphyrin excited triplet state was derived as 17 ps.

The CT state was found to decay rapidly (Figure 27c), with a lifetime of 50 ps, leaving a residual absorbance which was identified as the Au^{III} porphyrin neutral radical by virtue of its differential absorption spectrum. This latter species decayed relatively slowly, with a lifetime of 2.5 ns, to re-form the ground state of **Cu.20⁺**. As above, the rapid deactivation of the CT state is ascribed to a combination of direct reverse electron transfer (Eq. 18) and oxidation of the central copper(I) complex by the Zn porphyrin π -radical cation (Eq. 19). The yield of the $\text{Au}(\text{III})$ porphyrin neutral radical which escaped direct electron transfer was estimated from the transient absorption spectral changes to be 90 %. Thus, direct reverse electron transfer ($k_{18} = 2.0 \times 10^9 \text{ s}^{-1}$) accounts for only 10 %, and electron abstraction from the central copper(I) complex ($k_{19} = 1.8 \times 10^{10} \text{ s}^{-1}$) is the dominant decay route. The residual Au porphyrin neutral radical decays over several nanoseconds due to electron donation to the copper(II) complex (Eq. 20).

8.4.5 Comparison of the Electron Transfer Rates for both Systems

The reactions that lead to reoxidation of the Au^{III} porphyrin neutral radical are relatively slow and dissipate large amounts of energy, although there is no reason to suppose that they fall within the Marcus inverted region. The copper(I) complex exerts no significant effect on the rate of direct reverse electron transfer (compare k_{18} and k_{15}). That $k_{18} > k_{20}$ is in accord with the relative reaction exoergonicities, and the fact that reduction of the copper(II) complex, which is initially formed as a coordinatively unsaturated species, may involve a high reorganization energy.

It is noteworthy that the rate of reduction of the Zn porphyrin π -radical cation by the copper(I) complex is much faster than direct charge recombination between the porphyrin radicals, although the reaction exoergonicity for Eq. 19 is very much less than that for Eq. 18. The faster rate for Eq. 19 may arise because of the closer proximity of the reactants and/or because electron transfer occurs via a different route. In addition, k_{19} shows some dependence on the porphyrin donor. This effect could be due to a different spin multiplicity of the precursor excited state.

The most striking difference in reactivity between the bis-porphyrin **19** and the rotaxane **Cu.20**⁺ concerns the relative rates of *photoinduced* electron transfer. Regardless of which porphyrinic subunit is excited, the rate of photoinduced electron transfer is very much faster in **Cu.20**⁺ (k_{17}) than in **1** (k_{14}). This cannot be explained alone by higher reaction exoergonicities (see Table 16), which arise because the Zn porphyrin subunit in **Cu.20**⁺ has a higher excited singlet state energy [78]. Since the mutual arrangement of the two porphyrin nuclei of **Cu.20**⁺ is not expected to differ significantly from that in the bisporphyrin **19**, it is tempting to invoke a super-exchange effect to account for the large difference between k_{14} and k_{17} . There are at least two distinct ways for this to happen. Firstly, the copper(I) complex might modulate the energy of the relevant HOMO or LUMO orbitals on the bridging unit; this would be significant if electron transfer occurs through the spacer moiety. Secondly, the “accessory” 1,10-phenanthroline residue contained in the 30-membered macrocyclic ring of the rotaxane **Cu.20**⁺ could also mediate electron transfer since it is interspersed between the two porphyrin rings. This latter mechanism would be significant if electron transfer proceeded through space.

It is remarkable that the relative rates of electron transfer observed for both compounds can be qualitatively explained in terms of a simple orbital energy diagram of the type displayed in Figure 28. Here, the energies of the donating and accepting orbitals on the Zn^{II} and Au^{III} porphyrins are compared to the energies of the LUMO and HOMO on the 2,9-diphenyl-1,10-phenanthroline spacer moiety. For reaction to proceed via electron transfer through the LUMO of the spacer moiety, it is important to minimize the energy gap (B_-) between the donating orbital and the LUMO. Conversely, for reaction to proceed via hole transfer through the HOMO of the spacer moiety, it is important to minimize the energy gap (B_+) between the accepting orbital and the HOMO. The energy gaps have been calculated for each of the electron transfer reactions and are listed in Table 17.

The calculated energy gaps indicate that reaction from the first excited singlet state of the Zn porphyrin should proceed by way of electron transfer through the LUMO of the spacer. Accordingly, the rate of electron transfer is the highest for

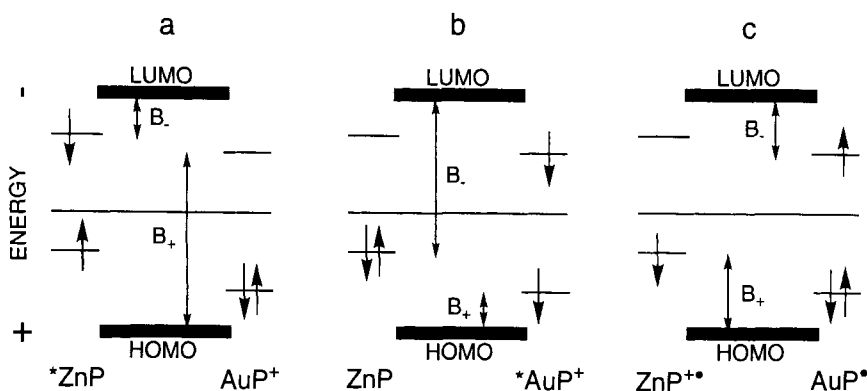


Figure 28. Orbital energy level diagram for (a) photoinduced ET from the excited singlet state of the Zn porphyrin, (b) photoinduced ET from the excited triplet state of the Au porphyrin, and (c) direct reverse ET. Values for the energy gaps (B_- and B_+) are listed in Table 17.

Table 17. Energy gaps for the various electron transfer steps between porphyrinic species within **19** and **Cu.20**⁺^a

	$k/10^8$ (s ⁻¹)	ΔG° (eV)	B_-^b (eV)	B_+^b (eV)
Electron transfer from *ZnP				
19	178	-0.75	0.56	2.44
Cu.20 ⁺	>10 000	-1.01	0.15	2.39
Electron transfer from *AuP ⁺				
19	76	-0.51	2.82	0.62
Cu.20 ⁺	530	-0.65	2.33	0.57
Direct reverse electron transfer				
19	17	-1.31	1.51	1.13
Cu.20 ⁺	20	-1.17	1.16	1.22

^aFrom Ref. [76b]; it is assumed that reaction proceeds by way of the spacer moiety.

^bCalculated using the appropriate redox potentials and the excited state energy values (Tables 14 and 15). The energy of the bridge LUMO was calculated using the reduction potential of free dpp (-2.00 V) in the case of **19**, and the reduction potential of [Cu(dpp)₂]⁺ (-1.65 V) for **Cu.20**⁺. The energy of the bridge HOMO was calculated using the oxidation potential of free dpp (+1.95 V) in the case of **19** and the ligand-centered oxidation potential of [Cu(dpp)₂]⁺ (+1.90 V) for **Cu.20**⁺.

Cu.20⁺, which has the lowest B_- . On the other hand, the Au^{III} porphyrin triplet is more likely to react via hole transfer through the HOMO of the spacer. However, there is a small decrease of the energy gap (B_+) upon coordination of a copper(I) cation to the bridging dpp moiety, which is nevertheless accompanied by an increase in the rate of electron transfer. This rate acceleration is modest by compari-

son with the former case, and could be explained, at least in part, by differing ΔG° values for electron transfer. The rate of direct reverse electron transfer (k_{15} or k_{18}) remains insensitive to the molecular architecture, within experimental limits. The slow rates observed appear consistent with the large energy gaps, and there seems to be no preferred pathway for this process. Overall, it appears that the rates of electron transfer between porphyrinic species are well explained in terms of the simple superexchange model involving electron or hole transfer through orbitals of the spacer moiety.

8.4.6 Conclusion

The studies described in this section were started shortly after the X-ray crystal structure of the RC of *Rh. viridis* was disclosed [73]. During these years, the role of the so-called accessory bacteriochlorophyll BCh was under debate [79]. In particular, the possibility was considered that it could play the role of a superexchange relay between SP and BPh (see Figure 22). In this respect, the copper(I)-complexed [2]rotaxane **Cu.20**⁺ represented a functional artificial model of the SP/BPh/BCh triad, the central Cu^I complex fragment between the Zn porphyrin donor and the Au porphyrin acceptor mimicking the function of BCh between SP and BCh. However, the kinetic scheme shown in Figure 22a has been revised, being now quite firmly established that (at least at room temperature) BCh is directly involved in the electron transfer reaction: the transfer from the electronically excited special pair SP* to BCh takes about 3 ps, and the next transfer step to the BPh, 0.65 ps [80]. In the earlier experiments, detection of the intermediate state SP⁺BCh[−] was prevented by its relatively slow population and fast decay.

Undoubtedly, if not a 273 K model of the SP/BCh/BPh triad, the copper(I)-complexed [2]rotaxane **Cu.20**⁺ remains a most elegant example of control by “external” complexation of the electron transfer rate between covalently linked donor and acceptor porphyrins.

8.5 Catenanes in Motion: Electrochemically and Photochemically Driven Machine-Like Molecules

8.5.1 Introduction

The early synthesis [1a, 81] of topological complex systems like catenanes, where the components are mechanically linked, allowed the chemical community to face unusual systems where large molecular motions could occur without implying any covalent bond breaking. This was intellectually very stimulating, but of mere academic interest until the development of synthetic methods based on various template effects [3b, 82, 83] which, affording a more accessible synthesis and allowing the inclusion of functional fragments in the structure of interlocked rings, made

these structures available in a large variety and good yields. The ambition to control by external stimuli the large amplitude motions allowed by this topology, with the possibility to store the delivered information, was the obvious consequence. Some of these systems, mostly those of amide-type [83] based on weak interactions such as hydrogen bonds, are characterized by the existence of several accessible minima in the coordinate relative to rotation of one ring around the other. Therefore, at room temperature a wide distribution of conformations can exist, which makes them ideal candidates for the study of dynamic processes in these compounds [84]. Though the relative distribution of the different “isomers” in these type of catenane can be controlled to some extent by a judicious use of solvent [85], or by geometric constraints due to bulky substituents [83, 86], more rigid systems can offer several advantages to the approach of externally driven ring motion. The relative ring position of a catenane which has to experience an external stimuli inducing rotation should, in fact, be constant during the time of action of the external stimuli and, to be effective in storing the information, should produce a different and stable geometry. In this respect catenanes based on stronger interactions as is the case of coordination bonds [28, 82, 87] and of electron donor–acceptor interactions [88] have to be preferred. As stressed above, the external stimuli has to produce a different “isomer” than the initial state, so some type of asymmetry is mandatory in a catenane which has to accomplish this task (Figure 29).

A critical parameter being reversibility, it should be possible to revert any externally induced motion to produce the starting structure so that the cycle can be repeated at will. A less critical, but not negligible, parameter is the time needed by the external action to be effective. Fast response times can be of great importance for some of the possible applications.

As far as the external action is concerned, several external stimuli can be conveniently used to achieve rotation of one ring into the other; some success has been achieved by chemical means like addition of protons [60, 89, 90], demetalation of catenates [90, 91] or change of solvent [85], but by far the most convenient system for its ease of control is a redox action which can be either chemically, electrochemically, or photochemically induced. The latter method, based on light-induced electron transfer processes, could take advantage of the development of laser technology and grant a complete control both in the space and in the time domain.

To date, few examples of electrochemically switchable [2]catenanes have been reported. One of those recently reported by Balzani and colleagues [92] incorporates

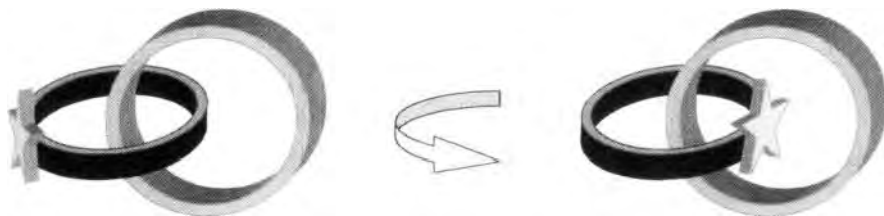


Figure 29. Schematic representation of a ring motion producing a different isomer in a [2]catenane.

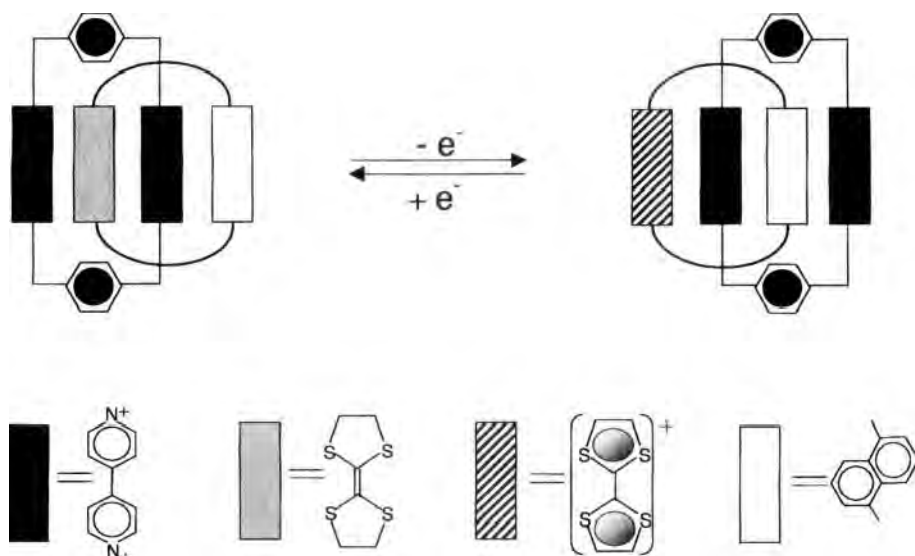
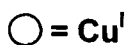
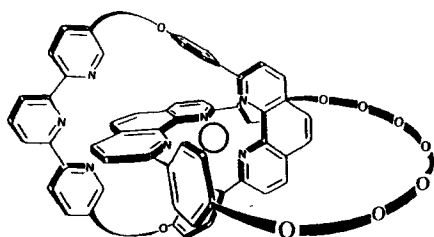


Figure 30. An example of externally induced ring rotation in a [2]catenane [92]. The motion could be triggered either electrochemically or chemically.

a tetrathiafulvalene (TTF) as redox active unit. In the solid state, the TTF unit resides in the inside of the cyclobis(paraquat-*p*-phenylene) tetracationic cyclophane by virtue of charge–transfer interactions; the same arrangement is maintained in acetonitrile solution, but upon oxidation of the TTF unit the 1,5-dioxynaphthalene moiety of the macrocycle moves to the inside of the tetracationic cyclophane to minimize charge repulsion.

The process (Figure 30)—which can be switched also chemically by using *o*-chloranil or $\text{Fe}(\text{ClO}_4)_3$ as oxidants, and $\text{Na}_2\text{S}_2\text{O}_5$ or ascorbic acid as reductants to complete the cycle—was detected both spectroscopically and by cyclic voltammetry, and is reversible and highly exclusive. A previously reported example by the same groups, of an electrochemically triggered ring rotation in a [2]catenane based on *trans*-bis(pyridinium)ethylene unit, was less exclusive than the present one, and was found to allow for some distribution of conformations [93]. For a detailed discussion of chemically, photochemically, and electrochemically induced motions in this kind of catenanes, see Volume III, Part 2, Chapter 7.

The other examples of electrochemically driven ring motions in [2]catenanes are from the class of metal complexed catenanes (i.e., catenates) that have been synthesized and studied in our groups. These compounds, the synthesis of which relies on the ability of copper(I) to gather the bidentate phenanthroline ligand around its tetrahedral coordination sphere, are produced in remarkable yield [9, 28, 57f]. The principle of operation is essentially based on the different stereoelectronic requirements of copper(I) and copper(II). Whereas a coordination number of 4, with a tetrahedral or distorted tetrahedral arrangement is preferred by copper(I),



Cu.25⁺

Figure 31. The nonsymmetrical copper [2]catenate **Cu.25⁺**.

copper(II) requires higher coordination numbers generally 5 or, even better, 6. The penta-coordination corresponds to either a square pyramidal or to a trigonal bipyramidal arrangement, the hexa-coordination to a distorted octahedral arrangement. If the interlocking rings can provide a tridentate ligand, in addition to the bidentate phenanthroline, the different requirements of the copper in the two oxidation states will provide the driving force for inducing the motion. Other transition metal complexes have been shown to undergo rearrangements following changes in the metal oxidation states [94].

8.5.2 A Nonsymmetrical Copper [2]Catenate

The first successful structure of this type is the catenate shown in Figure 31, where a gliding motion of one ring over the other could be triggered electrochemically [95, 96] and photochemically [96].

The nonsymmetrical catenate **Cu.25⁺** consists of the two different rings **26** and **27** reported in Figure 32: one includes the classical bidentate dpp and a polyoxoethylene chain; the other incorporates a dpp moiety and the terdentate ligand 2,2':6',2''-terpyridine (tpy), linked by three methylene groups. Both macrocycles have a 33 atom-long internal rim to minimize the hindrance toward rotation of one ring over the other.

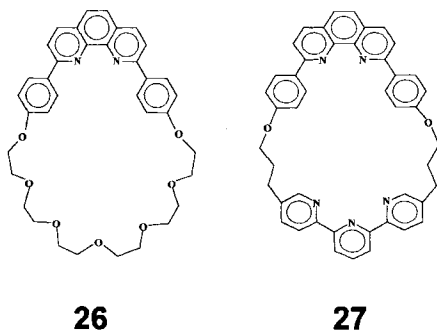


Figure 32. Macrocycles constituting the rings of the nonsymmetrical and symmetrical copper [2]catenate.

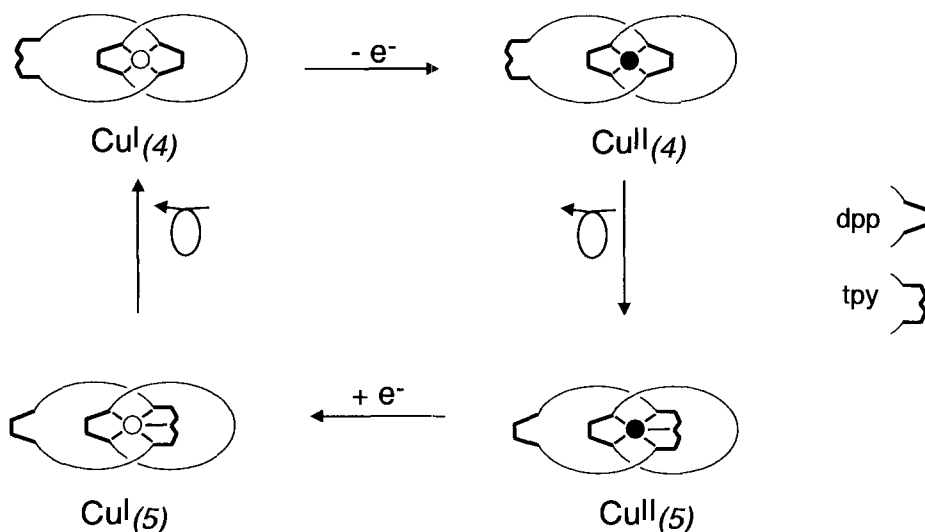


Figure 33. Principle of operation for inducing ring rotation in a nonsymmetrical [2]catenate. Horizontal arrows represent redox processes, vertical arrows represent rearrangements. Cu^{II} is a solid circle, whereas Cu^{I} is an open circle. The stable four-coordinate monovalent complex $\text{Cu}^{\text{I}}_{(4)}$ (top left) is oxidized to the intermediate tetrahedral divalent species $\text{Cu}^{\text{II}}_{(4)}$ (top right) which rearranges to the stable five-coordinate $\text{Cu}^{\text{II}}_{(5)}$ complex, bottom right. Upon reduction, the five-coordinated monovalent $\text{Cu}^{\text{I}}_{(5)}$ is formed (bottom left) which finally undergoes conformational changes to restore the starting $\text{Cu}^{\text{I}}_{(4)}$ (top left).

Electrochemical or chemical triggering

The principle of operation is shown schematically in Figure 33; horizontal arrows represent redox action, and vertical arrows represent rearrangements.

Following oxidation of the stable monovalent four-coordination state $\text{Cu}^{\text{I}}_{(4)}$, an intermediate tetrahedral divalent species $\text{Cu}^{\text{II}}_{(4)}$ is formed. The latter compound undergoes a complete rearrangement process which requires gliding of the macrocycle, to afford the stable five-coordinate bivalent complex $\text{Cu}^{\text{II}}_{(5)}$. Its reduction yields the transient five-coordinate monovalent copper $\text{Cu}^{\text{I}}_{(5)}$, which regenerates the starting species $\text{Cu}^{\text{I}}_{(4)}$ upon conformational change. The actual system and the changes corresponding to the redox steps discussed above are reported in Figure 34.

The species $\text{Cu}^{\text{I}}_{(4)}$ and $\text{Cu}^{\text{II}}_{(5)}$ are stable species which can be independently synthesized and characterized from a spectroscopic and electrochemical viewpoint. In acetonitrile solutions the monovalent species $\text{Cu}^{\text{I}}_{(4)}$ is brown-red in color, with a metal to ligand charge transfer (MLCT) absorption band around 470 nm ($\epsilon = 2500 \text{ M}^{-1} \text{ cm}^{-1}$) and a redox potential of the couple $\text{Cu}^{\text{II}}/\text{I}$ of +0.63 V versus SCE. The penta-coordinate $\text{Cu}^{\text{II}}_{(5)}$ ion in acetonitrile is characterized by an absorption band peaking around 640 nm ($\epsilon = 125 \text{ M}^{-1} \text{ cm}^{-1}$), which corresponds to a d-d transition, and a redox potential of -0.07 V versus SCE, indicating a strong stabilization of the bivalent copper in the penta-coordinate geometry.

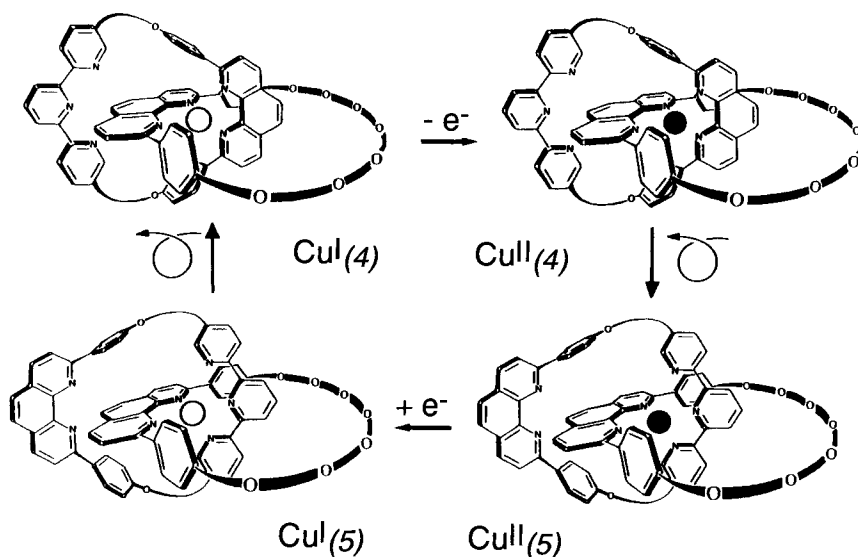


Figure 34. Square scheme illustrating the response of the catenane **Cu.25⁺** to an electrochemical signal. Oxidation and reduction generates metastable complexes which rearranges to adopt the best coordination mode for the new oxidation state of the copper center. Cu^{II} is a black circle and Cu^{I} is an open circle. (For the notation used here, see Figure 33.)

Upon chemical (by Br_2 or NOBF_4) or electrochemical oxidation on a platinum electrode (+0.8 V versus SCE), the red-brown colored solution of the $\text{Cu}^{\text{I}}_{(4)}$ catenane turns dark green. This corresponds to the progressive disappearance of the MLCT band with maximum at 470 nm typical of the $\text{Cu}^{\text{I}}_{(4)}$ and to the appearance of a new band with a maximum at 670 nm ($\epsilon = 800 \text{ M}^{-1} \text{ cm}^{-1}$). The position and intensity of this band is in agreement with tetra-coordinated dpp complexes of copper(II) [7, 28]. A cyclic voltammogram of the green solution shows a reversible wave centered at +0.63 eV, supporting the assignment. A thermal, slow reaction follows and changes the solution to a pale yellow-green color; this can be detected spectroscopically as a general decrease and shift to 640 nm of the original 670 nm band. Cyclic voltammograms on this solution indicate the appearance of a signal at -0.07 eV, while the +0.63 V signal decreases. On completion of the reaction the species in solution can be identified, by its spectral and electrochemical properties, as the penta-coordinate copper(II). This has occurred by rotation of the macrocycle with the two different units (bidentate and terdentate). A subsequent reduction by chemical (using ascorbic acid) or electrochemical methods regenerates the original red-brown color and a unique signal at +0.63 V, typical of the starting Cu^{I} catenane. Thus, a further gliding motion of the ring—opposite to the one triggered by oxidation—has occurred. More evidence of this rotation mechanism was obtained by electron paramagnetic resonance (EPR) spectroscopy, which also demonstrated for $\text{Cu}^{\text{II}}_{(4)}$ a distorted tetrahedral and for $\text{Cu}^{\text{II}}_{(5)}$ a square pyramidal coordination geometry [97]. The rates of the two changeover steps from tetra- to penta-coordination of the Cu^{II} and vice versa for Cu^{I} , are noticeably different. The pro-

cess involving rearrangement of the Cu^{I} coordination sphere is relatively fast (a few seconds at room temperature regardless of the solvent), whereas the Cu^{II} complex rearrangement is slow, allowing for the isolation of the intermediate $\text{Cu}^{\text{II}}_{(5)}$. The latter process depends strongly on the experimental conditions: a few minutes in anhydrous acetonitrile, but hours or even days in noncoordinating solvents or in the absence of coordinating counterions. Indeed, coordinating solvents and counterions can assist the rearrangement by stabilizing some intermediate state [96–98].

Photochemical triggering

One of the peculiarities of this system is that the motion can also be triggered photochemically [96]. The principle of operation is based on the fact that the MLCT excited state of the Cu^{I} complexes of polypyridine type can play the role of an electron transfer reagent. Its lifetime in aerated acetonitrile is sufficiently long (60 ns) to be able to intercept a reactant if this is in a sufficiently high concentration. The redox potential of the couple $\text{Cu}^{\text{II}}_{(4)}/\text{*Cu}^{\text{I}}_{(4)}$ (evaluated to be ca. -1 V versus SCE from the spectroscopic and electrochemical data) indicates that even a mild oxidant that is ineffective on the ground state $\text{Cu}^{\text{I}}_{(4)}$ can oxidize the photoexcited $\text{*Cu}^{\text{I}}_{(4)}$. The oxidant of choice, in addition to its ability to efficiently oxidize the excited state of the copper(I) during its short lifetime, must accomplish several requirements related to its spectroscopic features (i.e., no absorption in the visible region), and it must be possible to remove the reduced products from the solution mixture. This is necessary to prevent any back electron transfer in the reaction mixture. After a thorough search, the oxidant chosen—which could fulfill all the requirements—was *p*-nitrobenzylbromide. Illumination of the reaction mixture by visible light produced the spectral changes shown in Figure 35, indicating the disappearance of the MLCT band of $\text{Cu}^{\text{I}}_{(4)}$ complex and the concomitant formation of the $\text{Cu}^{\text{II}}_{(4)}$ band

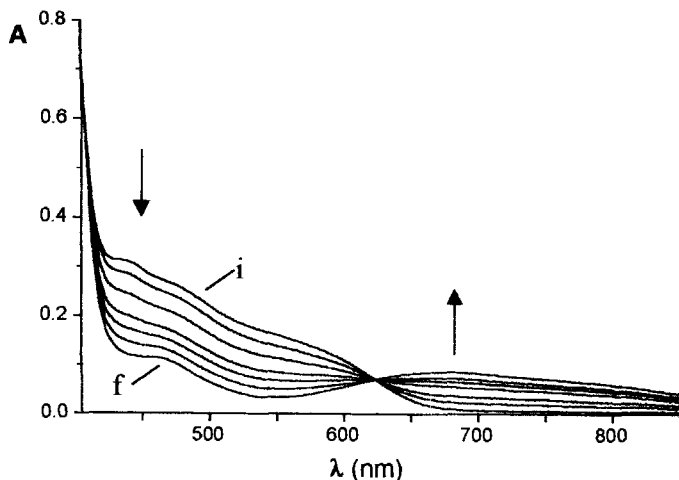


Figure 35. Spectral changes induced by excitation at 464 nm of an acetonitrile solution containing 1.0×10^{-4} M Cu.25^+ and 5×10^{-2} M *p*-nitrobenzylbromide. The initial spectrum (i) and final spectrum after 20 nm irradiation (f) are evidenced. The isosbestic point is at 625 nm.

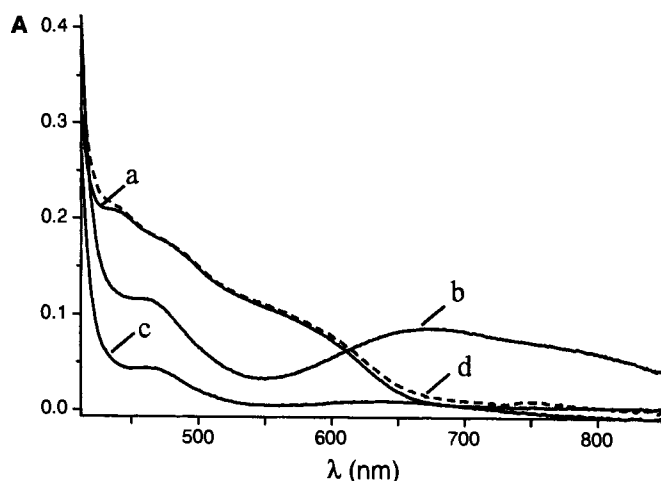


Figure 36. Absorption spectra of an acetonitrile solution of **Cu.25⁺**: (a) before light excitation; (b) at the end of the photoreaction with *p*-nitrobenzylbromide, (20 min irradiation); (c) 24 h later in the dark; (d) 30 min after addition of ascorbic acid.

with a maximum around 670 nm. On completion of the reaction, the spectrum slowly evolved to a new one characterized by a lower absorbance and a new band with low intensity around 640 nm. The latter spectrum is consistent with a complete conversion of the copper(II) complex to the penta-coordinate $\text{Cu}^{\text{II}}_{(5)}$. At this stage, in order to complete the cycle, ascorbic acid was used as reductant, and within 30 min a complete recovery of the initial $\text{Cu}^{\text{I}}_{(4)}$ spectral features occurred.

The spectra of the various stages of the reaction are shown in Figure 36. The complete agreement of the photochemical results with those induced electrochemically clearly shows that the ring motion can also be induced by light. The reduction step to complete the cycle was induced chemically, but in principle this could also be photochemically driven by using the excited state $^*\text{Cu}^{\text{II}}_{(5)}$ as an electron transfer reagent. The difficulty in this case resides in the short lifetime of the $^*\text{Cu}^{\text{II}}_{(5)}$ state, which would require a too high concentration of reductant to be able to interact with the short-lived excited state in a diffusional process. Furthermore, the presence in solution of the unreacted oxidant *p*-nitrobenzylbromide, which had to be used in high concentration to intercept the excited state, would be a complicating feature.

The same principle illustrated above was also used to trigger by electrochemical and photochemical techniques the motion of a dpp-containing macrocycle in a [2]rotaxane [99], see 8.6.

8.5.3 A Symmetrical Copper [2]Catenate

The scheme reported in Figure 33, which is based on two different states, can be further implemented if one could rely on three different geometries. An increase in

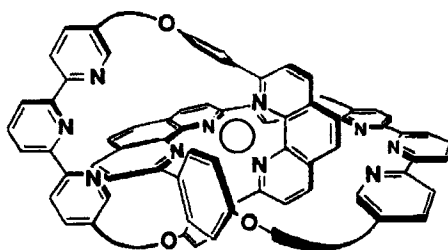
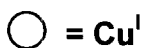


Figure 37. The symmetrical copper [2]catenate **Cu.28⁺**.



Cu.28⁺

the number of possible isomers would greatly enhance the information density which can be stored in this device. The quantity of information which could be stored by an array of n systems with three different states is 3^n , in contrast to the 2^n quantity which would be stored by an array containing the same number of systems but with only two states. This implementation was achieved by providing the conditions for the formation of a six-coordinated copper complex in the [2]catenate. The actual system **Cu.28⁺** is shown in Figure 37, and is based on the use of the two identical macrocycles **27** of Figure 32, both containing the bidentate dpp and the terdentate tpy ligands [100]. This would allow for the formation of a hexa-coordinated species, which incidentally is the coordination number preferred by the bivalent copper, via two terdentate ligands. The schematic diagram of the principle of operation of the system is shown in Figure 38 (the nature of the arrows is defined in Figure 33).

In this case the system can adopt three distinct geometries, which can interconvert and are triggered by an electrochemical action [100]. The initial tetra-coordinated Cu^I₍₄₎ complex can be oxidized to a tetra-coordinated copper(II), Cu^{II}₍₄₎, which then rearranges by gliding of one ring to the penta-coordinated Cu^{II}₍₅₎ as already seen in the previous case. However, the action can continue in this case and the more stable hexa-coordinate Cu^{II}₍₆₎ can be formed by gliding of the other macrocycle. The process can be reversed by reduction of the stable Cu^{II}₍₆₎ (bottom right); at first the Cu^I₍₆₎ is obtained which rearranges to Cu^I₍₅₎ and by a further gliding of one ring to the starting Cu^I₍₄₎. Some of the different conformations of **Cu.28⁺** could be independently synthesized and their spectroscopic and electrochemical properties probed. The visible spectrum of Cu^I₍₄₎ in acetonitrile has an absorption MLCT band at 439 nm ($\epsilon = 2750 \text{ M}^{-1} \text{ cm}^{-1}$), and its cyclic voltammetry shows a reversible oxidation process at +0.63 V versus SCE. Demetalation of this species and re-metalation by Cu^{II} afforded the Cu^{II}₍₆₎ species, with two terpyridine coordinated, as confirmed by its spectroscopic and electrochemical properties in agreement with reference Cu^{II}–tpy complexes [100]. In acetonitrile, this species is characterized by a very weak visible band with a maximum at 687 nm ($\epsilon = 100 \text{ M}^{-1} \text{ cm}^{-1}$) and by an irreversible reduction at –0.43 V versus SCE.

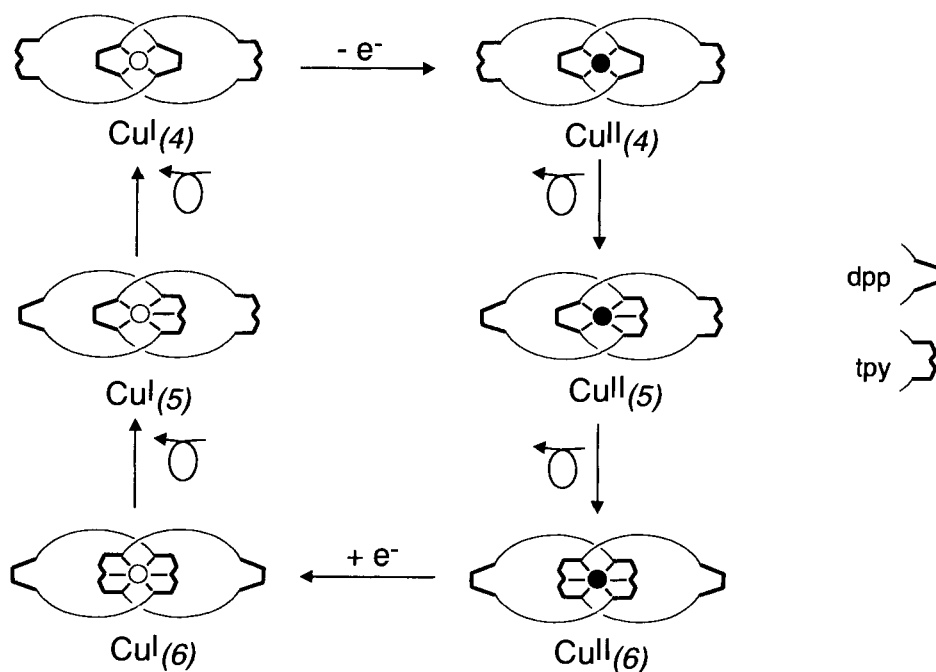
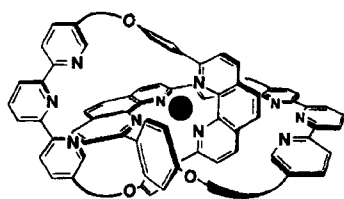
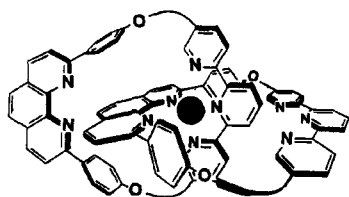


Figure 38. Principle of operation for inducing ring rotation in a symmetrical [2]catenate. Horizontal arrows represent redox processes, vertical arrows represent rearrangements. Cu^{II} is a black circle, whereas Cu^{I} is an open circle. The stable four-coordinate monovalent complex $\text{Cu}^{\text{I}}_{(4)}$ (top left) is oxidized to the intermediate tetrahedral divalent species $\text{Cu}^{\text{II}}_{(4)}$ (top right), which rearranges to the five-coordinate $\text{Cu}^{\text{II}}_{(5)}$ complex (middle right). Upon rearrangement of the other ring, the stable hexa-coordinate bivalent $\text{Cu}^{\text{II}}_{(6)}$ is formed (bottom right). Reduction of the latter yields the esa-coordinated monovalent $\text{Cu}^{\text{I}}_{(6)}$ (bottom left) which upon consecutive gliding motions converts at first to the five-coordinated monovalent $\text{Cu}^{\text{I}}_{(5)}$ (middle left) and finally to the starting $\text{Cu}^{\text{I}}_{(4)}$ (top left).

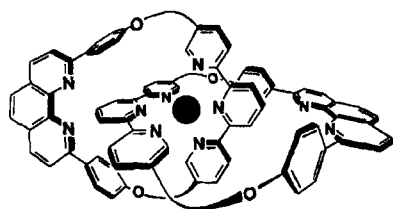
In practice this system was put to work by electrochemical action [100]. Oxidation of the starting $\text{Cu}^{\text{I}}_{(4)}$ yielded the $\text{Cu}^{\text{II}}_{(4)}$ species with its typical 670-nm band, as discussed for the previous bistable system. The rearrangements to $\text{Cu}^{\text{II}}_{(5)}$ and to $\text{Cu}^{\text{II}}_{(6)}$ could not be resolved, even if the overall process was rather slow (minutes or hours), and was strongly affected by the presence of coordinating solvents or ions, as previously discussed. The final point of the oxidation reaction, $\text{Cu}^{\text{II}}_{(6)}$, was clearly characterized by spectro- and electrochemical properties. Interestingly, the oxidation step from $\text{Cu}^{\text{I}}_{(4)}$, through the intermediate $\text{Cu}^{\text{II}}_{(5)}$, to $\text{Cu}^{\text{II}}_{(6)}$, could also be triggered chemically by using the oxidant NOBF_4 . The back reaction to close the cycle was electrochemically controlled. Reduction at 1 V of the hexa-coordinated copper(II) yielded quantitatively the $\text{Cu}^{\text{I}}_{(4)}$ starting compound, and the cycle was



$$\text{Cu}^{\text{II}}(4)/\text{Cu}^{\text{I}}(4); E^0 = +0.63\text{V}$$



$$\text{Cu}^{\text{II}}(5)/\text{Cu}^{\text{I}}(5); E^0 = -0.05\text{V}$$



$$\text{Cu}^{\text{II}}(6)/\text{Cu}^{\text{I}}(6); E^0 = -0.41\text{V}$$

Figure 39. Different coordination geometries for **Cu.28**⁺. The redox potential for the Cu²⁺/Cu⁺ couple in the different coordinations is also reported, showing the sequence of preferred stabilities for copper(II) versus copper(I).

completed. The changeover process for the copper(I) complexes was faster than the rearrangement of copper(II) complexes, as was previously observed with the bistable system. The existence of the three different coordination geometries for the monovalent metal was probed by cyclic voltammetry, which shows waves at +0.63 V (typical of tetravalent copper), −0.41 V, and −0.05 V, and these agree well with the six- and five-coordinated complexes. The three different coordination geometries with the pertinent redox potentials are shown in Figure 39.

The scheme shown in Figure 38 was put in operation, as shown by the spectro- and electrochemical characterization of the intermediates involved. Nevertheless, complete control of the cycle—with the possibility of isolating each of the three different topographies corresponding to the different coordination numbers 4, 5, and 6—has not been possible. The penta-coordinate species could not be isolated, i.e., the motion could not be stopped at this stage, neither in the oxidation nor in the reduction step.

The present examples are intended to demonstrate the potential of the copper catenanes as mobile, electro- and photoactive components in the design of molecular devices which may be of use in the development of electron transfer-driven molecular machines.

8.6 Rotaxanes: Gliding of the Ring on its Axle under the Action of an Electrochemical or Photochemical Signal

8.6.1 Introduction

A [2]rotaxane is a molecular system consisting of a ring threaded by a string, two blocking groups being attached at both ends of the string in order to prevent de-threading [1a]. Such compounds were first prepared long ago [101, 102], but in the past they have been mostly considered as chemical curiosities. Recently, rotaxanes underwent a real revival due not only to the newly developed efficient procedures for their preparation [103–105] but also to their electro- and photochemical properties [75, 76, 106, 107] and their aptitude to undergo controlled molecular motions [108–110].

In the molecular machines previously made and investigated (see Section 8.5), a general principle is utilized: by reducing or oxidizing the copper center, from a situation corresponding to a stable complex, the system is set out of equilibrium. The relaxation process of the compound implies a large-amplitude motion which will bring the system to its new equilibrium position. In previous work on catenanes, the gliding motion of a ring within the other was studied by setting in motion either one cycle or both rings [95–97, 100].

In the rotaxanes described here, a ring is translated along a rod-like component on which it is threaded (Figure 40) [99]. The ring incorporates a bidentate chelate, and the string contains both a bidentate coordinating unit and a terdentate fragment, the string being threaded through the ring via coordination of both components to the same metal center. The system can be switched from 4-coordinate (low oxidation state) to 5-coordinate (high oxidation state) and vice versa by oxidizing or reducing the transition metal, as shown in Figure 41.

The first approach towards threaded linear systems displaying electrochemically induced molecular motions involves the synthesis of the most simple system: pseudorotaxane **Cu.29⁺**, whose ring incorporates a 2,9-diphenyl-1,10-phenanthroline moiety and whose open-chain molecular string contains two different coordination sites; and a 2,9-disubstituted-1,10 phenanthroline bidentate chelate and a terdentate tpy ligand, covalently linked by a four-carbon aliphatic chain. Copper(I) was used as a gathering and templating metal center, forcing the string to thread through the coordinating ring while generating a bis-chelate complex between the metal ion and the two phen moieties.

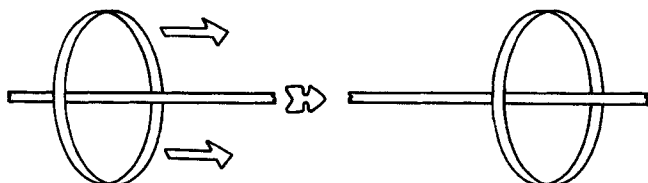
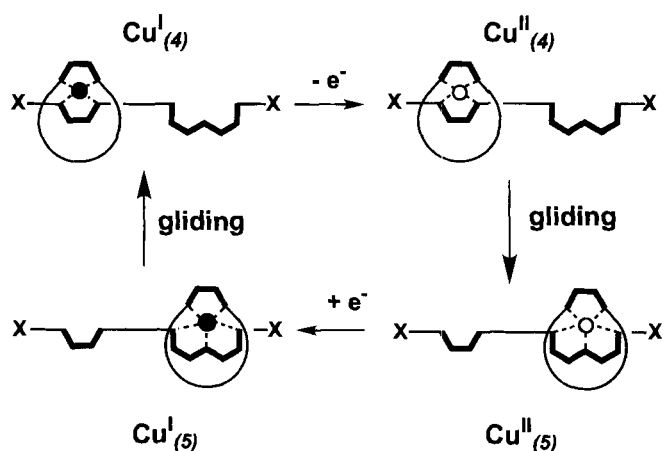


Figure 40. Motion of a ring on its axle.



X = small group or bulky stopper

Figure 41. Square scheme illustrating the principle of operation for the threaded compounds **Cu.29⁺**, **Cu.30⁺** or **Cu.31⁺**, reported in Figure 42. The subscripts 4 and 5 indicate the copper coordination number in each complex. The stable $\text{Cu}^{\text{I}}_{(4)}$ complex is oxidized to an intermediate tetrahedral divalent species $\text{Cu}^{\text{II}}_{(4)}$ which undergoes a rearrangement to afford the stable $\text{Cu}^{\text{II}}_{(5)}$ complex. Upon reduction, a $\text{Cu}^{\text{I}}_{(5)}$ species is formed as a transient which finally reorganizes to regenerate the starting complex. The solid circle represents Cu^{I} , and the open circle represents Cu^{II} .

The copper(I) rotaxane (**Cu.31⁺**) and its non- or partially stoppered analogues (**Cu.29⁺** and **Cu.30⁺** respectively) are shown in Figure 42.

8.6.2 Electrochemically Driven Motion

From the previously described electrochemical behavior of the catenane-type complexes [95–97], and assuming some analogous values for the redox couples $\text{Cu}^{\text{II}}_{(4)}/\text{Cu}^{\text{I}}_{(4)}$ and $\text{Cu}^{\text{II}}_{(5)}/\text{Cu}^{\text{I}}_{(5)}$, the same type of electron transfer-induced reaction is expected [111].

In the three systems **Cu.29⁺**, **Cu.30⁺**, and **Cu.31⁺**, a square scheme (as depicted in Figure 41) takes place. The electrochemical and chemical reactions are analyzed by cyclic voltammetry (CV) and controlled potential electrolysis experiments. From the CV measurements at different scan rate (from 0.005 to 2 V s⁻¹) both on the copper(I) and copper(II) species, it could be inferred that the chemical steps (motions of the ring from the phenanthroline to the terpyridine and vice-versa) are slow on the time scale of the experiments. As the two redox couples involved in these systems are separated by 0.7 V, the concentration of the species in each environment (tetra- or penta-coordination) are directly deduced from the peak intensities of the redox signals. Some voltammograms (curves a–e) obtained on different oxidation states of the rotaxane **Cu.31⁺** and at different times are displayed in Figure 43.

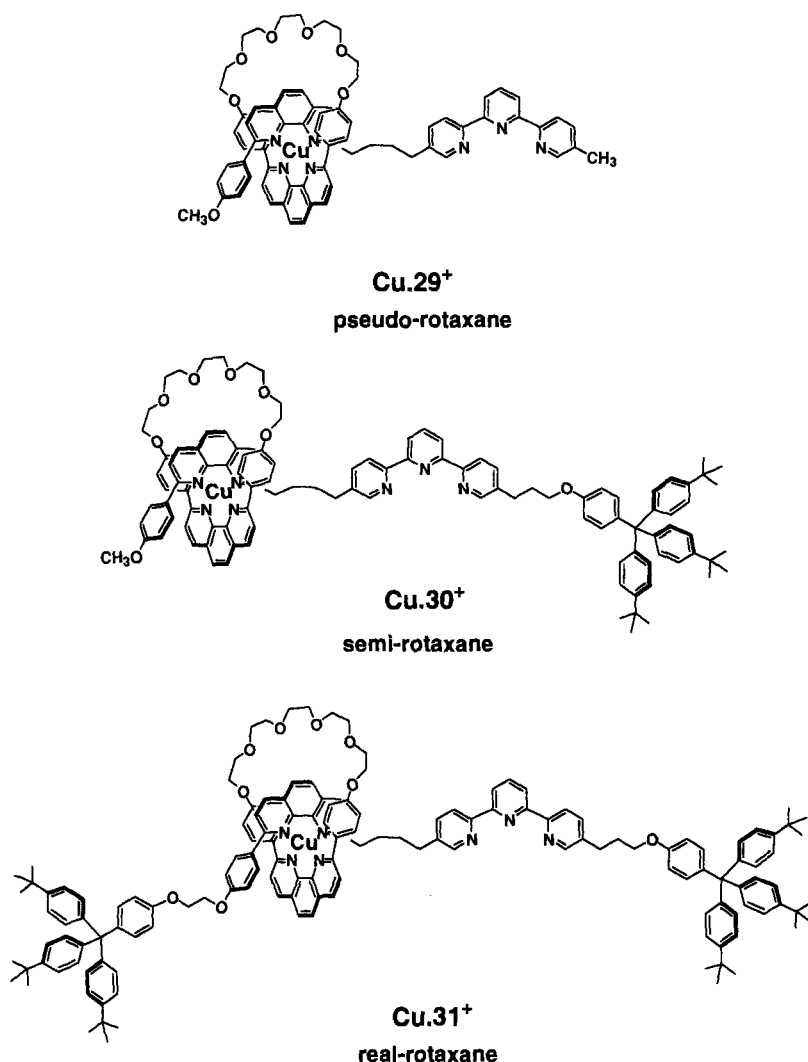


Figure 42. The copper(I) rotaxane and its nonstoppered analogues.

Curve (a) displays the voltammogram of a red solution of **Cu.31⁺** in degassed acetonitrile. A reversible redox wave at +0.68 V (versus SCE) is a fingerprint of the tetrahedral environment around the copper(I) atom [95–97, 100]. During the potential scan, for rates between 0.005 and 2 V s^{−1}, no redox signal corresponding to the penta-coordination could be observed. This fact evidences the high kinetic stability of the 4-coordinate copper(II) rotaxane generated at the electrode. At this stage, a controlled potential electrolysis (applied potential = +1.0 V) was performed until 1 Faraday was exchanged per mole of complex. During the electrolysis

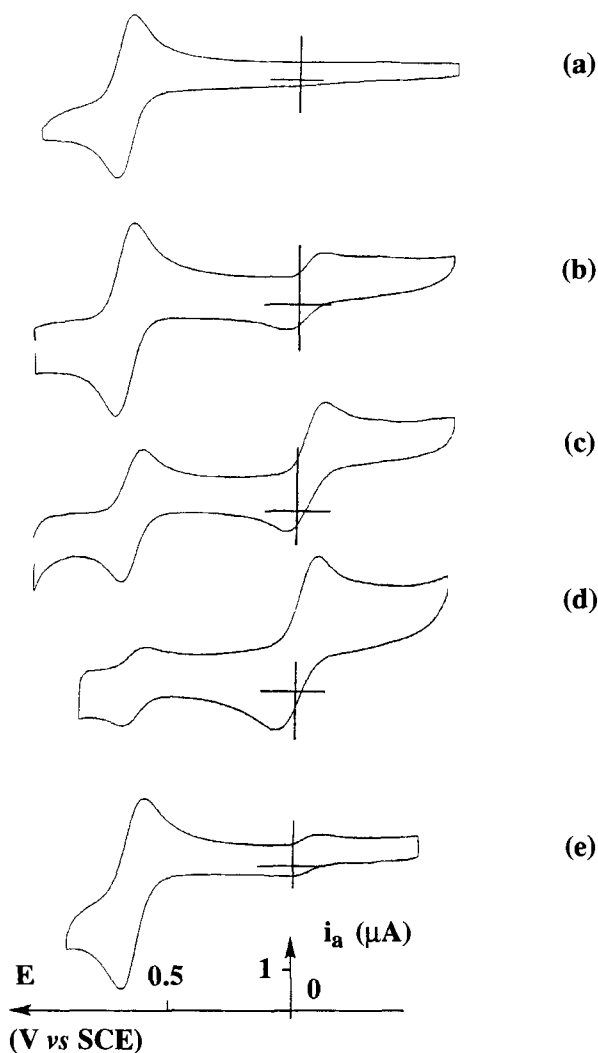


Figure 43. (a) Cyclic voltammogram of Cu.31^{2+} ; (b) after electrolysis during 1 h at +1.0 V; (c, d) evolution of Cu.31^{2+} solution with time: after 2 h (c) and after 4 h (d); (e) cyclic voltammogram immediately after electrolysis of Cu.31^{2+} solution at -0.3 V. Conditions: MeCN (0.1 M, $n\text{-Bu}_4\text{NBF}_4$), Pt electrode, scan rate (v) = 100 mV s^{-1} , 298 K.

the red color of the solution turned light green. Immediately after the coulometry, the voltammogram on the copper(II) species (curve (b)) showed the same peak at +0.68 V and an additional small reversible wave at -0.03 V. These signals are characteristic of the $\text{Cu}^{\text{II}}_{(4)}/\text{Cu}^{\text{I}}_{(4)}$ and $\text{Cu}^{\text{II}}_{(5)}/\text{Cu}^{\text{I}}_{(5)}$ couples, respectively [95–97, 100]. After several hours at room temperature, without any visible color change, the progressive disappearance of the wave at +0.68 V (4-coordinate state) and the simultaneous growth of the peak at -0.03 V (5-coordinate state) probed the coordination change around the copper (II) ion (curves (c) and (d)). The analysis of the concentration of the two different copper(II) species with time leads to a first-order rate constant of $1.5 \times 10^{-4} \text{ s}^{-1}$ for the chemical reaction $\text{Cu}^{\text{II}}_{(4)}$ giving $\text{Cu}^{\text{II}}_{(5)}$. Ac-

cording to the invariant shape of the signals with the scan rate of the copper (II) solution, it can be inferred that the rate constant for the reaction $\text{Cu}^{\text{I}}_{(5)}$ to $\text{Cu}^{\text{I}}_{(4)}$ is smaller than 10^{-2} s^{-1} . A second electrolysis at -0.3 V restores the initial red solution. The voltammogram (curve (e)) performed immediately after the reductive electrolysis displays the wave of Cu.31^+ , and is invariant with time. As all the $\text{Cu}^{\text{I}}_{(5)}$ species formed electrochemically are transformed quantitatively into $\text{Cu}^{\text{I}}_{(4)}$ species during the electrolysis, we can give a lower limit of 10^{-4} s^{-1} for the rate constant of the chemical reaction. The residual signal at -0.03 V simply reflects an incomplete electrolysis.

The behavior of the systems constituted by the unstoppered compound Cu.29^+ , or the semi-rotaxane Cu.30^+ [112], is related to the fully blocked rotaxane Cu.31^+ , i.e., the same redox couple can be observed. Some variations of peak intensities with the scan rate also indicate an acceleration of the chemical processes as compared to Cu.31^+ . However, additional signals corresponding to the species $\text{Cu}^{\text{I}}(\text{MeCN})_4^+$ ($E_{1/2} = +1.02 \text{ V}$) and $\text{Cu}^{\text{II}}_{(6)}$ (6-coordinate state, $E_{1/2} = -0.41 \text{ V}$) [95–97, 100] reveal that the dethreading process becomes significant and occurs primarily with the copper(II) species. The 6-coordinate complex evidenced by CV originates from the dethreading and coordination of the linear fragments via their tpy units to a copper center.

Of these three systems, Cu.31^+ is the most promising compound in relation with electrochemically induced molecular motions, due to the perfect chemical reversibility of the processes. Interestingly, the rates of the movements in rotaxane Cu.31^+ are very different from those measured for the related catenane Cu.25^+ (see Section 8.5) [95–97]. The conversion $\text{Cu}^{\text{II}}_{(4)}$ to $\text{Cu}^{\text{II}}_{(5)}$ is faster in Cu.31^+ than in Cu.25^+ . This difference could reflect a greater ability of $\text{Cu}^{\text{II}}_{(4)}$ in Cu.31^+ to interact with solvent molecules or anions, the copper(II) center being perhaps loosely bound to a fifth ligand which would thus stabilize intermediate states on the way to $\text{Cu}^{\text{II}}_{(5)}$.

8.6.3 Photochemically Driven Motion [99]

It is well known that Cu^{I} complexes of polypyridine ligands absorb light throughout the UV-visible spectral region, display luminescence from the lowest triplet MLCT excited state, have a reasonably long lifetime, and can play the role of electron transfer reductant [18, 49, 54, 60, 113]. This is also the case for the Cu^{I} -based chromophoric unit of rotaxane Cu.31^+ , which shows: (i) UV absorption bands due to $\pi\pi^*$ ligand-centered (LC) transitions; (ii) metal-to-ligand charge-transfer (MLCT) bands in the 400- to 700-nm spectral region (Figure 44); and (iii) a MLCT emission band with $\lambda_{\text{max}} = 785 \text{ nm}$ and $\tau = 34 \text{ ns}$ in aerated acetonitrile solution at 298 K (inset of Figure 44 and Table 18).

The spectroscopic properties and excited state properties of Cu.31^+ are similar, but not identical, to those of the analogous [2]catenane Cu.25^+ (Table 18) [95–97]. The most remarkable difference is the shorter excited state lifetime, which suggests that in the rotaxane the metal ion is less protected towards interaction with solvent molecules [29, 54g, 114]; this is probably due to the lower number of phenyl substituents onto the phenanthroline units of the rotaxane, with respect to the catenane

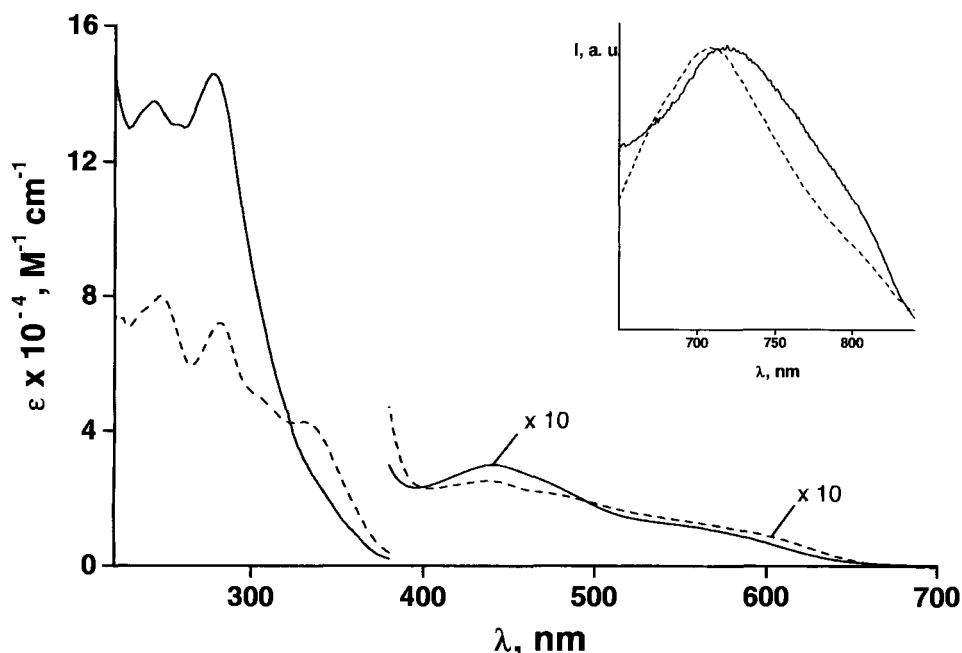
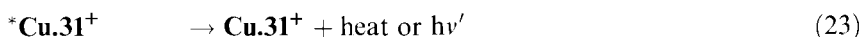


Figure 44. Absorption and (inset) uncorrected emission spectra in acetonitrile solution at 298 K of **Cu.31⁺** (solid line) and of the analogous, previously studied copper(1) [2]catenate **Cu.25⁺** (dashed line, Ref. [96]). The stronger absorption of the rotaxane in the UV spectral region is due to the presence of the aromatic-type stoppers.

[95–97]. In spite of the shorter excited state lifetime, we thought that it should be possible to cause the first step of the overall swinging process indicated in Figure 41, namely the conversion of **Cu.31⁺** into ***Cu.31⁺**, by light irradiation in the presence of a suitable electron acceptor (A), as described by Eqs. 22–26:



The occurrence of the excited-state electron transfer process (Eq. 24) competes with nonradiative deactivation and luminescence (Eq. 23), which is therefore a useful handle to evaluate whether Eq. 24 takes place. A necessary condition for the occurrence of Eq. 24 is, of course, that it takes place with negative free energy change. The reduction potential of the **Cu.31²⁺/*Cu.31⁺** couple can be evaluated

Table 18. Spectroscopic and kinetic parameters of the rotaxane **Cu.31⁺** and the analogous catenane **Cu.25⁺** (see Refs. [96, 99])^a

Property	Cu.31⁺	Cu.25⁺
λ_{max} (abs), nm ^b	439	439
ϵ_{max} (MLCT), M ⁻¹ cm ⁻¹	3000	2300
λ_{max} (em), nm ^c	785	735
τ , ns	34	60
τ , ns ^d	64	115
k_q , M ⁻¹ s ⁻¹ ^e	1.6×10^9	4.1×10^8
k_{conv} Cu ^{II} ₍₄₎ /Cu ^{II} ₍₅₎ , s ⁻¹ ^f	1.5×10^{-4}	2.8×10^{-5}
k_{conv} Cu ^I ₍₅₎ /Cu ^I ₍₄₎ , s ⁻¹ ^g	$10^{-4} \leq k \leq 10^{-2}$	1

^a 298 K, CH₃CN solution, unless otherwise noted.^b Absorption maximum in the visible spectra region.^c From emission maximum corrected for the photomultiplier response.^d CH₂Cl₂ solution.^e Bimolecular quenching constant obtained from Stern–Volmer plots, by using *p*-NO₂C₆H₄CH₂Br as quencher; for more details see text.^f Rate constant for the conversion from the tetra- to penta-coordination of Cu^{II}, upon electrolysis of a solution of Cu^I₍₄₎.^g Rate constant for the conversion from the penta- to tetra-coordination of Cu^I, upon electrolysis of a solution of Cu^{II}₍₅₎.

from the reduction potential of the **Cu.31²⁺/Cu.31⁺** couple (+0.68 V in acetonitrile) [112] and the energy of the ***Cu.31⁺** excited state (about 1.58 eV, as estimated from the maximum of the corrected emission band in the same solvent) by the following equation [115]:

$$E^\circ(\text{Cu.31}^{2+}/\text{*Cu.31}^+) \sim E^\circ(\text{Cu.31}^{2+}/\text{Cu.31}^+) - \xi_{0-0} = -0.90 \text{ V} \quad (27)$$

where ξ_{0-0} is the one-electron potential corresponding to the energy of the ***Cu.31⁺** excited state. This shows that even a mild oxidant should be capable of oxidizing the photoexcited ***Cu.31⁺** rotaxane (Eq. 24). As already pointed out in the previous chapter, the choice of the oxidant is not a trivial matter because other important requirements must be satisfied: (i) the oxidant should not compete with for light absorption; (ii) the reaction between ***Cu.31⁺** and the oxidant (Eq. 24) should be fast enough to compete with the intrinsic excited state decay (Eq. 23); and (iii) after reduction, the oxidant should undergo a very fast, irreversible decomposition reaction (Eq. 26) in order to prevent the occurrence of the back electron transfer reaction (Eq. 25). Such requirements are substantially met by *p*-NO₂C₆H₄CH₂Br (*p*-nitrobenzylbromide) [116–117], which was successfully used to cause photo-oxidation of the analogous catenane [96]. A Stern–Volmer analysis [118] of the quenching of the luminescence of ***Cu.31⁺** *p*-NO₂C₆H₄CH₂Br showed that the rate constant of the quenching process (Eq. 24) is $1.6 \times 10^9 \text{ M}^{-1} \text{ s}^{-1}$ in acetonitrile solution at 298 K, i.e., much larger than that found in the case of the catenane species

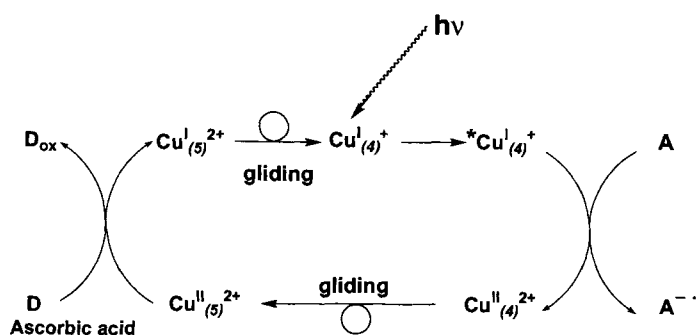


Figure 45. Principle of the photochemically and chemically triggered rearrangement of the rotaxane **Cu.31⁺**.

[96] (Table 18). This compensates for the shorter excited state lifetime of the rotaxane, and allows its photooxidation to occur in a relatively short time when a sufficiently high concentration of $p\text{-NO}_2\text{C}_6\text{H}_4\text{CH}_2\text{Br}$ is present in the solution. The principle of the photochemically triggered rearrangement of the rotaxane **Cu.31⁺** is shown in Figure 45.

Photochemical experiments were performed by irradiating with 464-nm light acetonitrile solutions containing 1.0×10^{-4} M **Cu.31⁺** and 1.8×10^{-2} M $p\text{-NO}_2\text{C}_6\text{H}_4\text{CH}_2\text{Br}$ in the presence of 0.1 M TBA(BF₄). Under these conditions, light excitation was found to cause the spectral changes shown in Figure 46, which clearly indicate the disappearance of **Cu.31⁺** and the simultaneous formation of **Cu.31²⁺** ($\text{Cu}^{\text{II}}_{(4)}$) as the only reaction product. At the end of the photoreaction, the irradiated solution was kept in the dark at 298 K. Spectrophotometric measurements showed that a slow reaction was occurring, responsible for a general decrease in absorbance, particularly in the 600- to 800-nm region (Figure 47), as expected for the transformation of **Cu.31²⁺** ($\text{Cu}^{\text{II}}_{(4)}$) into the more stable **Cu.31²⁺** ($\text{Cu}^{\text{II}}_{(5)}$) species (see Figure 45). After about 26 h, no further spectral change was observed. At this stage, the spectrum of the solution was that shown by curve (c) in Figure 47, which is that of the stable $\text{Cu}^{\text{II}}_{(5)}$ species. In order to close the cycle (Figure 45), an excess of ascorbic acid was added to the solution. A gradual, complete reappearance of the spectrum of **Cu.31⁺** ($\text{Cu}^{\text{I}}_{(4)}$) was observed, as happens when oxidation and successive reduction are carried out electrochemically. After about 8 h, the spectrum was practically coincident with the initial spectrum (Figure 47), showing that the cyclic process (Figure 45) is fully reversible even when oxidation is photo-induced and reduction is chemically induced [119].

The overall quantum yield of the photoreaction was about 3 %. Since under the experimental conditions used the fraction of ***Cu.31⁺** excited states reacting with the quencher is ~50 %, the fraction of quenching events that give rise to a permanent formation of **Cu.31²⁺** is ~6 %. Since $p\text{-NO}_2\text{C}_6\text{H}_4\text{CH}_2\text{Br}$ cannot quench ***Cu.31⁺** by energy transfer, the low efficiency of the photoinduced process must be attributed to a competition between back electron transfer (Eq. 25) and the irre-

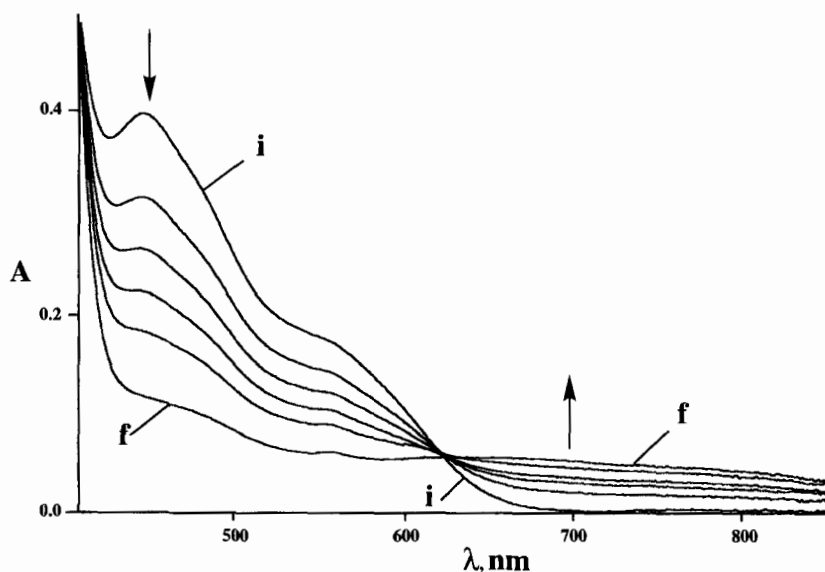


Figure 46. Spectral changes caused by photoirradiation of an acetonitrile solution containing 1.0×10^{-4} M **Cu.31**⁺, 1.8×10^{-2} M *p*-NO₂C₆H₄CH₂Br, and 1.0×10^{-1} M TBA(BF₄). The isosbestic point is at 626 nm. (i) Initial spectrum; (f) final spectrum obtained after 20 min of irradiation.

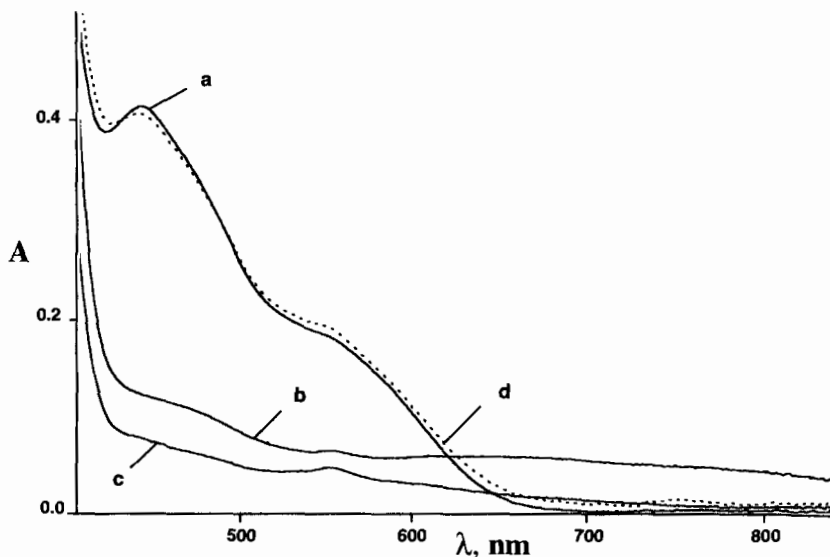


Figure 47. Absorption spectra of an acetonitrile solution of: **Cu.31**⁺ containing 1.0×10^{-1} M TBA(BF₄). (a) Before light irradiation; (b) at the end of the photoreaction (about 20 min irradiation) with *p*-NO₂C₆H₄CH₂Br; (c) after subsequent 26 h in the dark; (d) 8 h after subsequent addition of an excess of ascorbic acid.

versible decomposition of the primary reduced product of $p\text{-NO}_2\text{C}_6\text{H}_4\text{CH}_2\text{Br}$ (Eq. 26).

The motion of the ring and of the metal ion from the bidentate to the tridentate site on the string can be carried out either electrochemically or by an oxidative photochemical process, and can be fully reversed upon chemical reduction. A comparison with the analogous catenate **Cu.25**⁺ [95–97] shows that, for **Cu.31**⁺, the excited state lifetime is shorter, the rate constant for the excited state quenching reaction by $p\text{-NO}_2\text{C}_6\text{H}_4\text{CH}_2\text{Br}$ is higher, and the thermal $\text{Cu}^{\text{II}}_{(4)}/\text{Cu}^{\text{II}}_{(5)}$ conversion is less clean in the absence of $\text{TBA}(\text{BF}_4)$. These results show that the metal ion is less protected from interaction with external species in the rotaxane than in the catenate, as would be expected from structural considerations. This is also in agreement with the faster and, respectively, slower rate constant observed for the $\text{Cu}^{\text{II}}_{(4)}$ to $\text{Cu}^{\text{II}}_{(5)}$ and the $\text{Cu}^{\text{I}}_{(5)}$ to $\text{Cu}^{\text{I}}_{(4)}$ conversions in the rotaxane compared to the catenane species.

8.7 Conclusions

The topological properties of the compounds discussed in this chapter are of course novel and fascinating, and this is what had originally motivated their synthesis. However, their electron transfer properties turned out later to be equally interesting—which is an additional *a posteriori* justification for their preparation. Most of the present multicomponent systems which have been made and studied in our laboratories (Strasbourg and Bologna) are obtained via a template reaction involving copper(I)bis-2,9-*diaryl*-1,10-phenanthroline as precursors. These simple complexes were at first prepared in view of their photochemical and photophysical studies, following the pioneering work of McMillin and his group [54]. It is thus not surprising that the simple or complex catenanes or knots incorporating copper(I) display interesting photochemical properties. What was less expected was the variety of photochemical behaviors, with many different energy transfer processes or multimetallic effects (control of the excited state features by another metal present in the molecule).

In addition, the original series consisting of [2]catenanes and multi-ring interlocking compounds has later been expanded to lead to porphyrin-stoppered rotaxanes. These new molecules turned out to be particularly interesting models of simple fragments of the photosynthetic reaction center, permitting an effective control of the electron transfer rate between the porphyrinic chromophores by metallating or demetallating the rotaxane complexing site. This effect provided additional evidence for the importance of superexchange in electron transfer processes.

Photoinduced electron transfer, using the presently described molecular systems, remains an interesting and promising topic—particularly in relation to charge separation and ultimately artificial photosynthesis. Nevertheless, a new area has recently emerged, which is that of multicomponent molecular sets undergoing controlled motions, under the action of an external signal. There is no doubt that this

field of research has a bright future and that, in the long term, prospective, molecular devices based on such machines, motors, and switches will be developed. Catenanes and rotaxanes are ideally suited to become the working parts of such ensembles in motion, and it is thus clear that increasingly complex and efficient such assemblies will be designed, elaborated, and studied in the future, and will function under the action of signals of various nature, whether redox, photonic, or chemical.

Acknowledgments

This work was supported by the CNR (Italy) and the CNRS (France). We thank all the members of our respective teams whose name appear in the references, and who contributed to the work described in the present chapter with so much skill and enthusiasm.

References

1. (a) G. Schill, *Catenanes, Rotaxanes and Knots*, Academic Press New York, **1971**; (b) G. Schill, A. Lüttringhaus, *Angew. Chem.*, **1964**, 76, 567; (c) G. Schill, *Chem. Ber.*, **1967**, 100, 2021.
2. (a) S. A. Wasserman, N. R. Cozzarelli, *Science*, **1986**, 232, 951; (b) M. A. Krasnow, A. Stasiak, S. J. Spengler, F. Dean, T. Koller, N. R. Cozzarelli, *Nature (London)*, **1983**, 304, 559; (c) L. F. Liu, R. E. Depew, J. C. Wang, *J. Mol. Biol.*, **1976**, 106, 439.
3. (a) J.-P. Sauvage, C. Dietrich-Buchecker (Eds.), *Molecular Catenanes, Rotaxanes and Knots. A Journey through the World of Molecular Topology*, Wiley-VCH, Weinheim, **1999**; (b) D. B. Amabilino, J. F. Stoddart, *Chem. Rev.*, **1995**, 95, 2725.
4. (a) D. M. Walba, *Tetrahedron*, **1985**, 41, 3161; (b) C. Liang, K. Mislow, *J. Math. Chem.*, **1995**, 18, 1; (c) K. Mislow, *Top. Stereochem. Vol. 22*, (Ed.: S.C. Denmark), Wiley and Sons, **1999**.
5. (a) M. C. Thompson, D.H. Busch, *J. Am. Chem. Soc.*, **1964**, 86, 3651; (b) J. D. Curry, D. H. Busch, *J. Am. Chem. Soc.*, **1964**, 86, 592; (c) G. A. Melson, D. H. Busch, *J. Am. Chem. Soc.*, **1964**, 86, 4834.
6. (a) N. F. Curtis, *Coord. Chem. Rev.*, **1968**, 3, 3; (b) D. A. House, N. F. Curtis, *Chem. Ind. (London)*, **1961**, 1708; (c) N. F. Curtis, Y. M. Curtis, H. K. J. Powell, *J. Chem. Soc. A*, **1966**, 1015.
7. (a) C. O. Dietrich-Buchecker, J.-P. Sauvage, J.-P. Kintzinger, *Tetrahedron Lett.*, **1983**, 24, 5095; (b) C. O. Dietrich-Buchecker, J.-P. Sauvage, J. M. Kern, *J. Am. Chem. Soc.*, **1984**, 106, 3043.
8. H. L. Frisch, E. Wasserman, *J. Am. Chem. Soc.* **1961**, 83, 3789.
9. C. O. Dietrich-Buchecker, J.-P. Sauvage, *Biorganic Chemistry Frontiers, Vol. 2*, Springer-Verlag, Berlin, **1991**.
10. J.-C. Chambron, C. O. Dietrich-Buchecker, J.-P. Sauvage in *Comprehensive Supramolecular Chemistry Vol. 9*, 1st ed. (Eds. J.-P. Sauvage and M. W. Hosseini), Pergamon, London, **1996**.
11. A. A. Schilt, *Anal. Chem.* **1963**, 35, 1599.
12. N. Tanaka, Y. Sato, *Electrochimica Acta* **1968**, 13, 335.
13. W. R. McWhinnie, J. D. Miller, *Adv. Inorg. Radiochem.* **1969**, 12, 135.
14. F. A. Cotton, G. Wilkinson in *Advanced Inorganic Chemistry*, 4th ed., Wiley Interscience, New York, **1980**, pp. 119.
15. A. A. Schilt, in *Applications of 1, 10 Phenanthroline and related Compounds*, Pergamon, London, **1969**.
16. F. A. Cotton, G. Wilkinson in *Advanced Inorganic Chemistry*, 4th ed.; Wiley Interscience, New York, **1980**.

17. M. Cesario, C. O. Dietrich-Buchecker, J. Guilhem, C. Pascard, J.-P. Sauvage, *J. Chem. Soc., Chem. Commun.* **1985**, 244.
18. J.-M. Kern, J.-P. Sauvage, J.-L. Weidmann, N. Armaroli, L. Flamigni, P. Ceroni, V. Balzani, *Inorg. Chem.* **1997**, *36*, 5329.
19. L. Raehm, Thesis, Université Louis Pasteur de Strasbourg (France), **1999**.
20. J.-M. Kern, L. Raehm, J.-P. Sauvage, in *C.R. Acad. Sci. Paris*, t.2, Série II c, *41*, **1999**.
21. D. J. Cárdenas, P. Gaviña, J.-P. Sauvage, *J. Am. Chem. Soc.* **1997**, *119*, 2656.
22. D. J. Cárdenas, J.-P. Sauvage, *Inorg. Chem.* **1997**, *36*, 2777.
23. P. Federlin, J.-M. Kern, A. Rastegar, C. O. Dietrich-Buchecker, P. A. Marnot, J.-P. Sauvage, *New J. Chem.* **1990**, *14*, 9.
24. B. R. James, R. J. P. Williams, *J. Chem. Soc.* **1961**, 2007.
25. C. J. Hawkins, D. D. Perrin, *J. Chem. Soc.* **1963**, 2996.
26. O. Gürtler, K. P. Dietz, Ph. Thomas, *Z. Anorg. Allg. Chem.* **1973**, *396*, 277.
27. S. Sundararajan, E.L. Wehry, *J. Phys. Chem.* **1972**, *76*, 1528.
28. C.O. Dietrich-Buchecker, J.-P. Sauvage, J.-M. Kern, *J. Am. Chem. Soc.* **1989**, *111*, 7791.
29. M.T. Miller, P.K. Gantzel, T.B. Karpishin, *Inorg. Chem.* **1998**, *37*, 2285.
30. V. Gutman, R. Schmid, *Monatsh. Chem.* **1969**, *100*, 2113.
31. A. A. Vlcek, *Nature* **1957**, *180*, 753.
32. (a) N. Maki, T. Hirano, S. Musha, *Bull. Chem. Soc. Jpn.* **1963**, *36*, 756; (b) N. Tanaka, Y. Sato, *Bull. Chem. Soc. Jpn.* **1968**, *41*, 2059.
33. A. M. Tait, F. V. Lovecchio, D. R. Busch, *Inorg. Chem.* **1977**, *16*, 2206.
34. C. W. G. Ansell, J. Lewis, M. C. Liptrot, P. R. Raithby, M. Schröder, *J. Chem. Soc., Dalton Trans.* **1982**, 1593.
35. S. Musumeci, E. Rizzarelli, S. Sammartano, R. P. Bonomo, *J. Electroanal. Chem.* **1973**, *46*, 109.
36. B. C. Willet, F. C. Anson, *J. Electrochem. Soc.* **1982**, *129*, 1260.
37. G. Arena, R. P. Bonomo, S. Musumeci, E. Rizzarelli, *Z. Anorg. Allg. Chem.* **1975**, *412*, 161.
38. Y. W. D. Chen, K. S. V. Santhanaman, A. J. Bard, *J. Electrochem. Soc.* **1982**, *129*, 61.
39. C. O. Dietrich-Buchecker, J.-M. Kern, J.-P. Sauvage, *J. Chem. Soc. Chem. Commun.* **1985**, 760.
40. B. J. Henne, D. E. Bartak, *Inorg. Chem.* **1984**, *23*, 369.
41. N. Tanaka, T. Ogata, S. Niizuma, *Inorg. Nucl. Chem. Lett.* **1972**, *8*, 965.
42. M. Trouppel, Y. Rollin, O. Sock, G. Meyer, J. Perrichon, *Nouv. J. Chim.* **1986**, *10*, 593.
43. C.O. Dietrich-Buchecker, J. Guilhem, J.-M. Kern, C. Pascard, J.-P. Sauvage, *Inorg. Chem.* **1994**, *33*, 3498.
44. M. Billon, B. Divisia-Blohorn, J.-M. Kern, J.-P. Sauvage, *J. Mater. Chem.* **1997**, *7*, 1169.
45. A. J. Blake, C. O. Dietrich-Buchecker, T. I. Hyde, J.-P. Sauvage, M. Schröder, *J. Chem. Soc., Chem. Commun.* **1989**, 1663.
46. (a) C.O. Dietrich-Buchecker, A.K. Khémis, J.-P. Sauvage, *J. Chem. Soc. Chem. Commun.* **1986**, 1376; (b) C. O. Dietrich-Buchecker, C. Hemmert, A. K. Khémis, J.-P. Sauvage, *J. Am. Chem. Soc.* **1990**, *112*, 8002.
47. C. O. Dietrich-Buchecker, J. Guilhem, A. K. Khémis, J.-P. Kintzinger, C. Pascard, J.-P. Sauvage, *Angew. Chem.* **1987**, *99*, 711; *Angew. Chem. Int. Ed. Engl.* **1987**, *26*, 661.
48. C. O. Dietrich-Buchecker, C. Hemmert, J.-P. Sauvage, *New J. Chem.* **1990**, *14*, 603.
49. C. O. Dietrich-Buchecker, J.-F. Nierengarten, J.-P. Sauvage, N. Armaroli, V. Balzani, L. De Cola, *J. Am. Chem. Soc.* **1993**, *115*, 11237.
50. A.-M. Albrecht-Gary, C.O. Dietrich-Buchecker, J. Guilhem, M. Meyer, C. Pascard, J.-P. Sauvage, *Recl. Trav. Chim. Pays-Bas* **1993**, *112*, 427.
51. C. O. Dietrich-Buchecker, J.-P. Sauvage, A. De Cian, J. Fischer, *J. Chem. Soc. Chem. Commun.* **1994**, 2231.
52. (a) M. Meyer, A.-M. Albrecht-Gary, C. O. Dietrich-Buchecker, J.-P. Sauvage, *J. Am. Chem. Soc.* **1997**, *119*, 4599; (b) C. O. Dietrich-Buchecker, J.-P. Sauvage, N. Armaroli, P. Ceroni, V. Balzani, *Angew. Chem.* **1996**, *108*, 1190; *Angew. Chem. Int. Ed. Engl.* **1996**, *35*, 1119.
53. J.-P. Sauvage, M. Ward, *Inorg. Chem.* **1991**, *30*, 3869.
54. Some selected references: (a) D. R. McMillin, M. T. Buckner, B. T. Ahn, *Inorg. Chem.* **1977**, *16*, 943; (b) B. T. Ahn, D. R. McMillin, *Inorg. Chem.* **1981**, *20*, 1427; (c) J. R. Kirchhoff, R. E.

- Gamache Jr., M. W. Blaskie, A. A. Del Paggio, R. K. Lengel, D. R. McMillin, *Inorg. Chem.* **1983**, 22, 2380; (d) D. R. McMillin, J. R. Kirchhoff, K. V. Goodwin, *Coord. Chem. Chem. Rev.* **1985**, 64, 83; (e) C. C. Phifer, D. R. McMillin, *Inorg. Chem.* **1986**, 25, 1329; (f) A. K. Ichinaga, J. R. Kirchhoff, D. R. McMillin, C. O. Dietrich-Buchecker, P. A. Marnot, J.-P. Sauvage, *Inorg. Chem.* **1987**, 26, 4290; (g) R. M. Everly, D. R. McMillin, *Photochem. Photobiol.* **1989**, 6, 711; (h) A. K. I. Gushurst, D. R. McMillin, C. O. Dietrich-Buchecker, J.-P. Sauvage, *Inorg. Chem.* **1989**, 28, 4070; (i) R. M. Everly, D. R. McMillin, *J. Phys. Chem.* **1991**, 95, 9071; (j) F. Liu, K. A. Meadows, D. R. McMillin, *J. Am. Chem. Soc.* **1993**, 115, 6699; (k) K. L. Cunningham, C. R. Hecker, D. R. McMillin, *Inorg. Chim. Acta* **1996**, 242, 143; (l) M. K. Eggleston, D. R. McMillin, K. S. Koenig, A. J. Pallenberg, *Inorg. Chem.* **1997**, 36, 172; (m) D. R. McMillin, K. M. McNett, *Chem. Rev.* **1998**, 98, 1201; (n) C. T. Cunningham, K. L. H. Cunningham, J. F. Michalec, D. R. McMillin, *Inorg. Chem.* **1999**, 38, 4388.
55. K. C. Gordon, J. J. McGarvey, *Inorg. Chem.* **1991**, 30, 2986.
56. N. Armaroli, M. A. J. Rodgers, P. Ceroni, V. Balzani, C. O. Dietrich-Buchecker, J.-M. Kern, A. Bailal, J.-P. Sauvage, *Chem. Phys. Lett.* **1995**, 241, 555.
57. (a) J.-M. Lehn, A. Rigault, *Angew. Chem. Int. Ed.* **1988**, 27, 1095; (b) C. Piguet, G. Bernardinelli, G. Hopfgartner, *Chem. Rev.* **1996**, 97, 2005; (c) B. Hasenknopf, J.-M. Lehn, N. Boumediene, A. Dupont-Gervais, A. Van Dorsselaer, B. Kneisel, D. Fenske, *J. Am. Chem. Soc.* **1997**, 119, 10956; (d) O. Mamula, A. Von Zelewsky, G. Bernardinelli, *Angew. Chem. Int. Ed.* **1998**, 37, 290; (e) O. Mamula, A. Von Zelewsky, A. Bark, G. Bernardinelli, *Angew. Chem. Int. Ed.* **1999**, 38, 2945; (f) C. Piguet, *J. Incl. Phen. Macrocyc. Chem.* **1999**, 34, 361.
58. F. Vögtle, I. Lühr, V. Balzani, N. Armaroli, *Angew. Chem. Int. Ed.* **1991**, 30, 1333.
59. (a) G. S. Hanan, C. R. Arana, J.-M. Lehn, D. Fenske, *Angew. Chem. Int. Ed.* **1995**, 34, 1122; (b) G. S. Hanan, D. Volkmer, U. S. Schubert, J.-M. Lehn, G. Baum, D. Fenske, *Angew. Chem. Int. Ed.* **1997**, 36, 1842; (c) P. Ceroni, A. Credi, V. Balzani, S. Campagna, G. S. Hanan, C. R. Arana, J.-M. Lehn, *Eur. J. Inorg. Chem.* **1999**, 1409.
60. N. Armaroli, L. De Cola, V. Balzani, J.-P. Sauvage, C. O. Dietrich-Buchecker, J.-M. Kern, A. Bailal, *J. Chem. Soc. Dalton Trans.* **1993**, 3241.
61. N. Armaroli, L. De Cola, V. Balzani, J.-P. Sauvage, C. O. Dietrich-Buchecker, J.-M. Kern, *J. Chem. Soc. Faraday Trans.* **1992**, 88, 553.
62. M. Maestri, V. Balzani, C. Deuschel-Cornioley, A. Von Zelewsky, *Adv. Photochem.* **1992**, 17, 1.
63. N. Armaroli, V. Balzani, F. Barigelletti, L. De Cola, J.-P. Sauvage, C. Hemmert, *J. Am. Chem. Soc.* **1991**, 113, 4033.
64. N. Armaroli, V. Balzani, F. Barigelletti, L. De Cola, L. Flamigni, J.-P. Sauvage, C. Hemmert, *J. Am. Chem. Soc.* **1994**, 116, 5211.
65. C. K. Jørgensen, *Adv. Chem. Phys.* **1963**, 5, 33.
66. N. Armaroli, V. Balzani, L. De Cola, C. Hemmert, J.-P. Sauvage, *New J. Chem.* **1994**, 18, 775.
67. M. Cesario, C. O. Dietrich-Buchecker, A. Edel, J. Guilhem, J.-P. Kintzinger, C. Pascard, J.-P. Sauvage, *J. Am. Chem. Soc.* **1986**, 108, 6250.
68. D. J. Cárdenas, J.-P. Collin, P. Gaviña, J.-P. Sauvage, A. De Cian, J. Fischer, N. Armaroli, L. Flamigni, V. Vicinelli, V. Balzani, *J. Am. Chem. Soc.* **1999**, 121, 5481.
69. M. Maestri, N. Armaroli, V. Balzani, E. C. Constable, A. M. W. Cargill-Thompson, *Inorg. Chem.* **1995**, 34, 2759.
70. (a) J.-P. Sauvage, J.-P. Collin, J.-C. Chambron, S. Guillerez, C. Coudret, V. Balzani, F. Barigelletti, L. De Cola, L. Flamigni, *Chem. Rev.* **1994**, 94, 993; (b) V. Balzani, A. Juris, M. Venturi, S. Campagna, S. Serroni, *Chem. Rev.* **1996**, 96, 759.
71. (a) X. Zhang, M. A. J. Rodgers, *J. Phys. Chem.* **1995**, 99, 12797; (b) F. Wilkinson, D. J. McGarvey, A. F. Olea, *J. Phys. Chem.* **1994**, 98, 3762; (c) K. Kikuchi, C. Sato, M. Watabe, H. Ikeda, Y. Takahashi, T. Miyashi, *J. Am. Chem. Soc.* **1993**, 115, 5180.
72. L. Tan-Sien-Hee, L. Jacquet, A. Kirsch-De Mesmaeker, *J. Photochem. Photobiol. A* **1994**, 81, 169.
73. (a) J. Deisenhofer, O. Epp, K. Miki, R. Huber, H. Michel, *J. Mol. Biol.* **1984**, 180, 385; (b) J. Deisenhofer, O. Epp, K. Miki, R. Huber, H. Michel, *Nature* **1985**, 318, 618.
74. Some early and representative examples: (a) S. G. Boxer, R. R. Bucks, *J. Am. Chem. Soc.* **1979**, 101, 1883; (b) D. Gust, T. A. Moore, A. Moore, L. R. Makings, G. R. Seely, X. Ma,

- T. T. Trier, F. Gao, *J. Am. Chem. Soc.* **1988**, *110*, 7567; (c) T. Nagata, A. Osuka, K. Maruyama, *J. Am. Chem. Soc.* **1990**, *112*, 3054; (d) A. Harriman, D. J. Magda, J. L. Sessler, *J. Chem. Soc., Chem. Commun.* **1991**, 345.
75. (a) A. M. Brun, A. Harriman, V. Heitz, J.-P. Sauvage, *J. Am. Chem. Soc.* **1991**, *113*, 8657; (b) A. M. Brun, S. J. Atherton, A. Harriman, V. Heitz, J.-P. Sauvage, *J. Am. Chem. Soc.* **1992**, *114*, 4632.
76. (a) J.-C. Chambron, V. Heitz, J.-P. Sauvage, *J. Am. Chem. Soc.* **1993**, *115*, 12378; (b) J.-C. Chambron, A. Harriman, V. Heitz, J.-P. Sauvage, *J. Am. Chem. Soc.* **1993**, *115*, 6109; (c) J.-C. Chambron, A. Harriman, V. Heitz, J.-P. Sauvage, *J. Am. Chem. Soc.* **1993**, *115*, 7419; (d) A. Harriman, V. Heitz, J.-C. Chambron, J.-P. Sauvage, *Coord. Chem. Rev.* **1994**, *132*, 229.
77. (a) J.-P. Collin, A. Harriman, V. Heitz, F. Odobel, J.-P. Sauvage, *J. Am. Chem. Soc.* **1994**, *116*, 5679; (b) A. Harriman, F. Odobel, J.-P. Sauvage, *J. Am. Chem. Soc.* **1994**, *116*, 5481.
78. For the copper-free [2]rotaxane the rate of photoinduced electron transfer from the Zn porphyrin excited state to the Au porphyrin is $273 \times 10^8 \text{ s}^{-1}$ (as calculated from Ref. [76c]), which compares well with $k_{14} = 178 \times 10^8 \text{ s}^{-1}$.
79. (a) J. L. Martin, J. Breton, A. J. Hoff, A. Migus, A. Antonetti, *Proc. Natl. Acad. Sci. USA* **1986**, *83*, 957; (b) C.-K. Chan, T. J. Di Magno, L. X.-Q. Chen, J. R. Norris, G. R. Fleming, *Proc. Natl. Acad. Sci. USA* **1991**, *88*, 11202.
80. (a) T. Arlt, S. Schmidt, W. Kaiser, C. Lauterwasser, M. Meyer, H. Scheer, W. Zinth, *Proc. Natl. Acad. Sci. USA* **1993**, *90*, 11757; (b) K. Dressler, E. Umlauf, S. Schmidt, P. Hamm, W. Zinth, S. Buchanan, H. Michel, *Chem. Phys. Lett.* **1991**, *183*, 270.
81. E. Wasserman, *J. Am. Chem. Soc.* **1960**, *82*, 4433.
82. C. O. Dietrich-Buchecker, J.-P. Sauvage, *Chem. Rev.* **1987**, *87*, 795.
83. F. Vögtle, T. Dünwald, T. Schmidt, *Acc. Chem. Res.* **1996**, *29*, 451.
84. M. S. Deleuze, D. A. Leigh, F. Zerbetto, *J. Am. Chem. Soc.* **1999**, *121*, 2364.
85. D. A. Leigh, K. Moody, J. P. Smart, K. J. Watson, A. M. Z. Slawin, *Angew. Chem. Int. Ed. Engl.* **1996**, *35*, 306.
86. C. A. Hunter, *J. Am. Chem. Soc.* **1992**, *114*, 5303.
87. C. Piguët, G. Bernardinelli, A. F. Williams, B. Bocquet, *Ang. Chem. Int. Ed. Engl.* **1995**, *34*, 582.
88. (a) P. R. Ashton, T. T. Godnow, A. E. Kaifer, M. V. Reddington, A. M. Z. Slawin, N. Spencer, J. F. Stoddart, C. Vicent, D. J. Williams, *Angew. Chem. Int. Ed. Engl.* **1989**, *28*, 1396; (b) P. R. Ashton, C. L. Brown, E. J. T. Chrystal, T. T. Goodnow, A. E. Kaifer, K. P. Parry, A. M. Z. Slawin, N. Spencer, J. F. Stoddart, D. J. Williams, *Angew. Chem. Int. Ed. Engl.* **1991**, *30*, 1039; (c) P. R. Ashton, S. E. Boyd, A. Brindle, S. J. Langford, S. Menzer, L. Pérez-García, J. A. Preece, F. M. Raymo, N. Spencer, J. F. Stoddart, A. J. P. White, D. J. Williams, *New J. Chem.* **1999**, *23*, 587; (d) M. J. Gunter, D. C. R. Hockless, M. R. Johnston, B. W. Skelton, A. H. White, *J. Am. Chem. Soc.* **1994**, *116*, 4810; (e) Y.-Z. Hu, S. H. Bossmann, D. van Loyen, O. Schwarz, H. Durr, *Chem. Eur. J.* **1999**, *5*, 1267.
89. M. J. Gunter, M. R. Johnston, *J. Chem. Soc. Chem. Commun.* **1994**, 829.
90. D. B. Amabilino, C. O. Dietrich-Buchecker, A. Livoreil, L. Pérez-García, J.-P. Sauvage, J. F. Stoddart, *J. Am. Chem. Soc.* **1996**, *118*, 3905.
91. D. B. Amabilino, J.-P. Sauvage *New J. Chem.* **1998**, 395.
92. M. Asakawa, P. R. Ashton, V. Balzani, A. Credi, C. Hamers, G. Mattersteig, M. Montalti, A. N. Shipway, N. Spencer, J. F. Stoddart, M. S. Tolley, M. Venturi, A. J. P. White, D. J. Williams, *Ang. Chem. Int. Ed.* **1998**, *37*, 333.
93. P. R. Ashton, R. Ballardini, V. Balzani, A. Credi, M. T. Gandolfi, S. Menzer, L. Pérez-García, L. Prodi, J. F. Stoddart, M. Venturi, A. J. P. White, D. J. Williams, *J. Am. Chem. Soc.* **1995**, *117*, 11171.
94. See for example: (a) M. Sano, H. Taube, *J. Am. Chem. Soc.* **1991**, *113*, 2327; (b) L. Zeliko-vich, J. Libman, A. Shanzer, *Nature* **1995**, *374*, 790; (c) T. Pascher, J. P. Chesick, J. R. Winkler, H. B. Gray, *Science*, **1996**, *271*, 1558.
95. A. Livoreil, C. O. Dietrich-Buchecker, J.-P. Sauvage, *J. Am. Chem. Soc.* **1994**, *116*, 9399.
96. A. Livoreil, J.-P. Sauvage, N. Armaroli, V. Balzani, L. Flamigni, B. Ventura, *J. Am. Chem. Soc.* **1997**, *119*, 12114.
97. F. Baumann, A. Livoreil, W. Kaim, J.-P. Sauvage, *Chem. Commun.*, **1997**, 35.

98. J. P. Sauvage *Acc. Chem. Res.* **1998**, *31*, 611.
99. N. Armaroli, V. Balzani, J.-P. Collin, P. Gavina, J.-P. Sauvage, B. Ventura, *J. Am. Chem. Soc.* **1999**, *121*, 4397.
100. D. J. Cardenas, A. Livoreil, J.-P. Sauvage, *J. Am. Chem. Soc.* **1996**, *118*, 11980.
101. G. Schill, H. Zollenkopf, *Liebigs Ann. Chem.* **1969**, *721*, 53.
102. I. T. Harrison, S. Harrison, *J. Am. Chem. Soc.* **1967**, *89*, 5723.
103. H. Ogino, *J. Am. Chem. Soc.* **1981**, *103*, 1303.
104. M. Belohradsky, F. M. Raymo, J. F. Stoddart, *Collect. Czech. Chem. Commun.* **1996**, *61*, 1.
105. H. W. Gibson, M. C. Bheda, P. T. Egen, *Prog. Polym. Sci.* **1994**, *19*, 843.
106. (a) F. Diederich, C. O. Dietrich-Buchecker, J.-F. Nierengarten, J.-P. Sauvage, *J. Chem. Soc., Chem. Comm.* **1995**, 781; (b) N. Armaroli, F. Diederich, C. O. Dietrich-Buchecker, L. Flammigni, G. Marconi, J.-F. Nierengarten, J.-P. Sauvage, *Chem. Eur. J.* **1998**, *4*, 406.
107. S. S. Zhu, P. J. Carroll, T. M. Swager, *J. Am. Chem. Soc.* **1996**, *118*, 8713.
108. R. A. Bissell, E. Córdova, A. E. Kaifer, J. F. Stoddart, *Nature* **1994**, *369*, 133.
109. R. Ballardini, V. Balzani, M.T. Gandolfi, L. Prodi, M. Venturi, D. Philp, H.G. Ricketts, J.F. Stoddart, *Angew. Chem., Int. Ed. Engl.* **1993**, *32*, 1301.
110. J.-P. Collin, P. Gavina, J.-P. Sauvage, *J. Chem. Soc., Chem. Commun.* **1996**, 2005.
111. D.H. Evans, *Chem. Rev.* **1990**, *90*, 739.
112. J.-P. Collin, P. Gaviña, J.-P. Sauvage, *New J. Chem.*, **1997**, *21*, 525.
113. M. Ruthkoski, F.N. Castellano, G.J. Meyer, *Inorg. Chem.* **1996**, *35*, 6406.
114. J.R. Kirchhoff, D.R. McMillin, W.R. Robinson, D.R. Powell, A.T. McKenzie, S. Chen, *Inorg. Chem.* **1985**, *24*, 3928.
115. V. Balzani, F. Bolletta, M.T. Gandolfi, M. Maestri, *Top. Curr. Chem.* **1978**, *75*, 1.
116. In acetonitrile solution, $p\text{-NO}_2\text{C}_6\text{H}_4\text{CH}_2\text{Br}$ shows a band with $\lambda_{\text{max}} = 273\text{ nm}$ which does not interfere in the visible light absorption of $\text{Cu}^{\text{I}}\text{N}_4$. On reduction of $p\text{-NO}_2\text{C}_6\text{H}_4\text{CH}_2\text{Br}$, a benzylic radical is formed which undergoes a fast dimerization reaction. In the presence of dioxygen, the benzylic radical gives rise to a series of reaction which end with formation of benzaldehyde [117].
117. J.-M. Kern, J.-P. Sauvage, *J. Chem. Soc., Chem. Commun.* **1987**, 546.
118. (a) O. Stern, M. Volmer, *Z. Physik.* **1919**, *20*, 183; (b) A. Gilbert, J. Baggott, *Essentials of Molecular Photochemistry*, **1991**, Blackwell Scientific Publications, Oxford, UK.
119. Since Cu.31^{2+} is not photosensitive and does not exhibit any long-lived excited state, the reduction step cannot be induced by light (see Refs. [95–97]).

9 Dendrimers

Alberto Juris

9.1 Introduction

Dendrimers constitute a new class of highly branched, well-defined macromolecules which are usually built with repetitive syntheses [1]. Giving an IUPAC name to these intricate structures is almost impossible, so that several trivial names have been proposed. The term dendrimer, from the Greek word for “tree”, first suggested by Tomalia et al. [2], is now the most commonly used. The geometrical similarity between trees and dendrimers is illustrated in Figure 1.

Although it is simple to understand what a dendrimer is just by looking at the beautiful chemical structures drawn in the literature, there is at present no rigorous definition of the term “dendrimer”. It is generally agreed that monodispersity is an essential characteristic of dendrimers, which are thus sets of molecules all having the same identical constitution (and thus the same molecular weight), differently from hyperbranched polymers [1], which are a mixture of different, even if chemically similar, macromolecules.

From a topological viewpoint (Figure 1b), in dendrimers one can distinguish a multifunction core unit, a number of branches growing towards the periphery, ultimately terminating with end groups. The synthetic ingenuity employed by both organic and coordination chemists has produced a great variety of different chemical structures, which in turn are attracting more and more interest to this exponentially expanding field [3, 4].

Many recent reviews report on dendrimers in general [1, 3, 5–14], or focus on more specific topics like dendrimers containing metals [15–23], or elements of groups 13, 14 and 15 [23–27], or on redox-active dendrimers [16, 19, 28, 29]. For reasons of space, it is impossible here to review all the published literature concerning dendrimers involved in electron transfer processes; only selected examples will be presented to illustrate the diversity of chemical structures and research issues that can be encountered in this field. Synthetic procedures will not be dealt with; the interested reader should refer to the original literature.

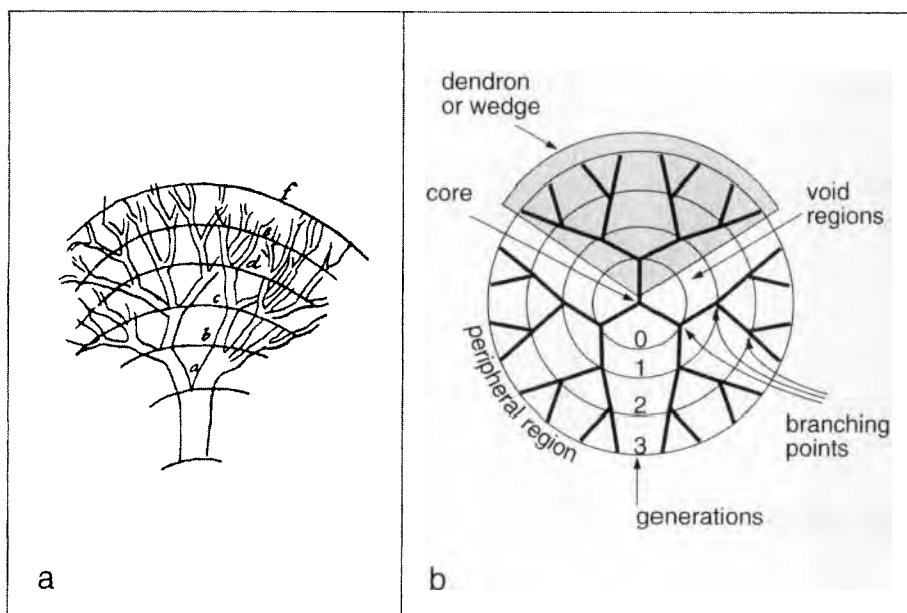


Figure 1. (a) A sketch by Leonardo da Vinci on tree branching; (b) schematic representation of a dendrimer, illustrating the basic terminology of these compounds.

9.2 Electroactive Units

As far as electron transfer properties directly involving dendrimers are concerned, it can be generally considered that these reactions may be observed whenever the macromolecular structure contains one or more units featuring redox levels at accessible potentials. The first dendrimers prepared were purely organic macromolecules, with no unit appropriate for electron transfer reactions. Later, however, the introduction of metal and organometallic complexes in the dendritic structure opened new possibilities to the chemistry of dendrimers. Indeed, the incorporated metal units exhibit important properties such as absorption and emission of visible light (relevant for the construction of antenna systems; see Volume V, Part 1, Chapter 7) and redox levels at accessible potential, which are necessary for electron transfer reactions. Successively, purely organic electroactive units have also been used to functionalize the dendrimers.

The electroactive unit may be incorporated in different positions of the dendrimer, giving rise to four prototypical kinds of functionalized structures (Figure 2a–d).

- 1) The electroactive unit is the core of the dendrimer (Figure 2a). The most commonly used units in this category are metal–polypyridine complexes and porphyrins.

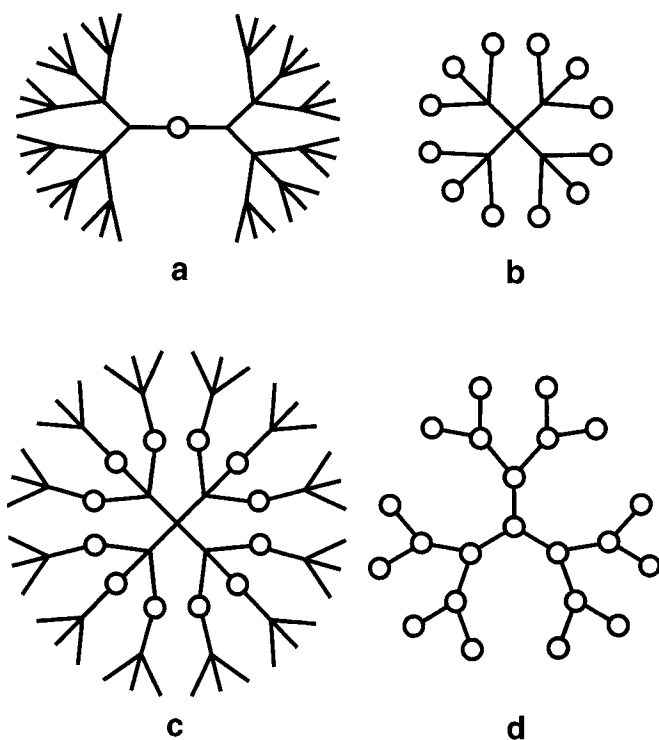


Figure 2. Different arrangements of the electroactive unit(s) in dendrimers. The electroactive units are represented with a circle, and can be used as core (a), at the periphery (b); along the branches (c); or at each branching point (d).

- 2) The electroactive units are the peripheral groups (Figure 2b). These dendrimers are functionalized on their surface, and all the units are equivalent. The most common units of this type are ferrocene and metal–polypyridine complexes.
- 3) The electroactive units are located in the branches (Figure 2c). There are examples where the units are used as connectors, and cases where these units are appended to a previously synthesized structure. Also, in these kind of dendrimers all the electroactive units are equivalent.
- 4) The electroactive units are used as branching centers in the whole structure (Figure 2d). Units of this type are typically metal complexes connected by suitable bridging polypyridine ligands.

Of course, there are also dendritic structures that belong to more than one of these categories. The most significant examples of electron transfer reactions involving dendrimers containing electroactive units will be presented in Section 9.4, arranged on the basis of the electroactive unit involved. Moreover, there are examples where the dendrimer itself does not contain any electroactive unit, but is in-

stead used as a “medium” to host species involved in electron transfer reactions. Electron transfer reactions occurring in the presence of such “electroinactive” dendrimers will be reviewed in Section 9.5.

9.3 Types of Electron Transfer Reactions

Dendrimers have been insofar involved in two main types of electron transfer processes, that is electrochemical reactions and photoinduced electron transfer reactions. A few general features of these reactions are introduced in the following Sections 9.3.1 and 9.3.2.

9.3.1 Electrochemical Reactions

Many studies have been carried out on the electrochemical characterization of dendrimers. In general, the observed electrochemical behavior depends on the position occupied by the active unit(s) in the molecular structure.

When the only electroactive unit of a dendrimer is the core of the structure (Figure 2a), the most interesting problem is whether and, in case, how much the electrochemical properties (potential value, kinetic reversibility) of the core are modified by the surrounding branches.

When the electroactive units are used for peripheral functionalization (Figure 2b) and/or are located along to the branches (Figure 2c) of a dendrimer, a number of equivalent redox-active centers are present, since dendrimers are usually highly symmetric species by their own nature. The active centers may or may not interact, depending on distance and nature of the connector units. Multielectron redox processes can therefore be observed, the specific patterns of which are related to the degree of interaction among the various units.

When each branching center is an electroactive unit (Figure 2d), the electrochemical behavior is even more complex since: (i) each unit of the dendrimer is electroactive; (ii) the chemical nature of the units constituting the dendrimer may be different; (iii) chemically equivalent units can be different from the topological viewpoint; and (iv) the degree of interaction among the moieties depends on their chemical nature and distance.

9.3.2 Photoinduced Electron Transfer Reactions

This type of electron transfer reaction requires the presence of a donor–acceptor couple, and is triggered by light excitation on one of the two reaction partners. The species which absorbs the exciting light must possess appropriate photophysical properties such as a long-lived excited state at suitable energy. The quencher, on the other hand, must possess appropriate redox levels.

A classification of these photoinduced electron transfer reactions can be based on the different arrangement that the two reaction partners can assume. Thus, one can observe:

- 1) Intermolecular reactions taking place between a unit incorporated in the dendrimer structure and an external partner. This is the most commonly observed situation. Often, well-known luminescent species like Ru^{II}–polypyridine complexes [30, 31] or metallo-porphyrin species [31] are used as dendrimer cores (Figure 2a). In this case, interesting issues are how the dendritic branches can influence the photophysical properties of the core, and to which extent quencher access to the core can be prevented.
- 2) Intramolecular reactions occurring with both partners being part of the dendrimer framework. At present, this is the most uncommon case, presumably due to synthetic difficulties.
- 3) Intermolecular reactions occurring between partners that are simply hosted by an “inactive” dendrimer. Poly(amidoamine) dendrimers are most commonly used in this area, probably because they are commercially available products.

9.4 Dendrimers Containing Electroactive Units

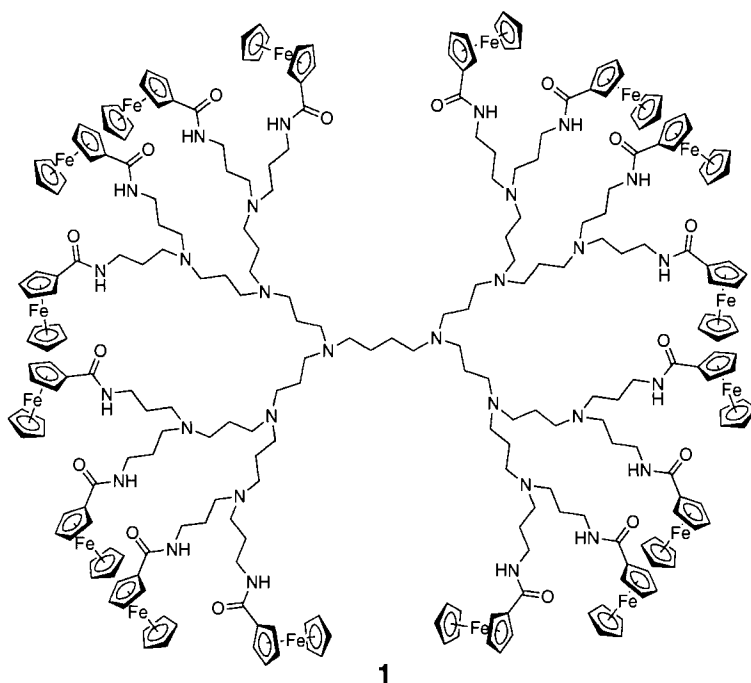
This section presents a literature survey on dendrimers containing at least one electroactive unit. The arrangement is on the basis of the electroactive unit incorporated in the dendrimer structure. In a few cases, different electroactive units are present in the same dendrimer, so that the classification is somewhat arbitrary.

9.4.1 Ferrocene and other Sandwich Compounds

Ferrocene is the most commonly used electroactive unit for functionalization of dendrimers. Only selected examples will be illustrated here, as the related literature is very extensive [29, 32–69].

The electrochemical behavior of ferrocene is relatively simple, giving rise to a reversible monoelectronic oxidation process at a very accessible potential. Most commonly, ferrocene has been used to functionalize the periphery of dendrimers, along the scheme illustrated in Figure 2b. Dendrimers **1** [42] and **2** [55] exemplify the commonly observed electrochemical behavior:

- 1) All the ferrocene units are oxidized at the same potential, with a number of exchanged electrons equal to the number of peripheral ferrocene units, thus indicating that these units behave independently from one another.
- 2) The potential value for ferrocene oxidation shows no or only minor dependence on dendrimer generation.



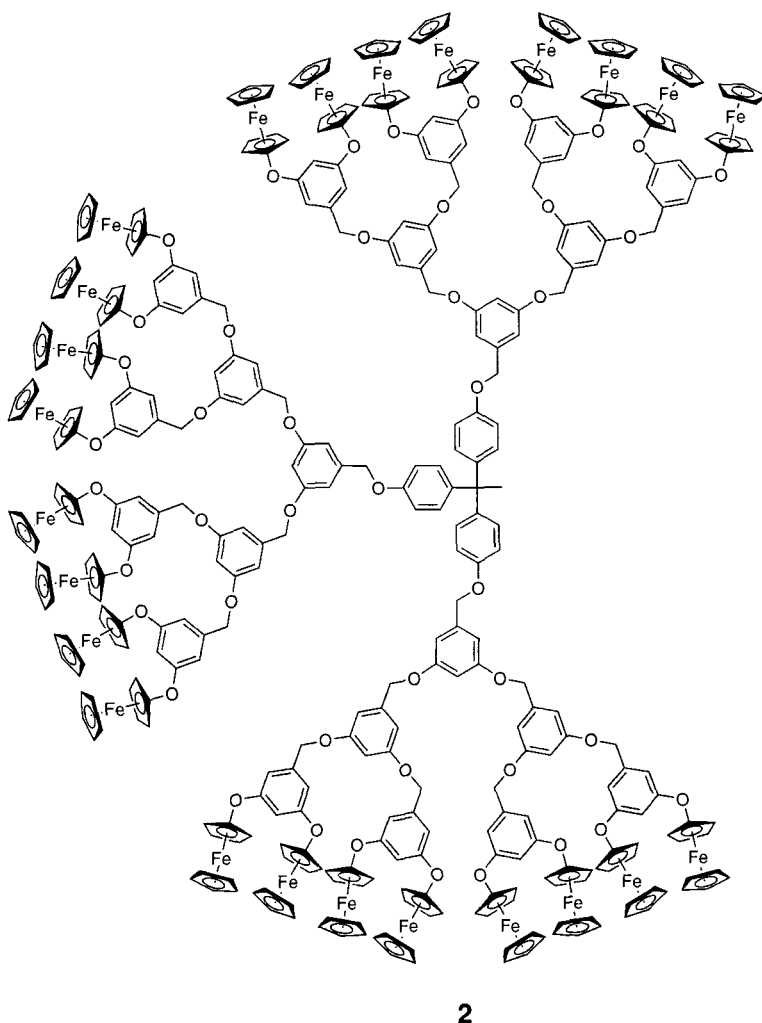
- 3) The oxidized product becomes insoluble in CH_2Cl_2 and is deposited on the electrode surface, as evidenced by the presence of a cathodic stripping peak in cyclic voltammetry experiments.

In particular, dendrimer **1** is a third-generation species with 16 ferrocenyl units based on a poly(propyleneamine) framework; dendrimers of different generation, carrying 64, 32, eight, and four ferrocenyl units, behave in analogous way, with only the number of exchanged electrons being different [42]. The thermodynamics and kinetics of the adsorption of these dendrimers on the electrode surface was also investigated [49].

Compound **2** is a third-generation dendrimer based on a poly(arylether) structure and contains 24 equivalent ferrocenyl units; even in this case the potential required for ferrocene oxidation was essentially the same observed in lower-generation analogues [55].

Compound **3** and its lower-generation analogues contain a cyclotetrasiloxane core terminated with ferrocenyl peripheral units [62]. Also in this case the potential for ferrocenyl oxidation was independent from dendrimer generation, but the oxidized species remained soluble in CH_2Cl_2 .

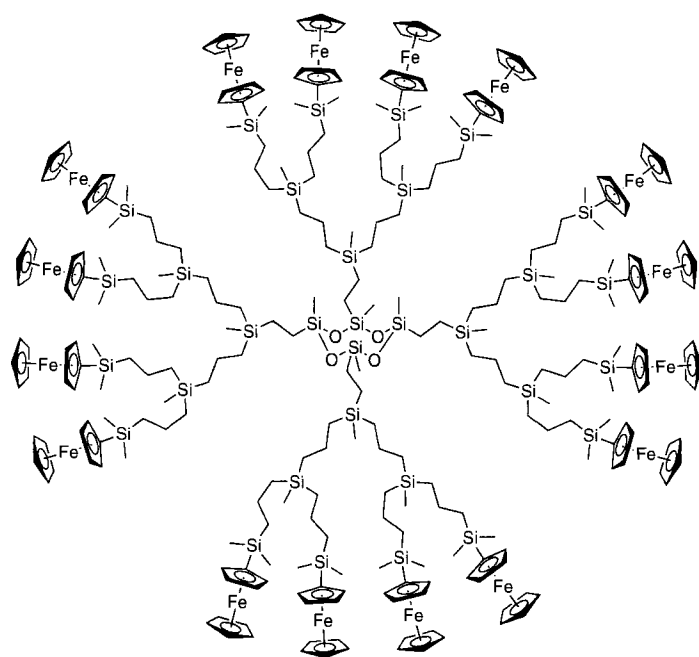
Compound **4** contains ferrocene both as a core and as a terminal unit [45]. Cyclovoltammetric experiments in CH_2Cl_2 showed that the equivalent peripheral ferrocenyl units are reversibly oxidized at the same potential. The core unit is chemically different from the peripheral ones and, as a consequence, it is oxidized at a



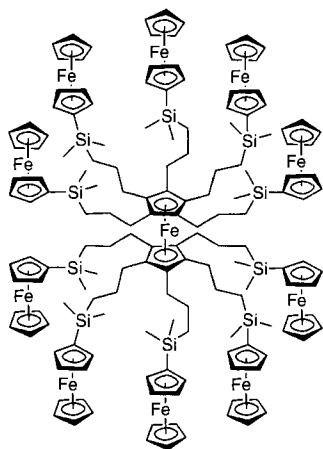
different potential. The ratio between the intensity of the two waves is not exactly 1:10; this has been attributed to adsorption at the electrode surface.

Mixed-metal dendrimers have also been prepared. In compound **5**, ferrocenyl units are present at the periphery, while platinum units play the role of connectors along the branches [56]. Electrochemical oxidation in acetonitrile involves only the ferrocenyl units and confirms the presence of multiple noninteracting sites. By combining different electrochemical techniques it was possible to measure the number of ferrocene units contained in the dendrimer, thus supporting the proposed structure.

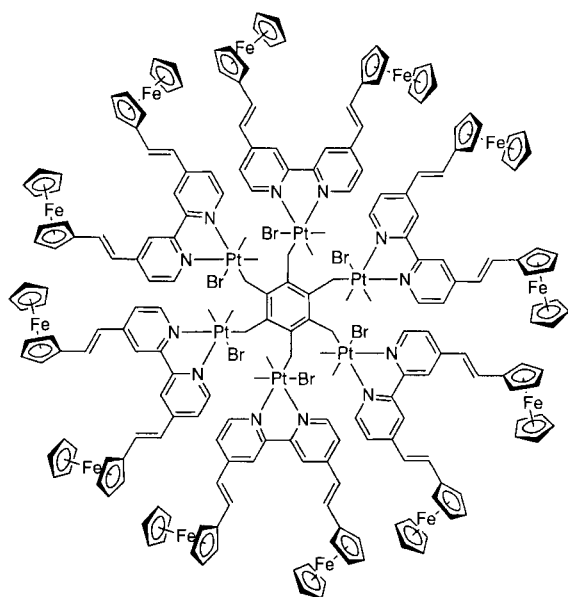
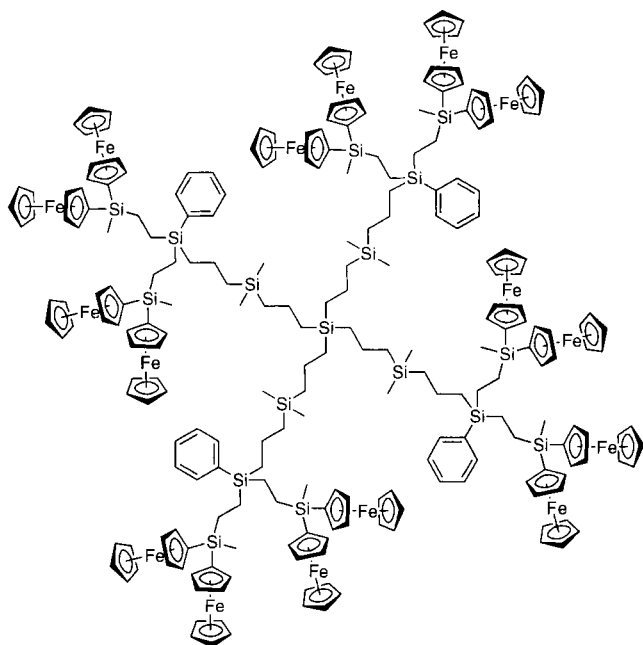
In a few cases, interaction between equivalent electroactive ferrocene units has been observed. One example is the silicon-based dendrimer **6**, containing 16 ferrocene units, which upon oxidation in CH_2Cl_2 shows two well-separated reversible

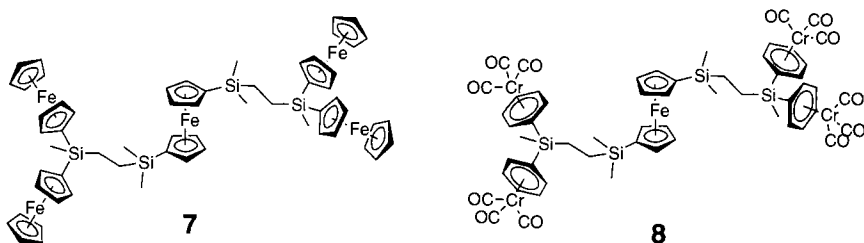


3



4

**5****6**

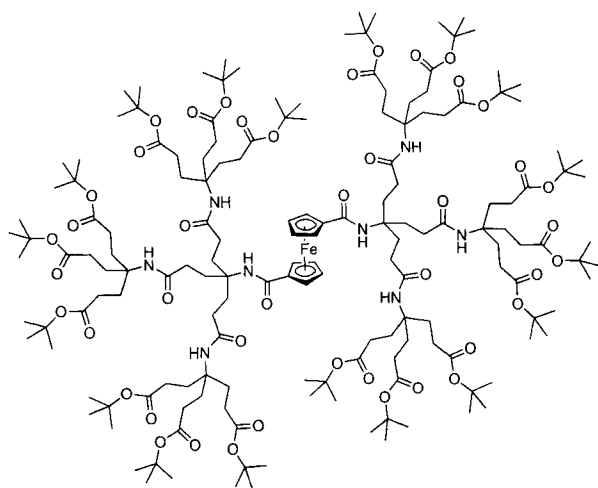
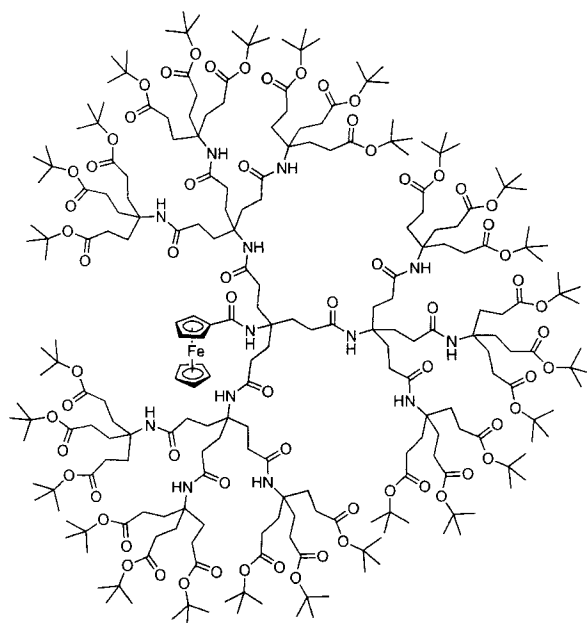
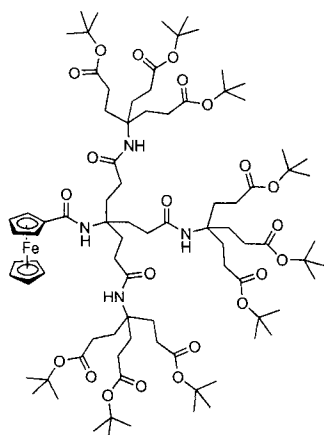
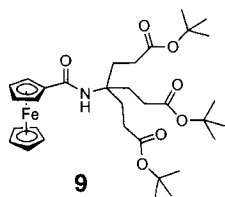


waves each accounting for eight electrons [47]. The same behavior was observed also in lower-generation analogues, and can be explained considering the interaction present between the two ferrocene units directly linked to the same silicon atom.

Compounds **7** and **8** can be considered as first-generation dendrimers [64]. In compound **7**, interaction of the peripheral ferrocenyl units is observed, and thus, oxidation in CH_2Cl_2 occurs in three consecutive processes, involving the exchange of two, one, and two electrons, respectively. The first process involves oxidation of two nonadjacent terminal ferrocenyls; the second is the oxidation of the central ferrocenyl, and the third corresponds to oxidation of the two remaining nonadjacent terminal units. Interestingly, in the similarly structured compound **8**, no interaction is observed between the adjacent η^6 -coordinated $\text{Cr}(\text{CO})_3$ units. Thus, oxidation of **8** gives rise to a first monoelectronic wave due to the central ferrocenyl unit, followed by a four-electron wave due to oxidation of the four chromium centers. This compound is also an example of a species where chemically distinct metal units (Fe- and Cr-based) are present, each being electroactive. Many other dendrimers incorporating different electroactive metal units can be found in Section 9.4.2.

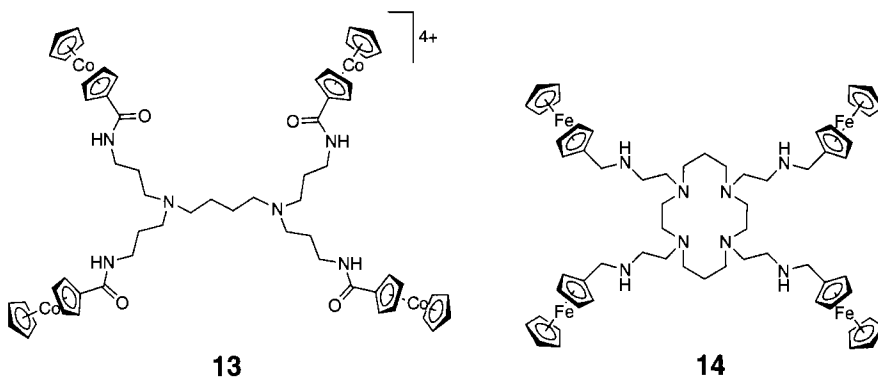
Compounds **9–11** represent three generations of asymmetric dendrimers containing a single ferrocene unit [58]. Their electrochemical oxidation occurs in a reversible, monoelectronic wave, whose potential in CH_2Cl_2 solution is 0.63, 0.60, and 0.54 V (versus Ag/AgCl), respectively, suggesting that formation of the ferricenium ion is favored in the dendritic structure. Digital simulation of the voltammetric data allowed estimation for the first time of the heterogeneous electron transfer rate constant between dendrimers and an electrode. The values found were about 80×10^{-3} , 17×10^{-3} , and $5 \times 10^{-3} \text{ cm s}^{-1}$, respectively, for compounds **9**, **10**, and **11**, indicating that electron accessibility to the electroactive core is quickly reduced with increasing dendrimer size. Moreover, it was found that the asymmetric compound **10** exhibits an electron transfer rate greater than that of the more symmetric bis-dendritic analogue **12** [58]. The slower kinetics of **12** was attributed to the greater shielding imposed by the two dendritic branches, which preclude close approach of the ferrocene unit to the electrode surface.

The electrochemical properties of ferrocene-functionalized dendrimers have been studied also in the presence of β -cyclodextrin (β -CD), which is a well-known inclu-

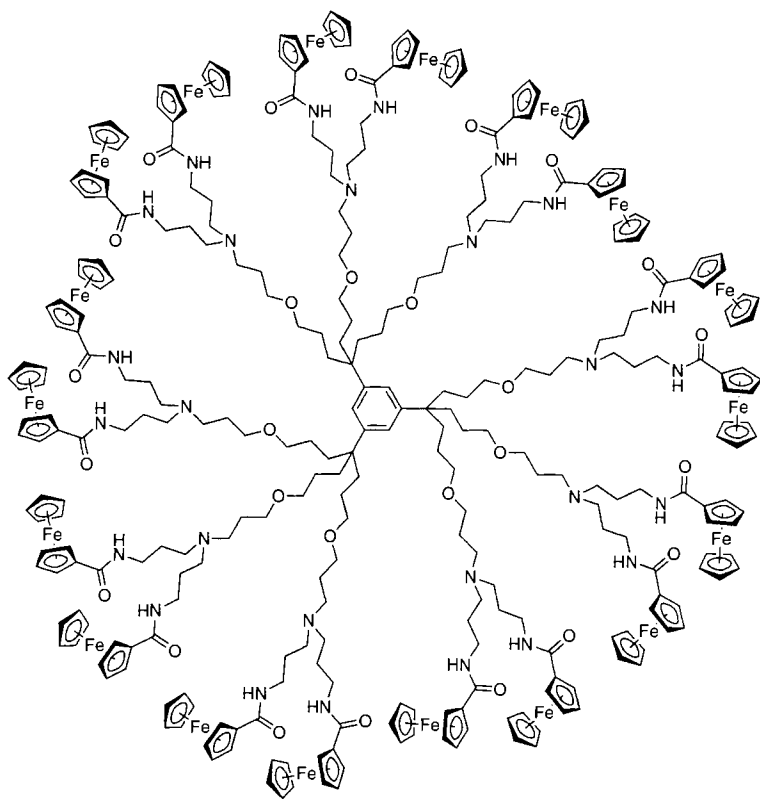


sion complexation host. Poly(propyleneamine) dendrimer **1**, functionalized with 16 ferrocene units, as well its lower generation analogues, interacts with β -CD giving rise to compounds where the β -CD cavity includes the peripheral ferrocene units [46]. As a result, the solubility in water of the dendrimer increases, and the potential for ferrocene oxidation is shifted to more positive values. In the lower-generation dendrimers containing four and eight ferrocene units, only one reversible voltammetric wave is observed, indicating that each ferrocene unit is complexed by β -CD and undergoes independent monoelectronic oxidation. In contrast, with dendrimer **1** two different voltammetric waves are observed, at the potentials corresponding to oxidation of uncomplexed and complexed ferrocene units. This finding indicates that steric congestion of the surface of the higher-generation dendrimer prevents inclusion of part of the ferrocene units.

The same poly(propyleneamine) framework has been used to obtain four dendrimers functionalized with four (**13**), eight, 16, and 32 cobaltocenium units [57]. Dendrimer **13** was examined in greater detail: electrochemical reduction in aqueous solution occurs in an irreversible single-wave process transforming the cobaltocenium into cobaltocene units. As a result, the dendrimer becomes hydrophobic and deposition on the electrode takes place. Addition of β -CD prevents dendrimer precipitation, and the cyclic voltammogram exhibits a shape which is consistent with that for a reversible process. This indicates that β -CD interacts with the *reduced* form of the dendrimer, forming an inclusion complex with cobaltocene. This system is an example where electrochemical activation is required in order to trigger the host–guest interaction. As far as the higher-generation analogues are concerned, their solubility in aqueous media decreased with increasing size, so that qualitatively similar results were obtained only in the species functionalized with eight and 16 cobaltocenium units.



Compounds containing several electroactive units can be used as sensors for ion recognition. In this field, recognition of cations was achieved with compound **14** [44]. The four ferrocene units are oxidized in a single, reversible, four-electron pro-

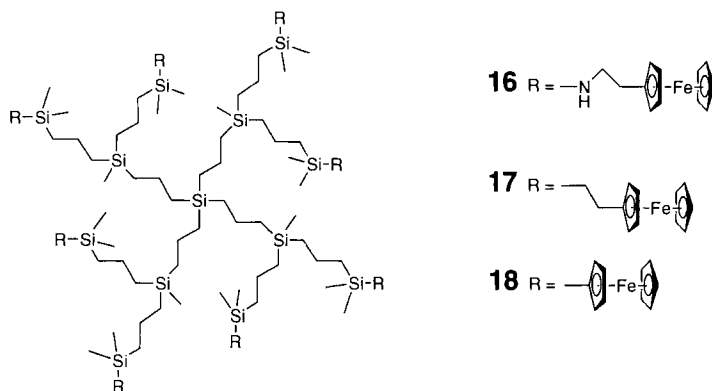


15

cess. In tetrahydrofuran/water the potential for oxidation depends on pH, and shifts on addition of Cu^{2+} , Zn^{2+} , or Cd^{2+} , which are coordinated by the central macrocycle. At $\text{pH} < 5$ the presence of Cu^{2+} is selectively recognized.

Recognition of anions is reported in several papers. Dendrimer **15** contains 18 equivalent and independent ferrocene units in the periphery, and only a single anodic reversible wave is observed in cyclic voltammetry experiments in CH_2Cl_2 solution [53]. Progressive addition of H_2PO_4^- induces the growing of a new wave at less positive potential, while the original wave is lowered in intensity. In contrast, addition of HSO_4^- , Cl^- , and NO_3^- only produces a cathodic shift of the original wave. The lower-generation analogues, carrying nine and three peripheral ferrocene units, were also tested; a clear dendritic effect is observed, in the sense that the ion-sensing ability increases with increasing dendrimer generation. Similar dendrimers using cobalticinium as electroactive units for anion sensing have also been studied [52, 60].

The silicon-based dendrimers **16**–**18** were also investigated as anion sensors in CH_2Cl_2 solution [63]. Compound **16** was found to be a much better sensor than **17** and **18**, and is more sensitive to H_2PO_4^- and HSO_4^- , with respect to Cl^- and Br^- .



The peculiar anion-sensing ability of dendrimers **15** and **16** has been related to a synergic effect between the electrostatic interaction of the anion with the ferricinium cation and the H-bonding of the anion with the close NH group. Dendrimer **16** was also deposited on electrodes, showing anion-sensing capability similar to that observed in homogeneous solution.

Compounds **17** and **18** (and their lower-generation analogues) were studied as amperometric biosensors for glucose determination in aqueous solution, using modified carbon-paste electrodes [48]. The response to glucose was found to increase with the length of the branches, and with the presence of a greater number of ethylene groups in the branches, so that dendrimer **17** gave the best response.

A new type of core is used in dendrimer **19** functionalized with 24 $[\text{FeCp}(\eta^6\text{-arene})]^+$ units, thus obtaining a 24+ polycationic species. Cyclic voltammetry in DMF features a single reversible 24-electron reduction wave [61]. ^1H NMR spectroscopy indicates that **19** recognizes Cl^- and Br^- ions, whereas electrochemistry was in this case an ineffective technique.

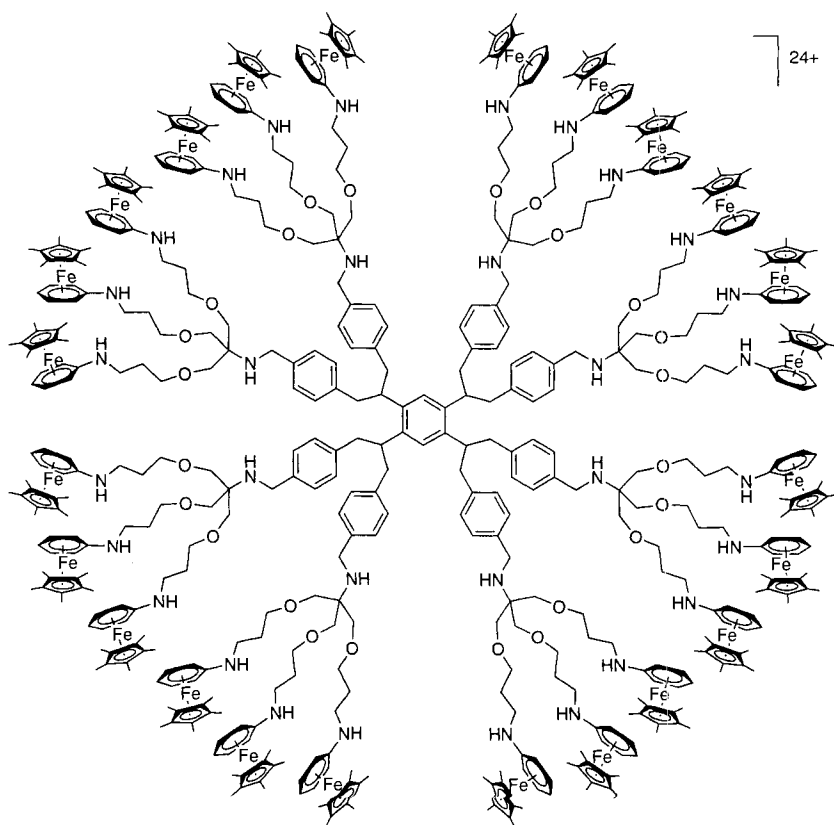
An example where ferrocenyl units of a dendrimer participate to an electron transfer reaction is discussed in Section 9.4.3.

9.4.2 Metal–Polypyridine Complexes

Metal–polypyridine complexes have been used extensively as electroactive units in dendrimers [50, 51, 70–115]. For reasons of space, only representative examples are presented here.

Electrochemical investigation of dendrimers containing metal–polypyridine units shows the presence of many redox processes, as usually oxidation is a metal-centered process, while reduction is centered on the polypyridine ligands.

Compound **20** is a third-generation dendrimer based on a $[\text{Fe}(\text{tpy})_2]^{2+}$ core (tpy = 2,2':6',2''-terpyridine) surrounded by a polyether framework [93]. Electrochemical characterization in CH_2Cl_2 or THF of dendrimers of generation 0–3 indicated that the reversibility of both the metal-centered oxidation and of the tpy-

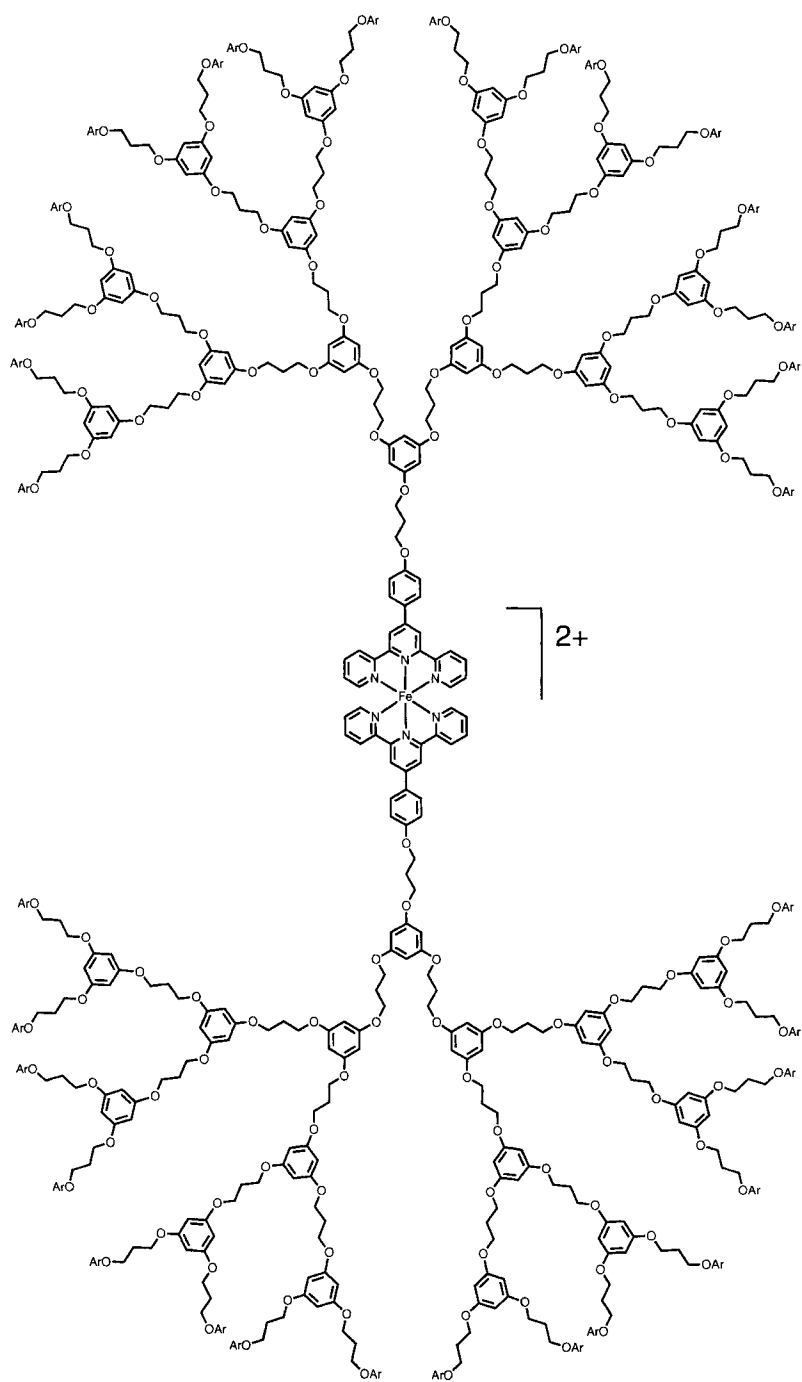


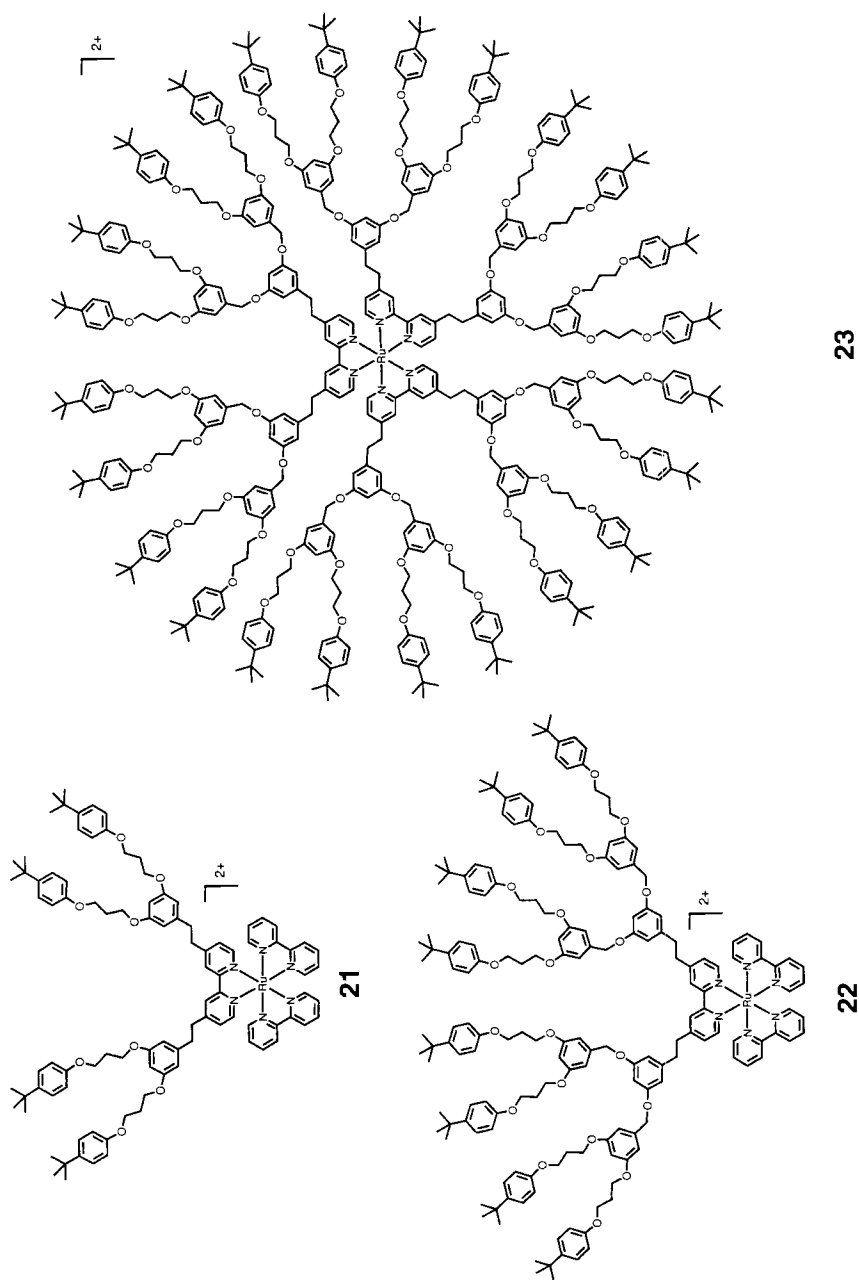
19

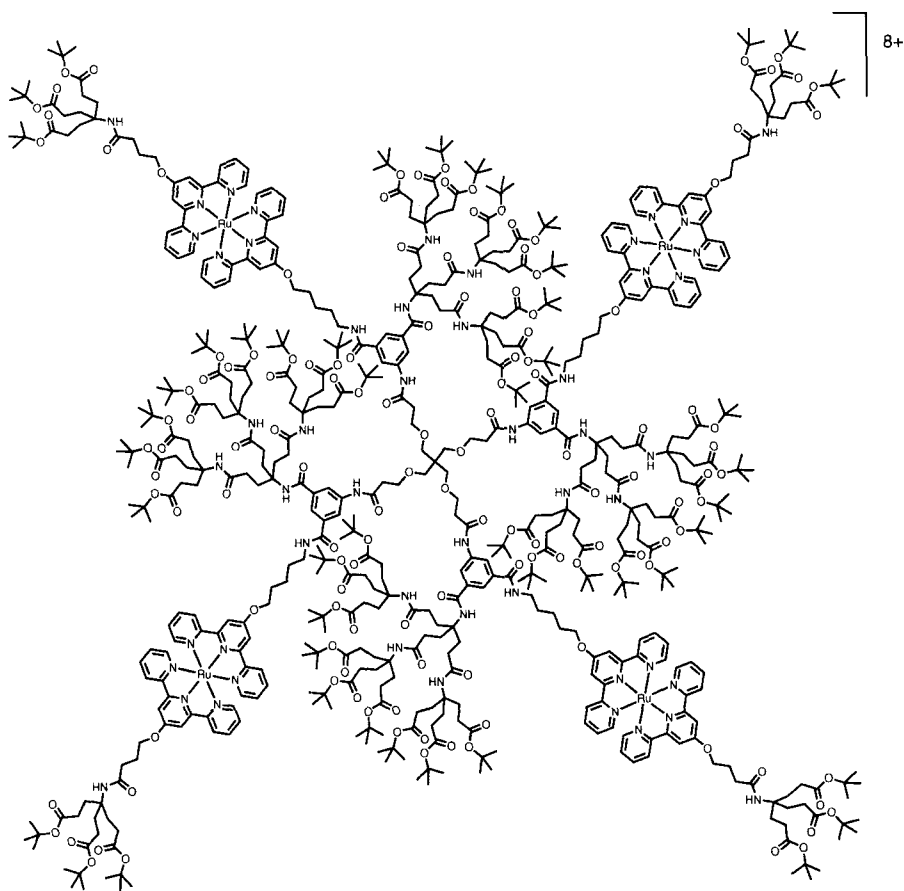
based reductions decreased on increasing dendrimer size. This effect is ascribed to encapsulation of the metal unit by the insulating polyether branches.

A similar organic framework was assembled around a $[\text{Ru}(\text{bpy})_3]^{2+}$ core (bpy = 2,2'-bipyridine) obtaining the three dendrimers **21**, **22**, and **23**, where the presence of many electroactive units was evidenced, giving rise to six redox processes in acetonitrile [115]. On oxidation, the reversible monoelectronic $\text{Ru}^{\text{II}} \rightarrow \text{Ru}^{\text{III}}$ wave is followed by two polyelectronic processes assigned to the dioxybenzene and oxybenzene units in the branches; in **23** the presence of a great number of these organic units gives rise to a huge unresolved wave. On reduction, three monoelectronic processes are due to the presence of the three coordinated bpy ligands. On increasing dendrimer size the processes involving the Ru–polypyridine core become more irreversible, as observed for encapsulated electroactive units.

$[\text{Ru}(\text{tpy})_2]^{2+}$ units are present in the branches of dendrimers **24** and **25**, which have identical molecular formula and are the first example of dendritic constitutional isomers [105]. These isomers feature similar solubility and decomposition temperature, whereas the electrochemical behavior (in acetonitrile), due to the four

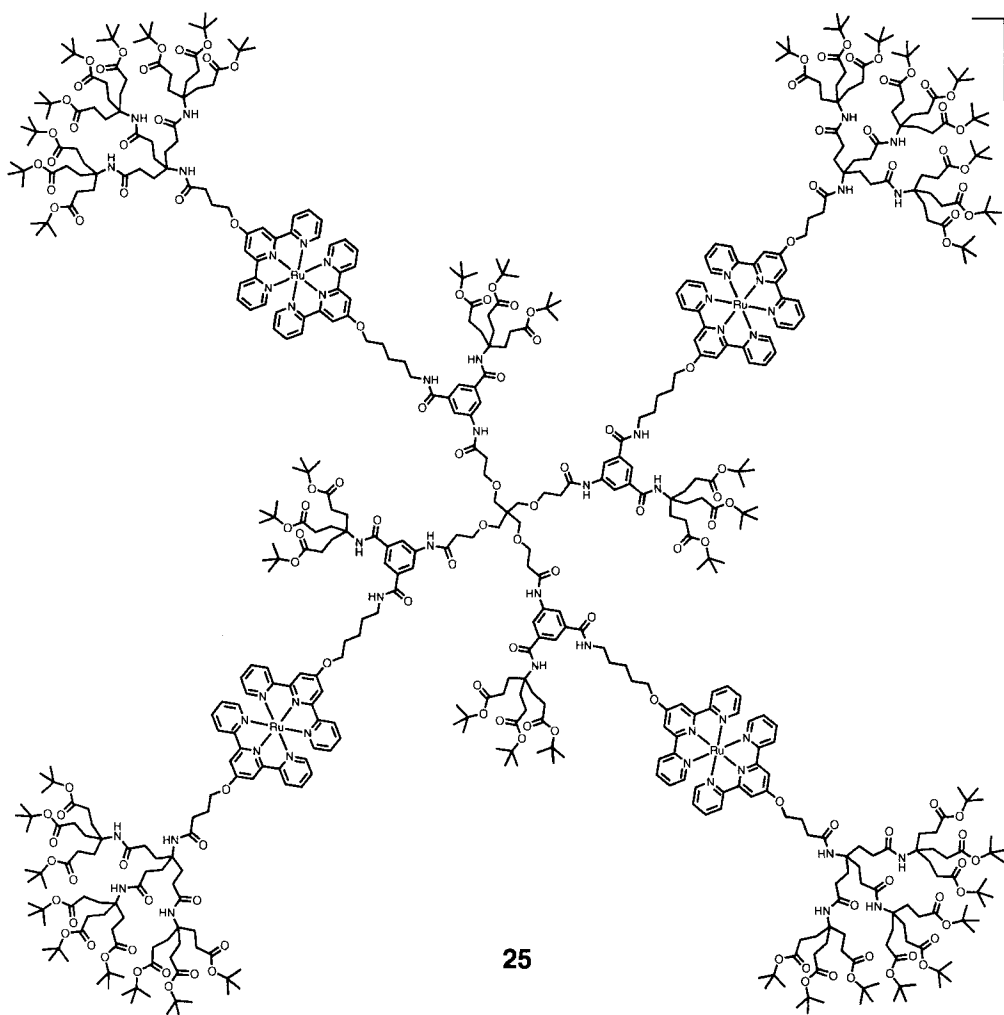




**24**

$[\text{Ru}(\text{tpy})_2]^{2+}$ units, is different. Reduction of the two isomers evidences two processes due to the terpyridine ligands; the values of the $E_{1/2}$ for isomer **25** are slightly more negative than those of **24**. Oxidation of the Ru^{2+} ions occurs in one process for isomer **25**, whereas two waves are observed in **24**. These differences suggest the presence of different chemical environments in the two isomers, due to different internal densities and void regions.

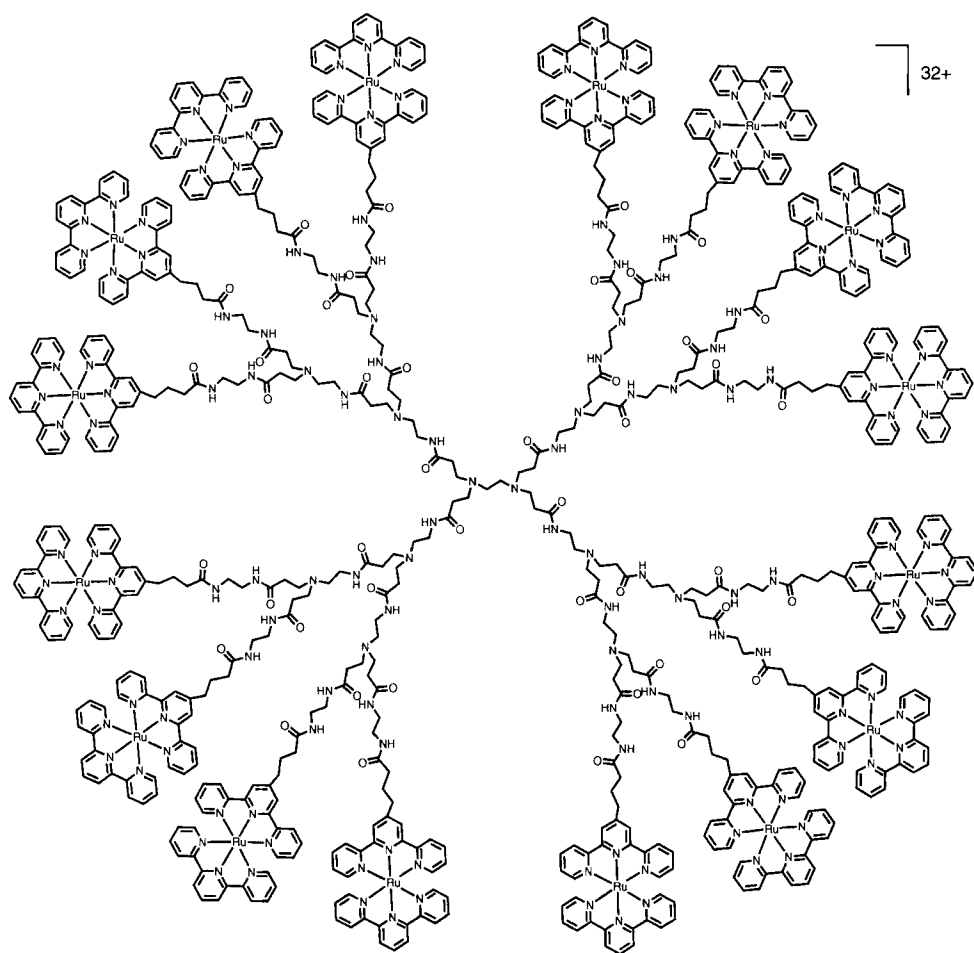
Poly(amidoamine) dendrimers of different generations have been surface functionalized with four, eight, 16 (compound **26**), 32, and 64 $[\text{Ru}(\text{tpy})_2]^{2+}$ units [114]. One oxidation ($\text{Ru}^{\text{II}} \rightarrow \text{Ru}^{\text{III}}$) and two reduction waves (one for each tpy ligand) are observed in acetonitrile, indicating that there is no significant interaction between the $[\text{Ru}(\text{tpy})_2]^{2+}$ units, independently on dendrimer generation. After the second reduction process the dendrimer becomes neutral and deposition occurs on the electrode surface. Cyclic voltammograms show also the presence of “charge-trapping peaks”, attributed to isolated domains of the redox centers. The peak current of these charge-trapping peaks increases with dendrimer generation. The authors suggest that such an effect is not observed in ferrocene-functionalized den-



drimers because in the latter case only one redox wave is present. The analogous $[\text{Ru}(\text{bpy})_3]^{2+}$ -functionalized dendrimers were also studied, with similar results.

Metal units both in the core and in the periphery are present in dendrimers **27** and **28** [107]. In **27**, oxidation of the core occurs in acetonitrile in an irreversible process, as often observed for encapsulated redox units. This process is followed, at more positive potential, by a single reversible wave due to the six Ru-based moieties, indicating that there is no interaction between the peripheral units. In **28**, the behavior of the Ru-based units is essentially the same as in **27**, but no oxidation due to the Co-based core was evidenced. Interestingly, also chemical treatment with chlorine was ineffective in this regard.

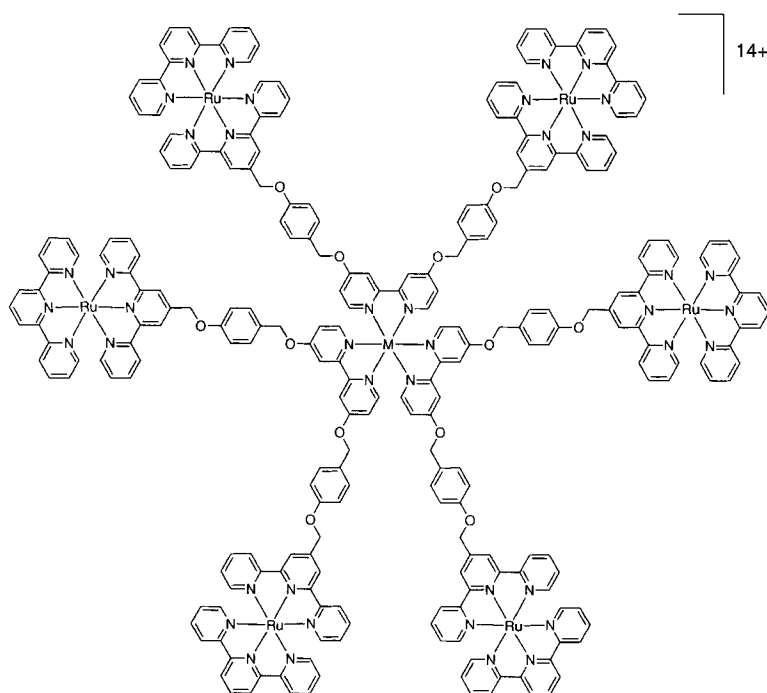
Compound **29** can be considered as a first-generation dendrimer where each branching center is an electroactive unit [99]. In the protonated form shown, a 3-1 oxidation pattern is observed in acetonitrile: simultaneous oxidation of the three



26

Os-based units is followed by one-electron oxidation of the core Ru-based unit. Interestingly, the redox pattern can be easily reversed. Removal of the six acidic protons changes the oxidation potential of the metal ions and the oxidation pattern becomes 1-3: the core Ru unit is oxidized first, followed by oxidation of the Os units at more positive potential.

Electrochemical characterization has been performed in acetonitrile solution on a great variety of dendrimers built with metal complexes as branching centers in the whole structure [16]. An interesting example is that represented by the decametallic dendrimers **30–32**, where the metal centers are linked by bridging ligands made of two, closely connected bis-chelating units such as 2,3-dpp (2,3-dpp = 2,3-bis(2-pyridyl)pyrazine) [76, 78]. In the dendritic species, each mononuclear component brings its own redox properties, more or less affected by intercomponent inter-



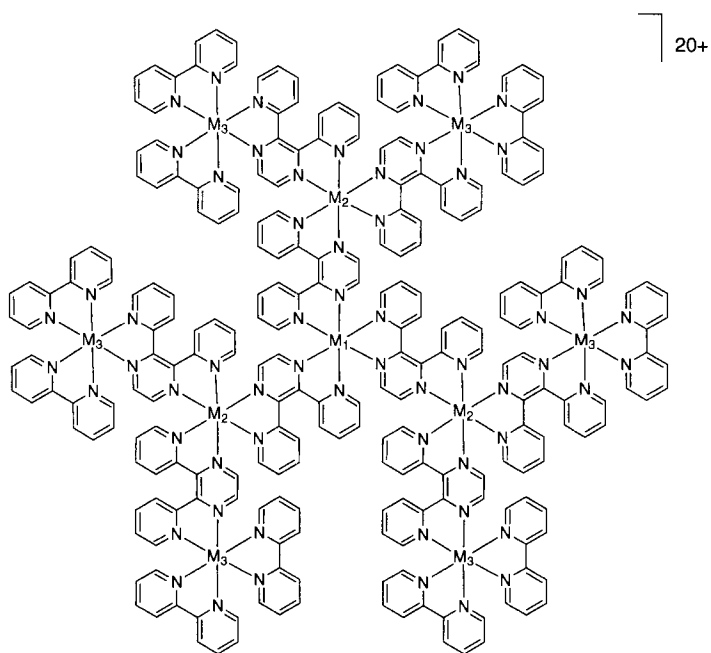
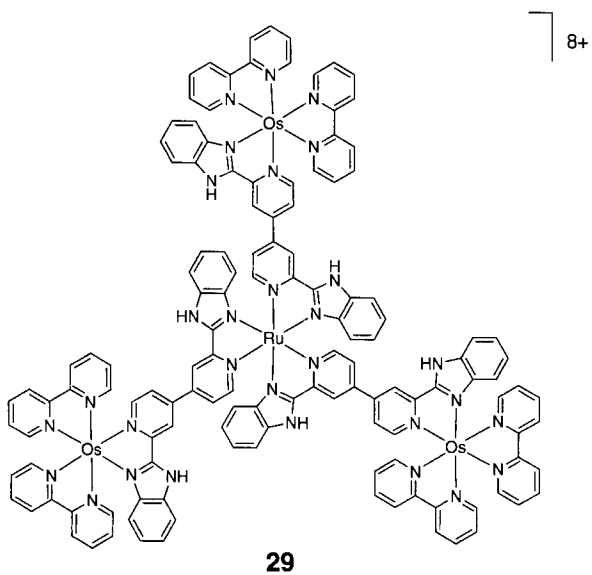
27, M = Fe

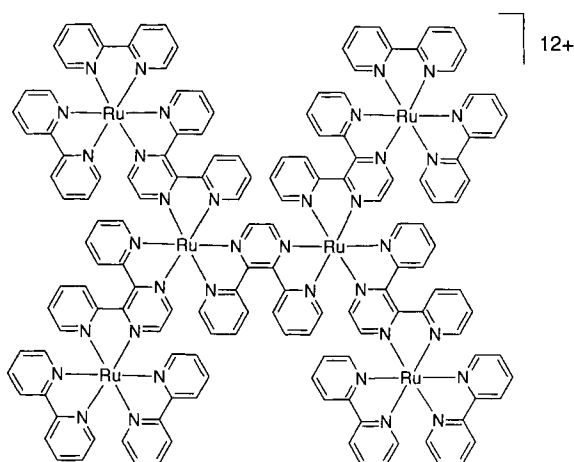
28, M = Co

actions. Metal–metal and ligand–ligand interactions are noticeable for metals coordinated to the same bridging ligand and for ligands coordinated to the same metal, whereas they are negligibly small for metals or ligands that are sufficiently far apart. Since chemically equivalent non-interacting units undergo electrochemical processes at the same potential, the number of electrons lost or gained at a certain potential can be synthetically controlled.

Dendrimer **30** contains ten Ru-based units. The six peripheral Ru^{II} ions are easier to oxidize than the inner ones, because the terminal bpy ligands are better electron donors than the 2,3-dpp bridging ligands. As a result, a single six-electron wave is observed on oxidation, indicating the equivalence of the peripheral metal units. Oxidation of inner units was not observed up to +2.0 V in acetonitrile, presumably because of the large positive charge accumulated on the periphery [78].

In **31** the central unit is a Os^{II} moiety, which is easier to oxidize than the corresponding Ru^{II} moiety. As a result, on oxidation two waves are observed, accounting for one (central Os^{II} unit) and six electrons (peripheral Ru^{II} units). Compound **32** is made of an Os^{II}-based core, three Ru^{II}-based units in the intermediate positions, and six Os^{II}-based units in the peripheral positions. In this case a 6-1 pattern



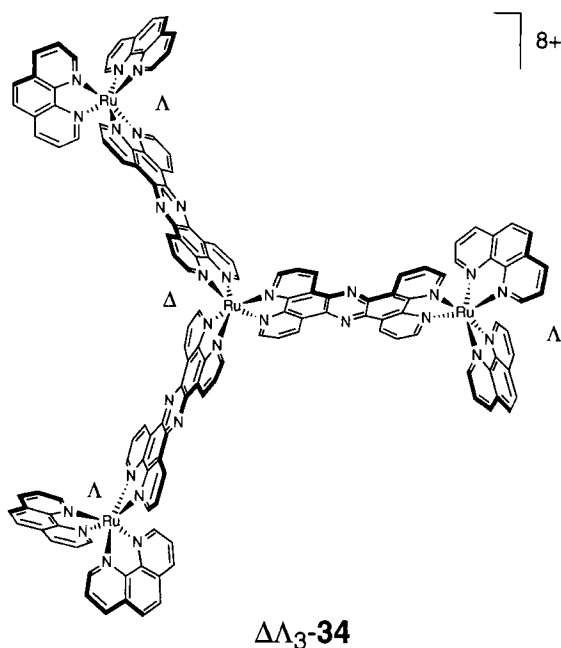
**33**

is observed on oxidation: the first wave involves the six peripheral Os^{II} -based units (which contain the stronger electron-donor bpy ligand in their coordination sphere), followed by the Os^{II} -based core. Oxidation of the intermediate Ru^{II} -based units is shifted to potentials inaccessible in acetonitrile solution because of their interaction with the already oxidized core and peripheral units [78].

In larger structures, the number of equivalent units becomes huge. In the doco-sanuclear dendrimer made of an Os^{II} -based core and 21 Ru^{II} -based units, a one-electron oxidation process, assigned to the Os^{II} -based unit, is followed by a 12-electron process, due to the simultaneous oxidation of the 12 equivalent and non-interacting peripheral Ru^{II} -based units [101].

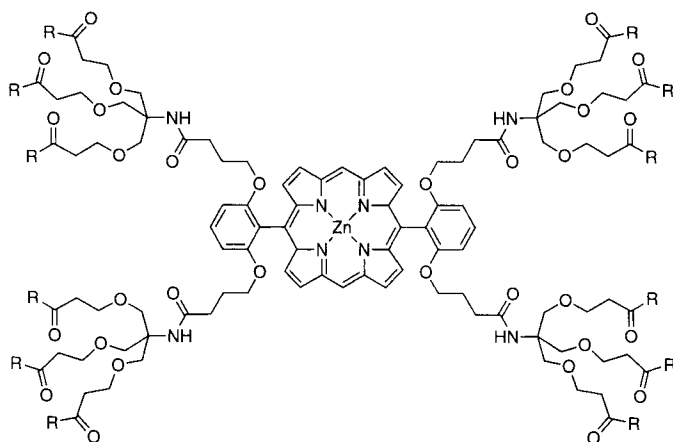
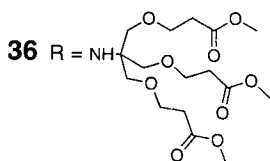
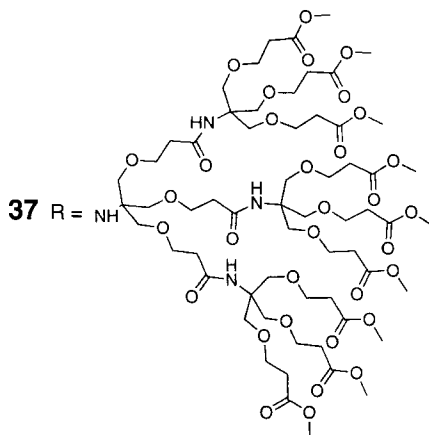
In this type of dendrimers the presence of many polypyridine ligands—each capable of several reduction processes—produces very complex reduction exchange patterns, with overlapping waves. In a smaller dendrimer as the hexametallic compound **33** it was possible to assign 26 reduction processes (in DMF at -54°C), that is all the reductions expected on the basis of the electrochemical behavior of the ligands present [110]. Oxidation of **33** up to $+4.3$ V versus SCE (in liquid SO_2) shows the presence of waves due to the metal units and also (above $+3.0$ V) to the bpy ligands, for a total of 14 electrons reversibly removed [104]. Thus, considering both cathodic and anodic processes, this compound gives rise to a redox series of 40 reversible one-electron processes, which is the largest one so far known for well-defined molecular systems.

Dendrimers based on octahedral metal complexes may be structurally not well defined because of the presence of several stereogenic centers [116]. Recently, the first examples of stereochemically pure tetrametallic Ru^{II} dendrimers have been described; compound **34** depicts the $\Delta\Lambda_3$ isomer [106]. On oxidation in acetonitrile, a three-electron wave due to the peripheral Ru^{II} units is followed by the mono-



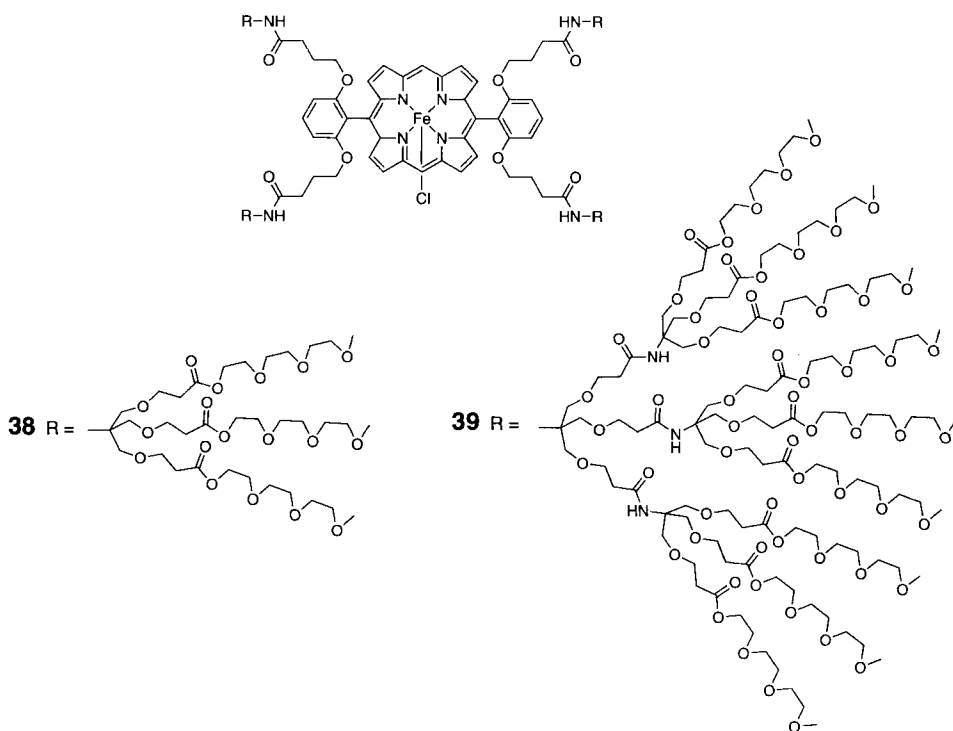
electronic oxidation of the central metal unit. On reduction, two trielectronic waves due to the bridging ligands and to the peripheral phen ligands (phen = 1,10-phenanthroline), respectively, are followed by other unresolved multielectron processes. The stereoisomers $\Lambda\Lambda_3$ and $\Delta\Delta_3$ were also examined, and their electrochemical (and also photophysical) behavior was indistinguishable from that of the $\Delta\Lambda_3$ isomer. Thus, in these compounds the stereochemical arrangement of the various redox units appears unimportant.

Electron transfer quenching processes in dendrimers containing metal-polypyridine units has been documented only in $[\text{Ru}(\text{bpy})_3]^{2+}$ -cored species. In dendrimers **21**, **22**, and **23** the luminescent $^3\text{MLCT}$ excited state of $[\text{Ru}(\text{bpy})_3]^{2+}$ was quenched using cationic (methylviologen, MV^{2+}), neutral (tetrathiafulvalene, TTF) and anionic (anthraquinone-2,6-disulfonate) species in acetonitrile solution [115]. Quenching takes place in all cases by a dynamic mechanism. In general, the values of the quenching rate constants decrease with increasing number and size of the dendritic branches. The greatest effect was observed with MV^{2+} : the quenching rate constant decreases by more than one order of magnitude on passing from the “naked” $[\text{Ru}(\text{bpy})_3]^{2+}$ complex to dendrimer **23**. Quenching of the luminescent $[\text{Ru}(\text{bpy})_3]^{2+}$ core by dioxygen was also observed in dendrimers **21–23** [115] as well in other [100, 113] dendrimers. It is found that the lifetime of the $[\text{Ru}(\text{bpy})_3]^{2+}$ core increases on increasing dendrimer generation, indicating a progressively increasing difficulty of dioxygen to reach the Ru-based core within the dendritic structure. Diminished interaction between dioxygen and the excited $[\text{Ru}(\text{bpy})_3]^{2+}$ complex in the presence of charged dendrimers has also been observed (see Section 9.5).

**35** R = OCH₃**36** R = NH**37** R = NH

9.4.3 Porphyrins and Phthalocyanins

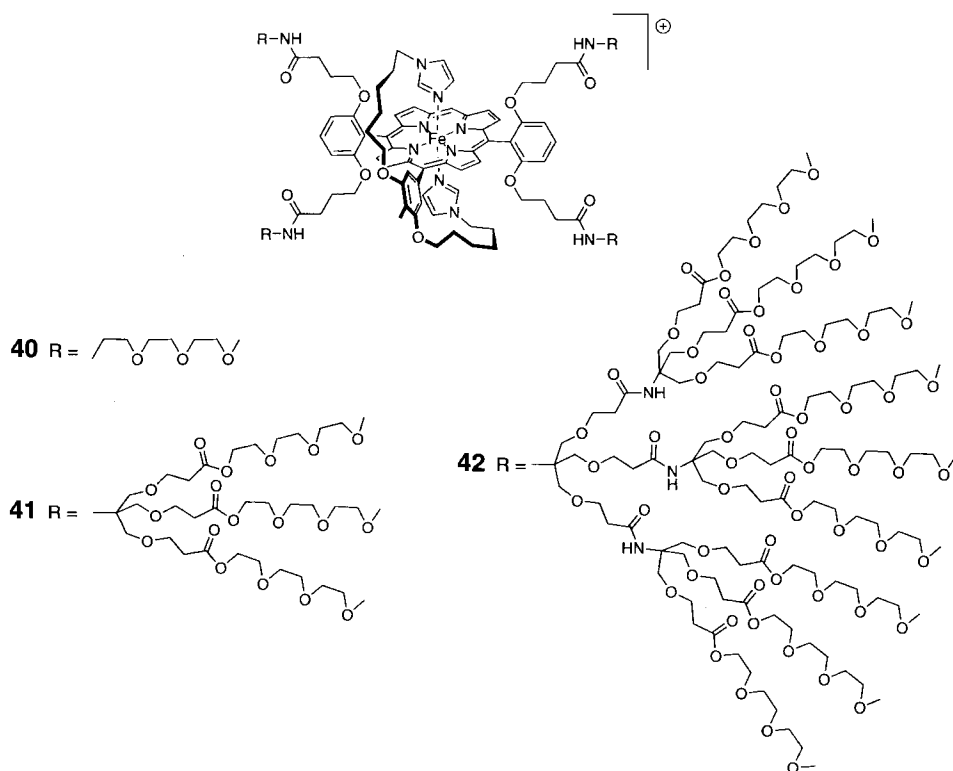
Various dendritic porphyrins were studied as functional mimics of globular electron transfer heme proteins [117–120]. Zn porphyrin has been used as a core to build dendrimers up to the third generation (compounds **35–37**) [117, 119]. Due to the poly(ether-amide) branches these compounds are soluble in organic solvents. The first-generation compound gives rise to two reversible monoelectronic reduction (in THF) and to two reversible oxidation processes (in CH₂Cl₂). By comparison to the model core, all of these processes are assigned to the macrocycle ring, the Zn²⁺ ion being electroinactive. On increasing the dendrimer generation all the observed potentials shift to more negative values, indicating that the branches induce an increasingly electron-rich microenvironment around the core. Moreover, with increasing dendrimer size the reversibility of all the observed redox processes



decreases, becoming irreversible in the third generation species **37**, as commonly happens for encapsulated redox units.

A better model for heme proteins was obtained by replacing the inactive Zn^{2+} ion with Fe^{3+} and using triethyleneglycol monomethyl ether surface groups to yield the water-soluble dendrimers of the first (**38**) and second (**39**) generations [118, 119]. Electrochemical oxidation of **38** and **39** in water occurs in one-electron irreversible processes, due to the macrocycle ring. On reduction, a first reversible process due to the $\text{Fe}^{3+/2+}$ couple is followed by a second irreversible wave due to the $\text{Fe}^{2+/1+}$ couple. Interestingly, whereas the potential for the $\text{Fe}^{2+/1+}$ couple is the same for the two dendrimers, the potential for the $\text{Fe}^{3+/2+}$ couple shifts about 420 mV towards more positive values on passing from **38** to **39**. This difference was attributed to the different environment around the iron core: whereas in the smaller dendrimer **38** the Fe^{3+} ion can be easily solvated by water, in **39** the denser dendritic structure reduces water access to Fe^{3+} , which is thus more destabilized relative to Fe^{2+} .

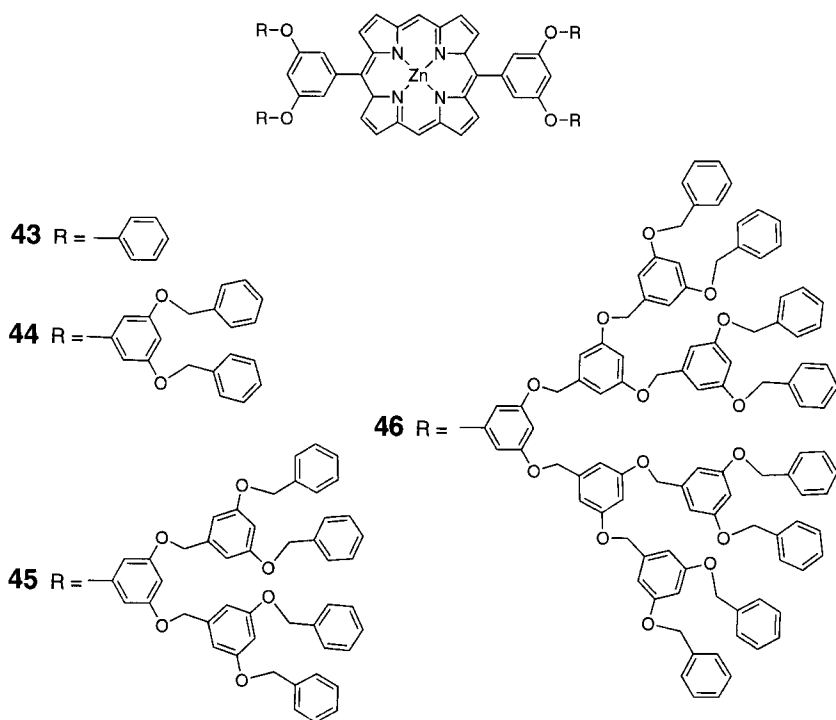
Very recently the iron porphyrin core has been modified in order to control the axial ligation to the iron center by means of two imidazoles tethered to the porphyrin ring [120]. The generation zero (**40**), one (**41**), and two (**42**) dendrimers have been prepared and the redox behavior of the $\text{Fe}^{3+/2+}$ couple has been examined in three solvents of increasing polarity, namely CH_2Cl_2 , acetonitrile, and water. The redox potential of the $\text{Fe}^{3+/2+}$ couple becomes more positive with increasing dendrimer generation, the process being reversible in all cases. For dendrimers **40** and



41 the potential value is solvent-dependent, increasing with increasing solvent polarity. Interestingly, for the larger dendrimer **42** the potential value is the same in all of the three solvents, indicating that the dendritic branches are dense enough to prevent solvent access to the iron core, which thus experiences a unique local microenvironment independently from the solvent. This shielding behavior is similar to that exercised by the peptide shell around the $\text{Fe}^{3+/2+}$ couple in cytochromes.

A compound where a porphyrin unit is linked to fullerene is described in Section 9.4.5.

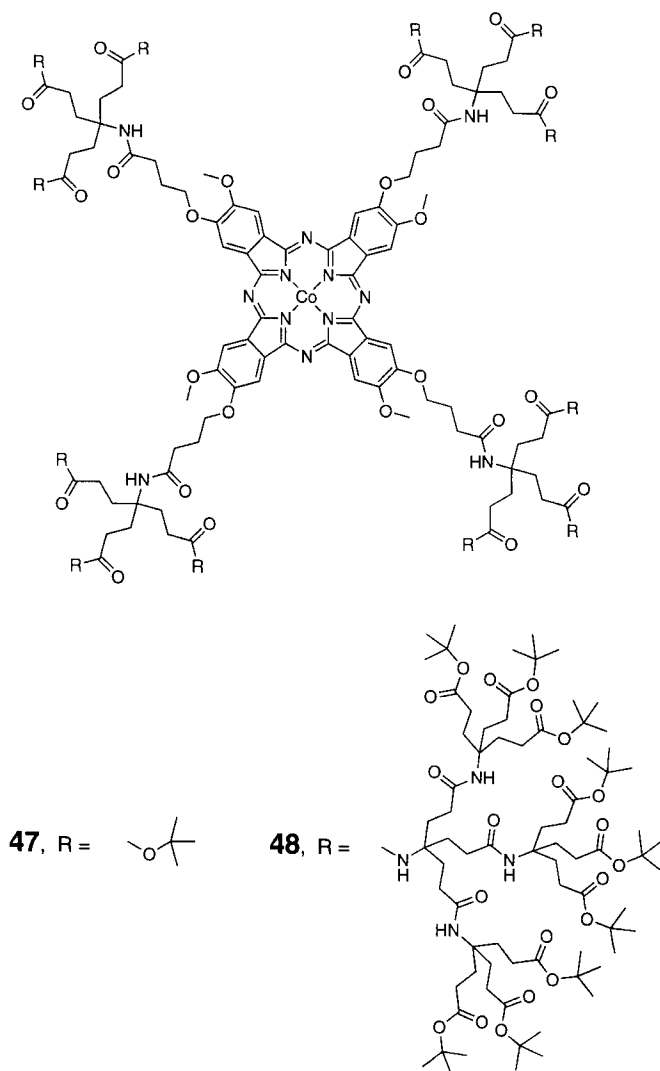
Zinc porphyrin has been also functionalized with a benzyl ether framework to obtain the dendrimers **43–46**, corresponding to generations 1–4 [121]. Electrochemical investigation was used to assess the rate of electron transfer between the electrode surface and the redox-active core. The smaller dendrimer **43** features four monoelectronic processes: the two oxidation waves (in CH_2Cl_2) and the first reduction wave (in DMF) are reversible, whereas the second reduction process is partially irreversible. Even in these compounds on increasing dendrimer generation the redox processes become more irreversible, complete irreversibility being reached with the third-generation species **45**. This effect is ascribed to the presence of the relatively rigid dendritic branches that hinder the approach of the core to the electrode surface.



Similar behavior has been very recently observed in cobalt phthalocyanines bearing dendritic substituents [122]. In **47**, Co^{II} is oxidized in methanol in a mono-electronic reversible wave, whereas in **48** no clear oxidative wave is observed, suggesting that the electroactive core is encapsulated in the dendritic structure. The ability of the Co-phthalocyanine core of **47** and **48** to catalyze oxidation of 2-mercaptoethanol in the presence of oxygen was also investigated. The two compounds exhibit similar catalytic activity, indicating that the dendritic structure does not hinder penetration of small molecules; **48** showed, however, an enhanced catalytic stability which was ascribed to the encapsulation of the core.

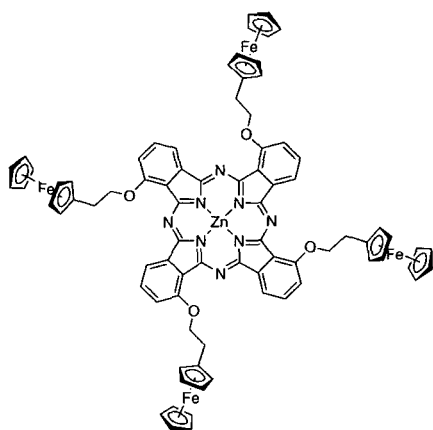
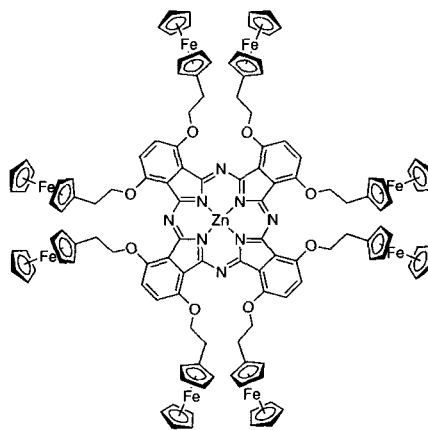
A phthalocyanine core was functionalized with four, eight, and 16 ferrocenyl units (compounds **49–51**) [67]. Cyclic voltammetry experiments in DMF or CH_2Cl_2 showed the presence of many quasi-reversible waves. All the ferrocenyl units behave independently, giving rise in all three compounds to a single oxidation wave, which is accompanied by one or two oxidation and by two or three reduction processes due to the phthalocyanine π -system. For **51**, the presence of a stripping peak indicates precipitation of the oxidized product in CH_2Cl_2 , as often observed in ferrocene-functionalized dendrimers (see Section 9.4.1).

Photoinduced electron transfer quenching of a porphyrin-cored dendrimer was first reported in compound **52**, where the fluorescence of the Zn core is quenched in acetonitrile by vitamin K_3 (2-methyl-1,4-naphthoquinone) [123].



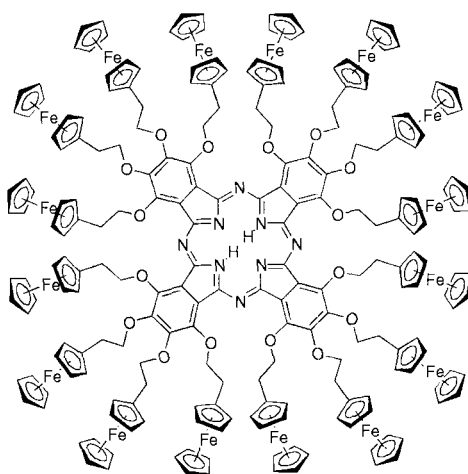
Later, generation 2 and 4 (**53**) water-soluble analogues were obtained [124]. In **53**, photophysical investigation showed that long-range photoinduced electron transfer *through* the dendrimer framework occurs between the encapsulated core and methylviologen molecules electrostatically interacting with the periphery of the dendrimer. In the generation 2 compound, on the other hand, quenching by methylviologen is much more efficient, because direct access to the core is possible.

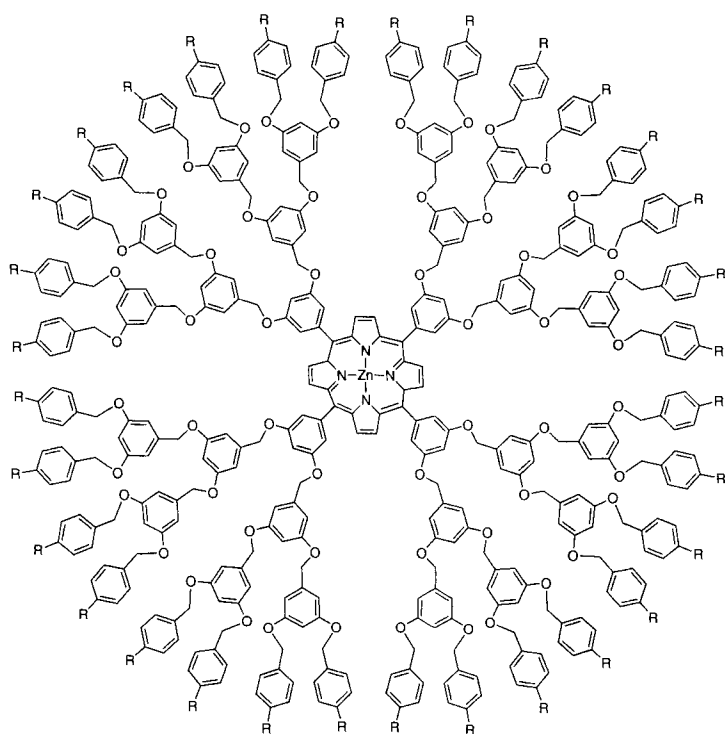
A similar quenching by methylviologen through the dendrimer architecture was also observed in the Zn-phthalocyanine-cored dendrimer **54** [125].

**49****50**

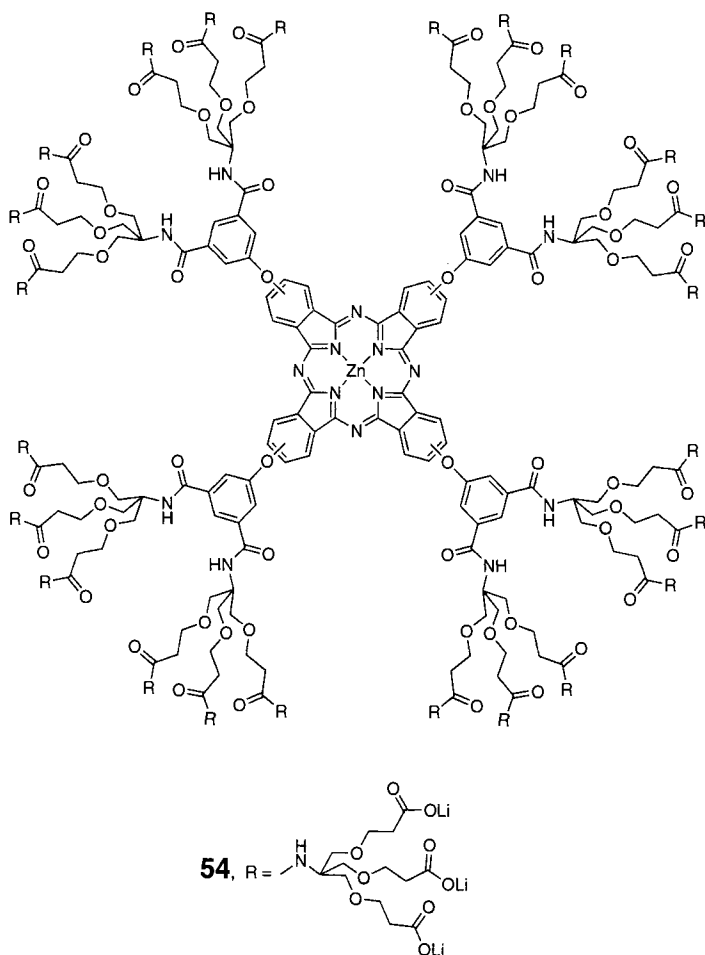
Electron transfer quenching of the excited metalloporphyrin core in compounds **43–46** was investigated in DMF using benzylviologen as electron acceptor [121]. The estimated electron transfer rate constants are similar in the four dendrimers, indicating that small molecules have no difficulties in approaching the porphyrin core. Thus, these porphyrin dendrimers may potentially be employed as catalysts.

The fluorescence of the zinc-phthalocyanine core in dendrimer **49** is completely quenched [67]. On the basis of energetic considerations, this quenching process was attributed to electron transfer from the connected ferrocenyl units to the excited phthalocyanine core. The photophysical behavior of **50** and **51** was not mentioned.

**51**

52, R = $-\text{O}-\text{CH}_3$ 53, R = $-\text{COOK}$

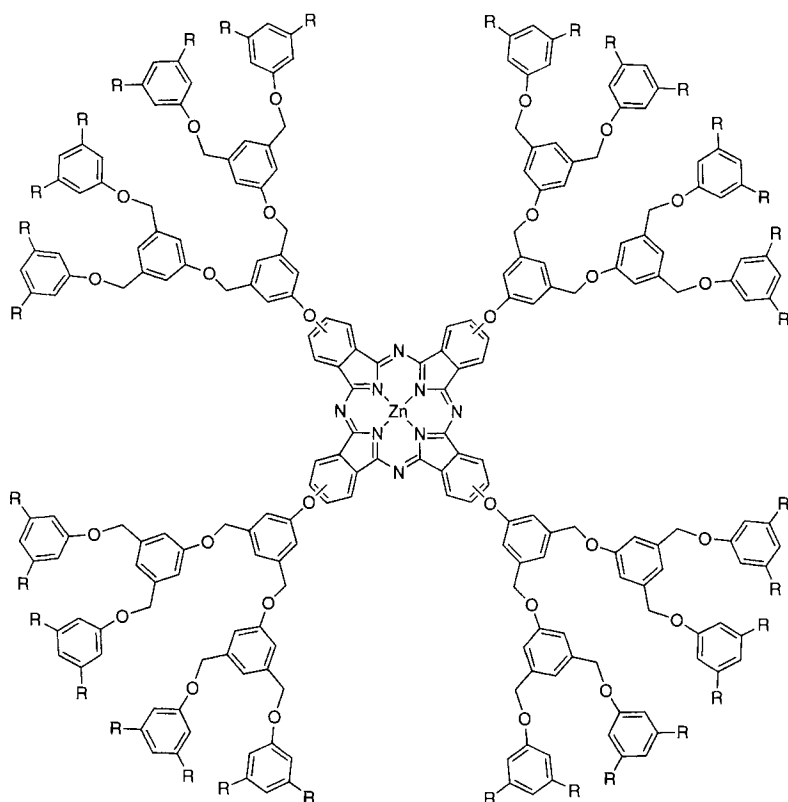
Two series of Zn-phthalocyanine dendrimers with aryl-ether branches were obtained as mixtures of constitutional isomers. Generation 0, 1, and 2 (dendrimer **55**) species, terminated with ester groups, are soluble in organic solvents, while the species terminated with carboxylate units (e.g., **56**), are soluble in water [126]. Photoinduced electron transfer quenching of the fluorescent core of the ester-terminated dendrimers was investigated using anthraquinone as electron acceptor. The quenching occurs through a dynamic mechanism, and the rate of the electron transfer process decreases with growing dendrimer size. The fluorescence of the core of the water-soluble series was quenched with anionic (picrate anion), and cationic (5,10,15,20-tetrakis(1-methyl-4-pyridyl)porphyrin) electron acceptors. With the picrate quencher, a sharp decrease of the bimolecular electron transfer rate constant is observed on increasing dendrimer generation, **56** being virtually unquenched. This behavior was ascribed to the highly negative dendrimer surface that repels electrostatically the picrate anion. In contrast, using the cationic quencher, the electrostatic interaction with the dendrimer results in a very efficient quenching through a static mechanism.



9.4.4 Tetrathiafulvalene

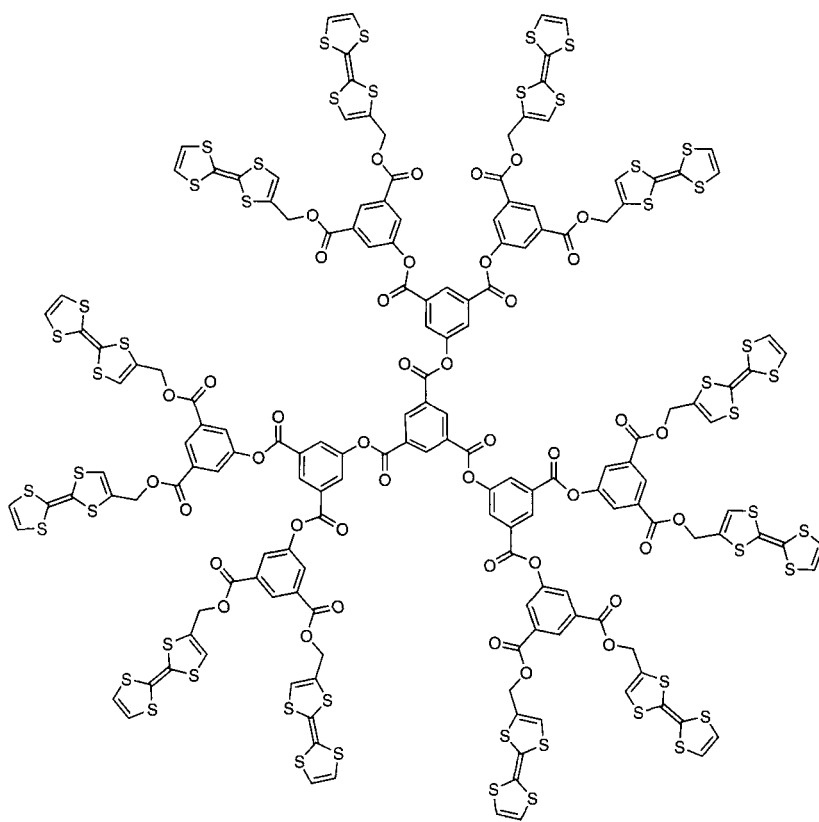
The tetrathiafulvalene (TTF) unit received attention owing to its possibility of being oxidized in two reversible monoelectronic steps at very accessible potential. Three generations of polyaryl-ester dendrimers containing three, six, and 12 (compound **57**) TTF units at the periphery were prepared, and their redox behavior examined in acetonitrile solution [127]. In each of the three dendrimers the TTF units are oxidized at the same potential in two multielectronic processes, indicating that they are noninteracting. Chemical oxidation of the TTF units in the three dendrimers was also achieved using iodine. Analogous results were obtained in other dendritic structures [128, 129].

The TTF unit was used also as core in dendrimers **58** and **59**, containing respectively four and 12 additional TTF units along the branches [130]. In both com-

**55**, R = COOC₅H₁₁**56**, R = COONa

pounds electrochemical oxidation in benzonitrile features the typical two redox reversible processes due to each TTF unit, indicating that all of these units behave independently, irrespective of their topological position. By applying for the first time to redox-active dendrimers the thin-layer cyclic voltammetry (TLCV) technique, it was also possible to measure the number of electrons exchanged in each oxidation wave, the result being five and about 13 for **58** and **59**, respectively, in CH₂Cl₂ solution. Thus, each TTF unit is oxidized simultaneously in both dendrimers.

Asymmetric functionalization was achieved in the two dendrimers **60** and **61**, which contain two branches terminated with electron-donor TTF units and one branch terminated with electron-acceptor anthraquinone (AQ) units [131]. Cyclic voltammetric investigation in acetonitrile showed that each of these electroactive units are noninteracting, giving rise to two waves on oxidation (due to TTF) and to two waves on reduction (due to AQ). The number of electrons exchanged in each of



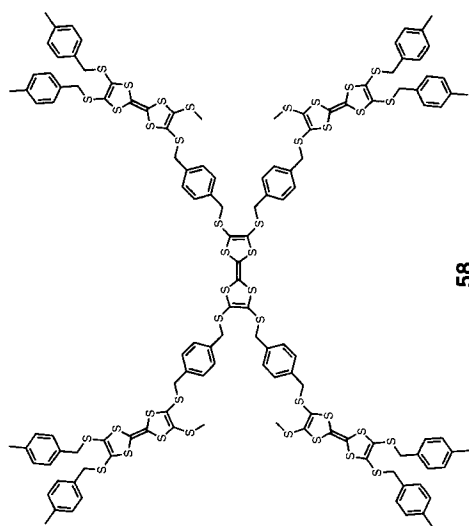
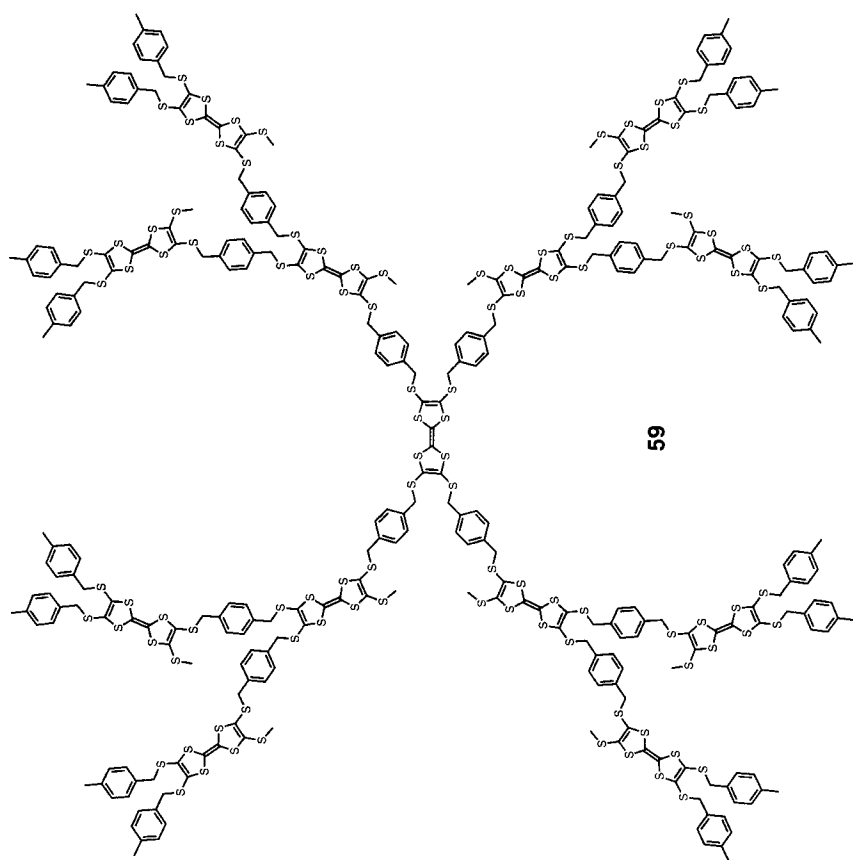
57

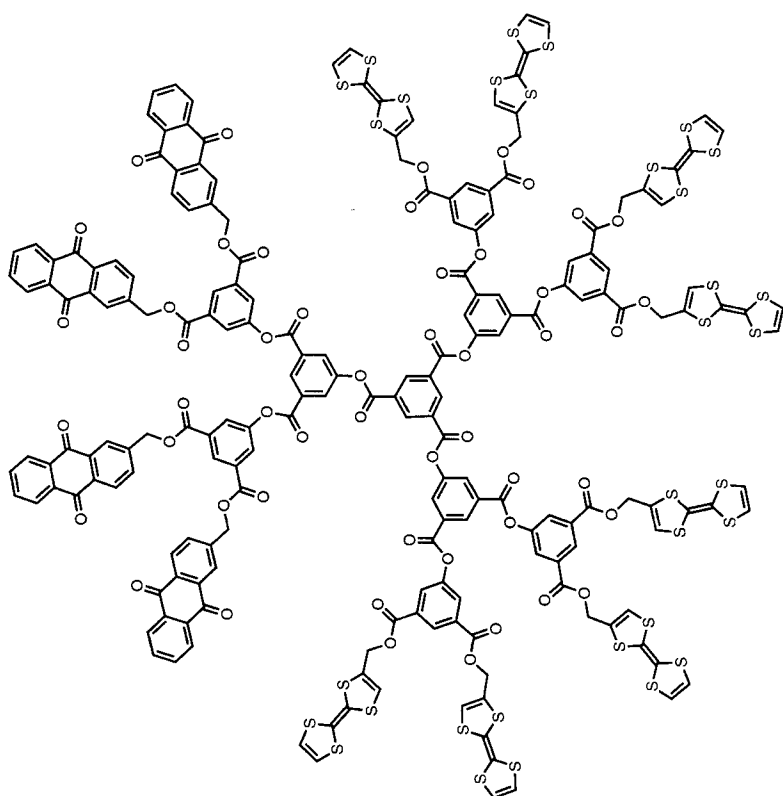
these reversible processes corresponds to the number of redox-active units present. Thus, these compounds can be switched reversibly between cationic and anionic states under electrochemical control; for example **60** can be switched between the +8, +4, 0, -2, and -4 states.

9.4.5 Fullerene

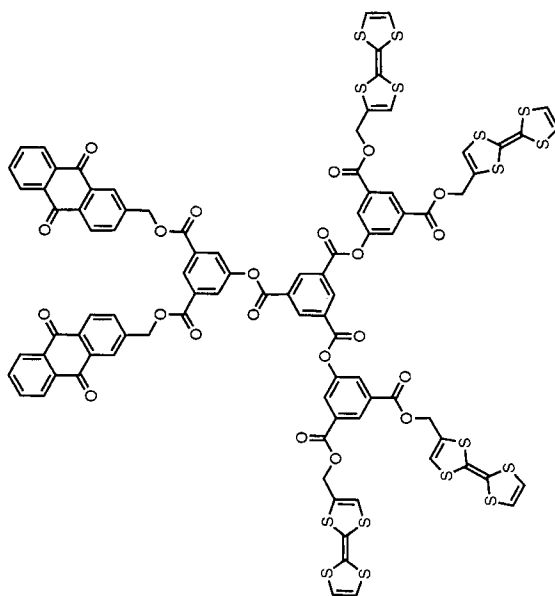
Fullerene has also been incorporated in redox-active dendrimers. In **62** the C_{60} unit has been modified by connecting a single polyaryl-ether dendritic branch [132]. Electrochemical reduction in CH_2Cl_2 of **62** features three reversible waves, which occur at a potential more negative than that of the free C_{60} molecule. This shift was ascribed to an insulating effect on the connected dendritic structure.

Starting from the fullerene-porphyrin dyad **63**, dendrimers **64** and **65** (generations 1 and 2) were obtained adding five dendritic branches to the remaining octahedral positions of C_{60} [133]. The π -system of fullerene is disrupted by the

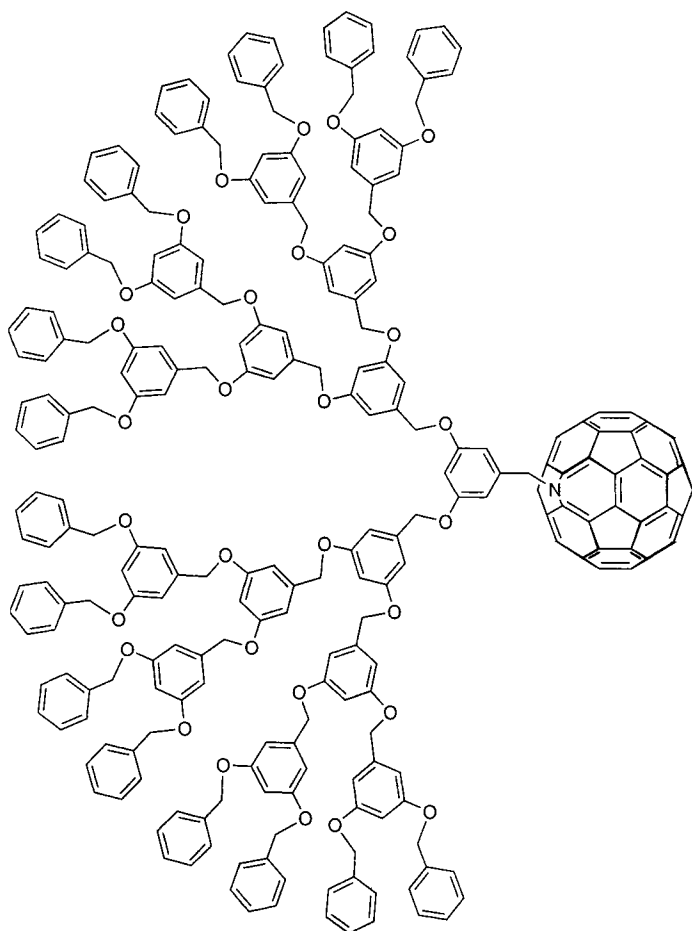




61

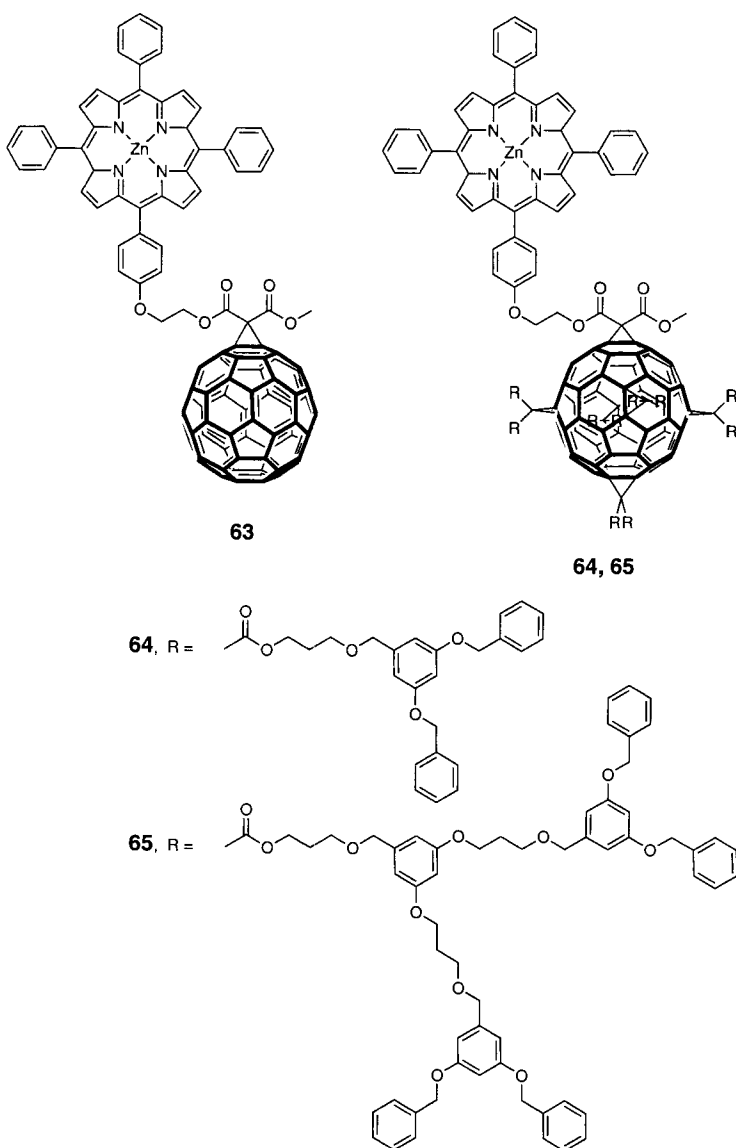


60



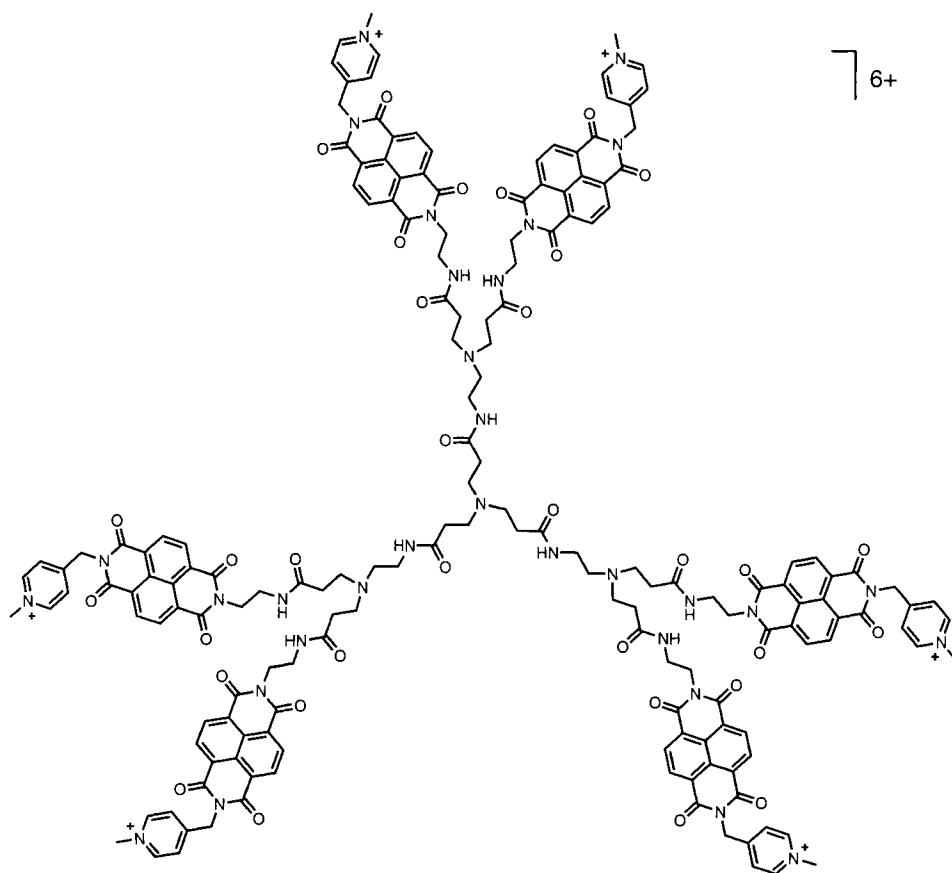
62

added units, so that its reduction in CH_2Cl_2 occurs in a single irreversible process at more negative potential with respect to the unsubstituted C_{60} . A further reduction process is observed, due to the porphyrin ring. On oxidation, two processes occur, also attributed to the Zn-porphyrin unit. Only the reduction waves are dendrimer generation-dependent, shifting to more negative potential on increasing dendrimer size. Quenching experiments of the Zn-porphyrin fluorescence were also performed. In dyad **63**, electron transfer quenching is observed, the C_{60} acting as electron acceptor. In contrast, in dendrimers **64** and **65**, no electron transfer occurs, due to the fact that the electron-accepting properties of C_{60} are greatly reduced in these species, as indicated by the electrochemical data.



9.4.6 Naphthalene Diimide

The naphthalene diimide electroactive unit was used to functionalize poly(amidoamine) dendrimers up to the sixth generation [134]. Compound **66** illustrates the first-generation dendrimer, containing six peripheral diimide units; in the sixth generation dendrimer the peripheral units number 192. Cyclic voltamme-

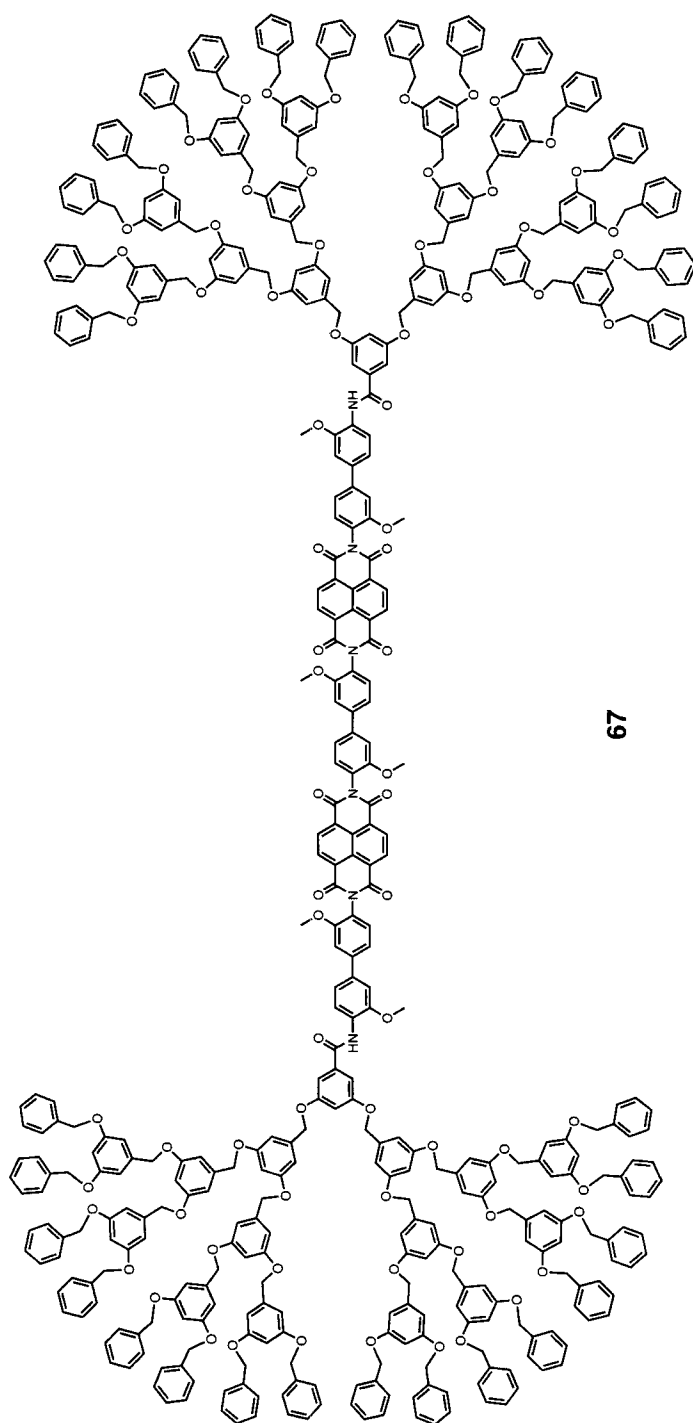


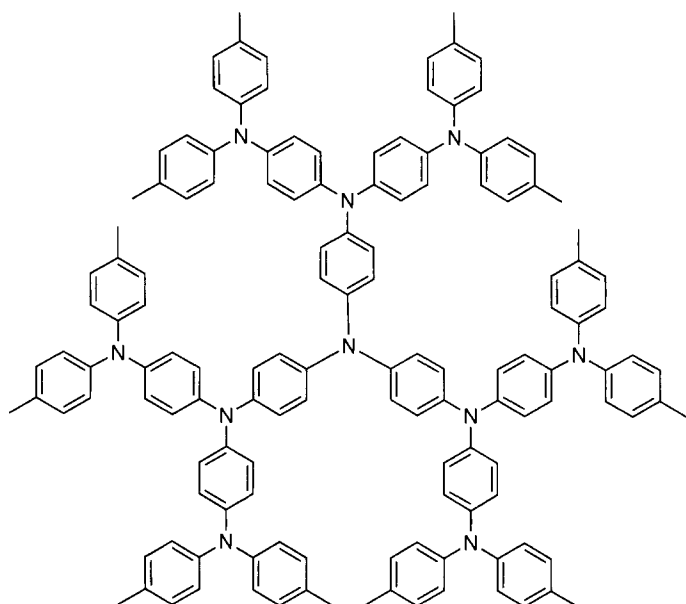
66

try in aqueous or DMF solution identifies two reduction processes, whose potential is independent from the dendrimer generation, while coulometry experiments indicate the exchange of one electron per imide group in both waves. The first reduction wave is very broad, indicating that the diimide units are not independent, probably because of π -stacking aggregation.

Generations 1–5 of dendrimers such as **66** were reduced with sodium dithionite in water or formamide to yield the diimide anion radicals [135, 136]. These reduced species were used to produce films that constitute the first example of electrically conducting dendrimers.

Dendrimer **67** contains two naphthalene diimide electroactive units in the core [137]. Electrochemical investigation in DMF showed the presence of two reversible bielectronic reduction processes at the potential typically featured by other naphthalene diimide-containing compounds. Thus, the two units behave independently and can be readily accessed from the electrode surface. The lack of encapsulating



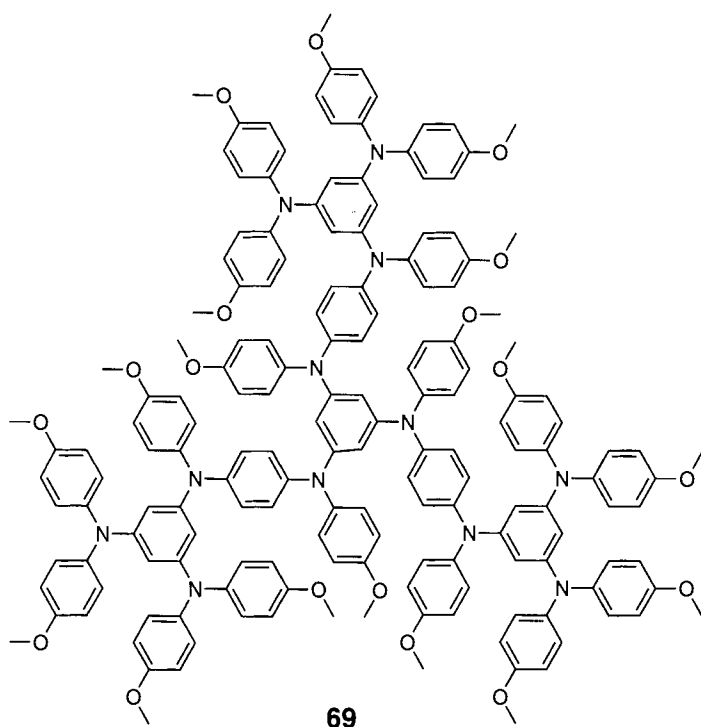
**68**

effect is ascribed to the structure of the core, which is rather long and rigid, and cannot be surrounded by the dendritic branches.

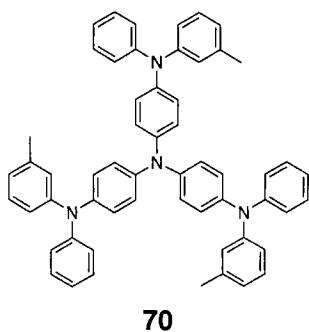
9.4.7 Triaryl Amines

Cyclic voltammetry in THF of the triarylamine-based dendrimer **68** indicated the presence of at least four unresolved waves, giving rise to delocalized radical cations [138].

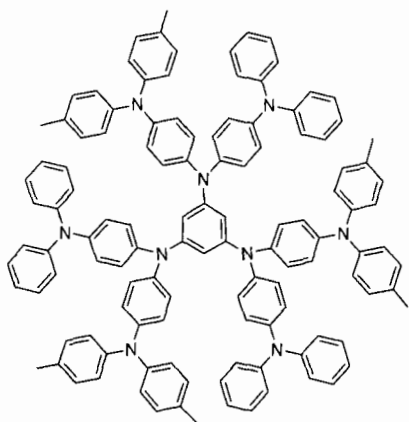
Dendrimer **69** contains different electroactive units arranged in order to obtain a radial redox gradient [139]. Three *p*-phenylenediamine units are located around the benzene core; these moieties are oxidized in two reversible waves in CH_2Cl_2 , corresponding to one- and two-electron processes. At more positive potential a reversible three-electron wave is observed, and assigned to the uncoupled peripheral arylamino groups. Further oxidation processes were also observed, but not discussed. Chemical oxidation of **69** was accomplished with NOPF_6 , and the self-exchange electron transfer rate between the neutral/cation phenylenediamine couple was measured in mixtures of 69/69^+ . The value obtained, $k_{\text{et}} = 1.8 \times 10^{-5} \text{ M}^{-1} \text{ s}^{-1}$ in CDCl_3 at 25°C , is 10^3 – 10^4 times lower than the self-exchange rate in model *p*-phenylenediamine compounds, indicating that the dendritic structure imparts a significant kinetic barrier to the intermolecular electron transfer exchange.



Several articles have addressed the possibility of using dendritic molecules as electroluminescent materials in organic light-emitting diodes (LEDs) [140–148]. For example, compound **70** works as an excellent hole transport material, and has been incorporated into multilayer devices that exhibit high luminance efficiency and significant thermal stability [140, 141, 144].



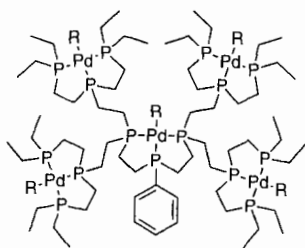
Another compound used in multilayer organic LEDs is dendrimer **71** [143], the electrochemical oxidation of this molecule having also been investigated in CH_2Cl_2 solution. A series of six reversible waves is observed, accounting for a total of nine

**71**

electrons removed, thus indicating that multiple electrons can be exchanged at the same potential. Another example of dendrimer used in LED devices is compound **90** (see Section 9.4.8).

9.4.8 Other Electroactive Units

Electroactive *palladium units* were incorporated in a series of dendrimers starting from a phosphorus–ethylene framework [149]. Compounds **72** and **73** depict two of the largest structures prepared. Cyclic voltammetry in DMF of **72** features a quasi-reversible cathodic wave assigned to two-electron reduction occurring at each palladium atom. In contrast, for **73** the cyclic voltammogram shows ill-defined, broad waves. Interestingly, the acetonitrile-containing dendrimers such as **73** were found to catalyze the electrochemical reduction of CO_2 to CO , with rates and selectivities similar to those seen with analogous monometallic complexes.

**72**, R = PEt_3 **73**, R = CH_3CN

Aryl-ether-based dendrons were used as stoppers in a series of rotaxanes containing one to three *bipyridinium units* surrounded by polyether macrocycles (compounds **74–76**) [150]. Electrochemical investigation in acetonitrile shows that a first reversible cathodic wave is due to the bipyridinium units, which are all reduced simultaneously and independently at the same potential. Electrode adsorption problems prevented accurate measurements for a second reduction process, also due to the bipyridinium units. On oxidation, two not fully reversible processes are observed, involving both the polyether macrocycle surrounding the bipyridinium units and the dioxybenzene units of the dendritic stoppers.

The inorganic *iron–sulphur cluster* $[\text{Fe}_4\text{S}_4(\text{SR})_4]^{2-}$ was used as a core to build the polyaryl-ether dendrimers **77–80**, corresponding to generations 1–4, respectively [151, 152]. The iron–sulphur core is electroactive, giving rise to a quasi-reversible monoelectronic reduction process in DMF solution. On increasing dendrimer generation the reduction potential moves to more negative values and the electron exchange becomes more irreversible, indicating that the electroactive center is progressively encapsulated by the dendritic structure.

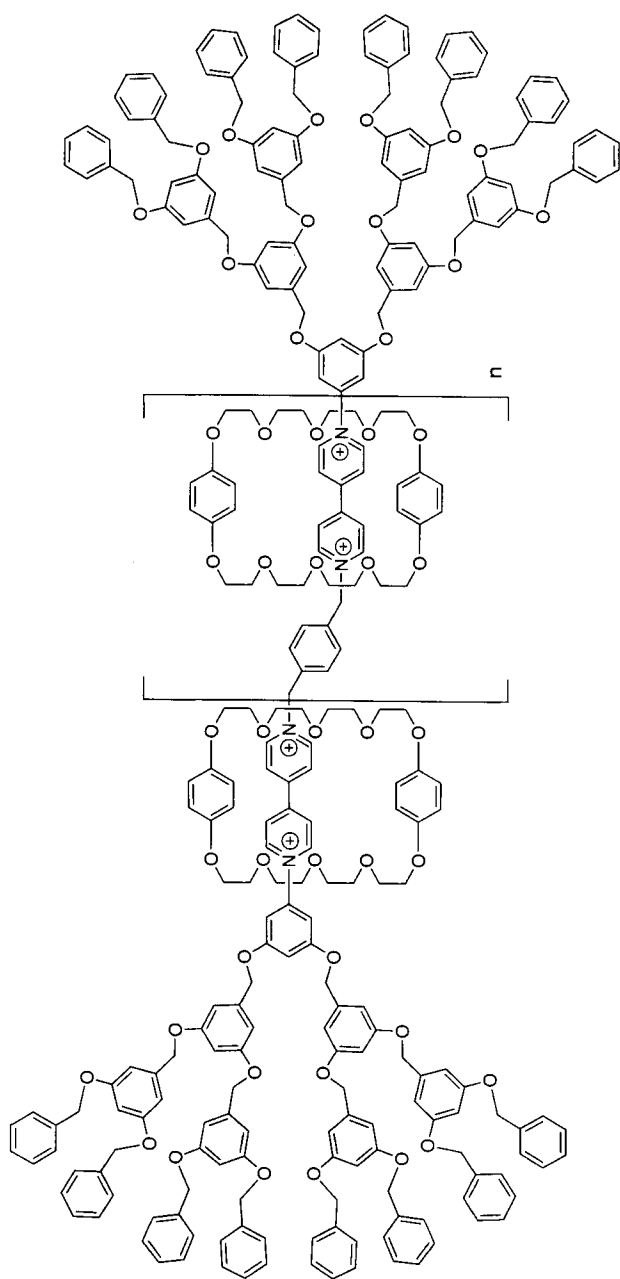
Very few cases exist where the electroactive units are located along the branches of the dendrimer. One example is represented by compound **81**, where four *anthraquinonoid units* are located near the core, with connected dendrons pointing outside [153]. Cyclic voltammetry experiments in acetonitrile showed that the four electroactive units are essentially noninteracting. The increasing irreversibility of the reduction waves with increasing dendron generation indicates a progressive encapsulation of the electroactive units.

A *tetrathienylenevinylene* core was used to obtain the dendrimers **82–84** (generations 1–3, respectively) [154]. Oxidation in CH_2Cl_2 of the electroactive core occurs in two reversible monoelectronic processes, with identical cyclovoltammetric waves for compounds **82–84**. The absence of any effect of the dendrimer generation indicates that the electroactive core is not encapsulated in the dendritic structure, as is commonly observed. The authors suggest that in this case the redox-active core is too long to be completely surrounded by the dendritic branches.

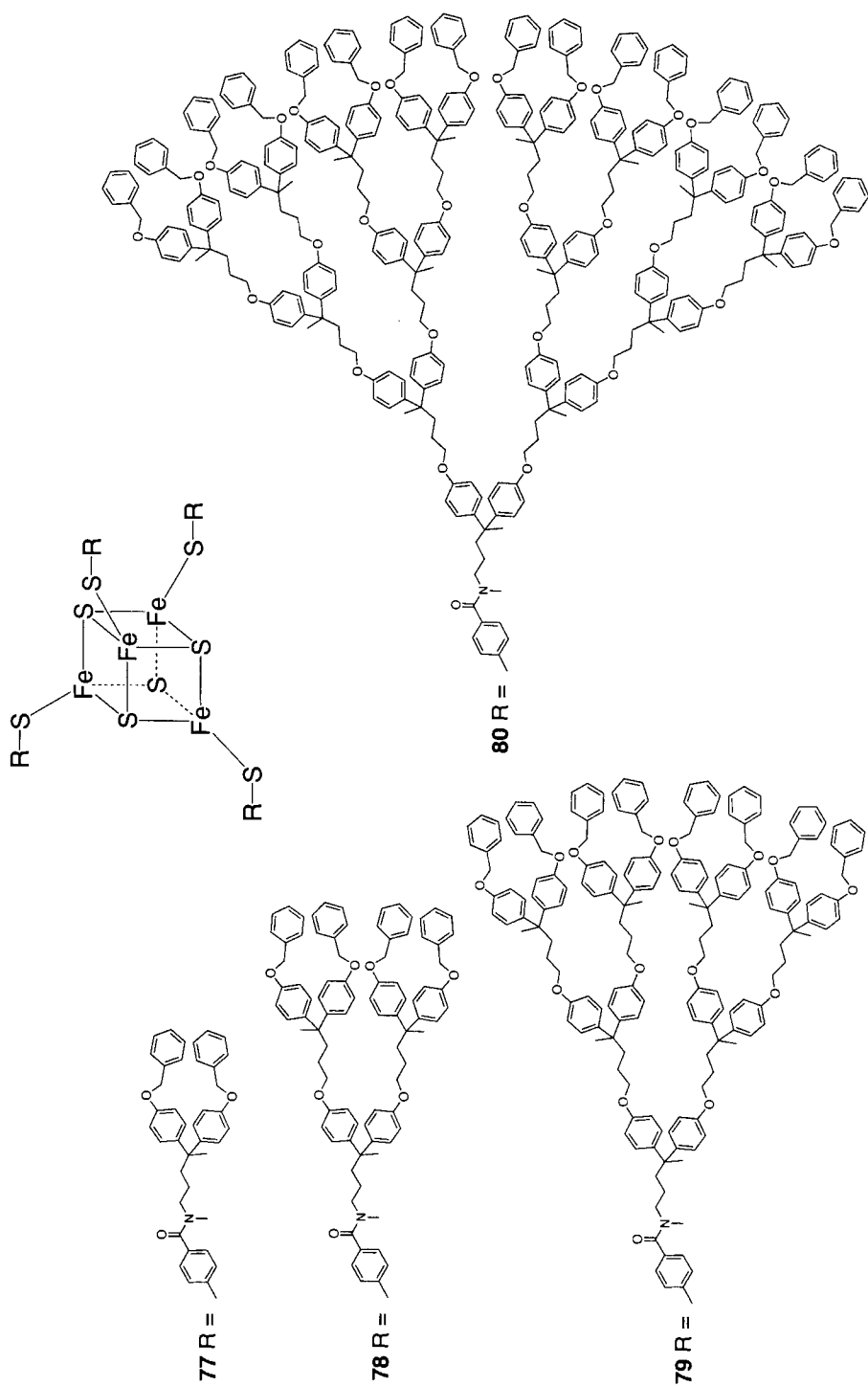
Very recently, poly(amidoamine) dendrimers were surface-functionalized with four, eight (**85**), 16, and 32 *nitroxyl radical units* [155]. In all these dendrimers electrochemical oxidation in acetonitrile of the appended radical units occurs at the same potential in a single reversible process, the number of exchanged electrons being equal to the number of units present. Thus, all the nitroxyl radical fragments in the dendrimer behave independently and are accessible from the electrode surface.

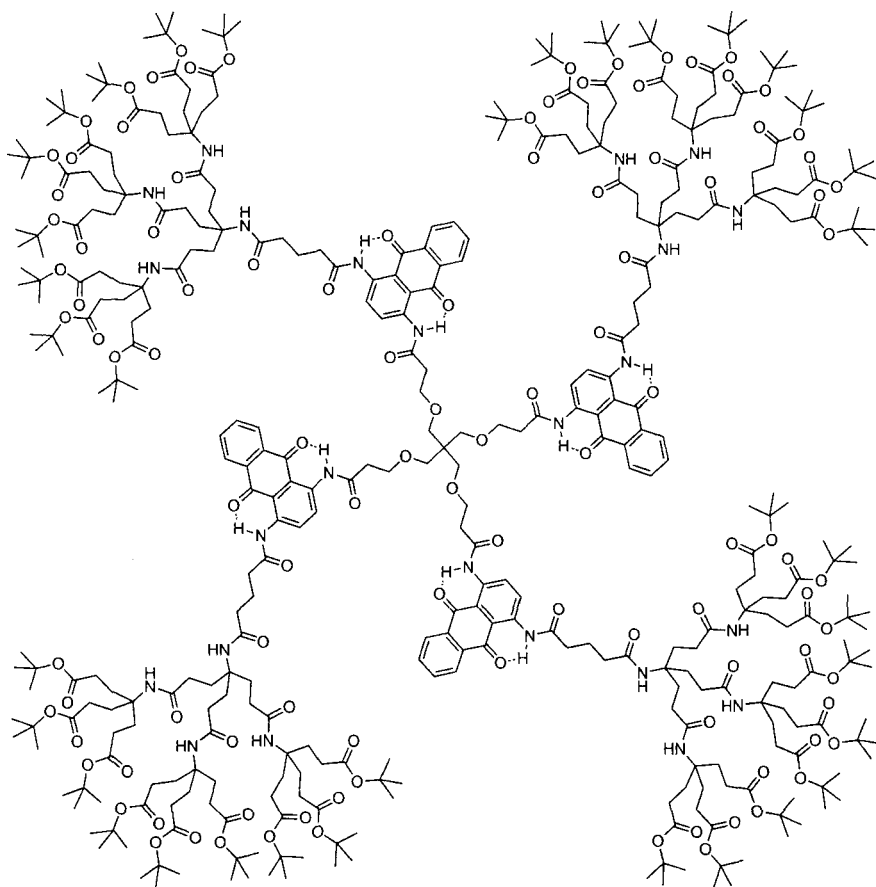
Dendritic branches of generations 1–3 (**86**) were built using aryl imides and a [5]helicene derivative [156]. In the three compounds a first reversible reduction in DMF, attributed to the *anhydride–imide* unit, is followed by a second process, assigned to the *o-terphenyl* moieties. The number of exchanged electrons was not measured. The second process, which is irreversible in the generation 1 species, becomes reversible in compounds of generations 2 and 3, suggesting that in the larger dendrimers the reduced species is stabilized by interaction with other *o-terphenyl* units.

The first investigation on photoinduced intramolecular electron transfer between units covalently attached to a dendritic framework was performed on a series of



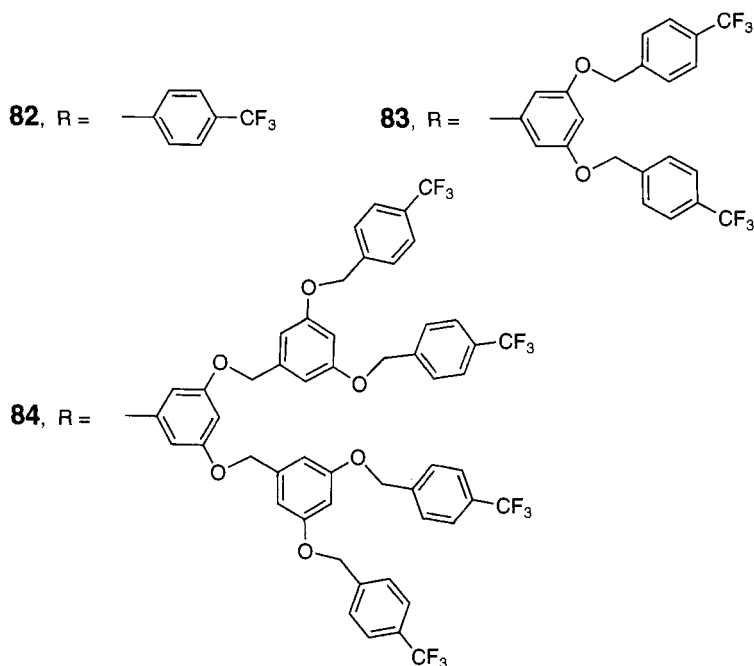
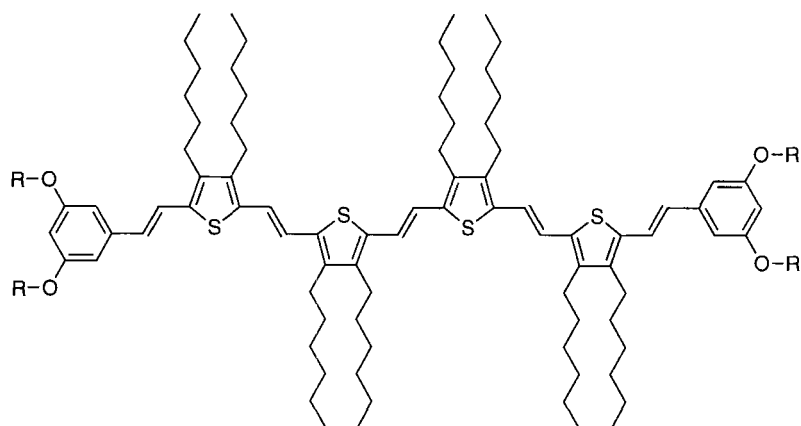
74, $n = 0$; **75**, $n = 1$; **76**, $n = 2$



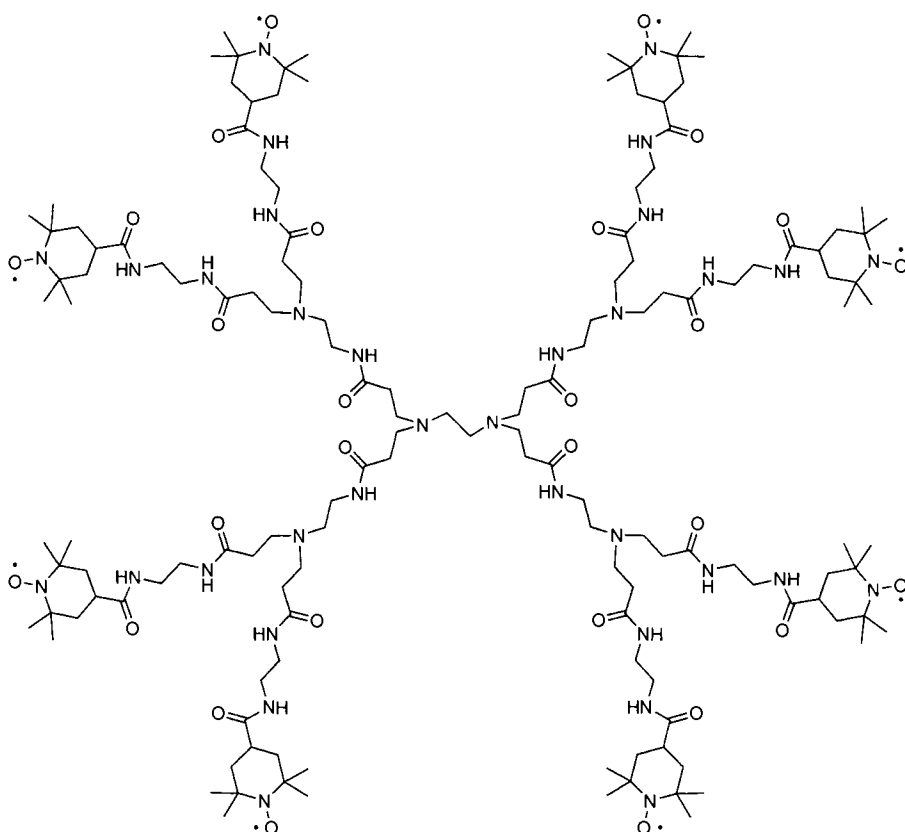
**81**

poly(arylether) dendrimers [157]. Compound **87** illustrates one of the largest dendrimers investigated. The peripheral excited states of *naphthyl* or *pyrenyl* chromophores are quenched by *triethylamino* or (*dimethylamino*)*phenoxy* groups, which play the role of electron donors. The efficiency of the process is function of dendrimer size and of solvent polarity (CH_2Cl_2 , THF, and acetonitrile were tested). As substantial electronic coupling exists within the dendrimer between chromophores and quenchers, these compounds appear promising as light-energy harvesters (see Volume V, Part 1, Chapter 7). Bimolecular quenching experiments were also performed using amines that were not connected to the dendrimer structure.

Intramolecular charge transfer interaction was investigated between *diphenylacetylene* electron donor groups and the *p*-*dimethoxybenzene* moiety in dendrimers of generations 1–6 [158]. Compound **88** illustrates the second generation species. Anomalous shifts of the emission spectrum (depending on the dendrimer generation and on the solvent used) suggested that a sudden change on size and shape of the dendrimer occurs, starting from the fifth-generation species.



Poly(propyleneamine) dendrimers of generations 1 and 4 (**89**) functionalized with azobenzene groups were investigated as hosts for eosin Y (eosin = 2',4',5',7'-tetrabromofluorescein dianion) in DMF solution [159]. The peripheral azobenzene groups can be switched by light excitation from the *E* to the *Z* form. The fluorescent excited state of eosin is reductively quenched by the *tertiary amine* units present in the dendrimer structure. This electron transfer quenching takes place with a static

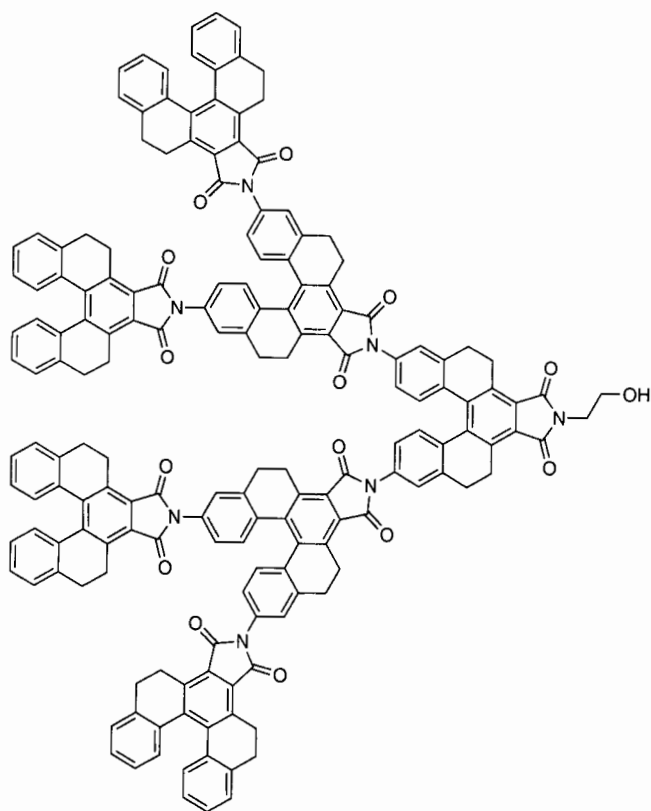


85

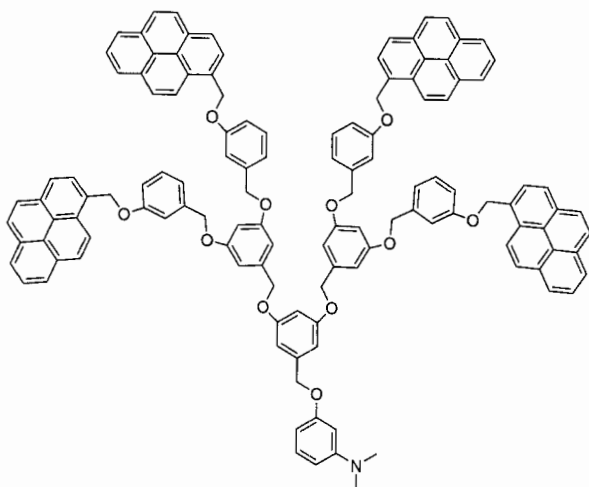
mechanism, indicating that the quenchable eosin molecules are hosted inside the dendrimer. It was also found that eosin is quenched (and thus, hosted) more effectively when the peripheral azobenzene groups are in the *Z* form.

Various generations of dendrimers based on *phenylenevinylene* units were incorporated into LED structures [145, 148]. Compound **90** depicts a second-generation species. The efficiency of the LED device depends on dendrimer generation, the maximum in efficiency being reached with the second-generation dendrimer **90**. By substituting the distyrylbenzene core with porphyrin or anthracene units, it is also possible to tune the electroluminescence emission in the blue, red, and green regions of the spectrum [146]. Other dendrimers used in LED fabrication can be found in Section 9.4.7.

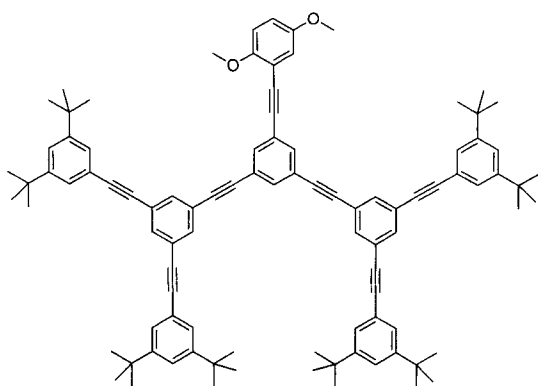
Finally, the ability of dendrimers to mediate electron transfer reactions has also been examined from a theoretical viewpoint [160, 161]. The electronic coupling in idealized dendrimers is predicted to be simply a function of the number of branches occurring at each branching point. The peculiar connectivity within the dendritic structure gives rise to hot and cold spots for electron transfer on the surface of the dendrimer—a behavior similar to that expected for the surface of proteins.



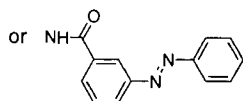
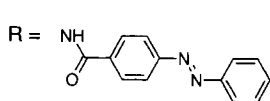
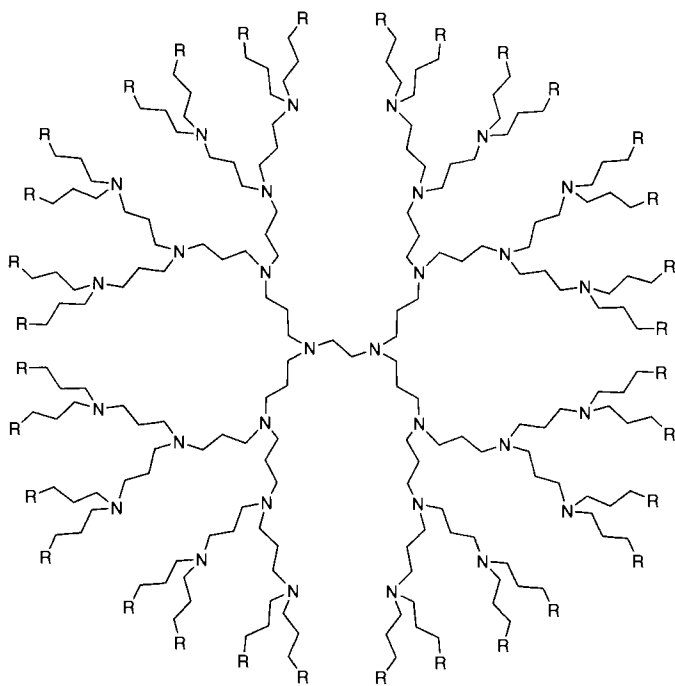
86



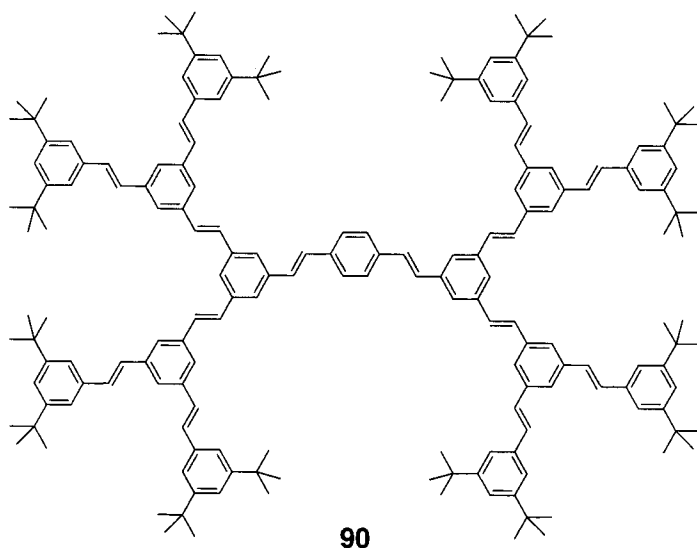
87



88



89



9.5 Electroinactive Dendrimers

This section describes cases where the dendrimer itself does not contain any electroactive unit, but is instead used as a “medium” to host species involved in electron transfer reactions.

Various generations of poly(amidoamine) dendrimers have been surface-terminated with carboxylate groups to investigate the effect of the negatively charged surface on the reactivity of small cationic molecules [162–167]. Compound **91** exemplifies a 2.5-generation dendrimer (this is a half-generation species on the basis of the dendrimer nomenclature). The photophysical properties of $[\text{Ru}(\text{bpy})_3]^{2+}$ or $[\text{Ru}(\text{phen})_3]^{2+}$ were investigated in the presence of these negatively charged dendrimers. In air-equilibrated aqueous solution, the excited Ru complex is quenched by oxygen [162, 163, 165, 167]. It is observed that the lifetime of the excited Ru complex increases on increasing dendrimer generation; this behavior has been related to a decrease of oxygen concentration near the dendrimer’s surface. Note that, by contrast, in dendrimers containing a $[\text{Ru}(\text{bpy})_3]^{2+}$ core dioxygen quenching is prevented because the branches encapsulate the luminescent complex (see Section 9.4.2).

Photoinduced electron transfer between photoexcited $[\text{Ru}(\text{bpy})_3]^{2+}$ (or $[\text{Ru}(\text{phen})_3]^{2+}$) and a variety of quenchers was also investigated in aqueous solution [162–167]. Different results were obtained depending on dendrimer generation. For example, with methylviologen as quencher in the presence of smaller poly(amidoamine) dendrimers (up to generation 2.5), the electron transfer process occurs with a bimolecular mechanism where the excited Ru complex is quenched outside the

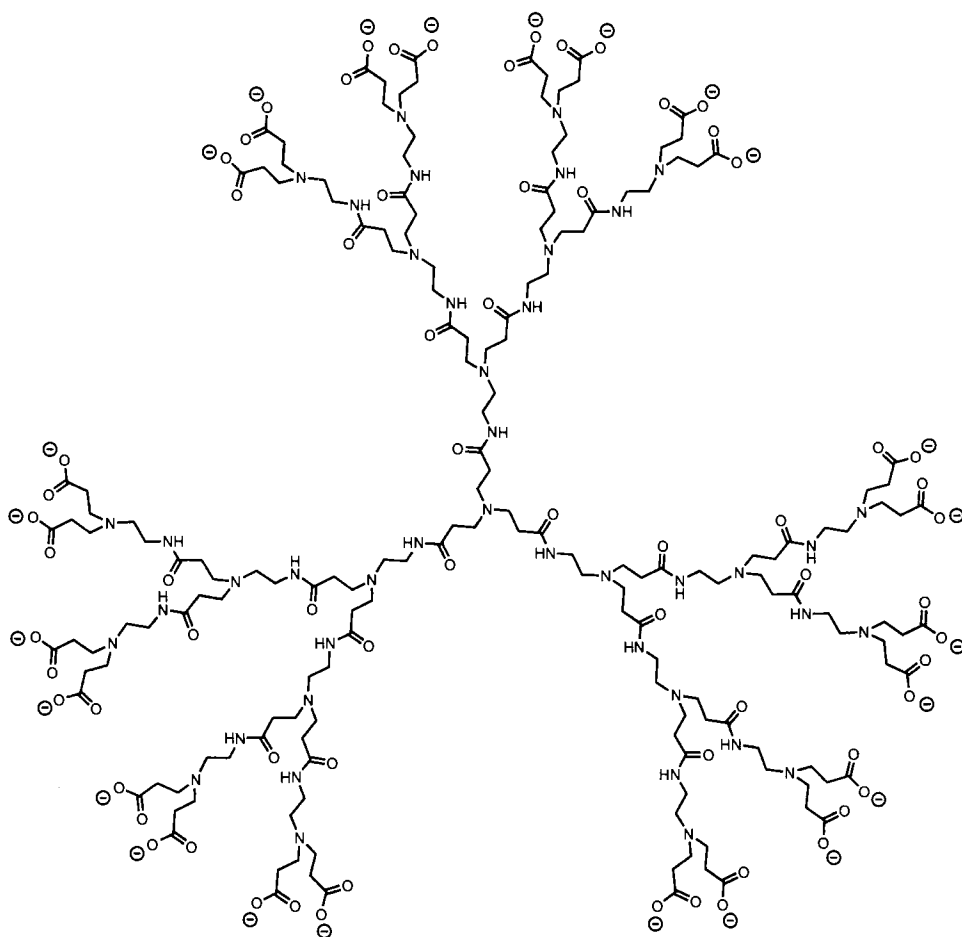
dendrimer surface. This is consistent with the notion that these dendrimers possess a open-surface structure, and their size is too small to host on their surface the two reaction partners. With higher generation (>3.5) dendrimers the quenching mechanism becomes monomolecular, indicating that the electron transfer quenching occurs while both partners are adsorbed on the dendrimer's surface. This behavior is related to the more closed and spherical surface structure of these later-generation dendrimers. Experiments performed using other cationic or anionic quenchers such as $[\text{Co}(\text{phen})_3]^{3+}$ [165, 166], and $[\text{Fe}(\text{CN})_6]^{4-}$ [162–164] substantiated this picture. Moreover, the photophysical properties of *anionic* Ru–polypyridine complexes in the presence of positively charged poly(amidoamine) dendrimers (terminated with protonated amine groups) were also studied, with similar results [168]. A statistical analysis of these quenching processes occurring at the surface of dendrimers has also been performed [166].

Poly(amidoamine) dendrimers such as **91**, which differ only in the presence of an ethylenediamine (instead of ammonia) core, were used to host the electron transfer reaction between photoexcited polycyclic aromatic hydrocarbons (PAHs) and nitromethane [169]. Quenching studies in aqueous solution indicate that the PAHs associate with the dendrimer, residing in the interior region, far from the charged surface. It was also found that within the dendrimer structure, nitromethane quenches alternant PAHs, while nonalternant PAHs are not quenched. This selective behavior of nitromethane parallels that commonly observed in solution, while in the presence of traditional micelles both classes of PAHs are quenched by nitromethane.

Poly(amidoamine) dendrimers of the fourth generation with $-\text{OH}$ terminal groups were used as templates to produce stable metal nanoparticles [170–172]. The dendrimers (in aqueous solution) are first loaded with a predetermined amount of Cu^{2+} or Pt^{2+} metal ions; following chemical reduction, metal nanoparticles are formed inside the dendrimer structure, where they are protected from agglomeration. This procedure permits both particle stability and control over particle size. Dendrimers containing Pt metal clusters were also attached to gold electrodes, and were found to be active as electrocatalysts for O_2 reduction [172]. This demonstrates that the nanoparticles inside the dendrimer can mediate electron transfer processes between the electrode surface and reactants in solution.

Functionalized gold electrodes were prepared by adding a monolayer of fourth-generation poly(amidoamine) dendrimer terminated with amine groups [173]. The response of these electrodes was examined in aqueous solution with the probe molecules $[\text{Ru}(\text{NH}_3)_6]^{3+}$ and $[\text{Fe}(\text{CN})_6]^{4-}$. At low pH values, when the dendrimer amine groups are protonated, only the $[\text{Fe}(\text{CN})_6]^{4-}$ probe can penetrate through the dendrimer structure to undergo electron exchange with the electrode surface. At higher pH values, when the amine groups are fully deprotonated, both probes can undergo electron transfer. These dendrimers can thus act as molecular gates, allowing selective mass transfer through the dendrimer. Similar pH-dependent behavior was also observed when grafting onto gold surfaces composite films formed from multilayers of amine-terminated dendrimers and an amphoteric random coil polymer [174]. In this case, depending on pH, selective access to the electrode surface can be obtained both for cationic and anionic probe molecules.

Poly(amidoamine) dendrimers of generations 2, 4, 6, and 8 have been tested as



91

adhesion promoters between vapor-deposited Au films and glass or other Si-based substrates [175]. The best adhesion properties are obtained with the higher generation dendrimer, which has a total of 1024 primary amine groups on the surface. The stability of electrodes built with glass/dendrimer/Au films was examined using $[\text{Ru}(\text{NH}_3)_6]^{3+}$ as redox probe in aqueous solution. After 4 h of continuous cycling the system did not show any performance reduction, indicating that electrodes built with this technique may be suitable for many common applications.

9.6 Concluding Remarks

This chapter on electron transfer reactions of dendrimers which, for reasons of space is not exhaustive, clearly indicates that, to date, two main topics have been investigated, namely electrochemical reactions and photoinduced electron transfer reactions.

As far as their electrochemical behavior is concerned, several interesting dendrimers have been synthesized, but in most cases these properties have not been investigated in great detail. Nevertheless, a few carefully performed studies have shown that electrochemistry is a powerful technique to: (i) elucidate the structure (and purity) of the dendrimers—a task that is not at all easy with these highly branched (and sometimes highly charged) compounds; (ii) evaluate the degree of electronic interaction of the various, chemically and/or topologically equivalent or nonequivalent moieties of a dendrimer; and (iii) study the endo- and exoreceptor capabilities of the dendrimers. Detailed electrochemical studies on dendrimers with an electroactive core promise to be rather useful in modeling natural electroactive species, and in investigating the problem of insulating such a unit from the electrode surface. Moreover, the importance of dendrimers as species capable of performing multielectron redox reactions has been highlighted since 1995 [176].

Photoinduced electron transfer studies have been performed in a more limited number of cases, due to the fact that the simultaneous presence of *two* reaction partners with appropriate characteristics is necessary. The study of suitably functionalized dendrimers can furnish information on the accessibility of the inner shell or core to external reagents (such as molecular oxygen or other small molecules) and on interchromophoric interactions within the dendritic structures. “Electroinactive” dendrimers can also be important in regulating the electron transfer reactions between hosted partners; in this sense dendrimers may also constitute a peculiar medium to investigate electron transfer reactions in restricted spaces.

Various recent papers have discussed possible applications of dendrimers [3, 4, 11, 14, 20, 23]. From the point of view of electron transfer, the interest in highly branched structures such as dendrimers is related not so much to their size, but rather to the presence of different components. In fact, an ordered array of different components can generate valuable properties, such as the presence of cavities with different size, surfaces with specific functions, gradients for photoinduced energy and electron transfer, and sites for multielectron transfer catalysis. At this point it is perhaps worth summarizing the practical applications of dendrimers encountered in this chapter. Dendrimers have already been used: (i) in catalytic processes [122, 149, 172]; (ii) in the functionalization of electrodes [48, 63, 172–175] which can also work as sensors [44, 48, 63]; (iii) in the fabrication of nanoparticles [170–172]; and (iv) in other devices such as LEDs [140–148] and molecular gates [173, 174]. Moreover, as many different exciting applications will certainly be added to this list in the future, it is easy to foresee a remarkable expansion in dendrimer related research.

References

1. G. R. Newkome, C. N. Moorefield, F. Vögtle, *Dendritic Macromolecules: Concepts, Syntheses, Perspectives*, VCH, Weinheim, 1996.
2. D. A. Tomalia, H. Baker, J. R. Dewald, M. Hall, G. Kallos, S. Martin, J. Roeck, J. Ryder, P. Smith, *Polym. J. (Tokyo)* **1985**, 17, 117–132.
3. M. Fischer, F. Vögtle, *Angew. Chem. Int. Ed. Engl.* **1999**, 38, 884–905.
4. M. Freemantle, *Chem. Eng. News* **1999**, November 1, 27–35.
5. B. I. Voit, *Acta Polymer.* **1995**, 46, 87–99.
6. *Advances in Dendritic Macromolecules, Vols. 1–5*, (Ed.: G. R. Newkome), JAI Press, Greenwich, 1994–1998.
7. N. Ardoin, D. Astruc, *Bull. Soc. Chim. Fr.* **1995**, 132, 875–909.
8. F. Zeng, S. C. Zimmerman, *Chem. Rev.* **1997**, 97, 1681–1712.
9. D. K. Smith, F. Diederich, *Chem. Eur. J.* **1998**, 4, 1353–1361.
10. A. Archut, F. Vögtle, *Chem. Soc. Rev.* **1998**, 27, 233–240.
11. O. A. Matthews, A. N. Shipway, J. F. Stoddart, *Prog. Polym. Sci.* **1998**, 23, 1–56.
12. M. H. P. van Genderen, E. W. Meijer, in *Supramolecular Materials and Technologies (Series: Perspectives in Supramolecular Chemistry)*, Vol. 4, (Ed.: D. N. Reinhoudt), John Wiley, Chichester, 1999, p. 47–88.
13. C. J. Hawker, *Adv. Polymer Sci.* **1999**, 147, 113–160.
14. A. W. Bosman, H. M. Janssen, E. W. Meijer, *Chem. Rev.* **1999**, 99, 1665–1688.
15. G. Denti, S. Campagna, V. Balzani, in *Mesomolecules: from Molecules to Materials*, (Eds.: G. D. Mendenhall, A. Greenberg, J. F. Liebman), Chapman & Hall, New York, 1995, p. 69–106.
16. S. Serroni, S. Campagna, G. Denti, A. Juris, M. Venturi, V. Balzani, in *Advances in Dendritic Macromolecules, Vol. 3*, (Ed.: G. R. Newkome), JAI Press, Greenwich, 1996, p. 61–113.
17. I. Cuadrado, M. Morán, J. Losada, C. M. Casado, C. Pascual, B. Alonso, F. Lobete, in *Advances in Dendritic Macromolecules, Vol. 3*, (Ed.: G. R. Newkome), JAI, Greenwich, 1996, p. 151–195.
18. E. C. Constable, *Chem. Comm.* **1997**, 1073–1080.
19. M. Venturi, S. Serroni, A. Juris, S. Campagna, V. Balzani, *Top. Curr. Chem.* **1998**, 197, 193–228.
20. C. Gorman, *Adv. Mater.* **1998**, 10, 295–309.
21. M. A. Hearshaw, J. R. Moss, *Chem. Commun.* **1999**, 1–8.
22. G. R. Newkome, E. He, C. N. Moorefield, *Chem. Rev.* **1999**, 99, 1689–1746.
23. I. Cuadrado, M. Morán, C. M. Casado, B. Alonso, J. Losada, *Coord. Chem. Rev.* **1999**, 193–195, 395–445.
24. H. Frey, C. Lach, K. Lorenz, *Adv. Mater.* **1998**, 10, 279–293.
25. A.-M. Caminade, R. Laurent, B. Chaudret, J. P. Majoral, *Coord. Chem. Rev.* **1998**, 178–180, 793–821.
26. J.-P. Majoral, A.-M. Caminade, *Chem. Rev.* **1999**, 99, 845–880.
27. C. Schlenk, H. Frey, *Monatsch. Chem.* **1999**, 130, 3–14.
28. M. R. Bryce, W. Devonport, in *Advances in Dendritic Macromolecules, Vol. 3*, (Ed.: G. R. Newkome), JAI Press, London, 1996, p. 115–149.
29. C. M. Casado, I. Cuadrado, M. Morán, B. Alonso, B. García, B. González, J. Losada, *Coord. Chem. Rev.* **1999**, 185–186, 53–79.
30. A. Juris, V. Balzani, F. Barigelletti, S. Campagna, P. Belser, A. von Zelewsky, *Coord. Chem. Rev.* **1988**, 84, 85–277.
31. K. Kalyanasundaram, *Photochemistry of Polypyridine and Porphyrin Complexes*, Academic Press, London, 1992.
32. P. D. Beer, E. L. Tite, *Tetrahedron Lett.* **1988**, 29, 2349–2352.
33. J.-L. Fillaut, D. Astruc, *Chem. Commun.* **1993**, 1320–1322.
34. F. Moulines, L. Djakovitch, R. Boese, B. Gloaguen, W. Thiel, J.-L. Fillaut, M.-H. Delville, D. Astruc, *Angew. Chem. Int. Ed. Engl.* **1993**, 32, 1075–1077.
35. M. Morán, C. M. Casado, I. Cuadrado, J. Losada, *Organometallics* **1993**, 12, 4327–4333.

36. B. Alonso, I. Cuadrado, M. Morán, J. Losada, *Chem. Commun.* **1994**, 2575–2576.
37. J.-L. Fillaut, J. Linares, D. Astruc, *Angew. Chem. Int. Ed. Engl.* **1994**, 33, 2460–2462.
38. C. M. Casado, M. Morán, J. Losada, I. Cuadrado, *Inorg. Chem.* **1995**, 34, 1668–1680.
39. C. M. Casado, I. Cuadrado, M. Morán, B. Alonso, F. Lobete, J. Losada, *Organometallics* **1995**, 14, 2618–2620.
40. B. Alonso, M. Morán, C. M. Casado, F. Lobete, J. Losada, I. Cuadrado, *Chem. Mater.* **1995**, 7, 1440–1442.
41. F. Lobete, I. Cuadrado, C. M. Casado, B. Alonso, M. Morán, J. Losada, *J. Organomet. Chem.* **1996**, 509, 109–113.
42. I. Cuadrado, M. Morán, C. M. Casado, B. Alonso, F. Lobete, B. García, M. Ibisate, J. Losada, *Organometallics* **1996**, 15, 5278–5280.
43. D. Astruc, C. Valério, J.-L. Fillaut, J. Ruiz, J.-R. Hamon, F. Varret, in *Magnetism: A Supramolecular Function*, (Ed.: O. Kahn), Kluwer, Dordrecht, 1996, p. 107–127.
44. M. J. Tendero, A. Benito, R. Martínez-Máñez, J. Soto, E. García-España, J. A. Ramírez, M. I. Burguete, S. V. Luis, *J. Chem. Soc., Dalton Trans.* **1996**, 2923–2927.
45. P. Jutzi, C. Batz, B. Neumann, H.-G. Stammer, *Angew. Chem. Int. Ed. Engl.* **1996**, 35, 2118–2121.
46. R. Castro, I. Cuadrado, B. Alonso, C. M. Casado, M. Morán, A. E. Kaifer, *J. Am. Chem. Soc.* **1997**, 119, 5760–5761.
47. I. Cuadrado, C. M. Casado, B. Alonso, M. Morán, J. Losada, V. Belsky, *J. Am. Chem. Soc.* **1997**, 119, 7613–7614.
48. J. Losada, I. Cuadrado, M. Morán, C. M. Casado, B. Alonso, M. Barranco, *Anal. Chim. Acta* **1997**, 338, 191–198.
49. K. Takada, D. J. Díaz, H. D. Abruña, I. Cuadrado, C. Casado, B. Alonso, M. Morán, J. Losada, *J. Am. Chem. Soc.* **1997**, 119, 10763–10773.
50. V. Marvaud, D. Astruc, *Chem. Commun.* **1997**, 773–774.
51. V. Marvaud, D. Astruc, E. Leize, A. Van Dorsselaer, J. Guittard, J.-C. Blais, *New J. Chem.* **1997**, 21, 1309–1319.
52. E. Alonso, C. Valerio, J. Ruiz, D. Astruc, *New J. Chem.* **1997**, 21, 1139–1141.
53. C. Valério, J.-L. Fillaut, J. Ruiz, J. Guittard, J.-C. Blais, D. Astruc, *J. Am. Chem. Soc.* **1997**, 119, 2588–2589.
54. S. Rigaut, M.-H. Delville, D. Astruc, *J. Am. Chem. Soc.* **1997**, 119, 11132–11133.
55. C.-F. Shu, H.-M. Shen, *J. Mater. Chem.* **1997**, 7, 47–52.
56. S. Achar, C. E. Immoos, M. G. Hill, V. J. Catalano, *Inorg. Chem.* **1997**, 36, 2314–2320.
57. B. González, C. M. Casado, B. Alonso, I. Cuadrado, M. Morán, Y. Wang, A. E. Kaifer, *Chem. Commun.* **1998**, 2569–2570.
58. C. M. Cardona, A. E. Kaifer, *J. Am. Chem. Soc.* **1998**, 120, 4023–4024.
59. J. Ruiz, E. Alonso, J.-C. Blais, D. Astruc, *J. Organometal. Chem.* **1999**, 582, 139–141.
60. C. Valério, J. Ruiz, J.-L. Fillaut, D. Astruc, *C. R. Acad. Sci. Paris, t. 2, Série II c* **1999**, 79–83.
61. C. Valério, E. Alonso, J. Ruiz, J.-C. Blais, D. Astruc, *Angew. Chem. Int. Ed. Engl.* **1999**, 38, 1747–1751.
62. C. M. Casado, I. Cuadrado, M. Morán, B. Alonso, M. Barranco, J. Losada, *Appl. Organometal. Chem.* **1999**, 13, 245–259.
63. C. M. Casado, I. Cuadrado, B. Alonso, M. Morán, J. Losada, *J. Electroanal. Chem.* **1999**, 463, 87–92.
64. B. García, C. M. Casado, I. Cuadrado, B. Alonso, M. Morán, J. Losada, *Organometallics* **1999**, 18, 2349–2356.
65. J. Ipaktschi, R. Hosseinzadeh, P. Schlaf, *Angew. Chem. Int. Ed. Engl.* **1999**, 38, 1658–1660.
66. D. K. Smith, *J. Chem. Soc., Perkin Trans. 2* **1999**, 1563–1565.
67. K.-W. Poon, Y. Yan, X. Li, D. K. P. Ng, *Organometallics* **1999**, 18, 3528–3533.
68. A. E. Kaifer, *Acc. Chem. Res.* **1999**, 32, 62–71.
69. H. Tokuhisa, M. Zhao, L. A. Baker, V. T. Phan, D. L. Dermody, M. E. Garcia, R. F. Peez, R. M. Crooks, T. M. Mayer, *J. Am. Chem. Soc.* **1998**, 120, 4492–4501.
70. S. Campagna, G. Denti, L. Sabatino, S. Serroni, M. Ciano, V. Balzani, *Chem. Commun.* **1989**, 1500–1501.

71. W. R. Murphy, Jr., K. J. Brewer, G. Gettliffe, J. D. Petersen, *Inorg. Chem.* **1989**, 28, 81–84.
72. G. Denti, S. Campagna, L. Sabatino, S. Serroni, M. Ciano, V. Balzani, *Inorg. Chem.* **1990**, 29, 4750–4758.
73. G. Denti, S. Campagna, L. Sabatino, S. Serroni, M. Ciano, V. Balzani, *Inorg. Chim. Acta* **1990**, 176, 175–178.
74. S. Campagna, G. Denti, S. Serroni, M. Ciano, V. Balzani, *Inorg. Chem.* **1991**, 30, 3728–3732.
75. G. Denti, S. Campagna, L. Sabatino, S. Serroni, M. Ciano, V. Balzani, in *Photochemical Conversion and Storage of Solar Energy*, (Eds.: E. Pelizzetti, M. Schiavello), Kluwer, Dordrecht, 1991, p. 27–45.
76. S. Serroni, G. Denti, S. Campagna, M. Ciano, V. Balzani, *Chem. Commun.* **1991**, 944–945.
77. G. Denti, S. Serroni, S. Campagna, V. Ricevuto, A. Juris, M. Ciano, V. Balzani, *Inorg. Chim. Acta* **1992**, 198–200, 507–512.
78. G. Denti, S. Campagna, S. Serroni, M. Ciano, V. Balzani, *J. Am. Chem. Soc.* **1992**, 114, 2944–2950.
79. G. Denti, S. Serroni, S. Campagna, A. Juris, M. Ciano, V. Balzani, in *Perspectives in Coordination Chemistry*, (Eds.: A. F. Williams, C. Floriani, A. E. Merbach), Verlag Helvetica Chimica Acta, Basel, 1992, p. 153–164.
80. S. Campagna, G. Denti, S. Serroni, M. Ciano, A. Juris, V. Balzani, *Inorg. Chem.* **1992**, 31, 2982–2984.
81. S. Serroni, G. Denti, S. Campagna, A. Juris, M. Ciano, V. Balzani, *Angew. Chem. Int. Ed. Engl.* **1992**, 31, 1493–1495.
82. V. Balzani, G. Denti, S. Serroni, S. Campagna, V. Ricevuto, A. Juris, *Proc. Indian Acad. Sci. (Chem. Sci.)* **1993**, 105, 421–434.
83. P. Belser, A. von Zelewsky, M. Frank, C. Seel, F. Vögtle, L. De Cola, F. Barigelletti, V. Balzani, *J. Am. Chem. Soc.* **1993**, 115, 4076–4086.
84. G. Denti, S. Serroni, S. Campagna, A. Juris, V. Balzani, *Mol. Cryst. Liq. Cryst.* **1993**, 234, 79–88.
85. V. Balzani, S. Campagna, G. Denti, A. Juris, S. Serroni, M. Venturi, *Coord. Chem. Rev.* **1994**, 132, 1–13.
86. S. Serroni, S. Campagna, A. Juris, M. Venturi, V. Balzani, G. Denti, *Gazz. Chim. Ital.* **1994**, 124, 423–427.
87. S. Serroni, A. Juris, S. Campagna, M. Venturi, G. Denti, V. Balzani, *J. Am. Chem. Soc.* **1994**, 116, 9086–9091.
88. S. Campagna, G. Denti, S. Serroni, A. Juris, M. Venturi, V. Ricevuto, V. Balzani, *Chem. Eur. J.* **1995**, 1, 211–221.
89. A. Juris, M. Venturi, L. Pontoni, I. Resino Resino, V. Balzani, S. Serroni, S. Campagna, G. Denti, *Can. J. Chem.* **1995**, 73, 1875–1882.
90. G. R. Newkome, R. Güther, C. N. Moorefield, F. Cardullo, L. Echegoyen, E. Pérez-Cordero, H. Luftmann, *Angew. Chem. Int. Ed. Engl.* **1995**, 34, 2023–2026.
91. D. Armspach, M. Cattalini, E. C. Constable, C. E. Housecroft, D. Phillips, *Chem. Commun.* **1996**, 1823–1824.
92. S. Campagna, S. Serroni, A. Juris, M. Venturi, V. Balzani, *New J. Chem.* **1996**, 20, 773–780.
93. H.-F. Chow, C. I.Y.-K., D. T. W. Chan, R. W. M. Kwok, *Chem. Eur. J.* **1996**, 2, 1085–1091.
94. E. C. Constable, P. Harverson, *Inorg. Chim. Acta* **1996**, 252, 9–11.
95. E. C. Constable, P. Harverson, *Chem. Commun.* **1996**, 33–34.
96. E. C. Constable, P. Harverson, M. Oberholzer, *Chem. Commun.* **1996**, 1821–1822.
97. G. Denti, S. Campagna, S. Serroni, V. Balzani, A. Juris, M. Venturi, in *Polymeric Materials Encyclopedia*, Vol. 3, (Ed.: J. C. Salamone), CRC Press, Boca Raton, 1996, p. 1799–1806.
98. K. Wärnmark, O. Heyke, J. A. Thomas, J.-M. Lehn, *Chem. Commun.* **1996**, 2603–2604.
99. M.-a. Haga, M. M. Ali, R. Arakawa, *Angew. Chem. Int. Ed. Engl.* **1996**, 35, 76–78.
100. J. Issberner, F. Vögtle, L. De Cola, V. Balzani, *Chem. Eur. J.* **1997**, 3, 706–712.
101. S. Serroni, A. Juris, M. Venturi, S. Campagna, I. Resino Resino, G. Denti, A. Credi, V. Balzani, *J. Mater. Chem.* **1997**, 7, 1227–1236.
102. H. E. Toma, T. E. Chavez-Gil, *Inorg. Chim. Acta* **1997**, 257, 197–202.

103. V. Balzani, S. Campagna, G. Denti, A. Juris, S. Serroni, M. Venturi, *Acc. Chem. Res.* **1998**, *31*, 26–34.
104. P. Ceroni, F. Paolucci, C. Paradisi, A. Juris, S. Roffia, S. Serroni, S. Campagna, A. J. Bard, *J. Am. Chem. Soc.* **1998**, *120*, 5480–5487.
105. G. R. Newkome, E. He, L. A. Godínez, *Macromolecules* **1998**, *31*, 4382–4386.
106. S. Campagna, S. Serroni, S. Bodige, F. M. MacDonnell, *Inorg. Chem.* **1999**, *38*, 692–701.
107. E. C. Constable, P. Harverson, *Polyhedron* **1999**, *18*, 1891–1901.
108. D. J. Díaz, G. D. Storrier, S. Bernhard, K. Takada, H. D. Abruña, *Langmuir* **1999**, *15*, 7351–7354.
109. M. Kimura, K. Mizuno, T. Muto, K. Hanabusa, H. Shirai, *Macromol. Rapid. Commun.* **1999**, *20*, 98–102.
110. M. Marcaccio, F. Paolucci, C. Paradisi, S. Roffia, C. Fontanesi, L. J. Yellowlees, S. Serroni, S. Campagna, G. Denti, V. Balzani, *J. Am. Chem. Soc.* **1999**, *121*, 10081–10091.
111. G. R. Newkome, A. K. Patri, L. A. Godínez, *Chem. Eur. J.* **1999**, *5*, 1445–1451.
112. G. R. Newkome, E. He, L. A. Godínez, G. R. Baker, *Chem. Commun.* **1999**, 27–28.
113. M. Plevoets, F. Vögtle, L. De Cola, V. Balzani, *New J. Chem.* **1999**, *23*, 63–69.
114. G. D. Storrier, K. Takada, H. D. Abruña, *Langmuir* **1999**, *15*, 872–884.
115. F. Vögtle, M. Plevoets, M. Nieger, G. C. Azzellini, A. Credi, L. De Cola, V. De Marchis, M. Venturi, V. Balzani, *J. Am. Chem. Soc.* **1999**, *121*, 6290–6298.
116. V. Balzani, A. Juris, M. Venturi, S. Campagna, S. Serroni, *Chem. Rev.* **1996**, *96*, 759–833.
117. P. J. Dandliker, F. Diederich, M. Gross, C. B. Knobler, A. Louati, E. M. Sanford, *Angew. Chem. Int. Ed. Engl.* **1994**, *33*, 1739–1742.
118. P. J. Dandliker, F. Diederich, J.-P. Gisselbrecht, A. Louati, M. Gross, *Angew. Chem. Int. Ed. Engl.* **1995**, *34*, 2725–2728.
119. P. J. Dandliker, F. Diederich, A. Zingg, J.-P. Gisselbrecht, M. Gross, A. Louati, *Helv. Chim. Acta* **1997**, *80*, 1773–1801.
120. P. Weyermann, J.-P. Gisselbrecht, C. Boudon, F. Diederich, M. Gross, *Angew. Chem. Int. Ed. Engl.* **1999**, *38*, 3215–3219.
121. K. W. Pollak, J. W. Leon, J. M. J. Fréchet, M. Maskus, H. D. Abruña, *Chem. Mater.* **1998**, *10*, 30–38.
122. M. Kimura, Y. Sugihara, T. Muto, K. Hanabusa, H. Shirai, N. Kobayashi, *Chem. Eur. J.* **1999**, *5*, 3495–3500.
123. R.-H. Jin, T. Aida, S. Inoue, *Chem. Commun.* **1993**, 1260–1262.
124. R. Sadamoto, N. Tomioka, T. Aida, *J. Am. Chem. Soc.* **1996**, *118*, 3978–3979.
125. M. Kimura, K. Nakada, Y. Yamaguchi, K. Hanabusa, H. Shirai, N. Kobayashi, *Chem. Commun.* **1997**, 1215–1216.
126. A. C. H. Ng, X. Li, D. K. P. Ng, *Macromolecules* **1999**, *32*, 5292–5298.
127. M. R. Bryce, W. Devonport, A. J. Moore, *Angew. Chem. Int. Ed. Engl.* **1994**, *33*, 1761–1763.
128. M. R. Bryce, W. Devonport, *Synth. Met.* **1996**, *76*, 305–307.
129. W. Devonport, M. R. Bryce, G. J. Marshallsay, A. J. Moore, L. M. Goldenberg, *J. Mater. Chem.* **1988**, *8*, 1361–1372.
130. C. Wang, M. R. Bryce, A. S. Batsanov, L. M. Goldenberg, J. A. K. Howard, *J. Mater. Chem.* **1997**, *7*, 1189–1197.
131. M. R. Bryce, P. de Miguel, W. Devonport, *Chem. Commun.* **1998**, 2565–2566.
132. C. J. Hawker, K. L. Wooley, J. M. J. Fréchet, *Chem. Commun.* **1994**, 925–926.
133. X. Camps, E. Dietel, A. Hirsch, S. Pyo, L. Echegoyen, S. Hackbarth, B. Röder, *Chem. Eur. J.* **1999**, *5*, 2362–2373.
134. L. L. Miller, T. Hashimoto, I. Tabakovic, D. R. Swanson, D. A. Tomalia, *Chem. Mater.* **1995**, *7*, 9–11.
135. R. G. Duan, L. L. Miller, D. A. Tomalia, *J. Am. Chem. Soc.* **1995**, *117*, 10783–10784.
136. L. L. Miller, R. G. Duan, D. C. Tully, D. A. Tomalia, *J. Am. Chem. Soc.* **1997**, *119*, 1005–1010.
137. L. L. Miller, B. Zinger, J. S. Schlechte, *Chem. Mater.* **1999**, *11*, 2313–2315.
138. J. Louie, J. F. Hartwig, *J. Am. Chem. Soc.* **1997**, *119*, 11695–11696.
139. T. D. Selby, S. C. Blackstock, *J. Am. Chem. Soc.* **1998**, *120*, 12155–12156.
140. Y. Shirota, Y. Kuwabara, H. Inada, T. Wakimoto, H. Nakada, Y. Yonemoto, S. Kawami, K. Imai, *Appl. Phys. Lett.* **1994**, *65*, 807–809.

141. Y. Kuwabara, H. Ogawa, H. Inada, N. Noma, Y. Shiota, *Adv. Mater.* **1994**, *6*, 677–679.
142. P.-W. Wang, Y.-J. Liu, C. Devadoss, P. Bharati, J. S. Moore, *Adv. Mater.* **1996**, *8*, 237–241.
143. K. Katsuma, Y. Shiota, *Adv. Mater.* **1998**, *10*, 223–226.
144. C. Glebeler, H. Antoniadis, D. D. C. Bradley, Y. Shiota, *Appl. Phys. Lett.* **1998**, *72*, 2448–2450.
145. M. Halim, J. N. G. Pillow, I. D. W. Samuel, P. L. Burn, *Synth. Met.* **1999**, *102*, 922–923.
146. M. Halim, I. D. W. Samuel, J. N. G. Pillow, P. L. Burn, *Synth. Met.* **1999**, *102*, 1113–1114.
147. M. Halim, I. D. W. Samuel, J. N. G. Pillow, A. P. Monkman, P. L. Burn, *Synth. Met.* **1999**, *102*, 1571–1574.
148. M. Halim, J. N. G. Pillow, I. D. W. Samuel, P. L. Burn, *Adv. Mater.* **1999**, *11*, 371–374.
149. A. Miedaner, C. J. Curtis, R. M. Barkley, D. L. DuBois, *Inorg. Chem.* **1994**, *33*, 5482–5490.
150. D. B. Amabilino, P. R. Ashton, V. Balzani, C. L. Brown, A. Credi, J. M. J. Fréchet, J. W. Leon, F. M. Raymo, N. Spencer, J. F. Stoddart, M. Venturi, *J. Am. Chem. Soc.* **1996**, *118*, 12012–12020.
151. C. B. Gorman, B. L. Parkhurst, W. Y. Su, K.-Y. Chen, *J. Am. Chem. Soc.* **1997**, *119*, 1141–1142.
152. C. B. Gorman, *Adv. Mater.* **1997**, *9*, 1117–1119.
153. G. R. Newkome, V. V. Narayanan, L. Echegoyen, E. Pérez-Cordero, H. Luftmann, *Macromolecules* **1997**, *30*, 5187–5191.
154. I. Jestin, E. Levillain, J. Roncali, *Chem. Commun.* **1998**, 2655–2656.
155. Y. Kashiwagi, F. Kurashima, C. Kikuchi, J. Anzai, T. Osa, *Electrochem. Commun.* **1999**, *1*, 305–308.
156. T. P. Bender, Y. Qi, P. Desjardins, Z. Y. Wang, *Can J. Chem.* **1999**, *77*, 1444–1452.
157. G. M. Stewart, M. A. Fox, *J. Am. Chem. Soc.* **1996**, *118*, 4354–4360.
158. C. Devadoss, P. Bharathi, J. S. Moore, *Angew. Chem. Int. Ed. Engl.* **1997**, *36*, 1633–1635.
159. A. Archut, G. C. Azzellini, V. Balzani, L. De Cola, F. Vögtle, *J. Am. Chem. Soc.* **1998**, *120*, 12187–12191.
160. S. M. Risser, D. N. Beratan, J. N. Onuchic, *J. Phys. Chem.* **1993**, *97*, 4523–4527.
161. J. N. Onuchic, S. M. Risser, S. S. Skourtis, D. N. Beratan, in *Molecular Electronics*, (Eds.: J. Jortner, M. Ratner), Blackwell, Oxford, 1997, p. 369–379.
162. M. C. Moreno-Bondi, G. Orellana, N. J. Turro, D. A. Tomalia, *Macromolecules* **1990**, *23*, 910–912.
163. N. J. Turro, J. K. Barton, D. A. Tomalia, *Acc. Chem. Res.* **1991**, *24*, 332–340.
164. K. R. Gopidas, A. R. Leheny, G. Caminati, N. J. Turro, D. A. Tomalia, *J. Am. Chem. Soc.* **1991**, *113*, 7335–7342.
165. C. Turro, S. Niu, S. H. Bossmann, D. A. Tomalia, N. J. Turro, *J. Phys. Chem.* **1995**, *99*, 5512–5517.
166. D. ben-Avraham, L. S. Schulman, S. H. Bossmann, C. Turro, N. J. Turro, *J. Phys. Chem. B* **1998**, *102*, 5088–5093.
167. S. Jockusch, J. Ramirez, K. Sanghvi, R. Nociti, N. J. Turro, D. A. Tomalia, *Macromolecules* **1999**, *32*, 4419–4423.
168. P. F. Schwarz, N. J. Turro, D. A. Tomalia, *J. Photochem. Photobiol. A: Chem.* **1998**, *112*, 47–52.
169. D. A. Wade, P. A. Torres, S. A. Tucker, *Anal. Chim. Acta* **1999**, *397*, 17–31.
170. M. Zhao, L. Sun, R. M. Crooks, *J. Am. Chem. Soc.* **1998**, *120*, 4877–4878.
171. L. Balogh, D. A. Tomalia, *J. Am. Chem. Soc.* **1998**, *120*, 7355–7356.
172. M. Zhao, R. M. Crooks, *Adv. Mater.* **1999**, *11*, 217–220.
173. M. Zhao, H. Tokuhisa, R. M. Crooks, *Angew. Chem. Int. Ed. Engl.* **1997**, *36*, 2596–2598.
174. Y. Liu, M. Zhao, D. E. Bergbreiter, R. M. Crooks, *J. Am. Chem. Soc.* **1997**, *119*, 8720–8721.
175. L. A. Baker, F. P. Zamborini, L. Sun, R. M. Crooks, *Anal. Chem.* **1999**, *71*, 4403–4406.
176. A. J. Bard, *Nature* **1995**, *374*, 13.

Volume IV

Part 1

Catalysis of Electron Transfer

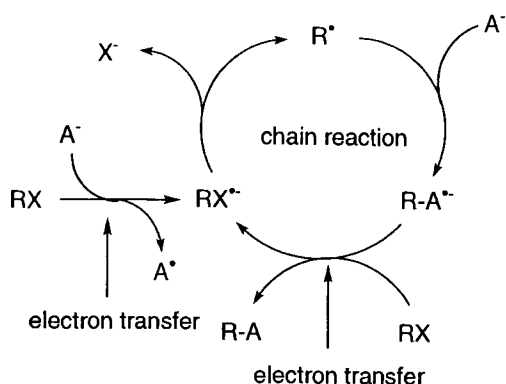
1 Fundamental Concepts of Catalysis in Electron Transfer

Shunichi Fukuzumi

1.1 Introduction

Catalysis is the most important concept to control any kind of chemical reaction, including enzymatic reactions in biological systems [1–4], contributing greatly to world industrial chemical output [5–11]. Among many types of chemical reactions, an electron transfer reaction is the most fundamental, since the electron is the minimal unit of the change in chemical reactions and any chemical bond is formed via electrons. The importance of electron transfer processes has been recognized in nearly every subdiscipline of chemistry, i.e., not only inorganic chemistry but also organic and organometallic chemistry [12–26]. Electron transfer processes often play an important role as a key elementary step in a variety of catalytic cycles [27–37]. This type of catalysis is called electron transfer catalysis (ETC) and it is characterized by a classical catalytic cycle which involves one or more electron transfer processes. In such cases, an electron transfer reaction often initiates a chain reaction in which the propagation step also involves an electron transfer process as shown in Scheme 1 [24–32].

Compared with electron transfer catalysis, which has been undergoing extensive exploration and expansion [24–34], catalysis of electron transfer reactions themselves has yet to emerge as an identifiable field of study. The conceptual lack of catalysis in electron transfer reactions seems to stem from a general belief that there may be no need for catalysis to accelerate further the electron transfer reaction, which is generally fast enough in a practical sense. This is largely true for reversible electron transfer reactions in which electron transfer occurs only when the free energy change of electron transfer is negative, i.e., the electron transfer is exergonic. If the electron transfer is endergonic, no net electron transfer would occur because of facile back electron transfer to regenerate the reactant pair. However, numerous chemical reactions, previously formulated by ‘movements of electron pairs’, are now understood as processes in which an initial electron transfer from a nucleophile (reductant) to an electrophile (oxidant) produces a radical ion pair, which leads to



the final products via the follow-up steps involving cleavage and formation of chemical bonds [12–23, 38–42]. The follow-up steps are usually sufficiently rapid to render the initial electron transfer the rate-determining step in an overall *irreversible* transformation as shown in Figure 1 [42]. In such a case, catalysis in the rate-determining electron transfer step, which is usually endergonic ($\Delta G_{\text{et}}^{\circ} > 0$) and thereby thermodynamically unfavorable, would play an essential role in accelerating the overall redox reaction.

Since photoexcitation induces significant enhancement of the reactivity of electron transfer, photochemical reactions via photoinduced electron transfer have been explored in homogeneous systems [43–52]. On the other hand, the term ‘photocatalysis’ has usually been used in heterogeneous systems involving photoinduced electron transfer across the gas–solid or liquid–solid interface [53–60]. Photocatalysis has been extensively studied using a semiconductor particle as a photocatalyst [53–60]. Photocatalysis is initiated by the absorption of a band gap photon

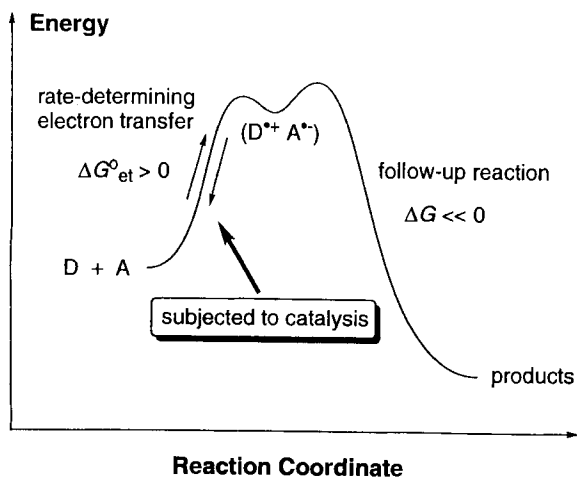


Figure 1. Energy diagram of irreversible electron transfer from an electron donor (D) to an acceptor (A).

at or near the surface of a semiconductor particle. This important field is covered in another chapter in this section [61].

Photochemical reactions involving photo-excited states can also be catalyzed as well as the thermal reactions of ground states. However, the lifetimes of excited states are usually very short, particularly for the singlet excited states, and accordingly reactions of the excited state should be fast enough to compete with the decay of the excited state to the ground state (typically the lifetime is 10^{-6} – 10^{-12} s). Hence there seems to be little chance of catalysis to accelerate the reactions of excited states, which are already fast. There are many cases, however, such that photochemical reactions can be accelerated by some added substances which act as catalysts in the photochemical reactions [62–65]. Photoinduced electron transfer reactions can also be accelerated by the presence of an appropriate catalyst [52].

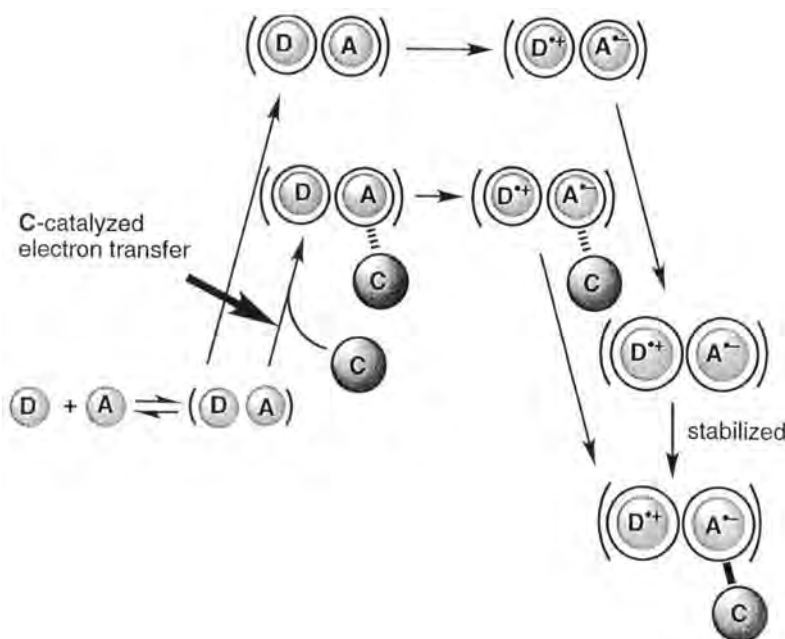
This chapter is intended to focus on catalysis in both thermal and photoinduced electron transfer reactions between electron donors and acceptors by investigating the effects of an appropriate substance that can reduce the activation barrier of electron transfer reactions. It is commonly believed that a catalyst affects the rate of reaction but not the point of equilibrium of the reaction. Thus, a substance is said to act as a catalyst in a reaction when it appears in the rate equation but not in the stoichiometric equation. However, autocatalysis involves a product acting as a catalyst. In this chapter, a catalyst is simply defined as a substance which affects the rate of reaction. This is an unambiguous classification, albeit not universally accepted, including a variety of terms such as catalyzed, sensitized, promoted, accelerated, enhanced, stimulated, induced, and assisted. Both thermal and photochemical redox reactions which would otherwise be unlikely to occur are made possible to proceed efficiently by the catalysis in the electron transfer steps. First, factors that accelerate rates of electron transfer are summarized and then each mechanistic viability is described by showing a number of examples of both thermal and photochemical reactions that involve catalyzed electron transfer processes as the rate-determining steps. Catalytic reactions which involve uncatalyzed electron transfer steps are described in other chapters in this section [66–68].

1.2 Factors to Accelerate Rates of Electron Transfer

According to the Marcus theory [69–71], the rate constants (k_{et}) of electron transfer are determined by the free energy change of electron transfer ($\Delta G^\circ_{\text{et}}$) and the reorganization energy associated with the electron transfer (λ) as given by:

$$k_{\text{et}} = \kappa Z \exp[-(\Delta G^\circ_{\text{et}} + \lambda)^2 / 4\lambda RT] \quad (1)$$

where κ is the probability for the electron transfer to occur normalized to the number of times the molecule acquires the correct nuclear configuration to pass through the intersection of the potential energy surfaces of the reactants and products, Z is the collision frequency in an intermolecular electron transfer reaction or



Scheme 2.

the vibrational frequency in an intramolecular electron transfer and λ is the nuclear reorganization energy including the solvent reorganization associated with electron transfer [69–71]. The κ value is taken as unity for an adiabatic process in solution when the interaction energy at the intersection is so large that formation of transition state can lead almost inevitably to the product.

As shown in Scheme 2, an electron is transferred from an electron donor (D) to an acceptor (A) instantaneously according to the Franck–Condon principle when the reactant pair (D – A) is activated to reach the nuclear configurations which include the solvation, where the energy before and after the electron transfer is the same. Figure 2 shows the dependence of $\log k_{\text{et}}$ on $\Delta G^{\circ}_{\text{et}}$ based on Eq. 1. The k_{et} value increases with decreasing (a) $\Delta G^{\circ}_{\text{et}}$ or/and (b) λ (Figure 2). Thus, in order to accelerate the rate of electron transfer, the $\Delta G^{\circ}_{\text{et}}$ or/and λ values should be decreased.

If a catalyst (C) which can interact with one of the products of electron transfer (e.g., $A^{\bullet -}$ in Scheme 2) is introduced into the D – A system, the factors to control the rate of electron transfer, $\Delta G^{\circ}_{\text{et}}$ and λ , may be altered. The $\Delta G^{\circ}_{\text{et}}$ value is shifted in the negative direction when the activation barrier of electron transfer is reduced to accelerate the rates of electron transfer as shown in Scheme 2, where C forms a complex with $A^{\bullet -}$. Since most organic compounds such as π acceptors in particular have small reorganization energies, the change of redox potentials due to the interaction of the corresponding radical anions with C may be the main factor to accelerate the rates of electron transfer. Thus, any catalyst C that can stabilize the products of electron transfer thermodynamically by complexation may act as an

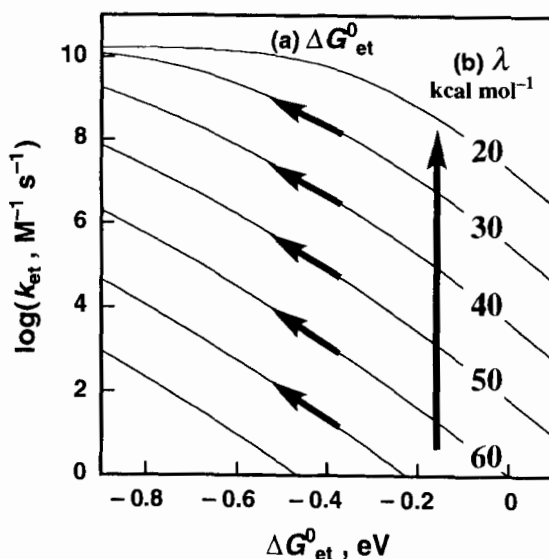
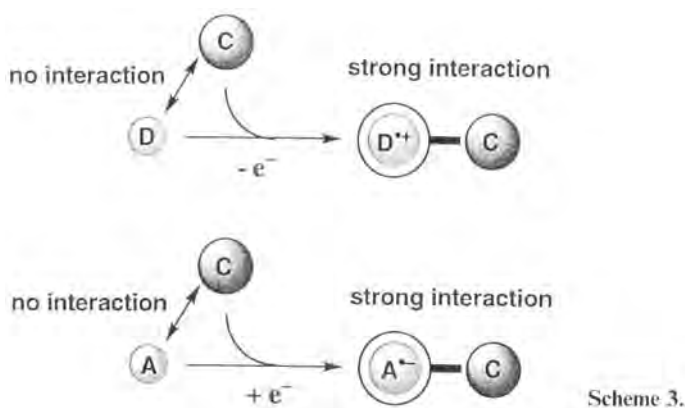


Figure 2. Dependence of $\log k_{et}$ on ΔG°_{et} for electron transfer reactions with different λ based on Eq. 1 [64–66].

efficient catalyst to accelerate the rates of electron transfer. The radical anions $A^{\bullet-}$ may be stabilized by the interaction with acids, while the radical cations $D^{\bullet+}$ may have a strong interaction with bases. The stronger the interaction of **C** (acid or base) with the radical anions or cations, the faster are the rates of electron transfer, as the free energy change of electron transfer decreases. This means that an electron is transferred instantaneously according to the Franck–Condon principle when the reactant pair is activated by the interaction with **C** to reach the nuclear configurations where the energy before and after the electron transfer is the same. Once an electron has been transferred, the interaction of **C** with the radical anions (or cations) becomes much stronger to give the thermodynamically more stable products as shown in Scheme 2.

It should be emphasized that there is no need to have an interaction of **C** with **A** and that the interaction with the reduced state ($A^{\bullet-}$) is sufficient to accelerate the rate of electron transfer. This contrasts well with the catalysis on conventional ionic or concerted reactions, in which the catalyst needs to interact with a reactant to accelerate the rate of reactions. In other words the strength of binding of catalyst (**C**) with an electron donor (**D**) or acceptor (**A**) is altered drastically depending on the redox state, as shown in Scheme 3. Even if there is no interaction between **D** (or **A**) and **C**, there can be a strong interaction between $D^{\bullet+}$ (or $A^{\bullet-}$) and **C**. As mentioned above, strong binding is expected between $A^{\bullet-}$ and an acid or between $D^{\bullet+}$ and a base, while there must be much less interaction between **A** and an acid or between **D** and a base. Thus, an acid can catalyze the electron transfer reduction of **A**, while a base can catalyze the electron transfer oxidation of **D**.

Much weaker intermolecular interactions such as hydrogen bonding and π stacking can also be altered depending on the redox state of **D** or **A** [72]. Generally, the gain or loss of an electron by a host (or guest) molecule modifies its charge and electronic distribution and often leads to very significant changes in the strength and



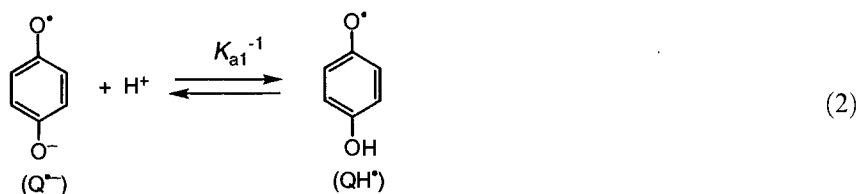
Scheme 3.

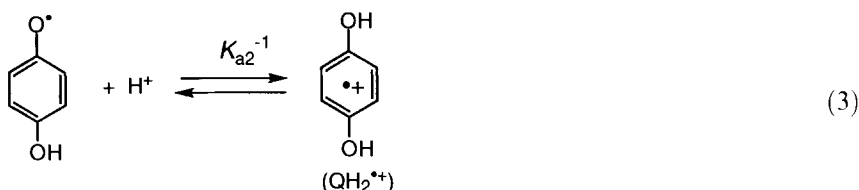
nature of the intermolecular forces between the host and guest molecules and their recognition patterns [73]. In such a case, the host (or guest) molecule can act as a catalyst (C in Scheme 3) to control the electron transfer reactions of the guest (or host) molecule. The effects of various molecular recognition elements on the redox behavior and physical properties of redox-active organic molecules including biological systems are discussed in another chapter in this Part [74].

1.3 Acid Catalysis in Electron Transfer

1.3.1 Catalysis of Brønsted Acid

The simplest substance which can act as a catalyst in the electron transfer reduction of an electron acceptor may be a proton ($C = H^+$), since the radical anion of an electron acceptor ($A^{•-}$) becomes a much stronger base as compared with the neutral form (A). The substrates first described here are *p*-benzoquinone derivatives (Q), since the redox and acid–base properties of Q and the reduced forms ($Q^{•-}$ and Q^{2-} as the one-electron and two-electron reduced form, respectively) have well been established and they exhibit important thermodynamic parameters in biological redox systems [75, 76]. The variations of the reduction potentials with pH are governed by the acid–base properties of the reduced species. Semiquinone radical anion ($Q^{•-}$) is not only singly protonated but also doubly protonated, as shown in Eqs. 2 and 3 [75, 76].





In such a case the one-electron reduction potential of Q (E_{red}) is shifted in the positive direction by the protonation of $\text{Q}^{\bullet-}$, according to Eq. 4:

$$E_{\text{red}} = E_{\text{red}}^{\circ} + (2.3RT/F) \log(1 + K_{a1}^{-1}[\text{H}^+] + K_{a1}^{-1}K_{a2}^{-1}[\text{H}^+]^2) \quad (4)$$

where K_{a1} and K_{a2} are the acid dissociation constants of QH^{\bullet} and $\text{QH}_2^{\bullet+}$, respectively. At high pH values ($\text{pH} > \text{p}K_{a1}$), $\text{Q}^{\bullet-}$ predominates as the one-electron reduced species, and thereby E_{red} is independent of pH, being equal to E_{red}° . In the region $\text{p}K_{a2} < \text{pH} < \text{p}K_{a1}$, QH^{\bullet} predominates as the reduced species when the E_{red} value is shifted to the positive direction with the slope of $2.3RT/F$ (F is the Faraday constant) which corresponds to 0.0592 at 298 K. Under more acidic conditions such that $\text{pH} < \text{p}K_{a2}$, the slope would be twice $2.3RT/F$ (0.118 at 298 K).

If one assumes that H^+ has no effect on the one-electron oxidation potential of an electron donor (D), the free energy change of electron transfer from D to Q in the presence of H^+ (ΔG_{et}) can be expressed by Eq. 5:

$$\Delta G_{\text{et}} = \Delta G_{\text{et}}^{\circ} - (2.3RT) \log(1 + K_{a1}^{-1}[\text{H}^+] + K_{a1}^{-1}K_{a2}^{-1}[\text{H}^+]^2) \quad (5)$$

where $\Delta G_{\text{et}}^{\circ}$ is the free energy change in the absence of H^+ . Thus, electron transfer from D to Q becomes more favorable energetically with an increase in the H^+ concentration. If such a change in the energetics is directly reflected in the transition state of electron transfer, the dependence of the rate constant of H^+ -catalyzed electron transfer (k_{et}) on $[\text{H}^+]$ may be given by Eq. 6:

$$k_{\text{et}} = k_{\text{et}}^{\circ}(1 + K_{a1}^{-1}[\text{H}^+] + K_{a1}^{-1}K_{a2}^{-1}[\text{H}^+]^2) \quad (6)$$

where k_{et}° is the rate constant in the absence of H^+ . Thus, the dependence of the rate constant (k_{et}) of H^+ -catalyzed electron transfer on $[\text{H}^+]$ is expected to change from zeroth order with respect to $[\text{H}^+]$ (independent of $[\text{H}^+]$) when $[\text{H}^+] \ll K_{a1}$ to first order with increasing $[\text{H}^+]$ when $[\text{H}^+] \gg K_{a1}$, and then to second order under more acidic conditions such that $[\text{H}^+] \gg K_{a2}$.

The dependence of k_{et} on $[\text{H}^+]$ in Eq. 6 has been reported for H^+ -catalyzed electron transfer from *cis*-dialkylcobalt(III) complexes (*cis*- $[\text{R}_2\text{Co}(\text{bpy})_2]^+$; R = Me, Et, PhCH_2 ; bpy = 2,2'-bipyridine) to Q as shown in Figure 3 [77]. The acid-catalyzed electron transfer from *cis*- $[\text{R}_2\text{Co}(\text{bpy})_2]^+$ to Q generates *cis*- $[\text{R}_2\text{Co}(\text{bpy})_2]^{2+}$ in which facile cleavage of a pair of cobalt-carbon bonds occurs to give R-R as shown in Scheme 4 [78, 79]. When a relatively strong oxidant such as 2,6- or 2,5-dichloro-*p*-benzoquinone is employed in the electron transfer oxidation of *cis*- $[\text{Et}_2\text{Co}(\text{bpy})_2]^+$, the k_{et} value is constant, independent of pH at high pH, $\text{pH} > \text{p}K_{a1}$

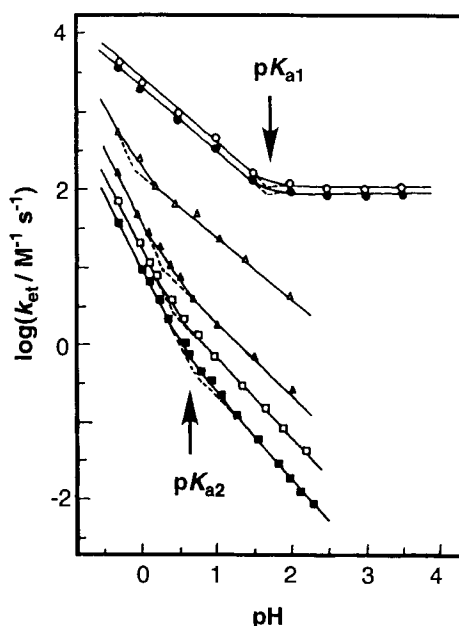
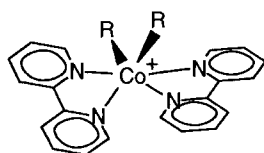
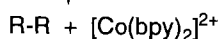
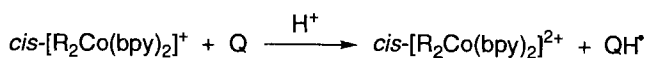


Figure 3. pH dependence of k_{et} for the electron transfer from $cis-[Et_2Co(bpy)_2]^+$ to p -benzoquinone derivatives in $H_2O-EtOH$ (5:1 v/v) at 298 K: 2,6-dichloro- p -benzoquinone (\circ); 2,5-dichloro- p -benzoquinone (\bullet); chloro- p -benzoquinone (\triangle); p -benzoquinone (\blacktriangle); methyl- p -benzoquinone (\square); and 2,6-dimethyl- p -benzoquinone (\blacksquare).

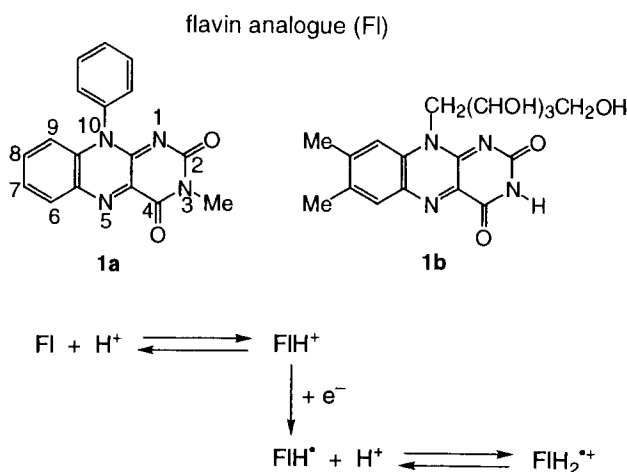


$cis-[R_2Co(bpy)_2]^+$



Scheme 4.

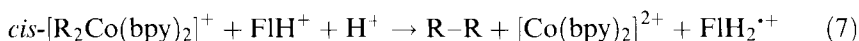
[77]. The acid catalysis starts to operate under acidic conditions, $pH < pK_{a1}$ (Figure 3) [77]. Under more acidic conditions such that $pH < pK_{a2}$, the slope changes from -1 to -2 , showing the second-order dependence of k_{et} on $[H^+]$, agreeing with the expectation based on Eq. 6 [77]. The pK_{a1} and pK_{a2} values of each p -benzoquinone derivative determined from the pH dependence of k_{et} in Figure 3 agree well with the known values in the literature [75, 77]. Thus, the acceleration of the rate of electron transfer is achieved by the protonation of $Q^{\cdot-}$ in Eqs. 2 and 3, and the number of protons which can form the chemical bond with $Q^{\cdot-}$ determines the kinetic order



Scheme 5.

(zeroth, first or second order) with respect to the acid concentration. It should be noted that no protonation of Q occurs in the pH region in Figure 3 [77].

Acid catalysis is also effective for the electron transfer reduction of flavins, which are also important coenzymes in the biological redox reactions [80–82]. Flavin analogues (FI: **1a** and **1b**) are known to be protonated at the N-1 position in a strongly acidic aqueous solution as shown in Scheme 5 ($\text{p}K_{\text{a}} \approx 0$) [83]. In an aprotic solvent such as acetonitrile (MeCN), the protonation of FI occurs much more readily than in H_2O [84]. The one-electron reduced radical FIH^* can also be protonated to give FIH_2^{*+} in acetonitrile (Scheme 5) [84]. In such a case, an acid-catalyzed electron transfer from $\text{cis-}[\text{R}_2\text{Co}(\text{bpy})_2]^+$ to FIH^+ in MeCN occurs to yield FIH_2^{*+} (Eq. 7) [84]:



The selective formation of FIH_2^{*+} is well characterized by the ESR spectra [84]. No reaction occurs without acid [84]. Since FI is already protonated at the oxidized state in the presence of HClO_4 in MeCN, the rate constant of electron transfer (k_{et}) from $\text{cis-}[\text{R}_2\text{Co}(\text{bpy})_2]^+$ to FIH^+ increases linearly with $[\text{H}^+]$ [84], in contrast to the case of the acid-catalyzed reduction of Q, in which the k_{et} value shows the second-order dependence with respect to $[\text{H}^+]$ when QH^* is further protonated to give QH_2^{*+} [77].

According to Eq. 6, the k_{et} value becomes larger with decrease in K_{a} , i.e., the larger $\text{p}K_{\text{a}}$ value. In general, the $\text{p}K_{\text{a}}$ value becomes larger in an aprotic solvent such as MeCN as compared with the value in water, since the solvation energy for proton in an aprotic solvent is much less than that in water [85]. Thus, acid catalysis in electron transfer reactions is expected to be much more efficient in acetonitrile than in water. In fact, the luminescence of $[\text{Ru}(\text{bpy})_3]^{2+*}$ (* denotes the excited state) is quenched by electron transfer from $[\text{Ru}(\text{bpy})_3]^{2+*}$ to acetophenone in the

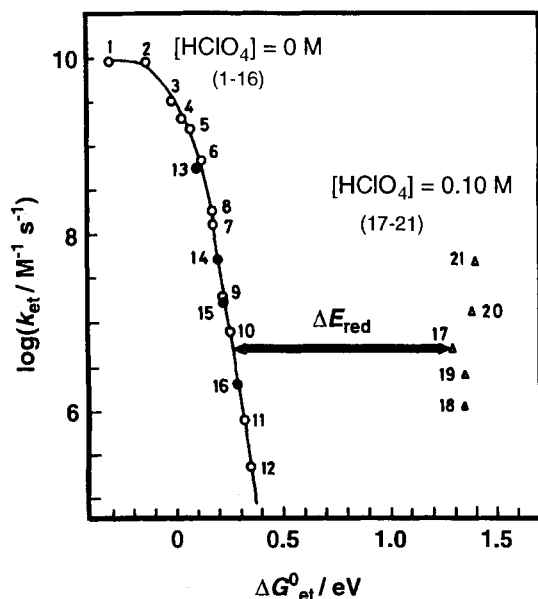
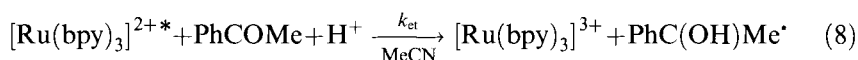
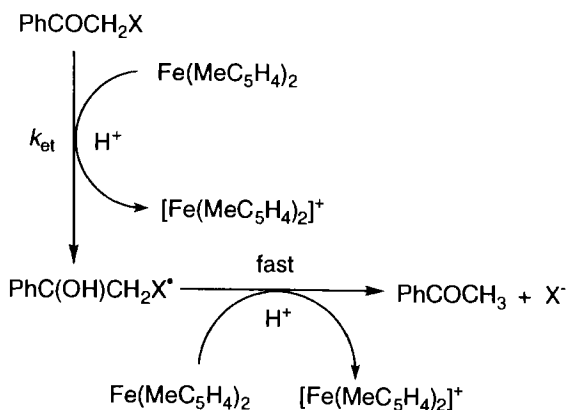


Figure 4. Plots of $\log k_{\text{et}}$ for photoinduced electron transfer reactions from $[\text{Ru}(\text{bpy})_3]^{2+}$ to nitrobenzene derivatives (Nos. 1–16) in the absence of HClO_4 and acetophenone derivatives (Nos. 17–21) in the presence of HClO_4 (0.10 mol dm^{-3}) in MeCN vs. the free energy change of electron transfer, $\Delta G^\circ_{\text{et}}$ {= the difference between the one-electron redox potentials of $[\text{Ru}(\text{bpy})_3]^{2+}$ and the electron acceptors in the absence of HClO_4 in MeCN, $E^\circ_{\text{ox}} - E^\circ_{\text{red}}$ } [77].

presence of HClO_4 in MeCN (Eq. 8):



although no electron transfer occurs in water [77, 86]. The k_{et} value increases linearly with the HClO_4 concentration ($\leq 0.10 \text{ M}$), indicating that the acetophenone radical anion is singly protonated under such experimental conditions as discussed above. The luminescence of $[\text{Ru}(\text{bpy})_3]^{2+}$ is quenched also by other acetophenone derivatives having more negative reduction potentials than acetophenone in the presence of HClO_4 (0.10 M) in acetonitrile at 298 K [77, 86]. Figure 4 shows plots of $\log k_{\text{et}}$ values for photoinduced electron transfer from $[\text{Ru}(\text{bpy})_3]^{2+}$ to nitrobenzene derivatives in the absence of HClO_4 in MeCN [87] and to acetophenone derivatives in the presence of HClO_4 (0.10 M) in MeCN at 298 K vs. the free energy change of electron transfer $\Delta G^\circ_{\text{et}}$ in the absence of HClO_4 [77]. The dependence of $\log k_{\text{et}}$ in the absence of HClO_4 on $\Delta G^\circ_{\text{et}}$ is typical for photoinduced electron transfer; the $\log k_{\text{et}}$ value increases linearly with decreasing $\Delta G^\circ_{\text{et}}$ value with a slope of $-F/(2.3RT)$, which is equal to -16.9 at 298 K , to reach the diffusion-limited value, $2.0 \times 10^{10} \text{ M}^{-1} \text{ s}^{-1}$ [88]. The $\log k_{\text{et}}$ values for acetophenone derivatives in

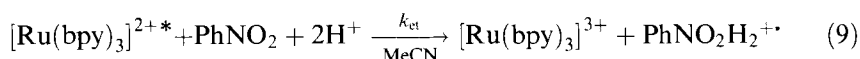


Scheme 6.

the presence of HClO_4 (0.10 M) are much larger than those extrapolated in the correlation between $\log k_{\text{et}}$ and $\Delta G^{\circ}_{\text{et}}$ (Figure 4). This indicates that the one-electron reduction potentials of acetophenone derivatives are shifted in the positive direction by the presence of HClO_4 due to the protonation of the corresponding radical anions. The positive shifts, ΔE_{red} , of acetophenone derivatives in the presence of HClO_4 (0.10 M) are readily evaluated as the difference in the abscissa between the value on the correlation of $\log k_{\text{et}}$ vs. $\Delta G^{\circ}_{\text{et}}$ and the value in the absence of HClO_4 as shown in Figure 4. The ΔE_{red} value of *p*-methoxyacetophenone in the presence of 0.10 M HClO_4 is as large as 1.19 eV, which corresponds to a *sextillion*-fold (10^{21} !) acceleration of the rate of electron transfer at 298 K.

Remarkable acid catalysis is also observed in thermal electron transfer from mild inorganic one-electron reductants, 1,1'-dimethylferrocene $[\text{Fe}(\text{MeC}_5\text{H}_4)_2]$ (or decamethylferrocene $[\text{Fe}(\text{Me}_5\text{C}_5)_2]$) to a series of α -halo ketones such as phenacyl halides (PhCOCH_2X , $\text{X} = \text{Br}, \text{Cl}$) in the presence of HClO_4 in MeCN at 335 K (Scheme 6) [89]. No reaction takes place in the absence of HClO_4 in MeCN or in the presence of HClO_4 in an aqueous solution [89]. The rate constant of electron transfer (k_{et}) increases linearly with increase in the HClO_4 concentration and thereby the second acid-catalyzed electron transfer from $\text{Fe}(\text{MeC}_5\text{H}_4)_2$ to $\text{PhCO}(\text{H})\text{CH}_2\text{X}^{\bullet}$ to yield $[\text{Fe}(\text{MeC}_5\text{H}_4)_2]^+$, PhCOCH_3 and X^- may be much faster than the initial electron transfer (Scheme 6).

Acid-catalyzed electron transfer plays an important role in reduction of not only carbonyl compounds but also other substrates such as O_2 [90, 91], NO_2^- [92], nitrobenzene derivatives [93, 94], nitrosobenzene derivatives [93, 94] and sulfoxides [95, 96]. The k_{et} value for the photoinduced electron transfer from $[\text{Ru}(\text{bpy})_3]^{2+*}$ to nitrobenzene increases parabolically with increase in $[\text{HClO}_4]$ [94]. This indicates that $\text{PhNO}_2^{\bullet-}$ is doubly protonated in the photoinduced electron transfer reaction to give $\text{PhNO}_2\text{H}_2^{+\bullet}$ (Eq. 9):



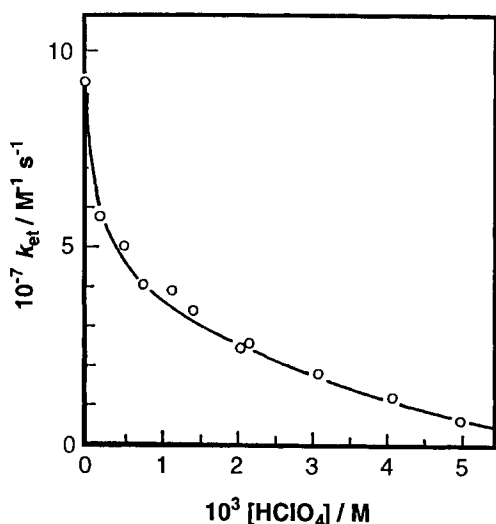
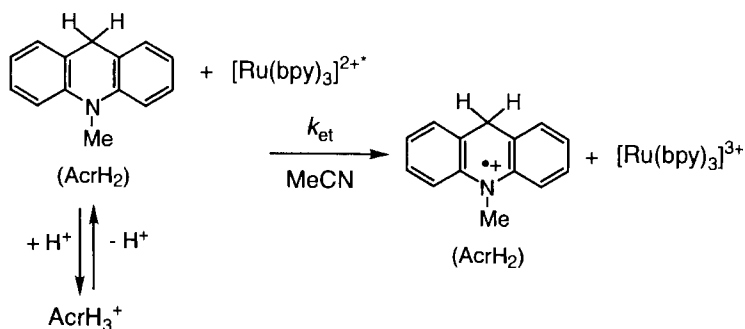


Figure 5. Dependence of the electron transfer rate constant (k_{et}) on $[\text{HClO}_4]$ for photoinduced electron transfer from AcrH_2 to $[\text{Ru}(\text{bpy})_3]^{2+*}$ in the presence of HClO_4 in MeCN at 298 K [102].

1.3.2 Deceleration and Acceleration Effects of Brønsted Acid

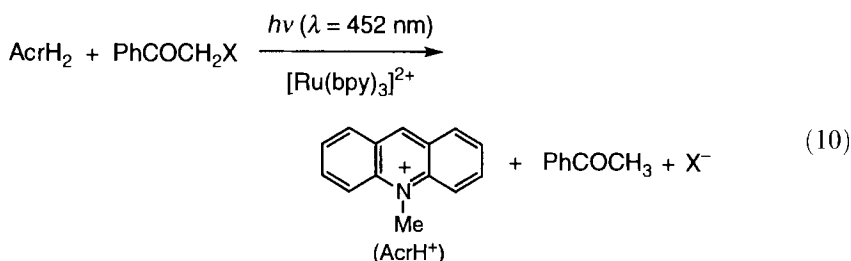
As described above, the protonation of radical anions of electron acceptors produced in thermal and photoinduced electron transfer reactions results in acceleration of the rate of electron transfer as given in Eq. 6, since the electron acceptor ability of electron acceptors is enhanced by the protonation. Conversely, the protonation of electron donors should result in deceleration of the rate of electron transfer, since the donor ability of electron donors is diminished by the protonation. No protonation of metal complexes such as ferrocene derivatives and $[\text{Ru}(\text{bpy})_3]^{2+*}$ used as electron donors occurs in the presence of HClO_4 in MeCN. In contrast to these metal complexes, strong organic electron donors can also be strong bases. For example, analogues of NADH (dihyronicotinamide adenine dinucleotide), which plays a vital role as an electron source in the biological redox reactions [97], are known to be readily protonated in the presence of acid [98–101]. Thus, the rate of photoinduced electron transfer from 9,10-dihydro-10-methylacridine (AcrH_2) to $[\text{Ru}(\text{bpy})_3]^{2+*}$ is decelerated with increasing the HClO_4 concentration as shown in Figure 5 [102]. The inhibitory effect of HClO_4 is ascribed to the protonation of AcrH_2 by which the electron donor ability of AcrH_2 is decreased significantly compared with that of unprotonated AcrH_2 . In such a case, only the unprotonated AcrH_2 can undergo photoinduced electron transfer to $[\text{Ru}(\text{bpy})_3]^{2+*}$ (Scheme 7) and the observed k_{et} value decreases as the concentration of unprotonated AcrH_2 decreases with increasing $[\text{HClO}_4]$.

On the other hand, photoinduced electron transfer from $[\text{Ru}(\text{bpy})_3]^{2+*}$ to PhCOCH_2X is accelerated in the presence of HClO_4 in MeCN as is the case of thermal electron transfer from $[\text{Fe}(\text{MeC}_5\text{H}_4)_2]$ to PhCOCH_2X (Scheme 6).



Scheme 7.

Thus, the $[\text{Ru}(\text{bpy})_3]^{2+}$ -catalyzed photoreduction of PhCOCH_2X by AcrH_2 (Eq. 10)



is initiated by the reductive quenching of $[\text{Ru}(\text{bpy})_3]^{2+*}$ by AcrH_2 in the absence of HClO_4 , while the quenching mechanism is changed to the acid-catalyzed oxidative quenching of $[\text{Ru}(\text{bpy})_3]^{2+*}$ by PhCOCH_2X in the presence of high concentrations of HClO_4 when the reductive quenching is inhibited [102]. The reductive quenching of $[\text{Ru}(\text{bpy})_3]^{2+*}$ by AcrH_2 gives $\text{AcrH}_2^{\bullet+}$ and $[\text{Ru}(\text{bpy})_3]^+$, followed by electron transfer from $[\text{Ru}(\text{bpy})_3]^+$ to PhCOCH_2X to yield $\text{PhCOCH}_2\text{X}^{\bullet-}$ accompanied by regeneration of $[\text{Ru}(\text{bpy})_3]^{2+}$. The acid-catalyzed oxidative quenching of $[\text{Ru}(\text{bpy})_3]^{2+*}$ by PhCOCH_2X gives $[\text{Ru}(\text{bpy})_3]^{3+}$ and $\text{PhC}(\text{OH})\text{CH}_2\text{X}^{\bullet}$, followed by electron transfer from AcrH_2 to $[\text{Ru}(\text{bpy})_3]^{3+}$ to yield $\text{AcrH}_2^{\bullet+}$ accompanied by regeneration of $[\text{Ru}(\text{bpy})_3]^{2+}$. In both cases, net electron transfer from AcrH_2 to PhCOCH_2X is attained and the subsequent electron transfer from $\text{AcrH}_2^{\bullet+}$, which is formed by the deprotonation of $\text{AcrH}_2^{\bullet+}$, to $\text{PhCOCH}_2\text{X}^{\bullet-}$ (or $\text{PhC}(\text{OH})\text{CH}_2\text{X}^{\bullet}$) yields the final product in Eq. 10 [102]. Direct UV irradiation of the absorption band due to AcrH_2 ($\lambda_{\text{max}} = 285 \text{ nm}$) in the presence of phenacyl halides (PhCOCH_2X) also results in photoinduced electron transfer from the singlet excited state of AcrH_2 to PhCOCH_2X , leading to the same products as obtained by the $[\text{Ru}(\text{bpy})_3]^{2+}$ -catalyzed photochemical reaction (Eq. 10) [103, 104].

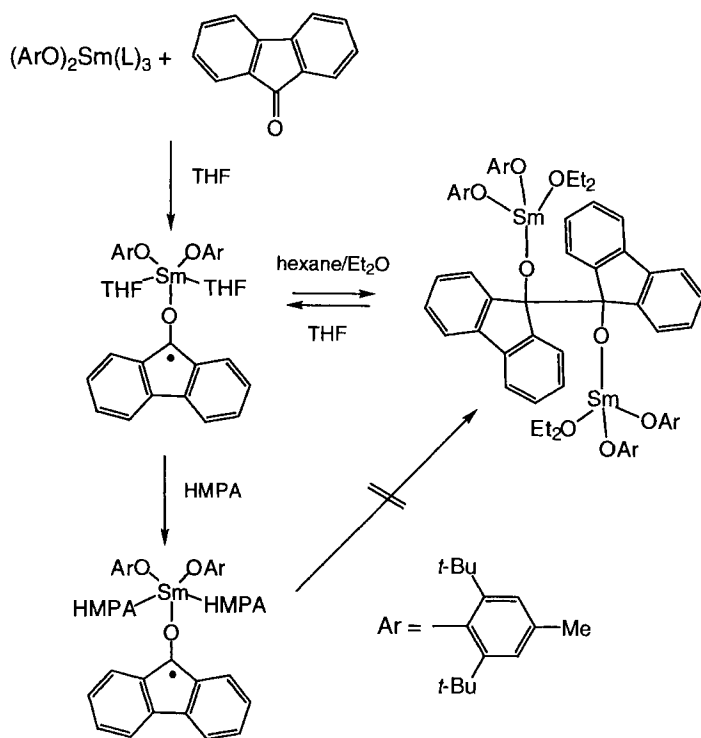
1.3.3 Catalysis of Metal Ions

Metal ion complexes with radical anions

Brønsted acid catalysis in electron transfer reactions can also be applied to catalysis of metal ions in electron transfer reactions, since not only protons but also metal

ions (M^{n+}) which can act as Lewis acids are able to form strong bond with radical anions. It is certainly desired to detect such radical anion–metal ion complexes. The complex formation between radical anions and metal ions has been known for a long time, since metal ion complexes of ketyls or radical anions of ketones can be readily produced by the one-electron reduction of ketones by reducing with metals [105, 106]. These radical anion–metal ion complexes have been utilized as key intermediates in a variety of organic reactions [107–115]. Although there have been a number of reports on the spectroscopic detection of metal ketyl species in situ [116–121], the high reactivity of the radical anion–metal ion complexes had precluded the isolation and structural determination.

The use of a sterically demanding samarium(II) reducing agent, $\text{Sm}(\text{OAr})_2(\text{THF})_3$ ($\text{Ar} = \text{C}_6\text{H}_2-2,6-t\text{-Bu}_2-4\text{-Me}$) and a highly conjugated aromatic ketone such as fluorenone can sufficiently stabilize the radical anion–metal ion complex with hexamethylphosphoric triamide (HMPA), which was isolated and structurally characterized by X-ray analysis [122]. This complex possesses a distorted trigonal bipyramidal structure with one fluorenone ketyl and two ArO ligands at the equatorial and two THF ligands at the apical positions (Scheme 8). When the fluorenone radical anion– Sm^{3+} complex is dissolved in hexane–diethyl ether, the two THF ligands are substituted by one molecule of Et_2O , and the radical anion complex dimerizes into a pinacolate (Scheme 8) [123]. The newly formed C–C bond in the

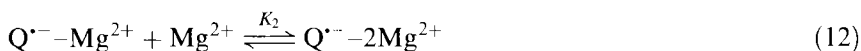


Scheme 8.

pinacolate, which is unusually long [1.613(9) Å], can be readily cleaved to regenerate the fluorenone radical anion–Sm³⁺ complex quantitatively (Scheme 8), and thereby the pinacol coupling process is completely reversible [123]. The THF ligand in the fluorenone radical anion–Sm³⁺ complex can be readily replaced by HMPA and the HMPA coordinated complex is stable against ether or hexane (Scheme 8) [123, 124]. The use of HMPA as a stabilizing ligand has been applied to isolate Na⁺ and Ca²⁺ complexes of fluorenone and benzophenone radical anions [123, 125, 126]. Similarly, a series of lanthanide ion (Sm³⁺ and Yb³⁺) complexes with benzophenone and fluorenone radical anions have been isolated and characterized [127]. Sm³⁺ complexes of 2,6-di-*t*-butylsemiquinone and azobenzene radical anions have also been isolated and structurally characterized [128–130]. Transition metal complexes of fluorenone radical anion are reported to be prepared via metathesis reactions of the corresponding alkali-metal complexes with transition metal chlorides as well as via deprotonation of pinacols with a transition metal base [131].

Metal ion catalysis in electron transfer by complexation with radical anions

A relation between complexation of metal ions with radical anions of electron acceptors and the metal ion catalysis in electron transfer reduction of electron acceptors was first clarified for the Mg²⁺ complex of semiquinone radical anions (see below) [132]. Although no electron transfer occurs from decamethylferrocene [Fe(Me₅C₅)₂] to *p*-benzoquinone (Q) in MeCN, the electron transfer is complete upon mixing [Fe(Me₅C₅)₂] and Q in the presence of Mg(ClO₄)₂. The transient electronic spectra of semiquinone radical anion in the presence of different concentrations of Mg(ClO₄)₂ are obtained by measuring the change in initial absorbance at various wavelengths with use of a stopped-flow spectrophotometer as shown in Figure 6 [132]. The transient absorption spectrum of Q^{•−} in the presence of 1.0 × 10^{−2} M Mg²⁺ (λ_{max} = 590 nm) is significantly red-shifted compared with that in the absence of Mg²⁺ (λ_{max} = 422 nm) [133]. Further addition of Mg²⁺ results in a blue shift to λ_{max} = 415 nm with a clean isosbestic point. Such spectroscopic changes clearly indicate the formation of complexes between Q^{•−} and Mg²⁺, which requires two steps. The first step is the formation of a 1:1 complex (Q^{•−}–Mg²⁺) and the second step is an additional addition of Mg²⁺ to form a 1:2 complex (Q^{•−}–2Mg²⁺), as shown in Eqs. 11 and 12:



Transient electronic spectra of the 1:1 and 1:2 complexes are also observed in the electron transfer reduction of 2,5-dichloro-*p*-benzoquinone and 2,5-dimethyl-*p*-benzoquinone [132]. Although the formation constant K_1 for the 1:1 complex is too large to be determined, the formation constant K_2 for the 1:2 complex can be determined as 4.5 M^{−1} and the K_2 value decreases with a decrease in the electron-donating ability of X-substituted semiquinone radical anion (X = 2,5-Me₂ > H > 2,5-Cl₂) [132]. Thus, Mg²⁺ acts as a Lewis acid which can bind with the radical anion base, although the radical anion–Mg²⁺ complexes are unstable owing to the facile disproportionation [132]. The formation of such complexes is also confirmed

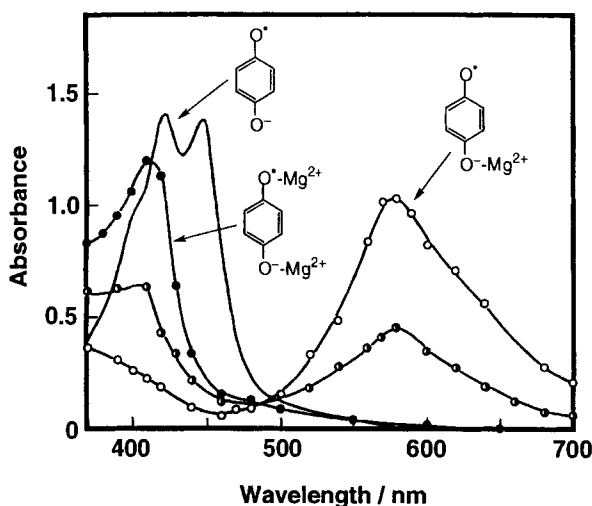


Figure 6. Transient absorption spectra of semiquinone radical anion formed in electron transfer reduction of *p*-benzoquinone (Q : 2.4×10^{-4} M) by $[Fe(Me_5C_5)_2]$ (2.4×10^{-3} M) in the presence of $Mg(ClO_4)_2$ [1.0×10^{-2} M (○), 2.0×10^{-1} M (◐)] and by $[Fe(MeC_5H_4)_2]$ (2.4×10^{-3} M) in the presence of $Mg(ClO_4)_2$ [1.6 M (●)] in deaerated MeCN at 198 K [132]. The solid line spectrum without symbols shows the absorption spectrum of $Q^{\bullet-}$ in the absence of $Mg(ClO_4)_2$, prepared by the reaction of Q (2.4×10^{-4} M) with $Me_4N^+OH^-$ (2.4×10^{-4} M) in deaerated MeCN at 298 K [132].

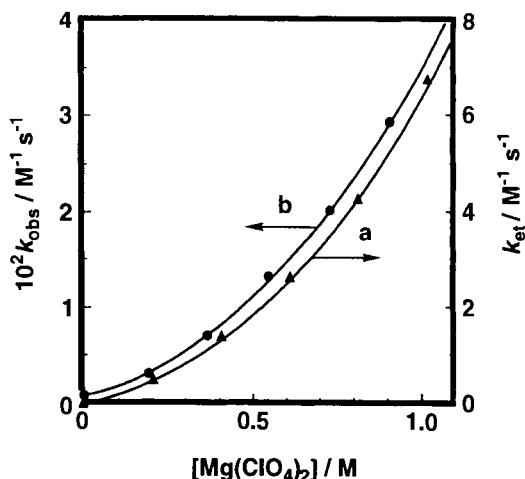
by the ESR spectra observed in the electron transfer reaction from $Fe(MeC_5H_4)_2$ to Q in the presence of Mg^{2+} in deaerated MeCN by applying a rapid-mixing ESR technique [132]. The g value of the $Q^{\bullet-}-2Mg^{2+}$ complex (2.0043) is appreciably smaller than that of free $Q^{\bullet-}$ because of the decrease in the spin density on the oxygen atom in the Mg^{2+} complex [132]. The strong binding between $Q^{\bullet-}$ and Mg^{2+} makes it possible to reduce Q by a weak electron donor which would otherwise have no ability to reduce Q .

Thus, an efficient electron transfer from (TPP)Co (TPP = tetraphenylporphyrin dianion) to Q occurs in the presence of $Mg(ClO_4)_2$ in MeCN at 298 K to yield $[(TPP)Co]^+$ (Eq. 13):



although no electron transfer from (TPP)Co to Q occurs without the metal ion [132]. The electron transfer rates obeyed second-order kinetics, showing a first-order dependence on each reactant concentration. The observed rate constant of electron transfer (k_{et}) increases with increase in $[Mg^{2+}]$ to exhibit a first-order dependence on $[Mg^{2+}]$ at low concentrations, changing to a second-order dependence at high concentrations as shown in Figure 7. Such a dependence of k_{et} on $[Mg^{2+}]$ in Figure 7 is essentially the same as the pH dependence of k_{et} for electron transfer from *cis*-

Figure 7. Dependence of k_{et} and k_{obs} on $[\text{Mg}(\text{ClO}_4)_2]$ for (a) electron transfer from $(\text{TPP})\text{Co}$ ($1.0 \times 10^{-5} \text{ M}$) to p -benzoquinone ($3.7 \times 10^{-3} \text{ M}$) and (b) Diels-Alder reaction of 9,10-dimethylantracene ($1.3 \times 10^{-3} \text{ M}$) with p -benzoquinone ($3.6 \times 10^{-1} \text{ M}$) in the presence of $\text{Mg}(\text{ClO}_4)_2$ in deaerated MeCN at 298 K, respectively [132].



$[\text{Et}_2\text{Co}(\text{bpy})_2]^+$ to Q (Scheme 4) in Figure 3, where the first-order dependence of k_{et} with respect to $[\text{H}^+]$ in the region of $\text{pH} < \text{p}K_{\text{a}1}$ (the slope being -1 for the plot of $\log k_{\text{et}}$ vs. pH) changes to a second-order dependence (the slope being -2) in the region of $\text{pH} < \text{p}K_{\text{a}2}$ [77]. Thus, Eq. (6) is rewritten as:

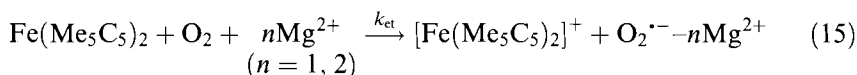
$$k_{\text{et}} = k^{\circ}_{\text{et}}(1 + K_1[\text{Mg}^{2+}] + K_1K_2[\text{Mg}^{2+}]^2) \quad (14)$$

the validity of which was confirmed by the linear plot of $k_{\text{et}}/[\text{Mg}^{2+}]$ vs. $[\text{Mg}^{2+}]$ for the data in Figure 7 ($k^{\circ}_{\text{et}} = 0$) [132]. From the slope and intercept the K_2 value (4.1 M^{-1}) is obtained, which agrees well with that (4.5 M^{-1}) determined directly from the spectral change of $\text{Q}^{\cdot-}$ in the presence of Mg^{2+} (Figure 6) [132]. The K_2 values for substituted semiquinone radical anions can also be determined from the dependence of k_{et} on $[\text{Mg}(\text{ClO}_4)_2]$ and they also agree with those determined from direct spectroscopic detection of 1:2 complexes between substituted semiquinone radical anions and Mg^{2+} [132]. Such agreements for each quinone indicate that the catalysis of the metal ion is ascribed to the 1:1 and 1:2 complex formation between semiquinone radical anions and the metal ion, which causes a positive shift of the one-electron reduction potential of the quinone. It should be noted that there is little interaction between Q and Mg^{2+} . As described earlier, there is no need to have an interaction between Q and Mg^{2+} and the interaction with the reduced state ($\text{Q}^{\cdot-}$) is essential to accelerate the rate of electron transfer.

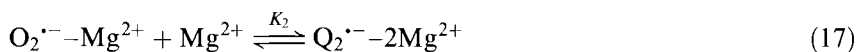
Electron transfer from $\text{cis-}[\text{R}_2\text{Co}(\text{bpy})_2]^+$ to Q also occurs efficiently in the presence of Mg^{2+} in MeCN, although no electron transfer occurs in the absence of Mg^{2+} [134, 135]. The observed rate constant of electron transfer (k_{et}) also exhibits a first-order dependence on $[\text{Mg}^{2+}]$ at low concentrations, changing to a second-order dependence at high concentrations [135]. The rate of electron transfer is further increased by the presence of both $\text{Mg}(\text{ClO}_4)_2$ and HClO_4 . Thus, the k_{et} value for electron transfer from $\text{cis-}[\text{Et}_2\text{Co}(\text{bpy})_2]^+$ to Q in the presence of $\text{Mg}(\text{ClO}_4)_2$

(1.0 M) and HClO_4 (0.10 M) in MeCN at 298 K is $5.2 \times 10^2 \text{ M}^{-1} \text{ s}^{-1}$, which is 5.2×10^{16} times faster than the rate constant without $\text{Mg}(\text{ClO}_4)_2$ or HClO_4 ($1.0 \times 10^{-14} \text{ M}^{-1} \text{ s}^{-1}$) which is estimated from the correlation between $\log k_{\text{et}}$ and E°_{red} of the oxidants [135]. Various metal ions, in particular rare earth metal ions such as scandium ion, have also been reported to act as very efficient catalysts in the electron transfer reduction of Q by complexation with $\text{Q}^{\bullet-}$ [136].

Mg^{2+} is also effective for electron transfer reduction of O_2 in acetonitrile [137]. Efficient electron transfer from $\text{Fe}(\text{Me}_5\text{C}_5)_2$ to O_2 occurs in the presence of $\text{Mg}(\text{ClO}_4)_2$ in MeCN at 298 K to yield $[\text{Fe}(\text{Me}_5\text{C}_5)_2]^+$ (Eq. 15):



although no electron transfer occurs from $[\text{Fe}(\text{Me}_5\text{C}_5)_2]$ to O_2 in the absence of Mg^{2+} under otherwise the same experimental conditions [137]. As observed in the Mg^{2+} -catalyzed electron transfer from (TPP)Co to Q in Figure 7a, the observed pseudo-first-order rate constant of electron transfer (k_{et}) in an O_2 -saturated MeCN solution exhibits a first- and second-order dependence on $[\text{Mg}^{2+}]$ at low and high Mg^{2+} concentrations, respectively. This indicates that $\text{O}_2^{\bullet-}$ forms complexes with Mg^{2+} with 1:1 and 1:2 stoichiometries at low and high Mg^{2+} concentrations (Eqs. 16 and 17), respectively:



From the linear plot of $(k_{\text{et}} - k_0)/[\text{Mg}^{2+}]$ vs. $[\text{Mg}^{2+}]$ based on Eq. 14 the K_2 value (3.2 M^{-1}) is obtained for the 1:2 complex between $\text{O}_2^{\bullet-}$ and Mg^{2+} [137].

Other metal ions such as Sc^{3+} can also form complexes with $\text{O}_2^{\bullet-}$ [138]. $\text{O}_2^{\bullet-}$ can be produced by photoinduced electron transfer from the excited state of dimeric 1-benzyl-1,4-dihydronicotinamide $[(\text{BNA})_2]$, which can act as a unique two-electron donor [139, 140], to O_2 in propionitrile at low temperatures (e.g. -30°C) [138]. Addition of scandium triflate $[\text{Sc}(\text{OTf})_3]$ to the $(\text{BNA})_2\text{-O}_2$ system results in the appearance of the sharp isotropic ESR signal under irradiation of the light in fluid solution at -30°C as shown in Figure 8 [138]. The clear eight-line *isotropic* spectrum is ascribed to the superhyperfine coupling of $\text{O}_2^{\bullet-}$ with the 7/2 nuclear spin of the scandium nucleus ($a_{\text{Sc}} = 4.26 \text{ G}$). The isotropic g value (2.0163) is appreciably smaller than the average value (2.030) [141] of the principal three g components of $\text{O}_2^{\bullet-}$ at 77 K, being consistent with the spin delocalization to the scandium nucleus as demonstrated by observation of superhyperfine. The $\text{O}_2^{\bullet-}\text{-Sc}^{3+}$ complex is fairly stable at -30°C but the signal intensity decreases with increase in temperature because of the faster disproportionation of the $\text{O}_2^{\bullet-}$ complex [138]. This is the first definitive detection of a $\text{O}_2^{\bullet-}$ -metal ion complex which is responsible for catalysis of metal ions in electron transfer reduction of oxygen.

The $\text{O}_2^{\bullet-}\text{-Sc}^{3+}$ complex can be stabilized by complexation with 3 equiv. of HMPA ligand as reported for the case of the fluorenone radical anion- Sm^{3+}

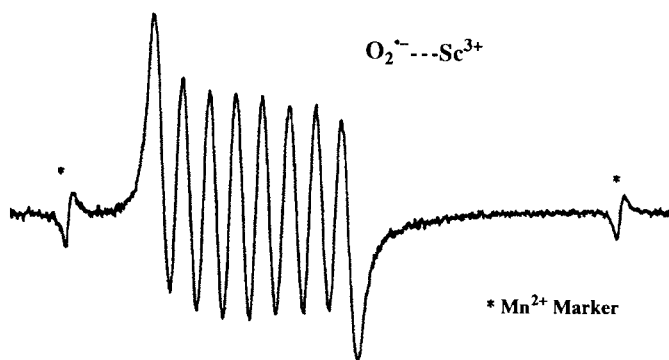


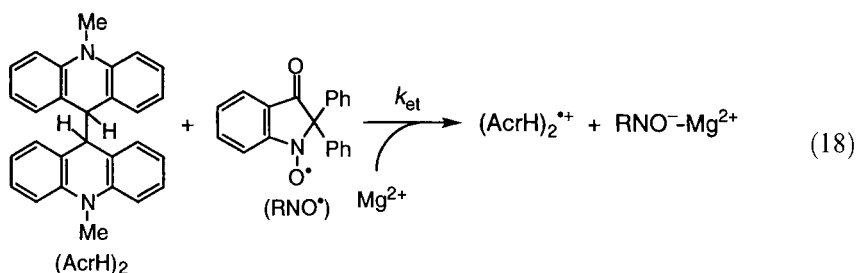
Figure 8. ESR spectrum observed during irradiation of an oxygen-saturated propionitrile solution containing $(\text{BNA})_2$ (1.7×10^{-3} M) and $\text{Sc}(\text{OTf})_3$ (2.7×10^{-2} M) with a high-pressure mercury lamp at -30°C [138].

complex [123, 124]. The ESR spectrum of the $\text{O}_2^{\bullet-}-\text{Sc}^{3+}-\text{HMPA}$ complex can be detected even at 60°C [138]. The g value increases with decrease in temperature from 2.0163 (60°C) to 2.0168 (-30°C), when the a_{Sc} value decreases from 3.88 G (60°C) to 3.77 G (-30°C). Such change in the g and a_{Sc} values with temperature may be attributed to the stronger coordination of HMPA to Sc^{3+} , which results in weaker coordination of $\text{O}_2^{\bullet-}$ to Sc^{3+} at lower temperature. The weaker the coordination of $\text{O}_2^{\bullet-}$ to Sc^{3+} , the closer to free $\text{O}_2^{\bullet-}$, and then the larger is the g value but the smaller is the a_{Sc} value.

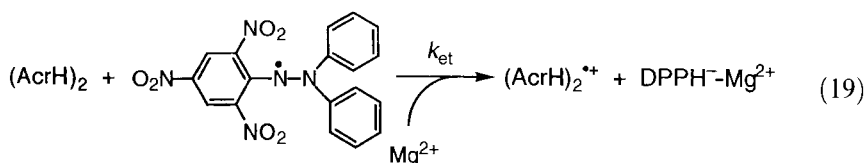
Oxygen enriched in ^{17}O gave the ESR spectrum of the $\text{O}_2^{\bullet-}-\text{Sc}^{3+}-\text{HMPA}$ complex with ^{17}O enriched oxygen, for which two inequivalent $a(^{17}\text{O})$ values (21 and 14 G) were obtained [138]. Such inequivalent $a(^{17}\text{O})$ values are fully consistent with an ‘end-on’ coordination form of $^{\bullet}\text{O}-\text{O}^--\text{Sc}^{3+}(\text{HMPA})$ in which the electron spin is more localized at the terminal oxygen. The unrestricted Hartree-Fock (UHF) SCF optimization using the 6-311++G** basis set also supports an ‘end-on’ coordination form of $^{\bullet}\text{O}-\text{O}^--\text{Sc}^{3+}$ [138]. Such an ‘end-on’ coordination of $\text{O}_2^{\bullet-}$ to Sc^{3+} results in the removal of degeneracy of the SOMO (singly occupied molecular orbital) orbital, decreasing the relaxation time significantly to make it possible to observe the ESR spectrum in fluid solution at temperatures even higher than room temperature. When $\text{O}_2^{\bullet-}$ is adsorbed on solid surfaces, both side-on and end-on coordinations have been reported depending on the metal oxide [142–145].

Metal ion catalysis in electron transfer reduction of radicals and radical anions

Metal ions can also drastically accelerate the electron transfer reduction of nitroxide and nitrogen centered radicals [146]. Electron transfer from 10,10'-dimethyl-9,9',10,10'-tetrahydro-9,9'-biacridine $[(\text{AcrH})_2]$, which can act as an organic electron donor [147, 148], to 2,3-dihydro-3-oxo-2,2-diphenyl-1*H*-indol-1-yloxy radical (RNO^{\bullet}) occurs efficiently in the presence of $\text{Mg}(\text{ClO}_4)_2$ in MeCN at 298 K (Eq. 18):



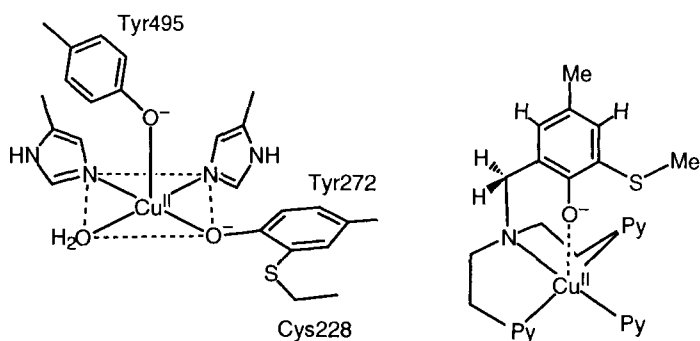
although no electron transfer occurs without Mg(ClO₄)₂ under otherwise the same experimental conditions. The k_{et} value increases linearly with an increase in [Mg²⁺], indicating 1:1 complex formation between the resulting RNO⁻ and Mg²⁺, since no interaction between Mg²⁺ and the RNO[•] radical has been detected in the electronic spectra in the presence of Mg²⁺ [146]. Similarly, electron transfer from (AcrH)₂ to 1,1-diphenyl-2-picrylhydrazyl (DPPH[•]) occurs efficiently in the presence of Mg²⁺ (Eq. 19):



and the k_{et} value also increases linearly with an increase in [Mg²⁺] [146].

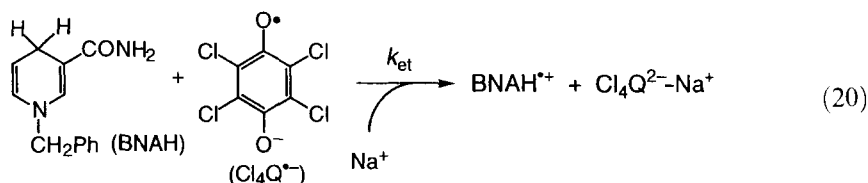
Metal ions also play an essential role in controlling the reactivity of protein radicals through coordination in several biologically important redox processes [149]. Galactose oxidase (GAO, EC 1.1.3.9) is one of the best characterized examples of such systems, where a tyrosyl radical directly coordinated to Cu(II) center is involved as the active species in the aerobic oxidation of D-galactose and primary alcohols to the corresponding aldehydes [150–153]. The crystal structure of galactose oxidase at 1.7 Å resolution has clearly shown that the tyrosine residue (Tyr 272, the precursor of the tyrosyl radical) is covalently bound to the sulfur atom of the adjacent Cys 228 at the α-position of the phenol ring as illustrated in Scheme 9 [151]. The strong binding of the organic cofactor as the phenolate form to the Cu(II) ion is expected to enhance the oxidizing ability of the phenoxyl radical as compared to the corresponding free radical. The GAO model study has shown that the one-electron reduction potential of a phenoxyl radical ($E^{\circ}_{red} = -0.31$ V vs. SCE) is shifted to a much more positive value ($E^{\circ}_{red} = +0.66$ V vs. SCE) when the corresponding phenolate is bound to the Cu(II) ion in Scheme 9 [154]. It has also been shown that such a synthetic model copper(II) complex of the active form of GAO possesses the alcohol-oxidation ability [155–158].

Compared with the electron transfer reduction of neutral radicals, the reduction of radical anions may be more readily catalyzed by metal ions which have weak Lewis acidity, since the binding to dianions produced in the electron transfer reduction of radical anions should be much stronger than the binding to monoanions. As such, even Na⁺ has been reported to accelerate electron transfer from 1-benzyl-1,4-



Scheme 9.

dihydronicotinamide (BNAH) to *p*-chloranil radical anion ($\text{Cl}_4\text{Q}^{\bullet-}$) in MeCN (Eq. 20) [159]:



The addition of NaClO_4 to the $\text{BNAH}-\text{Cl}_4\text{Q}^{\bullet-}$ system results in an increase in the rate of electron transfer from BNAH to $\text{Cl}_4\text{Q}^{\bullet-}$ where the k_{obs} value increases linearly with increase in $[\text{NaClO}_4]$, whereas no acceleration of the rates is observed by addition of *n*- Bu_4NClO_4 [159]. The significant catalytic effect of Na^+ on the electron transfer from BNAH to $\text{Cl}_4\text{Q}^{\bullet-}$ was also confirmed by a voltammetric study [159]. The reduction peak potential of $\text{Cl}_4\text{Q}^{\bullet-}$ is significantly shifted to the positive direction in the presence of 0.10 M NaClO_4 as compared with the position in the presence of 0.10 M *n*- Bu_4NClO_4 [159]. Such a positive shift in the presence of NaClO_4 indicates that the one-electron reduction of $\text{Cl}_4\text{Q}^{\bullet-}$ is accompanied by complex formation between the dianion (Cl_4Q^{2-}) and Na^+ , since no effect of Na^+ was observed on the electronic spectrum of $\text{Cl}_4\text{Q}^{\bullet-}$ [159]. In fact, the redox couple $\text{Cl}_4\text{Q}/\text{Cl}_4\text{Q}^{\bullet-}$ is unaffected by the presence of 0.10 M NaClO_4 compared with that in the presence of 0.10 M *n*- Bu_4NClO_4 [159]. Other metal ions such as Mg^{2+} , which is a relatively strong Lewis acid compared with Na^+ , can interact with the radical anion (see above), leading to rapid disproportionation of the radical anion [132].

Bimetallic catalysis in electron transfer

The biological catalytic activity of metalloproteins for redox reactions is usually associated with a particular coordination environment of the metal active site [160, 161]. In particular, there has been considerable interest in O_2 -binding and -activation by non-heme metalloenzymes [162–167]. A redox-active metal center is often associated with another metal center which can accelerate the redox process of O_2

in biological systems [160, 161]. A typical example is the copper–zinc superoxide dismutase (Cu,Zn-SOD) which contains an imidazolate-bridged Cu(II)–Zn(II) bimetallic center in its active site [168–171]. This enzyme catalyzes the disproportionation (dismutation) of toxic $\text{O}_2^{\bullet-}$ to O_2 and H_2O_2 [172, 173], thus preventing oxidative damage by the anticancer and antiaging mechanisms [174, 175]. The copper ion is coordinated to four imidazole N atoms of histidine residues in a distorted square-pyramidal geometry while the zinc ion located at a distance of 6.2 Å from the copper ion is coordinated to a carboxylato O atom of an aspartic acid residue and three imidazole N atoms of histidine residues in a distorted tetrahedral structure [168, 169]. A number of SOD model complexes have been designed and synthesized to provide valuable insights into the structure and catalytic function of the Cu,Zn-SOD active site [176–182].

The most important question to be answered is how the Cu,Zn-SOD active site can accelerate both the oxidation and reduction of $\text{O}_2^{\bullet-}$, required for the rapid disproportionation. Such a dual role would be made possible by the bimetallic system, since any monometallic system can only activate either the oxidation or reduction of $\text{O}_2^{\bullet-}$. The important role of Zn(II) ion in the bimetallic system to activate both the oxidation and reduction of $\text{O}_2^{\bullet-}$ has been implicated by a well-characterized SOD model, that is, an imidazolate-bridged Cu(II)–Zn(II) heterodinuclear complex containing a dinucleating ligand, Hbdpi {Hbdpi = 4,5-bis[di(2-pyridylmethyl)-aminomethyl]imidazole}, shown in Figure 9 [182]. The Cu(II)–Zn(II) distance of 6.197(2) Å in the Cu(II)–Zn(II) heterodinuclear complex agrees well with that of native Cu,Zn-SOD (6.2 Å), and each metal has the pentacoordinate geometry with the imidazolate nitrogen, two pyridine nitrogens, the tertiary amine nitrogen and a solvent (MeCN or H_2O) [182]. The ESR spectrum of complex of the Cu(II)–Zn(II) heterodinuclear complex gave the well-defined ESR parameters ($g_{\parallel} = 2.10$, $g_{\perp} = 2.24$, $|A_{\parallel}| = 11.7$ mT and $|A_{\perp}| = 12.4$ mT), which indicate that the Cu(II) ion in the complex has a trigonal bipyramidal environment and a d_{z^2} ground state

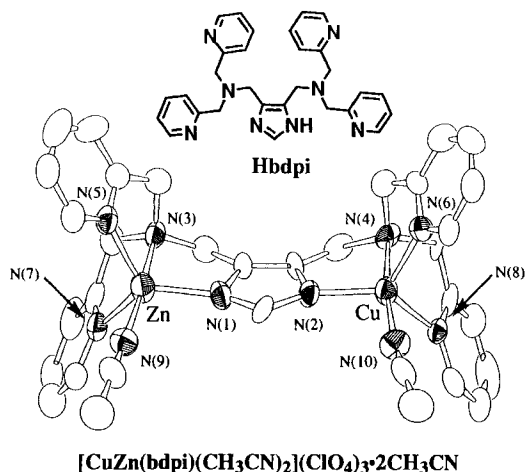
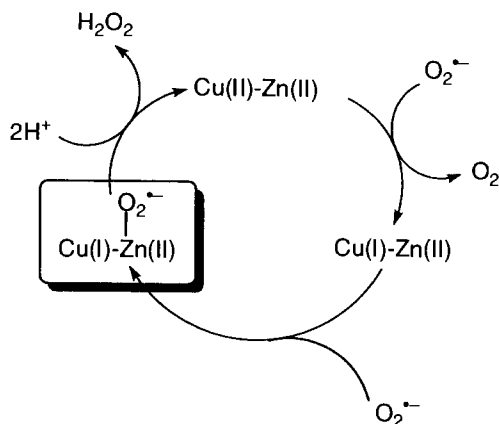


Figure 9. ORTEP view of [CuZn(bdpi)(MeCN)₂](ClO₄)₃·2MeCN [182]. The hydrogen atoms are omitted for clarity.

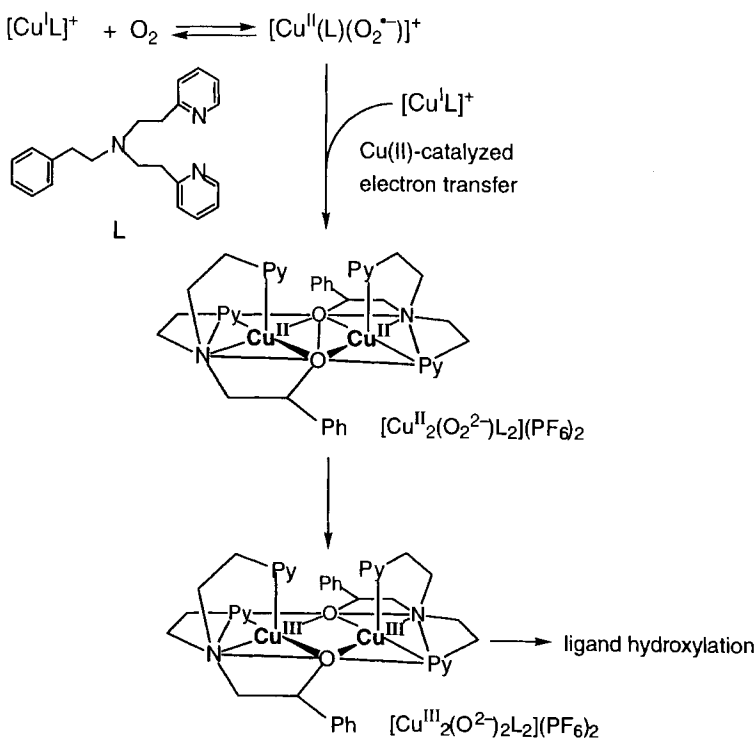
following the criteria given by Bencini et al. [183], in agreement with the X-ray structure in Figure 9 [182]. The observation of a well-defined ESR spectrum also confirms that the complex retains its imidazolate-bridged Cu(II)–Zn(II) heterodinuclear structure and that it is not a 1:1 mixture of Cu(II)–Cu(II) and Zn(II)–Zn(II) homodinuclear complexes. The Cu(II)–Zn(II)SOD model complex, which has a coordination site available for the binding of superoxide as shown in Figure 9, exhibits the highest activity among the structurally established SOD models reported so far [181, 184, 185].

A large positive shift (about 0.2 V) in the $E_{1/2}$ value of the Cu(II)–Zn(II) complex is observed compared with the corresponding Cu(II) mononuclear complexes [172]. This indicates that an important role of Zn(II) ion in the imidazolate-bridged Cu(II)–Zn(II) complex is to accelerate an outer-sphere electron transfer from $O_2^{\cdot-}$ to produce the Cu(I)–Zn(II) complex, when the free energy change of electron transfer becomes thermodynamically more favorable compared with that without Zn(II) ion. The presence of Zn(II) which can act as a Lewis acid is also able to accelerate an electron transfer from the Cu(I)–Zn(II) complex to $O_2^{\cdot-}$, since $O_2^{\cdot-}$ can form a complex with metal ions acting as a Lewis acid to accelerate the electron transfer reduction of $O_2^{\cdot-}$ (see above) [137, 138]. Such an acceleration for the reduction of $O_2^{\cdot-}$ can also be attained by a Brønsted acid instead of a Lewis acid since Valentine et al. reported that the reduction of $O_2^{\cdot-}$ for the zinc-deficient SOD form is acid-catalyzed [173, 186]. Thus, the essential role of Zn(II) ion in SODs is suggested to accelerate both the oxidation and reduction of superoxide by controlling the redox potentials of Cu(II) ion and superoxide in the catalytic cycle of SOD as shown in Scheme 10 [182]. A similar effect is also expected for another copper ion in the Cu(II)–Cu(II) homodinuclear complex containing the same Hbdpi ligand [182]. The role of Zn(II) ion may also lie in structural stabilization of the enzyme. The exact catalytic role of Zn(II) ion in SODs has yet to be examined in detail.

The binding of $O_2^{\cdot-}$ to Cu(II) ion can facilitate the further reduction of $O_2^{\cdot-}$ by Cu(I) ion to O_2^{2-} to give a $\mu\text{-}\eta^2\text{:}\eta^2$ -peroxodicopper complex [162, 187], which has been confirmed to exist in the enzyme active site of oxyhemocyanin [188, 189]. The



Scheme 10.



Scheme 11.

reaction of $[\text{Cu}^{\text{I}}\text{L}](\text{PF}_6)$ $\{\text{L} = N,N\text{-bis}[2\text{-(2-pyridyl)ethyl}]\text{-2-phenylethylamine}\}$ with O_2 in THF at -80°C was reported to give the $\mu\text{-}\eta^2\text{:}\eta^2\text{-peroxodicopper}$ complex, $[\text{Cu}^{\text{II}}_2(\text{O}_2^{2-})\text{L}_2](\text{PF}_6)_2$, the formation of which was confirmed by spectroscopic analyses [190, 191]. The kinetic study on formation of the peroxo complex indicates that the reaction of the Cu(I) complex and the monomeric superoxocopper(II) complex is rate-determining, as shown in Scheme 11 [191]. A superoxocopper(II) complex with a sterically hindered ligand which can prevent formation of the $\mu\text{-}\eta^2\text{:}\eta^2\text{-peroxodicopper}$ complex was isolated and the X-ray structure was determined to show a side-on binding of $\text{O}_2^{\bullet-}$ the Cu(II) ion [192]. The strong interaction between $\text{O}_2^{\bullet-}$ and the Cu(II) ion makes it possible to reduce $\text{O}_2^{\bullet-}$ to O_2^{2-} further by another $[\text{Cu}^{\text{I}}\text{L}]^+$, leading to the formation of the $\mu\text{-}\eta^2\text{:}\eta^2\text{-peroxodicopper}$ complex (Scheme 11). The change in the one-electron reduction potential of $\text{O}_2^{\bullet-}$ by the binding to the Cu(II) ion has yet to be determined.

The further intramolecular electron transfer from the two Cu(II) ions to O_2^{2-} in the $\mu\text{-}\eta^2\text{:}\eta^2\text{-peroxodicopper}$ complex may result in the O–O bond cleavage to give the bis- $\mu\text{-oxodicopper(III)}$ complex, which is suggested to be the actual reactive intermediate for the efficient benzylic ligand hydroxylation as also shown in Scheme 11 [191]. Interconversion between the $\mu\text{-}\eta^2\text{:}\eta^2\text{-peroxodicopper}$ complex and the bis- $\mu\text{-oxodicopper(III)}$ complex was observed using the $i\text{-Pr}_3\text{TACN}$ ligand ($i\text{-Pr}_3\text{TACN} =$

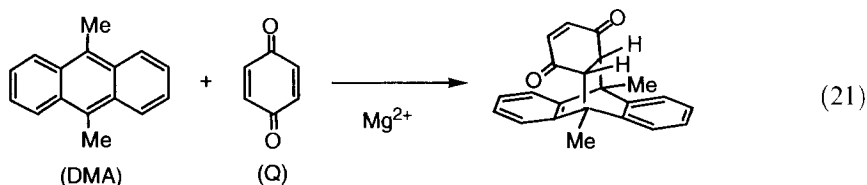
1,4,7-triisopropyl-1,4,7-triazacyclononane) just by changing the solvent between CH_2Cl_2 and THF, where the oxidative *N*-dealkylation occurs efficiently from the bis- μ -oxodicopper(III) complex [193, 194]. Thus, these two forms of the active oxygen dicopper complex may be similar in their energies.

1.3.4 Acid Catalysis in Overall Reactions

It has been extremely difficult to distinguish between conventional ionic or concerted mechanisms and electron transfer mechanisms, since the final products and kinetics are often the same regardless of the mechanisms. If an electron transfer step is the rate-determining step in an overall reaction, it would be almost impossible to detect the initial products of electron transfer because of the extremely short lifetimes. In such a case, the mechanistic distinction seems to be dubious and possibly even meaningless, unless one mechanism provides a more quantitative description of the energetic profiles of the reactions than the other does. If a particular reaction, which was previously formulated as an ionic or concerted reaction, undergoes a rate-determining electron transfer from an electron donor to an acceptor, which is catalyzed by metal ions, the dependence of the rate constant on the metal ion concentration for the overall reaction would be the same as that observed in the electron transfer reduction of the same electron acceptor. Hence the comparison of the catalytic function of metal ions in electron transfer reactions with that in apparently polar or concerted reactions of the same substrate would provide valuable insight into the mechanistic viability of electron transfer (see below).

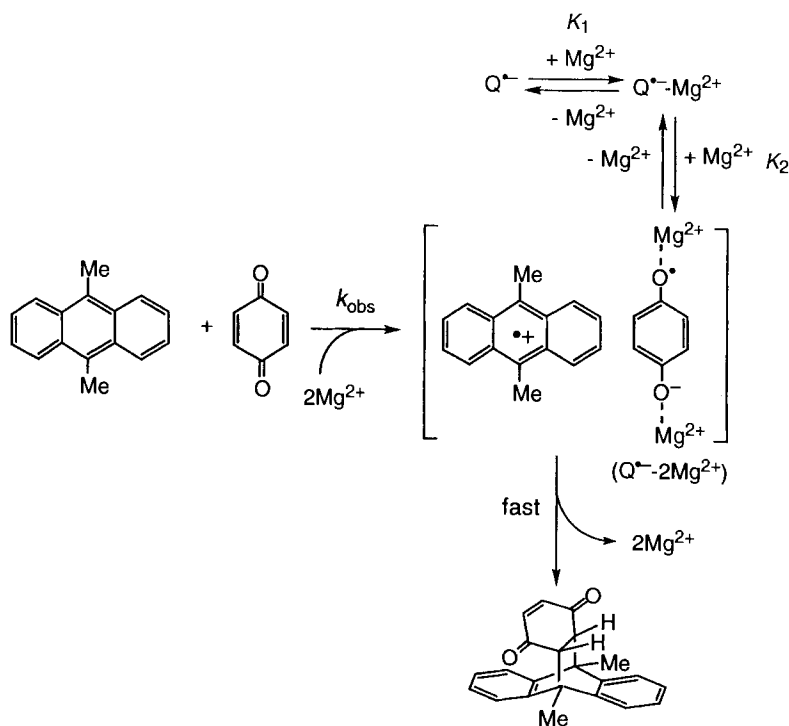
Diels–Alder reactions via electron transfer

Diels–Alder reactions are usually regarded as concerted processes where the interaction between HOMOs of dienes and LUMOs of dienophiles determines the reactivity [195–197]. When electron-rich dienes having high-lying HOMOs react with electron-deficient dienophiles having low-lying LUMOs, however, electron transfer from the diene to the dienophile in the charge-transfer complex formed between the diene and the dienophile plays an important role as the activation step [198–205]. The interaction of metal ions with radical anions of dienophiles may enhance the electron affinity of the dienophiles so that electron transfer may provide a favorable reaction pathway for such dienophiles. In fact, the $[4 + 2]$ cycloaddition of 9,10-dimethylantracene (DMA) with *p*-benzoquinone (Q) occurs efficiently in the presence of $\text{Mg}(\text{ClO}_4)_2$ to yield the adduct selectively (Eq. 21) [132]:



although *p*-benzoquinone derivatives have been regarded as inert or weak dienophiles [206, 207]. The $[4 + 2]$ cycloaddition of anthracene and 9-methylantracene

with other *p*-benzoquinone derivatives ($X-Q$: $X = 2,5\text{-Cl}_2$ and $2,5\text{-Me}_2$) also occurs efficiently in the presence of $\text{Mg}(\text{ClO}_4)_2$ to yield the corresponding adducts [132]. The observed second-order rate constant (k_{obs}) increases with increase in $[\text{Mg}^{2+}]$ to exhibit a first-order dependence on $[\text{Mg}^{2+}]$ at low concentrations, changing to a second-order dependence at high concentrations, as shown in Figure 7b [132]. There is a striking similarity with respect to the dependence of k_{obs} on $[\text{Mg}^{2+}]$ between the electron transfer reaction (Figure 7a) and the Diels–Alder reaction (Figure 7b), despite the large difference in their reactivities. Thus, the dependence of k_{obs} on $[\text{Mg}^{2+}]$ can be expressed by Eq. 14 in which k_{et} should be replaced by k_{obs} . The plot of $k_{\text{obs}}/[\text{Mg}^{2+}]$ vs. $[\text{Mg}^{2+}]$ as employed for the Mg^{2+} -catalyzed electron transfer also gives a straight line for the Diels–Alder reaction of DMA with Q [132]. The K_2 values obtained from the linear plots for the Diels–Alder reactions of DMA with $X-Q$ in MeCN at 298 K agree with those obtained directly from the spectral change of $X-Q^{\cdot-}$ in the presence of Mg^{2+} as well as those determined from the electron transfer reactions [132]. Such agreements for each quinone strongly suggest that the Mg^{2+} -catalyzed electron transfer from anthracenes to $X-Q$ is a rate-determining step of the Diels–Alder reactions as shown in Scheme 12. The electron transfer from DMA to Q is catalyzed by the complexation of Mg^{2+} with $Q^{\cdot-}$. The radical ion pair produced in the Mg^{2+} -catalyzed electron transfer yields the Diels–Alder ad-



Scheme 12.

duct via radical or ion coupling, accompanied by regeneration of Mg^{2+} . In contrast to the case of Mg^{2+} -catalyzed electron transfer from (TPP)Co to Q (Eq. 13), Mg^{2+} appears only in the rate equation and not in the stoichiometric equation for the Diels–Alder reaction. According to Scheme 12, the K_2 values should be the same, irrespective of anthracene derivatives or electron donors, since the formation of the 1:2 complex of $\text{Q}^{\cdot-}$ and Mg^{2+} is independent of anthracene derivatives or electron donors. In fact, the K_2 values derived from the Diels–Alder reactions of DMA, 9-methylanthracene and anthracene with Q in acetonitrile at 333 K are the same ($K_2 = 2.1 \pm 0.3 \text{ M}^{-1}$), despite the significant difference in their reactivities [132].

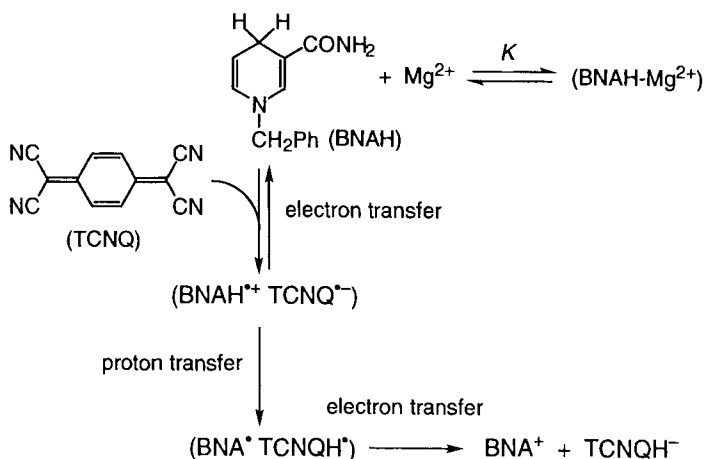
The catalytic role of Mg^{2+} in Scheme 12 is ascribed to the 1:1 and 1:2 complex formation of $\text{Q}^{\cdot-}$ and Mg^{2+} , which results in an increase in k_{obs} with an increase in $[\text{Mg}^{2+}]$, exhibiting first- and second-order dependences on $[\text{Mg}^{2+}]$, respectively (Figure 7). This contrasts with the Lewis acid catalysis in conventional concerted Diels–Alder reactions, in which the catalyst is believed to activate dienophiles (not the radical anions) by coordination to the acidic metal center [208–212]. However, the exact catalytic mechanism of numerous Lewis acid-catalyzed Diels–Alder reactions [208–212] has yet to be clarified, including a possible contribution of Lewis-acid catalyzed electron transfer step.

Lithium perchlorate in diethyl ether has also been reported to accelerate Diels–Alder reactions significantly and this system has been applied to obtain Diels–Alder adducts that were inaccessible via conventional means [213–219]. A linear dependence of k_{obs} on $[\text{Li}^+]$ is observed for the Diels–Alder reaction of DMA with acrylonitrile in $\text{LiClO}_4\text{--Et}_2\text{O}$ solution, while a second-order dependence of k_{obs} on $[\text{Li}^+]$ is involved for the reactions with fumaronitrile and dimethyl acetylenedicarboxylate [216]. This suggests the possible contribution of Li^+ -catalyzed electron transfer step in the Diels–Alder reaction as the case of Mg^{2+} -catalyzed Diels–Alder reaction in Scheme 12. However, such an electron transfer mechanism has not been confirmed in the Li^+ -catalyzed Diels–Alder reactions.

Redox reactions via metal ion-catalyzed electron transfer

The effects of metal ions such as Mg^{2+} and Zn^{2+} ions on hydride transfer reactions from NADH model compounds to substrates have attracted considerable interest in relation to the role of metal ions in the redox reactions of nicotinamide coenzymes [220]. Hydride transfer reactions from NADH analogues to organic oxidants such as *p*-benzoquinone derivatives have been shown to proceed via sequential transfer of electron, proton and electron in the charge-transfer (CT) complexes formed between NADH analogues and the organic oxidants based on the kinetic comparison with the electron transfer reactions between NADH and one-electron oxidants as well as the kinetic isotope effects for the proton transfer step [221, 222]. Negative activation enthalpies have been observed for hydride transfer reactions from NADH analogues to 2,3-dichloro-5,6-dicyano-*p*-benzoquinone (DDQ) in chloroform (the lower the temperature, the faster the rate), indicating unequivocally that the CT complex is a true intermediate for the hydride transfer reaction [223, 224].

The effects of Mg^{2+} on hydride transfer reactions from a typical NADH model compound, 1-benzyl-1,4-dihydronicotinamide (BNAH), to substrates are complex



Scheme 13.

[225]. When a strong organic oxidant such as 7,7,8,8-tetracyano-*p*-quinodimethane (TCNQ) is employed as a hydride acceptor, the addition of Mg^{2+} to the BNAH–TCNQ system in anhydrous MeCN causes a significant decrease in the reaction rate [223]. The observed rate constant of hydride transfer from BNAH to TCNQ decreases with increase in $[\text{Mg}^{2+}]$ to reach a constant value which is 23 times smaller than that in the absence of Mg^{2+} . Such a retarding effect of Mg^{2+} is well interpreted by formation of the 1:1 complex between BNAH and Mg^{2+} , in which the electron donor ability of BNAH is diminished significantly [225], and thereby free BNAH undergoes the hydride transfer reaction via sequential transfer of electron, proton and electron as shown in Scheme 13 [213]. In this case, Mg^{2+} cannot act as a catalyst, since no complex is formed between $\text{TCNQ}^{\bullet-}$ and Mg^{2+} (Scheme 13) [225]. The one-electron reduction potential of TCNQ ($E^\circ_{\text{red}} = 0.19 \text{ V}$ vs. SCE) is therefore not affected by the presence of Mg^{2+} [225], whereas the one-electron oxidation potentials of BNAH ($E^\circ_{\text{ox}} = 0.57 \text{ V}$ vs. SCE) [222] in MeCN is significantly shifted to the positive direction by the complexation with Mg^{2+} (0.80 V vs. SCE) [226]. Thus, the significant decrease in the reactivity of BNAH by the complexation with Mg^{2+} is ascribed to a decrease in the electron donor ability as observed in photo-induced electron transfer from AcrH_2 to $[\text{Ru}(\text{bpy})_3]^{2+*}$ in the presence of HClO_4 (Figure 5), where protonated AcrH_2 cannot act as an electron donor [102].

When TCNQ is replaced by a weaker oxidant such as 2,6-dichloro-*p*-benzoquinone, the Mg^{2+} ion shows both retarding and accelerating effects on the hydride transfer reaction depending on the Mg^{2+} concentration, as shown in Figure 10, where the observed second-order rate constant (k_{obs}) decreases sharply from the value in the absence of Mg^{2+} ($7.5 \times 10 \text{ M}^{-1} \text{ s}^{-1}$) with an increase in $[\text{Mg}^{2+}]$ at low concentrations ($\ll 0.10 \text{ M}$), while the k_{obs} value increases at higher concentrations ($> 0.10 \text{ M}$) [226]. Such decelerating and accelerating effects of Mg^{2+} on the hydride transfer rate can be well understood based on Scheme 14, in which Mg^{2+} -catalyzed electron transfer from BNAH to X–Q (X = 2,6-Cl₂) is the rate-determining step in

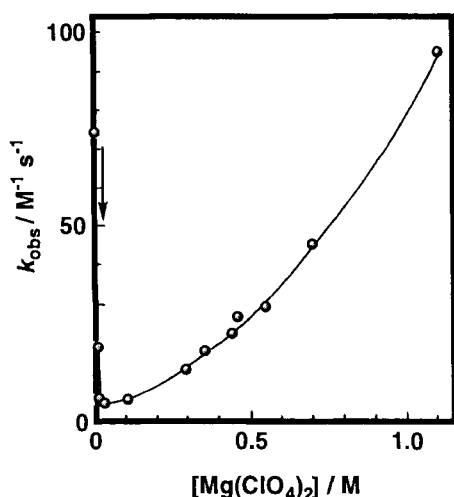
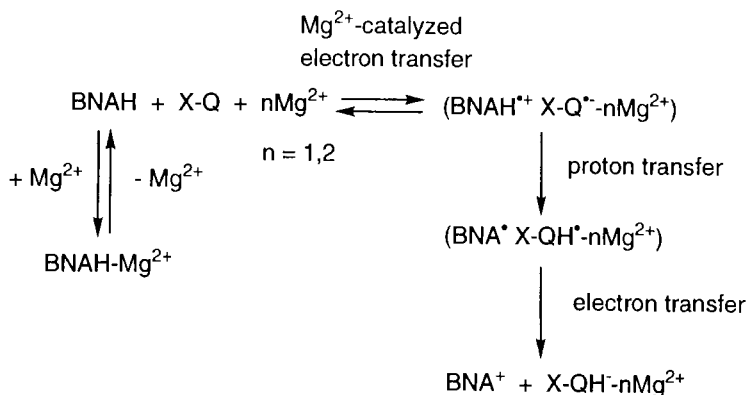


Figure 10. Plot of k_{obs} vs. $[\text{Mg}(\text{ClO}_4)_2]$ for the hydride transfer reaction from BNAH to 2,6- Cl_2Q in the presence of $\text{Mg}(\text{ClO}_4)_2$ in MeCN at 298 K [226].



Scheme 14.

the overall hydride transfer reactions in the absence and presence of Mg^{2+} [226]. The electron transfer from BNAH to X-Q is accelerated by the complexation of Mg^{2+} with X-Q⁻, while the complexation of Mg^{2+} with BNAH retards the electron transfer. The initial sharp decrease in the rate constant from the value in the absence of Mg^{2+} to those at low concentrations ($\ll 0.10$ M) is ascribed to the complexation of Mg^{2+} with BNAH. With an increase in the Mg^{2+} concentration, not only one Mg^{2+} but also two Mg^{2+} ions can form the complex with Q⁻ (Eqs. 11 and 12), resulting in a second-order dependence of k_{obs} with respect to $[\text{Mg}^{2+}]$ at high Mg^{2+} concentrations as shown in Figures 10 and 7. In this region, the positive shift of the E°_{red} value of the quinone is larger than the corresponding positive shift

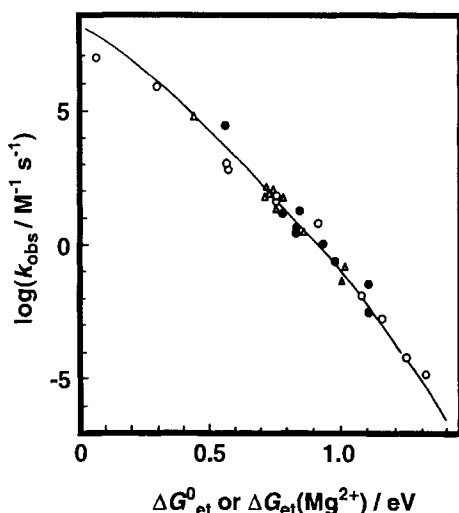
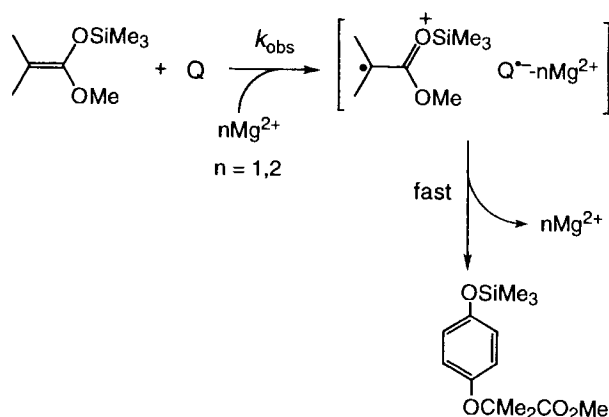


Figure 11. Plot of $\log k_{\text{obs}}$ for the hydride transfer reactions from BNAH to *p*-benzoquinone derivatives in the absence (○) and presence of Mg^{2+} [0.10 M (●), 1.6 M (△)] vs. the free energy change of electron transfer in the absence of Mg^{2+} ($\Delta G^\circ_{\text{et}}$) and in the presence of Mg^{2+} [$\Delta G_{\text{et}}(\text{Mg}^{2+})$] [226].

of BNAH (0.18 V), when the k_{obs} value increases with increasing $[\text{Mg}^{2+}]$ (Figure 6) [226].

The k_{obs} value should be correlated with the free energy change of electron transfer from BNAH to X–Q, which varies depending on X–Q and the Mg^{2+} concentration. The free energy change of electron transfer in the absence of Mg^{2+} ($\Delta G^\circ_{\text{et}}$) and that in the presence of Mg^{2+} [$\Delta G_{\text{et}}(\text{Mg}^{2+})$] are obtained from the E°_{ox} values of BNAH and the E_{red} values of *p*-benzoquinone derivatives in the presence of various concentrations of Mg^{2+} , which have been determined by the analysis of the cyclic voltammograms at various sweep rates [226]. Figure 11 shows plots of the $\log k_{\text{obs}}$ values in the absence and the presence of Mg^{2+} vs. $\Delta G^\circ_{\text{et}}$ and $\Delta G_{\text{et}}(\text{Mg}^{2+})$ [226]. The remarkable single and unified correlation in the absence and presence of Mg^{2+} in Figure 11 demonstrates clearly that the retarding and accelerating effects of Mg^{2+} on the rate constants of the overall hydride transfer reactions can be ascribed to the effects on the rate-determining electron transfer step in Scheme 14. The electron transfer step is followed by a proton transfer from $\text{BNAH}^{+\bullet}$ to $\text{Q}^{\bullet-}-\text{Mg}^{2+}$, and the subsequent electron transfer from BNA^\bullet to $\text{QH}^\bullet-\text{Mg}^{2+}$ may occur efficiently, judging from the largely negative oxidation potential of BNA^\bullet (–1.1 V vs. SCE) [222]. The observed primary kinetic isotope effects $k_{\text{H}}/k_{\text{D}}$ are well interpreted as those on the proton transfer step [226].

It is important to emphasize that three different types of reactions, i.e., electron transfer from (TPP)Co to Q (Eq. 13), Diels–Alder reaction of anthracenes with Q (Scheme 12) and hydride transfer from BNAH to Q (Scheme 14), have the common rate-determining step of Mg^{2+} -catalyzed electron transfer from these electron donors to Q. In each case, the relative catalytic dependence of k_{obs} on $[\text{Mg}^{2+}]$ is the same as indicated by Eq. 14, irrespective of different electron donors. The nucleophilic addition of a β,β -dimethyl-substituted ketene silyl acetal such as $\text{Me}_2\text{C}=\text{C}(\text{OMe})\text{OSiMe}_3$ is also catalyzed by Mg^{2+} in MeCN [227, 228]. No reaction takes



Scheme 15.

place between $\text{Me}_2\text{C}=\text{C}(\text{OMe})\text{OSiMe}_3$ and Q without Mg^{2+} in MeCN [227, 228]. The catalytic dependence of k_{obs} on $[\text{Mg}^{2+}]$ to Q has been shown to be the same as that for the Mg^{2+} -catalyzed electron transfer from (TPP)Co to Q (Eq. 14), changing from first- to second-order in $[\text{Mg}^{2+}]$ under the conditions that $\text{Q}^{\cdot-}$ forms the 1:2 complex with Mg^{2+} (Eq. 12). The β -methyl-substitution of ketene silyl acetals results in a significant increase in the electron donor ability to be becoming more susceptible to electron transfer oxidation than the less substituted counterparts [229–231]. The catalytic mechanism is shown in Scheme 15.

Electron transfer from $\text{Me}_2\text{C}=\text{C}(\text{OMe})\text{OSiMe}_3$ to Q is made possible by the strong interaction between $\text{Q}^{\cdot-}$ and Mg^{2+} (or 2Mg^{2+}) to produce the radical ion pair. Since the spin of the ketene silyl acetal radical cation is mainly localized on the terminal carbon atom [229], the carbon–oxygen bond is formed before the cleavage of the Si–O bond to yield the adduct (Scheme 15). This contrasts with the 1,2-addition of nonsubstituted ketene silyl acetal $[\text{H}_2\text{C}=\text{C}(\text{OEt})\text{OSiEt}_3]$ via nucleophilic attack to the positively charged carbonyl carbon of the quinone rather than via an alternative electron transfer pathway [228].

Hydride transfer from 1,5-dihydroflavin-2',3',4',5'-tetraacetate anion (FIH^-) to O_2 is also catalyzed by the presence of Mg^{2+} in acetonitrile [137]. The reduction of oxygen by the 1,5-dihydroflavin anion is known to be a key step in biological oxidation involving flavoproteins [80, 81]. An electron transfer mechanism has often been proposed for the reaction of 1,5-dihydroflavin with oxygen, since direct one-step reaction to give a covalent bond is spin-forbidden [232–234]. However, the facile follow-up reaction to give the covalent flavin 4a-hydroperoxide following the possible electron transfer has precluded the direct detection of the radical ion pair [232, 233]. In such a case, the comparison of the catalytic effects of Mg^{2+} on the hydride transfer reaction with that of electron transfer reduction of oxygen provides valuable insight into the viability of the electron transfer mechanism (see below).

The observed pseudo-first-order rate constant (k_{obs}) of the Mg^{2+} -catalyzed hydride transfer from FIH^- to O_2 increases linearly with increase in $[\text{Mg}(\text{ClO}_4)_2]$, as shown in Figure 12 [137]. There is an intercept which is much larger than the k_{obs}

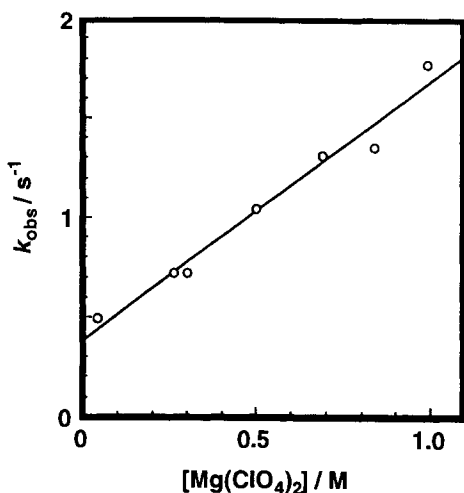


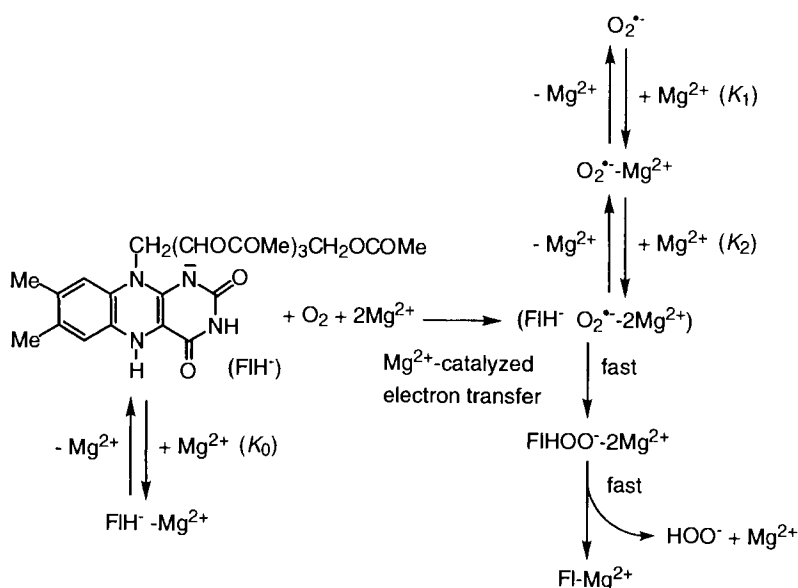
Figure 12. Plot of k_{obs} vs. $[\text{Mg}(\text{ClO}_4)_2]$ for reduction of O_2 ($1.3 \times 10^{-3} \text{ M}$) by FlH^- ($1.2 \times 10^{-4} \text{ M}$) in the presence of $\text{Mg}(\text{ClO}_4)_2$ in MeCN at 298 K [137].

value in the absence of Mg^{2+} . Such first-order dependence of k_{obs} on $[\text{Mg}^{2+}]$ with an intercept is apparently different from first- and second-order dependences on $[\text{Mg}^{2+}]$ observed in the Mg^{2+} -catalyzed electron transfer from $[\text{Fe}(\text{Me}_5\text{C}_5)_2]$ to O_2 due to the 1:1 and 1:2 complexes formed between $\text{O}_2^{\cdot-}$ and Mg^{2+} at low and high Mg^{2+} concentrations (Eqs. 16 and 17), respectively. Such a difference in dependence of k_{obs} on $[\text{Mg}^{2+}]$ can be well interpreted by the complex formation between FlH^- and Mg^{2+} [137], as shown in Scheme 16 [137]. Flavins themselves are known to form complexes with Mg^{2+} in acetonitrile [235]. The reduced flavin anion FlH^- has also been reported to form the complex with Mg^{2+} [236]. Since the Mg^{2+} complex of FlH^- is a much weaker one-electron donor than free FlH^- , only free FlH^- which is in equilibrium with $\text{FlH}^- - \text{Mg}^{2+}$ can undergo the Mg^{2+} -catalyzed electron transfer reaction with O_2 to give a radical pair ($\text{FlH}^{\cdot} \text{O}_2^{\cdot-} - 2\text{Mg}^{2+}$). Since the spin density of FlH^{\cdot} is greater at the C-4a position (0.30) than those at the other carbons, the radical coupling between FlH^{\cdot} and $\text{O}_2^{\cdot-} - 2\text{Mg}^{2+}$ occurs selectively at the C-4a position to give flavin 4a-hydroperoxide which decomposes to Fl and hydrogen peroxide (Scheme 16) [137].

According to Scheme 16, the dependence of k_{obs} on $[\text{Mg}^{2+}]$ is given by Eq. 22:

$$k_{\text{obs}} = k'_0 K_1 (1 + K_2 [\text{Mg}^{2+}]) / K_0 \quad (22)$$

where k'_0 is the rate constant in the absence of Mg^{2+} , K_0 is the formation constant of $\text{FlH}^- - \text{Mg}^{2+}$ and K_1 and K_2 are the formation constants of $\text{O}_2^{\cdot-} - \text{Mg}^{2+}$ and $\text{O}_2^{\cdot-} - 2\text{Mg}^{2+}$, respectively ($K_1 [\text{Mg}^{2+}] \gg 1$) [137]. The dependence of k_{obs} on $[\text{Mg}^{2+}]$ in Figure 12 agrees with Eq. 22. Thus, from the intercept and slope the K_2 value is obtained as $3.4 \pm 0.3 \text{ M}^{-1}$, which agrees well with the K_2 value ($3.2 \pm 0.3 \text{ M}^{-1}$) obtained independently from Mg^{2+} -catalyzed electron transfer from $\text{Fe}(\text{C}_5\text{Me}_5)_2$ to

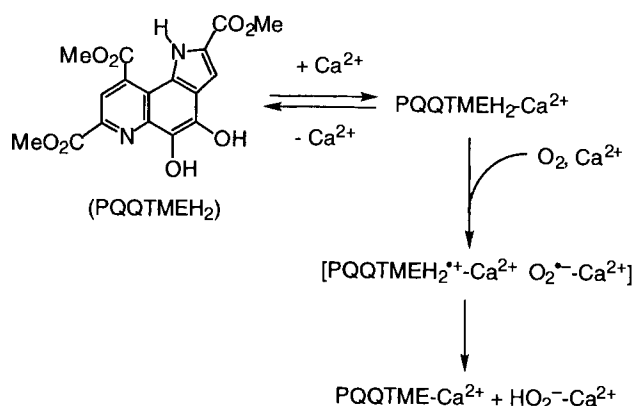


Scheme 16.

O_2 (Eq. 15) [137]. Such an agreement strongly indicates that Mg^{2+} -catalyzed electron transfer from FIH^- to O_2 is the rate-determining step for the hydride transfer from FIH^- to O_2 in the presence of Mg^{2+} (Scheme 16).

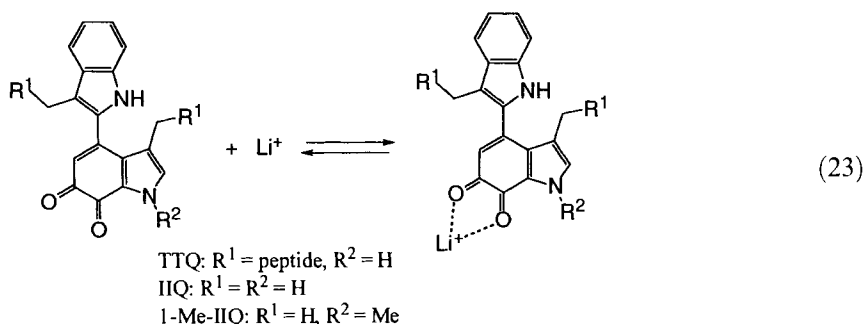
Metal ion catalysis is also effective for the reoxidation of reduced PQQ (pyrroloquinolinequinone) coenzyme by O_2 [237]. This coenzyme is the redox center of methanol dehydrogenases (MDH) that catalyze the oxidation of methanol to formaldehyde [238, 239]. The crystal structure of MDH from methylotrophic bacteria has shown that there is one calcium ion strongly bound to PQQ through its C-5 carboxylate group in the enzyme active site [240–243]. In this context, the oxidation of methanol to formaldehyde by the trimethyl ester of PQQ (PQQTME) has been shown to be catalyzed by Ca^{2+} [244]. The strong binding of Ca^{2+} to the pyridine nitrogen of $\text{PQQTME}^{\bullet-}$ is shown by the change in the hyperfine structure of the ESR spectrum due to the complexation [245]. This results in a 0.57 V positive shift in the one-electron reduction potential of PQQTME, indicating the enhancement of the oxidation power of PQQTME by a strong interaction between Ca^{2+} and $\text{PQQTME}^{\bullet-}$ [245]. The reduced PQQ also forms the Ca^{2+} complex, which is oxidized by O_2 via Ca^{2+} -catalyzed electron transfer from $\text{PQQTMEH}_2\text{--Ca}^{2+}$ to O_2 as shown in Scheme 17 [237].

Monovalent metal cations also influence the redox reactivity of tryptophan tryptophylquinone (TTQ) coenzyme in the amine oxidation and the subsequent electron transfer to the biological electron acceptor proteins such as amicyanin [246–251].



Scheme 17.

TTQ model compounds [252, 253] have been shown to form complexes with an alkali metal ion such as Li^+ (Eq. 23):



which can oxidize benzylamine in anhydrous MeCN, although no reaction takes place in the absence of Li^+ [254].

Hydride transfer via Brønsted acid-catalyzed electron transfer

Brønsted acid catalysis in electron transfer described in Section 1.3.1 has also been effective for redox reactions via the electron transfer step. As shown in the case of metal ion-catalyzed hydride transfer reactions (see above), hydride transfer reactions from an NADH analogue to *p*-benzoquinones also proceed via Brønsted acid-catalyzed electron transfer [255, 256]. Since NADH and ordinary NADH model compounds are subjected to the acid-catalyzed hydration [98, 257, 258], an acid-stable NADH model compound, 10-methyl-9,10-dihydroacridine (AcrH_2), was used as a hydride donor to *p*-benzoquinone (Eq. 24):

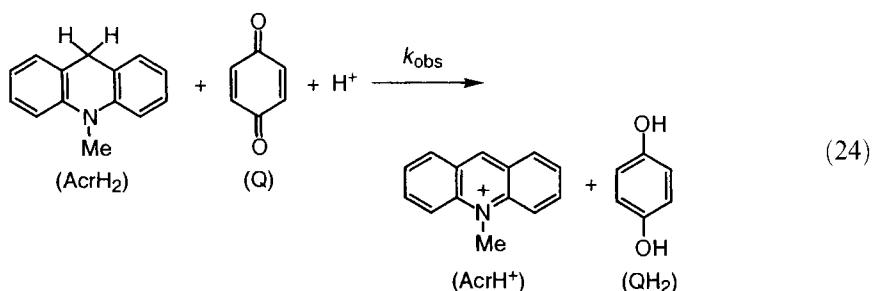


Figure 13 shows the pH dependence of the observed second-order rate constants ($\log k_{\text{obs}}$) for the hydride transfer from AcrH₂ to a series of hydride acceptors in H₂O-EtOH (5:1 v/v) at 298 K [256]. The $\log k_{\text{obs}}$ value of each Q in Figure 13 exhibits variation with pH in agreement with the pH dependence of $\log k_{\text{et}}$ of electron transfer from *cis*-[Et₂Co(bpy)₂]⁺ to Q in Figure 3. The $\log k_{\text{obs}}$ value of each Q is independent of pH in the region of pH > p*K*_{a1}, but increases with decreasing pH in the region pH < p*K*_{a1}. The p*K*_{a1} values thus determined for various *p*-benzoquinone derivatives agree well with the literature values [75]. In the case of 7,7,8,8-tetracyano-*p*-quinodimethane (TCNQ), the $\log k_{\text{obs}}$ value is independent of pH (Figure 13), since no protonation of TCNQ^{•−} has occurred in this pH region [256]. In general, the easier the reduction of a substrate, the more difficult is the protonation of the reduced species.

The kinetic deuterium isotope effects ($k_{\text{H}}/k_{\text{D}}$) are observed in the Brønsted acid-catalyzed hydride transfer reactions from AcrH₂ to the hydride acceptors (A) [259]. The pH dependence of the observed kinetic deuterium isotope effects ($k_{\text{H}}/k_{\text{D}}$) in-

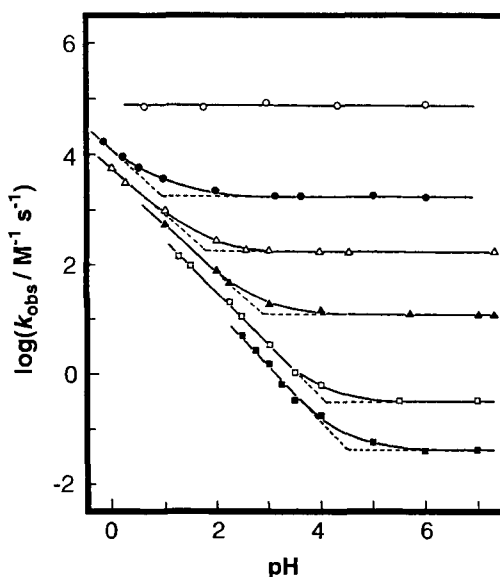
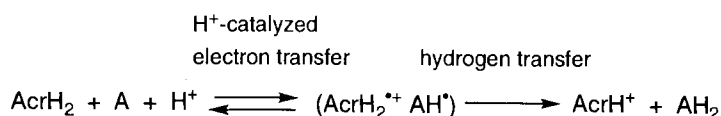


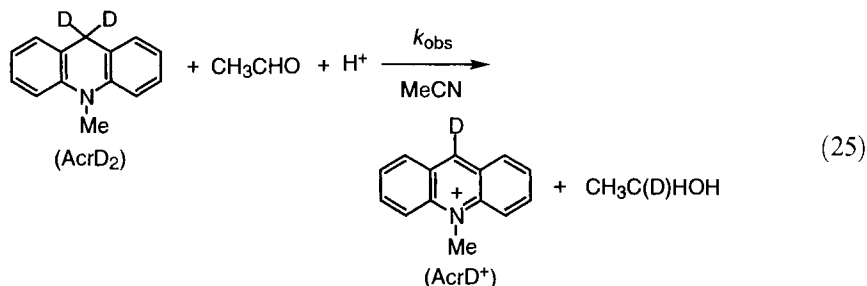
Figure 13. Plots of $\log k_{\text{obs}}$ vs. pH for hydride transfer reactions from AcrH₂ to TCNQ (○), *p*-chloranil (●), 2,6-dichloro-*p*-benzoquinone (△), chloro-*p*-benzoquinone (▲), *p*-benzoquinone (□) and methyl-*p*-benzoquinone (■) in H₂O-EtOH (5:1 v/v) at 298 K [256].



Scheme 18.

indicates that hydrogen is transferred from AcrH_2^{2+} to AH^* following the initial electron transfer from AcrH_2 to A , as shown in Scheme 18 [259].

In biological redox systems, acid catalysis operates in a hydrophobic environment where the acid strength may be enhanced significantly as compared with that in an aqueous solution. Thus, in the model system, the use of an aprotic solvent may be essential to achieve a high activity of acid catalysis. The enormous enhancement of the rate of electron transfer reduction of carbonyl compounds by acid catalysis in MeCN (Figure 4) is expected to cause a significant decrease in the activation barrier for the two-electron reduction as well, since the subsequent reduction by hydrogen (equivalent to one electron and one proton) following the initial electron transfer is usually highly exergonic. In fact, the two-electron reduction of acetaldehyde, which is the most important substrate with regard to the physiological significance of ethanol metabolism and ethanol fermentation [260], by AcrH_2 is made possible in the presence of HClO_4 in acetonitrile [261]. When AcrH_2 is replaced by the 9,9'-dideuterated compound, 9,9'-[$^2\text{H}_2$]-9,10-dihydro-10-methylacridine (AcrD_2), deuterium is introduced to ethanol (Eq. 25) [261]:



Other aliphatic and aromatic ketones and aldehydes can also be reduced by AcrH_2 in the presence of HClO_4 in acetonitrile at 333 K [86, 261].

When the $\log k_{\text{obs}}$ values of the acid-catalyzed reduction of aliphatic aldehydes and ketones by AcrH_2 in the presence of HClO_4 and the $\log k_{\text{et}}$ values of acid-catalyzed photoinduced electron transfer from $[\text{Ru}(\text{bpy})_3]^{2+*}$ to the same carbonyl compounds (cf. Eq. 8) are compared, there exists an excellent linear correlation between $\log k_{\text{obs}}$ and $\log k_{\text{et}}$ as shown in Figure 14 [261]. The kinetic deuterium isotope effects ($k_{\text{H}}/k_{\text{D}}$) for the acid-catalyzed reduction of aliphatic aldehydes and ketones are uniformly small. For example, the $k_{\text{H}}/k_{\text{D}}$ values of acetaldehyde and pivalaldehyde are 1.4 and 1.0, respectively [261]. Similar linear correlations between k_{obs} and k_{et} are also obtained for other aromatic carbonyl compounds [86, 89]. These correlations strongly indicate that the rate-determining step for the hydride transfer reactions in the presence of HClO_4 is the H^+ -catalyzed electron transfer

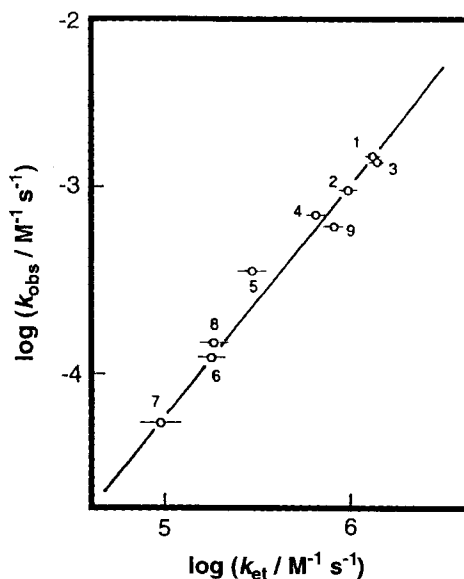


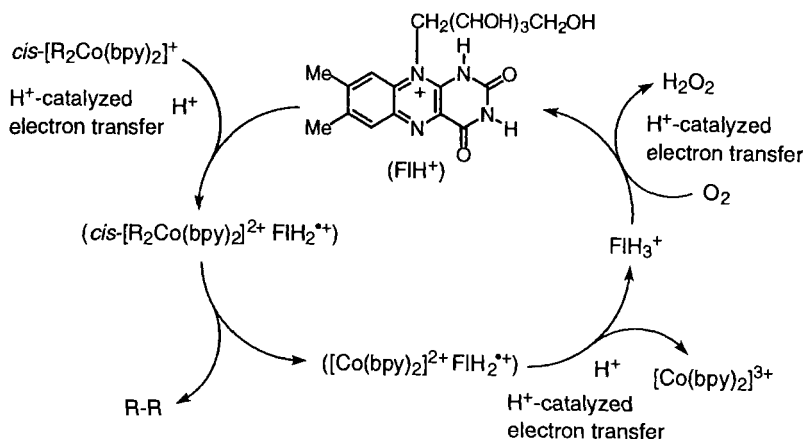
Figure 14. Plot of $\log k_{\text{obs}}$ for the acid-catalyzed reduction of aldehydes and ketones by AcrH_2 in the presence of HClO_4 (2.7×10^{-2} M) in MeCN at 333 K vs. $\log k_{\text{et}}$ for the acid-catalyzed electron transfer from $[\text{Ru}(\text{bpy})_3]^{2+*}$ to the same series of substrates in the presence of HClO_4 (2.0 M) at 298 K. Numbers refer to the aldehydes and ketones (1, acetaldehyde; 2, propionaldehyde; 3, butyraldehyde; 4, isovaleraldehyde; 5, isobutyraldehyde; 6, pivalaldehyde; 7, acetone; 8, fluoroacetone; 9, cyclohexanone; 10, pyruvic acid) [261].

from AcrH_2 to the carbonyl compounds. Similarly, hydride transfer reactions from AcrH_2 to O_2 [90, 91], NO_2^- [92], nitrobenzene derivatives [93, 94], nitrosobenzene derivatives [93, 94] and sulfoxides [95, 96] proceed via H^+ -catalyzed electron transfer from AcrH_2 to these hydride acceptors.

Alkylsilanes, which are relatively stable against strong acids compared with other metal hydrides, have frequently been used as effective hydride donors for the acid-catalyzed reduction of carbonyl compounds [262, 263]. Although triethylsilane shows no reactivity toward carbonyl compounds in acetonitrile, the carbonyl compounds are readily reduced by Et_3SiH in the presence of HClO_4 to yield the corresponding alcohol together with a minor amount of the corresponding ether [264, 265]. In contrast with the case of the acid-catalyzed reduction of carbonyl compounds by AcrH_2 , comparison of the k_{obs} values of Et_3SiH and the k_{et} values of $[\text{Ru}(\text{bpy})_3]^{2+*}$ revealed no apparent parallel relation in the reactivities of carbonyl compounds. Since the one-electron oxidation potential (E°_{ox}) of Et_3SiH is higher than 2.3 V (vs. SCE) [265], that is significantly higher than the E°_{ox} value of AcrH_2 (0.81 V vs. SCE) [266], there is no chance of Et_3SiH acting as an electron donor in the acid-catalyzed reduction of carbonyl compounds. The reactivity of carbonyl compounds in the acid-catalyzed reduction by Et_3SiH is determined mainly by the protonation ability of the carbonyl compounds, while that in the acid-catalyzed electron transfer is determined by two-reverse effects, i.e., the proton- and electron-acceptor abilities [265].

Acid catalysis in overall *catalytic* cycle

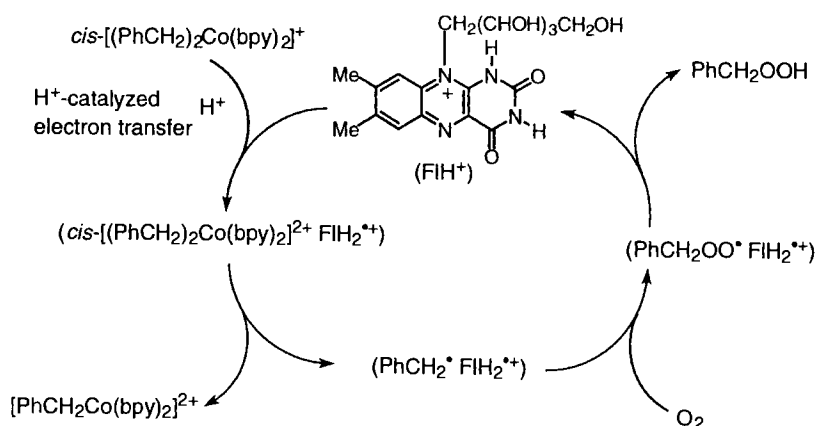
An acid-catalyzed electron transfer reaction can be combined with other reactions to construct an overall *catalytic* reaction, where catalysis in an overall reaction is



Scheme 19.

written in italics in order to distinguish it from catalysis in electron transfer. For example, an acid-catalyzed electron transfer from $cis\text{-}[\text{R}_2\text{Co}(\text{bpy})_2]^+$ ($\text{R} = \text{Me}, \text{Et}$) to FIH^+ (Eq. 7) is combined with an acid-catalyzed oxidation of FIH_2 by O_2 as shown in Scheme 19 [267, 268]. The overall reaction is the *FI-catalyzed* oxidative coupling of alkyl ligands of $cis\text{-}[\text{R}_2\text{Co}(\text{bpy})_2]^+$ ($\text{R} = \text{Me}, \text{Et}$) by O_2 in the presence of HClO_4 in MeCN to yield R-R , $[\text{Co}(\text{bpy})_2]^{3+}$ and H_2O_2 [268]. The *catalytic* cycle is started by an H^+ -catalyzed electron transfer from $cis\text{-}[\text{R}_2\text{Co}(\text{bpy})_2]^+$ to FI. This is followed by the facile reductive elimination of the alkyl ligands of $cis\text{-}[\text{R}_2\text{Co}(\text{bpy})_2]^{2+}$ to yield the coupling product R-R [84]. Then an H^+ -catalyzed electron transfer from the resulting cobalt(II) complex to FIH_2^{**+} occurs to give $[\text{Co}(\text{bpy})_2]^{3+}$ and a protonated dihydroflavin FIH_3^+ . The FIH_3^+ is oxidized by O_2 to regenerate the oxidized protonated form (FIH^+) via H^+ -catalyzed electron transfer from FIH_3^+ to O_2 , accompanied by the formation of H_2O_2 [268]. Thus, each step in the *catalytic* cycle is catalyzed by an acid. Other redox coenzymes such as lumazine and aminopterine can also act as *catalysts* in the presence of an acid [268]. In the absence of a coenzyme analogue, the cobalt-carbon bond of $cis\text{-}[\text{R}_2\text{Co}(\text{bpy})_2]^+$ in both the absence and presence of O_2 is cleaved by the electrophilic attack of proton to yield $[\text{RCo}(\text{bpy})_2]^{2+}$ and RH [268]. The rates of FIH^+ -catalyzed oxygenation of $cis\text{-}[\text{R}_2\text{Co}(\text{bpy})_2]^+$ increase linearly with increasing concentration of both HClO_4 and FI [268].

The product in the coenzyme-catalyzed oxidation of $cis\text{-}[\text{R}_2\text{Co}(\text{bpy})_2]^+$ by O_2 in the case of $\text{R} = \text{PhCH}_2$ is drastically changed from R-R in the case of $\text{R} = \text{Me}$ and Et (Scheme 19) to the oxygenated product PhCH_2OOH as shown in Scheme 20 [268]. The initial acid-catalyzed electron transfer from $cis\text{-}[(\text{PhCH}_2)_2\text{Co}(\text{bpy})_2]^+$ to FIH^+ occurs to give $cis\text{-}[(\text{PhCH}_2)_2\text{Co}(\text{bpy})_2]^{2+}$ and FIH_2^{**+} . The cobalt-benzyl bond of $cis\text{-}[(\text{PhCH}_2)_2\text{Co}(\text{bpy})_2]^{2+}$ is cleaved in a stepwise manner [79], and the benzyl radical formed is stable enough to be trapped by O_2 to give benzylperoxyl radical ($\text{PhCH}_2\text{OO}^\bullet$), which is reduced by hydrogen transfer from FIH_2^{**+} to yield benzyl



Scheme 20.

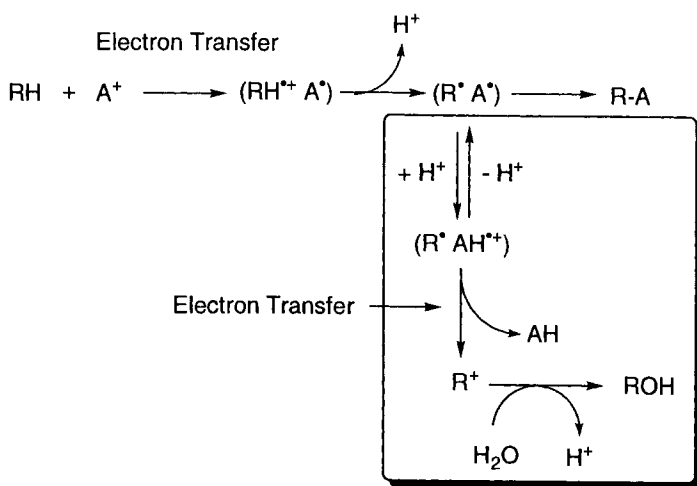
hydroperoxide, accompanied by regeneration of FIH^+ (Scheme 20). The benzyl hydroperoxide decomposes to yield the final oxygenated product, benzaldehyde [269].

In the absence of O_2 , the benzyl radical reacts with $[PhCH_2Co(bpy)_2]^{2+}$ in the cage to yield the coupling product, $PhCH_2CH_2Ph$ [79]. In the case of $cis-[R_2Co(bpy)_2]^+$ ($R = Me, Et$) also, the cleavage of the $Co-R$ bond in $cis-[R_2Co(bpy)_2]^{2+}$ may occur in a stepwise manner. However, the reaction of R^{\bullet} with $[RCo(bpy)_2]^{2+}$ may be so fast that R^{\bullet} cannot be trapped by oxygen and that only the net coupling of the alkyl ligands can occur to yield the coupling products even in the presence of O_2 . Thus, $cis-[(PhCH_2)_2Co(bpy)_2]^+$ is the least reactive in the electron transfer oxidation in the absence of O_2 because of the slow coupling process, but it becomes the most reactive in the FIH^+ -catalyzed oxidation by O_2 because of the facile trapping of the benzyl radical by O_2 [268]. Essentially the same reaction schemes (Schemes 19 and 20) are applied for other redox coenzyme analogues such as lumazine and aminopterine which act as catalysts in the oxidation of $cis-[R_2Co(bpy)_2]^+$ by O_2 in the presence of acid [268].

Metalloporphyrins can also act efficient *catalysts* in a variety of chemical and biological redox reactions. This area has been extensively studied and the catalytic functions of metalloporphyrins via electron transfer reactions have been reviewed Volume II, Part 2, Chapter 8 [270].

Change of reaction pathway by acid catalysis

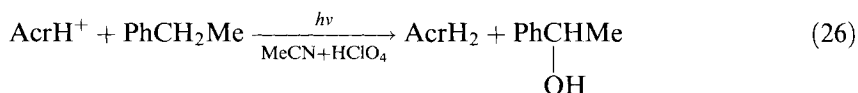
As shown above, acid catalysis in an electron transfer process accelerates the rate of the overall redox reaction via the electron transfer without affecting the final products. However, there is a case when acid catalysis in an electron transfer process results in a drastic change of the products in the overall redox reactions (see below). In general, the radical cations of organic compounds ($RH^{+\bullet}$) are much stronger carbon acids in solution as compared with the parent compounds (RH) [271], and



Scheme 21.

thereby they undergo proton loss from an α -carbon to yield carbon radicals [38, 272–275]. On the other hand, there are some electron-rich radicals (A^\bullet) such as 10-methylacridinyl radical (AcrH^\bullet) which can act as a base to accept H^+ to produce the radical cation ($\text{AH}^{\bullet+}$) [222]. In the absence of a strong acid, an electron transfer from RH to A^+ may be followed by deprotonation of $\text{RH}^{\bullet+}$ to give the radical pair ($\text{R}^\bullet \text{A}^\bullet$) and the facile radical coupling yields the adduct (R-A) as shown in Scheme 21. In strongly acidic media, the reaction pathway is changed from the adduct formation to the two-electron oxidation of RH , since A^\bullet may be protonated to produce $\text{AH}^{\bullet+}$ which can oxidize R^\bullet to give R^+ and AH (Scheme 21).

In the absence of a strong acid, photoinduced electron transfer from RH (alkylbenzenes [276] and alkenes [277]) to the singlet excited state of AcrH^+ ($^1\text{AcrH}^{+\bullet}$) is reported to lead to formation of the alkylated or allylated adducts, 9-R-10-methyl-9,10-dihydroacridine (AcrHR). Photoinduced electron transfer from a variety of organometallic compounds (RM) also gave the same type of adduct, AcrHR [278–282]. In the presence of HClO_4 (1.2 M), however, the photooxygenation of ethylbenzene to 1-phenylethanol occurs as shown in Eq. 26:



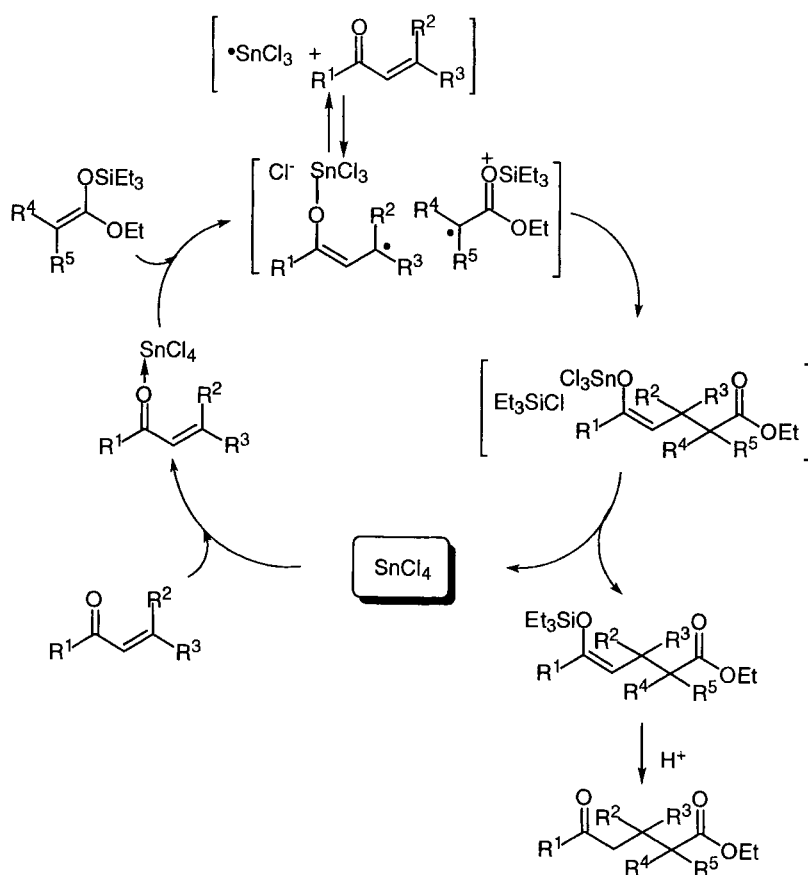
where AcrH^+ is reduced to AcrH_2 instead of the adduct [283]. Judging from the one-electron oxidation potential of benzyl radical and analogues (R^\bullet), being more negative ($E^\circ_{\text{ox}} = 0.73, 0.37, 0.16$ and 0.35 V vs SCE for PhCH_2^\bullet , PhCHMe^\bullet , PhMe_2^\bullet and $\text{Ph}_2\text{CH}^\bullet$, respectively) [284, 285] than the reduction potential of $\text{AcrH}_2^{\bullet+}$ ($E^\circ_{\text{red}} = 0.81$ V vs. SCE) [266], the electron transfer from R^\bullet to $\text{AcrH}_2^{\bullet+}$ is highly exergonic and thereby it may proceed efficiently to yield AcrH_2 and R^+ (Scheme 21). The benzylic cation and analogues (R^+) may undergo the nucleophilic

addition of H_2O to yield the oxygenated product, i.e. the corresponding benzyl alcohol derivatives (ROH). In the case of the other alkylbenzenes such as cumene and diphenylmethane, the photoinduced hydride reduction of AcrH^+ to AcrH_2 occurs in the presence of HClO_4 , accompanied by the oxygenation of alkylbenzenes to the corresponding benzyl alcohol [283]. When the HClO_4 concentration is reduced from 1.2 to 0.10 M in the photochemical reaction of AcrH^+ with diphenylmethane, comparable amounts of AcrH_2 and AcrHCHPh_2 are obtained in the ratio of 59:41 [283]. Thus, acid catalysis in electron transfer from R^* to AcrH^* plays an essential role to alter the products in the presence of HClO_4 (Scheme 21), although it does not affect the overall efficiency of the photochemical reaction significantly.

1.3.5 Lewis Acid Catalysis in C–C bond Formation via Electron Transfer

Lewis acids generally activate carbonyl substrates through coordination for nucleophilic attack [286–289]. In some cases, however, Lewis acids have been reported to act as an electron acceptor rather than an acid when relatively strong electron donors are employed as nucleophiles [290–296]. As described earlier, the β -methyl substitution of ketene silyl acetals increases the electron density rendering the donor more susceptible to the electron transfer oxidation than the less substituted counterparts [229], while it also generally increases the steric hindrance of the reaction center, thereby reducing the reactivity of the nucleophilic attack toward electrophiles [228, 297, 298]. When β,β -dimethyl-substituted ketene silyl acetal such as $\text{Me}_2\text{C}=\text{C}(\text{OEt})\text{OSiEt}_3$ is employed as a nucleophile, an electron transfer from $\text{Me}_2\text{C}=\text{C}(\text{OEt})\text{OSiEt}_3$ to a Lewis acid such as SnCl_4 is suggested to initiate the catalytic cycle for Mukaiyama–Michael reaction of the ketene silyl acetal as shown in Scheme 22 [292]. The SnCl_4 anion radical formed in the electron transfer step spontaneously decomposes to $^*\text{SnCl}_3$ and Cl^- . The $^*\text{SnCl}_3$ radical then reacts with an α -enone in a 1,4-fashion to give a stannyl enolate radical which subsequently couples with the cation radical to give a stannyl enolate of the Michael adduct (Scheme 22). Transmetalation of this intermediate with in situ-formed trialkylsilyl chloride produces the corresponding silyl enol ether and regenerates SnCl_4 (Scheme 22). In this process, the close contact between sterically demanding reaction sites at an early stage is of no virtual importance. Thus, the crossover reaction of an equimolar mixture of $\text{Me}_2\text{C}=\text{C}(\text{OEt})\text{OSiEt}_3$ and $\text{H}_2\text{C}=\text{C}(\text{OEt})\text{OSiEt}_3$ with a hindered α -enone in the presence of a Lewis acid gave the adduct of $\text{Me}_2\text{C}=\text{C}(\text{OEt})\text{OSiEt}_3$ bearing contiguous quaternary carbon centers exclusively [292]. Such a preferred connection of more hindered carbons is characteristic of radical coupling via electron transfer in Scheme 22.

The competition reaction employing various types of ketene silyl acetals also reveals that those bearing more substituents at the β -position react preferentially over less substituted ones [296]. However, when ketene silyl acetals involve bulky siloxy and/or alkoxy group(s), less substituted compounds react preferentially as expected for a ubiquitous nucleophilic reaction depending on Lewis acids [296, 299, 300]. Enhanced preference for the more sterically demanding Michael adducts is obtained with $\text{Bu}_2\text{Sn}(\text{OTf})_2$, SnCl_4 and $\text{Et}_3\text{SiClO}_4$ in the former reaction while TiCl_4 gives the highest selectivity for the less sterically demanding products in the latter



Scheme 22.

case [296]. Thus, the change in the reactivity of ketene silyl acetals particularly with β -methyl substitution provides valuable insight into the electron transfer vs. nucleophilic process dichotomy [229, 296].

A similar electron transfer mechanism has been proposed for photosensitized electron transfer catalysis of the Mukaiyama-aldol reaction of aldehydes and ketones with enol silanes [301]. Photoinduced electron transfer from enol silanes to a monocationic N²¹,N²²-bridged porphyrin [302, 303] leads to the production of a trimethylsilyl radical which can act as a chain carrier for the aldol reaction under the irradiation of visible light [301].

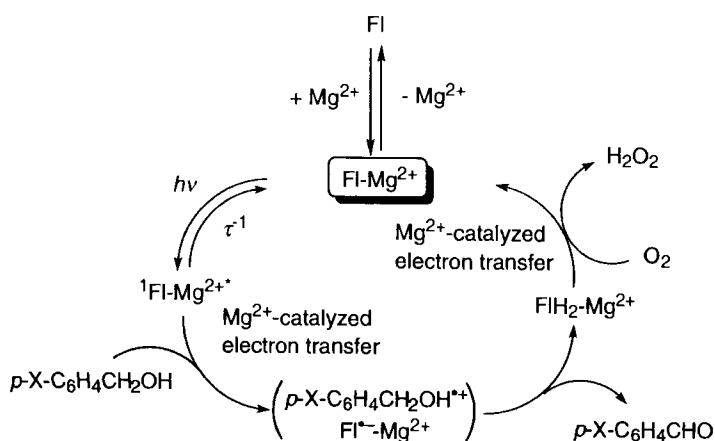
1.3.6 Acid Catalysis in Photoinduced Electron Transfer

A first remarkable catalytic effect of metal ions (Mg²⁺ and Zn²⁺) was also found in photoinduced electron transfer reactions from various electron donors to flavin analogs (Fl in Scheme 5) [235, 304]. The increase in the oxidizing ability of the

singlet excited states of FI by the complex formation with Mg^{2+} or Zn^{2+} is evaluated quantitatively as the positive shifts of the one-electron reduction potential of the singlet excited state [$E^\circ(^1\text{FI}^*/\text{FI}^{\cdot-})$] [235]. The magnitude of the shift is approximately constant (0.33 ± 0.01 V) for different FI–metal ion complexes [235]. The complex formation with metal ions not only increases the oxidizing ability of the ground and excited states of FI but also stabilizes FI against irradiation of the visible light to prevent the photodegradation [235, 305]. For example, the quantum yield Φ_d of photodegradation of FI– Mg^{2+} complex in deaerated MeCN is 6.2×10^{-4} , which is negligibly small compared with that of a free flavin **1a** ($\Phi_d = 1.6 \times 10^{-2}$) [235]. Thus, irradiation of the absorption band of **1a**– Mg^{2+} complex makes it possible to oxidize benzyl alcohol derivatives to the corresponding benzaldehydes efficiently, while irradiation of a free flavin (**1a**) results in no dehydrogenation of *p*-methylbenzyl alcohol [305]. The reduced flavin– Mg^{2+} complex, $\text{FIH}_2\text{--Mg}^{2+}$, produced in the photooxidation of benzyl alcohols by FI– Mg^{2+} is readily oxidized by O_2 via Mg^{2+} -catalyzed electron transfer [137] to regenerate the oxidized form FI– Mg^{2+} [235]. In such a case, flavin–metal ion complexes act as efficient photocatalysts for the dehydrogenation of benzyl alcohol derivatives ($\text{X--C}_6\text{H}_4\text{CH}_2\text{OH}$) as shown in Scheme 23 [235]. Flavin– Mg^{2+} complexes can also catalyze photoinduced oxygenation of R_4Sn via photoinduced electron transfer from R_4Sn to $^1\text{FI}^*\text{--Mg}^{2+}$ in acetonitrile at 298 K [306].

Protonated flavin and pteridine analogues formed in the presence of perchloric acid can also function as efficient photocatalysts for the photooxidation of benzyl alcohols by oxygen via H^+ -catalyzed photoinduced electron transfer [307–309]. In contrast to the case of flavin and pteridine analogues, the triplet excited state of coenzyme pyrroloquinolinequinone (PQQ) by itself can oxidize benzyl alcohols to the corresponding aldehydes via photoinduced electron transfer, since the oxidizing ability of the triplet excited state of PQQ is much higher than that of flavin and pteridine analogues [310].

Complexation of metal ions with substrates not only can enhance the oxidizing ability of the substrate, but also can change the excited state property [52, 311].



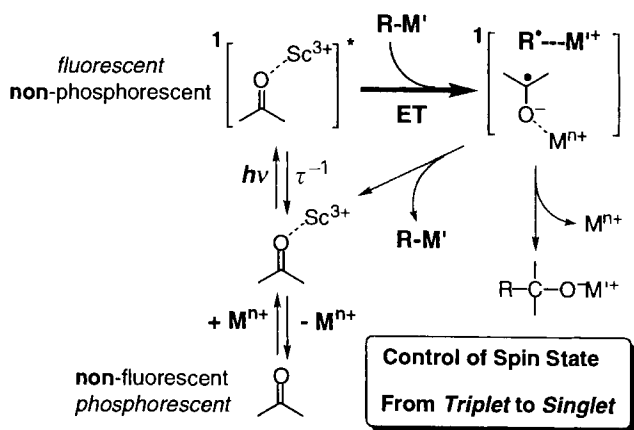
Scheme 23.

Aromatic carbonyl compounds with lowest $n-\pi^*$ singlet states are generally non-fluorescent, possessing large $\pi-\pi^*$ triplet formation quantum yields (ca. 0.7) via fast intersystem crossing [312, 313]. However, irradiation of the absorption band due to Mg^{2+} complex of 1- or 2-naphthaldehyde formed in the presence of $\text{Mg}(\text{ClO}_4)_2$ causes strong fluorescence at 430–440 nm. Other metal ions such as Sc^{3+} are also effective for the change in the excited states of carbonyl compounds from the triplet to the singlet states by the complex formation [136]. The coordination of carbonyl compounds to metal ions results in an increased energy of the $n-\pi^*$ singlet state relative to the fluorescent $\pi-\pi^*$ singlet excited state as reported for similar change in the photophysical and photochemical properties of carbonyl compounds by the complex formation with Lewis acids [314–316].

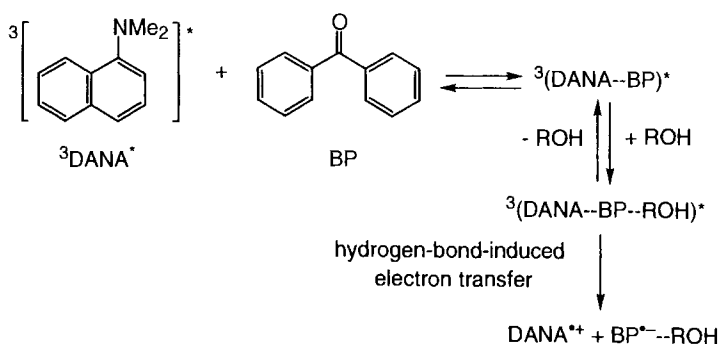
The E°_{red} values (vs. SCE) of the singlet excited states of the Mg^{2+} -carbonyl complexes are determined by adaptation of the electron transfer free energy relationship for photoinduced electron transfer from various aromatic electron donors to the singlet excited states of the Mg^{2+} -carbonyl complexes in the presence of Mg^{2+} (1.0 M) in MeCN at 298 K [311]. A remarkable positive shift (1.2 V) in the E°_{red} values of the singlet excited states of the Mg^{2+} -carbonyl complexes is reported compared with those of the triplet excited states of free carbonyl compounds [311]. Such a large positive shift results in a significant increase in the reactivity of the Mg^{2+} complexes vs. free carbonyl compounds in the photoinduced electron transfer reactions [311]. A more substantial positive shift (1.5 V) in the E°_{red} values is observed when $\text{Mg}(\text{ClO}_4)_2$ is replaced by $\text{Sc}(\text{OTf})_3$ compared with those of the triplet excited states of free carbonyl compounds [136]. It should be noted that the 1.5 V positive shift corresponds to 10^{25} -fold acceleration of the electron transfer rate at 298 K. Such a remarkable enhancement of the reactivities of the excited states of carbonyl compounds by the complexation with metal ions (M^{n+}) makes it possible to perform the photochemical C–C bond formation reactions of carbonyl compounds with various electron donors ($\text{R}-\text{M}'$, e.g. R_4Sn and allyl- or benzylsilanes) via the metal ion-catalyzed photoinduced electron transfer which would otherwise be impossible to occur as shown in a general manner in Scheme 24 [136, 311].

Reactivities of protons toward excited organic and inorganic molecules have received much attention, since the acid–base equilibria in the excited states are changed drastically compared with those in the ground states [317–321]. The changes in the electron transfer properties such as the one-electron redox potentials and the reorganization energies of electron transfer due to the protonation of the excited states have yet to be determined in detail. A catalytic effect of Brønsted acids has been reported for an electron transfer in the triplet exciplex formed between the triplet excited state of methoxynaphthalene and the ground state of benzophenone [322, 323]. The rate of electron transfer increased with an increase in proton concentration [322, 323].

An intraexciplex electron transfer is also induced by hydrogen bonding of ROH (H_2O and methanol) to the carbonyl group of benzophenone (BP) in the triplet exciplex formed between the triplet excited state of *N,N*-dimethyl-1-naphthalene and the ground state of benzophenone as shown in Scheme 25 [324]. The driving force for the intraexciplex electron transfer is hydrogen bonding between $\text{BP}^{\bullet-}$ and ROH, which should result in a positive shift in the one-electron reduction potential of BP. It has also been reported that an intermolecular electron transfer takes place



Scheme 24.

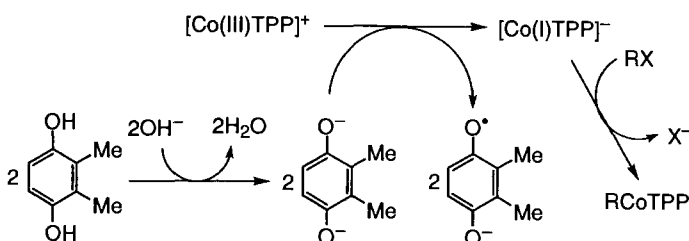


Scheme 25.

upon excitation of a hydrogen-bonded donor–acceptor complex in the ground state and that the proton-coupled electron transfer was induced by the proton movement on the hydrogen bond [325–329]. Such a proton-coupled electron transfer has been suggested to play an important role in biological electron transfer rates [329–332], stimulating experimental [325–329, 334, 335] and theoretical studies [336–339]. In Scheme 25, however, no proton movement is involved when no kinetic isotope effect is observed in the hydrogen bonding-induced electron transfer [324].

1.4 Base Catalysis in Electron Transfer

As demonstrated above, the interaction of Brønsted and Lewis acids with an electron acceptor or the one-electron reduced species results in remarkable acceleration of the rate of electron transfer from an electron donor to the acceptor due to the



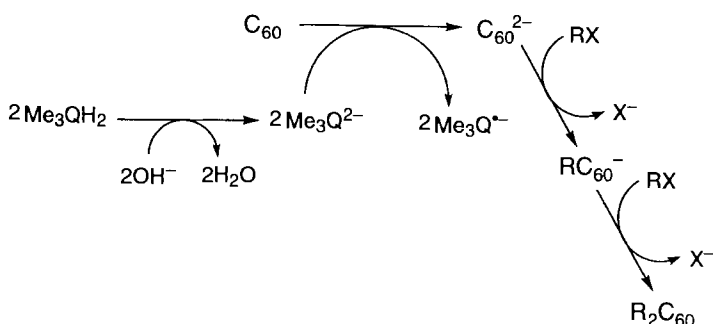
Scheme 26.

negative shift of the one-electron reduction potential of the acceptor (e.g., Eq. 4). Alternatively, the interaction of a base with an electron donor or the one-electron oxidized species should also result in acceleration of the rate of electron transfer from the electron donor to an acceptor due to the expected negative shift of the one-electron oxidation potential of the donor. Different types of base catalysis in electron transfer reactions are discussed below.

1.4.1 Base Catalysis by Deprotonation of Electron Donors

Various hydroquinone derivatives (X-QH₂) are readily deprotonated in the presence of 2 equiv. of Me₄N⁺OH⁻ in MeCN to produce the corresponding quinone dianion (X-Q²⁻) [340]. Although hydroquinones are weak electron donors, the corresponding quinone dianions, which are two-electron reduced species of quinones, are strong electron donors. Thus, stepwise electron transfer from 2 equiv. of 2,3-dimethylhydroquinone (Me₂QH₂) to [(TPP)Co]⁺ occurs in the presence of Me₄N⁺OH⁻ in MeCN to produce cobalt(I) tetraphenylporphyrin anion, [(TPP)Co]⁻, which can be further converted into the corresponding alkylcobalt(III) porphyrin, (TPP)Co(R), by an S_N2 reaction with alkyl halides (RX) as shown in Scheme 26 [341]. It should be noted that no electron transfer from Me₂QH₂ to [(TPP)Co]⁺ occurs in the absence of a base. The one-electron oxidation potential of Me₂Q²⁻ ($E^{\circ}_{\text{ox}} = -1.12$ V vs. SCE) is low enough to reduce (TPP)Co to [(TPP)Co]⁻ ($E^{\circ}_{\text{red}} = -0.85$ V vs. SCE) [341]. When a hydroquinone derivative with electron-withdrawing substituents such as tetrachlorohydroquinone or 2,3-dicyanohydroquinone is employed as an electron donor, no further reduction of (TPP)Co to [(TPP)Co]⁻ has been observed following the initial electron transfer from the dianion to [(TPP)Co]⁺ [340]. Whether the one- or two-electron reduction of [(TPP)Co]⁺ by X-QH₂ in the presence of 2 equiv. of Me₄N⁺OH⁻ occurs or not is determined by the difference in the E°_{ox} values of X-Q²⁻ or X-Q^{•-} and the E°_{red} values of (TPP)Co or [(TPP)Co]⁺ [340].

Similarly, the stepwise electron transfer from 2 equiv. of trimethylhydroquinone (Me₃QH₂) to C₆₀ occurs in the presence of Me₄N⁺OH⁻ in benzonitrile (PhCN) to produce C₆₀²⁻, which can be further converted into the corresponding dialkyl adduct (R₂C₆₀) by sequential electron transfer and S_N2 reactions with alkyl halides



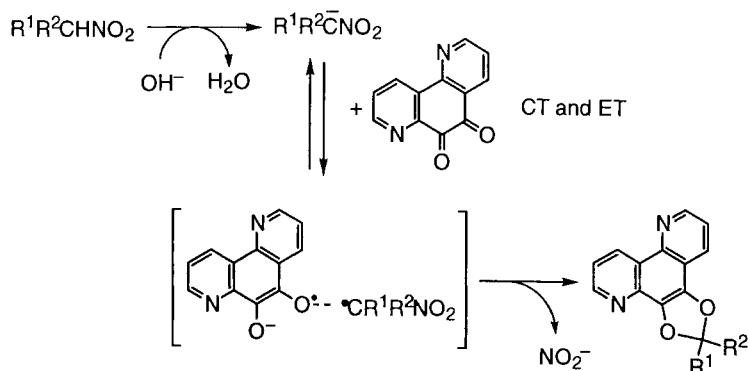
Scheme 27.

(RX) as shown in Scheme 27 [342, 343]. The E°_{ox} value of Me_3Q^{2-} is also low enough to reduce $\text{C}_{60}^{\cdot -}$ to C_{60}^{2-} ($E^\circ_{\text{red}} = -0.87$ V vs. SCE) in PhCN [344]. The electrochemically generated C_{60}^{2-} and C_{70}^{2-} also undergo the alkylation reactions with alkyl halides to obtain dialkyl and tetraalkyl adducts of C_{60} [345–347].

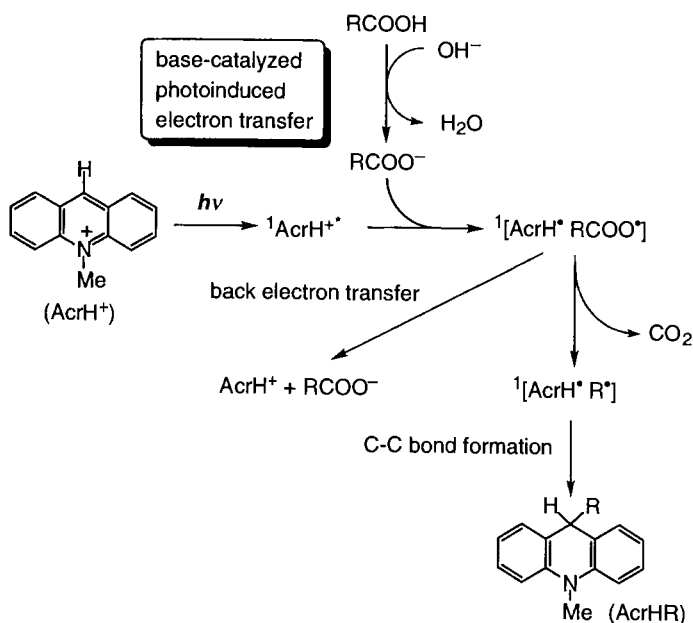
The rates of oxidation of hydroquinone by polypyridyl-oxo-Ru complexes, $[(\text{bpy})_2(\text{Py})\text{Ru}^{\text{IV}}(\text{O})]^{2+}$ and $[(\text{bpy})_2(\text{Py})\text{Ru}^{\text{III}}(\text{OH})]^{2+}$ (bpy = 2,2'-bipyridine, Py = pyridine) in aqueous solution were reported to be pH dependent, and the rate enhancement in basic solution arises from the appearance of hydroquinone anion (QH^-) acting as a stronger electron donor than QH_2 [334]. In the case of $[(\text{bpy})_2(\text{Py})\text{Ru}^{\text{III}}(\text{OH})]^{2+}$, the rate enhancement is also observed in highly acidic solution where the protonated complex, $[(\text{bpy})_2(\text{Py})\text{Ru}^{\text{III}}(\text{OH}_2)]^{3+}$, acts as a stronger electron acceptor than $[(\text{bpy})_2(\text{Py})\text{Ru}^{\text{III}}(\text{OH})]^{2+}$ [334].

2-Nitropropane is also readily deprotonated in the presence of 1 equiv. of $\text{Me}_4\text{N}^+\text{OH}^-$ in MeCN to produce the tetramethylammonium salt of 2-nitropropane anion [348]. The electron donor ability of 2-nitropropane anion is reduced when the Me_4N^+ counter cation is replaced by Li^+ owing to the strong binding between 2-nitropropane anion and Li^+ compared with Me_4N^+ . This is indicated by the more positive one-electron oxidation potential of the Li^+ salt ($E^\circ_{\text{ox}} = 0.48$ V vs. SCE) than that of the Me_4N^+ salt ($E^\circ_{\text{ox}} = 0.10$ V vs. SCE) [348]. Nitroalkane anions produced by deprotonation of nitroalkanes are known to play an essential role in radical chain nucleophilic substitutions (Scheme 1) [24–32]. An addition–cyclization reaction of nitroalkanes with tricyclic *o*-quinones has been reported to occur in the presence of $\text{Me}_4\text{N}^+\text{OH}^-$ in MeCN via electron transfer in the charge-transfer complex formed between nitroalkane anions and the *o*-quinones, followed by C–O adduct formation and subsequent cyclization to afford the 1,3-dioxole derivatives as shown in Scheme 28 [349].

The anodic oxidation of RCOO^- produced by deprotonation of RCOOH occurs at about 2 V (vs. SCE), known as the Kolbe reaction, producing the radical coupling products of the alkyl groups of RCOO^- , R–R and CO_2 [350]. Since the one-electron reduction potential of the singlet excited state $^1\text{AcrH}^{+*}$ (2.3 V vs. SCE) [351] is positive enough to oxidize RCOO^- , photoinduced electron transfer from RCOOH (R = H, Me, Et, *i*-Pr, *t*-Bu, $\text{C}_{11}\text{H}_{23}$, $\text{C}_{15}\text{H}_{31}$) to $^1\text{AcrH}^{+*}$ occurs in the



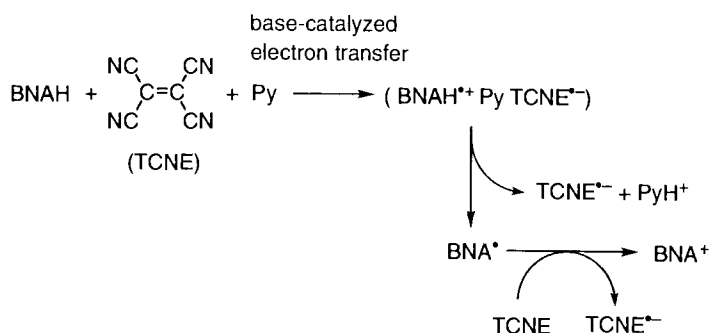
Scheme 28.



Scheme 29.

presence of NaOH to give a singlet radical pair $^1(AcrH^{\bullet} RCOO^{\bullet})$, in which $RCOO^{\bullet}$ undergoes facile decarboxylation in competition with the back electron transfer to give the reactant pair as shown in Scheme 29 [352]. The resulting radical pair $^1(AcrH^{\bullet} R^{\bullet})$ undergoes facile radical coupling to yield 9,10-dihydro-9-alkyl-10-methylacridine (AcrHR) selectively [352].

As discussed earlier, there is no need to have an interaction of a base catalyst with an electron donor (D) as is the case of an acid catalysis (Scheme 2). The interaction



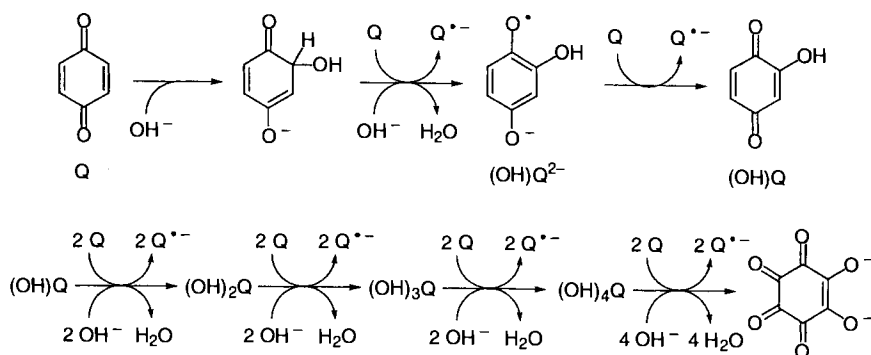
Scheme 30.

of a base with the oxidized state ($\text{D}^{*\bullet+}$) is sufficient to accelerate the rate of electron transfer from the electron donor to an acceptor. Such an example was reported for a base-catalyzed electron transfer from BNAH to tetracyanoethylene (TCNE) [353, 354]. Although there is no interaction between BNAH and pyridine, $\text{BNAH}^{*\bullet+}$ can be readily deprotonated by pyridine [222]. Since the one-electron oxidation potential of $\text{BNAH}^{*\bullet+}$ produced by deprotonation of BNAH ($E^\circ_{\text{ox}} = -1.08$ V vs. SCE) is much more negative than the one-electron reduction potential of TCNE ($E^\circ_{\text{red}} = 0.22$ V vs. SCE) [222], BNAH can reduce 2 equiv. of TCNE in the presence of pyridine as shown in Scheme 30 [354]. The observed second-order rate constant (k_{obs}) of the base-catalyzed electron transfer increases linearly with increasing the pyridine concentration [354].

The presence of a base is also essential for the efficient reductive dehalogenation of RX by BNAH via photoinduced electron transfer [355, 356]. Since the one-electron oxidation potential of the singlet excited state of BNAH ($^1\text{BNAH}^*$) is -3.1 V (vs. SCE) [351], which is more negative than the one-electron reduction potential of benzyl bromide (PhCH_2Br), photoinduced electron transfer from $^1\text{BNAH}^*$ to PhCH_2Br occurs efficiently with the diffusion-limited rate [356]. This fast process needs no base catalyst to accelerate the electron transfer rate further. However, the photoinduced electron transfer results in the formation of $\text{BNAH}^{*\bullet+}$, which is a strong acid to generate H^+ . Since BNAH is known to decompose efficiently via acid-catalyzed hydration [98, 257, 258], proton has to be removed in order to achieve the efficient photoreduction of PhCH_2Br by BNAH. As such the addition of pyridine (7.42×10^{-2} M) to the BNAH- PhCH_2Br system results in a significant increase in the product yield (toluene) of the photochemical reaction from 1.7 % in the absence of pyridine to 80 % [356, 357].

1.4.2 Base Catalysis via Formation of Base Adducts

Hydroxide ion (OH^-) in aprotic solvents has been reported to act as an electron donor in the one-electron reduction of quinones and other electron acceptors [358, 359]. However, the actual electron donor has been shown to be the quinone in the

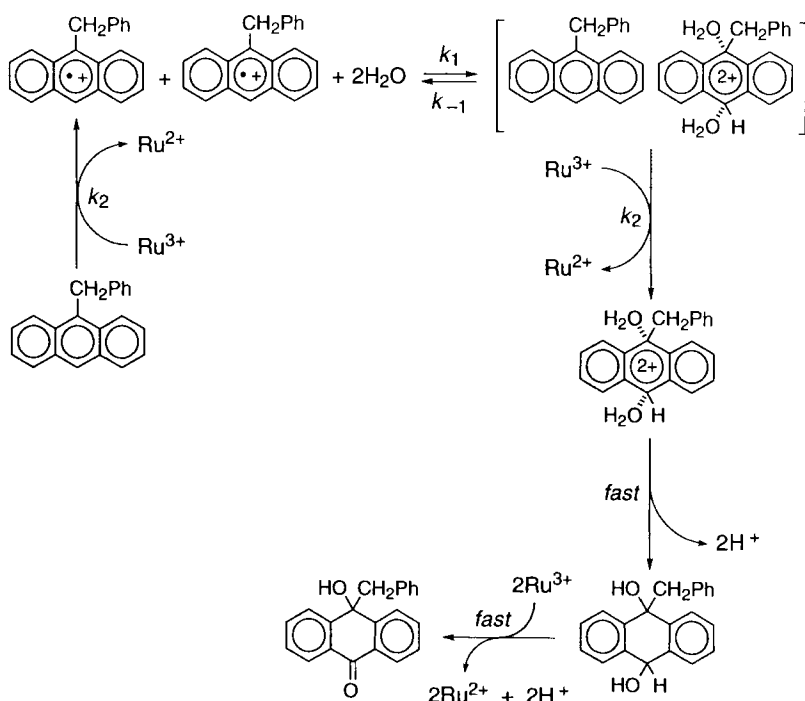


Scheme 31.

presence of OH^- in MeCN and therefore no oxidized product of OH^- is formed [133]. When OH^- is added to *p*-benzoquinone (Q), the adduct anion can act as a strong electron donor toward Q as shown in Scheme 31 [133]. Electron transfer from the adduct anion to Q occurs accompanied by deprotonation to yield OH-substituted semiquinone radical anion and $Q^{\bullet -}$. The subsequent electron transfer from the OH-substituted semiquinone radical anion to $Q^{\bullet -}$ occurs rapidly to yield OH-substituted quinone and $Q^{\bullet -}$. Thus, one-electron substitution of Q by OH, which corresponds to the two-electron oxidation of Q, results in the one-electron reduction of 2 equiv. of Q to yield two $Q^{\bullet -}$. In consequence, the successive substitution of Q by OH finally results in the formation of 10-electron oxidized species, accompanied by the one-electron reduction of 10 equiv. of Q to yield 10 $Q^{\bullet -}$ as shown in Scheme 31 [133]. Thus, such a novel disproportionation of *p*-benzoquinone, in which the quinone itself acts as a 10-electron donor in the presence of OH^- , is responsible for the apparently quantitative formation of semiquinone radical anion.

Reactions of *p*-benzoquinone and its derivatives with alkoxide ions (RO^- ; R = H, Me, Et, *i*-Pr, $PhCH_2$) in MeCN also result in formation of the corresponding semiquinone radical anions accompanied by the formation of RO-substituted *p*-benzoquinones, which are the oxidized products of *p*-benzoquinones [360]. Detailed product and kinetic analyses of the reactions indicate that RO-adduct anion of *p*-benzoquinone is an actual electron donor and that RO^- is acting as a very strong base or nucleophile rather than a one-electron reductant in an aprotic solvent, such as MeCN [360]. Similarly, the reaction of C_{60} with methoxide anion (MeO^-) in benzonitrile ($PhCN$) results in the disproportionation of C_{60} to yield both $C_{60}^{\bullet -}$ and the methoxy adduct [360]. Spectroscopic and kinetic studies also indicate that a methoxy adduct anion of C_{60} is a real electron donor and that MeO^- is acting as a very strong base or nucleophile rather than an electron donor in $PhCN$ [360].

A weak base such as H_2O can accelerate the rate of electron transfer disproportionation of anthracene radical cation in MeCN by the interaction between anthracene dication produced in the electron transfer and H_2O [361]. The four-electron oxidation of 9-benzylanthracene ($PhCH_2An$) with more than 4 equiv. of



Scheme 32.

$[\text{Ru}(\text{bpy})_3]^{3+}$ proceeds via the rate-determining electron transfer disproportionation of $\text{PhCH}_2\text{An}^{\bullet+}$ to yield 10-benzyl-10-hydroxy-9(10H)-anthracenone as shown in Scheme 32 [361, 362]. The dihydroxy adduct of $\text{PhCH}_2\text{An}^{2+}$ produced in the H_2O -catalyzed electron transfer disproportionation of $\text{PhCH}_2\text{An}^{\bullet+}$ is further oxidized to 10-alkyl-10-hydroxy-9(10H)-anthracenone by 2 equiv. of $[\text{Ru}(\text{bpy})_3]^{3+}$ (Scheme 32) [362]. The observed second-order rate constant (k_{et}) for the second-order decay of $\text{PhCH}_2\text{An}^{\bullet+}$ due to the electron transfer disproportionation increases with an increase in $[\text{H}_2\text{O}]$ to exhibit a first-order dependence on $[\text{H}_2\text{O}]$ at low concentrations, changing to a second-order dependence at high concentrations [361]. There is no kinetic deuterium isotope effect of water for the decay of $\text{PhCH}_2\text{An}^{\bullet+}$ when H_2O is replaced by D_2O [361]. The first- and second-order dependence of k_{obs} of $\text{PhCH}_2\text{An}^{\bullet+}$ on $[\text{H}_2\text{O}]$ can be explained by the complex formation of $\text{PhCH}_2\text{An}^{2+}$ with one and two H_2O molecules as shown in Scheme 32 [361].

The complex formation of $\text{PhCH}_2\text{An}^{2+}$ and H_2O should result in a negative shift of the one-electron oxidation potential of $\text{PhCH}_2\text{An}^{\bullet+}$ (E_{ox}). The Nernst equation may be expressed as

$$E_{\text{ox}} = E_{\text{ox}}^{\circ} - (2.3RT/F) \log K_1[\text{H}_2\text{O}](1 + K_2[\text{H}_2\text{O}]) \quad (27)$$

where E_{ox}° is the one-electron oxidation potential of $\text{PhCH}_2\text{An}^{\bullet+}$ in the absence

of H_2O and K_1 and K_2 are the formation constants for the complex between $\text{PhCH}_2\text{An}^{2+}$ and one and two H_2O molecules, respectively ($K_1[\text{H}_2\text{O}] \gg 1$) [361]. From Eq. 27 is derived the dependence of the rate constant of electron transfer disproportionation (k_{et}) on $[\text{H}_2\text{O}]$ as given by Eq. 28:

$$k_{\text{et}} = k_0 k_{\text{et}0} (1 + K_1[\text{H}_2\text{O}] + K_1 K_2 [\text{H}_2\text{O}]^2) \quad (28)$$

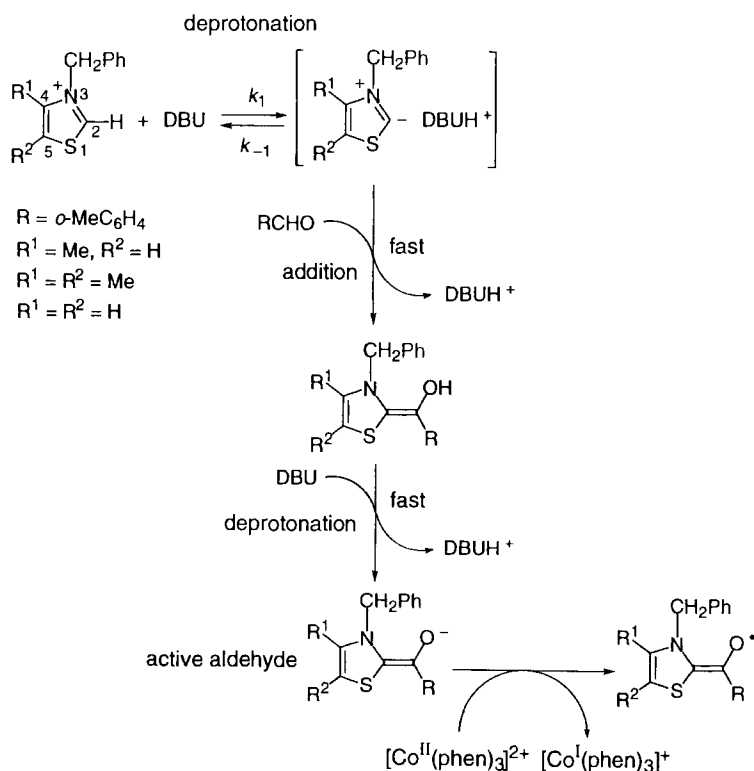
where $k_{\text{et}0}$ is the rate constant in the absence of H_2O . The experimental observation agrees with the dependence of k_{et} on $[\text{H}_2\text{O}]$ in Eq. 28 [361]. The six-electron oxidation of anthracene to anthraquinone also occurs with $[\text{Ru}(\text{bpy})_3]^{3+}$ in MeCN via the H_2O -catalyzed electron transfer disproportionation of anthracene radical cation [361].

The deprotonation and addition of a base to thiazolium salts are combined to produce an acyl carbanion equivalent (an active aldehyde) [363, 364], which is known to play an essential role in catalysis of the thiamine diphosphate (ThDP) coenzyme [365, 366]. The active aldehyde in ThDP dependent enzymes has the ability to mediate an efficient electron transfer to various physiological electron acceptors, such as lipoamide in pyruvate dehydrogenase multienzyme complex [367], flavin adenine dinucleotide (FAD) in pyruvate oxidase [368] and Fe_4S_4 cluster in pyruvate-ferredoxin oxidoreductase [369].

The active aldehydes are derived from the reaction of 3-benzylthiazolium salts with *o*-tolualdehyde in the presence of DBU (1,8-diazabicyclo[5.4.0]undec-7-ene) via deprotonation of thiazolium salts, addition of the aldehyde and deprotonation of the adduct as shown in Scheme 33 [364]. The anionic form of active aldehydes in Scheme 33 is confirmed by the direct detection of the one-electron oxidized species with use of ESR [364]. From the linewidth variations of the ESR spectra of the oxidized active aldehyde radicals were determined the rate constants $[(5-7) \times 10^8 \text{ M}^{-1} \text{ s}^{-1}]$ and the corresponding small reorganization energies ($\lambda = 12-13 \text{ kcal mol}^{-1}$) of electron transfer exchange reactions between the active aldehyde and the radicals [370]. The one-electron oxidation potentials of the active aldehydes are nearly the same ($E^\circ_{\text{ox}} = -0.93$ to -0.98 V) irrespective of parent aldehydes [364]. The small reorganization energies and the highly negative oxidation potentials of the active aldehydes indicate the high reducing ability to mediate electron transfer to an electron acceptor. This has been confirmed by using tris(1,10-phenanthroline)cobalt(II) complex, $[\text{Co}(\text{phen})_3]^{2+}$ (phen = 1,10-phenanthroline), which is reduced by the active aldehydes to $[\text{Co}(\text{phen})_3]^+$ (Scheme 33) [364]. Thus, the active aldehydes are suitable for fast electron transfer systems where they can act as efficient electron transfer *catalysts* [364].

1.4.3 Control of Reorganization Energy by Base Catalysis

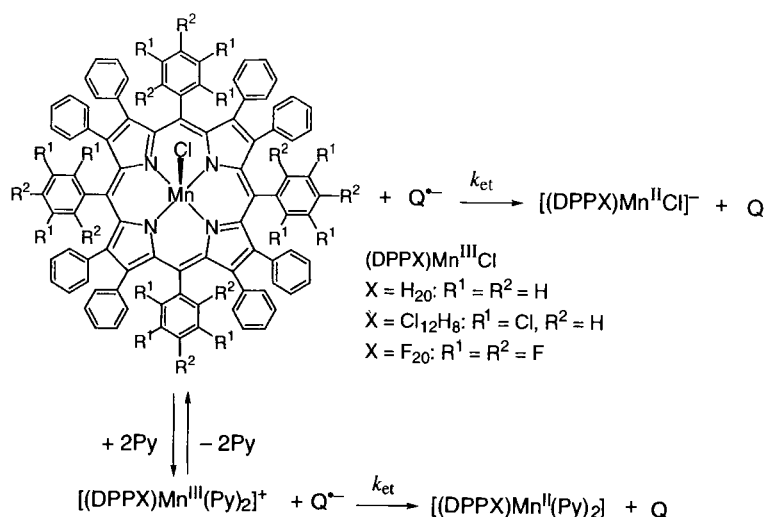
There are two factors to control the rate of electron transfer, i.e., the free energy change of electron transfer ($\Delta G^\circ_{\text{et}}$) and the reorganization energy of electron transfer (λ), as shown in Figure 2. When the λ values are relatively small in the electron transfer system as described so far, the main factor to accelerate the rates of



Scheme 33.

electron transfer by a catalyst is the change of redox potentials by the interaction of the products of electron transfer. When the λ value is large in an electron transfer system, a decrease in λ by the interaction with a catalyst would result in acceleration of the electron transfer rate. Such examples have been reported as described below [371, 372].

The electrochemical studies of (P)MnCl, where P represents either the dianion of tetraphenylporphyrin (TPP), which is planar, or of the dianion of dodecaphenylporphyrins (DPPX, X = H₂₀, Cl₁₂H₈, F₂₀), which are known to adopt a nonplanar conformation [373, 374], have shown that the Mn(III)/Mn(II) reduction is quasi-reversible [375], and that the separation between the cathodic and anodic peak potentials, $\Delta E_p = |E_{pc} - E_{pa}|$, increases in the order (TPP)MnCl < (DPPH)MnCl < (DPPCl₁₂)MnCl < (DPPF₂₀)MnCl [376, 377]. The large ΔE_p value (0.52 V) in the case of (DPPF₂₀)MnCl reduction is due to slow electron transfer kinetics, as has been reported for other (P)MnCl complexes [378]. The slow electron transfer reduction of (DPPX)MnCl was confirmed by determining the rate constant (k_{et}) of electron transfer from semiquinone radical anions (Q^{•-}) to each Mn(III) porphyrin (Scheme 34) [379]. The fit of the dependence of $\log k_{et}$ on the free energy change of



Scheme 34.

electron transfer ($\Delta G^\circ_{\text{et}}$) to the Marcus theory of adiabatic outer-sphere electron transfer [70] (Figure 15) indicates that the rate variations at a given $\Delta G^\circ_{\text{et}}$ value arise from the difference in the λ value given in Figure 15 and not from the non-adiabaticity [379].

The slow electron transfer reduction of $(\text{DPPH}_{20})\text{MnCl}$ can be accelerated significantly by axial coordination of a base, when the addition of a nitrogenous base such as pyridine (Py) to the five-coordinate complex gives the six-coordinate complex $[(\text{DPPH}_{20})\text{Mn}(\text{Py})_2]^+$ as shown in Figure 15 [371]. The reduction of $[(\text{DPPH}_{20})\text{Mn}(\text{Py})_2]^+$ occurs at $E^\circ_{\text{red}} = -0.41$ V vs. SCE, which is slightly more negative than the E°_{red} value (-0.36 V) of the five-coordinate complex, $(\text{DPPH}_{20})\text{MnCl}$ ($E^\circ_{\text{red}} = -0.36$ V) [371]. Such a small negative shift of E°_{red} by coordination of pyridine cannot account for the large acceleration in the rate of electron transfer for the six-coordinate complex as compared with the five-coordinate complex as shown by the arrows along the curve with a constant λ value in Figure 15. Thus, the acceleration in the rate of electron transfer upon axial coordination of pyridine results from a significant decrease in the reorganization energy associated with the electron-transfer reduction of $[(\text{DPPH}_{20})\text{Mn}(\text{Py})_2]^+$. This is shown by the vertical arrows in Figure 15, where the dependence of $\log k_{\text{et}}$ for the electron-transfer reduction of $[(\text{DPPH}_{20})\text{Mn}(\text{Py})_2]^+$, using a λ value of 30 kcal mol^{-1} , is given by the dashed line. The λ value becomes close to the value for the planar porphyrin [27 kcal mol^{-1} for $(\text{TPP})\text{MnCl}$] [371].

The addition of pyridine to the $(\text{OETPP})\text{Fe}(\text{C}_6\text{F}_5)-[\text{Fe}(4,7\text{-Me}_2\text{phen})_3]^{3+}$ system (OETPP = the dianion of 2,3,7,8,12,13,17,18-octaethyl-5,10,15,20-tetraphenylporphyrin) also results in a significant increase in the rate of electron transfer from $(\text{OETPP})\text{Fe}(\text{C}_6\text{F}_5)$ to $[\text{Fe}(4,7\text{-Me}_2\text{phen})_3]^{3+}$ [372]. The rate constant (k_{et}) of electron transfer of the six-coordinate complex $[(\text{OETPP})\text{Fe}(\text{C}_6\text{F}_5)(\text{Py})]$ in the presence of

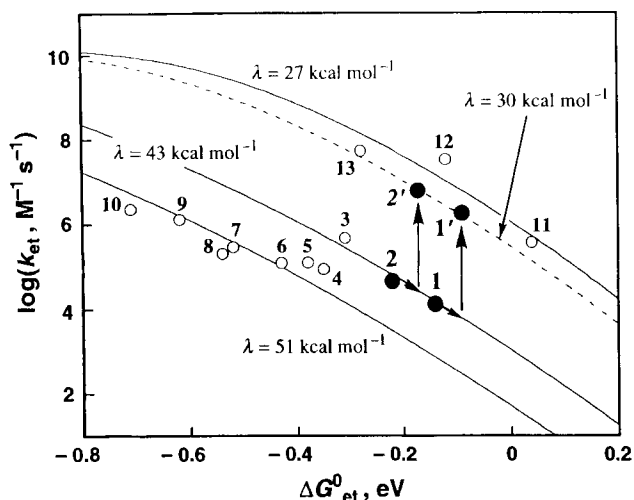


Figure 15. Dependence of $\log k_{\text{et}}$ on $\Delta G^{\circ}_{\text{et}}$ for electron-transfer from semiquinone radical anions to (P)MnCl in deaerated MeCN at 298 K. Numbers refer to the system: 1, (DPPH₂₀)MnCl/Q^{•-}; 1', [(DPPH₂₀)Mn(py)₂]⁺/Q^{•-}; 2, (DPPH₂₀)MnCl/MeQ^{•-}; 2', [(DPPH₂₀)Mn(py)₂]⁺/MeQ^{•-}; 3, (DPPH₂₀)MnCl/2,6-Me₂Q^{•-}; 4, (DPPCl₁₂H₈)MnCl/Q^{•-}; 5, (DPPF₂₀)MnCl/ClQ^{•-}; 6, (DPPCl₁₂H₈)MnCl/MeQ^{•-}; 7, (DPPCl₁₂H₈)MnCl/2,6-Me₂Q^{•-}; 8, (DPPF₂₀)MnCl/Q^{•-}; 9, (DPPF₂₀)MnCl/Q^{•-}; 10, (DPPF₂₀)MnCl/Q^{•-}; 11, (TPP)MnCl/2,5-Cl₂Q^{•-}; 12, (TPP)MnCl/ClQ^{•-}; 13, (TPP)MnCl/Q^{•-} [371]. The solid and dashed lines were drawn based on the Marcus theory of electron transfer using the λ values shown.

pyridine ($3.4 \times 10^9 \text{ M}^{-1} \text{ s}^{-1}$) is much larger than the k_{et} value of the five-coordinate complex [(OETPP)Fe(C₆F₅)] ($6.7 \times 10^4 \text{ M}^{-1} \text{ s}^{-1}$) [372]. The one-electron oxidation potential is expected to be shifted in a negative direction by the axial ligand coordination of pyridine, when the electron transfer oxidation becomes energetically more favorable. However, the observed positive shift in the oxidation potential in pyridine compared with the observed potential in MeCN is only 0.09 V, which cannot account for the remarkable acceleration of the rate of electron transfer for the pyridine-coordinated complex compared with the non-coordinated complex [372]. Thus, the acceleration in the rate of electron transfer upon axial coordination of pyridine results from a significant decrease in the reorganization energy associated with the electron transfer oxidation of the six-coordinate complex [(OETPP)Fe(C₆F₅)(Py)] than that for the five-coordinate complex [(OETPP)Fe(C₆F₅)]. The sixth axial coordination of a base minimizes the structural change associated with the electron transfer, since the six-coordinate iron atom may remain in the plane of the rather rigid porphyrin ligand irrespective of the oxidation state.

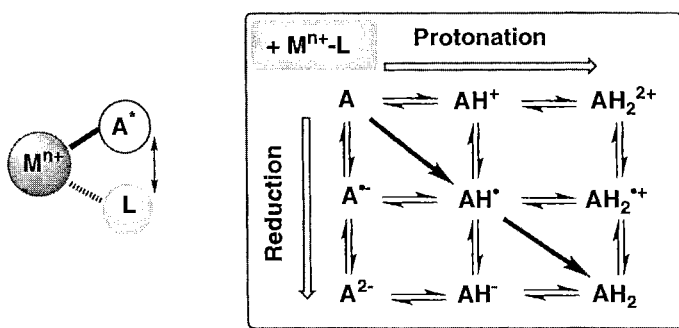
The sixth axial coordination of a base (L) also affects the rate of metal–carbon bond cleavage via an intramolecular electron transfer from the σ -bonded axial ligand (R) to the metal center in [(TPP)Co(R)(L)]⁺ produced by the one-electron oxidation of (TPP)Co(R), which leads to R group migration from the metal to ni-

trogen in $[(\text{TPP})\text{Co}(\text{R})]^+$ [380]. The migration rate of $[(\text{TPP})\text{Co}(\text{Ph})(\text{L})]^+$ increases by 1–2 orders of magnitude with increase in the ligand $\text{p}K_{\text{a}}$ [380].

1.5 Conclusions and Future Prospects

As demonstrated in this chapter, both thermal and photoinduced electron transfer reactions are accelerated by appropriate third components acting as catalysts when the products of electron transfer have strong interactions with the catalysts. Such interactions between the catalysts and the products of electron transfer result in significant changes in the free energy of electron transfer and the reorganization energies associated with the electron transfer. The catalysis in electron transfer processes is particularly important for controlling the redox reactions in which the electron transfer processes are involved as the rate-determining steps followed by facile follow-up steps involving cleavage and formation of chemical bonds. Once the thermodynamic properties of the complexation of acids or bases have been obtained, one can predict the kinetic formulation on the catalytic activity. There still remains a wealth of important fundamental questions with regard to catalysis in electron transfer, which have been only partially explored in the past, and which certainly deserve much more detailed attention in future.

When one thinks about only two-electron reduction of a substrate (A), the reduction and protonation give nine species at different oxidation and protonation states as shown in Scheme 35. Each species can have an interaction with a metal complex ($\text{M}^{n+}-\text{L}$) and such an interaction can control each redox step. Moreover, the interaction between the ligand L and a substrate has the possibility of controlling not only the reactivity but also the stereoselectivity of the redox reaction. With regard to multi-electron reduction or oxidation of a substrate, the much more redox and protonated or deprotonated states should be considered for the interaction with metal complexes. The scope and the application of catalysis in electron transfer are thereby expected to expand much further in the near future.



Scheme 35.

Acknowledgments

The author is deeply indebted for the work of all collaborators, co-workers and talented students whose names are listed in the references in this chapter (in particular, Prof. K. M. Kadish, Prof. J. Otera, Prof. S. Itoh and Dr. T. Suenobu). The author acknowledges continuous support of his studies on electron transfer chemistry by a Grant-in-Aid from the Ministry of Education, Science, Culture and Sports, Japan. The author also thanks Assoc. Prof. H. Imahori for helpful discussions.

References

1. M. L. Bender, *Mechanisms of Homogeneous Catalysis from Protons to Proteins*, Wiley, New York, **1971**.
2. W. Kaim, B. Schwederski, *Bioinorganic Chemistry: Inorganic Elements in the Chemistry of Life*, Wiley, New York, **1994**.
3. R. A. Sheldon (Ed.), *Metalloporphyrins in Catalytic Oxidations*, Marcel Dekker, New York, **1994**.
4. W. Rüttinger, G. C. Dismukes, *Chem. Rev.* **1997**, 97, 1.
5. I. M. Campbell, *Catalysis at Surfaces*, Chapman and Hall, London, **1988**.
6. R. A. Sheldon, M. Wallau, I. W. C. E. Arends, U. Schuchardt, *Acc. Chem. Res.* **1998**, 31, 485.
7. B. Cornils, W. Herrmann (Eds.), *Applied Homogeneous Catalysis*, VCH, Weinheim, **1996**.
8. G. W. Parshall, *Homogeneous Catalysis*, Wiley, New York, **1980**.
9. L. N. Lewis, *Chem. Rev.* **1993**, 93, 2693.
10. H. A. Wittcoff, B. G. Reuben, *Industrial Organic Chemistry in Perspective, Part I*, Wiley, New York, **1980**.
11. J. H. Clark, D. J. Macquarrie, *Chem. Soc. Rev.* **1996**, 25, 303.
12. J. K. Kochi, *Organometallic Mechanisms and Catalysis*, Academic Press, New York, **1978**.
13. L. Eberson, *Electron Transfer Reactions in Organic Chemistry; Reactivity and Structure*, Vol. 25, Springer, Heidelberg, **1987**.
14. Z. Jedlinski, *Acc. Chem. Res.* **1998**, 31, 55.
15. S. Hintz, A. Heidebreder, J. Mattay, *Top. Curr. Chem.* **1996**, 177, 78.
16. S. Steenken, *Top. Curr. Chem.* **1996**, 177, 125.
17. S. Fukuzumi, in *The Porphyrin Handbook*, Vol. 8 (Eds. K. M. Kadish, K. Smith, R. Guilard), Academic Press, San Diego, CA, **2000**, pp. 115–152.
18. S. Fukuzumi, J. K. Kochi, *Bull. Chem. Soc. Jpn.* **1983**, 56, 969.
19. E. C. Ashby, *Acc. Chem. Res.* **1988**, 21, 414.
20. R. J. Klingler, S. Fukuzumi, J. K. Kochi, *ACS Symp. Ser.* **1983**, 211, 117.
21. J. K. Kochi, *Angew. Chem., Int. Ed. Engl.* **1988**, 27, 1227.
22. J. K. Kochi, *Acc. Chem. Res.* **1992**, 25, 39.
23. G. Pandey, *Top. Curr. Chem.* **1993**, 168, 175.
24. S. Fukuzumi, in *Advances in Electron Transfer Chemistry*, Vol. 2 (Ed. P. S. Mariano), JAI Press, Greenwich, CT, **1992**, pp. 67–175.
25. M. Patz, S. Fukuzumi, *J. Phys. Org. Chem.* **1997**, 10, 129.
26. J. K. Kochi, *Adv. Phys. Org. Chem.* **1994**, 29, 185.
27. N. Kornblum, *Angew. Chem., Int. Ed. Engl.* **1975**, 14, 734.
28. J. F. Bunnett, *Acc. Chem. Res.* **1978**, 11, 413.
29. J. F. Bunnett, *Acc. Chem. Res.* **1992**, 25, 2.
30. M. Chanon, M. L. Tobe, *Angew. Chem., Int. Ed. Engl.* **1982**, 21, 1.
31. W. R. Bowman, in *Photoinduced Electron Transfer, Part C* (Eds. M. A. Fox, M. Chanon), Elsevier, Amsterdam, **1988**, pp. 487–552.
32. R. W. Alder, *J. Chem. Soc., Chem. Commun.* **1980**, 1184.
33. N. L. Bauld, *Tetrahedron* **1989**, 45, 5307.

34. M. Chanon, *Acc. Chem. Res.* **1987**, 20, 214.
35. N. L. Bauld, in *Advances in Electron Transfer Chemistry*, Vol. 2 (Ed. P. S. Mariano), JAI Press, Greenwich, CT, 1992, pp. 1–66.
36. J. P. Collman, L. S. Hegedus, J. R. Norton, R. G. Finke, *Principles and Applications of Organotransition Metal Chemistry*, University Science Books, Mill Valley, CA, **1987**, Chap. 4, p. 259.
37. L. Giannini, G. Guillemot, E. Solari, C. Floriani, N. Re, A. Chiesi-Villa, C. Rizzoli, *J. Am. Chem. Soc.* **1999**, 121, 2797.
38. M. Chanon, M. Rajzmann, F. Chanon, *Tetrahedron* **1990**, 46, 6193.
39. A. Pross, *Acc. Chem. Res.* **1985**, 18, 212.
40. S. S. Shaik, *Prog. Phys. Org. Chem.* **1985**, 15, 264.
41. J.-M. Savéant, *Acc. Chem. Res.* **1993**, 26, 455.
42. S. Fukuzumi, *Bull. Chem. Soc. Jpn.* **1997**, 70, 1.
43. M. A. Fox, M. Chanon (Eds.), *Photoinduced Electron Transfer*, Elsevier, Amsterdam, **1988**, Parts A–D.
44. M. Julliard, M. Chanon, *Chem. Rev.* **1983**, 83, 425.
45. U. C. Yoon, P. S. Mariano, *Acc. Chem. Res.* **1992**, 25, 233.
46. G. J. Kavarnos, N. J. Turro, *Chem. Rev.* **1986**, 86, 401.
47. F. D. Lewis, *Acc. Chem. Res.* **1986**, 19, 401.
48. K. Mizuno, Y. Otsuji, *Top. Curr. Chem.* **1994**, 169, 301.
49. E. R. Gaillard, D. G. Whitten, *Acc. Chem. Res.* **1996**, 29, 292.
50. F. Müller, J. Mattay, *Chem. Rev.* **1993**, 93, 99.
51. M. Mella, M. Fagnoni, M. Freccero, E. Fasani, A. Albini, *Chem. Soc. Rev.* **1998**, 27, 81.
52. S. Fukuzumi, S. Itoh, *Advances in Photochemistry*, Vol. 25 (Eds. D. C. Neckers, D. H. Volman, G. von Büнау), Wiley, New York, **1998**, pp. 107–172.
53. P. Pichat, M. A. Fox, in *Photoinduced Electron Transfer, Part D* (Eds. M. A. Fox, M. Chanon), Elsevier, Amsterdam, **1988**, pp. 241–302.
54. C. A. Koval, J. N. Howard, *Chem. Rev.* **1992**, 92, 411.
55. M. A. Fox, M. T. Dulay, *Chem. Rev.* **1993**, 93, 341.
56. P. V. Kamat, *Chem. Rev.* **1993**, 93, 267.
57. A. Hagfeldt, M. Grätzel, *Chem. Rev.* **1995**, 95, 49.
58. M. R. Hoffmann, S. T. Martin, W. Choi, D. W. Bahnemann, *Chem. Rev.* **1995**, 95, 69.
59. R. Memming, *Top. Curr. Chem.* **1994**, 169, 105.
60. A. Fujishima, K. Hashimoto, T. Watanabe, *TiO₂ Photocatalysis, Fundamentals and Applications*, Koyo Printing, Tokyo, **1999**.
61. H. Kisch, M. Hopfner, in *Electron Transfer in Chemistry*, Vol. IV (Ed. V. Balzani), Wiley-VCH, Weinheim, **2000**, pp. 232–275.
62. G. G. Wubbels, *Acc. Chem. Res.* **1983**, 16, 285.
63. A. Albini, *J. Chem. Educ.* **1986**, 63, 383.
64. F. D. Lewis, J. D. Oxman, *J. Am. Chem. Soc.* **1984**, 106, 466.
65. G. G. Wubbels, D. W. Celandier, *J. Am. Chem. Soc.* **1981**, 103, 7669.
66. E. Fujita, B. S. Brunschwig, in *Electron Transfer in Chemistry*, Vol. IV (Ed. V. Balzani), Wiley-VCH, Weinheim, **2000**, pp. 88–126.
67. E. Katz, A. N. Shipway, I. Willner, in *Electron Transfer in Chemistry*, Vol. IV (Ed. V. Balzani), Wiley-VCH, Weinheim, **2000**, pp. 127–201.
68. G. Tollin, in *Electron Transfer in Chemistry*, Vol. IV (Ed. V. Balzani), Wiley-VCH, Weinheim, **2000**, pp. 202–231.
69. R. A. Marcus, *J. Chem. Phys.* **1956**, 24, 966.
70. R. A. Marcus, *Annu. Rev. Phys. Chem.* **1964**, 15, 155.
71. R. A. Marcus, *Angew. Chem., Int. Ed. Engl.* **1993**, 32, 1111.
72. A. Niemz, V. M. Rotello, *Acc. Chem. Res.* **1999**, 32, 44.
73. A. E. Kaifer, *Acc. Chem. Res.* **1999**, 32, 62.
74. V. M. Rotello, in *Electron Transfer in Chemistry*, Vol. IV (Ed. V. Balzani), Wiley-VCH, Weinheim, **2000**, pp. 68–87.
75. P. R. Rich, D. S. Bendall, *Biochim. Biophys. Acta*, **1980**, 592, 506.
76. D. Meisel, G. Czapski, *J. Phys. Chem.* **1975**, 79, 1503.

77. S. Fukuzumi, K. Ishikawa, K. Hironaka, T. Tanaka, *J. Chem. Soc., Perkin Trans. 2* **1987**, 751.
78. S. Fukuzumi, K. Ishikawa, T. Tanaka, *J. Chem. Soc., Dalton Trans.* **1985**, 899.
79. K. Ishikawa, S. Fukuzumi, T. Tanaka, *Inorg. Chem.* **1989**, 28, 1661.
80. C. Walsh, *Acc. Chem. Res.* **1980**, 13, 148.
81. T. C. Bruice, *Acc. Chem. Res.* **1980**, 13, 256.
82. S. Fukuzumi, T. Tanaka, in *Photoinduced Electron Transfer, Part C* (Eds. M. A. Fox, M. Chanon), Elsevier, Amsterdam, **1988**, pp. 636–687.
83. P. F. Heelis, *Chem. Soc. Rev.* **1982**, 11, 15.
84. S. Fukuzumi, S. Kuroda, T. Goto, K. Ishikawa, T. Tanaka, *J. Chem. Soc., Perkin Trans. 2* **1989**, 1047.
85. D. T. Sawyer, J. L. Roberts, Jr., *Acc. Chem. Res.* **1988**, 21, 469.
86. S. Fukuzumi, M. Chiba, T. Tanaka, *Chem. Lett.* **1989**, 31.
87. C. R. Bock, J. A. Connor, A. R. Gutierrez, T. J. Meyer, D. G. Whitten, B. P. Sullivan, J. K. Nagle, *J. Am. Chem. Soc.* **1979**, 101, 4815.
88. D. Rehm, A. Weller, *Isr. J. Chem.* **1970**, 8, 259.
89. S. Fukuzumi, S. Mochizuki, T. Tanaka, *J. Am. Chem. Soc.* **1989**, 111, 1497.
90. S. Fukuzumi, S. Mochizuki, T. Tanaka, *Chem. Lett.* **1989**, 27.
91. S. Fukuzumi, S. Mochizuki, T. Tanaka, *Inorg. Chem.* **1989**, 28, 2459.
92. S. Fukuzumi, T. Yorisue, *Chem. Lett.* **1990**, 871.
93. S. Fukuzumi, M. Chiba, T. Tanaka, *J. Chem. Soc., Chem. Commun.* **1989**, 941.
94. S. Fukuzumi, M. Chiba, *J. Chem. Soc., Perkin Trans. 2* **1991**, 1393.
95. S. Fukuzumi, Y. Tokuda, *Chem. Lett.* **1991**, 897.
96. S. Fukuzumi, Y. Tokuda, *J. Phys. Chem.* **1993**, 97, 3737.
97. L. Stryer, *Biochemistry*, 3rd edn., Freeman, New York, **1988**, Chap. 17.
98. E. B. Skibo, T. C. Bruice, *J. Am. Chem. Soc.* **1983**, 105, 3316.
99. S. Fukuzumi, M. Ishikawa, T. Tanaka, *J. Chem. Soc., Chem. Commun.* **1985**, 1069.
100. S. Fukuzumi, M. Chiba, M. Ishikawa, K. Ishikawa, T. Tanaka, *J. Chem. Soc., Perkin Trans. 2* **1989**, 1417.
101. S. Fukuzumi, M. Ishikawa, T. Tanaka, *Tetrahedron* **1986**, 42, 1021.
102. S. Fukuzumi, S. Mochizuki, T. Tanaka, *J. Phys. Chem.* **1990**, 94, 722.
103. S. Fukuzumi, S. Mochizuki, T. Tanaka, *Chem. Lett.* **1988**, 1983.
104. S. Fukuzumi, S. Mochizuki, T. Tanaka, *J. Chem. Soc., Perkin Trans. 2* **1989**, 1583.
105. F. Bechman, T. Paul, *Liebigs Ann. Chem.* **1891**, 266, 1.
106. W. Schlenk, T. Weichel, *Chem. Ber.* **1911**, 44, 1182.
107. G. A. Molander, *Acc. Chem. Res.* **1998**, 31, 603.
108. T. Skrydstrup, *Angew. Chem., Int. Ed. Engl.* **1997**, 36, 345.
109. G. A. Molander, C. R. Harris, *Chem. Rev.* **1996**, 96, 307.
110. J. W. Huffman, in *Comprehensive Organic Synthesis*, Vol. 8 (Eds. B. M. Trost, I. Fleming), Pergamon Press, Oxford, **1991**, Chap. 1.4.
111. B. E. Kahn, R. D. Rieke, *Chem. Rev.* **1988**, 88, 733.
112. T. Wirth, *Angew. Chem., Int. Ed. Engl.* **1996**, 35, 61.
113. G. M. Robertson, in *Comprehensive Organic Synthesis*, Vol. 3 (Eds. B. M. Trost, I. Fleming), Pergamon Press, Oxford, **1991**, Chap. 2.6.
114. J. E. McMurry, *Chem. Rev.* **1989**, 89, 1513.
115. K. Maruyama, T. Katagiri, *J. Am. Chem. Soc.* **1986**, 108, 6263.
116. P. H. Rieger, G. K. Fraenkel, *J. Chem. Phys.* **1962**, 37, 2811.
117. N. Hirota, S. I. Weissman, *J. Am. Chem. Soc.* **1964**, 86, 2538.
118. S. W. Mao, K. Nakamura, N. Hirota, *J. Am. Chem. Soc.* **1974**, 96, 5341.
119. R. Dams, M. Malinowski, I. Westdorp, H. Y. Geise, *J. Org. Chem.* **1982**, 47, 248.
120. W. Kaim, *Coord. Chem. Rev.* **1987**, 76, 187.
121. K. J. Covert, P. T. Wolczanski, S. A. Hill, P. J. Krusic, *Inorg. Chem.* **1992**, 31, 66.
122. Z. Hou, T. Miyano, H. Yamazaki, Y. Wakatsuki, *J. Am. Chem. Soc.* **1995**, 117, 4421.
123. Z. Hou, Y. Wakatsuki, *Chem. Eur. J.* **1997**, 3, 1005.
124. Z. Hou, A. Fujita, H. Yamazaki, Y. Wakatsuki, *J. Am. Chem. Soc.* **1996**, 118, 7843.
125. Z. Hou, A. Fujita, H. Yamazaki, Y. Wakatsuki, *J. Am. Chem. Soc.* **1996**, 118, 2503.

126. Z. Hou, X. Jia, M. Hoshino, Y. Wakatsuki, *Angew. Chem., Int. Ed. Engl.* **1997**, *36*, 1292.
127. Z. Hou, A. Fujita, Y. Zhang, T. Miyano, H. Yamazaki, Y. Wakatsuki, *J. Am. Chem. Soc.* **1998**, *120*, 754.
128. J. Takats, *J. Alloy Compd.* **1997**, *249*, 52.
129. J. Takats, X. W. Zhang, V. W. Day, T. A. Eberspacher, *Organometallics* **1993**, *12*, 4286.
130. W. J. Evans, D. K. Drummond, L. R. Chamberlain, R. J. Doedens, S. G. Bott, H. Zhang, J. L. Atwood, *J. Am. Chem. Soc.* **1988**, *110*, 4983.
131. Z. Hou, A. Fujita, T. Koizumi, H. Yamazaki, Y. Wakatsuki, *Organometallics* **1999**, *18*, 1979.
132. S. Fukuzumi, T. Okamoto, *J. Am. Chem. Soc.* **1993**, *115*, 11600.
133. S. Fukuzumi, T. Yorisue, *J. Am. Chem. Soc.* **1991**, *113*, 7764.
134. S. Fukuzumi, K. Ishikawa, T. Tanaka, *Chem. Lett.* **1984**, 421.
135. S. Fukuzumi, K. Ishikawa, T. Tanaka, *Nippon Kagaku Kaishi* **1985**, 62.
136. S. Fukuzumi, in *Novel Trends in Electroorganic Synthesis* (Ed. S. Torii), Springer, Tokyo, **1998**, pp. 425–430.
137. S. Fukuzumi, T. Okamoto, *J. Chem. Soc., Chem. Commun.*, **1994**, 521.
138. S. Fukuzumi, M. Patz, T. Suenobu, Y. Kuwahara, S. Itoh, *J. Am. Chem. Soc.* **1999**, *121*, 1605.
139. S. Fukuzumi, T. Suenobu, M. Patz, T. Hirasaka, S. Itoh, M. Fujitsuka, O. Ito, *J. Am. Chem. Soc.* **1998**, *120*, 8060.
140. M. Patz, Y. Kuwahara, T. Suenobu, S. Fukuzumi, *Chem. Lett.* **1997**, 567.
141. R. N. Bagchi, A. M. Bond, F. Scholz, R. Stösser, *J. Am. Chem. Soc.* **1989**, *111*, 8270.
142. K. Dyrek, M. Che, *Chem. Rev.* **1997**, *97*, 305.
143. M. Che, A. J. Tench, *Adv. Catal.* **1983**, *32*, 1.
144. E. Giamello, Z. Sojka, M. Che, A. Zecchina, *J. Phys. Chem.* **1986**, *90*, 6084.
145. Z. Sojka, E. Giamello, M. Che, A. Zecchina, K. Dyrek, *J. Phys. Chem.* **1988**, *92*, 1541.
146. S. Fukuzumi, Y. Tokuda, Y. Chiba, L. Greci, P. Carloni, E. Damiani, *J. Chem. Soc., Chem. Commun.* **1993**, 1575.
147. S. Fukuzumi, T. Kitano, M. Ishikawa, *J. Am. Chem. Soc.* **1990**, *112*, 5631.
148. S. Fukuzumi, Y. Tokuda, *J. Phys. Chem.* **1992**, *96*, 8409.
149. J. Stubbe, W. A. van der Donk, *Chem. Rev.* **1998**, *98*, 705.
150. D. J. Kosman, in *Copper Proteins and Copper Enzymes*, Vol. 2 (Ed. R. Lontie), CRC Press, Boca Raton, FL, **1985**, pp. 1–26.
151. N. Ito, S. E. V. Phillips, C. Stevens, Z. B. Ogel, M. J. McPherson, J. N. Keen, K. D. S. Yadav, P. F. Knowles, *Nature* **1991**, *350*, 87.
152. M. M. Whittaker, D. P. Ballou, J. W. Whittaker, *Biochemistry* **1998**, *37*, 8426.
153. R. M. Wachter, M. P. Montague-Smith, B. P. Branchaud, *J. Am. Chem. Soc.* **1997**, *119*, 7743.
154. S. Itoh, S. Takayama, R. Arakawa, A. Furuta, M. Komatsu, A. Ishida, S. Takamuku, S. Fukuzumi, *Inorg. Chem.* **1997**, *36*, 1407.
155. S. Itoh, M. Taki, S. Takayama, S. Nagatomo, T. Kitagawa, N. Sakurada, R. Arakawa, S. Fukuzumi, *Angew. Chem., Int. Ed. Engl.* **1999**, *38*, 2774.
156. Y. Wang, J. L. DuBois, B. Hedman, K. O. Hodgson, T. D. P. Stack, *Science* **1998**, *279*, 537.
157. P. Chaudhuri, M. Hess, J. Müller, K. Hildenbrand, E. Bill, T. Weyhermüller, K. Wieghardt, *J. Am. Chem. Soc.* **1999**, *121*, 9599.
158. P. Chaudhuri, M. Hess, T. Weyhermüller, K. Wieghardt, *Angew. Chem., Int. Ed. Engl.* **1999**, *38*, 1095.
159. S. Fukuzumi, Y. Tokuda, *Chem. Lett.* **1992**, 1497.
160. W. KaIm, B. Schwederski, *Bioinorganic Chemistry: Inorganic Elements in the Chemistry of Life*, Wiley, New York, **1991**.
161. S. J. Lippard, *Science* **1993**, *261*, 699.
162. N. Kitajima, Y. Moro-oka, *Chem. Rev.* **1994**, *94*, 737.
163. S. Fox, K. D. Karlin, in *Active Oxygen in Biochemistry* (Eds. J. S. Valentine, C. S. Foote, A. Greenberg, J. F. Liebman), Chapman and Hall, London, **1995**, pp. 188–231.
164. L. Que, Jr., in *Active Oxygen in Biochemistry* (Eds. J. S. Valentine, C. S. Foote, A. Greenberg, J. F. Liebman), Chapman and Hall, London, **1995**, pp. 232–275.
165. A. L. Feig, S. J. Lippard, *Chem. Rev.* **1994**, *94*, 759.
166. E. I. Solomon, F. Tuzcek, D. E. Root, C. A. Brown, *Chem. Rev.* **1994**, *94*, 827.

167. L. Que, Jr., R. Y. N. Ho, *Chem. Rev.* **1996**, 96, 2607.
168. I. Fridovich, *J. Biol. Chem.* **1989**, 264, 7761.
169. I. Bertini, L. Banci, M. Piccioli, *Coord. Chem. Rev.* **1990**, 100, 67.
170. J. A. Tainer, E. D. Getzoff, J. S. Richardson, D. C. Richardson, *Nature* **1983**, 306, 284.
171. A. E. G. Cass, Superoxide dismutases, in *Metalloproteins, Part 1* (Ed. P. Harrison), Verlag, Chemie, Weinheim, **1985**, p. 121.
172. E. M. Fielden, P. B. Roberts, R. C. Bray, D. J. Lowe, G. N. Mautner, G. Rotilio, L. Calabrese, *Biochem. J.* **1974**, 139, 49.
173. L. M. Ellerby, D. E. Cabelli, J. A. Graden, J. S. Valentine, *J. Am. Chem. Soc.* **1996**, 118, 6556.
174. L. W. Oberley, G. R. Buettner, *Cancer Res.* **1979**, 39, 1141.
175. K. J. Farmer, R. S. Sohal, *Free Rad. Biol. Med.* **1989**, 7, 23.
176. G. Kolks, C. R. Frihart, H. N. Rabinowitz, S. J. Lippard, *J. Am. Chem. Soc.* **1976**, 98, 5720.
177. K. G. Strothkamp, S. J. Lippard, *Acc. Chem. Res.* **1982**, 15, 318.
178. B. P. Murphy, *Coord. Chem. Rev.* **1993**, 124, 63.
179. A. Gartner, U. Weser, *Top. Curr. Chem.* **1986**, 132, 1.
180. C. A. Salata, M.-T. Youinou, C. J. Burrows, *J. Am. Chem. Soc.* **1989**, 111, 9278.
181. J.-L. Pierre, P. Chautemps, S. Refaif, C. Beguin, A. E. Marzouki, G. Serratrice, E. Saint-Aman, P. Rey, *J. Am. Chem. Soc.* **1995**, 117, 1965.
182. H. Ohtsu, Y. Shimazaki, A. Odani, O. Yamauchi, W. Mori, S. Itoh, S. Fukuzumi, *J. Am. Chem. Soc.* **2000**, 122, 5733.
183. A. Bencini, I. Bertini, D. Gatteschi, A. Scozzafava, *Inorg. Chem.* **1978**, 17, 3194.
184. U. Weser, L. M. Schubotz, E. Lengfelder, *J. Mol. Catal.* **1981**, 13, 249.
185. G. Tabbi, W. L. Driessen, J. Reedijk, R. P. Bonomo, N. Veldman, A. L. Spek, *Inorg. Chem.* **1997**, 36, 1168.
186. P. J. Hart, M. M. Balbirnie, N. L. Ogihara, A. M. Nersissian, M. S. Weiss, J. S. Valentine, D. Eisenberg, *Biochemistry* **1999**, 38, 2167.
187. N. Kitajima, K. Fujisawa, Y. Moro-oka, K. Toriumi, *J. Am. Chem. Soc.* **1989**, 111, 8975.
188. K. A. Magnus, B. Hazes, H. Ton-That, C. Bonaventura, J. Bonaventura, W. G. J. Hol, *Proteins: Struct. Funct. Genet.* **1994**, 19, 302.
189. K. A. Magnus, H. Ton-That, J. E. Carpenter, *Chem. Rev.* **1994**, 94, 727.
190. S. Itoh, T. Kondo, M. Komatsu, Y. Ohshiro, C. Li, N. Kanehisa, Y. Kai, S. Fukuzumi, *J. Am. Chem. Soc.* **1995**, 117, 4714.
191. S. Itoh, H. Nakao, L. M. Berreau, T. Kondo, M. Komatsu, S. Fukuzumi, *J. Am. Chem. Soc.* **1998**, 120, 2890.
192. K. Fujisawa, M. Tanaka, Y. Moro-oka, N. Kitajima, *J. Am. Chem. Soc.* **1994**, 116, 12079.
193. J. A. Halfen, S. Mahapatra, E. C. Wilkinson, S. Kaderli, V. G. Young, Jr., L. Que, Jr., A. D. Zuberbühler, W. B. Tolman, *Science* **1996**, 271, 1397.
194. C. J. Cramer, B. A. Smith, W. B. Tolman, *J. Am. Chem. Soc.* **1996**, 118, 11283.
195. G. Maier, *Angew. Chem., Int. Ed. Engl.* **1988**, 27, 309.
196. J. Sauer, R. Sustmann, *Angew. Chem., Int. Ed. Engl.* **1980**, 19, 779.
197. K. N. Houk, J. González, Y. Li, *Acc. Chem. Res.* **1995**, 28, 81.
198. S. Fukuzumi, J. K. Kochi, *Tetrahedron* **1982**, 38, 1035.
199. M. Dern, H.-G. Korth, G. Kopp, R. Sustmann, *Angew. Chem., Int. Ed. Engl.* **1985**, 24, 337.
200. R. Sustmann, K. Lücking, G. Kopp, M. Rese, *Angew. Chem., Int. Ed. Engl.* **1989**, 28, 1713.
201. S. Yamago, S. Ejiri, M. Nakamura, E. Nakamura, *J. Am. Chem. Soc.* **1993**, 115, 5344.
202. K. Lücking, M. Rese, R. Sustmann, *Liebigs Ann.* **1995**, 1129.
203. K. Mikami, S. Matsumoto, T. Tono, Y. Okubo, T. Suenobu, S. Fukuzumi, *Tetrahedron Lett.* **1998**, 39, 3733.
204. K. Mikami, S. Matsumoto, Y. Okubo, M. Fujitsuka, O. Ito, T. Suenobu, S. Fukuzumi, *J. Am. Chem. Soc.* **2000**, 122, 2236.
205. K. E. Wise, R. A. Wheeler, *J. Phys. Chem. A* **1999**, 103, 8279.
206. K. T. Finley, in *The Chemistry of the Quinoid Compounds, Part 2* (Ed. S. Patai), Wiley, Chichester, **1974**, p. 877.
207. K. Kanematsu, S. Morita, S. Fukushima, E. Osawa, *J. Am. Chem. Soc.* **1981**, 103, 5211.
208. H. B. Kagan, O. Riant, *Chem. Rev.* **1992**, 92, 1007.

209. U. Pindur, G. Lutz, C. Otto, *Chem. Rev.* **1993**, 93, 741.
210. M. Lautens, W. Klute, W. Tam, *Chem. Rev.* **1996**, 96, 49.
211. D. M. Birney, K. N. Houk, *J. Am. Chem. Soc.* **1990**, 112, 4127.
212. S. Otto, J. B. F. N. Engberts, *J. Am. Chem. Soc.* **1999**, 121, 6798.
213. P. A. Grieco, J. J. Nunes, M. D. Gaul, *J. Am. Chem. Soc.* **1990**, 112, 4595.
214. H. Waldmann, *Angew. Chem., Int. Ed. Engl.* **1991**, 30, 1306.
215. P. A. Grieco, *Aldrichim. Acta* **1991**, 24, 59.
216. M. A. Forman, W. P. Dailey, *J. Am. Chem. Soc.* **1991**, 113, 2761.
217. G. Desimoni, G. Faita, P. P. Righetti, G. Tacconi, *Tetrahedron* **1991**, 47, 8399.
218. R. M. Pagni, G. W. Kabalka, S. Bains, M. Plesco, J. Wilson, J. Bartmess, *J. Org. Chem.* **1993**, 58, 3130.
219. P. A. Grieco, M. D. Kaufman, J. F. Daeuble, N. Saito, *J. Am. Chem. Soc.* **1996**, 118, 2095.
220. D. S. Sigman, J. Hajdu, D. J. Creighton, in *Bioorganic Chemistry*, Vol. IV (Ed. E. E. van Tamelen), Academic Press, New York, **1978**, p. 385.
221. S. Fukuzumi, N. Nishizawa, T. Tanaka, *J. Org. Chem.* **1984**, 49, 3571.
222. S. Fukuzumi, S. Koumitsu, K. Hironaka, T. Tanaka, *J. Am. Chem. Soc.* **1987**, 109, 305.
223. S. Fukuzumi, K. Ohkubo, Y. Tokuda, T. Suenobu, *J. Am. Chem. Soc.* **2000**, 122, 4286.
224. K. M. Zaman, S. Yamamoto, N. Nishimura, J. Maruta, S. Fukuzumi, *J. Am. Chem. Soc.* **1994**, 116, 12099.
225. S. Fukuzumi, Y. Kondo, T. Tanaka, *Chem. Lett.* **1983**, 485.
226. S. Fukuzumi, N. Nishizawa, T. Tanaka, *J. Chem. Soc., Perkin Trans. 2* **1985**, 371.
227. S. Fukuzumi, M. Fujita, G. Matsubayashi, J. Otera, *Chem. Lett.* **1993**, 1451.
228. M. Fujita, S. Fukuzumi, G. Matsubayashi, J. Otera, *Bull. Chem. Soc. Jpn.* **1996**, 69, 1107.
229. S. Fukuzumi, M. Fujita, J. Otera, Y. Fujita, *J. Am. Chem. Soc.* **1992**, 114, 10271.
230. S. Fukuzumi, M. Fujita, J. Otera, *J. Org. Chem.* **1993**, 58, 5405.
231. K. Mikami, S. Matsumoto, A. Ishida, S. Takamuku, T. Suenobu, S. Fukuzumi, *J. Am. Chem. Soc.* **1995**, 117, 11134.
232. G. Eberlein, T. C. Bruice, *J. Am. Chem. Soc.* **1983**, 105, 6685.
233. E. J. Nanni Jr., D. T. Sawyer, S. S. Ball, T. C. Bruice, *J. Am. Chem. Soc.* **1981**, 103, 2797.
234. K. Maeda-Yorita, V. Massey, *J. Biol. Chem.* **1993**, 268, 4134.
235. S. Fukuzumi, S. Kuroda, T. Tanaka, *J. Am. Chem. Soc.* **1985**, 107, 3020.
236. Y. Yano, T. Sakaguchi, M. Nakazato, *J. Chem. Soc., Perkin Trans. 2* **1984**, 595.
237. S. Itoh, H. Kawakami, S. Fukuzumi, *Chem. Commun.* **1997**, 29.
238. S. A. Salisbury, H. S. Forrest, W. B. T. Cruse, O. Kennard, *Nature* **1979**, 280, 843.
239. C. Anthony, M. Ghosh, C. C. F. Blake, *Biochem. J.* **1994**, 304, 665.
240. S. White, G. Boyd, F. S. Mathews, Z.-X. Xia, W.-W. Dai, Y.-F. Zhang, V. L. Davidson, *Biochemistry* **1993**, 32, 12955.
241. Z.-X. Xia, W.-W. Dai, Y.-F. Zhang, S. A. White, G. D. Boyd, F. S. Mathews, *J. Mol. Biol.* **1996**, 259, 480.
242. C. C. F. Blake, M. Ghosh, K. Harlos, A. Avezoux, C. Anthony, *Nature Struct. Biol.* **1994**, 1, 102.
243. S. Itoh, H. Kawakami, S. Fukuzumi, *J. Am. Chem. Soc.* **1997**, 119, 439.
244. S. Itoh, H. Kawakami, S. Fukuzumi, *Biochemistry* **1998**, 37, 6562.
245. S. Itoh, H. Kawakami, S. Fukuzumi, *J. Am. Chem. Soc.* **1998**, 120, 7271.
246. V. Kuusk, W. S. McIntire, *J. Biol. Chem.* **1994**, 269, 26136.
247. A. C. F. Gorren, J. A. Duine, *Biochemistry* **1994**, 33, 12202.
248. A. C. F. Gorren, S. de Vries, J. A. Duine, *Biochemistry* **1995**, 34, 9748.
249. A. C. F. Gorren, P. Moenne-Loccoz, G. Backes, S. de Vries, J. Sanders-Loehr, J. A. Duine, *Biochemistry* **1995**, 34, 12926.
250. P. Moenne-Loccoz, N. Nakamura, S. Itoh, S. Fukuzumi, A. C. F. Gorren, J. A. Duine, J. Sanders-Loehr, *Biochemistry* **1996**, 35, 4713.
251. G. R. Bishop, V. L. Davidson, *Biochemistry* **1997**, 36, 13586.
252. S. Itoh, M. Ogino, S. Haranou, T. Terasaka, T. Ando, M. Komatsu, Y. Ohshiro, S. Fukuzumi, K. Kano, K. Takagi, T. Ikeda, *J. Am. Chem. Soc.* **1995**, 117, 1485.
253. S. Itoh, N. Takada, S. Haranou, T. Ando, M. Komatsu, Y. Ohshiro, S. Fukuzumi, *J. Org. Chem.* **1996**, 61, 8967.

254. S. Itoh, M. Taniguchi, S. Fukuzumi, *Chem. Commun.* **2000**, 329.
255. S. Fukuzumi, M. Ishikawa, T. Tanaka, *Chem. Lett.* **1989**, 1227.
256. S. Fukuzumi, M. Ishikawa, T. Tanaka, *J. Chem. Soc., Perkin Trans. 2* **1989**, 1811.
257. C. C. Johnston, J. L. Gardner, C. H. Suelter, D. E. Metzler, *Biochemistry* **1963**, 2, 689.
258. P. van Eikeren, D. L. Grier, J. Eliason, *J. Am. Chem. Soc.* **1976**, 101, 7406.
259. M. Ishikawa, S. Fukuzumi, *J. Chem. Soc., Faraday Trans.* **1990**, 86, 3531.
260. M. Dixon, E. C. Webb, C. J. R. Thorne, K. F. Tipton, *Enzymes*, 3rd edn., Longman, London, **1979**.
261. M. Ishikawa, S. Fukuzumi, *J. Chem. Soc., Chem. Commun.* **1990**, 1353.
262. D. N. Kursanov, Z. N. Parnes, N. M. Loim, *Synthesis* **1974**, 633.
263. M. P. Doyle, D. J. DeBruyn, S. J. Donnelly, D. A. Kooistra, A. A. Odubela, C. T. West, S. M. Zonnebelt, *J. Org. Chem.* **1974**, 39, 2740.
264. S. Fukuzumi, M. Fujita, *Chem. Lett.* **1991**, 2059.
265. M. Fujita, S. Fukuzumi, J. Otera, *J. Mol. Catal.* **1993**, 85, 143.
266. S. Fukuzumi, Y. Tokuda, T. Kitano, T. Okamoto, J. Otera, *J. Am. Chem. Soc.* **1993**, 115, 8960.
267. S. Fukuzumi, T. Goto, K. Ishikawa, T. Tanaka, *Chem. Lett.* **1988**, 1923.
268. K. Ishikawa, S. Fukuzumi, T. Goto, T. Tanaka, *J. Am. Chem. Soc.* **1990**, 112, 1577.
269. S. Fukuzumi, K. Ishikawa, T. Tanaka, *Chem. Lett.* **1986**, 1.
270. S. Fukuzumi, H. Imahori, in *Electron Transfer in Chemistry*, Vol. II (Ed. V. Balzani), Wiley-VCH, Weinheim, **2000**, pp. 927-975.
271. F. G. Bordwell, J.-P. Cheng, M. J. Bausch, J. E. Bases, *J. Phys. Org. Chem.* **1988**, 1, 209.
272. E. Baciocchi, T. D. Giacco, F. Elisei, *J. Am. Chem. Soc.* **1993**, 115, 12290.
273. C. J. Schlessener, C. Amatore, J. K. Kochi, *J. Am. Chem. Soc.* **1984**, 106, 7472.
274. A. Sulpizio, M. Mella, A. Albini, *Tetrahedron* **1989**, 45, 7545.
275. E. Baciocchi, F. D'Acunzo, C. Galli, O. Lanzalunga, *J. Chem. Soc., Perkin Trans. 2*, **1996**, 133.
276. M. Fujita, S. Fukuzumi, *J. Chem. Soc., Chem. Commun.* **1993**, 1528.
277. M. Fujita, S. Fukuzumi, *J. Chem. Soc., Perkin Trans. 2* **1993**, 1915.
278. N. Satoh, S. Fukuzumi, *Rev. Heteroatom Chem.* **1999**, 20, 249.
279. S. Fukuzumi, S. Kuroda, T. Tanaka, *J. Chem. Soc., Chem. Commun.* **1986**, 1553.
280. S. Fukuzumi, M. Fujita, J. Otera, *J. Chem. Soc., Chem. Commun.* **1993**, 1536.
281. S. Fukuzumi, T. Kitano, K. Mochida, *Chem. Lett.* **1989**, 2177.
282. S. Fukuzumi, S. Noura, *J. Chem. Soc., Chem. Commun.* **1994**, 287.
283. M. Fujita, A. Ishida, S. Takamuku, S. Fukuzumi, *J. Am. Chem. Soc.* **1996**, 118, 8566.
284. D. D. M. Wayner, D. J. McPhee, D. Griller, *J. Am. Chem. Soc.* **1988**, 110, 132.
285. B. A. Sim, P. H. Milne, D. Griller, D. D. M. Wayner, *J. Am. Chem. Soc.* **1990**, 112, 6635.
286. T. Mukaiyama, *Angew. Chem., Int. Ed. Engl.* **1977**, 16, 817.
287. C. Gennari, in *Selectivities in Lewis Acid Promoted Reactions* (Ed. D. Schinzer), Kluwer, Dordrecht, **1989**, Chap. 4, p. 53.
288. D. A. Oare, C. H. Heathcock, in *Topics in Stereochemistry*, Vol. 20 (Ed. E. L. Eliel, S. H. Wilen), Wiley, New York, **1991**, p. 87.
289. R. Mahrwald, *Chem. Rev.* **1999**, 99, 1095.
290. M. T. Reetz, K. Schweltnus, F. Hübner, W. Massa, R. E. Schmidt, *Chem. Ber.* **1983**, 116, 3708.
291. S. M. Ali, G. Rousseau, *Tetrahedron* **1990**, 46, 7011.
292. T. Sato, Y. Wakahara, J. Otera, H. Nozaki, S. Fukuzumi, *J. Am. Chem. Soc.* **1991**, 113, 4028.
293. A. Quendo, S. M. Ali, G. Rousseau, *J. Org. Chem.* **1992**, 57, 6890.
294. W. Odenkirk, J. Whelan, B. Bosnich, *Tetrahedron Lett.* **1992**, 33, 5729.
295. Y. Fujita, S. Fukuzumi, J. Otera, *Tetrahedron Lett.* **1997**, 38, 2117.
296. J. Otera, Y. Fujita, N. Sakuta, M. Fujita, S. Fukuzumi, *J. Org. Chem.* **1996**, 61, 2951.
297. H. Mayr, M. Patz, *Angew. Chem., Int. Ed. Engl.* **1994**, 33, 938.
298. J. Burfeindt, M. Patz, M. Müller, H. Mayr, *J. Am. Chem. Soc.* **1998**, 120, 3629.
299. S. Fukuzumi, T. Okamoto, K. Yasui, T. Suenobu, S. Itoh, J. Otera, *Chem. Lett.* **1997**, 667.
300. J. Otera, Y. Wakahara, H. Kamei, T. Sato, H. Nozaki, S. Fukuzumi, *Tetrahedron Lett.* **1991**, 32, 2405.

301. K. Wada, M. Yamamoto, J. Setsune, *Tetrahedron Lett.* **1999**, 40, 2773.
302. J. Setsune, M. Ikeda, T. Iida, T. Kitao, *J. Am. Chem. Soc.* **1988**, 110, 6572.
303. H. J. Callot, R. Cromer, A. Louati, B. Metz, B. Chevrier, *J. Am. Chem. Soc.* **1987**, 109, 2946.
304. S. Fukuzumi, S. Kuroda, T. Tanaka, *Chem. Lett.* **1984**, 1375.
305. S. Fukuzumi, S. Kuroda, T. Tanaka, *Chem. Lett.* **1984**, 417.
306. S. Fukuzumi, S. Kuroda, T. Tanaka, *J. Chem. Soc., Perkin Trans. 2* **1986**, 25.
307. S. Fukuzumi, K. Tanii, T. Tanaka, *J. Chem. Soc., Chem. Commun.* **1989**, 816.
308. S. Fukuzumi, K. Tanii, T. Tanaka, *Chem. Lett.* **1989**, 35.
309. S. Fukuzumi, S. Kuroda, *Res. Chem. Intermed.* **1999**, 25, 789.
310. S. Itoh, T. Komori, Y. Chiba, A. Ishida, S. Takamuku, S. Fukuzumi, *Chem. Commun.* **1996**, 465; S. Fukuzumi, S. Itoh, T. Komori, T. Suenobu, A. Ishida, M. Fujitsuka, O. Ito, *J. Am. Chem. Soc.* **2000**, 122, 8435.
311. S. Fukuzumi, T. Okamoto, J. Otera, *J. Am. Chem. Soc.* **1994**, 116, 5503.
312. A. Samanta, R. W. Fessenden, *Chem. Phys. Lett.* **1988**, 153, 406.
313. D. W. Boldridge, B. L. Justus, G. W. Scott, *J. Chem. Phys.* **1984**, 80, 3179.
314. F. D. Lewis, D. K. Howard, J. D. Oxman, *J. Am. Chem. Soc.* **1983**, 105, 3344.
315. F. D. Lewis, S. V. Barancyk, E. L. Burch, *J. Am. Chem. Soc.* **1992**, 114, 3866.
316. F. D. Lewis, G. D. Reddy, J. E. Elbert, B. E. Tillberg, J. A. Meltzer, M. Kojima, *J. Org. Chem.* **1991**, 56, 5311.
317. K. R. Mann, N. S. Lewis, V. M. Miskowski, D. K. Erwin, G. S. Hammond, H. B. Gray, *J. Am. Chem. Soc.* **1977**, 99, 5525.
318. I. S. Sigal, K. R. Mann, H. B. Gray, *J. Am. Chem. Soc.* **1980**, 102, 7252.
319. H. Shizuka, *Acc. Chem. Res.* **1985**, 18, 141.
320. E. M. Kosower, D. Huppert, *Annu. Rev. Phys. Chem.* **1986**, 37, 127.
321. H. Shizuka, *Bull. Chem. Soc. Jpn.* **2000**, 73, 267.
322. H. Shizuka, H. Hagiwara, H. Satoh, M. Fukushima, *J. Chem. Soc., Chem. Commun.* **1985**, 1454.
323. M. Yamaji, T. Sekiguchi, M. Hoshino, H. Shizuka, *J. Phys. Chem.* **1992**, 96, 9353.
324. T. Kiyota, M. Yamaji, H. Shizuka, *J. Phys. Chem.* **1996**, 100, 672.
325. H. Tanaka, K. Nishimoto, *J. Phys. Chem.* **1984**, 88, 1052.
326. C. Turro, C. K. Chang, G. E. Leroi, R. I. Cukier, D. G. Nocera, *J. Am. Chem. Soc.* **1992**, 114, 4013.
327. H. Miyasaka, A. Tabata, K. Kamada, N. Mataga, *J. Am. Chem. Soc.* **1993**, 115, 7335.
328. J. A. Roberts, J. P. Kirby, D. G. Nocera, *J. Am. Chem. Soc.* **1995**, 117, 8051.
329. J. P. Kirby, J. A. Roberts, D. G. Nocera, *J. Am. Chem. Soc.* **1997**, 119, 9230.
330. M. Y. Okamura, G. Feher, *Annu. Rev. Biochem.* **1992**, 61, 861.
331. B. G. Malmström, *Acc. Chem. Res.* **1993**, 26, 332.
332. S. Ferguson-Miller, G. T. Babcock, *Chem. Rev.* **1996**, 96, 2889.
333. C. W. Hoganson, G. T. Babcock, *Science* **1997**, 277, 1953.
334. R. A. Binstead, M. E. McGuire, A. Dovletoglou, W. K. Seok, L. E. Roecker, T. J. Meyer, *J. Am. Chem. Soc.* **1992**, 114, 173.
335. M. H. V. Huynh, T. J. Meyer, P. S. White, *J. Am. Chem. Soc.* **1999**, 121, 4530.
336. R. I. Cukier, D. G. Nocera, *Annu. Rev. Phys. Chem.* **1998**, 49, 337.
337. R. I. Cukier, *J. Phys. Chem.* **1996**, 100, 15428.
338. R. I. Cukier, *J. Phys. Chem. A* **1999**, 103, 5989.
339. A. Peluso, M. Brahim, M. Carotenuto, G. Del Re, *J. Phys. Chem. A* **1998**, 102, 10333.
340. S. Fukuzumi, T. Yorisue, *Bull. Chem. Soc. Jpn.* **1992**, 65, 715.
341. S. Fukuzumi, J. Maruta, *Inorg. Chim. Acta* **1994**, 226, 145.
342. R. Subramanian, K. M. Kadish, M. N. Vijayashree, X. Gao, M. T. Jones, M. D. Miller, K. L. Krause, T. Suenobu, S. Fukuzumi, *J. Phys. Chem.* **1996**, 100, 16327.
343. S. Fukuzumi, T. Suenobu, T. Hirasaka, R. Arakawa, K. M. Kadish, *J. Am. Chem. Soc.* **1998**, 120, 9220.
344. D. Dubois, G. Moninot, W. Kutner, M. T. Jones, K. M. Kadish, *J. Phys. Chem.* **1992**, 96, 7137.
345. K. M. Kadish, X. Gao, E. Van Caemelbecke, T. Suenobu, S. Fukuzumi, *J. Am. Chem. Soc.* **2000**, 122, 563.

346. K. M. Kadish, X. Gao, E. Van Caemelbecke, T. Hirasaka, T. Suenobu, S. Fukuzumi, *J. Phys. Chem. A* **1998**, *102*, 3898.
347. K. M. Kadish, X. Gao, O. Gorelik, E. Van Caemelbecke, T. Suenobu, S. Fukuzumi, *J. Phys. Chem. A* **2000**, *104*, 2902.
348. S. Fukuzumi, M. Fujita, J. Maruta, M. Chanon, *J. Chem. Soc., Perkin Trans. 2* **1994**, 1597.
349. S. Itoh, J. Maruta, S. Fukuzumi, *J. Chem. Soc., Perkin Trans. 2* **1996**, 1429.
350. L. Ebersson, K. Nyberg, in *Encyclopedia of Electrochemistry of Elements, Organic Section* (Ed. A. J. Bard, H. Lund), Marcel Dekker, New York, **1978**, Chap. XII-2.
351. S. Fukuzumi, T. Tanaka, in *Photoinduced Electron Transfer, Part C* (Eds. M. A. Fox, M. Chanon), Elsevier, Amsterdam, **1988**, pp. 578–635.
352. S. Fukuzumi, T. Kitano, T. Tanaka, *Chem. Lett.* **1989**, 1231.
353. S. Fukuzumi, Y. Kondo, T. Tanaka, *Chem. Lett.* **1983**, 751.
354. S. Fukuzumi, Y. Kondo, T. Tanaka, *J. Chem. Soc., Perkin Trans. 2* **1984**, 673.
355. S. Fukuzumi, K. Hironaka, T. Tanaka, *Chem. Lett.* **1982**, 1583.
356. S. Fukuzumi, K. Hironaka, T. Tanaka, *J. Am. Chem. Soc.* **1983**, *105*, 4722.
357. K. Hironaka, S. Fukuzumi, T. Tanaka, *J. Chem. Soc., Perkin Trans. 2* **1984**, 1705.
358. D. T. Sawyer, J. L. Roberts, Jr., *Acc. Chem. Res.* **1988**, *21*, 469.
359. A. Ledwith, *Acc. Chem. Res.* **1972**, *5*, 133.
360. S. Fukuzumi, I. Nakanishi, J. Maruta, T. Yorisue, T. Suenobu, S. Itoh, R. Arakawa, K. M. Kadish, *J. Am. Chem. Soc.* **1998**, *120*, 6673.
361. S. Fukuzumi, I. Nakanishi, K. Tanaka, *J. Phys. Chem. A* **1999**, *103*, 11212.
362. M. Fujita, S. Fukuzumi, *Chem. Lett.* **1993**, 1911.
363. I. Nakanishi, S. Itoh, T. Suenobu, S. Fukuzumi, *Angew. Chem., Int. Ed. Engl.* **1998**, *37*, 992.
364. I. Nakanishi, S. Itoh, S. Fukuzumi, *Chem. Eur. J.* **1999**, *5*, 2810.
365. R. Kluger, in *The Enzymes*, 3rd edn., Vol. 20 (Ed. D. S. Sigman), Academic Press, New York, **1992**, pp. 271–318.
366. H. Bisswanger, A. Schellenberger, A. (Eds.), *The Biochemistry and Physiology of Thiamin Diphosphate Enzymes*, Intemann, Prien, Germany, **1996**.
367. L. J. Reed, *Acc. Chem. Res.* **1974**, *7*, 40.
368. Y. A. Muller, G. E. Schulz, *Science* **1993**, *259*, 965.
369. L. Kersch, D. Oesterhelt, *Eur. J. Biochem.* **1981**, *116*, 595.
370. I. Nakanishi, S. Itoh, T. Suenobu, S. Fukuzumi, *Chem. Commun.* **1997**, 1927.
371. I. Nakanishi, S. Itoh, S. Fukuzumi, *Eur. J. Inorg. Chem.* **2000**, *7*, 1557.
372. S. Fukuzumi, I. Nakanishi, K. Tanaka, T. Suenobu, A. Tabard, R. Guillard, E. Van Caemelbecke, K. M. Kadish, *J. Am. Chem. Soc.* **1999**, *121*, 785.
373. W. R. Scheidt, Y. J. Lee, *Struct. Bonding (Berlin)*, **1987**, *64*, 1.
374. C. J. Medforth, J. D. Hobbs, M. R. Rodriguez, R. J. Abraham, K. M. Smith, J. A. Shelnutt, *Inorg. Chem.* **1995**, *34*, 1333.
375. R. Guillard, K. Perié, J.-M. Barbe, D. J. Nurco, K. M. Smith, E. Van Caemelbecke, K. M. Kadish, *Inorg. Chem.* **1998**, *37*, 973.
376. X. H. Mu, F. A. Schultz, *Inorg. Chem.* **1992**, *31*, 3351.
377. X. H. Mu, F. A. Schultz, *Inorg. Chem.* **1990**, *29*, 2877.
378. K. M. Kadish, M. Sweetland, J. S. Cheng, *Inorg. Chem.* **1978**, *17*, 2795.
379. S. Fukuzumi, I. Nakanishi, J.-M. Barbe, R. Guillard, E. Van Caemelbecke, N. Guo, K. M. Kadish, *Angew. Chem., Int. Ed. Engl.* **1999**, *38*, 964.
380. S. Fukuzumi, K. Miyamoto, T. Suenobu, E. Van Caemelbecke, K. M. Kadish, *J. Am. Chem. Soc.* **1998**, *120*, 2880.

2 Redox Modulation by Molecular Recognition

Vincent M. Rotello

2.1 Introduction

The control of electron transfer processes through specific non-covalent interactions is a general phenomenon in biological systems. Enzymes containing redox-active organic molecules such as quinones [1], flavins [2], nicotinamides [3], and pterins [4] use specific enzyme–cofactor interactions to regulate the reactivity of the cofactor. Using hydrogen bonding, π -stacking and other electrostatic interactions, these enzymes exert powerful control over the redox behavior of the cofactor, selectively stabilizing specific oxidation and protonation states. Equally important to the proper function of redox enzymes are the more subtle consequences of enzyme–cofactor interactions, such as the control of molecular orbital distribution provided through enzyme–cofactor interactions. Finally, the protein matrix plays a crucial role in the regulation of both intra- and interprotein electron transfer pathways [5, 6]. Taken together, these modes of enzymatic regulation of redox events demonstrate that redox enzymes utilize molecular recognition to control all aspects of electron transfer processes.

Understanding the fundamental principles governing the interplay of redox processes and molecular recognition is invaluable both in the context of biochemistry as well as in the field of materials science [7], where complex biological systems can be used as prototypes for pragmatic devices [8, 9]. In this chapter, we will explore the role of noncovalent apoenzyme–cofactor interactions in controlling the redox processes of bioorganic cofactors [10, 11], including biochemical and structural studies of the parent biomolecular systems. Additionally, the application of supramolecular model systems [12] will be presented: through these model systems, the effects of hydrogen bonding, π -stacking and dipolar interactions on electron transfer processes can be decoupled in ways that are difficult or impossible to do within the complex biomolecular environment of the enzyme active site.

The role of enzyme–cofactor noncovalent interactions in controlling biological electron transfer processes can be divided into four key areas:

- 1) modulation of redox potentials;
- 2) control of molecular orbital geometries;
- 3) proton-coupled electron transfer processes;
- 4) electron transport through the protein matrix.

Each of these topics will be discussed in turn. Intra- and interprotein electron transport will not be discussed; they are covered in the contribution by Tollin in this volume.

2.2 Modulation of Redox Potentials by Noncovalent Interactions

The redox potentials of organic cofactors are directly responsible for controlling the equilibrium behavior of the corresponding cofactor-mediated electron transfer processes. The relative redox potentials of the cofactor and its redox partner are also intimately related to the rate of adiabatic electron transfer k_{ET} through the classical Marcus equation [13, 14], and nonadiabatic electron transfer through the semi-classical Marcus equation [15, 16]. The direct dependence of both the kinetics and thermodynamics of electron transfer processes on the cofactor redox potential makes the control of these potentials a key determinant of the activity of redox proteins.

Biochemical studies have shown that the redox potentials of bound cofactors are highly enzyme dependent. This variation in redox potentials arises from selective recognition of individual oxidation and protonation states of the cofactor by the apoenzyme. As an example, the one-electron reduction potential of the flavin cofactor (Figure 1a) in different flavoenzymes varies over a greater than 500 mV range, corresponding to a free energy differential ($\Delta\Delta G$) of over 12 kcal mol⁻¹ [17]. As the redox-active isoalloxazine nucleus is identical in all of these enzymes, this selective stabilization must arise from apoenzyme–cofactor noncovalent interactions. These interactions include charge–charge attraction and repulsion, as well as dipolar interactions such as hydrogen bonding. Additionally, recent studies (see below) have shown that less obvious multipolar interactions such as donor atom– π interactions and aromatic stacking can also strongly affect the redox properties of organic cofactors.

The fundamental origin of redox state-specific recognition can be seen from the changes in electrostatic potentials that occur when organic molecules undergo redox processes. Because noncovalent interactions such as hydrogen bonding, π -stacking and dipolar interactions are essentially electrostatic in nature [18], they are highly sensitive to changes in charge density distribution within the host–guest complex. The effect of redox state on charge distribution can be clearly observed in Figure 2, where we have calculated the changes in the electrostatic potential that occur when Q_{ox} is reduced to Q_{rad^-} , and Fl_{ox} is reduced to Fl_{rad^-} . These calculations were performed using the B3LYP-DFT hybrid DFT method on lumiflavin and ubiquinone Q_0 in both their oxidized and radical anion forms. This computational protocol has

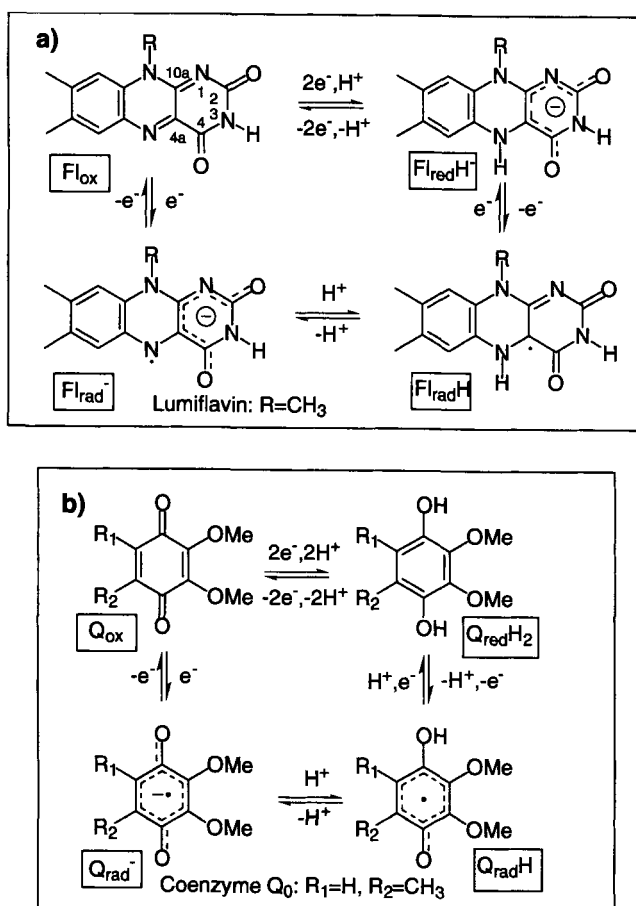


Figure 1. Common redox and protonation states for (a) flavin and (b) quinone cofactors.

been shown to reproduce accurately experimentally measured parameters including energetics and spin-density distributions (see below) [19], therefore the electrostatic potentials derived from the wavefunction are expected to reflect accurately those of the molecular system.

From the calculations for flavin, we can see that the one-electron reduction of flavin increases the negative potential of carbonyl oxygens O(2) and O(4) substantially: for O(2) this potential increases from $-45 \text{ kcal mol}^{-1}$ (Fl_{ox}) to $-116 \text{ kcal mol}^{-1}$ (Fl_{rad}⁻) at the van der Waals radius. This increase in charge density makes these carbonyl oxygens more basic, hence they are much stronger hydrogen bond acceptors.

In addition to increasing charge density at the carbonyls, reduction of flavin to the anion radical converts the electron-deficient aromatic framework of Fl_{ox} into the electron-rich Fl_{rad}⁻. In the Fl_{ox} state, the positive electrostatic potential of the atoms on the central ring allows Fl_{ox} to form favorable π -stacking interactions with electron-rich aromatic systems and complementary electrostatic interactions with electron-rich functional groups. Fl_{rad}⁻, in contrast, possesses negative electrostatic

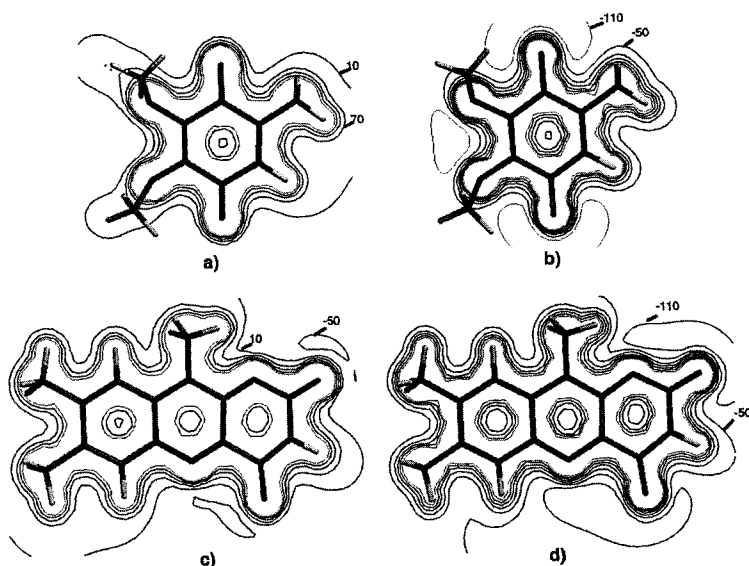


Figure 2. Electrostatic potentials derived from 6–31G* B3LYP-DFT//3–21G UHF calculations for Ubiquinone Q_0 in (a) the oxidized (Q_{ox}) and (b) the radical anion form (Q_{rad^-}) and lumiflavin in the oxidized (Fl_{ox}) and radical anion form (Fl_{rad^-}). Contour lines are at 60 kcal mol⁻¹ intervals.

potentials on the central and distal rings, making interactions with adjacent electron-rich systems highly unfavorable.

From the electrostatic potential maps, we can see how molecular recognition is related to the redox state of the guest/cofactor. The selective recognition of specific oxidation states is directly related to the potential required to shuttle between these oxidation states. This relationship can be quantified by the equation

$$\frac{K_a(\text{red})}{K_a(\text{ox})} = e^{(nF/RT)[E_{1/2}(\text{bound}) - E_{1/2}(\text{unbound})]} \quad (1)$$

where $K_a(\text{ox})$ and $K_a(\text{red})$ are the association constants in the oxidized and reduced form and $E_{1/2}(\text{unbound})$ and $E_{1/2}(\text{bound})$ are the standard reduction potentials in the unbound and receptor-bound forms. According to Eq. 1, enhanced binding [$K_a(\text{red})/K_a(\text{ox}) > 1$] inherently accompanies a positive shift in $E_{1/2}$ [$E_{1/2}(\text{bound}) - E_{1/2}(\text{unbound}) > 0$]. This direct correlation of redox and recognition is an important principle both in the understanding of biological systems and in the design of molecular devices.

2.2.1 Hydrogen Bonding

Hydrogen bonding is an efficient and specific recognition motif [20]. Depending on the directionality of the hydrogen bond donor–acceptor interaction, this interaction

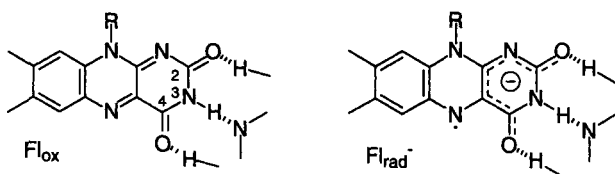


Figure 3. Redox state-selective recognition of flavin.

can selectively stabilize or destabilize individual oxidation states, thereby modulating the redox potential between these states. An example of hydrogen bond modulation of redox processes can be seen with the flavin cofactor, where hydrogen bonding to O(2) and O(4) of flavin is expected to be more favorable in the Fl_{rad}^- than the Fl_{ox} redox state, because of the greater negative charge present in these positions in the radical anion (Figure 3). As a consequence, these interactions selectively stabilize the Fl_{rad}^- redox state, making the reduction of Fl_{ox} to Fl_{rad}^- less unfavorable. In contrast, hydrogen bonding to N(3)–H is stronger with Fl_{ox} than with Fl_{rad}^- , owing to the greater positive charge at this position in Fl_{ox} . Therefore, interactions at this position would make the reduction of Fl_{ox} to Fl_{rad}^- more unfavorable.

There are a number of recent examples of recognition-modulated redox processes in host–guest complexes that are consistent with the above predictions (Figure 4). Three-point hydrogen bonding of diacyldiaminopyridine derivatives to flavin was shown to make the reduction of Fl_{ox} to Fl_{rad}^- 155 mV ($3.6 \text{ kcal mol}^{-1}$) less negative (Figure 4a) [21]. These interactions are partially self-canceling: recent solvent studies have shown that hydrogen bonding to N(3)–H makes flavin reduction 76 mV ($1.8 \text{ kcal mol}^{-1}$) more negative [22]. This more negative potential is in line with the

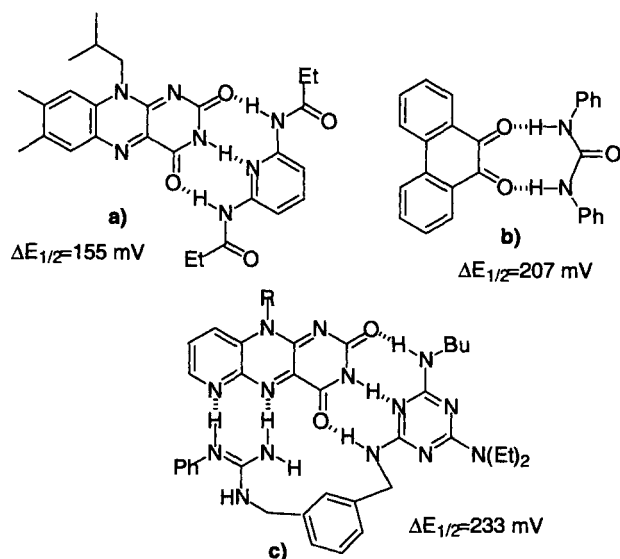


Figure 4. Modulation by supramolecular hosts of the redox potential for the reduction of oxidized guests to the radical anion state in CH_2Cl_2 at ambient temperature.

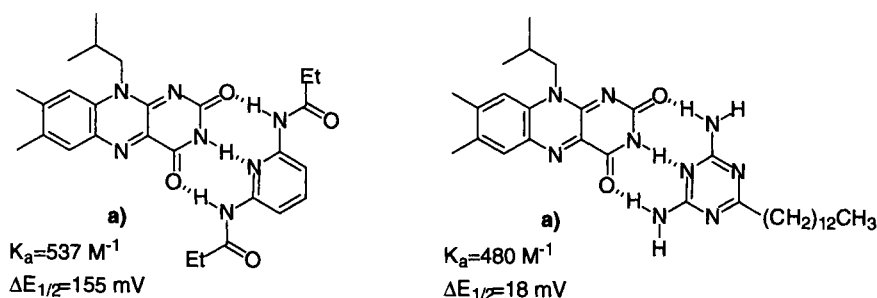


Figure 5. Recognition and redox modulation of flavin by (a) diacyldiaminopyridine receptors and (b) diaminotriazine-based receptors [25].

above predictions regarding the effect of hydrogen bonding at this position. Subtraction of this compensating effect from the potential shifts observed with the diacyldiaminopyridine receptor–flavin complexes indicates that hydrogen bonding at O(2) and O(4) shifts the reduction potential to 231 mV ($5.4 \text{ kcal mol}^{-1}$) less negative. Subsequent experiments have shown similar shifts for the reduction of *o*-quinones to their radical anions using ureas as host molecules (Figure 4b) [23]. The degree of redox modulation can be increased through the use of multi-point interactions: large shifts in $E_{1/2}$ were also observed in the multidentate host–guest system developed by Yano et al. [24] (Figure 4c).

From the limited number of experimental studies available, it can be seen that hydrogen bonding can have a profound impact on the reduction potential of redox-active organic systems. Host molecules that donate hydrogen bonds to redox-active guests can make the reduction of these guests more than 100 mV less negative per hydrogen bond. Conversely, systems that accept hydrogen bonds from these guests make reduction substantially more difficult. These results are obviously preliminary; as an example, diacyldiaminopyridines bind flavins with the same affinity that diaminotriazines do (Figure 5). The effects of these two different classes of receptors on flavin reduction potentials, however, are different: the diacyldiaminopyridine receptors make the flavin reduction potential less negative, whereas the diaminotriazine receptors have relatively little effect. Clearly, careful parametric study of these host–guest complexes will be required to understand fully the structure–function relationship in these systems.

An important caveat in the design of redox-active host molecules is that the recognition element apparently needs to be a direct part of the redox-active skeleton: recent studies of uracils attached to tetrathiafulvenes (TTF) [26] and amides attached to ferrocenes [27] have demonstrated much weaker (~ 15 – 20 mV per hydrogen bond) effects of recognition on redox processes. The weakness of this modulation is surprising, since there are examples of similar systems where simple substituent effects on aromatic units attached to ureas [28] and diaminotriazines [29] have had much larger effects on hydrogen bonding than those seen in the above TTF and ferrocene systems. This lack of redox modulation is in spite of

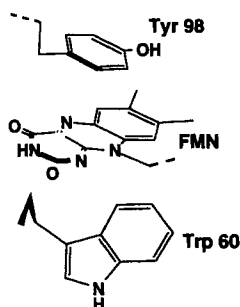


Figure 6. Flavin binding site of the flavodoxin isolated from *Desulfovibrio vulgaris* [36].

the fact that a far larger change in electron density of the system is expected in the systems undergoing redox processes.

2.2.2 Aromatic Stacking

Aromatic stacking interactions [30, 31] are a prominent feature in recognition-modulated redox processes. In biological systems, stacking of π -electron-deficient cofactors such as flavins and quinones with electron-rich side-chain residues and substrates strongly modulates the redox potential of the cofactor. This stacking motif has also seen widespread application in the creation of molecular shuttles, where redox-selective recognition has been used to drive the shuttling action [32, 33].

In biological systems, the most extensively studied examples of stacking-modulated redox processes are the flavodoxins, which are electron transferases isolated from microbial sources [34]. In these enzymes, mutation of aromatic residues near the flavin binding site (Figure 6) has been shown to modulate the reduction potential of the $\text{Fl}_{\text{rad}}\text{H}/\text{Fl}_{\text{red}}\text{H}^-$ couple 140 mV less negative [35]. The modulation provided by the tyrosine residue arises from redox-state specific interactions: reduction of the relatively electron-poor $\text{Fl}_{\text{rad}}\text{H}$ to the electron-rich anionic $\text{Fl}_{\text{red}}\text{H}^-$ species creates an electrostatically unfavorable interaction with the electron-rich phenolic tyrosine sidechain.

In model studies, the modulation of flavin redox potentials by aromatic stacking interactions has been studied through the use of bidentate hydrogen bonding-aromatic stacking receptors. (Figure 7). Using this host-guest complex, the favorable interactions between the electron-rich aromatic moiety on the receptor and the electron-deficient oxidized flavin were demonstrated through the increasing association constant (K_a) with increasing aromatic-aromatic overlap. Using the non-stacking phenyl receptor as a control, we can see that aromatic stacking in the anthracyl receptor-flavin complex is worth 2 kcal mol⁻¹ in free energy (ΔG). As with their biological prototype, aromatic-aromatic overlap makes the flavin reduction potential more negative. This change in potential arises from the loss of aromatic-

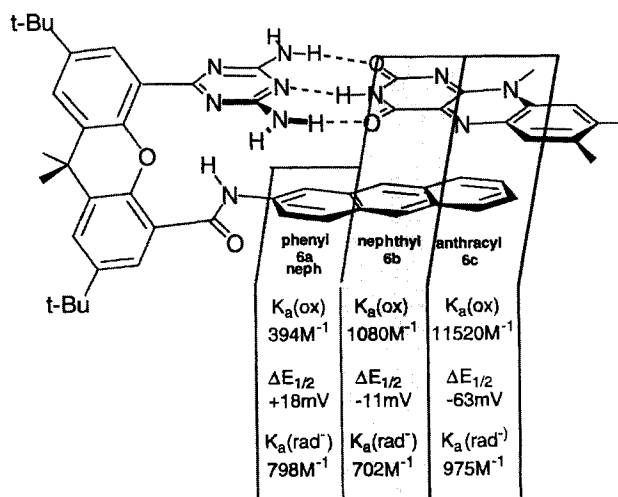


Figure 7. Molecular modeling structure (AMBER) of the flavin **1**–receptor **6** complex and thermodynamic constants for host–guest binding in CDCl₃ at 298 K.

aromatic recognition that arises when flavin is converted from the electron-deficient Fl_{ox} state to the electron-rich Fl_{rad⁻} state; the lack of aromatic–aromatic recognition can be seen from the virtually identical K_a s for the various receptors with Fl_{rad⁻}.

The virtually identical binding constants observed with Fl_{rad⁻} for each of the receptors strongly suggests the possibility of conformational switching upon reduction of Fl_{ox} to Fl_{rad⁻} (Figure 8). This switching could serve a variety of roles in biological systems, such as controlling protein–protein interactions. This kind of conformational adjustment also provides a potential tool for the creation of molecular devices.

To explore further the possibility of redox-controlled conformational switching in π -stacked systems, EPR experiments were performed on the above systems with analogous naphthalimide radical anion (N_{rad⁻}) systems (Figure 9). These systems behaved similarly to the flavin-based host–guest systems; aromatic stacking of the naphthalimide in the oxidized state with the anthracenyl receptor was manifested by a more than 10-fold increase in binding relative to the phenyl-substituted control. Likewise, analogous to the flavin redox system, this relative enhancement disappeared upon reduction of the naphthalimide to the radical anion (N_{rad⁻}). In EPR experiments, there was no visible difference in the EPR spectrum of N_{rad⁻} (Figure 10) when bound to either the nonstacking phenyl receptor (Figure 9a) or the an-

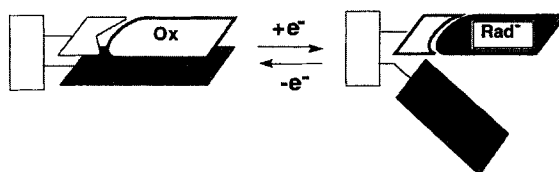


Figure 8. Redox-based conformational switching of π -stacked systems.

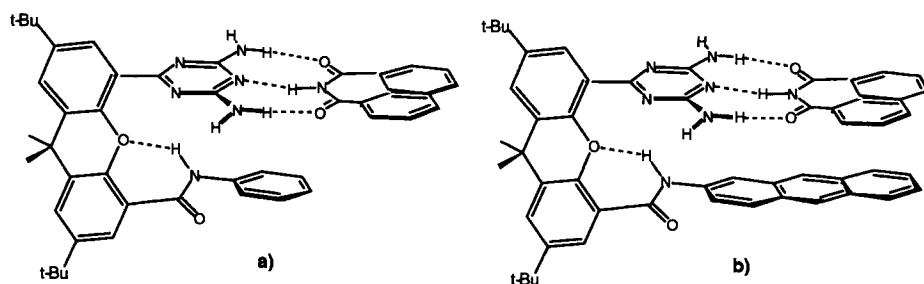


Figure 9. Naphthylimide bound to (a) phenyl-functionalized control receptor and (b) anthracyl receptor.

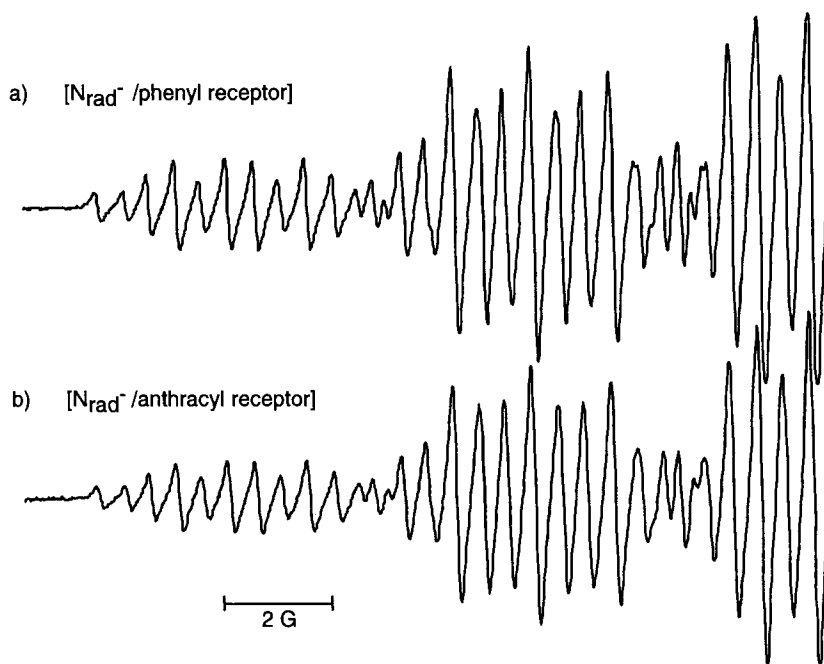


Figure 10. EPR spectra of N_{rad}^- bound to (a) phenyl receptor and (b) anthracyl receptor.

thracyl receptor (Figure 9b). This indicates a total lack of interaction between the two aromatic systems in the anthracyl system, consistent with the hypothesis that a conformational switch process is operative. A corollary of this observation is that the modulation of redox potentials observed in these flexible systems is a lower bound for that possible in their enzymatic counterparts, where the redox cofactor is unable to flip away, and can be forced into proximity with the aromatic stacking unit by the protein scaffold.

2.2.3 Other Electrostatic Interactions

In addition to hydrogen bonding and aromatic stacking, it is clear that other electrostatic interactions will influence the reduction potential of redox-active systems. These interactions can be either long-range or local in nature. One example of long-range electrostatic interactions on cofactor reduction potentials is provided by the flavodoxins. In these systems, Zhou and Swenson have shown that the anionic phosphate functionality on the flavin mononucleotide (FMN) side-chain makes the potential for flavin reduction more negative [37]. This effect was mirrored in a mutagenesis study of anionic (glutamate and aspartate) residues within 13 Å of the flavin binding site of the *D. vulgaris* flavodoxin. In these studies, it was found that neutralization of these residues through mutation made the reduction of the flavin from the neutral $\text{Fl}_{\text{rad}}\text{H}$ state to the anionic Fl_{red}^- state, an average of 15 mV per residue more negative.

In complementary computational studies, Gunner et al. have explored the role of long-range electrostatic interaction on electron transfer processes in the *Rhodospira sphaeroides* reaction center [38]. The interaction domains were identified by mapping electrostatic potentials, calculated from the Poisson–Boltzmann equation, on to calculated ‘encounter surfaces’ for each of the components of the reaction center. From qualitative correlation of electron transfer processes with these low-resolution potential maps, it is apparent that long-range interactions profoundly affect the reduction potential of the cofactors in the reaction center.

There has been far less research performed on the role of short-range electrostatic interactions such as cation– π [39] and other polar– π [40] effects on the reduction potential of organic cofactors. The effects of these interactions on biological systems are hard to assess: mutation of charged residues near the active site perturbs multiple aspects of the catalytic process [41], whereas dipolar interactions are often subtle, and are extremely distance dependent [42]. One model study has been performed on the ‘donor atom– π ’ interaction of electron-rich functionality with flavins [43]. These studies used a model system (Figure 11) to explore the role of this interaction

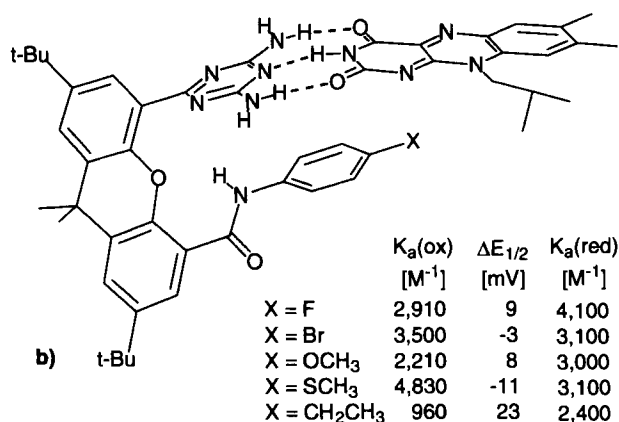


Figure 11. Modulation of flavin recognition and redox processes through donor atom– π interactions.

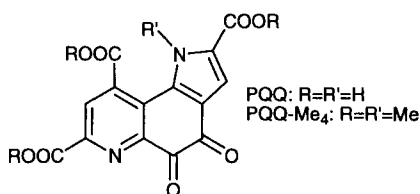


Figure 12. PQQ and trimethyl ester/methylated pyrrole analog.

in recognition and redox processes. These studies demonstrate once again the selective interaction of electron-rich functionality with the electron deficient Fl_{ox} state of the flavin. One interesting observation in this system is that the strongest donor atom- π interaction, and hence reduction potential modulation, occurs with the thiomethyl substituent. It remains an open question as to whether this stronger interaction arises from polarization or geometrical effects; preliminary computational studies suggest the latter [44].

Another aspect of electrostatic modulation of redox systems is metal-cofactor interactions. Although these interactions are surprisingly uncommon in biological systems, metal-cofactor interactions have been well documented in certain families of enzymes such as bacterial alcohol dehydrogenases. These enzymes utilize the pyrroloquinolinequinone (PQQ) system as a redox cofactor (Figure 12) [45]. In these systems, it has been established that Ca^{2+} serves as additional cofactors in the enzymatic processes catalyzed by PQQ-dependent proteins [46].

In recent model studies [47], Itoh et al. [48] used PQQ-Me₄ as an analog for PQQ to study the effects of Ca^{2+} interactions with PQQ. This peralkylated cofactor was chosen to simplify the electrochemistry of the naturally occurring cofactor which, as in the flavins, can serve as a proton source for electrochemical-chemical-electrochemical (ece) processes. Using this analog, it was established that Ca^{2+} binding had a profound impact on the reduction process, making the reduction of PQQ-Me₄ 570 mV (13 kcal mol⁻¹) less negative. The origin of this stabilization was explored using EPR studies coupled with semi-empirical calculations. Using this synergistic combination of methodologies, the structure of the PQQ-Me₄ radical anion was shown to chelate Ca^{2+} between the quinone carbonyl, the ester and the pyridine nitrogen as shown in Figure 13.

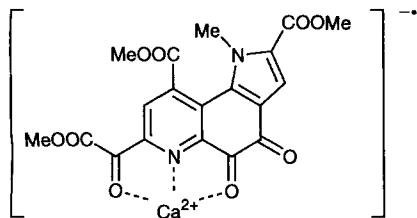


Figure 13. PQQ-Me₄ radical anion- Ca^{2+} complex.

2.3 Recognition-mediated Control of Molecular Orbital Geometries

In addition to modulating the reduction potentials of redox cofactors, noncovalent interactions affect the orbital geometries of these systems [49]. Changing the shape of the lowest unoccupied molecular orbital (LUMO) will alter the reduction of oxidized cofactors, while modification of the highest occupied molecular orbital (HOMO) will serve to modulate the oxidation of these cofactors when they are in their reduced states. The modification of redox properties arising from orbital distortion will be manifested thermodynamically through alteration of the reduction potentials of the cofactor. The distortion of orbital geometries should also alter the kinetics of electron transfer process by changing the vector of the transfer event, an effect that is not well explored. While clearly important to the understanding of redox processes, the structures of the HOMO and LUMO of molecular systems are not directly experimentally observable. This inability to correlate theory and experiment limits our ability to correlate orbital structure with molecular behavior and properties.

In contrast to the HOMO and LUMO, the singly occupied molecular orbital (SOMO) can be correlated both qualitatively and quantitatively with experimentally measurable EPR hyperfine couplings (hfcs). As a result, host-guest systems that have redox-active guests that are stable as radicals provide excellent tools for studying the effects of noncovalent interactions on redox properties.

One recent example of the redistribution of spin density by noncovalent interaction is the PQQ-Ca²⁺ system previously described (Figure 13). In this study, binding of the PQQ analog to Ca²⁺ increases the hfcs observed for the pyridine nitrogen, presumably indicating an increase in spin density at this position. Interestingly, the hfcs at the other positions of the cofactor analog were not substantially perturbed. The lack of longer range distortion of the SOMO is unusual, given the dramatic change in energetics observed upon complexation.

In recent studies, Rotello has quantitatively investigated the effect of hydrogen bonding on the spin density distribution of redox-active host radicals, using a combined EPR and density functional approach. In these studies, the radical anion of naphthalimide (N_{rad}^-) (Figure 14) was chosen as model for the flavin radical anion (Fl_{rad}^-) because of the high degree of symmetry of the naphthalene framework. This symmetry provides readily interpretable EPR spectra of high resolution, allowing direct determination of hfcs.

The spectra of N_{rad}^- and the N_{rad}^- -receptor complex that were acquired via simultaneous electrochemistry and EPR (SEEPR) are notably different. The spectrum of the hydrogen-bound radical, produced via addition of the diacyldiaminopyridine receptor, exhibits a greater overall signal width and concomitantly less overlap of hyperfine lines (Figure 15). Addition of the same receptor to *N*(1)-methylnaphthalimide radical anion, where the binding site is blocked through alkylation, had only negligible effects on the SEEPR spectrum of the control. This confirms that specific hydrogen bond interactions were the cause of the changes observed in the spectrum of N_{rad}^- .

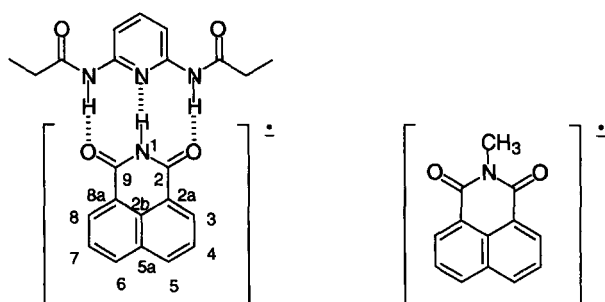


Figure 14. Hydrogen-bonded complex between naphthalimide radical anion (N_{rad}^-) and diacyl-diaminopyridine receptor, and the negative control *N*(1)-methyl-naphthalimide, in which the binding site is blocked via alkylation.

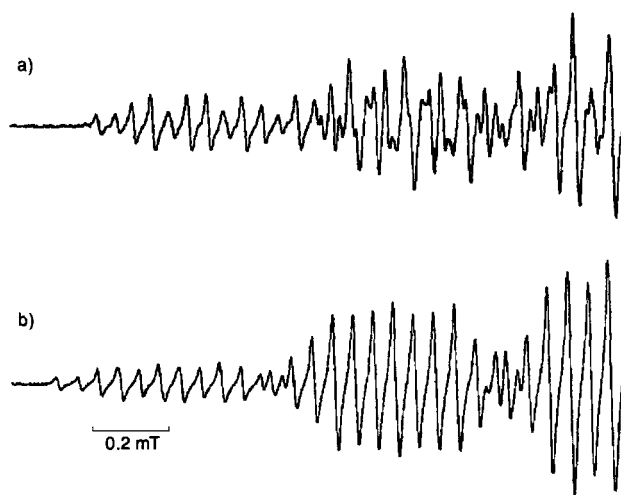


Figure 15. Low-field half of the SEEPR spectra of (a) N_{rad}^- and (b) the N_{rad}^- -receptor complex.

Despite the complexity of the observed spectrum of N_{rad}^- , spectral simulation and iterative curve fitting permitted the precise determination of hfcs for hydrogen-bound and free N_{rad}^- . Hydrogen bonding to the hydrogen-bonding receptor enhances the spin polarization of N_{rad}^- , which is manifested in the increased spectral width. Additionally, in contrast to the PQQ analog, changes are seen in all the observed hyperfine couplings, indicating an overall redistribution of spin density.

In addition to qualitative correlation to spin density distribution, the experimental hfcs provided critical benchmarks for the validation of *ab initio* computational studies of radical systems, through the relationship

$$a(\text{N}) = (8\pi/3)g_e\beta_e g_N\beta_N\rho(r_N) \quad (2)$$

Table 1. Experimental and calculated hfcs (G) of the naphthalimide radical anion.

Atom	Experimental hfcs ^{d)}			B3LYP 6-31G* hfcs		
	N_{rad^-} ^{a)}	$N_{\text{rad}^-} + \text{rec}^{\text{b)}}$	$\Delta^{\text{c)}}$	N_{rad^-} ^{a)}	$N_{\text{rad}^-} + \text{rec}^{\text{b)}}$	$\Delta^{\text{c)}}$
N(1)	1.424	1.492	0.068	-1.152	-1.281	0.129
H(1)	0.480	0.533	0.053	0.547	0.005	-0.542
H(3)/H(8)	5.112	5.282	0.170	-5.046	-5.747	0.701
H(4)/H(7)	0.908	1.028	0.120	0.992	1.520	0.528
H(5)/H(6)	5.744	5.763	0.019	-6.892	-7.055	0.163

^{a)} Naphthalimide radical anion alone.

^{b)} 1:1 complex between naphthalimide radical anion and diacyldiaminopyridine receptor.

^{c)} Difference in the absolute magnitude: $\Delta = |\text{hfc}(N_{\text{rad}^-} + \text{receptor})| - |\text{hfc}(N_{\text{rad}^-})|$.

^{d)} Absolute values, average dispersion approximately ± 0.005 G.

where the hfc of nucleus N, $a(\text{N})$, is proportional to the corresponding Fermi contact integral (spin density at the nucleus) $\rho(r_{\text{N}})$; g_e (g_{N}) represents the electronic (nuclear) g -factor and β_e (β_{N}) the Bohr (nuclear) magneton.

In the EPR studies of the N_{rad^-} host-guest complexes, DFT-B3LYP-predicted hfcs for N_{rad^-} and the N_{rad^-} -receptor system were in good overall quantitative agreement with experimental results (Table 1). This validates the wavefunction for N_{rad^-} and the hydrogen-bound complex, allowing us to predict properties not experimentally accessible, such as electrostatic potential (see above), electron density and spin density distribution (Figure 16).

According to the DFT-B3LYP calculations, complexation by the receptor shifts the spin density away from the carbonyl oxygens involved in hydrogen bonding, and towards the carbonyl carbons C(2) and C(9) (Figure 16). The largest increase in spin density, however, is observed in the naphthyl core of C(3)-C(8). This migration of spin density can be understood through examination of the molecular orbitals of N_{rad^-} . Since hydrogen bonding is a two-electron process, it will cause a distortion of lower, filled molecular orbitals towards the hydrogen-bonding recognition surface, leading to an increase in charge density at the carbonyl oxygens. To maintain orthogonality between wavefunctions, the SOMO will then be distorted away from the binding site, and into the naphthalene ring system. This

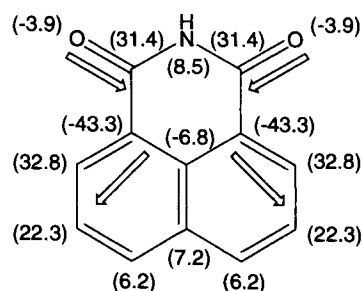


Figure 16. Change in the absolute spin density of N_{rad^-} upon complexation with diacyldiaminopyridine receptor, as predicted by DFT-B3LYP calculations. Numbers in parantheses: $1000 \times (|\text{sd}(N_{\text{rad}^-} + \text{receptor})| - |\text{sd}(N_{\text{rad}^-})|)$.

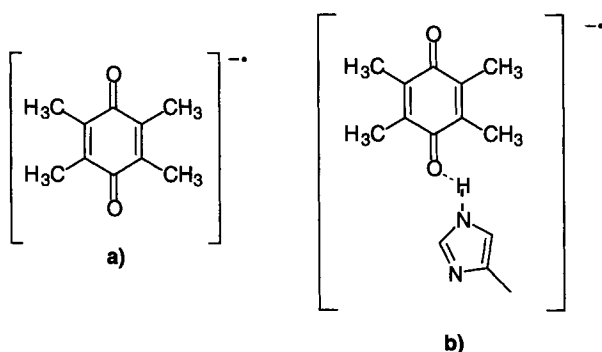


Figure 17. (a) Duroquinone radical anion. (b) Asymmetric duroquinone radical anion–imidazole complex.

result provides a possible solution to an apparent paradox in flavoenzyme electron transfer. In solution, spin density for Fl_{rad}^- is centered at N(5), whereas electron transfer processes occur through C(8) of the xylene ring. If an effect similar to that observed in the N_{rad}^- –receptor complex occurs in the flavin radical anion–protein complex, a movement of spin density away from the hydrogen bonding surface and towards the distal xylene ring will occur, facilitating the electron transfer event.

Computational methodologies also provide a powerful tool for the study of biological systems. In recent studies, O'Malley used DFT-B3LYP methods to explore the hydrogen bonding environment within the Q_a site of the *Rhodobacter sphaeroides* photosynthetic reaction center [50]. In these studies, the effects of symmetric and asymmetric hydrogen bonding on the hyperfine couplings of the duroquinone radical anion (Figure 17) were predicted using the B3LYP hybrid functional. In these studies, it was found that there was excellent agreement between the hfcs calculated for the duroquinone–imidazole complex and experimentally measured hfcs from a duroquinone-constituted photosynthetic reaction center [51].

2.4 Proton-coupled Electron Transfer

Proton-coupled electron transfer is a prominent theme in biological redox systems. There are three basic mechanisms for these processes (Figure 18). In the first mechanism (path A), electron transfer occurs prior to proton transfer. This mechanism is commonly observed for the electrochemical reduction and oxidation of quinones and flavins in protic media [52]. In this interfacial environment, proton transfer is manifested as an ECE (E represents an electron transfer at the electrode surface and C represents a homogeneous chemical reaction) two-electron reduction of these systems to their fully reduced states (Figure 19). As electron transfer occurs prior to the proton transfer event, proton transfer does not affect either the redox potential or the electron transfer rate to or from the cofactor.

In contrast to post-reduction proton transfer, transfer of the proton to the redox species prior to electron transfer (Figure 18, path B) has a profound impact on re-

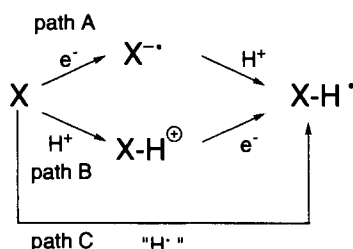


Figure 18. Proton-dependent electron transfer pathways.

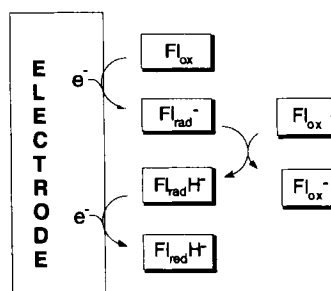


Figure 19. Schematic representation of the ECE pathway for two-electron reduction of flavins in aprotic media.

duction potentials and electron transfer rates. At the simplest level, protonation followed by electron transfer can be observed in acidic solutions, where the process has been termed ‘catalysis of electron transfer’ by Fukuzumi (see chapter 1 in this volume) [53]. In these systems the redox-active unit is protonated by the acidic solution, rendering the reduction potential of the redox system substantially less negative, directly analogous to the effects of hydrogen bonding previously mentioned. This lowering in reduction potential results in what is essentially specific acid catalysis of the electron transfer process.

While studies of specific acid catalysis of redox cofactors shed light on the intricacies of the electron transfer process [54], the conditions required for pre-protonation of the cofactor are highly acidic ($\text{pH} < 0$), and would not generally be found in biological systems. There are, however, systems such as Q_B reduction in the *Rhodobacter sphaeroides* reaction center [55], where kinetic data indicate proton transfer prior to or simultaneous with electron transfer. This would seem to indicate that a ‘general acid’ process is operative. At first glance, this sort of mechanism would seem to be contrary to the Born–Oppenheimer approximation. This apparent paradox can be avoided, however, if quantum chemical (nonadiabatic) processes are considered.

In recent research, the concept of simultaneous electron and proton transfer has been explored. In this process, directly coupled electron and proton transfer result in the formal transfer of a hydrogen atom (Figure 18, path C). In this pathway, two quantum events occur: electron tunneling and proton tunneling [56]. Whereas electron tunneling is a well-accepted phenomenon, proton tunneling is a far less commonly invoked property. Proton tunneling can be readily understood if we consider

the de Broglie wavelength of the proton, which is 0.5 \AA when the particle has an energy of $\sim 2 \text{ kcal mol}^{-1}$. Given that the distance required to transfer a proton from a hydrogen bond donor to an acceptor is on the order of 0.7 \AA , proton tunneling coupled to protein–cofactor motion is clearly a possibility.

Evidence for the dual proton and electron tunneling process required for simultaneous electron and proton transfer has been obtained from both enzymatic and model systems. In biomolecular systems, the strongest evidence for proton tunneling processes is obtained from kinetic isotope effects, where both anomalously high protium–tritium kinetic isotope effects and distinct temperature profiles for these isotope effects can be used as diagnostic tools for proton tunneling events [57].

For proton tunneling to occur efficiently, the donor and acceptor must be in the intimate proximity provided by hydrogen bonding. This contact is a natural feature in biological systems, and has been replicated in model systems through the use of hydrogen-bonded donor–acceptor pairs [58]. In one series of experiments, Therien et al. compared photoinduced charge transfer between covalently linked systems and the analogous transfer in hydrogen-bonded donor–acceptor pairs (Figure 20) [59]. In these studies, it was determined that the electron transfer rate in the hydrogen-bonded system (Figure 20a) was twice that of the covalently linked analog (Figure 20b), despite the fact that the thermodynamic driving force in the covalently linked system was more favorable (-0.87 versus -0.70 eV for the hydrogen-bonded system).

Further insight into the nature of proton-coupled electron transfer can be obtained from donor–acceptor pairs featuring an asymmetric hydrogen bonding in-

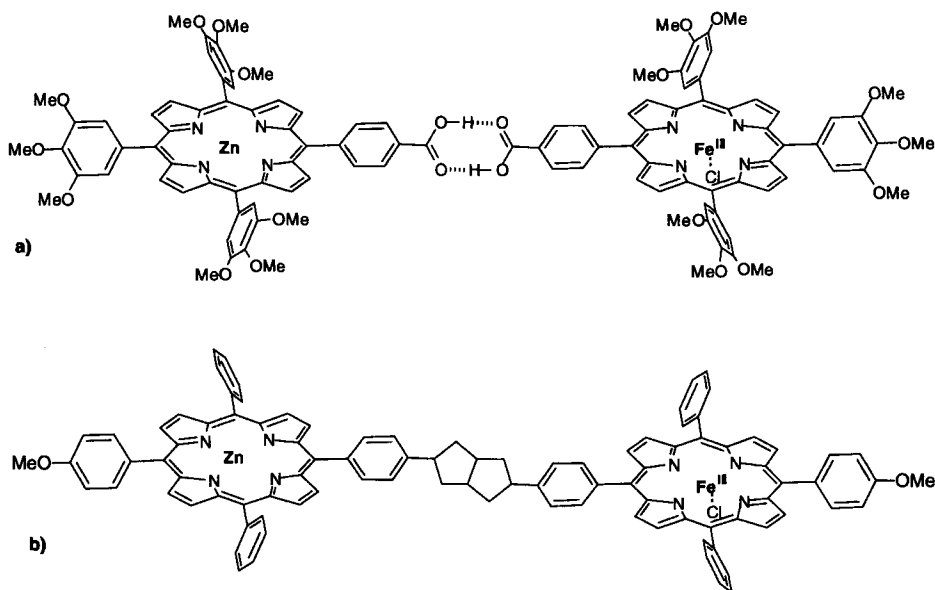


Figure 20. (a) Noncovalently and (b) covalently linked donor–acceptor pairs.

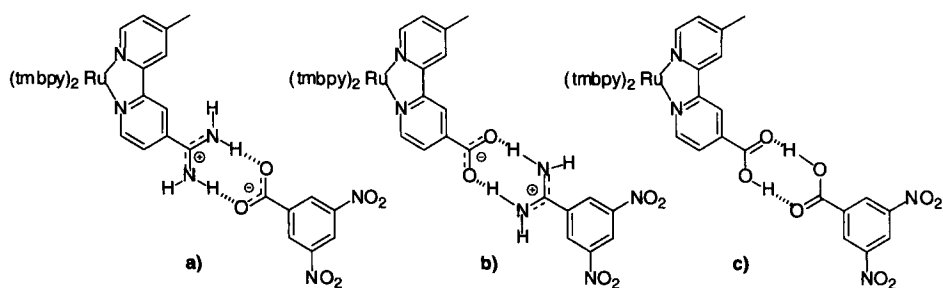


Figure 21. Hydrogen-bonded donor–acceptor pairs featuring (a) amidinium–carboxylate, (b) carboxylate–amidinium and (c) biscarboxylate interfaces.

terface. In recent studies, Nocera et al. used ruthenium tetramethylbipyridyl (tmby) systems to explore electron transfer processes (Figure 21) [60]. In these models, photoinduced electron transfer from the Ru^{2+} to the complementary dinitrobenzene acceptors provides an elegant system for the study of electron transfer in hydrogen-bonded systems. Using amidinium–carboxylate and carboxylic acid–carboxylic acid dimerization to provide the proton-transfer conduit, it was found that proton-coupled electron transfer in the carboxylate–amidinium system (Figure 21b) was 37-fold faster than the analogous amidinium–carboxylate donor–acceptor pair (Figure 21a), and seven-fold faster than the biscarboxylate system (Figure 21c). The difference in rates is attributed to the neutralization of the charged interface of the carboxylate–amidinium system upon electron or proton transfer. This highly favorable process is expected to play a key role in hydrophobic environments, and is probably a central factor in controlling electron transfer in biological systems [61].

2.5 Summary and Outlook

Recognition processes are clearly central to the control of cofactor redox properties in biological systems. This control is manifested in multiple aspects of the redox process, including redox potentials, orbital geometries, protonation states and electron transfer pathways. In all of these areas, study of model systems and their biological prototypes has provided considerable insight into the interplay of enzyme–cofactor noncovalent interactions and cofactor redox processes. While much remains to be explored with both biomolecular and model studies, perhaps the greatest challenge will be the integration of these two approaches, using the tools provided by computational chemistry. This integration will ultimately provide a comprehensive understanding of complex biomolecular processes at the electronic, molecular and supramolecular level. This understanding is important both biologically and synthetically, where redox-based molecular devices provide new solutions to pragmatic problems.

References

1. C. Anthony, *Biochem. J.* **1996**, 320, 697–711.
2. S. Ghisla, V. Massey, *Eur. J. Biochem.* **1989**, 181, 1–17.
3. V. Popov, V. S. Lamzin, *Biochem. J.* **1994**, 301, 625–643.
4. R. L. Blakley, S. J. Benkovic, *Chemistry and Biochemistry of Pterins*, Wiley, New York, **1985**.
5. R. E. Sharp, S. K. Chapman, G. A. Reid, *Biochemistry*, **1996**, 35, 891–899.
6. G. Tollin, J. Hurley, J. Hazzard, T. Meyer, *Biophys. Chem.*, **1993**, 48, 259–279.
7. A. E. Kaifer, *Acc. Chem. Res.* **1999**, 32, 62–71.
8. A. Roque, F. Pina, S. Alves, R. Ballardini, M. Maestri, V. Balzani, *J. Mater. Chem.* **1999**, 9, 2265–2269.
9. F. Diederich, L. Echegoyen, M. Gomez-Lopez, R. Kessinger, J. Stoddart, *J. Chem. Soc., Perkin Trans 2* **1999**, 1577–1586.
10. P. Mishra, D. Drueckhammer, *Curr. Opin. Chem. Biol.* **1998**, 2, 758–765.
11. V. Rotello, *Curr. Opin. Chem. Biol.* **1999**, 3, 747–751.
12. A. Niemz, V. Rotello, *Acc. Chem. Res.* **1999**, 32, 44–53.
13. I.-S. Lee, E. H. Jeoung, M. M. Kreevoy, *J. Am. Chem. Soc.* **1997**, 119, 2722–2728.
14. J. P. Guthrie, *J. Am. Chem. Soc.* **1996**, 118, 12878–12885.
15. For an excellent summary of electron transfer theory, see J. Bolton, M. Archer, in *Electron Transfer in Inorganic, Organic and Biological Systems*, ACS Advances in Chemistry Series 228 (Eds. J. Bolton, N. Mataga, G. McLendon), American Chemical Society, Washington, DC, **1991**, pp. 7–23.
16. S. J. Formosinho, L. G. Arnaut, R. Fausto, *Prog. React. Kinet.* **1998**, 23, 1–90.
17. For a comprehensive review of flavin redox chemistry, see F. Mueller (Ed.), *Chemistry and Biochemistry of Flavoenzymes*, CRC Press, Boca Raton, FL, **1990**, Vols. 1–3.
18. (a) F. G. Klärner, U. Burkert, M. Kamieth, R. Boese, J. Benet-Buchholz, *Chem. Eur. J.* **1999**, 5, 1700–1707; (b) S. Mecozzi, A. P. West, D. A. Dougherty, *Proc. Natl. Acad. Sci. USA* **1996**, 93, 10566–10571.
19. (a) M. Lozynski, D. Rusinska-Roszak, H.-G. Mack, *J. Phys. Chem. A* **1998**, 102(17), 2899–2903; (b) K. V. Alem, E. J. R. Sudholter, H. Zuilhof, *J. Phys. Chem. A* **1998**, 102, 10860–10868.
20. S. Scheiner, *Hydrogen Bonding*, Oxford University Press, Oxford, **1997**.
21. E. Breinlinger, A. Niemz, V. Rotello, *J. Am. Chem. Soc.* **1995**, 117, 5379–5380.
22. A. Cuello, C. McIntosh, V. Rotello, *J. Am. Chem. Soc.* **2000**, 122, 3517–3521.
23. Y. Ge, R. R. Lienthal, D. K. Smith, *J. Am. Chem. Soc.* **1996**, 118, 3976–3977.
24. T. Kajiki, H. Moriya, S. Kondo, T. Nabeshima, Y. Yano, *J. Chem. Soc., Chem. Commun.* **1999**, 2727–2728.
25. R. Deans, F. Ilhan, V. Rotello, *Macromolecules*, **1999**, 32, 4956–4960.
26. L. M. Goldenberg, O. Neilands, *J. Electroanal. Chem.* **1999**, 463, 212–217.
27. J. D. Carr, L. Lambert, D. E. Hibbs, M. B. Hursthouse, K. M. A. Malik, J. H. R. Tucker, *J. Chem. Soc., Chem. Commun.* **1997**, 1649–1650.
28. C. Wilcox, E. Kim, D. Romano, L. Kuo, A. Burt, D. Curran, *Tetrahedron* **1995**, 621–634.
29. R. Deans, G. Cooke, V. Rotello, *J. Org. Chem.* **1997**, 62, 836–839.
30. C. A. Hunter, *Chem. Soc. Rev.* **1994**, 23, 101–109.
31. Y. Chen, J. W. Kampf, R. G. Lawton, *Tetrahedron Lett.* **1997**, 5781–5784.
32. P. R. Ashton, V. Balzani, J. Becher, A. Credi, M. C. T. Fyfe, G. Matternsteig, S. Menzer, M. B. Nielsen, F. M. Raymo, J. F. Stoddart, M. Venturi, D. J. A. Williams, *J. Am. Chem. Soc.* **1999**, 121, 3951–3957.
33. A. E. Kaifer, *Acc. Chem. Res.* **1999**, 32, 62–71.
34. Z. Zhou, R. P. Swenson, *Biochemistry* **1996**, 35, 15980–15988.
35. R. P. Swenson, G. D. Krey, *Biochemistry* **1994**, 33, 8505–8514.
36. (a) W. Watt, A. Tulinsky, R. P. Swenson, K. D. Watenpaugh, *J. Mol. Biol.* **1991**, 218, 195–208; (b) L. J. Rogers, K. Fukuyama, H. Matsubara, *J. Mol. Biol.* **1992**, 225, 775–789.
37. Z. Zhou, R. Swenson, *Biochemistry* **1996**, 35, 12443–12454.
38. M. Gunner, A. Nicholls, B. Honig, *J. Phys. Chem.* **1996**, 100, 4277–4291.

39. J. P. Gallivan, P. Dougherty, *Proc. Natl. Acad. Sci. USA* **1999**, *96*, 9459–9464.
40. C.-T. Chen, J. S. Siegal, *J. Am. Chem. Soc.* **1994**, *116*, 5959–5960.
41. J. Basran, M. Mewies, F. S. Mathews, N. S. Scrutton, *Biochemistry* **1999**, *36*, 1989–1998.
42. A. J. Stone, *The Theory of Intermolecular Forces*, Clarendon Press, Oxford, 1996, pp. 45–48.
43. E. Breinlinger, C. Keenan, V. Rotello, *J. Am. Chem. Soc.* **1998**, *120*, 8606–8609.
44. V. Rotello, *Heteroatom. Chem.* **1998**, 605–606.
45. P. M. Goodwin, C. Anthony, *Adv. Microb. Physiol.* **1998**, *40*, 1–80.
46. G. Schurer, T. Clark, *J. Chem. Soc., Chem. Commun.* **1998**, 257–258.
47. For a comprehensive review of the PQQ and other related TPQ and TTQ cofactors, see A.C. Rinaldi, A. Rescigno, A. Rinaldi, E. Sanjust, *Bioorg. Chem.* **1999**, *27*, 253–288.
48. S. Itoh, H. Kawakami, S. Fukuzumi, *J. Am. Chem. Soc.* **1998**, *120*, 7271–7277.
49. (a) M. Takahashi, M. Matsuo, Y. Udagawa, *Chem. Phys. Lett.*, **1999**, *308*, 195–198; (b) L. Turi *J. Chem. Phys.* **1999**, *110*, 10364–10369.
50. P. O'Malley, *J. Phys. Chem. A* **1998**, *102*, 248–253.
51. P. O'Malley, G. Babcock, *J. Chem. Phys.* **1984**, *80*, 3912.
52. A. Niemz, J. Imbriglio, V. Rotello, *J. Am. Chem. Soc.* **1997**, *119*, 892–897.
53. (a) S. Fukuzumi, *Bull. Chem. Soc. Jpn.* **1997**, *70*, 1–28; (b) S. Fukuzumi, S. Itoh, in *Advances in Photochemistry*, Vol. 25 (Ed. D. C. Neckers, D. H. Volman, G. von Büna), Wiley, New York, **1998**, pp. 241–302.
54. S. Fukuzumi, S. Kuroda, T. Goto, K. Ishikawa, T. Tanaka, *J. Chem. Soc., Perkin Trans. 2* **1989**, 1047–1052.
55. M. S. Graige, M. L. Paddock, J. M. Bruce, G. Feher, M. Y. Okamura, *J. Am. Chem. Soc.* **1996**, *118*, 9005–9016.
56. R. Cukier, D. Nocera, *Annu. Rev. Phys. Chem.* **1999**, *49*, 337–369.
57. A. Kohen, J. Klinman, *Acc. Chem. Res.* **1998**, *31*, 397–404.
58. M. Greaves, V. Rotello, *J. Am. Chem. Soc.*, **1999**, *121*, 266–267.
59. P. J. de Rege, S. Williams, M. Therien, *Science* **1995**, *269*, 1409–1413.
60. J. Kirby, J. Roberts, D. Nocera, *J. Am. Chem. Soc.* **1997**, *119*, 9230–9236.
61. A.M. Baptista, P.J. Martel, C.M. Soares, *Biophys. J.* **1999**, *76*, 2978–2998.

3 Homogeneous Redox Catalysis in CO₂ Fixation

Etsuko Fujita and Bruce S. Brunschwig

3.1 Introduction

The twin problems of global warming and diminishing finite fossil fuels resources have stimulated research into CO₂ fixation and utilization [1, 2]. Natural photosynthetic CO₂ fixation utilizes sunlight and chlorophyll as the energy source and photocatalyst to generate carbohydrates and oxygen from CO₂ and H₂O. Natural photosynthesis occurring over a few hundred million years has created a vast quantity of fossil fuels that at present fill our energy needs. Unfortunately, current consumption rates are rapidly depleting our supply of fossil fuels. Even with the advent of fuel farms it is unlikely that natural photosynthesis will be able to balance the production and use of fuels. It is therefore necessary to explore alternative routes to fuel (and chemical) production and it is likely that artificial photosynthesis will play an increasingly important role in the future.

Because of the thermodynamic stability and chemical inertness of CO₂, both energy and catalysts are needed to transform CO₂ into fuels or useful chemicals [3–5]. The large energy input needed to fix CO₂ requires the use of renewable energy if artificial CO₂ fixation is carried out on a large scale. The reduction potential to convert CO₂ to CO₂^{•-} is –1.9 V vs. NHE, making this process highly unfavorable. In fact, 0.1 – 0.6 V overpotentials are typically for the single-electron reduction of CO₂ at Pt or Hg working electrodes. This overvoltage partially results from the kinetic barrier arising from the geometric changes required for one-electron reduction of CO₂ (CO₂ is linear whereas CO₂^{•-} is bent). Although CO₂ reduction by the proton-assisted multielectron steps shown in Table 1 is often kinetically difficult, these steps are more favorable thermodynamically than the one-electron process.

Since the two-electron reduction to formic acid or CO requires a lower potential, electrolysis using a multielectron transfer catalyst in aqueous or in low-protic media can be carried out at considerably lower voltages. The simplest electrocatalytic system for CO₂ reduction is an electrochemical cell that contains: a working electrode, a reference electrode, a homogeneous electrocatalyst, the supporting electro-

Table 1. Reduction potentials for CO₂ at pH 7 with all other solutes at 1 M.

Reaction	$E_{1/2}'$ (V) ^a	
$\text{CO}_2 + \text{e}^- \rightarrow \text{CO}_2^{\cdot -}$	-1.9	(1)
$\text{CO}_2 + 2\text{H}^+ + 2\text{e}^- \rightarrow \text{HCO}_2\text{H}$	-0.61	(2)
$\text{CO}_2 + 2\text{H}^+ + 2\text{e}^- \rightarrow \text{CO} + \text{H}_2\text{O}$	-0.53	(3)
$\text{CO}_2 + 4\text{H}^+ + 4\text{e}^- \rightarrow \text{C} + 2\text{H}_2\text{O}$	-0.20	(4)
$\text{CO}_2 + 4\text{H}^+ + 4\text{e}^- \rightarrow \text{HCHO} + \text{H}_2\text{O}$	-0.48	(5)
$\text{CO}_2 + 6\text{H}^+ + 6\text{e}^- \rightarrow \text{CH}_3\text{OH} + \text{H}_2\text{O}$	-0.38	(6)
$\text{CO}_2 + 8\text{H}^+ + 8\text{e}^- \rightarrow \text{CH}_4 + 2\text{H}_2\text{O}$	-0.24	(7)
$\text{CO}_2 + 2\text{e}^- \rightarrow \text{CO}_2^{2-}$	-1.55	(8)
$\text{CO}_2^- + \text{e}^- \rightarrow \text{CO}_2^{2-}$	-1.2	(9)

^a Values are for aqueous solution vs. NHE. The $E_{1/2}'$ values are close to the values in acetonitrile vs. SCE because the ferricenium/ferrocene redox potential shifts by 0.25 V (vs. SCE) on going from acetonitrile to water while the SCE potential in water is 0.24 V [6, 7].

lyte, CO₂ and an oxidizable species (often the solvent or CO₂). The electrodes, such as those made of Mg, can be used as the oxidizable species. A heterogeneous catalyst attached to the electrode surface can be used in place of the homogeneous electrocatalyst.

The prototypical photochemical system for CO₂ reduction contains a photosensitizer (or photocatalyst) to capture the photon energy, an electron relay catalyst (that might be the same species as the photosensitizer) to couple the photon energy to the chemical reduction, an oxidizable species to complete the redox cycle and CO₂ as the substrate. Figure 1 shows a cartoon of the photochemical CO₂ reduction system. An effective photocatalyst must absorb a significant part of the solar spectrum, have a long-lived excited state and promote the activation of small molecules. Both organic dyes and transition metal complexes have been used as photocatalysts for CO₂ reduction. In this chapter, CO₂ reduction systems mediated by cobalt and nickel macrocycles and rhenium complexes will be discussed.

3.2 Macrocyclic Complexes of Cobalt and Nickel

3.2.1 Overview of CO₂ Reduction Systems Mediated by Cobalt and Nickel Macrocycles

Many 14-membered tetraazamacrocyclic complexes of cobalt and nickel serve as catalysts for electrochemical CO₂ reduction to produce CO and H₂ in water, acetonitrile–water or organic solvents [8–11]. The structures of the macrocycles are shown in Figure 2. Among these, Ni(cyclam)²⁺ is a very effective and selective catalyst for the electrochemical reduction of CO₂ to CO [10, 11]. Ni(cyclam)⁺ ad-

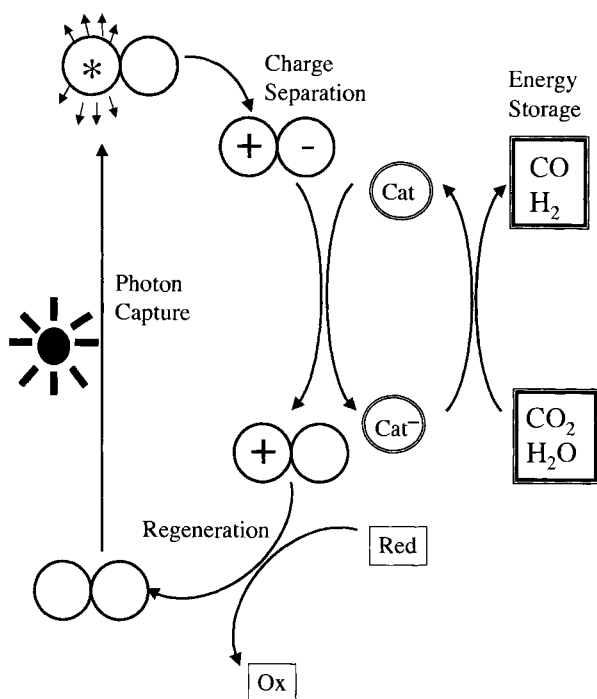


Figure 1. Artificial photo-synthetic scheme.

sorbed on the surface of the mercury electrode has been shown to be the active species. $\text{Ni}(\text{cyclam})^{2+}$ can have at least two isomers in solution (Figure 2) and studies on configurationally pure nickel complexes similar to $\text{Ni}(\text{cyclam})^+$ have been carried out to measure the activity of different isomers [12]. Structural differences are an important factor for both CO_2 binding and catalyst adsorption on mercury.

CoHMD^{2+} homogeneously catalyzes both electroreduction of CO_2 and water reduction in water, water–acetonitrile or DMF solutions [8, 9]. The CO -to- H_2 ratio produced is typically less than 1 and strongly depends on the experimental conditions used (i.e., applied potential, amount of water, electrolysis time, etc). The chiral N–H centers of the HMD macrocycle give rise to two isomers, *N-rac* and *N-meso*, as shown in Figure 2. The *N-rac* isomers of both $\text{Co}^{\text{II}}\text{HMD}^{2+}$ and $\text{Co}^{\text{I}}\text{HMD}^+$ predominate in MeCN (>90 %) and water at room temperature. The equilibrium between the *N-rac* and *N-meso* cobalt(II) isomers is very slowly established in acidic aqueous and organic media ($<2 \times 10^{-7} \text{ s}^{-1}$); by contrast, equilibration of the cobalt(I) isomers is relatively rapid ($>2 \times 10^3 \text{ s}^{-1}$) [13, 14].

Photochemical CO_2 reduction to CO (and formate in some cases) has been reported in a catalytic system using $\text{Ru}(\text{bpy})_3^{2+}$ as the sensitizer, nickel or cobalt macrocycles as the electron relay catalyst, and ascorbate as a sacrificial reductive quencher [9, 15, 16]. These systems also produce H_2 via water reduction. Although $\text{Ni}(\text{cyclam})^{2+}$ is an efficient and selective catalyst for electrochemical CO_2 reduc-

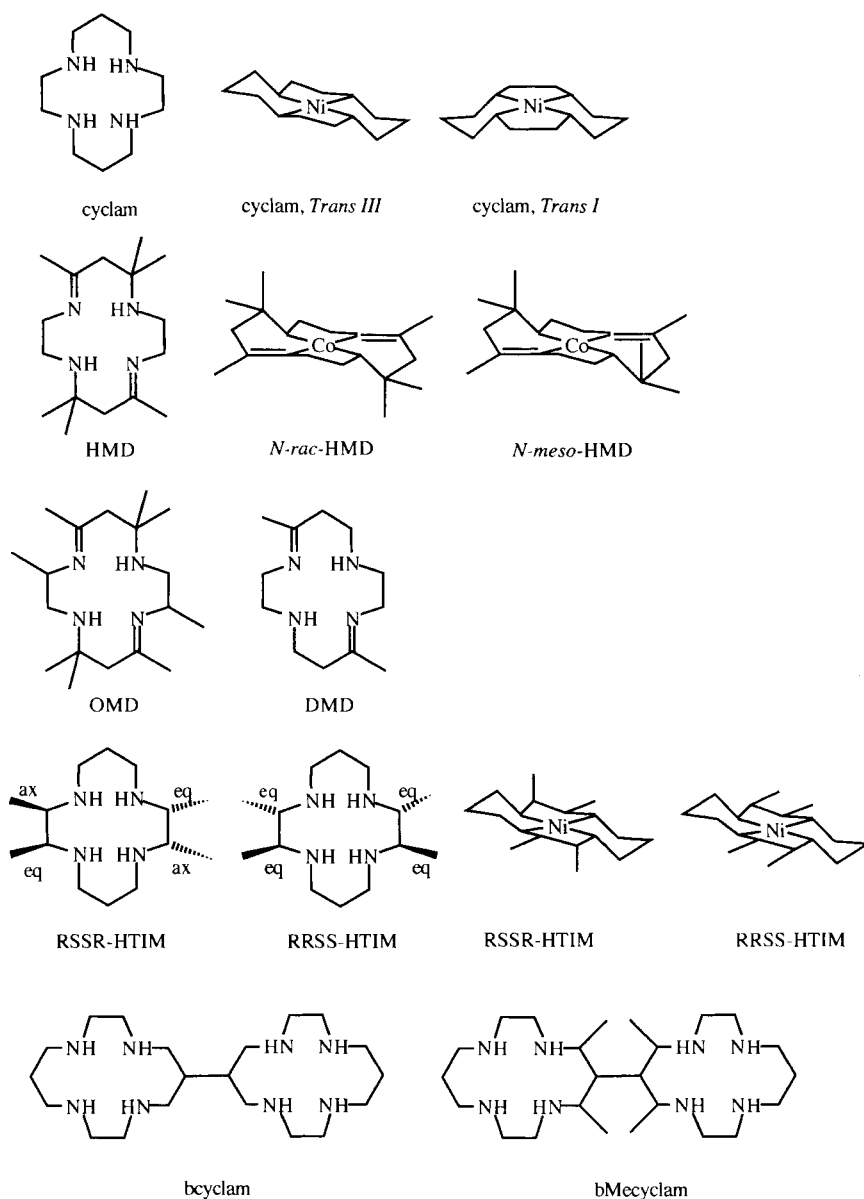


Figure 2. Structures and geometries of metal macrocycles.

tion, even in H_2O , when used as a homogeneous catalyst for photochemical reduction, the quantum yield and selectivity for CO formation are low. The yields of CO and H_2 are pH dependent and typically more H_2 than CO is produced.

Photoreduction of CO_2 with *p*-terphenyl as the photosensitizer and a tertiary

amine as a sacrificial electron donor has been demonstrated [49]. The addition of a cobalt macrocycle enhances the activity of the TP by suppressing degradative reactions of the TP and produces CO and formate efficiently with only small amounts of H₂ [17].

Metal(I), metal(III) hydride and metallocarboxylate complexes have all been postulated as intermediates in electro- and/or photochemical CO₂ reduction. These intermediates are discussed in the next sections.

3.2.2 Properties of the Cobalt and Nickel Macrocycles

M(I) complexes

Reduction potentials of Ni^{II}(cyclam)²⁺, *RRSS*-Ni^{II}HTIM²⁺ and Co^{II}HMD²⁺ are −1.44, −1.43 and −1.34 V (vs. SCE in MeCN), respectively [18]. The metal(I) complexes can be prepared by electrochemical or Na–Hg reduction, or pulse radiolysis. The spectra of all the M(I) species show a strong MLCT (metal-to-ligand charge transfer) band in the visible region (λ_{max} , ϵ): Ni^I(cyclam)⁺ at 384 nm, 4400 M^{−1} cm^{−1}; *RRSS*-Ni^IHTIM⁺ at 388 nm, 4340 M^{−1} cm^{−1} and Co^IHMD⁺ at 678 nm, 18000 M^{−1} cm^{−1} in MeCN [18]. In the square-planar d⁸-Co^IHMD⁺, the electron-rich cobalt(I) center donates significant electron density to the imine moiety, causing the C=N stretching frequency (1571 cm^{−1}) to be much lower than for Co^{II}HMD²⁺ (1661 cm^{−1}) [19]. Interestingly, the square-planar d⁹-NiHMD⁺ complex donates less electron density: the C=N stretching frequency only shifts from 1655 to 1647 cm^{−1} upon the reduction ($E_{1/2}$ = −1.22 V vs. SCE in MeCN) [20]. EXAFS and X-ray structures reveal that the Co–N bond distances remain almost the same upon the reduction of the Co(II) macrocycles in both solid and solution [20, 21].

Square-planar d⁸-Ni(cyclam)(ClO₄)₂ and *RRSS*-NiHTIM(ClO₄)₂ can be crystallized from water as low-spin complexes. However, in solution the Ni(II) complexes can exist as high-spin, octahedral complexes and/or as low-spin, square-planar complexes depending on solvent [18]. For example, Ni^{II}(cyclam)²⁺ and Ni^{II}HTIM²⁺ are low spin in MeNO₂, high spin in MeCN and the high- and low-spin complexes are in equilibrium in water. EXAFS studies reveal that *RRSS*-Ni^{II}HTIM²⁺ and *RRSS*-Ni^IHTIM⁺ are six- and four-coordinate with average Ni–N distances of 2.08 and 2.05 Å, respectively, in MeCN [22]. The X-ray structures of square-planar *RSSR*-Ni^{II}HTIM(ClO₄)₂ (average Ni–N distance 1.959 Å) and *RSSR*-Ni^IHTIM(ClO₄) (average Ni–N distance 2.068 Å) indicate that the bond lengths in the Ni(I) macrocycles increase by 0.11 Å on reduction [18]. This suggests that the Ni^{I/II} self-exchange rates of both Ni(cyclam) and NiHTIM complexes in H₂O or MeCN should be slow owing to the large structural changes upon electron transfer. The rate constant for the self-exchange reaction between Ni(cyclam)* and Ni(cyclam)²⁺ has been calculated to be 1 × 10^{−3} M^{−1} s^{−1} using the Marcus cross relation [25].

Some electron-transfer rates are summarized in Table 2. Owing to the large driving force for most of the reactions (>1.1 V except that involving Ru(bpy)₃⁺), the

Table 2. Comparison of electron transfer rates at 25 °C^a.

Reaction	Complex	k (M ⁻¹ s ⁻¹)	Ref.
$\text{ML}^{2+} + \text{e}^-_{\text{aq}} \rightarrow \text{ML}^+$	Ni(cyclam) ²⁺	5.6×10^{10}	23
	Ni(cyclam) ²⁺	4.1×10^{10}	24
	Ni(cyclam) ²⁺	3.8×10^{10}	25
	<i>N-rac</i> -CoHMD ²⁺	4.4×10^{10}	26
	<i>N-meso</i> -CoHMD ²⁺	4.7×10^{10}	14
$\text{ML}^{2+} + \text{TP}^{\bullet-} \rightarrow \text{ML}^+ + \text{TP}$	Ni(cyclam) ²⁺	4.3×10^9	27
	<i>N-rac</i> -CoHMD ²⁺	1.1×10^{10}	28
	CoOMD ²⁺	1.1×10^{10}	28
	CoDMD ²⁺	8.8×10^9	28
$\text{ML}^{2+} + \text{Ru}(\text{bpy})_3^+ \rightarrow \text{ML}^+ + \text{Ru}(\text{bpy})_3^{2+}$	<i>N-rac</i> -CoHMD ²⁺	1.8×10^8	29

^a The reaction rates with e^-_{aq} are measured in water. The electron-transfer rate from $\text{TP}^{\bullet-}$, which has a potential estimated at about -2.5 V, is measured in MeCN. The electron-transfer rate from $\text{Ru}(\text{bpy})_3^+$, which has a potential of -1.33 V, is measured in H₂O.

rates constants are mostly $>10^{10} \text{ M}^{-1} \text{ s}^{-1}$ and are at or near the diffusion-controlled limit.

M–H complexes

Although both cobalt(I) and nickel(I) macrocycles are stable in dry, degassed MeCN, their lifetimes in water are limited because the M(I) complexes can react with protons to form the corresponding metal hydrides, M(III)–H, as shown in Eq. 10 [14, 18]:



The thermodynamics and kinetics of H⁺ binding to cobalt(I) and nickel(I) macrocycles have been determined. The $\text{p}K_{\text{a}}$ of Ni(cyclam)(H)²⁺, *RRSS*-NiHTIM(H)²⁺ and *N-rac*-CoHMD(H)²⁺ are 1.8, 1.9 and 11.7, respectively [14, 24, 27]. As seen from Table 3, protonation rate constants for *N-rac*-CoHMD⁺ depend on acid strength. The results are consistent with an associative reaction of the square-planar complex with an acid, HA. Whereas the spectrum of *N-rac*-CoHMD(H)²⁺ suggests the formation of a $[\text{Co}^{\text{III}}(\text{H}^-)]^{2+}$ species with an absorption band at 440 nm ($520 \text{ M}^{-1} \text{ cm}^{-1}$), Ni(cyclam)(H)²⁺ shows no significant absorbance in the 300–700 nm region [14, 24].

M–CO₂ complexes

The reversible binding of CO₂ to M^IL⁺ has been studied using differential pulse polarography [30], cyclic voltammetry [19, 31], pulse radiolysis [14, 24], flash photolysis [24, 28] and conventional spectroscopic methods [19, 32]. The results

Table 3. Rate constants for protonation of M(I)L⁺ by acid (HA).

Complex	HA	pK _a of HA	I (M)	k (M ⁻¹ s ⁻¹)	Ref.
<i>N-rac</i> -Co ^I HMD ⁺	H ₃ O ⁺	-1.75	0.015	3.1 × 10 ⁹	26
	HCOOH	3.5	0.02	1.7 × 10 ⁸	14
	MeCOOH	4.5	0.1	1.1 × 10 ⁸	14
	MeCOOH	4.5	0.1	0.75 × 10 ⁸	26
	H ₂ PO ₄ ⁻	6.5	0.1	0.8 × 10 ⁸	14
	H ₂ PO ₄ ⁻	6.5	0.1	0.98 × 10 ⁸	26
	H ₂ PO ₄ ⁻	6.5	0.008	1.2 × 10 ⁸	14
	HCO ₃ ⁻	10.3	0.1	2.5 × 10 ⁶	14
	H ₃ BO ₃	9.3	0.1	0.7 × 10 ⁵	14
<i>N-meso</i> -Co ^I HMD ⁺	HPO ₄ ²⁻	12.25	0.2	1 × 10 ⁵	26
	H ₃ O ⁺	-1.75	0.015	2.3 × 10 ⁹	14
	HCOOH	3.5	0.02	1.8 × 10 ⁸	14
	MeCOOH	4.5	0.1	0.8 × 10 ⁸	14
	H ₂ PO ₄ ⁻	6.5	0.1	1.2 × 10 ⁸	14
Ni ^I (cyclam) ⁺	H ₃ O ⁺	-1.75	0.06–0.3	1.1 × 10 ⁵	23
	H ₃ O ⁺	-1.75	0.006	3 × 10 ⁷	24
	MeCOOH	4.5	0.015–0.3	1.2 × 10 ⁴	23
	H ₂ PO ₄ ⁻	6.5	0.01–0.1	<10 ⁴	23

are summarized in Table 4. The CO₂ binding constants of *N-meso*- and *N-rac*-Co^IHMD⁺ are different in both H₂O and MeCN.



The CO₂ binding constant for the *N-rac* isomer is about 100 times greater than that for the *N-meso* isomer in both solvents. The difference is primarily due to steric interactions between the bound CO₂ and the macrocycle. While hydrogen bonding between the bound CO₂ and amine protons of the macrocycle stabilizes both adducts, the *N-meso* adduct is destabilized by steric repulsion between the macrocycle methyl groups and the CO₂ molecule. The equilibrium constants for the formation of CoHMD(CO₂)⁺ and Ni(cyclam)(CO₂)⁺ are ~10⁴ and 4 times larger in water than in MeCN, respectively. Water may stabilize the CoHMD(CO₂) complex by forming hydrogen bonds to the bound CO₂ as found in crystals of [Ru(bpy)₂(CO)(COO)] · 3H₂O [33]. However, both CoHMD(CO₂)⁺ and Ni(cyclam)(CO₂)⁺ have shorter lifetimes in water than in MeCN owing to subsequent reactions.

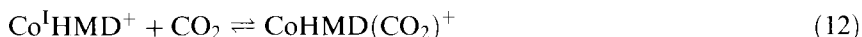
A redox potential threshold for CO₂ binding to the cobalt macrocycles seems to occur at ~-1.2 V vs. SCE [19]. The CO₂ binding constants for a series of Co(I) macrocycles show a strong correlation with the Co^{II/I} potential. This trend is consistent with charge transfer from the electron-rich cobalt center to the bound CO₂. The CO₂ binding rate constants in MeCN–MeOH seem also to correlate with the Co^{II/I} potential in MeCN: 1.1 × 10⁶ M⁻¹ s⁻¹ for Co^IOMD⁺, 1.7 × 10⁸ M⁻¹ s⁻¹ for Co^IHMD⁺ and 3.7 × 10⁸ M⁻¹ s⁻¹ for Co^IDMD⁺.

Table 4. Equilibrium and rate constants for the reaction of ML^+ with CO_2 in various solvents^a.

Complex	Solvent	$E_{1/2}$ (V)	K_{CO_2} (M^{-1})	k_f ($\text{M}^{-1} \text{s}^{-1}$)	k_r (s^{-1})	Ref.
$\text{Co}^{\text{I}}\text{HMD}^+$	DMSO	-1.29^b	7×10^4			30
<i>N-rac</i> - $\text{Co}^{\text{I}}\text{HMD}^+$	DMSO	-1.74^c	3.0×10^4			31
	PC	-1.54^c	4.0×10^4			31
	DMF	-1.77^c	1.8×10^4			31
	THF	-1.77^c	3.0×10^3			31
	H_2O	irr.	2.5×10^8	1.7×10^8	(0.38)	14
	MeCN^d	-1.34^b	1.2×10^4	1.8×10^8	(1.5×10^4)	19, 32
	MeCN	-1.34^b	1.4×10^4	1.8×10^8	(1.3×10^4)	28
	MeCN-MeOH		1.1×10^4	1.7×10^8	3×10^4	28
<i>N-meso</i> - $\text{Co}^{\text{I}}\text{HMD}^+$	DMSO	-1.74^c	260			31
	MeCN	-1.34^b	170			19
	H_2O	irr.	6.0×10^6	1.5×10^7	2.7	14
$\text{Co}^{\text{I}}\text{OMD}^+$	MeCN-MeOH		6	1.1×10^6	1.8×10^5	28
	MeCN	-1.28^b	4			34
$\text{Co}^{\text{I}}\text{DMD}^+$	MeCN-MeOH		$>5 \times 10^4$	3.7×10^8	$(<7 \times 10^8)$	28
	MeCN	-1.51^b	7×10^5			34
$\text{Ni}^{\text{I}}(\text{cyclam})^+$	MeCN	-1.44^b	4			12, 18
	H_2O	-1.52^b	16	(3.2×10^7)	2.0×10^6	24
<i>RRSS</i> - $\text{Ni}^{\text{I}}\text{HTIM}^+$	MeCN	-1.43^b	4			12, 18

^a Numbers in parentheses are calculated values.^b Measured vs. SCE.^c Measured vs. ferricenium/ferrocene.^d K_{CO_2} is assumed to be the same as K_{I_2} in Eq. 12.

Although the *N-rac*- $\text{CoHMD}(\text{CO}_2)^+$ adduct decomposes to *N-rac*- CoHMD^{2+} and CO in wet MeCN, it is stable in dry MeCN under a CO_2 atmosphere. The complex is thermochromic, being purple at room temperature and yellow at low temperature [34]. The 530 nm band diminishes in intensity and a 430 nm band increases in intensity as the temperature drops. Measurements over the range -40 to $+40^\circ\text{C}$ give $K_{13}(298) = 0.11 \pm 0.13$, $\Delta G^\circ(298) \approx 1.3 \text{ kcal mol}^{-1}$, $\Delta H^\circ = -7.0 \text{ kcal mol}^{-1}$ and $\Delta S^\circ = -28 \text{ cal K}^{-1} \text{ mol}^{-1}$ for Eq. (13) in MeCN.



A solid sample, obtained at -70°C from a THF–MeCN mixture, shows $\nu_{\text{C=O}} = 1558 \text{ cm}^{-1}$, $\nu_{\text{C=N}} = 1653 \text{ cm}^{-1}$ and two $\nu_{\text{C=N}}$, 2337 cm^{-1} (for coordinated MeCN) and 2272 cm^{-1} (for free MeCN), consistent with the formation of $[\text{S-CoHMD}(\text{CO}_2)]^+$ with $\text{S} = \text{MeCN}$. Increasing pressure also causes the color to change. An MeCN solution contains $\sim 80\%$ five-coordinate $[\text{CoHMD}(\text{CO}_2)]^+$ and $\sim 20\%$ six-coordinate $[\text{CoHMD}(\text{CO}_2)(\text{MeCN})]^+$ under atmospheric pressure at 15°C . Increasing pressure shifts the equilibrium toward the six-coordinate species

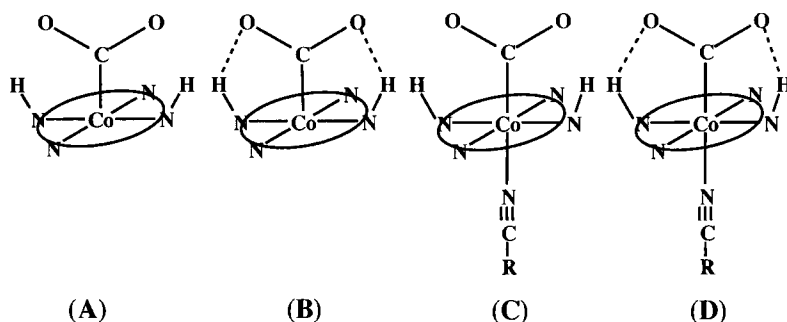


Figure 3. Structures of the CoHMD(CO₂)⁺ species observed by FTIR.

with an overall reaction volume $\Delta V^\circ = -17.7 \text{ mL mol}^{-1}$ [35]. Furthermore, the FTIR spectra measured over the range 25 to -75°C in a CD₃CN–THF mixture indicate the existence of four CO₂ adducts: a five-coordinate, non-hydrogen-bonded form **A** ($\nu_{\text{C=O}} = 1710 \text{ cm}^{-1}$, $\nu_{\text{NH}} = 3208 \text{ cm}^{-1}$), a five-coordinate intramolecular hydrogen-bonded form **B** ($\nu_{\text{C=O}} = 1626 \text{ cm}^{-1}$), a six-coordinate non-hydrogen-bonded form **C** ($\nu_{\text{C=O}} = 1609 \text{ cm}^{-1}$, $\nu_{\text{NH}} = 3224 \text{ cm}^{-1}$) and a six-coordinate intramolecular hydrogen-bonded form **D** ($\nu_{\text{C=O}} = 1544 \text{ cm}^{-1}$, $\nu_{\text{NH}} = 3145 \text{ cm}^{-1}$) (see Figure 3). The two five-coordinate (**A** and **B**) and two six-coordinate (**C** and **D**) species have similar UV–vis spectra, so only two species are observed by UV–vis spectroscopy.

The thermochromic behavior of the CO₂ adducts has been studied by X-ray absorption spectroscopy [20]. The metal coordination number, geometry and electronic properties can be studied using X-ray absorption near-edge spectroscopy (XANES) and metal–ligand bond distances can be obtained through analysis of the extended X-ray absorption fine structure (EXAFS). XANES spectra for a series of the CoHMD complexes are shown in Figure 4. The X-ray absorption edge position of the CoHMD complex is sensitive to the oxidation state of the cobalt. The edge energy of Co^{II}HMD²⁺ decreases (1 eV) upon reduction and increases (2 eV) upon oxidation, as can be seen in Figure 4a. The $1s \rightarrow 4p_z$ pre-edge peak, located $\sim 6 \text{ eV}$ below the main edge, in the XANES spectrum for Co^{II}HMD²⁺ is characteristic of a four-coordinate square-planar geometry. The XANES spectrum of the CO₂ adducts at room temperature and 150 K are shown in Figure 4b. At room temperature the Co–CO₂ adduct is 90 % five-coordinate CoHMD(CO₂)⁺ and 10 % six-coordinate S–CoHMD(CO₂)⁺, whereas cooling the solution to 150 K results in 100 % conversion to the six-coordinate species [19]. The edge position of CoHMD(CO₂)⁺ at room temperature is similar to that of Co^{II}HMD²⁺, consistent with theoretical predictions [36, 37] that the bound CO₂ receives significant electron density (~ 0.7 of an electron) mainly from the Co d_{z^2} orbital. The XANES spectrum for S–CoHMD(CO₂)⁺ at 150 K shows an increase of the $1s \rightarrow 3d$ peak ($\sim 11 \text{ eV}$ below the main edge) and almost complete loss of the $1s \rightarrow 4p_z$ transitions, indicative of six-coordinate distorted octahedral geometry. The six-coordinate S–CoHMD(CO₂)⁺ species shows a 1.2 eV shift towards Co(III) and is interpreted

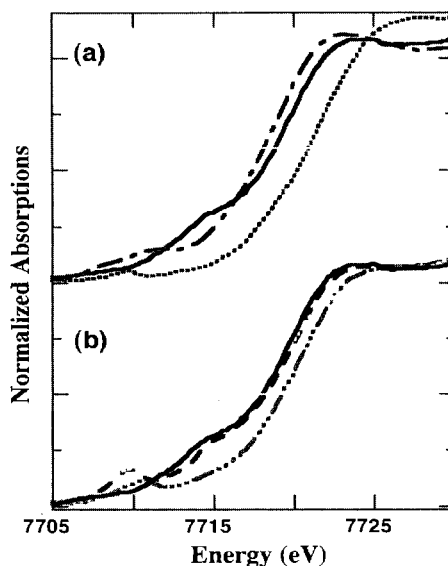


Figure 4. XANES for CoHMD complexes. (a) $[\text{Co}^{\text{II}}\text{HMD}](\text{ClO}_4)_2$ in acetonitrile at 150 K (—), $[\text{Co}^{\text{III}}\text{HMD}(\text{CO}_3^{2-})]\text{ClO}_4$ in H_2O at room temperature (\cdots) and $[\text{Co}^{\text{I}}\text{HMD}(\text{CO})]\text{ClO}_4$ in acetonitrile at room temperature (---). (b) $[\text{Co}^{\text{II}}\text{HMD}](\text{ClO}_4)_2$ in acetonitrile at 150 K (—), five-coordinate $[\text{CoHMD}(\text{CO}_2)]\text{ClO}_4$ in acetonitrile at room temperature (---) and six-coordinate $[\text{S-CoHMD}(\text{CO}_2)]\text{ClO}_4$ in acetonitrile at 150 K ($\cdots\cdots$).

as a $\text{Co}^{\text{III}}\text{-CO}_2^{2-}$ carboxylate complex. This assignment is consistent with the change of the CO_2 asymmetric stretch, $\nu_{\text{C=O}}$, from 1710 cm^{-1} for $\text{CoHMD}(\text{CO}_2)^+$ to 1544 cm^{-1} for $\text{S-CoHMD}(\text{CO}_2^{2-})^+$ discussed above. Although the cobalt(III) carboxylates have been postulated as intermediates in CO_2 reduction and water-gas shift reactions, the XANES results provide the first unambiguous evidence that active metal catalysts, such as $\text{Co}^{\text{I}}\text{HMD}^+$, can promote two-electron transfer to the bound CO_2 . The conversion of the $\text{M}^{\text{I}}\text{CO}_2$ species to a metallo-carboxylate, $\text{M}^{\text{III}}(\text{CO}_2^{2-})$, is an important step in catalytic CO_2 reduction since it avoids the very high-energy CO_2^- species.

3.2.3 Electrocatalytic Systems

$\text{Ni}(\text{cyclam})^{2+}$ is a very effective and selective catalyst for the electrochemical reduction of CO_2 [10, 11]. The advantages of the catalyst are high turnover frequencies (up to $10^3\text{ cycles h}^{-1}$), accessibility of the applied potential, high efficiency, good selectivity of CO formation at pH 4 and stability of the catalyst after a large number of turnovers ($>10^4$). $\text{Ni}(\text{cyclam})^+$ adsorbs on the surface of the mercury electrode and the adsorbed complex is the active catalyst. $\text{Ni}(\text{cyclam})^{2+}$ has configurational isomers in solution; the most stable two forms (*trans III*, 85 % and *trans I*, 14 % in water) are shown in Figure 2. It is possible to lock the cyclam ligand in one configuration (*trans III*) by adding methyl groups to the six-membered ring as in HTIM. The catalytic activities of pure stereoisomers, *RRSS*- and *RSSR*- NiHTIM^{2+} , have been studied [12]. These isomers do not show any isomerization in solution. *RRSS*- NiHTIM^{2+} , which has no axial methyl groups, shows much higher catalytic activity than *RSSR*- NiHTIM^{2+} . *RRSS*- NiHTIM^{2+} has larger cat-

alytic currents and more positive potentials for CO₂ reduction than Ni(cyclam)²⁺. The peak current density of the *RSSR*-NiHTIM²⁺, which has axial methyl groups, is lower than that of Ni(cyclam)²⁺ [12]. Thus structural differences may play an important role in adsorption of the metal complex on a mercury electrode and in CO₂ binding by the absorbed complex.

CoHMD²⁺ homogeneously catalyzes electroreduction of CO₂. However, it also catalyzes water reduction in water, water–acetonitrile and DMF solutions [8, 9]. The CO-to-H₂ ratio depends strongly on the experimental conditions used (i.e., applied potential, amount of water, electrolysis time, etc.) and is typically less than 1. Since the *pK_a* of CoHMD(H)²⁺ is 11.7, the hydride species also forms in CO₂-saturated water (pH ≈ 4) [8, 9] and is believed to be an intermediate in H₂ production.

3.2.4 Photocatalytic Systems

Systems with Ru(bpy)₃²⁺/Ni(cyclam)²⁺

CO₂ can be reduced using photogenerated reductants as shown in Figure 1. Photochemical CO₂ reduction has been reported in a catalytic system using Ru(bpy)₃²⁺ as the sensitizer, Ni(cyclam)²⁺ as the electron relay catalysts and ascorbate as a sacrificial reductive quencher (Table 5) [15, 16]. The quantum yield for CO production is ~10⁻⁴ at pH 4 with low selectivity for CO formation due to coproduction of H₂. The yields of both CO and H₂ are pH dependent. Without Ni(cyclam)²⁺, a system containing Ru(bpy)₃²⁺ and TEOA produces HCOO⁻ with a quantum yield of ~5 %, but no CO [38, 39]. In order to improve the CO yield, complexes that covalently link the sensitizer to the catalysts have been prepared. Complexes in which Ru(bpy)₃²⁺ or Ru(phen)₃²⁺ are bound to Ni(cyclam)²⁺ have been studied [40–43]. However, these supramolecular photochemical systems have low yields of CO due to competing processes in the quenching of the photoexcited complexes [40, 43]. Several pyridine derivatives of Ni(cyclam)²⁺, Ni(Pr-cyclam)²⁺, were prepared and used as catalysts together with Ru(bpy)₃²⁺. These systems produced up to five times more CO than the systems with underivatized Ni(cyclam)²⁺ [42].

Bismacrocylic nickel complexes, [Ni₂(bcyclam)]⁴⁺ and [Ni₂(bMe₂cyclam)]⁴⁺, have been prepared and tested as CO₂ reduction catalysts. The ligands bcyclam and bMe₂cyclam have two connected cyclam or dimethylcyclam units, respectively, as shown in Figure 2. While [Ni₂(bMe₂cyclam)]⁴⁺ shows good selectivity and a high yield for CO formation, [Ni₂(bcyclam)]⁴⁺ and the corresponding monomeric nickel complexes (Ni(cyclam)²⁺ and Ni(Me₂cyclam)²⁺) do not [44]. The authors attribute this to the configuration of the methyl groups, which occupy the axial positions of the six-membered chelate rings. However, why axial methyl groups increase the catalytic activity is not clear, since axial methyl groups normally hinder CO₂ binding.

Systems with *p*-terphenyl/CoL²⁺

Oligo(*p*-phenylene)s ranging from *p*-terphenyl (TP) to *p*-sexiphenyl sensitize the photoreduction of CO₂ to formic acid (Figure 5). The systems use triethylamine as a

Table 5. Photochemical CO₂ reduction with metal macrocycles.

Sensitizer	Catalyst or relay	Donor	Product(s)	CO/H ₂	Φ^a (mol einstein ⁻¹)	Ref.
Ru(bpy) ₃ ²⁺		TEOA	HCOO ⁻		0.049 ^b	38, 39
Ru(bpy) ₃ ²⁺		TEOA	HCOO ⁻		0.096 ^c	39
Ru(bpy) ₃ ²⁺	CoHMD ²⁺	H ₂ A	CO, H ₂			9
Ru(bpy) ₃ ²⁺	Ni(cyclam) ²⁺	H ₂ A	CO, H ₂	0.16	0.001 (CO)	15, 16
Ru(bpy) ₃ ²⁺	Ni(cyclam) ²⁺	H ₂ A	CO, H ₂	0.12		45
Ru(bpy) ₃ ²⁺	Ni(cyclam) ²⁺	H ₂ A	CO, H ₂	0.4		44
Ru(bpy) ₃ ²⁺	Ni(cyclam) ²⁺	H ₂ A	CO, H ₂	0.02–0.07		42
Ru(bpy) ₃ ²⁺	Ni(Pr-cyclam) ²⁺	H ₂ A	CO, H ₂	0.10–0.65	~0.005 ^d (CO)	42
Ru(bpy) ₃ ²⁺	[Ni ₂ (bcyclam)] ⁴⁺	H ₂ A	CO, H ₂		~0.0006 ^d (CO)	44
Ru(bpy) ₃ ²⁺	[Ni ₂ (bMe ₂ cyclam)] ⁴⁺	H ₂ A	CO, H ₂	15	~0.008 ^d (CO)	44
TP	Co(cyclam) ³⁺	TEOA	CO, HCOO ⁻ , H ₂	6	0.075 (HCOO ⁻) 0.05 (CO)	17, 46
TP	CoHMD ²⁺	TEOA	CO, HCOO ⁻ , H ₂	1.4		17
Phenazine	Co(cyclam) ³⁺	TEOA	HCOO ⁻		0.035	47

^a Unless noted, otherwise the quantum yield of product formation is defined as the formation rate divided by the light intensity.^b With 15 % water in DMF.^c With 15 % water and excess bpy in DMF.^d Assuming Φ for Ni(cyclam)²⁺ is 0.001.

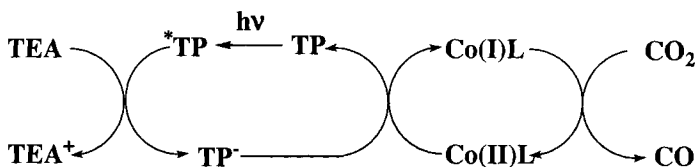
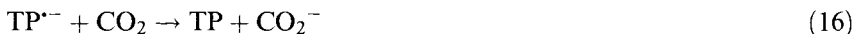


Figure 5. Schematic reaction mechanism for photochemical CO₂ reduction using TP and ML.

sacrificial electron donor in aprotic polar solvents such as DMF and MeCN [48, 49]. The photoreduction of CO₂ proceeds via electron transfer from the photo-generated anion radical of the *p*-phenylene directly to the CO₂ molecule. In the case of TP, the quantum yield of HCO₂⁻ formation is 3.6 % at 313 nm. Unfortunately, a photo-Birch reduction of the TP producing dihydroterphenyl derivatives occurs in parallel with the photoreduction process and photoactivity is quickly lost. The photodegradation is suppressed when metal macrocycles are added as electron mediators between the reduced terphenyl anion radical and the CO₂. Thus cobalt macrocycles mediate the photoreduction of CO₂ with TP and a tertiary amine (including the β -hydroxylated tertiary amine) as sacrificial electron donor in acetonitrile/methanol mixtures [17]. The system produces CO and formate efficiently with only small amounts of H₂. The combined quantum yield of CO and formate is 13 % at 313 nm in the presence of triethanolamine and Co(cyclam)³⁺.

Mechanistic and kinetic studies of the TEA–TP–CoHMD²⁺–CO₂ system have been undertaken [28] using flash photolysis techniques. In the absence of added CoHMD²⁺ and CO₂, the TP^{•-} spectrum was obtained in MeCN–MeOH, consistent with the reported rate constant for Eq. (14) of $3 \times 10^9 \text{ M}^{-1} \text{ s}^{-1}$ in THF [49]; decay of TP^{•-} in MeCN–MeOH solution follows first-order kinetics with a rate constant of 400 s^{-1} .



The transient absorption spectrum of a sample with added Co^{II}HMD²⁺ indicates the formation of the reduced cobalt complex, Co^IHMD⁺ (Eq. 15) [32, 34, 50]. The cobalt(I) complex is fairly stable with a lifetime of $>1 \text{ s}$ under the experimental conditions (Figure 6, bottom). The decay of the TP^{•-} absorption and the growth of the Co^IHMD⁺ absorption are shown in Figure 6, top left and right, respectively. The observed rates for the decay of TP^{•-} and growth of Co^IHMD⁺ are the same. The magnitudes of the changes in absorbance at 470 and 685 nm establish that the stoichiometry of the formation of Co(I) from TP^{•-} is $1:1 \pm 0.2$. A plot of the observed first-order rate constant (k_{obsd}) for the decay of TP^{•-} is linear in

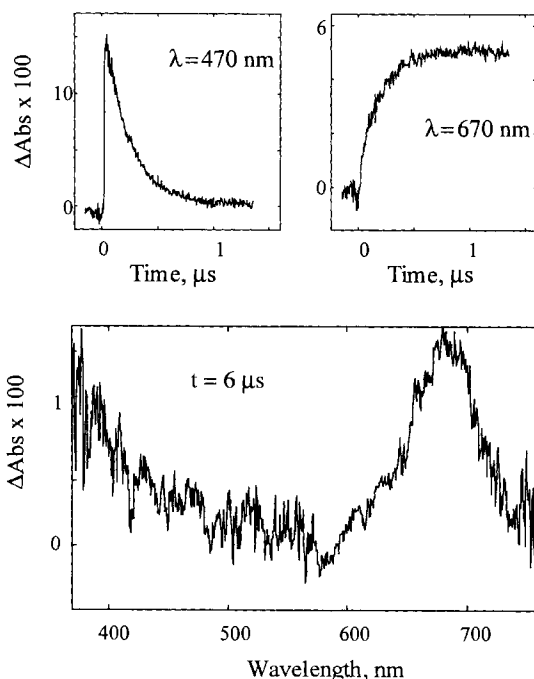


Figure 6. Top left: decay of $\text{TP}^{\bullet-}$ monitored at 470 nm. Top right: growth of $\text{Co}^{\text{I}}\text{HMD}^+$ monitored at 670 nm. Bottom: transient absorption spectrum of $\text{Co}^{\text{I}}\text{HMD}^+$ observed 6 μs after the excitation for a degassed sample containing 0.1 mM TP, 0.5 M TEA, 0.1 M TEAP and 1 mM $\text{Co}^{\text{II}}\text{HMD}^{2+}$ in MeCN–MeOH.

$[\text{Co}^{\text{II}}\text{HMD}^{2+}]$ and gives a second-order rate constant close to diffusion controlled as expected due to the reaction's large driving force (~ 1.1 V).

The dependence of the decay rate of $\text{TP}^{\bullet-}$ on $[\text{CO}_2]$, measured for solutions containing CO_2 with no cobalt macrocycle is not linear in CO_2 concentration [28]. A rate constant of $<10^6 \text{ M}^{-1} \text{ s}^{-1}$ is estimated for the $\text{TP}^{\bullet-}$ – CO_2 reaction. This sluggish rate constant is consistent with the large reorganization of the $\text{CO}_2/\text{CO}_2^-$ couple and modest driving force for the reaction (0.5 V). Under photocatalytic conditions (continuous photolysis) the $\text{TP}^{\bullet-}$ reacts much faster with the cobalt complex than with CO_2 and $>90\%$ the photochemically generated reducing equivalents are captured by the cobalt macrocycle.

When CO_2 is introduced into the photosystem, the lifetime of the $\text{Co}^{\text{I}}\text{HMD}^+$ changes dramatically [28]. The decay of $\text{Co}^{\text{I}}\text{HMD}^+$ is shown in Figure 7 (at 670 nm) and has a rate constant for CO_2 binding (Eq. 12) of $6.5 \times 10^4 \text{ s}^{-1}$. The observed rate constant for $\text{Co}^{\text{I}}\text{HMD}^+$ decay is linearly dependent on CO_2 concentration. The CO_2 binding rate constant (forward reaction in Eq. 12) is $1.7 \times 10^8 \text{ M}^{-1} \text{ s}^{-1}$. The decay of the $\text{Co}^{\text{I}}\text{HMD}^+$ under a CO_2 atmosphere results in a finite absorbance at long times (Figure 7). In addition, the transient spectra measured at 50, 25, 0 and -25°C indicate a mixture of the five- and six-coordinate CO_2 adducts, $\text{CoHMD}(\text{CO}_2)^+$ and $\text{S-CoHMD}(\text{CO}_2)^+$ (Eq. 13). Since the CO_2 adducts have no significant absorption at 670 nm (while $\text{Co}^{\text{I}}\text{HMD}^+$ does), the ratio of the

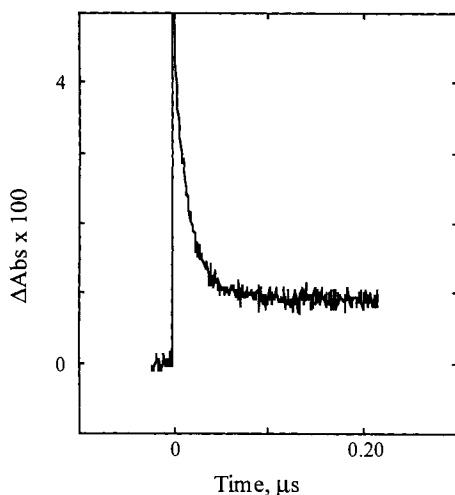


Figure 7. Transient decay curve of $\text{Co}^{\text{I}}\text{HMD}^+$ monitored at 670 nm for a sample containing 0.1 mM TP, 0.5 M TEA, 0.1 M TEAP, 1 mM $\text{Co}^{\text{II}}\text{HMD}^{2+}$ and 0.53 mM CO_2 in MeCN–MeOH.

total amount of cobalt– CO_2 complex, $[\text{Co}(\text{CO}_2)]_t$, to the unreacted complex, $[\text{CoHMD}^+]$, is given by the ratio of the change in the absorbance at 670 nm, $A_0 - A_\infty$, to the final absorbance at 670 nm (Figure 7). One can define an effective equilibrium constant

$$\begin{aligned} K_{\text{CO}_2} &= \frac{[\text{Co}(\text{CO}_2)]_t}{[\text{Co}^{\text{I}}\text{HMD}^+][\text{CO}_2]} \\ &= \frac{A_0 - A_\infty}{A_\infty [\text{CO}_2]} \end{aligned} \quad (17)$$

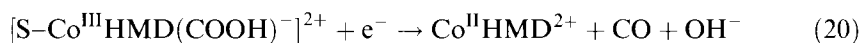
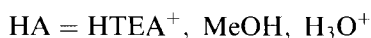
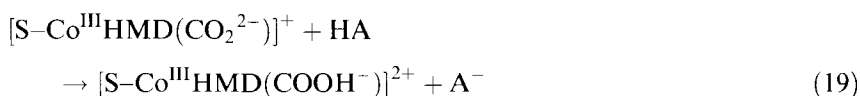
where $[\text{Co}(\text{CO}_2)]_t = [\text{CoHMD}(\text{CO}_2)^+] + [\text{S-CoHMD}(\text{CO}_2)^+]$ and A_∞ and A_0 are the absorbances at 670 nm at long times and at $t = 0$, respectively. The above assumes that the $\text{Co}^{\text{I}}\text{HMD}^+$ is rapidly formed, both $\text{Co}^{\text{I}}\text{HMD}^+$ and the CO_2 adduct are stable on the transient absorption time-scale, and only $\text{Co}^{\text{I}}\text{HMD}^+$ absorbs. When the CO_2 concentration is lowered, $A_0 - A_\infty$ is reduced and A_∞ increases. K_{CO_2} is calculated from Eq. 17 as $1.1 \times 10^4 \text{ M}^{-1}$ as shown in Table 4.

The equilibrium constant K_{CO_2} is also given by

$$K_{\text{CO}_2} = K_{12}(1 + K_{13}[\text{S}]) \quad (18)$$

where K_{12} and K_{13} are the equilibrium constants for Eqs. 12 and 13, respectively. Equilibrium studies in MeCN indicate that K_{12} and $K_{13}[\text{S}]$ are $1.2 \times 10^4 \text{ M}^{-1}$ and 0.17, respectively, for $\text{Co}^{\text{I}}\text{HMD}^+$ at 25 °C [19, 32, 34], yielding a value of $1.4 \times 10^4 \text{ M}^{-1}$ for K_{CO_2} . CO_2 binding rate constants determined by transient absorbance in MeCN–MeOH, by cyclic voltammetry in pure MeCN, and by pulse radiolysis in H_2O are all about $1.7 \times 10^8 \text{ M}^{-1} \text{ s}^{-1}$. The CO_2 binding constant obtained by transient methods is in good agreement with the value obtained from equilibrium methods [28]. These results also indicate that the CO formation proceeds via the

initial formation of a five-coordinate $\text{Co}^{\text{I}}\text{HMD}(\text{CO}_2)^+$ complex that quickly forms an equilibrium mixture with the six-coordinate complex, $[\text{S}-\text{Co}^{\text{III}}\text{HMD}(\text{CO}_2^{2-})]^+$. The production of CO in the photolysis solution probably proceeds by the subsequent reactions of $[\text{S}-\text{Co}^{\text{III}}\text{HMD}(\text{CO}_2^{2-})]^+$ shown in Eqs. 19 and 20:



The rate-determining step in the continuous photolysis system must be subsequent to the formation of the $\text{S}-\text{CoHMD}(\text{CO}_2)^+$ and is likely to be the C–O bond breakage in the bound carboxylic acid in Eq. 20. Recent developments in transient FTIR spectroscopy may allow the study of the reactions $\text{S}-\text{CoHMD}(\text{CO}_2)^+$ in the photocatalytic system.

Studies of catalytic systems with other cobalt macrocycles highlight some of the factors controlling the kinetics of the photoreduction of CO_2 [28]. Photogenerated $\text{Co}^{\text{I}}\text{DMD}^+$ (lifetime 16 μs) is unstable whereas $\text{Co}^{\text{I}}\text{OMD}^+$ is very stable (lifetime 6 h) in MeCN solution. The CO_2 binding constants (K_{CO_2}) are 6 and $>5 \times 10^4 \text{ M}^{-1}$ for $\text{Co}^{\text{I}}\text{OMD}^+$ and $\text{Co}^{\text{I}}\text{DMD}^+$, respectively, at room temperature. While the DMD complex with no axial methyl groups prefers the six-coordinate CO_2 adduct, formation of the six-coordinate $\text{S}-\text{CoOMD}(\text{CO}_2)^+$ is unfavorable owing to the steric hindrance of the four axial methyl groups. The $\text{Co}^{\text{II/I}}$ redox potentials, the CO_2 binding constants and the lifetimes show a strong correlation: $\text{Co}^{\text{I}}\text{OMD}^+$ (−1.28 V, 6 M^{-1} , 6 h), $\text{Co}^{\text{I}}\text{HMD}^+$ (−1.34 V, $1.2 \times 10^4 \text{ M}^{-1}$, ~2 s) and $\text{Co}^{\text{I}}\text{DMD}^+$ (−1.51 V, $>5 \times 10^4 \text{ M}^{-1}$, 16 μs).

Systems with phenazine/ CoL^{3+}

Recently photoreduction of CO_2 to HCOO^- (together with small amounts of CO and H_2) has been achieved by UV irradiation (313 nm) of a system involving phenazine as a photosensitizer, $\text{Co}(\text{cyclam})^{3+}$ as an electron mediator and TEA as an electron donor [47]. The quantum yield for the formation of HCOO^- is 0.035. Electron transfer from the photogenerated radical anion ($\text{Phena}^{\bullet-}$) to $\text{Co}(\text{cyclam})^{3+}$ ($k = 4.3 \times 10^9 \text{ M}^{-1} \text{ s}^{-1}$) results in the formation of $\text{Co}(\text{cyclam})^{2+}$. Since the reduction potential of $\text{Co}(\text{cyclam})^{2+/+}$ is ~−1.9 V vs. SCE in MeCN, $\text{Phena}^{\bullet-}$ (−1.18 V vs. SCE for a $\text{Phena}/\text{Phena}^{\bullet-}$ couple), unlike $\text{TP}^{\bullet-}$, is hardly capable of reducing $\text{Co}(\text{II})$ to $\text{Co}(\text{I})$. The authors suggest that PhenaH^{\bullet} , produced by the protonation to $\text{Phen}^{\bullet-}$, may transfer a hydrogen atom to $\text{Co}(\text{cyclam})^{2+}$ to form $\text{Co}(\text{cyclam})(\text{H})^{2+}$ and insertion of CO_2 into the hydride produces HCOO^- via the Co^{III} –formate complex. Although the results appear to support the proposed mechanism, the hydrogen-atom transfer step and the CO_2 insertion step have not been investigated in detail.

3.3 Re(α -diimine)(CO)₃X, Re(α -diimine)(CO)₂XX' and Similar Complexes

3.3.1 Overview of CO₂ Reduction System Mediated Rhenium Complexes

Complexes of the general formula *fac*-Re(α -diimine)(CO)₃X and Re(α -diimine)(CO)₂XX' (where α -diimine = bpy, phen, substituted bpy or phen, etc. and X, X' = halide, solvent, alkyl, benzyl, monodentate phosphine, CO, etc.), have attracted interest since the mid-1970s [51–53]. Many of these complexes show emission from their lowest long-lived MLCT state at room temperature in solution. Their catalytic properties for CO₂ reduction have also been investigated. Electrolysis of a solution containing *fac*-Re(bpy)(CO)₃Cl and 0.1 M Bu₄NPF₆ in freshly distilled CO₂-saturated MeCN at –1.5 V (vs. SCE) produces both CO and CO₃^{2–} with current efficiencies of 98 and 110 %, respectively [54]. Further, *fac*-Re(bpy)(CO)₃X (X = Cl[–], Br[–]) has been used successfully as a photocatalyst for CO₂ reduction to CO with TEOA in DMF [55–58]. When X = Cl[–], a quantum yield of 0.14 has been measured in the presence of excess Cl[–]. A formate–rhenium complex, *fac*-Re(bpy)(CO)₃(O₂CH), has been isolated in the absence of excess Cl[–].

Among rhenium catalysts for the photochemical reduction of CO₂, *fac*-Re(bpy)(CO)₃{P(OEt)₃}⁺ is the best catalyst and irradiation of DMF solutions containing CO₂ and TEOA yields CO with a quantum yield of 0.38 [59]. However, the formate complex *fac*-Re(bpy)(CO)₃(O₂CH) is also produced upon irradiation of Re(bpy)(CO)₃(PR₃)⁺ (R = O-*i*-Pr, OEt and Ph) in yields of 24, 73 and 55 %, respectively, based on *fac*-Re(bpy)(CO)₃(PR₃)⁺. It is generally believed that the formate complex is produced by CO₂ insertion into an Re–H bond and leads to the production of free formate. However, neither electrochemical nor photochemical CO₂ reduction using *fac*-Re(bpy)(CO)₃X produces any significant amount of free formate. Despite the great interest in CO₂ utilization, the mechanism of CO formation with *fac*-Re(bpy)(CO)₃X remains unclear. Below we discuss the possible involvement of intermediates such as Re–COO, Re–COOH, Re–CHO, Re–H, Re–CO, Re–O₂COH, Re–CH₂OH, etc. Some properties of the Re(α -diimine)(CO)₃X and Re(α -diimine)(CO)₂XX' complexes are summarized in Tables 6–8.

3.3.2 Properties of Re(α -diimine)(CO)₃X and Re(α -diimine)(CO)₂XX'

Redox properties

The complexes can be both oxidized and reduced; reduction potentials for many of the complexes are shown in Table 6. Cyclic voltammograms of Re(α -diimine)(CO)₃X show that in most cases the first oxidation is chemically irreversible at scan rates of 0.1–0.2 V s^{–1}; however, at much faster sweep rates (>100 V s^{–1}) a reversible wave is observed at 1.32 V (vs. SCE) in MeCN for Re(bpy)(CO)₃Cl [60]. The first oxidation is metal based and is followed by the rapid loss of carbon monoxide due to the weakening of the Re π -backbonding

Table 6. Redox properties of [Re(α -diimine)(CO)₃X]ⁿ⁺ and [Re(α -diimine)(CO)₂XX']ⁿ⁺ vs. SCE at room temperature.

Complex	Solvent		<i>E</i> _{1/2} (V)	Ref.
[Re(bpy)(CO) ₃ Br]	THF		−1.91 ^{a,b} , −2.33 ^{a,b}	62
[Re(bpy)(CO) ₃ Cl]	THF		−1.91 ^{a,b} , −2.38 ^{a,b}	62, 63
[Re(bpy)(CO) ₃ Cl]	THF–MeCN		−1.76 ^b , −2.21 ^{a,b}	61
[Re(bpy)(CO) ₃ Cl]	THF		−1.91 ^{a,b}	62
[Re(bpy)(CO) ₃ Cl]	MeCN	1.32 ^c ,	−1.35 ^c	54, 64
[Re(bpy)(CO) ₃ Cl]	MeCN or DMF	1.36,	−1.32	65
[Re(bpy)(CO) ₃ I]	THF		−1.91 ^{a,b} , −2.27 ^{a,b}	62
[Re(bpy)(CO) ₃ (H)]	MeCN	0.90,		66
[Re(bpy)(CO) ₃ (H)]	CH ₂ Cl ₂		−1.46	66
[Re(bpy)(CO) ₃ (O ₂ CH)]	MeCN	1.37,	−1.29, −1.71	66
[Re(bpy)(CO) ₃ (O ₂ CH)]	MeCN		−1.81 ^b , −2.33 ^{a,b}	61
[Re(bpy)(CO) ₃ (Otf)]	THF		−1.54 ^{a,b}	62
[Re(bpy)(CO) ₃ (P(OEt) ₃)] ⁺	MeCN	1.6 ^{d,e} ,	−1.59 ^d , −2.1 ^{a,d}	67
[Re(bpy)(CO) ₃ (P(OEt) ₃)] ⁺	MeCN		−1.63 ^b , −2.40 ^{a,b}	61
[Re(bpy)(CO) ₃ (PPh ₃)] ⁺	MeCN	1.6 ^{d,e} ,	−1.55 ^d , −1.98 ^{a,d}	67
[Re(bpy)(CO) ₃ (PPh ₃)] ⁺	THF		−1.62 ^{a,b} , −2.10 ^{a,b}	62
[Re(bpy)(CO) ₃ (PPh ₃)] ⁺	THF–MeCN		−1.58 ^b , −2.10 ^{a,b}	61
[Re(bpy)(CO) ₃ (MeCN)] ⁺	THF–MeCN		−1.58 ^b , −1.80 ^{a,b}	61
[Re(bpy)(CO) ₃ (MeCN)] ⁺	MeCN		−1.2	68
[Re(bpy)(CO) ₃ (PrCN)] ⁺	PrCN		−1.62 ^{a,b} , −1.97 ^{a,b}	63
[Re(bpy)(CO) ₃ (THF)] ⁺	THF		−1.73 ^{a,b} , −2.23 ^{a,b}	62
[Re(bpy)(CO) ₂ (P(OEt) ₃) ₂] ⁺	MeCN		−1.69 ^d , −2.45 ^{a,d}	69
[Re(bpy)(CO) ₂ (P(OEt) ₃) ₂] ⁺	MeCN		−1.79 ^b , −2.82 ^{a,b}	61
[Re(bpy)(CO) ₃] ₂	THF	−0.29 ^{b,e} ,	−0.6 ^{b,e} , −2.08 ^{a,b}	62
[Re(dmb)(CO) ₃ Cl]	MeCN	1.39 ^c ,	−1.43 ^c , −1.96 ^{a,c}	60
[Re(dmb)(CO) ₃ Cl]	MeCN or DMF		−1.32	65
[Re(dmb)(CO) ₃ Cl]	MeCN	1.3,	~−1.5, ~−1.8	70
[Re(phen)(CO) ₃ Cl]	MeCN or DMF	1.36,	−1.27	65
[Re(phen)(CO) ₃ Cl]	MeCN	1.33,	−1.34	71
[Re(phen)(CO) ₃ (P(OEt) ₃)] ⁺	MeCN		−1.55 ^d	72

^a *E*_{pc}.^b vs. Fc/Fc⁺.^c vs. SSCE.^d vs. Ag/AgNO₃.^e *E*_{pa}.

to CO. Oxidation of *fac*-Re(bpy)(CO)₃H occurs more easily than that of *fac*-Re(bpy)(CO)₃Cl, indicating the increased electron density on the Re center.

The electrochemical behavior of Re(α -diimine)(CO)₃X in the negative potential region usually shows several reduction waves. The first reduction wave is reversible and is assigned as a ligand-based reduction. The second wave is usually irreversible and assigned as a metal-based reduction followed by the rapid loss of X.

Table 7. UV–vis spectra and lifetimes for *fac*-Re(α -diimine)(CO)₃L complexes.

Complex	Solvent	λ_{max} (nm)	τ (ns)	$\lambda(\text{em})$ (nm)	Ref.
[Re(4,4'-bpy) ₂ (CO) ₃ Cl]	benzene		900/3300		73
[Re(4,4'-bpy) ₂ (CO) ₃ Cl]	CH ₂ Cl ₂		1010		74
[Re(4,4'-bpy) ₂ (CO) ₃ Cl]	benzene		2100		74
[Re(bpy)(CO) ₃ Cl]	CH ₂ Cl ₂	385	51	622	64
[Re(bpy)(CO) ₃ Cl]	MeCN	370	25	622	65
[Re(bpy)(CO) ₃ Cl]	MeCN	370, 318, 295	25/33		75
[Re(bpy)(CO) ₃ Cl]	DMF	373	26	620	65
[Re(bpy)(CO) ₃ Cl]	EtOH	372	36	610	65
[Re(bpy)(CO) ₃ Cl]	CH ₂ Cl ₂	384	50	615	65
[Re(bpy)(CO) ₃ Cl]	THF	388	65	622	65
[Re(bpy)(CO) ₃ Cl]	dioxane	390	62	626	65
[Re(bpy)(CO) ₃ Cl]	benzene	400	70	615	65
[Re(bpy)(CO) ₃ Cl] ^a	MeTHF	375	2700	532	76
[Re(bpy)(CO) ₃ (MeCN)] ⁺	CH ₂ Cl ₂	343	1201	536	64
[Re(bpy)(CO) ₃ (Otf)]	THF	355			62
[Re(bpy)(CO) ₃ (O ₂ CH)]	CH ₂ Cl ₂	382			66
[Re(bpy)(CO) ₃ (O ₂ COH)]	DMSO	362			66
[Re(bpy)(CO) ₃ (H)]	CH ₂ Cl ₂	415			66
[Re(bpy)(CO) ₃ (THF)] ⁺	THF	385			62
[Re(bpy)(CO) ₃ Br] ^a	MeTHF	378	3700	530	76
[Re(bpy)(CO) ₃ Br]	DMF	375	55	610	57
[Re(bpy)(CO) ₃ I]	THF	320 sh, 403			76
[Re(bpy)(CO) ₃ I] ^a	MeTHF	388	7500	525	76
[Re(bpy)(CO) ₃ CH ₃]	MeCN	410, 270			75
[Re(bpy)(CO) ₃ P(CH ₃) ₃] ⁺	CH ₂ Cl ₂	358	1169	544	64
[Re(bpy)(CO) ₃ {P(OEt ₃) ₃ }] ⁺	MeCN	317, 351 sh	920	521	59
[Re(bpy)(CO) ₃ PPh ₃] ⁺	THF	365, 330			62
[Re(bpy)(CO) ₃ PPh ₃] ⁺			416	517	77
[Re(dmb)(CO) ₃ Cl]	MeCN	360	27	592	65
[Re(dmb)(CO) ₃ CH ₃]	CH ₂ Cl ₂		35		78
[Re(dmb)(CO) ₃ CH ₃]	toluene		40		78
[Re(dmb)(CO) ₃ CH ₃]	THF		30		78
[Re(dmb)(CO) ₃ CH ₃] ^a	MeTHF	398	5000	644	78
[Re(phen)(CO) ₃ (MeCN)] ⁺	MeCN	360	2400	532	68
[Re(phen)(CO) ₃ Cl]	MeCN	364	178	612	65
[Re(phen)(CO) ₃ Cl]	DMF	366	155	614	65
[Re(phen)(CO) ₃ Cl]	EtOH	369	216	600	65
[Re(phen)(CO) ₃ Cl]	CH ₂ Cl ₂	374	288	604	65
[Re(phen)(CO) ₃ Cl]	THF	382	335	622	65
[Re(phen)(CO) ₃ Cl]	dioxane	384	340	620	65
[Re(phen)(CO) ₃ Cl]	benzene	388	320	610	65

^a 80 K.

Table 8. IR stretching frequencies for *Re*(α -diimine)(CO)₃L complexes^a.

Complex	Solvent	ν_{CO} (cm ⁻¹)	ν_{CO_2} or $\nu_{\text{O}_2\text{CH}}$ (cm ⁻¹)	Ref.
<i>Ground-state complexes:</i>				
[<i>Re</i> (4,4-bpy) ₂ (CO) ₃ (MeCN)] ⁺	KBr	2043, 1930 br		79
[<i>Re</i> (4,4-bpy) ₂ (CO) ₃ (MeCN)] ⁺	MeCN	2046, 1942 br		79
[<i>Re</i> (4,4-bpy) ₂ (CO) ₃ Cl]	CH ₂ Cl ₂	2027, 1926, 1891		74, 80, 81
[<i>Re</i> (4,4-bpy) ₂ (CO) ₃ Cl]	MeCN	2026, 1922, 1895		80, 81
[<i>Re</i> (4,4-bpy) ₂ (CO) ₃ Cl]	MeCN	2028, 1923, 1892		79
[<i>Re</i> (4,4-bpy) ₂ (CO) ₃ Cl]	KBr	2017, 1892 br		79
[<i>Re</i> (4,4-bpy) ₂ (CO) ₃ Cl] ⁺⁻	MeCN	2012, 1903, 1882		80, 81
[<i>Re</i> (4,4-bpy) ₂ (CO) ₃ Cl] ²⁻	MeCN	2002, 1890, 1868		80, 81
[<i>Re</i> (bpy)(CO) ₃ (MeCN)] ⁺	KBr	2040, 1954, 1929, 1920		79
[<i>Re</i> (bpy)(CO) ₃ (MeCN)] ⁺	MeCN	2041, 1936 br		79
[<i>Re</i> (bpy)(CO) ₃] ⁻	PrCN ^b	1944, 1843 br		63
[<i>Re</i> (bpy)(CO) ₃] ⁻	THF	1947, 1843 br		62
[<i>Re</i> (bpy)(CO) ₃] ⁻	MeCN	1948, 1846		61, 81
[<i>Re</i> (bpy)(CO) ₃ (Br)]	THF	2019, 1919, 1895		62
[<i>Re</i> (bpy)(CO) ₃ (Br)] ⁺⁻	THF	1997, 1888, 1867		62
[<i>Re</i> (bpy)(CO) ₃ Cl]	KBr	2012, 1903, 1880		79
[<i>Re</i> (bpy)(CO) ₃ Cl]	PrCN ^c	2021 s, 1916 m, 1897 m		63
[<i>Re</i> (bpy)(CO) ₃ Cl]	CH ₂ Cl ₂	2024, 1921, 1899		80, 81
[<i>Re</i> (bpy)(CO) ₃ Cl]	CH ₂ Cl ₂	2020, 1920, 1900		82
[<i>Re</i> (bpy)(CO) ₃ Cl]	DMF	2019, 1914, 1893		56
[<i>Re</i> (bpy)(CO) ₃ Cl]	THF	2019, 1917, 1895		62
[<i>Re</i> (bpy)(CO) ₃ Cl]	MeCN	2023, 1916, 1902		79
[<i>Re</i> (bpy)(CO) ₃ Cl]	MeCN	2023, 1917, 1899 m		62
[<i>Re</i> (bpy)(CO) ₃ Cl]	MeCN	2021 s, 1914 m, 1897 m		61
[<i>Re</i> (bpy)(CO) ₃ Cl] ⁻	PrCN ^c	1996 s, 1881 m, 1865 m		63
[<i>Re</i> (bpy)(CO) ₃ Cl] ⁺⁻	MeCN	1996, 1881, 1867		80, 81
[<i>Re</i> (bpy)(CO) ₃ Cl] ⁻	MeCN	1998 s, 1880 m, 1866 m		79
[<i>Re</i> (bpy)(CO) ₃ Cl] ⁻	DMF	1994, 1880, 1862		62, 82
[<i>Re</i> (bpy)(CO) ₃ Cl] ⁻	THF	1996, 1883, 1868		62
[<i>Re</i> (bpy)(CO) ₃ Cl] ⁺⁻	MeCN	1998, 1885, 1868		61
[<i>Re</i> (bpy)(CO) ₃ I]	THF	2020, 1921, 1900		62
[<i>Re</i> (bpy)(CO) ₃ I] ⁻	THF	1995, 1889, 1866		62
[<i>Re</i> (bpy)(CO) ₃ (O ₂ CH)]	KBr	2020, 1920, 1880	1630, 1280	56
[<i>Re</i> (bpy)(CO) ₃ (O ₂ CH)]	KBr	2018, 1918, 1893	1633, 1281	79
[<i>Re</i> (bpy)(CO) ₃ (O ₂ CH)]	THF	2019, 1916, 1894	1630, 1280	61
[<i>Re</i> (bpy)(CO) ₃ (O ₂ CH)] ⁻	THF	1997, 1879 br	1628, 1280	61
[<i>Re</i> (bpy)(CO) ₃ (CH ₂ OH)]	KCl	1987, 1865		83
[<i>Re</i> (bpy)(CO) ₃ (Ot ^f)]	THF	2034, 1930, 1914		62
[<i>Re</i> (bpy)(CO) ₃ (PPh ₃)] ⁺	THF	2037, 1950, 1922		62
[<i>Re</i> (bpy)(CO) ₃ (PPh ₃)] ⁺	THF	2015, 1919, 1892		62

Table 8 (continued)

Complex	Solvent	ν_{CO} (cm ⁻¹)	ν_{CO_2} or $\nu_{\text{O}_2\text{Cl}}$ (cm ⁻¹)	Ref.
[Re(bpy)(CO) ₃ (PrCN)] ⁺	PrCN	2039 s, 1936 s,br		63
[Re(bpy)(CO) ₃ (PrCN)] ⁺	PrCN	201, 1905, 1885		63
[Re(bpy)(CO) ₃ (PrCN)] ⁻	PrCN ^b	1980, 1861, 1851		63
[Re(bpy)(CO) ₃ (THF)] ⁺	THF	2019, 1917, 1894		62
[Re(bpy)(CO) ₂ {P(OEt) ₃ } ₂]Br	CH ₂ Cl ₂	1956, 1882		69
[Re(dmb)(CO) ₃ (CH ₃)]	EtCN–PrCN ^d	1987, 1874, 1867		78
[Re(dmb)(CO) ₃ (MeCN)] ⁺	MeCN	2039, 1934 br		79
[Re(dmb)(CO) ₃ (MeCN)] ⁺	MeCN	2039, 1948, 1935		70
[Re(dmb)(CO) ₃]	MeCN	1979, 1876, 1843		70
[Re(dmb)(CO) ₃] ₂	KBr	2020, 1940, 1860		56
[Re(dmb)(CO) ₃] ₂	MeCN	(1975), 1943		70
[Re(dmb)(CO) ₃] ⁻	MeCN	1943, 1828		70
[Re(dmb)(CO) ₃] ₂ ⁻	MeCN	1960, 1930, 1865, 1830		70
[Re(dmb)(CO) ₃ Cl]	MeCN	2023, 1906, 1893		70
[Re(dmb)(CO) ₃ Cl]	MeCN	2021, 1914, 1898		79
[Re(dmb)(CO) ₃ Cl] ⁻	MeCN	1993, 1875		70
[Re(dmb)(CO) ₃ (CO ₂ H)]	KCl	2012, 1916, 1892	1572, 1194	84
[Re(dmb)(CO) ₃ (CO ₂ H)] or [Re(dmb)(CO) ₃ (CO ₂)]	MeCN	2010, 1902, 1878		70
[Re(dmb)(CO) ₃ (CO ₂ H)] ⁻	MeCN	1997, 1860		70
[Re(dmb)(CO) ₃ (CO ₂ H)] ⁻	THF	2014, 1916, 1894		62
[Re(dmb)(CO) ₃ (CO ₂ H)] ⁻	MeCN	1986, 1868, 1852		62
[Re(dmb)(CO) ₃] ₂ (CO ₂)	KCl	1992, 1888, 1866	1485, 1155	84
[Re(dmb)(CO) ₃ H]	KCl	1992, 1887, 1865	2019, 2036 (ReH)	84
[Re(dmb)(CO) ₃ H]		1993, 1905, 1888	2018 (ReH)	66
<i>Excited-state complexes:</i>				
*[Re(CO) ₃ (4,4-bpy) ₂ (MeCN)] ⁺	MeCN	2068, 2031, 1992		79
*[Re(CO) ₃ (4,4-bpy) ₂ Cl]	CH ₂ Cl ₂	2055, 1992, 1957		74, 80, 81
*[Re(CO) ₃ (4,4-bpy) ₂ Cl]	MeCN	2065, 1993, 1961		79
*[Re(bpy)(CO) ₃ (MeCN)] ⁺	CH ₂ Cl ₂	2071, 2018, 1984		85
*[Re(bpy)(CO) ₃ (MeCN)] ⁺	MeCN	2070, 2017, 1982		79
*[Re(bpy)(CO) ₃ Cl]	CH ₂ Cl ₂	2065, 1991, 1951		86
*[Re(bpy)(CO) ₃ Cl]	CH ₂ Cl ₂	2064, 1987, 1957		81
*[Re(bpy)(CO) ₃ Cl]	MeCN	2067, 1990, 1874		79
*[Re(bpy)(CO) ₂ {P(OEt) ₃ } ₂]Br	CH ₂ Cl ₂	2012, 1927		69
*[Re(dmb)(CO) ₃ (CH ₃)]	EtCN–PrCN ^d	2029, 1950, 1925		78
*[Re(dmb)(CO) ₃ (MeCN)] ⁺	MeCN	2062, 2013, 1973		79
*[Re(dmb)(CO) ₃ Cl]	MeCN	2062, 1989, 1953		79

^a Room temperature.^b 183 K.^c 213 K.^d 195 K.

Spectroelectrochemical experiments using FTIR indicate that the reduced *Re*(bpy)(CO)₃Cl^{•−} shows a significant shift of the CO vibrational frequencies to lower energy (see Table 8). The electron, while primarily residing in the bpy ligand π^* orbital, increases the amount of charge on the Re center by reducing Re–bpy π -backbonding. This increases Re–CO π -backbonding and raises the electron density in the π^* orbital of the CO, and thus decreases the CO bond strength and vibrational frequencies. The IR absorption of the CO, ν_{CO} , shifts by about 30 cm^{−1} to lower energy.

The stability of the reduced complex depends on the ability of the X ligand to accommodate the increased electron density of the Re center. In the case of ligands that cannot easily accept electron density into a low-energy orbital the increased electron density on the Re weakens the Re–X bond and can lead to loss of the X ligand. Complexes such as *Re*(dmb)(CO)₃Cl tend to form the five-coordinate radical [*Re*(dmb)(CO)₃][•] species upon reduction even in MeCN [61]. This effect is stronger in the doubly reduced species that has added an electron directly to the Re center.

Excited-state photochemistry and photophysics

The photophysical properties of low-spin d⁶ complexes, *fac-Re*(α -diimine)(CO)₃X, are summarized in Table 7. These complexes are often emissive in solution and generally have an intense MLCT absorptions [*Re*^I $d\pi \rightarrow \pi^*$ (α -diimine)] between 340 and 500 nm depending on the α -diimine, X ligands and the solvent [53, 65]. Changes in solvent polarity lead to pronounced shifts of the absorption maxima (e.g. 370 nm in MeCN to 400 nm in benzene for *Re*(bpy)(CO)₃Cl) as shown in Table 7 [52]). Modification of the α -diimine ligand also affects the MLCT absorption with the λ_{max} shifting to shorter wavelength in the order dmb < phen < bpy [52, 53]. The replacement of Cl[−] by I[−] changes the excited-state character from MLCT to XLCT (X = halide) [76]. The MLCT absorption of *Re*(bpy)(CO)₃X (X = H or CH₃) is red shifted compared with that of *Re*(bpy)(CO)₃Cl. An excellent review of the photophysics of these complexes by Stufken and Vlcek has recently been published [53].

For *fac-Re*(α -diimine)(CO)₃Cl the initial absorption at ~400 nm populates a short-lived ¹MLCT state. This state rapidly decays to the long-lived ³MLCT states. These states are actually three closely spaced levels split by spin–orbit coupling. Since the splitting is small the states behave kinetically as a single level at temperatures above 77 K [53]. The ³MLCT excited state can be viewed as a charge-separated species * [*Re*^{II}(α -diimine^{•−})(CO)₃Cl]. Transient UV–vis spectra show that the excited-state absorption corresponds to the α -diimine^{•−} anion chromophore [65]. Transient IR spectroscopy of the excited state shows a significant shift (20 to 80 cm^{−1}) of the CO vibrational frequencies to higher energy. The shift is similar to but smaller than that observed on oxidation of the *Re*(α -diimine)(CO)₃Cl complex [70]. The charge transfer in the excited state decreases the amount of charge on the Re center. This reduces the π -backbonding between the Re center and the CO ligands, thereby increasing the CO bond strength and vibrational frequencies. Similar effects have also been observed in the time-resolved resonance Raman spectroscopy [53].

The complexes often undergo radiative decay from their lowest excited state both in fluid solutions at room temperature and in glassy media at 77 K [51, 63, 64, 71]. Emission lifetimes are typically 20 ns to 2 μ s at room temperature and are summarized in Table 7. The excited state can decay by two nonradiative pathways: by internal conversion to the ground state and by a thermally activated process through a higher energy excited state that rapidly decays to the ground state. The exact parameters for the two pathways depend on X, L, solvent and temperature.

The ³MLCT excited state is both a strong oxidant and a strong reductant and it can be quenched by either electron acceptors (oxidative) or donors (reductive quenching) [65, 71]. Table 9 gives rate constants for oxidative and reductive quenching of the MLCT excited state of a number of *fac*-Re(α -diimine)(CO)₃X complexes.

The relationship between the absorption (E_{abs}), emission (E_{em}), reorganization (λ_r), the singlet–triplet splitting (E_{st}) energies [87] and the energy difference between the thermally relaxed excited and ground states (E_{0-0}) is shown in Figure 8 [88]. In the equation

$$E_{\text{abs}} = E_{\text{em}} + E_{\text{st}} + 2\lambda_r \quad (21)$$

the reorganization energy, λ_r , is generally broken into contributions from the solvent and/or low-frequency internal modes of the complex, λ_s , and from the internal high-frequency modes of the complex, λ_i , with the total reorganization energy given by $\lambda_r = \lambda_s + \lambda_i$. A spherical continuum model [89] can be used to estimate the solvent contribution to λ_s . Using this model [90], $\lambda_s = 0.18$ eV for Ru(bpy)₃^{2+/*} in H₂O and 0.33 and 0.22 eV for Re(bpy)(CO)₃Cl in H₂O and CH₂Cl₂, respectively. The larger value for the Re (vs the Ru) complex is due to its smaller size while the decrease in the value of λ_s on going from water to CH₂Cl₂ reflects the decrease in the polarity of the solvent.

An alternative method of estimating the reorganization energies involves spectral fitting of the emission [91, 92]. For a number of rhenium complexes the λ_s and λ_r values are given in Table 10. In general, similar λ_s values are estimated by either method with λ_s typically being about half of the total reorganization energy. As expected, the inner-shell reorganization energy for the Re carbonyl complexes is significant as indicated by the shifts in the ν_{CO} frequencies. E_{0-0} and the E_{st} are estimated for a number of complexes in Table 10. One notes that E_{st} is approximately constant for the Ru(bpy)(CO)₃Cl and Ru(phen)(CO)₃Cl complexes if one excludes the two nonpolar solvents. The excited state energies, E_{0-0} , are important since they can be used to estimate the redox potential of the excited state.

The reduction potentials for either the oxidation ($E_{1/2}^{+/*}$) or the reduction ($E_{1/2}^{*/-}$) of the excited state can be calculated from the ground-state potential and the excited-state energy, E_{0-0} , by

$$E_{1/2}^{*/-} = E_{0-0} + E_{1/2}^{0/-} \quad (22)$$

$$E_{1/2}^{+/*} = E_{1/2}^{+/0} - E_{0-0} \quad (23)$$

Table 9. Oxidative and reductive quenching of MLCT excited state of $Re(\alpha\text{-diimine})(CO)_3X$ by Q in MeCN at room temperature.

α -Diimine	X	Q	E° vs. SCE (V)	$k_q \times 10^9$ ($M^{-1} s^{-1}$)	Ref.
<i>Oxidative quenching:</i>					
phen	Cl	tetracyanoethylene	+0.24	7.4	71
phen	Cl	1,1'-propylene-1,10-phenanthroline PF ₆	-0.27	3.3	71
phen	Cl	1,1'-ethylene-2,2'-bipyridinium PF ₆	-0.36	3.6	71
phen	Cl	<i>N,N'</i> -dibenzyl-4,4'-bipyridinium PF ₆	-0.36	2.7	71
phen	Cl	<i>N,N'</i> -dimethyl-4,4'-bipyridinium PF ₆	-0.45	3.1	71
phen	Cl	<i>N</i> -methyl-4-cyanopyridinium PF ₆	-0.79	2.3	71
phen	Cl	<i>p</i> -nitrobenzaldehyde	-0.86	2.6	71
phen	Cl	<i>N</i> -methyl-4-carbomethoxypyridinium PF ₆	-0.93	1.7	71
phen	Cl	4,4'-dinitrobiphenyl	-1.0	1.9	71
phen	Cl	<i>m</i> -nitrobenzaldehyde	-1.02	0.64	71
phen	Cl	4-chloronitrobenzene	-1.06	0.24	71
phen	Cl	4-methylnitrobenzene	-1.20	<0.02	71
Ph ₂ phen	Cl	<i>N,N'</i> -dibenzyl-4,4'-bipyridinium PF ₆	-0.36	3.3	71
Ph ₂ phen	Cl	<i>N,N'</i> -dimethyl-4,4'-bipyridinium PF ₆	-0.45	3.5	71
<i>Reductive quenching:</i>					
phen	Cl	<i>N,N,N',N'</i> -tetramethyl- <i>p</i> -phenylenediamine	+0.24	5.7	71
phen	Cl	<i>N,N'</i> -diphenyl- <i>p</i> -phenylenediamine	+0.35	3.7	71
phen	Cl	<i>N,N</i> -dimethyl- <i>p</i> -toluidine	+0.65	2.1	71
phen	Cl	10-methylphenothiazine	+0.83	1.7	71
phen	Cl	<i>N,N</i> -dimethylaniline	+0.78	0.98	71
phen	Cl	diphenylamine	+0.83	0.40	71
phen	Cl	triphenylamine	+0.86	0.33	71
phen	Cl	aniline	+0.98	0.058	71
phen	Cl	<i>p</i> -bromoaniline	+0.97	0.054	71
phen	Cl	<i>N,N</i> -dimethylbenzylamine	+1.01	<0.002	71
phen	Cl	<i>p</i> -dimethoxybenzene	+1.34	<0.002	71
phen	Cl	<i>N,N</i> -dimethylaniline	+0.78	0.98	65
phen	Cl	diphenylamine	+0.83	0.4	65
phen	Cl	<i>N,N',N'</i> -triphenylamine	+0.98	0.33	65
Ph ₂ phen	Cl	<i>N,N,N',N'</i> -tetramethyl- <i>p</i> -phenylenediamine	+0.24	8.7	71

Table 9 (continued)

α -Diimine	X	Q	E° vs. SCE (V)	$k_q \times 10^9$ (M ⁻¹ s ⁻¹)	Ref.
Ph ₂ phen	Cl	<i>N,N</i> -dimethyl- <i>p</i> -toluidine	+0.65	3.9	71
Ph ₂ phen	Cl	aniline	+0.98	0.20	71
Ph ₂ phen	Cl	<i>p</i> -dimethoxybenzene	+1.34	<0.002	71
bpy	Cl	TEOA	+0.80	0.08	65
bpy	{P(OEt) ₃ } ₂	1,4-diazabicyclo [2.2.2]octane		0.28	69
bpy	P(OEt) ₃	TEOA	+0.80	1.1	72
bpy	P(OEt) ₃	TEOA	+0.80	0.8	59
bpy	Br	TEOA	+0.80	0.06	57

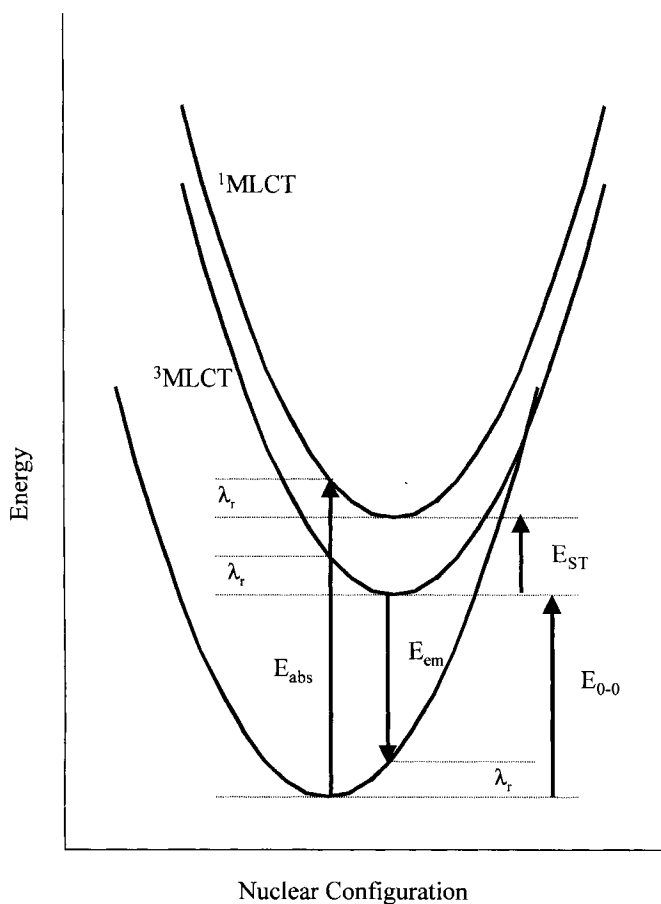
**Figure 8.** Potential energy surfaces for the ground, ³MLCT and ¹MLCT states of Re(α -diimine)(CO)₃X complexes. Note that all surfaces are assumed to have the same force constants.

Table 10. Reorganization energies, excited-state energies and singlet–triplet splitting for *Re*(α -diimine)(CO)₃X complexes^a.

α -Diimine	X	Solvent	E_{abs} (eV)	E_{em} (eV)	λ_{s} (eV)	λ_{r} (eV)	$E_{0,0}$ (eV)	E_{st} (eV)	Ref.
bpy	Br	DMF	3.31	2.03	0.28 ^a	0.48 ^b	2.51	0.31	57
bpy	Cl	benzene	3.10	2.02	0.00 ^a	0.20 ^b	2.22	0.68	65
bpy	Cl	CH ₂ Cl ₂	3.21	1.99	0.22 ^a	0.42 ^b	2.41	0.38	64
bpy	Cl	CH ₂ Cl ₂	3.22	1.99	0.22 ^a	0.42 ^b	2.41	0.39	65
bpy	Cl	CH ₂ Cl ₂	3.23	2.02	0.22 ^a	0.42 ^b	2.44	0.37	65
bpy	Cl	dioxane	3.18	1.98	0.02 ^a	0.22 ^b	2.20	0.76	65
bpy	Cl	DMF	3.32	2.00	0.28 ^a	0.48 ^b	2.48	0.36	65
bpy	Cl	EtOH	3.33	2.03	0.30 ^a	0.5 ^b	2.53	0.30	65
bpy	Cl	MeCN	3.35	1.99	0.31 ^a	0.51 ^b	2.50	0.34	65
bpy	Cl	MeTHF	3.10	1.93	<0.36 ^c	0.44 ^d	2.4 ^e	0.3	93
bpy	Cl	THF	3.20	1.99	0.21 ^a	0.41 ^b	2.40	0.38	65
bpy	4Etpy	EtOH–MeOH		2.11	0.21 ^c	0.51 ^d	2.45 ^e		95
bpy	4Etpy	CH ₂ Cl ₂	3.43	2.19	0.22 ^a	0.42 ^b	2.61	0.41	64
bpy	4Etpy	DCE	3.41	2.18	<0.48 ^c	0.52 ^d	2.86 ^e	0.52	97
bpy	3HOpy	MeCN	3.56	2.17	0.22 ^c	0.42 ^d	2.59 ^e	0.56	94
bpy	2Mepy	CH ₂ Cl ₂	3.25	2.03	0.22 ^a	0.42 ^b	2.45	0.37	64
bpy	2Mepy	MeCN	3.41	2.21	0.20 ^c	0.42 ^d	2.63 ^e	0.35	94
bpy	3Mepy	MeCN	3.41	2.19	0.20 ^c	0.42 ^d	2.61 ^e	0.38	94
bpy	MeCN	CH ₂ Cl ₂	3.61	2.31	0.22 ^a	0.42 ^b	2.73	0.46	64
bpy	Meimz	CH ₂ Cl ₂	3.42	2.11	0.22 ^a	0.42 ^b	2.53	0.47	64
bpy	NH ₂ py	CH ₂ Cl ₂	3.31	2.08	0.22 ^a	0.42 ^b	2.50	0.39	64
bpy	P(CH ₂) ₃	CH ₂ Cl ₂	3.46	2.28	0.22 ^a	0.42 ^b	2.70	0.34	64
bpy	P(CH ₃) ₃	CH ₂ Cl ₂	3.46	2.28	0.22 ^a	0.42 ^b	2.70	0.34	64
bpy	P(Oet) ₃	MeCN	3.91	2.38	0.25 ^a	0.45 ^b	2.83	0.62	59
bpy	py	CH ₂ Cl ₂	3.45	2.22	0.22 ^a	0.42 ^b	2.64	0.39	64
bpy	py	MeCN	3.39	2.22	0.20 ^c	0.44 ^d	2.66 ^e	0.29	94
Cl ₂ bpy	Cl	MeTHF	3.02	1.77	<0.39 ^c	0.47 ^d	2.24 ^e	0.32	93
Cl ₂ bpy	4Etpy	DCE		2.15	<0.36 ^c	0.31 ^d	2.73 ^e	0.31	97
(CO ₂ Et) ₂ bpy	Cl	MeTHF	2.88	1.73	<0.34 ^c	0.37 ^d	2.11 ^e	0.40	93
(isn) ₂ bpy	Cl	MeTHF	3.22	2.00	<0.34 ^c	0.49 ^d	2.49 ^e	0.25	93
(NEt) ₂ bpy	Cl	MeTHF	3.31	2.16	<0.55 ^c	0.63 ^d	2.79 ^e	−0.11	93
(NH ₂) ₂ bpy	Cl	MeTHF	3.44	2.16	<0.55 ^c	0.63 ^d	2.79 ^e	0.02	93
(OCH ₃) ₂ bpy	Cl	MeTHF	3.31	1.97	<0.48 ^c	0.54 ^d	2.51 ^e	0.25	93
Ph ₂ bpy	Cl	MeTHF	3.02	1.92	<0.39 ^c	0.44 ^d	2.36 ^e	0.22	93
Ph ₂ bpy	py	MeCN	3.48	2.18	0.15 ^c	0.37 ^d	2.55 ^e	0.56	94
CO ₂ Me	4Etpy	DCE		1.98	<0.34 ^c	0.36 ^d	1.50 ^e	0.36	97
dmb	Cl	MeCN	3.44	2.09	0.31 ^a	0.51 ^b	2.60	0.33	65
dmb	Cl	MeTHF	3.22	1.98	<0.45 ^c	0.52 ^d	2.50 ^e	0.20	93
dmb	4Etpy	DCE	3.48	2.30	<0.39 ^c	0.41 ^d	2.70 ^e	0.41	97
dmb	py	MeCN	3.48	2.25	0.18 ^c	0.42 ^d	2.65 ^e	0.44	94
phen	3Mepy	MeCN	3.23	2.25	0.20 ^c	0.42 ^d	2.67 ^e	0.14	94
phen	Cl	benzene	3.20	2.03	0.00 ^a	0.20 ^b	2.23	0.76	65
phen	Cl	CH ₂ Cl ₂	3.32	2.05	0.22 ^a	0.42 ^b	2.47	0.42	65
phen	Cl	CH ₂ Cl ₂	3.03	2.15	0.22 ^a	0.42 ^b	2.57	0.02	51
phen	Cl	dioxane	3.23	2.00	0.02 ^a	0.22 ^b	2.22	0.79	65

Table 10 (continued)

α -Diimine	X	Solvent	E_{abs} (eV)	E_{em} (eV)	λ_{s} (eV)	λ_{r} (eV)	E_{0-0} (eV)	E_{st} (eV)	Ref.
phen	Cl	DMF	3.39	2.02	0.28 ^a	0.48 ^b	2.50	0.41	65
phen	Cl	EtOH	3.36	2.07	0.30 ^a	0.50 ^b	2.57	0.29	65
phen	Cl	MeCN	3.41	2.03	0.31 ^a	0.51 ^b	2.54	0.36	65
phen	Cl	THF	3.25	1.99	0.21 ^a	0.41 ^b	2.40	0.43	65
phen	MeCN	MeCN	3.44	2.33	0.31 ^a	0.51 ^b	2.84	0.09	68
phen	py	MeCN	3.37	2.28	0.22 ^c	0.44 ^d	2.72 ^e	0.21	94
Brphen	Cl	CH ₂ Cl ₂	2.98	2.12	0.22 ^a	0.42 ^b	2.54	0.01	51
Clphen	Cl	CH ₂ Cl ₂	2.95	2.12	0.22 ^a	0.42 ^b	2.54		51
Mephen	Cl	CH ₂ Cl ₂	2.95	2.11	0.22 ^a	0.42 ^b	2.53	0.04	51
Ph ₂ phen	Cl	CH ₂ Cl ₂		2.14	0.22 ^a	0.42 ^b	2.51		51
Ph ₂ phen	py	MeCN	3.76	2.28	0.16 ^c	0.38 ^d	2.66 ^e	0.72	94
dpp	4Mepy	CH ₂ Cl ₂		1.97	0.36 ^c	0.45 ^d	2.42 ^e		96
dpp	4Phpy	CH ₂ Cl ₂		1.96	0.36 ^c	0.46 ^d	2.42 ^e		96
dpp	Cl	CH ₂ Cl ₂		1.72	0.39 ^c	0.47 ^d	2.19 ^e		96
dpp	MeCN	CH ₂ Cl ₂		1.98	0.36 ^c	0.45 ^d	2.43 ^e		96
dpp	Meimz	CH ₂ Cl ₂		1.86	0.39 ^c	0.48 ^d	2.34 ^e		96
dpp	P(CH ₃) ₃	CH ₂ Cl ₂		2.05	0.34 ^c	0.37 ^d	2.42 ^e		96
dpp	py	CH ₂ Cl ₂		1.98	0.34 ^c	0.44 ^d	2.42 ^e		96
dpq	4Mepy	CH ₂ Cl ₂		1.68	0.48 ^c	0.49 ^d	2.17 ^e		96
dpq	4Phpy	CH ₂ Cl ₂		1.68	0.48 ^c	0.50 ^d	2.18 ^e		96
dpq	MeCN	CH ₂ Cl ₂		1.74	0.59 ^c	0.61 ^d	2.35 ^e		96
dpq	Meimz	CH ₂ Cl ₂		1.60	0.45 ^c	0.47 ^d	2.07 ^e		96
dpq	P(CH ₃) ₃	CH ₂ Cl ₂		1.69	0.52 ^c	0.54 ^d	2.23 ^e		96
dpq	py	CH ₂ Cl ₂		1.69	0.48 ^c	0.50 ^d	2.19 ^e		96

^a Calculated from a single sphere model [89].^b $\lambda_{\text{i}} = 0.22$ eV [95].^c Calculated from spectral fitting [64, 91].^d Calculated as $E_{\text{em}} - E_{0-0}$.^e Calculated from spectral fitting as $E_0 + \lambda_{0,\text{s}}$ [64, 91].

The reduction potentials for the $\text{Re}(\text{phen})(\text{CO})_3\text{Cl}^+/\text{*Re}(\text{phen})(\text{CO})_3\text{Cl}$ and $\text{*Re}(\text{phen})(\text{CO})_3\text{Cl}/\text{Re}(\text{phen})(\text{CO})_3\text{Cl}^-$ couples have been estimated [71] to be approximately -1.0 and $+1.0$ V (vs. SCE in MeCN), respectively, using an excited-state energy of ~ 2.3 eV. Using the estimates in Table 10 one obtains -1.2 and $+1.2$ V. The data in Tables 6 and 10 allow redox potentials for a number of other complexes to be calculated.

Visible light irradiation of an Re-alkyl complex, $[\text{Re}(\text{dmb})(\text{CO})_3\text{R}]$ ($\text{R} = \text{CH}_3$, Et, *i*Pr, or Bz; dmb = 4,4'-dimethyl-2,2'-bipyridine), gives rise to a homolytic cleavage of the Re–R bond with the formation of the radicals $[\text{Re}(\text{dmb})(\text{CO})_3]^{\cdot}$ and R^{\cdot} [78]. The reaction proceeds with a quantum efficiency of 0.4 for $\text{R} = \text{CH}_3$ and 1 for $\text{R} = \text{Et}$, *i*Pr or Bz. The time-resolved UV–vis and IR absorption spectra reveal that for $\text{Re}(\text{dmb})(\text{CO})_3(\text{CH}_3)$ the initially formed excited

state is a ¹MLCT state. The ¹MLCT state can either pass over a thermal barrier of 1560 cm⁻¹ to the dissociative ³ $\sigma\pi^*$ state (and decompose into radicals) or decay nonradiatively to the ³MLCT state. In the case of R = Et, *i*Pr or Bz, the dissociative pathway to form the radical dominates. In all cases the radicals form in less than 10 ns.

Formate–rhenium complexes

fac-Re(bpy)(CO)₃H undergoes a thermally activated reaction with CO₂ in organic solvents to produce the stable formate adduct, *fac*-Re(bpy)(CO)₃(O₂CH) [98]. The rate of formation is first order in [CO₂] and [Re] with a rate constant of $2.0 \times 10^{-4} \text{ M}^{-1} \text{ s}^{-1}$ in THF and $2.7 \times 10^{-2} \text{ M}^{-1} \text{ s}^{-1}$ in MeCN. Kinetic studies using *fac*-Re(bpy)(CO)₃D reveals an inverse $k_{\text{H}}/k_{\text{D}}$ isotope effect of ~ 0.5 for both solvents. The reaction occurs by associative hydride-transfer. While the thermal reaction is very slow at room temperature, irradiation with 436 nm light increases the rate by a factor of more than 10 [66]. While the CO₂ insertion into the Re–H bond reduces the CO₂, the authors do not report CO or formate production. Nor is formate a product in photochemical CO₂ reduction systems that utilize *fac*-Re(bpy)(CO)₃X [56–58, 77], although the presence of Re(bpy)(CO)₃(O₂CH) was identified in such systems.

Re–CO₂ and Re–COOH complexes

Metallocarboxylates and metallocarboxylic acids are proposed as intermediates in photocatalytic reduction of CO₂ by *fac*-Re(α -diimine)(CO)₃X, but have not been directly observed in the photocatalytic systems. Re(dmb)(CO)₃(COOH), Re(bpy)(CO)₃(CH₂OH) and (CO)₃(dmb)Re–C(O)–O–Re(dmb)(CO)₃ have been prepared by different routes and characterized [83, 84]. Reaction of Re(dmb)(CO)₄(Otf) with aqueous KOH in water produces *fac*-Re(dmb)(CO)₃(COOH) as a yellow precipitate. This complex has IR carboxylate absorptions, ν_{OCO} , at 1572 and 1194 cm⁻¹, which are at lower energy than those of the ruthenium analog, [Ru(bpy)₂(CO)(COOH)]⁺ (1618 and 1240 cm⁻¹). The ruthenium complex has been prepared by a similar reaction [Ru(bpy)₂(CO)₂²⁺ with OH⁻] and characterized by X-ray crystal structure determination [99]. Reaction of Re(bpy)(CO)₄(Otf) with NaBH₄ in methanol leads to the formation of the red Re(bpy)(CO)₃(CH₂OH). Irradiation of Re(bpy)(CO)₃(CH₂OH) in dry MeOH yields a red solid, *fac*-Re(bpy)(CO)₃(OMe), in 97 % yield [83]. The authors suggest that a β -elimination converts Re–CH₂OH to Re–H, which upon photolysis reacts with MeOH to form Re–OMe.

The μ^2 – η^2 -CO₂-bridged complex (CO)₃(dmb)Re–C(O)–O–Re(dmb)(CO)₃ is isolated (together with several unidentified species) on standing from an acetone solution of *fac*-Re(dmb)(CO)₃(COOH). Their IR data are summarized in Table 8. Neither *fac*-Re(dmb)(CO)₃(O₂CH) nor *fac*-Re(dmb)(CO)₃(H) has been observed as a product in the decomposition of *fac*-Re(dmb)(CO)₃(COOH) [84]. However, *fac*-Re(dmb)(CO)₃(COOH) in DMSO containing small amounts of water is transformed into the bicarbonato complex, *fac*-Re(dmb)(CO)₃(OC(O)OH) [100]. The detail mechanisms involving these species need to be elucidated.

3.3.3 Electrochemical Systems: One- and Two-electron Pathways

Extensive electrochemical studies on *fac*-Re(bpy)(CO)₃Cl in MeCN, THF or DMF indicate that reduction of *fac*-Re(bpy)(CO)₃Cl gives the radical anion, Re(bpy)(CO)₃Cl^{•−}, which reacts with CO₂ after loss of chloride. As shown in Figure 9, CO₂ reduction is proposed [54, 61, 63] to occur by two independent routes, a 1e pathway via Re(bpy)(CO)₃[•] and a 2e pathway via Re(bpy)(CO)₃[−]. FTIR studies of Re(bpy)(CO)₃Cl^{•−} (ν_{CO} 1996, 1883, 1868 cm^{−1}) indicate that it is in equilibrium with Re(bpy)(CO)₃(solvent)[•] (ν_{CO} 2011, 1895 cm^{−1}) and [Re(bpy)(CO)₃]₂ (ν_{CO} 1988, 1951, 1887, 1859 cm^{−1}) in MeCN. Unfortunately, the equilibrium constants and the rate constant for Cl[−] loss from Re(bpy)(CO)₃Cl^{•−} have not been determined. Reduction of Re(bpy)(CO)₃(MeCN)⁺ in THF leads to the formation of three species: Re(bpy)(CO)₃(MeCN)[•], Re(bpy)(CO)₃(THF)⁺ and [Re(bpy)(CO)₃]₂. Re(bpy)(CO)₃(THF)[•] is not observed even in the reduction of Re(bpy)(CO)₃(Otf) in THF. Thus Re(bpy)(CO)₃(THF)[•] is unstable and rapidly dimerizes after loss of THF.

IR spectral changes during the further reduction of Re(bpy)(CO)₃Cl^{•−} indicate rapid loss of a Cl[−] ligand with formation of [Re(bpy)(CO)₃][−]. The further reduction of either [Re(bpy)(CO)₃(solvent)][•] or [Re(bpy)(CO)₃]₂ also yields [Re(bpy)(CO)₃][−]. This illustrates the instability of non- π -backbonding ligands coordinated to the formally Re⁰ center.

IR spectral changes of Re(bpy)(CO)₃Cl (with excess Cl[−]) or Re(bpy)(CO)₃(Otf) (without excess Cl[−]) in electrochemical reduction in THF under a CO₂ atmosphere indicate the disappearance of Re(bpy)(CO)₃X (X = Cl or Otf) and the formation of [Re(bpy)(CO)₃(O₂CH)]^{•−} (ν_{COO} 1628 cm^{−1}), CO₃^{2−} (ν_{COO} 1643 cm^{−1}), CO and an unidentified species with ν_{COO} at 1680 cm^{−1} (carboxylate?) [61]. It is reported that the ν_{COO} band of Re(bpy)(CO)₃(O₂CH) and [Re(bpy)(CO)₃(O₂CH)]^{•−} are coincident (see Table 8). IR spectral changes of Re(bpy)(CO)₃Cl in MeCN with excess Cl[−] under a CO₂ atmosphere have been reported to illustrate rapid formation of free CO₃^{2−} (ν_{COO} 1643 cm^{−1}) and CO, together with an unassigned product having ν_{COO} at 1679 cm^{−1}. The unassigned product appears before formation of CO₃^{2−}. The IR spectrum in the ν_{CO} region shows only small amounts of [Re(bpy)(CO)₃Cl]^{•−} and [Re(bpy)(CO)₃(MeCN)][•] compared with the parent Re(bpy)(CO)₃Cl and free CO₃^{2−}, indicative of the catalytic nature of CO₃^{2−} production. Both [Re(bpy)(CO)₃][•] (1e pathway) and [Re(bpy)(CO)₃][−] (2e pathway) are alleged to react with CO₂.

The authors suggest a modification of the original mechanism shown in Figure 9 [61]. In this mechanism, shown in Figure 10, the actual catalytic species is Re(bpy)(CO)₃S[•], i.e., the one-electron reduced species that has had X replaced by a solvent molecule. This species is formed from the original Re(bpy)(CO)₃Xⁿ⁺ upon one-electron reduction. It is asserted that the electron density on the Re center is of critical importance in the catalytic scheme. The Re center must be sufficiently electronically poor to allow coordination of Lewis bases such as phosphines or MeCN otherwise rapid dimerization will occur. The use of a slightly coordinating solvent or free Cl[−] in solution helps to suppress this reaction. Alternatively, the Re center must be electronically rich enough to coordinate and reduce CO₂.

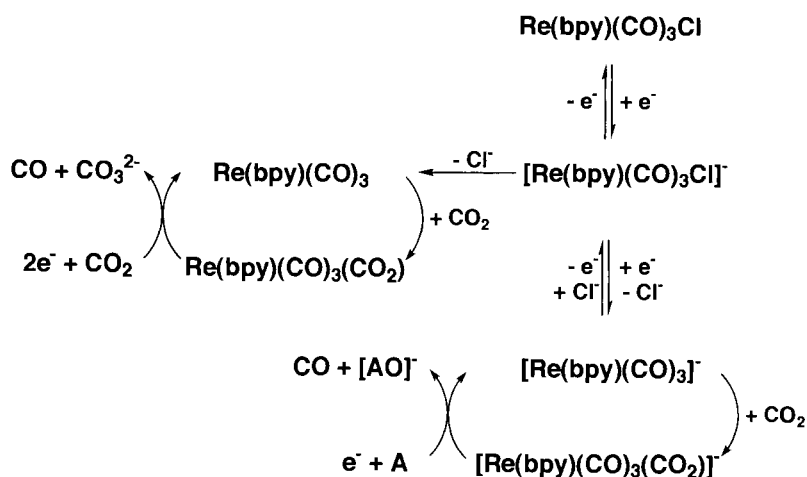


Figure 9. One- and two-electron pathways for CO_2 reduction. A = an oxide ion acceptor.

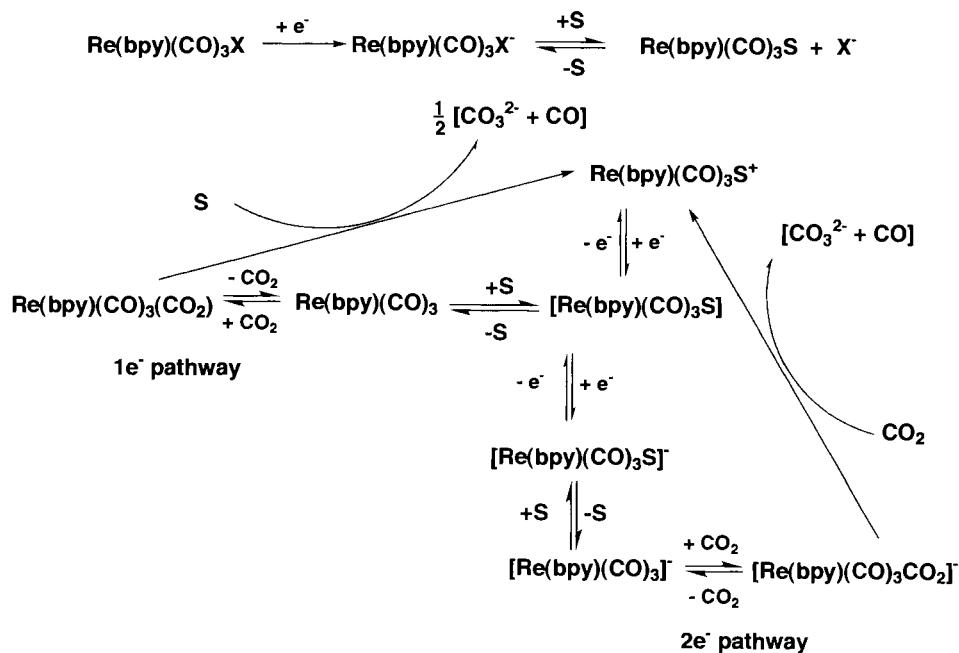


Figure 10. Modified one- and two-electron pathways for CO_2 reduction. S = solvent molecule.

The main products observed, CO and CO₃²⁻, are produced by both pathways. The authors assert [61] that production of the major side product Re(bpy)(CO)₃(O₂CH) (ν_{COO} 1630 cm⁻¹) is suppressed when the two-electron pathway dominates as it does when using [Re(bpy)(CO)₃{P(OEt)₃}]⁺ or Re(bpy)(CO)₃Cl in MeCN. They assume that Re(bpy)(CO)₃(O₂CH) is produced from either [Re(bpy)(CO)₃(CO₂)][•] or [Re(bpy)(CO)₃(CO₂)]⁻ by addition of e⁻ and H⁺ or H⁺, respectively. However, such transformations to metal-formate complexes are not well characterized. Rhenium carboxylates, [Re(bpy)(CO)₃(COO)] and [Re(bpy)(CO)₃(COO)]⁻, are generally proposed [5] as intermediates in the electrochemical reduction of CO₂ to CO (and CO₃²⁻) but no direct spectroscopic evidence has been obtained. Reported IR spectra involving an unidentified species, with ν_{COO} at 1680 cm⁻¹, show a relatively intense ν_{COO} band compared with the ν_{CO} bands. Normally, the molar absorptivity of the ν_{CO} band for bound CO is typically 3–5 times larger than that for bound CO₂ [19, 101, 102]. The correct identification of this species, which may be an organic carbonate, is essential.

3.3.4 Photochemical Systems

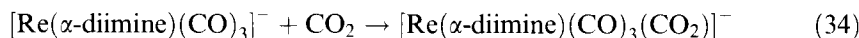
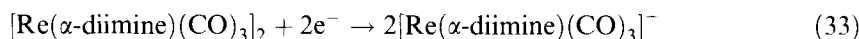
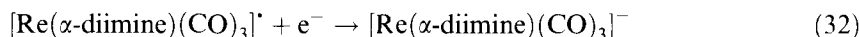
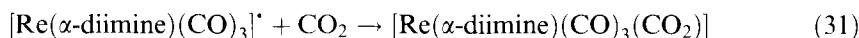
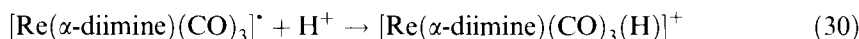
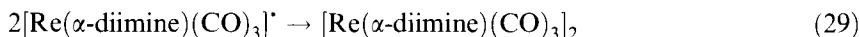
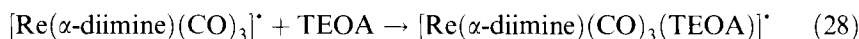
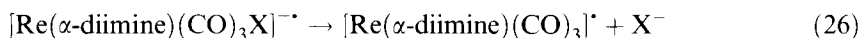
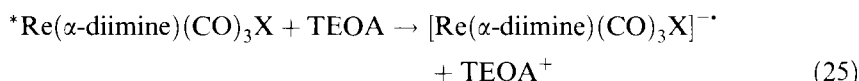
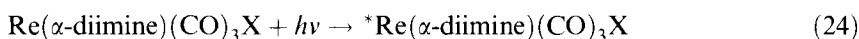
Re(α -diimine)(CO)₃X (X = halide, solvent, monodentate phosphine ligand, etc.) has been used as a photocatalyst for CO₂ reduction with TEOA in DMF [55–59, 72, 77] (Table 11). The ³MLCT excited states of these Re complexes are reductively quenched by TEOA (TEOA^{+/0} potential \approx 0.8 V) [52] to form

Table 11. Photocatalytic reduction of CO₂ with Re(bpy)(CO)₃X in DMF with TEOA as an electron donor.

Sensitizer	Additive	Product	Φ (mol einstein ⁻¹) ^b	Ref.
[Re(bpy)(CO) ₃ Cl]	Cl ⁻	CO	0.14	55, 56
[Re(bpy)(CO) ₃ Br]		CO	0.13	57, 58
[Re(bpy)(CO) ₃ Br]	10 % H ₂ O	CO	0.079	58
[Re(bpy)(CO) ₃ Br]	20 % EtOH	CO	0.11	58
[Re(bpy)(CO) ₃ Br]	Br ⁻	CO	0.14	58
[Re(bpy)(CO) ₃ P(OEt) ₃] ⁺		CO	0.38	59
[Re(bpy)(CO) ₃ P(OEt) ₃] ⁺		CO	0.16	72
[Re(bpy)(CO) ₂ {P(OEt) ₃ } ₂] ⁺		CO		69
[Re(bpy)(CO) ₃ (PPh ₃)] ⁺		CO	0.05	77
[Re(bpy)(CO) ₃ (PEt ₃)] ⁺		CO	0.024	72
[Re(bpy)(CO) ₃ {P(n-Bu) ₃ }] ⁺		CO	0.013	72
[Re(bpy)(CO) ₃ {P(O-i-Pr) ₃ }] ⁺		CO	0.20	72
[Re(bpy)(CO) ₃ {P(OMe) ₃ }] ⁺		CO	0.17	72
[Re(dmb)(CO) ₃ {P(OEt) ₃ }] ⁺		CO	0.18	72
[Re{(CF ₃) ₂ bpy}(CO) ₃ {P(OEt) ₃ }] ⁺		CO	0.005	72

[Re^I(bpy⁻)(CO)₃X]^{*}. Transient spectroscopy shows the expected bpy⁻ radical UV-vis absorption and ESR signals. When X = Br⁻, Cl⁻ or P(OEt)₃, the quenching rate constants are $6 \times 10^7 \text{ M}^{-1} \text{ s}^{-1}$ [57], $8 \times 10^7 \text{ M}^{-1} \text{ s}^{-1}$ [65] and $1.1 \times 10^9 \text{ M}^{-1} \text{ s}^{-1}$ [72], respectively, in MeCN or DMF. Transient IR spectra of both the ³MLCT excited state and the radical anion for Re(bpy)(CO)₃Cl [81], Re(4,4'-bpy)₂(CO)₃Cl [80], Re(4,4'-bpy)₂(CO)₃(MeCN)⁺ [79], Re(bpy)(CO)₂{P(OEt)₃}₂⁺ [69], Re(bpy)(CO)₃(MeCN)⁺ [85, 79], Re(dmb)(CO)₃(MeCN)⁺ [79] and Re(dmb)(CO)₃(CH₃) [78] have been measured. Transient IR shows the expected shifts of ν_{CO} for both the excited state to higher (20–80 cm⁻¹) and the reduced species to lower energy (–15 to –40 cm⁻¹) [74, 79–81] (see Table 8).

The subsequent reactions of the radical species depend on the nature of α -diimine, X, solvent and electron donor as also found in the electrochemical studies. The mechanism for photochemical CO₂ reduction must account for reactions of the electron donor (e.g., TEOA or TEA) and its reaction products. TEOA or TEA can coordinate to metal complexes and change their redox properties [27]. The following reactions can all become important under different conditions:



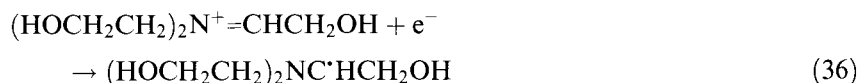
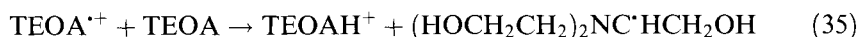
Both electrochemical and photochemical reduction of Re(bpy)(CO)₃X (X = halide), yield [Re(bpy)(CO)₃X]^{•-} [54]. It has been suggested that [Re(bpy)(CO)₃X]^{•-} reacts directly with CO₂ after loss of a CO [56]; however, electrochemical results [54, 61] indicate that CO₂ attachment only takes place after loss of X⁻. The labilization of X⁻ produces either a five-coordinate [Re(bpy)(CO)₃][•] or the six-coordinate [Re(bpy)(CO)₃S][•]. The five-coordinate species can dimerize but under photolysis conditions their low concentration makes this reaction slow. The intermediates may react with CO₂ or pick up a second electron and a proton to give Re(bpy)(CO)₃H. The formation of Re(bpy)(CO)₃H and Re(bpy)(CO)₃(O₂CH) has been reported for Re(bpy)(CO)₃X (X = Cl and Br) systems [38, 54, 55, 57, 58, 66].

Whereas formate complexes generally produce formate, metal carboxylates (or metal CO₂ adducts) generally lead to CO production [5]. Hawecker et al. [56] concluded that the Re(bpy)(CO)₃(O₂CH) is a side-product and an unlikely intermediate in the photochemical CO production. Re(bpy)(CO)₃(O₂CH) is only half as active as a CO₂ photoreduction catalysts than Re(bpy)(CO)₃(Cl). Re(bpy)(CO)₃(O₂CH) production is suppressed in the presence of excess Cl[−] whereas in the absence of excess Cl[−] ion Re(bpy)(CO)₃(O₂CH) accumulates. Further, Re(bpy)(CO)₃(O₂CH) is also formed as a side-product in the electrochemical reduction [61].

Re(bpy)(CO)₃{P(OEt)₃}⁺ produces CO with the highest quantum yield of up to 0.38 [59]. The quantum yield and turnover number using Re(bpy)(CO)₃{P(OEt)₃}⁺ depend on the intensity and wavelength of the exciting light; however, for Re(bpy)(CO)₃Cl neither quantum yield nor turnover number is intensity and wavelength dependent. Since the lifetime of [Re(bpy)(CO)₃{P(OEt)₃}][•] (514 s) is much longer than that of [Re(bpy)(CO)₃Cl][•] (6 s) under Ar in DMF, an inner filter effect by [Re(bpy)(CO)₃{P(OEt)₃}][•] may explain the wavelength and intensity dependence [59].

Electrochemical studies indicate that [Re(bpy)(CO)₃{P(OEt)₃}][•] is very stable and does not lose P(OEt)₃ or react with CO₂ in THF [61]. Only on further reduction does the complex lose P(OEt)₃ to form the five-coordinate anion [Re(bpy)(CO)₃][−] which can react with CO₂. The first and second reduction potentials of Re(bpy)(CO)₃{P(OEt)₃}⁺ are reported to be −1.25 and ∼−1.9 V vs. SCE in MeCN [61, 67], assuming the Fc/Fc⁺ and Ag/AgNO₃ potentials are 0.38 and 0.33 V vs. SCE, respectively. The *E*_{0−0} of the ³MLCT state of the Re(bpy)(CO)₃{P(OEt)₃}⁺ is ∼2.8 eV (Table 10), thus the excited-state reduction potential is ∼1.5 V (*E*_{1/2}^{+ / 0} = −1.25 V vs. SCE). Therefore the quenching of the *Re(bpy)(CO)₃{P(OEt)₃}⁺ by TEOA (*E*_{1/2}^{+ / 0} = 0.6 V vs. SCE [103]) has Δ*E*⁰ ≈ 0.9 = (1.5 − 0.6) V.

The TEOA^{•+} radical, (HOCH₂CH₂)₃N^{•+}, can react with another TEOA to form the carbon radical (HOCH₂CH₂)₂NC[•]HCH₂OH as shown in Eq. 35.



Although (HOCH₂CH₂)₂NC[•]HCH₂OH is known to be a strong reducing agent, its potential is not known. The reduction potentials of TEA^{•+} and TEOA^{•+} are 0.96 [104] and 0.6 V [103] vs. SCE in MeCN, respectively. Thus TEOA, with its electronegative oxygens, is a better reducing agent than TEA. The reduction potential of Et₂N⁺=CHCH₃ (Eq. 38) has been measured to be −1.12 V vs. SCE in MeCN [105], so the potential of (HOCH₂CH₂)₂N⁺=CHCH₂OH (Eq. 36) will be more negative than −1.12 V. Thus, while (HOCH₂CH₂)₂N⁺=CHCH₂OH may re-

duce $\text{Re}(\text{bpy})(\text{CO})_3\text{Cl}$ ($E_{1/2} = -1.35$ V) and $[\text{Re}(\text{bpy})(\text{CO})_3\{\text{P}(\text{OEt})_3\}]^+$ ($E_{1/2} = -1.25$ V), it is not expected to reduce $[\text{Re}(\text{bpy})(\text{CO})_3\text{Cl}]^*$ ($E_{1/2} \approx -1.7$ V) or $[\text{Re}(\text{bpy})(\text{CO})_3\{\text{P}(\text{OEt})_3\}]^*$ ($E_{1/2} \approx -1.9$ V). The above suggests that while the doubly reduced $[\text{Re}(\text{bpy})(\text{CO})_3]^-$ is formed in the electrochemical system, its formation is not possible in the photochemical system. Since $[\text{Re}(\text{bpy})(\text{CO})_3\{\text{P}(\text{OEt})_3\}]^*$ does not lose $\text{P}(\text{OEt})_3$ [59], it is hard to understand how the singly reduced Re complex can acquire a CO_2 ligand.

Koike et al. assumed that the monoreduced $[\text{Re}(\text{bpy})(\text{CO})_3(\text{PR}_3)]^*$ reacts with CO_2 or dimerizes in the photochemical system that they studied [72]. From the decay of $[\text{Re}(\text{bpy})(\text{CO})_3(\text{PR}_3)]^*$ observed during continuous photolysis under CO_2 , the CO_2 binding rate constants have been estimated: $\text{Re}(\text{bpy})(\text{CO})_3\{\text{P}(\text{OEt})_3\}$, $8.8 \times 10^{-3} \text{ M}^{-1} \text{ s}^{-1}$ [59]; $\text{Re}(\text{bpy})(\text{CO})_3\{\text{P}(\text{OEt})_3\}$, $5.6 \times 10^{-3} \text{ M}^{-1} \text{ s}^{-1}$ [72]; $\text{Re}(\text{bpy})(\text{CO})_3\{\text{P}(\text{O}-i\text{Pr})_3\}$, $9.4 \times 10^{-3} \text{ M}^{-1} \text{ s}^{-1}$ [72]; $\text{Re}(\text{dmb})(\text{CO})_3\{\text{P}(\text{OEt})_3\}$, $18.6 \times 10^{-3} \text{ M}^{-1} \text{ s}^{-1}$ [72]. These CO_2 binding rate constants are very slow compared with those of other metal complexes that act as photocatalysts: CoHMD^+ , $1.8 \times 10^8 \text{ M}^{-1} \text{ s}^{-1}$ [28]; $\text{Ni}(\text{cyclam})^+$, $3.2 \times 10^7 \text{ M}^{-1} \text{ s}^{-1}$ [24]; $\text{Pd}(\text{etpC})(\text{DMF})^+$, $53 \text{ M}^{-1} \text{ s}^{-1}$ [106]. The authors did not detect the formation of either the Re dimer or the CO_2 complex. Since they did not measure the dependence of the CO_2 binding rate on Re or CO_2 concentration, the actual pathway in the photochemical system is probably more complicated. Thus of fundamental importance in understanding photochemical CO_2 fixation is the elucidation of the mechanism that allows the singly reduced Re complex to bind CO_2 . One interesting possibility is that the reduced Re complex is photolabile and that the absorption of a second photon assists the loss of the sixth ligand. Detailed studies of the $\text{Re}(\text{bpy})(\text{CO})_3\text{X}$ ($\text{X} = \text{Cl}$ and Br) photochemical systems that report formation of $\text{Re}(\text{bpy})(\text{CO})_3\text{H}$, $\text{Re}(\text{bpy})(\text{CO})_3(\text{O}_2\text{CH})$ and $\text{Re}(\text{Mebpy})(\text{CO})_3\text{Br}$ in addition to the dimer [38, 54, 55, 57, 58, 66, 107] are needed.

3.4 Conclusions

Artificial photosynthetic systems offer the possibility of producing fuels and chemicals from CO_2 and sunlight in fewer steps and/or faster rates than in natural systems. It may also be possible to design such systems to operate under conditions and in environments where plant growth is not optimal or practical. Light capture, electron transfer and catalysis must be efficiently coupled. However, the approaches described in this chapter have several problems. All the systems require a sacrificial reagent. The stability of the systems is limited, the catalytic activities are too low and the overall costs are too high for commercialization. Dark reactions including the bond formation and cleavage steps are relatively slow. It is very important to investigate the factors controlling reaction rates and efficiencies through kinetic and mechanistic studies. At this stage, many questions remain. Hopefully, the insight obtained from a fundamental studies of the reactions occurring in the above systems

will provide the knowledge required for the design of useful systems. One fundamental and formidable challenge is the replacement of the 'sacrificial' electron donors by species that will lead to useful (or benign) chemicals in their own right.

Acknowledgments

We thank Drs. Norman Sutin and David Thompson (BNL) and Prof. Osamu Ishitani (Saitama University, Japan) for their helpful comments, and Prof. Shoichi Kita (Hirosaki University, Japan) for providing his unpublished data obtained during his stay at BNL. Brookhaven National Laboratory is funded under contract DE-AC02-98CH10886 with the US Department of Energy and supported by its Division of Chemical Sciences, Office of Basic Energy Sciences.

Abbreviations

bicyclam	6,6'-bis(1,4,8,11-tetraazacyclotetradecane)
bMe ₂ cyclam	6,6'-bis(5,7-dimethyl-1,4,8,11-tetraazacyclotetradecane)
4,4'-bpy	4,4'-bipyridine
bpy	2,2'-bipyridine
bpz	2,2'-bipyrazine
Brphen	5-bromo-1,10-phenanthroline
Cl ₂ bpy	4,4'-dichloro-2,2'-bipyridine
Clphen	5-chloro-1,10-phenanthroline
(CO ₂ Et) ₂ bpy	4,4'-bis(ethoxycarbonyl)-2,2'-bipyridine
cyclam	1,4,8,11-tetraazacyclotetradecane
DCE	1,2-dichloroethane
dmb	4,4'-dimethyl-2,2'-bipyridine
DMD	5,12-dimethyl-1,4,8,11-tetraazacyclotetradeca-4,11-diene
DMF	<i>N,N</i> -dimethylformamide
DMSO	dimethyl sulfoxide
dpp	2,3-di(2-pyridyl)pyrazine
dpq	2,3-di(2-pyridyl)quinoxaline
EtCN	propionitrile
EtOH	ethanol
etpC	bis[(dicyclohexylphosphino)ethyl]phenylphosphine
4Etpy	4-ethylpyridine
H ₂ A	ascorbic acid
HMD	5,7,7,12,14,14-hexamethyl-1,4,8,11-tetraazacyclotetradeca-4,11-diene
3HOpy	3-hydroxypyridine
HTIM	2,3,9,10-tetramethyl-1,4,8,11-tetraazacyclotetradecane
(isn) ₂ bpy	4,4'-isonitrile-2,2'-bipyridine
Me ₂ cyclam	5,7-dimethyl-1,4,8,11-tetraazacyclotetradecane
Mebpy	5-methyl-2,2'-bipyridine

MeCN	acetonitrile
Meimz	<i>N</i> -methylimidazole
MeOH	methanol
Mephen	5-methyl-1,10-phenanthroline
2Mepy	2-methylpyridine
3Mepy	3-methylpyridine
4Mepy	4-methylpyridine
MeTHF	2-methyltetrahydrofuran
MV ²⁺	methylviologen
(NEt ₂) ₂ bpy	4,4'-di(<i>N,N</i> -diethylamino)-2,2'-bipyridine
(NH ₂) ₂ bpy	4,4'-diamino-2,2'-bipyridine
(OCH ₃) ₂ bpy	4,4'-dimethoxy-2,2'-bipyridine
OMD	3,5,7,7,10,12,14,14-octamethyl-1,4,8,11-tetraazacyclotetradeca-4,11-diene
Otf	trifluoromethanesulfonate
PC	propylene carbonate
Ph ₂ bpy	4,4'-diphenyl-2,2'-bipyridine
Ph ₂ phen	4,7-diphenyl-1,10-phenanthroline
phen	1,10-phenanthroline
Phena	phenazine
4Phpy	4-phenylpyridine
PrCN	butyronitrile
Pr-cyclam	6-[(<i>N-p</i> -methoxybenzyl)pyridin-4-yl]methyl-1,4,8,11-tetraazacyclotetradecane or 6-[(<i>N</i> -benzyl)pyridin-4-yl]methyl-1,4,8,11-tetraazacyclotetradecane
py	pyridine
TEA	triethylamine
TEOA	triethanolamine
THF	tetrahydrofuran
TP	<i>p</i> -terphenyl
$E_{1/2}$	half-cell potential
E_{pa}	peak potential of the anodic scan
E_{pc}	peak potential of the cathodic scan
EXAFS	extended X-ray absorption fine structure
FTIR	Fourier transform Infrared
NHE	normal hydrogen electrode
SCE	saturated calomel electrode
SSCE	sodium-saturated calomel electrode
XANES	X-ray absorption near-edge structure

References

1. M. M. Halmann, M. Steinberg, *Greenhouse Gas Carbon Dioxide Mitigation*, Lewis, Boca Raton, FL, 1999.

2. T. Inui, M. Anpo, K. Izui, S. Yanagida, T. Yamaguchi (Eds.), *Advances in Chemical Conversions for Mitigating Carbon Dioxide, Studies in Surface Science and Catalysis*, Vol. 114, Elsevier, Amsterdam, **1998**.
3. J.-M. Lehn, R. Ziessel, *Proc. Natl. Acad. Sci. USA* **1987**, 79, 701–704.
4. E. Fujita, *Coord. Chem. Rev.* **1999**, 185–186, 373–384.
5. N. Sutin, C. Creutz, E. Fujita, *Comments Inorg. Chem.* **1997**, 19, 67–92.
6. S. Sahami, M. J. Weaver, *Electroanal. Chem.* **1981**, 122, 155–170.
7. S. Sahami, M. J. Weaver, *Electroanal. Chem.* **1981**, 122, 171–181.
8. B. Fisher, R. Eisenberg, *J. Am. Chem. Soc.* **1980**, 102, 7361–7365.
9. A. T. A. Tinnemans, T. P. M. Koster, D. H. M. W. Thewissen, A. Mackor, *Recl. Trav. Chim. Pays-Bas* **1984**, 103, 288–295.
10. M. Beley, J.-P. Collin, R. Ruppert, J.-P. Sauvage, *J. Chem. Soc., Chem. Commun.* **1984**, 1315–1316.
11. M. Beley, J.-P. Collin, R. Ruppert, J.-P. Sauvage, *J. Am. Chem. Soc.* **1986**, 108, 7461.
12. E. Fujita, J. Haff, R. Sanzenbacher, H. Elias, *Inorg. Chem.* **1994**, 33, 4627–4628.
13. D. J. Szalda, C. L. Schwarz, J. F. Endicott, E. Fujita, C. Creutz, *Inorg. Chem.* **1989**, 28, 3214–3219.
14. C. Creutz, H. A. Schwarz, J. F. Wishart, E. Fujita, N. Sutin, *J. Am. Chem. Soc.* **1991**, 113, 3361–3371.
15. J. L. Grant, K. Goswami, L. O. Spreer, J. W. Otvos, M. Calvin, *J. Chem. Soc., Dalton Trans.* **1987**, 2105.
16. C. A. Craig, L. O. Spreer, J. W. Otvos, M. Calvin, *J. Phys. Chem.* **1990**, 94, 7957.
17. S. Matsuoka, K. Yamamoto, T. Ogata, M. Kusaba, N. Nakashima, E. Fujita, S. Yanagida, *J. Am. Chem. Soc.* **1993**, 115, 601–609.
18. D. J. Szalda, E. Fujita, R. Sanzenbacher, H. Paulus, H. Elias, *Inorg. Chem.* **1994**, 33, 5855–5863.
19. E. Fujita, C. Creutz, N. Sutin, B. S. Brunshawig, *Inorg. Chem.* **1993**, 32, 2657–2662.
20. E. Fujita, L. R. Furenlid, M. W. Renner, *J. Am. Chem. Soc.* **1997**, 119, 4549–4550.
21. D. J. Szalda, E. Fujita, C. Creutz, *Inorg. Chem.* **1989**, 28, 1446.
22. L. R. Furenlid, M. W. Renner, E. Fujita, *Physica B* **1995**, 208–209, 739–742.
23. A. M. Tait, M. Z. Hoffman, E. Hayon, *Inorg. Chem.* **1976**, 15, 934–939.
24. C. A. Kelly, Q. G. Mulazzani, M. Venturi, E. L. Blinn, M. A. Rodgers, *J. Am. Chem. Soc.* **1995**, 117, 4911–4919.
25. N. Jubran, G. Ginzburg, H. Cohen, Y. Koresch, D. Meyerstein, *Inorg. Chem.* **1985**, 24, 251–258.
26. A. M. Tait, M. Z. Hoffman, E. Hayon, *J. Am. Chem. Soc.* **1976**, 98, 86.
27. E. Fujita, B. S. Brunshawig, D. Cabelli, M. W. Renner, L. R. Furenlid, T. Ogata, Y. Wada, S. Yanagida, in *Advances in Chemical Conversions for Mitigating Carbon Dioxide, Studies in Surface Science and Catalysis*, Vol. 114 (Eds. T. Inui, M. Anpo, K. Izui, S. Yanagida, T. Yamaguchi), Elsevier, Amsterdam, **1998**, pp. 97–106.
28. T. Ogata, S. Yanagida, B. S. Brunshawig, E. Fujita, *J. Am. Chem. Soc.* **1995**, 117, 6708–6716.
29. G. M. Brown, B. S. Brunshawig, C. Creutz, J. F. Endicott, N. Sutin, *J. Am. Chem. Soc.* **1979**, 101, 1298–1300.
30. D. A. Gangi, R. R. Durand, *J. Chem. Soc., Chem. Commun.* **1986**, 697.
31. M. H. Schmidt, G. M. Miskelly, N. S. Lewis, *J. Am. Chem. Soc.* **1990**, 112, 3420–3426.
32. E. Fujita, D. J. Szalda, C. Creutz, N. Sutin, *J. Am. Chem. Soc.* **1988**, 110, 4870.
33. H. Tanaka, H. Nagao, S.-M. Peng, K. Tanaka, *Organometallics* **1992**, 11, 1450–1451.
34. E. Fujita, C. Creutz, N. Sutin, D. J. Szalda, *J. Am. Chem. Soc.* **1991**, 113, 343–353.
35. E. Fujita, R. van Eldik, *Inorg. Chem.* **1998**, 37, 360–362.
36. S. Sakaki, A. Dedieu, *J. Organomet. Chem.* **1986**, 314, C63.
37. S. Sakaki, A. Dedieu, *Inorg. Chem.* **1987**, 26, 3278.
38. J. Hawecker, J.-M. Lehn, R. Ziessel, *J. Chem. Soc., Chem. Commun.* **1985**, 56–58.
39. J.-M. Lehn, R. Ziessel, *J. Organomet. Chem.* **1990**, 382, 157–173.
40. E. Kimura, S. Wada, M. Shionoya, T. Takahashi, Y. Iitaka, *J. Chem. Soc., Chem. Commun.* **1990**, 397.
41. E. Kimura, X. Bu, M. Shionoya, S. Wada, S. Maruyama, *Inorg. Chem.* **1992**, 31, 4542–4546.

42. E. Kimura, S. Wada, M. Shionoya, Y. Okazaki, *Inorg. Chem.* **1994**, *33*, 770–778.
43. E. Fujita, S. J. Milder, B. S. Brunschwig, *Inorg. Chem.* **1992**, *31*, 2079–2085.
44. K. Mochizuki, S. Manaka, I. Takeda, T. Kondo, *Inorg. Chem.* **1996**, *35*, 5132–5136.
45. E. Mejeritskaia, F. Luo, C. A. Kelly, B. Koch, E. M. Gundlach, E. L. Blinn, *Inorg. Chim. Acta* **1996**, *246*, 295–299.
46. S. Matsuoka, K. Yamamoto, C. Pac, S. Yanagida, *Chem. Lett.* **1991**, 2099–2100.
47. T. Ogata, Y. Yamamoto, Y. Wada, K. Murakoshi, M. Kusaba, N. Nakashima, A. Ishida, S. Takamuku, S. Yanagida, *J. Phys. Chem.* **1995**, *99*, 11916–11922.
48. S. Matsuoka, T. Kohzaki, C. Pac, S. Yanagida, *Chem. Lett.* **1990**, 2047.
49. S. Matsuoka, T. Kohzaki, C. Pac, A. Ishida, S. Takamuku, M. Kusaba, N. Nakashima, S. Yanagida, *J. Phys. Chem.* **1992**, *96*, 4437–4442.
50. J. Vasilevskis, D. C. Olson, *Inorg. Chem.* **1971**, *10*, 1228.
51. M. Wrighton, D. L. Morse, *J. Am. Chem. Soc.* **1974**, *96*, 998–1003.
52. K. Kalyanasundaram, J. Kiwi, M. Grätzel, *Helv. Chim. Acta* **1978**, *61*, 2720–2730.
53. D. J. Stufken, A. J. Vlcek, *Coord. Chem. Rev.* **1998**, *177*, 127–179.
54. B. P. Sullivan, C. M. Bolinger, D. Conrad, W. J. Vining, T. J. Meyer, *J. Chem. Soc., Chem. Commun.* **1985**, 1414–1416.
55. J. Hawecker, J.-M. Lehn, R. Ziessel, *J. Chem. Soc., Chem. Commun.* **1983**, 536–538.
56. J. Hawecker, J.-M. Lehn, R. Ziessel, *Helv. Chim. Acta* **1986**, *69*, 1990–2012.
57. C. Kutal, M. A. Weber, G. Ferraudi, D. Geiger, *Organometallics* **1985**, *4*, 2161–2166.
58. C. Kutal, A. J. Corbin, G. Ferraudi, *Organometallics* **1987**, *6*, 553–557.
59. H. Hori, F. P. A. Johnson, K. Koike, O. Ishitani, T. Ibusuki, *J. Photochem. Photobiol. A* **1996**, *96*, 171–174.
60. A. I. Breikss, H. D. Abruña, *J. Electroanal. Chem.* **1986**, *201*, 347–358.
61. F. P. A. Johnson, M. W. W. George, F. Hartl, J. J. Turner, *Organometallics* **1996**, *15*, 3374–3387.
62. G. J. Stor, F. Hartl, J. W. M. v. Outersterp, D. J. Stufkens, *Organometallics* **1995**, *14*, 1115–1131.
63. J. W. M. van Outersterp, F. Hartl, D. J. Stufkens, *Organometallics* **1995**, *14*, 3303–3310.
64. J. V. Caspar, T. J. Meyer, *J. Phys. Chem.* **1983**, *87*, 952–957.
65. K. Kalyanasundaram, *J. Chem. Soc., Faraday Trans.* **1986**, *82*, 2401–2415.
66. B. P. Sullivan, T. J. Meyer, *J. Chem. Soc., Chem. Commun.* **1984**, 1224–1245.
67. O. Ishitani, personal communication, **1999**.
68. D. P. Summers, J. C. Luong, M. S. Wrighton, *J. Am. Chem. Soc.* **1981**, *103*, 5238–5241.
69. O. Ishitani, M. W. George, T. Ibusuki, F. P. A. Johnson, K. Koike, K. Nozaki, C. Pac, J. J. Turner, J. R. Westwell, *Inorg. Chem.* **1994**, *33*, 4712–4717.
70. P. Christensen, A. Hamnett, A. V. G. Muir, J. A. Timney, *J. Chem. Soc., Dalton Trans* **1992**, 1455–1463.
71. J. C. Luong, L. Nadjo, M. S. Wrighton, *J. Am. Chem. Soc.* **1978**, *100*, 5790–5795.
72. K. Koike, H. Hori, M. Ishizuka, J. R. Westwell, K. Takeuchi, T. Ibusuki, K. Enjouji, H. Konno, K. Sakamoto, O. Ishitani, *Organometallics* **1997**, *16*, 5724–5729.
73. P. J. Giordano, M. S. Wrighton, *J. Am. Chem. Soc.* **1979**, *101*, 1067.
74. P. Glyn, M. W. George, P. M. Hodges, J. J. Turner, *J. Chem. Soc., Chem. Commun.* **1989**, 1655–1657.
75. L. A. Lucia, R. D. Burton, K. S. Schanze, *Inorg. Chim. Acta* **1993**, 103–106.
76. B. Rossenaar, D. J. Stufkens, A. J. Vlcek, *Inorg. Chem.* **1996**, *35*, 2902–2909.
77. H. Hori, F. P. A. Johnson, K. Koike, K. Takeuchi, T. Ibusuki, O. Ishitani, *J. Chem. Soc., Dalton Trans.* **1997**, 1019–1023.
78. C. J. Kleverlaan, D. J. Stufkens, I. P. Clark, M. W. George, J. J. Turner, D. M. Martino, H. van Willigen, A. J. Vlcek, *J. Am. Chem. Soc.* **1998**, *120*, 10871–10879.
79. S. Kita, B. S. Brunschwig, E. Fujita, unpublished work.
80. D. R. Gamelin, M. W. George, P. Glyn, F.-W. Grevels, F. P. A. Johnson, W. Klotzbucher, S. L. Morrison, G. Russell, K. Schaffner, J. J. Turner, *Inorg. Chem.* **1994**, *33*, 3246–3250.
81. M. W. George, F. P. A. Johnson, J. R. Westwell, P. M. Hodges, J. J. Turner, *J. Chem. Soc., Dalton Trans.* **1993**, 2977–2979.
82. C.-F. Shu, M. S. Wrighton, *Inorg. Chem.* **1988**, *27*, 4326–4329.

83. D. H. Gibson, B. A. Sleadd, X. Yin, A. Viji, *Organometallics* **1998**, *17*, 2689–2691.
84. D. H. Gibson, X. Yin, *J. Am. Chem. Soc.* **1998**, *120*, 11200–11201.
85. M. W. George, J. J. Turner, *Coord. Chem. Rev.* **1998**, *177*, 201.
86. I. P. Clark, M. W. George, F. P. A. Johnson, J. J. Turner, *J. Chem. Soc., Chem. Commun.* **1996**, 1587–1588.
87. For the complexes considered here, we expect the nuclear configuration of the singlet and triplet MLCT states to be similar. Hence the Stokes shift between the two states is small.
88. The singlet–triplet and ground–excited state energy differences and the absorption and emission energies are treated as unsigned quantities and taken as positive.
89. B. S. Brunschwig, S. Ehrenson, N. Sutin, *J. Phys. Chem.* **1986**, *90*, 3657–3668.
90. The spherical cavity model requires parameters for the solvent and the cavity to calculate the reorganization energy. The dimensions of the molecule have been obtained from models created in MacSparten. The cavity radius was calculated as $r = (\sqrt[3]{d_1 d_2 d_3})/2$, where d_i are the three principle diameters of the molecule (including van der Waals end radius for each atom) and are 7.8, 11.26 and 11.26, respectively, with $r = 5.0$ Å. The Re atom is placed off center by 1.3 Å and the electron transfer distance is 3.5 Å. The optical (square of the refractive index) and static dielectric constants of the solvent were used.
91. E. M. Kober, J. V. Caspar, R. S. Lumpkin, T. J. Meyer, *J. Phys. Chem.* **1986**, *90*, 3722.
92. J. V. Caspar, T. J. Meyer, *Inorg. Chem.* **1983**, *22*, 2444.
93. L. A. Worl, R. Duesing, P.-Y. Chen, L. D. Ciana, T. J. Meyer, *J. Chem. Soc.* **1991**, 849–858.
94. L. Sacksteder, A. P. Zipp, E. A. Brown, J. Streich, J. N. Demas, B. A. DeGraff, *Inorg. Chem.* **1990**, *29*, 4335–4340.
95. J. P. Claude, T. J. Meyer, *J. Phys. Chem.* **1995**, *99*, 51–54.
96. J. A. Baiano, R. J. Kessler, R. S. Lumpkin, M. J. Munley, J. W. R. Murphy, *J. Phys. Chem.* **1995**, *99*, 17680–17690.
97. P. Chen, R. Duesing, D. K. Graff, T. J. Meyer, *J. Phys. Chem.* **1991**, *95*, 5850–5858.
98. B. P. Sullivan, T. J. Meyer, *Organometallics* **1986**, *5*, 1500–1502.
99. K. Toyohara, H. Nagao, T. Adachi, T. Yoshida, K. Tanaka, *Chem. Lett.* **1996**, 27–28.
100. D. H. Gibson, X. Yin, *J. Chem. Soc., Chem. Commun.* **1999**, 1411–1412.
101. H. Tanaka, B.-C. Tzeng, H. Nagao, S.-M. Peng, K. Tanaka, *Inorg. Chem.* **1993**, *32*, 1508–1512.
102. J. R. Pinkes, C. J. Masi, R. Chiulli, B. D. Steffey, A. R. Cutler, *Inorg. Chem.* **1997**, *36*, 70–79.
103. H. Sun, M. Z. Hoffman, *J. Phys. Chem.* **1994**, *98*, 11719–11726.
104. J. W. Arbogast, C. S. Foote, M. Kao, *J. Am. Chem. Soc.* **1992**, *114*, 2277–2279.
105. D. D. M. Wayner, D. J. McPhee, D. Griller, *J. Am. Chem. Soc.* **1988**, *110*, 132–137.
106. D. L. DuBois, A. Miedaner, R. C. Haltiwanger, *J. Am. Chem. Soc.* **1991**, *113*, 8753–8764.
107. O. Ishitani, I. Namura, S. Yanagida, C. Pac, *J. Chem. Soc., Chem. Commun.* **1987**, 1153–1154.

4 The Electrochemical and Photochemical Activation of Redox Enzymes

Eugenii Katz, Andrew N. Shipway and Itamar Willner

4.1 Introduction

In the great majority of enzymes the redox center is located sufficiently far from the outermost surface to be electrically inaccessible. Consequently, most enzymes do not exchange electrons with electrodes on which they are adsorbed, i.e., their redox centers are neither electrooxidized nor electroreduced upon the application of potentials that are more positive or negative than the thermodynamic redox potential of the enzyme redox center [1]. It seems that part of the protein or glycoprotein shell serves as an insulator to prevent indiscriminate electron exchange between the different redox macromolecules of living systems. This isolation is necessary because such exchange would lead to an equipotential system, unable to sustain life. The distance dependence of the rate of electron transfer in proteins has been the subject of extensive experimental [2] and theoretical studies [3] during the past two decades.

Electron-transfer theory predicts that the electron-transfer rate constant between a donor-acceptor pair is given by Eq. 1:

$$k_{\text{et}} \propto e^{-\beta(d-d_0)} e^{[-(\Delta G^\circ + \lambda)^2 / (4RT\lambda)]} \quad (1)$$

where ΔG° and λ correspond to the free energy and reorganization energy accompanying electron-transfer and d_0 and d are the Van der Waals distance and actual distance separating the donor-acceptor centers, respectively. The electrode and the redox center embedded in the enzyme can be viewed as a donor-acceptor pair. Thus, the thick protein layer surrounding the active center introduces a spatial separation of the donor-acceptor pair and a kinetic barrier for electron transfer. This separation leads to the electrical insulation of the active sites of most redox proteins/enzymes. Various approaches have been developed and many bioelectrochemical systems have been designed to overcome this problem, providing efficient electrical contact of biocatalysts at electrode surfaces. These methodologies range from the simple application of soluble enzymes with diffusional electron-hole mediators to

systems with very sophisticated biomolecular architectures composed of numerous components. In addition to the electrochemical activation of biocatalytic systems, enzymes may be activated by light in artificial systems composed of the biocatalyst and a photosensitizer together with some additional components providing efficient interaction between them. The aim of this chapter is to review different kinds of systems where redox enzymes are activated either by electrical contact with electrodes or by light, and to address the potential applications of such assemblies.

4.2 The Electrochemical Activation of Enzymes

4.2.1 Direct, Nonmediated Electron Transfer Between Enzymes and Electrodes

The direct electron transfer between the redox-active sites of proteins and electrodes is normally prohibited as a consequence of steric insulation by the protein matrix. Early studies demonstrated, however, that certain enzymes or redox proteins can exhibit electrical communication with electrode supports, and that electrically stimulated biocatalytic transformations can be driven by that process (Figure 1A)

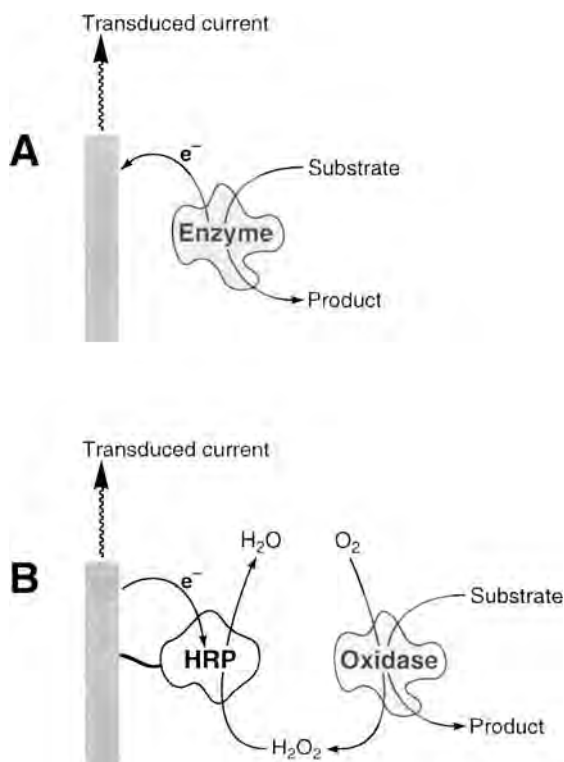


Figure 1. The direct, non-mediated electrical contacting of enzymes: (A) direct electron transfer between an electrode and an enzyme molecule located in close vicinity to the surface; (B) application of the direct electrical 'wiring' of HRP for the detection of H_2O_2 produced by an oxidase in response to a primary substrate.

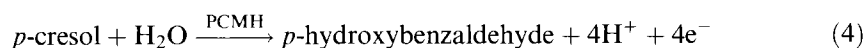
[4, 5]. The direct electroreduction of H_2O_2 by horseradish peroxidase (HRP):



has been demonstrated [6], and related heme-containing peroxidases, e.g., cytochrome *c* peroxidase [7], lactoperoxidase [8] and chloroperoxidase [9], have shown similar direct electron-transfer communication with electrode surfaces. Laccase (Lac, a copper-containing polyphenol oxidase) has been found to electrocatalyze the reduction of molecular oxygen [10]:



The ability of these enzymes to contact directly the electrode is attributed to the peripheral location of the redox center. A detailed kinetic study [11] of the peroxidase-catalyzed reduction of H_2O_2 revealed that 42 % of the enzyme molecules are aligned on the electrode surface in a configuration where the redox heme site is accessible for direct electron transfer. Other enzymes possess two redox sites, and electron transfer proceeds vectorially from a peripheral site to an inner component. For example, *p*-cresol methyl hydroxylase [PCMH, a flavin adenine dinucleotide (FAD)- and heme-containing redox enzyme] affects the direct oxidation of *p*-cresol to *p*-hydroxybenzaldehyde [12]:

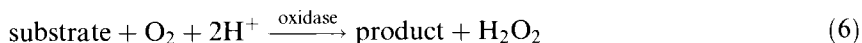


Similarly, flavocytochrome c_{552} (Cyt c_{552} , sulfide cytochrome *c* oxidoreductase), that includes FAD and two covalently linked heme groups, is bioelectrocatalytically active for the oxidation of sulfide to sulfur [13]:



The direct electronic communication of this series of redox enzymes allows their application as bioactive sensing interfaces: *p*-cresol [12], methylamine [14] and fructose [15] detection have been reported in the presence of *p*-cresol methyl hydroxylase, methylamine dehydrogenase and fructose dehydrogenase, respectively.

Sensors have also been constructed from some oxidases directly contacted to electrodes to give bioelectrocatalytic systems. These enzymes utilize molecular oxygen as the electron acceptor for the oxidation of their substrates. Enzymes such as catechol oxidase, amino acid oxidase, glucose oxidase, lactate oxidase, pyruvate oxidase, alcohol oxidase, xanthine oxidase and cholesterol oxidase catalyze the oxidation of their respective substrates with the concomitant reduction of O_2 to H_2O_2 :



The direct electron-transfer communication between HRP and electrodes allows the electroreduction of H_2O_2 in the potential range -0.2 to 0 V (vs. SCE) and its coupling to these oxidases can thus yield amperometric biosensors (Figure 1B). The

quantity of H_2O_2 generated is controlled by the substrate concentration, so the resulting current provides a quantitative measure for the analyte. Thus, amperometric biosensors based on HRP coupled with glucose oxidase for glucose analysis [16–20], with alcohol oxidase for alcohol detection [21], with choline oxidase for choline analysis [16] and with amino acid oxidase for amino acid determinations [22] have been constructed. Various conducting materials such as carbon black [6], pyrolytic graphite [23] and platinized carbon particles [24] have been used to support the enzymes, and carbon paste [25, 26] and polypyrrole [17, 25] have been used to entrap them.

Electrodes functionalized with some low molecular weight electrochemically inactive compounds have been found to effect electrical communication between redox proteins or redox enzymes and electrode supports. Reversible electrochemistry of Cyt *c*, which includes a partially exposed heme site, has been observed at Au, Pt and Ag electrodes modified with monolayers of various promoters [27–29]. Generally these promoters are linked to the electrode by a thiol or disulfide group and include an organic functional unit that interacts with the Cyt *c* protein backbone. The promoter monolayer prohibits the direct contact between the protein and the metal electrode surface, thus preventing irreversible unfolding of the protein. In addition, interactions between the promoter and the protein molecules can result in the specific alignment of the protein at the electrode surface, providing short electron-transfer distances that allow efficient electrical contact. The most common promoter for the activation of the interfacial electrochemistry of Cyt *c* is bis(4-pyridyl) disulfide [30], but several other thiol- or disulfide-derivatized molecules are also effective [31]. Amino acid and oligopeptide monolayers have been used as promoters for enhancing the interfacial electrochemistry of Cyt *c* [32] as well as other cytochromes [33]. Other promoters such as imidazole [34], thiophene [35] and iodide [36] deposited on Au or Ag electrodes have also been used to facilitate Cyt *c* electrochemistry. This electrochemically contacted Cyt *c* was applied to activate secondary biocatalytic processes stimulated by Cyt *c*-dependent enzymes (e.g., cytochrome oxidase, cytochrome reductase, ascorbate oxidase, laccase, etc.) [37, 38]. A similar methodology has been applied to other redox proteins and enzymes such as ferritin, blue copper proteins, azurin, pseudoazurin, umecyanin, stellacyanin, plantacyanin, plastocyanin and cucumber ascorbate oxidase [39]. 4-Mercaptopyridine (and other thiol and disulfide derivative) monolayer-modified Au electrodes have been used to enhance the electrochemistry of these proteins/enzymes. Protonated aminosiloxane-modified indium tin oxide electrodes have been reported to be efficient interfaces for stimulating electron transfer to negatively charged ferredoxin [40]. These promoters apparently align the protein molecules on the electrode surface in an orientation that facilitates efficient electron-transfer communication.

Direct electrical communication between enzyme active sites and electrodes may also be facilitated by the nanoscale morphology of the electrode. The modification of electrodes with metal nanoparticles allows the tailoring of surfaces with features that can penetrate close enough to the enzyme active site to make non-mediated electron transfer possible. Electrodes modified by unaggregated 12 nm diameter gold nanoparticles have been found to have the correct morphology to allow direct electron transfer between the cytochrome *c* active site and the electrode [41]. Elec-

trodes modified by different sizes or aggregation states of gold colloids do not exhibit this behavior. The electrical contacting of enzymes via Au nanoparticles has also been used for the construction of biosensing devices. In one example, 30 nm particles were used to establish efficient contact with HRP [42], and in another, a D-fructose dehydrogenase–Au colloid complex was immobilized on an electrode in a carbon paste [43].

Although enzymes with deeply embedded active centers do not normally allow significant non-mediated electron transfer [44], under carefully chosen conditions direct electron transfer is possible, and has been reported for glucose oxidase (GOx) at a bare Ag electrode [45] and in graphite paste electrodes [46]. These systems are unusual and the nonmediated mechanism of such long-range electron transfer is not fully understood.

Another way to effect direct electron transfer to the active sites of proteins is to shorten the electron-transfer distance by employing low molecular weight redox-active fragments of the native biomaterials. Microperoxidase-11 (MP-11, **1**), is a heme undecapeptide constituting the active site microenvironment of Cyt *c* [47]. Since the active site of MP-11 is not sufficiently isolated by the short oligopeptide chain, the direct electrochemistry of MP-11 can be observed in aqueous [48] and nonaqueous [49] solutions at unmodified electrodes. Microperoxidase-11 has been covalently linked to amino- [50] and carboxyl-functionalized [51] Au electrodes by its carboxylic and amino groups, respectively. The MP-11 monolayer reveals electrocatalytic activity for the reduction of H_2O_2 [50] in aqueous media and for organic peroxide reduction in nonaqueous solutions [52].

4.2.2 Electron Transfer Between Enzymes and Electrodes Provided by Diffusional Mediators

The electrical contacting of redox enzymes that defy direct electrical communication with electrodes can be established by mediated electron transfer using synthetic or biologically active charge carriers. Mediated electron transfer (MET) can be effected by a diffusional mechanism (Figure 2), where the electron relay is either oxidized or reduced at the electrode surface. Diffusional penetration of the oxidized or

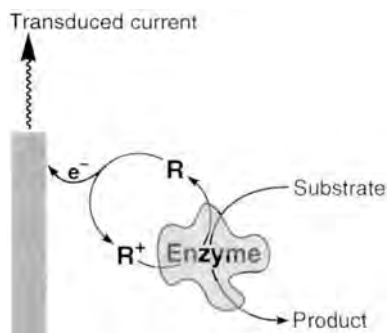


Figure 2. The electrical ‘wiring’ of a redox enzyme via a diffusional mobile electron-transfer mediator shuttling between an enzyme reaction center and an electrode.

Table 1. Diffusional electron transfer mediators applied to the immobilized enzymes.

Enzyme	Mediator	Mediator redox potential/mV (vs. SCE)	Ref.
Glucose oxidase, EC 1.1.3.4, from <i>Aspergillus niger</i>	1,4-Benzoquinone	39	57
	1,1'-Dimethylferrocene	100	58
	Ferrocenecarboxylic acid	275	59
	Phenazine methosulfate	-161	60
	Tetrathiofulvalene	300	61
	Tetracyanoquinodimethane	127	62
Xanthine oxidase, EC 1.2.3.3, from buttermilk	[Fe(CN) ₆] ⁴⁻	180	63
Cholesterol oxidase, EC 1.1.3.6, from <i>Pseudomonas</i> sp.	Ferrocenecarboxylic acid	275	64
Hydrogenase (Fe/S type)	Dimethylviologen	-681	65
Peroxidase, EC 1.11.1.7, from horseradish	[Fe(CN) ₆] ⁴⁻	180	66
Lactate dehydrogenase, EC 1.1.2.3 (Cyt. b ₂), from yeast	[Fe(CN) ₆] ⁴⁻	180	57a
Glucose dehydrogenase, EC 1.1.99.17, from <i>A.</i> <i>calcoaceticus</i>	1,1'-Dimethylferrocene	100	67
	Phenazine ethosulfate	-172	68
NADH dehydrogenase, EC 1.6.99, from <i>Bacillus</i> <i>stearothermophilus</i>	Ferrocenylmethanol	185	69
	Ferrocenecarboxylic acid	275	69

reduced relay into the protein yields a sufficiently short electron-transfer distance for the electrical activation of the biocatalyst. Ferrocene derivatives, ferricyanide, quinones, *N,N'*-dialkyl-4,4'-bipyridinium and other electroactive substrates have been employed for MET and the electrical activation of redox enzymes [53]. Diffusional MET can be applied to many biocatalytic systems lacking direct electrical contact with the conductive support, such as enzyme monolayers and multilayers [53] (including multilayer arrays composed of different enzymes [54]). Table 1 gives examples of immobilized enzymes that have been electrically contacted by the use of diffusional electron-transfer mediators. To improve the contact between electron relay molecules and redox enzymes, micellar systems composed of ferrocene-functionalized surfactants have been applied [55, 56]. Glucose oxidase has been electrically contacted using such redox-active micelles and an advantage in the electron-transfer efficiency over homogeneous electron relays was demonstrated.

Monolayers and multilayers of redox enzymes (e.g., glucose oxidase [70], bilirubin oxidase [71]) have been organized on electrode surfaces using bifunctional reagents (producing covalent bonding between the layers) [70, 71] or using bioaffinity

interactions (e.g., biotin–avidin [72] or antigen–antibody [73]). Multilayer arrays consisting of different enzymes (e.g., acetylcholine esterase and choline oxidase [54]) have been organized on electrode surfaces to provide cascades of enzymatic reactions. All these multilayer enzyme arrays were electrically contacted using diffusional mediators (e.g., ferrocenecarboxylic acid). The application of a rough electrode surface (an Au electrode with a roughness factor of ca. 15–30 [74]) allows an increase in the quantity of enzyme immobilized in mono- or multi-layer arrays, giving an improved amperometric response over architectures constructed on smooth electrodes [54].

Enantioselective MET has been addressed in a series of studies using diffusional chiral electron mediators [75–77]. The chiral electron relays (*S*)- and (*R*)-*N,N*-dimethyl-1-ferrocenylethylamine were reported to stimulate enantioselective bioelectrocatalyzed oxidation of glucose in the presence of glucose oxidase [75]. The bioelectrocatalyzed oxidation of glucose was enhanced ca. 2-fold in the presence of the (*S*)-isomer compared with the (*R*)-isomer. Kinetic analysis of the bioelectrocatalyzed oxidation of glucose by the two enantiomeric electron relays suggests that the protein induces chiral discrimination because of diastereoisomeric interactions during the mediator's penetration and dissociation pathways. Chiral discrimination in mediated electron transfer and subsequent bioelectrocatalyzed transformations has been observed using various diffusional electron relays and enzymes [76].

4.2.3 Electrochemistry of Enzymes at Electrodes Functionalized with Monolayers of Redox Relays

The electrochemical contacting of solution-state enzymes with surface-immobilized redox mediators is of interest in the study of the interfacial association of the enzyme with the mediators. The electrochemical kinetics of electrodes functionalized with layers of various mediators (e.g., viologens [78], C₆₀ derivative [79]) have been studied upon their interaction with diffusionally free enzymes. The temporary association of enzyme molecules to the relay-functionalized electrode surface has been demonstrated in these systems. This complexation results in enantioselective electrical contacting of redox enzymes when chiral electron mediator monolayers are used [80]. (*R*)- or (*S*)-2-methylferrocenecarboxylic acid (**2** or **3**) was assembled as a monolayer on an Au electrode (Figure 3A). The monolayer-mediated chiroselective oxidation of glucose in the presence of glucose oxidase and a ca. 1.9-fold enhanced biocatalytic oxidation of glucose was observed in the presence of the (*S*)-relay (**3**) enantiomer functionalized monolayer electrode (Figure 3B).

Microperoxidase-11 monolayers mediate electron transfer to hemoproteins [e.g., Cyt *c*, myoglobin (Mb) and hemoglobin (Hb)] by the formation of affinity complexes at the interface [81]. Microgravimetric analysis of these assemblies has determined the association constant of myoglobin to the MP-11 monolayer to be $K_a = 3.9 \times 10^2 \text{ M}^{-1}$. The MP-11–hemoprotein affinity complexes permit the mediated reduction of protein heme sites. Figure 4 shows the electrocatalytic cathodic currents originating from the MP-11 MET to the heme centers of Cyt *c*, Mb and Hb. The heme-containing monolayer can also stimulate MET to cytochrome-

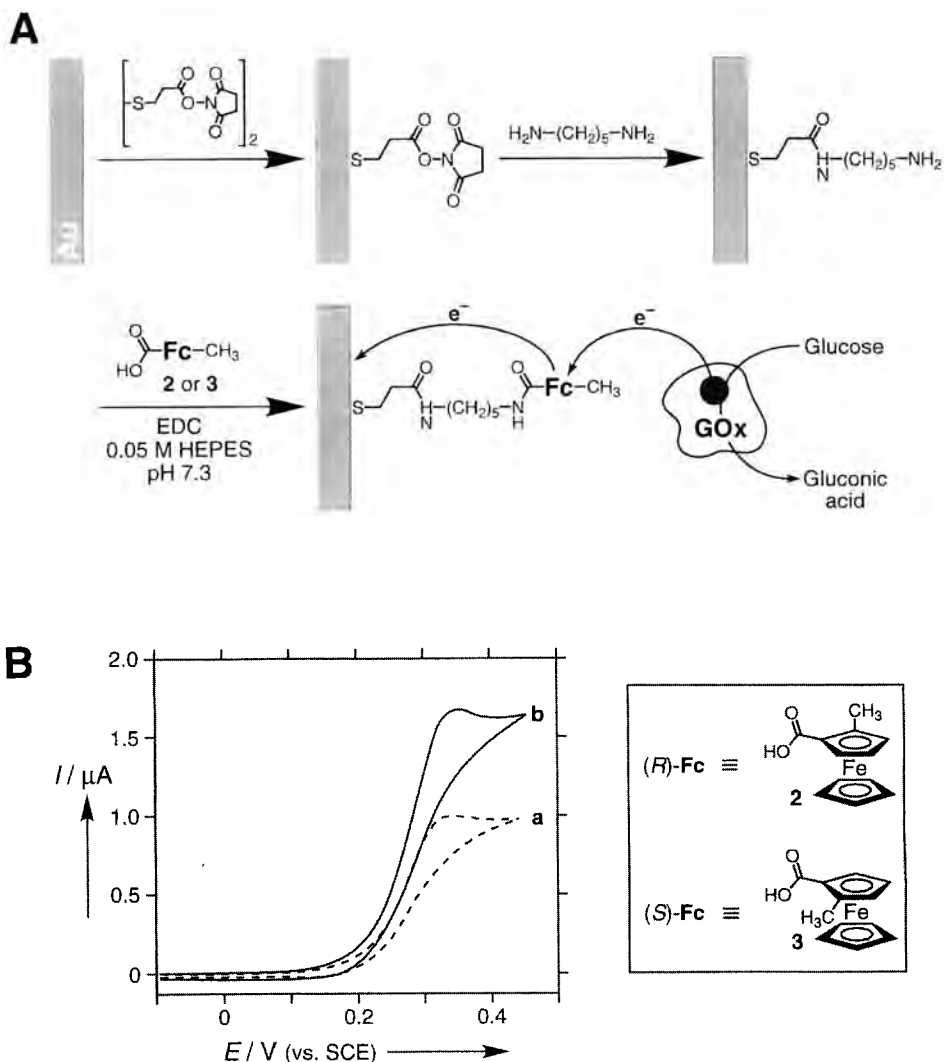


Figure 3. The enantioselective bioelectrocatalyzed oxidation of glucose by glucose oxidase at an electrode modified by a chiral electron-transfer mediator. (A) Organization of the chiral ferrocene monolayer-modified Au electrode and its interaction with soluble GOx. EDC = 1-(3-dimethylaminopropyl)-3-ethylcarbodiimide hydrochloride. (B) Cyclic voltammograms of the ferrocene-modified electrode (curves a and b for *(R)*-Fc (**2**) and *(S)*-Fc (**3**), respectively) in the presence of 1×10^{-5} M GOx and 50 mM glucose; 0.1 M phosphate buffer, pH 7.0; potential scan rate, 5 mV s^{-1} ; electrode area, 0.26 cm^2 .

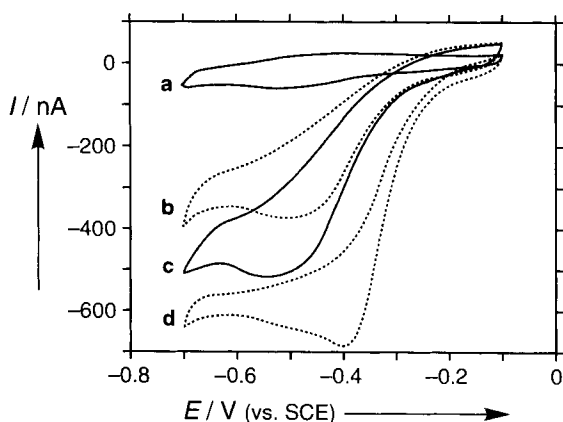


Figure 4. The electron-transfer process from an Au electrode to soluble heme proteins as mediated by a monolayer of microperoxidase-11. Cyclic voltammograms of a microperoxidase-11 monolayer-electrode in the absence (a) and presence of added hemoproteins: (b) with hemoglobin, 6×10^{-5} M; (c) with myoglobin, 2×10^{-4} M; (d) with cytochrome *c*, 2×10^{-4} M. Measurements recorded in 0.1 M phosphate buffer, pH 7.0, under Ar; potential scan rate, 5 mV s^{-1} .

dependent enzymes. The MP-11 monolayer was found to yield an affinity complex with the native cytochrome *b*₅-dependent nitrate reductase (NR, EC 1.9.6.1 from *Escherichia coli*), giving an NR surface coverage estimated as $3.8 \times 10^{-12} \text{ mol cm}^{-2}$ [82]. The association constant of the MP-11–nitrate reductase complex was determined by quartz crystal microbalance (QCM) measurements to be $K_a = 3.7 \times 10^3 \text{ M}^{-1}$. Electrocatalytic reduction of nitrate ions was achieved when the dissolved nitrate reductase was electrically contacted via the monolayer-immobilized MP-11.

4.2.4 Electrochemical Activation of Enzymes by the Attachment of Redox Relays to the Protein Backbone

The chemical modification of redox enzymes with electron relay groups permits the mediated electron transfer and the electrical ‘wiring’ of the proteins [83–85] (Figure 5A). The covalent attachment of electron-relay units at the protein periphery, as well as inner sites, yields short inter-relay electron-transfer distances. Electron ‘hopping’ or tunneling between the periphery and the active site allows electrical communication between the redox enzyme and its environment. The simplest systems of this kind involve electron relay-functionalized enzymes diffusively communicating with electrodes [83], but more complex assemblies including immobilized enzymes have also been reported.

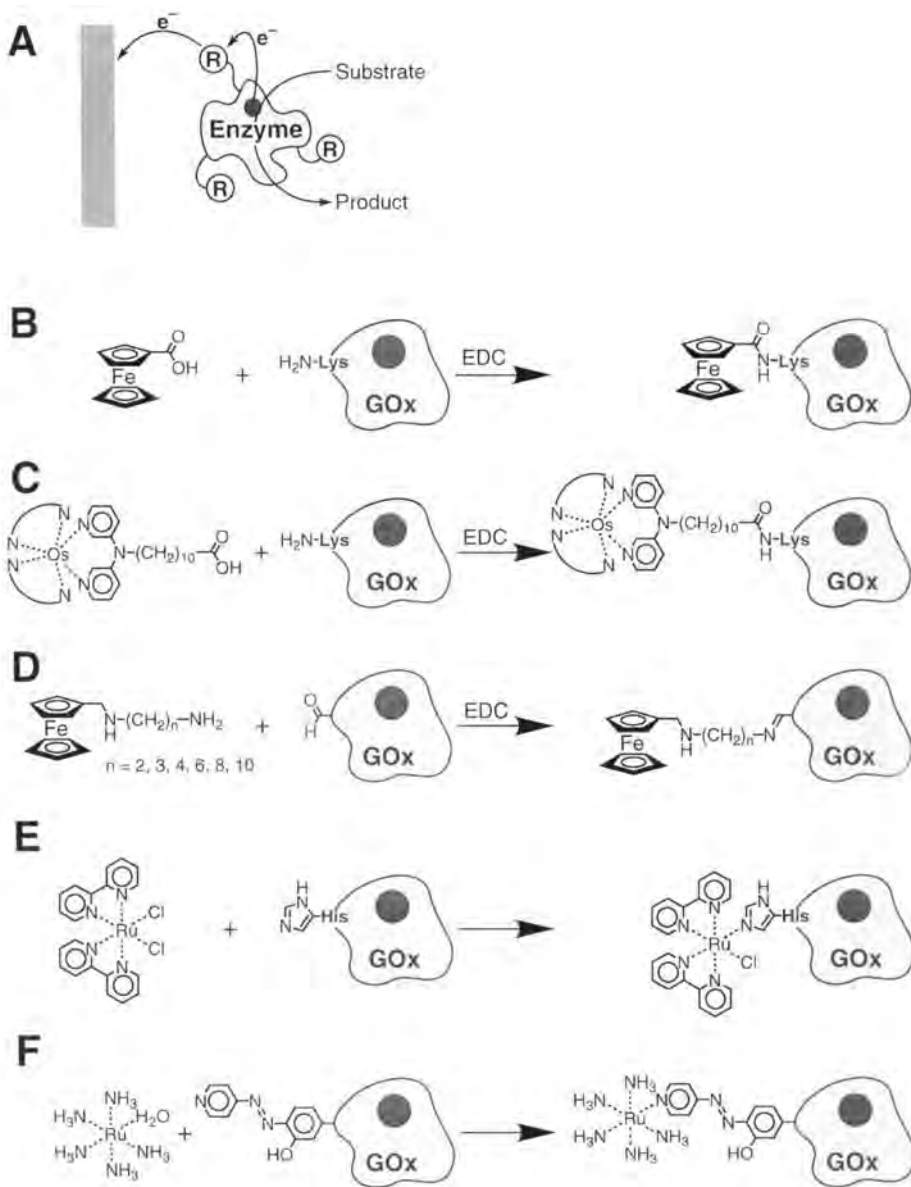


Figure 5. (A) A soluble enzyme electrically contacted with an electrode surface via redox-mediator groups covalently tethered to the protein backbone. (B)–(F) Different kinds of redox mediators tethered in various manners to the protein backbone. (B) A ferrocene unit linked to a lysine amino group via an amide bond generated in the presence of EDC. (C) An Os complex linked to a lysine amino group via an amide bond in the presence of EDC. (D) A ferrocene unit linked via a Schiff base to an aldehyde group generated in the protein backbone upon its oxidation with IO_4^- . (E) $Ru(bpy)_2Cl_2$ linked to histidine residues by the formation of a $Ru(bpy)_3His$ complex. (F) A Ru complex linked to a pyridine group by ligand exchange.

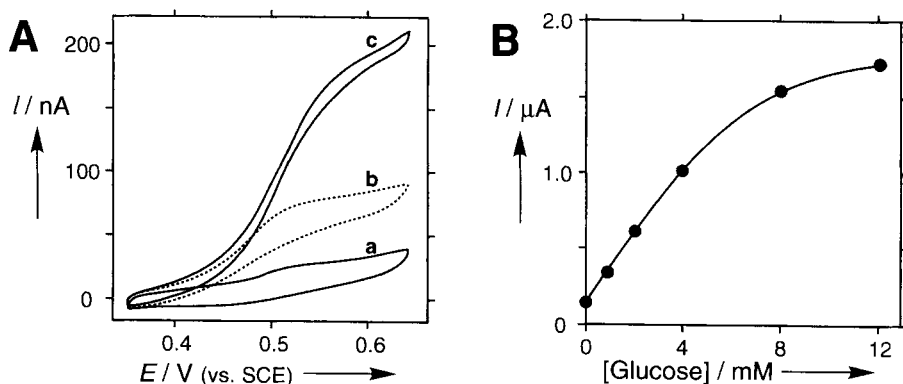


Figure 6. Electrical 'wiring' of glucose oxidase with ferrocene units tethered to lysine residues of the protein backbone (cf. Figure 5B). (A) Cyclic voltammograms of a bare Au electrode in the presence of modified GOx (10 mg mL^{-1}) and glucose at (a) 0, (b) 0.8 and (c) 5 mM. Experiments were performed in 0.085 M phosphate buffer, pH 7.0, under argon. (B) Glucose concentration dependence of the current at 0.26 V vs. SCE developed by the biocatalytic system (using a larger electrode). Adapted from Ref. [83] with permission.

Diffusional electrochemistry of enzymes functionalized with tethered redox relays

Glucose oxidase can be covalently modified with ferrocene electron-relay groups by the carbodiimide coupling of ferrocenecarboxylic acid [83] (Figure 5B) or osmium(bis-4,4'-diaminobutane-*N,N*-bis-2-pyridyl-11-aminoundecanoic acid) [55] (Figure 5C) to the amino functions of the protein backbone. Other chemical procedures have also been used to produce relay groups peripherally bound to proteins. For example, carbonyl groups generated in glycoproteins (e.g., glucose oxidase) by oxidative treatment with periodate have been coupled to an amino-functionalized ferrocene via Schiff bases (Figure 5D) [84]. In another approach, ruthenium complexes have been attached to glucose oxidase using either natural histidine residues [86] (Figure 5E) or artificially introduced pyridine groups [83b] (Figure 5F) in the protein backbone. The randomly distributed relay groups provide electrical contact between the enzyme redox center and the unmodified electrode surface. The resulting amperometric response was measured by cyclic voltammetry (Figure 6A) and a calibration curve was derived (Figure 6B). It has been demonstrated that longer spacer groups bridging the electron relay groups and the enzyme provide higher mobility, shorten the electron-transfer distance, and thus enhance the enzyme's bioelectrocatalytic activity (Figure 7) [84]. Partial and reversible unfolding of the enzyme (using urea) during the covalent modification of the protein with the relay is also important since it allows the attachment of the electron mediator to inter-protein positions close to the active site of the enzyme [87].

While an increased loading of an electron mediator on a protein enhances the effectiveness of electrical contacting, the enzyme activity suffers owing to changes in its structure. The chemical modification of redox proteins with synthetic

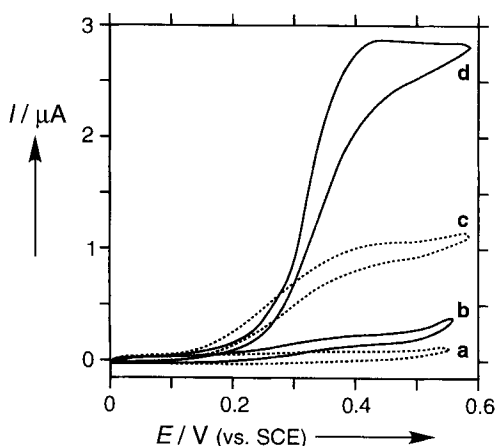


Figure 7. Cyclic voltammograms of a bare Au electrode in the presence of glucose oxidase with ferrocene units covalently tethered to lysine residues (cf. Figure 5D) (2 mg mL^{-1}); in the absence of glucose (a) and in the presence of glucose, 40 mM for spacers with $n = 2$ (b), $n = 3$ (c) and $n = 8$ (d). Experiments were performed in 0.1 M phosphate buffer, pH 7.2; potential scan rate, 10 mV s^{-1} . Adapted from Ref. [84] with permission.

electron mediators is always accompanied by this partial denaturing of the native biocatalyst, so the modification must be carefully controlled to achieve the optimum effect. With glucose oxidase modified by ferrocene units, the optimal mediated electron transfer was found at a loading corresponding to 12–13 electron relay units [87]. The rate constant of electron transfer between the enzyme's FAD site and the nearest electron relay group was found to be ca. 0.9 s^{-1} (substantially lower than electron transfer to the native dioxygen electron acceptor of the enzyme proceeding with a rate constant of ca. $5 \times 10^3 \text{ s}^{-1}$) [87]. Improvements in the efficiency of electrical contact may be possible by the use of protein engineering, genetic manipulation, or relay units placed at optimal positions in the enzyme structure.

Layered assemblies of enzymes functionalized with tethered redox relays

The immobilization of electron relay-functionalized enzymes on electrode supports allows the construction of integrated bioelectronic assemblies. Enzyme monolayers can be electrically contacted using electron relay units tethered to the protein [88, 89]. A glutathione reductase monolayer assembled on Au electrodes via a thiolate bridging unit (Figure 8A) was functionalized with *N*-methyl-*N'*-carboxyalkyl-4,4'-bipyridinium salts (**4**), where the chain length tethering the electron relay was systematically lengthened [88]. Electroreduction of the bipyridinium unit was found to activate the enzyme for the reduction of oxidized glutathione (GSSG). The effectiveness of GSSG reduction was controlled by the chain length tethering the electron relay to the protein, and longer bridging chains enhanced the electrobiocatalyzed reduction (Figure 8B). This phenomenon was rationalized in terms of shorter electron-transfer distances between the electron-relay sites and the enzyme redox center for the systems with long-chain tethered bipyridinium units. It was also found that in order to attain electron-transfer communication between the enzyme redox center and the electrode, it is important to modify the protein with the bipyridinium components in the presence of urea. Added urea partially unfolds the protein and permits the functionalization of inner lysine residues. These inner elec-

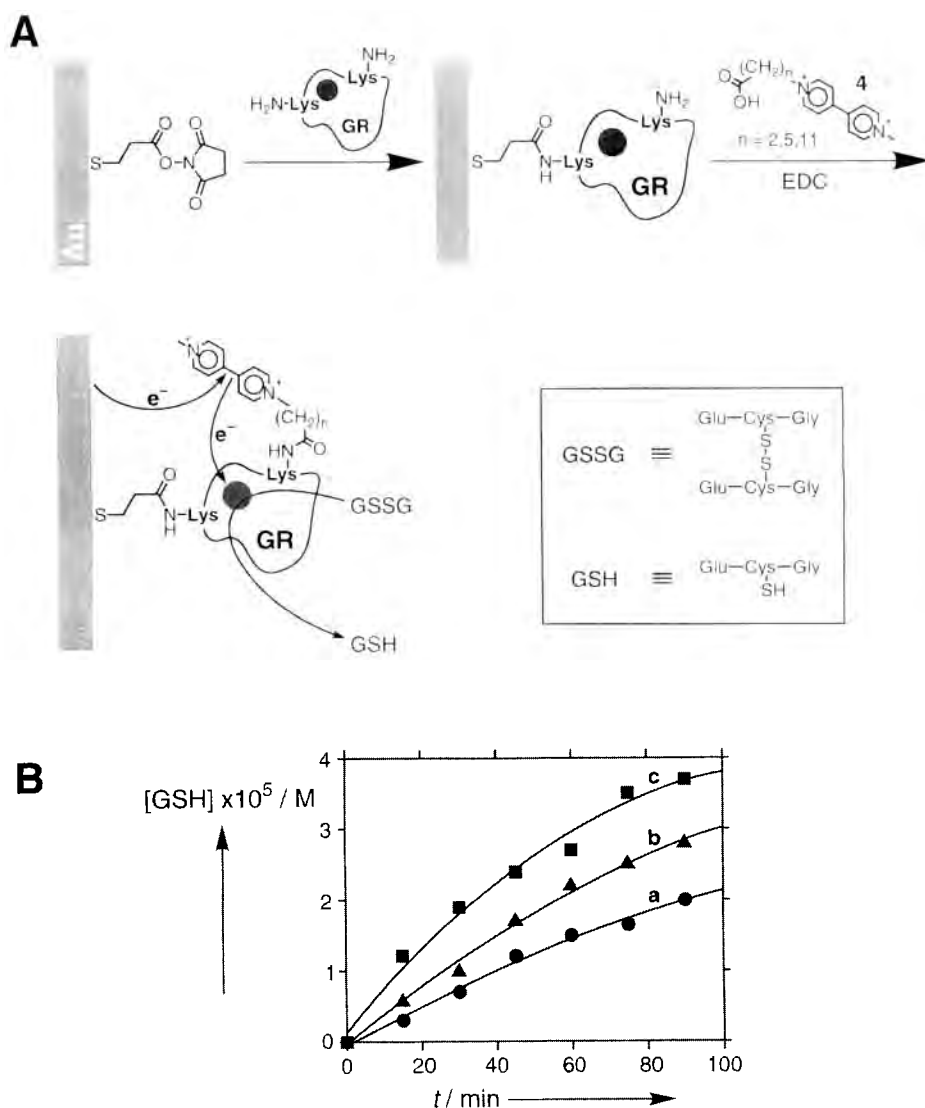


Figure 8. (A) The assembly of an electrically contacted glutathione reductase monolayer. (B) The rate of bioelectrocatalyzed reduction of oxidized glutathione (GSSG) by the electrically contacted enzyme electrode using various connecting chain lengths: (a) $n = 2$, (b) $n = 5$, (c) $n = 11$. Application of -0.72 V vs. SCE to the enzyme electrode in the presence of GSSG (10 mM). The experiments were performed in 0.1 M phosphate buffer, pH 7.2, under Ar.

tron relay units provide a route for electron 'hopping' between the electrode and the active redox center of the protein, and thus contribute to the electrical contacting of the enzyme layer with the electrode [88].

Non-organized multilayers of electron relay-tethered enzymes have been constructed both by cross-linking on an electrode surface [90] and by incorporation into a conductive polymer on electrode supports [5]. A thin-film glucose oxidase layer, electrically contacted by ferrocene units, was assembled on an Au electrode by the cross-linking of GOx, 2-aminoferrocene and a monolayer of *p*-mercaptoaniline with glutaric dialdehyde [90] (Figure 9A). The immobilized enzyme was electrically contacted via the electron relay groups, providing electron propagation throughout the assembly. A calibration curve for the modified electrode in the presence of glucose was derived by cyclic voltammetry (Figure 9B). More controlled superstructures can be constructed in a stepwise manner by the layer-by-layer deposition of enzymes and the covalent attachment of relay units to the enzyme backbone. A multilayer of glucose oxidase (GOx) (Figure 10A) was modified with *N*-aminomethylferrocenecaproic acid (**5**) [70]. The ferrocene relay units are oxidized by the electrode, and they in turn oxidize the enzyme redox sites. The amperometric responses of the layered electrodes were found to be controlled by the number of protein layers, implying that all of the enzyme layers are electrically contacted with the electrode by the ferrocene units. The rate-limiting process in the oxidation of glucose is the electron transfer between the substrate and the enzyme redox center. This results in different amperometric responses of the electrode at different glucose concentrations, and allows the application of the layered enzyme electrode as a glucose biosensor (Figure 10B, inset). This approach allows control of the enzyme array's sensitivity by the number of enzyme layers in the assembly (Figure 10B). Different enzymes can also be introduced into the structure in different layers, allowing the construction of thin films that facilitate cascades of the biocatalytic transformations.

4.2.5 Electrical 'Wiring' of Enzymes Entrapped in Polymeric Matrices on Electrode Supports

Many examples of polymer-embedded enzyme bioelectrocatalytic electrodes exist [91–93]. The electrical contacting of enzymes immobilized in polymer matrices is achieved either by virtue of a conducting polymer, or by incorporating electron relay groups within the polymer, providing electron hopping between the enzyme and the electrode support.

Enzyme entrapment in conductive polymers

The formation of conductive conjugated polymers [e.g., polyacetylene, polypyrrole, polythiophene, polyaniline and poly(*p*-phenylene)] [92, 94] on electrodes by electropolymerization has been studied thoroughly [95]. If the electropolymerization is performed in a solution containing both the monomer and enzyme, then enzymes present in the immediate vicinity of the electrode surface become trapped in the

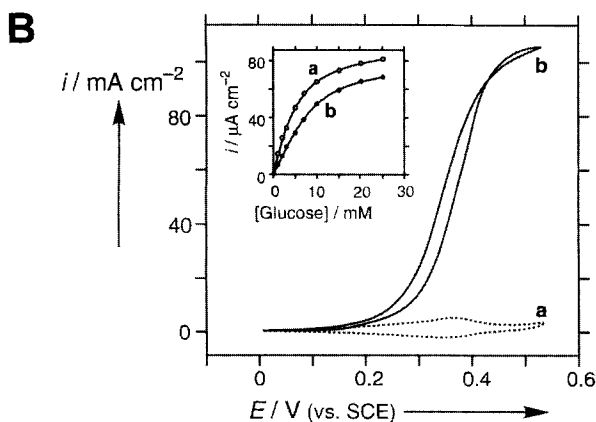
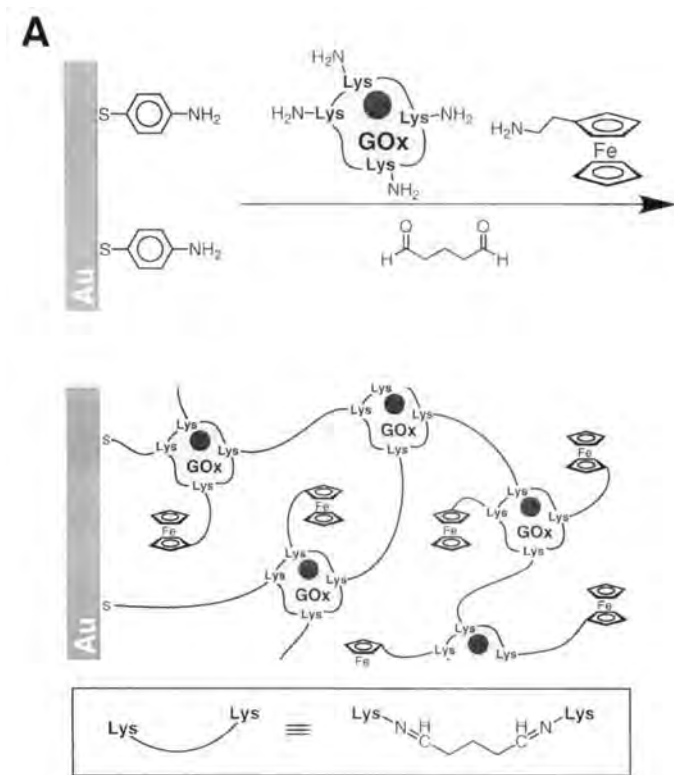


Figure 9. (A) The preparation of a nonordered polymeric layer of glucose oxidase electrically 'wired' by ferrocene groups incorporated in the polymer film. (B) Cyclic voltammograms of the GOx/ferrocene-modified electrode in the absence (a) and presence (b) of glucose, 30 mM. Performed under argon, in phosphate buffer, pH 7; potential scan rate, 10 mV s^{-1} . Inset: calibration curve for the amperometric response to glucose at 0.35 V vs. SCE measured under N_2 (a) and air (b). Adapted from Ref. [90] with permission.

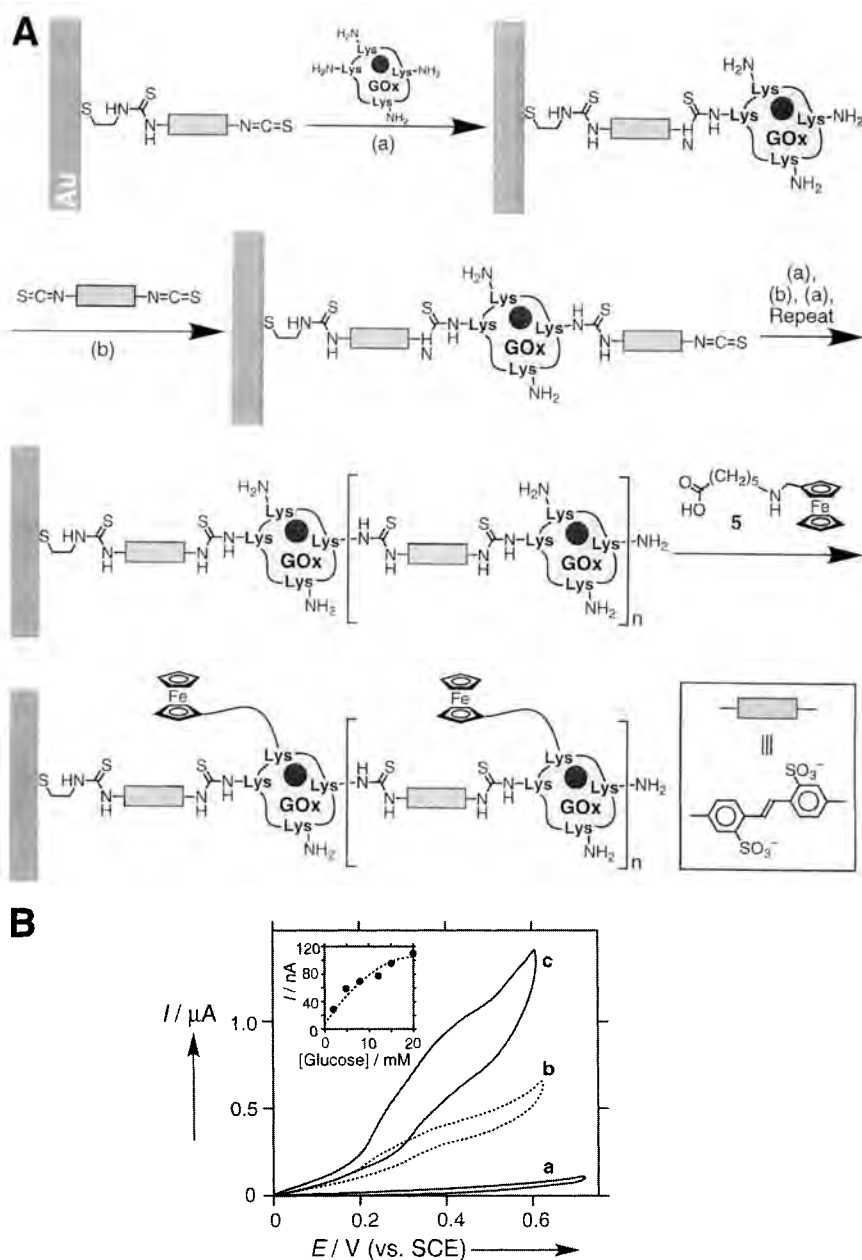


Figure 10. (A) The stepwise assembly and electrical contacting of a cross-linked organized multi-layer array of glucose oxidase (GOx) on an Au electrode. (B) Cyclic voltammograms of the GOx/ferrocene-modified electrode in the presence of glucose (20 mM) in (a) one-, (b) four- and (c) eight-layer configurations. Inset: amperometric responses of the four-layer GOx array at 0.4 V vs. SCE as a function of glucose concentration. Recorded in 0.1 M phosphate buffer, pH 7.3, under argon.

growing polymer. This kind of enzyme entrapment is desirable as it occurs without chemical reactions that could affect their activity. Electropolymerized films can be prepared easily in a rapid one-step procedure, and exact control of the layer thickness is possible based on the measurements of the electrical charge passed during the process. The method allows the precise electrogeneration of polymer coatings over small electrode surfaces of complex geometry, and is applicable to a very wide range of redox enzymes (e.g., glucose oxidase [60, 96, 97], horseradish peroxidase [18, 20, 98]). If the polymer is growing upon cyclic potential changes, charged reduced and oxidized states of the polymer are generated accordingly. This methodology has been used to assist the entrapment of charged enzyme molecules in the polymeric films. For example, negatively and positively charged enzymes have been incorporated into polyaniline films during the oxidation and reduction process, respectively [99].

Enzyme entrapment in conventional electrogenerated polymers such as polypyrrole, polyaniline or polyphenol occurs only due to presence of the enzyme molecules in the vicinity of the growing films [97, 100]. The ratio between biomolecules and the conductive polymer units is different from the ratio between the enzyme and monomer molecules in the original solution as it depends on the entrapment efficiency. An approach that allows control of this ratio is based on the application of amphiphilic monomers [101]. The procedure includes the solubilization of enzyme molecules (e.g., flavin reductase, horseradish peroxidase, galactose oxidase, choline oxidase, polyphenol oxidase, glucose oxidase, nitrate reductase, xanthine oxidase [92]) in an aqueous dispersion of amphiphilic pyrrole (e.g., derivatives **6–8**, Figure 11). Subsequently, the aqueous mixture is spread and dried on an electrode surface. The electropolymerization of the adsorbed mixture in an aqueous electrolyte provides the irreversible entrapment of a controlled amount of enzyme in the resulting polypyrrolic matrix. In contrast to simple monomers such as pyrrole, these amphiphilic monomers (e.g., **6**) possess a net positive charge, which promotes their association with anionic polar side-chains of enzyme molecules. This method also allows the tailoring of the local microenvironment for the enzyme molecules, e.g., highly hydrophobic or hydrophilic environments can be organized by the use of amphiphilic monomers **7** and **8**, respectively. The conductivity of the polypyrrole matrix allows the deposition and anodic polymerization of an additional amphiphilic monomer–enzyme mixture providing multienzyme structures with heterogeneous enzyme location [102]. For instance, the sequential deposition–electropolymerization of two different coatings has led to an amperometric flavin reductase/lactate dehydrogenase electrode for the interference-free determination of lactate.

Enzyme entrapment in polymers functionalized with redox relay units

Additional electron relay groups can be introduced into conductive polymer films to improve electrical ‘wiring’ of entrapped enzyme molecules [92]. The simplest approach involves the incorporation of ionic redox groups (e.g., ferrocyanide [103]) by employing the anion-exchange properties of the polymer. Consequently, co-entrapment of enzymes and anionic redox relays can be employed for electrical ‘wiring’ of the biocatalysts [97, 104]. The anion-exchange properties of regular

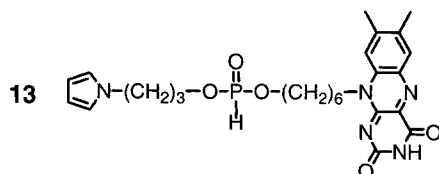
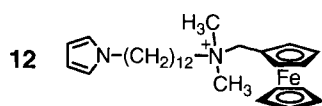
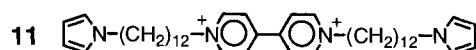
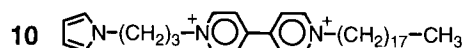
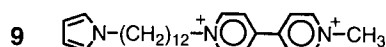
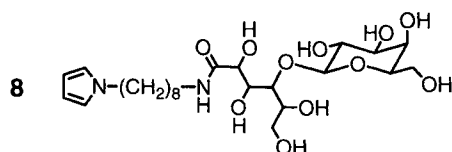
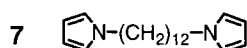
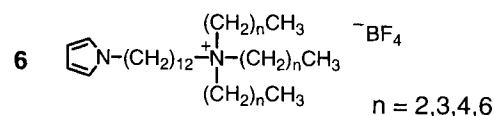


Figure 11. Structures of amphiphilic (6–8) and redox-functionalized (9–13) pyrrole derivatives applied for electropolymerization and entrapment of redox enzymes.

polypyrrole has been used to incorporate ferrocene carboxylate [59] and pyrrolo-quinoline quinone (PQQ) [105] for the electrical ‘wiring’ of glucose oxidase during the electrogeneration of a polypyrrole film. This simple approach to enhance the enzyme efficiency suffers from leakage of the noncovalently bound electron-transfer mediator from the polymeric matrix, however. Biocatalytic electrodes based on this technology therefore tend to be unstable and can not be utilized for *in vivo* measurements. To stabilize electron relays inside the polymeric matrix, new amphiphilic pyrrole derivatives (9–13) containing redox units have been synthesized (Figure 11) [92, 106], allowing the relay to be covalently incorporated into the polymer structure. A ferrocene-containing pyrrole derivative (12) and a flavin analog-functionalized pyrrole (13) have been employed to contact electrically glucose oxidase [92] and flavin reductase [107], respectively, realizing oxidative electron pathways for both

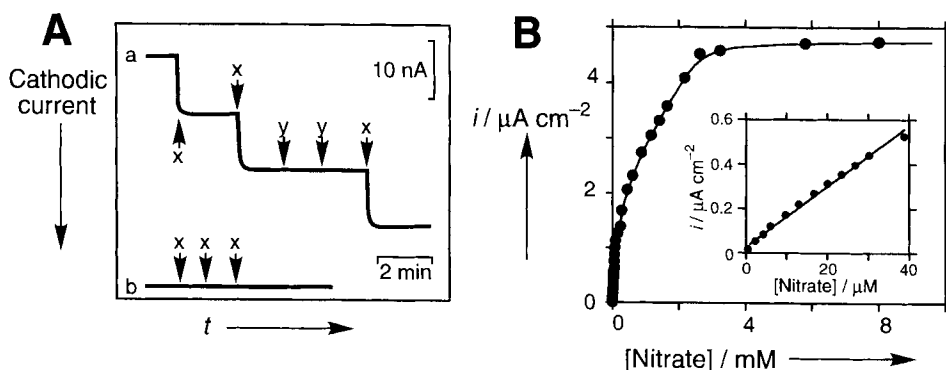


Figure 12. (A) The amperometric response of (a) a polypyrrole–viologen–nitrate reductase electrode and (b) an identical electrode constructed without the enzyme, in response to injections (x) increasing the nitrate concentration by 3.5 μM , and (y) of buffer. (B) Calibration curves (inset: smaller concentration range) for the response to nitrate of a polypyrrole–viologen–nitrate reductase electrode at -0.7 V vs. SCE. Adapted from Ref. [106a] with permission.

enzymes. Enzymes operating in reductive pathways (e.g., nitrate reductase, pyridine nucleotide oxidoreductase) have been electrically contacted in polymeric matrices by the use of the viologen-functionalized pyrrole derivatives **9–11** [106a, 108]. Nitrate reductase electrically contacted by the viologen units of a polymer matrix was used for the amperometric detection of nitrate ions (Figure 12A), leading to the calibration curve given in Figure 12B.

A further approach to contact electrically polymer-bound enzymes involves the use of chemically synthesized polymers functionalized with redox units [109]. Polyelectrolytes represent the best choice for the optimization of interactions with enzymes and electrodes. Hydrophilic, charged, flexible chains of polyelectrolytes can easily surround protein molecules, and even penetrate inside them slightly, providing good contact between the protein structures and polymer backbone (Figure 13). Each unit of a polyelectrolyte is weakly adsorbed on an electrode surface, but because of the very large amount of the units in the polymer chain, the total binding is strong and some domains of the chain remain unattached, providing binding areas for protein molecules. Three-dimensional redox polyelectrolyte networks that electrically connect enzyme redox centers to electrodes have been formed in several systems [110, 111], of which enzyme ‘wiring’ hydrophilic epoxy cements are an excellent example [111]. In this case, the polymeric chain consists of a poly(vinylpyridine) backbone of which approximately one-sixth of the pyridines are complexed to $[\text{Os}(\text{bpy})_2\text{Cl}]^{+/2+}$ and about one-fifth of the pyridines have been reacted with 2-bromoethylamine to form pyridinium-*N*-ethylamine polycationic domains (**14**). This redox polyelectrolyte easily interacts with enzymes and ‘wires’ their redox centers by penetrating into the protein shell of, e.g., lactate oxidase, glycerol-3-phosphate oxidase and cellobiose oxidase [109a, 112]. Although negatively charged enzymes can strongly interact with this polycationic polymer even without cross-

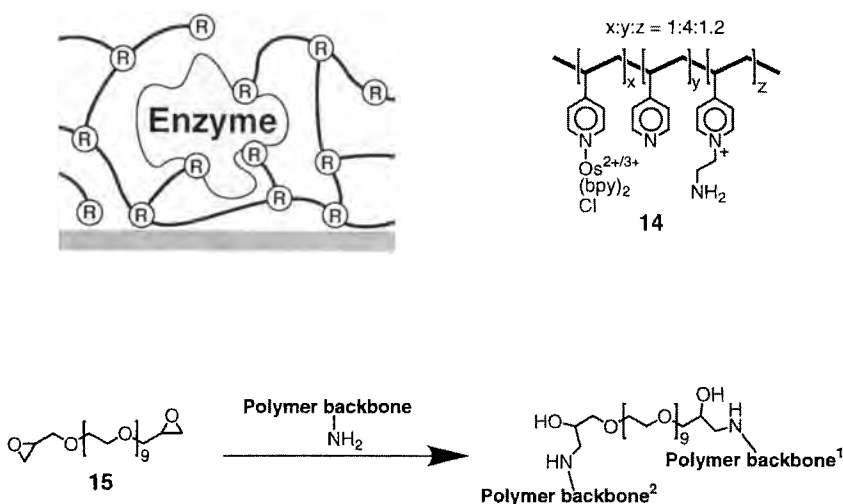


Figure 13. A redox enzyme electrically 'wired' to an electrode surface by flexible polymer chains functionalized with redox-mediator groups and surrounding the enzyme at the electrode surface.

linking, cross-linking with the water-soluble diepoxide poly(ethylene glycol) diglycidyl ether (**15**) can further stabilize the system. For example, glucose oxidase was incorporated into a cross-linked polymeric matrix containing $\text{Os}(\text{bpy})_2$ units coordinated with the pyridine groups in the protein backbone. This enzyme-modified electrode shows an electrocatalytic anodic current in the presence of glucose (Figure 14A), leading to the calibration curve given in Figure 14A (inset). A similar polymer composed of a positively charged copolymer of allylamine and ferrocene-functionalized acrylic acid with the negatively charged proteins can be cross-linked with glutaric dialdehyde in the presence of GOx to yield the stable electrically 'wired' biocatalytic matrix [113]. This enzyme electrode also demonstrates the electrocatalytic current of glucose oxidation (Figure 14B). Successive additions of glucose at a fixed oxidative potential result in increases in the current (Figure 14B, inset). A neutral polyacrylamide chain carrying ferrocene units was used for entrapment of GOx molecules without assistance of electrostatic interaction [109b]. Many other polymers functionalized with different redox groups (e.g., quinones [114]) have also been employed for the electrical 'wiring' of entrapped redox enzymes. The free-radical polymerization of redox hydrogels (as an alternative to the electropolymerization process) has also permitted the efficient entrapment of enzymes [115].

4.2.6 Electrical 'Wiring' of Enzymes Incorporated into Inorganic Matrices

The incorporation of enzymes into inorganic composite matrices provides very stable biocatalyst interfaces that have important practical applications. Cheap and versatile matrices composed of different kinds of inorganic components (e.g. sol-gel

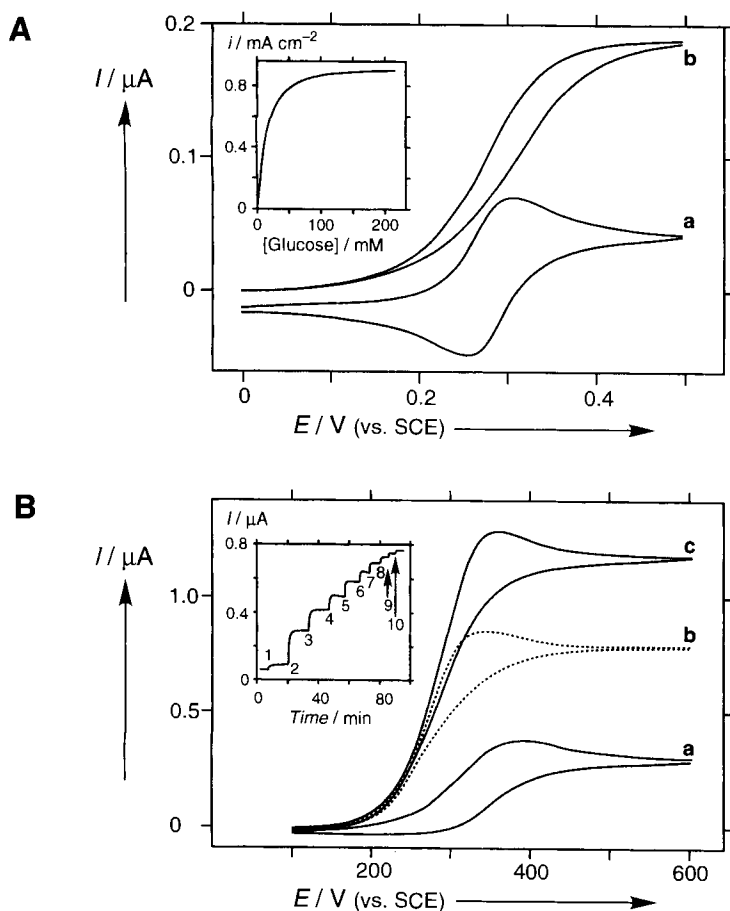


Figure 14. (A) Cyclic voltammograms of a graphite micro-electrode (7 μm diameter) modified with the Os complex-containing polymer **14**, cross-linked with the bi-epoxy reagent **15** with embedded glucose oxidase: (a) in the absence of glucose and (b) with glucose, 5 mM. Potential scan rate, 5 mV s^{-1} . Inset: calibration curve for the amperometric determination of glucose at 0.4 V vs. SCE. (B) Cyclic voltammograms of the electrode modified with ferrocene-containing cross-linked poly-allylamine-containing glucose oxidase in the polymer matrix: (a) in the absence of glucose, (b) with glucose, 1 mM, and (c) with glucose, 3 mM. Potential scan rate, 5 mV s^{-1} . Inset: amperometric responses of the enzyme electrode (at 0.6 V vs. SCE) upon successive additions of glucose. Numbers show glucose concentration in mM. Adapted from Refs. [109a] and [113] with permission.

[116], graphite paste [117]), impregnated with electron-transfer mediators, cofactors, etc., have been investigated for biosensor design.

Electrical 'wiring' of enzymes incorporated into sol-gel matrices

Enzymes entrapped by sol-gel processing have received increased attention in recent years [116]. Sol-gel matrices offer several advantages for enzyme entrapment and the development of new biosensors including inherent low-temperature processing

conditions, tunable porosity, chemical inertness, and negligible swelling of the final glass matrix. To date, silicon alkoxide precursors have been most extensively studied because they are inexpensive and exhibit relatively slow overall reaction kinetics. Thus, one can readily prepare silica sol–gels that are doped with a wide variety of reagents (e.g., enzymes, electron-transfer mediators, cofactors, promoters, etc.) and tune the characteristics of the final matrix by adjusting the processing conditions (pH, precursor ratios, etc.). The versatility of these doped sol–gel matrices has been exploited in the construction of enzyme biosensors. Initially, optical detection was found to be more efficient than electrochemistry because of the very low conductivities of the silicate network [118], but efficient electron shuttles (conductive particles or mediators) were soon used to overcome this limitation, bringing about the start of an extraordinary growth in the development of new amperometric biosensors based on sol–gel-prepared silicates. These materials can be classified into two main categories: (i) silica sol–gel biosensors (consisting of molecular components immobilized in the matrix) and (ii) composite carbon–ceramic bioelectrodes (where the properties of the matrix are enhanced by the addition of carbon or other conductive materials).

The electrical ‘wiring’ of sol–gel–enzyme matrices can be achieved by either the application of solution-state electron relays that can penetrate through the matrix, or by the immobilization of redox mediators into the sol–gel. Horseradish peroxidase films deposited on carbon paste substrates and then covered with a thin silica sol–gel layer have been used to detect H_2O_2 in aqueous medium [119] or organic peroxides in nonaqueous solutions [120] in the presence of $[\text{Fe}(\text{CN})_6]^{4-}$ or ferrocene, respectively, acting as a mediator. The extension of this electrode configuration to other enzymes has led to the development of new amperometric sensors for glucose [121] and phenolic compounds [122]. Glucose oxidase has been electrically contacted in a sol–gel matrix using a ferrocene mediator incorporated into the matrix (Figure 15A) [123]. In this construction, more than 80 % of the GOx remained active in the sol–gel and the amperometric response agreed well with theoretical predictions. Construction of sol–gel–enzyme multilayer matrices allowed the amperometric sensing of glucose [124] and L-lactate [125] with linear responses within large concentration ranges.

The application of additional electroconductive materials such as carbon powder or metal particles in the preparation of bioceramic films can result in improved biosensors (Figure 15B). These electrodes benefit from both the porosity and rigidity of the silica matrix and from the electrical conductivity of the additive [116]. Composite sol–gel electrodes containing GOx and co-immobilized redox mediators have been applied to the preparation of glucose biosensors [126–129]. In these procedures, the redox mediator is either added as an isolated molecule during the gelification process (resulting in its physical entrapment in the silicate structure) [127] or is chemically bound to the silicate network [e.g., *N*-(3-trimethoxysilylpropyl)-ferrocenylacetamide (**16**) may be used as a functionalized co-monomer] [129]. The electron relay may also be incorporated by tethering to the protein backbone. Relay-functionalized GOx has been entrapped in composite graphite–sol–gel matrices [128, 130]. The presence of the relay facilitates electron hopping between the enzyme active site and nearest graphite particle, from where the electrons are trans-

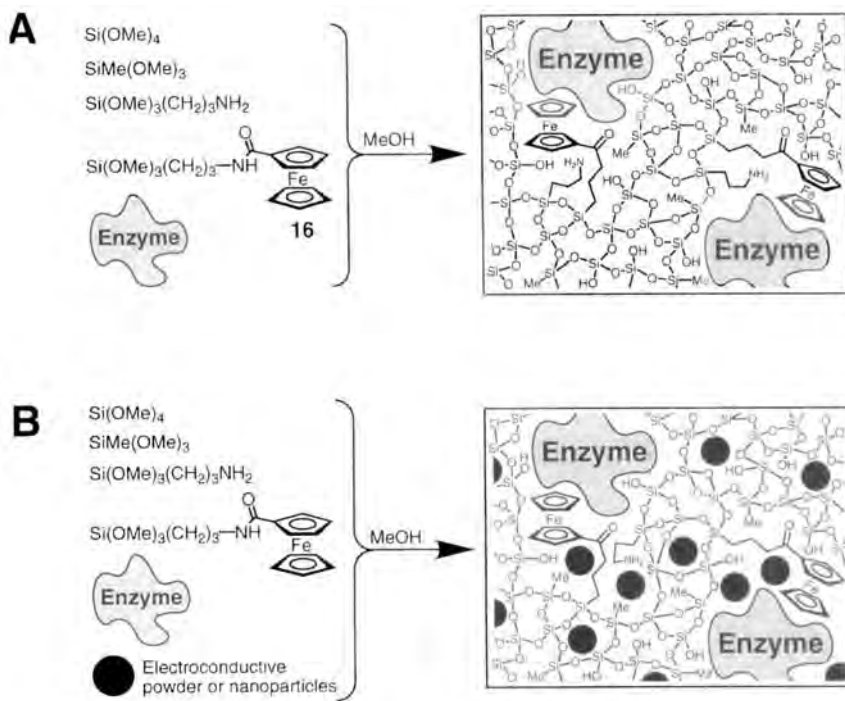


Figure 15. Encapsulation of enzyme molecules into a sol-gel matrix containing redox-mediator groups (A) and with the addition of conductive graphite (or metal) particles (B).

ported to the electrode through the conductivity of the graphite component. Ferrocene-mediated electrical ‘wiring’ of GOx resulted in an amperometric response for the electrode in the presence of glucose [116a] (Figure 16). Metallic components for the improvement the matrix conductivity are often composed of a graphite core covered with a metallic (e.g., palladium, rhodium) shell [131]. More recently, the percolating carbon particles have been replaced by gold nanoparticles embedded together with the enzyme in the porous silicate matrix [132].

Electrical ‘wiring’ of enzymes incorporated into carbon paste composites

During the last decade there has been a virtual explosion of reports on the subject of amperometric biosensors based on carbon paste electrodes [117]. The concept of simply mixing an enzyme, an electron relay and a conductive powder into a paste is very attractive. Bulk modification of the entire electrode allows renewal of the electrode surface by polishing or cutting to expose a new and fully bioactive surface in the event of fouling or deactivation. This feature is certainly attractive compared with surface-modified electrodes, which have to be discarded or at least remodified after deactivation. The main challenge in the construction of carbon paste biosensors is the establishment of efficient electrical ‘wiring’. Electron-transfer mediators have been introduced into GOx pastes either as conjugates with the particles

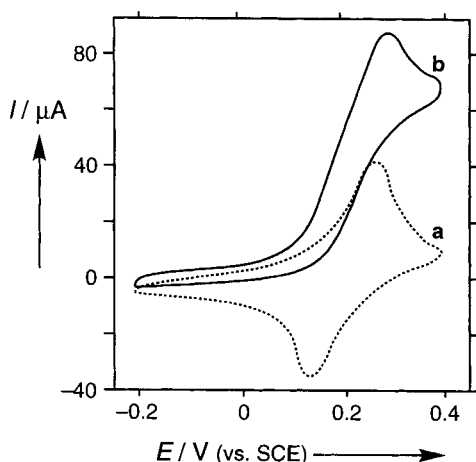


Figure 16. The electrochemical response of a GOx-ferrocene-sol-gel-modified electrode in the presence of glucose: cyclic voltammogram before (a) and after (b) the addition of 10 mM glucose solution; phosphate buffer, pH 5.6; potential scan rate, 10 mV s^{-1} . Adapted from Ref. [116a] with permission.

or enzyme, or simply as free molecules. Examples of mediators include ferrocene derivatives [133] (monomeric or polymeric), benzoquinone and benzoquinone-functionalized polymers [134], viologen derivatives [135], tetrathiafulvalene (TTF) [136], tetracyanoquinodimethane (TCNQ) [18, 20, 137], TTF-TCNQ conducting salts [138], cobalt phthalocyanine [139], Meldola blue [140], methylene green [141] and cupric hexacyanoferrate [142], among others [117]. Many other redox enzymes have been incorporated into graphite paste electrodes with appropriate electron-transfer mediators and used as amperometric biosensors for their respective substrates [117b]. It should be noted that (a) low-potential redox relays (particularly viologens [135]) provide effective oxidation of the FADH_2 cofactor under potentials negative enough to prevent the non-specific oxidation of interferants, and (b) the application of NAD^+ -dependent enzymes (e.g. glucose dehydrogenase [143], alcohol dehydrogenase [144]) requires the incorporation of NAD^+ cofactor and a redox catalyst for the oxidation of NADH.

Multienzyme systems have been used in carbon paste electrodes, providing biocatalytic cascades that result in an analytical amperometric signal. For example, acetylcholine esterase (AChE) and choline oxidase (ChOx) have been co-immobilized in carbon pastes, either with monomeric TTF [145] or flexible ferrocene-containing polymers [146] as electron mediators. The primary reaction includes the hydrolysis of acetylcholine biocatalyzed by AChE, then the choline produced is oxidized by the electrically contacted ChOx giving an analytical amperometric signal corresponding to the acetylcholine concentration.

Although many biocatalytic systems have been immobilized in carbon paste electrodes successfully, the method is not general. Some enzymes, e.g., fructose dehydrogenase [15, 134a] and aldose dehydrogenase [147], have defied efforts at incorporation into the paste matrix without losing their activity. It is possible to introduce these enzymes to the surface of preformed carbon paste electrodes while retaining their biocatalytic potential, but this procedure does not exploit the many advantages of the carbon paste technique [117]. The construction and optimization

of the multicomponent matrices composed of graphite powder, organic oils, enzymes, redox mediators, cofactors, etc., is still a subject of intensive study.

4.2.7 Electrical ‘Wiring’ of Nano-engineered Enzymes

The site-specific modification of enzymes with a single electron-relay group located near to the redox cofactor and providing efficient electrical contact with the conductive support has been achieved by the reconstitution of enzymes with cofactors covalently linked to redox groups. Affinity interactions between enzymes and their cofactors at the electrode interface can allow the efficient electrical contacting of aligned proteins.

Enzymes reconstituted with semi-artificial cofactors linked to redox relays

A novel means for the establishment of electrical contact between the redox center of enzymes and their environment that is based on a reconstitution approach has recently been suggested [148, 149]. This concept involves the site-specific positioning of a single mediator group directly linked to the enzyme redox center as an electron shuttle between the biocatalyst and the electrode. According to this method (Figure 17A) the FAD redox centers of glucose oxidase or D-amino acid oxidase (AOx) were removed to yield the respective apo-enzymes. The amino-functionalized semi-synthetic cofactor *N*⁶-(2-aminoethyl)-FAD (**17**) was covalently linked to *N*-aminomethylferrocenecaproic acid (**5**) (Figure 18), then the bifunctional redox-active ferrocene–FAD cofactor was reconstituted into apo-GOx or apo-AOx. The resulting semisynthetic enzymes revealed bioelectrocatalytic features for the oxidation of glucose or D-alanine, respectively. Figure 17B shows cyclic voltammograms recorded in a solution of ferrocene–FAD-reconstituted GOx at a cystamine-modified electrode and in the absence and presence of glucose. The bioelectrocatalytic features of these enzymes (‘electroenzymes’) originate from the single ferrocene electron-relay group that electrically contacts the FAD center with the electrode surface. Tailoring of enzyme electrodes by the covalent attachment of redox-tethered enzymes or redox-reconstituted enzymes to a base monolayer interface is conceptually limited owing to the random anchoring of the electrocatalyst to the monolayer. Covalent linkage of the enzyme to the monolayer results in multiple orientations of the redox-active site relative to the electrode surface. Hence attachment of the electrically wired redox relay units to the protein yields a mixture of bioelectrocatalysts with different electrical communication features, and the performance of the enzyme electrode represents the average activity of these randomly oriented bioelectrocatalysts.

A major advance in the construction of electrically contacted enzyme electrodes involves the structural alignment of the enzyme redox center with respect to the electrode interface in conjunction with the site-specific positioning of a redox relay component between the enzyme redox center and the electrode. The design of such electrodes promotes a new level of molecular architecture of biomolecules on surfaces, enabling us to optimize the electrical contact of the resulting enzyme elec-

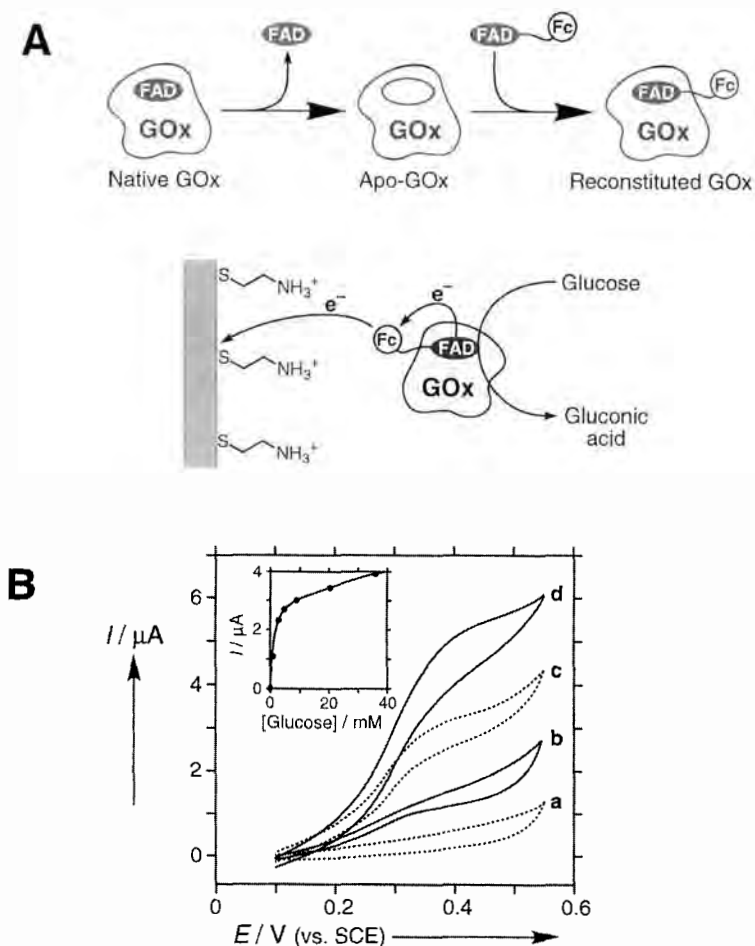


Figure 17. (A) The preparation of an electrically ‘wired’ enzyme by the reconstitution technique, involving the removal of the native FAD cofactor from the enzyme (e.g., GOx) and the incorporation of the artificial FAD–ferrocene dyad into the apo-enzyme. (B) Cyclic voltammograms of a system consisting of ferrocene–FAD–reconstituted GOx (1.75 mg mL^{-1}) at various concentrations of glucose: (a) 0, (b) 1, (c) 3 and (d) 20.5 mM. Experiments were performed in 0.1 M phosphate buffer, pH 7.3, at 35°C , using a cystamine-modified Au electrode, potential scan rate 2 mV s^{-1} , under argon. Inset: calibration curve of the biocatalytic current (0.5 V vs. SCE) at different glucose concentrations.

trode by the systematic alteration of the distances separating the electrode, catalyst and FAD components. The organization of an aligned reconstituted enzyme on a catalyst–FAD monolayer was recently realized by the reconstitution of an apo-enzyme on a surface functionalized with a relay–FAD monolayer [149, 150]. Figure 19A shows the method of assembly of the enzyme electrode. Pyrroloquinoline-quinone (**18**) was covalently linked to a base cystamine monolayer, and N^6 -(2-aminoethyl)-FAD (**17**) was then attached to the PQQ redox relay units. Following

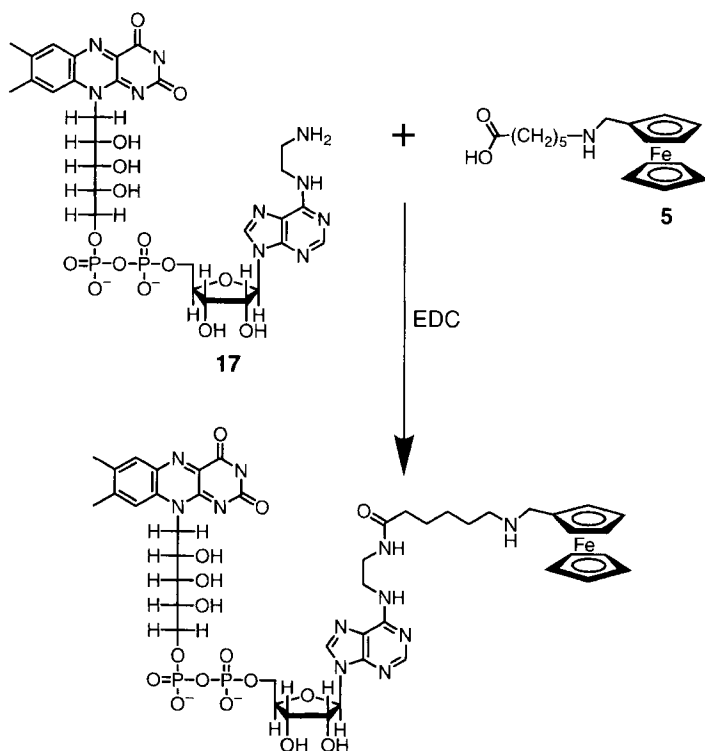


Figure 18. Synthesis of a FAD–ferrocene dyad for the reconstitution of FAD-containing enzymes.

the construction of this organized electrode–PQQ–FAD assembly, apo-GOx was reconstituted on the semisynthetic FAD unit to yield an immobilized biocatalyst on the electrode with a surface coverage of 1.7×10^{-12} mol cm $^{-2}$. The resulting reconstituted enzyme reveals bioelectrocatalytic properties. Figure 19B shows cyclic voltammograms of the enzyme electrode in the absence and presence of glucose. When the substrate is present, an anodic electrocatalytic current is observed, implying electrical contact between the reconstituted enzyme and the electrode surface leading to the bioelectrocatalyzed oxidation of glucose. The PQQ site located at the protein periphery is constantly oxidized by the electrode, and PQQ-mediated oxidation of the FAD center activates the bioelectrocatalytic oxidation of glucose. The resulting electrical current is controlled by the recycling rate of the reduced FAD by the substrate and the concentration of glucose. Figure 19B (inset) shows the derived calibration curve for the amperometric responses of the reconstituted enzyme electrode at different concentrations of glucose. The resulting current densities are unprecedentedly high in the area of biosensors and bioelectronic devices (300 μ A cm $^{-2}$ at 80 mM of glucose). Control experiments revealed that reconstituted GOx on an electrode–FAD assembly (lacking the PQQ component) does not exhibit direct electron-transfer communication with the electrode surface, demonstrating that the PQQ relay unit is indeed a key component in mediating electron transfer between the biocatalyst and the electrode [149, 150].

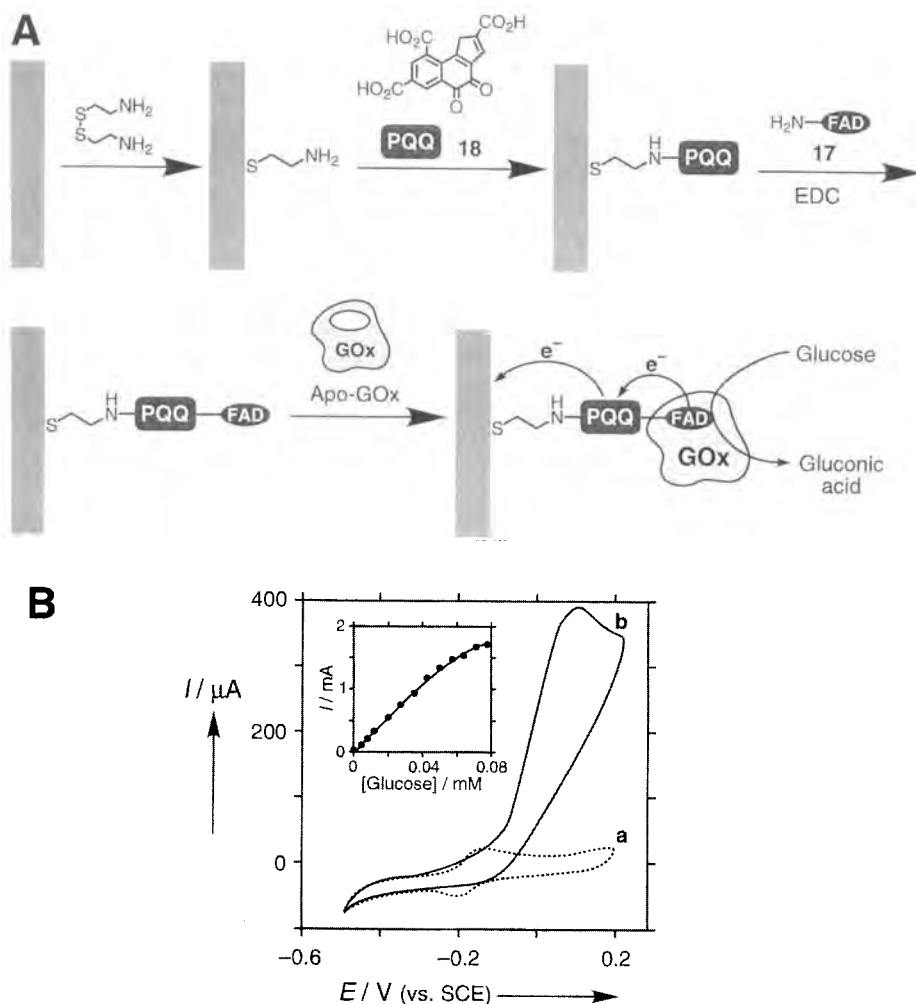


Figure 19. (A) The reconstitution of apo-glucose oxidase on a PQQ-FAD monolayer assembled on an Au electrode. (B) Cyclic voltammograms of the PQQ-FAD-reconstituted glucose oxidase on an Au electrode: (a) in the absence of glucose; (b) with glucose, 80 mM. Recorded in 0.1 M phosphate buffer, pH 7.0, under Ar, at 35 °C; potential scan rate, 5 mV s⁻¹. Inset: calibration curve corresponding to the amperometric responses (measured by chronoamperometry, $E = 0.2$ V vs. SCE) of the PQQ-FAD-reconstituted glucose oxidase enzyme electrode at different concentrations of glucose.

The electron-transfer turnover rate of GOx with molecular oxygen as the electron acceptor corresponds to ca. 600 s⁻¹ at 25 °C. Using an activation energy of 7.2 kcal mol⁻¹, the electron-transfer turnover rate of GOx at 35 °C is estimated to be ca. 900 s⁻¹ [149, 150]. A densely packed monolayer of GOx (ca. 1.7×10^{-12} mol cm⁻²) that exhibits the theoretical electron-transfer turnover rate is

expected to yield an amperometric response of ca. $300 \mu\text{A cm}^{-2}$. This figure indicates that reconstituted GOx on the PQQ–FAD monolayer exhibits an electron-transfer turnover of similar effectiveness to that observed with oxygen as mediator. In addition to the high sensitivity of the resulting enzyme electrode, the impressive efficiency of electrical contact has important consequences in the design of future enzyme electrodes. Amperometric glucose-sensing electrodes generally suffer from the non-specific oxidation of various interferants such as ascorbic acid or uric acid. Also, oxygen interferes with the current transduction as a result of nonelectrochemical oxidation of the enzyme redox site. The efficient electrical contact of the biocatalyst and the electrode, as well as the resulting effective electrobiocatalyzed oxidation of glucose suggest that the nonspecific oxidation of the interfering substrates and the reaction of the biocatalyst with oxygen should have little effect on the resulting current. Indeed, it was found that the transduced amperometric response at a glucose concentration of 5 mM was almost unaffected in the presence of oxygen or other interferents [149, 150]. The resulting selectivity of the reconstituted enzyme electrode and the high current densities achieved have further importance in the application of these electrodes as invasive glucose sensors. The pain accompanying the penetration of a needle electrode is proportional to its diameter, and microelectrodes are therefore being pursued for invasive sensing applications. The high electron-transfer turnover rate of the reconstituted biocatalyst in these systems suggests that even with the low surface area of the microelectrode, physically detectable current responses will be obtained.

The intermediate location of a redox relay between the electrode surface and the cofactor unit embedded into the enzyme is of key importance for the establishment of electrical contact between the enzyme and the electrode. For example, a pyrroloquinoline quinone monolayer assembled on an Au electrode was employed to reconstitute the PQQ-dependent apo-glucose dehydrogenase [151]. In this case the PQQ molecules play a role of the embedded cofactor and, since no additional electron relay was immobilized between PQQ cofactor and the electrode, the reconstituted enzyme was not electrically contacted with the electrode. The electrochemical oxidation of glucose by the reconstituted biocatalyst was only stimulated in the presence of a diffusional electron-transfer mediator. In other cases however, the orientation of the protein with respect to the electrode is sufficient to promote electron transfer without the need for a mediator. An Fe(III)–protoporphyrin IX complex was assembled as a monolayer on an Au electrode and apo-myoglobin was reconstituted with the heme–cofactor monolayer [152]. Although native myoglobin usually lacks direct electrical communication with electrode supports owing to insulation of the heme center, the surface-reconstituted myoglobin revealed electrical contact with the electrode. This property was attributed to the alignment of the heme center on the electrode surface in a structural orientation that facilitates electron transfer with the electrode.

Enzyme electrodes containing cross-linked cofactors, polypeptides or protein affinity complexes

Electrodes functionalized with monolayers of enzyme cofactors (e.g., NAD^+ monolayers) or redox proteins (e.g., heme proteins or heme polypeptides) demonstrate

the ability to form stable affinity complexes with the respective enzymes [153]. These interfacial complexes can be further cross-linked to produce integrated electro-biocatalytic matrices consisting of the biorelay units and the enzyme molecules. Electrically contacted biocatalytic electrodes of NAD^+ -dependent enzymes have been organized by the generation of affinity complexes between a catalyst- NAD^+ monolayer and the respective enzymes [154]. A PQQ monolayer covalently linked to an amino-functionalized nicotinamide adenine dinucleotide, N^6 -(2-aminoethyl)- NAD^+ (**19**), was assembled on an Au electrode. The resulting monolayer-functionalized electrode binds NAD^+ -dependent enzymes such as lactate dehydrogenase (LDH) and alcohol dehydrogenase (AlcDH) by affinity interactions between the cofactor and the biocatalyst (Figure 20A). These enzyme electrodes electrocatalyze the oxidation of the respective substrates, e.g., lactic acid or ethanol. The electro-biocatalytic transformations proceed via the biocatalyzed substrate-induced formation of NADH and its oxidation by the PQQ catalytic site. The resulting enzyme electrode reveals only temporary stability and ca. 25 % of the biocatalyst dissociates from the monolayer affinity complex to the electrolyte solution within 30 min. Cross-linking of the enzyme layer associated with the PQQ- NAD^+ cofactor monolayer with glutaric dialdehyde generates a stable, integrated, electrically contacted, cofactor-enzyme electrode (Figure 20A). The electrical response of a cross-linked layered PQQ- NAD^+ -LDH electrode in the absence (curve a) and presence (curve b) of lactate is given in Figure 20B, and a calibration curve for the amperometric responses of the integrated LDH layered electrode at different concentrations of lactate is shown in the Figure 20B (inset).

Protein-protein affinity interactions play a major role in biological electron transfer. For example, cytochrome *c* mediates electron transfer to different redox enzymes, e.g., cytochrome oxidase, lactate dehydrogenase, or copper enzymes [27, 38]. These mediated electron-transfer reactions proceed within interprotein affinity complexes [155]. Microperoxidase-11 (**1**) consists of the active-site microenvironment of cytochrome *c* [47], and is obtained by tryptic digestion of the native hemoprotein. Despite the structural similarities between MP-11 and cytochrome *c*, the heme sites of the oligopeptide and the native protein differ substantially in their redox-potentials ($E^\circ = -0.40$ V (vs. SCE) for MP-11 [50] and $E^\circ = +0.012$ V (vs. SCE) for cytochrome *c* [27, 38]). Microperoxidase-11 assembled [50, 82] as a monolayer on an Au electrode has been shown to stimulate electron transfer to hemoproteins such as myoglobin, hemoglobin and cytochrome *c* [81]. This mediated electron transfer is attributed to the formation of affinity complexes between the proteins and MP-11 at the electrode interface. The affinity interactions between MP-11 and hemoproteins or cytochrome-dependent enzymes have been used to assemble an electrically contacted nitrate reductase electrode [82]. The cytochrome-dependent nitrate reductase (NR) forms an affinity complex with the MP-11 monolayer associated with the electrode. Cross-linking of the enzyme-MP-11 affinity complex layer with glutaric dialdehyde generates a stable electrically contacted enzyme electrode that effects the bioelectrocatalyzed reduction of nitrate to nitrite (Figure 21A). The bioelectrocatalyzed transformation proceeds with a current efficiency of ca. 85 %, and the resulting enzyme electrode can be employed as an amperometric nitrate sensor (Figure 21B).

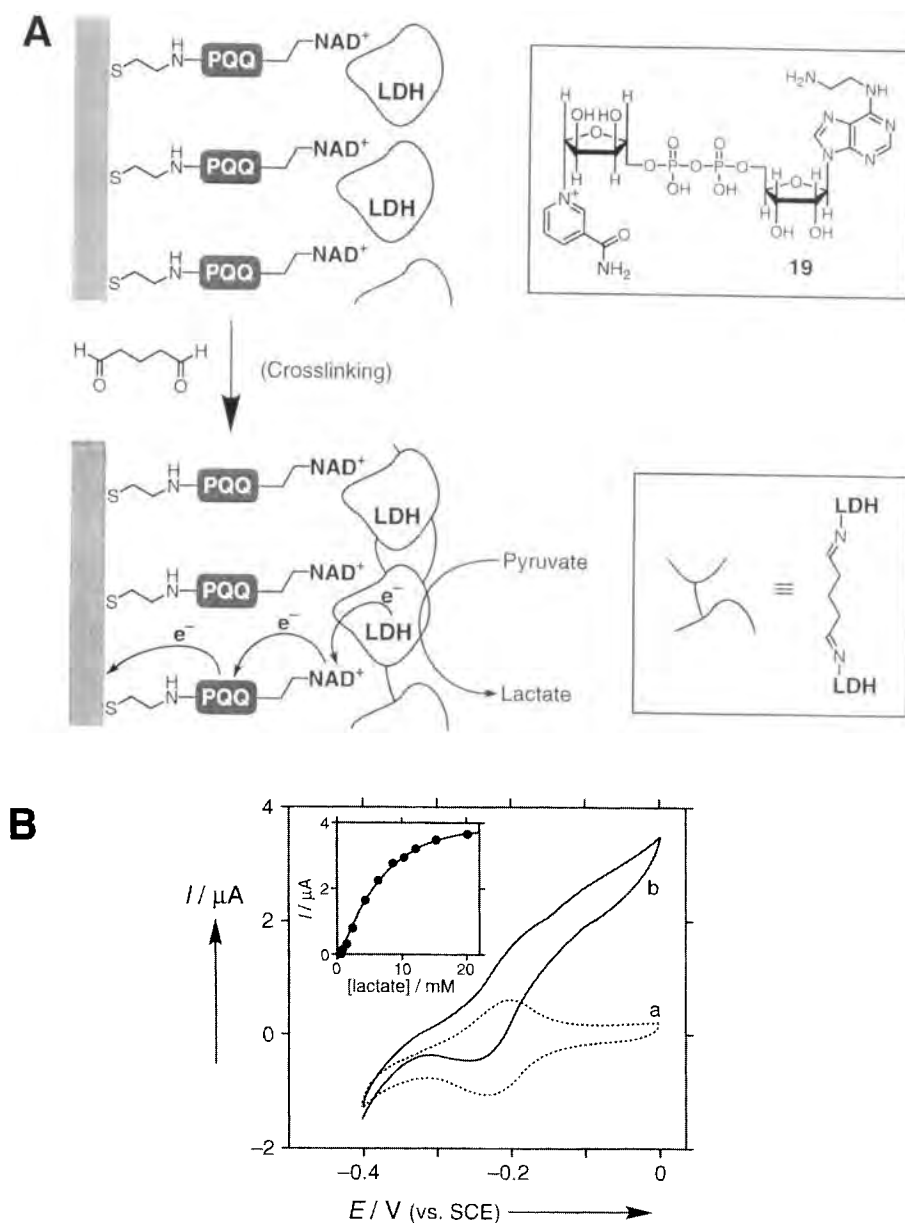


Figure 20. (A) The assembly of an integrated lactate dehydrogenase monolayer electrode by the cross-linking of an affinity complex formed between the enzyme and a PQQ–NAD⁺ monolayer-modified Au electrode. (B) Cyclic voltammograms of the integrated cross-linked PQQ–NAD⁺/lactate dehydrogenase electrode (roughness factor ca. 15): (a) in the absence of lactate; (b) with lactate, 20 mM. Recorded in 0.1 M Tris buffer, pH 8.0, in the presence of 10 mM CaCl₂, under Ar; potential scan rate, 2 mV s^{−1}. Inset: amperometric responses of the integrated electrode at different concentrations of lactate upon application of potential 0.1 V vs. SCE.

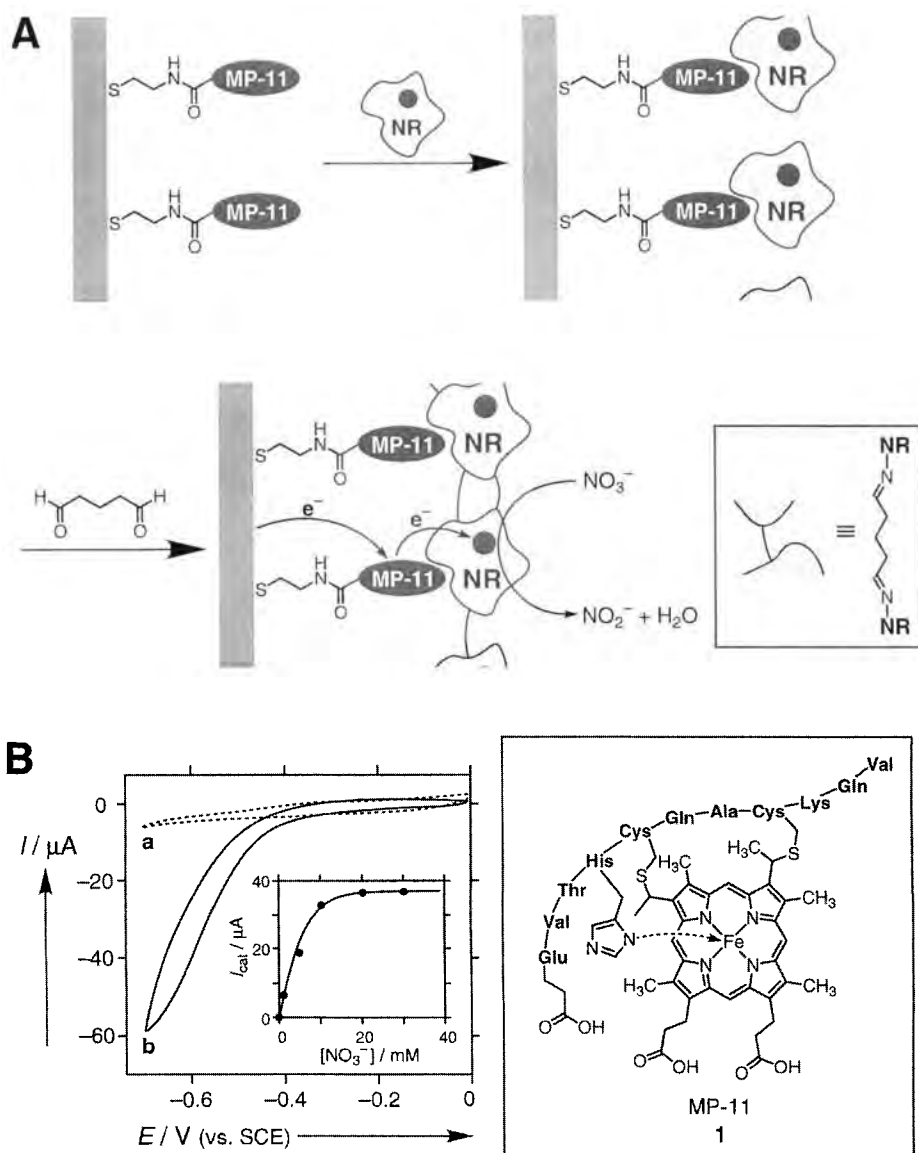


Figure 21. (A) The assembly of an integrated nitrate sensor electrode by the cross-linking of a microperoxidase-11-nitrate reductase (cytochrome-dependent, EC 1.9.6.1) affinity complex on an Au electrode. (B) Cyclic voltammograms of the integrated MP-11-NR monolayer-modified Au electrode (roughness factor ca. 15). (a) 0.1 M phosphate buffer, pH 7.0; (b) in the presence of KNO_3 , 20 mM. Potential scan rate, 5 mV s^{-1} . Inset: electrocatalytic cathodic currents ($E = -0.6 \text{ V}$ vs. SCE) transduced by the modified electrode at different concentrations of KNO_3 . Measurements were performed under argon.

Cobalt(II)–protoporphyrin IX-reconstituted myoglobin was also found to form an affinity complex with the MP-11 monolayer electrode [156]. The association constant of the affinity complex between the reconstituted myoglobin and MP-11 corresponds to $K_a = 1.6 \times 10^5 \text{ M}^{-1}$, and the electron-transfer rate constant in the resulting supramolecular complex is $k_{et} = 0.3 \text{ s}^{-1}$. The MP-11 mediates the electrocatalyzed reduction of Co(II)–myoglobin and the resulting cobalt hydride hydrogenates alkynes, e.g., acetylenedicarboxylic acid to maleic acid. Cross-linking of the Co(II)-reconstituted myoglobin affinity complex at the MP-11 monolayer with glutaric dialdehyde generates a stable electrode for the electrocatalytic hydrogenation of acetylenedicarboxylic acid with a current yield of ca. 80 %.

Recently, de novo-synthesized four-helix polypeptides were applied to mimic functions of cytochrome *b* and to tailor layered cross-linked electrocatalytic electrodes. A four-helix bundle de novo protein (14 728 Da) that includes four histidine units in the respective ‘A’-helices was assembled on Au electrodes (Figure 22A). Two units of Fe(III)–protoporphyrin IX were reconstituted into the assembly to yield a vectorial electron-transfer cascade [157]. The de novo-synthesized protein assembly forms affinity complexes with the cytochrome-dependent nitrate reductase (NR) and with Co(II)–protoporphyrin IX-reconstituted myoglobin [158]. The resulting layered complex of Fe(III)–de novo protein–NR or Fe(III)–de novo protein–Co(II)-reconstituted myoglobin was cross-linked with glutaric dialdehyde to yield electrically contacted electrocatalytic electrodes. The Fe(III)–de novo protein–NR electrode assembly was applied for the electrocatalyzed reduction NO_3^- to NO_2^- and acted as an amperometric NO_3^- sensor (Figure 22B). The Fe(III)–de novo protein–Co(II)-reconstituted myoglobin integrated electrode stimulated the electrocatalyzed hydrogenation of acetylenedicarboxylic acid to malic acid.

Artificial compounds capable of substituting natural materials and exhibiting affinity interactions with proteins have also been immobilized as monolayers on electrodes and used as ‘instruction matrices’ for assembling further protein layers. Artificial dyes exhibiting affinity interactions to NAD(P)⁺-dependent enzymes (e.g., Cibacron Blue F3G-A) have been assembled as monolayers on Au electrodes, which could then be used for the anchoring of NAD⁺-dependent enzymes such as lactate dehydrogenase [159]. The affinity complexes consisting of the layered dye–enzyme matrices exist in a bioactive configuration, but lack electrical contact with the electrode. Addition of the diffusional NAD⁺ cofactor was found to trigger biocatalytic activity from the enzyme electrodes.

4.2.8 Biosensor, Bioelectronic and Biotechnological Applications of Electrically ‘Wired’ Enzymes

Biosensors constructed from ‘wired’ enzyme assemblies

The electrochemical activation of enzyme electrodes results in the electrobiocatalyzed oxidation or reduction of a substrate specific to the biocatalyst. The rate of the biotransformation is dependent on the substrate concentration, hence these assemblies provide a basis for the construction of analytical biosensors [160]. The

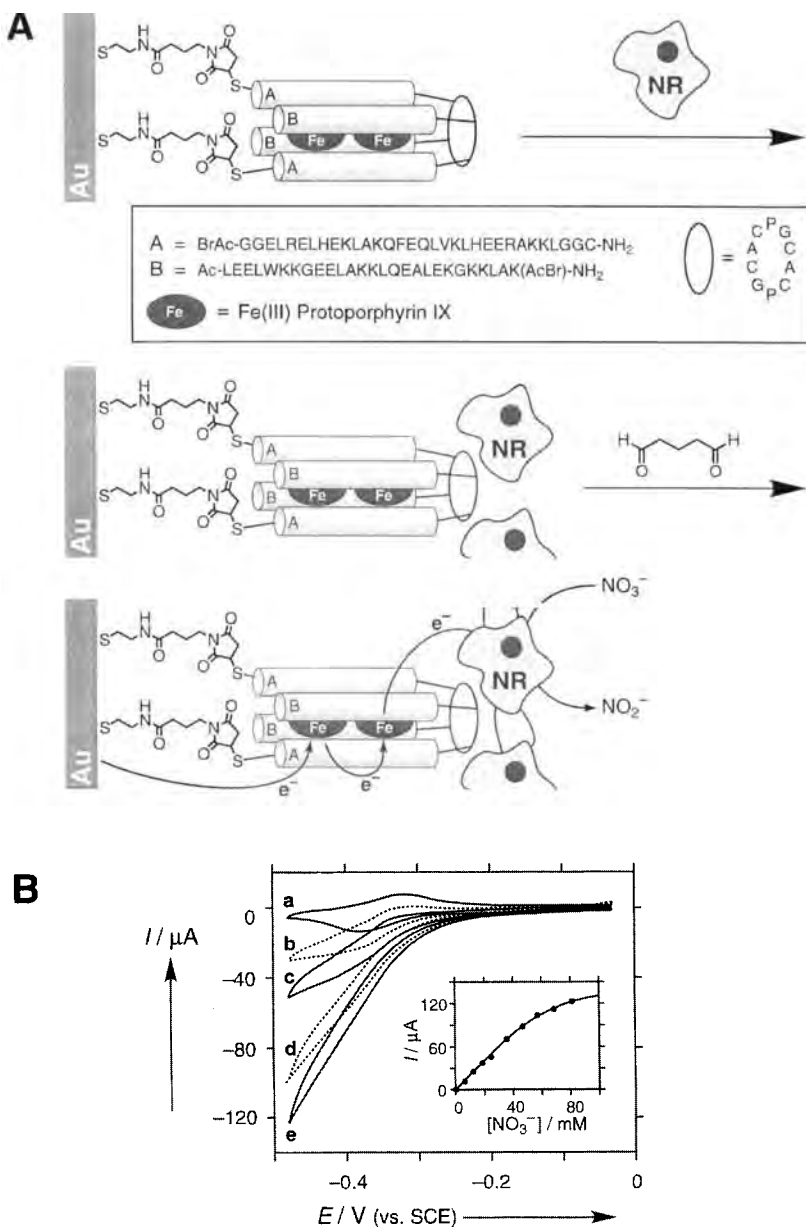


Figure 22. (A) The assembly of a nitrate-sensing electrode by the cross-linking of an affinity complex formed between nitrate reductase (cytochrome-dependent, EC 1.9.6.1), NR and an Fe(III)-protoporphyrin reconstituted de novo four-helix-bundle protein. (B) Cyclic voltammograms of the NR–two heme–reconstituted de novo protein-layered Au electrode at nitrate concentrations of (a) 0, (b) 12, (c) 24, (d) 46 and (e) 68 mM. Inset: calibration curve for the amperometric response of the electrode at different nitrate concentrations (at $E = -0.48 \text{ V vs. SCE}$). Potential scan rate, 5 mV s^{-1} ; 0.1 M phosphate buffer, pH 7.0, under argon; electrode roughness factor, ca. 20.

continuous monitoring of endogenous compounds or drugs by implantable biosensors permits the closer surveillance of patients via a rapid return of clinical information [161]. Such real-time measurements are thus highly desirable in intensive care units, during surgery or for the management of diabetes, as they offer an early warning of changes in a patient's condition, allowing rapid corrective action to be undertaken, possibly via an artificial biofeedback system. Much attention has been given to the probing of blood glucose levels as an aid to diabetes therapy [160]. Several other important metabolites can also be readily detected using amperometric biosensors based on electrically 'wired' enzymes (e.g., biosensors for lactate [162], bilirubin [71, 163], amino acids [164] and peptides [165] have been developed using lactate oxidase or lactate dehydrogenase, bilirubin oxidase, amino acid oxidase and tyrosinase, respectively). Amperometric biosensors for monitoring drugs have also received considerable attention (e.g., for assays of acetaminophen [166] and theophylline [167] using aryl acylamidase and theophylline oxidase, respectively). In addition to medical applications, electrically 'wired' redox enzymes have found many uses in food technology and biotechnology (e.g., for analysis of carbohydrates, organic acids, alcohols, additives, pesticides and fish/meat freshness [168]), in environmental monitoring (e.g., for analysis of pollutants and pesticides [169]) and in defense applications (e.g., for detection of toxins and pathogenic bacteria [170]).

Electrocatalyzed biosynthesis by 'wired' enzyme assemblies

Association between enzymatic and electrochemical reactions has provided efficient tools not only for analytical but also for synthetic purposes. In the latter field, the possibilities of enzymatic electrocatalysis, e.g., the coupling of glucose oxidation (catalyzed either by glucose oxidase or glucose dehydrogenase) to the electrochemical regeneration of a co-substrate (benzoquinone or NAD^+) have been demonstrated [171, 172]. An electroenzymatic reactor has also been developed [172] to demonstrate how the enzyme-electrode association can be used to produce biochemicals on a laboratory scale.

The electrochemical regeneration of cofactors required for the operation of redox enzymes is an important issue for the development of bioreactor technology. Most redox enzymes, dehydrogenases, require $\text{NAD(P)}^+/\text{NAD(P)H}$ coenzyme for their operation, hence the electrochemical regeneration of its oxidized or reduced form [NAD(P)^+ or NAD(P)H] is vitally important for the realization of biosynthetic reactions. Electrocatalytic oxidation of NAD(P)H using many different kinds of catalysts [173], such as *o*-quinones [174], *p*-quinones [175], phenazine, phenoxazine and phenothiazine derivatives [176], ferrocenes [177] and Os complexes [178], has been applied to the regeneration of NAD(P)^+ . Electrocatalytic or bioelectrocatalytic reduction of NAD(P)^+ using Rh complexes [179] or enzymes (e.g., diaphorase [180]) have been used to regenerate NAD(P)H . The regenerated NADH can be used to drive secondary enzymatic reactions with the participation of NADH-dependent enzymes, e.g. lactate dehydrogenase [179b, 180b]. NAD(P)^+ derivatives immobilized by covalent attachment to polymer matrices or protein backbones have been used in enzyme reactors [181]. Another important coenzyme Q, ubiqui-

uinone, playing an important role in metabolism, can be regenerated at an electrode [182] and applied to drive secondary enzymatic reactions with the participation of membrane enzymes (e.g., fumarate reductase), resulting in the production of biologically important compounds [183].

Low-potential electron-transfer mediators such as viologens can substitute natural cofactors (particularly NADH) in some enzymatic reactions [184]. The electrochemical reduction of viologens has been studied extensively [185] and they and other reductive electron mediators have been utilized to drive enzyme-catalyzed reactions [186]. For instance, the electrochemical reduction of NAD(P)^+ to NAD(P)H with a current efficiency of more than 97 % was achieved using alcohol dehydrogenase in the presence of acetophenone as an electron mediator [187]. The addition of acetone or acetaldehyde as a substrate to the above bioelectrocatalytic system allowed the reduction of the substrate to the corresponding alcohol at alcohol dehydrogenase accompanied by the oxidation of the resulting NAD(P)H .

Biocatalytic synthetic reactions also include carbon dioxide fixation with the production of methanol in artificial multi-enzyme systems [188]. Formate dehydrogenase (FDH, EC 1.2.1.2) can catalyze the reduction of carbon dioxide to formate, and methanol dehydrogenase (MDH, EC 1.1.99.8) can catalyze the reduction of formate to methanol. Both of these enzymes require NAD^+/NADH cofactor, and in the presence of the reduced dimethyl viologen mediator (MV^{+}), they can drive a sequence of enzymatic reactions. The cascade of biocatalytic reactions results in the reduction of CO_2 to formate catalyzed by FDH followed by the reduction of formate to methanol catalyzed by MDH. A more complex system composed of immobilized cells of *Parococcus denitrificans* has been demonstrated for the reduction of nitrate and nitrite [189].

Biofuel cells based on ‘wired’ enzyme assemblies

One of the more attractive applications of bioelectrocatalytic electrodes is the development of biofuel elements. The biofuel cell utilizes biocatalysts for the conversion of chemical energy to electrical energy [190]. Abundant raw materials (e.g., methanol, glucose) can be used as fuel substrates for the oxidation, and molecular oxygen or H_2O_2 can act as the oxidizer. The fact that an electrically ‘wired’ enzyme can catalyze the oxidation (e.g., glucose, methanol, lactic acid) or reduction (e.g., H_2O_2) of substrates allows the use of enzyme-modified electrodes as key elements of biofuel cells. Accordingly, a biofuel cell element based on the bioelectrocatalytic oxidation of glucose by H_2O_2 was constructed [191] (Figure 23A). An electrically contacted glucose oxidase monolayer (assembled on an electrode by the reconstitution of apo-glucose oxidase on a PQQ–FAD layer; cf., Section 4.2.7 and Figure 19) was used as the anode, whereas a microperoxidase-11-functionalized electrode acted as the cathode in the system. The bioelectrocatalyzed oxidation of glucose proceeds at the anode, whereas the MP-11 catalyzed reduction of H_2O_2 occurs in the catholyte compartment. The current–voltage behavior of the biofuel cell at different external loads and at optimized concentrations of the oxidizer and fuel substrates are shown in Figure 23B. The maximum power extracted was 32 μW at an external load of 3 k Ω (Figure 23B, inset). The configuration of this biofuel cell

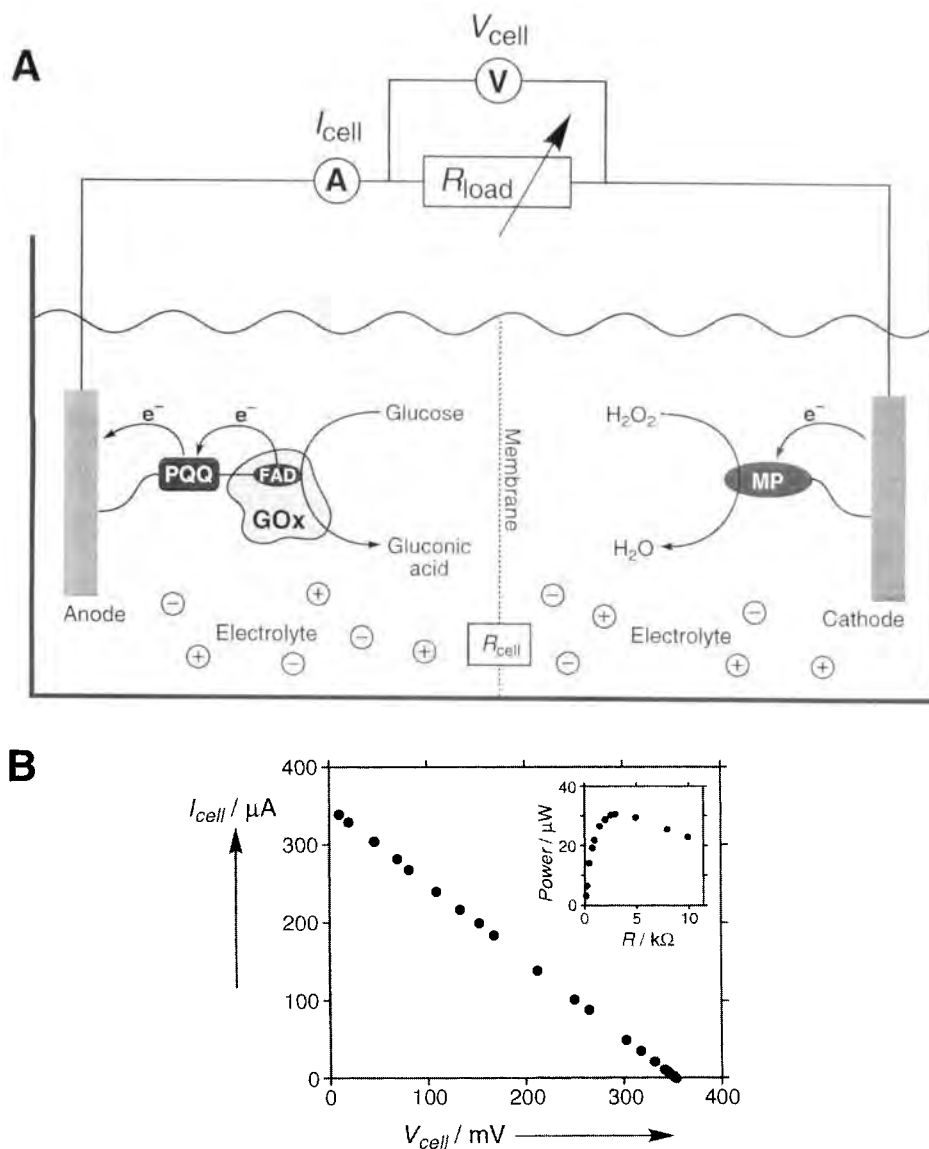


Figure 23. (A) Schematic configuration of a biofuel cell employing glucose and H_2O_2 as fuel and oxidizer, and using PQQ-FAD/reconstituted GOx and MP-11-functionalized electrodes as biocatalytic anode and cathode, respectively. (B) Current-voltage behavior of the biofuel cell at different external loads. Inset: electrical power extracted from the biofuel cell at different external loads.

represents a very general method for the development of future biofuel cell elements as it can be extended to other oxidative enzymes and fuel substrates such as methanol oxidase or lactate oxidase and the respective alcohol or lactic acid fuel substances.

The next generation of biofuel cells could utilize the anode described above (based on the reconstituted GOx) together with a cathode based on an aligned Cyt *c* (from *Saccharomyces cerevisiae*)–cytochrome oxidase couple providing the reduction of O₂ to water (Figure 24A). Since the reconstituted GOx provides extremely efficient biocatalyzed oxidation of glucose that is not affected by oxygen, the anode can operate in the presence of oxygen. Thus, this biofuel cell uses O₂ as an oxidizer and glucose as a fuel without the need for compartmentalization of the anode and cathode [192]. The cell operation was studied at different external loads (Figure 24B), and achieved a fill factor of ca. 40 % with a maximum power 4 μW at an external load of 0.9 kΩ.

Bioelectronic architectures based on ‘wired’ enzyme assemblies

Finally, electrochemically ‘wired’ enzymes and redox proteins can be applied as electronic elements in biomaterial-based electronic systems such as biomolecular switches, rectifies and amplifiers [193, 194]. One example utilized a four-helix bundle de novo protein reconstituted with two heme centers, each with a different potential. When the de novo protein was assembled as a monolayer such that the two redox centers were located at different distances from the electrode, the assembly was shown to display vectorial electron transfer, thus functioning as a biomolecular rectifier (Figure 25A) [158]. The Fe(III)–heme site close to the electrode support exhibits the more negative redox potential ($E^\circ = -0.43$ V vs. SCE). Electron transfer to this heme site is therefore accompanied by intramolecular electron transfer to the second heme center ($E^\circ = -0.36$ V vs. SCE) due to the potential gradient. Since the second process is fast, the electron-transfer rate of reduction is controlled by the primary electron-transfer rate to the heme site close to the electrode. The more negative potential of this site requires that each reduced heme must be oxidized directly, i.e., the oxidation of the reduced two-heme de novo protein cannot proceed by an intramolecular path, and the two reduced sites must be oxidized independently with different electron-transfer kinetics. A double-step chronoamperometric experiment was performed to demonstrate the rectifier function of this system (Figure 25B). The potential applied to the two-heme de novo protein assembly was stepped from -0.2 to -0.5 V (vs. SCE), and the step was interrupted after 70 ms. A reverse step from -0.5 to -0.2 V was then applied to oxidize the reduced assembly. The duration of the cathodic step (70 ms) was tuned to allow only a single electron transfer per protein assembly. As indicated previously, the heme center near the electrode surface is rapidly reduced, and mediates very fast electron transfer to the second site. Thus, upon the application of the cathodic step and the transfer of a single electron to the assembly, a fast cathodic current decay ($k_{\text{et}}' = 40$ s⁻¹) is observed, and the electron is ultimately positioned on the remote heme site. Upon application of the reverse potential step, the system exists in a configuration where the heme center close to the electrode is in the oxidized state,

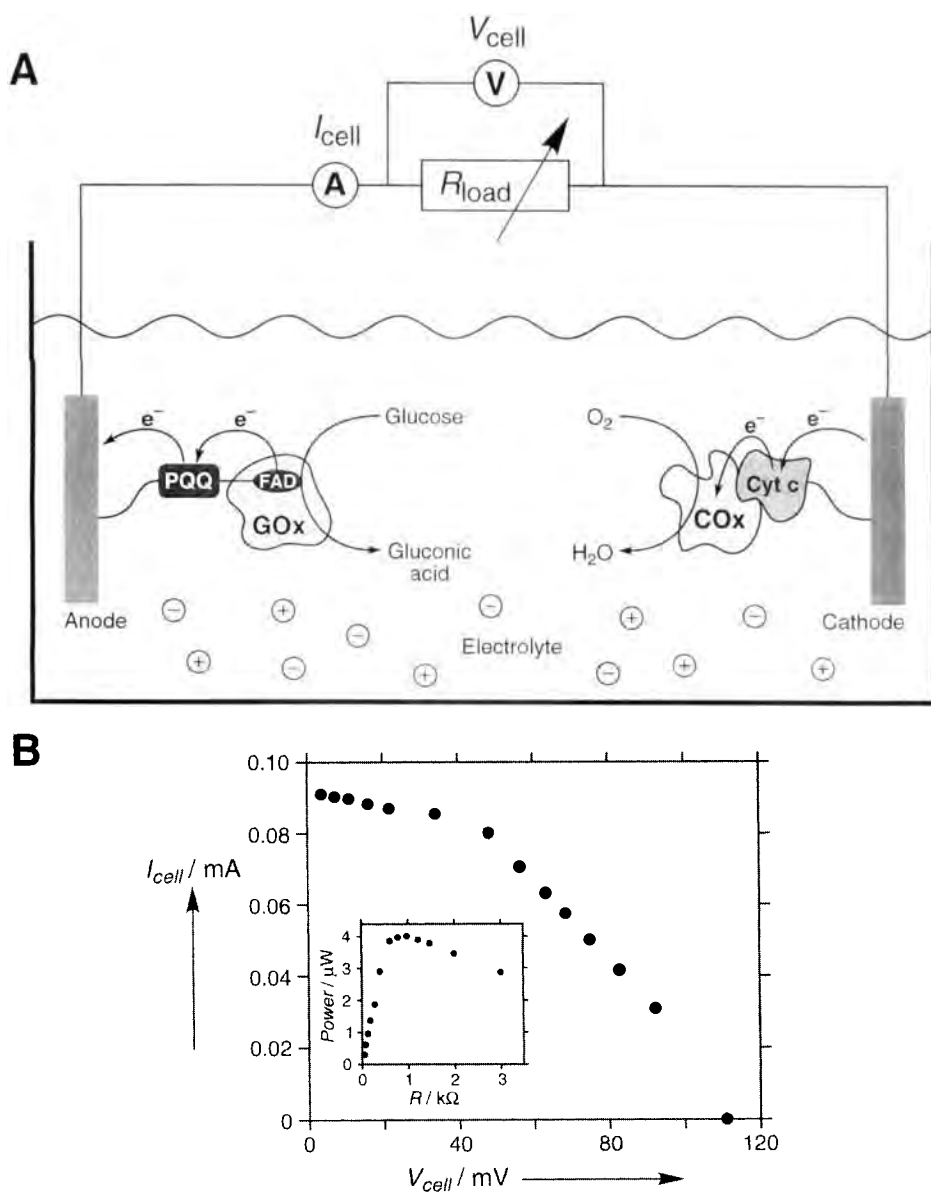


Figure 24. (A) Schematic configuration of a noncompartmentalized biofuel cell employing glucose and O_2 as fuel and oxidizer, and using PQQ–FAD/GOx- and Cyt *c*/COx-functionalized electrodes as biocatalytic anode and cathode, respectively. (B) Current–voltage behavior of the biofuel cell at different external loads. Inset: electrical power extracted from the biofuel cell at different external loads.

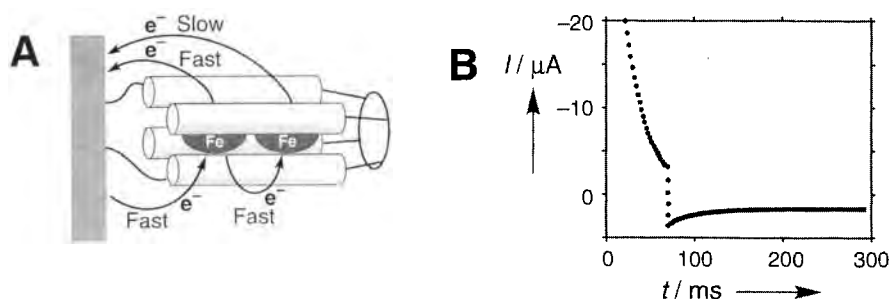


Figure 25. (A) Vectorial electron transfer in the two-heme-reconstituted de novo protein molecules organized as a monolayer at an electrode surface. (B) Transient current recorded with the two-heme reconstituted de novo protein monolayer during the double-potential step chronoamperometric experiment. The potential steps from -0.2 to -0.5 V (vs. SCE) to reduce the hemes in the protein, and after 70 ms the potential steps back, from -0.5 to -0.2 V, to oxidize the reduced hemes. The experiment was performed in 0.1 M phosphate buffer, pH 7.0, under argon.

whereas the remote heme site is reduced. Thus, only very slow oxidation of the remote heme site ($k_{\text{et}}'' = 1.0 \text{ s}^{-1}$) is observed. The system operates as a biomolecular rectifier, allowing fast electron transfer in one direction and only slow electron transfer in the other [158].

The photoswitchable electroactivation of biocatalytic processes can be achieved in systems where enzymes or redox proteins are electrically contacted using photoisomerizable ‘command’ interfaces or electron mediators [195–200]. For example, a mixed monolayer consisting of pyridine thiol and nitrospiropyran thiol (**20**) reveals properties of a light-controlled ‘command’ interface for the cytochrome *c* electrochemistry [195, 198]. On a gold surface, the pyridine thiol monolayer functions as a promoter for the Cyt *c* electrochemical reduction–oxidation process [27, 28]. The second monolayer component, nitrospiropyran thiol, is a photoisomerizable organic material that can be transformed by light ($360 \text{ nm} < \lambda < 400 \text{ nm}$) from the spiropyran state (**20a**) to the protonated merocyanine state (**20b**). The reverse photoisomerization from **20b** to **20a** proceeds upon illumination with visible light ($\lambda > 475 \text{ nm}$). The monolayer composed of the pyridine promoter groups and neutral molecules (**20a**) provides efficient reduction and oxidation of Cyt *c*, allowing enzymatic reactions that require the participation of a Cyt *c*-dependent enzyme. A biocatalytic cascade of reductive reactions was achieved in the presence of cytochrome oxidase (COx) and O_2 (Figure 26A). Oxidative reactions with the participation of lactate dehydrogenase resulted in the lactate oxidation (Figure 26B). When the photoisomerizable groups are transformed into the positively charged protonated merocyanine state (**20b**), the positively charged Cyt *c* molecules are repulsed from the electrode surface and are no longer electrically contacted (Figure 26C). In this case, not only is Cyt *c* electrochemistry inhibited, but so are any secondary reactions. Switching between the electrochemically contacted system and

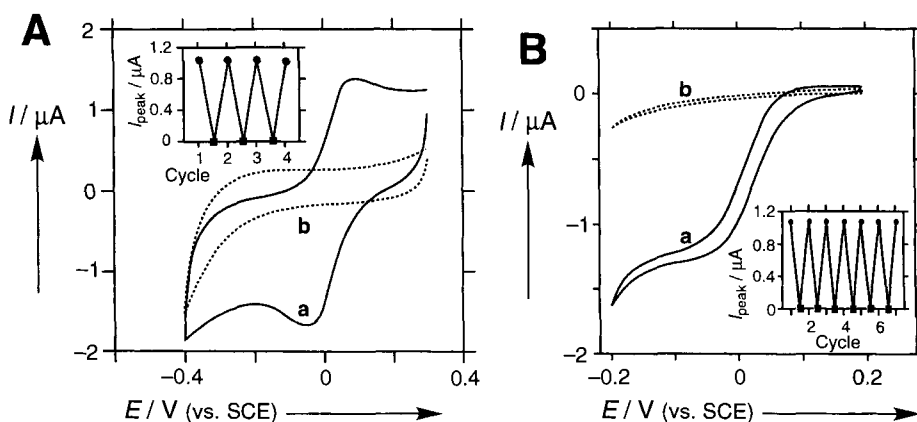


Figure 27. (A) Cyclic voltammetric response of Cyt *c* (0.1 mM) at a (20)-pyridine-modified electrode in (a) the neutral state (20a) and (b) the positively charged merocyanine state (20b), recorded at 50 mV s⁻¹. Inset: switching behaviour of the Cyt *c* peak current as a function of the monolayer state. (B) Cyclic voltammetric response of Cyt *c* (0.1 mM) with COx (1 μM) at a (20)-pyridine modified electrode in the presence of O₂ in (a) in the neutral state (20a) and (b) the cationic merocyanine state (20b). Inset: switching behavior of the electrode in the presence of O₂. All experiments were performed in 0.1 M phosphate buffer, pH 7.0.

mance of glucose oxidase [200, 201] and electrocatalytic regeneration of NAD⁺ cofactor [202].

Photoswitchable electrical communication between enzymes and electrodes has also been achieved by the application of photoisomerizable electron-transfer mediators [195, 199]. Diffusional electron mediators (viologen or ferrocene derivatives) were functionalized with photoisomerizable spiropyran/merocyanine units. These mediators can be reversibly photoisomerized from the spiropyran state to the merocyanine state ($360 < \lambda < 380$ nm) and back ($\lambda > 475$ nm). An enzyme multilayer array composed of glutathione reductase or glucose oxidase was electrically contacted only when the photoactive group linked to the redox relay (viologen or ferrocene derivative, respectively) was in the spiropyran state.

Similar photoisomerizable spiropyran/merocyanine (SP/MRH⁺) groups have been covalently tethered to the glucose oxidase backbone, resulting in control over the enzyme's activity [195, 197]. This control results from the influence of the isomeric state of the randomly tethered photoactive groups on the protein conformation. A more elegant approach involved the reconstitution of an apo-enzyme (e.g., apo-glucose oxidase) with the FAD cofactor covalently linked to a spiropyran/merocyanine photoisomerizable group [203] (Figure 28A). This single photoisomerizable group locates very near to the enzyme active site, providing a very strong effect on the enzyme activity. Cyclic voltammetry of a monolayer assembly consisting of reconstituted GOx in the presence of a diffusional electron relay revealed photoswitchable properties of the enzyme (Figure 28B).

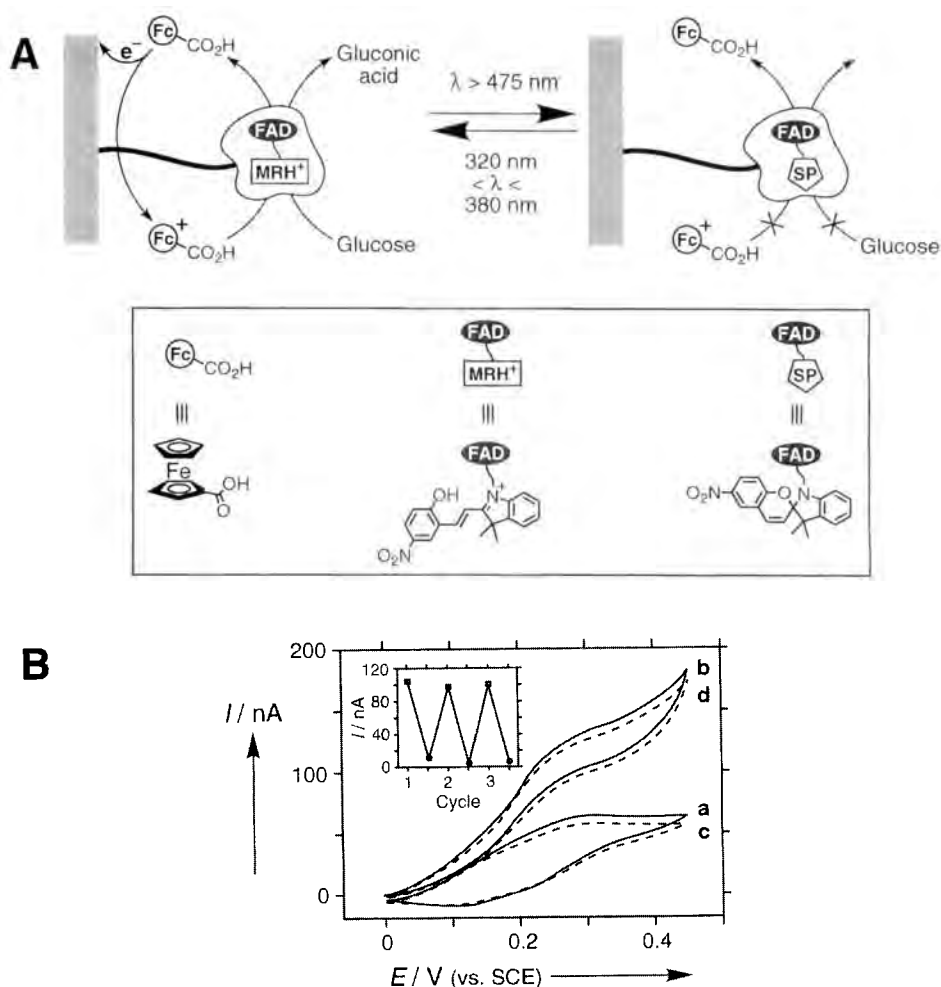


Figure 28. (A) The photoswitchable oxidation of glucose by immobilized GOx reconstituted with a spiropyran-modified FAD and with ferrocenecarboxylic acid as a diffusional electron mediator. (B) Cyclic voltammograms of the modified electrode in the presence of glucose (50 mM), Fc-CO₂H (50 μ M) and with the electrode (a, c) in the spiro (SP) state, and (b, d) in the merocyanine (MRH⁺) state. Recorded in 0.01 M phosphate buffer, pH 7.3; potential scan rate, 5 mV s⁻¹. Inset: switching behavior of the electrocatalytic current as a function of the state of the photoisomerizable group.

Command surfaces based on isomerizable monolayers have also been used to detect various signals (temperature change [204], pH change [205]) by the variation of redox cofactor regeneration rates (therefore by the control of enzymatic activity). Thus, they represent examples of biocatalytic switches. All the systems described above represent examples of bioelectronic devices that can be used for the trans-

duction of photonic signals into amperometric signals using electrically 'wired' enzymes. They can read out information written with light and amplify the signals using biocatalytic reaction cascades.

4.3 The Photochemical Activation of Enzymes

The biochemical processes performed by green plants and photosynthetic bacteria involve a primary photoinduced electron transfer that leads to charge separation and the formation of redox species. These redox species activate electron transfer to complex enzyme pathways that convert the energy of the separated charges into chemical energy that is used by plants and photosynthetic bacteria for their physiological needs. The photosynthetic apparatus in green plants is organized into two photosystems, photosystem I and photosystem II (PS-I and PS-II, respectively) schematically represented as the Z-scheme (Figure 29). Primary photoinduced charge separation in the both photosystems proceeds with the participation of chlorophyll and pheophytin molecules organized into complex assemblies. These units provide very fast and efficient vectorial electron transfer terminated by the formation of separated charges that can be stable at the final electron acceptor site for seconds. The reductive and oxidative equivalents generated during the primary photochemical step are then utilized in slow, dark enzymatic reactions. The first stable reduced product generated by PS-I is reduced ferredoxin, which induces a

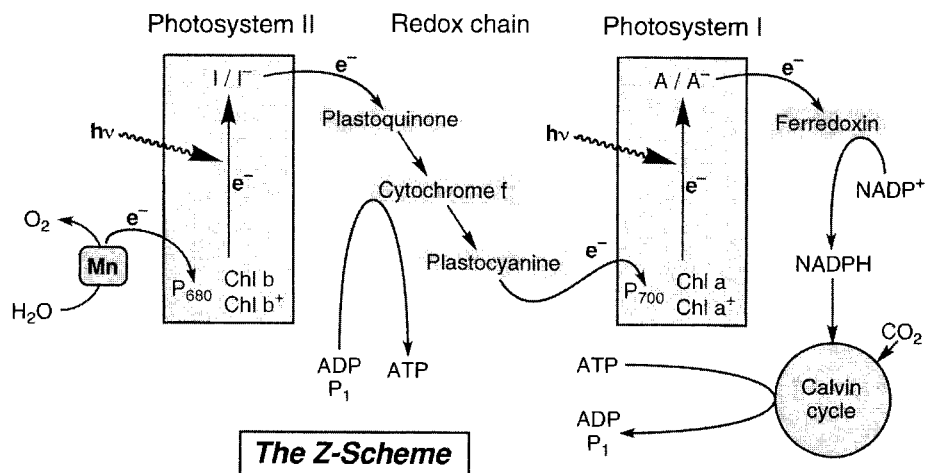


Figure 29. Z-scheme of the photoinduced electron-transfer and dark enzymatic reactions operating in the photosynthesis of green plants. **Mn** = Mn-containing enzyme complex catalyzing water oxidation and O_2 evolution; Chl a and Chl b = photoactivated primary electron acceptors in photosystems I and II, respectively; A and I = primary electron donors in photosystems I and II, respectively; ADP = adenosine diphosphate; ATP = adenosine triphosphate.

series of electron-transfer reactions that ultimately reduce the natural cofactor NAD^+ to NADH . This reduced cofactor provides the electron source for CO_2 fixation to form carbohydrates in a complex sequence of enzyme-catalyzed transformations (the Calvin cycle). The chlorophyll photooxidized in the PS-I is reduced by an electron coming from PS-II via an electron transport chain consisting of a quinone (the final electron acceptor in the reaction center of the PS-II) and electron-transporting proteins (cytochrome, plastocyanin). The oxidized chlorophyll of PS-II mediates the biocatalyzed oxidation of water to molecular oxygen catalyzed by a complex Mn-containing protein. This scheme emphasizes that the photosynthetic apparatus operates by a synchronous mechanism involving a photochemical part, where light energy is converted to chemical potential by electron-transfer reactions, followed by a set of dark reactions utilizing the chemical energy in driving CO_2 fixation and O_2 evolution.

Significant progress has been accomplished in the understanding of photoinduced electron-transfer and charge-separation processes by the characterization of the stepwise electron transfer in the photosynthetic reaction centers isolated from the photosynthetic bacteria *Rhodobacter sphaeroides* R-26 [206]. In contrast to green plants, photosynthetic bacteria contain a single photosystem, consisting of a protein matrix with embedded pigments and electron relays (Figure 30). This assembly includes four bacteriochlorophylls (BChl), two bacteriopheophytins (BPhe), two ubiquinones (UQ) and a nonheme iron. These units are organized in an almost symmetrical spatial configuration consisting of two arms, labeled L and M. Two of the BChls in this assembly (the 'special pair') form the primary electron donor site. The remaining two BChls, two BPhe's and two ubiquinones occupy analogous positions in the L and M arms. Photoinduced electron transfer initiated by excitation of $(\text{BChl})_2$ proceeds only across arm L and involves sequential electron transfer to BChl_L , BPhe_L , UQ_L and UQ_M . The important charge-separated intermediates and their lifetimes are represented in Figure 30. A vectorial electron-transfer process

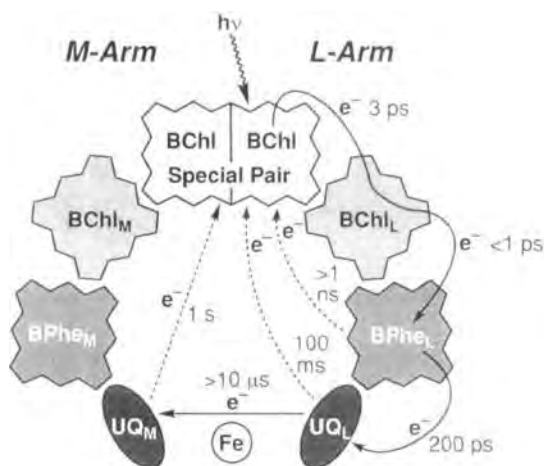


Figure 30. Charge-separated intermediates and their lifetimes in the bacterial photosynthetic reaction center.

proceeds in the photosynthetic reaction center and the lifetime of the intermediate redox products is lengthened as the distance between the components increases.

These photosynthetic reaction centers have been used for the construction of highly efficient photobioelectronic devices. The electrical ‘wiring’ of these natural photosensitive proteins (e.g., bacterial photosynthetic reaction centers [207]) on electrode surfaces results in electrodes that can be considered to be elements of photobioelectronic devices. More importantly, the study of photosynthetic reaction centers has resulted in a basic understanding of the mechanism of the photoinduced charge separation realized by nature. Specifically, photoinduced electron transfer in dye-functionalized proteins has been studied extensively and the kinetics of forward electron-transfer quenching and backward recombination have been characterized as a function of parameters including the free energy driving the electron transfer, the distance separating the donor–acceptor pair and protein structure [208–211].

4.3.1 Biological Transformations Driven by the Photochemical Regeneration of $\text{NAD(P)}^+/\text{NAD(P)H}$ Cofactors

As many redox enzymes depend on the common $\text{NAD(P)}^+/\text{NAD(P)H}$ cofactors, the development of photochemical regeneration cycles of these natural cofactors could provide a general means for the activation of numerous redox biotransformations. $\text{NAD(P)}^+/\text{NAD(P)H}$ -dependent enzymes usually operate reversibly. For example, Figure 31 outlines the biocatalyzed reduction of pyruvic acid (**21**) to lactic acid (**22**) by an alcohol in the presence of alcohol dehydrogenase and lactate dehydrogenase as well as NAD^+ cofactor. In an excess of lactic acid, however, the reverse process is possible and an equilibrium mixture of reactants and products is formed. This possibility can facilitate an ‘uphill’ endergonic process through the constant input of radiation energy. Thus, by the light-induced production of these cofactors the photosynthetic transformations may be envisaged [212–214].

Photochemical reductive systems providing regeneration of NAD(P)H

One photosystem for the reduction of NADP^+ to NADPH consists of *N,N'*-dimethyl-4,4'-bipyridinium (methylviologen, MV^{2+}) as an electron mediator,

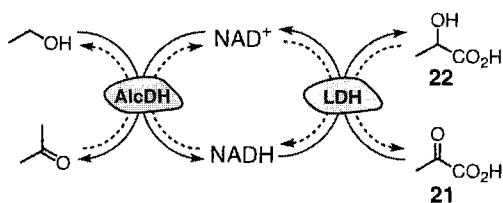


Figure 31. The biocatalyzed conversion of pyruvic acid (**21**) to lactic acid (**22**) by an LDH–AlcDH system and the use of the NAD^+/NADH cofactor. The transformation proceeds with the oxidation of ethanol, and is reversed in a high concentration of lactic acid.

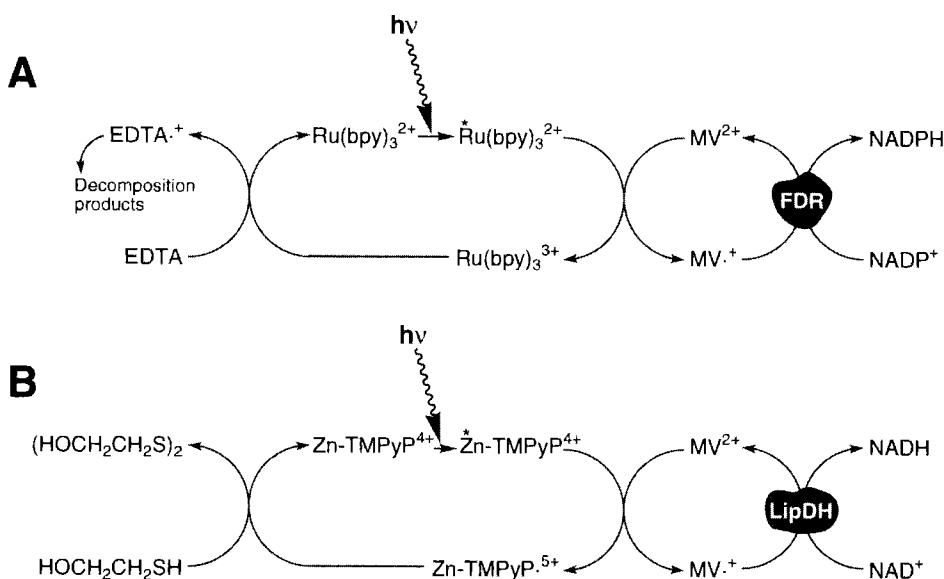


Figure 32. Photosensitized regeneration of NAD(P)H cofactor involving enzymes (FDR or LipDH) and the artificial electron-transfer mediator MV^{2+} , and using (A) $\text{Ru}(\text{bpy})_3^{2+}$ or (B) $\text{Zn}(\text{II})$ *meso*-(*N*-tetramethylpyridinium)porphyrin, Zn-TMPyP^{4+} , as a photosensitizer.

$\text{Ru}(\text{II})$ tris(bipyridine) [$\text{Ru}(\text{bpy})_3^{2+}$] as a photosensitizer, triammonium ethylenediaminetetraacetic acid [$(\text{NH}_4)_3\text{EDTA}$] as a sacrificial electron donor and the enzyme ferredoxin– NADP^+ reductase (FDR) [215, 216]. Oxidative electron-transfer quenching of the excited $\text{Ru}(\text{bpy})_3^{2+*}$ yields the *N,N'*-dimethyl-4,4'-bipyridinium radical cation (reduced methylviologen, $\text{MV}^{\cdot+}$), which mediates the reduction of NADP^+ in the presence of FDR as a biocatalyst (Figure 32A). The quantum efficiency for NADH production corresponds to $\phi = 1.9 \times 10^{-2}$. A related system that includes $\text{Zn}(\text{II})$ *meso*-(*N*-tetramethylpyridinium)porphyrin (Zn-TMPyP^{4+}) as a photosensitizer, mercaptoethanol as a sacrificial donor and lipoamide dehydrogenase (LipDH) as a biocatalyst has been applied for the photochemical reduction of NAD^+ to NADH (Figure 32B).

A different approach to the photochemical regeneration of NAD(P)H cofactors includes the integration of biomaterials with a semiconductor photocatalyst. Light-induced excitation of the semiconductor generates an electron–hole pair. While conduction-band electrons act as the electron source for the reduction of NAD(P)^+ to NADH, the valence-band hole oxidizes a solubilized donor. Heterogeneous semiconductor powders or colloids (TiO_2 , CdS) have been used to accomplish the photoreduction of the soluble electron mediator MV^{2+} in the presence of a sacrificial electron donor (e.g., mercaptoethanol or formate). Subsequent NADH regeneration was observed in the presence of LipDH [213, 217]. The direct coupling of an inorganic semiconductor with the active centers of NAD^+ -dependent enzymes is especially interesting as this could provide light-driven NADH regeneration without

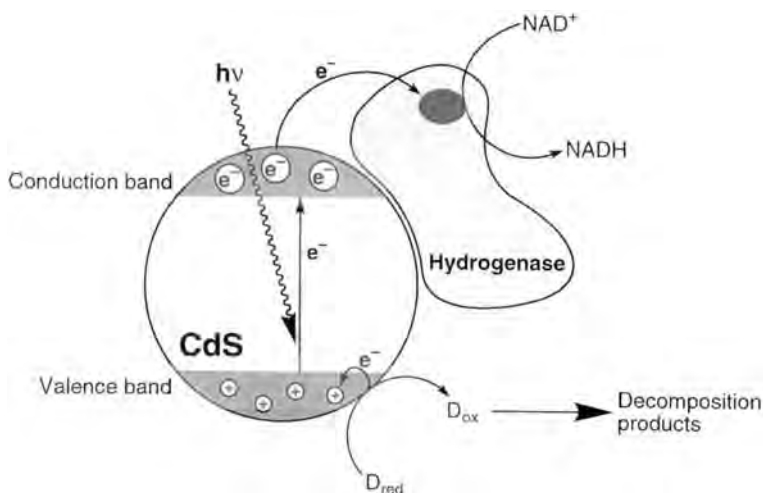


Figure 33. Regeneration of NADH by a photochemical system consisting of CdS–hydrogenase (from *Alcaligenes eutrophus*) and using formate as a sacrificial electron donor.

the need for any exogenous mediator. This goal has been achieved using the NAD^+ -dependent hydrogenase from *Alcaligenes eutrophus* immobilized on CdS particles [218]. Photoregeneration of NADH in a system composed of NAD^+ , hydrogenase–CdS and formate was obtained via direct electron transfer from the semiconductor to the enzyme in the absence of any mediating electron carriers (Figure 33).

The regeneration of NADH cofactor for subsequent biocatalytic transformations can also be accomplished by nonenzymatic means. Photosensitized regeneration of NADH proceeds in the presence of various rhodium complexes such as Rh(III) tris(bipyridine) $[\text{Rh}(\text{bpy})_3^{3+}]$ and Rh(III) tris(2,2'-bipyridyl-5-sulfonic acid) $[\text{Rh}(\text{bpysa})_3^{3+}]$ [219, 220]. Single-electron reduction of the rhodium complex is accompanied by the subsequent disproportionation of the product, resulting in a two-electron reduced product in the form of a hydridorhodium complex, capable of reducing NAD^+ to NADH. For example, in the photosystem composed of $\text{Ru}(\text{bpy})_3^{2+}$ as a photosensitizer, $\text{Rh}(\text{bpy})_3^{3+}$ as an electron acceptor and triethanolamine (TEOA) as a sacrificial electron donor, NAD^+ was reduced to NADH by the stepwise mechanism outlined in Figure 34 [219]. The primary process in this system includes the oxidative quenching of the excited state of the photosensitizer by the rhodium complex, followed by the reduction of its oxidized state by TEOA. The reduced state of the rhodium complex participates in the reduction of NAD^+ via the intermediate formation of the hydridorhodium complex. A related system includes $\text{Rh}(\text{bpysa})_3^{3+}$ as an electron relay and hydride transfer catalyst, $\text{Ru}(\text{bpy})_3^{2+}$ as a photosensitizer and ascorbate as a sacrificial electron donor [220]. The primary process in this system is the reductive quenching of $^*\text{Ru}(\text{bpy})_3^{2+}$ by ascorbate resulting in the formation of the reduced state of the photosensitizer

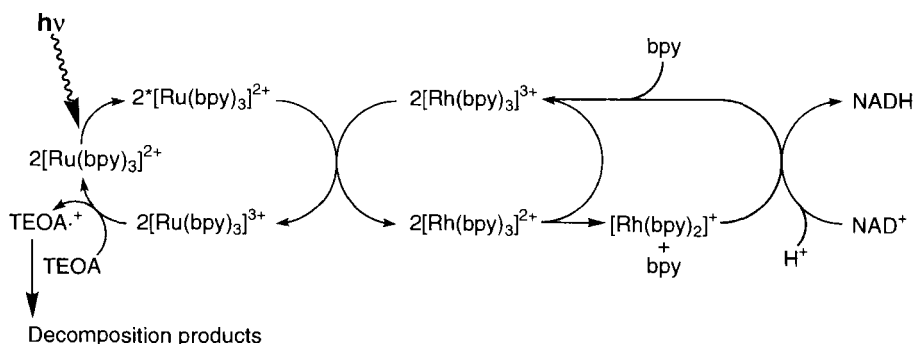
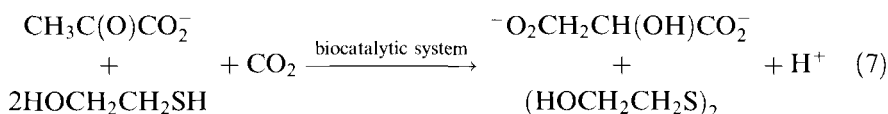


Figure 34. Nonenzymatic photosensitized regeneration of NADH using $\text{Rh}(\text{bpy})_3^{3+}$ as an electron-transfer mediator.

$[\text{Ru}(\text{bpy})_3^+]$. This reduced species is oxidized by $\text{Rh}(\text{bpy})_3^{3+}$, resulting in the formation of the reduced hydridorhodium complex, which provides further reduction of NAD^+ . The NADH regenerated in this photochemical system was coupled with the enzymatic reduction of acetaldehyde to ethanol in the presence of alcohol dehydrogenase.

Photochemically regenerated NAD(P)H cofactors may be used to drive secondary reductive biocatalytic transformations [212, 216, 221]. In these cases, it is important to avoid interactions between the photosystems and the biocatalysts. For example, NADPH regenerated photochemically in the presence of the $\text{Ru}(\text{bpy})_3^{2+}$ and ferredoxin reductase has been utilized for the reduction of ketones, e.g., 2-butanone in the presence of alcohol dehydrogenase (AlcDH) or for the reductive amination of α -ketoglutaric acid to glutaric acid. In addition, NADH regenerated by $\text{Zn}(\text{II})$ -porphyrin in the presence of lipoamide dehydrogenase has been used for the reduction of pyruvic acid to lactic acid in the presence of lactate dehydrogenase (LDH) and for the reductive amination of pyruvic acid to alanine.

Photogenerated cofactors can be employed to drive biocatalytic enzyme cascades including the photosynthetic carbon dioxide fixation process [184] (Figure 35). Photogenerated NADPH provides a two-electron relay for the insertion of CO_2 into α -ketoglutaric acid (**23**) and pyruvic acid (**21**) in the presence of isocitrate dehydrogenase (IcDH) and malic enzyme (MalE), respectively. In these photo-systems, $\text{Ru}(\text{bpy})_3^{2+}$ acts as a photosensitizer, MV^{2+} as a primary electron acceptor and 2-mercaptoethanol as the sacrificial electron donor. Photogenerated MV^{+} mediates the regeneration of NADPH in the presence of FDR, and the resulting cofactor provides the electrons for the dark fixation of CO_2 into keto acids. The net process accomplished in these transformations corresponds to the reductive insertion of CO_2 into keto acids by the oxidation of the sacrificial thiol donor (Eq. 7):



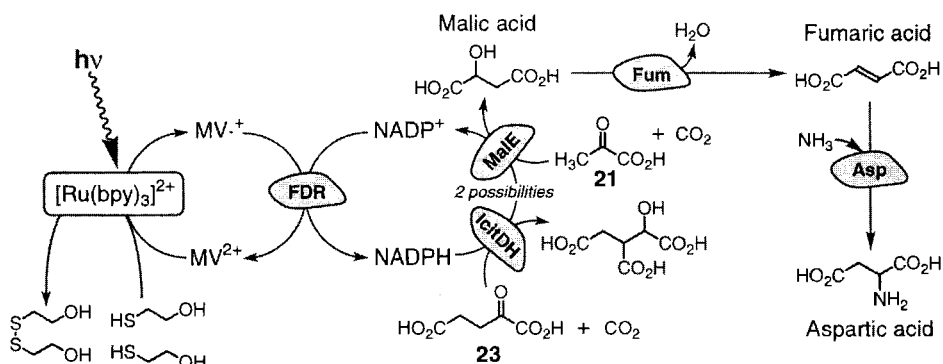


Figure 35. The application of the light-induced regeneration of NADPH to drive the biocatalyzed CO₂ fixation process and secondary transformations.

The photochemical carboxylation of pyruvic acid by this process is endergonic by about $\Delta G^\circ = 11.5 \text{ kcal mol}^{-1}$ and represents a true 'uphill' photosynthetic pathway. The carbon dioxide fixation product can then act as the source substrate for subsequent biocatalyzed transformations. For example, photogenerated malic acid can act as the source substrate for aspartic acid (Figure 35). In this case, malic acid is dehydrated by fumarase (Fum) and the intermediate fumaric acid is aminated in the presence of aspartase (Asp) to give aspartic acid.

Photochemical oxidative systems providing regeneration of NAD(P)⁺

The photochemical regeneration of NAD(P)⁺ proceeds by one of two possible mechanisms: (a) the reductive quenching of a photosensitizer by NAD(P)H results in the formation of NAD(P)⁺ and the reduced state of the photosensitizer, that is subsequently oxidized by an electron acceptor (Figure 36A); (b) oxidative quenching of a photosensitizer by an electron acceptor results in the formation of an oxidized state of the photosensitizer that is capable of oxidizing NAD(P)H (Figure 36B) [212]. Organic dyes such as methylene blue (**24**) and *N*-methylphenazonium methylsulfonate (**25**) have been used as photosensitizers for the photochemical regeneration of NAD(P)⁺. These photosensitizers operate by the reductive quenching route in the formation of NAD(P)⁺. The photoreduced dyes are re-oxidized by O₂ (Figure 37) [222, 223]. The quantum efficiencies for NAD⁺ formation using **24** and **25** correspond to $\phi = 0.30$ and 0.28, respectively. The oxidations of ethanol and lactic acid to acetaldehyde and pyruvic acid biocatalyzed by alcohol dehydrogenase or lactate dehydrogenase, respectively, have been photochemically driven by the regeneration of NAD⁺.

The photolysis of organic compounds to molecular hydrogen and the oxidized organic products has been reported by photogeneration of NAD⁺ (Eqs. 8–13) [224]:



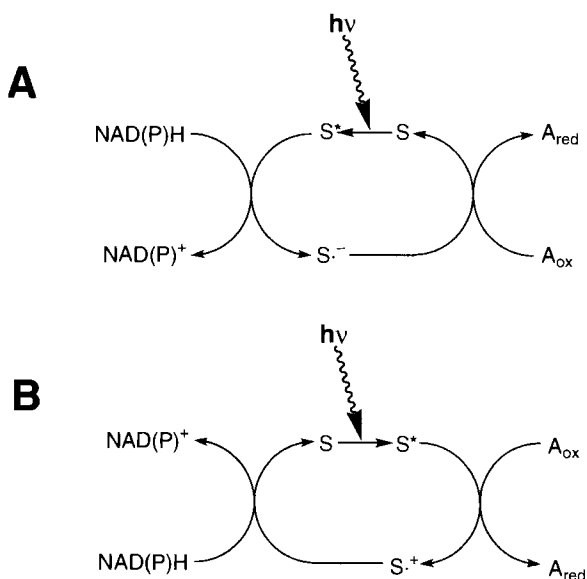


Figure 36. The photochemically induced oxidative regeneration of NAD(P)^+ cofactors: (A) when the primary step involves the reductive quenching of the photoexcited dye by NAD(P)H , and (B) when the primary step involves the oxidative quenching of the photoexcited dye by an electron acceptor.

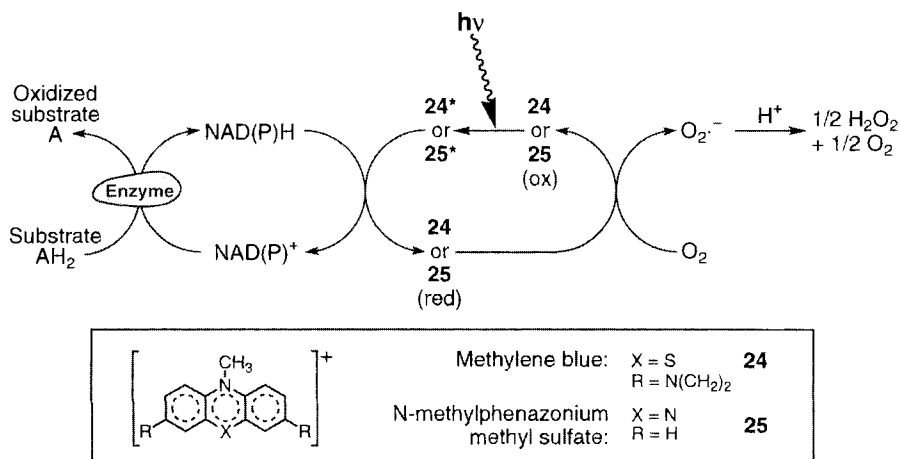
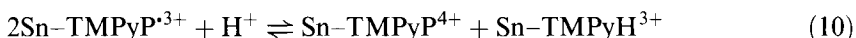
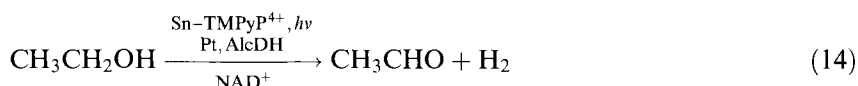


Figure 37. The photosensitized regeneration of NAD(P)^+ cofactor using organic dyes **24** and **25** as photosensitizers, and the application of the NAD(P)^+ to drive enzymatic reactions.

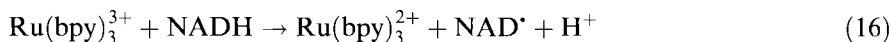


The photochemical assembly includes Sn(IV) *meso*-(*N*-tetramethylpyridinium)-porphyrin, (Sn-TMPyP⁴⁺) as a photosensitizer, a Pt colloid as a heterogeneous catalyst, the reduced cofactor NADH, an organic photolyzable substrate (e.g., ethanol) and the respective NAD⁺-dependent enzyme (alcohol dehydrogenase). The primary step involves reductive electron-transfer quenching of the excited state of the metalloporphyrin (Eq. 9). The resulting products undergo redox transformations that ultimately lead to NAD⁺ (Eq. 11) and the hydrogenated porphyrin (Eq. 10). These two photoproducts drive the oxidation and reduction of the organic material: while H₂ evolution is effected by the hydrometalloporphyrin in the presence of the Pt catalyst acting as charge storage site (Eq. 12), NAD⁺ mediates the oxidation of the alcohol using AldDH as a biocatalyst (Eq. 13). All of the photo-system components are recycled and the net transformation corresponds to the endergonic ($\Delta G^\circ = 10 \text{ kcal mol}^{-1}$) cleavage of ethanol (Eq. 14):



Thus this energy storage transformation represents a photosynthetic process in which H₂ fuel is produced.

The photolysis of organic materials has also been accomplished by the oxidative quenching of photosensitizers. For example, oxidative quenching of Ru(bpy)₃²⁺ by MV²⁺ in the presence of NADH leads to MV^{•+} and NAD⁺ through the sequence of reactions outlined in Eqs. 15–17. The reduced photoproduct, MV^{•+}, mediates H₂ evolution in the presence of Pt colloid (Eq. 18), while NAD⁺ mediates the two-electron oxidation of ethanol (Eq. 19) or lactic acid (Eq. 20) biocatalyzed by the respective enzyme [225].



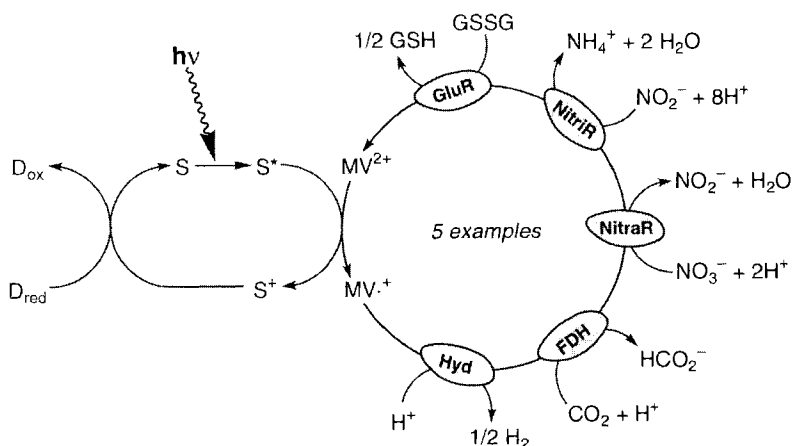


Figure 38. Biocatalyzed photosynthetic systems mediated by photochemically generated *N,N'*-dimethyl-4,4'-bipyridinium cation radical.

4.3.2 Enzymatic Reactions Driven by the Photochemical Regeneration of Synthetic Electron Relays

A variety of NAD(P)H-dependent enzymes recognize artificial electron carriers. These relays can substitute the native cofactors and activate electron-transfer reactions to the enzymes [212]. Photogenerated *N,N'*-dimethyl-4,4'-bipyridinium radical cation ($MV^{\bullet+}$) is recognized by various enzymes such as hydrogenase (Hyd) [226–228], formate dehydrogenase (FDH) [184], nitrate reductase (NitraR), nitrite reductase (NitriR) [229] and glutathione reductase (GluR) (Figure 38) [88b]. Various biocatalyzed photosynthetic systems using the light-induced regeneration of $MV^{\bullet+}$ by Zn-porphyrin, chlorophyll or $Ru(bpy)_3^{2+}$ photosensitizers and sacrificial electron donors such as EDTA (which may be in the form of any of a number of salts), cysteine and mercaptoethanol have been developed [184, 226–229]. For example, a photosystem composed of chlorophyll a (Chl) as a photosensitizer, MV^{2+} as an electron acceptor and ascorbate as a sacrificial electron donor has provided the photochemical reduction of MV^{2+} to $MV^{\bullet+}$. The resulting $MV^{\bullet+}$ can trigger H_2 evolution in the presence of hydrogenase [228]. Primary electron-transfer quenching reactions of $*Chl$ can be either oxidation by MV^{2+} or reduction by ascorbate depending on the pH of the medium [230]. Thus, different species can be involved in the formation of $MV^{\bullet+}$: the excited state of the photosensitizer ($*Chl$) or chlorophyll anion radical ($Chl^{\bullet-}$) in the case of oxidative or reductive quenching, respectively.

The reduction of carbon dioxide to formate in the presence of FDH represents a photochemical CO_2 -fixation process. In addition to $MV^{\bullet+}$, the enzyme recognizes other electron carriers such as 2,2'-bipyridinium radical cations [184]. Reduction of nitrate (NO_3^-) to nitrite (NO_2^-) and subsequently the reduction of nitrite to ammonia in the presence of NitraR and NitriR, respectively, allows the sequential $8e^-$

reduction of nitrate to ammonia in a photosystem that includes the two enzymes. The two enzymes are activated by photochemically regenerated MV^{+} . In a photosystem including $Ru(bpy)_3^{2+}$ as a photosensitizer, the fixation of NO_3^- to ammonia has been driven with a quantum efficiency of $\phi = 3 \times 10^{-2}$. Photobiocatalytic hydrogen evolution was achieved when hydrogenases were coupled to semiconductors and photosensitizers in the presence of artificial or natural electron carriers, usually MV^{2+} [226, 231]. It should be noted that hydrogenases isolated from mesophilic organisms are capable of evolving hydrogen in the presence of TiO_2 without electron carriers by direct electron transfer from the conduction band of the semiconductor to the enzyme [232].

For practical photoinduced synthetic biocatalyzed transformations, it is important to integrate biocatalysts in immobilized matrices that allow the recycling of the photosystems. The fact that bipyridinium sites act as electron mediators for various redox enzymes was used to develop two paradigms for the electrical contacting and photoactivation of the biocatalyst (Figure 39). By one approach, the bipyridinium electron relays are tethered by covalent bonds to the protein backbone (Figure 39A). These electron relays act as oxidative quenchers of the excited state of the dye and, upon photoreduction of the electron acceptor units, they act as electron carriers that activate the reductive functions of the enzyme. As an example, the

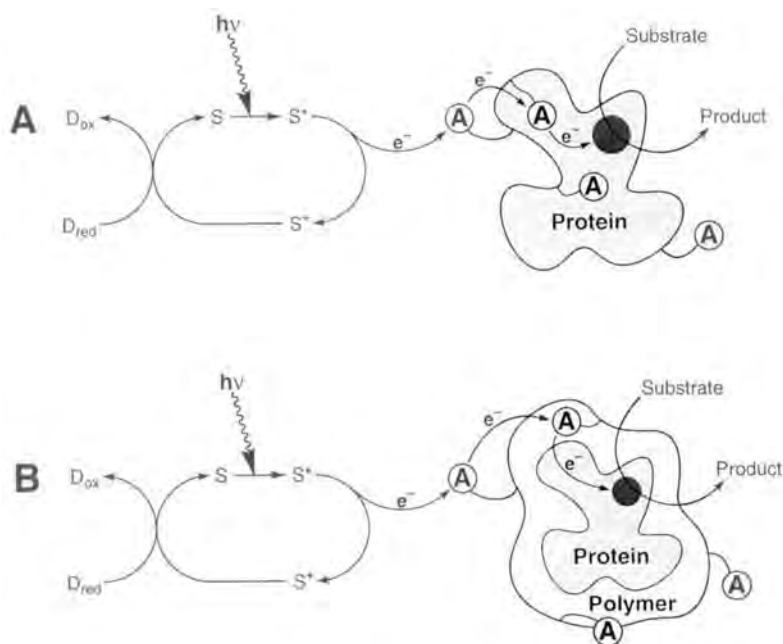


Figure 39. Electrical communication between an enzyme redox center and a photoexcited species attaining light-induced biocatalyzed transformations: (A) direct electrical 'wiring' of the protein by its chemical modification with tethered electron-relay units; (B) electrical communication by the immobilization of the protein into a redox-functionalized polymer matrix.

enzyme glutathione reductase was activated by the covalent tethering of *N*-methyl-*N'*-propionic acid-4,4'-bipyridinium (**4**) units to lysine residues of the protein backbone (Figure 39A) [233]. In a photochemical system composed of $\text{Ru}(\text{bpy})_3^{2+}$, EDTA and the bipyridinium-modified GluR, reduction of glutathione proceeds. Oxidative quenching of the photosensitizer by the tethered bipyridinium units results in the formation of bipyridinium radical cation units that mediate electron transfer to the enzyme active site that reduces the substrate. The oxidized photosensitizer, $\text{Ru}(\text{bpy})_3^{3+}$, takes an electron from the electron donor, EDTA, resulting in the recycling of the light-active compound.

By the second approach, the enzyme is immobilized in a redox polymer assembly (Figure 39B). Electron-transfer quenching of the photosensitizer by the polymer matrix generates an 'electron pool' for the activation of the enzyme. Photoreduction of nitrate to nitrite was accomplished by the physical encapsulation of NitraR in a redox-functionalized 4,4'-bipyridinium acrylamide copolymer [234]. In this photo-system, $\text{Ru}(\text{bpy})_3^{2+}$ was used as a photosensitizer and EDTA as a sacrificial electron donor. Oxidation of the excited photosensitizer results in electron transfer to the redox polymer, and the redox sites on the polymer mediate further electron transfer to the enzyme redox center, where the biocatalyzed transformation occurs. The rate constant for the MET from the redox polymer functionalities to the enzyme active site is $k_{\text{et}} = (9 \pm 3) \times 10^5 \text{ s}^{-1}$. Similarly, the enzyme glutathione reductase was electrically 'wired' by interacting the enzyme with a redox polymer composed of polylysine modified with *N*-methyl-*N'*-carboxyalkyl-4,4'-bipyridinium. The photosensitized reduction of oxidized glutathione (GSSG) (Eq. 21):



was examined in a photosystem composed of $\text{Ru}(\text{bpy})_3^{2+}$ as a photosensitizer, EDTA as a sacrificial electron donor, the redox-modified polylysine as an electron 'wiring' matrix and the enzyme glutathione reductase (GluR) [235]. The effectiveness of electrical communication between the excited species and the redox center was established as a function of the alkyl chain length bridging the bipyridinium salt to the polymer backbone. As the chain length tethering the bipyridinium relay to the polymer increases, electrical communication between the redox polymer and enzyme active site is enhanced since the redox group mediating electron transfer is more free to penetrate the protein active center.

Despite their advantages, the photobiocatalytic systems generally shown in Figure 39 still require diffusional components: the photosensitizer and sacrificial electron donor. Further efforts should be directed to the organization of photobiocatalytic systems where the photosensitizer is also immobilized in the matrix.

4.3.3 Photochemical Activation of Enzymes Using Dyes Covalently Tethered to the Protein Backbone

The covalent tethering of a photochemically active dye to a protein backbone can turn a native enzyme into a photoactive biocatalyst. Upon irradiation, the covalently

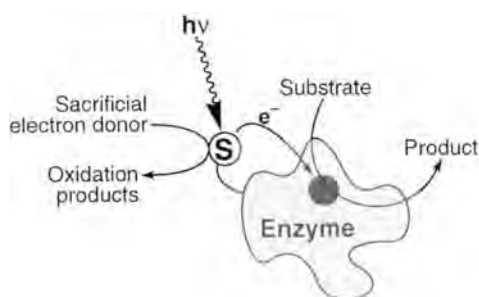
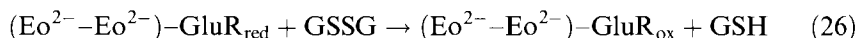
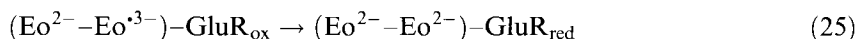
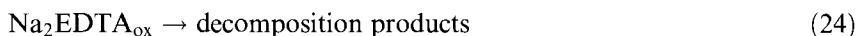
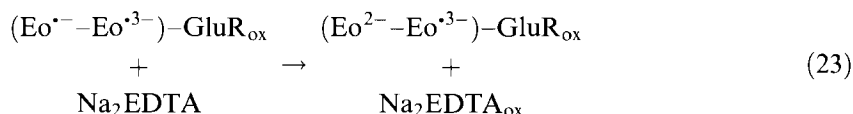
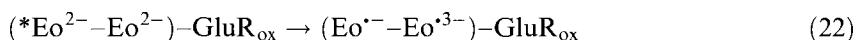


Figure 40. A biocatalytic reaction photochemically driven by the direct electron transfer from the photoexcited dye molecule covalently tethered to the enzyme backbone.

linked dye produces an excited state that is capable of transferring an electron to the enzyme active site. This induces a biocatalytic reaction at the reduced active site of the enzyme after which the active site is returned to the oxidized state. The initial ground state of the dye can be then regenerated in the presence of a sacrificial electron donor. This photochemically driven cyclic transformation results in the realization of a light-stimulated biocatalytic reaction (Figure 40). Glutathione reductase was transformed to a 'photoenzyme' by tethering photoactive eosin dye units (Eo^{2-}) to the protein [236]. The mechanism of the enzyme photoactivation is summarized in Eqs. 22–26:



The reaction scheme includes primary inter-dye electron-transfer quenching to yield the oxidized ($\text{Eo}^{\bullet-}$) and reduced ($\text{Eo}^{\bullet 3-}$) dye species both linked to the same protein (Eq. 22). The reduced dye stimulates electron transfer to the enzyme active site (Eq. 25) and the activation of the enzyme towards the reduction of oxidized glutathione (GSSG, Eq. 26). The oxidized dye species oxidizes EDTA (Eq. 23) and the two reactions regenerate the photoactive enzyme (Eqs. 25 and 26). Figure 41 shows the light-triggered activation of glutathione reductase for the reduction of GSSG.

Semi-synthetic enzymes are produced by the reconstitution of apo-proteins with artificial active sites that yield novel catalytic functions [237]. For example, reconstitution of apo-myoglobin with Co(II)-protoporphyrin IX results in a novel biocatalyst that is capable of hydrogenating acetylene derivatives or evolving hydrogen [209, 238]. By the modification of the reconstitution of apo-proteins with artificial redox-active cofactors and the covalent attachment of photosensitizer units, photo-

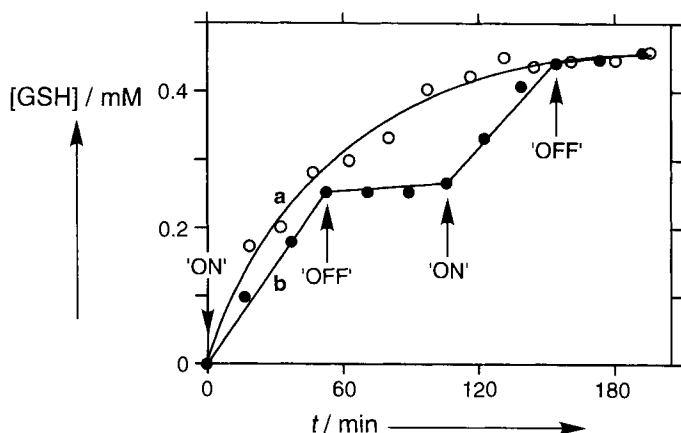
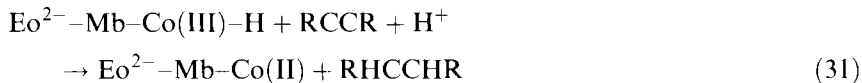
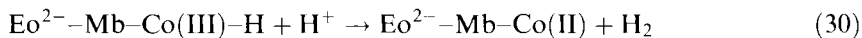
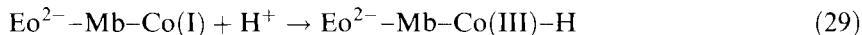
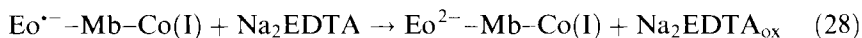
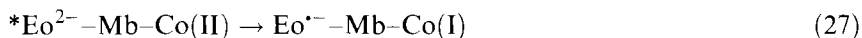


Figure 41. Rates of GSH formation under illumination at 475 nm. (a) $\text{Eo}^{2-}\text{-GR}$ (1 mg mL^{-1}), EDTA (10 mM), GSSG (10 mM); (b) a similar photosystem, but with the light switched on and off at the times indicated.

enzymes that stimulate photoinduced electron transfer and tailored biocatalytic transformations can be designed.

Apo-myoglobin was reconstituted with Co(II) -protoporphyrin IX and eosin dye units were tethered to lysine residues of the protein by the reaction of the Co(II) -protoporphyrin IX-reconstituted myoglobin with eosin isothiocyanate (**26**) [238]. The resulting eosin-functionalized, Co(II) -protoporphyrin IX-reconstituted myoglobin, $\text{Eo}^{2-}\text{-Mb-Co(II)}$, acts as a photobiocatalyst for H_2 evolution or the hydrogenation of acetylene to ethylene (Figure 42). Irradiation of $\text{Eo}^{2-}\text{-Mb-Co(II)}$ in an aqueous solution in the presence of EDTA yields H_2 evolution with a quantum yield of $\phi = 2 \times 10^{-4}$. Irradiation of the photobiocatalyst in the presence of acetylene and EDTA as sacrificial electron donor results in the hydrogenation of acetylene to ethylene with $\phi = 1 \times 10^{-2}$. The mechanisms that lead to the photoinduced H_2 evolution or the hydrogenation of acetylene are summarized in Eqs. 27–31:



Photoinduced electron transfer from the eosin dye to the Co(II) center yields a Co(I) species as an active site for the formation of a Co(III) hydride intermediate.

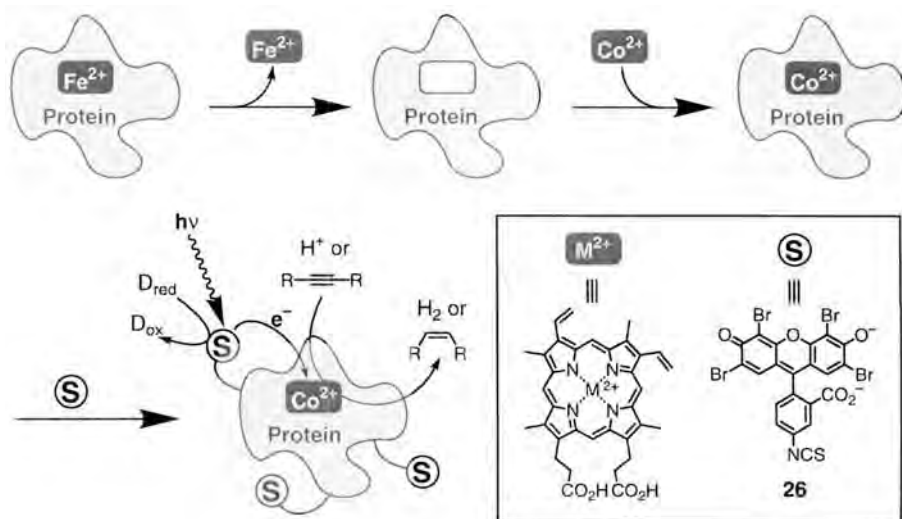


Figure 42. The preparation of a photoenzyme by the reconstitution of a heme protein with Co(II)-protoporphyrin IX and the chemical modification of the protein backbone with a tethered chromophore. Hydrogen evolution and hydrogenation of acetylene derivatives photobiocatalyzed by the assembly.

While the slow protonation of the hydride species leads to H_2 evolution, the ligation of acetylene to the Co(II)-protoporphyrin results in intramolecular hydride transfer and the hydrogenation of acetylene to ethylene. The oxidized dye is reduced by EDTA and thus the photobiocatalyst functions as a cyclic photoenzyme. Photoinduced hydrogenation of acetylenedicarboxylic acid proceeds stereoselectively and yields the thermodynamically less stable *cis* product, maleic acid.

Structurally defined photoenzymes for the hydrogenation of acetylene were tailored by the chemical modification of hemoglobin. The native hemoglobin tetramer was separated to the α -hemoglobin and β -hemoglobin units. The native hemoprotein fragments were then converted into the respective apo-proteins and further reconstituted with Co(II)-protoporphyrin IX. The eosin chromophore was tethered to the semi-synthetic protein by the coupling of eosin maleimide (**27**) to the cysteine-93 residue of Co(II)-protoporphyrin-reconstituted β -hemoglobin, $\text{Eo}^{2-}-\beta\text{-Hb}-\text{Co(II)}$, or to the single unknown lysine residue of Co(II)-protoporphyrin-reconstituted α -hemoglobin, $\text{Eo}^{2-}-\alpha\text{-Hb}-\text{Co(II)}$. The two chromophore-functionalized Co(II)-protoporphyrin IX-reconstituted hemoglobin units act as photocatalysts for the hydrogenation of acetylene [209]. In the presence of EDTA as a sacrificial electron donor, photoinduced hydrogenation of acetylene to ethylene by $\text{Eo}^{2-}-\alpha\text{-Hb}-\text{Co(II)}$ and $\text{Eo}^{2-}-\beta\text{-Hb}-\text{Co(II)}$ proceeds with quantum efficiencies of $\phi = 0.02$ and 0.004 , respectively. The mechanism that leads to the hydrogenation of acetylene by these two synthetic photoenzymes is identical to that described for the $\text{Eo}^{2-}-\text{Mb}-\text{Co(II)}$ photobiocatalyst.

The stabilization of the photogenerated redox products in the eosin-functionalized, Co(II)-protoporphyrin IX-reconstituted myoglobin, $\text{Eo}^{\bullet-}\text{-Mb-Co(I)}$, (slow charge recombination proceeds with the rate constant $k_b = 1.4 \times 10^5 \text{ s}^{-1}$) allowed the tailoring of an integrated photosynthetic reaction center that stimulates reductive and oxidative biocatalyzed transformations without the participation of any sacrificial component [209]. The reductive function of the photoenzyme $\text{Eo}^{2-}\text{-Mb-Co(II)}$ was coupled to that of lactate dehydrogenase (an oxidative enzyme) in the presence of *N*-aminomethylferrocenecaproic acid (**5**) as a diffusional electron mediator (Figure 43A). Steady-state irradiation of a photosystem composed of $\text{Eo}^{2-}\text{-Mb-Co(II)}$, LDH and **5** in the presence of acetylene and lactic acid results in the cyclic photoinduced hydrogenation of acetylene by lactic acid to yield ethylene and pyruvic acid, $\phi = 2 \times 10^{-3}$ (Figure 43B). The photogenerated redox species, $\text{Eo}^{\bullet-}\text{-Mb-Co(I)}$, exhibits sufficient stability against back electron transfer to allow the secondary reduction of acetylene by the Co(III)-hydrido intermediate and the concomitant oxidation of **5** by the oxidized dye. The oxidized electron mediator diffusionaly contacts LDH and oxidation of the biocatalyst active site activates the oxidation of lactic acid to pyruvic acid. This system may be further improved by the integration of its components to an electrically contacted rigid photosynthetic reaction center where the two biocatalytic components, LDH and $\text{Eo}^{2-}\text{-Mb-Co(II)}$, are covalently linked to each other and are modified with the tethered electron relay providing the electron transfer between them (Figure 43C). In fact, the photosynthetic transformation corresponding to the hydrogenation of acetylene by lactic acid that was accomplished in the artificial system, mimics the functions of the photosynthetic bacteria *Chloroflexus* [239].

The site-specific tethering of photoactive units to pre-designed protein mutants provides a means to control the photoinduced electron transfer and the stability of the photogenerated redox products. For example, artificial amino acids derivatized with bipyridyl units were incorporated into Cyt *c* and the Ru(II)-tris-bipyridine photosensitizer was anchored to the pre-designed ligand [240]. The effect of the structure of the resulting tethered hemoprotein assembly on the photoinduced electron transfer was characterized. Although Cyt *c* is inactive as biocatalyst, it acts as an electron-transfer cofactor for numerous redox enzymes [37, 38]. Also, the heme site of Cyt *c* might be reconstituted with other catalytically active metalloporphyrins or peripheral modification can result in its biocatalytic activity [241]. Thus, one envisages the future integration of Cyt *c* in other light-driven photosynthetic transformations.

4.3.4 Photochemical Activation of Semi-synthetic Enzymes Reconstituted with Non-natural Photosensitive Cofactors

A new strategy for the design of semi-synthetic proteins and enzymes bearing non-natural functional groups involves the replacement of the native cofactors by modified cofactors chemically linked to functional groups providing novel properties. This approach allows the placement of artificial groups at specific positions in close vicinity to the cofactor site [237]. The incorporation of photosensitizer-

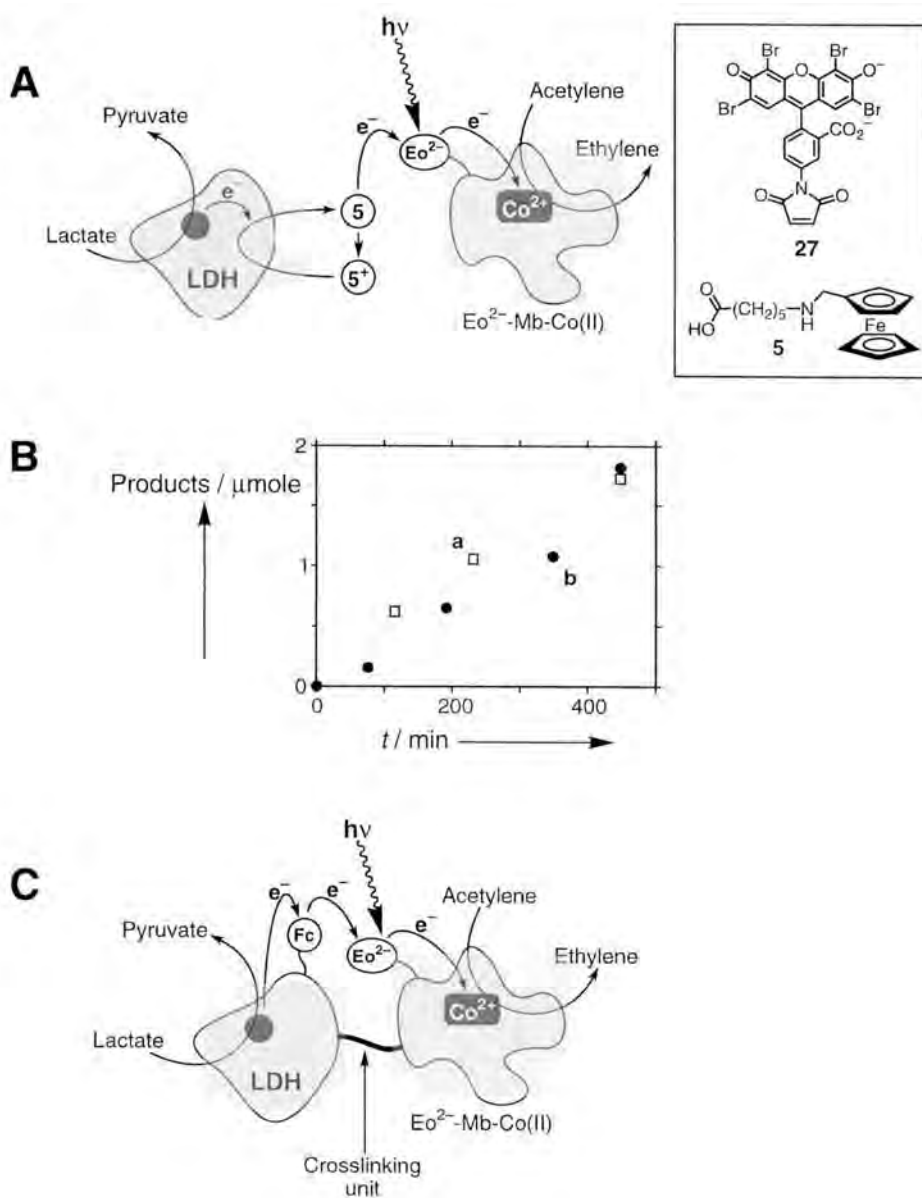


Figure 43. (A) Electron-transfer pathway for the cyclic photoinduced hydrogenation of acetylene by lactate using eosin-modified myoglobin reconstituted with $Co(II)$ -protoporphyrin IX working in cooperation with LDH. (B) Rates of formation of products upon illumination of a photosystem composed of myoglobin reconstituted with $Co(II)$ -protoporphyrin IX and modified with eosin (0.11 mg mL^{-1}), LDH ($0.6 \text{ units mL}^{-1}$), **5** ($8 \times 10^{-3} \text{ M}$) and lactic acid ($1 \times 10^{-2} \text{ M}$) under an atmospheric pressure of acetylene: (a) rate of ethylene formation and (b) rate of pyruvic acid formation. (C) Hypothetical improved system for the same photobiocatalytic system, where the two enzymes and electron mediator are covalently linked.

electron acceptor units in protein matrices has several important advantages over simple molecular photosensitizer–electron acceptor assemblies. The incorporation of the donor–acceptor pair in a rigid protein assembly permits the spatial separation of the electron-transfer photoproducts. This structural separation stabilizes the photoproducts against back electron transfer, and thus allows the effective use of the photogenerated redox species in secondary biocatalyzed transformations. Furthermore, the man-made active-site in the protein assemblies provides a unique microenvironment for stereoselective and chiroselective photobiocatalytic transformations.

Various dyads consisting of a heme unit bridged with the photoactive molecule $\text{Ru}(\text{bpy})_3^{2+}$ such as **28**, **29**, **30** have been synthesized for the generation of photoactivated hemo-proteins [210, 242]. Apo-myoglobin was reconstituted with the Fe(III)-heme– $\text{Ru}(\text{bpy})_3^{2+}$ dyad $[\text{Ru}(\text{bpy})_3^{2+}\text{-Mb}]$. The resulting protein yields the deoxy-Mb with the Fe(II) state of the heme upon irradiation under argon with visible light ($\lambda > 450$ nm) and in the presence of EDTA as a sacrificial electron donor. The resulting reduced species was rapidly converted into oxy-Mb upon exposure to air, confirming that Fe(II)–Mb was indeed the photoproduct (Figure 44A). It should also be noted that the photogeneration of the oxy species was not significantly affected by O_2 even though oxygen is a quencher of photoexcited $\text{Ru}(\text{bpy})_3^{2+}$. This effect was attributed to the accelerated intramolecular electron transfer from $^*\text{Ru}(\text{bpy})_3^{2+}$ to the Fe(III)-heme rather than to O_2 in the $\text{Ru}(\text{bpy})_3^{2+}\text{-Mb}$ protein assembly. Myoglobin reconstituted with **29** and **30** showed almost the same efficiencies of the heme photoreduction, but the myoglobin reconstituted with **28** revealed a substantially lower rate of photoreduction, demonstrating that the length of the spacer bridging the donor–acceptor pair has a significant effect on the photoreduction efficiency. Laser flash photolysis experiments have identified the electron-transfer mechanism in these systems [243]. It was concluded that the oxidative quenching of the excited state $^*\text{Ru}(\text{bpy})_3^{2+}$ ($E^\circ = -1.04$ V vs. SCE) by the Fe(III)-heme yields the redox photoproducts consisting of Fe(II)-heme and $\text{Ru}(\text{bpy})_3^{3+}$ and the oxidized species is reduced by the sacrificial electron donor. This process allows accumulation of the reduced photoproduct under continuous irradiation.

Photoinduced electron-transfer in the opposite direction was demonstrated upon irradiation of the $\text{Ru}(\text{bpy})_3^{2+}\text{-Mb}$ system in the presence of $\text{Co}^{3+}(\text{NH}_3)_5\text{Cl}$ as a sacrificial electron acceptor (Figure 44B) [244]. The photochemical reaction results in the formation of ferryl species (i.e., Fe(IV)-heme), with the intermediate formation of the porphyrin cation radical (as demonstrated using laser flash photolysis [237]). The electron-transfer cascade includes the primary oxidative quenching of the excited chromophore, $^*\text{Ru}(\text{bpy})_3^{2+}$, by $\text{Co}^{3+}(\text{NH}_3)_5\text{Cl}$ to yield $\text{Ru}(\text{bpy})_3^{3+}$ ($E^\circ = +1.01$ V vs. SCE). The resulting oxidant efficiently takes an electron from the porphyrin ring ($k_{\text{et}} = 8.5 \times 10^5 \text{ s}^{-1}$) and the porphyrin cation radical produced further oxidizes the central iron atom, converting it from the Fe(III) state to the Fe(IV) state ($k_{\text{et}} = 4.0 \times 10^4 \text{ s}^{-1}$ at pH 7.5).

An alternative approach to the preparation of ‘photoenzymes’ by the reconstitution of apo-proteins includes the application of metalloprotoporphyrins such as Zn(II)-protoporphyrin IX (Zn-P), which exhibits photophysical electron-transfer properties for the reconstitution of apo-proteins derived from hemoproteins. Func-

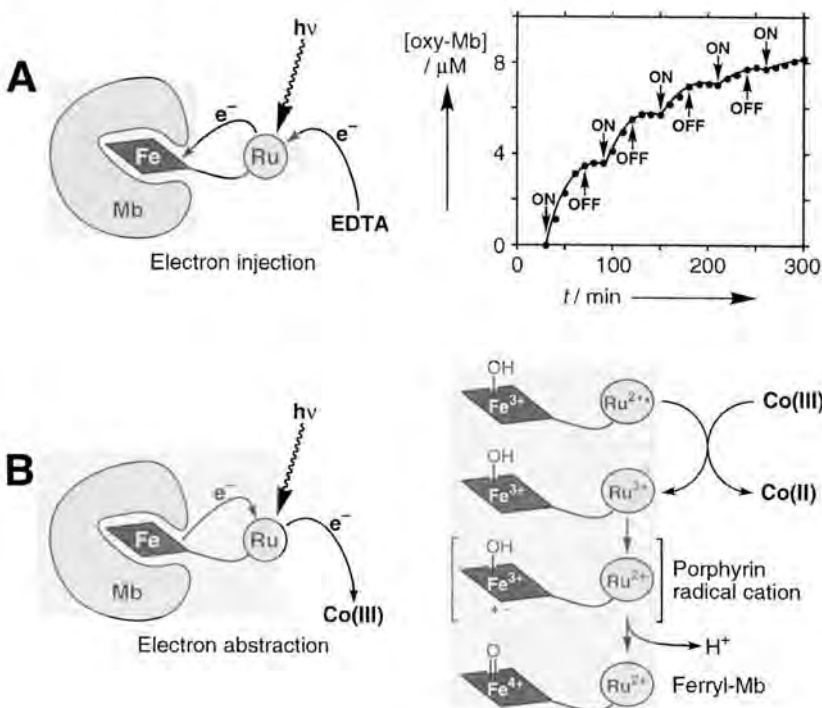


Figure 44. (A) Photoinduced electron transfer and ‘ON–OFF’ photoswitching of Ru(bpy)₃–Mb between the deoxy- and the oxy-heme states. Visible light ($\lambda > 450$ nm) results in switching according to the arrows. Adapted from Ref. [237] with permission. (B) Photooxidation of Ru(bpy)₃–Mb in the presence of a sacrificial Co(III) complex.

tionized Zn(II)-protoporphyrin–electron acceptor dyads such as **31** or **32** have been used to reconstitute apo-myoglobin [211, 245]. Vectorial photoinduced electron transfer proceeds in the semi-synthetic proteins, and the systems mimic functions of the photosynthetic reaction center. For example, in the Zn(II)-protoporphyrin IX–bis-viologen-reconstituted myoglobin, the vectorial electron transfer shown in Figure 45 and summarized in Eqs. 32–35 occurs:

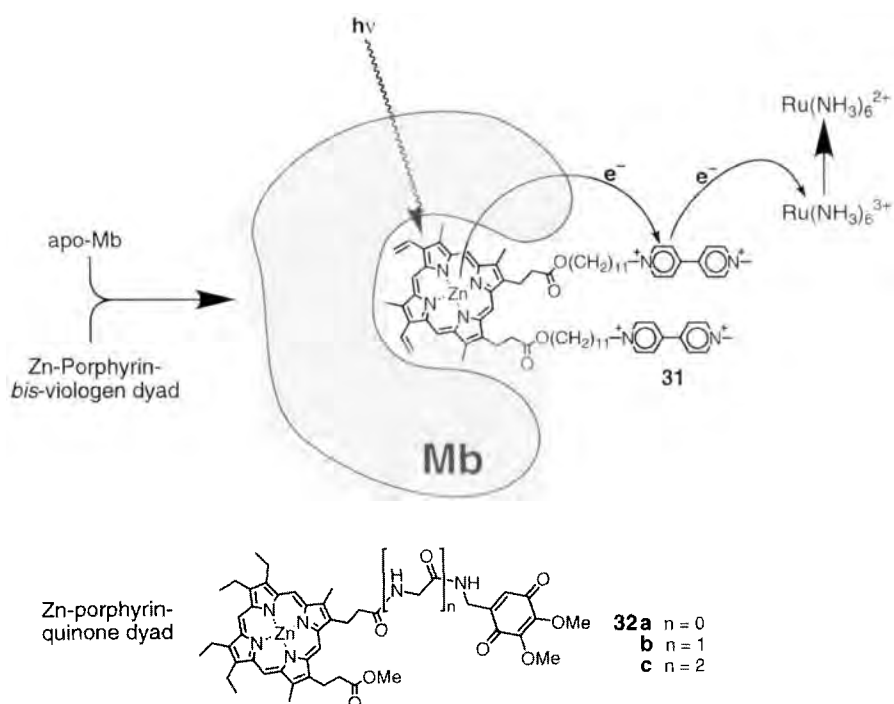
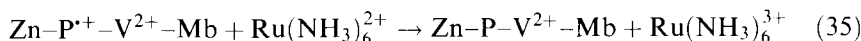
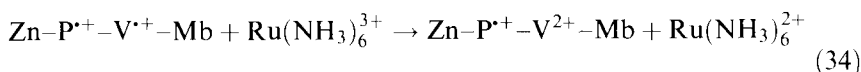
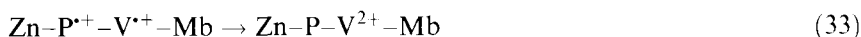


Figure 45. Reconstitution of apo-myoglobin with a Zn-protoporphyrin IX linked covalently to an electron acceptor (31 or 32) and vectorial photoinduced electron transfer in the assembly.



The excited triplet state of the Zn(II)-protoporphyrin IX, ${}^1\text{Zn-P}$, is quenched by the covalently linked viologen with $k_q = 1.55 \times 10^6 \text{ s}^{-1}$, resulting in charge separation, Eq. 32. The protein matrix spatially separates the primary redox products, resulting in a slow intermolecular recombination process ($k_b = 1.3 \times 10^6 \text{ s}^{-1}$), Eq. 33, thus allowing the reduction of the secondary electron acceptor $[\text{Ru}(\text{NH}_3)_6^{3+}]$ ($k_{et} = 6.5 \times 10^7 \text{ M}^{-1} \text{ s}^{-1}$), Eq. 34. The oxidized photosensitizer $\text{Zn-P}^{\bullet+}$ and the reduced acceptor $\text{Ru}(\text{NH}_3)_6^{2+}$ exhibit long lifetimes (ca. 2.6 ms), and are effectively stabilized against back electron transfer (Eq. 35) owing to the electrostatic repulsion of $\text{Ru}(\text{NH}_3)_6^{2+}$ from the positively charged protein interface.

The reconstituted photoactive proteins may act as light-triggered cofactors, activating enzyme cascades. For example, the electron-transporting protein cytochrome

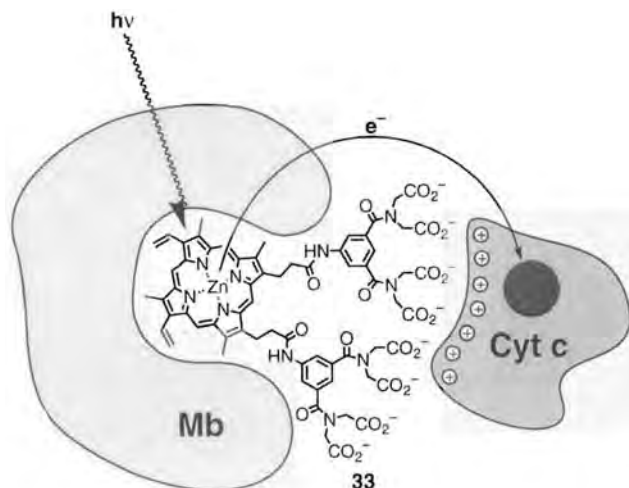


Figure 46. Interprotein photo-induced electron transfer in a system composed of positively charged cytochrome *c* and myoglobin reconstituted with Zn-protoporphyrin IX covalently bound to a negatively charged 'comb' providing association of the proteins in the assembly.

b_{562} was reconstituted with the Fe(III)-protoporphyrin IX–Ru(bpy)₃²⁺ dyad [246]. Photoirradiation of the system in the presence of a sacrificial electron donor results in the reduced Fe(II)-protoporphyrin site. In the presence of Cyt *c*, inter-protein electron transfer occurs, and the latter hemoprotein is reduced. Using a related approach [247], apo-myoglobin was reconstituted with the photoactive Zn(II)-protoporphyrin IX covalently linked to a negatively charged 'molecular comb' (**33**). Electrostatic association of the positively-charged Cyt *c* to the 'comb' aligns the hemoprotein, and vectorial electron transfer from the excited photosensitizer to the heme site of Cyt *c* is facilitated in the inter-protein complex (Figure 46).

4.3.5 Applications of Photoactivated Redox Enzymes

The major advantage of photoactivated redox enzymes is their ability to drive endergonic 'uphill' photosynthetic transformations, and therefore to transform light energy into chemical energy. The use of redox proteins in such artificial photosynthetic systems has several advantages. Evolutionally optimized enzymes promise superior catalysts for the fuel generation process. This is particularly true for multi-electron-transfer processes such as CO₂ or N₂ fixation. The tailoring of efficient catalysts for these multi-electron-transfer reactions, particularly catalysts operating in aqueous media, is still a challenging topic for future research. Polyfunctional redox-substituted proteins provide an attractive catalytic alternative for such photosynthetic transformations. In addition to the ability to drive photosynthetic transformations, the high efficiency of native biocatalysts is a major advantage as the effective utilization of the photogenerated redox species eliminates back electron-transfer reactions. An interesting photochemically induced photosynthetic transformation is the light-driven synthesis of formate in a photoelectrochemical cell consisting of a p-InP cathode (Figure 47) [248]. Photoexcitation of the semicon-

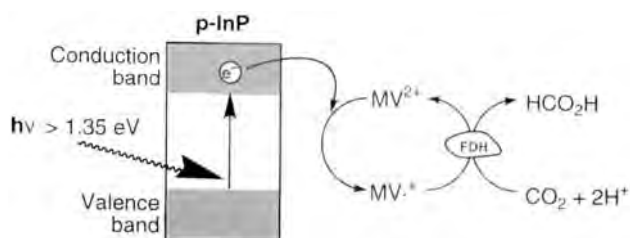


Figure 47. Photosystem for the reduction of CO_2 by FDH, powered by the photoexcitation of electrons in a p-InP cathode and mediated by MV^{2+} .

ductor results in the transfer of conduction band electrons to the *N,N'*-dimethyl-4,4'-bipyridinium electron acceptor (MV^{2+}). The resulting reduced acceptor ($\text{MV}^{\bullet+}$) acts as an electron carrier that activates formate dehydrogenase (FDH) for the reduction of CO_2 to formate. A further advantage of photoactivated enzymes is their ability to stabilize electron-transfer photoproducts by means of their spatial separation by the rigid protein assembly. This suggests that the tailoring of donor–acceptor components, e.g., a photosensitizer–electron relay, within a protein assembly could lead to improved photoelectrochemical cells. The use of photoenzymes as biocatalysts for photosynthetic transformations may have a future in stereoselective synthesis. One may envisage the photosynthesis of feedstocks from abundant raw material using cascades of biocatalytic transformations.

4.4 Conclusion and Perspectives

Substantial progress in the understanding of electron-transfer in proteins has led to the development of two interconnected research fields involving the electrochemical and the photonic activation of redox proteins (bioelectronics and optobioelectronics). Electroactivated and photoactivated redox proteins might find broad applications in various fields. Table 2 summarizes some of these potential uses. The tailoring of electrical contact between redox enzymes and electrodes provides a basis for electrochemical biosensors. Besides the broad application of electrically contacted enzyme electrodes for the amperometric analysis of enzyme substrates, one may apply electrically contacted enzymes as redox labels for the sensing of biorecognition events such as antigen–antibody [249] or oligonucleotide–DNA [250] complexation. The use of electrobiocatalytic electrodes as active components of biofuel cells is also appealing. In particular, the development of catalytic electrodes that can drive the reduction of O_2 to water may contribute important interfaces for biological or chemical fuel cell elements [192]. An important future direction for the application of electrically ‘wired’ enzyme electrodes is electrosynthesis. Efficient stereoselective synthesis is envisaged at these electrodes. The ability to design redox-active proteins exhibiting vectorial electron transfer and electrosynch-

Table 2. Potential applications of electroactivated and photoactivated redox proteins.

Type	Activated function	Field of application
Electroactivated redox proteins	1. Electrical communication with electrodes and the amperometric transduction of biorecognition	Biosensors, analytical tools for clinical diagnostics, environmental analyses, food control, etc.
	2. Activation of electrobiocatalytic processes	Electrobiocatalytic synthesis; stereoselective synthesis Biocatalytic electrodes for biofuel cells
	3. Vectorial electron transfer; switchable electron transfer; amplified electron transfer	Development of biomolecule-based electronic devices such as diodes, switches, amplifiers
	4. Photonic activation of electrobiocatalytic functions of redox proteins and the electrochemical transduction of recorded photonic signals	Information storage and design of write-read-erase functions Biomaterial-based electronic elements such as photoelectronic switches, amplifiers, actinometers Photolithographic patterning of surfaces by light-induced activation of redox processes
Photoactivated redox proteins	1. Photoinduced electron transfer and charge separation	Conversion of light energy to electrical energy; development of photo-electrochemical cells Light-driven photosynthesis; stereo-selective synthesis
	2. Photochemical activation of redox enzymes by the generation of cofactors or electron carriers	Endoergic photosynthesis of fuel products; CO ₂ fixation; N ₂ fixation; photolysis of water

able electron transfer suggests that such systems could act as electronic elements in future biomaterial-based devices.

All these bioelectrocatalytic functions of redox proteins are based on the control and enhancement of the electrical communication between the redox sites of the proteins and the electrode support. This is accomplished by the nano-engineering of the surfaces with covalently anchored proteins, the structural alignment of the proteins on the electrodes and the chemical modification of the proteins with redox-active units. Preliminary results suggest that two approaches will play important roles in the future development of bioelectronic systems: (i) protein mutagenesis with specific functional amino acid residues that can align the protein on the electrode surface and control the electrical contact with the electrode; (ii) the synthesis of de novo proteins with tailored bioelectronic and electrobiocatalytic functions.

The photonic activation and deactivation of the electrobiocatalytic functions of enzymes represent a challenging future perspective of redox proteins. The photonic activation of a redox enzyme provides a means to detect the light signal by the electrobiocatalyzed process and its resulting current. The 'ON' and 'OFF' photo-

triggered biocatalyzed transformations in these systems will allow their future development as optical storage systems, biomaterial-based computers and light-signal detectors. Furthermore, the photonic activation of redox enzymes may be applied to generate patterns on surfaces. The light-induced biocatalytic reduction of metal ions on surfaces may be used as a means to generate micro- or nano-scale electric circuits.

Photoactivated redox proteins will play important roles in the future development of artificial photosynthetic systems. The unique participation of the protein matrices in photoinduced charge separation and the possibility of implanting catalytic sites in the protein indicate that tailored photoenzymes will be important components for the light-driven synthesis of fuels and valuable chemicals, e.g., CO₂ and N₂ fixation and amino acid synthesis. The areas of bioelectronics and optobioelectronics represent exciting interdisciplinary ventures for chemists, biologists, physicists and materials scientists. The advances in these fields offer compelling opportunities for the development of electronic biomaterial-based devices.

Acknowledgments

This research is supported by the Israeli Ministry of Science, Infrastructure Project of Biomicroelectronics, and the MINERVA German–Israeli Program (DIP).

References

1. A. Heller, *Acc. Chem. Res.* **1990**, 23, 128–134.
2. (a) J.A. Cowan, H.B. Gray, *Chem. Scr.* **1988**, 28A, 21–26; (b) A.G. Sykes, *Chem. Soc. Rev.* **1985**, 14, 283–321; (c) S.S. Isied, *Prog. Inorg. Chem.* **1984**, 32, 443–517; (d) S.E. Peterson-Kennedy, J.L. McGourty, P.S. Ho, C.J. Sutoris, N. Liang, H. Zemel, N.V. Blough, E. Margoliash, B.M. Hoffman, *Coord. Chem. Rev.* **1985**, 64, 125–133; (e) G. McLendon, T. Guarr, M. McGuire, K. Simolo, S. Strauch, K. Taylor, *Coord. Chem. Rev.* **1985**, 64, 113; (f) T. Tanaka, K. Takehaka, H. Kawamura, Y. Beppu, *J. Biochem. (Tokyo)* **1985**, 99, 833; (g) J.R. Miller, in *Antennas and Reaction Centers of Photosynthetic Bacteria* (Ed. M.E. Michel-Beyerle), Springer, Berlin, **1985**, p. 234.
3. (a) M. Bixon, J.J. Jortner, *J. Phys. Chem.* **1986**, 90, 3795; (b) R.A. Marcus, N. Sutin, *Biochim. Biophys. Acta* **1985**, 811, 265; (c) D. DeVault, *Quantum Mechanical Tunneling in Biological Systems*, 2nd edn., Cambridge University Press, Cambridge, **1984**; (d) A.K. Churg, R.M. Weiss, A. Warshel, T. Takano, *J. Phys. Chem.* **1983**, 87, 1683–1694; (e) S. Larson, *J. Chem. Soc., Faraday Trans. 2* **1983**, 79, 1375; (f) J.J. Hopfield, *Proc. Natl. Acad. Sci. USA* **1974**, 71, 3640–3644; (g) J.N. Onuchic, D.N. Beratan, J.J. Hopfield, *J. Phys. Chem.* **1986**, 90, 3707–3721.
4. A.L. Ghindilis, P. Atanasov, E. Wilkins, *Electroanalysis* **1997**, 9, 661–674.
5. W. Schuhmann, *Biosens. Bioelectron.* **1995**, 10, 181–193.
6. A.I. Yaropolov, V. Malovik, S.D. Varfolomeev, I.V. Berezin, *Dokl. Akad. Nauk SSSR* **1979**, 249, 1399–1401.
7. (a) F.A. Armstrong, M. Lannon, *J. Am. Chem. Soc.* **1987**, 109, 7211–7212; (b) F.A. Armstrong, A.M. Bond, F.N. Büchi, A. Hamnett, H.A.O. Hill, A.M. Lannon, O.C. Lettington, C.G. Zoski, *Analyst* **1993**, 118, 973–978; (c) M.S. Mondal, H.A. Fuller, F.A. Armstrong, *J. Am. Chem. Soc.* **1996**, 118, 263–264.
8. E. Csöregi, G. Johnsson-Pettersson, L. Gorton, *J. Biotechnol.* **1993**, 30, 315–320.
9. T. Ruzgas, L. Gorton, J. Emneus, E. Csöregi, G. Marko-Varga, *Anal. Proc.* **1995**, 32, 207–208.

10. I.V. Berezin, V.A. Bogdanovskaya, S.D. Varfolomeev, M.R. Tarasevich, A.I. Yaropolov, *Dokl. Akad. Nauk SSSR* **1978**, *240*, 615–618.
11. (a) M.R. Tarasevich, in *Comprehensive Treatise of Electrochemistry*, Vol. 10, *Bioelectrochemistry* (Eds. S. Srinivasan, Y.A. Chizmadzhev, J.O'M. Bockris, B.E. Conway, E. Yeager), Plenum Press, New York, **1985**, pp. 275–301; (b) T. Ruzgas, L. Gorton, J. Emneus, G. Marko-Varga, *J. Electroanal. Chem.* **1995**, *391*, 41–49.
12. L.-H. Guo, H.A.O. Hill, G.A. Lawrance, G.S. Sanghera, D.J. Hopper, *J. Electroanal. Chem.* **1989**, *266*, 379–396.
13. L.-H. Guo, H.A.O. Hill, D.J. Hopper, G.A. Lawrance, G.S.S. Anghera, *J. Biol. Chem.* **1990**, *265*, 1958–1963.
14. A.L. Burrows, H.A.O. Hill, T.A. Leese, W.S. McIntire, H. Nakayama, G.S. Sanghera, *Eur. J. Biochem.* **1991**, *199*, 73–78.
15. T. Ikeda, F. Matsushita, M. Senda, *Biosens. Bioelectron.* **1991**, *6*, 299–304.
16. J.J. Kulys, R.D. Schmid, *Bioelectrochem. Bioenerg.* **1990**, *24*, 305–311.
17. T. Tatsuma, T. Watanabe, T. Watanabe, *Sens. Actuators B* **1993**, *13–14*, 752–753.
18. U. Wollenberger, V. Bogdanovskaya, S. Bobrin, F. Scheller, M. Tarasevich, *Anal. Lett.* **1990**, *23*, 1795–1808.
19. L. Gorton, G. Bremle, E. Csöregi, G. Jönsson-Pettersson, B. Persson, *Anal. Chim. Acta* **1991**, *249*, 43–54.
20. T. Tatsuma, T. Watanabe, T. Watanabe, *J. Electroanal. Chem.* **1993**, *356*, 245–253.
21. (a) T.A. Buttler, K. Johansson, L. Gorton, G.A. Marko-Varga, *Anal. Chem.* **1993**, *65*, 2628–2636; (b) G. Marko-Varga, K. Johansson, L. Gorton, *J. Chromatogr.* **1994**, *660*, 153–167.
22. V. Kacaniklic, K. Johansson, G. Marko-Varga, L. Gorton, G. Jönsson-Pettersson, E. Czöregi, *Electroanalysis* **1994**, *6*, 381–390.
23. R.M. Paddock, E.F. Bowden, *J. Electroanal. Chem.* **1989**, *260*, 487–494.
24. M.F. Cardosi, *Electroanalysis* **1994**, *6*, 89–95.
25. U. Wollenberger, J. Wang, M. Ozsoz, E. Gonzalez-Romero, F. Scheller, *Bioelectrochem. Bioenerg.* **1991**, *26*, 287–296.
26. I.C. Popescu, G. Zetterburg, L. Gorton, *Biosens. Bioelectron.* **1995**, *10*, 443–461.
27. F.A. Armstrong, H.A.O. Hill, N.J. Walton, *Q. Rev. Biophys.* **1986**, *18*, 261–322.
28. F.A. Armstrong, H.A.O. Hill, N.J. Walton, *Acc. Chem. Res.* **1988**, *21*, 407–413.
29. J.E. Frew, H.A.O. Hill, *Eur. J. Biochem.* **1988**, *172*, 261–269.
30. (a) I. Taniguchi, K. Toyosawa, H. Yamaguchi, K. Yasukouchi, *J. Chem. Soc., Chem. Commun.* **1982**, 1032–1033; (b) I. Taniguchi, S. Yoshimoto, K. Nishiyama, *Chem. Lett.* **1997**, 353–354; (c) B.D. Lamp, D. Hobara, M.D. Porter, K. Niki, T.M. Cotton, *Langmuir* **1997**, *13*, 736–741; (d) H.A.O. Hill, D.J. Page, N.J. Walton, *J. Electroanal. Chem.* **1987**, *217*, 141–158; (e) Y. Xie, S. Dong, *Bioelectrochem. Bioenerg.* **1992**, *29*, 71–79.
31. P.M. Allen, H.A.O. Hill, N.J. Walton, *J. Electroanal. Chem.* **1984**, *178*, 69–86.
32. (a) Z.-X. Huang, M. Feng, Y.-H. Wang, J. Cui, D.-S. Zou, *J. Electroanal. Chem.* **1996**, *416*, 31–40; (b) R. Santucci, A. Faraoni, L. Campanella, G. Tranchida, M. Brunori, *Biochem. J.* **1991**, *273*, 783–786.
33. S. Bagby, P.D. Barker, K. DiGleria, H.A.O. Hill, V.J. Lowe, *Biochem. Soc. Trans.* **1988**, *16*, 958–959.
34. G. Li, H. Chen, D. Zhu, *Anal. Chim. Acta* **1996**, *319*, 275–276.
35. X. Qu, T. Lu, S. Dong, C. Zhou, T.M. Cotton, *Bioelectrochem. Bioenerg.* **1994**, *34*, 153–156.
36. T. Lu, X. Yu, S. Dong, C. Zhou, S. Ye, T.M. Cotton, *J. Electroanal. Chem.* **1994**, *369*, 79–86.
37. (a) H.A.O. Hill, N.J. Walton, *J. Am. Chem. Soc.* **1982**, *104*, 6515–6519; (b) W. Jin, H. Wollenberger, E. Kázgel, W.-H. Schunck, F.W. Scheller, *J. Electroanal. Chem.* **1997**, *433*, 135–139; (c) W. Jin, H. Wollenberger, F.F. Bier, A. Makowez, F.W. Scheller, *Bioelectrochem. Bioenerg.* **1996**, *39*, 221–225.
38. (a) H.A.O. Hill, N.J. Walton, I.J. Higgins, *FEBS Lett.* **1981**, *126*, 282–284; (b) A.E.G. Cass, G. Davis, H.A.O. Hill, D.J. Nancarrow, *Biochim. Biophys. Acta* **1985**, *828*, 51–57.
39. (a) T. Sakurai, F. Nose, *Chem. Lett.* **1995**, 1075–1076; (b) T. Sakurai, F. Nose, T. Fujiki, S. Suzuki, *Bull. Chem. Soc. Jpn.* **1996**, *69*, 2855–2862; (c) T. Sakurai, *Chem. Lett.* **1996**, 481–482; (d) T.D. Martin, S.A. Monheit, R.J. Niichel, S.C. Peterson, C.H. Campbell, D.C. Zapien, *J. Electroanal. Chem.* **1997**, *420*, 279–290.

40. K. Nishiyama, H. Ishida, I. Taniguchi, *J. Electroanal. Chem.* **1994**, 373, 255–258.
41. K.R. Brown, A.P. Fox, M.J. Natan, *J. Am. Chem. Soc.* **1996**, 118, 1154–1157.
42. J. Zhao, R. Henkens, J. Stonehuerner, J.P. O'Daly, A.L. Crumbliss, *J. Electroanal. Chem.* **1992**, 327, 109–119.
43. S. Yabuki, F. Mitzutani, *Electroanalysis* **1997**, 9, 23–25.
44. S.D. Varfolomeev, I.N. Kurochkin, A.I. Yaropolov, *Biosens. Bioelectron.* **1996**, 11, 863–871.
45. Z. Wen, B. Ye, X. Zhou, *Electroanalysis* **1997**, 9, 641–644.
46. 190. C. Godet, M. Boujtita, N. El Murr, *New J. Chem.* **1999**, 23, 795–797.
47. (a) P.A. Adams, in *Peroxidases in Chemistry and Biology* (Eds. J. Everse, K.E. Everse), CRC Press, Boca Raton, FL, **1991**, Vol. 2, Chap. 7, pp. 171–200; (b) G. Ranghino, G. Antonini, P. Fantucci, *Isr. J. Chem.* **1994**, 34, 239–244.
48. R. Santucci, H. Reinhard, M. Brunori, *J. Am. Chem. Soc.* **1988**, 110, 8536–8537.
49. P.A. Mabrouk, *Anal. Chem.* **1996**, 68, 189–191.
50. T. Lötzbeier, W. Schuhmann, E. Katz, J. Falter, H.-L. Schmidt, *J. Electroanal. Chem.* **1994**, 377, 291–294.
51. L. Jiang, A. Glidle, C.J. McNeil, J.M. Cooper, *Biosens. Bioelectron.* **1997**, 12, 1143–1155.
52. A.N.J. Moore, E. Katz, I. Willner, *J. Electroanal. Chem.* **1996**, 417, 189–192.
53. P.N. Bartlett, P. Tebbutt, R.C. Whitaker, *Prog. React. Kinet.* **1991**, 16, 55–155.
54. A. Riklin, I. Willner, *Anal. Chem.* **1995**, 67, 4118–4126.
55. S.M. Zakeeruddin, M. Grätzel, D.M. Fraser, *Biosens. Bioelectron.* **1996**, 11, 305–315.
56. (a) A.D. Ryabov, A. Amon, R.K. Gorbatoeva, E.S. Ryabova, B.B. Gnedenko, *J. Phys. Chem.* **1995**, 99, 14072–14077; (b) C. Deshaies, J. Chopineau, J. Moiroux, C. Bourdillon, *J. Phys. Chem.* **1996**, 100, 5063–5069.
57. (a) D.L. Williams, A.P. Doig, Jr., A. Korosi, *Anal. Chem.* **1970**, 42, 118–121; (b) P. Janada, J. Weber, *J. Electroanal. Chem.* **1991**, 300, 119–124.
58. (a) A.E.G. Cass, G. Davis, G.D. Francis, H.A.O. Hill, W.J. Aston, I.J. Higgins, E.V. Plotkin, L.D.L. Scott, A.P.F. Turner, *Anal. Chem.* **1984**, 56, 667–671; (b) A.E.G. Cass, G. Davis, H.A.O. Hill, I.J. Higgins, E.V. Plotkin, A.P.F. Turner, W.J. Aston, in *Charge and Field Effects in Biosystems* (Eds. M.J. Allen, P.N.R. Usherwood), Abacus, **1984**, pp. 475–484; (c) G. Davis, H.A.O. Hill, I.J. Higgins, A.P.F. Turner, in *Implantable Sensors for Closed Loop Prosthetic Systems* (Ed. W.H. Ko), Futura, New York, **1985**, pp. 189–195; (d) G. Davis, M.J. Green, H.A.O. Hill, *Enzyme Microb. Technol.* **1986**, 8, 1203–1208; (e) S.L. Brooks, R.E. Ashby, A.P.F. Turner, M.R. Calder, D.J. Clarke, *Biosensors* **1987/88**, 3, 45–51; (f) J.M. Dicks, S. Hattori, I. Karube, A.P.F. Turner, T. Yokozawa, *Ann. Biol. Clin.* **1989**, 47, 607–619.
59. C. Iwakura, Y. Kajiya, H. Yoneyama, *J. Chem. Soc., Chem. Commun.* **1988**, 1019–1020.
60. N.C. Foulds, C.R. Lowe, *J. Chem. Soc., Faraday Trans. 1* **1986**, 82, 1259–1264.
61. A.P.F. Turner, S.P. Hendry, M.F. Cardosi, in *Biosensors, Instrumentation and Processing, The World Biotech. Report*, Vol. 1, Online Publications, Pinner, **1987**, pp. 125–137.
62. S.P. Hendry, A.P.F. Turner, *Horm. Metab. Res. Suppl. Ser.* **1988**, 20, 37–40.
63. R.M. Ianniello, T.J. Lindsay, A.M. Yacynych, *Anal. Chem.* **1982**, 54, 1980–1984.
64. Y. Kajiya, R. Tsuda, H. Yoneyama, *J. Electroanal. Chem.* **1991**, 301, 155–161.
65. (a) M.R. Tarasevich, *Bioelectrochem. Bioenerg.* **1979**, 6, 587–597; (b) H.A.O. Hill, I.J. Higgins, *Philos. Trans. R. Soc. London, Ser. A* **1981**, 302, 267–273.
66. J.J. Kulys, R.A. Vidzuite, *Anal. Lett.* **1983**, 16, 197–207.
67. E.J. D'Costa, I.J. Higgins, A.P.F. Turner, *Biosensors* **1986**, 2, 71–87.
68. W.H. Muller, S.J. Churchouse, P.M. Vadgama, *Analyst* **1985**, 110, 925–928.
69. T. Matsue, N. Kasai, M. Narumi, M. Nishizawa, H. Yamada, I. Uchida, *J. Electroanal. Chem.* **1991**, 300, 111–118.
70. I. Willner, A. Riklin, B. Shoham, D. Rivenzon, E. Katz, *Adv. Mater.* **1993**, 5, 912–915.
71. B. Shoham, Y. Migron, A. Riklin, I. Willner, B. Tartakovsky, *Biosens. Bioelectron.* **1995**, 10, 341–352.
72. (a) P. Pantano, T.H. Morton, W.G. Kuhr, *J. Am. Chem. Soc.* **1991**, 113, 1832–1833; (b) T. Hoshi, H. Takeshita, J. Anzai, T. Osa, *Anal. Sci.* **1995**, 11, 311–312; (c) X. Du, J. Anzai, T. Osa, R. Motohashi, *Electroanalysis* **1996**, 8, 813–816.

73. (a) C. Bourdillon, C. Demaille, J. Guerin, J. Moiroux, J.-M. Saveant, *J. Am. Chem. Soc.* **1993**, *115*, 12264–12269; (b) C. Bourdillon, C. Demaille, J. Moiroux, J.-M. Saveant, *J. Am. Chem. Soc.* **1994**, *116*, 10328–10329.
74. E. Katz, D.D. Schlereth, H.-L. Schmidt, *J. Electroanal. Chem.* **1994**, *367*, 59–70.
75. S. Marx-Tibbon, E. Katz, I. Willner, *J. Am. Chem. Soc.* **1995**, *117*, 9925–9926.
76. (a) S.J. Sadeghi, G. Gilardi, G. Nicolosi, A.E.G. Cass, *Chem. Commun.* **1997**, 517–518; (b) A.D. Ryabov, Y.N. Firsova, V.N. Gozal, E.S. Ryabova, A.N. Shevelkova, L.T. Troitskaya, T.V. Demeschik, V.I. Sokolov, *Chem. Eur. J.* **1998**, *4*, 806–813.
77. P. Alzari, N. Anicet, C. Bourdillon, J. Moiroux, J.-M. Savéant, *J. Am. Chem. Soc.* **1996**, *118*, 6788–6789.
78. V.J. Razumas, A.V. Gudavicius, J.J. Kulys, *J. Electroanal. Chem.* **1986**, *198*, 81–87.
79. F. Patolsky, G. Tao, E. Katz, I. Willner, *J. Electroanal. Chem.* **1998**, *454*, 9–13.
80. G. Tao, E. Katz, I. Willner, *Chem. Commun.* **1997**, 2073–2074.
81. A. Narvaez, E. Dominguez, I. Katakis, E. Katz, K.T. Ranjit, I. Ben-Dov, I. Willner, *J. Electroanal. Chem.* **1997**, *430*, 217–233.
82. F. Patolsky, E. Katz, V. Heleg-Shabtai, I. Willner, *Chem. Eur. J.* **1998**, *4*, 1068–1073.
83. (a) Y. Degani, A. Heller, *J. Phys. Chem.* **1987**, *91*, 1285–1289; (b) Y. Degani, A. Heller, *J. Am. Chem. Soc.* **1988**, *110*, 2615–2620.
84. W. Schuhmann, T.J. Ohara, H.-L. Schmidt, A. Heller, *J. Am. Chem. Soc.* **1991**, *113*, 1394–1397.
85. P.N. Bartlett, R.G. Whitaker, M.J. Green, J. Frew, *J. Chem. Soc., Chem. Commun.* **1987**, 1603–1604.
86. E.S. Ryabova, V.N. Goral, E. Csöregi, B. Mattiasson, A.D. Ryabov, *Angew. Chem., Int. Ed. Engl.* **1999**, *38*, 804–807.
87. A. Badia, R. Carlini, A. Fernandez, F. Battaglini, S.R. Mikkelsen, A.M. English, *J. Am. Chem. Soc.* **1993**, *115*, 7053–7060.
88. (a) I. Willner, E. Katz, A. Riklin, R. Kasher, *J. Am. Chem. Soc.* **1992**, *114*, 10965–10966; (b) I. Willner, N. Lapidot, A. Riklin, R. Kasher, E. Zahavy, E. Katz, *J. Am. Chem. Soc.* **1994**, *116*, 1428–1441.
89. E. Katz, A. Riklin, I. Willner, *J. Electroanal. Chem.* **1993**, *354*, 129–144.
90. S. Kuwabata, T. Okamoto, Y. Kajiya, H. Yoneyama, *Anal. Chem.* **1995**, *67*, 1684–1690.
91. S. Cosnier, *Electroanalysis* **1997**, *9*, 894–902.
92. S. Cosnier, *Biosens. Bioelectron.* **1999**, *14*, 443–456.
93. C. Kranz, H. Wohlschläger, H.-L. Schmidt, W. Schuhmann, *Electroanalysis*, **1998**, *10*, 546–552.
94. (a) P.C. Pandey, *J. Chem. Soc., Faraday Trans. 1* **1988**, *84*, 2259–2265; (b) H. Shinohara, T. Chiba, M. Aizawa, *Sens. Actuators* **1988**, *13*, 79–86; (c) P.N. Bartlett, J.M. Cooper, *J. Electroanal. Chem.* **1993**, *363*, 1–12.
95. A.R. Hillman, in *Electrochemical Science and Technology of Polymers* (Ed. R.G. Linford), Elsevier, New York, **1987**, Vol. 1, p. 241.
96. (a) M. Umana, J. Waller, *Anal. Chem.* **1986**, *58*, 2979–2983; (b) P.N. Bartlett, R. Whitaker, *J. Electroanal. Chem.* **1987**, *224*, 27–35; (c) S. Yabuki, H. Shinohara, M. Aizawa, *J. Chem. Soc., Chem. Commun.* **1989**, 945–946; (d) C.G.J. Koopal, B. Raiter, T.J.M. Nolte, *J. Chem. Soc., Chem. Commun.* **1991**, 1691–1692; (e) S. Kuwabata, C.R. Martin, *Anal. Chem.* **1994**, *66*, 2757–2762; (f) P.J.H.J. Van Os, A. Bult, C.G.J. Koopal, W.P. Van Bennekom *Anal. Chim. Acta* **1996**, *335*, 202–216.
97. W. Schuhmann, *Mikrochim. Acta* **1995**, *121*, 1–29.
98. T. Tatsuma, M. Gondaira, T. Watanabe, *Anal. Chem.* **1992**, *64*, 1183–1187.
99. (a) M. Shaolin, X. Huaiguo, Q. Bidong, *J. Electroanal. Chem.* **1991**, *304*, 7–16; (b) M. Shaolin, *J. Electroanal. Chem.* **1994**, *370*, 135–139; (c) Y. Yang, M. Shaolin, *J. Electroanal. Chem.* **1997**, *432*, 71–78.
100. P.N. Bartlett, D.J. Caruana, *Analyst*, **1992**, *117*, 1287–1292.
101. S. Cosnier, C. Innocent, *J. Electroanal. Chem.* **1992**, *328*, 361–366.
102. (a) S. Cosnier, P. Labbé, in *Uses of Biological Compounds* (Eds. G.G. Guibault, M. Mascini), Kluwer, Dordrecht, **1993**, pp. 231–244; (b) J.-L. Besombes, S. Cosnier, P. Labbé, G. Reverdy, *Anal. Chim. Acta* **1995**, *317*, 275–280; (c) S. Cosnier, I.C. Popescu, *Anal. Chim. Acta* **1996**, *319*, 145–151.

103. (a) H. Mao, P.G. Pickup, *J. Electroanal. Chem.* **1989**, 265, 127–142; (b) G. Lian, S. Dong, *J. Electroanal. Chem.* **1989**, 260, 127–136; (c) S. Dong, G. Lian, *J. Electroanal. Chem.* **1990**, 291, 23–29.
104. S. Yabuki, H. Shinohara, M. Aizawa, *J. Electroanal. Chem.* **1990**, 277, 179–187.
105. M.G. Loughram, J.M. Hall, A.P.F. Turner, *Electroanalysis* **1996**, 8, 870–875.
106. (a) S. Cosnier, C. Innocent, Y. Jouanneau, *Anal. Chem.* **1994**, 66, 3198–3201; (b) S. Cosnier, L. Allien, L. Coche-Guérente, C. Innocent, P. Labbé, P. Mailley, *Sens. Mater.* **1996**, 8, 169–177; (c) S. Cosnier, B. Galland, C. Innocent, *J. Electroanal. Chem.* **1997**, 433, 113–119.
107. S. Cosnier, J.-L. Décout, M. Fontecave, C. Frier, C. Innocent, *Electroanalysis* **1998**, 10, 521–525.
108. (a) S. Chao, M.S. Wrighton, *J. Am. Chem. Soc.* **1987**, 109, 5886–5888; (b) T. Parpaleix, J.M. Laval, M. Maida, C. Bourdillon, *Anal. Chem.* **1992**, 64, 641–646; (c) I. Willner, E. Katz, N. Lapidot, P. Bäuerle, *Bioelectrochem. Bioenerg.* **1992**, 29, 29–45; (d) S. Cosnier, K. Le Lous, *Talanta* **1996**, 43, 331–337; (f) G. Ramsay, S.M. Wolpert, *Anal. Chem.* **1999**, 71, 504–506.
109. (a) A. Heller, *J. Phys. Chem.* **1992**, 96, 3579–3587; (b) H. Bu, S.R. Mikkelsen, A.M. English, *Anal. Chem.* **1995**, 67, 4071–4076.
110. B.A. Gregg, A. Heller, *Anal. Chem.* **1990**, 62, 258–263.
111. (a) B.A. Gregg, A. Heller, *J. Phys. Chem.* **1991**, 95, 5970–5975; (b) B.A. Gregg, A. Heller, *J. Phys. Chem.* **1991**, 95, 5976–5980.
112. I. Katakis, A. Heller, *Anal. Chem.* **1992**, 64, 1008–1013.
113. (a) E.J. Calvo, C. Danilowicz, L. Diaz, *J. Electroanal. Chem.* **1994**, 369, 279–282; (b) S. Koide, K. Yokoyama, *J. Electroanal. Chem.* **1999**, 468, 193–201.
114. G. Arai, M. Masuda, I. Yasumori, *Bull. Chem. Soc. Jpn.* **1994**, 67, 2962–2966.
115. S.A. Emr, A.M. Yacynych, *Electroanalysis* **1995**, 7, 913–923.
116. (a) D. Avnir, S. Braun, O. Lev, M. Ottolenghi, *Chem. Mater.* **1994**, 6, 1605–1614; (b) A. Walcarius, *Electroanalysis* **1998**, 10, 1217–1235.
117. (a) K. Kalcher, J.-M. Kauffmann, J. Wang, I. Svancara, K. Vytras, C. Neuhold, Z. Yang, *Electroanalysis* **1995**, 7, 5–22; (b) L. Gorton, *Electroanalysis* **1995**, 7, 23–45.
118. (a) B.C. Dave, B. Dunn, J.S. Valentine, J.I. Zink, *Anal. Chem.* **1994**, 66, A1120–A1127; (b) U. Narang, P.N. Prasad, F.V. Bright, K. Ramanathan, N.D. Kumar, B.D. Malhotra, M.N. Kamalasanan, S. Chandra, *Anal. Chem.* **1994**, 66, 3139–3144; (c) U. Künzelmann, H. Böttcher, *Sens. Actuators B* **1997**, 38/39, 222–228.
119. J. Li, S.N. Tan, H.L. Ge, *Anal. Chim. Acta* **1996**, 335, 137–145.
120. J. Li, S.N. Tan, J.T. Oh, *J. Electroanal. Chem.* **1998**, 448, 69–77.
121. J. Li, L.S. Chia, N.K. Goh, S.N. Tan, H. Ge, *Sens. Actuators B* **1997**, 40, 135–141.
122. J. Li, L.S. Chia, N.K. Goh, S.N. Tan, *Anal. Chim. Acta* **1998**, 362, 203–211.
123. P. Audebert, C. Demaille, C. Sanchez, *Chem. Mater.* **1993**, 5, 911–913.
124. T.-M. Park, E.I. Iwuoha, M.R. Smith, B.D. MacCraith, *Anal. Commun.* **1996**, 33, 271–273.
125. T.-M. Park, E.I. Iwuoha, M.R. Smith, R. Freaney, A.J. McShane, *Talanta* **1997**, 44, 973–978.
126. M. Tsionsky, G. Gun, V. Glezer, O. Lev, *Anal. Chem.* **1994**, 66, 1747–1753.
127. I. Pankratov, O. Lev, *J. Electroanal. Chem.* **1995**, 393, 35–41.
128. S. Sampath, I. Pankratov, J. Gun, O. Lev, *J. Sol–Gel Sci. Technol.* **1996**, 7, 123–128.
129. (a) J. Gun, O. Lev, *Anal. Chim. Acta* **1996**, 336, 95–106; (b) J. Gun, O. Lev, *Anal. Lett.* **1996**, 29, 1933–1938.
130. S. Sampath, O. Lev, *Electroanalysis* **1996**, 8, 1112–1116.
131. (a) S. Sampath, O. Lev, *Anal. Chem.* **1996**, 68, 2015–2021; (b) S. Sampath, O. Lev, *J. Electroanal. Chem.* **1997**, 426, 131–137.
132. S. Bharathi, O. Lev, *Anal. Commun.* **1998**, 35, 29–31.
133. (a) B. Gründig, C. Krabisch, *Anal. Chim. Acta* **1989**, 222, 75–81; (b) H. Gunasingham, C.-H. Tan, T.-C. Aw, *Anal. Chim. Acta* **1990**, 234, 321–330; (c) P.D. Hale, T. Inagaki, H.I. Karan, Y. Okamoto, T.A. Skotheim, *J. Am. Chem. Soc.* **1989**, 111, 3482–3484; (d) L. Gorton, H.I. Karan, P.D. Hale, T. Inagaki, Y. Okamoto, T.A. Skotheim, *Anal. Chim. Acta* **1990**, 228, 23–30; (e) J. Wang, L.-H. Wu, Z.L. Lu, R.L. Li, J. Sanchez, *Anal. Chim. Acta* **1990**, 228, 251–257; (f) P.D. Hale, L.I. Boguslavsky, T. Inagaki, H.S. Lee, T.A. Skotheim, H.I. Karan, Y. Okamoto, *Mol. Cryst. Liq. Cryst.* **1990**, 190, 251–258; (g) P.D. Hale, L.I. Boguslavsky, T. Inagaki, H.I. Karan, H.S. Lee, T.A. Skotheim, Y. Okamoto, *Anal. Chem.* **1991**, 63, 677–

- 682; (h) P.D. Hale, H.L. Lan, L.I. Boguslavsky, H.I. Karan, Y. Okamoto, T.A. Skotheim, *Anal. Chim. Acta* **1991**, 251, 121–128; (i) A. Amine, J.-M. Kauffmann, G.J. Patriarche, *Talanta* **1991**, 38, 107–110; (j) A. Amine, J.-M. Kauffmann, G.J. Patriarche, A.E. Kaifer, *Anal. Lett.* **1991**, 24, 1293–1315; (k) F. Mizutani, S. Yabuki, A. Okuda, T. Katsura, *Bull. Chem. Soc. Jpn.* **1991**, 64, 2849–2851; (l) S. Sakura, R.P. Buck, *Bioelectrochem. Bioenerg.* **1992**, 28, 387–400; (m) P.D. Hale, H.S. Lee, Y. Okamoto, *Anal. Lett.* **1993**, 26, 1–16; (n) A. Amine, J.-M. Kauffmann, G.G. Guilbault, S. Bacha, *Anal. Lett.* **1993**, 26, 1281–1299; (o) I. Rosen-Margalit, J. Rishpon, *Biosens. Bioelectron.* **1993**, 8, 315–323; (p) J. Wang, N. Naser, *Electroanalysis* **1994**, 6, 571–575.
134. (a) T. Ikeda, *Bull. Electrochem.* **1992**, 8, 145–159; (b) T. Ikeda, I. Katasho, M. Senda, *Anal. Sci.* **1985**, 1, 455–457; (c) T. Ikeda, H. Hamada, K. Miki, M. Senda, *Agric. Biol. Chem.* **1985**, 49, 541–543; (d) T. Ikeda, H. Hamada, M. Senda, *Agric. Biol. Chem.* **1986**, 50, 883–890; (e) N. Motta, A.R. Guadalupe, *Anal. Chem.* **1994**, 66, 566–571; (f) T. Inagaki, H.S. Lee, P.D. Hale, T.A. Skotheim, Y. Okamoto, *Macromolecules* **1989**, 22, 4641–4643; (g) H.I. Karan, P.D. Hale, H.L. Lan, H.S. Lee, L.F. Liu, T.A. Skotheim, Y. Okamoto, *Polym. Adv. Technol.* **1991**, 2, 229–235; (h) T. Kaku, H.I. Karan, Y. Okamoto, *Anal. Chem.* **1994**, 66, 1231–1235.
135. P.D. Hale, L.I. Boguslavsky, H.I. Karan, H.S. Lee, Y. Okamoto, T.A. Skotheim, *Anal. Chim. Acta* **1991**, 248, 155–161.
136. (a) H. Gunasingham, C.-H. Tan, *Analyst* **1990**, 115, 35–39; (b) H. Gunasingham, C.-H. Tan, T.C. Aw, *Clin. Chem.* **1990**, 36, 1657–1661.
137. P.C. Pandey, A.M. Kayastha, V. Pandey, *Appl. Biochem. Biotechnol.* **1992**, 33, 139–144.
138. H. Gunasingham, C.-H. Tan, *Anal. Chim. Acta* **1990**, 229, 83–91.
139. I. Rosen-Margalit, A. Bettelheim, J. Rishpon, *Anal. Chim. Acta* **1993**, 281, 327–333.
140. J. Kulys, H.E. Hansen, T. Buch-Rasmussen, J. Wang, M. Ozsoz, *Anal. Chim. Acta* **1994**, 288, 193–196.
141. J. Kulys, L. Wang, H.E. Hansen, T. Buch-Rasmussen, J. Wang, M. Ozsoz, *Electroanalysis* **1995**, 7, 92–94.
142. J. Wang, X. Zhang, M. Prakash, *Anal. Chim. Acta* **1999**, 395, 11–16.
143. G. Bremle, B. Persson, L. Gorton, *Electroanalysis* **1991**, 3, 77–86.
144. F. Tobalina, F. Pariente, L. Hernández, H.D. Abruña, E. Lorenzo, *Anal. Chim. Acta* **1999**, 395, 17–26.
145. P.D. Hale, L.F. Liu, T.A. Skotheim, *Electroanalysis* **1991**, 3, 751–756.
146. L.I. Boguslavsky, P.D. Hale, L. Geng, T.A. Skotheim, H.-S. Lee, *Solid State Ionics* **1993**, 60, 189–197.
147. M. Smolander, G. Marko-Varga, L. Gorton, *Anal. Chim. Acta* **1995**, 303, 233–240.
148. A. Riklin, E. Katz, I. Willner, A. Stocker, A.F. Bückmann, *Nature* **1995**, 376, 672.
149. E. Katz, A. Riklin, V. Heleg-Shabtai, I. Willner, A.F. Bückmann, *Anal. Chim. Acta* **1999**, 385, 45–58.
150. I. Willner, V. Heleg-Shabtai, R. Blonder, E. Katz, G. Tao, A.F. Bückmann, A. Heller, *J. Am. Chem. Soc.* **1996**, 118, 10321.
151. (a) H.-L. Schmidt, W. Schuhmann, *Biosens. Bioelectron.* **1996**, 11, 127–135; (b) E. Katz, D.D. Schlereth, H.-L. Schmidt, A.J.J. Olsthoorn, *J. Electroanal. Chem.* **1994**, 368, 165–171.
152. L.-H. Guo, G. McLendon, H. Razafitrimo, Y. Gao, *J. Mater. Chem.* **1996**, 6, 369–374.
153. A.B. Kharitonov, L. Alfonta, E. Katz, I. Willner, *J. Electroanal. Chem.* **2000**, 487, 133–141.
154. A. Bardea, E. Katz, A.F. Bückmann, I. Willner, *J. Am. Chem. Soc.* **1997**, 119, 9114–9119.
155. M. Brunori, *Biosens. Bioelectron.* **1994**, 9, 633–636.
156. (a) V. Heleg-Shabtai, E. Katz, I. Willner, *J. Am. Chem. Soc.* **1997**, 119, 8121–8122; (b) V. Heleg-Shabtai, E. Katz, S. Levi, I. Willner, *J. Chem. Soc., Perkin Trans. 2* **1997**, 2645–2651.
157. E. Katz, V. Heleg-Shabtai, I. Willner, H.K. Rau, W. Haehnel, *Angew. Chem.* **1998**, 37, 3253–3256.
158. I. Willner, V. Heleg-Shabtai, E. Katz, H.K. Rau, W. Haehnel, *J. Am. Chem. Soc.* **1999**, 121, 6455–6468.
159. (a) D.D. Schlereth, *J. Electroanal. Chem.* **1997**, 425, 77–85; (b) D.D. Schlereth, R.P.H. Kooyman, *J. Electroanal. Chem.* **1997**, 431, 285–295; (c) L. Bertilsson, H.-J. Butt, G. Nellest, D.D. Schlereth, *Biosens. Bioelectron.* **1997**, 12, 839–852; (d) D.D. Schlereth, R.P.H. Kooyman, *J. Electroanal. Chem.* **1998**, 444, 231–240.

160. J. Wang, *J. Pharm. Biomed. Anal.* **1999**, *19*, 47–53.
161. (a) M.E. Collison, M.E. Meyerhoff, *Anal. Chem.* **1990**, *62*, 425A; (b) S. Jaffari, A.P. Turner, *Physiol. Meas.* **1995**, *16*, 1.
162. (a) M. Kyrolainen, H. Hakanson, R. Ekroth, B. Mattiasson, *Anal. Chim. Acta* **1993**, *279*, 149–153; (b) C. Meyerhoff, F. Bischof, F.J. Mennel, F. Sternberg, J. Bican, E.F. Pfeiffer, *Biosens. Bioelectron.* **1993**, *8*, 409–414; (c) D. Baker, D. Gough, *Anal. Chem.* **1995**, *67*, 1536.
163. J. Wang, M. Ozsoz, *Electroanalysis* **1990**, *2*, 647–650.
164. V. Kacanicklic, K. Johansson, G. Marko Varga, L. Gorton, G. Jonsson-Petterson, E. Csöregi, *Electroanalysis*, **1994**, *6*, 381–390.
165. H. Bramwell, A. Cass, P. Gibbs, M. Green, *Analyst* **1990**, *115*, 185.
166. A. Eremenko, A. Makower, C. Bauer, I. Kurochkin, F. Scheller, *Electroanalysis* **1997**, *9*, 288.
167. J. Wang, E. Dempsey, M. Ozsoz, M.R. Smyth, *Analyst* **1991**, *116*, 997–999.
168. (a) A. Maines, D. Ashworth, P. Vadgama, *Food Technol. Biotechnol.* **1996**, *34*, 31–42; (b) A.S. Bassi, D.Q. Tang, E. Lee, J.X. Zhu, M.A. Bergougnou, *Food Technol. Biotechnol.* **1996**, *34*, 9–22.
169. (a) C. Nistor, J. Emneus, *Waste Manage.* **1999**, *19*, 147–170; (b) J.L. Marty, B. Leca, T. Noguer, *Analisis* **1998**, *26*, M144–M149; (c) M.P. Marco, D. Barcelo, *Meas. Sci. Technol.* **1996**, *7*, 1547–1562.
170. (a) D. Ivnitski, I. Abdel-Hamid, P. Atanasov, E. Wilkins, *Biosens. Bioelectron.* **1999**, *14*, 599–624; (b) B.M. Paddle, *Biosens. Bioelectron.* **1996**, *11*, 1079–1113.
171. C. Bourdillon, J.M. Laval, D. Thomas, *J. Electrochem. Soc.* **1986**, *133*, 706–711.
172. (a) C. Bourdillon, R. Lortie, J.M. Laval, *Biotechnol. Bioeng.* **1988**, *31*, 553–558; A. Fassouane, J.M. Laval, J. Moiroux, C. Bourdillon, *Biotechnol. Bioeng.* **1990**, *35*, 935–939.
173. I. Katakis, E. Dominguez, *Mikrochim. Acta* **1997**, *126*, 11–32.
174. H. Jaegfeldt, T. Kuwana, G. Johansson, *J. Am. Chem. Soc.* **1983**, *105*, 1805–1814.
175. H. Huck, H.-L. Schmidt, *Angew. Chem., Int. Ed. Engl.* **1981**, *93*, 421–422.
176. L. Gorton, *J. Chem. Soc., Faraday Trans. 1* **1986**, *82*, 1245–1258.
177. B.W. Carlson, L.L. Miller, *J. Am. Chem. Soc.* **1983**, *105*, 7453–7457.
178. T. Vering, W. Schuhmann, D. Seiwald, H.-L. Schmidt, B. Speiser, L. Ye, *J. Electroanal. Chem.* **1994**, *364*, 277–279.
179. (a) R. Ruppert, S. Herrmann, E. Steckhan, *J. Chem. Soc., Chem. Commun.* **1988**, 1150–1151; (b) R. Ruppert, S. Herrmann, E. Steckhan, *Tetrahedron Lett.* **1987**, *28*, 6583–6586.
180. (a) K. Kano, K. Takagi, Y. Ogino, T. Ikeda, *Chem. Lett.* **1995**, 589–590; (b) K. Takagi, K. Kano, T. Ikeda, *Chem. Lett.* **1996**, 11–12.
181. (a) S. Furukawa, N. Katayama, T. Iizuka, I. Urabe, H. Okada, *FEBS Lett.* **1980**, *121*, 239–242; (b) Y. Yamazaki, H. Maeda, *Agric. Biol. Chem.* **1982**, *46*, 1571–1581; (c) J.R. Wykes, P. Dunnill, M.D. Lilly, *Biotechnol. Bioeng.* **1975**, *17*, 51–68.
182. (a) T. Erabi, H. Hiura, M. Tanaka, *Bull. Chem. Soc. Jpn.* **1975**, *48*, 1354–1356; (b) O.S. Ksenzhek, S.A. Petrova, M.V. Kolodyazhny, *Bioelectrochem. Bioenerg.* **1982**, *9*, 167–174; (c) R.S. Schrebler, A. Arratia, S. Sánchez, M. Haun, N. Durán, *Bioelectrochem. Bioenerg.* **1990**, *23*, 81–91; (d) K. Takehara, H. Takemura, Y. Ide, S. Okayama, *J. Electroanal. Chem.* **1991**, *308*, 345–350; (e) E. Katz, *Stud. Biophys.* **1988**, *125*, 211–217.
183. K.T. Kinneer, H.G. Monbouquette, *Biotechnol. Bioeng.* **1993**, *42*, 140–144.
184. D. Mandler, I. Willner, *J. Chem. Soc., Perkin Trans. 2* **1988**, 997–1003.
185. (a) C.L. Bird, A.T. Kuhn, *Chem. Soc. Rev.* **1981**, *10*, 49–82; (b) Y.S. Obeng, A. Founta, A.J. Bard, *New J. Chem.* **1992**, *16*, 121–129.
186. V.J. Razumas, A.V. Gudavicius, J.J. Kulys, *J. Electroanal. Chem.* **1986**, *198*, 81–87.
187. R. Yuan, S. Kuwabata, H. Yoneyama, *Chem. Lett.* **1996**, 137–138.
188. (a) S. Kuwabata, R. Tsuda, K. Nishida, H. Yoneyama, *Chem. Lett.* **1993**, 1631–1634; (b) S. Kuwabata, R. Tsuda, H. Yoneyama, *J. Am. Chem. Soc.* **1994**, *116*, 5437–5443.
189. K. Takayama, K. Kano, T. Ikeda, *Chem. Lett.* **1996**, 1009–1010.
190. (a) G. Prentice, *CHEMTECH* **1984**, *14*, 684–701; (b) G. Tayhas, R. Palmore, G.M. Whitesides, *Enzymatic Conversion of Biomass for Fuels Production*, ACS Symposium Series, No. 566, American Chemical Society, Washington, DC, **1994**, Chap. 14, pp. 271–290; (c) K. Kordes, *Ber. Bunsenges. Phys. Chem.* **1990**, *94*, 902–907; (d) C. Van Dijk, C. Laane, C. Veeger, *Recl. Trav. Chim. Pays-Bas* **1985**, *104*, 245–249.

191. I. Willner, E. Katz, F. Patolsky, A.F. Bückmann, *J. Chem. Soc., Perkin Trans. 2* **1998**, 1817–1822.
192. E. Katz, I. Willner, A.B. Kotlyar, *J. Electroanal. Chem.* **1999**, 479, 64–68.
193. I. Willner, E. Katz, B. Willner, R. Blonder, V. Heleg-Shabtai, A.F. Bückmann, *Biosens. Bioelectron.* **1997**, 12, 337–356.
194. S. Ueyama, S. Isoda, *J. Electroanal. Chem.* **1991**, 281–292.
195. I. Willner, M. Lion-Dagan, S. Marx-Tibbon, E. Katz, *J. Am. Chem. Soc.* **1995**, 117, 6581–6592.
196. I. Willner, A. Doron, E. Katz, S. Levi, A.J. Frank, *Langmuir* **1996**, 12, 946–954.
197. M. Lion-Dagan, E. Katz, I. Willner, *J. Am. Chem. Soc.* **1994**, 116, 7913–7914.
198. M. Lion-Dagan, E. Katz, I. Willner, *J. Chem. Soc., Chem. Commun.* **1994**, 2741–2742.
199. M. Lion-Dagan, S. Marx-Tibbon, E. Katz, I. Willner, *Angew. Chem., Int. Ed. Engl.* **1995**, 34, 1604–1606.
200. E. Katz, B. Willner, I. Willner, *Biosens. Bioelectron.* **1997**, 12, 703–719.
201. I. Willner, A. Doron, E. Katz, S. Levi, *Langmuir* **1996**, 12, 946–954.
202. E. Katz, M. Lion-Dagan, I. Willner, *J. Electroanal. Chem.* **1995**, 382, 25–31.
203. I. Willner, R. Blonder, E. Katz, A. Stocker, A.F. Bückmann, *J. Am. Chem. Soc.* **1996**, 118, 5310–5311.
204. E. Katz, I. Willner, *Electroanalysis* **1995**, 7, 417–419.
205. E. Katz, M. Lion-Dagan, I. Willner, *J. Electroanal. Chem.* **1996**, 408, 107–112.
206. (a) R. Huber, *EMBO J.* **1989**, 8, 2125–2147; (b) J. Deisenhofer, H. Michel, *EMBO J.* **1989**, 8, 2149–2170.
207. (a) E. Katz, A.Y. Shkuropatov, O.I. Vagabova, V.A. Shuvalov, *Biochim. Biophys. Acta* **1989**, 976, 121–128; (b) A.A. Solov'ev, E. Katz, V.A. Shuvalov, Y.E. Erokhin, *Bioelectrochem. Bioenerg.* **1991**, 26, 29–41; (c) E. Katz, *J. Electroanal. Chem.* **1994**, 365, 157–164.
208. (a) J.R. Winkler, H.B. Gray, *Chem. Rev.* **1992**, 92, 369–379; (b) K.M. Yocom, J.B. Shelton, J.R. Shelton, W.A. Schroeder, G. Worosila, S.S. Isied, E. Bordignon, H.B. Gray, *Proc. Natl. Acad. Sci. USA* **1982**, 79, 7052–7055; (c) D.G. Nocera, J.R. Winkler, K.M. Yocom, E. Bordignon, H.B. Gray, *J. Am. Chem. Soc.* **1984**, 106, 5145–5150; (d) H. Elias, M.H. Chou, J.R. Winkler, *J. Am. Chem. Soc.* **1988**, 110, 429–434; (e) H.B. Gray, *Aldrichimi. Acta* **1990**, 23, 87–93; (f) T.J. Meade, H.B. Gray, J.R. Winkler, *J. Am. Chem. Soc.* **1989**, 111, 4353–4356; (g) A.W. Axup, M. Albin, S.L. Mayo, R.J. Crutchley, H.B. Gray, *J. Am. Chem. Soc.* **1988**, 110, 435–439; (h) I. Hamachi, S. Tsukiji, S. Tanaka, S. Shinkai, *Chem. Lett.* **1996**, 751–752; (i) J. Sun, J.F. Wishart, *Inorg. Chem.* **1998**, 37, 1124–1126; (j) A.B. Kotlyar, N. Borovok, M. Hazani, *Biochemistry* **1997**, 36, 15828–15829.
209. E. Zahavy, I. Willner, *J. Am. Chem. Soc.* **1996**, 118, 12499–12514.
210. I. Hamachi, T. Matsugi, S. Tanaka, S. Shinkai, *Bull. Chem. Soc. Jpn.* **1996**, 69, 1657–1661.
211. V. Heleg-Shabtai, T. Gabriel, I. Willner, *J. Am. Chem. Soc.* **1999**, 121, 3220–3221.
212. I. Willner, B. Willner, in *Advances in Photochemistry* (Eds. D.C. Neckers, D.H. Volman, G. von Büchau), Wiley, New York, **1995**, Vol. 20, pp. 217–290.
213. I. Willner, D. Mandler, *Enzyme Microb. Technol.* **1989**, 11, 467–483.
214. H.K. Chenault, G.M. Whitesides, *Appl. Biochem. Biotechnol.* **1987**, 14, 147–162.
215. D. Mandler, I. Willner, *J. Am. Chem. Soc.* **1984**, 106, 5352–5353.
216. D. Mandler, I. Willner, *J. Chem. Soc., Perkin Trans. 2* **1986**, 805.
217. Z. Goren, N. Lapidot, I. Willner, *J. Mol. Catal.* **1988**, 47, 21–32.
218. I.A. Shumilin, V.V. Nikandrov, V.O. Popov, A.A. Krasnovsky, *FEBS Lett.* **1992**, 306, 125–128.
219. R. Wienkamp, E. Steckhan, *Angew. Chem., Int. Ed. Engl.* **1983**, 22, 497.
220. I. Willner, R. Maidan, M. Shapira, *J. Chem. Soc., Perkin Trans. 2* **1990**, 559–564.
221. D. Mandler, I. Willner, *J. Chem. Soc., Chem. Commun.* **1986**, 851–853.
222. M. Julliard, J. Le Petit, *Photochem. Photobiol.* **1982**, 36, 283.
223. R.P. Chambers, J.R. Ford, J.H. Allender, W.H. Baricos, W. Cohen, *Enzyme Eng.* **1974**, 2, 195.
224. J. Handman, A. Harriman, G. Porter, *Nature* **1984**, 307, 534–535.
225. I. Willner, R. Maidan, B. Willner, *Isr. J. Chem.* **1989**, 29, 289–301.
226. I. Okura, *Coord. Chem. Rev.* **1985**, 68, 53–99.

227. Y. Kinumi, I. Okura, *J. Mol. Catal.* **1989**, 52, L33–L36.
228. E. Katz, Y.N. Kozlov, B.A. Kiselev, *Biofizika* **1979**, 24, 801–805.
229. (a) I. Willner, N. Lapidot, A. Riklin, *J. Am. Chem. Soc.* **1989**, 111, 1883–1884; (b) I. Willner, N. Lapidot, S. Rubin, A. Riklin, B. Willner, in *Biotechnology: Bridging Research and Applications* (Eds. D. Kamely, A.M. Chakrabarty, S.E. Kornguth), Kluwer, Dordrecht, **1991**, pp. 341–369.
230. Y.N. Kozlov, E. Katz, B.A. Kiselev, V.B. Evstigneev, *Biofizika* **1979**, 24, 583–587.
231. (a) P. Cuendet, M. Grätzel, K.K. Rao, D.O. Hall, *Photochem. Photobiophys.* **1984**, 7, 331–340; (b) P. Cuendet, M. Grätzel, M.L. Pelaprat, *J. Electroanal. Chem.* **1984**, 181, 173–185; (c) V.V. Nikandrov, M.A. Shlyk, N.A. Zorin, I.N. Gogotov, A.A. Krasnovsky, *FEBS Lett.* **1988**, 234, 111–114.
232. (a) P. Cuendet, K.K. Rao, M. Grätzel, D.O. Hall, *Biochimie* **1986**, 68, 217–221; (b) N. Gogotov, N.A. Zorin, L.T. Serebriakova, *Int. J. Hydrogen Energy* **1991**, 16, 393–396.
233. I. Willner, N. Lapidot, *J. Am. Chem. Soc.* **1991**, 113, 3625–3626.
234. I. Willner, N. Lapidot, A. Riklin, *J. Am. Chem. Soc.* **1990**, 112, 6438–6439.
235. I. Willner, R. Kasher, E. Zahavy, N. Lapidot, *J. Am. Chem. Soc.* **1992**, 114, 10963–10965.
236. I. Willner, E. Zahavy, *Angew. Chem., Int. Ed. Engl.* **1994**, 33, 581–583.
237. I. Hamachi, S. Shinkai, *Eur. J. Org. Chem.* **1999**, 539–549.
238. I. Willner, E. Zahavy, V. Heleg-Shabtai, *J. Am. Chem. Soc.* **1995**, 117, 542–543.
239. N. Pfennig, in *Photosynthetic Bacteria* (Eds. R.K. Clayton, W.R. Sistron), Plenum Press, New York, **1978**, Chap. 1, p. 8.
240. D.S. Wuttke, H.B. Gray, S.L. Fisher, B. Imperiali, *J. Am. Chem. Soc.* **1993**, 115, 8455–8456.
241. I. Hamachi, O. Kimura, H. Takeshita, S. Shinkai, *Chem. Lett.* **1995**, 529–530.
242. (a) I. Hamachi, S. Tanaka, S. Shinkai, *Chem. Lett.* **1993**, 1417–1420; (b) I. Hamachi, S. Tanaka, S. Shinkai, *J. Am. Chem. Soc.* **1993**, 115, 10458–10459.
243. I. Hamachi, S. Tanaka, S. Tsukiji, A. Shinkai, S. Oishi, *Inorg. Chem.* **1998**, 37, 4380–4388.
244. I. Hamachi, S. Tsukiji, S. Tanaka, S. Shinkai, *Chem. Lett.* **1996**, 751–752.
245. T. Hayashi, T. Takimura, T. Ohara, Y. Hitomi, H. Ogoshi, *J. Chem. Soc., Chem. Commun.* **1995**, 2503–2504.
246. I. Hamachi, S. Tanaka, S. Tsukiji, S. Shinkai, M. Shimizu, T. Nagamune, *J. Chem. Soc., Chem. Commun.* **1997**, 1735–1736.
247. T. Hayashi, Y. Hitomi, H. Ogoshi, *J. Am. Chem. Soc.* **1998**, 120, 4910–4915.
248. B.A. Parkinson, P.F. Weaver, *Nature* **1984**, 309, 148–149.
249. (a) R. Blonder, E. Katz, Y. Cohen, N. Itzhak, A. Riklin, I. Willner, *Anal. Chem.* **1996**, 68, 3151–3157; (b) F. Patolsky, B. Filanovsky, E. Katz, I. Willner, *J. Phys. Chem. B* **1998**, 102, 10359–10367.
250. F. Patolsky, E. Katz, A. Bardea, I. Willner, *Langmuir* **1999**, 15, 3703–3706.

5 Interprotein and Intraprotein Electron Transfer Mechanisms

Gordon Tollin

5.1 Introduction

Protein electron transfer (ET) reactions are important components of a wide variety of key biological processes, including photosynthesis, respiration, nitrogen fixation, steroid biosynthesis, DNA biosynthesis, chemical carcinogenesis and drug detoxification. Many genetic diseases result from redox protein defects. ET reactions generally occur within either transient or pre-existing protein–protein complexes, in which the redox centers (heme, flavin, iron–sulfur, copper, etc.) can communicate either directly via orbital overlap, or indirectly via ligands or adjacent amino acid side-chains.

The field of biological electron transfer has undergone an enormous revitalization over the past decade or so, due both to theoretical and to experimental advances. Among the most significant developments [1] are the following:

- 1) Applications of Marcus ET theory [2] and the creation of theoretical methods for evaluating ET ‘pathways’ [3–5] have greatly enriched our understanding of protein-mediated ET mechanisms, and have provided a conceptual framework for describing these reactions. Marcus theory factors the ET process into electronic coupling matrix elements (H_{AB}), which describe the interactions between donor/acceptor electronic wave functions, and Franck–Condon terms, which describe nuclear motions required to reach the ET transition state, i.e., the crossover point between donor and acceptor potential energy surfaces. The pathways concept assumes that electrons ‘tunnel’ between localized redox centers, utilizing both through-bond and through-space routes which are highly sensitive to molecular structure. Although, in principle, quantum mechanical methods can be used to describe these processes, such applications to large and complex protein molecules are difficult [5].
- 2) High-resolution X-ray structures are now available for several multicenter ET proteins [6–9], as well as for redox protein–protein complexes [10–12]. These

have allowed many new questions to be asked regarding the detailed interplay between functional properties and 3-D structures.

- 3) New techniques have been developed for *directly* following intra- and inter-protein ET reactions in real time. These are based mainly upon photochemical methods for injecting or extracting electrons, and utilize laser flash photolysis and time-resolved spectrophotometry [13–16]. For interprotein reactions, this methodology permits the separation of protein–protein binding and ET processes, thus providing much more insight into structure–function relationships than can be obtained from steady-state kinetic analysis. This is especially true when this technology is combined with site-specific mutagenesis (see below).

Some of the important questions in this field, all of which are currently under intensive study in various laboratories, are the following. (i) What are the relative roles of electrostatic forces, hydrogen bonding and hydrophobic interactions in stabilizing intermediate complexes and in determining protein–protein orientations during ET? (ii) Which amino acid side-chains participate in complex formation and ET, and how do they function? Are π orbitals and hydrogen bonds directly involved in electron flow? To what extent do through-bond and through-space mechanisms contribute? Are specific charge pairs required, or are generalized electrostatic fields involved? (iii) How important is intermolecular orientation? Are multiple complexes involved, or is there a single, highly specific orientation required for optimal ET? (iv) What is the role of molecular dynamics in complex formation and ET? (v) Are highly specific (single or multiple) pathways utilized for ET? (vi) What are the quantitative relationships between ET rate constants, redox potentials and distances for both interprotein and intraprotein reactions?

According to the classical Marcus theory for weakly coupled (nonadiabatic) systems, the potential energy curves of reactants and products are modeled as intersecting simple harmonic oscillators, and the ET rate constant (k_{ET}) has a parabolic dependence on the free energy of the reaction. An optimum value (whose magnitude is determined by H_{AB}) is achieved when the free energy equals the reorganization energy (λ). The latter parameter reflects the energy required for rearranging the reactant nuclei and surrounding water molecules in order for ET to proceed, i.e., to achieve the geometry corresponding to the potential minimum of the products. Note that a hydrophilic active site will generally result in a larger λ than a hydrophobic one as a consequence of polarity changes resulting from the electron transfer process. The region beyond this optimum, in which k_{ET} decreases with increasing driving force, is referred to as the ‘Marcus inverted region’. According to Marcus theory, the distance dependence should be exponential, and it has been suggested that this is the dominating factor in protein ET reactions [17]. In contrast, the tunneling-pathway concept [5] emphasizes the importance of the relative coupling strengths of various through-bond (including hydrogen bonds) [18] and through-space routes between redox centers, rather than a linear through-space distance. Parameterized methods for calculating the effectiveness of these routes have been developed [5]. It should be noted that, because of the uncertainties involved in specifying the protein–protein contacts occurring in a transient intermediate complex, the application of the pathways formalism to interprotein ET is

considerably more difficult than for intraprotein reactions. Furthermore, protein conformational changes coupled to ET can introduce significant complications.

It is clear based on the present literature that we are far from having a satisfactory understanding of biological ET. Thus, the correlations between reaction rates, redox potentials and distance that are expected from simple Marcus theory are not always observed (for examples, see Refs. [17] and [19–25]). Furthermore, in many cases the detailed structure and composition of the intervening medium between redox centers must be taken into account [13, 24], which is often difficult to do. This lack of understanding is dramatically illustrated by the following example. In the three flavocytochromes for which crystal structures are available [6, 8, 9], the angle between the flavin and heme planes varies between 0° and 60°, the regions of the flavin ring through which ET apparently occurs differ substantially and the driving forces are different. As yet, no rationale is available for correlating the observed inter-prosthetic group k_{ET} values with these properties [9, 25].

Additional areas that are in serious need of further clarification involve the roles of electrostatics and of ET pathways. Thus, although electrostatic forces are clearly involved in complex formation and ET, there is growing evidence for the importance of hydrophobic interactions [26] and of dynamic rearrangements following initial collisions in which long-range electrostatic forces have pre-oriented the diffusing molecules [27–29]. Additionally, the relative importance of generalized electrostatic potentials and/or specific charge pairs is not always clear. Finally, although specific pathways for ET are often invoked [5, 30], it is difficult to assess experimentally the importance of one pathway over another in physiologically relevant systems [31]. Even when the structures of crystalline protein–protein complexes are known [11, 12], it must still be proven that these represent actual ET intermediates along the reaction pathway. Thus, lattice forces could selectively stabilize one of several structures present in solution, and not necessarily the most competent one for ET. Present information is sketchy. For the methylamine dehydrogenase system, slow ET has been observed in crystalline binary and ternary complexes of the participating proteins [32]. Crystals of a cytochrome c_2 –bacterial photosynthetic reaction center complex have comparable activity to that observed in solution, although a high-resolution structure for the complex was not obtained [33]. The crystal structures of binary complexes between two c -type cytochromes and cytochrome c peroxidase have been solved to high resolution [10], and an earlier computer model of one of the complexes was formulated based on maximizing electrostatic interactions between the two proteins [34]. These structures are very different; experiments indicate that the computer-generated structure is irrelevant to ET, and that the structures of the crystalline complexes are only partially relevant. The latter point will be discussed further below. Finally, for systems in which two or more redox cofactors are present within a single polypeptide chain organized into two or more domains, it may not be true that the structure of the fully oxidized protein accurately reflects the structures of partially reduced intermediate states or of variously liganded states. Examples of this will be described below.

Several redox protein systems have proven valuable as probes of these various questions. The main prerequisites for such models are the existence of a high-resolution 3-D structure for the reaction participants, the ability to express re-

combinant proteins at high levels and to carry out site-specific mutagenesis, and the ability to directly observe the individual steps involved in inter- and intraprotein ET. Among the most intensively studied systems are the following: (1) *interprotein*, ferredoxin–ferredoxin:NADP⁺ reductase; cytochrome *c*–cytochrome *c* peroxidase; cytochrome *f*–plastocyanin; (2) *intraprotein*, flavocytochrome *b*₂ (yeast lactate dehydrogenase); sulfite oxidase; cytochrome P450BM-3. In the following sections we will discuss these systems in some detail in order to illustrate the present state of our knowledge of the mechanisms of protein ET reactions.

5.2 Experimental Methods for Investigating Protein ET Reactions

In this section, we will briefly review some of the key techniques that have allowed the attainment of new levels of insight into inter- and intraprotein ET processes. Although our attention will be limited to kinetic methodology, this is not meant to imply that other approaches (e.g. spectroscopy) are not also of value.

5.2.1 Time-resolved Spectrophotometry

Although ET processes between redox centers can in principle be monitored by time-resolved spectrophotometry, a major requirement for the application of such methodology is the ability to synchronize observation with reaction progress. In the photosynthetic system, which is the paradigm for the use of time-resolved spectral methods to elucidate ET mechanisms, this is made possible by the fact that light absorption by chlorophyll molecules initiates the injection of electrons into the transport pathway, a process that occurs exceedingly rapidly (picoseconds). Thus, pulsed laser excitation can be used as the triggering event, and the progress of electrons through the various carriers can be observed by a variety of spectroscopic signatures. It is possible to mimic this in nonphotobiological redox systems [14, 25, 35–40] by utilizing the well-known excited state chemistry of riboflavin and its analogs as the means of reaction initiation. Flavin photoexcitation can be used to generate strong reductants or oxidants, which can either inject or remove electrons from the system under study.

Primary photochemical processes

The lowest triplet state of flavins (³F) can be populated in a few nanoseconds via intersystem crossing (ISC) from the first excited singlet state (¹F), and is a strong oxidant, capable of removing single H atoms or single electrons from a variety of molecules. Triplet state formation has a high quantum efficiency; for example, in the case of riboflavin, approximately 70 % of the absorbed photons generate the triplet species. The redox properties of the flavin triplet can be utilized either to produce a strong reductant, i.e., the neutral flavin semiquinone (FH[•]), by hydrogen

atom transfer from a sacrificial donor (AH_2), or to remove an electron from a reduced redox protein (P_{red}) to generate the anionic flavin semiquinone ($\text{F}^{\bullet-}$). These reactions are illustrated by the following equations:



Reactions 2 and 3 are generally diffusion-controlled, and thus can be made to occur on the microsecond time-scale. The exact time course depends upon the magnitude of the second-order rate constants for these reactions and the concentrations of AH_2 or P_{red} . Since the latter species are usually in large excess, these reactions follow pseudo-first-order kinetics. If EDTA (or similar donors) is used as the reactant in Eq. 2, the AH^\bullet species that is formed is highly unstable and rapidly ($\ll 1$ ms) undergoes decarboxylation, followed by reduction of an additional molecule of oxidized flavin to generate another neutral flavin semiquinone FH^\bullet , and fragmentation to produce stable products [41]. The flavin anion semiquinone ($\text{F}^{\bullet-}$) formed in reaction 3 will equilibrate, depending upon the pH and its pK_a , with the neutral semiquinone species (for example, the pK_a for riboflavin semiquinone is 8.4). The flavin semiquinones are kinetically unstable and are also strong reductants (at pH 7, the one-electron reduction potential for riboflavin semiquinone is -230 mV and that for 5-deazariboflavin semiquinone is -650 mV). Thus, in the absence of any other reducible species, the semiquinone will disproportionate to form oxidized and reduced flavin (Eq. 4), or, in the presence of an oxidized redox protein, will transfer a reducing equivalent to the protein prosthetic group (Eq. 5):



Reactions 4 and 5 are, of course, in competition with one another. Thus, if the concentration of P_{ox} is high enough, reaction 5 will predominate. However, one must keep this competition in mind in interpreting experimental data. An additional complication can arise due to the fact that FH_2 is also a strong reductant (at least in the case of ordinary flavins; with deazaflavins, the FH_2 species is much less reactive [42]). As a consequence, at low P_{ox} concentrations, a secondary protein reduction can occur via FH_2 , which contributes to the overall kinetics and must also be taken into account. This additional reaction can usually be recognized by two properties, i.e., it is slower than the initial reduction, and its amplitude diminishes with increasing protein concentration, which forces reactions to occur via the semiquinone. A similar complication occurs in the protocol of reaction 3; thus, the initial protein oxidation reaction generates a stoichiometric amount of flavin semiquinone, which can then react further via Eqs. 4 and 5. Again, however, this occurs on a much slower time scale than reaction 3, and can usually be readily deconvoluted. By

monitoring these reactions as a function of protein concentration, accurate values for the second-order rate constants for reactions 3 and 5 can be determined.

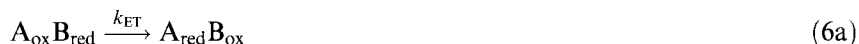
Although the ET processes represented by reactions 3 and 5 are nonphysiological, they can provide useful information. Thus, by varying the structure of the flavin it is possible to probe the steric and electrostatic environment of a protein redox center [38, 39]. This can be used as a method for assessing functional relationships between members of a homologous series of redox proteins (kinetic taxonomy). It is also possible to use these reactions to test the functional integrity of a redox center in a site-specific mutant [43].

Some additional features of the methodology are also worthy of note. (i) The intensity of the pulsed laser that is used to initiate the photochemistry is purposely kept low, so that substoichiometric quantities of flavin triplet and semiquinone are generated relative to the redox protein. This assures that pseudo-first-order conditions apply, and that only a single electron can be removed or added to each protein molecule. (ii) The irradiated volume in the sample cell is kept small ($<1\%$ of the total volume) so that only minor net conversion to products occurs. This allows samples to be subjected to multiple flashes for signal averaging and for the determination of protein concentration dependences by adding aliquots of protein to the sample. (iii) Because the oxidant and/or reductant are generated exogenously, no chemical modification of the protein is necessary. This last point is of some interest because it also provides one of the limitations of this methodology, i.e., since the initiation process depends upon *bimolecular* chemistry (reactions 2, 3 and 5), in some cases this becomes the major factor controlling the time resolution of the experiment. Another limitation of the present methodology derives from the fact that light absorption is used to initiate the reaction. Thus the wavelength range over which observation can be made without perturbing the sample is necessarily proscribed by this fact. The first of these limitations can be obviated by covalent attachment of the photoinitiator to a redox protein [13, 15, 16]. This allows a unimolecular process to be used to inject electrons, which achieves more rapid reaction initiation. However, this approach presents additional problems associated with the possibility of introducing structural perturbations into the system caused by the chemical modification. The second limitation, although intrinsic to all photochemical methodologies, is not a problem when high-energy radiation is used as the means of generating the initial electron donor or acceptor. Again, however, such pulse radiolysis procedures have their own unique difficulties, primarily associated with the exceedingly high reactivity (and therefore low specificity) of the free radical species formed under the conditions of the experiment. As is always true, one must accept trade-offs in using any of these procedures, and therefore each of them has a place in the armamentarium of the redox biochemist.

Intraprotein electron transfer reactions

If the reduced protein that is present in reaction 3, or the oxidized protein in reaction 5, has more than one redox center (denoted by A and B below, with the assumption that reaction occurs initially at site A), subsequent intraprotein ET processes can occur. This is shown in Eqs. 6a and 6b for oxidation and reduction

reactions, respectively:

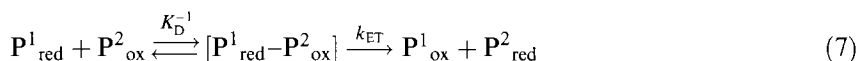


This, of course, is subject to both thermodynamic and kinetic constraints. Specifically, the initial reaction must occur predominantly (although not necessarily exclusively) at the center having the appropriate redox potential (the higher potential for reaction 6a and the lower potential for reaction 6b), and rapidly enough so that the secondary transfers shown in these equations are observable.

Interprotein electron transfer reactions

If a second redox protein is present under the conditions represented by Eq. 3 or 5, secondary protein–protein ET reactions can occur, again subject to thermodynamic and kinetic constraints. In this situation, however, the constraints can be modulated by having the higher potential (under oxidizing conditions) or lower potential (under reducing conditions) protein present in stoichiometric excess, thereby favoring removal of electrons from (or entry of electrons into) the appropriate protein in the initial reaction with exogenous flavin.

By varying the concentration of the higher potential protein, a second-order rate constant for the interprotein reaction can be obtained. In a situation in which the reaction proceeds via an intermediate complex, as shown by the (minimal) mechanism in Eq. 7, non-linear concentration dependences may be observed:



Data obtained under these conditions can be fitted using a least-squares procedure based upon the exact solution to the differential equations describing this mechanism [37, 44]. This yields values for the complex dissociation constant K_D and the limiting first-order rate constant k_{ET} (a minimum value for the second-order rate constant for complex formation can also be obtained from this analysis). Note that K_D refers to the interaction between reduced P^1 and oxidized P^2 , a situation that is observable *only* by kinetic methodology.

5.2.2 Use of Ionic Strength to Probe Electrostatic Interactions

Inasmuch as soluble proteins generally have highly charged surfaces, it is to be expected that electrostatic interactions play an important role in controlling ET reactions, especially those that occur between individual protein molecules. The dependence of reaction rate constants on the ionic strength of the solvent environment has long been used to probe such interactions for small-molecule systems [45]. However, the point charge approximation inherent in most theoretical models is inappropriate for protein molecules that have large radii and multiple charges asymmetrically distributed on their surfaces. An alternative approach [46], based on experimental observations indicating that localized charges near the active site are

generally the most important determinants of electrostatic interactions in protein ET reactions (see below), is the so-called ‘parallel plate’ model. This approximates the actual charge distribution in the region of intermolecular contact during an interprotein ET reaction by uniformly charged parallel plates of net charge Z , radius ρ and separation r_{12} , and uses averaged values for the dielectric constants and dipole moments within this region. This analysis results in the following relationship between the observed bimolecular rate constant k and the ionic strength I :

$$\ln k(I) = \ln k_{\infty} - V_{ii}X(I) - V_{id}Y(I)X(I) - V_{dd}Y(I)^2Z(I) \quad (8)$$

where k_{∞} is the diffusion-controlled rate constant at infinite ionic strength and the individual V terms correspond to monopole–monopole, monopole–dipole and dipole–dipole interactions, respectively. The latter quantities depend on the interaction domain radius, on the active site charges, on the distance between the charged plates, on the protein dipole moments and on the dielectric characteristics of the protein interior, the protein surface and the interprotein region (see [46] for details). The total electrostatic interaction energy is given by

$$V_{el} = kT(V_{ii} + V_{id} + V_{dd}) \quad (9)$$

The ionic strength dependence of the rate constant is completely contained within the X , Y and Z terms. Eq. 8 allows a non-linear least-squares fitting of experimental data to be carried out, yielding values for k_{∞} and V_{el} . In practice, the monopole and dipole terms cannot be uniquely characterized by this procedure, and using only the V_{ii} term in the fitting procedure yields a satisfactory value for V_{el} .

Figure 1 shows a typical example of results obtained using this procedure for two nonphysiological interprotein ET reactions involving reduction of spinach plastocyanin by reduced *c*-type cytochromes [28]. Cytochrome c_{555} has a net positive electrostatic charge, and displays an attractive electrostatic interaction during ET with the net negatively charged plastocyanin. The theoretical fit to the parallel plate model yields a value for V_{el} of $-10.9 \text{ kcal mol}^{-1}$ and $k_{\infty} = 3.9 \times 10^6 \text{ M}^{-1} \text{ s}^{-1}$. In contrast, cytochrome c_{551} has a net negative charge, and shows a repulsive electrostatic interaction during ET. In this case the theoretical fit yields $V_{el} = 6.3 \text{ kcal mol}^{-1}$ and $k_{\infty} = 2 \times 10^6 \text{ M}^{-1} \text{ s}^{-1}$. Although not shown here, the ionic strength dependence for the reaction of horse cytochrome *c* with plastocyanin yields a value for V_{el} of $-16.8 \text{ kcal mol}^{-1}$ and $k_{\infty} = 5 \times 10^5 \text{ M}^{-1} \text{ s}^{-1}$. It is interesting that, whereas the relative magnitudes of the V_{el} terms correlate well with the net protein charges, the k_{∞} values do not correlate with the relative thermodynamic driving forces for these reactions. Thus, the reduction potentials for the cytochromes are 145 mV for cytochrome c_{555} and 270 mV for both cytochrome c_{551} and horse cytochrome *c*. This would argue that other factors such as distance and orientation must be dominant.

It is also important to point out that the direction of the ionic strength effect on rate constants does not always correlate with the protein net charge. Thus, in reactions with FMN [47] and flavodoxin [48], three species of cytochrome c_2 having net charges of -7 , 0 and $+2$ all show attractive electrostatic interactions during ET with these negatively charged species. The reason for this behavior lies in the fact

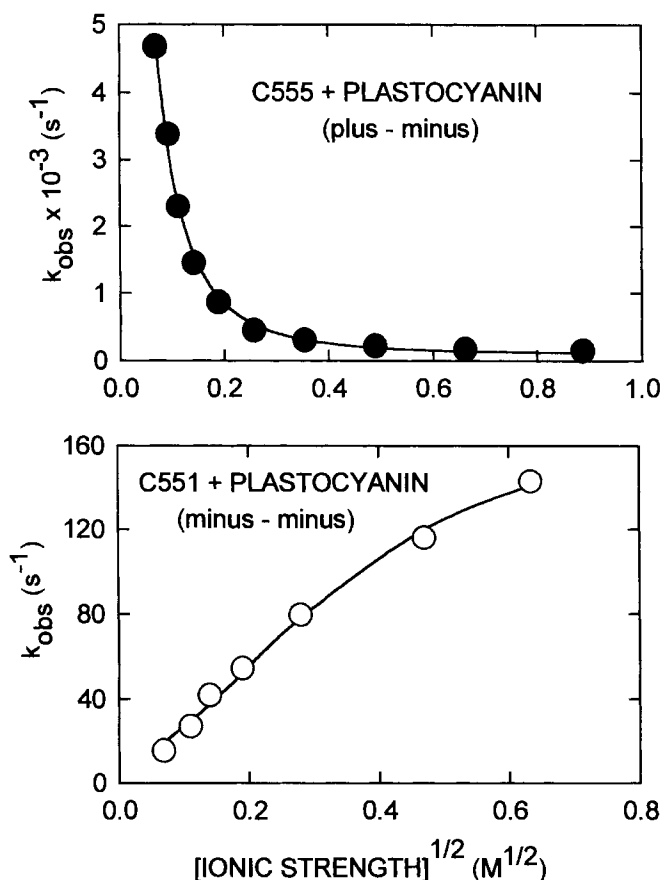


Figure 1. Ionic strength dependence of observed rate constants for ET from two reduced cytochromes (*c*₅₅₅ and *c*₅₅₁) to oxidized plastocyanin. Solid lines are theoretical fits to the data points using the parallel plate model (only the V_{ii} term is included).

that the distribution of acidic and basic residues in each of these cytochromes places a positive charge near the solvent-exposed edge of the heme. Thus, it is the *local* charge near the ET site that dominates the electrostatic interactions. More dramatic deviations from these patterns, obtained with several physiological interprotein reactions, will be described below.

5.3 Interprotein Electron Transfer Reactions

5.3.1 Ferredoxin (Fd)–Ferredoxin:NADP⁺ Reductase (FNR)

FNR is involved in the reductive side of photosynthesis, transferring electrons from reduced Fd to NADP⁺. The enzyme, as isolated from the cyanobacterium

Anabaena, is a 36 kDa basic protein having a noncovalently bound flavin (FAD) cofactor. Fd is a smaller (11 kDa) acidic [2Fe–2S] protein that is present in all photosynthetic organisms, and acts as a shuttle between larger proteins (in this case the iron–sulfur subunit of photosystem I and FNR), which are often anchored in membranes and have restricted mobility. Note that Fd is a one-electron carrier and NADP^+ requires the simultaneous addition of two electrons for its reduction.

Inasmuch as the FAD cofactor is capable of accepting two electrons in one-electron steps, with the intermediate formation of a neutral flavin semiquinone, reduction of NADP^+ proceeds via two Fd–FNR ET reactions. The one-electron reduction potentials for the proteins are as follows [49]. For FNR the values are –331 and –314 mV for the first and second reduction steps, respectively, and for Fd the value is –384 mV. Thus, both ET processes are slightly exoenergetic. Interestingly, complex formation between the two oxidized proteins increases the redox potential difference for the first ET reaction by about 30 mV, thereby increasing the thermodynamic driving force [49].

The 3-D structure of *Anabaena* FNR has been determined to 1.8 Å resolution (Figure 2, top), and shows two separate domains where the cofactor FAD and the substrate NADP^+ bind [50]. Several lines of evidence indicate that Fd binds within a concave surface that occupies both domains of FNR. The exposed dimethylbenzene ring of the flavin protrudes from this surface in a manner that probably allows close interaction (~ 5 Å) between the iron–sulfur center of Fd and the FAD in the enzyme [51, 52]. The 3-D structure of *Anabaena* Fd (Figure 2, bottom) has also been determined to high resolution [53]. The protein contains a large number of conserved acidic amino acid residues on its front surface surrounding the largely buried [2Fe–2S] center. However, the surface regions closest to the [2Fe–2S] center are electrically neutral. Both Fd and FNR from *Anabaena* have been cloned and overexpressed in *E. coli*, allowing site-specific mutagenesis to be applied, hence this system provides an ideal model for investigating protein–protein ET.

Laser flash photolysis time-resolved spectrophotometry, utilizing deazariboflavin–EDTA as a photochemical reductant, has been used with this system in order to characterize the initial step in the ET mechanism. Figure 3 shows examples of the type of data obtained in these studies. In the top panel, a transient is shown [54] that was obtained at 507 nm in 100 mM phosphate buffer, pH 7.0, containing 35 μM Fd, and in the middle panel, 10.3 μM FNR has been added to the solution prior to photolysis. This wavelength corresponds to an isosbestic point for the FAD cofactor of the reductase, and thus the absorbance change monitors the oxidation state of the [2Fe–2S] cluster of Fd (and also the formation and decay of the dRfH^\bullet species). As is evident, immediately after the laser flash there is a rapid rise in absorbance due to dRfH^\bullet formation. This is followed by a sharp absorbance decrease corresponding to Fd reduction and dRfH^\bullet oxidation. The subsequent slow increase in absorption shown in the middle panel is a consequence of Fd reoxidation that is due to electron transfer to FNR. The latter is confirmed by measurement at 610 nm (bottom panel), a wavelength which monitors FAD neutral semiquinone formation; the rate constant obtained from the 610 nm absorbance rise is the same as that obtained from the slow absorbance increase at 507 nm, consistent with this interpretation.

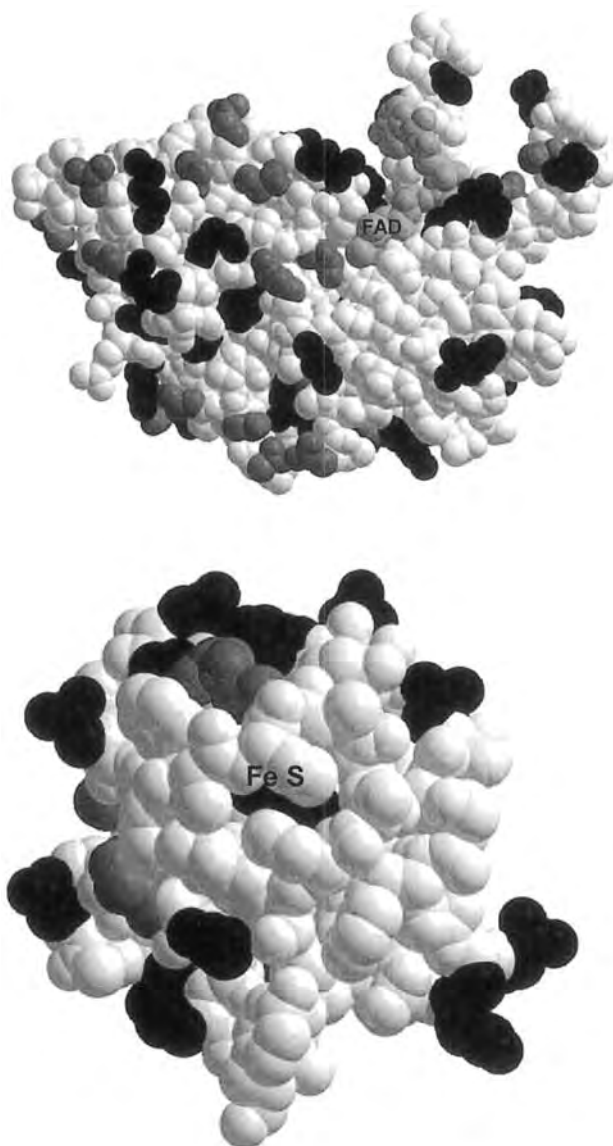


Figure 2. Space-filling models of the front surfaces of *Anabaena* FNR (top) and Fd (bottom). The FAD cofactor in FNR is partially exposed and shown in light shading. The buried iron-sulfur cofactor in Fd is shown in dark shading. For FNR, acidic amino acids are shown in light shading, basic amino acids in dark shading and uncharged amino acids are unshaded. For Fd, basic amino acids are shown in light shading and acidic amino acids in dark shading.

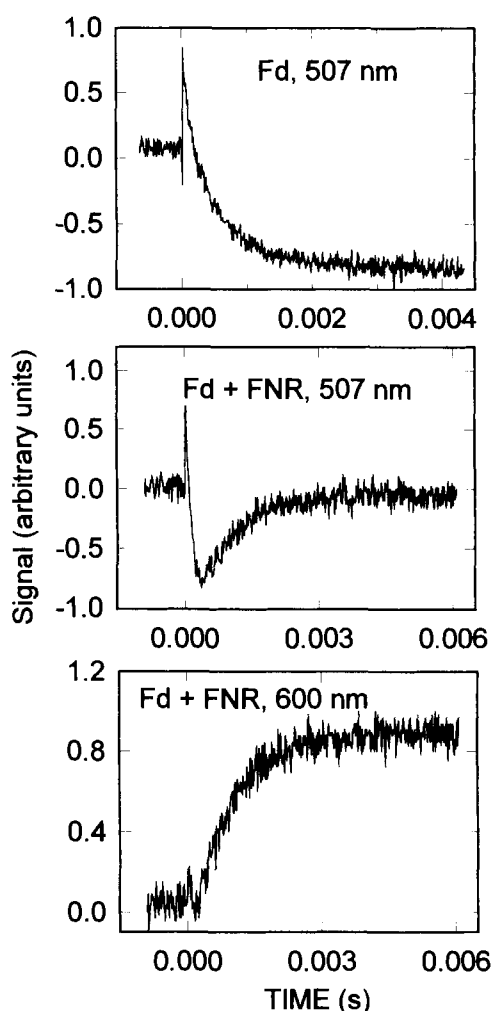


Figure 3. Kinetic transients obtained upon laser flash photolysis of the Fd–FNR system using dRf–EDTA.

Measurement of the FNR concentration dependence of the observed rate constant for reduction of the FAD cofactor yields a hyperbolic curve. After correction for the concentration of the unreactive pre-existing complex between the two oxidized proteins, a non-linear least-squares fit to the data for the two-step mechanism shown in Eq. 7 yields values of $1.7 \mu\text{M}$ for K_D and 5500 s^{-1} for k_{ET} . In comparison, the binding constant between the oxidized forms of the two proteins is $3.3 \mu\text{M}$ under these conditions. Thus, the reduced form of Fd binds more tightly to oxidized FNR than does the oxidized form, which is consistent with the direction of electron flow. The k_{ET} value is not especially large for an ET reaction proceeding over a relatively short distance [17]. Thus, the rate constant probably includes rate limitations imposed by the reorganizational processes accompanying the actual transfer of the electron, e.g., protein structural rearrangements around the active sites and within

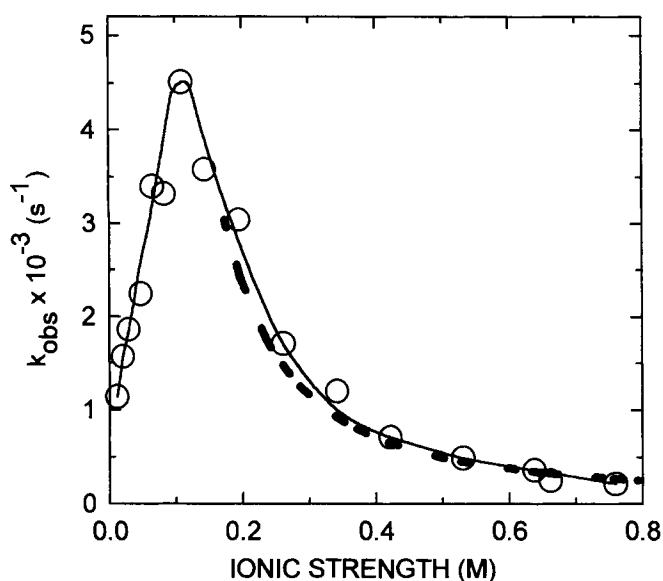


Figure 4. Ionic strength dependence of the observed rate constant for electron transfer from reduced Fd to oxidized FNR. The dashed line corresponds to a theoretical fit to the higher ionic strength data using the parallel-plate model. The solid line is a smooth curve drawn through the data points.

the interaction domain, water shell reorganization, etc. This aspect of the reaction mechanism needs further study.

Figure 4 shows the ionic strength dependence of the observed rate constant for ET from reduced Fd to oxidized FNR [26]. Note the biphasic nature of this curve, which is different from what is expected based on a simple electrostatic interaction between the two proteins (corresponding to the dashed curve drawn through the higher ionic strength points; compare with Figure 1). This type of biphasic behavior has also been observed with several other physiological redox protein systems, e.g. cytochrome *c*–cytochrome *c* peroxidase, cytochrome *c*–cytochrome oxidase and cytochrome *f*–plastocyanin (see below), so that it seems to be quite general. The following interpretation of this phenomenon has been given [26]. Both electrostatic and hydrophobic interactions contribute to complex stabilization. The decrease in ET rate constant observed below the optimum ionic strength is due to two effects: formation of a complex between the oxidized proteins that blocks the active site and strong electrostatic effects which force the intermediate ET complex to assume a less productive protein–protein orientation. The latter phenomenon is evident from the fact that the k_{ET} value at the lowest ionic strength ($I = 12 \text{ mM}$) is smaller than that at $I = 100 \text{ mM}$, even after correction for the formation of unreactive complexes between the oxidized proteins. At intermediate ionic strengths, hydrophobic forces become more important and complexes assume their most productive orientations. At ionic strengths above the optimum value, ET rate constants decrease again due to slowing of protein–protein encounters via screening of long-range electrostatic forces by salt ions. The occurrence of these deviant ionic strength effects can be ascribed to the fact that the front surfaces of both Fd and FNR (and also many other ET proteins) contain both charged and non-polar residues, with the charges asym-

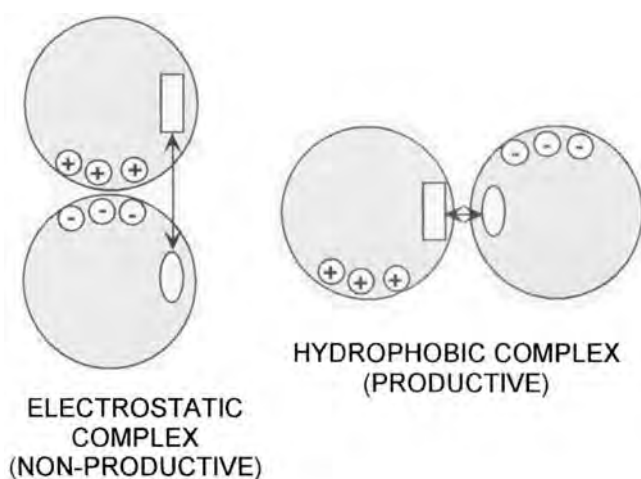


Figure 5. Schematic representation of the roles of electrostatic and hydrophobic interactions in the formation of ET complexes between redox proteins. Asymmetric placement of charged residues with respect to the prosthetic groups results in the electrostatically stabilized complex (left) being less optimal for ET than the complex stabilized by interactions between uncharged surfaces (right). This is a consequence of the larger distance between cofactors in the former complex than in the latter.

metrically located relative to the nonpolar regions immediately adjacent to the redox centers (see Figures 2 and 5). This represents an important insight into redox protein interactions.

The effects on the ET reaction of site-specific mutagenesis of surface residues close to the redox centers of both Fd and FNR have provided interesting insights into ET mechanisms [43, 49, 55, 56]. Nonconservative mutations in three positions (shown in Figure 6) in *Anabaena* Fd (S47A, F65A, F65I, E94K, E94Q) dramatically decrease the rate constant for ET from reduced Fd to oxidized FNR (by as much as a factor of 10^4), whereas conservative mutations at these sites (S47T, F65Y, F65W, E94D) result in retention of activity. Mutations of other surface residues in Fd have much smaller effects or none at all. Especially striking is the fact that a charge-reversal mutation at E95, which is spatially very close to E94, has only a minor effect on reactivity. Further, the T48A mutant maintains wild-type reactivity. A similar selectivity was found in the D67, D68, D69 cluster, where a charge-reversal mutation at D68 was found to increase k_{ET} at low ionic strengths, whereas such mutations at the other two positions were inhibitory under these conditions [57]. These results point to a very high level of specificity with regard to surface interactions between the two proteins during ET.

Appropriate experiments have shown that the inhibitory ET effects are not a consequence of changes in protein-protein binding affinity, in Fd redox potential or in the 3-D structures of the mutant proteins [49]. However, nonconservative mutations at the critical positions do have significant effects on a number of protein

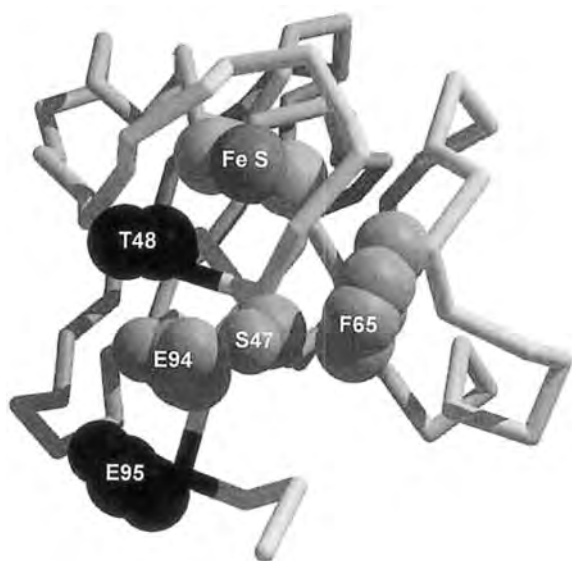


Figure 6. Front surface of *Anabaena* Fd showing critical residues for ET (E94, S47, F65), along with closely adjacent residues that have much smaller effects on ET upon mutagenesis (T48, E95). The iron–sulfur cofactor is labeled.

properties besides ET. Thus, in the S47A and E94K mutants, positive shifts of as much as 80 mV are observed in redox potentials, in the absence of any detectable structural changes in the immediate environment of the [2Fe–2S] cluster. Furthermore, protein stability to guanidine denaturation is decreased; this is especially notable in F65 mutants, and can be ascribed to increased solvent exposure of internal hydrophobic surfaces. Additionally, in the S47 and E94 mutants, the chain conformation in the C-terminal region is modified due to disruption of a hydrogen bond network which links the OH group of S47 to the COOH group of E94 and to the OH group of the C-terminal Y98 residue. The present interpretation of these data is that these three positions are critical points in the Fd structure that control the flexibility and/or conformation of a region of the surface which is close to the [2Fe–2S] cluster, and which is crucial for the interaction with FNR. Thus, it would appear that *parallel* effects on redox potential, protein stability and ET reactivity are occurring. In the ET process, it is the relative orientation of the two proteins within an intermediate complex that is being altered by the mutations, indicating that this is a highly sensitive parameter for controlling interprotein ET.

The laser photolysis results on the ET behavior of these mutants have been confirmed by steady-state kinetic measurements [58, 59]. Interestingly, the latter experiments have shown that nonconservative mutations at F65 and E94 not only severely inhibit reactivity with FNR, but also with two other ferredoxin-dependent enzymes, nitrite reductase and nitrate reductase [58]. Apparently, similar structural constraints in their interactions with Fd are also operative in these other enzymes.

Fd mutants have also been constructed in which each of the four Cys ligands to the [2Fe–2S] cluster have been mutated (one at a time) to Ser [60]. Of these, only the C79S mutant has an unstable iron–sulfur center. The other three mutants (i.e., C41S, C46S and C49S) are all reasonably stable, although clearly less so than the

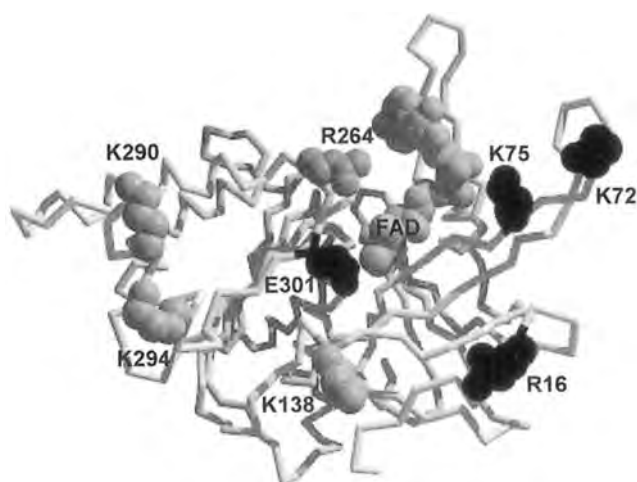


Figure 7. Front surface of *Anabaena* FNR showing residues subjected to mutagenesis. Those residues having the largest effects on Fd binding and ET are shown in dark shading, and those having smaller effects are shown in light shading. The FAD cofactor is labeled.

wild-type protein. They have relatively normal redox potentials (C46S is identical with wild-type FNR, and C49S is shifted by +50 mV), and can react with FNR (although k_{ET} values are smaller than the wild-type protein by factors of 2–3). These results indicate that whereas the cysteine sulfur atoms are not absolutely required for ET, they clearly make important contributions to protein properties, especially to cluster stability.

Mutagenesis of amino acid residues close to the exposed dimethylbenzene ring of the FAD cofactor of FNR has also provided interesting insights into the role of protein structural features in the interaction with Fd [61, 62]. Seven Lys and Arg residues in this region have been individually converted to Glu (Figure 7). The mutant proteins fall into two groups with respect to their ability to undergo ET with Fd. Thus, charge-reversal mutations at K75, R16 and K72 cause the most severe impairment (e.g., the ET rate constant for K75E is decreased by two orders of magnitude), whereas such mutations at K138, R264, K290 and K294 cause a much smaller degree of impairment. The severity of the ET effects clearly correlates with decreased stabilities of complexes between the two oxidized proteins. Those mutated residues that show the largest effects are located in a region of the protein in which positive charge predominates (see Figure 2), and thus charge reversals cause large changes in the local electrostatic surface potential. In contrast, the other residues are located within or close to regions of intense negative electrostatic potential (Figure 2) and therefore the introduction of additional negative charges has a much smaller net effect on the surface potential. Based on these results, it can be concluded that the positively charged region of the FNR surface located in the vicinity of K75, R16 and K72 is especially important in the binding and orientation of Fd during ET. The negatively charged surface located on the other side of the exposed

FAD cofactor may play a repulsive role during binding of the strongly negatively charged Fd, thereby facilitating the achievement of an appropriate orientation of the two molecules for the ET process. The importance of these electrostatic interactions is underscored by the observations that the degree of impairment of these mutations is strongly ionic strength dependent, and that replacement of K75 by Arg results in wild-type ET activity, whereas replacement by Gln or Ser does not [61].

A non-conservative replacement of a Glu residue (E301) close to the exposed portion of the FAD cofactor also results in a strong inhibition of ET with Fd [63]. In this case, it was shown that the carboxyl moiety of this residue was involved in stabilizing the one-electron reduced form of the FAD (i.e. FADH[•]). For both this mutation and the charge-reversal mutants noted above, steady-state experiments [64] support the laser flash photolysis results.

The results obtained thus far strongly support the following view of the Fd–FNR ET process. The opposite net surface charges of the two proteins play an important role in mediating long-range interactions that allow the molecules to approach each other in an orientation that, although not optimal, is approximately correct for ET. During collision, other forces, particularly hydrophobic interactions, become predominant, and align the proteins such that the closest possible distance, and the most effective orientation, between the prosthetic groups is attained. In the Fd–FNR case, this is probably close enough for outer-sphere ET between the [2Fe–2S] cluster and the isoalloxazine ring of the FAD to occur. If the electrostatic forces are too strong, an improper orientation is imposed, whereas if they are too weak, long-range pre-orientation is impaired. This leads to an ionic strength dependence that maximizes at approximately the value believed to exist *in vivo* (i.e., 100–150 mM). This general picture seems to be applicable to a large number of physiological ET protein pairs. However, as is often the case in biology, an all-encompassing generalization is dangerous.

5.3.2 Cytochrome *f* (Cyt *f*)–Plastocyanin (Pc)

The Cyt *f*–Pc redox pair is also involved in photosynthetic ET. Pc plays a role analogous to Fd, in that it serves as an electron acceptor from a membrane-bound complex, cytochrome *b₆f*. The latter mediates electron flow from photosystem II to photosystem I, coupled to proton translocation. Pc is a small, copper-containing protein, consisting of a single polypeptide chain forming an eight-stranded β -barrel. The coordination environment of the high-potential (~ 370 mV) ‘blue’ copper atom consists of two His nitrogen atoms, and sulfur atoms from Cys and Met residues. One of the His ligands (His87) is exposed at the surface in the center of a hydrophobic region. The Cyt *f* component of the complex, which also has a relatively high redox potential (~ 360 mV), is linked to the membrane by a single hydrophobic transmembrane segment, which allows the heme-containing domain to project out of the membrane surface and make contact with the soluble Pc. Note that the ET process is approximately isotopotential. The 3-D structure of the soluble domain of Cyt *f* is known to high resolution [65], as is the structure of Pc [66] (Figure 8). Laser flash photolysis studies (at 5 mM ionic strength) of the proteins isolated from spin-

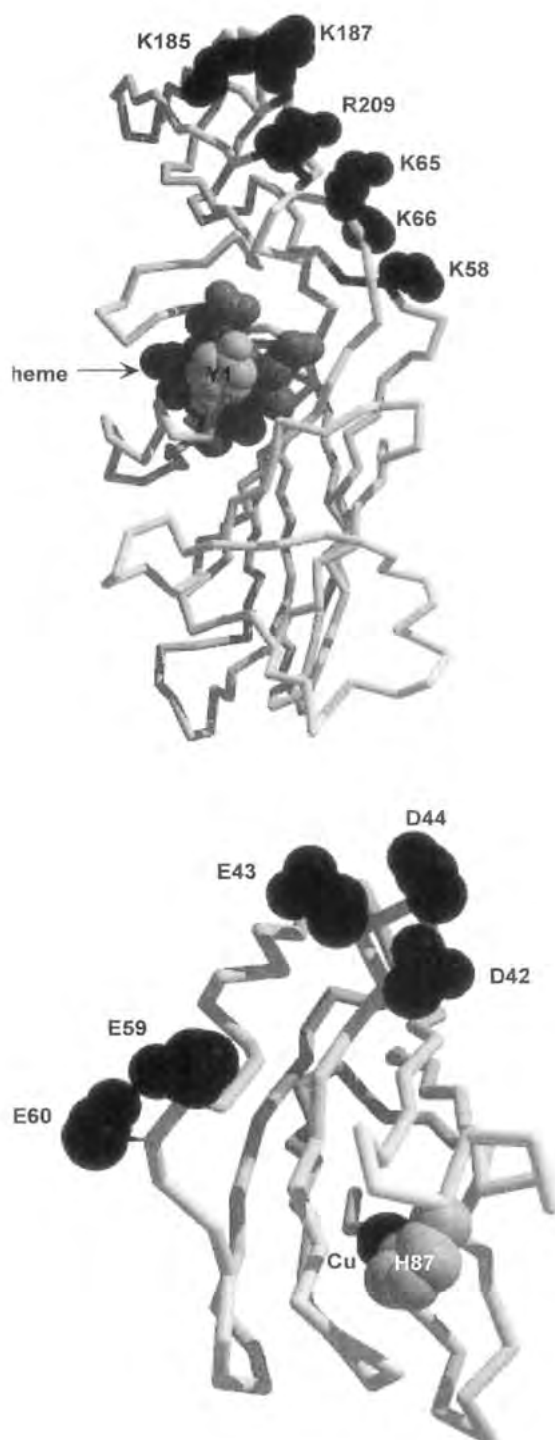


Figure 8. Front surfaces of Cyt *f* (top) and plastocyanin (bottom). Residues implicated in complex formation between the two proteins are shown in dark shading and are labeled. The heme cofactor in Cyt *f* and the Cu atom in plastocyanin are labeled. The Tyr ligand to the heme in Cyt *f* is shown in light shading and is labeled. The exposed ligand to the copper atom (His87) in plastocyanin is shown and labeled.

ach have yielded values of 23 μM for K_D and 2800 s^{-1} for k_{ET} [67]. The latter compares well with the k_{ET} value obtained in vivo [68]. The ionic strength dependence of the in vitro reaction [67], like that of the Fd–FNR reaction, is biphasic with a broad maximum centered at about 40 mM. It is interesting in this context that cytochromes which are not physiological partners of Pc display monophasic ionic strength effects in their reactions with Pc (see Figure 1). This is probably a consequence of a lack of specific regions of complementarity between the charge distributions on these cytochromes and that of Pc. Site-specific mutagenesis [69, 70] has shown that basic residues near the interface between the large and small domains in Cyt *f*, and acidic residues in Pc, are major contributors to the ionic strength dependence (see Figure 8). This implies that the initial interaction domain involves these regions of the two proteins. It is interesting that expression of these Cyt *f* mutations in vivo does not influence the rate of ET, indicating that the diffusion of the proteins to form an intermediate complex is not rate limiting under these conditions [70]. This may be a consequence of the small volume of the chloroplast intermembrane space.

Kinetic measurements [67] and chemical cross-linking studies [71] have indicated that the electrostatic interaction between Cyt *f* and Pc that occurs during the initial collisional encounter does not result in a complex which is optimal for ET, and that internal rearrangement within the collision complex is a necessary component of the reaction mechanism. The structural basis for this has been probed using NMR and molecular dynamics methods [72]. The initial, purely electrostatic, complex has been proposed to consist of an ensemble of relatively ‘loose’ structures which are in rapid equilibrium, and which undergo only slow ET reactions because of the large distances between redox centers that exist in these complexes. The collisional interaction is followed by the formation of a second well-defined, single-orientation complex, stabilized by both electrostatic and other types of forces (hydrogen bonds, hydrophobic interactions, van der Waals contacts). This latter complex is capable of rapid ET, owing to a smaller distance between redox centers. A specific structure for this ET complex has been proposed, in which the redox centers are approximately 11 Å apart, and in which electrostatic interactions occur between those acidic residues in Pc and basic residues in Cyt *f* that have been implicated by the site-specific mutagenesis studies (see Figure 8). In this model, the ET process occurs via the His87 ligand of the Pc Cu atom and the Tyr1 ligand of the heme iron.

5.3.3 Cytochrome *c* (Cyt *c*)–Cytochrome *c* Peroxidase (ccp)

Cytochrome *c* peroxidase, a heme protein isolated from yeast, catalyzes the two-electron reduction of H_2O_2 to H_2O , utilizing two molecules of reduced Cyt *c* as the source of reducing equivalents. In the first step of the catalytic cycle, ccp undergoes a two-electron oxidation by H_2O_2 . This produces an intermediate state in which one oxidizing equivalent is stored in the heme as an oxyferryl ion $[\text{Fe}^{\text{IV}}=\text{O}]^{2+}$, and the second equivalent as a cationic amino acid radical center located on Trp191 (see [16] for an overview). Catalysis is completed by two successive one-electron reductions by reduced Cyt *c*. A large body of evidence (see [73] for details) supports the

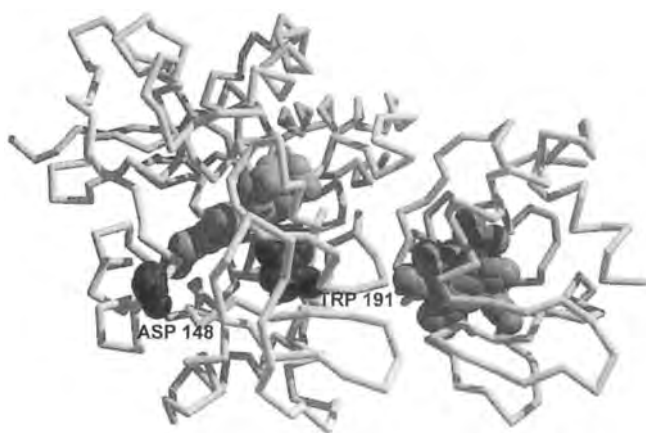


Figure 9. Structure of crystalline complex between cytochrome *c* (right) and cytochrome *c* peroxidase (left). The heme cofactors are shown (light shading) as well as two amino acid residues in the peroxidase (dark shading).

idea that two distinct Cyt *c* binding sites, with rather different affinities, exist on ccp. The high affinity site is associated with Trp radical reduction, and corresponds to the 1:1 complex formed between ccp and yeast iso-1 Cyt *c* whose structure has been solved by X-ray crystallography [10]. This structure is shown in Figure 9. Binding of Cyt *c* to the low-affinity site, which is suggested by electrostatic calculations to be located approximately 90° from the high-affinity site (near Asp148; see Figure 9), makes the predominant contribution to oxyferryl heme reduction [73]. In contrast to this proposed mechanism, observations using laser flash photolysis methodology with ruthenium-labelled Cyt *c* at low ionic strength [74] have suggested that two successive intracomplex ET reactions occur, involving transfer from reduced Cyt *c* molecules first to the Trp radical and then to the oxyferryl heme. Experiments with site-specific mutants indicated that both of these reactions occurred in the same region of the ccp molecule, i.e., the high-affinity site. The rate constants for these two reactions using reduced yeast iso-1 Cyt *c* were $2 \times 10^6 \text{ s}^{-1}$ and 5000 s^{-1} , respectively. Trp radical reduction by iso-1 Cyt *c* was shown to be independent of solvent viscosity, whereas a dependence on viscosity was observed for this reaction when horse Cyt *c* was used as the reductant [75]. This was interpreted as indicating that the iso-1 Cyt *c* reaction proceeded via the conformation shown in the crystal structure determination of the complex [10], whereas the slower horse Cyt *c* reaction ($k = 6.1 \times 10^4 \text{ s}^{-1}$) required a prior rearrangement within the complex from a less favorable orientation, as observed in the crystal structure of the horse Cyt *c* complex with ccp [10], to a more favorable iso-1-like orientation. The latter reaction provides another example of conformational control of interprotein ET.

It has also been proposed based on the laser photolysis studies [74] that both the Trp radical and the oxyferryl heme reduction reactions involve an initial ET to the Trp radical. This would require the occurrence of an intermediate step in the two-

reaction sequence that involves intramolecular ET from the reduced Trp radical to the oxyferryl heme in order to regenerate the radical species. Unfortunately, this reaction could not be directly observed in the laser photolysis experiments, and independent evidence exists that this is a very slow process, despite the fact that these two centers are close to one another. Further work appears necessary in order to resolve this matter. However, it is clear that site-specific mutagenesis of Trp191 to Phe strongly inhibits oxyferryl heme reduction [76].

The very large rate constant that is observed for the first step of Trp radical reduction is interesting. In the crystalline complex, the closest edge-to-edge distance between the heme of Cyt *c* and the indole ring of Trp191 is 16 Å. An ET pathway leading from the heme methyl group through ccp residues Ala194, Ala193 and Gly192 was proposed based on the crystallography [10]. Attempts to utilize the structure of the complex, along with estimated values for the reorganization energy (0.4–0.8 eV) and the driving force (0.4–0.5 eV), to calculate k_{ET} for this reaction were made using both Marcus theory and the pathways model [74]. These yielded values that were at least one order of magnitude too low. This points to the difficulties inherent in such calculations for complex protein systems.

5.4 Intraprotein Electron Transfer Reactions

5.4.1 Flavocytochrome b_2 (Fcyt *b*)

This interesting enzyme isolated from yeast is emerging as an important paradigm for intraprotein ET. It functions to catalyze the two-electron oxidation of lactate to pyruvate, utilizing an FMN and a b-type heme as intermediate electron carriers, and Cyt *c* as the terminal electron acceptor. Lactate oxidation occurs at the FMN site to produce the fully reduced flavin, followed by two successive intramolecular one-electron transfers to the heme cofactor, and from there to Cyt *c*. The 3-D structure of the enzyme from *Saccharomyces* [6] shows separate flavin and heme domains connected by a polypeptide bridge (Figure 10). This is a type of structural motif that is commonly found in multicenter redox proteins (see below for other examples), although ‘hard-wired’ connections between redox centers are also found in enzymes such as ascorbate oxidase and cytochrome *c* oxidase. In the Fcyt *b* case, the length of the bridging polypeptide has been shown to play a crucial role in the intraprotein ET reaction, presumably by constraining the relative distance and orientation of the two domains [77]. The propionate groups of the heme extend out of the heme pocket and point towards the FMN, with the closest edge-to-edge distance between the approximately coplanar cofactors being 9.7 Å. A Tyr residue (Y143) from the flavin domain lies between the two cofactors and forms an H-bond to the heme propionate. In the complex of the enzyme with the reaction product pyruvate, Y143 forms an H-bond to the pyruvate carboxylate. Interestingly, pyruvate binding results in stabilization of the FMN semiquinone form [78]. This is a thermodynamic effect achieved by increasing the midpoint potential of the oxidized–semiquinone

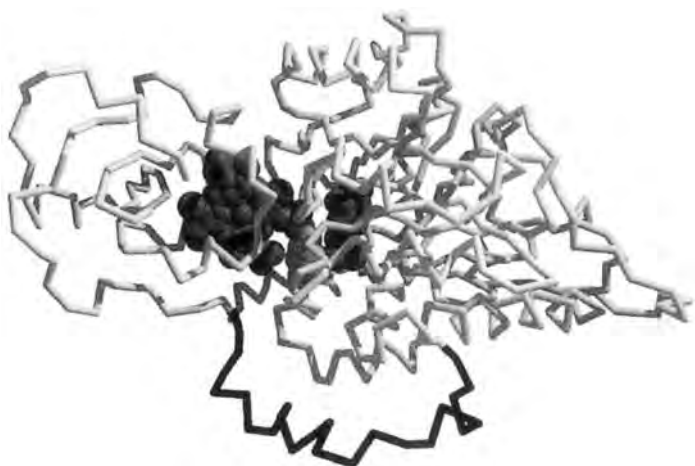


Figure 10. Structure of one of the subunits of flavocytochrome b_2 . The heme domain and the heme cofactor are shown on the left and the flavin domain and the FMN cofactor on the right. The connecting polypeptide bridge is shown in dark shading. Also shown is Tyr143 (in light shading), which lies between the two cofactors.

couple, and decreasing the potential of the semiquinone–fully reduced couple [79–81]. In the absence of pyruvate, these one-electron potentials for the native enzyme from *Saccharomyces* have been reported [82] to be -45 and -135 mV, respectively, and the heme potential -3 mV. In the presence of pyruvate, the heme potential is unchanged, the oxidized–semiquinone potential becomes 50 mV and the second potential becomes -125 mV. The structural basis for these effects is unclear at present.

Laser flash photolysis studies using the deazariboflavin system [80, 81] have shown that pyruvate binding also exerts a strong influence on intramolecular ET. In the one-electron reduced enzyme, ET from the FMN semiquinone to the oxidized heme can be observed *only* in the presence of pyruvate; for this reaction, $k_{\text{ET}} = 500 \text{ s}^{-1}$. When the enzyme is completely reduced by stoichiometric addition of lactate prior to laser photolysis with dRf alone, pyruvate binding *inhibits* ET from fully reduced flavin to oxidized heme. This reaction has an observed $k_{\text{ET}} = 2000 \text{ s}^{-1}$ in the absence of pyruvate [81]. Similar values for these two rate constants have been obtained by temperature-jump measurements [82].

A number of observations [6, 83, 84] have indicated that the heme domain of Fcyt b is mobile relative to the flavin domain, and it has been suggested that this conformational mobility may influence the intramolecular ET kinetics [80, 81, 85]. Inasmuch as the pyruvate effects on intramolecular ET do not correlate with the changes in redox potentials, they may provide an example of conformational gating [86, 87]. This remains to be established (see [82] for further discussion). In this context, it is interesting that in the Fcyt b crystal, bound pyruvate apparently acts to increase the mobility of the heme domain to the point where it is no longer visible in the X-ray electron density map [6].

Site-directed mutagenesis clearly demonstrates that changing Tyr143 to Phe strongly decreases the rate constant for flavin semiquinone to heme ET [27, 88]. Redox potential measurements [82] indicate that this mutation shifts the first FMN potential by about 60 mV in the positive direction, and the second potential by about 30 mV in the negative direction, with no change in the heme potential. This is similar to the effect of pyruvate on Fcyt *b* redox potentials, which was still observed in the mutant enzyme. Crystallography [89] indicates that no significant structural changes have occurred in the Y143F mutant, suggesting an important role for the interdomain hydrogen bond. This bond could function either as part of the ET pathway, or as a constraint on the relative positions of the two domains, or both.

5.4.2 Sulfite Oxidase (SO)

SO is found in various vertebrate liver tissues and catalyzes the two-electron oxidation of sulfite to sulfate coupled to the reduction of two molecules of oxidized Cyt *c*. It contains molybdopterin and b-heme cofactors in separate domains connected by a polypeptide bridge, analogous to Fcyt *b*. The smaller N-terminal heme domain resembles cytochrome *b*₅; the C-terminal domain contains Mo(VI) and catalyzes sulfite oxidation coupled to oxo group transfer. Two one-electron intramolecular ET steps, each followed by ET to Cyt *c*, complete the catalytic cycle.

The three-dimensional structure of SO [90] has been solved to 1.9 Å resolution (Figure 11). The distance between the heme and molybdopterin centers in this structure is fairly large (approximately 28 Å between the Mo atom and the edge of the heme ring), and the redox potential difference between the cofactors is small (approximately 10 mV at pH 6 [91]). Despite this, intramolecular ET between the two centers can be fairly rapid; using laser flash photolysis methods, k_{ET} values as large as 2400 s⁻¹ have been observed for the one-electron transfer between the reduced heme and oxidized Mo cofactors [91]. Arguments based on simple Marcus theory predict that k_{ET} should be less than or equal to 100 s⁻¹ for this process. This estimate assumes a coupling-decay constant (β) of approximately 0.9 Å⁻¹ and a zero activation energy. The latter value is improbable inasmuch as the driving force for the reaction is close to zero. Marcus theory predicts a zero barrier only when the reorganizational energy (λ) equals the driving force, and λ is unlikely to be zero in SO. Thus, k_{ET} values much less than 100 s⁻¹ are expected. This discrepancy has led to the suggestion [92] that the flexibility imparted by the long polypeptide tether that connects the two domains allows conformations that bring the heme and Mo centers much closer than shown in the crystal structure. This is supported by the observation [91] that sulfate ion binding at the molybdopterin site acts to inhibit the intramolecular ET reaction, another example of ligand-gated ET involving a reaction product (see above). It is noteworthy that, in the crystal structure, a sulfate anion sits at the bottom of a pocket in the molybdenum domain lined with basic amino acids, and is in contact with an oxygen ligand of the cofactor (Figure 11). This pocket lies on a surface of the molybdenum domain that is approximately 90° from that which is contacted by the heme domain in the crystal structure. Molecular graphics manipulation of the SO structure indicates that the polypeptide tether is

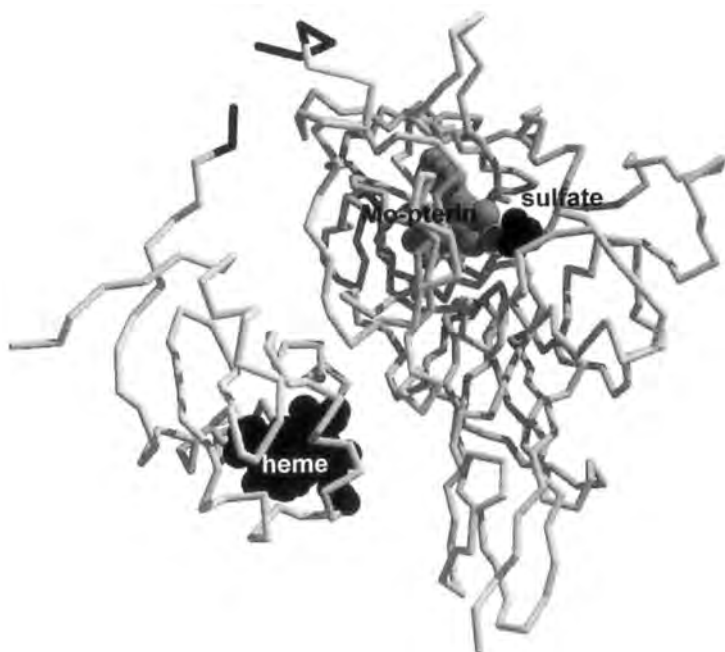


Figure 11. Structure of sulfite oxidase. The heme domain and the heme cofactor are shown on the left and the molybdopterin domain with its cofactor is shown on the right. The connecting polypeptide bridge is shown in dark shading (one residue is not visible in the electron density map). A bound sulfate ion is also shown in dark shading.

long enough to permit the exposed heme cofactor to make contact with this latter region. Furthermore, this region of the heme domain surface is negatively charged, and thus can interact electrostatically with the sulfate-binding pocket in the molybdenum domain. This can nicely account for both the relatively rapid intramolecular ET and the inhibition by sulfate binding. This interesting possibility needs further investigation.

5.4.3 Cytochrome P450BM-3

Cytochromes P450 are a large family of heme-containing monooxygenases that catalyze the hydroxylation of a variety of compounds. They may be either membrane-bound or soluble, and generally utilize either iron-sulfur proteins or flavoproteins as electron donors to the heme. The soluble bacterial fatty acid monooxygenase P450BM-3 is unique in that the flavoprotein reductase moiety, which contains both FAD and FMN cofactors, is fused with the cytochrome moiety within a single 119 kDa polypeptide [93], rather than being located in a separate protein as it is in most other P450 systems. Furthermore, polypeptides containing each of the three co-

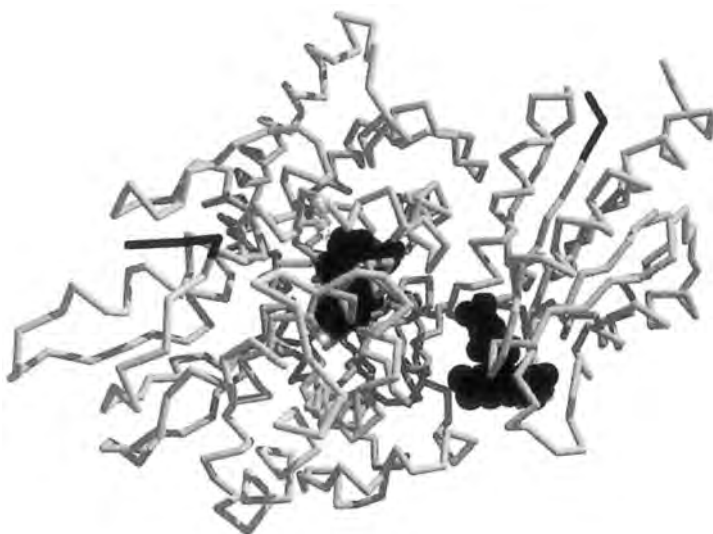


Figure 12. Structure of a crystalline complex between the heme (left) and FMN (right) domains of cytochrome P450BM-3. In this complex, the connecting polypeptide bridge (the ends are shown in dark shading) has been severed and a 20-residue segment is not visible in the structure. The heme and the FMN cofactors are shown in dark shading.

factors can be separately expressed [94], indicating the presence of separate domains connected by polypeptide linkers. Mutagenesis has shown that shortening the length of the linker region between the FMN and heme domains by six amino acid residues causes loss of enzymatic activity [95]. Presumably, this does not allow the domains to orient properly with respect to one another [96].

Although the 3-D structure of the holoprotein has not been determined, structures are available for the heme domain [97, 98] and for an FMN-heme construct [99] (the latter is shown in Figure 12). In the two-domain species, the connecting polypeptide bridge (located between residue 458 in the heme domain and residue 479 in the flavin domain) has been proteolytically severed and does not appear in the electron density map [99]. It is not known whether or not this has caused a change in conformation from the native protein. The heme is in a low-spin state, with a cysteine sulfur as the proximal ligand and a weakly bound water molecule on the distal side. The isoalloxazine ring of the FMN cofactor is at an approximately 90° angle to the plane of the heme, at a distance of about 17 Å from the heme edge.

Electron flow within the protein proceeds from the reducing substrate (NADPH) to FAD to FMN to heme. The initial reduction forms fully reduced FAD (FADH₂), which then transfers one-electron to FMN forming the neutral FAD semiquinone (FADH•) and the anionic FMN semiquinone (FMN^{•-}). When the fatty acid substrate is bound within a long hydrophobic channel adjacent to the distal face of the heme, it induces a low-spin to high-spin change and an increase in the heme potential [93]. This probably involves displacement of the water molecule in the sixth coordination position [100] and a decrease in the local dielectric con-

stant. This allows FMN^{•−} to reduce the ferric iron to the ferrous state. The reduction process is coupled to a structural change in the protein, which causes a 6 Å movement of the substrate into a position favorable for hydroxylation [101]. Upon dioxygen binding to the reduced heme iron, a second electron is delivered which generates an oxyferryl intermediate that carries out the hydroxylation reaction.

The redox potentials of the various P450BM-3 cofactors are as follows [99, 102]. For the heme in the absence of substrate, the potential is −370 mV; in the presence of the substrate arachidonic acid, this is raised to −240 mV. The estimated one-electron potentials of the flavins are as follows: FAD (ox/sq) \approx −285 mV; FAD (sq/hq) \approx −380 mV; FMN (ox/sq) \approx −250 mV; and FMN (sq/hq) \approx −150 mV. These values are consistent with electron flow from FAD semiquinone to FMN, and from FMN semiquinone to heme in the presence of bound substrate (ligand-gated ET).

Laser flash photolysis experiments with the FMN–heme domain using the deazariboflavin system [103] have shown that intramolecular ET from FMN semiquinone to heme cannot be observed in the absence of both substrate and CO, the latter serving as a non-redox active substitute for O₂ that binds to the reduced heme. In the presence of saturating amounts of CO (800 μ M), but no substrate, a slow transfer was observed ($k_{ET} \approx 20$ s^{−1}). Although this is against a thermodynamic gradient, trapping of the reduced heme by CO binding may allow this process to proceed. As CO binding is fairly rapid [104], the observed rate constant presumably reflects the ET step. As the substrate (myristic acid in these experiments) concentration was increased, the observed rate constant increased to 250 s^{−1} along a hyperbolic curve with a midpoint at a substrate concentration of 6.8 μ M. The latter value is in satisfactory agreement with the binding constant determined by spectral titration under the same conditions. This suggests that substrate binding is the rate-limiting step in this process, and that the actual value of k_{ET} must be greater than 250 s^{−1}. It was also observed that the rate constant for heme reduction via the FMN semiquinone in the presence of excess substrate increased linearly with increase in CO concentration. It is important that no heme reduction was detectable in the absence of CO, and that the observed rate constant only reached the limiting value of 250 s^{−1} in the presence of saturating concentrations of CO. Again, this indicates that a binding event, in this case one having low affinity and involving CO, is rate-limiting. As the ferric heme does not bind CO, this binding process must somehow convert the protein into a conformational state that enables the ferric iron to accept an electron from FMN^{•−}. Rapid CO binding to the ferrous heme then follows. Although the structural nature of this conversion is unclear, it provides still another example of the gating of intramolecular ET by ligand binding.

5.5 Conclusions

In the examples described above, we have seen that the interprotein ET reactions are controlled mainly by complementary interactions between the surfaces of the

two proteins involved that influence the mutual orientation of the reaction partners. These are mediated both by electrostatic effects between oppositely charged residues, which act at long distances and provide a mechanism whereby recognition and pre-orientation can be achieved prior to actual collision, and by hydrophobic effects, which act at short distances and provide for precise alignment of the prosthetic groups during the ET process. In contrast, the intraprotein ET reactions that have been discussed are strongly modulated by ligand binding effects, which act as gates to control electron flow (for further discussion, see [105]). It is probably significant that the latter systems are enzymes, which utilize much more complex reaction sequences than occur in redox proteins that are mainly designed for pure ET. Because of their domain structural organization, such multicenter enzymes do not require recognition and pre-orientation between individual polypeptides, and therefore control of ET reactions between redox sites must be exercised by other means, usually ligand-binding events. In at least some cases, gating effects are caused by shifts in redox potential upon ligand binding, and thus constitute thermodynamic control mechanisms. In other cases, ligand binding exerts kinetic control. The latter can involve changes in interdomain distance and/or orientation, or steric blockage of electron flow. At present, we know very little about the structural basis for these control processes. This is clearly a fertile area for future study.

Acknowledgments

The work described here was supported in part by NIH grant DK15057. The author also expresses his indebtedness to a large number of talented students, colleagues and collaborators, whose names appear on the papers from this laboratory that are cited in the text.

References

1. F. S. Millett (Ed.), *Minireview Series: Biological Electron Transfer*, *J. Bioenerg. Biomembr.* **1995**, 27, 261–362.
2. (a) R. A. Marcus, N. Sutin, *Biochim. Biophys. Acta* **1985**, 811, 265–322; (b) G. McLendon, *Acc. Chem. Res.* **1988**, 21, 160–167; (c) H. B. Gray, J. R. Winkler, *Annu. Rev. Biochem.* **1996**, 65, 537–561.
3. J. N. Betts, D. N. Beratan, J. N. Onuchic, *J. Am. Chem. Soc.* **1992**, 114, 4043–4046.
4. D. N. Beratan, J. N. Onuchic, J. R. Winkler, H. B. Gray, *Science* **1992**, 258, 1740–1741.
5. W. B. Curry, M. D. Grabe, I. V. Kurnikov, S. S. Skourtis, D. N. Beratan, J. J. Regan, A. J. A. Aquino, P. Beroza, J. N. Onuchic, *J. Bioenerg. Biomembr.* **1995**, 27, 285–293.
6. Z. X. Xia, F. S. Mathews, *J. Mol. Biol.* **1990**, 212, 837–863.
7. A. Messerschmidt, R. Ladenstein, R. Huber, M. Bolognesi, L. Avigliano, R. Petruzzelli, A. Rossi, A. Finazzi-Agro, *J. Mol. Biol.* **1992**, 224, 179–205.
8. J. Kim, J. H. Fuller, V. Kuusk, L. Cunane, Z. W. Chen, F. S. Mathews, W. S. McIntire, *J. Biol. Chem.* **1995**, 270, 31202–31209.
9. Z. W. Chen, M. Koh, G. Van Driessche, J. Van Beeumen, R. G. Bartsch, T. E. Meyer, M. A. Cusanovich, F. S. Mathews, *Science* **1994**, 266, 430–432.
10. H. Pelletier, J. Kraut, *Science* **1992**, 258, 1748–1755.

11. Z. W. Chen, R. Durley, B. J. Poliks, K. Hamada, Z. Chen, F. S. Mathews, V. L. Davidson, Y. Satow, E. Huizinga, M. D. Vellieux, W. G. J. Hol, *Biochemistry* **1992**, *31*, 4959–4964.
12. L. Chen, R. Durley, F. S. Mathews, V. L. Davidson, *Science* **1994**, *264*, 86–90.
13. M. J. Bjerrum, D. R. Casimiro, I. J. Chang, A. J. Di Bilio, H. B. Gray, M. G. Hill, R. Langen, G. A. Mines, L. K. Skov, J. R. Winkler, D. S. Wuttke, *J. Bioenerg. Biomembr.* **1995**, *27*, 295–302.
14. G. Tollin, *J. Bioenerg. Biomembr.* **1995**, *27*, 303–310.
15. B. Durham, J. L. Fairris, M. McLean, F. Millett, J. R. Scott, S. G. Sligar, A. Willie, *J. Bioenerg. Biomembr.* **1995**, *27*, 331–340.
16. F. Millett, M. A. Miller, L. Geren, B. Durham, *J. Bioenerg. Biomembr.* **1995**, *27*, 341–351.
17. C. C. Moser, J. M. Keske, K. Warncke, R. S. Farid, P. L. Dutton, *Nature* **1992**, *355*, 796–802.
18. P. J. F. De Rege, S. A. Williams, M. J. Therien, *Science* **1995**, *269*, 1409–1413.
19. J. R. Winkler, H. B. Gray, *Chem. Rev.* **1992**, *92*, 369–379.
20. R. S. Farid, C. C. Moser, & P. L. Dutton, *Curr. Opin. Struct. Biol.* **1993**, *3*, 225–233.
21. D. S. Wuttke, M. J. Bjerrum, J. R. Winkler, H. B. Gray, *Science* **1992**, *256*, 1007–1009.
22. D. N. Beratan, J. N. Onuchic, J. R. Winkler, H. B. Gray, *Science* **1992**, *258*, 1740–1741.
23. D. R. Casimiro, L. L. Wong, J. L. Colon, T. E. Zewert, J. H. Richards, I. J. Chang, J. R. Winkler, H. B. Gray, *J. Am. Chem. Soc.* **1993**, *115*, 1485–1489.
24. T. B. Karpishin, M. W. Grinstaff, S. Komar-Panicucci, G. McLendon, H. B. Gray, *Structure* **1994**, *2*, 415–422.
25. G. Tollin, J. T. Hazzard, *Arch. Biochem. Biophys.* **1991**, *287*, 1–7.
26. J. K. Hurley, M. F. Fillat, C. G. Gomez-Moreno, G. Tollin, *J. Am. Chem. Soc.* **1996**, *118*, 5526–5531.
27. G. Tollin, J. K. Hurley, J. T. Hazzard, T. E. Meyer, *Biophys. Chem.* **1993**, *48*, 259–279.
28. T. E. Meyer, Z. G. Zhao, M. A. Cusanovich, G. Tollin, *Biochemistry* **1993**, *32*, 4552–4559.
29. G. M. Ullmann, N. M. Kostic, *J. Am. Chem. Soc.* **1995**, *117*, 4766–4774.
30. J. N. Onuchic, D. N. Beratan, J. R. Winkler, H. B. Gray, *Annu. Rev. Biophys. Biomol. Struct.* **1992**, *21*, 349–377.
31. R. A. Friesner, *Structure* **1994**, *2*, 339–343.
32. A. Merli, D. E. Brodersen, B. Morini, Z. W. Chen, R. C. E. Durley, F. S. Mathews, V. L. Davidson, G. L. Rossi, *J. Biol. Chem.* **1996**, *271*, 9177–9180.
33. N. Adir, H. L. Axelrod, P. Beroza, R. A. Isaacson, S. H. Rongey, M. Y. Okamura, G. Feher, *Biochemistry* **1996**, *35*, 2535–2547.
34. T. L. Poulos, J. Kraut, *J. Biol. Chem.* **1980**, *255*, 10322–10330.
35. J. Jung, G. Tollin, *Biochemistry* **1981**, *20*, 5124–5131.
36. I. Ahmad, M. A. Cusanovich, G. Tollin, *Proc. Natl. Acad. Sci. USA* **1981**, *78*, 6724–6728.
37. R. P. Simonsen, G. Tollin, *Biochemistry* **1983**, *22*, 3008–3016.
38. G. Tollin, T. E. Meyer, M. A. Cusanovich, *Biochim. Biophys. Acta* **1986**, *853*, 29–41.
39. M. A. Cusanovich, T. E. Meyer, G. Tollin, in *Advances in Inorganic Biochemistry*, Vol. 7, *Heme Proteins* (Eds. G. L. Eichorn, L. G. Marzilli,) Elsevier, New York, **1988**, pp. 37–91.
40. G. Tollin, J. K. Hurley, J. T. Hazzard, T. E. Meyer, *Biophys. Chem.* **1993**, *48*, 259–279.
41. R. Traber, H. E. A. Kramer, P. Hemmerich, *Biochemistry* **1982**, *21*, 1687–1693.
42. D. E. Edmondson, B. Barman, G. Tollin, *Biochemistry* **1972**, *11*, 1133–1138.
43. J. K. Hurley, Z. Salamon, T. E. Meyer, J. C. Fitch, M. A. Cusanovich, J. L. Markley, H. Cheng, B. Xia, Y. K. Chae, M. Medina, C. Gómez-Moreno, G. Tollin, *Biochemistry* **1993**, *32*, 9346–9354.
44. R. P. Simonsen, P. C. Weber, F. R. Salemme, G. Tollin, *Biochemistry* **1982**, *21*, 6366–6375.
45. P. Debye, E. Hückel, *Phys. Z* **1954**, *24*, 185–206.
46. J. A. Watkins, M. A. Cusanovich, T. E. Meyer, G. Tollin, *Protein Sci.* **1994**, *3*, 2104–2114.
47. T. E. Meyer, J. A. Watkins, C. T. Przysiecki, G. Tollin, M. A. Cusanovich, *Biochemistry* **1984**, *23*, 4761–4767.
48. G. Tollin, G. Cheddar, J. A. Watkins, T. E. Meyer, M. A. Cusanovich, *Biochemistry* **1984**, *23*, 6345–6349.
49. J. K. Hurley, A. M. Weber-Main, M. T. Stankovich, M. M. Benning, J. B. Thoden, J. L. Vanhooke, H. M. Holden, Y. K. Chae, B. Xia, H. Cheng, J. L. Markley, M. Martínez-Júlvez, C. Gómez-Moreno, J. L. Schmeits, G. Tollin, *Biochemistry* **1997**, *36*, 11100–11117.

50. L. Serre, F. Vellicux, J. Fontecilla-Camps, M. Frey, M. Medina, C. Gómez-Moreno, in *Flavins and Flavoproteins* (Ed. K. Yagi), Walter de Gruyter, Berlin, **1994**, pp. 431–434.
51. C. M. Bruns, P. A. Karplus, *J. Mol. Biol.* **1995**, *247*, 125–145.
52. E. C. Apley, R. Wagner, *Biochim. Biophys. Acta* **1988**, *936*, 269–275.
53. W. R. Rypniewski, D. R. Breiter, M. M. Benning, G. Wesenberg, B. H. Oh, J. L. Markley, I. Rayment, and H. M. Holden, *Biochemistry* **1991**, *30*, 4126–4131.
54. M. C. Walker, J. J. Pueyo, J. A. Navarro, C. Gómez-Moreno, G. Tollin, *Arch. Biochem. Biophys.* **1991**, *287*, 351–358.
55. J. K. Hurley, H. Cheng, B. Xia, J. L. Markley, M. Medina, C. Gómez-Moreno, G. Tollin, *J. Am. Chem. Soc.* **1993**, *115*, 11698–11701.
56. J. K. Hurley, M. Medina, C. Gómez-Moreno, G. Tollin, *Arch. Biochem. Biophys.* **1994**, *312*, 480–486.
57. J. K. Hurley, J. L. Schmeits, C. Genzor, C. Gómez-Moreno, G. Tollin, *Arch. Biochem. Biophys.* **1996**, *333*, 243–250.
58. S. Schmitz, H. Böhme, *Biochim. Biophys. Acta* **1995**, *1231*, 335–341.
59. A. Aliverti, A. Livraghi, L. Piubelli, G. Zanetti, *Biochim. Biophys. Acta* **1997**, *1342*, 45–50.
60. J. K. Hurley, A. M. Weber-Main, A. E. Hodges, M. T. Stankovich, M. M. Benning, H. M. Holden, H. Cheng, B. Xia, J. L. Markley, C. Genzor, C. Gómez-Moreno, R. Hafezi, G. Tollin, *Biochemistry* **1997**, *36*, 15109–15117.
61. M. Martínez-Júlvez, M. Medina, J. K. Hurley, R. Hafezi, T. B. Brodie, G. Tollin, C. Gómez-Moreno, *Biochemistry* **1998**, *37*, 13604–13613.
62. J. K. Hurley, J. T. Hazzard, M. Martínez-Júlvez, M. Medina, C. Gómez-Moreno, G. Tollin, *Protein Sci.* **1999**, *8*, 1614–1622.
63. M. Medina, M. Martínez-Júlvez, J. K. Hurley, G. Tollin, C. Gómez-Moreno, *Biochemistry* **1998**, *37*, 2715–2728.
64. S. Schmitz, M. Martínez-Júlvez, C. Gómez-Moreno, H. Böhme, *Biochim. Biophys. Acta* **1998**, *1363*, 85–93.
65. S. E. Martinez, D. Huang, A. Szczepaniak, W. A. Cramer, J. L. Smith, *Structure* **1994**, *2*, 95–105.
66. J. M. Guss, H. D. Bartunik, H. C. Freeman, *Acta Crystallogr* **1992**, *B48*, 790–811.
67. T. E. Meyer, Z. G. Zhao, M. A. Cusanovich, G. Tollin, *Biochemistry* **1993**, *32*, 4552–4559.
68. G. M. Soriano, M. V. Ponamarev, G. S. Tae, W. A. Cramer, *Biochemistry* **1996**, *35*, 14590–14598.
69. A. Kannt, S. Young, D. S. Bendall, *Biochim. Biophys. Acta* **1996**, *1277*, 115–126.
70. G. M. Soriano, M. V. Ponamarev, R. A. Piskowski, W. A. Cramer, *Biochemistry* **1998**, *37*, 15120–15128.
71. L. Qin, N. M. Kostic, *Biochemistry* **1993**, *32*, 6073–6080.
72. M. Ubbink, M. Ejdebäck, B. G. Karlsson, D. S. Bendall, *Structure* **1998**, *6*, 323–335.
73. J. S. Zhou, S. T. Tran, G. McLendon, B. M. Hoffman, *J. Am. Chem. Soc.* **1997**, *119*, 269–277.
74. K. Wang, H. Mei, L. Geren, M. A. Miller, A. Saunders, X. Wang, J. L. Waldner, G. J. Pielak, B. Durham, F. Millett, *Biochemistry* **1996**, *35*, 15107–15119.
75. H. Mei, K. Wang, N. Peffer, G. Weatherly, D. S. Cohen, M. Miller, G. Pielak, B. Durham, F. Millett, *Biochemistry* **1999**, *38*, 6846–6854.
76. J. M. Mauro, L. A. Fishel, J. T. Hazzard, T. E. Meyer, G. Tollin, M. A. Cusanovich, J. Kraut, *Biochemistry* **1988**, *27*, 6243–6256.
77. R. E. Sharp, S. K. Chapman, G. A. Reid, *Biochemistry* **1996**, *35*, 891–899.
78. M. Tegoni, J. M. Janot, F. Labeyrie, *Eur. J. Biochem.* **1986**, *155*, 491–503.
79. M. Tegoni, M. C. Silvestrini, F. Labeyrie, M. Brunori, *Eur. J. Biochem.* **1984**, *140*, 39–45.
80. M. Walker, G. Tollin, *Biochemistry* **1991**, *30*, 5546–5555.
81. J. T. Hazzard, C. A. McDonough, G. Tollin, *Biochemistry* **1994**, *33*, 13445–13454.
82. M. Tegoni, M. C. Silvestrini, M. A. Guigliarelli, M. Brunori, P. Bertrand, *Biochemistry* **1998**, *37*, 12761–12771.
83. F. Labeyrie, J. C. Beloell, M. A. Thomas, *Biochim. Biophys. Acta* **1988**, *953*, 134–141.
84. M. Tegoni, C. Cambillau, *Protein Sci.* **1994**, *3*, 303–313.
85. M. C. Walker, G. Tollin, *Biochemistry* **1992**, *31*, 2798–2805.
86. P. Brzezinski, B. G. Malmström, *Biochim. Biophys. Acta* **1987**, *894*, 29–38.

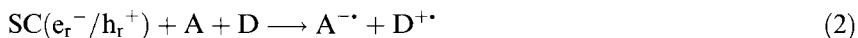
87. B. M. Hoffman, M. A. Ratner, *J. Am. Chem. Soc.* **1987**, *109*, 6237–6243.
88. C. S. Miles, N. Rouviere-Fourmy, F. Lederer, F. S. Mathews, G. A. Reid, M. T. Black, S. K. Chapman, *Biochem. J.* **1992**, *285*, 187–192.
89. M. Tegoni, S. Begotti, C. Cambillau, *Biochemistry* **1995**, *34*, 9840–9850.
90. C. Kisker, H. Schindelin, A. Pacheco, W. Wehbi, R. M. Garrett, K. V. Rajagopalan, J. H. Enemark, D. C. Rees, *Cell* **1997**, *91*, 973–983.
91. E. P. Sullivan, J. T. Hazzard, G. Tollin, J. H. Enemark, *Biochemistry* **1993**, *32*, 12465–12470.
92. A. Pacheco, J. T. Hazzard, G. Tollin, J. H. Enemark, *J. Biol. Inorg. Chem.* **1999**, in press.
93. L. O. Narhi, A. J. Fulco, *J. Biol. Chem.* **1986**, *261*, 7160–7169.
94. S. Govindaraj, T. L. Poulos, *J. Biol. Chem.* **1997**, *272*, 7915–7921.
95. S. Govindaraj, T. L. Poulos, *Biochemistry* **1995**, *34*, 11221–11226.
96. S. Govindaraj, T. L. Poulos, *Protein Sci.* **1996**, *5*, 1389–1393.
97. K. G. Ravichandran, S. S. Boddupalli, C. A., Hasemann, J. A. Peterson, J. Deisenhofer, *Science* **1993**, *261*, 731–736 (1993).
98. H. Y. Li, T. L. Poulos, *Nature Struct. Biol.* **1997**, *4*, 140–146.
99. I. Sevrioukova, H. Li, H. Zhang, J. A. Peterson, T. L. Poulos, *Proc. Natl. Acad. Sci. USA* **1999**, *96*, 1863–1868.
100. R. Raag, T. L. Poulos, *Biochemistry* **1989**, *28*, 917–922.
101. S. Modi, M. J. Sutcliffe, W. U. Primrose, L. Y. Lian, G. C. K. Roberts, *Nature Struct. Biol.* **1996**, *3*, 414–417.
102. S. N. Daff, S. K. Chapman, K. L., Turner, R. A. Holt, S. Govindaraj, T. L. Poulos, A. W. Munro, *Biochemistry* **1995**, *36*, 13816–13823.
103. J. T. Hazzard, S. Govindaraj, T. L. Poulos, G. Tollin, *J. Biol. Chem.* **1997**, *272*, 7922–7926.
104. M. A. McLean, H. Yeom, S. G. Sligar, *Biochimie* **1996**, *78*, 700–705.
105. R. E. Sharp, S. K. Chapman, *Biochim. Biophys. Acta* **1999**, *1432*, 143–158.

6 Novel Organic Syntheses Through Semiconductor Photocatalysis

Horst Kisch and Matthias Hopfner

6.1 Scope and Introduction

Photocatalysis at semiconductor surfaces is a growing field of photochemistry. In addition to its prime importance for the photochemical conversion and storage of solar energy, semiconductor photocatalysis per se is a promising part of general chemistry since it combines photochemistry with electrochemistry and heterogeneous catalysis. Different from homogeneous electron transfer photosensitization by a dissolved molecule, heterogeneous semiconductor photocatalysis opens up the possibility of performing reductive and oxidative reactions simultaneously. This is due to the fact that the light-generated electron–hole pair (e^-/h^+) is transformed into reducing and oxidizing surface centers (e_r^-/h_r^+ , Eq. 1), from which interfacial electron transfer (IFET) with adsorbed substrates (Eq. 2) may successfully compete with recombination (Eq. 3).



Thus, the semiconductor undergoes a double-electron exchange (Eq. 2). In contrast, in the homogeneous case sensitization proceeds via two consecutive one-electron steps (Eqs. 4–6):



In both cases the primary redox intermediates $A^{\cdot-}$ and $D^{\cdot+}$ are transformed into stable products.

The term *photocatalysis* implies that light and a catalyst are necessary to induce or accelerate a chemical transformation [1–9]. This definition includes *photosensitization*, ‘a process by which a photochemical alteration occurs in one molecular entity as a result of initial absorption of radiation by another molecular entity called photosensitizer’ [10], but it excludes the photoacceleration of a stoichiometric thermal reaction, exergonic or endergonic, and irrespective whether it occurs in homogeneous solution [11] or at the surface of an illuminated electrode [12], otherwise any photoreaction would be catalytic. Despite many attempts, there is no general accepted *mechanistic* definition of photocatalysis. It seems more appropriate to use a phenomenological definition by analogy to thermal catalysis. In the latter case a reaction is called *catalytic* when the turnover number, expressed as number of product molecules formed per number of active sites, is >1 [13]. When it is ≤ 1 , the reaction may be termed *assisted*, as commonly done in homogeneous organo-transition metal chemistry [14, 15]. The crucial point, of course, is that the number of active sites of a catalyst powder is usually unknown [16]. Therefore, in almost all cases the differentiation between a catalytic and assisted photoreaction may be impossible. Accordingly, many of the photoreactions conducted in the presence of semiconductor powders and claimed to be ‘photocatalytic’, in reality are semiconductor-assisted photoreactions [17]. An important example is the titanium dioxide-assisted photoreduction of dinitrogen [18]. What is then the difference between *photosensitization* and *photocatalysis*? Essentially there is none, except in a historical sense, since it became common to use the latter term when the sensitizer is a transition metal complex or a semiconductor particle. This usage has the advantage to signal the reader immediately that sensitization involves a complicated multi-step mechanism. In semiconductor photocatalysis the adsorbed substrate can be considered as a surface complex which is expected to change its structure even when light absorption occurs only by the photocatalyst. In addition to this direct effect of light, the original surface may be restructured to a catalytic surface during an induction period, a process well known from thermal heterogeneous catalysis.

Physico-chemical aspects of charge and current generation at semiconductor electrodes in contact with a liquid electrolyte are the classical topic of photoelectrochemistry [19]. They are treated in other parts of this book. Induced by the early observation of Bard et al. that irradiation of titania powder suspended in a liquid solvent promotes electron-transfer reactions of substrates in solution [20–23], a great variety of chemical transformations in the presence of semiconductor powders or colloids have been reported and summarized in recent review articles [24–27]. Some of these reactions are related to prebiotic chemistry, such as the TiO_2 - [18, 28] or CdS-assisted [29] photoreduction of N_2 , the generation of amino acids from CH_4 , N_2 and H_2O in the presence of platinized TiO_2 [30a] and the TiO_2 - or CdS-induced peptide formation from glycine [30b]. The fading of paints [31] and the detoxification of water and air [32] illustrate important technical and environmental aspects of semiconductor photocatalysis. Common to all these chemical processes is that well known products were formed in very low yields and identified spectroscopically rather than isolated. Although high quantum yields were reported in a few cases, it is recalled that quantum yields are measured at short irradiation times and therefore do not give any information on the synthetic usefulness of the

reaction. In general, photocorrosion, the self-destruction of the semiconductor by light-generated charges, often prevents a long-term reaction, indispensable to obtain the products on a preparative scale. In this chapter we shall therefore focus on the question of whether semiconductor photocatalysis at all is a useful alternative synthesis method and whether or not it may open novel pathways for chemical synthesis.

6.2 Heterogeneous Photocatalysis with Semiconductor Powders

6.2.1 Fundamentals

The mechanistic principles which enable a semiconductor powder, suspended in a solution of substrates, to catalyze a photoreaction originate in the field of photoelectrochemistry. For a critical discussion of the basic assumptions made in the deduction of the resulting theories and their relevance to catalysis, the reader is referred to recent review articles [33–35]. The use of a metallized semiconductor particle as a kind of ‘short-circuit’ micro-photoelectrochemical cell was introduced through the work of Kreutler and Bard on the photo-Kolbe reaction [36]. Differences from the macroelectrodes employed in more conventional photoelectrochemistry have been discussed [34, 37–40].

Almost all of the hitherto observed photoreactions can be rationalized by the simplified mechanistic scheme as depicted in Figure 1 for a platinized semiconductor particle. It is noted that platinization in most but not all cases is required in order to obtain acceptable reaction rates.

The light-generated electron–hole pair may undergo primary recombination through radiative and non-radiative pathways (process 1, Figure 1), or may be

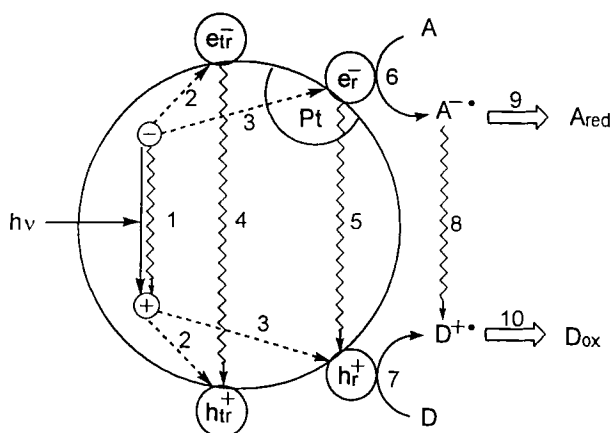


Figure 1. Schematic description of the photoredox reaction $A + D = A_{red} + D_{ox}$ catalyzed by a platinized semiconductor, a typical example of semiconductor photocatalysis type A; for secondary back electron transfer, see Eqs. 7 and 8.

trapped at unreactive (e_{tr}^-/h_{tr}^+) or reactive (e_r^-/h_r^+) surface sites (processes 2 and 3, Figure 1). For colloidal TiO_2 irradiated at low laser intensity, where about five electron–hole pairs are generated per particle, hole trapping occurs in a few hundred nanoseconds whereas electron trapping proceeds in the picosecond time regime. Secondary recombination (processes 4 and 5, Figure 1) is rather slow with a lifetime of the electron–hole pair in the range of 2 μs [41]. In competition with the recombination from reactive centers are the IFET processes (processes 6 and 7 in Figure 1) which afford the radical ions $A^{\cdot-}$ and $D^{\cdot+}$. From picosecond laser flash experiments at CdS colloids it was found that the IFET from e_r^- to an adsorbed viologen acceptor is finished within 18 ps whereas the IFET from adsorbed diethyldithiocarbamate to h_r^+ occurs within 200 ps [42]. Since the diameter of the semiconductor particles in most cases is smaller than the space-charge region, not band bending but competition between the two IFET reactions and the secondary recombination (process 5, Figure 1) is responsible for charge separation. This mechanism of charge separation is supported by the oxidation of alcohols at titania powder electrodes [43, 44]. The primary redox products $A^{\cdot-}$ and $D^{\cdot+}$ have to undergo a fast conversion to the final products A_{red} and D_{ox} in order to avoid primary (process 8, Figure 1) and secondary back-electron transfer (Eqs. 7 and 8):



Thus, in general, a reduced and an oxidized product are obtained, in complete analogy with a classical electrochemical reaction. Except for a very few examples, almost all reactions photocatalyzed by semiconductors fall within this scheme and we have proposed to classify such reactions as *semiconductor photocatalysis type A* [45].

It is generally assumed that owing to the short lifetime of the light-generated charges, only adsorbed substrates can undergo an efficient chemical reaction. However, in the case of the titania-photocatalyzed oxidation of benzyl alcohol and of rhodamine B weakly adsorbed substrates react faster than strongly adsorbed substrates [46–48]. However, this does not necessarily imply that the IFET occurs over a large distance, or that an initially formed OH radical oxidizes the substrate in the bulk solution, since the rate of a semiconductor-catalyzed photoreaction depends on many parameters not known in detail (see below). In Figure 2 a simple corresponding energy profile is displayed, illustrating substrate adsorption and product desorption assuming that the IFET is rate determining.

6.2.2 Thermodynamic Aspects

The thermodynamic feasibility of the IFET reactions can be predicted by comparing the redox potentials of e_r^- and h_r^+ with those of the two substrates A and D. Whereas the latter are easily accessible [49], this is not the case for the former. However, their values can be estimated by assuming that they are positioned close

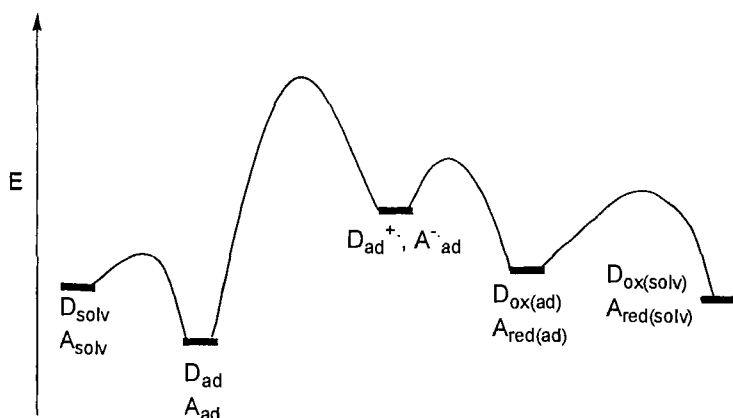


Figure 2. Energy profile of the reaction depicted in Figure 1.

to the edges of conduction and valence band. Figure 3 summarizes band-edge positions of TiO_2 , ZnS and CdS at pH 7 as measured photoelectrochemically. For single crystals in aqueous systems they usually shift cathodically with increase in pH by approximately 0.06 V per pH unit, as reported for ZnS [51], CdS [52] and TiO_2 [53]. In neutral aqueous solution the values for the conduction (E_{cb}) and valence band edges (E_{vb}) of ZnS [51, 54] and CdS [55] single crystals are $-1.84/+1.84$ V and $-0.9/+1.5$ V (vs. NHE), respectively. In addition to this pH dependence, surface impurities, adsorbed compounds and the change to organic solvents may induce strong band shifts. In the case of CdS it has been reported that removal of

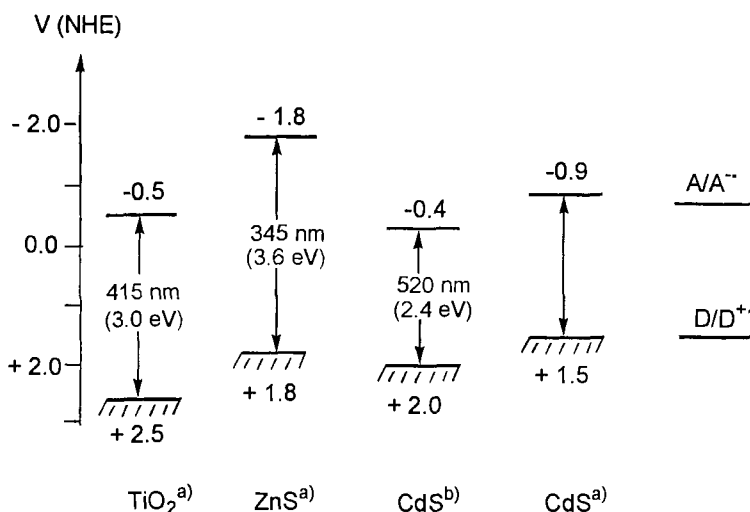


Figure 3. Band edge positions of some n-type semiconductors at pH 7. (a) Single crystal; (b) powder.

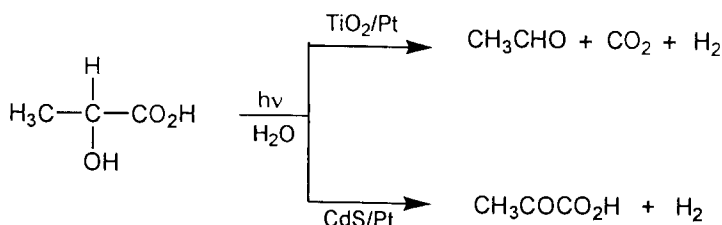


Figure 4. Influence of semiconductor nature on the chemoselectivity of lactic acid photo-oxidation.

traces of elemental sulfur and cadmium from the surface results in a cathodic shift of 1 V! [56]. Addition of neutral RSH has no influence whereas the charged RS^- shifts the band positions by 0.4 V cathodically [57]. The same shift of 0.4 V is observed when neutral water is replaced by acetonitrile as the solvent [25]. In the case of a TiO_2 powder electrode the latter shift amounts to 1.0 V [58]. Apparent differences in band positions of single crystals and powders are usually due to the presence of surface states in the latter [56]. In general, the IFET is assumed to occur from these surface states.

From the discussion above it follows that for a given semiconductor-photocatalyzed reaction the variation of catalyst preparation, kind of solvent and substrate adsorption may induce a shift of band positions. The estimation of the driving forces for the two IFET reactions is therefore connected with a large uncertainty. However, neglecting possible kinetic barriers, in many cases it rationalizes the observed experimental results. An example is the photo-oxidation of lactic acid. Whereas platinized TiO_2 catalyzes oxidation to acetaldehyde, platinized CdS induces oxidation of only the OH group affording pyruvic acid (Figure 4). This is in accordance with the less oxidizing property of $h\nu^+$ since the valence band edge of CdS is located about 0.5 V more cathodic as compared with TiO_2 [59]. The other possibility for introducing chemoselectivity is to vary the reduction potentials of the substrates but not to change the semiconductor. It was reported that the introduction of two methoxy groups in the *para*-positions of benzophenone shifts the reduction potential to the negative of the conduction band edge of highly pure cadmium sulfide and thus prevents the reduction to alcohols as observed with other aromatic ketones [60].

6.2.3 Kinetic Aspects

Owing to the heterogeneity of the reaction system, kinetic experiments are not as straightforward to conduct and interpret as in homogeneous photochemistry. Especially quantum yield determinations are ambiguous since it is difficult to correct for the amount of light scattered by the photocatalyst powder. Various attempts have been made to overcome these difficulties [61–63] in order to allow comparisons of quantum yields measured by different experimentalists. However, no general agreement has been reached so far.

The following qualitative considerations illustrate the problem of quantitative comparisons. Assuming that the efficiency of formation of the reactive electron-hole pair (η_r), the efficiency of the IFET (η_{ifet}) and the efficiency of product formation from the primary redox products (η_p) are given by the ratio of the rate constants for formation and consumption of the corresponding intermediate (Eqs. 9–11; see Figure 1; k_{sb} denotes the rate constant for the secondary back-electron transfer according to Eqs. 7 and 8), the rate of reaction is obtained according to Eq. 12, where I_a denotes the intensity of absorbed light:

$$\eta_r = \frac{k_3}{k_1 + k_2 + k_3} \quad (9)$$

$$\eta_{\text{ifet}} = \frac{k_{6,7}}{k_5 + k_{6,7}} \quad (10)$$

$$\eta_p = \frac{k_{9,10}}{k_8 + k_{\text{sb}} + k_{9,10}} \quad (11)$$

$$\text{rate} = \Phi_p I_a = \eta_r \eta_{\text{ifet}} \eta_p I_a \quad (12)$$

Accordingly, the quantum yield of product formation, Φ_p , can be formulated as the product $\eta_r \times \eta_{\text{ifet}} \times \eta_p$ and it is difficult to prove which term is decisive. The last term may be relatively independent on small changes of the semiconductor properties, whereas the two other terms may change considerably. Fairly minor alterations during the synthesis of the powder can lead, e.g., to different amounts of adsorbed ions and therefore vary the photophysical properties of the semiconductor-liquid interface. Furthermore, when the quantum yields for various substrates are compared, it is difficult to relate changes to a specific process of the multi-step reaction.

The dependence of quantum yield on the intensity of the absorbed light can be characterized by two limiting cases [64]. At high light intensity [65], the quantum yield increases linearly with the square root of the reciprocal intensity. This dependence is typical for homogeneous and heterogeneous photoreactions where recombination of primary products is predominant. It has been observed for the TiO_2 -catalyzed photooxidation of 2-propanol [66], the TiO_2/Pt -catalyzed photo-Kolbe reaction [67] and the CdS -catalyzed photoisomerization of *cis*-stilbene [68]. At low light intensity the quantum yield becomes independent of I_a and the reaction rate increases linearly with the first power of I_a . This is observed when the above-mentioned reactions [66, 68] are conducted at low light intensities.

From the discussion above, it is obvious that Φ_p may differ considerably upon minor changes in photocatalyst preparation and solution composition. Higher light intensities may increase recombination [69] and photophysical processes such as emission are strongly influenced by adsorbed impurities [70, 71]. It has been reported that increasing grinding times of ZnS powder enhance its photocatalytic activity in the isomerization of olefins [72] through the generation of reactive surface states; once formed, these catalyze the $[2 + 2]$ cycloaddition of phenyl vinyl ether even in the absence of further irradiation [73]. It is therefore not surprising that quantum yields and chemoselectivities reported by one research group may

differ from those obtained by another group. Furthermore, accurate measurement of Φ_p is difficult in these heterogeneous systems [61] owing to problems of light reflection and scattering, which may lower the effective absorbed light intensity by 15–80 % [62].

Increasing the temperature may influence the slowest chemical reaction step and the adsorption equilibria of substrates and products. Depending on the relation of the two latter steps and on the temperature range investigated, the measured activation energy, E_a , may be zero or larger or smaller than zero [74–79]. Since these factors depend on the detailed nature of the photocatalyst, minor modifications may induce variations of E_a . Accordingly, values of 1.7 and 4.2 kcal mol⁻¹ were reported for two different CdS samples used in the photodimerization of *N*-vinylcarbazole [80].

6.2.4 Surface Area and Particle Size

For the influence of the specific surface area of the semiconductor powder on the rate of product formation, two opposite effects are of major importance [81]. One is concerned with the rate of electron–hole recombination which increases linearly with surface area, and accordingly the reaction rate should decrease. The other is a linear increase in the reaction rate of the reactive electron–hole pair with the adsorbed substrates, which should increase product formation. It is therefore expected that, depending on the nature of semiconductor and substrates, the reaction rate, or Φ_p , may be constant, increase or decrease with increasing surface area. This is nicely reflected by the CdS/Pt-catalyzed photoreduction of water by a mixture of sodium sulfide and sulfite. The highest Φ_p values are observed with small surface areas and are constant up to 2 m² g⁻¹. From there a linear decrease to almost zero at a specific surface area of 6 m² g⁻¹ takes place. Upon further increase to 100 m² g⁻¹ this low quantum yield stays constant [82].

In addition to the rate, the chemoselectivity may also depend on the surface area, which is usually determined by the particle size [83]. Especially the possibility of whether one or more electrons are transferred from and to adsorbed substrates may be decided by the particle size as illustrated by the ZnS-catalyzed photo-oxidation of aqueous ethanol [84]. As summarized in Figure 5, only the nanometer-sized ZnS

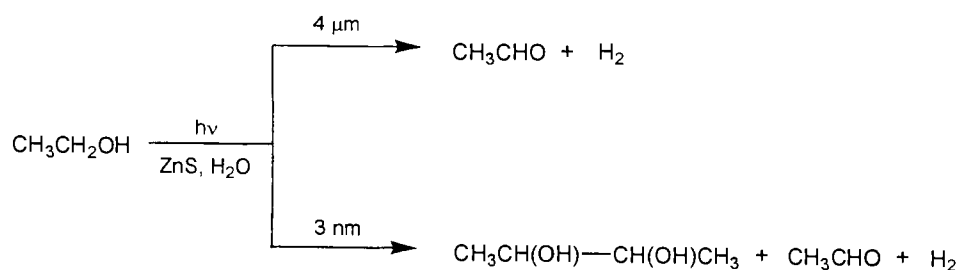


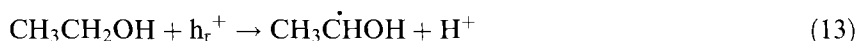
Figure 5. Influence of semiconductor particle size on the chemoselectivity of ethanol photo-oxidation.

Table 1. Some basic data for charge generation processes in nanometer- and micrometer-sized ZnS [84].

Parameter	Particle diameter	
	3 nm	4 μm
Absorption cross-section at 300 nm/cm ²	5.4×10^{-16}	1.25×10^{-7}
Photon flux/cm ² s ⁻¹	3.4×10^{16}	4.1×10^{17}
e ⁻ /h ⁺ pairs per particle and second, N/s^{-1}	18	5×10^{10}
Time interval $\Delta t = N^{-1}$	54 ms	20 ps

induces the formation of the 1h⁺ oxidation product 2,3-butanediol, whereas the 2h⁺ product acetaldehyde is produced by both photocatalysts.

Owing to the large difference in the absorption cross-sections of the 3 nm and 4 μm particles, the number of electron–hole pairs generated per particle and per second is estimated as 18 and 5×10^{10} , respectively (Table 1). Accordingly, the time interval Δt between the successive absorption of two photons is 54 ms and 20 ps for the nano- and microscale particles, respectively. Hence the chance of the semiconductor exchanging a second electron–hole pair with the substrates should be much greater at the larger particle. In agreement with this reasoning, the intermediate α -hydroxyethyl radical generated at the micrometer particle by the first reactive hole (Eq. 13) is immediately oxidized to acetaldehyde by the second hole (Eq. 14) and has no possibility of dimerizing to 2,3-butanediol or disproportionating to ethanol and acetaldehyde. In sharp contrast, considerable amounts of the diol are produced at the nanometer particle.



6.2.5 Photocorrosion

In 1922, Lenard [85] investigated the unfavorable darkening of the white pigment lithopone, a mixture of zinc sulfide and barium sulfate, that occurred upon prolonged exposition to sunlight. He assumed that the photocorrosion reaction afforded sulfur and metallic zinc. Shortly afterwards it was shown that UV light and the presence of water are necessary to observe this process [86]. Quantitative investigations by Platz and Schenk [87] revealed the additional formation of hydrogen, zinc sulfate and zinc hydroxide. The decomposition of photoexcited ZnS into its elements seems to be a consequence of the quasi-element electronic configuration, 'Zn(0)S(0)', of the lowest lying electron–hole pair [88]. Owing to the highly covalent character of the Zn–S bond, the effective charges of zinc and sulfur can be assumed to be +1 and –1, respectively [88–90]. Since the valence and conduction bands have

sulfur 3p and zinc 4s character, respectively [91, 92], the calculated quasi-element nature of excited ZnS becomes explainable.

The mechanism of photocorrosion seems to be the same for zinc and cadmium sulfide. For the latter it was investigated in detail for colloids [26] and crystals as discussed in the following [56]. In the absence of air, anodic photocorrosion (Eq. 15):



affords elemental sulfur and cadmium ions which are reduced to cadmium metal upon prolonged irradiation (Eq. 16):



This latter reaction competes with the reduction of lattice metal ions (Eq. 17):



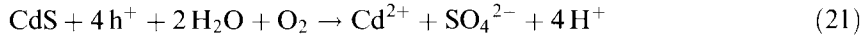
In the case of ZnS or metallized CdS powder, the reduction of water is a further competitive process (Eq. 18):



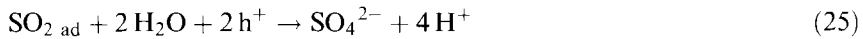
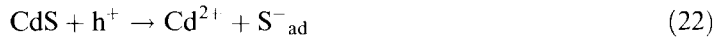
In the presence of air, at short illumination times the overall reaction is



with the cathodic and anodic parts according to Eqs. 20 and 21, respectively:



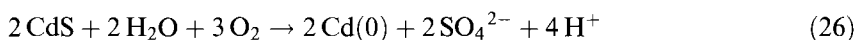
The anodic process consists of reactions (22)–(25), which are based on detailed comparative photocorrosion studies at single-crystal electrodes and at powder suspensions:



In the first step, lattice sulfide is oxidized to the S^- radical (Eq. 22), which then reduces oxygen according to Eq. 23. The resulting sulfur dioxide radical anion is

finally oxidized to the sulfate ion (Eqs. 24 and 25). Note the surprising feature that oxygen is reduced via a preceding *primary oxidation* step (Eq. 22). The intermediate S^- radical has been detected on ZnS powder by ESR [93, 94] and on colloidal zinc and cadmium sulfide by pulse radiolysis with UV–VIS detection (absorption maximum around 500 nm) [26, 95]. However, the sulfide radical anion can be also formed via the *primary reduction* $S + e^- \rightarrow S^-$ when elemental sulfur is present as an impurity.

At prolonged irradiation times in the presence of oxygen, the reduction of cadmium ions according to Eq. 16 becomes more important and the overall corrosion reaction follows Eq. 26:



All these photocorrosion processes are, of course, undesirable and it is obvious that their relative importance depends strongly on the presence of surface states which may facilitate recombination or redox reactions with adsorbed substrates. It is well known from ESR [69, 70, 94] and emission spectra [94] that most of these metal sulfide powders contain surface states. They are introduced during preparation of the powder as a result of lattice defects [72, 96], trapped holes [94], surface impurities [97] and metallization [38], and during the actual catalytic reaction as a consequence of irradiation and substrate adsorption. The stabilizing effect of platinization is exemplified by Figure 6 for the ZnS-catalyzed reduction of water in the presence of sodium formate [98]. Note that platinum does not accelerate the reaction but doubles the time of constant catalytic activity from 1 to 2 days. Similarly, the apparent product quantum yield of the 2,5-DHF dehydrodimerization is not increased but slightly decreases when platinizes ZnS is the photocatalyst [97].

6.2.6 Characterization of ZnS and CdS

From the results presented above it follows that catalytic activity and chemoselectivity of a semiconductor photocatalyst should depend on intimate details of the preparation method. In addition to careful description of these synthetic details, it is important to characterize the powder obtained by bulk and surface elemental analysis, by determination of crystal structure, specific surface area and surface charge, by ESR and electronic absorption and emission spectroscopy and by photoelectrochemical experiments to prove the semiconducting properties. The latter are of special importance in order to disfavor a general heterogeneous catalysis mechanism which usually does not involve simultaneous reductive and oxidative interfacial electron transfer steps [99, 100]. Their involvement may be demonstrated by the effects of electron and hole scavengers added to the reacting system. In the following we summarize the most important physical properties of the ZnS and CdS powders employed as photocatalysts in the syntheses of novel organic compounds.

Zinc sulfide was prepared from sodium sulfide or thiourea and zinc sulfate. The resulting porous powders contain about 2–3 % [101] water, have specific surface areas in the range 100–170 m² g⁻¹ and consist of 1–10 μm particles which are

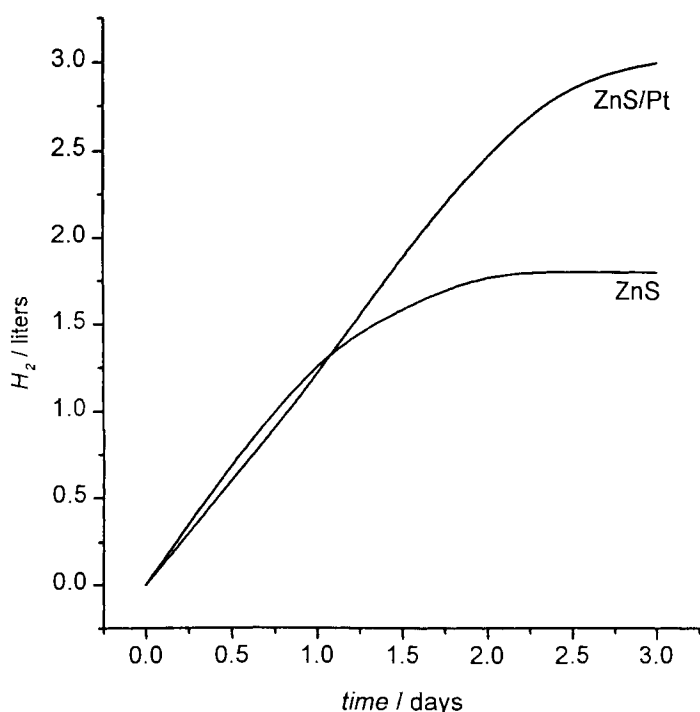


Figure 6. Effect of platinization on the ZnS-catalyzed photoreduction of water by sodium formate.

composed of cubic nanocrystals [102]. Elemental analyses of the bulk materials afford the ratio $\text{Zn:S} = 1.00:0.97$, whereas surface analyses reveal values of $\text{Zn:S} = 1.00:1.35$ to $1.00:1.60$. This significant excess of surface sulfur may be responsible for the pronounced photostability of these samples even when irradiated in an aqueous suspension in the absence of any other substrate. In contrast, zinc sulfides which have a surface excess of zinc immediately suffer photocorrosion [97]. Diffuse reflectance spectroscopy indicates a weak sub-bandgap absorption starting at about 400 nm followed by the steep onset of the band-to-band absorption at 360 nm; in some cases a weak absorption maximum is observable at 450 nm, most likely due to the presence of a surface sulfide species [97]. Accordingly, the emission spectrum of the powder contains, in addition to the bandgap emission at about 360 nm, broad bands around 400 and 490 nm which originate from recombination of the electron-hole pair scavenged at shallow and deep traps within the bandgap [97, 103]. Further emissions at 525 and 690 nm are due to traces of zinc oxide; at higher concentrations, ZnO completely inactivates the photocatalyst. Slightly different to the dry powders, the emission spectrum of an aqueous ZnS suspension exhibits, in addition to the band-to-band emission, only one further band at 430 nm. This *self-activated* emission [105, 106] is generated by excess surface zinc ions (sulfur vacancies) as indicated by its disappearance upon addition of sulfide ions [107]. From the difference

from the bandgap energy of 3.6 eV one can estimate that the corresponding surface state is located about 0.7 eV below the conduction band edge, i.e., at a potential of -1.1 V (at pH 7); a value of 1.0 V has been cited for another zinc sulfide sample [84].

Time-resolved emission spectra exhibit multi-exponential decay at 340 and 437 nm corresponding to lifetimes in the range 0.1–10 ns [107]. The longer lifetimes agree with those reported for other ZnS powders [108] and for colloids [26, 94]. It is recalled that multi-exponential decay may originate not only in different emitting states but also in the presence of various particle sizes [109–111].

The n-type character of these zinc sulfides is indicated by the observation of an anodic photocurrent upon illumination of a powder-coated electrode. The action spectrum of the photocurrent parallels the wavelength dependence of the apparent quantum yield of the photoreduction of water by sodium formate, except that hydrogen evolution starts already in the sub-bandgap region at 370 nm, a wavelength where no photocurrent was observable [98].

Cadmium sulfide was prepared from sodium sulfide and an aqueous ammonia solution of cadmium sulfate. Similarly to the zinc sulfides, the powders obtained contain 2–3 % water, have specific surface areas of about $160\text{ m}^2\text{ g}^{-1}$ and consist of nanoscaled micrometer aggregates as illustrated by Figure 7 [112]. An anodic photocurrent is also observable for a CdS/ITO electrode as displayed for various excitation wavelengths in Figure 8. Addition of methanol induces photocurrent doubling with a factor of about two, irrespective of the energy of excitation. From measurement of the flat-band potential according to the slurry method [52, 113], the position of the conduction band edge at pH 7 is found to be at -0.4 V (vs. NHE) [114].

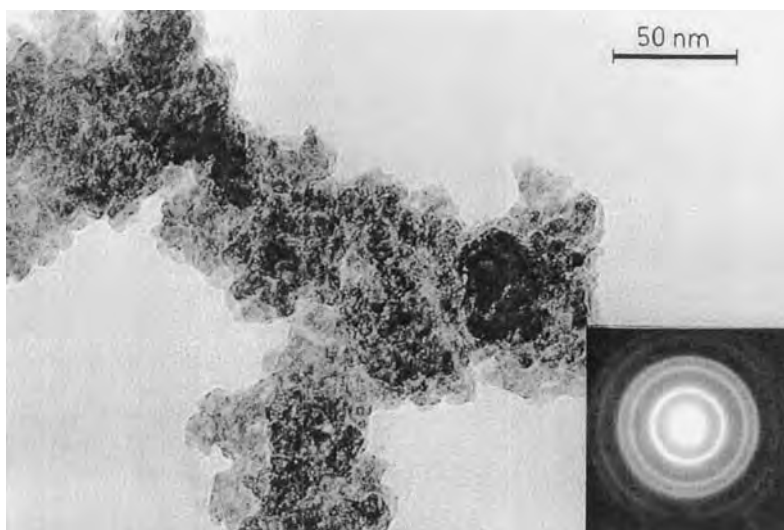


Figure 7. Transmission electron micrograph and electron diffraction pattern of CdS.

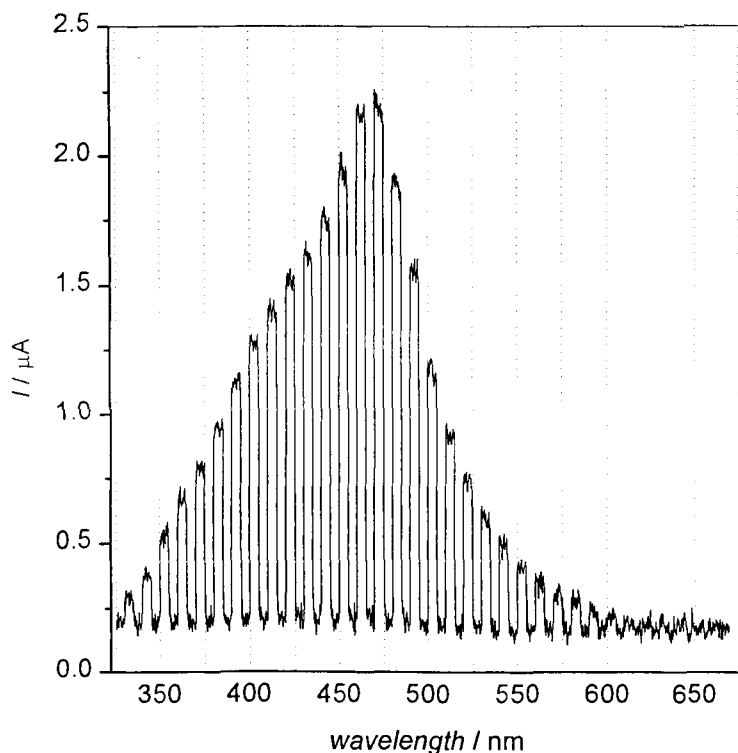


Figure 8. Photocurrent action spectrum of a CdS covered indium tin oxide (ITO) conducting glass electrode (0.5 V vs. Ag/AgCl) as obtained upon chopped irradiation (light and dark phases were 15 s); MeOH, 0.04 M NBu_4ClO_4 .

6.3 Semiconductor Photocatalysis Type A

6.3.1 Dealkylation, Cyclization and Hydroalkylation

Stimulated by the early work of Bard et al. on the TiO_2 -catalyzed photo-Kolbe reaction [36], many papers appeared in subsequent years dealing with *photocatalytic* organic reactions [115] in the presence of colloidal or suspended semiconductor particles. They include *cis-trans* isomerizations [68, 93, 116–119], valence isomerizations [120, 121], substitution and cycloaddition reactions [73, 80, 122–125], oxidations [126, 127], and reductions [128–130]. Characteristic of all these reactions is that in almost all cases well known compounds were formed, which were not isolated but only characterized by spectroscopic methods. The nature of the products can be rationalized within the mechanistic scheme of semiconductor photocatalysis type A, which means that at least one reduced and one oxidized compound are

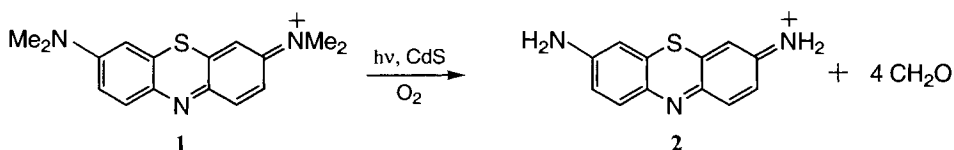


Figure 9. Exhaustive dealkylation of methylene blue photocatalyzed by CdS.

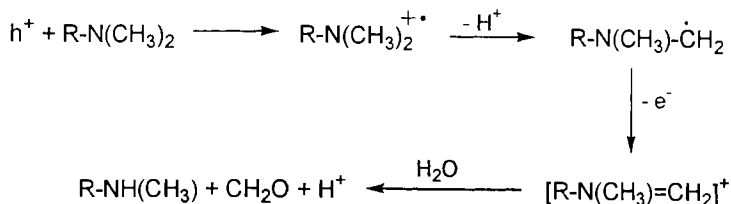


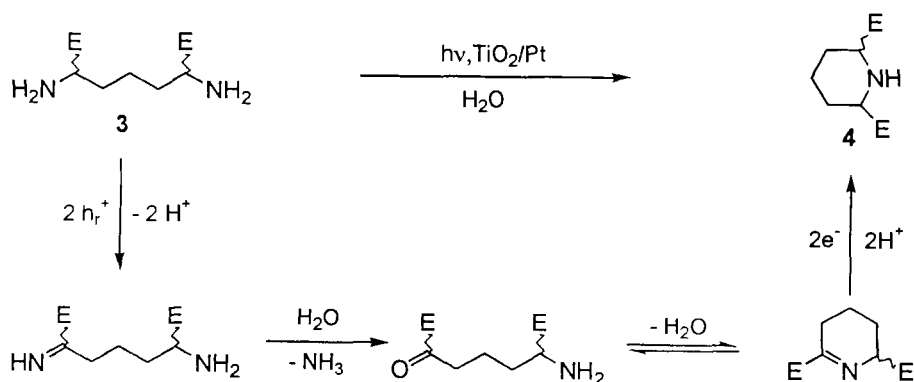
Figure 10. Exhaustive dealkylation: C–N bond cleavage of the of the intermediate radical cation.

obtained (see Figure 1). In most cases it is the oxidative part of the reaction where the organic substrate is involved. This means that the reactivity of the initially formed radical cation determines the kind of products formed finally. Typical reactions of radical cations are deprotonation, bond cleavage and electron transfer [131, 132]. An early example which illustrates two important mechanistic cases is the exhaustive photodealkylation of methylene blue and rhodamine B [133, 134] catalyzed by nonplatinized CdS (Figure 9) [135]. Photoexcitation of CdS is a prerequisite, since no reaction occurs when the dye **1** is absorbing exclusively.

In the primary reductive step, oxygen from air or Fe(III) ions function as electron acceptor. The radical cation $1^{+\bullet}$, generated in the oxidative counterpart, loses a proton, affording the strongly reducing α -amino radical (Figure 10), which injects an electron into the conduction band of CdS. Hydrolysis of the resulting iminium salt leads finally to the secondary amine. Repetition of this multi-step reaction affords the completely demethylated product **2**.

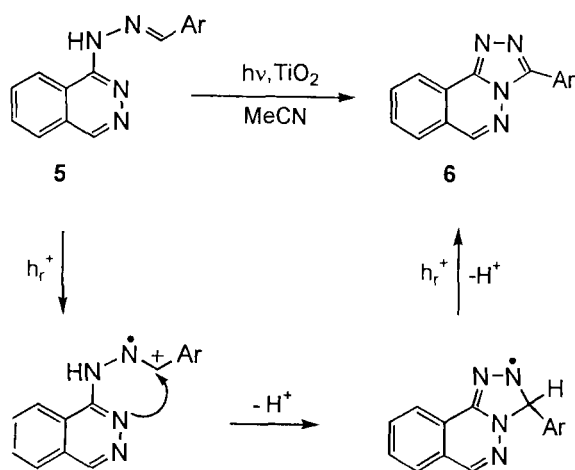
When methylene blue is replaced by rhodamine B, dealkylation occurs also if the dye is the light-absorbing species. In this case the reduction potential of the excited state is negative enough to inject an electron into the conduction band of CdS, followed by IFET to adsorbed oxygen. The remaining rhodamine radical cation is converted to the final product as summarized in Figure 10. This mechanistic case is rare since in general light is absorbed by the semiconductor and the radical cation is generated in the oxidative primary step through IFET from the substrate to the reactive hole (h_r^+). In addition to deprotonation via C–H cleavage, radical cations may be transformed to the corresponding radicals also by C–C, C–Si and other bond cleavages. The intra- or intermolecular consecutive reactions of these radicals usually determine the chemoselectivity of the overall reaction. Examples of *intra-molecular* reactions are the cyclizations of the diaminodicarboxylic acid **3** [136, 137] and the hydrazone **5** [138], both of which proceed via C–N coupling.

The postulated reaction sequences are summarized in Figures 11 and 12. It is



$E = \text{CO}_2\text{H}$

Figure 11. Cyclization of 1,5-diaminopimelic acid: intramolecular C–N bond formation of the intermediate radical cation.

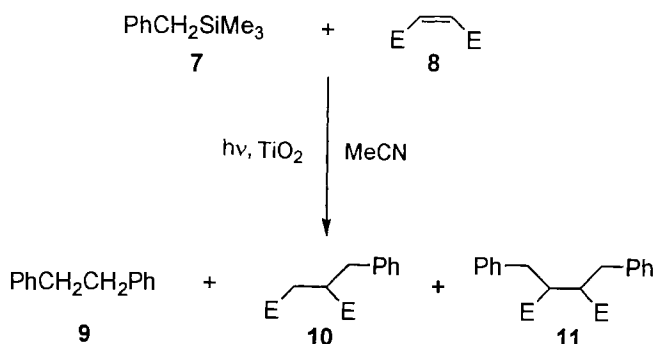


($\text{Ar} = p\text{-R-C}_6\text{H}_4$, $\text{R} = \text{H, Me, OMe, Br}$)

Figure 12. Cyclization of the hydrazone 5: intramolecular C–N bond formation of the radical cation.

assumed that water is reduced in the reductive part of the hydrazone cyclization. Note, that for both reactions two electron–hole pairs are necessary to produce one product molecule of 4 and 6 ($2 e^-/2 h^+$ process).

An example of an *intermolecular* consecutive reaction is the hydroalkylation of olefins [139, 140]. TiO_2 photocatalyzes the reaction of benzyltrimethylsilane



E = CO₂H

Figure 13. Hydroalkylation of maleic acid by benzyltrimethylsilane: C–Si bond cleavage of the intermediate radical cation followed by intermolecular addition of the generated radical to maleic acid.

(7) and maleic acid (8) to the hydroalkylation product 10; dibenzyl- (9) and 1,2-dibenzylsuccinic acid (11) are formed as by-products (Figure 13). It is proposed that in the reductive primary step 8 is reduced to the relatively stable radical anion 8^{•−}. The oxidatively formed radical cation 7^{•+} undergoes a fast C–Si bond cleavage to Me₃Si⁺ and PhCH₂[•]. Addition of the latter to 8 followed by proton-coupled reduction by 8^{•−} or e_r[−] affords 10. In contrast to the cyclizations mentioned above, only one electron–hole pair is required to obtain one molecule of the product 10 (1 e[−]/1 h⁺ process).

Hydrazone cyclization and hydroalkylation [138–140] are rare examples of reactions conducted on a preparative scale, since the products were isolated in milligram amounts and not just identified in solution. As already mentioned in Section 6.2.5, photocorrosion of the semiconductor photocatalyst often prevents its use in preparative chemistry. This is very true also for colloidal semiconductors; although the pseudo-homogeneous nature of their solutions allows one to conduct classical mechanistic investigations, until now they were too labile to be used in preparative chemistry [107, 141, 142]. In contrast to the above-mentioned reactions, in recent years we have isolated novel compounds on a gram-scale employing photostable zinc and cadmium sulfide powders as photocatalysts [97, 107, 143–145]. During this work we found also a new reaction type which was classified as *semiconductor photocatalysis type B* [45]. In contrast to type A reactions, where at least one oxidized and one reduced product is formed, type B reactions afford only one unique product, i.e., the semiconductor catalyzes a photoaddition reaction (see below).

6.3.2 Dehydrodimerization of Cyclic Enol/Allyl Ethers and Olefins

Irradiation of an aqueous 2,5-DHF suspension of ZnS ($E_{\text{bg}} = 3.6$ eV, $\lambda \leq 345$ nm) with UV light affords hydrogen and gram amounts of the hitherto unknown dehy-

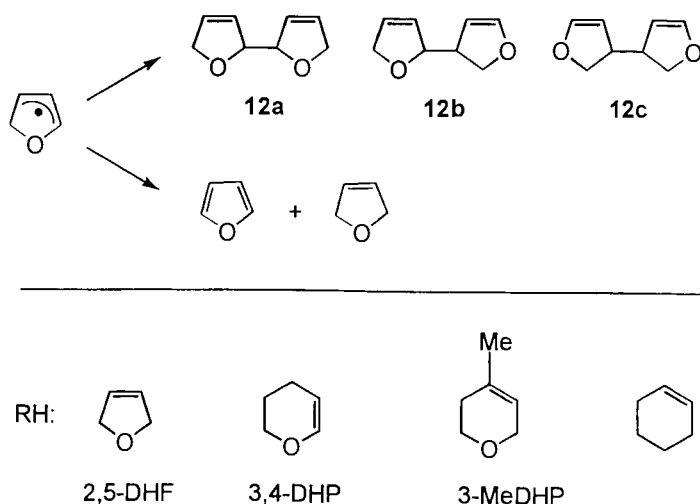
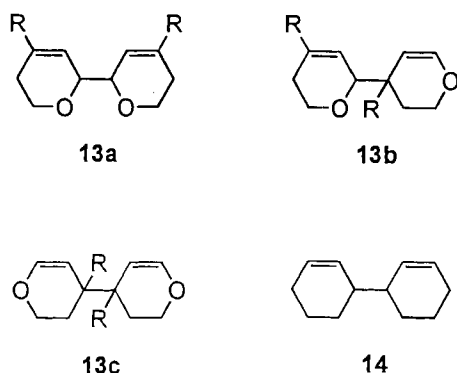


Figure 14. ZnS-photocatalyzed dehydrodimerization of 2,5-DHF: C–H bond cleavage followed by dimerization and to a very small extent by disproportionation of the generated radicals.

drodimers **12a–c** in isolated yields of 60 % (Figure 14) [143–145]. No reaction is observed in the absence of water and the initially evolved hydrogen gas contains about 90 % of D_2 when D_2O is employed. Colloidal zinc sulfide does not catalyze the dehydrodimerization [107]. The use of platinized CdS induces the reaction also with visible light, but with a lower rate and poorer yield [144]. The structures and statistical ratio of the three regioisomeric dehydrodimers suggest that the products are formed by dimerization of an intermediate dihydrofuryl radical. Accordingly, generation of this postulated radical through hydrogen abstraction by OH, produced by hydrogen peroxide photolysis in the absence of ZnS, also affords the dehydrodimers. However, in addition, 3-hydroxytetrahydrofuran is formed by addition of OH to the double bond and subsequent H-abstraction from 2,5-DHF. In sharp contrast to this result, no 3-hydroxytetrahydrofuran is detected in the ZnS-catalyzed photoreaction. The formation of the products can be rationalized within the scheme for *semiconductor photocatalysis type A* as depicted in Figure 1. In the reductive reaction step water is reduced to hydrogen (Eq. 27), whereas in the oxidative part 2,5-DHF is oxidized to the dihydrofuryl radical and a proton (Eq. 28):



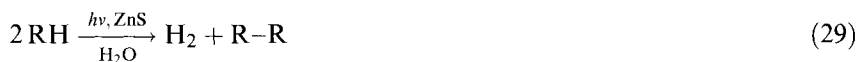
According to this, although water is reduced, it should not be consumed, since it is reformed as indicated by the sum of the two equations. In fact, even after production of 2–3 L of hydrogen, no water consumption could be measured. Further support stems from the observation that the initially observed D_2 content of 90 % drops to 40 % after evolution of 1 L of hydrogen, whereas the sum of HD and H_2



R = H, CH₃

Figure 15. Dehydrodimers isolated from the ZnS-photocatalyzed reactions of 3,4-DHP, 3-MeDHP and cyclohexene.

increased from 10 to 60 % [145]. From these results it is obvious that the formation of D₂ from D₂O in 'sacrificial' systems for water reduction is a necessary but not sufficient criterion for 'permanent' water cleavage [146].



Since the dehydrodimers **12a–c** were not known previously, this reaction is the first example of the preparation of a novel compound through semiconductor photocatalysis. The analogous products **13** and **14** are obtained from 3,4-dihydropyran (3,4-DHP), 3-methyl-2,3-dihydropyran (3-MeDHP) and cyclohexene in isolated yields of 30–60 % (Eq. 29, Figures 14 and 15) [97]. 1,4-Dioxane is not dehydrodimerized, contrary to in situ-prepared zinc sulfide, which otherwise photocatalyzes the same reactions [147].

To unravel the detailed mechanism, substrate adsorption, quenching, inhibition and kinetic studies were conducted for the ZnS-catalyzed photodehydrodimerization of 2,5-DHF [107, 148]. A plot of the amount of 2,5-DHF adsorbed (n_{eq}) against the residual concentration in solution (c_{eq}) exhibits saturation plateaus at $n_{\text{eq(max)}}$ of 2.8×10^{-3} and $65 \times 10^{-3} \text{ mol g}^{-1}$. The first plateau is due to the formation of a mixed solvent–solute surface monolayer and the second corresponds to multilayer adsorption. Assuming that the formation of the monolayer can be described by competitive adsorption between water and 2,5-DHF, the data can be analyzed according to Hiemenz (Eq. 30) [149]:

$$\frac{c_{\text{eq}}}{n_{\text{eq}}} = \frac{N_{\text{A}}\sigma^{\circ}}{A_{\text{sp}}K} + \frac{N_{\text{A}}\sigma^{\circ}}{A_{\text{sp}}}c_{\text{eq}} \quad (30)$$

A_{sp} and N_{A} denote the specific surface area of the powder and Avogadro's number, respectively, and σ° is the area covered by the molecule in the saturated solvent–

solute surface monolayer. A plot of $c_{\text{eq}}/n_{\text{eq}}$ vs. c_{eq} affords a straight line from which the adsorption constant K and the average area occupied by 2,5-DHF in the surface-solute monolayer are obtained as $170 \pm 30 \text{ L mol}^{-1}$ and 10.2 \AA , respectively. The latter value agrees well with 9.1 \AA as calculated for 2,5-DHF adsorbed *edge-on* to the ZnS surface [150]. From the surface density of zinc sites ($11.4 \times 10^{-6} \text{ mol m}^{-2}$) of cubic zinc sulfide [151a] and the specific surface area ($100\text{--}170 \text{ m}^2 \text{ g}^{-1}$) of the ZnS employed, one can estimate that the surface concentration of 2,5-DHF in the saturated monolayer is in the range $(1\text{--}2) \times 10^{-3} \text{ mol g}^{-1}$ [151b]. This agrees well with the measured value of $n_{\text{eq}(\text{max})}$. The small downfield shift of 1.5 ppm observed for the $\text{C}(\text{sp}^3)$ atoms of adsorbed 2,5-DHF by ^{13}C NMR suggests that the oxygen atom does not interact directly with zinc sites but rather indirectly through hydrogen bonding to coordinated water.

Only a very few studies have dealt with the problem of whether emissive (e_{tr}^- , h_{tr}^+) and reactive (e_{r}^- , h_{r}^+) surface sites are identical or not. As an example it is mentioned that diethylamine, although it is photo-oxidized at ZnS, does not affect the emission properties [108]. In order to clarify this important point for photo-dehydrodimerization, emission quenching and reaction inhibition studies were performed [107]. Addition of zinc or cadmium sulfate slightly increases or does not alter the emission intensity of an aqueous ZnS suspension, respectively; 2,5-DHF has no significant influence. Since, in contrast, both ions strongly inhibit the reaction, one can conclude that the emitting and reacting surface sites are different. A Stern–Volmer plot of the reduced reaction rate as a function of the initial inhibitor concentration affords a straight line only, when the concentration of *adsorbed* ions is employed (Figure 16). From the corresponding slopes, Stern–Volmer constants of 13×10^3 and $50 \times 10^3 \text{ M}^{-1}$ are calculated for Zn^{2+} and Cd^{2+} , respectively [152].

Inhibition by Cd^{2+} proceeds via competitive IFET (Eq. 31):



since even at the very low concentration of $3.9 \times 10^{-6} \text{ mol g}^{-1}$ the formation of elemental cadmium is observable; complete inhibition occurs at $6 \times 10^{-4} \text{ mol g}^{-1}$. This differs significantly from the effect of zinc ions in which case no elemental zinc could be detected, even at a high concentration of 0.8 mol g^{-1} . From this one can conclude that zinc ions either prevent the formation of the reactive electron–hole pair or efficiently promote its radiationless deactivation (Figure 17).

From detailed inhibition studies with various metal ions, it follows that Mn^{2+} , Fe^{2+} and Ni^{2+} accelerate the reaction whereas Cu^{2+} is weakly inhibiting [148]. At a given surface concentration of these ions, the relative reaction rate (v/v^0) increases approximately linearly with the exchange current density of hydrogen evolution at the corresponding metal electrode (Figure 18); there is no simple relation with the reduction potentials of the ions. This is clear experimental evidence that the water reduction at the photoexcited $\text{ZnS-M}_{\text{ad}}^{2+}$ surface occurs at small metal islands generated by photoreduction. Apparently, in the case of zinc the metal concentration is too low to be detected through the usually employed reduction of methylviologen [107].

From these results, the primary events at the ZnS surface can be summarized as

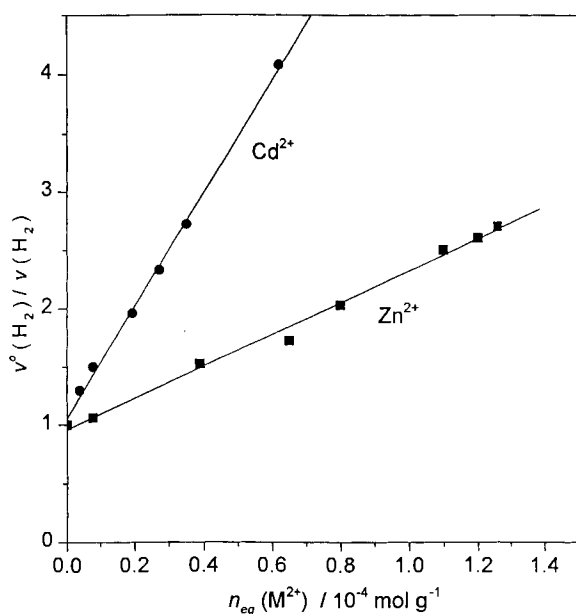


Figure 16. ZnS-photocatalyzed dehydrodimerization of 2,5-DHF: reduced product formation rate (v°/v) as a function of the concentration of *adsorbed* zinc and cadmium ions.

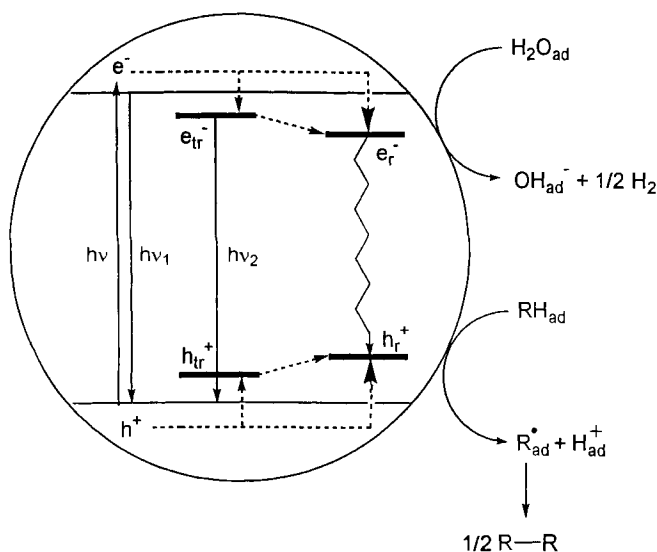


Figure 17. Dehydrodimerization of 2,5-DHF photocatalyzed by ZnS or CdS/Pt: schematic view of the mechanism. The circle represents a micrometer-sized semiconductor particle, wherein the two horizontal lines correspond to the upper and lower edge of the valence and conduction band, respectively.

Table 2. Characteristic data for the adsorption of 2,5-DHF (A) and azobenzene (B) on CdS, CdS-SiO₂ and SiO₂ from methanolic and aqueous solution [164].

	$A_{sp}/$ $m^2 g^{-1}$	K_{ad}/M^{-1}		$n_{eq(max)}/mol g^{-1}$		$\sigma^\circ/\text{\AA}^2$	
		A	B	A ($\times 10^{-3}$)	B ($\times 10^{-5}$)	A	B
CdS	157	18 ± 2	1130 ± 100	0.4 ± 0.1	0.7 ± 0.3	50 ± 5	2700 ± 300
		21 ± 3^a	—	2.1 ± 0.2^a	—	7 ± 1^a	—
CdS-SiO ₂	221	30 ± 1	1060 ± 220	1.6 ± 0.6	0.6 ± 0.1	20 ± 1	4400 ± 100
SiO ₂	340	30 ± 2	1090 ± 260	1.3 ± 0.2	0.6 ± 0.1	35 ± 2	7500 ± 500

^a Adsorption from aqueous solution; all other data from methanolic solution.

the photoaddition reaction [164]. The characteristic data as obtained from application of the Hiemenz model are summarized in Table 2. From the ¹³C NMR spectra of 2,5-DHF adsorbed from the gas phase on the dry powders, it is concluded that 2,5-DHF is adsorbed parallel to the surface. In the case of CdS-SiO₂ the data resemble those of unmodified SiO₂ and therefore suggest that adsorption of 2,5-DHF occurs primarily at the silica surface. In agreement with this conclusion, SiO₂ and CdS-SiO₂ afford the same adsorption constant of 30 M⁻¹, which is about 50 % larger than that for CdS (see below).

From the maximum surface concentration of $n_{eq(max)} = 0.4 \times 10^{-3} \text{ mol g}^{-1}$ found for 2,5-DHF and the maximum number of Cd²⁺ surface sites as calculated for cubic CdS [174], $1.54 \times 10^{-3} \text{ mol g}^{-1}$, it is estimated that 2,5-DHF is adsorbed at about every fourth Cd²⁺ center, in agreement with a parallel adsorption; however, the presence also of perpendicular adsorption cannot be excluded. In contrast, when 2,5-DHF is adsorbed on ZnS from aqueous suspension, it occupies each Zn²⁺ site and σ° matches the calculated molecular area [107]. The difference can be rationalized by comparing the polarities of the two sulfides with those of 2,5-DHF and the solvents employed. Since the surface polarity parameter E_T^N of CdS (0.68 ± 0.06) is comparable to the value for methanol ($E_T^N = 0.762$) [175], but is much higher than that of 2,5-DHF ($E_T^N = 0.366$) [176], displacement of MeOH_{ad} by 2,5-DHF should be disfavored. In contrast, the highly polar solvent water ($E_T^N = 1.0$) [175] is displaced almost completely from the less polar ZnS surface ($E_T^N = 0.57$) [148] by the less polar 2,5-DHF. This explanation is corroborated by the data obtained for 2,5-DHF when it is adsorbed on CdS from an aqueous solution. In this case comparison of the maximum surface concentration of $n_{eq(max)} = (2.1 \pm 0.2) \times 10^{-3} \text{ mol g}^{-1}$ with the calculated maximum number of Cd²⁺ surface sites reveals that about every Cd²⁺ center is occupied by 2,5-DHF. The σ° value of $7 \pm 1 \text{ \AA}^2$ matches fairly well the molecular area of 9 \AA^2 [150] calculated for a perpendicular adsorbed molecule. The change to the more polar solvent water permits an almost five-fold higher surface coverage of CdS. For CdS-SiO₂ the maximum surface concentration of 2,5-DHF ($1.6 \times 10^{-3} \text{ mol g}^{-1}$) is about the sum of the values for CdS-A ($0.4 \times 10^{-3} \text{ mol g}^{-1}$) and SiO₂.

The considerations outlined above are substantiated further by the σ° values as obtained from Hiemenz plots. The area covered by a 2,5-DHF molecule in the

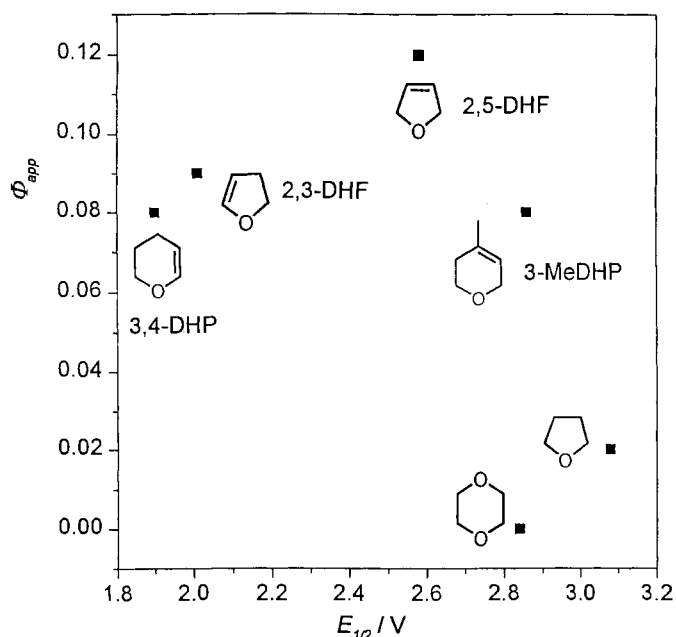


Figure 19. ZnS-photocatalyzed dehydrodimerization of 2,5-DHF: dependence of apparent product quantum yield on substrate oxidation potential.

apparent product quantum yield and redox potential when various substrates are compared (Figure 19). On the other hand, a similar estimation for the concerted process (Eq. 32):



reveals that the reaction is exergonic by at least 0.9 eV [160, 161]. Since the driving force of this reaction is the difference between the free enthalpy of C–H bond homolysis and the potential of the hydrogen electrode, the former value should be decisive when comparing apparent quantum yields of various substrates. Figure 20 displays the relation between the apparent quantum yield and calculated bond dissociation energy of the corresponding C–H bond. The expected increase with decreasing bond strength favors the concerted oxidation pathway. The deviation of 3-MeDHP most likely arises from steric hindrance of the radical C–C coupling step by the adjacent methyl group.

Once formed, the dihydrofuryl radicals may undergo a variety of reactions as known from homogeneous chemistry including disproportionation, addition to double bonds, electron transfer and dimerization. Surprisingly, the latter pathway is followed to about 90 % as indicated by the complete material balance [145]. It is therefore likely that C–C coupling occurs between radicals within the water–2,5-DHF surface layer. This is corroborated by the quadratic dependence of the initial

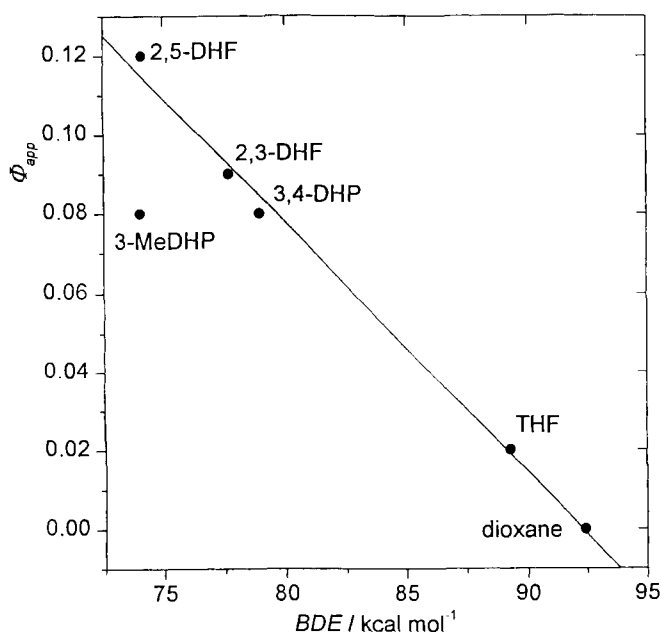


Figure 20. ZnS-photocatalyzed dehydrodimerization of 2,5-DHF: dependence of apparent product quantum yield on the calculated bond dissociation energy of the allylic C-H bond.

rate on the amount of adsorbed 2,5-DHF which is shown in the linearized form in Figure 21. This dependence corresponds to a heterogeneous catalytic dimerization by a modified Langmuir-Hinshelwood mechanism affording easily desorbable products [162]. It further suggests that at early reaction stages the concentration of adsorbed radicals increases linearly with the bulk concentration of 2,5-DHF. The latter relation breaks down as the reaction progresses, since the consumption of 2,5-DHF is faster than its adsorption from solution. Accordingly, the instantaneous rate decreases more strongly with time for lower than for higher starting concentrations and finally becomes diffusion controlled [148]. C-C coupling between radicals adsorbed in the water-2,5-DHF surface layer is further supported by competition experiments with THF. Although the unsaturated ether reacts only 10 times faster than the saturated ether, no THF dehydrodimers or cross-products are detected when THF is present in 10-fold excess over 2,5-DHF. Only at a 500-fold higher concentration are the expected products observed.

In summary, one can conclude that the formation of H_2 and the dehydrodimer occurs via subsequent adsorption of two photons ($2e^-/2h^+$ process). The intermediately adsorbed hydrogen atom and dihydrofuryl radical generated by the first photon must have lifetimes long enough to wait for the arrival of the second photon. This requirement is easily fulfilled since at a micrometer-sized ZnS particle the time interval between two successive photon absorptions can be estimated to be in range of 20 ps, much shorter than the lifetime of radicals and radical cations which

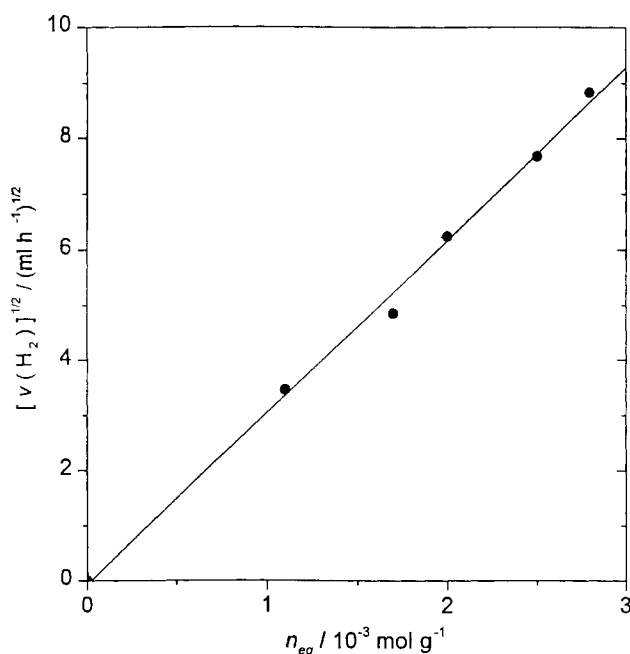


Figure 21. ZnS-photo-catalyzed dehydrodimerization of 2,5-DHF: dependence of square root of reaction rate on concentration of adsorbed 2,5-DHF.

are in the range of at least nanoseconds. However, the question arises of why the C–C homocoupling between two radicals is so highly favored over C–H heterocoupling with an adsorbed hydrogen atom to reform 2,5-DHF [163]. One possibility is that the first electron does not produce an adsorbed hydrogen atom, but is stored at the metallic zinc center and water is subsequently reduced in a two-electron step. Alternatively, the adsorbed hydrogen atom does not undergo coupling to the dihydrofuryl radical because of unknown kinetic barriers. Therefore, it seemed worthwhile to replace water by an organic acceptor which could produce a more stable one-electron reduction intermediate, perhaps capable of undergoing the postulated heterocoupling with the one-electron oxidation intermediate. The following section illustrates that this concept led to the catalysis of photoaddition reactions, classified as *semiconductor photocatalysis type B*.

6.4 Semiconductor Photocatalysis Type B

6.4.1 Linear Addition of Cyclic Enol/Allyl Ethers and Olefins to 1,2-Diazenes

Upon addition of azobenzene to a running ZnS-catalyzed photodehydrodimerization of 2,5-DHF, hydrogen evolution is completely inhibited in favor of formation of the novel allylhydrazine **13c**, a linear addition product of 2,5-DHF to azo-

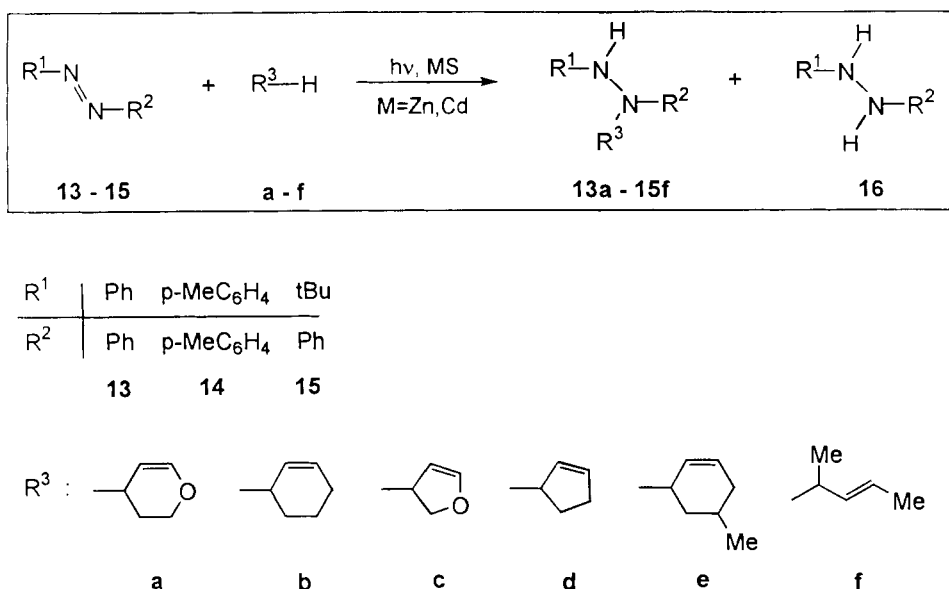


Figure 22. Synthesis of allyl hydrazines through addition of cyclic allyl/enol ethers and olefins to 1,2-diazenes photocatalyzed by ZnS or CdS.

benzene; small amounts of hydrazobenzene are formed as a by-product [141, 142]. When all the azobenzene is consumed and some excess 2,5-DHF is still present, hydrogen evolution starts again. Replacing ZnS by CdS or silica supported CdS (CdS/SiO₂) [164], allows one to conduct the reaction with visible light; a simple tungsten-halogen lamp can be used instead of the high-pressure mercury lamp. When colloidal CdS [165] is employed in the system 3,4-DHP-1,2-diphenyldiazene-MeOH, no photoaddition but efficient photocorrosion occurs. Figure 22 summarizes the novel allylhydrazines **13a–15f** prepared on a gram scale by this simple route employing methanol as the solvent [141, 142]. Owing to the poor crystallization properties, isolated yields are only in the range 10–40 % whereas HPLC yields are about twice larger. Structural assignments are based on an X-ray structural analysis of **13b** and on standard spectroscopic data. Dynamic NMR spectra of **13b** reveals that rotation around the N–N bond is hindered; the corresponding free activation enthalpy amounts to 14 kcal mol^{−1}.

From a few examples of limited synthetic utility, it is known that the same reaction type may occur in homogeneous solution when either the 1,2-diazene [166–169] or the olefin [170–172] is substituted by electron-withdrawing groups. Some other allylhydrazines have been prepared by more conventional thermal procedures [173].

The photoaddition exhibits a significant solvent dependence. No reaction occurs in dry *n*-hexane or THF, but upon addition of water or methanol the reaction is as fast as in pure methanol.

Substrate adsorption studies as conducted with ZnS in aqueous solution were performed also with CdS, CdS-SiO₂ and SiO₂ in methanol, the solvent employed in

Table 2. Characteristic data for the adsorption of 2,5-DHF (A) and azobenzene (B) on CdS, CdS-SiO₂ and SiO₂ from methanolic and aqueous solution [164].

	$A_{sp}/m^2 g^{-1}$	K_{ad}/M^{-1}		$n_{eq(max)}/mol g^{-1}$		$\sigma^\circ/\text{\AA}^2$	
		A	B	A ($\times 10^{-3}$)	B ($\times 10^{-5}$)	A	B
CdS	157	18 \pm 2	1130 \pm 100	0.4 \pm 0.1	0.7 \pm 0.3	50 \pm 5	2700 \pm 300
		21 \pm 3 ^a	—	2.1 \pm 0.2 ^a	—	7 \pm 1 ^a	—
CdS-SiO ₂	221	30 \pm 1	1060 \pm 220	1.6 \pm 0.6	0.6 \pm 0.1	20 \pm 1	4400 \pm 100
SiO ₂	340	30 \pm 2	1090 \pm 260	1.3 \pm 0.2	0.6 \pm 0.1	35 \pm 2	7500 \pm 500

^a Adsorption from aqueous solution; all other data from methanolic solution.

the photoaddition reaction [164]. The characteristic data as obtained from application of the Hiemenz model are summarized in Table 2. From the ¹³C NMR spectra of 2,5-DHF adsorbed from the gas phase on the dry powders, it is concluded that 2,5-DHF is adsorbed parallel to the surface. In the case of CdS-SiO₂ the data resemble those of unmodified SiO₂ and therefore suggest that adsorption of 2,5-DHF occurs primarily at the silica surface. In agreement with this conclusion, SiO₂ and CdS-SiO₂ afford the same adsorption constant of 30 M⁻¹, which is about 50 % larger than that for CdS (see below).

From the maximum surface concentration of $n_{eq(max)} = 0.4 \times 10^{-3}$ mol g⁻¹ found for 2,5-DHF and the maximum number of Cd²⁺ surface sites as calculated for cubic CdS [174], 1.54×10^{-3} mol g⁻¹, it is estimated that 2,5-DHF is adsorbed at about every fourth Cd²⁺ center, in agreement with a parallel adsorption; however, the presence also of perpendicular adsorption cannot be excluded. In contrast, when 2,5-DHF is adsorbed on ZnS from aqueous suspension, it occupies each Zn²⁺ site and σ° matches the calculated molecular area [107]. The difference can be rationalized by comparing the polarities of the two sulfides with those of 2,5-DHF and the solvents employed. Since the surface polarity parameter E_T^N of CdS (0.68 ± 0.06) is comparable to the value for methanol ($E_T^N = 0.762$) [175], but is much higher than that of 2,5-DHF ($E_T^N = 0.366$) [176], displacement of MeOH_{ad} by 2,5-DHF should be disfavored. In contrast, the highly polar solvent water ($E_T^N = 1.0$) [175] is displaced almost completely from the less polar ZnS surface ($E_T^N = 0.57$) [148] by the less polar 2,5-DHF. This explanation is corroborated by the data obtained for 2,5-DHF when it is adsorbed on CdS from an aqueous solution. In this case comparison of the maximum surface concentration of $n_{eq(max)} = (2.1 \pm 0.2) \times 10^{-3}$ mol g⁻¹ with the calculated maximum number of Cd²⁺ surface sites reveals that about every Cd²⁺ center is occupied by 2,5-DHF. The σ° value of $7 \pm 1 \text{\AA}^2$ matches fairly well the molecular area of 9\AA^2 [150] calculated for a perpendicular adsorbed molecule. The change to the more polar solvent water permits an almost five-fold higher surface coverage of CdS. For CdS-SiO₂ the maximum surface concentration of 2,5-DHF (1.6×10^{-3} mol g⁻¹) is about the sum of the values for CdS-A (0.4×10^{-3} mol g⁻¹) and SiO₂.

The considerations outlined above are substantiated further by the σ° values as obtained from Hiemenz plots. The area covered by a 2,5-DHF molecule in the

saturated surface-solute monolayer, is found to be 50 ± 5 , 35 ± 2 and $20 \pm 1 \text{ \AA}^2$ for CdS-A, SiO_2 and CdS– SiO_2 , respectively, and differs not too much from the area of 21 \AA^2 as calculated for an unsolvated molecule adsorbed parallel to the surface [177]. This qualitative agreement with the conclusions drawn from the maximum numbers of metal ion sites as well as the ^{13}C NMR data strongly suggests that 2,5-DHF adsorbs at surface [OH] or [SH] groups via hydrogen bonding.

Inspection of Table 2 reveals that the adsorption constants of 2,5-DHF on SiO_2 and CdS– SiO_2 are equal. This suggests predominant adsorption on the SiO_2 support in the latter case. The better adsorption on CdS– SiO_2 ($K_{\text{ad}} = 30 \pm 1 \text{ M}^{-1}$) than on CdS-A ($K_{\text{ad}} = 18 \pm 2 \text{ M}^{-1}$) is connected with a faster reaction and a higher product ratio of **13c**:**16**, which increases from 0.9 to 2.1. Since the amount of azobenzene adsorbed is the same for both photocatalysts, it is likely that the higher 2,5-DHF surface concentration induced by SiO_2 increases also the amount of 2,5-dihydrofuryl radicals adsorbed at CdS and therefore accelerates C–N coupling with the PhN–NPh radicals.

In comparison with 2,5-DHF, the maximum surface concentration $n_{\text{eq(max)}}$ for azobenzene of about $10^{-5} \text{ mol g}^{-1}$ is two orders of magnitude lower, whereas the adsorption constants are much higher and do not depend on the nature of the adsorbent. Comparison of the σ° values (Table 2) with the area covered by a flat, unsolvated molecule (52 \AA^2) [178] reveals that σ° for CdS, CdS– SiO_2 , and SiO_2 is 52, 85 and 145 times higher, respectively, than expected. It is estimated that in the case of CdS only every 220th Cd^{2+} site interacts with an azobenzene molecule. Depending on the adsorbent, only 0.7–2 % of the surface area is covered, which suggests that the more polar methanol ($\mu = 1.7 \text{ D}$) efficiently competes with the less polar *trans*-azobenzene [179] ($\mu_{\text{trans}} \approx 0 \text{ D}$) for adsorption sites at the relatively polar CdS surface. Together with the independence of the adsorption constant of the nature of the adsorbent, these results suggest that adsorption occurs through interaction with Brønsted acid sites [112, 164]. In this case the independence of the adsorption constant of the adsorbent can be rationalized since according to the literature CdS and SiO_2 have similar $\text{p}K_{\text{S}}$ values (6.1, 9.0 [180] and 6–8 [181], respectively) and the employed photocatalysts CdS or CdS– SiO_2 and SiO_2 have two surface centers of similar pH values [182].

Apparent quantum yields were measured at 366 nm, the wavelength where light absorption by the diazene is minimized. In the system CdS– R^3H –1,2-diphenyldiazene–MeOH, Φ_{app} of allylhydrazine formation increases from 0.02 (2,5-DHF) through 0.03 (cyclohexene) and 0.04 (3,4-DHP) to 0.05 (2,3-DHF). As also observed for the ZnS-catalyzed photodehydrodimerization, there is no simple relation with the oxidation potential of the donor, which is 2.6 V for 2,5-DHF and cyclohexene and 1.9 and 2.0 V for 3,4-DHP and 2,3-DHF, respectively. Although 3,4-DHP as compared with 2,5-DHF is more readily oxidized than 2,5-DHF by 0.7 V, its quantum yield is only twice as large. In contrast to this weak effect, lowering of the reduction potential of the diazene causes a strong increase in the *relative* quantum yield [183] of diazene disappearance. For cyclohexene addition in the series 1,2-bis(*p*-tolyl)diazene, 1,2-diphenyldiazene and 1,2-bis(*p*-chlorophenyl)diazene, E_{red} varies from -0.82 to -0.75 and -0.66 V [184] and Φ_{rel} increases from 0.5 to 1.0 and 5.0, respectively. Thus, although the *p*-chloro derivative is more easily reduced

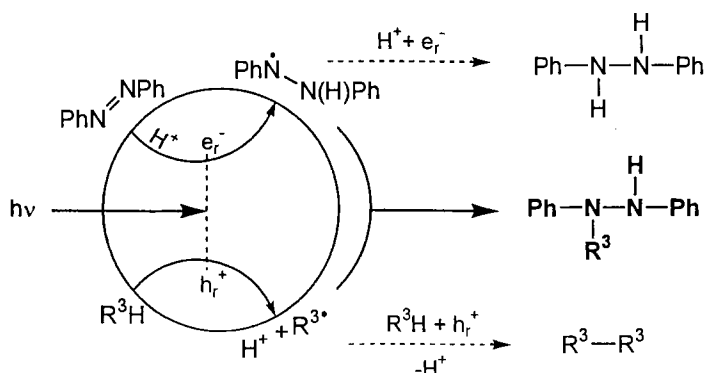
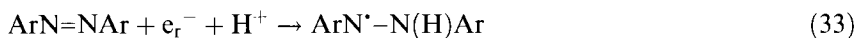


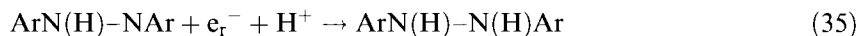
Figure 23. Linear addition of cyclic ally/enol ethers and olefins to 1,2-diazenes photocatalyzed by ZnS or CdS: schematic view of the mechanism.

than the *p*-methyl derivative by only 0.16 V, the quantum yield is 10 times larger. No photoaddition or reduction is observed in the case of 2,3-diazabicyclo[2.2.1]hept-2-ene. It is known that aliphatic diazenes are much more difficult to reduce than aromatic diazenes [185].

From the discussion at the end of Section 6.3.2 and the experimental results presented above, a simplified reaction scheme can be constructed (Figure 23). Since the presence of the diazene completely inhibits hydrogen evolution and the reaction proceeds only in protic solvents or in the presence of water, it is very likely that the reductive IFET is a proton-coupled reduction of the diazene to a hydrazyl radical (Eq. 33):



Hydrazyl radicals derived from 1,2 diaryl- and 1,2-dialkyldiazenes have been postulated [186] and identified in homogeneous solution by ESR [187]. The observation that the product **15a**, obtained from 1-*tert*-butyl-2-phenyldiazene, consists of only one isomer is in agreement with the expectation that the hydrazyl radical should be more stable when the unpaired electron is localized rather on the PhN than on the *t*BuN group. The oxidative IFET is assumed to proceed as described for the photodehydrodimerization. Heterocoupling of the hydrazyl and allyl radicals affords the allylhydrazine. Thus, formation of the addition product is a $1e^- - 1h^+$ process, whereas the by-products are formed via a $2e^- - 2h^+$ process, irrespective whether the hydrazobenzene derivative is formed by subsequent reduction or disproportionation of the hydrazyl radical (Eqs. 34 and 35):



The energetic relations between band positions and redox potentials are summarized in Figure 24.

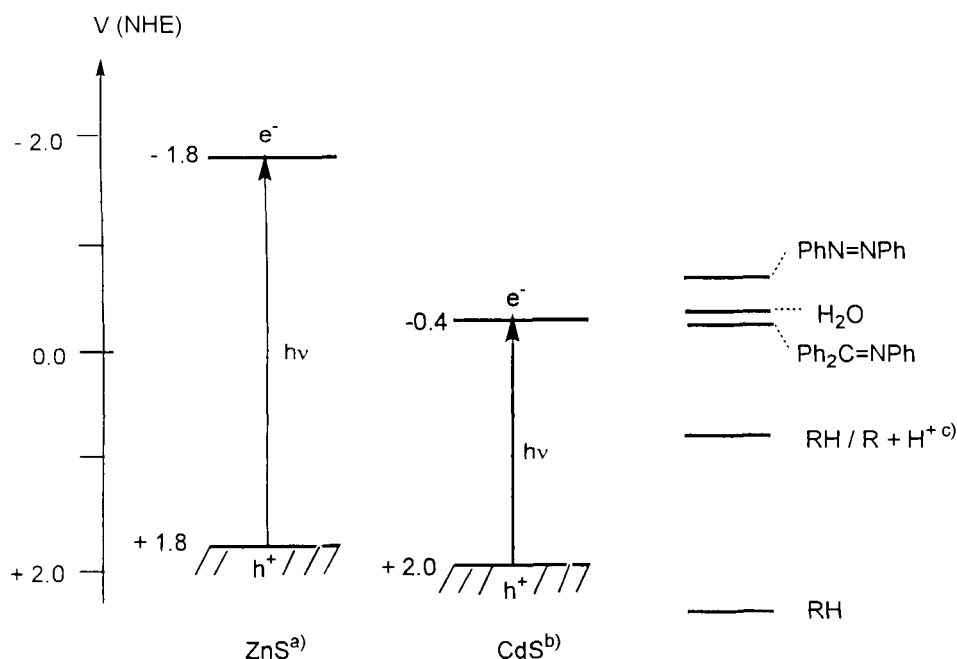


Figure 24. Band positions and substrate redox potentials at pH 7. (a) Single crystal; (b) powder as employed in the synthesis of allylhydrazines; (c) see Ref. [160]. RH = 2,5-DHF.

Table 3. Photocatalyzed addition of 3,4-dihydropyran to azobenzene: influence of various photocatalysts on product distribution (%) and relative rate [142].

	13a	PhNH–NHPh	v_{rel}^a
ZnS	90	5	1.0
ZnS/Pt	5	90	0.3
CdS	70	30	1.0
CdS/Pt	5	80	0.15
CdS-Colloid	–	–	Corrosion

^a Azobenzene disappearance.

Formation of the hydrazobenzene product is strongly favored when platinized zinc or cadmium sulfide is used as the photocatalyst (Table 3). In both cases the rate decreases considerably and hydrazobenzene becomes the major product. It is known that platinum favors multi-electron processes [34].

Model experiments in homogeneous solution support the involvement of the postulated intermediate radicals [142]. Irradiation ($\lambda > 290$ nm) of a dilute solution of benzophenone and 1,2-diphenyldiazene in 3,4-DHP as a reactive solvent affords the addition product **13a** in a yield of 30 % as indicated by HPLC analysis. The yield is negligible when the concentrations of the first two components are increased

or when an unreactive solvent is employed. It is assumed that benzophenone in its excited triplet state abstracts hydrogen from 3,4-DHP [188, 189] producing benzhydryl and dihydropyranyl radicals. The former transfer a hydrogen atom to the diazene [186] to afford the 1,2-diphenylhydrazyl radical, which couples with the latter to form **13a** [189]. Since it is known that hydrazyl radicals do not abstract hydrogen from C–H bonds [186, 190–192], the preference of the coupling reaction becomes understandable. Although in a much smaller yield of 5 %, the addition product **13a** is obtained also when the irradiation is performed in the absence of benzophenone. In this case the triplet π, π^* state of $\text{PhN}=\text{NPh}$ abstracts hydrogen from 3,4-DHP. No reaction except isomerization occurs upon monochromatic irradiation at $\lambda = 405$ nm which affords the triplet n, π^* state [190, 193].

Indirect evidence that intermediate R^3 radicals are involved stems from the formation of two regioisomers when an unsymmetrical olefin is employed, as indicated by the NMR spectrum of **13e**. More direct evidence is obtained upon conducting the reaction in the presence of the radical scavenger diphenylpicrylhydrazyl [194]. In the case of cyclohexene, formation of the corresponding addition product is indicated by MS analysis [142]. The cyclohexenyl radical was postulated also in the electrochemical oxidation of cyclohexene in methanolic solution [195].

The postulated C–N heterocoupling requires diffusion of the two radicals either in the solvent–solute surface layer or in the bulk solution. In both cases one expects that the reaction rate should decrease with increasing solvent viscosity. To achieve the latter, the CdS-SiO_2 -catalyzed photoaddition of 2,5-DHF to azobenzene was conducted at pressures ranging from 0.1 to 120 MPa [164]. Both the formation rates of the addition and reduction products **13c** and **16** ($\text{R}^1 = \text{R}^2 = \text{Ph}$) decrease with increasing pressure and from a plot of $\ln(\text{rate})$ vs. pressure activation volume ΔV^\ddagger are obtained as 17.4 ± 3.4 and 15.8 ± 2.3 $\text{cm}^3 \text{mol}^{-1}$, for **13c** and **16**, respectively (Figure 25).

However, since with increasing pressure the dielectric constant also increases, the observed effects may originate in the change in this property [196–199]. In order to differentiate between these two possibilities, the rates were measured in a series of alcohols for which viscosity and dielectric constant change in an opposite fashion. While the rates again decrease with increasing viscosity, they increase when plotted as function of increasing dielectric constant (Figure 26). This indicates that the rate decrease at higher pressure is a viscosity effect.

It is unlikely that the activation volume is connected with substrate adsorption or product desorption, since high pressure does not significantly affect the adsorption of uncharged substrates [200]. An influence on the interfacial electron transfer steps is also ambiguous since, contrary to homogeneous solution, where the rates of very fast electron transfer reactions can become diffusion controlled [201], no parallel explanation is possible for the heterogeneous case. Usually interfacial collision rates depend on molecular mass but not on diffusion rates [202]. Therefore, the activation volume measured for the formation of **13c** may stem from the diffusion of the intermediate radicals to each other or from the subsequent C–N coupling step itself. The latter case can be excluded since bond formation between neutral organic species in homogeneous solution in general has a negative activation volume [203–206]. The only exception is radical recombination in the termination step of polymerizations

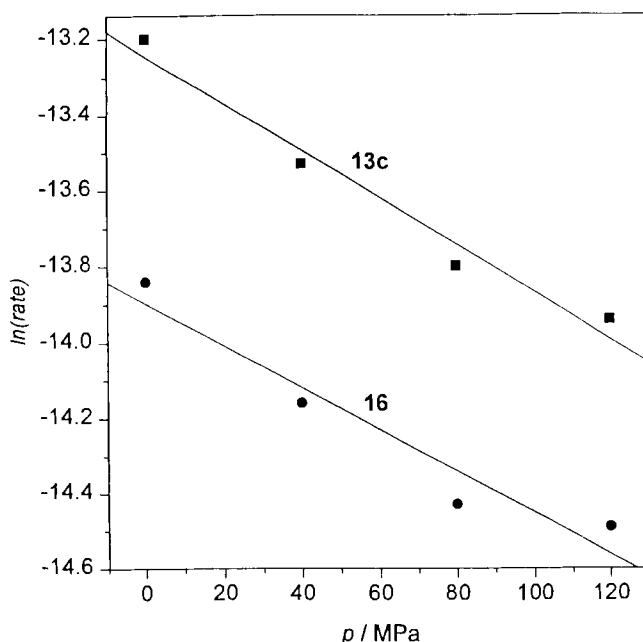


Figure 25. CdS-photo-catalyzed addition of 2,5-DHF to azobenzene: dependence of logarithm of product formation rates on applied pressure.

[207, 208]. These reactions possess ΔV^\ddagger values in the range of 13–25 cm³ mol⁻¹ which are composed of the large and positive contribution of diffusion and the small and negative part of radical C–C coupling. Hence the activation volume found for **13c** most likely originates primarily from diffusion of the intermediate radicals to each other and only to a minor part from C–N coupling and therefore should resemble the activation volume for the viscous flow of methanol. The fact that the latter value of 8 cm³ mol⁻¹ [209] is significantly smaller suggests that the radicals do not diffuse in the bulk homogeneous solution but in a solvent–solute surface layer. This should result in a higher viscosity and consequently the activation volume should become more positive. In accordance with this interpretation are also the small activation energies of 2.8 ± 0.3 kcal mol⁻¹ (**13c**) and 2.5 ± 0.2 kcal mol⁻¹ (**16**).

Since the same activation parameters as for **13c** were also found for the formation of the reduction product **16**, the disproportionation pathway (Eq. 34), which involves radical diffusion, is favored over the secondary reduction step (Eq. 35). However, the latter may be partly involved as suggested by the slightly smaller pressure effect compared with **13c**.

The conclusion that changes in solvent viscosity are responsible for the observed pressure and temperature effects is further corroborated by the same dependence of the product ratio **13c**:**16**. Irrespective whether the viscosity is calculated from the pressure or temperature experiments, a plot of the product ratio vs. viscosity affords two straight lines with slopes that are identical within experimental error (Figure

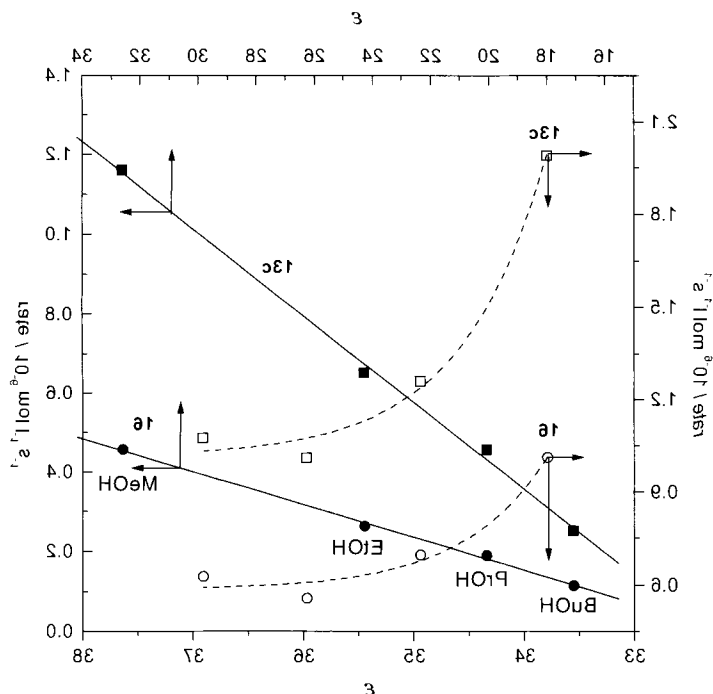


Figure 26. CdS-photocatalyzed addition of 2,5-DHF to azobenzene: dependence of product formation rates on solvent dielectric constant modified through application of pressure (dashed lines) or by changing the solvent from methanol over ethanol and 1-propanol to 1-butanol (solid lines).

27). When the different alcohols were used to change the viscosity, the product ratio also decreased with increasing viscosity.

6.4.2 Linear Addition of Cyclic Enol/Allyl Ethers and Olefins to Imines

According to the proposed mechanism for this novel photoaddition reaction, other substrates capable of forming radicals upon CdS photoinduced one-electron oxidation or reduction should undergo similar C–C coupling. Replacing the 1,2-diazene by the trisubstituted imine **17** indeed affords the new homoallyl amines **18a–g** in isolated yields of 30–75 % (Figure 28) [210].

The structure of the new compounds is confirmed by single-crystal X-ray analyses of **18a**, **c** and **d**, and by comparative NMR data in the case of the other products. The two expected regioisomers **18f** and **f'** were isolated in the case of 3,4-dihydropyran (Figure 29).

Thus, product formation can be rationalized by assuming that the allylic radical generated in the oxidative IFET as discussed above undergoes C–C heterocoupling

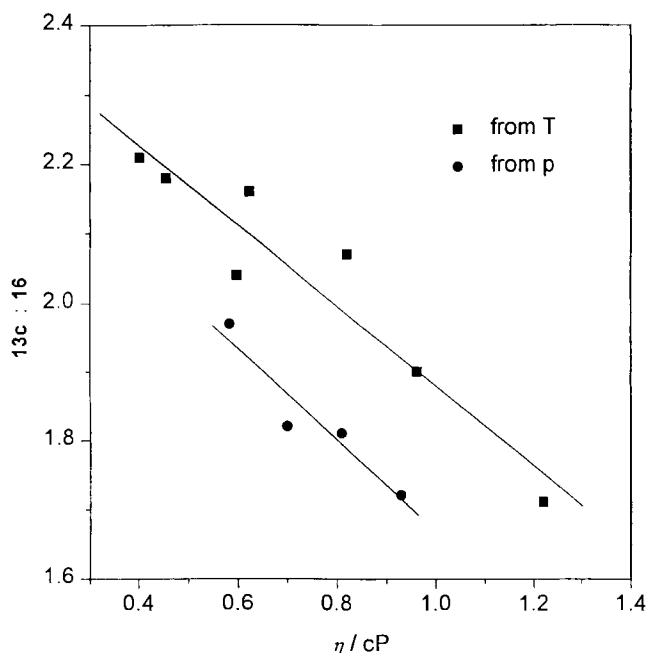
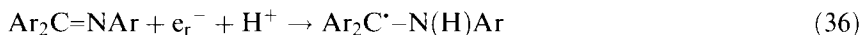


Figure 27. CdS-photo-catalyzed addition of 2,5-DHF to azobenzene: dependence of the product ratio on the viscosity modified by changing the pressure or temperature.

with the α -aminodiphenylmethyl radical produced according to Eq. 36:



In no cases could a product arising from C–N heterocoupling be observed. Thus, in contrast to thermal routes, which usually involve the use of organometallic intermediates [211–213], the reaction is regioselective and much easier to perform.

When a disubstituted imine (**19a–d**) is employed instead of the trisubstituted imine, in addition to the homoallylamine (**20**) also the hydrodimer (**21**) of the imine, i.e., the dimer of the postulated α -aminobenzyl radical, is isolated (Figure 30) [214, 45]. The observation that the hydrodimer is produced only from the disubstituted and not from the trisubstituted imine parallels the electrochemical reduction which affords hydrodimers from aldimines [215] but not from ketimines [215, 216].

Adsorption of **19a** on CdS was measured from methanolic solution. As observed for the adsorption of 2,5-DHF, the adsorption isotherm indicates the presence of mono- and multilayer adsorption. From the former a maximum surface concentration $n_{\text{eq(max)}}$ of $20 \times 10^{-7} \text{ mol g}^{-1}$ can be estimated. At higher concentrations a linear correlation seems to be present. A similar behavior was observed also for the adsorption of chlorophenols on TiO_2 [46]. Application of the Hiemenz model on the methanol–imine surface monolayer leads to an adsorption constant of $4400 \pm 950 \text{ M}^{-1}$ and a σ° value of 4000 \AA^2 . This is far too large, as indicated by comparison with 50 \AA^2 ($14 \times 3.5 \text{ \AA}$) estimated for a flat unsolvated molecule. This

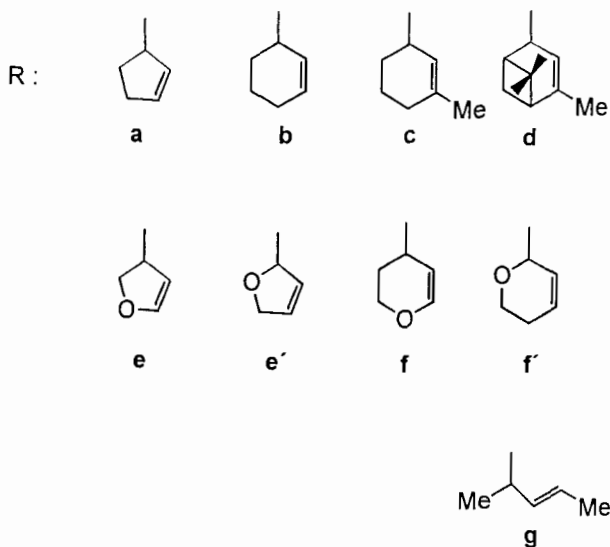
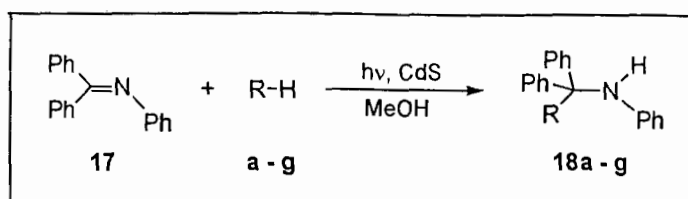


Figure 28. Linear addition of allyl/enol ethers or olefins to *N*-phenylbenzophenone imine photocatalyzed by CdS.

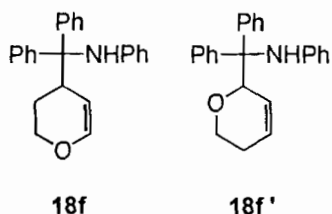
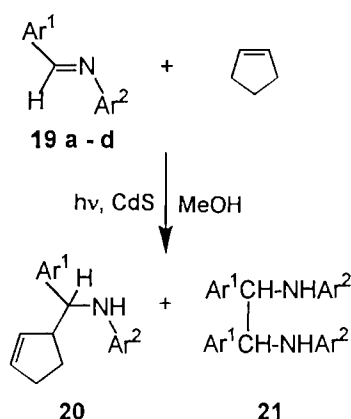


Figure 29. Regioisomers isolated from the CdS-photocatalyzed addition of 3,4-DHP to *N*-phenylbenzophenone imine.

suggests that only 1–2 % of the surface is covered by **19a** in competition with the solvent. The results resemble those obtained for the adsorption of azobenzene (see Table 2). Assuming a size of 8 \AA^2 for methanol, one arrives at the conclusion that methanol is present in a 500-fold excess over the imine in the methanol–imine surface monolayer. It therefore is rational that **19a** does not influence the photocurrent



	a	b	c	d
Ar ¹	4-ClC ₆ H ₄	2,6-Cl ₂ C ₆ H ₃	4-ClC ₆ H ₄	4-MeOC ₆ H ₄
Ar ²	4-ClC ₆ H ₄	C ₆ H ₅	3,5-Me ₂ C ₆ H ₃	4-MeC ₆ H ₄
20 ^{a)}	60	40	55	80
21 ^{a)}	20	10	40	--
a) isolated yield in %				.

Figure 30. Linear addition of cyclopentene to disubstituted imines photocatalyzed by CdS.

of a CdS electrode whereas methanol induces current doubling [217]. Although these numbers are only rough estimates, they are not unexpected since methanol should adsorb much more strongly than **1a** on the hydrous CdS surface [218].

Control experiments with **19a** showed that in the absence of olefins hydrodimers were also formed but the reaction rate was reduced by about 90 %. Either the CdS itself (under photocorrosion) or the solvent must be involved in the oxidative step of this reaction. Accordingly, irradiation of CdS in a solution of **19a** in different alcohols transforms the imine at different rates and the corresponding addition products **22a–e** and the hydrodimer **23** are isolated (Figure 31). Except for methanol and 2-propanol, the products are racemic diastereomeric mixtures which are isolated in low yields (5–20 %); they are often mixed with the two-electron reduction product *N*-4-chlorobenzyl-4-chloroaniline. The major product in all reactions is the hydrodimer **23**, obtained in yields of 10 % (MeOH), 28 % (BuOH), 29 % (PrOH), 42 %

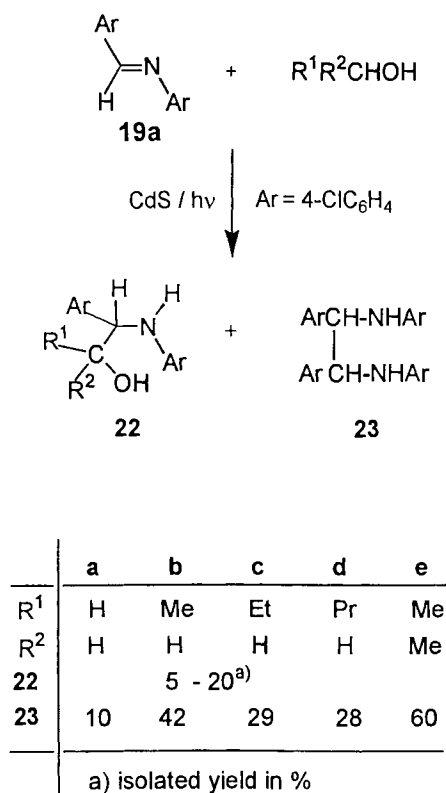


Figure 31. Linear addition of alcohols to a disubstituted imine photocatalyzed by CdS.

(EtOH) and 60 % (*i*PrOH). Upon prolonged irradiation the hydrodimer is partially decomposed. Other by-products were also formed but not isolated. The structure of **22** indicates that in all cases the α -CH bond of the alcohol is added to the imine in agreement with the preferred formation of α -hydroxyalkyl radicals from oxidation of the alcohols [219, 220].

The rate of imine disappearance increased from MeOH (relative rate 1.0) to EtOH (2.0), PrOH (2.0) and *i*PrOH (3.3), in agreement with the easier oxidation of these alcohols. BuOH does not follow this correlation since it induces a relative rate of only 1.8, giving rise to the formation of more side products. In the case of *i*PrOH, involvement of the intermediate hydroxyalkyl radical was corroborated through detection of its disproportionation product acetone. These results show that the solvent can be directly involved in the oxidative step. Formation of hydrodimers in the absence of olefins thus can be explained by the oxidation of the alcohols. It is noted that in the presence of olefins no alcohol addition products could be detected by HPLC analysis, although methanol is present in a 500-fold molar excess.

Decreasing the light intensity to 10–50 % of its original value results in a linear decrease in the reaction rate. Above 50 % a saturation effect is observed. This is in accord with other photoreactions catalyzed by semiconductor powders [66, 68].

At higher intensities the rate usually increases proportionally to $I_a^{1/2}$ owing to enhanced charge recombination as reported for the TiO_2 (specific surface area $7 \text{ m}^2 \text{ g}^{-1}$ [66]) catalyzed photo-oxidation of 2-propanol at light intensities above $10^{16} \text{ quanta s}^{-1}$. In the system investigated here this occurs only above intensities of $10^{18} \text{ quanta s}^{-1}$. It is noteworthy that the product ratio **20a:21a** = 0.9 does not depend on light intensity. Assuming that reductive and oxidative reaction steps are coupled, the rates of α -aminobenzyl and cyclopentenyl radical formation should be equal. When the concentrations of these radicals are taken as equal, one arrives at rate laws for the formation of the two products which differ only in the rate constants k_{add} and k_{dim} . Therefore, their ratio should determine also the ratio **20a:21a** [45]. The fact that the latter does not change suggests that these rate constants are independent of light intensity.

As observed for the photoreduction of methyl orange [218] and the oxidative photodimerization of olefins [80] catalyzed by CdS powder, the dependence of rate on CdS concentration increases approximately linearly and reaches a plateau at about 3 g L^{-1} . Surprisingly, in the same concentration range the ratio of addition to hydrodimer product (**20a:21a**) decreases from 2 to about 1. This can be rationalized by considering that the specific rate v_s , which is the measured rate divided by the amount of catalyst employed, decreases with increasing catalyst concentration (Figure 32).

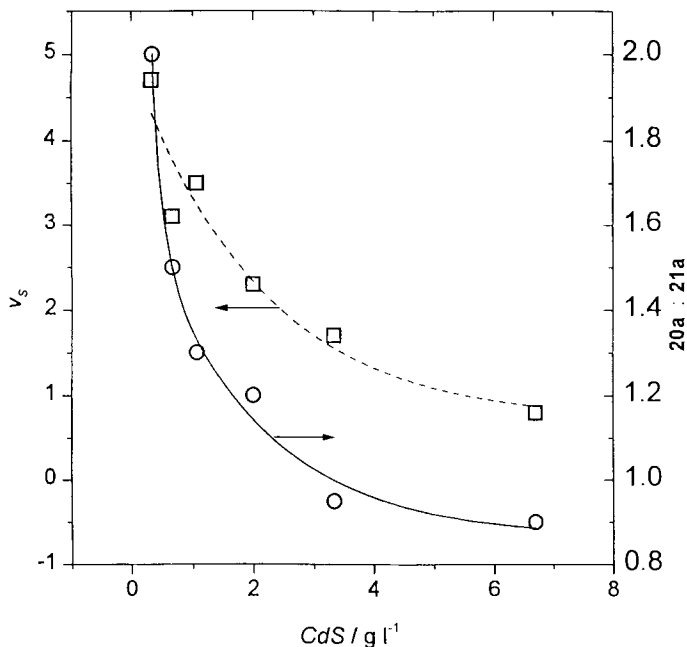


Figure 32. Dependence of specific rate ($10^{-7} \text{ mol g}^{-1} \text{ s}^{-1}$) and product ratio of addition to hydrodimerization on the concentration of CdS.

In the same direction, the surface concentration of the intermediate radicals should decrease although the ratio of α -aminobenzyl to cyclopentenyl radical concentration should not change. Therefore, the product ratio should stay constant. However, a lower concentration of the radicals increases their lifetime, assuming that they undergo only second-order decay reactions. This effect should favor hydrodimerization, which is a $2e^-/2h^+$ process and therefore requires that a second radical pair is generated during the lifetime of the first. Furthermore, one can make the plausible assumption that there is still some weak interaction within a reactive electron-hole pair and therefore the distance between the charges in a pair should be smaller than the distance between neighboring pairs. This means that the radical homocoupling most likely requires a longer diffusion path than heterocoupling. Accordingly, a longer radical lifetime should also allow more efficient diffusion and therefore additionally favor the hydrodimer formation.

6.5 Summary and Outlook

The unique property of the semiconductor-liquid interface to generate reducing and oxidizing surface sites upon absorption of light enables nanoscaled micrometer particles of zinc and cadmium sulfide powders to act as efficient heterogeneous electron transfer photocatalysts for novel organic syntheses. In most cases a reduced and an oxidized product are obtained, in complete analogy with an electrochemical synthesis (semiconductor photocatalysis type A). In a few cases, as observed only recently, the semiconductor catalyzes a linear photoaddition reaction between two unsaturated substrates affording a single product (semiconductor photocatalysis type B), a reaction type not known in classical electrochemistry. In both reaction types the semiconductor action is at least bifunctional. It allows proper assembly of the substrates through adsorption and it catalyzes a double interfacial electron transfer to and from substrates. The latter affords intermediate radicals which finally undergo regioselective C-C and C-N coupling reactions to stable products. The reactions are easy to perform and the heterogeneous sensitizer can be conveniently separated from the products by filtration. Especially the photoaddition reactions are promising examples of a 'green chemistry' since they do not produce waste materials and they can be driven by solar light. It may be expected that this multifunctional nature of the semiconductor powders can be utilized for further novel preparative reactions, especially in the field of solar energy conversion. In a formal way, the overall reaction resembles photosynthesis, where light absorption also generates reducing and oxidizing centers, which finally induce the synthesis of organic matter through C-C coupling reactions.

References

1. (a) V. Carassiti, *EPA Newsl.* **1984**, 21, 12; (b) H. Kisch, H. Hennig, *EPA Newsl.* **1983**, 19, 23; (c) A. Albini, *J. Chem. Educ.* **1986**, 63, 383.

2. H. Hennig, D. Rehorek, R. D. Archer, *Coord. Chem. Rev.* **1985**, 61, 1.
3. C. Kutal, *Coord. Chem. Rev.* **1985**, 64, 191.
4. L. Moggi, A. Juris, D. Sandrini, M. F. Manfrin, *Res. Chem. Intermed.* **1981**, 4, 171.
5. J. Plotnikov, *Allgemeine Photochemie*, Walter de Gruyter, Berlin, **1936**, p. 362.
6. R. G. Salomon, *Tetrahedron* **1983**, 39, 485.
7. S. J. Teichner, M. Formenti, in *Photoelectrochemistry, Photocatalysis and Photoreactors* (Ed. M. Schiavello), Reidel, Dordrecht, **1985**, p. 457.
8. M. S. Wrighton, D. S. Ginley, M. A. Schroeder, D. L. Morse, *Pure Appl. Chem.* **1975**, 41, 671.
9. G. G. Wubbels, *Acc. Chem. Res.* **1983**, 16, 285.
10. As defined in 'Glossary of Terms used in Photochemistry', *EPA Newsl.* **1985**, 25, 13.
11. V. Balzani, F. Boletta, M. Ciano, M. Maestri, *J. Chem. Educ.* **1983**, 60, 447.
12. A. J. Bard, *J. Photochem.* **1979**, 10, 59.
13. M. Boudart, G. Djega-Mariadassou, *Kinetics of Heterogeneous Catalytic Reactions*, Princeton University Press, Princeton, NJ, **1984**, p. 6.
14. F. Basolo, R. G. Pearson, *Mechanism of Inorganic Reactions*, Wiley, New York, **1967**.
15. S. G. Davies, *Organotransition Metal Chemistry: Applications to Organic Synthesis*, Pergamon Press, Oxford, **1982**.
16. It was proposed to take the number of molecules present in one monolayer, about 10^{14} per cm^2 , as an estimate [17].
17. L. P. Childs, D. F. Ollis, *J. Catal.* **1980**, 66, 383.
18. G. N. Schrauzer, T. D. Guth, *J. Am. Chem. Soc.* **1977**, 99, 7189.
19. H. Gerischer, in *Physical Chemistry*, Vol. 9A (Eds. M. Eyring, D. Henderson, W. Jost), Academic Press, New York, **1970**, p. 463.
20. S. N. Frank, A. J. Bard, *J. Am. Chem. Soc.* **1977**, 99, 4667.
21. S. N. Frank, A. J. Bard, *J. Am. Chem. Soc.* **1977**, 99, 303.
22. S. N. Frank, A. J. Bard, *J. Phys. Chem.* **1977**, 81, 1484.
23. B. Kraeutler, A. J. Bard, *J. Am. Chem. Soc.* **1977**, 99, 7729.
24. A. J. Nozik, R. Memming, *J. Phys. Chem.* **1996**, 100, 13061.
25. M. A. Fox, *Top. Curr. Chem.* **1987**, 142, 71.
26. A. Henglein, *Top. Curr. Chem.* **1988**, 143, 113.
27. N. Serpone, E. Pelizzetti, *Photocatalysis*, Wiley, New York, **1989**.
28. J. G. Edwards, J.-A. Davies, D. L. Boucher, A. Mennad, *Angew. Chem.* **1992**, 104, 489.
29. W. Hetterich, H. Kisch, *Chem. Ber.* **1989**, 122, 621.
30. (a) H. Reiche, A. J. Bard, *J. Am. Chem. Soc.* **1979**, 101, 3127; (b) J. Onoe, T. Kawai, S. Kawai, *Chem. Lett.* **1985**, 1667.
31. A. Heller, Y. Degani, D. W. Johnson, P. K. Gallagher, *J. Phys. Chem.* **1987**, 91, 43.
32. A. Fujishima, K. Hashimoto, T. Watanabe, *TiO₂ Photocatalysis, Fundamentals and Applications*, Koyo Printing, Tokyo, **1999**.
33. P. V. Kamat, *Chem. Rev.* **1993**, 93, 267.
34. R. Memming, *Top. Curr. Chem.* **1988**, 149, 137.
35. H. Tributsch, in Ref. [27], Chap. 11.
36. B. Kraeutler, A. J. Bard, *J. Am. Chem. Soc.* **1978**, 100, 5985.
37. H. Gerischer, *J. Phys. Chem.* **1984**, 88, 6096.
38. D. E. Aspnes, A. Heller, *J. Phys. Chem.* **1983**, 67, 4919.
39. A. J. Bard, *Science* **1980**, 207, 172.
40. G. Hodes, in *Energy Resources Through Photochemistry and Catalysis* (Ed. M. Grätzel), Academic Press, New York, **1983**, p. 421.
41. G. Rothenberger, J. Moser, M. Grätzel, N. Serpone, D. K. Sharma, *J. Am. Chem. Soc.* **1985**, 107, 8054.
42. P. V. Kamat, T. W. Ebbesen, N. M. Dimitrijevic, A. J. Nozik, *Chem. Phys. Lett.* **1989**, 157, 384.
43. G. Hodes, *J. Electrochem. Soc.* **1992**, 139, 3136.
44. A. Wahl, J. Augustynski, *J. Phys. Chem. B* **1998**, 102, 7820.
45. W. Schindler, H. Kisch, *J. Photochem. Photobiol. A: Chem.* **1997**, 103, 257.
46. (a) J. Cunningham, S. Srijaranai, *J. Photochem. Photobiol. A: Chem.* **1991**, 58, 361; (b) J. Cunningham, G. Al-Sayyed, P. Sedlak, J. Caffrey, *Catal. Today*, **1999**, 53, 145.
47. C. Anderson, A. J. Bard, *J. Phys. Chem. B* **1997**, 101, 2611.

48. C. Anderson, A. J. Bard, *J. Phys. Chem.* **1995**, 99, 9882.
49. The redox potential may change by almost 1 V when one form of the redox couple is adsorbed much more strongly than the other; see Ref. [50].
50. J. F. Rodriguez, J. E. Harris, M. E. Bothwell, Th. Mebrahtu, M. P. Soriaga, *Inorg. Chim. Acta* **1988**, 148, 123.
51. F.-R. F. Fan, P. Leempoel, A. J. Bard, *J. Electrochem. Soc.* **1983**, 130, 1866.
52. J. R. White, A. J. Bard, *J. Phys. Chem.* **1985**, 89, 1947.
53. J. R. White, A. J. Bard, *J. Am. Chem. Soc.* **1985**, 105, 27.
54. H. Tributsch, J. C. Bennett, *J. Chem. Tech. Biotechnol.* **1981**, 31, 565.
55. M. F. Finlayson, B. L. Wheeler, N. Kakuta, K.-H. Park, A. J. Bard, A. Campion, M. A. Fox, S. E. Webber, J. M. White, *J. Phys. Chem.* **1985**, 89, 5676.
56. D. Meissner, R. Memming, B. Kastening, *J. Phys. Chem.* **1988**, 92, 3476.
57. M. J. Natan, J. W. Thackeray, M. S. Wrighton, *J. Phys. Chem.* **1986**, 90, 4089.
58. G. Redmond, D. Fitzmaurice, *J. Phys. Chem.* **1993**, 97, 1426.
59. H. Harada, T. Sakata, T. Ueda, *J. Am. Chem. Soc.* **1985**, 107, 1773.
60. T. Shiragami, C. Pac, S. Yanagida, *J. Chem. Soc., Chem. Commun.* **1989**, 831.
61. N. Serpone, R. Terzian, D. Lawless, P. Kennepohl, G. Sauvé, *J. Photochem. Photobiol. A: Chem.* **1993**, 73, 11.
62. M. Schiavello, V. Augugliaro, L. Palmisano, *J. Catal.* **1991**, 127, 332.
63. L. Sun, J. R. Bolton, *J. Phys. Chem.* **1996**, 100, 4127.
64. For details see Ref. [66] and H. Kisch, *J. Prakt. Chem.* **1994**, 336, 635.
65. A typical value for a given set-up is $\geq 10^{15}$ photons s^{-1} .
66. T. A. Egerton, C. J. King, *J. Oil Colour Chem. Assoc.* **1979**, 62, 386.
67. S. Sato, *J. Phys. Chem.* **1983**, 87, 3531.
68. H. Al-Ekabi, P. de Mayo, *J. Phys. Chem.* **1985**, 89, 5815.
69. R. Rosetti, L. Brus, *J. Phys. Chem.* **1982**, 86, 4470.
70. G. Y. Myer, L. K. Leung, J. C. Yu, G. C. Lisensky, A. B. Ellis, *J. Am. Chem. Soc.* **1989**, 111, 5146.
71. T. Uchihara, M. Matsumara, H. Tsubomura, *J. Phys. Chem.* **1989**, 93, 3207.
72. M. Anpo, A. Matsumoto, S. Kodama, *J. Chem. Soc., Chem. Commun.* **1987**, 1038.
73. A. M. Draper, M. Ilyas, P. de Mayo, V. Ramamurthy, *J. Am. Chem. Soc.* **1984**, 106, 6222.
74. J. M. Herrmann, H. Courbon, P. Pichat, *J. Catal.* **1985**, 95, 539.
75. F. H. Hussein, R. Rudham, *J. Chem. Soc., Faraday Trans. 1* **1987**, 83, 1631.
76. L. V. Lyashenko, Y. B. Gorokhovatski, V. I. Stepanenko, F. A. Yamposkaya, *Teor. Eksp. Khim.* **1976**, 93, 35.
77. P. Pichat, M. N. Mozzanega, J. Disdier, J. M. Herrmann, *Nouv. J. Chim.* **1982**, 6, 559.
78. P. Pichat, J. M. Herrmann, in Ref. [27], Chap. 1.
79. A. Mills, R. Davies, *J. Photochem. Photobiol. A: Chem.* **1995**, 85, 173.
80. H. Al-Ekabi, P. de Mayo, *Tetrahedron* **1986**, 43, 6277.
81. A. Heller, Y. Degani, D. W. Johnson, P. K. Gallagher, *J. Phys. Chem.* **1987**, 91, 5987.
82. J. F. Reber, M. Rusek, *J. Phys. Chem.* **1986**, 90, 824.
83. Note that only for nonporous materials the surface area increases with smaller particle size; however, most of the powders employed are very porous.
84. B. R. Müller, S. Majoni, R. Memming, D. Meissner, *J. Phys. Chem. B* **1997**, 101, 2501.
85. P. Lenard, *Ann. Phys.* **1922**, 68, 553.
86. H. P. Weiser, A. D. Garrison, *J. Phys. Chem.* **1927**, 31, 1237.
87. H. Platz, P. W. Schenk, *Angew. Chem.* **1936**, 49, 822.
88. J. J. Hopfield, *J. Phys. Chem. Solids* **1959**, 10, 110.
89. J. L. Birman, C. Shakin, *Phys. Rev.* **1958**, 109, 810.
90. J. L. Birman, *Phys. Rev.* **1959**, 115, 1493.
91. M. Cardona, *Phys. Chem. Solids* **1963**, 24, 1543.
92. M. Cardona, G. Harbeke, *Phys. Rev.* **1965**, 137, 1467.
93. S. Yanagida, K. Mizumoto, C. Pac, *J. Am. Chem. Soc.* **1986**, 108, 647.
94. S. Yanagida, Y. Ishimura, Y. Miyake, T. Shiragami, C. Pac, K. Hashimoto, T. Sakata, *J. Phys. Chem.* **1989**, 93, 2576.
95. S. Baral, A. Fojtik, H. Weller, A. Henglein, *J. Am. Chem. Soc.* **1986**, 108, 375.
96. A. Kurian, C. V. Suryanarayana, *J. Appl. Electrochem.* **1972**, 2, 223.

97. R. K nneth, G. Twardzik, G. Emig, H. Kisch, *J. Photochem. Photobiol. A: Chem.* **1993**, 76, 209.
98. H. Kisch, J. B cheler, *Bull. Chem. Soc. Jpn.* **1990**, 63, 2378.
99. M. Anpo, S. C. Moon, K. Chiba, G. Martras, S. Coluccia, *Res. Chem. Intermed.* **1993**, 19, 495.
100. M. Anpo, *Surface Photochemistry*, Vol. 1, Wiley, New York, **1996**.
101. G. H rner, H. Kisch, unpublished work.
102. G. H rner, A. Fernandez, H. Kisch, unpublished work.
103. These bands are known as 'self-activated luminescence' [104].
104. A. S. Marfunin, *Spectroscopy, Luminescence and Radiation Centers in Minerals*, Springer, Berlin, **1979**, p. 176.
105. K. Sooklal, B. S. Cullum, S. M. Angel, C. J. Murphy, *J. Phys. Chem.* **1996**, 100, 4551.
106. L. Spanhel, M. Haase, H. Weller, A. Henglein, *J. Am. Chem. Soc.* **1987**, 109, 5649; A. Henglein, *Ber. Bunsenges. Phys. Chem.* **1982**, 86, 301.
107. G. H rner, P. Johne, R. K nneth, G. Twardzik, H. Roth, T. Clark, H. Kisch, *Chem. Eur. J.* **1999**, 5, 208.
108. S. Yanagida, H. Kawakami, K. Hashimoto, T. Sakata, C. Pac, H. Sakurai, *Chem. Lett.* **1984**, 1449.
109. W. J. Albery, P. N. Bartlett, C. P. Wilde, J. D. Darwent, *J. Am. Chem. Soc.* **1985**, 107, 1854.
110. W. J. Albery, G. T. Brown, J. R. Darwent, E. Saievar-Iranizad, *J. Chem. Soc. Faraday Trans. 1* **1985**, 81, 1999.
111. D. R. James, Y. S. Liu, P. d. Mayo, W. R. Ware, *Chem. Phys. Lett.* **1985**, 120, 460.
112. A. Reinheimer, A. Fernandez, H. Kisch, *Z. Phys. Chem.* **1999**, 213 II, 129.
113. A. M. Roy, G. C. De, N. Sasmal, S. S. Bhattacharyya, *Int. J. Hydrogen Energy* **1995**, 20, 627.
114. H. Weiss, Master Thesis, University of Erlangen **1999**.
115. In the literature, the expression 'photocatalysis' is often used in a misleading manner because in most cases it means that for a reaction the presence of a semiconductor is essential; however, it has been proven only in a few cases that the formation of products is catalytic; see H. Kisch, *J. Prakt. Chem.* **1994**, 336, 635.
116. M. Anpo, M. Yabuta, S. Kodama, Y. Kubokawa, *Bull. Chem. Soc. Jpn.* **1986**, 59, 259.
117. S. Kodama, N. Nakaya, M. Anpo, Y. Kubokawa, *Chem. Bull. Chem. Soc. Jpn.* **1985**, 58, 3645.
118. S. Kodama, S. Yagi, *J. Phys. Chem.* **1998**, 93, 4556.
119. M. Anpo, M. Sunamoto, *J. Phys. Chem.* **1989**, 93, 1187.
120. H. Ikezawa, C. Kutal, *J. Org. Chem.* **1987**, 52, 3299.
121. H. Al-Ekabi, P. de Mayo, *J. Phys. Chem.* **1986**, 90, 4075.
122. A. Maldotti, R. Amadelli, C. Martocci, V. Carassiti, *Photochem. Photobiol. A: Chem.* **1990**, 53, 263.
123. C. M. Wang, T. E. Mallouk, *J. Am. Chem. Soc.* **1990**, 112, 2016.
124. R. Barber, P. de Mayo, K. Okada, *J. Chem. Soc., Chem. Commun.* **1982**, 106, 1073.
125. M. Ilyas, P. de Mayo, *J. Am. Chem. Soc.* **1985**, 107, 5093.
126. M. A. Fox, T. Pettit, *J. Org. Chem.* **1985**, 50, 5013.
127. P. Boarini, V. Carassiti, A. Maldotti, R. Amadelli, *Langmuir* **1998**, 14, 2080.
128. C. Joyce-Pruden, J. K. Pross, Y. Li, *J. Org. Chem.* **1992**, 57, 5087.
129. F. Mahdavi, T. C. Bruton, Y. Li, *J. Org. Chem.* **1993**, 58, 744.
130. B. Ohtani, H. Osaki, S. Nishimoto, T. Kagiya, *J. Am. Chem. Soc.* **1986**, 108, 308.
131. M. Schmittel, A. Burghard, *Angew. Chem., Int. Ed. Engl.* **1997**, 36, 2551.
132. T. Linker, M. Schmittel, *Radikale und Radikationen in der Organischen Synthese*, Wiley-VCH, Weinheim, **1998**.
133. T. Takizawa, T. Watanabe, K. Honda, *J. Phys. Chem.* **1977**, 81, 1845.
134. T. Takizawa, T. Watanabe, K. Honda, *J. Phys. Chem.* **1978**, 82, 1391.
135. Here and in the following the use of the chemical formula indicates that the semiconductor was present as a powder suspension.
136. B. Ohtani, S. Kusakabe, S. Nishimoto, M. Matsumura, Y. Nakato, *Chem. Lett.* **1995**, 803.
137. B. Ohtani, S. Kusakabe, S. Nishimoto, K. Okada, S. Tsuru, K. Izawa, Y. Amino, *Tetrahedron Lett.* **1995**, 36, 3189.
138. K. H. Park, K. Jun, *Bull. Korean Chem. Soc.* **1998**, 19, 919.
139. L. Cermenati, C. Richter, A. Albini, *J. Chem. Soc., Chem. Commun.* **1998**, 805.
140. L. Cermenati, M. Mella, A. Albini, *Tetrahedron* **1998**, 54, 2575.

141. R. K nneth, C. Feldmer, H. Kisch, *Angew. Chem.* **1992**, 104, 1102.
142. R. K nneth, C. Feldmer, H. Kisch, *Chem. Eur. J.* **1995**, 1, 441.
143. J. B cheler, N. Zeug, H. Kisch, *Angew. Chem.* **1982**, 94, 792.
144. W. Hetterich, H. Kisch, *J. Photochem. Photobiol.* **1988**, 121, 15.
145. N. Zeug, J. B cheler, H. Kisch, *J. Am. Chem. Soc.* **1985**, 107, 1459.
146. An often neglected aspect in many 'sacrificial' systems of water splitting, i.e., hydrogen evolution can only be observed after adding a reducing agent.
147. (a) S. Yanagida, T. Azuma, Y. Midori, C. Pac, H. Sakurai, *J. Chem. Soc., Perkin Trans. 2* **1985**, 1487; (b) S. Yanagida, H. Kawakami, Y. Midori, H. Kizumoto, C. Pac, Y. Wada, *Bull. Chem. Soc. Jpn.* **1995**, 68, 1811.
148. G. H rner, H. Kisch, unpublished results.
149. (a) A. W. Adamson, *Physical Chemistry of Surfaces*, 4th edn., Wiley, New York, **1982**; (b) P.C. Hiemenz, *Principles of Colloid and Surface Chemistry*, 2nd edn., Marcel Dekker, New York, **1986**.
150. Estimated according to $3.8 \times 2.4 \text{ \AA}$.
151. (a) Q. Zhang, Z. Xu, J. A. Finch, *J. Colloid Interface Sci.* **1995**, 169, 414; (b) assuming that each zinc site is occupied by one 2,5-DHF molecule.
152. Although the lifetime of the reactive electron-hole pair is not known, the reasonable estimate of 10^{-6} – 10^{-9} s leads to an electron transfer rate constant between 10^{10} and $10^{13} \text{ M}^{-1} \text{ s}^{-1}$. In general, electron transfer reactions at the semiconductor-liquid interface are very fast [see Ref. [33] and N. Serpone, E. Pellizzetti (Eds.), *Homogeneous and Heterogeneous Photocatalysis*, Reidel, Dordrecht, **1986**, p. 51].
153. A. Henglein, M. Gutierrez, C.-H. Fischer, *Ber. Bunsenges. Phys. Chem.* **1984**, 88, 170.
154. S. Kodama, A. Matsumoto, Y. Kubokawa, M. Anpo, *Bull. Chem. Soc. Jpn.* **1986**, 59, 3765.
155. Y. Nakaoka, Y. Nosaka, *Langmuir* **1997**, 13, 708.
156. L. Lunazzi, G. Placucci, L. Grossi, *Tetrahedron* **1983**, 39, 159.
157. M. Bruening, E. Moons, D. Yaron-Marcovic, D. Cahen, J. Libman, A. Shanzer, *J. Am. Chem. Soc.* **1994**, 116, 2972.
158. M. Bruening, E. Moons, D. Cahen, A. Shanzer, *J. Phys. Chem.* **1995**, 99, 8368.
159. M. Bruening, R. Cohen, J. F. Guillemoles, T. Moav, J. Libman, A. Shanzer, D. Cahen, *J. Am. Chem. Soc.* **1997**, 119, 5720.
160. Calculated by using $E_0(\text{H}^+/\text{H}) = -2.40 \text{ V (H}_2\text{O)}$ [161] and a bond dissociation energy of 3.22 eV [106]; these were converted to the $\Delta G(\text{H}_2\text{O})$ values by subtracting 0.1 eV for the solvent contribution [161]. The same argument was used to explain the photooxidation of alcohols by ZnS [153].
161. V. D. Parker, *J. Am. Chem. Soc.* **1992**, 114, 7458.
162. F. Wilkinson, *Chemical Kinetics and Reaction Mechanism*, Van Nostrand Reinhold Co., Wokingham, **1980**.
163. It is noted that deuterium is not incorporated into unreacted 2,5-DHF and dehydrodimers when D_2O is employed [145].
164. A. Reinheimer, R. v. Eldik, H. Kisch, *J. Phys. Chem. B* **2000**, 104, 1014.
165. A. Fojtik, H. Weller, U. Knoch, A. Henglein, *Ber. Bunsenges. Phys. Chem.* **1984**, 89, 969.
166. G. O. Schenk, H. Formanek, *Angew. Chem.* **1958**, 70, 505.
167. R. C. Cookson, I. D. R. Stevens, C. T. Watts, *J. Chem. Soc., Chem. Commun.* **1965**, 259.
168. G. Ahlgren, *Tetrahedron Lett.* **1974**, 2779.
169. R. Askani, *Chem. Ber.* **1965**, 98, 2551.
170. I. Rosenthal, D. Elad, *Tetrahedron* **1967**, 23, 3193.
171. G. Ahlgren, *J. Org. Chem.* **1973**, 38, 1369.
172. I. Ninomiya, T. Naito, *Photochemical Synthesis*, Academic Press, New York, **1989**.
173. B. H. Al-Sader, R. J. Crawford, *Can. J. Chem.* **1970**, 48, 2745.
174. D. Chan, J. W. Perram, L. R. White, T. W. Healy, *J. Chem. Soc., Faraday Trans. 1* **1975**, 1046.
175. C. Reichardt, *Solvents and Solvent Effects in Organic Chemistry*, VCH, Weinheim, **1988**, p. 364.
176. (a) From comparison with the dipole moments of THF, 2,5-DHF and furan (1.63, 1.59 and 0.66 D, respectively) one would expect, however, that the E_1^{N} value of 2,5-DHF should be in the range 0.164–0.27, corresponding to furan and THF, respectively; (b) D. R. Lide, H. P. R.

- Raton (Eds.), *Handbook of Chemistry and Physics*, 75th edn., CRC Press, Boca Raton, FL, **1994**.
177. Estimated from a molecular model as $4.6 \times 4.5 \text{ \AA}$.
 178. Estimated from a molecular model as $10.8 \times 4.8 \text{ \AA}$.
 179. Since light could not be completely excluded in the dark adsorption experiments, *cis*-azobenzene was present at about 1 %.
 180. S. W. Park, C. P. Huang, *J. Colloid Interface Sci.* **1987**, *117*, 431.
 181. T. J. Bandosz, C. Lin, J. A. Ritter, *J. Colloid Interface Sci.* **1998**, *198*, 347.
 182. A. Reinheimer, H. Kisch, unpublished work.
 183. Φ_{app} of 1,2-diphenyldiazene was set to 1.0.
 184. A. J. Bard, W. Lund, *Encyclopedia of Electrochemistry of the Elements, Organic Section*, Marcel Dekker, New York, **1978**.
 185. R. Sustmann, R. Sauer, *J. Chem. Soc., Chem. Commun.* **1985**, 1248.
 186. P. S. Engel, W.-X. Wu, *J. Am. Chem. Soc.* **1989**, *111*, 1831, 5506.
 187. C. Lagercranz, J. Deinum, *Acta Chem. Scand.* **1984**, *48*, 670.
 188. This was observed in the system benzaldehyde–3,4-DHP; A. G. Griesbeck, S. Stadtmüller, *J. Am. Chem. Soc.* **1989**, *111*, 1830.
 189. An alternative mechanism could involve addition of the dihydropyranil radical to the diazene and subsequent H-abstraction from 3,4-DHP to produce the product **13a** and a new dihydropyranilradical. The latter should induce a radical chain reaction, the presence of which lacks any experimental evidence.
 190. S. Hashimoto, K. Kano, *Bull. Chem. Soc. Jpn.* **1972**, *45*, 852.
 191. L. Flamingi, S. Monti, *J. Phys. Chem.* **1985**, *89*, 3702.
 192. P. Neta, H. Levanon, *J. Phys. Chem.* **1977**, *81*, 2288.
 193. J. Griffiths, *Chem. Soc. Rev.* **1972**, *1*, 481.
 194. R. H. Poirier, E. J. Kahler, F. Benington, *J. Org. Chem.* **1952**, *17*, 1437.
 195. K. Yoshida, T. Kanbe, T. Fueno, *J. Org. Chem.* **1977**, *42*, 2313.
 196. K. Schäfer, *Landolt-Börnstein, Zahlenwerte und Funktionen*, Vol. 6, Bd. II/5a, Springer, Berlin, **1969**.
 197. K. R. Srinivasan, R. L. Kay, *J. Solution Chem.* **1977**, *6*, 357.
 198. D. W. Brazier, G. R. Freeman, *Can. J. Chem.* **1969**, *47*, 893.
 199. M. G. Gonikberg, *Chemical Equilibria and Reaction Rates at High Pressure*, Israel Program for Scientific Translations, Jerusalem, 1963.
 200. M. Miyahara, S. Iwasaki, T. Kotera, T. Kawamura, M. Okazaki, *J. Colloid Interface Sci.* **1995**, *170*, 335.
 201. M. E. Williams, J. C. Crooker, R. Pyati, L. J. Lyons, R. W. Murray, *J. Am. Chem. Soc.* **1997**, *119*, 10249.
 202. O. S. Anderson, S. W. Feldberg, *J. Phys. Chem.* **1996**, *100*, 4622.
 203. T. Asano, W. J. Noble, *Chem. Rev.* **1978**, *78*, 407.
 204. R. v. Eldik, T. Asano, W. J. L. Noble, *Chem. Rev.* **1989**, *89*, 549.
 205. A. Drljaca, C. D. Hubbard, R. v. Eldik, T. Asano, M. V. Basilevsky, W. J. L. Noble, *Chem. Rev.* **1998**, *98*, 2167.
 206. N. S. Isaacs, *Liquid Phase High Pressure Chemistry*, Wiley, New York, **1981**.
 207. A. E. Nicholson, G. W. Norrish, *Discuss. Faraday Soc.* **1956**, *22*, 104.
 208. M. Yokawa, Y. Ogo, *Makromol. Chem.* **1976**, *177*, 429.
 209. N. S. Isaacs, *Liquid Phase High Pressure Chemistry*, Wiley, New York, **1981**, p. 106.
 210. H. Keck, W. Schindler, F. Knoch, H. Kisch, *Chem. Eur. J.* **1997**, *3*, 1638.
 211. S. J. Jin, S. Araki, Y. Butsugan, *Bull. Chem. Soc. Jpn.* **1993**, *66*, 1528.
 212. B. Mauzé, L. Miginiac, *Bull. Soc. Chim. Fr.* **1973**, 1832.
 213. R. Arous-Chtara, J. L. Moreau, M. Gaudemar, *J. Soc. Chim. Tunis.* **1980**, *3*, 1.
 214. W. Schindler, F. Knoch, H. Kisch, *Chem. Ber.* **1996**, *129*, 925.
 215. K. Takaki, Y. Tsubaki, S. Tanaka, F. Beppu, Y. Fujiwara, *Chem. Lett.* **1990**, 203.
 216. H. Thies, H. Schöneberger, K. H. Bauer, *Arch. Pharm.* **1960**, *293*, 67.
 217. H. Weiss, H. Kisch, unpublished work.
 218. A. Mills, G. Williams, *J. Chem. Soc., Faraday Trans. 1* **1987**, *83*, 2647.
 219. L. Feng, H. Wang, Z. Jin, Q. Li, U. Shi, *J. Photochem. Photobiol. A: Chem.* **1991**, *56*, 89.
 220. R. L. Furey, R. O. Kan, *Tetrahedron* **1968**, *24*, 3085.

Volume IV

Part 2

Heterogeneous Systems

1 Electron Transfer at Semiconductor–Electrolyte Interfaces

Krishnan Rajeshwar

1.1 Introduction and Scope

The study of electron transfer across semiconductor–electrolyte interfaces has both fundamental and practical incentives. These interfaces have interesting similarities and differences with their semiconductor–metal and metal–electrolyte counterparts. Thus approaches to garnering a fundamental understanding of charge transfer across these interfaces have stemmed from both electrochemistry and solid-state physics perspectives and have proven to be equally fruitful. On the other hand, this knowledge base in turn impacts many technologies, including microelectronics, environmental remediation, sensors, solar cells and energy storage. Some of these are discussed elsewhere in this series of volumes.

Nonetheless, it is instructive first to examine the historical evolution of this field. Early work in the 1950s and 1960s undoubtedly was motivated by application possibilities in electronics and came on the heels of discovery of the first transistor. Electron transfer theories were also rapidly evolving during this period, starting from homogeneous systems to heterogeneous metal–electrolyte interfaces leading, in turn, to semiconductor–electrolyte junctions. The 1973 oil embargo and the ensuing energy crisis caused a dramatic spurt in studies on semiconductor–electrolyte interfaces once the energy conversion possibilities of the latter were realized. Subsequent progress at both fundamental and applied levels in the late 1980s and 1990s was more gradual and sustained. Much of this later research has been spurred by technological applicability in environmental remediation scenarios. Very recently, however, renewed interest in clean energy sources that are non-fossil in origin has provided new impetus to the study of semiconductor–electrolyte interfaces. As we also learn to understand and manipulate these interfaces at an increasingly finer (atomic) level, new microelectronics application possibilities may emerge, thus completing the cycle that first began in the 1950s!

The ensuing discussion of the progress that has been made in this field mainly hinges on studies that have appeared since 1990 or thereabouts. Several review

articles and book chapters have appeared since then dealing with semiconductor–electrolyte interfaces [1–10]; aspects related to electron transfer are featured in several of these. This author is also aware of at least three books/monographs/proceedings volumes that have appeared since 1990 [11–13]. The reader would be well advised, however, to consult the many authoritative accounts that exist prior to this timeframe for a thorough coverage of details on semiconductor–electrolyte interfaces in general. Entry to this early literature may be found in the references cited above. In some instances, however, the discussion that follows necessarily delves into research dating back to the 1970s and 1980s.

To facilitate a self-contained description, we will start with well-established aspects related to the semiconductor energy band model and the electrostatics at semiconductor–electrolyte interfaces in the ‘dark’. We shall then examine the processes of light absorption, electron–hole generation and charge separation at these interfaces. Finally, the steady-state and dynamic (i.e., transient or periodic) aspects of charge transfer will be considered. Nanocrystalline semiconductor films and size quantization are briefly discussed, as are issues related to electron transfer across chemically modified semiconductor–electrolyte interfaces.

Dye sensitization of semiconductor surfaces is not considered here, nor are issues related to semiconductor particles, photocatalysis and photoelectrolysis *per se*. These companion topics may be found elsewhere in Volumes I, IV and V. The discussion is phenomenological and is designed to provide an intuitive grasp of the key issues rather than detailed derivations that would have been prohibitive in terms of space constraints in any case. Indeed, the available theoretical framework is only examined in terms of how and with what confidence the pertinent conclusions can be experimentally verified with semiconductor electrodes.

1.2 Electron Energy Levels in Semiconductors and Energy Band Model

Unlike in molecular systems, the energy levels are so dense that they form, instead of discrete molecular orbital energy levels, broad energy bands. Consider a solid composed of N atoms. Its frontier band will have $2N$ energy eigenstates each with an occupancy of two electrons of paired spin. Thus, a solid having atoms with odd number of valence electrons (e.g., Al with [Ne] $3s^23p^1$) will have a partially occupied frontier band in which the electrons are delocalized. On the other hand, for a solid with an even number of valence electrons (e.g., Si having an electron configuration of [Ne] $3s^22p^2$) will have a fully occupied frontier band (termed a valence band, VB). The situation for Si is schematized in Figure 1.

As Figure 2 illustrates, the distinction between semiconductors and insulators is rather arbitrary and resides with the magnitude of the energy band-gap (E_g) between the filled and vacant bands. Semiconductors typically have E_g in the 1–4 eV range (Table 1). The vacant frontier band is termed a conduction band, CB (Figure 2). We shall see later that E_g has an important bearing on the optical response of a semiconductor.

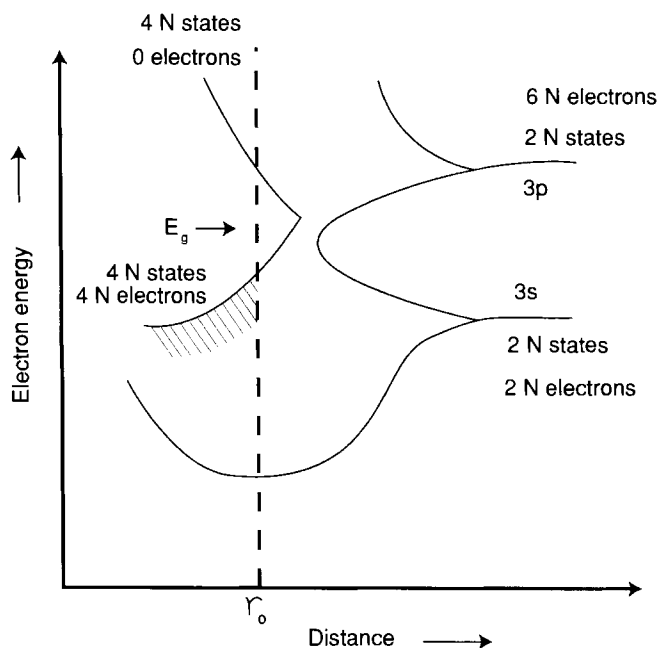


Figure 1. Schematic illustration of how energy bands in semiconductors evolve from discrete atomic states for the specific example of silicon.

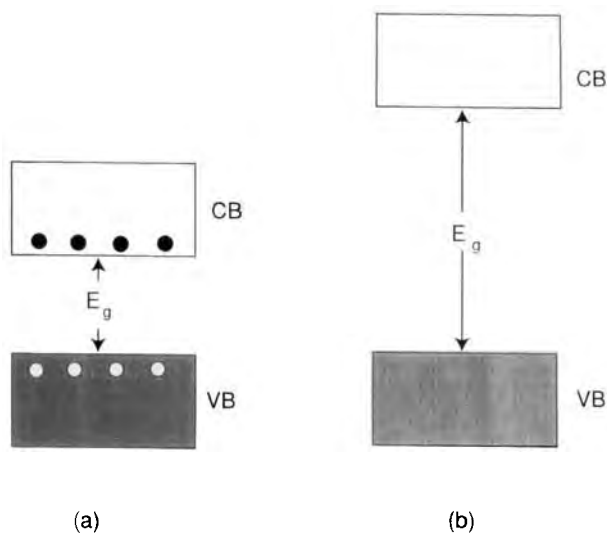


Figure 2. Relative disposition of the conduction band (CB) and valence band (VB) for a semiconductor (a) and an insulator (b). E_g is the optical band-gap energy.

For high-density electron ensembles such as valence electrons in metals, Fermi statistics are applicable. In a thermodynamic sense, the Fermi level, E_F (defined at 0 K as the energy at which the probability of finding an electron is 0.5) can be regarded as the electrochemical potential of the electron in a particular phase (in this

Table 1. Some elemental and compound semiconductors for photoelectrochemical applications.

Semiconductor	Conductivity type(s)	Optical band-gap energy eV ^a
Si	n, p	1.11
GaAs	n, p	1.42
GaP	n, p	2.26
InP	n, p	1.35
CdS	n	2.42
CdSe	n	1.70
CdTe	n, p	1.50
TiO ₂	n	3.00 (rutile) 3.2 (anatase)
ZnO	n	3.35

^aThe values quoted are for the bulk semiconductor. The gap energies increase in the size quantization regime (see Section 1.8).

case, a solid). Thus, all electronic energy levels below E_F are occupied and those above E_F are likely to be empty.

Electrons in semiconductors may be regarded as low-density particle ensembles such that their occupancy in the valence and conduction bands may be approximated by the Boltzmann function [14, 15]:

$$n_e \approx N_0 \exp\left(-\frac{E_0 - E_F}{kT}\right) \quad (1)$$

Now we come to another important distinction between metals and semiconductors in that two types of electronic carriers are possible in the latter. Consider the thermal excitation of an electron from VB to CB. This gives rise to a free electron in the CB and a vacancy or hole in the VB. A localized chemical picture for the case of Si shows that the hole may be regarded as a missing electron in a chemical bond (Figure 3). There is a crude chemical analogy here with the dissociation of a solvent such as water into H_3O^+ and OH^- . In either case, equal numbers of oppositely charged species are produced. Thus, Eq. 1 becomes

$$n_i \approx N_c \exp\left(-\frac{E_F - E_c}{kT}\right) \quad (2)$$

$$p_i \approx N_v \exp\left(-\frac{E_v - E_F}{kT}\right) \quad (3)$$

where N_c and N_v are the effective density of states (in cm^{-3}) at the lower edge and top edge of CB and VB, respectively. These expressions can be combined with the recognition that $n_i = p_i$ to yield

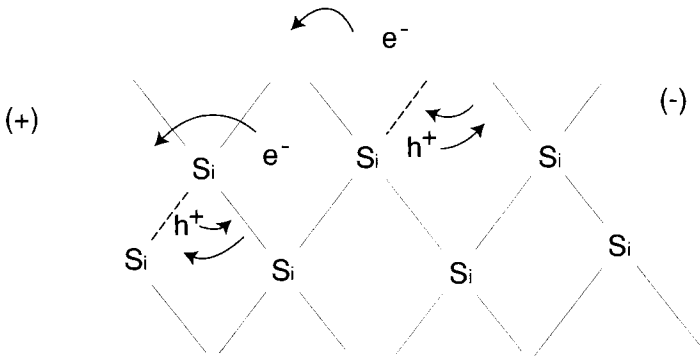


Figure 3. A localized picture of electron–hole pair generation (see also Figure 2a) in silicon.

$$\begin{aligned}
 n_i^2 &\approx N_0 \exp\left(-\frac{E_c - E_v}{kT}\right) \\
 &\approx N_0 \exp\left(-\frac{E_g}{kT}\right)
 \end{aligned} \tag{4}$$

To obtain a numerical feel of the situation, N_c and N_v are typically both $\sim 10^{19} \text{ cm}^{-3}$ so that the constant N_0 ($N_c N_v$) in Eq. 1 is about 10^{38} cm^{-3} . For a semiconductor such as Si (with $E_g = 1.11 \text{ eV}$, Table 1), n_i will be about 10^{10} cm^{-3} at 300 K according to Eq. 4. This rough calculation lends credence to the original rationale for the use of Boltzmann statistics for the electron energy distribution in semiconductors (see above).

The above case refers to the semiconductor in its intrinsic state with very low carrier concentrations under ambient conditions. The Fermi level, E_F , in this case lies approximately in the middle of the energy band-gap (Figure 4a). This simply reflects the fact that the probability of electron occupancy is very high in VB and very low in CB and does not imply an occupiable energy level at E_F itself.

In extrinsic semiconductors the carrier concentrations are perturbed such that $n \neq p$. Again, the analogy with the addition of an acid or base to water is instructive here. Consider the case when donor impurities are added to a neutral semiconductor. Since the intrinsic carrier concentrations are so low (sub-parts per trillion), even additions at parts per billion levels can have a profound electrical effect. This process is known as doping of the semiconductor. In this particular case, the Fermi level will shift toward the CB edge (Figure 4b). When the donor level is within a few kT in energy from the CB edge, appreciable electron concentrations are generated by the donor ionization process (at ambient temperatures) such that now $n \gg p$. This is termed n-type doping and the resultant (extrinsic) semiconductor is termed n-type. By analogy, p-type semiconductors have $p \gg n$. The terms minority and majority carriers now become appropriate in these cases. For a p-doped semiconductor case, the Fermi level now lies close to the VB edge (Figure 4c). The move-

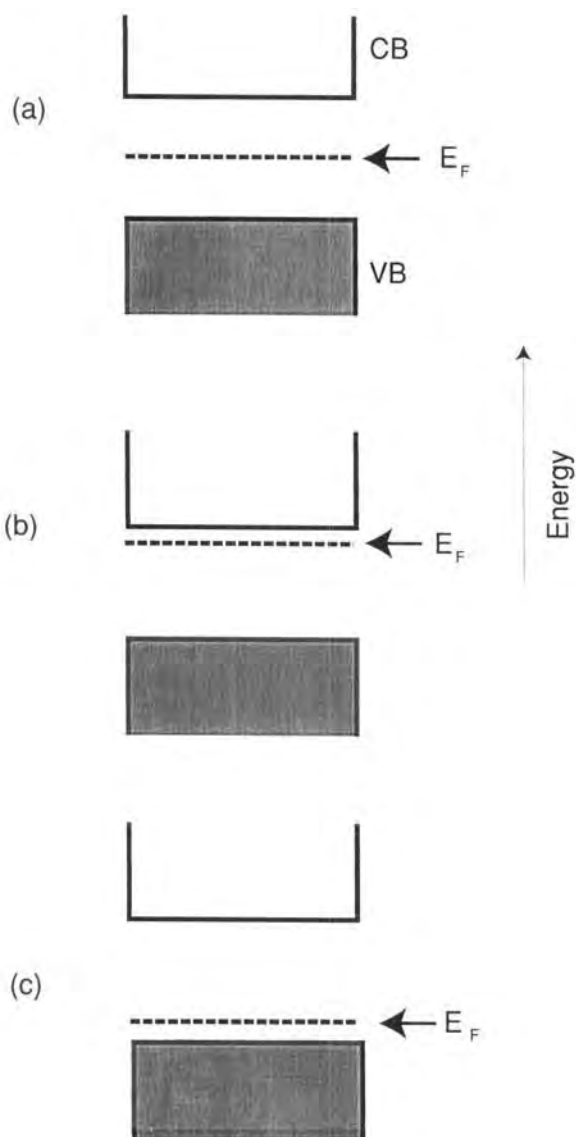


Figure 4. Relative disposition of the Fermi level (E_F) for an intrinsic semiconductor (a), for an n-type semiconductor (b) and for a p-type semiconductor (c).

ment of E_F with dopant concentration can also be rationalized via the Nernst formalism [6].

Doping can be done by adding altrivalent impurities to the intrinsic semiconductor. For example, P (a Group 15 or VA element) will act as a donor in Si (a Group 14 or IVA element). This can be rationalized on chemical terms by noting that P needs only four valence electrons for tetrahedral bonding (as in the Si lattice) —the fifth electron is available for donation by each P atom. The donor density,

N_D , nominally is $\sim 10^{17} \text{ cm}^{-3}$. Thus, assuming that $n \approx N_D$ (complete ionization at 300 K), p will be only $\sim 10^3 \text{ cm}^{-3}$ [recall that the product $n_i p_i$ is $\sim 10^{20} \text{ cm}^{-6}$ (see above)], bearing out the earlier qualitative assertion that $n \gg p$.

Impurity addition, however, is not the only doping mechanism. Nonstoichiometry in compound semiconductors such as CdTe (Table 1) also gives rise to n- or p-type behavior depending on whether Cd or Te is in slight excess, respectively. The defect chemistry in these solid chalcogenides controls their conductivity and doping in a complex manner, a discussion of which is beyond the scope of this chapter. Excellent treatises are available on this topic and on the solid-state chemistry of semiconductors in general [16–22].

The foregoing discussion strictly refers to semiconductors in single-crystal form. Amorphous and polycrystalline counterparts present other complications caused by the presence of defects, trap states, grain boundaries and the like. For this reason, we orient the subsequent discussion mainly toward single crystals, although comparisons with the less ideal cases are made where appropriate. The distinction between metal and semiconductor electrodes also becomes important when we consider the electrostatics across the corresponding solid–liquid interfaces; this is done next.

1.3 The Semiconductor–Electrolyte Interface at Equilibrium

1.3.1 The Equilibration Process

The electrochemical potential of electrons in a redox electrolyte is given by the Nernst expression:

$$E_{\text{redox}} = E_{\text{redox}}^{\circ} + \frac{RT}{nF} \ln \left(\frac{c_{\text{ox}}}{c_{\text{red}}} \right) \quad (5)$$

where c_{ox} and c_{red} are the concentrations (roughly activities) of the oxidized and reduced species respectively in the redox couple. The parameter ($E_{\text{redox}} = \tilde{\mu}_{e, \text{redox}}$) as defined by Eq. 5 can be identified with the Fermi level, $E_{F, \text{redox}}$, in the electrolyte. This was the topic of debate some years back [23], although this premise now appears to be well founded. The task now is to relate the electron energy levels in the solid and liquid phases on a common basis.

The semiconductor solid-state physics community has adopted the electron energy in vacuum as a reference whereas electrochemists have traditionally used the standard hydrogen electrode (SHE) scale. Although estimates vary [23–25], SHE appears to lie at -4.5 eV with respect to the vacuum level. We are now in a position to relate the redox potential, E_{redox} (as defined with reference to SHE), with the Fermi level, $E_{F, \text{redox}}$, expressed versus the vacuum reference (Figure 5a):

$$E_{F, \text{redox}} = -4.5 \text{ eV} - e_0 E_{\text{redox}} \quad (6)$$

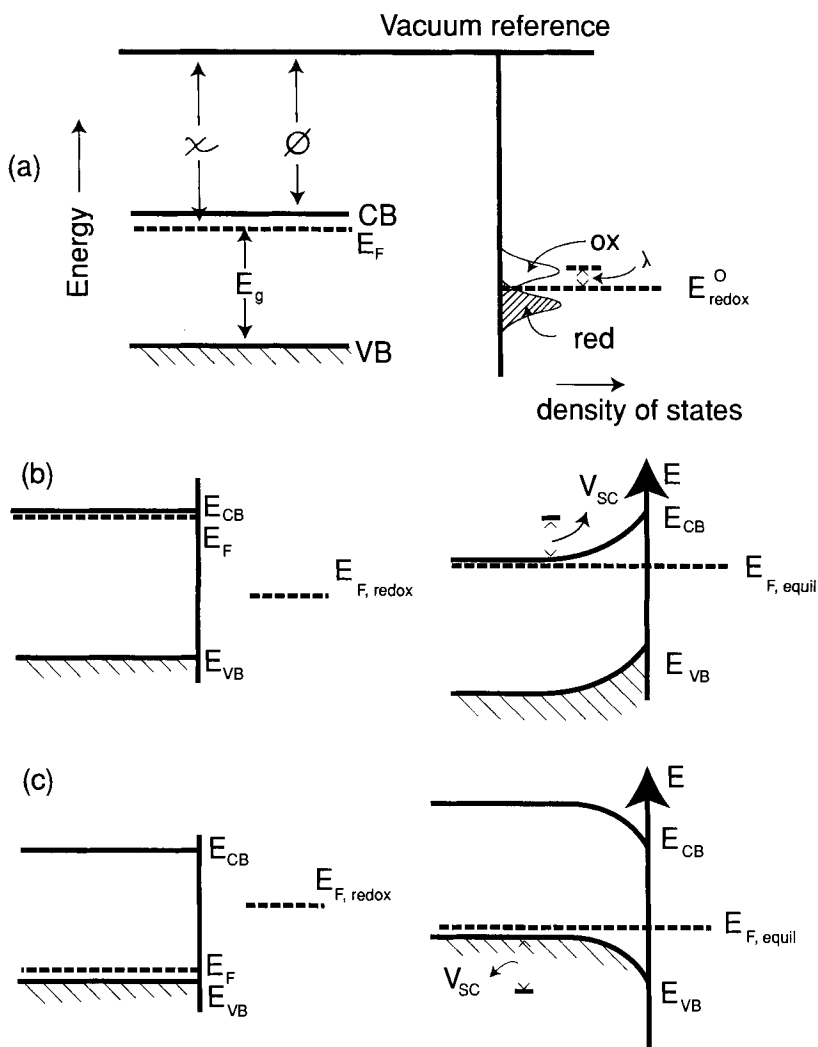


Figure 5. (a) Energy levels in a semiconductor (left-hand side) and a redox electrolyte (right-hand side) shown on a common vacuum reference scale. χ and ϕ are the semiconductor electron affinity and work function, respectively. (b) The semiconductor–electrolyte interface before (left) and after (right) equilibration (i.e., contact of the two phases) shown for an n-type semiconductor. (c) As in (b) but for a p-type semiconductor.

When a semiconductor is immersed in this redox electrolyte, the electrochemical potential (Fermi level) is disparate across the interface. Equilibration of this interface thus necessitates the flow of charge from one phase to the other and a ‘band-bending’ ensues within the semiconductor phase. The situation before and after contact of the two phases is illustrated in Figure 5b and c for an n-type and p-type

semiconductor, respectively. The net result of equilibration is that $E_F = E_{F,\text{redox}}$ and a ‘built-in’ voltage, V_{sc} , develops within the semiconductor phase as illustrated in the right-hand frames of Figure 5b and c.

It is instructive to examine this equilibration process further. Consider again an n-type semiconductor for illustrative purposes (Figure 5b). The electronic charge needed for Fermi level equilibration in the semiconductor phase originates from the donor impurities (rather than from bonding electrons in the semiconductor lattice). Thus, the depletion layer that arises as a consequence within the semiconductor contains positive charges from these ionized donors. The Fermi level in the semiconductor ($E_{F,n}$) moves ‘down’ and, of course, the process stops when the Fermi level is the same on either side of the interface. The substantial difference in the density of states on either side dictates that $E_{F,n}$ moves farther than the corresponding level, $E_{F,\text{redox}}$, in the electrolyte. A particularly lucid account of this initial charge transfer is contained in Ref. [6].

The band-bending phenomenon, shown in Figure 5b and c, is by no means unique to the semiconductor–electrolyte interface. Analogous electrostatic adjustments occur whenever two *dissimilar* phases are in contact (e.g., semiconductor–gas, semiconductor–metal). An important point of distinction from the corresponding metal case now becomes apparent. For a metal, the charge, and thus the associated potential drop, are concentrated at the surface penetrating at most a few ångströms into the interior. Stated differently, the high electronic conductivity of a metal cannot support an electric field within it. Thus, when a metal electrode comes into contact with an electrolyte, almost all the potential drop at the interface occurs within the Helmholtz region in the electrolyte phase. On the other hand, the interfacial potential drop across a semiconductor–electrolyte junction (see below) is partitioned both as V_{sc} and as V_H leading to a simple equivalent circuit model comprising of two capacitors (C_{sc} and C_H) in series (Figure 6). More refinements of the equivalent circuit description are given later but the point to note now is the rather variant behavior of a metal and a semiconductor at equilibrium with a redox electrolyte.

1.3.2 The Depletion Layer

There is a characteristic region within the semiconductor within which the charge would have been removed by the equilibration process. Beyond this boundary, the ionized donors (for an n-type semiconductor) have their compensating charge (electrons) and the semiconductor as a whole is electrically neutral. This layer is the space-charge region or the depletion layer, so termed because the layer is depleted of the majority carriers. The potential distribution in this interfacial region can be quantified by relating the charge density and the electric field strength as embodied by the Poisson equation [14, 26]. Under restrictive conditions, more fully discussed in Refs. [6] and [14], we obtain a particularly simple expression:

$$V(x) = -\left(\frac{e_0 N_D}{2\epsilon_s}\right)x^2 \quad (0 \leq x \leq W) \quad (7)$$

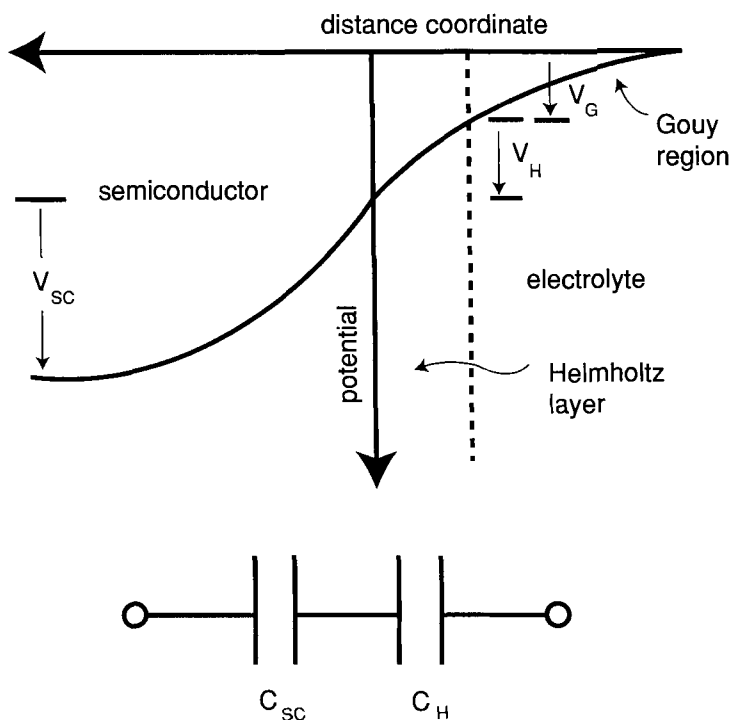


Figure 6. Electrostatics at a semiconductor–electrolyte interface. A very simplified equivalent circuit for the interface at equilibrium is shown at the bottom. The Gouy layer is neglected in the latter case (see text).

where e_0 is the electronic charge and ϵ_s is the static dielectric constant of the semiconductor. The potential distribution is mapped in Figure 6. We are now in a position to quantify the parameter V_{sc} :

$$V_{sc} = -\left(\frac{e_0 N_D}{2\epsilon_s}\right) W^2 \quad (8)$$

where W is the depletion layer width.

Further reflection shows how the magnitude of W should depend on the semiconductor parameter, N_D . Consider two cases of a semiconductor, one lightly doped (say $N_D \approx 10^{16} \text{ cm}^{-3}$) and another heavily doped ($N_D \approx 10^{18} \text{ cm}^{-3}$). Obviously in the former case, the charge needed for Fermi level equilibration has to come from deeper into the solid and so the magnitude W will be larger. This suggests a strategy for chemical control of the electrostatics at the semiconductor–electrolyte interface [6]. Nominal dimensions of W are in the 10–1000 nm range. This may be compared with the corresponding Helmholtz layer width, typically 0.4–0.6 nm. With the capacitor-in-series model (see above), we can see that the

semiconductor space-charge layer is usually the determinant factor in the total capacity of the interface. Once again, the contrast with the corresponding metal–electrolyte interface is striking. Only when the semiconductor is degenerately doped (leading to fairly large Q_{sc} and ‘thin’ depletion layer widths) or when its surface is in accumulation does the situation become akin to the latter (see below).

1.3.3 Mapping of the Semiconductor Band-edge Positions Relative to Solution Redox Levels

Considerations of interfacial electron transfer require knowledge of the relative positions of the participating energy levels in the two phases. Models for redox energy levels in solution are exhaustively treated elsewhere in this series of volumes. Besides the Fermi level of the redox system (Eq. 6), the thermal fluctuation model [27, 28] leads to a Gaussian distribution of the energy levels for the occupied (reduced species) and the empty (oxidized species) states, respectively, as illustrated in Figure 5a. The distribution functions for the states are given by

$$D_{ox} = \exp \left[-\frac{(E - E_{F, redox} - \lambda)^2}{4kT\lambda} \right] \quad (9a)$$

$$D_{red} = \exp \left[-\frac{(E - E_{F, redox} + \lambda)^2}{4kT\lambda} \right] \quad (9b)$$

where λ is the solvent reorganization energy.

Now consider the relative disposition of these solution energy levels with respect to the semiconductor band-edge positions at the interface. The total potential difference across this interface (Figure 6) is given by

$$V_t = V_{sc} + V_H + V_G \quad (10)$$

where V_t is the potential as measured between an ohmic contact on the rear surface of the semiconductor electrode and the reference electrode (Figure 6). The problematic factors in placing the semiconductor and solution energy levels on a common basis involve V_H and V_G . In other words, theoretical predictions of the magnitude of V_{sc} (and how it changes as the redox couple is varied) are hampered by the lack of knowledge of the magnitudes of V_H and V_G . A degree of simplification is afforded by employing relatively concentrated electrolytes such that V_G can be ignored.

As with metals, the Helmholtz layer is developed by adsorption of ions or molecules on the semiconductor surface, by oriented dipoles or, especially in the case of oxides, by the formation of surface bonds between the solid surface and species in solution. Recourse to band-edge placement can be sought through differential capacitance measurements on the semiconductor–redox electrolyte interface [29].

In the simplest case, as more fully discussed elsewhere [14, 15, 29], one obtains the Mott–Schottky relation (for the specific instance of an n-type semiconductor)

again by invoking the Poisson equation:

$$1/C_{\text{sc}}^2 = \frac{2}{N_{\text{D}}e_0\epsilon_s} \left[(V - V_{\text{fb}}) - \frac{kT}{e_0} \right] \quad (11)$$

where V_{fb} is the so-called flat-band potential, i.e., the applied potential (V) at which the semiconductor energy bands are ‘flat’ leading up to the solution junction. Several points with respect to the applicability of Eq. 11 must be noted.

The Mott–Schottky regime spans about ~ 1 V in applied bias potential for most semiconductor–electrolyte interfaces (i.e., in the region of depletion layer formation of the semiconductor space-charge layer, see above) [15]. The simple case considered here involves no mediator trap states or surface states at the interface such that the equivalent circuit of the interface essentially collapses to its most rudimentary form of C_{sc} in series with the bulk resistance of the semiconductor. Further, in all the discussions above, it is reiterated that the redox electrolyte is sufficiently concentrated that the potential drop across the Gouy layer can be neglected. Specific adsorption and other processes at the semiconductor–electrolyte interface will influence V_{fb} ; these are discussed elsewhere [29, 30], as are anomalies related to the measurement process itself [31]. Figure 7 contains representative Mott–Schottky

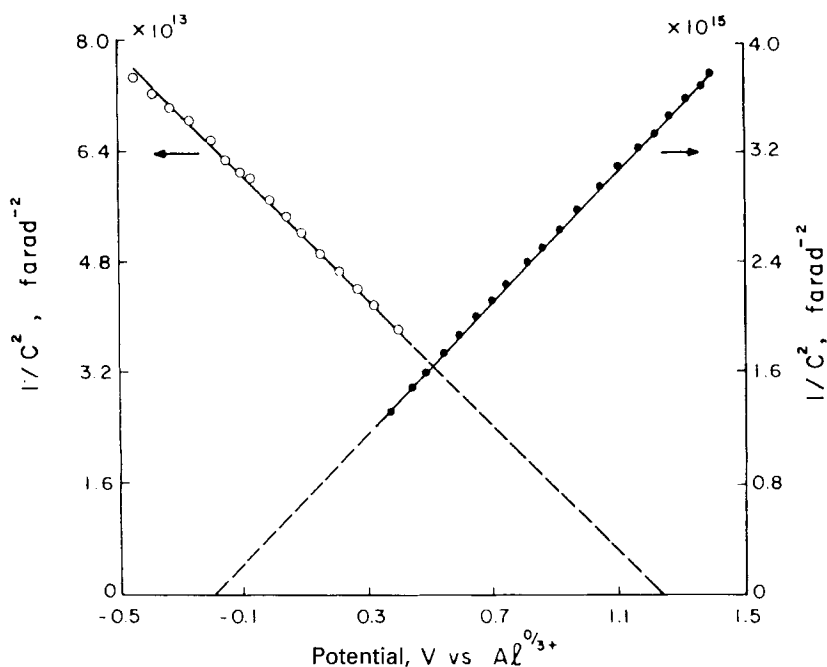


Figure 7. Mott–Schottky plots for n- and p-type GaAs electrodes in an AlCl_3 –*n*-butylpyridinium chloride molten-salt electrolyte. (Reproduced with permission from Ref. [32].)

plots for both n- and p-type GaAs electrodes in an ambient temperature molten salt electrolyte [32].

Once V_{fb} is known (from measurements), the Fermi level of the semiconductor at the surface is defined. It is then a simple matter to place the energies corresponding to the conduction and valence bands at the surface (E_{CB} and E_{VB} , respectively) if the relevant doping levels are known. The difference between E_{CB} and E_{VB} should roughly correspond to the semiconductor band-gap energy, E_g (see Figures 4 and 7). Alternatively, if V_{fb} is measured for one given state of doping of the semiconductor (n- or p-doped), the other band edge position can be fixed from knowledge of E_g . It is important to stress that the semiconductor surface band-edge position (as estimated from V_{fb} measurements) comprises of all the terms in Eq. 10 and reflects the situation in situ for a given set of conditions (solution pH, redox concentration, etc.) of the semiconductor–redox electrolyte. The situation obviously becomes complex when the charge distribution and mediation at the interface changes either via surface states, illumination or both. These complications are considered later. Figure 8 contains the relative dispositions of the surface band-edges thus mapped for a number of semiconductors in aqueous media.

Having located the semiconductor band-edge positions (relative to either the vacuum reference or a standard reference electrode), we can also place the Fermi level of the redox system, $E_{F, redox}$, on the same diagram. Energy diagrams such as those

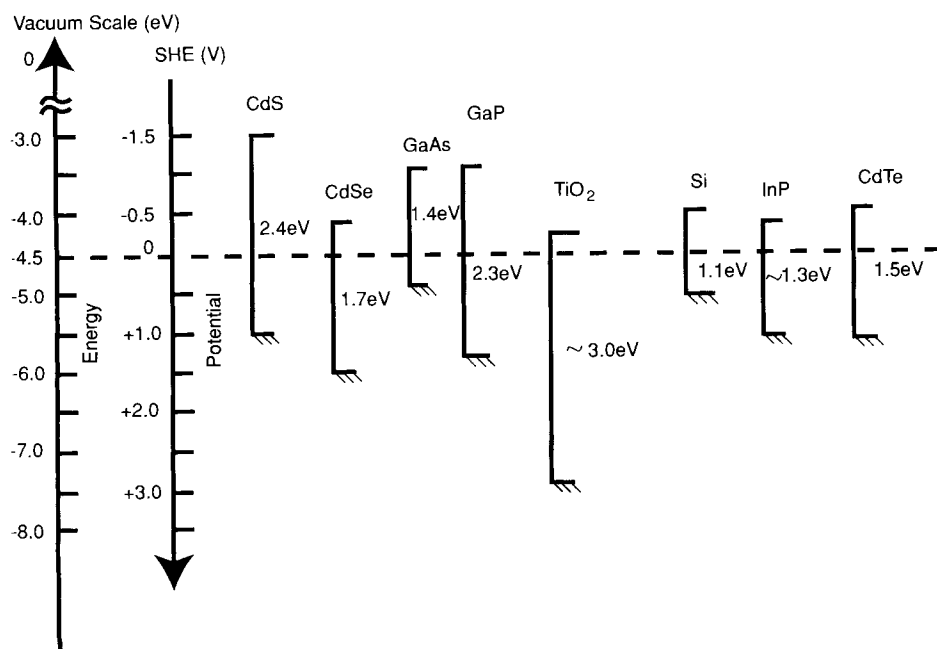


Figure 8. Relative dispositions of various semiconductor band-edge positions shown both on the vacuum scale and with respect to the standard hydrogen electrode (SHE) reference. These band-edge positions are for an aqueous medium of pH \approx 1.

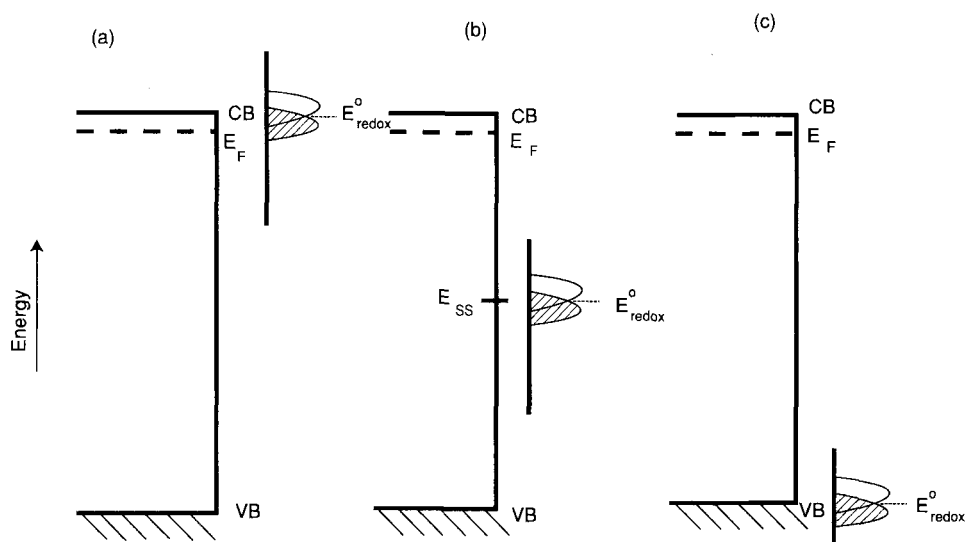


Figure 9. Three situations for an n-type semiconductor–electrolyte interface at equilibrium showing overlap of the redox energy levels with the semiconductor conduction band (a) with surface states (b) and with the semiconductor valence band (c). A discrete energy level is assumed for the surface states as a first approximation.

in Figure 8 are exceedingly important in considerations of charge transfer, as we shall see later. In anticipation of this discussion, it ought already to be apparent that the three situations illustrated in Figure 9 for an n-type semiconductor–electrolyte interface entail the participation of the semiconductor conduction band, valence band and even states in its band-gap in charge exchange with the solution species. Here again is a point of departure from the metal case, viz., for a semiconductor, hole, electron and surface-state pathways must all be considered.

Let us return to the band-bending process at the interface. For a given semiconductor, the expectation is that as the redox Fermi level is moved more positive (‘down’ on the energy diagram), V_{sc} should increase concomitantly. This is the ideal (band-edge ‘pinned’) situation. In other words [23],

$$\frac{d\Delta V_{sc}}{dE_{redox}} = 1 \quad (12)$$

which reflects the fact that the change in band-bending faithfully tracks the redox potential change. A measure of the former is the open-circuit photopotential (see below). Figure 10 shows that this ideal situation indeed is realized for selected semiconductor–electrolyte interfaces [33]. As further discussed below, the analogy with the corresponding metal–semiconductor junctions (Schottky barriers) is direct [5, 34–36].

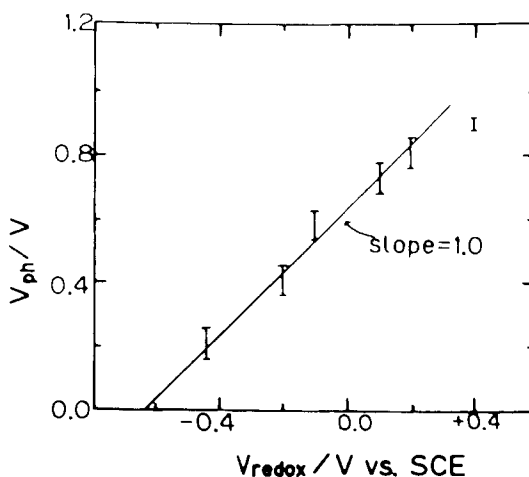


Figure 10. Plot of the open-circuit photo-voltage for amorphous Si–methanol interfaces containing a series of one-electron redox couples. (Reproduced with permission from Ref. [33].)

Complications arise when there are surface states that mediate charge exchange at the interface. When their density is high [37], they act as a ‘buffer’ in that in the extreme case, carriers in the semiconductor energy bands are completely excluded from the equilibration process.

1.3.4 Surface States and Other Complications

Surface states arise simply because of the abrupt termination of the crystal lattice at the surface; obviously, the bonding arrangement there is different from that in the bulk. Consider our prototype semiconductor, Si. The tetrahedral bonding characteristic of the bulk gives way to coordinative unsaturation of the bonds for the Si surface atoms. This unsaturation is relieved either by surface reconstruction or bonds with extraneous (e.g., solvent) species [29, 38–40]. The surface bonding results in a localized electronic structure for the surface that is different from the bulk. The energies of these localized surface orbitals nominally lie in the forbidden band-gap region. The corresponding states are thus able (depending on their energy location) to exchange charge with the conduction or valence bands of the semiconductor and/or the redox electrolyte [29].

Unlike in the case illustrated in Figure 10, changes in the solution redox potential have been observed to cause no change in the magnitude of V_{sc} . This situation is termed Fermi level pinning; in other words, the band-edge positions are *unpinned* in these cases so that the movement of E_{redox} is accommodated by V_{H} rather than by V_{sc} . As mentioned earlier, it appears [37] that surface state densities as low as 10^{13} cm^{-2} ($\sim 1\%$ of a monolayer) suffice to induce complete Fermi level pinning in certain cases. Of course, intermediate situations are possible. Thus, the ideal case manifests a slope of 1 in a plot of V_{sc} (or an equivalent parameter) versus E_{redox} (see Figure 10). On the other hand, complete pinning results in a slope of zero. Inter-

mediate cases of Fermi level exhibit slopes between 0 and 1 [41]. As stated earlier, there is a direct analogy here with the metal–semiconductor junction counterparts [42, 43]:

$$\phi_B = S\phi_m + \text{constant} \quad (13)$$

where ϕ_B is the Schottky barrier height, ϕ_m is the metal work-function and S is a dimensionless parameter. Attempts have been made to relate S to semiconductor properties [44–48].

To make matters worse, the nonideal behavior of semiconductor–electrolyte interfaces as noted above is exacerbated when the latter are irradiated. Changes in the occupancy of these states cause further changes in V_H so that the semiconductor surface band-edge positions are different in the dark and under illumination. These complications are considered later. The surface states as considered above are shallow (with respect to the band-edge positions) and can essentially be considered as completely ionized at room temperature. However, for many oxide semiconductors, the trap states may be deep and therefore are only partially ionized. Specifically, they may be disposed with respect to the semiconductor Fermi level such that they are ionized only to a depth that is small relative to W [49]. The manifestation of such deep traps in the AC impedance behavior of semiconductor electrolyte interfaces has been discussed [14, 49].

Finally, within the Mott–Schottky approximation (Eq. 11), large values of ϵ_s or N_D can lead to the ratio V_H/V_{sc} becoming significant. Figure 11 contains estimates of this ratio for several values of N_D for a semiconductor with a large ϵ_s value (TiO_2 , $\epsilon_s = 173$) mapped as a function of the total potential drop across the interface [50]. Clearly, V_H can become a sizeable fraction of the total potential drop (approaching the situation for metals) under certain conditions. It has been shown [51] that the Mott–Schottky plots will still be linear but the intercept on the potential axis is shifted from the V_{fb} value.

1.4 Experimental Methods for Studying Charge Transfer at Semiconductor–Electrolyte Interfaces

As Table 2 indicates, there is a wide array of tools available to the experimentalist to probe charge transfer at semiconductor–electrolyte interfaces. The references cited in this tabulation are meant only to provide illustrative examples of the application of a given technique, and by no means reflect a comprehensive listing. Space constraints also prohibit a detailed discussion of the principles underlying each method; the original references should be consulted instead. Several review articles [2, 4, 9, 10, 14, 52–54] have addressed the experimental aspects so that another detailed discussion here would be rather redundant. Some general comments, however, are in order prior to examining the consequences of potential- and light-induced perturbation of the semiconductor–electrolyte interface.

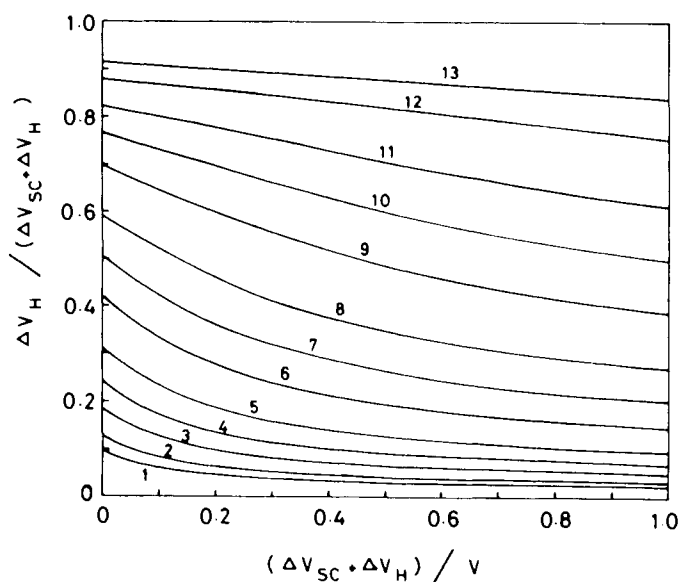


Figure 11. The ratio of the potential drop in the Helmholtz to the total potential change computed as a function of the total potential change. A static dielectric constant of 173 (typical of TiO_2) and a Helmholtz capacitance of $10 \mu\text{F cm}^{-2}$ were assumed and the doping density was allowed to vary from 10^{16} cm^{-3} (curve 1) to 10^{20} cm^{-3} (curve 13).

Table 2. Experimental techniques for studying charge transfer semiconductor–electrolyte interfaces^a.

Entry No.	Technique	Reference(s)
1	Cyclic and linear-sweep voltammetry	55–61
2	Hydrodynamic (rotating-disk and ring-disk) voltammetry	60, 62–72
3	AC impedance spectroscopy	31, 49, 73–86
4	Photoelectrochemical impedance spectroscopy	81, 87–92
5	Photocurrent spectroscopy	55, 76, 93
6	Photocapacitance spectroscopy	94–98
7	Intensity-modulated photocurrent spectroscopy	2, 9, 10, 99
8	Microwave conductivity	100–107
9	Surface conductivity	108, 109
10	Transient photocurrent and photovoltage measurements	99, 110–127
11	Electro- and photoluminescence spectroscopy	128–138
12	Reflectance spectroscopy	14, 139–143
13	Photothermal detection	144–150
14	Time-domain reflectometry	151
15	Quartz crystal microgravimetry	152, 153
16	Second-harmonic generation	154
17	Indirect laser-induced temperature jump	155

^aAlso see Refs. [4, 52–54].

Current–potential measurements, in the dark and under illumination of the semiconductor working electrode, are extremely useful for first defining the charge-transfer behavior across the interface before more sophisticated experiments are undertaken. The irradiation can be either continuous or intermittent (chopped); the latter mode has the distinct advantage that both the dark and light behavior can be examined in the same scan [55, 58]. Even some dynamic information can thus be extracted under the nominally ‘steady-state’ conditions typical of a cyclic or linear potential sweep experiment. Another useful steady-state experiment is photocurrent spectroscopy (performed at a fixed DC potential) [55], although this can also be dynamically performed via IMPS (see below). Such measurements not only yield the so-called photoaction spectrum of the semiconductor electrode, but also afford information on surface recombination and surface state activity at the interface as discussed below.

The parameters that are measured run a wide gamut from the routine (current, potential or some electrical parameter) to the exotic (e.g., beam deflection due to refractive index changes). A hierarchical approach to discussing these variant methods has been described [52]. Thus, the methods in Table 2 fall under the categories of purely electrical (entries 1–3, 8 and 9), purely optical (entry titled photoluminescence spectroscopy and entries 12 and 13), electro-optic (electroluminescence spectroscopy) or opto-electric (entries 4–7). We can also distinguish between frequency-resolved (entries 3–7) and time-resolved (entries 10 and 14) measurements, although it must be noted that in many instances (e.g., entries 8 and 11) both steady-state and time-resolved approaches are feasible.

A relatively recent development in frequency-resolved techniques is the perturbation of an electrochemical system (that is initially in a steady-state condition) by a periodic *nonelectrical* stimulus. One member in this family of techniques (IMPS, entry 7 in Table 2) has provided a wealth of information on charge transfer across semiconductor–electrolyte interfaces. Reviews are available [2, 9, 10], as is a summary of progress on the use of its electrical predecessor (AC impedance spectroscopy, entry 3 in Table 2) for the study of these interfaces [81]. These accounts should also be consulted for a discussion of the relevant time-scales in dynamic measurements on semiconductor–electrolyte interfaces.

1.5 Charge-transfer Processes in the Dark

1.5.1 Current–Potential Behavior

Let us return to the equilibrium situation of an n-type semiconductor in contact with a redox electrolyte and reconsider the situation in Figure 9a. This is shown again in Figure 12a to underline the fact that the interface is in a state of *dynamic* equilibrium. That is, the forward and reverse (partial) currents exactly balance each other and there is no *net* current flow across the interface. In fact, the situation here is much like that at a metal–redox electrolyte interface at the rest potential. We can

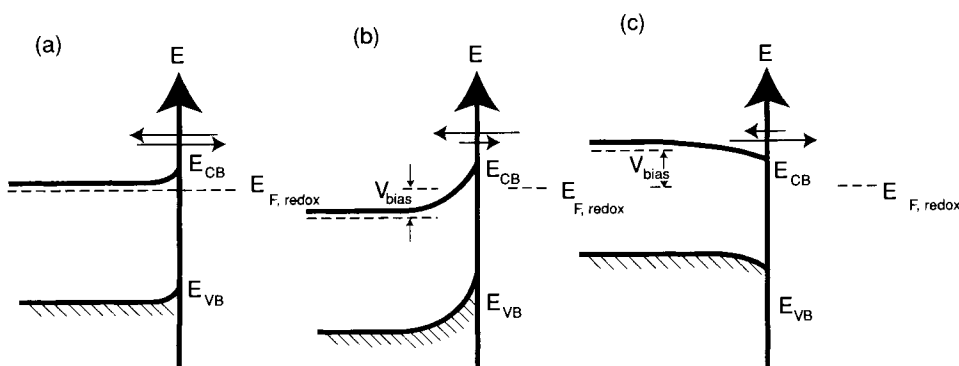


Figure 12. Three situations for an n-type semiconductor–electrolyte interface at equilibrium (a), under reverse bias (b) and under forward bias (c). The size of the arrows denotes the magnitudes of the current in the two (i.e., anodic and cathodic) directions.

write expressions for the net current using a kinetics methodology as in Ref. [6] with some minor changes in notation:

$$i_c = -e_0 A k_{et} c_{ox} (n_s - n_{s0}) \quad (14)$$

where k_{et} is the rate constant for electron transfer, c_{ox} is the concentration of empty (acceptor) state in the redox electrolyte and n_s and n_{s0} are the surface concentrations of electrons, the subscript 0 in the latter case denoting the equilibrium situation. Thus, as long as the semiconductor–electrolyte interface is not perturbed by an external (bias) potential, $n_s \equiv n_{s0}$ and the net current is zero. The voltage dependence of the current is embodied in the ratio n_s/n_{s0} , which can be regarded as a measure of the extent to which the interface is driven away from equilibrium. It must be noted that n_{s0} is *not* the bulk concentration of majority carriers (n) in the semiconductor because of the potential drop across the space charge layer [6, 35]:

$$n_{s0} = n \exp\left(-\frac{e_0 V_{sc}}{kT}\right) \quad (15)$$

A few words about the units of the terms in Eq. 14 are in order at this juncture. The term $i/e_0 A$ may be regarded as a flux (J) in units of number of carriers crossing per unit area per second [1, 3, 8]. The concentration terms are in cm^{-3} ; hence k_{et} has the dimensions $\text{cm}^4 \text{s}^{-1}$ because of the second-order kinetic nature stemming from the two multiplied concentration terms in Eq. 14 [1, 3, 8].

Consider now the application of a bias potential to the interface. Intuitively, when it is such that $n_s > n_{s0}$, a reduction current (cathodic current) should flow across the interface such that the oxidized redox species are converted to reduced species ($\text{Ox} \rightarrow \text{Red}$). On the other hand, when $n_{s0} > n_s$, the current flow direction is reversed and an anodic current should flow. Once again the situation here is similar

to the metal case. The major difference resides in the vastly different state densities in the solid and the existence of an energy gap region. The two nonequilibrium situations are shown in Figure 12b and c, respectively. Away from equilibrium, we have the analogous Boltzmann expression counterpart to Eq. 15:

$$n_s = n \exp \left[-\frac{e_0(V_{sc} + V)}{kT} \right] \quad (16)$$

leading, in turn, to

$$i_c = -e_0 A k_{et} c_{ox} n_{s0} \left[\exp \left(-\frac{e_0 V}{kT} \right) - 1 \right] \quad (17)$$

The assumption is inherent in the preceding discussion that *all* of the applied bias (V) drops across the space-charge layer such that we are modulating only the majority carrier population at the surface (and not the potential drop across the Helmholtz layer). In other words, the band-edge positions are pinned or there is *no* Fermi level pinning (see Section 1.3.4).

Analogous expressions may be developed for majority-carrier flow for a p-type semiconductor in contact with a redox electrolyte with the important caveat that the valence band is involved in this process instead.

Eq. 17 suggests that the cathodic current is exponentially dependent on potential for $V < 0$. This is the so-called forward bias regime. On the other hand, when $V > 0$ (reverse-bias regime) the current is essentially independent of potential and, importantly, is of opposite sign. Simply put, in this case, the electron flow direction (i.e., anodic) is from the occupied redox states into the semiconductor conduction band (Figure 12c). It should therefore not, be surprising that this process is independent of potential. Both bias regimes are contained in curve 1 in Figure 13.

Of particular interest to this discussion is the ‘pre-exponential’ term in Eq. 17:

$$i_0 = e_0 A k_{et} c_{ox} n_{s0} \quad (18)$$

Analogous to the metal case, we can call this term the exchange current; it is the current that flows at equilibrium when the partial cathodic and anodic components exactly balance one another. Of particular interest is the dependence of i_0 on n_{s0} . Also variations in c_{ox} will affect the magnitude of i_0 . Both of these trends can be readily rationalized. Finally, i_0 will increase with doping because of the ‘thinness’ of the resultant barrier at the surface.

When $E_{F, redox}$ is moved ‘down’, i.e., more positive, the band-bending increases, V_{sc} increases and therefore n_{s0} decreases. A similar alteration in c_{ox} affects $E_{F, redox}$ through the Nernst expression. In both instances, we are influencing the Fermi level at the interface at equilibrium. Thus, in a sense, i_0 is a quantitative measure of the extent of rectification of a given interface, i.e., a smaller i_0 value translates to better rectification.

The reverse bias current remains at a very low value because of the lack of minority carriers (i.e., holes for n-type semiconductor) in the dark. Alternatively,

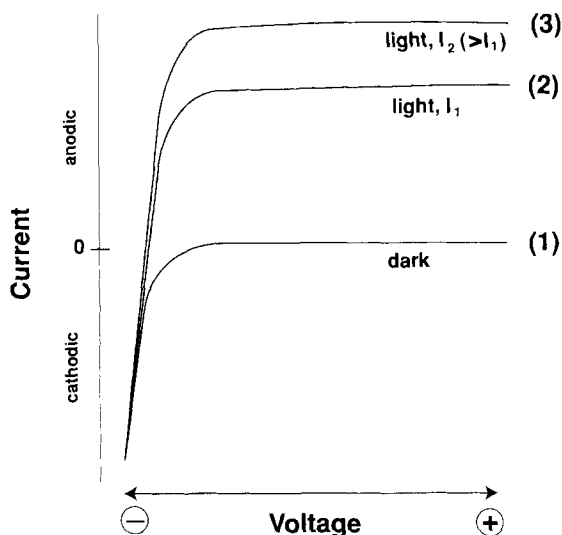


Figure 13. Current–potential curves for an n-type semiconductor in the dark (curve 1) and under band-gap illumination (curves 2 and 3). Two levels of photon fluxes are shown in the latter case.

injection of electrons from occupied redox levels (also an anodic current) has to thermally surmount the surface barrier [5, 34, 35]. Under extreme reverse bias, however, this barrier becomes ‘thin’ and electrons can tunnel through it leading to an abrupt increase in the anodic current. This process was studied even in the early days of semiconductor electrochemistry (see, e.g., Ref. [156]) and a detailed discussion can be found in a book chapter [14]. Ultimately the junction ‘breaks down’ (at the so-called Zener limit). This dark current flow is not shown in Figure 13 (curve 1).

Returning to the forward bias (cathodic) current flow, Eq. 17 bears some analogy to the famous Tafel expressions in electrochemical kinetics. Thus, ignoring the unity term within the square brackets, Eq. 17 predicts a Tafel slope of 60 mV per decade at 298 K. In many instances (see, e.g., Refs. [157, 158]), such a slope indeed is observed. In many cases, however, the slopes are higher than the ‘ideal’ value [14, 159–163].

The causes of this anomalous behavior are still not fully understood. It appears likely that many factors are involved: surface film formation, varying potential drop across the Helmholtz region caused, for example, by surface state charging, etc. Even crystallographic orientations appear to be important [163]. These aspects have been discussed by other authors [14, 159, 164].

We have so far considered only (majority carrier) processes involving the CB (again assuming for illustrative purposes an n-type semiconductor). Consider the interfacial situation depicted in Figure 9c. The energy states of the redox system now overlap with the VB of the semiconductor such that *hole injection* in the ‘dark’ is possible. When the band-bending is large, the injected holes remain at the surface and attack the semiconductor itself, causing the latter to undergo corrosion. If the

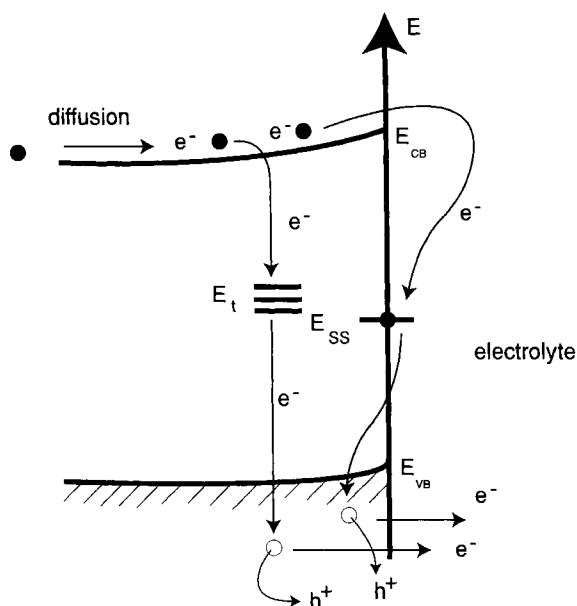


Figure 14. Hole injection into the VB of an n-type semiconductor from an oxidant (e.g., Fe^{3+}) and the injection/recombination pathway. Both surface-state mediated and depletion layer trap mediated routes are shown for the recombination.

bias potential is such that the band-bending is modest and the holes recombine with electrons (either via the surface states or in the space-charge region itself), a cathodic current flows that is carried by the majority carriers in the bulk. This recombination current pathway is schematized in Figure 14 and is further discussed in the next section. Hole injection has been extensively studied especially for III–V (Group 13–15) semiconductors such as GaAs and GaP because of the relevance of this process to electroless etching and device fabrication technology. This topic has been reviewed [165–168].

The invocation of either the conduction band or the valence band of the semiconductor in charge exchange in the dark with solution redox species is not always straightforward. This is particularly true for multi-electron redox processes to be discussed later. Movement of the semiconductor band-edge positions (i.e., band-edge unpinning) relative to the redox energy levels also presents a complicating situation (see below). Some cases (e.g., $\text{Eu}^{2+/3+}$ in contact with GaAs electrodes) are interesting in that the same couple can interact with both bands [159, 169]. Thus the oxidation of Eu^{2+} is a VB process (occurring at p-GaAs but not at n-GaAs in the dark), while the reduction of Eu^{3+} (a facile process reportedly occurring at rates close to the thermionic emission limit [159]) is mediated by CB electrons [169]. The $[\text{Cr}(\text{CN})_6]^{3-/4-}$ redox system behaves in a similar manner with respect to GaAs [170].

Electroluminescence, EL (Table 2), is a versatile probe for studying such carrier injection processes. Thus, hole injection into the VB of an n-type semiconductor leads to cathodic EL whereas electron injection into the CB of a p-type semiconductor leads to anodic EL [171]. Examples of studies of cathodic EL are common-

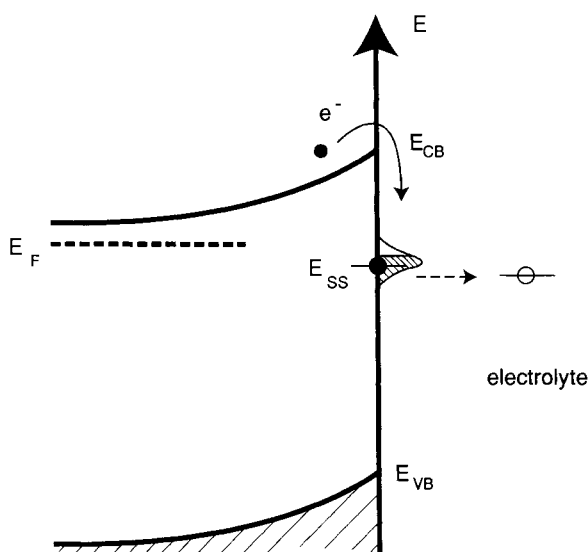


Figure 15. Surface-state mediated electron injection from the CB of an n-type semiconductor into the electrolyte.

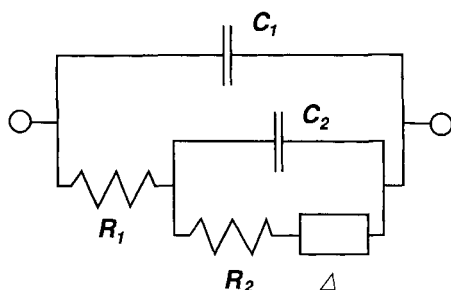
place (e.g., [129, 172, 173]); however, anodic EL is not very common because of the energy requirement for the redox couple to have a very negative redox potential. Nonetheless, anodic EL has been reported for the p-InP–[Cr(CN)₆]⁴⁻ interface [174]. Radical intermediates can also cause EL as discussed later for multi-electron redox processes.

This finally brings us to the comparability of the current–potential behavior of n- and p-type samples of a given semiconductor. It may be noted that for a redox process occurring via one of the bands (e.g., VB), the cathodic currents (electron transfer from VB to Ox) are expected to be equal for n- and p-type materials. This idea has been pursued using the so-called quasi-Fermi level concept [159, 175, 176]. This model has been proven quantitatively by studying the anodic decomposition of GaAs and the oxidation of redox species such as Cu⁺ and Fe²⁺ at n- and p-type GaAs electrodes [175, 176]. The original references should be consulted for details.

1.5.2 Dark Processes Mediated by Surface States or by Space Charge Layer Recombination

Surface states were considered earlier (Section 1.3.4) from an electrostatic perspective. Here we examine their dynamic consequences. There are two principal charge-transfer routes involving surface states. Consider again an n-type semiconductor; the forward bias current can either involve direct exchange of electrons between the semiconductor CB and Ox states in solution (see Figure 12b) or can be mediated by surface states (Figure 15). The second route involves hole injection into the semiconductor VB, again from Ox states in solution (Figures 9c and 14). The recomb-

(a)



(b)

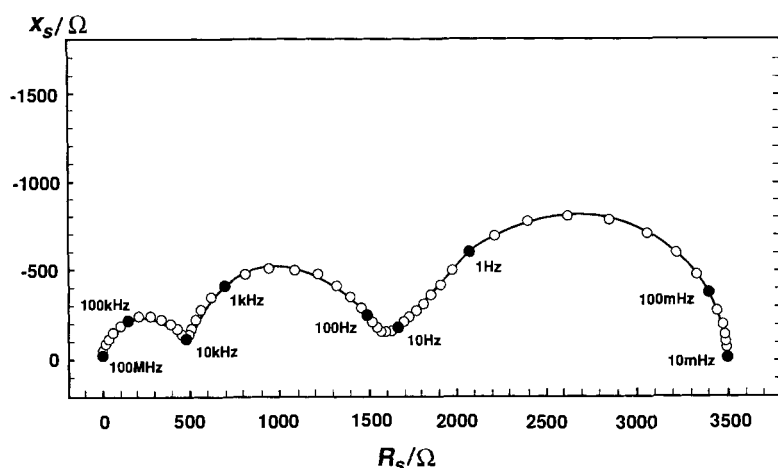


Figure 16. Equivalent circuit (a) and a simulated Nyquist plot (b) for the charge transfer pathway illustrated in Figure 15. The capacitance C_1 represents that of the space-charge layer and the parallel branch components represent the Faradaic charge transfer process. Refer to the original work for further details. (Reproduced with permission from Ref. [84].)

nation current is mediated either by surface states or via space-charge layer recombination. We shall consider first the CB process.

Initial evidence for the intermediacy of surface states came from dark current measurements on n-TiO₂ and n-SrTiO₃ in the presence of oxidizing agents such as [Fe(CN)₆]^{3−}, Fe³⁺, and [IrCl₆]^{2−} [177, 178]. Similar evidence that the charge-transfer process was more complex than direct transfer of electrons from the semiconductor CB also came early from AC impedance spectroscopy measurements on n-ZnO, n-CdS and n-CdSe in contact with [Fe(CN)₆]^{3−} species [179, 180].

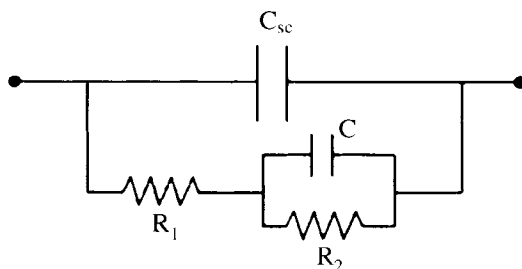


Figure 17. Equivalent circuit representation of the injection/recombination process. (Reproduced with permission from Ref. [81].)

The electrochemical impedance for surface state-mediated charge transfer has been computed recently [84]. The key results are summarized in Figure 16. Figure 16a contains the proposed equivalent circuit for the process and features a parallel connection of the impedance for the Faradaic process [$Z_F(\omega)$] (ω = angular frequency, $2\pi f$) and the capacitance of the semiconductor depletion layer, C_{sc} . The former also involves a diffusion impedance (Δ) of the Warburg type (see below). The complex plane (Nyquist) plot predicted for the circuit is illustrated in Figure 16b. The theoretically predicted AC impedance response was compared with experiments on n-GaAs rotating disk electrodes in sulfuric acid media [85]. The equivalent circuit in Figure 16a was also compared with previous versions proposed by other authors [181–183]. These alternative versions differ in their assumption of no variations in potential drop across the Helmholtz region (i.e., infinite C_H) and no concentration polarization in the electrolyte phase (infinite diffusion coefficient for the redox species). The same research group has also discussed the application of AC impedance spectroscopy for studying the kinetic reversibility of majority carrier charge transfer via the CB of an n-type semiconductor [83]. These original references should be consulted for further details.

AC impedance spectroscopy also has seen extensive utility in the study of the hole injection/recombination process depicted in Figure 14. An equivalent circuit for this process is illustrated in Figure 17; it resembles the circuit in Figure 16a except for the Warburg component [81]. Early studies [73, 74, 184, 185] utilized the recombination resistance parameter, R_r , that was extracted from model fits of the measured AC impedance data. This parameter was seen to be inversely related to the hole injection current, thus signifying that it is indeed related to the recombination process. However, the challenge is to differentiate whether recombination is mediated via surface states or whether it occurs in the depletion layer. Thus the parameter R_r alone cannot afford this information and both the real and the imaginary parts of this additional impedance must be considered. Subsequent studies have addressed this aspect [73, 186–190]. The admittance corresponding to recombination at the surface [189] and in the space-charge layer [190] was calculated from first principles. These computations show that the recombination *capacitance* increases monotonically with decreasing band-bending in the latter case while it shows a peak in the former case as a function of potential.

Experimental studies [188] show that in the case of n-GaAs electrodes in contact with Ce^{4+} as the hole injection agent, surface recombination prevails. On the other hand, with n-GaP electrodes, recombination in the depletion layer must also be

taken into account. Other discussions of the use of AC impedance spectroscopy for the study of hole injection/ recombination are contained in Refs. [81] and [84].

The consequences of potential drop variations across the Helmholtz layer in the hole injection process have been examined by a variety of techniques [191, 192]. For example, chemical reaction of the GaAs surface with iodine results in a downward shift of the semiconductor band-edge positions such that the reduction of iodine is mediated by conduction band electrons [192]. When sufficient negative charge accumulates at the surface, the potential is redistributed between the semiconductor space-charge layer and the Helmholtz region. Now iodine is reduced by hole injection as gauged by EL and AC impedance measurements [192].

1.5.3 Rate-limiting Steps in Charge-transfer Processes in the Dark

The assumption is implicit in the discussion in Section 1.5.1 (leading to Eq. 18) that charge-transfer kinetics at the semiconductor–electrolyte interface is the rate-limiting step. Fundamentally, we have to differentiate majority carrier *capture* and minority carrier *injection* processes in the dark. In the former case, transit through the semiconductor itself or charge exchange with the surface states can be potentially rate-limiting. In the latter case, there are three steps involved: hole injection into the semiconductor VB, charge exchange between the recombination center and the semiconductor CB and diffusion of majority carriers (electrons) from the neutral region. Finally, mass transport processes in the electrolyte phase itself can be a limiting factor in the overall current flow. We shall examine carrier capture and injection processes in turn.

Most outer-sphere, nonadsorbing redox systems to date have yielded values for k_{et} in the 10^{-17} – 10^{-16} $\text{cm}^4 \text{s}^{-1}$ range [3, 8]. These include n-Si–CH₃OH [193, 194], n-InP–CH₃OH [195], GaInP₂-coated n-GaAs–acetonitrile [196] and p-GaAs–HCl [197] interfaces. The redox couples in these studies have mostly involved metal-locenes that show a low proclivity to adsorb on the semiconductor surface. In these cases, the rate-determining step in the overall current flow undoubtedly lies in the electron transfer event at the interface itself. However, values for k_{et} roughly three orders of magnitude higher have also been reported for similar interfaces, e.g., n-GaAs–acetonitrile containing cobaltocenium [$\text{Co}(\text{Cp})_2^+$] acceptors [196, 198]. Similarly, high values were reported for p-GaAs–acetonitrile interfaces with ferrocenium and cobaltocenium redox species [199]. In these latter cases, alternative mechanisms (e.g., thermionic emission, see below) must be invoked in a rate-limiting role. Quartz crystal microbalance (Table 2) measurements have yielded evidence for adsorption of redox species (and consequently high *local* substrate concentration) in some of these ‘anomalous’ instances [198].

In the majority carrier capture process, if the interfacial charge-transfer kinetics are facile, the transport of majority carriers through the space-charge region can play a rate-limiting role. The thermionic emission theory [34] assumes that every electron that reaches the semiconductor surface and has the appropriate energy to overcome the potential barrier there will cross the interface with a tunnel probability of unity. However, if the interfacial kinetics are sluggish, some of the electrons will be reflected at the interface. In this case, the exchange current i_0 is no longer

described by Eq. 18 but by Eq. 19 [34]:

$$i_0 = AA^* \left(\frac{m^*}{m_e} \right) T^2 \left(\frac{n_s}{n} \right) \quad (19)$$

where A is the electrode area, A^* is the Richardson constant ($120 \text{ A K}^{-2} \text{ cm}^{-2}$), m^*/m_e is the relative effective electron mass in the conduction band and T is the absolute temperature.

In many of the reported instances [157, 159, 200], the current calculated from Eq. 19 is much higher than that measured experimentally, signaling that interfacial charge-transfer kinetics are limiting the overall rate. On the other hand, in the n-GaAs–acetonitrile– $\text{Co}(\text{Cp})_2^+$ case [198], AC impedance spectroscopic data appear to support the assumption that thermionic emission is the current-limiting transport mechanism.

Another factor that enters into this discussion is the mobility of the majority carriers. It has been argued [14] that in the case of low-mobility materials (e.g., $\mu_n \approx 1 \text{ cm}^2 \text{ V}^{-1} \text{ s}^{-1}$), carrier transport from the semiconductor bulk to the interface itself can become limiting. Clearly, a multitude of factors are important in majority carrier capture: k_{et} , acceptor concentration in the electrolyte and carrier mobility.

What about the minority carrier injection process depicted in Figure 14? Here, contrasting with the process considered above, the hole injection step itself is usually very fast (see below). Then the current is limited by diffusion/recombination described by the Shockley equation [201]:

$$i_0 = \frac{e_0 A D_p n_i^2}{n L_p} \quad (20a)$$

for bulk recombination and

$$i_0 = 0.5 e_0 A W \sigma v_{\text{th}} N_t n_i \quad (20b)$$

for recombination within the semiconductor space-charge region, where D_p is the diffusion coefficient for holes, L_p is the hole diffusion length, n_i is the intrinsic carrier concentration, σ is an average capture cross-section for electrons and holes, v_{th} is the thermal velocity of charge carriers and N_t is the areal density of recombination (trap) centers in the middle of the energy gap (see Figure 14).

The diffusion/recombination mechanism results in considerable overpotential for (cathodic) current flow in the dark (again assuming an n-type semiconductor for illustration). Such a rate-limiting process was found to describe the charge transfer at n-GaAs in 6 M HCl containing Cu^+ as the hole-injecting species [159, 176].

Whatever the limiting mechanism, ultimately the current becomes limited by concentration polarization, i.e., by the transport of redox species from the bulk electrolyte to the semiconductor surface. The situation in this regard is no different from that at metal electrode–electrolyte interfaces. As in the latter case, hydrodynamic (specifically RDE, Table 2) voltammetry is best suited to study mass transport. AC impedance spectroscopy can be another useful tool in this regard [82].

In the former case, the data can be processed via Levich plots of current vs. $\omega^{1/2}$ (ω = angular frequency). If processes other than solution mass transport become rate-limiting, then the plot will show a curvature and the current will even become independent of the electrode rotation rate. In this case, inverse Levich (or Koutecky–Levich) plots of $1/i$ vs. $\omega^{-1/2}$ can be used for further analyses. Such analyses have been done, for example, for n-GaAs–acetonitrile– $\text{Co}(\text{Cp})_2^+$ interfaces [198] and n- and p-GaAs electrodes in contact with the $\text{Cu}^{+/2+}$ redox couple in HCl electrolyte [159, 176].

The diffusion impedance at semiconductor electrodes has been considered recently [82]. Hens and Gomes described the applicability of AC impedance spectroscopy for the study of electron capture and hole injection processes at n-GaAs– $\text{H}_2\text{O}/\text{C}_2\text{H}_5\text{OH}$ –methylviologen, p-InP–aq. KOH – $\text{Fe}(\text{CN})_6^{3-}$, n-GaAs– H_2SO_4 – Ce^{4+} and n-InP–aq. KOH – $\text{Fe}(\text{CN})_6^{3-}$ interfaces. In the case of electron-capture processes, a Randles-like equivalent circuit was found to be applicable [82]. On the other hand, no Warburg component was present in the hole injection case when the reverse reaction was negligible (see Figure 17). For a nonideal semiconductor–electrolyte contact (see Section 1.3.4), a Warburg impedance appeared in the electrochemical impedance of an injection reaction as well, as exemplified by the n-InP– $\text{Fe}(\text{CN})_6^{3-}$ case [82].

1.6 Light Absorption by the Semiconductor Electrode and Carrier Collection

1.6.1 Light Absorption and Carrier Generation

The optical band-gap of the semiconductor (Section 1.2) is an important parameter in defining its light absorption behavior. In this quantized process, an electron–hole pair is generated in the semiconductor when a photon of energy $h\nu$ (ν = frequency and $h\nu > E_g$) is absorbed. Optical excitation thus results in a delocalized electron in the CB, leaving behind a delocalized hole in the VB; this is the band-to-band transition. Such transitions are of two types: direct and indirect. In the former, momentum is conserved and the top of VB and the bottom of CB are both located at $k = 0$ (k is the electron wavevector). The absorption coefficient (α) for such transitions is given by [202]

$$\alpha = A'(h\nu - E_g)^{1/2} \quad (21)$$

where A' is a proportionality constant. Indirect transitions involve phonon modes; in this case, Eq. 21 takes the form

$$\alpha = A'(h\nu - E_g)^2 \quad (22)$$

A given material can exhibit a direct or indirect band-to-band transition depending

on its crystal structure. For example, Si single crystals have an indirect transition located at 1.1 eV (Table 1). On the other hand, amorphous Si is characterized by a direct optical transition with a larger E_g value (shorter wavelengths). Even both types of transitions can be seen in the same material, e.g., GaP [203].

Within the present context, the important point to note is that the absorption depths (given by $1/\alpha$) are vastly different for direct and indirect transitions. Whereas in the former case absorption depths span the 100–1000 nm range, they can be as large as 10^4 nm for an indirect transition [9].

Optical transitions in semiconductors can also involve localized states in the band-gap. These become particularly important for semiconductors in nanocrystalline form (see below). Sub-band-gap transitions can be probed with photons of energy below the threshold defined by E_g .

1.6.2 Carrier Collection

The number of carriers collected (in an external circuit, for example) versus those optically generated defines the quantum yield (Φ), a parameter of considerable interest to photochemists. The difficulty here is to quantify the amount of light actually absorbed by the semiconductor since the cell walls, the electrolyte and other components of the assembly are all capable of either absorbing or scattering some of the incident light. Unfortunately, this problem has not been comprehensively tackled, unlike in the situation with photocatalytic reactors involving semiconductor particulate suspensions where such analyses are available [204–207]. Pending these, an *effective* quantum yield can still be defined.

Returning to the carrier collection problem, consider Figure 18 for an n-semiconductor–electrolyte interface. As can be seen, the electron–hole pairs are optically generated, both in the field-free and in the space-charge regions within the semiconductor. Recombination of these carriers must be considered in the bulk, in the space-charge layer and on the semiconductor surface (the latter in contact with the redox electrolyte). We are assuming here that light is incident from the electrolyte side. Rear illumination geometry can be profitably employed and is considered later for the nanocrystalline film case.

The direction of the electric field at the interface (Figure 6, Section 1.3.2) is such that the minority carriers (holes in this case) are swept to the surface and the electrons are driven to the rear ohmic contact. How fast the holes are drained away (by Faradaic reactions involving the redox electrolyte) will dictate how the Fermi levels compare with the equilibrium situation discussed earlier. The departure from equilibrium has been quantified in terms of the quasi-Fermi level concept discussed later.

The extent of collection of minority carriers from the region beyond the depletion layer is dictated by the diffusion process. A diffusion length, L , can be defined:

$$L_p = \sqrt{D_p \tau_p} = \sqrt{kT \mu_p \tau_p} \quad (\text{for n-type semiconductor}) \quad (23)$$

The subscripts in Eq. 23 remind us that we are dealing with minority carrier col-

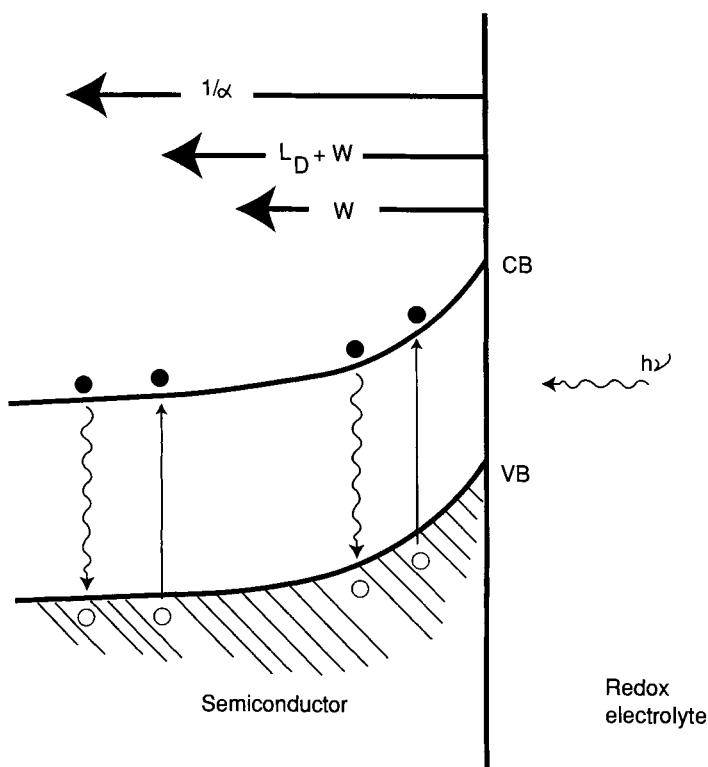


Figure 18. Photogeneration of electron–hole pairs in the field-free region and depletion layer for an n-type semiconductor–electrolyte interface. The characteristic regions defined by the depletion layer (W), Debye length (L_D) and the light penetration depth ($1/\alpha$) are also compared.

lection; μ_p is the hole mobility and τ_p is the hole lifetime. The characteristic length L_p defines the region within which electron–hole pair generation is fully effective. Thus, pairs generated at depths longer than the Debye length, L_D ($L_D = W + L$), will simply recombine. Thus, the effective quantum yield for a given interface will depend on the relative magnitudes of L_D and the light penetration depth, $1/\alpha$ (Figure 18) [9, 54, 55].

An expression for the flux of photogenerated minority carriers arriving at the surface was originally given for a solid-state junction [208] and subsequently adapted to semiconductor–liquid junctions [209]. The major weakness of these initial models hinges on their underlying assumption for the boundary condition that the surface concentration of minority carriers is zero. As pointed out elsewhere [14], this is a demanding condition necessitating very high magnitudes for the interfacial charge transfer rate constant, k_{et} (see above). A modicum of improvement to the basic Gärtner model was found [210] by defining a flux rather than a concentration expression for the holes and a characteristic length where the bulk diffusion current transitions into a drift current. However, this treatment still assumes that every hole

entering the depletion layer edge exits this region and out into the electrolyte phase.

The Gärtner equation [208] can be written in normalized form [55]:

$$\Phi \equiv \frac{j_{ph}}{I_0} = 1 - \frac{\exp(-\alpha W)}{1 + \alpha L_p} \quad (24)$$

where Φ is the effective quantum yield (see above), given by the ratio of the photo-current density (i_{ph}/A), j_{ph} , to the incident light flux, I_0 . Recasting Eq. 24 in the form

$$-\ln(1 - \Phi) = \ln(1 + \alpha L_p) + \alpha W \quad (25)$$

recalling that W is proportional to $V_{sc}^{1/2}$ (Eq. 8) and $V_{sc} = V - V_{fb}$, a test of the rudimentary model would lie in a plot of the left-hand side of Eq. 25 against $(V_{fb} - V)^{1/2}$. Such plots are shown in Figure 19 at four selected wavelengths for the p-GaP-H₂SO₄ electrolyte interface [211].

While adherence to the Gärtner model is satisfactory for large values of V_{sc} (i.e., large band-bending, see Figure 6), the model clearly fails close to the flat-band situation. Interestingly, this problem is exacerbated as the semiconductor excitation wavelength becomes shorter (Figure 19). Thus, another weakness of the basic Gärtner model [208, 209] is the complete neglect of surface recombination. At the

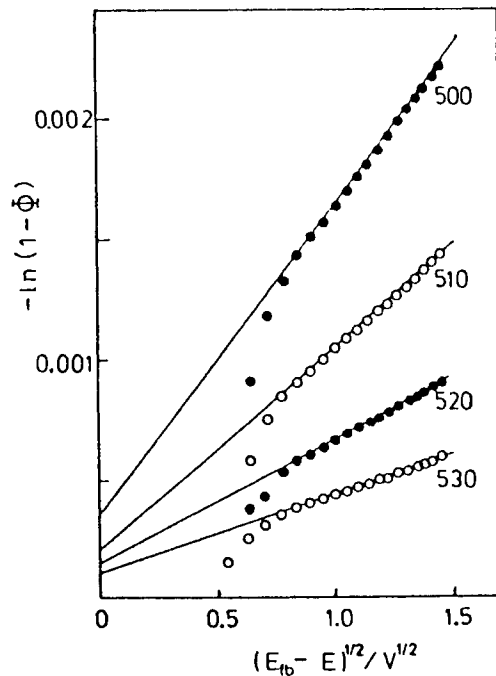


Figure 19. Gärtner plots (see Eq. 25) for the p-GaP-0.5 M H₂SO₄ interface. The numbers on the plots refer to the excitation wavelength; E_{fb} is the flat-band potential and E is the bias potential. (Note that this notation is different from that employed in the text.) (Reproduced with permission from Ref. [211].)

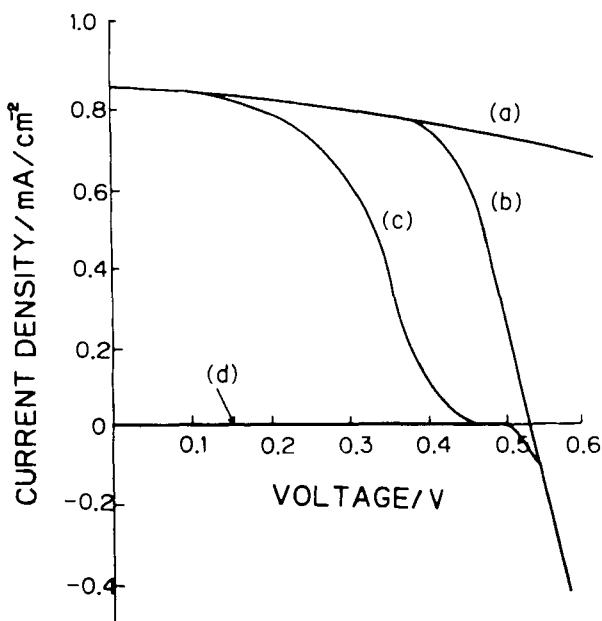


Figure 20. Comparison of calculated current voltage profiles in the dark (curve d) and under illumination (curves a–c). Curve a is obtained from the basic Gärtner model. Curve b considers surface recombination and curve c considers both surface recombination and recombination in the space-charge layer. These simulations are for an n-type semiconductor–electrolyte interface. (Reproduced with permission from Ref. [230].)

flat-band situation, this model still predicts finite current flow arising from the diffusive flow of minority carriers toward and out of the interface (see Figure 20).

A variety of refinements have been made to take into account the surface recombination effect [93, 211–225]. The earliest of these [212, 213, 216] involve some simplifying assumptions:

- 1) there is no recombination in the depletion layer, that is, all the holes optically generated in the bulk and within the depletion layer (Figure 18) are swept to the surface without loss;
- 2) the steady-state concentration of the optically generated minority carriers does not perturb the potential distribution in the dark (Figure 6); and
- 3) there is a quasi-thermodynamic distribution of minority carriers within the depletion layer, which translates to a constant product term np across this region.

Surface recombination in most of these treatments invokes the Hall–Shockley–Read model [226, 227]. Defining the Gärtner limiting expression (Eq. 24) as Φ_G , we obtain [14]

$$\Phi_{ss} = \Phi_G \left/ \left[1 + \frac{D_p \exp V_{sc}}{L_D(k_t + S_t)} \right] \right. \quad (26)$$

In Eq. 26, we have two new parameters, k_t and S_t . These are the first-order rate constant for hole transfer (units of cm s^{-1} , see below) and the surface recombination

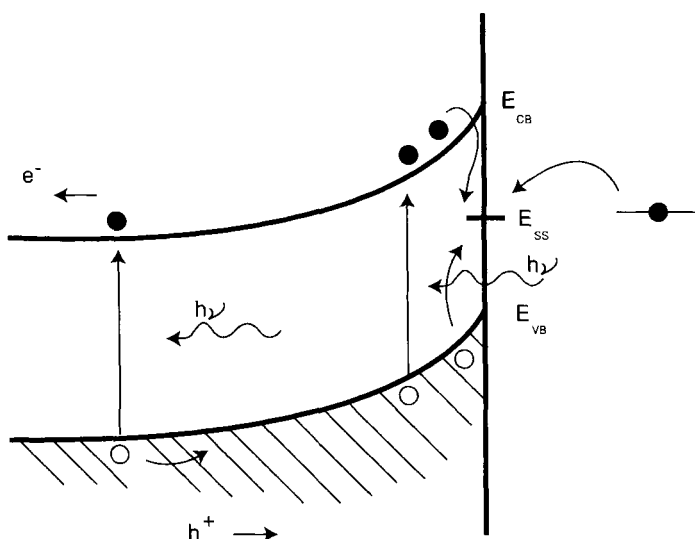


Figure 21. Surface-state mediation of both minority carrier (i.e., hole) transfer and recombination for an n-type semiconductor electrolyte interface.

velocity, S_t , respectively. In the combined situation of high L_D , high k_t and very low (or zero) S_t , Eq. 26 collapses to the Gärtner limit.

At this juncture, it is worth noting that only one trap state at the surface has been assumed until now; further, it is assumed that this surface state both functions as a carrier recombination site and as a charge transfer pathway (Figure 21). Both of these assumptions are open to criticism. An alternative model invoking two distinct types of surface states, one active in recombination and the other capable of mediating charge transfer, has been considered [228]. Nonetheless, the most serious flaw in the treatments above lies in the neglect of carrier recombination in the depletion layer itself (as distinct from recombination at the surface). Re-examination of Eqs. 24 and 26 shows that the larger the Debye length, L_D , and the depletion layer width, W , the higher is the quantum yield. However, recombination in the space-charge layer must become significant at some value of W , thus providing a further limit to carrier collection.

Recombination within the space-charge region is a non-trivial problem to treat from a computational perspective [14]. The methodology of Sah, Noyce, and Shockley [229] has been used by several authors [219, 220, 223, 230–232]. Figure 20 illustrates the sensitivity of the current–potential profiles at the semiconductor–electrolyte interface to this recombination mode [230].

Other models taking the above nonidealities to varying extents have been proposed; a detailed discussion of these lies beyond the scope of this chapter [233–239]. However, it is worth noting here that in some instances involving high-quality semiconductor–electrolyte interfaces the rate-determining recombination step does

indeed appear to lie in the bulk semiconductor [1, 240]. Silicon photoelectrodes in methanolic media containing fast, one-electron, outer-sphere redox couples were studied in these cases.

1.6.3 Photocurrent–Potential Behavior

The current–voltage characteristics of an illuminated semiconductor electrode in contact with a redox electrolyte can be obtained by simply adding together the majority and minority current components. The majority carrier component is given by the diode equation (Eq. 17) while the minority carrier current (i_{ph}) is directly proportional to the photon flux (see, e.g., Eq. 24). Thus, the net current is given by

$$i = i_{\text{ph}} - i_0 \left[\exp\left(-\frac{e_0 V}{kT}\right) - 1 \right] \quad (27)$$

The minus sign in Eq. 27 underlines the fact that the majority-carrier component flows opposite to (or ‘bucks’) the minority carrier current flow. This photocurrent component is shown as curves 2 and 3 in Figure 13.

Eq. 27 shows that the diode equation is offset by the i_{ph} term; this is exactly what is seen in Figure 13. The plateau photocurrent is proportional to the photon flux, I_0 , as illustrated for two different values of the incident light intensity in Figure 13. At the open-circuit condition of the interface, $i = 0$ (and neglecting the unity term within the square brackets relative to the exponential quantity), Eq. 27 leads to

$$V_{\text{oc}} \approx \frac{kT}{e_0} \ln\left(\frac{i_{\text{ph}}}{i_0}\right) \quad (28)$$

Eq. 28 underlines two important trends: first, V_{oc} increases logarithmically with the photon flux (with a slope of ~ 60 mV at 298 K). Second, V_{oc} decreases with an increase in i_0 (again logarithmically). This underlines the importance of ensuring that the majority carriers do not ‘leak’ through the interface. Because of the diode nature of the interface, from a device perspective, the semiconductor surface must be designed to have fast minority carrier transfer kinetics (and thus high i_{ph}) but must be blocking to the flow of majority carriers (from the CB for an n-type semiconductor) into the redox electrolyte. This challenge is not unlike what solid-state device physicists face but relative to metals (with a high density of acceptor states), *chemical* control of redox electrolytes offers a powerful route to performance optimization of liquid-based interfaces, as also pointed out by previous authors [1, 6, 8].

Referring back to Figure 13, the current–potential curves under illumination of the semiconductor simply appear shifted ‘up’ relative to the dark i – V counterpart. This, however, is the ideal scenario. Anomalous photoeffects (APEs) are often observed that manifest as a cross-over of light and dark current–voltage curves, as illustrated in Figure 22. Thus, the superposition principle [241] is not obeyed in this instance. The dashed line in Figure 22 is produced by translating the photocurrent–

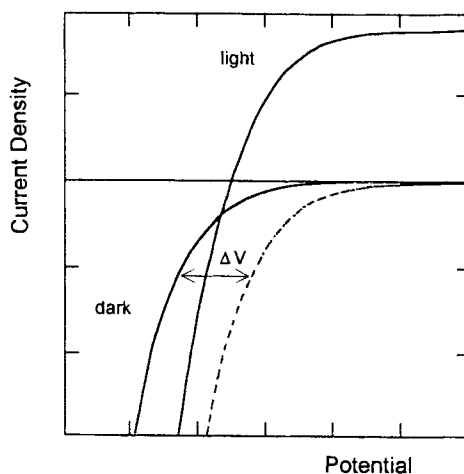


Figure 22. Anomalous photoeffect (APE) showing cross-over of the dark and light current–voltage curves for an n-type semiconductor-based interface. The dashed line is obtained as described in the text.

voltage data by j_{sc} , the short-circuit current density. If the superposition principle held, this dashed curve would have overlaid the dark current–voltage curve. Hence this ‘excess’ (forward bias) current embodies the APE, and the failure of superposition is quantified as the voltage difference (ΔV) between the dark j – V data and the dashed line.

What are the ramifications of the cross-over or the APE? First, mathematical modeling of carrier transport in a junction-based solar photovoltaic system, according to

$$j = j_{sc} - j_{bk}(V) \quad (27a)$$

not valid in the presence of this effect. (In Eq. 27a, j_{bk} is the ‘bucking’ current density in the forward-bias regime; see above.) That is, a fully linearized system of differential equations plus boundary conditions cannot be used to model the interface carrier transport. Second, computation and modeling of the open-circuit voltage for such devices by simply equating a constant photocurrent flux, j_{ph} , against the dark (recombination) current, j_0 , is no longer possible (see Eq. 28 and the accompanying discussion above).

Third, and perhaps practically of most significance, the ΔV component represents a loss pathway in the photovoltage deliverable by the given device. Thus, the (open-circuit) photovoltage is V_{oc} instead of $V_{oc} + \Delta V$ in the ideal case in the absence of the APE. Therefore, it is important to quantify and understand the molecular and chemical origins of this effect. This has not been done so far, at least to this writer’s knowledge, for semiconductor–electrolyte interfaces.

Of course, the cross-over effect is not confined to such interfaces. It is interesting that a recent textbook [241], dealing primarily with solid-state solar cell devices, makes only a fleeting reference to the underlying origin of the APE. Reference was made in this book to the cross-over of experimental dark and light j – V characteristics for a Cu_2S – CdS solid-state heterojunction solar cell but its origin was not

explored. A light-induced junction modification has also been reported for the (Cd,Zn)S–CuInSe₂ solid-state system [242]. The cross-over effect appears to have been treated in even lesser depth in some classical textbooks on semiconductor devices [201, 243].

Probably the first reported instance of observation of an APE was in 1977 for an n-TiO₂–NaOH electrolyte interface [244]. The APE was observed in the saturation region of cathodic current flow and was induced by sub-band-gap irradiation of the photoanode. A peak in the spectrum of the photoresponse at 800 nm (the corresponding photon energy being lower than the 3.0 eV bandgap of TiO₂) was used by the authors to invoke a surface-state mediated electron transfer to O₂ (in the electrolyte) as the origin of the photoeffect. Surface states were again invoked to explain a cathodic photoeffect at n-CdS–aqueous polysulfide interfaces [245]. This photoeffect was only observed for the (0001) single crystal face of n-CdS but not for the (0001) orientation. A subsequent study of photoelectrochemical effects at selenium films reported an anomalous *anodic* photocurrent at potentials positive of the flat-band location for the p-type film [246]. This effect was assigned to a hole injection process via a tunneling mechanism. An increase in the tunneling probability under illumination was accommodated by a shrinking of the space-charge layer at the interface. Photoenhancement of the forward current flow was observed again for n-CdS, in this instance in contact with a [Fe(CN)₆]^{3–/4–} redox electrolyte [247]. This effect was observed only with a mechanically damaged surface, and disappeared after it had been etched with concentrated HCl.

Subsequent work [248] describes suppression of the cathodic photocurrent for n-CdS–[Fe(CN)₆]^{3–/4–} interfaces upon mechanical polishing of the electrode. As with an earlier study [244], the spectral dependence of the photocathodic effect implicated sub-band-gap states. The suppression was explained by two alternative models involving a compensated insulating layer or by Fermi-level pinning. Illumination was claimed to result in a dramatic increase in the (suppressed) cathodic current, which interestingly enough was observed only for n-CdS films but not for crystals, including n-CdTe, n-CdSe, n-GaAs, n-ZnO, n-TiO₂ and n-ZnSe. On the other hand, a subsequent paper describes a photocathodic effect for n-CdSe–sulfite interfaces in which an interfacial layer of selenium was implicated [249].

More recent studies on n-CdS [250, 251] and n-TiO₂ photoanodes [252] implicate the formation of photoconductive layers in the APEs. Thus, the foregoing review suggests the following:

- 1) the APE is a very general phenomenon that has been observed for solid-state junctions for n- and p-type semiconductors alike, and for a wide variety of semiconductor materials;
- 2) the reported results and trends are often contradictory; it is possible that the experimental conditions in these studies were variant, thus precluding direct comparison of the results;
- 3) the mechanistic reasons given for the APE are possibly many and generalizations may not be warranted. Clearly, more research is needed on this topic.

Figure 23 contains an example of the APE for the n-GaAs–AlCl₃/n-butylpyridinium chloride molten salt electrolyte interface [253]. The bottom curve is

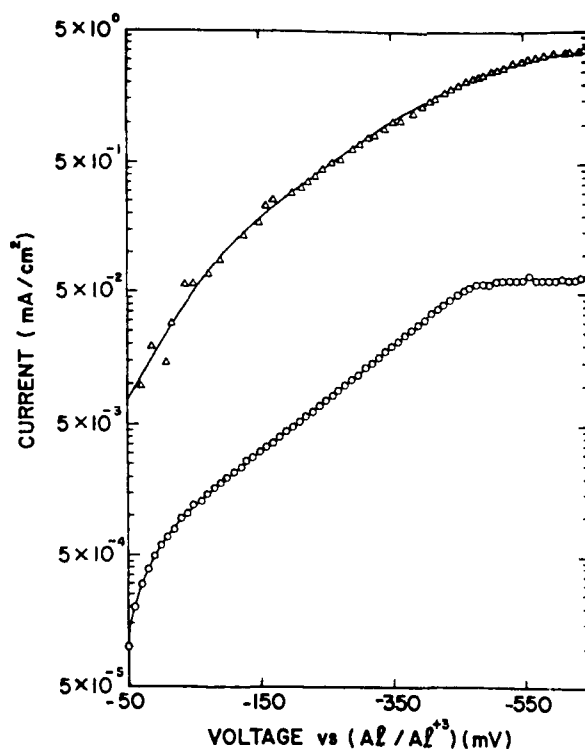


Figure 23. Experimental data embodying APE for the n-GaAs– AlCl_3 /n-butylpyridinium chloride molten-salt electrolyte interface. Refer to the text for details. (Reproduced with permission from Ref. [253].)

the measured dark current–voltage profile. The top curve was obtained from the photocurrent–voltage data (under irradiation of the semiconductor). Clearly, if the superposition principle held, the two curves would have coincided with one another.

APEs have also been observed for nanocrystalline and chemically modified films, as discussed in a subsequent section.

Light-induced changes in the electrostatics at the semiconductor–electrolyte interface are conveniently probed by capacitance–voltage measurements in the dark and under illumination of the semiconductor electrode. If charge trapping at the interface plays a decisive role (whatever be the mechanism), the voltage drop across the illuminated interface is altered, and consequently the semiconductor band-edge positions are shifted. This, of course, is the Fermi-level pinning situation that was encountered earlier (Section 1.3.4). Such measurements have been performed for a variety of interfaces and one example is shown in Figure 24 [217]. Another example concerns the CdTe–aqueous electrolyte interface [254].

1.6.4 Dynamics of Photoinduced Charge Transfer

So far, the discussion has centered on the steady-state aspects of carrier generation and collection at semiconductor–electrolyte interfaces. As with their metal electrode

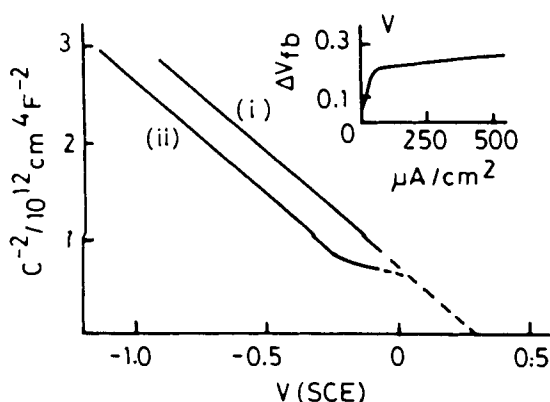


Figure 24. Mott–Schottky plots in the dark (i) and under illumination (ii) for a p-GaAs–0.5 M H₂SO₄ interface. The insert quantifies the shift in V_{fb} versus the limiting photocurrent density (or equivalently the photon flux). (Reproduced with permission from Ref. [217].)

counterparts, a wealth of information can be gleaned from perturbation–response type of measurements. An important difference, however, lies in the vastly different time-scale windows that are accessible in the two cases. The critical RC time constant of the cell in a transient experiment is given by

$$\tau_{\text{cell}} = C(R_m + R_{\text{el}}) \quad (29)$$

where R_m is the resistance of the measurement resistor (across which the current or photocurrent is measured) and R_{el} is the electrolyte resistance. The term C is the capacitance, which, in the metal case, is the Helmholtz layer capacitance, C_H . (Once again, the Gouy region is ignored here.) For semiconductor–electrolyte interfaces, we have seen that two layers are involved in a series circuit configuration with corresponding capacitances of C_{sc} and C_H (Figure 6). Since $C_H \gg C_{\text{sc}}$, $C \approx C_{\text{sc}}$. This assumption is usually justified since $C_H \approx 10^{-5} \text{ F cm}^{-2}$ and $C_{\text{sc}} = 10^{-8} \text{--} 1 \text{ F cm}^{-2}$. If the composite resistance ($R_m + R_{\text{el}}$) is 100Ω then τ_{cell} for metal electrodes is $\sim 10^{-3} \text{ s}$ and that for the semiconductor case is $10^{-6} \text{--} 10^{-7} \text{ s}$.

What are the processes important in a dynamic interrogation of the semiconductor–electrolyte interface? They are

- 1) carrier generation within the semiconductor;
- 2) diffusion of minority carriers from the field-free region to the space-charge layer edge;
- 3) transit through this layer;
- 4) charge transfer across the interface; and
- 5) carrier recombination via surface states or via traps in the space-charge layer.

Other phenomena such as thermalization also are important, as discussed below within the context of hot carrier effects. Complicating matters further and one that has caused some confusion in the interpretation of transient data is the time constant (τ_{cell}) of the cell and the measurement circuitry. If a potentiostat is not used, then this time constant is given by Eq. 29.

One can envision three types of perturbation: an infinitesimally narrow light pulse (a Dirac or δ -function), a rectangular pulse (characteristic of chopped or interrupted irradiation) or periodic (usually sinusoidal) excitation. All three types of excitation and the corresponding responses have been treated on a common platform using the Laplace transform approach and transfer functions [255]. These perturbations refer to the temporal behavior adopted for the excitation light. However, classical AC impedance spectroscopic methods employing periodic potential excitation can be combined with steady-state irradiation (the so-called PEIS experiment). In the extreme case, both the light intensity and potential can be modulated (at different frequencies) and the (nonlinear) response measured at sum and difference frequencies. The response parameters measured in all these cases are many but include the photocurrent, voltage, luminescence or microwave conductivity. Clearly semiconductor–electrolyte interfaces present a rich, albeit demanding, landscape for probing non-steady-state phenomena.

Perhaps the simplest to discuss is the rectangular excitation waveform. In fact, this method can even be combined with a slow voltammetric scan upon which the chopped irradiation response appears superimposed. This ‘photovoltammetry’ experiment is schematized in Figure 25. Two types of transient responses are apparent.

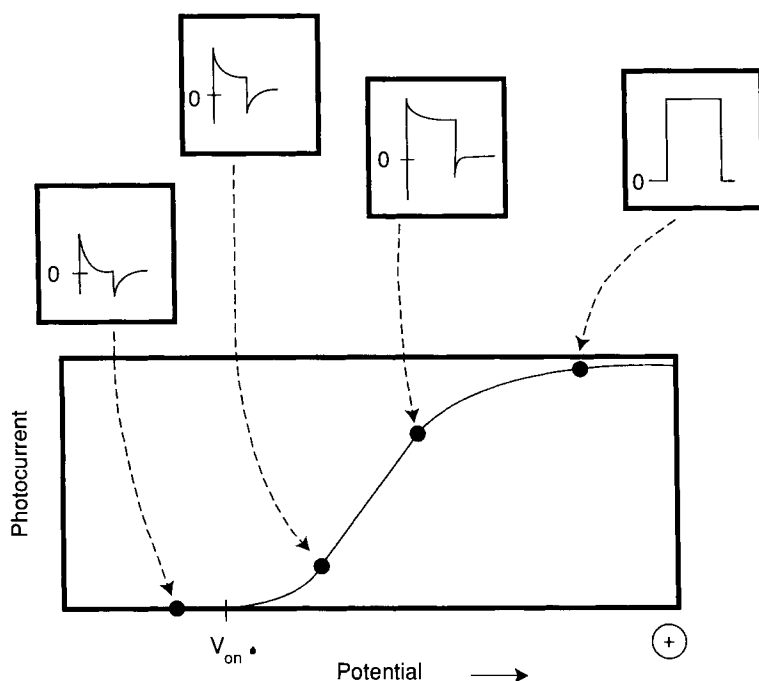


Figure 25. Schematic illustration of the transient profiles that would be seen under interrupted illumination as the potential is slowly scanned in the reverse bias regime. The situation as shown is for an n-type semiconductor–electrolyte interface. V_{on} is the potential for the onset of photoanodic current flow.

At potentials near the photocurrent onset (roughly V_{fb}), a spiked response is seen with a characteristic ‘overshoot’ when the light is turned off. At positive potentials near the plateau regime (again for the specific illustrative case of an n-type semiconductor), the response reverts to a rectangular profile that mimics the excitation waveform. Intermediate response patterns manifest at potentials in between.

The transient behavior in Figure 25 can be rationalized by invoking a surface-state mediated model of the sort shown in Figure 21. Model simulations and experiments have been reported for p-GaP photocathodes in acidic electrolyte [93, 211]. Similar experiments on n-CdSe electrodes have been reported [123].

Perhaps more challenging from both experimental and modeling perspectives is the δ -excitation case. Primary electron–hole pair separation occurs in the sub-nanosecond or picosecond time domain and light pulses with temporal resolution of $\sim 10^{-10}$ s (or better) are required. However, both nanosecond and picosecond light pulses have been employed [110–127] and although the analysis has been mostly confined to the slower (nanosecond) decay regime in the photocurrent (or photovoltage) transients, the rise-time domain has also been analyzed (see, e.g., Ref. [256]).

It appears that the carrier generation process is essentially complete within the picosecond time window; subsequent charging of C_{sc} manifests as a photovoltage that can be measured in the external circuit. If this photoinduced charge is discharged through R_m (strictly $R_m + R_{el}$), an exponential decay should appear with a time constant of τ_{cell} . However, faster photocurrent (or equivalently photopotential) transients have been observed (see, e.g., Figure 26 [113]). This initial decay has been

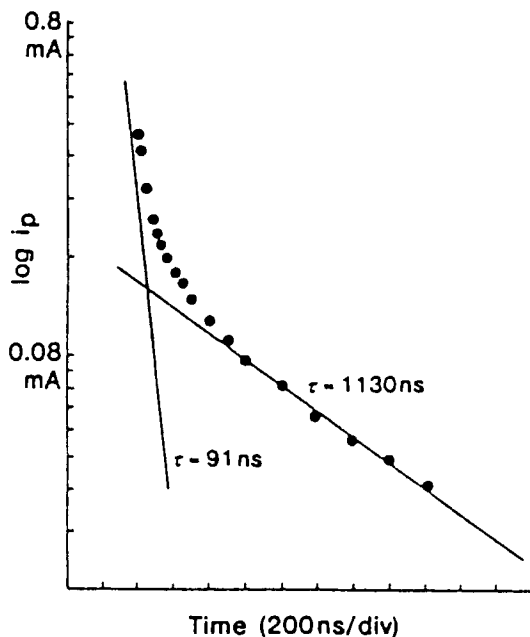


Figure 26. Transient photocurrent data plotted in semilogarithmic format for n-WSe₂ in 1.0 M KI at -0.30 V (vs. SCE) showing the rapid decay component at short times. (Reproduced with permission from Ref. [113].)

attributed to the flow of majority carriers into the hole-populated surface state(s) [2]. Note that this current flow is opposite in sign to the minority carrier component and accounts for the polarity of the ‘overshoot’ pattern in Figure 25.

The laser coulostatic experiment on semiconductor–electrolyte interfaces, in fact, has an early history dating back to ca. 1980. These and other similar works have been reviewed [2, 3, 9]. Luminescence decay experiments shed light on the competition between charge transfer, nonradiative recombination and luminescence, pathways. Once again, the reader is referred to the aforementioned reviews for further details.

Finally, light-modulated microwave conductivity measurements complement other non-steady-state methods in that when the rate constant for carrier recombination is zero, the photocurrent simply follows the perturbation profile (zero phase change) such that no information about the rate of interfacial charge transfer can be gleaned. On the other hand, light-modulated microwave reflectivity measurements still provide kinetic information at high semiconductor band-bending at the interface. Further details of the advantages and limitations of this technique are available [100–107].

Periodic excitation: the IMPS and PEIS experiments

As mentioned earlier, in these cases either the light intensity (IMPS) or the applied potential (PEIS) is sinusoidally varied. The potential is fixed in the former case and the light intensity is maintained constant in the latter. We shall consider IMPS mainly in what follows; further details and entry into the original literature, can be found elsewhere [2, 9, 10].

In IMPS, the light intensity has both a ‘DC’ and an ‘AC’ component:

$$I(t) = I_{\text{DC}} + I_{\text{AC}} \sin(\omega t) \quad (30)$$

where ω is the angular frequency (in rad s^{-1}). Generally, I_{AC} is chosen to be a small fraction of I_{DC} to insure a linear response. The corresponding Gärtner flux (Eq. 24) also has AC and DC components:

$$J(t) = J_{\text{DC}} + J_{\text{AC}} \sin(\omega t) \quad (31)$$

where J refers to the flux of minority carriers. After some algebra (see, e.g., Refs. [9, 10]), the dimensionless equivalent of Eq. 24 for the IMPS case becomes

$$\Phi(\omega) = \frac{j_{\text{ph}}(\omega)}{e_0 J_{\text{AC}}} = \frac{k'_{\text{et}} + i\omega}{k_{\text{rec}} + k'_{\text{et}} + i\omega} \quad (24a)$$

Note that both the quantum yield and the photocurrent density are a function of the modulation frequency, ω . The k s in Eq. 24a are *first-order* rate constants (with dimensions of s^{-1}) for electron transfer (k'_{et}) and carrier recombination (k_{rec}), respectively. The prime in k'_{et} distinguishes it from its bimolecular (second-order) counterpart discussed earlier (Section 1.5.1).

The complex function embodied in Eq. 24a can be broken down into its real and imaginary components:

$$\text{RE}\left(\frac{j_{\text{ph}}}{e_0 J_{\text{AC}}}\right) = \frac{(k'_{\text{et}} + k_{\text{rec}})k'_{\text{et}} + \omega^2}{(k'_{\text{et}} + k_{\text{rec}})^2 + \omega^2}$$

and

$$\text{IM}\left(\frac{j_{\text{ph}}}{e_0 J_{\text{AC}}}\right) = \frac{k_{\text{rec}}\omega}{(k'_{\text{et}} + k_{\text{rec}})^2 + \omega^2} \quad (32)$$

As with AC impedance spectroscopic data, IMPS data can be displayed in complex plane (Nyquist) format as exemplified by Figure 27.

In the low-frequency limit ($\omega \rightarrow 0$), Eq. 32 collapses to the ratio $k'_{\text{et}}/(k'_{\text{et}} + k_{\text{rec}})$. In the high-frequency limit ($\omega \rightarrow \infty$), Φ is unity (in the absence of RC attenuation effects, see below). The maximum of the semi-circular arc occurs at $\omega_{\text{max}} = k'_{\text{et}} + k_{\text{rec}}$. One of the advantages of IMPS (relative to DC measurements) is that surface recombination can be ‘frozen out’ at the high-frequency limit.

As with the transient measurements discussed earlier, τ_{cell} also sets a limitation on IMPS measurements. It has been shown [257–259] that τ_{cell} gives rise to an additional semi-circle in the positive-negative (fourth) quadrant. Further, if τ_{rec} is comparable to τ_{cell} , the normalized plot will cross the real axis at a point less than unity, unlike in the case in Figure 27a. In these original model simulations [257, 258], it was assumed, as usual, that $C_{\text{H}} \gg C_{\text{sc}}$. The more general case when C_{H} and C_{sc} are of comparable magnitude has been treated more recently [259].

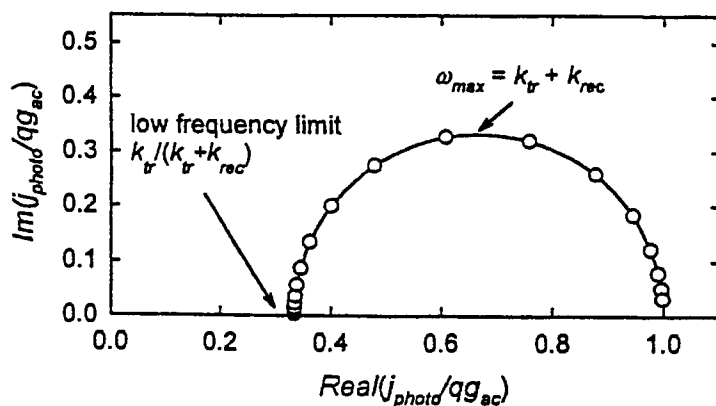
Figure 27b contains representative experimental IMPS plots for the n-InP– H_2SO_4 interface [92]; note that these data are displayed in non-normalized fashion, unlike the simulation in Figure 27a. Rate constants (k_{rec} and k'_{et}) were extracted from these data as was the branching ratio, $k'_{\text{et}}/(k'_{\text{et}} + k_{\text{rec}})$, all as a function of potential [92]. Many other semiconductor–electrolyte interfaces have been studied by IMPS, and Refs. [2], [9], and [10] should be consulted for citations of the original papers.

The relationship between IMPS and PEIS has been discussed by a number of authors [92, 260, 261]. In general, the information content appears to be equivalent.

1.6.5 Hot Carrier Transfer

Short-wavelength photons (of energy much greater than E_{g}) create ‘hot’ carriers. If, somehow, thermalization of these carriers can be avoided, photoelectrochemical reactions that would otherwise be impossible with the ‘cooled’ counterparts, i.e., at very negative potentials for n-type semiconductors, would be an intriguing possibility. The key issue here is whether the rate of electron transfer across the interface can exceed the rate of hot electron cooling. The observation of hot carrier effects at semiconductor–electrolyte interfaces is a controversial matter (see, e.g., Refs. [3],

(a)



(b)

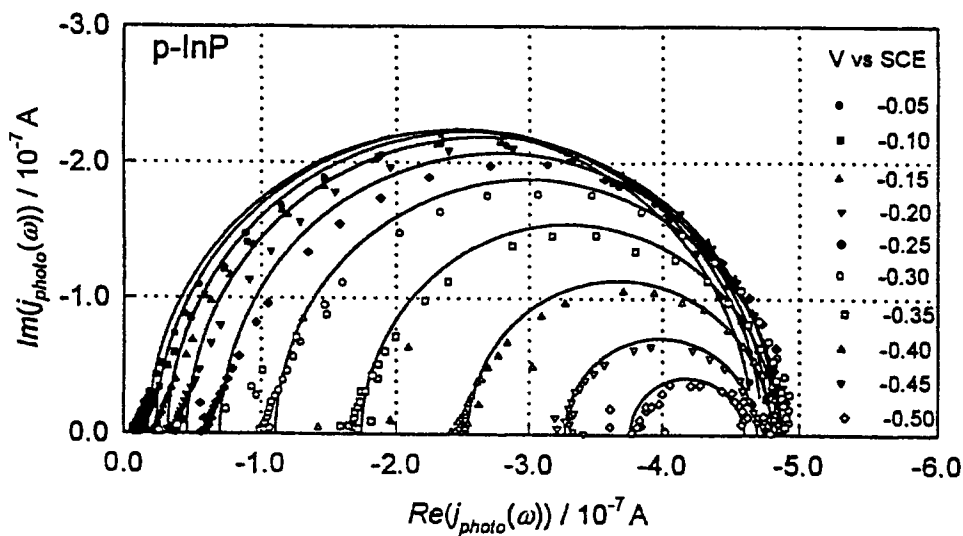


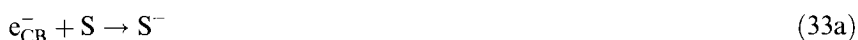
Figure 27. Simulated (a) and experimental (b) IMPS plots in Nyquist format. The latter are shown for the p-InP–1 M H₂SO₄ interface at various bias potentials. (Reproduced with permission from Refs. [10] and [92].)

[7], [11], [86]) and practical difficulties include problems with band-edge movement at the interface and the like [4]. Under certain circumstances (e.g., quantum-well electrodes, oxide film-covered metallic electrodes), it has been claimed that hot carrier transfer can indeed be sustained across the semiconductor–electrolyte interface [7, 262, 263].

1.7 Multi-electron Photoprocesses

Until now we have mainly considered redox electrolytes comprising one-electron oxidizing or reducing agents. Multi-electron redox processes, however, are important in a variety of scenarios. Consider the reduction of protons to H_2 (HER), a technologically important electrochemical process that has also been extensively studied from a mechanistic perspective on metallic electrodes.

Photoelectrolytic processes such as HER can be carried out on semiconductor electrodes. One can envision an HER mechanism on a p-type semiconductor of the following sort:



where S denotes a surface state and both direct (reactions 33c and 33d) and indirect (i.e., surface-state mediated) (reactions 33b and 33e) radical and H_2 generating pathways are shown. Reactions 33g and 33h represent recombination routes involving the reaction intermediates.

Admittedly this scheme is daunting in its complexity and the kinetic implications are as yet unclear. Early studies on p-GaP, p-GaAs and other Group III–V (13–15) semiconductors reported onset of cathodic photocurrents (attributable to HER) only at potentials far removed (ca. 0.6 V) from V_{fb} (see, e.g., Ref. [264]). This was attributed to steps 33b and 33h in the above scheme. More recent work [91] has shown that the HER at illuminated p-InP–electrolyte contacts is accompanied by a photocorrosion reaction, leading to indium formation on the semiconductor surface. Representative PEIS data from this study are shown in complex plane format in Figure 28. Note that unlike in the cases above (e.g., Figure 27), *multiple* relaxa-

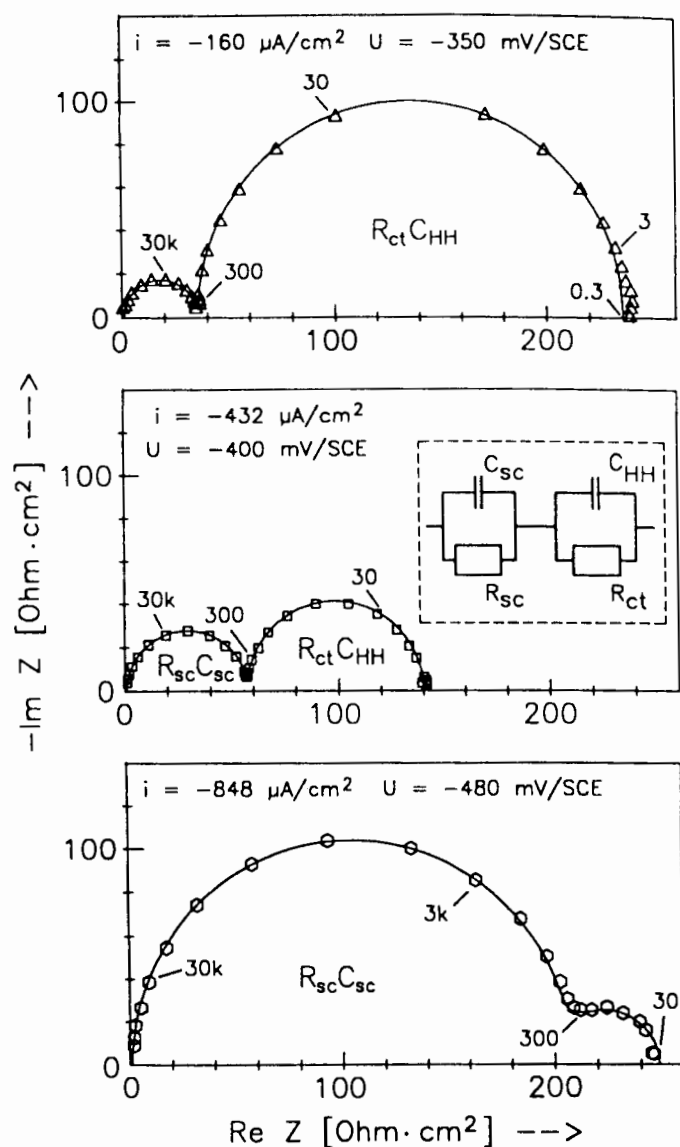


Figure 28. PEIS data for the p-InP-1 M H₂SO₄ interface at a constant illumination intensity and varying photocurrent densities and bias potentials as shown. Both data points and model fits are shown with the equivalent circuit employed shown in the inset. $R_{sc} \equiv R_r$ in our notation (refer to text). (Reproduced with permission from Ref. [91].)

tions are seen that were assigned to $R_r C_{sc}$ and $R_{ct} C_H$ combinations, respectively [91], where R_r is the recombination (diode) resistance (see Section 1.5.2) and R_{ct} is the Faradaic resistance. Multiple arcs are characteristic signatures of multi-electron redox processes, as we shall see soon.

Interestingly, surface states themselves were chemically identified with H^*_{ads} (adsorbed hydrogen atom intermediates) in the aforementioned study [264]. These species have also been implicated in accumulation layer formation and anodic EL at n- and p-GaAs–electrolyte interfaces [265–267].

Another interesting characteristic of many multi-equivalent redox systems is the phenomenon of photocurrent multiplication. This phenomenon may be illustrated for two systems utilizing illuminated n-type and p-type semiconductors:

n-type:



p-type:



Thus, the key feature of photocurrent multiplication is a majority carrier injection step (reaction 34b or 34d) from a reaction intermediate (usually a free radical) into the semiconductor CB or VB, respectively. Thus, in the examples above, each photon generates two carriers in the external circuit, affording a quantum yield (in the ideal case) of 2. This is the ‘current-doubling’ process.

Practically, however, quantum yields somewhat lower than 2 are usually measured because step 34b or 34d competes with the further photooxidation or photo-reduction of these intermediates, respectively. This is true especially at high photon flux values. Even multiplication factors as high as 4 are possible as in the photo-dissolution of n-Si in NH_4F media [268–271].

Photocurrent multiplication has been observed for a variety of semiconductors including Ge [269], Si [268–271], ZnO [272–278], TiO_2 [279–282], CdS [283, 284], GaP [285], InP [286] and GaAs [287–289]. These studies have included both n- and p-type semiconductors, and have spanned a range of substrates, both organic and inorganic. As in the Si case, this phenomenon can also be caused by photo-dissolution reactions involving the semiconductor itself. The earlier studies have mainly employed voltammetry, particularly hydrodynamic voltammetry (see, e.g., Ref. [282]).

As more recent examples (see Refs. [2], [9] and [10] for reviews) reveal, IMPS is a powerful technique for the study of photocurrent multiplication. Unlike in the cases discussed earlier (Figure 27), majority carrier injection leads to a component of the

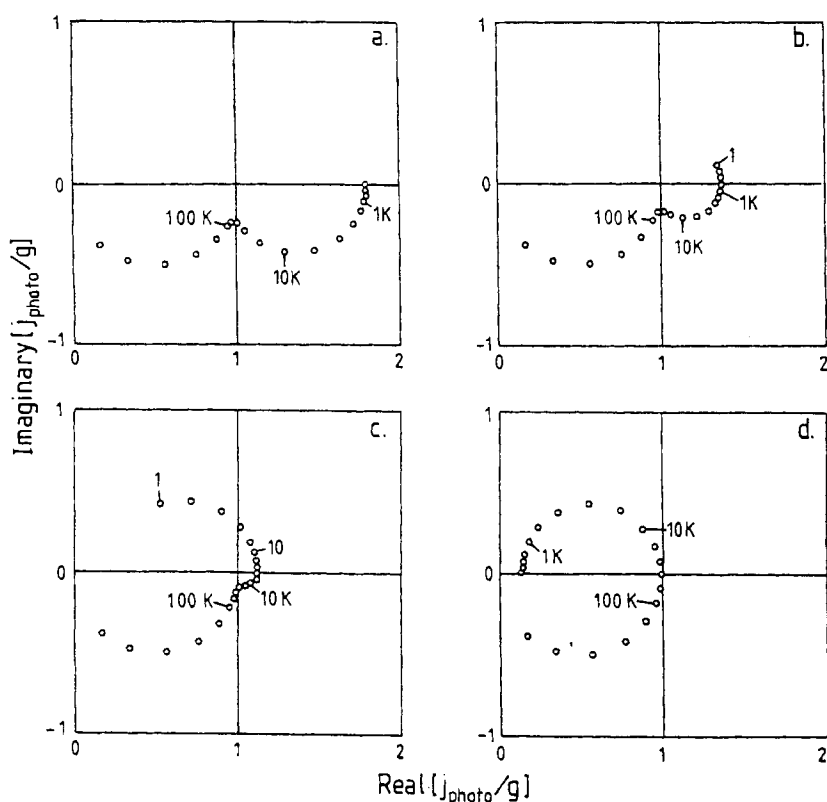


Figure 29. Simulated IMPS plots showing the competition between recombination and current doubling. The IMPS response switches from current doubling control in (a) to recombination control in (d). The band-bending values are 0.40, 0.35, 0.30 and 0.20 eV in (a), (b), (c) and (d) respectively. Refer to the original work for other simulation parameters. (Reproduced with permission from Ref. [284].)

photocurrent flux that lags behind the in-phase component associated with minority carrier processes. As the modulation frequency is increased, this injection component is progressively attenuated. Thus, the complex plane plot (that now lies in the *lower* quadrant) has a low-frequency intercept corresponding to 2 (in the ideal case). The high-frequency intercept tends toward a quantum yield of 1. In the presence of recombination, the plot becomes more complex.

Figure 29 contains a family of simulated IMPS plots showing the competition between recombination and current doubling [284]. At high band bending, the latter controls the response (along with the *RC* attenuation effect discussed in Section 1.6.4). On the other hand, recombination control manifests at 0.2 eV along with the lower-quadrant *RC* effect. Figure 30 contains simulated and experimental IMPS plots for the photodissolution of n-Si in NH_4F [270, 271]. As pointed out earlier,

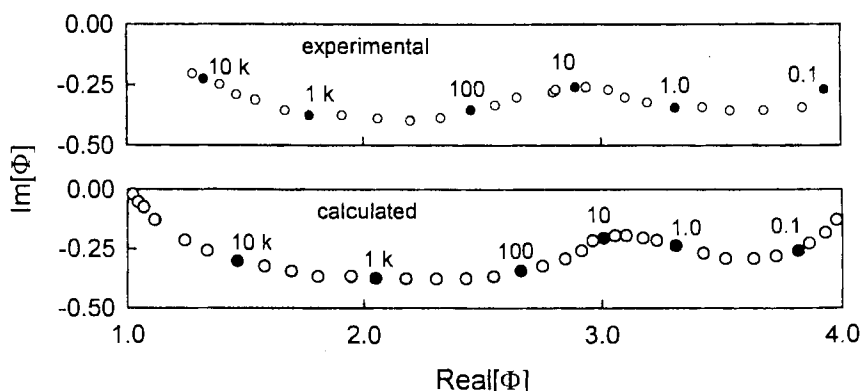
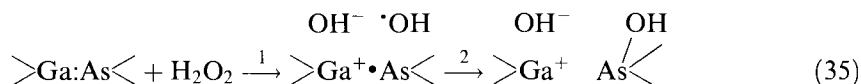


Figure 30. Experimental and simulated IMPS plots for the photodissolution of n-Si in 1.0 M NH_4F at pH 4.5. (Reproduced with permission from the authors of Ref. [9].)

multiple arcs are seen for the sequential injection of electrons from the dissolution intermediates.

The frequency windows for the study of photocurrent multiplication by IMPS is set by the dynamic response of the potentiostat (at high frequencies) and by the RC time constant attenuation. The injection rate constant, k_{inj} (first-order), can be calculated from the minimum of the arc, ω_{min} ; the upper limit to k_{inj} appears to be ca. 10^5 s^{-1} [9]. For example, k_{inj} for formic acid oxidation on n-CdS has been estimated to be $6 \times 10^4 \text{ s}^{-1}$ [284].

This leads us to another important category of multi-electron photoprocesses involving the semiconductor itself. While photocorrosion is a nuisance from a device operation perspective, it is an important component of a device fabrication sequence in the microelectronics industry. Two types of wet etching of semiconductors can be envisioned [290]. Both occur at open-circuit but one involves the action of chemical agents that cause the simultaneous rupture and formation of bonds. This is exemplified by the action of H_2O_2 on GaAs [291]:

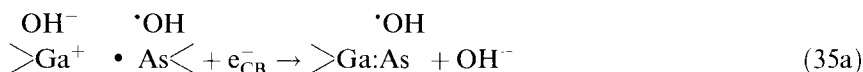


In the first step (1), the oxidant injects a hole into the surface bond between Ga and As. In the second step (2), a second hole is injected and the bond between Ga and As is broken with a new bond formed between As and hydroxyl species.

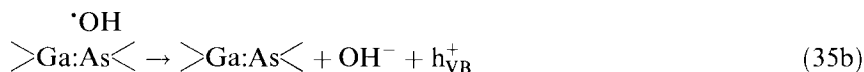
The second type of wet etching is called electroless etching [290]. This is based on the injection of a hole into the VB (for an n-type semiconductor). This dark process was discussed in some detail in Section 1.5.2.

The formation of an electron-deficient bond (as in reaction 35) can also be instigated by photogenerated holes. It has been shown that the resultant intermediates (especially for Group III–V materials) can act as effective electron traps for CB

electrons in the overall process [292, 293]:

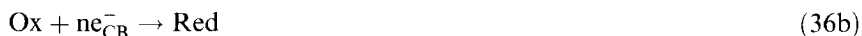


The 'surface state' is thus neutralized and the surface bond is repaired. The $\bullet\text{OH}$ radical can then efficiently inject a VB hole:



The net result is that the surface state is freed for a new reaction cycle to be re-initiated.

An important feature of wet etching is the possibility of changing the dissolution rate *locally* by application of photons with energy larger than E_g . Such photo-etching processes are relevant to several aspects of semiconductor technology including the production of highly anisotropic holes and grooves, specific geometric structures such as gratings and mesas, selective layer removal in heterostructures, and the like. Generically, photoetching can be represented by the following scheme:



A binary compound semiconductor (e.g., GaAs) has been assumed here and reaction 36b underlines the fact that charge neutrality in the system is maintained by reduction of Ox, an added oxidant (e.g., Ce^{4+}). Several aspects of photoetching have been reviewed [70, 166–168], including reaction mechanisms, morphology of the etched surfaces, and etching kinetics in the dark and under illumination. General rules for the design of anisotropic photoetching systems have also been formulated [294].

1.8 Nanocrystalline Semiconductor Films and Size Quantization

1.8.1 Introductory Remarks

From a materials perspective, the field of semiconductor electrochemistry and photoelectrochemistry has evolved from the use of semiconductor single crystals to polycrystalline thin films and, more recently, to nanocrystalline films. The latter have been variously termed membranes, nanoporous or nanophase films, mesoporous films, nanostructured films, etc.; they are all distinguished from their poly-

crystalline electrode predecessors by the crystallite size (nm versus μm in the former) and by their permeability to the electrolyte phase. We shall simply call these films ‘nanocrystalline’ in what follows. The above features render three-dimensional geometry to nanocrystalline films as opposed to the ‘flat’ or two-dimensional (planar) nature of single crystals or polycrystalline counterparts.

What are the virtues of these emerging photoelectrode materials? The first is related to their enormous surface area. Consider that the 3-D structure is built up of close-packed spheres of radius r . Then ignoring the void space, the specific area, A_s (area/volume), is given by $3/r$ [295]. For $r = 10\text{ nm}$, A_s is of the order of 10^6 cm^{-1} and for a 1 cm^2 film of $1\text{ }\mu\text{m}$ thickness, this value corresponds to an *internal* surface area of $\sim 100\text{ cm}^2$ (i.e., a ‘surface roughness factor’ of 100). Clearly, this becomes important if we want the electrolyte redox species to be adsorbed on the electrode surface (see below). Alternatively, a large amount of sensitization dye can be adsorbed on the support semiconductor although this dye sensitization approach is not considered in this chapter. By way of contrast, the amount of species that can be confined in a monolayer on a corresponding flat surface would be negligibly small.

As we shall see later, electron transport in nanocrystalline films is necessarily accompanied by charge-compensating cations because the holes are rapidly injected into the flooded electrolyte phase. This provides opportunities for studying ion transport processes in mesoporous media, that are coupled to electron motion. Ion insertion also has practical consequences as in energy storage device applications [296].

Surface state densities of the order of $\sim 10^{12}\text{ cm}^{-2}$ are commonplace for semiconductor electrodes of the sort considered in previous sections of this chapter. These translate to equivalent volume densities of $\sim 10^{18}\text{ cm}^{-3}$ for nanocrystalline films. Such high densities enhance light absorption by trapped electrons in surface states, giving rise to photochromic and electrochromic effects [297–299] (see below). Unusually high photocurrent quantum yields are also observed with sub-band-gap light with these photoelectrode materials. Corresponding sub-band-gap phenomena are rather weak and difficult to detect with single crystal counterparts.

1.8.2 Preparation of Nanocrystalline Electrode Films

These films can be prepared by a variety of routes, only a few of which are mentioned here. The original references should be consulted for more practical details. Titanium dioxide is used as an illustrative example below. First, colloidal solutions are prepared, e.g., from titanium isopropoxide. The resultant sol is concentrated under vacuum at room temperature until its viscosity increases. Then it is spin-coated on to suitable supports (e.g., conducting glass) and fired in an oven. The firing temperature critically controls the morphology of the resultant film as discussed elsewhere [300–303]. Films up to several micrometers thick can be prepared by this simple version of the sol–gel technology [304]. Aerosol or spray pyrolysis is a somewhat related approach [305, 306].

In another variant of this procedure, the oxide powder itself is used as a precursor. For example, a paste can be generated by grinding this powder with water and

acetylacetone along with other additives (e.g., Triton X-100) [301, 307–308]. The resultant dispersion can be either spread or brush-coated on to the support material. A final sintering at $\sim 400\text{--}450^\circ\text{C}$ in air completes the film preparation sequence.

Electrodeposition [309–311] and chemical bath deposition (CBD) [312, 313] are two other attractive routes for the preparation of nanocrystalline films. Oxides such as ZnO and TiO_2 [314–318] and other Group II–VI (12–16) semiconductors (e.g., CdS, CdSe, CdTe) [319, 320] can be prepared in nanocrystalline form via these routes. Hybrid electrochemical chemical synthesis routes have also been devised [321].

Finally, a single crystal itself provides a template for preparing a highly porous layer on top of it. This photoetch strategy, which was initially used for silicon from a luminescent device perspective [322], has been subsequently employed for enhancing the photoresponse of indirect band-gap semiconductors such as GaP [323, 324]. Interestingly, an early report on porous TiO_2 layers formed by anodization in the dark claimed a higher quantum yield in the long-wavelength regime relative to single-crystal rutile [325]. However, this behavior was ascribed by the authors to the formation of anatase ‘pockets’ in the anodic film or to the incomplete oxidation of the Ti foil that was employed [325].

1.8.3 The Nanocrystalline Film–Electrolyte Interface and Charge Storage Behavior in the Dark

Understanding of the electrostatics across nanocrystalline semiconductor film–electrolyte junctions presents interesting challenges, particularly from a theoretical perspective. Concepts related to space-charge layers, band-bending, flat-band potential and the like (Section 1.3) are not really applicable here because the crystallite dimensions comprising these layers are comparable to (or even smaller than) nominal depletion layer widths.

The fairly complete interpenetration of the electrode and electrolyte phases must mean that the Helmholtz double layer extends throughout the interior surface of the nanoporous network, much like a supercapacitor [9, 326] situation. Finally, unlike in the cases treated earlier, the semiconductor (especially if it is a metal oxide) is not heavily doped such that free majority carriers are not present in appreciable amounts. This is indicated, for example, by the sensitivity of the conductivity of nanocrystalline TiO_2 layers to UV light—the conductivity is strongly enhanced on UV exposure much like a photoconductive effect. This effect has been interpreted in terms of trap filling with recombination times considerably slower than the trapping processes under reverse bias [327, 328]. The light sensitivity also is diagnostic of the fact that the low electronic conductivity in the dark is not due to high inter-particle resistances (i.e., in the ‘neck’ regions), but rather is indicative of the low electron concentrations.

The electron concentration can be increased by forward biasing the nanocrystalline electrode–electrolyte interface potentiostatically. The interface is thus driven into the accumulation regime for the majority carriers and if a transparent rear contact (e.g., F-doped, SnO_2 or Sn-doped indium oxide) is used, the resultant blue

(or bluish black) coloration of the film can be monitored spectroscopically [298, 299, 329]. Whether the optical response arises from conduction band electrons or from electrons trapped in surface states is not entirely clear. It has been claimed [330] that the absorption spectrum of the latter differs significantly from that of conduction band electrons. Electrons in surface states can be chemically identified with Ti^{3+} defect sites that can be detected, for example, by electron paramagnetic resonance spectroscopy [307, 331].

In either case, the resultant negative charge generated by electron accumulation at the internal surfaces has to be balanced by cations (from the electrolyte phase) for charge compensation. Such ion insertion reactions have been studied using techniques such as voltammetry, reflectance or absorption spectroscopy, chronoamperometry and electrochemical quartz-crystal microgravimetry [329, 332–336]. Both aqueous and aprotic electrolytes have been deployed for these studies.

Unlike in the single-crystal cases treated earlier, placement of the semiconductor energy band positions at the interface via Mott–Schottky analyses is not straightforward for nanocrystalline films. Abrupt changes in slope and other nonidealities [307, 337, 338] have been observed, for example, in the Mott–Schottky plots for TiO_2 films and attributed to the influence of the conductive glass that is normally employed to support these films. This behavior is especially prevalent under reverse bias. The onset of majority carrier optical absorption (in the visible and near-IR range) under forward bias instead has been profitably employed to place the conduction band positions of TiO_2 in aqueous media [298].

Impedance spectroscopy and electrochemical dye desorption experiments have been employed [339] to study the electrical characteristics of TiO_2 nanocrystalline films in the dark. This study and the others cited above demonstrate how the conductivity changes (as a result of electron injection from the support electrode) can cause the porous/nanocrystalline layer to manifest itself electrically, such that the active region moves away (i.e., outward) from the support as the forward bias voltage is increased. The potential distribution has also been analyzed depending on whether the depletion layer width exceeds or is smaller than the typical dimension of the structural units in the nanocrystalline network [338].

1.8.4 Photoexcitation and Carrier Collection: Steady-state Behavior

Figure 31 contains a schematic representation of the nanocrystalline semiconductor film–electrolyte interface at equilibrium (Figure 31a) and the corresponding situation under bandgap irradiation of the semiconductor (Figure 31b) [9]. Since the diffusion length of the photogenerated carriers is usually larger than the physical dimensions of the structural units, holes and electrons can reach the impregnated electrolyte phase before they are lost via bulk recombination. This contrasts the situation with the single-crystal cases discussed earlier.

If, as is the case with TiO_2 nanocrystalline films, the holes are rapidly scavenged by the electrolyte redox (specifically Red) species, collection of the photogenerated electrons at the rear contact becomes the determinant factor in the quantum yield. Thus, the quasi-Fermi level for holes remains close to $E_{\text{F, redox}}$ and that for elec-

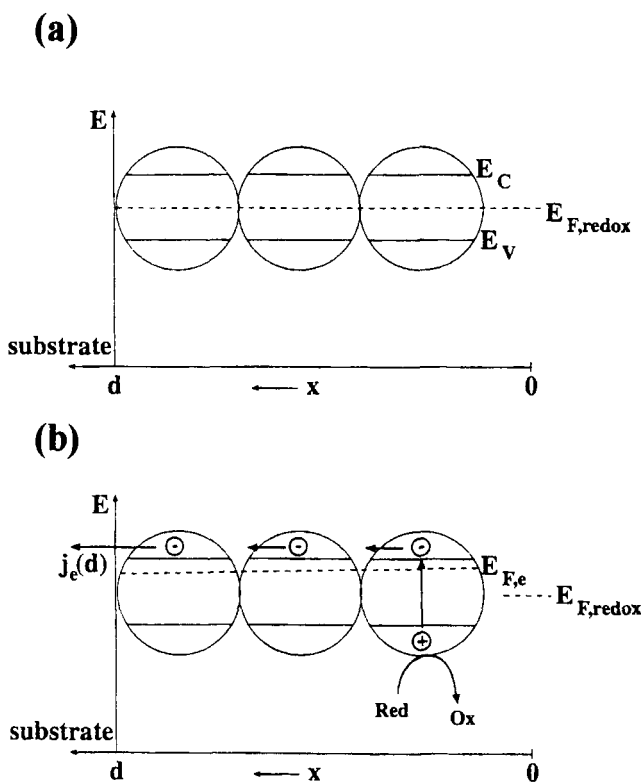


Figure 31. Schematic representation of a nanocrystalline semiconductor–electrolyte interface in the dark (a) and under illumination from the electrolyte side (b). E_c and E_v correspond to E_{CB} and E_{VB} in our notation. (Reproduced with permission from the authors of Ref. [9].)

trons, $E_{F,e}$, moves ‘up’ as depicted in Figure 31b. Illumination thus induces an electron flux, $J_n(x)$ through the nanocrystalline phase. Under steady-state conditions, the photocurrent density (j_{ph}) is equal to $e_0 J_n(x = d)$. The driving force for electron diffusion through the network of nanocrystallites has been calculated from first principles [340]. It has been found that the driving force is ca. kT/e_0 divided by the thickness of the network. Importantly, this free-energy gradient is found to be independent of the incident photon flux.

It is important to reiterate that the charge separation in a nanocrystalline semiconductor–electrolyte interface does not depend on a built-in electric field at the junction as in the single-crystal case. Instead, the differential kinetics for the reactions of photogenerated electrons and holes with electrolyte redox species accounts for the charge separation (and the generated photovoltage). The molecular factor(s) underlying the sluggish scavenging of electrons at the nanocrystalline film–electrolyte boundary (by the redox species) are as yet unclear. Of course, the competition between *surface* recombination of these electrons (with the photogenerated holes) and collection at the rear contact dictates the magnitude of the quantum yield experimentally measured for a particular junction.

Photocurrent losses have been recorded for electrolytes dosed with electron acceptors such as O_2 and iodine [341]. Nanocrystalline TiO_2 electrodes with thick-

nesses ranging from 2 to 38 μm were included in this study. In the presence of the above electron-capture agents, electron collection (i.e., photocurrent) at the rear contact was seriously compromised. On the other hand, as high as 10 % of the photons were converted to current for a 38 μm thick film in an N_2 -purged solution [341].

The above result was obtained with front-side illumination geometry. As one would intuitively expect, carrier collection is most efficient close to the rear contact. Indeed, marked differences have been observed for photoaction spectra with the two irradiation (i.e., through the electrolyte side vs. through the transparent rear contact) geometries for TiO_2 , CdS and CdSe nanocrystalline films [319, 342]. Obviously, the relative magnitudes of the excitation wavelength and the film thickness critically enter into this variant behavior.

In most cases, the iodide–triiodide redox couple has been employed (presumably because of its success in shuttling the photo-oxidized dye in the sensitization experiments) although other redox electrolytes {e.g., $\text{SCN}^-/(\text{SCN})_2^-$, [342]} have also been employed. For the chalcogenide films, sodium selenosulfite was employed [319]. It must be noted that, aside from losses due to the surface recombination and back-reactions, an additional loss component from the increase in film resistance must also be recognized especially as the film thickness is increased. The resistance loss manifests as a deterioration in the photovoltage and fill factor.

In the discussion to this point, we have not considered trapping/release of the photogenerated electrons as they undergo transit to the rear contact. However, electrons trapped in localized interfacial states induce a counter-charge in the Helmholtz double-layer, as discussed in the preceding discussion. The resultant voltage drop can introduce a non-negligible field component into the diffusional process. The time dependence of the electron density, $n(x, t)$, is given by [9]

$$\frac{\partial n(x, t)}{\partial t} = \eta \alpha I_0 e^{-\alpha x} + D_n \frac{\partial^2 n(x, t)}{\partial x^2} - \frac{n(x, t) - n_0}{\tau} \quad (37)$$

where η is the electron injection efficiency, D_n is the diffusion coefficient of electrons and τ is the pseudo-first-order lifetime of electrons determined by back-reaction with Ox.

Even if the migration component is negligible (but see below), solution of Eq. 37 presents difficulties because of the possible dependence of D_n on n and x . Similarly, τ may depend on these two variables also. Nonetheless, the steady-state solution of Eq. 37 has been obtained [343] by assuming that D and τ are constant and that $\eta = 1$. Under these conditions, the photocurrent is predicted to be independent of voltage—a rather physically implausible situation. In the forward bias regime, η is expected to decrease and back-reaction of the photogenerated electrons (with Ox) can no longer be neglected.

This brings us to the rear support–film interface. What sort of barrier exists at this junction? Are the electron exchange kinetics voltage-dependent at this interface? The effect of changing the work function of the substrate on the current–voltage curves (in the dark and under illumination) has been investigated for TiO_2 nanocrystalline films [344]. The onset potential for the photocurrent is found to be the

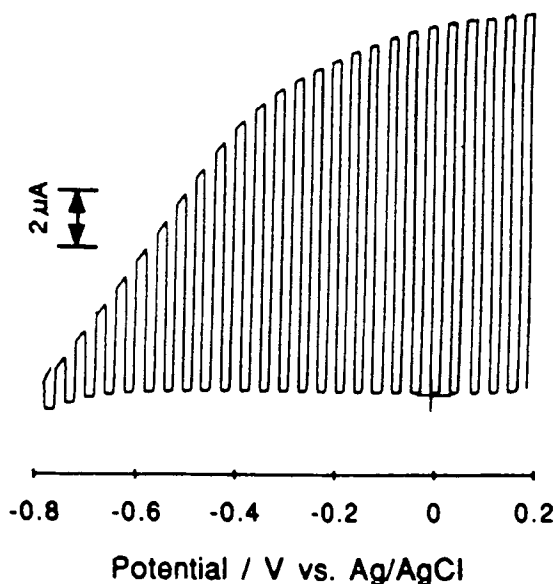


Figure 32. Photovoltammogram under interrupted illumination of a nanocrystalline CdS–sodium sulfite electrolyte interface in the reverse-bias regime.

same regardless of whether SnO_2 , Au or Pt is used to support the film. A Fermi level pinned *rear* interface was used to explain the results.

In general, the voltammograms for nanocrystalline electrodes are not unlike what is observed for their single-crystal counterparts. An example of a photovoltammogram for CdS is shown in Figure 32. The fact that an S-type profile is observed culminating in a photon flux-limited plateau regime is surprising given that the film is rather insulating and the electrolyte permeates into the network and possibly contacts the rear support electrode. The transition in the profiles from spiked at potentials near V_{on} (photocurrent onset) to more rectangular at positive bias potentials (not shown in Figure 32) must mean that the voltage does exert an effect on carrier transit through the network. No satisfactory explanation appears to exist at present to resolve this apparent anomaly.

1.8.5 Photoexcitation and Carrier Collection: Dynamic Behavior

In this section, we briefly consider the response of nanocrystalline semiconductor–electrolyte interfaces to either pulsed or periodic photoexcitation. Several points are worthy of note in this respect: (a) the photocurrent rise-time in response to an illumination step is nonlinear. Further, the response is *faster* when the light intensity is higher. (b) The decay profiles exhibit features on rather slow time-scales extending up to several seconds. (c) The photocurrent decay transients exhibit a peaking behavior. The time at which this peak occurs varies with the square of the film thickness, d . (d) A similar pattern is also seen in IMPS data where the transit time, τ , is seen to be proportional to d^2 .

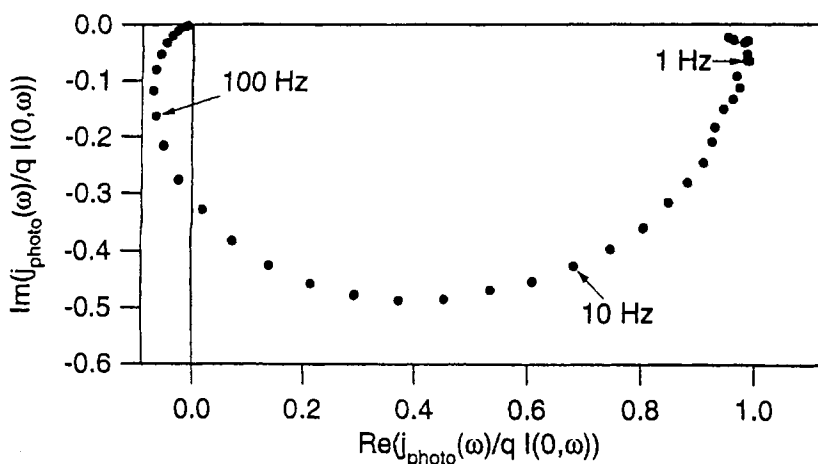


Figure 33. Complex plane IMPS plot for a nanocrystalline GaP–acid (pH 1.0) electrolyte with illumination from the electrolyte side. (Reproduced with permission from the authors of Ref. [9].)

The above observations have been interpreted within the framework of two distinct models, one involving trapping/detrapping of the photogenerated electrons [345, 346] and the other based on electron diffusion (or field-assisted diffusion) not attenuated by electron localization [347, 348]. The millisecond transit times also mean that the transit times are very long compared with equilibration of majority carriers in a bulk semiconductor or electron–hole pair separation within the depletion layer of a flat electrode. The slow transport is rationalized by a weak driving force and by invoking percolation effects [338].

It is interesting that the response patterns differ for different nanocrystalline electrodes [338]. For example, while trapping/detrapping effects appear to be relatively unimportant for GaP, the response for TiO₂, especially at low photon fluxes, is governed by electron trapping/detrapping kinetics. This accounts for the faster response at higher photon fluxes (see above).

As with the flat film counterparts, IMPS is also yielding a wealth of dynamic electron transport information for nanocrystalline films [346, 349–352]. An interesting point of contrast with the former is the fact that the imaginary component of the IMPS response is negative over most of the frequency range (Figure 33). In minority carrier processes for a semiconductor–electrolyte interface, on the other hand, the response lies in the upper complex plane (see, e.g., Figure 27). This stems from the fact that the phase delay is negative for majority carrier processes (i.e., there is a phase lag) whereas minority carriers involved in surface recombination ‘lead’ the illumination [9].

A further characteristic IMPS signature for nanocrystalline films is a spiral in the high-frequency regime as exemplified by the complex plane plot in Figure 33 [349]. This spiral is typical of a constant time lag (i.e., frequency-dependent phase shift), and it arises simply from the transit time required for the majority carriers to move

from the front face to the rear contact. In line with this notion, the spiral disappears for rear illumination geometry, i.e., for irradiation through the transparent film contact. The spiral pattern has also been accommodated within a model framework based on field-driven electron transport [349].

Several issues remain to be resolved in studies of electron transport at nanocrystalline semiconductor–electrolyte interfaces. Among these are those related to the variation of excess carrier density with distance (and consequent variations in D and τ across the film), the importance of field-assisted transport phenomena, the role of temporary localization of electrodes in traps, the influence of solution species on transient profiles and the like. However, rapid progress is being made in these directions as exemplified by several published studies [338, 349, 352, 353–355].

1.8.6 Size Quantization

When electronic particles such as electrons and holes are constrained by potential barriers to regions of space that are comparable to or smaller than their de Broglie wavelength, the corresponding allowed energy states become discrete (i.e., quantized) rather than continuous. This manifests in the absorption (or emission) spectra as discrete lines that are reminiscent of atomic (line) transitions; these sharper features often appear superimposed on a broader envelope. Another manifestation for semiconductors is that the energy band-gap (E_g) increases or, equivalently, the absorption threshold exhibits a blue shift. The critical dimension for size quantization (SQ) effects to appear in semiconductors depends on the effective mass (m^*) of the electronic charge carriers. For $m^* \approx 0.05$, the critical dimension is about 300 Å; it decreases approximately linearly with increasing m^* [7].

In general, charge carriers in semiconductors can be confined in one, two or three spatial dimensions, giving rise to quantum wells, quantum wires or quantum particles (or dots). There is much scientific and technological interest in SQ effects in semiconductors. One underlying reason is that the optical, electrical and redox properties of semiconductors can be tuned simply by manipulating their physical dimensions rather than their chemical composition. There is also a fundamental incentive to explore how atomic and molecular properties evolve into bulk ones. Much of this work, particularly that stemming from electrochemical and photochemical perspectives, has been reviewed elsewhere [356–358]. Therefore, in what follows, we merely summarize progress in the preparation of selected nanocrystalline semiconductor films and electrodes exhibiting SQ effects. Several reviews [4, 7, 312, 359] also contain closely related material and should be consulted for further details.

Much of the challenge from a preparation perspective concerns the size distribution of the nanocrystallites within the film. Ideally, this distribution should be as monodisperse as possible. Thus, CBD and electrodeposition have been utilized to prepare films showing SQ effects [312, 360–362]. Even hybrid methods have been employed wherein the chemical and electrodeposition steps are combined [321]. Other strategies to enhance SQ include selection of a particular substrate orientation (e.g., Au[111] planes) [360, 362], host matrix (e.g., clays, Nafion) [363, 364] or

chemically modified support (e.g., silane-functionalized tin oxide) [365, 366]. Techniques such as electrochemical atomic layer epitaxy allow the fabrication of ultra-thin films [367] or multilayered films [368] exhibiting SQ. Of course, molecular beam epitaxy (MBE) and metalloorganic chemical vapor deposition (MOCVD) have long been successfully employed for this purpose by the physics, materials science and engineering communities.

Another interesting photoelectrochemical approach employs selective corrosion or etching of a precursor film to secure SQ. This approach undoubtedly was inspired by the success with the preparation of porous Si (see Section 1.8.2 and Ref. [322]). The idea here is that the energy (or wavelength) of the light that is used for photoetching determines the particle size distribution [369, 370]. Simply put, larger crystallites will preferentially undergo photocorrosion and dissolve away in the medium, leaving behind ultra-small (ångström size) particles exhibiting the SQ effect.

Characterization of these materials presents new challenges. For example, the amounts of ‘active’ material in the film are extremely small, challenging the analytical sensitivity of many common optical absorption techniques. Optical interference from the (highly reflecting) supports (e.g., Au) can be a serious problem. Vibrational spectroscopy of ultra-thin overlayers, although highly desirable for probing SQ effects, demands even higher sensitivity (relative to the UV–visible spectral range) because of the inherently weaker transitions. Nonetheless, a battery of in situ measurement probes have been deployed for studying SQ effects in semiconductor nanocrystalline films. These include photocurrent spectroscopy [362], scanning probe microscopic methods such as AFM and STM [371], photoluminescence [321, 368], resonance Raman spectroscopy [372] and surface-enhanced Raman scattering [367].

The semiconductors in these studies also span a wide range and include CdS, CdSe, ZnO, Fe₂O₃ and TiO₂.

1.9 Charge Transfer Across Chemically Modified Semiconductor–Electrolyte Interfaces

1.9.1 Single Crystals

Much of the research in the early 1980s on chemically modified semiconductor–electrolyte interfaces was directed toward protecting them from photocorrosion; this body of work has been reviewed [373]. Parallel efforts also went into improving minority carrier transfer at the interface by chemisorbing metal ions such as Ru³⁺ on the semiconductor surface. Chemical agents such as sulfide ions are known to passivate the semiconductor against surface recombination [6]. A study [374] on electron transfer dynamics at p-GaAs–acetonitrile interfaces where the semiconductor surface was sulfide-passivated exemplifies this fact. In general, the mechanistic issue of whether the above chemical agents improve minority carrier charge

transfer by minimizing surface recombination or by a true catalytic action has not been completely resolved [1].

Yet another tactic involves perturbing the electrostatics at the semiconductor–electrolyte interface by adsorbing (or even chemically attaching) electron donors or acceptors on the semiconductor surface. In favorable cases, this increases the band-bending at the interface by thus introducing a fixed counter-charge of opposite polarity (negative for an n-type semiconductor) at the junction. Chloride ion adsorption on the n-GaAs surface from ambient-temperature AlCl_3 –*n*-butylpyridinium chloride melts [30, 375] is a case in point; this process serves to improve the junction and the photovoltage that it delivers. Of course, such ‘fixed-charge’ effects have long been known to the solid-state device physics and gas-phase catalysis communities. Other agents that have been deployed for chemical tuning of the interfacial energetics at the semiconductor–electrolyte interface are listed in Table 3.

Table 3. A summary of approaches^a to chemical modification of semiconductor–electrolyte interfaces.

Modification agent(s)	Semiconductor(s)	Modification objective ^b	Sample reference(s)
Ru^{3+}	n-GaAs	A	377, 378
Co^{3+}	n-GaAs	A	379
Os^{3+}	n-GaAs	A	379
Ag^+	p-InP	A	380
S^{2-}	p-GaAs	A	374
HS^-	CdS, CdSe	B	381
Thiolates	CdS, CdSe	B	382
Dithiocarbamate	CdS, CdSe	B	383, 384
Lewis acids	CdS, CdSe	B	385, 386
Lewis bases	CdS, CdSe	B	387
Cl^-	n-GaAs	B	30, 375
Benzoic acid derivatives	n^+ -GaAs	B	376
Noble metals	n- TiO_2	C	388
Noble metals	p-InP	C	377, 389–391
RuO_2^c	n-CdS	C	392, 393
RuO_2^c	n-Si	C	394
Pt^c	p-Si	C	394, 395
Pt^c	n-CdS	C	396
Noble metals	n-CdS	C	391
Noble metals ^d	p-InP	C	397

^a Approaches to photoanode stabilization based on polymer films containing redox functionalities have been reviewed elsewhere, e.g., Refs. [6, 373].

^b (A) minority carrier transfer catalysis and/or surface state passivation; (B) electrostatic modification; (C) catalysis of multi-electron photoprocesses (refer to text).

^c In these cases, the semiconductor electrode also contained a coating, either polymeric or indium tin oxide.

^d The chemically modified photocathode was used in conjunction with n-MoSe₂ (or n-WSe₂) in a two-photoelectrode cell configuration.

Native semiconductor surfaces are fairly inactive from a catalysis perspective. Thus, noble metal or metal oxide islands have been implanted on photoelectrode surfaces as electron storage centers to drive multi-electron redox processes such as HER, photo-oxidation of H_2O and photo-oxidation of HCl , HBr or HI . Examples of this sort of chemical modification strategy are also given in Table 3.

The advent of self-assembled monolayer (SAM) films on electrode surfaces has rendered a high degree of molecular order and predictability to the chemical modification approach. In particular, the use of these insulating, molecular spacers allows the interrogation of critical issues in electron transfer such as the influence of chemical bonding and distance between the support electrode and the redox moieties on the rate constant for electron transfer. Many such studies on gold-confined SAMs have appeared recently [398–400]. Corresponding studies on *semiconductor* surfaces (particularly Group II–V compounds such as GaAs and InP [401–403] and elemental semiconductors such as Si [404]) have also begun to appear.

Alkanethiol-based or alkylsiloxane-based SAMs have been profitably employed in all these instances to probe the distance effect in electron-transfer dynamics. The thiol-based SAMs have the virtue that the spacer length can be predictably altered simply by varying the number of methylene units in the chain. The distance dependence of k_{et} is embodied in the parameter β , the decay coefficient (for a critical discussion of the subtleties involved in the extraction and interpretation of this parameter, see Ref. [399]). A value of 0.49 ± 0.07 has been reported for β for n-InP–alkanethiol–ferrocyanide interfaces [403]. This value is smaller than its counterpart for corresponding films on gold surfaces which range from ~ 0.6 to 1.1 per methylene unit. The reason for this difference is not entirely clear, although several hypotheses were advanced by the authors [403].

1.9.2 Nanocrystalline Semiconductor Films and Composites

Dye sensitization of nanocrystalline semiconductor films certainly represents one popular approach to chemical modification of the interface. However, this topic is covered in detail elsewhere in this series of volumes. Other examples, from a non-dye sensitization perspective, are less common but two recent studies are noted [405, 406]. One utilizes the surface affinity of TiO_2 toward suitably derivatized viologens to construct chemically modified nanocrystalline films suitable for displays, electrochromic (smart) windows, sensors and the like [405]. In the other study [406], the TiO_2 film surface was modified with phosphotungstic acid (PWA). This compound belongs to a family of polyoxometallates that exhibit interesting electron- and proton-transfer/storage properties and also high thermal stability [407]. Hence these modified films would be applicable in areas such as catalysis, sensors, electronics and even medicine.

These TiO_2 –PWA films represent a logical bridge connecting single-phase semiconductor films and multi-component composite systems. Of course, highly evolved multi-component assemblies occur in nature and there is no better example than the plant photosynthetic system. The plant photosynthetic architecture contains synergistic components (e.g., light-harvesting antennae, membranes) each with a well-

defined and complementary function, to convert the incident photon energy, to move electrons vectorially and to store the reaction products. The design and implementation of artificial analogs have proved to be a daunting task, from both synthetic and characterization perspectives. This topic is covered elsewhere in this series of volumes, but we briefly discuss here some simple multi-component assemblies based on semiconductors.

Early examples in the 1980s were aimed at the design of composite systems for photoelectrolytic generation of H_2 . Thus, Nafion and SiO_2 were used as supports for coprecipitated ZnS and CdS for photoassisted HER from aqueous sulfide media [407]. Subsequent work has addressed the mechanistic role of the support in the photoassisted HER [408]. Vectorial electron transfer was demonstrated in bipolar TiO_2 -Pt or CdSe-CoS photoelectrode panels arranged in series arrays for the photodecomposition of water to H_2 and O_2 [409, 410].

More recently, matrix-semiconductor composites, i.e., films comprising of semiconductor particles that are dispersed in a nonphotoactive continuous matrix, have been developed. Examples of matrix candidates are metals and polymers [411–416]. Occlusion electrosynthesis is a versatile method for preparing such composite films, as exemplified by the Ni- TiO_2 and Ni-CdS family [417–419].

Matrix-semiconductor composite films have two virtues from a photoelectrochemical perspective. First, their components can be separately chosen and optimized for a specific function. Thus, the matrix component can be chosen to have good adsorption tendency toward a targeted substrate. The semiconductor component then functions in the role of photogenerating charge carriers either for reducing or oxidizing this sequestered substrate. This photocatalytic strategy has been recently demonstrated both for an organic substrate (formate ion) [420] and an inorganic substrate (sulfite) [421]. The net result in either case is an enhanced photocatalytic performance of the composite because of the high *local* concentration of the substrate resulting from the matrix adsorption process. In principle, high surface area supports of the sort that are normally used in the gas-phase catalysis community can also be used in conjunction with TiO_2 [422, 423]. These would include materials such as Al_2O_3 , SiO_2 and diatomaceous earth. The resultant composite films, however, cannot be used as electrodes because of their poor electronic conductivity.

The second important feature of a metal-semiconductor composite approach is that the metal can function as a template for chemical or electrochemical derivatization to afford a film comprising of molecular redox-semiconductor (or even semiconductor-semiconductor) contacts. Figure 34 generically illustrates the occlusion electrosynthesis approach for preparing M- TiO_2 composite films and a subsequent derivatization with ferri/ferrocyanide to afford the corresponding metal hexacyanoferrate (MHCF)- TiO_2 counterparts [424].

Such an approach was utilized for preparing NiHCF- TiO_2 [424–426] and CuHCF- TiO_2 [424] composites. These films have interesting photoelectrochromic and photoelectrochemical properties. For example, depending on the method of preparation, NiHCF- TiO_2 films exhibit different photoelectrochemical profiles (Figure 35). In the 'normal' case (Figure 35a), little photoactivity is evident at potentials up to the $Fe(II) \rightarrow Fe(III)$ redox point (ca. 0.4 V). Thereafter, photoanodic currents are observed as the photogenerated holes in TiO_2 oxidize the NiHCF(II)

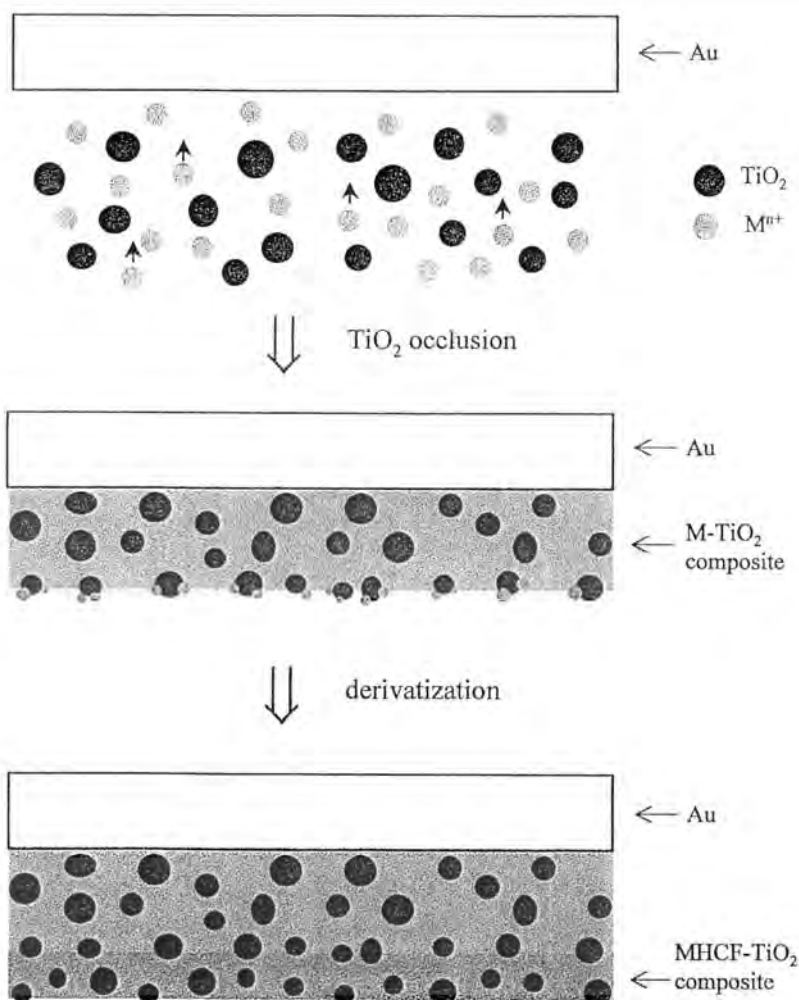


Figure 34. Schematic illustration of the occlusion electrosynthesis approach for the preparation of M-TiO_2 ($\text{M} = \text{metal}$) composite films and subsequent chemical derivatization to yield the metal hexacyanoferrate (MHCF)- TiO_2 counterparts. Refer to the text for further details.

redox centers. The electrons flow into the Ni phase and thence on to the rear Au contact.

On the other hand, in type II films (see inset in Figure 35b), the TiO_2 particles are not in electronic communication with the Ni phase. Hence *photocathodic* current flow is observed under light as the photogenerated electrons in TiO_2 flow into the electrolyte while the holes move into the NiHCF phase and ultimately into the Au contact (Figure 35b). That is, the carrier transit direction is reversed relative to the type I film case in Figure 35a.

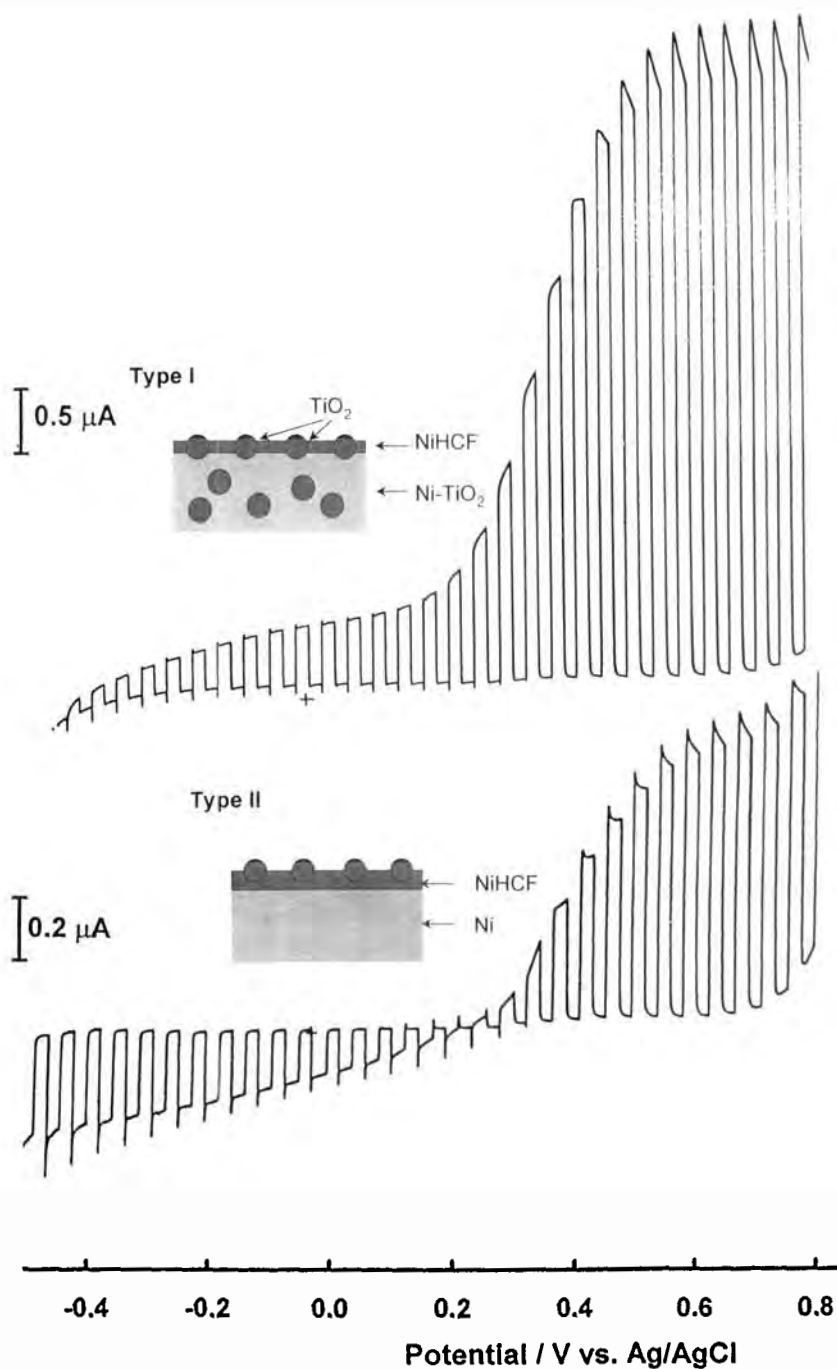


Figure 35. Photovoltammograms for NiHCF-TiO₂ composite films prepared by two variant routes (see Ref. [426]). The corresponding composite film architectures are shown schematically as insets.

As the potential is further increased, the Fe(II) redox centers in NiHCF are *electrochemically* oxidized. Now the photogenerated electrons (in TiO₂) can flow into the NiHCF phase and reduce the Fe(III) redox centers thus generated, whereas the holes flow into the electrolyte. In other words, the behavior reverts to the ‘normal’ carrier transit direction for an n-type semiconductor.

Such ‘bipolar’ photoelectrochemical behavior is not commonplace. It has been observed under certain conditions for nanocrystalline CdSe films [319]. Behavior of the sort shown in Figure 35b represents another type of APE (Section 1.6.3) and underlines the fact that the photoelectrochemical behavior of these types of films is dictated by differential electron and hole transfer kinetics rather than by factors related to band-bending as in semiconductor single crystals.

1.10 Concluding Remarks

The foregoing account hopefully illustrates the fact that the fields of semiconductor electrochemistry and photoelectrochemistry remain healthy and vibrant. Much progress has been made in our understanding of charge transfer across semiconductor–electrolyte interfaces, and the pace of research activity does not appear to have abated in the 1990s. In this author’s crystal ball, several profitable avenues will continue to be further explored in the future: chemically modified layers and their influence on charge transfer, nanocrystalline semiconductor films and semiconductor-based composite electrode assemblies. Concurrently, interfacial characterization probes will continue to improve, in terms of both sensitivity and time/space resolution, and new experimental and theoretical tools will also emerge. Indeed, it appears that this field is poised for exciting times ahead.

Acknowledgments

Research in the author’s laboratory on semiconductor electrochemistry and photoelectrochemistry since 1995 is funded, in part, by the Office of Basic Energy Sciences, US Department of Energy. A number of talented and dedicated co-workers and colleagues have been involved in collaborative research with the author over the past 20 years; their names appear in the publications cited from this laboratory. I also thank the University of Texas at Arlington for providing the facilities and infrastructure. My attempts to provide an updated account was facilitated by the receipt of reprints and preprints and many enjoyable discussions with my colleagues in this field. They include: Drs. S. W. Feldberg, D. Fitzmaurice, A. Fujishima, W. P. Gomes, A. Hagfeldt, A. Heller, J. T. Hupp, C. Koval, D. Lincot, S.-E. Lindquist, Y. Nakato, A. J. Nozik, L. M. Peter, K. Uosaki, D. Vanmaekelbergh, D. H. Waldeck and H. Yoneyama. Last but not least, I thank Ms. Gloria Madden for assistance with the preparation of this chapter. Finally, my thanks are due to the Part Editor,

Dr. T. E. Mallouk, for inviting me to undertake this project—while daunting at the outset, it turned out to be an enjoyable and stimulating experience after all!

References

1. N. S. Lewis, *Acc. Chem. Res.* **1990**, *23*, 176.
2. L. M. Peter, *Chem. Rev.* **1990**, *90*, 753.
3. N. S. Lewis, *Annu. Rev. Phys. Chem.* **1991**, *42*, 543.
4. C. A. Koval, J. N. Howard, *Chem. Rev.* **1992**, *92*, 411.
5. A. Kumar, W. C. Á. Wilisch, N. S. Lewis, *Crit. Rev. Solid State Mater. Sci.* **1993**, *18*, 327.
6. M. X. Tan, P. E. Laibinis, S. T. Nguyen, J. M. Kesselman, C. E. Stanton, N. S. Lewis, *Prog. Inorg. Chem.* **1994**, *41*, 21.
7. A. J. Nozik, R. Memming, *J. Phys. Chem.* **1996**, *100*, 13061.
8. N. S. Lewis, *J. Phys. Chem.* **1998**, *102*, 4843.
9. L. M. Peter, D. Vanmackelbergh, *Adv. Electrochem. Sci. Eng.* **1999**, *6*, 77.
10. L. M. Peter, in *Comprehensive Chemical Kinetics* (Eds. R. G. Compton, G. Hancock), Elsevier, Amsterdam, **1999**, pp. 223–280.
11. R. J. D. Miller, G. McLendon, A. J. Nozik, W. Schmickler, F. Willig, *Surface Electron-Transfer Processes*, VCH, New York, **1995**.
12. K. Rajeshwar, L. M. Peter, A. Fujishima, D. Meissner, M. Tomkiewicz (Eds.), *Photoelectrochemistry*, Proc. Vol. 97-20, Electrochemical Society, Pennington, NJ, **1997**.
13. N. Sato, *Electrochemistry at Metal and Semiconductor Electrodes*, Elsevier, Amsterdam, **1998**.
14. A. Hamnett, in *Comprehensive Chemical Kinetics* (Ed. R. G. Compton), Vol. 27, Elsevier, Amsterdam, **1987**, p. 61.
15. J. S. Newman, *Electrochemical Systems*, 2nd edn., Prentice-Hall, Englewood Cliffs, NJ, **1991**, p. 496.
16. R. A. Smith, *Semiconductors*, Cambridge University Press, Cambridge, **1964**.
17. F. A. Kröger, H. J. Vink, in *Solid State Physics* (Eds. F. Seitz, D. Turnbull), Vol. 3, Academic Press, New York, **1956**.
18. F. A. Kröger, *The Chemistry of Imperfect Crystals*, North-Holland, Amsterdam, **1964**.
19. N. B. Hannay (Ed), *Semiconductors*, Reinhold, New York, **1959**.
20. A. R. West, *Solid State Chemistry and Its Applications*, Wiley, New York, **1984**.
21. P. A. Cox, *The Electronic Structure and Chemistry of Solids*, Oxford University Press, Oxford, **1987**.
22. R. Hoffmann, *Solids and Surfaces*, VCH, New York, **1988**.
23. K. Uosaki, H. Kita, in *Modern Aspects of Electrochemistry* (Eds. R. E. White, J. O'M. Bockris, B. E. Conway), Vol. 18, Plenum Press, New York, **1986**, pp. 1–60, and references cited therein.
24. S. Trasatti, *The Absolute Electrode Potential: an Explanatory Note*, IUPAC Commission 1.3 (Electrochemistry), **1984**.
25. H. Reiss, *J. Electrochem. Soc.* **1978**, *125*, 937.
26. Yu. V. Pleskov, Yu. Ya. Gurevich, *Semiconductor Photoelectrochemistry*, Consultants Bureau, New York, **1986**.
27. H. Gerischer, *Adv. Electrochem. Eng.* **1961**, *1*, 139.
28. H. Gerischer, in *Physical Chemistry: An Advanced Treatise* (Eds. H. Eyring, D. Henderson, W. Jost), Vol. 9A, Academic Press, New York, **1970**.
29. S. R. Morrison, *The Chemical Physics of Surfaces*, Plenum Press, New York, **1977**.
30. P. Singh, R. Singh, R. Gale, K. Rajeshwar, J. DuBow, *J. Appl. Phys.* **1980**, *51*, 6286.
31. For example, K. Rajeshwar, in *Molten Salt Techniques* (Eds. R. J. Gale, D. G. Lovering), Vol. 2, Plenum Press, New York, **1984**, pp. 221–252.
32. R. Thapar, K. Rajeshwar, *Electrochim. Acta* **1983**, *28*, 198.
33. C. M. Gronet, N. S. Lewis, G. W. Cogan, J. F. Gibbons, G. R. Model, *J. Electrochem. Soc.* **1984**, *131*, 2873.

34. E. H. Rhoderick, *Metal–Semiconductor Contacts*, Clarendon Press, Oxford, **1980**.
35. S. Kar, K. Rajeshwar, P. Singh, J. DuBow, *Sol. Energy* **1979**, 23, 129.
36. G. Horowitz, P. Allongue, H. Cachet, *J. Electrochem. Soc.* **1984**, 131, 2563.
37. A. J. Bard, A. B. Bocarsly, F. R. F. Fan, E. G. Walton, M. S. Wrighton, *J. Am. Chem. Soc.* **1980**, 102, 3671.
38. A. Many, Y. Goldstein, N. B. Grover, *Semiconductor Surfaces*, North-Holland, Amsterdam, **1965**.
39. G. A. Somorjai, *Introduction to Surface Chemistry and Catalysis*, Wiley, New York, **1994**.
40. A. W. Adamson, A. P. Gast, *Physical Chemistry of Surfaces*, Wiley, New York, **1997**.
41. R. L. Van Meirhaeghe, F. Cardon, W. P. Gomes, *J. Electroanal. Chem.* **1985**, 188, 287.
42. J. Bardeen, *Phys. Rev.* **1947**, 71, 717.
43. A. M. Cowley, S. M. Sze, *J. Appl. Phys.* **1965**, 36, 3212.
44. S. Kurtin, T. C. McGill, C. A. Mead, *Phys. Rev. Lett.* **1969**, 22, 1433.
45. T. C. McGill, *J. Vac. Sci. Technol.* **1974**, 11, 935.
46. L. J. Brillson, *Phys. Rev. Lett.* **1978**, 40, 260.
47. L. J. Brillson, *J. Vac. Sci. Technol.* **1979**, 16, 1137.
48. W. E. Spicer, P. W. Chye, P. R. Skeath, C. Y. Su, I. Lindau, *J. Vac. Sci. Technol.* **1979**, 16, 1422.
49. G. Nogami, *J. Electrochem. Soc.* **1982**, 129, 2219.
50. K. Uosaki, H. Kita, *J. Electrochem. Soc.* **1983**, 130, 895.
51. R. de Gruyse, W. P. Gomes, F. Cardon, J. Vennik, *J. Electrochem. Soc.* **1975**, 125, 711.
52. J.-N. Chazalviel, *Electrochim. Acta* **1988**, 33, 461.
53. K. Rajeshwar, R. O. Lezna, N. R. de Tacconi, *Anal. Chem.* **1992**, 64, 429A.
54. K. Rajeshwar, *Spectroscopy* **1993**, 8, 16.
55. L. M. Peter, in *Comprehensive Chemical Kinetics* (Ed. R. G. Compton), Vol. 29, Elsevier, Amsterdam, **1989**, pp. 353–383.
56. O.-M. R. Chyan, K. Rajeshwar, *J. Electrochem. Soc.* **1985**, 132, 2109.
57. O.-M. R. Chyan, S.-I. Ho, K. Rajeshwar, *J. Electrochem. Soc.* **1986**, 133, 531.
58. K. K. Mishra, K. Rajeshwar, *J. Electroanal. Chem.* **1989**, 273, 169.
59. P. G. Santangelo, G. Miskelly, N. S. Lewis, *J. Phys. Chem.* **1988**, 92, 6359.
60. P. G. Santangelo, G. Miskelly, N. S. Lewis, *J. Phys. Chem.* **1989**, 93, 6128.
61. P. G. Santangelo, M. Lieberman, N. S. Lewis, *J. Phys. Chem. B* **1998**, 102, 4731.
62. T. Inoue, T. Watanabe, A. Fujishima, K. Honda, K. Kohayakawa, *J. Electrochem. Soc.* **1977**, 124, 719.
63. A. Fujishima, T. Inoue, K. Honda, *J. Am. Chem. Soc.* **1979**, 101, 5582.
64. K. W. Frese, Jr., M. J. Madou, S. R. Morrison, *J. Phys. Chem.* **1980**, 84, 3172.
65. B. H. Loo, K. W. Frese, Jr., S. R. Morrison, *Appl. Surf. Sci.* **1981**, 8, 290.
66. K. W. Frese, Jr., M. J. Madou, S. R. Morrison, *J. Electrochem. Soc.* **1981**, 128, 1527.
67. K. W. Frese, Jr., M. J. Madou, S. R. Morrison, *J. Electrochem. Soc.* **1981**, 128, 1939.
68. K. W. Frese, Jr., *J. Electrochem. Soc.* **1983**, 130, 28.
69. D. Vanmaekelbergh, W. P. Gomes, F. Cardon, *J. Electrochem. Soc.* **1982**, 129, 546.
70. W. P. Gomes, S. Lingier, D. Vanmaekelbergh, *J. Electroanal. Chem.* **1989**, 269, 237.
71. S. Lingier, W. P. Gomes, F. Cardon, *Ber. Bunsenges. Phys. Chem.* **1989**, 93, 2.
72. D. Vanmaekelbergh, J. J. Kelly, *J. Phys. Chem.* **1990**, 94, 5406.
73. P. A. Allongue, H. Cachet, *J. Electrochem. Soc.* **1985**, 132, 45.
74. J. E. A. M. Van der Meerakker, J. J. Kelly, P. H. L. Notten, *J. Electrochem. Soc.* **1985**, 132, 638.
75. B. L. Wheeler, G. Nagasubramanian, A. J. Bard, *J. Electrochem. Soc.* **1984**, 131, 1038.
76. K. Rajeshwar, L. Thompson, P. Singh, R. C. Kainthla, K. L. Chopra, *J. Electrochem. Soc.* **1981**, 128, 1744.
77. M. Tomkiewicz, *J. Electrochem. Soc.* **1979**, 126, 2220.
78. W. Siripala, M. Tomkiewicz, *J. Electrochem. Soc.* **1982**, 129, 1240.
79. J. F. McCann, S. P. S. Badwal, *J. Electrochem. Soc.* **1982**, 129, 551.
80. A. Goossens, J. Schoonman, *J. Electroanal. Chem.* **1990**, 289, 11.
81. W. P. Gomes, D. Vanmaekelbergh, *Electrochim. Acta* **1996**, 41, 967.
82. Z. Hens, W. P. Gomes, *J. Phys. Chem. B* **1997**, 101, 5814.

83. Z. Hens, W. P. Gomes, *Electrochim. Acta* **1998**, *43*, 2577.
84. Z. Hens, *J. Phys. Chem. B* **1999**, *103*, 122.
85. Z. Hens, W. P. Gomes, *J. Phys. Chem. B* **1999**, *103*, 130.
86. B. Ba, H. Cachet, B. Fotouhi, O. Gorochov, *Electrochim. Acta* **1992**, *37*, 309.
87. P. Allongue, H. Cachet, *J. Electroanal. Chem.* **1981**, *119*, 371.
88. J. Schefold, H. H. Kuhne, *J. Electroanal. Chem.* **1991**, *300*, 211.
89. J. Schefold, *J. Electrochem. Soc.* **1995**, *142*, 850.
90. F. Cardon, D. Vanmaekelbergh, *Electrochim. Acta* **1992**, *37*, 837.
91. J. Schefold, *J. Phys. Chem.* **1992**, *96*, 8692.
92. E. A. Ponomarev, L. M. Peter, *J. Electroanal. Chem.* **1995**, *397*, 45.
93. L. M. Peter, J. Li, R. Peat, *J. Electroanal. Chem.* **1984**, *165*, 29; **1984**, *165*, 41.
94. R. Haak, C. Ogden, D. Tench, *J. Electrochem. Soc.* **1982**, *129*, 891.
95. R. Haak, D. Tench, *J. Electrochem. Soc.* **1984**, *131*, 275.
96. R. Haak, D. Tench, *J. Electrochem. Soc.* **1984**, *131*, 1442.
97. C. E. Goodman, B. W. Wessels, R. G. P. Ang, *Appl. Phys. Lett.* **1984**, *45*, 442.
98. P. Allongue, H. Cachet, *Ber. Bunsenges. Phys. Chem.* **1987**, *91*, 386.
99. W. J. Albery, P. N. Bartlett, *J. Electrochem. Soc.* **1982**, *129*, 2254.
100. B. Messer, H. Tributsch, *J. Electrochem. Soc.* **1986**, *133*, 2212.
101. B. Messer, H. Tributsch, *Chem. Phys. Lett.* **1987**, *142*, 546.
102. G. Schlichthorl, E. A. Ponomarev, L. M. Peter, *J. Electrochem. Soc.* **1995**, *142*, 3062.
103. G. Schlichthorl, H. Tributsch, *Electrochim. Acta* **1992**, *37*, 919.
104. H. Tributsch, G. Schlichthorl, L. Elstner, *Electrochim. Acta* **1993**, *38*, 141.
105. H. J. Lewerenz, G. Schlichthorl, *J. Appl. Phys.* **1994**, *75*, 3544.
106. F. Wunsch, Y. Nakato, M. Kunst, H. Tributsch, *J. Chem. Soc., Faraday Trans.* **1996**, *92*, 4053.
107. M. D. E. Forbes, N. S. Lewis, *J. Am. Chem. Soc.* **1990**, *112*, 3682.
108. C. D. Jaeger, H. Gerischer, W. Kautek, *Ber. Bunsenges. Phys. Chem.* **1982**, *86*, 20.
109. A. Tardella, J.-N. Chazalviel, *Phys. Rev. B* **1985**, *2*, 2439.
110. S. P. Perone, J. H. Richardson, S. B. Deutscher, *J. Phys. Chem.* **1981**, *85*, 341.
111. S. Gottesfeld, S. W. Feldberg, *J. Electroanal. Chem.* **1983**, *146*, 47.
112. G. Bin-Daar, M. P. Dare-Edwards, J. B. Goodenough, A. Hamnett, *J. Chem. Soc., Faraday Trans. 1* **1983**, *79*, 1199.
113. T. Sakata, E. Janata, W. Jaegermann, H. Tributsch, *J. Electrochem. Soc.* **1986**, *133*, 339.
114. K. Bitterling, F. Willig, *J. Electroanal. Chem.* **1986**, *204*, 211.
115. K. Bitterling, F. Willig, F. Decker, *J. Electrochem. Soc.* **1987**, *228*, 29.
116. F. Willig, *Ber. Bunsenges. Phys. Chem.* **1988**, *92*, 1312.
117. S. Gottesfeld, *Ber. Bunsenges. Phys. Chem.* **1987**, *91*, 362.
118. S. Nakabayashi, S. Komuro, Y. Aoyagi, A. Kira, *J. Phys. Chem.* **1987**, *91*, 1696.
119. J. J. Kasinski, L. A. Gomez-Jahn, K. J. Faran, S. M. Fracewski, R. J. D. Miller, *J. Chem. Phys.* **1989**, *90*, 1253.
120. L. Min, R. J. D. Miller, *Chem. Phys. Lett.* **1989**, *163*, 55.
121. L. Min, R. J. D. Miller, *Appl. Phys. Lett.* **1990**, *56*, 524.
122. S. Prybyla, W. S. Struve, B. A. Parkinson, *J. Electrochem. Soc.* **1984**, *131*, 1587.
123. R. H. Wilson, T. Sakata, T. Kawai, K. Hashimoto, *J. Electrochem. Soc.* **1985**, *132*, 1082.
124. M. W. Verbrugge, C. W. Tobias, *J. Electrochem. Soc.* **1987**, *134*, 1437.
125. J.-N. Chazalviel, M. Strefenel, T. B. Truong, *Surf. Sci.* **1983**, *134*, 865.
126. F. Decker, M. Fracastoro-Decker, *J. Electroanal. Chem.* **1981**, *126*, 241.
127. P. V. Kamat, M. A. Fox, *J. Phys. Chem.* **1983**, *87*, 59.
128. J. F. Kauffman, B. A. Balko, G. L. Richmond, *J. Phys. Chem.* **1992**, *96*, 6374.
129. K. Uosaki, *Trends Anal. Chem.* **1990**, *9*, 98.
130. A. B. Ellis, in *Chemistry and Structure at Interfaces: New Laser and Optical Techniques* (Eds. R. B. Hill, A. B. Ellis), VCH, Deerfield Beach, FL, **1986**, p. 245.
131. B. Smandek, G. Chmiel, H. Gerischer, *Ber. Bunsenges. Phys. Chem.* **1989**, *93*, 1094.
132. H. Van Ryswyk, A. B. Ellis, *J. Am. Chem. Soc.* **1986**, *108*, 2454.
133. J. Z. Zhang, M. J. Geselbracht, A. B. Ellis, *J. Am. Chem. Soc.* **1993**, *115*, 7789.
134. G. Nogami, R. Shiratsuchi, S. Ohkubo, *J. Electrochem. Soc.* **1991**, *138*, 751.

135. E. Aharon-Shalom, A. Heller, *J. Phys. Chem.* **1983**, 87, 4913.
136. F. Decker, M. Abramovich, P. Motisuke, *J. Electrochem. Soc.* **1984**, 131, 1173.
137. D. Fichou, J. Kossanyi, *J. Electrochem. Soc.* **1986**, 133, 1607.
138. D. Huppert, E. Kolodney, *Chem. Phys.* **1981**, 63, 401.
139. A. V. Rao, J.-N. Chazalviel, F. Ozanem, *J. Appl. Phys.* **1986**, 60, 696.
140. A. Tardella, J.-N. Chazalviel, *Appl. Phys. Lett.* **1985**, 47, 334.
141. F. Ozanem, J.-N. Chazalviel, *J. Electroanal. Chem.* **1989**, 269, 251.
142. M. W. Peterson, J. A. Turner, C. A. Parsons, A. J. Nozik, D. J. Arent, C. Van Hoof, G. Borghs, R. Houdre, H. Morkoc, *Appl. Phys. Lett.* **1988**, 53, 2666.
143. K. Uosaki, Y. Shigematsu, H. Kita, K. Kunimatsu, *J. Phys. Chem.* **1990**, 94, 4623.
144. B. S. H. Royce, F. Sanchez-Sinencio, R. Goldstein, R. Muratore, R. Williams, W. M. Yim, *J. Electrochem. Soc.* **1980**, 129, 2393.
145. A. Fujishima, Y. Maeda, K. Honda, G. H. Brilmyer, A. J. Bard, *J. Electrochem. Soc.* **1980**, 127, 840.
146. A. Fujishima, Y. Maeda, K. Honda, *Bull. Chem. Soc. Jpn.* **1980**, 53, 2735.
147. Y. Maeda, A. Fujishima, K. Honda, *J. Electrochem. Soc.* **1981**, 128, 1731.
148. A. Fujishima, Y. Maeda, S. Suzuki, K. Honda, *Chem. Lett.* **1982**, 179.
149. Y. Maeda, A. Fujishima, K. Honda, *Bull. Chem. Soc. Jpn.* **1982**, 55, 3373.
150. M. A. Tamor, R. E. Hetrick, *Appl. Phys. Lett.* **1985**, 46, 460.
151. S. Nakabayashi, A. Fujishima, K. Honda, *J. Am. Chem. Soc.* **1985**, 107, 250.
152. N. Myung, C. Wei, N. R. de Tacconi, K. Rajeshwar, *J. Electroanal. Chem.* **1993**, 359, 307.
153. B. I. Lemon, J. T. Hupp, *J. Phys. Chem. B* **1999**, 103, 3797, and references cited therein.
154. Y. Liu, J. I. Dadap, D. Zimdars, K. B. Eisenthal, *J. Phys. Chem. B* **1999**, 103, 2480.
155. For example: J. F. Smalley, K. Chalfant, S. W. Feldberg, T. M. Nahir, E. F. Bowden, *J. Phys. Chem. B* **1999**, 103, 1676, and references cited therein.
156. J. C. Tranchart, L. Hollan, R. Memming, *J. Electrochem. Soc.* **1978**, 125, 1185.
157. S. R. Morrison, *Surf. Sci.* **1969**, 15, 363.
158. R. A. L. Vanden Berghe, F. Cardon, W. P. Gomes, *Surf. Sci.* **1973**, 39, 368.
159. D. Meissner, R. Memming, *Electrochim. Acta* **1992**, 37, 799.
160. H. Gerischer, *Ber. Bunsenges. Phys. Chem.* **1965**, 69, 578.
161. R. Memming, G. Schwandt, *Electrochim. Acta* **1968**, 13, 1299.
162. M. J. Madou, F. Cardon, W. P. Gomes, *Ber. Bunsenges. Phys. Chem.* **1977**, 81, 1186.
163. H. H. Goossens, W. P. Gomes, *J. Electrochem. Soc.* **1991**, 138, 1696.
164. D. Vanmaekelbergh, L. S. Yun, W. P. Gomes, F. Cardon, *J. Electroanal. Chem.* **1987**, 221, 187.
165. J. J. Kelly, J. E. A. M. van den Meerakker, P. H. L. Notten, R. P. Tijburg, *Philips Tech. Rev.* **1988**, 44, 61.
166. P. H. L. Notten, J. E. A. M. van den Meerakker, J. J. Kelly, *Etching of III–V Semiconductors: an Electrochemical Approach*, Elsevier, Oxford, **1991**.
167. H. H. Goossens, W. P. Gomes, *Electrochim. Acta* **1992**, 37, 811.
168. W. P. Gomes, H. H. Goossens, in *Advances in Electrochemical Science and Engineering* (Eds. H. Gerischer, C. W. Tobias), Vol. 3, VCH, Weinheim, **1994**.
169. D. Meissner, C. Sinn, R. Memming, P. H. L. Notten, J. J. Kelly, in *Homogeneous Photocatalysis* (Eds. E. Pelizzetti, N. Serpone), Reidel, Dordrecht, **1986**.
170. J. E. A. M. van den Meerakker, *J. Electroanal. Chem.* **1988**, 243, 161.
171. B. Pettinger, H.-R. Schöppel, H. Gerischer, *Ber. Bunsenges. Phys. Chem.* **1976**, 80, 849.
172. K. Uosaki, H. Kita, *Ber. Bunsenges. Phys. Chem.* **1984**, 91, 447.
173. A. Manivannan, A. Fujishima, *J. Lumin.* **1988**, 42, 43.
174. G. Oskam, E. A. Meulenlamp, *J. Electroanal. Chem.* **1992**, 326, 213.
175. R. Reincke, R. Memming, *J. Phys. Chem.* **1992**, 96, 1310.
176. R. Reineke, R. Memming, *J. Phys. Chem.* **1992**, 96, 1317.
177. J. Vandermolen, W. P. Gomes, F. Cardon, *J. Electrochem. Soc.* **1980**, 127, 324.
178. P. Salvador, C. Gutierrez, *J. Electrochem. Soc.* **1984**, 131, 326.
179. V. A. Tyagai, G. Ya. Kolbasov, *Surf. Sci.* **1971**, 28, 423.
180. W. P. Gomes, F. Cardon, *Ber. Bunsenges. Phys. Chem.* **1970**, 74, 431.
181. F. Cardon, *Physica* **1972**, 57, 390.

182. G. Horowitz, *J. Electroanal. Chem.* **1983**, 159, 421.
183. D. Vanmaekelbergh, *Electrochim. Acta* **1997**, 42, 1135.
184. K. Schröder, R. Memming, *Ber. Bunsenges. Phys. Chem.* **1985**, 89, 385.
185. D. Vanmaekelbergh, W. P. Gomes, F. Cardon, *Ber. Bunsenges. Phys. Chem.* **1986**, 90, 431.
186. D. Vanmaekelbergh, W. P. Gomes, F. Cardon, *Ber. Bunsenges. Phys. Chem.* **1985**, 89, 994.
187. D. Vanmaekelbergh, W. P. Gomes, F. Cardon, *J. Electrochem. Soc.* **1987**, 134, 891.
188. D. Vanmaekelbergh, R. P. ter Heide, W. Kruijt, *Ber. Bunsenges. Phys. Chem.* **1989**, 93, 1103.
189. D. Vanmaekelbergh, F. Cardon, *J. Phys. D: Appl. Phys.* **1986**, 19, 643.
190. D. Vanmaekelbergh, F. Cardon, *Semicond. Sci. Technol.* **1988**, 3, 124.
191. J. J. Kelly, P. H. L. Notten, *Electrochim. Acta* **1984**, 29, 589.
192. J. E. A. M. van den Meerakker, *Electrochim. Acta* **1985**, 30, 435.
193. A. M. Fajardo, N. S. Lewis, *Science* **1996**, 274, 969.
194. A. M. Fajardo, N. S. Lewis, *J. Phys. Chem. B* **1997**, 101, 11136.
195. K. E. Pomykal, N. S. Lewis, *J. Phys. Chem. B* **1997**, 101, 2476.
196. A. Meier, S. S. Kocha, M. C. Hanna, A. J. Nozik, K. Siemoneit, R. Reineke-Koch, R. Memming, *J. Phys. Chem. B* **1997**, 101, 7038.
197. I. Uhlendorf, R. Reincke-Koch, R. Memming, *J. Phys. Chem.* **1996**, 100, 4930.
198. A. Meier, D. C. Selmarten, K. Siemoneit, B. B. Smith, A. J. Nozik, *J. Phys. Chem. B* **1999**, 103, 2122.
199. Y. Rosenwaks, B. R. Thacker, R. K. Ahrenkiel, A. J. Nozik, *J. Phys. Chem.* **1992**, 96, 10096.
200. H. Gerischer, *J. Phys. Chem.* **1991**, 95, 1356.
201. For example, S. M. Sze, *Physics of Semiconductor Devices*, Wiley, New York, **1981**.
202. For example, J. L. Pankove, *Optical Processes in Semiconductors*, Prentice Hall, Englewood Cliffs, NJ, **1971**.
203. D. Vanmaekelbergh, B. H. Erne, C. W. Cheung, R. W. Tjekstra, *Electrochim. Acta* **1995**, 40, 686.
204. I. Rosenberg, J. R. Brock, A. Heller, *J. Mol. Catal.* **1992**, 96, 3423.
205. J. Valladares, J. R. Bolton, in *Photocatalytic Purification and Treatment of Water and Air* (Eds. D. F. Ollis, H. Al-Ekabi), Elsevier, Amsterdam, **1993**, p. 111.
206. M. I. Cabrera, O. M. Alfano, A. E. Cassano, *J. Phys. Chem.* **1996**, 100, 20043.
207. C. A. Martin, M. A. Baltanas, A. E. Casano, *Environ. Sci. Technol.* **1996**, 30, 2355.
208. W. W. Gärtner, *Phys. Rev.* **1959**, 116, 84.
209. M. A. Butler, *J. Appl. Phys.* **1977**, 48, 1914.
210. V. A. Tyagai, *Russ. J. Phys. Chem.* **1965**, 38, 1335.
211. J. Li, L. M. Peter, *J. Electroanal. Chem.* **1984**, 165, 41.
212. R. H. Wilson, *CRC Crit. Rev. Solid State Mater. Sci.* **1980**, 10, 1.
213. R. H. Wilson, *J. Appl. Phys.* **1977**, 48, 4297.
214. K. Rajeshwar, *J. Electrochem. Soc.* **1980**, 129, 1003.
215. J. F. McCann, D. Haneman, *J. Electrochem. Soc.* **1982**, 129, 1134.
216. R. Memming, *Surf. Sci.* **1964**, 1, 88.
217. J. J. Kelly, R. Memming, *J. Electrochem. Soc.* **1982**, 129, 730.
218. S. U. M. Khan, J. O'M. Bockris, *J. Phys. Chem.* **1984**, 88, 2504.
219. F. E. Guibaly, K. Colbow, B. L. Funt, *J. Appl. Phys.* **1981**, 52, 3480.
220. F. E. Guibaly, K. Colbow, *J. Appl. Phys.* **1982**, 53, 1737; **1983**, 54, 6488.
221. J.-N. Chazalviel, *J. Electrochem. Soc.* **1982**, 129, 963.
222. M. Nishida, *J. Appl. Phys.* **1980**, 51, 1669.
223. F. E. Guibaly, K. Colbow, *Can. J. Phys.* **1981**, 59, 1682.
224. D. L. Ullman, *J. Electrochem. Soc.* **1981**, 128, 1269.
225. S. Ramakrishna, S. K. Rangarajan, *J. Electroanal. Chem.* **1991**, 308, 49.
226. W. Shockley, W. T. Read, *Phys. Rev.* **1952**, 87, 835.
227. R. N. Hall, *Phys. Rev.* **1982**, 87, 387.
228. For example, S. J. Fonash, *Solar Cell Device Physics*, Academic Press, San Diego, CA, **1981**, Ch. 6, pp. 262–326.
229. C. T. Sah, R. N. Noyce, W. Shockley, *Proc. IRE* **1957**, 45, 1228.
230. J. Reichman, *Appl. Phys. Lett.* **1980**, 36, 574.

231. W. I. Albery, P. N. Bartlett, A. Hamnett, M. P. Dare-Edwards, *J. Electrochem. Soc.* **1981**, *128*, 1492.
232. W. J. Albery, P. N. Bartlett, *J. Electrochem. Soc.* **1983**, *130*, 1699.
233. H. Reiss, *J. Electrochem. Soc.* **1978**, *125*, 937.
234. J. Thomchick, A. M. Buoncristiani, *J. Appl. Phys.* **1980**, *51*, 6265.
235. W. Lorenz, M. Handschuh, *J. Electroanal. Chem.* **1980**, *111*, 181.
236. W. Lorenz, C. Aegerter, M. Handschuh, *J. Electroanal. Chem.* **1987**, *221*, 33.
237. M. Handschuh, W. Lorenz, *J. Electroanal. Chem.* **1988**, *251*, 1.
238. P. Lemasson, A. Etcheberry, J. Gautron, *Electrochim. Acta* **1982**, *27*, 607.
239. S. Ramakrishna, S. K. Rangarajan, *J. Electroanal. Chem.* **1994**, *369*, 289.
240. M. L. Rosenbluth, C. M. Lieber, N. S. Lewis, *Appl. Phys. Lett.* **1984**, *45*, 423.
241. S. J. Fonash, *Solar Cell Device Physics*, Academic Press, San Diego, CA, **1981**, pp. 206–207.
242. (a) R. R. Potter, J. R. Sites, *IEEE Trans. Electron Dev.* **1984**, *ED-31*, 571; (b) R. R. Potter, J. R. Sites, *Appl. Phys. Lett.* **1983**, *43*, 843.
243. For example, H. J. Hovel, *Semiconductors and Semimetals, Vol. 11, Solar Cells*, Academic Press, New York, **1975**.
244. H. Morisaki, M. Hariya, K. Yazawa, *Appl. Phys. Lett.* **1977**, *30*, 7.
245. H. Minoura, M. Tsuike, *Chem. Lett.* **1978**, 205.
246. W. Gissler, *J. Electrochem. Soc.* **1980**, *127*, 1713.
247. B. Vainas, G. Hodes, J. DuBow, *J. Electroanal. Chem.* **1981**, *130*, 391.
248. N. Müller, G. Hodes, B. Vainas, *J. Electroanal. Chem.* **1984**, *172*, 155.
249. R. Tenne, W. Girit, *J. Electroanal. Chem.* **1985**, *186*, 127.
250. D. P. Amalnerkar, S. Radhakrishnan, H. Minoura, T. Sugiura, Y. Ueno, *Sol. Energy Mater.* **1988**, *18*, 37.
251. D. P. Amalnerkar, S. Radhakrishnan, H. Minoura, T. Sugiura, Y. Ueno, *J. Electroanal. Chem.* **1989**, *260*, 433.
252. S.-E. Lindquist, H. Vidarsson, *J. Mol. Catal.* **1986**, *38*, 131.
253. P. Singh, R. Singh, K. Rajeshwar, J. DuBow, *J. Electrochem. Soc.* **1981**, *128*, 1145.
254. (a) D. Lincot, J. Vedel, *J. Electroanal. Chem.* **1987**, *220*, 179; (b) D. Lincot, J. Vedel, *J. Phys. Chem.* **1988**, *92*, 4103.
255. L. M. Peter, in *Photocatalysis and the Environment* (Ed. M. Schiavello), Vol. 237, Kluwer, Dordrecht, **1988**, p. 243.
256. F. Willig, K. Bitterling, K.-P. Charle, F. Decker, *Ber. Bunsenges. Phys. Chem.* **1987**, *88*, 374.
257. J. Li, L. M. Peter, *J. Electroanal. Chem.* **1985**, *193*, 27.
258. J. Li, L. M. Peter, *J. Electroanal. Chem.* **1986**, *199*, 1.
259. E. A. Ponomarev, L. M. Peter, *J. Electroanal. Chem.* **1995**, *396*, 209.
260. J. Schefold, *J. Electroanal. Chem.* **1992**, *341*, 111.
261. D. Vanmaekelbergh, A. R. de Wit, F. Cardon, *J. Appl. Phys.* **1993**, *73*, 5049.
262. Y.-E. Sung, F. Galliard, A. J. Bard, *J. Phys. Chem. B* **1998**, *102*, 9797.
263. Y.-E. Sung, A. J. Bard, *J. Phys. Chem. B* **1998**, *102*, 9806.
264. M. P. Dare-Edwards, A. Hamnett, J. B. Goodenough, *J. Electroanal. Chem.* **1981**, *119*, 109.
265. K. Uosaki, H. Kita, *J. Am. Chem. Soc.* **1986**, *108*, 4294.
266. S. Kaneko, K. Uosaki, H. Kita, *J. Phys. Chem.* **1986**, *90*, 6654.
267. K. Uosaki, Y. Shigematsu, S. Kaneko, H. Kita, *J. Phys. Chem.* **1989**, *93*, 6521.
268. M. Matsumura, S. R. Morrison, *J. Electroanal. Chem.* **1983**, *144*, 113.
269. M. Matsumura, S. R. Morrison, *J. Electroanal. Chem.* **1983**, *147*, 157.
270. H. J. Lewerenz, J. Stumper, L. M. Peter, *Phys. Rev. Lett.* **1988**, *61*, 1989.
271. L. M. Peter, A. N. Borazio, H. J. Lewerenz, J. Stumper, *J. Electroanal. Chem.* **1990**, *290*, 229.
272. S. R. Morrison, T. Freund, *J. Chem. Phys.* **1967**, *47*, 1543.
273. W. P. Gomes, T. Freund, S. R. Morrison, *Surf. Sci.* **1968**, *13*, 201.
274. W. P. Gomes, T. Freund, S. R. Morrison, *J. Electrochem. Soc.* **1968**, *115*, 818.
275. K. Micka, H. Gerischer, *J. Electroanal. Chem.* **1972**, *38*, 397.
276. J.-S. Lee, T. Kato, A. Fujishima, K. Honda, *Bull. Chem. Soc. Jpn.* **1984**, *57*, 1179.
277. G. H. Schoenmakers, D. Vanmaekelbergh, J. J. Kelly, *J. Phys. Chem.* **1996**, *100*, 3215.
278. G. H. Schoenmakers, D. Vanmaekelbergh, J. J. Kelly, *J. Chem. Soc., Faraday Trans.* **1997**, *93*, 1127.

279. M. Miyake, H. Yoneyama, H. Tamura, *Chem. Lett.* **1976**, 635.
280. N. Hykaway, W. M. Sears, H. Morisaki, S. R. Morrison, *J. Phys. Chem.* **1986**, 90, 6663.
281. D. J. Fermin, E. A. Ponomarev, L. M. Peter, in Ref. [12], p. 62.
282. G. Nogami, J. H. Kennedy, *J. Electrochem. Soc.* **1989**, 136, 2583.
283. W. J. Albery, N. L. Dias, C. P. Wilde, *J. Electrochem. Soc.* **1987**, 134, 601.
284. P. Herrasti, L. M. Peter, *J. Electroanal. Chem.* **1991**, 305, 241.
285. J. Li, L. M. Peter, *J. Electroanal. Chem.* **1985**, 182, 399.
286. B. H. Ern , D. Vanmaekelbergh, I. E. Vermeir, *Electrochim. Acta* **1993**, 38, 2559.
287. J. Li, R. Peat, L. M. Peter, *J. Electroanal. Chem.* **1986**, 200, 333.
288. R. Peat, L. M. Peter, *Electrochim. Acta* **1986**, 31, 731.
289. R. Peat, L. M. Peter, *J. Electroanal. Chem.* **1986**, 209, 307.
290. D. Vanmaekelbergh, J. J. Kelly, *J. Phys. Chem.* **1990**, 94, 5406.
291. B. P. Minks, D. Vanmaekelbergh, J. J. Kelly, *J. Electroanal. Chem.* **1989**, 273, 133.
292. J. J. Kelly, J. van de Ven, J. E. A. M. van den Meerakker, *J. Electrochem. Soc.* **1985**, 132, 3026.
293. D. Vanmaekelbergh, W. P. Gomes, F. Cardon, *Ber. Bunsenges. Phys. Chem.* **1985**, 89, 987.
294. J. van de Ven, H. J. P. Nabben, *J. Electrochem. Soc.* **1990**, 137, 1603.
295. G. A. Somorjai, *Chemistry in Two Dimensions: Surfaces*, Cornell University Press, Ithaca, NY, **1981**.
296. S. Y. Huang, L. Kavan, I. Exnar, M. Gr tzel, *J. Electrochem. Soc.* **1995**, 142, L142.
297. J. G. Highfield, M. Gr tzel, *J. Phys. Chem.* **1988**, 92, 464.
298. B. O'Regan, M. Gr tzel, D. Fitzmaurice, *Chem. Phys. Lett.* **1991**, 183, 89.
299. B. O'Regan, M. Gr tzel, D. Fitzmaurice, *J. Phys. Chem.* **1991**, 95, 10525.
300. B. O'Regan, J. Moser, M. Anderson, M. Gr tzel, *J. Phys. Chem.* **1990**, 94, 8720.
301. M. K. Nazeeruddin, A. Kay, I. Rodicio, R. Humphry-Baker, E. M ller, P. Liska, N. Vlachopoulos, M. Gr tzel, *J. Am. Chem. Soc.* **1993**, 115, 6382.
302. C. J. Barbe, F. Arendse, P. Comte, M. Jirousek, F. Lenzmann, V. Shklover, M. Gr tzel, *J. Am. Ceram. Soc.* **1997**, 80, 3157.
303. A. Hagfeldt, M. Gr tzel, *Chem. Rev.* **1995**, 95, 49.
304. F. N. Castellano, G. J. Meyer, in *Molecular Level Artificial Photosynthetic Materials* (Ed. G. J. Meyer), Wiley, New York, **1997**, p. 167.
305. L. Kavan, M. Gr tzel, *Electrochim. Acta* **1995**, 40, 643.
306. H. Maeda, K. Ikeda, K. Hashimoto, K. Ajito, M. Morita, A. Fujishima, *J. Phys. Chem. B* **1999**, 103, 3213.
307. F. Cao, G. Oskam, P. C. Searson, J. M. Stipkala, T. A. Heimer, F. Farzad, G. J. Meyer, *J. Phys. Chem.* **1995**, 99, 11974.
308. H. Rensmo, K. Keis, H. Lindstr m, S. S dergren, A. Solbrand, A. Hagfeldt, S.-E. Lindquist, L. N. Wang, M. Muhammed, *J. Phys. Chem. B* **1997**, 101, 2598.
309. K. Rajeshwar, *Adv. Mater.* **1992**, 4, 23.
310. G. Hodes, in *Physical Electrochemistry* (Ed. I. Rubinstein), Marcel Dekker, New York, **1995**, p. 515.
311. K. Rajeshwar, N. R. de Tacconi, in *Semiconductor Nanoclusters—Physical, Chemical, and Catalytic Aspects*, Elsevier, Amsterdam, **1997**, p. 321.
312. S. Gorer, G. Hodes, in Ref. [311], p. 297.
313. D. Lincot, M. Froment, H. Cachet, *Adv. Electrochem. Sci. Eng.* **1999**, 6, 165.
314. P. C. Searson, *Sol. Energy Mater. Sol. Cells* **1992**, 27, 377.
315. S. Peulon, D. Lincot, *Adv. Mater.* **1996**, 8, 166.
316. C. Natarajan, G. Nogami, *J. Electrochem. Soc.* **1996**, 143, 1547.
317. L. Kavan, T. Stoto, M. Gr tzel, D. Fitzmaurice, V. Shklover, *J. Phys. Chem.* **1993**, 97, 9493.
318. L. Kavan, B. O'Regan, A. Kay, M. Gr tzel, *J. Electroanal. Chem.* **1993**, 346, 291.
319. G. Hodes, I. D. J. Howell, L. M. Peter, *J. Electrochem. Soc.* **1992**, 139, 3136.
320. (a) D. Liu, P. V. Kamat, *J. Electroanal. Chem.* **1993**, 347, 451; (b) D. Liu, P. V. Kamat, *J. Phys. Chem.* **1993**, 97, 10769.
321. S. Gorer, R. M. Penner, *J. Phys. Chem. B* **1999**, 103, 5750.
322. For example, A. G. Cullis, L. T. Canham, *Nature* **1991**, 353, 335.
323. B. H. Ern , D. Vanmaekelbergh, J. J. Kelly, *Adv. Mater.* **1995**, 7, 739.

324. B. H. Ern , D. Vanmaekelbergh, J. J. Kelly, *J. Electrochem. Soc.* **1996**, *143*, 305.
325. D. Miller, S. Mamiche-Afara, M. J. Dignam, M. Moskovits, *Chem. Phys. Lett.* **1983**, *100*, 236.
326. For example, B. E. Conway, *J. Electrochem. Soc.* **1991**, *138*, 1539.
327. R. K nenkamp, R. Henninger, P. Hoyer, *J. Phys. Chem.* **1993**, *97*, 7328.
328. R. K nenkamp, R. Henninger, *Appl. Phys. A* **1994**, *58*, 87.
329. I. Bedja, S. Hotchandani, P. V. Kamat, *J. Phys. Chem.* **1996**, *100*, 19489.
330. G. Boschloo, D. Fitzmaurice, *J. Phys. Chem. B* **1999**, *103*, 2228.
331. R. F. Howe, M. Gr tzel, *J. Phys. Chem.* **1985**, *89*, 4495.
332. L. A. Lyon, J. T. Hupp, *J. Phys. Chem.* **1995**, *99*, 15718.
333. H. Lindstr m, S. S dergren, A. Solbrand, H. Rensmo, J. Hjelm, A. Hagsfeldt, S.-E. Lindquist, *J. Phys. Chem. B* **1997**, *101*, 7710.
334. H. Lindstr m, S. S dergren, A. Solbrand, H. Rensmo, J. Hjelm, A. Hagsfeldt, S.-E. Lindquist, *J. Phys. Chem. B* **1997**, *101*, 7717.
335. S. Lunell, A. Stashans, L. Ojam e, H. Lindstr m, A. Hagsfeldt, *J. Am. Chem. Soc.* **1997**, *119*, 7374.
336. L. A. Lyon, J. T. Hupp, *J. Phys. Chem. B* **1999**, *103*, 4623.
337. R. van de Krol, A. Goossens, J. Schoonman, *J. Electrochem. Soc.* **1997**, *144*, 1723.
338. J. J. Kelly, D. Vanmaekelbergh, *Electrochim. Acta* **1998**, *43*, 2773.
339. A. Zaban, A. Meier, B. A. Gregg, *J. Phys. Chem. B* **1997**, *101*, 7985.
340. D. Vanmaekelbergh, P. E. de Jongh, *J. Phys. Chem. B* **1999**, *103*, 747.
341. H. Rensmo, H. Lindstr m, S. S dergren, A.-K. Willstedt, A. Solbrand, A. Hagfeldt, S.-E. Lindquist, *J. Electrochem. Soc.* **1996**, *143*, 3173.
342. A. Hagfeldt, U. Bj rkst n, S.-E. Lindquist, *Sol. Energy Mater. Sol. Cells* **1992**, *27*, 293.
343. S. S dergren, A. Hagfeldt, J. Olsson, S.-E. Lindquist, *J. Phys. Chem.* **1994**, *98*, 5552.
344. A. Shiga, A. Tsujiko, T. Ide, S. Yae, Y. Nakato, *J. Phys. Chem. B* **1998**, *102*, 6049.
345. K. Schwarzburg, F. Willig, *Appl. Phys. Lett.* **1991**, *58*, 2520.
346. P. E. de Jongh, D. Vanmaekelbergh, *Phys. Rev. Lett.* **1996**, *77*, 3427.
347. A. Solbrand, A. Henningson, S. S dergren, H. Lindstr m, A. Hagfeldt, S.-E. Lindquist, *J. Phys. Chem. B* **1999**, *103*, 1078.
348. A. Solbrand, H. Lindstr m, H. Rensmo, A. Hagfeldt, S.-E. Lindquist, S. S dergren, *J. Phys. Chem. B* **1997**, *101*, 2514.
349. D. Vanmaekelbergh, F. Iranzo-Marin, J. van de Lagemaat, *Ber. Bunsenges. Phys. Chem.* **1996**, *100*, 616.
350. P. E. de Jongh, D. Vanmaekelbergh, *J. Phys. Chem. B* **1997**, *101*, 2716.
351. F. Cao, G. Oskam, G. J. Meyer, P. C. Searson, *J. Phys. Chem.* **1996**, *100*, 17021.
352. L. Dloczik, O. Ieperuma, I. Lauermann, L. M. Peter, E. A. Ponomarev, G. Redmond, N. J. Shaw, I. Uhlenhof, *J. Phys. Chem. B* **1997**, *101*, 10281.
353. A. Hagfeldt, H. Lindstr m, S. S dergren, S.-E. Lindquist, *J. Electroanal. Chem.* **1995**, *381*, 39.
354. N. S. Foster, C. A. Koval, J. G. Szczechowski, R. D. Noble, *J. Electroanal. Chem.* **1996**, *406*, 213.
355. J. Rabani, K. Yamashita, K. Ushida, J. Stark, A. Kira, *J. Phys. Chem. B* **1998**, *102*, 1689.
356. L. E. Brus, *J. Phys. Chem.* **1986**, *101*, 2555.
357. A. Henglein, *Chem. Rev.* **1989**, *89*, 1861.
358. L. E. Brus, *Annu. Rev. Mater. Sci.* **1989**, *19*, 471.
359. A. J. Nozik, in Ref. [311], p. 135.
360. Y. Golan, L. Margulis, I. Rubinstein, G. Hodes, *Langmuir* **1992**, *8*, 749.
361. Y. Golan, G. Hodes, I. Rubinstein, *J. Phys. Chem.* **1996**, *100*, 2220.
362. B. Alpers, H. Demange, I. Rubinstein, G. Hodes, *J. Phys. Chem. B* **1999**, *103*, 4943.
363. M. Miyoshi, S. Nippa, H. Uchida, H. Mori, H. Yoneyama, *Bull. Chem. Soc. Jpn.* **1990**, *63*, 3380.
364. H. Yoneyama, *Res. Chem. Intermed.* **1991**, *15*, 101.
365. S. Drouard, S. G. Hickey, D. J. Riley, *J. Chem. Soc., Chem. Commun.* **1999**, 67.
366. S. G. Hickey, D. J. Riley, *J. Phys. Chem. B* **1999**, *103*, 4599.
367. S. Zhou, M. J. Weaver, *J. Phys. Chem. B* **1999**, *103*, 2323.
368. A. Gichuhi, B. E. Boone, C. Shannon, *Langmuir*, **1999**, *15*, 763.

369. H. Matsumoto, T. Sakata, H. Mori, H. Yoneyama, *J. Phys. Chem.* **1996**, *100*, 13781.
370. A. van Dijken, D. Vanmaekelbergh, A. Meijerink, in Ref. [12], p. 79.
371. B. Alpers, S. Cohen, I. Rubinstein, G. Hodes, *Phys. Rev. B* **1995**, *52*, R17017.
372. B. A. Boone, A. Gichuhi, C. Shannon, *J. Phys. Chem. B* **1998**, *102*, 6499.
373. K. Rajeshwar, *J. Appl. Electrochem.* **1985**, *15*, 1.
374. Y. Rosenwaks, B. R. Thacker, R. K. Ahrenkiel, A. J. Nozik, *J. Phys. Chem.* **1992**, *96*, 10096.
375. S. Bastide, R. Butruille, D. Cahen, A. Dutta, J. Libman, A. Shanzer, L. Sun, A. Vilan, *J. Phys. Chem. B* **1997**, *101*, 2678.
376. P. Singh, K. Rajeshwar, *J. Electrochem. Soc.* **1981**, *128*, 1724.
377. A. Heller, *Acc. Chem. Res.* **1981**, *14*, 154.
378. B. A. Parkinson, A. Heller, B. Miller, *Appl. Phys. Lett.* **1978**, *33*, 521.
379. B. J. Tufts, I. L. Abrahams, L. G. Casagrande, N. S. Lewis, *J. Phys. Chem.* **1989**, *93*, 3260.
380. A. Heller, H. J. Leamy, B. Miller, W. D. Johnston, Jr., *J. Phys. Chem.* **1983**, *87*, 3239.
381. K. Uosaki, Y. Shigematsu, H. Kita, Y. Umezawa, R. Souda, *Anal. Chem.* **1989**, *61*, 1980.
382. M. J. Natan, J. W. Thackeray, M. S. Wrighton, *J. Phys. Chem.* **1986**, *90*, 4089.
383. J. W. Thackeray, M. J. Natan, P. Ng, M. S. Wrighton, *J. Am. Chem. Soc.* **1986**, *108*, 3570.
384. J. J. Hickman, M. S. Wrighton, *J. Am. Chem. Soc.* **1991**, *113*, 4440.
385. C. J. Murphy, A. B. Ellis, *J. Phys. Chem.* **1990**, *94*, 3082.
386. J. Z. Zhang, A. B. Ellis, *J. Phys. Chem.* **1992**, *96*, 2700.
387. C. J. Murphy, G. C. Lisensky, L. K. Leung, G. R. Kowach, A. B. Ellis, *J. Am. Chem. Soc.* **1990**, *112*, 8344.
388. C.-M. Wang, A. Heller, H. Gerischer, *J. Am. Chem. Soc.* **1992**, *114*, 5230.
389. E. Aharon-Shalom, A. Heller, *J. Electrochem. Soc.* **1982**, *129*, 2865.
390. A. Heller, E. Aharon-Shalom, W. A. Bonner, B. Miller, *J. Am. Chem. Soc.* **1982**, *104*, 6942.
391. D. E. Aspnes, A. Heller, *J. Phys. Chem.* **1983**, *87*, 4919.
392. K. Rajeshwar, M. Kaneko, A. Yamada, R. N. Noufi, *J. Phys. Chem.* **1985**, *89*, 806.
393. K. Rajeshwar, M. Kaneko, *J. Phys. Chem.* **1985**, *89*, 3587.
394. L. Thompson, J. DuBow, K. Rajeshwar, *J. Electrochem. Soc.* **1982**, *129*, 1934.
395. G. Hodes, L. Thompson, J. DuBow, K. Rajeshwar, *J. Am. Chem. Soc.* **1983**, *105*, 324.
396. A. W.-H. Mau, C.-B. Huang, N. Kakuta, A. J. Bard, A. Campion, M. A. Fox, J. M. White, S. E. Webber, *J. Am. Chem. Soc.* **1984**, *106*, 6537.
397. C. Levy-Clement, A. Heller, W. A. Bonner, B. A. Parkinson, *J. Electrochem. Soc.* **1982**, *129*, 1701.
398. C. E. D. Chidsey, *Science* **1991**, *251*, 919.
399. J. F. Smalley, S. W. Feldberg, C. E. D. Chidsey, M. R. Linford, M. D. Newton, Y.-P. Liu, *J. Phys. Chem.* **1995**, *99*, 13141.
400. S. B. Sachs, S. P. Dudek, R. P. Hsung, L. R. Sita, J. F. Smalley, M. D. Newton, S. W. Feldberg, C. E. D. Chidsey, *J. Am. Chem. Soc.* **1997**, *119*, 10563.
401. C. W. Sheen, J. X. Shi, J. Martensson, A. N. Parikh, D. L. Allara, *J. Am. Chem. Soc.* **1992**, *114*, 1514.
402. Y. Gu, D. H. Waldeck, *J. Phys. Chem.* **1996**, *100*, 9573.
403. Y. Gu, D. H. Waldeck, *J. Phys. Chem. B* **1998**, *102*, 9015.
404. A. Haran, D. H. Waldeck, R. Naaman, E. Moons, D. Cahen, *Science* **1994**, *263*, 948.
405. A. Hagfeldt, L. Walder, M. Grätzel, *Proc. SPIE* **1995**, *2531*, 60.
406. H. Lindstrom, H. Rensmo, S.-E. Lindquist, A. Hagfeldt, A. Henningsson, S. Södergren, H. Siegbahn, *Thin Solid Films* **1998**, *323*, 141.
407. N. Kakuta, K. H. Park, M. F. Finlayson, A. Ueno, A. J. Bard, A. Campion, M. A. Fox, S. E. Webber, J. M. White, *J. Phys. Chem.* **1985**, *89*, 732.
408. A. Ueno, N. Kakuta, K. H. Park, M. F. Finlayson, A. J. Bard, A. Campion, M. A. Fox, S. E. Webber, J. M. White, *J. Phys. Chem.* **1985**, *89*, 3828.
409. E. S. Smotkin, A. J. Bard, A. Campion, M. A. Fox, T. Mallouk, S. E. Webber, J. M. White, *J. Phys. Chem.* **1986**, *90*, 4604.
410. E. S. Smotkin, S. Cervera-March, A. J. Bard, A. Campion, M. A. Fox, T. Mallouk, S. E. Webber, J. M. White, *J. Phys. Chem.* **1987**, *91*, 6.
411. S. Kuwabata, N. Takahashi, S. Hirao, H. Yoneyama, *Chem. Mater.* **1993**, *5*, 437.
412. C. S. C. Bose, K. Rajeshwar, *J. Electroanal. Chem.* **1992**, *333*, 235.

- 413. Y. Son, N. R. de Tacconi, K. Rajeshwar, *J. Electroanal. Chem.* **1993**, 345, 135.
- 414. N. R. de Tacconi, Y. Son, K. Rajeshwar, *J. Phys. Chem.* **1993**, 97, 1042.
- 415. N. R. Avvaru, N. R. de Tacconi, K. Rajeshwar, *Analyst* **1998**, 123, 113.
- 416. S. Ito, T. Deguchi, K. Imai, M. Iwasaki, H. Tada, *Electrochem. Solid State Lett.* **1999**, 2, 440.
- 417. M. Zhou, W.-Y. Lin, N. R. de Tacconi, K. Rajeshwar, *J. Electroanal. Chem.* **1996**, 402, 221.
- 418. M. Zhou, N. R. de Tacconi, K. Rajeshwar, *J. Electroanal. Chem.* **1997**, 421, 111.
- 419. N. R. de Tacconi, H. Wenren, K. Rajeshwar, *J. Electrochem. Soc.* **1997**, 144, 3159.
- 420. N. R. de Tacconi, H. Wenren, D. McChesney, K. Rajeshwar, *Langmuir* **1998**, 14, 2933.
- 421. N. R. de Tacconi, M. Mrkic, K. Rajeshwar, *Langmuir*, in press.
- 422. C. Anderson, A. J. Bard, *J. Phys. Chem. B* **1997**, 101, 2611.
- 423. N. Takeda, M. Ohtani, T. Torimoto, S. Kuwabata, H. Yoneyama, *J. Phys. Chem. B* **1997**, 101, 2644.
- 424. N. R. de Tacconi, K. Rajeshwar, R. O. Lezna, *J. Electroanal. Chem.*, in press.
- 425. N. R. de Tacconi, J. Carmona, W. L. Balsam, K. Rajeshwar, *Chem. Mater.* **1998**, 10, 25.
- 426. N. R. de Tacconi, J. Carmona, K. Rajeshwar, *J. Phys. Chem. B* **1998**, 101, 10151.

2 Dye Sensitization of Electrodes

Ping Qu and Gerald J. Meyer

2.1 Dye Sensitization of Planar Electrodes

Sensitization of electrodes can be defined as the process by which interfacial electron transfers occurs as a result of selective light absorption by an entity called a *photosensitizer*, or simply a *sensitizer* [1]. The most common types of sensitizers are organic chromophores and inorganic coordination compounds, generically referred to as dyes. Interfacial electron transfer produces current or voltage response that can be measured in an external circuit. Thus sensitization provides a method for the conversion of a photon into an electrical signal that can be controlled at the molecular level.

The sensitization of electrodes to visible light by dye molecules is an old area of science with a rich history [2]. A dye-sensitized photoeffect was measured at a semiconductor surface as early as 1887 in Vienna [3]. The accepted mechanisms for the dye sensitization of electrodes emerged from photoelectrochemical studies in the 1960s and 1970s [4–6]. These studies were motivated by a desire to quantify interfacial electron transfer processes and develop cells useful for solar energy conversion. The two most common approaches are shown schematically in Figure 1.

The right-hand side depicts a simplified *photoelectrosynthetic cell*. This cell produces both electrical power and chemical products. Many of the early dye-sensitized cells were designed to operate in the manner shown with the goal of splitting water into hydrogen and oxygen. An excited sensitizer, S^* , injects an electron into the electrode and oxidizes a substrate in solution. The injected electron passes through an external circuit and returns to the counter electrode where it reduces another substrate. Shown on the left-hand side is a *regenerative cell* that converts light into electricity with no net chemistry. Dye-sensitized regenerative solar cells have recently achieved remarkably high solar energy conversion efficiencies that have renewed interest in this field. This is subject of Section 2.2. In the regenerative solar cell shown, the oxidation reactions that take place at the photoanode are reversed at the dark cathode.

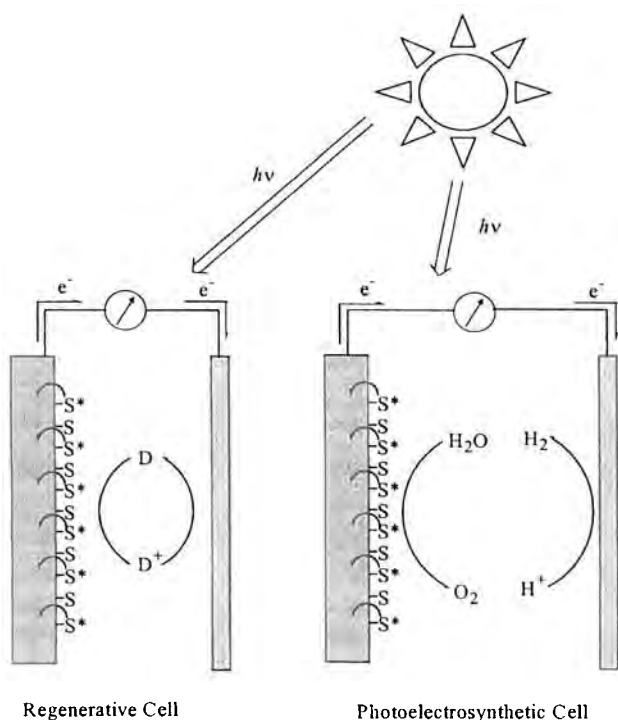


Figure 1. Schematic representation of regenerative and photoelectrosynthetic cells. S^* is the sensitizer excited state, D is an electron donor, and D^+ is the oxidized electron donor. Regenerative cells convert light into electricity while photoelectrosynthetic cells convert light into electricity and also produce chemical products.

In the remainder of this section we briefly overview fundamental concepts, vocabulary, photoelectrochemical characterization techniques and the dye-sensitization mechanisms developed for planar electrodes. We end the section with a short literature review of dye-sensitization studies.

2.1.1 Thermodynamics and Sensitization Mechanisms

Sensitization of electrodes to light relies on the fact that an excited state is simultaneously a stronger oxidant and a stronger reductant than is the ground state. Knowledge of the sensitizer's formal reduction potentials relative to the energy levels of the conductive substrate allows a priori determination of the direction of current flow and the sensitization mechanism. It is therefore of considerable interest to quantify the energetics of the sensitizer and the electrode with respect to one another. This can be accomplished, at least in principle, by spectroscopic and/or electrochemical measurements as described below.

Sensitizers

The formal reduction potentials, E° , for a sensitizer, S , that are most relevant to dye sensitization correspond to the ground, reduced and excited states. The first two can be directly measured by electrochemical techniques, such as cyclic voltammetry, and often in situ at the sensitized electrode of interest [7]. The excited state reduc-

tion and oxidation potentials of the thermally equilibrated, or thexi state are given by Eqs. 1 and 2 [8]:

$$E^{\circ}(S^{+}/*) = E^{\circ}(S^{+}/0) - \Delta G_{\text{es}} \quad (1)$$

$$E^{\circ}(S^{*}/-) = E^{\circ}(S^{0}/-) + \Delta G_{\text{es}} \quad (2)$$

where ΔG_{es} is the free energy stored in the thermally equilibrated excited state. ΔG_{es} can usually be estimated from the corrected photoluminescence (PL) spectra and is often equivalent to the E_{00} energy, the energy separation between the lowest vibrational levels of the excited state and the ground states. If the excited state is non-emissive, such as an organic triplet state, the free energy may be estimated from quenching studies with known triplet energies or by alternative techniques discussed elsewhere [9, 10].

It is generally assumed that vibrational relaxation occurs prior to interfacial electron transfer and therefore the energetics of the thexi states calculated through Eq. 1 or 2 are relevant [4]. This assumption is almost certainly valid when sensitization involves diffusional approach of an excited state to a conductive interface. However, when the sensitizer is proximate to the electrode surface, rapid interfacial electron transfer from 'hot' vibrational excited states may occur prior to and/or in competition with relaxation to the thexi state. The corresponding potentials of the excited state produced immediately upon light absorption, the Franck–Condon state, can be estimated by replacing ΔG_{es} in Eqs. 1 and 2 with the energy of the excitation light, $h\nu_{\text{ex}}$.

Metals

For metal electrodes, the Fermi level is embedded within a broad distribution of closely spaced electronic levels. The Fermi level describes the occupancy of energy levels of a system at equilibrium and can simply be thought of as the chemical potential of electrons in the solid [10]. When employed in the Fermi–Dirac distribution function, Eq. 3 results:

$$f(E) = [1 + \exp(E - E_{\text{F}})/kT]^{-1} \quad (3)$$

where k is Boltzmann's constant and $f(E)$ gives the occupation probability for an energy level E at an absolute temperature T [10]. Substitution of E_{F} for E demonstrates that the probability of occupation for an energy level at E_{F} at equilibrium is 0.5. For metal electrodes employed in a photoelectrochemical cells, an external bias allows E_{F} to be continuously tuned within the electrochemical window of the cell [7]. It is reasonable to assume that all states below E_{F} are filled and all those above are unfilled.

Semiconductors

Detailed descriptions of semiconductor terminology and photoelectrochemistry can be found in the previous chapter by Rajeshwar. Below are the basic concepts most relevant to dye sensitization followed by a description of sensitization mechanisms.

Terminology

Semiconductors are characterized by a forbidden energy gap, E_g , (band-gap) between the valence band (VB) maximum, E_{VB} , and the conduction band (CB) minimum, E_{CB} . The magnitude of the band-gap is what differentiates semiconductors from insulators: semiconductors have smaller band-gaps (<4 eV) than do insulators. Semiconductors are termed n-type if the majority charge carriers are electrons in the conduction band and p-type if the majority carriers are holes in the valence band. The Fermi level for most pure or intrinsic semiconductors lies near the middle of the band-gap [12]. The effect of doping is to shift the Fermi level closer to E_{CB} for n-type semiconductors and closer to E_{VB} for p-type semiconductors. For moderate dopant levels near room temperature this can be expressed quantitatively by Eqs. 4 and 5:

$$E_F = E_{CB} - kT \ln(N_C/N_D) \quad (4)$$

$$E_F = E_{VB} + kT \ln(N_V/N_A) \quad (5)$$

for n-type semiconductors and p-type semiconductors, respectively, where N_D and N_A are the concentration of donor and acceptor impurities, respectively, and N_C and N_V are the effective densities of states for the conduction band and valence band, respectively.

The two semiconductor potential distribution conditions most relevant to dye sensitization of planar n-type semiconductors are shown schematically in Figure 2. The flat band-condition applies to the case where the band edges are flat right up to the solution interface (Figure 2a). Under ideal conditions, a positive applied potential does not alter the energetic position of the bands at the semiconductor–

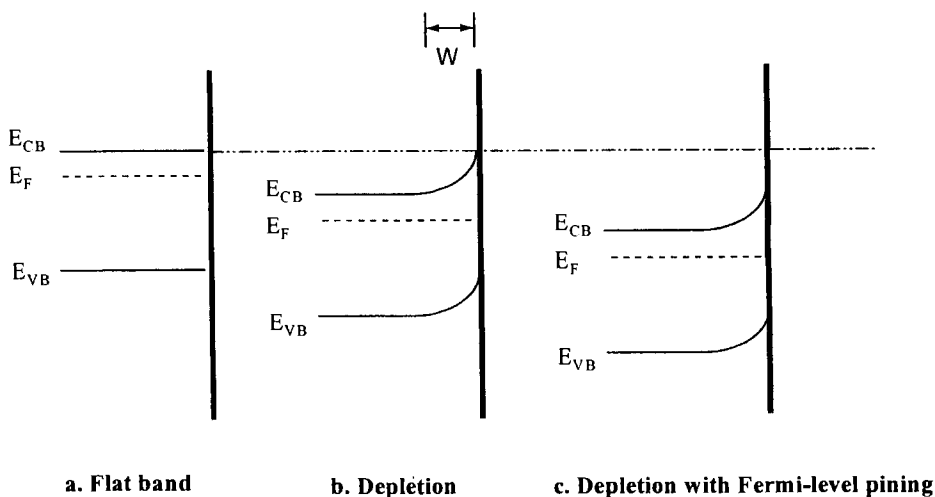


Figure 2. Three semiconductor potential distribution conditions for an n-type semiconductor: a) flat band condition, b) depletion condition, and c) depletion condition with Fermi-level pinning.

electrolyte interface. Instead an electric field that extends some distance W into the solid is produced as indicated by the bent bands (Figure 2b). The surface electric field (or space-charge region) thickness of a planar semiconductor is given by Eq. 6 in the Mott–Schottky approximation:

$$W = (2\epsilon\epsilon_0 V_b/qN_D)^{1/2} \quad (6)$$

where ϵ_0 is the permittivity of free space, ϵ is the dielectric constant of the semiconductor, q is the electronic charge and V_b is the amount of band bending [12]. Note that $W \propto (N_D)^{1/2}$, so highly doped semiconductors have thinner depletion layers than do more lightly doped materials at the same V_b .

Many semiconductor–electrolyte junctions do not behave ideally with respect to applied potential. When a high density of surface states exist within the forbidden energy gap, band edge movement (termed Fermi-level pinning or band edge unpinning) may be observed. Under these conditions the semiconductor appears to be metal-like (Figure 2c), and virtually all of the applied potential drops at the semiconductor–sensitizer interface rather than in the semiconductor space-charge layer. Surface states are created by oxide formation, dangling bonds or impurities, or they may be intrinsic to the semiconductor. Fermi-level pinning is common in the more covalent semiconductors and in highly doped, or degenerate, n-type semiconductors where E_F is within the CB continuum [12, 13].

Determination of band edge positions

Capacitance measurements are generally regarded as the most reliable method for determination of the band edge positions at a sensitized semiconductor–electrolyte interface [14]. The Mott–Schottky relationship, Eq. 7:

$$\frac{1}{C^2} = \frac{2}{\epsilon\epsilon_0 q N_D A^2} \left(V - V_{FB} - \frac{kT}{E} \right) \quad (7)$$

describes the dependence of the space-charge capacitance upon the corresponding electric field, where C is the capacitance and A is the electrode area. The intercept of the plot of $1/C^2$ versus applied potentials yields the flat-band potential from which the band edges can be determined if the band-gap and dopant levels are known.

The assumptions in the Mott–Schottky treatment of capacitance data have been discussed in detail elsewhere [15]. Capacitance measurements are performed in the dark in the absence of sensitizers. Any shift in the band edges that might occur with sensitizer adsorption or illumination is therefore unaccounted for in this analysis. Shifts in the band edge positions are known to occur under a variety of conditions, such as (1) specific ion adsorption, (2) trapping of photogenerated carriers and (3) changes in surface state occupation with applied potential [15]. The first of the three conditions has been exploited in dye sensitization of metal oxide semiconductors where the band edge positions shift 59 mV per pH unit through proton adsorption/desorption equilibria. The estimated positions of the band edges in pH 1 aqueous solution for semiconductors relevant to sensitization are shown.

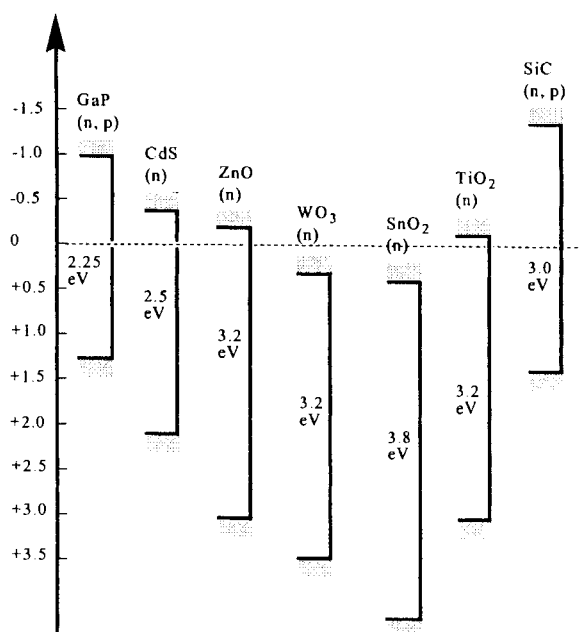


Figure 3. Semiconductor band edge positions vs NHE in pH = 1 aqueous solution.

When presenting a collection of band edge positions such as that shown in Figure 3, it is worth emphasizing that flat-band potentials, from which the band positions are calculated with Eq. 4 or 5, are *not* singular parameters. Under different experimental conditions the flat-band potential will shift. Furthermore, a flat-band potential for a specific electrode determined in situ by extrapolation from deep depletion (such as Mott–Schottky analysis), does not imply that the band edges will remain fixed as the Fermi level of the electrode is raised. Determination of the band edge positions relative to the sensitizers, as discussed further below, is necessary for comparison of experimental data with even the simplest interfacial electron transfer theory. The evaluation of the band edge positions under experimentally meaningful conditions represents a considerable experimental challenge in dye sensitization studies.

Sensitization mechanisms

Gerischer diagrams

Sensitization and interfacial electron transfer mechanisms have been described by Gerischer [4–6]. A basic assumption is that electron transfer, like light absorption, occurs under the restriction of the Franck–Condon principle. The time-scale for interfacial electron transfer is much shorter than that for nuclear motion. This means that the energy terms for electron transfer are different from the thermodynamic formal reduction potentials described above. Gerischer considered the appropriate energy levels and derived a distribution of energy levels when the sensi-

tizer behaves as an electron donor or as an electron acceptor, $W_{\text{don}}(E)$ and $W_{\text{acc}}(E)$ respectively. The distribution results from thermal fluctuations that, when treated classically, give rise to a Gaussian distribution function, Eqs. 8 and 9:

$$W_{\text{don}}(E) = A \exp \left[-\frac{(E - E^\circ)^2}{4kT\lambda} \right] \quad (8)$$

$$W_{\text{acc}}(E) = A \exp \left[-\frac{(E + E^\circ)^2}{4kT\lambda} \right] \quad (9)$$

where k is the Boltzmann constant, λ is the total reorganization energy for electron transfer and T is the absolute temperature. The reorganization energy, λ , contains terms from the sensitizer, the electrode and the solution. Interpretations of the pre-exponential term A have been discussed in the literature [16].

Gerischer's distribution curves can be interpreted as representing the energy dependence of the electron transfer rate constants involving the reduced and oxidized species. Only a few electrochemical studies have attempted to evaluate the model and quantify the distributions and reorganizational parameters [17, 18]. Nevertheless, it has become common practice to draw a pictorial representation of the distributions when discussing interfacial electron transfer kinetics relevant to dye sensitization.

In Gerischer diagrams, the interface is drawn as a perpendicular line with the electrode density of occupied and unoccupied states on the left and Gerischer's distributions for the sensitizer on the right. An example is shown in Figure 4 where the electrode density of states is not included. At first glance, Gerischer diagrams are confusing as there appear to be too many distributions. One must keep in mind that at least two different redox couples are involved, in the case shown a ground state and an excited state, each of which has its own λ and E° . In most literature diagrams, λ is assumed to be approximately the same for the ground and excited states and values between 0.8 and 2.0 eV are typical [19].

According to Gerischer, the simplest description for the rate of electron transfer, r , is given by Eq. 10:

$$r \sim \int \kappa(E) \cdot D_{\text{don}}(E) \cdot D_{\text{acc}}(E) dE \quad (10)$$

with the product of the transfer frequency, κ , the density of occupied and unoccupied electronic states, D_{don} and D_{acc} , and integrated overall energies, E [4]. For adiabatic electron transfer the maximum rate is controlled by the transfer frequency and is typically in the region of 10^{12} s^{-1} . In the cases of strong electronic coupling, nonadiabatic electron transfer is possible at much faster rates. When invoked in dye-sensitized electrode studies, non-adiabatic electron transfer is usually described by Fermi's golden rule.

Equation 10 represents a simple relation useful for predicting interfacial electron transfer rates relevant to dye sensitization. At this time more detailed descriptions

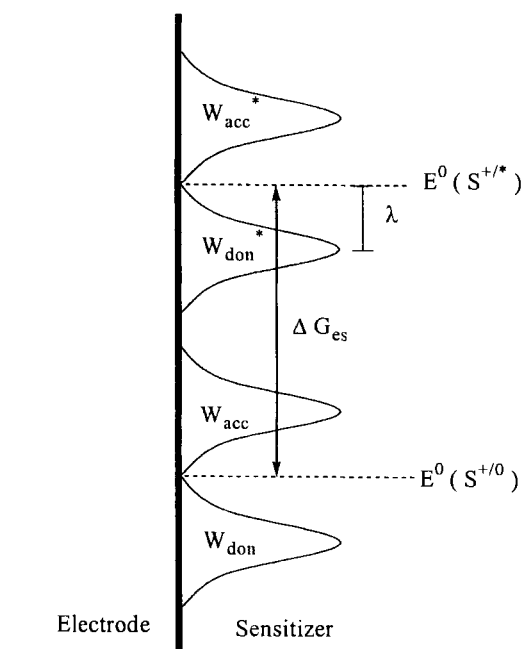


Figure 4. A Gerischer's diagram for a sensitizer, S^0 , and its excited state, S^* .

that account for the molecular details of the specific dye-sensitized electrode assembly are not available. In principle, Eq. 10 also provides an opportunity for experimental rates to be contrasted with theory. In practice, this is rarely done. The overlap of the sensitizer and semiconductor energy levels is critical for determining interfacial electron transfer rate constants and the experimental uncertainty in doing this is significant. This fact has prohibited extensive application of Eq. 10 to real dye-sensitized photoelectrochemical systems. The few cases where Gerischer theory has been successfully applied and tested involve changing only the solution pH while keeping all other variable constant. These studies are described in Section 2.2.2.

Metal sensitization

There are two possible excited state interfacial electron transfer processes that can occur from a molecular excited state, S^* , created at a metal surface: (a) the metal accepts an electron from S^* to form S^{+} ; or (b) the metal donates an electron to S^* to form S^{-} . Neither of these processes has been directly observed. The two processes would be competitive and unless there is some preference, no net charge will cross the interface. In order to obtain a steady-state photoelectrochemical response, back interfacial electron transfer reactions of S^{+} (or S^{-}) to yield ground-state products must also be eliminated. Energy transfer from an excited sensitizer to the metal is thermodynamically favorable and allowed by both Forster and Dexter mechanisms [20, 21]. There exists a theoretical [20] and experimental [21] literature describing 'energy transfer' quenching of molecular excited states by metals. How-

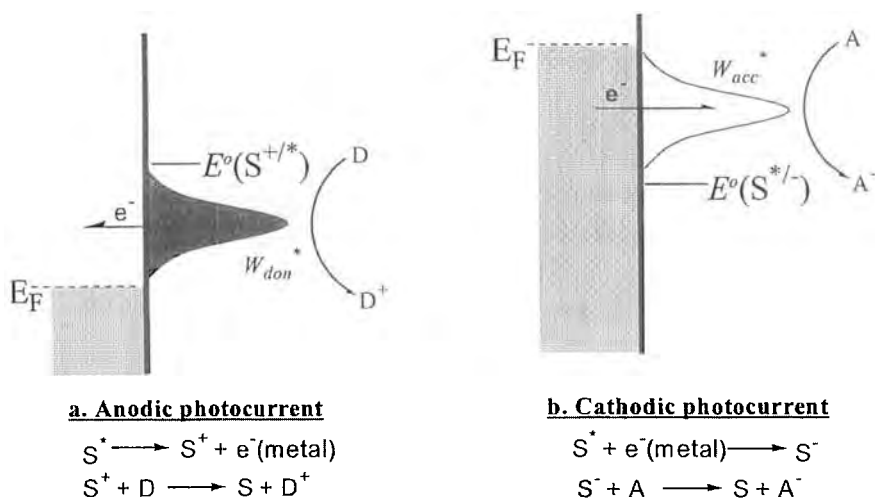


Figure 5. Excited state interfacial electron transfer reactions that can lead to a) anodic, and b) cathodic photocurrent at a metal surface in the presence of electron donor D and acceptor A respectively.

ever, these studies involve photoluminescence measurements and the actual quenching mechanism, electron or energy transfer, remains speculative. Nevertheless, competitive energy transfer quenching is often invoked to rationalize the low photocurrent efficiencies measured at sensitized metallic interfaces. However, there are many reasons to predict poor sensitization yields from metal electrodes [4].

The addition of electron donors or acceptors to the external electrolyte has allowed sustained photocurrents to be measured at sensitized metal interfaces, but the mechanism(s) often remain speculative. A photocurrent can be generated by excited state interfacial electron transfer like that shown in Figure 5, or by intermolecular excited state electron transfer followed by dark redox reactions at the electrode. It can be experimentally difficult to distinguish between these distinct mechanisms and strong evidence exists only for the latter pathway which forms the basis of the photogalvanic cell.

The celebrated 'photogalvanic cells' were the hallmark solar energy conversion devices of the 1940s and 1950s, and continue to be of interest [22, 23]. The cells generally contain a membrane or surface layer that serves to separate two dark metal electrodes and photogenerated redox equivalents. A simple regenerative cell arrangement is shown in Figure 6 with sensitizers embedded in a membrane that allows ion and charge transfer, yet physically separates electron donors, D, and acceptors, A. Clearly, this type of geometric arrangement precludes direct excited state electron transfer with the electrodes. A transmembrane Nernst potential can be generated by photodriven electron transfer occurring in the membrane. In photoelectrosynthetic galvanic cells, chemical fuels may also be formed. This general strategy for dye sensitization has been employed in many guises over the years, but the absolute efficiencies remain very low. Albery concluded that an efficiency of

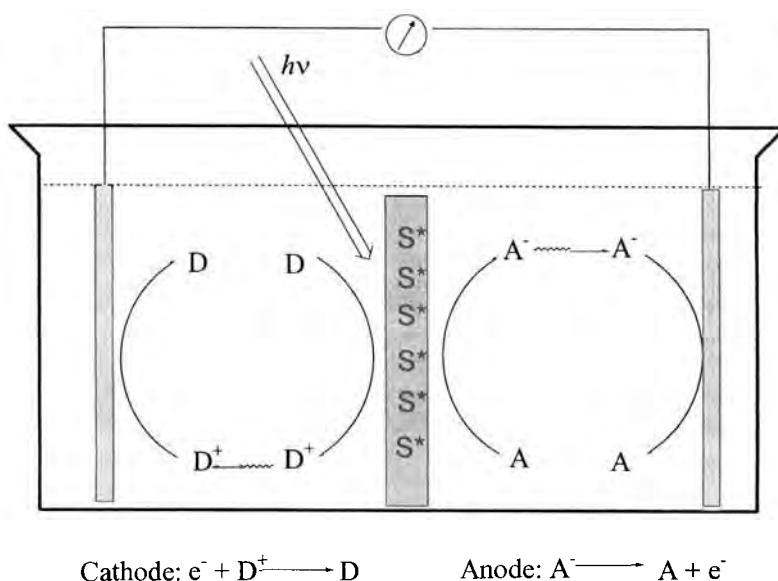


Figure 6. A regenerative photogalvanic cell where excited state electron transfer yields charge separated pair, D^+ and A^- , that are collected at dark electrodes.

~13 % could be theoretically achieved in a regenerative photogalvanic cell [22]. However, efficiencies realized to date are typically less than 2 %.

At negative potentials in the presence of electron acceptors, it is possible to produce cathodic photocurrents by a direct photoemission mechanism where electrons are photoejected from the metal directly into the solution [24]. Photoemission can be distinguished from dye sensitization by measuring the photocurrent yield as a function of excitation wavelength, a photocurrent action spectrum described further below. Barring competitive light absorption, the photoaction spectrum for dye sensitization is coincident with sensitizer absorptance spectrum, while photoemission currents increase continuously with the energy of the exciting photon. Photoemission is known to be inefficient in photoelectrochemical cells with quantum yields typically $< 10^{-4}$ [24].

Semiconductor sensitization

Anodic photocurrent generation is the most common and efficient mechanism by which photocurrents are generated at n-type semiconductors. A pictorial representation of a Gerischer diagram for the accepted mechanism is given in Figure 7. Corresponding diagrams for p-type sensitization have been proposed, but have received relatively little experimental attention [25]. For the case shown, the excited state reduction potential lies more than the reorganization energy above the conduction band edge, $E^\circ(S^{+/*}) - \lambda > E_{CB}$, and maximum overlap of the sensitizer excited state donor levels and the wide band is attained. This gives rise to the maximum electron transfer rate, i.e., activationless interfacial electron transfer. The excess

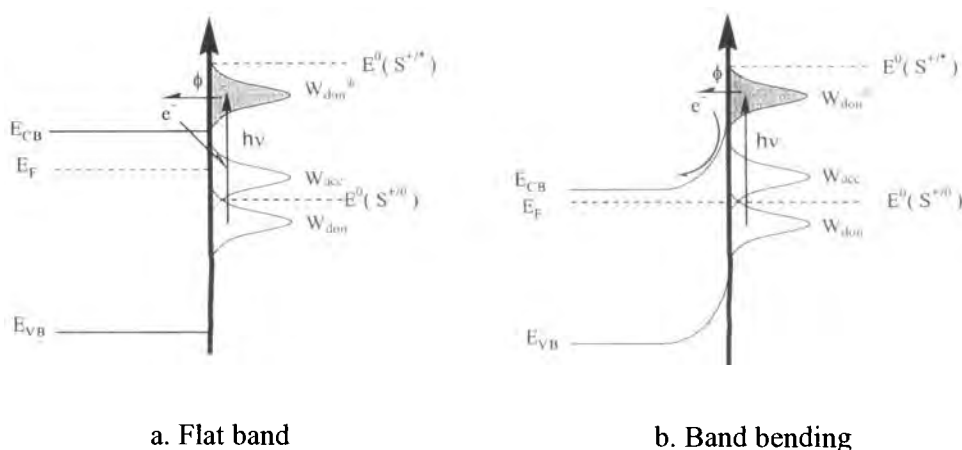


Figure 7. Gerischer's diagram for sensitization of a n-type semiconductor by an excited state sensitizer S^* .

energy of the injected electron is dissipated through lattice vibrations (phonons) as the electron thermalizes to the conduction band edge. Injection is therefore irreversible and repopulation of the excited state has never been observed.

The fate of the injected electron is expected to depend on the bias condition of the semiconductor. If injection occurs when the semiconductor is near the flat band condition (Figure 7a) then rapid recombination with the oxidized dye results because there is no electric field region to assist the spatial separation of the injected electron and oxidized hole. If the semiconductor is under depletion conditions, then the injected electron is swept toward the bulk by the surface electric field and recombination is inhibited (Figure 7b). Therefore, the current onset in photocurrent–voltage measurement can be taken as a crude estimation of the flat-band potential. The enhanced lifetime of the charge-separated state at molecular–semiconductor interfaces under depletion conditions allows the sensitizer to be regenerated by an external electron donor or by diffusional replacement with a new sensitizer and a net anodic photocurrent may flow. Spitler has proposed an Onsager model that predicts that a higher semiconductor doping level will result in more efficient spatial separation of the injected charge due to the larger average field [26]. Unfortunately, no experimental studies have been performed to test this model.

Photoelectrochemical techniques

Photocurrent–voltage behavior

Measurements of the photocurrent–voltage (i – V) and photovoltage properties describe the energy conversion properties of dye-sensitized photoelectrochemical cells and are probably the best fundamental method for their evaluation. This data can be acquired in a two- or three-electrode configuration. Figure 8 shows sche-

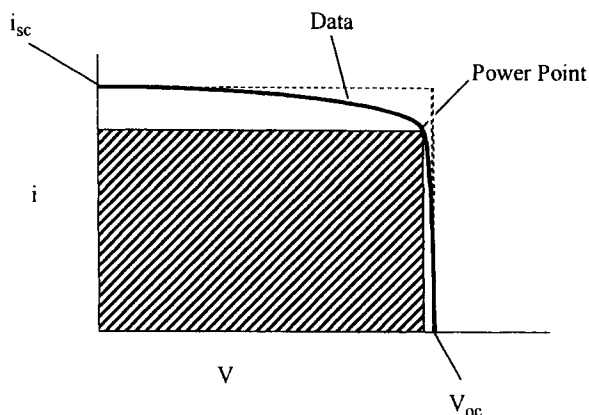


Figure 8. Hypothetical photo-current-voltage curve measured in a two-electrode arrangement. The short circuit photocurrent, i_{sc} , open circuit photovoltage, V_{oc} , and power point are indicated.

matically a hypothetical photocurrent-voltage curve measured in a two-electrode arrangement. The photocurrent measured under short-circuit conditions, i_{sc} , is often divided by the illuminated area and abbreviated j_{sc} . The open-circuit voltage, V_{oc} , is the potential of the illuminated electrode when no net current flows and represents the maximum Gibbs free energy that a regenerative solar cell will produce under conditions of constant irradiance [12]. The optimum conditions for solar energy conversion correspond to the maximum product of the cell voltage and photocurrent obtained along the i - V curve, and define the power point, pp. The maximum power is always assigned a positive value, regardless of the sign convention for photocurrent and photovoltage determination. The fill factor (FF) given by Eq. 11:

$$FF = (i_{pp} V_{pp}) / (i_{sc} V_{oc}) \quad (11)$$

in terms of the current and voltage measured at the power point, i_{pp} and V_{pp} , respectively. A fill factor of unity is ideal, but values <0.8 are most common owing to various resistive loss mechanisms and recombination. The maximum energy conversion efficiency, η_{max} , is defined by Eq. 12:

$$\eta_{max} = (i_{pp} V_{pp}) / (\text{absorbed optical input power}) \quad (12)$$

Maximum energy conversion efficiencies of $\eta_{max} = 0.1086$ have recently been measured and verified for dye-sensitized regenerative cells illuminated with air mass 1.5 simulated solar irradiation [27]. The efficiency of photoelectrosynthetic cells must also include contributions from the free energy stored in the chemical products of the reduction and oxidation reactions.

Models of i - V data for sensitized electrodes invariably begin with Gartner's treatment developed for solid-state junctions [28] that was later extended to photoelectrochemical cells by Butler [29]. In Gartner's model, light absorption by the semiconductor itself yields a photocurrent that contains a drift component asso-

ciated with carriers generated within the depletion region, and a diffusional component for minority carriers created in the neutral bulk that reach the depletion region before recombining [28]. The relative amplitudes of the two photocurrent components are controlled in part by the absorption coefficient of the exciting light, α . The optical generation of minority carrier is given by Eq. 13:

$$G(x) = I_0 \alpha e^{-\alpha x} \quad (13)$$

where $G(x)$ is the generation rate and I_0 is the intensity of the light. The generation rate in dye-sensitized electrodes can be defined analogously with the sensitizer's effective absorption coefficient. Gartner derived Eq. 14 for the photocurrent–voltage behavior:

$$i_{\text{ph}} = I_0 \left(1 - \frac{e^{-\alpha W}}{1 + \alpha L_p} \right) \quad (14)$$

where L_p is the diffusion length. Note that Gartner's expression predicts a substantial photocurrent at the flat-band potential ($W = 0$) [28]. This is due to the fact that in this simple model, important experimental variables, such as space-charge and surface state-mediated recombination and the dark current, are ignored. More complex models that take these and other variables into account, have been described in the literature [30–32].

The relevance of Gartner's model, in spite of its obvious shortcomings, underscores the inadequacy of simple i – V curves for understanding loss mechanisms in sensitized solar cells. The common, but crude, approach of using photocurrent onsets as a measure of the flat-band potential, alluded to above, is actually fraught with difficulties unless fill factors are high and the system behaves nearly ideally. In most cases, the determination of photocurrent onset requires high excitation irradiance (which may in itself shift the band edges) and abstraction of weak photocurrents from larger dark currents. When the sensitized material does not behave ideally, the actual flat-band potential is usually considerably more negative than that estimated from i – V curves.

Photoaction spectra

A plot of the photocurrent quantum yield versus excitation wavelength is termed the 'photoaction' or 'photocurrent action' spectrum. These spectra are obtained at short-circuit in a two-electrode arrangement or with an external bias in a three-electrode configuration. The photocurrent quantum yield is defined as the number of electrons measured in the external circuit divided by the number of absorbed photons. It is experimentally difficult to calculate the number of absorbed photons and corrections for scattered or transmitted light often appear to be 'fudge factors' that increase the uncertainty of the absolute photocurrent yield. Therefore, the incident photocurrent yield is often reported which represents a lower limit of the true photocurrent quantum yield.

Although it is often stated that the photoaction and absorption spectra should be coincident, this is not technically correct. Photoaction spectra of sensitized electrodes in photoelectrochemical cells are sensitive to the fraction of light absorbed by the sensitizer. The absorptance is the IUPAC recognized term for the fraction of incident radiant power absorbed by a chromophore [33]. The term 'light harvesting efficiency' (LHE) is occasionally employed in the dye-sensitization literature and is mathematically equivalent to the absorptance. The absorptance and absorption are approximately equal when the fraction of light absorbed is very small. For thick films of sensitizers or under conditions where species in the electrolyte absorb light, trivial inner filter effects and competitive light absorption can also affect the shape of the photocurrent action spectrum.

Time-resolved techniques

Steady-state photocurrent–voltage behavior quantifies the bottom line efficiency of operational solar cells. Unfortunately, it provides little molecular information, particularly when the photocurrent yields are low. A variety of transient, time and frequency domain electrochemical techniques have been employed to provide further insights into the molecular origin of loss mechanisms. Space restrictions do not allow these electrochemical techniques to be discussed here [34–37].

2.1.2 Examples of Sensitization Studies at Planar Electrodes

Metal electrodes

Photogalvanic cells

Some of the first examples of dye sensitization were the celebrated photogalvanic cells [22, 23, 38–42]. Recall that in these cells, charge separation occurs by excited state intermolecular electron transfer and the redox equivalents are collected at dark electrodes. Photogalvanic cells can be regenerative or photoelectrosynthetic. In many experimental studies, highly doped tin oxide electrodes were employed to allow uniform illumination of thin solutions. While the tin oxide electrodes could display semiconducting behavior, the materials are highly doped, degenerate semiconductor and space-charge contributions to electron collection are thought to be minimal. Indeed, in many cases the collection efficiencies of highly doped SnO_2 and metallic electrodes are found to be the same.

The Iron–thionine system

The first attempts to understand the mechanism of operation of photogalvanic cells was performed on the iron–thionine system [22, 23]. Here we summarize the main observations. Thionine (Th) is a cationic purple dye extremely soluble as the chloride salt. Two other forms of the compound, Leukothionine (L) and Semithionine (S[•]), are also important in the sensitization process and their structures are shown in Figure 9. According to Albery, the light driven redox reactions that lead to a photocurrent are as follows:

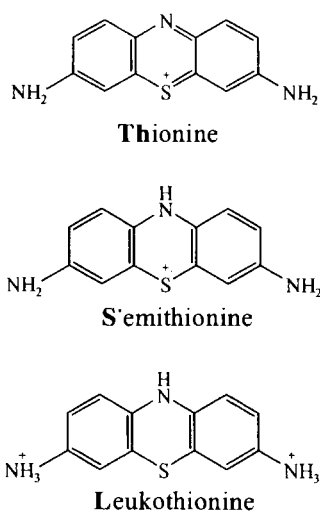
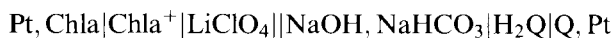


Figure 9. The compounds thionine (Th), semithionine (S), and leukothionine (L) proposed to exist in iron-thionine photogalvanic cells.



In competition with photocurrent production, the Fe^{III} can oxidize S^* or L. Experimental data strongly suggests that recombination with S^* is the main factor that lowers overall efficiency [20]. Attempts to increase the efficiency by replacing thionine with $\text{Ru}(\text{bpy})_3^{2+}$ were not successful from a practical point of view [38]. Other issues regarding the optimum diffusion length, solute concentration and selectivity of the electrodes have been considered. Theoretical solar conversion efficiencies of 0.13 are believed to be achievable by this general approach. The highest efficiency measured to date is only $\sim 3 \times 10^{-4}$ [23].

Photogalvanic cells with chlorophylls, porphyrins, phthalocyanines and other chromophores have been studied [38–42]. An example is the chlorophyll *a*–hydroquinone (Chla– H_2Q) galvanic cell [40]:



Light excitation of a Chla membrane deposited on Pt resulted in a weak photocurrent with the Pt/Chla behaving as a cathode. The photocurrent action spectrum resembled the Chla absorption spectrum which ruled out a direct photoemission process. The direction of the photocurrent was rationalized by invoking a p-type conductivity in the Chla films. Bolton and co-workers explored related monolayer assemblies with spatially organized quinones to increase efficiencies [41]. In a more promising system, Chla monolayers deposited on Al contacts with uboquinone ac-

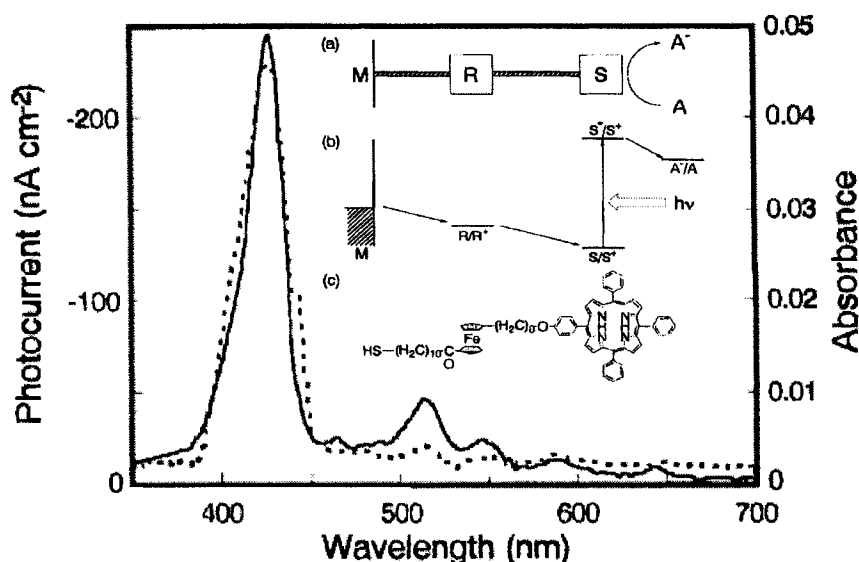


Figure 10. A self-assembled monolayer comprised of terminal porphyrins, intermediate ferrocenes, and surface thiols attached on gold surface. The solid line is the photoaction spectrum, the dashed line is the absorption spectrum. Panels a) and b) show the proposed mechanisms, and c) provides the structure of the thiol ferrocene-porphyrin complex.

ceptors yielded $V_{OC} = 270$ mV and $j = 140$ nA cm⁻² under 100 W m⁻² excitation irradiance [41]. Gust and co-workers described more elaborate donor-sensitizer-acceptor assemblies that yield a measurable photogalvanic response [42].

Self-assembled monolayers

An innovative approach for the sensitization of metal electrodes was recently reported [43]. Monolayers comprised of terminal porphyrins, intermediate ferrocenes and surface thiol were self-assembled on to gold surface. The strategy in the design of the self-assembled monolayers (SAMS), and the related energetics are shown schematically in Figure 10. Light absorption by the porphyrin initiates a series of electron transfer reactions that ultimately yield a reduced electron acceptor in solution and removal of an electron from the metal. A cathodic photocurrent was observed with a monochromatic quantum yield of 0.11 at the absorption maximum with methylviologen acceptors in solution. The sequence of photodriven electron transfer events remains unknown. It may in fact be best classified as a photogalvanic cell. Photocurrent versus potential measurements demonstrate that the efficiency increases significantly when the ferrocene iron is in the +2 oxidation state [43]. The mechanism, therefore, probably includes ferrocene-mediated electron transfer to the excited or oxidized porphyrin.

The photocurrent yield of these novel SAMS is higher than any previously measured at sensitized metal electrolyte interfaces [43]. It was suggested that the fixed distance imparted by the alkanethiol layer decreases the efficiency of energy transfer

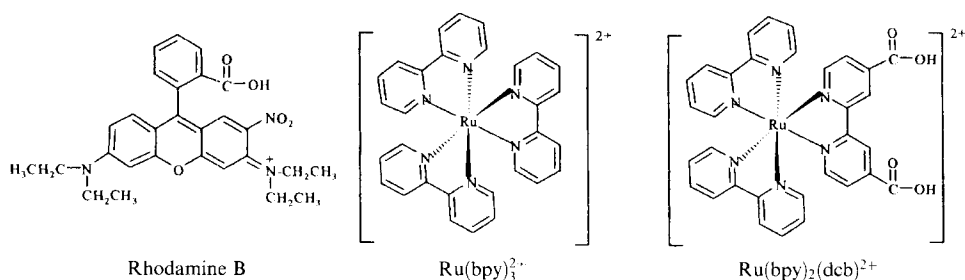


Figure 11. The structures of currently utilized sensitizers for the sensitization.

quenching or back electron transfer by the metallic electrode. Multistep electron transfer at a gold electrode modified with a ferrocene–porphyrin–C₆₀ triad SAMS has also been reported to yield sustained photocurrents [44, 45]. Photocurrents observed from the SAMS appear to be more stable than those observed with excitation of Langmuir–Blodgett monolayers [46–49]. These observations are encouraging and suggest that with further optimization it will be possible to efficiently harness solar energy with sensitized metal interfaces.

Metal oxide semiconductors

Early studies

Sensitization of wide band-gap, n-type metal oxide semiconductors to visible light was among the first sensitization studies in photoelectrosynthetic cells. The most common semiconductors were SnO₂, TiO₂ and SrTiO₃ and the sensitizers (Figure 11) were Rhodamine B [50–57], Ru(bpy)₃²⁺ [58–65], Ru(bpy)₂(dcb)²⁺ [66–68] and other organic chromophores [69–73]. This work was inspired, at least in part, by the famous water splitting experiments of Fujishima and Honda and the hope that sensitized materials could accomplish the same feat with visible light [74]. Although the photocurrent and water splitting yields were low, these studies provide important experimental data for current and future research. Below we summarize these findings from a historical point of view using Ru(bpy)₃²⁺ as the model sensitizer.

Gleria and Memming first sensitized tin oxide to visible light with Ru(bpy)₃²⁺ in pH 1 aqueous electrolyte [58]. A sustained photocurrent was observed under conditions of positive applied potentials. The photoaction spectra were reported to be slightly red-shifted, but otherwise closely resemble the absorption spectra of the sensitizer in fluid solution. The mechanism proposed was excited state electron transfer to the conduction band. The Ru(bpy)₃³⁺ product was thought to oxidize water with an apparent rate constant of $9 \times 10^2 \text{ s}^{-1}$ and the injected electron gave rise to the measured photocurrent [60]. Interestingly, the rate constant measured for water oxidation was over 1000 times greater than the rate measured previously in the dark [75]. This discrepancy has never been fully resolved [76].

An interesting potential dependence to the sensitized photocurrent was reported by Memming for heavily doped tin oxide semiconductors. At positive applied po-

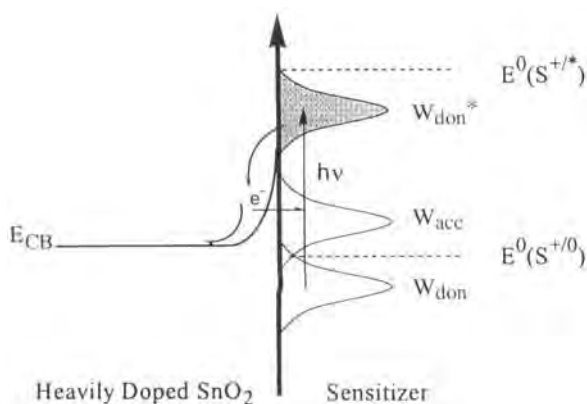


Figure 12. Enhanced electron tunneling from heavily doped SnO_2 to the oxidized sensitizer.

tentials, beyond the plateau in the photocurrent–voltage curve, the photocurrent decreased under conditions when a dark current also became significant [60]. Under the same conditions, weakly doped tin oxide showed no photocurrent decrease. Memming attributed this effect to enhanced electron tunneling to the oxidized sensitizer through the relatively thin space-charge layer of the heavily doped tin oxide electrode, as shown schematically in Figure 12. Similar behavior was observed by other researchers [52]. A related explanation for this behavior is that the dark currents that become significant at these potentials deplete the surface region of oxidizable species leaving a lower concentration to scavenge the oxidized sensitizer thereby allowing a larger fraction to recombine with electrons in the semiconductor.

Following Osa and Fujihira's studies with Rhodamine B [56], Goodenough and co-workers reported the covalent attachment of $\text{Ru}(\text{bpy})_2(\text{dcb})^{2+}$ to SnO_2 and TiO_2 surfaces, through the dehydrative coupling of surface hydroxyl groups with the carboxylic acid groups [66]. The product of this reaction was assumed to be surface ester linkages and water. It was proposed that surface ester linkage in the 4- and 4'-positions of bipyridine would enhance electronic coupling between the π^* orbitals of the bipyridine ligand and the Ti 3d orbital manifold of the semiconductor. The measured photocurrent yield was very low and the photoaction spectrum did not resemble the known solution absorption spectrum suggestive of direct charge transfer from the sensitizer ground state to the conduction band continuum [66]. A red shift in the photoaction spectra of the complex that increases with applied pressure was subsequently reported [68]. However, these authors concluded that sensitization involves excited state interfacial electron transfer rather than direct transfer to the CB [68].

Probing Gerischer's distributions

Clark and Sutin studied the photosensitization of rutile TiO_2 single crystals in dilute aqueous solution by $\text{Ru}(\text{bpy})_3^{2+}$ and two closely related Ru^{II} sensitizers that have different excited state reduction potentials, $\text{Ru}[4,7-(\text{CH}_3)_2\text{-phen}]_3^{2+}$, where 4,7-(CH_3)₂-phen is 4,4'-dimethyl-1,10-phenanthroline, and $\text{Ru}(5\text{-Cl-phen})_3^{2+}$ [63].

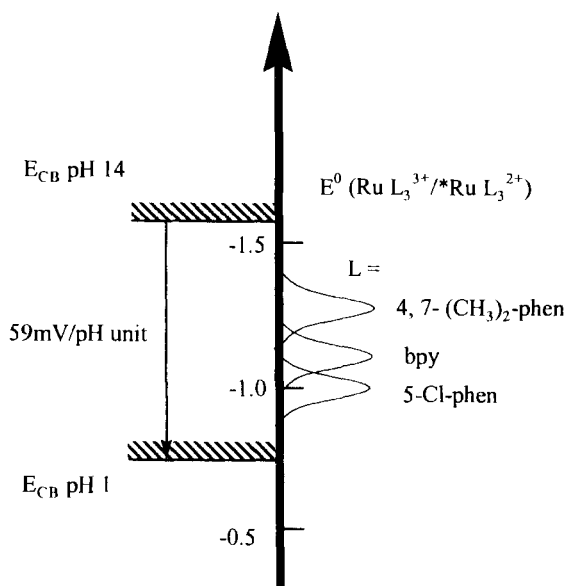


Figure 13. Conduction band edge, E_{CB} shifts as a function of solution pH relative to the indicated excited state distribution of RuL_3^* compounds, W_{don}^* , vs SCE reference.

Clark and Sutin took advantage of the known 59 mV per pH unit shift of the conduction band edge to probe Gerischer's distributions directly as shown schematically in Figure 13 [77]. An anodic photocurrent was observed in acidic solution under conditions of positive applied potential, consistent with excited state electron transfer to the TiO_2 . Watanabe and co-workers had previously observed decreased photocurrents at high pH relative to low pH for electrodes sensitized with Rhodamine B [52]. Photoelectrochemical measurements as a function of solution pH revealed that $Ru(5\text{-Cl-phen})_3^{2+}$ required the lowest pH to generate a measurable photocurrent while $Ru[4,7-(CH_3)_2\text{-phen}]_3^{2+}$ gave a photocurrent at the highest pH. The trend observed indicates that the pH onset originates from the variations of the sensitizer excited state reduction potentials. This finding suggests that the pH onset in photocurrent titration experiments of this kind could be used to determine the excited state reduction potential of nonemissive or unknown sensitizers. Furthermore, analysis of the pH–photocurrent data allowed the reorganization energy for excited state electron injection to be measured, $\lambda = 0.7$ eV. Spitler and co-workers calculated λ analogously from the pH-dependent sensitization of $SrTiO_3$ by two adsorbed dyes, 2,2'-diethylthiacarbocyanine and 2,2'-diethyloxadiazocarbocyanine. Values of between 0.3 and 0.4 eV were estimated and the authors concluded that the Gerischer formulation of electron transfer may be applied with confidence to reactions of species adsorbed at the semiconductor electrolyte interface [69].

Clark and Sutin [63] reported that the quantum yield for electron injection from $Ru[4,7-(CH_3)_2\text{-phen}]_3^{2+*}$ to rutile TiO_2 was unity at pH 1 but dropped to zero at higher pH. At that time, a quantum yield of unity had little precedence. Spitler and Calvin had measured adsorption isotherms and sensitized photocurrent quantum yields for Rose Bengal/ TiO_2 ⁷¹ and Rhodamine B/ ZnO [53] and reported surface coverage-independent values of less than 0.03. The results suggested that only a

small fraction of semiconductor adsorption sites allowed excited state electron injection. On the other hand, self-quenching of excited Rhodamine B* at high surface coverages on TiO_2 has been reported by several groups using luminescence and/or photoelectrochemical techniques [50, 51, 54].

'Supersensitization' mechanisms

Sensitized n-type semiconductors have been known to yield higher photocurrent efficiencies when electron donors such as iodide, hydroquinone or triethanolamine were added to an aqueous electrolyte. These donors are often referred to as 'supersensitizers' because their presence so dramatically increases the photocurrents. The mechanism of 'supersensitization' was often attributed to efficient reduction of the oxidized sensitizer allowing a greater fraction of the injected electrons to be converted to a photocurrent. This was a perfectly reasonable suggestion as most of these cells were designed to oxidize water at the photoanode, which is an inherently sluggish process.

An alternative reductive quenching mechanism for the 'supersensitizer' sensitization of metal oxide semiconductors has been explored in considerable detail by Kirsch-De Mesmaeker and co-workers [78–82]. These researchers found that unlike $\text{Ru}(\text{bpy})_3^{2+}$, sensitizers such as $\text{Ru}(\text{tap})_3^{2+}$ did not inject electrons into the semiconductor from the excited state, yet an anodic photocurrent was observed when an electron donor such as hydroquinone (H_2Q) was present in the electrolyte. The sensitization mechanism they proposed is distinctly different from 'trapping' the oxidized sensitizer described above, and is more similar to that proposed for photogalvanic cells. In the presence of H_2Q , excited state intermolecular electron transfer yields $\text{Ru}(\text{tap})_3^+$. The photogenerated $\text{Ru}(\text{tap})_3^+$ is a strong reductant (-0.76 V vs. SCE) that injects an electron into the SnO_2 conduction band which is measured as a photocurrent (Figure 14).

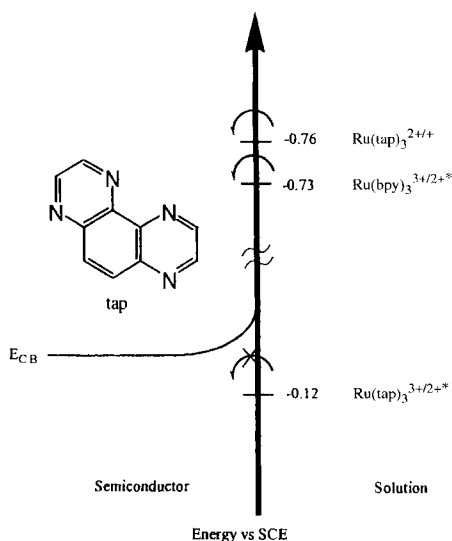


Figure 14. An alternative reductive quenching sensitization mechanism explored by Kirsch De Mesmaeker using $\text{Ru}(\text{tap})_3^{2+}$ which is not thermodynamically capable of injecting an electron into SnO_2 conduction band from the excited state, but can from reduced state.

Table 1. Photoluminescence quenching and steady-state photoelectrochemical data for $\text{Ru}(\text{tap})_3^{2+}$ – H_2Q systems.

Complex	τ_0/ns	$K_{\text{SV}}^{\text{PEC}}/\text{M}^{-1}$		$K_{\text{q}}^{\text{PEC}}/10^9\text{M}^{-1}\text{s}^{-1}$		$K_{\text{SV}}/\text{M}^{-1}$	$k_{\text{q}}/10^9\text{M}^{-1}\text{s}^{-1}$
		$E = 0.1\text{ V}$	$E = 0.2\text{ V}$	$E = 0.1\text{ V}$	$E = 0.2\text{ V}$		
$\text{Ru}(\text{tap})_3^{2+}$	200	1350	1510	6.7	7.5	900	4.9
$\text{Ru}(\text{Me}_2\text{tap})_3^{2+}$	90	465	521	5.1	5.7	470	5.2

Strong evidence for this sensitization mechanism came from a comparison of the excited state quenching rate constant and the photocurrent enhancement by the same donor. Photoelectrochemical Stern–Volmer constants were measured with the aid of Eq. 19:

$$\frac{I_{\infty} - I_0}{I - I_0} = 1 + \frac{1}{k_{\text{q}}^{\text{PEC}}\tau_0[\text{Q}]} = 1 + \frac{1}{K_{\text{SV}}^{\text{PEC}}[\text{Q}]} \quad (19)$$

where I , I_0 and I_{∞} are the steady-state potentials measured in the presence, absence and at high donor concentration, respectively, $k_{\text{q}}^{\text{PEC}}$ and $K_{\text{SV}}^{\text{PEC}}$ are the photoelectrochemical quenching and Stern–Volmer constants, respectively, τ is the excited state lifetime and $[\text{Q}]$ is the molar quencher concentration. The excited state was monitored by photoluminescence and the reductive quenching by D was monitored by the more familiar Stern–Volmer model, Eq. 20:

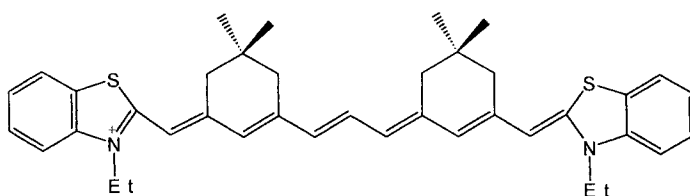
$$\frac{PLI_0}{PLI} = 1 + \frac{1}{k_{\text{q}}\tau_0[\text{Q}]} = 1 + \frac{1}{K_{\text{SV}}[\text{Q}]} \quad (20)$$

where PLI_0 and PLI are the photoluminescence intensity measured without and with quencher, Q, respectively.

Table 1 shows that the quenching and Stern–Volmer constants measured by the two techniques are in good agreement. This supports the idea that H_2Q quenches the excited state directly rather than reducing the oxidized sensitizer after electron transfer. The $\text{Ru}(\text{tap})_3^{+}$ produced from excited state quenching is a stronger reducing agent than is the excited state, by $\sim 640\text{ mV}$, as shown schematically. This additional driving force for interfacial electron transfer can allow sensitizers that are weak excited state reductants to sensitize semiconductors. Spectroscopic evidence for this mechanism has also recently been reported [83]. Taken together, these observations call into question the proposed ‘supersensitization’ mechanism(s) in early dye sensitization studies of wide band-gap metal oxide semiconductors.

Cathodic photocurrents

Cathodic photocurrents have been observed near the flat-band potential or at more negative potentials in the presence of dioxygen or other electron acceptors with sensitized and unsensitized wide band-gap semiconductor electrodes [84–88]. Al-



Thiapentacarbocyanine

Figure 15. Structure of thiapentacarbocyanine.

though alternative mechanisms have been proposed, it appears that all the data can adequately be rationalized by the mechanism previously described for photo-galvanic cells. The excited sensitizer transfers an electron to the acceptor and is then reduced by an electron in the semiconductor.

Small bandgap semiconductors

Layered semiconductors

The van der Waals surfaces of layered n-type semiconductor single crystals, such as SnS_2 , WS_2 and WSe_2 , have excellent characteristics for dye sensitization studies including atomically flat, defect-free surfaces that are renewable by cleavage under ambient conditions. Parkinson and others have explored the sensitization of this class of semiconductors with a wide variety of organic chromophores [89–93]. For example, efficient infrared dye sensitization of layered semiconductors n- WS_2 and n- WSe_2 was achieved with the thiapentacarbocyanine dye shown in Figure 15. The sensitized electrode behaves as a photoanode, as expected, and absorbed photon-to-current yields of 0.8 were estimated. The sensitized photocurrent densities were in excess of $40 \mu\text{A cm}^{-2}$ with aqueous hydroquinone electrolytes. Photocurrents reported at 1200 nm represent the longest wavelength semiconductor sensitization available in the photoelectrochemical literature [92].

An intriguing feature of the WSe_2 electrodes sensitized with the thiapentacarbocyanine was that the photocurrent action spectra were a function of the bias potential applied to the electrode. For example, the maximum conversion efficiency at $-0.4 \text{ V vs. Ag/AgCl}$ was 1100 nm but shifted to 1080 nm at $+0.05 \text{ V}$. The origin of these spectral shifts was attributed to sensitizer aggregates formed on the surface that have different conversion efficiencies [92].

Two research groups have measured the rate of excited state electron injection into SnS_2 with time-resolved fluorescence techniques. Willig and co-workers studied excited Cresyl Violet monomers at about 1 % of full monolayer coverage on SnS_2 [90]. Here the Cresyl Violet excited singlet-state reduction potential lies more than the reorganization energy above the estimated value of the conduction band edge, i.e., $E(S^{+/*}) - \lambda \gg E_{\text{CB}}$, so electron injection was expected to be activationless and the measured electron injection rate constant would correspond to the maximum in

Gerischer's distribution curve [89]. Injection was found to occur in less than 10 ps, providing the first clear indication of the relevant time-scale at the maximum of Gerischer's distribution. Two years later, Lanzafame and co-workers [89] reported femtosecond fluorescence studies of oxazine 1 adsorbed to the same semiconductor. Injection from the oxazine 1 singlet state was also activationless and an injection rate of approximately $3 \times 10^{13} \text{ s}^{-1}$, corresponding to an electron transfer time of $40 \pm 20 \text{ fs}$ was reported. The corresponding localization of the injected electron to the semiconductor conduction band edge was observed to occur in 1–10 ps. Theoretical justification for this rapid injection rate was also given [89].

Organic semiconductors

An important class of sensitized solar cells consists of an organic thin film, such as phthalocyanines, perylenes, chlorophylls or porphyrins, sandwiched between two metal electrodes. The interfacial regions are often modeled as Schottky junctions where the organic layer is considered to be small band-gap semiconductor with either n- or p-type photoconductivity [94–96]. In a related approach, a p-type organic film is deposited on top of an n-type organic film to form a p–n heterojunction. The sensitization mechanisms proposed for these materials often incorporate addition mechanistic steps such as excitonic energy transfer through the organic layer to the electrode where interfacial electron transfer takes place. It is not clear how important these proposed mechanistic steps are for most materials. The strategy of using thick sensitizer films to increase the fraction of light absorbed generally results in decreased photocurrent efficiency. For semiconducting sensitizer films, the reported excitonic diffusion lengths are short relative to the penetration depth of the light. Furthermore, excitons are readily quenched by impurities or incorporated solvent. In most cases it appears that the small photocurrents observed could simply be rationalized by interfacial electron transfer from localized excited states proximate to an electrode followed by charge migration in the organic layer to the opposite electrode.

In early studies, the two metals employed had different work functions that were incorporated to promote vectorial charge separation. Tang and Albrecht deposited chlorophyll-a (Chla) (Figure 16) on Cr or Al electrodes and then used a liquid metal, Hg or In, as the second electrode [97–99]. These cells are similar in some respects to the photogalvanic cells studied by Bolton and co-workers [41] and Fong and co-workers [40], except that no redox active electrolyte was employed. In the solid-state sandwich cells, the steady-state photocurrent and photovoltage transients resembled the solution absorption spectrum of Chla. The power conversion efficiencies were of the order of 10^{-4} – 10^{-5} with monochromatic light illumination. By applying a bias, the yield was increased to 0.03. In cells better optimized for solar energy conversion, merocyanine dyes have exhibited efficiencies greater than 1 % and monochromatic efficiencies near 100 % [100]. An impressive power efficiency of 1.8 % was reported for an organic heterojunction at low irradiance [101]. Some novel organic multilayer sensitized electrodes have also recently been fabricated [102, 103].

Bard and co-workers explored the effects of doping and illumination on the

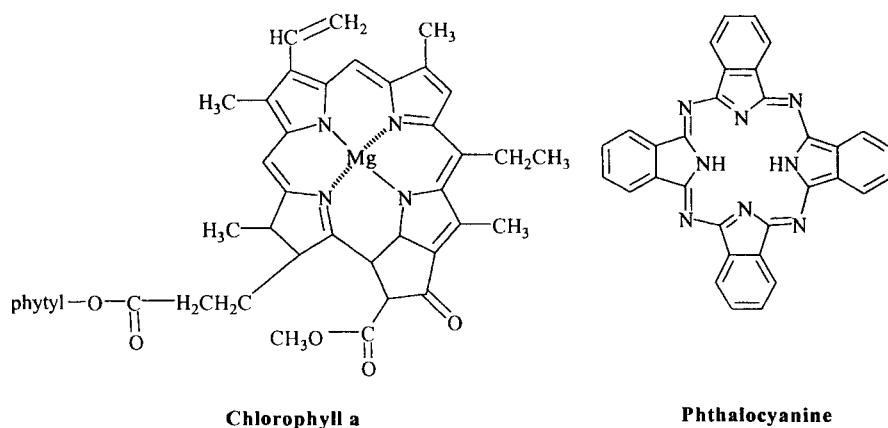


Figure 16. Structure of chlorophyll a and phthalocyanine.

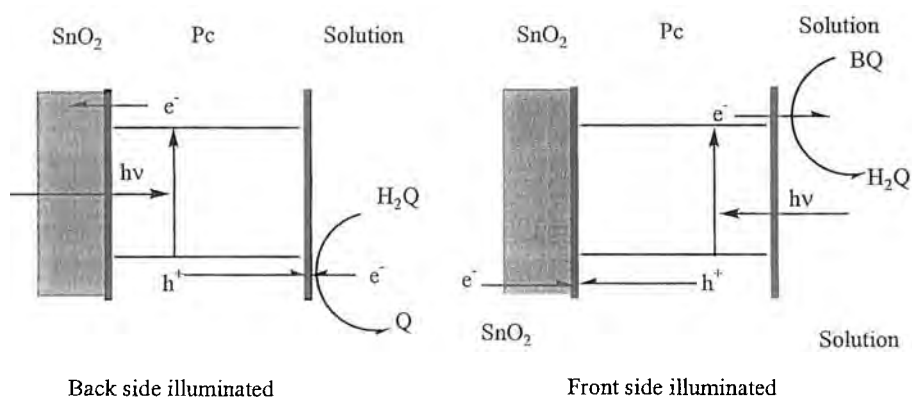


Figure 17. Effect of front side and back side illumination of semiconductor electrodes coated with phthalocyanine thin films. The direction of the photocurrent could be controlled by illumination direction and the redox couple in the solution.

photocurrent direction and magnitude for phthalocyanine (Pc) (Figure 16) films deposited on wide band-gap semiconductors and metals in wet photoelectrochemical cells [104–107]. For example, when Pc thin films (100–250 Å) deposited on tin oxide electrodes were illuminated in a hydroquinone (H_2Q)–benzoquinone (BQ) aqueous electrolyte (Figure 17), the sign of the photocurrent was dependent on the excitation wavelength and the applied potential. With back-side illumination, the Pc^* excited states were formed preferentially near the SnO_2 interface and electron injection into the solid was favored, giving rise to an anodic photocurrent. This process was also observed when the Fermi level is low, i.e., at positive applied potential. With front-side illumination the excited states were preferentially formed near the Pc–electrolyte interface where excited-state electron transfer to BQ was

avored. The hole was transferred to the SnO_2 interface, yielding a net reductive photocurrent. The magnitude and spectral distribution of the current were also sensitive to the metal ion in the Pc. Free base, Zn^{II} and Mg^{II} phthalocyanine gave large reductive photocurrents that are sensitive to E° of the electroactive couple present in the electrolyte. Interpretation of the photoaction spectra was complicated by competitive light absorption and the change in current direction for wavelengths of light with different penetration depths. The observed photoaction spectra could be qualitatively understood and, if only H_2Q was present, an anodic photocurrent was measured that agreed well with the solution absorption spectra.

More recently, liquid crystalline porphyrins sandwiched between two indium tin oxide electrodes were characterized by Bard and co-workers [108]. A memory effect was observed where upon irradiation of the organic film with the simultaneous application of an electric field, electron-hole pairs were generated and separated within the photoconductive porphyrin layer. These electron-hole pairs remained after the illumination of the cell was interrupted and could be released by irradiation of the cell, resulting in a transient short-circuit photocurrent. The high degree of order in the liquid crystalline layers appears to accentuate these processes relative to more disordered films prepared by spin coating or sublimation techniques. The authors suggested that this finding could be exploited for read-write data storage applications [108].

Usually the direction of current flow in sensitized cells is easily rationalized by considering the relative energetics and constructing a Gerischer-type diagram. Bard and co-workers' work provides an excellent example of this [104–107]. However, in some systems the direction of current flow is unexpected. A case in point is an unusual photoeffect reported by Gregg and co-workers [109–112]. Liquid crystalline porphyrins deposited between two tin oxides were found to yield a significant photovoltage and a small photocurrent. This is unexpected since the cell is symmetric with no built-in asymmetry or internal electric fields that might cause preferential vectorial charge transfer toward one electrode. Charge separation appears to be entirely driven by a kinetic effect. Electron injection from Pc^* into the tin oxide is more facile than is hole injection. Therefore, the illuminated surface yields an anodic photocurrent generated solely by the relative rate constants for interfacial electron transfer. Further studies of this behavior have been reported [109–111].

2.2 Dye Sensitization of Colloidal Semiconductor Electrodes

A practical disadvantage of the sensitized planar electrodes described in the previous section was their low solar energy conversion efficiencies. An experimental drawback was that characterization was limited to photoelectrochemical or luminescence techniques. Both of these issues arose from the poor light harvesting by monolayers on flat surfaces or inefficient interfacial electron transfer yields from thick films or concentrated solutions. In 1990, Grätzel and co-workers reported experimental studies of dye sensitized colloidal TiO_2 films that eliminated both of these problematic issues [112]. The effective surface area for sensitizer binding

was increased by about 1000-fold over that of a planar electrode and the interfacial injection yields were close to unity. Solar conversion efficiencies of $\sim 5\%$ were realized soon thereafter [113] and this efficiency has been optimized to 10.69% today [27]. The stability and current densities suggest a practical approach to solar energy conversion that has renewed interest in this area. Furthermore, time-resolved spectroscopic techniques can now be employed in conjunction with traditional photoelectrochemical techniques to probe dye sensitization mechanisms in molecular detail that was not previously possible [112].

The mechanism for anodic photocurrent generation at a sensitized n-type semiconductor, described in Section 1.1.1, is generally believed to be the operative mechanism for the sensitized nanocrystalline TiO_2 regenerative cells. A simplified schematic illustration is shown. An excited sensitizer, S^* , injects an electron into the semiconductor, with rate constant k_{inj} . The oxidized dye molecule accepts an electron from a donor present in the electrolyte, k_{red} . Iodide is the donor shown in Figure 18. The iodide oxidation products are reduced at the dark cathode. The net process allows an electrical current to be generated with light of lower energy than the semiconductor band-gap with no net chemistry. Charge recombination, k_{cr} , can occur to the oxidized sensitizer, S^+ , or donor.

Since the accepted mechanism for dye sensitization has been described in Section 1.1, it will not be elaborated on further here. Instead, the materials and spectroscopic, and photoelectrochemical properties of sensitized colloidal semiconductor films will be discussed in the next section. Nanocrystalline (anatase) TiO_2 films sensitized to visible light with Ru(II) coordination compounds are the best studied and will be focused upon here. Colloidal semiconductor films suitable for dye sensitization based on SnO_2 [114], Fe_2O_3 [115], Nb_2O_3 [116] and ZnO [117] have recently been developed but have received far less attention. Section 1.2.2 gives a progress report of photoinduced electron transfer studies that are ongoing in this active research area.

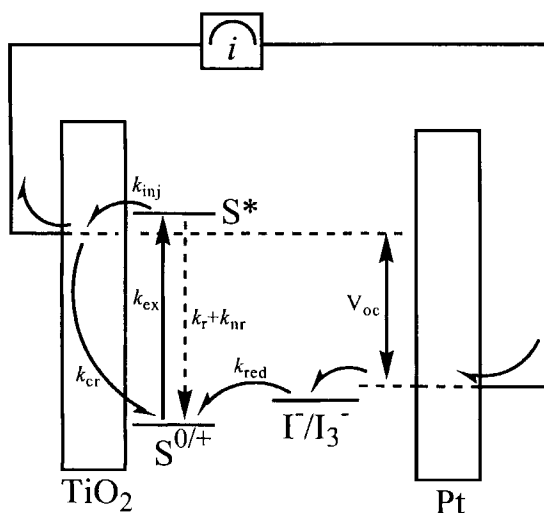


Figure 18. Simplified mechanism of a dye sensitized TiO_2 regenerative photoelectrochemical cells.

2.2.1 Materials, Spectroscopic and Electrochemical Properties of Nanocrystalline TiO_2

Materials

The preparation of nanocrystalline semiconductor films generally follows sol–gel procedures or takes advantage of commercially available particles, such as Degussa P-25 TiO_2 [118]. A typical sol–gel preparation is briefly described here. Titanium isopropoxide [$\text{Ti}(i\text{-PrO})_4$] is added to vigorously stirred acidic water, heated to 80°C , and subsequently heated under pressure for 12 h between 200 and 250°C . This procedure yields anatase particles that are between 8 and 20 nm in diameter depending on the temperature. The volume of the solution is then adjusted and a surfactant, such as poly(ethylene glycol), $\text{MW} = 20\,500$, is added to form a viscous white paste. The paste is deposited on conductive tin oxide glass dried in air for 15 min and heated at 450°C for 1 h.

The resulting material is a mesoporous film comprised of interconnected anatase particles. The scanning electron micrograph shows ~ 10 nm size particles interconnected in a sponge-like 8–10 μm thick film [119]. The materials are typically 50–70 % porous and about two-thirds of the tin oxide substrate is covered with particles. The colloidal films are highly resistive with dark conductivity of $\sim 10^{-9} \Omega \text{ cm}^{-1}$ at 330 K. An activation energy of 1.6 eV has been reported, which suggests that the Fermi level is near midgap [120]. X-ray analysis reveals the anatase structure shown in Figures 19 and 20.

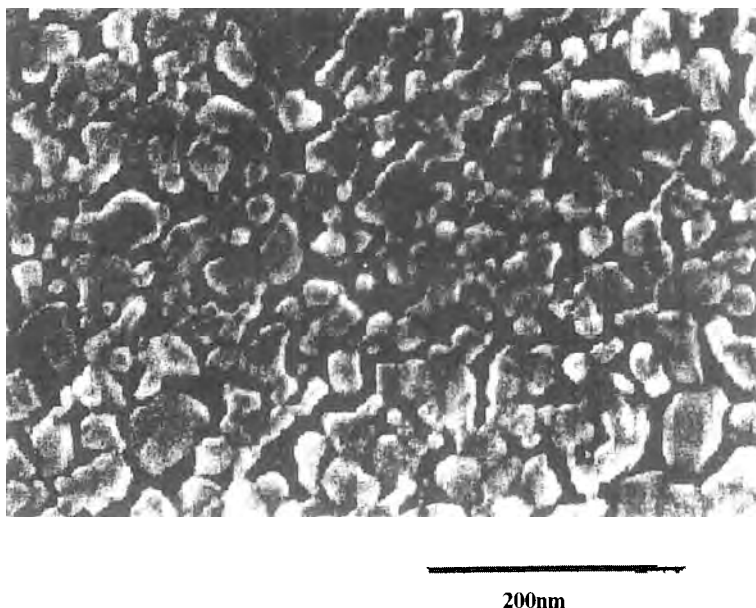


Figure 19. SEM image of a colloidal TiO_2 thin film.

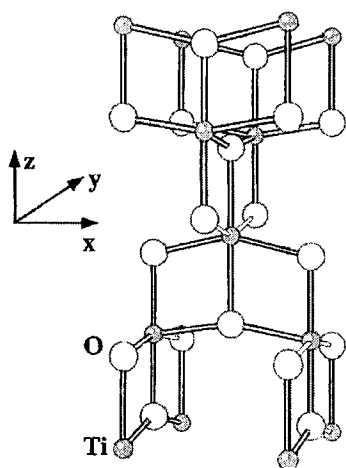


Figure 20. Anatase structure of TiO_2 where filled balls are titanium and open circles are oxygen.

The semiconductor films are transparent in the visible region. Around 380 nm a sharp absorption onset is observed below which the films are strongly absorbing. The absorption has been assigned to the fundamental $\text{VB} \rightarrow \text{CB}$ transitions consistent with the known anatase band-gap of 3.2 eV. However, it is not clear how intra-band-gap transitions from localized states alter the absorption edge. Owing to the large effective mass of electrons in TiO_2 , the Bohr radius of TiO_2 is smaller than 1 nm, which indicates that size quantization effects are not expected to be observable in nanometer-sized TiO_2 particles [121].

Sensitizers

Surface binding

The most common mode for surface binding inorganic and organic sensitizers is through the reaction of carboxylic acid groups with the metal oxide surface in neat acetonitrile or alcohol. Phosphonates [122], acetylacetonates [123], ether linkages [124] and cyano [125] groups have also been employed for binding to metal oxides but thus far have resulted in less efficient solar cells.

The reaction of carboxylic acids with surface hydroxyl groups to form ester linkages (Figure 21) was initially suggested by Goodenough et al. [67] for $\text{Ru}(\text{bpy})_2(\text{dcb})^{2+}$ and by Osa and Fujihira [56] for Rhodamine B. The nature of the surface linkage has been studied by several groups using vibrational spectroscopy [126–130]. Hester and co-workers used Raman spectroscopy to identify the binding mode(s) of $\text{Ru}(\text{dcb})_3^{2+}$ on colloidal TiO_2 particles suspended in acidic solution [126]. They concluded that the sensitizers hydrogen bond to the semiconductor surface. Many other groups have examined the chemistry of *cis*- $\text{Ru}(\text{dcb})_2(\text{NCS})_2$ and $\text{Ru}(\text{bpy})_2(\text{dcb})^{2+}$ anchored to colloidal TiO_2 films by infrared spectroscopy [127–129]. In all cases a low-energy asymmetric CO_2^- stretch is observed that is most consistent with carboxylate binding, rather than ester. It is likely that the nature of the surface linkage is dependent on the surface conditions. Even for X-ray

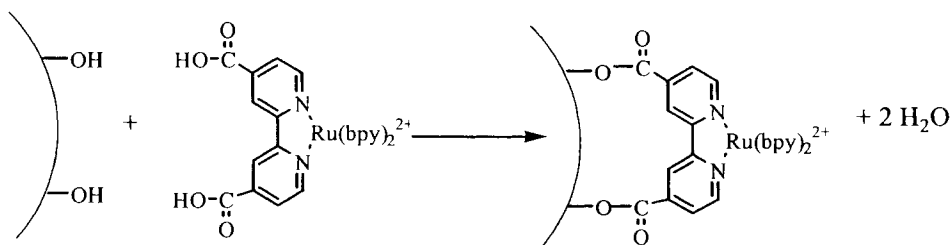


Figure 21. Surface binding through the dehydrative coupling of carboxylic acid groups with surface hydroxyl groups to yield ester linkages and water.

crystallographically characterized metal carboxylates, the coordination modes are known to be sensitive to sample preparation [130].

The concentration-dependent binding of Ru(dcb)-based sensitizers is well described by the Langmuir adsorption isotherm model from which adduct formation constants of $\sim 10^5 \text{ M}^{-1}$ have typically been abstracted [123, 132]. While it is often stated that monolayer coverage of the sensitizers is achieved, this is difficult to prove. The colloidal nature of the films makes absolute surface area determinations almost impossible. There is no evidence for multilayer formation, so the surface coverage is at most monolayer and probably sub-monolayer in most cases. The surface coverage for sensitizers in a 1 cm^2 geometric area is typically 10^{-8} mol , where $\sim 10^{-10} \text{ mol cm}^{-2}$ would be expected for a close-packed monolayer of 14 \AA diameter sensitizers on a flat surface.

Electrochemistry

Ru(bpy)₂(dcb)²⁺ anchored to nanocrystalline TiO₂ films displays quasi-reversible Ru^{III/II} redox chemistry [123, 132, 134]. The redox chemistry is termed quasi-reversible because the oxidation and reduction current are the same within experimental error and the peak-to-peak splitting is large [7]. This redox chemistry does not involve the semiconductor valence or conduction bands. Rather the proposed mechanism is that a small fraction of the sensitizers, $< 10^{-10} \text{ mol cm}^{-2}$, bound to the SnO₂ substrate are initially oxidized electrochemically. These oxidized sensitizers mediate the oxidation of TiO₂-bound sensitizers by self-exchange electron transfer across the nanocrystalline surface(s). Cyclic voltammetry is therefore a useful technique for characterizing the ground-state potentials of semiconductor-bound sensitizers. The technique has been utilized for sensitizers with only one carboxylic acid group and those bound through alternative linkages [123]. Unfortunately, it has not been successfully applied to the commonly used *cis*-Ru(dcb)₂(NCS)₂ sensitizer that displays irreversible electrochemistry in fluid solution at scan rates less than 200 mV s^{-1} [133].

Trammell and Meyer used cyclic voltammetry and chronoamperometry with absorption measurements to estimate the electron hopping rate across sensitized nanocrystalline semiconductor surfaces [134]. At high surface coverages of Ru(bpy)₂(dcb)²⁺ or Os(bpy)₂(dcb)²⁺, the apparent charge-transfer diffusion coefficients was measured to be $1.4 \times 10^{-9} \text{ cm}^2 \text{ s}^{-1}$ in acetonitrile electrolyte. Oxida-

tion of the surface-bound sensitizers could also be accomplished with a mediator present in the electrolyte. Bonhôte and co-workers applied a percolation model to the kinetics of cross-surface electron transfer for an organic triarylamine bound to nanocrystalline TiO_2 surfaces [135].

Zaban and co-workers reported the use of chemical redox titrations to measure the potential of sensitizers bound to TiO_2 [136]. An unexpected result from these studies is that redox couples that are not pH sensitive in fluid solution become pH dependent when bound to the semiconductor surface. The magnitude of the pH-induced shift varied from 21 to 53 mV per pH unit depending on the physical location of the sensitizer. Sensitizers inside the semiconductor double layer track the $\sim 59 \text{ mV pH}^{-1}$ shift of the semiconductor. When sensitizers were outside the double layer, their potential was almost independent of the semiconductor. This finding has important implications for the determination of interfacial energetics for dye sensitization and interfacial electron transfer studies [136].

Photophysics

In general, the absorption spectra of sensitizers bound to colloidal semiconductor films closely resemble those measured in fluid solution. In some cases small spectral shifts have been observed and attributed to Stark effects, acid–base chemistry or stabilization of the sensitizer excited states by the semiconductor surface. However, the effects are small, typically a few nanometers in the visible region.

The accepted model for photocurrent generation in the dye-sensitized nanocrystalline solar cells involves excited state interfacial electron transfer. It is therefore desirable to have a mechanistic understanding of excited-state behavior of the sensitizers. Since the most successful sensitizers for this application are Ru^{II} polypyridyl compounds, we include a brief review of their excited-state properties. More thorough reviews are available in the literature [137].

The parent compound $\text{Ru}(\text{bpy})_3^{2+}$ has been extremely well studied and a Jablonski-type diagram is shown in Figure 22 [137]. Light absorption forms a metal-to-ligand charge transfer (MLCT) excited state wherein an electron is formally promoted from the metal d-orbitals to a bipyridine ligand, $\text{Ru}^{\text{III}}(\text{bpy}^-)(\text{bpy})_2^{2+*}$. Rapid and quantitative intersystem crossing to a manifold of thermally equilibrated MLCT excited states is observed in fluid solution. The thexi state consists of three energetically proximate states that have significant Boltzmann population and behave as a single state near room temperature. This thexi excited state has a lifetime near 1 μs in fluid solution and is highly photoluminescent. Higher in energy is a fourth MLCT state and ligand field (LF) states. The LF states are antibonding with respect to metal–ligand bonds. Details regarding the time-scale for excited state evolution to the thexi state have only recently become available [138]. McCusker and co-workers performed ultrafast measurements of $\text{Ru}(\text{bpy})_3^{2+}$ in acetonitrile and found that the thexi state is reached within 300 fs at room temperature [138]. Ultrafast dynamics data for other Ru^{II} sensitizers are very sparse at present, which complicates assignments in ultrafast electron injection studies.

Molecular excited states are known to be sensitive to environment and dramatic changes in lifetimes, quantum yields and spectral distribution can arise from so-

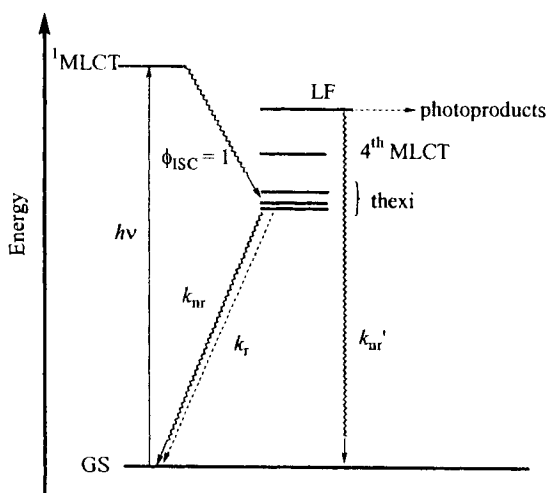
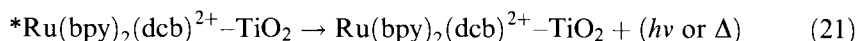


Figure 22. Jablonski type diagram for $\text{Ru}(\text{bpy})_3^{2+}$. See text for additional detail.

called ‘rigidochromic’ effects observed when chromophores are constrained in solid-state matrices [139]. Mechanistic information on semiconductor surfaces is difficult to obtain as interfacial electron transfer rapidly depletes the excited states under many conditions. The weak photoluminescence (PL) that remains has been studied by many groups and has been the subject of a recent review [140]. The difficulty with PL measurements, however, is that the observed PL may represent a small fraction of the surface-bound compounds and not the ensemble average.

The work of the groups of Clark, Sutin, Watanabe and Spitler described in Section 1.1 demonstrates convincingly that the efficiency of excited-state electron injection can be controlled by pH [52, 63, 69]. At low pH a sensitized photocurrent was measured but as the pH was raised the photocurrents decreased in a manner consistent with their excited-state reduction potentials [63]. Unfortunately, sensitizers bound to metal oxide surfaces through carboxylate linkages generally desorb rapidly when the pH is raised above 3. An alternative approach for controlling injection yields has been reported by Kelly et al., who found that the efficiency of electron injection for nanocrystalline TiO_2 films of $\text{Ru}(\text{bpy})_2(\text{dcb})^{2+}$ - TiO_2 , immersed in acetonitrile, could be widely ‘tuned’ by varying the electrolyte composition [141]. This finding allowed excited-state behavior to be quantified on semiconductor surfaces.

The excited-state decay kinetics of $\text{Ru}(\text{bpy})_2(\text{dcb})^{2+}$ - TiO_2 immersed in neat acetonitrile, probed by transient absorption spectroscopy, exhibited nonexponential kinetics. By minimizing the excitation irradiance, near exponential kinetics were observed for excited-state decay. However, at high excitation irradiance, second-order kinetics were found to fit the experimental data well. These observations are consistent with competitive first- and second-order processes attributed to radiative and nonradiative excited-state deactivation, Eq. 21, proceeding in parallel with excited-state annihilation, Eq. 22:



A second-order contribution to the excited-state decay of $\text{Ru}(\text{bpy})_3^{2+}$ adsorbed on surfactant- or polymer-modified nanocrystalline TiO_2 films has been reported by Rabani and co-workers [142]. The implied parallel first- and second-order kinetic model has been used successfully to fit many excited-state decays on semiconductor thin films in our laboratory. Energy migration across the nanocrystalline semiconductor surface, like that shown in Figure 23, has been confirmed by co-anchoring an energy transfer trap, $\text{Os}(\text{bpy})_2(\text{dcb})^{2+}$, to the same semiconductor surface [143]. Energy migration, $\text{Ru}(\text{bpy})_2(\text{dcb})^{2+*} + \text{Os}(\text{bpy})_2(\text{dcb})^{2+} \rightarrow \text{Ru}(\text{bpy})_2(\text{dcb})^{2+} + \text{Os}(\text{bpy})_2(\text{dcb})^{2+*}$, occurs with a quantum yield near unity under conditions of suppressed electron injection.

Very little is known about the excited-state properties of *cis*- $\text{Ru}(\text{dcb})_2(\text{NCS})_2$ anchored to semiconductor surfaces. However, the photophysical properties of *cis*- $\text{Ru}(\text{bpy})_2(\text{ina})_2^{2+}$, where ina is isonicotinic acid, 4-COOH-pyridine, on nanocrystalline TiO_2 and ZrO_2 surfaces were recently reported. An intriguing observation was that the activation energy for internal conversion from the thexi state to the ligand field states increased dramatically compared with fluid solution [129]. Similar behavior might be expected for *cis*- $\text{Ru}(\text{dcb})_2(\text{NCS})_2$.

Photoelectrochemistry

Depletion

Conventional models that describe the bias conditions for planar semiconductor–electrolyte junctions are not expected to be applicable to the nanocrystalline semiconductor films. The potential distribution within the complex three-dimensional

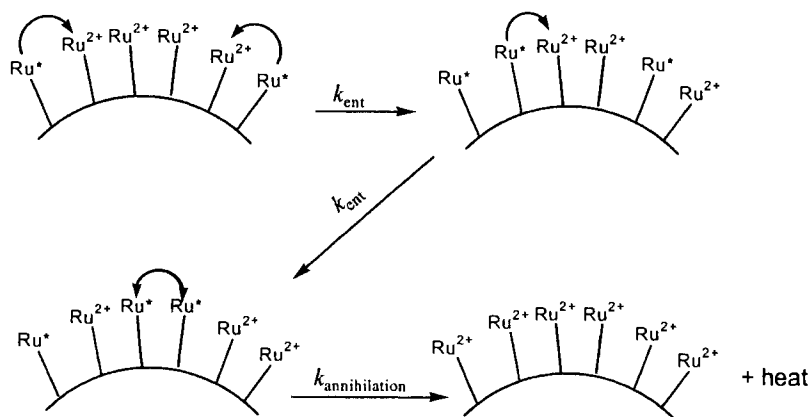


Figure 23. Proposal intermolecular energy migration between surface bound sensitizers. Excited states proximate to each other may annihilate and ultimately yield ground state products and heat.

semiconductor network is not well understood and represents a major challenge for future photoelectrochemical research. Below we highlight some significant contributions from theory and from experiments that address basic issues and have implications for the interfacial electron transfer processes relevant to dye sensitization.

For colloidal materials the small size of the semiconductor particles severely restricts the magnitude of the electric field that a particle can support. Albery and Bartlett first considered the potential distribution within spherical semiconductor particles [144]. For large particles, an expression equivalent to that for planar electrodes given in Eq. 6 was derived. For small semiconductor particles the total band bending within the semiconductor, V_b , is limited by the radius r , Eq. 23:

$$V_b = \frac{kT}{6e} \left(\frac{r}{L_D} \right)^2 \quad (23)$$

where L_D is the Debye length given by

$$L_D = \sqrt{\frac{\epsilon_0 \epsilon kT}{2e^2 N_D}} \quad (24)$$

in which these terms have been previously described. The key point is that nanometer-sized semiconductor particles cannot support a large electric field. For example, a 25 nm TiO_2 particle with a relative permittivity of 173 and $N_D = 10^{17} \text{ cm}^{-3}$ is completely depleted at a band bending of only 0.6 meV. Even though the potential drop across an individual particle is small, the average field may still be sufficient to play an important role in dye sensitization processes.

Accumulation and Fermi-level pinning

It has been known for some time that electrochemical, chemical or photoelectrochemical reduction of TiO_2 increases the conductivity, turns the solid blue or black, and the material becomes paramagnetic. The nature of the states created upon reduction has been the subject of much discussion and debate over the years. In 1986, Heller responded to a question by stating that TiO_2 reduction yields a ' Ti^{III} center or "state" that adds an electron to the conduction band. To add an electron the state must be either in the band or close to it' [145]. Today this issue remains very much unchanged and whether reduction yields Ti^{III} states or conduction band electrons is still unknown. How the two can be unambiguously differentiated is also unknown. The issue is important when considering interfacial electron transfer and the nature of the redox active states in TiO_2 . For example, does interfacial electron transfer involve the conduction band continuum or localized redox active $\text{Ti}^{\text{IV/III}}$ states? Some recent literature results that address this issue are described below.

A significant theoretical contribution to the potential distribution within nanocrystalline TiO_2 films was proposed by Rothenberger et al. [146]. These workers employed a Schottky junction model to derive the potential distribution within the TiO_2 particles at negative applied potentials. The model is based on the supposition

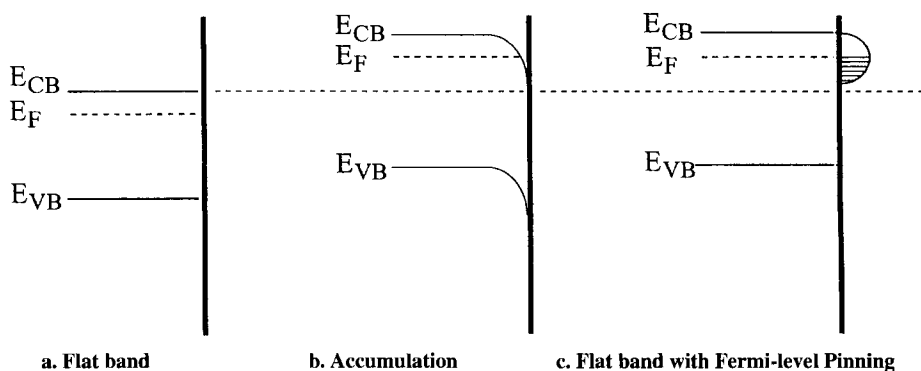


Figure 24. Potential distributions of a semiconductor at a) flat band condition, b) accumulation layer, and c) flat band condition with Fermi-level pinning.

that an accumulation layer can be created within each nanocrystalline particle as the potential is shifted negative of the flat-band potential. They demonstrated that an accumulation layer is thinner than a depletion layer when considering cases where the same amount of charge is transferred across the interface. Therefore, in small semiconductor particles an appreciable accumulation layer may be more likely than a depletion layer. Experimentally, a blue–black color, assigned to conduction band and trapped electrons, and a bleach of the UV absorption band, attributed to a Burnstein–Moss shift, were taken as evidence for accumulation layer formation. Spectroelectrochemical analysis in conjunction with this model has been used extensively by Fitzmaurice to calculate flat-band potentials.

Cao et al. reported an alternative Fermi-level pinning model to rationalize the potential distribution at negative applied potentials [147]. They suggested that the reduction of Ti^{IV} surface states to Ti^{III} , observed by low-temperature EPR spectroscopy, pins the Fermi level and, as the potential is raised further, the potential drops across the solution–semiconductor interface.

A simplified description of the limiting Fermi-level pinning and accumulation layer bias conditions is shown in Figure 24. Note that in an accumulation layer the Fermi-level at the surface is above the conduction band edge where free conduction band electrons accumulate. In the Fermi-level pinning model, reduction of the semiconductor, solvent or surface states unpins the band edges and, as E_F is raised further, the potential falls in the Helmholtz layer rather than the semiconductor. In principle, capacitance measurements can be used to characterize an accumulation layer and distinguish it from Fermi-level pinning. The potential dependence of an accumulation layer is given by Eq. 25:

$$C_{\text{SC}} \propto \exp\left(\frac{-eV_b}{2kT}\right) \quad (25)$$

For nanocrystalline TiO_2 films, the 120 mV per decade predicted by Eq. 25 was not realized by Cao et al. [143]. Instead ~ 360 mV per decade was measured, consistent

with a significant fraction of the applied potential falling across the Helmholtz layer. Zaban et al. also found that capacitance data were inconsistent with accumulation layer formation in sol–gel processed TiO₂ [148].

The electrochemical reduction of TiO₂ is known to be accompanied by the intercalation of small cations. This finding has been explored in sensitizing anatase films for battery applications [149]. Cation coordination to titanium alkoxide sol–gel precursors is also well known [150]. Lyon and Hupp used quartz crystal microbalance techniques to determine the mass of intercalating cations as the TiO₂ film is reduced [151]. Hagfeldt and co-workers have studied Li⁺ and Na⁺ intercalation into anatase TiO₂ both theoretically and experimentally [152, 153]. They found that the diffusion constants for Li⁺ and Na⁺ are temperature dependent with an activation barrier of 0.4 eV for insertion and 0.5 eV for extraction. The Li⁺ diffusion coefficient at 25 °C into the nanoporous structure was approximately $2 \times 10^{-17} \text{ cm}^2 \text{ s}^{-1}$ for insertion and $4 \times 10^{-17} \text{ cm}^2 \text{ s}^{-1}$ for extraction.

The issue of how to characterize reduced TiO₂ and the role of intercalation are still under much debate in the literature. In the dye-sensitized electrode field, the term ‘accumulation’ is used very loosely. Many authors use the term accumulation layer when they actually mean an increased concentration of trapped electrons. This language is unfortunate, as accumulation layers have well defined meanings in solid-state semiconductor devices. It is unclear what accumulated trapped electrons really means.

Photocurrent–voltage behavior

The state of the art regenerative solar cell consists of the sensitizer *cis*-Ru(dcb)₂(NCS)₂ anchored to colloidal anatase TiO₂ films with an I[−]I₂ organic electrolyte. An *i*–*V* curve recorded with 1000 W m^{−2} of air mass 1.5 illumination at 25 °C is shown in Figure 25 [154]. From these data, a *V*_{oc} of 0.79 V, an *i*_{sc} of 4.83 mA, a fill factor of 0.71 and an η_{max} of 0.11 were obtained. The active area of the electrode was kept low, 0.249 cm², to minimize resistive losses associated with the tin oxide glass and the nanocrystalline semiconductor film. The power efficiency was not significantly changed when the temperature was raised from 20 to 60 °C.

Photocurrent efficiencies near unity have been measured at single wavelengths for a wide variety of organic and inorganic sensitizers [119]. To circumvent the difficulty of correcting for transmitted light, the term incident photon-to-current efficiency (IPCE) has emerged. IPCE values are a lower limit of the actual photocurrent quantum yield of a sensitized cell. An experimentally useful expression for the determination of IPCE in photoaction spectra is

$$\text{IPCE} = \frac{(1240 \text{ eV nm})[\text{photocurrent density } (\mu\text{A cm}^{-2})]}{[\text{wavelength (nm)}][\text{irradiance } (\mu\text{W cm}^{-2})]} \quad (26)$$

The IPCE of sensitized electrodes is wavelength dependent. Occasionally, the IPCE is given as a percentage rather than a fraction from 0 to 1. In this case, an IPCE % of 80 % is equivalent to an IPCE of 0.8, and indicates that 80 of 100 incident photons are converted to electrons in the external circuit. It is important to distinguish

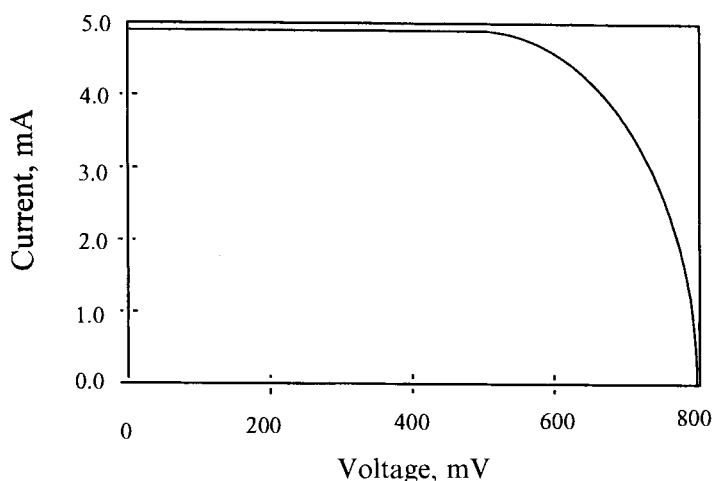


Figure 25. A typical i-V curve recorded with 1000 W/m^2 of air mass 1.5 illumination at 25°C for a regenerative solar cell based on *cis*-Ru(dcb)₂(NCS)₂/TiO₂.

between IPCE measurements made at a single wavelength and global efficiencies measured under sunlight or simulated sunlight conditions.

In most cases, the photoaction spectrum is coincident with the absorbance spectrum of the surface bound sensitizer, for all but one case. Assuming Beer's law is applicable, the LHE can be related to the molar extinction coefficient by

$$\alpha(\lambda) \equiv \text{LHE}(\lambda) = 1 - 10^{-[1000(\text{cm}^3 \text{ L}^{-1})\varepsilon(\text{mol}^{-1} \text{ L cm}^{-1})\Gamma(\text{mol cm}^{-2})]} \quad (27)$$

where ε is the molar extinction coefficient at wavelength λ and Γ is the surface coverage in mol cm^{-2} [33]. For thick films of sensitizers on planar surfaces or under conditions where species in the electrolyte absorb light, inner filter effects and competitive light absorption can also affect the shape of the photocurrent action spectrum.

The IPCE measured at a single wavelength of light is the product of three terms:

$$\text{IPCE} = (\text{LHE})(\phi)(\eta) \quad (28)$$

where ϕ is the quantum yield for electron injection and η is the efficiency with which the injected carriers reach the external circuit. Obviously, if either of the two terms is wavelength dependent, then the shape of a photoaction spectrum will change from that predicted solely on the absorbance spectrum. At the time of writing, there is only one example of a sensitizer whose absorption spectrum clearly does not match the photoaction spectrum. This sensitizer is $\text{Fe(dcb)}_2(\text{CN})_2$ and the importance of this observation is described in Section 1.2.2. By defining the absorbed photon to current efficiency (APCE) as IPCE/LHE , any wavelength dependence can be attributed to changes in ϕ and/or η .

Models for the photoelectrochemical behavior of colloidal semiconductor films have been described by Lindquist and co-workers [155]. Beginning with Gartner's model, a simple expression was derived:

$$\phi_{\text{FS}} = \frac{L}{d} (\phi_{\text{BS, max}}) \quad (29)$$

where ϕ_{FS} is the quantum efficiency for front side illumination, $\phi_{\text{BS, max}}$ is the quantum efficiency for back-side illumination, L is the electron diffusion length and d is the film thickness. This expression was derived assuming that (1) electron transport occurs by diffusion and (2) the diffusion length of the electron in the semiconductor is constant. With this equation, using front- and back-side illumination of sensitized films of known thickness, a diffusion length of 0.8–0.9 μm was calculated.

The shape of the i - V curve was predicted to follow Eq. 30:

$$I = I_{\text{L}} - I_{\text{S}}(e^{qv/kTm} - 1) \quad (30)$$

where I_{L} is the photocurrent, I_{S} is the saturation current, m is the ideality factor and the other terms have been described previously. With an ideality factor of 2.1, this expression accurately models the i - V behavior over a four-fold change in incident irradiance.

Carrier transport

A fascinating aspect of the sensitized colloidal semiconductor films is that injected electrons created throughout the semiconductor network are collected in the external circuit with high efficiency. This implies that carrier transport through the ~ 10 μm thick film occurs with no measurable recombination loss. The mechanisms of carrier transport have been studied in some detail. Carrier transport in a semiconductor film can be described by the continuity equation [155]:

$$\frac{\partial n}{\partial t} = \frac{1}{e} \frac{\partial J}{\partial x} + G - R \quad (31)$$

where n is the electron density under illumination, J is the current density in the film and G and R are the carrier generation rate and recombination rate, respectively. Recombination is assumed to be proportional to the electron concentration and can be written as $R = (n - n_0)/\tau_0$, where n_0 is the electron density in the dark and τ_0 is the position-independent electron lifetime. Both electron drift and diffusion can contribute to the current density:

$$J = en\mu_n \frac{\partial \phi_{\text{sc}}}{\partial x} + eD \frac{\partial n}{\partial x} \quad (32)$$

where μ_n is the electron mobility and D is the diffusion coefficient of the electron. Since the TiO_2 particles are too small to sustain significant band bending, the current density is dominated by the diffusion term. In the absence of migration, the continuity equation is given by

$$D \frac{\partial^2 n(x, t)}{\partial x^2} - \frac{\partial n(x, t)}{\partial t} - \frac{n(x, t) - n_0}{\tau_0} + \Gamma \alpha \exp(-\alpha x) = 0 \quad (33)$$

The first two terms represent the electron flux and the change in electron concentration with time, respectively. The third term represents the recombination rate and is assumed to be first order with electron density. The fourth term is the generation term that assumes the dye concentration is uniform throughout the film. Eq. 33 has been solved analytically. Södergren and co-workers [155] have shown that the steady-state photocurrent is consistent with this model and the assumption that electron transport occurs by diffusion.

The first time-resolved photocurrent measurements were employed by Schwarzbarg and Willig [156], who used Shockley–Reed kinetics to simulate their data numerically. Later, Cao et al. reported the first transient photocurrent measurements obtained in the frequency domain, using intensity-modulated photocurrent spectroscopy (IMPS), and compared them with data acquired in the time domain [157]. A characteristic feature of dye-sensitized nanocrystalline TiO_2 cells was the appearance of slow photocurrent transients that gave rise times varying from milliseconds to seconds depending on the experimental conditions. Several considerations led to the conclusion that the slow response was due to the transport of electrons in the semiconductor. First, the rate of excited-state electron transfer to the semiconductor was known to be at least six orders of magnitude faster. Second, sensitizer regeneration by the iodide electrolyte was known to occur rapidly and to contribute only to the observed transients at low concentrations or high irradiance. Therefore, the sluggish photocurrent transients are reasonably attributed to slow carrier transport. The apparent diffusion constants cannot correspond to the transport of free electrons in the conduction band of single-crystal rutile TiO_2 . Based on an electron mobility of about $1 \text{ cm}^2 \text{ V}^{-1} \text{ s}^{-1}$, the diffusion coefficient for free CB electrons determined from the Einstein equation is of the order of $10^{-2} \text{ cm}^2 \text{ s}^{-1}$ at room temperature. This value is much larger than what could be inferred from the transient photocurrent data.

The results imply that the diffusion coefficient represents the thermally activated transport of electrons through the particle network. Indeed, these and subsequent studies have been interpreted with models that involve trapping of conduction band electrons or electron hopping between trap sites [158, 159]. An unexpected feature of the diffusion constants reported by Cao et al. is that they are dependent on the incident irradiance. The photocurrent rise times display a power law dependence on light intensity with a slope of -0.7 . The data could be simulated if the diffusion constant was assumed to be second order in the electron concentration, $D \propto n^2$. The molecular origin of this behavior is not well understood and continues to be an active area of study [157, 159].

Open-circuit photovoltage

Since the nanocrystalline semiconductor particles are not expected to support large depletion layers, the origin of the 600–800 mV open-circuit photovoltage, V_{oc} , has been the subject of much discussion. Neglecting the contacts and leads, V_{oc} is de-

terminated by the difference in Fermi energies of the two current collectors. These are usually the tin oxide glass substrate of the sol–gel processed electrode and platinum at the counter electrode. V_{oc} represents the maximum Gibbs free energy a regenerative solar cell can produce under conditions of constant irradiance [160].

In a conventional single crystal or polycrystalline photoelectrochemical cells, the difference between the Fermi level of the semiconductor electrode and the counter electrode is expected to follow a logarithmic relationship with the light intensity described by the diode equation [160]. An analog of the diode equation for dye-sensitized cells can be obtained by equating the recombination rate to the injection flux under open-circuit conditions, Eq. 34:

$$V_{oc} = \frac{kT}{e} \ln \left(\frac{I_{inj}}{n_{s0} k_{et} N_{ox}} \right) \quad (34)$$

where N_{ox} is the concentration of the oxidized donor species, k_{et} is the rate constant for reduction by electrons in the TiO_2 , n_{s0} is the electron concentration in the dark and I_{inj} is the electron injection flux from the dye under illumination. Implicit in this equation is that the injection of charge carriers decreases the band bending in the space-charge layer and thus raises the Fermi level of the semiconductor electrode according to the Boltzmann equation [161]. For regenerative solar cells based on these nanocrystalline materials, V_{oc} increases exponentially with light intensity with a slope typically of the order of 100–120 mV per decade (i.e., an ideality factor of 1.5–2.5), suggesting that the diode equation captures the essential physics of the device [155].

Grätzel and co-workers first reported that treating the sensitized electrode with 4-*tert*-butylpyridine increased the open-circuit photovoltage by 200–300 mV without significantly altering the short-circuit photocurrent [161]. With Eq. 34, a 5.5×10^4 -fold decrease in the rate constant for the reduction of triiodide by electrons in TiO_2 was calculated. Frank and co-workers also observed increased V_{oc} on treating their sensitized electrodes with pyridine derivatives and pointed out that band edge shifts could also account for the effect [162].

Band edge positions

At present there is no unambiguous method for determining the energetic position of the conduction band edge of nanocrystalline semiconductor films under experimental conditions relevant to dye sensitization. Clearly, the lack of a depletion layer precludes traditional capacitance measurements with Mott–Schottky analysis described in Section 1.1. The onset of photocurrents in photocurrent–voltage plots can provide a crude working estimate under some conditions, but is problematic for the reasons described previously. This is unfortunate as accurate energetics are necessary to compare experimental results with even the simplest theory [4].

Fitzmaurice and co-workers have pioneered the use of spectroelectrochemical data to quantify flat-band potentials under a variety of conditions [163–167]. Table 2 gives data measured in the indicated solvents. Flat-band potentials for different cations and mixed solvents are also available in the literature. With this spectro-

Table 2. Flat-band potential (V_{fb}/V vs. SCE) of nanocrystalline TiO_2 films determined by spectroelectrochemistry^{a,b}.

Solvent	[LiClO ₄]/M		
	0.0	0.001	0.1
MeCN	−2.24	−1.97	−0.90
EtOH	−1.39	−1.37	−1.10
MeOH	−1.12	−1.11	−1.10
DMF	−2.04	−2.02	−1.09
THF	−2.34	−2.44	−1.20
H ₂ O (pH 11)	−1.06		−1.07
H ₂ O (pH 2)	−0.52		−0.49
EC	−1.59		

^a MeCN = acetonitrile; EtOH = ethanol; MeOH = methanol; DMF = dimethylformamide; THF = tetrahydrofuran; EC = ethylene carbonate. For all experiments, electrolyte is 0.2 M tetrabutylammonium perchlorate.

^b Data obtained from (a) Enright, B.; Redmond, G.; Fitzmaurice, D. *J. Phys. Chem.* **1994**, 98, 6195; (b) Redmond, G.; Fitzmaurice, D. *J. Phys. Chem.* **1993**, 97, 1426.

electrochemical approach, the flat-band potential shift the expected 59 mV per pH unit expected for metal oxide semiconductors. The potential calculated in 1.0 M LiClO₄ acetonitrile is very close to the Ti(IV/III) reduction potential, −1.0 V vs. SCE, measured by cyclic voltammetry of chemically vapor-deposited anatase films in the same electrolyte [153b,c]. Furthermore, the model predicts that electron injection from excited sensitizer should not occur in tetrabutylammonium perchlorate–acetonitrile and, at least in one case, this has been observed. Therefore, there is some reason to be optimistic that the tabulated values, or at least the trends, will be applicable to regenerative solar cells.

The accumulation layer model used to calculate the flat-band potentials with spectroelectrochemical data has been described above. Much like the difficulties of extrapolating flat-band potentials from conditions of strong depletion (i.e., Mott–Schottky analysis), extrapolation from strongly reducing conditions is also subject to systematic bias. Flat-band potentials are not singular parameters and there is no guarantee that the band edges will remain fixed as the Fermi level is lowered. Any degree of band edge unpinning will shift the tabulated potentials further in the negative direction, so the values listed are, perhaps, best thought of as lower limits for dye sensitization studies.

2.2.2 Examples of Interfacial Electron Transfer at Colloidal Semiconductor Electrodes

Nanocrystalline semiconductor films can be prepared with high transparency in the visible region [112]. This feature allows excited states and electron transfer to be characterized in considerable molecular detail by transmission-based spectroscopic

methods in addition to the more conventional photoelectrochemical techniques. In this final section we focus specifically on charge injection and recombination across molecular sensitizer–semiconductor interfaces quantified by direct spectroscopic techniques. The iodide redox chemistry critical for sensitizer regeneration and high conversion efficiencies is not well understood and will not be reviewed here [168–171]. The growing area of semiconductor sensitization by small band-gap semiconductors is also not included [172–174].

Table 3 gives a summary of the interfacial charge injection and recombination rate constants determined by direct spectroscopic techniques. The data are not directly comparable as different TiO_2 preparations, solvents, electrolytes, time-scales and kinetic models were used by different experimentalists. Nevertheless, the table demonstrates the wide range of sensitized materials reported in the literature and provides a basis for further discussion.

A key to the high energy conversion efficiencies of sensitized nanocrystalline semiconductors is that the rate of charge injection is orders of magnitude faster than is charge recombination. Why this fortuitous difference in rate constants exists has been the subject of much discussion. Shown schematically in Figure 26 are simplified models that are often invoked. For metal-to-ligand charge transfer (MLCT) excited states, electron injection is formally from a reduced ligand (typically dcb^-) and recombination is to the d-orbitals of the metal. On the semiconductor side, electron injection into a conduction band continuum followed by thermalization and/or trapping is generally proposed to precede recombination. Alternatively, injection and recombination may involve a well defined surface state and $\text{Ti}^{\text{IV/III}}$ redox chemistry. In any event, different molecular orbitals are involved in the electron injection and recombination processes. Furthermore, there is strong evidence that charge injection is activationless whereas charge recombination falls in the Marcus kinetic inverted region. Under some conditions charge recombination is sluggish because the injected electron is translated away from the oxidized sensitizer and electron transfer becomes rate-limited by diffusion back to the oxidized sensitizer. Other data suggest that proton-coupled electron transfer is important in controlling charge recombination rates. The experimental studies discussed below seek to develop a deeper understanding of these important interfacial electron transfer processes. The perfect portrait will emerge from the continued studies of many excellent research groups around the world.

Electron injection kinetics

The excited sensitizer that injects an electron into the semiconductor may be in either an equilibrated singlet or triplet ('thexi') states or a vibrationally 'hot' excited state. For organic chromophores, the singlet and triplet states are well defined and can be observed by many techniques such as fluorescence or low-temperature phosphorescence, respectively [9, 10]. For the excited states of second- and third-row transition metal compounds, spin is not a good quantum number [137]. The large metal center imparts significant spin–orbit coupling and emissive excited states generally possess both singlet and triplet character [137]. The nature of the injecting excited states for Ru^{II} compounds is discussed in the next section.

Table 3. Summary of electron transfer rate constants between sensitizer and semiconductor.

Sensitizer ^a	Semiconductor ^b	$k_{\text{inj}}^{\text{c}}/10^8 \text{ s}^{-1}$	$k_{\text{cr}}^{\text{c}}/10^8 \text{ s}^{-1}$	Technique ^d	Reference
Cresyl violet	SnO ₂	na	(0.62–1.58) × 10 ⁴	TA	175
Cresyl violet	TiO ₂	na	0.05	TA	176
9AC	TiO ₂ , anatase	≥ 10 ⁴	185	TA/TRANIP	177
9AC	TiO ₂ , anatase	> 5 × 10 ⁴	30	TA/TRANIP	178
9AC	TiO ₂ , amorphous	3.5 × 10 ⁴	18	TA/TRANIP	178
1AC	TiO ₂ , anatase	≥ 5 × 10 ⁴	56	TA/TRANIP	178
1AC	TiO ₂ , amorphous	6 × 10 ³	14	TA/TRANIP	178
2AC	TiO ₂ , anatase	≥ 5 × 10 ⁴	71	TA/TRANIP	178
2AC	TiO ₂ , amorphous	6 × 10 ³	18	TA/TRANIP	178
9AC	TiO ₂ , anatase		83–300	TA/TRANIP	179
Chlorophyll a, b	SnO ₂	>5		Microwave/ TRPL	180
Chlorophyll a	TiO ₂	3		TA	181
Copper chlorophyllin	TiO ₂	42		TA	182
Coumarin 343	TiO ₂ , anatase	5 × 10 ⁴	<100	TRPL	183
Coumarin 343	TiO ₂	8 × 10 ⁴	(30–6.67) × 10 ⁴	TR IR	184
Coumarin 343	TiO ₂	* 5 × 10 ⁹ M ⁻¹ s ⁻¹		FT-EPR	185
Eosin Y	TiO ₂	8.5	>0.002	TA	186
Eosin Y	TiO ₂	9.5		TA	187
Favonoid anthocyanin	TiO ₂	>10 ⁵	149, 1.92 × 10 ⁴	TRPL	188
Fluorescein 27	TiO ₂	3.3 × 10 ⁴	0.01–1000	TA	189
Fe(CN) ₆ ⁴⁻	TiO ₂	>2 × 10 ⁵	0.03–3330	TRIR/TA	190
Phenylfluorone	TiO ₂	>1	0.0028	TA	191
Perylene	TiO ₂ , anatase	5.26 × 10 ⁴		TRPL	192
Ru(dcb)(bpy) ₂ ²⁺	TiO ₂	1.0–5.5		TRPL	193
Ru(dcb)(bpy) ₂ ²⁺	TiO ₂	1–3		Microwave/ TRPL	194
Ru(dcb) ₂ (NCS) ₂	TiO ₂	>10 ⁵	0.1–1.43	TRIR	195
Ru(dcb) ₂ (NCS) ₂	TiO ₂	>10 ⁴	0.01–10	TA	196
Ru(deeb)(bpy) ₂ ²⁺	TiO ₂	>5 × 10 ²		TRIR	197
Ru(deeb)(dmb) ₂ ²⁺					
Rhodamine 6G	SnO ₂	5.5 × 10		TA	198

^a AC = anthracenecarboxylic acid; dmb = 4,4'-dimethyl 2,2'-bipyridine.^b There are variations in solvent, electrolyte and pH; see the reference for detail.^c Charge injection and charge recombination rate constants; for details about light source, light intensity, and excitation wavelength see the reference. The kinetic models used to obtain the rate constants varies; first-order, biexponential, multiexponential or second-order kinetic models are used; see references for detail. Listed units are not suitable for those who use second-order kinetic models.^d TA=transient absorption; TRANIP = time-resolved anisotropy; TRPL = time-resolved photoluminescence; TRIR = time-resolved IR; TR = EPR-time-resolved electron paramagnetic resonance spectroscopy.^e Units are μ⁻¹ s⁻¹.

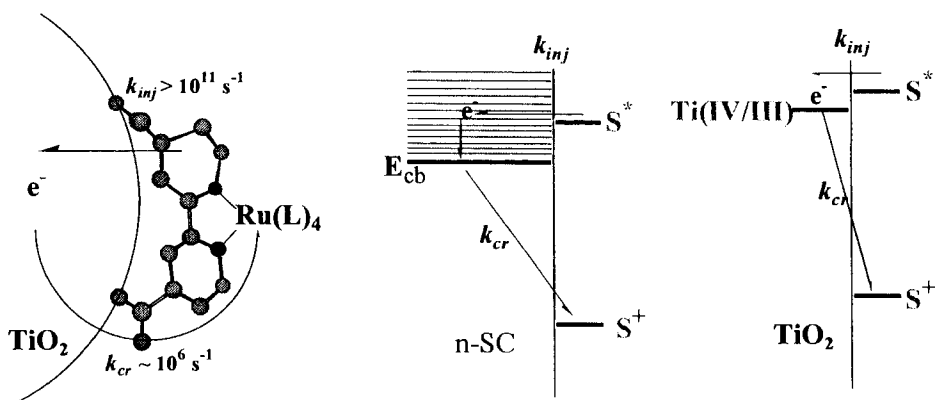


Figure 26. The middle and right hand figures show two possible acceptor states of TiO_2 for excited state electron injection. The right hand shows the apparent difference in rate constants for electron injection, k_{inj} , and charge recombination, k_{cr} , assuming first order kinetics.

Singlet and triplet excited state injection

Moser and Grätzel [186] described the dynamics of charge injection and recombination with eosin Y on $\sim 50 \text{ \AA}$ colloidal TiO_2 particles in aqueous solution. The triplet state of eosin decays with the same kinetics in free solution and when associated with TiO_2 , indicating that interfacial charge separation does not occur from the triplet state [186]. Rather, electron injection occurs from the singlet excited state. Time-resolved resonance Raman studies demonstrate the presence of the oxidized eosin and revealed significant surface-sensitizer interactions [199]. At pH 3, the quantum yield for charge separation was estimated to be 0.4 with rate constant $8.5 \times 10^8 \text{ s}^{-1}$. It was found that recovery of the oxidized eosin sensitizer, EO^+ , followed complex kinetics. Kinetic analysis with some assumptions yields a charge recombination rate of $2 \times 10^5 \text{ s}^{-1}$ and the mean lifetime of interfacial charge separated states is $\sim 5 \text{ \mu s}$. More recent picosecond studies have placed the charge separation rate at $k_{inj} = 9.5 \times 10^8 \text{ s}^{-1}$ [200].

Willig and co-workers time-resolved the rate of electron injection from a perylene derivative that contained a phosphonate functional group and two *tert*-butyl groups [192]. The phosphonate was used for binding to nanocrystalline TiO_2 thin films and the bulky organic groups were designed to prevent perylene association. A rough estimate of the excited-state donor levels of perylene relative to the E_{CB} indicated that the injection process should be activationless. Interfacial electron injection was probed with femtosecond resolution in ultra-high vacuum via transient absorption and fluorescence up-conversion techniques. Identical time constants were observed for the decay of the excited state and the formation of the oxidized perylene. A temperature-independent (300–22 K) 190 fs dominant fast rise time was measured, consistent with activationless electron injection.

Kamat and Patrick have shown that dynamic quenching by wide band-gap semiconductors does occur under some conditions [201]. Thionine was used to sensitize 20–40 \AA ZnO colloids. Both the ZnO particles and the thionine sensitizers were

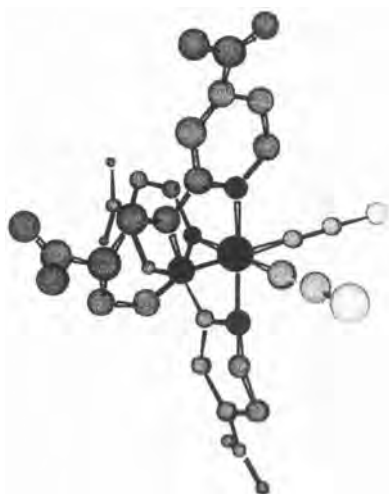


Figure 27. Chem 3-D minimized structure of *cis*-Ru(dcb)₂(NCS)₂. This sensitizer is referred to as N3 since it was the third dye prepared by Nazeeruddin.

positively charged, precluding significant ground-state interactions. Therefore, the luminescence and absorption properties of thionine were not significantly altered by exposure to ZnO. In contrast, the lifetime of the thionine triplet excited state decreased from 88 to 15 μ s as the concentration of ZnO colloid was increased and the appearance of the oxidized sensitizer demonstrated an electron transfer mechanism that proceeds with a quantum yield of 0.1. Grätzel and co-workers also concluded that copper 2- α -oxymesoisochlorin *e*₄ injects electrons into anatase TiO₂ thin films from the triplet state with a rate constant $k_{inj} = 3 \times 10^8 \text{ s}^{-1}$ [181].

'Hot' electron injection

Femtosecond absorption studies of *cis*-Ru(dcb)₂(NCS)₂ anchored to a mesoporous nanocrystalline TiO₂ thin films, shown schematically in Figure 27 and abbreviated *cis*-Ru(dcb)₂(NCS)₂-TiO₂, have recently been reported by several groups [195, 196, 202]. In these sensitized materials a direct electron transfer pathway from the Ru(II) metal center to the semiconductor is reasonably ruled out based on comparisons of the solution and semiconductor bound absorption spectra of *cis*-Ru(dcb)₂(NCS)₂ that are reported to be the same within experimental error. We note that direct charge transfer from inorganic sensitizers with ambidentate cyano ligands [127, 190, 203, 204] or organic chelates [205–207] is well known and the subject of intense research.

Durrant and co-workers performed ultra-fast interfacial electron injection studies with *cis*-Ru(dcb)₂(NCS)₂-TiO₂ in 1:1 ethylene carbonate–propylene carbonate solvent and were able to observe both the oxidized sensitizer and the electron in TiO₂ by time-resolved absorption spectroscopy [202]. Unfortunately, at long observation wavelengths, $\lambda = 650\text{--}900 \text{ nm}$, these absorption features overlapped with each other, making assignments and analysis difficult. Detailed analysis of the transient absorption data indicate that the electron injection process is at least bi-phasic with $\sim 50\%$ injecting in less than 150 fs and 50 % in 1.2 ps.

Willig and co-workers used near-infrared spectroscopy to measure excited-state interfacial electron transfer rates after pulsed light excitation of *cis*-Ru(dcb)₂(NCS)₂-TiO₂ in vacuum from 20 to 295 K [208]. They reported that excited-state electron injection occurred in less than 25 fs, prior to the redistribution of the excited-state vibrational energy, and that the classical Gerischer model for electron injection was inappropriate for this process. They concluded that the injection reaction is controlled by the electronic tunneling barrier and by the escape of the initially prepared wave packet describing the hot electron from the reaction distance of the oxidized dye molecule. It appears that some sensitizer decomposition occurred in these studies as the transient spectrum was reported to be similar to that of the thermal oxidation product of *cis*-Ru(dcb)₂(NCS)₂.

Lian and co-workers reported the femtosecond mid-IR properties of *cis*-Ru(dcb)₂(NCS)₂ in fluid ethanol solution and when anchored to nanocrystalline Al₂O₃ and TiO₂ thin films [195]. In this spectral window, the asymmetric and symmetric stretches of the thiocyanate ligands absorb strongly and serve as a marker for the ground, excited and oxidized states. In addition, the injected electron appears as a broad positive absorption band in this spectral range. Instrument response-limited excited-state formation, Ru^{III}(dcb⁻)(dcb)(NCS)*, was observed in ethanol. Excitation of *cis*-Ru(dcb)₂(NCS)₂-TiO₂ led to the appearance of a broad absorption assigned to the electron in TiO₂. The rise time was fitted to a biexponential model with a fast 50 ± 25 fs rate that comprised about 84 % of the signal and a slower 1.5 ± 0.5 ps component that accounted for the other 16 %. The fast component was assigned to the electron injection process. Because the signature of the slower component was sample dependent, its origin was less certain. These results were in general agreement with the previous studies by Durrant and co-workers. However, the results do not provide compelling evidence for injection from vibrationally hot excited states as suggested by Willig and co-workers.

Spectroscopic evidence for electron injection from ‘hot’ vibrational states came from the work of Moser and Grätzel [209]. They employed time-resolved absorption spectroscopy to quantify the injection yields of *cis*-Ru(dcb)₂(NCS)₂-TiO₂ and *cis*-Ru(dcb)₂(NCS)₂-Nb₂O₅ as a function of excitation wavelength. For TiO₂, the injection yield was found to be unity and independent of excitation wavelength within experimental error. In contrast, the quantum yield for injection on Nb₂O₅ dropped from 0.5 at 450 nm to ~0 at 640 nm. An alternative Ru^{II} sensitizer with a lower lying thexi state was found to give wavelength-dependent electron injection on anatase TiO₂. If injection occurred from the thexi state, the yield would be independent of excitation wavelength, contrary to what is observed. The authors concluded that injection occurs from a single state. Injection was modeled by Fermi’s Golden rule for non-adiabatic electron transfer:

$$k_{\text{inj}} = \frac{2\pi}{\hbar} |H|^2 \frac{1}{\hbar\omega} \quad (35)$$

By assuming $\omega = 1500 \text{ cm}^{-1}$ and an injection rate of $8 \times 10^{12} \text{ s}^{-1}$, an electronic coupling matrix element $H = 100 \text{ cm}^{-1}$ was estimated for injection from *cis*-Ru(dcb)₂(NCS)₂* to TiO₂.

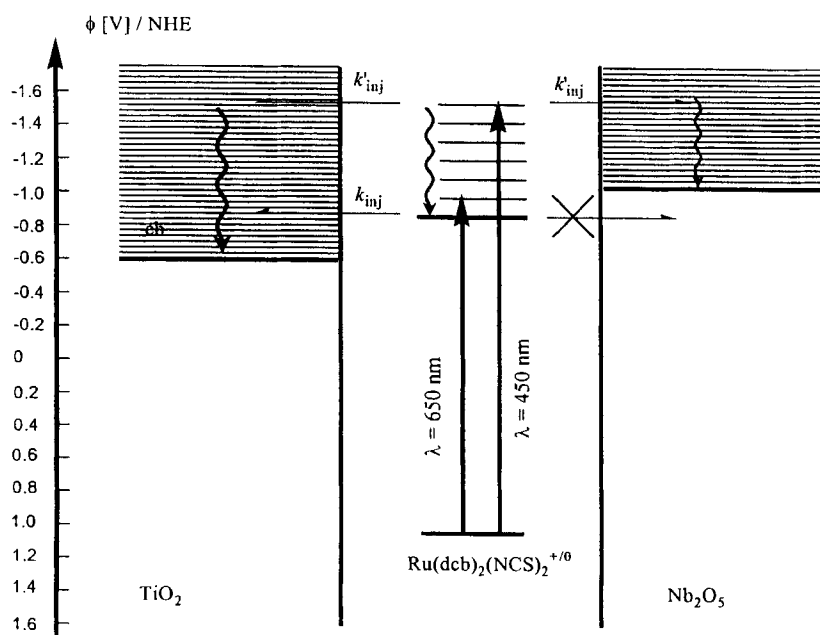


Figure 28. Strong evidence for hot interfacial electron injection. Nb_2O_5 has more negative conduction band edge and energetically requires a more potent reducing agent for electron injection. Blue light ($\lambda = 450 \text{ nm}$) excitation provides efficient sensitization of Nb_2O_5 while red light ($\lambda = 650 \text{ nm}$) does not.

The identification of electron injection as an ultra-fast process indicates that sensitizers with short excited-state lifetimes should be useful for energy conversion, provided that the transient spectroscopic data is at all relevant to the solar cell. Ferrere and Gregg have in fact reported sustained photocurrents from *cis*- $\text{Fe}(\text{dcb})_2(\text{CN})_2$ - TiO_2 thin films in regenerative solar cells [210]. By analogy with related iron polypyridyl compounds, this sensitizer's MLCT excited states are very short lived owing to rapid population of ligand field states. The fact that a sustained photocurrent is measured with this compound indicates that injection must also be very fast in the operational solar cell. A comparison of the solution absorption and photoaction spectra revealed evidence for preferential injection yields from 'upper' excited states as is shown in Figure 28 [210]. If 'hot' injection is commonplace in these materials, it is surprising that it does not manifest itself more often in photoaction spectra like this.

Manipulation of semiconductor-sensitizer energetics

Several reports have addressed how interfacial electron transfer rate constants vary with thermodynamic driving force. The driving force is tuned by manipulating the conduction band edge through adsorption of specific cations, utilizing different semiconductors, or by keeping the semiconductor constant with a series of sensitizers with known formal potentials. A difficulty in these studies is that the position

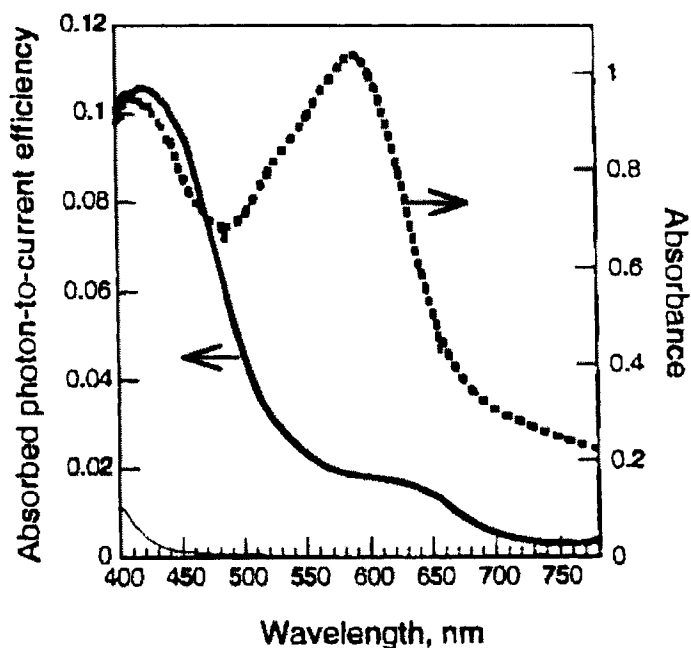


Figure 29. Absorption (solid line) and photoaction (dashed line) of *cis*-Fe(dcb)₂(CN)₂ adsorbed onto a nanocrystalline TiO₂ thin film.

of the band edges is not known precisely, nor are the formal potentials of the surface-bound sensitizers. One therefore hopes that solution electrochemical data translate directly to the sensitized interface so that trends and 'apparent' driving forces can be estimated [136]. These studies are important for the development of mechanistic descriptions of dye sensitization mechanisms and interfacial electron transfer.

Proton- and cation-induced shifts

Proton adsorption/desorption was utilized by Clark and Sutin to control electron injection yields and probe Gerisher's distributions at planar rutile electrodes. More recently, Grätzel and co-workers found that excited-state electron injection from tetrakis(4-carboxyphenyl)porphyrinato]Zn^{II} to colloidal TiO₂ particles was negligible at pH > 8 but increased substantially when the pH was lowered [211]. However, in this case it was difficult to rule out a trivial mechanism where the sensitizer simply desorbed from the surface at higher pH.

Yan and Hupp used nanosecond transient absorption to probe charge recombination after selective excitation of a hexaphosphonated Ru(bpy)₃²⁺ derivative bound to DeGussa TiO₂ as a function of pH [212]. They found that a fast first-order charge recombination process was insensitive to pH over 13 decades of H⁺ concentration. Assuming the sensitizer oxidation potential is independent of pH and

that electron transfer occurs from a TiO_2 donor state that displays the expected 59 mV per pH unit dependence, the driving force for charge recombination should have been varied by over 470 mV, yet there was no observed change in the measured rate constants. The authors suggested two possible explanations for this surprising lack of pH sensitivity. First, charge recombination occurred from a surface state with a pH-independent potential. Alternatively, proton-coupled back electron transfer occurred, where the rate-determining electron transfer preceded H^+ transfer, such that the kinetically relevant driving force was different from the overall reaction driving force. Based on previous work with sensitized rutile TiO_2 , it is surprising that the excited sensitizer injects electrons into TiO_2 over such a broad pH range and suggests that localized surface states play a key role.

Kelly et al. found that increasing the concentration of LiClO_4 in an acetonitrile electrolyte surrounding a *cis*- $\text{Ru}(\text{bpy})_2(\text{dcb})$ - TiO_2 film results in an enhancement of the interfacial electron injection yield [141]. Remarkably, the injection quantum yield could be reversibly controlled from below detection limits to near unity simply by varying the Li^+ concentration. Other alkali and alkaline earth metal cations were found to exhibit a similar effect, but at a magnitude related to the charge-to-radius ratio of the cation. The quantum yield for electron injection increased approximately with $\log[\text{Li}^+]$. The recombination of the injected electron with the oxidized sensitizer was fitted to a second-order kinetic model and the rate constants were independent of the Li^+ concentration. This Li^+ concentration range would correspond to an approximately 1 eV change in driving force based on spectroelectrochemical data (Table 2). However, there was no change in the measured rate constants or evidence for screening of the injected electron under these conditions.

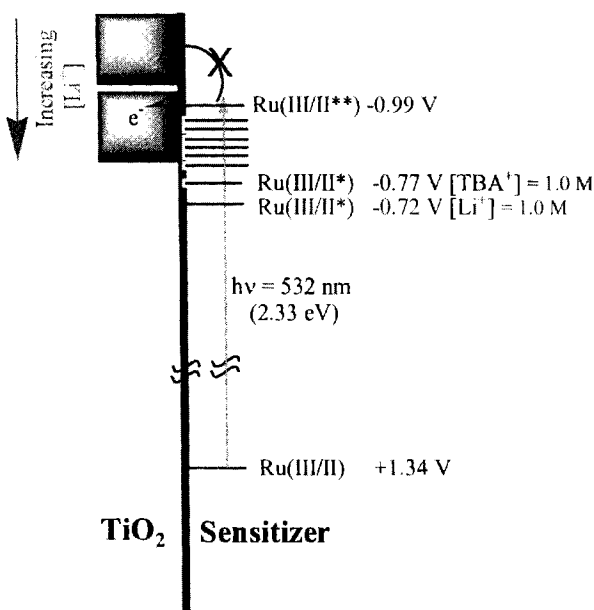


Figure 30. Proposed energy diagram showing the proposed mechanism for $[\text{Li}^+]$ enhancement of the injection yield for $\text{Ru}(\text{dcb})(\text{bpy})_2^{2+}/\text{TiO}_2$. Li^+ adsorption lowers the acceptor states of TiO_2 which results in energetically more favorable excited state injection.

Interestingly, the excited-state quenching with lithium cations was a static process [141]. If electron injection were occurring from the thexi state, one would expect the lifetime to decrease to $1/k_{\text{inj}}$, contrary to what was observed. One explanation is that only the sensitizers proximate to lithium adsorption sites are able to inject and surface heterogeneity underlies the largely static process. This explanation was not favored as efficient energy migration across the surface was known to occur and this same process should lead to sensitizers ‘finding’ an injection site. An alternative explanation is that the thexi state is thermodynamically unable to inject electrons. The conduction band edge position, estimated from spectroelectrochemical data in Table 2, is in fact midway between the Franck–Condon and the thexi states. Injection then is competitive with vibrational relaxation and the thexi state lifetime would not be quenched by electron injection as is observed. If this interpretation is correct it calls into question the common approach of using time-resolved photoluminescence data to estimate electron injection rate constants.

Qu et al. reported that *cis*-Ru(bpy)₂(ina)₂(PF₆)₂, where bpy is 2,2′-bipyridine and ina is isonicotinic acid, anchored to colloidal TiO₂ thin films displays injection yields that can be controlled with temperature and ionic strength [129]. The chromophoric bipyridine ligands do not bind directly to the semiconductor surface, so excited-state injection occurred by a remote process. The interfacial electron injection yields were measured by comparative actinometry. In 0.1 M LiClO₄–acetonitrile at 0 °C, the injection yield was unity, but decreased to 0.5 at room temperature. The injection quantum yield could be reversibly tuned between these extremes or to intermediate values by controlling the temperature. Photophysical properties of *cis*-Ru(bpy)₂(ina)₂(PF₆)₂ bound to TiO₂ and to insulating ZrO₂ samples led to the proposed excited-state deactivation routes shown in Figure 31.

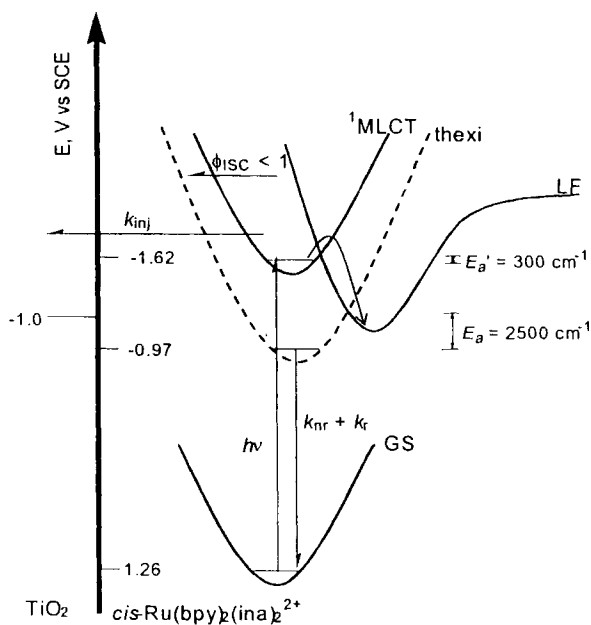


Figure 31. Jablonski type diagram invoked to rationalize the origin of temperature dependent injection quantum yield for *cis*-Ru(pby)₂(ina)₂²⁺ on TiO₂.

Temperature-dependent injection was attributed to a competitive population of low-lying state [thought to be a ligand field (LF) state] and the remote injection process. Regardless of the mechanism, the results demonstrate that sensitized electrodes can be fabricated for temperature-sensing applications.

Semiconductor-induced shifts

Fessenden and Kamat examined the photoluminescence and microwave conductivity properties of $\text{Ru}(\text{dcb})(\text{bpy})_2^{2+}$ anchored to colloidal ZnO , TiO_2 and SnO_2 films and estimated the electron injection rate constant from the data [194]. The energetics of the conduction band edge, E_{CB} , at pH 1 follows the trend $\text{SnO}_2 > \text{ZnO} > \text{TiO}_2$. PL decays at 650 nm were modeled as a biexponential decay, with an approximate order of magnitude difference between the fast and slow rates. Following selective excitation of the sensitizers, direct evidence for electron injection came from an absorption growth in the microwave region assigned to conduction band electrons. For SnO_2 and ZnO , the microwave kinetics agreed well with the electron injection rates from PL quenching measurements. The electron transfer rates calculated from these data, $k_{\text{inj}} = (1-3) \times 10^8 \text{ s}^{-1}$, showed an interesting correlation with the energy difference between the sensitizer excited-state oxidation potential and the energy of the semiconductor conduction band edge, ΔE (Figure 32). The rate was found to increase with ΔE . A similar behavior had previously been observed for $\text{Ru}(\text{bpy})_3^{2+}$ adsorbed in semiconductor powders [213]. In fact, the raw experimental data reflect this and the larger is ΔE the faster the PL decays to baseline. An implication of these observations, and one possible interpretation, is that the semiconductor density of unfilled states increases significantly at more negative potentials (closer to the vacuum level) resulting in better overlap with the excited sensitizer donor levels.

Charge recombination

Hupp and co-workers [214] studied interfacial charge recombination as a function of the driving force in considerable detail. Early work focused on ferrous cyano

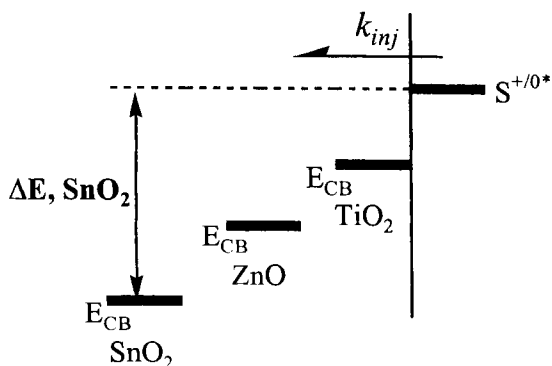


Figure 32. The relative energetic positions of semiconductor conduction band edges, E_{CB} , for SnO_2 , ZnO , and TiO_2 relative to a sensitizer excited state, S^* . ΔE is the apparent energy separation between the conduction band edge and the excited state sensitizers' reduction potential.

compounds bound to TiO_2 colloids through the ambidentate cyanide ligands. This interaction gives rise to direct interfacial intervalence charge-transfer bands in the visible region, i.e., $\text{Fe}^{\text{II}}-\text{CN}-\text{Ti}^{\text{IV}} \rightarrow \text{Fe}^{\text{III}}-\text{CN}-\text{Ti}^{\text{III}}$. A series of $\text{Fe}(\text{CN})_5\text{X}^{n-}$ compounds were prepared with known $\text{Fe}^{\text{III/II}}$ potentials [214]. The first-order rate constant for charge recombination was quantified by nanosecond absorption spectroscopy and found to decrease with increased driving force, thereby providing strong evidence for Marcus inverted kinetic behavior.

More recently, Dang and Hupp reported charge recombination studies for ruthenium tris(polypyridine) compounds electrostatically bound to tin oxide colloids [215]. Again, inverted behavior was observed and charge recombination rate constants decreased with driving force. Back electron transfer was also shown to be thermally activated consistent with the contention that variations in the Franck–Condon factors, and not the electronic coupling, are responsible for the inverted behavior. Hartland and co-workers also concluded that back electron transfer from TiO_2 colloids to oxidized anthracene isomers was inverted [178]. However, the inverted behavior stands in apparent conflict with the pH studies described above and other driving force studies performed at sensitized TiO_2 interfaces in water. Dang and Hupp speculated that this difference arises from localized $\text{Ti}^{\text{III/IV}}$ behavior and sequential electron transfer–proton transfer reaction sequences.

Moser and Grätzel reported temperature-dependent data for charge recombination from colloidal anatase TiO_2 particles to the cation radicals of three different sensitizers, alizarin, a merocyanin dye and a coumarin dye [216]. Although these reactions were believed to fall deep into the Marcus inverted region, they showed practically no activation energy. The largest temperature dependence was observed for alizarin, which showed an increase by only about a factor of 10 over a 200°C temperature change. The results were interpreted in terms of a quantum mechanical model for nonadiabatic electron transfer.

Hasselmann and Meyer prepared a series of Re^{I} coordination compounds, *fac*- $\text{Re}(\text{deeb})(\text{CO})_3(\text{X})$, where (deeb) is 4,4'-(COOEt)₂-2,2'-bipyridine and X is I^- , Br^- , Cl^- or CN^- , and [*fac*- $\text{Re}(\text{deeb})(\text{CO})_3(\text{py})$](OTf), where OTf^- is triflate anion and py is pyridine, specifically to probe charge recombination kinetics in colloidal TiO_2 films in 1.0 M LiClO_4 –acetonitrile solution at 22°C [217]. Recombination of the electron in TiO_2 with the oxidized sensitizer required milliseconds for completion and was quantified on a 10^{-7} – 10^{-3} s time-scale. Charge recombination kinetic rate constants were insensitive to an ~ 960 mV change in the apparent driving force, the sensitizer molecular geometry, the identity of the metal (Re, Ru or Os) and the number of carboxylic acid groups (two or four) present. The insensitivity to these factors suggested that interfacial electron transfer was not rate limiting. The authors speculated that charge recombination was limited by diffusional encounters of the injected electron and oxidized sensitizer under these conditions [217].

Effects of applied potential

The first transient absorption measurements of dye-sensitized nanocrystalline thin films under an external bias were carried out by O'Regan et al. [112]. These authors

followed the absorbance change at 480 nm following nanosecond pulsed excitation of Ru(dcb)_3^{2+} - TiO_2 films immersed in aqueous 0.2 M LiClO_4 at pH 3. The film was externally biased over the range -0.8 to 0.6 V vs. SCE. At negative applied bias, the excited state was found to luminesce strongly and current generation was near zero. Positively biasing the electrode resulted in quenching of the luminescence and optimized photocurrent generation. Transient absorption measurements over the potential range examined demonstrated a rapid loss of the Ru^{II} precursor that could not be time resolved from the laser pulse. The rapid formation of the transient signal was attributed to electron injection, $k_{\text{inj}} > 10^8 \text{ s}^{-1}$. At -0.45 V vs. SCE, the recovery of the ground state proceeds with a rate constant of $1.5 \times 10^6 \text{ s}^{-1}$, similar to that for excited-state decay of the complex in solution.

Kamat and co-workers studied electron injection following excitation of $\text{Ru(bpy)}_2(\text{dcb})^{2+}$ on SnO_2 thin films with an applied external bias [218]. Positive biasing results in quenching of the PL and improved photocurrent responses in functional solar cells. For negatively biased films, the low photocurrent may be due to either enhanced charge recombination following electron injection or decreased electron injection yields. The former would likely result in little change in the excited-state lifetime as the film is biased negative. In contrast, they observed longer excited-state lifetimes at negative bias, leading them to conclude that the applied bias controls the electron injection yield. The electron injection rate constant was estimated from a comparison of the emission decay rates for $^*\text{Ru(bpy)}_2(\text{dcb})^{2+}$ on SiO_2 (no injection) and SnO_2 at an applied potential of 0.6 V vs. Ag/AgCl , yielding 4.25×10^8 and $1.7 \times 10^7 \text{ s}^{-1}$ based on a biexponential fit. Transient absorbance measurements were used to estimate the yield of excited-state and oxidized complex. Based on the yield of oxidized sensitizer, with some assumptions, the electron injection rate increased with positive applied potential from -0.6 to 0.4 V vs. Ag/AgCl , reaching a plateau value of $4 \times 10^8 \text{ s}^{-1}$. The rate constant obtained from transient absorbance measurements, the fast component of the time-resolved photoluminescence experiments and previously reported transient microwave conductivity measurements were all in agreement.

It is surprising that Kamat, O'Regan and co-workers found a decreased injection yield at potentials near the flat-band condition. In the standard Gerischer model for sensitized planar electrodes, the low photocurrent near the flat band results because the injected carriers rapidly recombine with the oxidized sensitizer owing to the lack of a substantial depletion layer. Gerischer theory would not predict a decreased injection yield near the flat band, but this behavior can clearly be realized at sensitized nanocrystalline semiconductor films.

Durrant and co-workers reported time-resolved absorption studies of *cis*- $\text{Ru(dcb)}_2(\text{NCS})_2$ - TiO_2 at negative applied potentials [202]. In contrast to the previous studies, they did not report a change in injection quantum yield at negative potentials when compared with open-circuit or positive applied potentials. A significant increase in the charge recombination rate was observed when the semiconductor film was electrochemically reduced. Since light produces one injected electron and one oxidized sensitizer charge, recombination should formally follow a second-order equal concentration kinetic model, i.e. $[\text{Ru}^{3+}][\text{TiO}_2(\text{e}^-)]$. By electrochemically generating $\text{TiO}_2(\text{e}^-)$ the recombination rate increased substantially as expected.

2.3 Conclusions

Dye sensitization of electrodes is an old area of science with a rich history. The field has experienced renewed interest owing to the development of high surface area colloidal semiconductor electrodes. These materials yield impressive solar conversion efficiencies when employed in regenerative solar cells that have already found niche applications and have the real possibility of replacing traditional solid-state photovoltaics. Thus for the first time in history a solar cell designed to operate on a molecular level is useful from a practical point of view. It is also likely that other applications in the growing areas of molecular photonic materials will arise.

The long effective pathlength and high surface area afforded by these colloidal semiconductor materials allow spectroscopic characterization of interfacial electron transfer in molecular detail that was not previously possible. It is likely that within the next decade photoinduced interfacial electron transfer will be understood in the same detail now found only in homogeneous fluid solution. In many cases the sensitization mechanisms and theory developed for planar electrodes⁴ are not applicable to the sensitized nanocrystalline films. Therefore, new models are necessary to describe the fascinating optical and electronic behavior of these materials. One such behavior is the recent identification of ultra-fast 'hot' injection from molecular excited states. Furthermore, with these sensitized electrodes it is possible to probe ultra-fast processes using simple steady-state photocurrent action spectrum.

Figure 33 shows a Gerischer-like diagram which summarizes the kinetic processes that can be initiated with light excitation of a dye-sensitized nanocrystalline anatase

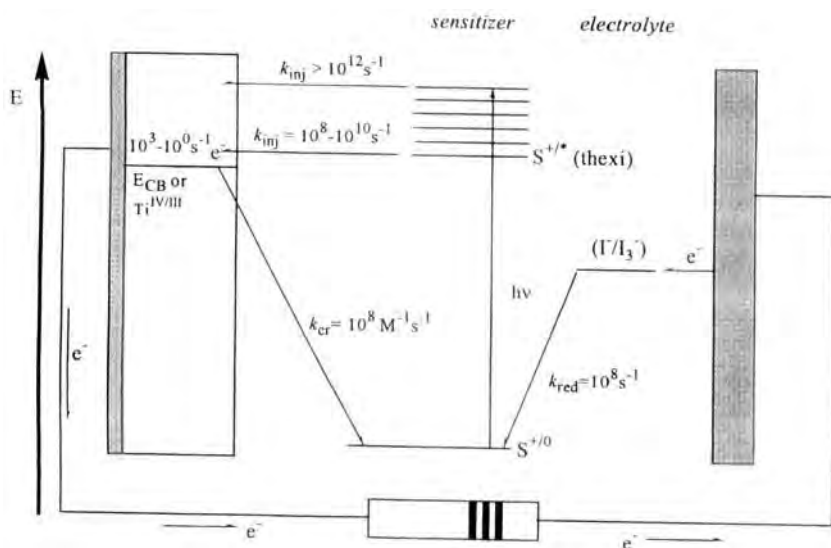


Figure 33. Gerischer-like diagram that summarizes the kinetic rate constants measured experimentally upon light excitation of a dye sensitized nanocrystalline TiO₂ (anatase) film.

film [119]. Injection from hot vibrational excited states occurs under some conditions, but injection from thermally equilibrated excited states (thexi) also has precedence. For some sensitizers, vibrational relaxation competes kinetically with electron injection and for other sensitizers injection from thexi states also occurs. Once injected, the electrons diffuse through the colloidal films on a slow millisecond to second time-scale. Carrier transport appears to involve the thermally activated hopping of electrons between trap sites. In the absence of iodide, charge recombination typically requires milliseconds for completion.

Details of this diagram, such as the nature of the redox-active states in the semiconductor, remain unknown. These and other important issues represent formidable challenges for experimentalists and theorists studying these and future generations of dye-sensitized electrodes.

Acknowledgments

The National Science Foundation (CHE-9322559, CHE-9402935) and the Division of Chemical Sciences, Office of Basic Energy Sciences, Office of Energy Research, US Department of Energy are gratefully acknowledged for research support.

References

1. Braslavsky, S. E.; Houk, K. N. *Pure Appl. Chem.* **1988**, *60*, 1055.
2. McEvoy, A. J.; Gratzel, M. *Sol. Energy Mater. Sol. Cells* **1994**, *32*, 221.
3. Moser, J. *Montash. Chem.* **1887**, *8*, 373.
4. Gerischer, H. *Photochem. Photobiol.* **1972**, *16*, 243.
5. Gerischer, H. *Pure Appl. Chem.* **1980**, *52*, 2649.
6. Gerischer, H.; Willig, F. *Top. Curr. Chem.* **1976**, *61*, 31.
7. Bard, A. J.; Faulkner, L. R. *Electrochemical Methods: Fundamentals and Applications*. Wiley, New York, **1980**.
8. Rehm, D.; Weller, A. *Isr. J. Chem.* **1970**, *8*, 259.
9. Turro, N. J. *Modern Molecular Photochemistry*, Benjamin/Cummings, Menlo Park, CA, **1978**.
10. Birks, J. B. *Photophysics of Aromatic Molecules*, Wiley, London, **1970**, p. 258.
11. Kittel, C. *Introduction to Solid State Physics*, 6th edn., Wiley, New York, **1986**.
12. Sze, S. M. *Physics of Semiconductor Devices*, Wiley, New York, **1981**.
13. Bard, A. J.; Boarsly, A. B.; Fan F.-R. F.; Walton, E. G.; Wrighton, M. S. *J. Am. Chem. Soc.* **1980**, *102*, 3671.
14. Macdonald, J. R. *Impedance Spectroscopy: Emphasizing Solid Materials and Systems*. Wiley, New York, **1987**.
15. Gomes, W. P.; Cardon, F. *Prog. Surf. Sci.* **1982**, *12*, 155.
16. Schmickler, W. *Interfacial Electrochemistry*, Oxford University Press, New York, **1996**.
17. Vanden Berghe, R. A. L.; Cardon, F.; Gomes, W. P. *Surf. Sci.* **1973**, *39*, 368.
18. Morrison, S. R. *Surf. Sci.* **1969**, *15*, 363.
19. Memming, R. *Top. Curr. Chem.* **1988**, *143*, 81.
20. Chance, R. R.; Prock, A.; Sibley, R. *Adv. Chem. Phys.* **1978**, *37*, 1, and references cited therein.
21. (a) Rossetti, R.; Brus, L. E. *J. Chem. Phys.* **1982**, *76*, 1146; (b) Campion, A.; Gallo, A. R.; Harris, C. B.; Robota, H. J.; Whitmore, P. M. *Chem. Phys. Lett.* **1980**, *73*, 447.

22. Albery, W. J. *Acc. Chem. Res.* **1982**, *15*, 142.
23. Gomer, R. *Electrochim. Acta* **1975**, *20*, 13.
24. Gale, R. J. *Spectroelectrochemistry Theory and Practice*, Plenum Press, New York, **1988**.
25. Memming, R.; Tributsch, H. *J. Phys. Chem.* **1971**, *75*, 562.
26. Spitler, M. T. *J. Electroanal. Chem.* **1987**, *228*, 69.
27. Gratzel, M. in *Future Generation Photovoltaic Technologies* (Ed. McConnell, R.D.), AIP Conference Proceedings 404, **1997**, p. 119.
28. Gartner, W.W. *Phys. Rev.* **1959**, *116*, 84.
29. Butler, M. A. *J. Appl. Phys.* **1977**, *48*, 1914.
30. Reiss, H. *J. Electrochem. Soc.* **1978**, *125*, 937.
31. Wilson, R. H. *J. Appl. Phys.* **1977**, *48*, 4292.
32. Hanemann, D.; McCann, J. F. *Phys. Rev. B* **1982**, *25*, 1241.
33. Sheppard, N.; Willis, H.A.; Rigg, J.C. *Pure Appl. Chem.* **1985**, *57*, 105.
34. Peter, L. M. *Chem. Rev.* **1990**, *90*, 753.
35. Dahnke, K. F.; Fratoni, Jr., S. S.; Perone, S. P. *Anal. Chem.* **1976**, *48*, 296.
36. (a) Harzion, Z.; Croitoru, N.; Gottesfeld, S. *J. Electrochem. Soc.* **1981**, *128*, 551; (b) Gottesfeld, S.; Feldberg, S. W. *J. Electroanal. Chem.* **1983**, *146*, 47.
37. Bitterling, K.; Willig, F. *J. Electroanal. Chem.* **1986**, *204*, 211.
38. Lin, C.-T.; Sutin, N. *J. Phys. Chem.* **1976**, *80*, 97.
39. (a) Osif, T. L.; Lichtin, N. N.; Hoffman, M. Z. *J. Phys. Chem.* **1978**, *82*, 1778; (b) Hall, D. E.; Eckert, J. A.; Lichtin, N. N.; Wildes, P. D. *J. Electrochem. Soc.* **1976**, *123*, 1705; (c) Hall, D. E.; Clark, W. D. K.; Eckert, J. A.; Lichtin, N. N.; Wildes, P. D. *Ceram. Bull.* **1977**, *56*, 408.
40. (a) Fong, F.K.; Winograd, N. *J. Am. Chem. Soc.* **1976**, *98*, 2287; (b) Fong, F.K.; Polles, J.S.; Galloway, L.; Fruge, D.R. *J. Am. Chem. Soc.* **1977**, *99*, 5802; (c) Fong, F.K.; Galloway, L. *J. Am. Chem. Soc.* **1978**, *100*, 3594.
41. (a) Lichtin, N. N.; Bolton, J. R. (Eds.), *Solar Power and Fuels*, Academic Press, New York, **1977**; (b) Janzen, A. F.; Bolton, J. R. *J. Am. Chem. Soc.* **1979**, *101*, 6342.
42. (a) Seta, P.; Bienvenue, E.; Moore, A. L.; Mathis, P.; Bensason, R. V.; Liddell, P. A.; Pessiki, P. J.; Joy, A.; Moore, T. A.; Gust, D. *Nature* **1985**, *316*, 653; (b) Steinberg-Yfrach, G.; Liddell, P. A.; Hung, S.-C.; Moore, A. L.; Gust, D.; Moore, T. A. *Nature* **1997**, *385*, 239; (c) Steinberg-Yfrach, G.; Rigaud, J.-L.; Durantini, E. N.; Moore, A. L.; Gust, D.; Moore, T. A. *Nature* **1998**, *392*, 479.
43. Uosaki, K.; Kondo, T.; Zhang X.-Q.; Yanagida, M. *J. Am. Chem. Soc.* **1997**, *119*, 8367.
44. Imahori, H.; Sakata, Y. *Eur. J. Org. Chem.* **1999**, 2445.
45. Imahori, H.; Yamada, H.; Ozawa, S.; Ushida, K.; Sakata, Y. *Chem. Commun.* **1999**, 1165.
46. Biesmans, G.; Van der Auweraer, M.; Cathy, C.; Meerschaut, D.; De Schryver, F. C.; Storck, W.; Willig, F. *J. Phys. Chem.* **1991**, *95*, 3771.
47. (a) Möbius, D. in *Topics in Surface Chemistry*, IBM Research Symposia Series, Sept. 7–9, (Ed. Kay, E.), Plenum Press, New York, **1978**; (b) Kuhn, H.; Möbius, D.; Bücher, H. in *Physical Methods of Chemistry, Part IIIB* (Eds. Weissberger, A.; Rossiter, B. W.), Wiley-Interscience, New York, **1972**; (c) Kuhn, H.; Möbius, D. *Angew. Chem.* **1971**, *10*, 620.
48. Liang, K.; Law, K.-Y.; Whitten, D. G. *J. Phys. Chem. B* **1997**, *101*, 540.
49. (a) Arden, W.; Fromherz, P. *Ber. Bunsenges. Phys. Chem.* **1978**, *82*, 868; (b) Arden, W.; Fromherz, P. *J. Electrochem. Soc.* **1980**, *127*, 370.
50. Liang, Y.; Moy, P. F.; Poole, J. A.; Ponte Goncalves, A. M. *J. Phys. Chem.* **1984**, *88*, 2451.
51. Liang, Y.; Ponte Goncalves, A. M. *J. Phys. Chem.* **1985**, *89*, 3290.
52. (a) Watanabe, T.; Fujishima, A.; Tatsvoki, O.; Honda, K. *Bull. Chem. Soc. Jpn.* **1976**, *49*, 8; (b) Nakao, M.; Itoh, K.; Honda, K. *J. Phys. Chem.* **1984**, *88*, 4906; (c) Nakao, M.; Itoh, K.; Watanabe, T. *Ber. Bunsenges. Phys. Chem.* **1985**, *89*, 134.
53. Spitler, M.; Calvin, M. *J. Chem. Phys.* **1977**, *67*, 5193.
54. Itoh, K.; Chiyokawa, Y.; Nakao, M.; Honda, K. *J. Am. Chem. Soc.* **1984**, *106*, 1620.
55. Fujihira, M.; Osa, T.; Hirsch, D.; Kuwana, T. *J. Electroanal. Chem.* **1978**, *88*, 285.
56. Osa, T.; Fujihira, M. *Nature* **1976**, *264*, 349.
57. Fox, M.A.; Nobs, F.J.; Voynick, T.A. *J. Am. Chem. Soc.* **1980**, *102*, 4036.
58. Gleria, M.; Memming, R. *Z. Phys. Chem. (Munich)* **1975**, *98*, 303.

59. Memming, R.; Schröppel, F.; Bringmann, U. *J. Electroanal. Chem.* **1979**, *100*, 307.
60. Memming, R. *Surf. Sci.* **1980**, *101*, 551.
61. Memming, R.; Schröppel, F. *Chem. Phys. Lett.* **1979**, *62*, 207.
62. Kirsch-De Mesmaeker, A.; Nasielski, J.; Willen, R. *Bull. Soc. Chim. Belg.* **1982**, *91*, 731.
63. Clark, W.D.K.; Sutin, N. I. *J. Am. Chem. Soc.* **1997**, *99*, 4676.
64. Ghosh, P. K.; Spiro, T. G. *J. Am. Chem. Soc.* **1980**, *102*, 5543.
65. Krishnan, M.; Zhang, X.; Bard, A. J. *J. Am. Chem. Soc.* **1984**, *106*, 7371.
66. (a) Anderson, S.; Constable, E. C.; Dare-Edwards, M. P.; Goodenough, J. B.; Hamnett, A.; Seddon, K. R.; Wright, R. D. *Nature* **1979**, *280*, 571; (b) Dare-Edwards, M. P.; Goodenough, J. B.; Hamnett, A.; Seddon, K. R.; Wright, R. D. *Faraday Discuss. Chem. Soc.* **1980**, *70*, 285.
67. Goodenough, J. B.; Hamnett, A.; Dare-Edwards, M. P.; Campet, G.; Wright, R. D. *Surf. Sci.* **1980**, *101*, 531.
68. Gulino, P. A.; Drizkamer, H. G. *J. Phys. Chem.* **1984**, *85*, 1173.
69. (a) Natoli, L.M.; Ryan, M.A.; Spitler, M. T. *J. Phys. Chem.* **1985**, *89*, 1453; (b) Sonntag, L.P.; Spitler, M. T. *J. Phys. Chem.* **1985**, *89*, 1453.
70. Harima, Y.; Yamashita, K. *J. Phys. Chem.* **1985**, *89*, 5325.
71. Spitler, M. T.; Calvin, M. *J. Chem. Phys.* **1977**, *64*, 4296.
72. Chamberlain, G. A.; Cooney, P. J. *Nature* **1979**, *289*, 45.
73. Harrison, S. E. *J. Chem. Phys.* **1969**, *50*, 4739.
74. Fujishima, A.; Honda, K. *Nature* **1972**, *238*, 37.
75. Creutz, C.; Sutin, N. *Proc. Natl. Acad. Sci. USA* **1975**, *72*, 2858.
76. (a) Daifuku, H.; Aoki, K.; Tokuda, K.; Matsuda, H. *J. Electroanal. Chem.* **1982**, *140*, 179; (b) Daifuku, H.; Aoki, K.; Tokuda, K.; Matsuda, H. *J. Electroanal. Chem.* **1985**, *183*, 1.
77. Finklea, H. O. *Semiconductor Electrodes*, Elsevier, New York, **1988**, p. 55.
78. Kirsch-De Mesmaeker, A.; Rochus-Dewitt, M.; Nasielski, J. *J. Phys. Chem.* **1986**, *90*, 6657.
79. Karlsson, K.; Kirsch-De Mesmaeker, A. *J. Phys. Chem.* **1991**, *95*, 10681.
80. Frippiat, A.; Kirsch-De Mesmaeker, A. *J. Phys. Chem.* **1985**, *89*, 1285.
81. Frippiat, A.; Kirsch-De Mesmaeker, A. *J. Electrochem. Soc.* **1987**, *134*, 66.
82. Ortmans, I.; Moucheron, C.; Kirsch-De Mesmaeker, A. *Coord. Chem. Rev.* **1998**, *168*, 233.
83. Thompson, D.W.; Kelly, C.A.; Farzad, F.; Meyer, G.J. *Langmuir* **1999**, *15*, 650.
84. Ginley, D. S.; Knotek, M. L. *J. Electrochem. Soc.* **1979**, *126*, 2163.
85. Grant, F. A. *Rev. Mod. Phys.* **1959**, *31*, 646.
86. Monnier, A.; Augustynski, J.; Stalder, C. *J. Electroanal. Chem.* **1980**, *112*, 383.
87. Tinnemans, A. H. A.; Koster, T. P. M.; Thewissen, D. H. M. W.; DeKreuk, C. W.; Mackor, A. *J. Electroanal. Chem.* **1983**, *145*, 457.
88. Augustynski, J. *J. Electroanal. Chem.* **1983**, *145*, 457.
89. Lanzafame, J. M.; Miller, R. J. D.; Muentner, A. A.; Parkinson, B. A. *J. Phys. Chem.* **1992**, *96*, 2820.
90. Willig, F.; Eichberger, R.; Sundaresan, N. S.; Parkinson, B. A. *J. Am. Chem. Soc.* **1990**, *112*, 2702.
91. Spitler, M.; Parkinson, B. A. *Langmuir* **1986**, *2*, 549.
92. Parkinson, B. A. *Langmuir* **1988**, *4*, 967.
93. Eichberger, R.; Willig, F. *Chem. Phys.* **1990**, *141*, 159.
94. Pope, M.; Swenberg, C. E. *Electronic Processes in Organic Solids*, Oxford University Press, New York, **1982**.
95. Simon, J.; Andre, J.-J. *Molecular Semiconductors*, Springer, Berlin, **1985**.
96. Gutman, F.; Lyons, L. E. *Organic Semiconductors, Parts A and B*, Krieger, Malabar, FL, **1981**.
97. Tang, C. W.; Albrecht, A. C. *J. Chem. Phys.* **1975**, *62*, 2139.
98. Tang, C. W.; Albrecht, A. C. *J. Chem. Phys.* **1975**, *63*, 953.
99. Tang, C. W. *Appl. Phys. Lett.* **1986**, *44*, 183.
100. Morel, D. L.; Ghosh, A. K.; Feng, T.; Stogryn, E. L.; Purwin, P. E.; Shaw, R. F.; Fishman, C. *Appl. Phys. Lett.* **1978**, *32*, 495.
101. Forrest, S.R.; Leu, L.Y.; So, F.F.; Yoon, W.Y. *J. Appl. Phys.* **1989**, *183*, 307.
102. Arbour, C.; Armstrong, N.R.; Brina, R.; Collins, G.; Danzinger, J.; Dodelet, J.-P.; Lee, P.; Nebesny, K.W.; Pankow, J.; Waite, S. *Mol. Cryst. Liq. Cryst.* **1990**, *183*, 307.

103. Hiramato, M.; Fukusumi, H.; Yokoyama, M. *Appl. Phys. Lett.* **1992**, *61*, 2580.
104. Jaeger, C.D.; Fan, F.-R.; Bard, A. J. *J. Am. Chem. Soc.* **1980**, *102*, 2592.
105. Giraudeau, A.; Fan, F.-R. F.; Bard, A. J. *J. Am. Chem. Soc.* **1980**, *102*, 5137.
106. Leempoel, P.; Castro-Acuna, M.; Fan, F.-R. F.; Bard, A. J. *J. Phys. Chem.* **1982**, *86*, 1396.
107. Leempoel, P.; Fan, F.-R. F.; Bard, A. J. *J. Phys. Chem.* **1983**, *87*, 2948.
108. Liu, C.-Y.; Pan, H.-I.; Fox, M. A.; Bard, A. J. *Science* **1993**, *261*, 887.
109. Gregg, B.A.; Fox, M.A.; Bard, A.J. *J. Phys. Chem.* **1990**, *94*, 1586.
110. Gregg, B.A.; Fox, M.A.; Bard, A.J. *Mater. Res. Soc. Symp. Proc.* **1990**, *173*, 199.
111. Gregg, B.A.; Kim, Y.I. *J. Phys. Chem.* **1994**, *98*, 2412.
112. O'Regan, B.; Moser, J.; Anderson, M.; Grätzel, M. *J. Phys. Chem.* **1990**, *94*, 8720.
113. O'Regan, B.; Grätzel, M. *Nature* **1991**, *353*, 737.
114. (a) Bedja, I.; Hotchandani, S.; Kamat, P. V. *J. Phys. Chem.* **1994**, *98*, 4133; (b) Nasr, C.; Hotchandani, S.; Kamat, P. V. *J. Phys. Chem. B* **1998**, *102*, 4944.
115. Björkstén, U.; Moser, J.; Grätzel, M. *Chem. Mater.* **1994**, *6*, 858.
116. Vogel, R.; Hoyer, P.; Weller, H. *J. Phys. Chem.* **1994**, *98*, 3183.
117. (a) Sakohara, S.; Tikanen, L. D.; Anderson, M. A. *J. Phys. Chem.* **1992**, *96*, 11086; (b) Redmond, G.; O'Keefe, A.; Burgess, C.; MacHale, C.; Fitzmaurice, D. *J. Phys. Chem.* **1993**, *97*, 11081; (c) Spanhel, L.; Anderson, M. A. *J. Am. Chem. Soc.* **1990**, *112*, 2278; (d) Rensmo, H.; Keis, K.; Lindström, H.; Södergren, S.; Solbrand, A.; Hagfeldt, A.; Lindquist, S.-E. *J. Phys. Chem. B* **1997**, 2598.
118. Brinker, C. J.; Scherer, G. W. *Sol-Gel Science: the Physics and Chemistry of Sol-Gel Processing*, Academic Press, San Diego, CA, **1990**.
119. Hagfeldt, A.; Grätzel, M. *Chem. Rev.* **1995**, *95*, 49.
120. Könenkamp, R.; Henninger, R.; Hoyer, R. *J. Phys. Chem.* **1993**, *97*, 7328.
121. (a) Brus, L. E. *J. Chem. Phys.* **1984**, *80*, 4403; (b) Brus, L. E. *J. Chem. Phys.* **1983**, *79*, 5566.
122. Péchy, P.; Rotzinger, F. P.; Nazeeruddin, M. K.; Kohle, O.; Zakeeruddin, S. M.; Humphry-Baker, R.; Grätzel, M. *J. Chem. Soc., Chem. Commun.* **1995**, 65.
123. Heimer, T.; D'Arcangelis, S. T.; Farzad, F.; Stipkala, J. M.; Meyer, G. J. *Inorg. Chem.* **1996**, *35*, 5319.
124. Zou, C.; Wrighton, M. S. *J. Am. Chem. Soc.* **1990**, *112*, 7578.
125. Vrachnou, E.; Grätzel, M.; McEvoy, A. J. *J. Electroanal. Chem.* **1989**, 258, 193.
126. Umphathy, S.; Cartner, A.M.; Parker, A.W.; Hester, R.E. *J. Phys. Chem.* **1990**, *94*, 1357.
127. Finnie, K.S.; Bartlett, J.R.; Woolfrey, J.L. *Langmuir* **1998**, *14*, 2744.
128. Argazzi, R.; Bignozzi, C.A.; Heimer, T.A.; Castellano, F.N.; Meyer, G.J. *Inorg. Chem.* **1994**, *33*, 5741.
129. Qu, P.; Meyer, G. J. *Langmuir* **2000**, *16*, 4662–4671.
130. Deacon, G. B.; Phillips, R. J. *Coord. Chem. Rev.* **1980**, *33*, 227.
131. Nazeeruddin, M. K.; Liska, P.; Moser, J.; Vlachopoulos, N.; Grätzel, M. *Helv. Chim. Acta* **1990**, *73*, 1788.
132. (a) Meyer, T. J.; Meyer, G. J.; Pfenning, B.; Schoonover, J. R.; Timpson, C.; Wall, J. F.; Kobusch, C.; Chen, X.; Peek, B. M.; Wall, C. G.; Ou, W.; Erickson, B. W.; Bignozzi, C. A. *Inorg. Chem.* **1994**, *33*, 3952; (b) Heimer, T. A.; Meyer, G. J. *Proc. Electrochem. Soc.* **1995**, *121*, 141.
133. (a) Wolfbauer, G.; Bond, A. M.; MacFarlane, D. R. *Inorg. Chem.* **1999**, *38*, 3836; (b) Bond, A. M.; Deacon, G. B.; Howitt, J.; MacFarlane, D. R.; Spiccia, L.; Wolfbauer, G. *J. Electrochem. Soc.* **1999**, *146*, 648.
134. Trammell, S. A.; Meyer, T. J. *J. Phys. Chem. B* **1999**, *103*, 104.
135. Bonhôte, P.; Gogniat, E.; Sophie, T.; Barbé, C.; Vlachopoulos, N.; Lenzmann, F.; Comte, P.; Grätzel, M. *J. Phys. Chem. B* **1998**, *102*, 1498.
136. (a) Zaban, A.; Ferrere, S.; Sprague, J.; Gregg, B. A. *J. Phys. Chem. B* **1997**, *101*, 55; (b) Zaban, A.; Ferrere, S.; Gregg, B. A. *J. Phys. Chem. B* **1998**, *102*, 452.
137. (a) Adamson, A. W. *J. Chem. Educ.* **1983**, *60*, 797; (b) Demas, J. N. *J. Chem. Educ.* **1983**, *60*, 803; (c) Crosby, G. A. *J. Chem. Educ.* **1983**, *60*, 791; (d) Caspar, J. V.; Meyer, T. J. *Inorg. Chem.* **1983**, *22*, 2444; (e) Hager, G. D.; Crosby, G. A. *J. Am. Chem. Soc.* **1975**, *97*, 7031; (f) Hager, G. D.; Watts, R. J.; Crosby, G. A. *J. Am. Chem. Soc.* **1975**, *97*, 7037; (f) Hipps, K. W.; Crosby, G. A. *J. Am. Chem. Soc.* **1975**, *97*, 7042.

138. Damrauer, N. H.; Cerullo, G.; Yeh, A.; Boussie, T. R.; Shank, C. V.; McCusker, J. K. *Science* **1997**, 275, 54.
139. Lakowicz, J. R. *Principles of Fluorescence Spectroscopy*, Plenum Press, New York, **1983**.
140. Kelly, C. A.; Meyer, G. J. *Coord. Chem. Rev.* **2000**, in press.
141. Kelly, C. A.; Farzad, F.; Thompson, D. W.; Stipkala, J. M.; Meyer, G. J. *Langmuir* **1999**, 20, 7047.
142. Rabani, J.; Ushida, K.; Yamashita, K.; Stark, J.; Gershuni, S.; Kira, A. *J. Phys. Chem. B* **1997**, 101, 3136.
143. Farzad, F.; Thompson, D. W.; Kelly, C. A.; Meyer, G. J. *J. Am. Chem. Soc.* **1999**, 121, 5577.
144. Albery, W. J.; Bartlett, P. N. *J. Electrochem. Soc.* **1984**, 131, 315.
145. Heller, A. *Conference on Chemical Research XXX. Advances in Electrochemistry: Photoelectrochemistry*, Houston, Texas, Nov. 3–5, **1986**.
146. Rothenberger, G.; Fitzmaurice, D.; Grätzel, M. *J. Phys. Chem.* **1992**, 96, 5983.
147. Cao, F.; Oskram, G.; Searson, P. C.; Stipkala, J.; Farzad, F.; Heimer, T. A.; Meyer, G. J. *J. Phys. Chem.* **1995**, 99, 11974.
148. Zaban, A.; Meier, A.; Gregg, B. *J. Phys. Chem. B* **1997**, 101, 7895.
149. Gerfin, T.; Grätzel, M.; Walder, L. *Prog. Inorg. Chem.* **1997**, 44, 345.
150. Hampden-Smith, M. J.; Williams, D. S.; Rheingold, A. L. *Inorg. Chem.* **1990**, 29, 4706.
151. Lyon, L. A.; Hupp, J. T. *J. Phys. Chem.* **1995**, 99, 15718.
152. Lunell, S.; Stashans, A.; Ojmäe, L.; Lindström, H.; Hagfeldt, A. *J. Am. Chem. Soc.* **1997**, 119, 7374.
153. (a) Stashans, A.; Lunell, S.; Bergström, R.; Hagfeldt, A.; Lindquist, S.-E. *Phys. Rev. B* **1996**, 53, 159; (b) Lindström, H.; Södergren, S.; Solbrand, A.; Rensmo, H.; Hjelm, J.; Hagfeldt, A.; Lindquist, S.-E. *J. Phys. Chem. B* **1997**, 101, 7717; (c) Lindström, H.; Södergren, S.; Solbrand, A.; Rensmo, H.; Hjelm, J.; Hagfeldt, A.; Lindquist, S.-E. *J. Phys. Chem. B* **1997**, 101, 7710.
154. McConnell, R. D. *Future Generation Photovoltaic Technologies: First NREL Conference*, Denver, CO, **1997**.
155. Södergren, S.; Hagfeldt, A.; Olsson, J.; Lindquist, S.-E. *J. Phys. Chem.* **1994**, 5552.
156. Schwarzburg, K.; Willig, F. *Appl. Phys. Lett.* **1991**, 58, 2520.
157. Cao, F.; Oskam, G.; Searson, P. C.; Meyer, G. J. *J. Phys. Chem.* **1996**, 100, 17021.
158. De Jongh, P. E.; Vanmaekelbergh, D. *J. Phys. Chem. B* **1997**, 101, 2716.
159. (a) Solbrand, A.; Henningson, A.; Södergren, S.; Lindström, H.; Hagfeldt, A.; Lindquist, S.-E. *J. Phys. Chem. B* **1999**, 103, 1078; (b) Lindström, H.; Rensmo, H.; Södergren, S.; Solbrand, A.; Lindquist, S.-E. *J. Phys. Chem.* **1996**, 100, 3084; (c) Solbrand, A.; Lindström, H.; Rensmo, H.; Hagfeldt, A.; Lindquist, S.-E. *J. Phys. Chem. B* **1997**, 101, 2514.
160. Fahrenbruch, A. L.; Bube, R. H. *Fundamentals of Solar Cells: Photovoltaic Solar Energy Conversion*, Academic Press, New York, **1983**.
161. Nazeeruddin, M. K.; Kay, A.; Rodio, I.; Humphry-Baker, R.; Müller, E.; Liska, P.; Vlachopoulos, N.; Grätzel, M. *J. Am. Chem. Soc.* **1993**, 115, 6382.
162. (a) Schlichthörl, G.; Huang, S. Y.; Sprague, J.; Frank, A. J. *J. Phys. Chem. B* **1997**, 101, 8141; (b) Huang, S. Y.; Schlichthörl, G.; Nozik, A. J.; Grätzel, M.; Frank, A. J. *J. Phys. Chem. B* **1997**, 101, 2576.
163. Redmond, G.; Fitzmaurice, D. *J. Phys. Chem.* **1993**, 97, 1426.
164. Enright, B.; Redmond, G.; Fitzmaurice, D. *J. Phys. Chem.* **1994**, 98, 6195.
165. Redmond, G.; Grätzel, M.; Fitzmaurice, D. *J. Phys. Chem.* **1993**, 97, 6951.
166. Boschloo, G.; Fitzmaurice, D. *J. Phys. Chem. B* **1999**, 103, 2228.
167. Boschloo, G.; Fitzmaurice, D. *J. Phys. Chem. B* **1999**, 103, 7860.
168. Huang, S. Y.; Schlichthörl, G.; Nozik, A. J.; Grätzel, M.; Frank, A. J. *J. Phys. Chem. B* **1997**, 101, 2576.
169. Argazzi, R.; Bignozzi, C. A.; Heimer, T. A.; Hasselmann, G. M.; Meyer, G. J. *J. Phys. Chem. B* **1998**, 102, 7577.
170. (a) Park, N.-G.; Schlichthörl, G.; van de Lagematt, J.; Cheong, H. M.; Mascarenhas, A.; Frank, A. J. *J. Phys. Chem. B* **1999**, 103, 3308; (b) Schlichthörl, G.; Park, N. G.; Frank, A. J. *J. Phys. Chem. B* **1999**, 103, 782.
171. Franco, G.; Gehring, J.; Peter, L. M.; Ponomarev, E. A.; Uhlendorf, I. *J. Phys. Chem. B* **1999**, 103, 692.

172. (a) Hotchandani, S.; Kamat, P. V. *J. Phys. Chem.* **1992**, *96*, 6834; (b) Patrick, B.; Kamat, P. V. *J. Phys. Chem.* **1992**, *96*, 1423.
173. Eychmüller, A.; VoBmeyer, T.; Mews, A.; Weller, H. *J. Lumin.* **1994**, *58*, 223.
174. Tennakone, K.; Senadeera, G. K. R.; Perera, V. P. S.; Kottogoda, I. R. M.; De Silva, L. A. A. *Chem. Mater.* **1999**, *11*, 2474.
175. Martini, I.; Hartland, G. V.; Kamat, P. V. *J. Phys. Chem. B* **1997**, *101*, 4826.
176. (a) Martini, I.; Hartland, G. V.; Kamat, P. V. *J. Phys. Chem.* **1997**, *101*, 4826; (b) Liu, D.; Fessenden, R. W.; Hug, G. L.; Kamat, P. V. *J. Phys. Chem.* **1997**, *101*, 2583.
177. Martini, I.; Hodak, J.; Hartland, G. V.; Kamat, P. V. *J. Chem. Phys.* **1997**, *107*, 8064.
178. Martini, I.; Hodak, J. H.; Hartland, G. V. *J. Phys. Chem. B* **1998**, *102*, 9508.
179. Martini, I.; Hodak, J. H.; Hartland, G. V. *J. Phys. Chem. B* **1998**, *102*, 607.
180. (a) Hotchandani, S.; Kamat, P. V. *Chem. Phys. Lett.* **1992**, *91*, 320; (b) Bedja, I.; Hotchandani, S.; Carpentier, R.; Fessenden, R. W.; Kamat, P. V. *J. Appl. Phys.* **1994**, *15*, 5444.
181. Kay, A.; Humphry-Baker, R.; Grätzel, M. *J. Phys. Chem.* **1994**, *98*, 952.
182. Kamat, P. V.; Chauvet, J.-P.; Fessenden, R. W. *J. Phys. Chem.* **1986**, *90*, 1389.
183. Rehm, J. M.; McLendon, G. L.; Nagasawa, Y.; Yoshihara, K.; Moser, J.; Grätzel, M. *J. Phys. Chem.* **1996**, *100*, 9577.
184. Ghosh, H. N.; Asbury, J. B.; Lian, T. *J. Phys. Chem. B* **1998**, *102*, 6482.
185. Martino, D. M.; Willegen, H. van; Spitler, M. T. *J. Phys. Chem. B* **1997**, *101*, 8914.
186. Moser, J.; Grätzel, M. *J. Am. Chem. Soc.* **1984**, *106*, 6557.
187. Moser, J.; Grätzel, M.; Sharma, D. K.; Serpone, N. *Helv. Chim. Acta* **1985**, *68*, 1686.
188. Cherepy, N. J.; Smestad, G. P.; Grätzel, M.; Zhang, J. Z. *J. Phys. Chem. B* **1997**, *101*, 9342.
189. Hilgendorff, M.; Sundström, V. *J. Phys. Chem.* **1998**, *102*, 10505.
190. Ghosh, H. N.; Asbury, J. B.; Weng, Y.; Lian, T. *J. Phys. Chem. B* **1998**, *102*, 10208.
191. Frei, H.; Fitzmaurice, D. J.; Grätzel, M. *Langmuir* **1990**, *6*, 198.
192. Burfeindt, B.; Hannappel, T.; Storck, W.; Willig, F. *J. Phys. Chem.* **1996**, *100*, 16463.
193. Vinodgopal, K.; Hua, X.; Dahlgren, R. L.; Lappin, A. G.; Patterson, L. K.; Kamat, P. V. *J. Phys. Chem.* **1995**, *99*, 10883.
194. Fessenden, R. W.; Kamat, P. V. *J. Phys. Chem.* **1995**, *99*, 12902.
195. Asbury, J. B.; Ellingson, R. J.; Ghosh, H. N.; Ferrere, S.; Nozik, A. J.; Lian, T. *J. Phys. Chem. B* **1999**, *103*, 3110.
196. Tachibana, Y.; Moser, J. E.; Grätzel, M.; Klug, D. R.; Durrant, J. R. *J. Phys. Chem.* **1996**, *100*, 20056.
197. Heimer, T. A.; Heilweil, E. J. *J. Phys. Chem. B* **1997**, *101*, 10990.
198. Nasr, C.; Liu, D.; Hotchandani, S.; Kamat, P. V. *J. Phys. Chem.* **1996**, *100*, 11054.
199. Rossetti, R.; Brus, L. E. *J. Am. Chem. Soc.* **1984**, *106*, 4336.
200. Moser, J.; Grätzel, M.; Sharma, D. K.; Serpone, N. *Helv. Chim. Acta* **1985**, *68*, 1686.
201. Kamat, P. V.; Patrick, B. *Electrochemistry in Colloids and Dispersions*, **1992**, pp. 447–455.
202. Haque, S. A.; Tachibana, Y.; Klug, D. R.; Durrant, J. R. *J. Phys. Chem. B* **1998**, *102*, 1745.
203. Vrachnou, E.; Vlachopoulos, N.; *J. Chem. Soc., Chem. Commun.*, **1987**, 868.
204. Blackburn, R. L.; Johnson, C. S.; Hupp, J. T. *J. Am. Chem. Soc.* **1991**, *113*, 1060.
205. Liu, Y.; Dadap, J. I.; Zimdars, D.; Eisenthal, K. B. *J. Phys. Chem. B* **1999**, *103*, 2480.
206. Moser, J.; Punchihewa, S.; Infelta, P. P.; Grätzel, M. *Langmuir* **1991**, *7*, 3012.
207. Houlding, V. H.; Grätzel, M. *J. Am. Chem. Soc.* **1983**, *105*, 5695.
208. Hannappel, T.; Burfeindt, B.; Storck, W.; Willig, F. *J. Phys. Chem. B* **1997**, *101*, 6799.
209. Moser, J. E.; Grätzel, M. *Chimia* **1998**, *52*, 160.
210. Ferrere, S.; Gregg, B. A. *J. Am. Chem. Soc.* **1998**, *120*, 843.
211. Kalyanasundaram, K.; Vlachopoulos, N.; Krishnan, V.; Monnier, A.; Grätzel, M. *J. Phys. Chem.* **1987**, *91*, 2342.
212. Yan, S. G.; Hupp, J. T. *J. Phys. Chem.* **1996**, *100*, 6867.
213. Sakata, T.; Hashimoto, K.; Hiramoto, M. *J. Phys. Chem.* **1990**, *94*, 3040.
214. Lu, H.; Preiskorn, J. N.; Hupp, J. T. *J. Am. Chem. Soc.* **1993**, *115*, 4927.
215. Dang, X.; Hupp, J. T. *J. Am. Chem. Soc.* **1999**, *121*, 8399.
216. Moser, J. E.; Grätzel, M. *Chem. Phys.* **1993**, *176*, 493.
217. Hasselmann, G. M.; Meyer, G. J. *J. Phys. Chem. B* **1999**, *103*, 7671.
218. (a) Bedja, I.; Hotchandani, S.; Kamat, P. V. *J. Phys. Chem.* **1994**, *98*, 4133; (b) Nasr, C.; Hotchandani, S.; Kamat, P. V. *J. Phys. Chem. B* **1998**, *102*, 4944.

3 Electron-transfer Processes in Zeolites and Related Microheterogeneous Media

Anand S. Vaidyalingam, Michael A. Coutant and Prabir K. Dutta

3.1 Introduction

The focus of this chapter is on electron-transfer processes occurring in porous media, with particular emphasis on zeolitic, mesoporous materials and sol-gel-derived materials. The definition of different classes of porous solids as specified by IUPAC is based on the pore diameter:

- microporous, if diameter < 2 nm;
- mesoporous, if diameter between 2 and 50 nm;
- macroporous, if diameter > 50 nm.

Zeolites are microporous materials with well-defined pores and crystalline frameworks. Sol-gel materials can have both micro- and mesopores, but both the framework and the pores are not well defined. Mesoporous materials have well-defined pores, but their framework structures are amorphous. These differences in structure and porosity are well reflected, as we discuss below, in the electron transfer reactions studied within these hosts. The link between these materials is the progressive increase in size of the molecules that can be encapsulated in the pores that undergo electron-transfer reactions, ranging in size from 1 nm in zeolites to enzymes of varying sizes in sol-gels. Another route to generate porosity is via pillaring of layered materials. The pillars push the layers apart and such a strategy to introduce porosity has been extensively studied with clays (smectites), layered double hydroxides, metal phosphates, etc., and forms the subject matter of a separate chapter.

As will be evident from this chapter, there is a significant body of work on electron-transfer (ET) reactions in porous materials driven by both fundamental research interests and applications in diverse areas such as sensors, catalysis and photochemical energy storage. Porous materials offer unique opportunities for ET reactions for several reasons. Porosity at the level of molecular size allows for novel spatial arrangements of molecules. Steric and electrostatic constraints can alter

chemical reactivity in ways that are impossible in a homogeneous medium. In some cases, the framework atoms can themselves play a role in the ET process. The freedom of adjusting the size of the pores to fit appropriately molecules of different shapes and sizes has made it possible to examine ET reactions involving a large number of ions and molecules.

We have restricted our discussion in this chapter to specific types of ET reactions. These include redox reactions with particular emphasis on oxidation chemistry because of the commercial importance of these reactions. In addition, photochemically induced ET reactions are extensively discussed. Numerous studies of electrochemistry with porous hosts have been reported, and there is considerable potential for the development of novel electrochemical sensors, which is discussed at length. This chapter is organized on the basis of the porosity of the materials that are discussed. The following section (Section 3.2) begins with a description of porosity in microporous, mesoporous and sol-gel materials and the synthesis routes for obtaining such porosities and assembly of molecules in these pores. ET reactions form the focus of the third section (Section 3.3). In the case of zeolites and microporous materials, redox and photoredox chemistry are treated separately (sub-sections in Section 3.3.1) since a large body of work exists in each of these areas. Electrochemical reactions involving zeolite-modified electrodes form a separate sub-section (in Section 3.3.1). For the mesoporous materials, the focus is primarily on redox reactions involving framework atoms and entrapped species (Section 3.3.2) whereas with the sol-gel materials, the photoredox chemistry of entrapped species and electrochemistry, especially the use of enzyme mediators, form the major focus of discussion (Section 3.3.3).

3.2 Description of Porous Media

3.2.1 Microporous Materials and Zeolites

Microporous materials include a large group of crystalline solids of varying chemical composition and porosity. These materials are characterized by channels and cavities of molecular dimensions. The framework structure is made up of interconnecting T–O–T' bonds, where T and T' can be Si, Al, P, Ga, Fe, Ti, Co, Zn, B and a host of other elements [1]. Materials with Si–O–Al bonding in the framework are called zeolites and are used extensively in many applications, including separations and catalysis [2]. The presence of Al in the zeolite framework leads to a charged framework and ion-exchange capabilities. In cases where the ion-exchange sites are occupied by hydrogen ions, the zeolites show remarkably strong superacid-type behavior [3]. Figure 1 shows the framework structures of some of the most extensively studied zeolites. Table 1 lists characteristic features of some zeolites, including their void volumes and the kinetic diameter of molecules that can enter the porous structure. Most of the work described in this chapter will be focused on zeolites shown in Figure 1, and the size limitation of the molecules that can be en-

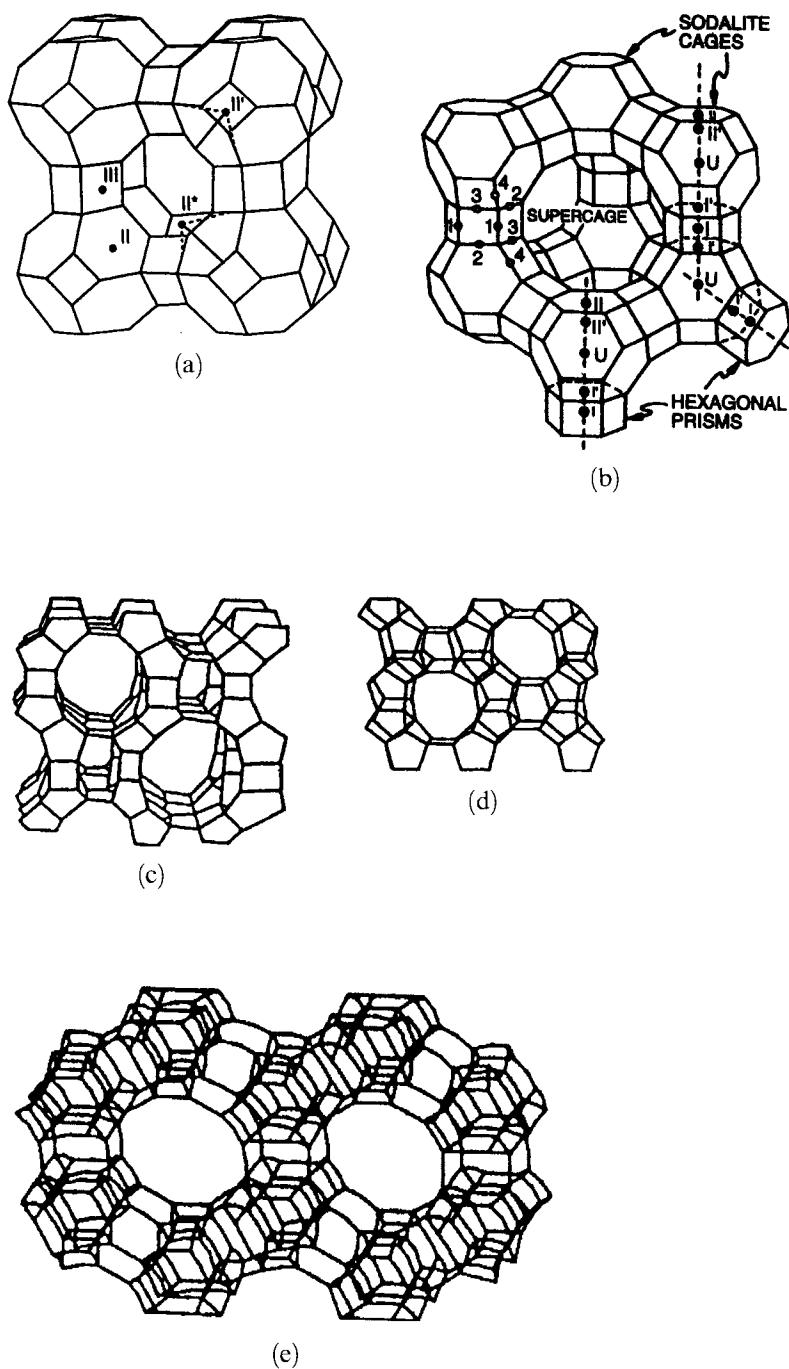


Figure 1. Framework structures of the most commonly studied zeolitic structures: (a) zeolite A; (b) zeolite X/Y; (c) mordenite; (d) ZSM-5; (e) zeolite L.

Table 1. Physical and chemical properties of some commercially important zeolites.

Type	Unit-cell compound (typical, fully hydrated)	Pore structure	Typical Si/Al ratio	Void volume/ cm ³ cm ⁻³	Kinetic diameter/ nm
A	Na ₁₂ [(AlO ₂) ₁₂ (SiO ₂) ₁₂] · 27H ₂ O	3D, 4.1 Å	1.0	0.47	0.39
X	Na ₈₆ [(AlO ₂) ₈₆ (SiO ₂) ₁₀₆] · 264H ₂ O	3D, 7.4 Å	1.0–1.5	0.50	0.81
Y	Na ₅₆ [(AlO ₂) ₅₆ (SiO ₂) ₁₃₆] · 250H ₂ O	3D, 7.4 Å	>1.5–3	0.48	0.81
L	K ₉ [(AlO ₂) ₉ (SiO ₂) ₂₇] · 22H ₂ O	1D, 7.1 Å	2.6–3.5	0.32	0.81
Mordenite	Na ₈ [(AlO ₂) ₈ (SiO ₂) ₄₀] · 24H ₂ O	1D, 6.5 × 7.0 Å	4.7–5	0.28	0.63
ZSM-5	(TPA, Na)[(AlO ₂)(SiO ₂) ₃₀] · 10H ₂ O	3D, 5.4 × 5.6 Å 5.1 × 5.5 Å	10 100	0.34	0.60

capsulated is of the order of 13 Å in zeolites X/Y (12-ring pores). Microporous frameworks with larger pores have only recently been synthesized, including aluminophosphate VPI-5 (18-ring pores, 13 Å channel), gallophosphate cloverite (20-ring pores, 13 Å window and 30 Å cavities) and aluminosilicate UTD-1 (14-ring pores, 10 Å channels) [4]. It is expected that reports of ET reactions in these hosts will be forthcoming.

Microporous materials are typically synthesized by a hydrothermal process, which involves mixing appropriate reactants in an aqueous medium followed by heat treatment [5]. Even though the process is relatively simple, the development and control of porosity, which determines the ultimate practical use of these materials, is not easy to predict. This is primarily because crystal growth of these materials is a very complicated chemical process [6]. For example, in zeolite formation, the silicon- and aluminum-containing reactants dissolve in the presence of base to produce many soluble species [7]. Speciation is strongly influenced by the pH, temperature, cations and structure-directing agents [8]. Insoluble aluminosilicates (commonly referred to as gel) are rapidly formed by reaction of the solubilized species. Thus, this system is typically in a state of supersaturation for many of the aluminosilicate species. After an induction period that can extend from hours to weeks, nuclei are formed. The nuclei grow using nutrients from the solution or the dissolving gel to form crystals. Figure 2 shows a schematic description of the crystallization process of microporous materials [9]. The complexity of the process is evident from the numerous chemical processes that occur during crystallization.

Typically, the interesting open porous structures are intermediates in the synthesis process and with longer crystallization times, condensed structures will form. Because kinetic stabilization is necessary for the formation of open pore structures, profound effects are manifested by changing the synthesis conditions. The interplay between the inorganic reactants and organic additives also influences the crystal growth process. Hence zeolite synthesis is an exciting area of research, with major discoveries of frameworks being reported on a regular basis. However, the critical

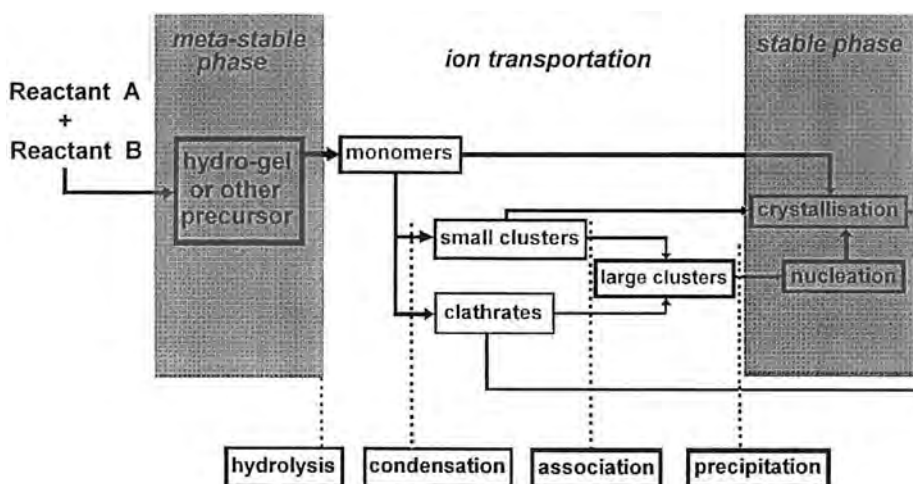


Figure 2. Schematic representation of the crystallization process of microporous materials.

discoveries of new frameworks usually occur by trial and error. Spectroscopic probes that have found considerable use in the past decade include NMR spectroscopy [10, 11] and Raman spectroscopy [12]. Other techniques that have provided information on the early stages of zeolite nucleation include small- and wide-angle X-ray and neutron scattering [13].

Assembling molecules within zeolites

The microporosity of zeolites and other microporous materials makes it very convenient to introduce molecules into the structure. Several strategies exist, depending on the size and nature of the species. Positively charged species can be ion exchanged into the zeolite from aqueous solution, provided that they are small enough to penetrate through the ring openings. Many inorganic and organometallic complexes, such as $[\text{Ru}(\text{NH}_3)_6]^{3+}$, $[\text{Co}(\text{NH}_3)_4]^{2+}$ and $[\text{Co}(\text{C}_5\text{H}_5)_2]^+$, as well as organic cations such as viologens can be readily exchanged into the zeolite [14]. The loading levels can be controlled by adjusting the concentration of the molecule in the ion-exchanging solution. For neutral molecules, the molecule can either be transported via the vapor phase into the empty space of the dehydrated zeolite, or introduced via a solvent into the dehydrated zeolite. Examples include the introduction of benzene into zeolite Y via vapor phase and the introduction of pyrene into zeolite Y using cyclohexane as solvent [15]. Metal carbonyl complexes of iron, ruthenium and molybdenum have also been introduced via the vapor phase [16].

A third approach is the construction of molecules inside the zeolite itself. Such a strategy has been particularly successful with the faujasitic zeolites, because of the possibility of synthesizing molecules within the supercage that are large enough that they cannot be introduced directly through the window openings. This procedure has been referred to as 'building a ship in a bottle' synthesis and typically incorpo-

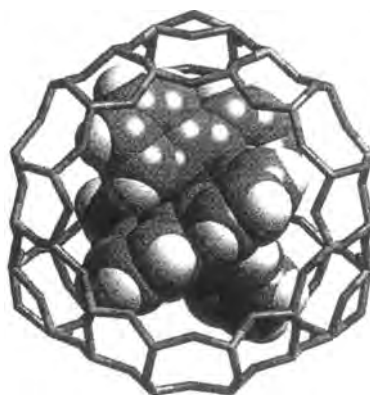
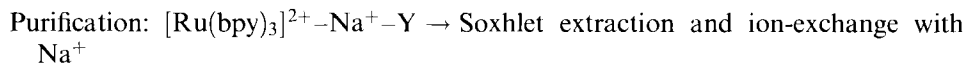
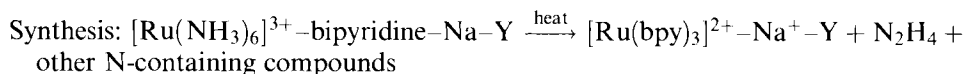
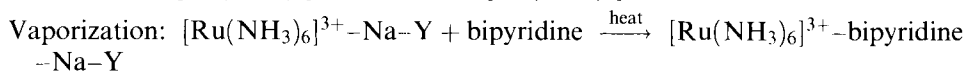


Figure 3. $\text{Ru}(\text{bpy})_3^{2+}$ entrapped inside a zeolite Y supercage synthesized by the ship-in-a-bottle approach.

rates steps to obtain the necessary building blocks into the supercage, followed by appropriate treatment to synthesize the desired complex. A good example is the synthesis of $[\text{Ru}(\text{bpy})_3]^{2+}$ in zeolite Y. This molecule has a dimension of 12 Å, and cannot be introduced through the 12-membered ring openings, as is obvious from Figure 3. The following scheme has been adapted from the pioneering work of Lunsford and co-workers [17]:



Under careful anaerobic conditions, $[\text{Ru}(\text{NH}_3)_6]^{2+}$ can also be used as the starting material, avoiding the formation of acidic compounds during the synthesis process. This is of particular importance in assembling complexes in low Si–Al zeolites such as zeolite X [18]. Recently, Kincaid and co-workers synthesized ruthenium polypyridyl complexes with mixed ligands in zeolite Y [19]. Intrazeolitic entrapped complexes $[\text{Ru}(\text{L})_n(\text{L}')_{3-n}]^{2+}$ where $\text{L}, \text{L}' = 2,2'$ -bipyridine, 2,2'-bipyrazine and 4-methyl- and 4,4'-dimethyl-2,2'-bipyridine have been synthesized. The strategy has been first to synthesize the bis-complex $[\text{Ru}(\text{L})_2(\text{H}_2\text{O})_2]^{2+}$ in the zeolite followed by insertion of a third ligand. This strategy opens up many more possibilities for the synthesis of new complexes. Phthalocyanine, Schiff base (salen) and tetraethylenediamine (tetren) complexes are examples of other ligands used for complex formation in zeolite Y [20]. Structures of several complexes and ligands used in zeolite Y are shown in Figure 4.

Another approach developed by Balkus and co-workers involves the use of organometallic complexes such as phthalocyanines and cobalticinium cations as tem-

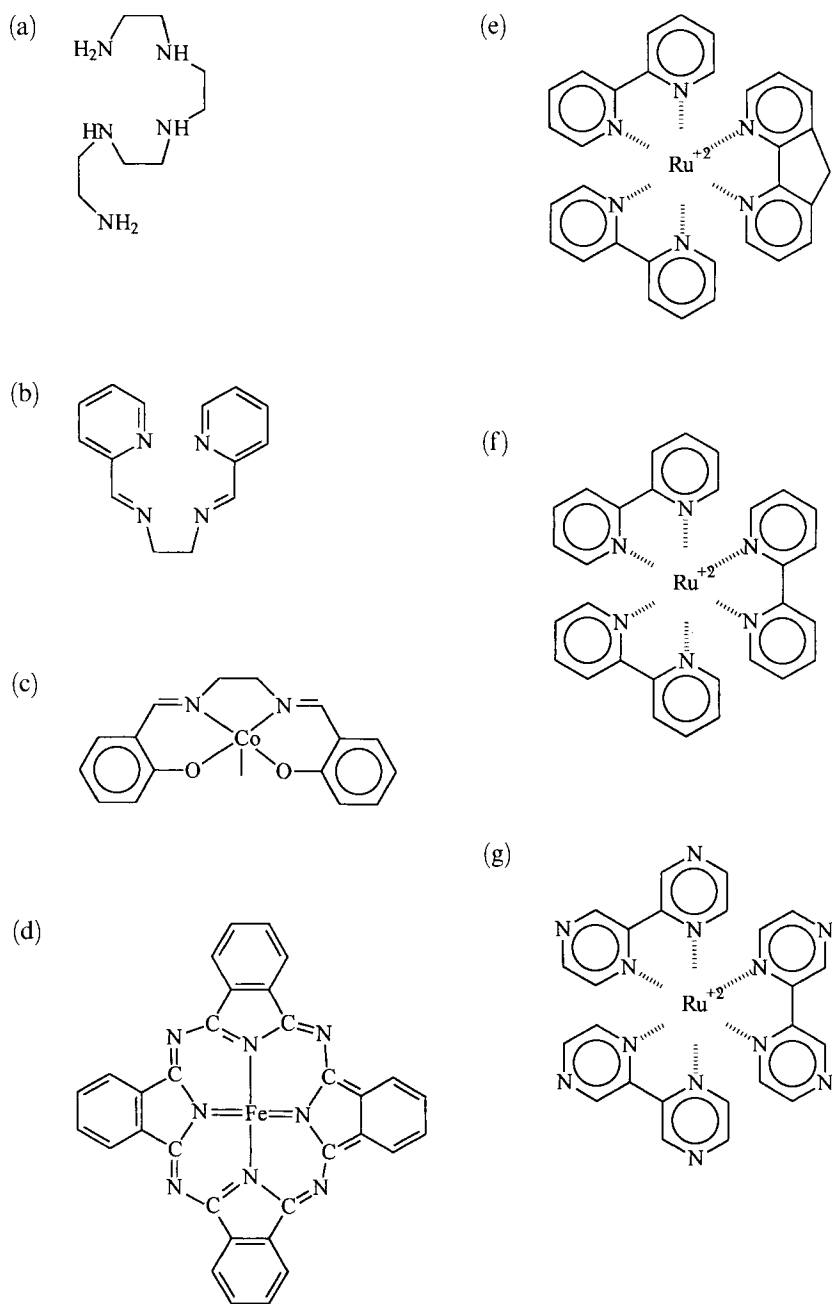


Figure 4. Structures of several ligands complexes synthesized in zeolite Y by the ship-in-a-bottle strategy: (a) tetren; (b) pyren; (c) Co(salen); (d) Fe(phthalocyanine); (e) [Ru(bpy)₂daf]²⁺; (f) [Ru(bpy)₃]²⁺; (g) [Ru(bpz)₃]²⁺. *N,N'*-Ethylenebis(salicylideneiminato) (2-) ion = salen, tetraethylenepentamine = tetren, 2,2'-bipyridine = bpy, 4,5-diazafluorene = daf, 2,2'-bipyrazine = bpz.

plates for the formation of microporous materials, thereby ensuring entrapment in micropores during the framework synthesis [21]. It is clear that our sophistication in synthesizing molecules within zeolite cages is continually being enhanced, with the ultimate goal being to develop chemistry parallel to that of conventional synthesis. The advantage of these synthetic advances in electron-transfer chemistry will become obvious as we proceed.

Environment within the zeolite structure

One of the important differences between molecules in zeolite cages and species isolated in other matrices such as cyclodextrins [22], micelles [23], vesicles [24] and polymers [25] arises from the fact that the zeolite can be an active host and influence the structure and reactivity of the encapsulated molecules. The nature of the intra-zeolitic environment has been extensively studied and the influence of polarity, steric and electrostatic effects on encapsulated molecules is beginning to be well understood.

Micropolarity

Optical spectroscopy of several polyaromatic hydrocarbon probes has provided information about the polarity of the intrazeolitic environment. The change in intensities of the two vibronic components (380 versus 370 nm) of the fluorescence of pyrene has been used for the estimation of micropolarity in micelles, cyclodextrins and other media [26]. This methodology has also been applied to zeolites [27]. Solvatochromic effects have also been exploited to obtain information about zeolite as a 'solvent' [28]. Using salicylidene as a probe and based on changes in its electronic and Raman spectra, it was concluded that Na⁺-exchanged zeolite Y behaved primarily like a solvent with α character, indicative of its ability to undergo hydrogen bonding. Polarity within faujasitic zeolites has recently been measured with the probe molecules Nile Red, pyrene-1-carboxyaldehyde and coumarin 500 [29]. The effect on the intrazeolitic polarity by the framework cations was negated by the presence of water or polar solvents. In the absence of solvent, the polarity was found to be controlled by the charge of the cation, and in all cases the zeolites were found to be more polar than water. This 'superpolarity' led to switching of the $n\pi^*$ and $\pi\pi^*$ states of acetophenones, an effect that is not found even in the most polar organic solvents [29].

Zeolite rigidity

The zeolite framework is relatively rigid under ambient conditions; however, at higher temperatures, there appears to be increased flexibility and typically excluded molecules can penetrate into the system [30]. For example, 1,3,5-triisopropylbenzene with a diameter of 9.3 Å will diffuse into zeolite X supercages at temperatures of 450–500 K. The rigidity of the framework is manifested most vividly if the entrapped molecule fits very tightly into the intrazeolitic space. Sodalite cages are the building blocks of zeolite X, Y and zeolite A (Figure 1a and b). The internal

diameter of these cages is 6.6 Å, and can accommodate the tetramethylammonium (TMA) cation, which is of the same size as the cage. Indeed, for TMA⁺ entrapped in sodalite cages, this fit was tight enough that the C–N symmetric stretching vibration of the TMA⁺ cation was shifted from 752 to 761 cm^{−1} upon encapsulation [31], comparable to what is observed for tetraalkylammonium salts under high pressures.

Kincaid and co-workers have exploited the steric effect in altering the excited-state photophysical properties of [Ru(bpy)₂(daf)]²⁺, where daf = 4,5 diazafluorene [32]. Aqueous solutions of this complex exhibit very weak luminescence, with lifetimes shorter than 10 ns at room temperature. Upon encapsulating this molecule into zeolite Y supercages, the fluorescence intensity increases by a factor of 100 and the excited-state lifetime is increased to 302 ns.

Similar dimensions of an entrapped molecule and the intrazeolitic volume can lead to novel structural perturbations. This is exemplified by the singlet excited lifetime of *trans,trans*-1,4-diphenylbutadiene [33]. In faujasitic zeolites, the lifetime is of the order of 0.6 ns, comparable to that in solution. However, upon incorporation into the channel crossings of ZSM-5, the lifetime increased to 12.7 ns, since the rotation around the π -bond is no longer possible. Entrapment of a molecule inside a zeolite cage can restrict access to it by other molecules. Reactive species can be trapped indefinitely, as is observed for cation radicals formed by the adsorption of α,ω -diphenylpolyenes (e.g. *trans*-stilbene, diphenylbutadiene, diphenylhexatriene) into Na–ZSM-5 [34]. These cation radicals are unstable in solution (lifetime of microseconds) or other solid matrices (lifetime of seconds), but are readily stabilized indefinitely in ZSM-5. This stability arises because the double bond is protected from external reagents by the phenyl rings that extend into the channels. We shall discuss how stabilization via entrapment of tropylium ion and Ru(bpy)₃³⁺ in zeolite Y gives rise to novel ET chemistry in Section 3.3.1.

Electrostatic effects

In the hydrated form of the zeolite, the intracrystalline space is filled with water molecules. However, upon dehydration, without the mediating effects of the high dielectric constant of water, the effects of the negatively charged aluminosilicate framework become apparent. In the early days of zeolite chemistry, it was calculated that electric fields could reach up to 6.3 V Å^{−1} at distances of a few ångströms from a cation site (S II in zeolite Y, Figure 1b) [35]. Fields of this magnitude can readily polarize absorbed molecules at close proximity to these sites, thereby altering the reactivity. Studies of the infrared spectra of adsorbed molecules such as CH₄ and N₂ in zeolite A show the evidence of Stark field splitting, and fields of the order of 1 V Å^{−1} were estimated [36]. How rapidly these fields fall off from the framework toward the center of the cage still needs to be determined. Calculations of electrostatic fields from X-ray diffraction data promises to be a good method for obtaining this information [37]. We shall discuss later how intrazeolitic electrostatic fields have been exploited for promoting ET reactions and hydrocarbon oxidation.

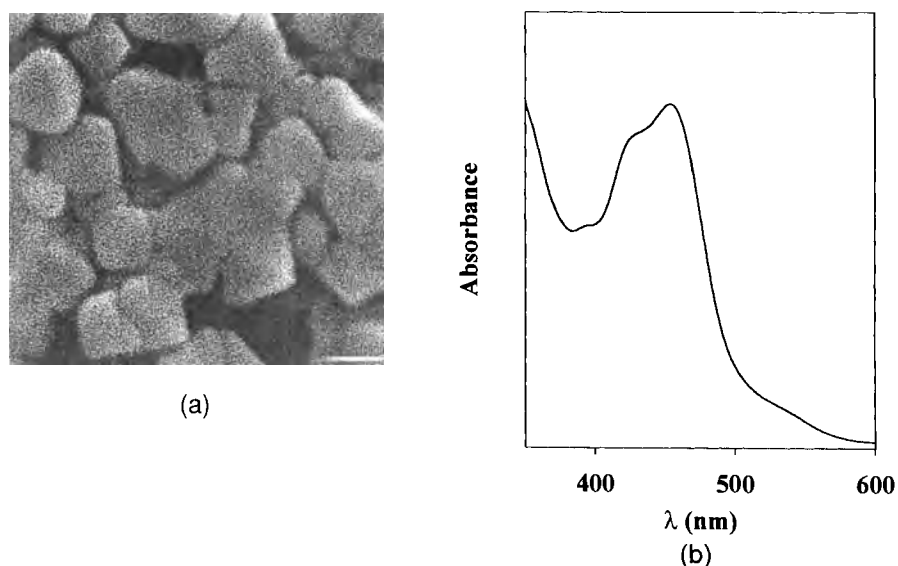


Figure 5. (a) SEM of nanocrystalline zeolite Y (bar = 100 nm). (b) Transmission electronic spectrum of a dispersion of $\text{Ru}(\text{bpy})_3^{2+}$ entrapped in nanocrystalline zeolite Y.

Nanocrystals and membrane forms of zeolites

Zeolites, as synthesized, are typically formed as powders. Most experimentation is done with the powder form, as such or in the form of pressed pellets. Two forms of zeolites that are of considerable interest for ET reactions are nanocrystals [38] and membranes [39]. In the case of nanocrystals, the dispersion in a solvent can be almost optically clear, which makes it possible to apply transmission optical spectroscopic studies to follow reactions occurring within the cages. Figure 5a shows a scanning electron micrograph (SEM) of nanocrystalline zeolite Y and Figure 5b shows the absorption spectrum of $\text{Ru}(\text{bpy})_3^{2+}$ –nanocrystalline zeolite Y obtained in the transmission mode [40]. Zeolites have also been embedded into poly(dimethylsiloxane) (PDMS) polymers to make transparent films [39]. Figure 6b shows the absorption spectrum (transmission mode) of the chromophore TMT^+ (Figure 6a) entrapped in zeolite Y and made into a PDMS film. The extinction coefficient of the dye in the zeolite is comparable to that in solution, indicating minimal perturbation by the zeolite framework. Transient species in zeolites can also be characterized via incorporation into films. It is also expected that quantitative parameters such as quantum yields will be more easily obtained with these forms of ‘transparent’ zeolites rather than powders. Another advance in this field is the development of self-standing zeolitic films [41]. Figure 7 shows the SEM pictures of top and side view of a chabazite film, which can be prepared readily with dimensions of centimeters [42].

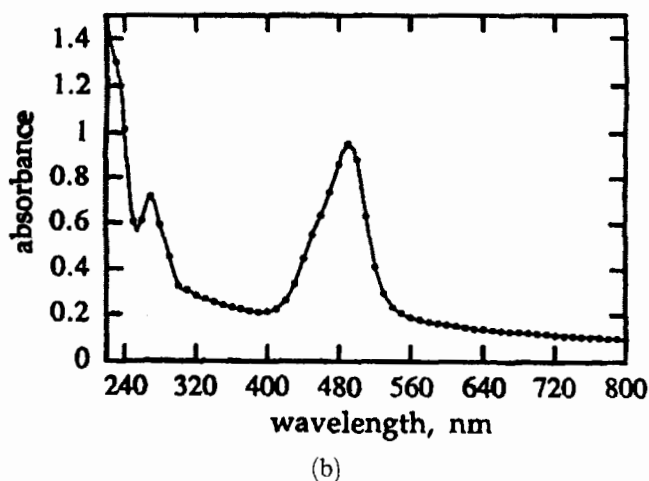
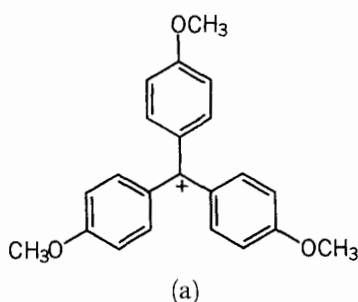
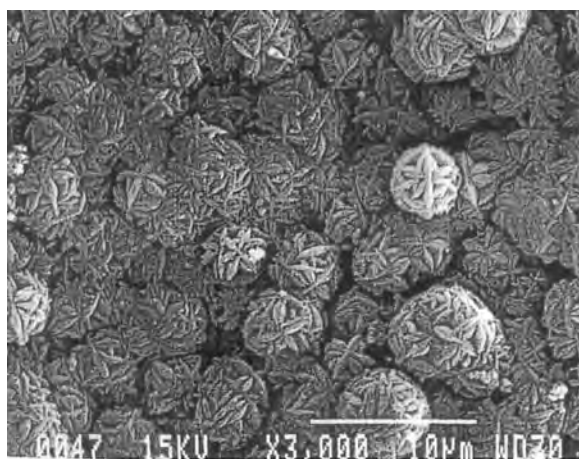


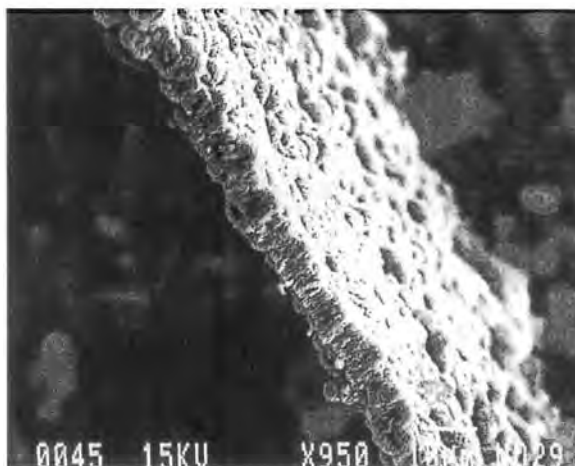
Figure 6. (a) Structure of TMT⁺. (b) Transmission optical spectrum of zeolite-entrapped TMT⁺–polymer film.

In summary, it is clear that the zeolite is a novel host for the entrapment of molecules and the rigidity and the charged nature of the framework allow for steric and electrostatic effects on the encapsulated molecules. Isolation of entrapped molecules can also influence their reactivity. The interest in zeolites as hosts for electron-transfer reactions stems from a combination of properties, including

- high surface area and adsorption capacity;
- redox-active framework elements;
- size of channels and cavities of molecular dimensions (5–13 Å);
- possibility of entrapment of molecules;
- electrostatic effects and unique solvation manifested in the intrazeolitic medium;
- formation of nanocrystals and films.



(a)



(b)

Figure 7. SEM of (a) top and (b) side view of a chabazite-type film.

3.2.2 Mesoporous Materials

As discussed above, zeolites and other microporous materials have channels and cages of 5–13 Å, which is typical of the size of many molecules of interest. Mesoporous materials serve to extend the range of porosities, with well-defined and controllable pores increasing readily from 15 Å. Research in the field of mesoporous materials began in earnest in 1992 with the discovery of the M41S class of materials by researchers at Mobil Research and Development Corporation [43]. Thus, of all the porous materials being discussed in this chapter, it is the most recent. However, the possibility of the precise tuning of pore sizes in a range that was previously

unattainable has generated intense excitement and large numbers of publications, including several review articles demonstrating the use of these materials as novel hosts, have appeared [44]. In this section, we provide a brief description of mesoporous materials and their synthesis and discuss ET reactions using these hosts in Section 3.3.2.

Mesoporous materials are defined as inorganic materials with pores with diameters in the range 20–500 Å and include sol–gel-derived aerogels, pillared layered structures and the M41S class materials. Since the sol–gel-derived materials have pore structures of varying dimensions, and have also been extensively studied, we shall discuss these materials separately. It is important to mention that the M41S class and the layered materials have a considerably better defined pore structure than the aerogels. The crystallinity in the M41S class arises from the long-range ordering of the pore structure rather than crystallinity of the framework, the latter being the case for zeolites.

The porosity in the M41S family of materials is typically generated with the use of surfactants as structure-directing agents. Most work has been done on the synthesis of silicate-based frameworks although, as we discuss later, other elements can also be incorporated into the framework (such as Al, V and Ti) and nonsilicon-containing frameworks can also be made (such as Ti and Zr). The first synthesis reports involved compositions including a silica source (tetraethylorthosilicate, Ludox®, fumed silica, sodium silicate), a cationic surfactant such as cetyltrimethylammonium bromide, a base (sodium hydroxide) and water. Upon heating these reactants to temperatures $>100^{\circ}\text{C}$ for several days, a solid crystalline material is obtained. Upon burning off the surfactant, the mesoporous material is obtained. Figure 8 shows a TEM picture of MCM-41, where the pores are arranged in a hexagonal geometry [43a]. Figure 9 shows the scheme proposed in the original publication detailing the synthesis of MCM-41 [43]. This mechanism, which was dubbed the ‘liquid crystal templating’ mechanism, suggests that the surfactant forms a liquid crystal phase and the silicate anions interact with the positively charged head groups and orient and condense to form the inorganic framework. The calcination step leaves the inorganic shell, which has the same structure as that

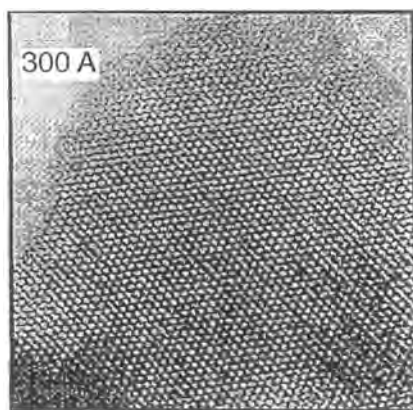


Figure 8. TEM of MCM-41 (text box corresponds to 300 Å).

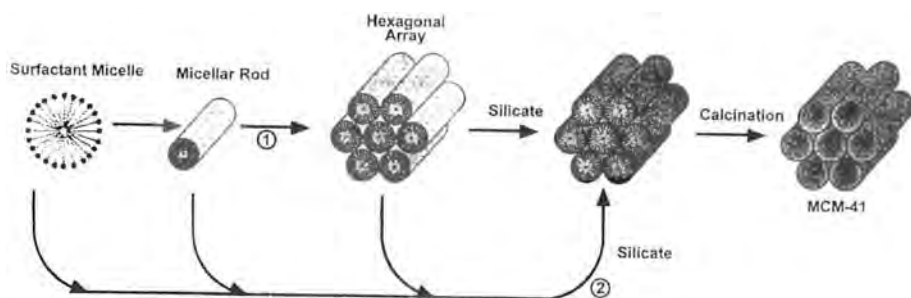


Figure 9. Schematic representation of formation of MCM-41 by a liquid crystal templating mechanism: (1) liquid crystal phase initiated and (2) silicate anion initiated.

of the hexagonal array of the surfactant. The pathway marked (2) in Figure 9 involves association of silicate ions with the micellar rods and self-assembly into the organized MCM-41 structure. A number of studies have since appeared focusing on the mechanism of formation of the MCM-type materials [44b] and, although the definitive chapter on this has not been written, it is agreed that the pathway (1) shown in Figure 9 is only possible if the surfactant concentration exceeds critical micelle concentration (CMC) so that liquid crystal phases exist in the medium [45]. Under most synthesis conditions [46], this is not the case and a more generalized version of the growth process begins with the interaction between the silicate species and the surfactant. These interactions may lead to the formation of an initial liquid crystalline [47] or a lamellar phase [48]. Figure 10 is a representation of a self-assembly process [49] that begins with specific interactions between silicate ions (such as $[\text{Si}_8\text{O}_{20}]^{8-}$ [50]) present at high pH and the surfactants to produce a silicatropic liquid crystal phase, followed by condensation of the silicate anions to form the inorganic framework.

It appears that the matching of the charge density of the surfactant with the ionic species is the important step in the assembly process [44b]. Thus, for example, a cationic surfactant S^+ can direct the formation of negatively charged inorganic species (I^-) through a direct $\text{S}^+ \text{I}^-$ interaction (e.g. MCM-41) or positively charged inorganic species I^+ through the mediation of an anion X^- as in $\text{S}^+ \text{X}^- \text{I}^+$ (e.g. silica, $\text{pH} < 2$).

Other types of interactions that can also lead to mesoporous silicas involve hydrogen bonding interactions of the structure-directing agent, such as an alkylamine or polyethylene oxide with neutral silicon containing species, such as hydrolyzed $\text{Si}(\text{OR})_4$ via an S^0I^0 route [51]. Mesoporous materials formed via these routes do not have the long-range order as in the M41S materials, but appear to have thicker framework walls, leading to enhanced thermal stability and worm-like pores. Also, the surfactant, since it is not ionically bound, can be extracted with solvents. In addition to the hexagonal MCM-41, cubic (MCM-48, SBA-1) and lamellar (MCM-50) structures have also been reported [52].

Another route to mesoporous materials is via intercalation of surfactants into layered silicates, such as kanemite. The flexible silicate sheets expand and cross-link

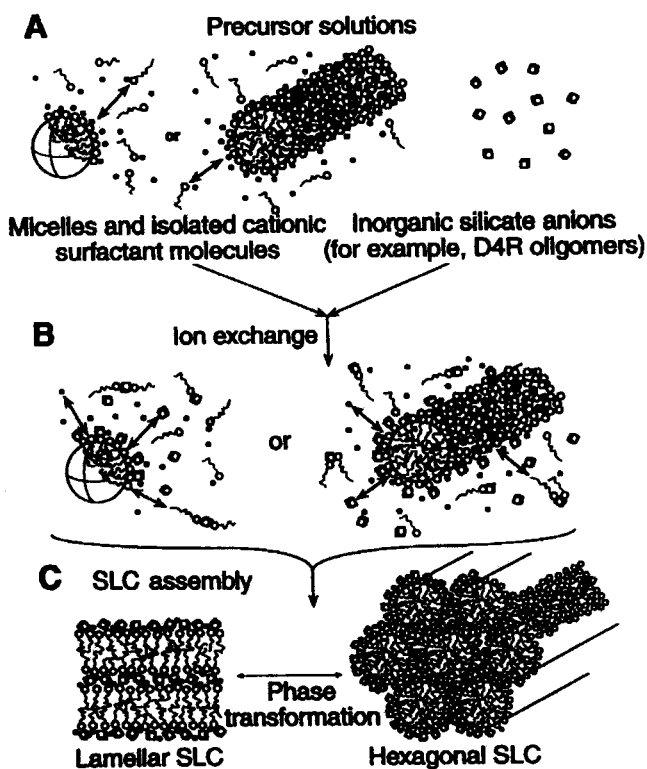


Figure 10. An electrostatic self-assembly process for forming mesoporous materials. (A) Organic and inorganic precursor solutions. (B) Ion-exchange of silicate oligomers with Br^- and OH^- to form inorganic-organic aggregates. (C) Self-assembly of SLC mesophases. D4R = double four ring; SLC = silicotropic liquid crystal.

with each other to develop the porosity [53]. These materials (abbreviated as the FSM family) tend to be more thermally stable than the MCM-type materials.

A considerable amount of research has also been done on incorporating other metal atoms into the mesoporous silicas. Establishing ion-exchange capability and acidity of mesoporous materials opens up many potential applications. This has primarily been done by insertion of tetrahedral Al into the framework. The level of substitution of silicon by tetrahedral Al depends on the reactants and method of preparation, with the highest amounts being in the region of 9 mol % [54]. Higher levels of Al could be inserted (up to 50 mol %), by using cube-like aluminosilicate species, but these materials will dealuminate, with conversion of the tetrahedral to octahedral Al [55]. Other metals that have been introduced into the framework include Ti, V, Cr, Mn, Fe, Mo, Zr and Nb, and some of these are relevant in ET reactions. Typical levels of these metals are in the range 1–2 mol %, although some exceptions, such as 17 mol % Zr insertion, have been reported [44b]. Several spectroscopic studies have confirmed that insertion of the metal into the framework occurs, rather than the formation of metal oxides. With Cr^{3+} , however, only small amounts will substitute into the framework, as is also observed with zeolites [56].

Typically, the synthesis conditions described above lead to the formation of mesoporous powders, with crystallite sizes of the order of microns. However, for

many applications, thin films of these materials would be of interest. Early attempts led to films where the pore channels were parallel to the substrate surface [57]. However, for practical applications, it would be necessary to have the pore channels perpendicular to the substrate in order to make them accessible to molecules. Use of external forces such as flow of reactants as well as strong magnetic fields have been shown to provide ordering of pores [58]. By manipulating the surfactant concentration at levels past the CMC, hexagonal as well as mixed cubic and hexagonal films with accessible pore channels have been made [59].

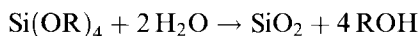
Nonsilicate compositions using the surfactant templating route did not result in making mesoporous materials, especially after surfactant removal. Alternative routes using metal alkoxides in the presence of a chelating agent, such as acetylacetone, yielded the first mesoporous titanium dioxide with a narrow pore size distribution and a surface area of $200 \text{ m}^2 \text{ g}^{-1}$ [60a]. Mesoporous niobium, tantalum and zirconium oxides have been reported [60b–d]. Of particular interest is mesoporous manganese oxide, with crystalline framework walls and semiconducting properties [61]. Mesoporous aluminas with surface areas as high as $400\text{--}710 \text{ m}^2 \text{ g}^{-1}$ have also been synthesized [62].

The larger pores of mesoporous materials have extended ET reactions to larger molecules than those studied in zeolites, but the amorphous nature of the framework and the presence of silanol groups along the pores have had other interesting consequences and are discussed later.

3.2.3 Sol–Gel Materials

Sol–gel processing is used to synthesize mainly inorganic materials starting from suitable monomers by a polycondensation process, and is an area of considerable research interest [63]. Various stages can be recognized in this process, including the formation of a colloidal suspension (sol) which via gelation leads to a solid phase (gel). Drying of the gel forms a xerogel (dry gel), which upon heating will transform into a denser and in some cases, a crystalline material. Almost all inorganic oxides, and also many mixed oxides, have been made by the sol–gel method, including SiO_2 , TiO_2 , ZrO_2 and Al_2O_3 .

The most extensive studies in this field have focused on SiO_2 and are reflected in this chapter. Typically, sol–gel materials are produced via controlled hydrolysis of alkoxides, as shown with silicon:



SiO_2 is a simplified representation of the final product, a more appropriate representation being $(\text{SiO}_m\text{H}_n)_p$ because of the presence of silanol groups and adsorbed water. The resulting materials can be highly porous, with pores typically in the range of tens of ångströms and surface areas that can reach hundreds of $\text{m}^2 \text{ g}^{-1}$.

The great interest in sol–gel chemistry arises not only because of the simplicity of the procedure required to generate the material and the ease of doping, but also for several technological reasons. It is straightforward to obtain a sol–gel material in a particular shape, be it in the form of powders, monoliths, thick/thin films or fibers.

The synthesis technology easily lends itself to miniaturization. Sol–gel processing can be adapted to ink-jet technology. The silica-like matrix which has been the most investigated is chemically, photochemically, electrochemically and thermally inert.

ET processes occurring inside the porous structure of sol–gel materials require entrapment of molecules in sol–gel matrices. Two basic strategies have been reported in the literature. Philipp and Schmidt, in a pioneering study, exploited the hydrolytic stability of Si–C bonds to prepare sol–gel materials with covalently held organic and organometallic groups [64]. Avnir and co-workers pioneered an alternative route to entrapment by carrying out sol–gel polymerization in the presence of a host molecule [65]. The advantage of the covalently bonded organic–inorganic system is the irreversibility of the bond, resulting in permanent entrapment. The doping procedure, on the other hand, is simpler and most molecules can be trapped in this fashion.

Nature of the porous structure

Considering that the focus of the chapter is to examine ET processes in the pores of sol–gel material, it is useful to summarize the nature of the porous structure. The chemical reactions involved in forming the oxide involve hydrolysis of the Si–OR group and the condensation of the Si–OH and Si–OR groups to form an Si–O–Si framework. Varying the synthesis conditions influences the different hydrolysis and condensation reactions and thereby allows for control of the porous property of the sol–gel-derived materials. Silica gels made under acidic conditions tend to exhibit microporosity, whereas processing under basic conditions leads to mesoporosity [66]. It has been proposed that in sol–gel oxides the porosity is controlled by both the nature of the internal structure of the primary particles and by how the particles aggregate [63g]. Acidic conditions tend to lead to smaller primary particles and hence microporosity, whereas basic conditions give larger particles, giving rise to mesoporosity. Figure 11 shows a transmission electron micrograph (TEM) of a xerogel derived from $\text{Si}(\text{OCH}_3)_4$, demonstrating the physical nature of the porosity [63g].

Considerable research has been done on optical properties of molecules entrapped in xerogels, providing information on porosity. With Rhodamine 6G as a probe, it was concluded that the matrix does an efficient job of isolating molecules in a reasonably polar environment due to nests of hydroxyl groups [65]. Because of the isolation of molecules from each other, materials with high extinction coefficients can be prepared by loading the sol–gel with dyes, although a limit to this process has been noted for $\text{Ru}(\text{bpy})_3^{2+}$ and proteins [67, 68]. The vibronic structure of the fluorescence spectrum of pyrene and excimer formation of pyrene have been used to monitor the generation of pore structure and it was found that the pyrenes ended up isolated in microporous cages [69].

Homogeneity of the pores was noted based on single excited-state lifetimes obtained for probes such as $\text{Ru}(\text{bpy})_3^{2+}$ on $\text{SiO}_2\text{--TiO}_2$ [70] and biphenylcarboxylic acid on SiO_2 [71]. The lifetime of $\text{Ru}(\text{bpy})_3^{2+}$ was found to increase from 0.6 μs in solution (1×10^{-3} M) to 1.9 μs upon encapsulation. This increase in the lifetime is characteristic of tight encapsulation, as has been noted previously for encapsulation of $\text{Ru}(\text{bpy})_3^{2+}$ into cellulose acetate and proposed to arise from destabilization of the ^3dd (metal-centered) state [72].

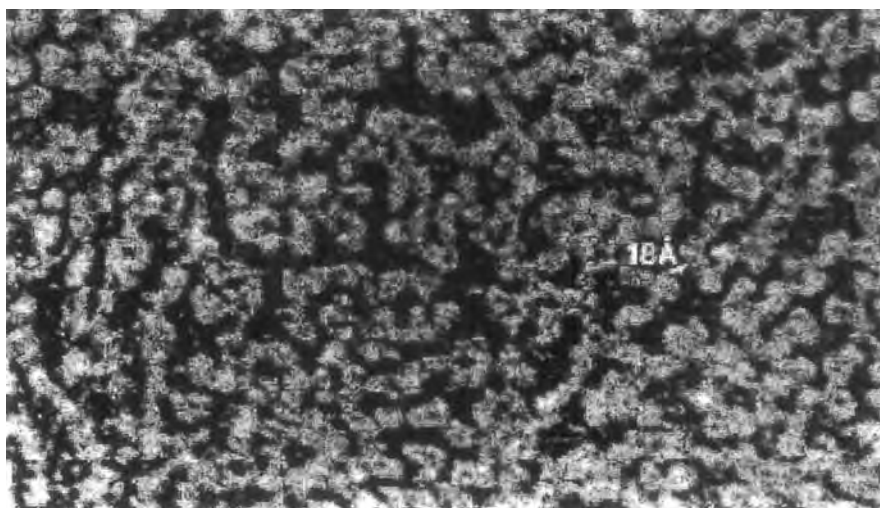


Figure 11. TEM of an $\text{Si}(\text{OCH}_3)_4$ -derived xerogel.

Photochemical stability is also increased upon encapsulation, e.g. the degradation half-life of 4-oxazine is increased fourfold by entrapment compared with solution [70]. Based on the emission spectrum of Eu^{3+} (in particular the $^5\text{D}_0 \rightarrow ^7\text{F}_2$ band at 615 nm), it has been noted that as the solvent is removed by heating, the symmetry around the cation decreases during the gel to glass transition [73]. Figure 12 shows the emission spectra of Eu^{3+} as the sol–gel is heated from 298 to 873 K [73]. At room temperature, the low intensity is due to electron–phonon coupling with the C–H and O–H groups. As the temperature increases, solvent begins to leave the gel and Eu^{3+} forms covalent and coordinative bonds with the sol–gel framework. Both of these events result in a lowering of the symmetry around the probe, causing band broadening and an increase in intensity of the $^5\text{D}_0 \rightarrow ^7\text{F}_2$ band at 615 nm. The degree of dryness of the sol–gel material controls both the rigidity of encapsulation and access to the probe molecule. Spiroyrans will exhibit photochromism via isomerization between the colorless spiro form and the colored mercocyanine zwitterion only in wet sol–gel SiO_2 [74].

3.3 Electron-transfer Reactions

3.3.1 Microporous Materials and Zeolites

Redox chemistry

Zeolites have found extensive applications in the field of petroleum cracking as solid acid catalysts [75]. With the introduction of redox metal atoms into the framework,

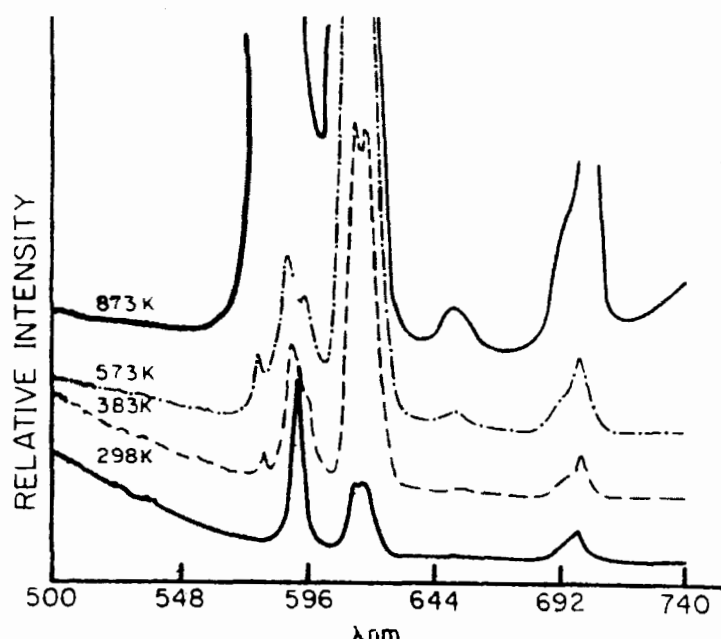


Figure 12. Emission spectra of Eu(III) at various temperatures during the gel to glass transformation of a silica sol-gel.

their potential extends into the realm of ET reactions and has been the subject of several reviews [76]. Redox molecular sieves, as they are popularly known, can be prepared in three different ways: (1) framework substitution, (2) ship-in-a-bottle encapsulation of complexes and (3) ion exchange with or without the formation of cluster species.

Involvement of framework atoms

The common means of introducing redox catalytic activity in zeolites is by the substitution of framework atoms such as Si, Al or P with redox-active metal cations. This has been accomplished by two different methods: (1) hydrothermal synthesis and (2) post-synthesis modification. Irrespective of the method of preparation, with the notable exception of titanium silicalites, these redox metals in the framework are susceptible to leaching due to the solvolysis of M–O bonds [77]. Even the Ti silicalites suffer from leaching under basic conditions [76a].

Various redox metals, including Ti, V, Cr, Mn, Fe, Co, Cu, Zn, As, Zr and Sn, have been incorporated into microporous materials such as silicalites through hydrothermal synthesis by the addition of the respective cations to the synthesis gel. The disadvantages of this method include the time-consuming optimization of synthesis procedure for each metal-zeolite combination and the necessity of Al for crystallization of certain structures. The presence of Al leads to Brønsted acidity

and increased hydrophilicity resulting in unwanted acid-catalyzed side reactions and reduced selectivity, respectively [78].

Post-synthesis modification involves isomorphous substitution of framework atoms with the desired redox metals either in aqueous media with soluble metal salts or in the gas phase with volatile chlorides. Incorporation of Ti into the framework of faujasite, zeolite- β and ZSM-5 has been accomplished by treating the zeolite with ammonium titanyl oxalate, TiCl_4 or $\text{Ti}(\text{O}i\text{-Pr})_4$. Substitution of V for framework atoms has been reported with VOCl_3 vapor. A more generalized method involving the reoccupation of the silanol nests created by the deboronation of borosilicates (ZSM-5 and zeolite- β) shows considerable promise for the incorporation of redox metals into the framework [79].

Interest in framework-substituted zeolites stems from their use as catalysts in liquid-phase oxidations. The most common mechanisms for oxidations involving the framework metal atoms are (1) free radical autoxidation and (2) catalytic oxygen transfer, represented schematically in Figure 13a and b, respectively [76]. Although both mechanisms could use O_2 , the commonly employed oxidants are hydrogen peroxide and alkyl hydroperoxides such as *tert*-butyl hydroperoxide (TBHP). Non-zeolitic microporous materials such as Co aluminophosphate (AIPO) with cobalt as the redox center could involve alkoxy and alkylperoxy radicals as intermediates and hence could be categorized as homolytic free radical autoxidation (Figure 13a). The catalytic oxygen transfer mechanism is heterolytic in nature, as shown in Figure 13b. In the case of early transition metals such as Ti, this mechanism involves the formation of a peroxometal and the metal center undergoes no change in oxidation state. In the case of first-row and late transition metals, an oxometal is involved and the metal undergoes a two-electron oxidation by the oxidant followed by reduction by the substrate. The oxometal route is the major pathway for gas-phase hydrocarbon oxidation (Mars–van Krevelan mechanism), but in the liquid phase it is much less common owing to the competing free radical autoxidation pathway.

Titanium silicalites

Of the various redox metal–zeolite systems that have been studied, none parallels titanium silicalites (TS-1, TS-2) in the extent of investigation, catalytic versatility and long-term stability [80]. The only limitation of these Ti silicalites is their small pore size ($5.1 \times 5.5 \text{ \AA}$ along the $\{100\}$ channels), restricting the size of substrates and oxidants. Larger substrates show much lower reactivity and turnover numbers and bulky oxidants such as TBHP are sluggish, limiting their usefulness. This significant limitation has been overcome with the use of larger pore systems such as zeolite- β , as will be discussed later.

Alkane oxidation to alcohols, aldehydes and ketones has been extensively studied and it was found that the smaller linear alkanes show higher turnovers than the longer linear, branched and cyclic alkanes [81]. Although the turnover numbers are found to increase with the addition of methanol as a co-solvent, the general role of the co-solvent in selectivity is still not clear. Catalytic epoxidations of relatively inert alkenes such as propylene and allyl chloride were found to be facile under mild

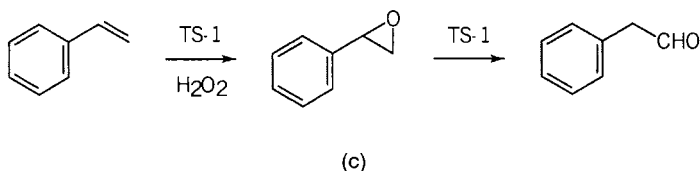
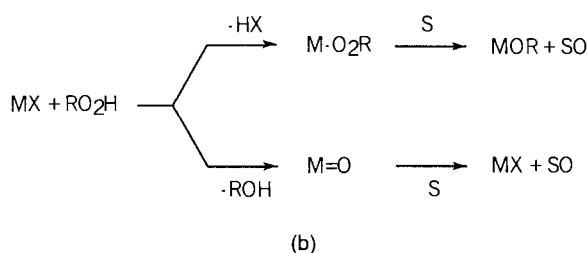
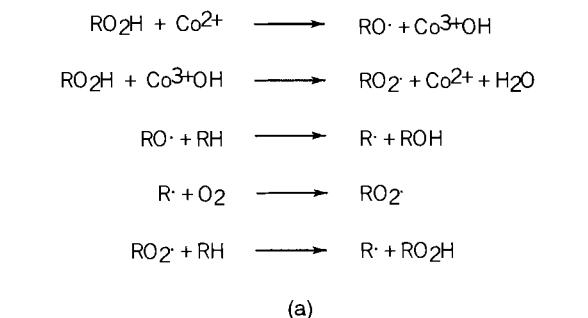


Figure 13. (a, b) Schematic representation of the oxidation pathways using redox molecular sieves: (a) homolytic free radical autoxidation and (b) heterolytic oxygen transfer. (c) Oxidation of styrene to styrene oxide and transformation to 2-phenylacetaldehyde using a bifunctional Ti-silicalite catalyst.

conditions [82]. The presence of Brønsted acid sites could be a boon or bane depending on the substrates and the desired product. One instance where the Brønsted acidity augments the catalytic ability through bifunctional catalysis is the oxidation of styrene to styrene oxide followed by the acid-catalyzed rearrangement to form 2-phenylacetaldehyde, shown in Figure 13c [83]. Selective oxidation of alcohols results in the conversion of primary alcohols to aldehydes and secondary alcohols to ketones as major products [84]. Methanol is not very reactive and tertiary alcohols are converted slowly to the corresponding alkyl hydroperoxides. Chemoselectivity has been illustrated by the oxidation of allyl alcohol, which results primarily in epoxidation of the double bond rather than oxidation of the OH group [85].

One of the most successful industrial applications of titanium silicalites has been the hydroxylation of phenol to yield a 1:1 mixture of catechol and hydroquinone

[86]. The selectivity to catalyze ring oxidation over side-chain oxidation has been illustrated in the case of nuclear hydroxylation of toluene, anisole and *m*-cresol [87]. Catalytic conversion of NH_3 to hydroxylamine has been cleverly exploited for the ammoximation of aldehydes and ketones via the reaction of the hydroxylamine and the carbonyl compound. Ammoximation of cyclohexanone to cyclohexanone oxime, a raw material for nylon-6 production, illustrates the use of redox molecular sieve catalysts for an industrially important and commercially viable process [88]. Other applications include oxidation of primary and secondary amines to the corresponding hydroxylamines and hydroximes, respectively [89], anilines to the corresponding symmetrical azobenzenes [90], thioethers to sulfoxides and sulfones [85a] and secondary amines to nitrones in the presence of methanol [91]. Cleavage of C=N groups in oximes, tosylhydrazones and imines has also been reported [92].

Other titanium frameworks

Large pore structures with Ti in the framework that can accommodate larger substrates and oxidants include Ti-zeolite- β [93], Ti- AlPO_4 -11 [94], Ti-ZSM-48 [95], Ti- AlPO_4 -5 [94] and Ti-Si AlPO_4 [96]. The aluminum content of these catalysts is a potential problem and requires the Brønsted acidity to be neutralized by ion exchange with alkali metals. Ti-zeolite- β can epoxidize branched and cyclic alkenes with the bulky TBHP as oxidant, but the epoxide undergoes cleavage or ring opening, if Brønsted acidity is present. A good example of such a system is the catalytic oxidation of 1-octene with H_2O_2 over ion-exchanged Ti-Al-zeolite- β , giving almost exclusively octane-1,2-diol in the case of H^+ -exchanged and epoxide in the case of Li^+ -exchanged zeolite [78a]. The product selectivity, due to pore size restriction, can be demonstrated with the oxidation of linalool using TBHP giving furans and not pyrans [76a]. An example of industrially important catalysis is the ammoximation of *p*-hydroxyacetophenone in the presence of hydrogen peroxide, ammonia and methanol to the corresponding oxime, a crucial intermediate in the synthesis of the analgesic paracetamol [97]. Cyclohexanone ammoximation with Ti-zeolite- β is not useful, as the oxime can undergo a Brønsted acid catalyzed, Beckmann rearrangement to form caprolactam, which polymerizes to nylon-6, blocking the pores [97]. Ti-zeolite- β can also catalyze phenol hydroxylation, alkane oxidation and conversion of anilines to symmetrical azobenzenes [76a]. Ti-Si AlPO_4 has been used for the oxidation of cyclohexene and the product selectivity has been reported to be dependent on the oxidant, the main product being the 1,2-diol with H_2O_2 and epoxide with TBHP [96]. Ti- AlPO_4 has also been reported to catalyze phenol hydroxylation [94].

Other redox microstructures

Redox silicalites with elements other than titanium have found catalytic applications in various organic oxidations. V-ZSM-11 is reported to catalyze alkane oxidation and is found to oxidize even primary C-H bonds [98]. Detailed studies indicate that V silicalites are better than Ti silicalites for alkane oxidation, as it is found that molecular oxygen can act as the oxidant in the former case [99]. V-ZSM-5 shows selectivity toward alcohol oxidation in allyl and methallyl alcohols

with hydrogen peroxide [85a]. Cr-ZSM-11 catalyzes the cleavage of the double bond in methyl acrylate to give methyl glyoxalate and is also capable of selective epoxidation of geraniol [100]. Silicalites with various structures and metals such as V-ZSM-12 [101], V-EU-1, V-THETA-1 [102], As-ZSM-5 [103] and Sn-ZSM-11 [104] are reported to catalyze phenol hydroxylation and V-ZSM-11, V-ZSM-5 [105], Sn-ZSM-11 [85a, 104], V-EU-1, V-THETA-1 [101] and Cr-ZSM-5 [106] are reported to catalyze arene side-chain oxidation. Oxidation of primary amine and various arylamines even with electron-withdrawing groups to the corresponding nitro compounds is possible with Cr-ZSM-11 [76a]. Oxidation of secondary amines to nitrones [91] and thioethers to sulfoxides and sulfones is possible with V-ZSM-5 [85a].

Redox catalytic applications of AlPOs include selective oxidation of secondary alcohols to ketones with Cr-AlPO₄-5 [106], oxidation of the allylic group to unsaturated ketones with Cr-AlPO₄-5 [107], selective oxidation of alkenes to epoxides with V-AlPO₄-5 [108], selective epoxidation of allylic alcohols with V-AlPO₄-5 [100], phenol hydroxylation with V-ZSM-48 [109], secondary amine oxidation with V-AlPO₄-5 [91] and arene side-chain oxidation with Cr-AlPO₄-5, AFI-AlPO₄-5 and Co-AlPO₄-11 [110]. Leaching of the active metal is a common problem with redox AlPOs. The use of large pore structures for bulky aromatic oxidations is illustrated in the case of V-NCL-1 catalyzed oxidation of naphthalene and trimethylbenzenes [85a, 98]. Zeolites such as V-zeolite- β and V-borosilicate- β are reported for arene side-chain oxidation [111]. Oxidation of ethanethiol and 2-mercaptoethanol to disulfides with O₂ is possible with Co-faujasite [112].

From the examples above, it is clear that oxidation reactions using redox-active molecular sieves is an active area of research for the synthesis of fine chemicals and intermediates. The novel chemistry is possible because of the location of the transition metal ions at specific crystallographic sites in the framework and also the pore structure of microporous materials.

Entrapped molecules and assemblies

Another route to making oxidation catalysts has been to take advantage of the microporosity of zeolites to incorporate catalytically active transition metal complexes, and forms the subject matter of several review articles [113]. Incorporation of homogeneous catalysts into frameworks offers potential advantages. Accessibility of the reactants to the catalytic site is guaranteed because of the porosity. The metal centers should be more stable to degradation from dismutation or autooxidation reactions. Recovery and re-use of the catalyst are also easy with the heterogenized catalysts. One of the first molecules to be encapsulated into zeolite Y was metal phthalocyanine (Pc) which was synthesized using a ship-in-a-bottle strategy via the condensation of dicyanobenzene molecules [114]. Iron Pc complexes in zeolites X/Y have been used as oxidation catalysts for hydrocarbons using iodosylbenzene (PhIO) as oxidant [115]. Although interesting shape selectivities were observed, the turnover numbers were of the order of 6. Jacobs and co-workers improved the performance of the catalyst by using TBHP as oxidant [116]. Turnover numbers as high as 6000 were reported for the oxidation of *n*-octane at low turn-

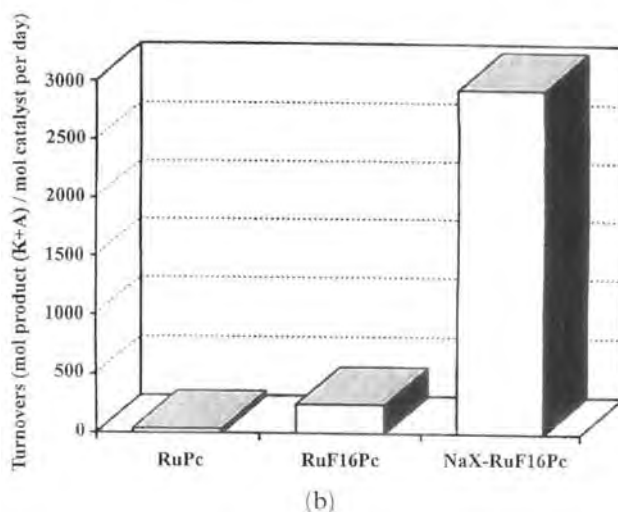
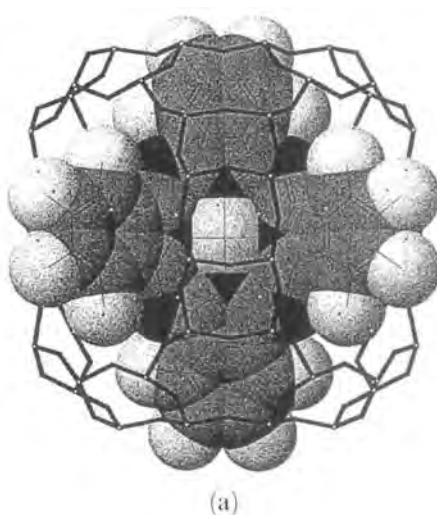


Figure 14. (a) Structure of a zeolite-entrapped perfluorinated ruthenium phthalocyanine (RuF_{16}Pc) complex used in epoxidation reactions. (b) Comparison of turnover numbers for cyclohexane oxidation using ruthenium phthalocyanine (RuPc), RuF_{16}Pc and zeolite X-entrapped RuF_{16}Pc .

over frequencies (12 h^{-1}). Significant improvement in turnover frequency for oxidation of cyclohexane (198 h^{-1}) was obtained by incorporating the FePc -zeolite into polymeric (PDMS) membranes [117]. The role of the polymer was to promote adsorption of the substrate into the zeolite. Balkus et al. entrapped ruthenium(II) perfluorophthalocyanine in zeolite X by using it as a template during the zeolite X synthesis. The fluorinated ligand is more stable, and a turnover number of 3000 per day in the oxidation of cyclohexane with TBHP was noted [118]. Figure 14a shows the entrapped Ru complex and Figure 14b compares the turnover numbers in the oxidation of cyclohexane for the Ru-Pc complexes in solution with the encapsu-

lated complex, clearly demonstrating the increased turnover numbers for the zeolite-encapsulated complex [118].

Metal complexes of other macrocyclic ligands such as salen, salophen, pyren and acacen (see Figure 4) have also been incorporated into zeolites and some of these have been examined in oxidation reactions [113]. A chiral Mn(III)–salen type of complex entrapped in zeolite EMT made it possible to obtain chiral products in alkene oxidation reactions using NaOCl as the oxidant [119]. As noted earlier, the oxidant in the epoxidation reactions using redox molecular sieves is typically H_2O_2 . Unfortunately, for metal complexes grafted into zeolites, H_2O_2 cannot be used since it decomposes, possibly by a Fenton-type reaction. This is the reason for the use of PhIO or organic hydroperoxides as oxidants. However, De Vos and Bein have reported that H_2O_2 can be used with the Mn complex of the ligand tmtacu (triamine-1,4,7-trimethyl-1,4,7-triazacyclononane) [120]. Higher selectivity using Mn(tmtacu)–zeolite Y was noted for the epoxidation of styrene, cyclohexane and norbornene. Dutta and Das have shown that the zeolite-encapsulated $[(\text{bpy})_2\text{Ru}(\text{OH}_2)_2]^{2+}$ can be oxidized by air to form the oxo complex $[(\text{bpy})_2\text{Ru}^{4+}=\text{O}]^{2+}$, which could oxidize PPh_3 to OPPh_3 [121]. In homogeneous media, the $\text{Ru}=\text{O}$ complex can only be formed electrochemically or by oxidation with Ce^{4+} [121].

The use of zeolite entrapped chiral complexes as enantioselective catalysts has been examined by Corma and co-workers [122]. Both reduction and oxidation chemistry has been explored. The zeolite used was ultrastable zeolite Y, which contains supermicropores of 12–30 Å, allowing for the encapsulation of larger complexes. These larger pores are formed by partial degradation of the framework during the ultrastabilization process. Upon catalytic hydrogenation of prochiral alkenes using Rh(I), Ru(II), Co(II) and Ni(II) chiral complexes of ligands based on L-prolinol, it was noted that the enantioselectivity was higher for zeolitic hosts than silica or unsupported complexes. Moderate enantioselectivity was also noted in the epoxidation reactions of allylic alcohols with TBHP using chiral dioxomolybdenum(VI) complexes derived from L-*trans*-4-hydroxyproline.

Even though the potential use of such entrapped catalytic systems is obvious, in practice there are problems. The reaction rates are often lower owing to the problems with diffusion of the reactants into the zeolite and pore blockage. These reasons have prompted the use of mesoporous materials and are discussed in Section 3.3.2.

Cluster species

Metal oxides on zeolites have also found use as redox catalysts. High-temperature (700–750 °C) dehydroaromatization of methane under nonoxidizing conditions has been explored with a number of zeolitic catalysts modified with transition metal ions. Although coke formation at these high temperatures is a problem, calcined molybdate-impregnated ZSM-5 shows unparalleled activity of up to 8 % methane conversion with 100 % selectivity towards aromatics. Surface studies of these Mo–HZSM-5 catalysts indicate that MoO_3 crystals are on the external zeolite surface [123].

MO_x –zeolites prepared by incorporation of metal complexes followed by mild oxidation offer unique control of activity. Comparison of Cu–ZSM-5 catalysts

prepared from $\text{Cu}(\text{OAc})_2$ and $[\text{Cu}(\text{en})_2]^{2+}$ precursors indicate that the former has higher activity for NO decomposition, whereas the latter is better for methanol conversion to higher hydrocarbons. It has been speculated that these differences in activity may be due to the fact that Cu-ZSM-5 catalyst prepared from $\text{Cu}(\text{OAc})_2$ shows a nearly equal distribution of the copper ions sited near pairs of Al^{3+} (site II) and isolated Al^{3+} ions (site I), whereas the catalyst prepared from $[\text{Cu}(\text{en})_2]^{2+}$ shows most of the copper ions sited near multiple Al^{3+} (site II) after reduction in CO [124].

Applications of cation-exchanged ZSM-5 include ammoximation of alkanes with Co-ZSM-5, water-tolerant oxidation of NH_3 to N_2 with Pd-ZSM-5, low-temperature catalytic combustion of CH_4 with Pd-ZSM-5, wet N_2O decomposition with Co-ZSM-5, NO_x reduction with CH_4 even in the presence of excess O_2 with Co-ZSM-5 and catalytic decomposition of NO in the absence of O_2 with Cu-ZSM-5. In most of these cases, the activity (rate, conversion and/or selectivity) of the redox ZSM catalysts is much higher than when the corresponding metal is supported on traditional oxides [125].

The examples discussed above demonstrate the unique advantages of zeolitic hosts; primarily stemming from highly dispersed exchange sites and the ligating effect of the framework on the cations.

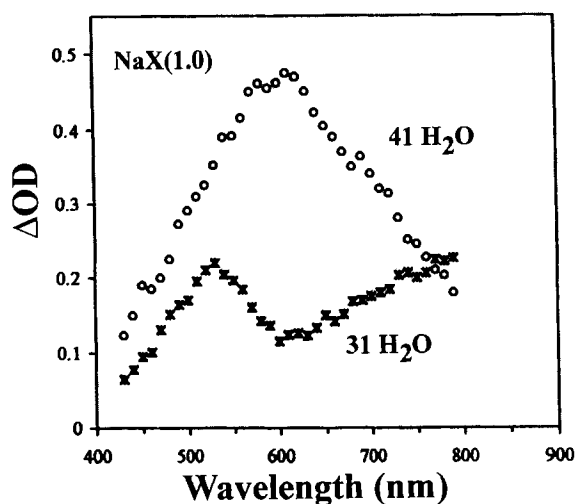
Photoredox chemistry

Active involvement of zeolitic framework in electron-transfer chemistry

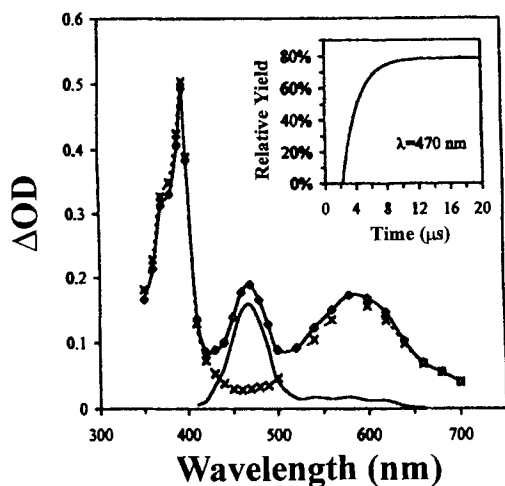
It was discovered several decades ago that spontaneous thermal electron transfer from encapsulated aromatic organics to the zeolite framework is possible. Although the exact location of the electron on the framework was not determined, dehydration of the zeolite, the zeolite topology and the nature of the co-cations in the zeolite were found to be important in generating the radical species. $\text{NH}_4\text{-Y}$ zeolite rather than Na-Y was necessary for formation of radical cations of 1,1-diphenylethylene, triphenylamine, quinoline, perylene, aniline and *p*-phenylenediamine [126]. Recent studies have shown that stable, radical cations of α,ω -diphenylpolyenes can be formed thermally on activated Na-ZSM-5 [127].

Photoexcitation of aromatics in zeolites also led to cation radicals, as reported by Iu and Thomas for pyrene and anthracene [128]. Ultraviolet photoexcitation of *trans*-stilbene in NaX formed the *trans*-stilbene radical cation (475 nm) and the zeolite-entrapped electron shows up as Na_4^{3+} (500 nm) [129]. Other organic species that form radical cations in zeolites upon high-energy UV excitation include 4-vinylanisole, *trans*-anethole, several styrenes and di(4-methoxyphenyl)ethylenes [130].

Thomas and co-workers found that high-energy γ -radiation will ionize the zeolite framework, forming holes and electrons [131]. In the presence of intrazeolitic water, hydrated electrons $(\text{H}_2\text{O})_n^-$ were formed, and characterized by their electronic spectra and short lifetimes. Figure 15a shows the transient absorption spectrum (20 ns) of the hydrated electron as a function of water content in zeolite X. For the zeolite with 41 water molecules per pseudo cell, the band at 600 nm was assigned to the hydrated electron. Upon decreasing the water content to 31 molecules per



(a)



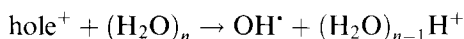
(b)

Figure 15. (a) Electronic spectra of hydrated electrons in zeolite X as a function of intrazeolitic water (taken 20 ns after electron pulse). (b) Transient absorption spectrum of MV^{2+} -zeolite Y after electron pulse. Inset show growth of 470 nm band, typical of the hydroxyl adduct of MV^{2+} .

pseudo cell, two bands at 540 and 750 nm were observed and assigned to a cation cluster trapped electron (Na_4^{3+}) and the hydrated electron, respectively [132]. Reactions of $(H_2O)_n^-$ with O_2 , N_2O and viologens were studied. In the case of methylviologen (MV^{2+}), electron transfer to form the MV^{+} radical occurred with the kinetics of ET being determined by the degree of hydration of the zeolite. From the quenching of the lifetime of $(H_2O)_n^-$ as a function of MV^{2+} , it was determined that the diffusion coefficient (D_e) of the hydrated electron through the zeolite medium is $1.2 \times 10^{-7} \text{ cm}^2 \text{ s}^{-1}$ for $(H_2O)_{31}^-$ and $3.5 \times 10^{-7} \text{ cm}^2 \text{ s}^{-1}$ for $(H_2O)_{38}^-$. The de-

crease in D_e with water content was considered to be a reflection of the activation barrier for the electron to pass from one supercage to another across a 7.4 Å window.

The holes generated by the high-energy radiation also reacted with organic molecules such as pyrene and methylviologen (MV^{2+}) to form radical cations [131]. Figure 15b shows the transient absorption spectrum of an MV^{2+} -zeolite Y after the electron pulse [131]. The bands at 390 and 600 nm are typical of MV^{+} , but the band at 470 nm that grows with time is typical of the hydroxyl adduct of MV^{2+} . Formation of OH^\bullet was explained by the following reaction:



Thus, exposure of zeolites to high-energy radiation leads to the formation of holes and electrons, both of which react with water to produce OH^\bullet and hydrated electrons.

Zeolite frameworks have also been reported to act as an electron donor via charge-transfer (CT) interactions. Yoon and co-workers examined the electronic spectra of a series of alkali metal ion-exchanged faujasitic zeolites containing about one MV^{2+} per eight supercages [133]. A new electronic band around 250–270 nm was observed in only the dehydrated zeolite X/Y samples, with the band red-shifting with increasing electropositivity of the metal ion: Li^+ (256 nm), Na^+ (258 nm), K^+ (263 nm) Rb^+ (265 nm) and Cs^+ (268 nm) (Figure 16) [133]. This band was assigned to a CT transition from the zeolite framework to methylviologen. A linear correlation, indicative of Mulliken's CT theory, was found between the energy of the CT band and the average charge on the framework oxygen atom, as calculated by Sanderson's electronegativity principle. This example represents a unique feature of the zeolite not only in the sense that it acts as an electron donor, but also because the degree of donation is tunable by the ion-exchanged cation. A related example of the zeolite acting as an electron donor is the detection of MV^{+} with lifetimes of

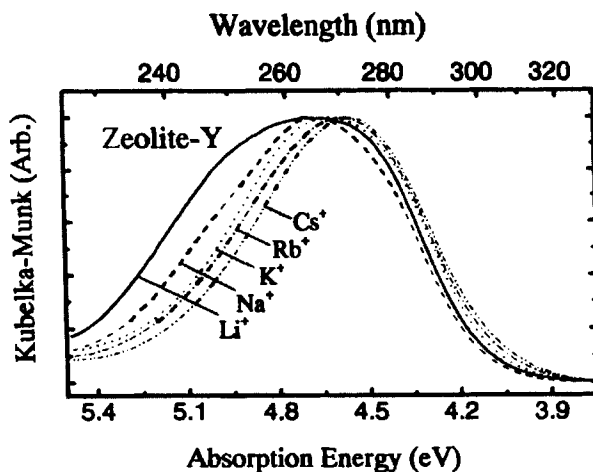


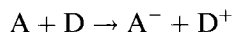
Figure 16. Electronic spectra of dehydrated MV^{2+} -alkali metal ion-exchanged zeolite Y as a function of alkali metal ion.

several hours upon UV photoexcitation of MV^{2+} in Rb- and Cs-zeolite Y [134]. Framework oxygen atoms were proposed as the electron-donating sites.

Electron-transfer reactions between entrapped species in zeolites

Transient spectroscopic studies

Extensive studies have been carried out on ET reactions between guest molecules in zeolites. The reaction of interest is



where A represents the electron acceptor and D the donor. In photoinitiated ET reactions, the major issues concern the efficiency of the forward ET process, the rate of the back ET reaction and the long-term stabilization of the charge-separated pairs. In photoinitiated ET reactions, the strong driving force for the back ET reaction limits the lifetime of the charge-separated states and thereby the usefulness of the photochemical process. Several review articles have appeared in the last few years in this research area [135]. We shall first examine the role of the zeolite as a host in influencing the dynamics of the photoelectron transfer reactions. Transient spectroscopic measurements are necessary to monitor the fate of charge-separated species. The time resolution of these experiments is controlled by the pulse width of the interrogating lasers and can be as brief as hundreds of femtoseconds. Considering that the zeolite matrix is a powder, transient studies typically involve diffuse reflectance spectroscopy, which provides information on the electronic spectra of the reactant/product species [136]. We discuss below three cases that clearly demonstrate the influence of the zeolite on the dynamics of ET reactions.

Aromatic hydrocarbons as donors: Charge-transfer complexes between aromatic hydrocarbons and bipyridinium in zeolites have been extensively studied [137]. Typically, MV^{2+} -exchanged zeolites are colorless but develop intense colors upon introduction of arene donors. This is reflected in the absorption spectra by the appearance of new CT bands, whose wavelength maxima relate well to the ionization potential of the donors, as expected from Mulliken's CT theory. Photoexcitation within the CT band of the anthracene (ANT)- MV^{2+} complex in zeolite Y with a 25 ps laser pulse led to the appearance of bands at 620 and 730 nm, which were assigned to the radical species $MV^{+\bullet}$ and $ANT^{+\bullet}$, respectively. The decay of these signals by the thermal back ET process occurred with a rate constant of $2.9 \times 10^9 \text{ s}^{-1}$, which was at least an order of magnitude slower than in acetonitrile ($4 \times 10^{10} \text{ s}^{-1}$). Interestingly, the signal due to the radical cations persisted beyond 4 ns, and for experiments done on the microsecond time-scale, residual absorptions were found beyond 1 ms. In zeolite L, which has channels of 7 Å, the decay rates were faster, e.g. for ANT-DQ $^{2+}$ (2,2'-bipyridinium ion) the rate constant was $2.2 \times 10^{10} \text{ s}^{-1}$ compared with $4.7 \times 10^9 \text{ s}^{-1}$ in zeolite Y. The three different decay regimes and the role of the zeolite topology on the back ET process have been explained as arising from electrostatic interactions with the zeolite. The radical ion pairs generated upon photoexcitation of the arene-pyridinium complexes are posi-

tively charged or neutral in all the cases that were examined. Since, the zeolite framework is negatively charged, Coulombic attraction of the radicals toward the zeolite walls will separate the charge pairs. The different decay regimes have been explained in terms of the acceptor and donor radicals being at different distances within the zeolite cages. Similar arguments justify that the back ET in zeolite L was faster than that in zeolite Y, because of the smaller size of the channels (7 Å) in zeolite L compared with the zeolite Y supercages (13 Å).

Charge-transfer complexes of neutral molecules in zeolites have also been examined. Transient experiments with 1,2,4,5-tetracyanobenzene (TCNB) as acceptor and arene donors have been reported. For naphthalene, transient absorption bands centered at 470 and 680 nm due to TCNB^{•-} and naphthalene radical were observed [138]. The decay was found to be biphasic and was 10 times slower in dehydrated zeolite Y than in the hydrated sample, indicating a strong interaction with the framework.

Sensitized electron-transfer reactions: The influence of the zeolite host on photo-sensitized ET reactions has also been investigated for a number of systems. Ramamurthy and co-workers found that the radical cation of *trans*-anethole was formed upon photoexcitation of 2,3-dicyanonaphthalene or 9-cyanoanthracene as sensitizers in zeolite NaX with 355 nm radiation [130a]. Figure 17 shows the transient diffuse reflectance spectra of the *trans*-anethole cation for two different loadings. From the decay of the signal, it was concluded that the radical cation was long-lived (half-lives in excess of 10 μs), and entrapment in the zeolite was slowing down the back ET reaction [130a].

Tris(bipyridyl) complexes of ruthenium: Another photosensitizer system that has been extensively studied in zeolites is tris(2,2'-bipyridine)ruthenium(II) [Ru(bpy)₃]²⁺,

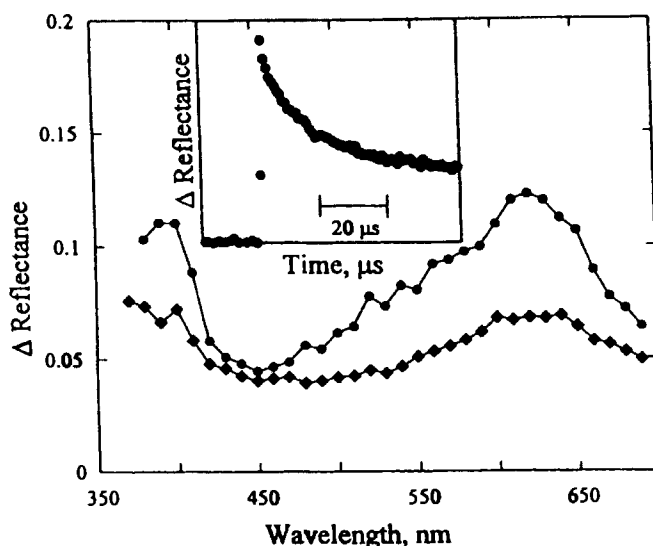


Figure 17. Transient spectra of nitrogen purged 2,3-dicyanonaphthalene ($10 \mu\text{mol g}^{-1}$) plus *trans*-anethole (\diamond , $32 \mu\text{mol g}^{-1}$; \bullet , $190 \mu\text{mol g}^{-1}$) in NaX measured $0.6 \mu\text{s}$ after 355 nm excitation. Inset shows decay of the signal at 610 nm for high loading of *trans*-anethole sample.

which has a long-lived (~ 500 – 600 ns) metal-to-ligand CT (MLCT) state, populated via visible excitation (peaked around 450 nm). Several transient spectroscopic studies have been reported for the $\text{Ru}(\text{bpy})_3^{2+}$ –bipyridinium photosensitized ET in zeolites. Mallouk and co-workers were the first to investigate the kinetics of photoelectron transfer from $\text{Ru}(\text{bpy})_3^{2+}$ on the surface of the zeolite to bipyridinium ions in the zeolite [139]. They linked a tris-ligated bipyridine complex of $\text{Ru}(\text{II})$ via an ethylene unit with a 2,2'-bipyridinium ion (2DQ^{2+}). The positive charge on the DQ^{2+} unit made it possible to exchange the RuL_3^{2+} – 2DQ^{2+} on to the surface of a zeolite that was previously exchanged with benzylviologen (BV^{2+}). The reduction potentials of $^*\text{RuL}_3^{2+}$, 2DQ^{2+} and BV^{2+} are -1.50 , -0.75 and -0.59 V (vs. SCE), respectively. Upon photoexcitation of the zeolite with a 10 ns, 532 nm laser pulse, the transient spectrum showed absorption maxima at 400 and 600 nm, assigned to the radical $\text{BV}^{+\cdot}$ and bleaching of the band at 480 nm due to formation of RuL_3^{3+} . The formation of the Ru^{3+} – $\text{BV}^{+\cdot}$ charge-separated pairs via the ET steps $\text{RuL}_3^{2+} \rightarrow 2\text{DQ}^{2+} \rightarrow \text{BV}^{2+}$ occurred within 100 ns. The back ET rate constant was determined as $2.7 \times 10^4 \text{ s}^{-1}$. The longer spatial separation of Ru^{3+} and $\text{BV}^{+\cdot}$ was suggested as the reason for the slow back ET.

In a more recent study, Mallouk and co-workers investigated the dynamics of ET of a series of $[\text{RuL}_3^{2+}-(\text{CH}_2)_n\text{-viologen}]^{2+}$ on the zeolite surface as a function of the length of the methylene spacer [140]. Several zeolites were examined, including zeolite Y, mordenite and zeolite L. In all cases, the viologen ends of the donor–acceptor pair ion-exchanged into the surface cages/channels of the zeolite, while the RuL_3^{2+} unit remained external to the zeolite. For small values of n (~ 2), the dynamics of the forward ET were too fast to be measured. For longer chains, it was found that the forward ET occurred 1–2 orders of magnitude slower ($\sim 10^8 \text{ s}^{-1}$) than in solution. Two reasons were proposed for this effect. First, the zeolite-exchanged complex has less flexibility than in solution and favorable conformations for ET may be restricted. Second, it was proposed that the ion exchange on to the zeolite surface may have modified the reduction potentials, and thereby the thermodynamic driving force for ET. The conformational argument for slowing of the ET is consistent with the fact that zeolite Y provides the greatest freedom followed by mordenite and zeolite L, and the forward ET rates followed the order zeolite Y > mordenite > zeolite L. The back ET dynamics were found to be complex and the rate constants were derived based on the Alberty model, which assumes heterogeneity of sites and, thereby, rate constants. It was found that for CH_2 spacer lengths ($n = 5$), the lifetime of $\text{Ru}(\text{III})$ –viologen $^{+\cdot}$ could be 10^5 times longer than in solution. Figure 18 demonstrates the decay of the viologen radical formed on a mordenite sample, measured by transient diffuse reflectance spectroscopy [140]. The inset shows the rapid rise in the $\text{MV}^{+\cdot}$ signal, followed by a slow decay. Such a large increase in lifetime was explained by a combination of slow back ET, and lateral ET between $\text{Ru}^{3+}/\text{Ru}^{2+}$ and $(\text{viologen})^{2+}/(\text{viologen})^{+\cdot}$ pairs, which would move the charges further apart.

Dutta and co-workers focused on the completely intrazeolitic $\text{Ru}(\text{bpy})_3^{2+}$ and bipyridinium ion systems [141]. Three N,N'-dialkyl-2,2'-bipyridinium ions and methylviologen (4,4'-bipyridinium ion) with reduction potentials varying from -0.37 to -0.65 V (vs. NHE) were studied. For the 2,2'-bipyridinium salts (members

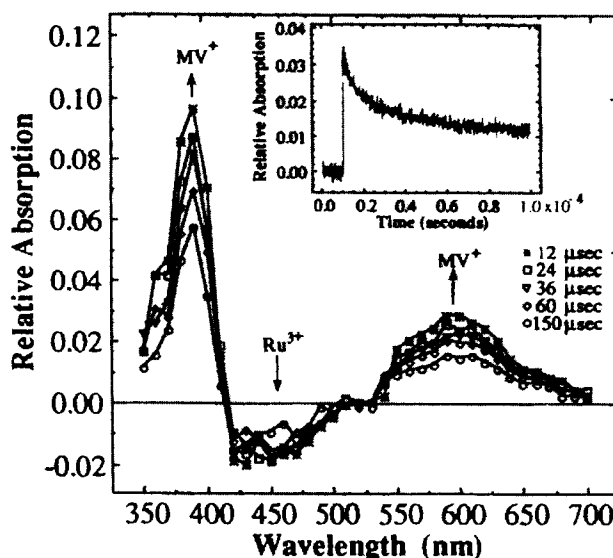


Figure 18. Time-resolved diffuse reflectance spectra 12–150 μ s after excitation from 532 nm laser pulse for $\text{Ru}(\text{bpy})_3^{2+}$ – $(\text{CH}_2)_5\text{-MV}^{2+}$ on mordenite. Inset shows the decay of methylviologen radical followed at 400 nm.

of the diquat family), two, three and four CH_2 bridging units, abbreviated 2DQ^{2+} , 3DQ^{2+} and 4DQ^{2+} , respectively, were examined. Because of the limitations of the time-resolved diffuse reflectance instrument, only a lower limit of the forward ET rate ($>10^7 \text{ s}^{-1}$) constant from $\text{Ru}(\text{bpy})_3^{2+}$ to the bipyridinium ion was obtained. The back ET from the photogenerated bipyridinium radical ions to $\text{Ru}(\text{bpy})_3^{3+}$ was monitored at different intrazeolitic bipyridinium concentrations. At low loadings of bipyridinium ions (one per 10–15 supercages), the transient signal between 360 and 390 nm had contributions from both $\text{Ru}(\text{bpy})_3^{2+}$ and the bipyridinium radical ions, since the bipyridinium ion concentration was not high enough to quench all of the $\text{Ru}(\text{bpy})_3^{2+}$. The decay of this signal (360–390 nm) could be fitted to the sum of two exponentials, representing the disappearance of unquenched $\text{Ru}(\text{bpy})_3^{2+}$ and the back ET from the bipyridinium radical ions to $\text{Ru}(\text{bpy})_3^{3+}$. The rate constants for the back ET for 2DQ^{2+} , MV^{2+} , 3DQ^{2+} and 4DQ^{2+} were found to be 4.0×10^4 , 1.7×10^4 , 1.1×10^4 and $7.3 \times 10^3 \text{ s}^{-1}$, respectively. The decrease in the ET rates with increasing driving force for the reaction indicates that the ET is occurring in the Marcus inverted region. At high loadings of the bipyridinium ions (1.2–1.7 molecules per supercage), the bipyridinium radical ions were considerably longer lived, as shown in Figure 19, and a simple exponential decay no longer described the loss of the bipyridinium radical signal [141]. A model that allowed for electron exchange processes between bipyridinium ions to compete with the back ET was necessary. The basis of the kinetic model is shown in Figure 20 and made it possible to extract the back ET rate constant (k_b) at high loadings along with the rate constants for electron hopping (k_{hop}) and a second-order electron (bipyridinium radical)–hole ($\text{Ru}(\text{bpy})_3^{3+}$) recombination process (k_2). For the series 2DQ^{2+} , MV^{2+} , 3DQ^{2+} and 4DQ^{2+} with high loading, the back ET rate constants were 2.5×10^5 , 9×10^4 , 1.8×10^5 and $1.2 \times 10^5 \text{ s}^{-1}$, respectively. In the high

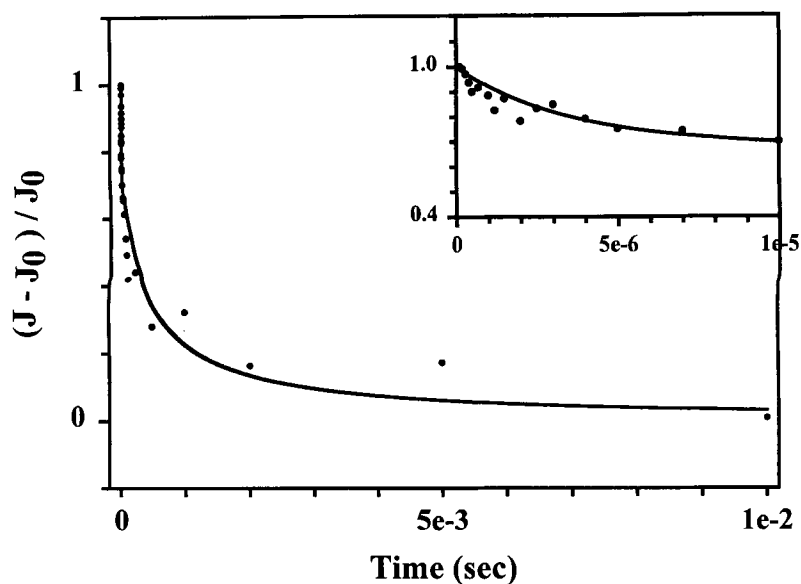


Figure 19. Decay of MV^{2+} for intrazeolitic $Ru(bpy)_3^{2+}-MV^{2+}$ -zeolite Y for high MV^{2+} loading. Inset shows the decay at shorter times and solid lines indicate best fit using the model shown in Figure 20.

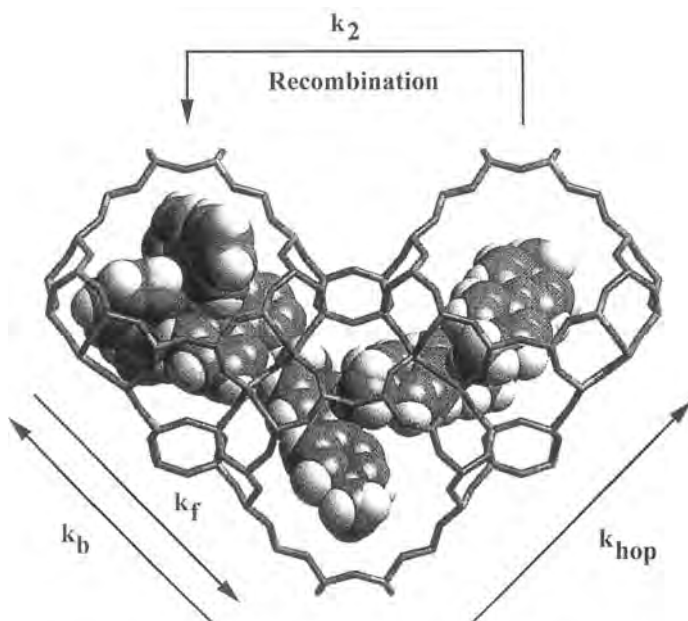


Figure 20. Model of the electron transfer process in $Ru(bpy)_3^{2+}-MV^{2+}$ -zeolite Y.

loading case, longer lived charge separation was observed because of the presence of a route for charge propagation by electron hopping via the densely packed viologen molecules.

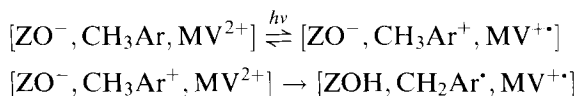
Steady-state photolysis studies

The above discussions on the transient spectroscopic studies of photoelectron transfer in zeolites clearly show that the dynamics of the ET can be strongly influenced by the host matrix. In particular, the energy-wasting back ET in all cases appears to be slowed inside the zeolite. Several research groups have taken advantage of the slower back ET in zeolites to develop novel synthetic schemes, and also to design systems that result in permanent charge separation. These experiments are typically done by steady-state photolysis followed by spectroscopic and/or chromatographic analysis of the products.

Synthetic schemes: Ramamurthy and co-workers have exploited the stabilization of arylalkene cation radical in zeolite X formed via photosensitized ET to examine the dimerization reaction of arylalkenes [130a]. Various photosensitizers, including cyanoaromatic compounds and quinolium and acridinium ions, have been examined. The radical cations react with the precursor alkenes to form the dimers shown in Figure 21 [130a]. Besides the role of the zeolite in stabilizing the radical cation by limiting the back ET, the spatial constraints in the zeolite also influenced the product distribution as compared with studies in homogeneous solution. Both *cis,syn* and *trans,anti* dimers were formed in solution and in the zeolite. However, in all cases the zeolite preferentially stabilized the more spherical *cis,syn* isomer rather than the elongated *trans,anti* dimer, reflecting the spherical geometry of the supercage [130a].

Permanent charge separation

Arene–bipyridinium CT complexes: As discussed above, long-lived charge-separated species were observed by transient spectroscopy upon excitation into the CT band of arene–bipyridinium complexes in Na-X zeolites. Interestingly, if the arene contained a CH₃ group (ArCH₃), as in pentamethylbenzene, mesitylene, durene, prehnitene and methylnaphthalene, and K⁺, Rb⁺ or Cs⁺ zeolite X were used as the host, photoexcitation led to permanent stabilization of the bipyridinium cation radical [135e]. Explanation of this effect hinges on the fact that the cation radical of the methylated arenes are acidic and that the zeolite framework is basic with ion exchange of the more basic alkali metal ions. The following scheme demonstrates the process (ZO represents the zeolite framework):



The CH₂Ar[·] radical can dimerize, leaving a steady-state population of MV⁺⁺. This example shows that the zeolite can be an active host and influence ET re-

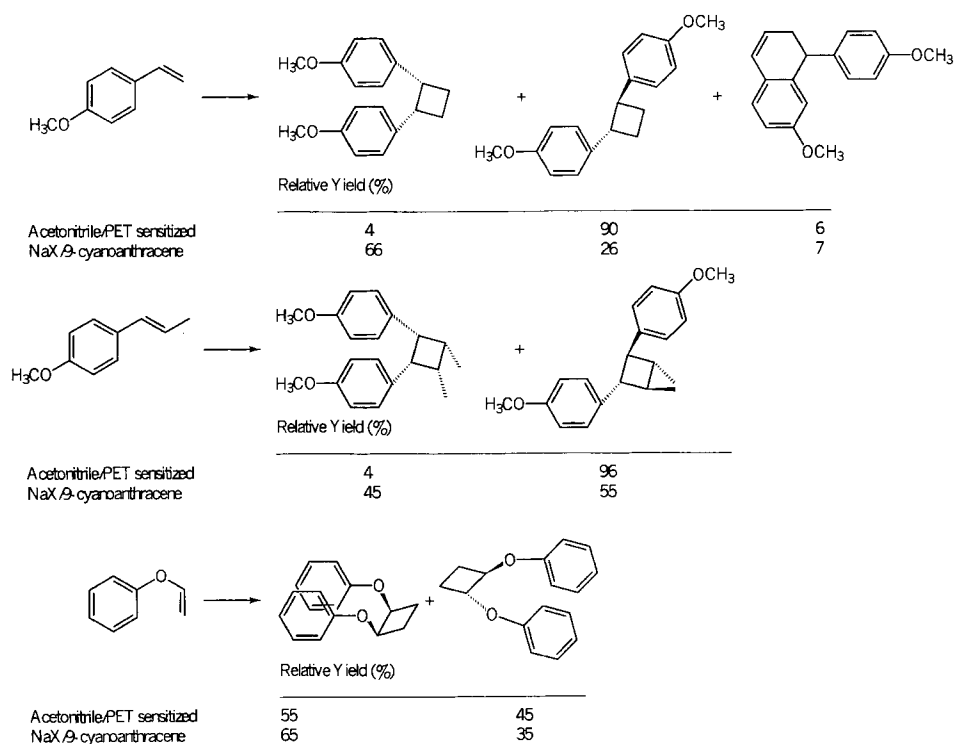


Figure 21. Reaction products of the photosensitized dimerization reactions of arylalkenes in NaX compared with solution studies.

actions both via electrostatics, leading to long-lived charge-separated species, and as a reactant in promoting permanent charge separation.

Ru(bpy)₃²⁺–bipyridinium system: From the transient studies on both zeolite-encapsulated and surface $\text{Ru}(\text{bpy})_3^{2+}$ –bipyridinium discussed above, it is clear that the zeolite promotes long-lived charge-separated states. Several strategies have been reported in translating the long-lived charge separation to permanent charge separation [142]. Dutta and co-workers surrounded the encapsulated $\text{Ru}(\text{bpy})_3^{2+}$ in zeolite Y with a 2,2'-bipyridinium ion (4DQ^{2+} , $E^\circ = -0.65$ V vs. NHE) and in turn suspended the zeolite in a solution of propylviologen sulfate (PVS, $E^\circ = -0.4$ V vs. NHE). Upon photoexcitation of the suspension in a deaerated environment, the aqueous solution turned blue and the absorption spectrum of the solution indicated the presence of $\text{PVS}^{\bullet+}$ radical cation. The model used to explain the data is shown in Figure 22 [142b]. As was pointed out in the section on transient spectroscopy of $\text{Ru}(\text{bpy})_3^{2+}$ –bipyridinium (high loading) zeolites, the initial process of ET quenching of the $\text{Ru}(\text{bpy})_3^{2+}$ system leads to the formation of the bipyridinium radical cation. Electron hopping can occur between neighboring bipyridinium molecules,

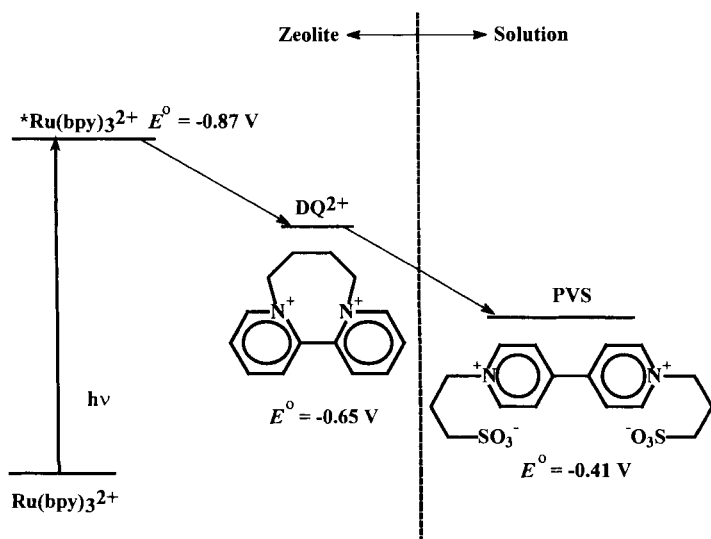


Figure 22. Model of permanent charge separation for the $\text{Ru}(\text{bpy})_3^{2+}$ – DQ^{2+} –PVS system.

leading to long-lived charge separation. If this charge migrates to the surface of the zeolite, then a directional ET to PVS can occur. The formation of $\text{PVS}^{\bullet-}$ will lead to repulsion from the zeolite framework and thereby permanent charge separation. Support for the electron hopping argument between the viologen molecules in neighboring cages is provided by a recent report [143]. It was found that a MV^{2+} –zeolite Y sample upon treatment with $\text{Na}^+\text{Mn}(\text{CO})_5^-$ turned blue, the characteristic color of $\text{MV}^{\bullet+}$, even though $\text{Mn}(\text{CO})_5^-$ cannot penetrate into the zeolite cages. The conversion of intrazeolitic MV^{2+} to $\text{MV}^{\bullet+}$ was quantitative. Electron migration into the zeolite must proceed through charge hopping after the surface MV^{2+} has been reduced by $\text{Mn}(\text{CO})_5^-$.

The problem with the $\text{Ru}(\text{bpy})_3^{2+}$ – 4DQ^{2+} zeolite Y, PVS solution system was its limited efficiency (quantum yield = 5×10^{-4}). This was related to both the back ET (even though it is slowed in the zeolite) and the ability of the charge to move to the surface by electron hopping. Improvements in both these areas have been reported. Kincaid and co-workers focused on influencing the back ET by adding a donor molecule in a cage neighboring the one containing the $\text{Ru}(\text{III})$ species and noticed a four-fold increase in the charge separation [142c, d]. Figure 23a shows the scheme of their ET process. The novelty of their system was the controlled intrazeolitic synthesis in which two molecules have been placed by design in neighboring supercages. Upon photoexcitation of $\text{Ru}(\text{bpy})_2\text{bpz}^{2+}$ in the zeolite, ET to DQ^{2+} occurs. The back ET from $\text{DQ}^{\bullet+}$ to $\text{Ru}(\text{bpy})_2\text{bpz}^{3+}$ is intercepted because of the ET from the neighboring $\text{Ru}(\text{mmb})_3^{2+}$ to $\text{Ru}(\text{bpy})_2\text{bpz}^{3+}$. As a result, there is increased efficiency of permanent charge separation ($\text{PVS}^{\bullet-}$). Figure 23b compares the $\text{PVS}^{\bullet-}$ yield for the adjacent cage system (AC), $\text{Ru}(\text{bpy})_2\text{bpz}^{2+}$ or $\text{Ru}(\text{mmb})_3^{2+}$ in zeolites

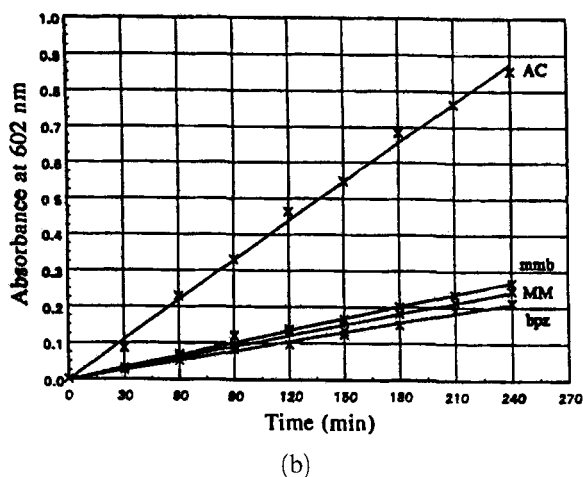
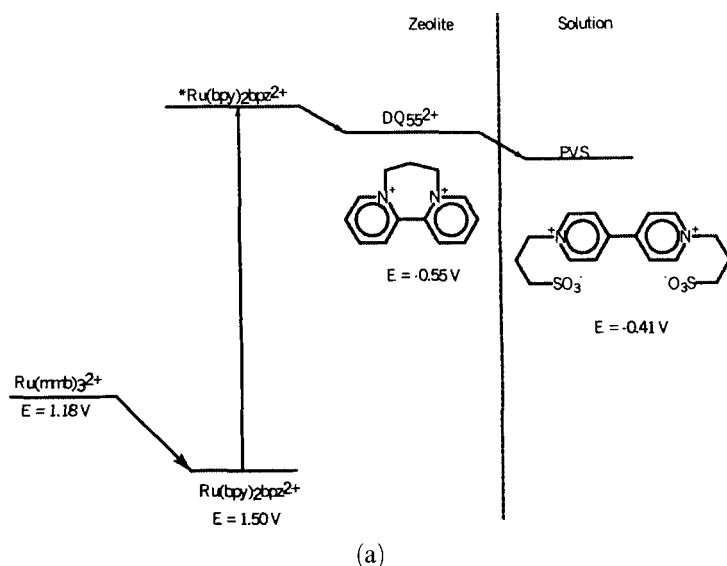


Figure 23. (a) Photochemical scheme of charge separation for Ru(mmb)_3^{2+} – $\text{Ru(bpy)}_2(\text{pbz})^{2+}$ – 3DQ^{2+} –zeolite Y with PVS in solution. (b) Comparison of the PVS radical generation for the adjacent cage dyad assemblies. PVS $^{\cdot-}$ growth as a function of time for (Z)-[$\text{Ru(bpy)}_2(\text{pbz})^{2+}$ – Ru(mmb)_3^{2+}] (AC), mechanically mixed (Z)- Ru(mmb)_3^{2+} and (Z)- $\text{Ru(bpy)}_2(\text{pbz})^{2+}$ (MM) and isolated systems of (Z)- Ru(mmb)_3^{2+} (mmb) and (Z)- $\text{Ru(bpy)}_2(\text{pbz})^{2+}$ (bpz).

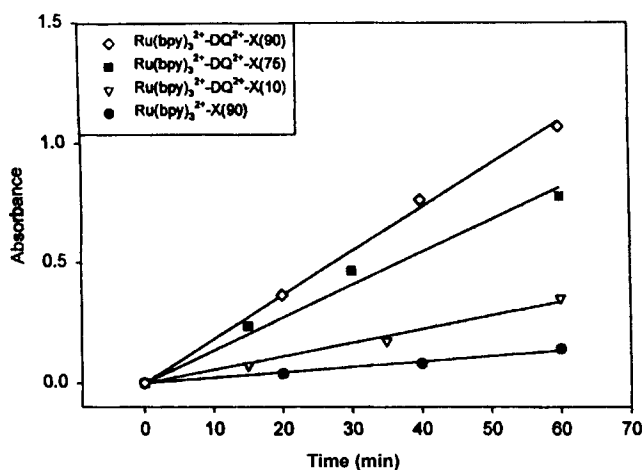
as lone electron donors and a mechanical mixture (MM) of two zeolites containing $\text{Ru(bpy)}_2\text{bpz}^{2+}$ and Ru(mmb)_3^{2+} .

Castagnola and Dutta investigated the use of nanocrystalline zeolites with high surface area as hosts [18]. The strategy to increase photochemical efficiency was

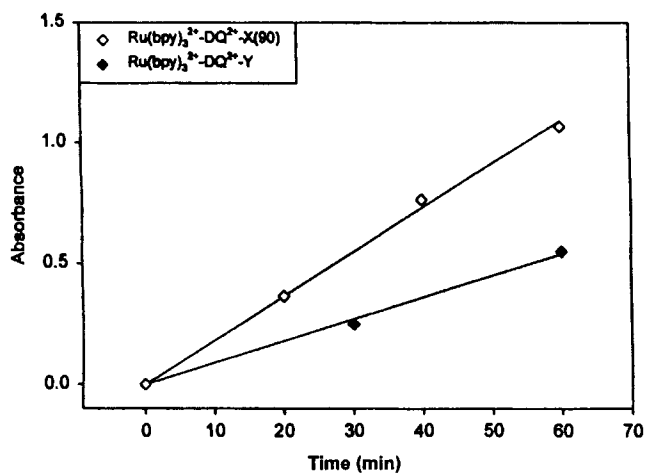
based on the fact that a larger fraction of the charge can migrate to the surface of nanocrystallites, and be transferred to the PVS in solution, as per the model in Figure 22. A patent procedure was followed to synthesize 250 nm aggregates of 30 nm crystallites of zeolite X. A low-temperature aging step and addition of sucrose to the reaction mixture were required to achieve optimum quality of crystals. Conventional ship-in-a-bottle synthesis of $\text{Ru}(\text{bpy})_3^{2+}$ in the cages of these nanocrystallites resulted in considerable framework degradation, with only 10 % of the crystallinity in the original crystals being retained. The degradation occurred owing to exposure to mild acidity and thermal treatment during the synthesis of $\text{Ru}(\text{bpy})_3^{2+}$. The procedure was modified by avoiding acidity in the initial ion exchange of $\text{Ru}(\text{NH}_3)_6^{3+}$, resulting in a $\text{Ru}(\text{bpy})_3^{2+}$ -zeolite with 75 % of the crystallinity retained. Acidity generated during conversion of $\text{Ru}(\text{NH}_3)_6^{3+}$ to $\text{Ru}(\text{bpy})_3^{2+}$ was thought to be responsible for the degradation. A third procedure starting with the highly air-sensitive $\text{Ru}(\text{NH}_3)_6^{2+}$ resulted in the formation of $\text{Ru}(\text{bpy})_3^{2+}$ -zeolite with about 90 % crystallinity. In all three procedures, the $\text{Ru}(\text{bpy})_3^{2+}$ molecules were entrapped within the framework. Ion exchange of viologen molecules and the fluorescence quenching of photoexcited $\text{Ru}(\text{bpy})_3^{2+}$ by intrazeolitic viologen increased with increase in zeolite crystallinity. Photolysis of $\text{Ru}(\text{bpy})_3^{2+}$ -viologen-zeolite in the presence of zwitterionic propylviologen sulfonate in solution also showed an increase in permanent charge separation efficiency as the crystallinity of the $\text{Ru}(\text{bpy})_3^{2+}$ -zeolite increased (Figure 24a) [18]. Because of the increased surface-to-volume ratio of the nanocrystallites compared with conventional micron-sized zeolite Y, the photochemical charge separation efficiency was found to be a factor of two better with the small crystallites (Figure 24b) [18].

These examples demonstrate that within the last few years, the sophistication for designing novel photochemical assemblies in zeolites has increased considerably and has resulted in our getting closer to architectures that provide permanent charge separation. The challenge continues to be in increasing the photochemical efficiency of the process.

Other permanent charge separation schemes: Fukuzumi and co-workers reported that permanent charge separation could be accomplished in a system consisting of Fe^{2+} /10-methylacridinium (AcrH^+)-zeolite Y sample suspended in an acetonitrile solution of 7,7,8,8-tetracyanoquinodimethane (TCNQ) [144]. A schematic diagram of their charge separation process is shown in Figure 25. Upon photoexcitation of AcrH^+ , its singlet excited state is quenched by intrazeolitic Fe^{2+} . The AcrH^+ can then transfer an electron to TCNQ in solution across the zeolite-solution interface to form $\text{TCNQ}^{\cdot -}$ in solution [144]. The rate of formation of $\text{TCNQ}^{\cdot -}$ depended on the Fe^{2+} loading of the zeolite. The upper limit of the rate constant was estimated to be $\sim 3 \times 10^{-8} \text{ mol dm}^{-3} \text{ s}^{-1}$ from their data. The back ET was measured by the loss of $\text{TCNQ}^{\cdot -}$ upon interaction with Fe^{3+} -exchanged zeolite Y. A decay rate of $1.5 \times 10^{-10} \text{ mol dm}^{-3} \text{ s}^{-1}$ was found, which is several orders of magnitude smaller than the rate of formation of $\text{TCNQ}^{\cdot -}$. In solution, the reaction between $\text{TCNQ}^{\cdot -}$ and Fe^{3+} is immediate, as expected from the reduction potentials. Thus, reaction between Fe^{3+} in the zeolites and $\text{TCNQ}^{\cdot -}$ in solution is drastically slowed because the $\text{TCNQ}^{\cdot -}$ is repelled by the negatively charged zeolite framework.



(a)



(b)

Figure 24. Photolytic charge separation with nanocrystalline zeolite: (a) correlation of percentage crystallinity of nanocrystals (shown in parentheses) with PVS^{••} production; (b) comparison of the rate of PVS^{••} radical generation for nanocrystalline zeolite X and micron-sized zeolite Y.

Photochemical oxidation of hydrocarbons in zeolites

Over the last several years, considerable research has been done on using zeolite hosts for examining oxidation reactions of hydrocarbons, using O₂ as the oxidant.

Singlet oxygen: Intrazeolitic singlet oxygen (¹O₂) can be generated with an ion-exchangeable sensitizer such as thionin in the zeolite. Drying of the zeolite sample is crucial to get the thionin in its monomeric form. Upon photoexcitation of the monomer, emission from singlet oxygen can be observed. The reaction of ¹O₂ with

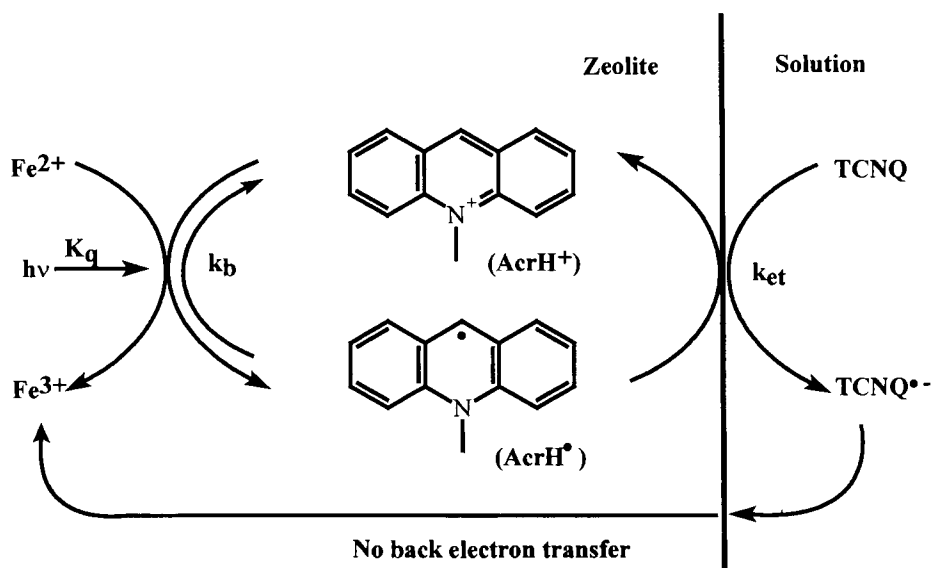
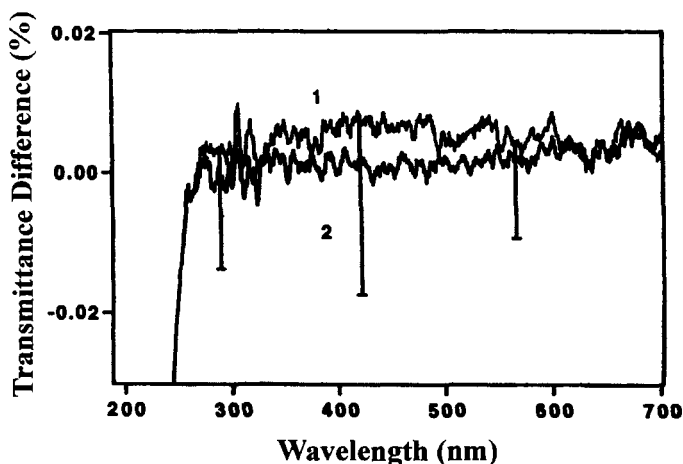


Figure 25. Schematic representation of the electron transfer process for Fe^{2+} - $AcrH^+$ -zeolite Y with TCNQ in solution.

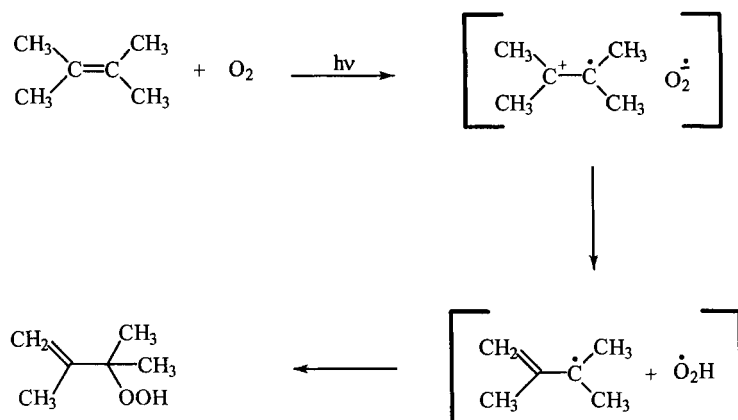
alkenes containing more than one distinct allylic hydrogen results in formation of several hydroperoxides in a homogeneous medium [145]. The role of the zeolite entrapment on the product distribution has been examined [146]. It was found that with most alkenes, a single hydroperoxide was formed within zeolite Na-Y. With 1-methylcycloalkenes, 100 % of the product was the result of the hydroperoxide formed by abstraction of the methyl protons. In solution, this product is usually formed in the lowest yield amongst three possible products. Two possible roles of the zeolite have been proposed for the high selectivity: control of the conformation of the alkene and/or polarization of the alkene. In both cases, the extra-framework cation of the zeolite was considered to play a major role, with smaller cations having a stronger effect on the selectivity.

Oxygen activated by charge-transfer reaction: It has been known since the 1950s that charge-transfer complexes of alkanes, alkenes or arenes with O_2 can be formed in O_2 -saturated hydrocarbon liquids or at high pressures of O_2 in the gas phase [147]. These charge-transfer bands, especially with small organic molecules, occur in the UV region and upon excitation at these wavelengths, photo-oxidation is observed with formation of many products. The initial step is the formation of superoxide ($O_2^{\bullet-}$), followed by proton transfer from the organic radical to form an HO_2^{\bullet} radical. The complex distribution of products is the result of secondary reactions of the radical intermediates.

Frei and co-workers reported that product distributions were much simpler if photoexcitation of hydrocarbon- O_2 complexes were carried out in zeolites [148].



(a)



(b)

Figure 26. (a) UV-Vis transmittance spectra of $\text{O}_2\text{-N}_2/\text{NaY}$ (1) and $\text{DMB/O}_2\text{-N}_2/\text{NaY}$ (2) for films of large Na-Y crystals at 253 K. Bars indicate the estimated DMB-O_2 absorption for scattered and unscattered transmitted light. (b) Proposed mechanism for the formation of 2,3-dimethyl-3-hydroperoxy-1-butene in $\text{DMB/O}_2\text{-NaY}$.

Several reasons were proposed to explain the cleaner chemistry. First, the electrostatic fields (0.3 and 0.9 V \AA^{-1} for Na-Y and Ba-Y, respectively) in the zeolite stabilize the hydrocarbon- O_2 charge transfer, thereby shifting the transition to visible wavelengths. Second, the use of visible excitation suppresses the secondary photochemistry rampant with UV light. Third, the steric constraints imposed by the zeolite promote product selectivity. This chemistry can be demonstrated by the reaction of 2,3-dimethyl-2-butene (DMB). Figure 26a shows the electronic spectrum

corresponding to the charge-transfer complex of DMB with O_2 in optically transparent crystals of large Na-zeolite Y on a CaF_2 support [148]. Trace 1 is the background spectrum in O_2 and trace 2 is with DMB. The difference between traces 1 and 2 shows an onset of absorption between 600 and 700 nm and a flat maximum between 400 and 500 nm. The red shift of the absorption band into the visible region in the zeolite as compared with solution was proposed to occur because of stabilization of the charge-transfer complex via the electrostatic fields in the zeolite. Visible excitation into the DMB- O_2 charge-transfer band at $-50^\circ C$ leads primarily to the formation of 2,3-dimethyl-3-hydroperoxy-1-butene, as identified by infrared spectroscopy. The proposed mechanism of formation of the hydroperoxide is shown in Figure 26b. The hydroperoxide intermediate was found to be common at the lower temperatures for a variety of substrates that were studied, including alkenes, alkyl-substituted benzenes and alkanes. Upon warming to room temperature, the hydroperoxide was found to be converted to more stable products, e.g. in the case of propylene oxidation, acrolein was formed. Frei and co-workers have recently summarized their photo-oxidation research on hydrocarbons [148d].

Several other research groups have also published papers in this area. A recent study by Larsen, Grassian and co-workers was focused on 1-alkene oxidation in a series of Ba-loaded zeolites, including zeolites X/Y, Z5M-5 and Beta [149]. They noticed that the intermediate hydroperoxide formation leads to selective product formation as long as temperatures are kept below $-20^\circ C$. At ambient temperature, a series of products can form, resulting in loss of selectivity. For example, in 1-butene photo-oxidation, mixtures of aldehydes, ketones, epoxides and alcohols were formed. Figure 27 shows the difference infrared spectra before and after photolysis of 1-butene and oxygen in Ba-Y. Comparison of the photolyzed samples (traces a, b and c) with that of methyl vinyl ketone (d) shows that several additional bands are observed [149]. NMR analysis of $CDCl_3$ extracts of the photolyzed samples showed that in addition to methyl vinyl ketone, crotonaldehyde, propionaldehyde, acetaldehyde, butyraldehyde, epoxybutane and 2-butanone are also formed. If acidic sites were present on the zeolite, then polymerization occurred. Thus, the generality of the photo-oxidation reactions in generating specific products can be limited because of the thermal reactions at ambient temperature and polymerization reactions. The reaction rates of the photo-oxidation reactions depended on the excitation wavelength. Since the intensity of the hydrocarbon- O_2 charge-transfer band increases at shorter wavelengths, the rate of photoproduct formation was found to increase, but the selectivity towards specific products decreased. For example, upon excitation of the propylene- O_2 complex at $\lambda > 285$ nm, short-chain saturated aldehydes (acetaldehyde, formaldehyde and propionaldehyde) were formed through a competing dioxetane chemistry (as compared with hydroperoxide).

Kojima and co-workers also examined the photo-oxidation of stilbenes in zeolite Y [150]. The presence of O_2 in the stilbene-NaY sample led to a red-shifting of the tail end of the diffuse reflectance spectrum and was assigned to the charge-transfer complex with O_2 . Upon excitation at 313/366 nm, both *cis*- and *trans*-stilbene undergo photo-oxygenation to form benzaldehyde. Phenanthrene, the expected product from the $[2 + 4]$ cycloaddition reaction of excited *cis*-stilbene, was also formed. The details of the mechanism leading to benzaldehyde and phenanthrene

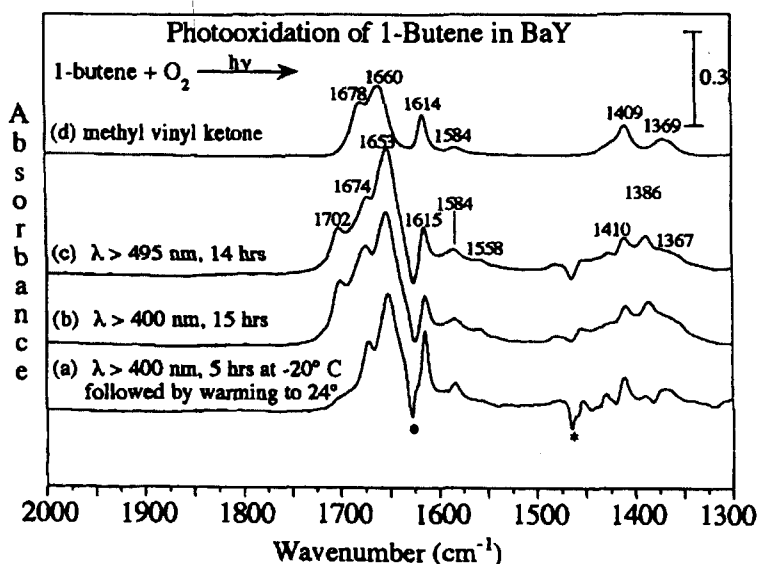


Figure 27. Difference infrared spectra (before and after photolysis) of 1-butene and oxygen in BaY. (a) $\lambda > 400$ nm at -20°C for 5 h followed by warm-up at 24°C for 18 h without O_2 ; (b) $\lambda > 400$ nm at room temperature for 1.5 h; (c) $\lambda > 495$ nm at 45°C for 14 hours; (d) reference spectrum of methyl vinyl ketone in BaY. Asterisks indicate the loss of 1-butene.

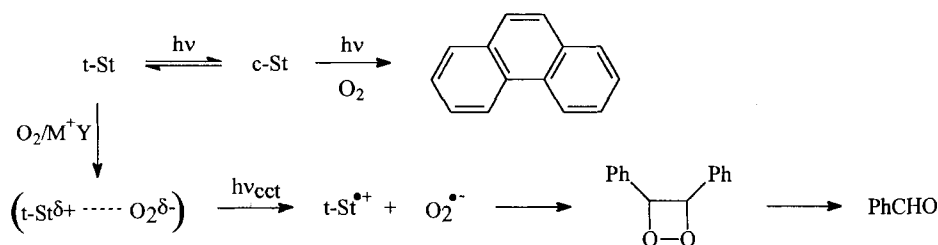


Figure 28. Mechanism of benzaldehyde and phenanthrene generation via photooxygenation of *cis*- and *trans*-stilbene within NaY.

formation are shown in Figure 28 [150]. It was noted that polymeric and bulky products were also formed via side reactions, and could not be extracted from the zeolite.

Stabilization via encapsulation

The geometric constraints and the immobilization of molecules in the zeolite supercages give rise to novel ET chemistry that is not observable in fluid media. We discuss two examples of such reactions. 2,4,6-Triphenylpyrylium ion (TP^+) can be synthesized inside zeolite Y supercages by a ship-in-a-bottle approach [151]. The

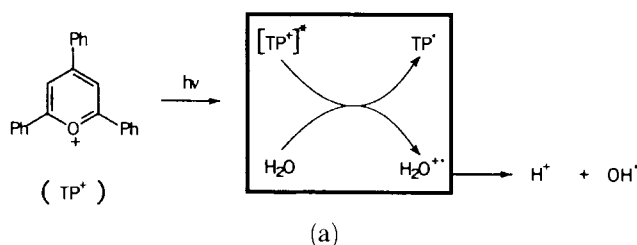
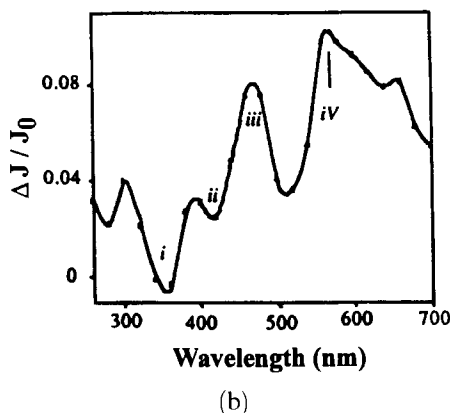


Figure 29. (a) Mechanism for the photo-oxidation of water by TP^+ . (b) TRDR spectrum of $\text{TP}^+-\text{MV}^{2+}-\text{Y}$ system 10 μs after 355 nm laser excitation: (i) and (ii) correspond to the bleaching of TP^+ ground state, (iii) is assigned to the $\text{MV}^{2+}-\text{OH}^\bullet$ adduct and (iv) is the absorption of TP^\bullet .



TP^+ molecule is unstable in water, but appears to be indefinitely stable in hydrated zeolite. The hydrolysis of TP^+ would require an intermediate state in which the phenyl substituent is displaced out of the molecular plane. This geometry cannot be accommodated in the zeolite cage, thus conferring stability to the TP^+ , and has led to some interesting photochemical studies. Upon photoexcitation of entrapped TP^+ , $^3\text{TP}^+$ is formed which has the appropriate potential to oxidize water and eventually results in the formation of OH^\bullet , as shown in Figure 29a [151]. The formation of OH^\bullet has been confirmed by trapping it as a DMPO adduct and investigating its EPR spectrum. Reactions of the OH^\bullet radical with ion-exchanged MV^{2+} have been studied. Figure 29b shows the transient diffuse reflectance spectrum 10 μs after photoexcitation of $\text{TP}^+-\text{MV}^{2+}-\text{Y}$ with a 355 nm laser pulse. The band marked (iii) is characteristic of the $\text{MV}^{2+}-\text{OH}^\bullet$ adduct [151]. The photocatalytic formation of OH^\bullet has also been exploited in pesticide degradation.

The reaction of water with low-loaded $[\text{Ru}(\text{bpy})_3]^{3+}$ entrapped in zeolite Y has been reported [152]. Since translational mobility of the Ru molecules cannot occur in the zeolite, the multimolecular degradation step observed in solution is no longer possible. Instead, O_2 was found to be formed from the reaction of $[\text{Ru}(\text{bpy})_3]^{3+}$ with water. It was possible to examine the evolution of this reaction at various pHs by spectroscopic methods, such as EPR, diffuse reflectance and Raman spectroscopy. Figure 30 shows the evolution of the diffuse reflectance spectra after exposure of $[\text{Ru}(\text{bpy})_3]^{3+}$ -zeolite Y to water at pH 7 [152]. Trace e is the spectrum of the

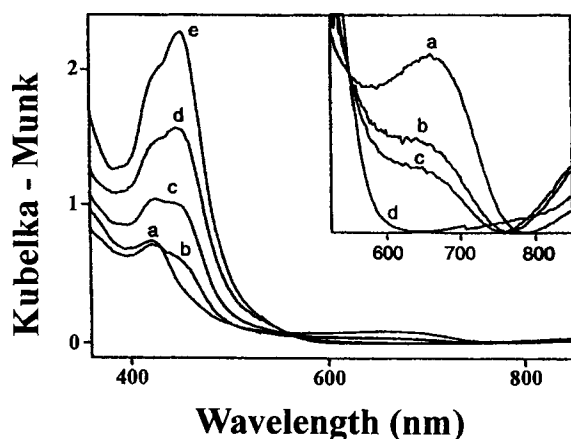
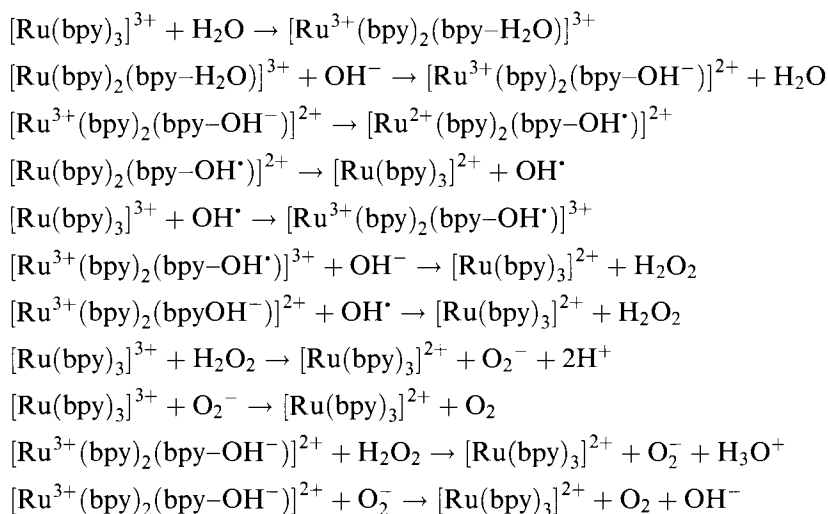


Figure 30. Diffuse reflectance spectra of $\text{Ru}(\text{bpy})_3^{3+}$ -zeolite-Y exposed to pH 7 deionized water for (a) 0, (b) 1, (c) 10 and (d) 42 h. Spectrum (e) is the spectrum of the initial $\text{Ru}(\text{bpy})_3^{2+}$ -Y.

$\text{Ru}(\text{bpy})_3^{2+}$ -zeolite Y used as the starting material for generation of $\text{Ru}(\text{III})$. Upon oxidation by Cl_2 , spectrum a is obtained with bands at 420 and 660 nm, typical of $\text{Ru}(\text{bpy})_3^{3+}$. With time, the band of $\text{Ru}(\text{bpy})_3^{2+}$ at 450 nm recovers. The intensity around 850 nm initially increases and then decreases. Bands in this region are typical of the hydroxylated complexes formed by water attack on the bpy ligands of $\text{Ru}(\text{bpy})_3^{3+}$. The overall mechanism for reaction of water with $\text{Ru}(\text{bpy})_3^{3+}$ was proposed to be as follows:



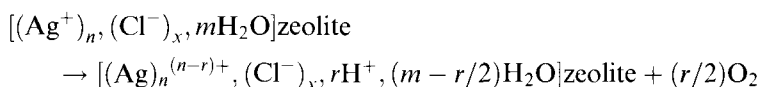
In the zeolite, owing to the lack of multimolecular degradation, oxidation of water by $[\text{Ru}(\text{bpy})_3]^{3+}$ becomes possible. The reaction is slow, and hydroxyl radicals, hydrogen peroxide and superoxide are created as intermediates. In plant photosynthesis, an Mn-based water-splitting catalyst system in which the reaction with water only occurs after four electrons have been stored in the water-splitting enzyme

complex [153] ensures that reactive oxygen metabolites are not formed. Development of catalysts is required in order to couple the conversion of intrazeolitic $\text{Ru}(\text{bpy})_3^{3+}$ with water oxidation and is discussed later.

Photochemical studies with cluster species

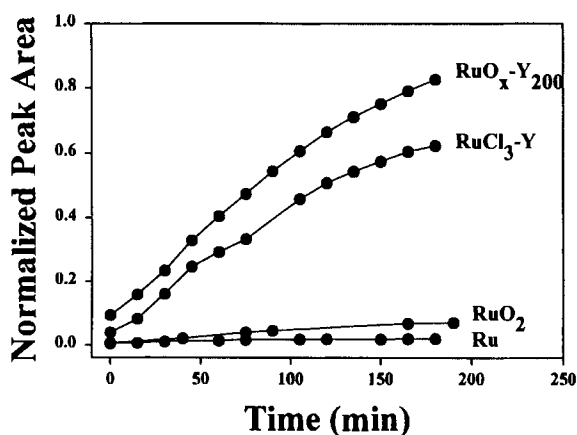
Metal clusters: Mallouk and co-workers reported on procedures to generate small particles of Pt inside zeolite L channels, which they used as catalysts for hydrogen formation [154]. The electron transport chain was composed of EDTA as sacrificial electron donor, zinc tetra(*N*-methyl-4-pyridyl)porphyrin (ZnTMPy^{4+}) as sensitizer and methylviologen (MV^{2+}) as electron acceptor. The zeolite host used was zeolite L, which has a one-dimensional tunnel-like structure (Figure 1e). Small Pt clusters were formed inside the zeolite and then loaded with MV^{2+} by ion exchange. Since $[\text{ZnTMPy}]^{4+}$ was too large to penetrate into the 7 Å zeolite L channels, it was ion exchanged on to the zeolite interface. The negatively charged EDTA^{2-} at pH 4 was intimately associated with the porphyrin. Upon photolysis, the singlet state of the porphyrin was quenched by the neighboring intrazeolitic viologen molecules. The sacrificial electron donor EDTA was oxidized by the porphyrin cation, thus stabilizing the MV^{+} radical, which in the presence of Pt catalysts formed H_2 . It was noted that significant H_2 evolution only resulted for high loading levels of MV^{2+} , necessary for close MV^{2+} – ZnTMPy^{4+} contact, as well as charge propagation by hopping into the zeolite, in agreement with the earlier discussions on page 447.

Calzaferri and co-workers have shown that upon illumination of Ag^+ -exchanged zeolite A which also contains occluded AgCl , the Ag^+ ions are reduced and molecular O_2 is formed [155]:



An interesting effect discovered during photolysis was self-sensitization, i.e. with increasing time, new chromophores were produced, which resulted in a bathochromic shift of the transition from the near-UV to the red region. The chromophores were proposed to be Ag_n^{m+} clusters, the ultimate growth of which was controlled by the size of the cavity.

Metal oxide clusters: Ruthenium oxide on zeolites has been studied as catalysts for the photochemical oxidation of water to oxygen. Thermal decomposition of $\text{Ru}_3(\text{CO})_{12}$ on zeolite Y at 170 °C produced Ru metal, which was readily oxidized by air to RuO_2 [156]. Under ambient oxidation conditions, the particles of RuO_2 were smaller than 2 nm and not observable in powder diffraction patterns. Oxidation by air at increasing temperatures led to sintering and growth of RuO_2 crystallites. The morphology of RuO_2 on the zeolite was found to be strongly dependent on the temperature at which air oxidation occurred. For samples prepared by air oxidation at 200 °C, fibrous structures (50 × 5 nm) of RuO_2 are formed. This material was found to be the best catalyst for water oxidation to O_2 by photochemically generated $\text{Ru}(\text{bpy})_3^{3+}$. Figure 31a compares the O_2 produced as a



(a)



(b)

Figure 31. (a) Comparison of oxygen produced by photolysis as a function of time for RuO_2 -zeolite Y prepared by the carbonyl route ($\text{RuO}_x\text{-Y}_{200}$), RuO_2 -zeolite Y prepared by impregnation ($\text{RuCl}_3\text{-Y}$), RuO_2 powder (RuO_2) and Ru metal (Ru). (b) TEM of fibrous RuO_2 on zeolite Y produced by thermal decomposition of $\text{Ru}_3(\text{CO})_{12}\text{-NaY}$.

function of photolysis time for RuO_2 -zeolite Y prepared via the carbonyl route, RuO_2 -zeolite Y prepared by RuCl_3 impregnation, RuO_2 powder and Ru metal. TEM of this material is shown in Figure 31b. It was concluded that the fibrous morphology of RuO_2 provided specific crystal faces that were optimal for the four-electron oxidation of water to O_2 [156].

Titanium oxides have been extensively studied for photocatalytic applications and several examples of TiO_2 -zeolite composites have also been examined. Sample preparation involved ion exchange or impregnation of titanium ammonium oxalate on zeolite Y followed by calcination at 450°C . TS-1, Ti-MCM-41 and Ti-MCM-48 were prepared by hydrothermal synthesis [157]. UV irradiation (260–290 nm) of the catalyst in the presence of a mixture of gas-phase CO_2 and H_2O led to the for-

mation of CH_4 and CH_3OH . The ion-exchanged and framework-substituted catalysts vastly outperformed the impregnated catalyst. Ti-MCM-48 was found to be better than TS-1 and Ti-MCM-41. XANES and EXAFS studies indicated that in the cases of ion-exchanged and framework-substituted catalysts, the Ti atoms are in an isolated tetrahedral environment and are photoluminescent, whereas the impregnated samples have Ti in an octahedral environment as anatase and do not exhibit photoluminescence. The addition of H_2O or CO_2 led to the efficient quenching of photoluminescence and a decrease in the excited-state lifetime. Water and CO_2 were proposed to react with the photoexcited state $(\text{Ti}^{3+}-\text{O}^-)^*$, resulting in decomposition of H_2O and reduction of CO_2 to form species that eventually end up as methane and methanol [157].

Another major application of Ti-oxide species prepared within the zeolite cavities includes the photocatalytic decomposition of environmentally noxious substances into benign compounds. Examples include photodecomposition of chlorophenol [158] and of NO_x into N_2 and O_2 [159]. TiO_2 -loaded MCM-41 shows a much lower apparent activation energy for the photodegradation of acetophenone than that of TiO_2 -loaded zeolite-X, -Y and -A. The differences in reactivity with different frameworks was related to the efficiency of trapping of the photogenerated electrons and/or holes [160].

Electrochemistry

Electrochemistry using chemically modified electrodes is an important area of research, since with modified electrodes, increase in selectivity of particular chemical reactions becomes possible [161]. Considering that the zeolite framework can impart added selectivity via molecular sieving, ion exchange or entrapment, it is not surprising that zeolite-based electrochemistry has been an active area of research for the past 15 years [162]. Research in this area has matured sufficiently that electroanalytical chemistry using zeolite-modified electrodes (ZME) is being extensively pursued, resulting in novel applications, particularly in the area of sensors.

Since zeolites are insulating in nature, it is necessary to design methodology to bring zeolite particles in to close contact with an electronically conducting material. The important strategies for fabricating ZME fall into three categories [162a]:

- 1) dispersing the zeolite crystallites onto a conducting phase, such as carbon paste, carbon polymer or graphite;
- 2) depositing a zeolite coating with a polymer, such as polystyrene or polyethylene oxide, on an electrode surface;
- 3) mechanically contacting a zeolite pellet with a solid electrode, in the presence or absence of carbon.

Three other methods of electrode preparation include photopolymerization of vinyl-saturated zeolites on a Pt electrode [163], direct synthesis of zeolite films on metal supports [164] (although electrochemical studies on this system have not been reported) and the use of agitated suspensions of zeolite, where zeolite particles contact the electrode at random [165].

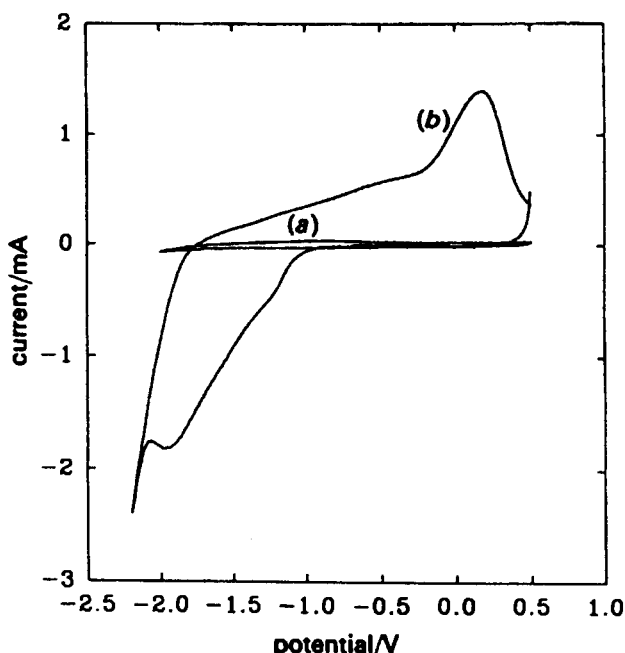


Figure 32. Cyclic voltammograms of Co^{2+} -Y ZME in the presence of (a) tetrabutylammonium ion and (b) Li^+ as supporting electrolyte ions.

There has been considerable debate about whether intrazeolitic species are electrochemically accessible and recent results on zeolite-encapsulated metal complexes are of interest in this regard. Before we discuss this topic, the role of ion exchange in electrochemical response is discussed. Electroactive transition metal ions can readily be ion exchanged into zeolites. Baker and co-workers reported that a Co^{2+} -zeolite Y-ZME resulted in reduction of cobalt ions if Li^+ was used as the supporting cation in the electrolyte solution, whereas the voltammetric response was absent in the presence of the larger tetrabutylammonium ion (TBA) [166]. Figure 32 compares the voltammetric data for Li^+ and TBA. There are two ways to interpret these data:

- 1) Co^{2+} -zeolite Y + $e^- \rightarrow \text{Co}^+$ -zeolite Y (electrochemistry)
 M^+ (solution) $\rightarrow \text{M}^+$ -zeolite Y (charge balance)
- 2) M^+ (solution) + Co^{2+} -zeolite Y $\rightarrow \text{M}^+$ -zeolite Y + Co^{2+} (solution) (ion exchange)
 $\text{Co}^{2+} + e^- \rightarrow \text{Co}^+$ (electrode)

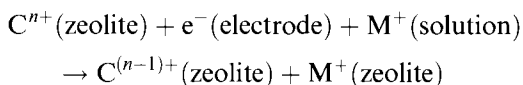
After much controversy [167], it now appears that whenever ion exchange is possible, mechanism 2 is the primary method by which an electrochemical response is observed in ZME. Much of the sensor-based research we discuss below is based on the principle of ion exchange, followed by electrochemistry.

Still controversial and of significant importance is the electrochemistry with zeolite-encapsulated complexes. Because of the unusual steric constraints and the

novel electrostatic environment within a zeolite, it can be expected that the electrochemical properties of an entrapped complex may differ significantly from that in solution. If so, then the zeolite host affords an incredible opportunity to influence electron transfer chemistry. Because the entrapped complexes are not ion exchangeable, the issue of extracrystalline redox chemistry as with ion-exchangeable cations will not be relevant.

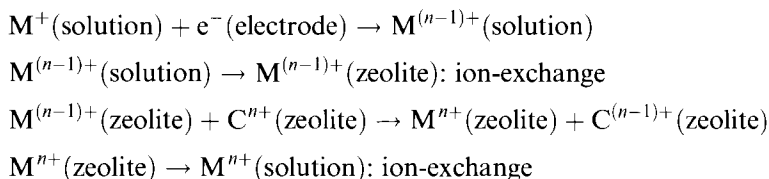
There are several routes by which intrazeolitic electrochemistry can occur.

1) Direct process:

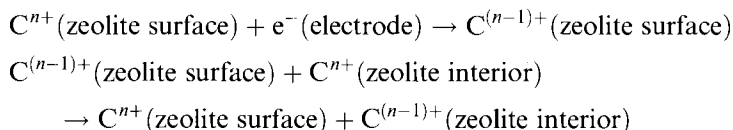


This would be the most direct way to monitor electrochemical properties of the entrapped complex, C^{n+} .

2) Mediated process:



3) Self-exchange:



Evidence for pathway 3 has been provided by the work of Mallouk and co-workers [168]. Using ZMEs, they showed that the rate of charge transfer from the electrode to metallocenes ion exchanged into the bulk of the zeolite was increased at least 10-fold if the surface of the zeolite was covered with $M(\text{bpy})_3^{2+}$ molecules ($M = \text{Ru}, \text{Os}$) [168a]. Charge diffusion from the zeolite surface to the bulk must be occurring by electron exchange. Similar results were obtained for cationic porphyrin molecules on the zeolite surface and viologen molecules within the bulk of the zeolite [168b]. Using electron and energy transfer quenching of zeolite-bound $\text{Ru}(\text{bpy})_3^{2+}$ with viologens and $\text{Os}(\text{bpy})_3^{2+}$ on other zeolite particles, Mallouk and coworkers concluded that intrazeolitic electron transfer was far more likely than reactions in solution after ion exchange of ions from zeolite. The electrolyte concentration in solution plays an important role in this process. It was concluded that if electrolyte concentrations were below 3 mM, as is typical for many electrochemical experiments, then intrazeolitic electron transfer as the primary route needs to be considered [168c]. Pathway 3 will also require migration of an external cation

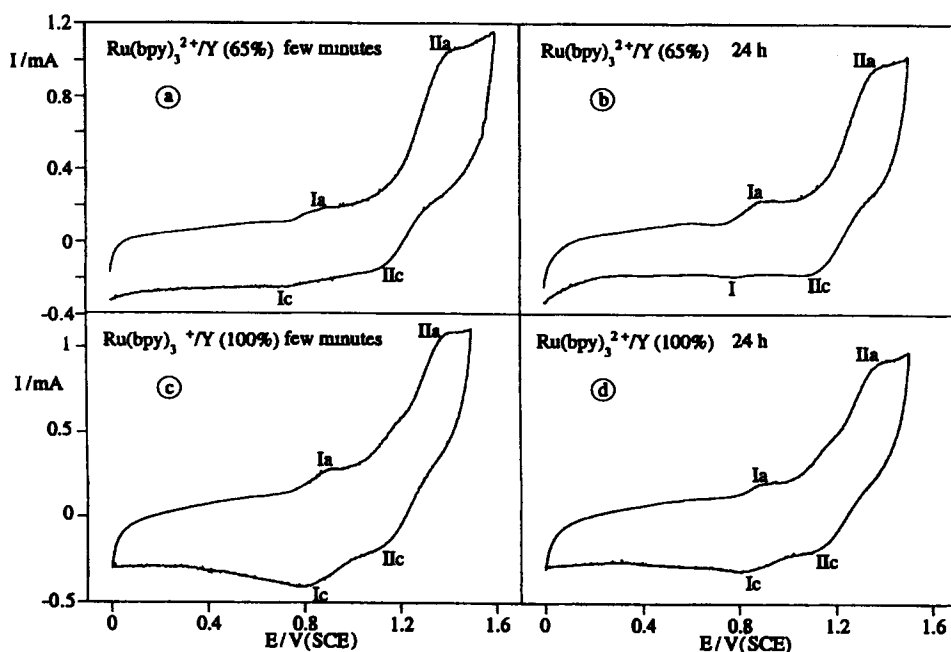


Figure 33. Cyclic voltammograms of zeolite Y-entrapped $\text{Ru}(\text{bpy})_3^{2+}$ at a pressed powder graphite electrode in acetonitrile (0.1 M LiBF_4). Scans taken for both 65 and 100 % loadings a few minutes and 24 h after electrode immersion.

into the zeolite to maintain charge balance. Pathway 2 is feasible, but not particularly interesting from either analysis or electrocatalysis points of view.

Pathway 1 is the most interesting and also the most controversial. There are two schools of thought [169]. The first is that pathway 1 does not occur and any voltammetric signal that is observed arises from complexes that have leached out of the zeolite, either from mechanical degradation during electrode preparation or by some other surface damage of the framework [169a–c]. The second group proposes that intrazeolitic redox does occur and is restricted to the complexes immobilized/entrapped near the surface [169de]. There is general agreement that the interior molecules are not directly accessible.

An example of the nature of electrochemical signal that is observed from zeolite entrapped complexes is shown in Figure 33 [169d]. It shows the cyclic voltammograms for $\text{Ru}(\text{bpy})_3^{2+}$ in zeolite Y at two different loading levels and collected after contact with the electrolytic solution for a few minutes and 24 h. Two redox couples (Ia, Ic) and (IIa, IIc) located at 0.63 and 1.26 V (vs. SCE), respectively, were observed immaterial of the loading or the exposure time [169d]. It was found that only 0.2 % of the entrapped species contributed to the electrochemical signal. $\text{Ru}(\text{bpy})_3^{2+}$ in solution shows a reversible, one-electron, $\text{Ru}^{2+}/\text{Ru}^{3+}$ process at 1.34 V. Two explanations were provided for the appearance of two voltammetric peaks. The first involved the assignment to two species, $\text{Ru}(\text{bpy})_2(\text{H}_2\text{O})_2^{2+}$ in addition to $\text{Ru}(\text{bpy})_3^{2+}$. The second proposed the presence of distorted $\text{Ru}(\text{bpy})_3^{2+}$ species due

to zeolite host–guest interactions. The latter explanation is difficult to rationalize since any influence of the zeolite host should be a continuum rather than two well-defined structural distortions. At the high loading levels examined in this study [65 and 100 % $\text{Ru}(\text{bpy})_3^{2+}$], it is possible that all the bis-complex $\text{Ru}(\text{bpy})_2(\text{H}_2\text{O})_2^{2+}$ has not converted to the tris form, and therefore the presence of two species is likely. Since voltammetric measurements were not reported on $\text{Ru}(\text{bpy})_2(\text{H}_2\text{O})_2^{2+}$ in zeolite Y, assignment of the voltammetric peaks (I, II, Figure 33) to specific molecular species is not possible.

Electroanalysis

Walcarius has recently summarized the status of the field of electroanalysis using ZME and so we shall only briefly highlight some of the basic principles [162c]. Ion-exchange properties of zeolites have been used to preconcentrate analytes, followed by electrochemical detection of the ion-exchanged species, in the analysis of both metal and organic cations. For example, the affinity of zeolite A was used for determining Ag^+ at concentrations of 1 mg L^{-1} in the presence of 10 mg L^{-1} of ions such as Co^{2+} , Mn^{2+} , Ca^{2+} , Pb^{2+} , Cu^{2+} and Ti^{2+} . The ions Bi^{3+} , U^{4+} , Ni^{2+} , Zn^{2+} , Ti^+ , Hg^{2+} and Fe^{3+} showed interference in Ag^+ determination [170a].

Walcarius and co-workers have used methylviologen-exchanged ZME for the detection of alkali metal cations in ion-exchange chromatography [170b–d]. The basis for detection was the ion exchange of the methylviologen out of the zeolite followed by amperometric detection. By using a mobile phase containing tetrabutylammonium bromide (TBABr), they ensured that the electrolyte cation would not enter into the zeolite, thereby minimizing interference with the smaller analyte ions. However, the presence of TBABr interfered with the ion-exchange chromatographic process. The electrolyte was avoided with the use of Cu^{2+} –ZME using carbon pastes. Figure 34 compares the chromatograms for a standard mixture of monovalent ions using a conductivity detector and an unmodified and a copper-modified zeolite carbon paste electrodes.

Zeolite electrodes modified with enzymes include tyrosinase and glucose oxidase and have shown good sensitivity for detection of various phenolic compounds and glucose [171]. It has been proposed that immobilization of the enzyme on the zeolite improved the enzyme activity. In the case of ZME using enzymes, the ion-exchange ability of the zeolite was exploited to immobilize mediator species such as methylphenazonium and TCNQ, which served as a shuttle between the enzymes and electrode. A problem with long-term use is the necessary loss of the mediator from the zeolite via ion exchange with supporting electrolyte cations.

Senaratne and Baker designed a humidity sensor based on the fact that Ag^+ –ZME in dimethylformamide will exhibit no electrochemical response related to Ag^+/Ag reduction, unless water is present to promote ion exchange. Using this technique, 100 ppb of water in DMF could be detected [172].

Electrocatalysis

Zeolite-supported transition metal complexes, such as Mn(III) porphyrin and Cu(II) tetraphenylporphyrin, have been used for the electrocatalytic oxidation of phenols and hydrazine, respectively [173]. Methylviologen-exchanged zeolites have

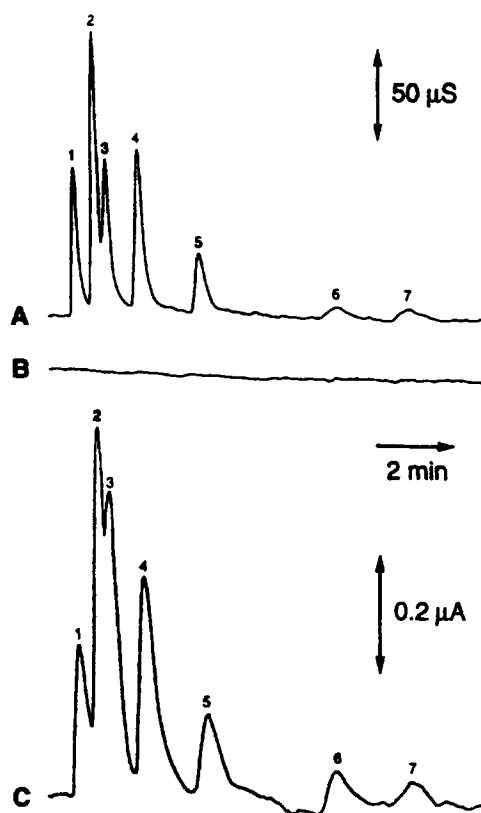


Figure 34. Use of MV^{2+} -ZME as an electrode for detection of alkali metal ions in ion-exchange chromatography. Detection using (A) a conductivity detector, (B) an unmodified and (C) Cu-modified ZME. Peaks 1–7 correspond to Li^+ , Na^+ , NH_4^+ , K^+ , Cs^+ , Mg^{2+} and Ca^{2+} respectively.

been used for the reduction of oxygen either in the dissolved state or in the gas phase at 425°C [174]. Rolison and co-workers dispersed zeolites in the absence of electrolytes to examine electrocatalysis of a number of systems [175]. Pt-zeolite Y was studied for the electrolysis of water. It was found that extrazeolitic Pt clusters of size 2.5 nm were the most effective catalysts. Another system that Rolison and co-workers examined is the Wacker oxidation of propene in pure water by dispersed Pd(II)- and Cu(II)-modified zeolite Y. Interestingly, both acetone, the normal oxidation product formed by the mechanism shown in Figure 35, and propylene oxide were found as products. Because they noticed partial degradation of the organic substrate, they examined alkali metal ion-exchanged zeolite Y for the detoxification of polychlorinated organic molecules [176]. It was interesting that the use of other solids such as silica, alumina or other zeolites led to oxygenation of the aromatic ring rather than complete mineralization, as observed for zeolite Y. It was unclear what unique feature of zeolite Y is promoting this process, since the zeolite is not directly involved in the electrochemistry.

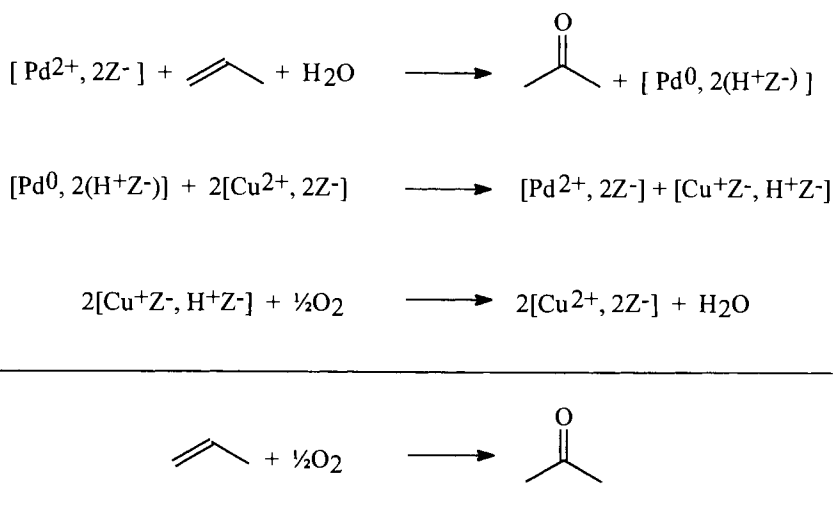


Figure 35. Mechanism for Wacker oxidation of propene in pure water by dispersed Pd(II)- and Cu(II)-modified zeolite Y.

3.3.2 Mesoporous Materials

Mesoporous materials extend the range of porosity to 500 Å, although most studies have been done with materials in the range 20–100 Å. The availability of the larger pores and control of the pore size within a narrow range made it possible to use mesoporous materials as hosts for reactions with molecules of varying sizes. Redox chemistry using metal-substituted frameworks, metallic oxides, entrapped complexes and enzymes has been reported. The major difference with zeolites is that the use of both larger substrates (that can readily penetrate the mesoporous framework) and grafting of larger catalytically active metal complexes has become possible. Several review articles summarize the research in this area [177].

Framework involvement

As we discussed in the section on zeolites, titanium-substituted zeolitic structures show very high catalytic activity and selectivity in oxidation reactions. Immediately after the report of the synthesis of MCM-41, it was realized that incorporation of Ti would make it possible to examine the oxidation of bulkier substrate molecules and to use larger oxidants. Indeed, Ti-MCM-41 showed higher catalytic activity for the epoxidation of norbornene with TBHP as the oxidant as compared with Ti-ZSM5 and Ti-zeolite β [178]. 2,6-Di-*tert*-butylphenol (2,6-DTBP) was oxidized to the quinone using H_2O_2 [179]. Vanadium-incorporated MCM-41 has also been found to be active for the partial oxidation of cyclododecane and 1-naphthol using H_2O_2 as the oxidant [180]. Interesting differences in catalytic activity have been noted for Ti-mesoporous materials made by different routes. For example, Ti-HMS (hexag-

onal mesoporous silicas) prepared by a neutral surfactant exhibited greater catalytic activity than Ti-MCM-41 for the oxidation of aniline [181]. Zr-HMS exhibited similar activity to the Ti analog and in both cases the turnover numbers were 10–50 times higher than with Ti-silicalite. Ti-MCM-41 incorporated into polymethoxysilane films was used for the epoxidation of *cis*-cyclooctene with TBHP as the oxidant [182]. Other organic reactions that have been reported with Ti-mesoporous materials include the oxidation of sulfides to sulfoxides and sulfones [183].

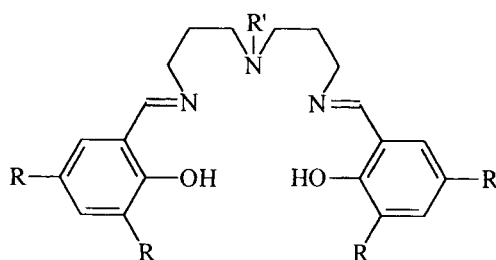
Few redox studies with cubic mesoporous materials have been reported [52]. The large, complex, three-dimensional pore system offers a unique environment. Ti- and Cr-substituted MCM-48 have been studied for the selective oxidation of methyl methacrylate and styrene to methyl pyruvate and benzaldehyde, respectively, using peroxides as oxidants and were found to outperform TS-1. Ti-MCM-48 has also been found to be better than Ti-MCM-41, TS-1 and TiO₂ for the photocatalytic reduction of CO₂ and H₂O to methane and methanol. Ti-grafted MCM-48 has also been reported as the first functional biomimic of vanadium bromoperoxidase, active at neutral pH and used in the peroxidative halogenation of bulky organic dyes.

Even though the metal-substituted, mesoporous solids allow the oxidation of molecules that is not possible with zeolites, there are several issues that still need to be addressed. First, the activity of the metal-loaded catalysts decreases with increased metal loading, e.g. for Ti-MCM-41, the peak activity for alkene epoxidation is attained at 2 wt. % [44a]. Second, metal leaching can occur and care needs to be exercised in concluding that oxidation is taking place at the framework site rather than via metal ions leached into solution [184, 185]. Leaching has been shown to occur for V-substituted mesoporous materials in the oxidation of alkanes [184]. X-ray absorption spectroscopy indicates that the inclination of the heteroatoms to remain in the MCM-41 framework after calcination follow the order Ti > Fe > V > Cr [56].

Few studies have also been reported with metal oxide clusters in mesoporous materials. MCM-41 modified by deposition of vanadium and titanium oxides exhibited catalytic activity for reduction of nitrogen oxides by NH₃ [186].

Entrapped species

Several routes to incorporating transition metal complexes in mesoporous materials have been reported. As in zeolites, Al incorporation in MCM-41 generates ion-exchange sites and has been used to introduce charged complexes into mesoporous materials. An example is phenanthroline iron(II) chloride, which was used as a catalyst for the oxidation of phenol with H₂O₂ [187]. Enhancement of activity was observed due to immobilization, but there were problems with leaching of the complex. Several strategies have been developed for chemically linking organometallic complexes on the inner walls of MCM-41, which alleviates leaching of the complexes during subsequent reactions. The anchoring methods have exploited the presence of silanol groups lining the pores. Titanium has been incorporated in MCM-41 by grafting of titanocene to triethylamine-activated silanol groups [188]. Upon calcination, the titanium was found to be tetrahedrally coordinated via the silanol groups and was a selective catalyst for the epoxidation of cyclohexene and



$R' = H, \quad R = H \quad : \text{Salpr}$

$R' = H, \quad R = t\text{Bu} \quad : \text{tSalpr}$

$R' = \text{CH}_3, \quad R = H \quad : \text{Smdpt}$

Figure 36. Schiff base ligands that have been covalently bound to MCM-41 framework.

pinene using TBHP as oxidant. The catalysts deactivated with 90 min of reaction, but could be regenerated by calcination.

Another strategy has been to condense the pore-lined OH groups of MCM-41 with a trialkoxysilane derivative to generate a stable $\text{O}_3\text{Si}-\text{R}$ linkage. The R group can then be modified with appropriate reactants to form a ligand. For example, Schiff base ligands have been formed by reacting MCM-41 with $(\text{CH}_3\text{O})_3\text{Si}(\text{CH}_2)_3\text{Cl}$, which generated $-\text{O}_3\text{Si}(\text{CH}_2)_3\text{Cl}$ groups bound to the MCM-41 framework. Treatment of the derivatized MCM-41 with ligands shown in Figure 36 led to bonding of the ligand at the R' site with the 3-chloropropylsilane moiety. The Schiff base ligands were then treated with an Mn^{2+} salt followed by oxidation to form the Mn^{3+} epoxidation catalyst [189]. Mesoporous silicas appear to possess patches of hydrophobic clusters made up of siloxanes and non-H-bonded silanol groups. The hydrophobic nature of the patches insures that the anchoring chloroalkylsilane chains migrate to these sites. For the parent mesoporous material the surface area and mesoporous volume were $947 \text{ m}^2 \text{ g}^{-1}$ and 0.72 mL g^{-1} , respectively, whereas for the $\text{Mn(III)}-\text{tSalpr}$ derivatized material these values were $672 \text{ m}^2 \text{ g}^{-1}$ and 0.41 mL g^{-1} respectively. The ligand grafting led to a decrease in surface area and mesoporous volume. However, as Figure 37 shows, the adsorption and desorption isotherms (type IV) were characteristic of the starting material, indicating that the textural properties were preserved. These complexes were examined as catalysts for styrene oxidation using PhIO as oxidant. For the $\text{Mn(III)}-\text{Salpr}$ and $\text{Mn(III)}-\text{tSalpr}$ complexes, the selectivity for epoxide formation was 58 and 24 %, respectively. The relatively low selectivity compared with unsupported complexes was explained as being due to the formation of by-products that were absorbed on the catalyst surface [177a].

Ru -porphyrin complexes covalently bound to MCM-41 were used as catalysts for the oxidation of alkenes, giving turnover numbers 20–40 times higher than the free complex [190]. Porphyrin complexes have also been attached to Nb dopants in the MCM-41 matrix, and behaved as cyclohexene epoxidation catalysts and were stable towards ligand degradation [44b]. Grafting of ethylenediamine ligands on

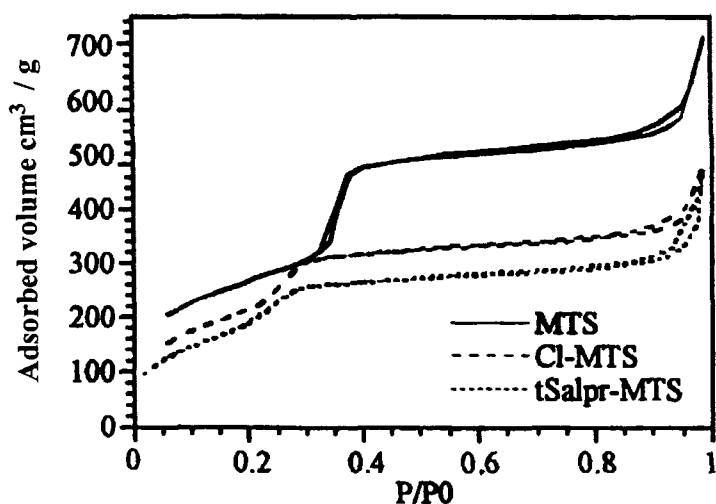


Figure 37. Nitrogen adsorption-desorption isotherms of parent mesoporous material MTS (solid line), Cl-MTS (dashed line) and tSalpr-MTS (dotted line). MTS = micelle templated silica, Cl-MTS = MTS modified by 3-chloropropylsilane and tSalpr-MTS = MTS modified with Mn(III) *N,N'*-bis[3-(3,5-di-*tert*-butylsalicylideneamino)propyl]amine.

walls of MCM-41 followed by complexation of Co(II) gave rise to the formation of a reversible dioxygen adduct [191]. The H_2O_2 -resistant ligand tmtacu (triamine-1,4,7-trimethyl-1,4,7-triazacyclononane) has also been grafted on mesoporous silicas and was found to be an excellent catalyst for styrene and cyclohexane epoxidation in the presence of Mn^{2+} and H_2O_2 [192].

Thus, mesoporous structures, because of their pores, make it possible to incorporate large catalytically active transition metal complexes. Covalently grafting these complexes in the hydrophobic patches provides better dispersion of the catalyst, as well as resistance to leaching. Improvement in catalytic performance is to be expected when materials with even larger pore diameters are studied. It will also be necessary to passivate the silanol groups responsible for promoting adsorption on the catalytic surface.

The large size of the pores of MCM-41 has also allowed the entrapment of enzymes, such as cytochrome *c*, papain and trypsin [193]. Enzyme entrapment has been extensively performed with sol-gel materials. The types of applications of redox catalysis using enzyme-mesoporous materials is expected to parallel the sol-gel materials, which is discussed in the last section of this chapter.

Electrochemistry

Electrochemical studies with mesoporous materials are only beginning to be explored [194]. Electroactive species can be introduced via ion exchange or by covalently attaching species in the mesopores. Balkus and co-workers were the first to examine the electrochemistry of anchored amine-ligated Co^{2+} complexes [191].

In particular, framework-bound ligands such as ethylenediamine (ED), diethylenetriamine (DET) and ethylenediaminetriacetic (EDT) acids were examined. Cobalt(II) complexes were formed by exposing the amine-derivatized MCM-41 to CoCl_2 solution. Working electrodes were made by pressing an MCM-41-graphite mixture on to a platinum grid, similar to the procedures used for making ZME. Electroactivity as measured by cyclic voltammetry (CV) was only observed if free uncomplexed ethylenediamine (en) ligand was present in the solution. The potential of the reversible redox couple was observed at -0.62 V vs. SCE and was similar to that of Co(en)_3^{2+} in solution. However, since the peak intensity did not decrease with time, it was proposed that the electroactive cobalt complexes were still grafted on to MCM-41. The excess en in solution was necessary to form mixed-ligand complexes (en, ED), (en, EDT), (en, DET) prior to observation of electrochemical activity. The CV signals observed corresponded to only a small fraction of the total cobalt in the MCM-41, indicative of electrochemical activity of only surface bound species.

Villemure and Pinnavaia examined the redox activity of Ru(bpy)_3^{2+} adsorbed or exchanged in mesoporous HMS and Al-HMS [195]. The electrochemical activities of the Ru(bpy)_3^{2+} ions that diffused out of the support were analyzed by CV. Walcarius and co-workers developed electroanalytical methods using MCM-41 [196]. The MCM-41-carbon paste electrode was found to be a good and selective preconcentrating medium for Cu^{2+} and Hg^{2+} in the presence of NH_3 . The preconcentration of millimolar levels of Cu^{2+} and Hg^{2+} was possible in the presence of a 1000-fold excess of alkali and alkaline earth metal cations and a 10-fold excess of other transition metal ions. After preconcentration, the analytes were exchanged out in a strongly acidic medium and analyzed by CV. In the case of mercury(II), the high discrimination against other cations was attributed to the fact that between pH 4 and 7, Hg(OH)_2 is the main soluble species and it can condense with the silanol groups of MCM-41, whereas other ions not in the hydroxide form cannot react with the silanol groups [197].

3.3.3 Sol-Gel Materials

Prior to the early 1980s there was minimal research on the incorporation of organic or biological compounds within ceramic materials [198]. Typical manipulation of ceramics occurs over 1000°C , well beyond the survival threshold for any biological or organic compound. However, sol-gel chemistry has altered this field since it lends itself well to the entrapment of chemically interesting species. The larger pores of sol-gel materials as compared with zeolites and MCM-41 type of materials have led to the encapsulation of many enzymatic systems. The entrapment of molecules is usually done by one of two methods: direct physical entrapment or by functional modification of the inorganic matrix by copolymerization with organo-metal alkoxides, and is represented schematically in Figure 38 [63i]. Direct doping of the sol-gel system is the easiest and most straightforward. In this procedure the dopant is added to the polymerizing mixture and, upon completion of the polycondensation, is entrapped within the inorganic polymeric network. Research on sol-gel-entrapped organic species has led to the realization of several general traits [199]. Most mole-

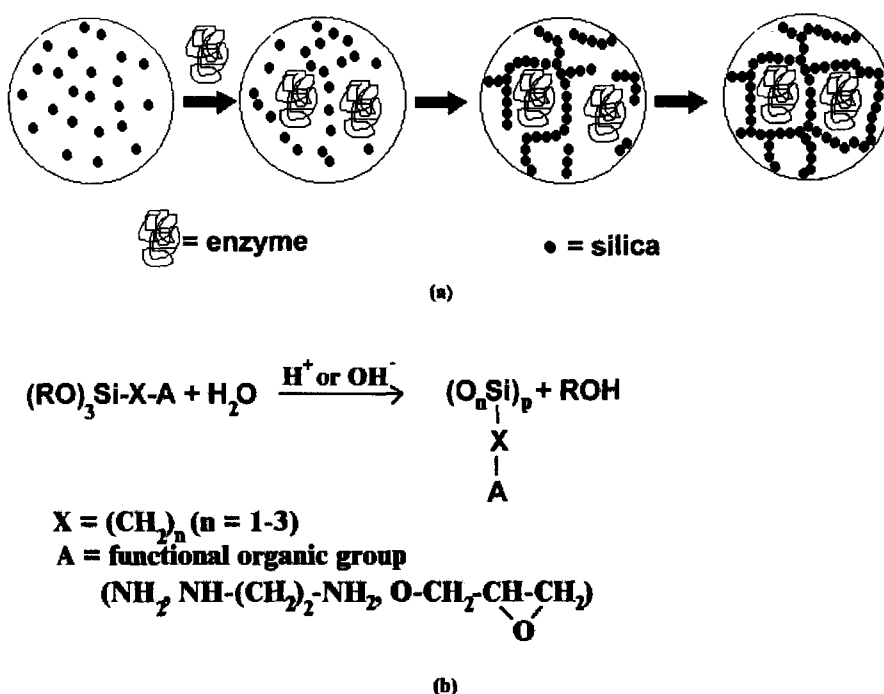
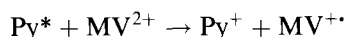


Figure 38. Schematic comparison of the entrapment procedures for sol-gel materials: (a) direct doping and (b) functional modification by copolymerization with organo-metal alkoxides.

cules can be entrapped within sol-gel matrices. Once entrapped, the dopant retains most of its physical and chemical properties. The pore network of the sol-gel permits the access of external reagents, allowing for chemical reactions and interactions. Materials made from sol-gel materials are optically transparent into the UV range, allowing for photochemical studies. Hydrocarbon oxidation using Ti-containing silicas has the potential to rival the studies done with mesoporous materials and, coupled with the fact that silica synthesis does not require templating agents, the possibilities are intriguing. Sol-gel techniques have led to materials with a high density of Ti-O-Si centers and 20 wt. % of titania with epoxidation catalytic activity poorer than 2 wt. % titania-MCM-41, but larger conversions than MCM-41, presumably because of the larger content of titanium [200].

Photochemical ET reactions

The photochemical inertness of the silica sol-gel makes it a good host for photochemical ET reactions. The porous architecture has been exploited to extend the lifetimes of charge-separated species [201]. For the system



where Py* is photoexcited pyrene and MV²⁺ is the methylviologen cation, Py⁺ and

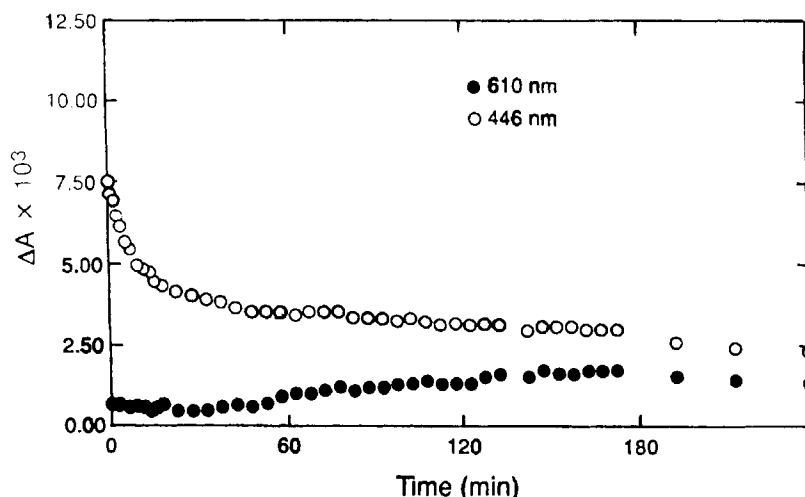
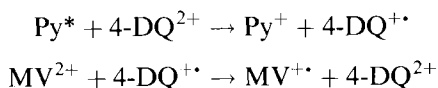


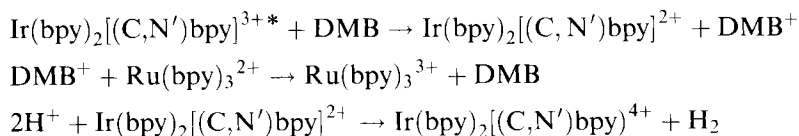
Figure 39. Changes in absorbance with respect to time for Py^+ (446 nm, \circ) and MV^+ (610 nm, \bullet) after irradiation of Py (4×10^{-5} M), DQ^{2+} (5×10^{-4} M), MV^{2+} (3×10^{-6} M) sol-gel system.

$\text{MV}^{+\bullet}$ are formed transiently and disappear quickly because of the back ET reaction. However, when the pyrene and methylviologen are entrapped within a silica sol-gel network in the presence of the mobile charge carrier N,N' -tetramethylene-2,2'-bipyridinium (4-DQ^{2+}), photoexcitation leads to the creation of long-lived $\text{MV}^{+\bullet}$ [201a]. This is because the 4-DQ^{2+} acts as a shuttle between the Py^* and MV^{2+} :



The photogenerated $\text{MV}^{+\bullet}$ and Py^+ can be monitored at 610 and 446 nm, respectively. As Figure 39 shows that, upon photolysis, the signal due to Py^+ decreases, whereas that due to $\text{MV}^{+\bullet}$ increases with time. At $[\text{MV}^{2+}] = 3 \times 10^{-6}$ M, the photogenerated redox species lasts up to 4 h and consists of $\sim 5\%$ of the radicals initially formed [201a].

Another important example of a photochemical ET reaction in a sol-gel is the reduction of H_2O to H_2 [201]. The donor $[\text{Ru}(\text{bpy})_3]^{2+}$ and acceptor $\{\text{Ir}(\text{bpy})_2[(\text{C},\text{N}')\text{bpy}]^{3+}\}$ were both entrapped in the sol-gel and dimethoxybenzene (DMB) was used to transport the charge between them. The following reactions were proposed for generation of H_2 :



After several thousand laser pulses at 390 nm, H₂ was detected using gas chromatography. H₂ was produced with a quantum yield of ~1 % and it was estimated that the turnover number for Ir(III) as a catalyst for H₂ generation was >100.

Enzymatic redox reactions

The redox chemistry of enzymes encapsulated within sol–gels has been an area of extensive research [198]. Initially, there was no reason to believe that enzymes would remain active upon sol–gel encapsulation. The enzyme could react with the alkoxide and be destroyed either by the pressure of matrix shrinkage or the release of toxic alcohols during the hydrolysis. In contrast to these expectations, it has been found that enzymes such as trypsin, which completely digests itself in solution, retains full activity for months upon sol–gel incorporation [202]. Other enzymes also show an increase in stability upon sol–gel entrapment [203]. Acid phosphatase experienced an increase of two orders of magnitude in its half-life, increasing from 0.1 min in solution to 12 min upon entrapment [203b]. The increase in stability can be attributed to the spatial restrictions placed upon the entrapped enzyme. The rigid structure of the sol–gel matrix may interfere with the unfolding of the enzyme associated with denaturation.

One of the most widely studied enzymes in sol–gels has been glucose oxidase on silica [202, 204]. Shtelzer and Braun developed a reversible optical glucose sensor based on the loss of color of the isoalloxazine moiety of the enzyme upon reductive complexation of glucose [204a]. The sol–gel/glucose oxidase system has also been used as a diagnostic tool. Hydrogen peroxide, a reaction product of glucose oxidase, was monitored via a second enzymatic reaction (peroxidase-based) with aromatic aza compounds [204]. The products of this reaction are colored and easily monitored spectroscopically. This system demonstrates the ability of the sol–gel matrix to play host to several working enzymes.

Enzyme encapsulation along with photochemical electron transfer within the sol–gel network has been studied by Shen and Kostic [205]. The enzyme zinc cytochrome *c* (Zncyt) has a long-lived triplet state that can be oxidatively quenched. Zncyt was entrapped in the sol–gel during the synthesis stage and the quencher, either [Ru(NH₃)₆]³⁺ or [Ru(NH₃)₅Cl]²⁺, was introduced by soaking the preformed sol–gel/enzyme system in a 2×10^{-4} M quencher solution [205a]. The ruthenium complex preferentially collected within the pore system and quenched the excited state of the enzyme. Figure 40 shows the decay of the transient absorption of ³Zncyt with and without quencher [205]. The upper decay corresponds to unquenched ³Zncyt and was fitted to a rate constant of 70 ± 10 s⁻¹. The lower decay is ³Zncyt upon quenching with [Ru(NH₃)₆]³⁺ and was fitted to three rate constants of 100, 570 and 3900 s⁻¹. The single exponential decay in the absence of quencher indicates a similar environment for all proteins, whereas the different decays upon quenching are indicative of a microheterogeneous media.

Another study involved native cytochrome *c* (iron containing) and the quenchers [Fe(CN)₆]³⁻, dioxygen and *p*-benzoquinone. The influences of ionic strength and pH on the quenching abilities of these molecules in solution were investigated [205b]. It was found that the assumption of uniform dispersion of small species

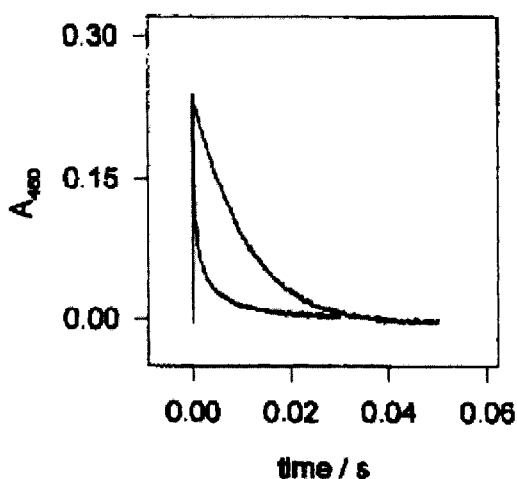


Figure 40. Transient absorbance (460 nm) of the triplet state of Zncyt ($^3\text{Zncyt}$) encapsulated in a sol-gel glass. Upper trace is in the absence of a quencher, lower trace in the presence of $[\text{Ru}(\text{NH}_3)_6]^{3+}$.

within sol-gel networks is not necessarily true and should be tested for each substrate.

Electrochemistry

Sol-gel systems provide several advantages in the design of electrochemical systems. They have favorable abrasion resistance, good optical characteristics and the ability to tailor the hydrophobicity and affinity of molecules towards the network. Leaching of active species from within the network is a problem and several methods are available to avoid or minimize this event [206]. The reagent of interest can be covalently bonded to the framework [207]. This eliminates all leaching, but requires the use of organic synthesis in the preparation and is usually accompanied by a change in the formal potential. Bulky dopants such as polymers can be used and will eliminate mobility of the encapsulated reagent, but also requires more in-depth synthesis schemes [208]. These two methods can only be used in situations where there is no requirement for the movement of the dopant. The sol-gel can also be modified to increase its affinity for the encapsulated species [198]. This is done by using organically modified sol-gels to tailor the degree of hydrophobicity to suit the encapsulated species. These systems tend to be easier to prepare and have less of an effect on the formal potential, but will also result in an eventual leaching of the reagent.

Electrochemistry has been used to study the effect of sol-gel entrapment on redox agents. Collinson and coworkers selected six redox probes based on size, shape and charge and investigated their entrapment, activity and stability [209]. It was determined that the sol-gel network is a dense, collapsed system that prohibits the majority of the probes from being able to move to the electrode and exchange electrons. Anionic probes were found to be more stable in the sol-gel, which was attributed to the diffusion of cationic and neutral species out of the sol-gel and into the solution. It was unclear as to why the anionic probes showed increased stability,

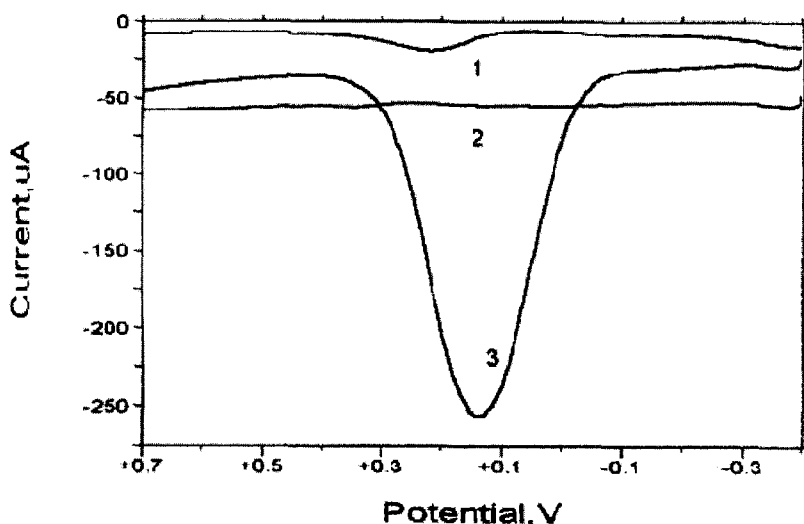


Figure 41. Square-wave voltammograms for 1.0 mM $\text{Fe}(\text{CN})_6^{4-}$, 0.1 M KCl at (1) a bare graphite electrode, (2) a sol-gel-modified electrode and (3) a sol-gel-PDMAAC-modified electrode after a 10 min exposure time.

especially considering that the sol-gel itself should be negatively charged. Two hypotheses were presented. The first was that the driving force to retain the probes was higher than the electrostatic repulsion and the second attributed the result to a concentration phenomenon. However, neither of these could be proven.

Sol-gels containing electroactive species have been used in the development of both amperometric and potentiometric electrodes. Films coated with anionic poly-(dimethyldiallylammonium chloride) (PDMDAAC) and cationic poly(vinylsulfonic acid) were used to concentrate $\text{Ru}(\text{bpy})_3^{2+}$ and the hexacyanoferrate anion, respectively, for use as amperometric electrodes [208a]. The detection limit by square-wave voltammetry improved by up to 50-fold compared with uncovered electrodes. In Figure 41, curve 1 corresponds to a bare graphite electrode, curve 2 to a sol-gel-covered electrode and curve 3 to a sol-gel-PDMDAAC-modified electrode after 10 min of exposure to $\text{Fe}(\text{CN})_6^{4-}$.

Ion-selective membranes have been developed using the carrier valinomycin and a 12-crown-4 derivative for the detection of potassium and sodium ions. Leaching was originally a problem, but was later avoided by using covalently bonded reagents [207, 210].

Several electrochemical studies have focused on the glucose oxidase system for sensor applications. Tatsu and co-workers reported an electrochemical oxygen sensor coupled to a sol-gel containing glucose oxidase using a nylon net and a cellulose membrane [211a]. The loss of oxygen from solution can be correlated with the glucose concentration, resulting in a glucose sensor. Figure 42 shows the response of the sensor to a series of glucose concentrations and a calibration curve [211a].

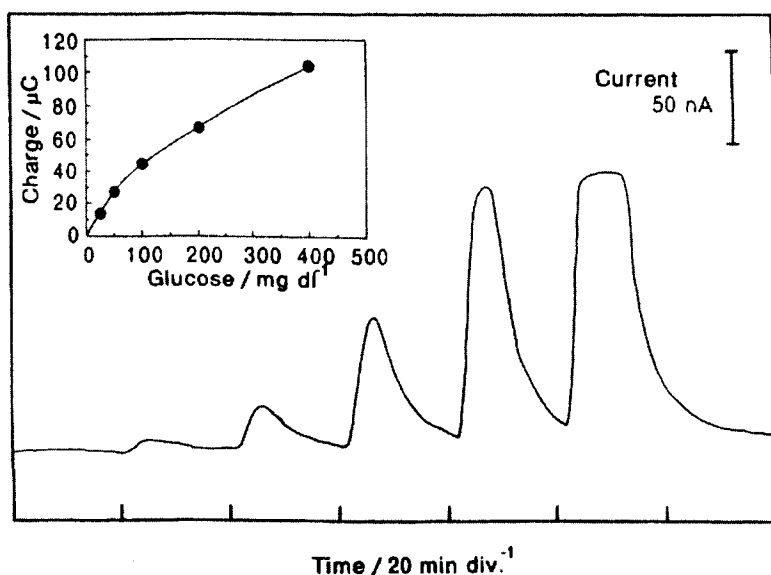
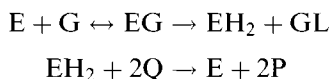


Figure 42. Output current of a sol-gel-entrapped glucose oxidase electrochemical sensor. Standard solutions of 0, 25, 50, 100, 200 and 400 mg dL^{-1} of glucose were injected over 20 min periods. Inset shows integrated peak area (charge) versus glucose concentration.

The response of the sensor peaked within 4 min and the calibration curve is applicable within the range of glucose concentrations in normal human serum. Another glucose sensor using sol-gel systems was based upon glucose oxidase in conjunction with a mediator compound (ferrocene or hexacyanoferrate) that transferred an electron to the enzyme [211]. This system can be represented as



where E and EH_2 are the oxidized and reduced form of the enzyme, Q and P are the oxidized and reduced form of the mediator, G is the substrate (glucose), GL is gluconolactone, and EG is the complex formed between the oxidized enzyme and the glucose [211b]. The mediator, P, can then be reoxidized to Q at the electrode surface. This results in a Faradaic current proportional to the glucose concentration that is completely independent of oxygen.

Horseradish peroxidase (HRP) has also been used in sol-gel electrochemical systems. In the presence of a mediator [hexacyanoferrate(II) or ferrocene], sol-gel-entrapped HRP was used as a peroxide sensor [212]. Chuit et al. used this system in a sandwich configuration to achieve good sensitivity [213].

In a departure from SiO_2 -based sol-gels, an amperometric biosensor was developed by Glezer and Lev [214]. Sol-gels of V_2O_5 doped with V^{4+} provide good

electrical conductivity and adhere well to conductive supports such as platinum. When glucose oxidase is entrapped within this system the hydrogen peroxide produced as a result of glucose oxidation is oxidized at the metal support, resulting in the analytical signal.

Another example of a nonsilicate biosensor was developed by Milagres and co-workers [215]. Silica gel was coated with TiO_2 using a sol-gel method. Ferrocene, carboxylic acid and glucose oxidase were then adsorbed on the surface. Large loadings of the enzyme were possible owing to the large surface area of the powder. The voltammogram response was found to be affected by the nature of the supporting anion, which caused a shift in midpoint potential. The sensor was tested by measuring glucose in blood serum and resulted in a correlation coefficient of 0.9996.

Lev and co-workers developed the composite carbon-silicate electrode (CCE) [216]. In these electrodes, the silica sol-gel is mixed with graphite or carbon black powder. At a critical concentration of carbon within the sol-gel (beyond the percolation threshold), there becomes a continuous path(s) of conductive carbon throughout the system. The sol-gel system used was a methyl silicate network (by using methyltrimethoxysilane as the sol-gel precursor, the resulting network has exposed SiCH_3 groups), which imparts hydrophobic properties to the electrode [217]. This prevents water penetration and only the exterior of the electrode is exposed to electrolytes. When used with 30 nm sized carbon black powder, the conductive area of the electrode in contact with the electrolyte consists of less than 1 % of the geometric cross-sectional area of the electrode. This has been compared with an ensemble of microelectrodes. These CCEs showed an improvement of up to three orders of magnitude in terms of Faradaic signal-to-noise compared with glassy carbon electrodes [218]. In addition, the sol-gel method of preparation affords a variety of structural configurations and it has been shown that CCEs can be produced by thick film and ink jet technology, which allows for their mass production [219].

In order to improve upon the poor electrocatalytic activity of graphite, trace amounts of metal or organometallic catalysts were added. This was done in several ways. The organometallic catalyst can be placed within the graphite powder prior to the addition to the sol-gel precursors, or added separately to the carbon/sol-gel precursor mixture [217, 219]. CCEs containing the catalysts cobalt phthalocyanine and cobalt porphyrin showed good activity toward the electrocatalytic reduction of molecular oxygen. This property has been demonstrated with the reduction of carbon monoxide and oxidation of sulfur dioxide. Owing to the porosity of the sol-gel network, these CCEs can be used as electrical sensors in the gas phase. Using these electrodes, a gas-phase oxygen sensor with a 0.8 s response time (90 % signal change) with a linear range of 0–0.21 atm was fabricated.

CCEs have also been used in conjunction with enzymes. Glucose oxidase was encapsulated within the methyl silicate (or silica)-graphite composite [216, 220]. Reduced oxygen from the enzymatic reaction results in the production of H_2O_2 , which is oxidized at the electrode. Palladium and rhodium catalysts have been added to the electrode to help lower the over voltage required for hydrogen peroxide oxidation [219, 221]. Glucose oxidase and horseradish peroxidase have been simultaneously entrapped within a CCE for a biosensor that does not require a

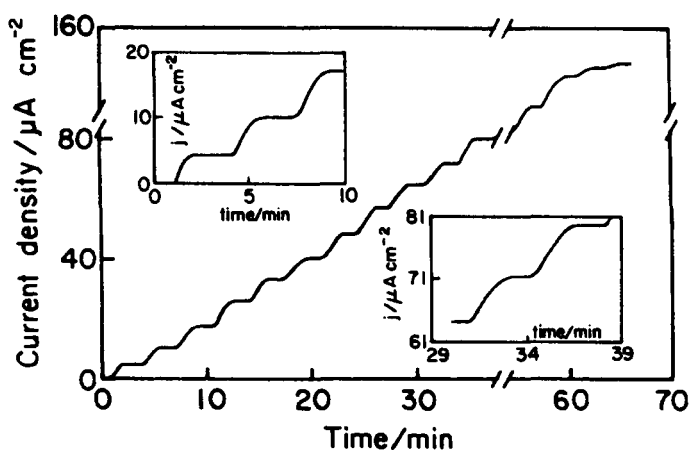


Figure 43. Response of 400 mV (vs. SCE) polarized TTF-mediated glucose oxidase-modified CCE upon sequential additions of 2.5 mM glucose solutions. Insets show details of response at the indicated times.

mediator [222]. The enzymatically generated H_2O_2 was detected at a potential of 0 V (vs. SCE), limiting the influence of interfering species. The performance was optimized by using two separate CCEs, each containing one enzyme, configured into a bilayer structure.

To improve further the characteristics of these systems, the use of mediators (either entrapped or chemically attached to the silicate network) has been investigated [220, 221]. Tetrathiafulvalene was used as a mediator with the glucose oxidase system to allow for oxygen-independent measurements. The performance of this sensor is shown in Figure 43 [220]. The electrode has a response time of 30–100 s upon addition of 2.5 mM glucose solution. The longer response times at higher concentrations are due to a lower reaction order. In another variation, ferrocenyl groups were covalently attached to the glucose oxidase itself before incorporation within the sol–gel [223].

The CCE–glucose oxidase system has evolved even further with the direct wiring of the enzyme [225]. The system consists of graphite powder and glucose oxidase in a ferrocene-, amine- and methyl-modified silicate sol–gel network. In the final electrode, each part makes its own contribution to the system. The silicate network provides the porous support, the graphite provides the conductivity, ferrocene provides the transduction of the signal from enzyme to the conductive surface, amino groups effect the anchoring of the enzyme to the surface via attraction to the negative charges of the enzyme surface and the methyl and amino groups provide the hydrophobicity to control the wetted area of the electrode.

Ruthenium-dispersed sol–gel thick-film electrodes were developed by Wang and co-workers [219]. All of these systems showed shelf-life stability in excess of 4 months and excellent selectivity over common interferents such as ascorbic acid, acetaminophen and uric acid. Based on this work, electrodes for lactate and amino

acid sensing were prepared using lactate oxidase and amino acid oxidase, respectively [224].

Bharathi and Lev developed a gold–ceramic composite and used it for glucose sensing [226]. This system is similar to CCEs with the graphite powder replaced by gold nanoparticles. In this system, the gold provides both the conductivity and the electrocatalytic activity required.

3.4 Conclusions

We have discussed in some detail ET reactions occurring in zeolites, mesoporous materials and sol–gels. The unifying theme across these three different types of materials is their porosity. ET reactions within the pores with molecules as small as propylene to complex enzymes such as glucose oxidase have been discussed. However, what is also apparent from the discussions are that each host matrix imposes its own unique characteristics on the reactions within its pores. We conclude by highlighting the uniqueness of each matrix.

Zeolites are microporous frameworks, and all of the ET chemistry that we have discussed is with molecules smaller than 13 Å. The unique features of zeolites are their ion-exchanging ability, a stable structure upon dehydration and a pore/channel structure that allows for a well-defined arrangement of molecules in space and the fact that redox-active atoms can be substituted on the framework. In most cases, the zeolite is an active host, influencing ET reactions via electrostatic fields or steric effects, a feature that is not found with the mesoporous and sol–gel materials. Packing of molecules/ions in the intrazeolitic space with very high densities is also possible and was found to be important in charge propagation and electrochemistry.

Mesoporous materials extend the range of porosities to the tens of ångströms scale. Although this provides a major advantage due to the increase in size of the molecules that can be introduced into the pores, several advantages of zeolitic-like systems are lost in the translation. The most important factor is that the framework of the mesoporous materials is amorphous. Thus, strong acidity and specific siting of redox active atoms on particular crystallographic sites are not possible. Increases in the size of the pores and the siliceous nature of the framework also limit the electrostatic effects that have been extensively exploited with zeolites. On the other hand, the silanol groups in the framework of mesoporous materials have found extensive use in anchoring of complexes. The ion-exchange properties of Al-doped mesoporous materials have not been exploited as yet. The major impact of mesoporous materials on ET reactions has been the study of the redox chemistry of larger substrates with metals doped into the framework. In the case of hydrocarbon oxidation, mesoporous materials have clearly broadened the scope of applications.

Sol–gel materials have found most promise in exploiting enzyme-based redox chemistry. The larger porosity and the very simple methods of entrapment have facilitated the use of enzyme–sol–gel systems. Lack of a regular pore structure makes the architecture of molecular assemblies difficult with sol–gel materials,

especially compared with zeolites. Attempts are being made to use doped sol-gel materials as redox catalysts, and could be in competition with mesoporous materials. However, issues regarding the use of H_2O_2 as oxidant, the long-term leaching of redox-active atoms and the regeneration of the catalyst by calcination need to be resolved if sol-gel materials are going to be important in hydrocarbon redox reactions.

Summarizing the field of ET using porous materials, it appears that zeolites act as active hosts and have advantages of manipulating reaction rates and product yields involving small molecules due to the close fits of the size of the molecule and cages. Mesoporous materials make it possible to examine the redox chemistry of larger molecules as compared with zeolites, while sol-gel materials form the primary hosts for enzyme-based redox reactions.

Acknowledgments

We acknowledge funding by the DOE and thank Prof. K. B. Yoon for providing us with a copy of his review article prior to publication.

References

1. R. Szostak, *Handbook of Molecular Sieves*, Van Nostrand, New York, **1992**.
2. J. Weitkamp, H. G. Karge, H. Pfeifer, W. Holderich, *Zeolites and Related Microporous Materials: State of the Art 1994*, Elsevier, Amsterdam, **1994**.
3. A. Corma, H. Garcia, *Catal. Today* **1997**, *38*, 257–308.
4. D. E. Akporiaye, *Angew. Chem., Int. Ed. Engl.* **1998**, *37*, 2456–2457.
5. D. W. Breck, *Zeolite Molecular Sieves*, Wiley, New York, **1974**.
6. M. E. Davis, R. F. Lobo, *Chem. Mater.* **1992**, *4*, 756–768.
7. C. T. G. Knight, *Zeolites* **1990**, *10*, 140–144.
8. R. M. Barrer, *Hydrothermal Chemistry of Zeolites*, Academic Press, London, **1982**.
9. E. N. Coker, J. C. Jansen, J. A. Martens, P. A. Jacobs, F. DiRenzo, F. Fajula, A. Sacco, Jr., *Microporous Mesoporous Mater.* **1998**, *23*, 119–136.
10. G. Engelhardt, H. Van Koningsveld, *Zeolites* **1990**, *10*, 650–656.
11. S. L. Burkett, M. E. Davis, *Chem. Mater.* **1995**, *7*, 920–928.
12. P. K. Dutta, *J. Inclusion Phenom. Mol. Recognit. Chem.* **1995**, *21*, 215–237.
13. P.-P. E. A. De Moor, T. P. M. Beelen, R. A. van Santen, *J. Phys. Chem. B* **1999**, *103*, 1639–1650.
14. (a) M. Goldwasser, J. F. Dutel, C. Naccache, *Zeolites* **1989**, *9*, 54–58; (b) P. K. Dutta, R. E. Zaykoski, *Inorg. Chem.* **1985**, *24*, 3490–3492; (c) P. K. Dutta, R. E. Zaykoski, M. A. Thomson, *Zeolites* **1986**, *6*, 423–426; (d) B. R. Shaw, K. E. Crearsy, C. J. Lanczycki, J. A. Sargeant, M. Tirhado, *J. Electrochem. Soc.* **1988**, *135*, 869–876.
15. (a) A. N. Fitch, H. Jovic, A. Renouprez, *J. Phys. Chem.* **1986**, *90*, 1311–1318; (b) X. Liu, K. K. Iu, J. K. Thomas, *J. Phys. Chem.* **1989**, *93*, 4120–4128.
16. (a) P. K. Dutta, M. Borja, *Zeolites* **1992**, *12*, 142–145; (b) H. Miessner, I. Burkhardt, D. Gutschik, A. Zecchima, C. Morterra, G. Spoto, *J. Chem. Soc., Faraday Trans.* **1990**, *86*, 2321–2327.
17. W. DeWilde, G. Peeters, J. H. Lunsford, *J. Phys. Chem.* **1980**, *84*, 2306–2310.
18. N. B. Castagnola, P. K. Dutta, *J. Phys. Chem. B* **1998**, *102*, 1696–1702.
19. K. Maruszewski, D. P. Strommen, J. R. Kincaid, *J. Am. Chem. Soc.* **1993**, *115*, 8345–8350.

20. (a) C. Bowers, P. K. Dutta, *J. Catal.* **1990**, *122*, 271–279; (b) R. F. Parton, I. F. J. Vankelecom, M. J. A. Casselman, J. B. Uytterhoeven, P. A. Jacobs, *Nature* **1994**, *370*, 541–544; (c) N. Herron, *Inorg. Chem.* **1986**, *25*, 4714–4717; (d) P. K. Dutta, C. Bowers, *Langmuir* **1991**, *7*, 937–940.
21. K. J. Balkus, Jr., C. D. Hargis, S. Kowalak, *Am. Chem. Soc. Symp. Ser.* **1992**, *499*, 347–354.
22. I. Willner, Y. Eichen, *J. Am. Chem. Soc.* **1987**, *109*, 6862–6863.
23. I. Okura, N. Naji, A. Aono, T. Nishisaka, *Bull. Chem. Soc. Jpn.* **1986**, *59*, 3967–3968.
24. J. K. Hurst, D. H. P. Thompson, *J. Membr. Sci.* **1986**, *28*, 3–29.
25. J.-S. Hsiao, A. R. Eckert, S. E. Webber, *J. Phys. Chem.* **1994**, *98*, 12032–12039.
26. F. M. Winnik, *Chem. Rev.* **1993**, *93*, 587–614.
27. (a) K. K. Iu, J. K. Thomas, *Langmuir* **1990**, *6*, 471–478; (b) V. Ramamurthy, *Photochemistry in Organized and Constrained Media*, VCH, New York, **1991**.
28. P. K. Dutta, W. Turbeville, *J. Phys. Chem.* **1991**, *95*, 4087–4092.
29. S. Uppili, K. J. Thomas, E. M. Crompton, V. Ramamurthy, *Langmuir* **2000**, *16*, 265–274.
30. J. Karger, D. M. Ruthven, *Diffusion in Zeolites and other Microporous Solids*, Wiley, New York, **1991**.
31. P. K. Dutta, B. Del Barco, D. C. Shieh, *Chem. Phys. Lett.* **1986**, *127*, 200–204.
32. K. Maruszewski, J. R. Kincaid, *Inorg. Chem.* **1995**, *34*, 2002–2006.
33. V. Ramamurthy, J. V. Caspar, D. R. Corbin, J. S. Kauffman, C. Dybowski, *J. Photochem. Photobiol. A* **1990**, *51*, 259–263.
34. V. Ramamurthy, J. V. Caspar, D. R. Corbin, *J. Am. Chem. Soc.* **1991**, *113*, 594–600.
35. (a) E. Dempsey, *Molecular Sieves*, Society of Chemical Industry, London, **1968**; (b) J. A. Rabo, C. L. Angell, P. H. Kasai, V. Schoemaker, *Discuss. Faraday Soc.* **1966**, *41*, 328–349.
36. B. Barrachin, E. Cohen de Lara, *J. Chem. Soc., Faraday Trans. 2* **1986**, *82*, 1953–1966.
37. M. A. Spackman, H. P. Weber, *J. Phys. Chem.* **1988**, *92*, 794–796.
38. B. J. Schoeman, J. Sterte, J. E. Otterstedt, *Zeolites* **1994**, *14*, 110–116.
39. M. Alvaro, H. Garcia, S. Corrent, J. C. Scaiano, *J. Phys. Chem. B* **1998**, *102*, 7530–7534.
40. R. Singh, P. K. Dutta, *Microporous Mesoporous Mater.* **1999**, *32*, 29–35.
41. A. Tavoraro, E. Drioli, *Adv. Mater.* **1999**, *11*, 975–996.
42. H. Lee, P. K. Dutta, *Microporous Mesoporous Mater.* **2000**, *38*, 151–159.
43. (a) C. T. Kresge, M. E. Leonowicz, W. J. Roth, J. C. Vartuli, J. S. Beck, *Nature* **1992**, *359*, 710–712; (b) J. S. Beck, J. C. Vartuli, W. J. Roth, M. E. Leonowicz, C. T. Kresge, K. D. Schmitt, C. T.-W. Chu, D. H. Olsen, E. W. Sheppard, S. B. McCullen, J. B. Higgins, J. L. Schlenker, *J. Am. Chem. Soc.* **1992**, *114*, 10834–10843.
44. (a) A. Corma, *Chem. Rev.* **1997**, *97*, 2373–2419; (b) J. Y. Ying, C. P. Mehnert, M. S. Wong, *Angew. Chem., Int. Ed. Engl.* **1999**, *38*, 56–77.
45. G. S. Attard, J. C. Glyde, C. G. Goltner, *Nature* **1995**, *378*, 366–368.
46. J. S. Beck, J. C. Vartuli, G. J. Kennedy, C. T. Kresge, W. J. Roth, S. E. Schramm, *Chem. Mater.* **1994**, *6*, 1816–1821.
47. A. Steel, S. W. Carr, M. W. Anderson, *J. Chem. Soc., Chem. Commun.* **1994**, 1571–1572.
48. (a) A. Monnier, F. Schuth, Q. Huo, D. Kumar, D. Margolese, R. S. Maxwell, G. D. Stucky, M. Krishnamurthy, P. Petroff, A. Firouzi, M. Janicke, B. F. Chmelka, *Science* **1993**, *261*, 1299–1303; (b) G. D. Stucky, A. Monnier, F. Schuth, Q. Huo, D. Margolese, D. Kumar, M. Krishnamurthy, P. Petroff, A. Firouzi, M. Janicke, B. F. Chmelka, *Mol. Cryst. Liq. Cryst. Sci. Technol., Sect. A* **1994**, *240*, 187–200.
49. A. Firouzi, D. Kumar, L. M. Bull, T. Besier, P. Sieger, Q. Huo, S. A. Walker, J. A. Zasadzinski, C. Glinka, J. Nicol, D. Margolese, G. D. Stucky, B. F. Chmelka, *Science* **1995**, *267*, 1138–1143.
50. C. A. Fyfe, G. Fu, *J. Am. Chem. Soc.* **1995**, *117*, 9709–9714.
51. (a) P. T. Tanev, T. J. Pinnavaia, *Science* **1995**, *267*, 865–867; (b) S. A. Bagshaw, E. Prouzet, T. J. Pinnavaia, *Science* **1995**, *269*, 1242–1244.
52. M. S. Morey, A. Davidson, G. D. Stucky, *J. Porous Mater.* **1998**, *5*, 195–204.
53. (a) T. Yanagisawa, T. Shimizu, K. Kuroda, C. Kato, *Bull. Chem. Soc. Jpn.* **1990**, *63*, 988–962; (b) Y. Fukushima, S. Inagaki, *Mater. Sci. Eng. A* **1996**, *A217/218*, 116–118; (c) S. Inagaki, Y. Fukushima, K. Kuroda, *J. Chem. Soc., Chem. Commun.* **1993**, 680–682.
54. Z. Luan, C.-F. Cheng, W. Zhou, J. Klinowski, *J. Phys. Chem.* **1995**, *99*, 1018–1024.

55. G. Fu, C. A. Fyfe, W. Schwieger, G. T. Kokotailo, *Angew. Chem., Int. Ed. Engl.* **1995**, *34*, 1499–1502.
56. F. Rey, G. Sankar, T. Maschmeyer, J. M. Thomas, R. G. Bell, G. Neville Greaves, *Top. Catal.* **1996**, *3*, 121–134.
57. (a) H. Yang, A. Kuperman, N. Coombs, S. Mamiche-Afara, G. A. Ozin, *Nature* **1996**, *379*, 703–705; (b) H. Yang, N. Coombs, I. Sokolov, G. A. Ozin, *Nature* **1996**, *381*, 589–592.
58. (a) H. W. Hillhouse, T. Okubo, J. W. v. Egmond, M. Tsapatsis, *Chem. Mater.* **1997**, *9*, 1505–1507; (b) S. H. Tolbert, A. Firouzi, G. D. Stucky, B. F. Chmelka, *Science* **1997**, *278*, 264–268.
59. Y. Lu, R. Ganguli, C. A. Drewien, M. T. Anderson, C. J. Brinker, W. Gong, Y. Guo, H. Soye, B. Dunn, M. H. Huang, J. I. Zink, *Nature* **1997**, *389*, 364–368.
60. (a) D. M. Antonelli, J. Y. Ying, *Angew. Chem., Int. Ed. Engl.* **1995**, *34*, 2014–2017; (b) D. M. Antonelli, A. Nakahira, J. Y. Ying, *Inorg. Chem.* **1996**, *35*, 3126–3136; (c) M. S. Wong, D. M. Antonelli, J. Y. Ying, *Nanostruct. Mater.* **1997**, *9*, 165–168; (d) J. S. Reddy, A. Sayari, *Catal. Lett.* **1996**, *38*, 219–223.
61. (a) J. Luo, S. L. Suib, *Chem. Commun.* **1997**, 1031–1032; (b) Z.-R. Tian, W. Tong, J.-Y. Wang, N.-G. Duan, V. V. Krishnan, S. L. Suib, *Science* **1997**, *276*, 926–930.
62. S. A. Bagshaw, T. J. Pinnavaia, *Angew. Chem., Int. Ed. Engl.* **1996**, *35*, 1102–1105.
63. (a) C. J. Brinker, G. W. Scherer, *Sol–Gel Science*, Academic Press, New York, **1990**; (b) C. Sanchez, M. L. McCartney, C. J. Brinker, A. K. Cheetham (Eds.), *Better Ceramics Through Chemistry, VI, Mater. Res. Soc. Symp. Proc.*, Vol. 346, Materials Research Society, Pittsburgh, Pa. **1994**; (c) J. Livage, M. Henry, C. Sanchez, *Prog. Solid State Chem.* **1988**, *18*, 259–341; (d) H. Dislich, *J. Non-Cryst. Solids* **1985**, *73*, 599–612; (e) L. L. Hench, J. K. West, *Chem. Rev.* **1990**, *90*, 33–72; (f) J. Zarzycki, *Heterogen. Chem. Rev.* **1994**, *1*, 243–253; (g) T. J. Barton, L. M. Bull, W. G. Klemperer, D. A. Loy, B. McEnaney, M. Misono, P. A. Monson, G. Pez, G. W. Scherer, J. C. Vartuli, O. M. Yaghi, *Chem. Mater.* **1999**, *11*, 2633–2656; (h) D. Avnir, L. Klein, D. Levy, U. Schubert, A. Wojcik, in *The Chemistry of Organic Silicon Compounds*, Vol. 2 (Eds. Z. Rappoport, Y. Apeloig), Wiley, New York, **1998**, pp. 2317–2362. (i) B. C. Dave, B. Dunn, J. S. Valentine, J. Zink, *Anal. Chem.* **1994**, *66*, 1120A–1127A.
64. G. Philipp, H. Schmidt, *J. Non-Cryst. Solids* **1984**, *63*, 283–292.
65. D. Avnir, D. Levy, R. Reisfeld, *J. Phys. Chem.* **1984**, *88*, 5956–5959.
66. A. J. Lecloux, J. Bronckart, F. Noville, C. Dodet, P. Marchot, J. P. Pirard, *Colloids Surf.* **1986**, *19*, 359–374.
67. V. R. Kaufman, D. Levy, D. Avnir, *J. Non-Cryst. Solids* **1986**, *82*, 103–109.
68. D. Anvir, S. Braun, O. Lev, M. Ottolenghi, *Chem. Mater.* **1994**, *6*, 1605–1614.
69. V. R. Kaufman, D. Avnir, *Langmuir* **1986**, *2*, 717–722.
70. D. Avnir, V. R. Kaufman, R. Reisfeld, *J. Non-Cryst. Solids* **1985**, *74*, 395–406.
71. T. Tani, H. Namikawa, K. Arai, A. Makishima, *J. Appl. Phys.* **1985**, *58*, 3559–3565.
72. R. S. Lumpkin, E. M. Kober, L. A. Worl, Z. Murtaza, T. J. Meyer, *J. Phys. Chem.* **1990**, *94*, 239–243.
73. D. Levy, R. Reisfeld, D. Avnir, *Chem. Phys. Lett.* **1984**, *109*, 593–597.
74. D. Levy, D. Avnir, *J. Phys. Chem.* **1988**, *92*, 4734–4738.
75. S. T. Sie, *Stud. Surf. Sci. Catal.* **1994**, *85*, 587–631.
76. (a) I. W. C. E. Arends, R. A. Sheldon, M. Wallau, U. Schuchardt, *Angew. Chem., Int. Ed. Engl.* **1997**, *36*, 1145–1163; (b) R. A. Sheldon, I. W. C. E. Arends, H. E. B. Lempers, *Catal. Today* **1998**, *42*, 387–407.
77. (a) B. Kraushaar-Czarnetzki, W. G. M. Hoogervorst, W. H. J. Stork, *Stud. Surf. Sci. Catal.* **1994**, *84*, 1869–1876; (b) M. P. J. Peeters, M. Busio, P. Leijten, J. H. C. van Hooff, *Appl. Catal. A* **1994**, *118*, 51–62.
78. (a) T. Sato, J. Dakka, R. A. Sheldon, *Stud. Surf. Sci. Catal.* **1994**, *84*, 1853–1860; (b) J. D. Chen, H. E. B. Lempers, R. A. Sheldon, *Colloids Surf. A* **1995**, *101*, 137–146.
79. (a) R. De Ruiter, J. C. Jansen, H. Van Bekkum, *Zeolites* **1992**, *12*, 56–62; (b) R. de Ruiter, A. P. M. Kentgens, J. Grootendorst, J. C. Jansen, H. van Bekkum, *Zeolites* **1993**, *13*, 128–138; (c) J. C. van der Waal, M. S. Rigutto, H. van Bekkum, *J. Chem. Soc., Chem. Commun.* **1994**, 1241–1242; (d) M. S. Rigutto, R. d. Ruiter, J. P. M. Niederer, H. v. Bekkum, *Stud. Surf. Sci. Catal.* **1994**, *84*, 2245–2252.

80. G. Bellussi, M. S. Rigutto, *Stud. Surf. Sci. Catal.* **1994**, *85*, 177–213.
81. T. Tatsumi, M. Nakamura, S. Negishi, H. Tominaga, *J. Chem. Soc., Chem. Commun.* **1990**, 476–477.
82. (a) M. G. Clerici, P. Ingallina, U. Romano, *J. Catal.* **1991**, *129*, 159–167; (b) M. G. Clerici, P. Ingallina, *J. Catal.* **1993**, *140*, 71–83.
83. C. Neri, F. Buonomo (to Anic SpA), *Eur. Pat.* EP-A 102097, **1984** [*Chem. Abstr.* **1984**, 100, 209389].
84. F. Maspero, U. Romano, *J. Catal.* **1994**, *146*, 476–482.
85. (a) P. Ratnasamy, R. Kumar, *Stud. Surf. Sci. Catal.* **1995**, *97*, 367–376; (b) A. Bhaumik, R. Kumar, P. Ratnasamy, *Stud. Surf. Sci. Catal.* **1994**, *84*, 1883–1888.
86. B. Notari, *Stud. Surf. Sci. Catal.* **1991**, *60*, 343–352.
87. A. Bhaumik, R. Kumar, *J. Chem. Soc., Chem. Commun.* **1995**, 349–350.
88. J. S. Reddy, S. Sivasanker, P. Ratnasamy, *J. Mol. Catal.* **1991**, *69*, 383–392.
89. J. S. Reddy, P. A. Jacobs, *J. Chem. Soc., Perkin Trans. 1* **1993**, 2665–2666.
90. H. R. Sonawane, A. V. Pol, P. P. Moghe, S. S. Biswas, A. Sudalai, *J. Chem. Soc., Chem. Commun.* **1994**, 1215–1216.
91. R. Joseph, A. Sudalai, T. Ravindranathan, *Synlett* **1995**, *11*, 1177–1178.
92. P. Kumar, V. R. Hegde, B. Pandey, T. Ravindranathan, *J. Chem. Soc., Chem. Commun.* **1993**, 1553–1554.
93. J. C. Van Der Waal, P. Lin, M. S. Rigutto, H. Van Bekkum, *Stud. Surf. Sci. Catal.* **1997**, *105B*, 1093–1100.
94. N. Ulagappan, V. Krishnasamy, *J. Chem. Soc., Chem. Commun.* **1995**, 373–374.
95. A. Tuel, Y. B. Taarit, *Zeolites* **1995**, *15*, 164–170.
96. A. Tuel, *Zeolites* **1995**, *15*, 228–235.
97. J. Le Bars, J. Dakka, R. A. Sheldon, *Appl. Catal. A* **1996**, *136*, 69–80.
98. K. R. Reddy, A. V. Ramaswamy, P. Ratnasamy, *J. Catal.* **1993**, *143*, 275–285.
99. F. J. Luna, S. E. Ukawa, M. Wallau, U. Schuchardt, *J. Mol. Catal. A* **1997**, *117*, 405–411.
100. R. Joseph, M. Sasidharan, R. Kumar, A. Sudalai, T. Ravindranathan, *J. Chem. Soc., Chem. Commun.* **1995**, 1341–1342.
101. A. Bhaumik, M. K. Dongare, R. Kumar, *Microporous Mater.* **1995**, *5*, 173–178.
102. M. Chatterjee, D. Bhattacharya, N. Venkatathri, S. Sivasanker, *Catal. Lett.* **1995**, *35*, 313–316.
103. A. Bhaumik, S. G. Hegde, R. Kumar, *Catal. Lett.* **1995**, *35*, 327–334.
104. N. K. Mal, V. Ramaswamy, S. Gonapathy, A. V. Ramaswamy, *Appl. Catal. A* **1995**, *125*, 233–245.
105. T. Selvam, A. P. Singh, *J. Chem. Soc., Chem. Commun.* **1995**, 883–884.
106. (a) J. D. Chen, R. A. Sheldon, *J. Catal.* **1995**, *153*, 1–8; (b) J. D. Chen, J. Dakka, E. Neeleman, R. A. Sheldon, *J. Chem. Soc., Chem. Commun.* **1993**, 1379–1380.
107. H. E. B. Lempers, R. A. Sheldon, *Appl. Catal. A* **1996**, *143*, 137–143.
108. M. S. Rigutto, H. van Bekkum, *J. Mol. Catal.* **1993**, *81*, 77–98.
109. A. Tuel, Y. B. Taarit, *Zeolites* **1994**, *14*, 18–24.
110. J. Dakka, R. A. Sheldon (to DSM NV), *Neth. Pat.* NL-A 9200968, **1992** [*Chem. Abstr.* **1994**, 120, 134031].
111. T. Sen, M. Chatterjee, S. Sivasanker, *J. Chem. Soc., Chem. Commun.* **1995**, 207–208.
112. G. Schulz-Ekloff, D. Wohlr, V. Iliev, E. Ignatzek, A. Andreev, *Stud. Surf. Sci. Catal.* **1989**, *46*, 315–325.
113. (a) D. E. de Vos, P. P. Knops-Gerrits, R. F. Parton, B. M. Weckhuysen, P. A. Jacobs, R. A. Schoonheydt, *J. Inclus. Phenom. Mol. Recognit. Chem.* **1995**, *21*, 185–213; (b) K. J. Balkus, Jr., A. G. Gabrielov, *J. Inclus. Phenom. Mol. Recognit. Chem.* **1995**, *21*, 159–184; (c) F. Bedioui, *Coord. Chem. Rev.* **1995**, *144*, 39–68.
114. V. Yu Zakharov, O. M. Zakharova, B. V. Romanovskii, R. E. Mardaleishvili, *React. Kinet. Catal. Lett.* **1977**, *6*, 133–137.
115. N. Herron, *J. Coord. Chem.* **1988**, *19*, 25–38.
116. F. Thibault-Starzyk, R. F. Parton, P. A. Jacobs, *Stud. Surf. Sci. Catal.* **1994**, *84*, 1419–1424.
117. B. M. Weckhuysen, A. A. Verberckmoes, I. P. Vannijvel, J. A. Pelgrims, P. L. Buskens, P. A. Jacobs, R. A. Schoonheydt, *Angew. Chem., Int. Ed. Engl.* **1995**, *34*, 2652–2654.

118. K. J. Balkus, Jr., M. Eissa, R. Levado, *J. Am. Chem. Soc.* **1995**, *117*, 10753–10754.
119. S. B. Ogunwumi, T. Bein, *Chem. Commun.* **1997**, 901–902.
120. (a) D. E. De Vos, T. Bein, *J. Organomet. Chem.* **1996**, *520*, 195–200; (b) D. De Vos, T. Bein, *Chem. Commun.* **1996**, 917–918.
121. P. K. Dutta, S. K. Das, *J. Am. Chem. Soc.* **1997**, *119*, 4311–4312.
122. A. Corma, A. Fuerte, M. Iglesias, F. Sanchez, *J. Mol. Catal. A* **1996**, *107*, 225–234.
123. Y. Xu, L. Lin, *Appl. Catal. A* **1999**, *188*, 53–67.
124. P. Van Der Voort, M. Mathieu, E. F. Vansant, S. N. R. Rao, M. G. White, *J. Porous Mater.* **1998**, *5*, 305–316.
125. J. N. Armor, *Microporous Mesoporous Mater.* **1998**, *22*, 451–456.
126. D. N. Stamires, J. Turkevich, *J. Am. Chem. Soc.* **1964**, *86*, 749–757.
127. V. Ramamurthy, J. V. Caspar, D. R. Corbin, *J. Am. Chem. Soc.* **1991**, *113*, 594–600.
128. K. K. Iu, J. K. Thomas, *J. Phys. Chem.* **1991**, *95*, 506–509.
129. (a) I. K. Lednev, N. Mathivanan, L. J. Johnston, *J. Phys. Chem.* **1994**, *98*, 11444–11451; (b) F. Gessner, J. C. Scaiano, *J. Photochem. Photobiol. A* **1992**, *67*, 91–100.
130. (a) L. Brancalion, D. Brousmiche, V. J. Rao, L. J. Johnston, V. Ramamurthy, *J. Am. Chem. Soc.* **1998**, *120*, 4926–4933; (b) F. I. Cozens, R. Bogdanova, M. Regimbald, H. Garcia, V. Marti, J. C. Scaiano, *J. Phys. Chem. B* **1997**, *101*, 6921–6928.
131. G. Zhang, X. Liu, J. K. Thomas, *Radiat. Phys. Chem.* **1998**, *51*, 135–152.
132. X. Liu, G. Zhang, J. K. Thomas, *J. Phys. Chem. B* **1997**, *101*, 2182–2194.
133. Y. S. Park, S. Y. Um, K. B. Yoon, *J. Am. Chem. Soc.* **1999**, *121*, 3193–3200.
134. M. Alvaro, H. Garcia, S. Garcia, F. Marquez, J. C. Scaiano, *J. Phys. Chem. B* **1997**, *101*, 3043–3051.
135. (a) K. B. Yoon, *Chem. Rev.* **1993**, *93*, 321–339; (b) P. K. Dutta, M. Ledney, *Prog. Inorg. Chem.* **1997**, *44*, 209–271; (c) J. C. Scaiano, H. Garcia, *Acc. Chem. Res.* **1999**, *32*, 783–793; (d) V. Ramamurthy, P. Lakshminarasimhan, C. P. Grey, L. J. Johnston, *Chem. Commun.* **1998**, 2411–2424; (e) K. B. Yoon, in *Molecular and Supramolecular Photochemistry* (Eds. V. Ramamurthy, K. Schanze), Marcel Dekker, New York, **2000**, Vol. 5, 143–251.
136. D. Oelkrug, W. Honnen, F. Wilkinson, C. J. Willsher, *J. Chem. Soc., Faraday Trans. 2* **1987**, *83*, 2081–2095.
137. K. B. Yoon, S. M. Hubig, J. K. Kochi, *J. Phys. Chem.* **1994**, *98*, 3865–3871.
138. S. Hashimoto, S. Ikuta, T. Asahi, H. Masuhara, *Langmuir* **1998**, *14*, 4284–4291.
139. J. S. Krueger, J. E. Mayer, T. E. Mallouk, *J. Am. Chem. Soc.* **1988**, *110*, 8232–8234.
140. E. H. Yonemoto, Y. I. Kim, R. H. Schmehl, J. O. Wallin, B. A. Shoulders, B. R. Richardson, J. F. Haw, T. E. Mallouk, *J. Am. Chem. Soc.* **1994**, *116*, 10557–10563.
141. M. Vitale, N. B. Castagnola, N. J. Ortins, J. A. Brooke, A. Vaidyalagam, P. K. Dutta, *J. Phys. Chem. B* **1999**, *103*, 2408–2416.
142. (a) P. K. Dutta, J. A. Incavo, *J. Phys. Chem.* **1987**, *91*, 4443–4446; (b) M. Borja, P. K. Dutta, *Nature* **1993**, *362*, 43–45; (c) M. Sykora, J. R. Kincaid, *Nature* **1997**, *387*, 162–164; (d) M. Sykora, K. Maruszewski, S. M. Treffert-Ziemelis, J. R. Kincaid, *J. Am. Chem. Soc.* **1998**, *120*, 3490–3498.
143. K. B. Yoon, Y. S. Park, J. K. Kochi, *J. Am. Chem. Soc.* **1996**, *118*, 12710–12718.
144. S. Fukuzumi, T. Urano, T. Suenobu, *Chem. Commun.* **1996**, 213–214.
145. M. Prein, W. Adam, *Angew. Chem., Int. Ed. Engl.* **1996**, *35*, 477–494.
146. X. Li, V. Ramamurthy, *J. Am. Chem. Soc.* **1996**, *118*, 10666–10667.
147. H. Tsubomura, R. S. Mulliken, *J. Am. Chem. Soc.* **1960**, *82*, 5966–5974.
148. (a) F. Blatter, H. Frei, *J. Am. Chem. Soc.* **1993**, *115*, 7501–7502; (b) F. Blatter, H. Frei, *J. Am. Chem. Soc.* **1994**, *116*, 1812–1820; (c) S. Vasenkov, H. Frei, *J. Phys. Chem. B* **1997**, *101*, 4539–4543; (d) F. Blatter, H. Sun, S. Vasenkov, H. Frei, *Catal. Today* **1998**, *41*, 297–309.
149. Y. Xiang, S. C. Larsen, V. H. Grassian, *J. Am. Chem. Soc.* **1999**, *121*, 5063–5072.
150. H. Takeya, Y. Kuriyama, M. Kojima, *Tetrahedron Lett.* **1998**, *39*, 5967–5970.
151. A. Sanjuan, M. Alvaro, G. Aguirre, H. Garcia, J. C. Scaiano, *J. Am. Chem. Soc.* **1998**, *120*, 7351–7352.
152. M. Ledney, P. K. Dutta, *J. Am. Chem. Soc.* **1995**, *117*, 7687–7695.
153. W. Ruettinger, G. C. Dismukes, *Chem. Rev.* **1997**, *97*, 1–24.

154. L. Persaud, A. J. Bard, A. Campion, M. A. Fox, T. E. Mallouk, S. E. Webber, J. M. White, *J. Am. Chem. Soc.* **1987**, *109*, 7309–7314.
155. (a) G. Calzaferri, S. Hug, T. Hugentobler, B. Sulzberger, *J. Photochem.* **1984**, *26*, 109–118; (b) G. Calzaferri, N. Gfeller, K. Pfanner, *J. Photochem. Photobiol., A* **1995**, *87*, 81–84.
156. S. K. Das, P. K. Dutta, *Microporous Mesoporous Mater.* **1998**, *22*, 475–483.
157. H. Yamashita, Y. Fujii, Y. Ichihashi, S. G. Zhang, K. Ikeue, D. R. Park, K. Koyano, T. Tatsumi, M. Anpo, *Catal. Today* **1998**, *45*, 221–227.
158. Y. Xu, C. H. Langford, *J. Phys. Chem.* **1995**, *99*, 11501–11507.
159. H. Yamashita, Y. Ichihashi, M. Anpo, M. Hashimoto, C. Louis, M. Che, *J. Phys. Chem.* **1996**, *100*, 16041–16044.
160. Y. Xu, C. H. Langford, *J. Phys. Chem. B* **1997**, *101*, 3115–3121.
161. R. W. Murray, *Techniques of Chemistry: Molecular Design of Electrode Surfaces*, Vol. 22, Wiley, New York, **1992**.
162. (a) D. R. Rolison, *Stud. Surf. Sci. Catal.* **1994**, *85*, 543–586; (b) E. Briot, F. Bedioui, *Curr. Top. Electrochem.* **1997**, *4*, 87–99; (c) A. Walcarius, *Anal. Chim. Acta* **1999**, *384*, 1–16; (d) J. Lipkowski, P. N. Ross, *Frontiers of Electrochemistry: The Electrochemistry of Novel Materials*, VCH, New York, **1994**.
163. G. Calzaferri, K. Haedener, J. Li, *J. Chem. Soc., Chem. Commun.* **1991**, 653–654.
164. S. Mintova, V. Valtchev, V. Engstrom, B. J. Schoeman, J. Sterte, *Microporous Mater.* **1997**, *11*, 149–160.
165. C. A. Bessel, D. R. Rolison, *J. Electroanal. Chem.* **1997**, *439*, 97–105.
166. M. D. Baker, C. Senaratne, J. Zhang, *J. Chem. Soc., Faraday Trans.* **1992**, *88*, 3187–3192.
167. (a) M. D. Baker, C. Senaratne, M. McBrien, *J. Phys. Chem.* **1995**, *99*, 12367; (b) J.-W. Li, K. Pfanner, G. Calzaferri, *J. Phys. Chem.* **1995**, *99*, 12368–12369.
168. (a) Z. Li, T. E. Mallouk, *J. Phys. Chem.* **1987**, *91*, 643–648; (b) Z. Li, C. M. Wang, L. Persaud, T. E. Mallouk, *J. Phys. Chem.* **1988**, *92*, 2592–2597; (c) E. S. Brigham, P. T. Snowden, Y. I. Kim, T. E. Mallouk, *J. Phys. Chem.* **1993**, *97*, 8650–8655.
169. (a) C. Senaratne, J. Zhang, M. D. Baker, C. A. Bessel, D. R. Rolison, *J. Phys. Chem.* **1996**, *100*, 5849–5862; (b) C. A. Bessel, D. R. Rolison, *J. Phys. Chem. B* **1997**, *101*, 1148–1157; (c) V. Ganesan, R. Ramaraj, *Langmuir* **1998**, *14*, 2497–2501; (d) E. Briot, F. Bedioui, K. J. Balkus, Jr., *J. Electroanal. Chem.* **1998**, *454*, 83–89; (e) F. Bedioui, L. Roue, E. Briot, J. Devynck, K. J. Balkus, Jr., J. F. Diaz, *New J. Chem.* **1996**, *20*, 1235–1241.
170. (a) J. Wang, T. Martinez, *Anal. Chim. Acta* **1988**, *207*, 95–102; (b) A. Walcarius, L. Lamberts, E. G. Derouane, *Electroanalysis* **1995**, *7*, 120–128; (c) A. Walcarius, L. Lamberts, *Anal. Lett.* **1998**, *31*, 585–599; (d) A. Walcarius, P. Mariaulle, C. Louis, L. Lamberts, *Electroanalysis* **1999**, *11*, 393–400.
171. (a) B. Liu, R. Hu, J. Deng, *Anal. Chem.* **1997**, *69*, 2343–2348; (b) H. Kotte, B. Grundig, K.-D. Vorlop, B. Strehlitz, U. Stottmeister, *Anal. Chem.* **1995**, *67*, 65–70; (c) G. Marko-Varga, E. Burestedt, C. J. Svensson, J. Emneus, L. Garton, T. Ruzgas, M. Lutz, K. K. Unger, *Electroanalysis* **1996**, *8*, 1121–1126.
172. C. Senaratne, M. D. Baker, *J. Electroanal. Chem.* **1992**, *332*, 357–364.
173. (a) B. De Vismes, F. Bedioui, J. Devynck, C. Bied-Charreton, M. Perree-Fauvet, *Nouv. J. Chim.* **1986**, *10*, 81–82; (b) S. V. Guerra, C. R. Xavier, S. Nakagaki, L. T. Kubota, *Electroanalysis* **1998**, *10*, 462–466.
174. K. E. Creasy, B. R. Shaw, *J. Electrochem. Soc.* **1990**, *137*, 2353–2354.
175. (a) D. R. Rolison, E. A. Hayes, W. E. Rudzinski, *J. Phys. Chem.* **1989**, *93*, 5524–5531; (b) D. R. Rolison, J. Z. Stemple, *J. Chem. Soc., Chem. Commun.* **1993**, 25–27; (c) C. A. Bessel, D. R. Rolison, *J. Am. Chem. Soc.* **1997**, *119*, 12673–12674.
176. E. A. Hayes, J. Z. Stemple, D. A. Rolison, in *Water Purification by Photocatalytic, Photoelectrochemical, and Electrochemical Processes*, Vol. 94-19, (Eds. T. L. Rose, O. Murphy, E. Rudd, B. E. Conway), The Electrochemical Society, Pennington, NJ, **1994**, pp. 120–131.
177. (a) D. Brunel, N. Bellocq, P. Sutra, A. Cauvel, M. Lasperas, P. Moreau, F. Di Renzo, A. Galarneau, F. Fajula, *Coord. Chem. Rev.* **1998**, *178–180*, 1085–1108; (b) P. Behrens, *Angew. Chem., Int. Ed. Engl.* **1996**, *35*, 515–518; (c) A. Sayari, *Chem. Mater.* **1996**, *8*, 1840–1852; (d) A. Corma, D. Kumar, *Stud. Surf. Sci. Catal.* **1998**, *117*, 201–222.
178. A. Corma, M. T. Navarro, J. Perez Pariente, *J. Chem. Soc., Chem. Commun.* **1994**, 147–148.

179. P. T. Tanev, M. Chibwe, T. J. Pinnavaia, *Nature*, **1994**, 368, 321–323.
180. K. R. Reddy, I. Moudrakovskiy, A. Sayari, *J. Chem. Soc., Chem. Commun.* **1994**, 1491–1492.
181. S. Gontier, A. Tuel, *J. Catal.* **1995**, 157, 124–132.
182. I. F. J. Vankelecom, N. M. F. Moens, K. A. L. Vercruysse, R. F. Parton, P. A. Jacobs, *Stud. Surf. Sci. Catal.* **1997**, 108, 437–444.
183. A. Corma, M. Iglesias, F. Sanchez, *Catal. Lett.* **1996**, 39, 153–156.
184. R. Neumann, A. M. Khenkin, *Chem. Commun.* **1996**, 2643–2644.
185. F. Rey, G. Sankar, T. Maschmeyer, J. M. Thomas, R. G. Bell, *Top. Catal.* **1996**, 3, 121–134.
186. J. S. Beck, R. F. Socha, D. S. Shihabi, J. C. Vartuli (assigned to Mobil Oil Corp.), U.S. 5143707, **1992** [*Chem. Abstr.* **1993**, 118, 26784].
187. C. Liu, X. Ye, Y. Wu, *Catal. Lett.* **1996**, 36, 263–266.
188. T. Maschmeyer, F. Rey, G. Sankar, J. M. Thomas, *Nature* **1995**, 378, 159–162.
189. P. Sutra, D. Brunel, *Chem. Commun.* **1996**, 2485–2486.
190. C.-J. Liu, W.-Y. Yu, S.-G. Li, C.-M. Che, *J. Org. Chem.* **1998**, 63, 7364–7369.
191. J. F. Diaz, K. J. Balkus, Jr., F. Bedioui, V. Kurshev, L. Kevan, *Chem. Mater.* **1997**, 9, 61–67.
192. Y. V. S. Rao, D. E. De Vos, T. Bein, P. A. Jacobs, *Chem. Commun.* **1997**, 355–356.
193. J. F. Diaz, K. J. Balkus, Jr., *J. Mol. Catal. B* **1996**, 2, 115–126.
194. A. Walcarius, *Electroanalysis* **1998**, 10, 1217–1235.
195. G. Villemure, T. J. Pinnavaia, *Chem. Mater.* **1999**, 11, 789–794.
196. A. Walcarius, C. Despas, P. Trens, M. J. Hudson, J. Bessiere, *J. Electroanal. Chem.* **1998**, 453, 249–252.
197. A. Walcarius, J. Bessiere, *Chem. Mater.* **1999**, 11, 3009–3011.
198. D. Avnir, L. Klein, D. Levy, U. Schubert, A. Wojcik, *Organo-silica Sol-gel Materials*, Vol. 2, Wiley, New York, **1998**.
199. D. Avnir, *Acc. Chem. Res.* **1995**, 28, 328–334.
200. R. Hutter, T. Mallat, D. Dutoit, A. Baiker, *Top. Catal.* **1996**, 3, 421–436.
201. (a) A. Slama-Schwok, M. Ottolenghi, D. Avnir, *Nature* **1992**, 355, 240–242; (b) A. Slama-Schwok, D. Avnir, M. Ottolenghi, *J. Phys. Chem.* **1989**, 93, 7544–7547; (c) A. Slama-Schwok, D. Avnir, M. Ottolenghi, *J. Am. Chem. Soc.* **1991**, 113, 3984–3985; (d) A. Slama-Schwok, D. Avnir, M. Ottolenghi, *Photochem. Photobiol.* **1991**, 54, 525–534; (e) F. N. Castellano, T. A. Heimer, T. M. Tandhasetti, G. J. Meyer, *Chem. Mater.* **1994**, 6, 1041–1048.
202. (a) S. Shtelzer, S. Rappoport, D. Avnir, M. Ottolenghi, S. Braun, *Biotechnol. Appl. Biochem.* **1992**, 15, 227–235; (b) S. Braun, S. Shtelzer, S. Rappoport, D. Avnir, M. Ottolenghi, *J. Non-Cryst. Solids* **1992**, 147–148, 739–743.
203. (a) S. Braun, S. Rappoport, R. Zusman, D. Avnir, M. Ottolenghi, *Mater. Lett.* **1990**, 10, 1–5; (b) S. Braun, S. Rappoport, S. Shtelzer, R. Zusman, S. Druckman, D. Avnir, M. Ottolenghi, in *Biotechnology: Bridging Research and Applications* (Eds. D. Kamely, A. M. Chakrabary, S. E. Kornguth), Kluwer, Boston, **1991**, pp. 205–218.
204. (a) S. Shtelzer, S. Braun, *Biotechnol. Appl. Biochem.* **1994**, 19, 293–305; (b) S. A. Yamanaka, F. Nishida, L. M. Ellerby, C. R. Nishida, B. Dunn, J. S. Valentine, J. I. Zink, *Chem. Mater.* **1992**, 4, 495–497; (c) U. Narang, P. N. Prasad, F. V. Bright, K. Ramanathan, N. D. Kumar, B. D. Malhotra, M. N. Kamalasanan, S. Chandra, *Anal. Chem.* **1994**, 66, 3139–3144.
205. (a) C. Shen, N. Kostic, *J. Electroanal. Chem.* **1997**, 438, 61–65; (b) C. Shen, N. Kostic, *J. Am. Chem. Soc.* **1997**, 119, 1304–1312.
206. O. Lev, Z. Wu, S. Bharathi, V. Glezer, A. Modestov, J. Gun, L. Rabinovich, S. Sampath, *Chem. Mater.* **1997**, 9, 2354–2375.
207. K. Kimura, T. Sunagawa, M. Tokayama, *Chem. Lett.* **1995**, 967.
208. (a) M. D. Petit-Dominguez, H. Shen, W. R. Heineman, C. J. Seliskar, *Anal. Chem.* **1997**, 69, 703–716; (b) L. Coche-Guerente, S. Cosnier, V. Desprez, P. Labbe, D. Petridis, *J. Electroanal. Chem.* **1996**, 401, 253–256.
209. M. Collinson, C. Rausch, A. Voight, *Langmuir* **1997**, 13, 7245–7251.
210. K. Kimura, T. Sunagawa, M. Yokoyama, *Chem. Commun.* **1996**, 745–746.
211. (a) Y. Tatsu, K. Yamashita, M. Yamaguchi, S. Yamamura, H. Yamamoto, S. Yoshikawa, *Chem. Lett.* **1992**, 1615–1618; (b) P. Audebert, C. Demaille, C. Sanchez, *Chem. Mater.* **1993**, 5, 911–913.

- 212. (a) J. Li, S. N. Tan, H. Ge, *Anal. Chim. Acta* **1996**, 335, 137–145; (b) J. Li, L. S. Chai, N. K. Goh, S. N. Tan, H. Ge, *Sens. Actuators B* **1997**, B40, 135–141; (c) J. Li, L. S. Chai, N. K. Goh, S. N. Tan, *Anal. Chim. Acta* **1998**, 362, 203–211.
- 213. S. L. Chuit, J. Li, S. N. Tan, *Analyst* **1997**, 122, 1431–1434.
- 214. V. Glezer, O. Lev, *J. Am. Chem. Soc.* **1993**, 115, 2533–2534.
- 215. B. G. Milagres, L. T. Kubota, G. de Oliveira Neto, *Electroanalysis* **1996**, 8, 489–493.
- 216. M. Tsionsky, G. Gun, V. Glezer, O. Lev, *Anal. Chem.* **1994**, 66, 1747–1753.
- 217. (a) M. Tsionsky, O. Lev, *J. Electrochem. Soc.* **1995**, 142, 2132–2138; (b) M. Tsionsky, O. Lev, *Anal. Chem.* **1995**, 67, 2409–2414.
- 218. G. Gun, M. Tsionsky, O. Lev, in *Better Ceramics Through Chemistry, VI, Mater. Res. Soc. Symp. Vol. 346* (Eds. C. Sanchez, M. L. Mecartney, C. J. Brinker, A. K. Cheetham), Materials Research Society, Pittsburgh Pa. **1994**, pp. 1011–1016.
- 219. J. Wang, P. V. A. Pamidi, D. S. Park, *Electroanalysis* **1997**, 9, 52–55.
- 220. I. Pankratov, O. Lev, *J. Electroanal. Chem.* **1995**, 393, 35–41.
- 221. (a) S. Sampath, O. Lev, *Anal. Chem.* **1996**, 68, 2015–2021; (b) S. Sampath, O. Lev, *Electroanal. Chem.* **1997**, 426, 131–137.
- 222. L. Coche-Guerente, S. Cosnier, P. Labbe, *Chem. Mater.* **1997**, 9, 1348–1352.
- 223. S. Sampath, I. Pankratov, J. Gun, O. Lev, *J. Sol–Gel Sci. Technol.* **1996**, 7, 123–128.
- 224. S. Sampath, O. Lev, *Electroanalysis* **1996**, 8, 1112–1116.
- 225. (a) J. Gun, O. Lev, *Anal. Lett.* **1996**, 29, 1933–1938; (b) J. Gun, O. Lev, *Anal. Chim. Acta* **1996**, 336, 95–106.
- 226. S. Bharathi, O. Lev, *Chem. Commun.* **1997**, 2303–2304.

4 Electron Transfer in Layered and Intercalated Compounds

Vasudeva Bhat and Kazunari Domen

4.1 Introduction

Layered compounds provide unique character for electron-transfer processes owing to their low dimensionality. Especially layered materials with ion-exchange and/or intercalation capabilities show behavior that is not seen in so-called bulk-type materials. Layered materials, which have been often used in studies of photoelectron transfer as well as photocatalysis, may be classified into two groups: compounds in which the host layers work as an active component for the photoexcitation and electron-transfer reactions, and materials in which the layers are inert for electron-transfer processes. Examples of the former are layered titanates and niobates and of the latter are clays. In the latter case, photoactive materials are intercalated in the interlayer spaces. Recently, the exfoliation of various layered compounds has become possible and artificial assemblies consisting of these exfoliated sheets have been formed. Electron transfer in such assemblies is also an attractive subject in this field.

4.2 Layered Oxides of Transition Metals

Transition metal elements such as Ti, Nb and Ta, which form d^0 cations, are known to form several oxides with layered structure exhibiting interlamellar activity. Figures 1 and 2 show the idealized structures of some of these oxides.

All of these oxides consist of titanate and/or niobate macropolyanion sheets and alkali metal cations in between to compensate the negative charges of the sheets. The alkali metal cations can be replaced by various kinds of cations, including protons. These oxides may be regarded as semiconductors/insulators owing to their large band-gap. The electronic state of the oxide sheets is excited when the photons with the energy larger than the band-gap (typically in the ultraviolet region) are

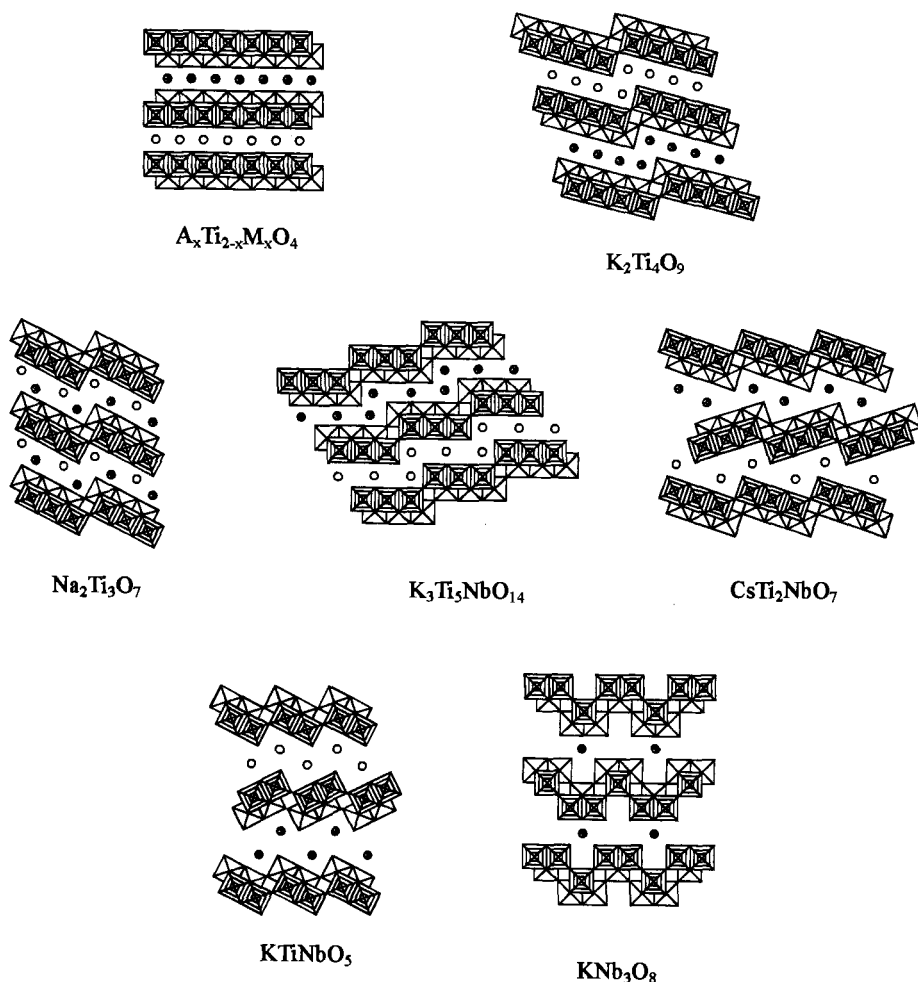


Figure 1. Idealized structures of some layered titanates and titanoniobates possessing edge- and corner-connected octahedra. Adapted from Refs. [1] and [2].

absorbed. This process may be regarded as the excitation of electrons from the valence band, mainly consisting of O 2p orbitals, to the conduction band, mainly consisting of Ti or Nb 3d orbitals. Based on the band models of the electronic states, the excitation process is depicted as the formation of electrons (e^-) in the conduction band and positive holes (h^+) in valence band. If electrons and holes are localized, they may be regarded as Ti^{3+} or Nb^{4+} and O^- species. The detailed dynamic behavior of these excited states has not been fully revealed. Judging from the results of photocatalytic reactions, the behavior of photoexcited electrons and holes seems to be more or less similar to that of bulk-type titanates and niobates. In principle, however, these photoexcited electrons and holes should be regarded as being confined in two-dimensional sheets of the oxides.

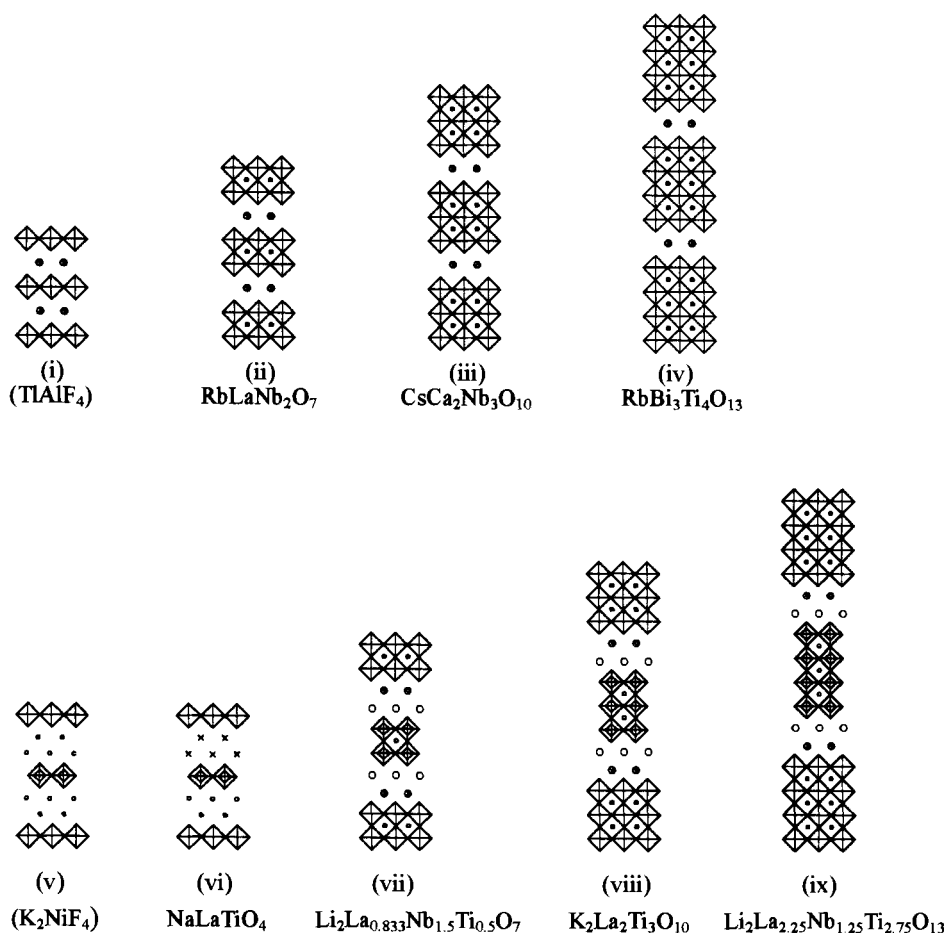


Figure 2. Idealized structures of some perovskite-related layered oxides and their fluoride relatives. Fluoride structures adapted from Ref. [3].

Among these oxides, $\text{K}_4\text{Nb}_6\text{O}_{17}$ has been studied in some detail, although the structure is rather unique. Hence studies on this oxide will be introduced first, followed by those on other layered oxides. Tables 1 and 2 list various systems studied for photocatalysis.

4.2.1 $\text{K}_4\text{Nb}_6\text{O}_{17}$

Structure and physico-chemical properties

Single crystals of $\text{K}_4\text{Nb}_6\text{O}_{17}$ can be obtained by slow cooling of the melt near 1200°C [4, 34, 35]. Powder samples can be prepared by conventional ceramic methods at about 1100°C . X-ray powder patterns have been reported [4]. The BET

Table 1. Unit cell data and electronic band energy data for $\text{K}_4\text{Nb}_6\text{O}_{17}$ and related oxides.

Composition	Unit cell dimensions	No. of H_2O of hydration	Estimated band-gap/absorption edge	Estimated conduction band edge/V vs. NHE
$\text{K}_4\text{Nb}_6\text{O}_{17}$	Orthorhombic, $a = 0.758$, $b = 3.23$, $c = 0.640$ nm [4], $a = 0.783$, $b = 3.32$, $c = 0.646$ nm [5]	0, 3 and 4.5 [4]; 3 [5]	3.52 eV [6], 3.3 eV [7], 360 nm [8]	-0.76 [6]
$\text{Rb}_4\text{Nb}_6\text{O}_{17}$	Orthorhombic, $a = 0.779$, $b = 3.319$, $c = 0.650$ nm [5]	3 [5, 9]	360 nm [8]	
$\text{Rb}_4\text{Ta}_6\text{O}_{17}$	Orthorhombic, $b = 3.45$ nm [8]	~ 3 [8]	295 nm [8], 4.4 eV [10]	
$\text{A}_4\text{Ta}_x\text{Nb}_{6-x}\text{O}_{17}$ (A = K, Rb; $x = 2, 3, 4, 6$)	Orthorhombic, $b = 3.32\text{--}3.45$ nm [8]		295–410 nm [8]	
$\text{K}_2\text{H}_2\text{Nb}_6\text{O}_{17}$			3.45 eV [6]	-0.265 [6]

surface area of the ceramic preparation [11] is typically of the order of $1 \text{ m}^2 \text{ g}^{-1}$. Hydrothermal synthesis can be used to prepare the single-phase oxide at temperatures as low as 280°C with four times the surface area [36]. Catalytic properties of such preparations have not been examined.

This oxide has a layered structure [5] consisting of $[\text{Nb}_6\text{O}_{17}]^{4-}$ macropolyanion sheets interleaved by K^+ ions, as shown in Figure 3. The K^+ ions can be replaced by various mono- and multivalent metal cations [12, 37, 38], protons [6, 12, 38, 39] and organic cations [40]. An important aspect of the structure is the presence of two types of interlayer regions [5, 9], referred to as interlayer-I and interlayer-II, with differing interlayer reactivities [37]. This makes the $[\text{Nb}_6\text{O}_{17}]^{4-}$ sheets non-symmetric with respect to mirror reflection about the sheet-planes. Besides the anhydrous compound of the above formula, it also forms two hydrates, one with about three water molecules of hydration, which is stable in the humidity range 25–85 %, and the other with about 4.5 molecules of water of hydration, which is stable above 85 % humidity [4]. These hydrates are structurally related to the anhydrous oxide: the H_2O molecules are accommodated in the interlayer-I together with the already existing K^+ ions, leaving the $[\text{Nb}_6\text{O}_{17}]^{4-}$ sheets and interlayer-II intact [5, 9]. The possible existence of higher hydrates being formed under aqueous environments has also been suggested [4]. Such spontaneous intercalation of water molecules is an important feature in making this oxide a photocatalyst, especially for water splitting.

$\text{K}_4\text{Nb}_6\text{O}_{17}$ crystals exhibit optical birefringence [34] and absorb in the UV region with an optical absorption edge between 320 and 330 nm. Figure 4 shows the wavelength dependences of the transmittance and absorption coefficient along the

Table 2. $K_4Nb_6O_{17}$ and related systems investigated for photocatalytic activity.

System	Promoter	Type of catalytic reaction	Ref.
$K_4Nb_6O_{17}$	—	H_2 and O_2 from H_2O	7, 11
	—	H_2 from aq. methanol	11–13
	Ni	H_2 and O_2 from H_2O	7, 11, 14–17
	Ni	Redn. of NO_3^- to NO_2^-	18
	Ni and a third component, metal oxide or hydroxide	H_2 and O_2 from H_2O	17
	Pt	H_2 and O_2 from H_2O	19
	Pt	H_2 from aq. methanol, O_2 from aq. $AgNO_3$	13
	MO_x , $M = Cr, Mn, Co,$ Ni, Cu, Pt, Ru, Rh	H_2 and O_2 from H_2O	7
$Rb_4Nb_6O_{17}$	Ni	H_2 and O_2 from H_2O	8
$Rb_4Ta_6O_{17}$	Ni	H_2 and O_2 from H_2O	8, 20
$A_4Nb_{6-x}Ta_xO_{17}$, A = K, Rb, $x = 2, 3, 4, 6$	Ni	H_2 and O_2 from H_2O	8
$K_{4-x}H_xNb_6O_{17}$	—	H_2 from aq. methanol	13, 20
	—	H_2 from C_1 – C_4 alcohols	21, 22
	—	H_2 from aq. Na_2SO_3	23, 24
	—	Redn. of NO_3^- to NO_2^-	18
	Pt	H_2 and O_2 from H_2O	25
	Pt	H_2 from aq. methanol, O_2 from aq. $AgNO_3$	13
	Pt	H_2 from C_1 – C_4 alcohols	22
	Pt, with RuL_3 as sensitizer	H_2 from aq. KI	6, 26
	—	Redn. of MV^{2+} to $MV^{•+}$ in H_2O and C_1 – C_3 alcohols	27
$MV-K_4Nb_6O_{17}$	—	Redn. of MV^{2+} to $MV^{•+}$	28–31
$K_{4-x}M_yNb_6O_{17}$, M = Cr, Fe, Co, Ni, Cu	—	H_2 from aq. methanol	12
$K_{4-x}H_xNb_6O_{17}-$ TiO_2	—	H_2 and O_2 from H_2O	32
	Pt	H_2 and O_2 from H_2O	25
	Pt	H_2 from aq. Na_2S and aq. Na_2SO_3	24
$K_{4-x}H_xNb_6O_{17}-$ Fe_2O_3	—	H_2 from aq. Na_2S and aq. Na_2SO_3	24
	Pt	H_2 from aq. Na_2SO_3	23
$K_{4-x}H_xNb_6O_{17}-$ CdS	—	Redn. of MV^{2+} to $MV^{•+}$ in H_2O and C_1 – C_3 alcohols	27
	Ni	H_2 from K_2SO_3	33
$K_{4-x}H_xNb_6O_{17}-$ $Cd_{0.8}Zn_{0.2}S$	—	H_2 from aq. Na_2S and aq. Na_2SO_3	24

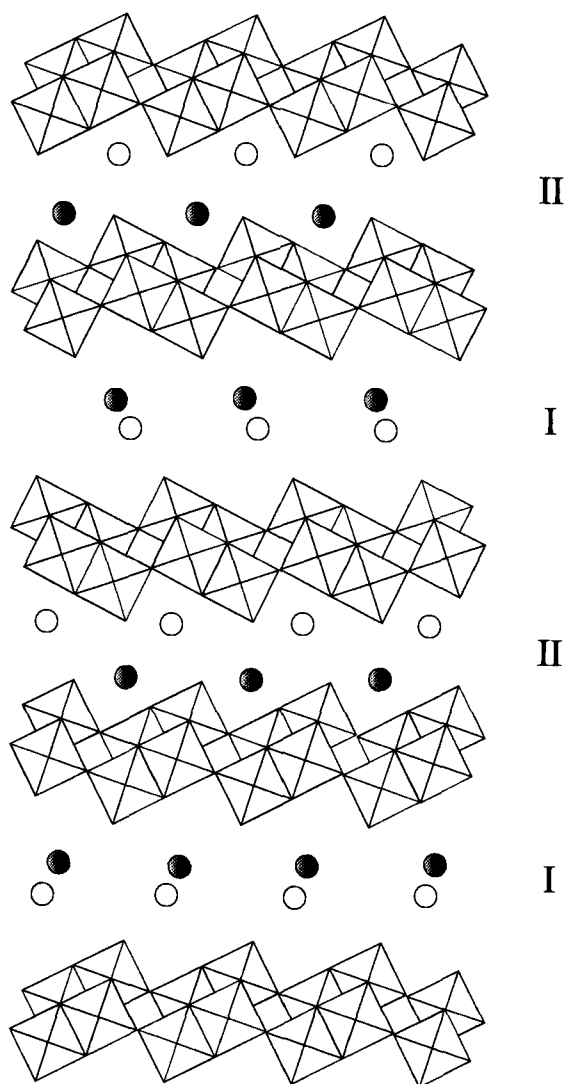


Figure 3. Schematic structure of $\text{K}_4\text{Nb}_6\text{O}_{17}$. Adapted from Ref. [5].

b -axis of a $\text{K}_4\text{Nb}_6\text{O}_{17}$ single crystal [41]. Figure 5 shows the photoluminescence spectra taken at 77 K [42]. Kudo and Sakata have reported on the effect of ion exchange on the luminescence properties [38, 39]. Photoconductivity measurements on single crystals [43] (Figure 6) also reveal UV light-assisted conductivity in the a - c plane. A band-gap of 3.3–3.5 eV has been estimated from diffuse reflectance measurements on powder samples [7] and on samples suspended in aqueous media [6].

Electrical conductivity measurements [41] along the b -axis and in the a - c plane reveal an extreme anisotropy: $\sigma = 2.0 \times 10^{-16} \text{ S cm}^{-1}$ in the b -direction and $1.4 \times 10^{-12} \text{ S cm}^{-1}$ in the a - c plane. The measurements were carried out on single crystals after the currents had reached a steady value to avoid the effect of ionic

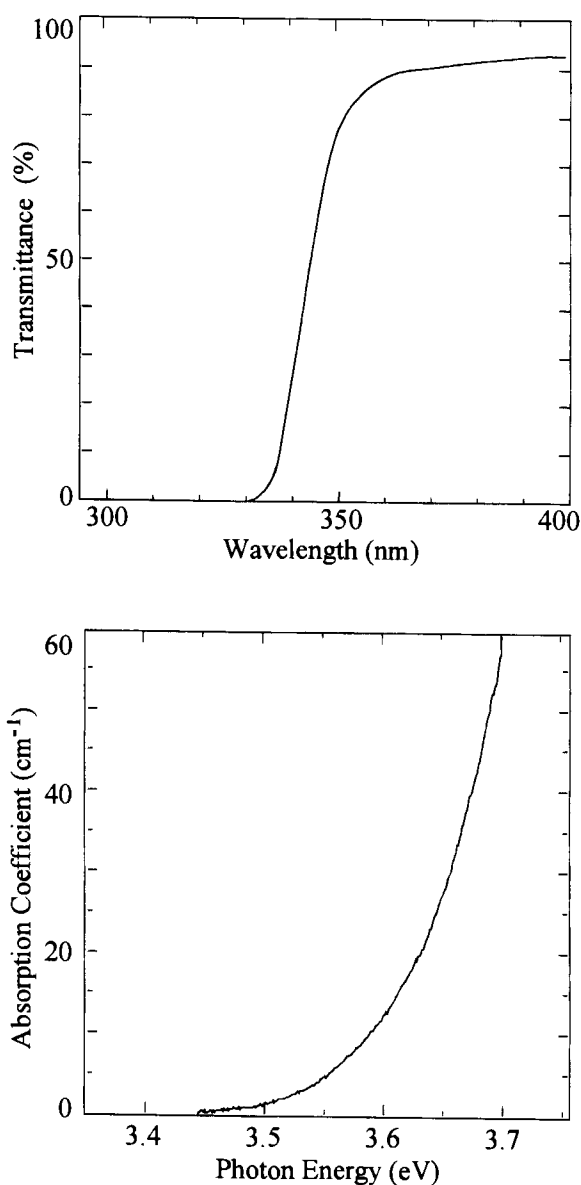


Figure 4. Transmittance and absorption spectra of single-crystal $\text{K}_4\text{Nb}_6\text{O}_{17}$ along b -axis. From Ref. [41].

conductivity. The applied voltages were 100 V/10 μm along the b -axis and 1 V/3 mm in the a - c plane.

Photocatalytic overall water splitting

In distilled water, $\text{K}_4\text{Nb}_6\text{O}_{17}$ without any modification evolves H_2 and O_2 under band-gap irradiation. This indicates that the photoexcited electrons and holes have enough potential to reduce and oxidize water. The rates of H_2 and O_2 evolution are,

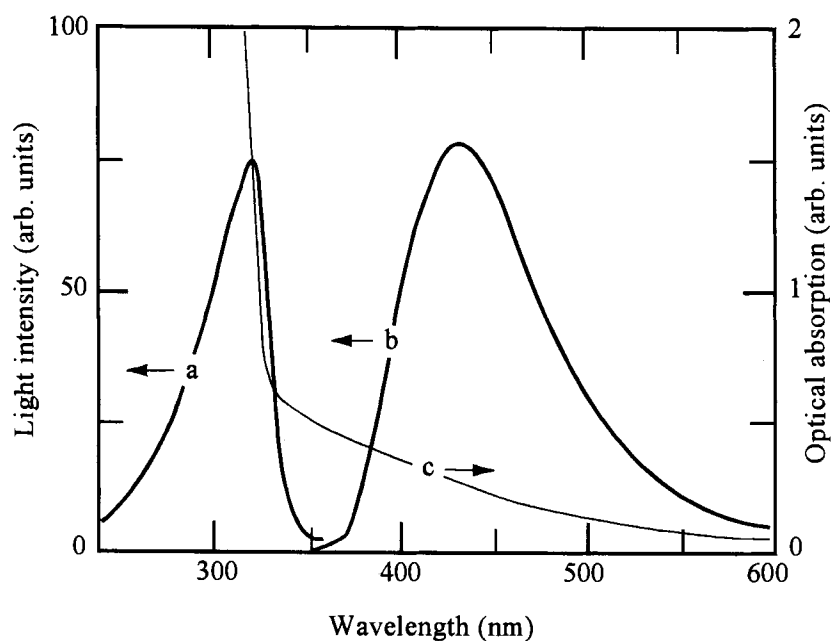


Figure 5. Photoluminescence spectra of $K_4Nb_6O_{17}$ taken at 77 K: (a) emission, excited at 320 nm; (b) excitation spectrum recorded at 440 nm. Optical absorption spectrum is shown in (c). From J.A. Sanz-Garcia, E. Dieguez and C. Zaldo, *Phys. Status. Solidi* **1988**, 108, K145. Reproduced by permission of Wiley-VCH.

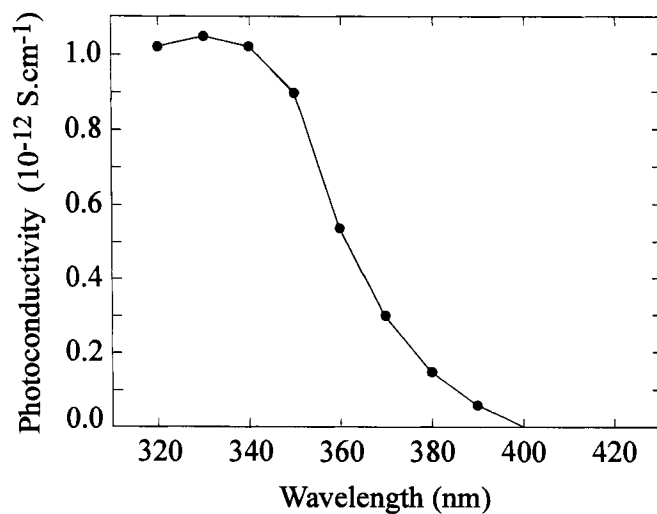


Figure 6. Photoconductivity of single-crystal $K_4Nb_6O_{17}$ in a - c plane. From Ref. [43].

Table 3. Photodecomposition of water over $\text{K}_4\text{Nb}_6\text{O}_{17}$ loaded with various metal oxides [14].

Metal oxide ^a	Pretreatment ^b	Amount of evolved gas/ $\mu\text{mol g}^{-1}$ per 10 h	
		H ₂	O ₂
None	R773–O473	63	7
Cr ₂ O ₃ (1 wt.%)	R773–O473	27	0
Mn ₃ O ₄ (1 wt.%)	R773–O473	6	0
Fe ₂ O ₃ (1 wt.%)	R773–O473	8	0
Co ₃ O ₄ (1 wt.%)	R873–O473	32	0
NiO (1 wt.%)	R773–O473	630	310
CuO (1 wt.%)	R773–O473	12	1
PtO (0.5 wt.%)	Untreated	19	0
PtO (0.5 wt.%)	R773–O473	12	0
RuO ₂ (0.5 wt.%)	Untreated	77	16
RuO ₂ (0.5 wt.%)	R773–O473	9	0
Rh ₂ O ₃ (0.5 wt.%)	Untreated	18	0
Rh ₂ O ₃ (0.5 wt.%)	R773–O473	3	0

^a Probable forms under experimental conditions.^b Rxxx–Oyyy: sample reduced at xxx K and then oxidized at yyy K.

however, very low. Various transition metal oxides have been used as promoters [14]. Table 3 gives the list of oxides used as promoters and the amount of hydrogen produced during water decomposition. As can be seen, NiO is found to be the best promoter.

Typically, Ni loading has been carried out as follows: the powdered $\text{K}_4\text{Nb}_6\text{O}_{17}$ is impregnated with dilute aqueous $\text{Ni}(\text{NO}_3)_2$ solution, evaporated to dryness with stirring and then calcined in air to decompose the nitrate to oxide. It is then subjected to evacuation and to activate the catalyst it is reduced in H_2 (at a pressure of about 40 kPa) at 500 °C for 2 h and then oxidized in O_2 (at a pressure of about 16 kPa) at 200 °C for 1 h. It is known that $\text{K}_4\text{Nb}_6\text{O}_{17}$, on treatment with NiCl_2 solution, exchanges the K^+ ions in interlayer-I with Ni^{2+} ions [37]. It was proved that a 0.1 wt.% loading of Ni with the above treatment procedure is the optimum condition for overall water splitting [7]. For such a sample, assuming 100 % exchange, less than 2 mol% of K^+ ions in interlayer-I are expected to be substituted. Figure 7 shows a typical time course of H_2 and O_2 evolution in distilled water for the optimally prepared catalyst. H_2 and O_2 are produced in a stoichiometric ratio and the total amounts of evolved H_2 and O_2 exceed that of catalyst. The quantum efficiency at 330 nm was estimated to be about 5 % [17] for the optimally loaded catalyst.

It should be noted that for $\text{K}_4\text{Nb}_6\text{O}_{17}$, irrespective of modification, the quantum efficiency reaches 20 % at 300 nm under low light intensities [41] (Figure 8). At higher light intensities, the rates of H_2 and O_2 evolution did not increase with light intensity; the dependence of the evolution rates on the light intensity was of the order of 0.52. This non-linearity at higher light intensity was attributed to the

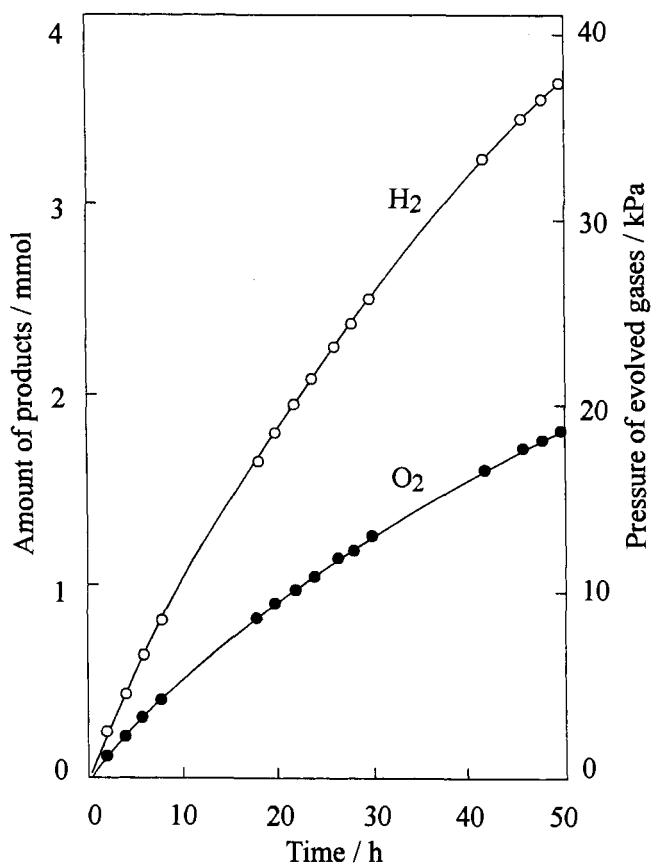


Figure 7. Time course of H₂ and O₂ evolution over 0.1 wt.% Ni loaded K₄Nb₆O₁₇. From Ref. [14].

dominance of the recombination reaction of photogenerated electrons and holes over the redox reactions with water.

The pH of a suspension of Ni-loaded K₄Nb₆O₁₇ in water is about 11 and the suspension acts as a kind of buffer for addition of small amounts of acid or base. When a small quantity (about 0.05 wt.%) of KOH was added, the activity increased by about 30 % [17] but the pH remained unchanged. On changing the pH to lower or higher values by adding considerable amounts of acid or base, the catalytic activity decreased [7]. For example, the rate of water decomposition reduced to about half the value on changing the pH from 11 to 9 or to 13. Complete suppression of oxygen evolution was observed on addition of excess alkali to the reaction mixture, although the activity is regained on neutralizing the excess alkali with acid.

The substitution of K⁺ by Rb⁺ gives Rb₄Nb₆O₁₇, which was found to decompose water at twice the rate as the K⁺ analog [8].

Structure of Ni-loaded K₄Nb₆O₁₇ and the reaction mechanism

Ni-loaded catalysts have been characterized using various techniques such as XPS, EXAFS, ESR and TEM.

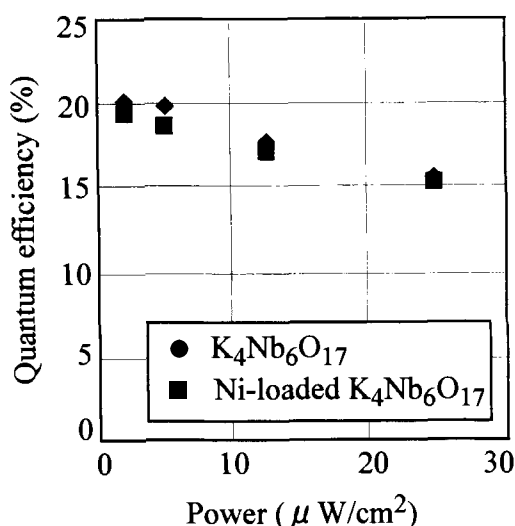


Figure 8. Quantum efficiency of $K_4Nb_6O_{17}$ samples as a function of power density of incident radiation. From Ref. [41].

XPS measurements demonstrated that loaded Ni predominantly locates between the layers of the catalyst and little remains on the external surface [15]. For sensitivity reasons, a sample with a 1 wt.% Ni loading was used. Comparison of the Ni $2p_{3/2}$ peak intensity in the catalyst with that in a reference sample (which was also 1 % Ni-loaded $KNbO_3$ with almost the same BET surface area as that of $K_4Nb_6O_{17}$) has shown that the surface concentration of Ni in the former is about 100 times less than that of the reference sample [7]. Table 4 presents the peak intensities normalized to Nb 3d peak intensities in these samples after various pretreatments.

EXAFS spectra for 1 wt.% Ni-loaded samples both before and after the reduction procedure, and also for Ni and NiO as standards, have also been examined [15], as shown in Figure 9. After reduction by H_2 at 500 °C for 2 h, the loaded Ni was completely reduced to the metallic state. Even after reoxidation by O_2 at 200 °C for 1 h, most of the Ni remained metallic. (By XPS, the Ni, which remained on the external surface, was found to be in the oxidized form.) The formation of metallic nickel on a 0.1 wt.% Ni-loaded catalyst was also confirmed by ESR measurements

Table 4. XPS peak intensity ratio of Ni $2p_{3/2}$ to Nb 3d [7].

Catalyst	Peak intensity ratio			
	Untreated	R773 ^a	R773–O473 ^a	R773–O773 ^a
NiO(1 wt.%)– $K_4Nb_6O_{17}$	0.026	0.004	0.004	0.05
NiO(1 wt.%)– $KNbO_3$	1.5	0.7	1.4	1.3
$NiNb_2O_6$	0.6			

^aR773: samples reduced at 773 K. R773–O473: samples reduced at 773 K and then oxidized at 473 K. R773–O773: samples reduced at 773 K and then oxidized at 773 K.

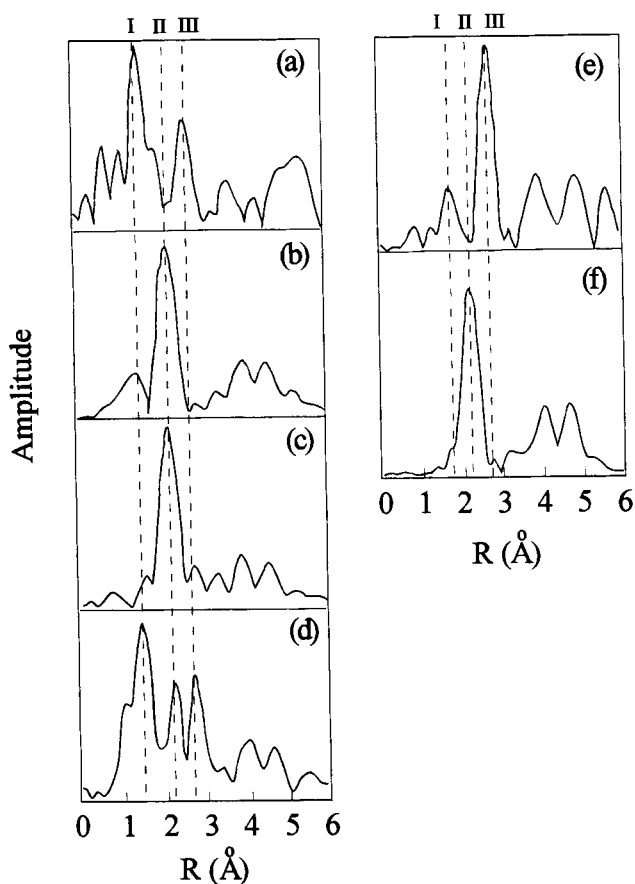


Figure 9. Fourier transforms of Ni K-edge EXAFS functions, $K^3X(K)$, of Ni (1 wt.%)– $K_4Nb_6O_{17}$ catalysts and reference samples. Phase shifts were not corrected. (a) Untreated; (b) reduced at 773 K; (c) reduced at 773 K and re-oxidized at 473 K; (d) reduced at 773 K and re-oxidized at 773 K; (e) NiO reference; (f) Ni metal reference. Interatomic distance I corresponds to Ni–O bond in NiO, II corresponds to Ni–Ni bond in Ni metal and III corresponds to Ni–Ni distance in NiO. From Ref. [15].

[7]. The appearance of an intense resonance line after the reduction and reoxidation indicates the formation of ferromagnetic metallic nickel in the sample.

TEM images of 0.1 % Ni-loaded samples showed the presence of ultra-fine particles of ca. 0.5–0.7 nm diameter, whereas for 1 % loaded samples, particles larger than 3 nm were also observed [15]. The rate of overall water splitting on the 0.1 wt.% Ni-loaded catalyst was twice that on the 1 wt.% Ni-loaded catalyst. Therefore, the Ni particles responsible for the enhancement of the activity are ultra-fine particles probably located at interlayer space-I. As mentioned above, XPS results indicated that these particles are present in the bulk of the catalyst. The larger particles observed in the 1 wt.% Ni-loaded sample are regarded as poisons because they exist in the bulk of the catalyst, leading possibly to destruction of the layered structure locally. X-ray powder diffraction did not show variations in d -spacing perpendicular to the $[Nb_6O_{17}]^{4-}$ sheets since the amount of Ni was very small.

Based on these characterizations, a model structure of 0.1 wt.% Ni-loaded $K_4Nb_6O_{17}$ was proposed as shown in Figure 10. During the loading of the catalyst with nickel, most of the nickel enters the interlayer region-I as Ni^{2+} by replacing K^+ ions, leaving a very small fraction on the external surface. During reduction at

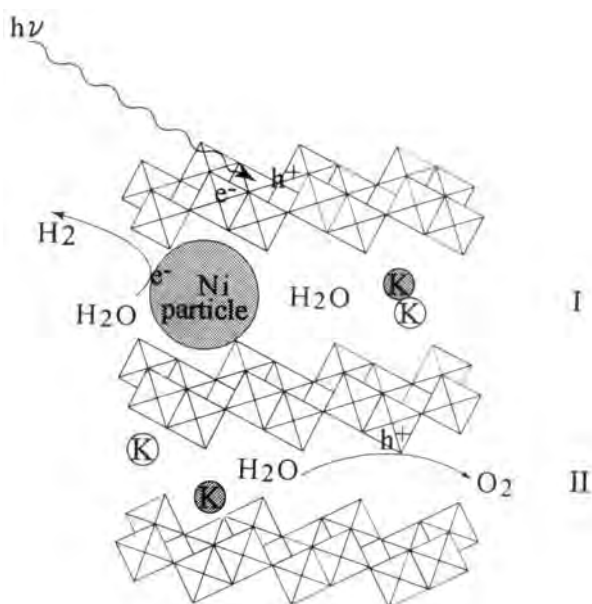


Figure 10. Proposed mechanism of catalytic water decomposition by Ni-loaded $\text{K}_4\text{Nb}_6\text{O}_{17}$. Adapted from Ref. [15].

700°C , the Ni^{2+} cations are reduced to metallic nickel in the form of ultra-fine particles of about 0.5 nm size.

On the basis of this model, a possible reaction mechanism for overall water splitting on Ni-loaded $\text{K}_4\text{Nb}_6\text{O}_{17}$ has been proposed as follows.

On band-gap irradiation, electrons and holes are generated in the host lattice of $[\text{Nb}_6\text{O}_{17}]^{4-}$. The electrons are transferred to the nickel particles on which the hydrogen formation takes place. The holes migrate to the other side of the niobate sheet where water is oxidized to O_2 . Such separation across the sheet may be facilitated by an electrostatic gradient existing across the niobate sheets due to unequal K^+ environments on the two sides of the sheets. However, since the quantum efficiency of overall water splitting is at most 20 % as described above, such an electron-hole separation must not be so efficient. Most of the electrons and holes recombine within the host lattice. Probably some holes may react at interlayer-I with water molecules or Ni metal particles, which causes the reverse reactions or degradation of the activity. The degradation of the catalyst with continued use, as seen by the decreasing rate of production of gases with time (see Figure 7), has been attributed to the decreasing amount of metallic nickel in the sample. It should be noted that this reaction mechanism was inferred from the structure of the active catalyst, and has not been confirmed by any spectroscopic methods.

Modified $\text{K}_4\text{Nb}_6\text{O}_{17}$ systems

CdS and Ni- $\text{K}_4\text{Nb}_6\text{O}_{17}$ mixture

Hydrogen evolution reaction in aqueous K_2SO_3 solutions using physical mixtures of CdS and $\text{K}_4\text{Nb}_6\text{O}_{17}$ or Ni- $\text{K}_4\text{Nb}_6\text{O}_{17}$ powders has been studied [33]. In these

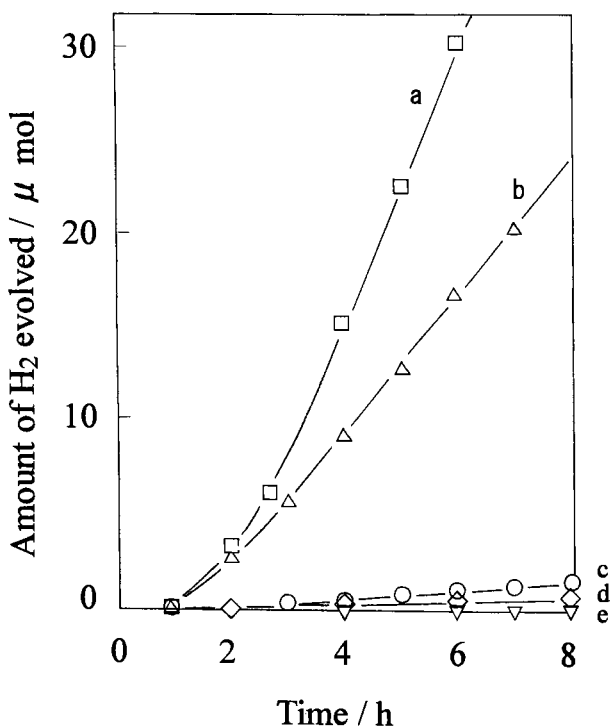


Figure 11. H_2 evolution under irradiation with visible light ($\lambda > 420$ nm) over several catalyst systems in aqueous K_2SO_3 solution (0.1 M, pH = 9.5, 250 mL): (a) $\text{CdS} + \text{NiO-K}_4\text{Nb}_6\text{O}_{17}$; (b) $\text{CdS} + \text{K}_4\text{Nb}_6\text{O}_{17}$; (c) CdS ; (d) $\text{NiO-K}_4\text{Nb}_6\text{O}_{17}$; (e) $\text{K}_4\text{Nb}_6\text{O}_{17}$. From Ref. [33].

experiments, light with $\lambda > 420$ nm was utilized. Figure 11 shows the time course of H_2 evolution using several catalytic systems. As can be seen, neither CdS nor $\text{Ni-K}_4\text{Nb}_6\text{O}_{17}$ is individually effective. On the other hand, a mixture of CdS and $\text{K}_4\text{Nb}_6\text{O}_{17}$ produces a considerable amount of H_2 gas. Ni -loaded $\text{K}_4\text{Nb}_6\text{O}_{17}$ showed much higher activity for H_2 generation. These results suggest that electrons excited in CdS by visible light are transferred to $\text{K}_4\text{Nb}_6\text{O}_{17}$. Furthermore, loaded Ni works as an H_2 evolution catalyst using electrons donated from CdS through the $[\text{Nb}_6\text{O}_{17}]^{4-}$ layer, because Ni exists as ultra-fine metal particles in the interlayer space as described in the preceding section. Optimization experiments have revealed that a mixture of 1 wt.% $\text{Ni-K}_4\text{Nb}_6\text{O}_{17}$ and CdS in a weight ratio of 1:1 at pH 10 is ideal for this system.

CdS-K₄Nb₆O₁₇

Under visible light irradiation, MV^{2+} (MV = methylviologen) was reduced in aqueous methanol in the presence of $\text{CdS-K}_4\text{Nb}_6\text{O}_{17}$ catalyst, even though CdS without niobate is ineffective under these conditions [27]. Here, the catalyst was prepared by partially (about 14 %) exchanging K^+ by Cd^{2+} in $\text{Cd}(\text{NO}_3)_2$ solution, followed by treatment with Na_2S solution. It is proposed that CdS particles are formed both in the interlayer region and on the external surface. Figure 12 shows

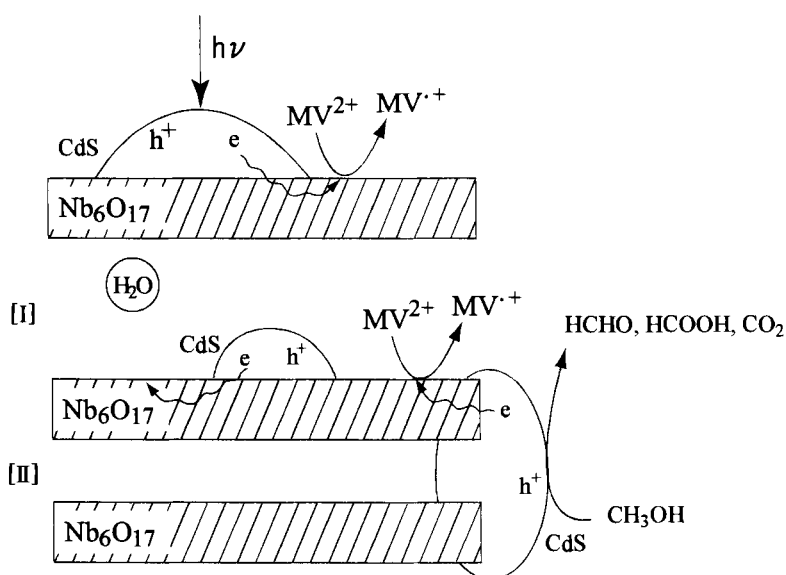


Figure 12. Scheme of CdS/ $K_4Nb_6O_{17}$ -catalyzed MV^{2+} formation using methanol as a reductant under visible light ($\lambda > 420$ nm) irradiation. From Ref. [27].

the mechanism proposed for the catalytic reaction. During the photocatalytic reduction of MV^{2+} , the amount of hydrogen produced was negligible.

Methylviologen and H^+ / $K_4Nb_6O_{17}$

Nakato et al. have intercalated $K_4Nb_6O_{17}$ with methylviologen by direct exchange of K^+ in aqueous solutions [28–31]. By carrying out reactions under two different conditions, they obtained two types of intercalates with differing amounts of MV^{2+} (Table 5). On band-gap irradiation, an intense blue color was observed, indicating the formation of $MV^{\cdot+}$ in the interlayers. The radical cations have high stability not only in vacuum but also in air and O_2 . The half-lives of the two systems are given in Table 5. It was found that the stability of $MV^{\cdot+}$ is higher in the case of $(MV)_{0.3}H_{0.7}K_{2.7}Nb_6O_{17}$. This is interpreted as being due to the spatial separation of the MV^{2+} ions by the co-existing K^+ ions, which prevents the inter-radical inter-

Table 5. Compositions and properties of MV^{2+} -intercalated $K_4Nb_6O_{17}$.

Composition	Basal spacing/nm	Half-life			Ref.
		in argon	in air	in oxygen	
$K_4Nb_6O_{17}$ (anh.)	1.64				
$(MV)_{0.3}H_{0.7}K_{2.7}Nb_6O_{17}$	2.05	Long	6 h	2 h	28, 30, 31
$(MV)_{0.4}H_{1.1}K_{2.1}Nb_6O_{17}$	2.07	2 h	45 min	15 min	29, 30, 31

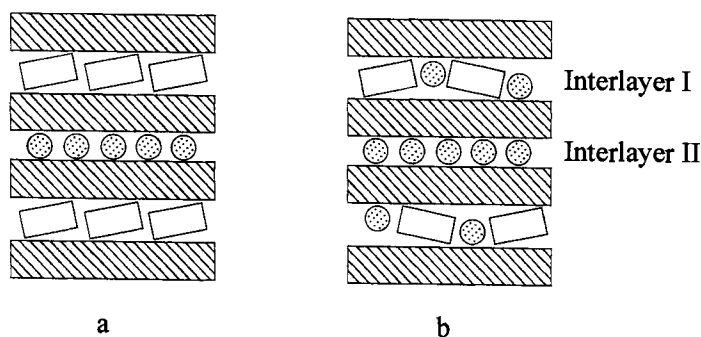


Figure 13. Schematic representation of structures of (a) $MV-K_4Nb_6O_{17}$ and (b) $MV/K--K_4Nb_6O_{17}$. Reprinted with permission from T. Nakato, K. Kuroda and C. Kato, *Chem. Mater.* **1992**, 4, 128. Copyright 1992 American Chemical Society.

action. Figure 13 gives a schematic representation of the structures of the two intercalates.

Kameyama et al. [27] reported on UV light-assisted reduction of MV^{2+} in water and in aqueous alcohols, in the presence of partially exchanged niobate, $H_{2.4}K_{1.6}Nb_6O_{17}$. Figure 14 shows the concentration of MV^{+} produced as a function of time in water and various aqueous alcohol solutions. It is found that methanol is the best reductant for MV^{2+} reduction.

Figure 15 shows the proposed mechanism for MV^{2+} reduction in aqueous methanol solutions. It should be noted that methanol oxidation proceeds to form CO_2 , without any detectable amounts of partially oxidized products, $HCHO$ or $HCOOH$, which suggests that intercalated methanol is completely oxidized in the interlayer space. Also, no noticeable amount of H_2 was detected, indicating that H^+ ions do not compete with MV^{2+} ions for capturing photogenerated electrons from the niobate sheets. The amount of MV^{+} leveled off with continued irradiation.

Photolysis of HI by $K_{4-x}H_xNb_6O_{17}$ loaded with Pt and sensitized with $Ru(bpy)_3^{2+}$

Mallouk and co-workers [6, 26, 206] reported the photodecomposition of acidic KI to H_2 and iodine under visible light irradiation. For this purpose, $K_4Nb_6O_{17}$ was internally loaded with Pt, ion exchanged partially with acid to obtain $K_{4-x}H_xNb_6O_{17} \cdot nH_2O$ ($x \approx 2.5$) and then sensitized with RuL_3 ($L = 4,4'$ -dicarboxy-2,2'-bipyridine). It was found that KI is the best reactant among the alkali metal iodides (Figure 16).

A sensitizer concentration of 5×10^{-7} mol g^{-1} , at which a monolayer of the sensitizer molecules on the external surface of the niobate would be formed, was found to be ideal for efficient photocatalysis. At higher concentrations, the activity diminished. Also, an initial Pt loading of 0.05 wt.% and a reduction temperature [for reducing $Pt(NH_3)_4^{2+}$ to Pt] of $450^\circ C$ were found to be optimum for this system.

It was proposed that the photoreduction involves production of H_2 in the interlayer sites and formation of iodine near the sensitizer molecule, as depicted in Fig-

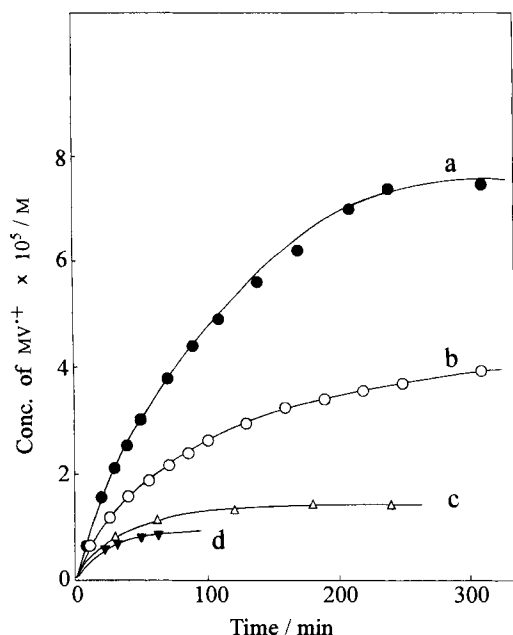


Figure 14. Effect of reductants, (a) methanol, (b) ethanol, (c) 2-propanol and (d) water, on the photoreduction of MV^{2+} catalyzed by $H^+/K_4Nb_6O_{17}$. From Ref. [27].

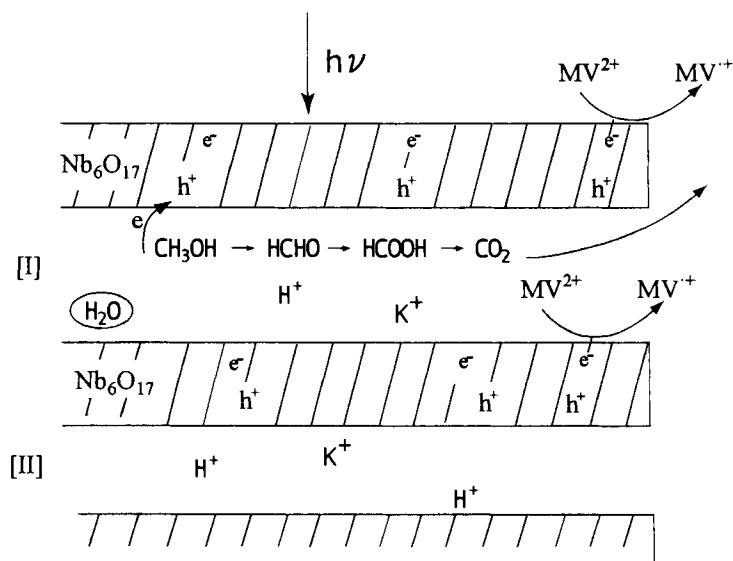


Figure 15. Schematic representation of $H^+/K_4Nb_6O_{17}$ -catalyzed MV^{2+} formation using methanol as reductant under band gap irradiation. From Ref. [27].

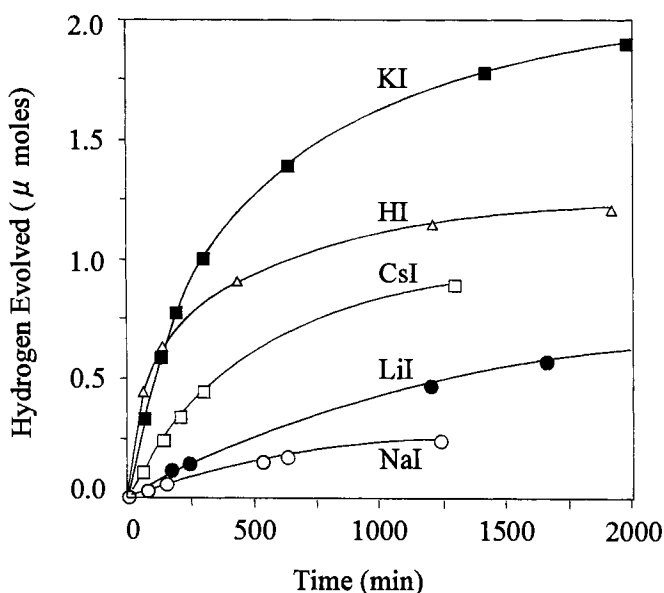


Figure 16. Photocatalytic H_2 evolution from $RuL_3^{2+}/K_2H_2Nb_6O_{17}/Pt$ (0.05 wt.%) in 0.7 M iodide solutions at pH 3. Reprinted with permission from Y. Kim, S.J. Atherton, E.S. Brigham and T.E. Mallouk, *J. Phys. Chem.* **1993**, 97, 11802. Copyright 1993 American Chemical Society.

ure 17. The initial quantum yield for product formation was about 0.3 %. The rate of the photolysis decreases with time, the reason given being the interception of photogenerated electrons by the reaction products (I_2^- and I_3^-), and *not* the reverse reaction. Since the reverse reaction was not operative, the concentration of the products did not change in the dark. The initial quantum yield was increased to 3 % when the reaction between the conduction band electrons and I_3^- ions was suppressed by electrostatically repelling the latter from the oxide surface through an anionic polyelectrolyte layer that was pre-adsorbed on the niobate surface [206].

Time-dependent measurements, where the transient concentration of ground-state sensitizer that was being formed by the reverse electron transfer from the layered oxide to RuL_3^{3+} was monitored as a function of time employing reflectance flash photolysis (in the absence of I^-), reveal a very slow reverse electron transfer. It is estimated that the process of reverse electron transfer is at least three orders of magnitude slower than the forward transfer.

Pillared $K_{4-x}H_xNb_6O_{17}$

Attempts have been made by Sato et al. [23–25, 32] to pillar proton-exchanged $K_4Nb_6O_{17}$ with TiO_2 , Fe_2O_3 and $Cd_{1-x}Zn_xS$. It is reported that incorporation of TiO_2 in the interlayer region enhances water cleavage on band-gap irradiation. On the basis of decreased fluorescence intensity and increased decay time constant of these pillars, it is argued that on irradiation, the photogenerated electron in the pillar is transferred to the layered host. Table 6 summarizes the results. Interestingly, the iron oxide intercalated material shows catalytic activity for irradiation with $\lambda > 400$ nm, whereas unsupported iron oxide found to be inactive.

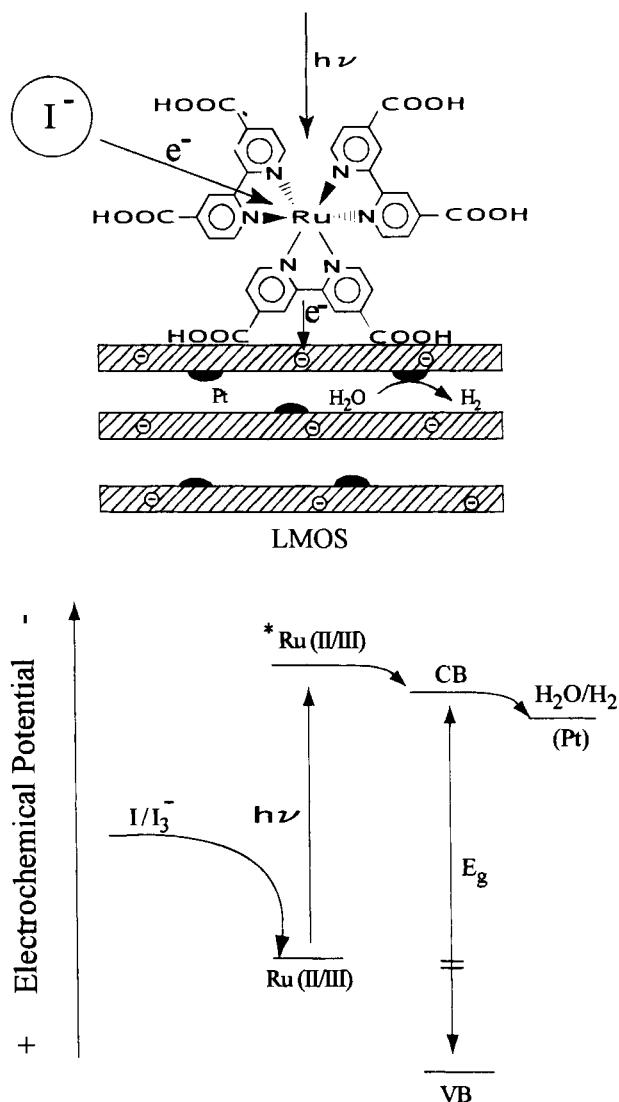


Figure 17. Schematic drawing and potential energy diagram of RuL₃²⁺-sensitized layered oxides for HI photolysis. Reprinted with permission from Y. Kim, S.J. Atherton, E.S. Brigham and T.E. Mallouk, *J. Phys. Chem.* **1993**, 97, 11802. Copyright 1993 American Chemical Society.

4.2.2 KTiNbO₅-type Oxides

Titanates and titanoniobates of the general formula A_{2-x}Ti_{n-x}Nb_xO_{2n+1} (A = alkali metal) crystallize in layered structures possessing [Ti_{n-x}Nb_xO_{2n+1}]^{(2-x)-} sheets stacked with interlayer A⁻ ions [1, 2]. The sheets may be obtained from edge-connected layers of double-ReO₃ units by shearing every *n*-octahedron perpendicular to the sheets. Idealized structures of some of these oxides are shown in Figure 1. Several oxides in this family are known to exhibit interlayer chemistry

Table 6. Materials data and activity data for $K_{4-x}H_xNb_6O_{17}$ and derived materials.

Catalyst ^a	Gallery height/ nm	Pillar content/ wt. %	Surface area/ m ² g ⁻¹	H ₂ from H ₂ O/ h ⁻¹ g ⁻¹	Ref.
H ₄ Nb ₆ O ₁₇	0.4	0	16.1	0	23 ^b , 24
H ₄ Nb ₆ O ₁₇	0.4	0	6.6	0	25
H ₄ Nb ₆ O ₁₇ /Pt		—		0	25
H ₄ Nb ₆ O ₁₇ /TiO ₂	0.48	7.3	38.6	0	25
H ₄ Nb ₆ O ₁₇ /TiO ₂ I	0.52	26.7	125.6	2 cm ³	32
H ₄ Nb ₆ O ₁₇ /TiO ₂ II	0.42	7.3	38.6	1 cm ³	32
H ₄ Nb ₆ O ₁₇ /Pt, TiO ₂	0.51	36.8	0.3 Pt	0.37 μmol	24
H ₄ Nb ₆ O ₁₇ /TiO ₂ , Pt	0.47	7.3 + 0.32 Pt	38.6	70 μmol	25
H ₄ Nb ₆ O ₁₇ /Fe ₂ O ₃	0.68	30.1 (Fe)	102	0	24
H ₄ Nb ₆ O ₁₇ /Fe ₂ O ₃ · 2.5H ₂ O	0.681	30.1 (Fe)	102	1.8 ^b	23
H ₄ Nb ₆ O ₁₇ /Fe ₂ O ₃ · <i>n</i> H ₂ O, Pt		0.1 % Pt		2.8 ^b	23
H ₄ Nb ₆ O ₁₇ /Cd _{0.8} Zn _{0.2} S	0.8	9.5 Cd, +0.09 Zn	96	0	24

^a Extent of exchange in proton exchange reaction is not available.^b H₂ from aqueous Na₂SO₃ solution.

such as ion exchange and intercalation [1]. Ion-exchange reactions have been reported for Ti₂Ti₄O₉ [44], H₂Ti₄O₉ [68, 207–209], K₃Ti₅MO₁₄ (M = Nb or Ta) [45], H₃Ti₅NbO₁₄ [46], KTiMO₅ (M = Nb or Ta) [47], and HTiNbO₅ [48]. Intercalation of organic amines has been reported for H₂Ti₄O₉ [49], K₂Ti₄O₉ [210], HTi₂NbO₇ [50], HTiNbO₅ [51–54], H₃Ti₅NbO₁₄ [46], Na₂Ti₃O₇ [210], Na₂Ti₂O₅ [55] and HNb₃O₈ [211]. Kudo et al. studied luminescence properties [56, 57]. Dielectric properties have also been reported [135]. Several of these oxides have been used for photocatalysis studies. Table 7 summarizes the structural and catalysis data for these oxides. Band-gaps calculated from reflectance measurements are available for some of these oxides and are included in the table.

Shibata *et al.* [64] studied hydrogen evolution from aqueous methanol under UV irradiation catalyzed by A₂Ti_{*n*}O_{2*n*+1} (A = Na or K, *n* = 2, 3, 4 and 6) and by partially (about 80–100 %) proton-exchanged products, with and without Pt loading. Table 8 lists the H₂ evolved from these oxides. It was found that, during a 10 h observation period, the catalytic activity remained stable after a short (about 2 h) induction period. Inoue et al. [61] carried out photodecomposition of water using these oxides with Ru as a promoter. It was found that whereas considerable amounts of hydrogen were produced, no oxygen was liberated. Sato et al. carried out studies with H₂Ti₄O₉ [23–25]. In water photolysis experiments, no activity was detected even after Pt-loading. However, on pillaring with TiO₂ or Fe₂O₃, considerable activity was observed for water decomposition and/or hydrogen evolution from aq. Na₂SO₃ solution.

Sekine et al. [72] studied CsNbTiO₅, CsNbTi₂O₇ and proton-exchanged compounds for hydrogen evolution from aqueous methanol and oxygen evolution from aqueous AgNO₃ solution. Flat-band potentials for these materials were determined

Table 7. Unit cell data, estimated electronic band level data and catalytic reactions studied for KTiNbO_5 -related oxides.

Composition	E_g/eV (Ref. [6])/ absorption edge	Conduction band edge/ eV vs. NHE [6]	Unit cell dimensions	No. of H_2O of hydration	Catalysis study	Promoter	Ref.
$\text{A}_3\text{Ti}_{2-x}\text{M}_x\text{O}_4$			Orthorhombic, $a = 0.38$ – 0.39 , $b = 1.55$ – 1.73 , $c = 0.29$ – 0.3 nm [58–60]				
$\text{K}_2\text{Ti}_4\text{O}_9$	3.48, (384–389 nm [61])	–0.98	Monoclinic, $a = 1.825$, $b = 0.3791$, $c = 1.201$ nm, $\beta = 106.4^\circ$ [62]	3 [63]	H_2 from CH_3OH H_2 and O_2 from H_2O Reduction of Cr(VI)	Pt RuO_x	64 61 65
$\text{H}_2\text{Ti}_4\text{O}_9$	3.25	–0.044	Monohydrate: monoclinic, $a = 1.988$, $b = 0.3735$, $c = 1.209$ nm, $\beta = 114.9^\circ$ [63]	0.25 [63], 1 [66, 67], 1.2 [68]	H_2 from CH_3OH H_2 from aq. Na_2SO_3 H_2 from aq. KI H_2 and O_2 from H_2O H_2 and O_2 from H_2O^a Redn. of MV^{2+} to MV^{+}	Pt Pt, RuL_3 Pt — —	64 23 6 25 24 29, 69
$\text{Na}_2\text{Ti}_3\text{O}_7$	3.47 384–389 nm [61]	–0.96	Monoclinic, $a = 0.8571$, $b = 0.3804$, $c = 0.9135$ nm, $\beta = 101.57^\circ$ [70]	—	H_2 and O_2 from H_2O^a H_2 from CH_3OH	Pillars ^b Pt	23, 24 64
$\text{H}_2\text{Ti}_3\text{O}_7$	3.27	0.015	Monoclinic, $a = 0.8080$, $b = 0.3752$, $c = 0.9178$ nm, $\beta = 101.27^\circ$ [66]	—	H_2 and O_2 from H_2O	RuO_x	61, 71
$\text{CsTi}_2\text{NbO}_7$	3.67, 3.56 [72]	–0.83, –0.56, pH 0 [72]	Orthorhombic, $a = 0.932$, $b = 1.841$, $c = 0.379$ nm [73]	—	H_2 from CH_3OH O_2 from AgNO_3	Pt —	64 72 72
HTi_2NbO_7	3.37 3.03 [72]	–0.054, –0.58, pH 3 [72]	Orthorhombic, $a = 0.9320$, $b = 0.3775$, $c = 1.600$ nm [1, 74]	1, 2 [1, 74]	H_2 from CH_3OH O_2 from AgNO_3 H_2 from aq. KI	Pt — Pt, RuL_3	72 72 6

Table 7 (continued)

Composition	E_g /eV (Ref. [6])/ absorption edge	Conduction band edge/ eV vs. NHE [6]	Unit cell dimensions	No. of H ₂ O of hydration	Catalysis study	Promoter	Ref.
KTiNbO ₅	3.50	-0.79	Orthorhombic, $a = 0.6459$, $b = 0.3792$, $c = 1.8472$ nm [75]	—	H ₂ and O ₂ from H ₂ O	Ni	76
CsTiNbO ₅	3.51 [72]	-0.30, pH 0 [72]	Orthorhombic, $a = 0.6498$, $b = 0.3826$, $c = 1.991$ nm [77]	—	H ₂ from CH ₃ OH O ₂ from AgNO ₃	Pt	72 72
A _{1-x} (Ti _{1-x} M _{1+x} O ₅), M = Nb/Ta			Orthorhombic, $a \cong 0.64$, $b \cong 0.38$, $c = 1.8-2.0$ nm [77]				
HTiNbO ₅	3.47, 3.24 [72]	0.021 -0.33, pH 3 [72]	Orthorhombic, $a = 0.6531$, $b = 0.3781$, $c = 1.6704$ nm [1, 47]	1, 2 [1]	H ₂ from CH ₃ OH O ₂ from AgNO ₃ H ₂ from aq. KI Redn. of MV ²⁺ to MV ⁺	Pt — Pt, RuL ₃ —	72 72 6 29-31, 78
KNb ₃ O ₈	3.53	-0.45	Orthorhombic, $a = 0.8903$, $b = 2.116$, $c = 0.3799$ nm [79]	—			
HNb ₃ O ₈	3.58	-0.073	Orthorhombic, $a = 0.887$, $b = 1.861$, $c = 0.3848$ nm [80]	1 [80]	Oxidation of I ⁻ in HI Redn. of MV ²⁺ to MV ⁺	Pt, RuL ₃ —	6 30, 31
A ₂ Ti ₂ O ₅ (A = K, Cs, H)			A = K, Monoclinic, $a = 1.1374$, $b = 0.3799$, $c = 0.6616$ nm, $\beta = 100.10^\circ$ [81]		H ₂ from CH ₃ OH	Pt (for A = H)	64 (A = K), 26

^a Also, hydrogen from aq. Na₂S/eq. Na₂SO₃ soln.^b (Pt, TiO₂), Fe₂O₃, (Fe₂O₃ · 2.39H₂O), (Pt, Fe₂O₃ · *n*H₂O), CdS, Cd_{0.8}Zn_{0.2}S.

Table 8. Catalytic activities of some layered titanates [64].

Catalyst	H ₂ evolution rate from aqueous CH ₃ OH/ $\mu\text{mol h}^{-1} \text{ g}^{-1}$				
	Original		H ⁺ exchanged		
	Alone	Pt loaded	Degree of H ⁺ exchange/%	Alone	Pt loaded
K ₂ Ti ₄ O ₉	7	9.6	~80	6.4	27.6
Na ₂ Ti ₃ O ₇	5.8	38	~80	3.8	11
K ₂ Ti ₂ O ₅	41.6	69.4	~100	66.8	83.8

Table 9. Photocatalytic activity data for CsTi₂NbO₇, CsTiNbO₅ and proton-exchanged forms [72].

Catalyst	H ₂ from aqueous methanol/ $\mu\text{mol h}^{-1} \text{ g}^{-1}$		O ₂ from $1.7 \times 10^{-2} \text{ M}$ aqueous AgNO ₃ solution/ $\mu\text{mol h}^{-1} \text{ g}^{-1}$
	Without Pt	With 0.1 wt.% Pt	
CsTi ₂ NbO ₇	4.6	8.5	19
H ⁺ /CsTi ₂ NbO ₇	1.9	87	51
CsTiNbO ₅	15	12	1.2
H ⁺ /CsTiNbO ₅	13	320	24

by the slurry electrode method and the band-gaps were estimated from reflectance spectra. Table 7 includes the flat-band potentials and band-gaps calculated in this study. Hydrogen evolution in aqueous methanol was studied using samples both before and after Pt loading (1 wt.%). Oxygen evolution was also studied, without promoter, in aqueous AgNO₃ solutions. Table 9 lists the rates of gas evolutions under steady-state conditions. Comparing the results, we see that a striking increase in the rate of H₂ evolution was found for protonated compounds after Pt loading. This was attributed to the intercalation of methanol and the catalytic role of Pt for H₂ formation.

Nickel-loaded KTiNbO₅ was studied by Takahashi et al. [76] for the photo-decomposition of water. It was found that the activity of compounds prepared by a polymerized complex (PC) method was 10 times higher than the activity of the oxide prepared by conventional methods. The increased activity for the PC preparation was attributed partly to the larger surface area (ca. 23 vs. ca. 3 m² g⁻¹) and partly to probable improvement in surface structure.

Kim et al. [6] reported hydrogen evolution from aqueous KI/CsI solutions under visible light irradiation ($\lambda > 400 \text{ nm}$) employing several KTiNbO₅-type oxides and KNb₃O₈ (see Table 7). In these experiments, internally Pt-loaded oxides were proton exchanged and then sensitized using a monolayer of Ru-L₃²⁺ (L = 4,4'-dicarboxy-2,2'-bipyridine). All the sensitized oxides exhibited photocatalysis. There was no

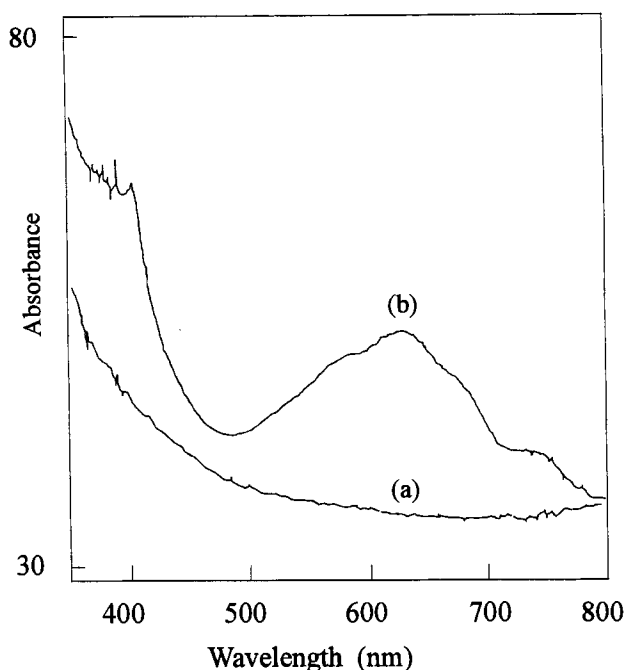


Figure 18. Visible absorption spectra of MV-HTiNbO₅ (a) before and (b) after irradiation. Reproduced from T. Nakato, H. Miyata, K. Kuroda and C. Kato, *React. Solids* **1988**, 6, 231, with permission from Elsevier Science.

activity in the absence of the sensitizer. Time-dependent measurements by flash photolysis revealed that reverse electron transfer from the oxide sheets is much slower compared to the forward electron transfer from the excited RuL₃²⁺.

Nakato et al. [29–31, 78] found that photogenerated electrons from the host can be transferred to methylviologen (MV²⁺) in HTiNbO₅ intercalated with methylviologen. MV²⁺ intercalates were prepared by first exchanging about 97 % of K⁺ in KTiNbO₅ by H⁺, then treating the proton-compound with propylamine to obtain a 66 %-intercalated compound and finally treating this with aqueous methylviologen to give the final product containing 0.25 mol of MV²⁺ per mole of [TiNbO₅][−].

The MV²⁺ intercalate turns blue on UV irradiation under an N₂ atmosphere owing to the formation of MV^{•+}. Formation of the latter was confirmed by absorption measurements. Figure 18 shows the absorption spectra in the visible region (a) before and (b) after UV irradiation. It is proposed that some Ti and/or Nb are present in lower oxidation states owing to probable oxygen deficiency in the host lattice, which makes these ions electron donors. It was found that the MV^{•+} species was fairly stable in N₂, as seen from the continued appearance of blue color even after turning the UV light off. The stability indicates that the reverse reaction does not occur at a considerable rate. However, the color disappears on exposure to O₂ indicating the reaction of MV^{•+} with O₂. Similar experiments have been carried out with K₂Ti₄O₉ [29, 69] and with HNb₃O₈ [30, 31].

4.2.3 Perovskite-related Layered Oxides

Perovskite-related layered oxides showing interlamellar activity belong to two main classes, (i) the Dion–Jacobson series (DJ series) of general formula $AM_{n-1}B_nO_{3n+1}$ (e.g., $KCa_2Nb_3O_{10}$ [82]) and (ii) the Ruddlesden–Popper series (RP series) of general formula $A_2M_{n-1}B_nO_{3n+1}$ (e.g., $Na_2Gd_2Ti_3O_{10}$ [83] and $K_2La_2Ti_3O_{10}$ [84]). Their structures are characterized by n -octahedra thick perovskite-like sheets stacked with interlayer A^- ions placed in between the sheets. Figure 2 shows idealized structures of some of these oxides. An intermediate series, where the amount of interlayer ions can be varied between the above two series, is also known [85].

Structurally, three types of stacking sequences are observed in which the neighboring sheets are (i) eclipsed (e.g. $RbCa_2M_3O_{10}$), (ii) ‘staggered’ (e.g., $NaCa_2M_3O_{10}$) or (iii) partially staggered (e.g., $KCa_2M_3O_{10}$, $M = Nb$ [86] or Ta [87]).

An important aspect of these structures is the possibility of varying the thickness of sheets in multiples of octahedron thickness. Thus, in the DJ series, oxides with $n = 2$ [86, 95], $n = 3$ [13, 82, 86, 93–102], $n = 4$ [86, 96, 103, 104], $n = 5$ [96, 103, 104], $n = 6$ [96] and $n = 7$ [96] are known. In the RP series, compounds with $n = 1$ are not known. However, the $NaLaTiO_4$ -type oxides [105–109], where Na^+ -occupied interlayer planes alternate with La^{3+} -occupied interlayer planes, or the corresponding H^+ analogs [212–218], may be considered as an ordered $n = 1$ system. Higher members in this series, namely with $n = 2$ [110], $n = 3$ [83, 84, 105, 111–115] and $n = 4$ [110] are known. The possibility of varying the chemical composition by choosing appropriate elements in three positions, namely (i) cubooctahedral, (ii) octahedral and (iii) interlayer sites, is another attractive feature of these oxides. Accommodation of vacancies in cubooctahedral sites [104, 110, 115], interlayer cation sites [85, 116] and oxygen sites [117, 118] is also known. In addition, the rich interlayer chemistry, such as spontaneous hydration, ion exchangeability and intercalation of alkylamines [88, 96, 101], makes them very attractive systems for catalysis studies. Other related studies include exchange of interlayer monovalent ions with divalent ions [67, 119–121], pillaring of $HLaNb_2O_7$ with AO_2 ($A = Ti, Zr$ or Si) [219], reductive intercalation of small ions [97, 102, 122–129], luminescence measurements [105, 109, 130–134] and dielectric property measurements [135].

Several oxides in the above family have been used for photocatalytic studies, especially for hydrogen and oxygen evolution reactions. Studies on the Dion–Jacobson series are presented first, followed by studies on the Ruddlesden–Popper series and finally on the intermediate series. Table 10 lists oxides employed for photocatalysis studies.

Dion–Jacobson Series, $AM_{n-1}Nb_nO_{3n+1}$

The Dion–Jacobson series of oxides of general formula $AM_{n-1}Nb_nO_{3n+1}$, ($A = K, Rb$ and Cs , $n = 2, 3$ and 4 , and protonated analogs) was investigated by Domen et al. [13] for hydrogen evolution from aqueous alcohol (with and without Pt loading) and for oxygen evolution from aqueous $AgNO_3$, under UV irradiation. Band-gaps were estimated from diffuse reflectance spectra. The photocatalytic per-

Table 10. Perovskite-related layered oxides studied for photocatalysis.

Composition	Unit cell dimensions	No. of H ₂ O of hydration	Band gap/ eV [13]/ absorption edge	Catalysis study
KLaNb ₂ O ₇	Orthorhombic, $a = 0.781$, $b = 0.767$, $c = 2.154$ nm [88]	—	3.2/330 nm [130]	^{a,b} [13]
RbLaNb ₂ O ₇	Tetragonal, $a = 0.3885$, $b = 1.0989$ nm [88]	—	3.35/330 nm [130]	^{a,b} [13]
CsLaNb ₂ O ₇	Tetragonal, $a = 0.3905$, $c = 1.1185$ nm [88]	—	3.3/340 nm [130]	^{a,b} [13]
HLaNb ₂ O ₇	Tetragonal, $a = 0.3894$, $b = 1.0459$ nm [88]	—	—	^{a,b} [13]
KCa ₂ Nb ₃ O ₁₀	Orthorhombic, $a = 0.7718$, $b = 0.7753$, $c = 2.945$ nm [82, 86]	—	3.35	^{b,c} [13]
RbCa ₂ Nb ₃ O ₁₀	Tetragonal, $a = 0.7725$, $b = 1.4909$ nm [82, 86]	—	3.5	^{a,b} [13]
CsCa ₂ Nb ₃ O ₁₀	Orthorhombic, $a = 0.7740$, $b = 0.7746$, $c = 3.0185$ nm [82, 98]	—	3.5	^{a,b} [13]
HCa ₂ Nb ₃ O ₁₀	Tetragonal, $a = 0.7706$, $b = 1.4387$ nm [86]	1.5 [86]	—	^{a,b} [13]
KSr ₂ Nb ₃ O ₁₀ [13]		—	3.16	^{a,b} [13]
HSr ₂ Nb ₃ O ₁₀ [13]				^{a,b} [13]
HSr ₂ Nb ₃ O ₁₀ -SiO ₂ pillars				^c [136]
RbPb ₂ Nb ₃ O ₁₀	Tetragonal, $a = 0.7863$, $b = 1.498$ nm [95]	—	500 nm [137]	^{a,b} [137]
HPb ₂ Nb ₃ O ₁₀	Orthorhombic, $a = 0.782$, $b = 0.786$, $c = 1.454$ nm [95]	0–3 [95]	—	^c [137]
RbLa ₂ Ti ₂ Nb O ₁₀	Tetragonal, $a = 0.3833$, $b = 1.524$ nm [85]		^e	^d [138]
CsLa ₂ Ti ₂ Nb O ₁₀	Tetragonal, $a = 0.3848$, $b = 1.539$ nm [101]		^e	^d [138]
Rb _{1.5} La ₂ Ti _{2.5} Nb _{0.5} O ₁₀	Tetragonal, $a = 0.3864$, $b = 3.251$ nm [85]	1 [85]	^e	^d [138]
Cs _{1.5} La ₂ Ti _{2.5} Nb _{0.5} O ₁₀ [138]		2 [138]	^e	^d [138]
K ₂ La ₂ Ti ₃ O ₁₀	Tetragonal, $a = 0.3871$, $b = 2.978$ nm [84]	1 [84], 2 [114]	^e	^d [138–141]
Rb ₂ La ₂ Ti ₃ O ₁₀	Tetragonal, $a = 0.3898$, $b = 3.05$ nm [84]	1 [85]	^e	^d [138]
Cs ₂ La ₂ Ti ₃ O ₁₀ [138]		3.5 [138]	^e	^d [138]
KCa ₂ NaNb ₄ O ₁₃	Orthorhombic, $a = 0.7730$, $b = 0.7745$, $c = 3.7274$ nm [86]	—	3.21	^{a,b} [13]

^a H₂ evolution from aq. CH₃OH using Pt-loaded catalyst.^b O₂ evolution from aq. AgNO₃ using catalyst without a promoter.^c H₂ from aq. C₁–C₄ alcohols using Pt-loaded catalyst.^d H₂ and O₂ evolution from water or alkaline water using Ni-loaded catalyst.^e 3.4–3.5 eV estimated from diffuse reflectance spectra [138].

Table 11. Photocatalytic activities of layered perovskite compounds and of TiO₂ [13].

Catalyst	Rate of gas evolution/ $\mu\text{mol h}^{-1} \text{ g}^{-1}$				
	H ₂ from aqueous methanol				O ₂ from Original compound
	Original compound		H ⁺ -exchanged compound		
	Alone	Pt-loaded	Alone	Pt-loaded	
KLaNb ₂ O ₇	28	54	760	3800	46
RbLaNb ₂ O ₇	60	90	740	2600	2
CsLaNb ₂ O ₇	12	28	300	2200	3
KCa ₂ Nb ₃ O ₁₀	14	100	5900	19000	8
RbCa ₂ Nb ₃ O ₁₀	3	26	3100	17000	16
CsCa ₂ Nb ₃ O ₁₀	2	10	970	8300	10
KSr ₂ Nb ₃ O ₁₀	10	110	8900	43000	30
KCa ₂ NaNb ₄ O ₁₀	5	280	790	18000	39
TiO ₂	—	7400	—	—	660

formance of these oxides is presented in Table 11. In these samples, Pt was loaded by the photodeposition method, from H₂PtCl₆ in aqueous methanol solution. Since PtCl₆²⁻ is an anion, it is not intercalated in the host oxide. Therefore, loaded-Pt particles are deposited on the external surface of the layered perovskite powder, and were observed by TEM [137].

It can be seen in Table 11 that the activities of protonated compounds are better than those of the non-protonated counterparts. The higher activity towards hydrogen evolution has been attributed to the easy accessibility of the interlayer space for CH₃OH molecules, which is facilitated by the spontaneous hydration of these proton-exchanged oxides. Platinum loading enhances the activity for all compounds. Considerable activity has been observed towards O₂ evolution from aqueous AgNO₃, although the activity is much less than that of TiO₂. This is attributed to the intercalated Ag⁺ cations that work probably as recombination centers for electrons and holes.

Photocatalytic activity towards oxidation of higher alcohols has also been investigated [13, 136]. For this purpose, KCa₂Nb₃O₁₀ was used as a representative system. Table 12 presents the results together with those for TiO₂. For each of the alcohols, the activity increases in the order KCa₂Nb₃O₁₀ < HCa₂Nb₃O₁₀ < HCa₂Nb₃O₁₀-Pt. Also, the shorter the chain length, the higher is the activity, especially for proton-exchanged forms.

By pillaring the layered oxides, it is possible to increase the interlayer space to make such space available for guest molecules. Ebina et al. [136] investigated the catalytic activity of silica-pillared Ca₂Nb₃O₁₀. Effective pillaring was achieved by intercalation of TEOS into HCa₂Nb₃O₁₀. The BET surface area of the pillared material was 200 m² g⁻¹. Since the interlayer space is now accessible for the alcohol with longer alkyl chains as well, the activity with these alcohols improves to a

Table 12. Activity of $\text{Ca}_2\text{Nb}_3\text{O}_{10}$ system and TiO_2 for H_2 evolution from various alcohols.

Catalyst	Rate of H_2 evolution/ $\mu\text{mol h}^{-1} \text{g}^{-1}$				Ref.
	Methanol	Ethanol	1-Propanol	1-Butanol	
$\text{KCa}_2\text{Nb}_3\text{O}_{10}$	7	7	3	2	13
$\text{HCa}_2\text{Nb}_3\text{O}_{10}^{\text{a}}$	920	73	27	19	13
$\text{HCa}_2\text{Nb}_3\text{O}_{10}\text{-Pt}^{\text{a}}$	4700	380	40	30	13, 136
$\text{Ca}_2\text{Nb}_3\text{O}_{10}\text{-SiO}_2$	8100	5500	1100	1060	136
Pt-TiO_2	4000	5200	3500	2800	13, 136

^aDegree of H^+ exchange >95 %.

greater extent. Table 12 includes the results with various alcohols. The effect of increased interlayer volume is clearly seen in an increase in performance with all alcohols and more so with 1-butanol.

The pillars are stable up to 400°C . At higher temperatures, the pillars collapse in height, as indicated by the shifting of the (001) line to higher angles in the powder X-ray diffraction patterns.

Visible light response was observed when the cubooctahedral Ca^{2+} ions in $[\text{Ca}_2\text{Nb}_3\text{O}_{10}]^-$ sheets were replaced by Pb^{2+} ions as in $\text{RbPb}_2\text{Nb}_3\text{O}_{10}$ [137]. In Figure 19, diffuse reflectance spectra of $\text{KCa}_2\text{Nb}_3\text{O}_{10}$ and $\text{RbPb}_2\text{Nb}_3\text{O}_{10}$ are shown. The reason for the absorption edge of $\text{RbPb}_2\text{Nb}_3\text{O}_{10}$ being at lower energies has not yet been fully revealed, but may be due to the interaction between $6s^2$ electrons of Pb^{2+} and $2p^6$ electrons of O^{2-} . Therefore, the top of the valence band shifts to higher electron energy and this results in a decrease in the band-gap. Figure 20 shows the time course of hydrogen evolution by this compound under visible

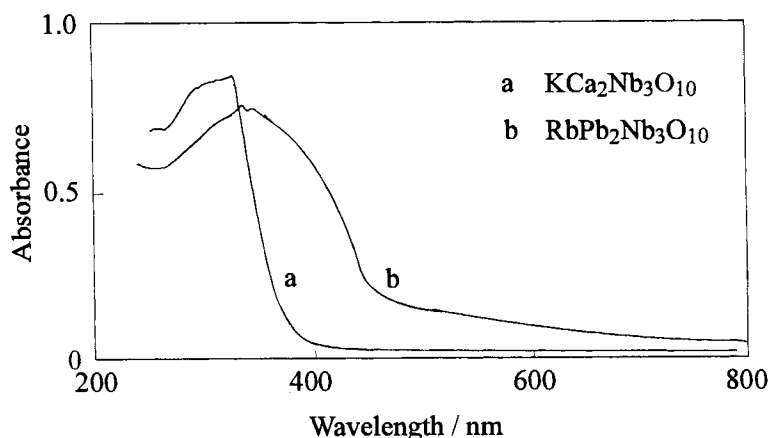


Figure 19. Diffuse reflectance spectra of (a) $\text{KCa}_2\text{Nb}_3\text{O}_{10}$ and (b) $\text{RbPb}_2\text{Nb}_3\text{O}_{10}$. From Ref. [137].

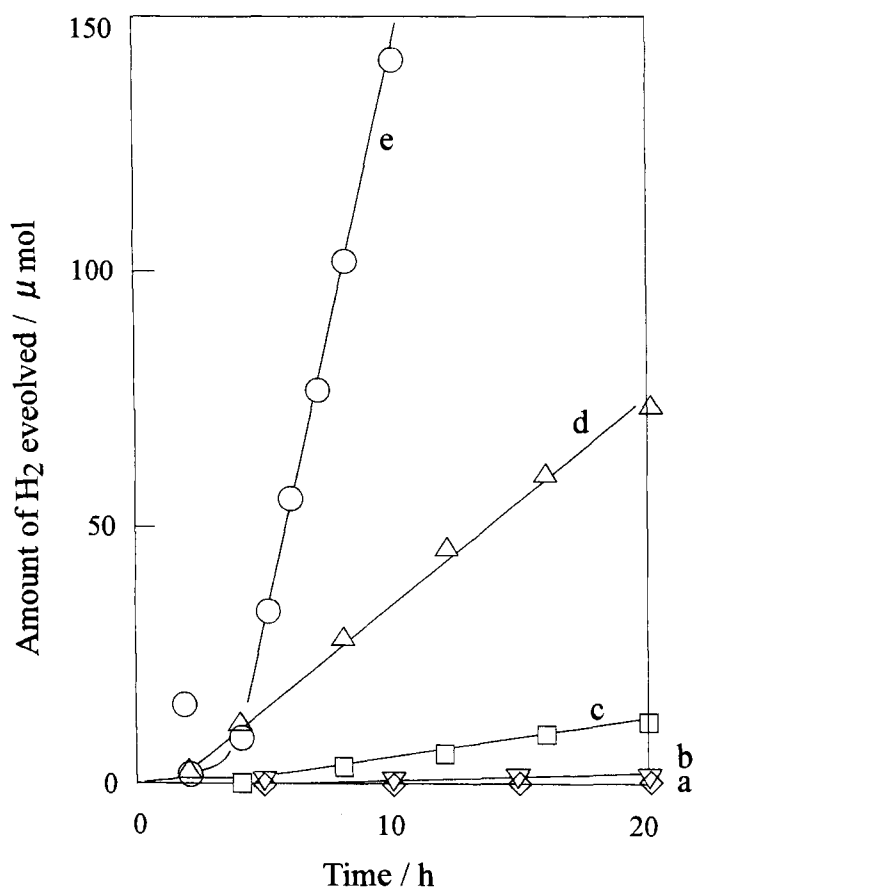


Figure 20. Time course of visible light-induced H_2 evolution from aqueous methanol solution over modified $\text{RbPb}_2\text{Nb}_3\text{O}_{10}$ catalysts: (a) $\text{RbPb}_2\text{Nb}_3\text{O}_{10}$; (b) Pt (0.1 wt.%) from $\text{H}_2\text{PtCl}_6/\text{RbPb}_2\text{Nb}_3\text{O}_{10}$; (c) $\text{HPb}_2\text{Nb}_3\text{O}_{10}$; (d) Pt (0.1 wt.%) from $\text{H}_2\text{PtCl}_6/\text{HPb}_2\text{Nb}_3\text{O}_{10}$; (e) Pt (0.1 wt.%) from $[\text{Pt}(\text{NH}_3)_4]\text{Cl}_2/\text{HPb}_2\text{Nb}_3\text{O}_{10}$. From Ref. [137].

light ($\lambda > 420$ nm) irradiation. Here also, as in the previous cases, $\text{HPb}_2\text{Nb}_3\text{O}_{10}$ shows better activity than the Rb form.

In this case, two types of Pt-loading procedures were adopted: (i) using H_2PtCl_6 as the precursor as described above, to produce Pt particles on the external surface of the catalyst, and (ii) using $\text{Pt}(\text{NH}_3)_4\text{Cl}_2$ to form Pt particles in the interlayer region. In the latter method, intercalation of $\text{Pt}(\text{NH}_3)_4^{2+}$ was achieved by treating $\text{HPb}_2\text{Nb}_3\text{O}_{10}$ with an aqueous solution of $\text{Pt}(\text{NH}_3)_4\text{Cl}_2$ for 1 week. This permits the formation of Pt particles in the interlayer region during photodecomposition of $\text{Pt}(\text{NH}_3)_4^{2+}$ by UV light. The locations of the Pt particles were confirmed by XPS and TEM. The catalytic activity was found to be higher (about fivefold) for the internally loaded samples. The difference in the catalytic activities for the two cases

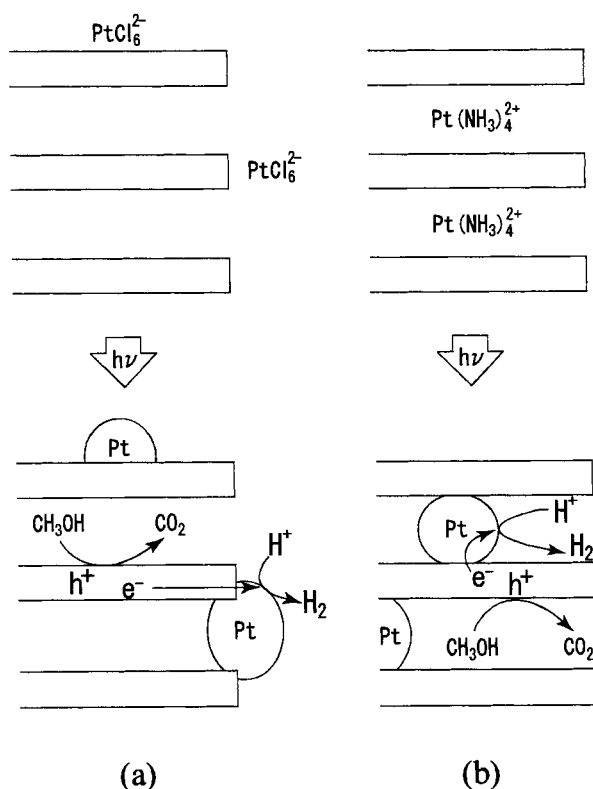


Figure 21. Schematic representation of mechanisms of H₂ evolution over Pt/HPb₂Nb₃O₁₀: Pt exists in the interlayer region in (b) and only on the external surface in (a). From Ref. [137].

is explained as follows (Figure 21): when Pt particles are on the external surface (Figure 21a), some of the photogenerated electrons, especially those produced in the interior region of the sample, have to move from the bulk towards the Pt site. During this travel, some of them may recombine with holes, thus making the photocatalytic process less effective. On the other hand, when the Pt is located in the interlayer region (Figure 21b), the travel length is considerably shorter, which leads to effective photoreaction.

Oxides, such as $\text{ALa}_2\text{Ti}_2\text{NbO}_{10}$ ($\text{A} = \text{Rb}$ or Cs), which have different sheet composition compared with $\text{KCa}_2\text{Nb}_3\text{O}_{10}$, have been investigated for their catalytic activity for overall water decomposition after Ni loading [138]. The results are included in Table 13 in the following section.

Ruddlesden–Popper series, $\text{A}_2\text{M}_{n-1}\text{B}_n\text{O}_{3n+1}$

$\text{K}_2\text{La}_2\text{Ti}_3\text{O}_{10}$ is a typical oxide in the Ruddlesden–Popper series exhibiting interlayer reactivity [84]. It forms a hydrate with about 1–2 H₂O molecules per formula unit under ambient conditions [84, 114]. Figure 22 shows schematic structures of anhydrous and hydrated oxides. Variation of the number of waters of hydration with humidity and exposure time has been reported for the analogous compound

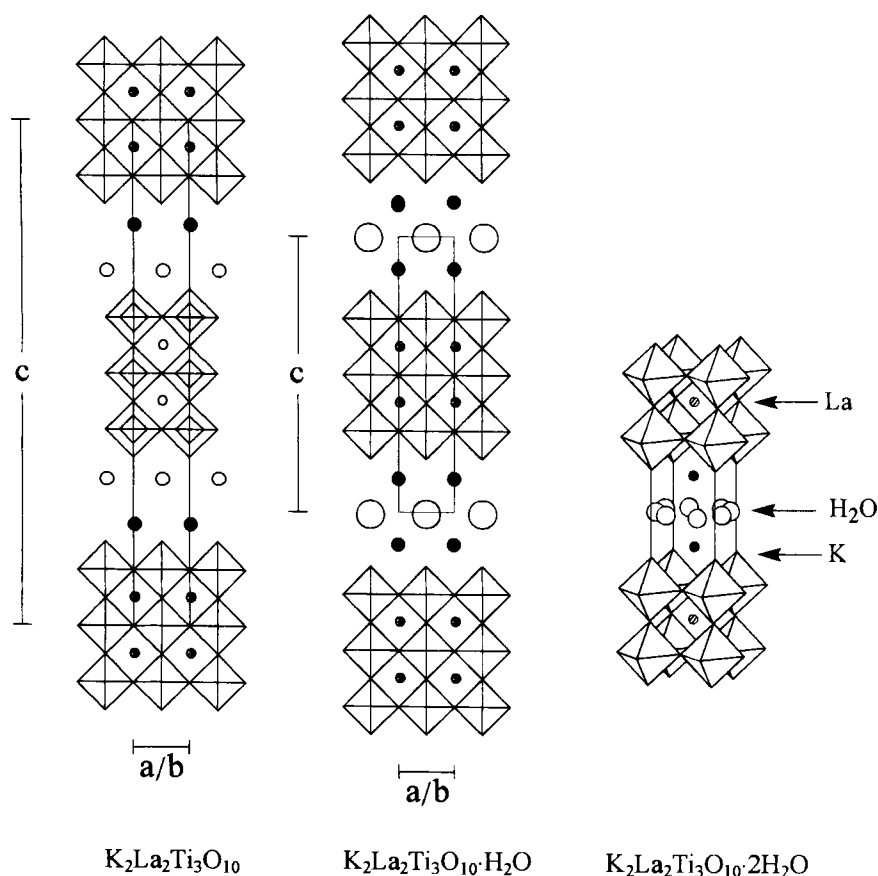


Figure 22. Schematic structures of $\text{K}_2\text{La}_2\text{Ti}_3\text{O}_{10}$, $\text{K}_2\text{La}_2\text{Ti}_3\text{O}_{10} \cdot \text{H}_2\text{O}$ and $\text{K}_2\text{La}_2\text{Ti}_3\text{O}_{10} \cdot 2\text{H}_2\text{O}$. Adapted from Refs. [84] and [114].

$\text{K}_2\text{Nd}_2\text{Ti}_3\text{O}_{10}$ [111]. A band-gap of 3.5 eV has been estimated for $\text{K}_2\text{La}_2\text{Ti}_3\text{O}_{10}$ from reflectance measurements [139].

Takata et al. [138, 139] and Ikeda et al. [140, 141] investigated $\text{K}_2\text{La}_2\text{Ti}_3\text{O}_{10}$ for photocatalysis. On loading with nickel, the oxide exhibits photocatalytic activity for overall water splitting under band-gap irradiation. The Ni-loading procedure is similar to that described earlier for $\text{K}_4\text{Nb}_6\text{O}_{17}$. The optimum amount of loaded nickel was 3 wt.%, which is considerably different from that for $\text{K}_4\text{Nb}_6\text{O}_{17}$ (0.1 wt.%). The activity depends on the KOH concentration. A 0.1 M concentration of KOH solution was the optimum for this system. Figure 23 shows a typical time course of water decomposition on Ni-loaded $\text{K}_2\text{La}_2\text{Ti}_3\text{O}_{10}$. Table 13 presents the activity data for this compound. Other promoters, such as Pt and RuO_2 , were also examined. However, only Ni was found to be effective.

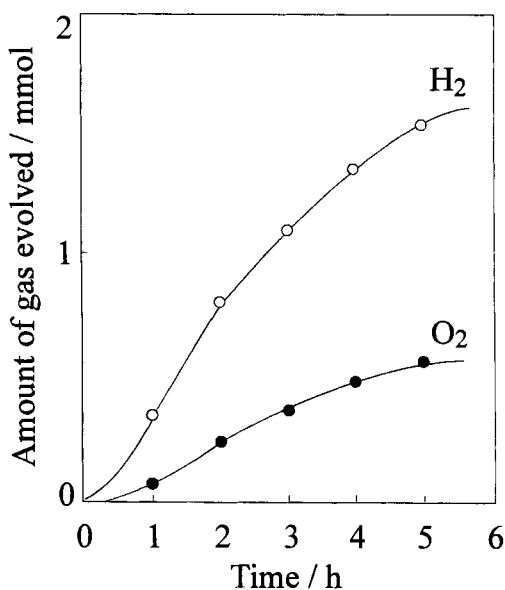


Figure 23. Time course of gas evolution over $\text{K}_2\text{La}_2\text{Ti}_3\text{O}_{10}$ with optimum loading (3.0 wt.% Ni) and optimum KOH concentration (0.1 M). From Ref. [139].

A scanning electron microscopic investigation of the morphology of the Ni-loaded catalysts revealed that most of the Ni was present as small particles on the external surface of the particles. On the basis of this observation, a reaction mechanism has been proposed [138], as depicted in Figure 24. According to this mechanism, electrons and holes are generated in the $\text{La}_2\text{Ti}_3\text{O}_{10}^{2-}$ sheets on band-gap irradiation. The electrons, having higher mobility than holes, migrate on to the external surface reaching the Ni particles where H_2O is reduced to H_2 . The holes travel a much shorter distance and react with water molecules in the interlayer region to generate oxygen.

Analogous compounds, $\text{Rb}_2\text{La}_2\text{Ti}_3\text{O}_{10}$ and $\text{Cs}_2\text{La}_2\text{Ti}_3\text{O}_{10}$, have also been studied for overall water splitting [138]. The optimum Ni loading for these was slightly higher, namely 4 wt.%. The catalytic activity was about twice that of $\text{K}_2\text{La}_2\text{Ti}_3\text{O}_{10}$, as shown in Table 13.

Series with intermediate cation density

Intermediate in interlayer ion density between $\text{KCa}_2\text{Nb}_3\text{O}_{10}$ and $\text{K}_2\text{La}_2\text{Ti}_3\text{O}_{10}$ are compounds of general formula $\text{A}_{2-x}\text{La}_2\text{Ti}_{3-x}\text{Nb}_x\text{O}_{10}$, where the cation density can be varied between the end members [85]. Photocatalysis of $x = 0.5$ members has been studied by Takata et al. [138]. Band-gaps of 3.4–3.5 eV were estimated from reflectance measurements. The photocatalytic activities for H_2O decomposition under UV irradiation are also listed in Table 13.

From the observation that such layered oxides, which undergo easy hydration under normal humidity, are associated with better catalytic activity, it appears that hydration behavior is one of the factors affecting the catalytic activity.

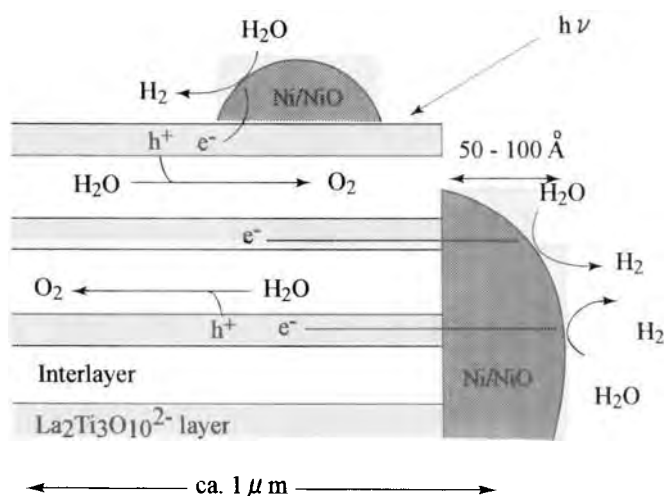


Figure 24. Proposed reaction mechanism for photocatalytic water decomposition on Ni-loaded $\text{K}_2\text{La}_2\text{Ti}_3\text{O}_{10}$. From Ref. [138].

Table 13. Photocatalytic activities of $\text{A}_2\text{La}_2\text{Ti}_3\text{O}_{10}$, $\text{ALa}_2\text{Ti}_2\text{NbO}_{10}$ and $\text{A}_{1.5}\text{La}_2\text{Ti}_{2.5}\text{Nb}_{0.5}\text{O}_{10}$ oxides [138].

Catalyst	Rate of gas evolution/ $\mu\text{mol h}^{-1} \text{g}^{-1}$		Optimum conditions		pH of the solution
	H_2	O_2	Ni loading/ wt.% of Ni	Alkali metal hydroxide concentration/ mol dm^{-3}	
$\text{K}_2\text{La}_2\text{Ti}_3\text{O}_{10}$	444	221	3	0.1	12.8
$\text{Rb}_2\text{La}_2\text{Ti}_3\text{O}_{10}$	869	430	4	0.1	12.8
$\text{Cs}_2\text{La}_2\text{Ti}_3\text{O}_{10}$	700	340	3	0	10.5
$\text{RbLa}_2\text{Ti}_2\text{NbO}_{10}$	49	30	0.3	0.1	12.8
$\text{CsLa}_2\text{Ti}_2\text{NbO}_{10}$	115	50	0.3	0	8.5
$\text{Rb}_{1.5}\text{La}_2\text{Ti}_{2.5}\text{Nb}_{0.5}\text{O}_{10}$	725	358	5	0.1	12.6
$\text{Cs}_{1.5}\text{La}_2\text{Ti}_{2.5}\text{Nb}_{0.5}\text{O}_{10}$	540	265	4	0	10.4

4.3 Clays

Clays are a class of silicates having layered structure, most of which occur in nature. They exhibit interlamellar reactivity, which makes them useful in catalysis. The sheets in clays consist of either two tetrahedral silicate units sandwiching an octahedral unit as in 2:1 clays or one tetrahedral unit joined to one octahedral unit as in 1:1 clays. Of these, 2:1 clays are more common in use.

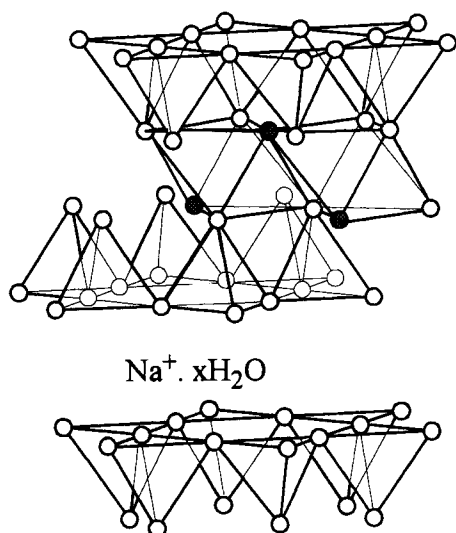


Figure 25. Schematic representation of 2:1 (trioctahedral and dioctahedral) cationic clays.

In 2:1 clays, the octahedral unit may either have all the octahedral sites occupied by metal ions (as in trioctahedral clays) or have only two-thirds of the octahedral sites occupied (as in dioctahedral clays). Talc $[\text{Si}_8\text{Mg}_6\text{O}_{20}(\text{OH})_4]$ and pyrophyllite $[\text{Si}_8\text{Al}_4\text{O}_{20}(\text{OH})_4]$ have representative structures of trioctahedral and dioctahedral clays, respectively. These two clays possess no net charge in their sheets, so they do not have charged species in the interlayer region, hence the name ‘neutral clays’. When the Si^{4+} in the tetrahedral unit and/or metal ions in the octahedral unit (Al^{3+} or Mg^{2+}) are partially substituted by ions of lower charges, the sheets attain a net negative charge. Charge neutrality can be maintained if the structure accommodates an appropriate number of additional cations in the interlayer region. Such clays are called cationic clays. Figure 25 shows a schematic representation of 2:1 (trioctahedral and dioctahedral) cationic clays. The interlayer cations are usually exchangeable with other cations by simple chemical methods. Cationic clays are classified according to the amount of cations present in the interlayer region.

Montmorillonite clay has been used as a host for accommodating photo-responsive species for photocatalytic and photochemical studies. Montmorillonite is a 2:1 dioctahedral cationic clay, which derives its charge in sheets due to partial substitution of Al^{3+} in $\text{Si}_8\text{Al}_4\text{O}_{20}(\text{OH})_4$ by Mg^{2+} . When sodium is present as a charge-compensating cation in the interlayer region, it is known as sodium montmorillonite. The charge may vary between 0.5 to 1.2 per unit cell. Guest species that have been studied include pillars of TiO_2 , Fe_2O_3 , $\text{CdS} + \text{ZnS}$ and several molecular species. Here, the host acts as an inert host in that it does not directly absorb photons in photoreactions.

4.3.1 TiO_2 in Montmorillonite

Yoneyama et al. [142, 143] formed TiO_2 pillars with thickness of about 1.5 nm in the galleries of montmorillonite by intercalation of titania sol followed by decom-

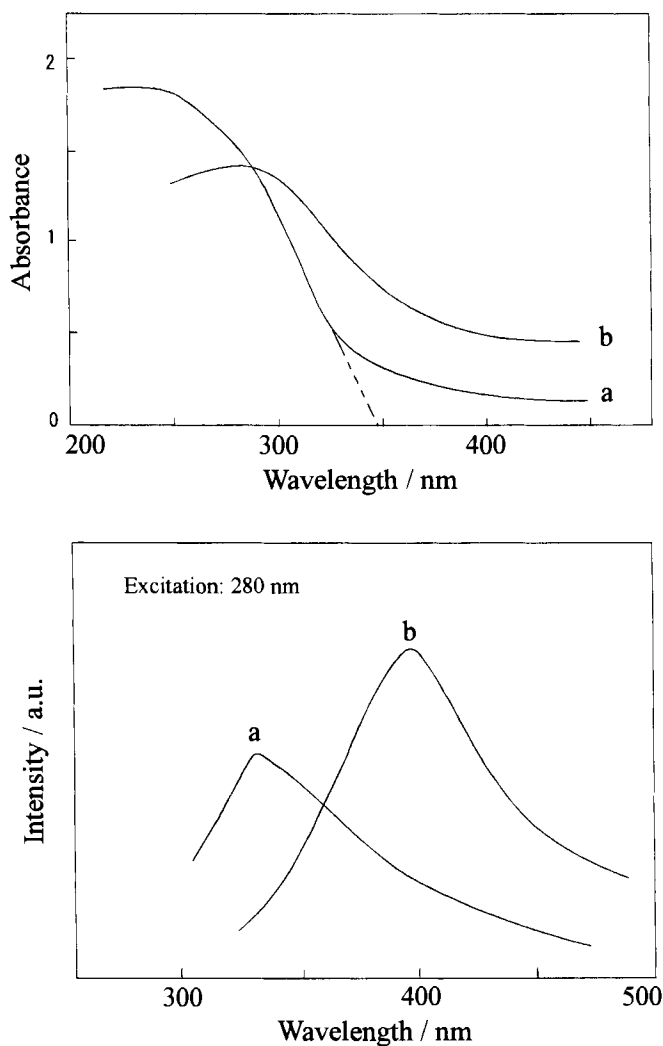


Figure 26. Absorption and fluorescence spectra of aqueous suspensions of (a) TiO₂-clay and (b) TiO₂ powder. Reprinted with permission from H. Yoneyama, S. Haga and S. Yamanaka, *J. Phys. Chem.* **1989**, 93, 4833. Copyright 1989 American Chemical Society.

position according to Yamanaka et al. [144, 145], which increased the surface area from 72 to 347 m² g⁻¹. The weight ratio of TiO₂ to clay was 1:1. The absorption and emission spectra of the TiO₂-clay system were blue shifted with respect to those of TiO₂ powders, indicating a wider band-gap in the TiO₂ pillars. Figure 26 shows the absorption and emission spectra of TiO₂-clay and TiO₂ powders. From the fluorescence blue shift, a band-gap of 3.58 eV was estimated, which is 0.58 eV greater than that of TiO₂ bulk material. This value agreed with their estimation from the absorption threshold (348 nm). From transient photocurrent measurements as a function of pH, the Fermi level of TiO₂-clay and TiO₂ powder were estimated to be -0.64 and -0.28 V vs. SCE, respectively, at pH 0.

Table 14. Photocatalytic decomposition of 2-propanol (reprinted with permission from H. Yoneyama, S. Haga and S. Yamanaka, *J. Phys. Chem.* **1989**, 93, 4833. Copyright 1989 American Chemical Society).

Catalyst	Rate of formation ^a /μmol h ⁻¹				
	H ₂	CH ₄	CO	CO ₂	(CH ₃) ₂ CO
TiO ₂	0.26	0.07	0.07	Trace	0.28
TiO ₂ /clay	1.34	0.35	0.12	0.15	1.4
Pt/TiO ₂ ^b	183	Trace	Trace	Trace	172
Pt/TiO ₂ /clay	697	4.0	Trace	Trace	661

^a Illumination with a 500 W high-pressure mercury arc lamp for 24 h of 3 mg of TiO₂ suspended in 8 ml of 2-propanol containing 0.2 ml of water. The data are given as time-averaged values for 24 h.

^b The amount of loaded Pt was 2 wt.-%.

The photocatalytic activity for decomposition of propanaol and various carboxylic acids has been studied, both with and without Pt loading. The activity of TiO₂-clay was found to be much higher than that of TiO₂ powder. This was attributed to the excited electronic state in pillars being higher by 0.36 eV, which is favorable for hydrogen evolution. Photodecomposition data for 2-propanol and for various acids are listed in Tables 14 and 15. As can be seen, the activity of TiO₂-clay is higher for all the acids except 1-decanoic acid. The lower activity for the latter has been attributed to the interlayer space being too narrow to accommodate large molecules.

4.3.2 Fe₂O₃ in Montmorillonite

Miyoshi and Yoneyama [146] incorporated microcrystals of Fe₂O₃ through insertion of a trinuclear complex of Fe(III) according to Yamanaka et al. [147] and studied the photodecomposition of acetic acid and propionic acid. The pillar height was about 0.66 nm as estimated from XRD. The blue shift in the absorption spectra was about 0.28 eV (Figure 27). Band-gaps of 2.48 and 2.2 eV were estimated for Fe₂O₃-clay and α-Fe₂O₃, respectively, from absorption spectra. Fermi levels at pH 0 were determined to be -0.01 and +0.22 V vs. SCE, respectively, by transient photocurrent measurements. Figure 28 shows the energy diagram. Table 16 and Figure 29 summarize the catalytic performance. Higher activity was observed for n-butyric acid also. As in the case of TiO₂-pillared clay, the higher activity was attributed to an upward shift of the Fermi level of Fe₂O₃ (Figure 28), resulting in increased reducing power.

4.3.3 CdS and ZnS Mixtures in Colloidal Montmorillonite

The mixed semiconductor system ZnS + CdS supported on Nafion films or on SiO₂ is known to liberate hydrogen from Na₂S solutions under visible light irradiation

Table 15. Photocatalytic decomposition of carboxylic acids (reprinted with permission from H. Yoneyama, S. Haga and S. Yamanaka, *J. Phys. Chem.* **1989**, 93, 4833. Copyright 1989 American Chemical Society).

Carboxylic acid	Catalyst	Rate of formation of major products ^a / $\mu\text{mol h}^{-1} \text{ g}^{-1}$		
		Alkane ^b	CO ₂	H ₂
1-Propanoic acid	TiO ₂	19.5	18.5	
	TiO ₂ /clay	44.1	44.9	
	Pt/TiO ₂	66.5	70.0	5.7
	Pt/TiO ₂ /clay	146	162	13.1
Lactic acid	TiO ₂	3.9	3.7	
	TiO ₂ /clay	19.3	20.1	
	Pt/TiO ₂	27.0	29.0	2.8
	Pt/TiO ₂ /clay	84.1	92.3	5.0
1-Octanoic acid	TiO ₂	2.67	2.98	
	TiO ₂ /clay	12.9	14.5	
	Pt/TiO ₂	19.9	19.7	1.9
	Pt/TiO ₂ /clay	54.1	56.6	2.8
1-Decanoic acid	TiO ₂	2.30	2.57	
	TiO ₂ /clay	1.02	1.33	
	Pt/TiO ₂	10.1	9.67	0.8
	Pt/TiO ₂ /clay	4.52	4.81	0.4

^a For experimental conditions, see footnotes a and b in Table 14.

^b With one C atom less than that in the acid.

without Pt, even though, individually, neither ZnS nor CdS is active [148]. Similar results have been reported for this system supported on colloidal montmorillonite clay [149]. Fermi levels were not determined, probably owing to the complex nature of the transient current vs. pH relationship. Comparing this system with the same system supported on SiO₂, it was reported that the activity in clay was about four times smaller.

4.3.4 Photoactive Species Intercalated into Lamellar Oxides

Layered materials serve as good hosts for accommodating photoresponsive molecular species. Ogawa and Kuroda [150] reviewed the photoprocesses in layered hosts.

Photoresponsive electron donor species such as Ru(bpy)₃²⁺ [151–159] and acceptor species such as MV²⁺ (MV = methylviologen) [153, 160] have been intercalated into montmorillonite/kaolin clays. Luminescence of Ru(bpy)₃²⁺ was found to be strongly quenched by lattice Fe³⁺ [152, 154]. A random distribution of quenching sites in the lattice has been proposed [155]. Self-quenching due to segregation has also been reported [153]. The segregation of Ru(bpy)₃²⁺ from co-intercalated

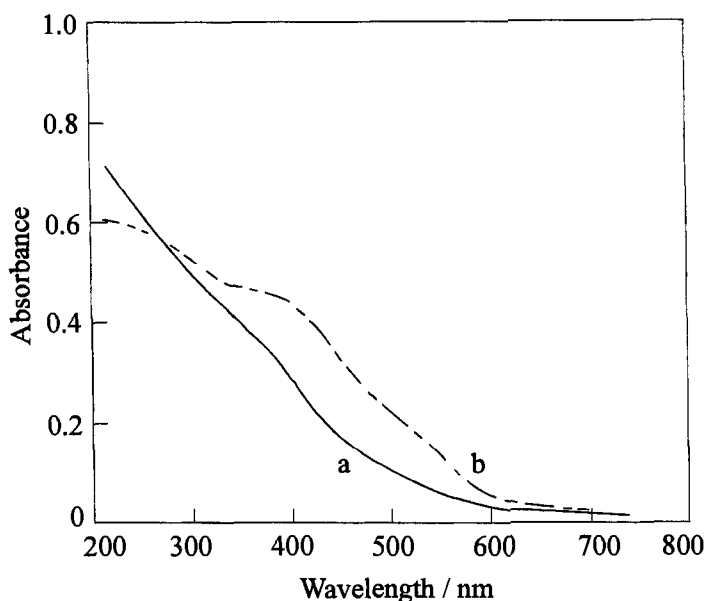


Figure 27. Absorption spectra of aqueous suspensions of (a) Fe_2O_3 -clay and (b) $\alpha\text{-Fe}_2\text{O}_3$. From H. Miyoshi and H. Yoneyama, *J. Chem. Soc., Faraday Trans. 1* **1989**, 85, 1873. Reproduced by permission of the Royal Society of Chemistry.

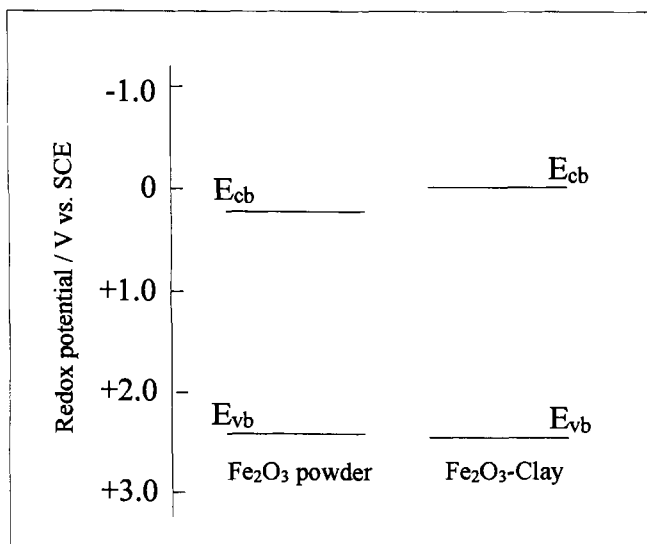


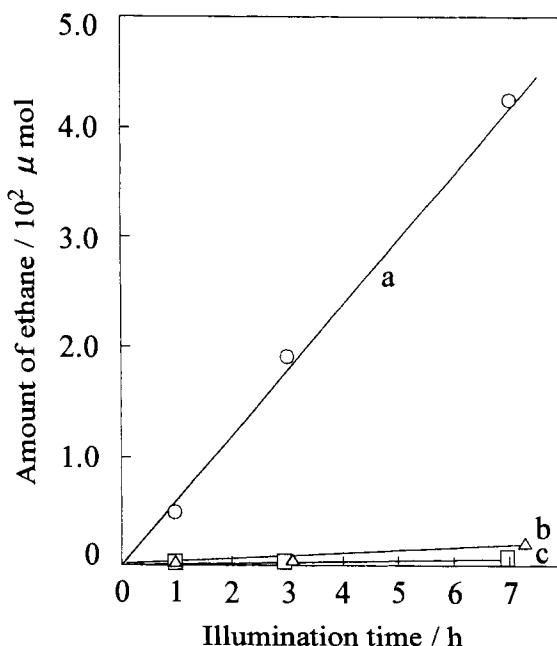
Figure 28. Energy diagram at pH 0 obtained by assuming that the Fermi level is equal to the bottom of the conduction band. From H. Miyoshi and H. Yoneyama, *J. Chem. Soc., Faraday Trans. 1* **1989**, 85, 1873. Reproduced by permission of the Royal Society of Chemistry.

Table 16. Major reaction products (μmol in 15 h) of photo-Kolbe reaction of 1 vol.% Acetic acid^a (from H. Miyoshi and H. Yoneyama, *J. Chem. Soc., Faraday Trans. 1* **1989**, 85, 1873. Reproduced by permission of the Royal Society of Chemistry).

Catalyst	CH ₄	CO ₂	C ₂ H ₆
$\alpha\text{-Fe}_2\text{O}_3$ powder	2.1	2.3	—
Fe ₂ O ₃ -clay	11.7	9.9	0.3

^a Irradiation with light of $\lambda > 330$ nm.

Figure 29. Time course of ethane gas produced by photodecomposition of propanoic acid solution (10 cm^3 of 1 vol.% aq. solution) over (a) Fe₂O₃-clay, (b) $\alpha\text{-Fe}_2\text{O}_3$, 3.6 mg, and (c) clay, 10 mg. From H. Miyoshi and H. Yoneyama, *J. Chem. Soc., Faraday Trans. 1* **1989**, 85, 1873. Reproduced by permission of the Royal Society of Chemistry.



MV²⁺ results in poor quenching by the latter compared with the quenching efficiency in homogeneous solutions. Co-intercalation of photoinactive Zn(bpy)₃²⁺ results in decreased self-quenching due to the random distribution of the luminescent molecules and the inactive molecules [153]. Also, whereas neutral propylviologen sulfonate (PVS) was found to be an effective quencher, MV²⁺ was not [153]. Studies with the aim of understanding racemic interactions between the optically active isomers of Ru(bpy)₃²⁺ have also been reported [156–158]. It may be noted that only 50 % intercalation of Ru(bpy)₃²⁺ occurs when the reactant contains only one isomer, whereas 100 % intercalation proceeds for racemic mixtures. Intercalation with a sequential arrangement of Δ - and Λ -isomers has been proposed for this observation [161, 162].

Hydrogen evolution under visible light irradiation, using triethanolamine as sacrificial electron donor, has been reported for the MV²⁺-clay (montmorillonite and

Table 17. Hydrogen production as a function of MV^{2+} and clay concentration, at Constant ratio (1.67 mmol MV^{2+} g⁻¹ clay) (from G. Villemure, H. Kodama and C. Detellier, *Can. J. Chem.* **1985**, 63, 1139. Reproduced with permission from the National Research Council of Canada).

Concentration of MV^{2+} / 10 ⁻³ M	Clay concentration/ g L ⁻¹	Amount of H ₂ ^a / μmol L ⁻¹ per 20 h
2.5	1.5	3.9
5.0	3.0	5.4
7.5	4.5	4.3
10.0	6.0	6.3

^aOther conditions: $Ru(bpy)_3^{2+}$ (5×10^{-4} M), triethanolamine (0.1 M), pH 7.0, argon atmosphere, 300 W tungsten halogen lamp, $\lambda > 395$ nm.

hectorite) system catalyzed by $Ru(bpy)_3^{2+}$ [163, 164]. The MV^{2+} to clay ratio was three times the cation exchange capacity of the clay. The internal surface was covered exclusively by MV^{2+} whereas the external surface was covered by MV^{2+} and $Ru(bpy)_3^{2+}$ in a 3:1 ratio. The excess MV^{2+} remained in solution. Nine different systems, differing in initial interlayer cations, were studied and the properties were found to be the same for all of these clays. Table 17 gives the results of a typical experiment.

Visible light-induced cleavage of water has been reported for a mixed colloidal clay system consisting of a mixture of sepiolite clay- RuO_2 - $Ru(bpy)_3^{2+}$ colloid (for O₂ production) and $Al_xEu_{1-x}(OH)_3$ -Pt colloid (for H₂ production) [165]. A turn-over number of 20 with respect to the sensitizer, $Ru(bpy)_3^{2+}$, was observed. It was reported that the gas (H₂ + O₂) evolution displayed a damped oscillatory behavior. Photo-oxidation of water by *trans*-diaqabis-(2,2'-bipyridine)ruthenium(2+) adsorbed on the surface of hectorite clay has also been reported [166].

A brief mention about gas evolution at clay modified electrodes, which is desirable in electrocatalysis, was made by Bard and co-workers [167, 168]. It should be noted that metal-bpy complexes and MV^{2+} bound on the internal and external surfaces of montmorillonite clay are *electroinactive*, and only about 15–30 % of the external electroactive species, which probably are present as ion pairs [170], reach the electrode [169].

4.4 Layered Double Hydroxides (LDHs) [171–174]

Layered double hydroxides, also known as anionic clays, belong to a class of lamellar hydroxides with a structure related to that of brucite. A large number of these hydroxides are naturally available and many more have been synthesized in laboratories. The structure of brucite, $Mg(OH)_2$, consists of sheets of edge-connected $Mg(OH)_6$ octahedra, which are held together by means of Van der Waals forces. The sheets have the composition $Mg(OH)_2$, and are electrically neutral.

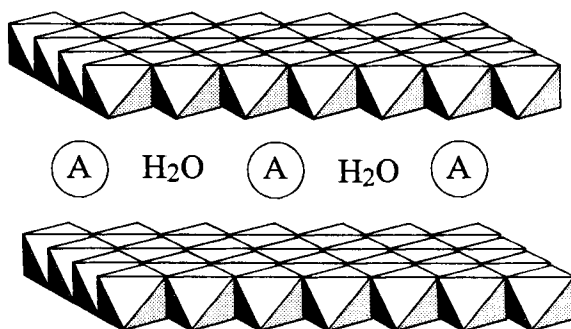


Figure 30. Schematic structure of anionic clays. A represents an anion.

When part of Mg^{2+} is replaced by an ion with higher charge, such as Al^{3+} , the sheets attain a positive charge. Overall charge neutrality is maintained through accommodation of anions in the interlayer region. Thus, substitution of 25 % of Mg^{2+} sites by Al^{3+} and placing CO_3^{2-} cations in the interlayer region, together with water molecules, give the formula $\text{Mg}_{0.75}\text{Al}_{0.25}(\text{OH})_2(\text{CO}_3)_{0.125} \cdot \frac{1}{2}\text{H}_2\text{O}$, which is the ideal composition of the mineral, hydrotalcite. Figure 30 gives a schematic view of the hydrotalcite structure.

The general formula of hydrotalcite-like compounds can be given as $\text{M}^{2+}_{1-x}\text{M}^{3+}_x(\text{OH})_2 \text{A}^{n-}_{x/n} \cdot m\text{H}_2\text{O}$, where $\text{M}^{2+} = \text{Mg}^{2+}, \text{Fe}^{2+}, \text{Co}^{2+}, \text{Ni}^{2+}, \text{Cd}^{2+}, \text{Cu}^{2+}$ or Zn^{2+} , $\text{M}^{3+} = \text{Al}^{3+}, \text{Ga}^{3+}, \text{Cr}^{3+}$ or Fe^{3+} and $\text{A}^{n-} = \text{CO}_3^{2-}, \text{SO}_4^{2-}, \text{OH}^-, \text{F}^-, \text{Cl}^-, \text{Br}^-$ or NO_3^- . The charge density of the hydroxide sheets depends on the $\text{M}^{2+}/\text{M}^{3+}$ ratio. Pure LDHs can be synthesized usually for $0.2 \leq x \leq 0.33$. Two types of stacking sequences of sheets are found, giving 2H and 3R structures. The interlayer anions (except CO_3^{2-}) can easily be exchanged by organic anions (such as carboxylates and sulfonates) and polyoxometallate anions.

4.4.1 Photocatalysis in LDHs Intercalated with CdS and CdS/ZnS

Sato et al. [175] reported on photocatalytic hydrogen evolution by CdS and CdS/ZnS (species obtained by sequential formation of CdS and then ZnS) incorporated into MgAl-LDH. The size of the sulfide particles was estimated to be about 0.3 nm. The optical absorption shows a slight blue shift, e.g. from 2.46 eV for bulk CdS to 2.64 eV for LDH-CdS. Photocatalytic hydrogen evolution was studied by using Na_2S and Na_2SO_3 as sacrificial electron donors. It was found that efficient H_2 evolution takes place in the intercalated system, although at a lower rate than that of the unsupported system, CdS/ZnS. The lower activity has been attributed to the restricted mass transfer in the interlayer region.

4.4.2 Photocatalysis in LDHs Pillared with Polyoxometallates

Polyoxometallates of Mo and W in homogeneous solutions are known to photocatalyze oxidation of alcohols [176, 177]. Such species can be intercalated into

the interlayer galleries of LDHs by ion-exchange reactions giving pillared structures with fairly high surface area. Kwon et al. [178, 179] synthesized several polyoxometallate-pillared LDHs and demonstrated photocatalytic properties for representative cases. Thus $\text{Zn}_2\text{Al}(\text{OH})_6\text{Cl} \cdot 2\text{H}_2\text{O}$ after pillaring with $\text{V}_{10}\text{O}_{29}^{6-}$ and $\text{Zn}_2\text{Al}(\text{OH})_6(\text{NO})_3 \cdot m\text{H}_2\text{O}$ after pillaring with polytungstates ($\text{BV}^{4+}\text{W}_{11}\text{O}_{40}^{11-}$, $\text{SiV}_3\text{W}_9\text{O}_{40}^{7-}$ or $\text{H}_2\text{W}_{12}\text{O}_{40}^{6-}$) oxidize catalytically 2-propanol to acetone under irradiation with light with $\lambda > 390$ nm in an oxygen atmosphere. Turnover numbers of 4–10 have been reported.

4.4.3 LDHs Intercalated with Photoresponsive Species

Robins and Dutta studied MV^{2+} reduction, in the presence of EDTA as sacrificial electron donor, by a *visible* light-excited Zn–porphyrin complex that was intercalated into LDH–tetradecanoate [180]. The rate of formation of viologen radical was higher when propylviologen sulfonate (PVS) was used. When TiO_x on the external surface (formed by hydrolysis of titanium butoxide) was present instead of intercalated Zn–porphyrin complex, UV light ($\lambda = 350$ – 450 nm)-assisted formation of viologen radicals was observed. The system, in which both the Zn complex and TiO_x were present, was also effective in the visible region ($\lambda = 420$ – 650 nm). It is argued on the basis of experimental results that, in this last system, sensitization of TiO_x particles by Zn–porphyrin complex *does* take place.

The luminescent anion $\text{Ru}(\text{BPS})_3^{4-}$ (PBS = 4,7-diphenyl-1,10-phenanthroline disulfonate) was intercalated into MgAl–LDH by Giannelis et al. [181]. Luminescence decay measurements indicated efficient self-quenching of the $\text{Ru}(\text{BPS})_3^{4-}$ emission. On co-intercalation of nonemissive $\text{Zn}(\text{BPS})_3^{4-}$, the self-quenching still persists and is attributed to the segregation of emitting ions. However, at higher concentrations of the Zn complex ($\text{Ru}:\text{Zn} = 1:9$), the emission kinetics of $\text{Ru}(\text{BPS})_3^{4-}$ were similar to the kinetics in solutions, indicating sufficient separation of emitting molecules in the galleries.

4.5 Artificially Built Multilayer Systems

Artificially built layered structures consisting of several components are attractive systems of interest in solid-state microelectronics, electrochemistry and catalysis [182, 183]. At present, artificial building has reached the level of incorporating desired species in a desired layer to obtain predictable properties [184, 185].

The deposition of molecular films on solid substrates was initially of the Langmuir–Blodgett type [186, 187], where layers preformed on a liquid–air interface are carefully transferred on to a solid surface. The difficulties associated with deposition of LB films are overcome in systems where molecules from a solution phase assemble themselves on a solid surface in the form of a one molecule thick film. If the interaction between the head groups of the molecules with the substrate surface is of the covalent type, as in the case of surface silanization [188, 189], then we can expect the film to be mechanically robust.

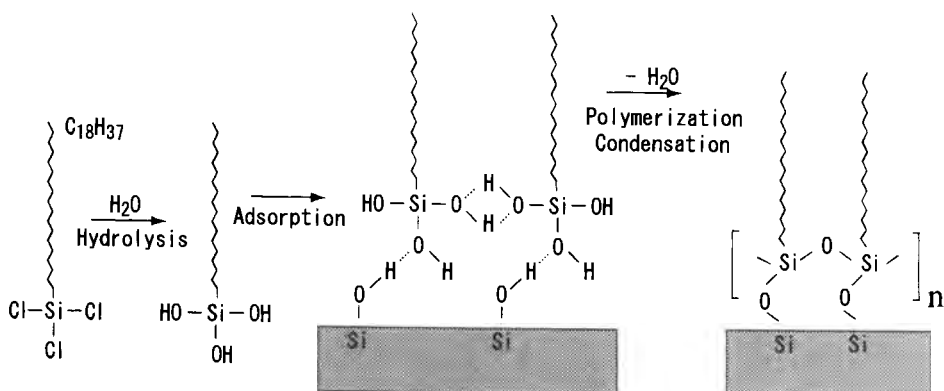


Figure 31. Chemisorption of *n*-octadecyltrichlorosilane on a glass slide. Reprinted with permission from J. Sagiv, *J. Am. Chem. Soc.* **1980**, 102, 92. Copyright 1980 American Chemical Society.

Various types of substrates have been used for layer deposition. Materials used as substrates include glass [188], SnO_2 [190], Al [188], Pt [191] and Au [192, 193]. In the case of glass or SiO_2 , the substrate surface is treated with alkylsilanes to form a 'primer' coating (anchor layer) on the surface. When gold is used as the substrate, thiols are found to be suitable for the anchor layer. Figure 31 shows the proposed bonding scheme for chemisorption of *n*-alkyltrichlorosilane on a silica glass surface.

Films grown in this manner are usually characterized by techniques such as ellipsometry, atomic force microscopy (AFM) and cyclic voltammetry. Ellipsometry gives the thickness of the layers and AFM the surface uniformity. Cyclic voltammetric measurements can give information about electron transfer across the film.

Once the anchoring layer has been deposited, a second layer can be grown on top of this layer when the tails of the molecules in the first layer are functionalized to link covalently to the head groups of the molecules in the second layer [189]. Figure 32 shows the scheme of formation of zirconyl phosphate layers. By repeating the deposition steps, such as steps 2 and 3 in Figure 32, a number of times, it is possible to deposit multilayer films [182, 183, 194].

Instead of covalent binding, an ionic bonding scheme can also be used. Thus, thin films of polymeric species are deposited by this method [195] (Figure 33).

Two-component systems, where one of the components is a polymeric film and the other is a clay sheet [196, 197], $\alpha\text{-ZrP}$, $[\text{Ti}_2\text{NbO}_7]^-$, $[\text{K}_2\text{Nb}_6\text{O}_{17}]^{2-}$ sheet [198], $[\text{Ca}_2\text{Nb}_3\text{O}_{10}]^-$ sheet [199] or graphite sheet [200], have been built. A combined ionic and covalent scheme can also be used as demonstrated [201] (Figure 34).

4.5.1 Towards Photoinduced Charge Separation

When viologens (MV^{2+}) are incorporated as part of the zirconium phosphate layers, and the resulting films are irradiated with solar radiation, stable viologen radicals

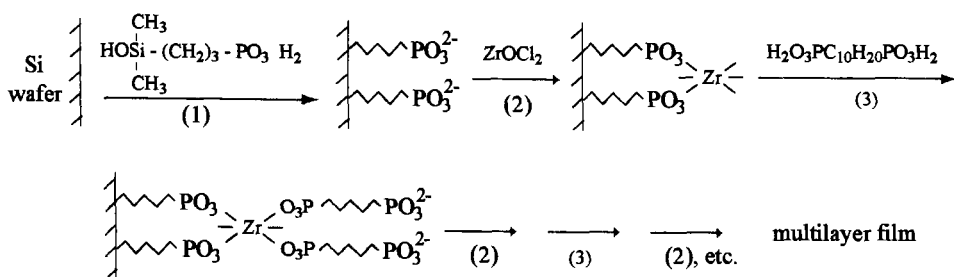


Figure 32. Scheme describing the steps in the formation of multilayer α -zirconyl phosphonate film. Reprinted with permission from H. Lee, L.J. Kepley, H.-G. Hong and T.E. Mallouk, *J. Am. Chem. Soc.* **1988**, 110, 618. Copyright 1988 American Chemical Society.

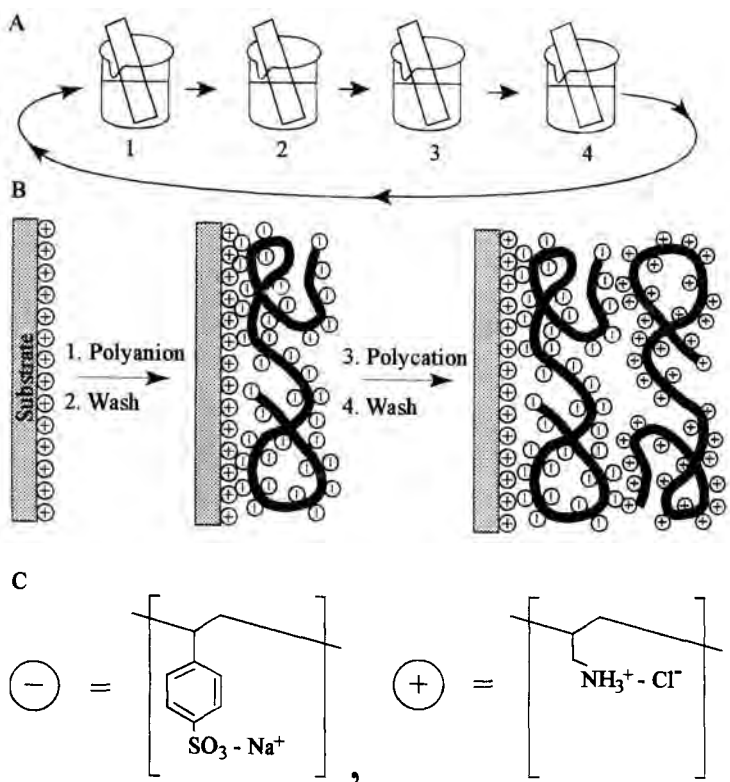


Figure 33. (A) Schematic representation of the deposition process using slides and beakers. Steps 1 and 3 represent the adsorption of a polyanion and polycation respectively and steps 2 and 4 are washing steps. (B) Simplified molecular picture of first two adsorption steps. (C) Structures of typical polyions. Reprinted with permission from G. Decher, *Science* **1997**, 277, 1232. Copyright 1997 American Association for the Advancement of Science.

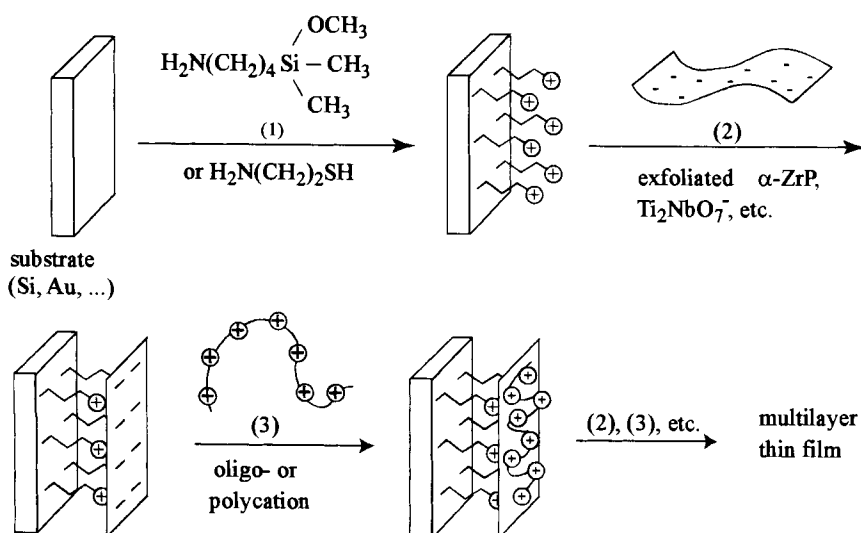


Figure 34. Sequential adsorption scheme for producing multilayer films by alternate adsorption of inorganic two-dimensional anions and oligomeric or polymeric cations. Reprinted with permission from S.W. Keller, H.-N. Kim and T.E. Mallouk, *J. Am. Chem. Soc.* **1994**, 116, 8817. Copyright 1994 American Chemical Society.

are produced, possibly by electron transfer from halide (Cl^- or Br^-) to MV^{2+} [202]. When porphyrins and viologens were incorporated as above in separate layers and irradiated with the excitation of porphyrin, the fluorescence of photoexcited porphyrin was quenched, indicating charge transfer from porphyrin donor to MV^{2+} acceptor [203]. In other methods, donor and acceptor species have been embedded in the multilayer films using the ability of polymeric ions to form monolayer films. For example, polymeric allylamine hydrochloride (PAH) was tagged with donor fluorescein (FI) and acceptor Rhodamine B (RHB) and the two species were confined to separate layers by sequential adsorption, with or without intermediate α -zirconium phosphate spacer layers [204]. Table 18 lists some such assemblies.

In steady-state fluorescence emission studies of these systems, good agreement between the experimental and theoretically calculated energy transfer efficiencies has been observed (Table 18), which indicates that the efficiencies in these systems are predictable. This is highly desirable in designing systems with high efficiencies.

Such multilayer systems can also be assembled on nonflat surfaces [185, 205]. Figure 35 shows the building scheme of a heterostructure on silica particles. In this case, MDESA-mediated electron transfer from Ru^{2+} to MV^{2+} proceeds through the following steps:

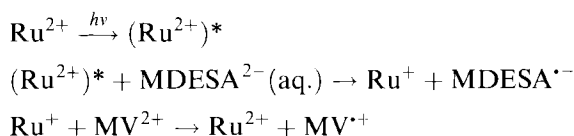
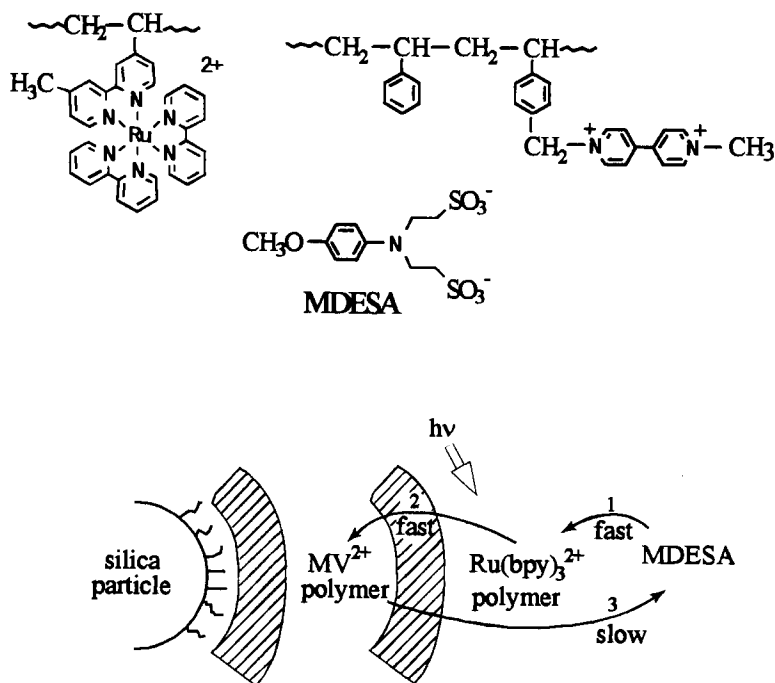


Table 18. Comparison of measured and calculated energy transfer efficiencies for different donor-acceptor geometries of multilayer assemblies (reprinted with permission from D. M. Kaschak and T. E. Mallouk, *J. Am. Chem. Soc.* **1996**, 118, 4222. Copyright 1996 American Chemical Society).

System ^a	χ measured (calculated)
RhB	0.89 (0.90)
RhB/FI/RhB	0.82 (0.81)
RhB/RhB/FI	0.72 (0.73)
RhB/PAH/FI/PAH/RhB	0.39 (0.41)
RhB/PAH/PAH/FI/PAH/PAH	0.13 (0.11)
RhB	
RhB/FI	0.62 (0.70)
RhB/PAH/FI	0.19 (0.27)
RhB/PAH/PAH/FI	0.05 (0.06)
RhB/RhB/FI/FI	0.35 (0.36)

^a A solidus (/) denotes an α -ZrP layer.**Figure 35.** Schematic representation of the $\text{Ru}(\text{bpy})_3^{2+}/\alpha\text{-ZrP/viologen}$ 'onion' structure grown on colloidal silica particles. The sequence of fast (1, 2) and slow (3) electron-transfer steps that follow photoexcitation of $\text{Ru}(\text{Me-vpy})(\text{bpy})_2^{2+}$ polymer is shown. Reproduced from D.M. Kaschak, S.A. Johnson, C.C. Waraksa, J. Pogue and T.E. Mallouk, *Coord. Chem. Rev.* **1999**, 185–186, 403, with permission from Elsevier Science.

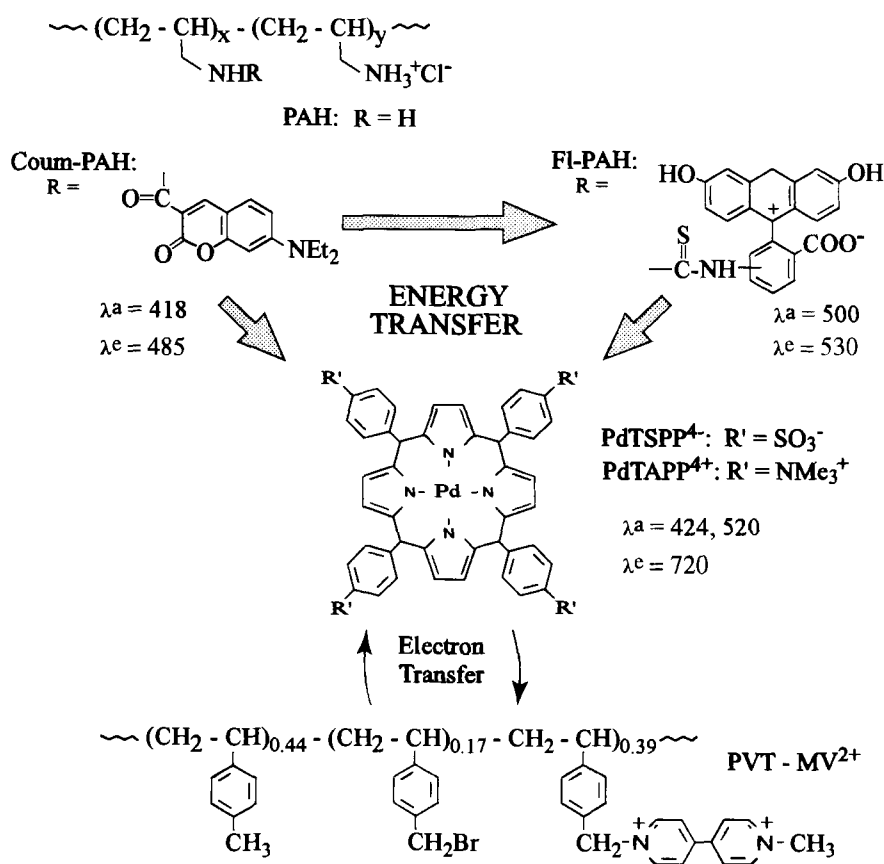


Figure 36. Energy and electron-transfer pathways (indicated by arrows) for the energy 'antenna' polymers Coum-PAH and Fl-PAH, the photosensitizers PdTAPP⁴⁺ and PdTSPP⁴⁻ and the electron-acceptor polymer PVT-MV²⁺. Reprinted with permission from D.M. Kaschak, J.T. Lean, C.C. Waraksa, G.B. Saupe, H. Usami and T.E. Mallouk, *J. Am. Chem. Soc.* **1999**, 121, 3435. Copyright 1999 American Chemical Society.

A multilayer system for photon harvesting from a wider region of visible light and to form a long-lived charge-separated state was built by Mallouk and co-workers [184, 185]. Two typical layer sequences are shown in Figures 37 and 38. In this system, coumarin, fluorescein, Pd-porphyrin and MV²⁺ (Figure 36) form an energy-harvesting chromophore group making a donor-acceptor sequence.

Molecules of chromophores were attached to appropriate ionic polymers to allow their confinement in desired layers. Good spectral overlap between donor emission and acceptor absorption spectra permits efficient energy transfer in the supramolecular assembly. Figure 36 summarizes the spectral characteristics of the four photoactive species [184]. The coumarin polymer (Coum-PAH) absorbs in the blue region of the visible spectrum ($\lambda_{\text{max}} = 412 \text{ nm}$), and its emission maximum, 485 nm,

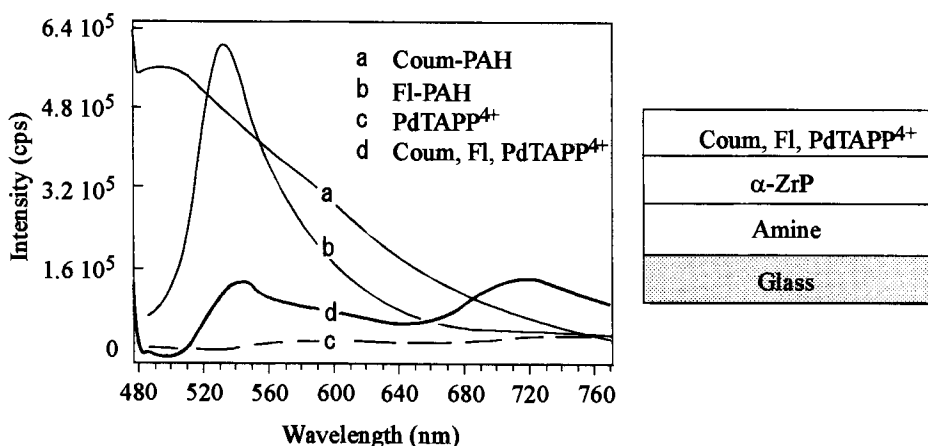


Figure 37. Steady-state emission spectra ($\lambda_{\text{ex}} = 450$ nm) of adsorbed monolayers of Coum-PAH and FI-PAH polycations, PdTAPP⁴⁺ and the co-adsorbed coumarin–fluorescein–porphyrin triad. Reproduced from D.M. Kaschak, S.A. Johnson, C.C. Waraksa, J. Pogue and T.E. Mallouk, *Coord. Chem. Rev.* **1999**, 185–186, 403, with permission from Elsevier Science.

coincides with the intense absorption band of the fluorescein polymer, FI-PAH ($\lambda_{\text{max}} = 500$ nm). The Coum-PAH emission also overlaps with the Q-band absorptions of porphyrin molecules. The emission maximum of FI-PAH (530 nm) completely overlaps the porphyrin Q-band absorbance maximum. In addition, porphyrins have a strong Soret absorbance band in the blue region. Together, these three chromophores are strong absorbers in the 380–530 nm region. The PVT–MV²⁺ polymer does not absorb in the visible region and so does not participate in the energy-transfer sequence. However, MV²⁺ is a good electron acceptor and is capable of accepting an electron from excited porphyrins.

In Figure 37, the photon-absorbing species are co-adsorbed in a single layer and the electron acceptor species is not present. Figure 37 also shows the emission spectra of the multilayer system, for exciting in the coumarin absorption band ($\lambda = 450$ nm). Luminescence spectra of single-component systems are also included. It is seen that efficient energy transfer takes place in this assembly: there is nearly complete quenching of the coumarin emission at 485 nm, substantial quenching of fluorescein emission at 530 nm and greatly enhanced porphyrin emission at 720 nm, with reference to individual emissions. The energy transfer quantum efficiency (χ) is 0.81 for this system. When the antenna molecules were placed in separate layers, χ was equal to 0.65.

Addition of an inorganic sheet and a PVT–MV²⁺ layer results in efficient quenching of the porphyrin phosphorescence at 720 nm, due to electron transfer from excited porphyrin to MV²⁺. Electron-transfer quantum yields were calculated as 0.58 and 0.76 for α -ZrP and HTiNbO₅ spacers, respectively. Figure 38 shows the steady-state emission spectrum of such a multilayer system.

Spectroscopic transient-state measurements indicate fast, biexponential electron transfer from porphyrin to MV²⁺, with either α -ZrP or HTiNbO₅ spacer sheets

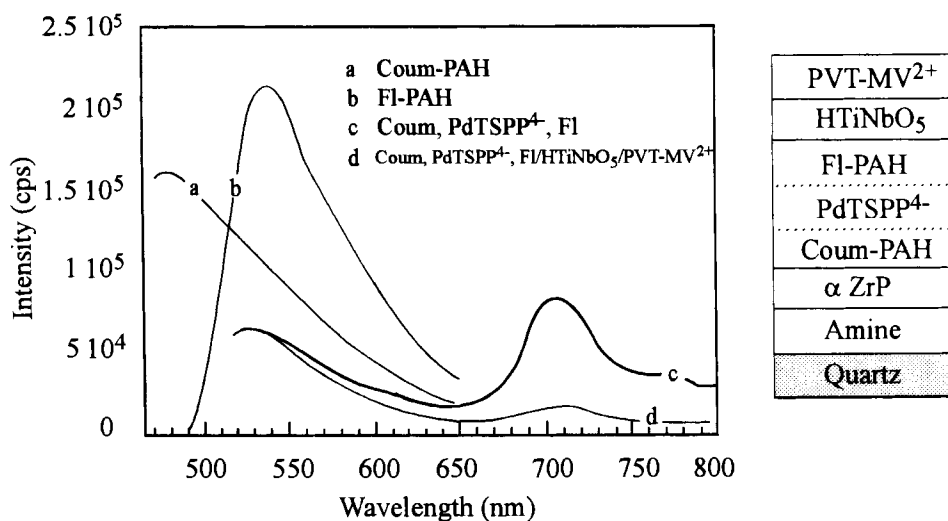


Figure 38. Emission spectra ($\lambda_{\text{ex}} = 450$ nm) of the photon-harvesting assembly having an electron-receiving PVT-MV²⁺ layer. Reprinted with permission from D.M. Kaschak, J.T. Lean, C.C. Waraksa, G.B. Saupe, H. Usami and T.E. Mallouk, *J. Am. Chem. Soc.* **1999**, 121, 3435. Copyright 1999 American Chemical Society.

(Figure 38). Of these, the HTiNbO₅ spacer efficiently blocks the reverse electron transfer.

4.6 Conclusion

Layered oxide systems belonging to different structural families, such as KTiNbO₅-type oxides, perovskite-related oxides, cationic clays and layered double hydroxides, provide a large number of materials with interlayer reactivity which can be employed in electron-transfer applications. In each of these families, the chemical composition of the systems can be varied without altering the main structural features, which provides a route for varying the composition-dependent properties such as acidity and hydration. Perovskite-related layered oxides are especially useful in this regard since an appropriate choice of cations can be made in octahedral and cubo-octahedral sites, in addition to interlayer sites. Also, vacancies can be accommodated in cubo-octahedral sites, interlayer sites and oxygen sites. This gives additional parameters, which can be varied in order to obtain desired material properties. Some of these oxides, and also other layered oxides, have already been used as electron-transfer systems as described in this chapter. The photogenerated electrons and holes have successfully been used for decomposing water into hydrogen and oxygen.

The photon absorption efficiency of the oxides can be greatly enhanced by the adsorption of organic dye molecules on the surface of the oxides. Such sensitized systems are promising in giving efficient electron-transfer systems.

Exploiting the weak interlayer chemical bonding in these oxides, the structures can be broken to form single sheets, as in exfoliation, where the two-dimensional structural integrity of the sheets is still retained. Such exfoliated sheets can be re-assembled by employing a layer-by-layer deposition technique together with other inorganic or organic layers in a desired sequence. Such techniques may be employed in designing and testing new application-oriented systems.

References

1. B. Raveau, *Rev. Chim. Miner.* **1984**, 21, 391.
2. B. Raveau, *Rev. Inorg. Chem.* **1987**, 9, 37.
3. A.F. Wells, *Structural Inorganic Chemistry*, 3rd edn., Clarendon, Press, Oxford, **1962**, pp. 383 and 499.
4. K. Nassau, J.W. Shiever and J.L. Bernstein, *J. Electrochem. Soc.* **1969**, 116, 348.
5. M. Gasperin and M.T. Le Bihan, *J. Solid State Chem.* **1982**, 43, 346.
6. Y. Kim, S.J. Atherton, E.S. Brigham and T.E. Mallouk, *J. Phys. Chem.* **1993**, 97, 11802.
7. A. Kudo, A. Tanaka, K. Domen, K. Maruya, K. Aika and T. Onishi, *J. Catal.* **1988**, 111, 67.
8. K. Sayama, H. Arakawa and K. Domen, *Catal. Today* **1996**, 28, 175.
9. M. Gasperin and M.-T. Le Bihan, *J. Solid State Chem.* **1980**, 33, 83.
10. A. Kudo, T. Shibata and H. Kato, *Chem. Lett.* **1999**, 959.
11. K. Domen, A. Kudo, A. Shinozaki, A. Tanaka, K. Maruya and T. Onishi, *J. Chem. Soc., Chem. Commun.* **1986**, 356.
12. K. Domen, A. Kudo, M. Shibata, A. Tanaka, K. Maruya and T. Onishi, *J. Chem. Soc., Chem. Commun.* **1986**, 1706.
13. K. Domen, J. Yoshimura, T. Sekine, A. Tanaka and T. Onishi, *Catal. Lett.* **1990**, 4, 339.
14. K. Domen, A. Kudo, A. Tanaka and T. Onishi, *Catal. Today* **1990**, 8, 77.
15. A. Kudo, K. Sayama, A. Tanaka, K. Asakura, K. Domen, K. Maruya and T. Onishi, *J. Catal.* **1989**, 120, 337.
16. S. Ikeda, A. Tanaka, K. Shinohara, M. Hara, J.N. Kondo, K. Maruya and K. Domen, *Microporous Mater.* **1997**, 9, 253.
17. K. Sayama, A. Tanaka, K. Domen, K. Maruya and T. Onishi, *Catal. Lett.* **1990**, 4, 217.
18. A. Kudo, K. Domen, K. Maruya and T. Onishi, *J. Catal.* **1992**, 135, 300.
19. K. Sayama, A. Tanaka, K. Domen, K. Maruya and T. Onishi, *J. Phys. Chem.* **1991**, 95, 1345.
20. T. Ishihara, H. Nishiguchi, K. Fukamachi and Y. Takita, *J. Phys. Chem. B* **1999**, 103, 1.
21. R. Abe, K. Shinohara, A. Tanaka, M. Hara, J.N. Kondo and K. Domen, *J. Mater. Res.* **1998**, 13, 861.
22. K. Domen, Y. Ebina, S. Ikeda, A. Tanaka, J.N. Kondo and K. Maruya, *Catal. Today* **1996**, 28, 167.
23. T. Sato, Y. Yamamoto, Y. Fujishiro and S. Uchida, *J. Chem. Soc., Faraday Trans.* **1996**, 92, 5089.
24. Y. Fujishiro, S. Uchida and T. Sato, *J. Inorg. Mater.* **1999**, 1, 67.
25. S. Uchida, Y. Yamamoto, Y. Fujishiro, A. Watanabe, O. Ito and T. Sato, *J. Chem. Soc., Faraday Trans.* **1997**, 93, 3229.
26. Y. Kim, S. Salim, M.J. Huq and T. E. Mallouk, *J. Am. Chem. Soc.* **1991**, 113, 9561.
27. A. Kameyama, K. Domen, K. Maruya, T. Endo and T. Onishi, *J. Mol. Catal.* **1990**, 58, 205.
28. T. Nakato, K. Kuroda and C. Kato, *J. Chem. Soc., Chem. Commun.* **1989**, 1144.
29. T. Nakato, Y. Sugahara, K. Kuroda and C. Kato, *Mater. Res. Soc. Symp. Proc.* **1991**, 233, 169.
30. T. Nakato, K. Kuroda and C. Kato, *Chem. Mater.* **1992**, 4, 128.

31. T. Nakato, K. Kuroda and C. Kato, *Catal. Today* **1993**, 16, 471.
32. M. Yanagisawa, S. Uchida, Y. Fujishiro and T. Sato, *J. Mater. Chem.* **1998**, 8, 2835.
33. J. Yoshimura, A. Kudo, A. Tanaka, K. Domen, K. Maruya and T. Onishi, *Chem. Phys. Lett.* **1988**, 147, 401.
34. A. Reisman and F. Holtzberg, *J. Am. Chem. Soc.* **1955**, 77, 2115.
35. M. Kestigian, F.D. Leipziger, J.R. Carter and F.G. Garabedian, *J. Am. Ceram. Soc.* **1966**, 49, 517.
36. S. Uchida, Y. Inoue, Y. Fujishiro and T. Sato, *J. Mater. Sci.* **1998**, 33, 5125.
37. N. Kinomura, N. Kumada and F. Muto, *J. Chem. Soc., Dalton Trans.* **1985**, 2349.
38. A. Kudo and T. Sakata, *J. Phys. Chem.* **1996**, 100, 17323.
39. A. Kudo and T. Sakata, *Chem. Lett.* **1994**, 2179.
40. G. Lagaly and K. Beneke, *J. Inorg. Nucl. Chem.* **1976**, 38, 1513.
41. S. Tabata, unpublished results.
42. J.A. Sanz-Garcia, E. Dieguez and C. Zaldo, *Phys. Status Solidi* **1988**, 108, K145.
43. S. Tabata, M. Ippommatsu, S. Nakabayashi and K. Domen, unpublished results.
44. A. Verbaere and M. Tournoux, *Bull. Soc. Chim. Fr.* **1973**, 1237.
45. M. Hervieu, H. Rebbah, G. Desgardin and B. Raveau, *J. Solid State Chem.* **1980**, 35, 200.
46. A. Grandin, M.M. Borel, G. Desgardin and B. Raveau, *Rev. Chim. Miner.* **1981**, 18, 322.
47. H. Rebbah, G. Desgardin and B. Raveau, *Mater. Res. Bull.* **1979**, 14, 1125.
48. A. Grandin, M.M. Borel and B. Raveau, *Mater. Res. Bull.* **1985**, 20, 1279.
49. P. Clement and R. Marchand, *C.R. Acad. Sci., Ser. II* **1983**, 296, 1161.
50. H. Rebbah, M. Hervieu and B. Raveau, *Ann. Chim. Fr.* **1981**, 6, 653.
51. H. Rebbah, M.M. Borel and B. Raveau, *Mater. Res. Bull.* **1980**, 15, 317.
52. A. Grandin, M.M. Borel and B. Raveau, *J. Solid State Chem.* **1985**, 60, 366.
53. H. Rebbah, M.-M. Borel, M. Bernard and B. Raveau, *Rev. Chim. Miner.* **1981**, 18, 109.
54. S. Kikkawa and M. Koizumi, *Mater. Res. Bull.* **1980**, 15, 533.
55. A. Weiss and A. Weiss, *Angew. Chem.* **1960**, 72, 413.
56. A. Kudo and T. Kondo, *J. Mater. Chem.* **1997**, 7, 777.
57. A. Kudo and E. Kaneko, *Microporous Mesoporous Mater.* **1998**, 21, 615.
58. A.F. Reid, W.G. Mumme and A.D. Wadsley, *Acta Crystallogr. B* **1968**, 34, 1228.
59. D. Groult, C. Mercey and B. Raveau, *J. Solid State Chem.* **1980**, 32, 289.
60. I.E. Grey, C. Li, I.C. Madsen and J.A. Watts, *J. Solid State Chem.* **1987**, 66, 7.
61. Y. Inoue, T. Kubokawa and K. Sato, *J. Phys. Chem.* **1991**, 95, 4059.
62. M. Dion, Y. Piffard and M. Tournoux, *J. Inorg. Nucl. Chem.* **1978**, 40, 917.
63. R. Marchand, L. Brohan, R. M'bedi and M. Tournoux, *Rev. Chim. Miner.* **1984**, 21, 476.
64. M. Shibata, A. Kudo, A. Tanaka, K. Domen, K. Maruya and T. Onishi, *Chem. Lett.* **1987**, 1017.
65. S. Zheng, D. Yin, W. Miao and G.K. Anderson, *J. Photochem. Photobiol. A: Chem.* **1998**, 117, 105.
66. H. Izawa, S. Kikkawa and M. Koizumi, *J. Phys. Chem.* **1982**, 86, 5023.
67. C.H. Mahler, B.L. Cushing, J.N. Lalena and J.B. Wiley, *Mater. Res. Bull.* **1998**, 33, 1581.
68. T. Sasaki, M. Watanabe, Y. Komatsu and Y. Fujiki, *Inorg. Chem.* **1985**, 24, 2265.
69. H. Miyata, Y. Sugahara, K. Kuroda and C. Kato, *J. Chem. Soc., Faraday Trans. I* **1988**, 84, 2677.
70. S. Andersson and A.D. Wadsley, *Acta Crystallogr.* **1961**, 14, 1245.
71. S. Ogura, M. Kohno, K. Sato and Y. Inoue, *J. Mater. Chem.* **1998**, 8, 2335.
72. T. Sekine, J. Yoshimura, A. Tanaka, K. Domen, K. Maruya, and T. Onishi, *Bull. Chem. Soc. Jpn.* **1990**, 63, 2107.
73. M. Hervieu and B. Raveau, *J. Solid State Chem.* **1980**, 32, 161.
74. H. Rebbah, M. Hervieu and B. Raveau, *Mater. Res. Bull.* **1981**, 16, 149.
75. A.D. Wadsley, *Acta Crystallogr.* **1964**, 17, 623.
76. H. Takahashi, M. Kakihana, Y. Yamashita, K. Yoshida, S. Ikeda, M. Hara and K. Domen, *J. Alloys Compd.* **1999**, 285, 77.
77. H. Rebbah, G. Desgardin and B. Raveau, *Solid State Chem.* **1980**, 31, 321.
78. T. Nakato, H. Miyata, K. Kuroda and C. Kato, *Solids*, **1988**, 6, 231.
79. P.M. Gasperin, *Acta Crystallogr. B* **1982**, 38, 2024.

80. R. Nedjar, M.M. Borel and B. Raveau, *Mater. Res. Bull.* **1985**, 20, 1291.
81. S. Anderson and A.D. Wadsley, *Nature*, **1960**, 187, 499;
S. Anderson and A.D. Wadsley, *Acta Chem. Scand.* **1961**, 15, 14.
82. M. Dion, M. Ganne and M. Tournoux, *Mater. Res. Bull.* **1981**, 16, 1429.
83. M. Gondrand and J.-C. Joubert, *Rev. Chim. Miner.* **1987**, 24, 33.
84. J. Gopalakrishnan and V. Bhat, *Inorg. Chem.* **1987**, 26, 4299.
85. S. Uma, A.R. Raju and J. Gopalakrishnan, *J. Mater. Chem.* **1993**, 3, 709.
86. M. Dion, M. Ganne and M. Tournoux, *Rev. Chim. Miner.* **1986**, 23, 61.
87. K. Toda, T. Teranishi, Z.-G. Ye, M. Sato and Y. Hinatsu, *Mater. Res. Bull.* **1999**, 34, 971.
88. J. Gopalakrishnan, V. Bhat and B. Raveau, *Mater. Res. Bull.* **1987**, 22, 413.
89. M. Sato, J. Abo and T. Jin, *Solid State Ionics* **1992**, 57, 285.
90. M. Sato, J. Watanabe and K. Uematsu, *J. Solid State Chem.* **1993**, 107, 460.
91. M. Sato, J. Abo, T. Jin and M. Ohta, *J. Alloys Compd.* **1993**, 192, 81.
92. K. Toda, T. Honma, Z.-G. Ye and M. Sato, *J. Alloys Compd.* **1997**, 249, 256.
93. K. Toda and M. Sato, *J. Mater. Chem.* **1996**, 6, 1067.
94. K. Toda, T. Suzuki and M. Sato, *Solid State Ionics* **1997**, 93, 177.
95. M.A. Subramanian, J. Gopalakrishnan and A.W. Sleight, *Mater. Res. Bull.* **1988**, 23, 837.
96. A.J. Jacobson, J.W. Johnson and J.T. Lewandowski, *Inorg. Chem.* **1985**, 24, 3727.
97. K. Toda, T. Teranishi, M. Takahashi, Z.-G. Ye and M. Sato, *Solid State Ionics* **1998**, 113–115, 501.
98. M. Dion, M. Ganne, M. Tournoux and J. Ravez, *Rev. Chim. Miner.* **1984**, 21, 92.
99. A.J. Jacobson, J.T. Lewandowski and J.W. Johnson, *J. Less Common Met.*, **1986**, 116, 137.
100. A.J. Jacobson, J.T. Lewandowski and J.W. Johnson, *Mater. Res. Bull.* **1990**, 25, 679.
101. J. Gopalakrishnan, S. Uma and V. Bhat, *Chem. Mater.* **1993**, 5, 132.
102. K. Toda, T. Teranishi, Z.-G. Ye, M. Sato and Y. Hinatsu, *Mater. Res. Bull.* **1999**, 34, 971.
103. R.A. Mohan Ram and A. Clearfield, *J. Solid State Chem.* **1991**, 94, 45.
104. J. Gopalakrishnan, T. Sivakumar, V. Thangadurai and G.N. Subbanna, *Inorg. Chem.* **1999**, 38, 2802.
105. K. Toda, Y. Kameo, M. Ohta and M. Sato, *J. Alloys Compd.* **1995**, 218, 228.
106. G. Blasse, *J. Inorg. Nucl. Chem.* **1968**, 30, 656.
107. G. Blasse and G.P.M. Van Den Heuvel, *J. Solid State Chem.* **1974**, 10, 206.
108. K. Toda, Y. Kameo, S. Kurita and M. Sato, *J. Alloys Compd.* **1996**, 234, 19.
109. P.A.M. Berdowski and G. Blasse, *J. Lumin.* **1984**, 29, 243.
110. M.P. Crosnier-Lopez, H. Duroy and J.L. Fourquet, *Mater. Res. Bull.* **1999**, 34, 179.
111. M. Richard, L. Brohan and M. Tournoux, *J. Solid State Chem.* **1994**, 112, 345.
112. A.J. Wright and C. Greaves, *J. Mater. Chem.* **1996**, 6, 1823.
113. K. Toda, J. Watanabe and M. Sato, *Solid State Ionics* **1996**, 90, 15.
114. K. Toda, J. Watanabe and M. Sato, *Mater. Res. Bull.* **1996**, 31, 1427.
115. N.S.P. Bhuvanesh, M.P. Crosnier-Lopez, O. Bohnke, J. Emery and J.L. Fourquet, *Chem. Mater.* **1999**, 11, 634.
116. S. Uma and J. Gopalakrishnan, *J. Solid State Chem.* **1993**, 102, 332.
117. J. Gopalakrishnan, S. Uma, N.Y. Vasanthacharya and G. N. Subbanna, *J. Am. Chem. Soc.* **1995**, 117, 2353.
118. S. Uma and J. Gopalakrishnan, *Chem. Mater.* **1994**, 6, 907.
119. B.L. Cushing and J.B. Wiley, *Mater. Res. Bull.* **1999**, 34, 271.
120. T. Matsuda, T. Fujita, N. Miyamae, M. Takeuchi and I. Kunou, *J. Mater. Chem.* **1994**, 4, 955.
121. K.-A. Hyeon and S.-H. Byeon, *Chem Mater.* **1999**, 11, 352.
122. R. Jones and W.R. McKinnon, *Solid State Ionics* **1991**, 45, 173.
123. M. Sato, T. Jin and H. Ueda, *Chem. Lett.* **1994**, 161.
124. C. Bohnke, O. Bohnke and J.L. Fourquet, *J. Electrochem. Soc.* **1997**, 144, 1151.
125. P. Gomez-Romero, M.R. Palacin, N. Casan and A. Fuertes, *Solid State Ionics* **1993**, 63–65, 424.
126. A.R. Armstrong and P.A. Anderson, *Inorg. Chem.* **1994**, 33, 4366.
127. H. Fukuoka, T. Isami and S. Yamanaka, *Chem. Lett.* **1997**, 703.
128. D. Hamada, M. Machida, Y. Sugahara and K. Kuroda, *J. Mater. Chem.* **1996**, 6, 69.

129. J.N. Lalena, B.L. Cushing, A.U. Falster, W.B. Simmons, Jr., C.T. Seip, E.E. Carpenter, C.J. O'Connor and J.B. Wiley, *Inorg. Chem.* **1998**, 37, 4484.
130. M. Wiegel, M. Hamoumi and G. Blassc, *Mater. Chem. Phys.* **1994**, 36, 289.
131. A. Kudo, *Chem. Mater.* **1997**, 9, 664.
132. K. Toda, T. Honma and M. Sato, *J. Lumin.* **1997**, 71, 71.
133. A. Kudo and E. Kaneko, *J. Mater. Sci. Lett.* **1997**, 16, 224.
134. A. Kudo and T. Sakata, *J. Phys. Chem.* **1995**, 99, 15963.
135. M.Fang, C.H. Kim and T.E. Mallouk, *Chem. Mater.* **1999**, 11, 1519.
136. Y. Ebina, A. Tanaka, J.N. Kondo and K. Domen, *Chem. Mater.* **1996**, 8, 2534.
137. J. Yoshimura, Y. Ebina, J. Kondo, K. Domen and A. Tanaka, *J. Phys. Chem.* **1993**, 97, 1970.
138. T. Takata, Y. Furumi, K. Shinohara, A. Tanaka, M. Hara, J. N. Kondo and K. Domen, *Chem. Mater.* **1997**, 9, 1063.
139. T. Takata, K. Shinohara, A. Tanaka, M. Hara, J.N. Kondo and K. Domen, *Photochem. Photobiol. A: Chem.* **1997**, 106, 45.
140. S. Ikeda, M. Hara, J.N. Kondo, K. Domen, H. Takahashi, T. Okubu and M. Kakihana, *J. Mater. Res.* **1998**, 13, 852.
141. S. Ikeda, M. Hara, J.N. Kondo, K. Domen, H. Takahashi, T. Okubo and M. Kakihana, *Chem. Mater.* **1998**, 10, 72.
142. H. Yoneyama and S. Nippa, *Chem. Lett.* **1988**, 1807.
143. H. Yoneyama, S. Haga and S. Yamanaka, *J. Phys. Chem.* **1989**, 93, 4833.
144. S. Yamanaka, T. Nishihara and M. Hattori, *J. Phys. Chem.* **1987**, 91, 4305.
145. S. Yamanaka, T. Nishihara and M. Hattori, *Mater. Chem. Phys.* **1987**, 17, 87.
146. H. Miyoshi and H. Yoneyama, *J. Chem. Soc., Faraday Trans. 1* **1989**, 85, 1873.
147. S. Yamanaka, T. Doi, S. Sako and M. Hattori, *Mater. Res. Bull.* **1984**, 19, 161.
148. N. Kakuta, K.H. Park, M.F. Finlayson, A. Ueno, A.J. Bard, A. Campion, M.A. Fox, S.E. Webber and J.M. White, *J. Phys. Chem.* **1985**, 89, 732.
149. O. Enea and A.J. Bard, *J. Phys. Chem.* **1986**, 90, 301.
150. M. Ogawa and K. Kuroda, *Chem. Rev.* **1995**, 95, 399.
151. R.A. Della Guardia and J.K. Thomas, *J. Phys. Chem.* **1983**, 87, 990.
152. R.A. Schoonheydt, P. DePauw, D. Vliers and F.C. DeSchrijver, *J. Phys. Chem.* **1984**, 88, 5113.
153. P.K. Ghosh and A.J. Bard, *J. Phys. Chem.* **1984**, 88, 5519.
154. D. Krenske, S. Abdo, H. Van Damme, M. Cruz and J.J. Fripiat, *J. Phys. Chem.* **1980**, 84, 2447.
155. A. Habeti, D. Keravis, P. Levitz and H. Van Damme, *J. Chem. Soc., Faraday Trans. 2* **1984**, 80, 67.
156. V. Joshi, D. Kotkar and P.K. Ghosh, *J. Am. Chem. Soc.* **1986**, 108, 4650.
157. V. Joshi and P.K. Ghosh, *J. Am. Chem. Soc.* **1989**, 111, 1964.
158. P.V. Kamat, K.R. Gopidas, T. Mukherjee, V. Joshi, D. Kotkar, V.S. Pathak and P.K. Ghosh, *J. Phys. Chem.* **1991**, 95, 10009.
159. S. Abdo, P. Canesson, M. Cruz, J.J. Fripiat and H. Van Damme, *J. Phys. Chem.* **1981**, 85, 797.
160. G. Villemure, C. Detellier and A.G. Szabo, *J. Am. Chem. Soc.* **1986**, 108, 4658.
161. A. Yamagishi and M. Soma, *J. Am. Chem. Soc.* **1981**, 103, 4640.
162. A. Yamagishi, *J. Coord. Chem.* **1987**, 16, 131.
163. G. Villemure, H. Kodama and C. Detellier, *Can. J. Chem.* **1985**, 63, 1139.
164. C. Detellier and G. Villemure, *Inorg. Chim. Acta* **1984**, 86, L19.
165. H. Nijs, J.J. Fripiat and H. Van Damme, *J. Phys. Chem.* **1983**, 87, 1279.
166. H. Nijs and H. Van Damme, *J. Chem. Soc., Chem. Commun.* **1981**, 1026.
167. D. Ege, P.K. Ghosh, J.R. White, J.-F. Equey and A.J. Bard, *J. Am. Chem. Soc.* **1985**, 107, 5644.
168. P.K. Ghosh, A.W.-H. Mau and A.J. Bard, *J. Electroanal. Chem.* **1984**, 169, 315.
169. W.E. Rudzinski and A.J. Bard, *J. Electroanal. Chem.* **1986**, 199, 323.
170. R.D. King, D.G. Nocera and T.J. Pinnavaia, *J. Electroanal. Chem.* **1987**, 236, 43.
171. S.P. Newman and W. Jones, *New J. Chem.* **1998**, p105-115.
172. A. Vaccari, *Catal. Today* **1998**, 41, 53-71.

173. S. Carlino, *Solid State Ionics* **1997**, 98, 73.
174. F. Cavani, F. Trifirò and A. Vaccari, *Catal. Today*, **1991**, 11, 169–301.
175. T. Sato, H. Okuyama, T. Endo and M. Shimada, *Reacti. Solids*, **1990**, 8, 63.
176. C.L. Hill and D.A. Bouchard, *J. Am. Chem. Soc.* **1985**, 107, 5148.
177. M. A. Fox, R. Cardona and E. Gillard, *J. Am. Chem. Soc.* **1987**, 109, 6347.
178. T. Kwon, G.A. Tsigdinos and T.J. Pinnavaia, *J. Am. Chem. Soc.* **1988**, 110, 3653.
179. T. Kwon and T.J. Pinnavaia, *J. Mol. Catal.* **1992**, 74, 23.
180. D.S. Robins and P.K. Dutta, *Langmuir* **1996**, 12, 402.
181. E.P. Giannelis, D.G. Nocera and T.J. Pinnavaia, *Inorg. Chem.* **1987**, 26, 203.
182. H. Lee, L.J. Kepley, H.-G. Hong and T.E. Mallouk, *J. Am. Chem. Soc.* **1988**, 110, 618.
183. G. Cao, H.-G. Hong and T.E. Mallouk, *Acc. Chem. Res.* **1992**, 25, 420.
184. D.M. Kaschak, J.T. Lean, C.C. Waraksa, G.B. Saupe, H. Usami and T.E. Mallouk, *J. Am. Chem. Soc.* **1999**, 121, 3435.
185. D.M. Kaschak, S.A. Johnson, C.C. Waraksa, J. Pogue and T.E. Mallouk, *Coord. Chem. Rev.* **1999**, 185–186, 403.
186. K.B. Blodgett, *J. Am. Chem. Soc.* **1935**, 57, 1007.
187. K.B. Blodgett and I. Langmuir, *Phys. Rev.* **1937**, 51, 964.
188. J. Sagiv, *J. Am. Chem. Soc.* **1980**, 102, 92.
189. L. Netzer and J. Sagiv, *J. Am. Chem. Soc.* **1983**, 105, 674.
190. P.R. Moses, L. Wier and R.W. Murray, *Anal. Chem.* **1975**, 47, 1882.
191. M.P. Soriaga and A.T. Hubbard, *J. Am. Chem. Soc.* **1982**, 104, 3937.
192. R.G. Nuzzo and D.L. Allara, *J. Am. Chem. Soc.* **1983**, 105, 4481.
193. T.T.T. Li and M.J. Weaver, *J. Am. Chem. Soc.* **1984**, 106, 6107.
194. H. Lee, L.J. Kepley, H.-G. Hong, S. Akhter and T.E. Mallouk, *J. Phys. Chem.* **1988**, 92, 2597.
195. G. Decher, *Science* **1997**, 277, 1232.
196. E.R. Kleinfeld and G.S. Ferguson, *Science* **1994**, 265, 370.
197. E.R. Kleinfeld and G.S. Ferguson, *Chem. Mater.* **1995**, 7, 2327.
198. S.W. Keller, H.-N. Kim and T.E. Mallouk, *J. Am. Chem. Soc.* **1994**, 116, 8817.
199. M. Fang, C.-H. Kim, G.B. Saupe, H.-N. Kim, C.C. Waraksa, T. Miwa, A. Fujishima and T.E. Mallouk, *Chem. Mater.* **1999**, 11, 1526.
200. N.A. Kotov, I. Dékány and J.H. Fendler, *Adv. Mater.* **1996**, 8, 637.
201. M. Fang, D.M. Kaschak, A.C. Sutorik and T.E. Mallouk, *J. Am. Chem. Soc.* **1997**, 119, 12184.
202. L. A. Vermeulen and M.E. Thompson, *Nature* **1992**, 358, 656.
203. S.B. Ungashe, W.L. Wilson, H.E. Katz, G.R. Scheller and T.M. Putvinski, *J. Am. Chem. Soc.* **1992**, 114, 8717.
204. D.M. Kaschak and T.E. Mallouk, *J. Am. Chem. Soc.* **1996**, 118, 4222.
205. S.W. Keller, S.A. Johnson, E.S. Brigham, E.H. Yonemoto and T.E. Mallouk, *J. Am. Chem. Soc.* **1995**, 117, 12879.
206. G.B. Saupe, T.E. Mallouk, W. Kim and R.H. Schmehl, *J. Phys. Chem. B* **1997**, 101, 2508.
207. T. Sasaki, M. Watanabe, Y. Komatsu and Y. Fujiki, *Bull. Chem. Soc. Jpn.* **1985**, 58, 3500.
208. T. Sasaki, Y. Komatsu and Y. Fujiki, *Mater. Res. Bull.* **1987**, 22, 1321.
209. T. Sasaki, Y. Komatsu and Y. Fujiki, *Inorg. Chem.* **1989**, 28, 2776.
210. H. Izawa, S. Kikkawa and M. Koizumi, *Polyhedron* **1983**, 2, 741.
211. R. Nedjar, M.M. Borel and B. Raveau, *Z. Anorg. Allg. Chem.* **1986**, 540/541, 198.
212. K. Toda, S. Kurita and M. Sato, *Solid State Ionics* **1995**, 81, 267.
213. S.-H. Byeon, K. Park and M. Itoh, *J. Solid State Chem.* **1996**, 121, 430.
214. K. Toda, Y. Kameo, S. Kurita and M. Sato, *Bull. Chem. Soc. Jpn.* **1996**, 69, 349.
215. S.-H. Byeon, J.-J. Yoon and S.-O. Lee, *J. Solid State Chem.* **1996**, 127, 119.
216. S.-H. Byeon, S.-O. Lee and H. Kim, *J. Solid State Chem.* **1997**, 130, 110.
217. V. Thangadurai, G.N. Subbanna and J. Gopalakrishnan, *Chem. Commun.* **1998**, 1299.
218. D. Chen, X. Jiao and R. Xu, *Mater. Res. Bull.* **1999**, 34, 685.
219. T. Matsuda, M. Udagawa and I. Kunou, *J. Catal.* **1997**, 168, 26.

5 Fundamental Aspects of Electron Transfer in Substrate-supported Organized Molecular Assemblies

Robert S. Clegg and James E. Hutchison

5.1 Introduction

Monolayer and multilayer thin films are technologically important materials that potentially provide well-defined molecular architectures for the detailed study of interfacial electron transfer. Perhaps the most important attribute of these heterogeneous systems is the ease with which their molecular architecture can be synthetically varied to tailor the properties of the ensemble. Assemblies incorporating specifically designed structures can, in principle, meet the needs of a variety of technological applications and be used as models for understanding fundamental interfacial reaction mechanisms. In fact, molecular assemblies are nearly ideal ‘laboratories’ for the fundamental study of electron-transfer reactions at interfaces. In this chapter, the use of monolayer and multilayer assemblies to probe fundamental questions regarding electron transfer in surface-confined molecular assemblies will be addressed.

Electron-transfer reactions in heterogeneous media are among the most important fundamental reactions in chemistry and biology, yet they remain to be completely understood. Heterogeneous electron-transfer processes are at the heart of technologically important systems, including processes at electrodes (e.g., electrocatalysis, chemical sensing and corrosion prevention), solar energy conversion, imaging (e.g., xerography and photography) and micro- and molecular electronics [1–3]. Complex heterogeneous biological systems permit exquisite control over the rates and directionality of electron transfer (e.g., the organized assemblies within membranes that are responsible for important processes such as oxidative phosphorylation and photosynthesis) [4]. Despite extensive study, the roles of electron-transfer reactions in artificial and biological systems continue to broaden. *The overarching goal of the investigations described within this chapter is understanding electron transfer in designed heterogeneous systems and, to a lesser extent, utilizing these systems for applications.*

Homogeneous systems have been extensively studied and most of the important parameters that affect electron transfer are established [5]. On the other hand,

electron-transfer processes in the more complex *heterogeneous* architectures are less well understood. Nevertheless, studies on homogeneous systems provide useful lessons (and a starting point) for understanding the more complex heterogeneous systems. Comprehensive theoretical treatments [6, 7] and numerous experimental investigations have been carried out on homogeneous systems. From this work, the dependence upon electron-transfer distance, molecular orientation, thermodynamic driving force, nature of the chemical environment (including solvent polarity and interactions), molecular spacer composition and temperature have been largely determined and are summarized concisely in a review by Bolton et al. [5]. The ability to obtain quantitative data on homogeneous populations of discrete, defined molecular systems using well-developed analytical tools (single-crystal X-ray diffraction, solution spectroscopic tools, etc.) has made these advances possible.

Why is it harder to determine how electron transfer depends upon structural and chemical parameters for heterogeneous systems? First, the nature of a heterogeneous system increases the probability that an inhomogeneous population of redox partners exists. The ideal system would be a defect-free sample where all electron-transfer partners were identically situated and would therefore exhibit the same kinetics. Such samples are difficult to prepare. Second, defects within a sample are often difficult to detect given the available structural tools that typically probe the bulk structure of an assembly. One often must rely upon indirect evidence (e.g., a single rate constant for electron transfer) of the structural homogeneity of electron-transfer assembly. To summarize, the difficulty in studying these heterogeneous systems is that *structural and compositional parameters that are hard to control (or determine) in molecular assemblies will affect electron-transfer rates*. Thus, the key challenge in performing detailed investigations of electron-transfer reactions in synthetic heterogeneous molecular assemblies is to strive continually to obtain better control over structure and make use of the best analytical methods that can detect inhomogeneous electron-transfer paths and/or defects within the sample.

Organized assemblies such as monolayer and multilayer thin-film samples offer a number of advantages as models with which to understand the fundamental aspects of electron transfer in heterogeneous systems:

- 1) Close-packed thin films enforce a conformational rigidity and thus impose a well-defined distance between redox partners, even if the bridge alone is not rigid.
- 2) The thin-film environment eliminates diffusion or reduces it to a low level.
- 3) Noncovalent organization of well-defined building blocks provides access to a large number of structural combinations without additional synthesis.
- 4) Assemblies on solid substrates can frequently be more easily analyzed with direct structural probes than heterogeneous aggregates in solution.
- 5) Organized assemblies provide a closer approximation to natural or synthetic organized assemblies than solution species.
- 6) In the case of conducting substrates, the electrode provides an infinitely tunable electrochemical driving force for electron transfer.

In the sections that follow, we will first outline the approaches that have been taken to use molecular assemblies to understand interfacial electron transfer and the

challenges faced in developing these systems. Next, the progress toward understanding electron transfer in well-defined assemblies will be discussed with emphasis on the interplay between structural parameters and electron-transfer kinetics in these assemblies. Finally, some of the continuing challenges and future directions of electron-transfer studies in molecular assemblies will be discussed.

5.2 Background

5.2.1 Monolayer and Multilayer Systems

Monolayer and multilayer assemblies supported on solid substrates *ideally* provide thin films of precise thickness and well-defined composition for the detailed study of the fundamental aspects of electron-transfer events in heterogeneous environments. These assemblies offer exquisite control over essentially all desirable experimental variables, including electron-transfer distance, molecular bridge chemical composition, redox probe or chromophore orientation, driving force for electron transfer, surrounding chemical environment, etc. In addition, the building blocks that make up these assemblies can be arranged on a variety of insulating and conducting substrates.

The challenge in employing these assemblies to obtain quantitative electron-transfer data is making sure that measurements made actually reflect the properties of the *intended* molecular architecture. In fact, electron-transfer measurements on such systems are often dominated by defects within the assembly or are made complex by multiple types of electron-transfer pathways within the film. Further complicating the situation is the fact that most available analytical tools provide data that are dominated by the bulk properties of the assembly rather than the local structure of the electron-transfer paths. Hence great care must be exercised in designing, assembling, characterizing and studying these assemblies so that data reflect the desired experimental system and are not the result of film defects, disorder or lateral heterogeneity.

Electron-transfer investigations have been made using both monolayer and multilayer assemblies prepared either by Langmuir–Blodgett techniques or through chemical self-assembly. Examples illustrating common structural motifs are shown in Figure 1. In the remainder of this section, the methods for preparing these assemblies will be briefly reviewed. Next, the relative strengths and limitations of each type of architecture and assembly method with respect to ease of preparation, experimental flexibility and structural integrity will be discussed. Finally, the methods used and challenges faced in characterizing these assemblies will be addressed.

Langmuir–Blodgett (LB) films

LB mono- and multilayers have been extensively studied as thin films with well-defined internal molecular architecture. This well-known method [8–13] involves a

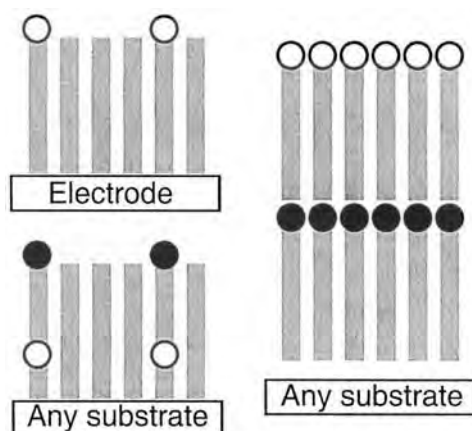


Figure 1. The use of monolayer and multilayer assemblies for electron-transfer study. Numerous other possible arrangements are not shown. (A) Mono- or multilayer on a conducting substrate (electrode) with pendant or soluble (not shown) redox probe. (B) Monolayer assembly on an insulating substrate with electron donors and acceptors in the same molecular chain. (C) Multilayer assembly with electron donors and acceptors in different layers of the assembly.

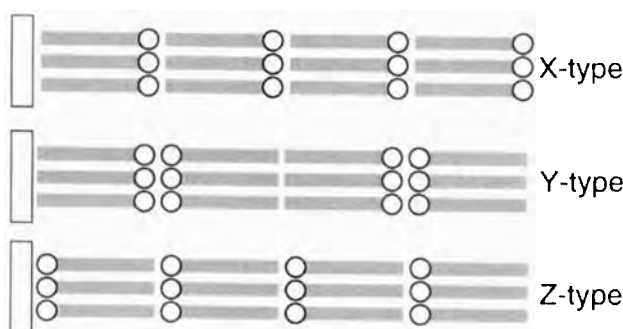
two-step process. In the first step, an organized monomolecular layer (Langmuir layer) of one of the components of the film is formed on an aqueous subphase. During the second step, the compressed Langmuir layer is transferred (by passing a clean substrate through the air–water interface) onto an appropriate support to form the LB film. The mechanism of transfer is not completely understood despite extensive study—obtaining complete transfer of the film and a *well-organized* assembly on the substrate can be difficult. In fact, the deposition conditions (including surface pressure during deposition, transfer speed, subphase composition and temperature) must be optimized for each new film building block [14].

The LB method is especially useful for preparing multilayered molecular assemblies. By passing the substrate through the air–water interface repeatedly, subsequent layers of molecules can be added to the initial film. A wide range of specialized transfer methods has been developed to control the orientation of layers with respect to one another and to prepare alternating layered films. The easiest multilayers to prepare (and hence most common) are those in which the orientation of the headgroup relative to the substrate alternates in each layer of the film (the Y-type). In principle, by varying the orientation of the headgroups within each layer and/or the surfactant composition within each layer, a wide variety of LB films can be prepared (Figure 2).

In addition to the relative ease of preparation of multilayered films, the primary advantage of LB films involves the flexibility with which the molecular architecture can be tuned. The composition within individual layers and from layer to layer can be precisely controlled by varying the composition of the mixed Langmuir monolayers. The relative spacing between active components (chromophores, redox probes, etc.) in the film can be systematically varied by controlling the adsorbate orientation and by varying the spacer length. Additionally, film deposition is possible on many substrates including both conductors and insulators.

Despite the numerous advantages, LB films have a number of potential disadvantages with regard to electron-transfer studies, including the difficulty of fabricating high-quality films and their fragility in electrochemical experiments. Al-

Figure 2. Examples of Langmuir–Blodgett multilayer assemblies. For simplicity, all surfactants are shown as the same type. Typically mixtures of surfactants are employed; composition can be varied within each layer and/or from layer to layer.



though the compression process results in fewer defects in the Langmuir layer, it can be difficult to optimize the film-transfer process. Inefficient transfer can result in poor film homogeneity and the incorporation of defects in the LB film. Additionally, it can be very difficult to control precise placement of chromophores/redox probes within the film. LB films typically do not withstand electrochemical investigation because they are usually stabilized only by van der Waals interactions and have limited stability unless they are covalently bound to the substrate.

Self-assembled monolayers (SAMs) and multilayers

An alternative to the LB method that eliminates the difficulties of film transfer and results in more stable films depends upon chemical self-assembly of adsorbates directly onto a solid support. In the self-assembly process, molecular assemblies are formed by soaking a substrate in a solution of a surfactant that interacts with the substrate through a reactive headgroup. Strong interactions between the headgroup and the surface drive the saturation of adsorbate binding sites and stabilize the film. Lateral interactions between neighboring adsorbate molecules provide added stability to the assembly and can lead to formation of 2-D crystals if the packing among the adsorbate chains is a reasonable match to the spacing between adsorbate binding sites on the surface.

As early as 1946, Bigelow et al. suggested the use of chemically-modified surfaces produced by self-assembly for applications such as control of wettability, ‘permanent’ lubrication and corrosion prevention [15]. Self-assembly of organic films on metals [16] and metal oxides (e.g., alkyl carboxylates on iron and aluminum oxide surfaces) [17] was extensively investigated; however, highly ordered self-assembled films that form covalent bonds to the substrate were not well known until the 1980s [18, 19]. Nuzzo and Allara’s 1983 report of facile formation of alkanethiol monolayers (from disulfides) on gold surfaces [20] rekindled interest in preparing well-defined molecular assemblies by self-assembly on surfaces.

A number of self-assembled systems have been thoroughly investigated, including organosilicon adsorbates on hydroxylated surfaces such as SiO_2 and Al_2O_3 , carboxylates on Al_2O_3 and organothiol derivatives on the coinage metals. Of these systems, the alkanethiols on gold provide a number of advantages for use in

electron-transfer experiments: They assemble readily to form stable, well-ordered molecular layers, methods for characterizing molecular films on metal surfaces are well developed, and the metallic surface can be used to probe electron transfer electrochemically. They exhibit enhanced solvent and thermal stability and are thus amenable to electrochemical investigation where the electrochemical driving force can be easily varied. Additionally, the effects of the composition of the contacting electrolyte solution can be addressed.

In certain cases, self-assembly methods can be employed to prepare *multilayered* thin films analogous to LB films. Typically, once the surface has been primed with a molecular adhesion layer, subsequent layers are assembled in a layer-by-layer fashion where the end group of the previously deposited layer directs the assembly of the next layer. Strong electrostatic or covalent interactions between the layers serve to stabilize the assemblies. The most notable examples of self-assembled multilayered films are those based upon metal phosphonates [21]. Although these multilayers are structurally analogous to LB films, their thermal and solvent stability makes them potentially more useful in many applications, including electron-transfer studies.

An important, practical advantage of molecular self-assembly is that, given proper adsorbate design, it offers a straightforward and rapid method to form well-ordered molecular films. Facile film formation can be induced with a wide variety of redox probes on the surface of the film. However, successful assembly of the highly ordered mono- or multilayer necessary for electron-transfer studies depends upon the molecular structure of the adsorbate. Careful selection (through design and screening) of the molecular adsorbate is necessary to ensure a well-assembled monolayer possessing a high degree of order and rigidity. The fact that not all adsorbates will form well-ordered assemblies is the major limitation of using self-assembled systems to investigate electron transfer.

5.2.2 Characterization of Molecular Assemblies

Given the dependence of electron transfer on spacer composition, conformation and length in homogeneous systems [5], it is evident that thorough characterization of an assembly's structure and its degree of order is necessary to support the validity of electron-transfer measurements in heterogeneous systems. Improved analytical methods have made it more feasible to determine whether the assemblies have the intended structure and degree of perfection. Even so, detailed characterization is a difficult task that is best met with an array of different analytical tools. In this section we briefly review the analytical methods used for the characterization of ultrathin organic films. A number of useful reviews are available [13, 19, 22, 23]. The material presented here is limited to film characterization that is most relevant to our subsequent discussion of electron-transfer studies. Given the heightened interest in how structure and defects affect electron-transfer measurements, the examples used will come from the more recent studies of self-assembled alkanethiol monolayers on gold. Most of these techniques have been or could be similarly applied to Langmuir–Blodgett film samples. We first consider methods that probe the 'bulk' or average film structure (see Figure 3), followed by methods that are either sensi-

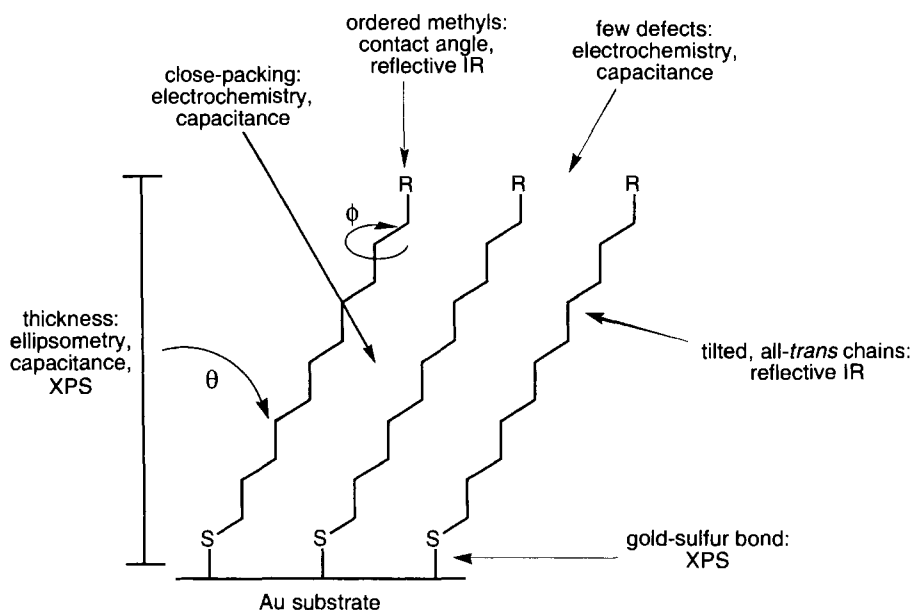


Figure 3. Structure elucidation of *n*-alkanethiol SAMs on gold by techniques excluding diffraction, STM and AFM.

tive to disorder or directly probe defects. Finally, we describe electrochemical studies that reveal defects that may influence (electrochemical) electron-transfer measurements.

Spectroscopic, structural and scanning probe studies

A consistent description of the structure of alkanethiol monolayers on gold has emerged from an array of spectroscopic and diffraction studies. X-ray photoelectron spectroscopic (XPS) studies support the presence of anisotropically chemisorbed alkanethiolates on gold [24–29]. Ellipsometric measurements [24–27, 30], capacitance studies [30] and XPS measurements [31] confirm monolayer film thickness. Fourier transform infrared external reflective spectroscopy (FTIR-ERS) shows that the chains tilt at about 30° off the surface normal, and the plane containing the carbon backbone is twisted out of the plane of tilt by about 50° [25–27, 30, 32, 33].

Diffraction techniques (low-energy electron diffraction [34, 35], helium diffraction [36, 37] and grazing incidence X-ray diffraction [38]), scanning tunneling microscopy (STM) [36, 39, 40] and atomic force microscopy (AFM) [41] served to solidify the conclusions inferred from the less direct spectroscopic methods and provide additional structural details. The sulfur atoms order epitaxially on the substrate in a $(\sqrt{3} \times \sqrt{3})R30^\circ$ structure [36–38, 40, 41]. The angle of the sulfur–carbon bond with respect to the substrate plane is approximately 104° for alkanethiol monolayers [38, 42] and 180° for arylthiol SAMs [42, 43]. Given the agreement between the results obtained from direct structural methods and indirect spectroscopic methods, one

can generally apply an array of complementary spectroscopic techniques with reasonable confidence in characterizing SAMs.

Many of the analytical techniques used to study SAMs provide measures of the average properties of SAMs, i.e., they may not be sensitive to disorder or defects. Contact angle goniometry, FTIR-ERS and electrochemical methods are convenient techniques that provide some information about the degree of order or presence of defects in monolayer assemblies. Contact angle goniometry has been used to probe the degree of order within the top few ångströms of methyl-terminated chains [24–26, 28]. Double-layer capacitance and electrochemical blocking experiments [30] probe the integrity of monolayer films and have shown that, for chain lengths greater than about 10 carbons (in air), the alkanethiol monolayers are close packed and contain few defects. FTIR-ERS studies support these findings and show that the alkyl chains occupy primarily all-*trans* conformations [25–27, 30, 32, 33].

Methods that probe local structure and defects, such as STM and AFM, show that nearly full coverage on the molecular scale is easy to achieve [36, 39, 40]. Defects for long-chain alkanethiol monolayers are restricted primarily to point defects such as missing single adsorbate molecules, grain boundaries between domains and step edges usually related to discontinuities in the substrate [39, 41].

Detecting disorder and defects under electrochemical conditions

To probe the microscopic order of SAMs (here we will treat only nonelectroactive SAMs; those containing tethered redox probes will be discussed later) under the conditions used during electrochemical electron-transfer measurements, functional characterization is performed by cyclic voltammetric techniques. In this subsection, electrochemical blocking effect (*EBE*) and double-layer capacitance (C_{dl}) experiments are detailed. When these experiments are carried out using a structural probe of molecular scale [30, 44, 45], they provide the greatest sensitivity to defects because the effects of defects and disorder dominate the electrochemical response.

If a defect-free molecular assembly covers an electrode surface completely, the assembly is an efficient electrochemical blocker [23, 30, 46, 47]. Electron transfer through the SAM to a solution redox probe is substantially slower than the rate of diffusion of the probe to the surface, and the voltammetric response is a quasi-exponential increase in Faradaic current resulting from electron transfer across the chains of the SAM [30, 46]. This type of response qualitatively supports the presence of a monolayer low in defect sites. A more quantitative measure of the *EBE* of a modified electrode is expressed as the percentage of total blocking achieved using a bare electrode as the standard [48]:

$$EBE = \left(1 - \frac{i_{\text{film}}}{i_{\text{bare}}} \right) \times 100 \% \quad (1)$$

A completely blocking electrode would yield an electrochemical blocking effect of 100 %.

If the molecular assembly coating the electrode contains defects greater than the size of the redox probe (but less the ca. 1 µm in diameter) [23], the electrode as-

sembly will function as an array of microelectrodes. The electrochemical response depends upon the size and separation of the defects. If the defects result in widely spaced bare spots, the current is limited by radial diffusion [23, 30, 46] with a hemispherical concentration profile centered on each pinhole [47]. In the cyclic voltammogram, the resulting sigmoidal current response levels off near $E^{o'}$ and remains constant at more extreme potentials [23, 30, 46, 47]. If, on the other hand, the pinholes are spaced closely enough that their concentration profiles overlap, the voltammetry becomes diffusion-limited at high overpotentials. In either case, the *maximum* pinhole area can be estimated [19, 30].

The double-layer capacitance is another useful electrochemical method for probing the integrity of molecular assemblies in contact with electrolyte solutions. If a cyclic voltammogram is recorded in a solution of electrolyte only, a non-Faradaic current results, and the double-layer capacitance, C_{dl} (or differential capacitance), is measured as half the width of the voltammogram charging envelope given by [30, 48]

$$C_{dl} = \frac{i_c - i_a}{2\nu A} \quad (2)$$

In a SAM-modified electrode, the SAM functions as a dielectric, reducing the permeability of the monolayer by electrolyte and decreasing the charging current [23, 30, 48]. However, a thinner film [30, 49], one with a higher dielectric constant (e.g., containing unsaturated carbons [50]), or one which is more permeable to electrolyte (i.e., a more defective SAM), exhibits increased C_{dl} because the resulting electrical double layer is better organized [23, 30, 48]. The double-layer capacitance is, thus, a convenient check of monolayer quality under the conditions of electrochemical electron-transfer measurements.

5.2.3 Measurement of electron-transfer rates

There are two primary methods of investigation of electron-transfer rates: photochemical and electrochemical. In photochemical experiments, a donor–acceptor pair is synthetically introduced into the system, ideally held at a well-defined separation. Photoexcitation of one of the partners provides the driving force for electron transfer. In systems designed to prohibit energy transfer, monitoring the decay (quenching) of the excited state provides a way to follow the electron-transfer reaction. A chief advantage of photochemical experiments is that electrical contact to the sample is not necessary. The main limitation is that the electrochemical driving force can only be varied by incorporation (usually through new synthesis) of different redox probes.

In electrochemical experiments, the molecular assembly is deposited on a conductive electrode surface that acts as one of the ‘redox partners’. The other partner is a redox molecule either tethered to the molecular film or free in solution. In either case, the film ideally provides a well-defined separation between the electrode and the redox probe. The electrode potential is either swept or stepped to increase the driving force for electron transfer. The chief advantage of the electrochemical elec-

tron-transfer experiment is that one can easily tune the thermodynamic driving force for electron transfer by simply varying the electrode potential. This method can only be applied to systems that are stable under electrochemical conditions.

5.3 Fundamental Studies of Electron Transfer in Organized Assemblies

Fundamental studies of electron transfer in substrate-supported, organized assemblies were pioneered by Kuhn, Möbius and others in the 1970s using specifically designed LB films. Experimentalists built upon this foundation over the last two decades but have increasingly focused on the use of LB systems for applications such as photoinduced charge separation rather than fundamental studies due, in part, to some of the experimental limitations of the LB systems. The pursuit of fundamental studies in organized assemblies was rejuvenated in the late 1980s as well-defined alkanethiol monolayers on coinage metals (particularly gold) became the new experimental paradigm. Recently, self-assembled multilayer systems and hybrid, self-assembled monolayer-LB systems have also been investigated. In this section, fundamental studies of electron transfer in LB systems will be reviewed, followed by a more thorough discussion of the recent work in self-assembled systems.

5.3.1 Electron Transfer in Langmuir-Blodgett Systems

The use of LB films for the study of electron transfer is an outgrowth of work aimed at photochemical charge separation [51–53]. In fact, Kuhn had proposed a light-driven electron pump before any details of the photochemical reaction center were available [52]. The LB technique was attractive because of the relative ease of preparing asymmetric bi- and multilayers needed for charge separation. In addition, compared with unsupported bilayers, LB films were more mechanically stable and were thought to eliminate flip-flop, the migration of a surfactant's headgroup from one side of the membrane to the other, which would randomize the position of redox partners in a multilayer assembly. The pioneering work of Kuhn, Möbius and co-workers on electron and energy transfer in engineered LB films has been extensively reviewed [54–57]. Here we will reiterate the key findings and unsolved challenges to lay the foundation for more recent studies of self-assembled systems.

Distance and material dependence

The rate of weakly coupled electron transfer by a tunneling mechanism is expected to decrease exponentially with increasing thickness of the spacer between donor and acceptor (due to the exponential decrease in electronic coupling with increasing separation [7]). Ideally, the thickness of the spacer in an organized assembly is the fully extended length of the spacer molecule. Any imperfections in a film will affect the spacer thickness and, thus, the electron-transfer rate. In properly designed and

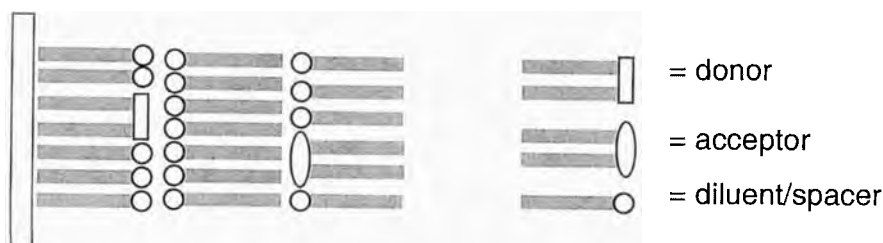


Figure 4. Langmuir–Blodgett multilayer systems pioneered by Kuhn and Möbius. Donor and acceptor surfactants are diluted with nontagged surfactants within each layer. The donor–acceptor separation is enforced by the inner layer spacing.

carefully prepared LB systems where it is possible to measure the dependence of the rate on distance accurately, the rate decays exponentially with distance.

Kuhn and Möbius first demonstrated the exponential distance dependence of electron-transfer rates in LB multilayers through fluorescence quenching experiments [56, 58, 59]. The multilayer assemblies were designed to eliminate energy-transfer reactions, yet permit electron transfer. These were composed of cyanine dye donors and viologen acceptors separated by a variable-length, fatty acid interlayer (e.g., Figure 4). Quenching of the cyanine's excited state by the viologen was used to follow the electron-transfer reaction. The electron-transfer distance was varied by adjusting the length of a single fatty acid interlayer spacer from C_{14} to C_{22} . Separation of the donor and acceptor by more than a single long hydrocarbon chain prevents electron transfer and, thus, fluorescence quenching, as expected. Plots of $\log(I/I_0 - 1)$ vs. distance are linear, which is consistent with an electron tunneling mechanism. The quenching rate is independent of temperature, consistent with a tunneling mechanism [58]. Subsequent work by Whitten's group [60] has shown that electron-transfer quenching studies in supported multilayers, containing *trans*-stilbene chromophores and a variety of different quenchers, yields the same linear dependence.

The LB method has been used to generate a number of well-spaced donor–acceptor pairs using surfactants, redox reagents and chromophores. In addition to the distance dependence studies described above, such systems have been used to investigate the effect of the spacer composition on the electronic coupling between the electron-transfer partners. Variation of the electronic nature and thickness of the spacer layer, without altering donor or acceptor layers, made possible the investigation of the material dependence of electron transfer in LB films. A variety of molecular and polymeric [61, 62] materials was investigated with the aim of understanding how the composition of the spacer layer affects the electron-transfer rate. In a number of cases, β , the material-dependent attenuation coefficient [the slope of the $\log(\text{rate})$ vs. distance plot] has been reported. The first systematic study of the material dependence of electron transfer was reported by Whitten's group [63]. For fatty acid spacers they found $\beta = 0.3 \text{ \AA}^{-1}$, consistent with the data obtained earlier in LB systems where β ranged from 0.3 to 0.4 \AA^{-1} [56, 58, 60, 64].

The incorporation of *trans*-stilbene groups into the spacer resulted in a decrease in β ($= 0.2 \text{ \AA}^{-1}$).

Few other systematic studies of β have been completed using LB films. The values obtained for aliphatic spacers are internally consistent but are not in good agreement with values found in organic glasses [65], bridged donor–acceptor systems [66] or self-assembled monolayer studies (see Section 5.3.2) that are typically in the region of 1 \AA^{-1} . The most likely explanation for this discrepancy is that electron transfer at defects increases the rate and decreases β . An exponential distance dependence has been shown in electrochemical experiments performed on self-assembled multilayers of zirconium bisphosphonates where electron transfer was shown to be dominated by defect sites [67]. If the lower β values are due to defects, given the similarity of the β values among the varied systems, the number and density of defects within the samples would have to be similar.

Probes that are most sensitive to defects [scanning probe microscopy (e.g., AFM and STM) and electrochemistry] are difficult to apply to the multilayered LB systems used for electron-transfer experiments. AFM studies are not sensitive to buried defects, and the insulating nature of the films complicates STM studies. These systems typically are unstable under conditions necessary to probe them electrochemically.

Dependence on the driving force

The rate of electron transfer within LB film assemblies depends upon the thermodynamic driving force, dictated by the redox potentials of the partners, just as it does in solution. The heterogeneous nature of LB assemblies introduces the added possibility of field-induced perturbations upon the driving force. Two field-induced effects, electrical double-layer effects at interfaces and the application of external fields, have been investigated. Fujihira's group showed that an internal double-layer effect influenced quenching rates of a ruthenium sensitizer and several ferrocene-based donors [68, 69]. They reported that 'up-hill' (thermodynamically unfavorable based upon solution redox potentials) electron transfer can occur in the LB assemblies under conditions where the electrical double layer acts to increase the driving force for the reaction. Application of an external field was reported to depress or enhance the rate of electron transfer by stabilizing or destabilizing radical ion pairs generated upon electron transfer [70] in LB films [71, 72].

5.3.2 Electron Transfer in Self-assembled Systems

As discussed earlier, SAMs of alkanethiols on gold surfaces offer access to highly ordered, surface-confined molecular structures. The use of these assemblies as stable, well-defined spacers for studies of electron transfer between the gold electrode and redox centers attached to the film surface [50, 73–83] or in solution [44, 46, 84] is depicted in Figure 5. The densely packed monolayer maintains a precise separation between a gold electrode surface and the pendant or dissolved redox center, and effectively eliminates conformational mobility that can complicate electron-transfer rate studies [73]. An advantage of using electrode-confined spacers is that

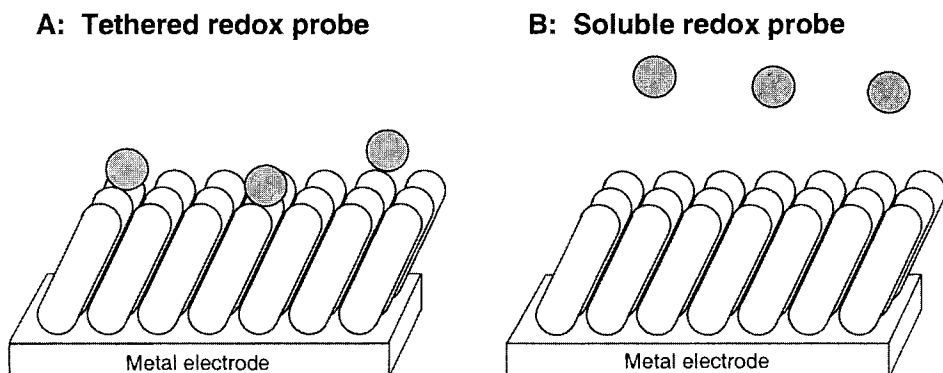
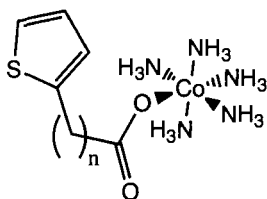


Figure 5. Self-assembled monolayers as rigid electrochemical spacers. Close packing of the SAM enforces a precise distance between the redox probes and the electrode. (A) In a tethered redox probe system, the probes are covalently attached to the outer surface of the monolayer. The probes may be undiluted (a probe attached to each chain in the monolayer) or mixed (probe-modified chains are diluted with nonelectroactive chains). (B) In a soluble redox probe system, the monolayer typically contains a single component that provides a well-defined separation between the soluble probe and the electrode surface.

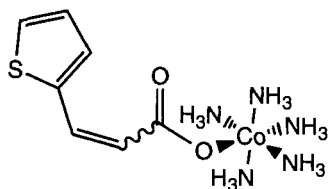
the driving force is infinitely tunable. Systematic variation of the molecular composition of the spacer is not limited to rigid linkers because full extension of the spacer is enforced by the monolayer [84]. However, the degree of order possible will depend upon the type and degree of substitution.

The advantages and challenges of using SAM models for the study of electron transfer in heterogeneous systems were defined in the early work by Weaver's group. They employed self-assembled monolayers to study the electroreduction of adsorbed $\text{Co}^{\text{III}}(\text{NH}_3)_5\text{L}$, where L is a thiophene-based headgroup containing a variable hydrocarbon linker. A large decrease in k_{et} is observed upon incorporation of saturated carbons (System 1) between the thiophene 'lead-in' and the carboxylate, whereas k_{et} is not decreased upon replacement of the saturated hydrocarbons with conjugated hydrocarbons (System 2). However, the monolayers were not structurally well enough defined to ascertain the quantitative dependence of k_{et} upon the degree of saturation or the length of the bridge [85]. An estimate of β ($= 1.45 \text{ \AA}^{-1}$) was obtained in a nonhomologous series of sulfides and disulfides containing 1–5 carbons [86]. Although the bond connectivities were known, the structures within the monolayer had not been determined. Thus, these studies illustrate the potential that SAMs offer as model systems and underscore the need for developing self-assembling systems that yield well-defined molecular assemblies.

This section describes the evolution of the systems and techniques that have made possible detailed studies in which electron transfer has been investigated using self-assembled monolayers. After a brief presentation of the important electrochemical methods for assessing the quality of the electroactive SAMs and determining k_{et} across monolayer spacers, studies of electron transfer across SAMs are presented.



System 1. Undiluted monolayers on gold, $n = 0-3$.



System 2. Undiluted monolayers on gold.

Electrochemical characterization of SAMs containing tethered redox probes

The importance of a well-defined, well-ordered organic film for reliable extraction of electron-transfer kinetics was discussed earlier. The methods of characterizing nonelectroactive SAMs were also presented. In this section, we address methods for assessment of the ideality of assemblies containing pendant redox probes (so-called electroactive SAMs) and strategies for optimizing the electron-transfer characteristics of these assemblies. When a tethered redox probe is used, it is typically incorporated into the film as the minor component, the major component being a nonelectroactive diluent adsorbate. In the ideal situation, the redox probes are well separated from one another and each is surrounded by a well-ordered monolayer of diluent. The ideality of the redox probe response is best determined electrochemically. Four major assessments are available by cyclic voltammetry, including measurement of (1) the charging current at the uncharged surface, (2) the degree of electrochemical blocking of the assembly, (3) the density of redox probe and (4) the ideality of the Nernstian response of the redox probe. Chronoamperometry is often used to measure electrode kinetics, as extraction of the kinetic data is more straightforward by this technique.

If the redox probe has an accessible uncharged state, then cyclic voltammograms may be measured *at potentials where the film surface is neutral* to check whether the capacitive charging matches that of the corresponding nonelectroactive SAM [74]. An increase in capacitive charging is evidence that the electroactive SAM is significantly disordered.

Mediation of electron transfer between a dissolved redox probe and the electrode by surface-confined redox groups has also been used to assess the integrity of electroactive monolayer assemblies. As an example, the reduction of $\text{Ru}^{\text{III}}(\text{NH}_3)_6$, normally occurring at about 0.1 V vs. Ag/AgCl, is fully blocked by an assembly containing tethered *N*-ethylviologen redox probes. However, at the observed reduction potential of the viologen probes (ca. -0.4 V), these probes mediate the reduction of $\text{Ru}^{\text{III}}(\text{NH}_3)_6$ [87]. Similarly, the delayed oxidation of $\text{Fe}^{\text{II}}(\text{CN})_6$ at

SAMs containing tethered ferrocenecarboxamide probes has been cited as an indication that through-chain electron transfer is preferred over electron transfer at defects [88].

The density of tethered redox probe at the surface is another useful parameter in electroactive assembly characterization. The amount of redox probe corresponds to the Faradaic charge of the redox process and is measured from the voltammogram using the area $i_F E$ under the voltammetric wave. The area is readily converted to the redox probe density (Γ , in mol cm^{-2}) [47]. For well-ordered *n*-alkanethiol SAMs, the total (electroactive plus diluent) surface density is one molecule of adsorbate per $\sim 20 \text{ \AA}^2$, or about $8 \times 10^{-10} \text{ mol cm}^{-2}$ [38]. To minimize disorder and electrochemical communication between tethered redox probes, the amount of redox probe should not exceed 10–20 % of the total adsorbate [23].

Assessment of the Nernstian behavior of the redox probe [47] is the most direct measure [23] of the reliability of information from a surface-confined electron-transfer experiment. For SAMs containing tethered redox probes, ideal Nernstian behavior is demonstrated by single voltammetric peaks with full widths at half maxima (FWHM) near $90.6/n \text{ mV}$ at room temperature. This ideal behavior strongly suggests that only a single, reversible redox process is occurring. Factors leading to increased FWHM include a number of processes such as aggregation of redox probes at the SAM surface, differential solvation of redox probe in the electrolyte and presence of redox probes at defect sites [82]. In addition to ideal peak shapes and widths, peak splittings ΔE_p are expected to be near 0 mV at slow scan rates [73–75, 79, 81] for a well-behaved system.

Chronoamperometry is more sensitive than cyclic voltammetry to defects in the SAM and serves as a stringent test of electroactive SAM order and integrity [73, 89]. The linearity of the appropriate plot (e.g., $\ln i$ versus t for a one-electron process) confirms that a single electrochemical process is occurring in the electroactive SAM [23].

It is often possible to optimize the response of a poorly assembled monolayer. In freshly adsorbed mixed SAMs, electroactive adsorbate is always present at defect sites [45, 74]. A distinct advantage of tethered redox probes over freely diffusing analyte is that a nearly perfect SAM is not required [23, 50, 73, 81, 90, 91].

The presence of electroactive adsorbate at defect sites can be reduced to insignificant levels using annealing methods such as the chemical annealing method of Chidsey and Loiacono [45] or the electrochemical annealing method of Finklea et al. [89].

Methods for determining electron-transfer rate constants

Cyclic voltammetric, chronoamperometric and AC impedance spectroscopic (ACIS) methods have typically been used to determine the electron-transfer rates in SAMs. Laviron developed a simple method for determining electron-transfer rate constants by cyclic voltammetry [92]. The method allows the determination of k^0 from the dependence of the cathodic/anodic peak separation, ΔE_p , upon sweep rate, but it is inherently inaccurate because it is based on Butler–Volmer kinetics [78, 93, 94].

Recently, the ability to simulate voltammograms based on the Marcus–DOS equation has allowed the extraction of reliable values of k^0 , νp and λ from CV data by curve fitting [78, 94]. In addition, Bowden and co-workers presented a method for calculating electron-transfer rate constants from voltammograms of electroactive SAMs, which provides a convenient shortcut for electrochemistry which is clearly reversible [93]. The advantages of this approach are that it permits the construction of Tafel plots for $\eta \geq 60$ mV from single voltammograms and that it is less time- and computer memory-intensive than the Murray–Creager method. However, this approach does not yield thermodynamic parameters directly from the voltammograms.

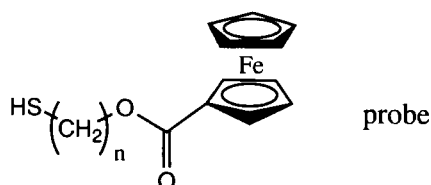
In chronoamperometry, the potential is stepped instantaneously from $E^{o'}$ to a positive or negative overpotential η , resulting in a current spike as oxidation or reduction occurs. The decay of the spike is recorded over time. For a one-electron electron-transfer process, k_η is calculated from chronoamperometry data as the slope of the $\log i$ vs. t plot following a potential step from $E^{o'}$. A Tafel plot is constructed from repeated potential steps. This technique has the advantage of minimizing the time spent at high overpotentials, preserving SAM integrity [23, 76] and allowing more data to be extracted from each sample.

In ACIS, a small-amplitude sine wave is superimposed on a constant potential, and the resulting current is recorded. The current lags behind the alternating potential by a degree proportional to the impedance of the SAM. From a plot of the imaginary versus real parts of the complex impedance, both the capacitance of the SAM and the electron-transfer kinetics can be extracted. Because the bulk of the studies described in this chapter make use of cyclic voltammetric or chronoamperometric methods, ACIS is not discussed further here. Leading references are provided for the interested reader [23, 43, 76].

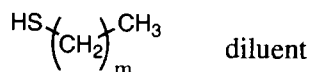
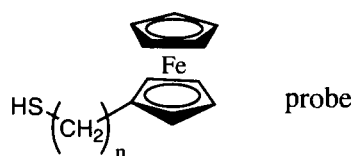
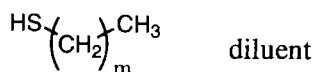
Fundamental studies of electron transfer across SAMs

In this section, the development of well-defined, self-assembled molecular systems and the key electron-transfer findings are discussed. First, pioneering studies in which fundamental processes in electron transfer across monolayers at metal electrodes are presented. These include electron transfer across well-ordered SAMs using tethered redox probes, freely diffusing redox probes and two juxtaposed electrodes. Next, the effect of changing the chemical environment of the redox probe is examined through a consideration of solvent effects, kinetic heterogeneity and vertical position of the redox probe with respect to the diluent molecules ('buried' versus 'dangling'). Distance dependence and material dependence of electron transfer are then addressed in turn. Finally, several mechanistic studies involving transition-state structures and the effects of ion pairing are summarized.

The development of alkanethiolate monolayers on gold as well-characterized, electrode-bound molecular assemblies sets the stage for electron-transfer measurements in more well-defined systems than has previously been available. Chidsey and co-workers began to adapt and test these systems for studying electron transfer across the monolayer [30, 45, 74]. They chose to employ a pendant ferrocene-carboxylate redox probe. Mixed monolayers were formed of the electroactive redox probes diluted with various amounts of methyl-terminated *n*-alkanethiols (Systems



System 3. Mixed monolayers on gold, $n = 11$ with $m = 9$ and $n = 16$ with $m = 15$.



System 4. Mixed monolayers on gold, $n = 16$ with $m = 15$.

3 and 4). Different combinations of chain lengths for diluent and electroactive adsorbates were used, and the spectrum of mole fractions in the mixed SAMs was investigated.

A number of important conclusions were drawn from this study, as follows. Electrochemical reversibility in electroactive self-assembled monolayers depends upon concentration and polarity of a covalently attached redox probe. Reversible surface electrochemistry is observed for the well-diluted ferrocenyl ester. However, reversibility decreases with steric congestion of redox probe because higher redox probe concentrations lead to disorder due to cross-sectional mismatch of the redox probe and the alkyl chain. Reversibility also decreases with a nonpolar redox probe; the alkylferrocene (System 4) yields broad peaks with long tails positive of $E^{o'}$, consistent with kinetic dispersion of the redox probes and their differential solvation in the SAM.

Chemical annealing steps decrease the surface concentration (Γ) of electroactive species and improve reversibility. Chemical exchange of electroactive with diluent adsorbate appears to take place at domain boundaries and defect sites. A 'domains/defects' model of monolayer structure was presented, whereby two populations of electroactive species are present: one which is fully desorbed after a few days of exposure to a nonelectroactive solution, and the other which remains unaffected by such chemical annealing for at least 10 days.

Based upon the results of this initial work, pendant redox probes appeared to provide two major advantages: (1) By exchanging electroactive adsorbate at defect sites for nonelectroactive adsorbate, electron transfer can be limited to that which occurs across the SAM (where coupling is mediated by the adsorbate chains); (2)

The transient currents (as opposed diffusion-limited currents in the case of freely diffusing redox probes) allow the ready identification of kinetic heterogeneity among the surface-confined redox sites [74].

In a subsequent investigation, Collard and Fox studied mixed electroactive monolayers that had been exchanged with a second electroactive probe, such that two redox tags could be distinguished by CV [95]. Upon exposure to the exchange solution, approximately one-third of the original probe is lost, and the voltammogram peak decreases in width (as had been observed by Chidsey and co-workers). The new electroactive component exhibits a broad peak that can largely be removed in a second exchange with a nonelectroactive thiol without further loss of the original redox species. These experiments confirm Chidsey and co-workers' 'domains/defects' model and provide certainty of control of the environment of electroactive species at the SAM–electrolyte interface [95].

With a structurally well-defined system in hand, Chidsey and co-workers were now able to investigate the relationship between electron transfer and thermodynamic driving force, and to study the activation energy of electron transfer. Using the best-behaved redox probe (System 3) from the previous study [74], k_{et} was measured by CV and chronoamperometry [73]. Single exponential chronoamperometric decays and reversible cyclic voltammograms suggest that a single reversible electrochemical process occurs. Using chronoamperometry, the kinetics were measured at overpotentials from -1.0 to $+0.8$ eV at temperatures from 1 to 47°C . All the k_{et} data were fitted with the Fermi–Dirac modified Marcus equation, which yields the same coupling prefactor ($7 \times 10^4 \text{ s}^{-1} \text{ eV}^{-1}$) at high overpotentials for each temperature. The temperature independence of the coupling prefactor shows that electron transfer across the SAM is nonadiabatic. The standard rate constant k^0 increases approximately twofold for every 15°C increase in temperature. This important report [73] showed that well-defined SAMs could be used to probe systematically the nature of electron-transfer processes in organized heterogeneous molecular assemblies and spurred many subsequent studies in these systems.

Shortly after Chidsey and co-workers' initial papers, Miller et al. reported full characterization of $\text{Au-S}(\text{CH}_2)_n\text{OH}$ monolayers (System 5, $n = 6\text{--}12, 14, 16$) by ellipsometry, XPS and electrochemical methods [44]. The nearly defect-free nature of the monolayers was attributed to hydrogen-bonding interactions between neighboring adsorbate chains at the film–electrolyte interface. The level of defects was probed by varying bridging halides, which should change electron-transfer processes at pinholes from outer to inner sphere. Electrochemical annealing was found to improve the *EBE* [44]. Later, they showed that defects in the SAMs are on the

$\text{HS}(\text{CH}_2)_n\text{OH}$ monolayer precursor

$\text{Fe}(\text{CN})_6^{3-}$
 OR
 Fe^{3+}

} soluble redox probes

System 5. Undiluted monolayers on gold.

nanometer scale or smaller and that the level of defects is sufficiently low as to be undetectable by CV. The passivating effect of 1-octanol upon defect sites decreases sequentially at adsorbate chain lengths longer than hexadecyl, suggesting defect sites account for a greater proportion of the measured current in the cases of shorter chains [96].

Rather than using covalently bonded redox probes, Miller et al. used electroactive species dissolved in the electrolyte (ferricyanide and ferric ion redox probes) to probe electron transfer across the SAMs (Figure 5B and System 5). Owing to the slow electron-transfer rate across the monolayers, the voltammetry was not diffusion limited, so the electron-transfer rates were extracted from the initial portions of the i - E curves. The temperature independence of k_{et} at high overpotentials shows that the electron transfer is nonadiabatic. The observed nonadiabaticity also supports high order. However, reorganization energies from the initial study are low (~ 0.5 eV), possibly due to difficulties in extracting k_{et} from voltammograms containing some contributions from diffusive processes. Qualitative Marcus behavior (the plateau region in Tafel plots) was observed in the initial study [44].

The distance decay constant β (see below) in Miller et al.'s original study was 0.9 per CH_2 , using ferricyanide and iron(III) hexahydrate [44]. In a later study which accounted more thoroughly for double layer effects, λ was determined to be ~ 1 eV for kinetically facile redox probes such as ferricyanide, 1.3 eV for Ru-hexamine and 2.1 eV for iron(III) hexahydrate. With a better understanding of the redox probe behavior, β was found to be 1.08 ± 0.20 per CH_2 and independent of the redox couple and electrode potential [96]. Pre-exponential factors were also extracted from the Tafel plots. The edge-to-edge rate constants (extrapolated) are approximately 10^4 – 10^5 s^{-1} for all redox probes, which is reasonable for outer-sphere electron transfer. The pre-exponential factors are $\sim 5 \times 10^{12}$ s^{-1} [96].

In another study, which extended the understanding of the behavior of both dissolved and tethered redox probes, the electrochemistry of a structurally related series of outer sphere redox complexes was compared at Au- $\text{S}(\text{CH}_2)_{13}\text{OH}$ monolayers (System 5). As bipyridyls replace cyano ligands in $\text{Fe}(\text{bpy})_n(\text{CN})_{6-2n}^{(2n-3)+}$ ($n = 0$ – 3), λ decreases as predicted by Marcus theory. However, the adiabaticity of the redox probe decreases discontinuously upon replacement of the last bipyridyl ligand, suggesting that the ligand hinders the approach of the complex to the film and that electronic coupling is not mediated by these ligands. Similar trends are also observed with methyl- and sulfonate-modified bipyridyl ligands and in $\text{M}(\text{bpy})_3^{3+}$ ($\text{M} = \text{Ru}, \text{Os}$) [97].

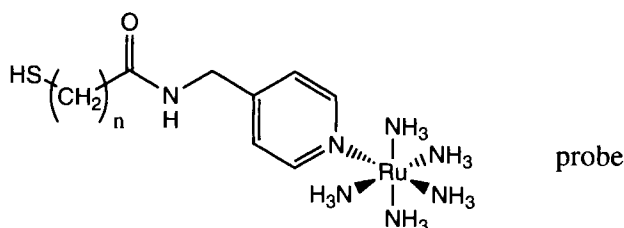
Recently, Majda and co-workers developed a new technique for measuring trends in electron-transfer rates through alkanethiol monolayers on mercury by forming mercury–mercury tunnel junctions between two micrometrically-controlled hanging drop mercury electrodes [98]. A SAM is adsorbed on each surface prior to formation of the tunnel junction; asymmetric junctions (with SAMs of different lengths) and voltage biases up to ± 1.5 V are employed. Inverse capacitance increases linearly with chain length, yielding a dielectric constant of 2.7 ± 0.3 . Tunneling currents increase quasi-exponentially with voltage bias. The plot of current versus chain length yields an electron transfer decay constant β of 0.89 ± 0.10 per CH_2 ,

consistent with through-chain coupling. Importantly, β varies only slightly with voltage bias, which is consistent with theoretical prediction for through-bond, but not through-space, electron transfer. Although parallel characterization of the actual molecular assemblies under study is difficult, if not impossible, the method shows promise for routine and direct measurements of electron transfer trends across nonelectroactive alkanethiol spacers without dependence on external redox probes.

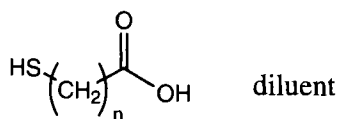
Chemical environment of tethered probes: kinetic heterogeneity and solvation sphere

The issues of kinetic heterogeneity (generally related to disorder) and dielectric nature of the solvation sphere are difficult to separate in the experimental arena. Decreasing the polarity of the solvent generally induces disorder in a nonpolar SAM, leading to decreased solvent reorganization energy either through differential solvation of the redox probe by the SAM (resulting in kinetic heterogeneity) or through direct interaction with the nonpolar solvent. Under these conditions, increased k_{et} also may result either from decreased average distance between redox probe and electrode (by virtue of increased disorder) or from decreased λ characteristic of a nonpolar solvent. Because ion pairing and the use of organic solvents are inextricably linked to the issues of kinetic heterogeneity and solvation sphere, all of these topics are addressed together in this section.

Since the first report of electrochemical measurements at SAM-modified electrodes in polypropylene carbonate by Groat and Creager [99], Murray's and Creager's groups have conducted extensive and systematic investigations of kinetic heterogeneity using tethered ferrocene redox probes diluted with methyl-terminated *n*-alkanethiols (analogous to System 3 with $n = 8$, $m = 7$; $n = 16$, $m = 15$; and $n = 18$, $m = 17$ or System 4 with $n = 8$, $m = 7$). Kinetic dispersity naturally makes the goodness of fit to Marcus kinetics suboptimal because a single electron-transfer process is not being considered [78]. The inhomogeneity is apparent from broadened voltammogram peaks and curved chronoamperometric log plots [81]. Analysis of the raw data yields average values for the fitting parameters [78]. The formal potential E^{of} of a redox probe generally moves positively by 60–400 mV upon immobilization at an electrode surface, due to either double-layer effects or destabilization of the positive ion, which is partially solvated by the organic film [23]. The latter effect causes an exaggeration of the average increase in E^{of} when a non-aqueous solvent is used [78]. The inhomogeneity causes analysis of voltammogram wave shapes and Tafel plots to yield artificially low values of λ [81]. However activation studies of diluted ferrocenecarboxyl- and ferrocenyloctanethiol monolayers (analogous to System 3 with $n = 8$, $m = 7$ and System 4 with $n = 8$, $m = 7$, respectively) in chloroethane–butyronitrile at 114–170 K yield a reasonable value of $\lambda = 0.95$ eV [81]. As expected, kinetic dispersion is more important in nonaqueous solvents. Interestingly, the kinetic dispersity is also increased at low temperature [83]. Three models were considered to account for this apparent kinetic dispersion: Gaussian distributions of (1) formal potentials, (2) reorganizational energies and (3) tunneling distances (i.e., electronic coupling parameters) were invoked, and the models were fitted to experimental data by adjusting the independent parameters [82]. The best fit to the broad CV peaks and multicomponent chronoamperometric



System 6. Mixed monolayers on gold, $n = 10-15$.

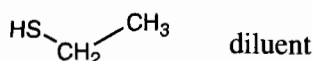
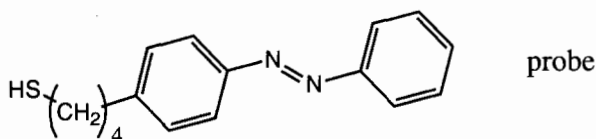
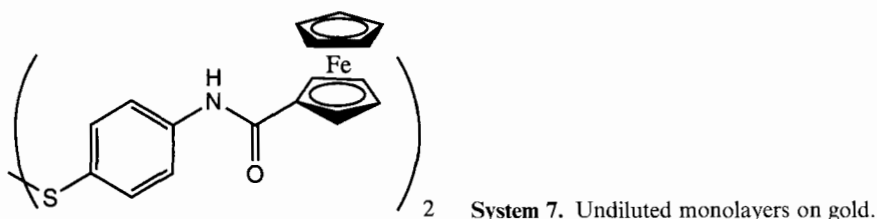


decays was obtained using the distribution of formal potentials [82]. Such a distribution would be reasonable if kinetically distinct states were 'frozen out' due to decreased thermal energy available for conformational interconversion. Strictly, this would represent not a kinetic dispersion but rather a thermodynamic dispersion of redox sites [82].

Ravenscroft and Finklea conducted extensive studies of ruthenated redox probes tethered to SAMs diluted with $\text{Au-S}(\text{CH}_2)_n\text{COOH}$ (System 6) in a wide range of organic solvents [76]. In nonaqueous media, ion pairing is strong and the monolayers are disordered. Fitting Tafel plots with Marcus theory yielded k^0 and λ . For the more polar solvents, $\lambda_{\text{ox}} = 0.9$ eV and $\lambda_{\text{red}} = 0.7-0.8$ eV. As calculated from the Tafel plots, λ decreases markedly for nonpolar solvents, but later Arrhenius and Tafel studies [100] in acetonitrile yielded a value of $\lambda = 0.8 \pm 0.1$ eV. In agreement with Murray et al.'s studies, the average k_{et} increases by up to an order of magnitude in nonaqueous solvents and does not correlate with solvent relaxation times, implicating SAM disorder as the major factor in the apparent kinetic dispersion in nonaqueous solvents [76].

The effect of solvent choice on ion pairing has been directly addressed by Ingram and Murray, who used tethered redox probes to study the effect of solvent dynamics on electrolyte behavior and the associated interfacial electron transfer [90]. The electron-transfer kinetics of methyl-diluted, tethered ferrocenecarboxylate redox probes (analogous to System 3, with $m = 16$, $n = 15$) were compared in dimethoxyethane (MW = 76) and two polyethers (MW = 400 and 1000). Although electron-transfer activation barriers are nearly constant for the series, k^0 falls off with the increasing molecular weight of the solvent. The change in rate constant was within a factor of two of the change predicted using a solvent dynamics model, indicating that solvent dynamics is responsible for at least part of the kinetic difference. Kinetic dispersion of the redox probes increases in the polymer solvents and at decreased temperature. In DME, k^0 is faster than in perchloric acid, which is consistent with a lower λ expected for the less polar solvent [90].

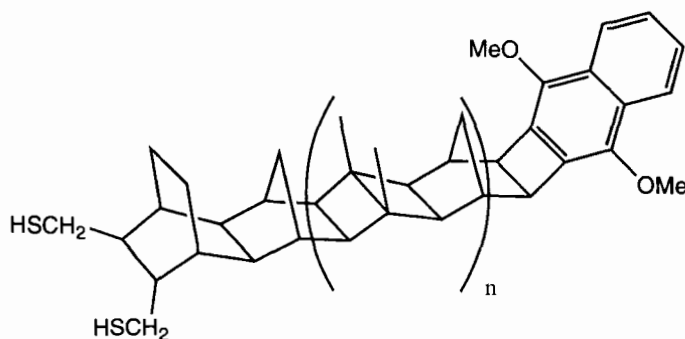
The relationship between ion pairing and steric congestion of the redox probes has been addressed in separate studies by Buttry's and Mirkin's groups. Ion pairing can be detected on the voltammetric time-scale if it kinetically limits electron transfer due to steric congestion. Using QCM, Buttry et al. measured chemically



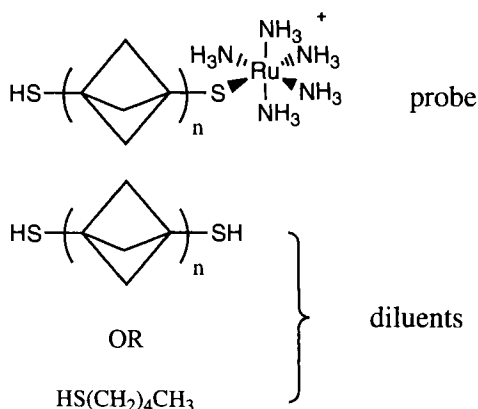
System 8. Mixed monolayers on gold.

reversible, potential-dependent changes in film mass consistent with ion pairing in undiluted, ferrocene-containing SAMs [101] (System 7). Mirkin et al. used SAMs to probe ion pairing by comparing azo-*n*-C₄H₈S-Au with the same redox probe successively diluted with C₂H₅S-Au [102] (System 8). Notably, the extensive characterization shows the undiluted monolayers to be densely packed. Azobenzene reduction is difficult in the SAM but facile in solution, and dilution with ethanethiol or the use of smaller cations results in more facile electron transfer, which is consistent with a kinetic limitation due to ion pairing in the congested films.

The effect of nonpolar solvents on the electrochemical behavior of surface-confined redox groups has also been studied by Geiger et al. Undiluted monolayers containing polynorbornyl spacers between dimethoxynaphthalene redox probes and the electrode were employed (System 9). Thiol, dithiol or disulfide head groups were used to increase SAM stability in nonpolar solvents [103]. Calculated by Laviron's method, the values of k_{et} are an order of magnitude faster than expected for a same-length alkanethiol spacer in an organic solvent [104]. The unexplained difference



System 9. Undiluted monolayers on gold, $n = 0, 1, 2$.



System 10. Undiluted monolayers or mixed monolayers on gold.

may result from possible structural disorder in the polynorbornyl assemblies, lack of dilution of the surface-confined redox probe with nonelectroactive adsorbate or possible differences in the material dependence of electron transfer between norbornylogous and *n*-alkyl linkers [105–107]. A relevant comparison is provided by the well-characterized ruthenated staffane monolayers (System 10) of Bard and co-workers, which provide reversible electrochemistry when well diluted with electroinactive *n*-alkanethiols. Like the polynorbornyl linkers, the undiluted staffane SAMs exhibit broad voltammetric peaks attributable to ion pairing and kinetic heterogeneity in organic solvents [108].

As a final note concerning solvent effects, amphiphilic alcohols added to hydrophobic electroactive *n*-alkanethiol SAMs in aqueous solution appear to aggregate on the monolayer surfaces, decreasing the capacitive envelope and enhancing the barrier properties [109, 110]. However, the formal potentials of the redox couples are shifted positively, and the electrochemical reversibility is decreased. This effect had previously been used by Becka and Miller to determine the pinhole current in the presence of a freely diffusing redox probe (see above) [96].

Effects of the chemical environment of tethered probes

Chidsey et al. first referred to the effect of ‘dangling’ redox probes in his studies of optimal conditions for forming well-ordered electroactive SAMs [74]. In an elegant series of experiments, Finklea and co-workers systematically varied the buried, matched or dangling position of a ruthenated redox probe tethered to SAMs containing an $\text{Au-S}(\text{CH}_2)_n\text{COOH}$ diluent (System 6, $n = 10\text{--}15$) [89]. Voltammograms indicate close-packed monolayers are formed, and the redox probes reside in the aqueous phase in all but the most buried cases. λ agrees with the predicted value of 1.0 eV. Plots of $\ln k^0$ vs. redox tether chain length are linear in all three cases, with $\beta_{\text{matched}} = 0.97 \pm 0.03$ per CH_2 , $\beta_{\text{dangling}} = 0.83 \pm 0.03$ per CH_2 and $\beta_{\text{buried}} = 0.16 \pm 0.02$ per CH_2 . The large value of β for the exposed cases is attributed to a significant contribution of chain–chain coupling between redox and diluent adsorbates to the overall electronic coupling. The slight decrease in β for the exposed cases compared with the matched cases may be due either to the decreased efficiency of coupling through *gauche* defects [111] or to the contribution of

through-chain coupling across the electroactive adsorbate chains. The very low β for the buried cases may be due to ion pairing or dielectric effects.

Distance dependence of electron transfer across SAMs

One of the fundamental parameters early workers desired to investigate in electron transfer across self-assembled monolayers was the dependence of k^0 on the distance between redox probe and electrode. Importantly, the potential dependence of the distance decay constant β directly addresses the nature of the nonadiabatic electron transfer. If β decays sharply with increasing overpotential according to Simmons theory of electron transfer across a square potential barrier [112], electron transfer through a square tunneling barrier is implicated; however, if only a weak dependence of β on the driving force is observed, the mechanism probably contains a large superexchange component (see below) [98, 113].

The results from selected studies in which β has been determined for *n*-alkanethiol self-assembled monolayers are presented in Table 1. The measurements made on

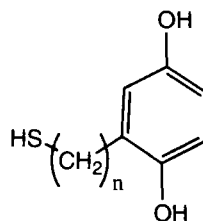
Table 1. Summary of electron-transfer distance decay constants for *n*-alkanethiol SAMs and related bilayer systems.

System ^a	β per CH ₂	Ref.
Co ^{III} (NH ₃) ₅ CO ₂ (CH ₂) _n S[(CH ₂) ₂]-Au, <i>n</i> = 1, 2, 3 (System 1) and a cyclic thiol and dithiol	1.84 ^b	Li and Weaver [86]
HO(CH ₂) _n S-Au, <i>n</i> = 6–14, 16–18; diffusing Ru(NH ₃) ₆ ³⁺ , Fe(H ₂ O) ₆ ³⁺ , Fe(CN) ₆ ³⁺ (System 5)	1.08 ± 0.02	Becka and Miller [96]
FeCO ₂ (CH ₂) _n S-Au in <i>n</i> -C _n H _{2n+1} S-Au, <i>n</i> = 10–18 (System 3)	1.07	Chidsey et al. [19]
Ru ^{III} (NH ₃) ₅ pyrCH ₂ NHC(O)(CH ₂) _n S-Au in HO ₂ C(CH ₂) _n S-Au, <i>n</i> = 10, 15 (System 6)	1.06 ± 0.04	Finklea and Hanshew [148]
FeCO ₂ (CH ₂) _n S-Au in <i>n</i> -C _n H _{2n+1} S-Au, <i>n</i> = 8, 12, 16 (MeCN solvent at 130–150 K) (System 3)	1.06	Murray et al. [83]
FeCO ₂ (CH ₂) _n S-Au in <i>n</i> -C _n H _{2n+1} S-Au, <i>n</i> = 5–9, 16 (ILIT method, except <i>n</i> = 16) (System 3)	1.21 ± 0.05	Chidsey et al. [80]
Ru ^{III} (NH ₃) ₅ pyrCH ₂ NHC(O)(CH ₂) _n S-Au in HO ₂ C(CH ₂) _n S-Au, <i>n</i> = 10–15 (System 6)	0.97 ± 0.03	Finklea et al. [89]
<i>n</i> -C _n H _{2n+1} S-Hg, <i>n</i> = 9, 10, 12, 14; HO(CH ₂) _n S-Au, <i>n</i> = 10, 11–14; diffusing Ru(NH ₃) ₆ ³⁺	1.14 ± 0.09	Majda et al. [133]
<i>n</i> -C _n H _{2n} S-Au, <i>n</i> = 9–16 (STM)	1.5	Weiss et al. [116]
<i>n</i> -C _n H _{2n} S-Hg bilayers, <i>n</i> = 6–14, 16, 18 (Hg-Hg tunnel junction, <i>i</i> - <i>E</i> plot)	0.9 ± 0.1	Majda et al. [98]
H ₂ Q(CH ₂) _n S-Au	0.99 ± 0.06	Hong et al. [115]

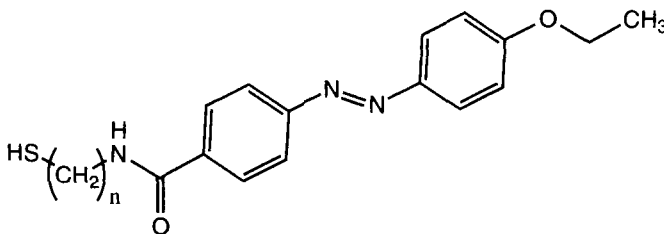
^a Adsorbed from solutions of 10–25% electroactive component compared with total adsorbate; where no diluent is indicated, none was used. Electron-transfer rates were determined by electrochemistry (CV, chronoamperometry or ACIS) using aqueous electrolyte except where noted in parentheses. Fc = ferrocenyl; pyr = pyridyl; azo = azobenzenyl; Q = quinone

^b Converted to per CH₂ using 1.27 Å per (sp³ C)–(sp³ C) bond [114].

System 11. Undiluted monolayers on gold, $n = 1, 4, 6, 8, 10$.



System 12. Undiluted monolayers on gold, $n = 2, 4, 6$.



well-defined, well-ordered films yield an average value of $\beta = 1.06 \pm 0.08$. The agreement of experimental results with the *ab initio* calculations of Liang and Newton is notable; $\beta = 1.08$ per CH_2 was determined from the chain length-dependent slope of transfer integrals for anion radicals for *n*-ethyl to *n*-octyl spacers [114]. The independence of β of the redox probe is most dramatically indicated in the study by Hong et al. [115] in which the observed rate constants are slowed by the two-electron/two-proton transfer mechanism of the hydroquinone probe (System 11), but an alkanethiol-like decay constant is obtained.

Extreme values arise in systems that may be significantly disordered owing to the use of short alkyl spacers or undiluted electroactive adsorbate. For example, the distance dependence of k^0 in undiluted ethoxyazobenzenyl–amide-functionalized alkanethiol SAMs (System 12) was studied with two, four and six methylenes in the alkyl spacer [91]. For azobenzene reduction, k^0 (by Laviron's method) falls off exponentially with increasing spacer length, yielding $\beta = 1.3 \pm 0.2$ per CH_2 . However, Γ varies greatly with chain length, and the inverse capacitance plot exhibits a nonzero intercept. These factors, along with Mirkin et al.'s detailed characterization of similar systems [102], suggest that these SAMs are increasingly disordered with decreasing chain length, leading to an artificially high decay constant. It has also been suggested that conformational changes required upon azobenzene reduction are responsible for the larger observed value of β [115]. For the STM study listed in Table 1 the seemingly high value of 1.5 per CH_2 may be due to difficulties in calibrating the tip height. Alternatively, it may be due to the vacuum conditions employed, suggesting that electron transfer across wetted monolayers differs from that for dry monolayers [116].

Material dependence of electron transfer

The value of $\beta \approx 1.1$ per CH_2 (0.9 \AA^{-1}) for all-alkyl spacers has become a benchmark for comparative studies of the material dependence of electron-transfer rates.

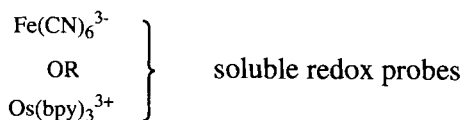
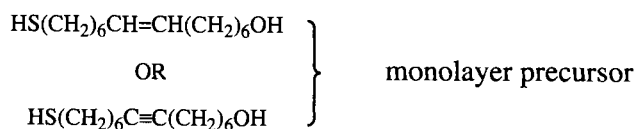
The effect of introducing new functionality into a structure comprising otherwise regular repeats is readily appreciated by consideration of the superexchange model of electron transfer [114, 117–121]. In the simplest form, the total nonadiabatic coupling across a molecular spacer is calculated as the product of individual couplings between atoms along the way from donor to acceptor. Successive approximations may be made in which coupling between first-, second- and third-nearest atoms are considered. Thus, single strong or weak couplings each affect the total coupling in a scalar way. Furthermore, a series of favorable couplings, as in the case of a conjugated spacer, increase the overall coupling by the product of the individual enhancements.

Electron transfer across monolayers and bilayers containing several types of variations in the material composition is considered in this subsection. SAMs have been studied that contain alkenes, alkynes, phenyl groups, ethers, carboxyl groups, amides, salt bridges, hydrogen bond links and through-space jumps. The effects of interposing these structural modifications in through-chain electron transfer pathways are discussed here.

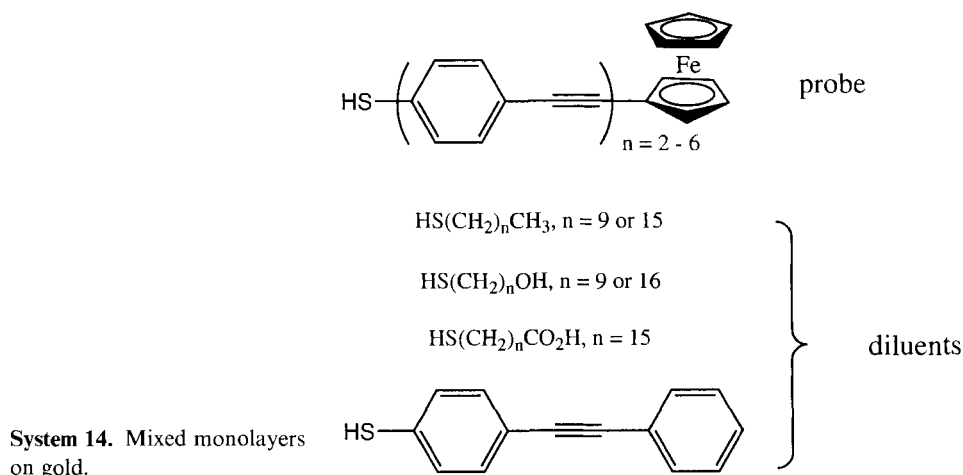
All-carbon, conjugated spacers

Miller et al. studied electron transfer across alkanethiol SAMs in which the adsorbates contain single alkene or alkyne bonds positioned in the center of the monolayers (System 13) [84]. Electronic coupling across the monolayers was decreased by each of these modifications. The electronic coupling might have been expected to increase as a result of the smaller band-gap of the conjugated linkers. However, the results are explained in terms of the superexchange model, which suggests that couplings between first-, second- and third-nearest neighbors with dissimilar electronics perturb the overall coupling and dominate over longer range couplings. This picture is supported by *ab initio* calculations of the neutral diradical splitting energies for modified and unmodified alkanes, which predict lower coupling for the modified spacers.

Electron transfer across ferrocene-substituted oligo(phenylene-ethynylene)thiols (System 14) on gold has been studied using the ILIT technique [122] (see above) and electrochemistry [50]. Values of $\beta = 0.57 \pm 0.02$ and 0.36 \AA^{-1} were obtained, respectively. Using the electrochemistry method, k^0 is 350 s^{-1} for the 43 Å, 36-bond, six-unit conjugated spacer, compared with 1.25 s^{-1} for the 23 Å, 18-bond alkanethiol



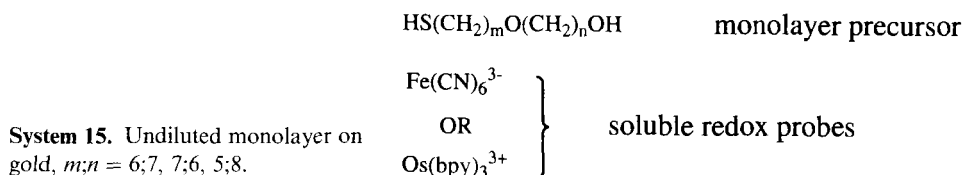
System 13. Undiluted monolayers on gold.

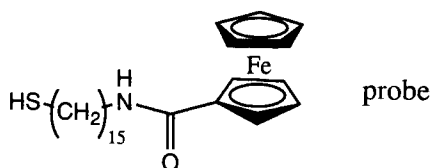


spacer used in Chidsey's seminal study [73]. The conductivity of single oligo(phenylene-ethynylene)thiols embedded in dodecanethiol monolayers on gold has also been investigated by STM. Groups of conjugated thiols were observed at alkanethiol domain boundaries and gold substrate step edges, but apparently single conjugated thiols were isolated on terraces. The apparent tunneling barrier height is at least twice as high over the conjugated spacers as over the domains in the alkanethiol monolayer, consistent with higher transconductance of the conjugated spacers [123, 124]. Efforts to quantify the transconductance of the phenylene-ethynylene spacers by STM are continuing [116].

Spacers containing covalently linked heteroatoms

In an example of careful structural characterization of internally modified SAMs intended for electron-transfer studies, Miller et al. fully characterized ω -hydroxy- n -alkanethiol SAMs on gold containing buried ether functionalities (System 15) [125]. Analysis of the potential of zero charge yielded values of the tilt and twist of the alkane chains in reasonable agreement with those found by reflective IR spectroscopy. The monolayers were concluded to exhibit crystalline packing due to the narrow ether asymmetric stretch, and the broadened and red-shifted methylene stretches were attributed to breaking of the degeneracy of the methylene dipoles by the internal ether dipole [125]. In subsequent measurements of electron transfer across the SAMs containing buried ether functionalities, electronic coupling was



HS(CH₂)₁₆OH

diluent

System 16. Mixed monolayers on gold.

decreased compared with *n*-alkanethiols of the same length. However, electron transfer across the ethers was significantly faster than for the SAMs containing buried alkenes and alkynes described above, as predicted by the *ab initio* calculations. In the context of superexchange theory, these results suggest that the effect of changing the electronic character of one of the bonds (from σ to π) in the chain perturbs coupling to a greater degree than changing one of the constituent atoms to a heteroatom [84].

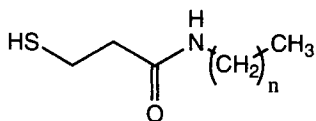
Spacers containing amide (peptide) groups

By analogy with proteins, the predictions of Beratan and co-workers [126–128] suggest that electron-transfer spacers containing amide groups should exhibit values of β equal to or slightly less than that of alkanes ($0.6\text{--}0.8\text{ \AA}^{-1}$). Three investigations of electron-transfer rates across amide groups in alkanethiol SAMs are summarized next.

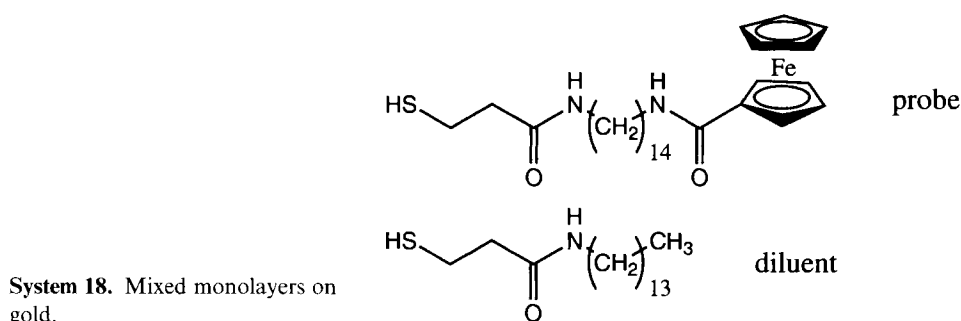
In SAMs of FcC(O)NH-*n*-C₁₅H₃₀S-Au diluted with HO-*n*-C₁₅H₃₀S-Au [94] (System 16), k^0 is 1.9 times faster than expected based on Chidsey's 1991 report [73] using $\beta = 1.07$ per CH₂ [19]. This difference could be due either to disorder in the amide-containing SAM or to the change in composition. The electrochemical responses of these amide-containing monolayers are well behaved, suggesting that the difference is due to variation in composition [94]. Thus, this result implies faster electron transfer through an amide group than a carboxylate moiety or two CH₂ groups.

In support of these findings, Majda et al. also recently published results of electron-transfer studies of amide-based adsorbates (System 17) using the Hg–Hg tunnel junction method [98]. The tunneling currents for the amide-containing bilayers are significantly higher than those for alkanethiol SAMs in the same study. A quantitative interpretation of these data is still awaited.

We have investigated the influence of amide bonds upon electron-transfer kinetics in well-organized assemblies of alkanethiolates possessing 'buried' amide groups within the chain [49, 129, 130]. Electron-transfer data obtained for a ferrocene-



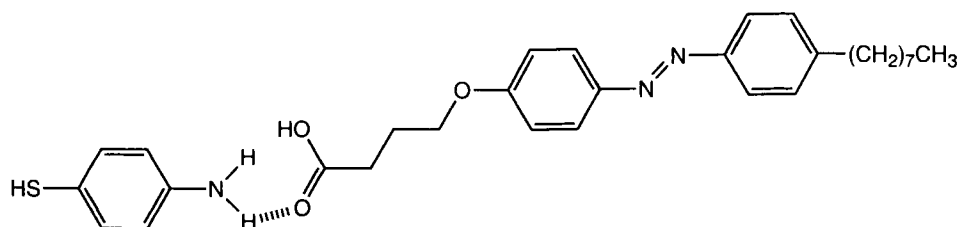
System 17. Undiluted bilayers at a mercury tunnel junction, $n = 9, 11$.



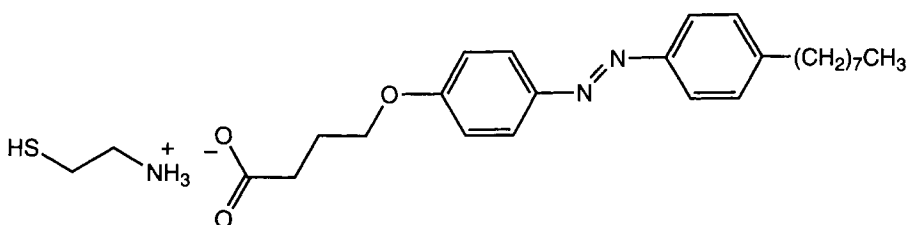
carboxamide redox probe diluted in methyl-terminated chains (System 18) from cyclic voltammetry and analyzed by Bowden et al.'s method [93] yield Tafel plots from which k^0 can be extrapolated. Fitting of the data and one-amide-containing SAMs to the Fermi–Dirac-modified Marcus equation [73] yields reasonable reorganization energies ($\lambda = 0.87$ eV) and coupling prefactors. This value of λ is in close agreement with previously published data and supports the kinetic homogeneity of the system [94]. The standard rate constants and coupling prefactors suggest that $\beta_{\text{amide}} \approx 0.8 \text{ atom}^{-1}$ ($\sim 0.7 \text{ \AA}^{-1}$) for electron transfer across peptide bonds in this model system.

Salt bridges, hydrogen bonds and through-space jumps

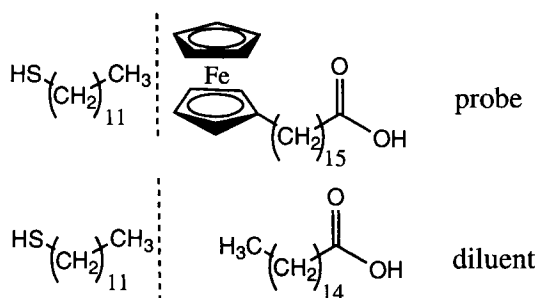
Liu et al. used self-assembled monolayers to explore electron transfer across non-covalent linkages. Self-assembly of aminoethanethiol and 4-mercaptoaniline monolayers was followed by LB deposition of azobenzene-containing carboxylic acid overlayers (Systems 19 and 20, respectively) [131]. Consideration of relative acid and base dissociation constants and FTIR-ERS suggest that two different ‘bridges’ are formed in the bilayers: (1) a salt bridge in the case of the 4-mercaptoaniline underlayer and (2) an interface with at least partial hydrogen-bonding character in the case of the aminoethanethiol underlayer. The apparent electron-transfer rate across the ionic bonding bridge is much more rapid than in the ‘hydrogen-bonded’ case. However, differences in molecular packing between these two systems, the different electron-transfer distances through the amine-containing underlayers and the



System 19. Undiluted monolayers on gold.



System 20. Undiluted monolayers on gold.



System 21. Hybrid SAM-LB mixed monolayers on gold.

poorly understood interfacial structures complicate the interpretation of these data. This study highlights the importance of interfacial structure on electron-transfer processes and underscores the need for well-defined models containing hydrogen bonding and ionic bonding links.

McLendon et al. studied the distance dependence of electron transfer in bilayers consisting of alkanethiol monolayers on gold with an overlying mixed LB monolayer of 16-ferrocenylhexadecanoic acid diluted with hexadecanoic acid [132] (System 21). In this system, a nonbonded, 'through-space' jump is required for electron transfer to occur between the ferrocene redox probe and the electrode. As expected, electron-transfer rates measured by CV decay exponentially with monolayer thickness. Interestingly, the rate constants are nearly two orders of magnitude lower than expected for a system with these dimensions if the nonbonding link is assigned the same decay constant as a covalent bond. The magnitude of the rate retardation is partially attributable to factors other than the presence of the through-space jump, such as the buried nature of the redox probe and associated constraints on ion pairing processes. However, these data suggest that electron transfer is much slower across noncovalent than covalent links, in accord with the expectations for chain-to-chain electron transfer [114, 117–121, 126–128].

Majda and co-workers provided an elegant demonstration of through-bond and chain-chain hopping processes as parallel mechanisms for electron transfer across SAMs [46, 133]. In *n*-alkanethiol monolayers formed on hanging drop mercury electrodes, the adsorbate coverage Γ is measured by chronocoulometry of the mercuric thiolate formed upon adsorption. For the as-adsorbed films, geometric con-

siderations show that the adsorbate chains are close packed and oriented perpendicular to the substrate. For $\text{Ru}(\text{NH}_3)_6^{3+}$ reduction at these SAM surfaces, k^0 decays exponentially with increasing chain length, yielding the ‘through-bond’ decay constant reported in Table I. Micrometrically driven changes in the surface area of the monolayer-covered mercury drop lead to directly proportional responses in C_{dl} , demonstrating a linear decrease in SAM thickness consistent with tilted chains and the absence of pinholes and bare spots. The increase in k^0 with increasing electrode area suggests that electron transfer can occur through van der Waals bridges between neighboring chains via a chain-hopping mechanism as well as by through-bond coupling along single chains. Fitting of the data to these parallel mechanisms yields a ‘through-space’ decay constant β_{ts} of 1.31 \AA^{-1} for the less efficient chain-to-chain pathway.

Use of SAMs to study mechanistic details of electron-transfer reactions

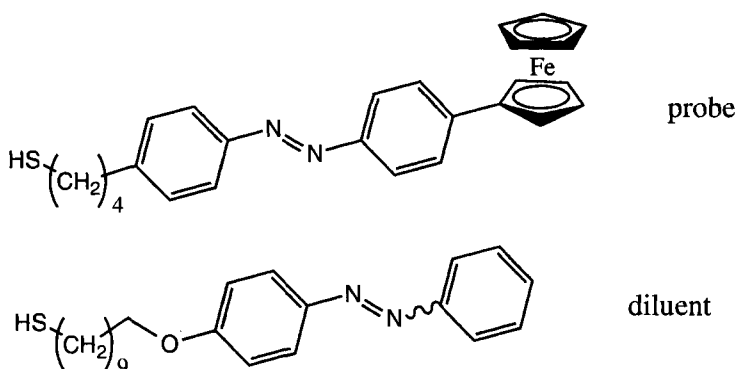
In this section, selected studies are presented in which self-assembled monolayers have been used to address topics such as transition-state structures and sequential electron transfer. These studies were selected because they address fundamental mechanistic processes. SAMs have also been used to investigate such basic electrochemical phenomena as the potential profile near an electrode [134, 135], interfacial capacitance [136], the influence of redox [134] or polarizable [137] moieties on double-layer structure and the behavior of ultramicroelectrodes approaching molecular size [138]. These important topics are beyond the scope of this chapter, and the interested reader is directed to the literature for more information.

Nuclear reorganization and transition-state structure

Faulkner et al. performed surface-confined electrochemistry at high pressures to probe the structure of the transition state during the oxidation of a tethered ferrocene probe (analogous to System 4) [139]. In these studies, the ferrocene-containing SAMs on gold were subjected to pressures between 1 and 6000 atm. The pressure dependence of the anodic peak potential reveals a positive volume of activation for oxidation, which is consistent with a solvent reorganization in the transition state, which allows ion complexation. This study demonstrates the importance of structural and environmental effects on surface-confined electron-transfer processes.

Electron transfer mediated by surface redox centers

Mirkin et al. studied the diode-like response of mediated ferrocyanide oxidation which occurs if oxidation potential of the surface-confined redox moieties is higher than that of the dissolved analyte [140]. This effect was previously reported by Uosaki et al. for the case of dissolved ferrous ion and an undiluted $\text{Fc}(\text{CH}_2)_{11}\text{S}-\text{Au}$ electrode [88]. Monolayers of azo-O-*n*- $\text{C}_{10}\text{H}_{20}\text{S}-\text{Au}$ containing 1 % $\text{Fc-trans-azo-O-}n\text{-C}_4\text{H}_8\text{S}-\text{Au}$ (System 22) are close packed according to extensive characterization [140]. Reduction of Fe^{3+} but not oxidation of Fe^{2+} is observed at the modified electrode, as ferricyanide reduction is thermodynamically disfavored, showing that ferrocyanide oxidation is mediated by ferrocenes [102, 141]. The diode-like response



System 22. Mixed monolayers on gold.

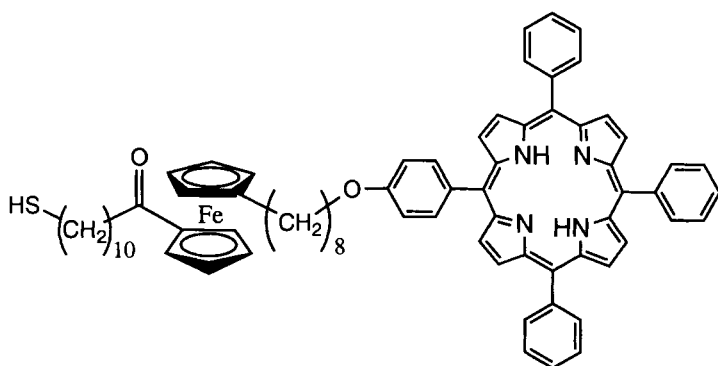
ceases upon photochemical isomerization of *cis*- to *trans*-azobenzene, consistent with increased free volume in the monolayer [140]. This study demonstrates the control of electron-transfer processes at SAMs by photochemical control of assembly structure and order.

Electron transfer mediated by buried redox centers

Hong and Mallouk [142] measured mediated electron transfer across 1,2-ethanedithylbis(phosphonate) (EDP) spacers in zirconium-containing thin-film multilayers. Ellipsometry shows a stepwise increase in multilayer thickness per EDP layer, suggesting that the degree of disorder is constant with film thickness. For ferrocyanide oxidation, k_{et} depends logarithmically on thickness, and $\beta = 0.43 \text{ \AA}^{-1}$. The low β is shown to be consistent with an electrochemical response dominated by disorder. However, the study demonstrates the potential to model long-range, mediated electron-transfer processes using sequential self-assembly [142]. Recent extensions and refinements of this approach include the construction of zirconium- and cesium-coordinated multilayers [143] and metalloporphyrin stacks immobilized on electrodes [144]. In an analogous monolayer system, a ferrocene group was synthetically placed midway between a metalloporphyrin chromophore and a thiol headgroup (System 23). Sequential electron transfer between the gold electrode and dissolved methylviologen is facile across the ferrocene-containing monolayer, but no electron transfer occurs if the ferrocene mediator is omitted [145].

5.4 Summary and Outlook

The use of mono- and multilayer molecular assemblies to investigate fundamental aspects of electron-transfer reactions in heterogeneous systems has been the focus of this chapter. We discussed the development, characterization and electron-transfer



System 23. Undiluted monolayers on gold.

studies of well-ordered molecular assemblies on solid supports. The relative merits of Langmuir–Blodgett and self-assembled systems were presented in the context of preparing well-defined electron-transfer models. To obtain reliable data from such systems, careful design, preparation and characterization of the assemblies are required. Thus, methods of characterizing the overall structures and assessing the extent of defects were also summarized. Techniques for measuring electron-transfer kinetics in electrode-bound assemblies were briefly reviewed.

Most of the work described in Section 5.3 involved organothiols monolayers on gold because of the relative ease of assembly of highly ordered and well-characterized assemblies in this system. *The key to collecting reliable electron-transfer data and an on-going challenge in this area is obtaining a well-defined system where all parallel electron-transfer paths are the same.* The studies reviewed in this chapter show that when the system is well defined, it has been possible to investigate, in detail, the effect upon electron transfer of (i) the chemical environment of the redox probe (e.g., the nature of the surrounding monolayer, contacting solvent and extent of ion pairing), (ii) the redox probe–electrode separation, (iii) the chemical composition of the spacer and (iv) the mechanisms of charge transfer across monolayers.

Well-defined electron-transfer systems, such as those described in this chapter, provide a number of opportunities for further fundamental study and development of new applications. Investigation of the mechanisms of electron transfer through new monolayer materials (e.g., those containing π -systems such as conjugated oligomers, charge-transfer salts and nucleic acids [146]) will be of increasing interest because these systems offer the possibility of promoting electron transfer over longer distances. As systems involving these new materials are developed, the efficiency of electron transfer will probably become limited by the ‘interconnect’ between the molecule and the electrode [146], hence there will be opportunities in engineering new attachment and linker functionalities.

There is still much to be learned about controlling the directionality or pathway of electron transfer within well-ordered assemblies despite the long-standing interest in mimicking biological processes such as photosynthesis and oxidative phosphor-

ylation. Thus, new systems designed to control the path of electron transfer through the incorporation of intermediate relay redox centers or through exploitation of lateral electron-transfer events [147] will be increasingly of interest. In addition, systems in which electron transfer can be switched or where the rate can be modulated will be important for both fundamental investigation and applications. We expect that designed electron-transfer paths that can control the timing, direction, rate and distance of electron transfer will be achieved and exploited in such applications as chemical sensing, molecular/nanoelectronics and catalysis.

References

1. A. Aviram, (Ed.) *AIP Conference Proceedings*, Vol. 262, American Institute of Physics, New York, 1992.
2. P.-W. Wang, Y.-J. Liu, C. Devadoss, P. Bharathi, J. S. Moore, *Adv. Mater.* 8 (1996) 237–241.
3. G. M. Stewart, M. A. Fox, *J. Am. Chem. Soc.* 118 (1996) 4354–4360.
4. I. Bertini, H. B. Gray, S. J. Lippard, J. S. Valentine, *Bioinorganic Chemistry*, University Books, Mill Valley, CA, 1994.
5. J. R. Bolton, J. A. Schmidt, T.-F. Ho, J.-Y. Liu, K. J. Roach, A. C. Weedon, M. D. Archer, J. H. Wilford, V. P. Y. Gadzekpo, in J. R. Bolton, N. Mataga, G. McLendon (Eds.), *Electron Transfer in Inorganic, Organic and Biological Systems*, Vol. 228, American Chemical Society, Washington, DC, 1991, pp. 117–131.
6. N. S. Hush, *Trans. Faraday Soc.* 57 (1961) 557.
7. R. A. Marcus, N. Sutin, *Biochim. Biophys. Acta* 811 (1985) 265–322.
8. I. Langmuir, *J. Am. Chem. Soc.* 39 (1917) 1848–1906.
9. K. B. Blodgett, *Phys. Rev.* 55 (1939) 391–404.
10. I. Langmuir, *Proc. Natl. Acad. Sci. USA* 3 (1917) 251–257.
11. G. G. Roberts, *Langmuir–Blodgett Films*, Plenum Press, New York, 1990.
12. M. C. Petty, *Langmuir–Blodgett Films: an Introduction*, Cambridge University Press, Cambridge, 1996.
13. A. Ulman, *An Introduction to Ultrathin Organic Films: from Langmuir–Blodgett to Self-assembly*, Academic Press, San Diego, 1991.
14. T. Richardson, *Chem. Br.* (1989) 1218–1222.
15. W. C. Bigelow, D. L. Pickett, W. A. Zisman, *J. Colloid Sci.* 1 (1946) 513–538.
16. L. C. F. Blackman, M. J. S. Dewar, *J. Chem. Soc.* (1957) 171–176.
17. W. G. Golden, C. D. Snyder, B. Smith, *J. Phys. Chem.* 86 (1982) 4675–4678.
18. A. Ulman, *Chem. Rev.* 96 (1996) 1533–1554.
19. L. H. Dubois, R. G. Nuzzo, *Annu. Rev. Phys. Chem.* 43 (1992) 437–463.
20. R. G. Nuzzo, D. L. Allara, *J. Am. Chem. Soc.* 105 (1983) 4481–4483.
21. G. Cao, H.-G. Hong, T. E. Mallouk, *Acc. Chem. Res.* 25 (1992) 420–427.
22. A. Ulman, *Materials Characterization Series: Surface, Interfaces, Thin Films*, Butterworth-Heinemann, Stoneham, MA, 1995.
23. H. O. Finklea, in A. J. Bard (Ed.), Marcel Dekker, New York, 1996, pp. 110–336.
24. C. D. Bain, E. B. Troughton, Y.-T. Tao, J. Evall, G. M. Whitesides, R. G. Nuzzo, *J. Am. Chem. Soc.* 111 (1989) 321–335.
25. E. B. Troughton, C. D. Bain, G. M. Whitesides, R. G. Nuzzo, D. L. Allara, M. C. Porter, *Langmuir* 4 (1988) 365–385.
26. P. E. Laibinis, G. M. Whitesides, D. L. Allara, Y.-T. Tao, A. N. Parikh, R. G. Nuzzo, *J. Am. Chem. Soc.* 113 (1991) 7152–7167.
27. R. G. Nuzzo, L. H. Dubois, D. L. Allara, *J. Am. Chem. Soc.* 112 (1990) 558–569.
28. P. E. Laibinis, G. M. Whitesides, *J. Am. Chem. Soc.* 114 (1992) 1990–1995.
29. C. D. Bain, H. A. Biebuyck, G. M. Whitesides, *Langmuir* 5 (1989) 723–727.

30. M. D. Porter, T. B. Bright, D. L. Allara, C. E. D. Chidsey, *J. Am. Chem. Soc.* **109** (1987) 3559–3568.
31. S.-W. Tam-Chang, H. A. Biebuyck, G. M. Whitesides, N. Jeon, R. G. Nuzzo, *Langmuir* **11** (1995) 4371–4382.
32. D. L. Allara, R. G. Nuzzo, *Langmuir* **1** (1985) 52–66.
33. R. G. Nuzzo, F. A. Fusco, D. L. Allara, *J. Am. Chem. Soc.* **109** (1987) 2358–2368.
34. L. Strong, G. M. Whitesides, *Langmuir* **4** (1988) 546–558.
35. L. H. Dubois, B. R. Zegarski, R. G. Nuzzo, *J. Chem. Phys.* **98** (1993) 678–688.
36. N. Camillone, III, P. Eisenberger, T. Y. B. Leung, P. Schwartz, G. Scoles, G. E. Poirier, M. J. Tarlov, *J. Chem. Phys.* **101** (1994) 11031–11036.
37. N. Camillone, III, C. E. D. Chidsey, G.-Y. Liu, G. Scoles, *J. Chem. Phys.* **98** (1993) 4234–4245.
38. P. Fenter, A. Eberhardt, P. Eisenberger, *Science* **266** (1994) 1216–1218.
39. B. E. Poirier, E. D. Pylant, *Science* **272** (1996) 1145–1148.
40. C. Schönenberger, J. Jorritsma, J. A. M. Sondag-Huethorst, L. G. J. Fokkink, *J. Phys. Chem.* **99** (1995) 3259–3271.
41. C. A. Alves, E. L. Smith, M. D. Porter, *J. Am. Chem. Soc.* **114** (1992) 1222–1227.
42. H. Sellers, A. Ulman, Y. Shnidman, J. E. Eilers, *J. Am. Chem. Soc.* **115** (1993) 9389–9401.
43. E. Sabatani, J. Cohen-Boulakia, M. Bruening, I. Rubinstein, *Langmuir* **9** (1993) 2974–2981.
44. C. Miller, P. Cuendet, M. Grätzel, *J. Phys. Chem.* **95** (1991) 877–886.
45. C. E. D. Chidsey, D. N. Loiacono, *Langmuir* **6** (1990) 682–691.
46. K. Slowinski, R. V. Chamberlain, II, R. Bilewicz, M. Majda, *J. Am. Chem. Soc.* **118** (1996) 4709–4710.
47. A. J. Bard, L. R. Faulkner, *Electrochemical Methods: Fundamentals and Applications*, Wiley, New York, 1980.
48. C.-H. Chen, J. E. Hutchison, T. A. Postlethwaite, J. N. Richardson, R. W. Murray, *Langmuir* **10** (1994) 3332–3337.
49. R. S. Clegg, J. E. Hutchison, *J. Am. Chem. Soc.* **121** (1999) 5319–5327.
50. S. Creager, C. J. Yu, C. Bamdad, S. O'Connor, T. MacLean, E. Lam, Y. Chong, G. T. Olsen, J. Luo, M. Gozin, J. F. Kayyem, *J. Am. Chem. Soc.* **121** (1999) 1059–1064.
51. H. Kuhn, D. Möbius, *Angew. Chem., Int. Ed. Engl.* **10** (1971) 620–637.
52. H. Kuhn, *Chem. Phys. Lipids* **8** (1972) 401–404.
53. K. P. Seefeld, D. Möbius, H. Kuhn, *Helv. Chim. Acta* **60** (1977) 2608–2632.
54. D. Möbius, *Acc. Chem. Res.* **14** (1981) 63–68.
55. H. Kuhn, *Pure Appl. Chem.* **53** (1981) 2105–2122.
56. H. Kuhn, *Pure Appl. Chem.* **51** (1979) 341–352.
57. M. Fujihira, *Thin Films* **20** (1995) 239–277.
58. D. Möbius, *Ber. Bunsenges. Phys. Chem.* **82** (1978) 848–858.
59. H. Kuhn, *J. Photochem.* **10** (1979) 111–132.
60. W. F. Mooney, D. G. Whitten, *J. Am. Chem. Soc.* **108** (1986) 5712–5719.
61. T. Murakata, T. Miyashita, M. Matsuda, *Macromolecules* **21** (1988) 2730–2733.
62. T. Yatsue, T. Miyashita, *J. Phys. Chem.* **99** (1995) 16047–16051.
63. Y. Hsu, T. L. Penner, D. G. Whitten, *J. Phys. Chem.* **96** (1992) 2790–2795.
64. T. Miyashita, Y. Hasegawa, M. Matsuda, *J. Phys. Chem.* **95** (1991) 9403–9405.
65. K. V. Mikkelsen, M. A. Ratner, *Chem. Rev.* **87** (1987) 113–153.
66. P. F. Barbara, T. J. Meyer, M. A. Ratner, *J. Phys. Chem.* **100** (1996) 13148–13168.
67. H. G. Hong, T. E. Mallouk, *Langmuir* **7** (1991) 2362–2369.
68. T. Kondo, M. Yanagisawa, M. Fujihira, *Electrochim. Acta* **36** (1991) 1793–1798.
69. T. Kondo, M. Fujihira, *Chem. Lett.* (1991) 191–192.
70. D. J. Lockhart, S. L. Hammes, S. Franzen, S. G. Boxer, *J. Phys. Chem.* **95** (1991) 2217–2226.
71. T. Ito, I. Yamazaki, N. Ohta, *Chem. Phys. Lett.* **277** (1997) 125–131.
72. N. Ohta, T. Nomura, I. Yamazaki, *J. Photochem. Photobiol. A* **106** (1997) 37–43.
73. C. E. D. Chidsey, *Science* **251** (1991) 919–922.
74. C. E. D. Chidsey, C. R. Bertozzi, T. M. Putvinski, A. M. Majsce, *J. Am. Chem. Soc.* **112** (1990) 4301–4306.
75. H. O. Finklea, D. D. Hanshew, *J. Electroanal. Chem.* **347** (1993) 327–340.

76. M. S. Ravenscroft, H. O. Finklea, *J. Phys. Chem.* **98** (1994) 3843–3850.
77. H. O. Finklea, M. S. Ravenscroft, D. A. Snider, *Langmuir* **9** (1993) 223–227.
78. L. Tender, M. T. Carter, R. W. Murray, *Anal. Chem.* **66** (1994) 3173–3181.
79. S. E. Creager, G. K. Rowe, *J. Electroanal. Chem.* **370** (1994) 203–211.
80. J. F. Smalley, S. W. Feldberg, C. E. D. Chidsey, M. R. Linford, M. D. Newton, Y.-P. Liu, *J. Phys. Chem.* **99** (1995) 13141–13149.
81. J. N. Richardson, S. R. Peck, L. S. Curtin, L. M. Tender, R. H. Terrill, M. T. Carter, R. W. Murray, G. K. Rowe, S. E. Creager, *J. Phys. Chem.* **99** (1995) 766–772.
82. G. K. Rowe, M. T. Carter, J. N. Richardson, R. W. Murray, *Langmuir* **11** (1995) 1797–1806.
83. M. T. Carter, G. K. Rowe, J. N. Richardson, L. M. Tender, R. H. Terrill, R. W. Murray, *J. Am. Chem. Soc.* **117** (1995) 2896–2899.
84. J. Cheng, G. Saghi-Szabo, J. A. Tossell, C. J. Miller, *J. Am. Chem. Soc.* **118** (1996) 680–684.
85. T. T.-T. Li, H. Y. Liu, M. J. Weaver, *J. Am. Chem. Soc.* **106** (1984) 1233–1239.
86. T. T.-T. Li, M. J. Weaver, *J. Am. Chem. Soc.* **106** (1984) 6107–6108.
87. S. A. John, T. Ohsaka, *J. Electroanal. Chem.* **477** (1999) 52–61.
88. Y. Sato, H. Itoigawa, K. Uosaki, *Bull. Chem. Soc. Jpn.* **66** (1993) 1032–1037.
89. H. O. Finklea, L. Liu, M. S. Ravenscroft, S. Punturi, *J. Phys. Chem.* **100** (1996) 18852–18858.
90. R. S. Ingram, R. W. Murray, *J. Chem. Soc., Faraday Trans.* **92** (1996) 3941–3946.
91. H. Z. Yu, H. B. Shao, Y. Luo, H. L. Zhang, Z. F. Liu, *Langmuir* **13** (1997) 5774–5778.
92. E. Laviron, *J. Electroanal. Chem.* **101** (1979) 19–28.
93. T. M. Nahir, R. A. Clark, E. F. Bowden, *Anal. Chem.* **66** (1994) 2595–2598.
94. K. Weber, S. E. Creager, *Anal. Chem.* **66** (1994) 3164–3172.
95. D. M. Collard, M. A. Fox, *Langmuir* **7** (1991) 1192–1197.
96. A. M. Becka, C. J. Miller, *J. Phys. Chem.* **96** (1992) 2657–2668.
97. S. Terrettaz, A. M. Becka, M. J. Traub, J. C. Fettinger, C. J. Miller, *J. Phys. Chem.* **99** (1995) 11216–11224.
98. K. Slowinski, H. K. Y. Fong, M. Majda, *J. Am. Chem. Soc.* **121** (1999) 7257–7261.
99. K. A. Groat, S. E. Creager, *Langmuir* **9** (1993) 3668–3675.
100. H. O. Finklea, M. S. Ravenscroft, *Isr. J. Chem.* **37** (1997) 179–184.
101. H. C. DeLong, J. J. Donohue, D. A. Buttry, *Langmuir* **7** (1991) 2196–2202.
102. D. J. Campbell, B. R. Herr, J. C. Hulteen, R. P. Van Duyne, C. A. Mirkin, *J. Am. Chem. Soc.* **118** (1996) 10211–10219.
103. A. J. Black, T. T. Wooster, W. E. Geiger, M. N. Paddon-Row, *J. Am. Chem. Soc.* **115** (1993) 7924–7925.
104. T. T. Wooster, P. R. Gamm, W. E. Geiger, A. M. Oliver, A. J. Black, D. C. Craig, M. N. Paddon-Row, *Langmuir* **12** (1996) 6616–6626.
105. M. J. Shephard, M. N. Paddon-Row, K. D. Jordan, *J. Am. Chem. Soc.* **116** (1994) 5328–5333.
106. K. W. Penfield, J. R. Miller, M. N. Paddon-Row, E. Cotsaris, A. M. Oliver, N. S. Hush, *J. Am. Chem. Soc.* **109** (1987) 5061–5065.
107. J. M. Warman, M. Hom, M. N. Paddon-Row, A. M. Oliver, J. Kroon, *Chem. Phys. Lett.* **172** (1990) 114–119.
108. Y. S. Obeng, M. E. Laing, A. C. Friedli, H. C. Yang, D. Wang, E. W. Thulstrup, A. J. Bard, J. Michl, *J. Am. Chem. Soc.* **114** (1992) 9943–9952.
109. S. E. Creager, G. K. Rowe, *Langmuir* **9** (1993) 2330–2336.
110. M. French, S. E. Creager, *Langmuir* **14** (1998) 2129–2133.
111. M. D. Newton, *Chem. Rev.* **91** (1991) 767–792.
112. J. G. Simmons, *J. Appl. Phys.* **34** (1963) 1793–1803.
113. T. Herz, P. Gedeck, T. Clark, *J. Am. Chem. Soc.* **121** (1999) 1379–1380.
114. C. Liang, M. D. Newton, *J. Phys. Chem.* **97** (1993) 3199–3211.
115. H. G. Hong, W. Park, E. Yu, *J. Electroanal. Chem.* **476** (1999) 177–181.
116. L. A. Bumm, J. J. Arnold, T. D. Dunbar, D. L. Allara, P. S. Weiss, *J. Phys. Chem. B* **103** (1999) 8122–8127.
117. M. A. Ratner, *J. Phys. Chem.* **94** (1990) 4877–4883.
118. C. A. Naleway, L. A. Curtiss, J. R. Miller, *J. Phys. Chem.* **95** (1991) 8434–8437.
119. K. D. Jordan, M. N. Paddon-Row, *J. Phys. Chem.* **96** (1992) 1188–1196.
120. C. Liang, M. D. Newton, *J. Phys. Chem.* **96** (1992) 2855–2866.

121. L. A. Curtiss, C. A. Naleway, J. R. Miller, *J. Phys. Chem.* 97 (1993) 4050–4058.
122. S. B. Sachs, S. P. Dudek, R. P. Hsung, L. R. Sita, J. F. Smalley, M. D. Newton, S. W. Feldberg, C. E. D. Chidsey, *J. Am. Chem. Soc.* 119 (1997) 10563–10564.
123. L. A. Bumm, J. J. Arnold, M. T. Cygan, T. D. Dunbar, T. P. Burgin, L. Jones, II, D. L. Allara, J. M. Tour, P. S. Weiss, *Science* 271 (1996) 1705–1707.
124. M. T. Cygan, T. D. Dunbar, J. J. Arnold, L. A. Bumm, N. F. Shedlock, T. P. Burgin, L. Jones, II, D. L. Allara, J. M. Tour, P. S. Weiss, *J. Am. Chem. Soc.* 120 (1998) 2721–2732.
125. K. Sinniah, J. Cheng, S. Terrettaz, J. E. Reutt-Robey, C. J. Miller, *J. Phys. Chem.* 99 (1995) 14500–14505.
126. J. N. Onuchic, D. N. Beratan, *J. Chem. Phys.* 92 (1990) 722–733.
127. J. N. Onuchic, P. C. P. de Andrade, D. N. Beratan, *J. Chem. Phys.* 95 (1991) 1131–1138.
128. J. N. Onuchic, D. N. Beratan, J. R. Winkler, H. B. Gray, *Annu. Rev. Biophys. Biomol. Struct.* 21 (1992) 349–377.
129. R. S. Clegg, J. E. Hutchison, *Langmuir* 12 (1996) 5239–5243.
130. R. S. Clegg, S. M. Reed, J. E. Hutchison, *J. Am. Chem. Soc.* 120 (1998) 2486–2487.
131. H. Z. Yu, N. Xia, J. Zhang, Z. F. Liu, *J. Electroanal. Chem.* 448 (1998) 119–124.
132. L.-H. Guo, J. S. Facci, G. McLendon, *J. Phys. Chem.* 99 (1995) 8458–8461.
133. K. Slowinski, R. V. Chamberlain, C. J. Miller, M. Majda, *J. Am. Chem. Soc.* 119 (1997) 11910–11919.
134. C. P. Smith, H. S. White, *Anal. Chem.* 64 (1992) 2398–2405.
135. R. Andreu, W. R. Fawcett, *J. Phys. Chem.* 98 (1994) 12753–12758.
136. S. D. Evans, A. Ulman, *Chem. Phys. Lett.* 170 (1990) 462–466.
137. C. P. Smith, H. S. White, *Langmuir* 9 (1993) 1–3.
138. W. Gorski, R. T. Kennedy, *J. Electroanal. Chem.* 424 (1997) 43–48.
139. M. T. Cruaños, H. G. Drickamer, L. R. Faulkner, *Langmuir* 11 (1995) 4089–4097.
140. D. G. Walter, D. J. Campbell, C. A. Mirkin, *J. Phys. Chem. B* 103 (1999) 402–405.
141. K. S. Alleman, K. Weber, S. E. Creager, *J. Phys. Chem.* 100 (1996) 17050–17058.
142. H.-G. Hong, T. E. Mallouk, *Langmuir* 7 (1991) 2362–2369.
143. A. Hatzor, T. Moav, H. Cohen, S. Matlis, J. Libman, A. Vaskevich, A. Shanzer, I. Rubinstein, *J. Am. Chem. Soc.* 120 (1998) 13469–13477.
144. D. A. Offord, S. B. Sachs, M. S. Ennis, T. A. Eberspacher, J. H. Griffin, C. E. D. Chidsey, J. P. Collman, *J. Am. Chem. Soc.* 120 (1998) 4478–4487.
145. K. Uosaki, T. Kondo, X.-Q. Zhang, M. Yanagida, *J. Am. Chem. Soc.* 119 (1997) 8367–8368.
146. S. O. Kelley, N. M. Jackson, M. G. Hill, J. K. Barton, *Angew. Chem., Int. Ed. Engl.* 38 (1999) 941–945.
147. C. A. Widrig, C. J. Miller, M. Majda, *J. Am. Chem. Soc.* 110 (1988) 2009–2011.
148. H. O. Finklea, D. D. Hanshew, *J. Am. Chem. Soc.* 114 (1992) 3173–3181.

6 Electron Transfer in Self-organizing Systems of Amphiphiles

James K. Hurst and Rafail F. Khairutdinov

6.1 Introduction

The chemical reactivities exhibited by molecules and ions organized around mesoscopic assemblies are often very different from their reactivities in homogeneous solution. The origins of these differences can be found primarily in (1) the non-homogeneous distributions of reactant concentrations and anisotropic and non-uniform mobilities arising from the simultaneous presence of hydrophilic and hydrophobic microdomains and (2) the influence of local electric fields and conformational restraints intrinsic to the particular supramolecular assembly upon adsorbed or partitioned reactants. In this chapter, we shall consider redox reactions in various microheterogeneous surfactant-based assemblies, including micelles, reversed micelles, vesicles and bilayer membranes. Emphasis will be placed upon principles controlling reactivity, which will be illustrated with selected examples taken from the large literature of experimental systems that have been investigated. No attempt will be made to be encyclopedic in scope; the reader is encouraged to consult the numerous available monographs and reviews for additional information on specific systems [1–3].

6.2 General Attributes of Surfactant Assemblies

Surfactants are amphiphilic compounds that contain hydrophobic segments, generally comprised of long-chain alkyl, acyl and/or aromatic groups, that are covalently linked to hydrophilic polar or ionized segments. When these amphiphilic molecules are dispersed in water, the hydrophilic part is easily solvated, whereas the hydrophobic part resists hydration and seeks to minimize the Gibbs energy of the system by aggregating to exclude water. The thermodynamics of surfactant self-organization

are complex, but the particular structures adopted are a result of the balance the energetics of the 'hydrophobic' effect and hydrophilic surfactant-solute interactions with steric constraints arising from the size and geometric shapes of the polar and nonpolar surfactant domains [4]. Although numerous different structures are possible, including rods, tubules and filamentous structures, dilute aqueous suspensions of surfactant molecules carrying two long alkyl chains generally form membranes and vesicles, which are closed bilayer membranes containing an aqueous core, whereas those carrying a single chain or two short chains (e.g., 6–8 carbons) tend to assemble into structurally simpler micelles characterized by a single aqueous-organic interface.

Surfactants can be classified in terms of their head-group charge as anionic, cationic, zwitterionic (i.e., carrying both positive and negative charges) or nonionic (uncharged, but polar). Several common membrane-forming and micelle-forming surfactants are given in Table 1.

6.2.1 Micelles and Reversed Micelles

Aggregation to form micelles usually occurs over a very narrow concentration range as the total concentration is raised, and is associated with an abrupt change in the turbidity of the solution. The concentration of the surfactant that corresponds to the point at which micelles first form in the solution (critical micelle concentration, cmc) usually decreases with increase in the hydrocarbon chain length. The cmc for sodium dodecyl sulfate (SDS), a 12-carbon anionic surfactant, is 8.1 mM; and the cmc for hexadecyltrimethylammonium bromide [cetyltrimethylammonium bromide (CTAB)], a 16-carbon cationic surfactant, is 0.92 mM. In general, the number of surfactant monomers per micelle, i.e., its aggregation number, can vary from less than 10 to more than 100.

A simplified model for ionic micelles given by Hartley [5] is useful for understanding general features of electron-transfer reactions in micellar suspensions (Figure 1). One should note, however, that this model does not accurately depict the hydrocarbon chain packing within the hydrophobic core, which is thought to be considerably more polar and microheterogeneous than implied by this model [6]. In any event, micelles are roughly spherical with radii that correspond approximately to the extended length of the hydrocarbon chain of the surfactant. The hydrocarbon chains constitute the liquid-like cores of the micelles, whose microviscosities have been estimated as ~ 8 cP from ^{13}C NMR spin-lattice relaxation times [7] (cf. H_2O , for which the viscosity is ~ 1 cP). The Stern layer, whose width is up to a few ångströms, consists of the surfactant head groups and bound counterions. Most of the counterions are dissociated from the micelle, however, and are located in the Gouy-Chapman double layer, whose width is up to several hundred ångströms. The net charge of the Stern layer generates a surface potential that is usually within the range 50–100 mV; this potential diminishes through the Gouy-Chapman layer with increasing distance from the micellar surface. It acts as an electrostatic barrier to the passage of charged ions to and across the micellar surface and promotes spatial separation of oppositely charged reactants and/or products.

Table 1. Chemical structures of some synthetic surfactants.

<i>Anionic surfactants</i>	
$\text{C}_{12}\text{H}_{25}\text{OSO}_3^- \text{Na}^+$	Sodium dodecylsulfate (SDS)
$\begin{array}{c} \text{C}_4\text{H}_9\text{CHCH}_2\text{OCOCH}_2\text{CHCO}_2\text{CH}_2\text{CHC}_4\text{H}_9 \text{Na}^+ \\ \qquad \qquad \qquad \qquad \qquad \qquad \\ \text{C}_2\text{H}_5 \qquad \qquad \text{SO}_3^- \qquad \qquad \text{C}_2\text{H}_5 \end{array}$	Sodium bis(2-ethylhexyl)sulfosuccinate (AOT)
$\begin{array}{c} \text{C}_{16}\text{H}_{33}-\text{O}-\text{P}(=\text{O}) \\ \qquad \qquad \qquad \\ \text{C}_{16}\text{H}_{33}-\text{O}-\text{O}^- \end{array} \text{H}^+$	Dihexadecyl phosphate (DHP)
<i>Cationic surfactants</i>	
$\text{C}_{16}\text{H}_{33}\text{N}^+(\text{CH}_3)_3 \text{Br}^-$	Hexadecyltrimethylammonium bromide (CTAB)
$\text{C}_{12}\text{H}_{25}\text{N}^+\text{H}_3 \text{C}_2\text{H}_5\text{COO}^-$	Dodecylammonium propionate (DAP)
$\begin{array}{c} \text{C}_{18}\text{H}_{37} \quad \text{CH}_3 \\ \diagup \quad \diagdown \\ \text{N}^+ \\ \diagdown \quad \diagup \\ \text{C}_{18}\text{H}_{37} \quad \text{CH}_3 \end{array} \text{Br}^-$	Diocetadecyldimethylammonium bromide (DODAB)
<i>Zwitterionic surfactants</i>	
$\begin{array}{c} \text{CH}_3 \\ \\ \text{C}_{14}\text{H}_{29}-\text{N}^+-\text{CH}_2\text{CH}_2\text{CH}_2\text{SO}_3^- \\ \\ \text{CH}_3 \end{array}$	Tetradecyl[N,N-dimethyl-3-ammonia-1-propane]sulfonate (Zwittergent 3-14)
$\begin{array}{c} \text{O} \\ \\ \text{C}_{15}\text{H}_{31}-\text{O}-\text{CH}_2 \\ \\ \text{O}-\text{CH} \\ \qquad \qquad \text{O} \\ \text{C}_8\text{H}_{17}\text{CH}=\text{CHC}_7\text{H}_{14}-\text{C} \quad \text{CH}_2-\text{O}-\text{P}-\text{O}-\text{CH}_2-\text{N}^+(\text{CH}_3)_3 \\ \qquad \qquad \qquad \qquad \qquad \qquad \\ \text{O} \qquad \qquad \qquad \text{O} \qquad \qquad \qquad \text{O}^- \end{array}$	1-Palmitoyl-2-oleoylphosphatidylcholine (PC)
<i>Nonionic surfactants</i>	
$\text{C}_8\text{H}_{17}-\text{C}_6\text{H}_4-(\text{OCH}_2\text{CH}_2)_n\text{OH}$	Polyethylene glycol mono-4-octylphenyl ether, $n = 9-10$ (Triton X-100)

Micelles are in dynamic equilibrium with their monomer surfactants. Two relaxation processes are related to this equilibrium, a fast one in the microsecond time domain associated with the exchange of individual monomers between the micelles and the bulk aqueous phase and a slower one on millisecond time-scale associated with the complete dissolution of the micelles into monomers [8]. For example, the exit rate for the SDS anion from its micelle is about 10^4 s^{-1} , which is considered to be a diffusion-controlled process [8a]. Nonpolar molecules are usually attracted to the relatively hydrophobic inner core of micelles, whereas ionic reactants and products are either associated with the Stern and Gouy–Chapman layers or repelled from the micelles, depending on the sign of electrostatic interaction. For example, NMR studies show that nonpolar molecules such as benzene and naphthalene are

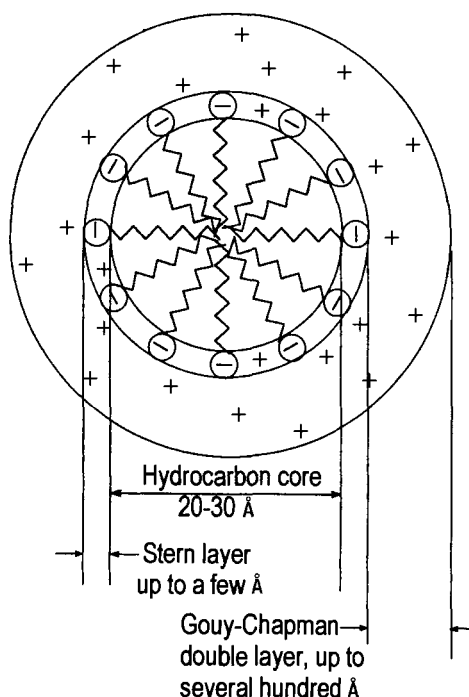


Figure 1. Schematic representation of the Hartley 'oil drop' model [5] for an anionic micelle.

located in a hydrocarbon-like environment in SDS micelles, whereas pyrenesulfonic acid is located at the micellar surface [9]. Compounds dissolved in micelles are also in dynamic equilibrium with those in the aqueous phase. Two distinct pathways have been identified for interparticle migration of adsorbates in micellar media; one involves desorption to the bulk medium and subsequent readsorption to a different micelle, and the other involves direct intermicellar transfer [10]. Exit rate constants for amphiphilic compounds from micelles can vary widely, depending upon the nature and size of the hydrophobic anchor and head-group charge; for example, they decrease dramatically with increasing alkyl chain lengths through homologous series [8a, 11].

Some surfactants form reversed micelles in hydrophobic solvents containing a small amount of water. In these structures, the water is dispersed as microdroplets surrounded by a shell of polar head groups [12]. When the water/surfactant ratio is less than ~ 12 , most of the water molecules are strongly hydrated to the ions or polar head groups of surfactant molecules, giving the aqueous core a viscosity and polarity very different from that of bulk water [13].

6.2.2 Vesicles and Membranes

When swollen in water, surfactant molecules with two long hydrocarbon chains can form single-compartmented (unilamellar) or multi-compartmented (multilamellar)

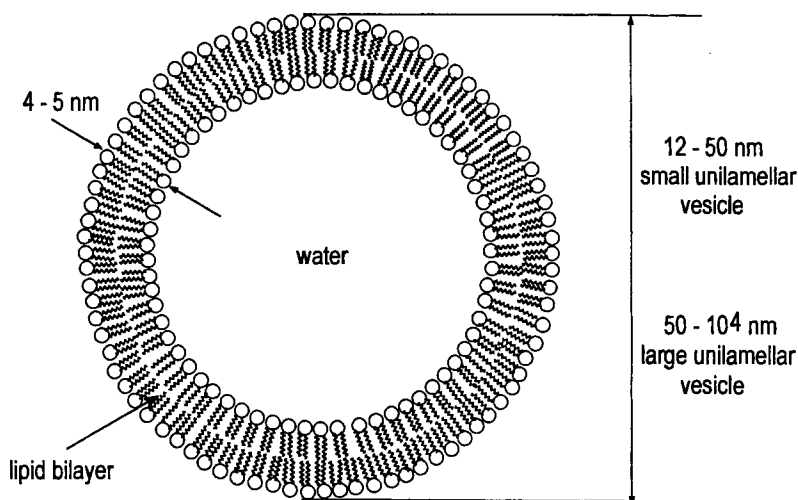


Figure 2. Schematic representation in cross-section of a unilamellar vesicle formed by surfactant molecules containing two long-chain *n*-alkyl substituents. Polar head groups of individual surfactants are indicated as circles and the two alkyl 'tails' as jagged lines.

closed bilayer structures; the latter consists of several concentric bilayers separated by aqueous shells. These structures are known generically as vesicles, although vesicles composed of phospholipids and other biologically derived surfactants are specifically referred to as liposomes. Unilamellar vesicles divide the reaction environment into three well-defined regions, i.e., the aqueous core is separated from bulk solvent by a thin continuous hydrophobic membrane that constitutes a barrier to ion and charge movement between the inner and outer aqueous phases [2a]. The structural organization of a unilamellar vesicle is shown in cross-section in Figure 2. The membrane is formed by a tail-to-tail orientation of the individual surfactant units, with the alkyl chains forming the anisotropic hydrocarbon phase. On lowering the temperature, the bilayer undergoes a thermotropic phase transition (T_c) from a relatively disordered liquid crystalline state characterized by alkyl chains in various *gauche* conformational states to a more ordered gel-like state in which the chains are aligned in parallel in all-*trans* configurations [4c, 14]. The vesicle shape is roughly spherical, [14b, 15] with diameters that range in size from hundreds to tens of thousands of ångströms; their actual sizes depend upon the ionic composition of the medium and inclusion of adsorbed solutes.

Multilamellar vesicles can be formed merely by raising the temperature of the lipid in water above a critical value [16]; unilamellar vesicles can be formed by a variety of dispersion techniques, including ultrasonic disruption [17], high-pressure extrusion through filters of uniform porosity [15], injection of solutions of the lipid dissolved in organic solvents into aqueous media [18], or reverse-phase evaporation [19]. As dynamic entities, vesicles are considerably less labile than micelles. Unlike the 'flickering clusters' that describe micelles, which are constantly dispersing and reforming in solution, individual vesicles, once formed, generally persist for periods

ranging from days to weeks, until a time at which they ultimately aggregate and precipitate from solution. Likewise, transverse diffusion of individual surfactant molecules from one bilayer leaflet to the other, termed 'flip-flop', occurs on time-scales ranging from minutes to days [4b, 20].

Analogous to micelles, vesicles can solubilize nonpolar molecules within their hydrocarbon membrane phase and adsorb polar molecules and charged ions at their aqueous-organic interfaces. Interventricular transfer of aromatic compounds appears to involve desorption-readsorption processes that are rate-limited by release of the vesicle-solubilized compound [21]; in cases where the dopant binding is strongly favored by both hydrophobic and head-group interactions, these reactions can be very slow. For example, the asymmetric *N*-methyl-*N'*-hexadecyl-4,4'-bipyridinium dication (hexadecylviologen, $C_{16}MV^{2+}$) binds very strongly to anionic dihexadecyl phosphate (DHP) vesicles [22]; measured exit rate constants are $\sim 4 \times 10^{-4} \text{ s}^{-1}$, corresponding to a $t_{1/2}$ of $\sim 30 \text{ min}$ [23]. These studies also revealed an unusual intervessel exchange mechanism in which a water-soluble tetraanionic zinc porphyrin, [5,10,15,20-tetrakis(4-sulfonatophenyl)porphinato]zinc(II), that strongly ion pairs viologens but is repelled from the DHP interface, functioned to 'chaperone' the $C_{16}MV^{2+}$ ion from vesicle to vesicle, presumably by interacting with the vesicle-bound viologen and thereby increasing its release rate.

The rate of transmembrane diffusion of ions and molecules across a membrane is usually described in terms of a permeability constant (P), defined so that the unitary flux of molecules per unit time (J) across the membrane is $J = P(c_0 - c_i)$, where c_0 and c_i are the concentrations of the permeant species on opposite sides of membrane; correspondingly, P has units of cm s^{-1} . Two theoretical models have been proposed to account for solute permeation of bilayer membranes. The most generally accepted description for polar nonelectrolytes is the solubility-diffusion model [24]. This model treats the membrane as a thin slab of hydrophobic matter embedded in an aqueous environment. To cross the membrane, the permeating particle dissolves in the hydrophobic region of the membrane, diffuses to the opposite interface, and leaves the membrane by redissolving in the second aqueous phase. If the membrane thickness and the diffusion and partition coefficients of the permeating species are known, the permeability coefficient can be calculated. In some cases, the permeabilities of small molecules (water, urea) and ions (proton, potassium ion) calculated from the solubility-diffusion model are much smaller than experimentally observed values. This has led to an alternative model wherein permeation occurs through transient hydrophilic defects, or 'pores', formed by thermal fluctuations of surfactant monomers in the membrane [25].

Permeability coefficients vary widely, from $P \approx 0$ for large, insoluble species to $P \approx 10^{-2} \text{ cm s}^{-1}$ for H_2O permeation through phosphatidylcholine (PC) membranes [24]. The permeabilities of small, nonpolar electrolytes are relatively high and, in a homologous series, are generally proportional to their partition coefficients in nonpolar solvents vs. water [26]. Lipophilic ions, i.e., those with a low charge/size ratio and/or hydrophobic substituents, can also show appreciable permeabilities, but transmembrane diffusion of small, charged ions such as normal electrolytes is exceedingly slow. The series, MV^0 , MV^+ , MV^{2+} [where $MV^{2+} = N,N'$ -dimethyl-4,4'-bipyridinium (methylviologen, etc.)] provides a useful comparison. First-order rate constants for transmembrane diffusion across this series are

1×10^3 , 2×10^{-2} , and $< 5 \times 10^{-7} \text{ s}^{-1}$ [27]. Thus, for each increase in electronic charge, the diffusion rate decreased by a factor of $\sim 5 \times 10^4$.

The effective barrier imposed by the bilayer membrane to movement of highly charged ions, coupled with the intrinsic vesicle stability, allows one to prepare asymmetrically organized vesicle systems in which the ionic composition of the inner aqueous phase is different from that of the bulk external phase, e.g., one phase containing aqueous reductants and the other aqueous oxidants. These 'vectorially' organized assemblies can often be conveniently prepared by forming the vesicles in solutions containing one of the reactants, then removing the external reactant by chromatographic means, followed by addition of the second reactant (or its precursors) to the external phase.

Planar lipid bilayer membranes (BLMs) have structural and dynamic properties that are similar to those of vesicles, although they are considerably more susceptible to irreversible degradation and mechanical disruption. They are generally formed at a small orifice in a cup dividing two bulk solutions; this arrangement has the experimental advantage that both sides of the membrane are readily accessible, allowing easy manipulation of the medium composition on both sides of the membrane, in addition to direct measurement of properties related to transmembrane dynamics, such as membrane conductivities. A schematic diagram illustrating measurement of a hypothetical transmembrane redox process mediated by a lipophilic electron carrier is given in Figure 3.

6.3 Surfactant Assembly Microenvironments

The microenvironment generates a spatially inhomogeneous distribution of reagents within the reaction volume. The local properties of a solubilization site can strongly affect the energetics of solvent-solute interactions and therefore the intrinsic reac-

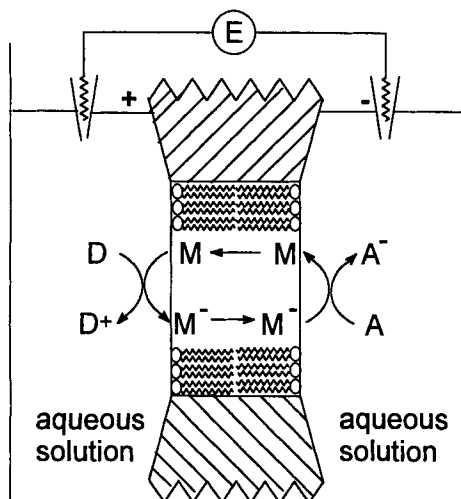


Figure 3. Schematic diagram of an apparatus for measuring transmembrane oxidation-reduction in a planar bilayer membrane. The mechanism described is simple carrier-mediated electron transport. D = aqueous electron donor; A = aqueous electron acceptor; M = membrane-soluble redox mediator; M^- = corresponding lipophilic anion.

tivity of ions and molecules involved in electron transfer. For bimolecular reactions, the geometry of the system and characteristics of the microenvironment in which the reactants are located also influence their capacity to interact. In this context, important effects include the microphase viscosity, local polarities and electric field gradients that exist at the phase interfaces and/or across the membrane. These factors can drastically alter the kinetics of oxidation–reduction reactions to the point that different elementary steps for a common reaction are often rate-limiting in microheterogeneous systems and in homogeneous solution.

6.3.1 Partitioning of Dopants in Micelles

In cases where migration of solute molecules between micelles occurs mainly via dissociation to the aqueous phase and readsorption [28], the reaction dynamics can be represented by the equation 1



where M_n is a micelle containing n solutes and S_{aq} is a solute in the aqueous phase, k_+ is the second-order rate constant for entry of a solute into a micelle and $(n+1)k_-$ is the first-order rate constant for exit of any one solute from a micelle containing $n+1$ solutes.

Taking into account the equilibrium condition, $d[M_n]/dt = 0$, one easily obtains from the set of equations represented by Eq. 1 that the distribution of solute among the micelles obeys a Poisson law [28], i.e.,

$$\frac{[M_n]}{[M]} = \frac{1}{n!} \bar{n}^n \exp(-\bar{n}) \quad (2)$$

where $[M] = \sum_{n=0}^{\infty} [M_n]$ is the total concentration of micelles and \bar{n} is the average number of solutes contained in a micelle. In many cases, Eq. 2 approximates the experimental data fairly well [29], whereas in other cases binomial or geometric distributions were used to describe solute distributions among micelles [30].

Ions adsorbed on the surface of ionic micelles by Coulombic attraction are thought to migrate between micelles primarily during micellar collisions [31]. If only one solute migrates per collision, the migration dynamics can be described by the equation



and the distribution of solutes will again obey the Poisson law [32]. An alternative mechanism that could lead to redistribution of solutes among micelles is the fusion of two micelles to form a short-lived larger aggregate, followed by the fission of this unstable micelle into two smaller micelles. Assuming that each solute of the fused micelle has an equal probability of being in either fragment following fission, a Poisson distribution was obtained for the solute distribution among micelles [33].

6.3.2 Partitioning of Dopants in Vesicles

When the partition dynamics are rapid, the solute distribution in vesicles will obey the same laws as the distributions in micelles. However, when the transmembrane diffusion time of molecules entrapped within the aqueous vesicle core or incorporated into the hydrocarbon phases exceeds the characteristic time of their chemical transformation in chemical reactions, then their partitioning is set by their initial statistical distribution rather than their migration dynamics. In this case also, a Poisson law is appropriate to approximate their distribution among vesicles. This follows because the volume of the inner aqueous phase generally exceeds 10^6 \AA^3 , and the maximum number of molecules that can be entrapped inside the vesicle is correspondingly large.

A complication apparently unique to the relatively static membranes is the tendency for amphiphilic dopants to aggregate in the membrane bilayer, even forming phase-separated domains in the lateral plane at relatively high dopant levels. This phenomenon is spectacularly demonstrated in Langmuir–Blodgett monolayers, where the extent and morphologies of the separated phases can be manipulated by varying the surface pressure and monitored by epifluorescence microscopy [34]. Irregular distributions of dopants can also occur in bilayer membranes [35]. Aggregation is often inferred in these cases from the kinetics of energy- or electron-transfer processes involving the adsorbate [36]; in several cases, fractal analyses have been successfully applied to describe the aggregate structures giving rise to the nonhomogeneous kinetics [37]. Direct observation of association of viologen radical cations (C_nMV^+) adsorbed on anionic DHP vesicles has been obtained by optical spectroscopy [38]. The monomeric species are blue, with characteristic absorption bands at 605 and 397 nm; upon association, the radical forms purple species whose optical bands are shifted to ~ 552 and ~ 366 nm. Several lines of evidence suggest that when the alkyl chain length exceeds $n = 10$, the alkylviologen can intercalate within the membrane, forming part of the bilayer structure [14a, 22, 38, 39]. In this configuration, lateral phase separation may be particularly favorable (Figure 4). Chemical or photochemical reduction of DHP-bound viologens to the corresponding radical cations gives a mixture of monomeric and multimeric species, with the proportion of multimers increasing with the alkyl chain length [38]. An interesting transverse asymmetry was also noted for MV^+ ; when bound to the external DHP surface, this ion was nearly completely dispersed as the monomer, but on the inner surface it was extensively aggregated [40]. Thus, the curvature of the charged interface (convex vs. concave) may also influence the distribution of the dopant in the lateral plane.

6.3.3 Microviscosities of Surfactant Assemblies

As commonly used, the term *viscosity* refers to isotropic systems of macroscopic dimensions. The term *microviscosity* is often used to describe the corresponding properties of the microphases in micelles, vesicles and membranes, despite the fact that this property can be highly anisotropic in these environments. Although am-

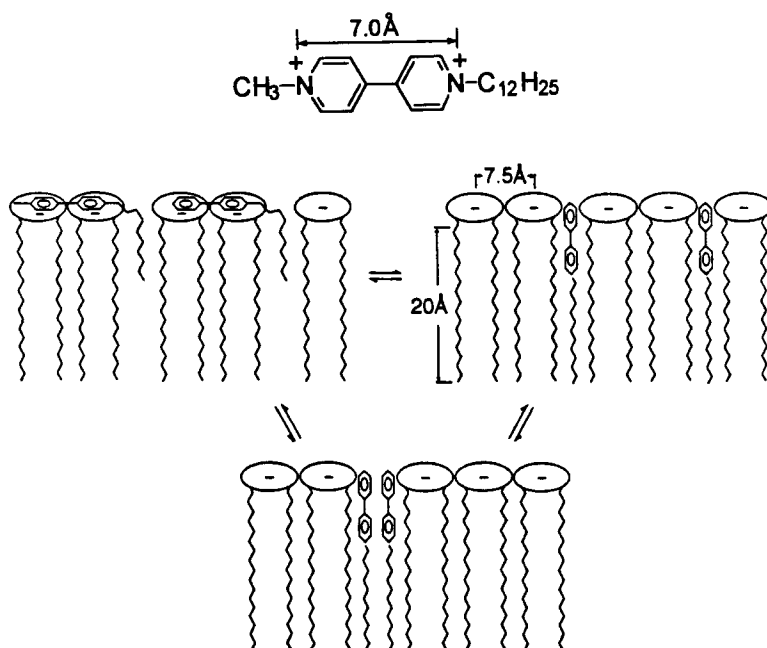


Figure 4. Hypothetical three-state model for binding of $C_{12}MV^{2+}$ in the lateral plane of anionic DHP vesicles. Top left, surface adsorption at the membrane interface; top right, intercalation within the bilayer as monomeric units; bottom, aggregation within the membrane bilayer. The average separation distance of the DHP head groups is 7.5 \AA [14a] and the distance between the quaternary nitrogen atoms of the viologen is $\sim 7.0 \text{ \AA}$.

biguous for this reason, microviscosity can be taken as a measure of the ease with which individual molecules in the assembly move with respect to one another. The microviscosity of surfactant assemblies is usually determined by fluorescence depolarization or magnetic resonance measurements, or by analyzing the kinetics of excimer formation or other diffusion-limited bimolecular reactions. A more useful parameter for kinetic purposes is the diffusion coefficient (D), related to microviscosity (η_m) through the standard Stokes–Einstein equation $D = kT/3\pi r\eta_m$.

In membranes, the motional anisotropies in the lateral plane of the membrane are sufficiently different from diffusion in the transverse plane that the two are separately measured and reported [4b, 20d,e]. Membrane ‘flip-flop’ and transmembrane diffusion of molecules and ions across the bilayer were considered in a previous section. The lateral motion of surfactants and additives inserted into the lipid bilayer can be characterized by the two-dimensional diffusion coefficient (D_l). Lateral diffusion of molecules in the bilayer membrane is often an obligatory step in membrane electron-transfer reactions, e.g., when both reactants are adsorbed at the interface, that can be rate-limiting [41]. Values of D_l have been determined for surfactant monomers and probe molecules dissolved in the membrane bilayer; typical values are given in Table 2. In general, lateral diffusion coefficients of molecules in vesicle

Table 2. Lateral diffusion coefficients measured for a variety of probes in vesicles and membranes.

Surfactant	Probe/method	<i>T</i> (°C)/phase	<i>D_l</i> × 10 ⁸ (cm ² s ⁻¹)	Ref.
<i>Vesicles</i>				
PC	PC/ ¹ H-NMR	25/LC	6.5	131
PC	PC/ ³¹ P-NMR	50/LC	2.6	132
PC	PC/ ³¹ P-NMR	20/LC	10	133
PC	Pyrene/EF	20/LC	3	134
PC	Pyrene/FQ	24/LC	21	135
DLPC	DLPC/ ¹⁴ N-NMR	31/LC	7	136
DLPC	Pyrene/FQ	15/LC	17	137
DLPC	Pyrene/EF	50/LC	59	138
DMPC	Pyrene/FQ	35/LC	31	137
DPPC	DPPC/ ¹ H-NMR	25/G	1.6 × 10 ⁻²	139
DPPC	DPPC/ ³¹ P-NMR	35/G	10 ⁻¹	132
DPPC	Pyrene/FQ	50/LC	63	137
DPPC	Pyrene/FL	60/LC	200	140
DOPC	Pyrene/PM	20/LC	44	103
DSPC	Pyrene/FQ	67/LC	64	137
DSPC	Pyrene/FL	59/LC	64	141
DOPE	Pyrene/FL	1/LC	14	103
DMPC	DOC/FR	24.5/LC	5	142
DMPC	DOC/FR	23/G	0.01	142
DMPC	DMPC/ESR	30/LC	7	143
<i>Membranes</i>				
DMPC	UQ ₁₀ /EC	30/LC	2	42d
DMPC	UQ ₂ /EC	30/LC	4.6	42d
DMPC	PQ ₂ /EC	30/LC	5.2	42d
PC	PC/ ¹⁴ N-NMR	20/LC	2.2	42e
DMPC	NBD/FRAP	26/LC	5	42f
DMPC	NBD/FRAP	16/G	0.007	42f
DPPC	DPPC/ ¹⁴ N-NMR	47/LC	5	42g
C ₁₈ V ²⁺	C ₁₈ MV ²⁺ /EC	23/LC	7.0	42h
C ₁₈ V ⁺	C ₁₈ MV ⁺ /EC	23/LC	2.3	42h
C ₁₈ Fe ²⁺	C ₁₈ Fe ²⁺ /EC	23/LC	3.5	42h
C ₁₈ Fe ⁺	C ₁₈ Fe ⁺ /EC	23/LC	2.7	42h

Abbreviations: PC = phosphatidylcholine; DLPC = dilauroylphosphatidylcholine; DPPC = dipalmitoylphosphatidylcholine; DOPC = dioleoylphosphatidylcholine; DSPC = distearoylphosphatidylcholine; DOPE = dioleoylphosphatidylethanolamine; DMPC = dimyristoylphosphatidylcholine; DOC = dioctadecyloxatricarbocyanine; UQ₂, UQ₁₀ = ubiquinone 2, 10; PQ₂ = plastoquinone 2; NBD = 4-nitrobenzo-2-oxa-1,3-diazol-4-ylphosphatidylethanolamine; C₁₈V²⁺ = N-octadecyl-*N*'-methyl-4,4-bipyridinium dication; C₁₈Fe²⁺ = octadecyl[*N,N*-dimethyl-3-ammonia-1-ethane]ferrocene; EF = excimer fluorescence; FL = fluorescence lifetime; FQ = fluorescence quenching; PM = monomer fluorescence; FR = fluorescence recovery; FRAP = fluorescence recovery after photobleaching; EC = electrochemical method; LC = liquid-crystalline phase; G = gel phase.

bilayers in their liquid-crystalline phase are about three orders of magnitude less than typical molecular diffusion coefficients in water. In the gel phase, where packing of the surfactant hydrocarbon chains is considerably more ordered, D_l values are further reduced by a factor of 100, reflecting the reduced fluidity of this phase. Numerous studies on oriented planar lipid multilayers have given D_l values that are similar to those of vesicles (Table 2 [41d, 42]). Calculations of D_l by molecular dynamics simulations have given values that are in good agreement with experimentally determined values [43].

Only a few D_l values have been reported for micellar systems. Most of the data have been determined by using NMR relaxation and fluorescence methods; D_l values range between 10^{-5} and 10^{-7} cm² s⁻¹ (Table 2 [44]), intermediate between vesicles and homogeneous solution. Reported values for diffusion coefficients within micelle interiors are very similar to those measured for surface diffusion (Table 2 [45]).

6.3.4 Local Polarity and Electric Field Gradients

Aqueous–organic interfaces

A universal feature of these surfactant-based organized assemblies is that electrical potentials exist at their interfaces. In the case of ionic surfactants, these potentials arise primarily from interfacial ionic gradients (e.g., Figure 1); for neutral and zwitterionic head groups, they are the resultant of aligned dipoles arising from geometries imposed by the anisotropic microphase structure and strongly adsorbed solvent molecules. The surface electrical potential of ionic assemblies can, in principle, be calculated from classical electrostatics for particles of known surface charge density [46]. The electrical potential of a charged surface can also be estimated experimentally by comparing the apparent pK_a shift of pH indicators bound to the surface of the charged surfactant assembly compared to a similarly structured neutral assembly. This pK_a shift (δpK_a) is related to the interfacial potential (Ψ_0) by the equation [47]

$$\Psi_0 = \frac{2.3RT}{F} \delta pK_a \quad (4)$$

The surface potential has also been measured by using EPR spectroscopy to determine the interfacial concentration of amphiphilic spin labels, which accumulate if the electrostatic interaction is attractive and are depleted if it is repulsive [48].

All three methods give similar values of interfacial potentials; typical results for some of micelles and vesicles are listed in Table 3. Also listed are estimates of interfacial dielectric constants (ϵ), determined by comparing the position of absorption bands of solvatochromic indicators in the surfactant assemblies with that of reference 1,4-dioxane–water mixtures with known ϵ values. More generally, luminescence probe analysis [49], thermal lensing [50] and absorption spectroscopy [47, 51] are techniques that have all been utilized to measure local polarities in micelles and vesicles. It is important to note that these methods presume knowledge of the loca-

Table 3. Interfacial potentials, Ψ_0 , and dielectric constants, ϵ , for a series of micelles and vesicles measured at 25 °C.

Surfactant	[Surfactant] (mM)	Ψ_0 (mV)	ϵ^a
<i>Micelles</i>			
SDS	20	−144	50
DBS	50	−63	52
Oleate	50	−131	46
CTAC	50	+168	29
CTAB	50	+151	29
DTAC	50	+154	34
DTAC (4 M NaCl)	50	+43	30
DTAB	50	+136	34
DTAB	65	+134	—
DTAB	162	+119	—
DTAB	324	+99	—
DTAB (4 M NaBr)	50	+19	34
<i>Vesicles</i>			
DHP	2.5	−153	53
DDDAB	2.5	+214	43
DMPC	2.5	−120	34
DPPC	2.5	−137	42
POPC–PCA (99:1)	—	−15	—
POPC–PCA (92:8)	—	−75	—

^a Average value obtained using 2,6-diphenyl-4-(2,4,6-triphenyl-1-pyridinio)phenoxide, 1-hexadecyl-4-[(oxocyclohexadienylidene)ethylidene]-1,4-dihydropyridine, 1-hexadecyl-5-hydroxyquinoline and 1-hexadecyl-6-hydroxyquinoline, average deviation $\leq 9\%$; calculated from [47d]. Abbreviations: SDS = sodium dodecyl sulfate; DBS = dodecyl benzenesulfonate; CTAC = hexadecyltrimethylammonium chloride; CTAB = hexadecyltrimethylammonium bromide; DTAC = dodecyltrimethylammonium chloride; DTAB = dodecyltrimethylammonium bromide; DHP = dihexadecyl phosphate; DDDAB = didodecyltrimethylammonium bromide; DMPC = dimyristoylphosphatidylcholine; DPPC = dipalmitoylphosphatidylcholine; POPC = 1-palmitoyl-2-oleoylphosphatidylcholine; PCA = phosphatidic acid.

tion of the probe; in a recent study, kinetic evidence was obtained for migration of an amphiphilic spirooxazine from the hydrocarbon interior of PC liposomes to the interface upon photoisomerization to the open-ring merocyanine form [52]. These studies indicate that subtle structural changes can lead to a relatively dramatic intracellular redistribution of dopants.

Microphase interiors

The solvent sensitivity of the emission spectrum and fluorescence quantum yield of pyrene and its derivatives have been used to sense the polarity of microphase interiors. By these methods, pyrene in SDS micelles is located within a micro-environment less polar than water, but more polar than typical hydrocarbons [53].

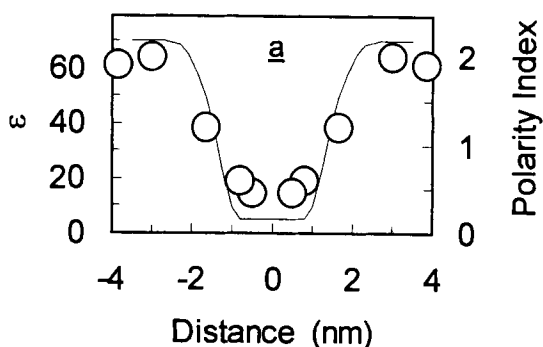
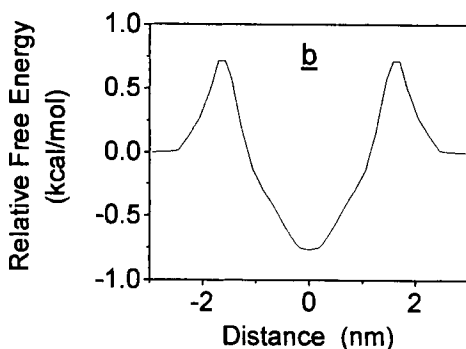


Figure 5. (a) Profile of the hydrophobic barrier in a phosphatidylcholine liposome. The circles are measured points based upon the polarity index [54]; the solid line is the dielectric constant as determined with fluorescent probes [55]. (b) Calculated relative free energy for diffusion of CH_4 across a dimyristoylphosphatidylcholine bilayer (adapted from [57h]). In both diagrams, distances are measured from the center of the bilayer.



In PC and 1,2-dipalmitoylphosphatidylcholine (DPPC) liposomes below the phase transition temperature, pyrene senses an environment similar to butanol and propanol, respectively, although above the transition temperatures the environment is less polar [49c].

To determine the shape of the hydrophobic barrier of bilayer membranes, fatty acids and PC molecules spin labeled with nitroxides at various positions along the lipid chains were diffused into vesicles and their solvent-sensitive isotropic ^{14}N coupling constants were measured [54]. Results are plotted in Figure 5 in terms of distance of the probe from the bilayer center. Also shown is the profile of the dielectric constant along the membrane normal evaluated from the fluorescence lifetime distribution of fluorescence probes in PC liposomes [55]. These data correlate well with results from neutron diffraction studies that map the positional distribution of water and lipid moieties along the bilayer normal [56].

Model calculations of interface-solute electrostatic interactions reproduce well the view of microenvironment polarities of micelles and bilayers obtained from experimental data [57]. According to molecular dynamics simulations, at ~ 1.2 nm from a bilayer interface, water has the properties of bulk water. At shorter distances, water movement slows as individual water molecules become attracted to the interface. At the true interface, which is a region containing both H_2O molecules and the surfactant polar head groups, the water molecules are oriented with

the positive ends of their dipoles shifted toward the bilayer center, generating a positive potential slightly within the bilayer [57h, 58]. The resulting relative free-energy profile for bilayer permeation by a simple hydrophobic molecule, CH_4 , is shown in Figure 5.

Transmembrane potentials

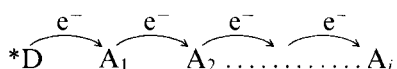
In compartmented systems such as vesicles and planar bilayer-divided volumes, uncompensated movement of charge across the membrane, whether by diffusion of a lipophilic ion or electron transport, violates electroneutrality. Consequently, the membrane becomes polarized, with the transmembrane potential that develops opposing further movement of charge. The magnitude of this effect can be calculated by assuming that the membrane acts as a simple capacitor. The actual value obtained is sensitive to the internal dielectric constant assumed; nonetheless, for small unilamellar vesicles, uncompensated transmembrane transfer of as few as 10 charges per vesicle generates a transmembrane potential of several hundred millivolts [2a]. This potential is sufficiently large to block many redox reactions. Thus, a carrier-mediated redox reaction such as that described in Figure 3 will progressively slow and ultimately cease after several cycles unless the membrane can be depolarized by cotransport of a cation with the electron or by counter-transport of an anion. A second point to note about this reaction is that the oxidative half-cycle, i.e., the sequence comprising oxidation of M^- by A, transmembrane diffusion of the uncharged M, and its reduction by D, is electroneutral, and therefore does not contribute or respond to the developing potential. In contrast, the reductive half-cycle, comprising reduction of M by D, transmembrane diffusion of the M^- anion and its reoxidation by A at the opposite membrane interface, is electrogenic, i.e., generates a potential, because it involves uncompensated translocation of a negative charge. Thus, unidirectional carrier-mediated transmembrane oxidation–reduction can be either responsive or unresponsive to existing transmembrane potentials, depending upon whether or not the carriers are charged or uncharged. In contrast, direct transmembrane electron transport is always electrogenic, and therefore tightly coupled to charge-compensating transmembrane diffusion of ions, a condition which can profoundly affect net transmembrane oxidation–reduction rates.

6.4 Electron-transfer Reactions in Micelles

6.4.1 Stabilization of Charge-separated States

As previously noted (Figure 1), a micellar interface generates an electrical double layer with a steep gradient attenuating over a few hundred ångströms. This electrical gradient has been used to retard the facile back electron transfer that often follows photochemical generation of high-energy redox partners in solution, thereby increasing the lifetimes of the charge-separated products. Effective charge separation can be achieved when one of the products is electrostatically attracted to the

micelle or, by virtue of overall reduction in formal charge, partitions favorably into the micellar interior, and the other product ion is electrostatically repelled from the micelle. A second means for micellar stabilization of high-energy photoproducts is through an electron relay system in which various donors or acceptors are partitioned in different regions of the microphase system, e.g., as in the following sequence:



where the electron transfer cascade increases the distance of physical separation of D^+ and A_i^- , significantly retarding back-electron transfer. This strategy mimics principles of biological photosynthesis and is analogous to numerous alternative approaches that utilize, e.g., covalently linked donor-sensitizer complexes and ordered polymeric arrays containing appended redox centers, zeolite-entrapped reagents and ordered organic multilayers and inorganic pillared systems, to achieve physical separation of reactive photogenerated species [1e].

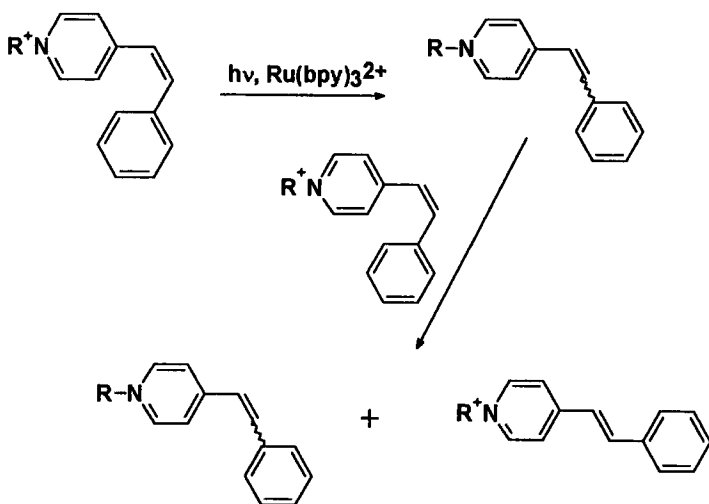
Stabilization via electrostatic interactions and proximity effects

The ability of micelles to enhance photoionization yields of hydrophobic molecules was demonstrated in the early 1970s. Thus, the photoionization yields of pyrene [59], phenothiazine [60] and tetramethylbenzidine [61] cations increased when these molecules were encapsulated in anionic micelles. The effect was attributed to efficient escape of electrons from the geminate charge-separated species formed within the micelle, which is accelerated by the anionic interface. The negative micellar surface imposes an electrostatic barrier between the cations, which remain with the micelle, and the aqueous electron in the bulk water phase, thus increasing the lifetimes of the photoredox products.

The use of micellar surface charge to modulate photochemical reactivity is also illustrated by oxidative quenching of hydrophobic 9-methylantracene fluorescence by the dibromide anion. The cationic CTAB micelle is about 10 times more efficient than the anionic SDS micelle in promoting quenching, an effect that was attributed to electrostatic adsorption of Br_2^- on the surface of the CTAB micelle [62].

Retardation of charge recombination rates by cationic CTAC micelles has been observed in investigations of $Ru(bpy)_3^{2+}$ [63] and [5,10,15,20-tetrakis(*N*-methylpyridinium-4-yl)porphinato]zinc(II) ($ZnTMPyP^{4+}$) [64] photo-oxidation by amphiphilic viologens (C_nMV^{2+}). In this case, the primary photoredox reaction takes place in the bulk solution. The viologen radical cations ($^{\bullet}C_nMV^+$) formed by oxidative quenching of the photoexcited sensitizer ions are considerably more lipophilic than the corresponding dications and, once formed, migrated to the micellar interior. However, the photo-oxidized $Ru(bpy)_3^{3+}$ and $ZnTMPyP^{5+}$ ions were repelled from the micelles by coulombic repulsion, leading to a significant increase (up to 20-fold for $^{\bullet}C_{14}MV^+$) in the photoproduct lifetimes.

Proximity effects arising from confining both reactants to the micellar microphase have also been demonstrated. For example, the efficiency of reductive quenching



Scheme 1.

of photoexcited $Ru(bpy)_3^{2+}$ by *N*-methylphenothiazine (MPH) was strongly increased in the presence of anionic tetradecyltrioxyethylenesulfate micelles [65]. In this case, both photoproducts remained associated with the micelle, resulting in fast back electron transfer. However, charge separation could be stabilized by secondary reactions involving reoxidation of $Ru(bpy)_3^+$ by neutral hydrophobic molecules that, upon reduction to negatively charged species, were sufficiently water-soluble to be ejected from the micelle.

Proximity effects have also been found in radical chain reactions of reactants adsorbed on micelles. $Ru(bpy)_3^{2+}$ -photosensitized *cis* to *trans* isomerization of stilbazolium ions is thought to proceed via intermediate formation of pyridyl radicals generated in the primary photochemical event [66]. The quantum yield of *cis* to *trans* isomerization was $\phi_i = 0.5$ in aqueous solution, whereas ϕ_i was as high as 100 when both $Ru(bpy)_3^{2+}$ and stilbazolium ions were adsorbed on SDS micelles. Calculations indicated that, on average, all the *cis*-stilbazolium molecules within a given micelle could be isomerized by absorption of a single photon. This result suggests operation of a highly efficient intramicellar electron-relay reaction (Scheme 1).

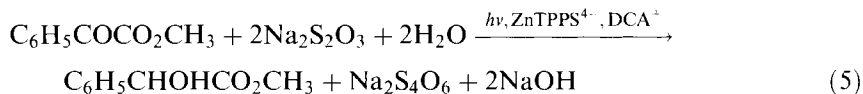
Rapid electron exchange has been directly observed by EPR spectroscopy between amphiphilic *N*-ethyl-*N'*-hexadecyl-4,4'-bipyridinium ($C_{16}C_2V^{2+}$) and the corresponding $\cdot C_{16}C_2V^+$ radical cations in mixed viologen-hexadecyltrimethylammonium cationic micelles [67]. From the measured line broadening of the radical signal in the micelles, the electron exchange rate constant was estimated to be $k \sim 5 \times 10^9 \text{ M}^{-1} \text{ s}^{-1}$ at room temperature. When incorporated into didodecyltrimethylammonium bromide vesicles, the same viologens exhibited even faster apparent electron exchange where, at dopant mole fractions above 0.2, the averaged EPR radical signal underwent exchange narrowing with increasing amounts of

added dopant [68]. However, these studies did not consider the possibility that lateral phase separation of the viologens in the membrane might be contributing to the rapid exchange rates.

Like reactions in normal micelles, rates of electron transfer in reversed micelles can be controlled by the mutual accessibility of the reactants. Electron-transfer reactions between viologen radical cations ($\cdot C_n MV^+$) and various quinones have been studied in aqueous solution and AOT–isooctane–H₂O reversed micelles [69]. For water-soluble anthraquinonesulfonate ions, the rate constants decreased with increasing length of aliphatic chain of viologens, an effect that was attributed to increasing association of the viologen with the surfactant interface. No electron transfer was observed with dimethylnaphthoquinone which, as a hydrophobic molecule, presumably occupied the bulk solvent. Analogously, the photoionization yield of alkylphenothiazines in AOT–isooctane–H₂O and CTAB–C₄H₉OH–H₂O reversed micelles was observed to decrease with increasing alkyl chain length on the phenothiazine [70]. This effect was interpreted as indicating a greater depth of penetration of the long-chain analogs into the organic phase, with attendant greater difficulty of electron ejection into the aqueous microphase. The rate constant for quenching of the luminescence of Ru(bpy)₃²⁺ and a surfactant analog by viologens was decreased by up to 10-fold in water-in-oil microemulsions compared with water [71]. This effect was attributed to restricted access of the viologens located in the aqueous phase to the interfacially adsorbed Ru(II) complex ions.

Vectorial electron transfer

The ability of micelles to partition reactants has been used to construct integrated photocatalytic systems for chemical syntheses. One such system consists of [5,10,15,20-tetrakis(4-sulfonatophenyl)porphinato]zinc(II) (ZnTPPS⁴⁻) as the sensitizer, quinolinium-3-carboxamide cation (DCA⁺) as an electron-transfer mediator, methyl benzoylformate (MBF) as an acceptor and thiosulfate ion (S₂O₃²⁻) as an electron source vectorially organized around cationic CTAB micelles [72]. The complete system as envisioned is shown schematically in Figure 6; methyl benzoylformate is in the hydrophobic core, the negatively charged photosensitizer adsorbed on the micellar surface and the hydrophilic electron donor and positively charged electron-transfer mediator (DCA⁺) residing primarily in the bulk water. The neutral dihydroquinoline (DHQ) produced by oxidative quenching of the triplet excited porphyrin carries an electron from the micellar surface to the hydrophobic interior. Reoxidation by methyl benzoylformate results in the formation of methyl mandelate (MM) with the DCA⁺ returning to the bulk aqueous phase. The overall reaction is given by the equation



From the reported yields [72], it appears that on average up to nine electron transport cycles/mediator had occurred. Significantly, no reduction of MBF by photo-excited ZnTPPS⁴⁻ was observed in the absence of the CTAB micelles.

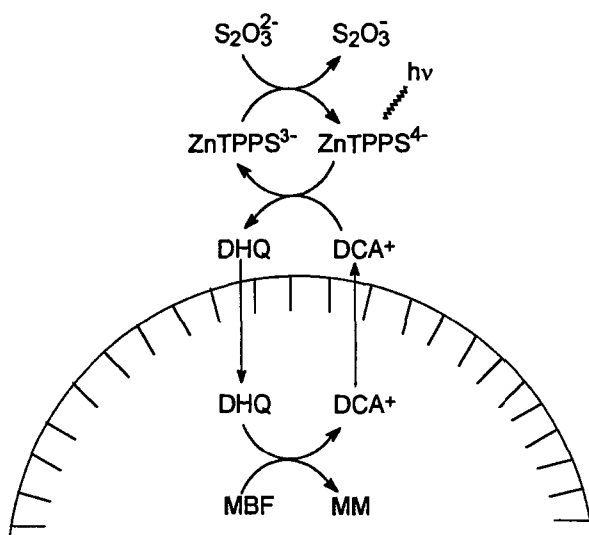


Figure 6. Reaction scheme for $ZnTPPS^{4-}$ photosensitized-quinolium (DHQ) ion-mediated reduction of methyl benzoylformate (MBF) to methyl α -hydroxyphenylacetate (MM) in CTAB micelles (adapted from [72]).

Photosensitized vectorial electron transfer from the (morpholine)ethanesulfonate anion (MES^-) to 1,5-anthraquinone disulfonate ($AQDS^{2-}$) mediated by dibutyl (BTDB) or diethyl (BTDE) esters of 2,1,3-benzothiadiazole-4,7-dicarboxylic acid solubilized in CTAB micelles has also been reported [73]. The proposed mechanism of BTDB-mediated electron transfer is shown in Figure 7, where reductive quenching of photoexcited BTDB by interfacially adsorbed MES^- is followed by electron transfer from reduced BTDB to the $AQDS^{2-}$, recycling the sensitizer.

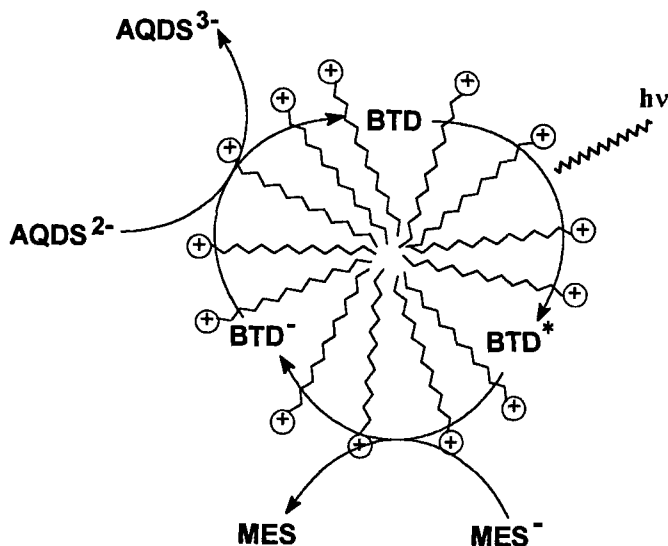


Figure 7. Proposed reaction scheme for BTDB-photosensitized reduction of $AQDS^{2-}$ by MES^- in CTAB micelles (adapted from [73]). BTDB is either BTDB or BTDE (see text for definitions).

6.4.2 Kinetic Analysis of Electron-transfer Reactions in Micelles

Quantitative approaches to describing reactions in micelles differ markedly from treatments of reactions in homogeneous solution primarily because discrete statistical distributions of reactants among the micelles must be used in place of conventional concentrations [74]. Further, the kinetic approach for bimolecular reactions will depend on how the reactants partition between micelles and bulk solution, and where they are located within the microphase region. Distinct microphase environments have been sensed by NMR spectrometry for hydrophobic molecules such as pyrene, cyclohexane and isopropylbenzene, which are thought to lie within a hydrophobic 'core', and less hydrophobic molecules such as nitrobenzene and *N,N*-dimethylaniline, which are preferentially located at the micelle–water interface [75]. Despite these complexities, relatively simple kinetic equations for electron-transfer reactions can be derived for cases where both donors and acceptors are uniformly distributed inside the micelle or on its surface.

Reactions in the interior of spherical micelles

Consider the diffusion-controlled electron transfer reaction $D + A \rightarrow D^+ + A^-$ in a spherical micelle of radius R with donors (D) and acceptors (A) located in the micelle interior. Electron transfer is presumed to require collisional interaction of the reactants. When one of the reactants, e.g., the donor, is immobile and placed at the center of the micelle and N acceptor molecules are initially uniformly distributed throughout the micelle interior, the kinetics of the donor decay are given by the expression [76]

$$\frac{n(t)}{n(0)} = \left\{ \sum_{i=1}^{\infty} H_i \exp\left(-\alpha_i^2 \frac{Dt}{R^2}\right) \right\}^N \quad (6)$$

where

$$H_i = \frac{6\left(\frac{d}{R}\right)^2}{\alpha_i^2 \left[1 - \left(\frac{d}{R}\right)^3\right] \left(\frac{\alpha_i^2}{1 + \alpha_i^2} - \frac{d}{R}\right)}$$

d is sum of the reactants radii, α_i are the positive roots of the equation $\tan[1 - (d/R)]\alpha = \alpha$ and D is the diffusion coefficient of the acceptor. When the observation time is sufficiently large, the kinetics are approximated by the first-order expression

$$\frac{n(t)}{n(0)} = H_1^N \exp(-k_D N t) \quad (7)$$

with the rate constant

$$k_D = \alpha_1^2 \frac{D}{R^2} \quad (8)$$

Monte Carlo calculations have shown that the exponential approximation to the decay kinetics is also valid when both electron donor and acceptors move freely within the micelle [77]. In this case, faster short-time components affect at most the first 15 % of the total decay. Equation 8 predicts that the rate constant of the reaction will decrease gradually with increasing micellar size, and will be only 20 % larger than the reaction in homogeneous solution when $d/R = 0.1$ [78].

To obtain the macroscopic kinetic behavior of an ensemble of micelles, one must average the intramicellar kinetics with a given number of reactants over the occupancy distribution. Assuming that decay kinetics in the individual micelles are exponential with a rate constant k_D for a Poisson distribution of acceptors and that acceptors can enter a micelle with the rate constant k_+ and exit it with the rate constant k_- , one has [79]

$$\frac{n(t)}{n(0)} = \exp\left(-\frac{k_+k_D\bar{N}}{k_- + k_D}t - \frac{k_+k_D^2\bar{N}}{k_-(k_- + k_D)^2}\{1 - \exp[-(k_- + k_D)t]\}\right) \quad (9)$$

Thus, the kinetics of diffusion-controlled bimolecular electron-transfer reactions in the micellar interiors differ from that in the homogeneous solution. Numerous data have shown that Eq. 9 reproduces the dynamics of electron-transfer reactions within micelle interiors [80]. Diffusion coefficients (D) estimated from Eqs. 8 and 9 are very similar to those obtained by independent measurements. For example, Eq. 8 gave $k_D = 7.5 \times 10^7 \text{ s}^{-1}$ for electron transfer from excited pyrene to CH_2I_2 in SDS micelles [79b]. One estimates from Eq. 8, with $R = 20 \text{ \AA}$ and $\alpha_1 = 1.5$ (calculated assuming $d = 7 \text{ \AA}$), a value of $D = 1.3 \times 10^{-6} \text{ cm}^2 \text{ s}^{-1}$, nearly identical with the experimentally determined value of $D = 10^{-6} \text{ cm}^2 \text{ s}^{-1}$ [45].

Reactions on the surface of spherical micelles

The survival probability $W(z, t)$ of a pair of reactants D and A that can diffuse on a spherical surface satisfies the equation [80]

$$\frac{\partial W(z, t)}{\partial t} = \frac{D_l}{R^2} \frac{\partial}{\partial z} (1 - z^2) \frac{\partial W(z, t)}{\partial z} \quad (10)$$

with $W(z, t = 0) = 1$ and $W(z = -\cos \alpha, t) = 0$ as initial and boundary conditions, respectively. In Eq. 10, $z = -\cos \theta$, where θ is the directed polar angle and α is the directed polar angle when the reactants are in contact with each other. The solution to Eq. 10 is expressed by a sum of exponentials [81]. When N acceptors are present on the surface of the micelle, the survival probability for a given initial configuration of acceptors is given by

Table 4. Examples of diffusion-controlled reactions on micellar surfaces.

Reaction	Micelle	R (Å)	D (10^{-7} cm ² s ⁻¹)	Ref.
$\text{Br}_2^- + \text{Br}_2^- \rightarrow \text{Br}_3^- + \text{Br}^-$	CTAB	13.5	0.8	144
$\text{Ag}_2^+ + \text{Ag}_2^+ \rightarrow \text{Ag}_2 + 2\text{Ag}^+$	SHDTE	28	0.6–1.4	31
$\text{Ru}(\text{bpy})_3^{3+} + \cdot\text{MV}^+ \rightarrow$ $\text{Ru}(\text{bpy})_3^{2+} + \text{MV}^{2+}$	SDS	16	6.0	145
$\text{Rh}^* + \text{DMA} \rightarrow \text{Rh}^- + \text{DMA}^+$	CTAB	22	6.2	82b
$\text{Rh}^* + \text{DMA} \rightarrow \text{Rh}^- + \text{DMA}^+$	DTAB	17	6.0	82b
$\text{Rh}^* + \text{DMA} \rightarrow \text{Rh}^- + \text{DMA}^+$	TTAB	19	5.4	82b

Abbreviations: CTAB = hexadecyltrimethylammonium bromide; SHDTE = sodium hexadecyltrioxyethylene sulfate; SDS = sodium dodecyl sulfate; DTAB = dodecyltrimethylammonium bromide; TTAB = tetradecyltrimethylammonium bromide; bpy = 2,2'-bipyridyl; MV^{2+} = *N,N'*-dimethyl-4,4'-bipyridinium; Rh = octadecylrhodamine; DMA = *N,N*-dimethylaniline.

$$W(z_1 \dots z_N, t) = \prod_{i=1}^N W(z_i, t) \quad (11)$$

Finally, the ensemble-averaged quantity $\langle W(z_1 \dots z_N, t) \rangle_N$ gives the probability of donors surviving to time t . Monte Carlo calculations have shown that in many cases the pair survival probability is approximated well by a single exponential except at very short times [79a, 81]. The rate constant k_D is related to the geometric and diffusional characteristics of the system by the equation [79a]

$$k_D = \frac{D_l}{R^2} \left[\frac{2}{1 - (d/2R)^2} \ln \frac{2R}{d} - 1 \right]^{-1} \quad (12)$$

Experimental studies of electron-transfer reactions occurring on the surface of micelles confirm the exponential character of the kinetics; results from some of these studies are summarized in Table 4. The values of the surface diffusion coefficients estimated from Eq. 12 using the measured rate constants are close to values determined by using NMR relaxation and fluorescence measurements [44].

Recent theoretical developments have been directed at incorporating the distance dependence of electron-transfer rate constants into the kinetic equations for diffusion-controlled reactions on the micelle surface, rather than assuming that these are collisional processes [82]. Both forward and back electron-electron transfers have been considered, with fitting of experimental data by numerical integration of appropriate differential equations. A standard Marcus-type expression was used to describe the electron-transfer rate constants. In the particular case of electron transfer from a donor to a single acceptor located initially at θ , one has instead of Eq. 10 [82c]

$$\frac{\partial W(z, t)}{\partial t} = \frac{D_l}{R^2} \frac{\partial}{\partial z} (1 - z^2) \frac{\partial W(z, t)}{\partial z} - k_f(z) W(z, t) \quad (13)$$

with $W(z, t = 0) = 1$ and

$$2\pi R^2 \sin \theta D_l \frac{\partial}{\partial \theta} W(z, t) \Big|_{\theta=\alpha} = 0$$

as initial and boundary conditions, respectively. The rate constant $k_f(z)$ is determined by the Marcus equation [83]:

$$k_f(z) = \frac{2\pi}{\hbar} J^2 \exp(-2r/a) \frac{1}{\sqrt{4\pi\lambda k_B T}} \exp \left[-\frac{(\Delta G_f + \lambda)^2}{4\lambda k_B T} \right] \quad (14)$$

where J denotes the electronic coupling at the donor–acceptor contact distance ($\theta = \alpha$), r is the distance between the donor and acceptor, a determines the distance dependence of k_f , ΔG_f is the reaction driving force and λ is the solvent reorganization energy.

An example of the goodness-of-fit attainable with these equations is given in Figure 8, where the decay kinetics for electron transfer from *N,N*-dimethylaniline to photoexcited octadecylrhodamine on the surface of CTAB micelles is compared with the theoretical fits for two different concentrations of the donor [82b]. The theoretical decay curves were obtained by numerical integration of Eq. 13, followed by ensemble averaging over the Poisson distribution of donors within the micelles; an exponential factor was also added to account for the spontaneous decay of the excited molecules. The parameters ΔG_f and λ were calculated by assuming that the donor and acceptor molecules are on the surface of a sphere of low dielectric

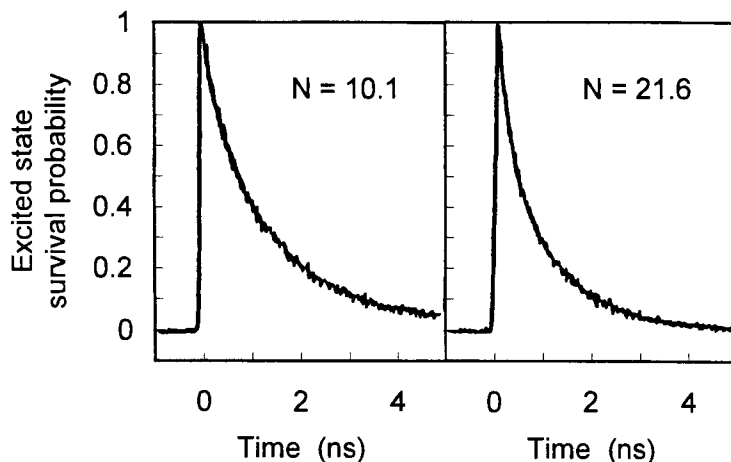


Figure 8. Fluorescence decay curves for octadecylrhodamine B and two concentrations of *N,N*-dimethylaniline on the surface of CTAB micelles. Also plotted as dashed lines are theoretical fits using Eqs. 13 and 14 with the parameters $J = 2 \times 10^{12} \text{ s}^{-1}$, $a = 1.0 \text{ \AA}$, $D = 6.2 \times 10^{-7} \text{ cm}^2 \text{ s}^{-1}$ and $\lambda = 0.93 \text{ eV}$, which are not visible because they reproduce the experimental data within the uncertainty of the linewidth. Adapted from [82b].

constant surrounded by a continuum at the higher dielectric constant of water. As seen from Figure 8, the fits are essentially indistinguishable from the data. For three alkyltrimethylammonium bromide micelles (tetradecyltrimethylammonium bromide, DTAB and CTAB) the overall electron-transfer rate was found to increase with increasing alkyl chain length. This result was attributed to a corresponding decrease in solvent reorganization energies, possibly due to varying extents of water penetration into the head-group regions [82b,d].

The transition from spherical to rod-like micelles changes the dimensionality of the diffusion space and affects the reaction dynamics [84]. The decay kinetics were predicted to follow approximate biphasic first-order kinetics, with the separate components corresponding to the two characteristic micelle dimensions. This behavior has been verified experimentally [85].

6.5 Electron-transfer Reactions in Vesicles and Membranes

6.5.1 Biological Electron Transport and ‘Artificial Photosynthesis’

Szent-Gyorgy first suggested 60 years ago that electron-transfer reactions across a biological membrane are responsible for many biological processes [86]. Since that time, thousands of publications have been devoted to various aspects of electron transfer in living cells, and the central role of electron transport in energy transduction via membrane polarization has been firmly established. Two distinct mechanisms have been delineated, one typified by photosynthetic systems that involves electrogenic vectorial transmembrane electron transfer occurring in a series of short hops between redox components embedded within a membrane-spanning multi-subunit protein complex [87], and the other typified by the mitochondrial terminal respiratory oxidase that involves electrogenic vectorial mechanical pumping of protons or other ions across the bilayer driven by redox-induced protein conformational changes [88]. In photosynthetic reaction centers, the highly organized, precisely defined spatial and energetic relationships of the membrane redox centers create a supramolecular device of incredible efficiency and photostability. The desire to duplicate these properties in simpler devices for practical applications associated with solar energy photoconversion and storage has spawned an area of research known as ‘artificial photosynthesis’. Indeed, spectacular achievements have recently been reported in constructing a liposomal membrane-based organized assembly utilizing a donor–sensitizer–acceptor molecular triad as a vectorially organized electron-transport chain. When a quinone pool was included in the membrane, photoexcitation of the sensitizer generated a proton electrochemical gradient [89] of sufficient magnitude to drive ATP synthesis by a membrane-incorporated F_0F_1 -ATP synthase [90], analogous to related processes in natural photosynthetic systems. However, in simple artificial systems devoted to high-flux applications such as photogeneration of fuels, it now appears that the most efficient systems will incorporate distinctly nonbiological redox processes in their design. For example, it

appears much more efficient in simple self-assembling arrays to initiate or stabilize charge separation in photoredox reactions across the membrane interface, rather than within the membrane plane, and to use electroneutral carriers to effect trans-membrane oxidation–reduction, rather than electrogenic processes such as trans-membrane electron transport.

6.5.2 Primary Charge Separation Events

As with micelles, vesicles can dramatically influence reaction dynamics by favorably partitioning the reactants in different microphase domains. One striking example is the oxidative quenching of photoexcited water-soluble zinc porphyrins by viologens. In homogeneous solutions containing electron donors, net quantum yields for photoreduction of C_nMV^{2+} dications to the corresponding $^{\bullet}C_nMV^+$ radical cations by triplet-excited $ZnTPPS^{4-}$ is low and concentration dependent because the sensitizer and electron acceptor tend to ion pair, forming a $ZnTPPS^{4-}-C_nMV^{2+}$ complex that undergoes static quenching [91]. However, in suspensions of anionic DHP vesicles, the C_nMV^{2+} is preferentially adsorbed at the vesicle interface and oxidative quenching occurs with near-unity quantum yields [92]. The quenching rate constants for the reactions of strongly adsorbed C_nMV^{2+} ions were only $\sim 10^7 M^{-1} s^{-1}$, which is about 100 times lower than bimolecular quenching in homogeneous solution. From the ionic strength dependence of this reaction, as well as chemical reduction of DHP vesicle-bound C_nMV^{2+} by $S_2O_4^{2-}$ [39a], the effective surface charges of the bound viologens were estimated to be -10 to -12 esu. Thus, the reactions are probably still nearly diffusion-controlled, with the reduced quenching rates arising from exclusion of $^3ZnTPPS^{4-}$ from the anionic vesicle interface in the vicinity of the bound viologen. One might note that the reaction is efficient only because the zinc porphyrin triplet lifetime is exceptionally long, i.e., of the order of milliseconds [93]. The use of several anionic sensitizers with excited state lifetimes in the microsecond range gave very inefficient formation of photo-products when reacted with DHP vesicle-bound C_nMV^{2+} ions [92]. Co-adsorption of the nominally water-soluble $ZnTMPyP^{4+}$ {[5,10,15,20-tetrakis(*N*-methylpyridinium-4-yl)porphinato]zinc(II)} ion also gave inefficient photoreduction of the bound viologens [36b]. Decay of $^3ZnTMPyP^{4+}$ was complex, and exhibited apparent triphasic behavior suggesting that aggregation had occurred. The low quantum yields were attributed to efficient triplet–triplet annihilation, charge recombination and other dissipative cross-reactions that increased when the reactants were confined in close proximity on the vesicle surface. In the $ZnTPPS^{4-}$ -photosensitized reaction, charge recombination was very slow, with decay half-times on the tens of milliseconds time-scales, an effect which can also be attributed to electrostatic repulsion, in this case between the lipophilic vesicle-bound $^{\bullet}C_nMV^+$ radical cation and the anionic $^{\bullet}ZnTPPS^{3-}$ π -cation radical.

Similar behavior has been reported for electron transfer between photoexcited [(trimethylammonio)propyl]thiadicyanobocyanine (TTDC $^{3+}$) and triphenylbenzylborate (TPBB $^-$) anions [94]. In aqueous solution, photoinduced charge separation was strongly attenuated by complex formation between the sensitizer and reducing

agent, but in the presence of DPPC, DOPC and L- α -dioleoylphosphatidic acid liposomes, reaction was facilitated by preferential localization of the lipophilic TPBB⁻ ion within the membrane interior, with adsorption of TTDC³⁺ occurring within the interfacial head-group region of the bilayer. These environments facilitate electron transfer since the net electrostatic charge is removed from the ion in the membrane interior and also decreased in the interfacial region. The electron-transfer efficiency for membranes in their gel phases was higher than in their liquid crystalline phases, possibly because the TPBB⁻ was excluded from the more ordered interior, thereby decreasing the donor-acceptor distance.

Comparative studies have also been made of the kinetics of electron transfer from photoexcited ³ZnTPPS⁴⁻ and ³ZnTMPyP⁴⁺ ions to DHP vesicle-bound *N*-alkyl-4-cyanopyridinium (C_{*n*}CP⁺) ions [95]. In homogeneous solution, oxidative quenching of these sensitizers obeyed simple exponential rate laws whose rate constants (*k_q*) were insensitive to the *N*-alkyl chain length of the oxidant. The quenching kinetics remained exponential in the presence of negatively charged DHP vesicles (Figure 9a), although now the *k_q* for ³ZnTPPS⁴⁻ quenching decreased progressively with increasing alkyl chain length through the series of C_{*n*}CP⁺ ions (Figure 9b). In contrast, *k_q* for the ³ZnTMPyP⁴⁺ ion increased progressively with increasing chain length (Figure 9b). The charge recombination rate constant for both zinc porphyrin π -cations decreased progressively with increasing chain length on the \cdot C_{*n*}CP radicals.

The chain length dependences of *k_q* are in quantitative accord with a dynamic model wherein the relative rate constants were determined by C_{*n*}CP⁺ partitioning between the aqueous phase and the aqueous-membrane interface, with only the aqueous-phase component being reactive toward ³ZnTPPS⁴⁻ and only the surface-bound component being reactive toward ³ZnTMPyP⁴⁺. The absence of ³ZnTPPS⁴⁻ quenching by DHP vesicle-bound C_{*n*}CP⁺ was attributed to strong repulsion between ³ZnTPPS⁴⁻ and negatively charged vesicle surface. The absence of appreciable reaction between DHP vesicle-bound ³ZnTMPyP⁴⁺ and C_{*n*}CP⁺ located in the aqueous phase was attributed to the fact that reduction of C_{*n*}CP⁺ is energetically more favorable when at the less polar membrane-water interface than in the bulk aqueous phase. The reduction in charge recombination rates with increasing chain length was rationalized in terms of the increasing hydrophobicity of the radical product. For the reaction with \cdot ZnTMPyP⁵⁺, this increasing hydrophobicity presumably leads to relocation of the neutral \cdot C_{*n*}CP radical more deeply within the bilayer, resulting in an increased separation distance from the membrane-bound oxidized porphyrin. Reaction with the aqueous \cdot ZnTPPS³⁻ π -ion radical is hindered by the electrostatic barrier provided by the DHP vesicle. In this case, the chain length dependence may arise from partially rate-limiting viologen radical exit rates, which are expected to decrease with increasing length. As in the study with C_{*n*}MV²⁺ ions as oxidative quenchers [36b, 92], net photoproduct yields were considerably higher when ZnTPPS⁴⁻ was used as the photosensitizer, i.e., when electron transfer was driven across the membrane interface, than when both sensitizer and quencher were membrane bound. Typically, quantum yields for the formation of charge-separated photoproducts were ~ 0.7 for ZnTPPS⁴⁻-photosensitized reactions and ~ 0.01 for ZnTMPyP⁴⁺-photosensitized reactions, the dominant factor limiting the latter quantum yield being the large rate constant for charge recombina-

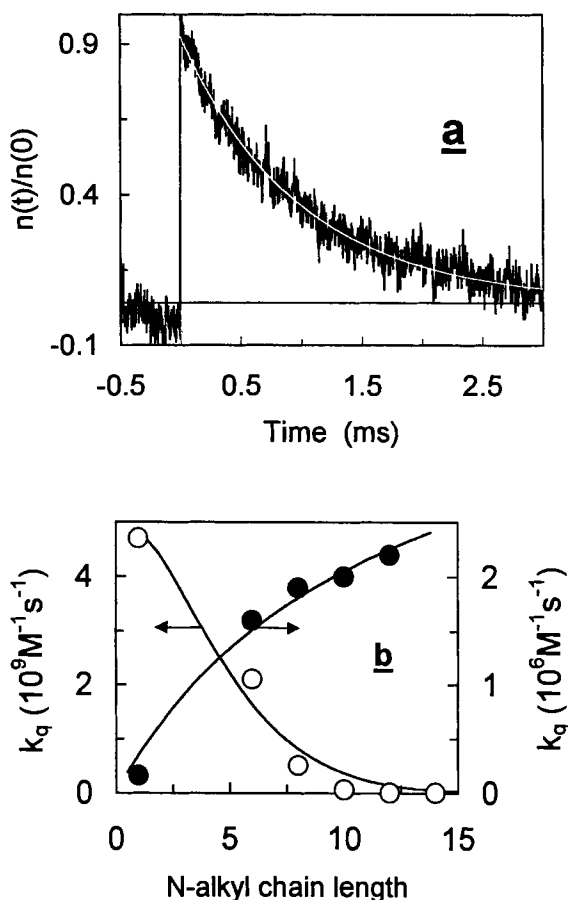
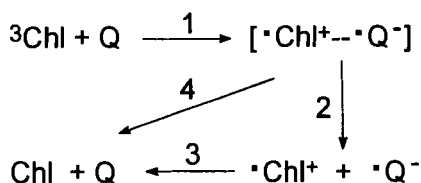


Figure 9. (a) Kinetics of ${}^3\text{ZnTMPyP}^{4+}$ quenching by C_{10}CP^+ in the presence of DHP vesicles. The solid line is the theoretical fit assuming exponential decay with a characteristic time $\tau = 0.9$ ms. (b) Rate constants for ${}^3\text{ZnTPPS}^{4-}$ (open circles) and ${}^3\text{ZnTMPyP}^{4+}$ (solid circles) quenching by C_nCP^+ in DHP vesicle suspensions. Data adapted from [93].

nation on the vesicle surface relative to processes that led to the formation of stable products.

The overall electrostatic charge of the vesicle can also exert more subtle effects on the electron-transfer dynamics of bound reactants. These effects are often complex and difficult to interpret because they can be expected to alter various elementary steps in the overall reaction in opposing ways. This complexity is well illustrated in the systematic study of the influence of the surface charge in mixed DPPC–DHP and DPPC–didodecyldimethylammonium (DDDMA) liposomes on photoinduced electron-transfer reactions involving chlorophyll and several electron acceptors [96]. The impetus for these studies was to find ways to increase the low efficiencies of photoinduced charge separation and the lifetimes of the immediate redox products, conditions that were inherent to binding of the sensitizer to the vesicles. Adding anionic or cationic surfactants had numerous effects, which could include altering the extent of quenching of the excited chlorophyll molecule, the yield of radicals formed by oxidative quenching and the rates of charge recombination. These effects



Scheme 2.

were modulated by the salt composition and ionic strength of the medium, and could be duplicated upon replacing the DHP or DDDMA with other charged surfactants. Thus, it appears that they were attributable primarily to the magnitude of the surface charge on the vesicle. A self-consistent rationalization of the observations could be made by assuming the reaction scheme shown in Scheme 2, where the oxidative quencher is a quinone (Q).

Reaction 1 represents formation of the geminate reaction products [the chlorophyll π -cation radical ($\cdot\text{Chl}^+$) and quinone radical anion ($\cdot\text{Q}^-$)] within the bilayer by electron-transfer quenching of the photoexcited chlorophyll triplet state; reaction 2 represents separation of the radical products by diffusion from the cage; reaction 3 represents charge recombination of the dissociated products; and reaction 4 represents geminate recombination within the cage resulting in no observable product formation. In many systems, step 3 was biphasic; this biphasic character was attributed to $\cdot\text{Q}^-$ partitioning between two different reaction environments, being either contained within the relatively hydrophilic head-group region of the membrane or expelled to a somewhat ill-defined more aqueous environment in the interface. Because the chlorophyll molecule was relatively strongly anchored within the head-group region of the membrane through its pendant phytol chain, emphasis was placed upon the influence of the surface charge on the mobility and distribution of the $\cdot\text{Q}^-$ ion. In principle, the surface charge can alter the reactivity by affecting any or all of the reaction steps in the scheme. Depending on the orientation of the reactants, the charge could stabilize or destabilize the geminate pair (reactions 1 and 4), promote or hinder cage escape by diffusion of $\cdot\text{Q}^-$ (reaction 2) and alter the distribution of sites occupied by $\cdot\text{Q}^-$, and thereby the overall rate of charge recombination (reaction 3). In practice, it was found for systems containing the membrane-soluble benzoquinone molecule that vesicles containing a negative surface charge gave increased photoproduct yields and increased lifetimes of the charge separated species, whereas vesicles containing a positive surface charge gave the opposite result relative to the uncharged system [96a]. The anionic charge was thought to promote expulsion of $\cdot\text{Q}^-$ from the membrane interior to a surface site relatively remote from $\cdot\text{Chl}^+$, effectively decreasing reactions 3 and 4 and promoting reaction 2. In contrast, the positively charged interface was viewed as providing an attractive interaction that held the $\cdot\text{Q}^-$ radical anion within the membrane plane, and therefore in close proximity to its reaction partner, $\cdot\text{Chl}^+$. This model was also used to rationalize the observed effects of surface charge upon reactions initiated by reaction of ${}^3\text{Chl}$ with water-soluble cationic and anionic quenchers, the most dramatic of which was a large (up to 7-fold) increase in photoproduct yields in anionic vesicles when anionic quinones were used as quenchers. This was attributed to

enhancement of reaction 2 by efficient expulsion of the highly charged $\cdot Q^{2-}$ radical dianion [96b]. An additional interesting observation was that charge effects were greater when the ionic strengths in the inner aqueous core and bulk solvent differed than when the salt compositions were identical [96c]. This effect was suggested to arise from changes in lipid packing, affecting the benzoquinone mobility.

Similar behavior has been reported for the dependence of photoionization yields and tetramethylbenzidine ($\cdot TMB^+$) radical cation lifetimes upon the surface charge of the solubilizing vesicles [97]. Specifically, the photoionization yield (ϕ_i) was found to decrease linearly with decreasing interfacial electric potential (Ψ_0) in negatively charged DHP vesicles. The photoionization process presumably involves electron ejection from photoexcited TMP into the bulk aqueous phase. This dependence mirrored that observed for photoionization of TMB and perylene solubilized in anionic sodium lauryl sulfate micelles [98]. Qualitatively, these effects were attributed primarily to inhibition of the geminate recombination of photogenerated electrons and cations by the negative interfacial potential (analogous to reaction 4 in the above scheme). The rate constant for $\cdot TMB^+$ decay is thought to proceed via interaction with nucleophiles in the bulk phase; in both DHP vesicles and the micellar system, the rate constant was found to decrease logarithmically with increasing negative Ψ_0 , implying that the potential presents an activation barrier to the movement of the nucleophile into the microphase. However, this interpretation was rendered ambiguous by the observation that in cationic dioctadecyldiammonium chloride (DODAC) vesicles, the decay rate was actually slower than in DHP vesicles and was promoted by addition of salt (which reduces the magnitude of the positive Ψ_0). In this case, it was suggested that the dominant effect of the surface potential was to change the intravesicular location of $\cdot TMB^+$, i.e., a positive potential would tend to exclude the cation from the vesicle interface, making accessibility to external nucleophiles more difficult.

The opposite result was obtained in a study of vesicle surface charge effects upon photoionization of ZnTPP [(5,10,15,20-tetraphenyl-21*H*,23*H*-porphinato)zinc(II)] in frozen mixed DPPC–DODAC and DPPC–DHP vesicles [99]. Optical spectroscopic measurements indicated that the zinc porphyrin molecules resided in very similar environments within the polar head-group region of the membrane in all of the vesicles. Photoionization efficiencies increased progressively with increasing mole fraction of the positively charged DODAC surfactant in the mixed vesicles and decreased progressively with addition of increasing amounts of the anionic DHP surfactant. These effects were interpreted as indicating that the negative surface potential generated by DHP hinders escape of the electron from the vesicle and thus from the photogenerated $\cdot ZnTPP^+$ π -cation radical. Correspondingly, addition of the positively charged DODAC molecules creates more favorable electrostatics for the electron to escape from the charge-separated geminate pair through the vesicle interface.

The reasons for the divergent effects of surface charge on TMB and ZnTPP photoionization yields in vesicular suspensions are unknown. Experimentally determined photoionization yields are complex quantities, which include as elementary processes primary ionization cross-section terms, dry electron escape probabilities, relatively complex electron hydration processes and recombination of various hy-

drated forms of the electron with the radical cation. The interfacial potential may affect each of these terms differently for different electron donors, which may further be dependent upon their location within the aggregate microphase.

The direction of electron transfer within the asymmetrically organized membrane can apparently also influence the reaction dynamics. As noted above, reductive quenching of photoexcited TTDC³⁺ by TBPP⁻ was more efficient below than above the membrane phase transition [93]. Given the solubility properties of the reactants, electron transfer almost certainly occurred in the transverse direction, i.e., normal to the plane of the interface. Diffusion-limited charge recombination reactions between pyrene radical anions and *N,N*-diethylaniline (DEA) radical cations formed by photoinduced electron transfer in liposomes exhibit an entirely different dependence upon membrane structure [100]. In this case, the reaction rate increased markedly around the vesicle gel-to-liquid crystalline transition, a region characterized by highly disordered side-chains and relatively low internal viscosity. By using pyrene molecules tethered to polar head groups through methylene chains of varying lengths, it was shown that these reactions were not influenced by the depth of penetration of the chromophore within the membrane bilayer, provided that it was not confined to the interface [101]. Presumably, then, these reactions were isotropic within the hydrocarbon microphase of the membrane and rate-limited primarily by the diffusion of [•]DEA⁺ [101]. In contrast, the transverse vectorial organization photoexcited TTDC³⁺ by TBPP⁻ apparently allows the effective distance between donor and acceptor to change upon undergoing the phase transition such that the increase in electron tunneling efficiency accompanying reduction in the separation distance outweighs the rate retarding effects of the increased microviscosity of the more ordered gel phase.

These examples should serve to underscore the difficulty in predicting the effects that interfacial potentials, membrane structure and microphase organization will have on electron-transfer reactions across the membrane interface and within the bilayer itself. The principles involved are common to micelles and vesicles, but the more anisotropic and highly ordered vesicles provide a more complex reaction environment for solubilized or adsorbed reactants.

6.5.3 Kinetic Analyses

Reactions that occur between components in the bulk solution and vesicle-bound components, i.e., reactions occurring across the membrane interface, can be treated mathematically as if they were bimolecular reactions in homogeneous solution. However, kinetic analyses of reactions on the surface of mesoscopic structures are complicated by the finiteness of the reaction space, which may obviate the use of ordinary equations of chemical kinetics that treat the reaction environment as an infinite surface populated with constant average densities of reactant molecules. As was noted above, the kinetics of electron-transfer reactions on the surface of spherical micelles and vesicles is expressed by a sum of exponentials that can be approximated by a single exponential function only at relatively long times [79a, 81]. At short times, the kinetics of the oxidative quenching of excited molecules on these surfaces are approximated by the equation [102]

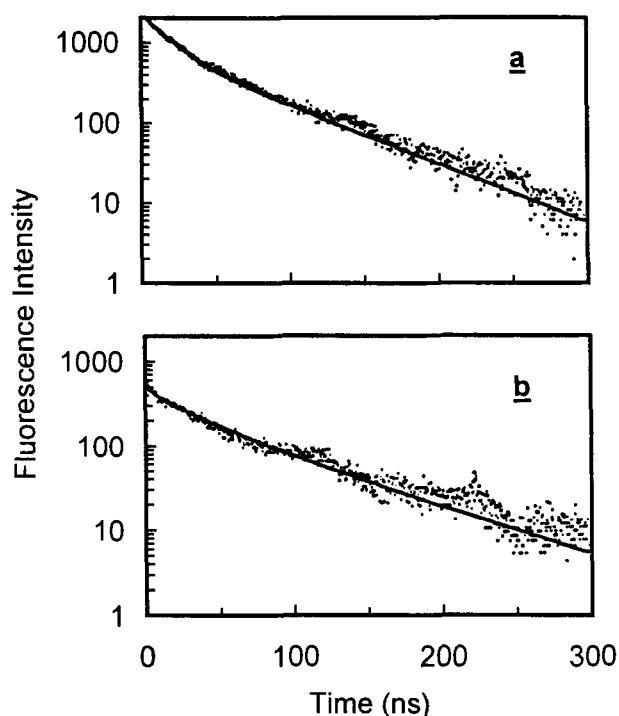


Figure 10. Kinetics of fluorescence quenching of OpyPC by HDP^+ in (a) the DOPC monolayer at $P = 30 \text{ mN m}^{-1}$ and (b) DOPC vesicles. The solid lines are theoretical curves calculated from Eq. 15 with $\tau = 115 \text{ ns}$, $R = 1 \text{ nm}$ and (a) $D_l = 5.2 \times 10^{-7} \text{ cm}^2 \text{ s}^{-1}$ and (b) $D_l = 4.1 \times 10^{-7} \text{ cm}^2 \text{ s}^{-1}$ symbols are defined in the text. Adapted from [102b].

$$\frac{n(t)}{n(0)} = \exp\left(-\frac{t}{\tau} - 7.44NR\sqrt{tD_l} - 2.28ND_l t\right) \quad (15)$$

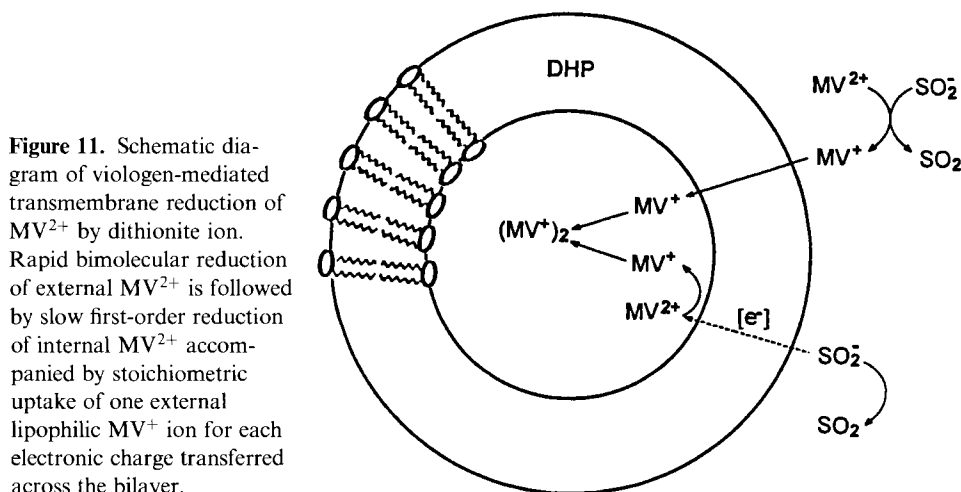
where τ is the fluorescence lifetime in the absence of a quencher, N is the quencher concentration in molecules per unit area, R is the radius of electron transfer from the excited molecule to the quencher and D_l is the lateral diffusion coefficient of the reactants. Typical kinetic data for oxidative quenching of fluorescence are presented in Figure 10 for reaction between photoexcited {10-[6(8)-octadecylpyrenyl]decanoyl}-2-hexanoylphosphatidylcholine (OpyPC) by the 4-(*N*-hexadecylpyridinium-4-yl)-pyridine cation (HDP^+) on the surface of a dioleoylphosphatidylcholine (DOPC) monolayer (a) and DOPC vesicles (b) [102b]. Fits obtained by using Eq. 15 are given as the solid lines, from which the lateral diffusion coefficients of the reacting species can be estimated. In this example, the lateral diffusion coefficient in the monolayer decreased with increasing surface pressure, P , from $D_l = 10^{-6} \text{ cm}^2 \text{ s}^{-1}$ at $P = 6 \text{ mN m}^{-1}$ to $5.2 \times 10^{-7} \text{ cm}^2 \text{ s}^{-1}$ at $P = 30 \text{ mN m}^{-1}$. The diffusion coefficient measured in the monolayer at higher surface pressures is comparable to that estimated for DOPC vesicles, for which $D_l = (4.1\text{--}4.4) \times 10^{-7} \text{ cm}^2 \text{ s}^{-1}$ [103]. More generally, Monte Carlo simulations based on $\text{H}_2\text{TMPyP}^{4+}$ triplet-triplet annihilation reactions on the surface of anionic DHP vesicles have been compared with more approximate methods commonly used to evaluate surface reactions to test their accuracy [104]. The comparisons indicate that these simpler methods gave

reasonably accurate estimations of D_l for spherical surfaces whose dimensions are equal to or greater than those of small unilamellar vesicles.

6.5.4 Transmembrane Oxidation–Reduction Reactions

Net reaction between hydrophilic oxidants and reductants separated by bilayer membranes has been convincingly demonstrated in numerous asymmetrically organized vesicle and planar bilayer systems [2a–c]. Particularly compelling examples are those in which electrogenic electron transport is accompanied by net translocation of lipophilic cations or anions, as is required to maintain electroneutrality. For example, MV^{2+} occluded within the inner aqueous phase of DHP vesicles can be completely reduced to the $\cdot MV^+$ radical cation by $S_2O_4^{2-}$ ion in the bulk phase, but only if an equal or greater amount of viologen is initially present in the external environment [40]. Neither MV^{2+} nor $S_2O_4^{2-}$ is membrane permeable. The reaction is biphasic, with rapid bimolecular reduction of external MV^{2+} being followed by slow first-order reduction of the internal MV^{2+} . Reduction of each internal MV^{2+} is accompanied by stoichiometric uptake of a single $\cdot MV^+$ radical ion. These events are depicted schematically in Figure 11. Under most conditions, the accumulation of lipophilic $\cdot MV^+$ ion occurs against its concentration gradient, and so its redistribution cannot be attributed to passive diffusion, but is driven by the thermodynamic potential of the redox reaction. This tight coupling between ion translocation and transmembrane oxidation–reduction establishes unequivocally that electron transport has occurred across a closed bilayer membrane.

A more difficult question to pursue is how electron transport occurs [38]. Three types of electron-transport mechanisms across bilayer membranes have been envisioned, including (i) direct electron tunneling from the donor to the acceptor located at the opposite membrane interfaces, (ii) electron carrier-mediated diffusional



transport across the bilayer and (iii) site-to-site electron hopping down a series of acceptors organized transversely across the membrane.

Transmembrane electron tunneling

Two celebrated early investigations of transmembrane oxidation–reduction were interpreted in terms of direct electron exchange between redox partners bound at the opposite vesicle interfaces. One involved apparent reduction of diheptylviologen [$(C_7)_2V^{2+}$] in the inner aqueous phase of phosphatidylcholine liposomes by EDTA in the bulk phase that was mediated by membrane-bound amphiphilic $Ru(bpy)_3^{2+}$ analogs; the ruthenium complexes acted as photosensitizers and were presumed to function as electron relays by undergoing $Ru(II)$ – $Ru(III)$ electron exchange across the bilayer [105]. The other apparently involved direct electron transfer between photoexcited $Ru(bpy)_3^{2+}$ and MV^{2+} bound at the opposite interfaces of asymmetrically organized anionic DHP vesicles [106]. What was remarkable about these reactions was their apparent rapidity. To compete with photophysical deactivation of $*Ru(bpy)_3^{2+}$, which occurs on the microsecond time-scale, transmembrane oxidative quenching across the DHP bilayer would have to occur with an apparent rate constant of $\sim 10^6 \text{ s}^{-1}$. Likewise, to account for the rate of transmembrane oxidation–reduction in the liposomal system, electron exchange would have to occur across the bilayer with a rate constant very nearly the same as that measured in aqueous solution where close approach of the reactants is possible. However, one expects electron transfer rates to fall off approximately exponentially with distance, as has been demonstrated for redox reactions in various other disordered media [107]. In these cases, the electron-transfer rate (k_{et}) constant can be estimated using the equation

$$k_{et} = k_0 \exp(-2r/a) \quad (16)$$

where k_0 is the rate constant when the reactants are in physical contact, r is the distance of separation and a is a constant whose experimental value typically ranges from 1.0 to 2.0 Å. For the average value of $a = 1.5 \text{ Å}$, one would predict a rate constant $k_{et} \approx 10^{-12} \text{ s}^{-1}$ for a reaction occurring across the full bilayer width of $\sim 40 \text{ Å}$ whose k_0 is 10^{11} s^{-1} ; this represents a characteristic decay time (τ) of over 10^{12} s , 18 orders of magnitude less than the values implied by the experimental data [105].

The dilemma posed by these considerations was resolved for the DHP-organized system when it was noted that upon illumination the initially compartmented MV^{2+} partially leaked out of the vesicles [108]. Thus, the observed reaction actually occurred between reactants adsorbed on the same vesicle surface. The mechanism of this unprecedented light-induced scrambling of MV^{2+} is still not understood. Likewise, subsequent investigations of the PC-organized system provided evidence for transmembrane leakage of a small amount of the compartmented $(C_7)_2V^{2+}$ ion, which then facilitated transmembrane electron transport [109]. Specifically, the reaction characteristics were duplicated when the amphiphilic $Ru(bpy)_3^{2+}$ analog was bound only to the opposite side of the membrane as the oxidative quencher

$[(C_7)_2V^{2+}]$ or when sensitizers that did not bind to the PC membrane at all were present in the external medium. Additional studies using ^{14}C -radiolabeled $(C_7)_2V^{2+}$ demonstrated that transmembrane diffusion of the viologen did occur on relevant time-scales, and a full kinetic analysis of apparent transmembrane reduction of viologens across PC liposomal membranes provided direct evidence for the proposed viologen-mediated transmembrane redox pathway [109]. Thus, in retrospect, it is clear that these reactions did not occur by electron tunneling across the bilayer.

Candidates for bona fide electron tunneling, at least part way across the bilayer, include the reactions of isoalloxazines that have been immobilized by covalent attachment at the β -alkyl position of a phosphatidylcholine surfactant [110], transmembrane reduction of an amphiphilic 4-alkylpyridinepentaammineruthenium(III) ion $[(NH_3)_5Ru-4-(11'-dodeceny)py^{3+}]$ [111] and photosensitized transmembrane oxidation–reduction of aqueous phase donors and acceptors mediated by chlorophyll *a* [112]. In the first of these, the flavophospholipid was shown to be incorporated into PC liposomes without perceptible perturbation of the normal bilayer structure. Reduction of the flavin by externally added $S_2O_4^{2-}$ was biphasic, with the rate of the slower step being independent of the $S_2O_4^{2-}$ concentration, consistent with electron transfer from the reduced flavin substituent in the outer bilayer leaflet to the flavin substituent in the inner leaflet. The flavin moieties were also shown to mediate transmembrane reduction of occluded $Fe(CN)_6^{3-}$ by external $S_2O_4^{2-}$ in a reaction that was weakly coupled to proton transport [113]. The rate constant for the transmembrane redox step was second-order, suggesting a mechanism in which uncorrelated lateral diffusion of the redox partners in the two membrane half-layers led to their transverse juxtaposition, followed by net transmembrane oxidation–reduction. In DPPC liposomes, an abrupt increase in the transmembrane electron transport was observed on going through the gel-to-liquid crystalline phase transition, consistent with this model. However, since the overall process is electrogenic, and requires membrane-depolarizing ion movement to proceed, an alternative interpretation is that ion permeation became rate limiting below the phase transition. The transmembrane redox step was fairly slow, with an apparent $t_{1/2} \approx 10$ s under the experimental conditions. Assuming that the flavophospholipids were incorporated in normal fashion into the bilayer, the flavin groups would be located ~ 7 Å from the membrane interface and, when transversely juxtaposed, separated by ~ 20 Å. Thus, the magnitude of the transmembrane redox step is consistent with an electron tunneling mechanism. Because the ‘flip-flop’ rate of the underivatized phospholipid is extremely slow ($t_{1/2} \geq 24$ h), it was assumed that the reaction could not occur by transverse diffusion of the derivatized phospholipid. It would have been useful to confirm this by direct measurement, however.

One-electron reduction of $(NH_3)_5Ru-4-(11'-dodeceny)py^{3+}$ by externally added reductants followed biphasic kinetics when the complex was bound at both interfaces of PC liposomes, but only the fast step was observed when binding was limited to the external surface [111]. The slow step was first order and independent of the identity and concentrations of added reductants. The rate constant, $k = 10^{-3} s^{-1}$, was unchanged upon adding either the potassium ionophore, valinomycin, or the proton carrier, carbonyl cyanide *m*-chlorophenylhydrazone, to the medium, indicating that, although electrogenic, the transmembrane reduction step was not rate-

limited by charge-compensating ion diffusion. The magnitude of the rate constant is consistent with an effective electron-tunneling distance of ~ 20 Å, which could be achieved if the ruthenium complexes intercalated within the bilayer in a manner envisioned for amphiphilic viologens bearing long alkyl chains (Figure 4). Kinetic 'mapping' studies established that neither the Ru(II) nor Ru(III) ions underwent net transmembrane diffusion on the time-scale of the transmembrane redox step. However, this does not preclude transverse "flip-flop" exchange between Ru(II) and Ru(III) as an alternative mechanism for the apparent transmembrane reduction step.

Based upon a detailed analysis of reaction transients, a mechanism was proposed for chlorophyll a-photosensitized transmembrane oxidation–reduction of aqueous phase donors and acceptors that included electron transfer between juxtaposed Chl a^+ π -cations and Chl a molecules as the transmembrane charge-transfer step [112]. The maximum apparent first-order rate constant for this step was $k \approx 10^4 \text{ s}^{-1}$, which seems large for thermal electron transfer between chlorophyll molecules located at the opposite membrane interfaces, even considering that nuclear activation barriers may be relatively small for this reaction. Transverse 'flip-flop' diffusion of Chl b across the membrane is 10^6 -fold slower than transmembrane redox under these conditions, so this alternative mechanism is almost certainly unimportant. Kinetic mapping studies have shown that some of the Chl a becomes localized within the membrane at sites that are inaccessible to aqueous phase electron acceptors, presumably within the membrane interior [114]. This suggests the possibility of a transverse 'hopping' mechanism involving electron transfer over relatively short distances from buried Chl a to interfacial Chl a^+ , followed by electron transfer from Chl a at the opposite interface to the buried Chl a^+ .

Several studies to probe distance dependences in electron-transfer reactions have been conducted using hydrophobic metalloporphyrins tethered through alkyl chains of varying lengths to hydrophilic groups, the basic idea being that the tether would limit the depth of penetration of the redox center within the bilayer. For example, hydrophilic polyethylenimine was attached to a hydrophobic manganese *meso*-tetratolylporphyrin that was capable of mediating transmembrane reduction of $\text{Fe}(\text{CN})_6^{3-}$ across PC liposomes by the highly hydrophilic dye indigotetrasulfonate (ITSAH₂) [115]. As discussed below, the mechanism of the untethered reaction is thought to be carrier-mediated transport. Electron transport in the tethered molecules was observed only for the longest chain derivatives, for which the minimal heme separation distance was estimated to be about 4 Å. Surprisingly, shorter chain analogs whose separation distance was limited to ~ 10 Å could not catalyze the transmembrane redox reactions. In another study, a series of hydrophobic zinc *meso*-tetraphenylporphine compounds was prepared that contained phosphatidylcholine groups attached via amide linkages to the phenyl rings [116]. Oxidative quenching of MV^{2+} by the triplet-excited zinc porphyrins incorporated into DPPC liposomes occurred only for those complexes for which the maximum distance from the liposomal interface was constrained to ~ 12 Å or less. These studies underscore the limitations of long-range electron transfer within bilayer membranes. However, the actual distances inferred from the data should probably be given only qualitative significance because the tethers are flexible and it has not been shown that the

derivatized complexes can assume their full extended length within the membrane bilayer. In the study with the 'picket fence' zinc porphyrins, for example, the fluorescence properties of the chromophores were consistent with an alcohol-like environment, suggesting an average location near the membrane interface, rather than buried within the membrane hydrocarbon phase [116].

Carrier-mediated electron transport

The mechanism of MV^{2+} -mediated electron transport across DHP vesicle membranes has been identified in systems where $^{\bullet}MV^{+}$ is generated chemically or photochemically in the bulk medium to react with a membrane-impermeable oxidant [$Co(bpy)_3^{3+}$] in the internal aqueous phase [27, 117]. Quantitative kinetic analyses of the decay profiles, including independent determination of the permeability coefficient of the $^{\bullet}MV^{+}$ radical, as well as determination of the extent of viologen uptake under varying reaction conditions, has provided conclusive evidence for two parallel pathways. One pathway involves electrogenic transmembrane diffusion of $^{\bullet}MV^{+}$ and the other involves electroneutral diffusion of the doubly reduced MV^0 species, the latter being formed in small concentrations by disproportionation of $^{\bullet}MV^{+}$, i.e., the reaction $2^{\bullet}MV^{+} = MV^0 + MV^{2+}$. The electrogenic pathway makes a relatively large contribution to the early stages of the reaction, but is sharply attenuated by the developing transmembrane potential; the latter stages are then carried primarily by the electroneutral pathway, which is insensitive to the transmembrane potential. Reaction by both pathways is relatively slow because the intrinsic permeability of $^{\bullet}MV^{+}$ is low and MV^0 , although highly permeable, is present in vanishingly small concentrations owing to the unfavorable disproportionation equilibrium. As a consequence, the flux of MV^0 through the membrane is low. An MV^0 diffusion pathway has also been proposed for viologen-mediated redox reactions across PC liposomes based upon the form of the rate law for transmembrane oxidation–reduction [118]. Analogous transmembrane diffusion mechanisms have been proposed for structurally similar *N*-alkyl-4-cyanopyridinium (C_nCP^{+}) ions, which act as combined oxidative quenchers and redox mediators in photoinitiated transmembrane reactions of aqueous phase-separated donors and acceptors [95]. Because in this case the cyanopyridinium radicals are both the majority carriers and neutral molecules, the transmembrane redox reactions are rapid, occurring on the millisecond time-scale. Surprisingly, the rate constants for diffusion of the $^{\bullet}C_nCP^0$ radicals, measured by transient spectrophotometry, were independent of the *N*-alkyl chain length over the range $n = 1$ –16. As with viologen-mediated electron transport, the oxidized C_nCP^{+} ion was membrane impermeable, and accumulated within the inner aqueous phase following reaction with the electron acceptor located there. By modifying the alkyl chain of the cyanopyridinium ion to include a terminal carboxyl substituent, it has been possible to demonstrate multiple electron transfers by a single mediator [119]. In this case, the reduced cyanopyridinium radical functions to co-transport a proton with the electron in the form of the carboxylic acid substituent. The acidity of the pendant carboxylic acid increases upon oxidation of the cyanopyridinium within the aqueous core of the vesicle, releasing a proton. The now zwitterionic oxidized species can also diffuse as an electroneutral species and

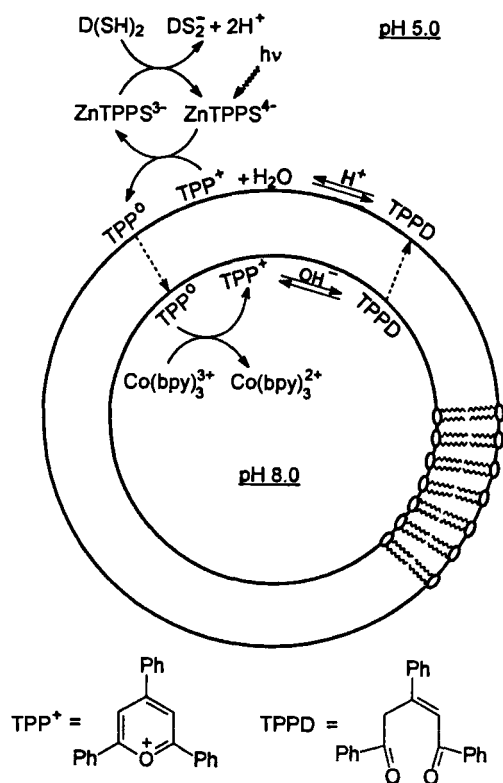


Figure 12. General reaction scheme for photoinduced transmembrane reduction of $\text{Co}(\text{bpy})_3^{3+}$ by dithiothreitol (DTT) across DHP bilayer membranes mediated by 2,4,6-triphenylpyrylium ion (TPP^+). The mediator acts both as an oxidative quencher of $^3\text{ZnTPPS}^{4-}$ and a cyclic electroneutral transmembrane e^-/OH^- antiporter (from [120]).

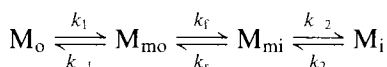
apparently has sufficient permeability to diffuse back across the membrane and engage in another redox cycle.

A similar strategy to achieve rapid (i.e., electroneutral) cyclic transmembrane diffusion of a redox mediator has been employed that makes use of pyrylium or thiopyrylium ions as combined oxidative quenchers and transmembrane electron carriers. In this case, advantage has been taken of the reversible hydrolytic ring opening to form 1,5-diketones to develop uncharged redox shuttles that function by counter-transport of the electron and OH^- ions [120]. The basic system is outlined in Figure 12. Photoreduction of the pyrylium cation in the external medium to the neutral radical is followed by transmembrane diffusion to the aqueous core, where it reduces an electron acceptor. The oxidized pyrylium ion undergoes hydrolysis according to the dictates of the thermodynamic equilibrium with its diketone form, the diketone diffuses outwardly and the cycle is closed by re-formation of the pyrylium ring. On average, 40 cycles of the redox carrier have been demonstrated without any evidence of degradation of the system; the limiting factor in these studies was the amount of electron acceptor that could be occluded within the vesicles.

Transmembrane reduction of $\text{Fe}(\text{CN})_6^{4-}$ by ITSAH_2 across PC liposomes is mediated by lipophilic iron and manganese porphyrins [121]. The relative rates increased with increasing heme lipophilicity, and were not influenced by adding

lipophilic ions or ionophoric compounds, indicating that the reaction was electro-neutral. This implies a carrier-mediated mechanism, rather than electron transfer between ferri- and ferrohemes in the opposite bilayer leaflets which would necessarily be electrogenic. A mechanism was proposed in which a proton was co-transported with the electron via a water molecule axially bound to the heme. Thus, the ferroheme diffused across the membrane as a neutral molecule bearing an aqua ligand, and the ferriheme diffused as the neutral hydroxo complex. This mechanism was shown to be consistent with changes in medium acidity accompanying the redox reaction; the ability of hemin dimethyl ester to carry SCN^- through a bulk liquid membrane was also demonstrated.

As noted previously, real membranes are characterized by nonuniform free-energy profiles for bilayer permeation. Consequently, molecular dynamics simulations have been used to treat the motion of a solute through a bilayer membrane. These calculations accurately reproduce experimentally estimated values of diffusion [43]. However, because this approach is mathematically complex, it has been applied only to the permeation of relatively small molecules. Approximate methods have been developed based on a simple kinetic scheme for the diffusion of solute molecules M in a four compartment system:



where the subscripts indicate the location of M in the bulk aqueous phase (o), inside the membrane near the outer (mo) and inner (mi) surfaces, and within the inner aqueous volume (i), k_1 , k_{-1} , k_2 and k_{-2} are constants for permeation across the membrane/water interface and k_f and k_r are constants for transmembrane diffusion [122, 123]. The equations which describe the flow of particles from each region are

$$\frac{dn_o}{dt} = k_{-1}[M_{mo}] - k_1[M_o] \quad (17)$$

$$\frac{dn_i}{dt} = k_{-2}[M_{mi}] - k_2[M_i] \quad (18)$$

$$\frac{dn_{mo}}{dt} = k_1[M_o] - k_{-1}[M_{mo}] + k_r[M_{mi}] - k_f[M_{mo}] \quad (19)$$

$$\frac{dn_{mi}}{dt} = k_2[M_i] - k_{-2}[M_{mi}] + k_f[M_{mo}] - k_r[M_{mi}] \quad (20)$$

where n_x and $[M_x]$ are the number and the concentration of molecules M in region x , respectively. The simultaneous solution of Eqs. 17–20 for n_o is an exponential function with the rate constant $\gamma \approx P[(S_o/V_o) + (S_i/V_i)]$ where S_o , S_i , V_o , and V_i are the outer and inner total surface areas and volumes, respectively [123]. Thus, the membrane permeability can be calculated from the transmembrane decay kinetics.

Site-to-site electron hopping

Transmembrane charge separation by sequential electron transfer between adjacent redox centers is epitomized by studies utilizing covalently linked donor–sensitizer–acceptor triad molecules that are vectorially organized across planar bilayer mem-

branes and liposomes [90, 92, 124]. In the studies with liposomes, transient spectrophotometry revealed that photoexcitation of the porphyrin sensitizer moiety is followed by electron transfer to the quinone acceptor and reduction of the porphyrin π -cation by electron donation from the appended carotene donor, the overall result being charge separation across nearly the full bilayer width. When the charge-separated species reacted with lipid-soluble quinones present in the membrane, a chemiosmotic proton gradient developed as a consequence of electrogenic proton translocation associated with the quinone oxidation–reduction cycling. This chemiosmotic potential, which is due solely to the transverse asymmetry of the electron-transport chain, was sufficient in magnitude to drive formation of the phosphoanhydride bond when a properly oriented ATP synthase was also incorporated into the membrane. As such, this system closely mimics biological photophosphorylation processes.

Less sophisticated and well-defined electron transport chains may also develop within bilayer membranes simply by aggregation of redox components. In one study, the protein cytochrome (cyt) c_3 incorporated within PC liposomes was found to mediate electrogenic transmembrane reduction of entrapped $\text{Fe}(\text{CN})_6^{3-}$ by externally added donors with cotransport of protons [125]. Transmembrane electron transfer was suggested to occur through an electron-transport chain formed by dimerization of cyt c_3 because the dominant term in the rate law was second order in cyt c_3 . Aggregation can indeed be expected to lead to an electron-hopping pathway because this remarkable protein contains a cluster of four nonidentical hemes whose center-to-center distances range from 10 to 18 Å. Furthermore, electromagnetic interactions between the iron centers are detectable, and dried films of the protein have anomalously high electrical conductivities [126]. There are several unexplained anomalies associated with these reactions [2a], so the mechanism cannot be taken as established.

An interesting case of metalloporphyrin-mediated photoinitiated transmembrane oxidation–reduction between aqueous donors and acceptors has been reported in which the efficiency of reaction was proportional to the square of the incident light intensity [127]. This dependence implies a two-photon excitation mechanism. Optical spectroscopic and EPR evidence were presented indicating that the lipophilic metalloporphyrins were extensively aggregated within the membrane bilayer. A mechanism involving reaction initiated by oxidative quenching of a doubly excited metalloporphyrin dimer by the aqueous electron acceptor was proposed, although it was acknowledged that an alternative mechanism involving stepwise electron transfer with reaction between a photoexcited triplet porphyrin and a porphyrin π -cation radical as an obligatory second step could not be excluded from the data. Two-step activation schemes involving synchronous photochemical reactions at the opposite interfaces of a bilayer membrane have been suggested for more complex vesicle assemblies containing both lipid-soluble zinc porphyrins and electron acceptors (alloxazines), as well as aqueous donors and acceptors [128]. As envisioned, photoexcitation of a zinc porphyrin near the donor interface results in oxidative quenching by the alloxazine, followed by electron transfer from the donor to the porphyrin π -cation radical. At the other interface, oxidative quenching of a second triplet-excited zinc porphyrin by the aqueous phase acceptor generates another π -cation radical, which is subsequently reduced by an oxidized alloxazine that diffuses

across the bilayer. Cyclic oxidation–reduction of the alloxazine at the opposite interfaces is thought to shuttle a proton, as is required to maintain electroneutrality. Overall, although it cannot be taken as established, the proposed mechanism appears to incorporate elements of long-range electron transfer, carrier mediated proton–electron co-transport and possibly electron hopping.

Strong evidence exists for electron hopping in photoinduced transmembrane redox reactions mediated by C_{60} and C_{70} fullerenes across planar bilayer membranes [129]. Reductive quenching of the triplet-excited fullerene by an aqueous donor (e.g., ascorbate) followed by oxidation of an acceptor (e.g., anthraquinone sulfonate) in the opposite compartments was monitored by measuring the induced photocurrents. The influence of factors such as membrane thickness, dependence upon applied photopotentials and membrane electrostatic charge were inconsistent with a transbilayer diffusional mechanism for the reduced fullerene radical anions [129c]. Furthermore, the charge transient time, measured from photovoltage and photocurrent transients following illumination of a sensitizer adsorbed at the membrane interface in the presence and absence of acceptors, was less than 10^{-6} s [129b]. This is considerably shorter than the time for transmembrane diffusion of large anions (10^{-4} – 10^{-6} s), and provides convincing evidence of charge movement by electron transfer, rather than ion diffusion. Because the diameters of the individual fullerenes are only 7–11 Å, it is assumed that they are aggregated within the membrane to span the bilayer. Rapid electron transport then occurs by electron transfer from particle to particle within the aggregate.

Photoinduced electron transfer across planar bilayer membranes doped with discrete cofacially stacked porphyrin trimers and tetramers has been demonstrated [130]. The proposed mechanism involves a sequence of steps initiated by interfacial oxidation of a photoexcited porphyrin ring adjacent to the aqueous phase containing the electron acceptor, followed by migration of the positive charge by electron hopping to the ring adjacent to the aqueous phase containing the electron donor and electron transfer across that interface [130c].

To summarize, electron transfer across the full width of a bilayer membrane has not been demonstrated and almost certainly does not occur, although direct transfer from one bilayer leaflet to the other may be possible if the redox centers are embedded within the membrane, reducing the effective distance to less than 20 Å. Site-to-site electron hopping also occurs when transversely aligned redox centers or membrane-spanning aggregates of redox molecules form in the bilayer. These processes are electrogenic and must be associated with charge-compensating ion movement to proceed to completion. Transmembrane oxidation–reduction can also occur by transbilayer carrier-mediated diffusion when lipophilic redox-active molecules and ions are present in the membrane; these reactions can be either electrogenic or electroneutral.

Acknowledgments

Research in Dr. Hurst's laboratory receives financial support from the Office of Basic Energy Sciences, US Department of Energy (grant No. DE-FG03-99ER14943).

References

- (a) M. Calvin, *Photochem. Photobiol.* **1983**, 37, 349–360; (b) J. H. Fendler, *J. Phys. Chem.* **1985**, 89, 2730–2740; (c) N. J. Turro, *Pure Appl. Chem.* **1986**, 58, 1219–1228; (d) K. Kalyanasundaram, *Photochemistry in Microheterogeneous Systems*, Academic Press, New York, **1988**; (e) V. Ramamurthy (Ed.), *Photochemistry in Organized and Constrained Media*, VCH Publishers, New York, **1991**; (f) M. A. Fox, *Top. Curr. Chem.* **1991**, 159, 67–101; (g) Y. Moroi, *Micelles. Theoretical and Applied Aspects*, Plenum Press, New York, **1992**; (h) M. H. Gehlen, F. C. Schryver, *Chem. Rev.* **1993**, 93, 199–221; (i) V. Barzykin, M. Tachiya, *Heterog. Chem. Rev.* **1996**, 3, 105–167.
- (a) J. K. Hurst, in *Kinetics and Catalysis in Microheterogeneous Systems*, Surfactant Science Series, Vol. 38 (Eds. M. Gratzel, K. Kalyanasundaram), Marcel Dekker, New York, **1991**, pp. 183–226; (b) S. Lymar, V. N. Parmon, K. I. Zamaraev, *Top. Curr. Chem.* **1991**, 159, 1–66; (c) J. N. Robinson, D. J. Cole-Hamilton, *Chem. Soc. Rev.* **1991**, 20, 49–94; (d) K. I. Zamaraev, S. V. Lymar, M. I. Khramov, V. N. Parmon, *Pure Appl. Chem.* **1988**, 60, 1039–1046; (e) F. Baros, A. Naoumi, M. L. Viriot, J. C. Andre, *J. Chem. Soc., Faraday Trans.* **1991**, 87, 2039–2046; (f) K. Takagi, Y. Sawaki, *Crit. Rev. Biochem. Mol. Biol.* **1993**, 28, 323–367.
- (a) H. Ti Tien, *Prog. Surf. Sci.* **1985**, 19, 169–274; **1989**, 30, 1–199; (b) H. Kuhn, *Pure Appl. Chem.* **1979**, 51, 341–352; (c) P. Seta, E. Bienvenue, *Mol. Electron. Mol. Electron. Dev.* **1994**, 3, 59–78; (d) K. Sun, D. Mauzerall, *J. Phys. Chem.* **1998**, 102, 6440–6447.
- (a) C. Tanford, *The Hydrophobic Effect*, Wiley, New York, **1973**; (b) M. N. Jones, D. Chapman, *Micelles, Monolayers, and Biomembranes*, Wiley, New York, **1995**; (c) R. B. Gennis, *Biomembranes: Molecular Structure and Function*, Springer, New York, **1989**; (d) P. Yeagle, *The Structure of Biological Membranes*, CRC Press, Boca Raton, FL, **1992**; (e) J. N. Israelachvili, *Intermolecular and Surface Forces: with Applications to Colloidal and Biological Systems*, 2nd edn., Academic Press, London, **1992**; (f) M. Ahlers, W. Muller, A. Reichert, H. Ringsdorf, J. Venzmer, *Angew. Chem., Int. Ed. Engl.* **1990**, 29, 1269–1285; J. M. Lehn, *Angew. Chem., Int. Ed. Engl.* **1990**, 29, 1304–1319.
- G. S. Hartley, *Q. Rev. Chem. Soc.* **1948**, 2, 152–183.
- (a) K. A. Dill, P. J. Flory, *Proc. Natl. Acad. Sci. USA* **1981**, 78, 676–680; (b) F. M. Menger, *Acc. Chem. Res.* **1979**, 12, 111–117.
- J. H. Fendler, *J. Phys. Chem.* **1980**, 84, 1485–1491.
- (a) E. A. G. Aniansson, S. N. Wall, M. Almgren, H. Hoffman, I. Kielmann, W. Ulbricht, R. Zana, J. Lang, C. Tondre, *J. Phys. Chem.* **1976**, 80, 905–922; (b) T. Inoue, R. Tashiro, Y. Shibuya, R. Shimozawa, *J. Colloid. Interface Sci.* **1980**, 73, 105–114; (c) J. Gormally, W. J. Gettins, E. Wyn-Jones, in *Molecular Interactions*, Vol. 2 (Eds. H. Ratajczak, W. J. Orville-Thomas), Wiley, New York, **1980**, Ch. 3; (d) J. Lang, R. Zana, in *Surfactant Solutions—New Methods of Investigation* (Ed. R. Zana), Marcel Dekker, New York, **1987**, Ch. 8.
- (a) S. J. Renfeld, *J. Phys. Chem.* **1970**, 74, 117–122; (b) K. Kalyanasundaram, M. Gratzel, J. K. Thomas, *J. Am. Chem. Soc.* **1975**, 97, 3915–3922.
- (a) P. P. Infelta, in *Energy Resources through Photochemistry and Catalysis* (Ed. M. Gratzel), Academic Press, New York, **1983**, pp. 49–70; (b) M. Almgren, J.-E. Lofroth, J. van Stam, *J. Phys. Chem.* **1986**, 90, 4431–4437.
- P. P. Infelta, P.-A. Brugger, *Chem. Phys. Lett.* **1981**, 82, 462–468.
- A. Verbeck, E. Gelade, F. C. DeSchryver, *Langmuir* **1986**, 2, 448–456.
- (a) M. Wong, T. Nowak, J. K. Thomas, *J. Am. Chem. Soc.* **1977**, 99, 4730–4736; (b) H. F. Eicke, *Top. Curr. Chem.* **1980**, 87, 86–145; (c) N. Sarkar, A. Datta, S. Das, K. Brattacharyya, *J. Phys. Chem.* **1996**, 100, 15483–15486; (d) D. Mandal, S. K. Pal, A. Datta, K. Brattacharyya, *Anal. Sci.* **1998**, 14, 199–202.
- (a) R. Humphry-Baker, D. H. Thompson, Y. Lei, M. J. Hope, J. K. Hurst, *Langmuir* **1991**, 7, 2592–2601; (b) I. W. Levin, in *Advances in Infrared and Raman Spectroscopy*, Vol. 11 (Eds. R. J. Clark, R. E. Hester), Wiley-Heyden, Chichester, **1984**, pp. 1–48; (c) I. W. Levin, T. E. Thompson, Y. Barenholz, C. Huang, *Biochemistry* **1985**, 24, 6282–6286.
- M. J. Hope, M. B. Bally, G. Webb, P. R. Cullis, *Biochim. Biophys. Acta* **1985**, 812, 55–65.
- A. D. Bangham, R. W. Horne, *J. Mol. Biol.* **1964**, 8, 660–668.

17. C. H. Huang, *Biochemistry* **1969**, 8, 334–352.
18. (a) S. Bartzi, E. D. Korn, *Biochim. Biophys. Acta* **1973**, 298, 1015–1019; (b) D. W. Deamer, A. D. Bangham, *Biochim. Biophys. Acta* **1976**, 443, 629–634; (c) D. Deamer, A. D. Bangham, *Biochim. Biophys. Acta* **1976**, 629–634.
19. F. Szoka, D. Papahadjopoulos, *Proc. Natl. Acad. Sci. USA* **1978**, 75, 4194–4198.
20. (a) K. L. Mittal (Ed.), *Micellization, Solubilization and Microemulsions*, Vols. 1 and 2, Plenum, New York, **1977**; (b) S. L. Hardt, *J. Membr. Biol.* **1979**, 48, 299–323; (c) S. B. Hladky, *Curr. Top. Membr. Transp.* **1979**, 12, 53–164; (d) R. D. Kornberg, H. M. McConnell, *Proc. Natl. Acad. Sci. USA* **1971**, 68, 2564–2568; (e) A. Blume, in *Phospholipids Handbook* (Ed. G. Cavc), Marcel Dekker, New York, **1993**, pp. 455–509.
21. M. Almgren, *J. Am. Chem. Soc.* **1980**, 102, 7882–7887, and references cited therein.
22. Y. Lei, J. K. Hurst, *J. Phys. Chem.* **1991**, 95, 7918–7925.
23. B. C. Patterson, J. K. Hurst, *Langmuir* **1993**, 9, 16–18.
24. A. Finkelstein, *Water Movement Through Lipid Bilayers, Pores, and Plasma Membranes: Theory and Reality*, Wiley-Interscience, New York, **1987**.
25. D. W. Deamer, A. G. Volkov, in *Permeability and Stability of Lipid Bilayers* (Eds. E. A. Disalvo, S. A. Simons), CRC Press, Boca Raton, FL, **1995**, pp. 161–177.
26. A. Walter, J. Gutknecht, *J. Membr. Biol.* **1986**, 90, 207–217.
27. S. V. Lymar, J. K. Hurst, *J. Phys. Chem.* **1994**, 98, 989–996.
28. M. Tachiya, *Chem. Phys. Lett.* **1975**, 33, 289–292.
29. (a) M. A. J. Rodgers, M. F. S. Wheeler, *Chem. Phys. Lett.* **1978**, 53, 165–169; (b) B. K. Selinger, A. R. Watkins, *Chem. Phys. Lett.* **1978**, 56, 99–104; (c) S. S. Atik, L. A. Singer, *Chem. Phys. Lett.* **1978**, 59, 519–524.
30. (a) T. F. Hunter, *Chem. Phys. Lett.* **1980**, 75, 152–155; (b) T. Nakamura, A. Kira, M. Imamura, *J. Phys. Chem.* **1983**, 87, 3122–3125; (c) G. Rothenberg, P. P. Infelta, M. Gratzel, *J. Phys. Chem.* **1979**, 83, 1871–1876; (d) R. C. Dorrance, T. F. Hunter, *J. Chem. Soc., Faraday Trans. 1* **1974**, 70, 1572–1580.
31. A. Henglein, T. Proske, *Ber. Bunsenges. Phys. Chem.* **1978**, 82, 1107–1112.
32. M. Tachiya, M. Almgren, *J. Chem. Phys.* **1981**, 75, 865–870.
33. P. P. Infelta, R. Gaglia, C. Minero, E. Pelizzetti, *Colloids Surf.* **1987**, 28, 289–299.
34. (a) H. M. McConnell, L. K. Tamm, R. M. Weiss, *Proc. Natl. Acad. Sci. USA* **1984**, 81, 3249–3253; (b) H. Mohwald, *J. Mol. Electron.* **1988**, 4, 47–55; (c) J. Y.-J. Uang, D. P. Parazak, H. Y. Chiu, K. J. Stine, *J. Colloid Interface Sci.* **1995**, 171, 366–376.
35. (a) T. Kunitake, H. Ihara, Y. Okahata, *J. Am. Chem. Soc.* **1983**, 105, 6070–6078; (b) E. J. Shimshick, H. M. McConnell, *Biochemistry* **1973**, 12, 2351–2360; (c) J. W. Smalley, S. W. Feldberg, S. H. Wool, *J. Phys. Chem.* **1989**, 93, 2570–2575.
36. (a) R. A. Cellarius, D. Mauzerall, *Biochim. Biophys. Acta* **1966**, 112, 235–255; (b) J. K. Hurst, L. Y. C. Lee, M. Gratzel, *J. Am. Chem. Soc.* **1983**, 105, 7048–7056.
37. I. Yamazaki, N. Tamai, T. Yamazaki, *J. Phys. Chem.* **1990**, 94, 516–525.
38. B. C. Patterson, J. K. Hurst, *J. Phys. Chem.* **1993**, 97, 454–465.
39. (a) D. H. P. Thompson, W. C. Barrette, Jr., J. K. Hurst, *J. Am. Chem. Soc.* **1987**, 109, 2003–2009; (b) J. K. Hurst, D. H. P. Thompson, *Inorg. Chem.* **1987**, 26, 39–43; (c) M. J. Colaneri, L. Kevan, D. H. P. Thompson, J. K. Hurst, *J. Phys. Chem.* **1987**, 91, 4072–4077.
40. B. C. Patterson, D. H. Thompson, J. K. Hurst, *J. Am. Chem. Soc.* **1988**, 110, 3656–3657.
41. (a) D. Axelrod, *J. Membr. Biol.* **1983**, 75, 1–10; (b) C. R. Hackenbrock, B. Chazotte, S. S. Gupte, *J. Bioenerg. Biomembr.* **1984**, 87, 331–368; (c) P. Mitchel, J. Moyle, in *Coenzyme Q* (Ed. G. Lenaz), Wiley, New York, **1985**, pp. 12–19; (d) F. Zhang, G. M. Lee, K. Jacobson, *BioEssays* **1993**, 15, 579–588.
42. (a) Tocanne, J.-F., L. Dupou-Cezanne, A. Lopez, *Prog. Lipid Res.* **1994**, 33, 203–237; (b) G. L. Schutz, H. Schindler, Th. Schmidt, *Biophys. J.* **1997**, 73, 1073–1080; (c) M. Hetzer, S. Heinz, S. Grage, T. M. Bayerl, *Langmuir* **1998**, 14, 982–984; (d) D. Marchal, W. Boireau, J. M. Laval, J. Moiroux, C. Bourdillon, *Biophys. J.* **1998**, 74, 1937–1948; (e) Kanazava, K. Koga, *Biochem. Biophys. Res. Commun.* **1980**, 95, 269–272; (f) J. L. R. Rubinstein, B. A. Smith, H. M. McConnell, *Proc. Natl. Acad. Sci. USA* **1979**, 76, 15–18; (g) A. L. Kuo, C. G. Wade, *Biochemistry* **1979**, 18, 2300–2308; (h) C. A. Goss, C. J. Miller, M. Majda, *J. Phys. Chem.* **1988**, 92, 1937–1942.

43. (a) R. W. Pastor, S. E. Feller, in *Biological Membranes: a Molecular Perspective from Computation and Experiment* (Eds. K. M. Merz, B. Roux), Birkhauser, Boston, **1996**, pp. 3–29; (b) S. J. Marrink, H. J. C. Berendsen, *J. Phys. Chem.* **1996**, *100*, 16729–16738; (c) U. Essmann, M. L. Berkowitz, *Biophys. J.* **1999**, *76*, 2081–2089; (c) H. E. Alper, T. R. Stouch, *J. Phys. Chem.* **1995**, *99*, 5274–5731.
44. (a) J. Charvolin, P. Rigny, *J. Chem. Phys.* **1973**, *58*, 3999–4008; (b) F. Grieser, C. J. Drummond, *J. Phys. Chem.* **1988**, *92*, 5580–5593; (c) T. Shikata, S. Imai, Y. Morishima, *Langmuir* **1997**, *13*, 5229–5234; (d) T. Shikata, S. Imai, Y. Morishima, *Langmuir* **1998**, *14*, 2020–2026; (e) M. A. Hink, A. Hoek, A. J. W. G. Visser, *Langmuir* **1999**, *15*, 992–997.
45. O. Soderman, G. Carlstrom, U. Olsson, T. C. Wong, *J. Chem. Soc., Faraday Trans 1* **1988**, *84*, 4475–4486.
46. (a) G. Gunnarson, B. Johnsson, H. Wennerstrom, *J. Phys. Chem.* **1980**, *84*, 3114–3121; (b) D. Bratko, B. Lindman, *J. Phys. Chem.* **1985**, *89*, 1437–1440; (c) J. F. Rathman, J. F. Scamehorn, *J. Phys. Chem.* **1985**, *89*, 5807–5816; (d) E. Rodenas, F. Ortega, *J. Phys. Chem.* **1987**, *91*, 837–840; (e) A. Bunton, J. R. Moffatt, *J. Phys. Chem.* **1988**, *92*, 2896–2902.
47. (a) P. Mukerjee, K. Banerjee, *J. Phys. Chem.* **1964**, *68*, 3567–3574; (b) M. S. Fernandez, P. Fromherz, *J. Phys. Chem.* **1977**, *81*, 1755–1761; (c) F. C. Tsui, D. M. Ojcius, W. L. Hubbell, *Biophys. J.* **1986**, *49*, 459–468; (d) C. J. Drummond, F. Grieser, T. W. Healy, *J. Phys. Chem.* **1988**, *92*, 2604–2613; (e) C. J. Drummond, F. Grieser, *Photochem. Photobiol.* **1987**, *45*, 19–34.
48. J. D. Castle, W. L. Hubbell, *Biochemistry* **1976**, *15*, 4818–4831.
49. (a) K. Kalyanasundaram, J. K. Thomas, *J. Phys. Chem.* **1977**, *81*, 2176–2180; (b) N. J. Turro, T. Okubo, *J. Phys. Chem.* **1982**, *86*, 159–161; (c) P. Lianos, A. K. Mukhopadhyay, S. Georgiou, *Photochem. Photobiol.* **1980**, *32*, 415–419.
50. C. D. Tran, *Proc. SPIE* **1988**, *910*, 66–72.
51. K. A. Zachariasse, N. V. Phuc, B. Kozankiewicz, *J. Phys. Chem.* **1981**, *85*, 2676–2683.
52. R. F. Khairutdinov, K. Giertz, J. K. Hurst, E. N. Voloshina, N. A. Voloshin, V. I. Minkin, *J. Am. Chem. Soc.* **1998**, *120*, 12707–12713.
53. K. Kalyanasundaram, J. K. Thomas, *J. Am. Chem. Soc.* **1977**, *99*, 2039–2044.
54. O. H. Griffith, P. J. Dehlinger, S. P. Van, *J. Membr. Biol.* **1974**, *15*, 159–192.
55. I. Konopasek, P. Kvasnicka, E. Amler, A. Kotyk, G. Curatola, *FEBS Lett.* **1995**, *374*, 338–340.
56. M. C. Wiener, S. H. White, *Biophys. J.* **1992**, *61*, 434–447.
57. (a) P. Ram, E. Kim, D. S. Thomson, K. P. Howard, J. P. Prestegard, *Biophys. J.* **1992**, *63*, 1530–1535; (b) M. Milik, J. Skolnick, *Proteins Struct. Funct. Genet.* **1993**, *15*, 10–26; (c) C. R. Sanders, J. P. Schwonek, *Biophys. J.* **1993**, *65*, 1207–1218; (d) J. C. Shelley, M. Sprik, M. L. Klein, *Langmuir* **1993**, *9*, 916–926; (e) L. Laaksonen, J. Rosenholm, *Chem. Phys. Lett.* **1993**, *216*, 429–434; (f) A. D. MacKerell, *J. Phys. Chem.* **1995**, *99*, 1856–1865; (g) J. C. Shelley, M. Sprik, M. L. Klein, *Prog. Colloid. Polym. Sci.* **1997**, *103*, 146–154; (h) T. R. Stouch, *Prog. Colloid. Polym. Sci.* **1997**, *103*, 116–120.
58. (a) H. E. Alper, D. A. Bassolino, T. R. Stouch, *J. Chem. Phys.* **1993**, *98*, 9798–9807; (b) T. R. Stouch, D. A. Bassolino, in *Biological Membranes* (Eds. J. K. Merz, B. Roux), Birkhauser, Boston, **1996**, pp. 255–277.
59. J. K. Thomas, *Chem. Rev.* **1980**, *80*, 283–299.
60. S. A. Alkaitis, M. Gratzel, *J. Am. Chem. Soc.* **1976**, *98*, 3549–3555.
61. S. A. Alkaitis, G. Beck, M. Gratzel, *J. Am. Chem. Soc.* **1975**, *97*, 5723–5728.
62. K. Takagi, N. Miyake, E. Nakamura, H. Usami, Y. Sawaki, *J. Chem. Soc., Faraday Trans. 1* **1988**, *84*, 3475–3486.
63. P.-A. Brugger, P. P. Infelta, A. M. Braun, M. Gratzel, *J. Am. Chem. Soc.* **1981**, *103*, 320–326.
64. M. P. Pileni, R. A. Mackay, *J. Dispers. Sci. Technol.* **1989**, *10*, 45–57.
65. M. Maestri, P. P. Infelta, M. Gratzel, *J. Chem. Phys.* **1978**, *69*, 1522–1526.
66. K. Takagi, K. Aoshima, Y. Sawaki, H. Iwamura, *J. Am. Chem. Soc.* **1985**, *107*, 47–52.
67. K. Takuma, T. Sakamoto, T. Nagamura, T. Matsuo, *J. Phys. Chem.* **1981**, *85*, 619–621.
68. K. Takuma, T. Sakamoto, T. Matsuo, *Chem. Lett.* **1981**, 815–818.
69. S. M. Hubig, M. A. J. Rogers, *J. Phys. Chem.* **1990**, *94*, 1933–1936.
70. L. Kevan, *Radiat. Phys. Chem.* **1991**, *39*, 333–344.

71. K. I. Zamaraev, V. N. Parmon, in *Energy Resources Through Photochemistry and Catalysis* (Ed. M. Gratzel), Academic Press, New York, **1983**, pp. 123–162.
72. I. Tabushi, S. Kugimya, T. Mizutani, *J. Am. Chem. Soc.* **1983**, *105*, 1658–1659.
73. C. J. Grubb, D. J. Cole-Hamilton, M. K. Whittlesey, *J. Chem. Soc., Faraday Trans.* **1996**, *92*, 5005–5012.
74. (a) D. A. McQuarrie, *J. Chem. Phys.* **1963**, *38*, 433–436; (b) D. A. McQuarrie, C. J. Jachimowski, M. E. Russel, *J. Chem. Phys.* **1964**, *40*, 2914–2921.
75. (a) J. C. Eriksson, G. Gilberg, *Acta Chem. Scand.* **1966**, *20*, 2019–2027; (b) M. Gratzel, K. Kalyanasundaram, J. K. Thomas, *J. Am. Chem. Soc.* **1974**, *96*, 7869–7874.
76. (a) M. Hatley, J. J. Kozak, G. Rothenberger, P. P. Infelta, M. Gratzel, *J. Phys. Chem.* **1980**, *84*, 1508–1519; (b) M. Tachiya, *Chem. Phys. Lett.* **1980**, *69*, 605–607.
77. (a) U. Gosele, U. K. A. Klein, M. Hauser, *Chem. Phys. Lett.* **1979**, *68*, 291–295; (b) G. Rothenberger, M. Gratzel, *Chem. Phys. Lett.* **1989**, *154*, 165–171.
78. R. F. Khairutdinov, N. Serpone, *Prog. React. Kinet.* **1996**, *21*, 1–88.
79. (a) M. Tachiya, in *Kinetics of Nonhomogeneous Processes* (Ed. G. R. Freeman), Wiley, New York, **1987**, pp. 575–650; (b) P. P. Infelta, M. Gratzel, J. K. Thomas *J. Phys. Chem.* **1974**, *70*, 190–195; (c) P. P. Infelta, M. Gratzel, *J. Chem. Phys.* **1983**, *78*, 5280–5282.
80. M. Almgren, in *Kinetics and Catalysis in Microheterogeneous Systems* (Eds. M. Gratzel, K. Kalyanasundaram), Marcel Dekker, New York, **1991**, pp. 63–113.
81. H. Sano, M. Tachiya, *J. Chem. Phys.* **1981**, *75*, 2870–2878.
82. (a) K. Weidemaier, M. D. Fayer, *J. Phys. Chem.* **1996**, *100*, 3767–3774; (b) K. Weidemaier, H. L. Tavernier, M. D. Fayer, *J. Phys. Chem. B* **1997**, *101*, 9352–9361; (c) K. Weidemaier, H. L. Tavernier, K. T. Chu, M. D. Fayer, *Chem. Phys. Lett.* **1997**, *276*, 309–315; (d) H. L. Tavernier, A. V. Barzykin, M. Tachiya, M. D. Fayer, *J. Phys. Chem. B* **1998**, *102*, 6078–6088; (e) K. Seki, A. V. Barzykin, M. Tachiya, *J. Chem. Phys.* **1999**, *110*, 7639–7649.
83. (a) R. A. Marcus, *Annu. Rev. Phys. Chem.* **1964**, *15*, 155–196; (b) R. A. Marcus, N. Sutin, *Biochim. Biophys. Acta* **1985**, *811*, 265–332; (c) R. A. Marcus, *Angew. Chem., Int. Ed. Engl.* **1993**, *32*, 1111–1121.
84. M. D. Hatlee, J. J. Kozak, M. Gratzel, *Ber. Bunsenges. Phys. Chem.* **1982**, *86*, 157–161.
85. (a) M. Almgren, J. Alsins, J. Van Stam, E. Mukhtar, *Prog. Colloid Polym. Sci.* **1988**, *76*, 68–74; (b) M. Van der Auweraer, S. Reekmans, N. Boens, F. C. De Schryver, *Chem. Phys.* **1989**, *132*, 91–113; (c) M. Almgren, J. Alsins, *Prog. Colloid Polym. Sci.* **1990**, *81*, 9–12.
86. A. Szent-Gyorgy, *Nature* **1941**, *148*, 157–159.
87. J. Drenthofer, H. Michel, *Angew. Chem., Int. Ed. Engl.* **1989**, *28*, 829–847.
88. (a) S. Iwata, C. Ostermeier, B. Ludwig, H. Michel, *Nature* **1995**, *376*, 660–669; (b) T. Tsukihara, H. Aoyama, E. Yamashita, T. Tomizaki, H. Yamaguchi, K. Shinzawa-Itoh, R. Nakashima, R. Yaono, S. Yoshikawa, *Science* **1995**, *269*, 1069–1074.
89. G. Steinberg-Yfrach, P. A. Liddell, S.-C. Hung, A. L. Moore, D. Gust, T. A. Moore, *Nature* **1997**, *385*, 239–241.
90. G. Steinberg-Yfrach, J.-L. Rigaud, E. N. Durantini, A. L. Moore, D. Gust, T. A. Moore, *Nature* **1998**, *392*, 479–482.
91. M. Rougee, T. Ebbesen, F. Ghetti, R. V. Bensasson, *J. Phys. Chem.* **1982**, *86*, 4404–4412.
92. J. K. Hurst, D. H. P. Thompson, J. S. Connolly, *J. Am. Chem. Soc.* **1987**, *109*, 507–515.
93. K. Kalyanasundaram, M. Neumann-Spallart, *J. Phys. Chem.* **1982**, *86*, 5163–5169.
94. B. Armitage, D. F. O'Brien, *J. Am. Chem. Soc.* **1992**, *114*, 7396–7403.
95. (a) S. V. Lymar, R. F. Khairutdinov, V. A. Soldatenkova, J. K. Hurst, *J. Phys. Chem. B* **1998**, *102*, 2811–2819; (b) R. F. Khairutdinov, J. K. Hurst, *J. Phys. Chem. B* **1998**, *102*, 6663–6668.
96. (a) Y. Fang, G. Tollin, *Photochem. Photobiol.* **1983**, *38*, 429–439; (b) V. Senthilathipan, G. Tollin, *Photochem. Photobiol.* **1985**, *42*, 437–445; (c) Y. Fang, G. Tollin, *Photochem. Photobiol.* **1984**, *39*, 685–695.
97. T. B. Chaabane, A. Bernas, D. Grand, S. Hauteclouque, *J. Phys. Chem.* **1987**, *91*, 6055–6060.
98. A. Bernas, D. Grand, S. Hauteclouque, C. Giannotti, *J. Phys. Chem.* **1986**, *90*, 6189–6194.
99. M.-P. Lanot, L. Kevan, *J. Phys. Chem. B* **1989**, *93*, 998–1000.
100. S. Neumann, R. Korenstein, Y. Barenholtz, M. Ottolenghi, *Isr. J. Chem.* **1982**, *22*, 125–132.
101. Y. Barenholz, T. Cohen, R. Korenstein, M. Ottolenghi, *Biophys. J.* **1991**, *59*, 110–124.

102. (a) B. Medhage, M. Almgren, *J. Fluorescence* **1992**, 2, 7–21; (b) L. Li, L. K. Patterson, *J. Phys. Chem.* **1995**, 99, 16149–16154.
103. S. Y. Chen, K. H. Cheng, D. M. Ortalano, *Chem. Phys. Lipids* **1990**, 53, 321–329.
104. R. F. Khairutdinov, J. K. Hurst, *J. Phys. Chem.* **1999**, 103, 3682–3686.
105. W. E. Ford, J. W. Otvos, M. Calvin, *Proc. Natl. Acad. Sci. USA* **1979**, 76, 3590–3593.
106. M. S. Tunuli, J. H. Fendler, *J. Am. Chem. Soc.* **1981**, 103, 2507–2513.
107. R. F. Khairutdinov, K. I. Zamaraev, V. P. Zhdanov, *Electron Tunneling in Chemistry*, Elsevier, Amsterdam, **1987**.
108. L. Y.-C. Lee, J. K. Hurst, M. Politi, K. Kurihara, J. H. Fendler, *J. Am. Chem. Soc.* **1983**, 105, 370–373.
109. E. R. Kuhn, J. K. Hurst, *J. Phys. Chem.* **1993**, 97, 1712–1721.
110. (a) I. Tabushi, I. Hamachi, Y. Kobuke, *J. Chem. Soc., Perkin Trans. 1* **1989**, 383–390; (b) I. Tabushi, I. Hamachi, Y. Kobuke, *Tetrahedron Lett.* **1987**, 28, 5899–5902.
111. L. Y. C. Lee, J. K. Hurst, *J. Am. Chem. Soc.* **1984**, 106, 7411–7418.
112. W. E. Ford, G. Tollin, *Photochem. Photobiol.* **1982**, 35, 809–819; **1983**, 38, 441–449.
113. Y. Kobuke, I. Hamachi, *J. Chem. Soc., Chem. Commun.* **1989**, 1300–1302.
114. W. E. Ford, G. Tollin, *Photochem. Photobiol.* **1982**, 36, 647–655; **1984**, 40, 249–259; S. Rong, G. Tollin, *Photochem. Photobiol.* **1988**, 47, 277–284.
115. T. J. Dannhauser, M. Nango, N. Oku, K. Anzai, P. A. Loach, *J. Am. Chem. Soc.* **1986**, 108, 5865–5871.
116. E. Tsuchida, M. Kaneko, H. Nishide, M. Hoshino, *J. Phys. Chem.* **1986**, 90, 2283–2284.
117. S. V. Lymar, J. K. Hurst, *J. Am. Chem. Soc.* **1992**, 114, 9498–9503.
118. L. Hammerstrom, M. Almgren, T. Norrby, *J. Phys. Chem.* **1992**, 96, 5017–5024.
119. L. D. Lucchesi, R. F. Khairutdinov, J. K. Hurst, *Colloids Surf.* **2000**, 169, 329–335.
120. R. F. Khairutdinov, J. K. Hurst, *Nature* **1999**, 402, 509–511.
121. J. A. Runquist, P. A. Loach, *Biochim. Biophys. Acta* **1981**, 637, 231–244.
122. J. H. Byrne, *An Introduction to Membrane Transport and Bioelectricity*, Raven Press, New York, **1988**.
123. R. G. Males, P. S. Phillips, F. G. Herring, *Biophys. Chem.* **1998**, 70, 65–74.
124. P. Seta, E. Bienvenue, A. L. Moore, P. Mathis, R. V. Bensasson, P. Liddel, P. J. Pessiki, A. Joy, T. A. Moore, D. Gust, *Nature* **1985**, 316, 653–655.
125. I. Tabushi, T. Nishiyama, M. Shimomura, T. Kunitake, H. Inokuchi, T. Yagi, *J. Am. Chem. Soc.* **1984**, 106, 219–226.
126. T. Yagi, H. Inokuchi, K. Kimura, *Acc. Chem. Res.* **1983**, 16, 2–7.
127. R. G. Yusupov, A. N. Asanov, R. F. Khairutdinov, *Bull. Acad. Sci. USSR, Div. Chem. Sci.* **1985**, 34, 252–256.
128. T. Matsuo, K. Itoh, K. Takamura, K. Hashimoto, T. Nagamura, *Chem. Lett.* **1980**, 1009–1012.
129. (a) K. C. Hwang, D. Mauzerall, *Nature*, **1993**, 361, 138–140; (b) K. C. Hwang, D. Mauzerall, *Proc. Electrochem. Soc.* **1994**, 94, 845–853; (c) R. V. Bensasson, J.-L. Garaud, S. Leach, G. Miquel, P. Seta, *Chem. Phys. Lett.* **1993**, 210, 141–148.
130. (a) P. Seta, E. Bienvenue, P. Maillard, M. Momenteau, *Photochem. Photobiol.* **1989**, 49, 537–543; (b) A. Lamrabte, J. M. Janot, E. Bienvenue, M. Momenteau, P. Seta, *Photochem. Photobiol.* **1991**, 54, 123–126; (c) A. Lamrabte, J. M. Janot, E. Bienvenue, G. Miquel, P. Seta, *Bioelectrochem. Bioenerg.* **1992**, 27, 449–463; (d) J. L. Garaud, E. Bienvenue, J. M. Janot, G. Miquel, P. Seta, P. Maillard, M. Momenteau, *Mol. Cryst. Liq. Cryst. Sci. Technol., Sect. A* **1993**, 235, 59–66.
131. G. Lahanjnar, I. Zupancic, *Period. Biol.* **1981**, 83, 159–162.
132. P. R. Cullis, *FEBS Lett.* **1976**, 70, 223–228.
133. D. W. Larsen, J. G. Boylan, B. R. Cole, *J. Phys. Chem.* **1987**, 91, 5631–5643.
134. J. M. Vanderkooi, J. B. Callis, *Biochemistry* **1974**, 13, 4000–4006.
135. M. F. Blackwell, K. Gounaris, S. J. Zara, J. Barber, *Biophys. J.* **1987**, 51, 735–744.
136. A. L. Kuo, C. G. Wade, *Biochemistry* **1979**, 18, 2300–2308.
137. E. Garcin, F. Baros, J. C. Andre, D. Daveloose, J. Viret, M. L. Viriot, M. Donner, *Stud. Phys. Theor. Chem.* **1990**, 71, 265–272.
138. J. F. Tournier, A. Lopez, N. Gas, J. F. Toccaner, *Exp. Cell Res.* **1989**, 181, 375–384.

139. M. S. Crawford, B. C. Gerstein, A. L. Kuo, C. G. Wade, *J. Am. Chem. Soc.* **1980**, 102, 3728–3732.
140. D. Daems, M. Van den Zegel, N. Boens, F. C. Schryver, *Eur. Biophys. J.* **1985**, 12, 97–105.
141. F. Baros, A. Naoumi, M. L. Viriot, J. C. Andre, *J. Chem. Soc., Faraday Trans.* **1991**, 87, 2039–2046.
142. R. Peters, R. J. Cherry, *Proc. Natl. Acad. Sci. USA* **1982**, 79, 4317–4321.
143. A. Kotyk, K. Janáček, J. Koryta, *Biophysical Chemistry of Membrane Functions*, Wiley, New York, **1988**.
144. A. J. Frank, M. Gratzel, J. J. Kozak, *J. Am. Chem. Soc.* **1976**, 98, 3317–3221.
145. M. A. J. Rodgers, J. C. Becker, *J. Phys. Chem.* **1980**, 84, 2762–2768.

Volume IV

Part 3

Gas-phase Systems

1 Introduction and Theoretical Background

Yehuda Haas

Electron transfer is usually carried out in bulk, condensed matter. In the gas phase, the lower concentrations of the donor and acceptor reduce the chance of an encounter between them in comparison with condensed phases. Furthermore, in the absence of a solvent, no stabilization of the separated ions by solvation is possible, enhancing the chance of charge recombination. The volume of published papers in this field is therefore much smaller for gaseous systems than for condensed matter. Nonetheless, gas-phase systems are in principle simpler to analyze and comparison with theory is more straightforward. The analysis of electron transfer in condensed systems usually starts from the (sometimes experimentally inaccessible) gaseous system. Therefore, efforts to study electron transfer in the gas phase continue, and have indeed shed much light on the mechanism of the process.

This Part deals with gas-phase systems in general, but the emphasis is on systems studied in supersonic jets. Chapter 2 by Soep and Mestdagh in this Part introduces the subject. Gas-phase electron-transfer reactions have been studied since the 1930s in the bulk, and later in crossed molecular beams. When the electron donor is easily ionized, as is the case with the alkali and alkaline earth metals, large reaction cross-sections are measured with acceptors having a large electron affinity. The very large cross-sections were explained by the harpoon mechanism, still the starting point for the analysis of these reactions. Ground-state reactions are usually characterized by a barrier, requiring energy input into the reactants. Efforts to understand better the stereochemical requirements of these reactions led to increased interest in well-defined binary structures containing the donor and the acceptor. Supersonic jet cooling is a relatively simple method for preparing weakly bound van der Waals complexes in the gas phase.

The jet-cooling method is now so widely spread that it does not need a separate introduction. In principle, all that is needed is mixture of the system under study in a suitable carrier gas (e.g., helium) which is expanded from a moderately high pressure (1–5 atm) to high vacuum through a small orifice. This rapid expansion creates a jet that emerges from the orifice and very efficiently cools the system to

temperatures as low as 1–10 K. Adding a ‘solvent’ molecule to the mixture provides a means to prepare solvated clusters of different sizes. The study of photoinduced electron transfer in gas-phase systems has been almost completely dominated in the last 10 years or so by this method. The reasons for this are obvious:

- For electron transfer to happen, two molecules are required—a donor and an acceptor. The easy formation of van der Waals adducts in the cold environment of the supersonic jet allows the future donor and acceptor to be in close contact before absorbing the light. This makes it possible to work under collision-free conditions.
- The low temperature prevailing removes spectral congestion due to hot rotational and vibrational bands. Therefore, subtle effects can easily be measured. In particular, different structural isomers can be studied.
- It is possible, in principle and in practice, to synthesize clusters of different sizes and shapes. In particular, it is possible to prepare an adduct and ‘solvate’ it with a gradually increasing number of solvent molecules. This allows, in principle, the study of the effects of solvents on the electron-transfer process.
- In recent years, several new techniques have become available for the more detailed study of jet-cooled systems. These techniques, to be described briefly below, and at greater length in the following chapters, open up new ways for characterizing the species formed in the jet expansion.
- The collision-free situation is in principle easier to compare with theory, since complications due to interactions with the solvent or other surrounding entities are removed.

Supersonic jets have limitations. The very low number density of the adducts requires special methods for analysis. These are usually state specific, and can be easily applied to the reactants, which are produced in a small number of quantum states. The products are usually formed in many quantum states, making them difficult to observe in real time. The method allows the preparation of a limited number of binary clusters—those structures that form stable adducts in the ground state. In the bulk, thermal energy allows the formation (perhaps only for a short time) of many other conformations. It is not clear at this point whether the structures studied in supersonic jets are the ones important in the bulk. The low temperature prevailing in the jet usually precludes observation of ground-state reactions. It is necessary to initiate the reaction by some means of excitation, usually realized by the absorption of a photon. Excitation is subject to Franck–Condon restrictions, and the subsequent dynamics of the cluster may be dominated by the vibrational modes controlling the departure from the Franck–Condon region. In particular, long-range interactions (i.e., for distances exceeding the van der Waals equilibrium distance) cannot be studied.

In this Part, the emphasis is on experimental advances, mainly over the last dozen years. This introductory chapter outlines some unifying aspects of the work to be presented in the following chapters, and also reviews briefly the theoretical background.

1.1 Some Novel Experimental Advances

The main advantages of jet-cooled systems are as follows:

- Direct probing of isolated molecules.
- The stepwise study allows, in principle, the role of the solvent in the photo-physical process under investigation to be established, in the present case the promotion of electron transfer by the solvent.
- These systems are better suited to detailed comparison with theory than any other experimental arrangement.

Early studies, using a simple one-photon excitation of fluorescence, or resonance-enhanced multi-photon ionization (REMPI), established the fact that electrons can be transferred in gas-phase systems (Chapters 2 to 5 of this Part). Mass selection sometimes allowed the discrimination between different-sized clusters of the type AD_n or AD_nX_m , where A and D are the acceptor and donor molecules, respectively, X a solvent molecule and n and m integers. However, it soon became evident that in the jet, several isomers having the same molecular formula are synthesized simultaneously. Their photophysical properties were different, making the elucidation of structure–reactivity relationships a major research goal. Some new techniques have been developed to address this issue. They are usually based on the use of several laser sources, taking advantage of the high power and high resolution available. Examples are as follows.

In hole-burning spectroscopy, used in conjunction with either fluorescence or ionization detection, two pulsed lasers are used, usually both in the nanosecond regime. One (the ‘burn’ laser) is operated at high power, and is scanned across the absorption spectrum. It excites one of the isomers, depleting the population of this particular species. A second, low-power laser (the ‘probe’ laser), fired after a suitable time delay, is tuned to one of the excitation spectrum vibronic bands of the system, and the fluorescence (or ionization) induced by it (the ‘signal’) is monitored. Whenever the frequency of the burn laser corresponds to excitation of the isomer that absorbs the probe laser, the signal is reduced. This reduction appears as a ‘hole’ that is burned in the signal intensity due to the probe laser. If a different isomer is excited (or a different vibrational level of the same isomer), no change in signal intensity is incurred. The method has been widely used to establish the number of different isomers (Chapter 4, of this part). A recent variant used infrared laser as the probe (Chapter 3 of this Part), although application to electron transfer has not yet been reported.

Charge transfer to solvent (CTTS) has long been studied in liquid solutions of negative ions. The method is now widely investigated in supersonic jets (Chapter 5 of this Part). Size selection of these charged species is easily accomplished using magnetic and electric fields. The mass-selected ions are then subjected to monochromatic laser excitation, causing photodetachment of the electron. The kinetic energy of the electron is monitored as a function of cluster size, allowing the prob-

ing of electron transfer between the anion and solvent molecules. A connection with bulk properties is easily established in this way. Pump–probe techniques are employed in the time-resolved study of the photodynamics of monoanions. A femto-second laser pulse (the pump) electronically excites the anion, and a second femto-second pulse (the probe) induces the photodetachment of the electron. The kinetic energy of the released electron is found to depend strongly on the cluster size.

Examples of such systems include alkali metal atoms solvated by ammonia and by water; four solvent molecules appear to fill the first solvation layer. Thus, in $\text{Li}(\text{H}_2\text{O})_n$, when $n > 4$, the valence electron appears to move out into the second solvation layer, forming $\text{Li}^+(\text{H}_2\text{O})_n^-$. Another example is solvated iodine anions [such as $\text{I}^-(\text{CH}_3\text{CN})_n$]; photoexcitation leads to the transfer of an electron to the solvent even for $n = 2$. The nature of the excited state is determined by the entire arrangement of the solvent molecules, as expected for a CTTS state.

Still another technique uses one laser to prepare the initial state and a different laser to photodissociate the electron donor. The second laser competes with the rate of electron transfer (Chapter 4 of this Part). This method has been used so far only in the nanosecond regime, and could not probe fast electron-transfer rates. Its extension to picosecond or even femtosecond time-scales should be most fruitful.

As detailed in Chapter 3 of this Part, TICT molecules are an example of the extreme importance of solvation in promoting electron transfer. Almost all molecules studied in isolation do not exhibit the characteristic CT fluorescence. When solvated in the jet, some show pronounced CT emission. The role of solvation has been shown to be crucial also in excited-state proton transfer reactions—there is a minimum size at which a proton is transferred in clusters of potential proton donors solvated by ammonia (or water). A similar trend appears to be found in the TICT systems. A major factor is the change in the energy level diagram—the charge-transfer state is affected by solvation in a different manner than the locally excited state. Thus, the crossing point between the states is changed apparently in a way that promotes electron transfer. The application of modern experimental methods to the detailed study of these systems is expected to unravel the factors controlling their dynamics.

These examples are only a few demonstrations of the general effort to use cluster reactions as a bridge between isolated binary systems and bulk reactions. The cluster isolated chemical reaction (CICR) technique elaborated in Chapter 2 of this Part is an important advance in that direction.

1.2 Theoretical Background

The theory of photoinduced electron transfer is based on the classical work of Marcus, Hush, Mulliken, Murrell and many others and it has been extensively reviewed in Chapter 1 of Part 1. The study of isolated, ultra-cold systems provides an opportunity to check some of the basic assumptions of these theories. In particular, one can easily discriminate between different structural isomers of a given system

and probe separately locally excited (LE) and charge-transfer (CT) states. As explained in Chapters 2 to 4 of this Part, it is often possible to monitor the evolution of an LE state to a state. In that sense, the jet studies support the three-state model for weakly coupled systems: the acceptor and donor are viewed as separate species, weakly interacting. The Hamiltonian operator of the complete system may be written as the sum of the Hamiltonians of the two systems, with only weak interaction. This leads to the widespread use of the Fermi golden rule, as is often done in radiationless transition theory. In this picture, initial photoexcitation is into the LE state, which is coupled to the lower lying CT state by a coupling term V . Irreversibility is ensured by the higher density of vibrational states of the CT state.

In some cases, however, electron transfer is very rapid. This has been demonstrated for systems consisting of two separate molecules (e.g., anthracene and dimethylaniline), for solvated TICT molecules (not for the isolated ones) and for some rigid bridged systems. In these cases, it may be inappropriate to use the weak coupling scheme and one has to consider some curve-crossing mechanism. The classical Marcus curve-crossing model assumes motion along a single coordinate. Recent studies of TICT molecules indicate that at least two coordinates are involved. This situation is typical of cases where conical intersections are involved. These unique loci on the molecular potential surfaces are believed to lead to very efficient curve crossing. Their connection with photoinduced electron transfer has not yet been elucidated.

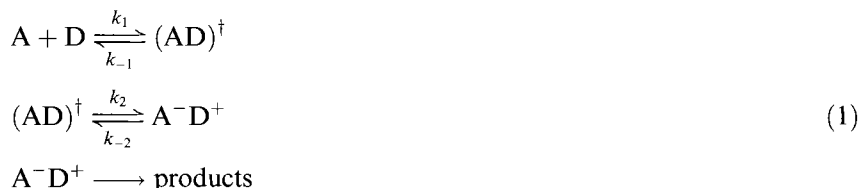
2 Electron-transfer Reactions Involving Atoms, Molecules and Clusters

Benoit Soep and Jean Michel Mestdagh

2.1 Introduction

This chapter reviews several gas-phase studies involving atoms, simple molecules, van der Waals complexes and clusters. Electron-transfer reactions are central processes in a variety of scientific disciplines as outlined in a recent review by Bixon and Jortner [1]. We highlight here the current understanding in the dynamics of the gas-phase electron-transfer reactions, and end the chapter by presenting work which intends to bridge the gap between the standard knowledge of electron-transfer reactions in the gas phase and in condensed phases.

Electron-transfer reactions between a donor D and an acceptor A have been widely studied in liquid solutions. Marcus first proposed the following multistep mechanism to account for these reactions [2, 3]:



The first step forms the activation complex $(\text{AD})^\ddagger$ along a reaction coordinate which is a combination of the nuclear coordinates of the reactant pair with those of the solvent. The activation complex is actually doubly degenerate. Besides the form $(\text{AD})^\ddagger$ where no electron has transferred, which is hence close to the reactant electronic configuration, a second form exists where an electron has jumped from the donor to the acceptor for forming the ion pair A^-D^+ . The second step of the reaction corresponds to the electron jump. The resulting ion pair then evolves to the reaction products. Gibbs energy G is the essential quantity to follow along the reaction coordinate [in the gas phase, however, as we shall deal mostly with direct reactions

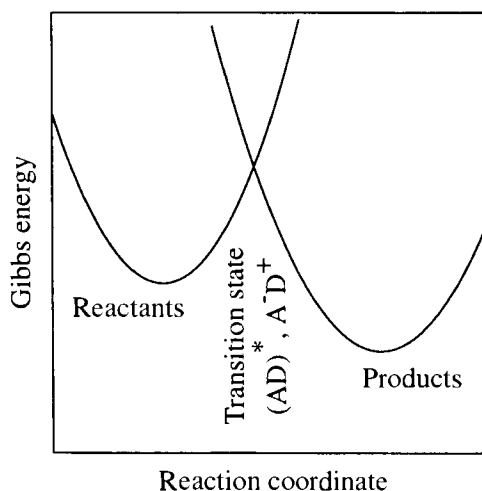


Figure 1. Gibbs energy diagram of a typical electron transfer reaction $A + D \rightarrow A^-D^+$ in solution. Adapted from Ref. [3].

under isolated conditions, the relevant quantity is the energy E (see below)]. Its variation is shown in Figure 1. As shown, this early mechanism was assumed to follow a single coordinate, and the electron jump at the transition state was assumed to be Franck–Condon limited [no atomic movement during the $(AD)^{\ddagger} \rightarrow A^-D^+$ transfer]. This mechanism is described in many review papers, e.g., [4–7]. The modern approach to excited-state electron transfer in solution has abandoned the picture of a movement along a single reaction coordinate. It has adopted a quantum mechanical picture where electron transfer appears as a radiationless process between two states. The *doorway states* describing the reactant pair AD in its environment are then coupled to a dissipative manifold describing the solvated ion pair A^-D^+ [1]. In excited-state electron-transfer processes, this can also be termed the excitation of a locally excited state decaying into the charge-transfer quasi-continuum.

Electron-transfer reactions are also gas-phase processes, which truly correspond to the aims and model examples for reaction dynamics. They have been studied for more than 60 years, and appear as invaluable benchmarks to unravel the interplay between forces during chemical reactions. As a first approximation, electron transfer can be considered as localized and proceeds instantaneously when the reactants move towards each other along the reaction path. The electron transfer leads to a sudden release of forces which drive the further dynamics of the reaction. Hence visualizing and modeling the effect of these forces should be a fairly easy task.

An important class of the gas-phase electron-transfer reactions is well described, at least qualitatively, by the model named pictorially the ‘harpoon model’, which was proposed originally by Michael Polanyi [8] to account for exceptionally large cross-sections in the oxidation reaction of alkali metal atoms by halogen molecules. It is striking to observe that such a simple model is still a useful tool to rationalize these reactions. It is illustrated in Figure 2.

Figure 2, which describes harpoon reactions in the gas phase, has strong relationships with Figure 1, which pictures the Marcus mechanism of an electron-

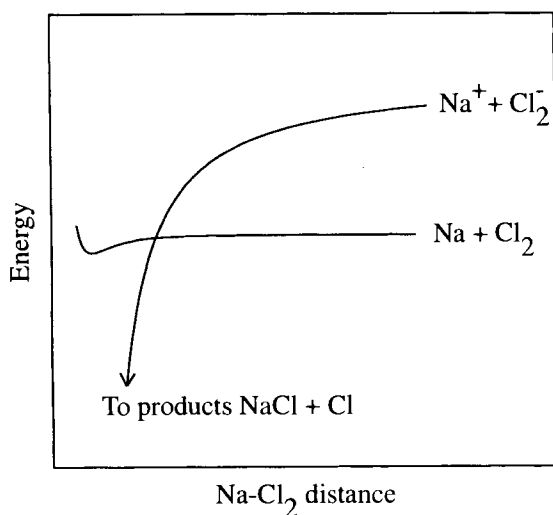


Figure 2. Schematic energy diagram of the harpoon model for describing the $\text{Na} + \text{Cl}_2 \rightarrow \text{NaCl} + \text{Cl}$ reaction.

transfer reaction in solution. In both cases, the transition state of the reaction corresponds to the crossing between an ion-pair curve with a covalent curve. The essential difference is in the way this crossing is accessed. This difference shows up in the definition of the reaction coordinate, which is obviously much simpler in the gas-phase process. This simplification also has its counterpart in the fact that energy considerations prevail in gas-phase processes whereas free energy terms, including level densities and a transition state, must be considered in solution. Moreover, it must also be borne in mind that the condensed phase not only affects the coordinates defining the ion-pair intermediate but also helps to stabilize it.

The gas phase has many advantages when studying primary reaction mechanisms, since all the physical parameters which characterize the reaction product or the reaction intermediate are, in principle, accessible to the experiment: mass, energy, internal energy distribution (E, V, R), product velocity mapping and charge distribution. Also, interestingly, the use of clusters of increasing size allows one to approach the conditions of 'real' reactions in the condensed phase. In this context, electron-transfer reactions between neutral reactants are convenient probes to follow the forces in the course of chemical reactions.

Of course, the very simple harpoon model at the beginning has been considerably refined and more sophisticated approaches are currently used also. This chapter aims to review such reactions. This has obliged us to omit interesting reactions which are not directly relevant to the harpoon model, such as the electron-transfer reactions of buckminsterfullerene, C_{60} [9], and charge-transfer reactions, which have also produced a considerable literature [10]. Reactions of metal ions are also not treated here. They appear elsewhere in this Part (see Chapter IV.3.5). Moreover, although not centered exclusively on electron-transfer reactions, extensive reviews are available on the ion chemistry of transition metals, either bare [11] or ligated [12].

2.2 Experimental Methods

Gas-phase electron-transfer reactions have been studied using all the experimental methods which are of common use in the reaction dynamics community. These methods have been extensively described in the literature, and it is not necessary to describe them again in detail. We just need to recall a few points, which are necessary to understand the origin of the results discussed in the remainder of the chapter, and only the most recent and comprehensive reviews and a few original papers describing the principal techniques are referred to hereafter. It must be mentioned that the techniques used to study reactive collisions are in very wide use and have also been used to investigate non-reactive collisions, both inelastic and elastic.

Except for a very few studies, experimental investigations in the field of reaction dynamics use one or two molecular beams to prepare the reactants. An impressive compilation of information concerning both the molecular beam technique and its use in reaction dynamics can be found in a book edited by Scoles [13]. The book also includes a thorough description of the tools used to characterize the reaction products.

Crossed molecular beam machines count among the experimental arrangements which allowed a significant breakthrough in reaction dynamics. A recent review by Casavecchia et al. shows how improvements in the crossed molecular beam technique made possible recent progresses in the understanding of gas-phase reaction dynamics [14].

The first aims of crossed molecular beam techniques were to ensure the single collision regime and to define well the kinematics of the collision by fixing the collision energy and the direction of the relative velocity of the colliding partners. The first property was necessary to isolate a single reactive event and to study its dynamics, free of external perturbations. The last two properties allowed one to investigate reaction cross-sections as a function of the collision energy, and also, very important, to determine how cross-sections vary when changing the spatial orientation of one or both reactants with respect to the relative velocity vector of the collision. This led to the determination of scalar quantities in the first case (cross-sections describe the transfer of population into final states) and of vector quantities in the second case, i.e., quantities describing the transfer of orientation, of alignment or of higher tensorial orders from a non-spherical state into another. The systematic search of vector quantities in reaction dynamics led to a new field, *reaction stereodynamics* [15]. Its progress is covered by several special issues of the *Journal of Physical Chemistry*, the latest one appearing in 1997 [16]. Reaction stereodynamics now reveals its true nature, an elegant way of controlling atomic and molecular collisions [17].

An important issue in reaction stereodynamics must be considered. Experiment and vector preparations are usually performed in the laboratory reference frame (space fixed) whereas the important preparation for the reaction is the molecular reference frame (body fixed) which rotates during the collisions at a non-constant angular velocity. This leads to numerous difficulties, which have motivated an important literature reviewed in Ref. [18]. As far as stereodynamics considerations are

concerned, the multi-coincidence detection of all the products of the same reaction must be highlighted as a very promising direction. The description of the technique and important achievements are given in Refs. [19–23].

When the crossed molecular beam geometry is associated with a movable detector, rotatable about the crossing zone of the molecular beams, it is possible to measure both the angular and translational energy distribution of the reaction products. The important breakthrough came with the use of a universal detector which allowed one to go beyond the simple alkali metal atom chemistry [24, 25]. The full dynamic picture of many types of reactions then became available. The latest generation of crossed molecular beam equipment was constructed recently. It improves the sensitivity of the detection in several ways: (i) by arranging the detector in ultra-high-vacuum oil-free chambers [26, 27]; (ii) by using tunable synchrotron radiation rather than electron impact to ionize the reaction product to be detected [28, 29] (several applications illustrating the possibilities opened by this technique appear in Refs. [30–32]); (iii) by using the *velocity map imaging* technique, which gives easy access to the velocity–flux contour map, which summarizes the dynamics of the reaction [33–36].

The crossed-beam geometry can also be used to map the angular distribution of chemiluminescent reaction products. The videochemiluminescence technique has been introduced for this purpose. It was exemplified on the $\text{Ba}({}^1\text{P}_1) + \text{N}_2\text{O} \rightarrow \text{BaO}({}^1\Pi) + \text{N}_2$ reaction where the angular distributions of the long-lived $\text{BaO}^*({}^1\Pi)$ product were imaged using a CCD camera [37, 38].

A variant of the crossed-beam geometry, simpler but efficient in some cases, is the beam-gas arrangement. It leads usually to much larger signal than in the crossed-beam configurations, at the expense of a less accurate definition of the reaction kinematics. It is used fairly often to study the total cross-sections of chemiluminescent processes, especially when the species which is to be put into the beam is refractory, as are the transition metals [39, 40]. Reactions of alkaline earth metal atoms have been studied by this technique [41].

The use of optical techniques, either associated with crossed-beam or beam-gas arrangements, was an important landmark in reaction dynamics since it allowed both the preparation of the reactants and the analysis of the reaction products by laser-induced fluorescence. The reactant preparation consists in depositing energy into a specific state, in order to investigate its reactivity, and also to change its spatial orientation and alignment when the system is not spherically symmetric. The introduction of this technique into reaction dynamics was pioneered by Zare's group. A lot of insight can be found in Ref. [42].

An optical technique involving Doppler spectroscopy can also serve to gain insight into the angular and velocity distributions of reaction products, as reviewed in Ref. [43]. Finally, the Doppler method has been associated with the imaging technique. This is the so-called *Doppler-selected time-of-flight* technique, which is the most powerful one to obtain information on the three-dimensional (3D) velocity and angular distribution of the reaction products [44–46].

The experiments performed under the crossed-beam or the beam-gas arrangement document full collisions, where the system evolves on a single or on several

potential surfaces, from an infinite separation of the reactant to the infinite separation of the reaction products through the transition state of the reaction. The technique of van der Waals clusters is an elegant way to bypass the entrance channel of the reaction, by blocking the reactants close together in a fairly well-defined geometry. The reaction is initiated by laser excitation, near the transition state. Varying the wavelength of the laser allows the reaction to be initiated at various configurations about the transition state. It therefore allows one to study spectroscopically the access to the transition-state region of the reactions. This gives, of course, a very different and complementary insight into the reaction to full collisions [47–50].

More recently, the use of picosecond and femtosecond lasers in reaction dynamics opened up the field of femtochemistry, which was pioneered by Zewail [51–54]. The idea of these reactions is to photoinitiate the reactive process in a van der Waals complex. Sometimes, the process that is initiated is a simple dissociation or the isomerization of a free molecule. In each case, the reaction is initiated by a first ultrashort laser pulse (the pump pulse). It is analyzed after a certain delay by a second pulse (the probe pulse). This gives access to the reaction dynamics on the pertinent time-scale where chemical bonds are broken and others are formed. Depending on the system, this typically lasts between a few tenths of femtoseconds to hundredths of picoseconds. Recently the techniques of stereodynamics have been combined by Zewail and co-workers with femtosecond analysis [55, 56] to label specific reaction channels in electron-transfer reactions.

2.3 The Harpoon Model and Beyond: a Historical Review

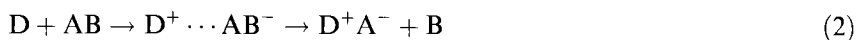
2.3.1 The Early Age: the Harpoon, a Model to Describe Reactions of Ground-state Alkali Metal Atoms

The reactions of ground-state alkali metal atoms with halogen molecules have been studied extensively over many decades. The flame experiments by Michael Polanyi's group revealed their exceptionally large cross-sections in the early 1930s [8]. These reactions have attracted detailed crossed molecular beam studies for over 30 years [57–59]. The well-accepted picture to interpret these reactions is the harpoon mechanism, which was proposed originally by Polanyi [8] and was put in a semi-quantitative form by Magee [60]. Gislason has reviewed the early efforts to make it quantitative [61].

According to the harpoon model, the reaction of a ground-state alkali metal atom M with a halogen molecule X_2 proceeds through a long-range electron transfer from the HOMO (highest occupied molecular orbital) of the alkali metal atom (the electron donor) to the LUMO (lowest unoccupied molecular orbital) of the halogen molecule (the electron acceptor), thus forming an $M^+-X_2^-$ complex, which decays to $M^+X^- + X$. In this mechanism one electron has left the HOMO of the alkali metal atom M and has entered into the LUMO orbital of the halogen mole-

cule X_2 . It is the origin of the force which pulls the molecule apart and, as we shall see below, determines both the angular distribution of the reaction product and its internal energy.

The harpoon model has been used on a large variety of systems, far beyond the alkali metal–halogen systems for which it was proposed originally. It is therefore necessary to describe the model on a more general basis by considering the reaction



where D is the electron donor (often a metal atom or an electronically excited metal atom of low ionization potential) and AB a molecule, which acts as an electron acceptor to form temporarily AB^- , which then comes apart as $A^- + B$.

Two crucial parameters determine the dynamics of the reaction. The first is the $D \cdots AB$ distance at which the electron transfer occurs, i.e., the distance R_c for which the ion-pair potential $D^+ \cdots AB^-$ crosses the covalent curve $D \cdots AB$. Assuming a flat covalent curve and R_c large enough for the Coulomb interaction to be dominant, the crossing occurs at

$$R_c = \frac{14.4}{IE - EA} \quad (3)$$

where R_c is in Å and the energies IE and EA in eV, IE being the ionization energy of the electron donor D and EA the electron affinity of the acceptor AB . This expression, sometimes called Magee's equation, could be refined [61], but it is often sufficient to anticipate the important aspects of the reaction.

At this point, when following the terminology of Truhlar and Dixon [62], the harpoon mechanism appears as an *entrance-channel model in a single-surface reaction*. This terminology highlights the fact that the access to the transition state of the reaction involves a movement along a single coordinate in the entrance channel of the reaction, on a single potential energy surface (PES). It is obvious that, even when staying with simple models, efforts have to be made to include the necessary multi-coordinate character of the reaction. This is the role of the second dynamic parameter, which is discussed in the next paragraph.

The second important dynamic parameter mentioned above is the shape of the AB^- potential, which promotes the AB^- dissociation [57, 63]. As we shall see, this parameter is the key to account for the shape of the differential cross-sections measured experimentally. Figure 3 shows the angular distribution of the monohalide product in a family of reactions. All these reactions are called *reaction* according to reaction dynamics terminology. The reaction is dominated by the *impulsive regime* and the product angular distribution has a strong forward–backward asymmetry. In the extreme situations of the $K + CH_3I$ and $K + Br_2$ reactions, the product is respectively backward (scattering angle 180° from the incoming direction of potassium) or strongly forward peaked. This regime occurs when the collision complex breaks up before it can rotate through a half turn. In contrast, an *indirect reaction* involves a long-lived (or persistent) complex, and the product angular distribution has a forward–backward symmetry [64]. One such example is shown later in Figure

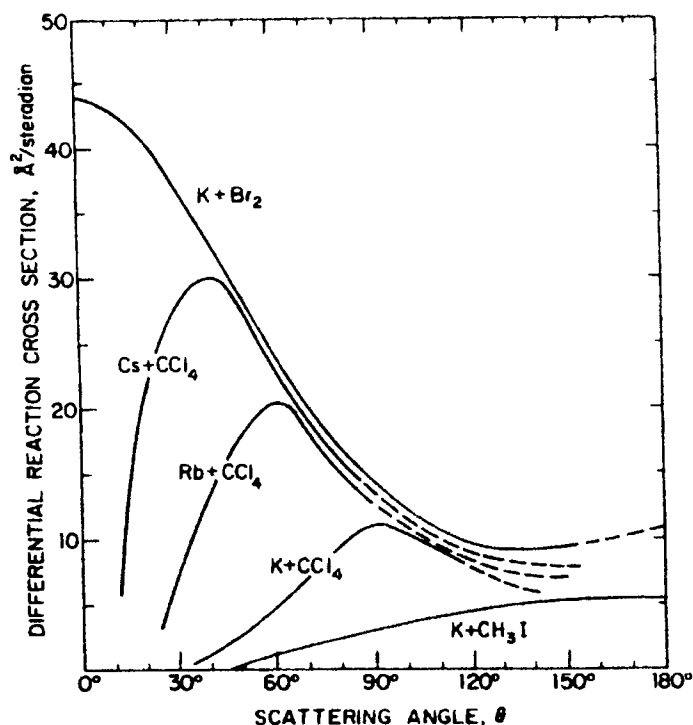


Figure 3. Center-of-mass angular distributions of an alkali metal monohalide compound in five gas-phase electron-transfer reactions as labeled. Forward scattering is to be found around 0° and backward scattering at 180° . Adapted from Ref. [63].

5. Grice has derived a microcanonical theory of reactions decaying from a persistent complex [65].

Let us discuss the two extreme situations of direct reactions observed in Figure 3. Then we shall examine an example of an indirect reaction.

When the electron is transferred to an antibonding orbital, the AB^- potential is strongly repulsive along the $A^- \cdots B$ coordinate, thus kicking the $D^+ A^-$ product away from B . Sideways or backward scattering is expected in this case. A representative example is the reaction [66]



which is probably one of the most often studied in the whole field of reaction dynamics. It exhibits further constraints: the distance R_c is short and the acceptance angle $K-I-C$ for an efficient electron transfer is small [67–69]. This makes the reaction of the rebound reaction type, with most products scattered in the backward hemisphere. It must be mentioned, however, that despite many efforts, the dynamics

of this reaction are still not fully understood. A recent paper extensively reviews the current knowledge about this reaction and identifies the problems still open [69].

In contrast, forming AB^- near its dissociation limit requires the Coulomb field of the positive ion to stimulate dissociation of the molecular anion. This situation is encountered when the molecule has a large electron affinity. In this case, the crossing distance R_c is large and the dynamics of the reaction are well described by the spectator stripping model, where the reaction product is strongly forward peaked [70]. This pictorial formulation leaves unaffected the neutral moiety of the molecular reaction partner, which plays the part of a spectator in the reaction. A representative example is the reaction [71]



After these two examples, it should not be thought that reactions described by the harpoon model are necessarily direct. This was the case with reactions 4 and 5 because they are very exoergic and the molecular negative ion is unstable. In contrast, in the almost thermoneutral reaction of Cs with NO_2 , NO_2^- is a stable ion, and the charge-transfer complex $Cs^+ \cdots NO_2^-$ corresponds to a deep well along the reaction coordinate. Hence the reaction proceeds from a persistent complex, with a forward-backward symmetry in the angular distribution of the reaction product CsO [72].

These three examples illustrate the goal of the reaction dynamics community during the late 1960s and 1970s: to build a catalog of some major features of potential-energy surfaces and to indicate, in a qualitative fashion, the consequences of these features for the reaction dynamics. Developing this concept led to an impressive series of papers, which are summarized in comprehensive review papers by J. C. Polanyi [70, 73, 74a]. These dynamic approaches were constructed on very general potential energy surfaces, with no reference to a particular process. The same methodology is currently revisited in order to help understanding the global shape of the product energy distribution in indirect three-atom-reactions going through the temporary formation of a collision complex [74b]. Of course, these very general approaches can therefore be applied to any class of gas-phase reaction, including the present electron-transfer reactions. However, the electron-transfer reactions, which are relevant to the harpoon mechanism are relatively simple as the electron transfer is sudden, and the shape of the potential surface on which the reaction proceeds is fairly simple to guess qualitatively.

The mechanism of the electron transfer and the subsequent dynamics of the system have both been oversimplified at the moment. A more refined model of the dynamics is discussed in the next section: the direct interaction with product repulsion (DIPR) model and its variant called DIPR-DIP (DIP-distributed as in photodissociation). The purpose of sections 2.4 and 2.5 is to explicit the multi-dimensional and multi-PES character of the electron jump step.

2.3.2 A First Multi-dimensional Reaction Model: the DIPR-DIP Model

Readers may wonder why we focus our attention on simple models when modern high-speed computers can handle full quantal calculations. A very recent example of this is furnished by the work of Truhlar and co-workers on the $Na \cdots HF$ system

[75]. However, simple reaction models are very useful in giving a clear, although often semi-quantitative, understanding of reaction mechanisms. Several simple classical models of this type have been proposed to account for direct reactions [62, 76].

We focus our attention on the DIPR (direct interaction with product repulsion) model and its variant, the DIPR-DIP model, mainly because it can be used to predict an entire range of dynamic observables in chemical reactions: angular and recoil velocity distributions, rotational energy and orientation and vibrational energy of the reaction products. It is also able to account for the switch from the rebound to the stripping reaction mechanism for a given system when the collision energy is increased. The beauty of the model is its ability to include semiempirical parameters, each of which is related to a different physical phenomenon.

The DIPR model presumes that the reaction is initiated by a sudden change of coordinate, as suggested by the harpoon model, when the valence electron of the donor D is transferred to the electron acceptor AB. The basic dynamic idea of the model is that the angular and energy distributions of the product AD are mainly determined by a monotonic energy release along the A^--B coordinate after the electron jump. This model was proposed originally by Kuntz and co-workers to account for the direct reactions of an alkali metal atom with a halogen or a halide molecule to give an alkali metal halide product [77–80].

More precisely, the DIPR model is founded on the following set of assumptions, as shown in the pictorial representation in Figure 4.

- AB is initially in the ground rotational and vibrational level.
- The $D + AB$ system evolves on an essentially flat potential surface. This initial movement has a negligible effect on the dynamic behavior of the reactive trajectories.
- The electron jump forming the complex $D^+ \cdots AB^-$ takes place at a distance R_c between reactants. A parameter linked to stereodynamics can easily be introduced at this point into the model: the electron jump probability as a function of the $D-A-B$ angle at the electron jump distance.

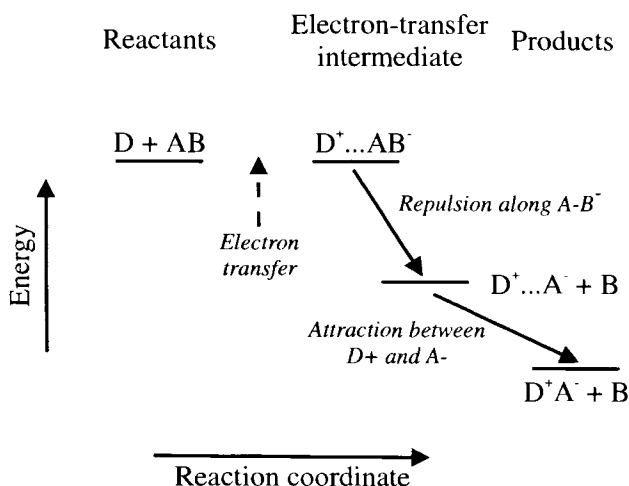


Figure 4. Schematic description of the energy release according to the DIPR-DIP reaction mechanism.

- A change of coordinate follows the electron jump, which turns on the sudden repulsion between A^- and B. Considering that the electron distance R_e is large, no interaction is assumed between D^+ and the departing B moiety.
- An attractive interaction between D^+ and A^- follows the $A^- \cdots B$ repulsion. The attractive and repulsive energy releases are presumed to be separable, and the attraction is assumed to be slower than the repulsion.

If the energy release along the A–B coordinate is a substantial fraction of the total exoergicity (more than 10 %), then the model was found to do very well in reproducing product state distributions [77].

Herschbach [58] noted a striking similarity between the recoil energy distribution of Cl atoms in the $H + Cl_2$ reaction and that observed in the photodissociation of Cl_2 . This suggests that the electron attachment to the molecule is essentially a vertical process, hence he proposed the DIP extension to the model, which makes the AB repulsion after the electron jump analogous to that encountered in photodissociation experiments. This provided the necessary empirical basis for estimating the parameter of the repulsive interaction. All the mathematical expressions relevant to the model were given by Truhlar and Dixon [62]. Zare and co-workers extended the model to chemiluminescent reactions and a full account of the new model is given in Ref. [81]. It was used to predict successfully the product state distribution in the reaction $Ca(^1S_0) + F_2 \rightarrow CaF(B^2\Sigma^+) + F$.

The DIPR model is often used to help in understanding the stereodynamics of direct reactions [82–85]. The important parameter of the model is thus the electron-transfer probability as a function of the molecular orientation. The same parameter, which actually defines the best geometry of the system in the electron transfer step, also plays a role in determining the product alignment in chemiluminescent reactions [86, 87]. A new model has been introduced recently, the anisotropic impulsive model [88]. It is conceptually close to the DIPR model, and also helps to determine the preferred angle of approach between the reactants.

2.3.3 The Double Harpoon: a Mechanism Adapted to Alkaline Earth Metal Atom Reactions

Alkaline earth metal atoms have fairly low ionization potentials, as have alkali metal atoms (e.g., 5.21 and 5.14 eV for barium and sodium, respectively [89]). Hence the reactions of alkaline earth metal atoms with oxidizing molecules are also expected to be initiated by an electron transfer and should follow the harpoon mechanism. However, alkali metal atoms are monovalent species, whereas alkaline earth metal atoms have two valence electrons. Hence peculiarities are to be expected in the alkaline earth metal reaction dynamics, especially when doubly charged products such as BaO are to be formed [90]. The second valence electron also opens up the possibility of chemiluminescent reactions, which are largely absent in alkali metal atom reactions [91, 92]. The second electron causes the existence of low-lying excited states in the product.

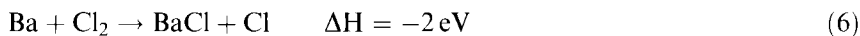
Reactions of ground-state alkaline earth metal atoms have been the subject of too

numerous studies to be reviewed here thoroughly. A comprehensive compilation of work prior to 1988 was made by Menzinger [92]. Many references can also be found in earlier review papers and book chapters [91, 93, 94]. We restrict ourselves here to studies, which highlight a concept not yet introduced in the present chapter, the double harpoon, which involves both singly and doubly charged ion-pair intermediates in the reaction. This concept was introduced originally by Menzinger to account for chemiluminescence in reactions with halogen molecules [91]. It was refined further by Lee and co-workers to account for crossed molecular beam studies of the formation of ground-state products [90]. We shall use the model again when considering reactions of electronically excited alkaline earth metal atoms.

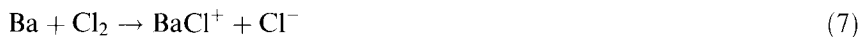
Since alkaline earth metal atoms have two valence electrons, it is convenient to distinguish between reaction products, which have a single ionic bond such as BaCl (Ba^+Cl^-) from products having a double ionic bond in the ground state such as BaO (BaO has the structure $\text{Ba}^{2+}\text{O}^{2-}$ in the ground state and Ba^+O^- in the lowest excited states).

Reaction products with a single ionic bond

The reactions of alkaline earth metal atoms with halogen molecules, either forming alkaline earth metal monohalides or leading to chemi-ionization, represent an important case study in the reaction dynamics of divalent systems [91, 92, 95–100]. Let us take as an example the reaction



The reaction product BaCl has the structure Ba^+Cl^- where a single electron is transferred from barium to chlorine. This reaction channel thus correlates adiabatically to the single electron-transfer intermediate Ba^+Cl_2^- . Chemi-ionization is also observed as a minor channel in the $\text{Ba} + \text{Cl}_2$ collision:



The structure of the product BaCl^+ is close to $\text{Ba}^{2+}\text{Cl}^-$. The product channel of reaction 7 thus correlates to the double electron-transfer intermediate, whose structure is probably $\text{Cl}^-\text{Ba}^{2+}\text{Cl}^-$ [91, 92].

Herm and co-workers have measured the BaCl angular and recoil velocity distribution from reaction 6 [101]. As expected, this reaction channel tells little about the role of the second valence electron of barium. The product is forward peaked as in alkali metal–halogen reactions, and is close to the spectator stripping limit. This contrast with reaction 7, where the product BaCl^+ is backscattered [96, 97]. This suggests a very restricted geometry for the reaction: a low impact parameter and a near collinear approach. A scenario of the collision could be as follows: following the first electron transfer, the newly formed Cl_2^- molecular ion is stretched rapidly as in the DIPR-DIP mechanism above. For collinear, low impact parameter trajectories, the stretching cannot be as rapid because of momentum conservation which pushes the nascent Ba^+Cl^- and Cl moieties together. Hence the close-packed inter-

mediate can transfer the second valence electron. It is transformed into $\text{Ba}^{2+}\text{Cl}^-\text{Cl}^-$ which dissociates very rapidly as $\text{BaCl}^+ + \text{Cl}^-$ because of the Coulomb repulsion between the two negative Cl^- ions. The same picture has also been proposed in $\text{Ba} + \text{Br}_2$ collisions [98].

The reactions of alkaline earth metal atoms with halogenated molecules, of which reaction (6) is an example, are sufficiently exoergic to lead to chemiluminescence [91]. The picture due to Menzinger for the branching to chemiluminescence is a broadside approach of Ba and Cl_2 in a near C_{2v} geometry. The outer harpoon forming Ba^+Cl_2^- with Ba^+ in its ground state $6s^2\ ^2\text{S}$ is forbidden for symmetry reasons (conical intersection between the covalent $\text{Ba} \cdots \text{Cl}_2$ and ion-pair $\text{Ba}^+ \cdots \text{Cl}_2^-$ states in C_{2v} geometry). This allows the system to reach an inner harpoon crossing where Ba^+ is formed in an electronically excited state. The resulting excited $\text{Ba}^{*+} \cdots \text{Cl}_2^-$ intermediate then decays into the chemiluminescent product BaCl . According to this scheme, chemiluminescence appears as due to the conservation of the electronic excitation of the positive ion as it goes from the ion-pair intermediate into the exit channel of the reaction.

Reaction products with a double ionic bond

Lee and co-workers distinguished three different classes for these reactions [90, 96, 102]:

- 1) Reactions going through a long-range transfer of the first valence electron, in a situation where the resulting molecular anion is stable. This is best illustrated by the $\text{Ba} + \text{NO}_2$ reaction.
- 2) Reactions with still a first long-range electron transfer, but in a situation where the molecular anion could promptly dissociate. The illustrative example will be the $\text{Ba} + \text{O}_3 \rightarrow \text{BaO} + \text{O}_2$ reaction.
- 3) Reactions involving a close collision for the first electron transfer. They will be exemplified by the $\text{Ba} + \text{H}_2\text{O}$ system.

Let us start with the first class of processes, which we illustrated by the reaction



A long-range electron transfer is possible in this reaction, as in alkali metal atom reactions. However, the resulting electron-transfer complex Ba^+NO_2^- does not correlate to the ground-state products BaO which has the structure $\text{Ba}^{2+}\text{O}^{2-}$. Moreover, the NO_2^- ion is stable and its dissociation into $\text{NO} + \text{O}^-$ is endoergic. Hence the Ba^+NO_2^- complex may survive for many rotational periods despite the availability of a very exoergic reaction channel. This is expected to dissociate after the transfer of the second valence electron of barium, which is probably hindered by an energy barrier.

This picture was first proposed by Lee and co-workers. It helps to interpret the angular and energy distributions of the product BaO observed in reaction 8, and shown as a 3D plot in Figure 5 [90, 96]. Panel D indicates that the reaction yields

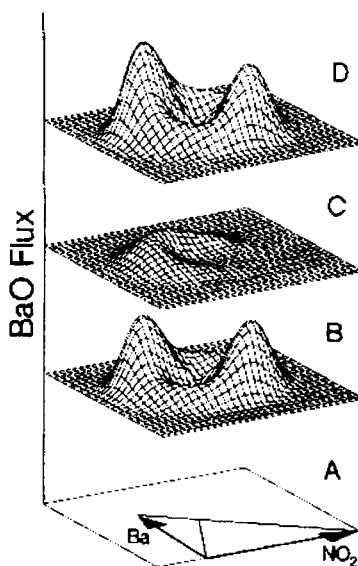


Figure 5. (A) Newton diagram of the reaction, which was studied in a crossed-beam experiment. The other three panels are 3D plots showing the velocity and angular distribution of the product BaO in reaction (8). Panel D is the full signal, which is resolved into two components, a forward-backward symmetric component shown in panel B + a forward component shown in panel C. Adapted from Ref. [102].

mostly ground-state BaO with a forward-backward symmetry in the angular distribution. This suggests that BaO decays from a long-lived collision complex, in agreement with the mechanism proposed above. However, a direct forward product, which is believed to be vibrationally excited BaO(X), is superimposed on this dominant channel (see the slight forward-backward asymmetry in Figure 5 D, which is further resolved as the superposition of the forward component shown in panel C plus the long-lived complex component of panel B). An electron transfer is also conjectured to account for this channel, but in unfavorable geometries for the formation of a long-lived complex, for instance when Ba approaches very close to one of the oxygen atoms of NO₂. Figure 6 is a correlation diagram, which shows the two reaction channels accessible from Ba(¹S₀) + NO₂ collisions.

Besides reaction 8, formation of BaNO is also observed in Ba + NO₂ collisions. It is a minor reaction channel and the corresponding velocity-angle contour map reveals that the corresponding reaction channel goes through a very restricted range of collision geometries. It is believed to result from trajectories which are able to avoid the electron transfer, as this could happen when Ba approaches NO₂ on the N end of the molecule, off the C_{2v} axis. This kind of geometry is likely to maintain the system on a covalent surface and to promote the asymmetric stretching of the NO₂ molecule which is necessary for the formation of the BaNO product.

The reaction of barium with NO₂ has also a chemiluminescent channel, which was studied in a beam-gas arrangement [103]. The chemiluminescence originates from BaO(A ¹Σ⁺, A' ¹Π). The correlation diagram in Figure 6 indicates that both the direct and the indirect channel forming ground-state BaO may also lead to excited BaO through a non-adiabatic coupling. The product state distribution of the chemiluminescent product analyzed by Cheong and Parson is close to a prior distribution [103]. This suggests that the chemiluminescent product decays essentially

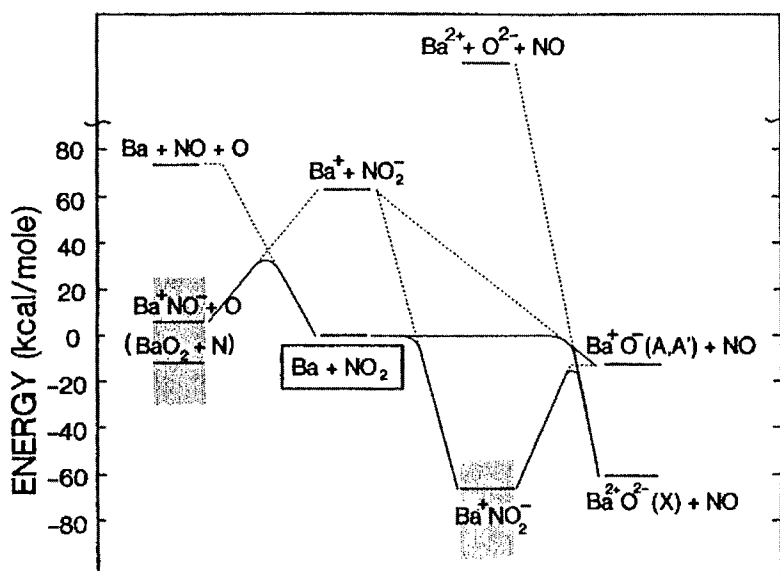
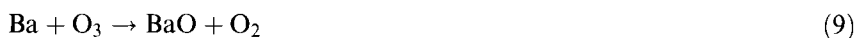


Figure 6. Correlation diagram for the reaction $\text{Ba}(^1\text{S}_0) + \text{NO}_2$. Adapted from Ref. [102].

from the long-lived complex, as it is waiting for the second electron transfer ultimately to form ground-state BaO.

The second class of processes also corresponds to a long-range transfer of the first valence electron, as in the reaction



but the complex Ba^+O_3^- formed in this case is very different from the Ba^+NO_2^- complex encountered in the previous example. The important point here concerning the dynamics of the subsequent reaction is the dissociation property of the negative molecular ion. Let us follow the simple dynamics considerations recalled in Section 2.3.1. Whereas the O^- production is endoergic from NO_2^- , it is exoergic from O_3^- . In the former case this has led to the existence of a persistent complex because NO_2^- was not going to dissociate spontaneously. On the contrary the complex had to wait for the second electron transfer before dissociating. No such delay is expected with O_3 and a spectator stripping character could be anticipated for the dynamics of the reaction. Nevertheless, one should not forget that the complex formed from a single electron transfer does not correlate to the ground-state reaction product. Hence the dynamics of the reaction cannot correspond purely to a spectator stripping reaction. It is therefore not surprising that the experiment reveals a mixed character of both a spectator stripping and a long lived complex reaction [96].

We switch now to the last class of reactions where a long-range electron transfer is not possible because the possible electron acceptor has a negative electron affinity. This is the case of water.

A crossed molecular beam study of $\text{Ba} + \text{H}_2\text{O}$ collisions by Lee and co-workers has shown that BaO is the major reaction product, even at collision energies well above the barrier of endoergicity for the formation of the BaOH product [90, 104]. This result precludes the formation of an intermediate where barium is inserted into an OH bond. On the contrary, it was interpreted on the ground of a concerted mechanism, with abstraction of the central O atom of HOH and simultaneous formation of H_2 . This process is induced by a very short distance ($< 2 \text{ \AA}$) electron transfer, and two points make it realistic. First, the valence electron of barium is transferred into the $4a_1$ orbital of water, which is antibonding with respect to both OH bonds. Second, the electron jump distance is close to the bond length of ground-state BaO , which has the structure $\text{Ba}^{2+}\text{O}^{2-}$. The system is therefore in a good position to transfer readily the second electron required for the formation of the BaO product at the same time as the H_2 molecule is formed. The kick of barium into water in near C_{2v} geometry, by stimulating the bending of the molecule, also favors the formation of H_2 .

In reaction with methanol, barium leads to the methoxide, and not to BaO . This is surprising at first glance since the barium + alcohol reaction should have a similar mechanism to the barium + water reaction. In fact, the reaction starts the same with a close collision between barium and methanol, but the concerted formation of the H-H bond in the water mechanism has no equivalent when H-O-H (water) is replaced by H-O-CH_3 (methanol). Its equivalent would be the concerted formation of H-CH_3 , which should go through a three-center transition state, and would necessitate the rotation of the sp^3 carbon to put it into position for bonding with the H atom leaving OH . This is very unfavorable and the H atom prefers to migrate, hence forming temporarily the insertion intermediate HBaOCH_3 , which decays to $\text{BaOCH}_3 + \text{H}$ [104].

The above two scenarios for the reactions with water and methanol not only are supported by the nature of the reaction products, but also account for the product angular and recoil velocity distributions observed experimentally. In particular, the concerted three-center elimination of H_2 implies a substantial bond rearrangement, which implies energy barriers in the entrance and in the exit valley of the reaction, hence resulting in a certain duration of the collision complex, in agreement with the observed forward-backward symmetrical angular distribution of the product BaO [104]. Interestingly, these scenarios are close to those encountered in the chemiluminescent reactions of alkaline earth metal atoms (Ca , Sr , Ba) with stronger oxidizing agents: H_2O_2 , $t\text{-BuOOH}$ and HNO_3 . A near-statistical distribution of the product energy states was observed, thus suggesting again that these products decay from a long-lived complex [103, 105].

2.3.4 Beyond the Harpoon Model: the HOMO/LUMO Matching to Describe Transition Metal Reactivity

The gas-phase chemistry of ground-state transition metals is much less well understood and has attracted far fewer studies than the reaction dynamics of alkali and alkaline earth metal atoms. Three reasons explain this situation. The first is experi-

mental. Owing to the refractory nature of most transition metals, it is difficult to generate the intense beams which are necessary for reaction dynamic studies. Second, the electronic structure of the transition metal compounds involves the participation of d electrons, which complicates tremendously the interpretations, especially because of the third reason: many oxidation reactions of transition metals are very exoergic, with the consequence that many product states are populated. Despite these difficulties, significant progress has been made in this field and three very recent achievements can be quoted: (i) the beam-gas investigation by Parson and co-workers of the chemiluminescent reaction between manganese and ozone [40], (ii) the work performed by Levy's group where the laser ablation of Mn and MnO₂ targets was employed to investigate the reactions $\text{Mn}(a^6\text{S}, a^6\text{D}_J, \dots) + \text{Cl}_2 \rightarrow \text{MnCl}^* + \text{Cl}$ in a beam-gas configuration [39], and (iii) the crossed beam study of Vetter et al. on the oxidation reactions of $\text{Ti}(a^3\text{F}_J, a^5\text{F}_J)$ atoms by O₂, NO and N₂O [106].

Reactions of transition metals with oxidizing molecules cannot be interpreted so simply on the basis of the harpoon model, even when considering reactions with a good oxidizing agent such as ozone or Cl₂. The ionization energy of the ground-state metal falls in the 7 eV range, which precludes a long-range electron transfer. For example, manganese has an ionization potential of 7.43 eV [89], hence the crossing between the covalent Mn + O₃ curve and the ion-pair curve occurs at a distance of 2.7 Å, which is only 1.6 times the equilibrium distance of the expected reaction product MnO (1.7 Å). Moreover, and for the same reason, reaction products such as MnO are largely covalent in nature [40]. Despite this, reactions such as



do proceed via an electron-transfer reaction, but not according to the simple harpoon model picture. In the case just mentioned, manganese is the donor and ozone the acceptor. This reaction was investigated by Parson and co-workers, whose interpretation is summarized in Figure 7 [40]. These authors suggested that the behavior of the system could be essentially adiabatic and interpreted based on the correlation of frontier orbitals (see Ref. [107] for an illuminating discussion of how electron transfers from HOMOs into LUMOs control reactions). A consideration of the electronic structure of the reactants and products suggests the picture called 'forward σ -donation' in the top left corner of Fig. 7. The sd_{z^2} hybridized orbital of Mn takes the part of the HOMO and, when manganese approaches perpendicular to the O₃ plane with the sd_{z^2} pointing toward a terminal O atom of O₃, this orbital overlaps the LUMO of ozone ($2b_1$), hence producing a bonding σ -orbital centered on the O atom and an antibonding σ^* -orbital centered on the Mn atom. This corresponds to a newly formed polar covalent Mn–O bond which is further strengthened by the back-donation a π -electron from the 2p π -orbital of the terminal O atom into the empty 3d π -orbital of manganese (see the middle panel of Figure 7. This results in a slackening of the O₂–O bond and energy is released as in the above-mentioned DIPR model (see Section 2.3.2) along the O₂–OMn bond, in agreement with the observed high product rotational excitation.

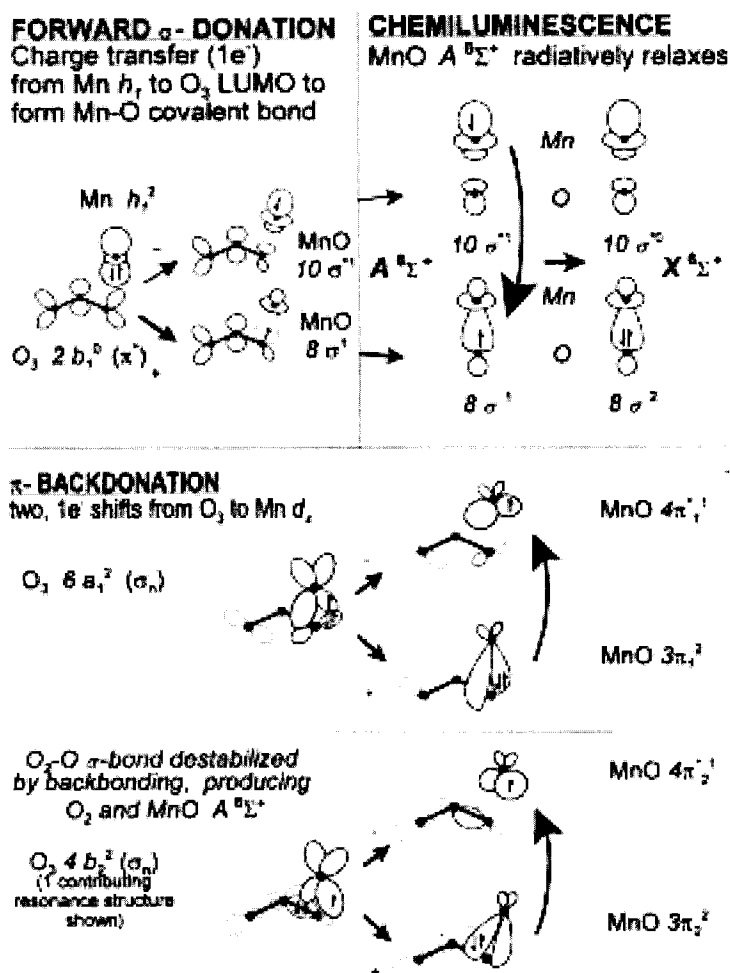


Figure 7. Frontier orbital correlation diagram for the $Mn + O_3 \rightarrow MnO^* + O_2$ reaction. Adapted from Ref. [40].

2.3.5 Multicenter Harpoon Reactions

These reactions were pioneered by Grice and co-workers who first addressed the reactivity of alkali metal dimers with halogen molecules [108–111]. These reactions are four-center harpoon reactions. They are interesting because of the possibility of two sequential electron jumps [112].

Let us take the collision $K_2 + Br_2$ as an example. The dominant reaction channels are



Chemiluminescent channels have also been observed in this type of reaction [113]. Reactions of alkali metal dimers with oxygen molecules have also been reported [114–116].

The electron jump forming $\text{K}_2^+ \cdots \text{Br}_2^-$ in the $\text{K}_2 + \text{Br}_2$ collision occurs at a 7 Å distance. The resulting complex has the biradical structure $\text{K}^* \text{K}^+ \text{Br}^- \text{Br}^*$ [108, 109, 111]. Its principal decay mode is the formation of the di-alkali metal complex $\text{K}^* \text{K}^+ \text{Br}^-$ because, as in alkali metal–halogen reactions, the excess electron of the Br_2^- moiety induces its dissociation. Most reactive trajectories lead to further dissociation of the complex to $\text{K}^* + \text{K}^+ \text{Br}^-$, which corresponds to the dominant channel of the reaction, i.e. process 11. The two other reaction channels require a second electron jump, hence forming temporarily $\text{K}^+ \text{K}^+ \text{Br}^- \text{Br}^-$. The bent geometry of the latter complex tends to produce two KBr molecules as in reaction 12, whereas its linear geometry leads to reaction 13.

A number of chemiluminescent studies of chemiluminescent multicenter reactions of transition metal dimers and trimers have been reported [117], namely



Reactions of Mn_3 have also been reported. The analysis of the observed emissions served essentially to unravel the complex spectroscopy of the manganese halides rather than investigating the dynamics of the corresponding reactions.

2.3.6 Harpoon Reactions with Surfaces

The harpoon model, in the simple form given in Section 2.3.1, has been used recently in a very different, although related, context to gas-phase reactions. It has been used to account for the observation of Cl^- ions embedded in a potassium surface when colliding a beam of Cl_2 molecules with the surface at suprathreshold energies (0.08–0.68 eV) [118]. A four step model is proposed. Its first step is the harpoon: at 4 Å from the surface, an electron is transferred from potassium to the antibonding orbital of Cl_2 , which dissociates to $\text{Cl} + \text{Cl}^-$, as in the gas-phase process. The differences from the gas-phase process are found in the next three steps where the metal surface transfers a further electron to the Cl moiety and emits an Auger electron. Similar experiments have also been done by colliding vibrationally excited SF_6 molecules with a barium surface [119] and CH_3I molecules with an Ag(111) surface [120].

More recently, N_2O molecules have been collided with a monolayer of Li on Rh(100). Two different reaction channels were observed. First, a direct reaction channel with an Eley–Rideal mechanism, i.e., an abstraction reaction that pro-

ceeds during the impact of the N_2O where harpooning is the key step that triggers the reaction. Second, an indirect reaction channel, which follows the Langmuir–Hinshelwood scheme where the reacting molecules are adsorbed on the surface with complete energy accommodation and thus a complete loss of the information on their initial orientation in the gas phase [121, 122]. As in the previous example, the gas-phase harpoon-like mechanism is invoked to account for the observed phenomena.

2.4 Effect of Changing the Internal State of the Reactants

Adding energy to a reactive system is, of course, a way to overcome a possible endoergicity. In a more subtle way this can also serve to pass an activation barrier placed somewhere along the reaction path. With this in mind, the addition of energy is expected to affect the dynamics of the reaction. If the reaction is direct and if the reactants do not have too many degrees of freedom, this effect could be different, whether the additional energy appears as translation, vibration or electronic excitation of the system.

One of the first attempts to compare the effect of different forms of energy on gas-phase reactions was done in a very general way by John Polanyi [70, 73]. When the reaction barrier is in the entrance or the exit channel of the reaction, translational or vibrational energy, respectively, is more efficient at promoting the reaction. These rules, known as *Polanyi's rules*, are not linked specifically to electron-transfer reactions. On the contrary, they were derived without reference to a specific reaction. As an illustration of these rules in an electron-transfer reaction, vibrational excitation of HCl gives easier access than translation to a late barrier in the $\text{K} + \text{HCl}$ reaction [123, 124].

In the context of this chapter, we shall focus on work where the additional energy deposited into the system directly affects the electron-transfer step and consequently changes the dynamics of the reaction.

2.4.1 Changing the Vibrational State of the Molecular Reactant

The geometry of molecular anions generally differs from that of the neutral molecule. For instance, N_2O^- is bent whereas the N_2O molecule is linear. This is one of the reasons why the vertical electron affinity of N_2O^- is negative. This is also the reason why bending excitation increases the electron affinity (EA) of the molecule. From Magee's equation (see Eq. 3), we know that the increase in EA results in a larger distance R_c for the harpoon. A larger cross-section is therefore expected. This effect has actually been observed semiquantitatively in the chemiluminescent reaction $\text{Ba} + \text{N}_2\text{O} \rightarrow \text{BaO} + \text{N}_2$ [125, 126]. The same effect was confirmed later in an experiment where the internal excitation of N_2O was carefully prepared [127]. It

should be noted that the full interpretation of the $\text{Ba} + \text{N}_2\text{O}$ reaction cannot rest on the simple harpoon model since barium is an alkaline earth metal atom with two valence electrons (see Section 2.3.3).

The dependence of the harpoon crossing radius R_c on the geometry of the molecules was pointed out a long time ago for the stretching of the C–I bond in CH_3I [128, 129] and appears as a major feature in the most recent mechanistic interpretation of the $\text{K} + \text{CH}_3\text{I} \rightarrow \text{KI} + \text{CH}_3$ reaction [69].

The same phenomenon has shown up as a very spectacular effect in a study by Kleyn and co-workers looking at collisions between cesium and O_2 at hyperthermal collision energies (25–100 eV) [130–133]. Let us consider the reaction



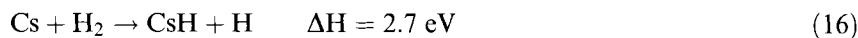
The following picture emerges from their illuminating work [131]. The initial electron transfer forms the anion O_2^- with the bond length of the neutral molecule, shorter than that of the anion. Hence the newly formed O_2^- is compressed and starts to oscillate with a period of 3×10^{-14} s. At the chosen collision energy, depending on the impact parameter, the collision time varies between 0.5 and 3 times the vibration period. As a result, there is a family of impact parameters where O_2^- is back in position to return the captured electron on the exit channel of the collision, but there is another family also, for which the electron return is impossible. This leads to oscillations in the angular distribution of the Cs atoms, which can be related to the vibrational period of O_2^- .

2.4.2 Electronic Excitation to Overcome an Endoergicity Barrier

Reactions of electronically excited atoms were investigated many years ago [134–137], and have been the subject of continuous efforts [91, 138–140]. Recent reviews cover the subject [42, 90, 141–143]. It is useless to review these studies again in a general way. We prefer to focus our attention on a limited number of studies which illustrate the various effects that electronic excitation can have on the reaction dynamics.

The first effect is simply energetics. Electronic energy corresponds in general to a large amount of energy (up to several eV), which is deposited in one step into the system. This is often more than enough to satisfy the energy requirement of a substantially endoergic reaction. A large number of studies illustrate this point. For a large part, they are reviewed in the papers quoted above.

$\text{Na} + \text{HF}$ is one of the systems where electronic excitation promotes the reaction. In this case, $\text{NaF} + \text{H}$ is formed. This reaction has been studied both in the gas phase and in van der Waals complexes, and we reserve its discussion to the section on van der Waals complexes (Section 2.6). We focus our attention here on a related system, the reaction



Owing to its large endoergicity, it needs laser excitation to be turned on.

Reaction 16 was first laser induced by Happer and co-workers in a cell experiment under a multi-collision regime, which allowed, spectacularly, the product CsH to condense as powder, the so-called *laser snow* [144]. The dynamic picture of this reaction has emerged from a series of studies by Vetter and co-workers using a crossed-beam machine where cesium was excited to both the levels $6d\ ^2D$ [145] and $7p\ ^2P$ [146–150]. The most interesting result concerns the reaction dynamics of cesium in the $(7p\ ^2P_{1/2})$ level, which was interpreted after *ab initio* potential energy surface, semi-classical and quantal dynamics calculations [151–153]. The reaction of cesium in the $8p\ ^2P$ and $9p\ ^2P$ Rydberg levels with hydrogen molecules has also been studied [154].

We now summarize the results of Vetter and co-workers on the reaction dynamics of $Cs(7p\ ^2P)$ [146–150]. Although molecular hydrogen has a negative electron affinity, the reaction appears as an harpoon reaction with an electron-transfer distance of about 4 Å. Despite this significantly large distance, the measured reactive cross-section is very small, $0.6\ \text{\AA}^2$. This effect is due to the large electronic excitation needed to overcome the endoergicity barrier. The $7p\ ^2P$ level is indeed higher in energy than many other cesium levels, namely the $6s\ ^2S$, $6p\ ^2P$, $5d\ ^2D$ and $7s\ ^2S$ levels. Hence the attractive ion-pair surface $Cs^+H_2^-$ crosses the covalent surfaces correlating to these lower levels, and more than 90 % of the trajectories end up on these states after back-transfer of the electron to cesium rather than leading to dissociation of H_2^- and forming the reaction product Cs^+H^- . This example is interesting because the large electronic excitation needed to open the reactive channel also opens non-reactive quenching processes which enter in competition with the reactive channel.

The similar system $K^* + H_2 \rightarrow KH + H$ has also been studied, with similar information on the reaction dynamics [155, 156]: the reaction of electronically excited potassium follows a collinear geometry, producing KH via the ion-pair intermediate K^+H^-H . Very interestingly, this reaction is state specific: $K(7s\ ^2S)$ leads to reaction, whereas $K(5d\ ^2D)$ does not. We shall come back to this important question later.

Before leaving this section, let us make a short digression to the mechanism invoked above, where the forward and back electron transfer between cesium and H_2 is responsible for the quenching of the electronic excitation of cesium. This mechanism was proposed a long time ago to account for the quenching of the first electronic state of sodium by collision with nitrogen, a non-reactive molecule. This model, plus a few related ones, have been reviewed by Schermann et al. [139]. According to the model, the covalent potential curves describing the excited and ground states of the $Na + N_2$ system are coupled together by the ion-pair curve $Na^+N_2^-$. This model was proposed originally by Jerre and Nikitin [157]. It was rediscovered by Bauer et al. [158] and was further developed by Gislason and Sachs [61, 159]. It has been used widely to account for quenching experiments by Hertel's group [160] and was put eventually into the more correct form of the *bond-stretch* model. Molecules such as N_2 and H_2 do not accept an electron easily, hence the electron transfer on the molecule is only partial and progressive along the entrance channel of the collision. It is accompanied by stretching of the molecule which also results in coupling between the electronically excited state of the system and its ground state, hence leading to quenching [161].

2.4.3 Effect of Electronic Excitation on the Reaction Dynamics

The idea behind these studies is that electronic excitation of one of the reactants certainly affects the dynamics of the reaction and in some cases allows one to control the outcome of the reaction. An important aspect of electronic excitation is the possibility of selecting the potential energy surface on which the reaction is initiated, just by exciting the reactants to states of various symmetries. In other words, the motivation for studying the excited-state reaction dynamics comes from the anticipation that the dynamics of the reaction are determined not only by the amount of energy which is available in the system, but also by the nature of the excited potential energy surface on which the reaction proceeds. Of course, this can occur only if one of two conditions is met: the electronic energy deposited in the system is not randomized too rapidly as a hot ground state of the system, or the electron-transfer step does not connect the system directly on the ground-state surface of the exit valley.

Dramatic effects of electronic excitation on the reaction mechanisms have been demonstrated in several cases. One of the first reported examples must be recalled here also as it falls outside the scope of this chapter. Electronically excited $O(^1D)$ is much more reactive than ground-state $O(^3P)$ and inserts into the C–H bonds of methane [162]. Similar state specificity in the reactivity has also been encountered in electron-transfer reactions and seems to be the rule in light systems. Its origin has been explored systematically in alkali and alkaline earth metal atom reactions. Before discussing some of the studies, it is appropriate to survey a much simpler situation where electronic excitation affects the dynamics of the reaction just by changing the location of the electron-transfer region.

Dynamic effects associated with the change of the electron-transfer distance

This effect is best viewed in single harpoon reactions such as those of alkali metal atoms with halogen-containing molecules discussed in Section 2.3.1. A series of studies conducted in a crossed-beam experiment by Lee's group at Berkeley have demonstrated how the electronic excitation of sodium affects the dynamics of these reactions.

The reaction $K + CH_3I \rightarrow KI + CH_3$ has been revisited very recently [69]. Let us start our discussion with another reaction of the same family:



This is a classical rebound reaction. When sodium is in the ground state, 84 % of the reaction product NaBr is scattered in the backward hemisphere. This phenomenon arises from two factors: a close approach distance for the electron transfer to proceed, and a *steric factor*, where sodium must approach the Br end of CH_3Br to bounce back as NaBr. If approaching the wrong end of CH_3Br , sodium does not react. This leads to the concept of the *acceptance angle* for the reaction [163].

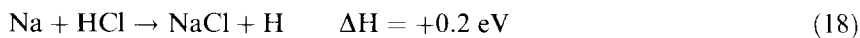
When exciting sodium electronically to the $3p^2P$ and $4d^2D$ levels, the reactive cross-section increases, the center-of-mass angular distribution widens, but the re-

action still proceeds via the rebound mechanism [the backwards scattered fraction is 79 % for reaction of $\text{Na}(4d\ ^2D)$]. This has been interpreted as the relaxation of the steric factor and an opening up of the acceptance angle [164]. The origin of this effect is clear when following the recent interpretation of the acceptance angle given for the reaction $\text{K} + \text{CH}_3\text{I} \rightarrow \text{KI} + \text{CH}_3$ [69]. The assumption that the electron transfer which initiates the reaction is localized is only a first approximation. The more correct picture with a molecule such as CH_3I , which does not have a large positive electron affinity, is given by the *bond-stretch* model considered at the end of Section 2.4.2. A partial and progressive electron transfer initiates the elongation of the molecule, but importantly for the following, elongation of the C–I bond takes time. This makes the $\text{K} + \text{CH}_3\text{I} \rightarrow \text{KI} + \text{CH}_3$ reaction mimic a concerted reaction where the old bond stretches as the new bond begins to form. The stereodynamics of the reaction and, in Ref. [69], its dependence on the collision energy, stem from the ease of the final electron transfer. Of course, the more the $\text{CH}_3\text{–I}$ bond has had time to elongate during the early stage of the reaction, the easier is the final electron transfer which promotes the reaction, the longer is the distance at which it occurs and the less restrictive are the geometry requirements which allow the final electron transfer. In other words, a change in the partial electron transfer, which gives more time for the C–I bond to stretch, is expected to widen the acceptance angle of the reaction.

With this model in mind, the observation recalled above of the effect of increasing the electronic energy of sodium in the $\text{Na} + \text{CH}_3\text{Br} \rightarrow \text{NaBr} + \text{CH}_3$ reaction becomes clear. Since the excited orbitals of sodium are increasingly more diffuse on switching from $3s\ ^2S$ to $3p\ ^2P$ and $4d\ ^2D$, the first partial electron transfer occurs at larger and larger distances and allows more time for the CH_3Br molecule to stretch. Hence the final electron transfer is expected to be possible at a larger distance than simply deduced from the sole use of Magee's equation (see Eq. 3). At the same time, the steric requirements for the reaction are also expected to relax, in agreement with the experiment.

Opposite to rebound reactions is the reaction $\text{Na} + \text{Cl}_2 \rightarrow \text{NaCl} + \text{Cl}$ which proceeds via the spectator stripping mechanism. In this case, the crossing between the nonreactive covalent Na–Cl_2 curve and the Na^+Cl_2^- ion-pair curve, which promotes the reaction, occurs at a large distance ($R_c = 5.22\ \text{\AA}$, when using the chlorine adiabatic electron affinity in Magee's equation). This distance increases to $22.3\ \text{\AA}$ when sodium is excited to the $3p\ ^2P$ level. One would expect an increased reaction cross-section, but this is not observed because electron transfers at such large distance are inefficient. The overlap between the sodium HOMO and the Cl_2 LUMO is very small at these distances. As a result, when the crossing radius increases substantially, there is only a small effect on the dynamics of the reaction [164, 165].

The reaction



is very interesting because the dynamics of the reaction change completely when sodium switches from the ground state, where the reaction is endoergic, to $3p\ ^2P$ and either $4d\ ^2D$ or $4s\ ^2S$.

Excitation of sodium to the $3p\ ^2P$ level enhances tremendously the reaction cross-section and leads to a backscattered product with a broad velocity distribution. The qualitative agreement of the observed velocity and angular distribution of the NaCl product with fits by the DIPR-DIP model allows one to draw two conclusions: first, a near-isotropic distribution of the HCl molecule at the moment of the electron jump, with however a slight preference for the $\text{Na} \cdots \text{Cl}-\text{H}$ approach; and second, a partial breakdown of the basic DIPR-DIP assumption, which separates the breakage of the H-Cl bond from the formation of the Na-Cl bond. This suggests a concerted reaction (as above in the $\text{Na} + \text{CH}_3\text{Br}$ reaction), essentially because the electron jump distance is not very large (3.7 \AA). Additionally, the fact that the NaHCl system is close packed at the transition state, rather like a compressed spring, explains also why a lot of the energy release goes into translation after the reaction [166].

Excitation of sodium to the $4d\ ^2D$ and $4s\ ^2S$ levels, which are ca. 4.2 eV above the ground state, changes drastically the dynamics of the reaction. The electron-jump distance moves further away (ca. 8 \AA) and the system is no longer close packed at the transition state. As a result, although the system contains 2 eV more energy, the translational energy release between the products is smaller than in the $\text{Na}(3p\ ^2P)$ reaction. Most of the excess energy shows up as vibrational excitation of the product NaCl. Despite this, the reaction does not follow the spectator stripping mechanism. The product NaCl is mainly backward scattered [165, 167], bringing evidence for this continuous e-transfer.

State selectivity in alkali metal atom reactions

State-specific reactions of excited alkali metal atoms have been encountered a number of times. We have mentioned already the $\text{K} + \text{H}_2 \rightarrow \text{KH} + \text{H}$ reaction which is turned on by excitation of potassium to the $7s\ ^2S$ level (ca. 3.7 eV above the ground state), and not by the excitation to the $5d\ ^2D$ level, although it is only 0.01 eV below the $7s\ ^2S$ level [155, 156]. Such a change in reactivity is, of course, linked to the different potential energy surface on which the reaction is promoted, but owing to the equivalent energy of the $7s\ ^2S$ and $5d\ ^2D$ levels the difference in reactivity is connected with orbital symmetry.

Another striking example is provided by the $\text{Na} + \text{O}_2 \rightarrow \text{NaO} + \text{O}$ reaction, which is endoergic by 2.5 eV. Excitation of sodium to the $3p\ ^2P$ level provides the system with 2.1 eV electronic excitation, and the reaction could become possible with the help of translational energy. However, no such reaction is observed. The NaO product is observed only at a sufficiently high translational energy when sodium is excited with ca. 4 eV electronic energy in the $4d\ ^2D$ level [168]. In contrast, the $5s\ ^2S$ level, which has approximately the same energy, does not lead to reaction.

The nonreactivity of $\text{Na}(3p\ ^2P)$ finds a fairly simple explanation when the stability of the O_2^- ion is taken into account. Electronic excitation of Na to $3p\ ^2P$ actually promotes the formation of the intermediate Na^+O_2^- , but when the negative ion is formed in its ground state $X^2\Pi_g$ it does not dissociate spontaneously and the Coulomb field due to the Na^+ core is not enough to tear it apart. The only possibility

open for the intermediate $\text{Na}^+\text{O}_2^-(X^2\Pi_g)$ is to back-transfer the electron from O_2^- to Na^+ and to dissociate as $\text{Na} + \text{O}_2$. The temporary formation of the Na^+O_2^- intermediate resulted in this case in quenching of the electronic excitation of sodium. Presumably the formation of the NaO product is observed when the electron transfer from Na to O_2 forms the negative molecular ion in the dissociative excited state $A^2\Pi_u$ [169, 165, 170]. For this to occur, long-range electron transfer has to be avoided and the reaction proceeds only at restricted geometries and state symmetries. This could be the explanation of why the $4d\ ^2D$ level is reactive, and not $5s\ ^2S$. Again, orbital symmetry is seen to play a role in reaction dynamics. The control of chemical reactions by orbital symmetry is a very important issue in stereodynamics. It is the subject of Section 2.5 and is invoked in Section 2.6.1.

Interestingly, the necessity to transfer the electron to an excited O_2^- orbital for breaking the O–O bond has also been invoked in other circumstances when investigating the $\text{Na}_2 + \text{O}_2$ reaction [116].

Changing the reaction mechanism by changing the PES initiating the reaction

The two previous sections have shown that the largest changes in the reaction dynamics are to be expected when the electronic excitation added to the system moves the electron-transfer distance from a close-packed geometry where the harpoon mechanism is hardly applicable to distances at which the access to the electron-transfer region is easy. Similarly, when turning to reaction implying a double harpoon, the most dramatic changes in the reaction mechanism are expected for systems like $\text{Ba} + \text{H}_2\text{O}$ where the first electron transfer occurs at a short distance (see Section 2.3.3). This is confirmed by experiment. Whereas ground-state barium leads essentially to the product BaO on reaction with water, electronically excited barium, in either the $6s5d\ ^1D$ or the $6s6p\ ^1P$ level, leads to BaOH as reaction product [104, 171, 172]. This finds an easy interpretation within the framework provided by the double harpoon mechanism given in Section 2.3.3. Formation of BaO in the ground-state reaction has to wait for the second electron transfer in order to have its correct structure $\text{Ba}^{2+}\text{O}^{2-}$. Since the first electron jump occurs in a closed-pack geometry, the system is readily in position for the second valence electron of barium to transfer. The reaction forming BaO is thus of concerted nature. Promotion of one valence electron of barium to the $5d$ or the $6p$ orbital favors a longer range electron transfer. The system is then far from the favorable geometry for the second electron transfer. The weakly bonded H atom of the $\text{Ba}^+\text{H}_2\text{O}^-$ complex therefore has time to migrate and form the insertion intermediate $\text{H}-\text{Ba}-\text{OH}$, which dissociates to $\text{BaOH} + \text{H}$ [104]. The reaction paths corresponding to reaction of the ground-state $6s^2\ ^1S$ and the excited-state $6s5d\ ^1D$ of barium are shown as a correlation diagram in Figure 8.

A similar correlation diagram can be drawn to interpret the exclusive observation of BaOH chemiluminescence in the reaction of $\text{Ba}(6s6p\ ^1P)$ with water [172]. Here again, the reaction of excited barium can be explained by H-atom migration and formation of the intermediate HBaOH . This mechanism definitely carries some generality since it has been used also by Oberlander and Parson to account for re-

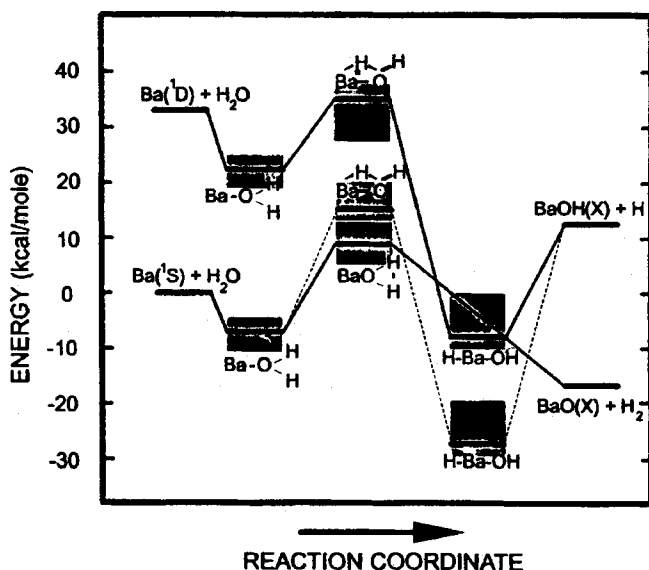


Figure 8. Correlation diagram for the reaction $\text{Ba} + \text{H}_2\text{O}$. The shaded areas indicate the uncertainties in energies of the collision complexes. Solid and dashed lines show the dominant and minor reaction paths, respectively. Adapted from Ref. [104].

actions of laser-excited calcium and strontium atoms with water and alcohols [173]. Related reactions of alkaline earth metal atoms with peroxide molecules have also been investigated by Parson's group, but the reaction mechanism differs since barium seems to insert into the O–O bond of the peroxides [103, 105].

The reactivity of excited alkaline earth metal atom reactions has attracted considerably more attention than reported above. Among the work that we shall not review here we must mention the investigations of Dagdigan and co-workers who explored the spin–orbit effects on the reactivity of metastable calcium and barium [174–181]. For example, significant differences in reactivity were observed between the three components $J = 0, 1$ and 2 of $\text{Ba}(6s5d\ ^3\text{D}_J)$. Spin–orbit effects have also been observed as a drastic change of reactivity between $\text{Cs}(7p\ ^2\text{P}_{1/2}) + \text{H}_2$ and $\text{Cs}(7p\ ^2\text{P}_{3/2}) + \text{H}_2$ [150]. Gonzalez Ureña's group has also contributed considerably to unraveling the reactivity of excited alkaline earth metal atoms, especially with halogen-containing molecules [37, 38, 182–187]. Part of this work is recalled in Section 2.6. Finally, the same kind of systems have also been investigated by the groups of Husain [188–190], Kowalski [41, 191–193], Lou [86, 194–196], Menzinger [197, 198] and Stolte [199, 200].

Conservation of the ion core electronic configuration

Work performed by the groups of Levy [39, 201–207], Parson [208, 209] and Sadeghi [210, 211, 212, 213, 214] have drawn attention to reactions of electronically excited multivalent atoms. These groups investigated reactions of copper and manganese atoms with halogen and halide molecules. Again, these reactions are well interpreted on the basis of the harpoon model, but in this case, owing to the variety of electronic levels of the halide product that may be excited, the interpretation implies a hierarchy of inner electron transfers. This question has been examined in

detail for reactions of Mn and $\text{Mn}^*(a^6D_J)$ with Cl_2 [39], SF_6 [205] and SiCl_4 [206]. The situation turns out to be very complicated because the covalent and the ion-pair curves corresponding to $\text{Mn}^*(a^6D_J)$ and $\text{Mn}^{+*}(a^5D_J)$ are split into several components by the interaction with the molecular partner, allowing a number of crossings at different approach distances and energies [205].

It is simpler for our present purpose to consider the reactions [210, 211, 214, 208]



The point which draws our attention here is the very strong increase in the CuF chemiluminescence when Cu switches from the ground-state $3d^{10}4s^2S$ to the excited-state $3d^94s^2^2D$.

Sadeghi and co-workers first pointed out that the electronic configuration of excited CuF is essentially $\text{Cu}^+(3d^94s)\text{F}^-$, and that it resembles to that of the excited ion pair $\text{Cu}^+(3d^94s) \cdots \text{F}_2^-$. This ion pair is thus likely to correlate to the excited-state product. Conversely, the ground-state ion pair $\text{Cu}^+(3d^{10}) \cdots \text{F}_2^-$ is likely to correlate to the ground-state product of dominant configuration $\text{Cu}^+(3d^{10})\text{F}^-$. This leads to the potential energy diagram shown in Figure 9. As suggested by Sadeghi and co-workers, the harpoon process in the entrance channel of the reaction corresponds to the minimal electronic rearrangement when ground-state $\text{Cu}(3d^{10}4s^2S)$ transfers one of the 4s electrons to molecular fluorine, thus forming the ground-state ion pair. Similarly excited $\text{Cu}(3d^94s^2^2D)$, by transferring one 4s electron, forms the excited ion pair, which correlates to the excited-state product. This correlation helps

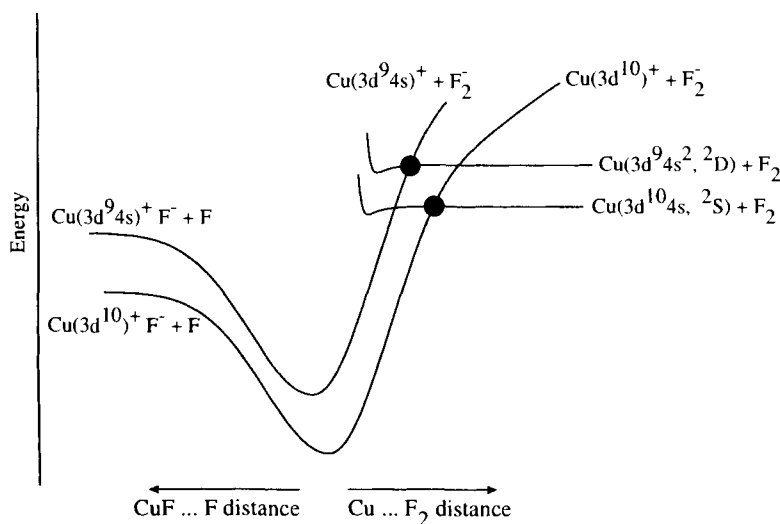


Figure 9. Potential energy diagram for the $\text{Cu} + \text{F}_2$ reaction. The circles indicate the crossing regions where the electron jump takes place. Adapted from Ref. [210].

in understanding why the electronic excitation of copper increases tremendously the chemiluminescence yield of the reaction [208, 210, 211, 214]. Conservation of the electronic configuration of the metal ion core along the reaction path thus appears important in the branching to chemiluminescence.

2.5 Stereodynamics of the Electron Transfer

Stereodynamics is focused on the dependence of forces on reactant orientation (or alignment) in the course of chemical reactions [15]. One of the ideas behind this is to use these forces to control chemical reactions [17]. Continuous efforts have been made toward this goal in recent years, and the ultimate step at the moment is coherent control [215]. We shall not consider these questions here. We prefer to follow a second idea behind stereodynamic studies, which is more simply to refine our understanding of how reactive systems access the transition state region of the reaction.

We have encountered in several places in this chapter that orbital symmetry plays a role in the reactivity of excited-state metals. Such symmetry effects are best observed in vector correlation experiments where the effect of orienting and aligning reactants is explored systematically and correlated to the angular distribution of the reaction products [216–220].

Two routes have been followed in reaction stereodynamics. One is to orient a molecular reactant in space and see how the reaction cross-section varies with the molecular orientation. This direction has been pioneered in molecular beam experiments using focusing of an electric hexapole field to control the molecular orientation [221–223a]. Numerous studies have applied this technique to electron-transfer reactions of alkaline-earth atoms [223b]. This technique is now complemented by the so-called *brute force* technique, where polar molecules are oriented in extremely strong electric fields [83].

The other route applies when the reactivity of laser-excited species is to be studied. It is then possible to polarize the excited orbital and observe how this polarization affects the dynamics of the reaction. This was first demonstrated by observing the alignment-dependent chemiluminescence in reactions of aligned $\text{Ca}(4s4p\ ^1\text{P})$ with halogen-containing molecules [224, 225]. This work will serve to rationalize the branching to chemiluminescence observed in reactions induced in van der Waals complexes (see Section 2.6.1). It has been extended very recently to other molecular reactants [196].

There is a bridge between the two routes when bimolecular collisions are initiated by a prior photodissociation to produce aligned reactants [226].

Within the framework of this chapter, a section on stereodynamics must focus on the heart of harpoon reactions: the electron transfer itself. Hence we review studies which directly inform on the extent to which the electron transfer is affected by the relative polarization of the donor (HOMO) and acceptor (LUMO) orbitals.

The electron-transfer step can almost be isolated when observing ion-pair for-

mation in hyperthermal collisions. Such experiments have been done recently by Brooks and co-workers [227–229]. For example, a beam of potassium atoms has been crossed with a beam of acetonitrile molecules which had been oriented spatially prior to collision. Collision energies of 5–30 eV are sufficient to separate the charged species after the collision if a K atom has transferred its valence electron to the acetonitrile molecule. The most abundant negative ion, CN^- , is preferentially formed upon attack at the CN end of the molecule, whereas the CH_3CN^- ion is observed at large collision energies with attack at the CH_3 end of the molecule. These results have been rationalized by assuming that the CN^- production results from an initial electron transfer into the π_{CN}^* LUMO (located on the CN group), followed by migration into the σ_{CC}^* . Conversely, formation of CH_3CN results from the electron transfer into a σ_{CH}^* LUMO at the other end of the molecule [229].

Such preference in molecular orientation for electron transfer certainly should show up in the reaction dynamics, especially when seeking to direct reactions. This was exemplified for the first time in the reaction of sodium with a different molecule [230]:



This reaction was studied using a crossed-beam apparatus. It was found that the favorable alignment of the D orbital of sodium varies only slightly with the scattering angle of the product NaCl. The best geometry is when the d_{z^2} orbital of sodium is aligned along the relative velocity vector of the collision.

In interpreting these experiments, the following difficulty must be noted. The orbital preparation is performed in the laboratory reference frame at infinite separation between the reactant, and might be different from the actual orbital alignment in the molecular frame, at finite separation between reactants when the system is close to the electron-transfer region. This difficulty refers to the concept of *locking radius*, involving the locking of orbitals to the rotating molecular frame in the course of a collision [231, 232]. With this in mind, it has been concluded from experimental observations that the reaction $\text{Na}(4d^2D) + \text{HCl} \rightarrow \text{NaCl} + \text{H}$ goes through a long-range electron transfer, and that the Na–HCl axis dominates over the Cl–H axis in determining the most favorable alignment angle. In other words, the d_{z^2} orbital of sodium just needs to be pointing at the HCl molecule for the reaction to proceed, but the Na, Cl and H atoms do not need to be collinear at the transition state [230]. Of course this picture complements that drawn in Section 2.4.3 when discussing reactions of electronically excited sodium.

Measuring the polarization of the reaction product is also an important issue in stereodynamics. A lot of the activity in this field concerns the reactivity of alkaline earth metal atoms since the corresponding reaction products are easy to probe by optical techniques. A full account of methods to measure product alignment and orientation in bimolecular collisions has been given by Orr-Ewing and Zare [18]. Such measurements, with the help of simple models such as the DIPR-DIP model considered Section 2.3.2, give insight into the shape of the reactive system at the moment where forces are released [86, 87, 184, 195, 233, 234].

2.6 Van der Waals Complexes: a Tool to Explore the Potential Energy Surface in the Electron-transfer Region

We now present a new tool to investigate in further detail the potential energy surfaces for electron transfer, especially those involving excited states of the reacting metal. One could think that the models introduced in the previous sections, namely the double harpoon originally described by Menzinger [91, 92] and the DIPR-DIP model refined by Zare and co-workers [81], are oversimplified. Instead, the present section confirms their simplicity and predictivity in explaining the branching of excited-state metal reactions to luminescent products.

The preceding sections have emphasized the role of the relative orientation of the reagents: geometric orientation or orbital orientation of an electronically excited metal with respect to the collision axis. This applies to excited metal orbitals with p or d symmetry and has been termed polarization effects, where in the laboratory frame the polarization of the light aligns the excited orbital. Instead, reactions initiated within the molecular 'body fixed frame', within a van der Waals complex formed by the reagents, offer a powerful way to study this problem of the relative orientation of the excited orbital of the metal, directly in the frame of the reactants. When an electron-transfer reaction is initiated in the complex by light, the relative orientation of the orbital with the approach coordinate of the reagents is dictated by the orbital symmetry of the accessed state and in this electronic state the reagents have a fixed, specific orientation. The resulting bimolecular excited-state reactions promoted by optical excitation of a van der Waals complex formed by the reactants are accessed directly via the excited reaction complex. This allows the direct spectroscopic investigation of the reaction surface when occurring in the excited state, through the laser-induced spectra of the reaction. This was first shown by Jouvét and Soep [47–49]. Also, it must be emphasized that in the perspective of a half-collision the reactants are prealigned and this allows stereodynamic studies, as shown by Wittig and co-workers [50]. The reactions within van der Waals complexes are also closely related to laser-assisted collisions, as developed for chemical reactions by Setser and co-workers [235–237], where the reaction complex is attained from the dissociative collision pair in the ground-state complex instead of the bottom of the potential well of the interaction van der Waals potential. In a scheme later called laser photoassociation [238], the colliding ground-state collision pair is transferred into the quasi-bound potential domain of the reacting excited complex. The studied systems involve harpoon-type reactions in xenon–halogenated compounds. In this manner, laser-assisted reactions have been performed in low-pressure gas mixtures of Xe with Br₂, CCl₄, CCl₃Br, CCl₂Br₂ and I₂. The products are XeCl(B, C), XeBr(B, C) or XeI(B, C) following two-photon promotion to the reactive ion-pair potentials. The utilization of a two-color scheme enhances the two-photon, laser-assisted reactions because of better match with an intermediate state of the reagent molecule. In this work, interesting preferences in the reactions with mixed halogenated compounds were found for the final excited-state products.

A typical van der Waals complex experiment consists in recording the reactive signal as a function of the wavelength of the laser inducing the reaction. The re-

sulting spectra are called *action spectra*. They usually appear as a series of broad bands, the spacing (vibrational) of which characterizes ‘modes’ on the reaction surface that are weakly coupled to the reaction coordinate, the *perpendicular modes*. Excitation along the reaction coordinate does not produce any vibrational structure in the action spectrum, because there is no bonding along this coordinate. Such spectra are intrinsically diffuse and analogous to bound-free spectra in molecules. In turn, the breadth of the diffuse perpendicular bands is related to the dynamics of the reaction through the kinetics of departure from the Franck–Condon accessed region on the surface. This spectroscopy is similar to that of bound molecules for the so-called perpendicular modes where the observed vibrations are directly related to an equivalent potential surface. This can be done by either Franck–Condon overlap [49, 239, 240] or wavepacket calculations [241–243]. Hence the explored region in the reaction on the reaction surface depends on the Franck–Condon allowed window from the ground state.

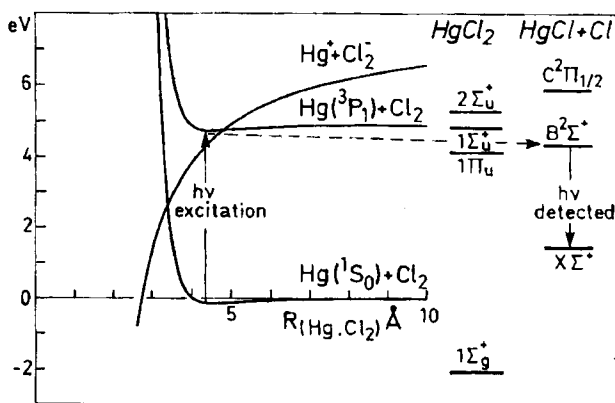
The van der Waals initiated reaction explores ideally excited-state harpoon reactions. The latter occur at intermolecular distances in the range 3–10 Å, a region which is Franck–Condon accessible from ground-state van der Waals complexes, whose equilibrium distance is typically $R = 3\text{--}4\text{ Å}$.

2.6.1 Local Excitation and Subsequent Electron Transfer

Excited mercury chemiluminescent reactions

The first example of such reactions is the reaction of excited mercury, $\text{Hg}(6s6p\ ^3P_1) + \text{Cl}_2$ [47], in which the crossing seam of the neutral and ionic [correlating with $\text{Hg}(6s\ ^2S) + \text{Cl}_2^-$] surfaces, can be directly observed. The excited-state mercury atom becomes open shell with an ionization energy close to 5 eV, almost a sodium atom, and the resulting ionic covalent crossing occurs at 4 Å! The schematics of the reaction and observation conditions are described in Figure 10, where the reaction has sufficient energy to produce excited-state products $\text{HgCl}(\text{B}\ ^2\Sigma^+)$. Thus, the laser scans the potential energy surface of the reaction and produces chemiluminescent

Figure 10. Potential energy diagram of the reaction of Hg with Cl_2 along the $R_{\text{Hg}-\text{Cl}_2}$ coordinate. The excitation Franck–Condon region is reproduced and the positions of energy levels of the HgCl product are reproduced at scale, together with the insertion product ClHgCl levels. This latter product is not observed. Adapted from Ref. [47].



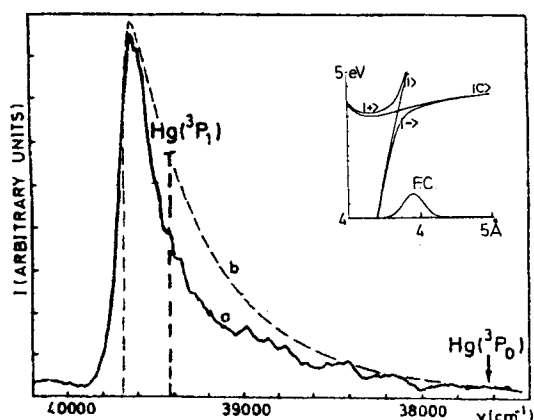


Figure 11. Action spectrum monitoring the HgCl emission while scanning the laser inducing the reaction in the region of the Hg resonance line. The spectrum is broad and falls off sharply after this line. The simulation is obtained using the potential in the inset and the ground-state wavefunction as pictured in the diagram. The contribution to the spectrum comes essentially from the $|-\rangle \rightarrow |+\rangle$ branch of the potential in the inset. Adapted from Ref. [49].

products that are detected via the HgCl B–X emission. The resulting action spectrum appears in Figure 11, where a broad continuum of width 1000 cm^{-1} falls abruptly, shortly after the mercury line. This indicates that the transition relates to the local excitation of the mercury joining on to the neutral asymptote correlating with $\text{Hg}(6s6p\ ^3P_1) + \text{Cl}_2$. Therefore, the state accessed by the excitation laser has a compound character with a mixing coefficient that depends on $R_{\text{Hg-Cl}_2}$, the mercury–chlorine distance. The mixing coefficient depends simply on the energy gap $\Delta E(R)_{\text{IC}}$ between the covalent and ionic potentials:

$$\frac{H_{\text{IC}}}{\Delta E(R)_{\text{IC}}} \quad (22)$$

where H_{IC} is the ionic–covalent matrix element. There results a mixed adiabatic potential represented in the inset in Figure 11. In the hypothesis (verified) that the reaction is fast, all excited complexes will have reacted and the intensity of the spectrum has been shown to be proportional to the Franck–Condon factor connecting the ground-state complex with the locally excited state accessed by optical excitation at each energy:

$$(\langle \Psi_{\text{Hg-Cl}_2} | \Psi_{\text{Hg}^+-\text{Cl}_2(E)} \rangle)^2 \quad (23)$$

The potential $E(R)$ corresponds to the mixed ionic covalent state and takes into account the R -dependent coupling via the ionic–covalent matrix element H_{IC} . In simulating the experimental curve in Figure 11, this coupling was found to be small 0.1 eV , which is unusual for this type of allowed reaction. This small value results from the geometry of the reacting molecule, T-shaped as produced by the Franck–Condon excitation of the ground-state Hg–Cl₂ complex, T-shaped. The T-shaped geometry with C_{2v} symmetry of the excited reacting complex has an unfavorable overlap for the electron transfer [49] from a $6p\sigma$ mercury orbital to the

antibonding orbital of the chlorine for symmetry reasons. In this experiment, no evidence was found for the observation of the other orbital orientation.

This experiment allowed the direct exploration of the radial part of the excited-state electron-transfer surface, here at the transition-state level and also partially in the exit valley. It has also provided further evidence of the angular dependence of the electron transfer which is addressed in the following example. This example does not take into account the correlations with excited ionic surfaces accessed by 6s electron transfer because these surfaces lie at too high energy in the case of mercury. This type of electron transfer will be described in the following section.

Ca–HX excited-state reactions

The reaction of excited-state calcium with hydrogen chloride had been considered by Bernstein et al. [15] as an example where an excited-state body-fixed orientation could be achieved, in relation with the polarization collision experiments of Rettner and Zare [225]. The reactions of locally excited calcium, in $4s4p\ ^1P_1$ and $4s3d\ ^1D_2$ states, within complexes with the hydrogen halides HF, HCl, HBr and HI have been observed within the body frame of the excited van der Waals complex, while detecting the excited-state reaction products [243–245] by luminescence or the ground-state products by laser-induced fluorescence (in the case of Ca–HCl) [246]. Also, full collision experiments conducted by Gonzalès-Ureña's group [233, 247] have yielded interesting comparisons. In the full and half collisions of excited Ca with HX, the open decay channels are:

- $\text{Ca}^{**} + \text{HX} \rightarrow \text{Ca}^* + \text{HX}$: electronic relaxation of Ca, where Ca^{**} represents the $4s4p\ ^1P_1$ and $4s3d\ ^1D_2$ states and Ca^* one of the lower calcium states.
- $\text{Ca}^{**} + \text{HX} \rightarrow \text{CaX} + \text{H}$: ground-state product formation.
- $\text{Ca}^{**} + \text{HX} \rightarrow \text{CaX}(\text{A}, \text{B}) + \text{H}$: excited-state product formation. Notably the only system that comes at threshold for the production of the A and B states is the $\text{Ca}(4s3d\ ^1D_2) + \text{HF}$ system.

The ground and excited states A, B of the CaX product are observed to be the essential outcomes of the half collision, where electronic relaxation does not seem to be able to compete. Detecting excited- or ground-state products yields expectedly different results.

Local excitation of the metal

Here we encounter a new situation: the local excitation of the calcium chromophore from the ground-state $\text{Ca} \cdots \text{HCl}$ complexes transfers the complex in a strongly attractive van der Waals potential amidst two electron-transfer regions: the transfer of the 4p or 3d electron at long $R_{\text{Ca} \cdots \text{HX}}$ distances to form $\text{Ca}^+(^2\text{S})\text{--HX}^-$ and at short distances the transfer of the 4s electron to the excited $\text{Ca}^+(^2\text{D})\text{--HX}^-$. Both crossings will differ from one halogen to the other owing to the variation in the electron affinity of HX (negative for free HF to positive for HI) and will also vary with the locally excited region of the potential. This will condition the dynamics of

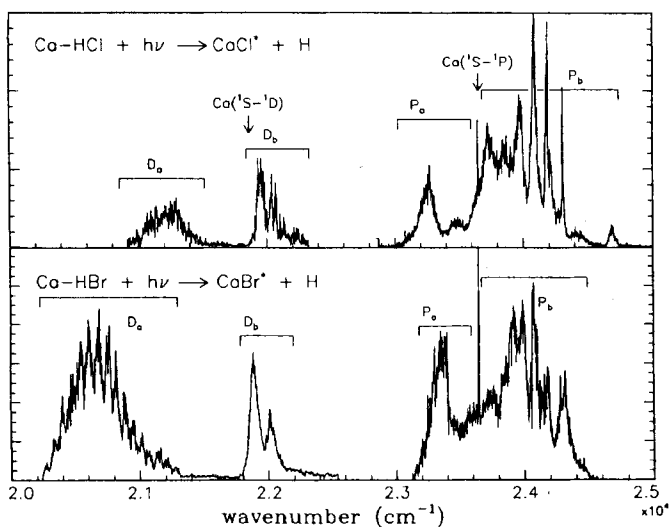


Figure 12. Action spectra recording the $\text{CaX}(\text{A}^2\Pi)$ emission while scanning the laser inducing the excited-state reaction; top $\text{X} = \text{Cl}$, bottom $\text{X} = \text{Br}$. The van der Waals precursor has been created in a supersonic beam resulting from the mixing of laser-ablated calcium in argon containing HX . One notes the great similarity of the spectra extending from $20\,000\text{ cm}^{-1}$ (500 nm) to $25\,000\text{ cm}^{-1}$ (400 nm) and the prominence of vibrational structure. The $4s^2\ ^1\text{S}_0\text{--}4s4p\ ^1\text{P}_1$ calcium line arising from collisions is indicated as a reference while the $4s^2\ ^1\text{S}_0\text{--}4s3d\ ^1\text{D}_2$ line is not observed but marked; therefore, the bands are labeled according to the locally induced transition P or D after the neighboring calcium line. Adapted from Ref. [243].

the excited-state reaction and its branching to excited-state products among which the Ca-HBr system is the most efficient.

To investigate excited-state potentials of these complexes, in the same manner as for Hg-Cl_2 , action spectra were recorded, detecting the $\text{A}^2\Pi$, $\text{B}^2\Sigma$ states of CaX . These spectra are remarkably similar in appearance from Ca-HF through Ca-HI . What is striking, in contrast to the former example Hg-Cl_2 , is the presence of extended structures corresponding to vibrational progressions in the spectra, as seen in Figure 12.

The spectra indicate that the excitation is local, corresponding to the promotion of a 4s calcium electron to a 4p or 3d orbital. This stems from the general appearance of the action spectra with two regions on the side of each atomic transition $\text{Ca}^1\text{P}_1 \leftarrow \text{Ca}^1\text{S}_0$ or $\text{Ca}^1\text{D}_2 \leftarrow \text{Ca}^1\text{S}_0$. The spectral distribution of these transitions is similar to the equivalent transitions of nonreacting van der Waals complexes with metal chromophores. The spectral distributions and the vibrational progressions have been interpreted with model potentials. This interpretation was confirmed by the calculations of Dubernet and Hutson on the open-shell van der Waals complexes Ca-HX correlating with Ca^1P_1 [248]. They found that the electrostatic interaction between the excited Ca (quadrupole) and HX (dipole) yields the following potentials, which are labeled according to the C_2 symmetry group:

- two states of A' symmetry, one with a linear equilibrium geometry similar to that expected for the ground state of the complex and another with an in-plane 4p calcium orbital. The two potentials exhibit an avoided crossing and states in separate energy domains result: the low-energy linear complex with $p\sigma$ configuration and a high-energy nonlinear complex with an in-plane 4p orbital.
- another of A'' symmetry with a T-shaped equilibrium geometry and an out-of-plane 4p orbital.

In the action spectra the states have been well identified. The first A' transition corresponds to the $4p\sigma$ linear complex observed in the red part of the spectrum with respect to atomic line (labeled P_a in Figure 12) and the A'' excited T-shaped follows with an extended vibrational progression (labeled P_b in Figure 12). On the blue side of P_b bands, the remaining transition A' can be found in the case of Ca–HCl at $24\,700\text{ cm}^{-1}$, as a broad, distinct, weak structure. From the ground-state geometry of the complex with a linear $\text{Ca} \cdots \text{HX}$ structure, the general features of the observed spectra are reproduced in the model of local excitation: similar red shifted to the $\text{Ca } ^1P_1$ line corresponding to the $A' \rightarrow A'$ absorption within the complex and blue shifted absorption with intense bending transitions corresponding to a 90° geometry change in the $A' \rightarrow A''$ transition.

The same line of argument can be invoked for the 1D domain in terms of the local excitation of the calcium. The observation of two domains, D_a and D_b , is clear for all the complexes except for Ca–HF, where only the blue-shifted domain D_b is apparent in the action spectra. The observation of the atomic forbidden transition $4s3d\ ^1D_2 \rightarrow 4s^2\ ^1S_0$ within the complex has been interpreted for HCl, HBr and HI [249, 245] as a lifting of the S–D forbiddenness in the complex through mixing with the nearby 1P_1 states of A' and A'' symmetry.

As an example, the dynamics of the reacting complexes in the A'' state (T-shaped complex with the $4p\pi$ orbital out of the plane) are well described by wavepacket calculations. The experimental result is shown in the left panel of Figure 13 (top curve), where only the group of bands located on the blue side of the calcium line, which were labeled P_b in Figure 12 are relevant to the A'' excitation. A two-dimensional potential has been used for the Ca–HBr complex to model the evolution of the hydrogen motion for a fixed Ca–Br distance. The surface is constructed from the bending Ca–HBr van der Waals potential [244] and the Morse potential representing HBr. The reaction on the surface corresponds to the H atom passing the transition state, which is a narrow channel at a 120° bent configuration of the Ca–H–Br molecule (see the upper right panel of Figure 13. The reactive trajectories initiated from the Franck–Condon region represented at 0° in the same panel can find this channel either directly or after one or several oscillations. Quantal calculations of the reactive flux are made numerically by wavepacket propagation [241, 242]. This is the quantal analog of classical trajectories. The probability of returning close to the origin is given by the autocorrelation function shown in the bottom right panel of Figure 13. The Fourier transform of this function simulates the action spectrum of the reaction. The result of this simulation is shown as the bottom curve in the left panel of Figure 13. The potential surface shown and more specifically the position and width of the funnel were adjusted for the simulation to reproduce the

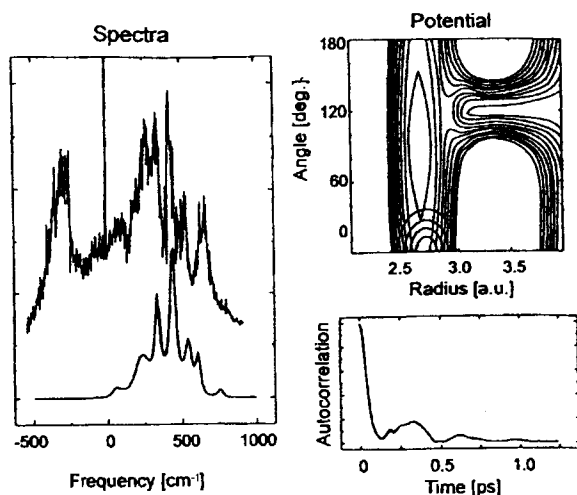


Figure 13. Result of the two-dimensional calculation for Ca-HBr. The calculation and the spectrum of the $P_b(A' \leftarrow A'')$ transition are compared on the left. The two-dimensional surface built on the reaction coordinate R_{H-X} and the Ca-HX bending angle is displayed in the top-right panel. The propagation was performed over 1.25 ps. Each contour corresponds to 500 cm^{-1} . The contour of the Gaussian wavepacket issued from the ground state by vertical excitation is also shown in this surface. The bottom panel on the right shows the resulting modulus of the autocorrelation function with clear recurrences. Adapted from Ref. [243].

positions and width of the experimental action spectrum [243]. It must be mentioned that the fit is not very sensitive to the bending angle, but the essential conclusion is that the transition state is far from linear.

The picture of the reaction is that of the Ca-HBr complex having bending oscillations on either side of the channel where it reacts with high efficiency. Outside this geometry no reaction occurs. This is a one-potential picture whereas two potential surfaces are expected in harpoon reactions: a covalent and an ion-pair surface. This is due to the locally high efficiency of the coupling between both surfaces at the bent configuration of Ca-H-Br. Presumably, this can be due, at least partly, to an optimum overlap between the diffuse antibonding orbital (LUMO) of HBr, mainly localized on the hydrogen, and the 4s orbital of calcium at nonlinear geometries of the Ca-HBr complex. In the same manner, the action spectrum for the reaction in the Ca \cdots HI complex is broad and almost featureless, corresponding to an even broader intersection between the ion-pair and covalent surfaces.

In contrast, this single-surface model does not apply to Ca-HCl, and a two-surface calculation was performed where the H-atom departure is induced by the electron jump from the van der Waals potential to the electron transfer potential. The quantal nature of this nonadiabatic transition allows one to reproduce all the features of the spectrum. This includes the small linewidth of some transitions and, more important, the inverse energy dependence observed in the spectrum, where the broadest bands are those of lowest energy [244], in figure 13.

Lastly, the action spectra in Ca–HF close to the energy threshold to chemiluminescence display very narrow lines, indicating the partial closure of the corresponding reactive excited-state channel. This indicates that the observed channel luminescence is independent of the ground-state channel that could also contribute to the broadening of the lines in the spectrum and confirms the model of the 4s electron hop separated from the 3d hop. We shall now examine the effect of this hop on the efficiency of production of excited states.

Mechanism of production of excited states: excited ionic curves

The mechanism for the production of excited states has already been invoked in the case of excited-state barium reactions. It was also discussed by Rettner and Zare when investigating polarization effects in the chemiluminescent reaction of aligned $\text{Ca}(4s4p\ ^1P_1) + \text{HCl}$ and other halogenated molecules [224, 225]. Following their analysis, the excited states of the calcium product correlate directly with an excited ionic electron-transfer potential; here the lowest is the $\text{Ca}(3d\ ^2D)^+ + \text{HX}^-$ potential. The reaction results from the crossing of the locally excited potential correlating with $\text{Ca}^* + \text{HX}$, with this excited ionic potential $\text{Ca}(3d\ ^2D)^+ + \text{HX}^-$. Specifically, it is shown that the crossing is possible within the range 3–5 Å of the excited van der Waals potential [245]. There result symmetry effects, termed core symmetry conservation, where the excitation of a specific excited state of the complex (of a given orbital symmetry) yields CaX products in the equivalent symmetry. A'' and A' states of the Ca–HX complex yield preferentially states of CaX with Π or Σ symmetries, respectively. This corresponds to the covalent–ion-pair crossing where the 4s electron of the calcium has transferred to HX leaving the Ca core with the initial symmetry. In Figure 14 an example is given of this preferred core conservation where the A'' symmetry excited Ca–HBr complexes form preferentially the CaBr $A^2\Pi$ state and conversely A' states of the complex will populate the CaBr $B^2\Sigma$ state, despite the unfavorable energetics: the lowest energy state of the product should always be the most populated. The flux to the CaBr $A^2\Pi$ state, although being modulated by the excitation in either the P_a (A') or P_b (A'') transitions, is always important. The reason for the lesser correlation of the A' excited state of the $\text{Ca}\cdots\text{HBr}$ complex with $\text{CaBr}(B^2\Sigma^+)$ emission, may be found in the outer electron transfer, at the crossing of the ground-state ionic curve and the locally excited state. Reactive trajectories passing through this crossing are not expected to yield chemiluminescence, but ground-state CaBr instead. Here, in A' symmetry with the Ca 4p orbital pointing towards HCl in σ symmetry, the electron transfer will trap states of core Σ symmetry and divert them from chemiluminescence. The flux to $B\Sigma$ states will be decreased accordingly.

As outlined above, the mechanism for channeling reactive flux into the chemiluminescent channels via the inner crossing with the excited ionic potential accounts well for the effect of the preferential population of $\text{CaCl}(A^2\Pi)$ observed in the full collision experiment $\text{Ca}4s4p\pi + \text{HCl}$ performed by Rettner and Zare [225]. It is supported further by elegant experiments performed by Gonzalez Ureña's group on full collisions of $4s3d\ ^1D_2$ metastable calcium atoms with HX molecules ($X = \text{Cl}, \text{Br}$) at variable translational energies. The production of chemiluminescent

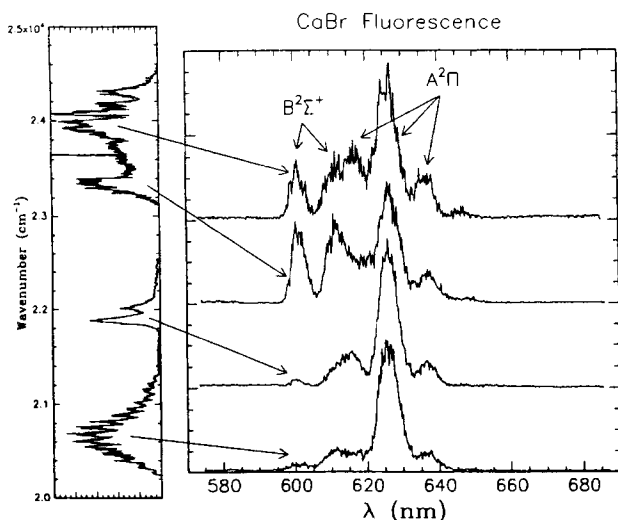


Figure 14. Chemiluminescence spectra of CaBr following different excitations of the $\text{Ca} \cdots \text{HBr}$ complex, as indicated by arrows connecting the excitation region on the action spectrum (displayed vertically at the left of the figure) to the corresponding chemiluminescence spectrum (shown horizontally). From top to bottom P_b , P_a the ratios, from simulations, are $(\text{A/B})_{\text{P}_b} = 2$ and $(\text{A/B})_{\text{P}_a} = 1.1$, respectively. Next come D_b and D_a whose ratios are 11 and 5, respectively. Adapted from Ref. [245].

species CaX in the $\text{A}^2\Pi$ or $\text{B}^2\Sigma$ states shows a clear threshold at 280 meV for HCl [250] and 215 meV for HBr [251]. This threshold was modeled as a barrier due to the crossing with the excited ionic potential correlating with the excited ion $\text{Ca}(3\text{d},^2\text{D})^+$ [252]. This crossing labeled 2 in Figure 15 results in 4s electron transfer to HX, thus forming an excited ionic complex. In order to access this inner crossing the system has to pass the crossing labeled 1 that mixes the $\text{Ca}(4\text{s}3\text{d } ^1\text{D}_2) + \text{HX}$ and $\text{Ca}(4\text{s}4\text{p } ^1\text{P}_1) + \text{HX}$ covalent potentials. The coupling is, as we have seen, important and therefore the process is efficient. This mechanism proposed by Rettner and Zare [225] finds quantitative confirmation here. In turn, the formation of the ground-state products proceeds directly at the outer crossing 3 with the ground-state ion curve by Ca 4p electron transfer to HX.

Quasi-direct excitation of the electron-transfer potential surface in the Ca–HCl complex

The other important channel in the decay of the Ca-HX complex, ground state of the product CaCl , can be observed by laser-induced fluorescence and a very high vibrational excitation is detected. This high vibrational excitation arises from the sudden release at 4 Å of the ground-state CaCl molecule, and thereby in a highly excited vibrational state, the distribution, maximum at $v = 30$, extends to $v = 60$. The resultant energy distribution has been interpreted with the use of the DIPR-DIP model [246].

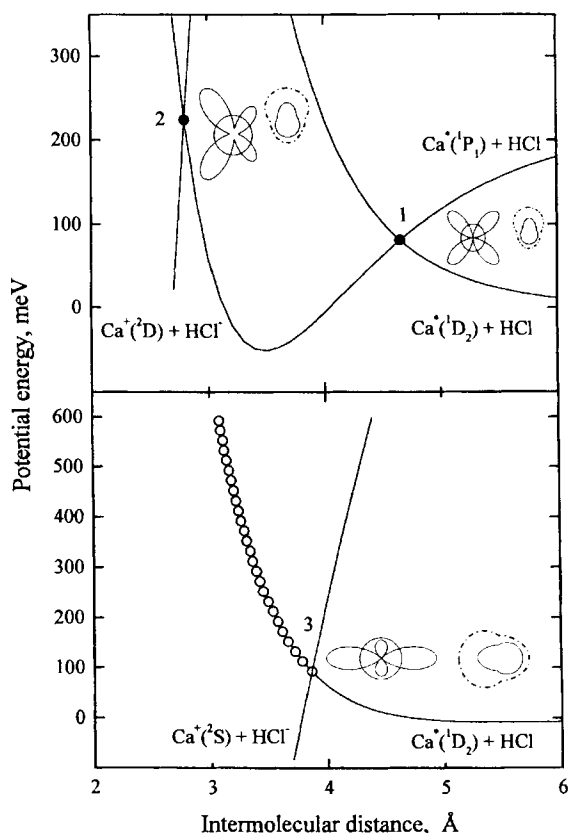


Figure 15. Schematic diagrams of the one-dimensional interaction potentials between Ca and HX in the vicinity of the 1P_1 and 1D_2 states of calcium. The crossings with the ground-state 2S and 2D electron transfer potentials are indicated by the numbers 1, 2 and 3. Also represented is the most favorable electronic configuration of the calcium for this transition. Adapted from Ref. [252].

The action spectra when monitoring the high vibrational levels of the ground state of CaCl appear strikingly different from the preceding structured spectra when detecting the chemiluminescence. In the case of excited product detection, the action spectra are assigned to local electronic excitation of the calcium within the Ca–HCl complex, resulting in states of A' or A'' electronic symmetry correlating with the optically accessible calcium states $4s4p\ ^1P$ or $4s3d\ ^1D$, within the complex. On the other hand, the continuous action spectrum exhibiting a Gaussian shape when detecting ground-state CaCl is assigned here to an excitation of a different nature, i.e., the direct excitation of the charge-transfer surface Ca^+HCl^- with A' symmetry correlating with the $\text{Ca}^+\ ^2S_0$ ground-state ion. The excitation region corresponds to a fairly steep potential surface, the lowest charge-transfer potential surface $\text{Ca}^+(4s\ ^2S) - \text{HCl}^-$, that correlates with the ground-state products $\text{CaCl}(X) + \text{H}$. Vertical excitation of this surface from the ground state of the Ca–HCl complex is possible owing to its partial ionic character [253]. The transition intensity can be represented by excitation to a Coulomb potential along the coordinate $R_{\text{Ca-HCl}}$, with the equilibrium distance of the ground-state complex as 3.8 Å and the width of the potential as 0.5 Å. With this simulation there is reasonable agreement, given the simplicity of the model.

Absorption of the Ca–HCl complex at different frequencies can be linked with different regions of the potential energy surface and the resulting branching to the different product states is noticeably different. The yield of chemiluminescent products is only important for excitation of certain regions of the potential surface that cross at reasonable distance from the equilibrium with a potential surface correlating with an excited ion core $\text{Ca}^+ \text{ } ^2\text{D}$. Also, it can be expected that the decay of the initially excited state in the case of the local excitation of the calcium and in the latter case of the direct excitation of the charge-transfer potential have different appearances.

The latter excitation of the ionic region in the red of the action spectrum will result in immediate Cl abstraction to form CaCl while the local A'' excitation in the same spectral region will necessitate a reasonable rearrangement before the excited CaCl^* product is formed. Time-resolved experiments have been conducted on the Ca–HBr system within the $\text{Ca}(4s4p \text{ } ^1\text{P}_1)$ region and a 200 fs decay time of the initially excited complex has been observed [254]. This confirms the local nature of the excited state of the calcium. The 200 fs decay might correspond to the time necessary to reach the transition state from the Franck–Condon region.

Ground-state products from locally excited reactions in alkali metals

The detection of nonfluorescent ground states within a large population distribution is a difficult problem, as we have just seen for Ca–HCl. A new and general method has been proposed by John Polanyi's group to address this problem in clusters. Here also the reacting system composed of a metal and a molecule or an aggregate of molecules is prepared in a locally excited state of the metal, yielding short-lived quasi-bound states whose resonances are analyzed to unravel the electron-transfer reaction.

The equivalent of an absorption spectrum of the short-lived reaction complex can be measured by depletion spectroscopy. The absorption spectrum of the reacting intermediate is monitored via the decrease in the ground-state population of the ground-state van der Waals complex of the reagents, due to the reaction from the excited state. This is achieved by the use of two lasers, one probing, by ionization, the population of the ground-state complex formed by the reagents and the other, intense, exploring the reacting excited surfaces, thus causing a decrease in this population by funneling population into the reaction channel. The major advantage of this method compared with laser-induced fluorescence, used in the preceding section, is that it is sensitive to electron-transfer reactions of nonchemiluminescent or nonluminescent products. This occurs especially in the case of polyatomic molecules such as fluorobenzene and methyl fluoride with sodium [255, 256]. However, the method yields the detection of the sum of all nonradiative decay channels of the excited state, fluorescent or nonfluorescent. It has the advantage of giving the absolute excitation cross-section, by measuring the dependence of the ion signal on the intensity of the depletion laser. The absorption cross-section can be directly derived from the relative disappearance of the ion signal as

$$\log\left(\frac{N_0}{N}\right) = \sigma_{\text{depletion}} F \quad (24)$$

where F is the laser fluence of the depletion loss expressed in photons per unit area [257]. This cross-section is directly related to the absorption and decay process:

$$\sigma_{\text{dep}} = \frac{4\pi^2\omega}{c} |\mu_{if}|^2 \frac{\Gamma_f}{(E - E_f)^2 + \Gamma_f^2} \quad (25)$$

where μ_{if} is the $i \rightarrow f$ transition dipole moment and Γ_f represents the linewidth derived from the golden rule expression. This formulation of σ_{dep} is similar to the intensity in the absorption spectra derived in the case of $\text{Hg}-\text{Cl}_2$ where it is assumed that all the excited molecules have reacted ($\Gamma_f \gg$ determining).

Moreover, using high laser fluences one can saturate the $i \rightarrow f$ transition in a manner that depends on the excited-state lifetime. Measuring the energy saturation threshold will relate directly to the decay time of this accessed reactive excited state: a long decay will correspond to a low saturation threshold, and the converse.

Various systems have been investigated: $\text{Na}_2 \cdots \text{ClCH}_3$, $\text{Na}_2 \cdots (\text{ClCH}_3)_2$, $\text{Na} \cdots \text{FPh}$ [255], $\text{Na} \cdots (\text{FCH}_3)_n$ ($n = 1-4$) [256]. The photoinduced charge-transfer dissociation spectra observed for these systems all reveal the local nature of the excitation. In the case of $\text{Na} \cdots (\text{FCH}_3)_n$ ($n = 1-4$), for each value of n three broad peaks appear on the red and blue sides of the sodium D line. As before, the interaction of $\text{Na}(3^2\text{P}_J)$ with CH_3F results in the formation of these electronic excited states $|\Lambda = 1/2, \Omega = 1/2\rangle$, $|\Lambda = 3/2, \Omega = 1/2\rangle$, $|\Lambda = 3/2, \Omega = 3/2\rangle$. Vibrational structure is most prominent for the largest complexes with a spacing of 270 cm^{-1} , a standard value for strongly bound van der Waals clusters.

A relatively large cross-section (1.2 \AA^2) was obtained for the photoreaction of the excited state of the $\text{Na} \cdots (\text{FCH}_3)$ complex, this seems indicative of a very favorable geometry to reaction. It compares with a negligible cross-section for reaction in collisions within crossed beams [164]. The reasonably high value of the cross-section implies also that the electron transfer can proceed without a barrier. If the electron affinity of the CH_3F molecule were that of the free molecule, there would be a very high barrier at ca. 6 eV. This suggests that the $\text{F}-\text{CH}_3$ bond is substantially released at the transition state to accommodate the electron and allow a crossing of the ionic potential $\text{Na}^+ \cdots (\text{FCH}_3)^-$ van der Waals potential at the distance $R_{\text{Na} \cdots \text{FCH}_3} \approx 3 \text{ \AA}$, close to the Franck-Condon excitation region accessed from the ground-state complex. The increase in the electron affinity in stretching the $\text{F}-\text{CH}_3$ bond can be understood, since at infinite distance the electron affinity must reach +3.45 eV (atomic fluorine), starting from -6.2 eV in the molecule. The different intensities of the different peaks in the depletion spectrum were inferred from the different perturbations of the sodium by the complexing FCH_3 molecule. The peak cross-section also decreased with the size of the complex in a way that may reflect the formation of an inner solvation shell closed at $n = 3$. This system represents the first one where gradual solvation effects have been observed on an electron-transfer reaction.

The prototypical $\text{Na} \cdots \text{HF}$ system has been investigated by the same method. It represents an excellent example where elaborate and accurate calculations (MRDCI)[75] are possible for the ground and excited states of the complex. Also,

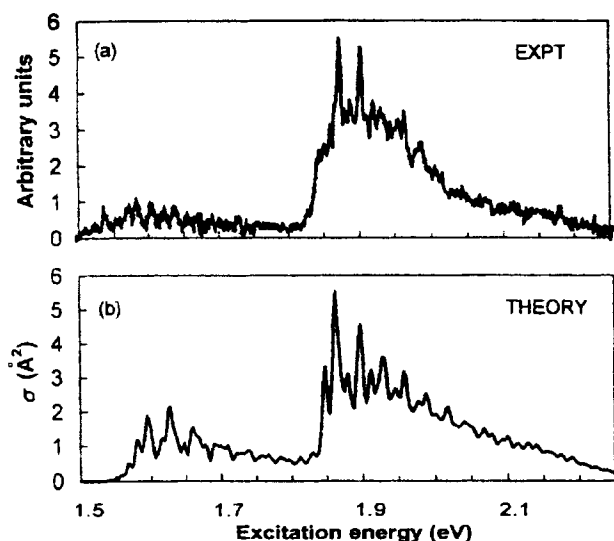


Figure 16. (a) Experimental photodepletion spectrum of the Na...FH complex and (b) calculated absorption spectrum assuming $T = 250$ K. Adapted from Ref. [75].

the reaction is best activated by electronic excitation since it is endoergic by ca. 1.3 eV. The depopulation spectrum represented in Figure 16 displays two bands, a small one at 780 nm and a strong one at 650 nm in the immediate red region of the sodium D line. In contrast to the preceding case of Na...FCH₃^{*}, the number of bands is only two in the depopulation spectrum instead of three and the spectrum extends also over a considerable range. There is an extensive vibrational structure within these bands. The calculations reproduce with great accuracy the position of the bands, their shape and the detailed vibrational structure. These bands have in essence the same origin as in the case of Na...CH₃F and result from the interaction of excited Na(3p²P) with HF, which is very strong in this case and explains the extent of the spectrum over 1 eV. It is interesting to note the geometries of the three states, the lowest energy state $\tilde{A}(2A')$ of quasi-diatomic symmetry Σ , correlating with Na(3p²P_{1/2}), is bound by 0.53 eV and bent at 60°; in contrast, the next two degenerate states, B(3A', 1A''), correlating with Na(3p²P_{3/2}), are linear and bound by 0.34 eV. The geometry changes between the ground state (0.076 eV) and the excited states account for the extensive vibrational structure both in the Na–FH stretch and bends.

The dynamics of the photoreactive intermediate are complex and still need to be elaborated in detail. There is a strong avoided crossing, the locus of the electron transfer between the exciplex $\tilde{A}(2A')$ state and the ground X state where the reaction occurs. Dynamic calculations show [258] that the system is trapped in the excited $\tilde{A}(2A')$ exciplex before undergoing a nonadiabatic relaxation to the ground state and that this relaxation is quantal owing to the large energy gap between the two states. The calculations also show the very long lifetime of the excited state (several hundred picoseconds) which can be dramatically decreased by the H/D

isotope effect and excitation of the HF vibration. There is a complex process where conical intersections come into play to funnel the system from the B to the \tilde{A} state and the avoided crossing further funnels the excited-state reagents to the ground state. The reactive process can no longer be understood as a classical process leading through a crossing between the electron-transfer potential and the initial covalent potential to the reaction products involving a nonadiabatic process. This also showed up in the preceding section in modeling the sharp resonances observed in the Ca–HF reacting complex [246].

2.6.2 Time-resolved Observation of Electron Transfer in Excited-state Reactions: the Ba–FCH₃ case

The spectrum of the Ba–FCH₃ complex has also been probed via photodepletion spectroscopy and it displays strong transitions in the region of the Ba 1P_1 line with a 60 Å² cross-section [259, 260]. This corresponds to the local excitation observed in the preceding section which results in the corresponding splitting (here doubling) of the p transitions.

The dynamics of the system have been explored by femtosecond pump–probe techniques [261] through the excitation of the intense band observed at 618 nm. This band, although being slightly asymmetric, can be assigned a homogeneous linewidth of 220 fs from the uncertainty principle. The decay of the parent (270 fs) was found to match exactly the appearance time of the fragment BaF with no delay and populated in an excited C electronic state quasi-exclusively. The lack of delay between the disappearance of the parent and the appearance of the product BaF* is surprising in a scheme where the locally excited parent complex should undergo an evolution on the reaction surface bringing it from the Franck–Condon accessed region to the transition state and the products. What can be concluded, however, is a rapid, direct passage over the electron-transfer transition state Ba⁺–FCH₃[–] involving a nonmeasurable delay between the excited state of the reagents and the products; this must correspond to the absence of a barrier separating them.

2.6.3 Direct Excitation of an Electron-transfer Complex

Direct excitation of electron-transfer states may yield surprising results. This is the case with the bimolecular benzene–iodine charge-transfer complex. In solutions this system is the prototypical case of charge transfer as reported by Mulliken [262]. The characteristic 280 nm absorption band of the benzene–iodine system is distinct from any absorption features of neat iodine or benzene. It has been identified as being due to a promotion of the HOMO benzene π electron to a σ^* LUMO orbital on iodine resulting in benzene–iodine electron transfer.

Hence, in a benzene–iodine cluster, excitation at 266 nm leads to the charge-transfer potential energy surface. Using femtosecond excitation one can detect the decay of the initially populated state, the appearance of the products and their kinetic energy distribution and alignment (with respect to the pump laser) [55, 56,

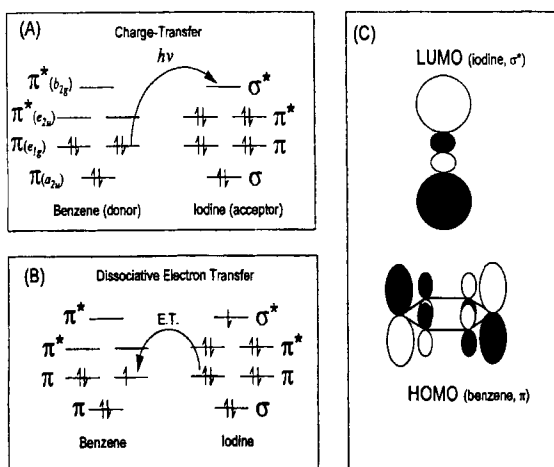


Figure 17. (A) schematic diagram showing the electronic configurations of benzene and molecular iodine. The arrow represents the electron transfer excitation from the HOMO of the donor to the LUMO of the acceptor, iodine. (B) Schematic diagram of the back electron transfer process which leaves the molecular iodine electronically excited. (C) Pictorial representation of the HOMO in benzene and the LUMO of iodine. Adapted from Ref. [55].

263, 264]. The decay of the parent is biexponential with a short time constant, typically 250 fs, and a longer one, 800 fs. The kinetics appear to be parallel, i.e., correspond to different and competing decay channels. Their pre-exponential factors are different, with the short one dominating. The short decay has been assigned to an ionic to covalent back electron transfer pictured in Figure 17, resulting in iodine dissociation. A back transfer from the iodine π^* orbital to the half-filled benzene π orbital leaves iodine in a dissociative state. The reaction channel forms $(\text{benzene})^+ \text{I}^- + \text{I}$, and corresponds to the minor decay component of the parent.

The neutral decay channels have been shown to outnumber the ionic channels and are carefully analyzed by determining the energy distribution (kinetic) of the released iodine atom and its recoil direction via polarization measurements. A double energy distribution has been found with a low-energy component and another one located at $+4000 \text{ cm}^{-1}$. The latter high-velocity iodine recoils directly away from the benzene ring in a very short time (700 fs) while the slower velocity component is detected and presumably corresponds to the other iodine atom lying closer to the benzene ring as shown in Figure 17. The geometry of the cluster corresponds to an iodine molecule slightly tilted away (30°) from the C_6 axis of the benzene molecule and during the dissociation one of the atoms rebounds on the plane of benzene with lesser energy and appears after a longer time. This is confirmed by polarization measurements and appears also in molecular dynamics simulations. A very interesting feature of this work is to analyze the results of iodine caged in large benzene, or benzenic, clusters; there the escaping iodine atom appears with a considerable delay (up to 75 ps), as might be expected, and with lesser energy. This type of experiment has been compared with liquid-phase results [265] and a major difference is the observation of a benzene $\cdots \text{I}$ cage complex resulting from the I_2 dissociation.

This charge-reverse electron-transfer process has been studied systematically with a variety of electron donors and iodine and ICl as acceptors in the precursor. The

general phenomena of reversible and dissociative electron back transfer are observed for all systems studied. However, in the case of diethyl sulfide and iodine complexes [56] trapping can occur at the transition-state level where the reversible electron transfer can be delayed by 500 fs followed by the release of the first iodine atom. One notes that this mechanism of bond breaking due to the reverse transfer of the electron is symmetric with that developed in the harpoon model where the negative ion resulting from the direct transfer is dissociated.

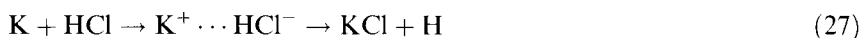
2.7 Prereactive Behavior in Ground States

Within the framework of the harpoon reactions described at the beginning of this chapter, ground-state reactions occur between an electron donor and an electron acceptor, because an electron is totally transferred from the donor to the acceptor. Of course, situations must exist where an electron is transferred but the reaction does not occur owing to energetics. Thus the charge-transfer complex can be stabilized before reaction. Other situations can be encountered where the electron transfer is only partial. These situations can be named prereactive to highlight the fact that the reaction is blocked somewhere along the reaction path.

2.7.1 Stabilizing an Electron-transfer Complex

Prereactive behaviors were identified very early and an impressive series of examples was listed in a book by Klabunde in 1980 [266]. Electron spin resonance (ESR) studies reveal that in low-temperature matrices electron-transfer reactions are blocked as a rule and most, if not all, charge-transfer complexes involved in standard gas-phase harpoon reactions have been stabilized and observed in matrices. The ESR spectra of these systems revealed nearly complete electron transfer. Similar conclusions have also been drawn from infrared spectroscopy. For example, outside the field of alkali metal atoms, evidence of an Al^+NO^- complex has been obtained by this technique [267]. It should not be thought that every metal atom is able to make charge transfer with every molecule. For example, no indication exists of a charge transfer between Cu and NO in an argon matrix [268].

Let us consider an illuminating example concerning an alkali metal atom: the harpoon reaction



which was extensively studied in the gas phase by Brooks and co-workers [123, 124]. The K–HCl system has also been studied in an argon matrix [220]. The ESR spectrum in the matrix study, which is normally very sensitive to the presence of atomic hydrogen, indicates only a very little tendency to form $\text{KCl} + \text{H}$ compared with a very easy formation and stabilization of the electron-transfer $\text{K}^+ \cdots \text{HCl}^-$ complex.

Of course, this suggests a barrier on the potential energy surface, which prevents further reaction of the complex to form $\text{KCl} + \text{H}$. With the classification of Polanyi such a barrier is a *late barrier*, localized somewhere in the exit channel of the reaction [70, 73]. With such a barrier, translational energy is less efficient at promoting the reaction than a comparable increase in the vibrational energy of the HCl reaction partner [269]. This anticipation based on the ‘Polanyi rule’ for barrier location was exactly confirmed by the gas-phase measurements of Brooks and co-workers [123, 124].

2.7.2 Observing Partial Electron Transfers in the Gas Phase

When facing a full collision process, the existence of such a partial electron transfer state is elusive and usually difficult to evidence experimentally. A major difficulty comes from its transient character. A convenient approach to stabilize the electron transfer between two encounters is to consider a complex formed with both of them. This was the case with the $\text{Au}^+(\text{H}_2\text{O})$ complex mentioned above. This is also the case with the neutral van der Waals complexes considered hereafter. In this case, the characterization of the charge-transfer state requires a careful experimental investigation. We review here how spectroscopy of these clusters can characterize partial electron transfers.

This is probably the most delicate and quantitative way of characterizing partial charge transfer in binary pairs. These pairs are stabilized for an ‘infinite’ time within a molecular complex where the charge-transfer properties can be examined. Two methods have been used: Stark spectroscopy and pulsed Fourier transform rotational spectroscopy. The first method diagnoses the dipole moment of the molecular complex under study, and hence the distribution of charges. If the dipole moment has increased within the complex due to charge transfer, a positive signal is observed. This direct method has been mainly applied to cooled gas mixtures containing a small fraction of dimers. This method could be enhanced by the development of Stark spectroscopy in supersonic molecular beams [271]. A systematic study of the charge-transfer properties in various complexes of electron donors with electron acceptors, has been performed by Legon [270, 272] by rotational spectroscopy (pulsed Fourier transform). The electron transfer is monitored here via the hyperfine splitting observed in these spectra.

In an atom, the nuclear quadrupole having unpaired electrons interacts with the field gradient in its vicinity. This provides an accurate measurement of the charge distribution around this atom. The hyperfine splitting, precisely measured with microwave accuracy, yields the hyperfine coupling constant $\chi = eqQ$, where e is the proton charge, Q is the nuclear quadrupole and q is a quantity depending on the charge distribution around the nucleus. In this case, q relates to the average field gradient $\langle \partial^2 V / \partial r^2 \rangle_{\text{ave}}$ about the atom and is given by the following expression:

$$q = e \int \Psi_{JJ}^* \frac{3 \cos^2 \theta - 1}{r^3} \Psi_{JJ}^* d\tau \quad (28)$$

where J relates to a state of total electronic angular momentum J and $mJ = J$. In a method originally developed by Townes and Dailey [273], q is now measured in molecules but the atom is bound within a chemical bond. However, on average one unpaired electron remains about this atom and the wavefunction can be expanded as a linear combination of atomic orbitals. In the case of an atom Cl, for example, accepts a second charge becoming Cl^- , and becomes spherically symmetric and $q = 0$. It is then found that, in the case where the molecule is partially ionic, the wavefunction is a superposition of neutral and ionic contributions with probabilities $1 - x$ and x , respectively. Hence q becomes a linear combination of the neutral and ionic contributions: $q_{\text{neutral}}(1 - \delta) + \delta q_{\text{neutral}} (= 0) = q_{\text{neutral}}(1 - \delta)$. This has been successfully applied to molecules of increasing electronegativity [273]. Of course, the q value of ^{35}Cl in NaCl , i.e., Na^+Cl^- , is zero.

In a cluster formed by a donor molecule D with an acceptor A, partial charge transfer may occur between these units, but the derivation of q from quadrupole splitting measurements of one atom requires a detailed analysis. Considering the acceptor subunit ClBr , for example:

- $\chi(\text{Br})$ is increased while $\chi(\text{Cl})$ is decreased by the charge distribution of the nearby donor;
- the $\chi(\text{X})$ values will be decreased by angle averaging the large amplitude oscillations of ClBr about the axis of the complex, $\chi(\text{Cl}) = \chi(\text{Cl})_0(3 \cos^2 \beta - 1)$ [274].

The results are conclusive since in clusters with Cl_2 and BrCl as acceptors with a manifold of donors, a direct relationship of the amount of charge transfer δ with the force constant of the intermolecular mode $\text{D} \cdots \text{A}$ was found, as seen in Figure 18. This increased force constant results from the interaction between the induced

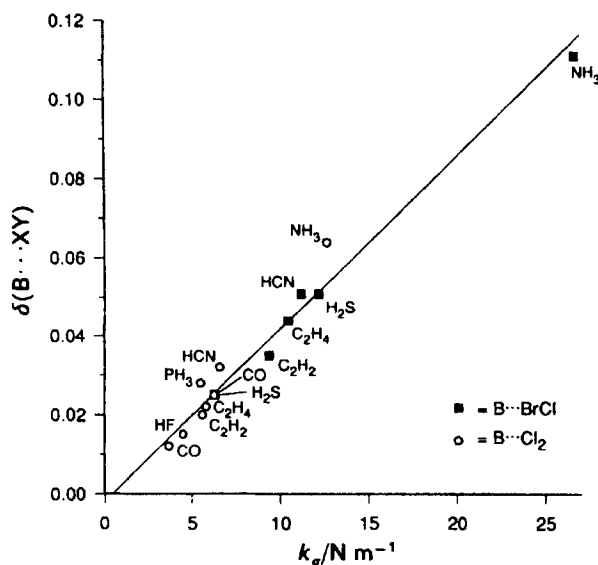


Figure 18. Partial electron transfer $\delta(\text{B} \cdots \text{XY})$ versus the van der Waals bond force constants. Adapted from Ref. [270].

charges in the cluster. From these measurements it appears that the amount of charge transfer is much smaller than expected, even for well known systems such as $\text{NH}_3 \cdots \text{HCl}$, that could be believed to be ionic. In Figure 18 very small amounts of charge transfer δ are observed for an ensemble of donors and acceptors, which shows the power of the approach and also correlates the strength of the bond with the partial charge transfer δ .

2.8 Towards Electron-transfer Reactions in Condensed Phases

Few experiments allow one to bridge gas-phase electron transfer mechanism to liquid (or condensed)-phase electron transfer reactions. The major problem is to model the so-called solvent coordinates in the gas phase. Of course, clusters seems to be the ideal medium to build solvent effects in a stepwise manner. However, clusters are much colder than liquids, with the consequence that only a limited number of isomers are explored, as compared with the room temperature configurations involved in liquid processes. Discrepancies are observed in the case of cluster solvation of ionic molecules in clusters: NaI remains at the surface of water clusters whereas it dissolves in bulk water [275]. Clusters thus do not allow one to explore in a single step all the aspects of a liquid-phase electron-transfer reaction. Their main advantage arises from this limitation since they allow one to study separate aspects of the solution processes.

Hence there is no gas-phase experiment yet which fully encompasses all aspects of an electron-transfer reaction in solution. In solution, the solvent acts first as a polarization medium, which affects the energetics of direct transfers from the donor to the acceptor. It can also act as a transport medium for indirect electron transfers. The first aspect has been addressed in various cluster experiments [276]. The second aspect was addressed more recently by considering the femtosecond dynamics of iodide-(water) $_n$ anion clusters, as reviewed below [277]. Finally, clusters present the advantage of isolating one reaction pair free from secondary collisions, except those, which are desired, with the solvent molecules (or atoms). The latter consideration motivated the cluster isolated chemical reaction (CICR) technique reviewed in Section 2.8.3.

2.8.1 Solvent-induced Electron Transfer in Clusters

Metals with low ionization potentials such as the alkali metals (lithium through cesium) dissolve in polar solvents such as ammonia and the electron of the metal is solvated in a small cage surrounded by the polar molecules, while the corresponding metal ion is strongly stabilized by the solvent dipoles. This represents an example of solvation effects inducing charge separation and the process can be essential in stabilizing reaction intermediates resulting from electron transfer.

The effect of the medium inducing this electron transfer can be modeled experimentally in the corresponding metal-molecule clusters where the gradual onset of

electron transfer is monitored by measuring their ionization potentials. Excellent experiments by Schulz et al. [278] and Haberland and co-workers [279] have achieved that goal: the ionization potential of sodium–ammonia clusters decreases in size and suitable extrapolation of the ionization potential yields the value of 1.45 eV for the infinite size cluster. On the other hand, the photodetachment of the electron attached to a cluster of ammonia of infinite size is also 1.45 eV, as shown by Haberland and co-workers [279]. Thus in sodium clusters within ammonia, the lone electron from the sodium atom becomes increasingly delocalized within the cluster as its size increases finally to form a volume/surface solvated electron whose detachment energy from both experiments is 1.45 eV. The same experiments performed with other alkali metal atoms [280] reach the same detachment value, indicating that it is a property of the solvated electron and not of the metal. Also similar experiments have been made on the equivalent water clusters and the ionization potential of the clusters quickly reach the limiting value of 3.3 eV for clusters containing five water molecules. This demonstrates the efficiency of a limited number of polar molecules to stabilize the charged intermediates resulting from the electron transfer.

2.8.2 Dynamics of Electron Solvation in Finite Water Clusters

Solvent-mediated electron-transfer reactions involves the transient transfer of an electron to the solvent acting as a bridge between the donor and the acceptor [1]. Clusters offer the possibility to split this sequential process, the first step of which is the transfer of an electron from the donor to the solvent. In the absence of an acceptor, this step also occurs in solution, but cluster experiments allow a more direct characterization as follows.

Electron solvation dynamics in photoexcited anion clusters of $\text{I}^-(\text{D}_2\text{O})_{4-6}$ and $\text{I}^-(\text{H}_2\text{O})_{4-6}$ have been studied by Neumark's group at Berkeley, using femtosecond photoelectron spectroscopy. The experiment follows the pump–probe scheme, where the pump prepares the cluster analog of charge transfer to solvent by transferring the electron of I^- to the attached water moiety of the cluster. The system is probed by photodetaching the excess electron. Evidence is given of electron solvation dynamics of the excess electron by rearrangement of the solvent molecules for cluster sizes $n = 5$ and 6. This arises from an isomerization from an initially formed dipole bound state (very diffuse electron outside the water cluster) to a conformer where the excess electron is more localized (solvated). This step lasts ca. 1 ps, as shown by the shift of the photoelectron detachment energy to lower values. It corresponds to an important rearrangement of the solvent, prefiguring what should become a cage formed by water molecules.

2.8.3 Cluster Isolated Chemical Reactions

The cluster isolated chemical reaction (CICR) technique was developed in Saclay to permit quantitative studies of heterogeneous chemical processes at a microscopic level. The ultimate goal is to document the coupling between a reaction coordinate

and the degrees of freedom of a reaction medium. An ideal experiment in this direction would consist in isolating a single pair of reactants in a controlled environment, i.e., in a medium of known size, structure, internal energy, and interaction with the solute, and to observe its dynamics. The (CICR) technique is a way to approach such control. It consists in depositing reactants on free nanometric van der Waals clusters, that play the role of a reaction medium. A full account of the method is given in Ref. [281].

This section gives some details on the CICR method, then reviews results concerning the electron-transfer reactions of barium atoms and small barium aggregates with oxidizing molecules such as Cl_2 , CO_2 and SF_6 on argon clusters. More extensive descriptions of our work can be found in Refs. [281–287]. The CICR technique is now beginning to be developed outside our group; for example, it has been used to investigate the $\text{Ba} + \text{N}_2\text{O}$ reaction in helium clusters [288] and a charge-transfer reaction forming the Kr^+F^- excimer after excitation of the $\text{Kr}_n(\text{NF}_3)_m$ clusters with synchrotron radiation [289, 290].

Brief survey of the CICR technique

The CICR method is based on two important features, which are actually not independent of each other.

The first is the choice of fairly large, finite-sized van der Waals clusters for the environment of the chemical reaction (10^2 – 10^3 atoms or molecules in our case). At such sizes, the number of surface atoms is relatively important compared with the number of atoms staying inside the cluster, and in our case the reactants deposited on the clusters stay at the surface, but are free to migrate, to collide with each other and eventually to react.

The second important point on which the CICR technique is based is the strict control of the average number $\langle m \rangle$ of reactants deposited on the clusters. This is achieved by using the pick-up technique originally developed by Scoles and co-workers [291]. It consists in capturing the reactants by sticky collisions between the clusters and a low-pressure gas. Of course, the number of particles trapped is not the same for every cluster, but the important point is that the capture process has known statistics, being a random Poisson process. Hence the probability distribution $P_q(\langle m \rangle)$ of finding exactly q reactant molecule per cluster follows the Poisson law of order q :

$$P_q(\langle m \rangle) = \frac{\langle m \rangle^q}{q!} \exp(-\langle m \rangle) \quad (29)$$

The principle of the experiment is to record the reaction signal (e.g., a chemiluminescence signal) as a function of the average number $\langle m \rangle$ and to fit it by a Poisson distribution or by a linear combination of Poisson distributions. The order of the Poisson distribution which best fits the experimental data is a direct measure of the exact number of reactants involved in the chemical process under study, since the reactants are confined on a cluster of finite size. For instance, if the reaction signal is well fitted by the Poisson distribution $P_2(\langle m \rangle)$, when varying the average

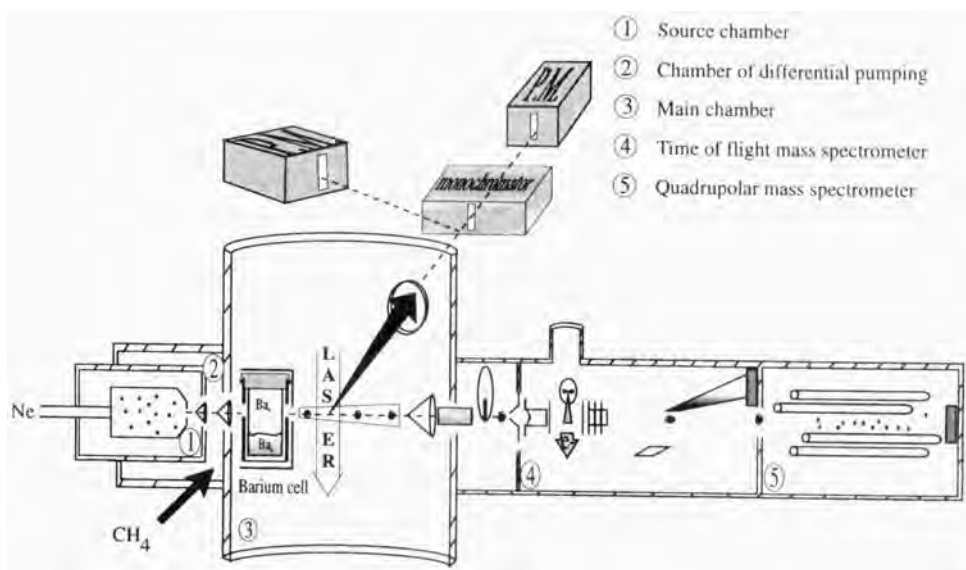


Figure 19. Scheme of the experimental set-up.

number $\langle m \rangle$ of the reactant 'r' deposited per cluster, then we know that the reaction signal originates from the reaction of two reactants 'r', and only two. Since the binding energy between the two is usually much larger than the cluster temperature, these two reactants group together as a dimer. For instance, the binding energy of Ba_2 has recently been calculated to be 0.2 eV [292], a value that is much larger than the thermal energy available on clusters. This is the approach we used to investigate the reactivity of small barium aggregates Ba_2 , Ba_3 , etc. [283, 285, 293].

The apparatus used in CICR experiments is shown schematically in Figure 19 [285, 287]. The beam source (chamber 1), which generates the cluster beam, is complemented by three pick-up regions (chambers 2 and 3) in order to deposit reactants having different chemical natures at various places along the cluster beam. Two mass spectrometers (chambers 4 and 5) are used to characterize the cluster beam, according to procedures extensively described in Ref. [281]. The most important characterization is that of the average number of reactants deposited per cluster. Finally, two laser beams, a monochromator and a photon detection system are used to interrogate the reaction events through fluorescence measurements (chemiluminescence or laser-induced fluorescence).

The fate of the reaction product in cluster isolated chemical reactions

A series of studies by our group of the $\text{Ba} + \text{N}_2\text{O} \rightarrow \text{BaO} + \text{N}_2$ and $\text{Ba}_3 + \text{SF}_6 \rightarrow \text{BaF} + \dots$ reactions have led to the following scenario of CICRs [285, 294–298].

When a very exoergic, chemiluminescent reaction such as $\text{Ba} + \text{N}_2\text{O}$ takes place at the cluster surface, there is competition between ejection of the electronically excited product BaO from the cluster and its solvation. The reaction path of this

reaction is not much perturbed by the cluster and the chemiluminescence of the ejected product is very similar to that observed in the gas-phase reaction. In contrast, the cluster has a profound influence on the solvated product. It changes the branching to chemiluminescence, and affects the vibrational population of the electronically excited state.

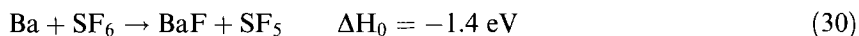
From our work on the Ba–N₂O and Ba–SF₆ systems, a hierarchy in the degree of interaction between the cluster and the reaction product has been found. As just mentioned, the chemiluminescent product of very exoergic reactions is almost unaffected by the cluster. It is vibrationally and rotationally hot, presumably because it is ejected very rapidly after the reaction with not enough time to interact and to be cooled by the cluster. In contrast, free products, when electronically in the ground state, are also much colder rotationally and vibrationally, suggesting more interaction with the cluster [297]. As could easily be anticipated, the cluster effect is dramatic on the solvated products. Very strongly interacting clusters such as nitrogen clusters quench totally the chemiluminescence of the Ba + N₂O reaction. Instead, argon clusters, which interact much less with the product BaO*, do not quench its chemiluminescence. Nevertheless, within its lifetime, electronically excited BaO* is cooled vibrationally, down to $v = 0$. Only the less interacting neon clusters let BaO*, $v = 1$, be observed [286]. Finally, progressive embedding of the product BaO is reported, but this process turns out to be very slow. For instance, it takes place on a time-scale of a few tens of microseconds in neon clusters [298].

Electron-transfer reactions of barium and barium aggregates with oxidizing molecules

The CICR method has also been used to stabilize small barium aggregates (Ba₂, Ba₃, etc.), in order to explore their reactivity with oxidizing molecules ranging from very good to very poor oxidizing agents: Cl₂, O₂, CO₂ and SF₆ [283, 285, 293].

Multiple chemiluminescent channels are observed in the reaction of Cl₂ with barium dimers. They correspond to all the electronically excited products BaCl, BaCl₂ and Ba that are energetically accessible [293]. In contrast, only the most exoergic chemiluminescence channel corresponding to the formation of BaO is observed in the reaction of O₂ with Ba₂.

The most interesting results concern the reaction with the lesser oxidizing molecules, CO₂ and SF₆. Barium monomers do not react with these molecules at the cluster temperatures. This result is actually surprising considering that such reactions have been observed in the gas phase. Let us focus on the Ba + SF₆ reaction, which can be written as



Its energetics are deduced from Refs. [299, 300].

Process 30 has been studied in the gas phase using a crossed-beam apparatus [301]. The reaction product has not been clearly identified as being BaF or BaF₂, but its measured angular and velocity distributions reveal that the reaction proceeds via the formation of a long-lived BaSF₆ intermediate, which is believed to be the electron-transfer complex Ba⁺–SF₆[–]. Hence the reaction can be tentatively in-

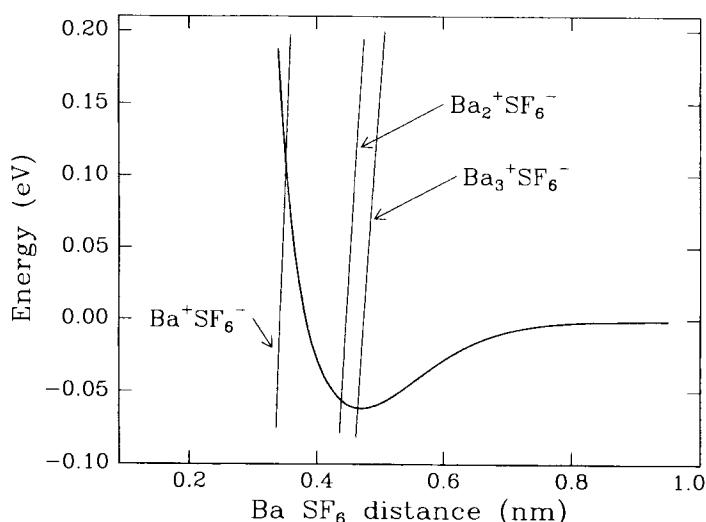


Figure 20. Scheme of covalent and ion-pair curves describing the BaSF_6 , Ba_2SF_6 and Ba_3SF_6 systems. The construction details for these curves are given in Ref. [285].

interpreted on the basis of the harpoon model shown in Figure 20. The important point to observe is the crossing point between the ion-pair curve and the covalent curve. It is located at a short enough distance between Ba and SF_6 to experience the repulsive wall of the $\text{Ba} + \text{SF}_6$ covalent interaction. This leads to an activation barrier of about 0.1 eV height in the entrance channel of the reaction. We have already mentioned the existence of such barriers in electron-transfer reactions when considering the $\text{K} + \text{HCl}$ example in Section 2.7.1. However, this was a late barrier, which was overcome by vibrational excitation of the molecule. In the present $\text{Ba} + \text{SF}_6$ case, it is more probably an early barrier since it was overcome in the crossed-beam study of Herm et al. performed at 0.11 eV collision energy [301]. In the context of a CICR experiment on argon clusters, such a barrier blocks the reaction. The collision energy is then given by the cluster temperature and is too small (ca. 0.003 eV) to overcome the reaction barrier.

In contrast, $\text{Ba}_{\geq 2}$ aggregates react with CO_2 and $\text{Ba}_{\geq 3}$ aggregates react with SF_6 [283, 285]. This is exemplified in Figures 21 and 22 where the chemiluminescence of the barium- SF_6 system is considered. The chemiluminescence spectrum is shown in Figure 21 and the variation of its intensity is shown in Figure 22 as a function of the average number of both barium and SF_6 per cluster. It appears that only clusters carrying one SF_6 molecule and barium aggregates larger than Ba_3 lead to chemiluminescence. Hence chemiluminescence originates from reactions of one SF_6 molecule with $\text{Ba}_{\geq 3}$ aggregates.

The above results suggest that small barium aggregates are better reducing agents than atomic barium. This may be understood with the help of Figure 20, by considering that barium aggregates more easily transfer an electron in a redox reaction than barium atoms. Chevalyre and co-workers measured the ionization potentials

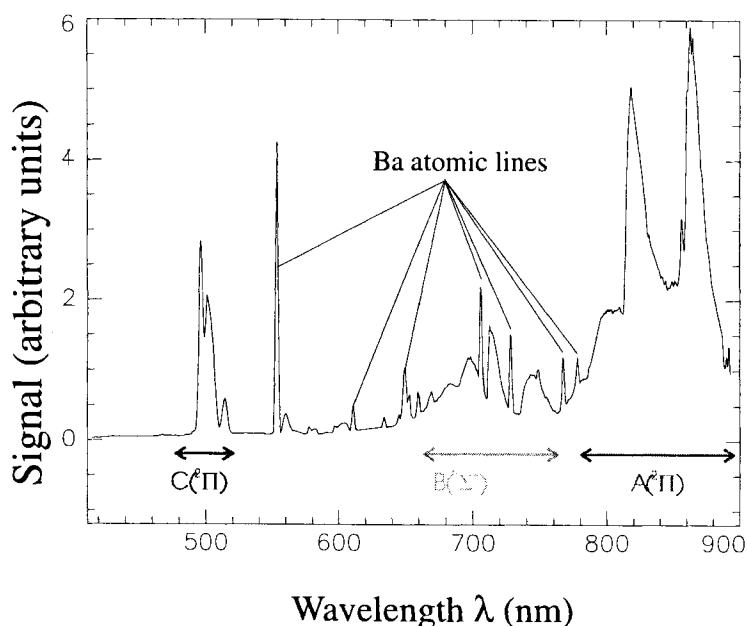


Figure 21. Chemiluminescence observed with Ba-SF₆ mixtures on argon clusters.

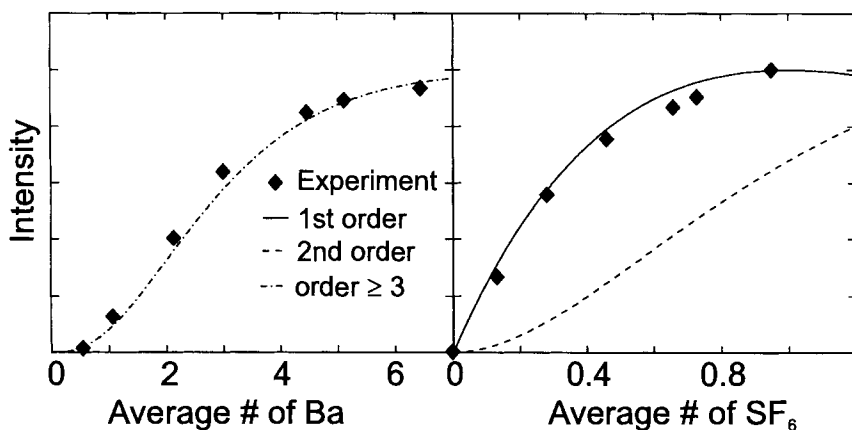


Figure 22. Chemiluminescence intensity as a function of the average number of barium atoms ($\langle m \rangle_{\text{Ba}}$, left) and SF₆ molecules ($\langle m \rangle_{\text{SF}_6}$, right) deposited per cluster. The curves show the variation of Poisson distributions of various orders as labeled.

of small barium aggregates and found 4.2, 4.0, 4.0 and 3.6 eV for Ba₂, Ba₃, Ba₄ and Ba₅, respectively, whereas the ionization potential of barium is 5.2 eV [302]. This leads to a larger distance for the electron transfer, and the lowering of the entrance barrier when switching from barium monomers to dimers, trimers, etc. The experi-

mental observation suggests that the barrier is low enough with $\text{Ba}_{\geq 3}$ to open the route to the electron transfer, and hence to the reaction.

2.9 Summary and Conclusions

The experimental and theoretical studies reported in this chapter have shown the central role of electron-transfers processes in the reactions of metals with oxidizing compounds. The electron-transfer process provides, at the transition-state level of the reaction, the driving force for the reactive evolution towards the products, as was first recognized by Polanyi [8]. In this framework, the reaction dynamics can be accurately described, and this is manifested in the recoil direction of the fragments and in the disposal of energy into the vibration and translation of the product of ionic character. The reaction mechanism via an electron transfer also applies to excited-state metals of higher ionization potentials, these excited-state metals being transformed by electronic excitation into open-shell facile electron donors. Further, excited-state reactions can produce excited-state products and this results from an electron transfer from excited covalent states to excited ion-pair potentials. Symmetry propensity rules correlate these excited-state reagents with the excited-state products.

The ion-pair potentials are usually one-dimensional and experiments have given recurring indications of their dependence on other coordinates (angular, for instance). As an example, the electron transfer needs an additional bond stretching for molecules having a negative electron affinity, as exemplified in the case of the $\text{K} + \text{CH}_3\text{I}$ reaction [69]. The ion-pair potentials that are used to interpret the experiments are mostly empirical; this follows from the difficulty of precise quantum chemical calculations for the diffuse negative ion. In this respect we can cite the case of $\text{Mg}^1\text{P}_1 + \text{H}_2$, where the electron transfer is readily identified with the saddle point for the 'insertion' reaction of Mg^* into H_2 [303]. This emphasizes the difficulty in assigning by quantum calculations the transition region of the reaction to an electron-transfer intermediate; the previous example involves H^- and hence has been more easily characterized. Thus we require developments in quantum calculations where charge analysis is performed; a recent example of this is the charge delocalization in clusters that involves a transfer of an electron from a metal to the solvent, and this process has been fairly accurately reproduced in the case of $\text{Na} + (\text{NH}_3)_n^-$ clusters, [304]. Similarly, there are few calculations describing accurately excited states; the example given by Truhlar and co-workers [75] on Na-HF is probably a singular case. Given the recent developments in calculations, it will be less of a challenge to perform them on excited states.

The observation of excited products in metal-molecule reactions is mostly limited to the simplest molecules. The formation of excited species is probably much more general and should be probed since the electron transfer can correlate excited-state reagents and excited-state products. In fact, the nascent excited-state products from reactions yielding complex polyatomic systems are quenched by nonadiabatic

transitions to the ground states of these molecules and remain unobserved except for special cases. These excited nascent states can be detected by femtosecond methods in the case of complex reagents but also in the case of excited-state reactions within clusters.

Solvation effects at the transition-state level of electron-transfer reactions is a field that is opening up by means of clusters reactions. Reactions within clusters (see Section 2.7) or at the surface of clusters (see Section 2.8) provide an experimental tool to observe the effect of gradual solvation on electron-transfer reactions. Femtosecond methods appear highly valuable for characterizing the electron transfer in reactions within clusters, since in neutral clusters the electrostatic effects of solvation will show up intensely at the electron-transfer level and for a short period of time, before the products are fully developed. In the gas phase the solvation of electrons is directly sensed by photoelectron spectroscopy, as exemplified in the (nonreactive) case of ultrafast solvation of electrons in water clusters [305].

The model of electron transfer in gas-phase metal-molecule reactions can be extended to more complex systems such as the collisions of metastable rare gas atoms with molecules to produce negative molecular ions [306]. In surface chemistry the harpoon model describes the forces between the reagents after the electron transfer has been applied to reactions of molecules with metal surfaces [120]. Another domain, involving the reaction of metal ions with complex systems could be interpreted in the framework of electron transfers: in the porphyrin site of the heme within hemoglobin, addition of oxygen to the Fe^{2+} results in an electron transfer from the metal to the oxygen. The dynamics of this attachment and of the photo-induced detachment could be viewed in that perspective.

In essence, electron transfer, characterized at the transition-state level of simple metal-molecule reactions, should provide a simple framework to study a variety of much more complex and important reaction mechanisms.

References

1. M. Bixon and J. Jortner, *Adv. Chem. Phys.* **106**, 35 (1999).
2. R. A. Marcus, *J. Chem. Phys.* **24**, 966 (1956).
3. R. A. Marcus, *Rev. Mod. Phys.* **65**, 599 (1993).
4. R. D. Cannon, *Electron Transfer Reactions*, Butterworth, London, 1980.
5. K. F. Purcell and B. Blaive, Theory of Electron Transfer Reactions, in *Photoinduced Electron Transfer, Part A*, edited by M. A. Fox and M. Chanon, Chapter I.3, pp. 123–160, Elsevier, Amsterdam, 1988.
6. D. F. Calef, Theoretical treatments of Solvent Effects, in *Photoinduced Electron Transfer, Part A*, edited by M. A. Fox and M. Chanon, Chapter I.9, pp. 362–390, Elsevier, Amsterdam, 1988.
7. N. Sutin, *Adv. Chem. Phys.* **106**, 7 (1999).
8. M. Polanyi, *Atomic Reactions*, Williams and Northgate, London, 1932.
9. D. K. Bohme, *Int. Rev. Phys. Chem.* **13**, 163 (1994).
10. W. Lindinger, A. Hansel and Z. Herman, *Adv. At. Mol. Opt. Phys.* **43**, 243 (2000).
11. K. Eller and H. Schwartz, *Chem. Rev.* **91**, 1121 (1991).
12. L. Capron, H. Mestdagh and C. Rolando, *Coord. Chem. Rev.* **178–180**, 269 (1998).
13. G. Scoles, *Atomic and Molecular Beam Methods*, Oxford University Press, Oxford, 1988.
14. P. Casavecchia, N. Balucani and G. G. Volpi, *Annu. Rev. Phys. Chem.* **50**, 347 (1999).

15. R. B. Bernstein, D. R. Herschbach and R. D. Levine, *J. Phys. Chem.* **91**, 5365 (1987).
16. Special issue of *J. Phys. Chem.*, **101**, No. 41, 1997.
17. J. P. Simons, *Faraday Discuss.* **113**, 1 (1999).
18. A. J. Orr-Ewing and R. N. Zare, Orientation and Alignment of the Products of Bimolecular Reactions, in *The Chemical Dynamics and Kinetics of Small Radicals*, edited by K. Liu and A. Wagner, Part 2.20, pp. 936–1063, World Scientific, Singapore, 1995.
19. K. Goudjil, J. C. Brenot, M. Durup-Ferguson and J. A. Fayeton, *Chem. Phys.* **179**, 573 (1994).
20. M. Barat, J. C. Brenot, H. Dunet and J. A. Fayeton, *Z. Phys. D: At. Mol. Clusters* **40**, 323 (1997).
21. M. Barat, J. C. Brenot, H. Dunet, J. A. Fayeton and Y. J. Picard, *Comments At. Mol. Phys.* **34**, 329 (1999).
22. M. Barat, J. C. Brenot, H. Dunet, J. A. Fayeton and Y. J. Picard, *J. Chem. Phys.* **110**, 10758 (1999).
23. M. Barat, J. C. Brenot, H. Dunet, J. A. Fayeton, Y. J. Picard, D. Babikov and M. Sizun, *Chem. Phys. Lett.* **306**, 233 (1999).
24. Y. T. Lee, J. D. McDonald, P. R. LeBreton and D. R. Herschbach, *Rev. Sci. Instrum.* **40**, 1402 (1969).
25. Y. T. Lee, Reactive Scattering I: Non-optical Methods, in *Atomic and Molecular Beam Methods*, edited by G. Scoles, Part 1.22, pp. 553–568, Oxford University Press, Oxford, 1988.
26. N. Balucani, O. Asvany, A. H. H. Chang, S. H. Lin, Y. T. Lee, R. I. Kaiser, H. F. Bettinger, P. v. R. Schleyer and H. F. Schaefer, III, *J. Chem. Phys.* **111**, 7457 (1999).
27. N. Balucani, O. Asvany, A. H. H. Chang, S. H. Lin, Y. T. Lee, R. I. Kaiser, H. F. Bettinger, P. v. R. Schleyer and H. F. Schaefer, III, *J. Chem. Phys.* **111**, 7472 (1999).
28. P. A. Heimann, M. Koike, C. W. Hsu, D. Blank, X. M. Yang, A. G. Suits, Y. T. Lee, M. Evans, C. Y. Ng, et al., *Rev. Sci. Instrum.* **68**, 1945 (1997).
29. X. Yang, J. Lin, Y. T. Lee, D. A. Blank, A. G. Suits and A. M. Wodtke, *Rev. Sci. Instrum.* **68**, 3317 (1997).
30. A. S. Bracker, E. R. Wouters, A. G. Suits, Y. T. Lee and O. S. Vasyutinskii, *Phys. Rev. Lett.* **80**, 1626 (1998).
31. D. A. Blank, A. G. Suits, Y. T. Lee, S. W. North and G. E. Hall, *J. Chem. Phys.* **108**, 5784 (1998).
32. D. A. Blank, N. Hemmi, A. G. Suits and Y. T. Lee, *Chem. Phys.* **231**, 261 (1998).
33. M. Ahmed, D. S. Peterka and A. G. Suits, *Chem. Phys. Lett.* **317**, 264 (2000).
34. M. Ahmed, D. S. Peterka and A. G. Suits, *Phys. Chem. Chem. Phys.* **2**, 861 (2000).
35. M. Ahmed, D. S. Peterka and A. G. Suits, *Chem. Phys. Lett.* **301**, 372 (1999).
36. M. Ahmed, D. Blunt, D. Chen and A. G. Suits, *J. Chem. Phys.* **106**, 7617 (1997).
37. C. M. Rinaldi, C. A.; Santiveri, G. Tardajos and A. Gonzalez Ureña, *Chem. Phys. Lett.* **274**, 29 (1997).
38. C. A. Rinaldi, M. de Castro, S. Skowronek and A. Gonzalez Ureña, *Phys. Chem. Chem. Phys.* **2**, 723 (2000).
39. T. J. Hughes and M. R. Levy, *Phys. Chem. Chem. Phys.* **2**, 651 (2000).
40. K. M. Green, R. P. Kampf and J. M. Parson, *J. Chem. Phys.* **112**, 1721 (2000).
41. B. Pranszke, P. Kierzkowski and A. Kowalski, *Chem. Phys. Lett.* **317**, 220 (2000).
42. A. Gonzalez Ureña and R. Vetter, *Int. Rev. Phys. Chem.* **15**, 375 (1996).
43. J. M. Mestdagh, J. P. Visticot and A. G. Suits, Doppler Spectroscopy, a Powerful Tool for Studying Molecular Collision Dynamics, in *The Chemical Dynamics and Kinetics of Small Radicals*, edited by K. Liu and A. Wagner, pp. 668–729, World Scientific, Singapore, 1995.
44. P. Hermine, Y.-T. Hsu and K. Liu, *Phys. Chem. Chem. Phys.* **2**, 571 (2000).
45. Y.-T. Hsu, K. Liu, L. A. Pederson and G. C. Schatz, *J. Chem. Phys.* **111**, 7921 (1999).
46. Y.-T. Hsu, K. Liu, L. A. Pederson and G. C. Schatz, *J. Chem. Phys.* **111**, 7931 (1999).
47. C. Jouvét and B. Soep, *Chem. Phys. Lett.* **96**, 426 (1983).
48. W. H. Breckenridge, C. Jouvét and B. Soep, *J. Chem. Phys.* **84**, 1443 (1986).
49. C. Jouvét, M. Boivineau, M. C. Duval and B. Soep, *J. Phys. Chem.* **91**, 5416 (1987).
50. S. K. Shin, Y. Chen, S. Nickolaissen, S. W. Sharpe, R. A. Beaudet and C. Wittig, *Adv. Photochem.* **16**, 249 (1991).

51. A. H. Zewail, *Science* **242**, 1645 (1988).
52. C. Lienau, J. C. Williamson and A. H. Zewail, *Chem. Phys. Lett.* **213**, 289 (1993).
53. A. H. Zewail, Femtochemistry, in *Ultrafast Phenomena VIII*, edited by J. L. Martin, A. Migus, G. A. Mourou and A. H. Zewail, Springer Series in Chemical Physics, pp. 43–48, Springer, Berlin, 1993.
54. A. H. Zewail, Femtochemistry: Concepts and Applications, in *Femtosecond Chemistry*, edited by J. Manz and L. Wöste, pp. 15–128, VCH, Weinheim, 1995.
55. P. Y. Chen, D. Zhong and A. H. Zewail, *J. Chem. Phys.* **105**, 6216 (1996).
56. D. Zhong, T. M. Bernhardt and A. H. Zewail, *J. Phys. Chem.* **103**, 10093 (1999).
57. D. R. Herschbach, Reactive Scattering in Molecular Beams, *Adv. Chem. Phys.* **10**, 319 (1966).
58. D. R. Herschbach, *Faraday Discuss. Chem. Soc.* **55**, 233 (1973).
59. P. Davidovits, Cross-sections for the Reaction of Alkali Atoms with Halogen Molecules, in *Alkali Halide Vapors, Structure, Spectra and Reaction Dynamics*, edited by P. Davidovits and D. L. McFadden, Chapter 9, p. 331, Academic Press, New York, 1979.
60. J. L. Magee, *J. Chem. Phys.* **8**, 687 (1940).
61. E. A. Gislason, Reaction Model for Alkali Halide Systems, in *Alkali Halide Vapors, Structure, Spectra and Reaction Dynamics*, edited by P. Davidovits and D. L. McFadden, Chapter 13, p. 415, Academic Press, New York, 1979.
62. D. G. Truhlar and D. A. Dixon, Direct-mode Chemical Reactions II. Classical Theories, in *Atom–Molecule Collision Theory: a Guide for the Experimentalist*, edited by R. B. Bernstein, Chapter 18, pp. 595–646, Plenum Press, New York, 1979.
63. D. R. Herschbach, *Chem. Scr.* **27**, 327 (1987).
64. D. R. Herschbach, *Pure Appl. Chem.* **47**, 61 (1976).
65. R. Grice, *Int. Rev. Phys. Chem.* **14**, 315 (1995).
66. D. R. Herschbach, G. H. Kwei and J. A. Norris, *J. Chem. Phys.* **34**, 1842 (1961).
67. D. H. Parker, K. K. Chakravorty and R. B. Bernstein, *J. Phys. Chem.* **85**, 466 (1981).
68. D. H. Parker, K. K. Chakravorty and R. B. Bernstein, *Chem. Phys. Lett.* **86**, 289 (1982).
69. A. E. Wiskerke, S. Solte, H. J. Loesch and R. D. Levine, *Phys. Chem. Chem. Phys.* **2**, 757 (1999).
70. J. C. Polanyi and J. L. Schreiber, The Dynamics of Bimolecular Reactions, in *Physical Chemistry, An Advanced Treatise*, Vol. 6-A, edited by W. Jost, pp. 383–487, Academic Press, New York, 1974.
71. J. H. Birely and D. R. Herschbach, *J. Chem. Phys.* **44**, 1690 (1966).
72. R. R. Herm and D. R. Herschbach, *J. Chem. Phys.* **52**, 5783 (1970).
73. J. C. Polanyi, *Acc. Chem. Res.* **5**, 161 (1972).
74. a) J. C. Polanyi, *Chem. Scr.* **27**, 229 (1987); b) L. Bonnet, J. C. Rayez, *J. Chem. Phys. A*, **101**, 9318 (1997); *Eur. Phys. J. D.*, **4**, 169 (1998); *PCCP*, **1**, 2383 (1999); *J. Chem. Phys.*, **110**, 4772 (1999).
75. M. S. Topaler, D. G. Truhlar, Y. C. Xiao, P. Picuch and J. C. Polanyi, *J. Chem. Phys.* **108**, 5378 (1998).
76. J.-B. Song, E. A. Gislason and M. Sizun, *J. Chem. Phys.* **102**, 4885 (1995).
77. P. J. Kuntz, E. M. Nemetz and J. C. Polanyi, *J. Chem. Phys.* **50**, 4607 (1969).
78. P. J. Kuntz, E. H. Mok and J. C. Polanyi, *J. Chem. Phys.* **50**, 4623 (1969).
79. P. J. Kuntz, *Trans. Faraday Soc.* **66**, 2980 (1969).
80. P. J. Kuntz, *Mol. Phys.* **23**, 1035 (1972).
81. M. G. Prisant, C. T. Rettner and R. N. Zare, *J. Chem. Phys.* **81**, 2699 (1984).
82. H. J. Loesch and J. Moeller, *J. Phys. Chem. A* **101**, 7534 (1997).
83. H. J. Loesch, *Annu. Rev. Phys. Chem.* **46**, 555 (1995).
84. H. J. Loesch and F. Stienkemeier, *J. Chem. Phys.* **98**, 9570 (1993).
85. L. Banares and A. Gonzalez Ureña, *J. Chem. Phys.* **93**, 6473 (1990).
86. G. Ding, W. Yang, W. Sun, D. Xu, G. He and N. Lou, *Chem. Phys. Lett.* **220**, 1 (1994).
87. R. J. Hennessy, Y. Ono and J. P. Simons, *Mol. Phys.* **43**, 181 (1981).
88. P. E. Siska and D. R. Herschbach, *Can. J. Chem.* **72**, 762 (1994).
89. R. C. Weast, M. J. Astle and W. H. Beyer (Eds.), *Handbook of Chemistry and Physics*, 65th edn., CRC Press, Boca Raton, FL, 1984.
90. H. F. Davis, A. G. Suits and Y. T. Lee, Reaction Dynamics of Ground State and Electronically Excited Barium Atoms., in *Gas-Phase Metal Reactions*, edited by A. Fontijn, pp. 319–347, North-Holland, Amsterdam, 1992.

91. M. Menzinger, The $M + X_2$ Reactions: a Case Study, in *Gas-Phase Chemiluminescence and Chemi-Ionization*, edited by A. Fontijn, pp. 25–66, Elsevier, Amsterdam, 1985.
92. M. Menzinger, *Acta Phys. Pol., A* **73**, 85 (1988).
93. R. R. Herm, Reactive Scattering at Thermal Energies, in *Alkali Halide Vapors, Structure, Spectra and Reaction Dynamics*, edited by P. Davidovits and D.L. McFadden, Chapter 7, pp. 189–253, Academic Press, New York, 1979.
94. J. C. Whitehead, The Distribution of Energy in the Products of Simple Reactions, in *Comprehensive Chemical Kinetics, Vol. 24: Modern Methods in Kinetics*, Chapter 5, pp. 357–506, Elsevier, Amsterdam, 1983.
95. C. D. Jonah and R. N. Zare, *Chem. Phys. Lett.* **9**, 65 (1971).
96. H. F. Davis, A. G. Suits, H. Hou and Y. T. Lee, *Ber. Bunsen-Ges. Phys. Chem.* **94**, 1193 (1990).
97. A. G. Suits, H. Hou and Y. T. Lee, *J. Phys. Chem.* **94**, 5672 (1990).
98. A. G. Suits, H. Hou, H. F. Davis and Y. T. Lee, *J. Phys. Chem.* **95**, 8207 (1991).
99. A. G. Suits, H. Hou, H. Floyd Davis, Y. T. Lee and J. M. Mestdagh, *J. Chem. Phys.* **95**, 8178 (1991).
100. L. Banares and A. Gonzalez Ureña, *THEOCHEM* **90**, 271 (1992).
101. S. M. Lin, C. A. Mims and R. R. Herm, *J. Chem. Phys.* **58**, 327 (1973).
102. H. F. Davis, A. G. Suits and Y. T. Lee, *J. Chem. Phys.* **96**, 6710 (1992).
103. B. S. Cheong and J. M. Parson, *J. Chem. Phys.* **100**, 2637 (1994).
104. H. F. Davis, A.G. Suits, Y. T. Lee, C. Alcaraz and J. M. Mestdagh, *J. Chem. Phys.* **98**, 959 (1993).
105. M. D. Oberlander, R. P. Kampf and J. M. Parson, *Chem. Phys. Lett.* **176**, 385 (1991).
106. R. Vetter, C. Naulin and M. Costes, *Phys. Chem. Chem. Phys.* **2**, 643 (2000).
107. L. Salem, *Electrons in Chemical Reactions: First Principles*, Wiley, New York, 1982.
108. P. B. Foreman, G. M. Kendall and R. Grice, *Mol. Phys.* **23**, 117 (1972).
109. J. C. Whitehead, D. R. Hardin and R. Grice, *Mol. Phys.* **25**, 515 (1973).
110. S. M. Lin, D. J. Mascord and R. Grice, *Mol. Phys.* **28**, 975 (1974).
111. S. M. Lin, J. C. Whitehead and R. Grice, *Mol. Phys.* **27**, 741 (1974).
112. W. S. Struve, J. R. Krenos, D. L. McFadden and D. R. Herschbach, *J. Chem. Phys.* **62**, 404 (1975).
113. R. C. Oldenborg, J. L. Gole and R. N. Zare, *J. Chem. Phys.* **60**, 4032 (1973).
114. H. Figger, R. Straubinger and H. Walther, *J. Chem. Phys.* **75**, 179 (1981).
115. H. Figger, W. Schrepp and X. H. Zhu, *J. Chem. Phys.* **79**, 1320 (1983).
116. H. Hou, K.-T. Lu, V. Sadchenko, A.G. Suits and Y.T. Lee, *Springer Ser. Chem. Phys.* **61**, 79 (1996).
117. T. C. Devore and J. L. Gole, *J. Phys. Chem.* **100**, 5660 (1996).
118. L. Hellberg, J. Stroemquist, B. Kasemo and B. I. Lundqvist, *Phys. Rev. Lett.* **74**, 4742 (1995).
119. J. Castano Aspas and A. Gonzalez Ureña, *Laser Chem.* **14**, 201 (1994).
120. E. T. Jensen and J. C. Polanyi, *J. Phys. Chem.* **97**, 2257 (1993).
121. M. Brandt, F. Kuhlmann, T. Greber, N. Bowering and U. Heinzmann, *Surf. Sci.* **439**, 49 (1999).
122. T. Greber, *Surf. Sci. Rep.* **28**, 1 (1997).
123. a) T. J. Odiorne, P. R. Brooks and J. V. V. Kasper, *J. Chem. Phys.* **55**, 1980 (1971); b) S. Stolte, *Ber. Bunsenges. Phys. Chem.* **86**, 413 (1982); H. Jalink, F. Harren, D. ran den Ende, S. Stolte, *Chem. Phys.* **108**, 391 (1986); H. Jalink, D. H. Parker, K. H. Meiwes-Broer, S. Stolte, *J. Phys. Chem.* **90**, 552 (1986); H. Jalink, M. H. M. Janssen, M. Geijsberts, S. Stolte, *NATO ASI Ser. Ser. C*, **245**, 195 (1988); H. Jalink, G. Nicolassen, S. Stolte, *J. Chem. Soc. Faraday Trans. Z* **85**, 1115 (1989); M. H. M. Janssen, D. H. Parker, S. Stolte, *J. Phys. Chem.* **95**, 8142 (1991); J. Bulthuis, S. Stolte, *J. Phys. Chem.* **95**, 8180 (1991); J. Bulthuis, J. B. Milan, H. M. M. Janssen, S. Stolte, *J. Chem. Phys.* **97**, 7181 (1991); M. J. J. Vrakking, S. Stolte, *Chem. Phys. Lett.* **271**, 209 (1997).
124. J. G. Pruett, F. R. Grabiner and P. R. Brooks, *J. Chem. Phys.* **63**, 1173 (1975).
125. D.J. Wren and M. Menzinger, *J. Chem. Phys.* **63**, 4557 (1975).
126. D.J. Wren and M. Menzinger, *Faraday Discuss. Chem. Soc.* **67**, 97 (1979).
127. H. Jalink, F. Harren, D. Van den Ende and S. Stolte, *Chem. Phys.* **108**, 391 (1986).

128. R. A. LaBudde, P. J. Kuntz, R. B. Bernstein and R. D. Levine, *J. Chem. Phys.* **59**, 6286 (1972).
129. R. A. LaBudde, P. J. Kuntz, R. B. Bernstein and R. D. Levine, *Chem. Phys. Lett.* **19**, 7 (1973).
130. J. Los and A. W. Kleyn, Ion-pair Formation [in Alkali-Halogen Reactions], in *Alkali Halide Vapors, Structure, Spectra and Reaction Dynamics*, edited by P. Davidovits and D.L. McFadden, Chapter 8, pp. 275–330, Academic Press, New York, 1979.
131. A. W. Kleyn, V. N. Khromov and J. Los, *J. Chem. Phys.* **72**, 5282 (1980).
132. A. W. Kleyn, V. N. Khromov and J. Los, *Chem. Phys.* **52**, 65 (1980).
133. A. W. Kleyn, E. A. Gislason and J. Los, *Chem. Phys.* **52**, 81 (1980).
134. R. J. Donovan and H. M. Gillespie, *React. Kinet.* **1**, 14 (1975).
135. D. L. King and D. W. Setser, *Annu. Rev. Phys. Chem.* **27**, 407 (1976).
136. D. Husain, *Ber. Bunsenges. Phys. Chem.* **81**, 168 (1977).
137. R. J. Donovan, *Prog. React. Kinet.* **10**, 253 (1979).
138. W. H. Breckenridge, Reactions of Electronically Excited Atoms, in *Reactions of Small Transient Species*, edited by A. Fontijn, Chapter 4, pp. 157–230, Academic Press, London, 1983.
139. J. P. Schermann, J. P. Astruc, C. Desfrancois and R. Barbé, Electron Transfer Between Excited Atoms and Molecules, in *Photoinduced Electron Transfer, Part A*, edited by M. A. Fox and M. Chanon, Chapter I.2, pp. 60–122, Elsevier, Amsterdam, 1988.
140. W. H. Breckenridge, *Acc. Chem. Res.* **22**, 21 (1989).
141. J. M. Mestdagh, C. Alcaraz, J. Berlande, J. Cuvellier, T. Gustavsson, P. Meynadier, P. de Pujo, O. Sublemontier and J. P. Visticot, *Laser Chem.* **10**, 389 (1990).
142. A. Gonzalez-Ureña and R. Vetter, *J. Chem. Soc., Faraday Trans.* **91**, 389 (1995).
143. R. Vetter, *J. Chin. Chem. Soc. (Taipei)* **45**, 219 (1998).
144. A. Tam, C. Moe and W. Happer, *Phys. Rev. Lett.* **35**, 1630 (1975).
145. V. Caverio, J. M. L'Hermite, G. Rahmat and R. Vetter, *J. Chem. Phys.* **110**, 3428 (1999).
146. R. J. Vetter, *Isr. J. Chem.* **29**, 393 (1989).
147. J. M. L'Hermite, G. Rahmat and R. Vetter, *Laser Chem.* **10**, 377 (1990).
148. J. M. L'Hermite, G. Rahmat and R. Vetter, *J. Chem. Phys.* **93**, 434 (1990).
149. R. J. Vetter, *Laser Chem.* **11**, 177 (1991).
150. J. M. L'Hermite, G. Rahmat and R. Vetter, *J. Chem. Phys.* **95**, 3347 (1991).
151. F. X. Gadéa, G. H. Jeung, M. Pélissier, J. P. Malrieu, J. L. Picqué, G. Rahmat, J. Vergès and R. Vetter, *Laser Chem.* **2**, 361 (1983).
152. F. X. Gadéa, F. Spiegelmann, M. Pélissier and J. P. Malrieu, *J. Chem. Phys.* **84**, 4872 (1986).
153. J. M. L'Hermite, *J. Chem. Phys.* **97**, 6215 (1992).
154. X. Huang, J. Zhao, G. Xing, X. Wang and R. Bersohn, *J. Chem. Phys.* **104**, 1338 (1996).
155. D.-K. Liu and K.-C. Lin, *J. Chem. Phys.* **105**, 9121 (1996).
156. D.-K. Liu and K.-C. Lin, *J. Chem. Phys.* **107**, 4244 (1997).
157. A. B. Jerre and E. E. Nikitin, *Chem. Phys. Lett.* **1**, 179 (1967).
158. E. Bauer, E. R. Fisher and F. R. Gilmore, *J. Chem. Phys.* **51**, 4173 (1969).
159. E. A. Gislason and J. G. Sachs, *J. Chem. Phys.* **62**, 2678 (1975).
160. I. V. Hertel, *Adv. Chem. Phys.* **45**, 341 (1981).
161. I. V. Hertel, *Adv. Chem. Phys.* **50**, 475 (1982).
162. P. Casavecchia, R. J. Buss, S. J. Sibener and Y. T. Lee, *J. Chem. Phys.* **73**, 6351 (1980).
163. S. E. Choi and R. B. Bernstein, *J. Chem. Phys.* **83**, 4463 (1985).
164. P. S. Weiss, H. Schmidt, M. H. Covinsky, Y. T. Lee and J. M. Mestdagh, *J. Phys. Chem.* **95**, 3005 (1991).
165. J.-M. Mestdagh, B. A. Balko, M. H. Covinsky, P. S. Weiss, M. F. Vernon, H. Schmidt and Y. T. Lee, *Faraday Discuss. Chem. Soc.* **84**, 145 (1987).
166. M. F. Vernon, P. S. Schmidt, H. and Weiss, M. H. Covinsky and Y. T. Lee, *J. Chem. Phys.* **84**, 5580 (1986).
167. P. S. Weiss, J.-M. Mestdagh, M. H. Covinsky, B. A. Balko and Y. T. Lee, *Chem. Phys.* **126**, 93 (1988).
168. H. Schmidt, P. S. Weiss, J.-M. Mestdagh and Y. T. Covinsky, M. H. and Lee, *Chem. Phys. Lett.* **118**, 539 (1985).

169. J.-M. Mestdagh, D. Paillard and J. Berlande, *J. Chem. Phys.* **88**, 2398 (1988).
170. D. Paillard and J.-M. Mestdagh, *J. Chem. Phys.* **91**, 6866 (1989).
171. C. Alcaraz, J.-M. Mestdagh, P. Meynadier, P. de Pujo, J.-P. Visticot, A. Binet and J. Cuvellier, *Chem. Phys. Lett.* **156**, 191 (1989).
172. P. de Pujo, O. Sublemontier, J. P. Visticot, J. Berlande, J. Cuvellier, C. Alcaraz, T. Gustavsson, J. M. Mestdagh and P. Meynadier, *J. Chem. Phys.* **99**, 2533 (1993).
173. M. D. Oberlander and J. M. Parson, *J. Chem. Phys.* **105**, 5806 (1996).
174. H. J. Yuh and P. J. Dagdigian, *J. Chem. Phys.* **81**, 2375 (1984).
175. P. J. Dagdigian, Spin-Orbit Effects in Chemiluminescent Reactions of State-selected Calcium (3PJ0), in *Gas-Phase Chemiluminescence and Chemi-Ionization*, edited by A. Fontijn, pp. 203–219, Elsevier, Amsterdam, 1985.
176. N. Furio, M. L. Campbell and P. J. Dagdigian, *J. Chem. Phys.* **84**, 4332 (1986).
177. M. L. Campbell and P. J. Dagdigian, *J. Am. Chem. Soc.* **108**, 4701 (1986).
178. M. L. Campbell, N. Furio and P. J. Dagdigian, *Laser Chem.* **6**, 391 (1986).
179. M. L. Campbell and P. J. Dagdigian, *Faraday Discuss. Chem. Soc.* **84**, 127 (1987).
180. P. J. Dagdigian and M. L. Campbell, *Chem. Rev.* **87**, 1 (1987).
181. P. J. Dagdigian, *NATO ASI Ser., Ser. C* **245**, 147 (1988).
182. R. de Castro Vitores, M. Candori, F. Pirani, V. Aquilanti, M. Menendez, M. Garay and A. Gonzalez Ureña, *J. Phys. Chem.* **100**, 7997 (1996).
183. J. M. Garay, M. Orea and A. Gonzalez Ureña, *Chem. Phys.* **207**, 451 (1996).
184. J. M. Orea, A. Laplaza, C. A. Rinaldi, G. Tardajos and A. Gonzalez Ureña, *Chem. Phys.* **220**, 337 (1997).
185. M. Garay, C. A. Rinaldi, J. M. Orea and A. Gonzalez Ureña, *Chem. Phys.* **236**, 343 (1998).
186. M. Garay Garay Salazar, J. M. Orea Rocha, A. Gonzalez Ureña and G. Roberts, *Mol. Phys.* **97**, 967 (1999).
187. R. De Castro, M. Candori, F. Pirani, V. Aquilanti, M. Garay and A. Gonzalez Ureña, *J. Chem. Phys.* **112**, 770 (2000).
188. F. Beitia, F. Castano, M. N. Sanchez Rayo, S. Carl, D. Husain and L. Santos, *Z. Phys. Chem.* **171**, 137 (1991).
189. J. Geng, D. Husain, J. Lei, F. Castano and M. N. Sanchez Rayo, *An. Quim., Int. Ed.* **94**, 279 (1998).
190. D. Husain, J. Geng and J. Lei, *Combust. Flame* **113**, 566 (1998).
191. P. Kierzkowski, B. Pranszke and A. Kowalski, *Chem. Phys. Lett.* **254**, 391 (1996).
192. B. Pranszke, P. Kierzkowski and A. Kowalski, *Chem. Phys. Lett.* **309**, 183 (1999).
193. B. Pranszke, P. Kierzkowski and A. Kowalski, *Z. Naturforsch., Teil A* **54**, 191 (1999).
194. H. Liu, J. Li, L. Peng, F. Li, R. Lu, G. He and N. Lou, *Wuli Huaxue Xuebao* **6**, 437 (1990).
195. J. P. Zhan, H. P. Yang, W. Q. Deng, G. Z. He and N. Q. Lou, *J. Phys. Chem. A* **101**, 7486 (1997).
196. G. Ding, W. Sun, W. Yang, D. Xu, G. He and N. Lou, *Mol. Phys.* **96**, 1349 (1999).
197. A. Kowalski and M. Menzinger, *J. Phys. Chem.* **94**, 1899 (1990).
198. A. Kowalski and M. Menzinger, *Int. J. Mass Spectrom. Ion Processes* **135**, 63 (1994).
199. J. M. Teule, M. H. M. Janssen, J. Bulthuis and S. Stolte, *J. Chem. Phys.* **110**, 10792 (1999).
200. J. M. Teule, J. Mes, J. Bulthuis, M. H. M. Janssen and S. Stolte, *J. Phys. Chem. A* **102**, 9482 (1998).
201. M. R. Levy, *J. Phys. Chem.* **95**, 8500 (1991).
202. M. R. Levy, *J. Phys. Chem.* **95**, 8491 (1991).
203. D. L. Herbertson, D. A. Newnham and M. R. Levy, *Can. J. Chem.* **72**, 850 (1994).
204. D. A. Newnham and M. R. Levy, *J. Phys. Chem.* **100**, 2799 (1996).
205. D. L. Herbertson and M. R. Levy, *J. Phys. Chem.* **100**, 2809 (1996).
206. D. L. Herbertson and M. R. Levy, *J. Phys. Chem.* **100**, 14584 (1996).
207. M. A. Spence and M. R. Levy, *J. Phys. Chem. A* **101**, 7490 (1997).
208. J. M. Parson and C. C. Fang, *J. Chem. Phys.* **92**, 4823 (1990).
209. C. C. Fang and J. M. Parson, *J. Chem. Phys.* **95**, 6413 (1991).
210. P. Baltayan, F. Hartmann, I. Hikmet, J. C. Pebay-Peyroula and N. Sadeghi, *Chem. Phys. Lett.* **160**, 549 (1989).
211. P. Baltayan, F. Hartmann and N. Hikmet, I. and Sadeghi, *J. Chem. Phys.* **97**, 5417 (1992).

212. I. Hikmet, P. Kowalczyk and N. Sadeghi, *Chem. Phys. Lett.* **188**, 287 (1992).
213. P. Kowalczyk, I. Hikmet and N. Sadeghi, *Chem. Phys.* **160**, 73 (1992).
214. N. Sadeghi, I. Hikmet, I. Colomb and D. W. Setser, State-to-State Dynamics for the Reactions of Metastable Copper Atoms with Fluorine, Chlorine and Bromine, in *Gas-Phase Metal Reactions*, edited by A. Fontijn, pp. 363–392, North-Holland, Amsterdam, 1992.
215. M. Shapiro and P. Brumer, *Adv. At. Mol. Opt. Phys.* **42**, 287 (2000).
216. D. A. Case and D. R. Herschbach, *Mol. Phys.* **30**, 1537 (1975).
217. D. A. Case and D. R. Herschbach, *J. Chem. Phys.* **64**, 4212 (1976).
218. D. A. Case and D. R. Herschbach, *J. Chem. Phys.* **69**, 150 (1978).
219. G. M. McClelland and D. R. Herschbach, *J. Phys. Chem.* **83**, 1445 (1979).
220. D. M. Lindsay, M. C. R. Symons, D. R. Herschbach and A. L. Kwiram, *J. Phys. Chem.* **86**, 3789 (1982).
221. P. R. Brooks, *Science* **193**, 11 (1976).
222. D. H. Parker and R. B. Bernstein, *Annu. Rev. Phys. Chem.* **40**, 561 (1989).
223. S. Stolte, Scattering Experiments with State Selector, in *Atomic and Molecular Beam Methods*, edited by G. Scoles, Part 1.25, pp. 631–652, Oxford University Press, Oxford, 1988.
224. C. T. Rettner and R. N. Zare, *J. Chem. Phys.* **75**, 3636 (1981).
225. C. T. Rettner and R. N. Zare, *J. Chem. Phys.* **77**, 2416 (1982).
226. M. Brouard and J. P. Simons, The Stereodynamics of Photon Initiated Bimolecular Reactions, in *The Chemical Dynamics and Kinetics of Small Radicals*, edited by K. Liu and A. Wagner, Part 2.18, pp. 795–841, World Scientific, Singapore, 1995.
227. P. R. Brooks, *Int. Rev. Phys. Chem.* **14**, 327 (1995).
228. S. A. Harris, S. D. Wiediger and P. R. Brooks, *J. Phys. Chem. A* **103**, 10035 (1999).
229. S. A. Harris, P. W. Harland and P. R. Brooks, *Phys. Chem. Chem. Phys.* **2**, 787 (2000).
230. P. S. Weiss, M. H. Covinsky, H. Schmidt, B. A. Balko, Y. T. Lee and J.-M. Mestdagh, *Z. Phys. D* **10**, 227 (1988).
231. I. V. Hertel, H. Schmidt, A. Baehring and E. Meyer, *Rep. Prog. Phys.* **48**, 375 (1985).
232. M. Ben-Nun, T. J. Martinez and R. D. Levine, *J. Phys. Chem. A* **101**, 7522 (1997).
233. M. Garay, M. Menendez, E. Verdasco, J. Castano and A. Gonzalez Ureña, *J. Phys. Chem.* **97**, 5836 (1993).
234. M. Garay, E. Esteban, M. Verdasco and A. Gonzalez Ureña, *Chem. Phys.* **195**, 235 (1995).
235. J. Qin and D. W. Setser, *Chem. Phys. Lett.* **184**, 121 (1991).
236. J. Qin, T. O. Nelson and D. W. Setser, *J. Phys. Chem.* **95**, 5374 (1991).
237. F. Huang, D. W. Setser and B. S. Cheong, *Isr. J. Chem.* **34**, 127 (1994).
238. P. Backhaus, B. Schmidt and M. Dantus, *Chem. Phys. Lett.* **306**, 18 (1999).
239. A. Weaver, R. B. Metz, S. E. Bradforth and D. M. Neumark, *J. Phys. Chem.* **92**, 5558 (1988).
240. I. M. Waller, T. N. Kitsopoulos and D. M. Neumark, *J. Phys. Chem.* **94**, 2240 (1990).
241. S. E. Bradforth, A. Weaver, D. W. Arnold, R. B. Metz and D. M. Neumark, *J. Chem. Phys.* **92**, 7205 (1990).
242. R. B. Metz, S. E. Bradforth and D. M. Neumark, *Adv. Chem. Phys.* **81**, 1 (1992).
243. A. Keller, R. Lawruszczuk, B. Soep and J. P. Visticot, *J. Chem. Phys.* **105**, 4556 (1996).
244. A. Keller, J. P. Visticot, S. Tsuchiya, T. S. Zwier, M. C. Duval, C. Jouvet, B. Soep and C. Whitham, *NATO ASI Ser.* **227**, 103 (1990).
245. B. Soep, S. Abbès, A. Keller and J. P. Visticot, *J. Chem. Phys.* **96**, 440 (1992).
246. R. Lawruszczuk, M. Elhanine and B. Soep, *J. Chem. Phys.* **108**, 8374 (1998).
247. M. Menendez, M. Garay, E. Verdasco and A. Gonzalez Ureña, *J. Chem. Soc., Faraday Trans.* **89**, 1493 (1993).
248. M. L. Dubernet and J. M. Hutson, *J. Chem. Phys.* **101**, 1939 (1994).
249. B. Soep, C. Whitham, A. Keller and J. P. Visticot, *J. Chem. Soc., Faraday Trans.* **91**, 191 (1991).
250. M. De Castro Vittores, M. R. Candori, F. Pirani, V. Aquilanti, M. Menendez, M. Garay and A. Gonzalez Ureña, *J. Phys. Chem.* **100**, 7997 (1996).
251. M. De Castro Vittores, M. R. Candori, F. Pirani, V. Aquilanti, M. Garay and A. Gonzalez Ureña, *J. Phys. Chem.* **10**, 9537 (1998).
252. M. De Castro Vittores, M. R. Candori, F. Pirani, V. Aquilanti, M. Garay and A. Gonzalez Ureña, *J. Chem. Phys.* **112**, 770 (2000).

253. M. De Castro Vittores, M. R. Candori, F. Pirani, V. Aquilanti, M. Garay and A. Gonzalez Ureña, *Chem. Phys. Lett.* **263**, 456 (1996).
254. C. P. Schulz, C. Bobbert and B. Soep, *J. Chem. Phys.* unpublished.
255. K. Liu, J.C. Polanyi and S. Yang, *J. Chem. Phys.* **98**, 5431 (1993).
256. J.C. Polanyi and J.-X. Wang, *J. Phys. Chem.* **99**, 13691 (1995).
257. U. Buck, *NATO ASI Ser.* **B227** (1990).
258. Y. Zeiri, G. Katz, R. Kosloff, M.S. Topaler, D.G. Truhlar and J.C. Polanyi, *Chem. Phys. Lett.* **300**, 523 (1999).
259. S. Skowronek, J. B. Jimenez and A. Gonzalez Ureña, *Chem. Phys. Lett.* **303**, 275 (1999).
260. S. Skowronek, J. B. Jimenez and A. Gonzalez Ureña, *J. Chem. Phys.* **111**, 460 (1999).
261. P. Farmanara, V. Stert, W. Radloff, S. Skowronek and A. Gonzalez Ureña, *Chem. Phys. Lett.* **304**, 127 (1999).
262. R. S. Mulliken, *J. Am. Chem. Soc.* **72**, 610 (1950).
263. P. Y. Cheng, D. Zhong and A. H. Zewail, *Chem. Phys. Lett.* **242**, 369 (1995).
264. P. Y. Cheng, D. Zhong and A. H. Zewail, *J. Chem. Phys.* **103**, 5153 (1995).
265. E. Lenderink, K. Duppen and D. W. Wiersma, *Chem. Phys. Lett.* **211**, 503 (1993).
266. K. J. Klabunde, *Chemistry of Free Atoms and Particles*, Academic Press, New York, 1980.
267. D. W. Ruschel, G. K. and Ball, *High Temp. Mater. Sci.* **37**, 63 (1997).
268. J. Chiarelli and D. W. Ball, *J. Phys. Chem.* **98**, 12828 (1995).
269. J. C. Polanyi and W. H. Wong, *J. Chem. Phys.* **51**, 1439 (1969).
270. A. C. Legon, *J. Chem. Soc., Faraday Trans.* **91**, 1881 (1995).
271. K. W. Jucks and R. E. Miller, *J. Chem. Phys.* **87**, 5629 (1987).
272. A. C. Legon, *Chem. Soc. Rev.* **19**, 197 (1990).
273. C. H. Townes and B. P. Dailey, *J. Chem. Phys.* **17**, 782 (1949).
274. H. I. Bloemink, C. M. Evans, J. H. Holloway and A. C. Legon, *Chem. Phys. Lett.* **248**, 260 (1996).
275. G. Grégoire, M. Mons, C. Dedonder-Lardeux and C. Jouvet, *Eur. Phys. J. D* **1**, 187 (1998).
276. J. A. Syage, *J. Phys. Chem.* **99**, 5772 (1995).
277. L. Lehr, M. T. Zanni, C. Frischkorn, R. Weinkauff and D. M. Neumark, *Science* **284**, 635 (1999).
278. C. P. Schulz, A. Gerber, C. Nitsch and I.V. Hertel, *Z. Phys. D* **20**, 65 (1991).
279. G. H. Lee, S. T. Arnold, J. G. Eaton, H. W. Sarkas, K. H. Bowen, C. Ludewigt and H. Haberland, *Z. Phys. D* **20**, 9 (1991).
280. T. Takasu, K. Hashimoto and K. Fuke, *Chem. Phys. Lett.* **258**, 94 (1996).
281. J. M. Mestdagh, M. A. Gaveau, C. Gée, O. Sublemontier and J. P. Visticot, *Int. Rev. Phys. Chem.* **16**, 215 (1997).
282. A. I. Krylov, R. B. Gerber, M. A. Gaveau, J. M. Mestdagh, B. Schilling and J. P. Visticot, *J. Chem. Phys.* **104**, 3651 (1996).
283. C. Gée, M. A. Gaveau, J. M. Mestdagh, M. A. Osborne, O. Sublemontier and J. P. Visticot, *J. Phys. Chem.* **100**, 13421 (1996).
284. M. Osborne, M. A. Gaveau, C. Gée, O. Sublemontier, J. M. Mestdagh and J. P. Visticot, *J. Chem. Phys.* **106**, 1449 (1997).
285. C. Gée, M. A. Gaveau, O. Sublemontier, J. M. Mestdagh and J. P. Visticot, *J. Chem. Phys.* **107**, 4194 (1997).
286. M. A. Gaveau, C. Gée, J. M. Mestdagh and J. P. Visticot, *Comments At. Mol. Phys.* **34**, 241 (1999).
287. M. A. Briant, M. Gaveau, J. M. Mestdagh and J. P. Visticot, *J. Chem. Phys.* **112**, 1744 (2000).
288. J. P. Toennies, Personal communication, 2000.
289. L. Moussavizadeh, K. von Haeften, L. Museur, A. V. Kanaev, M. C. Castex, R. von Pietrowski and T. Moller, *Chem. Phys. Lett.* **305**, 327 (1999).
290. L. Museur, A. V. Kanaev, M. C. Castex, L. Moussavizadeh, R. von Pietrowski and T. Möller, *Eur. Phys. J. D* **7**, 73 (1999).
291. T. E. Gough, M. Mengel, P. A. Rowntree and G. Scoles, *J. Chem. Phys.* **83**, 4958 (1985).
292. A. R. Allouche, M. Aubert-Frécon, G. Nicolas and F. Spiegelmann, *Chem. Phys.* **200**, 63 (1995).
293. X. Biquard, O. Sublemontier, J. Berlande, M. A. Gaveau, J. M. Mestdagh and J. P. Visticot, *J. Chem. Phys.* **103**, 957 (1995).

- 294. A. Lallement, J. Cuvellier, J. M. Mestdagh, P. Meynadier, P. de Pujo, O. Sublemontier, J. P. Visticot, J. Berlande and X. Biquard, *Chem. Phys. Lett.* **189**, 182 (1992).
- 295. A. Lallement, J. M. Mestdagh, P. Meynadier, P. de Pujo, O. Sublemontier, J. P. Visticot, J. Berlande, X. Biquard, J. Cuvellier and C. G. Hickman, *J. Chem. Phys.* **99**, 8705 (1993).
- 296. M. A. Gaveau, B. Schilling, C. Gée, O. Sublemontier, J. P. Visticot, J. M. Mestdagh and J. Berlande, *Chem. Phys. Lett.* **246**, 307 (1995).
- 297. J.P. Visticot, M.A. Gaveau, P. Eulry, M. Lengaigne, J.M. Mestdagh and C. Gée, *Faraday Discuss.* **108**, 401 (1997).
- 298. M.-A. Gaveau, M. Briant, P.-R. Fournier, J.-M. Mestdagh and J.-P. Visticot, *Phys. Chem. Chem. Phys.* **2**, 000 (2000).
- 299. M. W. Chase, J. L. Curnutt, R. A. McDonald and A. N. Syverud, *J. Phys. Chem. Ref. Data* **7**, 793 (1978).
- 300. K. K. Irikura, *J. Chem. Phys.* **102**, 5357 (1995).
- 301. R. R. Herm, S. M. Lin and C. A. Mims, *J. Phys. Chem.* **77**, 2931 (1973).
- 302. V. Boutou, A. R. Allouche, F. Spiegelmann, J. Chevaletyre and M. Aubert Frécon, *Eur. Phys. J. D* **2**, 63 (1998).
- 303. N. Adams, W.H. Breckenridge and J. Simons, *Chem. Phys.* **56**, 327 (1981).
- 304. K. Hashimoto and K. Morokuma, *J. Am. Chem. Soc.* **117**, 4151 (1995).
- 305. V. S. Batista, M. T. B. Zanni, J. Greenblatt, D. M. Neumark and W. H. Miller, *J. Chem. Phys.* **110**, 3736 (1999).
- 306. C. Desfrancois, H. Abdoul-Carime, N. Khelifa and J. P. Schermann, *J. Chim. Phys.* **92**, 409 (1995).

3 TICT Molecules

Jerzy Herbich and Bernhard Brutschy

3.1 Photoinduced Electron Transfer in Donor–Acceptor (D–A) Molecules in Solutions

3.1.1 Introduction

Excited-state electron transfer (ET) is a fundamental complex phenomenon playing a crucial role in a variety of photophysical, photochemical and biochemical reactions (for reviews see, for example, Refs. [1–3]). Owing to the essential role of ET in many processes and in photochemical applications (e.g., solar energy conversion and storage [4–6], photocatalysis [7], photopolymerization [8], information processing and storage [9] and photomedicine [10]) the understanding of the factors which determine the thermodynamics, kinetics and dynamics of the ET processes is very important.

Most investigations of photoinduced ET are performed in solutions. In this work the discussion of the excited-state ET is restricted to bichromophoric molecules where the donor (D) and acceptor (A) are formally linked by a single bond. In recent years, a large number and variety of D–A compounds have been characterized. These molecules can be classified into different families with respect to the angular relaxation of the D and A moieties. A class of these, which shows solvent-dependent characteristic dual fluorescence [11], is thought to form, upon excitation, a twisted intramolecular charge-transfer (TICT) state with an orbitally decoupled perpendicular geometry (the model was proposed by Grabowski and co-workers [12, 13]; see Sections 3.1.2 and 3.1.4). On the other hand, in larger D–A π -systems (which reveal non-negligible π – π interaction strongly depending on the torsional angle Θ_{A-D} between the planes of the A and D subunits) excited-state electron transfer can lead to a more planar mutual conformation [14] (see Section 3.1.3). Various processes which can occur upon excitation are summarized in Figure 1. Important issues related to the photophysics of such D–A systems are (i) the relative energy and interactions between the primary excited and charge-transfer singlet and triplet states ($^1,^3CT$), (ii) the electronic structure and conformation of the D–A molecules

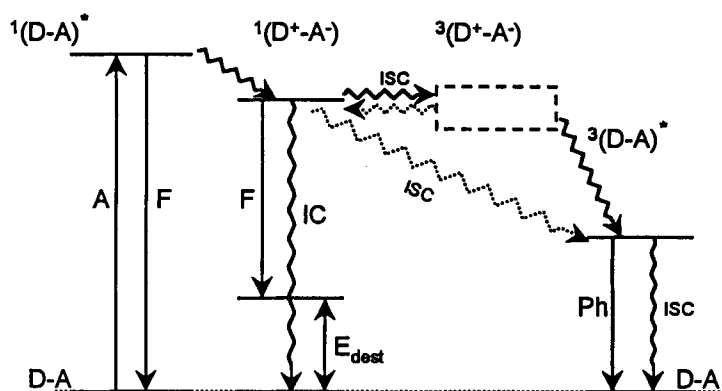


Figure 1. Jablonski-type diagram of the lowest energy levels of electron donor–acceptor molecules formally linked by a single bond which show dual fluorescence phenomenon. D–A, $^1(D-A)^*$, $^1(D^+-A^-)$, $^3(D^+-A^-)$ and $^3(D-A)^*$ denote the ground state, the primary excited and charge-transfer (CT) singlet states, and CT and locally excited triplet states, respectively. The arrows correspond to the radiative (absorption, A, fluorescence, F, and phosphorescence, Ph) and the radiationless (internal conversion, IC, and intersystem crossing, ISC) processes.

in these states and (iii) the intramolecular and environmental factors controlling the kinetics and dynamics of the passage of electrons.

3.1.2 Solvent-dependent Dual Luminescence

A class of the electron D–A molecules shows a dual luminescence phenomenon [11]. The best known examples are *p*-cyano-*N,N*-dimethylaniline (CDMA) and its derivatives [11–13, 15–20], 4-dialkylamino derivatives of benzaldehyde and acetophenone [21, 22] and dialkylaminobenzoic acid esters [16, 23, 24] (Figure 2). The fluorescence originates from two different excited states (Figure 3). In nonpolar solvents and rigid low-temperatures glasses or for model systems constrained such that the electron-donating (dialkylamino) group lies in the plane of the aromatic acceptor ring, only a short-wave emission **b** is observed. An additional low-energy fluorescence band **a** is observed for the flexible molecules which have an internal degree of freedom for internal D–A rotation (e.g., CDMA) in a sufficiently polar and mobile environment or for compounds with a fixed, highly twisted conformation (e.g., TMCA) [12, 15].

The nature of this dual fluorescence phenomenon has been the subject of intense interest. The currently most widely accepted explanation assumes that dielectric polarization of the solvent permits excited-state rotational isomerization, leading to a highly polar fluorescent TICT state with a conformation of the D^+ and A^- moieties close to perpendicular [12, 13, 15–24]. This model predicts that the π -electronic decoupling of the D^+ and A^- subunits leads to full charge separation and, consequently, to a large dipole moment and a considerable solvent reorientational en-

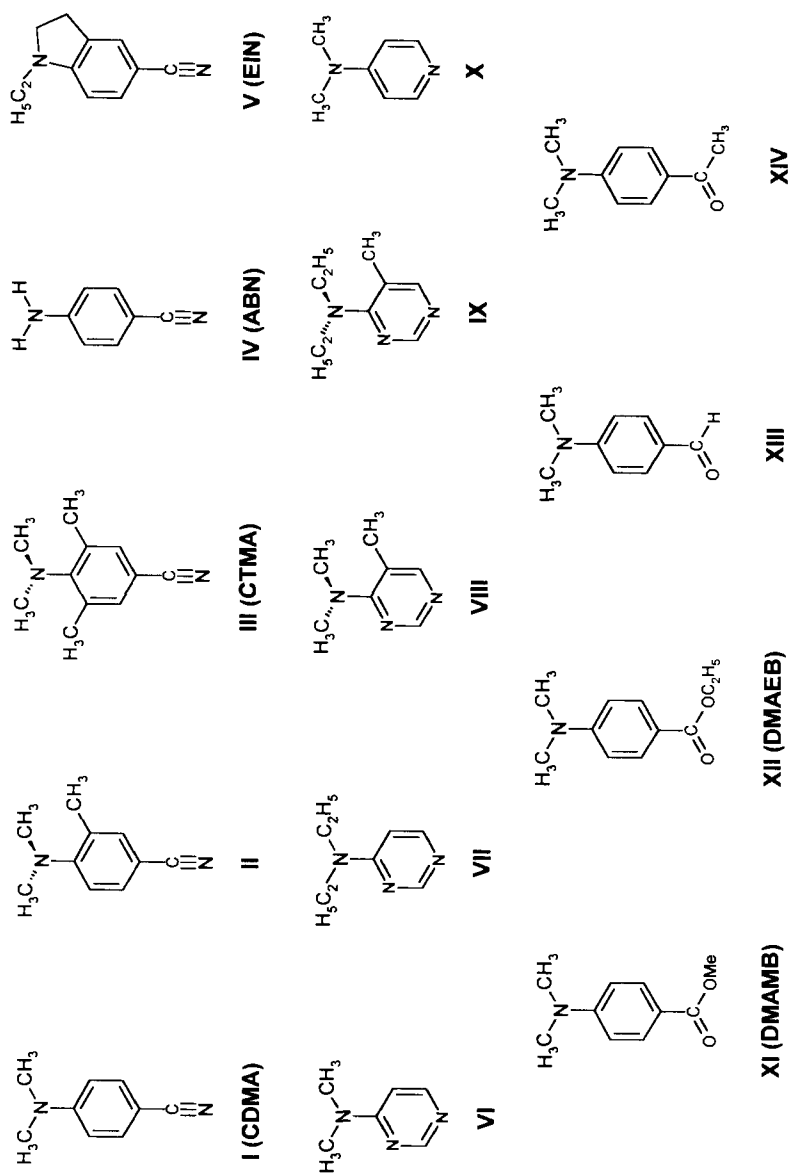


Figure 2. Formulas of selected D–A compounds which contain 4-dialkylamino group as an electron donor and reveal dual fluorescence behaviour. Top: *p*-cyano-*N,N*-dimethylaniline (**I**, CDMA) and its model derivatives: *p*-cyano-2,6,*N,N*-trimethylaniline (**II**), *p*-cyano-2,6,*N,N*-tetramethylaniline (**III**, CTMA), *p*-aminobenzonitrile (**IV**, ABN) and 1-ethyl-2,3-dihydro-indole-5-carbonitrile (**V**, EIN). Middle: 4-(dimethylamino)pyrimidine (**VI**), 4-(diethylamino)pyrimidine (**VII**), 4-(dimethylamino)-5-methylpyrimidine (**VIII**), 4-(diethylamino)-5-methylpyrimidine (**IX**) and 4-(dimethylamino)-pyridine (**X**). Bottom: methyl 4-(dimethylamino)benzoate (**XI**, DMAMB), ethyl 4-(dimethylamino)benzoate (**XII**, DMAEB), *p*-(dimethylamino)-benzaldehyde (**XIII**) and *p*-(dimethylamino)acetophenone (**XIV**).

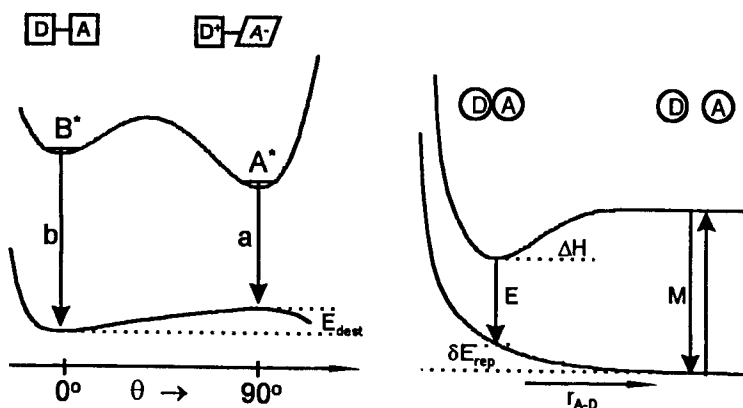


Figure 3. Schematic cross-section of the ground-state and the lowest excited singlet-state potential hypersurfaces along the reaction coordinate corresponding to the TICT state model (left, the reaction coordinate represented by the D–A twist angle) and exciplex model (right, the reaction coordinate represents the distance between reaction partners). The TICT state model proposes that dual fluorescence (**b** and **a**) is due to emission from the substrate (primary excited state B*) and product (A* \equiv TICT state) of the intramolecular excited state electron transfer (cf. Ref. [12]). E_{dest} is the energy difference between the Franck–Condon ground state and the solvent-equilibrated ground state. The term exciplex denotes a collision complex between the electronically excited species with any polar (or polarizable) ground-state molecule (cf. Refs. [28b, 29]). Donor and acceptor properties may be attributed to the reaction partners, since most exciplexes are stabilized by charge transfer interactions (ΔH denotes a stabilization enthalpy). Dual fluorescence, **M** and **E**, corresponds to the excited monomeric and exciplex species, respectively. The ground-state collision complexes are unstable (the Franck–Condon ground state is destabilized with respect to an equilibrated pair of molecules in the ground state by the repulsion energy δE_{rep}).

ergy. Dual luminescence is due to emission from the substrate (the primary excited B* state of low polarity; the conformation of the D–A molecule in this state is similar to that in the ground state [25]) and the product (A* \equiv TICT state) of the excited state intramolecular ET (Figure 3). The CT fluorescence carries a low electronic transition dipole moment, M_{flu} . This model has been adopted to explain the photophysical properties of the compounds related to the nucleic acid bases, such as 4-(dialkylamino)pyrimidines [26] and N^6,N^6 -dimethyladenosine [27].

An alternative intermolecular mechanism proposed by Chandross [30] and developed by Varma and co-workers [31] assumes that the long-wave emission *E* originates from solute–solvent exciplexes of CDMA (Figure 3). The binding between the polar nonaromatic solvent molecule and CDMA in the exciplex has been suggested to arise from local interactions with the solvent restricted to a single site in the solute (it has been proposed [31b] that the binding is due to an overlap between the lone pair orbitals on the solvent and the lone pair orbital on the amino nitrogen atom of the electronically excited CDMA). In aromatic solvents (e.g., benzene and toluene) a sandwich-like configuration of the 1:1 and 1:2 CDMA–solvent exciplexes has been proposed [31j]. Wang and Eisenthal [18b] attributed the

long-wave emission of CDMA in mixed solvents containing *n*-butanol to a complex between excited CDMA and an alcohol molecule. They postulated that in alcohol solutions the dominant stabilization of the fluorescent ^1CT state is due to a short-range specific interaction and a further stabilization of the complex occurs by a long-range polarization interactions with polar molecules. In view of the principal role of the solvent, a localized 1:1 solvation must be taken into account, at least in mixed solvents.

Still another explanation has been given by Zachariasse and co-workers [32]. According to this hypothesis, the CT fluorescence arises from vibronic coupling between closely spaced S_1 and S_2 (or S_3) states leading to a solvent-induced ‘pseudo–Jahn-Teller interaction’. In other words, a distortion of the molecule lowers its symmetry, permitting electronic coupling between the lowest excited singlet state, S_1 , and a higher one, S_i ($i = 2$ or 3), which has a large dipole moment. A solvent of high polarity would stabilize the dipolar component of the emissive state, hence increasing the mixing of the S_1 and S_i states. The reaction coordinate involves rehybridization of the amino nitrogen group from sp^3 to sp^2 and a deformation of the phenyl ring similar to that corresponding to radical anion formation of benzene.

It seems, in view of the experimental results, that the excited-state geometric rearrangement accompanying ET in the D–A amino compounds is complex and involves the twisting of the D and A moieties and the pyramidalization at the amino nitrogen; both effects have to be considered simultaneously. The systems which show dual fluorescence are very good models for theoretical studies trying to establish the links between structure and reactivity. The significance of the dimethyl-amino group torsion for ET in CDMA has so far not been proved; in fact, recent *ab initio* [33a–e] and semiempirical [15h, 26c, 33f–h] calculations of various quality confirm the TICT state model (the rehybridization coordinate seems to be less important). It has also been proposed [33i] that the distortion that lowers energy of the ^1CT state in this molecule is a bending of the $\text{C}=\text{C}\equiv\text{N}$ bond with respect to the ring and rehybridization of the cyano carbon atom from sp to sp^2 (RICT model). Such a bending would cause a stabilization of an intramolecular ^1CT state which is formed by transferring an electron from an aromatic π -orbital to the quasi- π^* -orbital of the cyano group. In recent and refined *ab initio* calculations by Sobolewski et al. [33e], however, the plausibility of the RICT model was not confirmed.

3.1.3 Electronic and Molecular Structure of Large D–A π -Systems

During the last three decades, ample experimental evidence has been accumulated which confirms that the photoinduced intramolecular electron transfer plays a key role in the photophysics of large D–A π -systems such as 9,9'-bianthryl (BA) [34–39], other biaryls [34d, 40] and their substituted analogues [41], aryl and heteroaryl derivatives of aromatic amines [42–50] and *N*-arylcarbazoles [51]. There is an important difference between the luminescence properties of the latter molecules and the former molecules containing 4-dialkylamino group as an electron donor (cf., Figure 2): the large D–A π -systems show single strongly allowed CT fluorescence at room temperature. Three of the most intriguing aspects of the photophysics of these

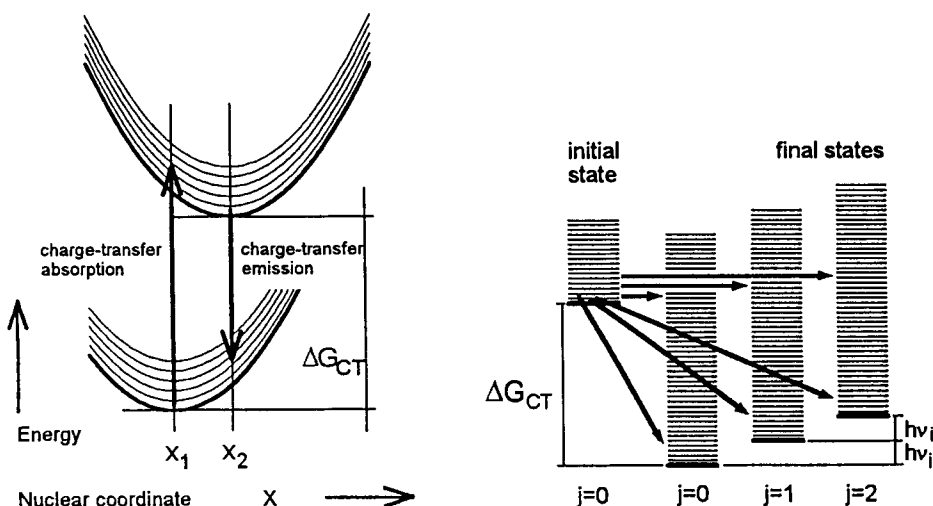


Figure 4. Left, radiative transitions in the inverted Marcus region: CT absorption (arrow up) and CT emission (arrow down). Right, schematic illustration of the relationship between radiative (diagonal arrows) and nonradiative (horizontal arrows) charge recombination in the inverted Marcus region. A quasi-continuum of the sublevels representing the low-frequency motions (mainly solvent modes) is associated with each quantized vibronic state, j , related to the high-frequency motions represented by a single 'averaged' mode characterized by ν_i . Charge recombination occurs from the lowest vibrational level ($j = 0$) of the initial CT state to the various vibrational sublevels (with $j = 0, 1, 2, \dots$) of the ground state. Adapted from Refs. [54b, 135].

D–A molecules relate to (i) the mechanism of the radiative and nonradiative charge recombination $^1\text{CT} \rightarrow \text{S}_0$, (ii) the electronic structure and conformation of the molecules in the fluorescent ^1CT state and (iii) the role of the charge-transfer triplet states (^3CT) in the intramolecular energy and electron transfer.

It has been shown recently by Kapturkiewicz and co-workers [14] that the analysis of the CT absorption $^1\text{CT} \leftarrow \text{S}_0$ and the radiative and radiationless charge recombination processes $^1\text{CT} \rightarrow \text{S}_0$ (Figure 4) in selected D–A π – π interacting systems sterically hindered to coplanarity (such as 9-anthryl and 9-acridyl derivatives of aromatic amines [14a,b], carbazol-9-yl derivatives of aromatic nitriles [14c] and ketones [14d] and D–A derivatives of indoles [14e] or phenoxazines and phenothiazines [14f]) in terms of the theory of photoinduced ET processes in absorption [52, 53] and emission [53–55] and Mulliken and Murrell models of molecular CT complexes [56, 57] leads to the determination of the quantities relevant for the rate of the radiative ET processes (exemplified by the CT absorption and emission) and to the estimation of the electronic structure and molecular conformation of the states involved in the photoinduced ET. A similar approach can be applied to describe the properties of the fluorescent singlet ^1CT states and phosphorescent triplet ^3CT states [58]. It should be pointed out that the relatively large values of the electronic transition dipole moments M_{flu} of the CT fluorescence indicate a non-

orthogonal geometry of the D and A subunits in the lowest ^1CT states of these compounds.

The time-dependent perturbation theory of the rates of radiative ET is based on the Born–Oppenheimer approximation [59] and the Franck–Condon principle (i.e. on the separation of electronic and nuclear motions). The theory predicts that the ET rate constant, k_{ET} , is given by a ‘golden rule’-type equation, i.e., it is proportional to the product of the square of the donor–acceptor electronic coupling (V) and a Franck–Condon weighted density of states (FC):

$$k_{\text{ET}} = \frac{4\pi^2}{h} V^2 (FC) \quad (1)$$

A challenging problem for large organic solute–solvent systems is the accurate evaluation of the FC term. An analysis of the CT absorption (Eq. 2 [14a–c, 52, 53]) and emission spectra (Eq. 3 [14, 53–55]), within the semiclassical approach employing a single intramolecular quantized mode yields the reaction driving force (the Gibbs free energy of the CT process, ΔG_{CT} , Figure 4) and estimates the low-frequency (λ_o) and the high-frequency (λ_i) reorganization energies, and the average energy spacing ($h\nu_i$) of the effective quantized mode undergoing reorganisation upon electron transfer:

$$\frac{\varepsilon(\tilde{\nu}_a)}{n\tilde{\nu}_a} = \frac{8\pi^3}{3c \ln 10} M_{\text{abs}}^2 \sum_{j=0} \frac{e^{-S} S^j}{j!} \sqrt{\frac{1}{4\pi\lambda_o k_B T}} \exp \left[-\frac{(jh\nu_i + \lambda_o - hc\tilde{\nu}_a + \Delta G_{\text{CT}})^2}{4\lambda_o k_B T} \right] \quad (2)$$

$$\frac{I(\tilde{\nu}_f)}{n^3 \tilde{\nu}_f^3} = \frac{64\pi^4}{3h} M_{\text{flu}}^2 \sum_{j=0} \frac{e^{-S} S^j}{j!} \sqrt{\frac{1}{4\pi\lambda_o k_B T}} \exp \left[-\frac{(jh\nu_i + \lambda_o + hc\tilde{\nu}_f + \Delta G_{\text{CT}})^2}{4\lambda_o k_B T} \right] \quad (3)$$

where S is the electron–vibration coupling constant:

$$S = \lambda_i / h\nu_i \quad (4)$$

and where electronic transition dipole moments of the CT absorption (M_{abs}) and CT fluorescence (M_{flu}) may depend, in principle, on the wavenumber $\tilde{\nu}_a$ and $\tilde{\nu}_f$ of the absorption and emission, respectively. $\varepsilon(\tilde{\nu}_a)$ is the molar CT absorption coefficient for photons with energy $hc\tilde{\nu}_a$. $I(\tilde{\nu}_f)$ denotes the CT fluorescence intensity, i.e., the rate of the emission of photons with energy $hc\tilde{\nu}_f$ expressed in photons per molecule per unit time per unit spectral energy [integration of $I(\tilde{\nu}_f)$ over the whole range of $\tilde{\nu}_f$ leads to the radiative rate constant k_f]. n and T are the refractive index of the surrounding medium and temperature, respectively. k_B , h and c are the Boltzmann and Planck constants and the speed of light, respectively. The reorganization energy λ_o is related to the low-frequency motions such as reorientation of the solvent shell (λ_s) as well as any other low-frequency ($\tilde{\nu}_L < 200 \text{ cm}^{-1}$) and

medium-frequency ($\tilde{\nu}_M \approx 300\text{--}600\text{ cm}^{-1}$ [14c, 55]) nuclear motions of the solute ($\delta\lambda_o$). The inner reorganisation energy λ_i corresponds to the high-frequency motions (represented by a single 'averaged' mode ν_i) associated with the changes in the solute bond lengths and angles.

The electronic coupling elements between the lowest excited ^1CT state and the ground state (V_0) or the locally excited state lying most closely in energy (V_1) can be estimated from the CT absorption and fluorescence investigations [14, 54, 57]. Applying a simple kinetic model of an irreversible excited CT state formation (with 100 % efficiency) the radiationless (k_{nr}) and radiative (k_{r}) rate constants can be determined from the CT fluorescence quantum yields Φ_{f} and lifetimes τ :

$$k_{\text{nr}} = (1 - \Phi_{\text{f}})/\tau \quad (5)$$

$$k_{\text{r}} = \Phi_{\text{f}}/\tau \quad (6)$$

and the resulting electronic transition dipole moments M_{flu} are given by [60]

$$k_{\text{r}} = \frac{64\pi^4}{3h} (n\tilde{\nu}_{\text{flu}}^{\text{CT}})^3 |M_{\text{flu}}|^2 \quad (7)$$

The electronic transition dipole moments M_{abs} corresponding to the CT absorption can be determined from an approximate expression [60]

$$|M_{\text{abs}}|^2 = \frac{3 \ln 10}{8\pi^3 N_{\text{A}}} \frac{hc}{n\tilde{\nu}_{\text{abs}}^{\text{CT}}} \int_{\text{band}} \varepsilon(\tilde{\nu}_{\text{a}}) d\tilde{\nu}_{\text{a}} \quad (8)$$

where $\tilde{\nu}_{\text{abs}}^{\text{CT}}$ is the wavenumber of the CT absorption maximum and N_{A} is Avogadro's number.

The comparison of the M_{flu} values with those of M_{abs} allows one to obtain information about the changes in the electronic structure and molecular conformation between the Franck–Condon excited state initially reached upon excitation and the solvent-equilibrated fluorescent state [14]. Electronic transition dipole moments are mainly determined by the direct interactions between the lowest ^1CT state and the ground state (S_0), and by the contributions from the locally excited configurations [14, 54, 56, 57]. For example, for the fluorescent ^1CT state one can obtain

$$M_{\text{flu}} \approx \frac{V_{0\text{F}}(\vec{\mu}_{\text{e}} - \vec{\mu}_{\text{g}})}{hc\tilde{\nu}_{\text{flu}}^{\text{CT}}} + \sum_i \frac{V_{i\text{F}}\vec{M}_i}{E_i - hc\tilde{\nu}_{\text{flu}}^{\text{CT}}} \quad (9)$$

where $hc\tilde{\nu}_{\text{flu}}^{\text{CT}}$ is the energy of the solvent-equilibrated CT fluorescence maxima, $\vec{\mu}_{\text{g}}$ and $\vec{\mu}_{\text{e}}$ are the dipole moments of the D–A molecule in the ground and excited state, respectively, and $V_{0\text{F}}$ and $V_{i\text{F}}$ denote the electronic coupling elements between the fluorescent ^1CT state and the ground state or the locally excited (^1LE)_{*i*} states, respectively. The first term in Eq. 9 is related to the Mulliken two-state model [56a] (i.e., the direct interactions between the fluorescent ^1CT state and the Franck–

Condon ground state) and the second term represents the Murrell ‘borrowing’ mechanism [56b] [i.e., the contributions from the $(^1\text{LE})_i$ states of energy E_i]. The electronic transition dipole moments M_i correspond to the radiative transitions $(^1\text{LE})_i \rightarrow S_0$. The above relation allows one to estimate the values of the electronic coupling elements V_{0F} and V_{1F} (i.e., between the fluorescent ^1CT state and the locally excited state lying most closely in energy). The matrix elements V_{0A} and V_{1A} corresponding to the Franck–Condon excited CT state reached in absorption can be estimated from a relation analogous to Eq. 9 [14].

An interesting challenge in the study of the intramolecular electron-transfer reactions is to identify structural elements that promote electronic coupling between an electron donor and an acceptor. It has been shown by Kapturkiewicz and co-workers [14] that the appropriate values of the electronic coupling elements, which are mainly determined by the interactions between the atoms forming the A–D bond, can be theoretically predicted following the formalism proposed by Dogonadze et al. [61]. Neglecting contributions from the σ -orbitals, one can obtain for π -electronic systems [14]

$$V_0 = C_{\text{LUMO}}^{\text{A}} C_{\text{HOMO}}^{\text{D}} \beta_{\text{AD}} \cos(\Theta_{\text{A-D}}) + \text{constant} \quad (10a)$$

$$V_1^{\text{A}} = C_{\text{HOMO}}^{\text{A}} C_{\text{HOMO}}^{\text{D}} \beta_{\text{AD}} \cos(\Theta_{\text{A-D}}) + \text{constant} \quad (10b)$$

$$V_1^{\text{D}} = C_{\text{LUMO}}^{\text{A}} C_{\text{LUMO}}^{\text{D}} \beta_{\text{AD}} \cos(\Theta_{\text{A-D}}) + \text{constant} \quad (10c)$$

where $\Theta_{\text{A-D}}$ denotes the angle between the planes of the A and D subunits, C_{HOMO} and C_{LUMO} are the LCAO coefficients (as obtained for the individual chromophores) of the $2p_z$ atomic orbitals (where z is the axis perpendicular to the acceptor or donor rings) of the highest occupied molecular orbital (HOMO) and of the lowest unoccupied molecular orbital (LUMO) located on the atoms forming the A–D bond, β_{AD} is the resonance integral for these atoms and the constant is related to the electronic interactions between the remaining pairs of atoms in the D–A molecule (this contribution is usually small and negligible because β_{AD} is an exponential function of the distance). Expressions 10b and 10c assume that the locally excited ^1LE state which interacts with the ^1CT state and is localized either in the acceptor or in the donor subunit, respectively, is mainly described by a configuration corresponding to the HOMO \rightarrow LUMO excitation (e.g., $^1\text{L}_a$ state in Platt’s notation).

The studies reported in Refs. [14a–f] show that the conformation of the investigated D–A systems in the fluorescent ^1CT states (and its dependence on the solvation effects) can be explained in terms of a simple model assuming the competition between: (i) the stabilization of the highly polar ^1CT state by a polar surrounding (this could lead to the decoupled perpendicular conformation, i.e. the TICT state, of the molecule resulting from the large dipole moment due to the full electron transfer), (ii) the stabilization effects related to the electronic interactions between the donor and acceptor subunits (these could result in the planar conformation of the molecule) and (iii) the steric repulsion between both moieties. For example, 9-anthryl and 9-acridyl derivatives of aromatic amines, as has been suggested by Mataga and co-workers [42], show the dependence of the electronic structure and conformation of the fluorescent ^1CT state on solvation [47]. In a low-

polarity environment, the interactions between the ^1CT state and the locally excited states (mainly with the $^1\text{L}_a$ state localized on the acceptor ring) lead to a more planar mutual conformation (of $\Delta\Theta_{\text{A-D}} \approx 15\text{--}20^\circ$) of the D and A moieties than that in the ground state [14a,b]. In highly polar solvents the relatively strong solute–solvent interactions prevent the flattening of the excited D–A system and its conformation is similar to that in the ground state. It has been also shown that the angle $\Theta_{\text{A-D}}$ in the fluorescent ^1CT state of N-bonded D–A derivatives of 3,6-*di-tert*-butylcarbazole containing benzonitrile, nicotinonitrile or various dicyanobenzenes [14c] and ketones [14d] as an electron acceptor, and also of the D–A systems containing indole [14e] and phenothiazines and phenoxazines [14f] as an electron donor, do not change the geometry significantly upon excitation.

3.1.4 TICT Molecules

The influence of *o*-methylation on the photophysical properties of the molecules which show dual luminescence phenomenon (Figure 2) and the low electronic transition dipole moments, M_{flu} , corresponding to the $^1\text{CT} \rightarrow \text{S}_0$ transition, and also the large dipole moments, μ_e , of the fluorescent ^1CT states indicate a small overlap between the donor (i.e., the lone pair orbital on the amino nitrogen) and the acceptor π -orbitals. The determined values of M_{flu} do not correspond, however, to an orthogonal molecular geometry. The large energy gap (especially in polar solvents) between the fluorescent ^1CT state and the lowest $^1(\pi, \pi^*)$ state of the acceptor subunit such as benzonitrile (which lies about $36\,000\text{ cm}^{-1}$ [62a]), pyrimidine ($40\,000\text{ cm}^{-1}$ [62b,c]), pyridine ($38\,000\text{ cm}^{-1}$ [62b,c]), methyl benzoate ($35\,600\text{ cm}^{-1}$ [62d]) and acetophenone ($35\,000\text{ cm}^{-1}$ [62e]), strongly suggests that the first term in Eq. 9 is dominant in the description of the CT fluorescence of the compounds shown in Figure 2. Neglecting the second term in Eq. 9, one obtains $V_0 \approx 0.18\text{ eV}$ for 4-(dimethylamino)-5-methylpyrimidine (**VIII**) in acetonitrile from the data collected in Table 3 in Ref. [26c]. Following the discussion presented in Section 3.1.3, one can estimate the mutual conformation of the D (dimethylamino group) and A (pyrimidine ring) subunits (i.e., the angle $\Theta_{\text{A-D}}$ between the axis, z , perpendicular to the acceptor ring and the axis of the lone pair orbital, l , located on the amino nitrogen atom N_a):

$$V_0 = C_{\text{LUMO}}^{\text{A}} C_{\text{HOMO}}^{\text{D}} \beta_{\text{CN}} \cos(\Theta_{\text{A-D}}) + \text{constant} \quad (10\text{d})$$

where $C_{\text{LUMO}}^{\text{A}}$ and $C_{\text{HOMO}}^{\text{D}}$ are the LCAO coefficients of the $2p_\pi$ atomic orbitals located on the carbon atom and of the l orbital on the adjacent N_a atom of the LUMO and the HOMO, respectively and β_{CN} is the resonance integral for these atoms which form the A–D bond. The values of $C_{\text{LUMO}}^{\text{A}} \approx 0.56$ and $C_{\text{HOMO}}^{\text{D}} \approx 0.87$ were calculated by the INDO/S method [26c] for the perpendicular conformation of **VIII**. Assuming $\beta_{\text{CN}} = 2.3\text{ eV}$ [63], one can estimate the angle $\Theta_{\text{A-D}}$. The values of 81° (constant = 0) and 84° (constant = 0.06 eV , as taken from the investigations of the carbazol-9-yl derivatives of aromatic nitriles [14c]) can be regarded as the lower and upper limits. Thus, the conformation of these relatively small compounds

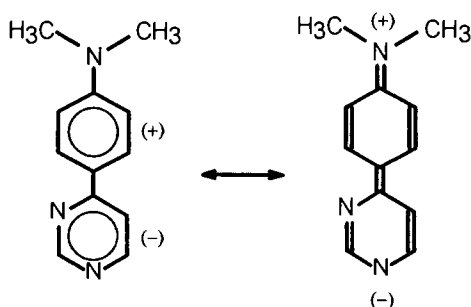


Figure 5. Resonance structures of the zwitterionic forms of 4-(dimethylanilino)pyrimidine.

containing dialkylamino group as an electron donor in the fluorescent ^1CT state is nearly orthogonal (most probably because of the strong solute–solvent interactions which in the theory of continuum polarization depend on the magnitude of the ratio μ_e^2/a_o^3 , where a_o denotes the effective radius of the Onsager cavity [64]). The small deviation from perpendicularity is due to the effects related to the electronic delocalization from the lone-pair orbital on the amino nitrogen to the acceptor ring.

The photophysical behavior of these compounds turned out to be very different from that of the conjugate donor–acceptor π -systems such as 4-(dimethylanilino)-pyrimidine (4-DAAP) [26c] and other D–A biphenyl derivatives [65]. In contrast to the TICT state model, the CT fluorescence of 4-DAAP is strongly allowed. Absorption and luminescence of the compound indicate that the conformation of both the Franck–Condon state initially reached upon excitation and the solvent equilibrated fluorescent state is similar and close to planarity. Owing to the large π -overlap, mesomeric interaction between the donor and acceptor subunits (Figure 5) is significant, and the excitation can involve only a partial charge transfer.

3.2 Supersonic Jet Spectroscopy of Selected D–A Molecules

3.2.1 Introduction

Most investigations of photoinduced electron transfer have been performed in condensed phases. Much less is known about conditions that permit the occurrence of intramolecular ET in isolated (collision-free) molecular D–A systems. A powerful method for this kind of study is the supersonic jet expansion technique (which was originally developed by Kantrowitz and Grey in 1951 [66]) combined with laser-induced fluorescence (LIF) spectroscopy and time-of-flight mass spectrometry (TOF-MS). On the other hand, the molecular aspects of solvation can be studied by investigations of isolated gas-phase ‘solute–solvent’ clusters which are formed in a supersonic jet expansion [67] (jet cooling under controlled expansion conditions [68] permits a stepwise growth of size-selected solvation clusters [69–71]). The formation of van der Waals complexes between polyatomic molecules in a supersonic jet pro-

vides a way to study exciplex [72–77] and excimer [78, 79] formation in a gas phase (see Chapter IV.3.4). Crossing from an excited state of a van der Waals complex to the exciplex at low excess of excitation energy has been discussed by Deperasińska and Prochorow [80]. Studies of electron D–A molecules such as CDMA (Figure 2) and its derivatives [81–92], dialkylaminobenzoic acid esters [82d, 85, 88, 91–95], 4-(dialkylamino)pyrimidines [90, 92d], 9,9'-bianthryl [96–98], 4-(9-anthryl)-*N,N*-dimethylaniline (ADMA) [99], 4-(9-anthryl)aniline (AA) [100], 9-(*N*-carbazolyl)-anthracene [101] and 4-(carbazol-9-yl)benzonitrile [86e, 102] in a free jet expansion have attempted to investigate the properties and significance of isolated molecules and their complexes with polar and/or protic partners with respect to CT emission.

The conditions for photoinduced charge separation and recombination in solvent-free molecules have recently been analyzed theoretically by Jortner et al. [103]. The important factors that could lead to intramolecular ET are (i) sufficiently large electronic coupling V and significant Franck–Condon vibrational overlap factors between the excited state $^1(\text{D-A})^*$ and the vibronic state of the $^1\text{CT} (\text{D}^+-\text{A}^-)$ manifold (Figure 6) and (ii) a large density of effectively coupled vibronic levels

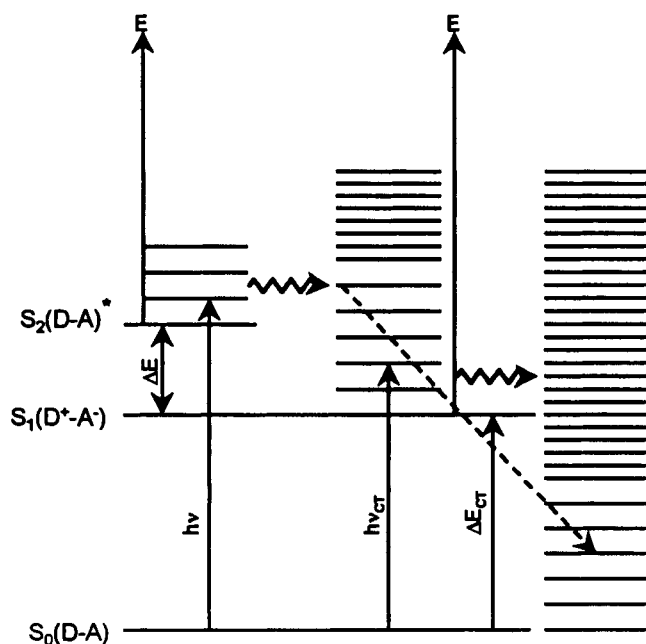


Figure 6. Schematic molecular level structure for electron transfer processes in an isolated molecule. Excitation $S_0(\text{D-A}) \rightarrow S_2[(\text{D-A})^*]$ selects the vibronic level(s), which undergo(es) intramolecular charge separation (denoted by horizontal arrow) to the $S_1(\text{D}^+-\text{A}^-)$ vibronic manifold quasi-degenerate with it. Excitation $S_0 \rightarrow S_1$ selects the vibronic levels of the charge-transfer singlet state, which undergo intramolecular charge recombination (denoted by a horizontal arrow) to the ground-state vibronic manifold. Radiative electron transfer exemplified by the CT fluorescence is labeled with a broken arrow. Adapted from Refs. [103a–d].

(this situation could be realized for a sufficiently large electronic energy gap ΔE between the origins of the two interacting states). Excited-state electron transfer in jet-cooled bare molecules has been already reported for a few cases of D–A molecules {such as CTMA [81b, 90a] and (*p*-cyanophenyl)pentamethyldisilane [104]} and donor–bridge–acceptor (D–B–A) systems [73i, 105–108].

The supersonic jet expansion technique generates ‘supercooled’ species: translational and rotational ‘temperatures’ could be as low as 0.5 K, vibrational ‘temperatures’ are higher [68]. Jet cooling decongests an otherwise dense spectrum of the solute molecule. The cooling and a consequent spectral simplification offer a chance to study the structural changes and the dynamics of the excited-state processes. For example, the application of high-resolution LIF spectroscopy and/or resonance-enhanced multiphoton ionization mass spectrometry (REMPI-MS) [109] allows one to probe the structures via rotational band-contour analysis [86–89, 90c,d, 92b, 95, 97–101], to identify alternative intramolecular conformers {e.g., via the stimulated emission pumping (SEP) technique [110]} and cluster geometries and to explore the dependence of solvent-induced spectral shifts on both the nature and the local structure of the solute–solvent cluster.

This section describes the application of high-resolution LIF spectroscopy combined with REMPI-TOF-MS to probe the conditions that permit the occurrence of electron transfer in the excited state of isolated bare molecules and also in their size-selected microsolvated clusters (in order to assess the incidence of solvent molecular perturbations in a controlled manner). A schematic diagram of the supersonic beam apparatus, developed by Brutschy and co-workers [92], is shown in Figure 7. The equipment was described in detail in Ref. [92a]. Briefly, with helium as the carrier gas, the chromophore and solvent molecules are expanded by a pulsed solenoid valve with a nozzle diameter of 500 μm into two differentially pumped, sequentially aligned vacuum chambers, which are connected via a 5.0 mm diameter skimmer. The sample is heated in an oven very near to the nozzle to achieve sufficient vapor pressure. The low-pressure solvent vapor is mixed with the carrier gas before introducing it into the nozzle. Its amount is controlled with needle valves regulating the flow conditions and by the temperature of the solvent reservoir. UV excitation is provided by the pulsed, frequency-doubled output of an Nd:YAG pumped optical parametric oscillator (OPO) (Continuum, Sunlite) tunable within the range 450–710 nm. The bandwidth of the laser running at a repetition rate of 10 Hz is about 0.1 cm^{-1} and the pulse width is about 8 ns. In chamber 1 (expansion chamber) the molecules and clusters are excited by laser radiation in order to observe the dispersed emission spectra. Fluorescence is collected at a right-angle to both the jet and the laser beam, dispersed by a spectrograph (Chromex 250 IS with 1200 and 300 grooves mm^{-1} gratings) and detected with a CCD camera coupled to an image intensifier (LaVision, FL-III). In chamber 2, the molecules and clusters are ionized by one-color resonant two-photon ionization (1C-R2PI) via a resonant excitation into the S_1 vibronic manifold and a non-resonant second step into the ionization continuum. Subsequently, the ions are mass analyzed in a reflectron TOF mass spectrometer equipped with a microchannel plate detector and a digital oscilloscope. A variable time delay between laser pulse and valve opening pulse is used to ensure that the same portion of the inhomogeneous gas pulse is probed for the dis-

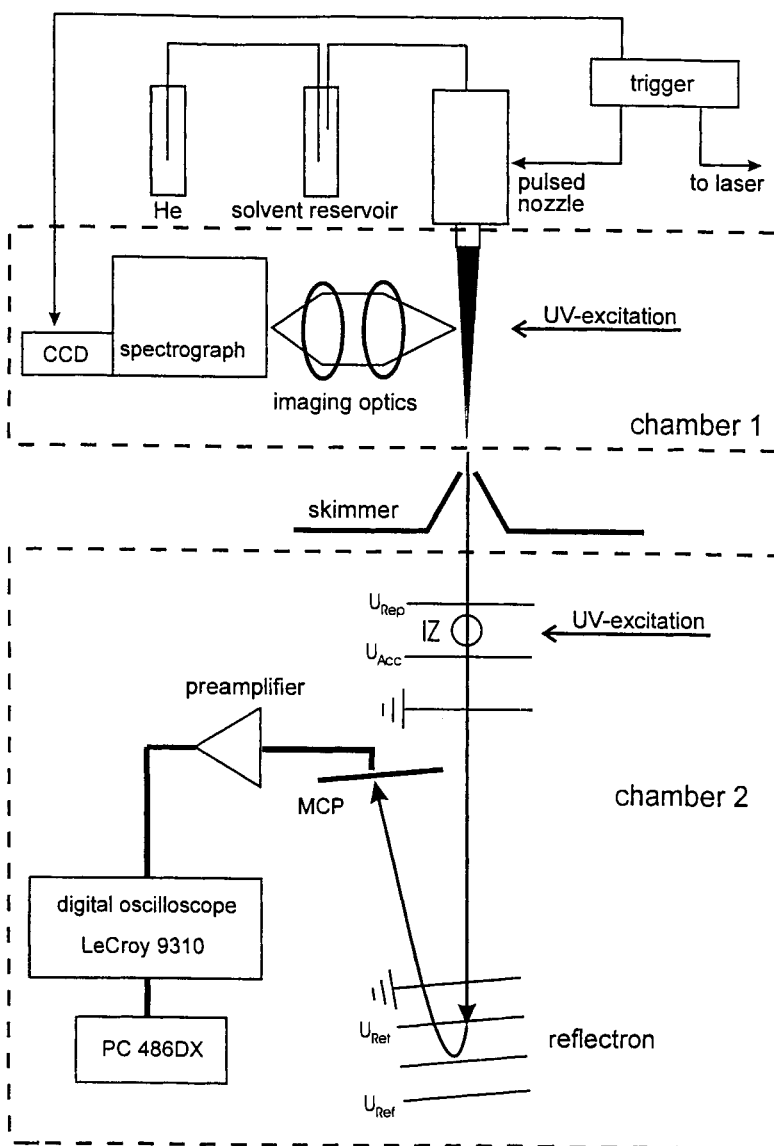


Figure 7. Schematic diagram of the supersonic beam apparatus which combines laser-induced fluorescence spectroscopy with time-of-flight mass spectrometry. Reproduced with permission from Ref. [92a].

persed emission spectrum in the first chamber and for the cluster size analysis in the second chamber (correction of flight time between the two chambers).

The present discussion is restricted to D-A molecules which show dual fluorescence in solutions, i.e., 4-dialkylamino derivatives of benzonitrile (**I–III**, Figure

2), pyrimidine (VI–IX) and benzoic acid esters XI, XII (the investigations of larger D–A π -systems, such as ADMA, are reviewed in Chapter IV.3.5). The main variables in the studies were (i) the conformation of the ground-state molecule, being close to planarity (I, VI, VII, XI, XII) or ‘pretwisted’ due to the *o*-methylation in the acceptor ring (II, III, VIII, IX) and (ii) the use of different solvent partners (e.g., water, methanol, tetrahydrofuran, acetonitrile). It is known from X-ray investigations [25] that for CDMA (I) and CTMA (III) the torsional angle between the dimethylamino group and acceptor ring is 10° and 59.3° , respectively (the amino nitrogen atom deviates slightly from the plane of the acceptor ring). The photo-physical behavior of the TICT molecules has been compared with that of the model compounds such as ABN (IV) and EIN (V) which do not show the CT fluorescence band in solutions. 4-(Dialkylamino)pyrimidines (VI–IX) seemed to be an attractive family of D–A molecules to study the influence of hydrogen bonding on the ET processes.

3.2.2 Bare Molecules

In recent years, the study of D–A molecules containing the dialkylamino group as an electron donor in supersonic jet conditions has received considerable interest. Particularly extensive investigations have been performed for CDMA (I) and its derivatives (e.g., II–V). It has been reported by Kobayashi et al. [81a], Phillips and co-workers [82], Peng et al. [83] and Bernstein and co-workers [84] that jet-cooled I did not show the excited ^1CT state formation. Figure 8 presents LIF emission and excitation spectra of I and its two *o*-methylated derivatives (II, III) [90a]. Compounds I [81a, 82, 83, 85, 86, 88–91] and II [90] exhibit the structured LIF excita-

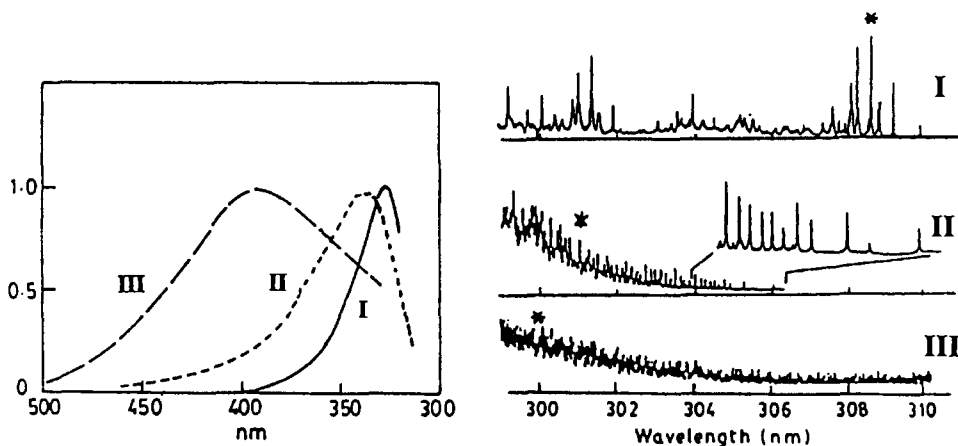


Figure 8. Left, LIF emission spectra and right, LIF excitation spectra of jet-cooled I, II and III [90]. The fluorescence spectra were recorded with a spectral resolution of the detection monochromator of 10–15 nm (the position of excitation is indicated by an asterisk). The detection wavelength for the excitation spectra was 340 nm (I and II) or 400 nm (III).

tion spectra (and very similar R2PI-TOF mass spectra [84, 87a, 92a,b]). The excitation spectrum of **III** is diffuse. A possible explanation of the diffuseness is the broadening of the individual lines as a result of a short lifetime of the optically excited state caused by rapid vibrational redistribution (IVR) and/or internal conversion (IC). Emission spectra of the compounds have been recorded with low resolution of the detection monochromator [90a,b], hence they are structureless. The relatively narrow fluorescence of **I**, which is centered at about 330 nm, has been assigned to a nearly planar delocalized state **B*** (cf. Figure 3). On the other hand, the fluorescence of CTMA is markedly broader and red shifted. The shape and position of the emission of **III** in a thermalized vapor [15d] and in a supersonic jet [81b] depend on the excitation (higher energy excitation leads to the blue shift of the fluorescence maximum). The emission was found to be composed of two transitions: first, **a** (Figure 3), from the ^1CT state, and the second, **b**, from a higher excited $^1(\pi, \pi^*)$ state. The long-wave emission $^1\text{CT} \rightarrow \text{S}_0$ dominates upon direct excitation to the ^1CT state and the intensity of the short-wave emission $\text{S}_2(^1\pi, \pi^*) \rightarrow \text{S}_0$ increases with excess excitation energy.

The shape and position of the LIF emission spectrum of **II** as a function of the excitation energy has been examined [90, 92d]. The molecule has been excited up to 4400 cm^{-1} above the 0,0 transition. As can be seen in Figure 9, the maximum shifts to the red and the half-width of the spectrum increases markedly (from 4900 to 6800 cm^{-1}) with excess excitation energy. However, no distinct shoulder was found in the expected region of the CT emission (comparison of the spectra of **II** and CTMA leads to the conclusion that the ^1CT state is not markedly populated in **II**). In this respect the behavior of **II** is similar to that of CDMA: (i) no evidence for the CT emission from **I** could be found upon excitation up to 4500 cm^{-1} above the electronic origin [82d, 83], and (ii) the half-width of the spectrum increases with excitation energy. Increasing the excitation energy could give rise to a red shift and broadening of the dispersed emission when the vibrational frequencies are smaller in the excited electronic state than those in the ground state. The diffuseness of the spectrum is due to the diversity of these frequency shifts since, as a result of IVR, the emission originates from a number of vibronic levels. The red shift and broadening of the emission from **II**, observed with increasing excess excitation energy, is relatively strong with respect to the magnitude of these effects for molecules of similar size. Such behavior can occur if the emitting vibronic states contain vibrational modes with strongly reduced frequencies in the upper electronic state. The torsional and inversion modes of the dialkylamino group could act as such vibrations.

Similarly to CDMA and **II**, and in contrast to CTMA, the LIF excitation spectra for the other molecules considered (i.e., ABN [86, 92b], EIN [92b], 4-dialkylamino derivatives of pyrimidine (except **VIII**) [90] and benzoic acid esters, **XI** and **XII** [88, 91, 94]) show the characteristic pattern of low-frequency vibrations (Table 1). Similar patterns have been analyzed for alkylbenzenes and toluenes [111], fluorotoluene [112, 113a,b], *m*-cresol [113c], toluidines [113d] and dialkylanilines [87a, 114] in terms of the internal rotation of the methyl groups, torsion of the dialkylamino group and inversion. The precise nature of the vibrations active in the LIF spectra of the considered compounds is not yet clear, but it is most probably associated with torsion and inversion of the dialkylamino group [86, 87, 88b, 90c]. The lowest

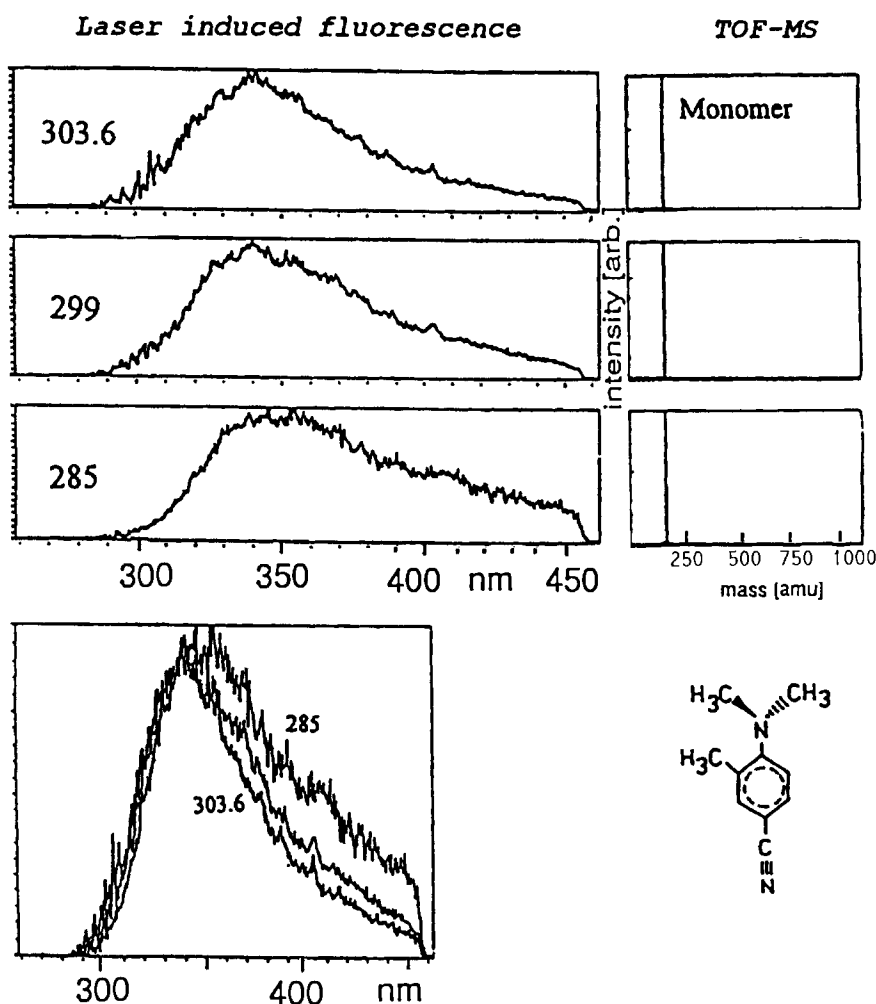


Figure 9. Effect of increasing the excess excitation energy on the LIF spectra of **II** in a supersonic jet expansion. TOF mass spectra (right) indicate that the emission spectra (left, bottom) correspond to the monomer. The numbers indicate the wavelengths of excitation (in nm).

energy transitions of the excitation spectra were assigned to the 0,0 transition, in spite of their weakness. The low intensity of the first vibronic band and the progression of the low-frequency vibrations suggest a change of the geometry of the compounds in the fluorescent states with respect to that in the ground state.

Analysis of the vibrational structure and rotational contours of the LIF emission and excitation spectra offers the possibility of studying the conformational changes of the molecules and clusters upon excitation. However, the assignment of the low-frequency modes observed in the LIF excitation spectra of the investigated compounds is difficult in view of the complexity of the dialkylamino group which may

Table 1. Spectral position of the origin ($\tilde{\nu}_{\text{vac}}$ in cm^{-1}) and the vibrational bands observed in the LIF excitation spectra of the monomers of CDMA (**I**, Figure 2), its *o*-methylated derivative (**II**) and 4-(dialkylamino)pyrimidines (**VI**, **VII** and **IX**) in the supersonic jet expansion^{a,b,c}

I	II	VI	VII	IX
32246.5 B	32654.8 B	33023.8 C	32971.2 A	32950.8 A
76.1 B	57.6 B	64	52	26
113.2	83.5 B	80 C	88	51
118.5 B	122.1 B	126 C	147	75
136.4 C	138.4 B	135	152	82
145.3	154.0	143	162 A	86
171.1 B	167.1	152	166	95
176.4 B	178.3	176	171	113 A
190.1	192.7	216	208	121
193.7	204.8	260	214	132
242.6	220.4 B	271	219	140
573.2	236.8	286	249	145
632.6 B	244.6	293	266	152
674.8	250.3	299	277	164
729.7	259.5 C	328	287	170
855.9	274.8	347	291	173
895.4	288.5	354	297	187
916.4 M	299.9	360	307	191
957.1	303.1	363	322	201
972.7	314.3	377	338	214
1004.6	317.9	384	341	220
1023.5	320.5	429	344	226
1061.2	331.2	440	361	234
1103.5	341.7	452	375	247
1158.2 M	357.5	456	391	256
	395.7	525	408	261 A
	412.4	586	430	269
	420.7	614	449	275
	424.5	635	454	280
	427.0	641	460	287

^a Accuracy of results: $\pm 0.5 \text{ cm}^{-1}$ [90a,b].^b A, B, C and M (\equiv mixed) denote the type of rotational contour [90c,d].^c The positions of the vibrational transitions obtained by IC-R2PI-TOF-MS [92] are very similar to those given in this Table.

undergo *N*-aryl torsion, *N*-methyl rotation and inversion. Microwave investigations of dimethylaniline (DMA) [115a] provide an estimate for the frequency of the NMe_2 group torsion about the *N*-aryl bond; the torsional frequency appears to be less than 100 cm^{-1} . The frequency of *N*-methyl rotation is expected to be somewhat higher. Its value is about 257 cm^{-1} in dimethylamine [116] (the barrier to this motion in *N*-methylaniline [115b,c] has been estimated to be comparable to that in dimethylamine). The torsional barrier in DMA is expected to be higher than that in *N*-methylaniline. On the basis of the above information, the lowest energy vibronic

transitions in the LIF excitation spectra of the studied compounds seem to be associated with torsion and inversion of the dialkylamino group [86, 87]. Assuming that the pattern of seven low-frequency transitions in the vicinity of the electronic origin of the LIF excitation spectrum of CDMA corresponds to the progressions of the NMe₂ group torsion and inversion, and using a Franck–Condon intensity analysis, Grassian et al. [87a] determined that the D–A twist angle (Θ_{A-D}) in the excited state is about 30° ($\Theta_{A-D} = 0^\circ$ in the ground state has been assumed). On the other hand, the effects of deuterium on the vibrational structure of the LIF spectra of DMA [94] and diethylaniline (DEA) [114] led Weersink and Wallace to the assignment of the low-frequency bands to the *N*-methyl or *N*-ethyl rotation, respectively.

Rotational contour analysis of the number of vibrational transitions in **I**, **II**, **VI**, **VII** and **IX** has been performed by Pérez Salgado et al. [90c,d]. For CDMA most bands near to the origin are of B-type rotational contour [86, 88, 89, 91, 92b], indicating that the electronic transition dipole moment is polarized along the short in-plane molecular axis (i.e., it is the $^1L_b \leftarrow S_0$ transition as in aniline [117] and benzonitrile [118]). The simulation procedure of these contours (which is based on the asymmetric-top rigid-rotor approximation [119] and assumes the separation of the rotational and vibrational motions) suggests that jet-cooled **I** undergoes small changes in conformation upon excitation. Kajimoto et al. [89] and Lommatzsch and Brutschy [92b] (Figure 10) reported that this analysis leads to a torsional angle between the donor and acceptor moieties in the fluorescent state of $\Theta_{A-D} \approx 20\text{--}30^\circ$. Concerning the inversion potential, the most stable conformations have been found [89] to correspond to the angles 15° and 0° for the ground and excited state, respectively. The rotational contour analysis for several vibronic bands in the first 250 cm^{−1} range above the origin of the LIF excitation spectra of 4-(dialkylamino)pyrimidines (**VI**, **VII** and **IX**) reflects the complex spectroscopy of these compounds [90c]. In contrast to CDMA and **II**, and similarly to pyrimidine [120], the 0,0 transition of **VI** exhibits a mixed-type of rotational contour with a dominant contribution of the C-type transition (which is characteristic for the out-of-plane polarized electronic transitions [e.g., $^1(n, \pi^*) \leftarrow S_0$]). On the other hand, **VII** and **IX** show mainly A-type transitions, i.e., polarized along the long in-plane axis. The simulation of the rotational contours suggests that the conformation of these molecules is similar to that in the ground state.

The lack of mirror symmetry between the LIF excitation spectra and high-resolution dispersed fluorescence spectra of CDMA upon 0,0 excitation (i.e. excitation into the lowest energy band centered at 310.022 nm) has been observed [90c,d]. Excitation into the origin and of the single vibronic levels such as 0,0 + 76 cm^{−1}, 0,0 + 113 cm^{−1}, 0,0 + 136 cm^{−1} and 0,0 + 176 cm^{−1} (Table 1) leads to different fluorescence spectra. Moreover, the high-resolution emission spectra of CDMA become severely congested upon exciting higher energy transitions, e.g., 0,0 + 632 cm^{−1}, 0,0 + 916 cm^{−1} and 0,0 + 1158 cm^{−1}. To explain these findings, the hypothesis that the fluorescence is preceded by a fast (i.e., on the picosecond time-scale) radiationless intramolecular process (probably internal conversion from the primary excited state to another excited electronic state of lower potential energy minimum) has been proposed [90c,d].

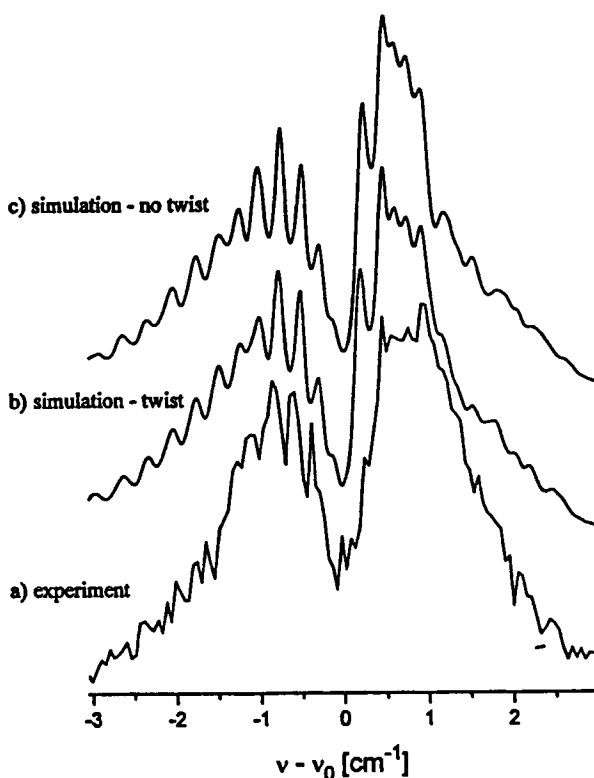


Figure 10. Experimental (a) and simulated (b, c) rotational band contours of the 0–0 +76.1 cm⁻¹ vibronic band of the LIF excitation spectrum of CDMA. The band contour (b) is based on *ab initio* geometries (the torsional angle between the donor and acceptor moieties is 22°). The band contour (c) assumes that the dimethylamino group is not twisted in the ground and excited states. Reproduced with permission from Ref. [92 b].

3.2.3 Microsolvation Effects

Electron donor–acceptor molecules linked by a single bond have been widely used for studying structural requirements and solvation effects upon photoinduced intramolecular charge transfer processes. Polarity, acidity and viscosity may all act to influence the relative accessibility and stability of the CT state and the kinetics of its population. Solvation may affect the barrier height, the well depth and the electron transfer probability. Molecular aspects of solvation can be studied by the investigation of isolated gas phase solute–solvent clusters, which are formed in a supersonic jet expansion. Among the issues concerning the excited-state CT process are (i) critical number of solvent partners of the defined polarity; (ii) relative contributions of the local and the long-range stabilizing forces and (iii) details of the solute–solvent interactions, e.g., steric effects, solvation site(s), solvent orientation and hydrogen bonding.

Experiments with clusters in a supersonic jet can advantageously be employed to study the effects of solvation of a chromophore on its emission spectrum. Hence it is desirable to characterize the composition and the structure of the solute–solvent clusters as precisely as possible. The cluster size distributions can be determined by TOF-MS after resonant two-photon ionization, R2PI [84, 92a,c]. This allows for a

better characterization of the cluster sizes in the emission experiments than correlation with expansion parameters such as sample temperature and the stagnation pressure of the carrier gas (e.g., [82, 83, 85–91, 93–95]). The former method presumes that fragmentation induced by the ionization is negligible, which is generally not the case. However, with the use of very low laser intensities and of ionization energies very near to the ionization threshold, one can correlate the species contributing to the fluorescence spectra with the cluster ion mass spectra. To avoid falsification of the mass spectra by fragmentation of larger clusters, the intensity dependence of an ion mass signal on laser power and excitation wavelength should be tested. The cluster size distribution can be varied by changing the sample/nozzle temperature and by adjusting the time delay between the laser pulse and the opening pulse of the valve.

Homogeneous aggregates

The dimers of 4-(dialkylamino)pyrimidines (**VI–IX**), show structured LIF excitation spectra (an example is shown in Figure 11) [90a–c]. The origin is shifted to the red with respect to that of the bare molecule by about $600\text{--}700\text{ cm}^{-1}$ (Table 2). The dispersed fluorescence spectra of the dimers are surprisingly narrow and the spectral position of its maximum (centered at about $330\text{--}335\text{ nm}$) is similar to that of the bare molecule. It is plausible to assume for these dimers a nearly planar geometry with a head-to-tail conformation stabilized by a hydrogen bond between the dialkylamino hydrogen and the pyrimidine ring nitrogen atoms. It is noteworthy that for the nonplanar compounds **VIII** and **IX** two kinds of dimers are observed. The second type of dimers show structureless excitation spectra and their fluorescence is markedly red shifted (the maximum is centered at about 400 nm). This finding suggests the transformation of these ground-state van der Waals (vdW) complexes into excimers (see below).

The LIF excitation spectrum of the dimers of jet-cooled CDMA is structureless and the low-energy part is red shifted by about 1500 cm^{-1} with respect to the $0,0$ transition of the monomer [84b]. The emission spectra for a homogeneous expansion of **I** in helium depend strongly on the size of excited clusters. The dimers show significantly broader and red-shifted fluorescence with respect to that of the monomer. The emission maximum is centered at 390 nm [82c,d, 83, 92a]. Formation of larger clusters ($n \geq 3$) shifts this maximum to 410 nm [92a]. Similarly, the structureless excitation spectra and the red-shifted emission spectra centered at 405 and 400 nm are observed for the dimers of **II** and EIN (the latter does not show dual luminescence phenomenon in solutions), respectively. On the other hand, the formation of clusters does not change markedly the position of the fluorescence maximum of the monomers of CTMA (however, the increase of the intensity of the long-wave part of the spectrum is observed). Luminescence properties of ABN clusters differ from those observed for CDMA and its other derivatives. Under expansion conditions where only small clusters ($n \leq 3$) are observed in the TOF ion mass spectrum, an additional long-wave band is not observed in the fluorescence spectrum (Figure 12). The appearance of larger aggregates results in a red-shifted emission with a maximum centered at 395 nm [92a].

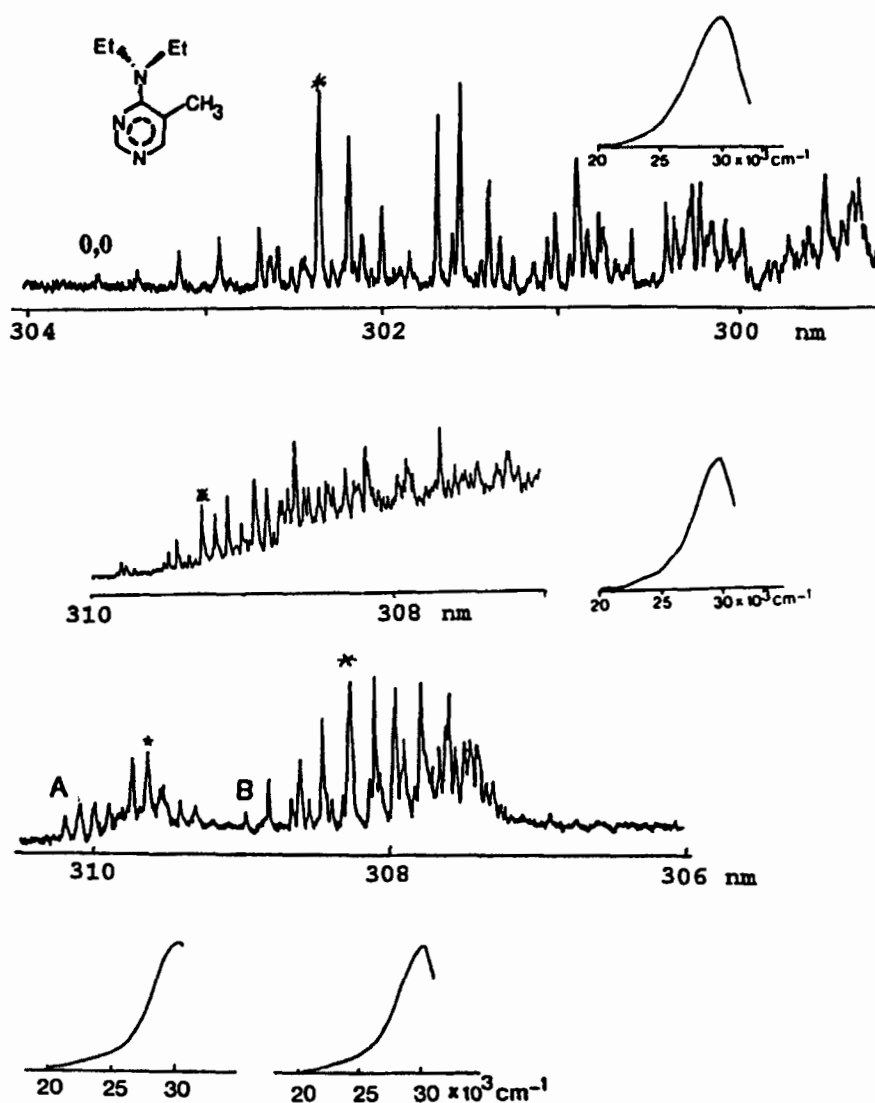


Figure 11. LIF excitation and emission spectra of jet-cooled monomer and clusters of IX [90a–c]: top, monomer; middle, dimer; bottom, van der Waals complexes between IX and acetonitrile. The electronic origins of the excitation spectra of the latter complexes are labelled A (1:2 complex) and B (1:1). Low-intensity features of the 1:3 complex are observed in the red part of the spectrum with the high pressure of acetonitrile. The fluorescence spectra were recorded with a spectral resolution of the detection monochromator of 10–15 nm (the position of excitation is indicated by an asterisk).

Table 2. Electronic origin (in nm) of the excitation spectra (as obtained from the LIF spectroscopy and REMPI-TOF-MS) of 4-dialkylamino derivatives of benzonitrile (**I**, **II**, **IV**)^a and pyrimidine (**VI–IX**), methyl 4-dimethylaminobenzoate (**XI**) and their clusters with various polar solvent molecules [the displacement in cm⁻¹ (- denotes the red shift and + the blue shift) of the 0,0 transitions of the clusters with respect to the monomer origin are included]

Compound	Monomer	Dimer	Complexes with acetonitrile			Complexes with methanol			Complexes with water		
			1:1	1:1	1:2	1:3	1:1	1:1	1:1	1:1	Others
I	310.022 ^b	c	307.52 ^d +252	~318.5 ^d ~-850			309.11 ^e +95		309.89 ^{f,g} +14	308.12 ^f +199	306.21 ^f +401
II	306.145 ^h	c									
IV	298.57 ⁱ		296.48 ^j +236				297.75 ^k +92	296.71 ^k +210	297.82 ^k +84	296.83 ^k +196	295.80 ^k +314
VI	302.725 ^l	309.19 ^l -690						298.50 ^l +468			
VII	303.208 ^l	308.96 ^l -613	300.65 ^l +281 [?]	308.03 ^l -518			300.41 ^l +307	304.71 ^l -163	299.86 ^l +367	304.58 ^l -149	
VIII	c	308.20 ^l									
IX	303.396 ^l	309.815 ^l -683	308.975 ^l -595	310.185 ^l -721							
XI	302.79 ⁿ	o		310.67 ^l -770					~302.4 ^p ~+38		

^a The monomer, dimer and heterogeneous complexes of **III** show structureless excitation spectra [81b, 90a, 92a,d].

^b cf. Refs. [84a, 88c, 90a,d, 92a,b].

^c The excitation spectra are structureless [82c,d, 83, 90a–c, 92a,d].

^d cf. Refs. [84a–c].

^e cf. Refs. [82a, 83].

^f cf. Refs. [84a–c].

^g Kajimoto and co-workers [81a] and Peng et al., however, determined the origin of the 1:1 complex at about 309.12 nm (i.e. shifted about 94 cm⁻¹ with respect to the origin of the monomer).

^h cf. Refs. [90a–c].

ⁱ cf. Refs. [86a–c, 88c, 92a,b].

^j cf. Refs. [86b,e].

^k cf. Refs. [86e, 88d].

^l cf. Refs. [90a–c, 92d].

^m 1:2 complex [90a,c, 92d].

ⁿ cf. Refs. [88c, 91, 94].

^o The excitation spectra are structureless [91].

^p cf. Ref. [91].

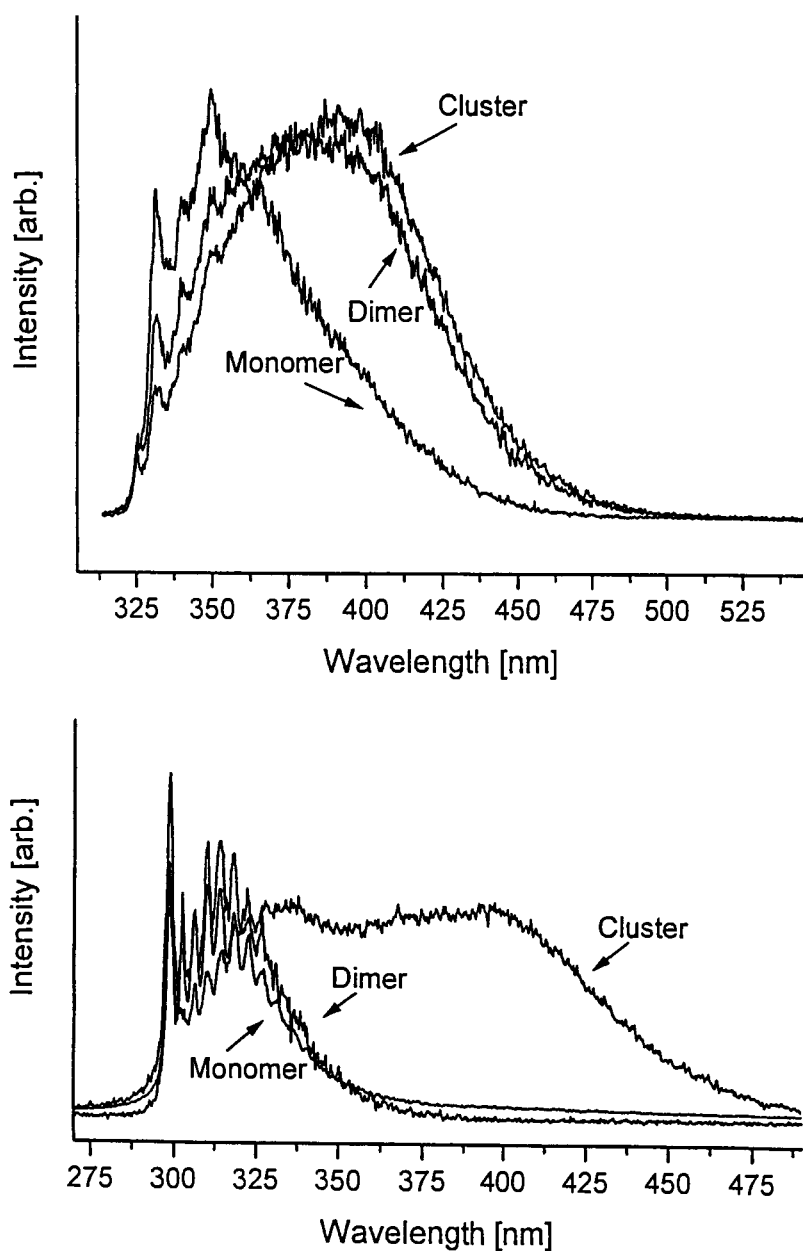


Figure 12. Dispersed emission spectra of jet-cooled monomer, dimer and larger homoaggregates upon 0,0 excitation: top, E1N; bottom, ABN. Reproduced with permission from Ref. [92a].

The changes in the emission spectra of DMAEB resulting from the cluster formation in the supersonic beam are presented in Figure 13 [92a]. The long-wave emission band (which is centered at 410 nm) was previously observed by Phillips and co-workers [82c, 93] and attributed to dimers, owing to its concentration dependence. Similar spectra have been observed for monomers and dimers of DMAMB [91, 93, 94]. The LIF excitation spectra of the dimers of both molecules are structureless and extend far to the red (about 1800 cm^{-1}) with respect to the monomer 0,0 transition.

Correlation between the mass and emission spectra demonstrates that the observed long-wave emission in all the compounds under consideration is due to the formation of self-complexes. The origin of this band has been a subject of intense discussion. Following the arguments given by Phillips and co-workers [82c,d] the red-shifted fluorescence of the CDMA dimer can be due to its transformation into an excimer or the transition into an intramolecular ^1CT state (e.g., TICT state) of one chromophore is induced by its polar partner. There is no doubt that detailed characterization of the conformational reaction coordinate is crucial for understanding of the mechanism of the excited-state process, an extremely difficult task for jet studies of transitions terminating on a repulsive ground-state potential energy surface(s) at the geometry of the relaxed excited state (cf. Figure 18). Some help, however, comes from comparative studies of the investigated compounds. The occurrence of the long-wave fluorescence for dimers of EIN and for larger than trimeric homoaggregates of ABN suggests that this band is not due to the TICT state formation (neither ABN nor EIN show dual fluorescence in solutions). It has been proposed by Lommatzsch et al. [92a] that the absence of dual fluorescence for the ABN dimer is due to a planar head-to-tail conformation (stabilized by a hydrogen bond between the amino hydrogen and the nitrogen of the cyano group) which prevents the formation of excimers. For the same reasons, a cyclic structure for the trimer has been proposed. The comparison of the effects of dimer formation of CDMA and benzoic acid esters (**XI** [93, 94], **XII**) on the emission spectra strongly suggests the transformation of the ground-state vdW complexes into excimers. In the vdW dimer two partners (M) are identical. The excimer state is stabilized by configuration interaction with charge resonance states ($M^-M^+ \leftrightarrow M^+M^-$) and exciton resonance states ($M^*M \leftrightarrow MM^*$) [28a, 37b, 60a]. The stabilization of an excimer due to charge resonance is given by the potential energy function:

$$V = IP - EA - C(r) \quad (11)$$

where IP is the ionization potential, EA is the electron affinity of the monomer subunit and $C(r)$ is the Coulomb attraction. When both molecules are in a suitably arranged contact, an exciton interaction can mix the two S_1 states of the monomers and split them by equal amount of energy $\pm \Delta E_{\text{exc}}$. The corresponding potential energy function in the dipole–dipole approximation can be obtained from the relation

$$V = E_M \pm \Delta E_{\text{exc}} = E_M \pm \frac{\vec{M}_1 \vec{M}_2}{r^3} \quad (12)$$

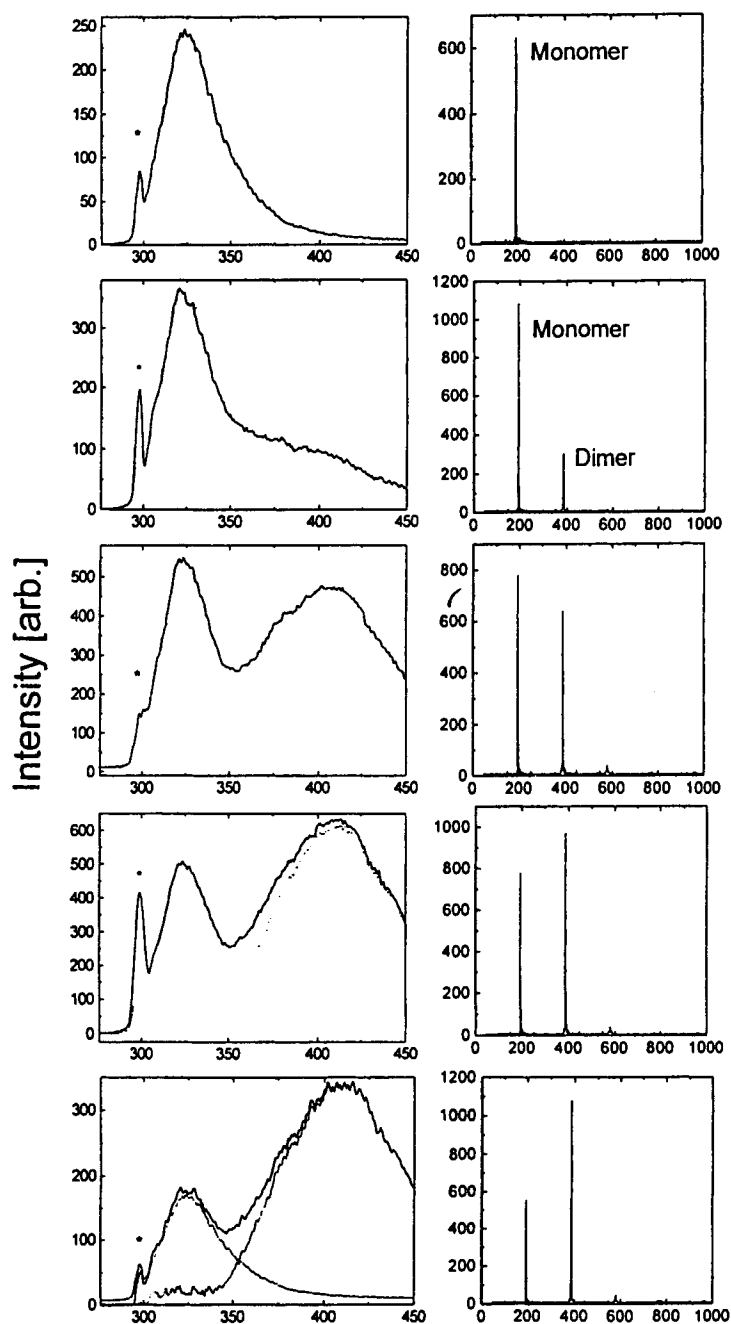


Figure 13. Left, dispersed emission spectra (recorded with a low resolution of the detection part) of jet-cooled monomer and self-clusters of DMAEB (XII). Right, time-of-flight mass spectra. The cluster size distribution was varied by changing the operating conditions of the pulsed nozzle. Reproduced with permission from Ref. [92a].

where \vec{M}_i ($i = 1, 2$) is the transition dipole moment, E_M is the unperturbed energy of the monomer excited state and r is the intermolecular distance between the monomer moieties in the excimer. Thus, the exciton interaction of the 1L_a states results in the larger stabilization of the excimer than that connected with the interaction of the 1L_b states. The magnitude and sign of ΔE_{exc} depend on the mutual orientation of both partners. The favorable geometry of the vdW dimer for singlet excimer formation is a sandwich-like conformation. When the transition dipole moments are parallel the exciton interaction is strong and when they are perpendicular the interaction vanishes. In the case of the ideal sandwich geometry, the out-of-phase combination ($-$) of the (M^*M) and (MM^*) wavefunctions is the lower exciton state, whereas for an in-plane head-to-tail orientation, the in-phase combination ($+$) is the lower exciton state. To estimate the stabilization of the CDMA excimer due to exciton resonance interactions, both the 1L_b and 1L_a states have to be considered [28a, 92a] (see the schematic diagram in Figure 14). The excimer of CDMA is expected to be stabilized about 0.28 eV below the 1L_b state of the monomer. The exciton stabilization effects in benzoic acid esters (**XI**, **XII**) should lead to a larger red shift of the emission spectra (even if the sequence of the 1L_b and 1L_a states in DMAMB and DMAEB is the same as in CDMA the energy gap is expected to be much smaller [23, 85, 91, 94]), and this is observed.

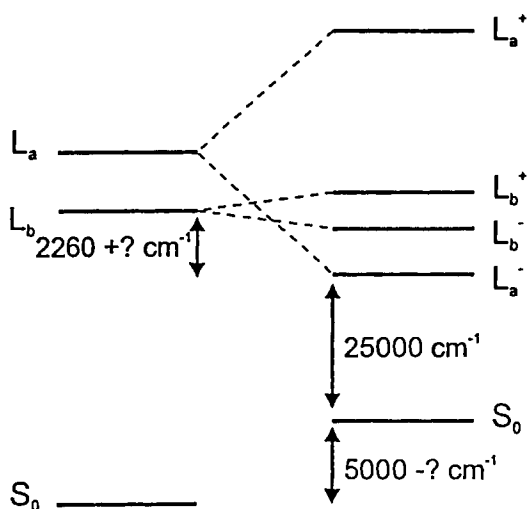


Figure 14. Schematic diagram of the stabilization of the CDMA excimer due to exciton resonance interaction. An ideal sandwich-like conformation with opposite orientation of the two monomers is assumed for the excimer. The values of the excited-state energies and the corresponding transition dipole moments were taken from Ref. [33c]. The exciton splitting of the 1L_b state is only 39 cm^{-1} , owing to the low transition dipole moment M_{lu} corresponding to the $^1L_b \leftarrow S_0$ emission. The much larger M_{lu} value for the $^1L_a \leftarrow S_0$ fluorescence makes the exciton splitting of the 1L_a state the dominant stabilization. The in-phase and the out-of-phase combinations of the exciton resonance states are labeled L^+ and L^- , respectively. The unknown contributions of the charge resonance interaction are indicated by a question mark. Reproduced with permission from Ref. [92a].

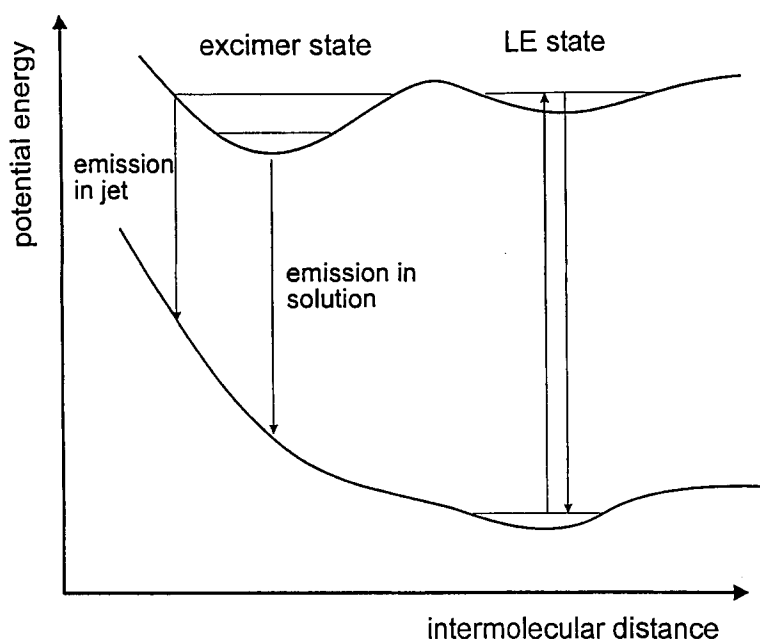


Figure 15. Potential energy surface(s) for excimer formation. Reproduced with permission from Ref. [92a].

The excimer fluorescence (with respect to the excited vdW dimer emission) is red shifted and structureless because the emission is terminated in a repulsive ground-state potential energy surface (Figure 15). For parallel transition moments, emission from the out-of-phase exciton state to the ground state is forbidden and for the in-phase exciton state emission is allowed [28a]. It should be noted, however, that the forbidden emission from the out-of-phase exciton state is expected to have a similar transition dipole moment as the $^1L_b \rightarrow S_0$ emission. The actual dynamics of the initially excited vdW dimer depend on the energy gap and the coupling strength between the primary excited (LE) state and the excimer state.

Heterogeneous clusters

Specific effects on spectroscopy and photophysics induced by complexation of the D–A chromophores with various solvent molecules have been examined for all the compounds under consideration. The idea of the beam work is to generate 1:*n* solute–solvent complexes and to determine thereby the relation between the solute–solvent interactions and the excited-state CT process. Kajimoto et al. [81a,c, 89], Phillips and co-workers [82], Peng et al. [83], Bernstein and co-workers [84] and others [85, 88, 90–92] have shown that solute–solvent complexes of CDMA were readily produced by varying the partial pressure of the compounds and the stagnation pressure of the carrier gas. Cyclohexane, chloroform, carbon tetrachloride, methyl fluoride, trifluoromethane, dichloromethane, acetone, acetonitrile, metha-

nol, water, ammonia and dimethylamine have been used as solvents. Some of the complexes show structured excitation spectra (a few examples are collected in Table 2) and narrow short-wave LIF emission spectra (which strongly resemble the fluorescence spectra of the bare molecule). The fluorescence has been assigned to the primary excited state of the vdW complexes.

Similar results have been obtained for the complexes between benzoic acid esters (**XI**, **XII**) [88d, 91, 94] or 4-dialkylaminopyrimidines (**VI–IX**) [90, 92d] and polar and protic solvent molecules. The results in Table 2 show that polar partners induce a wide range of both bathochromic and hypsochromic shifts. The two most important interactions are dipole–dipole and hydrogen bonding, both of which are strong and directional in nature. Thus, the magnitude and direction of solvent shifts with polar solvents are very sensitive to the binding site and relative orientation of the solvent molecule. In many cases, several distinct isomers have been detected, with different solvent shifts for the same complex stoichiometry. For example, the excitation spectrum of **VII** complexed with methanol (Figure 16) exhibits four different regions, all of them giving rise to short-wave fluorescence [90a–c]. The spectral origin is either blue (**D**) or red shifted (**A**, **B** and **C**) with respect to that of the monomer (Table 1). TOF-MS experiments [92d] proved that the complexes **C** and **D** are of 1:1 and **B** and **A** of 1:2 and 1:3 stoichiometry, respectively (the 1C-R2PI-TOF mass spectra show a structure very similar to that observed by LIF spectroscopy). The LIF spectra of the complexes of **IX** with acetonitrile are presented in Figure 11. The LIF [90a–c] and 1C-R2PI-TOF-MS [92d] experiments indicate that the excitation spectrum corresponds to three complexes of different stoichiometry. The 0,0 transitions of these complexes are shifted to the red by 595 cm^{-1} (1:1 complex), 721 cm^{-1} (1:2) and 770 cm^{-1} (probably 1:3) with respect to the origin of the monomer. The vibrational structure of the excitation spectra of the complexes differs markedly from that of the bare molecule (the spectra show different Franck–Condon envelope and smaller frequency spacings between the vibronic bands). For these complexes the first vibronic band is fairly intense, which suggests that in the complexes the displacement of the equilibrium conformation is smaller than that in the bare molecule.

The effects of the mixed supersonic expansion of CDMA with various solvent molecules (such as cyclohexane, carbon tetrachloride, acetone, acetonitrile, methanol, dichloromethane and chloroform) on the emission spectra have been investigated by Phillips and co-workers [82d]. The cluster size distribution was varied by changing the nozzle temperature and the partial pressure of the solvent. Two emission components were observed in each case. The long-wave emission was attributed to dimers (which can be isolated or solvated) and to monomer complexed with chloroform or dichloromethane (of unknown stoichiometry). On the other hand, it has been reported by Bernstein and co-workers [84] that CDMA forms with acetonitrile two kinds of 1:1 complexes of different geometry. The first cluster has a structured excitation spectrum, similar to that of the bare molecule, but blue shifted by about 252 cm^{-1} . The second exhibits a broad excitation spectrum with some resolvable features between $31\,400$ and $31\,600\text{ cm}^{-1}$ (Table 2). The complexes show different fluorescence spectra; excitation into the broad absorption leads to the red-shifted emission with respect to that of the monomer (Figure 8) and of the ‘blue’

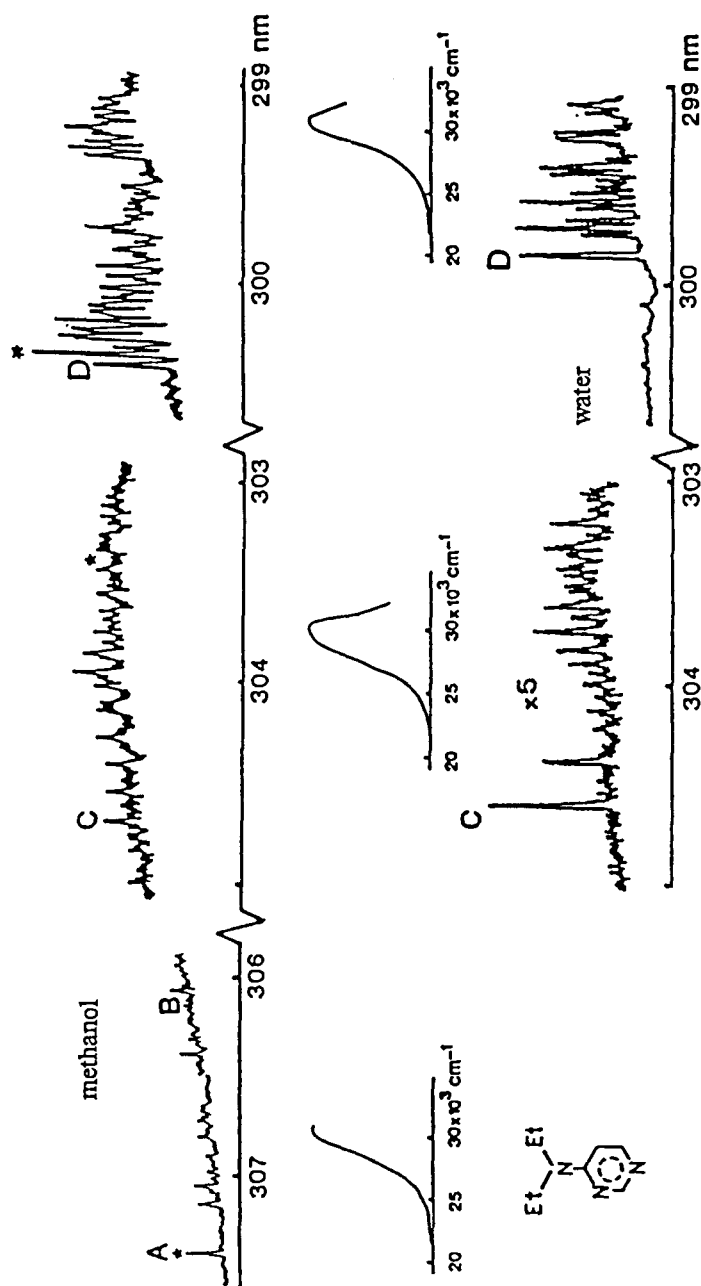


Figure 16. LIF excitation (scale in cm^{-1}) and emission (scale in nm) spectra of VII with methanol and water [90a–c]. The electronic origins of the LIF excitation spectra of various complexes are labeled A (complex of stoichiometry 1:3), B (1:2), C (1:1) and D (1:1). The spectra of the complexes with water do not show the low-energy parts A and B. The fluorescence spectra were recorded with a spectral resolution of the detection monochromator of 10–15 nm (the position of excitation is indicated by an asterisk).

cluster (with a maximum centered at about 345 nm). The effects of the gradual complexation of CDMA, ABN and EIN by acetonitrile, tetrahydrofuran (THF) and cyclohexane on the fluorescence spectra have been investigated by Lommatzsch et al. [92c] with the use of the experimental set-up that combines TOF-MS with dispersed emission spectroscopy (Figure 7). Two different (chromophore)_m–(solvent)_n cluster size distributions were studied: (i) complexes containing one chromophore molecule ($m = 1$) and a small number of solvent molecules ($n = 1–4$) and (ii) complexes of one chromophore and a large number of solvent molecules ($n = 1–12$). As discussed above in this Section, the homogeneous clusters of CDMA and its derivatives exhibit dual fluorescence, because of excimer formation [82c,d, 92a]. Therefore, to avoid interference of excimer emission with the emission from the heterogeneous clusters, the formation of homogeneous dimers should be suppressed. Figure 17 shows the emission spectra of ABN and EIN complexed with a small number of solvent molecules. For both chromophores an increasing red shift of the emission maximum with respect to the uncomplexed chromophore is observed with increasing polarity of the solvent partners. No significant changes of the emission are observed with increasing size of the ‘solvent shell’ (i.e. from $n \leq 4$ to $n \leq 12$). It is noteworthy, that the emission maxima of the complexed chromophores in the jet resemble closely those in the respective solutions. In particular, no second, anomalous and red-shifted emission band is found under these expansion conditions. CDMA–solvent clusters seem to show different behavior. Under the expansion conditions favoring the formation of monomers and clusters between CDMA and acetonitrile of 1:1 stoichiometry, the observed emission shows two maxima centered at 325 and 345 nm. The formation of 1: n clusters (with $n \geq 5$) gives rise to a strongly red-shifted and clearly separated second emission with a maximum centered at about 425 nm. The contributions of dimers and 2: n complexes were excluded by the correlation of the increase of the intensity of the long wavelength emission with the concentrations of various mass analyzed ionic clusters [92c]. The effects of the gradual complexation of CDMA by methanol and THF on the luminescence are qualitatively very similar, but dispersed fluorescence spectra show different shape and spectral position of the long-wavelength band. This finding agrees with previous results for the jet-cooled 1:1 complexes between CDMA (**I**) and water [81a, 83], methanol [82a, 83], acetonitrile or ammonia [83] which showed that one polar solvent molecule is definitively not enough to observe this emission. It is noteworthy that this result for CDMA is different from the behavior of methyl 4-dimethylaminobenzoate (**XI**) where the long-wave fluorescence has been reported for 1:1 complexes with water [91].

Hence the detailed investigations demonstrate that the luminescence properties of the heterogeneous clusters of ABN and EIN differ from those of **I** and **XI**. Whereas for the clusters of the two former compounds with polar solvent molecules only one emission band appears (being red shifted with respect to the monomer), those of **I** [probably of 1: n ($n \geq 5$) stoichiometry] and **XI** with water (of 1:1 stoichiometry) show dual fluorescence. This finding may be discussed in terms of a qualitative model presented in Figure 18. In general, the equilibrium conformation of a vdW cluster and the shape of the potential energy curves in the ground and primary excited state are usually different owing to a larger binding energy in the excited state

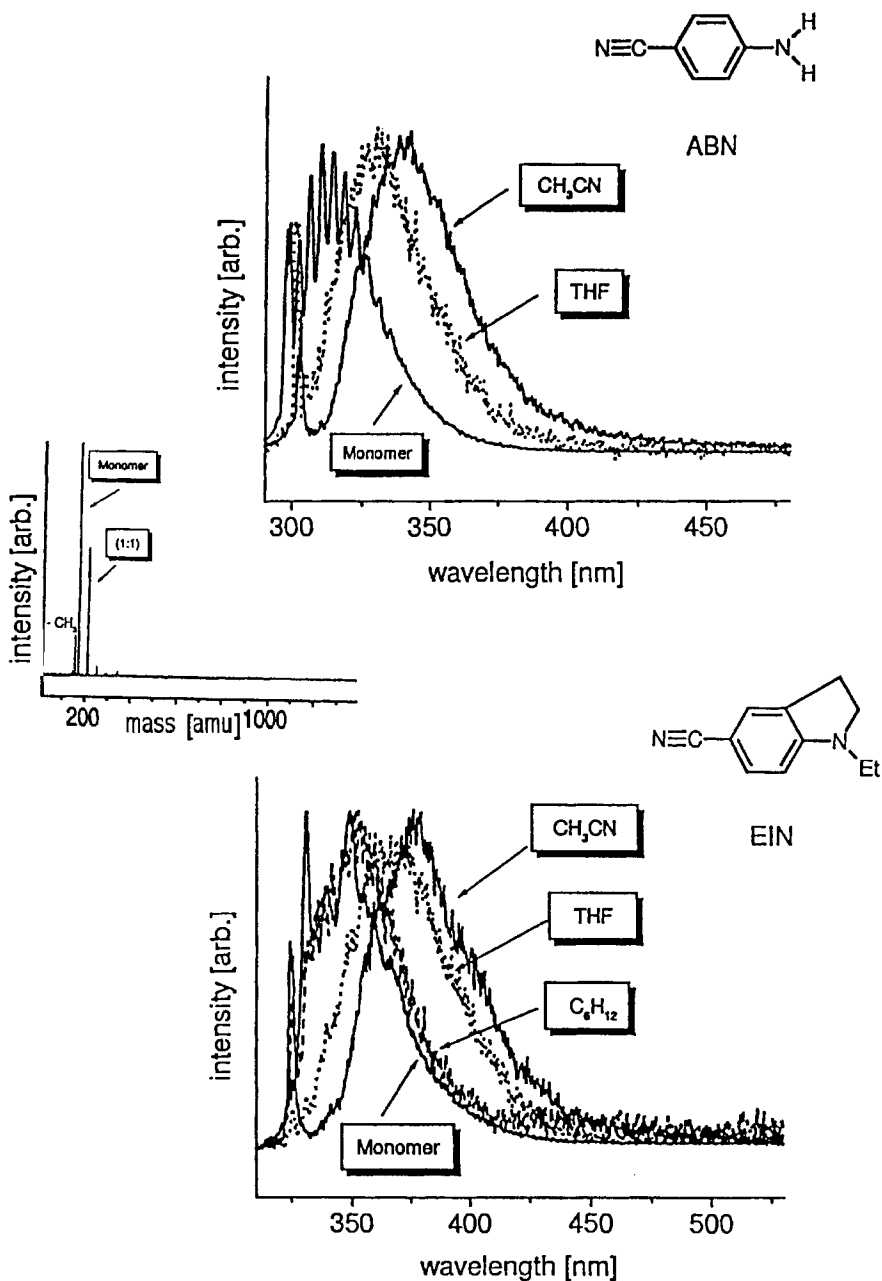


Figure 17. Dispersed fluorescence spectra of ABN (top, excitation wavelength 300 nm) and EIN (bottom, excitation wavelength 325.60 nm) and their complexes with a small number ($n = 1-4$) of solvent molecules such as cyclohexane (C₆H₁₂), tetrahydrofuran (THF) and acetonitrile (CH₃CN). The 1C-R2PI-TOF mass spectrum of EIN + CH₃CN expansion is also shown (middle).

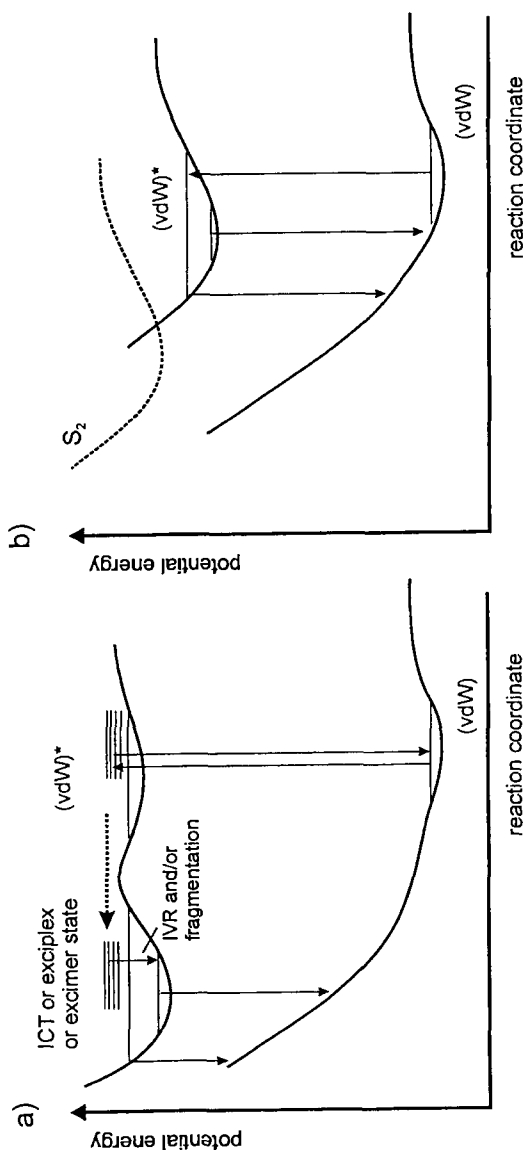


Figure 18. Schematic representation of the potential energy surfaces of the ground and excited states along the reaction coordinate corresponding to the transformation of the vdW clusters (in the ground state represented by a shallow potential energy minimum) into excimers, exciplexes or intramolecular charge-transfer (ICT) states. These systems possess a double minimum potential in the resultant adiabatic excited state; the relative energy of the minima, the barrier height and the well depth is dependent on the electronic structure of the chromophore and the interactions with solvent molecules. (b) The barrier is high enough to prevent formation of excimers, exciplexes or ICT states. This is the case of the clusters that show structured excitation spectra and a short-wave emission from the primary excited state of the vdW complex. (a) The case with the clusters that are 'prepared' for the excited-state reaction. The diffuse excitation spectra are most likely due to the short lifetime of the primary excited vibronic levels of the vdW cluster which leads to the broadening of the individual lines. The difference between the geometry of the product of the excited-state reaction with respect to that of the ground-state vdW cluster generates a broad, red-shifted emission. The reaction coordinate of the excited-state reaction is complex, e.g., should be related to the intermolecular distance and the mutual orientation of the complexing partners combined with the intramolecular motions in the D-A chromophore such as torsion and inversion.

with respect to the ground state. This could result from the increase in the dipole moment and/or the polarizability of the D–A molecule, from exciton or CT interactions and/or from the interactions with the solvent molecules. The actual dynamics of a particular, electronically excited vdW complex depend on the electronic structure of the chromophore (e.g., the energy gap between the interacting electronic states) and on the intracluster interactions (which may depend strongly on the electron donor–acceptor properties of the solute and the equilibrium geometry of the solute–solvent clusters). It is most likely that the relatively small red shift of the emission of jet-cooled clusters between ABN and EIN and polar partners compared with that of the monomers and clusters with nonpolar molecules is caused by the change of the potential energy surface together with intramolecular vibrational redistribution, IVR (by the latter, various low-frequency vibronic states in the S_1 state can be populated). The striking appearance of dual luminescence in jet-cooled CDMA and DMAMB clusters with polar molecules must be of different origin. Following the arguments given by Bixon and Jortner [103c,d], Phillips and co-workers [82], Wersink and Wallace [94] and Yip and Levy [72b], the origin of a long-wave emission band can be due to the transformation of the vdW cluster into an exciplex (1: n complexes), a solvated excimer (2: n complexes) or the transition into an intramolecular CT state of the D–A chromophore which is induced by its polar partner. Most probably, the latter mechanism is responsible for the red-shifted emission of 1: n solute–solvent complexes. Its appearance is probably related to the lower ionization potential of **I** (and **XI**) compared with ABN, with energy difference amounting to at least 0.6 eV [121]. This value may be even larger in the case of the TICT state formation owing to the decoupling of the amino group. Thus, the relatively strong interactions between the primary excited state (S_1) and CT state (S_2) due to the small energy gap (Eq. 11, Ref. [122]) are expected for **I** and **XI**. The exclusion of an exciplex mechanism is suggested by the relatively low electron affinity and high ionization potential of the solvent molecules. However, it should be noted that larger subclusters of solvent molecules show a decreasing ionization potential [70b] and an increased electron affinity [123] in comparison with the monomer.

A critical evaluation of the findings described here needs some further remarks. As already mentioned, the determination of the cluster size distribution in the beam by R2PI-TOF-MS is limited by the intermolecular fragmentation of the vdW clusters in the ionic and, possibly, also in the fluorescent state. Clusters between aromatic chromophores and water, methanol and other polar molecules usually dissociate upon 1C-R2PI by losing one solvent molecule [124]. This fragmentation is mostly due to an excess energy in the ion after a non-resonant ionization transition and/or by a rearrangement of the ionized cluster due to the charge–dipole interaction. In addition to the fragmentation after ionization, an unknown amount of fragmentation could occur in the electronically excited state due to an exothermic process from the primary excited state of a vdW cluster to a CT state (Figure 18a). The system transforms a certain amount of electronic energy into vibrational energy which could be imparted by IVR to the solvent partners, followed by a fast predissociation of a vdW cluster. The dissipation of energy by fragmentation could be slowed with increasing number of coupled vibrational degrees of freedom (i.e.,

with increasing number of solvent molecules) in the vdW complex. Thus, in larger clusters under collision-free conditions IVR and internal conversion could be the dominant energy dissipation channels.

One of the methods which allows one to characterize the size and structure of the vdW complexes which are responsible for the specific photophysical properties is double resonance (IR/R2PI) laser depletion spectroscopy [70b]. This method combines the structurally sensitive infrared (IR) vibrational predissociation spectroscopy (VPS) with the highly mass-selective R2PI-TOF-MS. The VPS of clusters, pioneered by Gough and co-workers [125] and by Vernon and co-workers [126], has been described theoretically by Beswick and Jortner [127]. The IR/R2PI technique was subsequently applied to the study of jet-cooled molecular clusters by several groups [124, 128–130]. In such a pump and probe experiment, the cluster beam is irradiated by a pulsed, tunable IR laser. The absorption of IR photons matching a particular intramolecular vibration of a molecular subunit within the vdW complex leads to its predissociation. This depletion of selected complexes can be probed with a certain delay time (e.g., of about 100 ns) by R2PI-MS. Centering the UV probe laser on a size-specific band of a product ion while tuning the wavelength of the IR laser leads to an ion depletion spectrum corresponding to the IR absorption of the probed cluster in its neutral state. The comparison of the experimental spectrum with quantum chemical *ab initio* calculations gives information about the structure of the clusters. Moreover, the IR/R2PI method allows one to obtain the hole-burning spectra. The latter are recorded by keeping the wavelength of the IR laser fixed on a particular intramolecular vibrational transition while tuning the wavelength of the UV probe laser. The respective IR/R2PI spectrum differs from the normal R2PI spectrum (i.e., the excitation spectrum of a neutral complex observed via measurement of the ion yield as a function of the scanning wavelength of the UV laser) because of the depletion of all the bands corresponding to the clusters containing a particular IR absorber. With this method the spectroscopic features in an R2PI spectrum originating from fragmenting larger clusters, isomers or hot bands can clearly be identified and often assigned. It should be pointed out that this IR/R2PI hole-burning spectroscopy offers a unique chance to determine a cluster-specific fluorescence within a broad cluster size distribution. It can be done by comparing the LIF emission spectra recorded with and without the IR predissociation laser matching a particular intramolecular vibration. For example, if the difference emission spectrum contains an anomalous long-wave component, the formation of the excited CT state in this specific cluster can be determined unequivocally.

3.2.4 Concluding Remarks

Under jet-cooled conditions, no long-wave emission is observed for a series of the D–A compounds that show dual luminescence in solutions, except **III** (Figure 2). The observed broad emission (Figure 8) of the latter, highly ‘pretwisted’, molecule is a manifestation of the overlap of two fluorescences, **a** and **b** (Figure 3). The long-wave emission **a** dominates upon direct excitation to the ¹CT state and the intensity

of the short-wave emission **b** [corresponding to the $S_2(^1\pi, \pi^*) \rightarrow S_0$ transition] increases with excess excitation energy. High-resolution spectral investigations and quantum chemical studies provide a method for the elucidation of geometries in the ground and excited states.

Solute–solvent complexes of different stoichiometry have been observed between all the D–A compounds under consideration and various solvent molecules. Some of the clusters show structured excitation spectra and a narrow short-wave emission that has been assigned to the primary excited state of the vdW complex. The broad, red-shifted emission of other clusters can be explained in terms of the transformation of the vdW complexes of stoichiometry $2:n$ ($n \geq 0$) into excimers or the transition into an intramolecular CT state of the D–A chromophore which is induced by its polar partner(s) (for the complexes of stoichiometry $1:n$). The main conclusion from the fluorescence behaviour of the jet-cooled vdW clusters is that dual luminescence is obviously connected with the preference of specific solute–solvent geometries.

As has been discussed above, molecular clusters produced in a supersonic expansion are preferred model systems to study solvation-mediated photoreactions from a molecular point of view. Under such conditions, intramolecular electron transfer reactions in D–A molecules, traditionally observed in solutions, are amenable to a detailed spectroscopic study. One should note, however, the difference between the possible energy dissipation processes in jet-cooled clusters and in solution. Since molecular clusters are produced in the gas phase under collision-free conditions, they are free of perturbations from many-body interactions or macromolecular structures inherent for molecules in the condensed phase. In addition, they are frozen out in their minimum energy conformations which may differ from those relevant at room temperature. Another important aspect of the condensed phase is its role as a heat bath. Thus, excess energy in a molecule may be dissipated to the bulk on a picosecond time-scale. On the other hand, in a cluster excess energy may only be dissipated to a restricted number of oscillators and the cluster may fragment by losing solvent molecules.

A peculiarity of the cluster beams discussed above which has to be taken into account in the luminescence studies of intramolecular electron transfer processes is that even under beam conditions optimized for the production of small D–A solute–solvent complexes, the simultaneous appearance of homogeneous clusters is nearly inevitable. Hence excimer fluorescence and the fluorescence of the mixed clusters are often superimposed. Therefore, only the careful characterization of the clusters with respect to their constitution, size and structure can allow the unequivocal assignment of the processes observed.

3.3 Summary and Perspectives

The advent of supersonic molecular beam expansion techniques and high spectral- and time-resolved laser spectroscopic probing has transformed experimental

molecular spectroscopy, photophysics and photochemistry (e.g., [67, 70, 131]). Jet expansion of organic molecules allows the stabilization of both intramolecular conformers and intermolecular clusters. Analysis of their vibrational pattern and rotational band contours can provide detailed insights into their structures and their state-selective photophysics and photochemistry. Studies of molecular aspects of solvation of large jet-cooled organic chromophores lie at the intersection of many important types of research. The chromophore can be used to address questions of site selectivity (in polyfunctional molecules), the topography of intermolecular potentials and fundamental aspects of molecular recognition. LIF (or ionization) probing of jet-cooled clusters can be used to reveal both structural and dynamical information.

The recent development of tunable, ultraviolet, high-resolution dye lasers has opened up a new region of the spectrum to high-resolution studies [132]. For example, using such techniques combined with quantum chemical calculations, Kaya and co-workers [132e] determined the geometric structure of various jet-cooled complexes between 7-azaindole and water of 1: n ($n = 1-3$) stoichiometry. Femtochemistry, pioneered by Zewail [131], fulfilled the chemists' dream of being able to study the dynamics of chemical reactions in real time. For example, femtosecond molecular dynamics of phototautomerization in jet-cooled model DNA base pairs (7-azaindole dimers) containing two hydrogen bonds has been studied [133]. The stepwise (versus concerted) mechanism has been proved by using the phenomenon of Coulomb explosion of the reaction complex (caused by an intense femtosecond probe laser pulse) to arrest and interrogate directly the intermediates (by TOF-MS) in the latter reaction [134].

Clusters are (in spite of limitations and differences with respect to the condensed phase) adequate model systems to investigate the molecular roots of various processes with cluster-specific spectroscopic methods. The use of double resonance IR/R2PI laser depletion spectroscopy will probably have a great impact on future studies of the charge-transfer processes in mixed solute-solvent complexes. Other experimental methods that can be proposed for this kind of study are cluster-specific static and transient photoelectron spectroscopy (PES). In the latter case two synchronized, wavelength-tunable picosecond lasers are used, both for the excitation and the ionizing steps of R2PI. From the photoelectron spectra sampled at different delays of the ionization relative to the exciting laser, the CT dynamics may be investigated in real time. From the transient photoelectron spectra also the site of the charge separation may presumably be deduced. For example, after an intramolecular CT process in microsolvated CDMA the photoelectron spectrum should resemble that of the solvated benzonitrile anion, while a charge transfer to or from the solvent molecule (i.e., exciplex mechanism) should contain the signature of the solvent cluster ion.

Acknowledgments

We thank Professors Zbigniew R. Grabowski, Andrzej Kapturkiewicz, R.P.H. Rettschnick and Wolfgang Rettig and Dr. Uwe Lommatzsch for cooperation and

illuminating discussions. J.H. is grateful to the Polish Committee of Scientific Research, the Netherlands Organization for Scientific Research (NWO) and the Deutsche Forschungsgemeinschaft for generous support.

References

1. *Photoinduced Electron Transfer, Parts A–D* (Eds. M.A. Fox, M. Chanon), Elsevier, Amsterdam, **1988**.
2. *Electron Transfer in Biology and the Solid State*, Advances in Chemistry Series 226 (Eds. M.K. Johnson, R.B. King, D.M. Kurtz, Jr., Ch. Kutal, M.L. Norton, R.A. Scott), American Chemical Society, Washington, DC, **1990**.
3. *Dynamics and Mechanisms of Photoinduced Electron Transfer and Related Phenomena* (Eds. N. Mataga, T. Okada, H. Masuhara), Elsevier, Amsterdam, **1992**.
4. (a) T.F. Ho, A.R. McIntosh, J.R. Bolton, *Nature* **1980**, 286, 254; (b) T.A. Moore, D. Gust, P. Mathis, J.-C. Mialosq, C. Chachaty, R.V. Bensasson, E.J. Land, D. Doizi, P.A. Liddell, W.R. Lehman, G.A. Nemeth, A.L. Moore, *Nature* **1984**, 307, 630; (c) P. Seta, E. Bienvenue, A.L. Moore, P. Mathis, R.V. Bensasson, P. Liddell, P.J. Pessiki, A. Joy, T.A. Moore, D. Gust, *Nature* **1985**, 316, 653; (d) M. R. Wasielewski, M.P. Niemczyk, W.A. Svec, E.B. Pewitt, *J. Am. Chem. Soc.* **1985**, 107, 1080; (e) M. Bixon, J. Jortner, M.E. Michel-Beyerle, *Biochim. Biophys. Acta* **1991**, 1056, 301; (f) A. Osuka, S. Nakayama, K. Maruyama, N. Mataga, T. Asahi, I. Yamazaki, Y. Nishimura, T. Ohno, K. Nozaki, *J. Am. Chem. Soc.* **1993**, 115, 4577.
5. (a) J.S. Connolly, J.R. Bolton, in *Photoinduced Electron Transfer, Part D* (Eds. M.A. Fox, M. Chanon), Elsevier, Amsterdam, **1988**, p. 303; (b) M. Grätzel, in *Photoinduced Electron Transfer, Part D* (Eds. M.A. Fox, M. Chanon), Elsevier, Amsterdam, **1988**, p. 394.
6. *Perspectives in Photosynthesis, The Jerusalem Symposia on Quantum Chemistry and Biochemistry*, Vol. 22 (Eds. J. Jortner, B. Pullman), Kluwer, Dordrecht, **1990**.
7. P. Pichat, M.A. Fox, in *Photoinduced Electron Transfer, Part D* (Eds. M.A. Fox, M. Chanon), Elsevier, Amsterdam, **1988**, p. 241.
8. (a) *New Trends in the Photochemistry of Polymers* (Eds. N.S. Allen, J.F. Rabek), Elsevier, New York, **1985**; (b) Y. Shirota, in *Photoinduced Electron transfer, Part D* (Eds. M.A. Fox, M. Chanon), Elsevier, Amsterdam, **1988**, p. 441.
9. (a) *Molecular Electronic Devices II*, Marcel Dekker, New York, **1987**; (b) M.V. Alfimov, V.A. Sazhnikov, in *Photoinduced Electron Transfer, Part D* (Eds. M.A. Fox, M. Chanon), Elsevier, Amsterdam, **1988**, p. 474.
10. N. Paillous, M. Comtat, in *Photoinduced Electron Transfer, Part D* (Eds. M.A. Fox, M. Chanon), Elsevier, Amsterdam, **1988**, p. 578.
11. E. Lippert, W. Lüder, H. Boss, in *Advances in Molecular Spectroscopy* (Ed. A. Mangini), Pergamon Press, Oxford, **1962**, p. 443.
12. Z.R. Grabowski, K. Rotkiewicz, A. Siemiarczuk, D.J. Cowley, W. Baumann, *Nouv. J. Chim.* **1979**, 3, 443.
13. (a) K. Rotkiewicz, K.H. Grellmann, Z.R. Grabowski, *Chem. Phys. Lett.* **1973**, 19, 315; (b) Z.R. Grabowski, K. Rotkiewicz, W. Rubaszewska, E. Kirkor-Kamińska, *Acta Phys. Pol.* **1978**, A54, 767; (c) Z. R. Grabowski, K. Rotkiewicz, A. Siemiarczuk, *J. Lumin.* **1979**, 18/19, 420; (d) Z. R. Grabowski, J. Dobkowski, *Pure Appl. Chem.* **1983**, 55, 245; (e) M. Van der Auweraer, Z.R. Grabowski, W. Rettig, *J. Phys. Chem.* **1991**, 95, 2083.
14. (a) J. Herbich, A. Kapturkiewicz, *Chem. Phys. Lett.* **1997**, 273, 8; (b) J. Herbich, A. Kapturkiewicz, *J. Am. Chem. Soc.* **1998**, 120, 1014; (c) A. Kapturkiewicz, J. Herbich, J. Karpiuk, J. Nowacki, *J. Phys. Chem. A* **1997**, 101, 2332; (d) A. Kapturkiewicz, J. Nowacki, *J. Phys. Chem. A* **1999**, 103, 8145; (e) P. Borowicz, J. Herbich, A. Kapturkiewicz, J. Nowacki, *Chem. Phys.* **1999**, 244, 251; (f) P. Borowicz, J. Herbich, A. Kapturkiewicz, J. Nowacki, M. Opallo, *Chem. Phys.* **1999**, 249, 49.
15. (a) K. Rotkiewicz, Z.R. Grabowski, A. Krówczyński, W. Kühnle, *J. Lumin.* **1976**, 12/13, 877; (b) E. Kirkor-Kamińska, K. Rotkiewicz, A. Grabowska, *Chem. Phys. Lett.* **1978**, 58, 379;

- (c) K. Rotkiewicz, W. Rubaszewska, *Chem. Phys. Lett.* **1980**, 70, 444; (d) K. Rotkiewicz, W. Rubaszewska, *J. Lumin.* **1982**, 27, 221; (e) H. Bischof, W. Baumann, N. Detzer, K. Rotkiewicz, *Chem. Phys. Lett.* **1985**, 116, 180; (f) K. Rotkiewicz, *Spectrochim. Acta* **1986**, A42, 575; (g) G. Köhler, K. Rotkiewicz, *Spectrochim. Acta* **1986**, A42, 1127; (h) J. Herbich, K. Rotkiewicz, J. Waluk, B. Andresen, E.W. Thulstrup, *Chem. Phys.* **1989**, 138, 105.
16. (a) W. Rettig, *Angew. Chem., Int. Ed. Engl.* **1986**, 25, 971; (b) E. Lippert, W. Rettig, V. Bonačić-Koutecký, F. Heisel, J.A. Miehe, in *Adv. Chem. Phys.*, **1987**, 68, 1; (c) W. Rettig, W. Baumann, *Progr. Photochem. Photophys.* **1992**, 6, 79; (d) W. Rettig, *Top. Curr. Chem.*, **1994**, 169, 253; (e) K. Bhattacharyya, M. Chowdhury, *Chem. Rev.* **1993**, 93, 507.
17. (a) W. Rettig, *J. Lumin.* **1980**, 26, 21; (b) W. Rettig, *J. Phys. Chem.* **1982**, 86, 1970; (c) W. Rettig, *J. Mol. Struct.* **1982**, 84, 303; (d) W. Rettig, K. Rotkiewicz, W. Rubaszewska, *Spectrochim. Acta* **1984**, A40, 241; (e) W. Rettig, R. Gleiter, *J. Phys. Chem.* **1985**, 89, 4676; (f) W. Rettig, *Ber. Bunsenges. Phys. Chem.* **1991**, 95, 259; (g) W. Baumann, H. Bischof, J.-C. Fröhling, C. Brittinger, W. Rettig, K. Rotkiewicz, *J. Photochem. Photobiol. A: Chem.* **1992**, 64, 49.
18. (a) Y. Wang, M. McAuliffe, F. Novak, K.B. Eisinger, *J. Phys. Chem.* **1981**, 85, 3736; (b) Y. Wang, K.B. Eisinger, *J. Chem. Phys.* **1982**, 77, 6076; (c) J.M. Hicks, M. Vandersaal, Z. Babarogić, K.B. Eisinger, *Chem. Phys. Lett.* **1985**, 116, 18; (d) J.M. Hicks, M.T. Vandersaal, E.V. Sitzmann, K.B. Eisinger, *Chem. Phys. Lett.* **1987**, 135, 413.
19. (a) P. Suppan, *Chem. Phys. Lett.* **1986**, 128, 160; (b) D. Pilloud, P. Suppan, L. van Haelst, *Chem. Phys. Lett.* **1987**, 137, 130.
20. T. Okada, N. Mataga, W. Baumann, *J. Phys. Chem.* **1987**, 91, 760.
21. C. Rullière, Z.R. Grabowski, J. Dobkowski, *Chem. Phys. Lett.* **1987**, 137, 408.
22. (a) S. Dähne, W. Freyer, K. Teuchner, J. Dobkowski, Z.R. Grabowski, *J. Lumin.* **1980**, 22, 37; (b) J. Dobkowski, E. Kirkor-Kamińska, J. Koput, A. Siemiarz, *J. Lumin.* **1982**, 27, 339; (c) Z.R. Grabowski, J. Dobkowski, W. Kühnle, *J. Mol. Struct.* **1984**, 114, 93; (d) J. Dobkowski, W. Rettig, C. Rullière, J. Waluk, W. Wang, *Radiat. Phys. Chem.* **1992**, 39, 149; (e) J. Dobkowski, J. Waluk, W. Yang, C. Rullière, W. Rettig, *New J. Chem.* **1997**, 21, 429.
23. (a) W. Rettig, G. Wermuth, E. Lippert, *Ber. Bunsenges. Phys. Chem.* **1979**, 83, 692; (b) G. Wermuth, W. Rettig, E. Lippert, *Ber. Bunsenges. Phys. Chem.* **1981**, 85, 198; (c) G. Wermuth, W. Rettig, *J. Phys. Chem.* **1984**, 88, 2729; (d) W. Rettig, G. Wermuth, *J. Photochem.* **1985**, 28, 351.
24. (a) R.K. Guo, N. Kitamura, S. Tazuke, *J. Phys. Chem.* **1990**, 94, 1404; (b) J.A.T. Revell, R.G. Brown, *Chem. Phys. Lett.* **1992**, 188, 433.
25. (a) W. Rettig, D. Braun, P. Suppan, E. Vauthey, K. Rotkiewicz, R. Luboradzki, K. Suwińska, *J. Phys. Chem.* **1993**, 97, 13500; (b) A. Gourdon, J.-P. Launay, M. Bujoli-Doeuff, F. Heisel, J.A. Miehe, E. Amouyal, M.-L. Boillot, *J. Photochem. Photobiol. A: Chem.* **1993**, 71, 13; (c) A. Heine, R. Herbst-Irmer, D. Stalke, W. Kühnle, K.A. Zacharias, *Acta Crystallogr.* **1994**, B50, 363; (d) G.B. Jameson, B.M. Sheikh-Ali, R.G. Weiss, *Acta Crystallogr.* **1994**, B50, 703.
26. (a) J. Herbich, Z.R. Grabowski, H. Wójtowicz, K. Golankiewicz, *J. Phys. Chem.* **1989**, 93, 3439; (b) J. Herbich, J. Karpiuk, Z.R. Grabowski, N. Tamai, K. Yoshihara, *J. Lumin.* **1992**, 54, 165; (c) J. Herbich, J. Waluk, *Chem. Phys.* **1994**, 188, 247.
27. (a) B. Albinsson, *J. Am. Chem. Soc.* **1997**, 119, 6369. (b) J. Andréasson, A. Holmén, B. Albinsson, *J. Phys. Chem. B* **1999**, 103, 9782.
28. (a) Th. Förster, *Pure Appl. Chem.* **1962**, 4, 121; (b) Th. Förster, *Angew. Chem., Int. Ed. Engl.* **1969**, 8, 333.
29. H. Beens, A. Weller, in *Organic Molecular Photophysics*, Vol. 2 (Ed. J.B. Birks), VCH, Weinheim, **1975**, p. 159.
30. E.A. Chandross, in *The Exciplex* (Eds. M. Gordon, W.R. Ware), Academic Press, New York, **1975**, p. 187.
31. (a) R. J. Visser, C.A.G.O. Varma, *J. Chem. Soc., Faraday Trans. 2* **1980**, 76, 453; (b) R.J. Visser, C.A.G.O. Varma, J. Konijnenberg, P. Bergwerf, *J. Chem. Soc., Faraday Trans. 2* **1983**, 79, 347; (c) R.J. Visser, P.C.M. Weisenborn, C.A.G.O. Varma, M.P. de Haas, J.M. Warman, *Chem. Phys. Lett.* **1984**, 104, 38; (d) R.J. Visser, P.C.M. Weisenborn, C.A.G.O. Varma, *Chem. Phys. Lett.* **1985**, 113, 330; (e) R.J. Visser, P.C.M. Weisenborn, J.M. van Kan, A.H. Huizer, C.A.G.O. Varma, J.M. Warman, M.P. de Haas, *J. Chem. Soc., Faraday Trans. 2*

- 1985, 81, 689; (f) R.J. Visser, P.C.M. Weisenborn, J. Konijnenberg, A.H. Huizer, C.A.G.O. Varma, *J. Photochem.* **1986**, 32, 217; (g) P.C.M. Weisenborn, C.A.G.O. Varma, M.P. de Haas, J.M. Warman, *Chem. Phys. Lett.* **1986**, 129, 562; (h) P.C.M. Weisenborn, A.H. Huizer, and C.A.G.O. Varma, *Chem. Phys.* **1989**, 133, 437; (i) P.C.M. Weisenborn, A.H. Huizer, C.A.G.O. Varma, *J. Chem. Soc., Faraday Trans. 2* **1989**, 85, 1895; (j) M.C.C. de Lange, D. Thorn Leeson, K.A.B. van Kuijk, A.H. Huizer, C.A.G.O. Varma, *Chem. Phys.* **1993**, 174, 425.
32. (a) U. Leinhos, W. Kühnle, K.A. Zachariasse, *J. Phys. Chem.* **1991**, 95, 2013; (b) W. Schuddeboom, S.A. Jonker, J.M. Warman, U. Leinhos, W. Kühnle, K.A. Zachariasse, *J. Phys. Chem.* **1992**, 96, 10809; (c) K.A. Zachariasse, Th. von der Haar, A. Hebecker, U. Leinhos, W. Kühnle, *Pure Appl. Chem.* **1993**, 65, 1745; (d) Th. von der Haar, A. Hebecker, Yu.V. Il'ichev, Y.-B. Jiang, W. Kühnle, K.A. Zachariasse, *Recl. Trav. Chim. Pays-Bas* **1995**, 114, 430; (e) K.A. Zachariasse, M. Grobys, Th. von der Haar, A. Hebecker, Yu.V. Il'ichev, Y.-B. Jiang, O. Morawski, W. Kühnle, *J. Photochem. Photobiol. A: Chem.* **1996**, 102, 59; (f) K.A. Zachariasse, M. Grobys, Th. von der Haar, A. Hebecker, Yu.V. Il'ichev, Y.-B. Jiang, O. Morawski, I. Ruckert, W. Kühnle, *J. Photochem. Photobiol. A: Chem.* **1997**, 105, 373.
33. (a) W. Rettig, V. Bonačić-Koutecký, *Chem. Phys. Lett.* **1979**, 62, 115; (b) S. Kato, Y. Amamatsu, *J. Chem. Phys.* **1990**, 92, 7241; (c) L. Serrano-Andrés, M. Merchán, B.O. Ross, R. Lindh, *J. Am. Chem. Soc.* **1995**, 117, 3189; (d) U. Lommatzsch, B. Brutschy, *Chem. Phys.* **1998**, 234, 35; (e) A.L. Sobolewski, W. Sudholt, W. Domcke, *J. Phys. Chem. A* **1998**, 102, 2716; (f) J. Lipiński, H. Chojnacki, Z.R. Grabowski, K. Rotkiewicz, *Chem. Phys. Lett.* **1980**, 70, 449; (g) D. Majumdar, R. Sen, K. Bhattacharyya, S.P. Bhattacharyya, *J. Phys. Chem.* **1991**, 95, 4324; (h) P. Gedeck, S. Schneider, *J. Photochem. Photobiol. A: Chem.* **1997**, 105, 165; (i) A. Sobolewski, W. Domcke, *Chem. Phys. Lett.* **1996**, 250, 428 and **1996**, 259, 119.
34. (a) F. Schneider, E. Lippert, *Ber. Bunsenges. Phys. Chem.* **1968**, 72, 1155; (b) *Ber. Bunsenges. Phys. Chem.* **1970**, 74, 624; (c) W. Rettig, M. Zander, *Ber. Bunsenges. Phys. Chem.* **1983**, 87, 143; (d) M. Zander, W. Rettig, *Chem. Phys. Lett.* **1984**, 110, 602; (e) H. Lück, M.W. Windsor, W. Rettig, *J. Phys. Chem.* **1990**, 94, 4550; (f) W. Rettig, W. Majenz, R. Lapouyade, M. Vogel, *J. Photochem. Photobiol. A: Chem.* **1992**, 65, 95.
35. (a) N. Nakashima, N. Murakawa, N. Mataga, *Bull. Chem. Soc. Jpn.* **1976**, 49, 854; (b) N. Mataga, H. Yao, T. Okada, W. Rettig, *J. Phys. Chem.* **1989**, 93, 3383; (c) H. Yao, T. Okada, N. Mataga, *J. Phys. Chem.* **1989**, 93, 7388; (d) N. Mataga, S. Nishikawa, T. Okada, *Chem. Phys. Lett.* **1996**, 257, 327.
36. (a) T.J. Kang, M.A. Kahlou, D. Giser, S. Swallen, V. Nagarayan, W. Jarzęba, P.F. Barbara, *J. Phys. Chem.* **1988**, 92, 6800; (b) T. J. Kang, W. Jarzęba, P.F. Barbara, T. Fonseca, *Chem. Phys.* **1990**, 149, 81; (c) K. Tominaga, G.C. Walker, W. Jarzęba, P.F. Barbara, T. Fonseca, *J. Phys. Chem.* **1991**, 95, 10485.
37. (a) V. Bonačić-Koutecký, J. Koutecký, J. Michl, *Angew. Chem.* **1987**, 99, 216; (b) J. Michl, V. Bonačić-Koutecký, *Electronic Aspects of Organic Photochemistry*, VCH, Weinheim, **1990**.
38. (a) R. Wortman, K. Elich, S. Lebus, W. Liptay, *J. Chem. Phys.* **1991**, 95, 6371; (b) R. Wortman, S. Lebus, K. Elich, S. Assar, N. Detzer, W. Liptay, *Chem. Phys. Lett.* **1992**, 198, 220; (c) K. Elich, S. Lebus, R. Wortman, F. Petzke, N. Detzer, W. Liptay, *J. Phys. Chem.* **1993**, 97, 9947.
39. M. Schütz, R. Schmidt, *J. Phys. Chem.* **1996**, 100, 2012.
40. J. Dobkowski, Z.R. Grabowski, B. Paepelow, W. Rettig, K.H. Koch, K. Müllen, R. Lapouyade, *New J. Chem.* **1994**, 18, 525.
41. (a) F. Lahmani, E. Breheret, A. Zehnacker-Rentien, C. Amatore, A. Jutand, *J. Photochem. Photobiol. A: Chem.* **1993**, 70, 39; (b) F. Lahmani, E. Breheret, O. Benoist d'Azy, A. Zehnacker-Rentien, J.F. Delouis, *J. Photochem. Photobiol. A: Chem.* **1995**, 89, 191.
42. (a) N. Mataga, Y. Murata, *J. Am. Chem. Soc.* **1969**, 91, 3144; (b) T. Okada, T. Fujita, M. Kubota, S. Masaki, N. Mataga, R. Ide, Y. Sakata, S. Misumi, *Chem. Phys. Lett.* **1972**, 14, 563; (c) T. Okada, T. Fujita, N. Mataga, *Z. Phys. NF* **1976**, 101, 57; (d) S. Masaki, T. Okada, N. Mataga, Y. Sakata, S. Misumi, *Bull. Chem. Soc. Jpn.* **1976**, 49, 1277; (e) T. Okada, M. Kawai, T. Ikemachi, N. Mataga, Y. Sakata, S. Misumi, S. Shionoya, *J. Phys. Chem.* **1984**, 88, 1976; (f) T. Okada, N. Mataga, W. Baumann, A. Siemiarczuk, *J. Phys. Chem.* **1987**, 91, 4490; (g) W. Baumann, B. Schwager, N. Detzer, T. Okada, N. Mataga, *J. Phys. Chem.* **1988**, 92, 3742; (h) N. Mataga, S. Nishikawa, T. Asahi, T. Okada, *J. Phys. Chem.* **1990**, 94, 1443.

43. (a) A. Siemiarz, Z. R. Grabowski, A. Krówczyński, M. Asher, M. Ottolenghi, *Chem. Phys. Lett.* **1977**, 51, 315; (b) A. Siemiarz, J. Koput, A. Pohorille, *Z. Naturforsch., Teil A* **1982**, 37, 598; (c) A. Siemiarz, *Chem. Phys. Lett.* **1984**, 110, 437.
44. W. Baumann, F. Petzke, K.D. Loosen, *Z. Naturforsch., Teil A* **1979**, 34, 1070; (b) W. Baumann, H. Bischof, *J. Mol. Struct.* **1982**, 84, 181; (c) N. Detzer, W. Baumann, B. Schwager, J.C. Fröhling, C. Brittinger, *Z. Naturforsch., Teil A* **1987**, 42, 395.
45. (a) J.C.C. Tseng, S. Huang, L.A. Singer, *Chem. Phys. Lett.* **1988**, 153, 401; (b) J.C.C. Tseng, L.A. Singer, *J. Phys. Chem.* **1989**, 93, 7092.
46. (a) P.F. Barbara, W. Jarzęba, *Adv. Photochem.*, **1990**, 15, 1, and references cited therein; (b) K. Tominaga, G.C. Walker, W. Jarzęba, P.F. Barbara, *J. Phys. Chem.* **1991**, 95, 10475.
47. (a) J. Herbich, A. Kapturkiewicz, *Chem. Phys.* **1991**, 158, 143; (b) J. Herbich, A. Kapturkiewicz, *Chem. Phys.* **1993**, 170, 221.
48. A. Wiesner, G. Huttmann, W. Kühnle, H. Staerk, *J. Phys. Chem.* **1995**, 99, 14923.
49. (a) A. Onkelinx, F.C. De Schryver, L. Viaene, M. Van der Auweraer, K. Iwai, M. Yamamoto, M. Ichikawa, H. Masuhara, M. Maus, W. Rettig, *J. Am. Chem. Soc.* **1996**, 118, 2892; (b) A. Onkelinx, G. Schweitzer, F.C. De Schryver, H. Miyasaka, M. Van der Auweraer, T. Asahi, H. Masuhara, H. Fukumura, A. Yashima, K. Iwai, *J. Phys. Chem. A* **1997**, 101, 5054; (c) M. Maus, W. Rettig, S. Depaemelaere, A. Onkelinx, F.C. De Schryver, K. Iwai, *Chem. Phys. Lett.* **1998**, 292, 115.
50. S. Lee, K. Arita, O. Kajimoto, K. Tamao, *J. Phys. Chem. A* **1997**, 101, 5228.
51. W. Rettig, M. Zander, *Chem. Phys. Lett.* **1982**, 87, 229.
52. N.S. Hush, *Coord. Chem. Rev.* **1985**, 64, 135, and references cited therein.
53. R.A. Marcus, *J. Phys. Chem.* **1989**, 93, 3078, and references cited therein.
54. (a) I.R. Gould, R.H. Young, R.E. Moody, S. Farid, *J. Phys. Chem.* **1991**, 95, 2068; (b) I.R. Gould, S. Farid, *J. Photochem. Photobiol. A: Chem.* **1992**, 65, 133; (c) I.R. Gould, D. Noukakis, L. Gomez-Jahn, R.H. Young, J.L. Goodman, S. Farid, *Chem. Phys.* **1993**, 176, 439; (d) I.R. Gould, D. Noukakis, L. Gomez-Jahn, J.L. Goodman, S. Farid, *J. Am. Chem. Soc.* **1993**, 115, 4405; (e) I.R. Gould, R.H. Young, L.J. Mueller, S. Farid, *J. Am. Chem. Soc.* **1994**, 116, 8176; (f) I.R. Gould, R.H. Young, L.J. Mueller, A.C. Albrecht, S. Farid, *J. Am. Chem. Soc.* **1994**, 116, 8188.
55. J. Cortes, H. Heitele, J. Jortner, *J. Phys. Chem.* **1994**, 98, 2527.
56. (a) R.S. Mulliken, *J. Am. Chem. Soc.* **1952**, 74, 811; (b) J.N. Murrell, *J. Am. Chem. Soc.* **1959**, 81, 5037; (c) R.S. Mulliken, W.B. Person, *Molecular Complexes: a Lecture and Reprint Volume*, VCH, Weinheim, **1969**.
57. (a) M. Bixon, J. Jortner, J.W. Verhoeven, *J. Am. Chem. Soc.* **1994**, 116, 7349; (b) J.W. Verhoeven, T. Scherer, B. Wegewijs, R.M. Hermant, J. Jortner, M. Bixon, S. Depaemelaere, F.C. De Schryver, *Recl. Trav. Chim. Pays-Bas* **1995**, 114, 443.
58. J. Herbich, A. Kapturkiewicz, J. Nowacki, *Chem. Phys. Lett.* **1996**, 262, 633.
59. M. Born, J.R. Oppenheimer, *Ann. Phys.* **1927**, 84, 457.
60. (a) J.B. Birks, *Photophysics of Aromatic Molecules*, VCH, Weinheim, **1970**, p. 51; (b) J. Michl, E.W. Thulstrup, *Spectroscopy with Polarized Light*, VCH, Weinheim, **1986**, pp. 28 and 75.
61. R.R. Dogonadze, A.M. Kuznetsov, T.A. Marsagishwili, *Electrochim. Acta* **1980**, 25, 1.
62. (a) *The Sadtler Handbook of Ultraviolet Spectra*, Sadtler Research Laboratory, Philadelphia, 1979; (b) K.K. Innes, I.G. Ross, W.R. Moomaw, *J. Mol. Spectrosc.* **1988**, 132, 492; (c) A. Castellan, J. Michl, *J. Am. Chem. Soc.* **1978**, 100, 6824; (d) J.C. Baum, D.S. McClure, *J. Am. Chem. Soc.* **1979**, 101, 2335; (e) S.K. Ghoshal, S.K. Sarkar, G.S. Kastha, *Bull. Chem. Soc. Jpn.* **1981**, 54, 3556.
63. F.P. Billingsley, J.E. Bloor, *Theor. Chim. Acta* **1968**, 11, 325.
64. (a) L. Onsager, *J. Am. Chem. Soc.* **1936**, 58, 1486; (b) C.J.F. Böttcher, *Theory of Electric Polarization*, Vols. 1 and 2 (Eds. O.C. Van Belle, P. Bordewijk, A. Rip), Elsevier, Amsterdam, **1973**.
65. (a) W. Rettig, M. Maus, R. Lapouyade, *Ber. Bunsenges. Phys. Chem.* **1996**, 100, 2091; (b) M. Van Damme, J. Hofkens, F.C. De Schryver, T.G. Ryan, W. Rettig, A. Klock, *Tetrahedron* **1989**, 45, 4693; (c) D.S. Bulgarevich, O. Kajimoto, K. Hara, *J. Phys. Chem.* **1994**, 98, 2278.
66. A. Kantrowitz, J. Grey, *Rev. Sci. Instrum.* **1951**, 22, 328.
67. (a) D.H. Levy, *Annu. Rev. Phys. Chem.* **1980**, 31, 97; (b) D.H. Levy, *Adv. Chem. Phys.* **1981**, 47, 323; (c) J.A. Beswick, J. Jortner, *Adv. Chem. Phys.* **1981**, 47, 363.

68. (a) H. Ashkenas, F.S. Sherman, in *Rarefied Gas Dynamics*, Vol. 2 (Ed. J.M. De Leeuw), Academic Press, New York, **1966**, p. 84; (b) J.B. Anderson, in *Molecular Beams and Low Density Gas Dynamics* (Ed. P.P. Wegener), Marcel Dekker, New York, **1974**.
69. A.W. Castleman, Jr., R.G. Keesee, *Annu. Rev. Phys. Chem.* **1986**, 37, 525.
70. (a) B. Brutschy, *J. Phys. Chem.* **1990**, 94, 8637; (b) B. Brutschy, *Chem. Rev.* **1992**, 92, 1567.
71. *Clusters of Atoms and Molecules. I. Theory, Experiment and Clusters of Atoms*, Springer Series in Chemical Physics 52 (Ed. H. Haberland), Springer, Berlin, **1994**.
72. (a) T.D. Russel, D.H. Levy, *J. Phys. Chem.* **1982**, 86, 2718; (b) W.T. Yip, D.H. Levy, *J. Phys. Chem.* **1996**, 100, 11539.
73. (a) M. Castella, J. Prochorow, A. Tramer, *J. Chem. Phys.* **1984**, 81, 2511; (b) M. Castella, A. Tramer, F. Piuze, *Chem. Phys. Lett.* **1986**, 129, 105; (c) M. Castella, A. Tramer, F. Piuze, *Chem. Phys. Lett.* **1986**, 129, 112; (d) A. Amirav, M. Castella, F. Piuze, A. Tramer, *J. Phys. Chem.* **1988**, 92, 5500; (e) M. Castella, P. Millié, F. Piuze, J. Caillet, J. Langlet, P. Claverie, A. Tramer, *J. Phys. Chem.* **1989**, 93, 3941; (f) *J. Phys. Chem.* **1989**, 93, 3949; (g) F. Piuze, A. Tramer, *Chem. Phys. Lett.* **1990**, 166, 503; (h) F. Piuze, *Chem. Phys. Lett.* **1993**, 209, 484; (i) V. Brenner, P. Millié, F. Piuze, A. Tramer, *J. Chem. Soc., Faraday Trans.* **1997**, 93, 3277; (j) A. Tramer, V. Brenner, P. Millié, F. Piuze, *J. Phys. Chem. A* **1998**, 102, 2798 and 2808.
74. (a) H. Saigusa, M. Itoh, *Chem. Phys. Lett.* **1984**, 106, 391. (b) H. Saigusa, M. Itoh, *J. Chem. Phys.* **1984**, 81, 5692; (c) H. Saigusa, M. Itoh, M. Baba, I. Hanazaki, *J. Chem. Phys.* **1987**, 86, 2588; (d) M. Itoh, M. Sasaki, *Chem. Phys. Lett.* **1988**, 149, 40; (e) M. Itoh, M. Sasaki, *J. Phys. Chem.* **1990**, 94, 6544; (f) H. Saigusa, E.C. Lim, *J. Phys. Chem.* **1990**, 94, 2631; (g) H. Saigusa, E.C. Lim, *J. Phys. Chem.* **1991**, 95, 7580; (h) H. Saigusa, S. Sun, E.C. Lim, *J. Phys. Chem.* **1992**, 96, 2083.
75. (a) O. Anner, Y. Haas, *Chem. Phys. Lett.* **1985**, 119, 199; (b) O. Anner, Y. Haas, *J. Phys. Chem.* **1986**, 90, 4298; (c) O. Anner, E. Zarura, Y. Haas, *Chem. Phys. Lett.* **1987**, 137, 121; (d) O. Anner, Y. Haas, *J. Am. Chem. Soc.* **1988**, 110, 1416; (e) Y. Haas, O. Anner, in *Photo-induced Electron Transfer, Part A* (Eds. M.A. Fox, M. Chanon), Elsevier, Amsterdam, **1988**, p. 305; (f) E. Zingher, Y. Haas, *Chem. Phys. Lett.* **1993**, 202, 442.
76. F. Lahmani, A. Zehnacker-Rentien, F. Breheret, *J. Phys. Chem.* **1991**, 95, 3647.
77. P.B. Bisht, H. Petek, K. Yoshihara, *Chem. Phys. Lett.* **1993**, 213, 75.
78. (a) H. Saigusa, M. Itoh, *J. Phys. Chem.* **1985**, 89, 5486; (b) M. Itoh, H. Morita, *J. Phys. Chem.* **1988**, 92, 5693; (c) M. Itoh, M. Takamatsu, *Chem. Phys. Lett.* **1990**, 170, 396; (d) T. Ebata, M. Ito, M. Itoh, *J. Phys. Chem.* **1991**, 95, 1143; (e) M. Itoh, M. Takamatsu, N. Kizu, Y. Fujiwara, *J. Phys. Chem.* **1991**, 95, 9682.
79. (a) H. Saigusa, S. Sun, E.C. Lim, *J. Phys. Chem.* **1992**, 96, 2083; (b) H. Saigusa, S. Sun, E.C. Lim, *J. Chem. Phys.* **1992**, 97, 9072.
80. (a) I. Deperasińska, J. Prochorow, *Chem. Phys.* **1987**, 114, 251; (b) I. Deperasińska, *Chem. Phys.* **1988**, 120, 359; (c) I. Deperasińska, J. Prochorow, *Chem. Phys. Lett.* **1989**, 163, 257; (d) I. Deperasińska, J. Prochorow, *J. Phys. Chem.* **1991**, 95, 2001.
81. (a) T. Kobayashi, M. Futakami, O. Kajimoto, *Chem. Phys. Lett.* **1986**, 130, 63; (b) T. Kobayashi, M. Futakami, O. Kajimoto, *Chem. Phys. Lett.* **1987**, 141, 450; (c) M. Itoh, O. Kajimoto, in *Dynamics of Excited Molecules* (Ed. K. Kuchitsu), Elsevier, Amsterdam, **1994**, p. 333, and references cited therein.
82. (a) E.M. Gibson, A.C. Jones, D. Phillips, *Chem. Phys. Lett.* **1987**, 136, 454; (b) R. Howell, H. Petek, D. Phillips, K. Yoshihara, *Chem. Phys. Lett.* **1991**, 183, 249; (c) D. Phillips, R. Howell, A.G. Taylor, *Proc. Indian Acad. Sci. (Chem. Sci.)* **1992**, 104, 153; (d) R. Howell, D. Phillips, H. Petek, K. Yoshihara, *Chem. Phys.* **1994**, 188, 303, and references cited therein.
83. L.W. Peng, M. Dantus, A.H. Zewail, K. Kemnitz, J.M. Hicks, K.B. Eisenthal, *J. Phys. Chem.* **1987**, 91, 6162.
84. (a) J.A. Warren, E.R. Bernstein, J.I. Seeman, *J. Chem. Phys.* **1988**, 88, 871; (b) Q. Shang, E.R. Bernstein, *J. Chem. Phys.* **1992**, 97, 60; (c) E.R. Bernstein, *J. Phys. Chem.* **1992**, 96, 10105.
85. J. August, T.F. Palmer, J.P. Simons, C. Jouvet, W. Rettig, *Chem. Phys. Lett.* **1988**, 145, 273.
86. (a) E.M. Gibson, A.C. Jones, D. Phillips, *Chem. Phys. Lett.* **1988**, 146, 270; (b) E.M. Gibson, A.C. Jones, A.G. Taylor, W.G. Bouwmann, D. Phillips, J. Sandell, *J. Phys. Chem.* **1988**, 92, 5449; (c) H. Yu, E. Joslin, B. Crystall, T. Smith, W. Sinclair, D. Phillips, *J. Phys. Chem.* **1993**,

- 97, 8146; (d) H. Yu, E. Joslin, S.M. Zain, H. Rzepa, D. Phillips, *Chem. Phys.* **1993**, 178, 483; (e) D. Phillips, *J. Photochem. Photobiol. A: Chem.* **1997**, 105, 307.
87. (a) V.H. Grassian, J.A. Warren, E.R. Bernstein, H.V. Secor, *J. Chem. Phys.* **1989**, 90, 3994; (b) R.D. Gordon, *J. Chem. Phys.* **1990**, 93, 6908; (c) J.P. LaFemina, G.K. Schenter, *J. Chem. Phys.* **1991**, 94, 7558.
88. (a) B.D. Howells, M.T. Martinez, T.F. Palmer, J.P. Simons, A. Walters, *J. Chem. Soc., Faraday Trans.* **1990**, 86, 1949; (b) B.D. Howells, J. McCombie, T.F. Palmer, J.P. Simons, A. Walters, *J. Chem. Soc., Faraday Trans.* **1992**, 88, 2587; (c) *J. Chem. Soc., Faraday Trans.* 2595; (d) *J. Chem. Soc., Faraday Trans.* 2603.
89. O. Kajimoto, H. Yokoyama, Y. Ooshima, Y. Endo, *Chem. Phys. Lett.* **1991**, 179, 455.
90. (a) J. Herbich, F. Pérez Salgado, R.P.H. Rettschnick, Z.R. Grabowski, H. Wójtowicz, *J. Phys. Chem.* **1991**, 95, 3491; (b) J. Herbich, F. Pérez Salgado, J. Karpiuk, *Proc. Indian Acad. Sci. (Chem. Sci.)* **1992**, 104, 117; (c) F. Pérez Salgado, PhD Thesis, University of Amsterdam, **1992**; (d) F. Pérez Salgado, J. Herbich, A. Kunst, R.P.H. Rettschnick, *J. Phys. Chem. A* **1999**, 103, 3184.
91. C. Dedonder-Lardeaux, C. Jouvet, S. Martrenchard, D. Solgadi, J. McCombie, B.D. Howells, T.F. Palmer, A. Subaric-Leitis, C. Monte, W. Rettig, P. Zimmermann, *Chem. Phys.* **1995**, 191, 271.
92. (a) U. Lommatzsch, A. Gerlach, C. Lahmann, B. Brutschy, *J. Phys. Chem. A* **1998**, 102, 6421, and references cited therein; (b) U. Lommatzsch, B. Brutschy, *Chem. Phys.* **1998**, 234, 35; (c) O. Krauß, U. Lommatzsch, C. Lahmann, B. Brutschy, W. Rettig, J. Herbich, *Phys. Chem. Chem. Phys.*, submitted; (d) J. Herbich, B. Brutschy, unpublished results.
93. R. Howell, A.C. Jones, A.G. Taylor, D. Phillips, *Chem. Phys. Lett.* **1989**, 163, 282.
94. R.A. Weersink, S.C. Wallace, *J. Phys. Chem.* **1994**, 98, 10710.
95. (a) R. Pereira, I. Alava, F. Castaño, M.T. Martinez, *J. Chem. Soc., Faraday Trans.* **1994**, 90, 2443; (b) R. Pereira, T. Calvo, F. Castaño, M.T. Martinez, *Chem. Phys.* **1995**, 201, 433.
96. R. Khundar, A.H. Zewail, *J. Chem. Phys.* **1986**, 84, 1302.
97. (a) K. Yamasaki, K. Arita, O. Kajimoto, K. Hara, *Chem. Phys. Lett.* **1986**, 123, 277; (b) K. Arita, K. Yamasaki, K. Honma, O. Kajimoto, K. Tabayashi, K. Shobatake, *Chem. Phys. Lett.* **1986**, 125, 184; (c) K. Honma, K. Arita, K. Yamasaki, O. Kajimoto, *J. Chem. Phys.* **1991**, 94, 3496; (d) T. Fujiwara, Y. Fujiwara, O. Kajimoto, *J. Chem. Phys.* **1996**, 261, 201; (e) T. Ishida, Y. Fujiwara, T. Fujiwara, O. Kajimoto, *J. Chem. Phys.* **1998**, 288, 433.
98. A. Subaric-Leitis, C. Monte, A. Roggan, W. Rettig, P. Zimmermann, J. Heinze, *J. Chem. Phys.* **1990**, 93, 4543.
99. O. Kajimoto, S. Hayami, H. Shizuka, *Chem. Phys. Lett.* **1991**, 177, 219.
100. (a) S. Lee, K. Arita, O. Kajimoto, *Chem. Phys. Lett.* **1997**, 265, 579; (b) S. Lee, O. Kajimoto, *J. Phys. Chem. A* **1997**, 101, 5232.
101. C. Monte, A. Roggan, P. Subaric-Leitis, W. Rettig, P. Zimmermann, *J. Chem. Phys.* **1993**, 98, 2580.
102. R. Howell, A.G. Taylor, D. Phillips, *Chem. Phys. Lett.* **1992**, 188, 119.
103. (a) J. Jortner, M. Bixon, H. Heitele, M.E. Michel-Beyerle, *Chem. Phys. Lett.* **1992**, 197, 131; (b) J. Jortner, M. Bixon, B. Wegewijs, J.W. Verhoeven, R.P.H. Rettschnick, *Chem. Phys. Lett.* **1993**, 205, 451; (c) M. Bixon, J. Jortner, *J. Phys. Chem.* **1993**, 97, 13061; (d) J. Jortner, M. Bixon, *J. Photochem. Photobiol. A: Chem.* **1994**, 82, 5.
104. Y. Tajima, H. Ishikawa, T. Miyazawa, M. Kira, N. Mikami, *J. Am. Chem. Soc.* **1997**, 119, 7400.
105. P.M. Felker, J.A. Syage, W.R. Lambert, A.H. Zewail, *Chem. Phys. Lett.* **1982**, 92, 1; (b) J.A. Syage, P.M. Felker, A.H. Zewail, *J. Chem. Phys.* **1984**, 95, 2233.
106. (a) H. Shou, J.C. Alfano, N.A. van Dantzig, D.H. Levy, N.C. Yang, *J. Chem. Phys.* **1991**, 95, 711; (b) N.A. van Dantzig, H. Shou, J.C. Alfano, N.C. Yang, D.H. Levy, *J. Chem. Phys.* **1994**, 100, 7068.
107. (a) N. Kizu, M. Itoh, *J. Phys. Chem.* **1992**, 96, 5796; (b) N. Kizu, M. Itoh, *J. Am. Chem. Soc.* **1993**, 115, 4799.
108. (a) B. Wegewijs, R.M. Hermant, J.W. Verhoeven, A.G.M. Kunst, R.P.H. Rettschnick, *Chem. Phys. Lett.* **1987**, 140, 587; (b) R.M. Hermant, B. Wegewijs, J.W. Verhoeven, A.G.M. Kunst, R.P.H. Rettschnick, *Recl. Trav. Chim. Pays-Bas* **1988**, 107, 349; (c) J.W. Verhoeven, B.

- Wegewijs, J. Kroon, R.P.H. Rettschnick, M.N. Paddon-Row, A.M. Oliver, *J. Photochem. Photobiol. A: Chem.* **1994**, 82, 161; (d) J.W. Verhoeven, B. Wegewijs, R.M. Hermant, R.J. Willemse, A.M. Brouwer, *J. Photochem. Photobiol. A: Chem.* **1996**, 95, 3.
109. (a) U. Boesl, *J. Phys. Chem.* **1991**, 95, 2949; (b) U. Boesl, R. Weinkauff, E.W. Schlag, *Int. J. Mass Spectrom. Ion Processes* **1992**, 112, 121.
110. (a) C. Kittrell, E. Abramson, J.L. Kinsey, S.A. McDonald, D.E. Reiser, R.W. Field, *J. Chem. Phys.* **1981**, 75, 2056; (b) T. Ebata, M. Furukawa, T. Suzuki, M. Ito, *J. Opt. Soc. Am. B* **1990**, 1890.
111. (a) P.J. Breen, J.A. Warren, E.R. Bernstein, J.I. Seeman, *J. Chem. Phys.* **1987**, 87, 1917; (b) *J. Chem. Phys.* 1927; (c) P.J. Breen, E.R. Bernstein, J.I. Seeman, *J. Chem. Phys.* 3269; (d) J.I. Seeman, H.V. Secor, P.J. Breen, V.H. Grassian, E.R. Bernstein, *J. Am. Chem. Soc.* **1989**, 111, 3140.
112. D.B. Moss, C.S. Parmenter, G.E. Ewing, *J. Chem. Phys.* **1987**, 86, 51.
113. (a) K. Okuyama, N. Mikami, M. Ito, *J. Phys. Chem.* **1985**, 89, 5617; (b) M. Ito, *J. Phys. Chem.* **1987**, 91, 517; (c) H. Mizuno, K. Okuyama, T. Ebata, M. Ito, *J. Phys. Chem.* **1987**, 91, 5589; (d) K. Okuyama, N. Mikami, M. Ito, *Laser Chem.* **1987**, 7, 197.
114. R.A. Weersink, S.C. Wallace, *J. Phys. Chem.* **1993**, 97, 6127.
115. (a) R. Cervellati, A. Dal Borgo, D.G. Lister, *J. Mol. Struct.* **1982**, 78, 161; (b) R. Cervellati, G. Corbelli, A. Dal Borgo, D.G. Lister, *J. Mol. Struct.* **1981**, 73, 31; (c) H. Yu, E. Joslin, D. Phillips, *J. Chem. Soc. Faraday Trans.* **1993**, 89, 2345.
116. (a) W.G. Fateley, F.A. Miller, *Spectrochim. Acta* **1962**, 18, 977; (b) K.D. Möller, A.R. DeMeo, D.R. Smith, L.H. London, *J. Chem. Phys.* **1967**, 47, 2609.
117. (a) N. Mikami, A. Hiraya, I. Fujiwara, M. Ito, *Chem. Phys. Lett.* **1980**, 74, 531; (b) D.E. Powers, J.B. Hopkins, R.E. Smalley, *J. Chem. Phys.* **1980**, 72, 5721.
118. (a) T. Kobayashi, K. Honma, O. Kajimoto, S. Tsuchiya, *J. Chem. Phys.* **1987**, 86, 1111; (b) T. Kobayashi, O. Kajimoto, *J. Chem. Phys.* **1987**, 86, 1118.
119. J.M. Hollas, *High Resolution Spectroscopy*, Butterworths, London, **1982**.
120. (a) A.E.W. Knight, C.M. Lawburgh, C.S. Parmenter, *J. Chem. Phys.* **1975**, 63, 4336; (b) J.A. Konigs, W.A. Majewski, Y. Matsumoto, D.W. Pratt, W.L. Meerts, *J. Chem. Phys.* **1988**, 89, 1813; (c) R.E. Bandy, J. Nash, T.S. Zwier, *J. Chem. Phys.* **1991**, 95, 2317.
121. (a) A. Modelli, G. Distefano, *Z. Naturforsch., Teil. A* **1981**, 36, 1344; (b) A. Buchs, *Helv. Chim. Acta* **1970**, 53, 2026.
122. A. Weller, *Z. Phys. Chem. NF* **1982**, 133, 93.
123. Ch. Desfrancois, H. Abdoul-Carime, J.-P. Schermann, *Int. J. Mod. Phys.* **1996**, 10, 1339.
124. H.-D. Barth, K. Buchhold, S. Djafari, B. Reimann, U. Lommatzsch, B. Brutschy, *Chem. Phys.* **1998**, 239, 49.
125. (a) T.E. Gough, R.E. Miller, G.J. Scoles, *J. Chem. Phys.* **1978**, 69, 1588; (b) T.E. Gough, R.E. Miller, G.J. Scoles, *J. Phys. Chem.* **1981**, 85, 4041; (c) R.E. Miller, *Science* **1988**, 240, 447.
126. (a) M.F. Vernon, D.J. Krajnovich, H.S. Kwok, J.M. Lisy, Y.R. Shen, Y.T. Lee, *Faraday Discuss. Chem. Soc.* **1982**, 73, 387; (b) M.F. Vernon, D.J. Krajnovich, H.S. Kwok, J.M. Lisy, *J. Chem. Phys.* **1982**, 77, 47.
127. J.A. Beswick, J. Jortner, *J. Chem. Phys.* **1981**, 74, 6725.
128. (a) Ch. Riehn, Ch. Lahmann, B. Wassermann, B. Brutschy, *Chem. Phys. Lett.* **1992**, 197, 443; (b) Ch. Riehn, Ch. Lahmann, B. Wassermann, B. Brutschy, *Ber. Bunsenges. Phys. Chem.* **1992**, 96, 1161; (c) S. Djafari, G. Lembach, H.-D. Barth, B. Brutschy, *Z. Phys. Chem.* **1996**, 195, 253; (d) S. Djafari, H.-D. Barth, K. Buchhold, B. Brutschy, *J. Chem. Phys.* **1997**, 107, 10573; (e) K. Sugawara, J. Miyawaki, T. Nakanaga, H. Takeo, G. Lembach, S. Djafari, H.-D. Barth, B. Brutschy, *J. Phys. Chem.* **1996**, 100, 17145.
129. (a) S. Tanabe, T. Ebata, M. Fujii, N. Mikami, *Chem. Phys. Lett.* **1993**, 215, 347; (b) A. Fujii, S. Okuyama, A. Iwasaki, T. Maeyama, T. Ebata, M. Mikami, *Chem. Phys. Lett.* **1996**, 256, 1.
130. (a) R.N. Pribble, T.S. Zwier, *Faraday Disc.* **1994**, 97, 229; (b) C.J. Gruenloh, J.R. Carney, C.A. Arrington, T.S. Zwier, S.Y. Fredericks, K.D. Jordan, *Science* **1997**, 276, 1678; (c) R.N. Pribble, F. Hagenmeister, T.S. Zwier, *J. Chem. Phys.* **1997**, 106, 2145.
131. A.H. Zewail, in *Femtochemistry. Ultrafast Dynamics of the Chemical Bond*, Vols. 1 and 2, World Scientific, Singapore, **1997**.

132. (a) L.A. Philips, D.H. Levy, *J. Chem. Phys.* **1986**, 85, 1327; (b) L. Yu, S.C. Foster, J.M. Williamson, T.A. Miller, *J. Chem. Phys.* **1990**, 92, 5794; (c) G. Berden, M.L. Meerts, M. Schmitt, K. Kleinermanns, *J. Chem. Phys.* **1996**, 104, 972; (d) A. Held, D.W. Pratt, *J. Am. Chem. Soc.* **1993**, 115, 9708; (e) A. Nakajima, M. Hirano, R. Hasumi, K. Kaya, H. Watanabe, C.C. Carter, J.M. Williamson, T.A. Miller, *J. Phys. Chem. A* **1997**, 101, 392.
133. A. Douhal, S.K. Kim, A.H. Zewail, *Nature* **1995**, 378, 260.
134. D.E. Folmer, L. Poth, E.S. Wisniewski, A.W. Castleman, Jr., *Chem. Phys. Lett.* **1998**, 287, 1.
135. A. Kapturkiewicz, *Adv. Electrochemi. Sci. Engi.* **1997**, 5, 1.

4 Exciplexes of Large Molecules

Yehuda Haas

4.1 Introduction

In this chapter we discuss electron transfer between closed-shell donors and acceptors. Important oxidation–reduction reactions of free radicals, such as take place in the gas-phase combustion of hydrocarbons, are excluded. We also shall not discuss systems in which an electron is transferred in the ground state. The only interaction assumed for the ground state is due to weak van der Waals forces. Under ambient gas-phase conditions, these forces cannot support a lasting bond between the two partners. In solution, these forces are of the same magnitude as solute–solvent interactions, and the large concentration excess of the solvent results in effective separation between the two. In the gas phase, thermal energies are of the same order as the binding energy, so that, on average, a very small fraction of these molecules are close enough for electron transfer to take place.

Electronic excitation can change, in principle, the nature of the interaction. A bound charge-transfer state is often found at excitation energies of 2–4 eV. Its origin has been discussed in several chapters in this series (see Volume I). The ionization energy of a molecular electron donor to be considered in this chapter is typically 8–10 eV. The electron affinity of the acceptor is of the order of 0.5–1.5 eV, so that at infinite separation charge transfer from the neutral pair requires a 7–9 eV photon—the far-UV region. Strong Coulomb attraction between the opposite charges leads to reduction of the total energy as the two charged components approach each other. The distance between the two components cannot become very small, as it is limited by Pauli repulsion forces between the electron clouds of the two partners as they come nearer to each other. The balance between the attractive and repulsive forces determines the distance between the two components at the minimum (equilibrium) energy of the ion pair. The Coulomb interaction at the equilibrium geometry of the ion pair (~ 3 Å) is about 3–5 eV, and the minimum is often found to be between 2.5 and 5 eV, an easily accessible range with available light sources.

In the bulk, the low concentration of ground-state pairs excludes their observation by absorption. The formation of the excited-state complex, termed exciplex, is a collisional process: electronic excitation of either the acceptor or the donor leads to the formation of a locally excited state (for instance, in hydrocarbon molecules, it is a $\pi\pi^*$ state). During the lifetime of this state, a collision with the other partner (which is in the ground state) leads to the formation of the exciplex. This mechanism is compatible with the fact that the absorption and fluorescence *excitation* spectra of the system are identical with those obtained by superimposing the spectra of the individual components. At the same time, the fluorescence *emission* spectrum changes drastically—a broad band, red shifted with respect to the bare molecule's emission spectrum, appears. It is usually devoid of vibrational structure, and is shifted to longer wavelengths as the solvent polarity increases [1].

The wavefunctions of these systems have been traditionally represented by superpositions of the wavefunctions of the separated systems plus those due to charge transfer: $\psi_g(\text{DA})$ is the ground state represented by the product of the wavefunctions of the separate components [$\psi_g(\text{DA}) = \psi_g(\text{D})\psi_g(\text{A})$]. Likewise, $\psi_1(\text{DA}^*) = \psi_g(\text{D})\psi(\text{A}^*)$, and $\psi_{\text{CT}}(\text{D}^+\text{A}^-) = \psi(\text{D}^+)\psi(\text{A}^-)$. In a simple model, these three states combine to form three diabatic states: the ground state, Ψ_G , a locally excited state, Ψ_{LE} , and an exciplex, Ψ_{Exc} :

$$\Psi_G = a_0\psi_g(\text{DA}) + a_1\psi_1(\text{DA}^*) + a_{\text{CT}}\psi_{\text{CT}}(\text{D}^+\text{A}^-) \quad (1)$$

$$\Psi_{\text{LE}} = b_0\psi_g(\text{DA}) + b_1\psi_1(\text{DA}^*) + b_{\text{CT}}\psi_{\text{CT}}(\text{D}^+\text{A}^-) \quad (2)$$

$$\Psi_{\text{Exc}} = c_0\psi_g(\text{DA}) + c_1\psi_1(\text{DA}^*) + c_{\text{CT}}\psi_{\text{CT}}(\text{D}^+\text{A}^-) \quad (3)$$

(In principle, other charge-transfer states, such as due to the D^-A^+ pair, as well as other locally excited states, such as the D^*A pair, should be included. Their contribution, however, usually turns out to be less important).

In the ground state, one finds that $a_0 \gg a_1$, $a_0 \gg a_{\text{CT}}$, in the locally excited state, $b_1 \gg b_0$, $b_1 \gg b_{\text{CT}}$, and in the CT (exciplex) state, $c_{\text{CT}} \gg c_0$, $c_{\text{CT}} \gg c_1$. The $\psi(\text{DA}^*)$ state is referred to as a locally excited state, since its character is basically that of an electronically excited acceptor molecule, A, van der Waals bound to the ground state donor, D.

As mentioned in the Introductory Chapter of this Part, jet cooling allows the easy synthesis of van der Waals (vdW) adducts between two molecules. This technique has been widely used by microwave spectroscopists to elucidate the structure and binding characteristics of loose vdW complexes [2]. Temperatures of the order of 1–10 K are easily achieved, so that the binding energy of the complex is much larger than the average thermal energy. A potential electron donor and acceptor may therefore be brought together to a short distance in their ground state, possibly facilitating electron transfer if proper energetic conditions are met. The energy required for the electron transfer is provided by a photon, but after photoexcitation, the system may undergo several competing processes in addition to electron transfer. One of the difficulties encountered in gas-phase systems is the fact that charge separation is not a favoured process, in the absence of the stabilizing effect of the solvent. Hence back electron transfer often dominates the overall yield of the process.

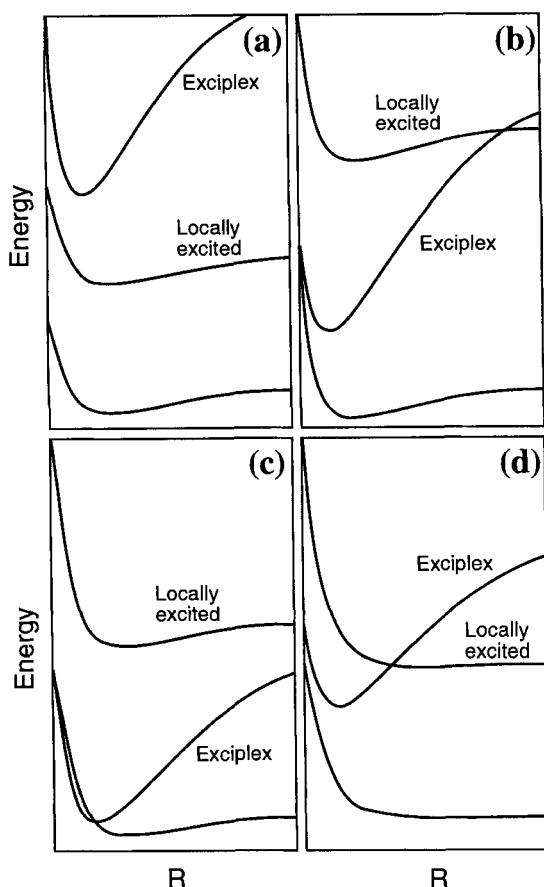


Figure 1. Schematic energy level diagram of exciplex systems. Adapted from Ref. [3]. See text for details.

Within the three-state model represented by Eqs. 1–3, the photophysics of potential exciplex systems are often discussed in terms of the simplified energy level diagrams shown in Figure 1 [3]. The two electronically excited states considered are the locally excited (LE) state, which in this chapter will be in general the first valence electronically excited state of the acceptor molecule, and an exciplex-type state, extrapolating at infinite distance to the separated ions. The diagrams are drawn along a single coordinate, R , the separation between the donor and the acceptor. This is a gross over-simplification for polyatomic systems. In fact, it is recognized that the system's energy depends on other coordinates, which may be most important for the understanding of the dynamics of electron transfer. In most cases, R is taken as the centre of mass separation, but sometimes the edge-to-edge distance is used.

Four schematic situations are shown in Figure 1. In (a), the exciplex state is at a much higher energy than the LE state at all intermolecular separations; excitation of the LE state cannot lead to electron transfer. It is noted that solvation may considerably reduce the energy of the exciplex state, so that the two energy curves may

cross in solution. In (b) the exciplex state is at a much lower energy than the LE state at about the equilibrium distance in the ground state. Franck–Condon excitation into the LE state is not likely to lead to charge separation, since the crossing of the two curves is near the dissociation energy of the LE state into A^* and D. In (c), the exciplex state is strongly stabilized, and mixes with the ground state. This situation leads to the formation of an ion-pair ground-state system, and the absorption spectrum of the system is characterized as a charge-transfer transition [4].

The situation depicted in (d) is the one most relevant to this chapter. Here, the crossing between the exciplex and the LE state is near the minimum of the latter. According to the Franck–Condon principle, absorption into the LE state is much favored over direct excitation of the exciplex. Nonetheless, excitation of the LE state creates a non-stationary state, which evolves in time. The transition between the two states is most likely to occur near the curve-crossing point. Therefore, analysis of these systems is in terms of radiationless transitions from the initially excited LE state to the exciplex state. Experimentally the latter is observed directly by its characteristic emission, or indirectly by its photochemical consequences. Inspection of the figure shows that the minimum of the exciplex state energy curve is at a smaller R than that of the ground-state van der Waals complex. Emission will therefore be strongly red shifted with respect to the excitation frequency. In addition, the emission is mostly to the repulsive part of the ground-state curve, so that the pair dissociates and the emission spectrum is broad and devoid of vibrational structure. These are the characteristic indications of exciplex-type emission.

The topic of electron transfer in jet-cooled systems has been reviewed several times in the past, in some cases with special attention to exciplex formation [3, 5]. These reviews covered the literature up to 1993 fairly extensively. We shall concentrate on the main advances made since that time, while giving an overview of the current understanding of these systems.

4.1.1 Evidence for Electron Transfer in Isolated Systems

When a potential acceptor molecule (such as anthracene) is cooled in a rare gas jet, its absorption and emission spectra are considerably simplified compared with the bulk: vibrational and even rotational bands are easily separated, and hot bands are eliminated, leading to removal of spectral congestion. Owing to the low number density characterizing supersonic jets (10^6 – 10^9 molecules cm^{-3}), absorption spectroscopy is rarely used in the UV range, and is replaced by more sensitive detection methods such as fluorescence or ionization. Thus, the fluorescence excitation spectrum or the ionization action spectra are frequently used. (In microwave [2] or high-resolution infrared spectroscopy [6], the very narrow bandwidth available allows the use of absorption spectroscopy in jet-cooled systems). The UV spectrum consists of a series of vibrational bands whose widths (for aromatic molecules) are of the order of 1 cm^{-1} , determined by the rotational envelope. The rotational structure of clusters can be analyzed by increasing the spectral resolution to 0.01 cm^{-1} and beyond. Fluorescence excitation has been used to record the rotationally resolved spectra of fairly large clusters such as argon and methane van der Waals complexes of naph-

thalene derivatives [7] and the cyanonaphthalene–trimethylamine complex [8]. The spectra allow the determination of the moments of inertia of the ground and excited states of these clusters, and hence the approximate determination of their structures. Mass-selected resonance-enhanced two-photon ionization was used to probe clusters of benzene and argon at a similar resolution [9]. These few examples (which are far from exhaustive) demonstrate the power of current spectroscopic instrumentation to provide very detailed information on the structure and energetics of van der Waals clusters in both the ground and excited electronic states.

Under lower resolution, the linewidths of the vibronic bands are of the same order as those of the bare molecule in both fluorescence excitation and emission. In some cases, the *emission* fluorescence spectrum is different, exhibiting broad emission bands. This situation is encountered when the co-seeded molecule is a potential electron donor, such as an aromatic or aliphatic amine. The jet spectrum in this case is very similar to solution spectra: it is broad (typical width $\sim 3000\text{ cm}^{-1}$), strongly red shifted from the excitation wavelength and is usually characterized by a long decay time. For instance, whereas the fluorescence lifetime of bare anthracene is about 20 ns in the jet, the anthracene–dimethylaniline adduct has a decay time of about 300 ns [10]. Based on a comparison with solution-phase studies, in which these spectra were identified as being due to the formation of an electronically excited charge-transfer complex, the broad emission spectra were assigned to an excited state having a strong charge-transfer character.

It should be noted that broad emission spectra are also observed in some cases for molecular dimers and larger aggregates, e.g., in the case of naphthalene [11]. The excited state in these homogeneous clusters is characterized as an excimer, and the interaction between the two components is mainly due to exchange interactions, although the contribution from charge-transfer states such as A^-A^+ is also important [12, 13].

Charge transfer can take place also when the acceptor and the donor are linked covalently by an ‘inert’ bridge. The bridge can be a flexible chain of CH_2 groups, a semi-flexible structure made, for instance, of cyclohexane or piperidine rings, or a rigid bridge of fused norbornane and bicyclo[2.2.0]hexane units. These bridges are considered to be inert in the sense that they act only to transmit the charge and not as charge sources or sinks. This topic is covered elsewhere in the chapter by Paddon-Row (Chapter III.2.1). Several excellent reviews are available; the most recent one by Wegewis and Verhoeven discusses extensively the jet work of the Amsterdam group [14].

When the bridge itself contains a potential electron donor or acceptor, the situation can be more complex. Thus, Tsujiya et al. [15] studied the intramolecular electronic interaction between anthracene (An) and dimethylaniline (DMA) in bridged systems, when the bridge contained an ethereal oxygen. In these systems it was found that the appearance of exciplex emission depended strongly on the relative position of the ethereal oxygen with respect to the anthracene part of the molecule. For 1-An-O-(CH_2)₂-DMA, one conformer was found to exhibit no exciplex emission at all in the jet, whereas another showed both locally excited and exciplex emission. For 1-An- CH_2 -O- CH_2 -DMA (and also for 9-An- CH_2 -O- CH_2 -DMA), no exciplex emission was found in the jet, although the same molecules show exciplex emission in solution! It appears that the interaction between

$\text{CH}_2\text{--O--CH}_2$ and anthracene is sufficiently strong in the jet to prevent population of the charge-transfer state. The mechanism of this interaction needs further clarification.

4.2 Structure–Reactivity Relationships

Early work (prior to 1990) concentrated on the gross features of jet-cooled exciplexes. In the absence of collisions, and at the very low temperature prevailing, it was hoped that it would be possible to find whether certain structures are more inclined than others to permit charge transfer in the excited state. It was soon realized from the pioneering work of Itoh's group on intermolecular clusters [16] and of Zewail's group on linked pairs [17] that in certain systems, excess energy is required in order to induce charge transfer. Changing the excitation wavelength varied the energy content of the system. In this case, the energy initially resides in the internal vibrational degrees of freedom of the acceptor, and has to be transferred to intermolecular degrees of freedom, to allow electron transfer. It was assumed that structural reorganization was necessary, for instance that the donor and acceptor moieties must achieve a certain relative alignment so that the necessary curve crossing can take place.

Levy and co-workers [18] studied a number of linked donor acceptor systems. The acceptor was anthracene and the donor an aniline derivative. The donor and acceptor were linked by a $(\text{CH}_2)_n$ chain with n varying between 1 and 4, the link to the aniline moiety being through the nitrogen atom [$9\text{-An}-(\text{CH}_2)_n\text{-N}(\text{CH}_3)\text{C}_6\text{H}_5$]. Only excitation near the origin was investigated—the goal was to find out whether the system could transfer an electron upon electronic excitation without adding excess vibrational energy. It was found that in the short-chain systems, only locally excited fluorescence was present. With $n = 4$, two different spectra were recorded, one exhibiting the narrow, well-resolved, vibrational structure of a locally excited state and the other showing a typical exciplex spectrum in both excitation and emission. The former was assigned to an all-*trans* conformer, in which the donor and acceptor are too far apart to allow electron transfer. In the latter, a folded conformation was assumed, based on a geometric calculation that showed that the donor and acceptor were at a van der Waals contact with each other. In this case it was argued that the charge-transfer state is lower in energy than the locally excited state, and that it interacts strongly with the ground state. In fact, the interaction is strong enough to impart a partial charge-transfer character to the ground state [4]. Under these conditions, the lowest lying electronic transition is of a charge-transfer character.

A similar situation is encountered in other systems. For instance, in the case of the pair pyrene (acceptor)–dimethylaniline (donor) connected by a propyl [$(\text{CH}_2)_3$] chain, one of the conformers is found to exhibit a charge-transfer band at the origin [19]. Another conformer, possibly a stretched one, shows only locally excited fluorescence at the origin, and exciplex type as the vibronic energy is increased. It seems that for strong acceptors, such as pyrene, an $n = 3$ chain is sufficiently long to allow

strong electrostatic interaction between the two components even in the ground state. Another example is the 1-(9,10-dicyanoanthryl)-3-(2-naphthyl)propane molecule, which exhibits a broad charge-transfer band in absorption. This is due to the fact that 9,10-dicyanoanthracene is a strong electron acceptor, allowing ground-state charge-transfer interaction with naphthalene when the two are connected with a propyl ($n = 3$) link.

In the early developments of this field, only energetic requirements were considered, and statistical methods were used to analyze the data [17]. The current effort is concentrated on a more detailed analysis, both experimentally and theoretically.

4.2.1 The Co-existence of Several Isomers

The very first fluorescence spectra of jet-cooled exciplexes indicated the existence of two types of ground-state van der Waals adducts. For instance, the anthracene–dimethylaniline system displayed two types of cluster bands in the fluorescence excitation spectrum: broad ($\sim 150\text{ cm}^{-1}$) and structureless, leading to typical exciplex emission, and narrow (1 cm^{-1}), leading to resonance-type emission [10, 20]. It was assumed that they are due to different 1:1 adducts, distinguished by different geometries. Recently, laser-based techniques were developed that allow the discrimination of different species. One is hole-burning spectroscopy and another—mass-selected photoionization.

4.2.2 Hole-burning Spectroscopy

In this method, two pulsed lasers are used, both usually in the nanosecond regime. One (the ‘burn’ laser) is operated at high power, and is scanned across the absorption spectrum. It excites molecules (or clusters) from the particular vibrational level (usually the $v = 0$ level) to an electronically excited state. The upper state relaxes (radiatively or otherwise) back to the ground state, but not necessarily to $v = 0$. Thus, depletion in the population of this species is achieved. A second, low-power laser (the ‘probe’ laser) is fired after a suitable time delay (to allow complete decay of the emission induced by the pump laser). It is tuned to one of the excitation spectrum vibronic bands of the system, and the fluorescence induced by it (the ‘signal’) is continuously monitored. Whenever the frequency of the burn laser corresponds to excitation of the species giving rise to the absorption of the probe laser, the signal is reduced. This reduction appears as a ‘hole’ that is burned in the spectrum—hence the name of the method. If a different species is excited (another molecule or a different vibrational level) no change in fluorescence intensity is incurred.

Itoh’s group and also Tramer, Piuze and their co-workers used this method extensively for the study of jet-cooled exciplexes. Examples of hole-burning spectra are shown in Figures 2 and 3.

The results of these studies may be summarized as follows. The first published application of hole burning to exciplex-forming systems in supersonic jets appears

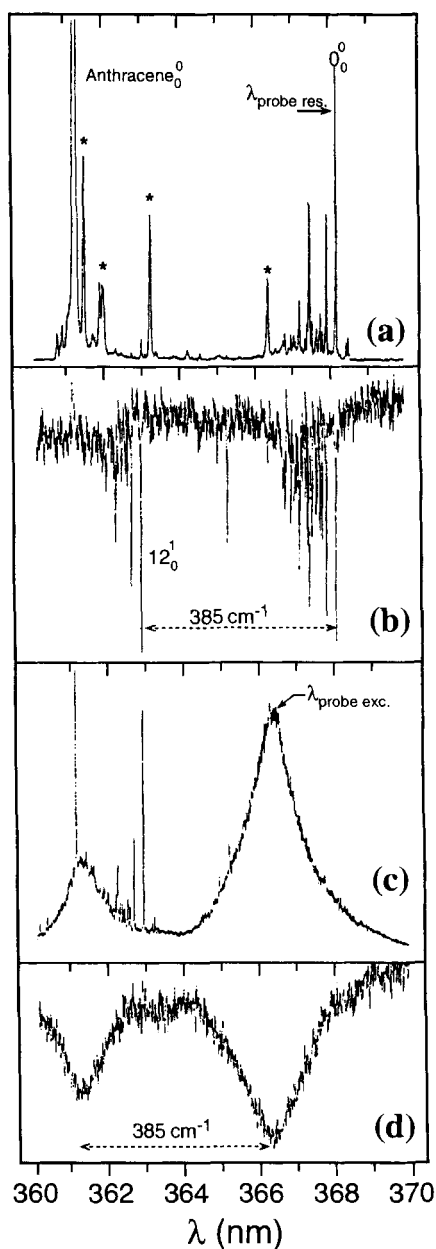


Figure 2. Characterization of intermolecular exciplexes by hole-burning spectroscopy. Adapted from Ref. [22a]; (a) Fluorescence excitation ($\lambda_{\text{emission}}$ set at 375 nm) and (b) hole-burning spectra of the R-isomer of the anthracene–dimethylaniline (An–DMA) adduct in a supersonic jet. The probe laser was tuned on the most intense line of the adduct. Lines marked with asterisks are due to bare anthracene. (c) Fluorescence excitation ($\lambda_{\text{emission}}$ set at 450 nm) and (d) hole-burning spectra of the E-isomer of the An–DMA adduct in a supersonic jet. The probe laser was tuned to the maximum of the broad exciplex excitation band.

to be Piuze's 1993 paper [21]. A comprehensive summary of the group's results is given in two 1998 papers [22] and further information may be found in other papers [23, 24]. The acceptor in these systems was anthracene (An), and several aniline derivatives (see Scheme 1 for their structures) were used as donors. Early on, these

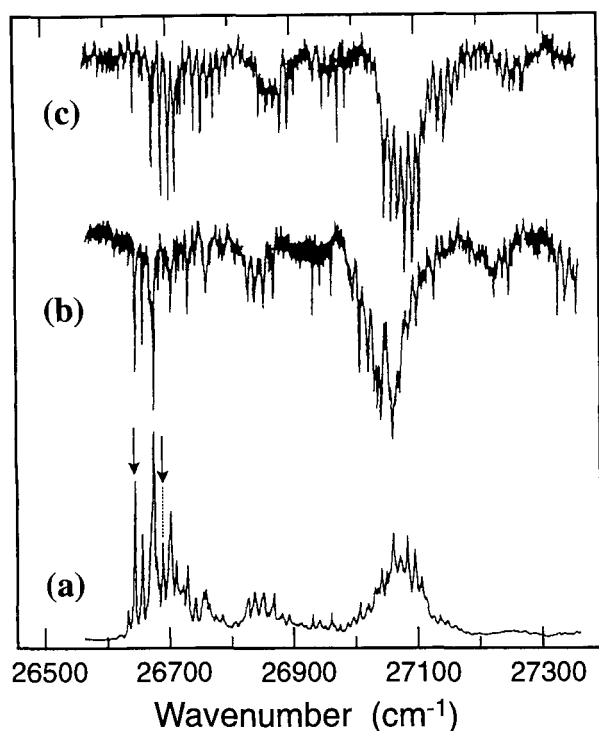
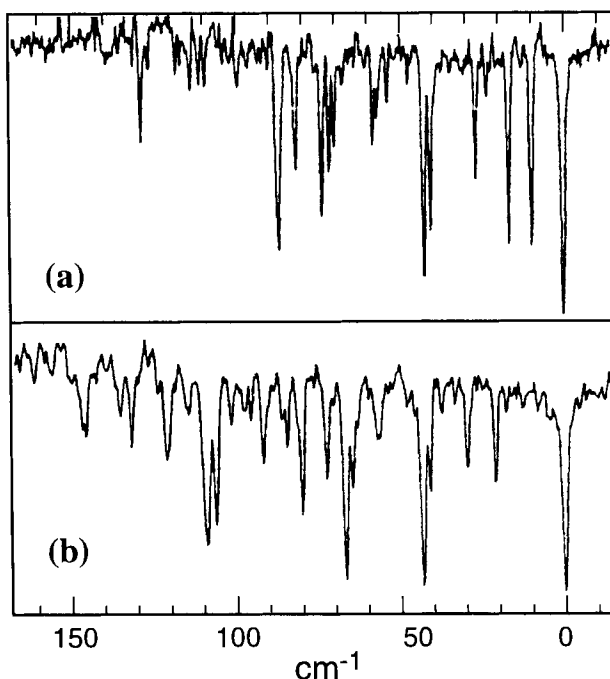


Figure 3. Example of fluorescence excitation and hole-burning spectra of an intramolecular exciplex: the fluorescence excitation spectrum ($\lambda_{\text{emission}}$ set at 395 nm, locally excited fluorescence) of 9-An-*m*-DMA (see Scheme 1 for structure) (b), along with two hole-burning spectra, (a) the probe laser set at $26\,644\text{ cm}^{-1}$ and (c) the probe laser set at $26\,689\text{ cm}^{-1}$. The arrows in (a) indicate the bands used for the probe lasers. Adapted from Ref. [19b].

workers [20], in agreement with other groups [10], showed that two different fluorescence spectra were observed in the jet-cooled An-DMA systems. These spectra were assigned to locally excited (LE) states, and to exciplex states. The former (termed R-isomers by Tramer and co-workers) were characterized by narrow-band systems in both emission and excitation. R stands for resonance, since the origin of these bands in excitation and emission coincided. The latter, termed E-isomers, showed broad and vibrationally unresolved emission spectra. E stands for exciplex; in this case, the structureless emission spectrum is strongly red shifted with respect to excitation. Mass-selective multiphoton ionization (MPI) showed that under appropriate expansion conditions, only 1:1 adducts were present in the jet expansion. The appearance of different excitation series in the fluorescence spectrum must therefore be assigned to isomers.

Hole-burning spectroscopy revealed one E-isomer and one to five R-isomers for each donor–acceptor pair. The E-isomer spectra, having broad bands, may in fact be due to several overlapping bands (see below). The spectra of the R-isomers, on the other hand, could be easily separated and analyzed. The number of isomers appears to depend on the complexity of the donor's structure: there is only one isomer for the parent molecule (DMA), and the largest number is found for DMOT (see scheme 1), in which the two N-bound methyl groups strongly interact with the *ortho*-substituted methyl group. Figure 4 shows the hole-burning spectra of two isomers and it can be seen that they are readily distinguishable.

Figure 4. Hole-burning spectra of the anthracene–dimethyl-*o*-toluidine (An–DMOT) pair, demonstrating the existence of two R-isomers. The vibrational structures of the electronic transitions of the two isomers are clearly different. The probe laser was set at the origins of the two isomers, respectively, which are separated by 97 cm^{-1} from each other; the spectrum shown in (a) is red shifted from that of bare anthracene by 493 cm^{-1} and that shown in (b) is shifted by 396 cm^{-1} . Adapted from Ref. [22a].



The relative populations of the different isomers were calculated from the fluorescence intensities assuming that the fluorescence quantum yields were the same. This assumption, in turn, is based on the experimental finding that the measured decay times were the same for all R-isomers. A semi-empirical method due to Claverie and co-workers [25] was used to calculate the relative energy stabilization of the ground-state isomers (see Section 4.6), and good agreement between the number of experimental and calculated isomers was found. This may eventually allow the tentative assignment of different spectroscopic features to molecular structures with reasonable confidence. It was calculated that the barriers for conversion of one isomer to another on the ground state surface are typically very small, of the order of 1 kcal mol^{-1} . Hence their presence cannot be observed under usual experimental conditions (room temperature, solution phase); jet cooling is the method of choice to discern these fine details. R-isomers are easily transformed in to E-isomers in the excited state: they are mostly observed near the origin, and at excess energies of $0\text{--}200\text{ cm}^{-1}$ they show exciplex emission. This transition is interpreted as a photoinduced electron transfer, the rate of which is discussed in the Section 4.4.

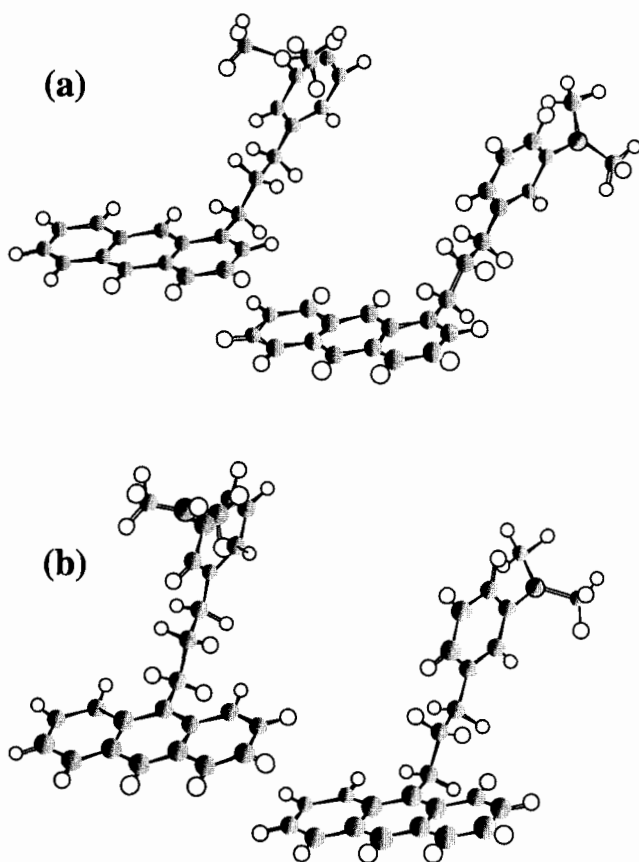
The co-existence of several isomers allows one, in principle, to check possible differences in their photophysical properties. In a recent paper, two-color mass-selective MPI was used to estimate the relative efficiency of the ionization of isomeric forms of DMOT–anthracene adducts [24]. It was found that photodetachment of an electron from the exciplex excited state is about 10 times more efficient than that from LE excited states. A similar observation was made in the case of NaI

[26]. The reason for this difference is not yet obvious, nor is it clear whether this is a general phenomenon. In fact, an opposite trend was reported for the styrene–trimethylamine system [27]. In any case, the difference in ionization efficiency may become another tool for studying gas-phase systems. In cases where several R-isomers co-exist in the jet, some differences were recorded in their photophysical behavior. The change in the rate of R → E isomerization was found to depend on the internal energy in a different way. However, the differences were in general small.

Itoh and co-workers applied the hole-burning method to the study of intermolecular donor–acceptor pairs, linked by a flexible covalent chain. Two of the molecules studied by this group are depicted schematically in Scheme 1. Rotation around single CC (or CO) bonds allows the co-existence of several conformational isomers, which may be present in the jet after the expansion. The goal of these studies was to identify such isomers and study their photophysics. Previous work indicated that several different excitation and emission spectra may be observed from a given sample. In particular, both exciplex-type and locally excited fluorescence were often observed. For the latter it was found that increasing the vibrational energy content of the excited state beyond a certain threshold value led to a gradual increase in the exciplex-type emission. One of the goals of the hole-burning experiments was to find out whether the transition from the locally excited state to the exciplex-type state transition depended on the nature of the different conformational isomers.

The results may be summarized as follows. For 4-(2',3'-dimethylbutenyloxy)-methyl-1-cyanonaphthalene (4-DMB-CNN) [28], hole-burning spectroscopy revealed three different excitation bands. In all, locally excited fluorescence dominated the spectrum at low excitation energies, and a gradual shift to exciplex-type emission was observed as the vibrational energy of the excited electronic state increased. The cyanonaphthalene moiety acts as an electron acceptor and the dimethylbutene moiety as the electron donor. The rate of the transition to the exciplex emission varied among the different isomers, but beyond a certain excess energy (1100 cm^{-1}), no significant difference in exciplex formation could be detected. The three conformers were assigned to the *trans*, *anti-gauche* and *syn-gauche* structures of the molecule.

The 1-(1-anthryl)-3-phenylpropane (1-An-Ph) structure [and the 9-anthryl analog (9-An-Ph)] for which no exciplex emission was observed was studied as a reference system [29]. For both molecules, several conformers are possible, but exciplex-type emission is unlikely, since the two moieties (anthracene and benzene) linked by the flexible propane bridge do not tend to form a donor–acceptor pair. Two major fluorescence excitation series were revealed in both. As the vibrational energy was increased, the decay times of one isomer (isomer I) hardly changed in the range $0\text{--}2000\text{ cm}^{-1}$, whereas a threefold decrease was found in the other (isomer II). The form of the emission spectrum also changed—for both isomers the emission spectrum becomes more diffuse as the internal energy is increased. This change takes place at a higher energy for isomer II than for isomer I. Based on comparison with previous work on rotational conformers (e.g., propylbenzene [30]), it was suggested that isomer I is the *gauche/trans* (*g/t*) isomer, and isomer II is the *trans/trans* (*t/t*) isomer. Torsional motion appears to be important for intramolecular vibrational



Scheme 1 (continued)

energy redistribution (IVR), which is the process responsible for the increased diffuseness of the spectrum and the decrease in fluorescence decay time. In the more tightly folded *g/t* conformer, IVR is restricted, leading to the observed behavior. Simple semi-empirical calculations supported the interpretation.

Several linked molecules in which the donor is an aniline derivative and the acceptor an anthracene moiety were investigated. In the case of anthracene linked to *N,N*-dimethylaniline by a trimethylene bridge, two molecules were investigated. In both the link was to the *meta* (3-) position of the aniline. In one anthracene was linked in the 9-position, (9-anthryl)-3-[*m*-(*N,N*-dimethylamino)phenyl] propane (9-An-*m*-DMA), and in the other the link was to the 1-position (1-An-*m*-DMA). In both cases hole-burning spectroscopy revealed two distinct species, that were assigned to two isomeric forms (possible structures are shown in Scheme 1). The emission spectra of both forms at the origin bands were essentially of the locally excited type. As the internal energy was increased, the exciplex emission spectrum

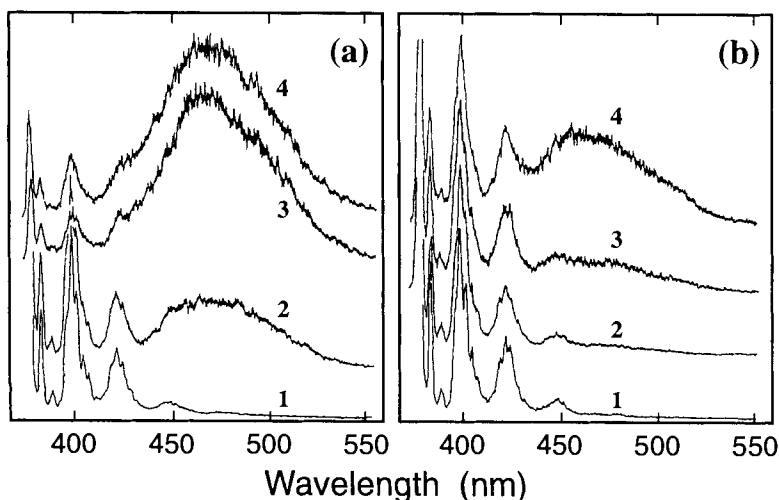


Figure 5. Changes in the fluorescence spectrum of two isomeric intramolecular adducts of 9-An-*m*-DMA as a function of excitation energy: (a) the isomer having an origin at $26\,644\text{ cm}^{-1}$ and (b) the isomer having an origin at $26\,689\text{ cm}^{-1}$. Adapted from Ref. [19b].

gradually increased in intensity, until it dominated the spectrum. The rate at which the exciplex-type emission increases was different for the two isomers. Figure 5 shows the changes in the fluorescence spectra of the two forms of 9-An-*m*-DMA as the excitation energies are increased. A qualitatively similar situation was observed for 1-An-*m*-DMA. The threshold for the onset of exciplex emission was different for the two forms in the two molecules, as shown in Figure 6. It was suggested that the two species are conformational isomers, and that in order to form the exciplex, the molecule must undergo an intramolecular conformational change that will allow electron transfer. The exact nature of the two conformers could not be established, although on the basis of comparison with the non-exciplex-forming 1-An-Ph and 9-An-Ph, it was proposed that they were probably due to *trans/trans* and *trans/gauche* structures.

The photodynamics of linked systems are thus a sensitive function of their structure, and the excess energy dependence of the electron transfer depends on the details of the intramolecular dynamics. IVR and electron transfer are two important processes that may compete with each other or, conversely, operate in harmony. One way to check the role of IVR without significantly changing the electronic structure of the molecule is by isotopic substitution. The main change is in the vibrational energy-level density. Itoh and co-workers [31] applied this method to the 9-An-*m*-DMA system mentioned above. It was found that the S_1 vibrational energy thresholds for formation of the exciplex were considerably *smaller* in the deuterated molecules than those for the respective protonated molecules. This result is consistent with the assumption that the transition from the locally excited state (the one is initially excited) to the exciplex state, is aided by an increase in the energy level

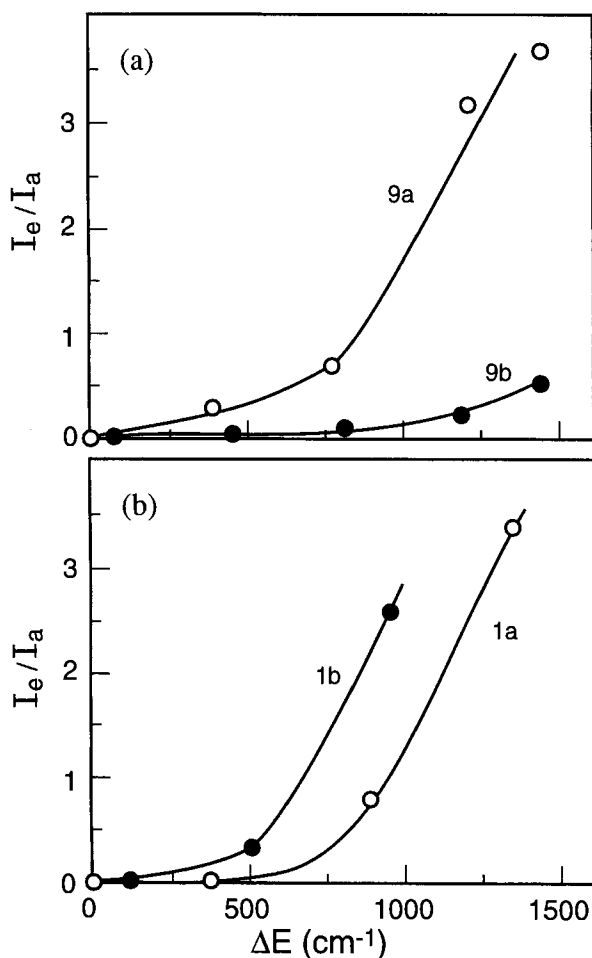


Figure 6. Ratio of the exciplex-type fluorescence intensity (I_e) to that of the locally excited-type fluorescence intensity (I_a) in an intramolecular adduct as a function of excitation energy. The upper panel shows the data for two isomers of 9-An-*m*-DMA and the lower panel for two 1-An-*m*-DMA isomers. The different onsets of exciplex emission are clearly displayed for different isomers. For possible structures of these isomers, see Scheme 1. Adapted from Ref. [19b].

density in the locally excited A^*D complex. The increased density increases the IVR rate, which in turn enhances the rate of internal rotation. Thus, the folding into the 'right' conformer suitable for electron transfer is promoted, leading to faster exciplex formation. This paper [31] therefore provides almost direct experimental evidence for the role of IVR. It would be interesting to find out by direct monitoring of the absorption of the exciplex state whether the rate of its formation is indeed increased upon deuteration.

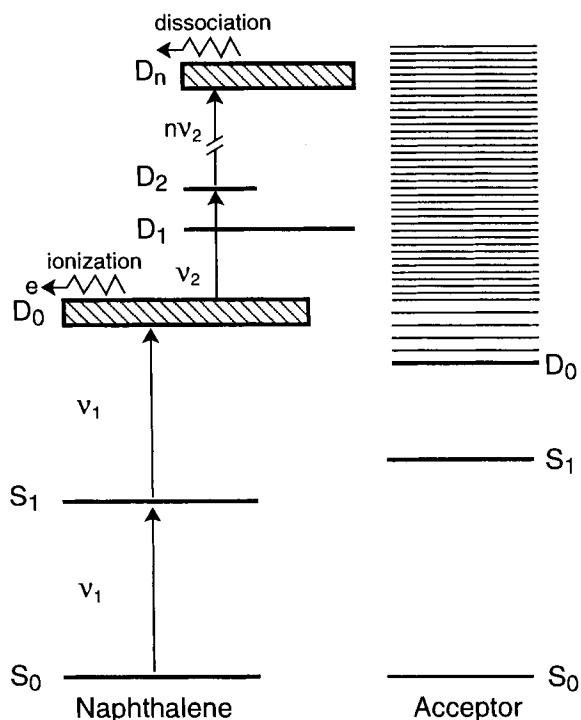


Figure 7. Schematic energy level diagram showing the principle of the ionization method for detecting electron transfer in gas-phase adducts. Naphthalene cation (the hole donor) is formed by resonance-enhanced two-photon ionization of the neutral. A hole acceptor, whose ionization potential is lower than that of naphthalene, is not ionized, since its S_1 level is not resonant with the UV photons used (ν_1). The vibrational levels of the ionic form of the acceptor are resonant with the naphthalene cation, and accept the hole easily. Detection is by photodissociation, using photons of different frequency (ν_2) that dissociate the naphthalene cation in a resonance-enhanced multiphoton absorption process. Charge transfer is detected by the diminution of the product ion signal in the presence of a suitable acceptor. Adapted from Ref. [32].

4.2.3 Two-color Photoionization

UV absorption spectroscopy is usually not sensitive enough to monitor ions directly in the jet. Even if the original ion pair is somehow dissociated into two separate ions having a characteristic absorption, their detection by high-resolution absorption spectroscopy is often impractical. The nascent product ions are formed in a large number of quantum states, and the small population of a single state cannot be detected with reasonable signal-to-noise ratio.

Ionization is much more sensitive, and may serve in principle as another tool for detecting ions or charge transfer. Levy and co-workers [32, 33] offered a scheme by which charge transfer between two species linked by a suitable bridge may be detected. The scheme is outlined in Figure 7. The donor is ionized by a two-photon

process, in which an excited state acts as a resonance enhancer. A potential acceptor (of positive charge), that has a lower ionization potential than the donor, is linked to the donor. Its direct ionization by the laser is avoided by choosing an acceptor whose intermediate electronic excited state is higher in energy than that of the donor. Once the donor ion is formed, it may transfer its charge to the acceptor. The process is monitored using a second laser source *of a different frequency* that induces fragmentation of the molecule. The second laser is tuned to the absorption spectrum of the donor ion, thus ensuring selective dissociation. In particular, if charge is quickly transferred to the acceptor, no adsorption of the second laser light takes place, and therefore no fragments can be observed. The amount of photoproducts thus serves as a measure for the efficiency of charge transfer.

The method was applied to systems similar to those previously studied in solution [34]. Naphthalene was used as a donor and a variety of molecules as acceptors. The spacer was either a cyclohexane ring or a steroid (androstane). It was found that the idea works in principle: when the other molecule had a higher ionization potential than naphthalene, extensive fragmentation was induced by the second laser, as was the case in the absence of the second molecule (a naphthalene-spacer system). When the donor had a lower ionization potential, fragmentation virtually disappeared. This was interpreted as indicating that complete charge transfer took place within the time resolution of the experiment (~ 2 ns). Attempts to slow the charge transfer by using longer spacers failed. It is likely that applying picosecond laser pulses to this system will enable the charge-transfer rate to be followed in real time.

4.3 Distance Dependence of Charge Separation; Mechanisms

In all systems discussed above, relative motion of the donor and acceptor was possible either since they were separate species or because the 'bridge' connecting them was flexible. Verhoeven and co-workers have studied since the early 1980s systems in which that motion was limited by progressively using more rigid spacers. Early work was in solution, revealing solvent dependence as also found in the classical work of Closs, Miller and co-workers [34] and Wasielewsky [35]. In order to find out whether electron transfer could proceed over long distances in the absence of a solvent, Verhoeven and co-workers prepared a series of compounds that could be studied in a supersonic jet, i.e., under solvent-free conditions. This work was recently reviewed in detail [14], so we shall only summarize the essential features.

Electron transfer was followed by the exciplex fluorescence method: LE and exciplex-type emissions were recorded as a function of internal energy, as in the previously cited papers (Section 4.2). Here, however, the initial excitation was either of the electron donor or the acceptor. The electron-donating power was varied by simple substitution, with minimal interference with the nature of the spacer. Typical donors were *para*-substituted anilines or substituted naphthalenes. Typical acceptors were cyano-substituted naphthalenes (when anilines served as the donors) and dicyanoethylene or dicarbomethoxyethylene when naphthalenes served as donors. Spacers were of varying flexibility: semi-flexible (a piperidine ring which may have a

chair or boat form, attached to a methylene group, for instance **1r**, **2r** and **3r** in Scheme 1). More rigid ones, such as a piperidine ring attached to a vinyl group, for instance **1**, **2** and **3** in Scheme 1), and a most rigid spacer based of a norbornyl bridge, such as **7** in Scheme 1.

In these experiments, excitation was by absorption into the naphthalene moiety, and emission was monitored as a function of excitation energy. In the ground state, the semi-flexible molecule has a stretched conformation, so that the donor and acceptor are separated by at least 5.4 Å. Excitation near the origin led only to LE emission, as in the case of the systems studied by Zewail's [17] and Itoh's groups [19]. Considerable vibrational excitation was required for the appearance of exciplex-type emission. A harpoon mechanism (see Chapter IV.3.2 by Soep and Mestdagh) was suggested to account for the data: the donor sends out the electron to the acceptor over a long distance, and the system folds later on due to the Coulomb attraction between the separated charges. This mechanism was suggested for **1r** because the onset of exciplex emission was observed at 4.8 kcal mol⁻¹, whereas the estimated barrier for folding is 10 kcal mol⁻¹. This mechanism was supported by further experiments: the stretched form of the exciplex could not be observed in the gas phase, but a new emission, centered at 380 nm, was seen in cooled cyclohexane solution. It was assigned to the stretched exciplex by time-resolved studies [36]. The harpoon mechanism was also supported by using a more efficient electron donor (i.e., a molecule with a lower ionization potential). A methyl (**2r**) or methoxy (**3r**) group was placed *para* to the aniline nitrogen. In the resulting molecule, the spacer was identical with that of **1r**, so that the barrier to conformational change was the same. The acceptor unit was also identical, so the excitation spectrum was essentially the same. However, it was found that the threshold energy for exciplex emission was reduced from 4.8 to about 2.1 kcal mol⁻¹. This result is in line with the idea that the barrier to exciplex formation is not due to folding, but an intrinsic barrier to the harpooning. Its height is determined by the crossing point of the two potential surfaces in the classical Marcus mechanism, rather than to a nuclear motion. In terms of Figure 1, it is determined by the height of the crossing point between the LE state of the DA pair, and the exciplex state.

Molecules **1**, **2** and **3** are similar to **1r**, but instead of a flexible single bond connection between the piperidine ring and the acceptor, the vinyl bond makes the system much more rigid. In fact, the donor and acceptor moieties cannot come into close contact by folding. This was verified in solution studies, where the measured dipole moment for the exciplex state (23 D) is consistent with an *extended* rather than folded conformation. In the jet, the excitation spectrum of systems **1**, **2** and **3** were found to be red shifted (by about 5 nm at the origin) and much more congested than for **1r** (Figure 8). The emission spectra are broad and structureless, as expected for an exciplex state, even upon excitation at the longest wavelength, which is assumed to be the origin. The absence of locally excited fluorescence was interpreted as indicating rapid charge separation. From the known radiative lifetime of the parent system (vinylcyanonaphthalene, VCN) and width of the excitation bands, the charge separation rate constant was estimated to be 10¹⁰–10¹¹ s⁻¹ (see Section 4.4 for details).

Even more rigid donor–acceptor systems were constructed using a norbornyl bridge (systems **7** and **8**, Scheme 1). For **7**, the fluorescence excitation spectrum

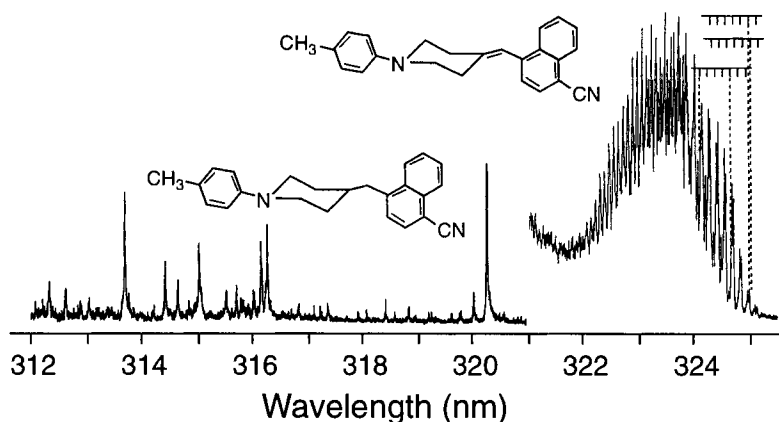


Figure 8. Excitation spectrum of two acceptor—donor systems, differing only by the spacer module connecting them. The left side shows the spectrum of **2r** (Scheme 1) and the right side that of **2**. Species **2** is the more rigid of the two and its spectrum is more red shifted and congested than that of **2r**. The vibrational progressions shown have a frequency of 13.5 cm^{-1} . Adapted from Ref. [14].

showed no vibrational structure at all, and only exciplex-type emission was observed. The conclusion was that in these systems, the charge-transfer state lies below the LE state, and is directly excited. In terms of Eqs. 1–3, it appears that the transition from the semi-flexible system **1r** to the more rigid molecule **1** and on to the completely rigid **7** involves a gradual change in the relative values of a_{CT} and c_{CT} . One could interpret the results in the time domain: initial excitation is into the LE state, and charge transfer follows. This is the weak coupling approximation, assuming that the donor and acceptor are weakly coupled, so that the system may be considered on the short time-scale characteristic of the light absorption process as being separate entities. An alternative interpretation is that the interaction between the donor and acceptor increases as the system becomes more rigid, so that the exciplex-type and LE states are strongly mixed even in absorption. This approach accounts for the difference between the excitation spectra of **2** and **2r** (Figure 8): the coupling between the two states causes the red shift in the spectrum of **2** compared with **2r**. Rather than viewing the spectrum of **2** as being a pure local excitation, it may actually be excitation of a mixed state, with a large contribution of charge transfer in the excited state. In that case, further time development of the system is controlled by statistics—the exciplex part has a higher density of states than the LE state, and emission is primarily from eigenstates of the exciplex. In solution, the exciplex state is further stabilized, and vibrational relaxation leads to the population of levels below the origin of the LE state.

In the fully rigid system (such as **7**), mixing is complete, and the charge-transfer character dominates even the absorption. It would be interesting to study the photophysics of donor–acceptor systems separated by several norbornyl groups. Such experiments are hampered by the low vapor pressure of these large molecules, but offer an opportunity for studying distance dependence in strongly coupled systems.

Recent experiments [37] showed that electronic energy transfer is very rapid in such systems.

4.4 Rate of Electron Transfer

Tramer et al. [22] discussed the rate of electron transfer in jet-cooled systems. Direct measurement is not always possible, but the rate may be estimated from the changes in fluorescence decay times and from linewidths. The estimate is based on the following data and assumptions:

- Initial excitation is always into the locally excited (LE) state, which then may decay either radiatively back to the ground state or non-radiatively to the exciplex state. Other processes are negligibly slow compared with these two.
- The fluorescence decay time of the locally excited state of the A*D complex (where A is anthracene and D the donor) is about 20 ns, hence the rate constant for depletion of this state, k_A , is $5 \times 10^7 \text{ s}^{-1}$.
- The rate constant for electron transfer is defined as the rate constant of formation of the exciplex state.
- The exciplex state is detected by the exciplex emission, which can be easily distinguished from the locally excited state owing to its much longer decay time (150–300 ns), the large red shift and the broad and structureless spectrum.
- The absence of exciplex emission following photoexcitation in a given system indicates that the rate constant for exciplex formation is at least an order of magnitude smaller, namely $k_{ET} = 5 \times 10^6 \text{ s}^{-1}$.
- If dual fluorescence is observed (both exciplex and LE), then k_{ET} is of the order of magnitude of k_A , namely $5 \times 10^6 \text{ s}^{-1} < k_{ET} < 5 \times 10^8 \text{ s}^{-1}$. Its value may be deduced from direct measurement of the fluorescence decay time of the LE state.

A simple kinetic scheme yields the following equation for the ratio of the integrated exciplex emission intensity, I_{EXC} , to the LE integrated emission intensity, I_{LE} :

$$I_{EXC}/I_{LE} = (k^r_{EXC}/k_{EXC})/(k^r_{LE}/k_{ET}) \quad (4)$$

where k^r_{EXC} is the radiative rate constant of the exciplex, k^r_{LE} is the radiative rate constant of the locally excited state and k_{EXC} is the observed decay rate constant of the exciplex. This expression holds for a short pulse excitation and when $k_{ET} \gg k_{EXC}$. Hence k_{ET} may be deduced if the intensity ratio and the radiative rate constants are known. If only exciplex emission is observed (as is the case when the E-isomer is excited), the electron-transfer rate is at least one order of magnitude larger than k_A , namely $5 \times 10^8 \text{ s}^{-1} < k_{ET}$. An upper limit for the rate constant may be estimated from the linewidths of the excitation bands. Assuming that broadening beyond the rotational envelope width ($\sim 1 \text{ cm}^{-1}$) is due to the electron-transfer rate means that as long as no broadening is observed, k_{ET} is $< 2 \times 10^{11} \text{ s}^{-1}$. When the linewidth exceeds $2 \times 10^{11} \text{ s}^{-1}$ the rate constant may be calculated directly from

the width σ , in cm^{-1} :

$$k_{\text{ET}} = 2\pi c\sigma \quad (5)$$

where c is the velocity of light.

The width of the excitation bands of the E-isomers was about $100\text{--}150\text{ cm}^{-1}$. If that width is due entirely to homogeneous broadening caused by electron transfer, k_{ET} would be of the order of the order of $2 \times 10^{13}\text{ s}^{-1}$. Usually, the observed bands are not purely Lorentzian; they appear to be a superposition of many closely lying bands, whose width is of the same order as their spacing, i.e., about $10\text{--}20\text{ cm}^{-1}$. Hence a more realistic rate constant for the electron-transfer rate constant in these systems is 10^{12} s^{-1} . A similar rate constant is deduced for R-isomers when they are excited to higher vibrational levels. Likewise, the shape of the excitation bands of linked systems [31], when excited to higher vibrational levels, is compatible with similar values.

The excess energy above the origin of the LE state required to reach these high rate constants differs somewhat among different systems. In the intermolecular systems, it is in the range $20\text{--}400\text{ cm}^{-1}$, whereas the linked systems, it may be as high as 1000 cm^{-1} or more. The difference may be due to the more stringent restrictions on the relative motion of the donor and acceptor in the linked systems.

In the linked systems studied by Wegewis and Verhoeven [14], electron-transfer rates were estimated by the same methods—quenching of the acceptor fluorescence and linewidth measurements. The rates were found to vary over many orders of magnitude: in the weakly coupled systems they are $10^7\text{--}10^9\text{ s}^{-1}$ (for the reduced forms **1r**–**3r**), increasing to 10^{11} s^{-1} for the double bond conjugated forms **1**–**3**, and up to 10^{14} s^{-1} for strongly coupled systems such as **7**. The latter conclusion, which is based on linewidths, may be overestimated—if the width of individual lines exceeds their separation, the lines appear to be broad and one sees only the envelope [22]. It may be fortuitous, but these values appear to agree nicely with the results obtained with simpler inter- and intramolecular systems [10, 19, 20].

The next chapter by Ohshima, Kajimoto and Fuke reviews some results obtained with linked systems, in which charge transfer is facilitated by torsional motion around a single bond. Picosecond time-resolved experiments allowed the direct measurement of the decay of the LE state and the rise of the CT state fluorescence. In some cases a third excited state, also characterized as a charge-transfer state, was observed. It was assigned to a charge-transfer state in which the two connected moieties (anthracene and aniline in this case) are twisted from the planar conformation characteristic of the ground state, but not to a fully perpendicular conformation. The photophysics of twisted intramolecular charge-transfer (TICT) states, were studied extensively in the gas phase and in solution (see the previous chapter by Herbich and Brutschy).

Although this chapter deals exclusively with gas-phase systems, it appears appropriate to compare briefly the data with liquid solution work.

In favorable cases, the rate of charge transfer in solutions can be measured directly by following changes in absorption due to the formation of separated ions [38]. Furthermore, the distance dependence of the electron-transfer rate may be

studied extensively—the increased molecular weight makes gas-phase studies extremely difficult.

In some bridged A–br–D systems, in which the donor and acceptor are rigidly linked by a norbornylogous bridge (Ref. [39], pp. 623–626), it was found that the rate of electron transfer could be fitted to an exponential distance-dependent form:

$$k = A \exp(-\beta r) \quad (6)$$

where r is the edge-to-edge distance between A and D. Similar distance dependences of the rate constant in condensed phases were reported by other workers [34, 35] (see also Chapter III.2.1 by Paddon-Row). The charge separation pre-exponential factor A was found to be solvent dependent for a given system. As a typical example, for a group of molecules in which dimethoxynaphthalene (DMN) was a donor, and dicyanovinyl (DCV) the acceptor, the A factor was found to vary between $9.3 \times 10^{13} \text{ s}^{-1}$ for tetrahydrofuran (THF) and $104 \times 10^{13} \text{ s}^{-1}$ for di-*n*-butyl ether (DNBE). The β factor was 0.92 per bond in THF and 1.25 per bond in DNBE [39]. However, the actual values of the rate constants in these two solvents are not necessarily very different. Thus, for eight intervening σ -bonds, they vary only over a factor of 1.4 for these two solvents (4.7×10^{10} for DNBE and 6.7×10^{10} for THF; see Table IV in Ref. [39]). The solvent effects involve several factors, including changes in the overall free energy release, solvent rearrangement, changes in the relative stabilization of excited states, etc. Studies in the gas phase provide a means to study the 'pristine' donor–acceptor system, removing these complications, and thus perhaps to obtain a model for electron transfer that may be compared with quantum mechanical-based theory.

4.5 Exciplexes in Reactive Systems

The role of exciplexes in chemical reactions has been controversial ever since they were discovered. Their most prominent manifestation, the characteristic fluorescence, has actually been taken as an indication that they are not important as reactive intermediates, because of the relatively long decay times. It has been argued that there may be reactive exciplexes which are not observed spectroscopically in emission. Evidence for their presence is deduced mostly from solvent polarity effects.

Jet cooling may reveal weakly fluorescing systems, since some non-radiative decay processes become less efficient in that environment, particularly bimolecular interactions. Thus, exciplexes formed between aromatic molecules acceptors and tertiary amine donors have long been known to fluoresce, whereas under ambient conditions exciplex emission from pairs in which the tertiary amine has been replaced by a secondary or primary amine is rare. Anner and Haas observed exciplex emission from an anthracene–ammonia adduct in a jet [40] and Drescher et al. [41] reported weak exciplex emission from a β -methylstyrene–diethylamine adduct

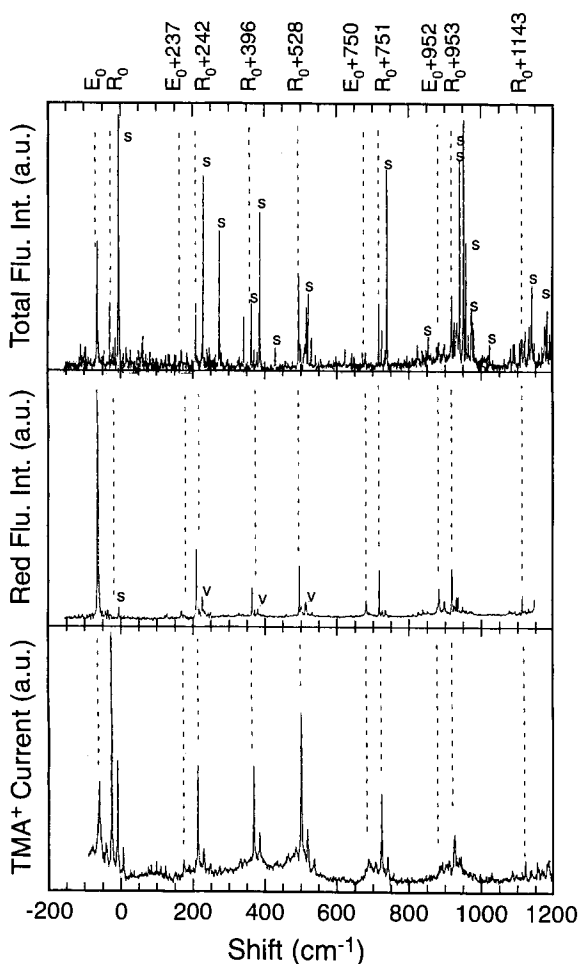


Figure 9. Fluorescence and REMPI excitation spectra of the styrene-TMA adduct in a supersonic jet. The top panel shows the fluorescence excitation spectrum of the total emission; bands marked S are due to bare styrene. The middle panel shows the fluorescence excitation spectrum observed through a filter transmitting at 385 ± 3 nm and the bottom panel the excitation spectrum of the trimethylamine ion (a fragment of the cluster ion). Two vibronic band systems are clearly observed, one being assigned to an R-isomer and the other to an E-isomer, as shown at the top of the figure. Adapted from Ref. [27].

An attempt to establish the role of exciplexes in a reactive system was made by Kendler and Haas [27]. The fluorescence characteristics of the styrene-trimethylamine (TMA) adduct were studied in a supersonic jet. In the bulk, this system is known to exhibit exciplex emission and also to form photoproducts [42]. In the jet, fluorescence excitation of the STY-TMA 1:1 adduct revealed two isomers, an R-type and an E-type (Figure 9) (labeled n-type and w-type, respectively, in the original paper). The resonance-enhanced multiphoton ionization (REMPI)

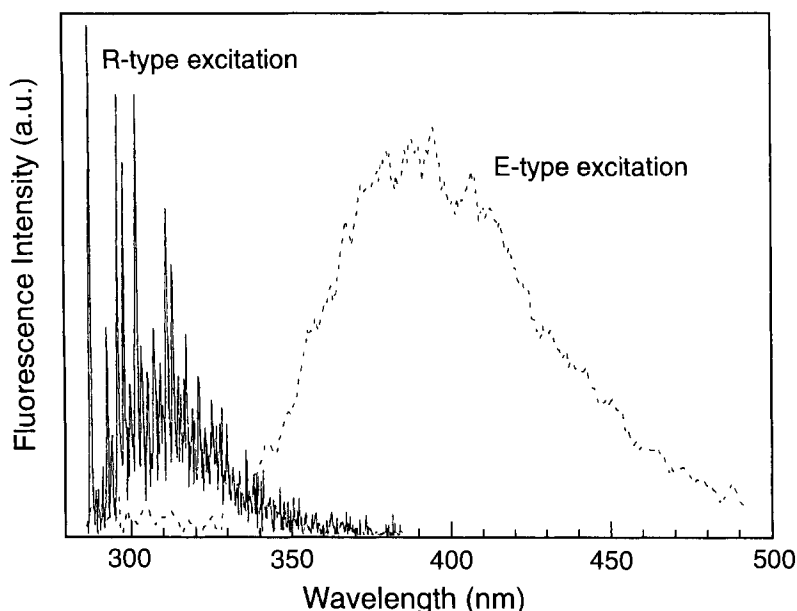


Figure 10. Fluorescence spectra of the R- and E-isomers of the styrene-TMA adduct in a supersonic jet. Adapted from Ref. [27].

excitation spectrum is also shown. It is clear that the R-type isomer yields a much stronger ionisation signal than the E-type isomer. The dissociation energy of the R-type isomer in the locally excited state was estimated from MPI measurements to be 1100 cm^{-1} . The emission spectra of the two isomers obtained upon excitation at the origin are shown in Figure 10. Evidently, the R-isomer shows LE-type fluorescence only, while the E-type shows exciplex emission. At higher excitation energies, the R-isomer rapidly develops exciplex emission: at an excess energy as low as 242 cm^{-1} , emission was already largely of exciplex type also from the R-isomer. This finding is reminiscent of the energy dependence of the LE to exciplex conversion in the anthracene-DMA clusters discussed in Section 4.2.

The decay times and the relative fluorescence intensities of both bands were measured as a function of excess energy. Figure 11 reproduces the results. It is seen that in the case of the R-isomer, the decay times and the fluorescence intensity decrease in parallel as the excess energy is increased up to 1100 cm^{-1} . For the E-isomer, the decay time shows a similar behavior, but the fluorescence intensity decreases sharply (by a factor of 10) within 200 cm^{-1} , and then remains almost constant.

These results were rationalized using the energy level diagram reproduced in Figure 12. The scheme is necessarily oversimplified, since it summarizes energy changes along different coordinates under the title 'reaction coordinate'. In the jet, IVR is assumed to be rapid, but the total energy in the cluster is conserved as long as there is no dissociation or photon emission. Initial excitation of the adduct leads

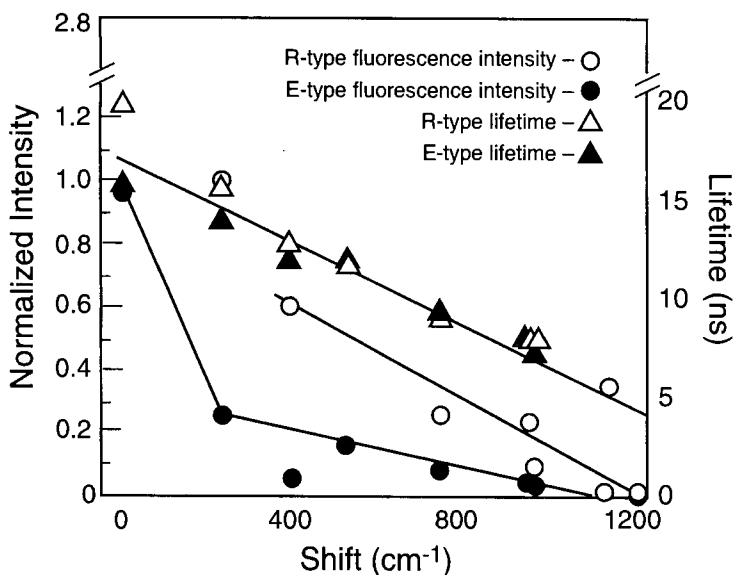


Figure 11. Plot of the decay times and the relative intensities of the fluorescence of the styrene-TMA adduct as a function of excess energy (expressed as frequency shift from the system's origin). Note the different pattern observed for the intensity and lifetime in the case of exciplex-type emission. Adapted from Ref. [27].

either to an excited E-isomer or an excited R-isomer. Both are formed with a relatively large energy excess over the equilibrium structure of the exciplex, which has a different geometry than that of the ground-state adduct. The system is non-stationary in the Franck–Condon (FC) region, and may evolve by different routes. The different excess energy dependence of the exciplex yield vs. decay time may be accounted for as follows: the emitting exciplex is formed in competition with another process, leading to a conical intersection between the excited state and the ground state. Once the emitting exciplex is formed, it may fluoresce in competition with some internal non-radiative processes, such as inter-system crossing. The latter affect the change in decay time, whereas the initial process starting at the FC region determines the yield. The rapid initial decrease may indicate a small barrier on the way to the conical intersection region.

After reaching the conical intersection, the system may evolve to form the radical pair that leads to the final products, or revert back to the ground-state precursors. These processes cannot be observed in the jet, since the products of both routes are formed in a huge number of quantum states, and the detection efficiency of a single product is prohibitively small. This mechanism is also in line with available data in liquid solution. It supports the notion, suggested by some workers [43], that the formation of the exciplex is in competition with formation of stable products. At the same time, it agrees with the important role of the charge-transfer state (or some polar structure), denoted in the scheme as the CT,FC state. The complicated Stern–

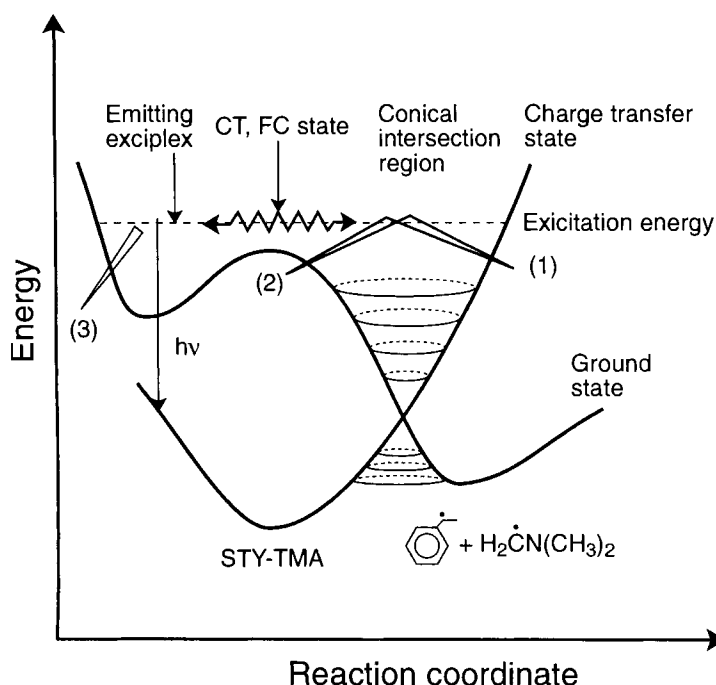


Figure 12. Schematic energy level diagram of the styrene–TMA system. The ‘reaction coordinate’ is a general coordinate along which different chemical processes occur. Initial excitation is from the bottom of the ground-state potential surface of the styrene–TMA van der Waals adduct. Excitation is into the Franck–Condon region, which contains an appreciable charge-transfer character and is designated the CT,FC state. This non-stationary state develops along two main routes: one carries the system to the emitting exciplex state, shown on the left. This process competes with rearrangement towards the conical intersection region, in which re-crossing to the ground state takes place. In this region the charge-transfer state is converted to the ground state, where the separated pair may be formed, and also a radical pair, which later leads to the observed products. Note that the dimethylmethyleamino radical $[\text{H}_2\text{CN}(\text{CH}_3)_2]$ may be formed as two isomers, as the nitrogen atom is pyramidal. Adapted from Ref. [27].

Volmer behavior observed for the exciplex emission [43] may also be explained using the model if the quenchers are reactive enough to interact with the transient species formed in the system en route to the conical intersection.

The possible involvement of an exciplex state in quenching the fluorescence of tryptophan and of indole by molecular oxygen has been discussed [44]. No emission was found from this exciplex, but its presence is strongly suggested by photodetachment experiments on the $[\text{indole} \cdot \text{O}_2]^-$ anion in a supersonic jet. The experiment revealed an onset of photoelectrons at about 3.2 eV. This process was assigned to the formation of a neutral charge-transfer complex $[\text{indole}^+ \cdot \text{O}_2^-]$ for several reasons, including the following:

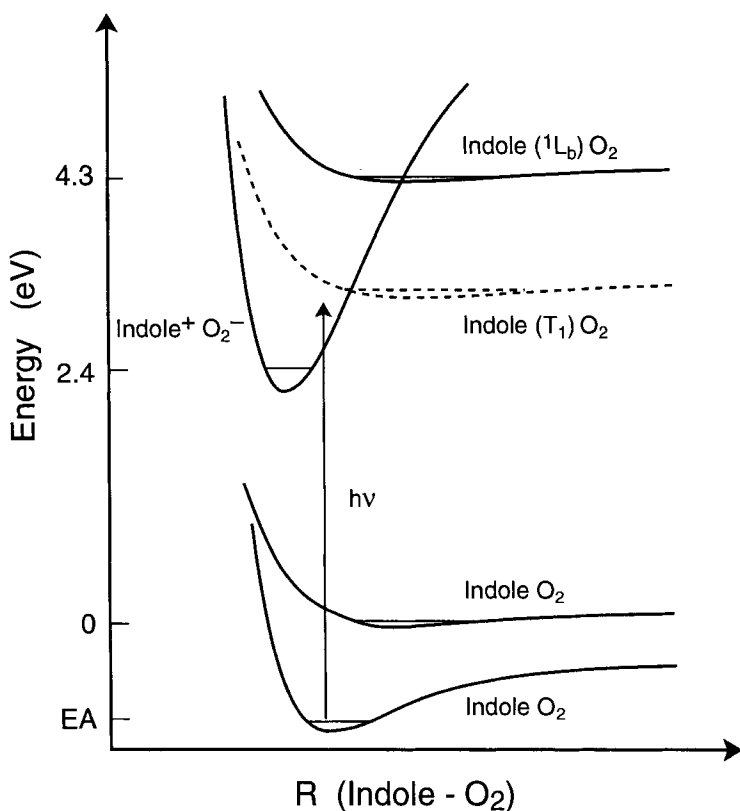


Figure 13. Energy level diagram suggested for the photoinduced electron transfer between molecular oxygen and indole. Adapted from Ref. [44].

- The energetics fit with a reasonable calculation for this ion pair, and not with any other species of the same mass.
- Electron photodetachment from molecular oxygen or from indole can be excluded.
- The absence of clear vibrational structure is consistent with the involvement of a cluster, not a molecule.

The energy level diagram, reproduced in Figure 13, is essentially identical with those suggested for other exciplexes. Emission from exciplexes containing molecular oxygen has not been reported, possibly because of rapid intersystem crossing.

4.6 Modeling

One of the most important motivations for the study of gaseous systems, as repeatedly hinted at, is the hope of obtaining a better connection with theory and theoretical modeling. The structure of solvated adducts and charge-transfer pairs in solution cannot be deduced directly from experimental data. In the gas phase, rotationally resolved spectroscopy provides information on the structure. The method also allows a much better vibrational resolution than liquid-phase spectroscopy, allowing in principle the elucidation of subtle effects such as the role of torsional motion. All of these advantages are enhanced in supersonic jets, where only a small number of quantum states are initially populated.

One of the goals of current efforts in the field is to discriminate between possible ground-state isomers of inter- and of intramolecular adducts. The basic idea behind this effort is that the geometry of the molecular pair involved in the electron transfer may affect the probability of electron transfer. The work of several groups (Piuze, Levy, Itoh) showed that this is indeed the case: several different spectroscopic series of lines were found for a given system, which were assigned to different structural isomers. As discussed in Section 4.2, the barrier to electron transfer appears to be different for different isomers. The task is to correlate the observed spectra with calculated structures.

The simplest model uses atom–atom pairwise potentials, as was done for clusters of molecules with rare gas atoms [45] and with other molecules [46]. The Haas group suggested such models for the anthracene– and perylene–ammonia adducts, in which an electrostatic interaction [47] was added to account for the charge distribution in the molecules [40], and also as for the larger donors (dimethylaniline). The potential is written as

$$V_{\text{Tot}} = \sum_{i=1}^{n_A} \sum_{j=1}^{n_D} (V_{ij}^{\text{vdW}} + V_{ij}^{\text{EL}}) \quad (7)$$

where

$$V_{ij}^{\text{vdW}} = 4\epsilon_{ij} \left[\left(\frac{\sigma_{ij}}{R_{ij}} \right)^{12} - \left(\frac{\sigma_{ij}}{R_{ij}} \right)^6 \right] \quad (8)$$

or

$$V_{ij}^{\text{vdW}} = \beta \exp(-\gamma R_{ij}) - \left(\frac{\alpha_{ij}}{R_{ij}} \right)^6 \quad (9)$$

and

$$V_{ij}^{\text{EL}} = \frac{q_i q_j}{DR_{ij}} + \text{higher terms} \quad (10)$$

Here n_A and n_D are the number of atoms in the acceptor and the donor, respectively, R_{ij} is the distance between atoms i and j and V^{vdW} and V^{EL} are the van der Waals and electrostatic potentials, respectively. The van der Waals potential is often represented by a Lennard–Jones potential (Eq. 8) or by a Buckingham potential (Eq. 9). The parameters α , β , γ and σ are obtained from solid-state crystal data. The leading term in the electrostatic potential is the Coulomb interaction (first term in Eq. 10), where D is the effective dielectric constant (usually $1 \leq D \leq 2$). Other terms may be added to represent induced polarization, etc. [40]. The geometries of the two components of the cluster are obtained from microwave or electron diffraction data or from quantum chemical calculations. It is assumed that these geometries do not change upon adduct formation. An initial guess is made for the structure of the adduct, and then the relative positions of the two (or more) components are varied until a local energy minimum is obtained.

This model was successful in showing that two isomers are expected for the styrene–trimethylamine system [27, 48] (Figure 14). The structures found were consistent with chemical intuition inasmuch as electron transfer may be correlated

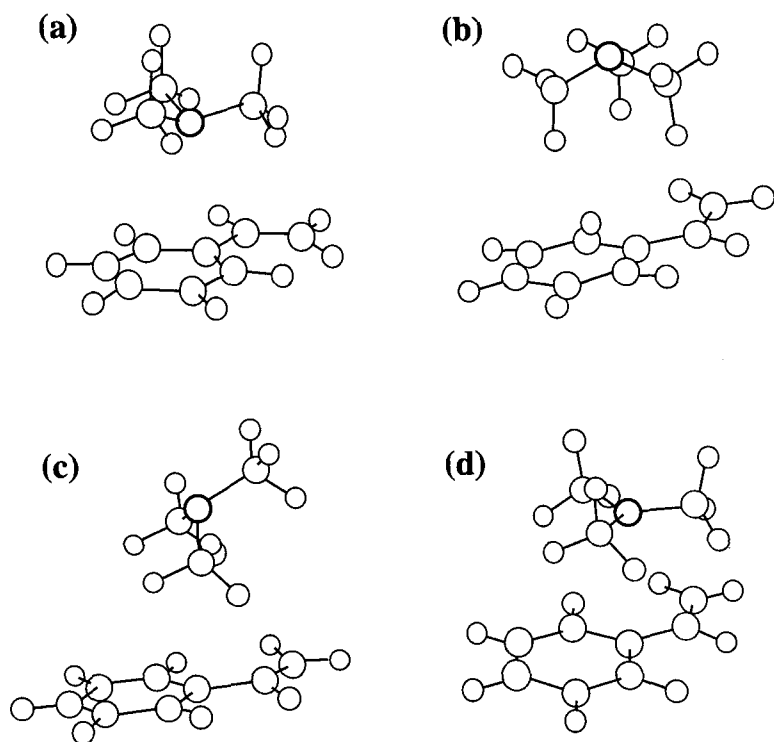


Figure 14. Structures calculated for the styrene (S)–trimethylamine (TMA) system: (a) and (b) the two neutral structures having a minimum on the ground-state potential surface, (a) being assigned to the E-isomer and (b) to the R-isomer; (c) structure of the transition state between (a) and (b); (d) structure of the ion pair S^- – TMA^+ . Adapted from Ref. [47].

with well-defined molecular orbitals. In one isomer the lone pair orbital of the amine nitrogen atom (the donor orbital) overlapped nicely with the lowest unoccupied molecular orbital (LUMO) of styrene. In the other structure, the overlap was poor. The method allows also the calculation of the transition state between the two structures. The result for the ground state (a barrier of $\sim 100 \text{ cm}^{-1}$) is consistent with the low barrier observed in the excited state for the $R \rightarrow E$ isomerization. This method can be used only for ground-state systems, for which reasonable potentials have been worked out.

A more sophisticated model has been developed by Milli  and co-workers [49], based on the exchange perturbation method of Claverie and co-workers [25]. This is a semi-empirical, second-order perturbation method: A and D are treated first as separate entities, and then the intermolecular potential is used as the perturbation Hamiltonian. Its most straightforward application is for the ground-state potential. The potential surface of the two components is known (or obtained by quantum chemical calculations). The intermolecular energy is written as a sum of electrostatic, polarization and dispersion terms. The quantum mechanical application requires the consideration of Pauli's principle and antisymmetrization of the wavefunction with respect to electron exchange. It turns out that the polarization exchange term can usually be neglected; therefore, it is possible to write the energies of the ground and excited states of these systems as a sum of terms, as follows.

Ground electronic states

- Electrostatic term: for each component, an *ab initio* calculation is carried out to obtain the wavefunction. The charge distribution is then written as a sum of multipolar, multicentric terms, up to quadrupole. It has been shown that the system can be represented by a relatively small number of point charges, one for each atom and one for each chemical bond [25]. The electrostatic term is the sum of all intermolecular multipole–multipole interactions.
- Polarization term: atomic and bond polarizabilities are taken from experimental data. The polarization energy is the sum of the polarization energies of each component due to the electric field created by the multipoles of the other component.
- Dispersion and repulsion terms: these are calculated as sums of atom–atom contributions, in the same way as in the simpler pairwise potential described by Eq. 7.

Locally excited electronic states

For these, empirical values are usually not available. One calculates first the wavefunction of the excited state, A^* , using SCF-CI techniques. The charge distribution of this state is obtained, and expressed as a sum of multipolar, multicentric terms, up to quadrupole. From this expression, the electrostatic interactions are calculated as in the ground state. The polarization term is harder to calculate, it is often taken to be equal to the ground-state term. The dispersion term may be calculated approximately by considering the interaction between two dipolar distributions due to the excited states of A and D. This approximation is valid when the first excited state

may be described by a single electron excitation, and when the $S_0 \rightarrow S_1$ transition is allowed [50].

Ionic excited states

For these, the electrostatic and polarization terms are dominant. The ground-state wavefunctions of the D^+ cations are calculated; the charge distribution is obtained from them, and used to calculate the interaction. For the anion, it is usually assumed that the extra electron occupies the LUMO of the neutral.

This method was recently applied to the calculation of the ground-state isomers of the anthracene–dimethylaniline derivatives discussed in Section 4.2.2 [22]. It was noted that for each isomer found, the total interaction energy was about the same as the dispersion energy, the other terms largely cancelling each other. In other words, the attractive stabilization of the electrostatic and polarization terms was offset by the repulsive Pauli term. The resulting geometries were different from those based on chemical intuition—the aromatic ring of the aniline was found not to be parallel to the aromatic anthracene. Up to now (early 2000), no high-resolution study of these systems has been carried out experimentally; therefore, the validity of these calculations awaits confirmation.

4.7 Conclusions

The brief survey presented in this chapter demonstrates the wealth of information obtainable from jet-cooled systems. The presence of several conformational isomers has been definitely proven. It may be argued that the small barriers separating them ($50\text{--}400\text{ cm}^{-1}$) mean that in bulk systems rapid exchange takes place between them, so that they are kinetically and spectroscopically indistinguishable. Nonetheless, the fact that electron transfer can be practically blocked by a barrier of only about 50 cm^{-1} in the jet is remarkable. It must mean that in addition to height, the width of the barrier is also important. If the barrier is narrow, tunneling is bound to make electron transfer measurable for such small barriers. The width may be correlated with nuclear configuration and the need to obtain proper overlap between the donating and accepting molecular orbital.

The approximate treatment of these systems composed of an electron donor and an electron acceptor as two separate entities appears to be best justified for the van der Waals adducts. As the interaction between the two components becomes stronger, the distinction between two-component systems and two-state systems becomes hazy. In particular, the rigid systems studied by Verhoeven, Paddon-Row and their co-workers are most interesting. The very strong interaction does not express itself in rapid electron transfer only, but also in energy transfer [37]. In these systems, the concept of stepwise electron transfer between different parts of the molecule may be inappropriate. When the interaction between donor and acceptor states becomes appreciable, the system has to be treated as a single quantum me-

chanical entity. The transition from one state to the other is then perhaps better described as an internal conversion between two electronically excited states of a single system.

The theoretical understanding of electron-transfer processes in molecular systems is still lagging behind experiment. This is understandable in view of the intrinsic complexity of these systems. It appears that in order to design an efficient light-driven electron-transfer system, the complete assembly has to be considered. Electron transfer can be very rapid, but so is recombination. For the systems considered in this chapter to be useful in practical applications, one needs to consider the fate of both the electron and hole formed in the initial step. The multi-bridged systems that have recently been constructed may be the first step in that direction.

Acknowledgments

The Farkas Center for Light Induced Processes is supported by Minerva Gesellschaft mbH. Special thanks and appreciation are due to my co-workers who helped me in untangling some of the mysteries of jet-cooled exciplexes: Drs. Oded Anner, Hanna Zuckermann, Wolfgang Drescher, Eyal Zingher and Shai Kendler and Mr. Ismael Zarura.

References

1. A. Weller, in M. Gordon, W.R. Ware (Eds.), *The Exciplex*, Academic Press, New York, 1975, p. 25.
2. A. Bauder, in R. Fausto (Ed.), *Low Temperature Molecular Spectroscopy*, Kluwer Academic Publishers, Amsterdam, 1996, p. 291.
3. Y. Haas, O. Anner, in M.A. Fox, M. Chanon (Eds.), *Photoinduced Electron Transfer, Part A*, Elsevier, Amsterdam, 1988, p. 305.
4. R.S. Mulliken, W.B. Person, *Molecular Complexes: a Lecture and Reprint Volume*, Wiley, New York, 1969.
5. M. Itoh, O. Kajimoto, in K. Kuchitsu (Ed.), *Dynamics of Excited Molecules, Studies of Physical and Theoretical Chemistry*, Elsevier, Amsterdam, 1994, Chapter 10.
6. D.J. Nesbitt, *Chem. Rev.* **88**, 843 (1988).
7. B.B. Champagne, J.F. Pfanstiel, D.W. Pratt, R.C. Ulsh, *J. Chem. Phys.* **102**, 6432 (1995).
8. G. Berden, W.L. Meerts, *Chem. Phys. Lett.* **224**, 405 (1994).
9. Th. Weber, A. von Bargaen, E. Riedle, H.J. Neusser, *J. Chem. Phys.* **92**, 90 (1990).
10. O. Anner, Y. Haas, *Chem. Phys. Lett.* **119**, 199 (1985).
11. H. Saigusa, E.C. Lim, *J. Phys. Chem.* **96**, 2083 (1992).
12. Th. Foerster, *Angew. Chem., Int. Ed. Engl.* **8**, 333 (1969).
13. J.B. Birks, *Photophysics of Aromatic Molecules*, Wiley-Interscience, New York, 1970.
14. B. Wegewis, J.W. Verhoeven, *Adv. Chem. Phys.* **106**, 221 (1999).
15. N. Tsujiya, K. Kitaura, Y. Kumamoto, M. Itoh, *J. Phys. Chem.* **101**, 31 (1997).
16. H. Saigusa, M. Itoh, *Chem. Phys. Lett.* **106**, 391 (1984).
17. J.A. Syage, P.M. Felker, A.H. Zewail, *J. Chem. Phys.* **81**, 2233 (1984).
18. N.A. van Dantzig, H. Shou, J.C. Alfano, N. C. Yang, D.H. Levy, *J. Chem. Phys.* **100**, 7068 (1994).
19. (a) M. Kurono, M. Itoh, *J. Phys. Chem.* **99**, 17113 (1995); (b) M. Kurono, R. Takasu, M. Itoh, *J. Phys. Chem.* **99**, 9668 (1995).
20. M. Castella, J. Prochorow, A. Tramer, *J. Chem. Phys.* **81**, 2511 (1984); M. Castella, A. Tramer, F. Piuze, *Chem. Phys. Lett.* **129**, 112 (1986).

21. F. Piuze, *Chem. Phys. Lett.* **209**, 484 (1993).
22. (a) A. Tramer, V. Brenner, P. Millié, F. Piuze, *J. Phys. Chem. A* **102**, 2798 (1998); (b) A. Tramer, V. Brenner, P. Millié, F. Piuze, *J. Phys. Chem. A* **102**, 2808 (1998).
23. V. Brenner, P. Millié, F. Piuze, A. Tramer, *J. Chem. Soc., Faraday Trans.* **93**, 3277 (1997).
24. F. Piuze, D. Uridat, I. Dimicoli, M. Mons, A. Tramer, K. LeBarbu, F. Lahmani, A. Zehnacker-Rentier, *Acta Phys. Pol.* **95**, 121 (1999).
25. J. Langlet, P. Claverie, P. Boeuvre, *Int. J. Quantum Chem.* **20**, 299 (1981); P. Claverie, in B. Pulman (Ed.), *Intermolecular Interactions from Diatomics to Biopolymers*, Wiley, New York, 1978, p. 69; F. Vigne-Maeder, P. Claverie, *J. Chem. Phys.* **88**, 4934 (1989).
26. C. Jouvet, S. Martrenchard-Barra, D. Solgadi, C. Dedonder-Lardeux, M. Mons, G. Gregoire, I. Dimicoli, F. Piuze, J.P. Visticot, J.M. Mestdag, P. d'Oliviera, P. Meynadier, M. Perdrix, *J. Phys. Chem. A* **101**, 2555 (1997).
27. S. Kendler, Y. Haas, *J. Phys. Chem.* **101**, 2578 (1997).
28. M. Kurono, R. Takasu, M. Itoh, *J. Phys. Chem.* **98**, 5925 (1994).
29. R. Takasu, N. Kizu, M. Itoh, *J. Phys. Chem.* **98**, 7364 (1994).
30. J.B. Hopkins, D.E. Powers, R.E. Smalley, *J. Chem. Phys.* **72**, 5039 (1980).
31. M. Kurono, C. Mitsuhashi, S. Kohtani, M. Itoh, *J. Phys. Chem. A* **101**, 3102 (1997).
32. M. Chattoraj, S.L. Laursen, B. Paulson, D.D. Chung, G.L. Closs, D.H. Levy, *J. Phys. Chem.* **96**, 8778 (1992).
33. D.H. Levy, *Adv. Chem. Phys.* **106**, 203 (1999).
34. G.L. Closs, L.T. Calcaterra, N.J. Green, K.W. Penfield, J.R. Miller, *J. Phys. Chem.* **90**, 3673 (1986).
35. M.R. Wasielewski, in M.A. Fox, M. Chanon, (Eds.), *Photoinduced Electron Transfer, Part A*, Elsevier, Amsterdam, 1988, p. 161; *Chem. Rev.* **92**, 435 (1992).
36. B. Wegewijs, R.M. Hermant, J.W. Verhoeven, M.P. de Haas, J.M. Warman, *Chem. Phys. Lett.* **168**, 185 (1990); B. Wegewijs, A.K.F. Ng, J.W. Verhoeven, *Recl. Trav. Chim. Pays-Bas* **114**, 6 (1995).
37. N. Lokan, M.N. Paddon-Row, T.A. Smith, M. La Rosa, K.P. Ghiggino, S. Speiser, *J. Am. Chem. Soc.* **121**, 2917 (1999).
38. N. Orbach, M. Ottolenghi, *Chem. Phys. Lett.* **35**, 175 (1973).
39. J.W. Verhoeven, *Adv. Chem. Phys.* **106**, 603 (1999).
40. O. Anner, Y. Haas, *J. Phys. Chem.* **90**, 4298 (1986).
41. W. Drescher, S. Kendler, E. Zingher, Y. Haas, *Chem. Phys. Lett.* **224**, 391 (1994).
42. F.D. Lewis, D. Bassani, *J. Photochem. Photobiol. A: Chem.* **81**, 13 (1994).
43. H. Aoyama, J. Sugiyama, M. Yoshida, H. Hatori, A. Hosomi, *J. Org. Chem.* **57**, 3037 (1992).
44. R. Weinkauff, J. Scheidt, *Photochem. Photobiol.* **66**, 569 (1997).
45. U. Even, A. Amirav, S. Leutwyler, M.J. Ondrechen, Z. Berkovitch-Yellin, J. Jortner, *Faraday Discuss Chem. Soc.* **73**, 153 (1982).
46. S. Sun, E.R. Bernstein, *J. Phys. Chem.* **100**, 13348 (1992).
47. F.A. Momany, L.M. Caruthers, R.F. McGuire, H.A. Scheraga, *J. Phys. Chem.* **78**, 1595 (1974).
48. S. Kendler, Y. Haas, *Chem. Phys. Lett.* **236**, 324 (1995); E. Zingher, S. Kendler, Y. Haas, *Chem. Phys. Lett.* **254**, 213 (1996).
49. M. Castella, Ph. Millié, F. Piuze, J. Caillet, J. Langlet, P. Claverie, A. Tramer, *J. Phys. Chem.* **93**, 3941 (1989).
50. V. Brenner, A. Zehnacker, F. Lahmani, Ph. Millié, *J. Phys. Chem.* **97**, 10570 (1993).

5 Isolated Supermolecules

Yasuhiro Ohshima, Okitsugu Kajimoto and Kiyokazu Fuke

5.1 Introduction

Owing to recent advances in gas-phase experimental methods, ensembles composed of a finite number of molecules bound by non-covalent forces, e.g., electrostatic (including hydrogen-bonding) and dispersion interactions, can be formed and studied under isolated conditions. Investigations on electron-transfer (ET) processes that take place in such supermolecular systems are of substantial importance since we can explore the functionality that becomes operative only when the constituents are assembled as a total system. In addition, a precise knowledge of how the composition and configuration of the constituents affect ET can be extracted from studies on the finite ensembles, which are virtually free from perturbations by environments. In particular, the supermolecule approach for the experimental exploration of ET processes is most suitable for combination with detailed quantum mechanical calculations, which have also been developing with extreme rapidity.

The most extensively studied supermolecular systems which exhibit ET are binary gas-phase clusters. In most cases, one constituent has a low ionization potential and thus acts as an electron donor, whereas the other with positive electron affinity acts as an electron acceptor. An electron is transferred from the donor to the acceptor in the system spontaneously or after electronic and/or vibrational excitation. Detailed discussions on the ET processes in such donor–acceptor pairs have already been given in preceding chapters (see Chapters 2 and 4 in this Part). Here, we will mainly focus on supermolecular systems of another type, in which aggregation of more than two constituents is essential for ET to proceed. Even when the electron affinity of an isolated molecule is negative (i.e., the molecule cannot form a stable anion), a group of a certain number of the molecules may act as an electron acceptor. This is entirely due to the collective polarization which stabilizes the electron located inside the molecular ensemble. The ET to such a cooperative electron-accepting unit is strongly related to electron redistribution phenomena in condensed phases, e.g., excitation into the conduction band from an impurity level and formation of

solvated electrons in polar liquids. As an electron donor, two typical systems, i.e., alkali metal atoms and a halide anion (I^- in this case), will be discussed in this chapter. Their simple and well-evaluated electronic energy levels make them ideal electron donors to be investigated. In addition, their low ionization potentials afford the opportunity for the application of various experimental methods utilizing recently developed laser techniques. Because of these advantages, the gas-phase clusters containing alkali metal atoms and the I^- ion have been most actively studied as supermolecular systems displaying cooperative ET.

As a final part of this chapter, we shall briefly discuss the intramolecular ET processes in relatively large aromatic molecules. This is a supplement to Chapter 3 in this Part, in which twisted intramolecular charge-transfer (TICT) phenomena were described for isolated donor–acceptor molecules and their clusters. Here we present the charge-transfer dynamics in some selected anthryl derivatives in which the donor and acceptor parts are linked directly or by alkyl chains, and also microscopic solvation effects on the dynamic properties in their clusters, which were not discussed in the earlier chapter. The emphasis resides on a detailed description of the torsional motions and the solvation structure, which are strongly correlated with the intramolecular charge transfer in these systems.

5.2 Stepwise Charge Separation in Alkali Metal Atom-containing Clusters

Solvated electrons play important roles in chemical and biological phenomena and have been the subject of numerous investigations [1]. Especially the process of excess electron solvation in the alkali metal–polar solvent systems has been one of the central issues. Many experimental and theoretical efforts have been made to understand the nature of solvated electrons and the dynamics of electron solvation in these systems [2]. However, the microscopic properties of solvated electrons are not yet fully understood [3].

Advances in charged-cluster formation have afforded new approaches to microscopic investigations of the solvated electron. Anionic water and ammonia clusters, $(H_2O)_n^-$ and $(NH_3)_n^-$, have been prepared via capture of low-energy electrons by solvent neutral clusters [4, 5]. Their vertical detachment energies (VDEs) have been measured with n up to ~ 70 [6, 7]. On the other hands, Hertel's and Fuke's groups have prepared prototypes such as solvated alkali metal atom clusters, i.e., $M \cdot (H_2O)_n$ and $M \cdot (NH_3)_n$, where $M = Li, Na$ and Cs [8–10]. These clusters serve as a good model for elucidating the microscopic aspect of the electron transfer from the alkali metal atom to solvent molecules. Figure 1 shows a schematic energy diagram for the covalent and ion-pair states in the neutral form and the positive and negative ionic states for metal–solvent clusters as a function of the solvent number (n). The ionic ground states are stabilized monotonically with increasing n , as can be seen from the enthalpies of solvation for the metal ion [11]. For small clusters, the ground state is of the covalent type and expected to be stabilized very slowly

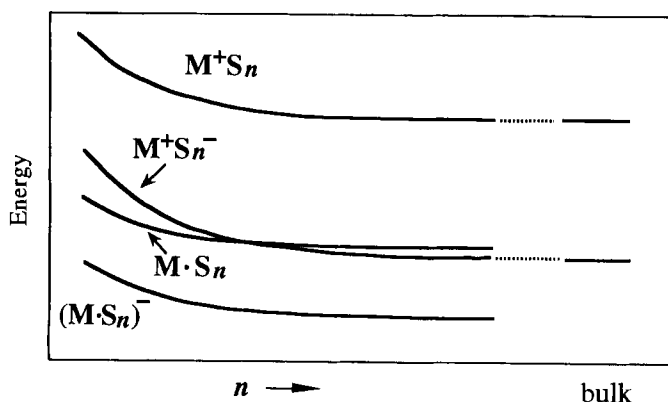


Figure 1. Schematic diagram of the energies of the anion ground state $(M\cdot S)_n^-$, the lowest covalent state $(M\cdot S)_n$, ion-pair state $(M^+S_n^-)$ and cation ground state (M^+S_n) versus n (M = alkali metal atom; S = solvent molecules). The ion-pair state is expected to correlate with the ground state of the solvated electron plus the solvated M^+ ion in bulk fluids. The ground-state electronic character of the neutral cluster changes from covalent to ion-pair type at a certain critical size.

with increasing number of solvents (Figure 1). On the other hand, the energy level of the ion-pair state is more sensitive to the solvation. In analogy with the bulk behavior of an alkali metal in polar fluids [1], the ion-pair state may correlate with the ground state of the solvated electron plus the solvated metal cation. As a result, the electronic character of the ground-state clusters is expected to change from the covalent type to the ion-pair type at a certain critical size. This transition has been investigated by photoionization and photoabsorption experiments on water and ammonia clusters containing a neutral alkali metal atom [8–10, 12]. The solvation of alkali metal atoms has also been probed by photoelectron spectroscopy of the solvated clusters containing alkali metal anions [10, 13–15]. We discuss below the photoionization and photoelectron spectroscopy of these clusters in relation to the electron transfer from an alkali metal atom to solvent molecules and the formation of the solvated electrons.

5.2.1 Alkali Metal Atom Clusters Solvated with Ammonia Molecules

The ionization potentials (IPs) of ammonia clusters containing alkali metal atoms, such as Li [10], Na [8] and Cs [9], have been reported by Hertel's and Fuke's groups. These clusters have been prepared by pickup sources coupled with a heated oven (Na and Cs) or a laser-vaporization source (Li). The $IP(n)$ values decrease almost linearly with $(n+1)^{-1/3}$, which is approximately proportional to the inverse of the cluster radius. Although the IPs of free atoms are different (5.392, 5.139 and 3.894 eV for Li, Na and Cs, respectively), those of the clusters ($n \geq 5$) are almost the same irrespective to the metal atoms. The intercept at $(n+1)^{-1/3} \rightarrow 0$

of the fitted line (1.4 eV) agrees with the photoelectric threshold of liquid ammonia (1.47 eV) and that from the fitted line of VDEs for $(\text{NH}_3)_n^-$ [7]. Fuke and co-workers [9, 10] discussed these observations in terms of the change in the electronic character of the neutral ground-state clusters from the covalent type to the one-center ion-pair type with increasing n (see Figure 1). Stampfli and Bennemann [16] calculated the IPs of metal–ammonia clusters using a polarizable electropole model and suggested a single-center structure for intermediate size ($6 < n < 25$) and a transition to a two-center structure for larger clusters. They predicted that the metal cation and electron are completely separated in the larger clusters, as in the case of bulk solution. *Ab initio* calculations on the geometric structures for both $\text{Na} \cdot (\text{NH}_3)_n$ and $\text{Na}^+ \cdot (\text{NH}_3)_n$ ($n \leq 6$) were conducted by Hashimoto and Morokuma [17]. According to their calculations with the 6–31+G(d) basis set and the Hartree–Fock and second-order many-body perturbation (MP2) methods, both the neutral and ionic clusters with $n \geq 4$ have an interior structure where Na is surrounded by four ammonia molecules in the first solvent shell. These calculations also reproduce the observed IPs reasonably well.

The electronic structures of the neutral clusters have also been investigated by photoelectron spectroscopy (PES) of the solvated clusters of alkali metal anions, $\text{M}^- \cdot (\text{NH}_3)_n$ [10, 13]. The anion clusters have been successfully prepared with a laser vaporization technique coupled with a supersonic expansion method. The PE spectra of mass-selected cluster anions have been studied by using a magnetic-bottle type PE spectrometer [18]. Figure 2 shows the PE spectra of $\text{Na}^- \cdot (\text{NH}_3)_n$ ($n \leq 12$) [13]. The PE spectrum of bare Na^- exhibits a strong band at 0.55 eV and a weak band at 2.65 eV. These bands correspond to the transitions from the ionic ^1S state to the neutral ground (3^2S) and first excited (3^2P) states, respectively. $\text{Na}^- \cdot \text{NH}_3$ exhibits a broad 3^2S -type band at around 0.5 eV, which is an overlap of two transitions. The PE spectrum with higher resolution (not shown) exhibits two separate transitions at 0.42 and 0.67 eV [19]. These bands are ascribed to the transitions of two different isomers. According to the calculations at the MP2 level with extended basis set, $\text{Na}^- \cdot \text{NH}_3$ has two structural isomers with total binding energies (corrected for zero-point vibrations) of 4.3 and 2.9 kcal mol $^{-1}$ [20]. The more stable isomer has a structure similar to that of the neutral complex, in which ammonia molecule is bound to Na^- by the nitrogen atom, whereas in the less stable isomer, NH_3 is bound to Na^- by the hydrogen atoms as in the case of the hydrated anions, such as $\text{Na}^- \cdot (\text{H}_2\text{O})_n$ [10], $\text{Cu}^- \cdot (\text{H}_2\text{O})_n$ [18] and $\text{X}^- \cdot (\text{H}_2\text{O})_n$ ($\text{X} = \text{Cl}, \text{Br}$ and I) [21–23]. The VDEs to the 3^2S -type state of the isomers with the $\text{Na}^- \cdots \text{N}$ and $\text{Na}^- \cdots \text{H}$ bonds have been calculated as 0.35 and 0.65 eV, respectively, at the CCSD(T) level with a frozen core approximation. From these theoretical results, the peaks at 0.43 and 0.67 eV have been assigned to the 3^2S -type transitions of the more and less stable isomers, respectively. The very weak bands at near 2.4 eV shown in Figure 2b have been assigned to the 3^2P -type transitions of the two isomers. The PE spectrum of $\text{Li}^- \cdot \text{NH}_3$ also exhibited a slight red shift in the 2^2S -type band and a large red shift for the 2^2P -type transition, but no indication of the isomers [10, 13]. *Ab initio* calculations also predicted two isomers having $\text{Li}^- \cdots \text{N}$ and $\text{Li}^- \cdots \text{H}$ interactions, but the latter is substantially less stable (>8 kcal mol $^{-1}$) than the former in this case [20].

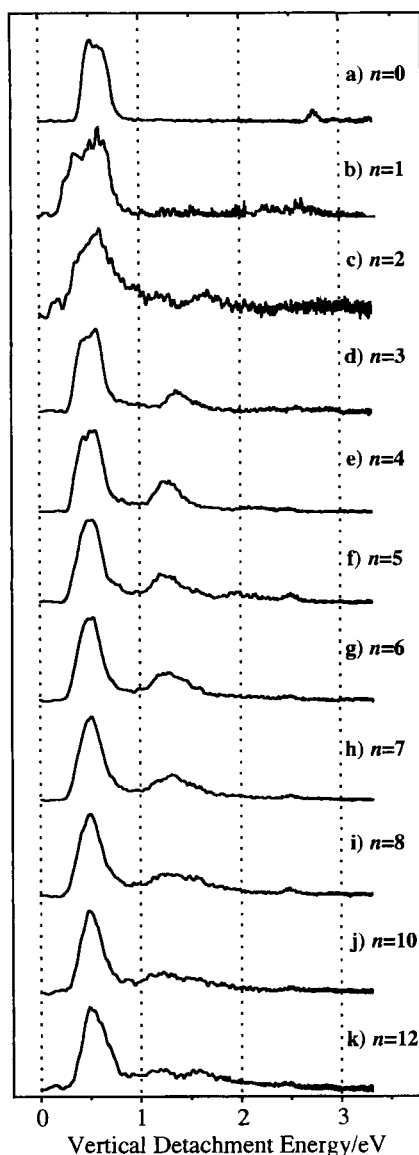


Figure 2. Photoelectron spectra of $\text{Na}^-\cdot(\text{NH}_3)_n$ clusters ($n = 0-12$), collected using a photodetachment energy of 3.50 eV (355 nm). The spectra are normalized to the peak of the $3^2\text{S}-^1\text{S}$ transition.

For the large Li^- and Na^- clusters solvated with ammonia, both the experimental and theoretical results suggest that the isomer with the metal $\cdots\text{N}$ interaction is much more favored with increasing n as in the case of the neutral clusters. Thus the photodetachment process of the clusters with $n \geq 2$ is considered to involve the transition from the anionic state to near the potential minimum of the neutral states. For $n = 2$, the VDE to the 3^2S -type state does not change appreciably from $n = 1$ (Figure 2c), whereas the 3^2P -type transition shifts to a lower electron binding

energy (EBE) and peaks at about 1.7 eV. For $n \geq 2$, VDEs of the 2S type shift slightly to lower EBE with respect to that of Na^- as seen in Figure 2. The results clearly indicate that the solvation energies of the neutral clusters are larger than those of the anion clusters. The amount of the shift in the 3^2P -type transition is >1.4 eV at $n = 5$ with respect to free Na^- (2.65 eV). The transition to the 2^2P -type state in $\text{Li}^-(\text{NH}_3)_n$ ($n = 2-9$) has also been found to be shifted to lower EBE, as low as 1.4 eV, and almost becomes degenerate with the transition to the neutral ground state (2^2S) for $n \geq 10$ [10]. The large red shift in the 2^2P -type transitions suggests the extensive change in the electronic structure of the metal atom in the clusters. As seen in Figure 2, the successive changes in the VDEs for the 3^2P -type state are >0.2 eV for $\text{Na}^-(\text{NH}_3)_n$ ($n \leq 4$), whereas they are negligibly small for $n = 5-8$. The rapid change in the rate of the shift for this transition between $n = 4$ and 5 indicates the filling of the first solvent shell around Na^- at $n = 4$. The theoretical calculations also predicted that the first solvent shell around the Li and Na atoms is closed with four or five ammonia molecules [17, 24]. Figure 2 also shows that the bandwidth of the 3^2P -type transition increases systematically with increasing n up to 12, although the band shift is almost the same for $n \geq 5$. Moreover, the 2S -type transition stays slightly lower in EBE than that of bare Na^- . The binding energy of the neutral clusters is larger than that of the corresponding anions even after the first solvation shell is closed. These spectral features clearly indicate that the electronic structure of the metal atom is affected further with the addition of ammonia molecules in the second solvent shell. In other words, the valence electron of the alkali metal atom is delocalized over the clusters and interacts directly with the second-shell ammonia molecules. In accord with the above experimental findings, calculations also predicted extensive delocalization of a singly occupied molecular orbital (SOMO) for the clusters with $3 \leq n \leq 6$ [17]. The IPs which are independent of the metal for $\text{M}(\text{NH}_3)_n$ with $n \geq 5$ ($\text{M} = \text{Li}, \text{Na}$ and Cs), as mentioned previously, can be explained by the diffuse character of the SOMO. These results suggest that the alkali metal atom is partially ionized and forms a one-center ion-pair state, which extends over more than the first solvent shell in the clusters.

Recently, Hertel and co-workers investigated the first electronically excited state of $\text{Na}(\text{NH}_3)_n$ with n up to 22 by photodepletion spectroscopy [12]. They observed a drastic decrease in the excitation energy of the 3^2P -type state. The value for the free atom is 16950 cm^{-1} , whereas it is only 6000 cm^{-1} for $\text{Na}(\text{NH}_3)_4$. For larger clusters ($n > 4$), it increases slightly and reaches the bulk value at 6300 cm^{-1} , which corresponds to the absorption of the solvated electron. They have explained the switching of the spectral shift at $n = 4$ as the closure of the first solvent shell. The observed spectral features are very similar to those of the photoelectron spectra of $\text{Na}^-(\text{NH}_3)_n$ (see Figure 2). As mentioned above, both the neutral and anion clusters have similar structures and thus the energy separation between the first and second transitions in the PE spectra corresponds well to the absorption bands of $\text{Na}(\text{NH}_3)_n$ observed by photodepletion spectroscopy.

Farrar and co-workers recorded the photodissociation spectra of the isoelectronic $\text{Sr}^+(\text{NH}_3)_n$ system and observed similar large spectral shifts for the 5^2P-5^2S transition [25, 26]. They carried out a moment analysis of the absorption spectra and found a large increase in the electronic radial distribution in the ground state with

increasing n . Based on the results, they proposed the involvement of an increasing ion-pair character, $\text{Sr}^{2+} \cdot (\text{NH}_3)_n^-$, in both the ground (5^2S) and the first excited (5^2P) electronic states. This argument is similar to that for the alkali metal atom– NH_3 systems. Because a neutral alkali metal atom is isoelectronic with a singly charged alkaline earth metal cation, we might argue that the large red shifts in the absorption bands for $\text{Sr}^+ \cdot (\text{NH}_3)_n$ correspond to the large decrease in VDE for the $\text{Na } ^2\text{P}$ -type state seen in Figure 2. However, since Sr^+ has much larger ionization potential (11.0 eV) than those for alkali metal atoms and has other transitions derived from the d-type atomic orbital between the ground and ^2P -type states, more careful analysis might be required to apply a simple analogy.

5.2.2 Hydrated Clusters of Alkali Metal Atoms

In contrast to the clusters solvated with ammonia, the vertical ionization potentials (IPs) of $\text{Li} \cdot (\text{H}_2\text{O})_n$ [10], $\text{Na} \cdot (\text{H}_2\text{O})_n$ [8] and $\text{Cs} \cdot (\text{H}_2\text{O})_n$ [9] exhibit an anomalous size dependence. For $\text{Li} \cdot (\text{H}_2\text{O})_n$, the IP decreases with cluster size up to $n = 4$ and then becomes constant at 3.12 eV for larger clusters. Similar results have also been observed for $\text{Na} \cdot (\text{H}_2\text{O})_n$ and $\text{Cs} \cdot (\text{H}_2\text{O})_n$ with constant IPs of 3.10 and 3.17 eV ($n \geq 4$), respectively. These values are nearly equal to the estimated photoelectric threshold of bulk ice (3.3 eV) and the VDE of $(\text{H}_2\text{O})_n^-$ [7]. The difference in size dependence of alkali metal clusters with water and ammonia clearly suggests that the IP(n) with $n \geq 4$ in the water systems is determined entirely by the solvents. Several theoretical efforts have been made to interpret the characteristic size dependence of the IPs for $\text{M} \cdot (\text{H}_2\text{O})_n$ [16, 27–29]. Barnett and Landman [28] calculated the geometrical and electronic structures of $\text{Na} \cdot (\text{H}_2\text{O})_n$ ($n \leq 8$) using the local spin density functional method and shown that the structure of the neutral $\text{Na} \cdot (\text{H}_2\text{O})_n$ clusters resembles that of $\text{Na}^+ \cdot (\text{H}_2\text{O})_n$. They also predicted that the saturation of IP for $n > 4$ is due to the formation of a molecular shell around the Na atom for $n \approx 4$, accompanied by exclusion of the valence electron of the alkali metal atom from the hydration cavity. The electron is distributed in a surface Rydberg-like state, where the electron is delocalized and spreads equally around water molecules. Hashimoto and Morokuma [29] calculated the structures and IPs of $\text{Na} \cdot (\text{H}_2\text{O})_n$. According to their calculations, the most stable structure is the surface-type clusters, in which only three or four water molecules are directly bound to the Na atom, and their calculated IPs agree well with the observed values for $n \geq 4$. The calculations also predicted that the excess-electron distribution is localized in the surface region of the clusters at around Na and extend widely in space opposite to the water molecules. With this geometry, the effect of the hydration in the second and/or third solvent shells on the metal atom is expected to be very weak and, as a result, the IPs of these clusters may not change appreciably with increasing n . They also evaluated the IPs of the interior-type structures for $n \geq 4$, but the calculated IPs differ from the experimental values. Recently, Hashimoto and Kamimoto also calculated the geometries and the electronic structures of $\text{Li} \cdot (\text{H}_2\text{O})_n$ ($n \leq 8$) [24]. The theoretical IPs of both the most stable interior and the less stable threefold forms of $\text{Li} \cdot (\text{H}_2\text{O})_n$ were found to be in good agreement with the observed values. Recently, Tsurusawa and Iwata

also examined the IPs and the excess-electron distribution of $\text{Li} \cdot (\text{H}_2\text{O})_n$ using the *ab initio* method and reached similar conclusions [30]. The details will be discussed later.

As in the case of the alkali metal–ammonia systems, the photoelectron spectra of negatively charged water clusters containing alkali metal atoms have been investigated for exploring the electronic structure of the metal atom in neutral clusters. In contrast to metal–ammonia systems, both the $\text{Na}(3^2\text{S})\text{--Na}^-(^1\text{S})$ and $\text{Na}(3^2\text{P})\text{--Na}^-(^1\text{S})$ transitions in the PE spectra of $\text{Na}^-(\text{H}_2\text{O})_n$ ($n \leq 7$) have been found to shift to the higher EBE (see Figure 3). The spectral shifts of the 3^2S -type transition

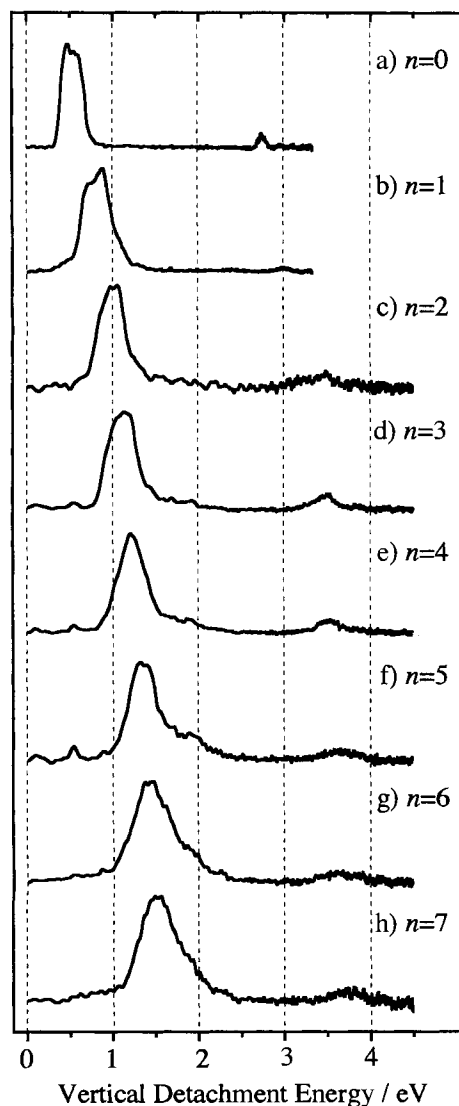


Figure 3. Photoelectron spectra of $\text{Na}^-(\text{H}_2\text{O})_n$ clusters ($n = 0\text{--}7$), collected using photo-detachment energies of 3.50 eV (355 nm) for $n \leq 1$ and 4.66 eV (266 nm) for $n \geq 2$. The spectra are normalized to the peak of the $3^2\text{S}\text{--}^1\text{S}$ transition.

from that of the bare anion ($3^2\text{S}^{-1}\text{S}$, 0.55 eV) are 0.21, 0.44 and 0.58 eV for $n = 1, 2$ and 3 , respectively. A similar trend in spectral shifts has been observed for the PE spectra of solvated cluster anions such as $\text{Cu}^{-}\cdot(\text{H}_2\text{O})_n$ [18] and $\text{I}^{-}\cdot(\text{H}_2\text{O})_n$ [21, 22]. For $\text{Cu}^{-}\cdot(\text{H}_2\text{O})_n$ ($n \leq 2$), Zhan and Iwata [31] calculated the structures and VDEs using the *ab initio* method and found that the Cu^{-} ion is symmetrically hydrated with $\text{Cu}^{-}\cdots\text{H}$ bonds. On the other hand, the clusters with $\text{Cu}\cdots\text{O}$ bonds were found to be the most stable in the neutral ground state. Thus, the observed blue shift of the photodetachment transition arises from the excitation of the electrostatically stabilized anion into the neutral state with a configuration far from the equilibrium geometry. For $\text{Na}^{-}\cdot(\text{H}_2\text{O})_n$, Hashimoto et al. [20] calculated the structures, total binding energies and VDEs for $n \leq 4$. Their calculations predict that the isomer having symmetrical $\text{Na}^{-}\cdots\text{H}$ bonds is more stable than the other isomer with the $\text{Na}^{-}\cdots\text{O}$ bond by 1 kcal mol $^{-1}$. For $n \geq 2$, the isomers with $\text{Na}^{-}\cdots\text{H}$ bonds are also more stable by 3–5 kcal mol $^{-1}$ than the isomers having only $\text{Na}^{-}\cdots\text{O}$ bonds. Thus, the theoretically predicted structures of $\text{Na}^{-}\cdot(\text{H}_2\text{O})_n$ are different from those for the neutral $\text{Na}\cdot(\text{H}_2\text{O})_n$ clusters having $\text{Na}\cdots\text{O}$ bonds. The calculations also reproduced the observed VDEs reasonably well (0.74, 0.94 and 1.09 eV for $n = 1, 2$ and 3 , respectively) [20]. These theoretical results indicate that the observed PE spectra are mainly due to the isomers with $\text{Na}\cdots\text{H}$ interactions. The much larger electrostatic interaction in the anionic state than that in the neutral state results in a blue shift of VDE. Therefore, the observed features in the PE spectra and the theoretical results indicate that the potential energy minimum of $\text{Na}\cdot(\text{H}_2\text{O})_n$ cannot be accessed by anion PES because of the large difference in the structures of the relevant states. The other interesting feature in the observed PE spectra of $\text{Na}\cdot(\text{H}_2\text{O})_n$ is that there is no appreciable change in the energy separation between the 3^2S - and 3^2P -type states for $n \leq 7$. These results suggest that the electronic structure of the neutral alkali metal atoms is not affected substantially by hydration when the metal $\cdots\text{H}$ interaction is dominant. The 3s electron density should be localized on the Na atom as expected from the theoretical calculations [20].

As mentioned above, the similarity of the geometrical structures between the anionic and neutral clusters is a key to probing the potential energy surface of the neutral state via anion PES. Fortunately, the structures of $\text{Li}\cdot(\text{H}_2\text{O})_n$ in the neutral and anionic forms have been found to be similar to each other. These clusters have similar interior structures with $\text{Li}\cdots\text{O}$ bonds and hydrogen-bonding networks for solvent water molecules for $n \leq 8$ [20, 24]. Hence these clusters are good targets to explore the electronic structure of the neutral clusters by PES. Figure 4 shows the PE spectra of $\text{Li}^{-}\cdot(\text{D}_2\text{O})_n$ ($n \leq 10$) recorded at a photon energy of 3.50 eV. The spectra of $\text{Li}^{-}\cdot(\text{H}_2\text{O})_n$ have been found to be essentially the same as those of $\text{Li}^{-}\cdot(\text{D}_2\text{O})_n$. The bare Li^{-} exhibits a strong band at 0.62 eV and a weak band at 2.47 eV, corresponding to the $\text{Li}(2^2\text{S})\text{--Li}^{-}(^1\text{S})$ and $\text{Li}(2^2\text{P})\text{--Li}^{-}(^1\text{S})$ transitions, respectively. The spectrum for $\text{Li}^{-}\cdot\text{D}_2\text{O}$ consists of two peaks at 0.56 and 1.97 eV, corresponding to the two transitions in Li^{-} . Interestingly, these bands are shifted to the lower EBE with respect to those of bare ion by 0.06 and 0.5 eV for the 2^2S and 2^2P transitions, respectively. For $\text{Li}^{-}\cdot\text{D}_2\text{O}$, the calculations have predicted two isomers with $\text{Li}\cdots\text{O}$ and $\text{Li}\cdots\text{D}$ bonds, of which the former is more stable than the

latter by about 5 kcal mol⁻¹ [20]. The VDEs of the 2²S-type states are calculated to be 0.45 and 0.85 eV for the stable and less stable isomers, respectively, at the CCSD/6-311++G(d,p)//MP2/6-311++G(d,p) level. From these theoretical predictions and the experimental results on the alkali metal–ammonia clusters, the observed bands have been assigned to the transitions of the 1:1 complex with Li···O interaction. The large shift in the Li(2²P)–Li⁻(¹S) transition (ca. 0.5 eV) from the bare atom indicates a large increase in the binding energy between the Li atom and the solvent molecule in the first excited state (as large as ca. 0.90 eV) owing to a much larger electron-transfer interaction.

The PE spectra for Li⁻·(D₂O)_n with *n* ≥ 4 show that the band to the 2²S-type state shifts slightly to the red with respect to the 1:1 complex, while the band to the 2²P-type state shows much larger red shift, 1.43 eV for *n* = 4, as shown in Figure 4c. The theoretical calculations have predicted that the most stable isomers of these clusters also have Li···O bonds, and the other isomers with Li···D bonds become energetically unfavorable with increasing *n* [20]. Moreover, the calculated VDEs to the 2²P-type state for the most stable isomers have been found to be close to 0.50 eV, whereas those of the less stable isomers become larger with increasing *n* as in the case of Na⁻·(H₂O)_n shown in Figure 3. From the comparison of these experimental results with the theoretical data, the observed PE spectra for *n* ≤ 10 have been assigned to the transitions of the most stable clusters.

The spectral features in the PE spectra of Li⁻·(D₂O)_n (*n* ≤ 4) are similar to those of Na⁻·(NH₃)_n, and completely different from those of Na⁻·(H₂O)_n mentioned previously. The observed red shifts of the 2²S-type transition with respect to that of the bare anion clearly indicate that the solvation energies of the neutral clusters are larger than those of the anionic forms. The large binding energy in the neutral forms has been ascribed to the extensive charge-transfer interaction induced by the strong Li···O interaction. The large reduction in the 2²P–2²S energy separation, suggesting a complete change in the electronic structure of the Li atom in the clusters, may support this conclusion. These experimental findings are consistent with recent theoretical calculations on the distribution of the 2s valence electron of Li in neutral Li·(H₂O)_n clusters reported by Hashimoto's and Iwata's groups [24, 30]. According to the calculations, the valence electron of Li in the *n* ≤ 2 clusters is strongly polarized in the direction opposite to the water molecules, but is mainly distributed around the Li atom. In Li·(H₂O)₄, the electron distribution is further altered and the electron density is separated from the Li atom; it extends mostly on and between the H₂O molecules. The calculations also reproduced the observed IPs for *n* ≤ 4 with sufficient accuracy. The rapid decrease in IPs has been ascribed to the redistribution of the valence electron on the surface of the cluster where the positive charge is screened with water molecules. Therefore, the red shift of the 2²S- and 2²P-type transitions of Li·(H₂O)_n observed in the PE spectra and the theoretical calculations suggest that the Li atom is gradually ionized with increasing *n* up to 4.

For Li·(H₂O)_n (*n* ≥ 5), both the 2²S- and 2²P-type transitions come to be shifted to the *higher* EBE with respect to those with *n* = 4. This trend may indicate that the first solvent shell around Li is closed with four water molecules in both the neutral and anionic forms. In addition to the spectral shifts, the bandwidths of these transitions become broader for *n* ≥ 5. The gradual increase in the bandwidth indicates

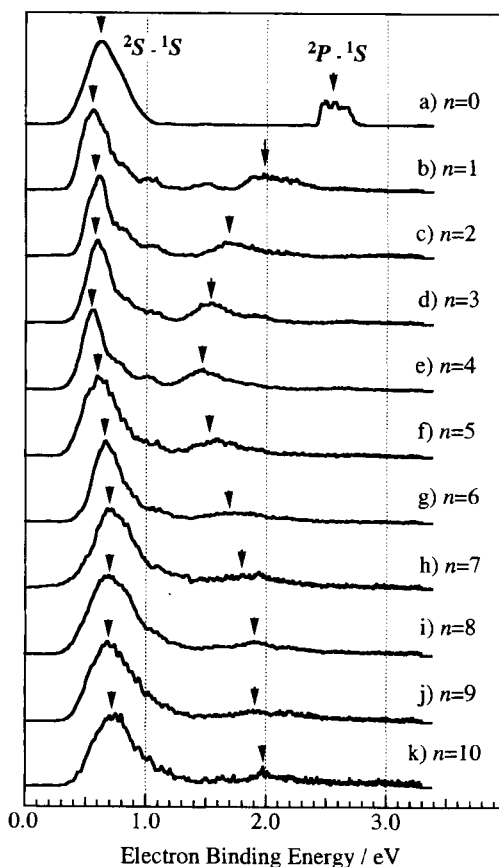


Figure 4. Photoelectron spectra of $\text{Li}^-\cdot(\text{D}_2\text{O})_n$ clusters ($n = 0-10$), collected using a photodetachment energy of 3.50 eV (355 nm). The spectra are normalized to the peak of the $2^2\text{S}-1^1\text{S}$ transition.

an enlargement of the structural difference between the anionic and neutral ground states after the first solvent shell is closed. According to the calculations [24, 30], a $2s$ valence electron of Li in the $n \geq 5$ clusters is squeezed out from the first solvent-shell cavity, forming $[\text{Li}\cdot(\text{H}_2\text{O})_4]^+$, and starts to be trapped on the second-shell waters. For $n = 8$, the electron is localized near the cluster surface to form a two-center ion-pair structure. The electron that has escaped from the first solvent shell interacts with some dangling H atoms in the second-shell waters [30]. Because of the electron $\cdots \text{H}-\text{O}$ bond interaction in the second shell in $\text{Li}\cdot(\text{H}_2\text{O})_n$ ($n \geq 5$), their structures may be distorted from a centrosymmetric form. The extent of the electron localization in the anion clusters is expected to be much smaller because the excess electron in the anion may occupy the same highest occupied orbital being accommodated by the valence electron and they may repel each other. This difference in the electron-localization modes may cause a significant change in the structures of the anion and neutral clusters and may reflect on the bandwidth and also the shift of the PES bands. Although the theoretical results on the larger anion clusters are not available at present, these arguments seem to suggest that the formation of the two-

center ion-pair state in the neutral clusters may be responsible for the observed switching of the spectral shift.

5.3 Charge Transfer in Solvated Anion Clusters

As the second topic in this chapter, the following charge transfer in anionic cluster systems is discussed in this section:



where $\text{X}^{\cdot-}$ and S represent a stable valence anion and a solvent molecule, respectively. In the $\text{X}^{\cdot-}(\text{S})_n$ state, the negative charge is localized exclusively in the $\text{X}^{\cdot-}$ anion core. Even if all the valence anionic states of S are unstable to autodetachment, there can be a different bound (or quasi-bound) anionic state, denoted $[\text{X} \cdot (\text{S})_n]^-$ here, in which the excess electron resides in a diffuse orbital extending over the whole cluster system. Such a diffuse electron trapping can originate from the electrostatic interaction between the excess electron and molecules/atoms. For example, a polar system with a sufficiently large permanent dipole moment can support a weakly bound anionic state, which is well known as a ‘dipole-bound state’ [32]. The excess electron can also be trapped at polar parts in the system, such as a cavity surrounded by dangling hydrogens in anionic water clusters [33, 34]. Even in totally non-polar systems such as pure rare-gas atom clusters, the polarization-induced electrostatic field is strong enough to support a diffuse bound or quasi-bound state [35–39].

If the localized state, $\text{X}^{\cdot-}(\text{S})_n$, is the most stable electronic state in the anion cluster, photoexcitation from the $\text{X}^{\cdot-}(\text{S})_n$ ground state to the diffuse $[\text{X} \cdot (\text{S})_n]^-$ excited state is inherently accompanied by a substantial change in the electronic character and charge distribution. If most of the negative charge is distributed over the solvent moiety, the diffuse anionic state can be represented by $\text{X} \cdot (\text{S})_n^-$ and we may regard the transition from $\text{X}^{\cdot-}(\text{S})_n$ to $[\text{X} \cdot (\text{S})_n]^-$ as a kind of ‘charge transfer to solvent’ (CTTS). This is a cluster analog for CTTS of solvated anions in condensed phases. The observation of CTTS states in solutions dates back to the 1920s [40]. Stable anions, e.g., halide ions, OH^- and NO_3^- , exhibit distinct absorption in the UV region, whose excitation energy is insufficient for the valence excitation of the anion or the creation of free electron [41, 42]. This absorption has been assigned to the electron ejection from the anion into the solvent, i.e.,



Since the beginning of its observation, CTTS has attracted much attention owing to its great importance as a source of solvated electrons, and has been explored extensively in relation to the solvation dynamics of electrons [43–51]. The cluster analog in Eq. 1 has been expected to be a useful model system for microscopic

characterization of CTTS, and has become a focus of recent studies with state-of-the-art methodologies [52]. In such studies, I^- was chosen as a reactant anion because of its stability, the excess electron being bound by 3.04 eV relative to the neutral $\text{I}(^2\text{P}_{3/2})$. The solvents thus far examined are relatively small polyatomic molecules with substantial polarity, e.g., acetone [53], acetonitrile [54] and water [55, 56], in addition to a highly polarizable closed-shell atom, Xe [57]. The studies on I^- clusters with organic molecular solvents, hydrated clusters and $\text{I}^-(\text{Xe})_n$ will be described in some detail in this section.

5.3.1 Dipole-bound Excited States in I^- Clusters Solvated with Small Organic Molecules

Experimental studies on charge-transfer excitation from the localized ground state to the diffuse dipole-bound excited state have been pioneered by Johnson and co-workers [53]. They studied the I^- -acetone cluster via PES and photofragmentation action spectroscopy. The anion cluster was formed by expanding a mixture of several atmospheres of Ar with vapor of methyl iodide and acetone, which was intersected by a 1 keV electron beam at the throat of the expansion. For PES, the anion complex thus formed was mass selected and irradiated with 4.66 eV laser light. The kinetic energy of the ejected electron was analyzed using a time-of-flight (TOF) spectrometer. After the electron-detachment threshold had been determined by PES, photofragmentation was examined by scanning an excitation laser around the detachment threshold. Action spectra for both anionic and neutral products were recorded. The anion fragments were detected in a mass-selected manner by using a tandem TOF spectrometer, while all the photo-neutrals were monitored with a fast neutral detector.

The PE spectrum of I^- -acetone shows a single band peaking at an electron binding energy of 3.49 eV. This value corresponds to the vertical detachment energy (VDE) of the anion complex. Stronger binding (by 0.43 eV) with almost identical bandshape relative to the free I^- ion confirms that the ground-state complex is essentially the intact I^- ion stabilized by solvation with acetone. The action spectrum for the neutrals has an onset about 0.12 eV below the VDE. This indicates the existence of an electronic state slightly below the electron-detachment threshold, which is typical of a dipole-bound state [32]. The action spectrum peaks at the VDE and gradually declines at higher energy, probably owing to the direct photodetachment. It has been noted that the neutral action spectrum is approximated as the absorption spectrum of anion clusters, since all the following reaction channels (Eqs. 3a–c) after photoexcitation produce neutral products:



where $S = \text{acetone}$ in this case. Product analysis has shown that only $(\text{acetone})^-$ is formed as an anion fragment, indicating predominance of channel 3b over 3a. The action spectrum monitoring $(\text{acetone})^-$ indicates a band which looks similar to that in the PE spectrum. Especially, the shapes in the lower energy region are fairly close each other, except that the action spectrum is shifted slightly lower (by ~ 10 meV). In the region above the VDE, the $(\text{acetone})^-$ action spectrum falls more sharply than the PE spectrum. This has been explained by the efficient autodetachment in vibrationally excited states of the dipole-bound complex. The dissociation into I and $(\text{acetone})^-$ after photoexcitation below the VDE should proceed via thermal decomposition of vibrationally hot clusters or excitation to a repulsive region of the I-acetone neutral potential energy surface. In any case, the remarkable result that the excess electron is preferentially trapped by acetone rather than I with much larger electron affinity indicates strong similarity of the dipole-bound state of the $[\text{I} \cdot (\text{acetone})]^-$ precursor and the $(\text{acetone})^-$ product.

To confirm the generality of a diffuse dipole-bound excited state existing in anion clusters with polar solvent molecules, Johnson and the co-workers extended the study to I^- clusters solvated with acetonitrile molecules, i.e., $\text{I}^- \cdot (\text{CH}_3\text{CN})_n$ ($n = 1$ and 2) [54]. Acetonitrile was chosen as a suitable solvent, since it has no anionic valence state lying in the lower energy region and its dipole moment is large (3.92 D).

Experimental methods for exploring excited dipole-bound anions are almost identical for the study of $\text{I}^- \cdot (\text{acetone})$ mentioned above. The VDEs were determined via PES, then the action spectra for negative and neutral photoproducts were observed across the VDEs for $\text{I}^- \cdot (\text{CH}_3\text{CN})_n$ ($n = 1$ and 2). The behavior of the $n = 1$ cluster is remarkably similar to that of the $\text{I}^- \cdot (\text{acetone})$ complex. First, the PE spectrum of $\text{I}^- \cdot (\text{CH}_3\text{CN})$ indicates a band with almost the same shape as the bare I^- band, but shifted by 0.48 eV higher electron binding energy. Second, the absorption cross-section has an onset 0.1 eV lower than the VDE, and increases significantly toward a peak just below the detachment threshold. Third, $(\text{CH}_3\text{CN})^-$ is the only anion product after photoexcitation below the VDE. Fourth, the band appearing in the $(\text{CH}_3\text{CN})^-$ action spectrum is almost identical with that in the PE spectrum, besides the slight red shift. In addition, the PE spectrum of the product $(\text{CH}_3\text{CN})^-$ ion was obtained by a two-color experiment, in which $\text{I}^- \cdot (\text{CH}_3\text{CN})$ was excited into the dipole-bound state by the first laser (at 355 nm) to produce $(\text{CH}_3\text{CN})^-$ and the product was sequentially irradiated with the second laser (at 1064 nm) to photodetach the excess electron. The PE spectrum shows a sharp peak at almost zero electron binding energy, confirming that the $(\text{CH}_3\text{CN})^-$ thus generated is in the dipole-bound ground state.

The notable difference from the $\text{I}^- \cdot (\text{acetone})$ complex is the much larger enhancement of absorption just below the VDE, which corresponds to the excitation to the diffuse $[\text{I} \cdot (\text{CH}_3\text{CN})]^-$ state. The enhancement has been explained as being due to the much larger dipole moment of acetonitrile than acetone, which makes the dipole-bound electron more localized, resulting in larger overlap between the diffuse orbital and the HOMO of the ground state, mostly localized in the 5p orbital of I^- . This implies that, for clusters with more than two solvent molecules, the absorption cross-section to an excited dipole-bound state provides information on the net dipole moment of the solvent system. This has been demonstrated in the $\text{I}^- \cdot (\text{CH}_3\text{CN})_2$ clusters, as mentioned below.

The PE spectrum of $\text{I}^- \cdot (\text{CH}_3\text{CN})_2$ has shown some different features to the bare I^- and $\text{I}^- \cdot (\text{S})$ anions (S = acetone and acetonitrile). It consists of two bands at 3.88 and 4.02 eV in binding energy, of which the higher one (denoted band I) is much stronger than the other (band II). The shift for the major peak (I) relative to bare I^- is exactly twice of that for $\text{I}^- \cdot (\text{CH}_3\text{CN})$, strongly implying symmetric solvation of the I^- core by two CH_3CN , i.e., the solvent molecules reside in equivalent sites, as $\text{NCCH}_3 \cdots \text{I}^- \cdots \text{CH}_3\text{CN}$. Two possible origins of the minor peak (II) have been considered, i.e., a hot band associated with the stronger peak or an isomer with a different configuration. The observed neutral action spectrum also indicates two bands, but the shapes and the relative intensities are very different from those in the PE spectrum. This observation supports the co-existence of two structural isomers in the anion ground state, since a hot band should have a similar shape to a cold band with relative intensity the same as that in the PE spectrum. The lower band (denoted band A) has a feature typical of a dipole-bound excited state, correlating with the detachment threshold of band II in the PE spectrum. The higher band (band B) is much weaker and peaks at the VDE of band I in the PE spectrum.

The large absorption cross-section for band A indicates that the structural isomer with ~ 3.9 eV electron binding energy should have a very large net dipole moment for the solvent unit. An asymmetric colinear geometry, as $\text{I}^- \cdots \text{CH}_3\text{CN} \cdots \text{CH}_3\text{CN}$, has been considered as most probable. The symmetric solvated isomer ($\text{NCCH}_3 \cdots \text{I}^- \cdots \text{CH}_3\text{CN}$) has no net dipole moment in a linear configuration, and the slightly bent form or large-amplitude librations of two dipoles have been suggested to support the dipole-bound state correlating with the weak band (B). Anion photoproduct analysis has provided further information for structural assignments. Photoexcitation into band A produces both CH_3CN^- and $(\text{CH}_3\text{CN})_2^-$ anions but no I^- , whereas excitation into band B results only in electron detachment. The $(\text{CH}_3\text{CN})_2^-$ thus generated should be a dipole-bound cluster with a linear $(\text{CH}_3\text{CN} \cdots \text{CH}_3\text{CN})^-$ configuration. This strongly supports colinear geometry in the asymmetric isomer, as the photodissociation from the $[\text{I} \cdot (\text{CH}_3\text{CN})_2]^-$ state cannot induce a large geometrical change. The difference in the electron binding energies corresponds directly to the anion stability, as the van der Waals binding energies in the neutral isomers should not be very different. Hence the symmetric isomer is more stable than the asymmetric isomer by 0.14 eV.

The most important point in this study is that the dipole-bound excited states of the $\text{I}^- \cdot (\text{CH}_3\text{CN})_2$ cluster cannot be considered as a result of further solvation of the $[\text{I} \cdot \text{CH}_3\text{CN}]^-$ ion core. Instead, the nature of diffuse excited states is determined by the entire arrangement of solvent molecules around the solute anion, as mentioned above. This situation is more akin to CTTS in bulk solutions than solvated ion cores, which are common to most ionic clusters and electrolytic solutions without photoexcitation.

5.3.2 CTTS Precursor States in $\text{I}^- \cdot (\text{water})_n$ Clusters

Evolution of the diffuse excited state with increasing degrees of solvation is of great interest with respect to the correlation with the bulk CTTS. The first examination of this issue was conducted with the I^- clusters solvated with water molecules. John-

son and co-workers [55] observed the absorption spectra of $\text{I}^-\cdot(\text{H}_2\text{O})_n$ ($n = 0-4$) by monitoring photofragments after excitation of mass-selected ions. Among the three photodecomposition channels in Eq. 3, only electron detachment (Eq. 3c) has been observed for all the $n = 1-4$ clusters. The observed photodetachment spectra reveal that onsets of absorption are gradually blue shifted as the cluster sizes become larger. The shifts are well correlated with the VDEs determined via the PE spectra of $\text{I}^-\cdot(\text{H}_2\text{O})_n$ observed by Cheshnovsky and co-workers [22]. Interestingly, the bandshape in absorption changes considerably with increasing degree of hydration. The bare I^- spectrum shows a sharp onset at the threshold energy for $\text{I}^- \rightarrow \text{I}(^2\text{P}_{3/2}) + \text{e}^-$, and the cross-section remains almost constant once it has risen to the threshold. This behavior is typical of direct photodetachment. The gross feature for $n = 1$ is similar to that for bare I^- , but there is a small absorption enhancement just above the VDE. The enhancement around the VDE becomes more prominent for larger n , and the step-like absorption turns to a band with a distinct peak. The peaks for $n \geq 2$ come to be located lower in energy than the VDEs, and the difference from the VDE increases as the cluster size becomes larger. The absorption cross-section also increases with n . Strikingly, the small cluster with only four solvent molecules already has $\sim 70\%$ of the peak intensity of the band in aqueous I^- solution. In short, absorption bands of the hydrated I^- clusters are rapidly approaching the bulk CTTS band with respect to both shape and intensity.

The above-mentioned change in absorption for $\text{I}^-\cdot(\text{H}_2\text{O})_n$ ($n = 0-4$) demonstrates the evolution of diffuse excited states supported by the solvent networks. A schematic energy diagram is illustrated in Figure 5. The slight absorption enhance-

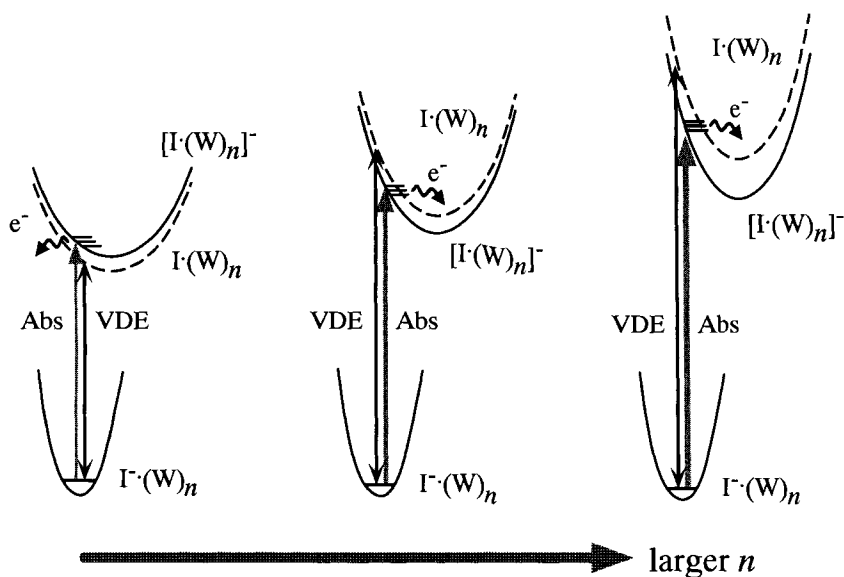


Figure 5. Schematic energy diagram for photoexcitation into CTTS precursor states in $\text{I}^-\cdot(\text{water})_n$ clusters. Abs and VDE represent CTTS-type absorption and vertical detachment energy from the anion ground state, respectively.

ment in the monohydrate is considered as resonance in the detachment continuum, which is due to a long-range attractive potential originating from the electrostatic field by the neutral solvent. Since the dipole moment of H_2O is not very large (1.9 D), it can only support the *virtual* dipole-bound state. For the larger clusters, the dipole-bound states become stabilized below the detachment threshold. This has been rationalized by *ab initio* calculations on the ground-state anion geometry [58–60]. The most stable anions have been predicted to have a so-called ‘surface’ structure, in which water molecules are hydrogen-bonded each other with their dangling hydrogens pointing to the I^- ion. The net solvent dipole moments in the clusters (3.2, 3.5 and 4.4 D for $n = 2, 3$ and 4, respectively) are larger than the critical value (~ 2.5 D) to support a dipole-bound state [32]. Recently, the ‘surface’ structures for $n = 1\text{--}3$ have been confirmed by the results of vibrational predissociation spectroscopy [61]. The increasing dipole moments for the larger clusters are well correlated with increasing stabilization of the dipole-bound state relative to electron detachment. The resultant enhancement in localization of the diffuse orbital should provide a larger transition moment to the excited state, which is consistent with the observed increase in absorption intensity. It has been noted that the solvent orientations in the anion and neutral states should be very different each other for the larger clusters, since the estimated *adiabatic* detachment energies (ADEs) are much smaller than the VDEs. Thus excitation into the dipole-bound states produces vibrationally hot dipole-bound clusters according to the Franck–Condon (FC) principle, and the excess electron is eventually ejected, as its binding in the excited states is much weaker than the hydrogen bonding between the solvents and the I atom.

Following the above-mentioned spectroscopic study by Johnson and co-workers [55], Neumark and co-workers [56] explored the ultrafast real-time dynamics that occur after excitation into the CTTS precursor states of $\text{I}^-(\text{water})_n$ ($n = 4\text{--}6$) by applying a recently developed novel method with ultimate time resolution, i.e., femtosecond photoelectron spectroscopy (FPES). In anion FPES, a size-selected anion is electronically excited with a femtosecond laser pulse (the *pump*), and a second femtosecond laser pulse (the *probe*) induces photodetachment of the excess electron, the kinetic energy of which is determined. The time-ordered series of the resultant PE spectra represents the time evolution of the anion excited state projected on to the neutral ground state. In the study of $\text{I}^-(\text{water})_n$, 263 nm (4.71 eV) and 790 nm (1.57 eV) pulses of ~ 100 fs duration were used as pump and probe pulses, respectively. The pump pulse is resonant with the CTTS bands for all the clusters examined.

The results for FPES on $\text{I}^-(\text{water})_n$ have shown that the dynamic behavior changes substantially on going from $n = 4$ to 5 and 6. For $\text{I}^-(\text{D}_2\text{O})_4$, the relatively sharp (~ 0.3 eV, FWHM) band rises to a maximum during the first 200 fs with the electron kinetic energy (eKE) centered at 1.38 eV. Subsequently, it becomes weaker to some extent at longer times ($\sim 20\%$ after 2 ps), with its position and shape essentially unchanged. The band for $\text{I}^-(\text{D}_2\text{O})_5$ remains constant (centered at 1.38 eV eKE) during ~ 200 fs, then becomes shifted to lower eKE by ~ 0.2 eV with a time constant of 390 fs. The intensity of the PE signal starts to increase after the initial period, reaching a maximum at around 2 ps, and then slowly decreases with a decay

constant of 37 ps. The width of the spectrum also increases slightly (from 0.27 to 0.34 eV) along with the band shift and intensity increase. The gross features of the PE spectrum of $\text{I}^{\cdot-}(\text{D}_2\text{O})_6$ are similar to those of $\text{I}^{\cdot-}(\text{D}_2\text{O})_5$, with the exceptions of a change in the center eKE (from 1.33 to 1.05 eV) and the time constants of the fast band shift (560 fs) and slow intensity decay (96 ps). Isotopic substitution from D_2O to H_2O has also been examined, and all the hydrated clusters are shifted by 20 meV to higher eKE relative to the corresponding deuterated species, owing to the zero-point energy difference. The $n = 4$ clusters shows no other difference, whereas the band shifts for $n = 5$ and 6 start earlier by ~ 100 fs and the time constant of the band shift is slightly smaller for $\text{I}^{\cdot-}(\text{H}_2\text{O})_6$ (470 fs).

For the $n = 4$ cluster, the small (0.19 eV) VDE from the excited state, i.e., difference between the probe photon energy and eKE, and the relatively sharp band width confirmed that the excited state is of ‘dipole-bound’ type, which is supported by the large net dipole moment for the solvent network, as a dipole-bound state is in general located slightly below the detachment threshold and its potential energy surface is similar to that of the neutral, giving almost diagonal FC activity [32]. Therefore, the time evolution in the PE spectrum for $n = 4$ is well ascribed to the population change of the dipole-bound excited state. Because the pump photon energy is larger than the estimated ADE (4.36 eV), dipole-bound clusters generated by the pump pulse excitation are vibrationally hot. The slow decrease of the PE signal on the picosecond time-scale corresponds to a pure population decay via vibrational autodetachment.

The time evolution for the $n = 5$ and 6 clusters shows more elaborate dynamics than the population change of the excited state. The schematic energy level diagram is presented in Figure 6. Because the early-time PE spectra are similar to that for $n = 4$ in location and width, the initially prepared state is considered to be a dipole-

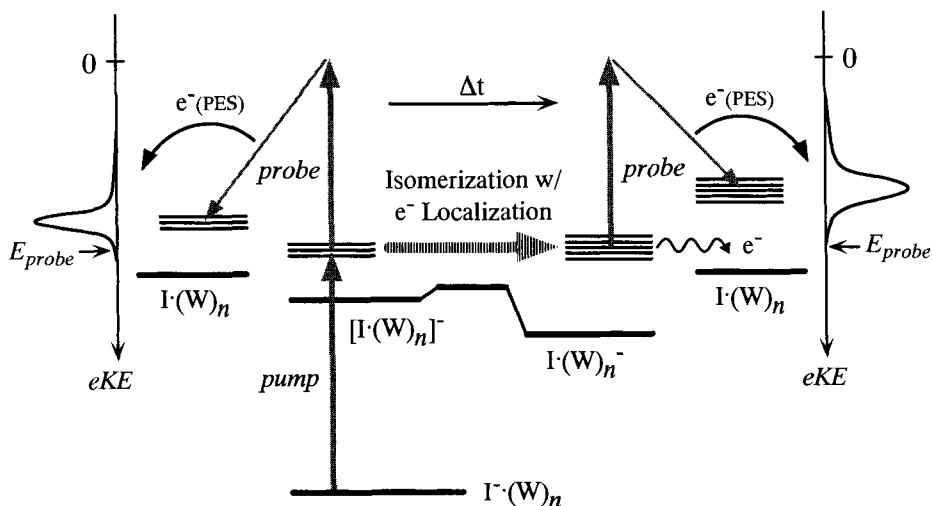


Figure 6. Schematic diagram of femtosecond photoelectron spectroscopy of $\text{I}^{\cdot-}(\text{water})_n$ clusters.

bound state, in which the excess electron is in a diffuse orbital extending over the solvent network. The shifts of the PE signals toward lower eKE indicate that the electron binding becomes stronger on a time-scale of several hundred femtoseconds. This stabilization should be accompanied by a substantial change in the electronic character, as the intensity gain in the PE signals is certainly due to the increase in the photodetachment cross-section. These facts have been interpreted by invoking isomerization into a more stable conformer, in which the hydrogen-bond network of the solvent water molecules is rearranged to make a more stable trapping site for the excess electron. The trapped electron after isomerization is much more localized than that in the initial dipole-bound state, resulting in a change in detachment cross-sections. The observed isotopic effects also support the structural rearrangement. The fact that the eKE shifts in $\text{I}^{\cdot-}(\text{H}_2\text{O})_5$ and $\text{I}^{\cdot-}(\text{H}_2\text{O})_6$ start earlier than in the corresponding deuterated species indicates that isomerization takes place more rapidly in the hydrated species, and strongly implies that the librational motions of the solvents must be involved in the structural rearrangement to stabilize the excess electron.

A possible isomerization pathway for the $n = 6$ cluster has been proposed on the basis of the quantum chemical calculations of Conbariza et al. [59] and Kim et al. [33]. In the predicted most stable structure for the ground state [59], the I^- ion lies on the surface of a V-shaped solvent network. It has been assumed that the initially excited state has a similar geometry, in which the excess electron is weakly bound by the net dipole moment of the solvent network. The supposed form after isomerization resembles the stable ‘half-cage’ structure for the water hexamer anion [33], in which the excess electron is confined by dangling hydrogens of waters.

Neumark and co-workers [56] pointed out the similarity of the cluster results to the transient behavior in aqueous I^- solution, which has been studied via ultrafast pump–probe measurements [50]. Bradforth and co-workers [50] observed IR (800 nm) transient absorption after UV (255 nm) excitation with 50 fs time resolution. In I^- solution, a promptly arising transient disappears within ~ 50 fs, and absorption due to solvated electron rises with a ~ 200 fs time constant. For longer time-scales, the trapped electron shows a biexponential decay with time constants of 8 and 60 ps, which is due to recombination with the nearby iodine atom. The close resemblance of time-scales for the rise of the solvated electron and isomerization in $\text{I}^{\cdot-}(\text{water})_n$ ($n = 5$ and 6) implies that the electron trapping pathway in solution can be modeled as a rearrangement of the solvent hydrogen-bond network in gas-phase clusters.

5.3.3 Dipole-bound Excited State in $\text{I}^{\cdot-}(\text{Xe})_n$ Clusters

Unlike molecular solvents, charge–dipole interaction cannot be expected between closed-shell atoms and excess electrons. However, finite and infinite ensembles of rare-gas atoms can support a bound and/or quasi-bound state for electrons, due solely to the collective polarization of the surrounding atoms. In bulk Xe, for instance, the conduction band lies ~ 0.7 eV below the vacuum level [62]. The formation of negatively charged clusters has also been reported for He [35–37], Ne [38]

and Xe [39]. This has promoted the idea that clusters of stable anions, e.g., I^- , solvated with a sufficient number of rare-gas atoms can support a diffuse excited state, in which the excess electron is essentially transferred to the solvent moiety, such as polar molecular solvents mentioned above. This idea was confirmed by the study of I^- clusters solvated with a number of Xe atoms, the polarizability of which is fairly large.

Cheshnovsky and co-workers [57] characterized diffuse excited states in $\text{I}^-(\text{Xe})_n$ ($n = 1-54$) via PES and photofragment action spectroscopy. It was noted that the $n = 12$ cluster predominates in the mass spectrum, i.e., $n = 12$ is a 'magic number'. This implies that the cluster has an icosahedral structure in which the first solvent shell becomes closed. All the PE spectra measured with excitation by ~ 5 eV photons indicate two Gaussian-like bands with an ~ 1 eV interval. The band lower in binding energy corresponds to the detachment to $\text{I}(^2\text{P}_{3/2})$, and the higher energy band to $\text{I}(^2\text{P}_{1/2})$. The VDEs for both channels gradually increase with increasing cluster size: from 3.06 to 3.96 eV ($^2\text{P}_{3/2}$) and from 4.01 to 4.90 eV ($^2\text{P}_{1/2}$) from $n = 0$ to 54. The VDE indicates an almost linear dependence on n for $n = 0-12$, then the slope suddenly becomes smaller for $n \geq 12$. This abrupt change is consistent with the first solvent shell closure.

Examination of the photodecomposition products revealed that electron emission is the only discernible channel after photoexcitation around the VDEs. The size evolution of action spectra for smaller clusters ($n = 0-12$) is similar to that which appears in $\text{I}^-(\text{H}_2\text{O})_n$ ($n = 0-4$). The step-like spectrum of bare I^- shows an enhancement around the VDE to the $^2\text{P}_{3/2}$ channel, which becomes narrower to form a distinct band as n increases. The absolute peak position in absorption becomes higher in parallel with the VDE, but the peak shifts toward lower energies relative to VDE with larger size. Therefore, the absorption peak lies above the VDE for $n = 0-3$ and becomes lower for $n \geq 4$. The relative absorption cross-section increases gradually by about two orders of magnitude from $n = 1$ to 12. In the vicinity of the VDE ($^2\text{P}_{1/2}$), a small peak with a relatively narrow width appears at $n = 4$, and it becomes stronger and lower in energy relative to the VDE as n increases. The energy shift of the band peak from the VDE is the same for the $^2\text{P}_{3/2}$ channel within the experimental accuracy. All the observations are well ascribed to a gradual stabilization of a diffuse excited state by the increasing polarization of the Xe solvent shell. The crossover from a quasi-bound excited state to a bound state takes place at $n = 4$. This critical size is consistent with the observation that a pure Xe cluster as small as $n = 6$ can support a stable anionic form [39].

For clusters with $n \geq 13$, the action spectra show a drastic change, i.e., the lower energy band correlating to the $^2\text{P}_{3/2}$ channel disappears almost completely, while the upper band to the $^2\text{P}_{1/2}$ channel appears for all the clusters as in the cases with $n \leq 12$. Because the bound state to the $^2\text{P}_{3/2}$ channel is gradually stabilized for $n \leq 12$, it must exist below the VDE for larger clusters. The disappearance in the action spectrum should be attributed to inefficiency in electron emission after excitation into the bound state. This was proved by performing two-photon action spectroscopy (2PAS), in which a UV pulse excited the cluster into the $^2\text{P}_{3/2}$ band and the second near-IR light pulse induced the electron detachment. The $^2\text{P}_{3/2}$ bands for $n \geq 13$ have been observed clearly by 2PAS, and it has been confirmed that the excited bound state is regularly stabilized in the whole range of cluster sizes examined.

The inefficient electron emission from the $^2P_{3/2}$ band for the larger clusters has been explained in terms of temperature which depends on the cluster size. Excitation above the $VDE(^2P_{3/2})$ can be followed by autodetachment via direct coupling with the electron continuum to form $e^- + I(^2P_{3/2})$. However, electron ejection after excitation below the $VDE(^2P_{3/2})$ needs additional vibrational energy, which is converted through non-adiabatic relaxation to electronic energy to overcome the electron binding. Vibrational excitation in the excited state is achieved with off-diagonal FC activity in electronic transitions, or simply transferred from vibrationally hot clusters in the ground state. Considering the narrow bandwidth in absorption, the latter is more probable for $I^-(Xe)_n$. Hence the $^2P_{3/2}$ absorption band appearing in the action spectra are due mainly to vibrationally hot ground-state clusters. It has been considered that the temperature of a cluster ensemble with definite size is determined by evaporative cooling [63]. Since binding between the I^- core and Xe atoms in the first solvent shell is fairly strong, evaporation in the clusters with $n = 1-12$ is not so active, resulting in a higher temperature. On the other hand, binding for second-shell Xe atoms is estimated as less than half that for the first-shell atoms, and therefore the temperature for the larger clusters is much lower owing to efficient evaporation. This is consistent with the abrupt disappearance of the $^2P_{3/2}$ band in the action spectra.

5.4 Electron-transfer Reactions in Large Donor–Acceptor Molecules Studied Under Jet-cooled Conditions

Studies on electron donor–acceptor (EDA) molecules in condensed phases have a long history. Since the EDA interaction was first proposed by Mulliken [64], an appreciable number of reviews on this subject have been published during the latter half of the 20th century [65]. Similar studies under isolated jet-cooled conditions started in the 1980s and have supplied detailed information on the static and dynamic characters of excited electronic states responsible for the electron transfer [66]. The present section does not intend to cover all the details of the EDA studies in jet-cooled conditions but rather focuses on selected EDA molecules consisting of anthracene derivatives. Although limited in scope, the subject provides the most essential aspects of the EDA phenomena observed in an isolated system or in solvated clusters.

EDA molecules consist of the donor and acceptor parts within a single molecular frame. N,N' -Dialkylaniline constitutes the most familiar donor part and anthracene is the most frequently used acceptor part. Anthracene can also be used as a donor moiety. A group of molecules where the donor and acceptor parts are separated by a saturated hydrocarbon chain $-(CH_2)_n-$ as in Figure 7 are called *bridged* EDA molecules. All the EDA molecules composed of anthryl and dimethylanilino moieties were reported to form a charge-transfer (CT) state in polar liquid solvents [67]. In isolated jet-cooled conditions, however, only the specific bridged EDA molecules can form the CT state. To enable the other bridged EDA molecules to form the CT state, at least one polar solvent molecule should be attached to the parent EDA molecule.

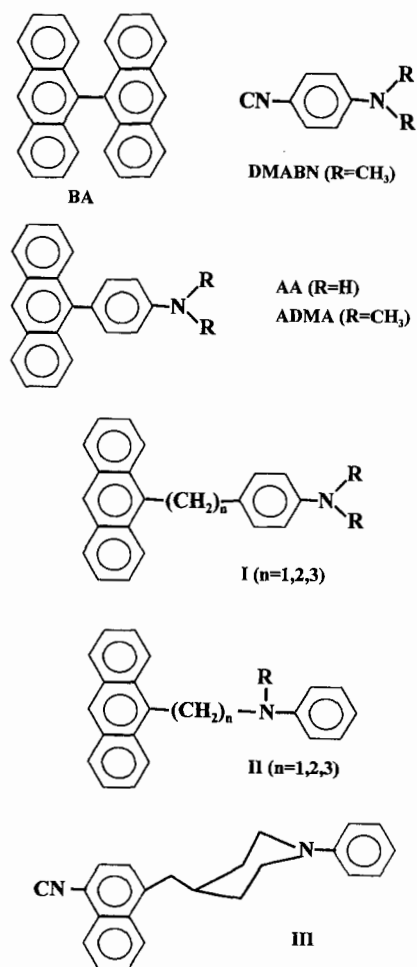


Figure 7. Typical EDA molecules with anthryl moieties.

In the present section, we first describe the details of the intramolecular charge-transfer (ICT) state formation in several directly connected (i.e., $n = 0$) EDA molecules from our recent studies, and then review the reported features of the bridged EDA molecules.

5.4.1 Directly Connected EDA Molecules

9,9'-Bianthryl

In 9,9'-bianthryl (BA) shown in Figure 7, the anthryl moiety acts as both a donor and an acceptor. On photoexcitation in a polar solvent, BA forms the ICT state via the ordinary S_1 state or so-called locally excited (LE) state. Although CT state for-

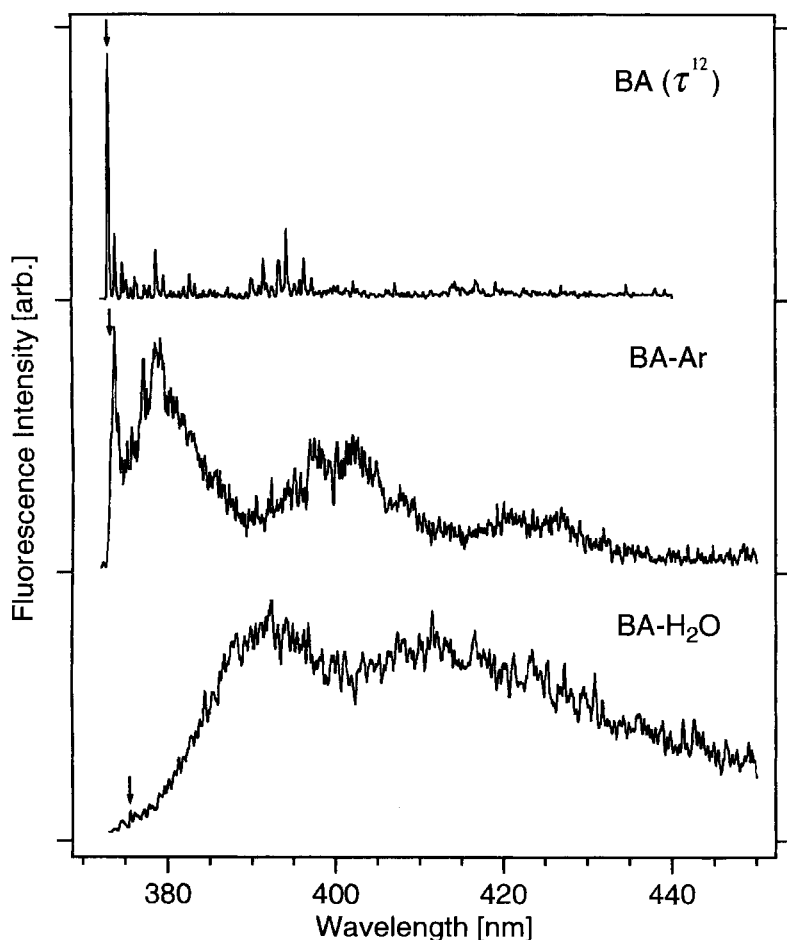


Figure 8. Dispersed fluorescence spectra of free BA, 1:1 BA-Ar and 1:1 BA-H₂O complexes. The 1:1 BA-H₂O complex shows red-shifted CT emission whereas the BA-Ar complex gives fluorescence from the vibrationally relaxed LE state.

mation in polar liquid solvents has been extensively studied for many decades [68], the precise determination of the torsional potential around the 9,9'-bond became possible only about 10 years ago with the combined use of jet cooling and laser excitation [69–71]. The torsional potential was found to be seriously affected by an attached solvent atom or molecule [72]. A water molecule, as a polar solvent, enables a BA molecule to form the CT state by stabilizing the polar state. The fluorescence of the 1:1 BA-H₂O complex is considerably red shifted as in Figure 8 and shows a long lifetime which is characteristic of the intramolecular CT state [73].

The time dependence of the fluorescence at several wavelengths is illustrated in Figure 9. The resonance fluorescence at the excitation wavelength, 375 nm, dies away within 20 ps while the fluorescence at 380 nm rises with the same time con-

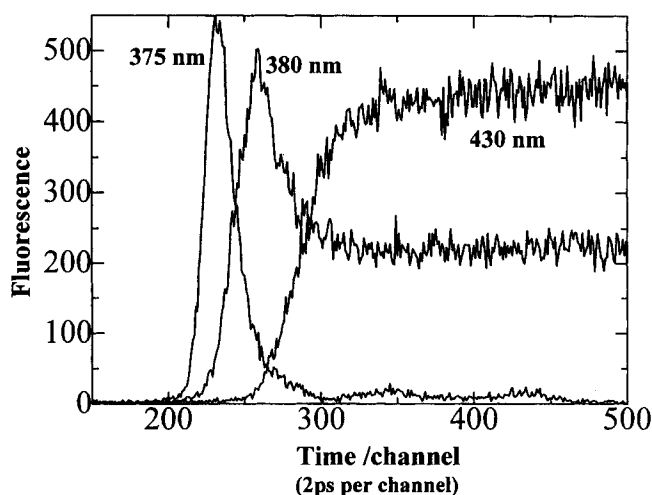


Figure 9. Time-resolved fluorescence of the 1:1 BA-H₂O complex at selected wavelengths after the excitation at 375 nm. The rapid decay of the resonance fluorescence at 375 nm coincides with the fluorescence increase at 380 nm, which then decays with a time constant of 50 ps. The CT emission from the equilibrated state at >400 nm grows simultaneously with the decay of the 380 nm emission.

stant. As the latter fluorescence decays, the CT fluorescence at longer wavelength (>400 nm) appears with the common time constant of 50 ps. Such features suggest the simultaneous occurrence of CT state formation and intramolecular vibrational-energy redistribution (IVR). The IVR in the LE state and the formation of the CT state may take place within 20 ps and the 380 nm fluorescence probably comes from the highly vibrationally excited CT state, which eventually relaxes to the vibrationally equilibrated CT state. This equilibrated CT state emits the ordinary red-shifted CT fluorescence [73].

The structure of the 1:1 BA-H₂O complex in its ground state has been determined by rotational coherence spectroscopy (RCS) using the fluorescence depletion scheme [74, 75]. The empirical minimum-energy calculation supplemented the insufficient information obtained from the RCS measurement [74]. In the structure giving the best fit to the RCS signal, the water molecule sits on the terminal aromatic ring of the one anthracene moiety. Thus the two anthracene moieties are stabilized by the water molecule in a different manner, and such asymmetry in the stabilization, i.e., symmetry breaking, facilitates the electron jump from one anthracene to the other [76].

4-(9-Anthryl)-aniline and 4-(9-anthryl)-*N,N'*-dimethylaniline

The second typical EDA molecule is 4-(9-anthryl)-*N,N'*-dimethylaniline (ADMA), where the anthracene acts as an acceptor and directly links to dimethylaniline, the donor. Studies in the condensed phase revealed that ADMA and BA offered a sharp contrast in their dynamic behaviors of ICT state formation [77–80]. The dy-

namics of BA can be analyzed simply in terms of the two-state model including only the LE and CT states. In contrast, the dynamics of ADMA are complex. One has to assume many intermediate states between the LE and the CT states. This contrasting behavior probably originates from the difference in their torsional potentials in both the ground and excited states. However, the precise determination of the torsional potential of ADMA is difficult because of the significant complexity of the vibrational features appearing in the LIF spectrum [81]. We then synthesized 4-(9-anthryl)-aniline (AA), which possessed only one internal rotor, and demonstrated that the LIF spectrum became much simpler than that of ADMA to facilitate the estimation of the torsional potential [82–85].

The characteristic features of the CT formation dynamics in AA proved similar to those of ADMA [83]. The detailed analysis of the vibrational structure revealed the presence of a new low-lying CT state in addition to the LE state [84]. Taking account of a coupling between this CT state and the LE state, we successfully reproduced the spectra and evaluated the torsional potentials of the ground, the LE and the CT states, as shown in Figure 10. In an isolated AA molecule, the CT state is non-perpendicular and charge separation is incomplete. The presence of the NH_2 substituent is responsible for the low-lying CT state while the flexibility in torsional

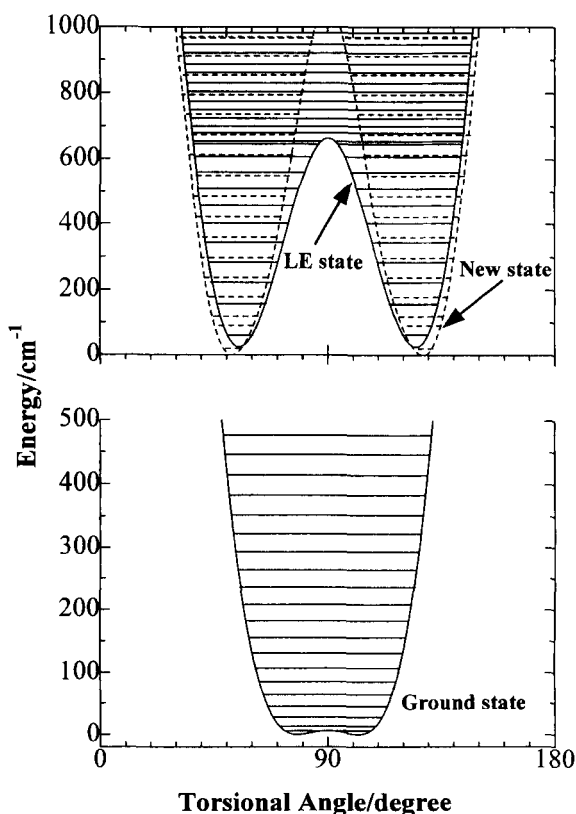


Figure 10. Ground- and excited-state torsional potentials of AA. In addition to the ordinary LE state, a new low-lying excited state with partial CT character exists in the vicinity of the LE state.

motion yields the non-perpendicular CT state. These findings are the key to understanding the so-called multistate CT in ADMA and its homologs.

The effect of microscopic solvation on the electronically excited states of AA was then studied by using solvated clusters of AA produced in a free jet [85]. The magnitude of the red shift and the broadness in the dispersed fluorescence spectra depended on the solvent polarity and the clustering number. Both the low-lying partial CT state and the ordinary full CT state are involved as the fluorescing state, and their relative contributions depend on the polarity and the number of solvent molecules.

5.4.2 Bridged EDA Molecules

In the bridged EDA molecule **I** (Figure 7) where the donor dimethylaniline and the acceptor anthracene are bridged by a saturated hydrocarbon chain $-(CH_2)_n-$, the features of the electron-transfer reaction are known to be strongly dependent on the chain length n . Mataga and co-workers demonstrated that in the condensed phase bridged EDA molecules with $n = 0, 1$ and 2 formed the CT state only in polar solvents. In the case of $n = 3$, the CT state was formed even in non-polar solvents [86]. The rise time of the CT emission in 2-propanol was 54 and 93 ps for $n = 1$ and 2 , respectively. In n -hexane solvent, a rise time of 2.6 ns was reported for the $n = 3$ molecule.

Zewail and co-workers first observed the behavior of the CT formation for the $n = 3$ bridged EDA molecule in isolated jet-cooled conditions [87, 88]. They found that the rate of electron transfer depends on the excess energy given to the EDA molecule and not on the vibrational mode to be excited. This implies that the IVR in the LE state precedes the CT reaction. They confirmed this mechanism by demonstrating that an RRKM calculation could reproduce the energy dependence of the CT rate. The IVR accelerates the structural change, i.e., folding, of the EDA molecule in the LE state so that the donor part most favorably overlaps the acceptor part.

Levy and co-workers showed that the similar bridged EDA molecule **II** (Figure 7) in isolated conditions gave CT fluorescence only for $n = 2$ (actually $n = 3$ when including the N atom) and one isomer of $n = 4$ [89]. This finding again indicates the essential role of the overlap between the donor and acceptor parts. Verhoeven and co-workers then demonstrated that, even in the rigidly bridged EDA molecule **III** where the donor and acceptor are apart by 6.7 Å, CT could occur as a result of the chair-boat isomerization [90, 91]. They assumed the existence of an extended CT state which is produced by a rapid electron jump in the chair form. This extended CT state then isomerizes to the boat form CT state with the aid of Coulomb interaction between the donor and the acceptor just like in the harpooning scheme. They also showed that the CT rate depends on the given total excess vibrational energy in the LE state.

In summary, for bridged EDA molecules in isolated jet-cooled conditions, folding is essential for the electron transfer to intensify the overlap between the donor and acceptor. In the condensed phase, a polar solvent assists the electron transfer even for molecules which cannot form a folded structure. The 1:1 bianthryl-H₂O

complex provides such an example of 'solvent-assisted electron transfer' in isolated conditions.

5.5 Conclusion and Outlook

In the first two parts of this chapter, electron transfer (ET) from atomic donors, e.g., alkali metals or the iodine anion, to an accepting unit composed of simple molecular or atomic solvents was discussed. It was demonstrated that even for a molecule without a stable anionic state or large dipole moment, e.g., water and ammonia, an ensemble of a relatively small number of the molecules can act as an electron acceptor. In the case of the solvated alkali metal atom clusters, ET takes place spontaneously as the number of solvent molecules increases, while the ET in the solvated I^- clusters is induced by photoexcitation into the diffuse electronic excited states just below the vertical detachment thresholds. These ET processes in isolated supermolecular systems resemble the charge delocalization phenomena in condensed phases, e.g., excess-electron ejection from alkali metals into polar solvents and the charge transfer to solvent in a solution of stable anions.

The key feature which has allowed remarkable advances in studies of the ET in these supermolecular systems is close agreement of experiment and theory. Detailed comparison of the results from photoabsorption and photoelectron spectroscopy with molecular orbital calculations has revealed the stepwise evolution of the excess-electron distribution after the ET. Such an intimate interplay between theoretical and experimental work will certainly be enhanced in the future to gain more discerning insights into the ET processes in isolated supermolecules. At present, information on the solvation structure is mainly derived from quantum-mechanical or empirical-model calculations. It is highly desirable that the experimental methods for definite structural characterization, e.g., spectroscopy with vibrational and/or rotational resolution, be applied more extensively to various systems that execute ET to solvent networks. Time-resolved experiments utilizing ultrafast laser facilities are another promising direction for exploring dynamic aspects of the ET in supermolecules. Owing to the recent advances in ultrafast laser technology, real-time ET dynamics in condensed media can be probed in great detail. Comparison of the two closely related systems should be fruitful, although the results derived from one cannot simply be transferred to the other.

In the last part of this chapter, intramolecular charge transfer (ICT) in anthryl derivatives with linked donor–acceptor parts was discussed. Ultrafast spectroscopy has been applied both for structural characterization and for real-time probing of the ICT in this case. Microscopic solvation effects on the torsional motions and the ICT in the molecules have been examined by the use of their clusters with polar solvents. One of the most important problems which awaits for further studies is an ambiguous description of the electronic character of the charge-separated states in the systems. So far, high-level quantum-mechanical calculations have not been able to deal with such large molecular systems, but reliable evaluation of electronically

excited states in these molecules will soon be achieved thanks to the rapid progress in computational capability. Of course, their transient nature after photoexcitation should be more thoroughly characterized experimentally, and time-resolved measurements with sufficient state selectivity, e.g., femtosecond pump–probe absorption and photoelectron spectroscopy, will be utilized in future.

References

1. *The Chemical Physics of Solvation, Part C* (Eds. R. R. Dogonadze, E. Kalman, A. A. Kornyshev, J. Ulstrup), Elsevier, Amsterdam, **1988**.
2. Y. Gauduel, in *Ultrafast Dynamics of Chemical Systems* (Ed. J. D. Simon), Kluwer Academic, Dordrecht, **1994**, p. 81.
3. T. R. Tuttle, Jr., S. Golden, *J. Phys. Chem.* **1991**, *95*, 5725.
4. H. Haberland, H.-G. Schindler, D. R. Worsnop, *Ber. Bunsenges. Phys. Chem.* **1984**, *88*, 270.
5. H. Haberland, C. Ludewigt, H.-G. Schindler, D. R. Worsnop, *Surf. Sci.* **1985**, *156*, 157.
6. J. V. Coe, G. H. Lee, J. G. Eaton, H. W. Sarkas, K. H. Bowen, C. Ludewigt, H. Haberland, D. R. Worsnop, *J. Chem. Phys.* **1990**, *92*, 3980.
7. G. H. Lee, S. T. Arnold, J. G. Eaton, H. W. Sarkas, K. H. Bowen, C. Ludewigt, H. Haberland, *Z. Phys. D* **1991**, *20*, 9.
8. I. V. Hertel, C. Hüglin, C. Nitsch, C. P. Schulz, *Phys. Rev. Lett.* **1991**, *67*, 1767.
9. F. Misaizu, K. Tsukamoto, M. Sanekata, K. Fuke, *Chem. Phys. Lett.* **1992**, *188*, 241.
10. R. Takasu, F. Misaizu, K. Hashimoto, K. Fuke, *J. Phys. Chem. A* **1997**, *101*, 3078.
11. R. T. Rodgers, P. B. Armentrout, *J. Phys. Chem.* **1997**, *101*, 1238.
12. P. Brockhaus, I. V. Hertel, C. P. Schulz, *J. Chem. Phys.* **1999**, *110*, 393.
13. R. Takasu, K. Hashimoto, K. Fuke, *Chem. Phys. Lett.* **1996**, *258*, 94.
14. R. Takasu, T. Taguchi, K. Hashimoto, K. Fuke, *Chem. Phys. Lett.* **1998**, *290*, 481.
15. K. Fuke, K. Hashimoto, S. Iwata, *Adv. Chem. Phys.* **1999**, *110*, 431.
16. P. Stampfli, K. H. Bennemann, *Comput. Mater. Sci.* **1994**, *2*, 578.
17. K. Hashimoto, K. Morokuma, *J. Am. Chem. Soc.* **1995**, *117*, 4151.
18. F. Misaizu, K. Tsukamoto, M. Sanekata, K. Fuke, *Laser Chem.* **1995**, *15*, 195.
19. R. Takasu, H. Ito, K. Nishikawa, K. Hashimoto, R. Okuda, K. Fuke, *J. Electron Spectrosc. Relat. Phenom.* **2000**, *106*, 27.
20. K. Hashimoto, T. Kamimoto, K. Fuke, *Chem. Phys. Lett.* **1997**, *266*, 7.
21. G. Markovich, R. Giniger, M. Levin, O. Cheshnovsky, *J. Chem. Phys.* **1991**, *95*, 9416.
22. G. Markovich, S. Pollack, R. Giniger, O. Cheshnovsky, *J. Chem. Phys.* **1994**, *101*, 9344.
23. D. W. Arnold, E. H. Bradforth, E. H. Kim, D. M. Neumark, *J. Chem. Phys.* **1995**, *102*, 3510.
24. K. Hashimoto, T. Kamimoto, *J. Am. Chem. Soc.* **1998**, *120*, 3560.
25. M. H. Shen, J. M. Farrar, *J. Chem. Phys.* **1991**, *94*, 3322.
26. S. G. Donnelly, J. M. Farrar, *J. Chem. Phys.* **1993**, *98*, 5450.
27. G. J. Martyna, M. L. Klein, *J. Phys. Chem.* **1991**, *95*, 515.
28. R. N. Barnett, U. Landman, *Phys. Rev. Lett.* **1993**, *70*, 1775.
29. K. Hashimoto, K. Morokuma, *J. Am. Chem. Soc.* **1994**, *116*, 11436.
30. T. Tsurusawa, S. Iwata, *J. Phys. Chem. A* **1999**, *103*, 6134.
31. C.-G. Zhan, S. Iwata, *Chem. Phys. Lett.* **1995**, *232*, 72.
32. J. H. Hendricks, H. L. de Clercq, S. A. Lyapustina, C. A. Fancher, T. P. Lippa, J. M. Collins, S. T. Arnold, G. H. Lee, K. H. Bowen, in *Structure and Dynamics of Clusters* (Eds. T. Kondow, K. Kaya, A. Terasaki), Universal Academic, Tokyo, **1995**, p. 321.
33. K. S. Kim, S. Lee, J. Kim, J. Y. Lee, *J. Am. Chem. Soc.* **1997**, *119*, 9329; S. Lee, J. Kim, S. J. Lee, K. S. Kim, *Phys. Rev. Lett.* **1997**, *79*, 2038.
34. T. Tsurusawa, S. Iwata, *Chem. Phys. Lett.* **1998**, *287*, 553.
35. J. Gspann, *Physica B* **1991**, *169*, 519.
36. T. Jiang, C. Kim, J. A. Northby, *Phys. Rev. Lett.* **1993**, *71*, 700.
37. U. Henne, J. P. Toennies, *J. Chem. Phys.* **1998**, *108*, 9327.

38. K. Martini, J. P. Toennies, C. Winkler, *Chem. Phys. Lett.* **1991**, 178, 429.
39. H. Haberland, T. Kolar, T. Reiners, *Phys. Rev. Lett.* **1989**, 63, 1219.
40. J. Franck, G. Scheibe, *Z. Phys. Chem. A* **1928**, 139, 22.
41. E. Rabinowitch, *Rev. Mod. Phys.* **1942**, 14, 112.
42. M. J. Blandamer, M. F. Fox, *Chem. Rev.* **1970**, 70, 59.
43. J. Jortner, M. Ottolenghi, G. Stein, *J. Phys. Chem.* **1964**, 68, 247.
44. J. M. Wiesenfeld, E. P. Ippen, *Chem. Phys. Lett.* **1980**, 73, 47.
45. A. Migus, Y. Gauduel, J. L. Martin, A. Antonetti, *Phys. Rev. Lett.* **1987**, 58, 1559.
46. F. H. Long, H. Lu, K. B. Eisenthal, *Phys. Rev. Lett.* **1990**, 64, 1469; *Chem. Phys. Lett.* **1990**, 169, 165; F. H. Long, X. Shi, H. Lu, K. B. Eisenthal, *J. Phys. Chem.* **1994**, 98, 7252.
47. W.-S. Sheu, P. J. Rossky, *Chem. Phys. Lett.* **1993**, 213, 233; *J. Am. Chem. Soc.* **1993**, 115, 7729.
48. Y. Kimura, J. C. Alfano, P. K. Walhout, P. F. Barbara, *J. Phys. Chem.* **1994**, 98, 3450; C. Silva, P. K. Walhout, K. Yokoyama, P. F. Barbara, *Phys. Rev. Lett.* **1998**, 80, 1086.
49. A. Staib, D. Borgis, *J. Chem. Phys.* **1996**, 104, 9027.
50. J. A. Klopfer, V. H. Vilchiz, V. A. Lenchenkov, S. E. Bradforth, *Chem. Phys. Lett.* **1998**, 298, 120.
51. M. Assel, R. Laenen, A. Laubereau, *J. Chem. Phys.* **1999**, 111, 6869.
52. C. E. H. Dessent, M. A. Johnson, I. Becker, O. Cheshnovsky, *Adv. Chem. Phys.* **1999**, 106, 265.
53. C. E. H. Dessent, C. G. Bailey, M. A. Johnson, *J. Chem. Phys.* **1995**, 102, 6335.
54. C. E. H. Dessent, C. G. Bailey, M. A. Johnson, *J. Chem. Phys.* **1995**, 103, 2006.
55. D. Serxner, C. E. H. Dessent, M. A. Johnson, *J. Chem. Phys.* **1996**, 105, 7231.
56. L. Lehr, M. T. Zanni, C. Frischkorn, R. Weinkauff, D. M. Neumark, *Science* **1999**, 284, 635.
57. I. Becker, G. Markovich, O. Cheshnovsky, *Phys. Rev. Lett.* **1997**, 79, 3391; I. Becker, O. Cheshnovsky, *J. Chem. Phys.* **1999**, 110, 6288.
58. L. Perera, M. L. Berkowitz, *J. Chem. Phys.* **1994**, 100, 3085.
59. J. E. Combariza, N. R. Kestner, J. Jortner, *J. Chem. Phys.* **1994**, 100, 2851; *Chem. Phys. Lett.* **1994**, 221, 156.
60. S. S. Xantheas, *J. Phys. Chem.* **1996**, 100, 9703.
61. P. Ayotte, C. G. Bailey, G. H. Weddle, M. A. Johnson, *J. Phys. Chem. A* **1998**, 102, 3067; P. Ayotte, G. H. Weddle, J. Kim, M. A. Johnson, *J. Am. Chem. Soc.* **1998**, 120, 12361; *Chem. Phys.* **1998**, 239, 485; P. Ayotte, G. H. Weddle, J. Kim, J. Kelley, M. A. Johnson, *J. Chem. Phys. A* **1999**, 103, 443; P. Ayotte, G. H. Weddle, M. A. Johnson, *J. Chem. Phys.* **1999**, 110, 7129.
62. R. Reininger, U. Asaf, I. T. Steinberger, *Chem. Phys. Lett.* **1982**, 90, 287.
63. C. E. Klotz, *J. Chem. Phys.* **1985**, 83, 5854.
64. R. S. Mulliken, *J. Am. Chem. Soc.* **1950**, 72, 600; **1952**, 74, 811.
65. G. Briegleb, *Electron Donor-Acceptor Complexes*, Springer, Berlin, **1961**; R. Foster, *Organic Charge-Transfer Complexes*, Academic Press, New York, **1969**; N. Mataga, M. Ottolenghi, in *Molecular Association*, Vol. 2 (Ed. R. Foster), Academic Press, London, **1979**, p. 1; M. A. Fox, *Photoinduced Electron Transfer* (Ed. M. Chanon), Elsevier, Amsterdam, **1988**.
66. M. Ito, O. Kajimoto in *Dynamics of Excited Molecules* (Ed. K. Kuchitsu), Elsevier, Amsterdam, **1994**, p. 333.
67. T. Okada, T. Fujita, M. Kubota, S. Masaki, N. Mataga, R. Ide, Y. Sakata, S. Misumi, *Chem. Phys. Lett.* **1972**, 14, 563.
68. F. Schneider, E. Lippert, *Ber. Bunsenges. Phys. Chem.* **1968**, 72, 1155; **1970**, 74, 624.
69. K. Yamasaki, K. Arita, O. Kajimoto, *Chem. Phys. Lett.* **1986**, 123, 277.
70. L. R. Khundkar, A. H. Zewail, *J. Chem. Phys.*, **1986**, 84, 1302.
71. A. Subaric-Leitis, C. Monte, A. Roggan, W. Rettig, P. Zimmermann, J. Heinze, *J. Chem. Phys.* **1990**, 93, 4543.
72. T. Fujiwara, K. Egashira, Y. Ohshima, O. Kajimoto, *Phys. Chem. Chem. Phys.* **2000**, 2, 1365.
73. T. Ishida, Y. Fujimura, T. Fujiwara, O. Kajimoto, *Chem. Phys. Lett.* **1998**, 288, 433.
74. T. Fujiwara, PhD Thesis, Kyoto University, **2000**.
75. T. Fujiwara, Y. Fujimura, O. Kajimoto, *Chem. Phys. Lett.* **1996**, 261, 201.
76. K. Honma, K. Arita, K. Yamasaki, O. Kajimoto, *J. Chem. Phys.* **1991**, 94, 3496; K. Honma, O. Kajimoto, *J. Chem. Phys.* **1994**, 101, 1752.
77. W. Rettig, M. Zander, *Ber. Bunsenges. Phys. Chem.* **1983**, 87, 1143.

78. T. J. Kang, M. A. Kahlow, D. Giser, S. Swallen, V. Nagarajan, W. Tarzeba, P. F. Barbara, *J. Phys. Chem.* **1988**, 92, 6800.
79. A. Siemiarczuk, W.R. Ware, *J. Phys. Chem.* **1987**, 91, 3677.
80. N. Mataga, S. Nishikawa, T. Asahi, T. Okada, *J. Phys. Chem.* **1990**, 94, 1443.
81. O. Kajimoto, S. Hayami, H. Shizuka, *Chem. Phys. Lett.* **1991**, 177, 219.
82. S. Lee, K. Arita, O. Kajimoto, *Chem. Phys. Lett.* **1997**, 265, 579.
83. S. Lee, K. Arita, O. Kajimoto, K. Tamao, *J. Phys. Chem. A* **1997**, 101, 5228.
84. S. Lee, O. Kajimoto, *J. Phys. Chem. A* **1997**, 101, 5232.
85. S. Lee, PhD Thesis, Kyoto University, **1997**.
86. M. Migita, T. Okada, N. Mataga, Y. Sakata, S. Misumi, N. Nakashima, K. Yoshimura, *Bull. Chem. Soc. Jpn.* **1981**, 54, 3304.
87. P. M. Felker, J. A. Syage, W. R. Lambert, A. H. Zewail, *Chem. Phys. Lett.* **1982**, 92, 1.
88. J. A. Syage, P. M. Felker, A. H. Zewail, *J. Chem. Phys.* **1984**, 81, 2233.
89. N. A. Dantzig, H. Shou, J. C. Alfano, N. C. Yang, D. H. Levy, *J. Chem. Phys.* **1994**, 100, 7068.
90. B. Wegewijs, A. K. F. Ng, R. P. H. Rettschnick, J. W. Verhoeven, *Chem. Phys. Lett.* **1992**, 200, 357.
91. J. Jortner, M. Bixon, B. Wegewijs, J. W. Verhoeven, R. P. H. Rettschnick, *Chem. Phys. Lett.* **1993**, 205, 451.

Volume V

Part 1

Molecular-Level Electronics

1 Wires Based on Metal Complexes

Jean-Pierre Launay and Christophe Coudret

1.1 Introduction

Polymetallic complexes with suitable bridging ligands can be useful models of molecular wires. In the present chapter, we shall consider mainly bimetallic systems in which two metal atoms are connected by a bridging ligand, with the general topology shown in Figure 1.

By extension, some compounds in which the bridging ligand contains a metal unit will also be considered. The present chapter will be focused on the case of mixed-valence compounds, for which reviews covering the basic processes are already available [1, 2].

In most cases, the metal atoms are in fact end groups necessary to define a starting site and an arrival site, while the spacer is usually purely organic. The concept of a molecular wire requires something to be transferred between these two sites more efficiently than if the two sites were separated by empty space. The present chapter will deal essentially with electron (or hole) transfer, but the related topic of energy transfer (treated extensively in Part 1, Chapter 3 of this volume) will be also evoked. Representative examples of electron and energy transfer in polynuclear transition metal complexes can also be found in recent reviews by Juris, Balzani et al. [3a] and by De Cola and Belser [3b].

The distinction between the end groups and the spacer (the wire itself) is not a trivial one. It seemed to us logical to incorporate in the definition of the end groups the immediate coordination sphere, for instance the coordinated pyridine ring in the complexes of the Creutz–Taube family. Thus the spacer would be all the rest of the structure, even if it has no independent chemical existence. In a number of cases, the spacer is made of several *repeat units*, in order to allow the construction of long molecules by repetitive synthesis or even polymerization. Finally, one has to distinguish the *spacer* from the *bridge*, the latter including the coordination sites. The definition of all these terms is made clear by the example of Figure 2.

Among the numerous bimetallic complexes known in the literature, we have selected those for which the metal–metal distance exceeds a minimum value, taken

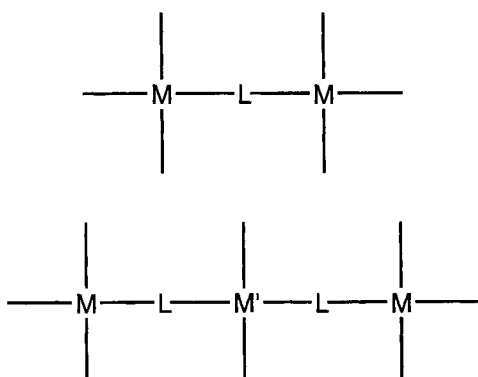


Figure 1. General topology of the complexes.

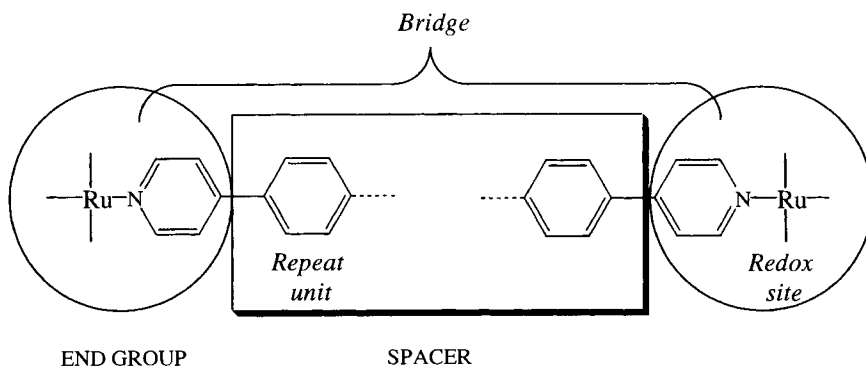


Figure 2. Nomenclature used in the present review: end groups and spacers.

as 10 Å. The metal–metal distance provides an easy way to compare structures, and the 10 Å limit selects complexes for which relatively uncommon processes may occur. Note that with the above definition, complexes with the ligand 4,4'-bipyridine would present only the end sites, but not *stricto sensu* a spacer. However, we have kept these complexes in the scope of this review, since the M–M distance is 11.3 Å, and they have been the subject of a large number of fundamental studies and tests of new methods and concepts.

1.2 Bimetallic Metal Complexes as Models of Molecular Wires

By reference to macroscopic electrical devices, the concept of a wire is fundamentally based on intramolecular electron transfer, and this will be the main focus of

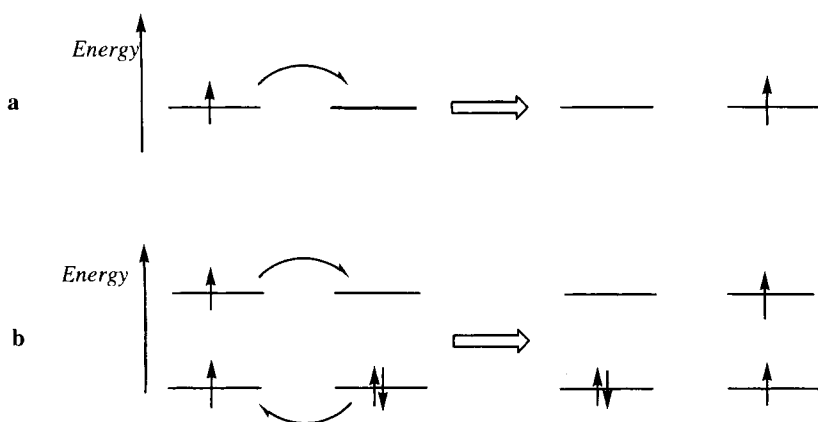


Figure 3. a) Electron transfer and b) Dexter-type energy transfer.

this review. Electron transfer occurs in its simplest form in mixed-valence complexes. It is also encountered in some excited-state processes where charge separation occurs after a photochemical excitation. Energy transfer bears some analogy to electron transfer when it occurs by the Dexter mechanism [4], i.e. a double electron transfer in which an electron jumps from the LUMO of the donor to the LUMO of the acceptor, while simultaneously an electron moves from the HOMO of the acceptor to the HOMO of the donor (see Figure 3).

Why study electron transfer in bimetallic metal complexes? A first justification is that this is a fundamental and ubiquitous process occurring in diverse fields of chemistry, physics, and biology. Of particular importance is the question of the decay law of electronic interaction or electron transfer rates with distance, which is of paramount significance for biological electron transfer. Another interesting topic is the development of molecular switches (in the electrical sense of the word), i.e., molecules able to allow or block intramolecular electron transfer according to a definite perturbation. This development clearly requires the mastering of long-distance electron transfer (over 15–20 Å), because the switching unit must be inserted on the electron transfer path.

Finally, molecular wires based on metal complexes can be used as models to understand the basic processes occurring in (bulk metal)/molecule/(bulk metal) nanojunctions (Figure 4). Such nanojunctions can now be prepared by several methods: “broken junction” [5a], nanodeposition on ultrathin metallic wires [5b], deposition of a suitable molecule on atomic steps of a metallic surface [5c], etc., and they allow the measurement of an electron flux (i.e., a current) through a single molecule. In the case of bimetallic metal complexes, there is just one atom connected at each end, and just one electron moving. In addition, the bimetallic complex involves only one or a few energy levels at each end, while there is a continuum of such levels in the case of ultrathin metallic wires. However, the electron transfer involves the same general principles; in particular, in complexes as in nanojunctions, it is governed by the tunnel effect: the energy levels of the coordinated metals fall in the “gap” be-

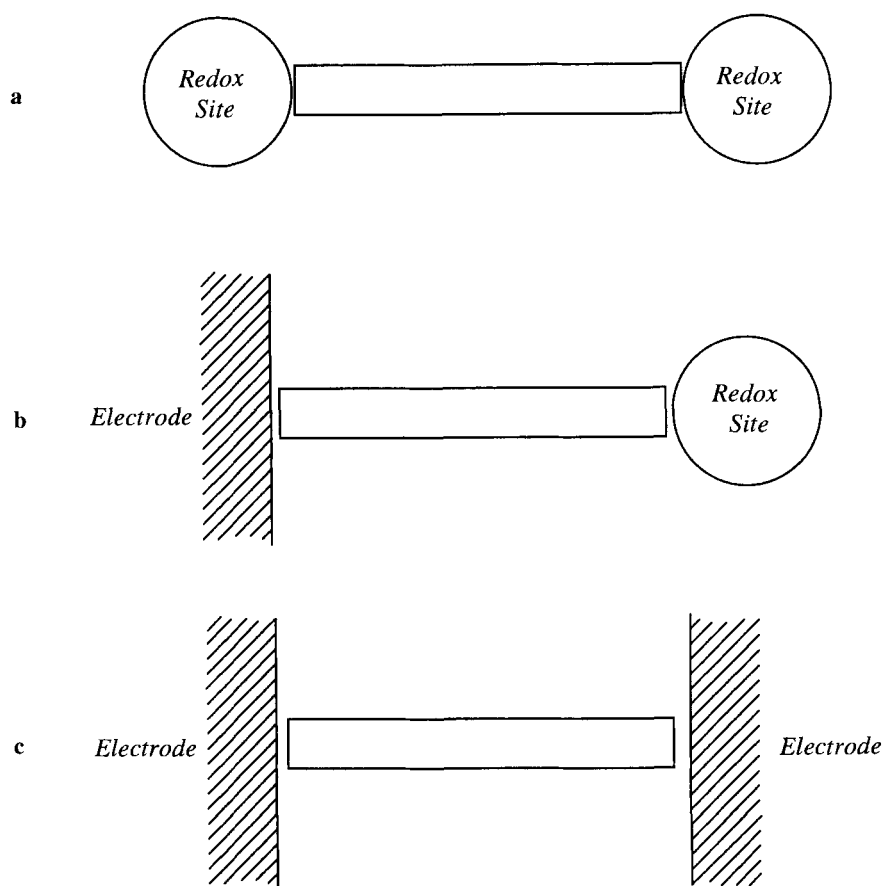


Figure 4. a) Bimetallic metal complex, b) monometallic complex linked to a surface, and c) metal/molecule/metal nanojunction.

tween the ligand's HOMO and LUMO, and thus the situation in which one electron or hole has been transferred to the bridge is a high-energy one. The advantage of metal complexes is that they are chemically and geometrically well defined at the metal–molecule connection. Thus the study of bimetallic metal complexes could be a rapid screening procedure to identify efficient molecules or molecular fragments in order to build molecular nanojunctions.

1.3 Synthetic Strategies

The lack of systematic studies, sustained by theoretical calculations, may explain the large variety of molecular wires (as well as a very poor definition of this notion)

that can be found throughout the literature. However, the proposed syntheses can be sorted according to two general strategies:

- a “classic” strategy, in which the bridging ligand is prepared before the complexation step. This allows a large versatility, since such a ligand would be suitable for various studies including energy transfer. This strategy is appropriate for short ligands, or if the organic precursors are easily available. One of the main difficulties, apart from the handling of a chemical species with free coordination sites (i.e., basic atoms) which may not be trivial, is the final complexation step of a sophisticated and high added-value molecule.
- a “metal complex as building block” strategy in which metallic complexes are used as special organic synthons, the key step being their grafting on an organic core. This strategy is used routinely for complexes with unstable anionic ligands, the most common example being ferrocene. However, it is now applied even for non-organometallic species, especially for chiral complexes since enantiomer resolution can be achieved relatively early in the synthesis on very simple mononuclear precursors [6b]. It has been used in the case of a complex acting as bridging moiety (the “complex as ligand” approach) [7–10].

Eventually, regardless of the strategy used, a recurrent problem is the solubility of the final wire. It is known that rod-like molecules tend to aggregate, especially if they are relatively rigid. Such a problem is usually circumvented by grafting alkyl groups [11]. Another solution is to use ionic complexes, whose charge is expected to allow an efficient solvation of the molecule. However, aggregation in solution can never be ruled out [12a].

Since the synthetic reactions are intended to build the redox centers on one hand, and the conjugated spacer on the other, we have followed this order to present selected examples of syntheses.

1.3.1 Redox Centers

Since metallic ions are supposed to be the only part of the molecule where the extra electron has to reside, one has to be sure that all the interesting redox processes are metal-centered. It is usually true that most of the organic molecules display a moderate reactivity in redox reactions: a large HOMO–LUMO gap, and subsequent rearrangements, tend to decrease electron transfer rates and destabilize the oxidized (or reduced) form of the spacer—thus moving the bridge’s redox couple out of the solvent’s electroactivity window. However this is not true for unsaturated molecules, and as the length of the conjugated part increases, one has to think about redox processes involving the spacer.

Another difficulty comes from the spectroscopic technique used to probe the degree of electronic interaction, which relies basically on the observation of a metal-to-metal charge transfer band (intervalence band) in the near-infrared (NIR). A simple analysis based on the Franck–Condon principle leads to the conclusion that its shape and energy may depend on the geometry change between the reduced and

oxidized form (vide infra, Section 1.4.1 and Figure 13). Thus limiting this distortion should keep the intervalence band in the NIR region, i.e., separated from the other bands. Complexes having a rigid coordination sphere made of multidentate ligands appear promising candidates. However, other low-energy charge transfers originating from low-lying ancillary ligand π or π^* orbitals (such as LMCT), may nevertheless overlap with the intervalence band.

Chemical stability, and more precisely *kinetic* stability to avoid ligand scrambling, is needed for all the concerned oxidation degrees, not only during the redox titration but also for synthetic purpose, especially in the building block approach. The use of heavy transition metals (second or third row), known to give slow ligand exchange reactions, is helpful, but the counterpart is harsh complexation conditions. A careful choice of the ancillary ligand will also bring the interesting redox couple away from the borders of the electroactivity domain of most of the solvents. It may be also important not to populate anti-bonding orbitals (i.e., e_g for an octahedral or pseudo-octahedral geometry) of the metallic complex during the redox processes. Finally, it is more convenient from an analytical point of view (NMR identification) to work with diamagnetic complexes as primary forms. The most common redox groups are listed in Table 1.

For all the above reasons, ruthenium has become a very popular redox site: as a (relatively cheap) heavy metal, its complexes are kinetically stable and its crystal field Δ parameter value is relatively high. Hence, for most common complexes of ruthenium(II) of pseudo-octahedral geometry, the d^6 electronic configuration is a low-spin diamagnetic state, and frontier orbitals, involved in the redox processes are essentially of the nonbonding “ t_{2g} ” type. Eventually its rich photochemistry may be used to probe excited-state behaviors.

Classic strategy

Classically, the redox site are obtained by a “traditional” complexation reaction. This supposes the substitution of a labile ligand from the coordination sphere of the metallic precursor by the desired coordinating ligand. Among the most common, we can find neutral sites made of basic di- or trigonal nitrogens (nitriles, heterocycles), or anionic sites usually based on heteroatoms, digonal or trigonal carbides (acetylides, σ - or π -aryl). Chelation, and especially for heavy metals changes in the degree of oxidation of the metal, enhance the reaction rate. Labile ligands of the metallic precursors are usually halide or solvent [13], and sometimes nitrosyl [14a]. Several examples are shown in Figure 5.

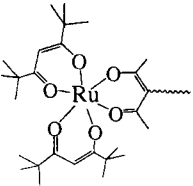
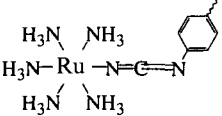
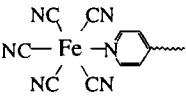
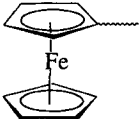
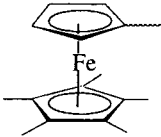
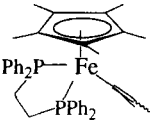
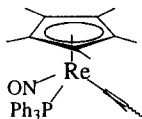
“Metal complexes as building blocks” strategy

In some cases, it is more convenient to handle a complexed ligand rather than a free one. This is especially true for organometallic complexes since free and complexed ligands may have a totally different chemistry. The latter point can be used to achieve easily a functionalization which would be tedious with the free species [11, 17b, 18, 22]. When the latter is impossible (the complex is destroyed during functionalization, or no special activation is gained by complexation), the alternative

Table 1. Structure and redox properties (E° [V] vs. SCE) of the end groups.

End group ^a	Couple	E° [V]	Ref.
	Ru(III)/Ru(II)	0.4	[13]
	Ru(III)/Ru(II)	0.05	[13]
	Ru(III)/Ru(II)	0.45	[8]
	Ru(III)/Ru(II)	0.9	[14]
	Ru(III)/Ru(II)	0.7	[15]
	Ru(III)/Ru(II)	1.00	[13]
	Ru(III)/Ru(II)	1.25	[16]
	Ru(III)/Ru(II)	0.5	[17]
	Ru(III)/Ru(II)	0.45	[18]

Table 1 (continued)

End group ^a	Couple	E° [V]	Ref.
	Ru(IV)/Ru(III)	0.9	[19]
	Ru(III)/Ru(II)	-0.3	[20]
	Fe(III)/Fe(II)	0.37	[21]
	Fe(III)/Fe(II)	0.4	[22]
	Fe(III)/Fe(II)	0.13	[71b]
	Fe(III)/Fe(II)	-0.05	[23]
	Re(III)/Re(II)	0.25	[24]

^acharges are omitted for clarity.

route is to use “prefunctionalized ligands” [6, 17b, 26a]. Examples of the “building blocks” strategy are given in Figure 6.

The other aims of such a strategy are: (i) to maintain fairly good solubility of the growing wire, and (ii) especially for heavy metals, to avoid submitting the final wire, usually a very conjugated hence fragile molecule, to complexation conditions.

On the other hand, most of the disadvantages come from the fact that the free

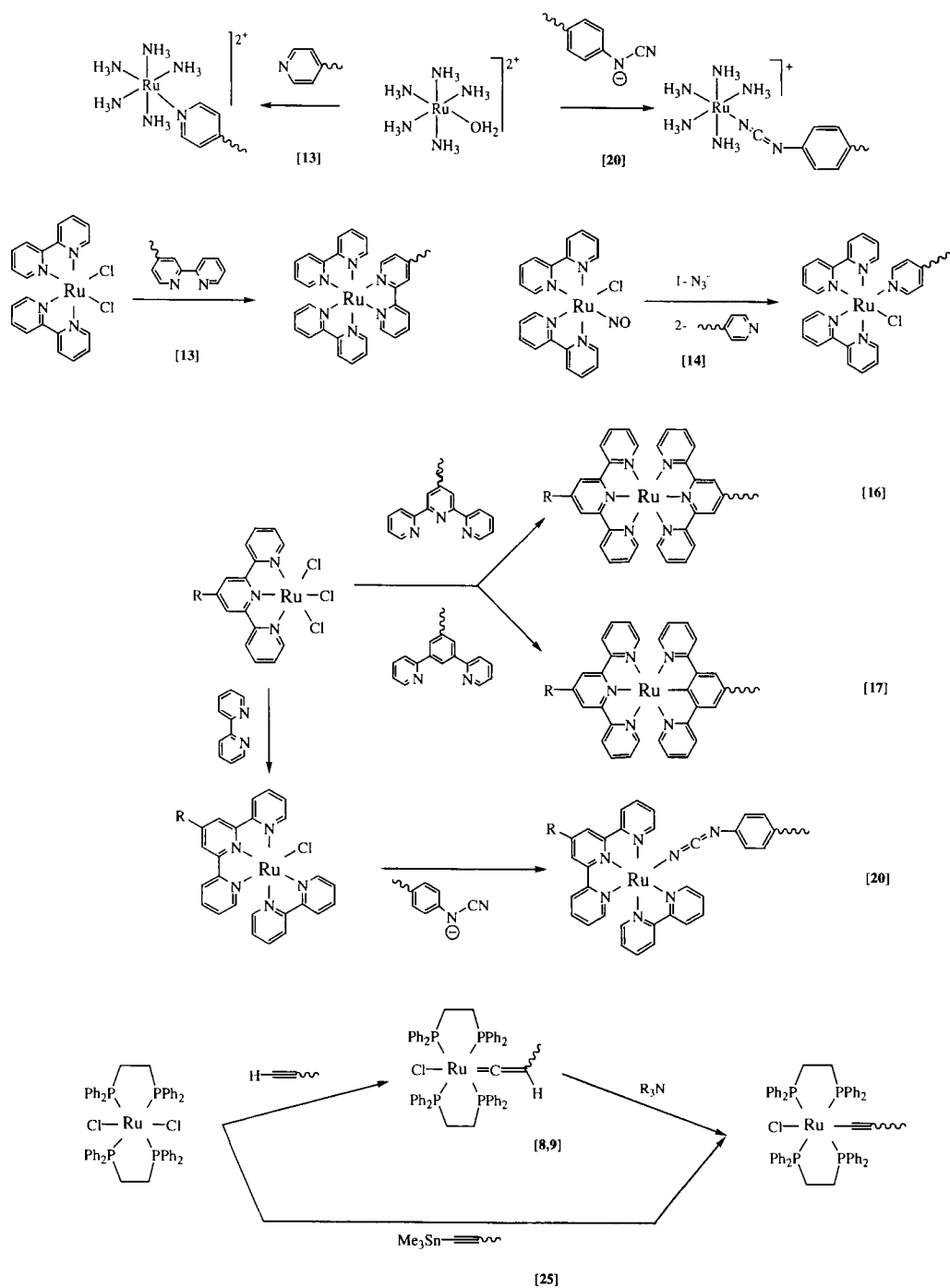


Figure 5. Examples of redox site syntheses, with literature references in bold.

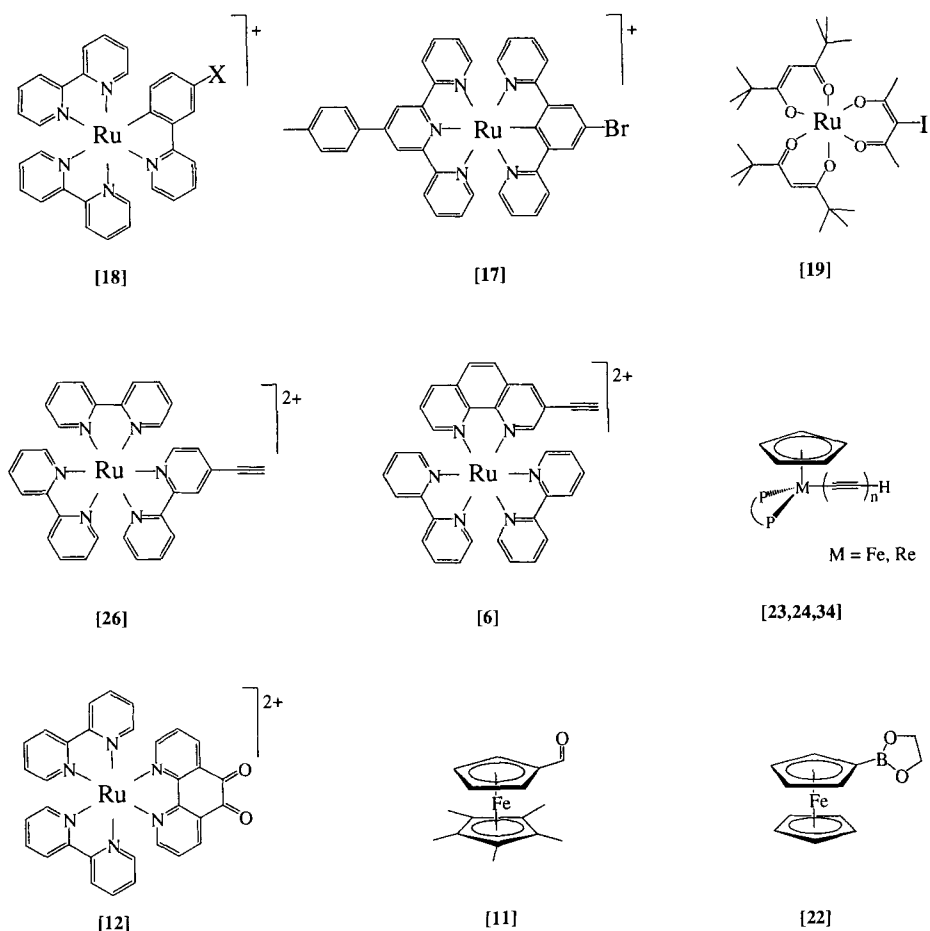


Figure 6. Some metal complexes used as building blocks, with literature references in bold.

ligand remains unknown, and, because of the “hybrid” nature of this “metallo-synthon” (a term coined by Ziessel) [26a] the adaptation of the reaction conditions (i.e., solvents, use of strong bases, etc.) is sometimes difficult.

1.3.2 Conjugated Bridges

Molecular wires may be considered as a special case of conjugated and rigid rod-like molecules. A recent review by Michl and co-workers [27] gives an exhaustive view of this field, and our purpose here is only to give additional clues in order to appreciate the synthetic choices.

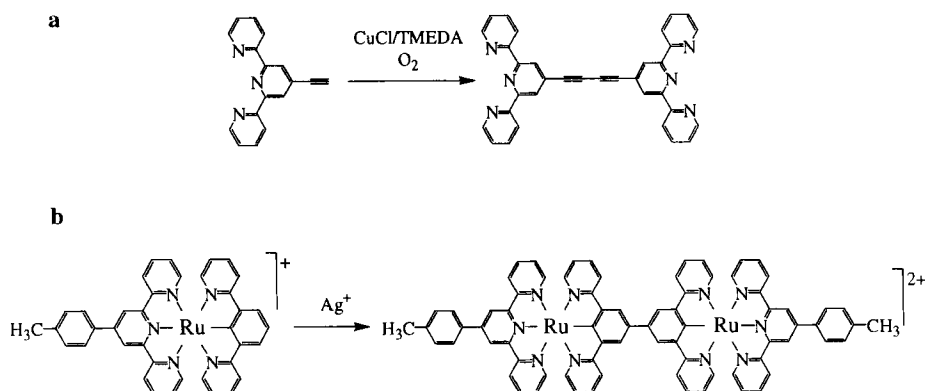


Figure 7. Examples of oxidative couplings.

Traditionally, the very unsaturated bridges can be viewed as an alternation of conjugated units (triple bond, double bond, aromatic nucleus ...) and simple bonds. In most of the strategies, the synthetic effort is focused on the creation of these simple bonds by redox dimerizations, or metal-catalyzed cross-couplings. In some cases, especially for double bonds, it is the unsaturated unit which will be the target of the synthesis. This is usually achieved by a condensation reaction (with the important exception of the McMurry reaction [28]). Other routes to polyunsaturated systems do exist, but they may have not been used yet to build bridging ligands or they are too marginal; hence our list is certainly not exhaustive.

Redox dimerizations

Such reactions are used to prepare bridging ligands having one main symmetry element (mirror plane or C_2 axis) passing between two (carbon-) bonded atoms. Except for some metal-catalyzed reactions, redox dimerizations are generally interpreted as the recombination of two radical species—followed, if needed, by a dehydrogenation step—hence generating a simple bond.

Oxidative dimerizations (see Figure 7)

Controlled oxidation of organometallic species may lead to the creation of a C–C bond. In acetylene chemistry, the Glaser reaction and its variations [29] are among the most ancient reactions of this type, and rely on the oxidation by air (or cupric ions) of alkynyl copper(I) species generated in situ. These very mild conditions allow the use of a large range of terminal alkynes, such as ethynylated heterocycles (Figure 7a) [26b].

Biaryls can also be obtained by oxidation of arenes, as long as these are electron-rich enough. Some very short dinuclear complexes have been obtained in this way. Thus, a bis-cyclometallated dinuclear complex has been obtained by a smooth oxidation of a nonfunctionalized precursor by silver(I) ions (Figure 7b) [17a].

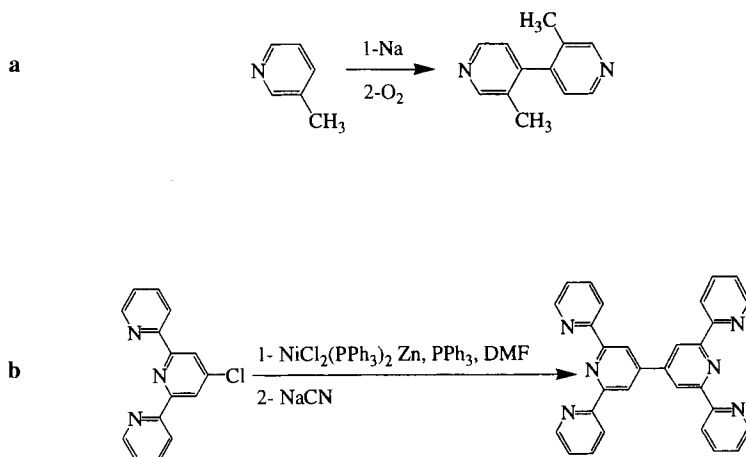


Figure 8. Examples of reductive couplings.

Reductive dimerizations (see Figure 8)

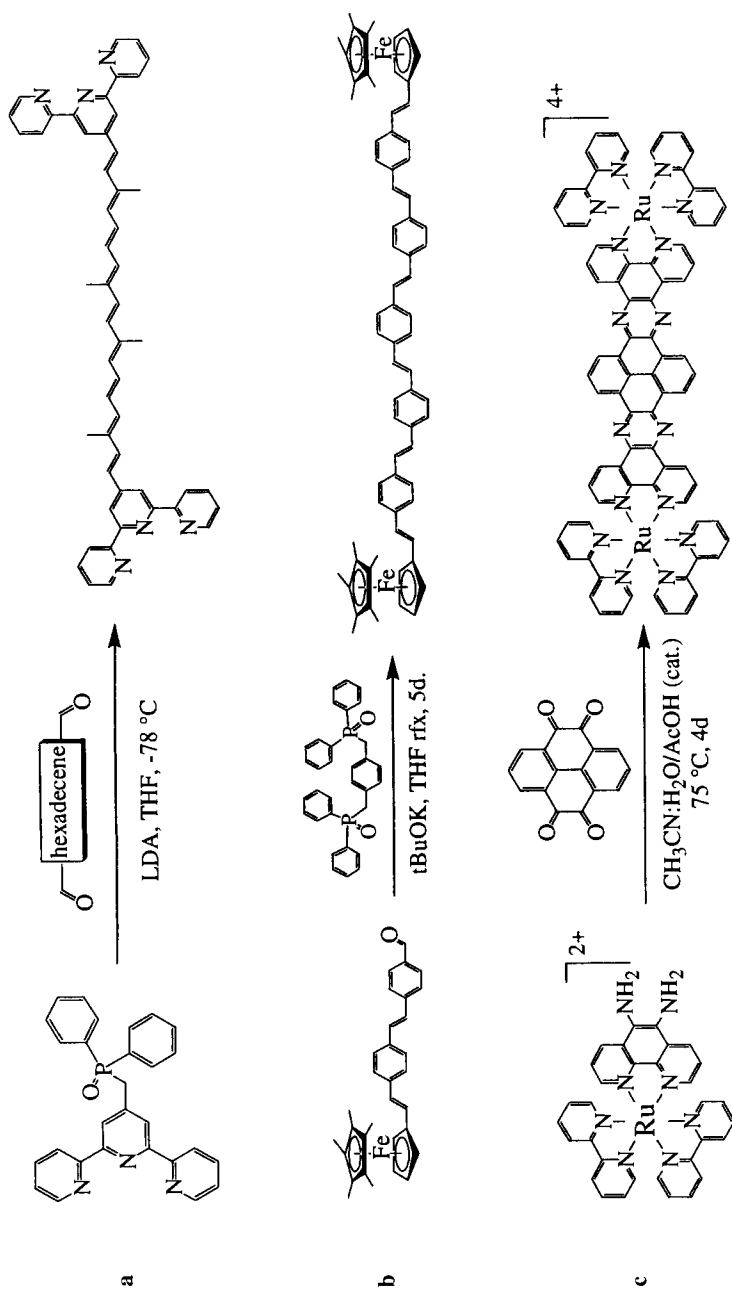
A radical species may also be generated by reduction of an electron-deficient compound and a classical entry to 4,4'-bipyridines is the reduction of a pyridine by sodium and subsequent rearomatization. Figure 8a illustrates the use of such a reduction in order to prepare the precursor of a sodium-ion molecular switch [30].

A more general route, derived from the ancient copper-catalyzed Ullmann coupling, is the metal-induced dimerization of an aryl halide. The key step is a reductive elimination within the coordination sphere of the metal. A nickel(0) complex, in stoichiometric quantities, is usually selected for this purpose. Constable and Ward have used such a reaction to prepare a bis-terpyridine from an interesting synthon, which would have otherwise required a more specialized strategy with dedicated intermediates (Figure 8b) [31].

Condensations

Examples are shown in Figure 9. Reactions between an active methylene compound and a ketone or an aldehyde are an attractive entry to double bonds, as long as one can control the final stereochemistry. Among them, the Wittig–Horner reaction, requiring relatively mild reaction conditions (i.e., a strong base), gives excellent results and has been used successfully by Lehn [32] and Ziessel [33] to introduce coordinating sites, respectively a bipyridine, or a terpyridine (Figure 9a) unit on a carotenoid. The reaction, under thermodynamic control, produces only the *trans*-isomer with no isomerization of the other double bonds. A similar approach was used to prepare oligo(phenylene-vinylene) bridging ferrocenyl units (Figure 9b) [11].

The condensation between a carbonyl and an amine leads to the rather fragile imine link. However, its stability is greatly increased when it is included in a heterocycle. This may be used to prepare “ladder molecules” such as polyquinoxalines.

**Figure 9.** Examples of condensation reactions.

Thus, the reaction between a diamino building block and tetraketopyrene gives a dinuclear complex with a metal–metal distance of 20 Å (Figure 9c) [12].

Metal-catalyzed hetero cross-couplings

Recent developments in the chemistry of polyunsaturated compounds are due to an extensive use of metals as catalysts to create single bonds between sp - or sp^2 -hybridized carbon centers. At first copper, and now palladium and nickel, are routinely used in such reactions, which may be viewed as a formal nucleophilic displacement of an electronegative substituent, denoted X, i.e., a halogen, by an organometallic species, denoted Rm. For transition metal catalysts (Pd, Ni), the catalytic cycle involves an oxidative addition of the “electrophilic moiety”, i.e., the organic halide RX, on the most reduced form of the catalyst, followed by a transmetalation step with the “nucleophilic moiety” Rm, leading to a complex containing two formally carbanionic ligands. Such a complex is unstable and evolves through a reductive elimination process to a reduced form of the catalyst, and the desired cross-coupled compound. (In the Heck reaction, the “nucleophilic moiety” is an alkene: hence coupling goes through successive *cis*-migration and β -elimination reactions).

Rate-determining steps are usually the oxidative addition (the more electron-deficient the RX, the faster the addition), and/or the transmetalation of Rm to palladium.

Copper

In order to prepare nonsymmetrical diynes, one can use the Cadiot–Chodkiewicz reaction. It involves a haloalkyne such as an iodoalkyne or a bromoalkyne. Combined with the Glaser dimerization, this reaction provides a powerful entry to oligoynes bridging ligands and has been used extensively by Gladysz (see Figure 10) [34].

Palladium

Excellent reviews on the use of this metal as catalyst in cross-coupling reactions are now available [35]. The mild reaction conditions, as well as the wide scope of compatible functionalities, characterize palladium couplings, leading to a considerable simplification of the retrosyntheses—hence its increasing popularity. Examples are shown in Figure 11. Among the most common skeletons encountered in molecular wires, we have selected two representative examples now easily available by palladium chemistry: tolanses and biaryls.

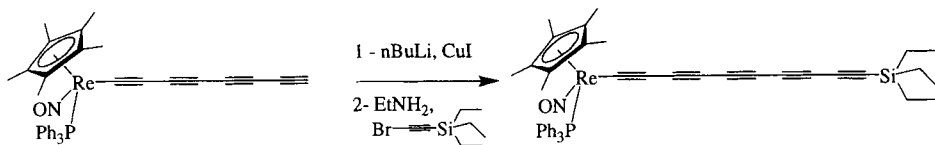
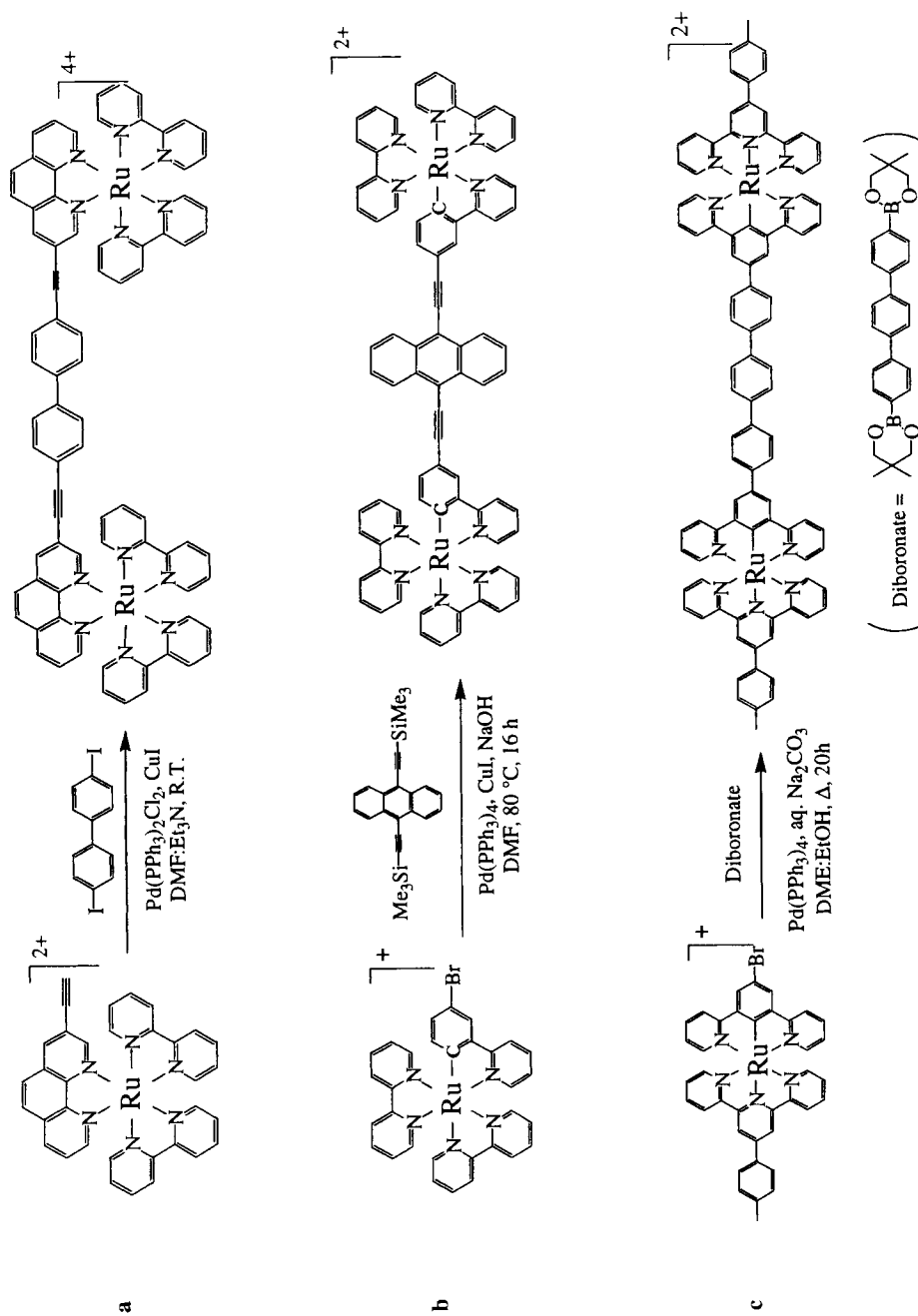


Figure 10. Synthesis of poly-yne bridges [34].

**Figure 11.** Examples of palladium-catalyzed couplings.

Tolanes

An alternation of triple bonds and aromatic nuclei, “polytolane”, is easily achieved by the Hagihara–Sonogashira coupling of a terminal (poly)alkyne and an aromatic (poly)halide, combined, if needed, with a suitable sequence of alkyne protection and deprotection. Reaction conditions involve a mixture of a cuprous salt and a palladium(II) or (0) complex, and a necessary base, usually an amine. Yields are usually high, especially for aryl iodides (Figure 11a) or electron-deficient heteroaryl bromides [6]. If the reaction is too slow, alkyne degradation may be prevented by an in-situ deprotection, hence releasing the reagent at a very low rate (Figure 11b) [18].

Biaryls

Replacing the terminal alkyne by an arylzinc, an aryltin, or an arylboron compound leads respectively to the Negishi, Stille, or Suzuki aromatic cross-coupling reactions. There is no need for a cocatalyst, but the Suzuki reaction requires a nucleophilic base such as aqueous carbonate (Figure 11c) (or fluoride) [17b, 22].

Other bridges

Some architectures require specific synthesis, and we wish to focus on three other types of structures (cyanines, porphyrins, and metallic complexes) as bridging ligands (see Figure 12).

Cyanines

The conjugation of a carbanion (or a carbocation) to an even number of double bonds gives rise to a cyanine-like system, the negative (positive) charge being delocalized over an odd number of trigonal carbons. In an example reported by Tolbert (Figure 12a) [14a], a pentadienyl anionic system is used to bridge two ruthenium complexes via two pyridyl residues. The carbanion is obtained by a mere deprotonation of the twice-allylic methylene group. However, such a bridge is relatively unstable, and the conditions used for the deprotonation may destroy the metallic complexes. More recently, the same group has achieved the synthesis of the cationic counterpart bridging two ferrocenes, creating a carbocation by a hydride abstraction [14b].

Porphyrins

Very few reports are about the use of porphyrins as bridges connecting redox centers, although their annulene character may be of interest. Recently, Officer and co-workers [36] have prepared a 5,15-diferrocenylporphyrin by condensation of ferrocenecarboxaldehyde and a substituted dipyrromethane (Figure 12b). The considerable steric hindrance of the resulting macrocycle gives rise to two remarkable features: the “saddle” conformation of the porphyrin ring, as already noted for crowded porphyrins, and more surprisingly, the full conjugation of the two ferrocenyl moieties to the porphyrin ring despite their *meso* position. See Figure 12 (inset) for a sketch of the geometry.

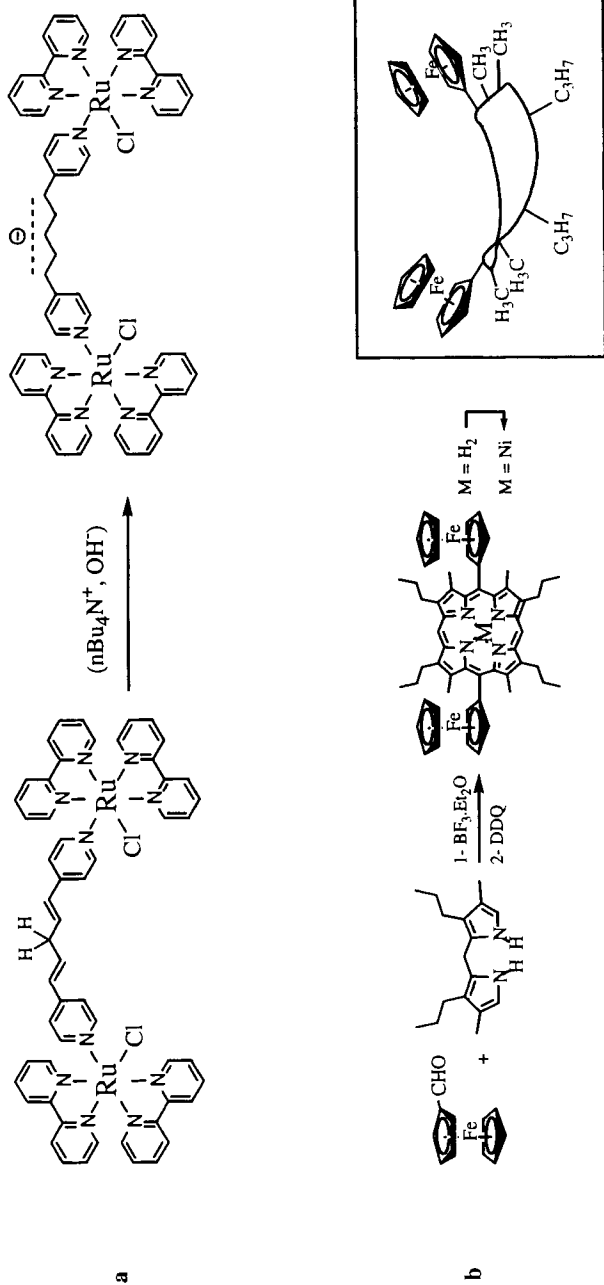


Figure 12. Examples of a) a cyanine spacer and b) a porphyrin spacer, showing the strong distortion of the molecule in the latter case (inset).

Metal complexes

Attempts have been made to include metals within the bridge, which allow the study of new geometries, and more interestingly, the impact of the presence of an electropositive element with variously occupied d orbitals on the electron transmission. For such a goal, the most efficient strategy is to use a “metallic complex as ligand” approach, either by capping a metallic complex bearing free peripheral coordinating sites, or, since metallic ions are efficient templates, by complexing on the metallic ion two ligands bearing a redox site. The most abundant literature on this subject involves diethynyl metal complexes and relies on synthetic concepts already mentioned in this review [7–10].

1.4 Theory

1.4.1 Outline of the Theoretical Treatment of Mixed-valence Compounds

Only a brief outline will be presented here since electron transfer theory is extensively treated in Volume I. Let us just recall that electron transfer reactions are currently represented by potential energy curves of the Marcus type (Figure 13). We concentrate here on weakly coupled systems (class II according to Robin and Day’s classification) [37] for which two minima are observed on the lowest potential energy curve. (For delocalized systems (class III), it is not always clear that for long bridges, the oxidation/reduction is truly metal-centered since extensive delocalization must involve the bridge.) Returning to class II systems, the two minima are of

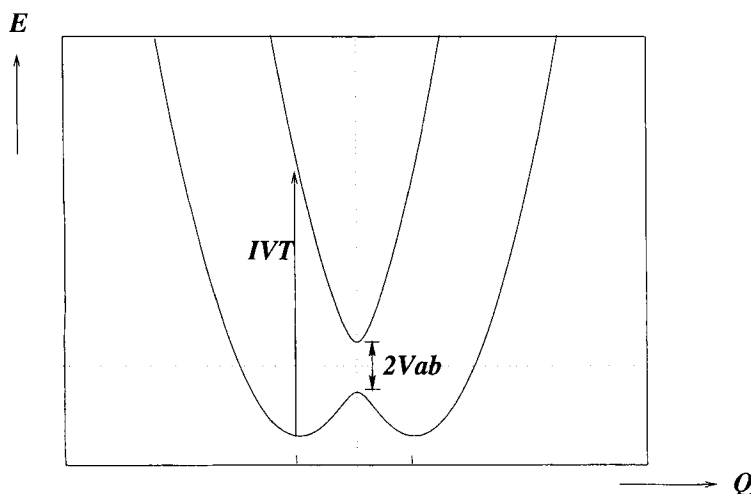


Figure 13. Potential energy curves for a class II mixed-valence compound.

equal height if the system is chemically symmetrical. As shown by Hush [38], there are two kinds of intramolecular electron transfer: a thermal one, and an optical one corresponding to the so-called intervalence transition (IVT) (Figure 13). A key parameter is the electronic coupling V_{ab} , also called “tunneling matrix element”, “resonance exchange integral”, “coupling element”..., which corresponds to the avoided crossing between the two zero-order parabolas. From an experimental point of view, the role of V_{ab} is twofold: 1) it allows the system to jump from one zero-order parabola to the other when arriving in the avoided crossing region, which corresponds to the thermal electron transfer process, the rate of which is proportional to V_{ab}^2 ; 2) it mixes the electronic wave functions of the ground state with that of the excited state, which determines the intensity of the intervalence transition, also proportional to V_{ab}^2 .

Since V_{ab} plays a central role in the theory, its determination in the largest possible series of compounds is of great interest. In a two-state model, a simple evaluation of the transition moment, using Mulliken’s approach of donor–acceptor systems, yields Hush’s (1967) equation [38b]:

$$V_{ab} = \frac{2.05 \times 10^{-2} \sqrt{\bar{\nu} \Delta \bar{\nu}_{1/2} \epsilon_{\max}}}{R_{MM}} \quad (1)$$

V_{ab} is obtained in cm^{-1} , ϵ_{\max} is the maximum extinction coefficient for the intervalence transition, $\bar{\nu}$ is its energy (cm^{-1}), $\Delta \bar{\nu}_{1/2}$ is its full width at half-maximum, and R_{MM} is the direct (through space) metal–metal distance. Although more than 30 years old, this equation is still widely used. A recent reinvestigation has shown in particular that its range of validity is wider than previously believed [39]. Note that for a class III system, V_{ab} is merely one-half of the optical transition energy (see Volume I).

Since the practical use of Eq. (1) requires the determination of the intervalence band for the pure mixed-valence compound, two corrections are generally applied to the experimental spectra:

a correction for the comproportionation equilibrium linking the mixed valence species with the fully reduced and fully oxidized ones:



It is easy to show that when the composition of the solution corresponds to the mixed-valence stoichiometry, the proportion P of complex present as mixed-valence form is given by:

$$P = \frac{\sqrt{K_c}}{2 + \sqrt{K_c}} \quad (3)$$

The spectrum of the equilibrium mixture can thus be corrected by subtracting the absorptions due to the fully reduced and fully oxidized forms. The K_c value

can be determined either from a redox titration [40a], or from the determination of the standard potentials of the Ox–Ox/Red–Ox and Red–Ox/Red–Red couples. This is conveniently realized by electrochemical methods such as differential pulse voltammetry [40b].

a spectral deconvolution. The intervalence band profile is very frequently polluted by the tail of more intense charge transfer (either metal-to-ligand or ligand-to-metal) transitions. The spectrum must then be decomposed as a sum of gaussian components [41].

Returning now to the comproportionation equilibrium, it is interesting to notice that for large systems ($R_{MM} \rightarrow \infty$) the comproportionation constant tends towards a statistical limit of 4 (see below). Then a single electrochemical wave is observed, a fact which has frequently dissuaded researchers from further studies on such binuclear complexes. However, even in this apparently unfavorable case, the proportion of mixed-valence species at half-oxidation (reduction) is, according to Eq. (3), a comfortable 50 %, nevertheless allowing a meaningful correction.

1.4.2 Processes Related to the V_{ab} Coupling

We now consider several phenomena or processes related to the electronic interaction. They are listed below in order of decreasing parentage with the electronic interaction defined as above.

Thermal electron transfer rate constant

This is the most direct experimental manifestation of the existence of an electronic interaction. It can occur spontaneously in mixed-valence complexes, but also in bimetallic systems after a photochemical excitation (photoinduced electron transfer). The general theory considers electron transfer as a special case of radiationless transition, with a perturbative treatment based on Fermi's Golden Rule [42]. In the nonadiabatic case, the rate constant can be written as [43]:

$$k_{et} = \frac{2V_{ab}^2}{h} \left(\frac{\pi^3}{E_\lambda kT} \right)^{1/2} \exp\left(-\frac{\Delta G^\ddagger}{RT}\right) \quad (4)$$

where E_λ is the total reorganization energy, ΔG^\ddagger is the free enthalpy of activation, and the other symbols have their usual meaning. This equation is valid for very weakly coupled systems (nonadiabatic ones), a situation which is expected to occur for long molecules. It should be noted that the rate of electron transfer in a symmetrical system such as a mixed-valence compound has rarely been determined because the thermal reaction is accompanied by no net chemical change. (For an example, but with organic end groups, see [44]). Direct measurements of the electron transfer rate constant are preferably performed by flash photolysis experiments (excited-state electron transfer).

A different experimental setup has been used in recent years to measure electron transfer rates through molecular wires. Conjugated molecules with a redox group (ferrocene) on one end and a thiol group at the other were attached to gold electrodes and embedded in monomolecular aliphatic monolayers [45]. The electrochemical response in AC voltammetry was used to measure the rate of electron transfer between the ferrocene group (accessible from the solution side of the monolayer) and the electrode. Here again, the rate depends on an electronic coupling factor V_{ab} (Eq. (5)).

$$k_{et} = \rho(E) V_{ab}^2 \left(\frac{2\pi kT}{h} \right) \sqrt{\frac{\pi}{E_\lambda kT}} \int_{-\infty}^{\infty} \exp \left[\frac{-((\varepsilon_F - \varepsilon) + E_\lambda)^2}{4E_\lambda kT} \right] f(\varepsilon) \frac{d\varepsilon}{kT} \quad (5)$$

where $\rho(E)$ is the density of states of gold near the Fermi energy, $f(\varepsilon)$ the Fermi function, ε_F the Fermi energy, and E_λ the reorganization energy.

Note the analogy between Eqs. (4) and (5): electron transfer at the interface can be considered as a special case of intramolecular electron transfer, the integration taking into account the existence of a continuum of energy levels on the electrode side. Thus the experimental setup is somewhat intermediate between a molecular mixed-valence complex in solution and a metal/molecule/metal nanojunction.

Dexter-type energy transfer rate

As mentioned above, this is an energy transfer process occurring by a double electron exchange, so that no net charge moves from one site to the other. A simple argument due to Closs et al. [46a] suggests that the rate of triplet–triplet energy transfer k_{TT} should be proportional to the products of the corresponding electron and hole transfer rates k_E and k_H :

$$k_{TT} = c k_E k_H \quad (6)$$

This relation was indeed verified experimentally in a series of organic molecules with naphthyl and biphenyl groups linked by rigid spacers. Assuming that each rate constant is proportional to the square of an electronic coupling element gives:

$$V_{TT} = c' V_E V_H \quad (7)$$

Thus the matrix coupling element for energy transfer would be proportional to the product of the coupling terms for electron and hole transfers. This was later confirmed by ab-initio calculations [46b].

Magnetic coupling

This corresponds to the existence of a dipolar coupling between magnetic ions in a homovalent bimetallic complex. The interaction is usually described by the following Hamiltonian:

$$\hat{H} = -J \hat{S}_A \hat{S}_B \quad (8)$$

where S_A and S_B are local spin operators and J is the coupling constant, positive for a ferromagnetic interaction and negative for an antiferromagnetic one. Although this process occurs in a homovalent complex, while electron transfer is studied in a mixed-valence complex, the two effects are related. One of the simplest theories is based on the use of magnetic orbitals [47] Φ_A and Φ_B , i.e., orbitals mainly localized on a metal site (A or B), but with some extension on the coordinated ligands. The magnetic coupling parameter is then given by:

$$J = J_F + J_{AF} \quad (9)$$

where J_F is the ferromagnetic contribution, and J_{AF} the antiferromagnetic one. J_F is given by

$$J_F = 2 \left\langle \Phi_A(1)\Phi_B(2) \left| \frac{1}{r_{12}} \right| \Phi_A(2)\Phi_B(1) \right\rangle \quad (10)$$

The antiferromagnetic contribution is given by:

$$J_{AF} = -2S_{AB}\Delta \quad (11)$$

where S_{AB} is the overlap integral between magnetic orbitals, and Δ is the difference in energy between the two canonic molecular orbitals obtained from Φ_A and Φ_B . To a first approximation $\Delta = 2V_{ab}$ and is proportional to S_{AB} .

Frequently J_{AF} dominates the J_F term, so that the observed coupling is antiferromagnetic. Equation (11) shows that J_{AF} is proportional to the square of the splitting between molecular orbitals, i.e., to the square of V_{ab} .

Nonlinear optical activity

In the simplest case of a donor–acceptor (D–A) molecule, the nonlinear optical activity arises from the electric-field-induced mixing of electronic states such as D–A and $D^+ - A^-$. This makes the response (polarizability) of the molecule different according to the sense of the electric field, and a second-order hyperpolarizability (β coefficient) is observed. If D and A are connected by some bridge, its role in promoting the electronic interaction will be quite similar to the bridge role in mixed-valence complexes. Metal complexes can play the role of donor or acceptor groups. Recent examples have been described with ferrocene or ruthenium(pentaammine) groups [48], but they are either monometallic or too short to be considered in this review.

Electrochemical wave splitting

In a bimetallic complex, the oxidation or reduction may occur in one or several steps. The corresponding difference in redox potentials, noted as $\Delta E_{1/2}$, is easy to determine, and is frequently used as a measure of the “electronic communication” between redox sites. However, one has to be careful before relating this parameter with the V_{ab} coupling. While V_{ab} is a *spectroscopic-like* quantity which depends only on the electronic properties of the mixed-valence species, by contrast $\Delta E_{1/2}$ is a

thermodynamic quantity depending on the properties of three species: the mixed-valence one, and the two adjacent homovalent forms. This is made clear by the relation between $\Delta E_{1/2}$ and the comproportionation constant K_c for the equilibrium:

$$F\Delta E_{1/2} = \Delta G_C = -RT \ln K_c \quad (12)$$

where F is the Faraday and ΔG_C the free enthalpy change for comproportionation.

To date, the best analysis of the factors determining K_c (and thus ΔG_C and $\Delta E_{1/2}$) is based on Sutton and Taube's work [49] considering mixed-valence complexes obtained by oxidation of a bimetallic ruthenium(II) complex. Four factors were recognized as contributing to ΔG_C : (i) a statistical factor $-RT \ln(4)$ since there are two equivalent redox sites, (ii) an electrostatic factor ΔG_E since the oxidation of the first metal site renders the second one more difficult to oxidize, owing to the repulsion between the two additional charges, (iii) a resonance factor ΔG_R coming from the mixing of the electronic ground state with the one of the redox isomer, and (iv) a synergistic factor ΔG_S . The last of these is the most mysterious but its existence appears nevertheless undoubtedly established. In the case of ruthenium complexes, it is due to the Ru(II) backbonding interaction. Once ruthenium(II) has been oxidized to ruthenium(III), the energy of the ligand π^* orbital is decreased, and its interaction with the other site in oxidation state (II) is amplified [50].

The original treatment by Sutton and Taube has later been refined by the addition of effects such as "structural distortion" [51] or "magnetic interaction" [52]. They do not seem to be as general as the others, and will not be discussed further.

Among the above factors, only ΔG_R , the resonance stabilization due to electron delocalization in the mixed-valence species, depends clearly on V_{ab} . The synergistic factor ΔG_S seems to correspond to some form of electronic interaction, but this is less clear than for ΔG_R . Unfortunately, the careful analysis of Sutton and Taube reveals that for long systems of the type considered here, the ΔG_R factor makes a minor contribution to ΔG_C . On the other hand, the electrostatic factor seems to give an important contribution to ΔG_C ($\Delta E_{1/2}$), but this is not interesting in the frame of Molecular Electronics: the electrostatic interaction is a through-space interaction influenced little or not at all by the nature of the bridging ligand (except through its effective dielectric constant). Thus it does not exhibit the strong directional selectivity required for a wire.

To be complete, one has also to consider the analysis by Kaim and co-workers [53], according to which K_c would be determined by the coefficients of the LUMO on the coordinating atoms of the ligands (in his case, nitrogen atoms of bis-chelating polyimine ligands).

It should be mentioned finally that, in a number of cases, the location of the oxidation or reduction (on the metal sites or on the bridging ligand?) has not been clearly established.

All of these considerations cast doubt on the use of $\Delta E_{1/2}$ (ΔG_C) for measuring the electronic "communication" between redox sites and the ability of the molecule to function as a wire. Regardless of its true nature, the wave splitting resembles some kind of polarization effect. It *does not correspond to a transfer process*, and has no counterpart in the usual behavior of a macroscopic wire.

1.5 Review of the Different Studies

In the following, the investigations are ranked by type of process, starting with intervalence electron transfer, which is the most direct way to determine the fundamental parameter V_{ab} . An important issue is the rate of decay with distance, and in most cases it follows, or nearly follows, an exponential law, i.e.,

$$V_{ab} = V_{ab}^0 \exp(-\gamma R) \quad (13)$$

Ideally, a good molecular wire should exhibit a strong coupling even for large distances, i.e., a low γ and a high V_{ab}^0 . A number of processes depend on the *square* of V_{ab} (cf. Eqs. (4), (5)), or the square of an analogous parameter (in the case of magnetic coupling, or Dexter energy transfer). In such cases, the observable quantity decays with a slope of 2γ .

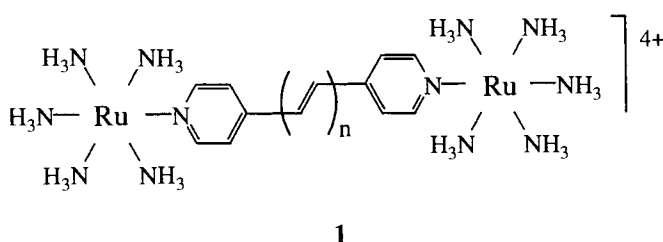
1.5.1 Intervalence Electron Transfer

Intervalence electron transfer implies generally a symmetrical system, i.e., two chemically equivalent metal sites. The literature shows that most authors concentrate on a type of terminal redox group, rather than on a particular type of spacer. Thus in the following, the metal complexes will be listed according to their coordination sphere, with an indication of the ligand on which the spacer is attached (e.g., “py-” means that the substitution leading to the molecular wire is performed on the pyridine ligand). A number of reviews have already been devoted to the subject, in particular by Creutz (1983) [1], Crutchley (1994) [2], and Lapinte (1998) [23], the first two concentrating on coordination complexes, and the last one on organometallic complexes. Here, particular attention will be paid to *series* of complexes with spacers of various lengths, for the purpose of studying the role of distance. The through-space metal–metal distance (the one entering Hush’s equation) will be considered, unless otherwise stated.

$(\text{NH}_3)_5\text{Ru}(\text{py}-)$

The simplest complex is the association of two such end groups without a spacer, i.e., $[(\text{NH}_3)_5\text{Ru}-4,4'\text{-bipy}-\text{Ru}(\text{NH}_3)_5]^{n+}$. This is one of the most studied complexes as a representative example of a weakly coupled (class II) mixed-valence system [1]. In particular, it allowed the study of several original or intriguing effects: multiple intervalence transitions [54], contributions of high-frequency librations [55], and effects of unsymmetrical solvation [56]. This is also the longest mixed-valence complex for which electroabsorption spectroscopy (Stark effect) has been performed [57]. This experiment provided the value of the change in dipole moment ($\Delta\mu$) associated with the intervalence transition, a key parameter for testing new theories: while very large in the absolute sense (ca 28 D), the $\Delta\mu$ value is about one-half of the theoretical value for a full charge transfer over 11.3 Å.

Inserting one or several conjugated double bonds gives rise to complexes of α,ω -dipyridylpolyenes, $\text{py}-(\text{CH}=\text{CH})_n\text{-py}$, the first examples ($n = 0, 1$) being described by Sutton and Taube [49], and the longer ones ($n = 2$ to 4) by Launay, Spangler, and co-workers et al. [58] (series 1). Analysis of the intervalence transitions showed a slow decrease of the V_{ab} coupling term according to an exponential law, within the uncertainties of the measurements. For the longest systems, the intervalence transitions were increasingly ill-resolved. However, the inclusion of furan and thiophene heterocycles in place of two double bonds improved the resolution, probably for reasons of better coplanarity and rigidity. For the series of α,ω -dipyridylpolyene bridged systems, the experimental decay slope γ was found to be 0.070 \AA^{-1} .



Theoretical values of the coupling term were obtained by extracting the V_{ab} values from an Extended Hückel calculation, either by the “dimer splitting method”, or by the Effective Hamiltonian technique [59]. The order of magnitude of the coupling was satisfactorily reproduced, and the role of bond length alternation as a limiting factor in the long-distance transmission of electronic coupling was recognized.

An alternative theoretical treatment of α,ω -dipyridylpolyene complexes was proposed in 1990 by Reimers and Hush [41], in which the quantum calculation is performed at the CNDO level with an empirical adjustment of the d levels of ruthenium with respect to the bridging ligand orbitals. This calculation gave a higher decay slope of -0.13 \AA^{-1} . In more recent work, the explicit treatment of the solvent allowed reproduction of experimental coupling within 25 % of experimental data, with a decay slope of -0.127 \AA^{-1} [60].

The insertion of a triple bond was performed by Sutton and Taube [49]. Curiously the V_{ab} coupling was found to be smaller through dipyridylacetylene than through dipyridylethylene, a fact attributed to the almost free rotation of the two pyridine rings with respect to each other. This point is discussed later, however.

The insertion of a polyphenylene unit (up to two phenylenes) unfortunately gave particularly weak and ill-resolved intervalence transitions, precluding a quantitative exploitation [61].

Bridging by a cyanine-like ligand has been attempted by Tolbert [14a]: in the bis(pentaammine)ruthenium complex of 1,5-dipyridyl-1,3-pentadiene, deprotonation of the methylene group was expected to give a complex bridged by a pyridocyanine ligand, but the complex dissociated upon deprotonation. The concept is nevertheless interesting since bridges with an *odd* number of carbon atoms are expected to enhance strongly the coupling between redox centers [62] (see below).

(NH₃)₅Ru(NC⁻) and py(NH₃)₄Ru(NC⁻)

Complexes with 1,4-dicyanobenzene, 1,5-dicyanonaphthalene, 1,6-dicyanonaphthalene, 2,6-dicyanonaphthalene, and 2,7-dicyanonaphthalene as bridging ligands, prepared by Richardson and Taube [51], exceed the 10 Å limit for the metal–metal distance. Metal–metal couplings have been obtained by Hush’s formula and the bridging ligand role has been clarified with the help of INDO calculations. The coupling decreases exponentially with the total number of conjugated atoms. (Note that since the structures and composition of the ligands are markedly different, the exponential law is no longer obtained when plotting V_{ab} as a function of the through-space metal–metal distance). An alternation rule has been established, i.e., the most efficient bridges are those for which an even number of atoms separate the metal sites. However, even when restricted to ligands of this category (1,4-dicyanobenzene, 1,5-dicyanonaphthalene, 2,6-dicyanonaphthalene), the couplings are modest in comparison with other series, and decay rapidly with distance.

Trimetallic complexes built around a central ruthenium complex of *cis*-[Ru(bpy)₂(CN)₂] have been described by Bignozzi and co-workers [10]. Cyanide ligands are N-bonded to external py(NH₃)₄Ru sites. The general topology is therefore “bent”, with a metal–metal through-space distance of only 7 Å between the outer metal sites, but the sequence of atoms constituting the trimetallic complex is Ru–NC–Ru–CN–Ru, and would correspond for a linear geometry to a 10 Å distance. The V_{ab} coupling deduced from the intervalence band is ca 0.037 eV.

(NH₃)₅Ru(NCN⁻)

The bridging ligand dicyanamidobenzene and its dichloro- and tetrachloro-substituted variants have been studied extensively by Crutchley and co-workers [20]. It exhibits unusual properties from the point of view of antiferromagnetic coupling when ruthenium is in oxidation state III, and provokes also large wave splitting in cyclic voltammetry for metal–metal distances of 13.1 Å. For intervalence transitions, the situation is complicated by the overlap with intense LMCT bands of the ruthenium(III) chromophore. An intriguing effect is the great sensitivity of the intervalence transition to the solvent, the band appearing as a simple shoulder in D₂O, but as a well-resolved and isolated band in acetonitrile [20d]. This is attributed to the specific interaction between the solvent and ammine protons. In acetonitrile, the dicyanamido ligand gives a 980 cm⁻¹ (0.122 eV) coupling from Hush’s formula [63]. It is possible to prepare longer homologs of dicyanamidobenzene, such as the 4,4′-dicyanamidobiphenyl dianion, the metal–metal distance reaching 17.2 Å [64, 65]. The corresponding complex gives a 400 cm⁻¹ (0.050 eV) coupling.

(NH₃)₄(py)Ru(NCN⁻) and (NH₃)₃(bpy)Ru(NCN⁻)

Again, complexes with these end groups derived from the dicyanamido ligand are reported by Crutchley [66, 63]. Intervalence transitions have been observed and exploited to give V_{ab} values which are found, through Hush’s equation [63], in the 800–1100 cm⁻¹ range (0.1–0.13 eV). Another estimation of the metal–metal coupling was performed through the CNS model [66], giving much higher values.

However, this treatment [39] is an *indirect* estimation, because it is not based on the intervalence transition, but on the parameters of the ligand-to-metal charge transfer transition appearing in the ruthenium(III) chromophore. The values obtained by this procedure are thus difficult to compare to the other ones mentioned in this review.

(bpy)₂(Cl)Ru(py⁻) and (bpy)₂Ru(bpy⁻)

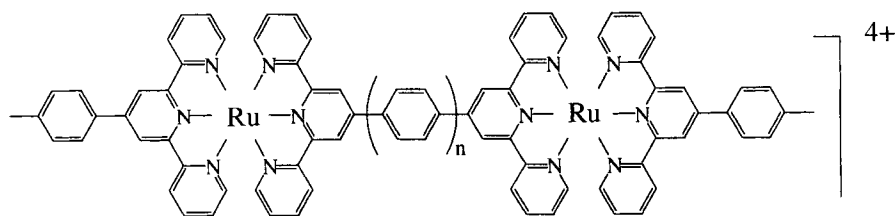
Complexes with (bpy)₂(Cl)Ru bridged by 4,4'-bipyridine, or bipyridylethylene were prepared by Meyer et al., but unfortunately they exhibit lower couplings when compared to the analogous ruthenium(pentaammine) compounds [1, 67a]. This is attributed to the competitive effect of π -acceptor ancillary ligands which drain the electron density away from the bridging ligand [67b].

Deprotonation of a binuclear complex with (bpy)₂ClRu moieties and 1,5-dipyridyl-1,3-pentadiene as bridging ligand yielded the cyanine-bridged complex, contrarily to the unsuccessful case of the bis(pentaammine)ruthenium complex (cf. (NH₃)₅Ru(py⁻) above) [14a]. However, cyclic voltammetry and spectroelectrochemical studies revealed that oxidation occurred at the cyanine bridging segment rather than on ruthenium atoms, thus precluding the preparation of a mixed-valence species.

A mixed-valence complex of Ru(bpy)₂ bridged by 1,10-bis[4'-methyl(2,2'-bipyridyl)]-3,8-dimethyl-1,3,5,7,9-decapentene, i.e., with five double bonds constituting the spacer between 2,2'-bipyridine ligands, has been described by Lehn and co-workers [32b]. Hush's analysis of the intervalence transition gave $V_{ab} = 0.018$ eV for a 24 Å metal-metal distance.

(terpy)Ru(terpy⁻)

These complexes, prepared by Collin and Sauvage, are made from a bridging ligand in which two terpyridine groups are connected either directly back-to-back, or via a polyphenylene spacer (C₆H₄)_n, $n = 1, 2$ (series **2**). Starting from the ruthenium(II) complexes, the oxidation by Ce(IV) in acetonitrile yielded the mixed-valence species, and Hush's analysis gave the corresponding V_{ab} couplings [16b]. The decay slope for the $\ln(V_{ab})$ vs. R plot was -0.084 Å^{-1} . The high values of the redox potentials (ca 1.3 V vs. SCE) was however a drawback of this series, since oxidized species were not stable for long periods and titrations had to be performed rapidly.



Cyclometallated species (see (terpy)Ru(dpb-) below) represent a significant improvement in this respect.

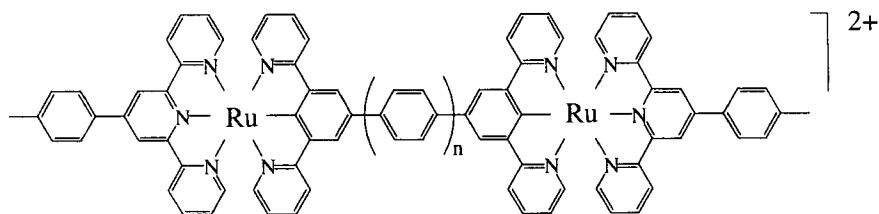
(bpy)(terpy)Ru(NCN-)

A complex with Ru(bpy)(terpy) moieties bridged by the dicyanamido ligand has been described by Crutchley [15a]. The mixed-valence ion presents an intervalence band at 1090 nm, and the authors assign the system to class III, resulting in a high V_{ab} coupling (half the optical energy, giving 0.57 eV). However, since the band is moderately intense ($\epsilon = 5600 \text{ mol}^{-1} \text{ L cm}^{-1}$), a class II nature could also have been considered, and in such a case, from the published values, Hush's equation would give a 0.058 eV value. (Treating such complexes either as class II or class III systems results in large changes in V_{ab} .)

(terpy)Ru(dpb-)

These complexes, prepared by Collin and Sauvage, are structurally similar to those of the bis(terpy) family ((terpy)Ru(terpy-) described above), but with the nitrogen atom of the central ring replaced by a carbon atom (cyclometallated species). The spacer between the dipyridylbenzene coordination sites can be made of 0 to 3 phenylene units, the metal-metal distance ranging from 11 to 24 Å (series 3). Starting from the ruthenium(II) state, the oxidation occurred more easily (ca. 0.5 V vs. SCE) than for the corresponding bis(terpyridine) complexes, and a much stronger coupling was observed for the mixed-valence species [17c,d]. However the rate of decay in the $\ln(V_{ab})$ vs. R plot was faster (-0.118 Å^{-1} instead of -0.084 Å^{-1}). This key observation is discussed in more detail in the conclusion. Note that the mechanism of electronic coupling, and in particular the effect of replacing a nitrogen atom by a carbon, can be addressed by molecular orbital calculations [17d]. It was found that the theoretical predictions were very sensitive to the energy of the Ru(4d) orbitals, which unfortunately are somewhat arbitrarily positioned in conventional Extended Hückel calculations. However, with the help of the ZINDO method, it was possible to justify the choice of the ruthenium orbital energies, and to reproduce the main features of the series.

This series also allowed an investigation of the influence of the position of the carbon atom substituting for nitrogen in the basic bis(terpyridine) framework. The highest efficiency for intervalence electron transfer was found when the carbon atom was located on the metal-metal C_2 axis of the molecule.

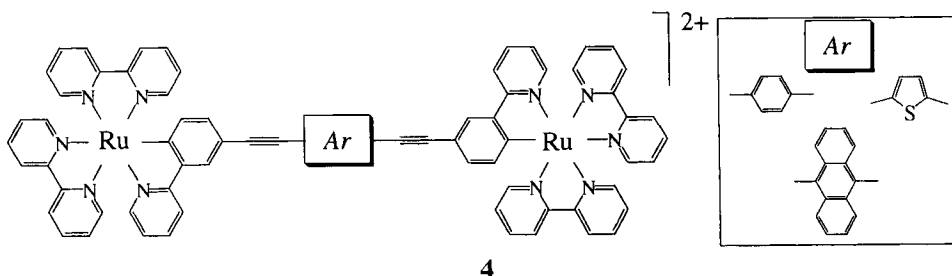


(terpy)Ru(bdmab⁻) (bdmap = bis(dimethylaminomethyl)benzene)

The bis(dimethylaminomethyl)benzene ligand (“pincer”) developed by Van Koten is an interesting cyclometallating ligand giving complexes very similar to the ones of dipyridylbenzene ((terpy)Ru(dpb⁻)). With two such complexing parts connected back-to-back (“bis-pincer”), it is possible to prepare strongly coupled bimetallic complexes with 10.8 Å metal–metal distance [68]. An intense intervalence band ($\epsilon = 33\,000 \text{ mol}^{-1} \text{ L cm}^{-1}$) was observed, and computing V_{ab} from the Hush formula gives 0.165 eV, i.e., more than for the analogous bis(dipyridylbenzene) complex. (Considering the system as class III would even give $V_{ab} = 0.33 \text{ eV}$).

(bpy)₂Ru(pp⁻)

These are also cyclometallated species, but based on complexation by the 2-phenylpyridine part. The spacer can be one or two triple bonds, or diethynylaryl groups (aryl = 9,10-anthrylene, 2,5-thienylene, or 1,4-phenylene), constituting series 4. As for cyclometallated complexes of the dipyridylbenzene family, the oxidation is easy (ca. 0.5 V vs. SCE), and the intervalence transitions are relatively intense, although partly overlapped by a nearby charge transfer transition of ruthenium(III) [18b,c]. For a given length, the couplings obtained are generally intermediate between those of the bis(terpy) and dipyridylbenzene families, and the decay slope is -0.104 Å^{-1} if the complex with a diethynylanthracene spacer is excluded. The latter exhibited a particularly strong coupling, which is discussed below (see Section 1.6.3)

**(bpy)₂Ru(N–N) (N–N = benzimidazolyl-pyridine site)**

In these complexes, the two Ru(bpy)₂ terminal moieties are bridged by a 2,2'-bis(benzimidazol-2-yl)-4,4'-bipyridine ligand, the metal–metal distance reaching 11 Å [69]. An intervalence band has been observed at 1200 nm, from which a 120 cm⁻¹ coupling (0.015 eV) is determined. Although this value is low in comparison with other complexes, the system is extremely appealing, since the intervalence band, and thus the coupling, can be switched OFF upon deprotonation.

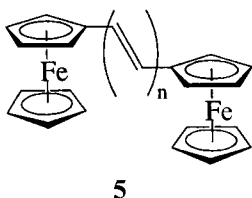
(NC)₅Fe(py⁻)

Mixed-valence complexes based on this end group were first developed by Felix and Ludi [70], and their basic properties are reviewed elsewhere [1]. The longest system is based on the bis(pyridyl)ethylene ligand, and the metal–metal separation (14 Å) is

large enough to study ionic association effects in a situation where the redox centers interact independently with the environment [21]. It can be shown for instance that stepwise ion pairing occurs when highly charged counterions are added, with symmetry reduction, and subsequent restoration when the two ends of the mixed-valence ion are associated with counterions to the same extent.

(Cp)Fe(Cp-)

A series of α,ω -diferrocenylpolyenes with $n = 1-6$ conjugated double bonds have been prepared and studied upon electrochemical oxidation in dichloromethane by Launay, Spangler, and co-workers [71a] (series 5). Intervalence transitions were obtained and gave the electronic coupling terms as a function of the number of double bonds. Although the decrease with distance was essentially exponential, a small but significant deviation was observed for $n = 3$, suggesting that there could be two regimes for the decay law, one from one to three double bonds, and the other one beyond.



Ferrocene-containing molecules present some drawbacks, however, such as a weak solubility and a tendency to decompose upon oxidation. Substituted ferrocenes, in particular pentamethylferrocenes, are interesting alternatives. With a spacer made of three phenylene and four vinylene units, an intervalence band has been obtained, corresponding to a 0.01 eV coupling for a metal-metal distance of 26.5 Å [71b].

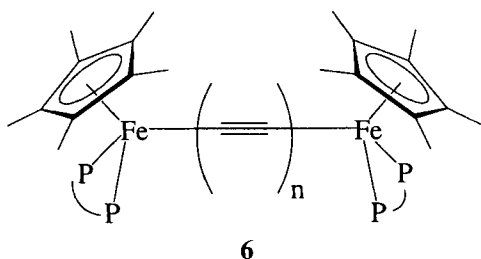
An interesting spacer is provided by the ruthenium bisacetylide group. When inserted between two ferrocene end groups, it gives a rigid linear system for which iron-iron intervalence bands have been observed [72]. The metal-metal distance is modest, however (ca. 10 Å); from the published spectra, one can compute V_{ab} values in the 0.06–0.08 eV range.

Another special spacer consists of porphyrin (either metallated or not) substituted in the 5,15 positions (see Figure 12b). Intervalence transitions have been observed when the ferrocene groups are electrochemically oxidized [36]. The metal-metal distance is >10 Å. No estimation of the V_{ab} coupling was reported, but the mixed-valence compounds would correspond to class III, or II/III.

(Cp*)(dppe)Fe(C≡C)-

Organometallic species presenting intervalence transitions through bridges essentially made of carbon atoms have been described by Lapinte and co-workers. The end group is (Cp*)(dppe)Fe(C≡C)-, where dppe = ethylenebis(diphenylphosphine),

and the spacer is either a phenylene unit or two triple bonds. The bridging ligand (see Figure 2 for the distinction with respect to spacer) is either 1,4-bis(ethynyl)-benzene (metal–metal distance 11.9 Å) [73] or octatetrayne (metal–metal distance 12.6 Å) [74], i.e., a chain of eight sp-hybridized carbon atoms (series **6**). The synthesis gives initially the 18e–18e species (formally Fe(II)–Fe(II)), which can be quantitatively oxidized to the 35e mixed-valence species, thanks to a large comproportionation constant (wave splittings 0.26 and 0.43 V respectively).



For the complex bridged by 1,4-bis(ethynyl)benzene, the experimental evidence (Mössbauer, ESR, IR) shows a borderline behavior between classes II and III. The electronic coupling is then either 0.064 eV (class II) or 0.31 eV (class III) [73]. For the complex bridged by octatetrayne, the class III behavior appears most likely (from the IR spectrum, and the sharp intense intervalence transition), giving $V_{ab} = 0.32$ eV [74]. This appears to be the largest coupling observed for such a distance (the less likely treatment as class II would give 0.09 eV) and shows the promise of all-carbon bridges if the synthesis can be extended. Still longer all-carbon bridges are described later (Section 1.5.5, under “Electrochemical wave splitting”), but they have not been studied for intervalence transitions.

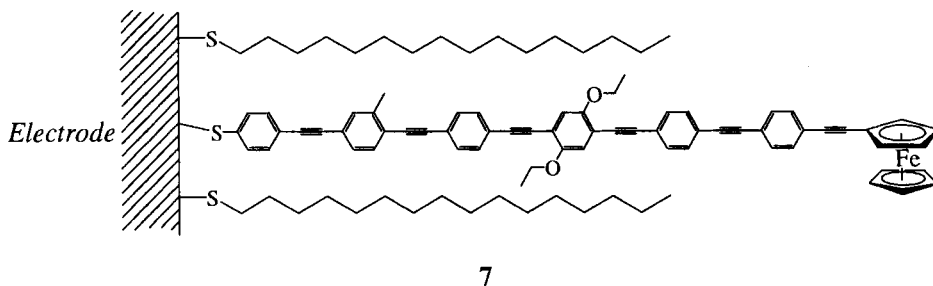
(dppe)(Cp)Fe(N≡C)–

In these organometallic species, terminal Fe(Cp)(dppe) units are linked by a square-planar Pt complex, either *trans*–[(py)₂Pt(CN)₂], or [Pt(CN)₄]^{2–}, resulting in a trinuclear Fe–Pt–Fe assembly with a 10 Å Fe–Fe distance [75]. Chemical oxidation in dichloromethane afforded the mixed-valence complexes which exhibited intervalence transitions near 1400 nm. From the published values, one can compute $V_{ab} = 0.038$ and 0.034 eV respectively.

1.5.2 Electron Transfer through a Monolayer at an Electrode

This kind of measurement being in its infancy, there is only one example for which systematic measurements on long molecules have been made [45]. It involves a series of rigid molecules with thiol at one end, linked to a ferrocene group through a poly(tolane) bridge. They were embedded in an inert long-chain thiol monolayer deposited on gold, and probed by AC voltammetry. With two to five tolane units,

the electrode–ferrocene length varies from 25 to 42 Å (series 7). The study by Creager et al. [45] yielded the intramolecular electron transfer rate constant and the $\ln k$ vs. R plot exhibited a slope of -0.36 Å^{-1} . Since k is proportional to V_{ab}^2 (cf. Eq. 5), this corresponds to a -0.18 Å^{-1} decay slope for V_{ab} .



1.5.3 Excited-state Electron Transfer

Among the large number of systems investigated [3], we concentrate on compounds for which a systematic study as a function of bridge length is possible. Several of them are based on the (terpy)Ru(terpy⁻) end group, and phenylene units are frequently used as spacers.

Bisporphyrin compounds linked by one to three phenylene spacers have been used by McLendon et al. to probe electron transfer between excited zinc porphyrin and Fe(III)(bisimidazole) porphyrin as acceptor site [76]. Electron transfer rates were deduced from the decrease in the lifetime of the first excited singlet state of the zinc porphyrin. The variation with the edge-to-edge distance between porphyrins gave a decay slope of -0.4 Å^{-1} . This dependence was attributed by the authors to the poor conjugation between adjacent phenylene rings twisted by 55° from each other.

Triads containing two Ru(II)(terpy)₂ end groups connected by one or two ethynyl spacers to a central Co(terpy)₂ moiety have been described by Ziessel, Harriman, and co-workers [77]. Upon excitation of the ruthenium chromophore, excited-state electron transfer from the central cobalt site occurs, as shown by spectral identification of the transient species. The electron transfer thus occurs at a distance of 15 Å.

Dyads of general formula [(ttpy)Ru(tpy)–(ph)_n–Rh(tppy)]⁵⁺ where ttpy = tolylterpyridine, and ph = phenylene spacer, with $n = 0–2$, have been studied by Sauvage, Scandola, and co-workers. Ru(II) and Rh(III) are thus rigidly fixed at distances varying between 11 and 20 Å. Time-resolved emission spectroscopy was first performed at low temperatures [78a], with the hope of observing the quenching of ruthenium(II) luminescence by electron transfer from excited Ru(II) to Rh(III). At 150 K, electron transfer quenching was only observed for the shortest member of the series ($n = 0$), while for the others it was too slow to compete with the decay of the excited state. This can be qualitatively rationalized using theoretical formulas for the electron transfer rate constant with V_{ab} values taken from the related work on

ruthenium mixed-valence complexes (see Section 1.5.1, under (terpy)Ru(terpy⁻)). At room temperature, electron transfer is fast enough to be detectable for the $n = 1$ complex, provided that emission measurements are brought to the picosecond domain [78b]. Although the decrease in the electron transfer rate constant with distance is evident, in practice the experimental window for studying the complete series is too narrow.

A very fascinating effect and still an open question is the wire-like behavior of DNA, in relation to radiation-induced damage. In an elegant study, Barton and co-workers, using well-defined systems, showed that DNA could facilitate photo-induced electron transfer between intercalated ruthenium and rhodium complexes with in particular a low decay coefficient (0.2 \AA^{-1} in terms of rate constant) [79a,b]. This value would correspond to 0.1 \AA^{-1} for the decay of the V_{ab} parameter, i.e., a behavior only encountered so far with really conjugated bridges of the type displayed in Figure 14. This appeared to conflict with other studies, in particular Brun and Harriman's work using organic intercalant molecules [79c], and also with theoretical expectations [79d] based on the similar case of electron transfer through proteins. Although the controversy is probably not finished [79e], an element of the solution could come from a recent theoretical work by Jortner et al. [79f], according to which two mechanisms could operate according to the nature of the intercalated donor and acceptor: a tunneling mechanism, strongly distance-dependent, and a hopping mechanism, much less dependent on distance.

1.5.4 Dexter-type Energy Transfer

Starting from the (terpy)Ru(terpy⁻) end group, bimetallic Ru(II)–Os(II) dyads with zero to two phenylene units have been studied (cf. Section 1.5.3). Energy transfer from Ru to Os has been observed, and assigned to a Dexter-type process from order-of-magnitude arguments [80]. Unfortunately, only a lower limit for k ($>10^{10} \text{ s}^{-1}$ for all complexes at 293 and 77 K) could be obtained.

With the Ru(II)–Rh(III) complexes mentioned above (Section 1.5.3), energy transfer from excited Rh(III) to Ru(II) occurs [78a]. Unfortunately, here also, only a lower limit for k ($>4 \times 10^5 \text{ s}^{-1}$ at 77 K, or $>3 \times 10^7 \text{ s}^{-1}$ at 150 K for all complexes) could be given, without the possibility of discriminating between the different compounds.

In the case of (terpy)Ru(terpy⁻) and (terpy)Os(terpy⁻) end groups linked by one or two ethynyl units studied by Ziessel and co-workers, triplet energy transfer from Ru to Os was also observed, but in this case rate constants could be obtained [81]. From these, assuming an exponential decay of k_{TT} with distance, the decay slope would be -0.17 \AA^{-1} for the rate constant, corresponding to -0.085 \AA^{-1} for the matrix element V_{TT} (cf. Eq. (7)).

Cyclometallated compounds of the type described in Section 1.5.1 under “terpyRu(dp⁻)”, but used as Ru(II)–Os(II) dyads, present remarkably different properties with respect to their bisterpyridine counterparts. In this case, the rates are appreciably lower and could be measured at 298 and 77 K from the quenching of

Ru-based luminescence [83]. The variation with bridge length (spacer of zero to two phenylene units) gave -0.33 \AA^{-1} for the decay law of the coupling.

A very interesting series has been prepared and studied by Balzani, Belser, De Cola and co-workers [82], in which $\text{Ru}(\text{bpy})_3$ and $\text{Os}(\text{bpy})_3$ end groups are connected by three, five or seven phenylene units, the metal-metal distance ranging from 24 to 42 Å. Energy transfer is deduced from the observed quenching of the Ru(II) phosphorescence, with a parallel sensitization of the Os(II) phosphorescence. Energy transfer rate constants vary from $6.7 \times 10^8 \text{ s}^{-1}$ for $n = 3$ to $1.3 \times 10^6 \text{ s}^{-1}$ for $n = 7$ at 293 K in acetonitrile, and a decay rate of -0.32 \AA^{-1} was established for the rate constants, corresponding to -0.16 \AA^{-1} for the matrix elements.

1.5.5 Other Effects

Spectroscopic evidence for delocalization

Several bimetallic complexes of Ru(II) present a special behavior, suggesting that in the excited state, an electron is promoted to an extended π^* orbital spanning the complete bridging ligand, which consequently plays the role of a wire. This is described on ethynyl-bridged binuclear ruthenium(II) complexes for which the triplet lifetime is abnormally long [84]. Incidentally, it is this property which allowed Ziessel and co-workers to develop bimetallic complexes in which excited-state electron transfer or energy transfer could be measured [77, 81]. With the bimetallic ruthenium complex bridged by bis(bipyridyl)decapentene (Section 1.5.1, under “ $(\text{bpy})_2\text{ClRu}(\text{py}-)$ and $(\text{bpy})_2\text{Ru}(\text{bpy}-)$ ”) [32b], the triplet lifetime was also long, which was attributed to the promotion of an electron on an extended orbital, with possible mixed-valence delocalization between the two bipyridyl subunits at either end of the polyene.

In the bimetallic ruthenium(II)–osmium(II) complex bridged by tetrapyridophenazine (tpphz) reported by Chiorboli, Gourdon, and co-workers [85a], the two metal atoms are fixed at a distance of 12.7 Å by the “ladder-like” polyquinoxaline ligand [85b]. Complete quenching of the $\text{Ru} \rightarrow \text{tpphz}$ MLCT emission, with sensitization of the $\text{Os} \rightarrow \text{tpphz}$ MLCT emission, was observed. Since here also the LUMO appears delocalized on the bridging tpphz ligand, the process can be viewed alternatively as energy transfer as well as electron transfer [85a].

In other respects, a bis(ferrocenyl)polymethine cation, in which two ferrocene end groups are connected by a polymethine spacer with up to 13 CH units, has been described by Tolbert et al. [14b]. The “molecular-wire behavior” is claimed, from the optical properties, in particular the absorption energy varying as the reciprocal of the chain length. In addition, separate oxidation potentials were observed for up to 13 carbon atoms between the metal centers.

Electrochemical wave splitting

As stated above, electrochemical wave splitting in itself cannot be actually considered as a manifestation of wire-like properties. However, some spectacular or intriguing examples deserve to be quoted.

Bimetallic molybdenum nitrosyl complexes, (containing Mo(I), i.e. a 17e species) with conjugated bridging ligands of the bipyridine family, or the bisphenolate family, present widely separated reduction waves, as shown by McCleverty, Ward, and others [86]. The separation can be observed with spacers containing up to four double bonds, or four phenylene units.

Bridges essentially made of carbon are also efficient in promoting such large wave splittings. Thus Lapinte and co-workers' organometallic iron complexes bridged by 1,4-bis(ethynyl)benzene or octatetrayne [73, 74] gave $\Delta E_{1/2}$ values of 0.26 and 0.43 V for metal-metal distances of 11.9 and 12.6 Å respectively. Longer systems, described by Gladysz and co-workers [34], are made of two (Cp*)Re(NO)(PPh₃) groups connected by a poly-yne chain reaching eventually 20 carbon atoms. Wave splitting is observed up to 16 carbon atoms (ca. 23 Å metal-metal distance).

Finally, complexes with (acac)Ru(III)(acac-) end groups and diethynylanthracene, diethynylthiophene, or triethynyl spacers, described by Hoshino et al. [19], exhibit wave splittings for the Ru(IV/III) couple (but not for Ru(III/II)). Interestingly, the diethynylanthracene spacer proved particularly efficient (cf. Section 1.5.1, under "(bpy)₂Ru(pp-)" for its role in mixed-valence compounds).

Magnetic effects

Intramolecular magnetic couplings are generally measured on compounds presenting relatively short metal-metal distances. A review of antiferromagnetic couplings reported up to 1979 by Coffman and Buettner [87] led to an empirical relation (Eq. (14)) for the maximum J values:

$$|J|[\text{cm}^{-1}] = 1.35 \times 10^7 \exp(-1.80 R_{\text{MM}}) \quad (14)$$

where R_{MM} is in Å.

Thus, for a 10 Å separation, the limit would be only -0.2 cm^{-1} . This small value arises from the fact that most known compounds at this time involved σ orbitals to propagate the exchange interaction. In particular, with copper(II) complexes, the unpaired electrons reside in a $d_{x^2-y^2}$ orbital which mixes with the σ system, but not the π one.

However, in 1978, Hendrickson and co-workers reported a value of -9 cm^{-1} for a binuclear copper(II) complex bridged by benzidine ($R_{\text{MM}} = 12.2 \text{ Å}$). The interaction was supposed to be propagated mainly by σ orbitals, with a possible role of π orbitals [88a]. Measurements on this complex *in solution*, to avoid intermolecular couplings, later gave a maximum value of 3.5 cm^{-1} for the $|J|$ parameter [88b].

Another attempt was performed by Julve, Verdager, et al. on copper(II) complexes bridged by 4,4'-bipyridine ($R_{\text{MM}} = 11.1 \text{ Å}$). Only a very weak coupling was obtained (-0.9 cm^{-1}), with no possibility of proving its intramolecular character [89].

Binuclear complexes with 17e molybdenum fragments of the type Mo(NO)Tp*Cl or MoOTp*Cl lead to larger couplings, as shown by Ward, McCleverty and co-workers. With 4,4'-bipyridine or 4,4'-bipyridylethylene as bridges ($R_{\text{MM}} = 11.3$ and 13.8 Å respectively), the couplings (-33 and -18 cm^{-1}) could be measured by

magnetic susceptibility down to 3 K [90]. Using bisphenates as bridging ligands, a coupling of -13.2 cm^{-1} was obtained for a distance estimated at 13.9 \AA . For all these complexes, studies with positional isomers, or crowded systems twisting the 4,4'-bipyridine ligand, demonstrated clearly the intervention of the π system.

At the present time, the largest couplings are reported by Crutchley and co-workers [20c], using dicyanamidobenzene bridging ligands (or chloro-substituted variants) with rutheniumpentaammine fragments. Unprecedented couplings in the -120 to -200 cm^{-1} range for a metal-metal distance of 13.2 \AA were reported, one of the complexes even being diamagnetic ($|J| > 800 \text{ cm}^{-1}$). This was explained by the strong mixing between $\text{Ru}(4d)$ orbitals and the HOMO or second HOMO of the bridging ligand. However, the analysis failed to recognize that it is not the properties of a single orbital (even spanning the whole molecule) which determines a strong coupling, but the *difference* in mixing between in-phase and out-of-phase combinations of metal orbitals with ligand orbitals.

To summarize, it appears that few systems have been devised to exhibit long-distance magnetic couplings. Compounds derived from dicyanamido complexes appear promising candidates, and for longer systems, magnetic susceptibility studies could be complemented by EPR, which is more appropriate to measure small couplings.

1.6 Conclusions

1.6.1 The Decay Law

A number of effects or parameters vary with distance according to exponential, or almost exponential, laws. This is of course the case for the basic V_{ab} parameter, and this occurs also for several related experimental observables, such as electron and energy transfer rate constants, and also magnetic J couplings. This general behavior is ultimately linked to orbital overlap considerations, and is discussed in more detail below for the case of mixed-valence compounds.

In the case of nanojunctions, an exponential law is also predicted [91], and was very recently amenable to an experimental verification [5c]. This confirms the relationship between molecular model systems studied in solution, and actual devices involving an electrical connection to the outside world.

Magnetic couplings seem also to decrease exponentially with distance, but as stated above, there have been few systematic studies of the rate of decay through conjugated bridges, the compilation by Coffman and Buettner being empirical, and limited to σ -mediated interactions [87].

Let us consider in more detail the case of mixed-valence complexes, for which systematic studies on several series of compounds are available. Most results can be summarized in Table 2, and Figure 14, where the key parameter V_{ab} , on a log scale, is plotted against R_{MM} . As stated above, it usually displays an exponential decrease (except in the case of bis(ferrocenyl)polyenes, for which a small but significant de-

Table 2. Parameters of the intervalence bands, V_{ab} values from Hush's formula, and decay slope for compounds constituting a series.

Series or complex, bridge or spacer, [Ref.]	R_{MM} [Å]	K_c	ν [cm ⁻¹]	$\Delta\nu_{1/2}$ [cm ⁻¹]	ϵ [L mol ⁻¹ cm ⁻¹]	V_{ab} [eV]	γ [Å ⁻¹]
1 ruthenium bipyridylpolyene complexes, 0–4 vinylene units [49, 58]	11.1 13.4 15.8 18.1 20.6	20 14 11 10 9	9700 10400 10200 10900 11000	5200 5300 5340 6000 5700	920 760 740 640 630	0.047 0.039 0.032 0.028 0.024	0.071
2 ruthenium bis(terpyridyl) complexes, 0–2 phenylene [16b]	11.0 15.5 20.0	15 7 5	6330 7720 8700	4000 6040 4930	1600 730 710	0.047 0.030 0.022	0.084
3 cyclometallated ruthenium complexes, bipyridylbenzene family, 0–3 phenylene units [17c,d]	11.0 15.5 20.0 24.0	690 16 6 4	5160 6060 8240 10150	2660 5110 5710 7500	22000 6600 2200 920	0.127 0.074 0.041 0.028	0.118
4 cyclometallated ruthenium complexes, phenylpyridine family [18b,c]	13.7 16.4 20.1 20.6 20.7	44 22 9 14 9	5550 6660 7690 8330 7000	4680 5170 3900 3620 4150	5800 2480 2430 2350 6800	0.070 0.045 0.034 0.033 0.055	0.104 ^a
5 diferrocenylpolyenes, 2–6 vinylene units [71a]	9.2 11.5 13.9 16.3 18.7	155 60 40 25 7	5500 6010 6070 5860 5565	4340 3800 3700 3600 3600	1570 2100 1670 1600 1600	0.053 0.048 0.035 0.028 0.022	0.097

Table 2 (*continued*)

Series or complex, bridge or spacer, [Ref.]	R_{MM} [Å]	K_c	ν [cm ⁻¹]	$\Delta\nu_{1/2}$ [cm ⁻¹]	ε [L mol ⁻¹ cm ⁻¹]	V_{ab} [eV]	γ [Å ⁻¹]
Ru complex, bipyridylacetylene bridge [1, 49]	14.0	14	10 900	5400	640	0.035	
Ru complexes, dicyano bridging ligands [51]							
1,4-dicyanobenzene	11.8	23	11 600	5600	510	0.039	
1,5-dicyanonaphthalene	12.1	7	12 800	5900	135	0.021	
2,6-dicyanonaphthalene	14.0	10	13 000	6000	140	0.018	
Trimetallic Ru complexes, <i>cis</i> -[Ru(bpy) ₂ (CN) ₂] [10]	7.0		10 000			0.037	
Ru(NH ₃) ₅ complex, dicyanamidobenzene, AN [20d, 63] ^b	13.1	6.8×10^4	6 900	2760	19 400	0.122	
Ru(NH ₃) ₄ (py) complex, dicyanamidobenzene, AN [63, 66] ^b	13.1	1.5×10^6	7 130	1900	25 500	0.120	
Ru(NH ₃) ₃ (bpy) complex, dicyanamidobenzene, AN [63, 66] ^b	13.1	9.3×10^6	7 580	1940	18 500	0.095	
Ru(NH ₃) ₅ complex, dicyanamidobiphenyl [64]	17.2	16	8 400	3300	3 300	0.050	
Ru(bpy) ₂ , 5 double bonds [32b]	24.2		10 400	4150	680	0.018	
Ru(bpy)(terpy) complex, dicyanamidobenzene [15a]	13.1	2.7×10^7	9 100	1800	5 600	0.058 ^d 0.57 ^e	
Ru complex, "bis-pincer" ligand [68]	10.8	1250	5 300	2900	33 000	0.165 ^d 0.33 ^e	
Ru complex, bis(benzimidazolyl)bipyridine [69]	11.0	4	8 300	4800	170	0.015	
Pentamethylferrocene, 3 phenylene and 4 vinylene [71b]	26.5	11	8 300	2900	420	0.010	
(Cp*)(dppe)Fe, bis(ethynyl)benzene [73]	11.9	2.6×10^4	4 960	3000	5 940	0.064 ^d 0.31 ^e	
(Cp*)(dppe)Fe, octatetrayne [74]	12.6	2×10^7	5 100	1300	31 000	0.32 ^e	
(Cp)(dppe)Fe linked by Pt complex [75]							
Pt(py) ₂ CN ₂	10.0	10 ^c	7 600	5200	560	0.038	
PtCN ₄	10.0	68 ^c	6 400	4700	600	0.034	

^aslope computed from the first four compounds of the series only, ^bsee refs. [20d, 63, 66] for additional values with related ligands and different solvents, ^ccomputed from reported $E_{1/2}$ values, ^{d,e} V_{ab} values when considered as a class II system (Hush equation), or class III ($V_{ab} = \bar{\nu}/2$), respectively.

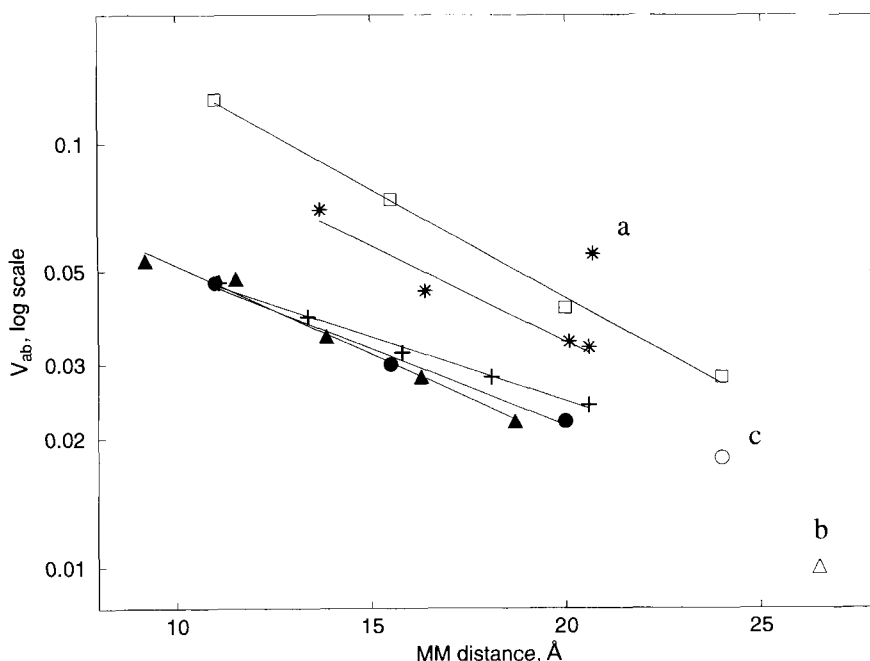


Figure 14. V_{ab} values, from intervalence measurements, on a log scale, as a function of the through-space metal–metal distance: +, ruthenium bipyridylpolyene complexes (series 1); ●, ruthenium bis(terpyridyl) complexes (series 2); □, ruthenium bis(cyclometallated) complexes, dipyritylbenzene family (series 3); *, ruthenium bis(cyclometallated) complexes, phenylpyridine family (series 4); ▲, bis(ferrocenyl)polyenes (series 5). Additional measurements: a, bis(cyclometallated) complexes, phenylpyridine family with diethynylantracene as spacer; b, bis(ferrocene) with three phenylene and four vinylene units as spacer; c, bis[ruthenium(trisbipyridyl)] with five double bonds as spacer. Note that the $\text{Cp}^*(\text{dppe})\text{Fe}$ system bridged by octatetrayne (13 Å, 0.32 eV) is outside the graph.

parture has been observed, i.e., there are two slopes, one up to three double bonds, and another one thereafter [71a]).

A simple tight-binding model has been proposed by McConnell [92], which describes a donor–bridge–acceptor system (this can be adapted to mixed-valence systems composed of two terminal sites and N repeat units) with three parameters: α , the coupling between equivalent repeat units constituting the bridge; β , the coupling between the last unit of the bridge and one terminal site; and “a”, the energy difference between terminal and bridge sites (Figure 15).

This model allows the determination of the effective coupling V_{ab} , and its decay with distance. However, while the original McConnell treatment relied on perturbation theory, an exact analysis was performed by Joachim et al. [59, 93], and shortly afterward developed by Hush and co-workers [62, 94]. The complete analysis predicts a wide variety of behaviors according to the values of the parameters: slow or fast decay, exponential or nonexponential character, oscillations, and even

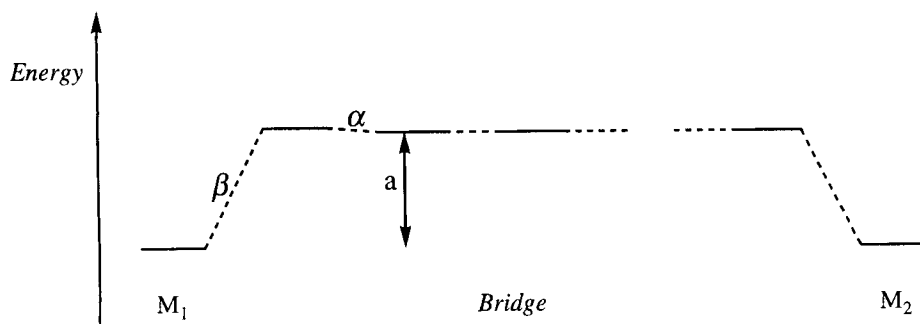


Figure 15. The simple tight-binding model, with α , β , and “a” parameters.

an increase in coupling with distance [62]. In a refinement of the original model, the effect of alternation, i.e., the existence of two different intra-bridge couplings β_1 and β_2 , was also considered [59, 62]. The frequent occurrence of exponential decay [95] is a general behavior when, as usual with most conjugated bridges used in mixed-valence chemistry, the metal energy levels fall in the “gap” of the bridge backbone, i.e., they are far from resonance.

Finally, when compared to intervalence electron transfer, Dexter-type energy transfer gives widely different decay laws (expressed in terms of $\ln V_{\text{TT}}$ vs. R), i.e., from -0.085 to -0.33 \AA^{-1} . No simple explanation appears at present, due to the higher complexity of the process. One can only remark that, since the matrix element V_{TT} appears as the *product* of matrix elements for electron transfer and hole transfer (Eq. (7)), one can expect the rate of decay with distance to be the *sum* of the rates of decay for these two processes [46a, 83]. This would explain why the decay is generally faster than for electron transfer, with the curious exception of Ziessel’s acetylene-bridged complexes (see Section 1.5.4).

1.6.2 Cyclometallated Compounds

The most striking point from Figure 14 is that many compounds with very diverse structures fall in the same area, giving similar V_{ab} values, and decay slopes in the range -0.07 to -0.10 \AA^{-1} . Cyclometallated compounds, on the other hand, exhibit a special behavior, characterized by a larger V_{ab} , but also a *larger decay slope*. This is particularly true for compounds where the coordinating site is of the bipyridyl-benzene family (Section 1.5.1, “(terpy)Ru(dpbb-)”), but the trend is also very clear with compounds of the phenylpyridine family (Section 1.5.1, “(bpy)₂Ru(pp-)”). To use the simple tight-binding model above as an explanatory tool, it is necessary to have at least a rough idea of the change in the formal α , β , “a” parameters from one compound to the other.

According to molecular orbital calculations, the main difference between bis(terpyridyl) complexes and cyclometallated ones lies in the tail of the wave functions with mainly metal character. In the case of cyclometallated compounds,

they have a greater extension on the carbon atom located *para* to the ruthenium–carbon bond, thus ensuring a better communication with the spacer [17d]. In the framework of the simple model above, this is equivalent to an increase in β , and the model indeed predicts an increase in V_{ab}^0 , and an increase in the γ decay coefficient.

Thus it does not seem possible, in general, to win on V_{ab}^0 and γ at the same time [59]. In other words, the “ V_{ab}^0 vs. γ ” competition appears inherent to the structure of any compound made of repeat units. The above tight-binding model is however limited, because assigning just one energy level to one repeat unit does not take into account the detailed structure of the latter. Actually, each of the repeat units may exhibit several energy levels with different energies and symmetries. More recent treatments take this explicitly into account [91], and could help in the selection of the most efficient structures.

1.6.3 Puzzling Compounds

Among the values reported in Figure 14, several compounds are really exceptional:

complexes linked by bridges made of pure carbon, which exhibit record values of the coupling, although for modest distances. In addition, they produce record values of the length/width ratio. Very long systems of this kind have not yet been studied as mixed-valence compounds.

compounds involving a diethynylanthracene spacer. With (acac)Ru(III)(acac–) end groups they give a high wave splitting (cf. Section 1.5.5, “Electrochemical wave splitting”), and with (bpy)₂Ru(pp–) end groups (Section 1.5.1, “(bpy)₂Ru(pp–)”) the V_{ab} coupling is *higher than without the anthracene part of the spacer*. This very strange effect has been also observed with dimers of porphyrins linked by a 9,10-diethynylanthracene spacer [96]. The electronic communication, measured by the red shift of luminescence, is higher than for a shorter dimer *without* the anthracene part.

These two intriguing classes of compounds have a common point: the possibility to write an alternate mesomeric structure, either quinoidal or cumulenic, for the fully oxidized form containing ruthenium(III) or iron(III) [23, 68, 73, 96]. The relationship with the high value of the coupling in the mixed-valence state is at present unknown, but deserves further investigation.

1.6.4 Mixed-valence Complexes and Metal/Molecule/Metal Nanojunctions

The comparison with theoretical estimations on metal/molecule/metal nanojunctions could be fruitful since, in both approaches, one tries to optimize the pre-exponential term and the decay slope. A recent systematic theoretical study by Joachim and Magoga has ranked a large number of bridge structures, made of several repeat units [91]. They were characterized by the value of the conductance, and its rate of decay with distance. The comparison with the compounds of the

present review cannot be pushed too far, however, because there are relatively few repeat units common to the two studies, and moreover, the existing mixed-valence compounds usually involve a small number of repeat units in the bridge (a maximum of three vs. more than ten in the theoretical work on nanojunctions). But several intriguing facts appear: a) again, bridges made of ethynylanthracene units appear very promising, giving here a small rate of decay of the conductance with distance; b) conjugated triple bonds (which have not been very much used in mixed-valence chemistry) appear better than double bonds, provided they are not introduced alone in the structure, but associated with an aromatic cycle. This is contrary to naïve intuition since, for an infinite system, triple bonds give a higher gap than double bonds, but the study demonstrates that the band gap is not the only factor determining the efficiency.

References

1. C. Creutz, *Prog. Inorg. Chem.* **1983**, 30, 1.
2. R. J. Crutchley, *Adv. Inorg. Chem.* **1994**, 41, 273.
3. a) V. Balzani, A. Juris, M. Venturi, S. Campagna, S. Serroni, *Chem. Rev.* **1996**, 96, 759; b) L. De Cola, P. Belser, *Coord. Chem. Rev.* **1998**, 177, 301.
4. D. L. Dexter, *J. Chem. Phys.* **1953**, 21, 836.
5. a) M. A. Reed, C. Zhou, C. J. Muller, T. P. Burgin, J. M. Tour, *Science* **1997**, 278, 252; C. Kergueris, J.-P. Bourgoin, S. Palacin, D. Esteve, C. Urbina, M. Magoga, C. Joachim, *Phys. Rev. B* **1999**, 59, 12505; b) S. J. Tans, M. H. Devoret, H. Dai, A. Thess, R. E. Smalley, L. J. Geerligs, C. Dekker, *Nature* **1997**, 386, 474; S. Gerdes, T. Ondarçuhu, S. Cholet, C. Joachim, *Europhys. Lett.* **1999**, 48, 292; c) V. J. Langlais, R. R. Schlittler, H. Tang, A. Gourdon, C. Joachim, J. K. Gimzewski, *Phys. Rev. Lett.* **1999**, 83, 2809.
6. a) D. Tzalis, Y. Tor, *Chem. Commun.* **1996**, 1043; b) D. Tzalis, Y. Tor, *J. Am. Chem. Soc.* **1997**, 119, 852.
7. D. Osella, O. Gambino, M. Ravera, M. V. Russo, G. Infante, *Inorg. Chim. Acta* **1994**, 225, 35.
8. O. Lavastre, J. Plass, P. Bachmann, S. Guesmi, C. Moinet, P. H. Dixneuf, *Organometallics* **1997**, 16, 184.
9. M. Uno, P. H. Dixneuf, *Angew. Chem. Int. Ed. Engl.* **1998**, 37, 1714.
10. F. Scandola, R. Argazzi, A. Bignozzi, C. Chiorboli, M. T. Indelli, M. A. Rampi, *Coord. Chem. Rev.* **1993**, 125, 283.
11. A. Hradsky, B. Bildstein, N. Schuler, H. Schottenberger, P. Jaitner, K.-H. Ongania, K. Wurst, J.-P. Launay, *Organometallics* **1997**, 16, 392.
12. a) E. Ishow, A. Gourdon, J.-P. Launay, *Chem. Commun.* **1998**, 1909; b) E. Ishow, A. Gourdon, J.-P. Launay, C. Chiorboli, F. Scandola, *Inorg. Chem.* **1999**, 38, 1504.
13. E. A. Seddon, K. R. Seddon, *The Chemistry of Ruthenium*, Elsevier, Amsterdam, **1984**.
14. a) L. M. Tolbert, X. Zhao, Y. Ding, L. A. Bottomley, *Inorg. Chim. Acta* **1996**, 251, 29; b) L. M. Tolbert, X. Zhao, Y. Ding, L. A. Bottomley, *J. Am. Chem. Soc.* **1995**, 117, 12891.
15. a) A. R. Rezvani, C. E. B. Evans, R. J. Crutchley, *Inorg. Chem.* **1995**, 34, 4600; b) J. Bonvoisin, personal communication.
16. a) J.-P. Sauvage, J.-P. Collin, J.-C. Chambron, S. Guillerez, C. Coudret, V. Balzani, F. Barigelletti, L. De Cola, L. Flamigni, *Chem. Rev.* **1994**, 94, 993; b) J.-P. Collin, Ph. Lainé, J.-P. Launay, J.-P. Sauvage, A. Sour, *J. Chem. Soc. Chem. Commun.* **1993**, 434.
17. a) M. Beley, J.-P. Collin, R. Louis, B. Metz, J.-P. Sauvage, *J. Am. Chem. Soc.* **1991**, 113, 8521; b) S. Chodorowski-Kimmes, M. Beley, J.-P. Collin, J.-P. Sauvage, *Tetrahedron Lett.* **1996**, 37, 2963; c) M. Beley, S. Chodorowski-Kimmes, J.-P. Collin, P. Lainé, J.-P. Launay, J.-P. Sauvage, *Angew. Chem. Int. Ed. Engl.* **1994**, 33, 1775; d) C. Patoux, J.-P. Launay, M. Beley, S. Chodorowski-Kimmes, J.-P. Collin, S. James, J.-P. Sauvage, *J. Am. Chem. Soc.* **1998**, 120, 3717.

18. a) C. Coudret, S. Frayssé, J.-P. Launay, *Chem. Commun.* **1998**, 663; b) S. Frayssé, C. Coudret, J.-P. Launay, *Tetrahedron Lett.* **1998**, 39, 7873; c) S. Frayssé, Thesis, Université Paul Sabatier, Toulouse, **1999**.
19. Y. Hoshino, T. Suzuki, H. Umeda, *Inorg. Chim. Acta* **1996**, 245, 87.
20. a) M. A. S. Aquino, A. E. Bostock, R. J. Crutchley, *Inorg. Chem.* **1990**, 29, 3641; b) M. A. S. Aquino, F. L. Lee, E. J. Gabe, J. E. Greedan, R. J. Crutchley, *Inorg. Chem.* **1991**, 30, 3234; c) M. A. S. Aquino, F. L. Lee, E. J. Gabe, C. Bensimon, J. E. Greedan, R. J. Crutchley, *J. Am. Chem. Soc.* **1992**, 114, 5130; d) M. L. Naklicki, R. J. Crutchley, *Inorg. Chim. Acta* **1994**, 225, 123; e) M. L. Naklicki, R. J. Crutchley, *J. Am. Chem. Soc.* **1994**, 116, 6045.
21. R. Blackburn, Y. Dong, L. A. Lyon, J. T. Hupp, *Inorg. Chem.* **1994**, 33, 4446.
22. C. Patoux, C. Coudret, J.-P. Launay, C. Joachim, A. Gourdon, *Inorg. Chem.* **1997**, 36, 5037.
23. F. Paul, C. Lapinte, *Coord. Chem. Rev.* **1998**, 178–180, 431.
24. W. Weng, T. Bartik, M. Brady, B. Bartik, J. A. Ramsden, A. M. Arif, J. A. Gladysz, *J. Am. Chem. Soc.* **1995**, 117, 11922.
25. C. W. Faulkner, S. L. Ingham, M. S. Khan, J. Lewis, N. J. Long, P. R. Raithby, *J. Organomet. Chem.* **1994**, 482, 139.
26. a) M. Hissler, R. Ziessel, *New J. Chem.* **1997**, 21, 843; b) V. Grossshenny, F. M. Romero, R. Ziessel, *J. Org. Chem.* **1997**, 62, 1491.
27. P. F. H. Schwab, M. D. Levin, J. Michl, *Chem. Rev.* **1999**, 99, 1863.
28. J. E. McMurry, *Chem. Rev.* **1989**, 89, 1513.
29. G. Eglinton, W. McCrae, *Adv. Org. Chem.* **1963**, 4, 225.
30. A. Gourdon, *New J. Chem.* **1992**, 16, 953.
31. E. C. Constable, M. D. Ward, *J. Chem. Soc., Dalton Trans.* **1990**, 1405.
32. a) T. S. Arrhenius, M. Blanchard-Desce, M. Dvornitzky, J.-M. Lehn, J. Malthête, *Proc. Natl. Acad. Sci. USA*, **1986**, 85, 5355; b) A. C. Benniston, V. Goulle, A. Harriman, J.-M. Lehn, B. Marczinke, *J. Phys. Chem.* **1994**, 98, 7798.
33. G. Pickaert, R. Ziessel, *Tetrahedron Lett.* **1998**, 39, 3497.
34. T. Bartik, B. Bartik, M. Brady, R. Dembinski, J. A. Gladysz, *Angew. Chem. Int. Ed. Engl.* **1996**, 35, 414.
35. a) Boron: N. Miayura, A. Suzuki, *Chem. Rev.* **1995**, 95, 2457; b) Zinc: P. Knochel, R. S. Singer, *Chem. Rev.* **1993**, 93, 2117; c) Tin: J. K. Stille, *Angew. Chem. Int. Ed. Engl.* **1986**, 25, 508; d) Leading reference: *Metal Catalyzed Cross-coupling Reactions*, F. Diederich, P. J. Stang (Eds.), Wiley-VCH, Weinheim **1998**.
36. P. D. W. Boyd, A. K. Burell, W. M. Campbell, P. A. Cocks, K. C. Gordon, G. B. Jameson, D. L. Officer, Z. Zhao, *Chem. Commun.* **1999**, 637.
37. M. B. Robin, P. Day, *Adv. Inorg. Chem. Radiochem.* **1967**, 10, 247.
38. a) N. S. Hush, *Prog. Inorg. Chem.* **1967**, 8, 391; b) N. S. Hush, *Coord. Chem. Rev.* **1985**, 64, 135.
39. CNS model: C. Creutz, M. D. Newton, N. Sutin, *J. Photochem. Photobiol. A: Chem.* **1994**, 82, 47.
40. a) J. E. Sutton, P. M. Sutton, H. Taube, *Inorg. Chem.* **1979**, 18, 1017; b) D. E. Richardson, H. Taube, *Inorg. Chem.* **1981**, 20, 1278.
41. J. R. Reimers, N. S. Hush, *Inorg. Chem.* **1990**, 29, 3686; J. R. Reimers, N. S. Hush, *Inorg. Chem.* **1990**, 29, 4510.
42. A. Gilbert, J. Baggott, *Essentials of Molecular Photochemistry*, Blackwell, Oxford, **1991**, p. 123.
43. B. S. Brunshwig, N. Sutin, *Coord. Chem. Rev.* **1999**, 187, 233.
44. J. Bonvoisin, J.-P. Launay, C. Rovira, J. Veciana, *Angew. Chem. Int. Ed. Engl.* **1994**, 33, 2106.
45. a) S. Creager, C. J. Yu, C. Bamdad, S. O'Connor, T. MacLean, E. Lam, Y. Chong, G. T. Olsen, J. Luo, M. Gozin, J. F. Kayyem, *J. Am. Chem. Soc.* **1999**, 121, 1059; b) K. Weber, L. Hockett, S. Creager, *J. Phys. Chem. B* **1997**, 101, 8286. Note that in eq. 2) of ref. a), E_{λ} is missing in the denominator of the square root.
46. a) G. L. Closs, M. D. Johnson, J. R. Miller, P. Piotrowiak, *J. Am. Chem. Soc.* **1989**, 111, 3751; b) N. Koga, K. Sameshima, K. Morokuma, *J. Phys. Chem.* **1993**, 97, 13117.
47. O. Kahn, *Angew. Chem. Int. Ed. Engl.* **1985**, 24, 834.
48. W. M. Laidlaw, R. G. Denning, T. Verbiest, E. Chauchard, A. Persoons, *Nature* **1993**, 363, 58; B. J. Coe, S. Houbrechts, I. Asselberghs, A. Persoons, *Angew. Chem. Int. Ed. Engl.* **1999**, 38, 366.

49. J. E. Sutton, H. Taube, *Inorg. Chem.* **1981**, 20, 3125.
50. For very long systems, all effects decrease with distance except the statistical factor (*i*). Thus when the metal-metal distance is large enough, K_c should approach 4 as a lower limit. Then the electrochemical wave shape becomes indistinguishable from the case of a complex undergoing a single electron transfer, apart from the fact that the concentration has doubled.
51. D. E. Richardson, H. Taube, *J. Am. Chem. Soc.* **1983**, 105, 40.
52. V. Palaniappan, R. M. Singru, U. C. Agarwala, *Inorg. Chem.* **1988**, 27, 181.
53. S. Ernst, V. Kasack, W. Kaim, *Inorg. Chem.* **1988**, 27, 1146.
54. J. T. Hupp, T. J. Meyer, *Inorg. Chem.* **1987**, 26, 2332.
55. J. T. Hupp, T. J. Meyer, *J. Phys. Chem.* **1987**, 91, 1001.
56. J. T. Hupp, J. Weydert, *Inorg. Chem.* **1987**, 26, 2657.
57. D. H. Oh, S. G. Boxer, *J. Am. Chem. Soc.* **1990**, 112, 8161; D. H. Oh, M. Sano, S. G. Boxer, *J. Am. Chem. Soc.* **1991**, 113, 6880.
58. S. Woitellier, J.-P. Launay, C. W. Spangler, *Inorg. Chem.* **1989**, 28, 758; A.-C. Ribou, J.-P. Launay, K. Takahashi, T. Nihira, S. Tarutani, C. W. Spangler, *Inorg. Chem.* **1994**, 33, 1325.
59. C. Joachim, J.-P. Launay, S. Woitellier, *Chem. Phys.* **1990**, 147, 131.
60. J. R. Reimers, N. S. Hush, *J. Phys. Chem. A* **1999**, 103, 3066.
61. Y. Kim, C. M. Lieber, *Inorg. Chem.* **1989**, 28, 3990.
62. J. R. Reimers, N. S. Hush, *J. Photochem. Photobiol. A: Chem.* **1994**, 82, 31, and references therein.
63. C. E. B. Evans, M. L. Naklicki, A. R. Rezvani, C. A. White, V. V. Kondratiev, R. J. Crutchley, *J. Am. Chem. Soc.* **1998**, 120, 13096.
64. M. A. S. Aquino, C. A. White, C. Bensimon, J. E. Greedan, R. J. Crutchley, *Can J. Chem.* **1996**, 74, 2201.
65. Refined values are 13.3 and 17.2 Å for complexes linked by dicyanamido and dicyanamidobiphenyl ligands respectively: R. J. Crutchley, private communication.
66. A. R. Rezvani, C. Bensimon, B. Crompton, C. Reber, J. E. Greedan, V. V. Kondratiev, R. J. Crutchley, *Inorg. Chem.* **1997**, 36, 3322; C. E. B. Evans, G. P. A. Yap, R. J. Crutchley, *Inorg. Chem.* **1998**, 37, 6161.
67. a) M. J. Powers, T. J. Meyer, *J. Am. Chem. Soc.* **1980**, 102, 1289; b) R. W. Callahan, F. R. Keene, T. J. Meyer, D. J. Salmon, *J. Am. Chem. Soc.* **1977**, 99, 1064.
68. J.-P. Sutter, D. M. Grove, M. Beley, J.-P. Collin, N. Veldman, A. L. Spek, J.-P. Sauvage, G. van Koten, *Angew. Chem. Int. Ed. Engl.* **1994**, 33, 1282.
69. M.-a. Haga, Md. M. Ali, S. Koseki, K. Fujimoto, A. Yoshimura, K. Nozaki, T. Ohno, K. Nakajima, D. J. Stufkens, *Inorg. Chem.* **1996**, 35, 3335.
70. F. Felix, A. Ludi, *Inorg. Chem.* **1978**, 17, 1782.
71. a) A.-C. Ribou, J.-P. Launay, M. L. Sachtleben, H. Li, C. W. Spangler, *Inorg. Chem.* **1996**, 35, 3735; b) M. Trezies, B. Bildstein, J.-P. Launay, unpublished results.
72. Y. Zhu, O. Clot, M. O. Wolf, G. P. A. Yap, *J. Am. Chem. Soc.* **1998**, 120, 1812.
73. N. Le Narvor, C. Lapinte, *Organometallics* **1995**, 14, 634; N. Le Narvor, Thesis, University of Rennes 1, **1993**.
74. F. Coat, C. Lapinte, *Organometallics* **1996**, 15, 477; F. Coat, Thesis, University of Rennes 1, **1996**.
75. G. N. Richardson, U. Brand, H. Vahrenkamp, *Inorg. Chem.* **1999**, 38, 3070.
76. A. Helms, D. Heiler, G. McLendon, *J. Am. Chem. Soc.* **1992**, 114, 6227.
77. V. Grossshenny, A. Harriman, R. Ziessel, *Angew. Chem. Int. Ed. Engl.* **1995**, 34, 2705.
78. a) M. T. Indelli, F. Scandola, J.-P. Collin, J.-P. Sauvage, A. Sour, *Inorg. Chem.* **1996**, 35, 303; b) M. T. Indelli, F. Scandola, L. Flamigni, J.-P. Collin, J.-P. Sauvage, A. Sour, *Inorg. Chem.* **1997**, 36, 4247.
79. a) C. J. Murphy, M. R. Arkin, Y. Jenkins, N. D. Ghatlia, S. H. Bossmann, N. J. Turro, J. K. Barton, *Science* **1993**, 262, 1025; b) M. R. Arkin, E. D. A. Stemp, R. E. Holmlin, J. K. Barton, A. Hörmann, E. J. C. Olson, P. F. Barbara, *Science*, **1996**, 273, 475; c) A. M. Brun, A. Harriman, *J. Am. Chem. Soc.* **1992**, 114, 3656; d) T. L. Netzel, *J. Chem. Ed.* **1997**, 74, 646; e) E. K. Wilson, *Chem. Eng. News*, **1999**, 43; f) J. Jortner, M. Bixon, T. Langenbacher, M. E. Michel-Beyerle, *Proc. Nat. Acad. Sci. USA*, **1998**, 95, 12759.

80. F. Barigelletti, L. Flamigni, V. Balzani, J.-P. Collin, J.-P. Sauvage, A. Sour, E. C. Constable, A. M. W. Cargill Thompson, *J. Am. Chem. Soc.* **1994**, *116*, 7692; F. Barigelletti, L. Flamigni, V. Balzani, J.-P. Collin, J.-P. Sauvage, A. Sour, E. C. Constable, A. M. W. Cargill Thompson, *Coord. Chem. Rev.* **1994**, *132*, 209.
81. V. Grosshenny, A. Harriman, R. Ziessel, *Angew. Chem. Int. Ed. Engl.* **1995**, *34*, 1100.
82. B. Schlicke, P. Belser, L. De Cola, E. Sabbioni, V. Balzani, *J. Am. Chem. Soc.* **1999**, *121*, 4207.
83. F. Barigelletti, L. Flamigni, M. Guardigli, A. Juris, M. Beley, S. Chodorowski-Kimmes, J.-P. Collin, J.-P. Sauvage, *Inorg. Chem.* **1996**, *35*, 136.
84. A. C. Benniston, V. Grosshenny, A. Harriman, R. Ziessel, *Angew. Chem. Int. Ed. Engl.* **1994**, *33*, 1884.
85. a) C. Chiorboli, C.-A. Bignozzi, F. Scandola, E. Ishow, A. Gourdon, J.-P. Launay, *Inorg. Chem.* **1999**, *38*, 2402; b) J. Bolger, A. Gourdon, E. Ishow, J.-P. Launay, *J. Chem. Soc. Chem. Commun.* **1995**, 1799.
86. M. D. Ward, *Chem. Soc. Rev.* **1995**, 121; J. A. McCleverty, M. D. Ward, *Acc. Chem. Res.* **1998**, *31*, 842, and references therein.
87. R. E. Coffman, G. R. Buettner, *J. Phys. Chem.* **1979**, *83*, 2387.
88. a) T. R. Felthouse, D. N. Hendrickson, *Inorg. Chem.* **1978**, *17*, 2636; b) F. Tinti, Thesis, Université Paris Sud, Orsay, **1987**, pp. 158-163.
89. M. Julve, M. Verdaguer, J. Faus, F. Tinti, J. Moratal, A. Monge, E. Gutiérrez-Puebla, *Inorg. Chem.* **1987**, *26*, 3520.
90. A. M. W. Cargill Thompson, D. Gatteschi, J. A. McCleverty, J. A. Navas, E. Rentschler, M. D. Ward, *Inorg. Chem.* **1996**, *35*, 2701; V. A. Ung, A. M. W. Cargill Thompson, D. A. Bardwell, D. Gatteschi, J. C. Jeffery, J. A. McCleverty, F. Totti, M. D. Ward, *Inorg. Chem.* **1997**, *36*, 3447.
91. M. Magoga, C. Joachim, *Phys. Rev. B* **1997**, *56*, 4722.
92. H. M. McConnell, *J. Chem. Phys.* **1961**, *35*, 508.
93. C. Joachim, *Chem. Phys.* **1987**, *116*, 339.
94. J. R. Reimers, N. S. Hush, *Chem. Phys.* **1990**, *146*, 89.
95. M. A. Ratner, *J. Phys. Chem.* **1990**, *94*, 4877.
96. P. N. Taylor, A. P. Wylie, J. Huuskonen, H. L. Anderson, *Angew. Chem. Int. Ed. Engl.* **1998**, *37*, 986.

2 Approaches to an Optically Controlled Molecular Switch

Aaron S. Lukas and Michael R. Wasielewski

2.1 Introduction

At the dawn of the 21st century our fundamental understanding of complex processes such as photosynthesis and gene replication has reached the molecular level. The ability to observe ultrafast chemical and physical processes as well as these events occurring in single molecules [1] was unknown a mere 30 years ago. In the coming decade researchers hope to synthesize concepts gleaned from research in these fields and develop a computer whose operation is based on the interactions of single molecules with one another. This computer has the potential to be orders of magnitude smaller, faster, and more efficient than those based on semiconductor technology [2–4]. Massive size reductions using molecular switches will most likely be limited by quantum statistical considerations, if reasonable data error rates are to be maintained [5]. Nevertheless, molecular devices that use visible light for addressing and control purposes have a realizable data density of $\sim 2 \times 10^9$ bits cm^{-2} just through diffraction-limited spot size considerations alone. Recent results suggest that three-dimensional addressing [6], the use of excitonic waveguides [7, 8], and near-field optical techniques [9, 10] can greatly increase this resolution. Furthermore, since energy and electron transfer processes can occur on a sub-picosecond time scale, it is possible to produce devices that respond with equal rapidity. Employing high quantum efficiency, fast photo-driven processes will also decrease the heat load produced by the current computing devices. This results in a more energy efficient system, and may result in economically viable molecular electronic devices.

Nonetheless, a working device has yet to be realized. Successful examples of molecular systems capable of rectification [11, 12], wiring [13–44], memory storage [6, 45–49], and switching [50–57] have been demonstrated; however, integration of these various components has proved difficult.

The development of a paradigm to guide this undertaking is an active area of research [58, 59]. One promising approach is to base such a device on the interaction of light with these various components [60–64]. There are several advantages to performing switching operations via optical inputs and outputs. Electronic ab-

sorption is an extremely rapid process, and it should be possible to create switching devices that respond equally rapidly. The excited states of molecules can fluoresce, undergo electron and energy transfer, and lead to bond making and bond breaking. Each of these processes can be used for switching and storing data. Variable addressing of molecular states can be achieved by modulating the wavelength, intensity [65], polarization, and temporal and spatial properties of laser pulses. Information can be read from these systems via fluorescence [66], spectral bleaching [67–76], circular dichroism [77–79], the readout of electronic spin states, and other techniques.

Great strides have been made in recent years towards the development of electronic devices based on the interaction of single molecules with light. Switching systems based on photochromic behavior [30, 45–47, 66, 80–101], optical control of chirality [78, 79, 102], fluorescence [103–108], intersystem crossing [109–113], electro- and photochemically induced changes in liquid crystals [114–119], thin films [73, 120–129], and membranes [130, 131], and photoinduced electron and energy transfer [132–150] have been synthesized and studied. This review will briefly discuss recent developments in photochromic-type devices as well as giving a detailed look at the development and applications of molecular switches based on photoinduced energy and electron transfer processes.

Experimental work has focused mainly on approaches to molecular switches that make use of photochemical and electrochemical conformational changes within molecules. The general class of molecules to be discussed has several distinguishing properties. It is any molecule or array of molecules capable of absorbing a photon at a first wavelength, λ_1 , which induces a change in its electronic and/or nuclear structure. This structural change does two things: it attenuates the absorption of a second photon at λ_1 and introduces a new absorption at a second wavelength, λ_2 . The switch has been turned “on”. The switch can be turned “off” in one of several ways. We will examine systems whose lifetime is modulated thermally, magnetically, and also via absorption of a photon at this second wavelength, λ_2 , or in some other part of the spectrum. The lifetime of the “on” state determines the turnover time and also the potential applications of a switch. Molecules with very long state lifetimes are no longer switches, but are considered to be memory devices.

The operation of any optically controlled device is critically dependent upon the efficiency of light absorption by the input chromophore, and its ability to undergo electron transfer. Three characteristics make an excellent input chromophore: a large ground state extinction coefficient, long-lived excited state (in the region of several nanoseconds), and high fluorescent quantum yield. The most commonly used chromophores for light absorption are fused polycyclic aromatic hydrocarbons, metallated and free-base porphyrins, and derivatives of other light absorbers found in nature.

The electronic state of the switch is often read by using optical transient absorption and fluorescence emission spectroscopies. Fluorescence is a much more sensitive technique, and can be used even at the single molecule level. It also requires a much smaller density of photons to provide a stable signal; however, very few charge-separated ion pair states exhibit radiative charge recombination. In these cases transient absorption is often used because it allows direct nondestructive observation of a molecule’s electronic configuration. Problems with this technique

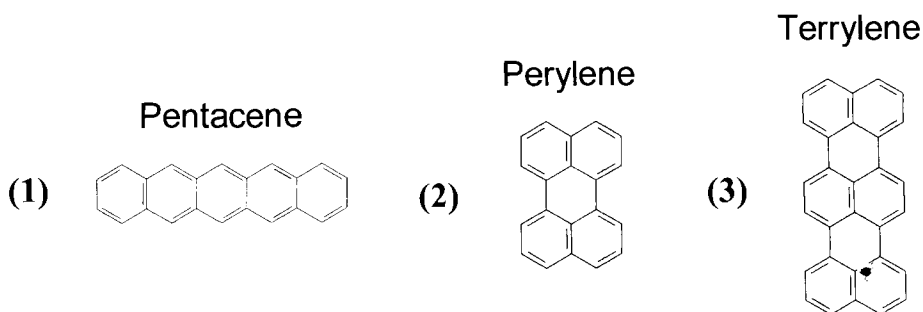
include photodegradation of more sensitive biological systems. Also, transient absorption is difficult to perform on monolayers or in the solid state, where absorption cross-sections are much lower than in solution. For this reason monolayers and thin-film assemblies are generally characterized by fluorescence emission or other more sensitive techniques.

2.2 Systems Consisting of Single Molecules

Perhaps the simplest optically controlled switches are single molecules embedded in a solid host matrix. These systems consist of an amorphous, polycrystalline, or crystalline film doped with dilute concentrations of impurity molecules. The most commonly used dopant molecules are fused polycyclic aromatic hydrocarbons and porphyrins. In addition to facilitate sample preparation, these planar molecules absorb in the visible to near-IR regions of the spectrum, possess large extinction coefficients in both the ground and excited states, and have high fluorescence quantum yields.

2.2.1 Two-level Systems

Theoretically the simplest molecular switch is a two-level system (TLS) consisting of a double well potential in which two near-degenerate states are separated by a potential barrier [151]. Single molecules embedded as dilute impurities in solid media demonstrate TLS properties. The study of these systems for optically controlled molecular switching is an active area of research [152–158]. The most commonly studied impurity molecules are pentacene (**1**), perylene (**2**), and terrylene (**3**). The coupling of single or multiple nearby TLSs results in spectral diffusion in the emission spectra from these single molecules. The TLS behavior may arise from structural relaxation within the single molecule, or more likely from small rearrangements of the surrounding medium. Structural fluctuations in the medium are likely to be coupled to phonon excitations in the impurity molecule. Although initial work on TLSs suggested this effect should be observed only in amorphous solids, it has also been observed in polycrystalline matrices [154] and crystalline [158] solids.



The switching lifetime of the resonance frequency has been observed to exhibit an exponential dependence on the intensity of irradiation [154]. The intensities of the emission lines from each state are proportional to the probability of the TLS population in that site. This ratio is given by

$$\exp(-\Delta E/kT) \quad (1)$$

where ΔE is the energy separation between sites. When many TLSs are coupled to a single molecule, multiple resonance frequencies are observed [154].

Investigation of the microscopic origin of these TLSs has demonstrated the ability to modulate resonance shifts in single molecules by interrogation of neighboring solvent molecules coupled to the system [155]. Doping of poly(methyl methacrylate) with free-base phthalocyanine and small amounts of water shows that reorientation of nearby water molecules is the source of spectral diffusion observed in the phthalocyanine.

These systems demonstrate the possibility that an optical switch can be based on photochemical manipulation of a single molecule's electronic state and local environment. However, these systems also possess several limitations. First, these switching phenomena are observed only at liquid helium temperatures. Second, these systems suffer from photobleaching at relatively low photon densities. Third, single molecules do not allow for broad spectral coverage. Whereas perylene, terrylene, and porphyrins all have large extinction coefficients, their absorption bands are only 20–50 nm wide. In some cases it may be desirable to incorporate light-absorbing antenna complexes to enhance this spectral coverage. By selecting molecules on the basis of their spectral and electrochemical properties it should be possible to cover any region of the visible spectrum. This should also improve the lifetime of these systems because a single molecule need not absorb photons during each clock cycle, which can lead to photodegradation. Fourth, switching events based on a TLS are on the order of seconds to minutes, and are likely to have greater application to optical data storage. Lastly, one cannot take full advantage of the gains in data storage density provided by such systems unless improvements are made in our ability to address single molecules. These experiments are performed in dilute solid solutions wherein single impurity molecules can be easily addressed without interference from neighboring molecules. This technology has yet to be applied to arrays of molecules in close contact with one another. This leap must be made before consideration can be given to devising high-density data storage systems based on TLS switching.

2.3 Photochromic Systems

Photochromic molecules undergo reversible photoinduced color changes based on structural rearrangement. Generally, there is a stable configuration of the molecule which, when irradiated (often with ultraviolet light), undergoes a large change in its absorption spectrum. Conversion back to the original form of the species is com-

monly achieved via irradiation at a second wavelength or by the application of heat. Photochromic molecules undergo efficient internal conversion, taking excited-state electronic energy into vibrational and torsional modes of the molecule. Thus, these molecules are characteristically nonfluorescent.

Photochromic processes are often observed both in solution and in the solid state, thus making for facile incorporation of photochromics in films, in membranes, and as dopants in host matrices—prerequisites for the construction of molecular optoelectronic devices. Section 2.3.1 focuses on the materials and supramolecular systems prepared from photochromic systems. For more comprehensive descriptions of the basic photochemical processes the reader is referred to any of the numerous reviews on the subject [47, 51, 89, 159–162].

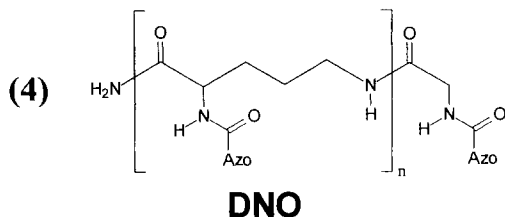
2.3.1 Photoisomerizations

The most basic photochromic systems are those that undergo a light-induced structural rearrangement. Isomerizations often involve large nuclear rearrangements which, for example, can change the symmetry or convert from a linear to bent structure. This property is especially useful for doping of liquid crystals and thin films, in which the microscopic structure of individual dopant molecules can be used to modulate the macroscopic properties of a host system.

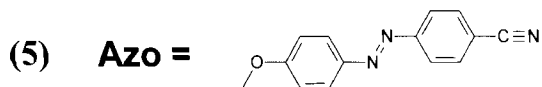
One of the most frequently exploited photochromic processes is the *cis-trans* isomerization of azobenzene. Irradiation of the more stable *trans* configuration with 360 nm ultraviolet light induces conversion to the *cis* isomer, which is stable for long periods in the absence of heat or light. Exposure to moderate heat or irradiation in the visible spectrum induces the transformation back to the *trans* species.

Azobenzenes have been incorporated into monolayers [124, 163], membranes [130, 164], Langmuir–Blodgett films [45, 165, 166], molecular sieves [167], oligomers [168], dendrimers [96, 169], polymers [170], and liquid crystals [116–119, 171–179]. When azobenzenes in an ordered environment are irradiated with polarized light a series of *trans-cis-trans* isomerization cycles is induced until a stable conformation is found. This alignment occurs with the optical transition moment of the azobenzenes oriented in the plane perpendicular to the polarization of the laser beam [180, 181]. The anisotropic alignment of the azobenzenes gives rise to local modulation of the refractive index of the material, forming the basis of optical data storage. In the absence of light or heat the azobenzene alignment is highly robust.

Berg et al. synthesized peptide oligomers that incorporated 4-cyanoazobenzene for erasable holographic data storage [168]. The oligomer is a diamino acid- N^{α} -substituted peptide (DNO) repeat unit, compound **4**, with an azobenzene side chain



(5). The DNO backbone imposes a helical stacking on the azobenzenes similar to that observed in DNA, with a twist angle of 36° between adjacent azobenzenes, as shown in Figure 1. Most importantly, the helical stacking imposed by the oligo-peptide limits considerably the number of potential stable stationary orientations that the azobenzenes may assume upon irradiation.



The DNO oligomers were cast as isotropic films $5\text{ }\mu\text{m}$ thick. Optical writing was achieved by overlapping two beams of circularly polarized 488 nm light from a continuous-wave argon ion laser at 2 W cm^{-2} . The writing time was observed to depend on the oligomer length, with the most efficient gratings forming in decamers ($n = 10$), implying a cooperative dynamic effect between adjacent azobenzene units. Optical reading was performed with the circularly polarized 633 nm output from a He:Ne laser at 4.2 mW . The gratings could be erased by irradiation with a single beam of circularly polarized 488 nm light. No fatigue in the system was observed for several read–write–erase cycles. The authors also discuss the effects of oligomeric stereochemistry, size, and side chain flexibility.

A second type of isomerizable system is a chiral molecule that can be photo-switched between two enantiomers. Changing the handedness of the light used for writing controls the relative concentrations of each enantiomer, and can provide the basis for a molecular switch. Each enantiomer has the same absorption spectrum

4 - UNIT HAIRPIN

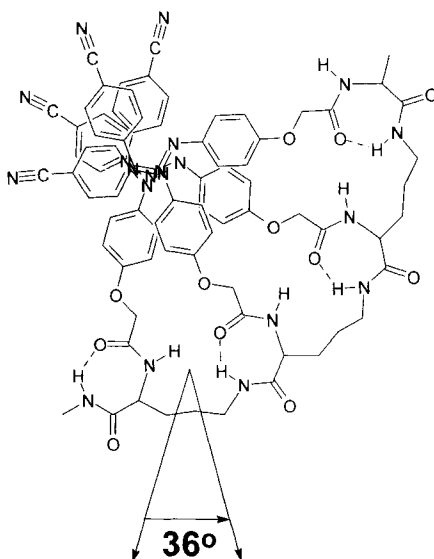
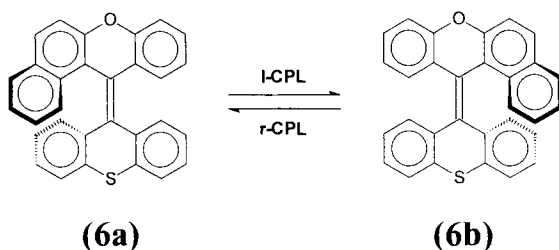


Figure 1. The oligomer (4) forms a single-stranded helix in which adjacent azobenzene side groups are off-axis from one another by 36° . This stacking arrangement is nearly identical to that observed in DNA base pairs.

but the left- and right-handed isomers can be differentiated on the basis of their ability to rotate incident polarized light used for reading the state of the system [77, 78, 102, 127, 182].

An example of such a system is 12-(9'*H*-thioxanthene-9'-ylidene-12*H*-benzo[*a*]-xanthene, which can exist in two distinct states, compounds **6a** and **6b**. The free energy barrier for racemization is 25.9 kcal mol⁻¹. Irradiation of the **6a** isomer with circularly polarized light (CPL) at 300 nm resulted in photoisomerization to the **6b** isomer. The same wavelength of light was used for reading the state of the system, although with linear polarization. Circular dichroism (CD) measurements detect an ensemble average of a local domain determined by the spot size of the laser beam, and thus the racemic conversion need not be quantitative. The anisotropy factor [183] of the system determines the racemic excess that can be formed, and in hexane solutions of **6a** and **6b** an enantiomeric excess of only $\pm 0.07\%$ was achieved. However, this was easily detectable in the CD spectrum. The system is “erased” using linearly polarized 300 nm light. This effect was also demonstrated in the nematic phase of liquid crystals. Thus, such a system can be used as an optical switching device with the advantage of employing a single wavelength of light for writing, reading, and erasing. The same research group also synthesized a system in which the absorption spectrum was shifted to the visible part of the spectrum [77]. Operation at these more convenient wavelengths was achieved by the addition of electron-donating [$-\text{N}(\text{CH}_3)_2$] and -withdrawing groups ($-\text{NO}_2$) on the xanthene chromophore which produced an absorption at 435 nm. Furthermore, substitution of a sulfur atom at the 1-position of the xanthene resulted in a more robust switch.



Photoisomerizations can often occur by several different mechanisms. Systems that isomerize via a controlled mechanism are potential candidates for molecular machines [184]. Energy in the form of light is absorbed and converted to controlled mechanical force on the molecular scale. Examples of a mono-directional rotor [185, 186], a switchable rotor [187], and a molecular shuttle [188] have been demonstrated. These systems are light-controlled, but there are also examples of systems which control molecular motion based on electro- and/or chemical modulation, such as the threading/unthreading of (pseudo)rotaxanes [189–196].

Biological molecules are often switched on and off by controlling the ligation environment or oxidation state of a metal center. The selective binding of ions [104, 197] and modulation of the binding environment of metal centers [79, 92, 198–204] have also been demonstrated as mechanisms for switching. The second of these examples is based on chemical modulation of the valence state of a metal or its

ligands, which induces nuclear rearrangement. This same principle can also be applied to organic chromophores.

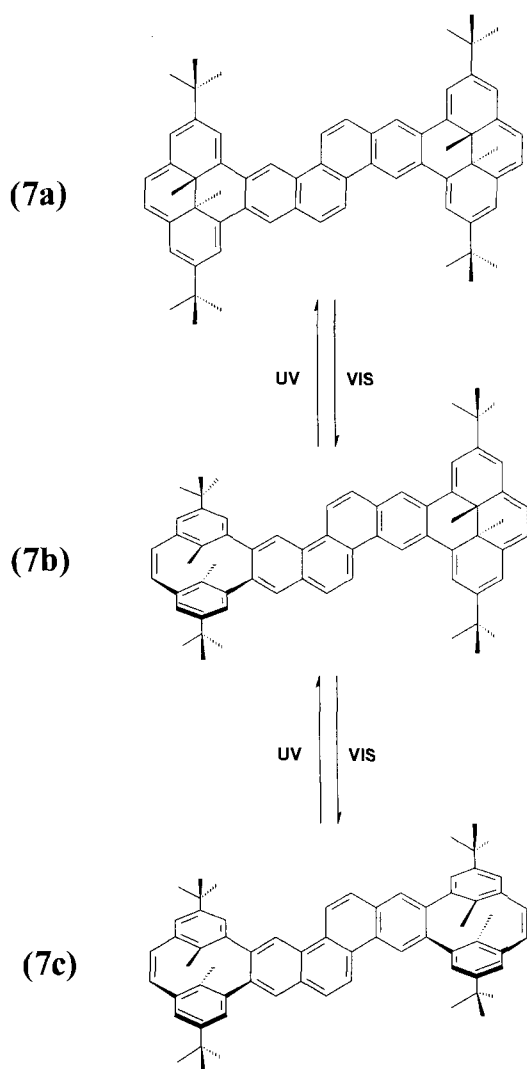
A problem in constructing memory devices from photochromic systems is the inability to read the state of the switch nondestructively. Irradiation with visible light oftentimes leads to photodegradation, and erases the data after several read cycles. Thus, it is desirable to have some other means of reading the state of a switch: for example, the measurement of refractive index, IR absorption, or optical rotation. Another approach is to couple two reversible processes, such that once written to, the switch can be locked into a particular configuration. This can be effected electrochemically, via absorption of a second photon, or through binding of a free metal ion or proton. In essence, one has created a three-level switching system.

Most switches based on isomerizations are bistable; there are few examples of tristability [97, 98] or greater. Higher orders of stability in a single molecule preclude the need for high connectivity between adjacent switches. Thus, one switching device could accomplish the same logic operation as two switches linked together. One such example of a tristable organic molecular switch is a system that incorporates two dimethyldihydropyrene (DHP) units via a conjugated naphthalene bridge [97]. The switch is based on the photoinduced valence isomerization between the fully conjugated compound, **7a**, which contains two DHP groups and the nonconjugated bis(cyclophane)diene (CDP), compound **7c**. Irradiation with 427 nm light induced the **7a** \rightarrow **7b** \rightarrow **7c** switching process, resulting in the formation of a band in the ultraviolet region ($\lambda_{\text{max}} = 268$ nm) of the spectrum. The nonconjugated system was returned to its original state via irradiation at 313 nm, and furthermore displayed no degradation after 80 switching cycles. The advantage of this three-level system is that it is all-optically controlled; however, it is also difficult to stop at the intermediate state (**7b**). The creation of three-level systems in which all the forms are stable and distinguishable generally leads to coupling some other switching mechanism to a photochromic property.

A three-level switching device has been demonstrated in which photochromic properties are used to control electrical properties, and vice versa. Such a system has been realized in the form of thiophene bisphenol [90, 91]. Conversion of the open (**8a**) to the closed (**8b**) form of the thiophene was achieved by absorption of 312 nm light, and reversed by absorption of 600 nm light. The bisphenol oxidation occurs at +0.735 V (vs. SCE), forming the closed-ring bisquinone, compound **8c**. This species has large absorptions at 400 and 534 nm. The optical properties of the quinone–phenol couple have previously been used in a bianthrone-based system [87]. The bisquinone (**8c**) cannot be converted to the open thiophene, and locks the system in the closed form. The thiophene has also been incorporated as a component in two-level molecular switches [99, 128] and switchable molecular wires [30].

2.3.2 Open–Closed Ring Systems

Perhaps the most promising materials for all-optical write–read–erase switches are systems in which ultraviolet irradiation induces ring opening. One of the most studied systems are spiropyrans in which writing and nondestructive reading are based on successive two-photon and one-photon processes [46, 205–209].



Rentzepis and co-workers have employed spiropyran in methanol and a variety of polymer matrices [6], creating a three-dimensional arrangement of switching sites. Sites are selected within the polymer matrix via temporal and spatial overlap of two orthogonal laser beams tuned to the same or different wavelengths. The closed form of the spiropyran absorbs in the near-UV and was excited via two-photon absorption, from either the fundamental and second harmonic (355 nm), or two photons of the second harmonic (266 nm) output from a 1064 nm Nd:YAG laser. Rapid conversion to the open form placed the system in the “on” state and induced an absorption at 600 nm. This open system is also fluorescent, and excitation with either two photons of the fundamental or a single photon of the second harmonic (both 532 nm) resulted in a red-shifted emission. An energy level diagram of this system is shown in Figure 2. Writing to, addressing, and reading from the

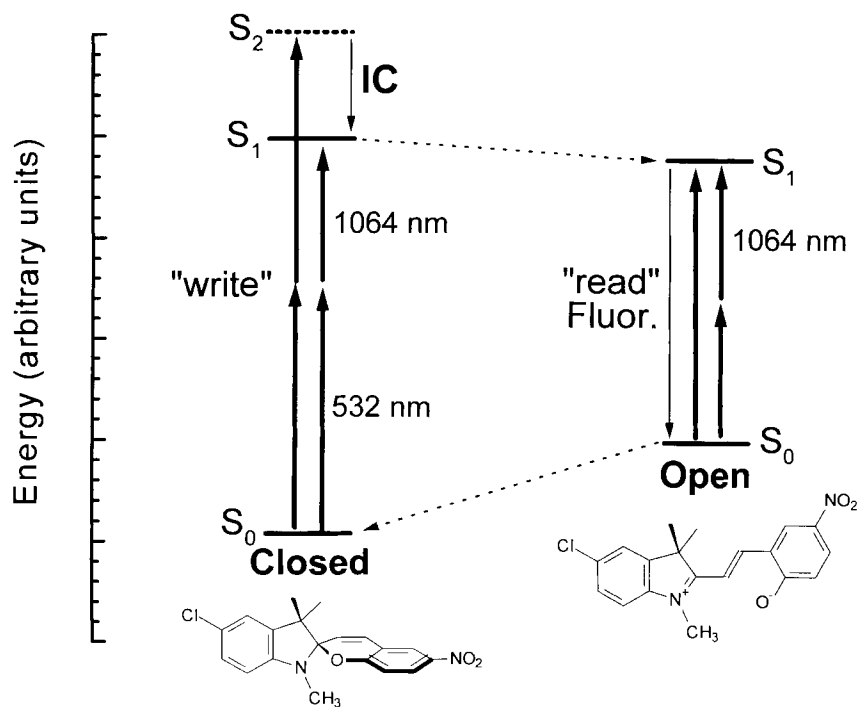
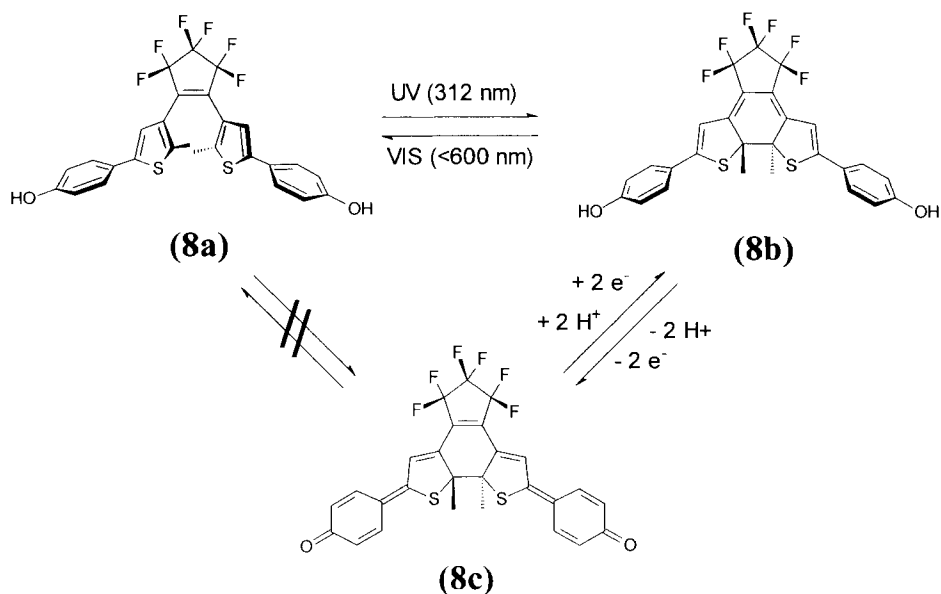
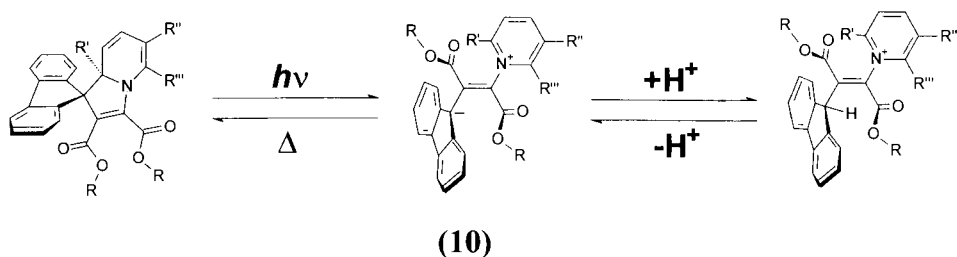
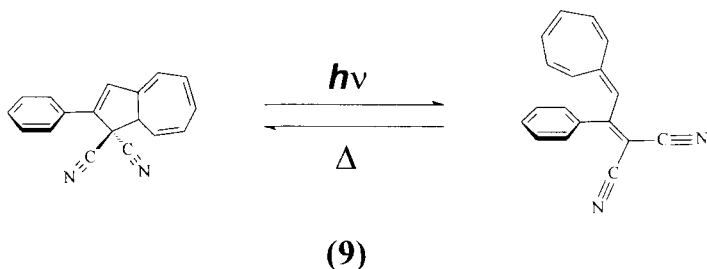


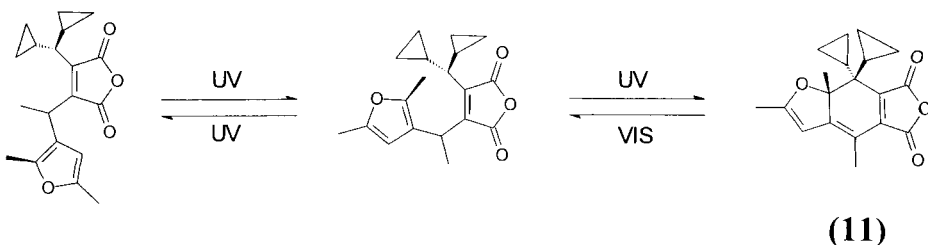
Figure 2. Two-photon excitation of the closed spiropyran to the S_1 or S_2 state results in ring opening, and fluorescence from the S_1 state of the open-ring merocyanine species. The latter is stable and can be accessed for numerous “read” cycles via two-photon excitation with 1064 nm light. Switching back to the closed-ring spiropyran is achieved with mild heat.

sites all occur in different regions of the spectrum so that there is no cross-talk. This system is attractive because of the potentially high density of switches, parallel addressing capabilities, high sensitivity, and low cross-talk. Applying heat switched the system back to the closed-ring form. Further work has implemented spiropyrans as side groups on polymers [210], as dopants in films [211], and as single crystals [100]. This two-photon technique has also been implemented for the dimerization of anthracene [212] and the salicylideneaniline systems [213], in which the mechanism is proton transfer instead of ring opening.

The dihydroazulene–vinylheptafulvene couple (**9**) [85, 98], dihydroindolizine (**10**) [95], and fulgides are further examples of photochromic open–closed ring systems



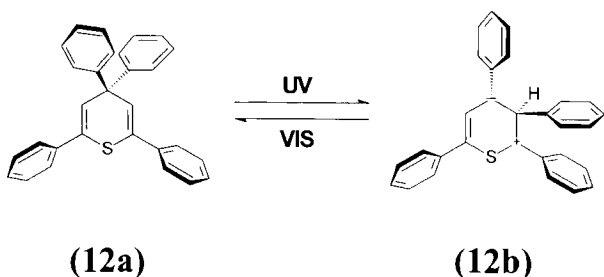
that are potential three-level systems. Fulgides are derivatives of dimethylene-succinic anhydride, and their deactivated colorless form consists of *cis* and *trans* isomers, of which only the latter is convertible into the activated colored form [88, 214–217]. Similarly to spiropyran systems, fulgides consist of an open and closed ring system, and retain their photochromic properties when doped in films [94, 216, 218, 219] and liquid crystals [220]. The three forms of the 111D fulgide (Lancaster) can be interconverted based on their absorption of UV and visible light. Ultraviolet light induces a buildup of the closed form (**11**), which has a large absorption in the



visible region of the spectrum ($\lambda_{\text{max}} = 562 \text{ nm}$). The formation of **11** depends on the relative rates of the UV-initiated processes. The incorporation of fulgides into films presents the possibility of a molecular switch whose visible absorption or transmission can be modulated by UV light. Poly(methyl methacrylate) films of $1.2 \mu\text{m}$ thickness were doped with **11** and 611TD fulgide (Lancaster) [216]. Transmittance of visible light measured at 532 nm was modulated by irradiation of a pulsed UV emission, which resulted in 50 % attenuation of the visible transmittance.

2.3.3 Photorearrangements

Aromatic systems are apt to undergo rearrangements when irradiated with ultraviolet light. When the photoproducts are stable compounds with distinct absorption spectra, these reactions lend themselves to the construction of solid-state optical switches. One such system is 1-nitronaphthaldehyde [49]. A second system is the 2,4,4,6-tetraphenyl-4*H*-pyran and pyridine systems. They undergo a photoinduced rearrangement, converting compound **12a** to **12b** [83, 84]. The nonconjugated zwitterionic species (**12b**) has an absorption in the visible region which can be tuned by applying the appropriate electron-donating or -withdrawing substituents to the various phenyl rings [86].



There is no limit to the number of photochromic systems possible. The systems discussed are excellent candidates for integration into solid-state devices because nearly all retain their photochromic properties in the absence of solvent. The organization of these systems in tandem with other molecular systems is being pursued. For the switching applications many of these systems have much too slow a turn-over rate to be explored as working devices. That is unless the connectivity in these systems can be increased. In the meantime, photochromic systems will probably be explored as possible optical memory devices. The most promising switches are those based on the much faster processes of electron and energy transfer. We will now examine research in these areas.

2.4 Electron Transfer Based Systems

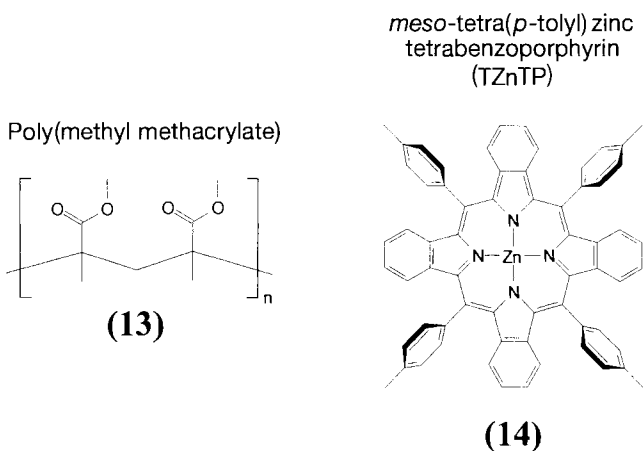
Theoretical work strongly supports the idea that an electron transfer reaction can form the basis for a molecular switch [12, 48, 221–223]. Yet the field has been slow to develop because the optimal use of electron transfer processes requires careful

control of molecular structure, electronic coupling, and thermodynamics in a complex array of donors and acceptors.

2.4.1 Intermolecular Electron Transfer

Photoinduced spectral hole burning [67–76] uses small fluctuations in the local environment to store bundles of information in a single molecule. In these systems the presence (or absence) of a spectral hole at a particular frequency is utilized to encode numerous bits of digital information within a single focused laser spot. In some systems the absorption of two photons encodes the data, while the readout is performed with a one-photon process [71]. These systems have the advantage of greatly increased readout speeds allowing for fast switching in small laser spots.

Carter and co-workers demonstrated spectral hole burning via an intermolecular electron transfer mechanism. In this experiment poly(methyl methacrylate) (**13**) films were doped with zinc tetrabenzoporphyrin (**14**) electron donors and chloro-



form (CHCl₃) electron acceptors. The formation of gated holes occurred when both the singlet–singlet and triplet–triplet absorptions were excited, as seen in the Jablonski diagram in Figure 3. Excitation of the ground state with 627 nm light (λ_1) results in triplet population with a quantum yield of 0.8. The lifetime of the triplet state is $\tau = 39$ ms. If a second photon arrives before this state decays then triplet–triplet transitions can occur. This excited state readily donates electrons to nearby acceptors, in this case chloroform molecules. The color of the second photon need not be specific, although the highest yield for electron transfer occurred with $\lambda_2 = 488$ nm. Electron transfer from two-photon absorption results in hole formation in the singlet manifold, and the observed photobleaching. The energy of the reduced CHCl₃ was not determined, but this system is likely to work with other electron acceptor groups. It is unclear if the free electrons can migrate between chloroform molecules, adding to the stability of the system; this is likely, however, considering the high concentrations of CHCl₃ used. Optimal electron transfer was

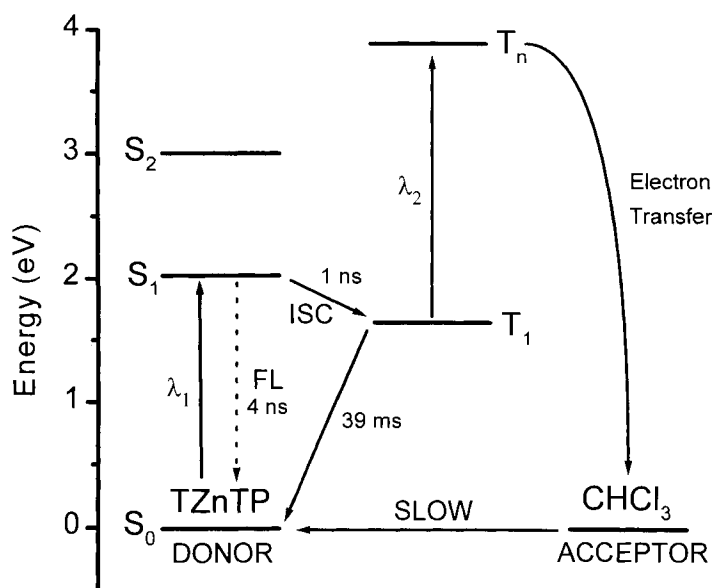


Figure 3. Energy level diagram for the zinc tetrabenzoporphyrin donor–chloroform acceptor system.

observed when chloroform was used in a molar excess of $10^5:1$. Furthermore, a weak electron acceptor such as chloroform makes the charge recombination a highly Marcus inverted process.

In their current form these systems have far more application to the construction of high-density optical memory devices. Several fundamental issues remain to be resolved before single molecules are widely used. At present these switching effects are observed only at liquid nitrogen temperatures or below. It should be possible to observe the same effects at ambient conditions. Also, cross-talk between molecules is likely to occur as the concentration of the dopant molecules increases and nearest neighbor interactions become important. But this may not be a problem, as the density of states should also increase in this situation, making possible even greater gains in the data storage capacity. It is clear that many of these questions will not be answered until the experiments are performed. Work on the single molecule level can also lend insight to covalently bound systems consisting of multiple subunits. We now examine such systems.

2.4.2 Intramolecular Electron Transfer

Covalently linked arrays of electron donors and acceptors can be used to perform switching operations. In addition, systems can be designed to store and transport digital information. One can tune both the optical and electrochemical properties of a multicomponent system by selecting the appropriate electron donors and ac-

ceptors. These systems are inherently more complex, yet allow for a wider range of applications than devices based on single molecules. Generally these systems consist of an input chromophore, a bridging group, and an output chromophore. Absorption of a photon results in one of two processes: stepwise photoinduced electron transfer resulting in a charge-separated state, or energy transfer followed by fluorescence.

An early hypothesis for a molecular switch based on stepwise photoinduced electron transfer appeared in 1988 [48]. The design describes a polymer consisting of a $[D-A_1-A_2]_n$ monomer unit wherein D is an electron donor moiety and A_1 and A_2 are primary and secondary electron acceptors, respectively. The system is designed to form a rigid photoactive chemical bridge capable of storing and transferring digital information between two electrodes. This is done via the synchronization of two processes: oxidation/reduction of the termini at an electrode and photoexcitation of the electron donor within the polymer.

The clock cycle for the switching process begins with photoexcitation of every electron donor in the polymer, forming the $[^1D-A_1-A_2]_n$ state. There are three potential deactivation pathways from this state to consider: fluorescence back to the ground state (dot), forward electron transfer to A_1 (solid), or backward electron transfer to A_2 in the adjacent monomer unit (dash-dot). A HOMO/LUMO scheme for these processes in the first three units of such a polymer is shown in Figure 4(a). The donor-terminated end of the polymer can decay only via the first two paths. It should be relatively simple to enhance the coupling between 1D and A_1 so that forward electron transfer is the preferential process. Spontaneous thermal electron transfer resulting in the state $[D^+-A_1-A_2^-]_n$, Figure 4(b), follows this initial charge separation step. This places free electrons and holes adjacent to one another on neighboring monomers. The basis for switching in this system is that electron tunneling between monomer units in this state (solid), which results in charge recombination, is kinetically preferred over charge recombination to the ground state within a single $[D-A_1-A_2]$ monomer (dash-dot). If one can control the electronic coupling to favor charge recombination across the unit, this leaves a single hole on the donor adjacent the cathode. The next phase in the clock cycle is the data writing process, which is done electrochemically. If cathodic current flows and returns the donor to its ground-state electronic configuration, then photoinduced electron transfer can occur from this donor site during the next clock cycle. However, if no reduction occurs, the hole will propagate along the polymer during the next clock cycle, leaving positive charge on the first two electron donors in the system. The holes are read out at the anode as 0s. The system must register n cycles before data entered at the cathode are read at the anode.

The authors discuss several parameters related to optimizing the efficiency of such a device. First, the chromophore that is photoexcited must possess a distinct absorption band having a large extinction coefficient. Other chromophores in the polymer should not absorb in this spectral region. The second concern is the ability for charge recombination to occur between monomer units. This process must be favored over charge recombination within a single monomer, or a switching error occurs. The free energy for each process is identical, and thus preference for one path over the other is based exclusively on the electronic coupling between the var-

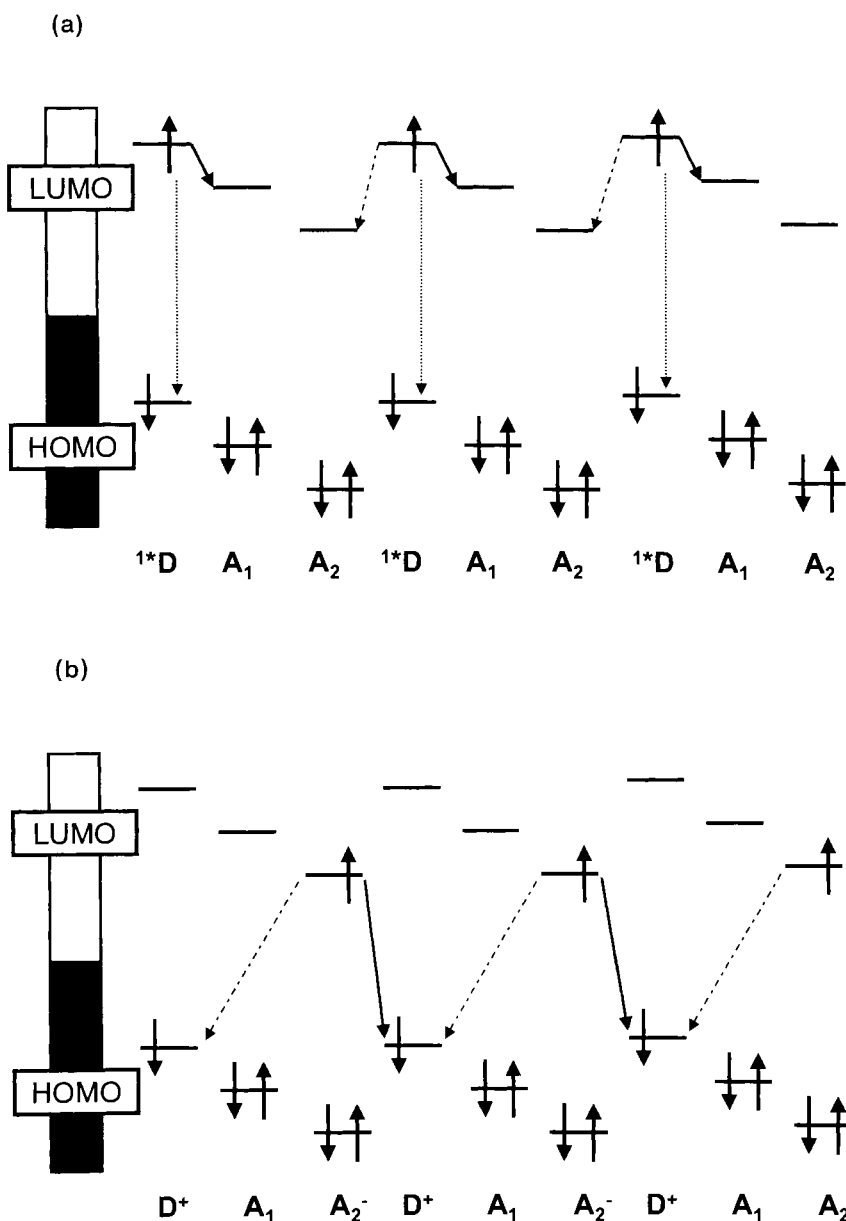


Figure 4. HOMO/LUMO scheme for operation of a proposed molecular shift register [48]. a) The clock cycle is initiated by photoexcitation of the donor moiety, resulting in the electronic configuration shown. Decay pathways from this excited state are forward electron transfer within the same monomer unit (solid), back electron transfer to the adjacent monomer unit (dash-dot), and fluorescence (dot). b) Electronic configuration resulting from successive forward electron transfer steps. The charge-separated state $[D^+-A_1-A_2^-]_n$ can recombine charge within a single monomer unit (dot-dash) or with the adjacent monomer unit (solid).

ious sites. There are many examples of molecules with long-lived charge-separated states that would be appropriate for such a system. Even if tunneling through the barrier separating monomer units were slow, on the order of hundreds of nanoseconds, this could be much faster than charge recombination within the $[D-A_1-A_2]$ monomer. Bottlenecks can be avoided by encoding data to the polymer only on alternate clock cycles. This also improves the yield for charge shift between monomers. Thus, if tunneling had a quantum efficiency of 0.95, after two clock cycles this improves to 0.99 for transfer from a single monomer to the next. However, even a device with 99 % efficiency is not sufficient for a polymer with more than several repeat units. For a polymer of 100 repeat units the yield of transmission for a single bit through the polymer drops to 36 %. Many systems have been designed which undergo highly efficient long-lived charge separation appropriate for such a device [132, 224, 225], but as of yet no working system has been constructed.

In the proposed device the transport of holes is the basis for data transmission; however, polymeric and oligomeric systems capable of soliton propagation have also been synthesized and studied [15, 17, 32, 33, 35, 36, 38, 40, 43, 226]. Further examination shows that one could operate this system to transport negative charge along the polymer. In this scheme the clock cycle begins with the electrochemical encoding of data into the polymer. Reduction (or lack of reduction) of the ground electronic state of the donor adjacent to the electrode places a free electron into its LUMO. This reduced species undergoes spontaneous stepwise thermal electron transfer until the negative charge is localized on the last acceptor group in the first monomer, Figure 5(a). Radical anions of many organic chromophores have distinct spectral signatures with large extinction coefficients. Selective photoexcitation of the $[D-A_1-A_2^-]$ state gives an excited doublet state, with the electronic configuration shown in Figure 5(b). Optical switching is achieved by preferential charge shift from this excited state to the LUMO of the donor in the next monomer unit. Competitive charge shift to the adjacent acceptor will result in switching errors.

While such a device has not yet been constructed, Debreczeny and co-workers synthesized and studied a linear $D-A_1-A_2$ triad suitable for implementation in one [227]. In this system, compound **15**, a 4-aminonaphthalene monoimide (ANI) electron donor, is excited selectively with 400 nm laser pulses. Electron transfer from the excited state of ANI to A_1 , naphthalene-1,8:4,5-diimide (NI), occurs across a 2,5-dimethylphenyl bridge with $\tau = 420$ ps and a quantum yield of 0.95. The dynamics of charge separation and recombination in these systems has been well characterized [228]. Spontaneous charge shift to A_2 , pyromellitimide (PI), is thermodynamically uphill and does not occur. The mechanism for switching makes use of the large absorption cross-section of the NI^- anion radical at 480 nm ($\epsilon = 28\,300$). A second laser pulse at 480 nm can selectively excite this chromophore and provide the necessary energy to move the electron from NI^- to PI. These systems do not rely on electrochemical oxidation–reduction reactions at an electrode. Thus, switching occurs on a sub-picosecond time scale.

Excitation of the NI^- anion radical within ANI^+-NI^-PI with a 480 nm laser pulse rapidly forms the $ANI^+-^*NI^-PI$ excited doublet state. Its electronic configuration is analogous to that in Figure 4(b). There are two pathways for decay from this excited state: charge recombination back to yield the 1ANI excited state or charge shift to PI. The driving force for each of these paths is nearly identical, and

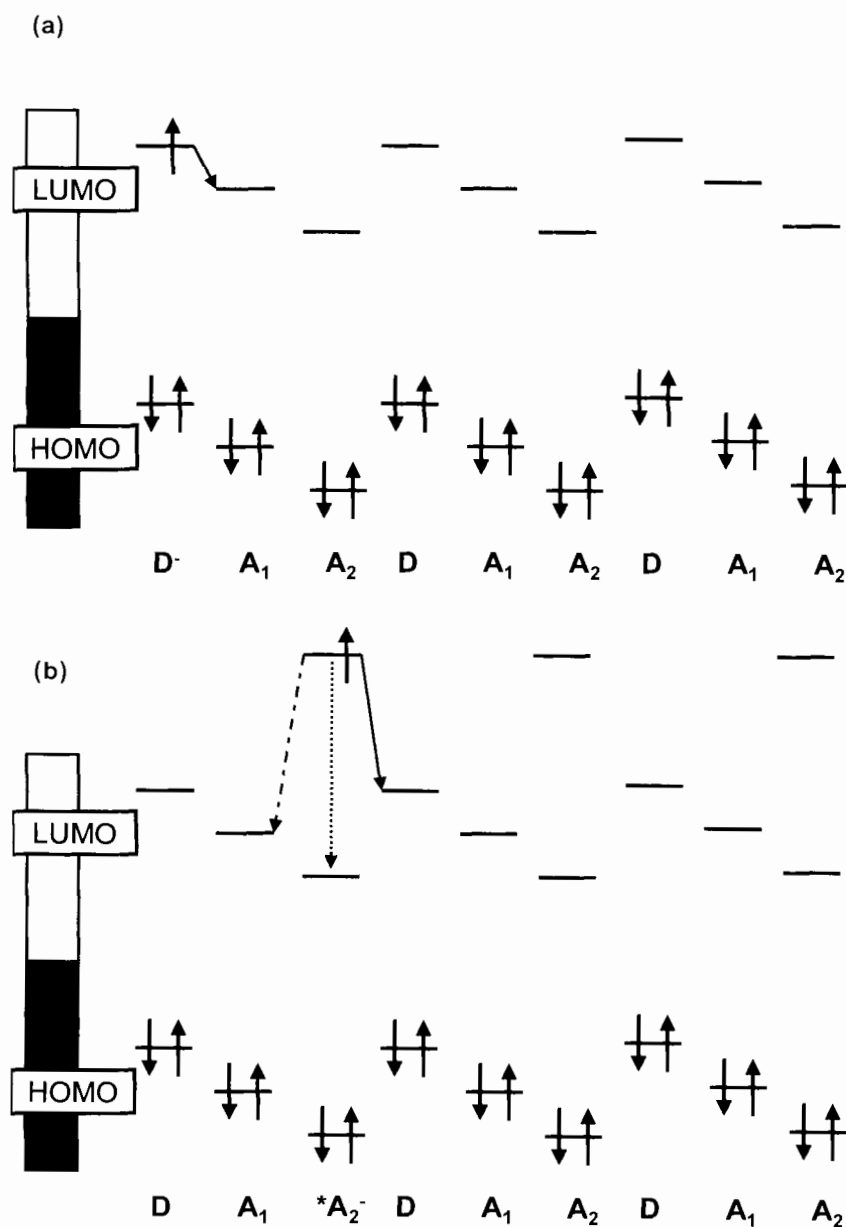
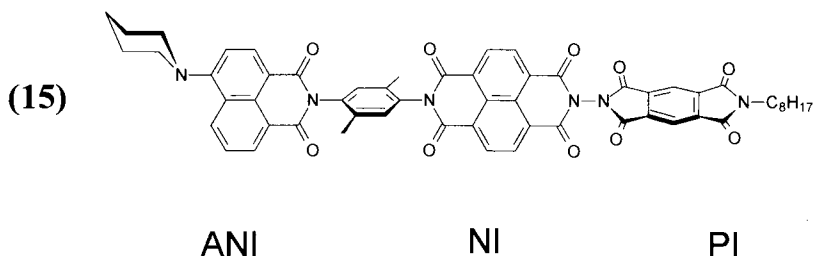
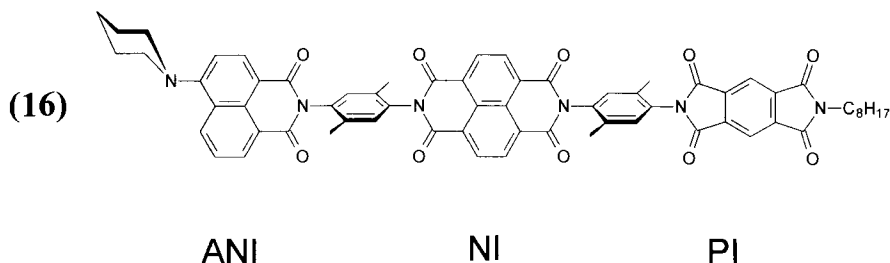


Figure 5. HOMO/LUMO scheme for a modified molecular shift register in which bits are encoded and propagate as free electrons instead of the hole transfer based system described in Figure 4. a) Data are encoded via electrochemical reduction of the donor moiety adjacent the cathode, resulting in the electronic configuration shown. Subsequent stepwise thermal electron transfer localizes the free electron on A₂. b) Excited doublet state resulting from photoexcitation of this species; it can decay via forward electron transfer (solid), back electron transfer (dash-dot), or internal relaxation processes (dot). Tuning of the energetics and electronic coupling to favor the forward electron transfer pathway propagates the charge to the next monomer unit.

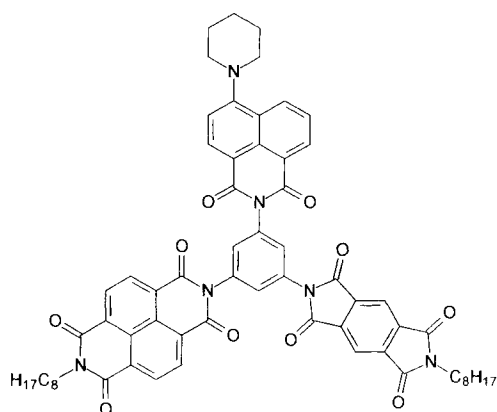


thus the yield for each process is determined by electronic coupling. The electronic coupling between NI and PI is much greater than that between NI and ANI because no phenyl bridge separates them. As expected, this is the preferential path for deactivation, and can be observed directly by monitoring the formation of PI^- at 720 nm. Charge shift to PI occurs with $\tau = 300$ fs and a quantum yield of 0.88. The overall yield for the switching process is 0.84.

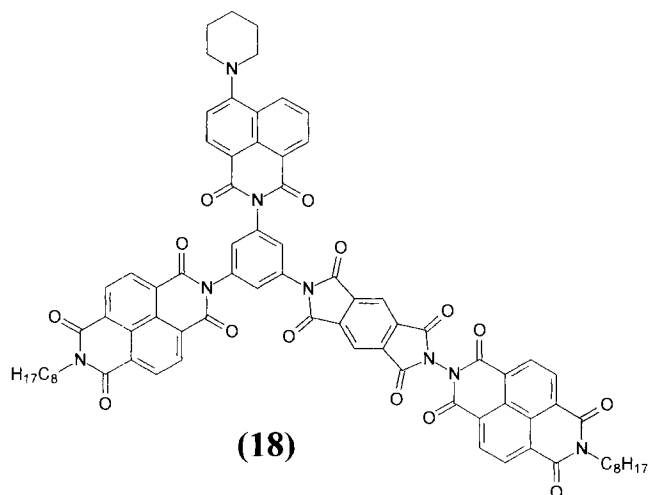
The electronic coupling can be changed by the insertion of a phenyl bridge between the NI and PI, compound **16**. Identical excitation of the NI^- with 480 nm laser pulses results in a much slower charge shift to PI, $\tau = 4$ ps, and a quantum yield of only 33 % [229]. It is clear that, as hypothesized, the ability to control electronic coupling between various sites is the determining factor in realizing the construction of a working device. However, enhancing the electronic coupling to favor the charge shift reaction from NI^- to PI also increases the rate for back electron transfer from PI^- to NI. The PI^- state undergoes back electron transfer to NI with $\tau = 600$ fs in **15** and $\tau = 312$ ps in **16**. It is likely that the addition of a third electron acceptor attached to PI could provide a lower-energy electronic state into which the system could relax, thereby reducing back electron transfer to NI. This would be more analogous to the polymeric systems described earlier.



Recent work has investigated the potential to control the partitioning of charge in branched arrays [230]. This has many potential applications to the development of photoactive networks and dendritic systems capable of electron transfer. Compounds **17** and **18** employ 1,3,5-triaminobenzene as the central branch point. In each molecule ANI is attached to the 1 position and serves as the electron donor. The electron acceptors again are NI and PI, and are attached to the 3 and 5 positions, respectively in compound **17**. Excitation of ANI with 400 nm laser pulses results in electron transfer exclusively to the NI branch. This is due to the 0.3 V



(17)



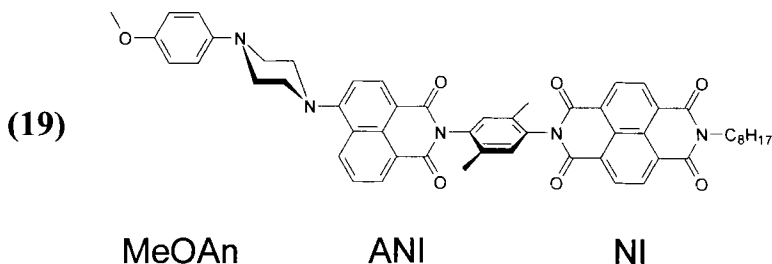
(18)

difference in reduction potentials between NI and PI. Excitation of NI^- within $\text{NI}^- - \text{ANI}^+ - \text{PI}$ with 480 nm laser pulses 2 ns after formation of this initial ion pair results in formation of an excited doublet state. This excited state can decay via charge recombination back to ANI or charge-shift to PI. The 720 nm absorption band of PI^- appears with $\tau = 600$ fs, and a quantum yield of 0.44. Competitive charge recombination to the $^1\text{ANI}^*$ excited state also occurs quite rapidly, $\tau = 500$ fs, and is the reason for the observed yield. The $\text{NI}^- - \text{ANI}^+ - \text{PI}^-$ state is 0.3 eV above that of the $\text{NI}^- - \text{ANI}^+ - \text{PI}$ state, and 2.7 eV above the ground state. Charge recombination to the ground state is a Marcus inverted process, and thus charge shift back to the initial charge-separated state, $\tau = 400$ ps, is the exclusive decay path. The lifetime of the electron on the second branch of the system was significantly enhanced by the addition of a lower-energy acceptor on the end of PI, in this case a second NI moiety. In compound **18** the rate of switching from branch 2 back to

branch 1 is $\tau = 2$ ns; however, the yield for the initial switching between branches decreases to 0.36.

The spin properties of charge-separated ion pairs can also be exploited for the purposes of all optical switching. Radical pair intersystem crossing (RP-ISC) of the form $^1[D^+-A^-] \rightleftharpoons ^3[D^+-A^-]$ to yield the spin-correlated triplet state is observed in the photosynthetic reaction center, but is seen rarely in synthetic systems. The reason for this observation is that the spin–spin interactions are generally strong, even in systems which undergo charge separation over large distances. However, the time for charge recombination within the triplet manifold is usually very different than that of the singlet state. An all-optical switch based on this property can be devised by controlling the rate, and thus the yield, of the intersystem crossing.

Wasielewski and co-workers [110] developed the first multistep donor(1)–donor(2)–acceptor molecule, MeOAn–ANI–NI, compound **19**, that mimics all of the primary spin-dependent charge separation and recombination dynamics of the photosynthetic reaction center. This makes it possible to use the same strategy as an entry point to a molecular switch based on photocontrollable spin dynamics. Transient absorption spectroscopy carried out on **19** in toluene determined the nature of the intermediates and the rate constants for intramolecular electron transfer between the electronic states in the energy level diagram displayed in Figure 6. At 295 K excitation with 420 nm, 130 fs laser pulses selectively excites the ANI chromophore within MeOAn–ANI–NI. The lowest excited singlet state of ANI accepts an electron from MeOAn with $\tau = 8$ ps. A subsequent dark electron transfer step with $\tau = 430$ ps forms the final radical ion pair, $^1[MeOAn^{+*}-ANI-NI^-]$, with a lifetime of 310 ns. Photoexcitation of **19** oriented in a solid liquid-crystal matrix results in the two broad electron paramagnetic resonance (EPR) spectra, shown at two orientations in Figure 7, with additional narrow lines superimposed at the center of the spectra. The broad spectra are due to a triplet state.



In all covalent electron donor–acceptor systems produced earlier, triplet states observed by EPR were formed via a spin–orbit intersystem crossing (SO-ISC) mechanism. Another possible mechanism of triplet formation is RP-ISC, mentioned above, which results from radical ion pair recombination, and which had been observed previously by time-resolved electron paramagnetic resonance spectroscopy (TREPR) only in bacterial reaction centers and in the green plant Photosystem I and II reaction centers. These two mechanisms can be differentiated by the polarization pattern of the six EPR transitions at the canonical orientations. In SO-ISC,

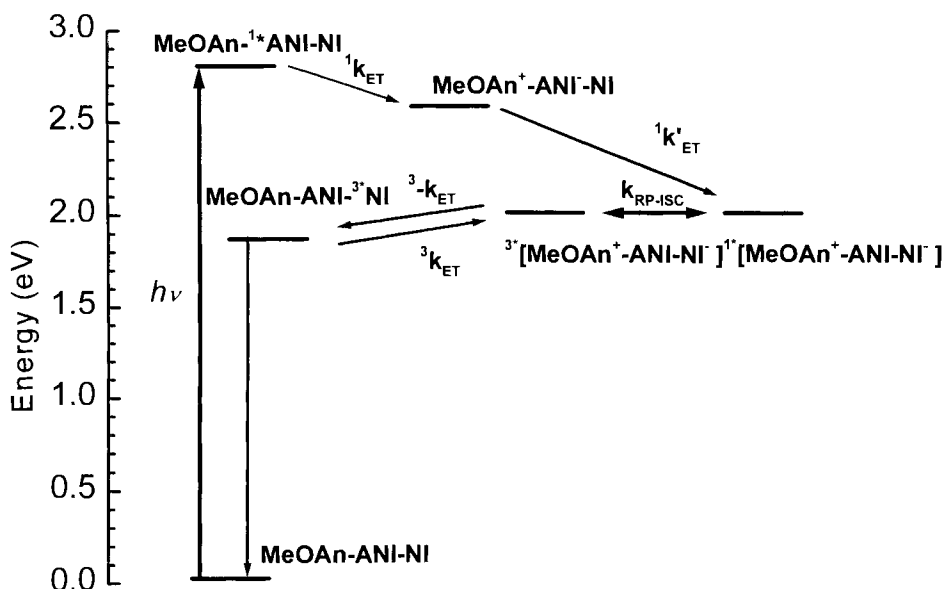
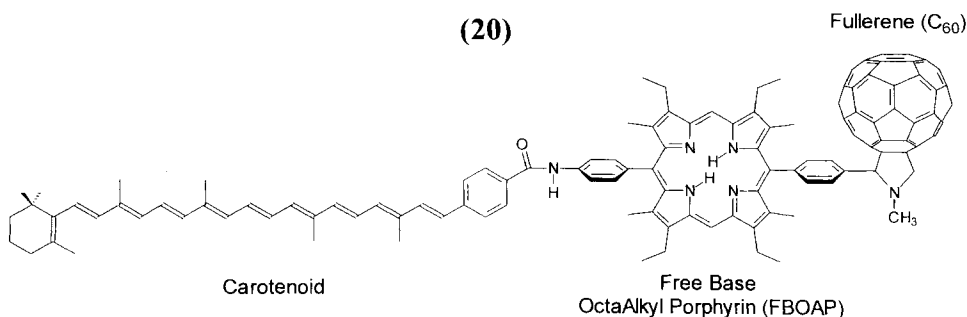


Figure 6. Energy level scheme for **19**. Internal conversion occurs in the fully charge-separated state to give the triplet. Charge recombination gives the T_1 state localized on the NI chromophore.

the three zero-field levels are selectively populated and this selectivity is carried over to the high-field energy levels. RP-ISC is also selective, but acts directly on the high-field triplet sublevels via singlet–triplet mixing $S-T^0$ (or $S-T^{\pm 1}$). Thus, SO-ISC results in mixed absorption (a) and emission (e) lines within a particular EPR transition, i.e., $T^i \leftrightarrow T^0$ ($i = \pm 1$), while in RP-ISC a mixed polarization pattern is impossible. Inspection of the triplet spectra (Figure 7) in the $B \perp L$ and $B \parallel L$ orientations shows that the polarization pattern of a,e,e,a,a,e can only be attributed to an RP-ISC mechanism, as found for reaction center proteins. This unique triplet state is localized on C, and exhibits zero-field splitting parameters identical to those obtained by direct observation of C itself.

In a subsequent study, Gust and co-workers synthesized and studied a compound **20**, consisting of a carotenoid and free base octaalkyl porphyrin (FBOAP) electron



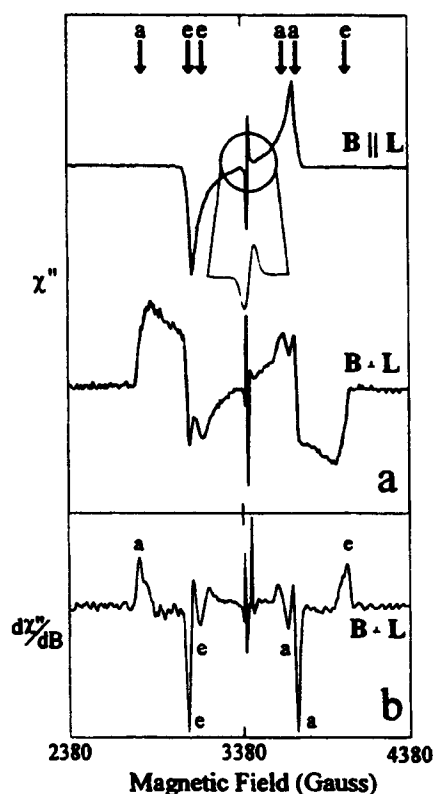
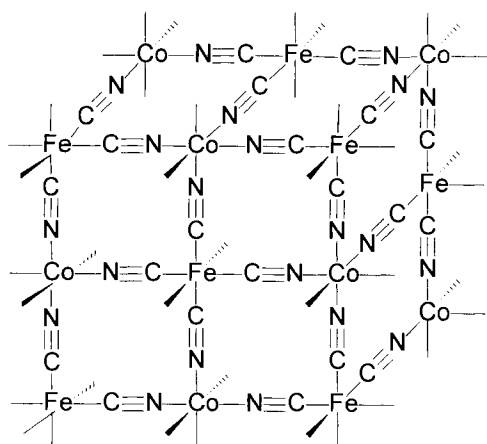


Figure 7. a) Direct detection TREPR spectra of MeOAn-ANI-^{3*}NI in the nematic liquid-crystal mixture E-7 (Merck) at two orientations of the liquid-crystal director, L, taken 700 ns after a 420 nm laser pulse at 150 K. The narrow signal is an expansion of the radical pair signal. b) Numerical differentiation of the B ⊥ L spectrum.

donors, and a fullerene (C₆₀) electron acceptor [231]. In the fully charge-separated state this molecule decays exclusively to the triplet. The lifetime of the excited triplet state can be modulated by applying an external magnetic field at 77 K [111]. Excitation of the FBP with 416 nm laser pulses resulted in electron transfer to form the C-P⁺-C₆₀⁻ charge-separated state with $\tau = 10$ ps, and a quantum efficiency of unity. Hole transfer from the FBP to C competes with charge recombination and occurs with $\tau = 270$ ps and a yield of 0.14. This final charge-separated state decays exclusively to the carotenoid triplet state, ³C-P-C₆₀, with $\tau = 1.3$ μ s in the absence of a magnetic field. Application of a relatively weak magnetic field, B = 4.1 mT, resulted in a 50 % increase in the lifetime of the triplet state to $\tau = 2.0$ μ s. No effect was observed at ambient temperatures. Modulation of charge recombination on the picosecond time scale has also been observed in ferrocene complexes, albeit in a field of several Tesla [232].

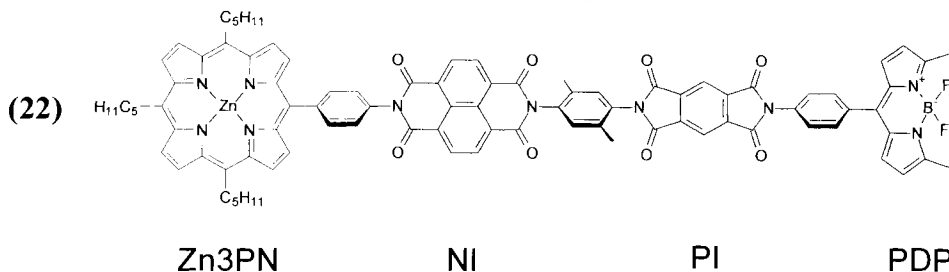
Sato and co-workers presented the first example of the ability to optically change the magnetic field in a single crystal. The magnetic field is a macroscopic property, but the principle behind the switching mechanism is photoinduced electron transfer within the crystalline lattice. Sato and co-workers employed a Prussian Blue complex with the stoichiometry K_{0.2}Co_{1.4}[Fe(CN)₆] · 6.9 H₂O. It formed the rock-salt

crystalline lattice (21). The Curie temperature, T_c , below which long-range ordering of the electron spins results in the creation of a magnetic material, was 14 K. Illumination with 660 nm flashes of light raised this temperature to 19 K. The mechanism for switching of the magnetic properties is photoinduced electron transfer from the diamagnetic low-spin complex, $\text{Fe}^{\text{II}}-\text{CN}-\text{Co}^{\text{III}}$, to the high-spin $\text{Fe}^{\text{III}}-\text{CN}-\text{Co}^{\text{II}}$ electronic configuration. At 5 K this results in a doubling of the magnetic field strength. Furthermore, the lattice can be switched back to the low-spin diamagnetic state by the application of a second laser pulse at 450 nm. The overall time for both switching processes is on the order of several seconds, but this result is an important example of the ability to control macroscopic properties by switching on the molecular level. One can also envision the integration of switches based on spin control with this technology to yield an all-optical magnetic device.



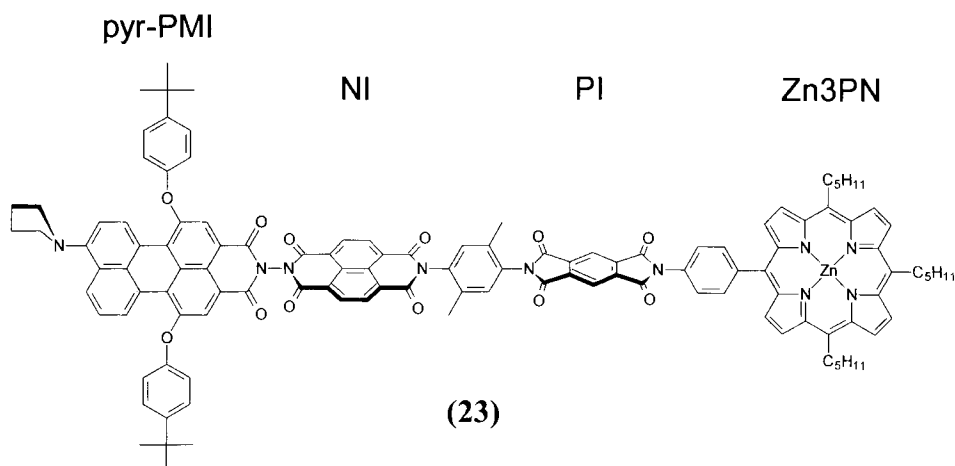
(21)

The systems examined thus far have all been based on the propagation of positive or negative charge using consecutive laser pulses. Alternatively, it should be possible to base optical switches on the application of consecutive laser pulses to cause charge recombination. Electric fields can also have a profound effect on the lifetimes of charge-separated states. Debreczeny et al. demonstrated the all-optical control of an ion pair lifetime via the large, anisotropic, local electric field generated by a second ion pair [233]. The molecular tetrad (22) consists of zinc triphenylpor-

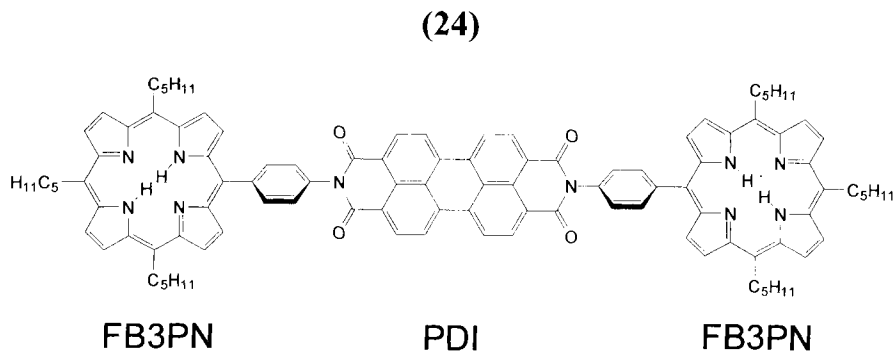


phyrin (Zn3PN) and phenyldimethylpyrromethene (PDP) electron donors and NI and PI electron acceptor groups. Selective excitation of PDP with 513 nm laser pulses resulted in electron transfer to form the $\text{Zn3PN-NI-PI}^--\text{PDP}^+$ charge-separated state with $\tau = 700$ ps and a quantum yield of unity. The lifetime of this charge-separated state is $\tau = 1.3$ ns. However, if a 416 nm laser pulse excites the tetrad 700 ps after the formation of the ion pair, its decay to the ground state is accelerated by an order of magnitude.

In further work, a similar system completely inhibited the formation of a second ion pair using the electric field of an initial ion pair. In compound **23**, Zn3PN and 9-(*N*-pyrrolidinyl)perylene-3,4-dicarboximide (pyr-PMI) are the electron donors, while once again NI and PI are electron acceptors [234]. Photoinduced electron transfer from Zn3PN to PI with 416 nm laser pulses occurs with $\tau = 27$ ps; however, if a 645 nm laser pulse is used to excite pyr-PMI, first this event is completely inhibited.



In addition to modulating the wavelength and timing of laser pulses, one can also perform photoinduced electronic switching by modulating the intensity of the laser pulses. This was demonstrated by O'Neil et al. using a molecule consisting of two free base triphenylporphyrin (FB3PN) electron donors covalently bound to either end of a perylene-3,4:9,10-tetracarboxylic diimide (PDI) electron acceptor, **24** [65].



Excitation of the FBP with 585 nm laser pulses results in single electron transfer to PDI, forming the state $\text{FB3PN}^+-\text{PDI}^--\text{FB3PN}$. When the intensity of the laser pulse is increased, both FBP moieties are excited, resulting in double electron transfer to PDI, forming the state $\text{FB3PN}^+-\text{PDI}^{2-}-\text{FB3PN}^+$. This effect is detected because the PDI anion absorbs at 713 nm, while the dianion absorbs at 546 nm. Thus, by modulating the laser intensity one can either singly or doubly reduce the perylene acceptor. This is possible because only 0.2 V separates the one- and two-electron reductions of PDI. Other molecules whose reduction potentials are closely spaced, such as terrylene, quaterrylene, and many metal complexes, should also display this behavior.

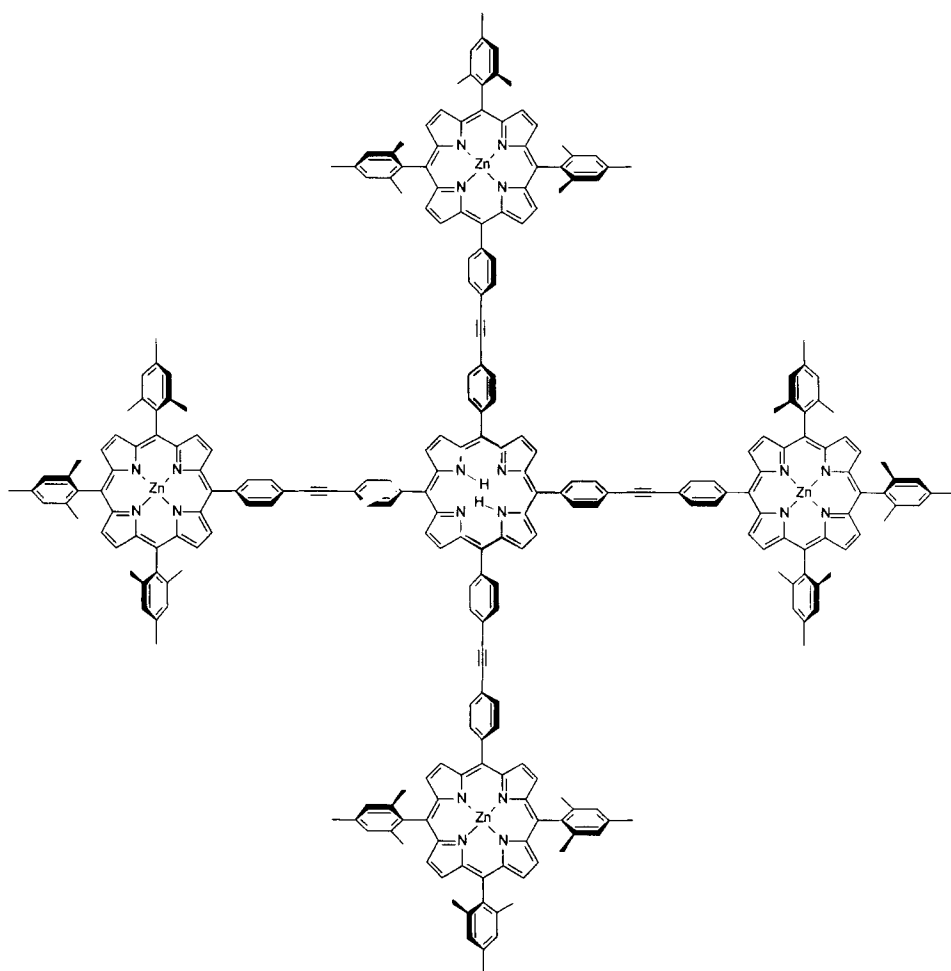
2.5 Energy Transfer Based Systems

Whereas electron transfer reactions that occur via a superexchange mechanism depend exponentially on the distance between electron donor and acceptor, Förster type, through-space (TS) energy transfer has a distance dependence of $1/r^6$. Thus, it is known to occur efficiently over much larger distances. Energy transfer is also known to occur via a Dexter, through-bond (TB) mechanism. For most of the rigidly linked systems described here, in which site-to-site distances are less than 20 Å, the Dexter mechanism is predominant. Within an antenna of mixed chromophores, energy transfer proceeds downhill in a site-to-site fashion until energy is localized on the chromophore with the lowest excited state energy. One advantage of using an antenna is that excitation is not site-specific, and absorption of a photon by any chromophore results in energy transfer to the same low-energy site. Fluorescence, nonradiative decay, electron transfer, or a combination of these processes follows energy transfer. Thus, employing light absorbers with large extinction coefficients allows versatility in the choice of electron donors or fluorophores. Designing systems for efficient light absorption across the visible spectrum that can transfer this energy to chromophores capable of converting the energy to chemical potential is an active area of research [132, 235, 236]. It also has applications for the design of efficient optical switching devices.

Many of the molecules discussed in the previous section are not highly robust and photodegrade rapidly under intense visible irradiation. However, switching errors are more likely to occur at low photon densities. A simple solution to this problem is to use a light-absorbing antenna that can efficiently transfer energy to the input chromophore. This greatly increases the lifetime of the devices, and in addition makes it possible to design an antenna that absorbs either at specific wavelengths, or across the entire visible spectrum. By a careful choice of chromophores energy transfer can alleviate many of the problems inherent in devising efficient robust all-optical switches employing electron transfer reactions. Many antenna complexes based on mixed metalloporphyrins have been studied [137, 138, 141–143, 146–148, 150, 237]. Porphyrins are often used because their electrochemical and spectral properties can be tuned by substitution of appropriate metals.

A synthetic system should meet several requirements in order for researchers to

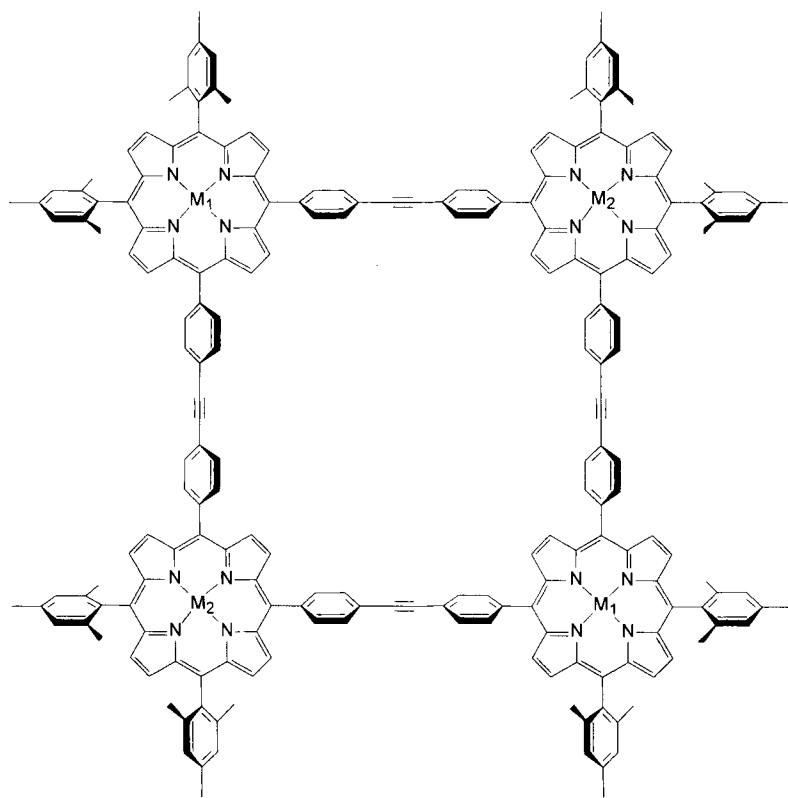
learn useful information about the transfer of energy among the chromophores. It should be structurally rigid, soluble in organic solvents, and incorporate controlled metallation sites including free base and metalloporphyrins. Even so, there is no limit to the variety of architectures that can be constructed from arrays of covalently linked chromophores. Porphyrins are natural candidates for the creation of arrays with four-fold symmetry. Lindsey and co-workers synthesized a pentamer (**25**) consisting of four ZnP_s surrounding a central FBP [134]. This system undergoes energy transfer from the $^1\text{ZnP} \rightarrow ^1\text{FBP}$ with a quantum yield of approximately 90 % based on quenching of the ZnP emission. Further work from this laboratory has enabled the placement of eight light-harvesting chromophores about the periphery of a single free base or zinc porphyrin [144]. The phenyl rings of the



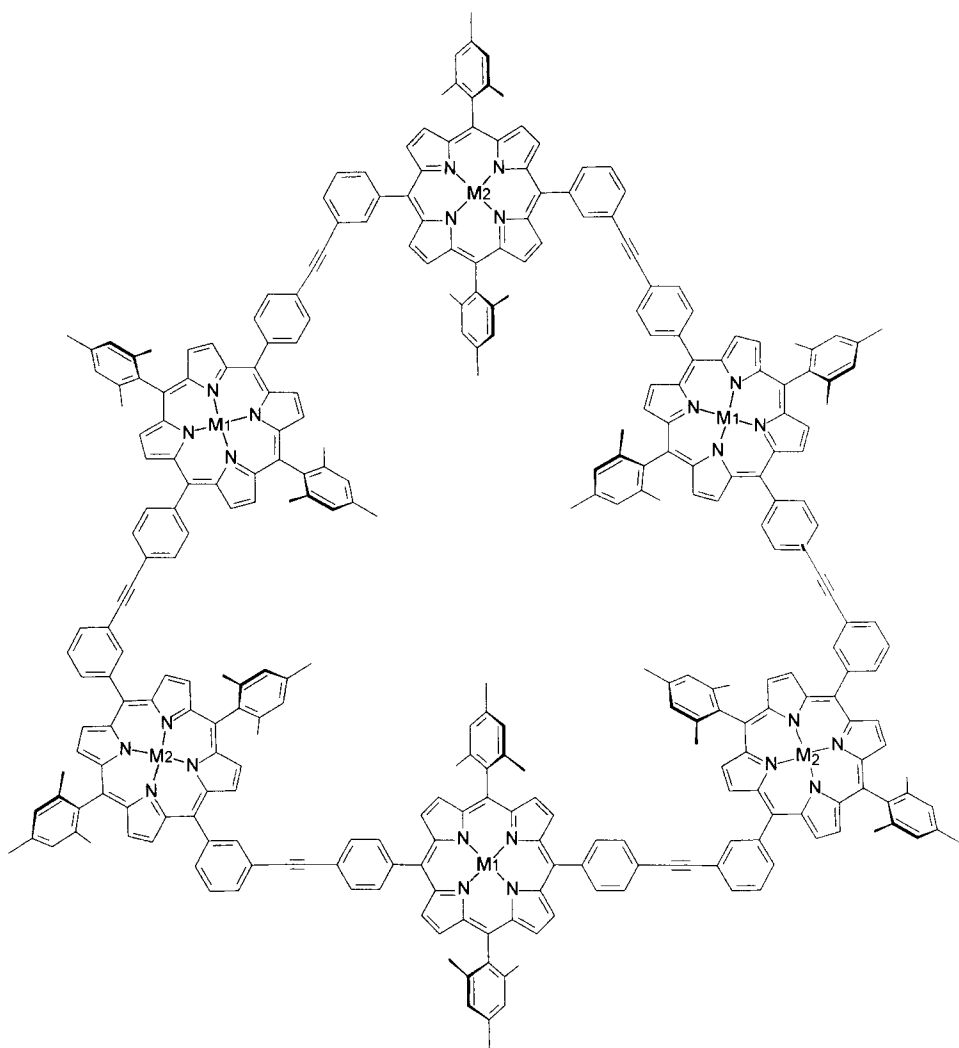
(25)

porphyrin are substituted at the 3 and 5 positions with ethynyl groups linked to boron dipyrromethene dye molecules.

Lindsey and co-workers also constructed macrocyclic square (**26**) and hexagonal (**27**) structures in which the alternating metallo- and free-base porphyrins form the subunits [143, 150]. The all free-base, zinc-, and magnesium-substituted arrays ($M_1 = M_2$) were synthesized as reference systems. In each system the dominant electronic mechanism was TB energy transfer; however, the rate decreased by 50 % between the square ($\tau_{TB} = 12$ ps) and hexagonal architectures ($\tau_{TB} = 17$ ps). This occurred despite there being one fewer chemical bond and a slight decrease in the center-to-center distance separating the chromophores. This effect was attributed to the change in substitution pattern from a *para* to *meta* linker. Thus, energy transfer in these architectures occurs via mediation of the conjugated linker groups, and not through the σ -bonded framework. Although these competitive rates are quite similar due to the proximity of the two chromophores, it should be possible to control energy transfer over greater distances on the basis of this effect.

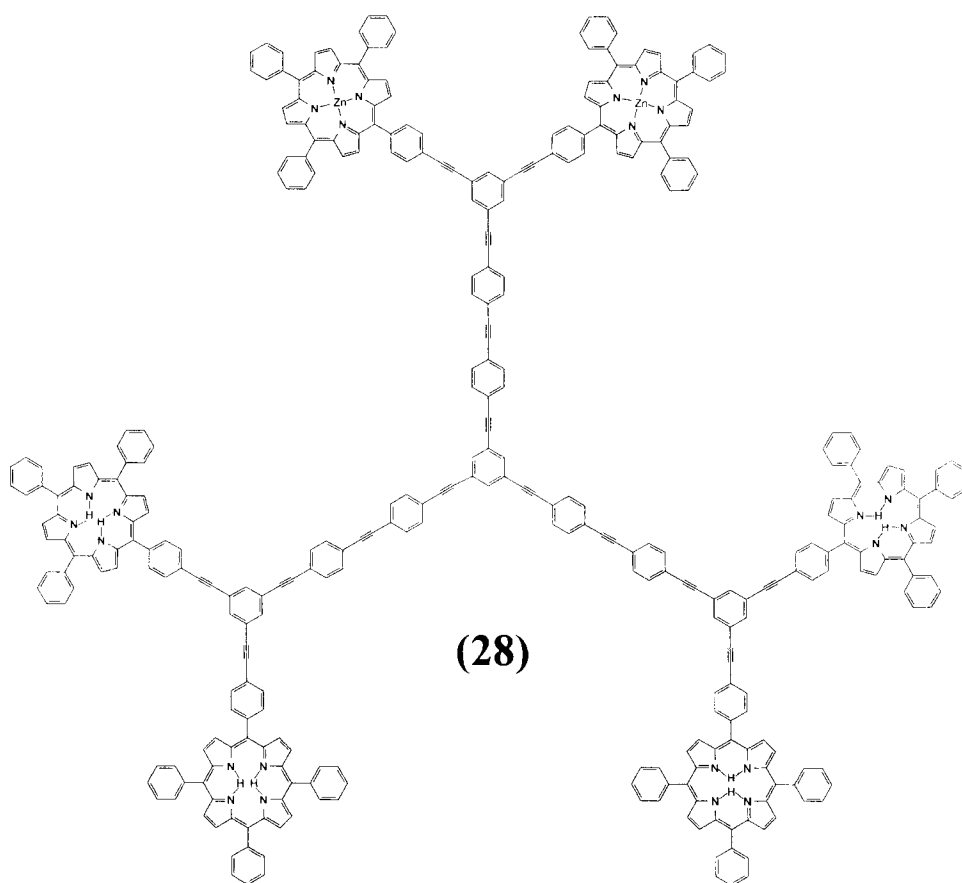


(26)



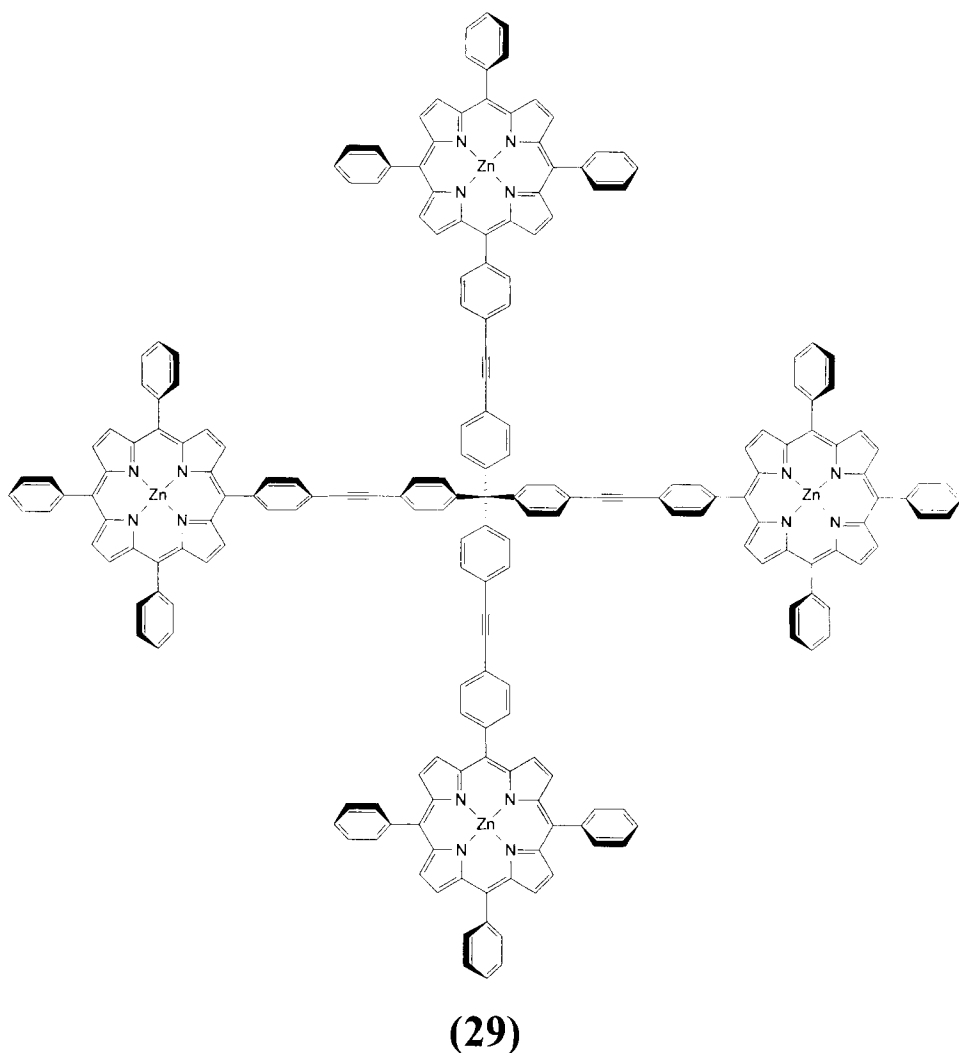
(27)

The trigonal and tetrahedral macromolecules, **28** and **29**, respectively, are systems in which these ideas might be applied and were synthesized by Vauthey and co-workers [147]. Interestingly, these systems show significant contributions from both TB and TS energy transfer mechanisms. In **28** the ZnP to FBP distance is 35.5 Å along a shortest line, and 67.5 Å via the bonded pathway. The rate of ZnP → FBP energy transfer is $\tau = 62$ ps, and occurs primarily via a TS mechanism. Only when the bonded pathway becomes smaller, <45 Å, do the authors observe a shift to the TB mechanism. However, in compound **29**, where the interchromophore distance is 27 Å through space, and 32 Å through the bonded pathway, the TS mechanism



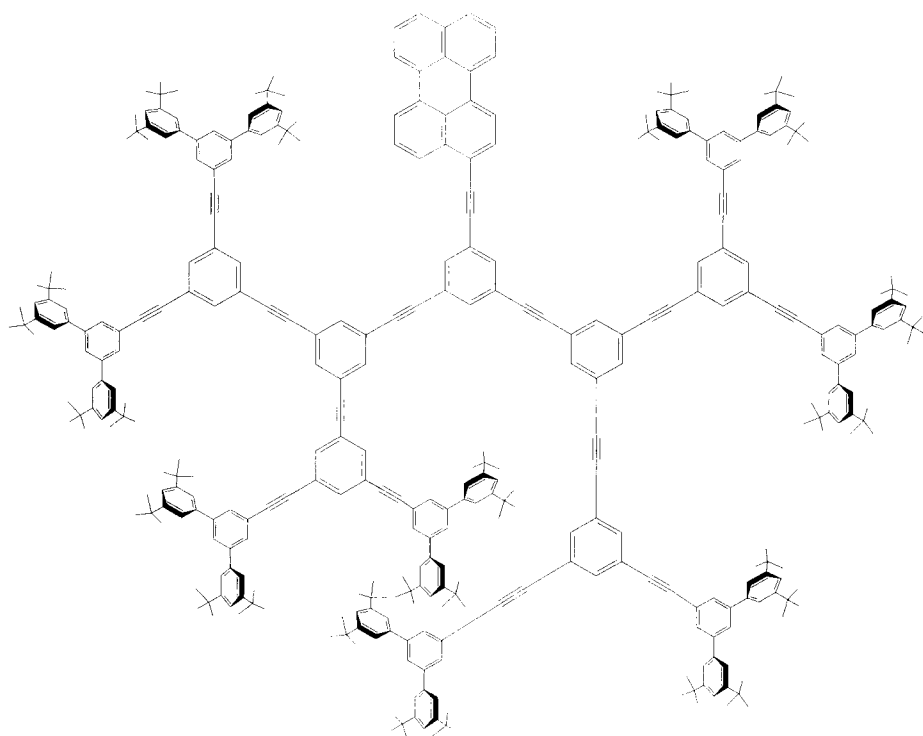
is still dominant. The TB mechanism is disrupted by the sp^3 -hybridized central carbon. This again demonstrates the need to give significant consideration to the electronic structure of the medium through which electronic communication must occur. The conjugation of the linker is especially important when energy and electron transfer events occur across large distances.

In **28** the array of chromophores is beginning to take on a dendritic type of architecture where the termini are capped with light-harvesting antennae. Recent work has demonstrated the construction of not only dendritic antenna complexes, but also of systems wherein the dendrimer itself is the light harvester [136, 139, 149]. The great advantage of using dendritic architectures is that the number of light-harvesting chromophores increases as 2^n for each additional generation. Unfortunately, this increase in photon absorption efficiency is countered by a decrease in energy transfer efficiency. The dendritic compounds **30** and **31** synthesized by Moore and co-workers again demonstrated the requirements for constructing efficient energy transfer dendrons. As before, the electronic structure of the intervening medium is crucial in designing an efficient system. Although **30** and **31** each contain

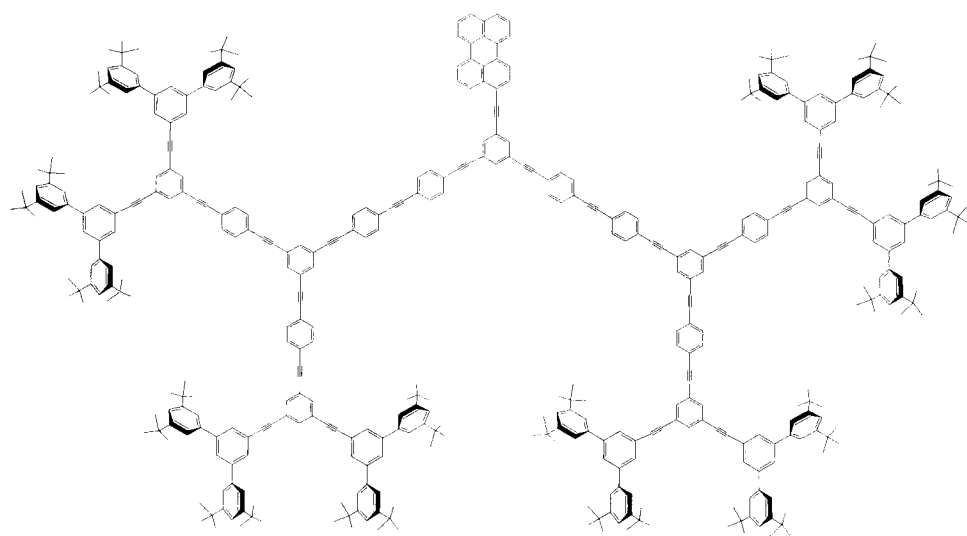


16 light-absorbing groups, the linking groups between absorber and collector are different. Compound **30** is a dendrimer with a simple fan-out macromolecular structure, while **31** contains localized regions of π -conjugation between the absorber and collector. This creates an energy gradient, which results in a directional energy flow, and is reflected in the rates of energy transfer. Energy transfer occurs with $\tau = 311$ ps in **30**, and despite the greater interchromophore distance the rate of energy transfer in **31** increases almost two orders of magnitude to $\tau = 5.3$ ps, with a yield of 98 %.

It is also possible to incorporate dendritic design motifs into polymeric systems. Sato and Aida have recently demonstrated the feasibility of constructing light-harvesting dendritic side chains on polymer chains of fluorophores [149]. The repeat

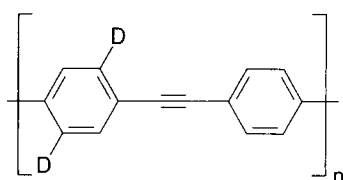


(30)

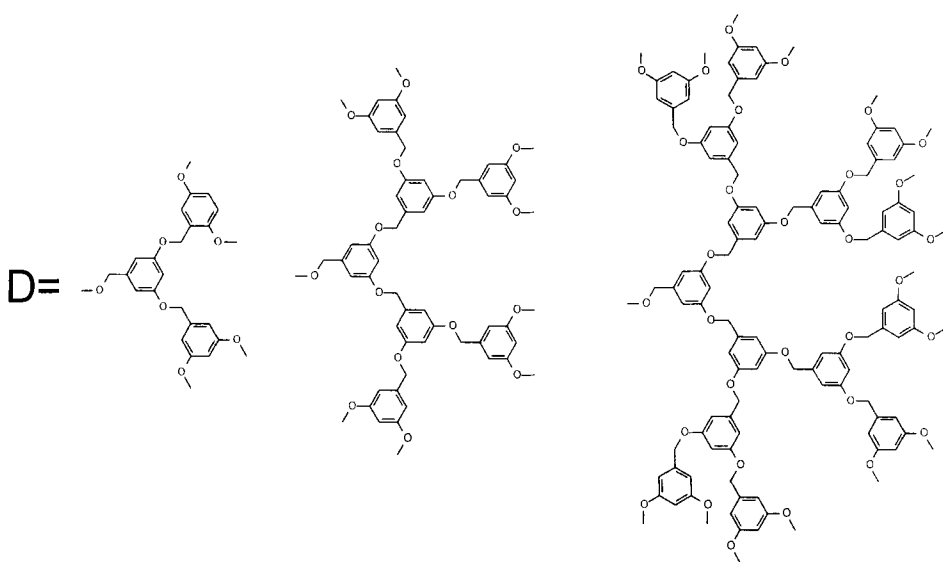


(31)

units of the dendrimer are 1,3,5-poly(benzyl) ether moieties. Polymers with dendritic side chains of between two and four generations were synthesized (**32**). The attachment of these groups to the poly(phenylene-ethynylene) polymer introduces a large absorption band at 278 nm in the ultraviolet region of the spectrum. Excitation in this region results in energy transfer to the polymer backbone with a quantum efficiency of unity, and is observed as fluorescence at 454 nm. In addition to acting as efficient light absorbers, the dendrimers also increase the fluorescent quantum yield. This is because the bulky side groups prevent interchain collisional deactivation. Similar types of dendrimers are readily applicable to polymers of the $[-D-A_1-A_n-]_n$ monomer type [238] both to improve solubility and to act as light-harvesting antennae.



(32)

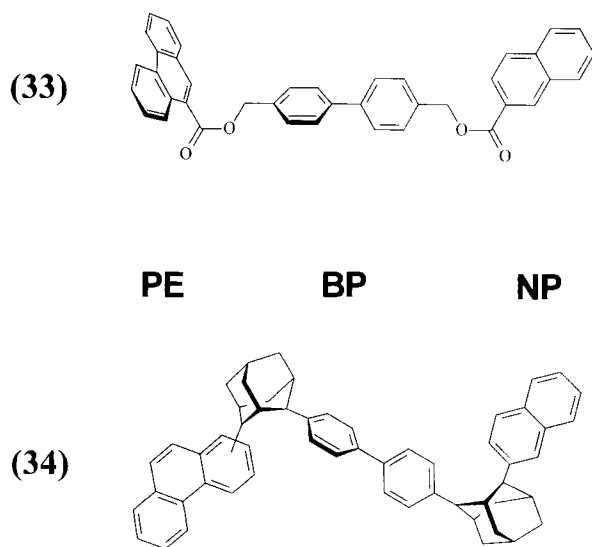


It should be possible to employ intramolecular energy transfer reactions to perform logic operations similar to those discussed for intramolecular electron transfer. McGimpsey and co-workers synthesized and studied trichromophoric systems designed for a molecular shift register based on singlet-singlet and triplet-triplet energy transfer processes [239, 240]. Digital information is encoded as excitation

energy, which is propagated from one monomer unit to the next using consecutive laser pulses. The authors note that the chromophores in such a device would logically be arranged in order of descending excited-state energies. The series of chromophores ${}^1\text{A} < {}^1\text{B} < {}^1\text{C}$ would function so that excitation of A resulted in consecutive energy transfer steps becoming localized on C, similarly to the electron transfer scheme in Figure 5. Subsequently, a second laser pulse is used to excite ${}^3\text{C} \rightarrow {}^3\text{C}^*$, from which energy transfer to chromophore A on the next monomer unit occurs. Thus, data are encoded to the system in the singlet manifold, and propagate along the register in the triplet manifold. The use of singlet–singlet and triplet–triplet energy transfer also allows for potential control of relative rates within these systems with applied external magnetic fields, as discussed earlier.

Compounds **33** and **34** were designed to test this hypothesis using monomeric model compounds. A biphenyl (BP) was employed as a light absorber, held rigidly between phenanthrene (PE) and naphthalene (NP) chromophores using ester and adamantyl linkers in **33** and **34**, respectively. The saturated adamantyl bridge lowered the excited-state energies of each chromophore by approximately 0.1 eV; however, the driving force for energy transfer remained constant between the two systems. Excitation of the BP moiety within **33** and **34** with a 226 nm flashlamp resulted in the formation of the $\text{PE}-{}^1\text{BP}-\text{NP}$ state. The energy level diagram for this system is displayed in Figure 8. A series of singlet–singlet energy transfer steps, k_1 and k_2 , resulted in localization of the excited-state energy on the phenanthrene. In each system k_1 occurred with $t < 30$ ps; however, the rate for k_2 differed significantly: $k_{2,33} = 2.5 \times 10^8 \text{ s}^{-1}$, while $k_{2,34} = 2.5 \times 10^6 \text{ s}^{-1}$. This is due to the differences in coupling for the through-bond energy transfer process. Intersystem crossing within the phenanthrene yielded the ${}^3\text{PE}-\text{BP}-\text{NP}$ triplet excited state.

Excitation within the triplet manifold of PE is possible because of its $\text{T}_1 \rightarrow \text{T}_n$ absorption near 500 nm. Application of a second laser flash at 488 nm resulted in



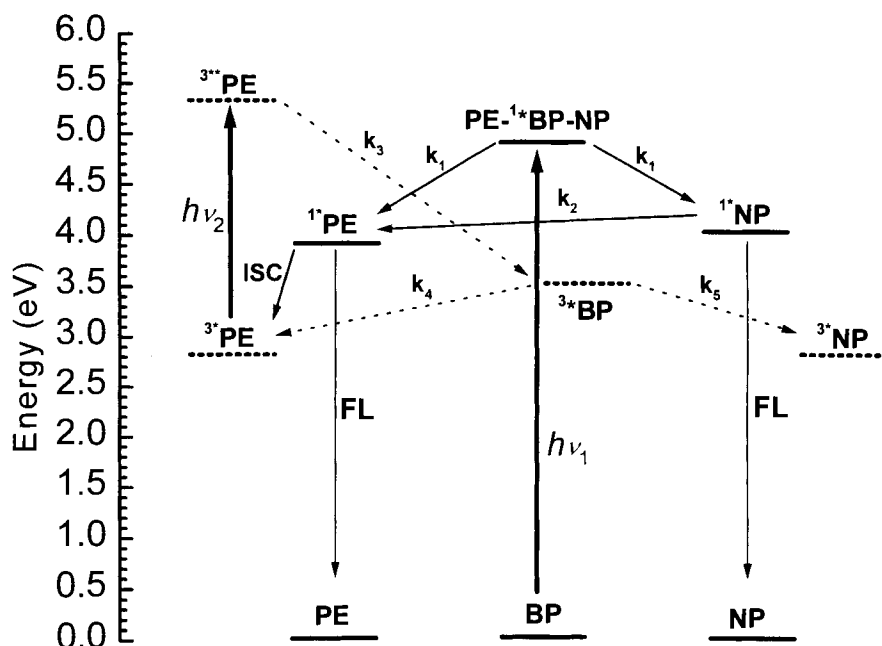
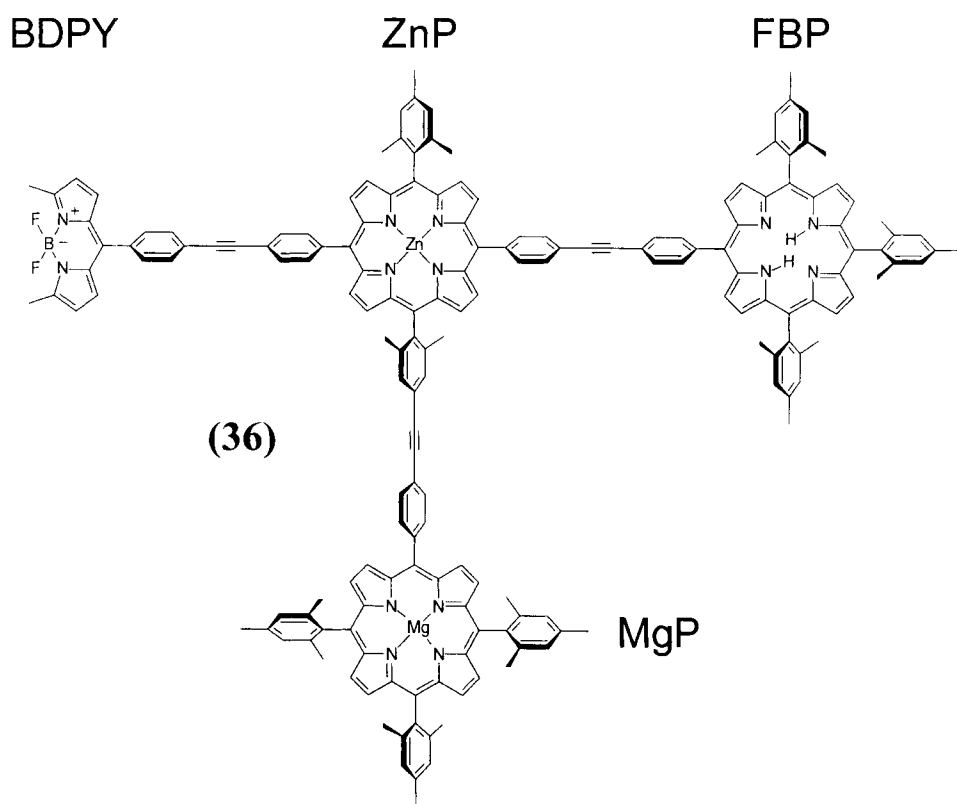
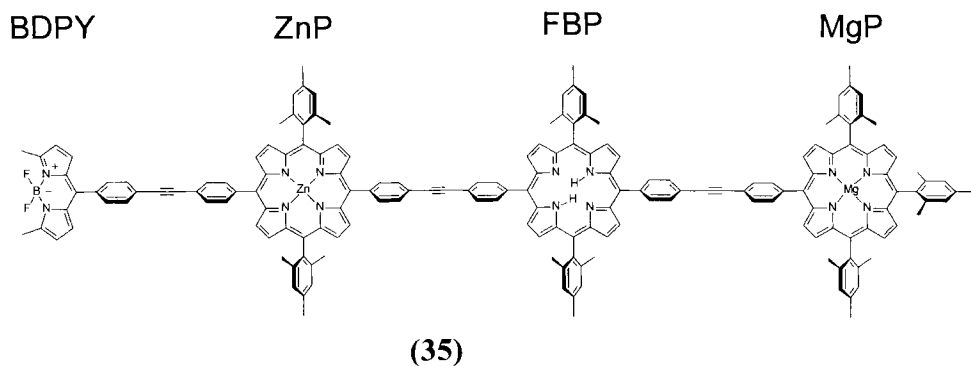


Figure 8. Energy level scheme for **33** and **34**. Excitation with 226 nm light populates 1^*BP , which undergoes efficient energy transfer to 1^*PE and 1^*NP . Subsequent energy transfer and intersystem crossing populate the triplet state of the phenanthrene, 3^*PE . Excitation to the 3^{**}PE state with 488 nm light results in stepwise energy transfer to 3^*BP and 3^*NP , the latter of which acts as an energy well.

triplet–triplet energy transfer to 3^*BP , k_3 , followed by energy transfer both to 3^*NP , k_5 , and back to 3^*PE , k_4 . The ratio $k_4/(k_4 + k_5)$ determines the efficiency of the switching operation. For these systems the switching efficiency was approximately 50 %; however, tuning the coupling and energetics of the chromophores could optimize this.

Thus far we have examined systems which were designed for the absorption of energy by one chromophore, transferring the excitation, and finally dissipating this energy via emission by some other chromophore. It is also possible to modulate this emission and create a molecular switch based on competing routes of energy transfer, one of which is nonradiative. An example of such a switch employing energy transfer in porphyrin arrays is an optoelectronic gate synthesized by Lindsey and co-workers [148]. It consisted of three porphyrins and a light-absorbing dye in a linear or branched arrangement (compounds **35** and **36**); their operation is identical. The branched design, **36**, consists of a tri-substituted zinc porphyrin (ZnP) with a boron dipyrromethene dye (BDPY), and magnesium and free-base porphyrins (MgP and FBP, respectively) on its periphery. The FBP *para* to the BDPY has the lowest-energy excited state, and is highly fluorescent. A HOMO/LUMO scheme for this array is shown in Figure 9. Excitation of the BDPY with 485 nm light initiates



a stepwise energy transfer. The energy becomes localized on the FBP and is dissipated radiatively as fluorescence centered at 650 nm. The quantum yield for the total process is approximately 0.8 in both the linear and branched architectures. Activation of a nonradiative decay pathway within the system can modulate this emission. The MgP has the lowest oxidation potential (${}^{+1}E_{1/2} = 0.34$ V vs. SCE) and a vacancy in its HOMO can be easily created by electrochemical or chemical

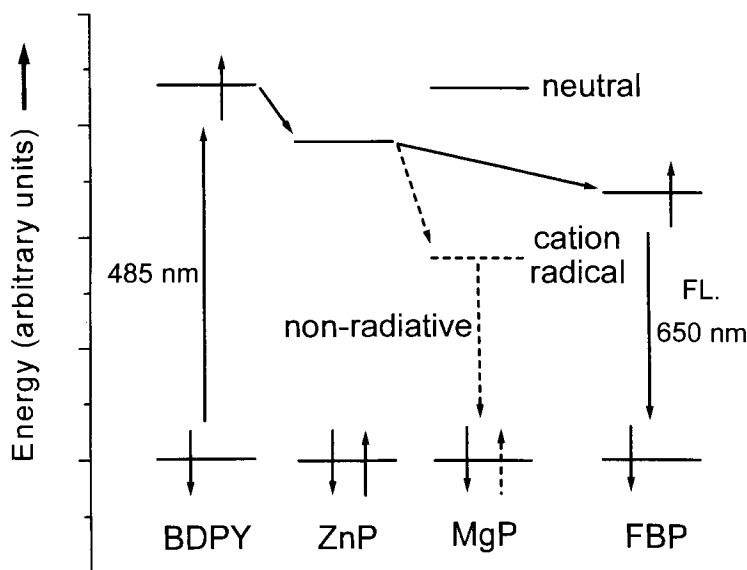
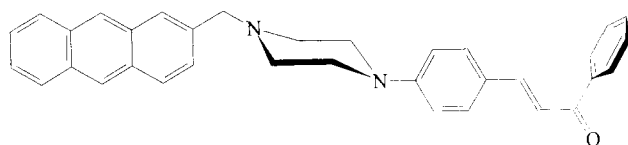


Figure 9. Energy level scheme for **35** and **36**. Excitation with 485 nm light initiates a series of energy transfers which localizes the excitation onto the chromophore with the lowest-energy excited state. In the neutral state (solid), this is the FBP. Electrochemical oxidation of MgP lowers its excited state energy (dash) and activates a nonradiative decay pathway.

oxidation. For this experiment iron perchlorate, $\text{Fe}^{\text{III}}(\text{ClO}_4)_3$, was used as the chemical oxidant. Once oxidized, energy transfer occurs to the MgP^+ , which has low-lying absorptions indicative of a manifold of low-energy singlet–singlet transitions. These are nonradiative, and thus no emission is observed from the monocationic species. Furthermore, the fluorescence signal was fully restored by returning to the neutral species via addition of triethylamine or electrochemical reduction. This system demonstrates the ability to modulate energy transfer in large arrays; however, the ON/OFF switching of fluorescence is limited by diffusional processes which are relatively slow compared to the energy transfer events [66].

A tri-chromophoric system (**37**) studied by Wang and Wu switches between energy and electron transfer pathways in a single molecule via proton binding [106].

(**37**)



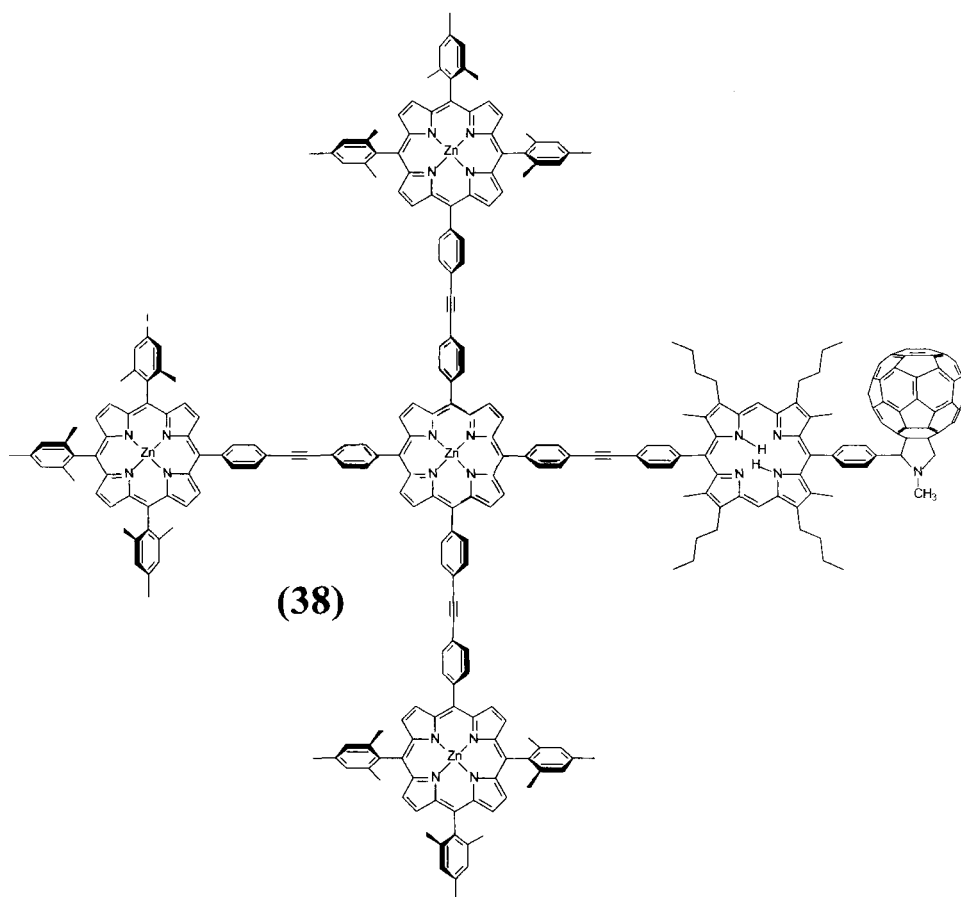
Anthracene

Piperazine

Chalcone

In **37**, absorption of near-ultraviolet light by the anthracene results in quenching by electron transfer from a nearby piperazine. Bound to the other side of the piperazine is a chalcone moiety, an α,β -unsaturated carbonyl group, which has a lower-energy excited state than the anthracene. When H^+ ions are added to solution, electron transfer is quenched via H^+ binding at the piperazine site, and energy transfer can proceed from the anthracene to the chalcone. There are also examples of electron transfer controlled by reversible proton binding in ruthenium complexes [241, 242]. While these systems are highly efficient, they rely upon the slow processes of diffusion and ion binding in solution to modulate the much faster electron transfer reaction.

Gust and co-workers designed a synthetic antenna reaction center capable of undergoing energy transfer followed by electron transfer [146]. Four ZnP chromophores arranged in a cross are covalently linked to an FBP electron donor and C_{60} electron acceptor, **38**. Excitation of a ZnP results in energy transfer, $\tau = 240$ ps, to the FBP with a quantum yield of 0.69. The excited state of the FBP decays exclusively via electron transfer, $\tau = 3$ ps, giving rise to the charge-separated ZnP_4^-

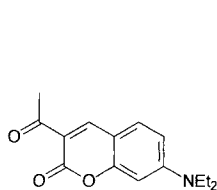


FBP⁺-C₆₀⁻ state which has a lifetime of $\tau = 1$ ns. The authors discuss several parameters that determine the efficiency of energy transfer in light-harvesting antennas. The choice of metal for substitution in the porphyrin is key in determining the rate and yield for energy transfer because the metal exercises control over both the electrochemical properties and excited-state lifetime. As stated previously, a through-bond energy transfer mechanism is dominant for most antenna complexes, and the choice of linkage is thus critical in determining electronic coupling between sites. This includes factors such as substitution site and steric hindrance in addition to site-to-site distance and bond type. Several small, fast, and highly efficient energy transfer steps are likely to be much more efficient than a single one-step energy transfer.

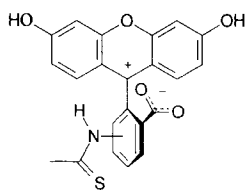
One of the foremost concerns in this field is the leap to be made from studying isolated complexes to the synthesis of large assemblies that will retain the characteristics of single molecules. The synthesis of large, covalently linked, light-harvesting and switching assemblies becomes increasingly complex as more chromophores and redox-active units are added. It is clear that many of the design considerations that apply to the single-molecule level are not suitable for the synthesis of macromolecules. Thus, it is desirable to construct architectures via self-assembly [243–250] or other techniques [251] which have exceedingly high yields and arrange themselves with minimal defect sites. Dendrimers [96, 252–257], polymers [258–261], membranes [262–266], and zeolites [267–275] have been employed as supports for the construction of well-defined supramolecular arrays. However, it may be unnecessary to construct entire arrays in which the local environment of each subunit is rigorously controlled.

Recent work has demonstrated the deposition of consecutive nanometer-thick thin films of light-harvesting and redox-active molecular subunits to create a layered structure capable of stepwise energy and electron transfer [276]. The light-harvesting chromophores coumarin (**39**) and fluorescein (**40**) are synthesized as ionic polymers of poly(allylamine hydrochloride) (**41**). They are deposited sequentially and absorb light across a large portion of the visible spectrum and funnel it to a palladium(II) tetrakis(4-sulfonatophenyl)porphyrin (**42**). This chromophore has a long-lived excited triplet state, and can transfer an electron to an acceptor in the next layer. In this case the electron acceptor is viologen-substituted polyvinyltoluene (**43**).

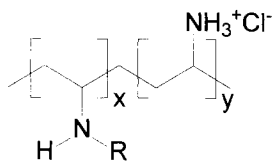
A key aspect of this system is the insertion of semiconductor layers between the layers of chromophores. Local control is exerted over the network of covalent bonds, but there is no rigorous control over the local environment during film for-



(39)



(40)



(41)

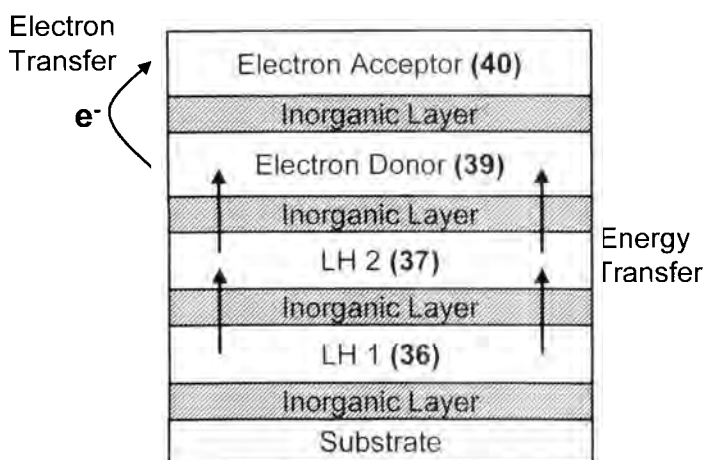
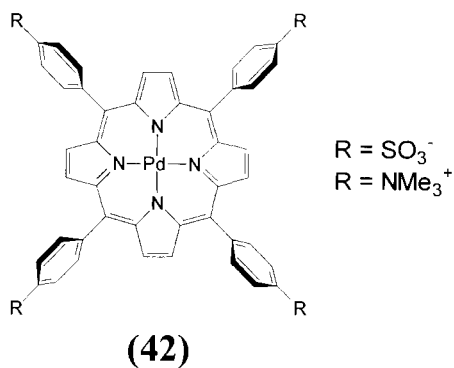
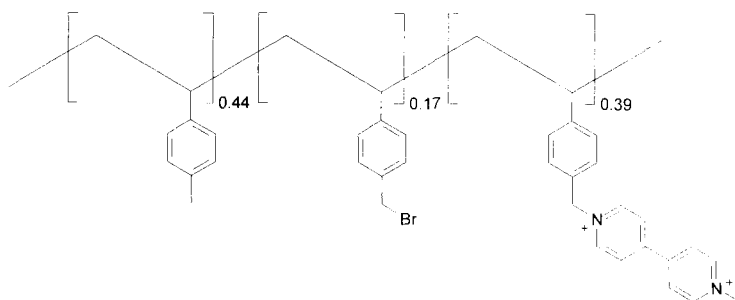


Figure 10. Schematic representation of the organic–inorganic solid-state hybrid synthesized by Mallouk and co-workers [276]. Absorption of a photon by any of the organic layers results in energy transfer to the electron donor layer. This initiates an intermolecular electron transfer reaction. Interestingly, the yield of both energy and electron transfer can be modulated by changing the electronic characteristics of the inorganic semiconductor material.

mation. The inorganic spacers ensure that each layer maintains a homogeneous distribution of chromophores, and that there is no interlayer migration. No covalent bonds link any of the redox-active chromophores. The semiconductors both increase the yield and the rate of electron transfer from the excited state of the donor and inhibit the back electron transfer reaction from the acceptor. These layers consist of anionic $\text{Zr}(\text{HPO}_4)_2 \cdot \text{H}_2\text{O}$ (α -ZrP) or HTiNbO_5 sheets. Figure 10 shows the scheme for this assembly. Energy and electron transfer occurred with quantum yields of 0.47 and 0.61 in the α -ZrP and HTiNbO_5 spaced assemblies, respectively. The rate of energy and electron transfer in any of these systems is an ensemble average of all sites within the layered assembly, and thus there is no single rate for any of the processes in the assemblies. Nonetheless, in addition to the increased quantum yield, assemblies constructed with the HTiNbO_5 spacer exhibit a long-lived charge-separated state component not observed in the α -ZrP spaced assemblies, $\tau = 900 \mu\text{s}$. While there is still much to be learned from the study of multichromophore arrays, this synthetic approach appears to hold much promise for the creation of organic–inorganic hybrid solid-state devices. This research also lends credence to the idea that the three-dimensional location of individual components within a molecule-based computer need not be rigorously controlled to take full advantage of their photochemical properties.



(43)



2.6 Conclusions and Future Prospects

The creation of ever more complex systems designed to exhibit single-molecule switching is an ongoing process. There are still many hurdles to cross before optical molecular switches are integrated with other components to build all-optical computing devices. The synthesis of large arrays of molecule-sized switches into a network capable of processing information is a major challenge. Whereas covalent attachment schemes can be used to test a variety of switch concepts, ultimately a molecular self-assembly strategy is necessary to carry out organization of these elementary units into large, working arrays. Much of the current research on molecular switches is oriented toward the implementation of individual components operating in a solid, organized matrix. Surface attachment and/or three-dimensional order induced by incorporation into a crystalline matrix may be necessary to achieve full functionality for such systems. However, our understanding of membrane-based switches in living cells and biological regulators points toward applying basic thermodynamic principles to arrange appropriately functionalized chromophores noncovalently using a potential gradient.

Addressing molecular switches remains a problem as well. The use of diffraction-limited focused light pulses provides a useful start, but subdiffraction optical techniques need to be improved and implemented to transfer information into and out of these molecular arrays. At present near-field optical techniques are relatively slow, so that although they provide better spatial resolution, the speed of information access is somewhat limited.

Finally, the fundamental quantum mechanical challenges of using molecules themselves to store and process information needs to be more fully explored. While the fundamental limitations dictated by the Heisenberg uncertainty principle place stringent criteria on such information processing, the intrinsic properties of quantum systems may be exploited for molecule-based computation. The ability of quantum systems to function as coherent superpositions of states [277] may make it possible to design molecules that take advantage of these properties to implement quantum computation schemes [278–280]. The future of this area is quite promising, especially when one considers the vast possibilities provided by molecular design and synthesis coupled with utilization of the numerous photophysical properties of molecules.

Acknowledgment

The authors thank the National Science Foundation for support of this work (CHE-9732840).

References

1. Tamarat, P.; Maali, A.; Orrit, M. *J. Phys. Chem. A* **2000**, *104*, 1–16.
2. Miller, J. S. *Adv. Mater.* **1990**, *2*, 378–379.
3. Miller, J. S. *Adv. Mater.* **1990**, *2*, 495–497.
4. Miller, J. S. *Adv. Mater.* **1990**, *2*, 601–603.
5. Haddon, R. C.; Lamola, A. A. *Proc. Natl. Acad. Sci. USA* **1985**, *82*, 1874–1878.
6. Parthenopoulos, D. A.; Rentzepis, P. M. *Science* **1989**, *245*, 843–845.
7. Lieberman, K.; Harush, S.; Lewis, A.; Kopelman, R. *Science* **1990**, *247*, 59.
8. Thylen, L.; Karlsson, G.; Nilsson, O. *IEEE Commun. Mag.* **1996**, *February*, 106–113.
9. Feldstein, M. J.; Vohringer, P.; Wang, W.; Scherer, N. F. *J. Phys. Chem.* **1996**, *100*, 4739–4748.
10. Higgins, D. A.; Vanden Bout, D. A.; Kerimo, J.; Barbara, P. F. *J. Phys. Chem.* **1996**, *100*, 13794–13803.
11. Tour, J. M.; Schumm, J. S. *J. Am. Chem. Soc.* **1991**, *113*, 7064–7066.
12. Waldeck, D. H.; Beratan, D. N. *Science* **1993**, *261*, 576–577.
13. Patil, A. O.; Heeger, A. J.; Wudl, F. *Chem. Rev.* **1988**, *88*, 183.
14. Wasielewski, M. R.; Johnson, D. G.; Svec, W. A.; Kersey, K. M.; Cragg, D. E.; Minsek, D. W. *Long-distance Photoinitiated Electron Transfer through Polyene Molecular Wires*; Norris, J. R., Ed.; Elsevier: New York, NY; Chem. Div., Argonne Natl. Lab.: Argonne, IL 60439, USA, 1989; pp. 135–147.
15. Sundram, M.; Chalmers, S. A.; Hopkins, P. F.; Gossard, A. C. *Science* **1991**, *254*, 1326–1335.
16. Blanchard-Desce, M.; Arrhenius, T. S.; Dvornitzky, M.; Kugimiya, S. I.; Lazrak, T.; Lehn, J. M. *AIP Conf. Proc.* **1992**, *262*, 48–57.
17. Tolbert, L. M. *Acc. Chem. Res.* **1992**, *25*, 561–568.

18. Wagner, R. W.; Lindsey, J. S. *J. Am. Chem. Soc.* **1994**, *116*, 9759–9760.
19. Kemp, M.; Mujica, V.; Ratner, M. A. *J. Chem. Phys.* **1994**, *101*, 5172–5178.
20. Schumm, J. S.; Pearson, D. L.; Tour, J. M. *Angew. Chem.* **1994**, *106*, 1445–1448.
21. Reimers, J. R.; Craw, J. S.; Bacskey, G. B.; Hush, N. S. *BioSystems* **1995**, *35*, 107–111.
22. Tolbert, L. M.; Zhao, X.; Ding, Y.; Bottomley, L. A. *J. Am. Chem. Soc.* **1995**, *117*, 12891–12892.
23. Shimidzu, T.; Segawa, H.; Wu, F.; Nakayama, N. *J. Photochem. Photobiol. A* **1995**, *92*, 121–127.
24. Shimidzu, T. *Synth. Met.* **1996**, *81*, 235–241.
25. Kemp, M.; Roitberg, A.; Mujica, V.; Wanta, T.; Ratner, M. A. *J. Phys. Chem.* **1996**, *100*, 8349–8355.
26. Harriman, A.; Ziessel, R. *Chem. Commun.* **1996**, 1707–1716.
27. Bumm, L. A.; Arnold, J. J.; Cygan, M. T.; Dunbar, T. D.; Burgin, T. P.; Jones, L., II; Allara, D. L.; Tour, J. M.; Weiss, P. S. *Science* **1996**, *271*, 1705–1707.
28. Reimers, J. R.; Lu, T. X.; Crossley, M. J.; Hush, N. H. *Chem. Phys. Lett.* **1996**, *256*, 353–359.
29. Jones, L., II; Schumm, J. S.; Tour, J. M. *J. Org. Chem.* **1997**, *62*, 1388–1410.
30. Tsvigoulis, G. M.; Lehn, J. M. *Adv. Mater.* **1997**, *9*, 39–42.
31. Pearson, D. L.; Tour, J. M. *J. Org. Chem.* **1997**, *62*, 1376–1387.
32. de Silva, G. M. *Synth. Met.* **1997**, *86*, 2245–2246.
33. de Silva, G. M.; Acioli, P. H. *Synth. Met.* **1997**, *87*, 249–256.
34. Tans, S. J.; Devoret, M. H.; Dai, H.; Thess, A.; Smalley, R. E.; Geerligs, L. J.; Dekker, C. *Nature* **1997**, *386*, 474–477.
35. Frank, S.; Poncharal, P.; Wang, Z. L.; de Heer, W. A. *Science* **1998**, *280*, 1744–1746.
36. Davis, W. B.; Svec, W. A.; Ratner, M. A.; Wasielewski, M. R. *Nature* **1998**, *396*, 60–63.
37. Hu, J.; Odom, T. W.; Lieber, C. M. *Acc. Chem. Res.* **1999**, *32*, 435–445.
38. Schlicke, B.; Belsner, P.; De Cola, L.; Sabbioni, E.; Balzani, V. *J. Am. Chem. Soc.* **1999**, *121*, 4207–4214.
39. Constable, E. C.; Housecroft, C. E.; Schofield, E. R.; Encinas, S.; Armaroli, N.; Barigelletti, F.; Flamigni, L.; Figgemeier, E.; Vos, J. G. *Chem. Commun.* **1999**, 869–870.
40. Creager, S.; Yu, C. J.; Bamdad, C.; O'Connor, S.; MacLean, T.; Lam, E.; Chong, Y.; Olsen, G. T.; Luo, J.; Gozin, M.; Kayyem, J. F. *J. Am. Chem. Soc.* **1999**, *121*, 1059–1064.
41. Anderson, H. L. *Chem. Commun.* **1999**, 2323–2330.
42. Cotton, F. A.; Daniels, L. M.; Murillo, C. A.; Wang, X. *Chem. Commun.* **1999**, 2461–2462.
43. Ness, H.; Fisher, A. J. *Phys. Rev. Lett.* **1999**, *83*, 452–455.
44. Barigelletti, F.; Flamigni, L. *Chem. Soc. Rev.* **2000**, *29*, 1–12.
45. Liu, Z. F.; Hashimoto, K.; Fujishima, A. *Nature* **1990**, *347*, 658–660.
46. Hunter, S.; Kiamilev, F.; Esener, S.; Parthenopoulos, D. A.; Rentzepis, P. M. *Appl. Opt.* **1990**, *29*, 2058–2066.
47. Feringa, B. L.; Jager, W. F.; de Lange, B. *Tetrahedron* **1992**, *49*, 8267–8310.
48. Hopfield, J. J.; Onuchic, J. N.; Beratan, D. N. *Science* **1988**, *241*, 817–819.
49. Dvornikov, A. S.; Taylor, C. M.; Liang, Y. C.; Rentzepis, P. M. *J. Photochem. Photobiol. A* **1998**, *112*, 39–46.
50. Aviram, A. *J. Am. Chem. Soc.* **1988**, *110*, 5687–5692.
51. Lehn, J.-M. *Angew. Chem. Int. Ed. Engl.* **1988**, *27*, 89–112.
52. Lehn, J.-M. *Angew. Chem. Int. Ed. Engl.* **1990**, *29*, 1304–1319.
53. Ebbesen, T. W. *New J. Chem.* **1991**, *15*, 191–197.
54. Mirkin, C. A.; Ratner, M. A. *Annu. Rev. Phys. Chem.* **1992**, *43*, 719–754.
55. Ball, P.; Garwin, L. *Nature* **1992**, *355*, 761–766.
56. Gust, D.; Moore, T. A.; Moore, A. L. *IEEE Eng. Med. Biol.* **1994**, *94*, 58–66.
57. Willner, I.; Willner, B. *J. Mater. Chem.* **1998**, *8*, 2543–2556.
58. Heath, J. R.; Kuekes, P. J.; Snider, G. S.; Williams, R. S. *Science* **1998**, *280*, 1716–1721.
59. Tour, J. M.; Kozaki, M.; Seminario, J. M. *J. Am. Chem. Soc.* **1998**, *120*, 8486–8493.
60. Neff, J. A. *Opt. Eng.* **1987**, *26*, 2–9.
61. Shirakawa, M.; Takemori, T.; Ohtsubo, J. *Opt. Commun.* **1996**, *124*, 333–344.
62. Wherrett, B. S. *Synth. Met.* **1996**, *76*, 3–9.

63. Bjornholm, T. *Isr. J. Chem.* **1996**, 36, 349–356.
64. Yatagai, T.; Kawai, S.; Huang, H. *IEEE Proc.* **1996**, 84, 828–852.
65. O'Neil, M. P.; Niemczyk, M. P.; Svec, W. A.; Gosztola, D.; Gaines, G. L., III; Wasielewski, M. R. *Science* **1992**, 257, 63–65.
66. Daub, J.; Beck, M.; Knorr, A.; Spreitzer, H. *J. Pure Appl. Chem.* **1996**, 68, 1399–1404.
67. Burkhalter, F. A.; Suter, G. W.; Wild, U. P. *Chem. Phys. Lett.* **1983**, 94, 483–487.
68. Wild, U. P.; Bucher, S. E.; Burkhalter, F. A. *Appl. Opt.* **1985**, 24, 1526–1530.
69. Winnacker, A.; Shelby, R. M.; Macfarlane, R. M. *Opt. Lett.* **1985**, 10, 350–352.
70. Lee, H. W. H.; Gehrtz, M.; Marinero, E. E.; Moerner, W. E. *Chem. Phys. Lett.* **1985**, 118, 611–616.
71. Moerner, W. E.; Carter, T. P.; Brauchle, C. *Appl. Phys. Lett.* **1987**, 50, 430–432.
72. Carter, T. P.; Brauchle, C.; Lee, V. Y.; Manavi, M.; Moerner, W. E. *Opt. Lett.* **1987**, 12, 370–372.
73. Wild, U. P.; Bernet, S.; Kohler, B.; Renn, A. *Pure Appl. Chem.* **1992**, 64, 1335–1342.
74. Kohler, B.; Bernet, S.; Renn, A.; Wild, U. P. *Opt. Lett.* **1993**, 18, 2144–2146.
75. Maniloff, E. S.; Altner, S. B.; Bernet, S.; Graf, F. R.; Renn, A.; Wild, U. P. *Appl. Opt.* **1995**, 34, 4140–4148.
76. Shen, X. A.; Nguyen, A.-D.; Perry, J. W.; Huestis, D. L.; Kachru, R. *Science* **1997**, 278, 96–100.
77. Jager, W. F.; de Jong, J. C.; de Lange, B.; Huck, N. P. M.; Meetsma, A.; Feringa, B. L. *Angew. Chem. Int. Ed. Engl.* **1995**, 34, 348–350.
78. Huck, N. P.; Jager, W. F.; de Lange, B.; Feringa, B. L. *Science* **1996**, 273, 1686–1688.
79. Zahn, S.; Canary, J. W. *Angew. Chem. Int. Ed. Engl.* **1998**, 37, 305–307.
80. Bouas-Laurent, H.; Castellan, A.; Desvergne, J.-P. *Pure Appl. Chem.* **1980**, 52, 2633–2648.
81. Nagamura, T.; Sakai, K.; Ogawa, T. *J. Chem. Soc., Chem. Commun.* **1988**, 1035–1037.
82. Ashwell, G. J. *Nature* **1990**, 347, 617.
83. Nespurek, S.; Schwartz, M.; Bohm, S.; Kuthan, J. J. *Photochem. Photobiol. A* **1991**, 60, 345–353.
84. Nespurek, S.; Schnabel, W. J. *Photochem. Photobiol. A* **1991**, 62, 151–159.
85. Achatz, J.; Rischer, C.; Salbeck, J.; Daub, J. J. *J. Chem. Soc., Chem. Commun.* **1991**, 504–507.
86. Sebek, P.; Nespurek, S.; Hrabal, R.; Adamec, M.; Kuthan, J. J. *Chem. Soc. Perkin Trans. 2* **1992**, 1301–1308.
87. Jorgensen, M.; Lerstrup, K.; Frederiksen, P.; Bjornholm, T.; Sommer-Larsen, P.; Schaumburg, K.; Brunfeldt, K.; Bechgaard, K. *J. Org. Chem.* **1993**, 58, 2785–2790.
88. Walz, J.; Ulrich, K.; Port, H.; Wolf, H. C.; Wonner, J.; Effenberger, F. *Chem. Phys. Lett.* **1993**, 213, 321–324.
89. Nespurek, S.; Sworakowski, J. *IEEE Eng. Med. Biol.* **1994**, 94, 45–57.
90. Kawai, S. H.; Gilat, S. L.; Lehn, J. M. *J. Chem. Soc., Chem. Commun.* **1994**, 1011–1013.
91. Kawai, S. H.; Gilat, S. L.; Ponsinet, R.; Lehn, J.-M. *Chem. Eur. J.* **1995**, 1, 285–293.
92. DelMedico, A.; Fielder, S. S.; Lever, A. B. P.; Pietro, W. J. *Inorg. Chem.* **1995**, 34, 1507–1513.
93. Otsuki, J.; Tsujino, M.; Iizaki, T.; Araki, K.; Seno, M.; Takater, K.; Watanabe, T. *J. Am. Chem. Soc.* **1997**, 119, 7895–7896.
94. Seibold, M.; Handschuh, M.; Port, H.; Wolf, H. C. *J. Lumin.* **1997**, 72–74, 454–456.
95. Weber, C.; Rustemeyer, F.; Durr, H. *Adv. Mater.* **1998**, 10, 1348–1351.
96. Archut, A.; Vogtle, F.; De Cola, L.; Azzellini, G. C.; Balzani, V.; Ramanujam, P. S.; Berg, R. H. *Chem. Eur. J.* **1998**, 4, 699–706.
97. Mitchell, R. H.; Ward, T. R.; Wang, Y.; Dibble, P. W. *J. Am. Chem. Soc.* **1999**, 121, 2601–2602.
98. Gobbi, L.; Seiler, P.; Diedrich, F. *Angew. Chem. Int. Ed. Engl.* **1999**, 35, 674–678.
99. Kawai, S. H.; Gilat, S. L.; Lehn, J.-M. *Eur. J. Org. Chem.* **1999**, 2359–2366.
100. Benard, S.; Yu, P. *Adv. Mater.* **2000**, 12, 48–50.
101. Dvornikov, A. S.; Rentzepis, P. M. *Opt. Commun.* **1997**, 136, 1–6.
102. Westermeier, C.; Gallmeier, H.-C.; Komma, M.; Daub, J. *Chem. Commun.* **1999**, 2427–2428.
103. Fabbrizzi, L.; Poggi, A. *Chem. Soc. Rev.* **1995**, 197–202.
104. de Silva, A. P.; Gunaratne, H. Q. N.; Gunnlaugsson, T.; Huxley, A. J. M.; McCoy, C. P.; Radmacher, J. T.; Rice, T. E. *Chem. Rev.* **1997**, 97, 1515–1566.

105. Mitchell, K. A.; Brown, R. G.; Yuan, D.; Chang, S.-C.; Utecht, R. E.; Lewis, D. E. *J. Photochem. Photobiol. A* **1998**, *115*, 157–161.
106. Wang, P.; Wu, S. *J. Photochem. Photobiol. A* **1998**, *118*, 7–9.
107. Kimura, E.; Koike, T. *Chem. Soc. Rev.* **1998**, *27*, 179–184.
108. Kijima, H.; Takeuchi, M.; Robertson, A.; Shinkai, S.; Cooper, C.; James, T. D. *Chem. Commun.* **1999**, 2011–2012.
109. Wu, Z.-Z.; Morrison, H. *J. Am. Chem. Soc.* **1989**, *111*, 9267–9269.
110. Hasharoni, K.; Levanon, H.; Greenfield, S. R.; Gosztola, D. J.; Svec, W. A.; Wasielewski, M. R. *J. Am. Chem. Soc.* **1995**, *117*, 8055–8056.
111. Kuciauskas, D.; Liddell, P. A.; Moore, A. L.; Moore, T. A.; Gust, D. *J. Am. Chem. Soc.* **1998**, *120*, 10880–10886.
112. Klumpp, T.; Linsenmann, M.; Larson, S. L.; Limoges, B. R.; Burssner, D.; Krissinel, E. B.; Elliott, C. M.; Steiner, U. E. *J. Am. Chem. Soc.* **1999**, *121*, 1076–1087.
113. Wiederrecht, G. P.; Svec, W. A.; Wasielewski, M. R. *J. Am. Chem. Soc.* **1999**, *121*, 7726–7727.
114. Kondo, K.; Takezoe, H.; Fukuda, A.; Kuze, E. *Jpn. J. Appl. Phys., Part 2* **1983**, *22*, 85–87.
115. Bawa, S. S.; Biradar, A. M.; Saxena, K.; Chandra, S. *Jpn. J. Appl. Phys., Part 1* **1987**, *26*, 1952–1958.
116. Ikeda, T.; Tsutsumi, O.; Sasaki, T. *Synth. Met.* **1996**, *81*, 289–296.
117. Shishido, A.; Tsutsumi, O.; Kanazawa, A.; Shiono, T.; Ikeda, T.; Tamai, N. *J. Am. Chem. Soc.* **1997**, *119*, 7791–7796.
118. Kurihara, S.; Sakamoto, A.; Nonaka, T. *Macromolecules* **1998**, *31*, 4648–4650.
119. Wu, Y.; Mamiya, J.-I.; Kanazawa, A.; Shiono, T.; Ikeda, T.; Zhang, Q. *Macromolecules* **1999**, *32*, 8829–8835.
120. Chiang, C. *Appl. Phys. Lett.* **1997**, *31*, 553–555.
121. Kawamura, S.; Tsutsui, T.; Saito, S.; Murao, Y.; Kina, K. *J. Am. Chem. Soc.* **1988**, *110*, 509–511.
122. Wild, U. P.; Rebane, A.; Renn, A. *Adv. Mater.* **1991**, *3*, 453–456.
123. Iwamoto, M.; Majima, Y.; Naruse, H.; Noguchi, T.; Fuwa, H. *J. Chem. Phys.* **1991**, *95*, 8561–8567.
124. Iwamoto, M.; Noguchi, T.; Fuwa, H.; Majima, Y. *Jpn. J. Appl. Phys., Part 1* **1991**, *30*, 1020–1023.
125. Iwamoto, M.; Ohnishi, K.; Xu, X. *Jpn. J. Appl. Phys., Part 1* **1995**, *34*, 3814–3819.
126. Vermeulen, L. A.; Thompson, M. E. *Nature* **1992**, *358*, 656–658.
127. Oosterling, M. L. C. M.; Schoevaars, A. M.; Haitjema, H. J.; Feringa, B. L. *Isr. J. Chem.* **1996**, *36*, 341–348.
128. Owrutsky, J. C.; Nelson, H. H.; Baronavski, A. P.; Kim, O.-K.; Tsvigoulis, G. M.; Gilat, S. L.; Lehn, J.-M. *Chem. Phys. Lett.* **1998**, *293*, 555–563.
129. Willner, I.; Doron, A.; Katz, E. *J. Phys. Org. Chem.* **1998**, *11*, 546–560.
130. Kano, K.; Tanaka, Y.; Ogawa, T.; Shimomura, M.; Okahata, Y.; Kunitake, T. *Chem. Lett.* **1980**, 421–424.
131. Cremer, P. S.; Groves, J. T.; Kung, L. A.; Boxer, S. G. *Langmuir* **1999**, *15*, 3893–3896.
132. Gust, D.; Moore, T. A.; Moore, A. L. *Acc. Chem. Res.* **1993**, *26*, 198–205.
133. Alpha, B.; Lehn, J.-M.; Mathis, G. *Angew. Chem. Int. Ed. Engl.* **1987**, *26*, 266–267.
134. Prathapan, S.; Johnson, T. E.; Lindsey, J. S. *J. Am. Chem. Soc.* **1993**, *115*, 7519–7520.
135. Holl, N.; Port, H.; Wolf, H. C.; Strobel, H.; Effenberger, F. *J. Chem. Phys.* **1993**, *176*, 215–220.
136. Vogtle, F.; Frank, M.; Vieger, M.; Belser, P.; von Zelewski, A.; Balzani, V.; Barigelletti, F.; De Cola, L.; Flamigni, L. *Angew. Chem. Int. Ed. Engl.* **1993**, *32*, 1643–1645.
137. Seth, J.; Palaniappan, V.; Johnson, T. E.; Prathapan, S.; Lindsey, J. S.; Bocian, D. F. *J. Am. Chem. Soc.* **1994**, *116*, 10578–10592.
138. Wagner, R. W.; Johnson, T. E.; Lindsey, J. S. *J. Am. Chem. Soc.* **1996**, *118*, 11166–11180.
139. Devadoss, C.; Bharathi, P.; Moore, J. S. *J. Am. Chem. Soc.* **1996**, *118*, 9635–9644.
140. Gust, D. *Nature* **1997**, *386*, 21–22.
141. Van Patten, P. G. S.; A. P.; Lindsey, J. S.; Donohoe, R. J. *J. Phys. Chem. B* **1998**, *102*, 4209–4216.

142. Yang, S. I.; Lammi, R. K.; Seth, J.; Riggs, J. A.; Arai, T.; Kim, D.; Bocian, D. F.; Holten, D.; Lindsey, J. S. *J. Phys. Chem. B* **1998**, *102*, 9426–9436.
143. Wagner, R. W.; Seth, J.; Yang, S. I.; Kim, D.; Bocian, D. F.; Holten, D.; Lindsey, J. S. *J. Org. Chem.* **1998**, *63*, 5042–5049.
144. Li, F.; Yang, S. I.; Ciringh, Y.; Seth, J.; Martin III, C. H.; Singh, D. L.; Kim, D.; Birge, R. R.; Bocian, D. F.; Holten, D.; Lindsey, J. S. *J. Am. Chem. Soc.* **1998**, *120*, 10001–10017.
145. Gust, D.; Moore, T. A.; Moore, A. L.; Kuciauskas, D.; Liddell, P. A.; Halbert, B. D. *J. Photochem. Photobiol. B* **1998**, *43*, 209–216.
146. Kuciauskas, D.; Liddell, P. A.; Lin, S.; Johnson, T. E.; Weghorn, S. J.; Lindsey, J. S.; Moore, A. L.; Moore, T. A.; Gust, D. *J. Am. Chem. Soc.* **1999**, *121*, 8604–8614.
147. Brodard, P.; Matzinger, S.; Vauthey, E.; Mongin, O.; Papamical, C.; Gossauer, A. *J. Phys. Chem. A* **1999**, *103*, 5858–5870.
148. Wagner, R. W.; Lindsey, J. S.; Seth, J.; Palaniappan, V.; Bocian, D. F. *J. Am. Chem. Soc.* **1996**, *118*, 3996–3997.
149. Sato, T. J.; D-L.; Aida, T. *J. Am. Chem. Soc.* **1999**, *121*, 10658–10659.
150. Li, J.; Ambroise, A.; Yang, S. I.; Diers, J. R.; Seth, J.; Wack, C. R.; Bocian, D. F.; Holten, D.; Lindsey, J. S. *J. Am. Chem. Soc.* **1999**, *121*, 8927–8940.
151. Phillips, W. A. *J. Low Temp. Phys.* **1972**, *7*, 351–360.
152. Basche, T.; Moerner, W. E. *Nature* **1992**, *355*, 335–337.
153. Fleury, L.; Zumbusch, A.; Orrit, M.; Brown, R.; Bernard, J. *J. Lumin.* **1993**, *56*, 15–28.
154. Moerner, W. E.; Plakhotnik, T.; Irngartinger, T.; Croci, M.; Palm, V.; Wild, U. P. *J. Phys. Chem.* **1994**, *98*, 7382–7389.
155. Barth, K.; Richter, W. *J. Lumin.* **1995**, *64*, 63–67.
156. Kummer, S.; Basche, T.; Brauchle, C. *Chem. Phys. Lett.* **1994**, *229*, 309–316.
157. Basche, T.; Kummer, S.; Brauchle, C. *Nature* **1995**, *373*, 132–134.
158. Kulzer, F.; Kummer, S.; Matzke, R.; Brauchle, C.; Basche, T. *Nature* **1997**, *387*, 688–691.
159. Dessauer, R.; Paris, J. P. *Photochromism*; Interscience Publishers: New York, 1963; Vol. 1.
160. Cabrera, I.; Engel, M.; Haubling, L.; Mertesdorf, C.; Ringsdorf, H. *Photoinduced Structural Changes in Organized Supramolecular Systems*; Schneider, H.-J. and Duerr, H., Ed.; VCH: Weinheim, Germany, 1991; pp. 311–336.
161. Ashwell, G. J. *Adv. Spectrosc.* **1993**, *22* (*Spectroscopy of New Materials*), 61–85.
162. Martin, P. J. *Photochromism*; Petty, M. C., Bryce, M. R. and Bloor, D., Ed.; Arnold: London, UK, 1995; pp. 112–141.
163. Maack, J.; Ahuja, R. C.; Mobius, D.; Tachibana, H.; Matsumoto, M. *Thin Solid Films* **1994**, *242*, 122–126.
164. Xu, X. B.; Majima, Y.; Iwamoto, M. *Thin Solid Films* **1998**, *331*, 239–247.
165. Tachibana, H.; Nakamura, T.; Matsumoto, M.; Komizu, H.; Manda, E.; Niino, H.; Yabe, A.; Kawabata, Y. *J. Am. Chem. Soc.* **1989**, *111*, 3080–3081.
166. Tachibana, H.; Manda, E.; Azumi, R.; Nakamura, T.; Matsumoto, M.; Kawabata, Y. *Appl. Phys. Lett.* **1992**, *61*, 2420–2421.
167. Hoffman, K.; Marlow, F.; Caro, J. *Adv. Mater.* **1997**, *9*, 567–570.
168. Berg, R. H.; Hvilsted, S.; Ramanujam, P. S. *Nature* **1996**, *383*, 505–508.
169. Mekelburger, H.-B.; Rissanen, K.; Vogtle, F. *Chem. Ber.* **1993**, *126*, 1161–1169.
170. Kumar, G. S.; Neckers, D. C. *Chem. Rev.* **1989**, *89*, 1915–1925.
171. Ikeda, T.; Horiuchi, S.; Karanjit, B.; Kurihara, S.; Tazuke, S. *Macromolecules* **1990**, *23*, 36–42.
172. Ikeda, T.; Horiuchi, S.; Karanjit, B.; Kurihara, S.; Tazuke, S. *Macromolecules* **1990**, *23*, 42–48.
173. Ikeda, T.; Kurihara, S.; Karanjit, D. B.; Tazuke, S. *Macromolecules* **1990**, *23*, 3938–3943.
174. Ikeda, T.; Sasaki, T.; Kim, H.-B. *J. Phys. Chem.* **1991**, *93*, 509–511.
175. Tsutsumi, O.; Shiono, T.; Ikeda, T.; Galli, G. *J. Phys. Chem. B* **1997**, *101*, 1332–1337.
176. Kurihara, S.; Kanda, T.; Nagase, T.; Nonaka, T. *Appl. Phys. Lett.* **1998**, *73*, 2081–2083.
177. Tsutsumi, O.; Demachi, Y.; Kanazawa, A.; Shiono, T.; Ikeda, T.; Nagase, Y. *J. Phys. Chem. B* **1998**, *102*, 2869–2874.
178. Wu, Y.; Demachi, Y.; Tsutsumi, O.; Kanazawa, A.; Shiono, T.; Ikeda, T. *Macromolecules* **1998**, *31*, 349–354.

179. Tsutsumi, O.; Kanazawa, A.; Shiono, T.; Ikeda, T.; Park, L.-S. *Phys. Chem. Chem. Phys.* **1999**, *1*, 4219–4224.
180. Eich, M.; Wendorff, J. H. *J. Opt. Soc. Am. B* **1990**, *7*, 1428–1436.
181. Gibbons, W. M.; Shannon, P. J.; Sun, S.-T.; Swetlin, B. J. *Nature* **1991**, *351*, 49–50.
182. Jager, W. F.; De Lang, B.; Feringa, B. L. *Mol. Cryst. Liq. Cryst. Sci. Technol., Sect. A* **1992**, *217*, 133–138.
183. Rau, H. *Chem. Rev.* **1983**, *83*, 535.
184. Gakh, A. A.; Sachleben, R. A.; Bryan, J. C. *Chemtech* **1997**, *27*, 26–33.
185. Koumura, N.; Zijlstra, R. W.; van Delden, R. A.; Harada, N.; Feringa, B. L. *Nature* **1999**, *401*, 152–155.
186. Kelly, T. R.; De Silva, H.; Silva, R. A. *Nature* **1999**, *401*, 150–152.
187. Schoevaars, A. M.; Kruizinga, W.; Zijlstra, R. W.; Veldman, N.; Spek, A. L.; Feringa, B. L. *J. Org. Chem.* **1997**, *62*, 4943–4948.
188. Benniston, A. C.; Harriman, A. *Angew. Chem. Int. Ed. Engl.* **1993**, *32*, 1459–1461.
189. Balzani, V.; Gomez-Lopez, M.; Stoddart, J. F. *Acc. Chem. Res.* **1998**, *31*, 405–414.
190. Amabilino, D. B.; Asakawa, M.; Ashton, P. R.; Ballardini, R.; Balzani, V.; Belohradsky, M.; Credi, A.; Higuchi, M.; Raymo, F. M.; Shimizu, T.; Stoddart, J. F.; Venturi, M.; Yase, K. *New J. Chem.* **1998**, 959–972.
191. Bissell, R. A.; Cordova, E.; Kaifer, A. E.; Stoddart, J. F. *Nature* **1994**, *369*, 133–137.
192. Asakawa, M.; Iqbal, S.; Stoddart, J. F.; Tinker, N. D. *Angew. Chem. Int. Ed. Engl.* **1996**, *35*, 976–978.
193. Ballardini, R.; Balzani, V.; Credi, A.; Gandolfi, M. T.; Langford, S. J.; Manzer, S.; Prodi, L.; Stoddart, J. F.; Venturi, M.; Williams, D. J. *Angew. Chem. Int. Ed. Engl.* **1996**, *35*, 978–981.
194. Credi, A.; Balzani, V.; Langford, S. J.; Stoddart, J. F. *J. Am. Chem. Soc.* **1997**, *119*, 2679–2681.
195. Ashton, P. R.; Balzani, V.; Becher, J.; Credi, A.; Fyfe, M. C. T.; Mattersteig, G.; Menzer, S.; Nielsen, M. B.; Raymo, F. M.; Stoddart, J. F.; Venturi, M.; Williams, D. J. *J. Am. Chem. Soc.* **1999**, *121*, 3951–3957.
196. Matthews, O. A.; Raymo, F. M.; Stoddart, J. F.; White, A. J.; Williams, D. J. *New J. Chem.* **1998**, 1131–1134.
197. de Silva, A. P.; Gunaratne, H. Q. N.; Rice, T. E.; Stewart, S. *Chem. Commun.* **1997**, 1891–1892.
198. Steenwinkel, P.; Grove, D. M.; Veldman, N.; Spek, A. L.; van Koten, G. *Organometallics* **1998**, *17*, 5647–5655.
199. Plenio, H.; Aberle, C. *Angew. Chem. Int. Ed. Engl.* **1998**, *37*, 1397–1399.
200. Belle, C.; Pierre, J.-L.; Saint-Aman, E. *New J. Chem.* **1998**, 1399–1402.
201. Laine, P.; Marvaud, V.; Gourdon, A.; Launay, J. P.; Argazzi, R.; Bignozzi, C.-A. *Inorg. Chem.* **1996**, *35*, 711–714.
202. Tysoe, S. A.; Kopelman, R.; Schelzig, D. *Inorg. Chem.* **1999**, *38*, 5196–5197.
203. Ward, T. R.; Lutz, A.; Parel, S. P.; Ensling, J.; Gutlich, P.; Buglyo, P.; Orvig, C. *Inorg. Chem.* **1999**, *38*, 5007–5017.
204. Collins, G. E.; Choi, L.-S.; Ewing, K. J.; Michelet, V.; Bowen, C. M.; Winkler, J. D. *Chem. Commun.* **1999**, 321–322.
205. Ford, J. E.; Hunter, S.; Piyaket, R.; Fainman, Y.; Esener, S.; Dvornikov, A. S.; Rentzepis, P. M. *Proc. SPIE-Int. Soc. Opt. Eng.* **1993**, 2026(*Photonics for Processors, Neural Networks, and Memories*), 604–613.
206. Ford, J. E.; Hunter, S.; Piyaket, R.; Fainman, Y.; Esener, S. E.; Dvornikov, A. S.; Rentzepis, P. M. *Proc. SPIE-Int. Soc. Opt. Eng.* **1993**, 1853(*Organic and Biological Optoelectronics*), 5–13.
207. Piyaket, R.; Cokgor, I.; Esener, S. C.; Solomon, C.; Hunter, S.; Ford, J. E.; Dvornikov, A. S.; Tomov, I.; Rentzepis, P. M. *Proc. SPIE-Int. Soc. Opt. Eng.* **1994**, 2297(*Photonics for Processors, Neural Networks, and Memories II*), 435–446.
208. Dvornikov, A. S.; Malkin, J.; Rentzepis, P. M. *J. Phys. Chem.* **1994**, *98*, 6746–6752.
209. Akimov, D. A.; Fedotov, A. B.; Koroteev, N. I.; Magnitskii, S. A.; Naumov, A. N.; Sidorov-Biryukov, D. A.; Sokolyuk, N. T.; Zheltikov, A. M. *Proc. SPIE-Int. Soc. Opt. Eng.* **1998**, 3402(*Optical Memory and Neural Network*), 137–148.

210. Bobrovsky, A. Y.; Boiko, N. I.; Shibaev, V. P. *Adv. Mater.* **1999**, *11*, 1025–1028.
211. Yitzchaik, S.; Berkovic, G.; Krongauz, V. *Adv. Mater.* **1990**, *2*, 33–36.
212. Dvornikov, A. S.; Cokgor, I.; McCormick, F.; Piyaket, R.; Esener, S.; Rentzepis, P. M. *Opt. Commun.* **1996**, *128*, 205–210.
213. Sekikawa, T.; Kobayashi, T. *J. Phys. Chem. B* **1997**, *101*, 10645–10652.
214. Whittall, J. *Stud. Org. Chem.* **1990**, *40* (Photochromism: Mol. Syst.), 467–92.
215. Kurita, S.; Takeda, J.; Yokoyama, Y.; Kurita, Y. *Photochromic Fulgides Applicable to Optical Information Storage*; Tsuruta, T., Ed.; Elsevier: Amsterdam, 1993; Vol. C, pp. 357–362.
216. Francini, F.; Ottavi, G.; Sansoni, P.; Tiribilli, B. *Opt. Commun.* **1996**, *130*, 235–240.
217. Liang, Y.; Dvornikov, A. S.; Rentzepis, P. M. *Tetrahedron. Lett.* **1999**, *40*, 8067–8069.
218. Kardinahl, T.; Franke, H. *Appl. Phys. A: Mater. Sci. Proc.* **1995**, *A61*, 23–27.
219. Kardinahl, T.; Franke, H. *Holographic Gratings in Organic Photochromics: Nonlinear and Switchable Gratings*; 1996; Vol. 2688 (Holographic Materials II), pp. 52–58.
220. Janicki, S. Z.; Schuster, G. B. *J. Am. Chem. Soc.* **1995**, *117*, 8524–8527.
221. Aviram, A.; Ratner, M. A. *Chem. Phys. Lett.* **1974**, *29*, 277–283.
222. Metzger, R. M.; Panetta, C. A.; Heimer, N. E.; Bhatti, A. M.; Torres, E.; Blackburn, G. F.; Tripathy, S. K.; Samuelson, L. A. *J. Mol. Electron.* **1986**, *2*, 119.
223. Metzger, R. M. *Adv. Chem. Ser.* **1994**, *240*, 81–129.
224. Wasielewski, M. R.; Gaines, G. L., III; Gosztola, D.; Niemczyk, M. P.; Svec, W. A. *Supramolecular Structures Modeling Photosynthetic Reaction Center Function*; Murata, N., Ed.; Kluwer: Dordrecht, 1992; Vol. 2; pp. 795–800.
225. Kurreck, H.; Huber, M. *Angew. Chem. Int. Ed. Engl.* **1995**, *34*, 849–866.
226. *Photoresponsive Polymers*, Irie, M.; Ikeda, T. Eds.; Dekker: New York, NY, 1997.
227. Debreczeny, M. P.; Svec, W. A.; Marsh, E. M.; Wasielewski, M. R. *J. Am. Chem. Soc.* **1996**, *118*, 8174–8175.
228. Greenfield, S. R.; Svec, W. A.; Gosztola, D.; Wasielewski, M. R. *J. Am. Chem. Soc.* **1996**, *118*, 6767–6777.
229. Debreczeny, M. P.; Svec, W.; Wasielewski, M. R. unpublished results.
230. Lukas, A. S.; Miller, S. E.; Wasielewski, M. R. *J. Phys. Chem.* **2000**, *104*, 931–940.
231. Carbonera, D.; Di Valentin, M.; Corvaja, C.; Agostini, G.; Giacometti, G.; Liddell, P. A.; Kuciauskas, D.; Moore, A. L.; Moore, T. A.; Gust, D. *J. Am. Chem. Soc.* **1998**, *120*, 4398–4405.
232. Gilch, P.; Pollinger-Dammer, F.; Musewald, C.; Michel-Beyerle, M. E.; Steiner, U. E. *Science* **1998**, *281*, 982–984.
233. Debreczeny, M. P.; Svec, W. A.; Wasielewski, M. R. *Science* **1996**, *274*, 584–587.
234. Gosztola, D.; Niemczyk, M. P.; Wasielewski, M. R. *J. Am. Chem. Soc.* **1998**, *120*, 5118–5119.
235. Wasielewski, M. R. *Chem. Rev.* **1992**, *92*, 435–461.
236. Steinberg-Yfrach, G.; Liddell, P. A.; Hung, S.-C.; Moore, A. L.; Gust, D.; Moore, T. A. *Nature* **1997**, *385*, 239–241.
237. Feirong, L.; Yang, S. I.; Ciringh, Y.; Seth, J.; Martin III, C. H.; Singh, D. L.; Kim, D.; Birge, R. R.; Bocian, D. F.; Holtz, D.; Lindsey, J. S. *J. Am. Chem. Soc.* **1998**, *120*, 10001–10017.
238. Zhang, Q. T.; Tour, J. M. *J. Am. Chem. Soc.* **1998**, *120*, 5355–5362.
239. McGimpsey, W. G.; Samaniego, W. N.; Chen, L.; Wang, F. *J. Phys. Chem. A* **1998**, *102*, 8679–8689.
240. Tan, Z.; Kote, R.; Samaniego, W. N.; Weininger, S. J.; McGimpsey, W. G. *J. Phys. Chem. A* **1999**, *103*, 7612–7620.
241. Launay, J.-P.; Turrel-Pagis, M.; Lipskier, J.-F.; Marvaud, V.; Joachim, C. *Inorg. Chem.* **1991**, *30*, 1033–1038.
242. Marvaud, V.; Launay, J.-P. *Inorg. Chem.* **1993**, *32*, 1376–1382.
243. Stupp, S. I.; LeBonheur, V.; Walker, K.; Li, L. S.; Huggins, K. E.; Kcseser, M.; Amstutz, A. *Science* **1997**, *276*, 384–389.
244. Gellman, S. H. *Acc. Chem. Res.* **1998**, *31*, 173–180.
245. Valiyaveetil, S.; Mullen, K. *New J. Chem.* **1998**, *22*, 89–95.
246. Huck, W. T. S.; Rohrer, A.; Anikumar, A. T.; Fokkens, R. H.; Nibbering, N. M. M.; van Veggel, F. C. J. M.; Reinhoudt, D. N. *New J. Chem.* **1998**, *22*, 165–168.
247. Kishikawa, K.; Tsubokura, S.; Kohmoto, S.; Yamamoto, M. *J. Org. Chem.* **1999**, *64*, 7568–7578.

248. Schoonbeek, F. S.; van Esch, J. H.; Wegewijs, B.; Rep, D. B. A.; de Haas, M. P.; Klapwijk, T. M.; Kellogg, R. M.; Feringa, B. L. *Angew. Chem. Int. Ed. Engl.* **1999**, *38*, 1393–1397.
249. Gong, B.; Yan, Y.; Zeng, H.; Skrzypczak-Jankunn, E.; Kim, Y. W.; Zhu, J.; Ickes, H. *J. Am. Chem. Soc.* **1999**, *121*, 5607–5608.
250. Giribabu, L.; Rao, T. A.; Maiya, B. G. *Inorg. Chem.* **1999**, *38*, 4971–4980.
251. Tour, J. M. *Chem. Rev.* **1996**, *96*, 537–553.
252. Serroni, S.; Juris, A.; Venturi, M.; Campagna, S.; Resino, I. R.; Denti, G.; Credi, A.; Balzani, V. *J. Mater. Chem.* **1997**, *7*, 1227.
253. Issberner, J.; Voegtle, F.; De Cola, L.; Balzani, V. *Chem. Eur. J.* **1997**, *3*, 706.
254. Serroni, S.; Campagna, S.; Denti, G.; Juris, A.; Venture, M.; Balzani, V. *Adv. Dendritic Macromol.* **1996**, *3*, 61.
255. Balzani, V.; Campagna, S.; Denti, G.; Juris, A.; Serroni, S.; Venturi, M. *Acc. Chem. Res.* **1998**, *31*, 26–34.
256. Constable, E. C.; Housecroft, C. E.; Cattalini, M.; Phillips, D. *New J. Chem.* **1999**, *22*, 193–200.
257. Felder, D.; Gallani, J.-L.; Guillon, D.; Heinrich, B.; Nicoud, J.-F.; Neirengarten, J.-F. *Angew. Chem. Int. Ed. Engl.* **2000**, *39*, 201–204.
258. Slate, C. A.; Striplin, D. R.; Moss, J. A.; Chen, P.; Erickson, B. W.; Meyer, T. J. *J. Am. Chem. Soc.* **1998**, *120*, 4885.
259. Sassoon, R. E.; Gershuni, S.; Rabani, J. *J. Phys. Chem.* **1992**, *96*, 4692.
260. Watkins, D. M.; Fox, M. A. *J. Am. Chem. Soc.* **1996**, *118*, 4344.
261. Fossum, R. D.; Fox, M. A. *J. Am. Chem. Soc.* **1997**, *119*, 1197.
262. Rebek Jr., J. *Acc. Chem. Res.* **1999**, *32*, 278–286.
263. Brugger, P.-A.; Gratzel, M. *J. Am. Chem. Soc.* **1980**, *102*, 2461.
264. Kang, Y. S.; McManus, H. J. D.; Liang, K.; Kevan, L. *J. Phys. Chem.* **1994**, *98*, 1044.
265. Humphry-Baker, R.; Thompson, D. H.; Lei, Y.; Hope, M. J.; Hurst, J. K. *Langmuir* **1991**, *7*, 2592.
266. Patterson, B. C.; Thompson, D. H.; Hurst, J. K. *J. Am. Chem. Soc.* **1988**, *110*, 3656.
267. Dutta, P. K.; Incavo, J. A. *J. Phys. Chem.* **1987**, *91*, 4443.
268. Incavo, J. A.; Dutta, P. K. *J. Phys. Chem.* **1990**, *94*, 3075.
269. Dutta, P. K.; Turbeville, W. *J. Phys. Chem.* **1992**, *96*, 5024.
270. Sankaraman, S.; Yoon, K. B.; Yake, T.; Kochi, J. *J. Am. Chem. Soc.* **1991**, *113*, 1419.
271. Liu, X.; Liu, K.-K.; Thomas, J. *J. Phys. Chem.* **1989**, *93*, 4120.
272. Borja, M.; Dutta, P. K. *Nature* **1993**, *362*, 43.
273. Maruszewski, K.; Strommen, D. P.; Kincaid, J. R. *J. Am. Chem. Soc.* **1993**, *115*, 8345.
274. Ledney, M.; Dutta, P. K. *J. Am. Chem. Soc.* **1995**, *117*, 7687.
275. Kim, Y. I.; Mallouk, T. E. *J. Phys. Chem.* **1992**, *96*, 2879.
276. Kaschak, D. M.; Lean, J. T.; Waraksa, C. C.; Saupe, G. B.; Usami, H.; Mallouk, T. E. *J. Am. Chem. Soc.* **1999**, *121*, 3435–3445.
277. Nakamura, Y.; Pashkin, Y. A.; Tsai, J. S. *Nature* **1999**, *398*, 786–788.
278. Gershenfeld, N.; Chuang, I. L. *Sci. Am.* **1998**, *278*, 66–71.
279. Brassard, G.; Chuang, I.; Lloyd, S.; Monroe, C. *Proc. Natl. Acad. Sci. USA* **1998**, *95*, 11032–11033.
280. Yamaguchi, F.; Yamamoto, Y. *Appl. Phys. A: Mater. Sci. Proc.* **1999**, *A68*, 117–123.

3 Photonic Wires Containing Metal Complexes

Luisa De Cola and Peter Belser

3.1 Introduction

The control of the electronic properties in molecular systems has acquired a growing importance in chemistry, especially in the field of molecular electronics and nanotechnology in connection with electronic and photonic applications [1–9]. The burgeoning of supramolecular architectures [10–16] that could perform functions that the simplest systems do not [17–20], the need to realize nanosized systems to fill the gap between the molecular and the macroscopic world, and the development of new synthetic strategies have contributed strongly to the design and realization of rods and wire-type systems [21–25]. Many organic conjugated oligomeric systems [4, 23] and conductive polymers [2, 3, 9] have been described and the possibility of tailoring their electronic and structural properties to accomplish a desired function and use them in optoelectronic devices has been described by several authors [4, 9]. Despite the increasing number of rod- and wire-type molecules, the assembly of such molecules with metal complexes units to build up multicomponent systems, the simplest being dinuclear complexes, is rather limited [18, 24–27]. Many dinuclear complexes have been studied with the aim of obtaining quantitative statements on the motion of charge or excitation energy along one or another type of rod. The role played by σ or π symmetry orbitals, the effect of the substituents on the peripheral ligands, and the difficulties associated with a localized vs. delocalized model in highly conjugated species surely need more investigation. We have tried in this chapter to collect some, in our opinion representative, examples of “rigid” systems containing metal complexes covalently linked through a bridging ligand. We have selected some “nonconductive” species and compare their properties with some that show a conductive or “wire-type” behavior. We have restricted our discussion only to dinuclear compounds containing Ru, Os, or Rh complexes as electron and/or energy donor/acceptor (D/A) moieties. We have divided the compounds according to the nature of the bridging ligand and we have included, at the

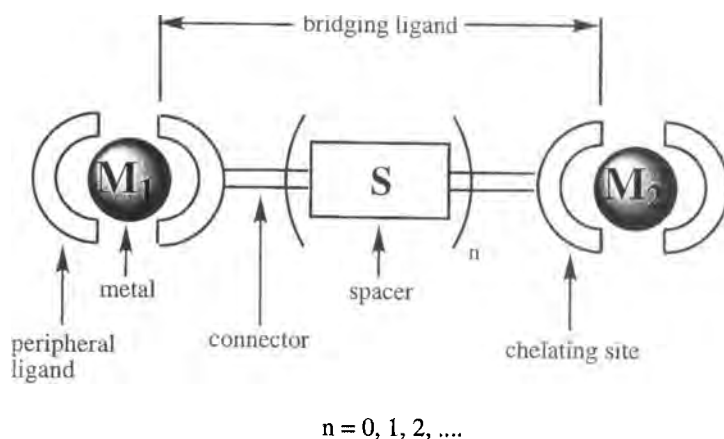


Figure 1. Schematic representation of a simple dinuclear compound.

end of each section, a table containing the most important photophysical data, related to species where photoinduced processes were observed.

3.2 Choice and Assembly of the Components for Photoactive Systems

In order to have a rod-type system where photoinduced energy transfer or electron transfer processes can occur, great attention must be devoted to the separated components and to the way they are connected [24, 26–29]. The simplest system conceivable for the occurrence of a photoinduced process, a dyad, is depicted in Figure 1.

As shown schematically, we can recognize three important elements in the construction of a dyad: the donor and acceptor sites that in our discussion are metal-based units, the connectors, and the bridging ligand. Many multicomponent systems incorporating photoactive and electroactive units based on metal transition complexes have been constructed [24, 26–28], especially with the attractive electrochemical and excited-state properties of $M(N-N)_3^{n+}$ or $M(N-N-N)_2^{n+}$ complexes, where M is a metal ion of the second or third transition rows, $N-N$ is a bidentate bpy-type or phen-type ligand (bpy = 2,2'-bipyridine, phen = 1,10-phenanthroline), and $N-N-N$ is generally a tpy-type ligand (tpy = 2,2':6',2''-terpyridine). Extensive investigations performed on $[Ru(bpy)_3]^{2+}$ and $[Os(bpy)_3]^{2+}$ and related complexes [12, 26, 27, 30–32] have shown that:

- 1) their high-intensity absorption bands in the 250–300 nm spectral region are due to spin-allowed ligand-centered (LC) transitions;

- 2) their absorption bands in the 400–550 nm region are due to spin-allowed metal-to-ligand charge-transfer (MLCT) transitions;
- 3) for the compounds of the heavier (Os) metal, spin-forbidden MLCT bands can also be seen in the 550–700 nm region;
- 4) luminescence takes place from the lowest-energy triplet MLCT excited state;
- 5) the luminescent excited state is very rapidly populated with unit efficiency regardless of the excitation wavelength.

At room temperature in fluid solution $[\text{Ru}(\text{bpy})_3]^{2+}$ and $[\text{Ru}(\text{phen})_3]^{2+}$ exhibit a strong and long-lived luminescence (τ of the order of 10^2 – 10^3 ns) [30, 31]. A different behavior is shown by terpyridine compounds, which offer important geometrical advantages (the possibility of constructing linear and rigid arrays) but poor emitting properties [33]. In fact $[\text{Ru}(\text{tpy})_2]^{2+}$ is very weakly luminescent (τ ca. 0.25 ns) [33] because of the low energy of the metal-centered states, ^3MC , which can be thermally populated from the luminescent $^3\text{MLCT}$ state. Besides ruthenium and osmium, other luminescent metal units have been used to construct multinuclear compounds. $\text{Re}(\text{I})$ diimine complexes of general formula $\text{ReL}(\text{CO})_3\text{X}^+$ exhibit luminescence at room temperature which is usually due to $d\pi \rightarrow \pi^*$ ($^3\text{MLCT}$) or $\pi \rightarrow \pi^*$ (^3LC) transitions, but these will not be discussed in this chapter. $\text{Rh}(\text{III})$ and $\text{Ir}(\text{III})$ complexes containing polypyridine or cyclometallating chelating ligands $\text{N}-\text{C}^-$ have also been used in the construction of multinuclear systems and some examples will be given.

In order to assemble these metal-containing building blocks it is necessary to have a connection between the metal units. Such a structural component, the bridging ligand, should contain sites able to coordinate the metal center, and suitable spacers in order to control distance and orientation of the chromophores (see Figure 1). The main requirements for the bridging ligand are therefore: control of the overall geometry, rigidity, and length modulation. The first two requirements have been achieved for several systems, but a modular nature of the bridging ligand is often difficult to attain for synthetic reasons, solubility being the most important [11, 22, 27]. In order to provide a way of varying the distance and the electronic interaction between the two chromophores, the bridging ligand must contain spacers, conjugated or saturated molecules that can be modular units. With such an arrangement it is clear therefore that one can tune the rates of the energy and electron transfer processes with an appropriate choice of components. It is important to notice, however, that even the use of rigid spacers, such as polyphenylenes or saturated molecules, provides in some cases a fixed metal–metal distance, but does not prevent conformational effects. In fact rotation around formally single bonds will confer some conformational freedom, and if the intercomponent interaction proceeds via the π system of the bridge, the tilt angle between the spacers can have relevant consequences for metal–metal interactions and for electron transfer rates. Therefore the connections between the spacers and/or the chelating sites is another factor that should not be neglected.

Another important consideration concerns the peripheral ligands. Figure 2 shows the peripheral ligands that are employed in the systems discussed here.

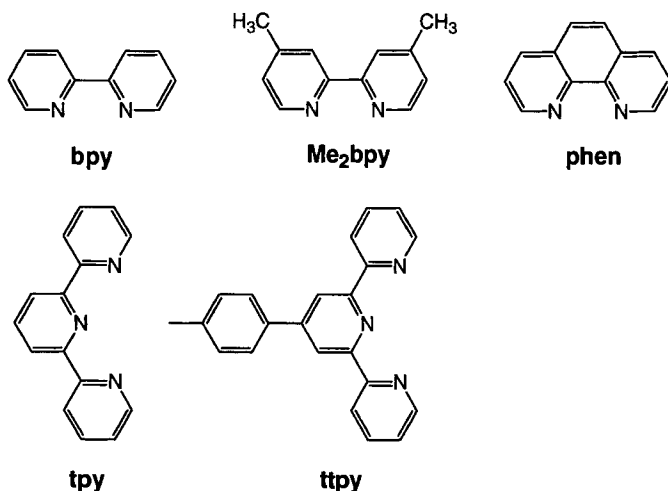


Figure 2. Peripheral ligands and their abbreviations.

In many dinuclear compounds the lowest excited states involve the bridging ligand, since very often the lowest LUMO is localized on the more delocalized π system of the bridge. Therefore in such cases the peripheral ligands play only a minor role in the excited-state properties of the complexes. On the other hand, when the peripheral ligands have excited states lower in energy than the bridging ligand, upon light excitation the lowest MLCT will involve the ancillary ligands and the distance between the two chromophoric groups will be greater (for an example see Section 3.5.3). This consideration allows the construction of dinuclear compounds in which the lowest excited state can involve either the bridging or the peripheral ligand, depending on the substituents (electron donor or acceptor groups) on the ancillary ligands. A similar situation has been observed in the case of electron-rich bridging ligands for instance pyridyltriazole ligands, in which the lowest excited state is often localized on the peripheral ligands [34].

3.3 Intercomponent Photoinduced Processes

For a simple dinuclear compound D–S–A the photoinduced energy and electron transfer processes are represented schematically in Figure 3.

Since theoretical treatment of photoinduced processes may be found in recent review articles and books [35–47] and will be treated in other chapters, we recall only a few fundamental features below.

In an absolute rate formalism, the Marcus model [41a], the rate constant for an electron transfer process can be expressed as:

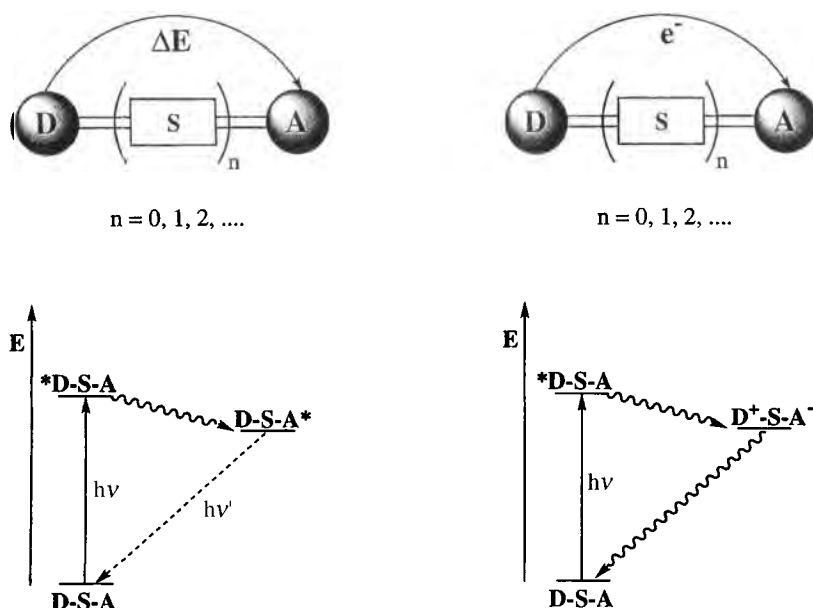


Figure 3. Schematic energy level diagrams for photoinduced energy transfer (left) and electron transfer (right) processes.

$$k_{\text{el}} = \nu_{\text{el}} \exp(-\Delta G_{\text{el}}^{\ddagger}/RT) \quad (1)$$

where ν_{el} is an effective frequency for nuclear motion, and $\Delta G_{\text{el}}^{\ddagger}$ is the free activation energy. $\Delta G_{\text{el}}^{\ddagger}$ depends on the driving force of the reaction and on the reorganizational energy λ , as expressed by the Marcus equation [41a]:

$$\Delta G_{\text{el}}^{\ddagger} = (\lambda/4) \left(1 + \frac{\Delta G^{\circ}}{\lambda} \right)^2 \quad (2)$$

Dealing with dinuclear metal complexes, the electronic interaction (often through-bond interaction) is strongly dependent on the length, electronic nature and geometry of the bridging ligand. The role of the bridging ligand in enhancing the electronic coupling between the two chromophoric groups in a multicomponent system has been described in terms of superexchange theory [35–37, 48–53]. This theory provides an approach where overlap between the metal-based components is mediated by overlap with the orbitals of the bridging ligands (through-bond interaction). The parameters which govern the extent of the interaction are therefore the orbital overlap and the energy gap between the relevant metal orbitals and LUMO/HOMO orbitals of the bridging ligand. In the case of modular bridging ligands constituted by a different number of spacers, an exponential dependence of the

electronic coupling on the number of spacers must be considered [35, 37, 51–53]:

$$H = H(0) \exp - [(\beta/2)(r - r_0)] \quad (3)$$

where r is the (through-bond) length of the spacer, r_0 is the distance between the donor and acceptor components without the spacer, $H(0)$ is the corresponding electronic coupling value and β , the attenuation factor, is a term which contains the interactions between the spacers. Most of the above-mentioned parameters and the rates for the electron transfer processes can be obtained by photophysical measurements [54].

The energy transfer processes can occur by two mechanisms: the Förster-type mechanism (through-space) [55], based on coulombic interactions, and the Dexter-type mechanism (through-bond) [56], based on exchange interactions. The energy transfer rate constants according to the Förster and Dexter treatments can be evaluated by Eqs. (4) [55] and (5) [56], respectively:

$$k_F = \frac{8.8 \times 10^{-25} K^2 \Phi}{n^4 \tau r^6} J_F \quad (4)$$

$$k_D = \frac{4\pi^2 H^2}{h} J_D \quad (5)$$

where H is the intercomponent electronic interaction energy, K is a geometric factor, Φ and τ are the luminescence quantum yield and the lifetime of the donor, respectively, n is the refractive index of the solvent, and J_F and J_D , according to the two different theories, are the overlap integrals between the luminescence spectrum of the donor, and the absorption spectrum of the acceptor, respectively [55–58].

In the weak-interaction limit, the exchange mechanism can be described in terms of thermodynamic quantities, according to a classical approach which parallels that for nonadiabatic electron transfer (see Eqs. (1) and (2)) [59–63].

The free energy change, ΔG° , for the energy transfer reaction can be expressed by the difference between the zero-zero spectroscopic energies of the donor and the acceptor excited states, which can be estimated from the luminescence band maxima of the reference complexes taken at 77 K [57, 64, 65].

Both through-bond and through-space transfer mechanisms can operate in donor-acceptor systems. Very often these mechanisms occur competitively and in some cases they can practically add to each other; their relative contributions are difficult to evaluate.

An evaluation of the rate constant of the energy transfer process can be obtained from Eqs. (6a) and (6b):

$$k_{en} = 1/\tau^\circ (I^\circ/I - 1) \quad (6a)$$

$$k_{en} = 1/\tau - 1/\tau^\circ \quad (6b)$$

where I° and τ° are the luminescence intensity and lifetime, respectively, of the species that can be quenched, the donor component, and I and τ are the residual luminescence intensity and lifetime after quenching. Long-lived excited states and

high luminescence quantum yields are preferred in the study of photoinduced processes and for the construction of supramolecular photochemical systems. This is simply due to the fact that short-lived excited states will decay to ground states before the desired reaction is accomplished.

In dinuclear metal complexes electronic interactions between the mononuclear components may range from very strong (with profound changes in the absorption spectrum on passing from mononuclear to dinuclear species) to very weak (with almost equal properties for separated and bridged units), depending on the type of bridge. If the interaction between the two metal-based units (for instance, polypyridine units $M(L)_n^{n+}$) in a dinuclear or multinuclear compound are weak, the following results are usually obtained:

- 1) the absorption spectra in the visible region of the homodinuclear $[M(L)_n-LSL-M(L)_n]^{n+}$ (LSL = a bridging ligand constituted by a spacer S and two chelating sites L) species are practically identical to those of the corresponding $[M(L)_n]^{n+}$ model compound;
- 2) the absorption spectra in the visible region of the heteronuclear complexes $[M(L)_n-LSL-M'(L)_n]^{n+}$ are practically identical to those of 1:1 mixtures of their corresponding homodinuclear $[M(L)_n-LSL-M(L)_n]^{n+}$ and $[M'(L)_n-LSL-M'(L)_n]^{n+}$ parent compounds;
- 3) the emission maximum, lifetime, and (in the homodinuclear complexes) quantum yield of the phosphorescence band of each $[M(L)_n]^{n+}$ unit are unaffected by the length of the spacer and by the nature of the metal contained in the $[M'(L)_n]^{n+}$ unit.

It should be recalled, however, that even an interaction of a few cm^{-1} (which cannot be noticed in spectroscopic experiments) may be sufficient to cause inter-component energy transfer or electron transfer processes. As already mentioned, the nature and length of the bridging ligand can contribute strongly to the rate of the photoinduced processes. Many compounds have been labeled wire molecules, but in most cases the wire-type behavior could not be observed. However, one should first define what is a molecular wire and what are the expectations for such a system.

3.4 What is a Molecular Wire?

One of the most important components of an integrated electronic system is the connection between the active units: the so-called wire. As in the macroscopic world, a (molecular) wire is a (molecular) structure that transmits a signal between two termini. The wire can transfer excitation energy or move electron or hole charges [3, 5, 66]. In our chapter we will refer to systems in which the charge or energy transport is due to a photoinduced intramolecular process and the molecular wire is indeed the bridging ligand between the donor and the acceptor sites. A molecular system, in order to behave as a wire, must have some structural features such as rigidity and modularity, and when used as a bridging ligand, in a donor–acceptor

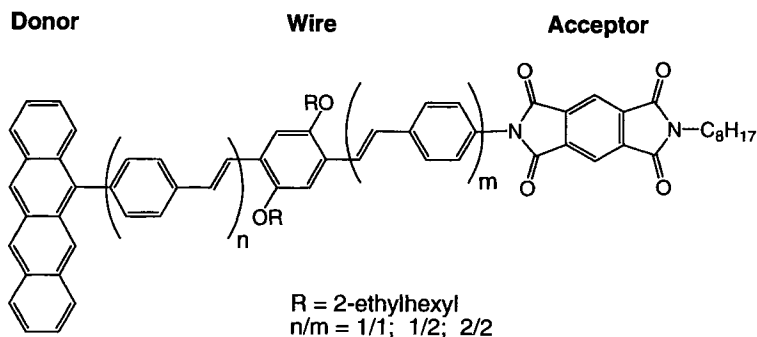


Figure 4. Schematic formula of the molecular wire reported by Wasielewski et al. [66].

system to perform photoinduced processes, this behavior should be independent of distance [3, 5, 24, 66, 67]. Such ideal behavior is hard to achieve for molecular wires, and in most of the compounds investigated an exponential decay of the rate of photoinduced processes has been observed. The growing interest in this field has led to a search for systems in which long-distance energy and electron transfer can be achieved, the rates of the photoinduced processes being fast ($k > 10^9 \text{ s}^{-1}$) and relatively independent of the length of the system. For example, Wasielewski and co-workers have recently reported a weak length dependence in highly conjugated systems [66]. In their system, schematized in Figure 4, the molecular wire behavior can be attained when there is an energy match between the donor and the bridge components; such requirements are indeed achieved in their multicomponent system when the bridging ligand contains more than three spacer units.

Also in metal-containing systems several attempts have been made to design systems that could show a wire behavior (see, for example, Refs. [24, 25, 67–70]). The use of metal complexes as D or A units is particularly attractive since the photo-physics and excited-state redox properties of many transition metal chromophores are tunable and therefore a tailor-made system can be obtained. It is interesting to recall that for metal complexes the excited state responsible for energy and electron transfer is often the lowest-lying triplet state, and that the photostability of such building blocks is generally very high [31, 71]. We will discuss some of these dinuclear systems, which we have divided into families depending on the type of the bridging ligand.

3.5 Systems Containing Saturated Spacers

Some dinuclear complexes, **1–10** [24–28, 38, 72–89], containing rigid saturated spacers are shown in Figure 5 and, for the species for which photoinduced processes have been observed, the photophysical properties are reported in Table 1.

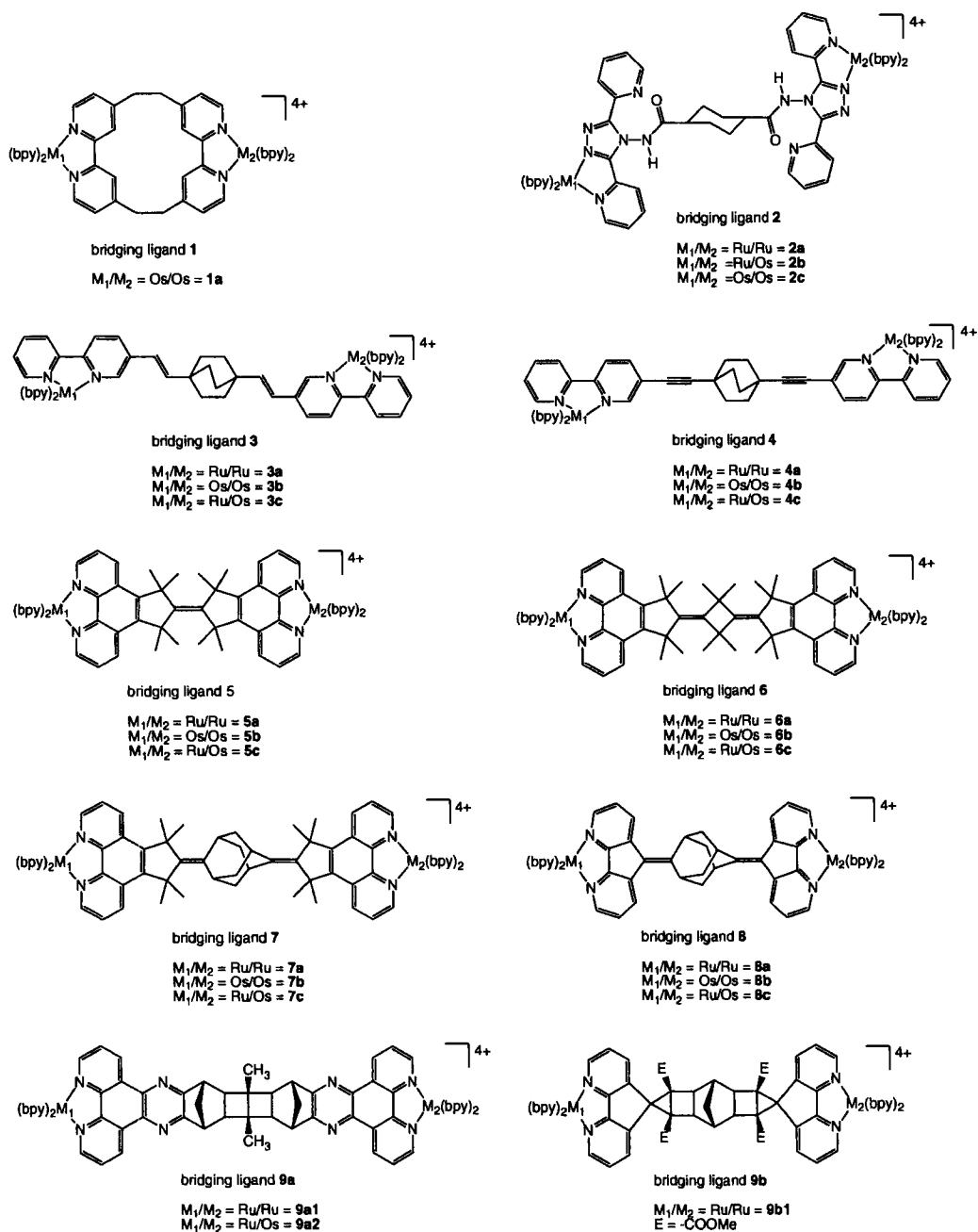


Figure 5. Dinuclear complexes containing saturated rigid bridging ligands.

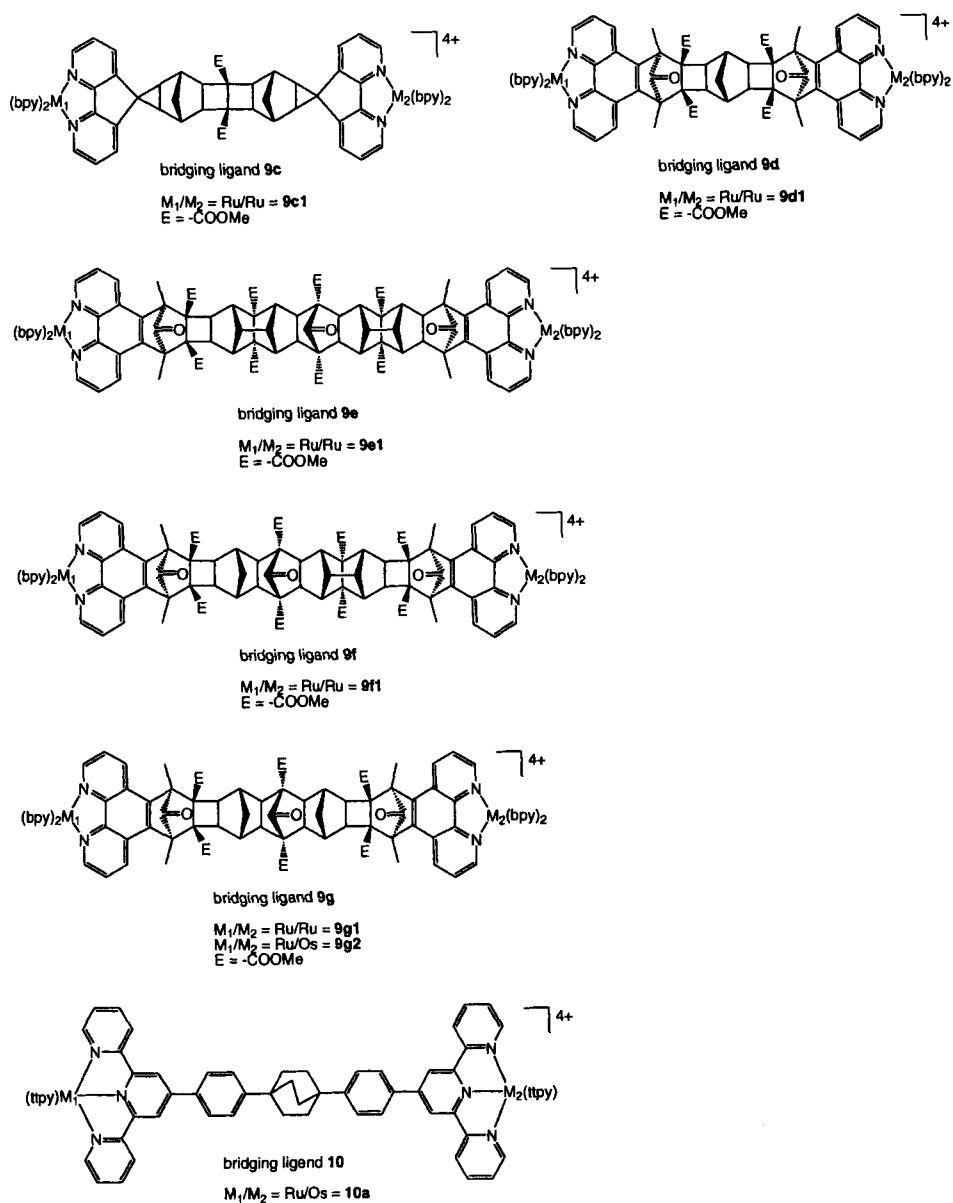


Figure 5 (continued)

Table 1 (continued)

Compound (conditions) ^a	298 K		77 K		k [s ⁻¹]	ΔG [eV]	d_{MM} [nm]	Ref(s).
	M_1	M_2	M_1	M_2				
	E_m^b [nm]	τ [ns]	Φ	E_m [nm]	τ [ns]	Φ	E_m [nm]	τ [μs]
$[(bpy)_2Ru(7)Os^{III}(bpy)_2]^{5+}$ (AN)								
$[(bpy)_2Ru^{III}(7)Os(bpy)_2]^{5+}$ (AN)								
$[(bpy)_2Os(7)Os^{III}(bpy)_2]^{5+}$ (AN)								
$[(bpy)_2Ru(8)Os(bpy)_2]^{4+}$ (RT, AN; 77 K, BuCN)	605	0.29		720	40		577	0.0039
$[(bpy)_2Ru(8)Os^{III}(bpy)_2]^{5+}$ (AN)		0.24					703	1.1
$[(bpy)_2Ru^{III}(8)Os(bpy)_2]^{5+}$ (AN)								
$[(bpy)_2Os(8)Os^{III}(bpy)_2]^{5+}$ (AN)		2.4						
$[(bpy)_2Ru(9a)Os(bpy)_2]^{4+}$ (AN)	588		0.0021					
$[(ttpy)Ru(10)Os(ttpy)]^{4+}$ (RT; DMF/CH ₂ Cl ₂)	640	1.1		736	125		634	0.22
$[(ttpy)Ru(10)Os^{III}(ttpy)]^{5+}$ (RT; DMF/CH ₂ Cl ₂)	640	1.1					632	10.5

^a abbreviations are defined in a separate section in the text, ^b E_m , Emission maximum.

We have prepared and investigated several systems containing saturated molecules, **3–8** [20, 27, 28, 38, 77–81, 83–86]. In our investigations the distance between the metal centers ranges from 16 to 21 Å. In the dinuclear compounds **5–8**, where the two metal units are connected to the spacer by double bonds, or in systems **9**, we can really talk about rigid rod-like molecules. The electronic coupling is extremely small (a few wavenumbers), but both photoinduced energy and electron transfer processes are still fast enough to compete efficiently with the decay of the excited state of the ruthenium moiety (see Table 1). In donor–acceptor systems bridged by saturated species, large attenuation factors have been reported for such groups ($\beta = 0.85 - 0.95 \text{ Å}^{-1}$) [90], and we can conclude that such spacers behave as insulating units. Rigid homometallic dinuclear complexes containing similar saturated spacers in the bridging ligand have been reported by Paddon-Row [21, 52, 76, 87] and Keene [73, 88, 89]. In complex **9a** [76] a similar rate constant for intramolecular energy transfer has been observed and a through-bond (Dexter-type) mechanism was postulated (see Table 1).

3.6 Systems Containing Conjugated Spacers

A π -conjugated system is a molecule along the backbone of which occurs a continuous path of carbon atoms or heteroatoms, each carrying a p atomic orbital. The determination of the electronic structure of conjugated systems and their properties in terms of energy, electron and hole transport is very difficult. Electron correlation effects must be taken into account and the strong connection between, and mutual influence of, the electronic and geometric structures should be evaluated [91].

π -conjugated molecules, such as polyalkenes, polyalkynes, poly(*p*-phenylene) (PPP), poly(phenylene-vinylene) (PPV), and poly(phenylene-ethylene) (PPE), (see, for instance, Refs. [2, 4, 9, 23, 92]) have been extensively studied since they possess unique geometrical, optical, and electronic properties. They can be prepared as defined oligomers with discrete numbers of repetitive units or as conjugated polymers. Their colors and optical properties can be changed upon introduction of substituents or side chains [4]. Introduction of solubilizing side chains has been an essential choice in order to achieve the solubility necessary to build up large oligomers. Their behavior and applications are the focus of this chapter; we shall discuss their use as bridging ligands (BL) in donor (D)/acceptor (A) systems (D–BL–A), and their molecular wire behavior.

3.6.1 Polyene-bridged Bimetallic Compounds

Despite the great number of oligoene systems and their use as molecular wires in donor–acceptor compounds containing organic fragments [22, 23], only a few dinuclear compounds containing oligoene oligomers as bridging ligands have been synthesized and investigated (see Figure 6: compounds **11–16**) [93–98].

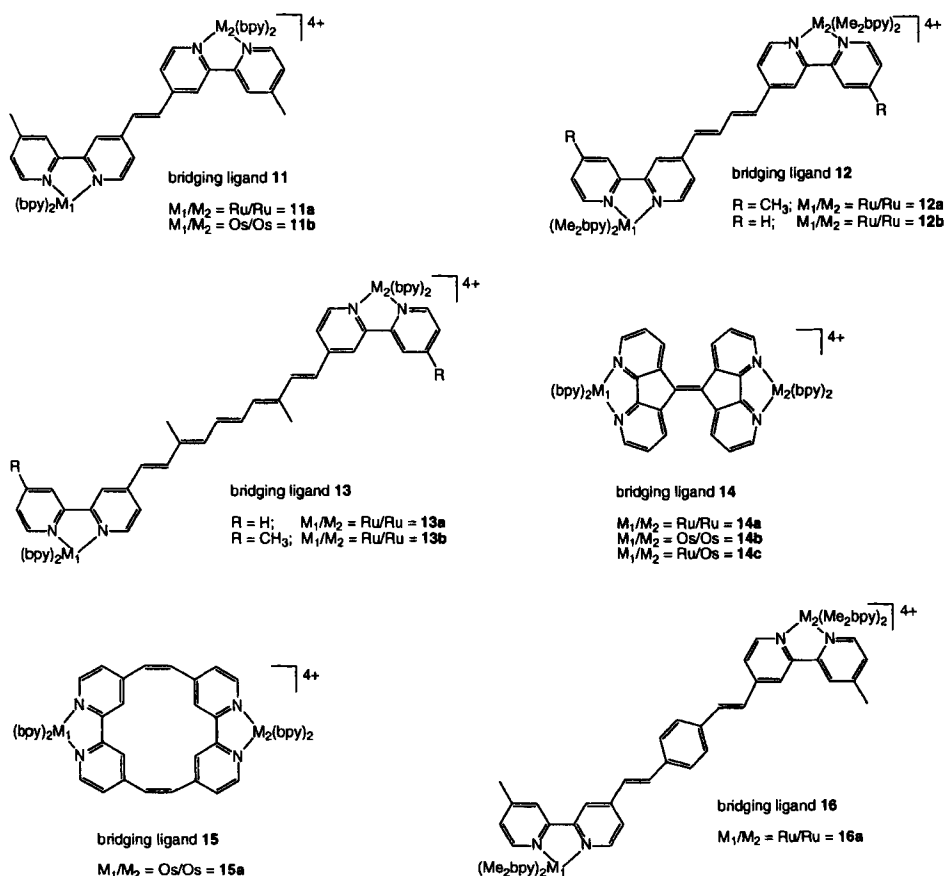


Figure 6. Dinuclear complexes containing oligoenes as bridging ligands.

Most of them, however, are monometallic species for which no information about photoinduced processes has been reported. Due to strong electronic coupling between the two metal units, the compounds containing polyene-bridged bis(bipyridine) exhibit large differences in electrochemical and photophysical behavior between the monometallic and dinuclear complexes. Lehn and co-workers [94] have reported for compounds **13** an electronic coupling matrix of 140 cm^{-1} over a distance of 24 \AA . An attenuation factor β of 0.06 \AA^{-1} has been calculated [94]. For the dinuclear complexes **11** [95], **12** [96, 97], and **16** [95] the authors reported low-lying emitting states with rather long excited-state lifetimes. The assignment of the excited state was not clear, but mixing of the $^3\text{MLCT}$ levels with the close triplet Intra-Ligand (^3IL) states of the bridging ligands was suggested [96]. Hosseini and co-workers have recently reported [75] the synthesis of the complexes **15** and their photophysical properties are under investigation [98].

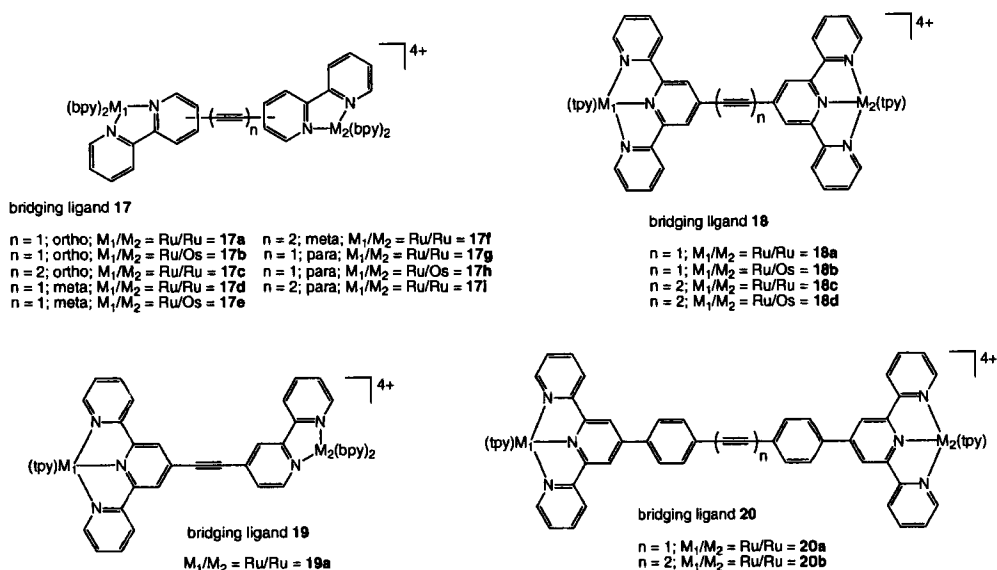


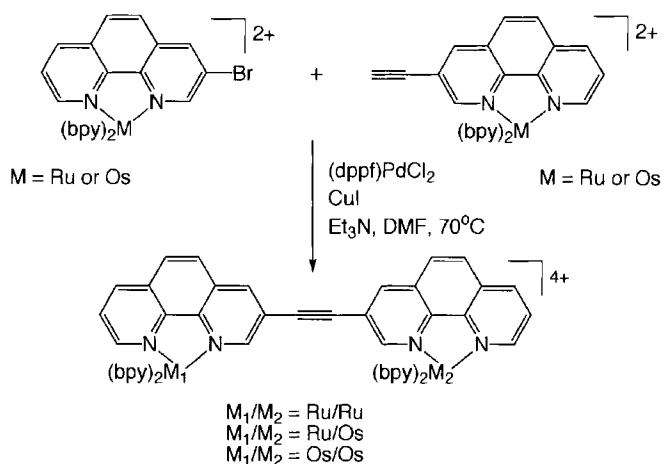
Figure 7. Dinuclear complexes containing oligoynes as bridging ligands.

3.6.2 Oligoyne-bridged Bimetallic Compounds

An important class of conjugated bridging ligand comprises those containing $\text{C}\equiv\text{C}$ as spacers. Oligoynes can be easily accessible bridging ligands; however, due to the flexibility and poor stability and solubility of the longer oligomers and complications arising with increasing chain length, lowering of the triplet energy and decrease of the redox potentials of the polyalkyne, their use has been restricted to short oligoyne linkers. The short systems have quite a good thermal and photochemical stability, and can be easily functionalized in the terminal CH group. They have been used as bridging ligands to construct inorganic dyads such as the complexes **17–20** [67c, 70, 99–109] reported in Figure 7.

In general these bridging ligands are good electron conductors, but worse than oligoenes, presumably because of the large bond-length alternation between the single and the triple bonds. The synthesis of the corresponding dinuclear compounds has been achieved by normal procedures, reacting the bridging ligand with the metal complex precursor [67c, 70, 99–105], or more recently by a direct coupling of two metal-based components, a strategy developed by Tor and co-workers [106–109] (Scheme 1). In such a way the synthesis of heterometallic complexes can be achieved in one coupling step using complementary functional groups on each metal fragment.

Most of the systems shown in Figure 7 have been obtained by Ziessel and co-workers, who have carried out detailed investigations on their photophysical properties and intramolecular photoinduced processes [67c, 70, 99–103, 110, 111]. Some



Scheme 1. The reaction used by Tor and co-workers to prepare oligoyne-bridged homo- and heteronuclear compounds (see text).

of the results are summarized in Table 2. The general behavior of these dinuclear compounds is consistent with the assessment that oligoyne spacers are electronic conductors at the molecular level. In complexes **18d**, for example, even though the intramolecular energy transfer process is only slightly exoergic, $\Delta G = -0.11$ eV, a very fast rate has been observed (see Table 2) [99]. The electronic coupling matrix element has been estimated to be ca. 12 cm^{-1} and so fast a process has been attributed to a Dexter-type energy transfer mechanism.

A similar result was obtained for complexes **18b** and an attenuation factor $\beta = 0.17\text{ \AA}^{-1}$ was reported [99]. It should be pointed out that for the terpyridine complexes the presence of the second metal unit increases the excited-state lifetimes. Such an observation can be rationalized by the presence of extensive electron delocalization in these dinuclear compounds. This desired improvement in the photo-physical properties precludes, however, a clear description of the electronic excitation path and of the distinction between donor, bridging ligand, and acceptor site. The authors suggested that the electron delocalization could be reduced by introduction of small insulators into the carbon bridge which could also help to decrease the direct participation of the bridge in subsequent photochemical or redox processes involving the active terminal chromophores. The introduction of a phenyl ring between a polypyridine ligand and a polyalkyne spacer, in complexes **20** [99–101], causes a dramatic reduction in the electron delocalization. A similar behavior has been observed by insertion of a Pt(II) bis-*s*-acetylide complex, or by the incorporation of chelating heterocycle unit for this purpose [67c, 70, 99, 101, 105, 110]. In the last case the possibility of tuning the energy levels of the bridging ligand upon complexation seemed quite appealing (see Section 3.7).

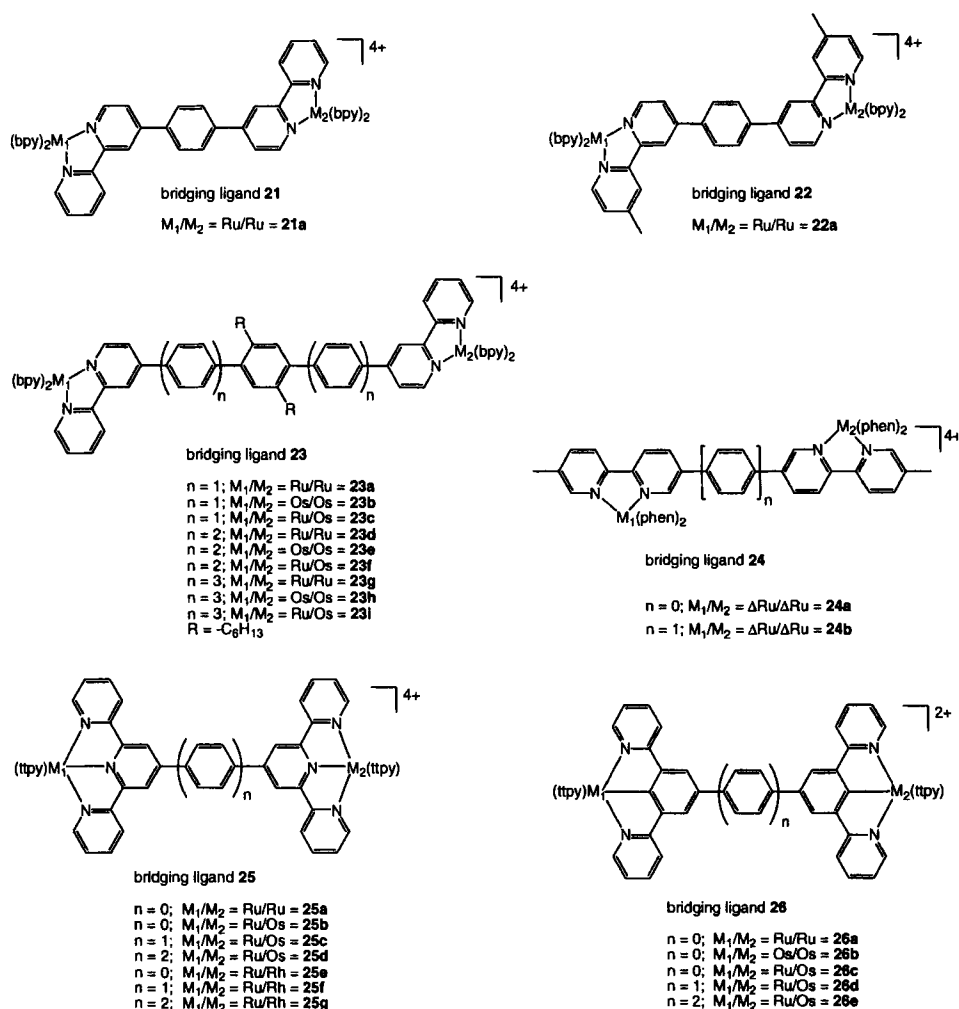


Figure 8. Dinuclear complexes containing *p*-phenylene oligomers as bridging ligands.

3.6.3 Phenylene-bridged Bimetallic Compounds

Oligophenylene rods [92, 112] have attracted much interest as spacers [113], because of their thermal and photochemical stability, and their interesting tunable photo-physical properties. Until recently their use as bridging ligands was limited to species containing only one or two phenylene units (see compounds **23–26**, Figure 8) because of synthetic difficulties related to solubility problems [24, 33, 74, 97, 114–117].

This difficulty has recently been overcome by Schlüter and co-workers, who reported oligomers containing up to 16 phenylene units bearing solubilizing groups

in good yields [11, 118–120]. Using this strategy we have recently reported [69] homodinuclear and heteronuclear complexes containing the bridging ligand **23**. In heterodinuclear Ru23Os compounds, besides complete quenching of the fluorescence of the oligophenylene spacers, a quenching of the phosphorescence of the $[\text{Ru}(\text{bpy})_3]^{2+}$ chromophoric unit and a parallel sensitization of the phosphorescence of the $[\text{Os}(\text{bpy})_3]^{2+}$ chromophoric unit were observed, indicating the occurrence of electronic energy transfer (see Figure 9). Such an observation was clearly confirmed by the observed rise time at 77 K (Figure 9b).

The rate of the energy transfer process from the $[\text{Ru}(\text{bpy})_3]^{2+}$ to the $[\text{Os}(\text{bpy})_3]^{2+}$ unit is practically independent of temperature and decreases with increasing length of the oligophenylene spacer (see Table 3) [69].

It was shown that such an energy transfer process takes place via a Dexter-type mechanism (superexchange interaction) with an attenuation coefficient of 0.32 \AA^{-1} . It is interesting to notice that the planes of the rings of adjacent phenylene moieties in *p*-polyphenylenes form an angle of $20\text{--}40^\circ$ because of the steric repulsion between the *ortho* hydrogens [121–124]. Substitution of the rings leads to an increase in the twist angles. For instance, in our systems, due to the presence of the alkyl chain on the central ring, the tilt angle between the phenyl rings is rather large ($60\text{--}70^\circ$), causing a partial electronic decoupling between the phenyls (reduction of π -orbital delocalization between the aromatic rings). Photoinduced electron transfer reactions in the case of Ru23Os(III) are under investigation at the moment. Other authors have investigated homonuclear compounds containing bipyridine as chelating site and a phenyl as spacer (see complexes **21** and **22** in Figure 8) [113] and chiral dinuclear compounds, **24**, have been reported by Lehn and co-workers [114].

Polyphenylene bridging ligands containing terpyridine (tpy)-type chelating sites and different metal complexes as donor/acceptor units, (**25**, **26**) have been reported and their photophysical properties investigated in great detail [24, 33, 36, 74, 115–117]. Due to the short lifetime of Ru(II) terpyridine complexes at room temperature most of the data on the photoinduced processes for this class of compounds have been obtained at 77 K or at 150 K. Photophysical investigation of the Ru–Os complexes has shown that in such compounds a very efficient energy transfer process takes place from the excited ruthenium unit to the osmium moiety (see Table 3) [24, 33, 74, 114–117]. It is interesting to notice that the insertion in the bridging ligand of a saturated unit such as bicyclooctane (bco) (see Figure 5, complex **10a**) causes a dramatic decrease in the energy transfer rate (see Table 1) [74]. This effect is only partly due to increasing distance and can surely be attributed to the insulating character of the saturated bco group.

When tpy groups in the bridging ligand are substituted by cyclometallating units [115c, 125] (complexes containing the bridging ligand **26**; see Figure 8), the rates of energy transfer in the heterometallic compounds **26c**, **26d**, and **26e** are orders of magnitude slower than in the analogous series of noncyclometallated compounds (see Table 3) [115c]. The reason for such a decrease has been explained on the basis of the localization of the lowest excited state on the peripheral ligands and not on the bridging ligands as reported for the analogous noncyclometallated series. In fact, when the N atom of a terpyridine ligand is substituted by a C[–] the σ -donating ability of that coordinating site is much stronger than that of the normal tpy ligand

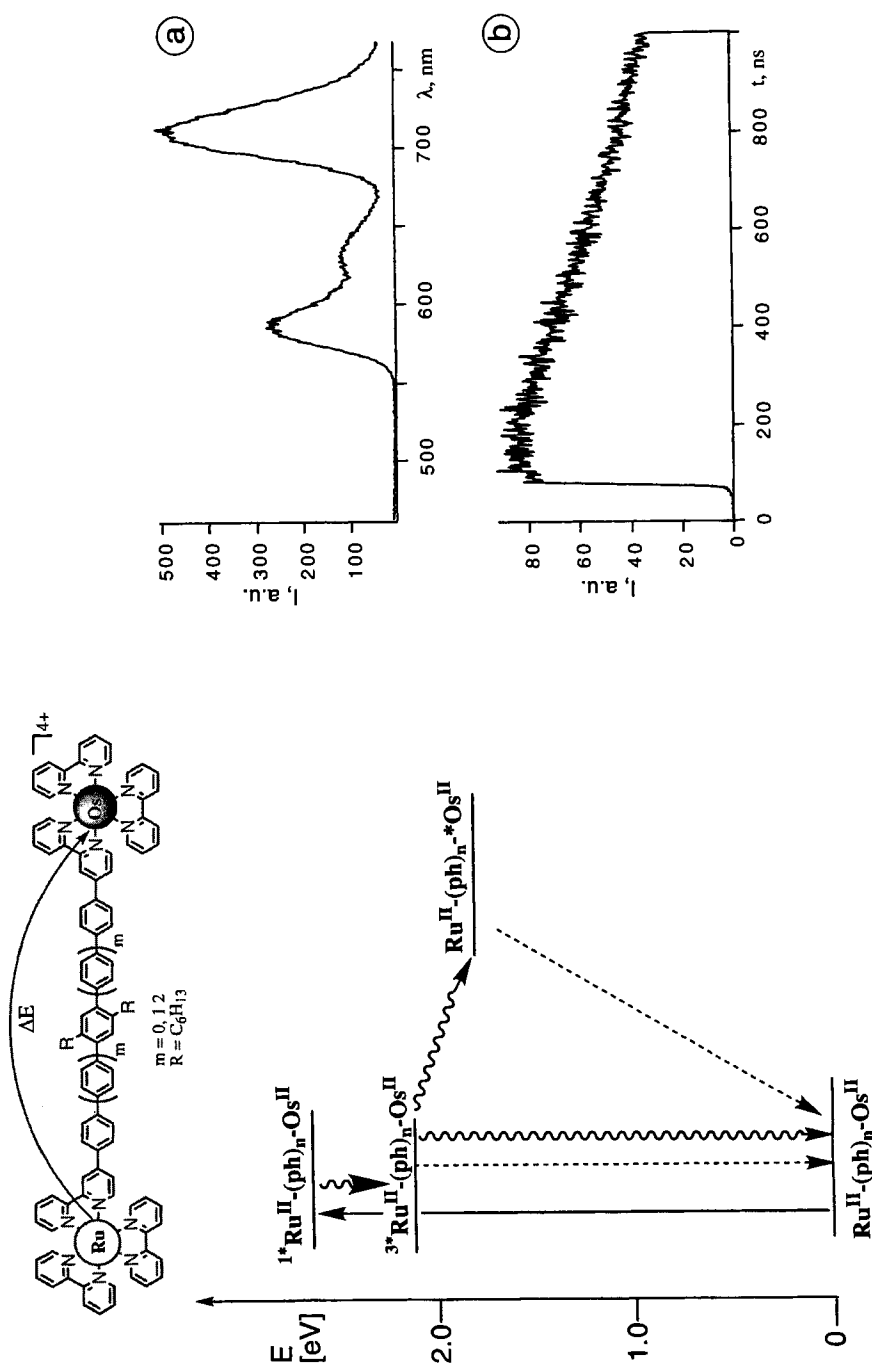


Figure 9. Schematic energy level diagram (left) for Ru23Os compounds. Evidence for the photoinduced energy transfer process can be obtained from a) the emission spectrum (quenching of the ruthenium emission and sensitization of the osmium) and b) the rise time.

Table 3. Photophysical data of dinuclear complexes containing *p*-phenylene oligomers as bridging ligands.

Compound (conditions) ^a	298 K		77 K				<i>k</i> [s ⁻¹]	ΔG [eV]	<i>d</i> _{MM} [nm]	Ref(s).				
	M ₁		M ₂		M ₁						M ₂			
	<i>E</i> _m [nm]	τ [ns]	Φ	<i>E</i> _m [nm]	τ [ns]	Φ	<i>E</i> _m [nm]	τ [μs]	<i>E</i> _m [nm]	τ [μs]				
[(bpy)₂Ru(23c)Os(bpy)₂]⁴⁺ (RT, AN; 77 K, BuCN)	622	1.5		740	42		596	2.2×10^{-3}	715	1.1	6.7×10^8 (298 K) 4.5×10^8 (77 K)	-0.37	2.40	[69]
[(bpy)₂Ru(23f)Os(bpy)₂]⁴⁺ (RT, AN; 77 K, BuCN)	622	68		740	41		596	0.093	718	1.1	1.0×10^7 (298 K) 1.1×10^7 (77 K)	-0.37	3.25	[69]
[(bpy)₂Ru(23i)Os(bpy)₂]⁴⁺ (RT, AN; 77 K, BuCN)	624	163		740	41		594	0.612	717	1.2	1.3×10^6 (298 K) 1.4×10^6 (77 K)	-0.37	4.20	[69]
[(tpy)Ru(25b)Os(tpy)]⁴⁺ (BuCN)				800	110	0.0013			753	1.8	$\geq 10^{10}$ (77 K)	-0.25	1.10	[74, 115a]
[(tpy)Ru(25c)Os(tpy)]⁴⁺ (BuCN)			≤ 0.03	746	190	0.015			726	2.8	$\geq 10^{10}$		1.53	[74, 115a]
[(tpy)Ru(25d)Os(bpy)₂]⁴⁺ (BuCN)			≤ 0.03	738	200	0.013			725	2.8	$\geq 10^{10}$		1.96	[74, 115a]
[(tpy)Ru(25e)Rh(tpy)]⁵⁺ (EtOH/MeOH)	<0.1 (150 K)						674	12.5				0.01	1.10	[117]
[(tpy)Ru(25f)Rh(tpy)]⁵⁺ (EtOH/MeOH)	0.24 3.0 (150 K)						636	13.0				-0.1	1.55	[117]

Table 3 (continued)

Compound (conditions) ^a	298 K		77 K				k [s ⁻¹]	ΔG [eV]	d_{MM} [nm]	Ref(s).
	M ₁		M ₂		M ₂					
	E_m [nm]	τ [ns]	Φ	E_m [nm]	τ [ns]	Φ	E_m [nm]	τ [μs]	E_m [nm]	τ [μs]
[(ttpy)Ru(25g)Rh(tpy)] ⁵⁺ (EtOH/MeOH)	816	0.39		629 (77 K)	13.2 (77 K)		<0.5 × 10 ⁸	-0.14	2.00	[117]
					3.5 (150 K)					
[(ttpy)Ru(26c)Os(tpy)] ⁴⁺ (BuCN)	816	0.39	940	750	7.2 × 10 ⁻⁴ (150 K)	0.4	2.6 × 10 ⁹ 1.4 × 10 ⁹ (77 K)	1.10	[74, 115c]	
[(ttpy)Ru(26d)Os(tpy)] ⁴⁺ (BuCN)	800	3.5	920	750 837	0.042 0.370	0.37	6.3 × 10 ⁷ 2.2 × 10 ⁷ (77 K)	1.53	[74, 115c]	
[(ttpy)Ru(26e)Os(tpy)] ⁴⁺ (BuCN)	792	4.9	916	750	0.178	840	<2.2 × 10 ⁷ 3.6 × 10 ⁶ (77 K)	1.96	[74, 115c]	

^a abbreviations are defined in the text.

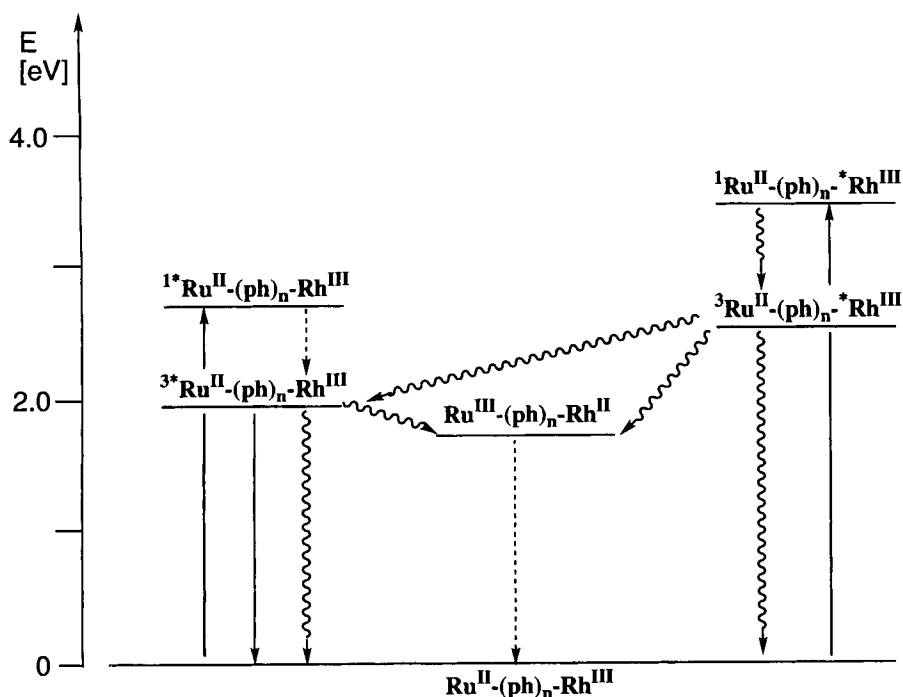


Figure 10. Schematic energy levels diagram for the system Ru25Rh.

and therefore a remarkable increase in the electron density in the metal center occurs. As a consequence the first reduction and the lowest-lying MLCT states are centered on the terminal ttpy ligands. According to the above discussion the energy transfer process will occur over a distance greater than that of the analogous non-cyclometallated series. An attenuation factor, β , of 0.33 \AA^{-1} has been reported [74].

Scandola et al. have investigated the behavior of heterometallic dyads Ru(II)–Rh(III), **25e–25g**, at room temperature and at low temperature to elucidate the mechanism for photoinduced electron transfer processes [117]. In such systems the energy level diagram schematized in Figure 10 clearly shows that electron transfer can occur upon excitation of one of the metal-based components. However, due to the low exergonicity of the electron transfer process, no evidence for photoinduced electron transfer in compounds **25e–25g** was obtained at low temperature [117a]. At room temperature, however, some data were reported suggesting a quite efficient electron transfer able to compete with the short-lived excited state of the ruthenium moiety, see Table 3 [117b].

3.6.4 Other Conjugated Systems

A special class of conjugated systems are those containing triple bonds and aromatic units as part of the bridging ligand and schematically represented by the

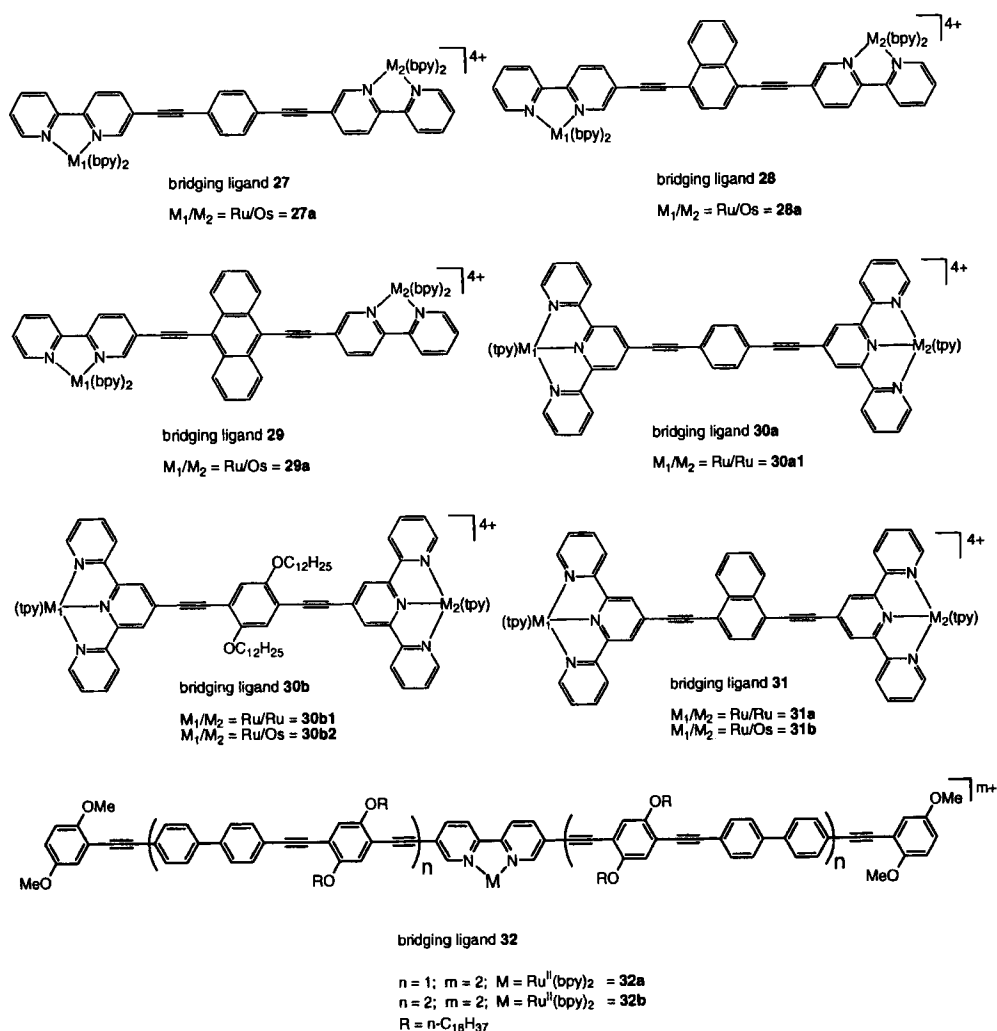


Figure 11. Dinuclear complexes containing aromatic units and oligoynes as bridging ligands.

compounds **27–32** [70, 72c, 100] reported in Figure 11. The compounds **30** and **31** [70] exhibit different rates for photoinduced energy transfer processes, due to the variation of the triplet state energy localized on the connector (phenylene or naphthalene). Assuming a superexchange mechanism for the energy transfer process, the energy gap between the donor and the lowest excited state of the bridging ligand becomes an important factor for the rate of the photoinduced process. The rates observed for such compounds (see Table 4) are in agreement with the observation that the triplet energy of the naphthalene-based connector is much lower than that of the phenylene-bridged system, therefore favoring the energy transfer process. More complicated is the situation for complexes **28** and **29** since in the latter case

Table 4. Photophysical data of dinuclear complexes containing aromatic units and oligoynes as bridging ligands.

Compound (conditions) ^a	298 K		77 K				k [s ⁻¹]	ΔG [eV]	d_{MM} [nm]	Ref(s).	
	M_1		M_2		M_1						
	E_m [nm]	τ [ns]	Φ	E_m [nm]	τ [ns]	Φ	E_m [nm]	τ [μs]	E_m [nm]	τ [μs]	
$[(bpy)_2Ru(27)Os(bpy)_2]^{4+}$ (AN)	606	1.4		725	80			7.1×10^8	-0.34	1.83	[67]
$[(bpy)_2Ru(28)Os(bpy)_2]^{4+}$ (AN)	606	0.085		725	60			1.2×10^{10} (Ru \rightarrow na) ^b 1.5×10^9 (na \rightarrow Os) ^c 4.0×10^{10} (Ru \rightarrow an) ^b 7.6×10^9 (Os \rightarrow an) ^b 1.16×10^8	-0.12 (Ru \rightarrow na) ^b -0.22 (na \rightarrow Os) ^c	1.83	[67, 70]
$[(bpy)_2Ru(29)Os(bpy)_2]^{4+}$ (AN)	606	0.025		725	0.13					1.83	[67, 70]
$[(tpy)_2Ru(30b)Os(tpy)_2]^{4+}$ (AN)	639	135	0.0028							1.98	[70]
$[(tpy)_2Ru(31)Os(tpy)_2]^{4+}$ (AN)	702	475	0.0040					1.06×10^9		1.98	[70]

^a abbreviations are defined in the text, ^bRu → na, Ru → an and Os → na denote rate constants for the processes involving the ruthenium or osmium moiety and the anthracene (an) or naphthalene (na) contained in the bridging ligand (for more details see text), ^cna → Os is the rate constant for the process involving the naphthalene contained in the bridging ligand and the osmium moiety.

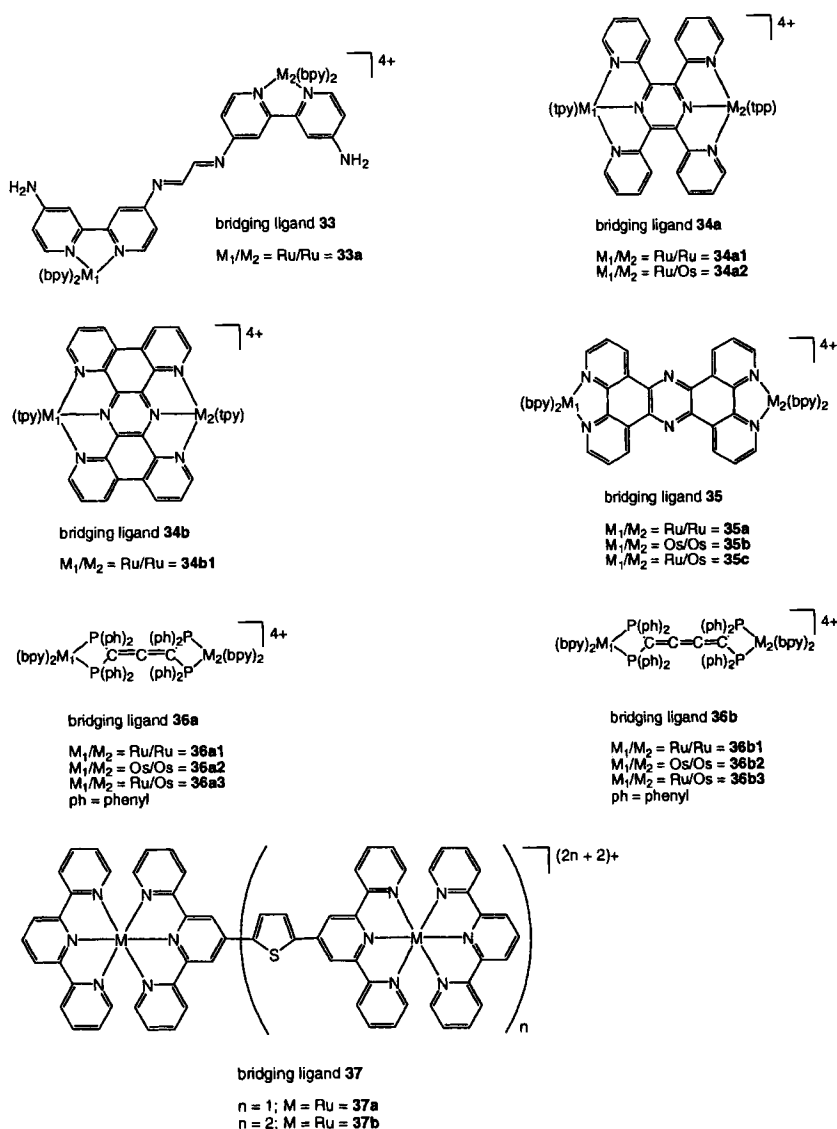


Figure 12. Other dinuclear complexes containing conjugated bridging ligands.

energy transfer proceeds by intermediate population of the triplet localized on the bridging ligand. In such a situation forward and back processes can occur (see Table 4).

Schanze and co-workers have reported several studies on oligomers and polymers containing Re and Ru units in the ligand **32** [126, 127].

Among other dinuclear compounds (see Figure 12) containing rigid bridging ligands, **33–37** [68, 128–130], those based on tpphz (tetrapyrido[3, 2-*a*:2',3'-*c*:3'',2''-

h:2'''-3'''-*j*]phenazine, **35**, are particularly interesting for their aromatic character, planarity, and lack of flexibility [68]. In the complex **35c** a very efficient energy transfer process has been observed (see Table 5) [68]. The energy transfer mechanism was assigned in a first approximation as a Dexter-type process. However, the authors pointed out that for such a bridging ligand the excited electron remains in a common localized LUMO positioned on the bridging ligand and it is therefore more appropriate to discuss the process of interconversion between the lowest excited states as an electron transfer process [68].

Hong and co-workers have investigated the photophysical behavior of complexes **36a** and **36b** containing cumulene systems as bridging ligands [128]. It is interesting to note that even though the structure is similar to acetylenyl chains the electronic properties are very different and depend on the number of carbon atoms. Whereas acetylenyl ligands are conjugated, in the cumulenic chains each additional carbon will cause the terminal groups to be rotated 90° relative to each other. Therefore the two metal units will be perpendicular in the system when the bridging ligand contains three carbons (C₃) (**36a1**–**36a3**) whereas the C₄ bridge will arrange the two terminal metal complexes in a coplanar structure (**36b1**–**36b3**). The electronic interaction and therefore the rates of energy and electron transfer processes will therefore be strongly influenced by the difference in electronic communication due to the different structures in chains of different lengths. Such observation has been recently confirmed and the energy transfer process for the compounds **36b3** resulted indeed faster [128a] than for the analogous shorter dinuclear complex **36a3** [128b] (see Table 5). The authors suggested a Dexter-type mechanism for the photo-induced triplet energy transfer processes.

In the systems **37** reported by Constable et al., 2,5-thiophenediyl spacers have been used for the assembly of ruthenium units [129]. Photoinduced processes have not been published yet to clarify the role of the thiophenediyl as linker.

3.7 Modulation of the Electronic Interactions in Dinuclear Complexes

The rate of photoinduced processes can be tuned by changing the solvent or temperature, but more interestingly by changing the geometry and/or electronic properties of the bridging ligand. In principle there are several approaches to achieve the change in conductivity and therefore to gate electron transfer reactions. Among the most interesting ways to tune the electronic interactions between the donor and acceptor moieties, those that can induce a reversible modification, by an external stimulus, of the geometric and/or electronic properties of the bridging ligand are the most appealing. The changes in geometry of the bridging ligand that are due to planarization of a conjugated bridging ligand or to coordination of a cation or anion in suitable sites of the bridging ligand have been the most investigated [4, 100, 131, 132].

All of the conjugated systems that have been reported in the past few years [2, 4, 22, 23] exhibit a more or less rapid saturation of the effective conjugation length

Table 5. Photophysical data of dinuclear complexes containing other conjugated bridging ligands.

Compound (conditions) ^a	298 K		77 K				k [s ⁻¹]	ΔG [eV]	d_{MM} [nm]	Ref(s).
	M_1		M_2		M_1					
	E_m [nm]	τ [ns]	Φ	E_m [nm]	τ [ns]	Φ	E_m [nm]	τ [μs]	E_m [nm]	τ [μs]
$[(\text{tpy})\text{Ru}(\mathbf{34a})\text{Os}(\text{tp})]^{4+}$ (AN)				820	120				0.67	[130]
$[(\text{bpy})_2\text{Ru}(\mathbf{35})\text{Os}(\text{bpy})_2]^{4+}$ (CH ₂ Cl ₂)				790	1.5		707	0.65	-0.38	[68]
$[(\text{bpy})_2\text{Ru}(\mathbf{36a})\text{Os}(\text{bpy})_2]^{4+}$ (AN)	0.33 5.9		0.007	590	410				-0.14	[128]
$[(\text{bpy})_2\text{Ru}(\mathbf{36b})\text{Os}(\text{bpy})_2]^{4+}$ (AN)	0.01		0.0025	660	340				-0.21	[128]

^a abbreviations are defined in the text.

(ECL) and hence of the HOMO–LUMO gap for chain lengths noticeably shorter than the maximum dimension [4, 133, 134]. Since this saturation originates from π -electron confinement related to structural factors such as rotational disorder or resonance stabilization energy, oligomeric structures with a more planar geometry should in principle exhibit improved π -electron delocalization. Planarization is not the only way to improve the electronic conduction of the bridge, however, and in some cases the elongation of the bridging ligand, increasing the number of spacers, can play an important role [66]. The possibility of modulating the rate of a photoinduced process or reaching a quasi-wire behavior relies on the mechanism of transfer. In many cases the long-range electron/energy transfer reactions in metal complexes occur via a superexchange-type mechanism due to the large gap between the HOMO orbital of the donor and the LUMO orbital of the bridging ligand (see Figure 13, case a).

When the molecular orbital energy levels of the bridge are very close in energy (nearly resonant) to the levels of the donor, the superexchange is no longer the mechanism responsible for the charge transport. Electron hopping becomes the main mechanism and in principle the rate of the photoinduced processes becomes independent of the length of the bridging ligand, which behaves as a real molecular wire (Figure 13, case b). If the lowest excited state of the bridging ligand lies below the lowest excited state of the acceptor unit the occurrence of photoinduced processes between the components is precluded (Figure 13, case c). Therefore, a careful

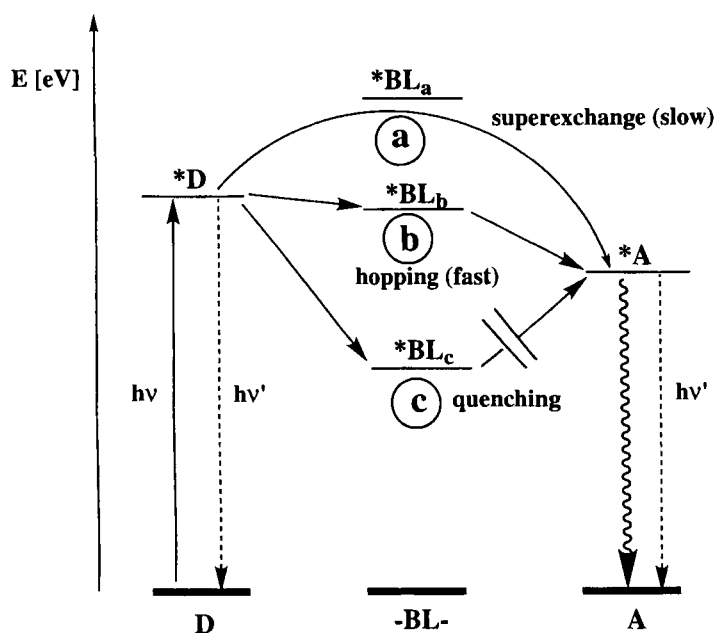


Figure 13. Schematic representation of the energy levels of a dinuclear system and tuning of the rate for a photoinduced process changing the excited-state properties of the bridging ligand, BL (for more details see text).

design for a multicomponent system could lead to molecular wire behavior for systems of a certain length. The increase in the number of monomer units in a π -conjugated oligomer causes a decrease in the energy of the triplet excited state due to an increased delocalization length until the convergent limit (ECL) is reached [133, 134]. Taking advantage of this decrease in the triplet state energy of the π -conjugated spacer, one could switch the energy or electron transfer mechanism from superexchange-mediated to exoergonic hopping, Figure 13, with a dramatic increase in the rate of the process, similar to that described for photoinduced electron transfer in the organic system reported by Wasielewski [66]. In such a case one could observe a decrease in the rate of photoinduced processes for a certain number of units and then a sudden increase for longer systems.

It should be pointed out, however, that the modification of the electronic properties of the bridging ligand often has profound influence on the photophysical and electrochemical behavior of the donor and acceptor moieties. Furthermore, the energetic situation depicted in Figure 13, case b, could lead to complete delocalization of the electronic energy or charge and control of the excitation site could be prevented. Therefore the insertion of an “insulating” unit between the donor and the bridging ligand could prevent this undesirable situation.

To our knowledge no examples of inorganic systems showing a wire-type behavior with increasing length of the bridging ligand have been reported.

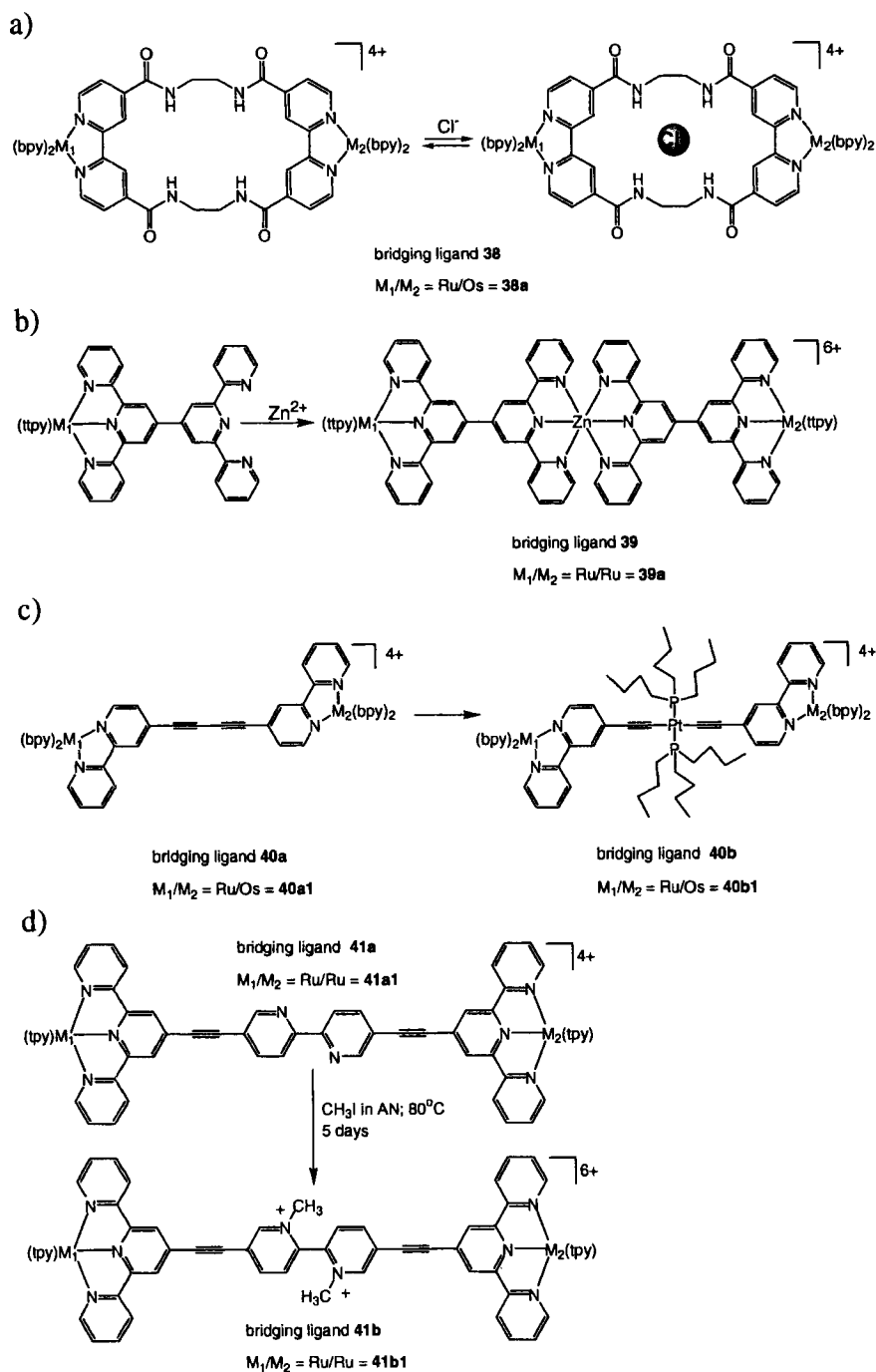
Some examples have been reported where, upon coordination of an anion [131] or cation [110, 132] or methylation [100] of a unit inserted in the bridging ligand, it is possible to modify the electronic interaction between the terminal units (see Scheme 2).

In particular, concerning the photoinduced processes it has been shown that in the heterometallic system **40** (Scheme 2c) the energy transfer process (Dexter-type mechanism) is slowed down 3000-fold by insertion of a Pt(II) center into the butadiynyl bridge ($k = 1.3 \times 10^7 \text{ s}^{-1}$) [67c, 111]. The authors explained this behavior by the change in the HOMO–LUMO energy gap between donor and bridging ligand, induced by coordination of the Pt moiety that raised the energy of the ethynyl units. As a consequence, a lower magnitude of electronic coupling and therefore a slower rate for the photoinduced processes is expected. Furthermore, the authors suggest that coulombic energy transfer could play an important role in the Ru–Pt–Os system [110].

A similar behavior has been reported by Beer et al. [131] for the complex **38** (see Scheme 2a) for which upon coordination of chloride anions the rate constant of the energy transfer process decreases, indicating a weaker electronic interaction between the excited Ru-based unit and the (Os-based) acceptor component.

Another example of modulation of the electronic interaction between two metal units is schematically represented by compound **41** in Scheme 2(d), for which upon complexation of the vacant 2,2'-bipyridine a perturbation of the luminescence properties of the ruthenium moiety was reported [100]. Methylation caused a quenching of the emission, most likely due to photoinduced electron transfer from the terminal chromophores to the central viologen-type unit.

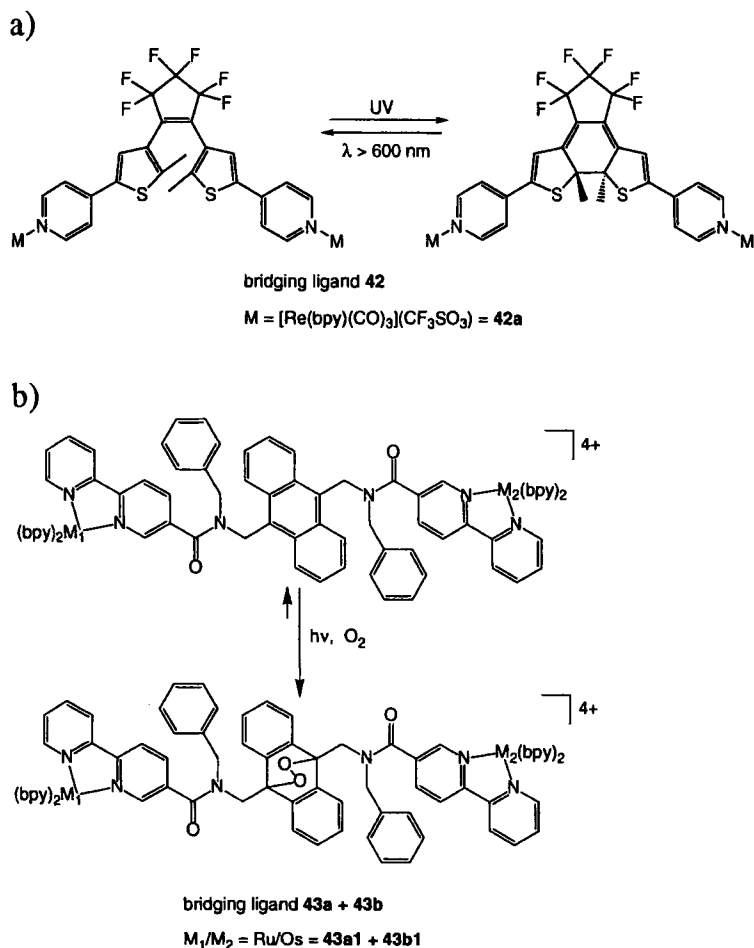
Finally the possibility to switch photochemically or electrochemically the electronic nature of the bridging ligand to build up tunable systems is still the dream of



Scheme 2. Modulation of the electronic interactions in dinuclear complexes upon coordination of a) an anion; b) and c) a cation; or d) methylation of a central unit (for more details see text).

many researchers. Recently Lehn and co-workers have reported metal complexes connected to a photochromic system, a dithienylethylene derived from a perfluorocyclopentene, **42** (Scheme 3a), in which the electronic interaction could be controlled by the state of the bridging ligand (see Scheme 3) [135]. Upon light excitation interconversion of the bridging ligand between a nonconjugated ("open form", colorless) isomer to a conjugated ("closed form", deeply colored) one occurs [135]. At the moment no data have been reported for photoinduced processes in homo- or heterometallic systems.

We have reported a three-component **Ru–An–Os** species, complex **43a1** (see Scheme 3b), in which an efficient energy transfer from the ruthenium unit to the Os-based component occurs in deaerated solution [136, 137]. The rate constant for the process was found to be $4.7 \times 10^8 \text{ s}^{-1}$ [136]. The occurrence of energy transfer from



Scheme 3. Examples of photoactive bridging ligands.

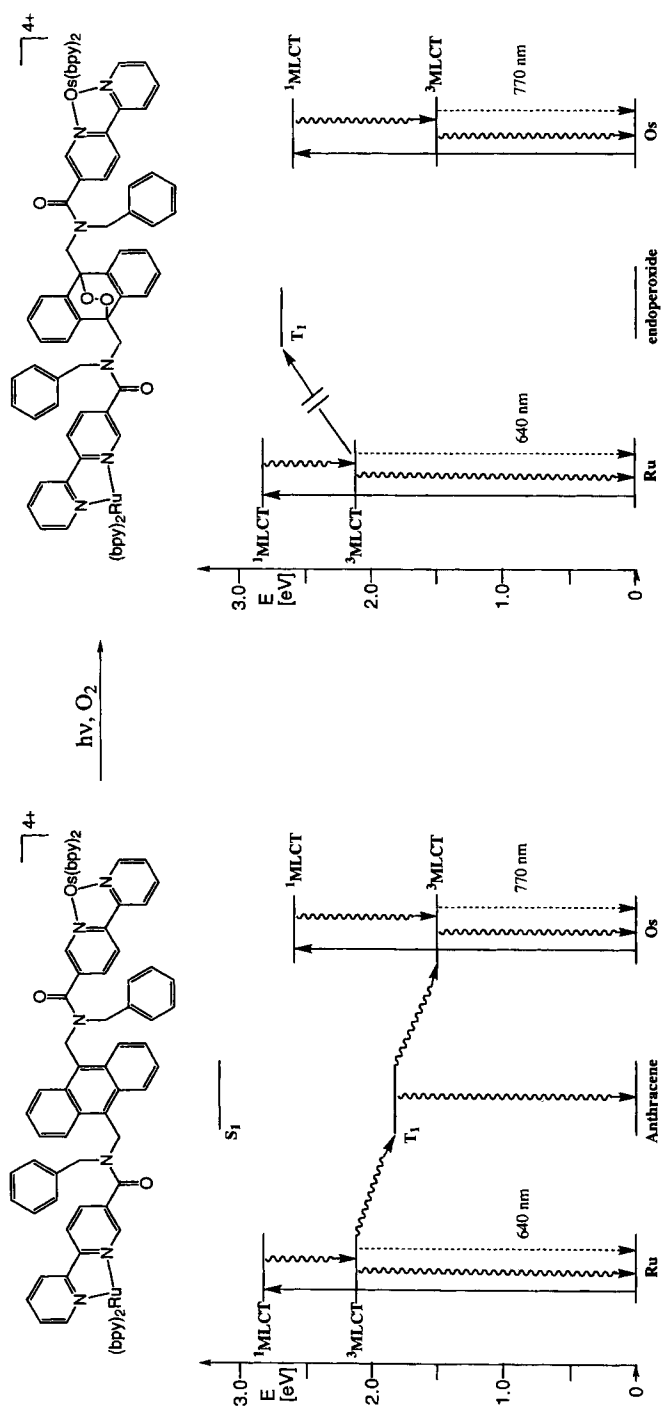


Figure 14. Schematic formulas and energy level diagram of a species where energy transfer occurs (left) and can be switched off (right).

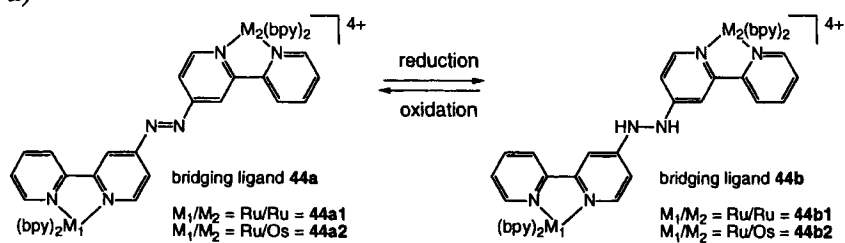
the Ru-based to the Os-based component of **Ru–An–Os** can be explained on the basis of the relative energy positions of the ^3CT levels of the two metal-containing units (Figure 14a). The structure of the supramolecular species and the energy level diagram suggest that the lowest triplet excited state of anthracene (T_1) is directly involved in the photoinduced process. In air-equilibrated solutions, continuous irradiation causes a photoreaction, formation of singlet oxygen, followed by attack of singlet oxygen on an anthracene ring to form an endoperoxide derivative. As a consequence of this photooxidation the delocalization on the bridge is reduced and the T_1 excited state moves to much higher energy. The lack of a suitable energy level in the bridge precludes the occurrence of energy transfer from the Ru-based to the Os-based component (Figure 14b) [136].

An interesting example of a redox-responsive bridging ligand, **44**, Scheme 4, has been reported by Otsuki et al [138]. They have investigated the behavior of homo- and heterometallic dinuclear compounds containing a 4,4'-azo-(2,2'-bipyridine) ligand as bridging unit. They observed that in the **Ru44aOs** compound the emission of the luminescent units is quenched because of the low-lying excited state localized on the azo group. No energy transfer can be observed with the neutral bridging ligand that acts as an energy trap. Reduction of the azo group, **44b**, causes a rise in the energy of the lowest excited state of the bridging ligand. As a result an efficient energy transfer from the ruthenium component to the osmium center in **Ru44bOs** is observed ($k_{\text{en}} = 6.3 \times 10^8 \text{ s}^{-1}$) [138]. In system **45** a similar concept is applied since the spacer inserted in the bridging ligand is a quinone derivative [139]. However, the system is more flexible and no rate constants for photoinduced processes have been reported. An interesting potential redox-active bridging ligand, Scheme 4(c), is the polyaniline derivative, but such a system has not yet been investigated for this purpose.

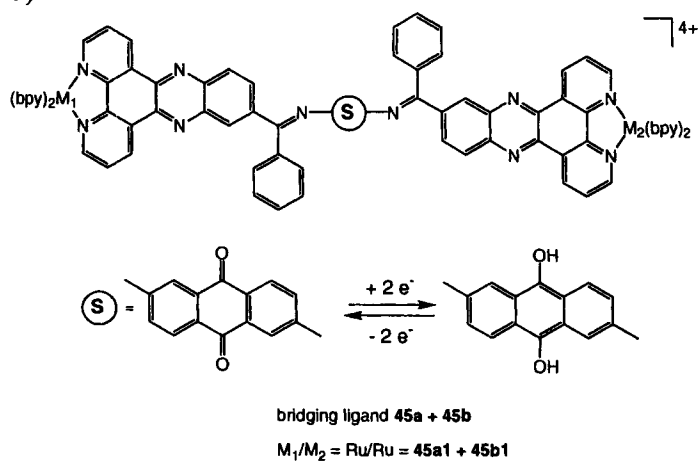
3.8 Conclusions

New synthetic routes make available every day many rigid, long, and tunable systems able to transport charge over a long distance, which could ultimately be used as components for nanoscale electro-optical devices. By comparison of the species containing saturated bridging ligands with those containing conjugated systems, it is clear that the rates of the photoinduced processes are strongly influenced by the electronic nature of the bridging ligands used to build up such dinuclear compounds. We have tried to define some fundamental requirements for a wire-type behavior and to summarize some of the recent achievements in this field. We believe, however, that a deeper understanding of the intramolecular processes is still needed, and we are still far from being able to control and modulate by reversible changes the rates of photoinduced processes.

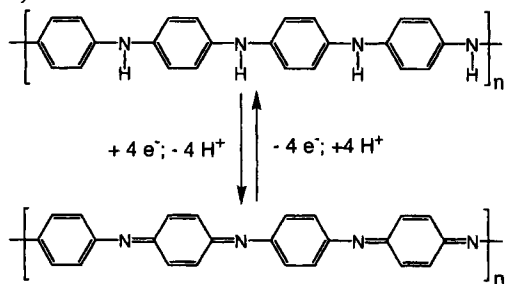
a)



b)



c)



Scheme 4. Examples of redox-active bridging ligands.

Abbreviations

A	acceptor
an	anthracene
AN	acetonitrile
bco	bicyclooctane
biq	2,2'-biquinoline
BL	bridging ligand
bpy	2,2'-bipyridine
BuCN	butyronitrile
D	donor
DMF	dimethylformamide
dppf	1,1'-bis(diphenylphosphino)ferrocene
EtOH	ethanol
Me ₂ bpy	4,4'-dimethyl-2,2'-bipyridine
MeOH	methanol
na	naphthalene
ph	phenyl
phen	1,10-phenanthroline
RT	room temperature
S	spacer
tpp	2,3,5,6-(2'-pyridyl)pyrazine
tpy	2,2':6,2''-terpyridine
ttpy	4'-(p-tolyl)-2,2':6',2''-terpyridine

References

1. P. J. Martin, *Introduction to Molecular Electronics*, Edward Arnold, London, **1995**.
2. R. H. Friend, R. W. Gymer, A. B. Holmes, J. H. Burroughes, R. N. Marks, C. Taliani, D. D. C. Bradley, D. A. Dos Santos, J. L. Brédas, M. Löglund, W. R. Salaneck, *Nature* **1999**, 397, 121.
3. A. Aviram, M. Ratner, *Molecular Electronics: Science and Technology*, New York Academy of Science Press, New York, **1998**.
4. K. Müllen, G. Wegener, *Electronic Materials: the Oligomer Approach*, Wiley-VCH, Weinheim, **1998**.
5. a) S. N. Yaliraki, M. Kemp, M. A. Ratner *J. Am. Chem. Soc.* **1999**, 121, 3428; b) M. Ratner, *Nature* **2000**, 404, 137.
6. D. Mendenhall, A. Greensberg, J. Liebman, *Mesomolecules: from Molecules to Materials*, Chapman and Hall, New York, **1995**.
7. F. L. Carter, R. E. Siatkowski, H. Wohltjen, *Molecular Electronic Devices*, North-Holland, Amsterdam, The Netherlands, **1988**.
8. K. E. Drexler, *Nanosystems. Molecular Machinery, Manufacturing, and Computation*, Wiley, New York, **1992**.
9. Special Issue on Molecular Materials in Electronic and Optoelectronic Devices, *Acc. Chem. Res.* **1999**, 32.
10. J.-M. Lehn, *Supramolecular Chemistry, Concepts and Perspectives*, VCH, Weinheim, **1995**.

11. A. D. Schlüter, V. Hensel, P. Liess, K. Lützwow, *Modular Chemistry*, Kluwer, Dordrecht, The Netherlands, **1997**.
12. a) L. Fabbrizzi, A. Poggi, *Transition Metals in Supramolecular Chemistry*, Kluwer, Dordrecht, The Netherlands, **1994**; b) *Transition Metals in Supramolecular Chemistry (Perspectives in Supramolecular Chemistry, v. 5)*, J.-P. Sauvage (Ed.), Wiley, New York, **1999**.
13. a) H.-J. Schneider, H. Dürr, *Frontiers in Supramolecular Organic Chemistry and Photochemistry*, VCH, Weinheim, Germany, **1991**; b) H.-J. Schneider, A.K. Yatsimirski *Principles and Methods in Supramolecular Chemistry*, Wiley, New York, **1999**.
14. F. Vögtle, *Supramolecular Chemistry*, Wiley, Chichester, UK, **1991**.
15. V. Balzani, L. De Cola, *Supramolecular Chemistry*, Kluwer, Dordrecht, The Netherlands, **1992**.
16. *Comprehensive Supramolecular Chemistry* J. L. Atwood, J.-M. Lehn, J.E.D. Davies, D.D. MacNicol, F. Vogtle (Eds.), Pergamon Press, Oxford, **1996**.
17. V. Balzani, F. Scandola, *Supramolecular Photochemistry*, Horwood, Chichester, UK, **1991**.
18. a) V. Balzani, F. Scandola, in: *Comprehensive Supramolecular Chemistry*, Pergamon Press, Oxford, **1996**; b) V. Balzani, *Supramolecular Photochemistry*, D. Reidel, Dordrecht, The Netherlands, **1987**.
19. *Organic and Inorganic Photochemistry (Molecular and Supramolecular Photochemistry)*, V. Ramamurthy, K. S. Schanze (Eds.), Marcel Dekker, New York, **1999**.
20. P. Belser, S. Bernhard, C. Blum, A. Beyeler, L. De Cola, V. Balzani, *Coord. Chem. Rev.* **1999**, 190–192, 155.
21. M. N. Paddon-Row, *Acc. Chem. Res.* **1982**, 15, 245.
22. P. F. H. Schwab, M. D. Levin, J. Michl, *Chem. Rev.* **1999**, 99, 1863.
23. R. E. Martin, F. Diederich, *Angew. Chem., Int. Ed. Engl.* **1999**, 38, 1351.
24. F. Barigelletti, L. Flamigni, *Chem. Soc. Rev.* **2000**, 29, 1.
25. M. Ward, *Chem. Ind.* **1996**, 568.
26. V. Balzani, A. Juris, M. Venturi, S. Campagna, S. Serroni, *Chem. Rev.* **1996**, 96, 759.
27. L. De Cola, P. Belser, *Coord. Chem. Rev.* **1998**, 177, 301.
28. L. De Cola, *Chimia* **1996**, 50, 214.
29. J. A. McCleverty, M. Ward, *Acc. Chem. Res.* **1998**, 31, 842.
30. A. Juris, V. Balzani, S. Campagna, P. Belser, A. von Zelewsky, *Coord. Chem. Rev.* **1988**, 84, 85.
31. K. Kalyanasundaram, *Photochemistry of Polypyridine and Porphyrin Complexes*, Academic Press, London, **1992**.
32. K. M. Omberg, G. D. Smith, D. A. Kavaliunas, P. Y. Chen, J. A. Treadway, J. R. Schoonover, R. A. Palmer, T. J. Meyer, *Inorg. Chem.* **1999**, 38, 951.
33. J.-P. Sauvage, J.-P. Collin, J.-C. Chambron, S. Guillerez, C. Coudret, V. Balzani, F. Barigelletti, L. De Cola, L. Flamigni, *Chem. Rev.* **1994**, 94, 993.
34. C. G. Coates, T. E. Keyes, J. J. McGarvey, H. P. Hughes, J. G. Vos, P. M. Jayaweera, *Coord. Chem. Rev.* **1998**, 171, 323.
35. L. A. Curtiss, C. A. Naleway, J. R. Miller, *J. Phys. Chem.* **1995**, 99, 1182.
36. H. M. McConnell, *J. Chem. Phys.* **1961**, 35, 508.
37. M. D. Todd, A. Nitzan, M. A. Ratner, *J. Phys. Chem.* **1993**, 97, 29.
38. V. Balzani, F. Barigelletti, P. Belser, S. Bernhard, L. De Cola, L. Flamigni, *J. Phys. Chem.* **1996**, 100, 16786–16788.
39. G.J. Kavarnos, *Fundamentals of Photoinduced Electron Transfer*, VCH, Weinheim, **1993**.
40. M. A. Fox, M. Chanon, *Photoinduced Electron Transfer, Parts A–D*, Elsevier, New York, **1988**.
41. a) R. A. Marcus, *Annu. Rev. Phys. Chem.* **1964**, 15, 155; b) R. A. Marcus, N. Sutin, *Biochim. Biophys. Acta* **1985**, 811, 265.
42. R. A. Marcus, *Angew. Chem., Int. Ed. Engl.* **1993**, 32, 1111.
43. M. R. Wasielewski, *Chem. Rev.* **1992**, 92, 435.
44. G. L. Closs, J. R. Miller, *Science* **1988**, 240, 440.
45. P. Piotrowiak, *Chem. Soc. Rev.* **1999**, 28, 143.
46. P. F. Barbara, T. J. Meyer, M. A. Ratner, *J. Phys. Chem.* **1996**, 100, 13148.
47. N. J. Turro, *Modern Molecular Photochemistry*, Benjamin, Menlo Park, **1978**.

48. D. E. Richardson, H. Taube, *J. Am. Chem. Soc.* **1983**, 105, 40.
49. J. R. Miller, J. V. Beitz, *J. Chem. Phys.* **1981**, 74, 6746.
50. M. R. Wasielewski, *Photoinduced Electron Transfer*, Elsevier, New York, **1988**.
51. M. D. Newton, *Chem. Rev.* **1991**, 91, 767.
52. K. D. Jordan, M. N. Paddon-Row, *Chem. Rev.* **1992**, 92, 395.
53. C. Liang, D. Newton, *J. Phys. Chem.* **1993**, 97, 3199.
54. a) N. S. Hush, *Prog. Inorg. Chem.* **1967**, 8, 391; b) D. Graff, J.P. Claude, T.J. Meyer, *Adv. Chem. Ser.* **1997**, 253, 183.
55. T. H. Förster, *Discuss. Faraday Soc.* **1959**, 27, 7.
56. D. L. Dexter, *J. Chem. Phys.* **1953**, 21, 836.
57. V. Balzani, F. Bolletta, F. Scandola, *J. Am. Chem. Soc.* **1980**, 102, 2552.
58. G. L. P. Closs, J. R. Miller, *Science* **1989**, 244, 35.
59. K. Deshayes, D. W. Place, E. Piatnitski, Z. S. Romanova, *Inter-American Photochemical Society Newsletter* **1998**, 21, 27.
60. V. Balzani, F. Bolletta, F. Scandola, *J. Am. Chem. Soc.* **1980**, 102, 2152.
61. G. Orlandi, S. Monti, F. Barigelletti, V. Balzani, *Chem. Phys.* **1980**, 52, 313.
62. N. Sutin, *Acc. Chem. Res.* **1982**, 15, 275.
63. F. Scandola, V. Balzani, *J. Chem. Educ.* **1983**, 60, 814.
64. T. J. Meyer, *Pure Appl. Chem.* **1990**, 62, 1003.
65. C. K. Ryu, R. H. Schmehl, *J. Phys. Chem.* **1989**, 93, 7961.
66. W. B. Davies, W. A. Svec, M. A. Ratner, M. R. Wasielewski, *Nature* **1998**, 396, 60.
67. a) V. Grossshenny, A. Harriman, M. Hissler, R. Ziessel, *Platinum Metals Rev.* **1996**, 40, 26; b) V. Grossshenny, A. Harriman, M. Hissler, R. Ziessel, *Platinum Metals Rev.* **1996**, 40, 72; c) R. Ziessel, M. Hissler, A. El-ghayoury, A. Harriman, *Coord. Chem. Rev.* **1998**, 177, 1251.
68. C. Chiorboli, C. A. Bignozzi, F. Scandola, E. Ishow, A. Gourdon, J.-P. Launay, *Inorg. Chem.* **1999**, 38, 2402.
69. B. Schlicke, P. Belser, L. De Cola, E. Sabbioni, V. Balzani, *J. Am. Chem. Soc.* **1999**, 121, 4207.
70. A. El-ghayoury, A. Harriman, A. Khatyr, R. Ziessel, *Angew. Chem., Int. Ed. Engl.* **2000**, 39, 185.
71. C. A. Bignozzi, J. R. Schoonover, F. Scandola, *Prog. Inorg. Chem.* **1997**, 44, 1.
72. L. Hammarström, F. Barigelletti, L. Flamigni, N. Armaroli, A. Sour, J.-P. Collin, J.-P. Sauvage, *J. Am. Chem. Soc.* **1996**, 118, 11972.
73. F. R. Keene, *Coord. Chem. Rev.* **1997**, 166, 121.
74. F. Barigelletti, L. Flamigni, J.-P. Collin, J.-P. Sauvage, *Chem. Commun.* **1997**, 333.
75. J.-J. Lagref, M. W. Hosseini, J.-M. Planeix, A. De Cian, J. Fischer, *Chem. Commun.* **1999**, 2155.
76. P. T. Gulyas, T. A. Smith, M. N. Paddon-Row, *J. Chem. Soc., Dalton Trans.* **1999**, 1325.
77. S. Bernhard, P. Belser, *Synthesis* **1996**, 192.
78. M. Frank, M. Nieger, F. Vögtle, P. Belser, A. von Zelewsky, L. De Cola, F. Barigelletti, L. Flamigni, V. Balzani, *Inorg. Chim. Acta* **1996**, 242, 281.
79. C. Blum, Dissertation No. 1286, **2000**, CH-1700 Fribourg, Switzerland.
80. (a) M. Frank, M. Nieger, F. Vögtle, P. Belser, A. Von Zelewsky, L. De Cola, V. Balzani, F. Barigelletti, L. Flamigni, *Inorg. Chim. Acta* **1996**, 242, 281; (b) L. De Cola, V. Balzani, F. Barigelletti, L. Flamigni, P. Belser, S. Bernhard, *Rec. Trav. Chim. Pays-Bas* **1995**, 114, 534.
81. F. Vögtle, M. Frank, M. Nieger, P. Belser, A. von Zelewsky, V. Balzani, F. Barigelletti, L. De Cola, L. Flamigni, *Angew. Chem., Int. Ed. Engl.* **1993**, 32, 1643.
82. a) G. Giuffrida, G. Calogero, V. Ricevuto, S. Campagna, *Inorg. Chem.* **1995**, 34, 1957; b) G. Giuffrida, G. Calogero, G. Guglielmo, V. Ricevuto, S. Campagna, *Inorg. Chim. Acta*, **1996**, 251, 255.
83. L. De Cola, F. Barigelletti, V. Balzani, P. Belser, A. von Zelewsky, M. Frank, F. Vögtle, *Mol. Cryst. Liq. Cryst. Sci. Technol., Sect. A* **1993**, 234, 115.
84. L. De Cola, V. Balzani, F. Barigelletti, L. Flamigni, P. Belser, A. von Zelewsky, M. Frank, F. Vögtle, *Inorg. Chem.* **1993**, 32, 5228.
85. S. Bernhard, P. Belser, *Synth. Commun.* **1996**, 26, 3559.

86. L. De Cola, V. Balzani, F. Barigelletti, L. Flamigni, P. Belser, A. von Zelewsky, M. Frank, F. Vögtle, *Mol. Cryst. Liq. Cryst. Sci. Technol., Sect. A* **1994**, 252, 97.
87. J. W. Verhoeven, M. N. Paddon-Row, J. M. Warman, *Photoprocesses in Transition Metal Complexes, Biosystems and Other Molecules*, Kluwer, Dordrecht, The Netherlands, **1992**.
88. a) F. R. Keene, *Chem. Soc. Rev.* **1998**, 27, 185; b) F. R. Keene, *Angew. Chem., Int. Ed. Engl.* **1996**, 35, 2485.
89. A. C. Schultz, L. S. Kelso, M. R. Johnston, R. N. Warrener, F. R. Keene, *Inorg. Chem.* **1999**, 38, 4906.
90. M. N. Paddon-Row, M. J. Shephard, K. D. Jordan, *J. Phys. Chem.* **1993**, 97, 1743.
91. See for example: J.-L. Brédas, J. Cornil, D. Beljonne, D. A. Dos Santos, Z. Shuai, *Acc. Chem. Res.* **1999**, 32, 267, and references therein.
92. J. M. Tour, *Chem. Rev.* **1996**, 96, 537.
93. S. C. Rasmussen, D. W. Thompson, V. Singh, J. D. Petersen, *Inorg. Chem.* **1996**, 35, 3449.
94. A. C. Benniston, V. Goulle, A. Harriman, J.-M. Lehn, B. Marczinke, *J. Phys. Chem.* **1994**, 98, 7798.
95. G. F. Strouse, J. R. Schoonover, R. Duesing, S. Boyde, W. E. Jones, Jr., T. J. Meyer, *Inorg. Chem.* **1995**, 34, 473.
96. A. I. Baba, J. R. Shaw, J. A. Simon, R. P. Thummel, R. H. Schmehl, *Coord. Chem. Rev.* **1998**, 171, 43.
97. A. I. Baba, H. E. Ensley, R. H. Schmehl, *Inorg. Chem.* **1995**, 34, 1198.
98. L. De Cola, M. W. Hosseini, manuscript in preparation.
99. A. Harriman, R. Ziessel, *Chem. Commun.* **1996**, 1707.
100. M. Hissler, A. El-ghayoury, A. Harriman, R. Ziessel, *Angew. Chem., Int. Ed. Engl.* **1998**, 37, 1717.
101. A. Harriman, R. Ziessel, *Coord. Chem. Rev.* **1998**, 171, 331.
102. V. Grosshenny, A. Harriman, R. Ziessel, *Angew. Chem., Int. Ed. Engl.* **1995**, 34, 1100.
103. A. C. Benniston, V. Grosshenny, A. Harriman, R. Ziessel, *Angew. Chem., Int. Ed. Engl.* **1994**, 33, 1884.
104. J. R. Shaw, R. T. Webb, R. H. Schmehl, *J. Am. Chem. Soc.* **1990**, 112, 1117.
105. R. Ziessel, *J. Chem. Educ.* **1997**, 74, 673.
106. P. J. Connors, Jr., D. Tzalis, A. L. Dunnick, Y. Tor, *Inorg. Chem.* **1998**, 37, 1121.
107. D. Tzalis, Y. Tor, *Angew. Chem., Int. Ed. Engl.* **1997**, 36, 2666.
108. D. Tzalis, Y. Tor, *Chem. Commun.* **1996**, 1043.
109. D. Tzalis, Y. Tor, *J. Am. Chem. Soc.* **1997**, 119, 852.
110. V. Grosshenny, A. Harriman, M. Hissler, R. Ziessel, *J. Chem. Soc., Faraday Trans.* **1996**, 92, 2223.
111. V. Grosshenny, A. Harriman, R. Ziessel, *Angew. Chem., Int. Ed. Engl.* **1995**, 34, 2705.
112. a) J. N. Onuchic, D. N. Beratan, *J. Am. Chem. Soc.* **1987**, 109, 6771; b) M. Yamaji, T. Tanaka, K. Suto, H. Shizuka, *Chem. Phys. Lett.*, **1996**, 261, 289; c) J. Grimme, M. Kreyenschmidt, F. Uckert, K. Müllen, U. Scherf, *Adv. Mater.* **1995**, 7, 292.
113. a) Y. Kim, C. M. Lieber, *Inorg. Chem.* **1989**, 28, 3990; b) A. Osuka, K. Maruyama, N. Mataga, T. Asahi, I. Yamazaki, N. Tamai, *Inorg. Chem.* **1990**, 112, 4958; c) A. Helms, D. Heiler, G. McLendon, *J. Am. Chem. Soc.* **1991**, 113, 4325; d) A. Helms, D. Heiler, G. McLendon, *J. Am. Chem. Soc.* **1992**, 114, 6227; e) A. Osuka, N. Satoshi, K. Maruyama, N. Mataga, T. Asahi, I. Yamazaki, Y. Nishimura, T. Onho, K. Nozaki, *J. Am. Chem. Soc.* **1993**, 115, 4577.
114. K. Wärnmark, P. N. W. Baxter, J.-M. Lehn, *Chem. Commun.* **1998**, 993.
115. a) F. Barigelletti, L. Flamigni, V. Balzani, J.-P. Collin, J.-P. Sauvage, A. Sour, E. C. Constable, A. M. W. Cargill Thompson, *J. Am. Chem. Soc.* **1994**, 116, 7692; b) F. Barigelletti, L. Flamigni, V. Balzani, J.-P. Collin, J.-P. Sauvage, A. Sour, *New J. Chem.* **1995**, 19, 793; c) F. Barigelletti, L. Flamigni, M. Guardigli, A. Juris, M. Beley, S. Chodorowski-Kimmes, J.-P. Collin, J.-P. Sauvage, *Inorg. Chem.* **1996**, 35, 136.
116. L. Hammarström, F. Barigelletti, L. Flamigni, M. T. Indelli, N. Armaroli, G. Calogero, M. Guardigli, A. Sour, J.-P. Collin, J.-P. Sauvage, *J. Phys. Chem.* **1997**, 101, 9061.
117. a) M. T. Indelli, F. Scandola, J.-P. Collin, J.-P. Sauvage, A. Sour, *Inorg. Chem.* **1996**, 35, 303; b) M. T. Indelli, F. Scandola, L. Flamigni, J.-P. Collin, J.-P. Sauvage, A. Sour, *Inorg. Chem.* **1997**, 36, 4247.

- 118. M. Rehahn, A. D. Schlüter, *Makromol. Chem.* **1990**, *191*, 1991.
- 119. P. Liess, V. Hensel, A. D. Schlüter, *Liebigs Ann.* **1996**, 1037.
- 120. V. Hensel, A. D. Schlüter, *Liebigs Ann./Recueil* **1997**, 303.
- 121. J. M. Tour, J. J. S. Lamba, *J. Am. Chem. Soc.* **1993**, *115*, 4935.
- 122. S. Tsuzuki, K. Tanabe, *J. Phys. Chem.* **1991**, *95*, 139.
- 123. B. L. Farmer, B. R. Chapman, D. S. Dudis, W. W. Adams, *Polymer* **1993**, *34*, 1588.
- 124. E. P. Socci, B. L. Forner, W. W. Adams, *J. Polym. Sci., Part B* **1993**, *31*, 1975.
- 125. F. Barigelletti, B. Ventura, J.-P. Collin, R. Kayhanian, P. Gauina, J.-P. Sauvage, *Eur. J. Inorg. Chem.* **2000**, 113.
- 126. a) K. D. Ley, K. S. Schanze, *Coord. Chem. Rev.* **1998**, *171*, 287.
- 127. K. D. Ley, Y. Li, J. V. Johnson, D. H. Powell, K. S. Schanze, *Chem. Commun.* **1999**, 1749.
- 128. a) J. V. Ortega, B. Hong, S. Ghosal, J. C. Hemminger, B. Breedlove, C. P. Kubiak, *Inorg. Chem.* **1999**, *38*, 5102; b) B. Hong, J. V. Ortega, *Angew. Chem., Int. Ed. Engl.* **1998**, *37*, 2131; c) B. Hong, S. R. Woodcock, S. K. Saito, J. V. Ortega, *J. Chem. Soc., Dalton Trans.* **1998**, 2615; d) B. Hong, *Comments Inorg. Chem.* **1998**, *29*, 177.
- 129. E. C. Constable, C. E. Housecroft, E. R. Schofield, S. Encinas, N. Armaroli, F. Barigelletti, L. Flamigni, E. Figgemeier, J. G. Vos, *Chem. Commun.* **1999**, 869.
- 130. L. M. Vogler, K. J. Brewer, *Inorg. Chem.* **1996**, *35*, 818.
- 131. P. D. Beer, F. Szemes, V. Balzani, C. M. Salà, M. G. B. Drew, S. W. Dent, M. Maestri, *J. Am. Chem. Soc.* **1997**, *119*, 11864.
- 132. F. Barigelletti, L. Flamigni, G. Calogero, L. Hammarström, J.-P. Sauvage, J.-P. Collin, *Chem. Commun.* **1998**, 2333.
- 133. H. Meier, U. Stalmach, H. Kolshorn, *Acta Polym.* **1997**, *48*, 379.
- 134. G. Zerbi, E. Galbati, M. C. Gallazzi, C. Castiglioni, M. Del Zoppo, R. Schenk, K. Müllen, *J. Chem. Phys.*, **1990**, *23*, 2509.
- 135. a) A. Fernández-Acebes, J.-M. Lehn, *Adv. Mater.* **1998**, *10*, 1519; b) A. Fernández-Acebes, J.-M. Lehn, *Chem. Eur. J.* **1999**, *5*, 3285.
- 136. P. Belser, R. Dux, M. Baak, L. De Cola, V. Balzani, *Angew. Chem., Int. Ed. Engl.* **1995**, *34*, 595.
- 137. L. De Cola, V. Balzani, P. Belser, R. Dux, M. Baak, *Supramol. Chem.* **1995**, *5*, 297.
- 138. J. Otsuki, M. Tsujino, T. Iizaki, K. Araki, M. Seno, K. Takatera, T. Watanabe, *J. Am. Chem. Soc.* **1997**, *119*, 7895.
- 139. L. Mishra, C.-S. Choi, K. Araki, *Chem. Lett.* **1997**, 447.

4 Rectifiers

Alan C. Brady and J. Roy Sambles

4.1 Introduction

In 1959 the eminent physicist Richard Feynman gave a talk to the American Physical Society [1] which is widely regarded as one of the most influential early heralds of nanotechnology. He suggested that the future lay in miniaturization—that it should be possible to manufacture machines and electronic devices from components made of only a handful of atoms. He foresaw that computers could become very useful tools if they were smaller and more complex, by being reduced from room-sized to a size where “the wires should be 10 or 100 atoms in diameter, and the circuits should be a few thousand ångströms across”.

The rapid progress of microelectronics in the guise of semiconductor integrated-circuit technology has followed this trend of miniaturization. Indeed, since the early 1970s Moore’s law—that the number of transistors on a chip will double every 18 months—has been followed. The present cutting-edge devices are fabricated lithographically with a track width of 0.18 µm, while in research systems widths down to 70 nm have been demonstrated. Until very recently it was believed that current MOSFET technology could not function below about 30 nm due to Zener breakdown of the source/substrate junction and current leakage through the gate oxide layer [2]. Even this limit seems to have been bettered; a 20 nm MOSFET transistor has been demonstrated by a group from the CEA at Geneva, and devices such as the dual-gate MOSFET and the vertical-gate transistor are predicted to scale to 5 nm. Building devices which are this small require elaborate electron or ion beam lithography to carve structures which are just a handful of atoms across, and which must not contain any defects. At this scale it would be useful to be able to assemble the materials atom by atom, or molecule by molecule. Organic molecules can be fine-tuned to produce very specific properties, and could be used as the building blocks of nanometer-scale “molecular electronics”. In this section we shall consider the fundamental unit of a molecular-scale logic device, the molecular rectifier.

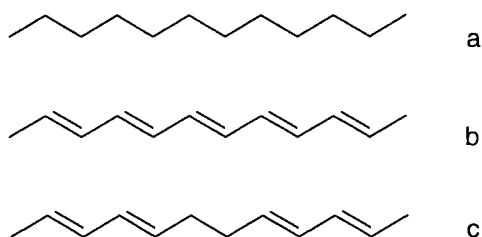


Figure 1. a) A σ -bridged aliphatic chain; b) a π -bridged molecular wire; c) a σ -bridged molecular wire.

4.2 Molecular Conduction

The principal mechanism for molecular conduction is electron transport through part-filled or empty molecular states [3]. The primary candidates for mediating conduction in organic molecules are perhaps π -bonds, as they have a relatively low excitation energy (the π - π^* gap is typically 1.5–3 eV) and can overlap with neighbouring π -bonds or lone-pair orbitals. This overlap can produce an extended conjugated wavefunction which can facilitate electron transfer over several nanometers. However, the degree of delocalization between two π -bridged moieties, and hence the π - π^* gap width, are highly dependent on the orbital overlap in the plane of the bond. If a torsion is applied to the bond, for example by geometric constraints, the degree of conjugation between the π -orbitals at each end of the bond will fall off rapidly as the twist angle increases [4]. There are no such distortions in the simple polyalkene shown in Figure 1(a), an example of the simplest type of extended molecular conductor or molecular wire. Molecular wires are discussed in detail in other chapters in this section; it is enough for us to know that the ideal molecular wire is a material which has a π - π^* gap which is small enough to allow ballistic transport through the extended system [5].

In contrast, long-chain aliphatic molecules such as the one illustrated in Figure 1(b) are excellent insulators and conduction through such materials occurs by tunneling. This is because saturated bonds (σ -bonds) are very localized along the axis of the bonded atomic centres, and the corresponding antibonding states have relatively high energies in molecular terms (i.e., the σ - σ^* gap is typically of the order of 8 eV for C–C bonds). However, σ -bonds can be used to spatially separate π -bonded regions such as the two ends of the molecule illustrated in Figure 1(c), whilst still allowing electron transfer between them. This is because, whereas “through-space” tunneling becomes vanishingly small beyond the length of two σ -bonds [6], “through-bond” interactions between lone-pair orbitals or isolated π -bonds can be mediated through one or several σ -bonds, although the electron transfer (ET) probability decreases exponentially with the length of the bridge. Marcus ET theory [7] (also see Figure 2) suggests that such transfer can occur rapidly; this has been borne out in spectroscopic studies.

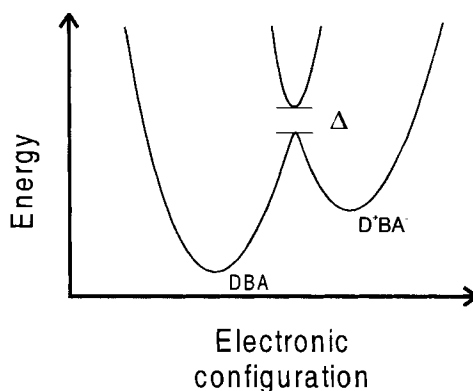


Figure 2. Marcus electron transfer plot for the process $\text{DBA} \rightarrow \text{D}^+\text{BA}^-$ [7]. The electronic coupling between the two states is defined as the energy difference Δ at the avoided crossing. Δ decreases exponentially with bridge length.

4.3 Molecular Rectifier

In the early 1970s researchers at IBM explored the possibility of exploiting the properties described above by using organic molecules as electronic components. In 1974 Aviram and Ratner, working at New York University with support from IBM, proposed that a suitably engineered molecule could act as a rectifier, exhibiting a diode-like electrical response when placed between two metallic electrodes [8]. Their deceptively simple idea is illustrated in Figure 3. The molecule would consist of three parts: an electron donor, an electron acceptor and a rigid “bridge” which would serve to keep the donor and acceptor spatially and electronically distinct. The electronic asymmetry of the molecule would allow electron transfer between the molecule and an external circuit to occur at low applied bias in one direction, and to be hindered in the opposite bias sense.

This mechanism is illustrated in more detail in Figure 4. The junction is simplified so that we consider only the highest occupied (HO) and lowest unoccupied (LU) energy levels of the donor, bridge, and acceptor regions of the molecule and the highest of the electronic states of the metal electrodes. Note that even with no

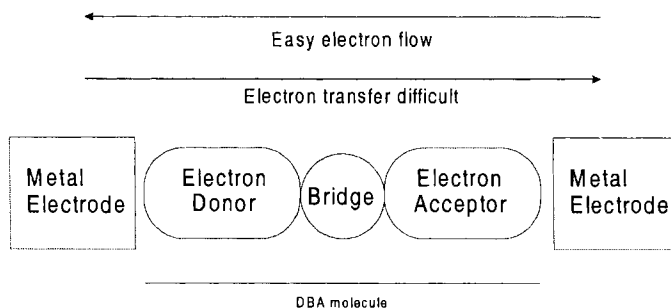


Figure 3. Schematic of a donor-bridge-acceptor molecular rectifier.

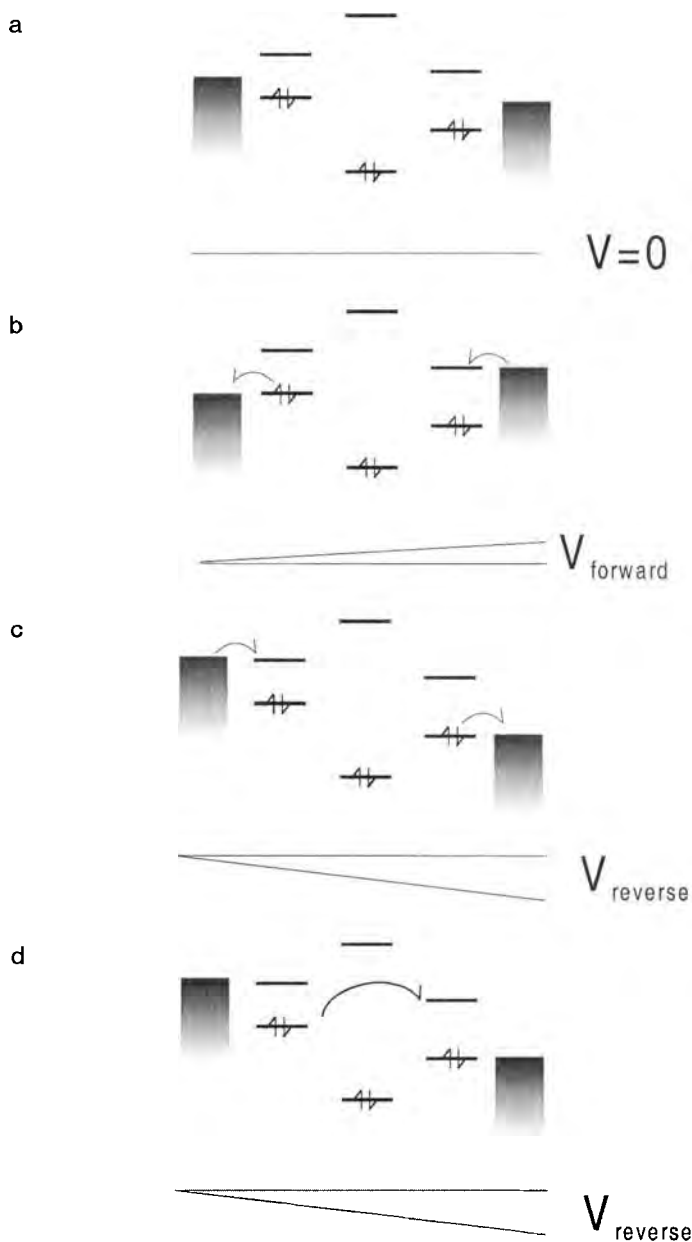


Figure 4. The energy levels of an Aviram and Ratner molecular rectifier [8]. a) Zero applied field, ground state configuration; b) forward bias; c) reverse bias (note that $V_{\text{reverse}} > V_{\text{forward}}$); d) reverse bias, alternative mechanism.

applied electric field (Figure 4a) the interaction between these electronic states and the adjacent molecular orbitals will lead to a broadening of the molecular states, and the Fermi edges of the metal electrodes will shift to lie at the centre of local HO–LU gap. Consequently the position of the Fermi edges of the two electrodes will not be symmetric unless the molecule has a symmetric charge distribution at its extremities.

An external voltage applied across the electrodes will induce a potential gradient and hence realign the energy level diagram. In Figure 4(b) there has been an energy shift such that an electron can transfer from the right-hand electrode into the vacant LU level of the acceptor, and an electron from the HO donor level can transfer into the left-hand electrode. Rapid internal recombination will now restore the $D^+\sigma A^-$ molecule to the $D\sigma A$ ground state. This bias sense, which results in “easy” electron transfer, is referred to as the forward bias direction. Figure 4(c) shows how a much larger reverse bias is required for electron transfer to occur in the opposite direction. Electron transport across the molecule is asymmetric with respect to applied bias, and hence the molecule acts as a rectifier. However, there is a further mechanism, shown in Figure 4(d), which can occur under reverse bias. If the energy gap between the HO donor state and the LU acceptor state is small, internal electron transfer can occur. This will be a rapid process, analogous to carrier excitation in a semiconductor, and the right coupling conditions between the donor and the acceptor could result in significant current flow.

Aviram and Ratner carried out a series of calculations using a semi-empirical INDO/CNDO technique to compare the electronic structure and electrical response of a hemiquinone (shown in Figure 5) and a hypothetical candidate molecular rectifier molecule [9]. They chose analogues of tetrathiofulvalene (TTF), a strong donor with an ionization potential of 6.83 eV, and tetracyanoquinodimethane (TCNQ), a strong acceptor with an electron affinity of 2.8 eV, separated by a rigid, cage-like aliphatic bridge to construct the rectifier shown in Figure 6. The calculated electrical response of this material showed a clear rectifying step.

It is reasonable to assume that any molecule that has an asymmetry in its electronic structure, such as carbon monoxide, is potentially a molecular rectifier. An Aviram and Ratner rectifier is merely an extension of this principle in that it is a modular assembly of parts which are well understood from charge transfer studies. The electronic asymmetry of the rectifier is obtained by placing an electron donor at one end of the molecule and an electron acceptor at the other. Some common

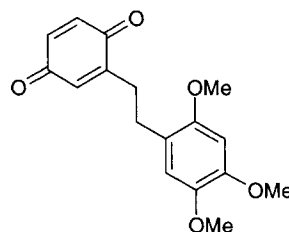


Figure 5. The hemiquinone studied by Aviram [9].

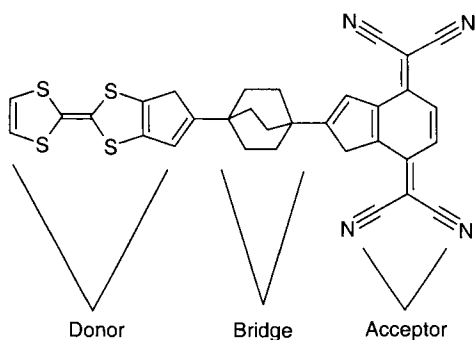
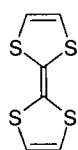
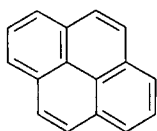


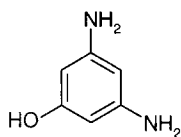
Figure 6. The Aviram and Ratner molecular rectifier [8].



a

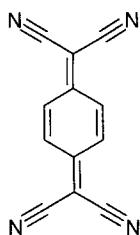


b

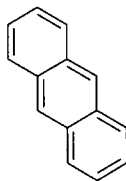


c

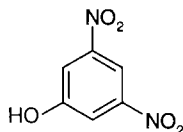
Figure 7. Examples of donor molecules: a) tetrathiofulvalene (TTF), b) pyrene, and c) di-aminophenol.



a



b



c

Figure 8. Examples of acceptor molecules: a) tetracyanoquinodimethane (TCNQ), b) anthracene, and c) dinitrophenol.

examples of organic donors and acceptors are illustrated in Figures 7 and 8. C_{60} (Figure 9) also acts as an acceptor in its native state, and as its chemistry is unlocked it is likely to become an important addition to the molecular electronics tool kit.

The third and perhaps the most important component of the Aviram and Ratner rectifier is the bridge. The purpose of the bridge is to electronically separate the donor and acceptor and to create a ground-state electronic structure that has the HOMO and LUMO localized on different parts of the molecule. It has already been mentioned that σ -bonded bridges can mediate electron transfer between π -orbitals, and indeed the majority of molecules synthesized as molecular rectifiers have used σ -bridges. However, the large σ - σ^* gap means that such systems are limited by an exponential loss of transfer probability with bridge length. Furthermore, the flexi-

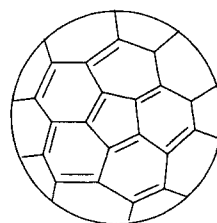


Figure 9. Buckminsterfullerene, C_{60} .

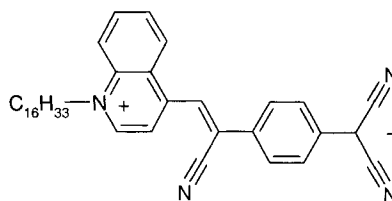


Figure 10. $C_{16}H_{33}^+Q3CNQ$.

bility of the bridge resulting from the freedom of rotation about the σ -bonds means that it is difficult to ensure effective donor–acceptor separation.

It is also possible to keep the molecular orbitals of the donor and acceptor separate by ensuring that they are not coplanar, exploiting the fall-off of π -coupling with twist angle described earlier. $C_{16}H_{33}^+Q3CNQ$ (Figure 10) has such a twisted chromophore, arising from steric hindrance, which stabilizes the ground state of the molecule in a charge-separated zwitterionic form. This effect has been further utilized by Ashwell and co-workers in an attempt to produce a material for Second Harmonic Generation (SHG) which does not have a charge transfer absorption band near the SHG emission band [10]. The modified bridge of the dye in Figure 11 effectively splits the chromophore in two, despite the fact that it is π -bridged. Such a molecule may also be a candidate molecular rectifier.

One cannot discuss the manufacture of molecular rectifiers without mentioning the huge volume of work, both in terms of papers published and molecules synthesized, undertaken by Robert Metzger and Charles Panetta [11]. They have refined the complicated techniques required for the synthesis of these materials and produced a large catalogue of potential rectifiers, a selection of which is shown in Figures 12–15. The molecule shown in Figure 12 is very close to the archetypal Aviram and Ratner rectifier. However, a pure sample has never been isolated. The molecules represented in Figures 13, 14, and 15 have been selected to give examples of molecules with different donor and acceptor combinations. In addition, all three

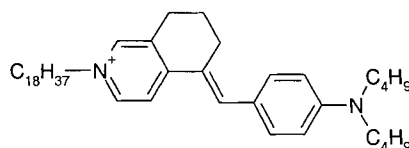


Figure 11. Hemicyanine dye with a sterically hindered bridge which gives it a twisted chromophore.

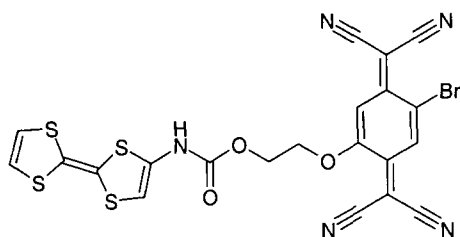


Figure 12. TTF-C-BHTCNQ.

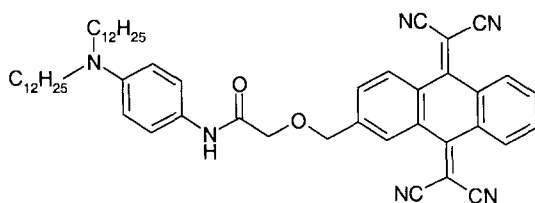


Figure 13. BDDAP-C-HMTCAQ.

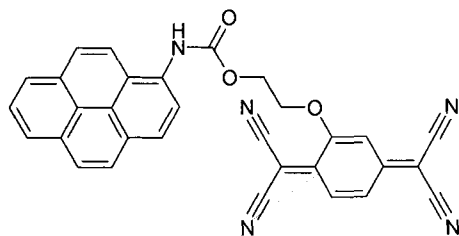


Figure 14. Py-C-HETCNQ.

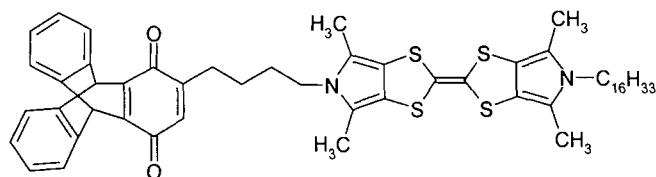


Figure 15. Hdpyr-TTf-Pyr-C4-TrpQ.

have aliphatic tails for Langmuir–Blodgett assembly (see below). The molecule in Figure 15 is also unusual because it has a nonplanar acceptor.

There already exist a large number of materials in general use or synthesized for other purposes that possess many if not all of the properties of a molecular rectifier. Many liquid crystal materials are designed with a weak donor–acceptor structure in order to give the molecules a large dipole moment (Figure 16 shows a typical cyano–biphenyl nematic material), but as a side effect some of these may have potential as molecular electronic devices. Donor–bridge–acceptor molecules such as the “antenna” material shown in Figure 17 have been synthesized in an attempt to artificially replicate photosynthesis, i.e., to use light to drive chemical reactions.

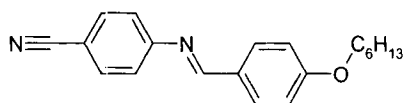


Figure 16. A typical cyano-biphenyl nematic liquid crystal molecule.

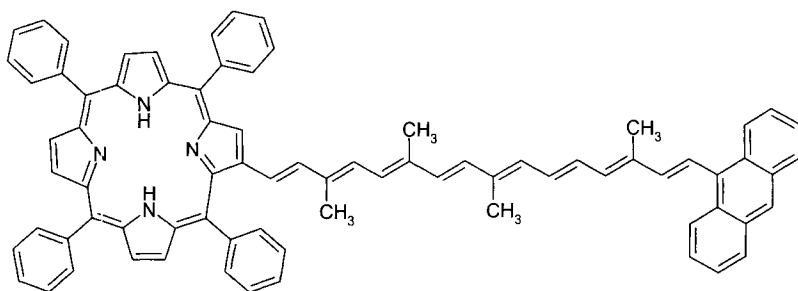


Figure 17. A donor-bridge-acceptor antenna molecule.

These materials are effectively molecular photodiodes. It is highly possible that future applications of molecular electronic devices will arise through this overlap of technologies.

4.4 Practical Investigation of a Molecular Rectifier

We have described how a molecule which has an internal electronic asymmetry should exhibit rectifying properties. However, since we are interested in current flow rather than simply charge separation within the molecule, we must characterize the molecule as part of a circuit. It is important to realize that the measurements being made are of the junction as a whole rather than just the molecular properties. That is to say, the electrical response is a convolution of the molecular properties, the external circuit and, in particular, the contacts between the molecule and the electrodes. The interactions at the interfaces are responsible for many of the effects that are observed in metal-insulator-metal devices.

Aviram and Ratner envisaged that their hypothesis could be tested by sandwiching a monolayer of the rectifier molecules between metallic electrodes, i.e., measuring a two-dimensional (2D) assembly of identically oriented molecules rather than a single molecule. The monolayer would be assembled using the Langmuir-Blodgett (LB) technique, which at the time was the only reliable means of constructing an ordered molecular monolayer. There are a number of more recently developed techniques which could clearly now also be used. The major candidate is self-assembly, which utilizes the propensity of thiols to chemisorb onto noble metal surfaces, and

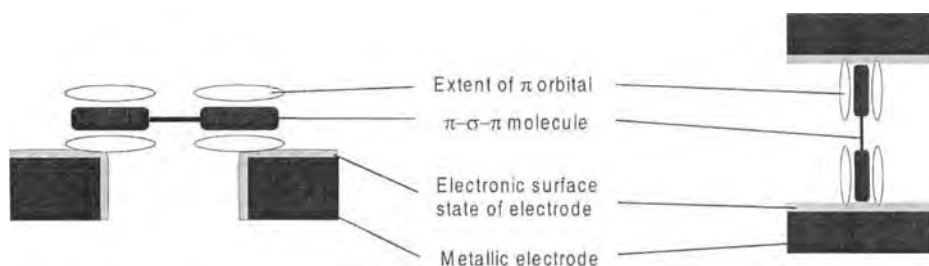


Figure 18. Possible orientations of π -orbitals with respect to the electronic surface states of the electrodes. The normal LB geometry would be the right hand case.

has major possibilities for device fabrication. However, the sulphur–metal bond can in itself act as a tunnel barrier and exhibit rectifying effects.

Even within a monolayer there is the possibility of in-plane intermolecular interaction [12]. Adjacent π -systems can interact to form a 2D band or a pseudo-1D band structure within the layer, resulting in dispersion of the individual molecular orbital levels. It should be possible to isolate single-molecule effects by diluting the rectifier material in an inert matrix, e.g., a fatty acid. The current should then scale with the area fraction of active molecules within the matrix, if it is assumed that the rectifying current is the dominant conduction mechanism.

The use of a 2D film of molecules raises a further consideration related to the interface states. The orientation of the molecular π -cloud with respect to the surface states of the metal electrode will very strongly influence the ET probability. In LB films and self-assembled monolayers, the π -orbitals are generally aligned so that they are almost orthogonal to the plane of the metallic substrate. Consequently the overlap with the surface states of the metal is poor, and hence the ET probability between the two is low. Ideally the junction should be arranged so that the molecular states lie in the same plane as the surface states of the metal, as shown in Figure 18. This has not yet been attempted with rectifying molecules; the coupling efficiency has been reliant upon the native layer tilt of the molecules within the LB film.

Langmuir–Blodgett films have been at the heart of the majority of molecular rectifier studies to date. A brief description of the technique follows.

4.5 The Langmuir–Blodgett Technique

An amphiphilic molecule will preferentially sit at an air/water interface with the hydrophilic group immersed in the water and the hydrophobic part clear of the surface. A direct consequence of this is that insoluble amphiphiles will form a monolayer at the interface. With no external constraints this will be disordered, but as the available surface is restricted, the molecules will align and pack into an ordered 2D pseudo-crystalline state (as shown in Figure 19b). This ordered semi-rigid structure

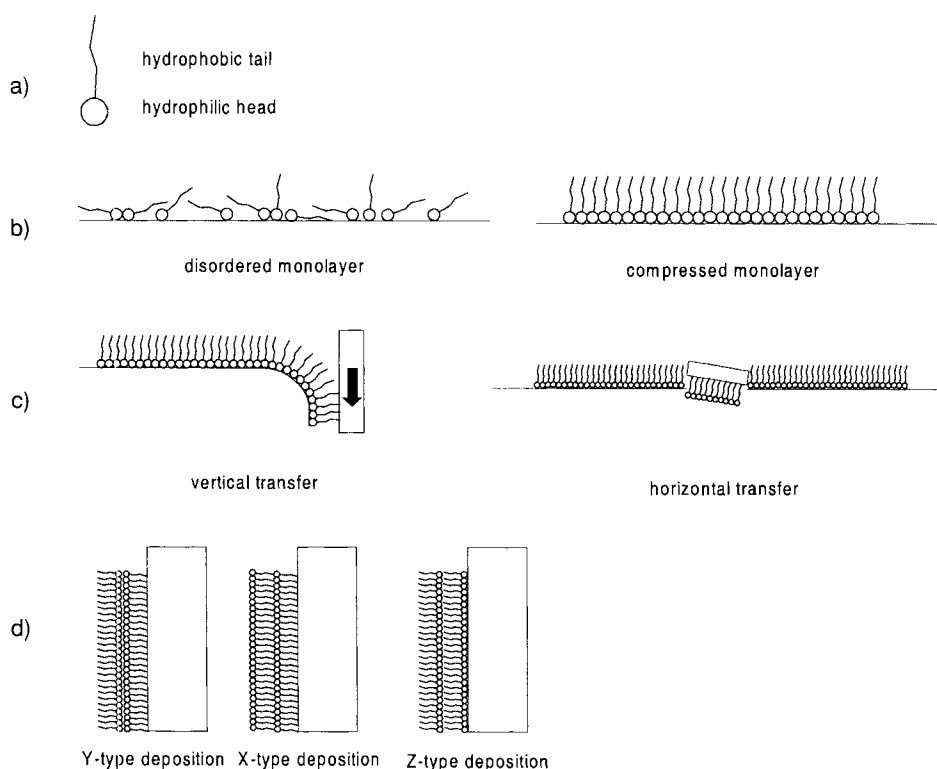


Figure 19. a) Simple representation of an amphiphile; b) Langmuir monolayer in expanded and compressed states; c) vertical and horizontal Langmuir–Blodgett film transfer; d) X-, Y-, and Z-type LB films.

can be transferred onto a solid support by either vertical or horizontal transfer (Figure 19c). Many amphiphilic materials can be built into multilayered structures using repeated monolayer deposition. Three different orientational structures are shown in Figure 19(d).

A drawback of the LB technique for producing electrical samples is its reliance on amphiphiles. Aviram and Ratner suggested that the donor part of their rectifier would be sufficiently hydrophobic for LB deposition. It is more generally found that a long aliphatic tail has to be added to one end of the molecule to make it strongly hydrophobic. This is a tunnel barrier, and can result in the through-space tunnel current being of a similar magnitude to the transmitted current in a monolayer. Furthermore, LB films have inherent defects at grain boundaries such as that illustrated in Figure 20, and these defects tend to be more prevalent in more complex, heavily substituted materials. It is critically important to produce films which are as defect-free as possible in order to make a junction which is not a short circuit. The majority of workers have chosen to study multilayer structures, despite the complication of interpretation arising from multiple interfaces. There will be a potential

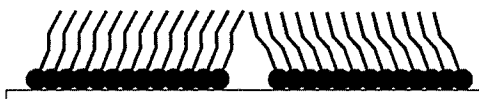


Figure 20. Grain-boundary defect in a LB film.

drop at every interface, and as a result it is by no means clear what the electric field will be across each layer (see Figure 21). Furthermore, in order not to have reversed the electrical response of the molecules in every other layer, the structure must be noncentrosymmetric, i.e., X- or Z-type. Even then tunnelling may overshadow the molecular conduction process.

Tunneling in multilayered LB films is defect-mediated via trap sites within the conduction band of the molecules (Poole conduction), or by Schottky emission between widely spaced trap sites (Poole–Frenkel conduction) in thicker samples [13]. With good molecular conductors the current from molecular conduction should dominate the small contribution from tunneling. However, the conduction mechanism between adjacent layers is not always obvious, due to the complexity of the interface structure.

Careful use of the Langmuir–Blodgett technique allows the assembly of an oriented molecular film onto a solid support, which could be one of the electrodes in our electrical circuit. This circuit must now be completed by adding a second metallic contact on top of the film.

4.6 Junction Design

Defects in the film are perhaps the primary cause of short circuits in junctions. The junction design, that is to say the electrode geometry and materials, has to be chosen to minimize defect formation. There are broadly two classes of junction geometry, and these are illustrated in Figure 22. The simplest structure consists of a linear base electrode on an insulating substrate; a linear top electrode is then deposited perpendicular to the base electrode. This strategy can be used to make very small junction areas, minimizing the probability of including a defect while distancing the connection to the external circuit. However, the edges of the base electrode (and the penumbra associated with it if the electrode is thermally evaporated) are in themselves prime sites for defect formation in the LB film. The second geometry eliminates the edge problem by utilizing a planar base electrode and small pads for top electrodes. The problem with this geometry is that making a connection to the top electrode is difficult with most fragile molecules.

In both cases the base electrode should be flat and smooth, and free from any contamination or oxide layers. Ideally both of the electrodes should be noble metals so that there is no possibility of any oxide layers in the junction. However, the majority of LB films are not very thermally stable, and are easily damaged during top electrode deposition. This is a particular problem with noble metals, which

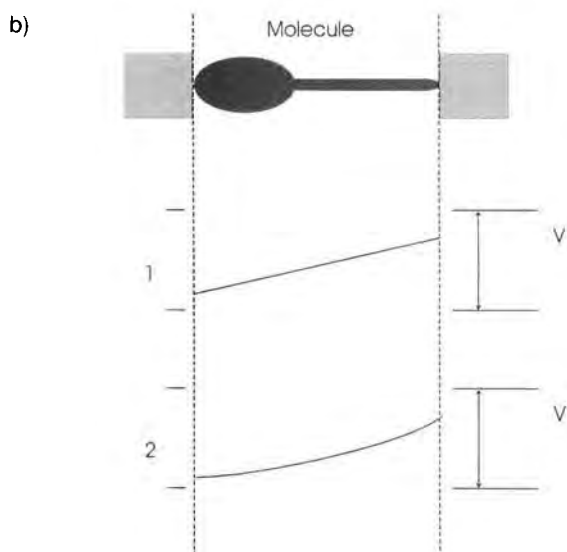
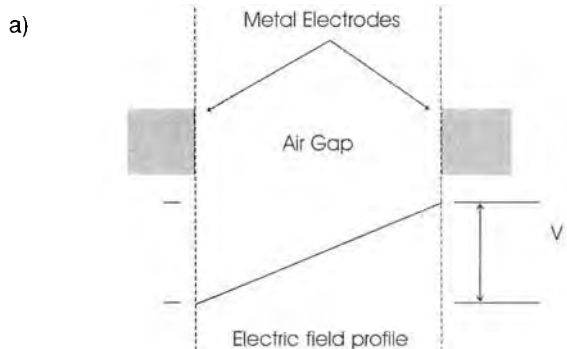
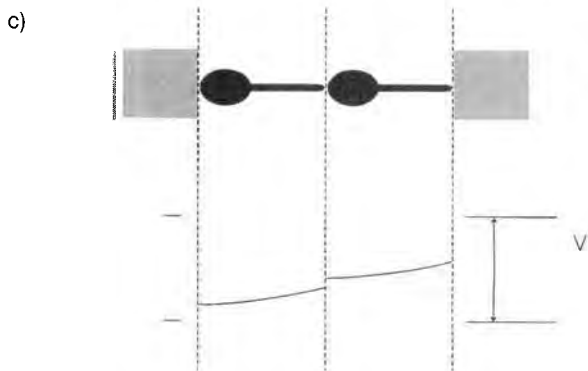


Figure 21. Electric field profile across multiple interfaces: a) across an air gap the potential gradient is uniform; b) with a molecule in the gap, there will be a potential drop which can be different at each interface (note that the potential gradient along the length of the molecule is not necessarily uniform, as illustrated in case 2); c) with a multilayer of molecules, there is an extra interface between each layer.



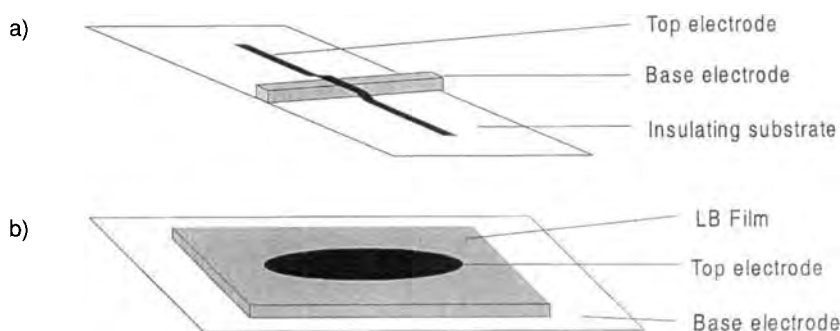


Figure 22. Classes of electrode geometry: a) crossed-wire electrodes; b) planar base electrode with pad top electrode.

have high evaporation temperatures (1500 °C for gold) and a large latent heat of condensation.

Thus, so far, few measurements have been conducted on the ideal gold|LB|gold system—instead, other top electrodes are used which inflict less thermal damage on the LB film. The measurements that have been made are outlined below.

4.7 Electrical Characterizations of LB Films

The first measurements of the electrical properties of LB films appear to have been carried out by Buchwald et al. in the 1930s using an electrolyte in place of a second electrode [14]. It was not until the 1960s the first metal|LB|metal experiments were undertaken by Handy and Scala [15] and were followed by a major contribution by Mann and Kuhn which included the first Al|LB|Al experiment [16]. Aluminum has an insulating native oxide which strongly influences the results of characterizations carried out using it as an electrode [17]. Only in the late 1980's was the first electrical characterization of LB films without oxide layers on the electrodes carried out by Geddes et al. [18], in the first study to emphasize the critical importance of producing defect-free LB films for junction fabrication. They used a junction geometry with a planar platinum base electrode and magnesium top electrodes which were capped with silver contacts, similar to the geometry shown in Figure 23 (which actually shows a later refinement of this original innovative solution). Connection was made using droplets of gallium/indium eutectic to bridge between the silver pads and a gold wire. Geddes also reported seeing the asymmetric I/V response shown in Figure 24 from LB films of DDOP-C-TCNQ (Figure 25), although the molecular origin of the effect was never fully explained [19].

Rectification in a monolayer and multilayers of $C_{16}H_{33}\gamma Q3CNQ$ (Figure 10) was observed by Martin and co-workers [20]. Typical data from a multilayer sample are shown in Figure 26. The rectification was convincingly shown to be molecular in

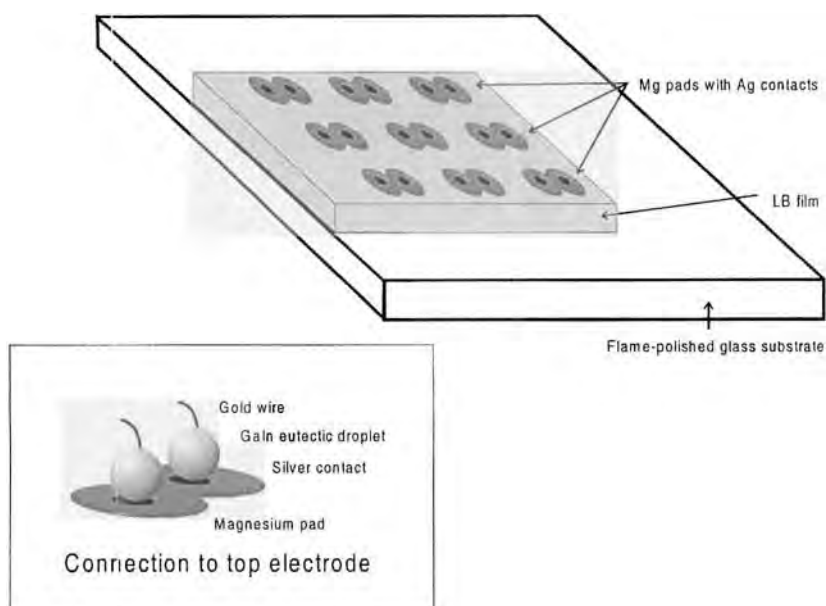


Figure 23. Junction geometry used by Geddes et al., Martin and co-workers, and Brady et al. [19, 20, 23].

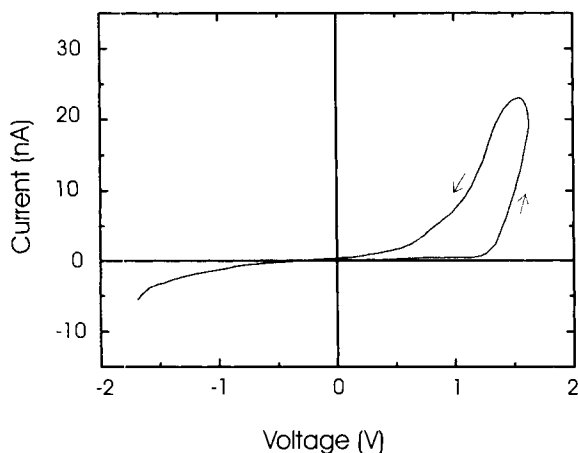


Figure 24. I/V characteristics of a monolayer of DDOP-C-TCNQ [19].

origin by insulating the active molecule from the electrodes with inert layers [21]. These measurements have recently been repeated and confirmed by Metzger et al., who have carried out a large number of corroborative spectroscopic studies [22]. Unfortunately this group has taken the retrograde step of moving back to aluminum electrodes in an attempt to produce “symmetric” junctions. There will always

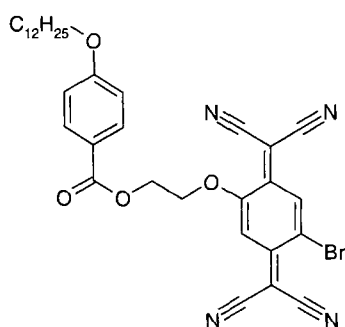
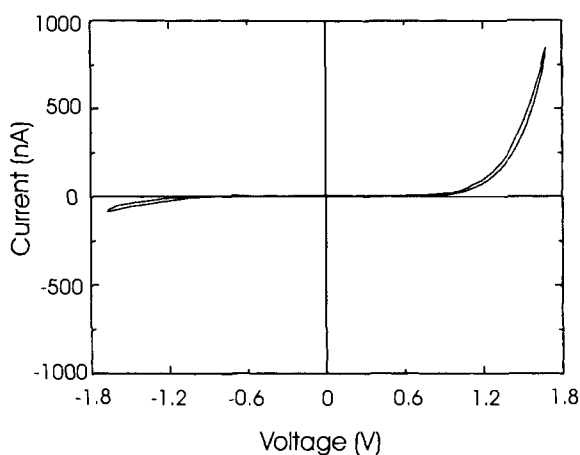


Figure 25. DDOP-C-TCNQ.

Figure 26. I/V characteristics of a five-layer film of $C_{16}H_{33}/Q3CNQ$ [20].

be a large element of uncertainty in the interpretation of any measurements obtained from a junction containing oxide barriers.

A σ -bridged material, OHAPy-C-DNB (Figure 27) has been studied by Brady et al. [23]. This material exhibits very strong rectifying effects (Figure 28), but the direction of high current flow does not fit the simple Aviram and Ratner model. Instead, it is believed that this material acts more like an organic semiconductor, in a manner similar to the “alternative” reverse-bias mechanism shown in Figure 2(d).

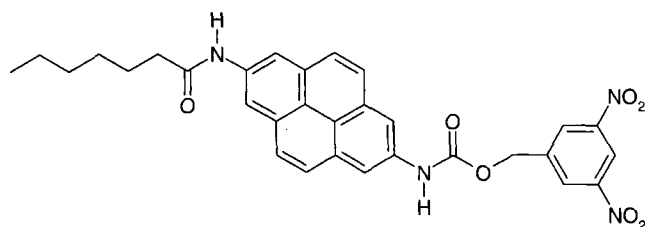


Figure 27. OHAPy-C-DNB.

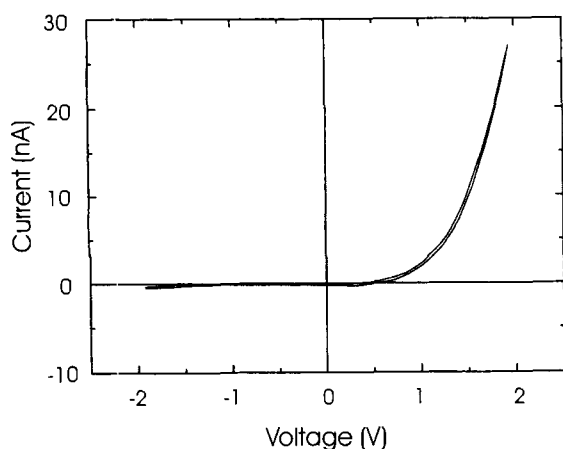


Figure 28. I/V characteristics of a five-layer film of OHAPy-C-DNB [23].

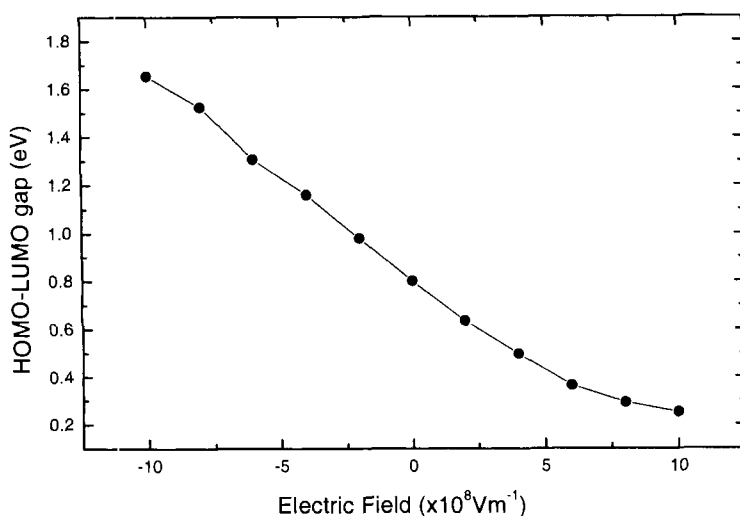


Figure 29. Behavior of computationally modeled HOMO–LUMO gap under applied electric field [23].

Ab-initio modeling indicates that the HOMO–LUMO gap changes in width in the high electric fields involved in these experiments, as shown in Figure 29, and this probably dominates the rectification behavior. Furthermore, it is believed that the distortion of the molecular orbitals in the huge electric fields is responsible for the nonlinear conduction observed.

The crucial step of manufacturing gold|LB|gold junctions which can be cooled to 4.2 K has been achieved by a group from Stuttgart [24]. They have observed rectification from multilayer heterostructures, and recorded what are believed to be

the signatures of molecular orbitals filling and emptying. The materials they have studied to date have been thermally robust phthalocyanines and porphyrins, but the importance of the technological step cannot be understated.

4.8 Other Techniques

Other technologies are also emerging which allow single molecules to be addressed. Scanning probe microscopy allows a conducting tip to be placed on a partial or complete monolayer with atomic precision. A number of materials, including benzene and C₆₀, have been probed with a scanning tunneling microscope (STM) [25]. Nanoelectrodes are being fabricated with gaps down to 10 nm [26], and a single dithiol molecule has been trapped in a break junction [27]. These studies herald the arrival of truly molecular electronics.

4.9 Conclusions

Unimolecular rectifiers are a reality. They have been made and they have been measured. However, there is still substantial room for improvement in the experimental techniques used to study the molecules and in the molecules used to give improved thermal stability. Current experiments need to be modified so that noble metal electrodes may be used to study a dilute monolayer, ideally at low temperature where molecular orbital signatures will be observable. This already has been achieved with “robust” molecules such as phthalocyanines, which suggests that the technological step to be made is not too great.

At the moment molecular electronic circuits and logic devices are still some distance away, but the building blocks are there and the tools are being assembled.

References

1. R.P. Feynman, “There’s plenty of room at the bottom”, a talk given to the annual meeting of the American Physical Society at Caltech, December 29, 1959. A transcript is available online at <http://www.zyvex.com/nanotech/feynman.html>.
2. Y. Taur, D.A. Buchanan, W. Chen, D.J. Frank, K.E. Ismail, S-H. Lo, G.A. Sai-Halasz, R.G. Viswanthan, H-J. C. Wann, S.J. Wind, H-S. Wong, *Proc. IEEE* **1997**, *85*, 486–504.
3. E.G. Petrov, I.S. Tolokh, A.A. Demidenko, V.V. Gorbach, *Chem. Phys.* **1995**, *193*, 237–253; M.P. Samanta, W. Tian, S. Datta, J.I. Henderson, C.P. Kubiak, *Phys. Rev. B* **1996**, *53*, 7626–7629.
4. A. Broo, M.C. Zerner, *Chem. Phys.* **1995**, *196*, 423–436; A. Broo, M.C. Zerner, *Chem. Phys.* **1995**, *196*, 407–422; A. Broo, *Chem. Phys.* **1993**, *169*, 135–150; A. Broo, *Chem. Phys.* **1993**, *169*, 151–163.

5. C. Joachim, J.F. Vinuesa, *Europhys. Lett.* **1996**, 33, 635–640; M. Magoga, C. Joachim, *Phys. Rev. B* **1997**, 56, 4722–4729; M. Magoga, C. Joachim, *Phys. Rev. B* **1998**, 57, 1820–1823.
6. M. Braga, A. Broo, S. Larsson, *Chem. Phys.* **1991**, 156, 1–9; A. Broo, S. Larsson, *Chem. Phys.* **1990**, 148, 103–115.
7. R.A. Marcus *J. Chem. Phys.* **1965**, 43, 679.
8. A. Aviram, M.A. Ratner, *Chem. Phys. Lett.* **1974**, 29, 277–283.
9. A. Aviram, PhD Thesis, **1975**, NewYork University.
10. G.J. Ashwell, G. Jefferies, C.D. George, R. Ranjan, R.B. Charters, R.P. Tatam, *J. Mater. Chem.* **1996**, 6, 131.
11. See R.M. Metzger, *J. Mater. Chem.* **1999**, 9, 2027–2036 and references therein.
12. I.A. Levine, *Quantum Chemistry*, 3rd ed., Allyn & Bacon Inc., Boston, **1983**.
13. R.M. Hill, *Philos. Mag.* **1971**, 23; R.O. Carlson, *Phys. Rev.* **1955**, 100.
14. CE Buchwald, D.M. Gallagher, C.P. Haskins, E.M. Thatcher, P.A. Zahl, *Proc. NAS* **1938**, 24, 204–208.
15. R.M. Handy, L.C. Scala, *J. Electrochem. Soc.* **1966**, 113, 109.
16. B. Mann, H. Kuhn, L. Szentpály, *Chem. Phys. Lett.* **1971**, 8, 82.
17. K.H. Gundlach, J. Kadlec, *Chem. Phys. Lett.* **1973**, 25, 293–295.
18. N.J. Geddes, J.R. Sambles, D.J. Jarvis, N.R. Couch, *Thin Solid Films* **1988**, 167, 261.
19. N.J. Geddes, J.R. Sambles, D.J. Jarvis, W.G. Parker, D.J. Sandman, *Appl. Phys. Lett.* **1990**, 56, 1916–1918.
20. G.J. Ashwell, J.R. Sambles, A.S. Martin, W.G. Parker, M. Szablewski, *J. Chem Soc., Chem. Commun.* **1990**, 19, 1734–1736.
21. A.S. Martin, J.R. Sambles, G.J. Ashwell, *Phys. Rev. Lett.* **1993**, 79, 218–221.
22. R.M. Metzger, B. Chen, U. Höpfner, M.V. Lakshmikantham, D. Vuillame, T. Kawai, X. Wu, H. H. Tachibana, T.V. Hughes, H. Sakurai, J.W. Baldwin, C. Hosch, M.P. Cava, L. Brehmer, G.J. Ashwell, *J. Am. Chem. Soc.* **1997**, 119, 10455.
23. A.C. Brady, B. Hodder, A.S. Martin, J.R. Sambles, C.P. Ewels, R. Jones, P.R. Briddon, A.M. Musa, C.A. Panetta, D.L. Mattern, *J. Mater. Chem.* **1999**, 9, 2271–2275.
24. C.M. Fischer, M. Burghard, S. Roth, K. v. Klitzing, *Europhys. Lett.* **1994**, 28, 129–134.
25. V.J. Langlais, R.R. Schlitter, H. Tang, A. Gourdon, C. Joachim, J.K. Gimzewski, *Phys. Rev. Lett.* **1999**, 83, 2809–2812; C. Joachim, J.K. Gimzewski, R.R. Schlitter, C. Chavy, *Phys. Rev. Lett.* **1995**, 74, 2102; A. Yazdani, D.M. Eigler, N.D. Lang, *Science* **1996**, 272, 1921; S. Datta, W. Dang, S. Hong, R. Reifengerge, J.I. Henderson, C.P. Kubiak, *Phys. Rev. Lett.* **1997**, 79, 2530–2533.
26. M.A. Reed, C. Zhou, C.J. Muller, T.P. Burgin, J.M. Tour, *Science* **1997**, 278, 252–254.
27. A. Bezryadin, C. Dekker, G. Schmid, *Appl. Phys. Lett.* **1997**, 71, 1273–1275; A. Bezryadin, C. Dekker, *J. Vac. Sci. Technol. B* **1997**, 15, 793–799.

5 Logic Gates

A. Prasanna de Silva, Nathan D. McClenaghan, and Colin P. McCoy

5.1 Introduction

It is hard to ignore the influence the information technology revolution has had on the practice of chemistry. Then it is only fair that we as practitioners of chemistry apply our particular skills to examining some of the principal revolutionaries—the logic gates [1, 2]. If nothing else, such efforts will infuse the computational ways of thinking into our culture, and besides causing such cross-fertilization, they can access niche applications of single molecules (or small populations of them) with logic capabilities. Applying chemical or optical inputs and receiving optical output from molecules according to various logic types is no longer a dream. Therefore sensory applications of these molecular-scale logic gates are to be expected, especially for use in small spaces. Other approaches to information processing with molecules or atoms have also come to the fore. The spectral hole-burning approach has already led to parallel arithmetic operations. The huge parallelism inherent in DNA-based computation has been demonstrated. The possibilities of quantum computing in several of its manifestations have excited interest. When compared with current semiconductor devices, the far smaller size of molecules and atoms remains an important feature to exploit in this and other ways.

Other features of current molecular logic systems, such as the rudimentary logic capability, the solution-phase operation, and the difficulty of physical “wiring” of simpler systems into more complex ones, are viewed as fatal disadvantages by those bent on channeling current research slavishly along the beaten track of silicon technology. These issues can be debated. When we view them more generally, we realize that the logic capabilities are being steadily generalized and developed in spite of the relatively meager resources invested thus far, i.e., with a rather high benefit/cost ratio. We also notice that wet operation of molecule-based information processors has served humankind well ever since its beginning [3]. Furthermore, molecular logic systems can be transplanted to surfaces when so desired. The physical “wiring” problem has been circumvented, at least in some prototype cases.

Designers of molecular logic gates have the prerogative to be educated by silicon technology and yet not be bound by its attitudes and culture, all-pervasive though it may be. This debate aside, one general way of addressing this challenge will be to look for applications where these issues are not involved.

The area of molecular logic and information processing, like any embryonic field, faces several common issues. On the one hand, in order to grow it needs new exponents. On the other hand, these new exponents may occasionally make over-enthusiastic extrapolations leading to criticism by the chemical community. We must carefully consider cautionary remarks, expressed most recently by Bard [4], if this field is to prosper.

Even though molecular electronics [5, 6] has been a sphere of scientific effort since the 1980s, it is only since 1993 that molecular-scale logic gates have become available in the primary literature [7]. Coincidentally, some of the experimental tools required to examine these gates at the single-molecule limit became available [8, 9]. These examinations should be a priority for the future. As the following sections will demonstrate, molecular-scale logic gates arrived rather suddenly without going through intermediary stages. In contrast, molecular-scale electronic logic gates have not yet been realized, although steady progress is being made with the development of wires [10], switches [11], and diodes [12]. On the other hand, the current generation of molecular-scale logic gates are being generalized as we write. Logic functions of various types have been arranged within single molecules. These cover over half of the nontrivial cases out of the four single-input and the sixteen two-input logic families [13]. The emphasis in this chapter will be on tracking the progress of these ideas and related developments in other approaches to atomic/molecular-scale information processing. We provide this status report for all interested scientists to ponder and build on. As this is a naturally interdisciplinary subject, everything here is offered as a series of thumbnail sketches from a chemist's perspective. For deeper analysis, the reader is encouraged to consult the original references.

5.2 Photochemical Approaches to Molecular-scale Logic

5.2.1 Chemical/Optical Input/Output

Combination of ideas from organic, coordination, supramolecular, and photochemistry provides a simple approach to logic operations at the molecular scale. It is straightforward to marshal inputs, outputs, and power supplies if they are all distinguishable. Truly molecular devices thus arise naturally [14–16]. The subsections below show how this can be done by using a mix of various chemical species and different wavelengths of light. In most cases so far, the optical output is considered in the fluorescence mode because of its ease of detection even at the single-molecule limit [17, 18]. Using light absorption (or transmission) as an output is normally a less sensitive approach, though single-molecule experiments are becoming possible even here, albeit under special conditions [19, 20]. If the absorption

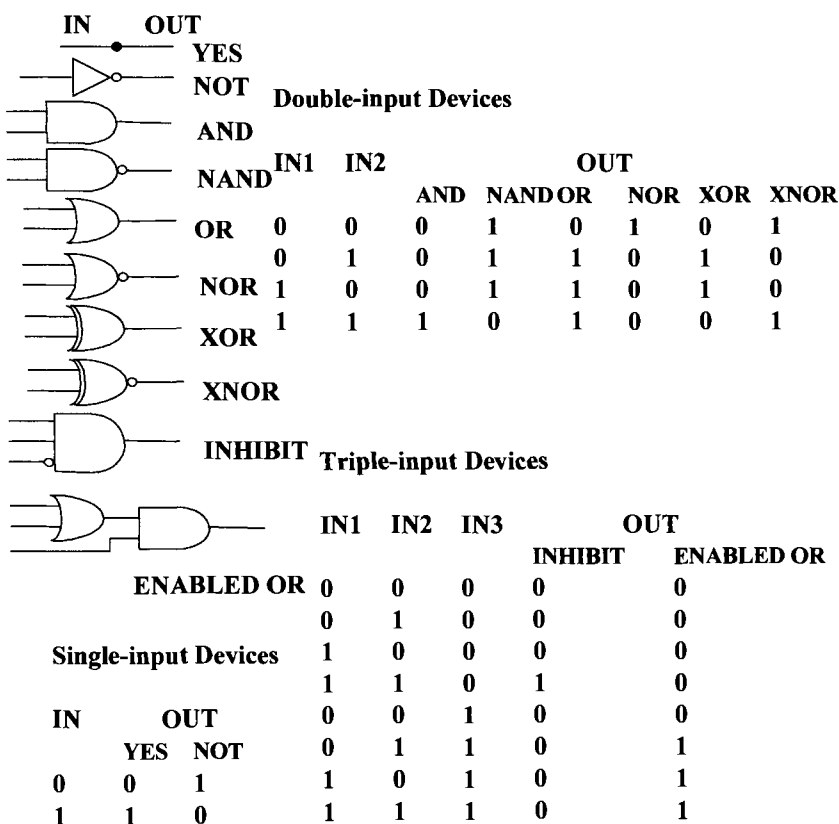


Figure 1. Electronic symbols for logic gates and corresponding truth tables.

mode is considered more seriously, many earlier experiments from the analytical chemistry area [21] also become available for discussion in the present context. In spite of this bounty the discussion is limited to an example or two of each type, owing to space constraints and also to maintain balance between the different sections. More detailed discussion on the photochemical approach is available in two companion reviews [22, 23].

YES logic

A YES logic gate is the simplest of all gates, with a single input channel and a single output channel. A low input (input 0) gives a low output (output 0) (Figure 1). Conversely, a high input (input 1) results in a high output (output 1).

There are literally hundreds of examples of this type of behavior, most of which have been developed for other applications by their original authors and are therefore not recognized in this logical context. Using appropriate codings any bistable system with an easily recognizable physical output would fall into this category. A fluorescent photoionic example can be seen in Figure 2 with 1 [24], whereby protons

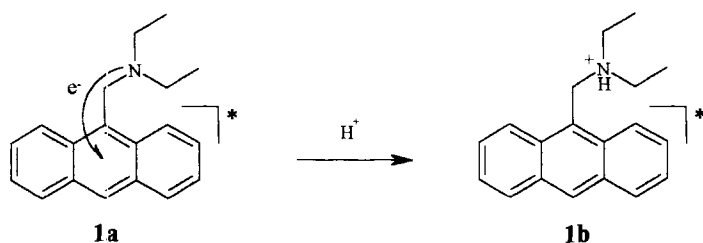


Figure 2. Molecule **1** displaying YES logic via fluorescence output from a proton input.

are considered as the input and fluorescence emission intensity at a chosen wavelength within the emission band is the output. In the absence of protons (input 0) an electron can be freely transferred from the amine to the anthryl fluorophore in its excited state, with a resulting quenching effect on the fluorescence emission (output 0). This is photoinduced electron transfer (PET) [25–29]. Introduction of protons of sufficiently high concentration (input 1) causes binding of the amine receptor, which has the effect of ceasing this relatively long-range electron transfer and hence restoring the fluorescence output (output 1), **1b**. Thus **1** can be seen to convert two different kinds of signal (ionic to photonic). Many variations in the input species employed and output measured have been reported. The literature of absorptiometric and fluorescent reagents for protons and metal ions in analytical chemistry is a particularly rich source, provided that adequate care is paid to binding reversibility [21, 30, 31].

NOT logic

Another one-input, one-output gate is a NOT gate. This gate can be considered an inverted YES gate, as can be seen by the electronic representation in Figure 1. The corresponding truth table for this logic situation can also be seen.

In the example seen in Figure 3, a PET process is again implemented. However,

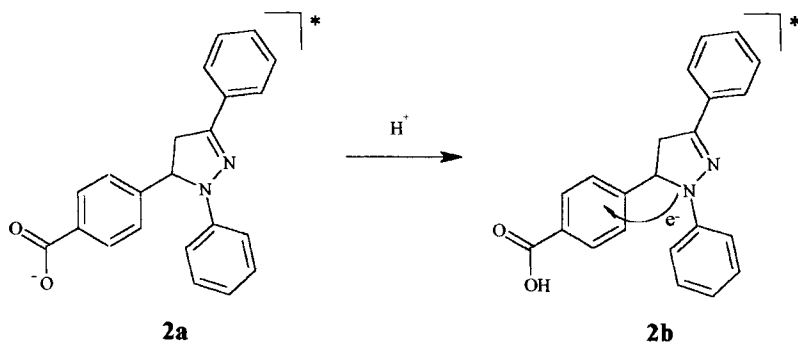


Figure 3. Molecule **2** displaying NOT logic via fluorescence output from a proton input.

in this example the quenching mechanism is set in place only upon protonation. Therefore the input is again protons and the output is fluorescence emission. The deprotonated carboxylic acid group in **2a** [32] exhibits a near-zero Hammett substituent constant, resulting in a small net effect on the adjacent benzene ring. Therefore this substituent has only a small effect on the reduction potential of this entity. However, protonation of the carboxylic acid group results in a much greater electron-withdrawing ability which is conferred upon the adjacent benzene ring, **2b**. The lowered reduction potential of this moiety makes the quenching mechanism favorable. Thus introduction of a high proton concentration (input 1), 10^{-2} M, yields a low fluorescence emission (output 0). At a low proton concentration (input 0), 10^{-6} M, the inefficient PET process results in switching “on” fluorescence (output 1).

Again, it is important to note that there are many examples of NOT logic gates scattered throughout the fluorescence literature, of analytical reagents for metals for instance [31]. This is to be expected since the quenching of fluorescence is a common phenomenon, especially with the transition metal ions.

AND logic

Previous examples considered required a one-input, one-output format. In the AND logic situation and subsequent gates under consideration, a minimum of two inputs are required. This two-input, one-output situation can be seen in Figure 1 along with the resulting truth table.

As two inputs are required, two different ionic species can be considered as the inputs when supplied in sufficiently high concentration. In the case of **3** [33] (Figure 4), Na^+ and protons are employed. The benzo-15-crown-5 ether and tertiary amine nitrogen serve as the respective binding sites. An essentially digital action is seen in this case; in other words, the low-fluorescence cases are characterized by measurable emission being almost absent, due to the efficient PET processes in this molecule. With neither Na^+ nor H^+ present (input 00), **3a**, PET can occur from either receptor with no resulting fluorescence emission (output 0). With only Na^+ (or H^+) present, electron transfer from its receptor is halted (output 0). However, electron transfer from the other receptor can continue unabated and so no fluorescence is detected. This corresponds to the input 10, **3b** (or input 01, **3c**), output 0, situation. With both Na^+ and H^+ present (input 11), the PET mechanism cannot function from either receptor and so fluorescence is switched “on”, giving an output 1, **3d**. The PET process shown in **3c** deserves special comment. A quick look at the relevant electrochemical data would show that PET from a *o*-dialkoxybenzene unit to an anthracene is thermodynamically unfavorable. The intramolecular nature of the current situation does not change this conclusion, as confirmed experimentally with the appropriate model compound [34]. However, the substitution of anthracene in a *meso* position with a strongly electron-withdrawing substituent swings this situation around. Now PET thermodynamics becomes favorable, as seen with 9-cyanoanthracene derivatives, for example [34]. The fact that **3c** contains a protonated aminomethyl substituent in a *meso* position of the anthracene is therefore pivotal to the successful operation of AND gate **3**.

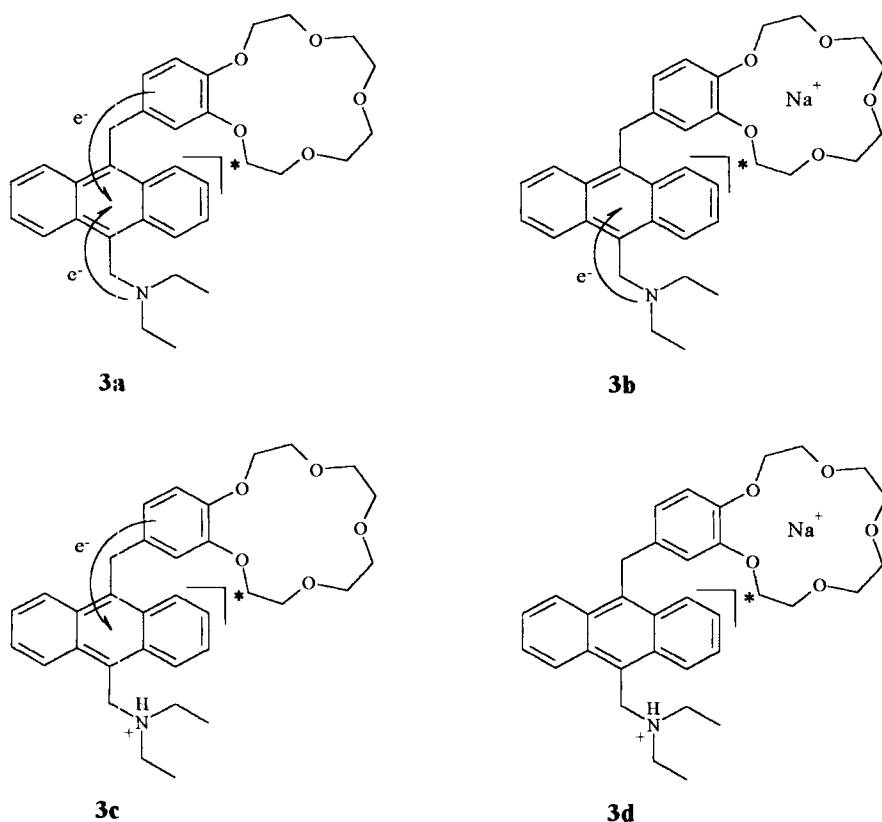
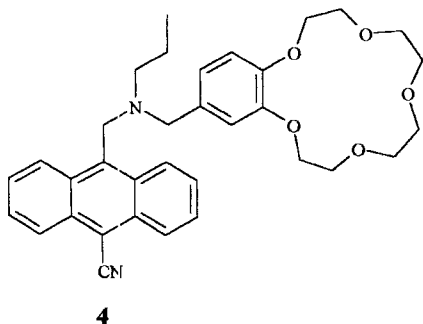


Figure 4. Molecule 3 displaying AND logic via fluorescence output using sodium and proton inputs. Note that only one of the two PET paths shown would occur in a given excited state 3a.

In a preceding case [7], indeed the first example of this behavior, **4** was seen to behave in a similar fashion employing the same inputs and outputs being constructed from similar components. However, the same degree of switching between “on” (output 1) and “off” states (output 0) was not seen. This was attributed to the



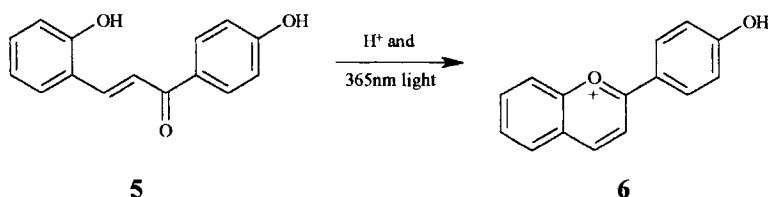
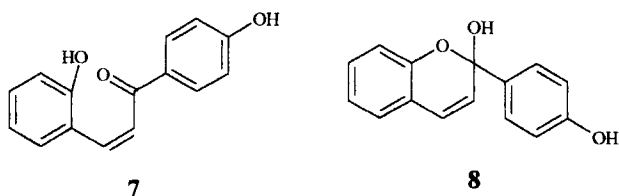


Figure 5. AND logic with **5** via fluorescence output with combined ionic (H^+) and photonic inputs (365 nm light).

arrangement of components, with the benzo-15-crown-5 ether receptor three atoms away from the fluorophore.

Pina, Balzani, and their colleagues developed a different approach to molecular-scale AND logic. In the case of **5** [35] (Figure 5), protons and 365 nm light were utilized as the inputs, thereby differing from the all-ion input strategy shown previously. The proton input is considered low at a concentration of 10^{-4} M, and high at 10^{-1} M. This combination of an ionic input followed by photonic one then consummated in the photochemical isomerization seen in Figure 5. Unlike its precursor, the newly formed molecule emitted fluorescence, and thus emission (515 nm) served as the output. Irradiation of **5** caused smooth *E*- to *Z*- isomerization of the alkene to produce **7**, which then allows proton-induced cyclization to **6** via intermediate **8**. These systems are elegant because of their extreme structural simplicity and understandable mechanistic/operational complexity, because of which their importance extends beyond logic operations to include the “write–lock–read–unlock–erase” cycles [36] as well as shallow and deep memories.



We must again draw attention to venerable analytical reagents which show features of AND logic. The importance of pH control is stressed during assays of metal ions, for instance. Therefore, alkaline conditions (proton input 0) produce no signal (output 0) even if the metal ion is present (metal input 1). Upon adjustment of pH to neutral conditions (proton input 1), the presence of metal ion (metal input 1) produces an analytically useful fluorescence/absorption signal (output 1) [31]. Further increase of the proton level is detrimental to many of these cases, resulting in the loss of fluorescence/absorption. Simpler systems, some of which are metal-free, can be predictively designed to show such “window” or “off–on–off” effects [37–40].

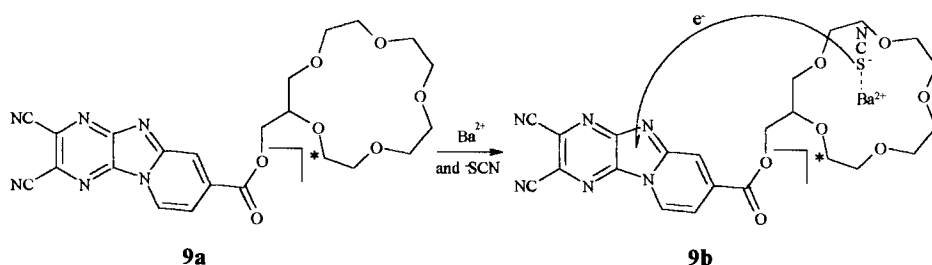


Figure 6. NAND logic with **9** via fluorescence output using Ba^{2+} and SCN^- inputs.

NAND logic

In operational terms a NAND operation can be considered as an AND logic gate with a NOT logic function imposed upon its output. The symbols used and the corresponding truth table are shown in Figure 1.

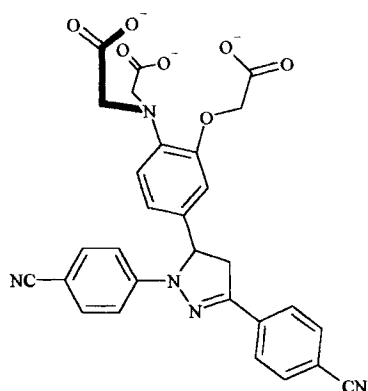
Even though not originally discussed as such [41], **9** was the first case of a well-behaved fluorescent NAND logic gate. The strategy employed in the derivation of this system can be seen in Figure 6, whereby a cation receptor is coupled to multi-heteroatom fluorophore. The action displayed here is noncommutative in the sense that binding of a thiocyanate ion, which is one of the inputs, can only occur if the other input, Ba^{2+} , has previously been bound. The Ba^{2+} is bound at the 15-crown-5 ether site, but as this ion is large in comparison with the crown ether cavity, the possibility exists for cooperation of the ester carbonyl group as a lariat. The large residual charge is counteracted by the binding of an SCN^- to the Ba^{2+} in an apical fashion. This easily oxidizable SCN^- can undergo PET to the excited fluorophore, **9b**, with a resultant quenching action. Thus a photoactive dyad can be seen to be formed, where the receptor is not directly involved in electron transfer. The incorporation of two nitrile groups and an ester group into the fluorophore make the reduction of the fluorophore in the excited state more facile and the resulting PET process is not surprising. The authors discussed this in a logical AND context but it would be more consistent with other systems discussed in these pages if it were interpreted as a NAND gate.

OR logic

Another two-input, one-output gate is the OR gate whose electronic symbol and corresponding truth table can be seen in Figure 1. The output can be seen to be high in the presence of one or two high inputs. The output is low only when no high input is present. It should be noted that the number of input channels could potentially be increased, two being the minimum number necessary to identify this behavior.

At the molecular scale, an OR gate can be constructed from a PET system which emits luminescence when a receptor is occupied by any one of several guests, thereby blocking a PET channel. Thus the ideas employed for YES logic can be re-

applied here provided that the receptors are deliberately chosen to be poorly chemo-selective. A well-behaved OR gate should additionally have more or less the same high level of luminescence output when switched “on”. This condition is not always easy to satisfy in a rational manner. Molecule **10** [42] illustrates these points. The amino acid receptor within **10** successfully binds Ca^{2+} or Mg^{2+} , although with quite different stability constants (10^5 or 10^3 M^{-1} , respectively). Thus $10^{-3} \text{ M Ca}^{2+}$ or 0.5 M Mg^{2+} are sufficient to engage the receptor site and block PET from the receptor. Thus the nonselectivity of binding is sufficient for our present purpose, though it should be noted in passing that this receptor is selective enough to permit physiological monitoring of Mg^{2+} [43, 44]. Our purpose requires more than non-selectivity of binding: we need nonselectivity of the ion-induced luminescence response. Once either ion is in the receptor site, it arranges the ligating groups around itself into a coordination shell such that the conjugation between the amine and the benzene ring is cut off even though the two ions have quite different radii and charge densities. Thus the PET process is blocked to the same degree. In other words, the control of PET prevention in **10** is conformational rather than electrostatic.

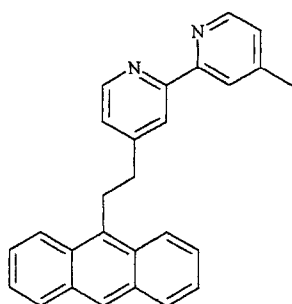
**10**

NOR logic

NOR logic can be considered as an OR gate feeding into a NOT gate. This inversion of an OR action can be seen in Figure 1 with the appropriate truth table. Similarly a minimum of two inputs is required, but the number of input channels can be extended.

Our **11** [45] builds on the known ability of protonated pyridine units to quench the emission from fluorophores in their neighborhood [46]. The electron deficiency of such units makes them good acceptors in PET processes. Compound **11** possesses a 2,2'-bipyridyl unit which can be a receptor for H^+ , but it can also bind Zn^{2+} [47]. In either case the 2,2'-bipyridyl unit is rendered more electron-deficient. Hence, the fluorescence of the anthracene unit is quenched upon input of either ion in sufficiently high concentrations. The requirement for nonselectivity of the ion-induced luminescence response is not as stringent as for the OR gate described above,

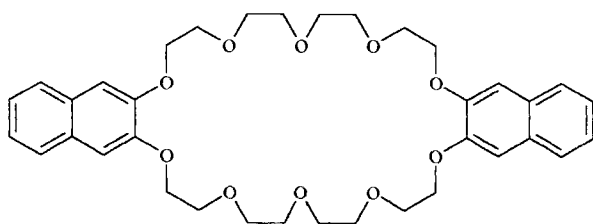
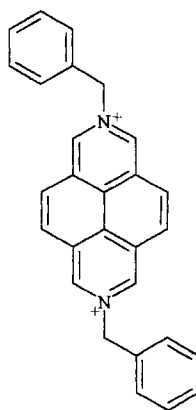
provided that the quenching is efficient enough. More generally, **11** illustrates how integration of two logic operations can be achieved functionally within one molecule without resorting to physically “wiring up” two separate molecules—a much tougher proposition.

**11**

XOR logic

An exclusive-OR gate is one in which the presence of only one input out of two registers a high output value. Considering the two-input situation, presence of neither input or presence of both inputs gives a low output signal. This situation can be seen in Figure 1 along with its truth table. Another way of viewing this situation is that the gate compares the inputs and if they are different then an output 1 is given, whereas if they are the same an output 0 is derived.

This logic type proved particularly difficult to emulate at the molecular scale until Credi et al. provided the breakthrough [48]. Following a mechanochemical line of attack (see Section 5.3.1), an electron-rich macrocycle **12** serves as a “bead” sliding on a “string” which is made from an electron-deficient heteroaromatic **13**. The complex **12**·**13** is held together by charge transfer (CT) interactions. This same CT

**12****13**

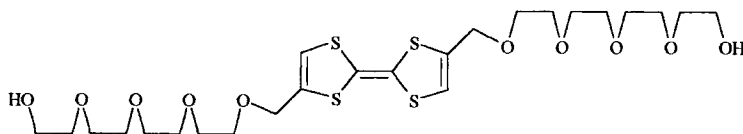
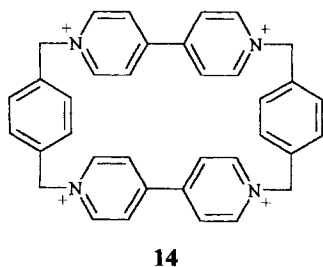
interaction causes efficient quenching of emissions both from **12** and from **13**. Protons and Bu_3N are the two inputs and the fluorescence of **12** is the output for the present purpose. Application of protons alone, at sufficiently high concentration, causes protonation of the oxygen atoms in **12**, forcing the “bead” to slip off the “string”. Freed of the suffocating CT interaction, both **12** and **13** recover their fluorescence emissions. Interestingly, protonation of **12** does not perturb its emission compared with the neutral form. Thus the output becomes digital 1. Conversely, application of Bu_3N alone causes attachment to **13** via a strong CT interaction, again forcing collapse of the complex **12**·**13**. A strong fluorescence output (digital 1) is seen from the liberated **12**. Finally, simultaneous application of both inputs in stoichiometric amounts for acid–base neutralization results in the complex **12**·**13** being left untouched in its nonemissive state, i.e., digital 0 output.

XNOR logic

Exclusive-NOR logic is analogous to an XOR gate feeding into a NOT gate. The electronic symbol and corresponding truth table can be seen in Figure 1.

Controlled perturbation of a “bead-on-a-string” complex again provides entry into this logic type [49]. CT complex **14**·**15** has the necessary electron-rich and

electron-poor components except that, this time, the bead **14** is electron-deficient and the “string” **15** is electron-rich. A more critical difference compared with **12**·**13** is that the output is viewed as the CT absorption band. The virtually mutual exclusivity of CT absorption and component fluorescence provides a way to evolve XNOR logic systems from their XOR cousins. The two inputs are the application of reductive and oxidative potentials sufficient to cause one-electron reduction of **14** and to cause one-electron oxidation of **15** within complex **14**·**15**. In either case, the complex collapses and the CT absorption band dies with it. Thus the supply of either input on its own produces an output of digital 0. As we saw, the absence of both electrochemical inputs (both inputs at digital 0) preserves the complex **14**·**15**

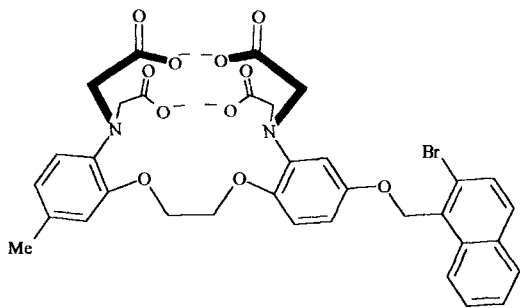


and its signature CT absorption (output digital 1). Again the final row of the truth table is arranged with a neutralization of reductive and oxidative potentials of equal magnitude. The net potential of zero leaves complex **14-15** untouched with its CT absorption intact, i.e., output digital 1. Notably, the fourth row of the truth table is indistinguishable from the first row in this case.

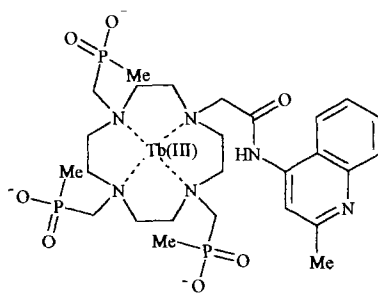
INHIBIT logic

INHIBIT logic in its three-input manifestation is more complex than other logic types presented in previous sections, as can be seen from the electronic symbol and the corresponding truth table in Figure 1. A NOT gate confronts the third input signal before it can reach the AND gate. Thus, at first sight, a “wiring” of two molecular-scale gates is required. As mentioned under NOR logic, such challenges can be successfully sidestepped by functional, rather than physical, integration. In this instance we require the presence of the third input to disable the entire device. The powerful quenching influence of O_2 on relatively long-lived triplet states fits the bill. Phosphorescent bromonaphthalene is built into system **16** [45], which also contains a polyaminoacid receptor, not unrelated to that found in OR gate **10** described above, which launches a PET process to quench phosphorescence unless blocked by Ca^{2+} complexation. The AND logic action is completed by arranging for β -cyclodextrin to bind and encapsulate the bromonaphthalene phosphor [50] so that the excited state of the latter is protected from collisional triplet-triplet annihilation [51]. Thus, the presence of Ca^{2+} and β -cyclodextrin and the absence of O_2 is the condition under which phosphorescence output is observed from **16**.

The simpler two-input INHIBIT gate **17** was unveiled very recently by Gunnlaugsson et al. [52]. The disabling second input is, again, O_2 . Tb(III) complexes occasionally display luminescence which is quenched by O_2 because the metal-centered excited state is only slightly lower in energy than the triplet excited state of the aromatic ligand. The two-way energy transfer between these two excited states mixes them sufficiently for the usual O_2 -sensitivity of organic triplets, as seen in **16** above, to show up in the Tb(III) luminescence. The first input which supports luminescence is H^+ , which protonates the quinoline and shifts the absorption band into contact with the excitation wavelength. In other words, absorption is denied to **17** unless H^+ is present at sufficient concentration. Thus the line-like luminescence of Tb(III) is seen only if H^+ is present and if O_2 is absent.



16



17

ENABLED OR logic

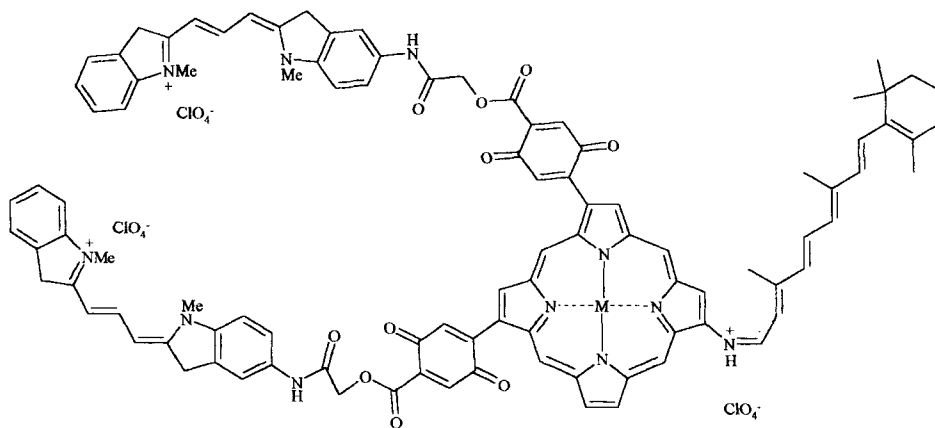
A recent report from the Lisbon–Bologna collaboration shows how their AND logic gate (discussed under “AND logic”, above) can be expanded into three-input ENABLED OR logic systems [53]. The electronic symbol and corresponding truth table in Figure 1 illustrates its relative complexity. The expansion is achieved by noting that anionic micelles such as sodium dodecyl sulfate (SDS) present highly negatively charged surfaces to locally trapped fluorophores such as **5**. Such surfaces concentrate protons locally [54, 55]. Thus SDS above its critical micellar concentration serves as an enabler for protons, even at relatively high bulk pH, by concentrating them sufficiently to activate the process shown in Figure 5.

The last few examples clearly illustrate how photochemical systems can emulate integrated logic gates at the molecular scale. It is clear that more and more logic types will fall to chemists’ ingenuity in the coming months and years.

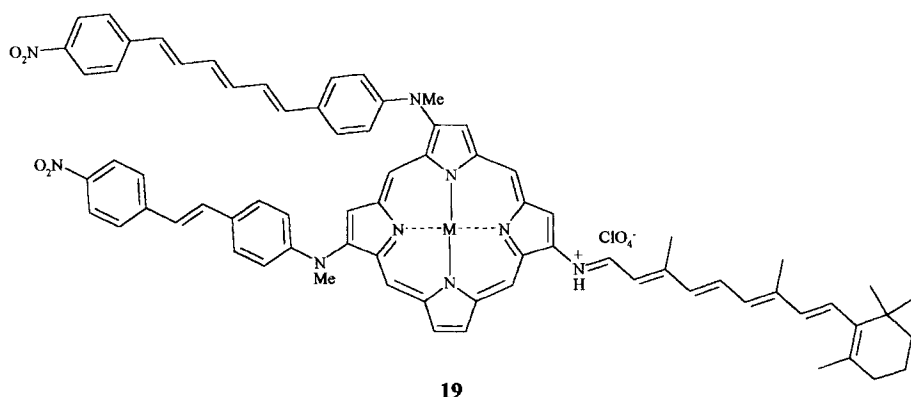
5.2.2 All-optical Input/Output

Multichromophoric systems

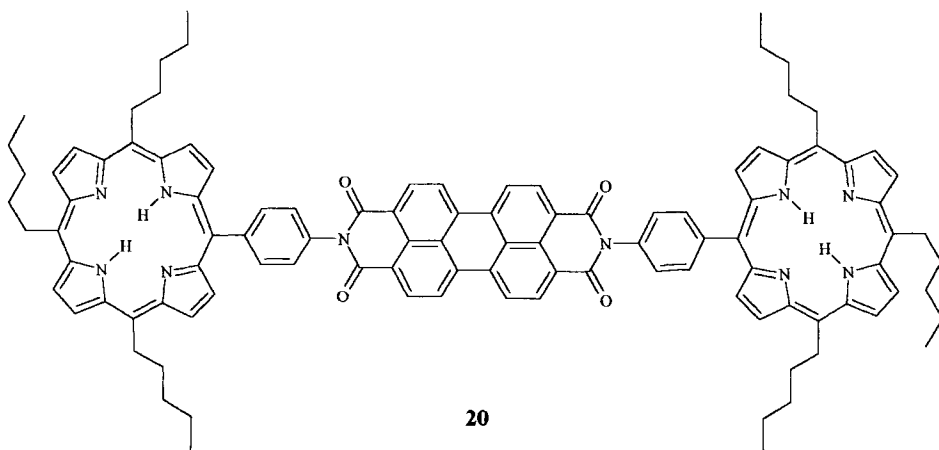
The NAND gate molecules **18** and **19** proposed by Birge [56] are designed to contain two input chromophores to which light can be directed. A retinal Schiff base derivative is used as the output chromophore whose absorption band is expected to shift upon electric charging of the porphyrin which is to serve as a charge integrator. The input chromophores are stated to be selectively excitable although their structures do not differ significantly in **18**. The electric charging upon excitation of the input chromophores is considered to arise from electron transfers (PET) in **18** and from internal charge transfer (ICT) in **19**. We await detailed information on these molecules in the primary literature before attempting any mechanistic discussion.



18



The donor–acceptor molecule **20** [57, 58] has been shown by Wasielewski and his colleagues to be capable of acting as an ultrafast molecular switch with potential logic capabilities. The two terminal porphyrin donor moieties are independently capable of reducing the central perylene tetracarboxydiimide acceptor moiety via PET. When only one porphyrin is excited by a femtosecond laser pulse, the absorption due to the perylene tetracarboxydiimide radical anion is seen. If both porphyrins are excited simultaneously by a higher-intensity laser pulse, two PET processes to the central acceptor can occur, giving a dianion, with a different absorption band. It is envisaged that this molecule should be capable of performing the AND logic operation if two different excitation wavelengths of light are used as inputs, and monitoring of the dianion absorption is used to read the output resulting from the various combinations of optical inputs. This is possible for molecule **20** since excitation of the perylene tetracarboxydiimide moiety will induce the first electron transfer process, and the second input wavelength can be the porphyrin absorption. Substitution of one of the porphyrins with a moiety capable of reducing the perylene tetracarboxydiimide in the excited state, but with a different absorption profile, should also function in this way. The extreme speed of such optical molec-



ular switches and gates is testimony to the lightness of their only “moving part”—the electron.

Systems based on spectral hole-burning

Not only can the technique of persistent photochemical spectral hole-burning (PSHB) be useful for molecular information processing but it has also been discussed for some time in the context of extremely dense frequency-domain optical data storage [59, 60].

Brief background

If molecules are embedded in solid hosts (e.g., in glassy or crystalline states) and temperatures are sufficiently low, sharp homogeneous absorption bands begin to show up within the broad inhomogeneous absorption band of the dopant [61]. A solute molecule and its noncovalently bonded solvent shell can be classified as a supermolecule [62]. Each solute molecule will thus create a unique supermolecule with its own arrangement of the solvent shell. Each supermolecule exists in a local energy well with a potential energy barrier which cannot be overcome at low temperatures. These supermolecules can show different physical properties—specifically, a spread in their absorption. In essence every supermolecule is different and can be addressed individually.

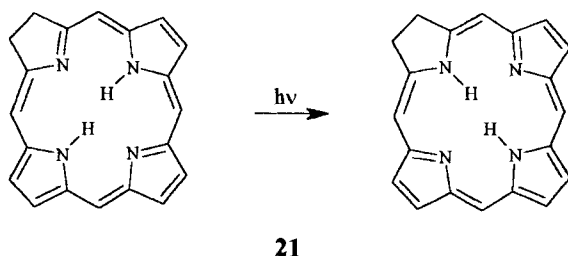
Selective irradiation of a given supermolecule will cause its photoconversion to another species. Hence its original spectral signature will disappear. This photochemically etched information is the spectroscopic “hole”, in that the essential profile of the absorption band remains but, at the precise frequency corresponding to the etching energy, a large absorption change will be observed. Monitoring this change allows for an information read-out process. This information can be re-read provided the hole persists [63], which is the case at low temperatures [64]. Single-molecule detection is thus possible via fluorescence [65] or absorption [66] detection.

Most frequently PSHB has been employed or studied in the context of data and image storage. The storage of information relies upon writing of information onto micrometer-scale spots. This hole-burning technique allows unique addressing of numerous domains within each spot, each of which represents one data bit (up to a density of 10^{12} bits cm^{-2}) [67]. An analogy would be a number of people, each with his/her own mobile telephone, in a single room. As well as these frequency-domain optical storage systems, the use of a controllable electric field provides the potential for even higher storage densities [68].

Spectral hole-burning and molecular-scale information processing

Wild [62, 69] described the potential application of spectral hole-burning in developing a parallel information processor by combining it with the Stark effect (the interaction of molecular energy levels with an applied electric field) and the interferometric properties of holography. Data stored in two-dimensional arrays can be directly combined in parallel, without the use of an external processor. A four-

dimensional space is effectively created with two geometrical dimensions from the sample along with a third dimension from the burning wavelength and the fourth from the electric field. A laser beam is split into reference and object beams. The object beam is overlapped with the reference beam at the sample, a chlorin guest **21** in a polyvinylbutyral matrix. The two phototautomeric forms of **21** involved in the key photochemical reaction are shown.



By synchronous exposure of the sample to object and reference beams and by adjusting the laser frequency and electric fields appropriately, holograms were obtained. Each hologram is thus associated with specific values of electric field and laser frequency. The image could be reconstructed by illuminating the sample with the reference beam alone. Specific images were selected by choosing the laser frequency and electric field strength used during the recording process. An applied electric field changes the shape of the spectral hole as it interacts with the dipole moments and polarizabilities of the guest molecules. Pairs of holograms can therefore be stored at the same optical frequency and with slightly different electric fields.

At the burning coordinates the recorded images can be constructed separately. The individually recorded holograms can be reconstructed simultaneously. This results in coherent superposition, the nature of which depends on the relative hologram phases selected during the recording process. By control of the hologram phase during recording, constructive or destructive interference of the hologram is observed. Thus, with the appropriate combination of holograms of two-dimensional objects, logical operations between data arrays can be performed with a new resultant image. The logical operation performed depends on the relative phase used during the recording process: constructive interference results in an increase in intensity where the images overlap and the images are added, and destructive interference results in a subtraction of the images [70, 71].

The amplitudes of each component add in the interferometric holographic operation. From these efficiencies truth tables can be derived by looking at corresponding pixel elements and employing a certain level of discrimination. Logical operations performed correspond to the OR, AND, and XOR functions. These operations are performed in parallel on the basis of individual pixels. Thus these systems demonstrate parallel information processing at the molecular scale.

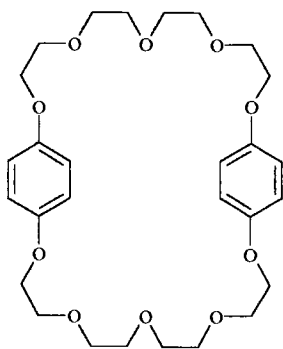
5.3 Other Approaches to Molecular-scale Information Processing

5.3.1 Mechanochemical Approach

The classical mechanical device used for information processing is the abacus. Even today human operators perform arithmetical calculations at speed with these “beads-on-wires”. Molecular emulation of the form and function of the abacus could allow rapid switching speeds and calculation rates, with bead position and position read-out being performed by external physical stimuli rather than human manipulation and observation. Approaches to the type of materials suitable for use as thread and beads and to the manipulation and determination of bead position have been made via self-assembling rotaxanes [72].

Such rotaxanes incorporate a macrocyclic structure (representative of a bead) on an acyclic chain (thread), with bulky stopper groups at their ends to prevent dethreading. The position of the bead on the thread, and hence representation of information, is controlled by the incorporation of “stations” on the thread upon which the bead preferentially resides. Requirements of a successful system are that the bead can be controllably shuttled between stations by an external stimulus and that the position of the bead can be subsequently read out.

The problem of controlling the bead on its thread can be addressed by using the charge transfer interaction between π -electron-rich and π -electron-deficient aromatic rings. In particular the interaction of cyclobis(paraquat-*p*-phenylene) **14** with π -electron-rich aromatic rings [73] and the interaction of bis(*p*-phenylene)-34-crown-10 ether **22** with paraquat [74, 75] have been used.

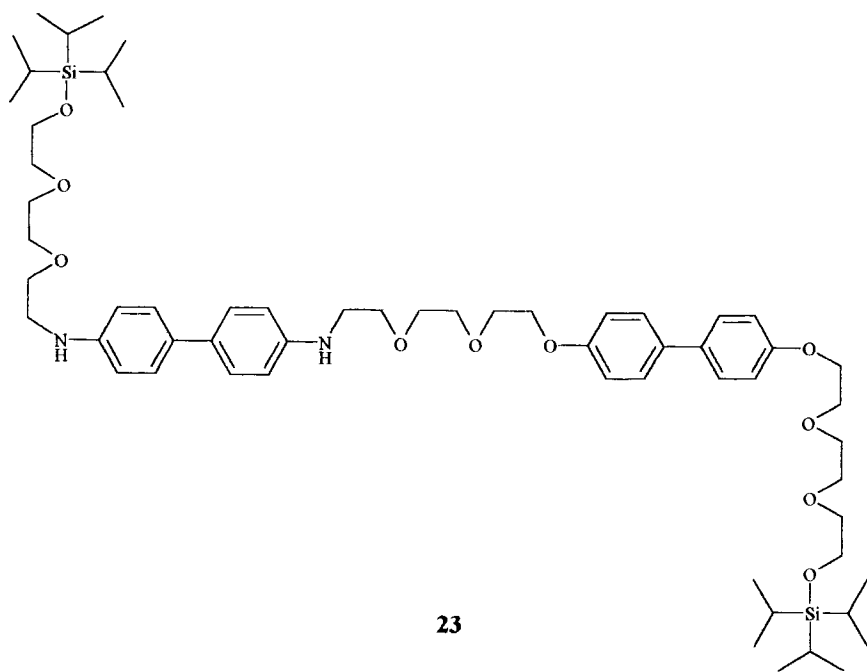


22

In these cases **14** and **22** act as beads, threaded on stoppered polyether chains containing the π -electron-rich or π -electron-deficient stations. This noncovalent interaction simplifies the synthetic procedures necessary, as the unstoppered thread and its bead will self-assemble, and the resulting charge transfer complex can be stoppered with bulky terminal groups to give the functional rotaxane. Other suc-

cessful approaches include clipping an uncyclized bead which interacts with a thread station to its cyclized rotaxane and thermal “slipping” of the bead over the stoppers [72].

Using the bead **14**, a rotaxane has been synthesized which contains two π -electron-rich moieties, namely biphenol and benzidine [76]. The thread portion **23** of this rotaxane therefore contains two stations upon which the tetracationic bead can potentially reside. For such a device, stability of the bead at its preferred station must be considered. This implies that a large energy difference ($>kT$) between stations must exist at the operating temperature to prevent dynamic shuttling of the bead between the stations.



Manipulation of the bead in this instance is accomplished in one of two ways. Firstly and most successfully, an ionic stimulus can be used. When the benzidine nitrogens are protonated with $\text{CF}_3\text{CO}_2\text{H}$, electrostatic repulsion causes the energy bias between stations to switch and forces the tetracationic bead to translate along the thread; the bead then preferentially resides at the biphenol station. This situation can be reversed using pyridine. Secondly, the benzidine moiety can be electrochemically oxidized to give the corresponding radical cation, which again switches the energy bias, leading to preferential residence of the bead at the biphenol station. Electrochemical reduction restores the bias toward the benzidine station. In common with other systems [77], determination of the bead position can be made either

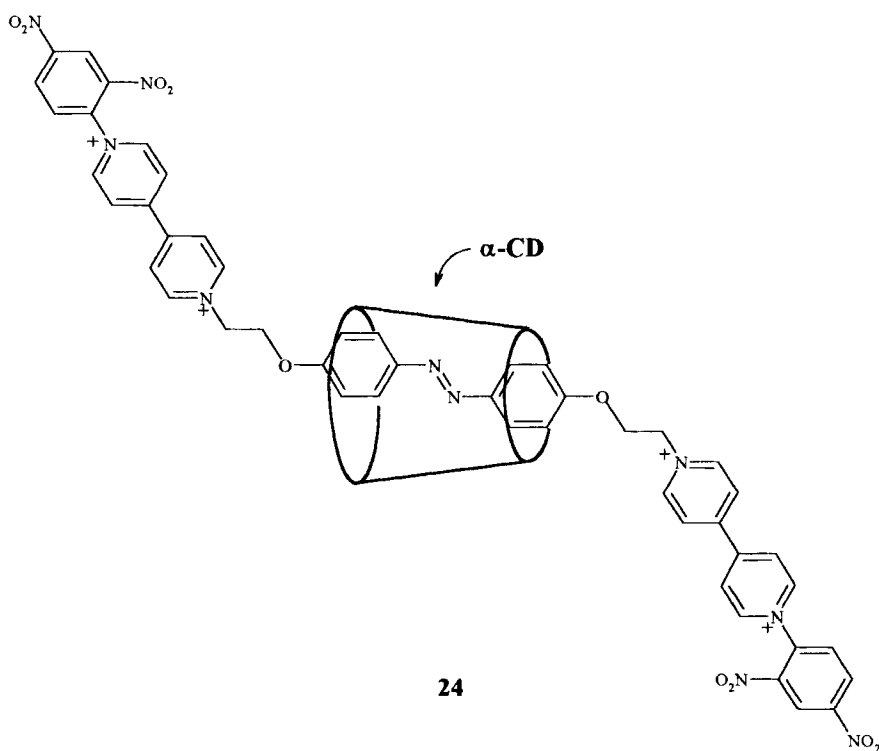


Figure 7. A light-driven molecular shuttle.

from NMR signals or by optical monitoring of the charge transfer bands due to two possible interactions of the bead and the interactions between the bead and spacing polyether chains.

Nakashima took up the challenge to build a light-driven rotaxane-based molecular shuttle **24** [78] (Figure 7). On photoirradiation of the aqueous solution with ultraviolet light a photoisomerization of the azobenzene unit from *E*- to *Z*- occurred, forcing the movement of the shuttle to a new station, a hydrocarbon spacer. Subsequent irradiation with visible light caused reversion to the *E*-form accompanied by movement of the shuttle to its original station. This cycle could then be repeated at will. Further development of this important system should reduce the timescale of switching.

In addition to these molecular shuttles, other dynamic supramolecular systems have been reported with the development of molecular trains utilizing catenanes [79], where one catenane ring can continually cycle around another via several stations. Sauvage and co-workers [80–83] reported electrochemically induced ring gliding in copper catenanes which exploits the differing preferred geometries associated with Cu(I)/Cu(II).

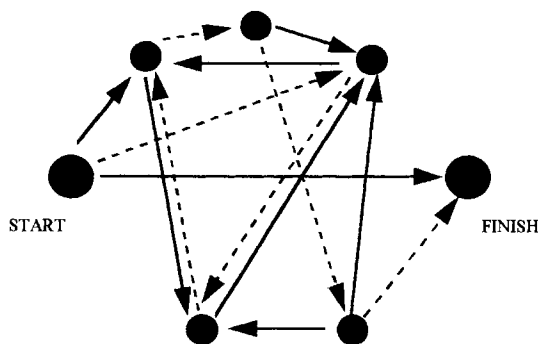


Figure 8. A directed graph with a unique Hamiltonian path, where circles represent vertices (cities) and arrows represent edges (routes).

5.3.2 Oligonucleotide Approach

Seminal work by Adleman demonstrated that molecular biological methods could be successfully employed to solve a mathematical problem [84, 85]. The problem he solved was a Hamiltonian path problem, in common parlance referred to as a travelling salesman problem. This is a hard computational problem for which no satisfactory algorithm is known allowing solution with electronic computers in polynomial time [86]. The potential of this DNA-based methodology relies on the inherent parallelism a DNA molecule affords.

The solution to Adleman's problem (Figure 8) is the correct combination of routes between several vertices (or cities), fulfilling several criteria. These are that the starting and finishing cities in the directed graph are defined, each city must be visited, each city can only be visited once, and there is a defined set of one-way edges (or routes) connecting different cities. A Hamiltonian path may not exist, if all the above criteria cannot be satisfied.

Different 20-residue oligonucleotide sequences (20-mers) containing unique, randomized sequences of A, T, C, and G bases were used to code for each of the cities. Selection of random sequences made it improbable that oligonucleotides associated with different cities would share long common sequences that might result in noncognate binding occurring (particularly during the ligation step). Each route was coded with a 20-mer, such that one-half (a 3'-10-mer) formed the Watson-Crick complement to half of one city, whilst the other half (a 5'-10-mer) could similarly anneal with the first half of the adjacent city. Thus neighbouring cities could be linked by the appropriate route.

Each route was phosphorylated at the 5'-hydroxy position, permitting the joining of the appropriate route 20-mer with the 3'-hydroxy position of another. Equimolar quantities of the complementary 20-mer of each city and each route were then mixed together in a single template-directed ligation step. The complementary 20-mers of each city served as splints to bring oligonucleotides associated with the compatible routes together for ligation. This reaction resulted in the formation of DNA molecules encoding random paths throughout the graph.

To implement the next step of the algorithm, the product of the previous step was

amplified by the polymerase chain reaction (PCR). Primers were used which bind to the ends of the DNA strand to promote the replicating action, by activating the enzyme. The primers chosen were such that they bound only to the 20-mers associated with the start and finish. The presence of both results in an exponential amplification in sequences terminating with the correct starting and finishing cities, satisfying the first criterion. Gel electrophoresis provided a means of separating the polyanionic, double-stranded DNA based on molecular weight. Isolation of the 140-basepair band gave a population of molecules satisfying the condition that exactly seven cities were visited. This set was then amplified and further purified.

The final step of the algorithm determined whether all the cities were visited, via use of combinatorial methods. This was achieved by affinity purification with biotin-avidin magnetic bead systems. Firstly, the double-stranded DNA product of the previous step was dissociated to give single-stranded DNA. Secondly, the microscopic beads were introduced upon which the complementary sequence to one of the cities was previously attached. Therefore sequences containing this city could specifically bind to it. Removal of the beads, washing, and releasing the bound strands then gave the molecules fulfilling part of the solution. This subset was further reduced by repeating this iteration sequentially with different sets of beads, each set containing the complement of a different city (start and finish cities had already been accounted for). The product of this step was PCR-amplified and run on a gel. The bands obtained demonstrated that these molecules encoded for the correct Hamiltonian path, proving that the route did exist. Absence of any bands would therefore mean that no appropriate path existed.

This type of problem is so complex that, with certain graphs containing less than 100 cities utilizing current algorithms it would take hundreds of years to solve [85]. Whilst electronic computers require exponentially increasing amounts of time to solve more complex problems, DNA would require a linear increase in time. However, whilst the time required to perform these calculations increases linearly, the quantity of material required for the purpose increases exponentially [87]. Despite the progress achieved, practical and theoretical obstacles to creating a DNA computer remain.

Theoretical limitations concern the versatility of DNA computers and their capacity to accommodate efficiently a variety of computational problems. DNA computing generated much excitement, mainly caused by the capability for massively parallel searches. This in turn showed its potential to yield tremendous advantages from the point of view of speed (10^{18} operations s^{-1}) and energy consumption (10^{19} operations J^{-1}), and could allow for an extremely high information density (1 bit nm^{-3}). A single strand of DNA can be likened to a string consisting of a combination of four different symbols A, G, C and T. Mathematically, this means that a four-letter alphabet can encode information, whereas an electronic computer uses only two digits, 0 and 1, for the same purpose.

DNA computation can be built on the large array of bio-operations, as exemplified in the previous case, which could be used to write programs [88]. A program will receive a tube containing DNA strands encoding information as input and output, either “yes” or “no” or a set of tubes. A bio-computation will consist of a sequence of bio-operations performed on tubes containing DNA strands. A rela-

tively simple solid-phase method for solving Hamiltonian path problems using DNA has been introduced. In this approach all, and only, the possible pathways are generated stepwise using molecules. Therefore, the entire procedure requires significantly less time than the previous one. Since its selection operation is not by the length of DNA, this method can be employed in other molecular applications using the DNA length.

DNA computation may hold the key for certain complex problems, where existing electronic computers are very inefficient and where massively parallel searches can be organized. Potential development of this field therefore relies on the recognition of algorithms better suited to these molecular methods. Lipton [89] suggested methods to extend this idea to solve other difficult problems, again relying heavily on the huge parallelism inherent in DNA-based computation. Various modifications of Lipton's model based on DNA manipulation have been systematically investigated.

Other approaches to DNA computation have been suggested, including a method to calculate the product of Boolean matrices containing positive numbers [90]. In the case of matrices containing real numbers, the manipulation of reaction conditions allows a quantitative calculation to be performed. This use of DNA to perform an analog calculation is a new approach to computing with DNA.

Besides this approach based on oligonucleotides, there have been some notable efforts by Lotan and co-workers to use the enzymic activity of polypeptides as logic gates [91, 92]. These are particularly interesting because enzymatic activity can be viewed as an amplification process.

5.3.3 Quantum Approach

The distinctive feature of a quantum computer is the ability to store and process superpositions of numbers [93]. This potential for parallel computation has led to the discovery that certain problems would be more efficiently solved on a quantum computer than on a classical computer [94, 95]. The most dramatic example is an algorithm presented by Shor [96], showing that a quantum computer should be able to factorize large numbers very easily. This would have a large social impact since the security of many data encryption systems relies on the inability of classical computers to factorize large numbers.

A quantum computational network can be decomposed into quantum logic gates [94, 95], analogously to the situation for classical computers. Quantum logic gates provide fundamental examples of conditional quantum dynamics, in which one subsystem undergoes a coherent evolution, which depends on the quantum state of another subsystem.

Experimental realization of a quantum computer requires isolated quantum systems that act as the quantum bits (qubits), and the presence of controlled unitary interactions between the qubits. As pointed out by many authors [97–99], if the qubits are not sufficiently isolated from outside influences, decoherences can destroy the quantum interferences that actually form the computation.

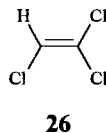
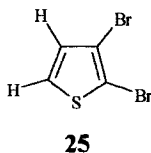
Nuclear magnetic resonance

Recently, nuclear magnetic resonance (NMR) techniques have been adapted as an approach to quantum computation. This has the attraction that most chemists are familiar with NMR spectrometers, though perhaps not with this adaptation. Quantum calculations rely on controlled time evolution of a system of coupled qubits. In the current context a qubit can be considered as a nuclear spin vector which in an applied magnetic field can spin in one of two states (α and β), equivalent to a digital 0 or 1. Qubits can exist in superposition states where they are simultaneously 0 and 1. Therefore, a system of qubits represents all possible values at the same time. When a quantum gate performs a function it operates on all the numbers simultaneously. For example, 32 qubits hold over four billion numbers and a quantum gate performs a function on all of them, whilst a normal computer works on one at a time. Qubits also have a property called entanglement. In a system with several qubits, changing or measuring one will simultaneously change the others. This property is used to “wire” together all the qubits in a quantum computer so that they act as a complete system.

Therefore the NMR computer consists of a molecule, which is the “circuitry”, and the NMR spectrometer, which acts as the gate array and provides a method of reading the answer. Application of the correct sequence of radiofrequency pulses therefore determines the operations the molecule can perform [100].

Gershenfeld and Chuang’s two-qubit system [101] uses an NMR machine and the protons in **25**. They demonstrated a nonlinear interaction between spins, a prerequisite for quantum logic gates. This was realized through the controlled-NOT operation (CNOT) which conditionally flips one spin based on the value of another [102]. This gate can be considered as a quantum XOR gate.

Laflamme et al.’s three-qubit system [103] is **26**. In this molecule the two carbon nuclei are in different chemical environments and therefore represent two qubits, whilst the proton serves as the third. Compound **26** therefore represents the binary numbers 000, 010, 011, 100, 110, and 111. A pulse of radio waves causes the nuclei to be thrown into the entangled superposition state, where they can act as qubits. The NMR machine then initiates the quantum computer program—a series of radiofrequency pulses that act like gates on the qubits and carry out the calculation. The superposition state is then collapsed to give an answer.



NMR techniques suffer an exponential drop in signal-to-noise ratio as the number of nuclei are increased; thus larger-scale implementation using the methodology outlined previously may be prevented. Other limitations associated with the scaling-up involve distinguishing qubits on a molecule by their chemical identities in larger molecules, the large number of molecules in solution required to perform the com-

putation, and the lack of a properly initialized starting state (e.g., all spin α). This latter problem arises from thermal equilibration between the two states corresponding to a Boltzmann-type distribution.

Cold trapped ions

Cirac and Zoller's [104] idea was that a set of N cold ions, interacting with laser light and moving in a trap [105, 106], provides a different physical system for implementation of a quantum computer. The key features of this system are that it allows the implementation of N -bit quantum gates between any set of ions (even nonvicinal ions), decoherence is made negligible during the whole computation, and the final read-out can be performed efficiently. In this proposal, the qubits are the ions themselves. The two states of the n th qubit are identified with two of the internal states of the corresponding ion, either the ground or excited state. Independent manipulation of each individual qubit was accomplished by directing different laser beams to each of the ions.

The quantum-controlled NOT gate with the trapped ions can be implemented by exciting the collective quantized motion of the ions with lasers. The coupling of the motion of the ions is provided by the coulombic repulsion which is the dominant interaction for small ion-ion separations of the order of a wavelength. The final read-out of the quantum register (state measurement of the individual qubits) at the end of the computation can be accomplished using quantum jumps with unit efficiency [107, 108].

Coupled quantum dots

Previously, the dipole-dipole interaction between the two qubits through magnetic dipoles (nuclear spins in an external magnetic field) was seen through NMR logic. Qubits can also be seen to interact through their electric dipoles (single-electron quantum dots). Mathematically the two cases are identical [109]. While the subjects of this subsection are not molecules as such, the relatively small size of quantum dots justifies their brief discussion here.

A quantum dot is a charge in a zero-dimensional space, an electron confined in an extremely small box. In the current context, presence or absence of an electron gives the requisite 1/0 states. Bate et al. [110] imagine a large two-dimensional array of devices that couple with their neighbors. Coupling may be achieved through short-wire connections or, preferably, by utilizing device-device interaction. Input/output of data occurs at the periphery of the array. They show an example of a system where the device (or cell) is a quantum dot and the coupling is electron tunneling between discrete levels. As examples of these proposed architectures, Randall [111] suggests multi-gate field-effect transistor-type devices. In these devices, a series of quantum dots is controlled by a third terminal added to each dot (called a "quantum logic cell"). By switching the tunneling current through the cell, various binary-output logic functions become possible. Because coupling using tunneling is short-range from the fabrication point of view, alternative coupling using long-range electrostatic interaction has been proposed. Bakshi et al.'s [112] system has elongated quantum dots (quantum dashes) arranged in an array. The

dipole moment in each dash is spontaneously polarized and the antiferroelectric phase appears. If a flip of dipole moments on individual dashes could be enforced, the resulting electrostatic perturbation would generate a domino-type response, flipping the dipole in the remaining dash which is viewed as cellular automata. Lent et al. [113, 114] elaborate on this idea using cells consisting of a central dot with four neighboring dots occupied by two electrons, instead of a dash. The cell has strong bistability of polarization which is encoded to the binary data, which are transferred by the inter-cell coulomb interaction as in the quantum-dash array. Arrays of AND, OR, and NOT become possible.

Nomoto et al. [115] have proposed another version based upon locally interconnected architecture, demonstrating AND/OR logic consisting of an asymmetric coupled quantum dot pair. The dots are coupled by both tunneling and the coulomb interaction. The device exploits the difference between the one-electron ground state and the two-electron ground state for the operation. In other words, the electron-number dependent ground state is viewed as a result of the operation. In their logic device, coupled quantum dots in which single-electron tunneling is influenced by electron–electron interaction were used. With occupation or not by a single electron in a quantum dot being equivalent to a bit 1 or 0, the device can be seen to perform (N)AND and (N)OR operations simultaneously. Data input/output was performed by irradiation/absorption of photons. The (N)AND and (N)OR operations were performed by the relaxation of the electronic system to the ground state, which depends on the number of electrons in the dots. When the device is constructed of semiconductor nanostructures, the main energy-loss channel is phonon emission from an electron. This scheme is particularly interesting because data processing is performed by electrons (fermions) whereas data input/output is done with photons (bosons).

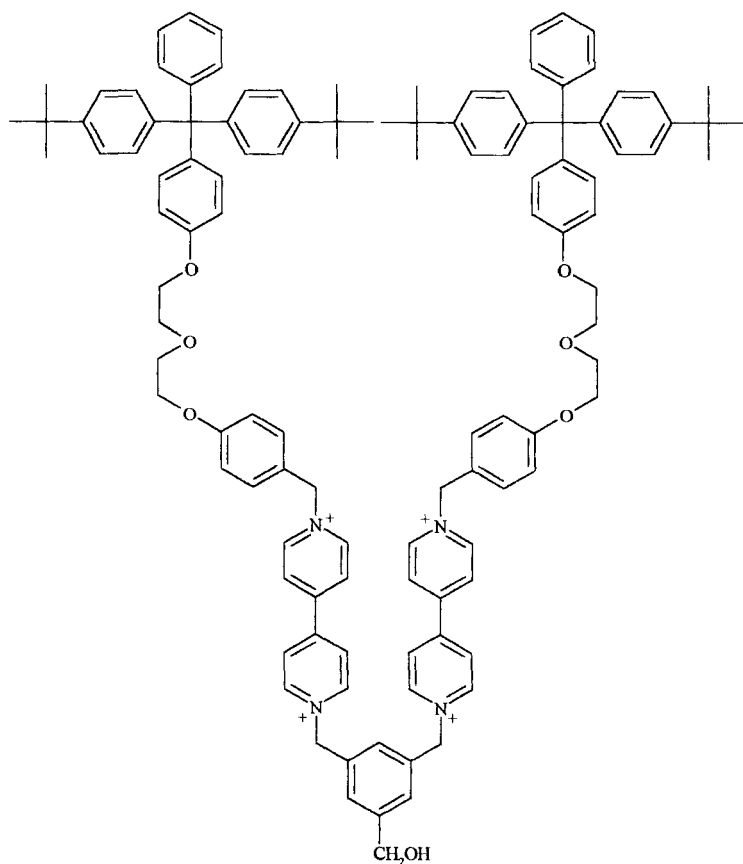
5.3.4 Electronic Approach

As pointed out above, this approach has not yet yielded molecular-scale logic gates [116]. Nevertheless, its direct link to the culture of current computer industries appears to guarantee the greatest investment (intellectual and financial) so far. Also, there are many good discussions in the literature [6] and within this volume. We focus on a single recent achievement to put things in some kind of perspective.

For some time now, monolayers between two electrical conducting terminals (usually metallic) have given rise to asymmetric current–voltage curves indicating diode, or rectifying, behavior [12, 117, 118]. In some cases, the tip of a scanning tunneling microscope has been seen to act as one of these conducting terminals [119]. Electrical conduction across the single molecular thickness is generally ascribed to resonant tunneling where the Fermi levels of the metallic terminals are energetically close to the molecular frontier orbitals. The latter energy values can be derived from voltammetric measurements in solution. Though not without controversy, such work opens the way to interesting extensions.

In such an extension, Collier et al. [120] use a similar arrangement of a unimolecular layer sandwiched between metallic terminals with an additional barrier at

each molecular interface. Molecule **27** was used, but the actual chemical structure does not matter in this instance provided that surface-active viologen units are available. These viologen derivatives conduct through resonant tunneling provided they are contacted with a titanium surface and interrogated with a negative voltage (from the titanium side). However, the molecules are much poorer conductors at positive voltages, i.e., they exhibit a diode-like action. Furthermore, application of a positive voltage leads to irreversible oxidative damage which prevents any conduction, even upon returning to a negative voltage. The oxidative setting of the molecular switch in an “open” state is exploited to electrically reconfigure individual switches in an array.



27

Combinations of these switches, appropriately wired, lead to molecular logic gates. Collier et al. illustrate this by setting up two-input AND and three-input OR gates with a small array of switches containing several million viologen molecules in each. The excellent “on/off” discrimination in the output current can be ascribed to the diode-like nonlinearity in the switches when in their “closed” states.

The reconfiguring is illustrated by converting a three-input OR gate to a two-input version by oxidatively “opening” a switch in one of the input lines. This is somewhat reminiscent of certain programmable logic devices in silicon technology [13] where chosen links between individual logic gates are opened irreversibly so that the resulting device is customized according to the needs of the circuit designer.

In summary, molecule-based, but not molecular-scale, switches can be metal-lically wired to produce logic gates. However, this methodology is yet to be extended to truly molecular-scale counterparts.

5.4 Conclusion

We feel convinced that the diversity and depth of the approaches currently available for performing computational operations at the atomic/molecular scale offers a solid springboard for growth of the subject. The systems described so far may be rudimentary, the enthusiasm of some exponents may be excessive, and the criticism of some skeptics may be heavy: but at the end of the day, the subject will live or die according to the eventual uses to which the systems are put.

Acknowledgements

We appreciate the support of the Engineering and Physical Sciences Research Council (UK), the Department of Education in Northern Ireland, and the European Social Fund for our efforts in this area.

References

1. A.P. Malvino, J.A. Brown, *Digital Computer Electronics*, 3rd Edn., Glencoe, Lake Forest, 1993.
2. A.P. de Silva, C.P. McCoy, *Chem. Ind.* **1994**, 992.
3. *Principles of Neural Science*, 3rd Edn, E.R. Kandel, J.H. Schwartz, T.M. Jessel, Eds., Elsevier, New York, 1991.
4. A.J. Bard, *Chem. Eng. News* 1999, Sept 6, 5.
5. *Molecular Electronic Devices*, F.L. Carter, R.E. Siatkowski, H. Wohltjen, Eds., Elsevier, Amsterdam, 1988.
6. *Molecular Electronics*, J. Jortner, M. Ratner, Eds., Blackwell, Oxford, 1997.
7. A.P. de Silva, H.Q.N. Gunaratne, C.P. McCoy, *Nature* **1993**, 364, 42.
8. S.L. Sharp, R.J. Warmack, J.P. Goudonnet, I. Lee, T.L. Ferrell, *Acc. Chem. Res.* **1993**, 26, 377.
9. X.S. Xie, *Acc. Chem. Res.* **1996**, 29, 598.
10. M.T. Cygan, T.D. Dunbar, J.J. Arnold, L.A. Bumm, N.F. Shedlock, T.P. Burgin, L. Jones, D.L. Allara, J.M. Tour, P.S. Weiss, *J. Am. Chem. Soc.* **1998**, 120, 2721.
11. D. Gosztola, M.P. Niemczyk, M.R. Wasielewski, *J. Am. Chem. Soc.* **1998**, 120, 5118.
12. A.S. Martin, J.R. Sambles, *Nanotechnology* **1996**, 7, 401.
13. J. Millman, A. Grabel, *Microelectronics*, McGraw-Hill, London, 1988.

14. V. Balzani, F. Scandola, *Supramolecular Photochemistry*, Ellis-Horwood, Chichester, 1991.
15. R.A. Bissell, A.P. de Silva, H.Q.N. Gunaratne, P.L.M. Lynch, G.E.M. Maguire, K.R.A.S. Sandanayake, *Chem. Soc. Rev.* **1992**, 21, 187.
16. J.-M. Lehn, *Supramolecular Chemistry*, VCH, Weinheim, 1995.
17. J. Wolfrum, M. Sauer in *Applied Fluorescence in Chemistry, Biology and Medicine*, W. Rettig, B. Strehmel, S. Schrader, H. Seifert, Eds., Springer Verlag, Berlin, 1999, p 39.
18. S. Weiss, *Science* **1999**, 283, 1676.
19. W.E. Moerner, T. Basche, *Angew. Chem. Int. Ed. Engl.* **1993**, 32, 457.
20. R. Bornemann, E. Thiel, *Abstr. VI Int. Conf. Methods and Applications of Fluorescence Spectroscopy*, Paris, **1999**, P7.
21. E.B. Sandell, *Colorimetric Determination of Traces of Metals*, 3rd Edn., Interscience, New York, 1965.
22. A.P. de Silva, D.B. Fox, T.S. Moody in *Stimulating Concepts in Chemistry*, M. Shibasaki, J.F. Stoddart, F. Vogtle, Eds., Wiley-VCH, Weinheim, 2000, in press.
23. A.P. de Silva, N. D. McClenaghan, C.P. McCoy in *Molecular Switches*, B.L. Feringa, Ed., Wiley-VCH, Weinheim, 2000, in press.
24. A.P. de Silva, R.A.D.D. Rupasinghe, *J. Chem. Soc., Chem. Commun.* **1985**, 1669.
25. G.J. Kavarnos, *Fundamentals of Photoinduced Electron Transfer*, VCH, Weinheim, 1993.
26. B. Valeur, in *Probe Design and Chemical Sensing (Top. Fluoresc. Spectry, Vol. 4)*, J.R. Lakowicz, Ed., Plenum, New York, 1994, p 21.
27. L. Fabbri, M. Licchelli, P. Pallavicini, *Acc. Chem. Res.* **1999**, 32, 846.
28. A.P. de Silva, H.Q.N. Gunaratne, T. Gunnlaugsson, A.J.M. Huxley, C.P. McCoy, J.T. Rademacher, T.E. Rice, *Chem. Rev.* **1997**, 97, 1515.
29. *Chemosensors for Ion and Molecule Recognition*, A.W. Czarnik, J.-P. Desvergne, Eds., Kluwer, Dordrecht, 1997.
30. *Indicators*, E. Bishop, Ed., Pergamon, Oxford, 1972.
31. A. Fernandez-Gutierrez, A. Munoz de la Pena in *Molecular Luminescence Spectroscopy. Methods and Applications, Part 1*, S.G. Schulman, Ed., Wiley, New York, 1985, p 371.
32. A.P. de Silva, S.A. de Silva, A.S. Dissanayake, K.R.A.S. Sandanayake, *J. Chem. Soc., Chem. Commun.* **1989**, 1056.
33. A.P. de Silva, H.Q.N. Gunaratne, C.P. McCoy, *J. Am. Chem. Soc.* **1997**, 119, 7891.
34. A.P. de Silva, K.R.A.S. Sandanayake, *Tetrahedron Lett.* **1991**, 32, 421.
35. F. Pina, M. Maestri, V. Balzani, *Chem. Commun.* **1999**, 107.
36. F. Pina, M.J. Melo, M. Maestri, R. Ballardini, V. Balzani, *J. Am. Chem. Soc.* **1997**, 119, 5556.
37. A.P. de Silva, H.Q.N. Gunaratne, C.P. McCoy, *Chem. Commun.* **1996**, 2399.
38. S.A. de Silva, A. Zavaleta, D.E. Baron, O. Allam, E.V. Isidor, N. Kashimura, J.M. Percarpio, *Tetrahedron Lett.* **1997**, 38, 2237.
39. L. Fabbri, F. Gatti, P. Pallavicini, L. Parodi, *New J. Chem.* **1998**, 22, 1403.
40. Y. Kubo, S. Obara, S. Tokita, *Chem. Commun.* **1999**, 2399.
41. S. Iwata, K. Tanaka, *J. Chem. Soc., Chem. Commun.* **1995**, 1491.
42. A.P. de Silva, H.Q.N. Gunaratne, G.E.M. Maguire, *J. Chem. Soc., Chem. Commun.* **1994**, 1213.
43. L.A. Levy, E. Murphy, B. Raju, R.E. London, *Biochemistry* **1988**, 27, 4041.
44. B. Raju, E. Murphy, L.A. Levy, R.D. Hall, R.E. London, *Am. J. Physiol.* **1989**, 256, C540.
45. A.P. de Silva, I.M. Dixon, H.Q.N. Gunaratne, T. Gunnlaugsson, P.R.S. Maxwell, T.E. Rice, *J. Am. Chem. Soc.* **1999**, 121, 1393.
46. A.P. de Silva, H.Q.N. Gunaratne, P.L.M. Lynch, *J. Chem. Soc., Perkin Trans. 2* **1995**, 685.
47. A.E. Martell, R.M. Smith, *Critical Stability Constants*, Plenum, New York, 1974.
48. A. Credi, V. Balzani, S.J. Langford, J.F. Stoddart, *J. Am. Chem. Soc.* **1997**, 119, 2679.
49. M. Asakawa, P.R. Ashton, V. Balzani, A. Credi, G. Mattersteig, O.A. Matthews, M. Montalti, N. Spencer, J.F. Stoddart, M. Venturi, *Chem. Eur. J.* **1997**, 3, 1992.
50. M. Bender, M. Komiyama, *Cyclodextrin Chemistry*, Springer-Verlag, New York, 1971.
51. J.D. Bolt, N.J. Turro, *Photochem. Photobiol.* **1982**, 35, 305.
52. T. Gunnlaugsson, D.A. MacDonail, D. Parker, *Chem. Commun.* **2000**, 93.
53. A. Roque, F. Pina, S. Alves, R. Ballardini, M. Maestri, V. Balzani, *J. Mater. Chem.* **1999**, 9, 2265.

54. M.S. Fernandez, P. Fromherz, *J. Phys. Chem.* **1977**, 81, 1755.
55. R.A. Bissell, A.J. Bryan, A.P. de Silva, C.P. McCoy, *J. Chem. Soc., Chem. Commun.* **1994**, 405.
56. R. Birge, *Nanotechnology, Research and Perspectives*, B.C. Crandall, J. Lewis, Eds., MIT Press, Cambridge, MA, 1992, p 156.
57. M.R. Wasielewski, M.P. O'Neil, D. Gosztola, M.P. Niemczyk, W.A. Svec, *Pure Appl. Chem.* **1992**, 64, 1319.
58. M.P. O'Neil, M.P. Niemczyk, W.A. Svec, D. Gosztola, G.L. Gaines III, M.R. Wasielewski, *Science* **1992**, 257, 63.
59. B.M. Kharlamov, R.I. Personov, L.A. Bykovskaya, *Opt. Commun.* **1974**, 12, 191.
60. A.A. Gorokhovskii, R.K. Kaarli, L.A. Rebane, *JETP Lett.* **1974**, 20, 216.
61. R. Jankowiak, J.M. Hayes, G.J. Small, *Chem. Rev.* **1993**, 93, 1471.
62. U.P. Wild, S. Bernet, B. Kohler, A. Renn, *Pure Appl. Chem.* **1992**, 64, 1335.
63. *Persistent Spectral Hole Burning: Science and Applications (Top. Curr. Phys. Vol. 44)*, W.E. Moerner, Ed., Springer-Verlag, Berlin, 1988.
64. A. Furusawa, K. Horie, *J. Chem. Phys.* **1991**, 94, 80.
65. W.E. Moerner, T. Basché, *Angew. Chem. Int. Ed. Engl.* **1993**, 32, 457.
66. W.E. Moerner, L. Kador, *Phys. Rev. Lett.* **1989**, 62, 2535.
67. K.K. Rebane, L.A. Rebane, Ref. [63], p 17.
68. U.P. Wild, S.E. Bucher, F.A. Burkhalter, *Appl. Opt.* **1985**, 24, 1526.
69. U.P. Wild, A. Renn, S. DeCaro, S. Bernet, *Appl. Opt.* **1990**, 29, 4329.
70. A. Rebane, R. Kaarli, P. Saari, A. Anijalg, K. Timpmann, *Opt. Commun.* **1983**, 47, 173.
71. F.A. Burkhalter, G.W. Suter, U.P. Wild, V.D. Samoilenko, N.V. Rasumova, R.I. Personov, *Chem. Phys. Lett.* **1983**, 94, 483.
72. D.B. Amabilino, J.F. Stoddart, *Pure Appl. Chem.* **1993**, 65, 2351.
73. B. Odell, M.V. Reddington, A.M.Z. Slawin, N. Spencer, J.F. Stoddart, D.J. Williams, *Angew. Chem. Int. Ed. Engl.* **1988**, 27, 1547.
74. B.L. Allwood, N. Spencer, H. Shahriari-Zavareh, J.F. Stoddart, D.J. Williams, *J. Chem. Soc., Chem. Commun.* **1987**, 1064.
75. C. Reichardt, S. Asharin-Farid, *Angew. Chem. Int. Ed. Engl.* **1991**, 30, 958.
76. R.A. Bissell, E. Córdova, A.E. Kaifer, J.F. Stoddart, *Nature* **1994**, 369, 133.
77. E. Córdova, R.A. Bissell, N. Spencer, P.R. Ashton, J.F. Stoddart, A.E. Kaifer, *J. Org. Chem.* **1993**, 58, 6550.
78. H. Murakami, A. Kawabuchi, K. Kotoo, M. Kunitake, N. Nakashima, *J. Am. Chem. Soc.*, **1997**, 32, 7605.
79. J.F. Stoddart, P. Ashton, C.L. Brown, E.J.T. Chrystal, K.P. Parry, M. Pietraszkiewicz, N. Spencer, *Angew. Chem. Int. Ed. Engl.* **1991**, 30, 1042.
80. A. Livoreil, C.O. Dietrich-Buchecker, J.-P. Sauvage, *J. Am. Chem. Soc.* **1994**, 116, 9399.
81. P. Gaviña, J.-P. Sauvage, *Tetrahedron Lett.* **1997**, 38, 3521.
82. J.-P. Collin, P. Gaviña, J.-P. Sauvage, *J. Chem. Soc., Chem. Commun.* **1996**, 2005.
83. D.J. Cárdenas, A. Livoreil, J.-P. Sauvage, *J. Am. Chem. Soc.* **1996**, 118, 11980.
84. L.M. Adleman, *Science* **1994**, 266, 1021.
85. L.M. Adleman, *Sci. Am.* **1998**, 279, 54.
86. D.K. Gifford, *Science*, **1994**, 266, 993.
87. Q. Ouyang, P.D. Kaplan, S. Liu, A. Libchaber, *Science* **1997**, 278, 446.
88. L. Kari, *Proc. Bio-computing Emergent Computation*, **1997**, 146.
89. R.J. Lipton, *Science* **1995**, 268, 542.
90. J.S. Oliver, *J. Mol. Evolution* **1997**, 45, 161.
91. N. Lotan, G. Ashkenazi, S. Tuchman, S. Nehamkin, S. Sideman, *Mol. Cryst. Liq. Cryst.* **1993**, 236, 95.
92. G. Ashkenazi, D.R. Ripoli, N. Lotan, H.A. Scheraga, *Biosensors Bioelectronics* **1997**, 12, 85.
93. R.P. Feynman, *Int. J. Theor. Phys.* **1982**, 21, 467; R.P. Feynman, *Opt. News* **1985**, 11, 11.
94. D. Deutsch, *Proc. Roy. Soc. London A* **1989**, 425, 73.
95. D. Deutsch, R. Jozsa, *Proc. Roy. Soc. London A* **1992**, 439, 554.
96. P. Shor, *Proc. 35th Ann. Symp. Foundations of Computer Science* **1994**, 14.
97. Q.A. Turchette, R.J. Thompson, H.J. Kimble, *Appl. Phys.* **1995**, 74, 4091.

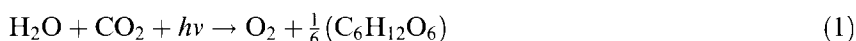
98. S. Lloyd, *Phys. Rev. Lett.* **1995**, 75, 346.
99. A. Barenco, D. Deutsch, A. Ekert, *Proc. Roy. Soc. London A* **1995**, 449, 669.
100. A. Fahmy, T. Havel, *Proc. Natl. Acad. Sci. USA* **1997**, 94, 1634.
101. N.A. Gershenfeld, I.L. Chuang, *Science* **1997**, 275, 350.
102. D.P. DiVincenzo, *Phys. Rev. A* **1995**, 50, 1015.
103. R. Laflamme, E. Knill, W.H. Zureck, P. Catasti, S.V.S. Mariappan, *Proc. Roy. Soc. London A* **1998**, 356, 1941.
104. J.I. Cirac, P. Zoller, *Phys. Rev. Lett.* **1995**, 74, 4091.
105. M.G. Raizen, J.M. Gilligan, J.C. Bergquist, *Phys. Rev. A* **1992**, 45, 6493.
106. H. Walther, *Adv. At. Mol. Opt. Phys.* **1994**, 32, 379.
107. W. Nagourney, J. Sandberg, H. Dehmelt, *Phys. Rev. Lett.* **1986**, 56, 2797.
108. J.C. Bergquist, R.G. Hulet, W.M. Itano, D.J. Wineland, *Phys. Rev. Lett.* **1986**, 57, 1699.
109. A. Barenco, D. Deutsch, A. Ekert, *Phys. Rev. Lett.* **1995**, 74, 4083.
110. R.T. Bate, G.A. Frazier, W.R. Frensley, J.W. Lee, M.A. Reed, *SPIE* **1987**, 792, 26.
111. J.N. Randall, *Nanotechnology* **1993**, 4, 43.
112. P. Bakshi, D.A. Broido, K. Kempa, *J. Appl. Phys.* **1991**, 70, 5150.
113. C.S. Lent, P.D. Tougaw, W. Porod, *Appl. Phys. Lett.* **1993**, 62, 714.
114. C.S. Lent, P.D. Tougaw, W. Porod, *J. Appl. Phys.* **1993**, 74, 6227.
115. K. Nomoto, R. Ugajin, T. Suzuki, I. Hase, *J. Appl. Phys.* **1996**, 79, 291.
116. A. Aviram, *J. Am. Chem. Soc.*, **1988**, 110, 5687.
117. R.M. Metzger, B. Chen, U. Hopfner, M.V. Lakshmikantham, D. Vuillaume, T. Kawai, X. Wu, H. Tachibana, T.V. Hughes, H. Sakurai, J.W. Baldwin, C. Hosch, M.P. Cava, L. Brehmer, G.J. Ashwell, *J. Am. Chem. Soc.* **1997**, 119, 10455.
118. A. Stabel, P. Herwig, K. Mullen, J.P. Rabe, *Angew. Chem. Int. Ed. Eng.* **1995**, 34, 1609.
119. D.L. Allara, T.D. Dunbar, P.S. Weiss, L.A. Bumm, M.T. Cygan, J.M. Tour, W.A. Reinert, Y. Yao, M. Kozaki, L. Jones, *Ann. N.Y. Acad. Sci.* **1998**, 852, 145. P.S. Weiss, L.A. Bumm, T.D. Dunbar, T.P. Bagin, J.M. Tour, D.L. Allara, *Ann. N.Y. Acad. Sci.* **1998**, 852, 349.
120. C.P. Collier, E.W. Wong, M. Belohradsky, F.M. Raymo, J.F. Stoddart, P.J. Kuekes, R.S. Williams, J.R. Heath, *Science* **1999**, 285, 391.

6 Antennas

Sebastiano Campagna, Scolastica Serroni, Fausto Puntoriero, Cinzia Di Pietro, and Vittorio Ricevuto

6.1 Introduction

Light energy from the Sun is vital for powering the living world. It is collected and used by plants to turn water and carbon dioxide into complex energy-rich molecules such as carbohydrates. Each year, more than 10^{17} kJ of energy from sunlight is captured and used by natural organisms (beside green plants, photosynthetic bacteria also concur to convert sunlight into more convenient forms of energy) to produce chemical fuels which provide the basis for life on Earth [1]. The basic process by which the natural photochemical energy conversion is accomplished is schematized in Eq. (1).



Such a reaction is highly endoergonic (as much as $114 \text{ kcal mol}^{-1}$ can be obtained from the opposite combustion reaction) and can only occur thanks to the energy input of the incoming photons.

The sunlight-generated fuels are used by photosynthetic organisms to drive their own metabolic processes, and also provide energy for higher organisms by supporting the food chain. Over billions of years, energy from the Sun also formed fossil fuels, which our civilization consumes at an increasing and alarming rate. Life and civilization are therefore basically founded on sunlight. To develop artificial systems capable of using the influx of solar energy on Earth to supply man's energy needs directly, providing a renewable and nonpolluting solution to man's increasing energy demands, therefore looks like a Holy Grail: taking the words of a famous lecture [2] delivered by one of the pioneers of photochemistry, Giacomo Ciamician, at the beginning of the 20th century, "... If our black and nervous civilization, based on coal, shall be followed by a quieter civilization based on the utilization of solar energy, that will not be harmful to the progress and to human happiness."

After a boost in research for artificial photosynthesis in the 1970s as a conse-

quence of the oil crisis, the field has been recently revitalized because of the environmental problems connected with release of carbon dioxide in the atmosphere from the burning of fossil fuels. It is now clear that man cannot tolerate the present conventional energy production processes any more. Looking at the present foreboding situation and at the outstanding recent developments in the field, it is conceivable that artificial photosynthesis may play a key role in providing a cheap and clean energy source in the 21st century [3].

The first functions an artificial photosynthetic system has to perform, similarly to the natural systems, are to collect solar light and to redirect it in the form of electronic energy to a specific site in its own structure (in the case of photosynthetic bacteria, for example, such a site is a properly organized pair of chromophores, called the special pair [4]). From this site a series of photoinduced electron transfer processes take place, with the final result of converting electronic energy into chemical (redox) energy. The absorption of light energy is performed by Nature by means of organized arrays of suitable chromophores; the funneling of the light energy absorbed by the various chromophores to specific sites is accomplished by migration of the electronic energy stored in each chromophore within the array, via a series of interchromophoric energy hopping and/or transfer processes. Early time-resolved measurements [5] showed that in natural systems this migration process is typically finished within ~ 100 ps, explaining the high, $\sim 95\%$, overall quantum yield of the process. More recently, it has been demonstrated that some of the individual energy transfer steps within the light-harvesting systems are in the subpicosecond timescale [6].

The arrays of molecular entities which perform the functions cited above (absorption of light and energy migration to a specific site) are called *antennas*. Like the other active components of the photosynthetic organisms, which have the role of performing other specific functions in the complex solar energy conversion scheme, the antenna is essential for the effective conversion of the solar energy input: its function, in summary, is actually to enhance the probability of catching the solar energy by increasing the molar absorptivity of the systems in the visible region of the solar spectrum. It has been estimated that the efficiency of conversion by the photosynthetic organisms of the input of solar energy into fuels (i.e., the ratio between moles of fuels produced and energy of solar rays incident on Earth) would be hundreds of times lower without the antenna effect [1]. This leads to an overall solar energy conversion which would have been insufficient to sustain life on Earth throughout the millennia if the antenna effect were not effective.

The aim of this article is to discuss the basic requirements that an antenna system has to fulfill and to summarize some examples of the various artificial antennas reported in the literature. For the sake of comparison, brief comments on natural antennas are also presented.

It should also be noted that, although the main interest in antennas comes from the search for an effective artificial photosynthesis, antennas may be relevant for any kind of application involving light-induced processes, such as luminescent sensors, photochemical reactions, and so on. The efficiency of any photoinduced process may actually be significantly enhanced by using suitable antennas, when the overall light energy incident on the system is considered.

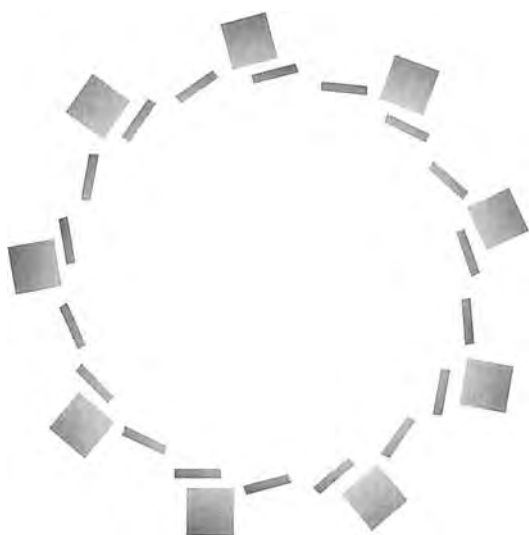


Figure 1. Schematic representation of the LH2 antenna complex from *Rps. acidophila* [7]. Only bacteriochlorophyll molecules are considered, for clarity. The squares represent bacteriochlorophyll molecules which lie in the plane of the page. Their assembly is called the B800 system (see text). The rectangles represent the BChl molecules which are perpendicular to the plane of the page. These latter are in almost a face-to-face arrangement and constitute the B850 system.

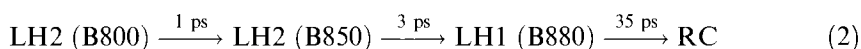
6.2 Natural Antennas

The better-known natural antennas are the light-harvesting complexes of the photosynthetic bacteria, so our discussion will be limited to these species. A major breakthrough in the field has been the structural determination of the light-harvesting antenna complex (LH2) from *Rhodospseudomonas acidophila* in 1995 [7]. This structure (for a schematization, see Figure 1) is amazingly both simple and elegant: nine identical units, each consisting of two fairly short α -helical polypeptides and associated bacteriochlorophyll (BChl) molecules, combine into a ring. The helices are more or less perpendicular to the plane of the membrane. Within each unit, each pair of polypeptides coordinates three bacteriochlorophylls and one carotenoid. Two BChls are held near the periplasmic, carboxy-terminal end of the helices, and one is suspended between the helices near their middle. The antenna complex LH2 is therefore composed of two rings of bacteriochlorophylls, one set of 18 close to the membrane surface, in almost a face-to-face arrangement like a turbine wheel, and another set of nine all lying in the same plane which is perpendicular to the rings of the bacteriochlorophylls of the first type, in the middle of the bilayer. These nine chromophores are also arranged in the form of a wheel.

Because of their different chemical environments, the two sets of bacteriochlorophylls have different absorption and photophysical properties. The bacteriochlorophylls belonging to the larger wheel have the lower-energy absorption maximum at 850 nm (and are named B850) and the nine in the middle of the bilayer have the lower-energy absorption maximum at 800 nm (and are named B800). There are other significant differences between the two sets of pigments, as evidenced by a

series of spectroscopic studies [8]: the B800 BChl molecules are largely monomeric, whereas the B850 ones are strongly exciton-coupled [9], with the so-called exciton states delocalized over several (most likely four) BChl molecules. All the BChl are maintained in a fixed spatial relationship by the polypeptides. Carotenoids are also associated within the LH2 structure and have the function of contributing to the light-harvesting process [10] and of playing the role of photoprotecting species. The various BChl molecules absorb a significant proportion of solar light. The light absorbed by the B800 array is transferred to the B850 “wheel” within ~ 1 ps. Energy migration among the various exciton states of B850 then occurs on the 300 fs timescale [8].

LH2 is sometimes referred to as the *outer antenna*, because the energy it collects flows to its final destination through another antenna complex, named LH1, which immediately surrounds the reaction center, the site where the light energy has to be ultimately transferred and where charge separation takes place. The structure of LH1 is not known at the same level of definition as that of LH2, but an impressive result has recently been obtained by electron crystallography of two-dimensional crystals of the LH1 complex of *Rhodospirillum rubrum* [11]. This structure evidences a clear similitude between LH2 and LH1; LH1 is formed by 32 BChl molecules in the same arrangement as the B850 BChl molecules of LH2. Clearly, the “wheel” defined by the LH1 complex is much larger than that defined by the LH2 complex because of the larger number of molecules involved. Furthermore, LH1 absorbs at lower energy, so its BChl wheel is named B880. LH1 and LH2 are in a close contact (a shorter 30 Å distance between bacteriochlorophylls of the two complexes has been estimated), so that $\text{LH2} \rightarrow \text{LH1}$ energy transfer occurs with a time constant of 3 ps at room temperature. The reaction center (RC) is embedded within LH1, and energy transfer from LH1 to RC takes place with a time constant of 35 ps. This last step is therefore the slowest step of the entire process over the antenna network, which may be summarized in Eq. (2):



The overall energy migration within the antenna network to reach the reaction center is also schematized in Figure 2. The relatively slow rate of the final energy transfer to the RC is a consequence of the size of the RC protein, which prevents a short antenna–RC distance [8, 12]. It should also be borne in mind that the BChl molecules of B880 in LH1 are exciton-coupled like those of B850, and in view of the structural similarity between the two complexes, even in this case the exciton delocalization is probably relatively small and extends over about four BChl molecules [8]. This would imply that the energy is transferred from approximately eight sites of LH1 (each one composed of four delocalized BChl subunits) to the RC (assuming 1 RC per 32 BChl LH1 molecules).

To summarize, the natural photosynthetic processes occurring in bacteria are based on a clever modular design of the active subunits and on a series of downhill energy transfer steps. By indirect evidence, a similar organization appears to be present in the green plants [1, 8]. Ultrafast energy migration within almost iso-energetic subunits is used to transfer the energy within a single complex until it

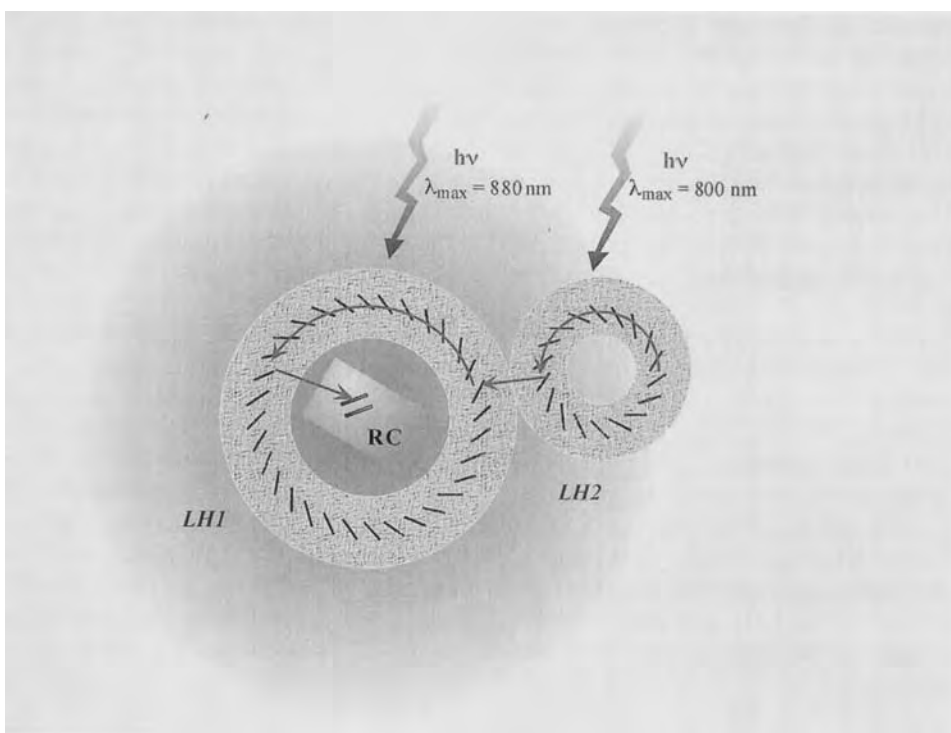


Figure 2. Schematization of the overall energy migration within the antenna network to reach the reaction center. The small and large wheels represent the LH2 and LH1 complexes, respectively. For the LH1 complex, only the B850 system is represented.

reaches a site suitable for transferring the energy to a lower-energy complex, so allowing for a minimal loss. The various energy transfer steps mainly occur by the Förster singlet–singlet mechanism [13].

6.3 Artificial Antennas

6.3.1 Principles of Design

It should be borne in mind that the bacterial light-harvesting complexes described above have some differences from the plant light-harvesting complexes [1], although the basic principles of construction, in particular the modular approach, are common, as well as the occurrence of the sequential energy transfer steps via an energy cascade. This suggests that, just as Nature has responded in some slightly different

ways to the problem of converting solar energy, the design of effective artificial antennas can be tackled by a number of different approaches. Here we will be outlining the basic principles that appear to be necessary for designing an effective artificial antenna and in the next section we will discuss some representative examples of the artificial systems reported in the literature.

If an artificial system has to be developed, the obvious choice is probably to think of it as a modular system, as Nature did. This leads us to focus directly on the individual modules to be used (the building blocks). The requirements that the building blocks have to fulfill are the following: i) stability in the ground and excited states; ii) the capability to absorb solar light significantly [14]; iii) a relatively long-lived excited state, to allow energy transfer to occur with minimal loss of energy. In particular, point i) is even more important for artificial antennas than for natural ones, in that self-repairing processes, available in Nature, are difficult to reproduce in artificial systems.

After the building blocks have been selected, the next step is to connect them together. This is not a trivial point, in that suitable spatial connection is crucial for fast energy transfer. Of course, the connections should be selected to assure the necessary electronic coupling (through-space or through-bond) between the building blocks. In this regard, one can take advantage of both coulombic (Förster) [13] and electron exchange (Dexter) [15] mechanisms for the energy transfer. Nature makes use of noncovalent connections and the membrane elements guarantee the right arrangements among the chromophores. From a synthetic viewpoint, although supramolecular chemistry has made impressive progress recently as far as noncovalent made-to-order synthesis is concerned [16], noncovalent synthesis has not yet reached the necessary stage of development to allow the design of well-defined, controlled, and robust architectures to satisfy all the requirements of an effective antenna. Thus, covalent linkage is still probably the preferred choice.

The choice of connectors generally succeeds to the choice of building blocks. This is made clear on considering that the connectors have to allow interchromophore energy transfer fast enough to overcome the intrinsic decay rates of the individual chromophores. In other words, if the chromophores C_1 , C_2 , and C_3 are arranged in the series C_1 – C_2 – C_3 , so that the energy must flow from C_1 to C_3 , the energy transfer rate from C_1 to C_2 must dominate over the intrinsic excited-state decays of C_1 , and the same must hold for the couple of chromophores C_2 and C_3 . This is made evident in Figure 3. Because the chemical nature of the connectors affects the interchromophoric energy transfer rates, it is clear that connectors that are effective for antenna systems based on chromophores having slow intrinsic decays may be not suitable for antenna systems based on chromophores having shorter excited-state lifetimes. As a consequence, the connectors have to be properly designed for each type of antenna. The solution of the connector problem may also be related to the development of molecular wires [17] (see also Part 1, Chapters 1 and 3, in this volume).

For an artificial antenna to be effective, it should contain as much chromophore as possible. This point immediately calls for the development of suitable substrates to which the chromophores should be linked and/or of properly designed synthetic

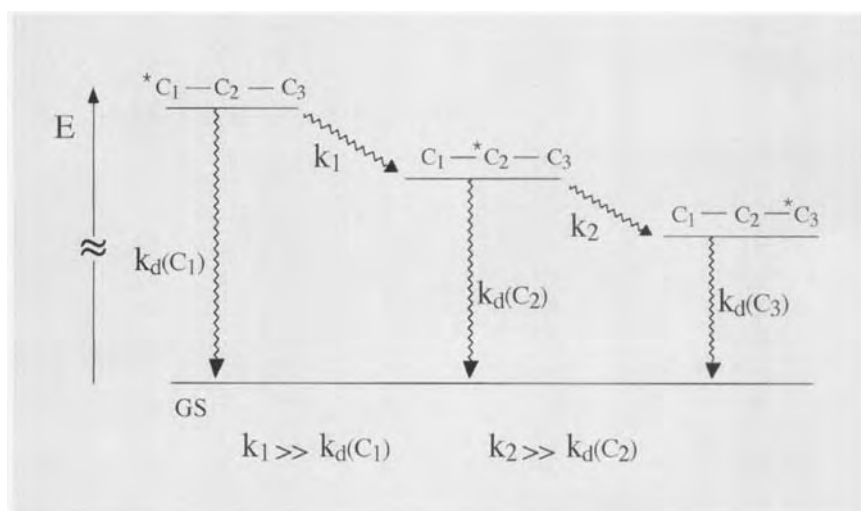


Figure 3. Energy level diagram and restrictions on kinetic parameters for the series of chromophores C_1 , C_2 , C_3 . $k_d(C_n)$ represents the intrinsic decay rates for C_n , regardless the radiative or nonradiative nature of the processes; k_1 and k_2 are energy transfer rate constants.

approaches. Furthermore, to funnel the electronic energy to a specific point of the antenna, to which a charge-separation system should be connected, an energy gradient is necessary. As Nature uses essentially the same type of chromophore (porphyrins and derivatives), tuning their excited-state energies by means of environmental effects, a possible answer is to select building blocks whose properties are tunable by slight chemical modifications, and to insert these building blocks in the correct position of the array in order to create the desired excited-state energy gradient. The synthetic approaches needed therefore should be able to allow a topological control of the final array. This also introduces a further requirement, the tunability of the absorption and photophysical properties for the building blocks to be used.

The ideal sequence of choices which has usually been followed for the construction of artificial antennas up to now is shown in Figure 4. However, this sequence could be revolutionized if quite different approaches for the assembly of chromophores (e.g., self-assembly) should emerge.

All the antennas are easily schematizable, as in Figure 5 [18]. In this representation, each "floor" of chromophores contains identical subunits, and moving between floors one encounters chromophores which differ in excited-state energy, in such a way as to create an energy gradient. The chromophore at the basis of the array is the lowest-energy one, which plays the role of energy collector (energy trap, T). The energy gradient drives the antenna effect. The various "floors" of the artificial systems in this schematization play the role of the various "wheels" which assist the natural systems.

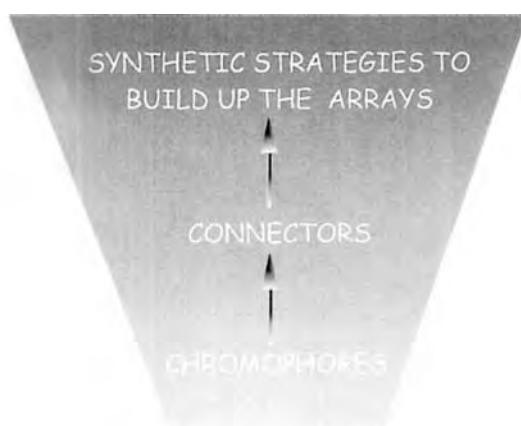


Figure 4. The sequence of choices usually employed to build up artificial antennas.

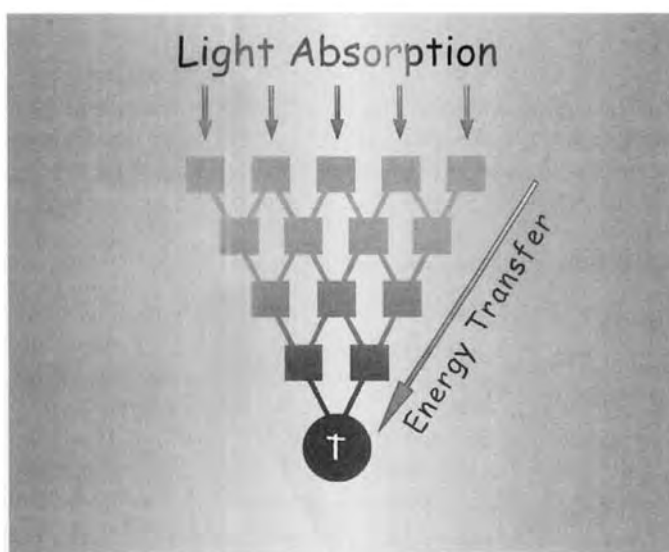


Figure 5. Schematization of an antenna system. † stands for the energy trap.

6.3.2 Examples

By definition, an antenna is a multichromophoric array in which the light energy captured by each active component (each single chromophore) is funneled by a series of elementary energy transfer steps to a single, specific site. So, two individual *actions*, light absorption and energy migration, are integrated to perform a multiple, more valuable *function*, the *antenna effect*.

Many systems, sometimes also very different from one another, have been designed to act as antennas. Here we will review only a few typical cases. We will focus on systems in fluid solution, leaving aside solid-state devices.

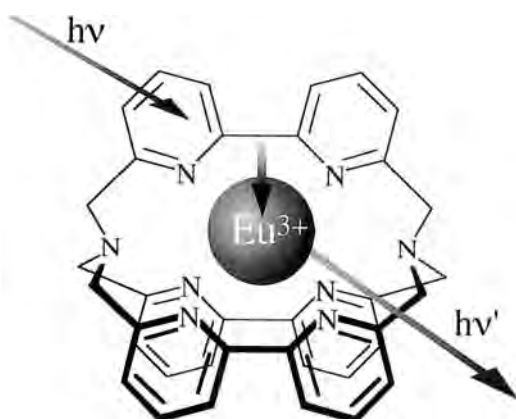


Figure 6. A typical europium cryptate featuring the antenna effect [19].

Although different synthetic approaches have been used, the experimental techniques employed to verify the properties of the systems are very often similar, and generally include steady-state and time-resolved absorption and luminescence spectroscopy.

Small antennas: lanthanide complexes

Maybe some of the simplest antennas are lanthanide complexes containing chelating polypyridine ligands, such as the Eu(III) cryptates developed by Lehn and co-workers [19]. In these simple antennas, the role of light-harvesting units is played by the N-heterocyclic ligands, which transfer the excitation energy in a sub-picosecond timescale to the lanthanide cations, which ultimately emit the collected energy with a high luminescence quantum yield (Figure 6). In spite of their simplicity and of the similarity of these systems to usual coordination compounds such as $\text{Ru}(\text{bpy})_3^{2+}$ ($\text{bpy} = 2,2'$ -bipyridine) and analogous species [20], in which the light absorbed by the ligand is also transferred to lowest-lying, luminescent, metal-to-ligand charge transfer (MLCT) states, we decided to include these lanthanide compounds in this chapter because they exemplify very well the importance of the antenna effect: in fact, the “free” lanthanide cations had previously been known to exhibit very good luminescence properties (quantum yields close to unity under certain conditions) but they were very poor absorbers, so their interesting photophysical properties remained almost useless. Light energy absorption is accomplished by the ligands in the cryptates, and the electronic energy is transferred successively to the lanthanides, making the whole species at the same time good absorbers (although usually only in the UV region) and emitters.

Following the initial reports of the antenna effect in lanthanide cryptates, many other lanthanide complexes containing additional chromophoric ligands have been investigated and found to be useful as luminescent labels for biological substrates, and in general as sensors based on luminescent properties [21].

Polymer-based antennas

Many artificial antennas have been based on polymers containing chromophores as appended photoactive units. An example of this class is the series of antennas developed by Guillet and co-workers [22]. In these species the energy traps are condensed aromatic hydrocarbons such as naphthalene derivatives to which the other (peripheral) chromophores, usually also of aromatic nature, transfer the excitation energy. Guillet's antennas are water-soluble polyelectrolytes, and have been termed *photozymes*, i.e., artificial photochemical enzymes, in that the antenna effect is used to amplify the photodegradation ability of the energy trap with regard to various hydrophobic substrates (pollutants) which are surrounded by the polyelectrolyte arrays in water solution, giving rise to a microheterogeneous photocatalysis. Similar antennas have been employed recently by the same group to evolve hydrogen from water under irradiation [23].

The approach based on derivatized polymers with appended chromophores has also been developed by Meyer and co-workers [24]. They used as chromophores polypyridyl complexes of Ru(II) and Os(II) which have high absorptivities in the visible region based on intense MLCT bands. An early synthetic strategy [24a] involved attachment of the chromophores to polystyrene by an ether linkage (Figure 7a). Successively [24b], the authors developed a new route based on amide linkage (Figure 7b), finding a dramatic enhancement in the ability of the polymeric arrays to promote intrastrand energy transfer. In a typical preparation, the amide polymer was obtained from a 1:1 styrene-*p*-aminomethylstyrene copolymer of polydispersity

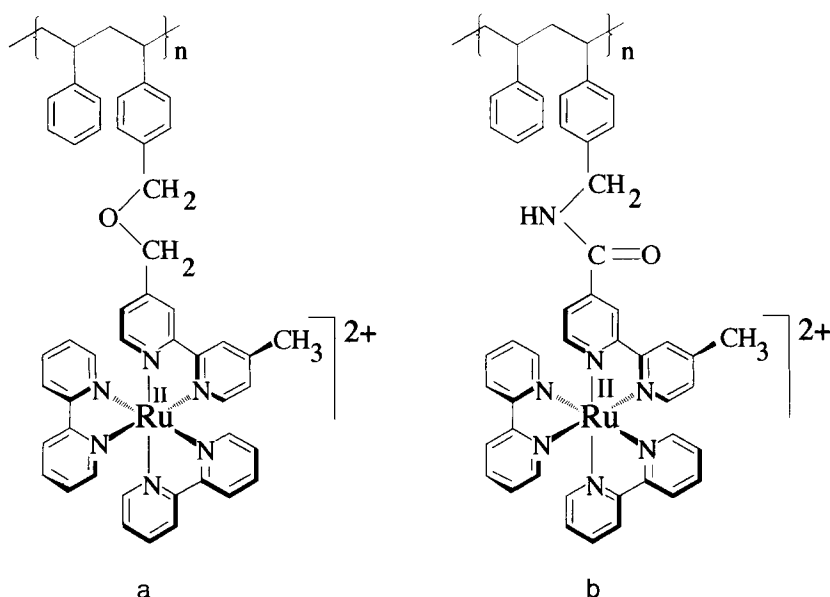


Figure 7. Chromophores used as the photoactive appended subunits in Meyer's light-harvesting soluble polymers [24].

1.5 and an average of 16 repeating units. The amide link was formed by reaction with the acid-derivatized complexes, $[M(b)_2(b-COOH)](PF_6)_2$ ($M = Ru, Os$; $b = bpy$; $b-COOH = 4'$ -methyl-2,2'-bipyridine-4'-carboxylic acid) by using standard coupling conditions. A mixed polymer was prepared by sequential coupling, first with the $Os(II)$ complex (which is less reactive) in a limited amount and then with the more reactive $Ru(II)$ complex to fill all the free polymeric sites. In the mixed polymers, containing the lower-energy Os -based chromophores and the higher-energy Ru -based ones in a 3:13 ratio (so therefore the $Os(II)$ chromophores act as the energy traps), triplet-triplet energy transfer from excited Ru chromophores to the Os ones occurred with efficiency higher than 0.90 in acetonitrile solution.

It was pointed out that energy transfer from $*Ru$ to Os requires two processes: $*Ru$ -to- Ru energy migration (a self-exchange process) and the actual energy step from $*Ru$ to a nearby Os . For both processes the rate constants exceeded $2 \times 10^8 \text{ s}^{-1}$ for the amide-linked polymer, whereas in the ether-linked polymer the rate constant for intrastrand energy migration from $*Ru$ to Ru was orders of magnitude slower. The rate constants for the amide-linked species, coupled with the relatively long intrinsic lifetime of the $*Ru$ chromophores (910 ns), accounts for the ability of the polymer arrays containing the amide-linked chromophores to act as efficient antennas. The reason for the different behavior of the ether-linked and amide-linked arrays lies in the direction of the excited-state MLCT dipole of the chromophores involved in the energy transfer processes. This dipole is directed toward the polymer backbone in the most effective amide-linked antenna systems, whereas it acts out from the polymer backbone in the less efficient ether-linked arrays. This difference affects the electronic coupling between donor and acceptor sites of the energy transfer and migration processes. This finding demonstrates that in polymer-based antennas, slight modifications in the chromophore linkage may have large effects on the antenna performance. Recently, the same group also used poly(amino acid)s as polymer backbones to construct antenna systems [25].

Interesting antenna systems based on polymers have also been designed by Fox and co-workers [26]. They prepared a series of well-defined block copolymers labeled with aromatic chromophores and demonstrated that directional singlet energy migration across the block interface takes place, whereas extensive exciplex formation, a decay channel which dissipates electronic energy in flexible polymers, is strongly inhibited in these special polymers.

Within the class of antennas made of chromophores appended to polymers, there may be included the quite peculiar systems developed by Valeur, Lehn, and co-workers in a series of intriguing papers [27]. These species are based on β -cyclodextrins (which may be considered as cyclic oligomers) containing seven 2-naphthoxyloxy chromophores as substituents appended to the lower rim (Figure 8). In these systems, and in general in artificial antenna systems containing a large number of identical chromophores, an interesting problem to be considered is whether excitation hopping between identical units can occur in a truly chaotic fashion. By using fluorescence anisotropy in low-temperature glasses, the authors demonstrated that solvation heterogeneity causes inhomogeneous broadening in the spectrum of the chromophores, and this drives the energy hopping in the systems toward the lower-energy chromophore(s). Such an energy hopping occurs in the

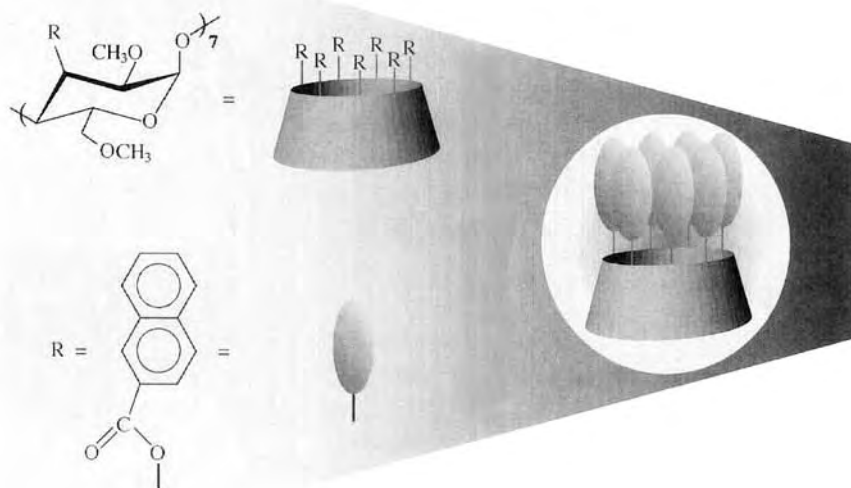


Figure 8. Schematic representation of the cyclodextrin-based antennas [27].

systems studied with an average rate constant of $2 \times 10^9 \text{ s}^{-1}$ [27c]. When the cyclodextrin cavity encloses a merocyanine dye, a species having an excited state lower in energy than the naphthoyloxy chromophores, the light energy absorbed by the chromophores of the cyclodextrin rim is transferred to the merocyanine pigment with a quantum efficiency close to unity [27d]. The authors have also performed chemical reactions of substrates enclosed in the cavity, powered by the energy absorbed via the cyclodextrin antennas [27e].

Multiporphyrin arrays

Because Nature elected porphyrin derivatives as components of the natural antennas, it cannot be surprising that many artificial antennas are based on these chromophores. This represents surely the largest class of artificial antennas studied. Even for this class, we discuss just a few representative examples [28].

In a series of elegant and fascinating papers, Lindsey and co-workers developed a set of porphyrin building blocks and used them in a modular approach for the construction of a large series of light-harvesting arrays having highly-controlled geometries [29]. The porphyrin building blocks were facially encumbered to enhance solubility in organic solvents, were employed in defined metallation states (free base or zinc chelate), and carried peripheral functional groups such as iodo or ethyne for joining the porphyrins via covalent bonds by means of highly efficient hetero-coupling reactions. Figure 9 depicts a star-like pentameric array, together

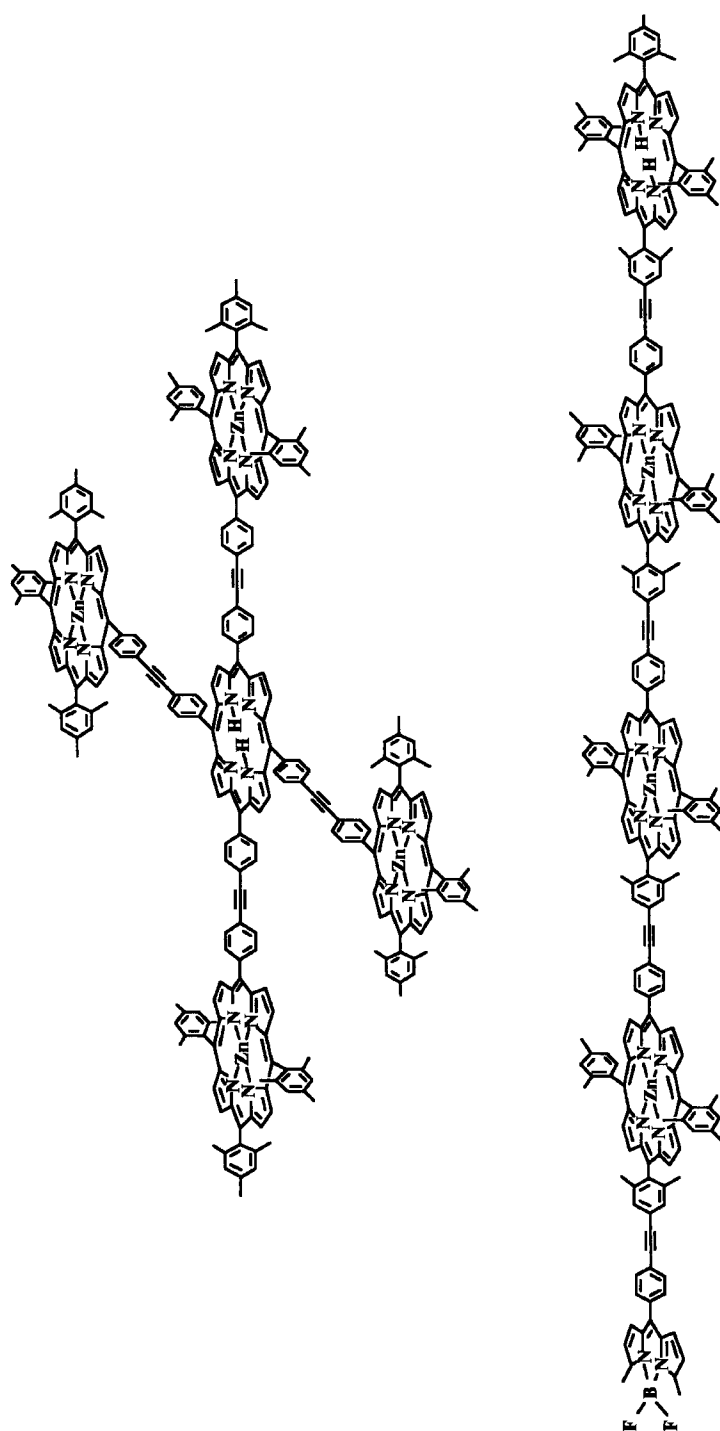


Figure 9. Examples of star-like (top) and linear (bottom) arrays synthesized by Lindsey and co-workers [29].

with a linear array of four porphyrins and one accessory pigment. The latter array can be regarded both as an antenna and as a molecular wire. The quantum efficiency of energy migration from the high-energy boron–dipyrrole pigment through the medium-energy zinc porphyrins to the low-energy free-base porphyrin is 76 %, while the quantum efficiency of energy transfer from the peripheral, high-energy zinc porphyrins to the central, low-energy free-base porphyrin in the star-like pentameric array is quantitative. The effect of the geometry on the energy transfer efficiency was also investigated in variously arranged trimers and dimers. The mechanism of the energy transfer is in all the cases through-bond, as clearly shown by the dependence of the energy transfer rate on the nature of the linker, orbital tuning, and linker location [30].

Some of the largest light-harvesting arrays introduced by this research group, in collaboration with the groups of Birge, Bocian, and Holten, are nine-chromophore species containing a central porphyrin (free base or zinc-metallated) [31a], which act as the energy sink, and eight peripheral boron–dipyrrole accessory pigments (Figure 10). It was demonstrated that the light absorbed by the eight accessory pigments is transferred to the central subunit (the sink) with a quantum efficiency which exceeds 85 %, with an average rate constant of $5 \times 10^{10} \text{ s}^{-1}$. Quite recently, even light-harvesting arrays composed of eight porphyrins and one phthalocyanine acting as the energy trap have been reported [31b].

Lindsey, Donohoe, and co-workers also developed a matrix-formulated eigenvalue/eigenvector approach, using empirical data from a small set of prototypical molecules, to predict the quantum efficiency of energy migration in a variety of arrays as a function of rates, competitive processes, and architectures [32]. Following this approach, they demonstrated, among other findings, that:

- 1) branched and cyclic array architectures exhibit higher quantum efficiencies than linear architectures with an equal number of chromophores;
- 2) large improvements are achieved when energy transfer is directed by a progressive downward cascade in excited-state energy; and
- 3) the most effective light-harvesting arrays are those in which isolated pools of donors each have independent paths directly to the terminal energy collectors.

Of great interest is the recent coupling of some of the above-mentioned multiporphyrin antennas with the charge-separation artificial systems mastered by Gust, Moore, and co-workers [33]. This coupling led to the synthesis of one of the first effective artificial photosynthetic antenna–reaction center complexes (Figure 11). As revealed by time-resolved absorption and emission studies, excitation of any peripheral zinc porphyrin moiety (P_{ZP}) in 2-methyltetrahydrofuran solution is followed by singlet–singlet energy transfer to the central zinc porphyrin with a time constant of ~ 50 ps. The excitation is then transferred to the free-base porphyrin in 240 ps, and this latter species decays by oxidative electron transfer to the fullerene with a time constant of 3 ps. The $(P_{ZP})_3\text{-}P_{ZP}\text{-}P^{\bullet+}\text{-}C_{60}^{\bullet-}$ charge-separated state thus formed has a lifetime of 1330 ps, and is generated with a quantum yield of 0.7, based on the light absorbed by the zinc porphyrin antenna [33a].

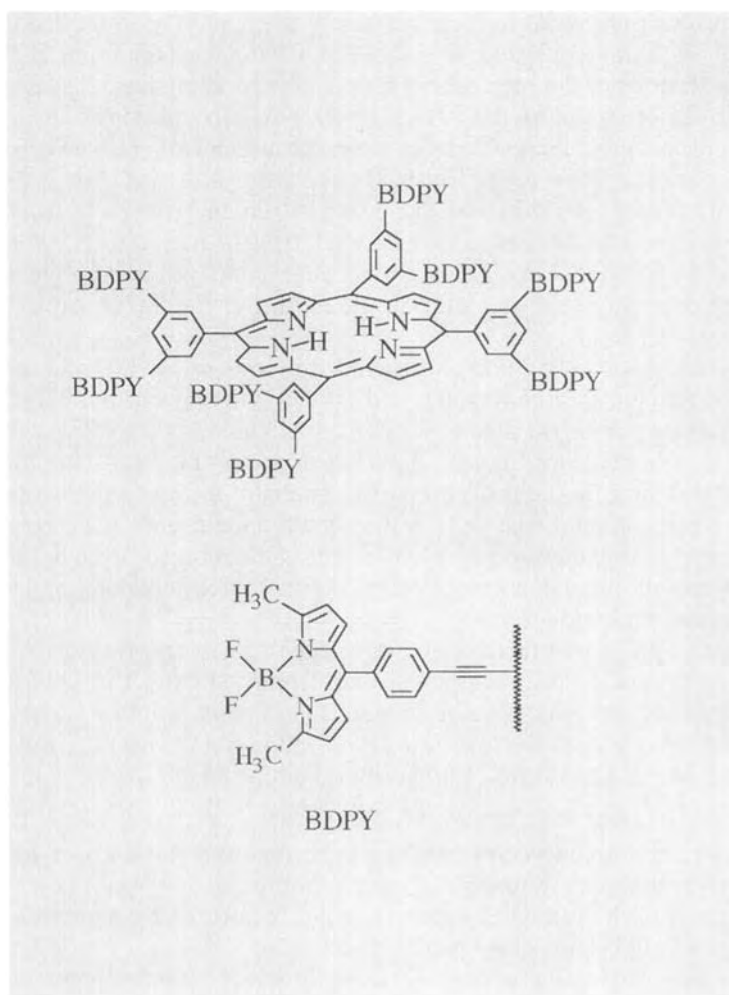


Figure 10. A nine-chromophore species made of eight peripheral boron–dipyrrole pigments and one central porphyrin, acting as the energy sink [31a].

A representative example of multiporphyrin species in which the subunits are assembled by relatively weak coordination links is the three-chromophore species studied by Hunter and Hyde (Figure 12). In this system, the light absorbed by the zinc porphyrins is partially transferred to the free-base porphyrin subunit [34].

Dendrimers

In the very last few years, a molecular architecture which has received more and more attention in view of the construction of artificial antennas is that typical of dendrimers. Dendrimers are highly branched molecules which resemble the shape of

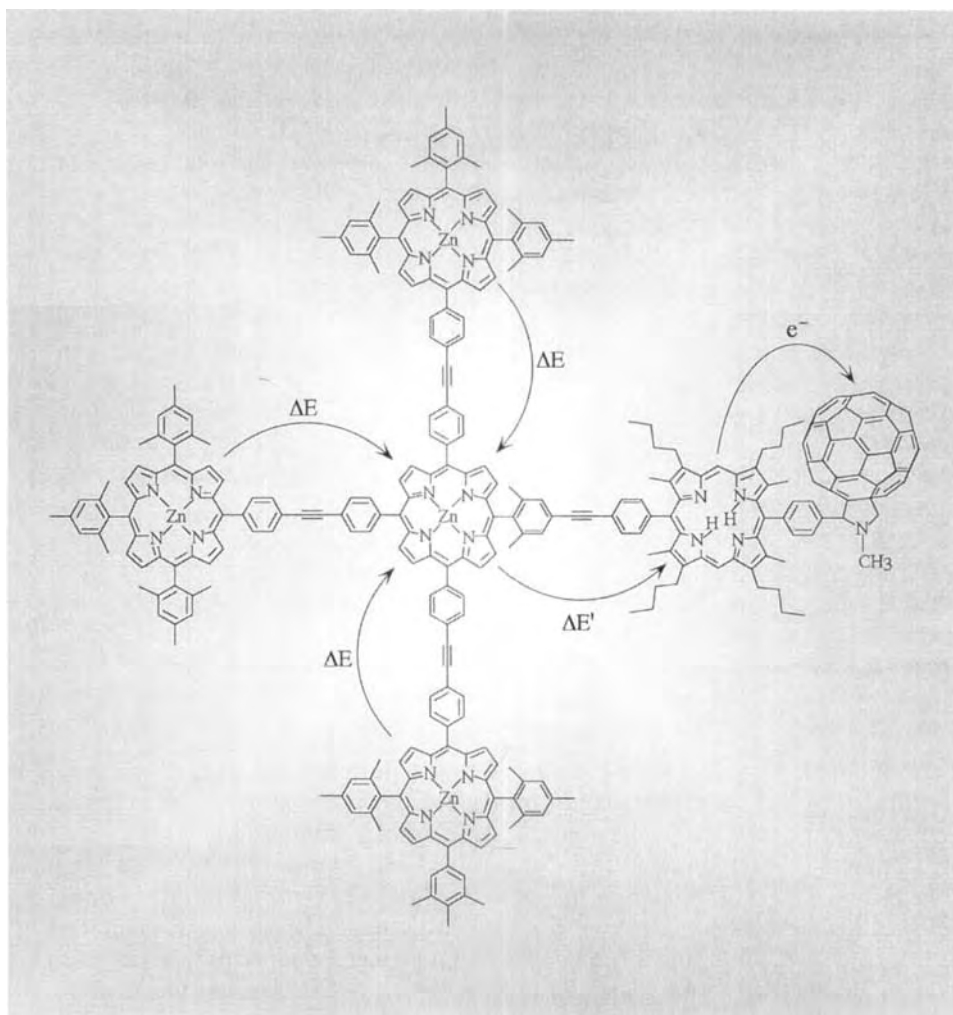


Figure 11. An antenna–reaction center complex [33a]. For details, see text.

a tree (*dendrimer* comes from the term *dendron*, the Greek word for tree, and *polymer*) originating from a core subunit and evolving into three dimensions [35]. Within their globular shape, subunits (and species) of various generations may be identified in the dendrimer structures. Without any doubt, the fact that the convergent and/or divergent synthesis of dendrimers allows assembly, in relatively few synthetic steps, of a large number of subunits (i.e., chromophores) in a restricted space and with a high topological control, is quite attractive for antenna designers. The peculiar characteristics of dendrimer molecules as far as the design of antenna systems is concerned have also been faced from a theoretical viewpoint [36].

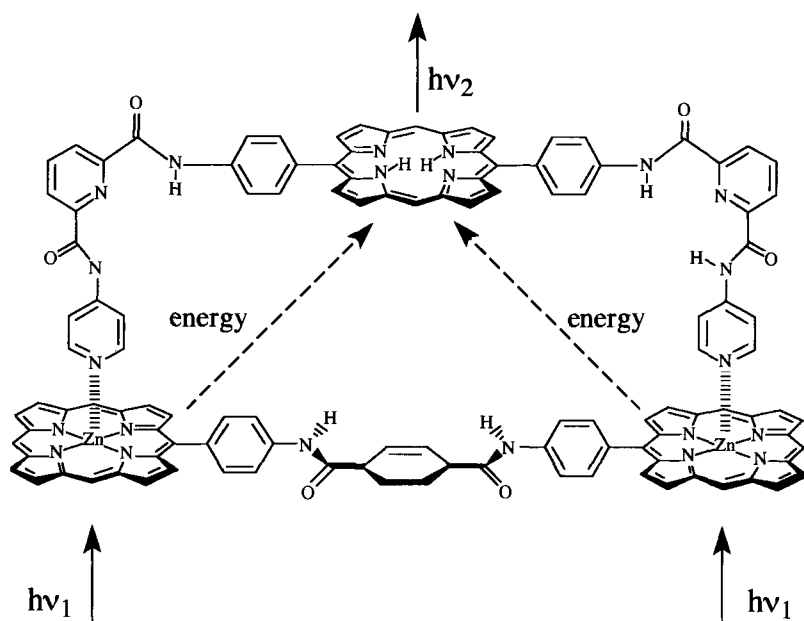


Figure 12. Multi-chromophoric species assembled by weak coordination bonds [34].

Probably the largest class of light-harvesting dendrimers investigated up to now is constituted by the dendrimers based on Ru(II) and Os(II) polypyridine complexes, and the most extensive studies within these species involve the systems containing 2,3-bis(2-pyridyl)pyrazine (2,3-dpp) as bridging ligands [37, 38]. The synthetic approach is based on chelating ligand protection/deprotection iterative steps, developed within the framework of the so-called *complexes as ligands/complexes as metals* strategy [39]. Figure 13 shows the metal ions and the peripheral and bridging ligands mostly used in the course of this study, as well as their graphical representation, and Figure 14 schematizes the iterative synthetic strategy [37g, 38]. Dendrimers containing up to 22 chromophores have been synthesized by this approach [37c,g,i]; such species represent the dendrimers of the third generation within this particular series, and are characterized by a huge light absorption which extends throughout all the visible region (ϵ exceeds $2 \times 10^5 \text{ M}^{-1} \text{ cm}^{-1}$ at the visible absorption maximum, around 550 nm, and is still significant even at 750 nm). Such species are probably some of the best artificial antennas ever reported as far as the cross-section with sunlight is concerned. The MLCT excited-state levels of the various subunits constituting the dendrimers can be quite different from one another, as a function of the metal ion, of its immediate coordination sphere, and also, although to a minor extent, of its second coordination sphere; as a consequence, the excited-state energies of the various subunits depends on their composition and on their position in the array. This allowed the authors the opportunity of generating energy gradients within the dendrimers and of obtaining efficient energy migration

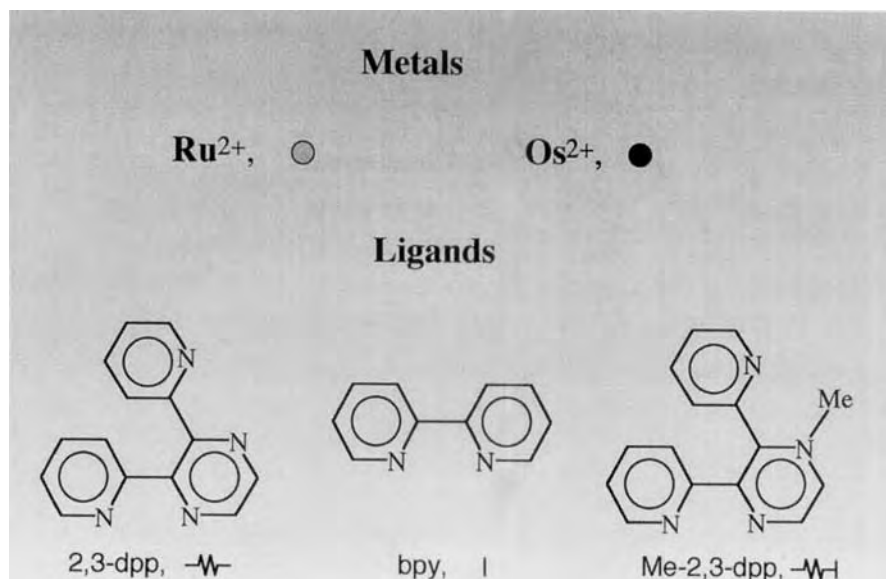


Figure 13. Structural formulas and schematic representation of some components used for the construction of light-harvesting metal-based dendrimers [37, 38].

among the “shells” of suitably designed dendrimers (see Figure 15) [38]. The complete topological control of the systems, a consequence of the synthetic approach, can actually translate into different, made-to-order energy migration patterns within the dendritic arrays. Several examples of such different energy migration patterns have indeed been obtained [38, 40]. The mechanism of the energy transfer steps has been proposed to be triplet–triplet electron exchange (Dexter-type), which is typical of photoinduced energy transfer in multicomponent species containing heavy transition metal coordination compounds [41]. The photophysical studies showed that energy transfer between nearby chromophores occurs with unitary efficiency and within a sub-nanosecond timescale, whereas energy transfer between indirectly connected chromophores has poor efficiency. Therefore, when a correct energy cascade is not obtained and endoergonic energy transfer steps are interposed in the energy pathway to the trap, as occurs in some of the largest dendrimers, the energy migration processes have poor efficiency. The situation is summarized in Figure 16. However, the authors indicated that suitable modifications in the peripheral ligands could permit to overcome this problem [38].

Purely organic light-harvesting dendrimers have been prepared by Moore and co-workers [42]. In these systems (Figure 17), the light absorbed by the peripheral chromophores (phenylacetylene monodendrons) is transferred to the core (perylene) via a coulombic mechanism. The efficiency of the process depends on the

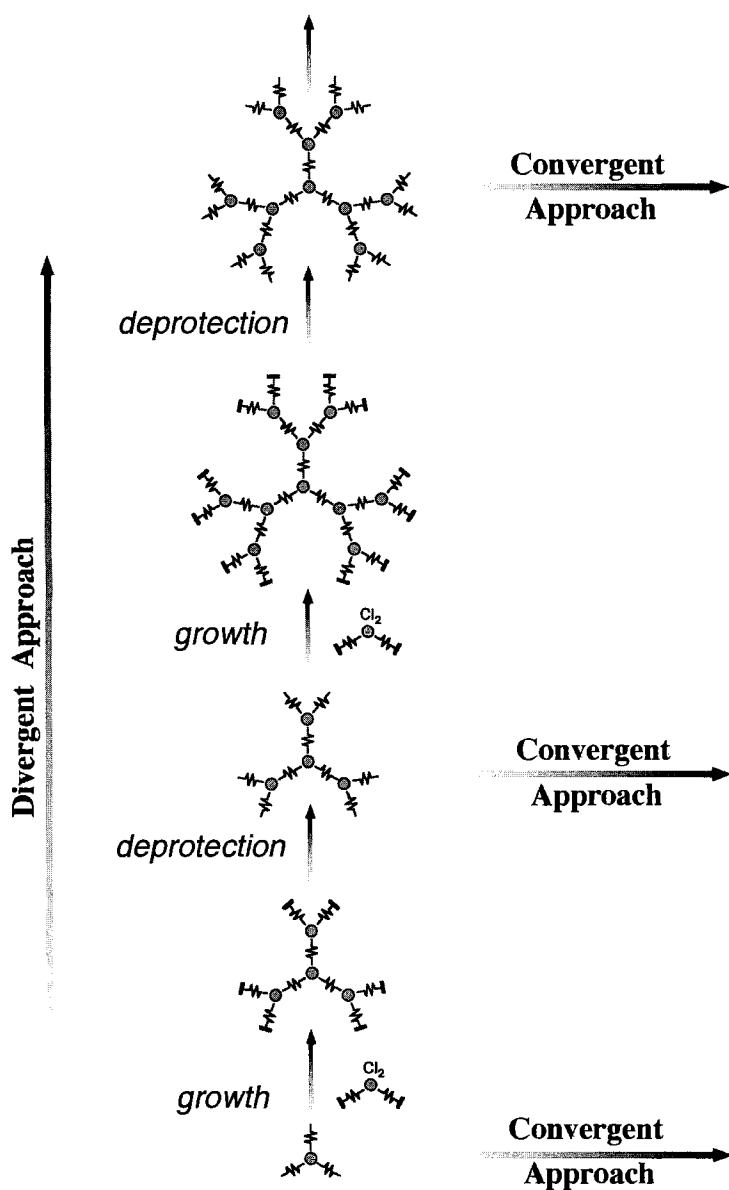


Figure 14. Iterative synthetic strategy for metal-based dendrimers [38].

generation of the dendrimers. As expected, the quantum efficiency decreases with increasing generation. Compound **1** represents a particular case, in that the excitation energy is funneled to the focal point very efficiently (around 98 %), compared with the dendrimers of corresponding dimension of the series **2–7**. In contrast to

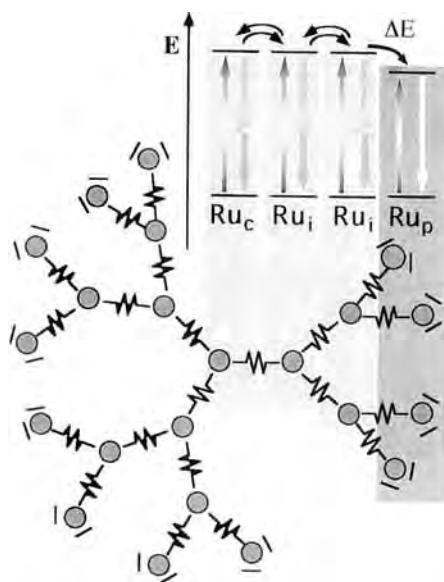


Figure 15. Energy migration pattern across dendritic shells in metal-based dendrimers. In the species represented, all the building blocks contain Ru(II) chromophores and the energy migration from the center to the periphery is quantitative [38].

monodendrons **2–7**, in fact, **1** possesses a variable monomer type at each generation which creates an energy cascade. The ultrafast energy transfer (calculated rate constant for energy transfer from periphery to the core in **1**, $1.9 \times 10^{11} \text{ s}^{-1}$) in this antenna is therefore explained by the presence of the energy gradient.

Other totally organic light-harvesting dendrimers have been developed by Fréchet and co-workers [43]. These species (Figure 18) typically contain coumarin 2 as the donor terminal chromophores and coumarin 343 as the acceptor focal dye. Favorable intramolecular charge transfer takes place in the excited state of these dyes, and this accounts for their high extinction coefficients and high dipole moments, which enhance the dipole–dipole interaction leading to fast singlet–singlet energy transfer via a coulombic mechanism. The energy transfer is thus highly efficient in the first three generations (at least 97 % of quantum efficiency for the process was calculated), and remains significantly efficient for the fourth-generation species (86 %).

Morphology-dependent antenna properties in dendrimers have been reported by Jiang and Aida [44]. They synthesized and investigated a series of dendrimers, of general formula $(L5)_n P$ ($n = 1–4$) having a porphyrin (P) as energy collector, which bear different numbers (n) of five-layered dendron subunits (L5) at the *meso* position of the central porphyrin (Figure 19). Upon irradiation of the dendron subunits in dichloromethane at room temperature, $(L5)_n P$ showed an intramolecular singlet energy transfer which leads to excitation of the central porphyrin core. It was found that tetrasubstituted $(L5)_4 P$ with a spherical morphology exhibited a much higher energy transfer quantum yield (80 %) than the partially substituted $(L5)_1 P$ – $(L5)_3 P$ species (32 % in the most favorable case). Fluorescence depolarization studies of

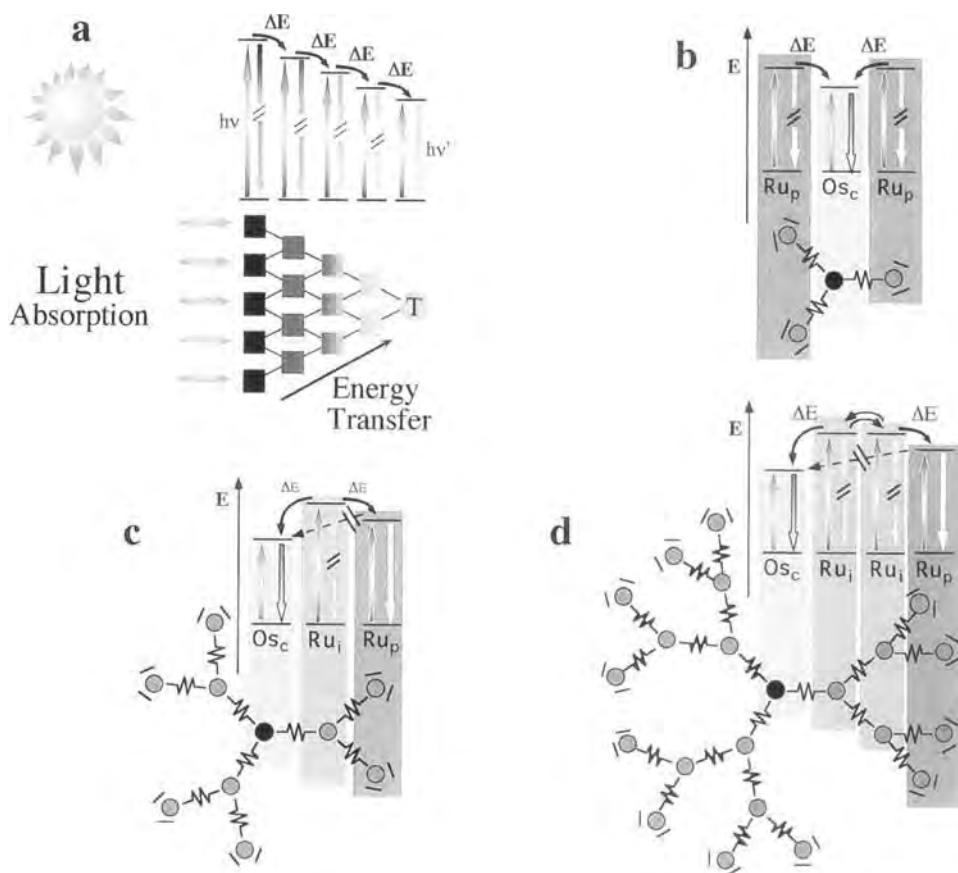


Figure 16. Schematic representation of a) a generic light-harvesting system and b) energy migration patterns for a tetranuclear compound, c) a decanuclear compound, and d) a docosanuclear compound containing one Os(II) species at the center and Ru(II) chromophores in intermediate and peripheral positions. In decanuclear and docosanuclear species, the intermediate chromophores have excited-state energies higher than those of both central and peripheral chromophores. As a consequence, uphill energy transfer steps are present for the energy migration from the peripheral chromophores to the central one and the overall process has poor efficiency [38].

(L5)₄P showed that the excitation energy migrates very efficiently over the various dendron units within the lifetime of the excited state. The four dendrons therefore behave as a single, large chromophore surrounding the energy trap. Consequently, the probability of energy transfer to the porphyrin core may be enhanced.

This hypothesis is schematized in Figure 20 and suggests an interesting similarity between the behavior of this type of antennas and the “wheels” of the natural photosynthetic systems (see above). The energy hopping between the various dendrons enhances the overall efficiency of the antenna, like the way in which ultrafast energy migration within the various chromophores arranged as wheels of LH2 and

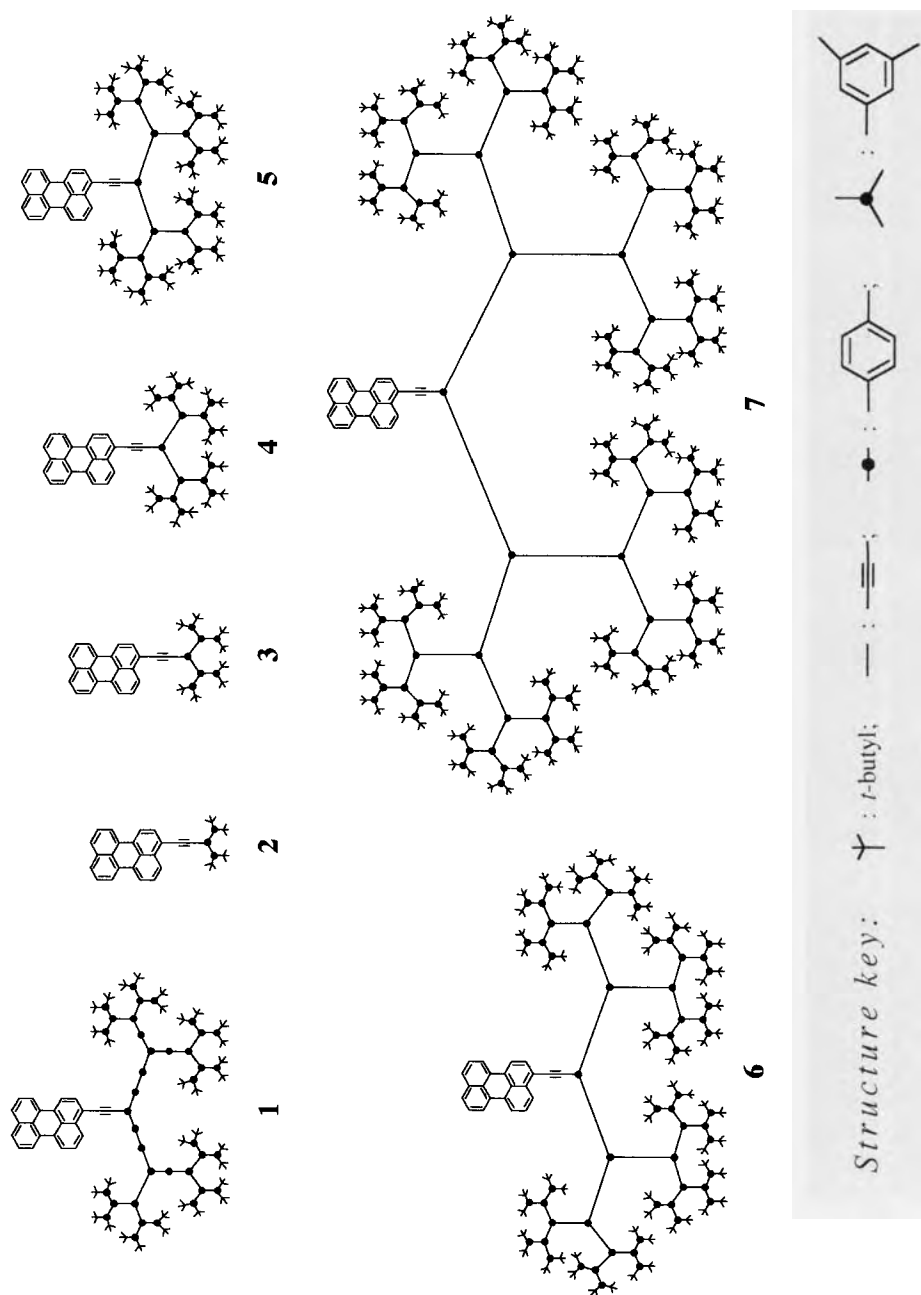


Figure 17. Schematic representation of the light-harvesting dendrimers prepared by Moore and co-workers [42].

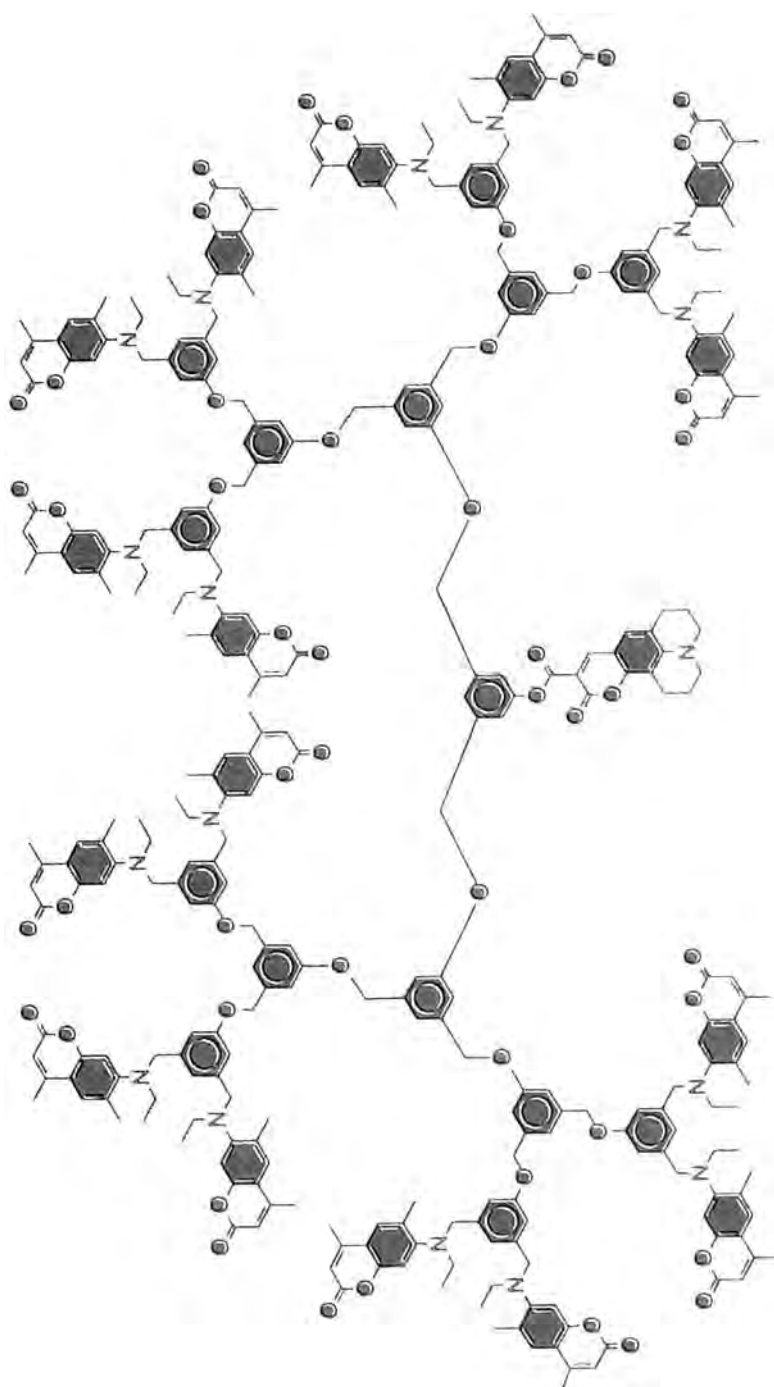


Figure 18. Fréchet's light-harvesting dendrimers [43].

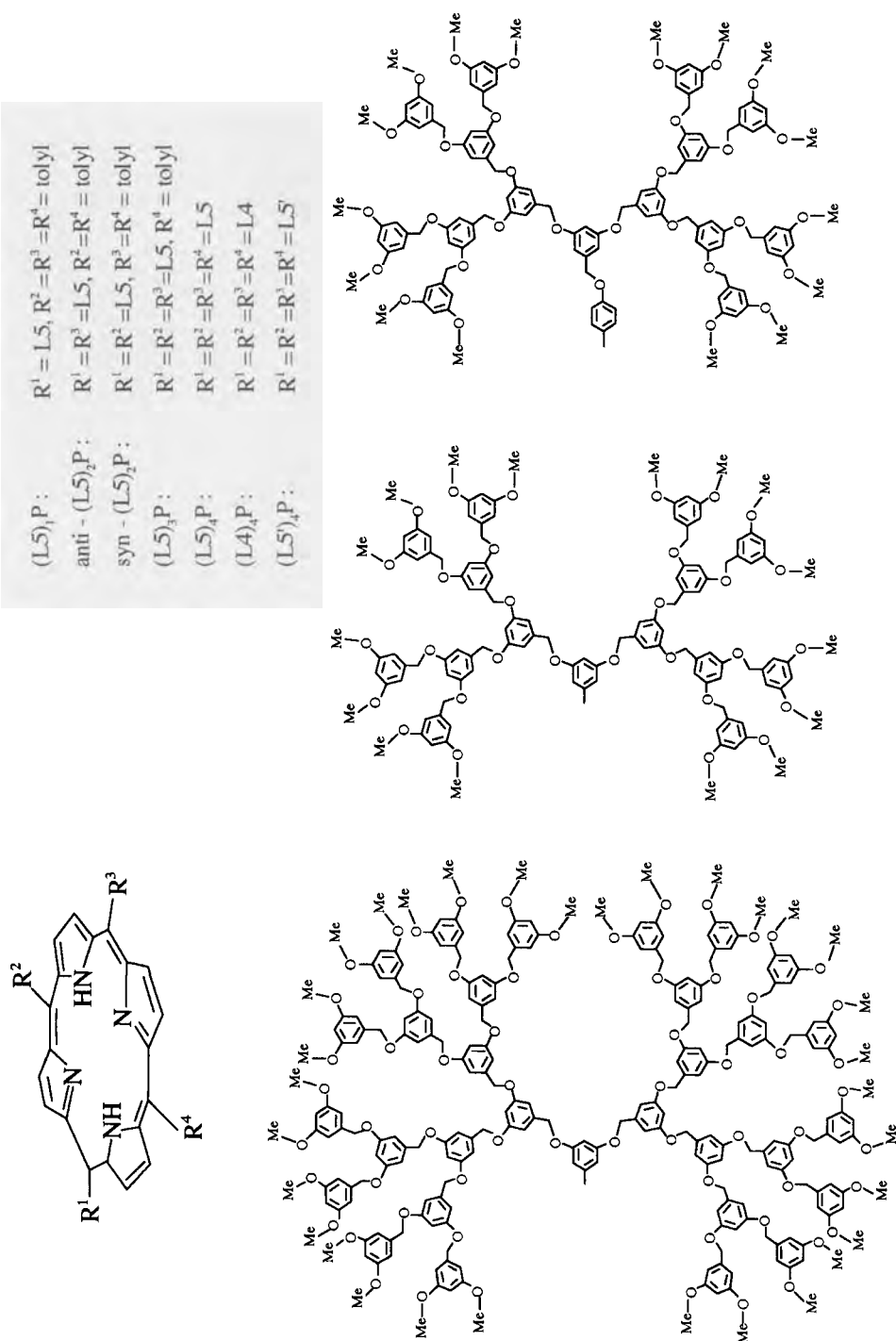


Figure 19. Schematic representation of the antennas reported by Aida and co-workers [44].

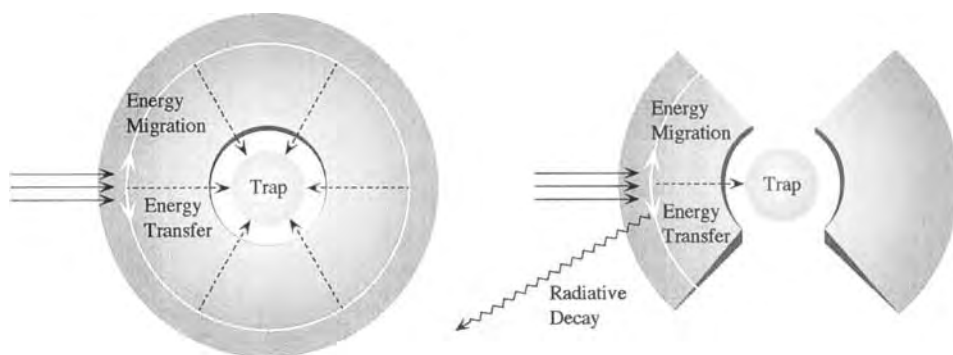


Figure 20. Schematic representations of photochemical events in aryl ether dendrimer porphyrins of spherical (left) and nonspherical (right) morphologies [44].

LH1 systems allows for a quite efficient energy transfer to the reaction center in the natural systems [8].

Stewart and Fox prepared a series of polyether dendrimeric segments (dendrons) end-capped with various chromophores such as pyrenyl and naphthyl groups. They used these species to investigate the possibility of quenching the aromatic chromophores by a suitable electron donor (e.g., a 3-(dimethylamino)phenoxy group), when it was covalently attached to the dendron focal point. The occurrence of the excited-state quenching of the chromophores definitively demonstrated substantial electronic coupling between appended chromophores and quenchers across the dendritic framework [45]. This is a somewhat unusual antenna, anyway, because energy transfer among the chromophores is not necessary to the process.

Miscellaneous

Many other systems, not included in the classes discussed above, are of interest as far as the development of artificial antennas is concerned. Among them, we would like to recall the trichromophoric species developed by McGimpsey and co-workers [46], in which phenyl, naphthyl, and phenanthryl groups are linked by adamantyl and methyl ester bridges. The authors demonstrated that energy migration from the highest-lying chromophore to the lowest-lying one occurs by sequential singlet–singlet and/or triplet–triplet energy transfer steps. Another interesting system is the light-harvesting bilayer membrane studied by Kimura and co-workers [47]. This latter system is composed of two amphiphiles: one having an antenna group (containing *N*-ethylcarbazoyl chromophores, ECz) and the other having an energy-accepting group (an anthryl chromophore) and an electron-accepting group (a viologen). It was demonstrated that efficient energy migration among ECz groups occurs in the membrane until it reaches an ECz which is close to the anthryl group. Then energy transfer from the excited ECz to the anthryl chromophore takes place, and the excited anthryl group successively reduces the viologen electron acceptor. The quantum yield of the overall process depends of course on the ratio of the various

components. However, the number of possible energy migration steps among the ECz molecules, calculated from experimental data and computer simulation, is 78. This figure looks promising for possible developments of this approach.

6.4 Concluding Remarks

In this report we have attempted to summarize briefly the basic principles of construction and functioning of the natural antenna systems, and we have pointed out some of the factors that one should carefully consider in designing artificial antennas for photochemical energy conversion. Then we presented selected examples of different types of artificial antennas recently reported in the literature. Far from pretending to be exhaustive, this list tends to be just an example of the ingenuity of the chemists and of the large and increasing efforts devoted to this field in the last few years. We mainly examined antennas which have been somewhat arbitrarily classified as soluble polymers with appended photoactive subunits (including the special case of cyclodextrin-appended chromophores), multiporphyrins, and dendrimers. Various mechanisms have been found to be responsible for the antenna effect in the different systems, with singlet–singlet (Förster and Dexter) energy transfer usually dominating the purely organic antennas and triplet–triplet energy transfer (mostly of the Dexter type) governing the processes for systems containing heavy transition metals such as Ru(II) and Os(II). This variety of artificial antennas and possible mechanisms, instead of suggesting uncertainty over which systems should be preferred, strongly indicates that there is not a single answer to the problem of designing efficient antennas, and the exploitation of multiple solutions certainly will enrich our possibilities.

On the basis of the studies reported in the last few years, it is clear that the recent significant progress both in mapping the natural systems and in designing sophisticated artificial systems has been made possible by the recent notable advancements of experimental techniques and made-to-order synthesis. Because both the experimental techniques and made-to-order synthesis are continuing to improve fast at the moment, further impressive developments in the field are expected in the near future [48], so bringing the photochemical conversion of solar energy closer.

References

1. a) D. S. Halacy, Jr., *The Coming Age of Solar Energy*, Harper & Row, New York, **1973**; b) D. P. Hader, M. Tevini, *General Photobiology*, Pergamon, Oxford, **1987**; c) *The Photosystems: Structure, Function and Molecular Biology* (Ed.: J. Barber), Elsevier, Amsterdam, **1992**.
2. G. Ciamician, "The Photochemistry of the Future", *Science* **1912**, 36, 38.
3. a) V. Balzani, *New Scientist*, **1994**, issue 1951, p. 30; b) J. M. Durrant, *Chem. Ind.* **1998**, October 19, 838; c) M. Freemantle, *Chem. Eng. News* **1998**, October 26, 37. d) V. Balzani, S. Serroni, *Sci. Spectra*, **2000**, issue 22, p. 28.

4. J. Deisenhofer, O. Epp, K. Miki, R. Huber, H. Michel, *Nature* **1985**, 318, 618.
5. a) A. Yu. Borisov, A. M. Friedberg, V. I. Godik, K. K. Rebane, K. K. Timpmann, *Biochim. Biophys. Acta* **1985**, 807, 221; b) V. Sundström, R. Van Grondelle, H. Bergström, E. Åkesson, T. Gillbro, *Biochim. Biophys. Acta* **1986**, 851, 431.
6. a) M. Du, X. Xie, Y. Jia, L. Mets, G. R. Fleming, *Chem. Phys. Lett.* **1993**, 210, 535; b) S. Hess, E. Åkesson, R. Cogdell, T. Pullerits, V. Sundström, *Biophys. J.* **1995**, 69, 2211; c) Y.-Z. Ma, R. J. Cogdell, T. Gillbro, *J. Phys. Chem. B* **1998**, 102, 881.
7. G. MacDermott, S. M. Prince, A. A. Freer, A. M. Hawthornthwaite-Lawless, M. Z. Papiz, R. J. Cogdell, N. W. Isaacs, *Nature* **1995**, 374, 517.
8. T. Pullerits, V. Sundström, *Acc. Chem. Res.* **1996**, 29, 381 and references therein.
9. R. J. Cogdell, H. Scheer, *Photochem. Photobiol.* **1985**, 42, 669.
10. *Carotenoids in Photosynthesis* (Eds.: A. Young, G. Britton), Chapman & Hall, London, **1993**.
11. S. Karrash, P. A. Bullough, R. Ghosh, *EMBO J.* **1995**, 14, 631.
12. a) A. M. Kleinherenbrink, G. Deinum, S. C. M. Otte, A. J. Hoff, J. Ames, *Biochim. Biophys. Acta*, **1992**, 1099, 175; b) K. Timpmann, F. G. Zhang, A. Freiberg, V. Sundström, *Biochim. Biophys. Acta* **1993**, 1183, 185; c) K. Timpmann, A. Freiberg, V. Sundström, *Chem. Phys.* **1995**, 194, 275.
13. Th. Förster, *Discuss. Faraday Soc.* **1959**, 27, 7.
14. The emission spectrum of the sun consists approximately of 9 % UV light, 40 % visible, and 51 % IR [1]. Only UV, visible, and a small fraction of the near-IR can cause electronic excitation. Furthermore, we have to take into account that the excitation energy collected should be enough to drive the chemical reactions we would like to use to store the solar energy. Therefore, any practical photochemical solar energy conversion system has to be based on visible light absorption.
15. D. L. Dexter, *J. Chem. Phys.* **1953**, 21, 836.
16. a) J.M. Lehn, *Supramolecular Chemistry*, VCH, Weinheim, **1995**; b) V. Balzani, F. Scandola, *Supramolecular Photochemistry*, Horwood, Chichester, **1991**.
17. a) P. F. H. Schwab, M. D. Levin, J. Michl, *Chem. Rev.* **1999**, 99, 1863; b) *Molecular Electronics: Science and Technology* (Eds.: A. Aviram, M. A. Ratner), New York Academy of Sciences, New York, **1998**; c) W. B. Davies, W. A. Svec, M. A. Ratner, M. R. Wasielewski, *Nature* **1998**, 369, 60; d) F. Barigelletti, L. Flamigni, *Chem. Soc. Rev.* **2000**, 29, 1.
18. V. Balzani, A. Credi, F. Scandola in *Transition Metals in Supramolecular Chemistry* (Eds.: L. Fabbrizzi, A. Poggi), Kluwer, Amsterdam, **1994**, p. 1.
19. a) N. Sabbatini, S. Perathoner, V. Balzani, B. Alpha, J.-M. Lehn in *Supramolecular Photochemistry* (Ed.: V. Balzani), Reidel, Dordrecht, **1987**, p. 187; b) N. Sabbatini, M. Guardigli, J.-M. Lehn, *Coord. Chem. Rev.* **1993**, 123, 201 and references therein.
20. a) G. A. Crosby, R. J. Watts, D. H. Carstens, *Science* **1970**, 170, 1195; b) T. J. Meyer, *Pure Appl. Chem.* **1986**, 58, 1193; c) A. Juris, V. Balzani, F. Barigelletti, S. Campagna, P. Belser, A. von Zelewsky, *Coord. Chem. Rev.* **1988**, 88, 85.
21. See, for example: a) D. Parker, J. A. G. Williams, *J. Chem. Soc. Dalton Trans.* **1996**, 3613; b) C. Piguet, G. Bernardinelli, G. Hopfgartner, *Chem. Rev.* **1997**, 97, 2005; c) T. Gunnlaugsson, D. Parker, *Chem. Commun.* **1998**, 511; d) S. W. Magennis, S. Parsdons, A. Corval, J. D. Woollins, Z. Pikramenou, *Chem. Commun.* **1999**, 61; e) M. H. V. Werts, M. A. Duin, J. W. Hofstra, J. W. Verhoeven, *Chem. Commun.* **1999**, 799 and references therein.
22. a) M. Nowakowska, B. White, J. E. Guillet, *Macromolecules* **1988**, 21, 3430; b) M. Nowakowska, E. Sustar, J. E. Guillet, *J. Am. Chem. Soc.* **1991**, 113, 253; c) M. Nowakowska, V. P. Foyle, J. E. Guillet, *J. Am. Chem. Soc.* **1993**, 115, 5975; d) D. M. Gravett, J. E. Guillet, *Macromolecules* **1996**, 29, 617.
23. M. Nowakowska, J. E. Guillet, *J. Photochem. Photobiol. A: Chem.* **1998**, 112, 285.
24. a) L. A. Worl, G. F. Strouse, J. N. Younathan, S. M. Baxter, T. J. Meyer, *J. Am. Chem. Soc.* **1990**, 112, 7571; b) S. M. Baxter, W. E. Jr. Jones, E. Danielson, L.A. Worl, G. Strouse, J. Younathan, T. J. Meyer, *Coord. Chem. Rev.* **1991**, 111, 47; c) J. Younathan, W. E. Jones, Jr., T. J. Meyer, *J. Phys. Chem.* **1991**, 95, 488; d) W. E. Jones, Jr., S. M. Baxter, G. Strouse, T. J. Meyer, *J. Am. Chem. Soc.* **1993**, 115, 7363; e) L. M. Dupray, M. Devenney, D. R. Striplin, T. J. Meyer, *J. Am. Chem. Soc.* **1997**, 119, 10234; f) D. A. Friesen, T. Kajita, E. Danielson, T. J. Meyer, *Inorg. Chem.* **1998**, 37, 2756.

25. C. A. Slate, D. R. Striplin, J. A. Moss, P. Chen, B. W. Erickson, T. J. Meyer, *J. Am. Chem. Soc.* **1998**, *120*, 4885 and references therein.
26. a) D. M. Watkins, M. A. Fox, *Macromolecules* **1995**, *28*, 4939; b) B. Hong, M. A. Fox, *New J. Chem.* **1995**, *73*, 2101; c) D. M. Watkins, M. A. Fox, *J. Am. Chem. Soc.* **1996**, *118*, 4344.
27. a) M. N. Berberan-Santos, J. Canceill, J. C. Brochen, L. Julien, J.-M. Lehn, J. Pouget, P. Tauc, B. Valeur, *J. Am. Chem. Soc.* **1992**, *114*, 6427; b) M. N. Berberan-Santos, J. Pouget, B. Valeur, J. Canceill, L. Julien, J.-M. Lehn, *J. Phys. Chem.* **1993**, *97*, 11376; c) M. N. Berberan-Santos, J. Canceill, E. Gratton, L. Julien, J.-M. Lehn, P. So, J. Sutin, B. Valeur, *J. Phys. Chem.* **1996**, *100*, 15; d) L. Julien, J. Canceill, B. Valeur, E. Bardez, J.-P. Lefèvre, J.-M. Lehn, V. Marchi-Artzner, R. Pansu, *J. Am. Chem. Soc.* **1996**, *118*, 5432; e) P. F. Wang, L. Julien, B. Valeur, J. S. Filhol, J. Canceill, J.-M. Lehn, *New J. Chem.* **1996**, *20*, 895; f) P. Choppinet, L. Jullien, B. Valeur, *Chem. Eur. J.* **1999**, *5*, 3666.
28. Other representative examples of this family of light-harvesting molecules, not discussed in detail in this overview, can be found in the following references: a) P. Tecilla, R. P. Dixon, G. Slobodkin, D. S. Alavi, D. H. Waldeck, A. D. Hamilton, *J. Am. Chem. Soc.* **1990**, *112*, 9408; b) J. L. Sessler, V. L. Capuano, A. Harriman, *J. Am. Chem. Soc.* **1993**, *115*, 4618; c) J.-P. Collin, A. Harriman, V. Heitz, F. Odobel, J.-P. Sauvage, *J. Am. Chem. Soc.* **1994**, *116*, 5679; d) D. Officer, A. K. Burrell, D. C. W. Reid, *Chem. Commun.* **1996**, 1657; e) C. C. Mak, N. Bampos, J. K. M. Sanders, *Angew. Chem. Int. Ed.* **1998**, *37*, 3020; f) T. E. Clement, D. J. Nurco, K. M. Smith, *Inorg. Chem.* **1998**, *37*, 1150; g) W. T. S. Huck, A. Roher, A. T. Anilkumar, R. H. Fokkens, N. M. M. Nibbering, F. C. J. M. van Veggel, D. N. Reinhoudt, *New J. Chem.* **1998**, 165; h) A. Nakano, A. Osuka, I. Yamazaki, T. Yamazaki, Y. Nishimura, *Angew. Chem. Int. Ed.* **1998**, *37*, 3023; i) M. R. Johnston, M. J. Gunter, R. N. Warrener, *Chem. Commun.* **1998**, 2739; j) R. Kumble, S. Palese, V. S. Y. Lin, M. J. Therien, R. M. Hochstrasser, *J. Am. Chem. Soc.* **1999**, *120*, 11489; k) L. Flamigni, F. Barigelletti, N. Armaroli, B. Ventura, J.-P. Collin, J.-P. Sauvage, J. A. G. Williams, *Inorg. Chem.* **1999**, *38*, 661; l) A. Prodi, M. T. Indelli, C. J. Kleverlaan, F. Scandola, E. Alessio, T. Gianferrara, L. G. Marzilli, *Chem. Eur. J.* **1999**, *5*, 2668; m) M. S. Vollmer, F. Würthner, F. Effenberger, P. Emele, D. U. Meyer, T. Stümpfig, H. Port, H. C. Wolf, *Chem. Eur. J.*, **1998**, *4*, 260.
29. a) S. Prathapan, T. E. Johnson, J. S. Lindsey, *J. Am. Chem. Soc.* **1993**, *115*, 7519; b) R. W. Wagner, J. S. Lindsey, *J. Am. Chem. Soc.* **1994**, *116*, 9759; c) R. W. Wagner, T. E. Johnson, J. S. Lindsey, *J. Am. Chem. Soc.* **1996**, *118*, 11166; d) J. Seth, V. Palaniappan, R. W. Wagner, T. E. Johnson, J. S. Lindsey, *J. Am. Chem. Soc.* **1996**, *118*, 11194; e) A. A. Bothner, J. Dadok, T. E. Johnson, J. S. Lindsey, *J. Phys. Chem.* **1996**, *100*, 17551; f) S. I. Yang, R. K. Lammi, J. A. Riggs, T. Arai, D. Kim, D. F. Bocian, D. Holten, J. S. Lindsey, *J. Phys. Chem. B* **1998**, *102*, 9426.
30. S. I. Yang, J. Seth, T. Balasubramanian, D. Kim, J. S. Lindsey, D. Holten, D. F. Bocian, *J. Am. Chem. Soc.* **1999**, *121*, 4008.
31. a) F. Li, S. I. Yang, Y. Ciringh, J. Seth, C. H. M. Martin III, D. L. Singh, D. Kim, R. R. Birge, D. F. Bocian, D. Holten, J. S. Lindsey, *J. Am. Chem. Soc.* **1998**, *120*, 10001; b) J. Li, J. S. Lindsey, *J. Org. Chem.* **1999**, *64*, 9101.
32. P. G. Van Patten, A. P. Shreve, J. S. Lindsey, R. J. Donohoe, *J. Phys. Chem. B* **1998**, *102*, 4209.
33. a) D. Kuciauskas, P. A. Liddell, S. Lin, T. E. Johnson, S. J. Weghorn, J. S. Lindsey, A. L. Moore, T. A. Moore, D. Gust, *J. Am. Chem. Soc.* **1999**, *121*, 8604. For some examples of charge-separation devices developed by Gust, Moore, and co-workers, see: b) D. Gust, T. A. Moore, A. L. Moore; *Acc. Chem. Res.* **1993**, *26*, 198 and references therein; c) D. Kuciauskas, P. A. Liddell, S. C. Hung, S. Lin, S. Stone, G. R. Seely, A. L. Moore, T. A. Moore, D. Gust, *J. Phys. Chem. B* **1997**, *101*, 429; d) G. Steinberg-Yfrach, P. A. Liddell, S. C. Hung, A. L. Moore, T. A. Moore, D. Gust, *Nature* **1997**, *385*, 239; e) J. P. Sumida, P. A. Liddell, S. Lin, A. N. Macpherson, G. R. Seely, A. L. Moore, T. A. Moore, D. Gust, *J. Phys. Chem. A* **1998**, *102*, 5512.
34. C. A. Hunter, R. K. Hyde, *Angew. Chem. Int. Ed. Engl.* **1996**, *35*, 1936.
35. a) D. A. Tomalia, A. M. Naylor, W. A. Goddard III, *Angew. Chem. Int. Ed. Engl.* **1990**, *29*, 138; b) J. M. J. Fréchet, *Science* **1994**, *263*, 1710; c) N. Ardoin, D. Astruc, *Bull. Soc. Chim. Fr.* **1995**, *132*, 875; d) G. R. Newkome, C. N. Moorefield, F. Vögtle, *Dendritic Molecules. Concepts, Syntheses, Perspectives*, VCH, Weinheim, **1996**; e) M. Venturi, S. Serroni, A. Juris, S. Campa-

- gna, V. Balzani, *Topics Curr. Chem.* **1998**, 197, 193; f) A. W. Bosman, H. M. Janssen, E. W. Meijer, *Chem. Rev.* **1999**, 99, 1665; g) G. R. Newkome, E. He, C. N. Moorefield, *Chem. Rev.* **1999**, 99, 1689.
36. a) A. Bar-Haim, J. Klafter, R. Kopelman, *J. Am. Chem. Soc.* **1997**, 119, 6197; b) A. Bar-Haim, J. Klafter, *J. Phys. Chem. B* **1998**, 102, 1662; c) J. N. Onuchic, S. M. Risser, S. S. Skourtis, D. N. Beratan in *Molecular Electronics, Chemistry for the 21st Century* (Eds.: J. Jortner, M. Ratner), Blackwell Science, Oxford, **1997**, p. 369.
 37. a) G. Denti, S. Campagna, L. Sabatino, S. Serroni, M. Ciano, V. Balzani, *Inorg. Chem.* **1990**, 29, 4750; b) G. Denti, S. Campagna, S. Serroni, M. Ciano, V. Balzani, *J. Am. Chem. Soc.* **1992**, 114, 2944; c) S. Serroni, G. Denti, S. Campagna, A. Juris, M. Ciano, V. Balzani, *Angew. Chem. Int. Ed. Engl.* **1992**, 31, 1493; d) A. Juris, V. Balzani, S. Campagna, G. Denti, S. Serroni, G. Frei, H. U. Güdel, *Inorg. Chem.* **1994**, 33, 1491; e) S. Serroni, A. Juris, S. Campagna, M. Venturi, G. Denti, V. Balzani, *J. Am. Chem. Soc.* **1994**, 116, 9086; f) S. Serroni, S. Campagna, A. Juris, M. Venturi, V. Balzani, G. Denti, *Gazz. Chim. Ital.* **1994**, 124, 423; g) S. Campagna, G. Denti, S. Serroni, A. Juris, M. Venturi, V. Ricevuto, V. Balzani, *Chem. Eur. J.* **1995**, 1, 211; h) S. Serroni, S. Campagna, G. Denti, T. E. Keyes, J. G. Vos, *Inorg. Chem.* **1996**, 35, 4513; i) S. Serroni, A. Juris, M. Venturi, S. Campagna, I. Resino Resino, G. Denti, A. Credi, V. Balzani, *J. Mater. Chem.* **1997**, 7, 1227; j) M. Marcaccio, F. Paolucci, C. Paradisi, S. Roffia, C. Fontanesi, L. J. Yellowlees, S. Serroni, S. Campagna, G. Denti, V. Balzani, *J. Am. Chem. Soc.* **1999**, 121, 10081.
 38. V. Balzani, S. Campagna, G. Denti, A. Juris, S. Serroni, M. Venturi, *Acc. Chem. Res.* **1998**, 31, 26.
 39. G. Denti, S. Serroni, S. Campagna, A. Juris, M. Ciano, V. Balzani in *Perspectives in Coordination Chemistry* (Eds.: A.F. Williams, C. Floriani, A.E. Merbach), Verlag Helvetica Acta, Basel, **1992**, p. 153.
 40. a) V. Balzani, S. Campagna, G. Denti, A. Juris, S. Serroni, M. Venturi, *Solar Energy Materials and Solar Cells* **1995**, 38, 159; b) V. Balzani, A. Juris, M. Pink, M. Venturi, S. Campagna, S. Serroni in *Conjugated Polymers, Oligomers, and Dendrimers: from Polyacetylene to DNA* (Ed.: J.-L. Brédas), De Boeck-Université, Bruxelles, **1999**, p. 291 and references therein.
 41. a) V. Balzani, F. Scandola, *Supramolecular Photochemistry*, Horwood, Chichester, **1991**, chapter 6; b) J. R. Shaw, G. S. Sadler, W. F. Wacholtz, C. K. Ryu, R. H. Schmehl, *New J. Chem.* **1996**, 20, 749; c) V. Balzani, A. Juris, M. Venturi, S. Campagna, S. Serroni, *Chem. Rev.* **1996**, 96, 759 and references therein.
 42. C. Devadoss, P. Bharathi, J. S. Moore, *J. Am. Chem. Soc.* **1996**, 118, 9635 and references therein.
 43. S. L. Gilat, A. Adronov, J. M. J. Fréchet, *Angew. Chem. Int. Ed.* **1999**, 38, 1422 and references therein.
 44. D.-L. Jiang, T. Aida, *J. Am. Chem. Soc.* **1998**, 120, 10895 and references therein.
 45. G. M. Stewart, M. A. Fox, *J. Am. Chem. Soc.* **1996**, 118, 4354.
 46. a) W. G. McGimpsey, W. N. Samaniego, L. Chen, F. Wang, *J. Phys. Chem. A* **1998**, 102, 8679; b) Z. Tan, R. Kote, W. N. Samaniego, S. J. Weininger, W. G. McGimpsey, *J. Phys. Chem. A* **1999**, 103, 7612.
 47. T. Morita, S. Kimura, Y. Imanashi, *J. Am. Chem. Soc.* **1999**, 121, 581.
 48. For example, artificial antennas based on noncovalent interactions can contribute extensively to the field. A typical recent case is reported in Ref. [49]. Other, still rarely considered, aspects of the natural systems could also play a role in the development of artificial systems. In this regard, of particular interest appear to be some investigations [50] dealing with the design of artificial light-harvesting systems which may spontaneously evolve toward greater efficiency under light illumination, a feature that at the moment remains mostly peculiar to the natural systems.
 49. S. L. Springs, D. Gosztola, M. R. Wasielewski, V. Kral, A. Andrievsky, J. L. Sessler, *J. Am. Chem. Soc.* **1999**, 121, 2281.
 50. a) K. K. Rebane, *J. Phys. Chem.* **1992**, 96, 9583; b) B. A. Gregg, U. Resch, *J. Photochem. Photobiol. A: Chem.* **1995**, 87, 157.

7 Memories

Masahiro Irie and Kenji Matsuda

7.1 Introduction

Information storage technologies, which provide high memory density, high capacity, and fast access, are indispensable to a highly developed information-based society. Although magnetic recording media such as magnetic tapes and hard disks have been used in mass memories, they are being challenged on several fronts with optical recording. Optical digital recording utilizes focused laser light to effect some optical property changes in the memory media which can be subsequently read back by the laser. The memory spot size can be reduced to as small as the wavelength of light. Therefore, the area memory density is higher than that of conventional magnetic recording. Optical digital recording is one of the most promising information storage technologies.

Although it has long been a dream of organic photochemists to use organic molecular materials as the optical memory media, the media mainly developed so far have been inorganic ones, which utilize the magneto-optic (MO) effect or phase change (PC) as the basis of optical recording. Nowadays, the situation is dramatically changing. CD-R (compact disk—recordable) disks which use organic dyes as the memory media have been developed and widely accepted as data storage as well as audio–video recording media. The number of CD-R disks supplied to the worldwide market in 1999 was as large as 2×10^9 , which was similar to the number of floppy disks. CD-Rs are compatible with CDs and CD-ROMs and the memory density is 650 MB. A new version, the DVD-R (digital versatile disk—recordable), has a density as high as 3.95 GB. The memory layer of a CD-R is prepared by spin-coating the organic dyes on the polycarbonate disk covered with gold or silver and used as the memory layer. The coated dyes are photoexcited with the focused laser light and decomposed thermally as well as photochemically. The decomposition of dyes results in changes in the shape and the refractive index of the recorded areas, which induce the reflection changes. The reflection changes can be read out by the laser. Organic dyes are the third generation of organic molecular materials, which

are used practically in opto-electronic devices (the first generation was liquid crystals; the second, organic photoconductors).

In principle, any kinds of organic dyes which undergo photochemical reactions by irradiation with visible laser light (635–830 nm) can be used as the memory media. The photochemical reactions can be detected by changes in refractive index as well as in absorption properties. Although most of photochemical reactions are irreversible, some organic dyes undergo reversible photochemical reactions (*photochromism*) and the photochromic dyes are potentially applicable to erasable optical memory media.

In this chapter the properties of organic molecules which are potentially useful as archival digital optical memory media, mainly erasable media, will be described. The memory media which require wet development/fixing processes will not be mentioned. Photopolymers and photoresists are also beyond the scope of this chapter.

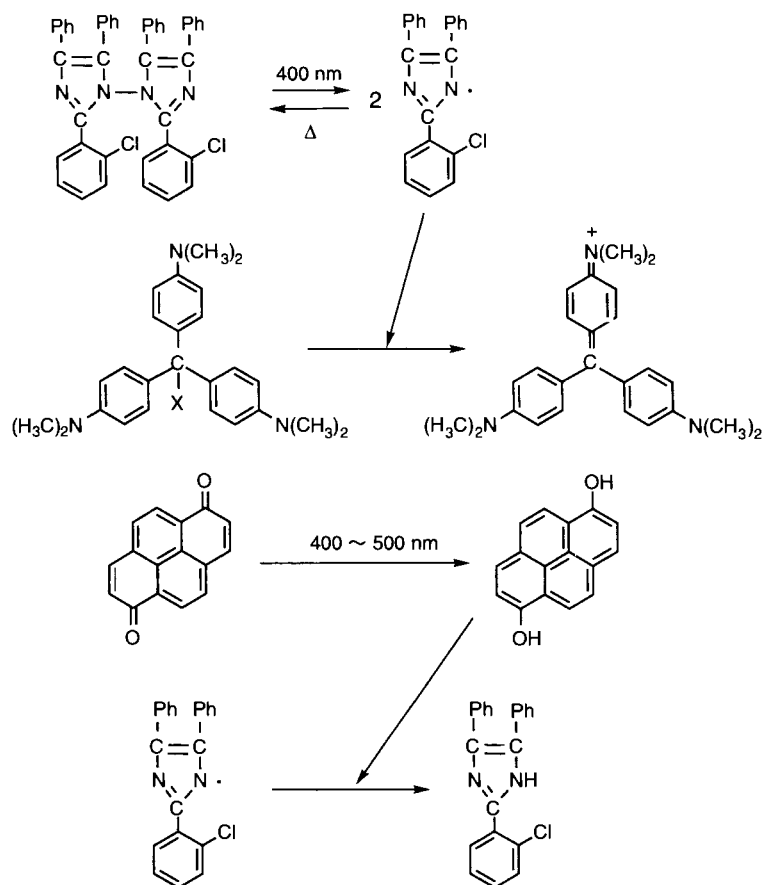
7.2 Irreversible Memory Media

In the 1960s various types of photosensitive organic molecular materials were developed in an attempt to apply them to non-silver photographic systems. Although those materials and processes cannot be directly applied to modern digital optical memory systems, it is worthwhile to note them because useful basic ideas for constructing photosensitive systems were involved. Typical examples are shown in Table 1. In the first case the colored species are formed by radicals, which are produced by the electron transfer reaction from photoexcited amines to tetrabromomethane (Scheme 1) [1–3]. The tetrabromomethane can be eliminated from the systems just by heating. Thus, photogenerated images are fixed by heating. Although relatively high-sensitivity systems were developed, instability during storage prevented their practical use.

In the second case a violet-colored species (crystal violet) is produced by the photogenerated imidazole radical (Scheme 2). 1,6-Hydroxypyrene which is produced from 1,6-pyrenequinone by visible irradiation quenches the imidazole radical, and the system is fixed.

Other interesting photosensitive materials are alkylborates of cyanine dyes [5, 6]. An electron transfer from the alkylborate anion to the photoexcited cyanine dye causes the decomposition of the alkylborate to produce colorless alkyl-substituted cyanine dye derivatives (Scheme 3). The color of the cyanine dyes is bleached by photoirradiation. By mixing three kinds of alkylborates of cyanine dyes, yellow, magenta, and cyan, with vinyl monomers it is possible to construct a full color printing system.

As described in Section 7.1, a modern digital optical memory system, the CD-R, uses organic dyes as the memory layer. The dyes used are shown in Figure 1. All these dyes have absorption tails around 780 nm, where the recording laser has the emitting line. At the absorption tails the dyes show the maximum refractive index



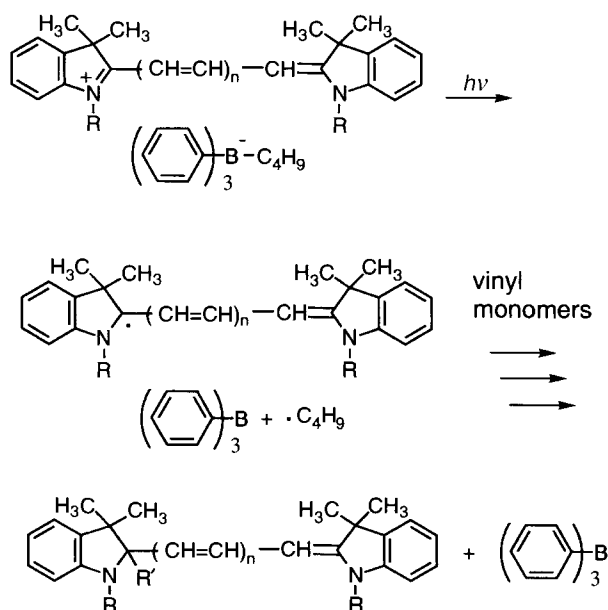
Scheme 2.

changes. Therefore, their decomposition by laser light induces large changes in the refractive index or the reflection in the recorded area. At present much effort has been put into developing dyes suitable for DVD-Rs, which have absorption tails around 635–650 nm.

Various photopolymer systems have also been developed for analog as well as digital holographic memories and photoresists (see Refs. [7, 8] for details).

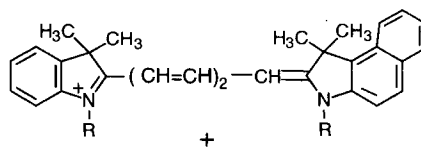
7.3 Reversible Memory Media

As described above, write-once optical disks (CD-R and DVD-R) using organic molecular materials are now commercially available. The next target is to develop erasable memory media. At present inorganic materials, such as magneto-optic or

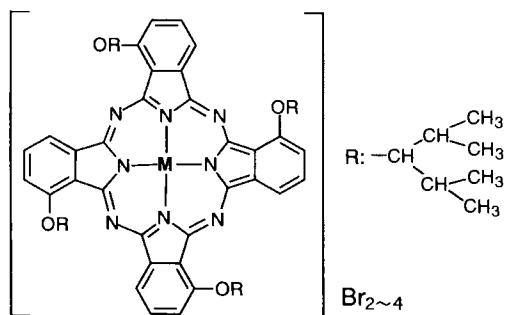
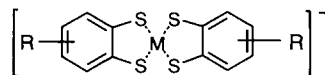


Scheme 3.

Cyanine Dyes



Phthalocyanine Dyes



Metal Chelates of Azo Dyes

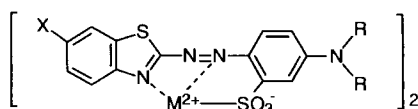


Figure 1.

phase-change materials, are used as the erasable media. These media are driven by a heat-mode optical recording method. Photon energy of the laser light is converted to heat energy on the recording media and used for recording. The memory density of the heat-mode recording is restricted by the diffraction limit of the laser light. Therefore, it is impossible in principle to increase the area memory density further. One possible way to overcome the limit is to explore photon-mode recording, which fully utilizes the versatile functions of light, such as wavelength (frequency), phase, polarity, and so on [9]. One of the candidates for photon-mode erasable media is photochromic molecules.

Photochromic molecules which can be used as the erasable memory media are required to have following properties.

- 1) archival storage capability (thermal stability of both isomers);
- 2) low fatigue (can be cycled many times without loss of performance);
- 3) high sensitivity and rapid response;
- 4) nondestructive reactivity.

Among these requirements, the most important are the thermal stability of both isomers and fatigue resistance. Although so many photochromic molecules have been reported, molecules which undergo thermally irreversible photochromic reactions are limited. Table 2 shows some typical photochromic molecules and their reactions. Thermally reversible photochromic molecules, such as azobenzene, spirobenzopyran, naphthopyran, thioindigo, anthracene dimer, dihydroazulene, and dihydroindolizine, cannot be used as the memory media. Although several attempts have been carried out to stabilize such unstable photochromic molecules by dispersing them in high- T_g polymer matrices [10], the stability is not sufficient for practical applications. Aggregate formation is another approach to stabilizing the photogenerated isomers [11], but the reversibility of the system is poor. So far, thermally irreversible molecules are limited to diarylethenes with heterocyclic aryl groups, furyl fulgides, naphthacenequinone, and sterically overcrowded stilbene derivatives. The photochromic properties of these molecules and their application to memory media will be described below.

7.3.1 Diarylethenes

cis-Stilbene is known to undergo a reversible photocyclization reaction to produce dihydrophenanthrene in the absence of oxygen. In the presence of air, however, the dihydrophenanthrene is irreversibly converted to phenanthrene by hydrogen elimination with oxygen (Eq. (1)).

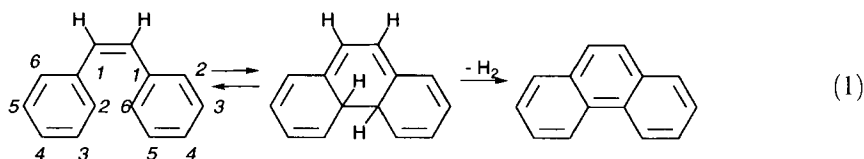


Table 2. Photochromic molecules.

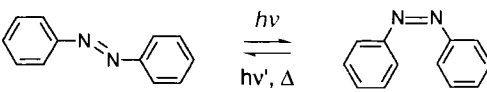
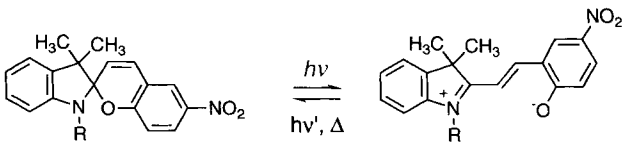
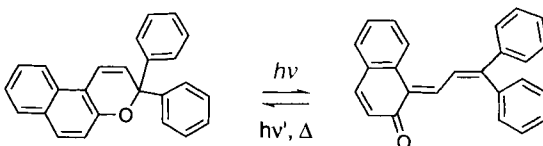
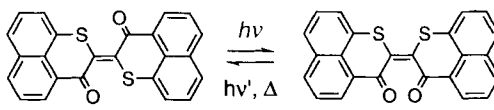
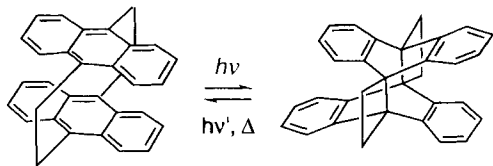
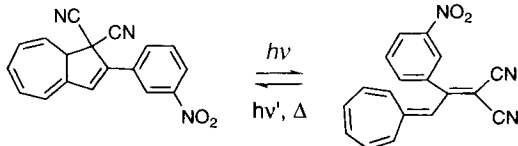
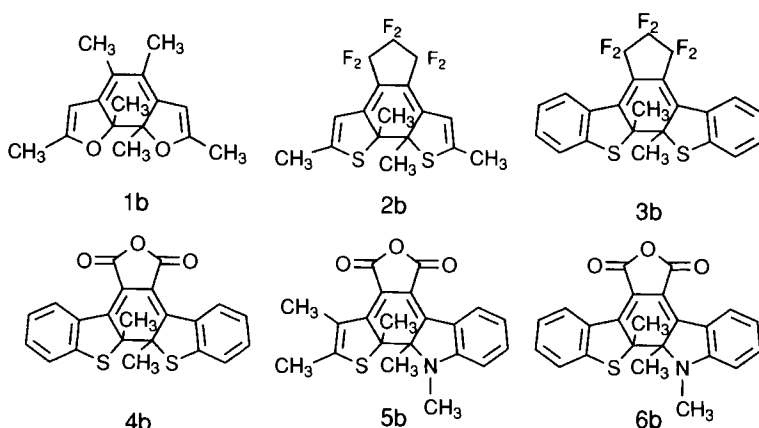
Name	Reaction
Azobenzene	
Spirobenzopyran	
Naphthopyran	
Thioindigo	
Anthracene dimer	
Dihydroazulene	

Table 2 (continued)

Name	Reaction
Dihydroindolizine	
Diarylethene	
Furyl fulgide	
Naphthacene quinone	
Stilbene derivative	

When methyl groups were substituted at the 2- and 6-positions of the phenyl rings, the molecule underwent a reversible photocyclization reaction, even in the presence of oxygen [12]. The lifetime of the dihydro-type yellow closed-ring isomer was, however, very short and it quickly returned to the colorless open-ring isomer. When the phenyl groups were replaced with heterocyclic five-membered rings, as in bis(2,5-dimethylthiophen-3-yl)perfluorocyclopentene **1a**, the closed-ring isomer **1b** became thermally stable and never returned to the open-ring isomer, even at 100 °C. The red closed-ring isomer **1b**, however, returned to the colorless open-ring isomer

Thermally Stable Compounds



Thermally Unstable Compounds

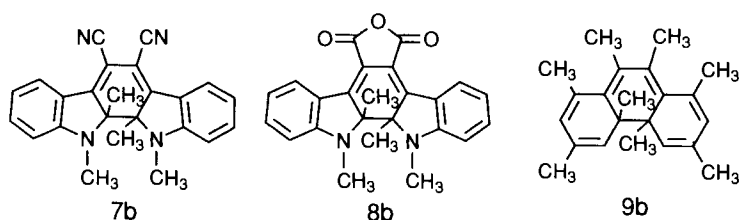
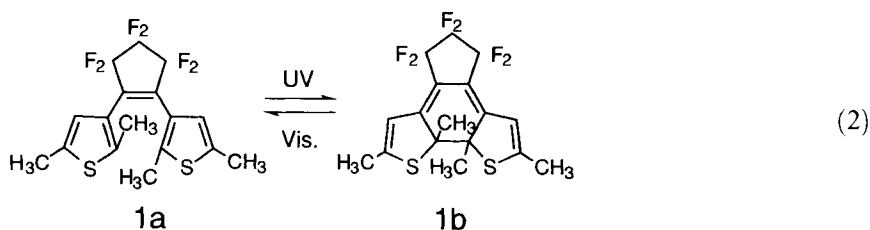


Figure 2. Thermally stable and unstable diarylethenes. The lifetimes of the closed-ring isomers of the thermally stable diarylethenes were longer than 12 h at 80 °C.

by irradiation with visible light (Eq. (2)). The diarylethenes with thiophene aryl groups underwent thermally irreversible photochromic reactions [13].

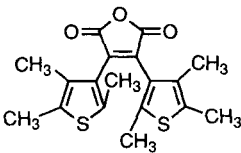
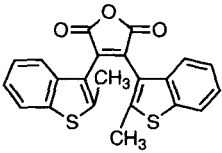
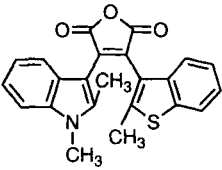
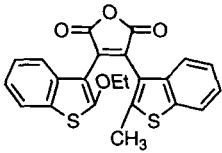
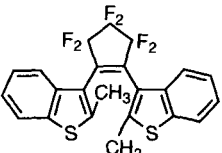


The stability was dependent on the type of aryl group, as shown in Figure 2. When the aryl groups were furan or thiophene rings, which have low aromatic stabilization energies, the closed-ring isomers were thermally stable and did not return to the open-ring isomers in the dark. On the other hand, photogenerated closed-ring isomers of diarylethenes with phenyl or indole rings, which have rather high aromatic stabilization energies, were thermally unstable. The photogenerated yellow color of the closed-ring isomer of 2,3-dimesitylbutene **9b** disappeared with a

half-life of 1.5 min at 20 °C. It returned quickly to the open-ring isomer. The closed-ring isomers of diarylethenes with indole rings, **7b** and **8b**, exhibited thermally reversible reactions. The different thermal stability behavior between diarylethenes with furan or thiophene rings and those with phenyl or indole rings agrees well with the theoretical prediction that the thermal stability depends on the aromatic stabilization energies of the aryl groups [14].

Diarylethenes undergo fatigue-resistant photochromic reactions [13]. Table 3 shows the fatigue-resistant properties of various diarylethenes. Benzene solutions

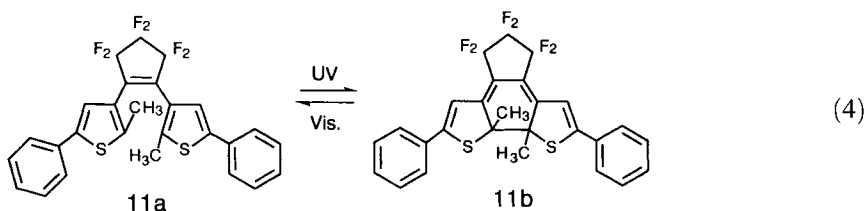
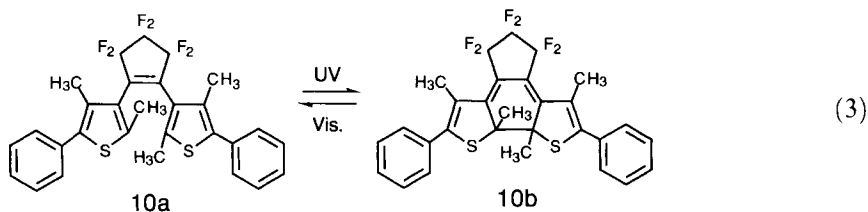
Table 3. Fatigue-resistant properties of diarylethenes in benzene.

Compound	Repeatable cycle number ^a	
	in air	under vacuum
	70	480
	3.7×10^3	1.0×10^4
	—	$>1.1 \times 10^4$
	$>1.0 \times 10^4$	—
	$>1.3 \times 10^4$	—

^a the number of repeatable cycles by which the absorbance of the closed-ring (or open-ring) isomer had decreased to 80 % of that in the first cycle.

containing diarylethenes (ca. 10^{-4} mol L $^{-1}$) were irradiated with shorter-wavelength light until the absorption intensity of the colored isomers reached 90 % of the photostationary state, then the colored isomers were completely bleached by irradiation with longer-wavelength light. This operation was repeated many times. Although diarylmaleic anhydride with thiophene rings cannot repeat the photochromic cycle more than 70 times in the presence of air, bis(2-methyl-1-benzothiophen-3-yl)-perfluorocyclopentene can repeat the cycles more than 1.3×10^4 times. Benzothiophene has much lower reactivity to singlet oxygen, which decomposes diarylethenes, and does not undergo a rearrangement reaction to produce by-products (see below). Diarylethenes with benzothiophene aryl groups undergo thermally irreversible and fatigue-resistant photochromic reactions [13].

It is worthwhile to note the difference in fatigue resistance of compounds **10** and **11** (Eqs. (3) and (4)) [15].



Compound **10a** has methyl groups at the 4- and 4'-positions of the thiophene rings, whereas compound **11a** has no methyl groups at these positions. Figure 3 shows the cycle number dependence of the absorbance of the bleached samples. The absorbance of **10a** remained almost constant even after 850 cycles, while the absorbance of **11a** gradually declined. At the same time a photostable violet product with an absorption maximum at 547 nm was formed. The molecular structure of the by-product is shown in Figure 4. Such by-product formation is the main fatigue process of dithienylethenes which have no methyl groups at the 4- and 4'-positions of the thiophene rings, in the absence of oxygen. The methyl substituents at the 4- and 4'-positions play an important role in improving the fatigue resistance of dithienylethenes.

Most diarylethenes show very large spectral shifts upon photoisomerization from the open- to the closed-ring isomers (>6600 cm $^{-1}$). These shifts are due to π -electron delocalization throughout the two condensed aryl rings. It is interesting to compare the spectral shift among dithienylethenes in which the substitution position of the thiophene rings on the ethene moiety is different, as shown in Eq. (5) [16].

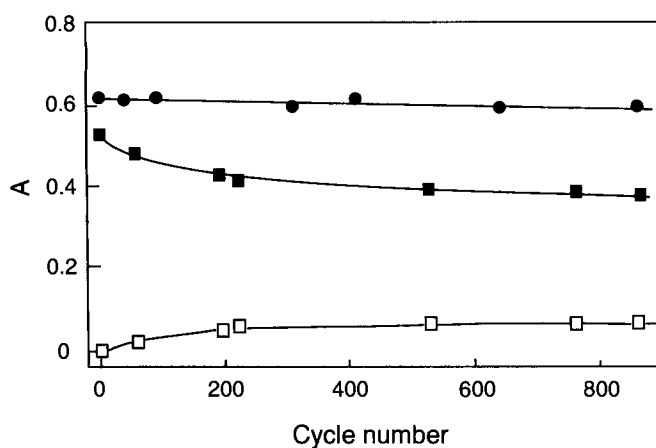


Figure 3. Fatigue resistance of **10** and **11** in deaerated hexane solution. Absorbances of **10a** (●) and **11a** (■) were plotted after irradiation with visible light. The visible absorbance at 547 nm (□), which remained after visible irradiation of a hexane solution containing **11**, was also plotted.

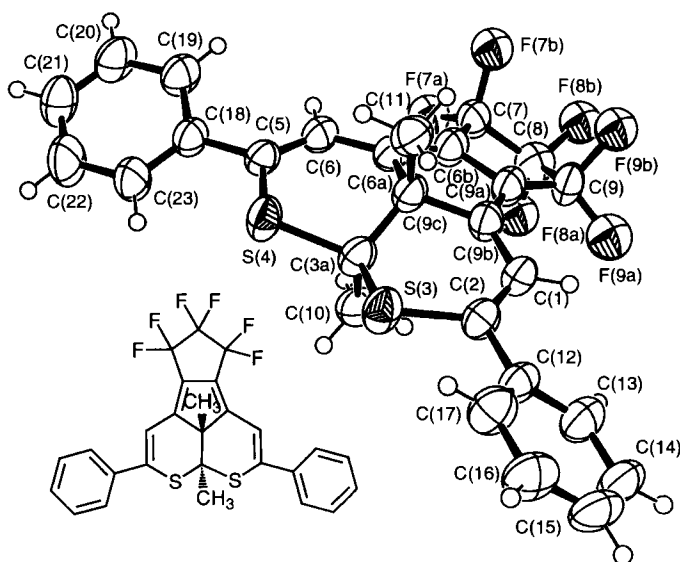
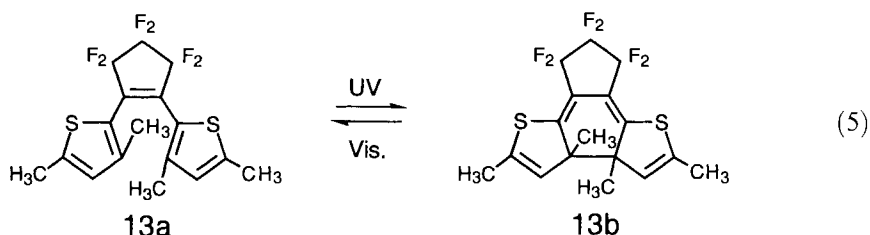


Figure 4. ORTEP view of the by-product from **11a** and its chemical structure.



Photoirradiation of a hexane solution of **13a** with 366 nm light led to a decrease in the absorption at 336 nm and formation of a yellow solution, in which a new band appeared at 425 nm. The absorption maximum is blue-shifted as much as 109 nm in comparison with the maximum of **1b** (see Eq. (2)), in which thiophene rings are attached to the ethene moiety at the 3-positions. The open-ring isomer **13a**, on the other hand, gave an absorption band longer than that of **1a**. The red shift indicates that π -conjugation in the open-ring isomer extends further in the molecule. On the other hand, in **1a** π -conjugation is localized in each thiophene ring. By changing the substitution positions it is possible to control the extent of π -conjugation or the color of the open- and the closed-ring isomers. The diarylethenes so far synthesized cover all colors in the visible region from yellow to blue-green [13].

Practical optical memory media should have nondestructive readout capability. Photochromic reactions, in general, proceed in proportion to the number of photons absorbed by the compounds. Such linear-response characteristics cannot be used as the basis of memory media, because recorded memories are destroyed after many readout operations. There are two approaches to avoid such inconvenience: one is to introduce gated photochromic reactivity to the molecules, and another is to read the recorded memories by using light whose energy cannot induce photochromic reactions. The former approach will be described in this section. The latter approach will be discussed in Section 7.4.

A diarylethene with heterocyclic aryl groups has two conformations with the two rings in mirror and C_2 symmetries, and the cyclization reaction can proceed only from the C_2 symmetry, as shown in Figure 5. The photocyclization is prohibited when the compound is fixed in the mirror symmetry conformation. This means that compounds having special substituents which reversibly fix the conformation undergo gated photochromic reactions (Scheme 4) [17, 18].

The photochromic reaction of **14a** was completely prohibited in cyclohexane because the molecule is fixed in photoinactive mirror symmetry, or parallel conformation, by the intramolecular hydrogen bonding. The addition of a very small amount of ethanol to the cyclohexane solution gained the photochromic reactivity. The addition of ethanol converts the conformation into a photoactive anti-parallel conformation. Ethanol acts as a switch which controls the reactivity of the diarylethene molecule.

The hydrogen bonds can also be broken upon heating. In decalin the photocyclization did not occur below 60°C, but it was clearly observed above 100°C. This molecule has both chemical- and thermal-gated reactivity.

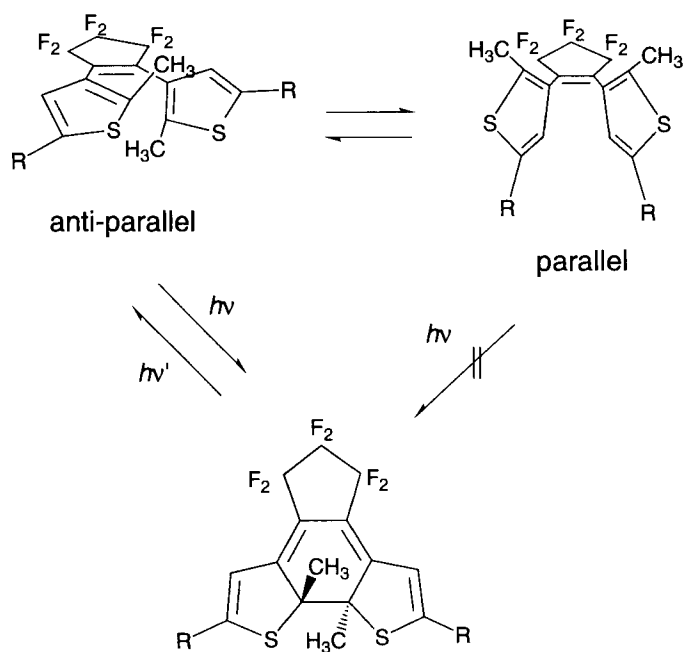
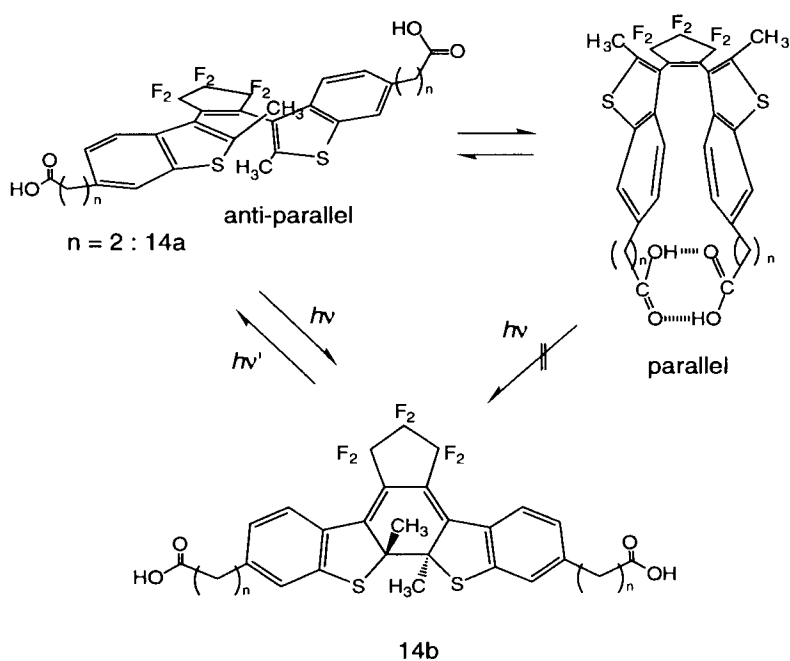
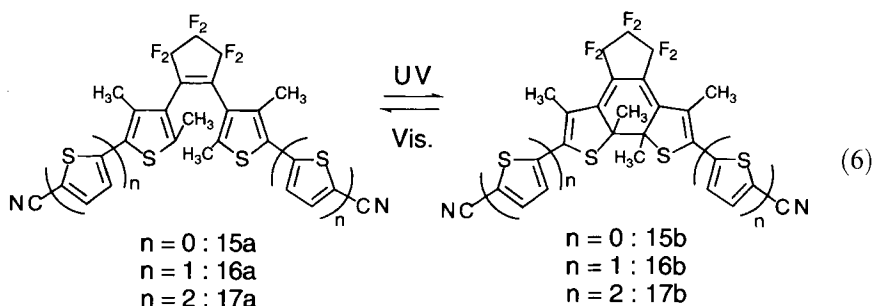


Figure 5. Conformations and photoreactivities of diarylethenes.



Scheme 4.

The diarylethenes **15**–**17** with oligothiophene aryl groups showed a thermal-gated reactivity (Eq. (6)) [19].

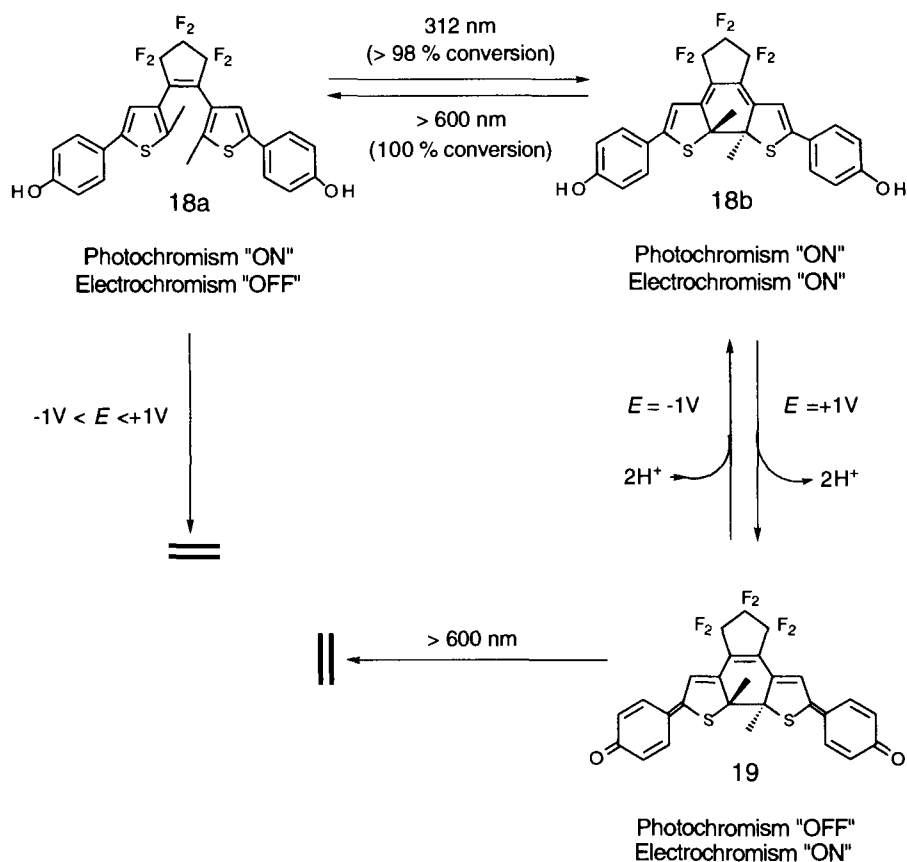


The cycloreversion quantum yield of **17b** ($\Phi = 0.00013$) was much lower than that of **15b** ($\Phi = 0.075$). The very low cycloreversion quantum yield was found to increase steeply as much as 34-fold when the temperature was raised from 25 to 150 °C. The large temperature dependence provides **17** with thermal-gated reactivity. The recorded memory in this system can be read many times with a weak laser, which does not raise the temperature of the medium. The memory can be erased with a high-intensity laser, which can raise the temperature of the medium to as high as 100–150 °C.

Dual-mode switching systems, which combine two reversible processes that can be addressed by two independent stimuli, can be used for nondestructive readout. Such a molecule, **18**, having photochromic and electrochromic active units has been synthesized [20, 21]. Upon irradiation with 312 nm light an acetonitrile solution containing **18a** turned deep blue, for which absorption maxima were observed at 590 and 340 nm. The absorption was due to the closed-ring isomer **18b** (Scheme 5). The conversion was over 98 %. The blue color disappeared upon irradiation with >600 nm light. The electrochemical activity of the two isomers, **18a** and **18b**, was examined in acetonitrile. Whereas the open-ring isomer was electrochemically inert within the –1 to +1 V domain, the closed-ring isomer, which is an extended hydroquinone, presented a reversible oxidation wave at +735 mV (with respect to SCE) corresponding to the formation of quinonoid form **19**. The quinonoid form **19** was photochemically inactive. Irradiation of the acetonitrile solution of **19** with >600 nm light for 8 h resulted in less than a 2 % decrease in the absorbance at the maximum. Thus, in the reduced hydroquinone form **18b** the system is photochromic, while oxidation to the quinonoid form **19** can be used to effectively block the photochemical coloration. Such multi-mode switching was also observed in a photochromic mixture system [22].

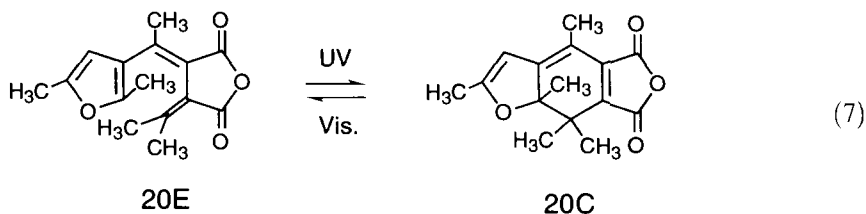
7.3.2 Furyl Fulgide Derivatives

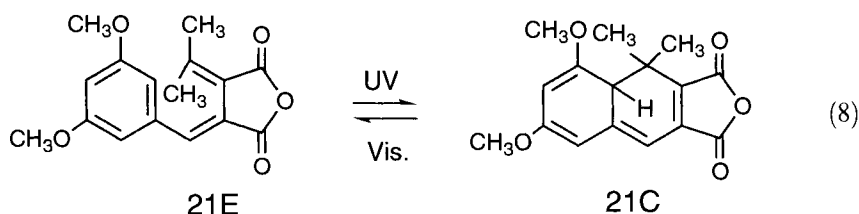
Furyl fulgide **20** (Eq. (7)) is the first known example of thermally irreversible photochromic molecules. Although phenyl fulgides such as **21** have been known to show photochromic reactions, photogenerated dihydronaphthalene derivatives such as **21C** (Eq. (8)) are thermally unstable and undergo irreversible side reactions, i.e., 1,5-hydrogen shifts to produce 1,2-dihydronaphthalene derivatives [23–26]. This



Scheme 5.

undesirable performance was much improved by replacing the phenyl group with a furyl group [27]. Compound **20E** underwent a thermally irreversible photocyclization reaction to produce the closed-ring isomer **20C** quantitatively (Eq. (7)). The rather low cycloreversion quantum yield and the weak absorption band of **20C** in the UV region ($\sim 366 \text{ nm}$) yielded high conversion from the open- to the closed-ring isomer.





The thermal irreversibility of the closed-ring isomer was ascribed to the steric hindrance of the methyl groups at the reactive center; these methyl groups were said to prevent the disrotatory thermal cycloreversion reaction [27, 28]. This is not the case. The thermal stability of the closed-ring isomer of the furyl fulgide is due to the low aromatic stabilization energy of the furyl group, as evidenced in the case of diarylethenes with heterocyclic aryl groups [14]. Because of the low aromatic stabilization energy the ground-state energy difference between the open- and closed-ring isomers becomes small, and this stabilizes the closed-ring isomer.

One of the serious defects of the furyl fulgide is low fatigue resistance. Tomoda and co-workers prepared fulgide derivatives with various types of heterocyclic aryl groups and compared the thermal stability of the colored closed-ring isomers in poly(methyl methacrylate) (PMMA) film and the fatigue resistance [29, 30]. The results are shown in Figures 6 and 7, from which it can be seen that the colored closed-ring isomer of furyl fulgide is not stable. The absorbance of **20C** disappeared after one-day storage in PMMA film at 80 °C. The disappearance is not due to cycloreversion but to decomposition. Furthermore, the coloration/decoloration cycles are limited to fewer than 50 in toluene in the presence of oxygen. Feryl fulgide itself is not fatigue-resistant.

The fatigue resistance was improved when the furyl group was replaced with indole or oxazole [29, 30]. The coloration/decoloration cycles of oxazolyl fulgide **26** could be repeated more than 500 times in toluene, even in the presence of oxygen. The fatigue resistance strongly depends on the aryl groups.

Another defect of fulgide derivatives is solvolysis. The maleic anhydride structure is destroyed in alcohols or protic solvents. To avoid such solvolysis the maleic anhydride structures were changed to maleimides; the maleimide derivatives were stable in alcohol solutions.

Upon UV irradiation the furyl fulgide undergoes not only cyclization but also an *E*–*Z* photoisomerization reaction (Scheme 6). The ratio between the cyclization and the *E*–*Z* isomerization depends on the steric hindrance of substituent R¹. Feryl fulgide derivatives with various R¹ substituents were prepared and the quantum yields were compared [31–34]. The results are summarized in Table 4.

When R¹ was changed from methyl to *n*-propyl, the *E*–*Z* isomerization quantum yield decreased from 0.13 to 0.04. It became almost zero when bulky substituents, such as isopropyl or *t*-butyl, were introduced. At the same time the cyclization quantum yield (Φ_{EC}) increased. The cyclization quantum yield of **31** is four times larger than that of **20**. Introduction of bulky substituents is effective in increasing the coloration quantum yield.

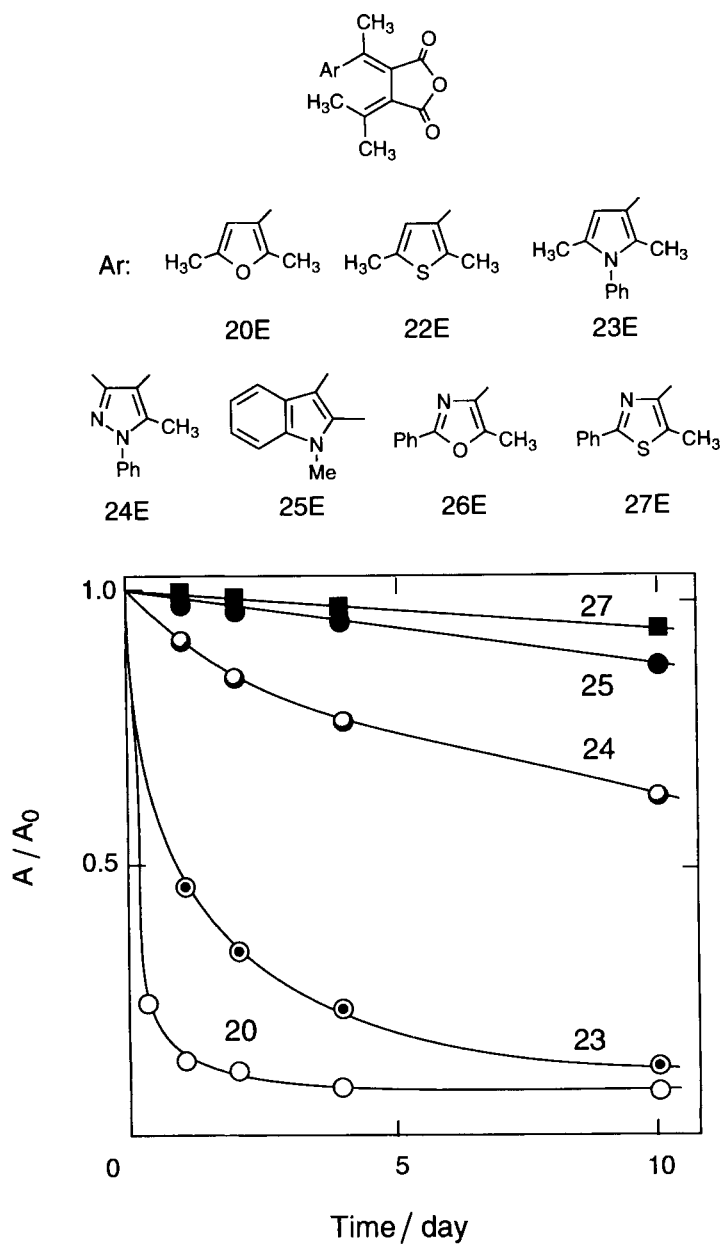


Figure 6. Thermal stability at 80°C of the closed-ring isomers of fulgide derivatives (15–20 wt. % in PMMA film).

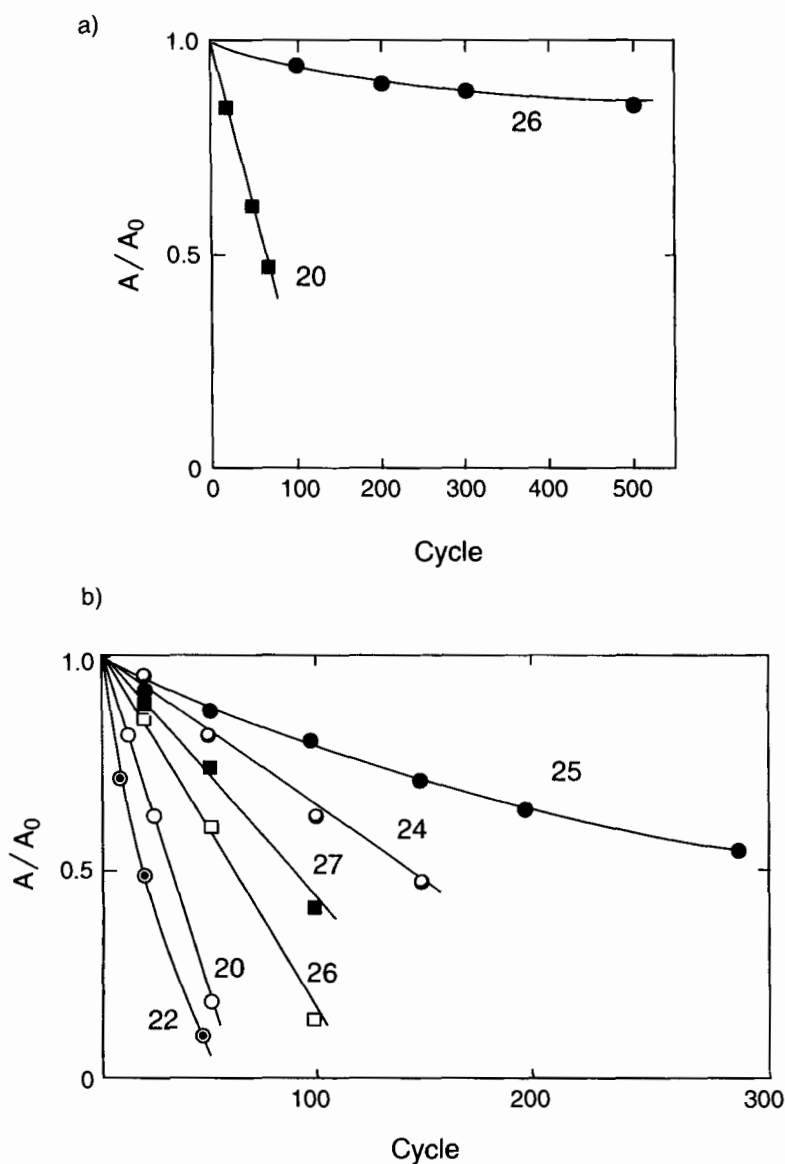
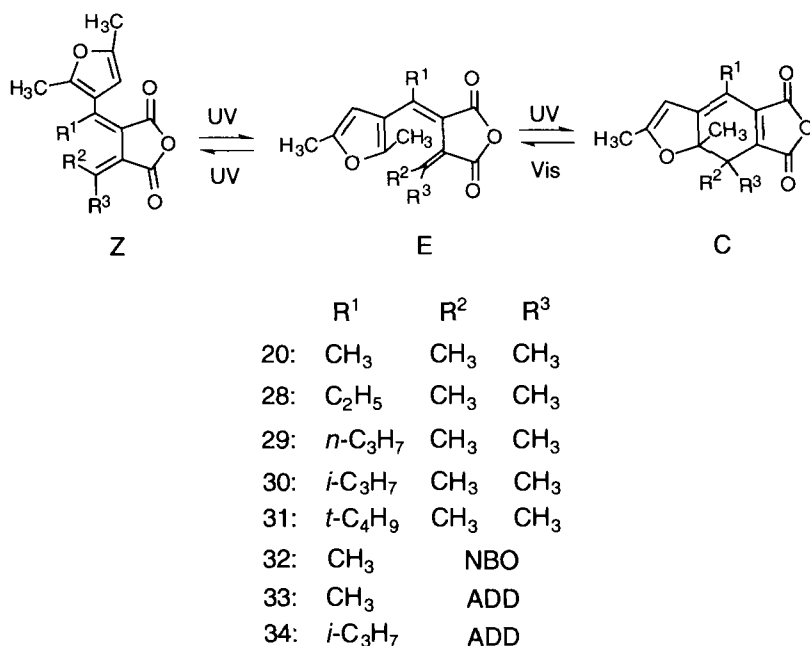


Figure 7. Fatigue resistance of fulgide derivatives a) in toluene and b) in PMMA film. A_0 and A were the absorbances of the first cycle and after n coloration/decoloration cycles, respectively.

Replacement of isopropylidene groups with bulky norbornylidene or adamantylidene groups was carried out with the aim of increasing the cycloreversion quantum yield [32, 35, 36]. Although norbornylidene groups were not effective, adamantylidene groups dramatically increased the yield. Finally, both isopropyl and adamantylidene groups were introduced into the fulgide molecular structure.



NBO : 7- norbornylidene

ADO : 2 - adamantylidene

Scheme 6.

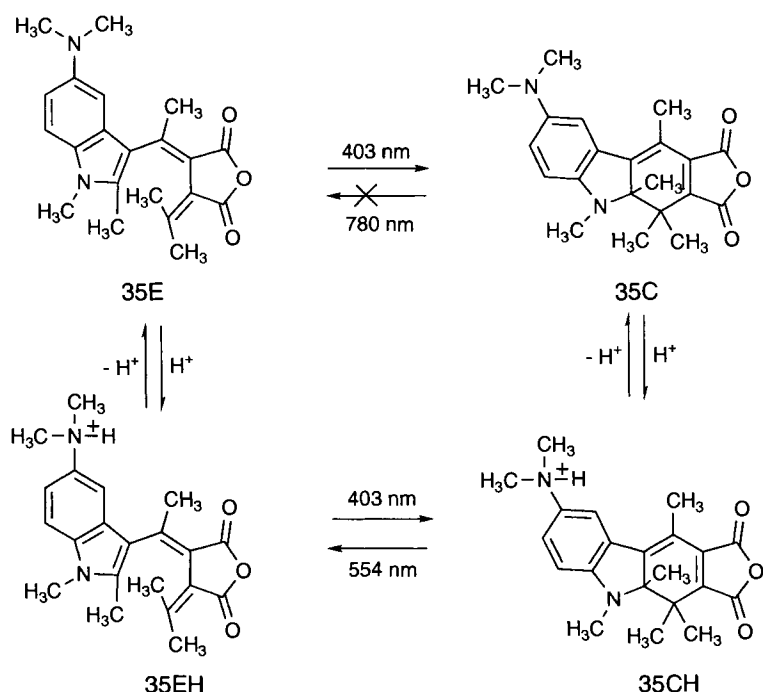
Table 4. Quantum yields of furyl fulgide derivatives in toluene.

Compound	Φ_{EC}	Φ_{EZ}	Φ_{ZE}	Φ_{CE}
20	0.18	0.13	0.11	0.048
28 ^a	0.34	0.06	0.12	0.027
29 ^a	0.45	0.04	0.10	0.044
30 ^a	0.62	0.00	0.06	0.040
31 ^a	0.79	0.00	—	0.034
32	0.20	0.30	0.42	0.057
33	0.12	0.10	0.10	0.21
34	0.51	0.02	0.05	0.26

^ain chloroform.

The cyclization and cycloreversion quantum yields of **34** were increased to 0.51 and 0.26, respectively. Both yields of **34** were reasonably high.

Indolyl fulgide, having a dimethylamino substituent at the 5-position of the indole ring **35**, undergoes an acid-gated photochromic reaction as shown in Scheme 7 [37]. In the absence of acid, the open-ring isomer **35E** converts to the closed-ring isomer **35C**, but the reverse process is strongly suppressed. The quantum yield is less than



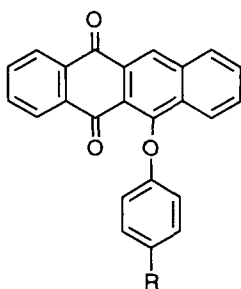
Scheme 7. Acid-gated photochromic reactions of an indolyl fulgide **35** with a dimethylamino substituent.

10^{-4} . Upon addition of an acid, such as trichloroacetic acid, the absorption maximum showed the hypsochromic shift and the cycloreversion quantum yield increased as much as 10^3 -fold. Protonation to the dimethylamino group decreased the electron-donating ability of the substituent and resulted in the change in reactivity. This acid-gated reactivity is potentially applicable to nondestructive readout in a polymer memory medium.

7.3.3 Phenoxynaphthacene Quinones

Another class of thermally irreversible photochromic molecules comprises phenoxynaphthacene quinone derivatives (**36–40**). The photogenerated orange isomer (*ana* form) never returns to the colorless isomer (*trans* form) at ambient temperature. Although the derivative in which R is hydrogen only slightly shows photochromic reactivity, all derivatives having amino or alkyl substituents in the *para* position of the phenoxy group undergo normal photochromism.

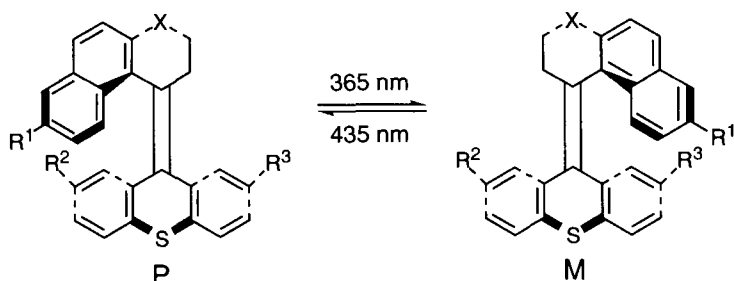
The *trans*-to-*ana* and the reverse quantum yields of **40** were determined to be 0.60 and 0.10, respectively. The coloration/decoloration cycle could be repeated more than 500 times. The quantum yield of side product formation was also determined to be 5×10^{-4} , which agrees with the fatigue resistance of this molecule [41]. Vari-

36: $R = -NH_2$ 37: $R = -CH_2COOH$ 38: $R = -CH_2CH \begin{matrix} \nearrow COOCH_3 \\ \searrow NH_2 \end{matrix}$ 39: $R = -CH_2CH \begin{matrix} \nearrow COOC_4H_9 \\ \searrow NH_2 \end{matrix}$ 40: $R = -CH_2CH \begin{matrix} \nearrow COOC_4H_9 \\ \searrow NHCOOC(CH_3)_3 \end{matrix}$

ous types of polymers containing the chromophores were prepared and their photochromic performance was also examined [39, 40].

7.3.4 Stilbene Derivatives

Stilbene derivatives also undergo thermally irreversible photochromic reactions. Among the derivatives, the thioxanthenes **41** and **42** are of the most interest from the viewpoint of their application to memory media [42–44].

41 : $X = CH_2$, $R^1 = CH_3$, $R^2 = OCH_3$, $R^3 = H$ 42 : $X = S$, $R^1 = H$, $R^2 = NO_2$, $R^3 = N(CH_3)_2$

Major advantages of **41** and **42** over other photochromic systems are:

- 1) the photoswitching between **P** and **M** isomers can be detected by more discriminative detection techniques, such as circular dichroism (CD) or optical rotation dispersion (ORD) spectra, which change the sign between the isomers; and
- 2) the recorded memory can be read out without affecting the ratio of the two isomers by using ORD and employing a wavelength outside the absorption region.

Irradiation of hexane solutions of **P-42** at 365 and 435 nm resulted in two distinct photostationary states. Upon irradiation with 365 nm light the photostationary state was composed of 70 % **M-42** and 30 % **P-42**, whereas the photostationary

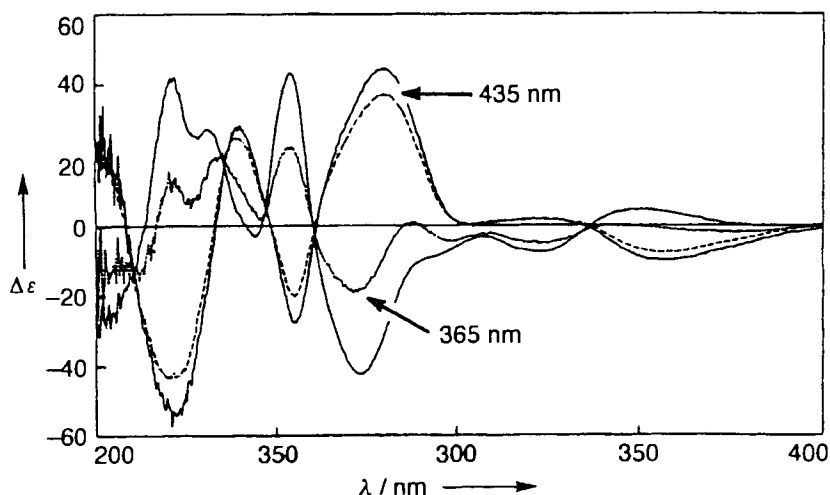


Figure 8. CD spectra of **M-42** (negative) and **P-42** (positive), and the photostationary states generated by irradiation at 365 and 435 nm in hexane.

state with 435 nm light was composed of 10 % **M-42** and 90 % **P-42**. The interconversion between **M-42** and **P-42** was reversible and any racemization was not observed after 60 cycles. Figure 8 shows the CD spectra of the two photostationary states. The CD spectra changed the sign by alternate irradiation with 365 and 435 nm light. The change in ORD spectra can be detected in principle by using visible light of wavelength longer than 500 nm, which does not induce the photochromic reaction. The two states could also be detected by the fluorescence intensity change [44]. One serious defect of this system is that the photochemical reactivity is strongly suppressed in rigid solid matrices.

The photochemical interconversion between two states, **P-42** and **M-42**, was prohibited by the addition of trifluoroacetic acid [44]. The fluorescence was also quenched by the acid. The protonation of the dimethylamino group lost the effective donor–acceptor system and changed the photoreactivity.

The sterically overcrowded stilbene derivatives were also useful dopants which caused photoinduced transition between induced cholesteric and nematic phases of liquid crystals [45, 46]. By alternate irradiation with light of different wavelengths, or left or right circularly polarized light, the phase transitions were successfully induced.

7.4 Nondestructive Readout

Several methods using fluorescence or infrared absorption as readout signals have been proposed to avoid destructive readout. A diarylethene having dithieno(thiophene) units **43a** [47, 48] shows fluorescence in the open-ring isomer (Eq. (9)).

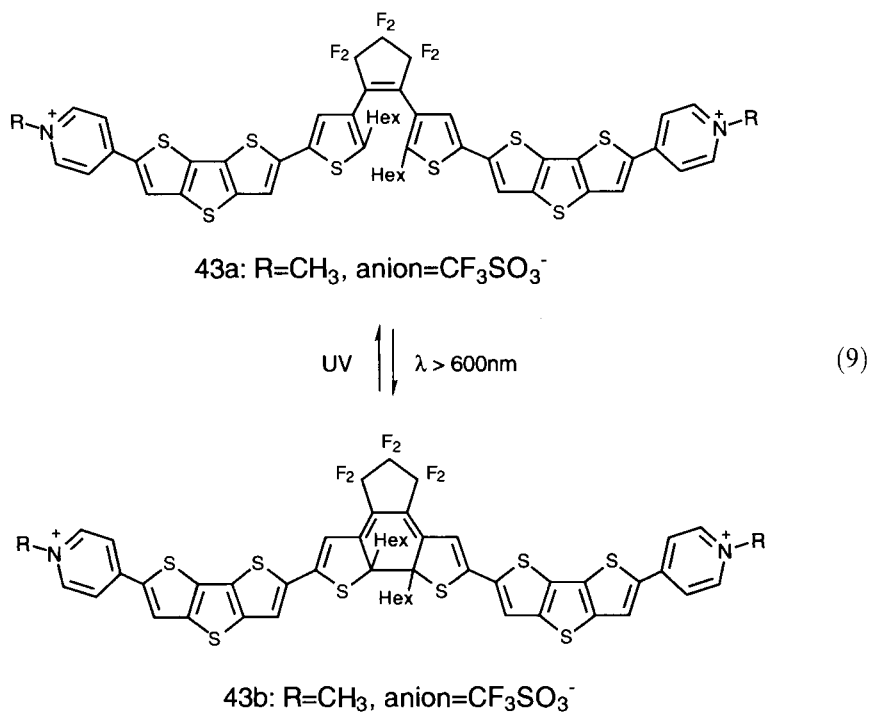


Figure 9 shows the absorption spectra of **43a** and **43b**. Irradiation of the main band of the open-ring isomer **43a** at 400–500 nm gave no reaction, while the cyclization reaction proceeded by irradiation at wavelengths less than 400 nm. The closed-ring isomer presented an intense broad absorption band at 704 nm. Cycloreversion

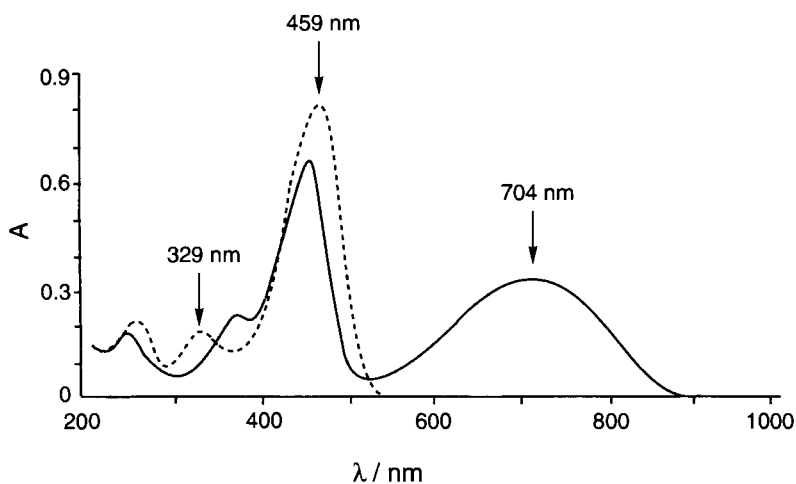


Figure 9. Absorption spectra of **43a** (···) and **43b** (—) in methanol.

occurred upon irradiation with >600 nm light. The open-ring isomer was found to present a strong emission at 589 nm when excited in the 400–500 nm region. In contrast, the closed-ring isomer displayed only a weak fluorescence. The large change in fluorescence intensity between the open- and closed-ring isomers makes it possible to use the change as the readout signal. When the fluorescence can be detected without influencing the ratio of the two isomers, the readout method becomes non-destructive. The absorption band at 459 nm of the open-ring isomer was photochemically inactive. The analogous band of the closed-ring isomer ($\lambda_{\text{max}} = 454$ nm) also had very low activity; a slow conversion of less than 10 % h^{-1} was observed. Therefore, the spectral change during fluorescence detection using a narrow range of exciting wavelengths was negligible. Although the system does not give a perfect performance of nondestructive readout, a very large number of fluorescence readings can in principle be performed before significant change takes place.

As described in Section 7.3.4, the recorded information can be read many times without destruction by light whose energy cannot cause any molecular change [49, 50]. Infrared light can be used to detect the difference between the open- and closed-ring isomers. The region of C=C stretching ($1400\text{--}1650\text{ cm}^{-1}$) is highly selective and suitable for detecting the difference. In the spectral region, the open-ring isomer **11a** has three bands at 1637, 1592, and 1544 cm^{-1} . The first one is due to the C=C bond of perfluorocyclopentene, and the others can be ascribed to the double bonds of the thiophene rings. In the closed-ring forms three new bands appeared at 1612, 1574, and 1503 cm^{-1} , which are assigned to the C=C bonds of the newly generated conjugated system. It is possible to detect the difference in the isomers using infrared spectra. Conceptually it is proposed to construct an optical memory system in which the information is written and erased by UV and visible photons that activate the photochromic process; the reading is achieved by infrared photons unable to cause any molecular rearrangement.

7.5 Near-field Memory

Various approaches have been proposed to increase the memory density: decreasing the spot diameter by use of short-wavelength lasers [51], three-dimensional recording [52, 53], and multi-wavelength recording [54]. One of the approaches to the ultra-high-density optical memory is near-field optical recording [55, 56]. The recording density in conventional optical recording is limited by the diffraction limit of light and the numerical aperture of the lens. Therefore, efforts have been focused on developing shorter-wavelength lasers [51]. In near-field recording, in contrast, the size of the recording mark depends only on the diameter of the probe tip aperture. Therefore, the recording density can be increased at will, in principle, if a small aperture tip is available. Photochromic media are suitable for near-field recording because of their ultra-high resolution and writing speed.

Amorphous thin recording medium (300 nm) was prepared by vacuum evaporation of dithienylethene **10a** on a glass substrate and used for the near-field optical

recording. The film was first colored by irradiation with UV light ($300\text{ nm} < \lambda < 400\text{ nm}$) and then bleached with 529 nm light from a small probe tip. The diameter of the mark was as small as $\sim 100\text{ nm}$. The mark could be erased by irradiation with UV light. The result represents a 60-fold improvement in recording density compared with current conventional MO and PC recording systems.

7.6 Conclusions

When we intend to apply organic molecular materials, especially photochromic dyes, to optical memory media, the indispensable condition is stability, both thermal and photochemical. The photogenerated isomers are required never to return to the initial isomers in the dark, even at elevated temperatures, e.g., 80°C . In addition, the coloration/decoloration can be cycled many times while the photochromic performance is maintained, and the memory media are provided with nondestructive readout capability. Although several molecules which fulfill the former condition have been developed, some problems still remain to gain access to molecules and systems which fully satisfy the latter condition.

At present the most robust photochromic molecules are diarylethenes with benzothiophene aryl groups [13]. They undergo more than 1.3×10^4 photochromic cycles in the presence of oxygen without destruction. Recently crystalline photochromic diarylethenes have been developed [57, 58] which could repeat the cycles more than 10^5 times.

Although several attempts to develop gated photochromic systems have been made to avoid destructive readout as described in Section 7.3, their functions are not adequate for practical application. Recently a new practical technology to avoid destructive readout has been developed [53], using a reflection confocal microscope as a readout system. The wavelength of the readout laser light is longer than the absorption edge of the colored isomer. The method was successfully applied to nondestructive readout of data stored in three-dimensional photochromic memory. We are now close to the goal of constructing an erasable optical memory system using organic molecular materials.

References

1. R. H. Sprague, H. L. Fichter, E. Wainer, *Photogr. Sci. Eng.* **1961**, 5, 98.
2. R. H. Sprague, M. Roscow, *Photogr. Sci. Eng.* **1964**, 8, 91.
3. R. H. Sprague, H. L. Fichter, *Photogr. Sci. Eng.* **1964**, 8, 95.
4. R. Dessauer, Preprint of SPSE Seminar, *Novel Imaging System*, **1969**, p. 7.
5. N. A. Koska, S. R. Wilson, G. B. Schuster, *J. Am. Chem. Soc.* **1993**, 115, 11628.
6. S. Murphy, B. Sauerwein, H. G. Drichamer, G. B. Schuster, *J. Phys. Chem.* **1994**, 98, 13476.
7. *Photochemistry and Polymeric Systems* (Eds.: J. M. Kelly, C. B. McArdle, M. J. de F. Maun-der), Royal Society of Chemistry, Cambridge, **1993**.
8. *Introduction to Microlithography*, *ACS Symposium Series 219* (Eds.: L.F. Thompson, C. G. Wilson, M. J. Bowden), American Chemical Society, Washington DC, **1983**.

9. *Photo-reactive Materials for Ultrahigh Density Optical Memory* (Ed.: M. Irie), Elsevier, Amsterdam, **1994**.
10. K. Horie, I. Mita, *Adv. Polym. Sci.* **1989**, 88, 77.
11. J. Hibino, T. Hashida, M. Suzuki in Ref. [9], p. 25.
12. M. Irie, M. Mohri, *J. Org. Chem.* **1988**, 53, 6136.
13. M. Irie, K. Uchida, *Bull. Chem. Soc. Jpn.* **1998**, 71, 985.
14. S. Nakamura, M. Irie, *J. Org. Chem.* **1988**, 53, 6136.
15. M. Irie, T. Lifka, K. Uchida, S. Kobatake, Y. Shindo, *Chem. Commun.* **1999**, 747.
16. K. Uchida, M. Irie, *Chem. Lett.* **1995**, 969.
17. M. Irie, O. Miyatake, K. Uchida, *J. Am. Chem. Soc.* **1992**, 114, 8715.
18. M. Irie, O. Miyatake, K. Uchida, T. Eriguchi, *J. Am. Chem. Soc.* **1994**, 116, 9894.
19. M. Irie, T. Eriguchi, T. Takada, K. Uchida, *Tetrahedron* **1997**, 53, 214.
20. S-H. Kawai, S.L. Gilat, J.-M. Lehn, *J. Chem. Soc., Chem. Commun.* **1994**, 1011.
21. S-H. Kawai, S.L. Gilat, R. Ponsinet, J.-M. Lehn, *Chem. Eur. J.* **1995**, 1, 285.
22. G.M. Tsivgoulis, J.-M. Lehn, *Adv. Mater.* **1997**, 9, 627.
23. J. Whittall in *Photochromism: Molecules and Systems* (Eds.: H. Dürr, H. Bouas-Laurent), Elsevier, Amsterdam, **1990**, pp. 467–492.
24. J. Whittall in *Applied Photochromic Polymer Systems* (Ed.: C.B. McArdle), Blackie, Glasgow, **1992**, pp. 80–120.
25. M. G. Fan, L. Yu, W. Zhao in *Organic Photochromic and Thermochromic Compounds* (Eds.: J. C. Crano, R. J. Guglielmetti), Plenum, New York, **1999**, pp. 141–206.
26. H. G. Heller, R. M. Megit, *J. Chem. Soc., Perkin Trans. 1*, **1974**, 923.
27. P. J. Darcy, H. G. Heller, P. J. Strydom, J. Whittall, *J. Chem. Soc., Perkin Trans. 1*, **1981**, 202.
28. H. G. Heller, *IEE Proceedings*, **1983**, 130, 209.
29. A. Kaneko, A. Tomoda, M. Ishizuka, H. Suzuki, R. Matsushima, *Bull. Chem. Soc. Jpn.* **1988**, 61, 3569.
30. H. Suzuki, A. Tomoda, M. Ishizuka, A. Kaneko, M. Furui, R. Matsushima, *Bull. Chem. Soc. Jpn.* **1989**, 62, 3968.
31. Y. Yokoyama, T. Goto, T. Inoue, M. Yokoyama, T. Kurita, *Chem. Lett.* **1988**, 1049.
32. Y. Yokoyama, T. Iwai, N. Kera, I. Hitomi, Y. Kurita, *Chem. Lett.* **1990**, 263.
33. Y. Yokoyama, T. Inoue, M. Yokoyama, T. Goto, T. Iwai, N. Kera, I. Hitomi, Y. Kurita, *Bull. Chem. Soc. Jpn.* **1994**, 67, 3297.
34. J. Kiji, T. Okano, H. Kitamura, Y. Yokoyama, S. Kubota, Y. Kurita, *Bull. Chem. Soc. Jpn.* **1995**, 68, 616.
35. A. P. Glaze, H. G. Heller, J. Whittall, *J. Chem. Soc., Perkin Trans. 2* **1992**, 591.
36. K. Ulrich, H. Port, H. C. Wolf, J. Wonner, F. Effenberger, H.-D. Ilge, *Chem. Phys.* **1991**, 154, 311.
37. Y. Yokoyama, T. Yamame, Y. Kurita, *J. Chem. Soc., Chem. Commun.* **1991**, 1722.
38. Y. E. Gerasimenko, N. T. Poteleschenko, V. V. Romanov, *J. Org. Chem. USSR (Eng. Transl.)* **1980**, 16, 1651.
39. F. Buchholtz, A. Zelichenok, V. Krongauz, *Macromolecules* **1993**, 26, 906.
40. A. Zelichenok, F. Buchholz, E. Fischer, J. Ratner, V. Krongauz, *J. Photochem. Photobiol. A: Chem.* **1993**, 76, 135.
41. J. Malkin, A. Zelichenok, V. Krongauz, A. S. Dvornikov, P. M. Rentzepis, *J. Am. Chem. Soc.* **1994**, 116, 1101.
42. B. L. Feringa, W. F. Jager, B. de Lange, *J. Am. Chem. Soc.* **1991**, 113, 5468.
43. W. F. Jager, J. C. de Jong, B. de Lange, N. P. M. Huck, A. Meetsma, B. L. Feringa, *Angew. Chem. Int. Ed. Engl.* **1995**, 34, 348.
44. N. P. M. Huck, B. L. Feringa, *J. Chem. Soc., Chem. Commun.* **1995**, 1095.
45. B. L. Feringa, N. P. M. Huck, H-A. van Doven, *J. Am. Chem. Soc.* **1995**, 117, 9929.
46. N. P. M. Huck, W. F. Jager, B. de Lange, B. L. Feringa, *Science* **1996**, 273, 1686.
47. G.M. Tsivgoulis, J.-M. Lehn, *Angew. Chem. Int. Ed. Engl.* **1995**, 34, 1119.
48. G.M. Tsivgoulis, J.-M. Lehn, *Chem. Eur. J.* **1996**, 2, 1399.
49. H. Seibsl, H. Port, *Chem. Phys. Lett.* **1996**, 252, 133.
50. F. Stellacci, C. Bertarelli, F. Toscano, M.C. Gallazzi, G. Zerbi, *Chem. Phys. Lett.* **1999**, 302, 563.

51. S. Nakamura, M. Senoh, S. Nagahama, N. Iwata, T. Yamada, T. Matsushita, Y. Sugimoto, H. Kiyoku, *Jpn. J. Appl. Phys.* **1997**, 36, L1059.
52. D.A. Parthenopoulos, D.M. Rentzepis, *Science* **1989**, 245.
53. A. Toriumi, S. Kawata, *Opt. Lett.* **1998**, 23, 1924.
54. T. Tsujioka, Y. Shimizu, M. Irie, *Jpn. J. Appl. Phys.* **1994**, 33, 1914.
55. M. Hamano, M. Irie, *Jpn. J. Appl. Phys.* **1996**, 35, 1764.
56. M. Irie, H. Ishida, T. Tsujioka, *Jpn. J. Appl. Phys.* **1999**, 38, 6114.
57. S. Kobatake, T. Yamada, K. Uchida, N. Kato, M. Irie, *J. Am. Chem. Soc.* **1999**, 121, 2380.
58. S. Kobatake, M. Yamada, T. Yamada, M. Irie, *J. Am. Chem. Soc.* **1999**, 121, 8450.

8 Nonlinear Optics

*Stephan Houbrechts, Eric Hendrickx, Thierry Verbiest, Koen Clays, and
André Persoons*

Nonlinear optics is a rapidly evolving field that studies the interaction of strong electric fields (e.g., high-intensity light) with matter. Historically, it had to await the advent of laser sources (high-intensity radiation sources) before most of the small optical nonlinearities could be addressed [1, 2]. Though, since its genesis the field has been continuously expanding. For several decades now, nonlinear optics has been recognized for its applications in the domain of opto-electronics and photonics [3, 4]. High-performance electro-optical switches for telecommunications and optical information processing are all based on materials with high nonlinear optical (NLO) properties. In addition, NLO materials also found their use as eye or photo-sensor protection materials due to their light-intensity-dependent transmission properties [5]. This chapter is intended as an introduction to nonlinear optics. Emphasis is on organic structures that exhibit second-order NLO properties, on various strategies to enhance the molecular nonlinearities, and on the methods used to determine them. More extensive discussions of the work performed in this field can be found in the literature [3–9].

8.1 Introduction to Nonlinear Optics

8.1.1 The Basics of Nonlinear Optics

The interaction of light with a molecule can be described by the influence of its electric field on the electron density. The electric field E acting on the molecule (or material) induces a distortion of the electron density, with (induced) dipole moment μ_{ind} (or polarization P on the macroscopic level). For weak electric fields the magnitude of this induced moment (polarization) can be expected to be linear with the amplitude of the electric field. This linear proportionality suffices to explain the linear optical properties, e.g., refraction and optical activity. Yet, when the electric

field strength approaches that of the internal electric field within the molecule, the linear relationship no longer holds and nonlinear terms have to be taken into account. In these circumstances, the induced dipole moment (induced polarization) can be expressed in terms of a power series (Eqs. (1) and (2)).

$$\mu_{\text{ind}} = \alpha E + \beta EE + \gamma EEE + \dots \quad (1)$$

$$P_{\text{ind}} = \chi^{(1)} E + \chi^{(2)} EE + \chi^{(3)} EEE + \dots \quad (2)$$

The molecular constants α , β , and γ are called the linear polarizability, the quadratic (or first) hyperpolarizability, and the cubic (or second) hyperpolarizability respectively. The related macroscopic quantities $\chi^{(n)}$ defined by Eq. (2) denote respectively the first-, second-, and third-order susceptibility. Although the precise relationship between $\mu_{\text{ind}}(P_{\text{ind}})$ and E is tensorial by nature, it is sufficient for the present section to use the scalar notation. The quadratic terms β and $\chi^{(2)}$ are responsible for second-order NLO effects such as the linear electro-optic or Pockels effect and frequency doubling (or second-harmonic generation, SHG). In like manner do the cubic terms γ and $\chi^{(3)}$ account for third-order NLO properties such as the Kerr effect and third harmonic generation (THG). Nevertheless, as the nonlinear terms βEE and γEEE in general are much smaller than αE , NLO effects were seldom observed before lasers were at hand. Utilizing the correct trigonometric relations, the appearance of SHG and THG can easily be verified by expressing the electric field of a light wave as $E = E_0 \cos(\omega t)$.

$$\begin{aligned} \mu_{\text{ind}} &= \alpha E_0 \cos(\omega t) + \beta (E_0 \cos(\omega t))^2 + \gamma (E_0 \cos(\omega t))^3 + \dots \\ &= \frac{\beta E_0^2}{2} + \left(\alpha + \frac{3\gamma E_0^2}{4} \right) E_0 \cos(\omega t) + \frac{\beta E_0^2}{2} \cos(2\omega t) + \frac{\gamma E_0^3}{4} \cos(3\omega t) + \dots \end{aligned} \quad (3)$$

Apart from SHG and THG, Eq. (3) also reveals a second-order DC contribution (optical rectification) and the optical Kerr effect (i.e., the dependence of the term at the original frequency upon the light intensity $I \propto E_0^2$). A similar expression can be derived for the macroscopic polarization. Other NLO effects can be described utilizing different frequencies and/or static $E(0)$ or magnetic $B(0)$ fields (see Table 1).

In the literature however, other related parameters, besides $\chi^{(2)}$, are often used to describe the macroscopic second-order NLO properties of materials. The SHG nonlinear coefficient d and the linear electro-optic coefficient r are the parameters commonly used for second-harmonic generation and the Pockels effect respectively [3, 5]. They are related to $\chi^{(2)}$ according to Eqs. (4) and (5).

$$d = \frac{\chi^{(2)}}{2} \quad (4)$$

$$r = -\frac{8\pi\chi^{(2)}}{n_0^4} \quad (5)$$

Table 1. Certain NLO contributions to the induced dipole moment.

Dipole moment contribution	NLO effect
$\mu(0) \propto \beta E(\omega)E(\omega)$	optical rectification
$\mu(\omega) \propto \beta E(0)E(\omega)$	Pockels effect
$\gamma E(0)E(0)E(\omega)$	DC Kerr effect
$\gamma E(\omega)E(\omega)E(\omega)$	optical Kerr effect
$\mu(2\omega) \propto \beta E(\omega)E(\omega)$	SHG
$\gamma E(0)E(\omega)E(\omega)$	electric-field induced SHG
$\gamma B(0)E(\omega)E(\omega)$	magnetic-field induced SHG
$\mu(\omega_1 \pm \omega_2) \propto \beta E(\omega_1)E(\omega_2)$	frequency mixing
$\mu(3\omega) \propto \gamma E(\omega)E(\omega)E(\omega)$	THG

8.1.2 Symmetry Restrictions

The anisotropy of molecules and matter imposes that the proportionality factors (Eqs. (2) and (3)) are tensorial quantities (vide supra). As such, the relations between the dipole moment vector and the electric field vector can be defined by Eq. (6),

$$\begin{aligned}\mu_i &= \sum_j \alpha_{ij} E_j + \sum_{j,k} \beta_{ijk} E_j E_k + \sum_{j,k,l} \gamma_{ijkl} E_j E_k E_l \\ &= \alpha_{ij} E_j + \beta_{ijk} E_j E_k + \gamma_{ijkl} E_j E_k E_l\end{aligned}\quad (6)$$

where summation over the repeated indices is implied. Consequently, α is a second-rank tensor (or a 3×3 matrix), β a third-rank tensor ($3 \times 3 \times 3$ matrix), and γ a fourth-rank tensor ($3 \times 3 \times 3 \times 3$ matrix) with respectively 9, 27, and 81 tensor components. Fortunately, the number of independent tensor components is severely restricted by molecular symmetry (or the symmetry of the medium in case of the susceptibilities) as many components are equivalent or equal to zero. As an example, let us consider the quadratic hyperpolarizability, and a particular physical situation (molecule, electric fields, and induced moments are fixed in space) described by Eq. (6). This situation can now also be described in an alternative coordination frame. Like the vectors, the new β'_{lmn} and old β_{ijk} tensor components of the first hyperpolarizability relate to each other through a transformation matrix t .

$$\begin{aligned}\mu'_l &= t_{li} \mu_i \\ E'_m &= t_{mj} E_j \\ \beta'_{lmn} &= t_{li} t_{mj} t_{nk} \beta_{ijk}\end{aligned}\quad (7)$$

If we consider t to be a symmetry operation T , than all properties are described identically in both frames. As each symmetry operation produces an expression like Eq. (8), the number of independent tensor components is restricted.

$$\beta_{lmn} = T_{li} T_{mj} T_{nk} \beta_{ijk}\quad (8)$$

Note that the inversion transformation $T_{li} = -\delta_{li}$ yields $\beta_{lmn} = -\beta_{lmn}$ and thus $\beta_{lmn} = 0$. As a consequence, no second-order, or more general even-order, NLO effects can be present for molecules that are centrosymmetric. Moreover, the absence of an inversion center is required for the macroscopic symmetry of the medium [3, 5].

For certain macroscopic nonlinear parameters the tensor notation can be simplified due to the intrinsic symmetry of the experiment, e.g., second-harmonic generation and the linear electro-optic effect. Let us first consider SHG. The second-order contribution to the polarization is given by Eq. (9).

$$P_i^{(2)} = \chi_{ijk}^{(2)} E_j(\omega) E_k(\omega) \propto d_{ijk} E_j(\omega) E_k(\omega) \quad (9)$$

As $E_j(\omega)$ and $E_k(\omega)$ are indistinguishable (experimentally only one laser beam is used), the two last indices may be interchanged ($d_{ijk} = d_{ikj}$) and the third-rank tensor d_{ijk} can be represented as a two-dimensional matrix (Eq. (10)).

$$\begin{aligned} d_{ijj} &= d_{ij} \\ d_{i23} &= d_{i32} = d_{i4} \\ d_{i13} &= d_{i31} = d_{i5} \\ d_{i12} &= d_{i21} = d_{i6} \end{aligned} \quad (10)$$

In contrast to the SHG coefficient, the electro-optic coefficient r_{ijk} is symmetric in its first two indices for a lossless, not optically active, material. This follows from Eq. (11), which relates the electro-optical coefficient to the impermeability tensor η_{ij} (the matrix inverse of the dielectric permeability tensor ϵ_{ij}), a real and symmetric tensor under the stated conditions [3],

$$\eta_{ij} = \eta_{ij}^0 + r_{ijk} E_k + \cdots \quad (11)$$

with η_{ij}^0 the linear impermeability. As such the electro-optic coefficient can be contracted as in Eq. (12).

$$\begin{aligned} r_{iik} &= r_{ik} \\ r_{23k} &= r_{32k} = r_{4k} \\ r_{13k} &= r_{31k} = r_{5k} \\ r_{12k} &= r_{21k} = r_{6k} \end{aligned} \quad (12)$$

8.1.3 Systems of Units

The system of units most frequently employed in nonlinear optics is the Gaussian (or cgs) system. Sporadically, the SI unit system is used. It is important to be able to convert between the two systems. However, not only do the units need to be con-

Table 2. Some units and conversion factors in nonlinear optics.

Property		cgs ^a	SI	Conversion factor N^b
Dipole moment	μ	sC cm	C m	2.998×10^{11}
Polarization	P	sC cm ⁻²	C m ⁻²	2.998×10^5
Electric field	E	sV cm ⁻¹	V m ⁻¹	3.334×10^{-5}
Linear polarizability	α	cm ³	C m ² V ⁻¹	$(2.998)^2 \times 10^{15}$
1st hyperpolarizability	β	cm ⁵ sC ⁻¹ (esu)	C m ³ V ⁻²	$(2.998)^3 \times 10^{19}$
2nd hyperpolarizability	γ	cm ⁷ sC ⁻² (esu)	C m ⁴ V ⁻³	$(2.998)^4 \times 10^{23}$
Linear susceptibility	$\chi^{(1)}$	dimensionless	C m ⁻¹ V ⁻¹	$(2.998)^2 \times 10^9$
2nd-order susceptibility	$\chi^{(2)}$	cm sV ⁻¹	C V ⁻²	$(2.998)^3 \times 10^{13}$
3rd-order susceptibility	$\chi^{(3)}$	cm ² sV ⁻²	C m V ⁻³	$(2.998)^4 \times 10^{17}$

^a 1 C = 2.998×10^9 sC, 299.8 V = 1 sV, ^b SI $\times N$ = cgs.

verted correctly, but the quantities need to be treated according to their different definitions in different systems as well. Table 2 lists the conversion factors for the quantities of importance in second- and third-order nonlinear optics.

Note that for the macroscopic nonlinear parameters ($\chi^{(2)}$, d and r) the MKS system is frequently used ($1 \text{ pm V}^{-1} = 3.387 \times 10^{-9} \text{ esu}$).

8.2 Measurement Techniques

8.2.1 Electric-field-induced Second-harmonic Generation (EFISHG)

For the experimental determination of the second-order first hyperpolarizability, some sort of non-centrosymmetry has to be present in the solution. This can be achieved by applying a static electric field over a solution of neutral molecules with dipolar chromophores. Implicitly, this description limits the applicability of this Electric-field-induced second-harmonic generation (EFISHG) technique:

- 1) No ionic species can be measured: they would migrate rather than orient under the influence of the static field.
- 2) Only dipolar molecules can be measured, because reorientation in the electric field is necessary to induce the non-centrosymmetry.

The latter limitation did not prove a disadvantage until recently. The paradigm of second-order nonlinear optics used to be an asymmetrically *para*-substituted (azo)-benzene or stilbene, and hence a dipolar molecule.

EFISHG [10–12] is inherently a third-order process: two optical fields are necessary to generate the optical harmonic, but a third (static) field is also present. A complete analysis of the different contributions to the second-order signal obtained

from EFISHG reveals that there are different contributions to the molecular third-order nonlinear optical polarizability which are inherently determined by the third-order process. There is a purely electronic third-order contribution, inherently third-order; a purely vibrational contribution, also third-order in nature; and a so-called average dipolar rotational contribution, γ_r . The latter contribution is in fact a combination of a second-order parameter with another field, yielding a third-order contribution. For the analysis toward a value for the second-order nonlinear polarizability β of dipolar molecules, we have to focus on this contribution. The experimental conditions are parallel polarizations of fundamental, second harmonic, and static field.

The rotational contribution stems from the second harmonic that is generated by partially oriented dipolar molecules. The orientation is induced by the lowering of the energy when a dipole moment orients parallel to the field. The orientation of the molecules induces a specific phase relation that leads to the generation of a coherent second-harmonic signal. The coherence length of the solution and the interaction length, i.e., the length of the cell containing the solution, ultimately determine the magnitude of this coherent signal. The wedge-shaped cell is therefore instrumental to factor out this length dependence and to accurately determine the amplitude. Referencing can be done in different ways. Either quartz can be used, with the appropriate $\chi^{(2)}$ value, or a solution of known concentration of a dipolar chromophore with known first hyperpolarizability value can be used.

The important question in EFISHG, especially in the light of the complementarity with hyper-Rayleigh scattering (HRS), is: What is actually experimentally determined? The expression for the rotational contribution is determined by the scalar product of the dipole moment vector with the vector part of the third-rank hyperpolarizability tensor (Eq. (13)).

$$\gamma_r = \frac{\mu \cdot \beta_{\text{vec}}}{5kT} \quad (13)$$

As will be explained in Section 8.3.3, the reduction spectrum of rank-three tensors contains, in the general case, one (pseudo)scalar, three vectors, two (pseudo)deviators, and one septor [13]. Here, we only have to deal with the vectorial parts. They transform as a vector. Hence, the scalar product of the dipole moment vector with a vector part of the first hyperpolarizability tensor can be written as the simple product of two scalars, when we designate θ as the angle between the molecular axis (z -axis) and the dipole moment axis (Eq. (14)).

$$\gamma_r = \frac{\mu_z \beta_z \cos \theta}{5kT} \quad (14)$$

The assumption is often made that the two vectors are collinear, leading to the familiar expression, Eq. (15), for EFISHG.

$$\gamma_r = \frac{\mu_z \beta_z}{5kT} \quad (15)$$

From the measurement of the intensity of the generated second harmonic for a dipolar molecule and with knowledge of the value of the dipole moment, an experimental value for β can be obtained. The relation of this value to the hyperpolarizability tensor components, in the completely general case ($\beta_k = \frac{1}{3}(\beta_{kmn}\delta_{nm} + \beta_{nkm}\delta_{nm} + \beta_{nmk}\delta_{nm})$), is given by Eq. (16).

$$\beta_z = \beta_{zzz} + \frac{1}{3}(\beta_{zyy} + \beta_{zxx} + \beta_{yyz} + \beta_{xzx} + \beta_{yyz} + \beta_{xxz}) \quad (16)$$

In the more specific case of second-harmonic generation, with degeneracy between the optical fields ($\beta_{ijk} = \beta_{ikj}$), Eq. (16) reduces to Eq. (17).

$$\beta_z = \beta_{zzz} + \frac{1}{3}(\beta_{zyy} + \beta_{zxx} + 2\beta_{yyz} + 2\beta_{xzx}) \quad (17)$$

When Kleinman [14] symmetry is applicable (i.e., $\beta_{ijk} = \beta_{jik}$), Eq. (18) holds.

$$\beta_z = \beta_{zxx} + \beta_{zyy} + \beta_{zzz} \quad (18)$$

These relations between the experimental observable in EFISHG, β_z , and the molecular third-rank hyperpolarizability tensor components do not reflect the (approximate) symmetry of the molecule yet. When we accept (approximate) C_{2v} symmetry for a molecule with a planar conjugated π -electron system (in the xz -plane), we are still left with these three non-zero and independent tensor components.

For $C_{\infty v}$ symmetry, there are only two independent tensor components β_{zzz} ; $\beta_{zyy} = \beta_{zxx}$, resulting in Eq. (19).

$$\beta_z = \beta_{zxx} + \beta_{zzz} \quad (19)$$

In most cases, for charge transfer molecules, only a single major non-zero tensor component can be assumed. Then, Eq. (19) finally reduces to Eq. (20).

$$\beta_z = \beta_{zzz} \quad (20)$$

It is important to make the distinction, and state the exact relation, between the measured observable and the actual hyperpolarizability tensor component(s), even if, for specific experimental conditions and molecular symmetries, their values turn out to be identical. What is also important is the fact that only one experimental condition is favorable for EFISHG, namely parallel polarizations for all optical and static fields. This leads to only one observable, resulting in only a single value to be deduced. It is not possible with EFISHG to determine more than one tensor component; hence, one often contends either with the approximation that β_{zzz} was determined, or with the statement that β_z was obtained, in any of the above-mentioned relations to the individual tensor components. Even then, the assumption that the dipole moment vector and the vector part of the third-rank tensor along the molec-

ular z -axis are collinear, is implicitly made. However, even if one was to be interested in checking this assumption, it would not be possible, since EFISHG can only provide one independent observable.

8.2.2 Hyper-Rayleigh Scattering (HRS)

In hyper-Rayleigh scattering (HRS) [15–17], no extrinsic non-centrosymmetry is induced in a solution. Advantage is taken of the temporal and spatial deviation from the average centrosymmetry caused by fluctuations. Due to the isotropic distribution of chromophores in the solution without an orienting field, the relations between the experimental observable and the hyperpolarizability tensor components are determined by the averaging of direction cosines over all possible orientations. The results have been obtained for the general case, i.e., as a function of all 27 possible hyperpolarizability tensor components [18, 19]. Again, degeneracy of the optical fields in hyper-Rayleigh scattering ($\beta_{ijk} = \beta_{jik}$, dispersive HRS) [20] reduces this number to 18, while Kleinman symmetry ($\beta_{ijk} = \beta_{jik}$) results in only 10 independent components. Molecular symmetry then ultimately determines the number of non-zero components.

Since, in HRS, there is no preferred orientation induced by an additional static field, there is the possibility of varying the experimental conditions in order to increase the number of independent observables. The number of theoretically possible independent observations, and hence the number of tensor components that can be obtained by HRS, is at most five. For parametric light scattering, this number is six, due to the possibility of distinguishing between the two optical fundamental fields [20]. The experimental difficulty has precluded the determination of this number of components. What is experimentally realistic in HRS is an additional depolarization measurement, apart from the classical measurement of the intensity of the second-order incoherent scattered light. The two measurements, the total intensity measurement and the depolarization ratio (or two intensity measurements, one with parallel and one with perpendicular polarization for fundamental and second harmonic), represent two independent observables and allow the experimental determination of two tensor components. For molecules of C_{2v} symmetry, these are β_{zzz} and β_{zxx} , resulting for the total intensity measurement in Eqn. (21),

$$\langle \beta_{\text{HRS}}^2 \rangle = \frac{6}{35} \beta_{zzz}^2 + \frac{16}{105} \beta_{zzz} \beta_{zxx} + \frac{38}{105} \beta_{zxx}^2 \quad (21)$$

and for the depolarization ratio ρ , measured under 90° , in Eqn. (22).

$$\rho = \frac{15 + 18q + 27q^2}{3 - 2q + 11q^2} \quad \text{with } q = \frac{\beta_{zxx}}{\beta_{zzz}} \quad (22)$$

The total-intensity hyper-Rayleigh scattering experiment basically consists of measuring the amount of incoherently scattered optical second harmonic (parallel and perpendicular output polarizations) versus a reference. When only this single measurement is done, only one independent tensor component can be obtained. For charge transfer molecules, this is generally approximated by β_{zzz} . The depolariza-

tion measurement is generally performed with a rotating analyzer inserted between the scattering cell and photomultiplier, but with a reduced numerical aperture of the condensing system [21–23]. From the theoretical depolarization ratio calculated as a function of β_{zxx}/β_{zzz} (Eq. (22)), it is then possible to derive, from the experimentally observed depolarization ratio, the ratio of β_{zxx}/β_{zzz} . This then not only gives a value for β_{zxx} , but additionally a relative sign and a check on the assumption that β_{zzz} was responsible for most of the scattered light. For donor–acceptor charge transfer molecules, this is always the case. Measurement of the depolarization ratio for more complex molecules also reveals the tensorial nature of the hyperpolarizability [24].

From the complementary nature of EFISHG and HRS, application of both techniques to (neutral and dipolar) molecules can lead to the measurement of more tensor components, to the experimental determination of structural parameters [22], or to the independent confirmation of experimentally obtained values for hyperpolarizability tensor components [25].

Ever since HRS has been developed as an experimental technique to determine the first hyperpolarizability β of molecules in solution, it has been realized that multi-photon fluorescence is a competing nonlinear process, contributing to the HRS signal [26]. For the classical dipolar and neutral molecules that may exhibit multi-photon fluorescence, electric-field-induced second-harmonic generation (EFISHG) experiments are possible. However, for ionic and non-dipolar compounds, no electric field can be applied over the solution. Hence, no EFISHG measurements are possible. Then it is very tempting to rely on the HRS measurement only. When there is, however, a multi-photon fluorescence (MPF) contribution, an overestimation of the first hyperpolarizability value results [27].

A number of experimental approaches have been suggested to overcome this fluorescence contribution. Since the fluorescence has a very broad spectral signature, versus a narrow spectral response for the hyper-Rayleigh scattering, subtracting the background from the peak is feasible, but time-consuming [28]. A fundamental and elegant approach is based on the intrinsic difference in temporal profile between the immediate scattering and the time-delayed fluorescence [29]. The high-frequency demodulation of the multi-photon fluorescence is, in fact, the implementation in the Fourier domain of this approach. A straightforward way to obtain high modulation frequencies is by using the higher harmonics of the pulse repetition frequency of a femtosecond laser [30]. The use of the generic femtosecond pulse laser—the titanium–sapphire laser—then leads to a fundamental wavelength of around 800 nm. For second-order nonlinear optical effects, this wavelength often leads to strong two-photon resonance enhancement, due to the closeness of the second-harmonic wavelength and the wavelength of electronic absorption. Although this may facilitate the measurement of the enhanced hyperpolarizability, it also strongly suggests the use of longer wavelengths as the fundamental. Accurate knowledge of the dispersion of the first hyperpolarizability can lead to an assessment of the two-level model (see Section 8.3.1). With the use of a femtosecond optical parametric oscillator (OPO), accurately measuring the first hyperpolarizability β at the signal wavelengths of this OPO has now become possible [31]. Together with the measurements of β at the titanium–sapphire output wavelength itself, a significant dispersion of the first hyperpolarizability is now attainable.

To obtain a fluorescence-free hyperpolarizability value of these fluorescent chromophores, HRS experiments have to be performed at different amplitude modulation frequencies. The frequencies are the higher harmonics of the pulse repetition frequency (80 MHz). At each amplitude modulation frequency, an apparent hyperpolarizability value is calculated by the external reference method. Plotting the determined apparent hyperpolarizability value of the measured compound versus the applied amplitude modulation frequency then results in a typical demodulation curve. If no demodulation is observed, i.e., a constant value of the first hyperpolarizability versus frequency, no fluorescence contribution to the HRS signal is present. This indicates that the chromophore does not fluoresce; that the fluorescence present is spectrally filtered out; or that the fluorescence lifetime is too short for its corresponding demodulation to be observed within the bandwidth of the instrument. Much care has to be taken when interpreting the result, then. When there is an MPF contribution to the HRS signal, the fluorescence contribution will diminish for the higher modulation frequencies, since the fluorescence can no longer follow the modulated excitation. The same principle is applied in multi-frequency phase fluorometry to determine the fluorescence lifetime. The finite fluorescence lifetime(s) cause a delay between the excitation and the fluorescence. In the frequency domain, this temporal delay is translated to a phase shift between excitation and fluorescence, and thus a decrease in the amplitude of the fluorescence for increasing modulation frequencies. In the limit of high modulation frequencies, the fluorescence contribution is completely demodulated, essentially zero, and the measured signal is solely due to HRS. The apparent hyperpolarizability as a function of modulation frequency can be analyzed toward the fluorescence contribution and lifetime(s), and the intrinsic, fluorescence-free, hyperpolarizability in the high-frequency limit. Depending on the actual value for the fluorescence lifetime, this limit can be experimentally achieved (for long lifetimes), or its value has to be calculated from a high-frequency extrapolation. The technique of high-frequency demodulation of the MPF contribution has been successfully applied to newly designed chromophores that intrinsically show MPF, such as subphthalocyanines [32] and stilbazolium dyes [33]. It was also instrumental in validating the inclusion strategy as a promising technique, not only to induce non-centrosymmetry in the bulk, but also to increase the molecular nonlinearity [34]. The inclusion leads to a more rigid structure, thereby reducing the number of nonradiative relaxation pathways, and hence, inducing (multi-photon) fluorescence.

8.3 Second-order Nonlinear Optical Molecules

8.3.1 Dipolar Molecular Structures

Molecules are suitable for nonlinear optics devices, only if they satisfy several requirements [35]. Amongst others are demands, due to the high temperatures needed

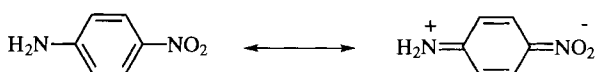


Figure 1. Resonance forms of the benchmark 4-nitroaniline molecule.

for poling and the intense optical fields used in nonlinear optics, for a high thermal and photochemical stability. To improve device performance, the molecules must also have a high transparency and an optimized nonlinearity. Here we treat mainly the design of molecules with an optimized nonlinearity.

The general quantum chemical description of the nonlinear susceptibilities and hyperpolarizabilities in the density matrix formalism was developed by Bloembergen and Shen [36]. A simplification of this model for dipolar organic molecules, by only considering the transition between the ground state and the first excited state, led to the well-known two-state expression for the first hyperpolarizability [37] (Eq. (23)).

$$\beta_{zzz}(-2\omega; \omega, \omega) = \frac{3\Delta\mu_{eg,z}M_{eg,z}^2}{(\hbar\omega_{eg})^2} \frac{\omega_{eg}^4}{(\omega_{eg}^2 - 4\omega^2)(\omega_{eg}^2 - \omega^2)} \quad (23)$$

where $\Delta\mu_{eg,z}$, $M_{eg,z}$ and $\hbar\omega_{eg}$ are the dipole moment difference along the z -axis, the electronic transition moment along the z -axis, and the energy of transition, respectively, between the ground state and the first excited state. The contribution from bond-additivity in Ref. [37] was shown not to contribute to β [38]. The first factor corresponds to the intrinsic value of the hyperpolarizability for $\omega = 0$, β_0 , and the second factor is the dispersion factor. This model is a widely used tool to describe the β response in terms of the electronic and spectroscopic properties of organic molecules.

The charge distribution in the ground and first excited state of dipolar donor–acceptor-substituted molecules can be described in terms of the resonance forms in Figure 1. For donor–acceptor-substituted aromatic conjugated systems, the ground state is described mainly by the first resonance form. Upon excitation, an electron is transferred from the donor to the acceptor, a strong increase in the dipole moment occurs, and the charge distribution in the excited state is described better by the second resonance form. For aromatic systems, increasing donor and acceptor strengths, and lengthening the conjugated bridge, are approaches that have led to significant improvements in β .

Marder et al. have shown that an increase in donor and acceptor strength does not necessarily result in an increase in β_0 for donor–acceptor-substituted polyenes, but that β_0 has a sinusoidal evolution with the donor and acceptor strength [39]. The evolution of $\Delta\mu_{eg,z}$, $M_{eg,z}$, and $\hbar\omega_{eg}$ appearing in the parameters of the static hyperpolarizability β_0 was calculated semi-empirically [40, 41]. If the donor and acceptor strength increase, the polarization of the ground state will also increase. The structural parameter used to describe the ground-state polarization is the average difference in length between adjacent carbon–carbon bonds in the polyenic

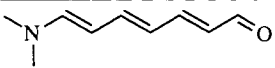
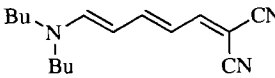
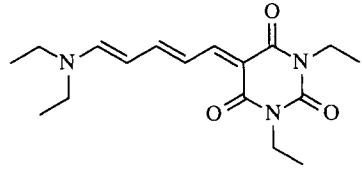
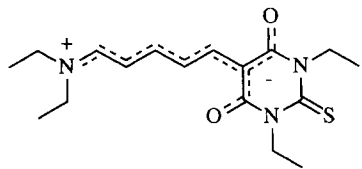
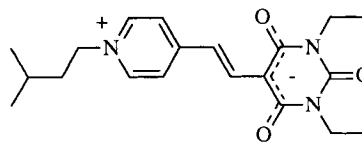
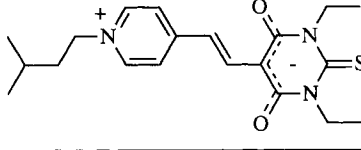
bridge, or bond order alternation (BOA). Initially, an increase in donor and acceptor strength leads to an enhancement of β_0 ($-11 \text{ pm} > \text{BOA} > -4 \text{ pm}$). An optimum in the hyperpolarizability is found for polyenes having an intermediate BOA value ($-4 \pm 1 \text{ pm}$) [42]. If the donor and acceptor strength increase further, both resonance forms will contribute equally to the ground state and first excited state. The polyene ground-state structure is then that of a symmetric cyanine ($\text{BOA} \approx 0$) and $\beta_0 \approx 0$ because of the small polarity difference between the ground state and excited state ($\Delta\mu_{\text{eg},z} \approx 0$). Thus, β_0 decreases for $-4 \text{ pm} > \text{BOA} > 0 \text{ pm}$. As the donor and acceptor strength increase even further, the ground-state structure is described by the charge-separated canonical form, $11 \text{ pm} > \text{BOA} > 0 \text{ pm}$. Since the first excited state is then described by the first resonance form, $\Delta\mu_{\text{eg},z} < 0$ and $\beta_0 < 0$. Experimental evidence for the calculated evolution was presented in a series of papers [43–47]. An example of the observed evolution of the parameter $\mu\beta_0$ with donor–acceptor strength is given in Table 3. The ground-state dipole moment increases monotonically with increasing ground-state polarization.

Based on the BOA theory, Barzoukas and Blanchard-Desce developed a two-state two-form model for the β_0 of push–pull compounds [48]. The β_0 was expressed as a function of the newly defined parameter *MIX*, which is related to the degree of mixing between the neutral and zwitterionic resonance forms in the ground and excited state. This treatment has the advantage of conceptual simplicity and that it relies on a structural parameter that can be more easily used for other push–pull molecular systems than polyenes. The evolution of β_0 observed with *MIX* is identical to that with BOA. The BOA theory was later also used to optimize the figure-of-merit of dyes for photorefractive applications [49, 50].

This theory yielded valuable guidelines for the further optimization of the β_0 of aromatic systems. These systems are not able to pass the peak of the β_0 curve due to the large ground-state aromaticity that limits the electronic polarizability. A further optimization was thus achieved by increasing the ground-state polarization through the use of conjugated systems with lower aromaticity [51] and stronger electron acceptors [52]. Simultaneously, functional groups were introduced to improve the processability and stability of the chromophores and to prevent chromophore–chromophore interactions. The substitution of a chromophore with bulky alkyl groups reduces the risk of unwanted chromophore aggregation in the solid state and improves the translation of a large hyperpolarizability into a large second-order nonlinearity [53]. An example of such a chromophore is given in Figure 2 [54].

Apart from purely electronic effects, an asymmetric nuclear relaxation in the electric field can also contribute to the first hyperpolarizability in processes that are partly induced by a static field, such as the Pockels effect [55, 56], and much attention is currently devoted to the study of the vibrational hyperpolarizability, β_v . β_v can be deduced from experimental data in two different ways [57, 58], and a review of the theoretical calculations of β_v is given in Refs. [59] and [60]. The numerical value of the static β_v is often similar to that of static electronic hyperpolarizabilities, and this was rationalized with a two-state valence-bond charge transfer model. Recent ab-initio computational tests have shown, however, that this model is not always adequate and that a direct correlation between static electronic and vibrational hyperpolarizabilities does not exist [61].

Table 3. Ground-state structure of a series of donor–acceptor substituted polyenes with increasing ground-state polarization, and the corresponding $\mu\beta_0$ values and wavelengths of maximum absorption λ_{\max} in CHCl_3 .

Ground-state structure	λ_{\max} [nm]	$\mu\beta_0$ [10^{-48} esu]
	420	247
	478	281
	510	133
	536	-14
	510	-248
	526	-386

8.3.2 Rigid Multichromophoric Molecules

Since the first nonlinear susceptibility $\chi^{(2)}$ is a third-rank tensor, it is only non-zero in non-centrosymmetric media. To break the centrosymmetry of the macroscopic media, poling techniques using optical and electric fields have been developed, or use was made of the inherent polar ordering in Langmuir–Blodgett films and crystals with non-centrosymmetric point groups.

It is also possible to covalently bind dipolar molecules together in a non-centrosymmetric conformation. In this approach, the requirement of molecular

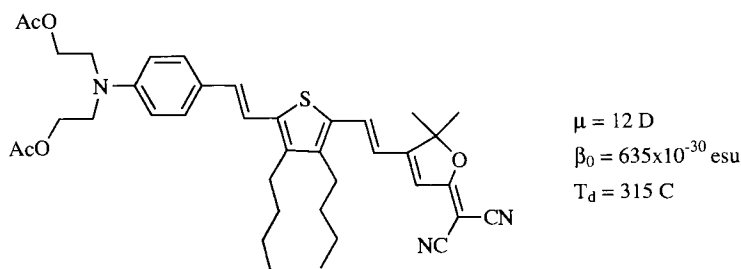


Figure 2. Example of a chromophore optimized for electro-optic applications. A PMMA-doped film with this chromophore had $r_{33} = 83 \text{ pm V}^{-1}$.

alignment is partly incorporated at the molecular level. Theoretically, this can result in a significant enhancement of the nonlinear susceptibility tensor. If n dipolar molecules with dipole moment μ_M and a dominant hyperpolarizability tensor component β_M along the dipole moment are covalently bonded together in a parallel fashion, the resulting multimer will have dipole moment $n\mu_M$ and hyperpolarizability $n\beta_M$. For a polymer film with a number density of N_M multimers and poled by a poling field with amplitude E , the macroscopic nonlinear susceptibility is equal to:

$$\chi_{ZZZ}^{(2)} = \frac{n^2 N_M f^2(\omega) f(2\omega) \mu_M \beta_M E}{5kT} \quad (24)$$

or n times the susceptibility of a poled film with nN_M monomer number density. Here we have assumed that, to a first approximation, there are no changes in the electronic structure due to intramolecular dipolar interactions. Note that this enhancement in the nonlinear susceptibility is only obtained by an improved orientation, and does not result in a transparency loss.

In addition to this enhancement, several other effects can be induced by the new conformation at the microscopic scale, such as the appearance of off-diagonal molecular hyperpolarizability tensor components. The study of these microscopically aligned molecules has also provided new fundamental insights and was only made possible through creative synthetic chemistry. The systems that have been studied so far include dimers and tetramers such as the binaphthyl ethers and the calixarenes, and polymers with rigid backbones that force the pendant D- π -A chromophores into a non-centrosymmetric conformation.

Tetramers: calixarenes

In a calixarene, four dipolar donor-acceptor molecules are covalently bonded in a non-centrosymmetric conformation [62, 63]. As shown in Figure 3, a functionalized calix[4]arene can occur in four different extreme conformations with different relative orientations of the NLO-phores: *cone*, *paco*, *1,2-alt* and *1,3-alt*. If the donor groups are alkylated by groups larger than ethyl, the different conformations are

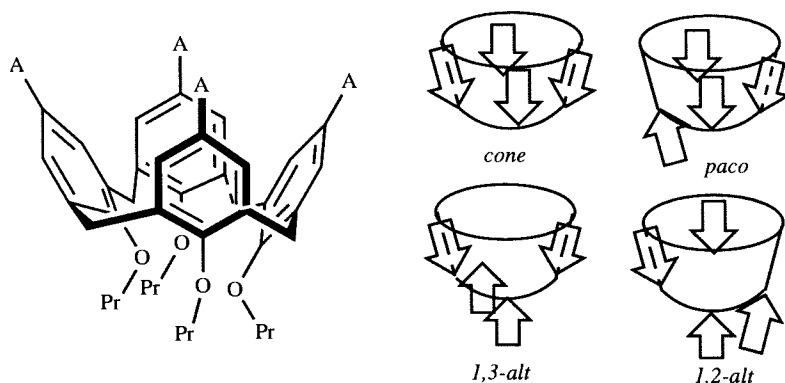


Figure 3. Molecular structure of a propoxycalix[4]arene in the *cone* conformation and a schematic representation of the four possible calix[4]arene conformations. A, electron-accepting group.

not interconvertible [64]. Since the synthesis starts from cyclophanes of four phenol moieties connected by methylene bridges, the electron donor groups are ether groups.

For the *cone* conformation, and with propoxynitrostilbene as a constituent chromophore, a threefold improvement in the static hyperpolarizability β_0 and tenfold improvement in $\mu\beta_0$ were reported for the calixarene compared with the monomeric chromophore, methoxynitrostilbene [65]. Upon poling of calixarenes in a thin film, a higher degree of orientation than for single D- π -A systems was observed.

The hyperpolarizability tensor of the four tetranitropropoxycalix[4]arene conformers using hyper-Rayleigh scattering (HRS) was studied systematically by Kenis et al. [66]. The dihedral angles of the four conformers (the angle between the planes of the different *p*-nitropropoxyphenyl units and the molecular plane through the four methylene groups that connect the four chromophoric units) were calculated by molecular dynamics and compared with the values from X-ray diffraction. The relative values of the hyperpolarizabilities of the different conformers could be well accounted for by using an additive approach for the calixarene hyperpolarizability. In this approach, the four chromophoric units are considered to contribute independently to the hyperpolarizability of the calixarene, which is calculated by performing a coordinate transformation of the monomeric hyperpolarizability tensor components to the coordinate system of the calixarene and adding the four contributions. A review of this approach used to analyze the hyperpolarizability tensor of rigid multi-chromophoric molecules is given in Ref. [67]. Although the 1,2-*alt* and 1,3-*alt* conformations can be considered as being close to centrosymmetry, this calculation showed that the relatively large hyperpolarizability for these conformations (β_0 is 1/2 and 1/4 of the cone conformation, respectively) could be attributed to an octopolar contribution in the calixarene hyperpolarizability.

Sum-over-state calculations by Morley and Naji [68] have shown that, for *cone* tetranitropropoxy[4]calixarene, steric interactions force the propoxy donor groups into an orientation that does not allow an optimal overlap of the oxygen donor lone

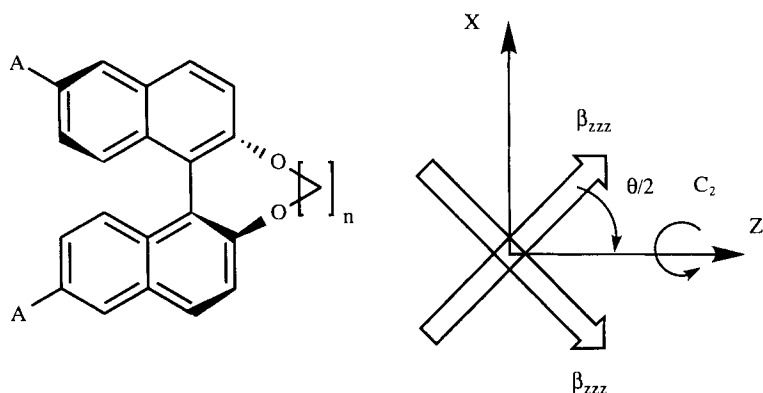


Figure 4. Structural formula and simplified geometry of a binaphthyl ether derivative. A is an electron acceptor. In the simplified geometry, β_{zzz} is in a plane parallel to the XZ -plane.

pairs with the conjugated system. This effect should reduce the total hyperpolarizability of the *cone* conformer. The evolution of the calixarene β with respect to changes in conformation was studied theoretically by Brouyère et al. [69]. According to these calculations, strong π - π cofacial interactions shift the calixarene charge transfer bands to shorter wavelengths.

Dimers: binaphthol and carbazole derivatives

An interesting class of multi-chromophoric chromophores are the binaphthol derivatives. In this class of molecules, two naphthyl ether units are covalently attached to each other in the 1,1'-positions, as shown in Figure 4 [70–72].

Apart from the possibility of obtaining a larger hyperpolarizability, these molecules are also interesting since they occur as two enantiomers. The molecular geometry of the binaphthyl rings is not planar due to the steric interactions between the hydrogen atoms in the 8,8'-positions as the molecule approaches planarity [73]. From the geometry in Figure 4, it is clear that the binaphthyl ethers cannot be superimposed on their mirror image, and hence are axially chiral. A free interconversion between the two forms does not occur at room temperature. If the starting point for the synthesis is optically pure 2,2'-dihydroxy-1,1'-binaphthyl, optically pure push-pull binaphthol derivatives can be prepared, with an ether group as electron donor. Since chiral molecules guarantee a non-centrosymmetric point group in the crystalline phase, it was anticipated that this family of compounds would provide crystals with large susceptibilities.

The hyperpolarizability tensor components of the dimer can again be calculated using an additive approach for the dimer hyperpolarizability. In the dimer coordinate frame, which has the C_2 axis as Z -axis, the dimer hyperpolarizability tensor components are:

$$\beta_{ZZZ} = 2 \left(\cos \frac{\theta}{2} \right)^3 \beta_{\text{mono}} \quad (25)$$

$$\beta_{ZXX} = \beta_{XZX} = \beta_{XXZ} = 2 \left(\cos \frac{\theta}{2} \right) \left(\sin \frac{\theta}{2} \right)^2 \beta_{\text{mono}} \quad (26)$$

where β_{mono} is the dominant β_{zzz} tensor component of the dipolar subunit. A series of binaphthol derivatives was studied using a combination of HRS and EFISHG [25, 74]. Each of these techniques measures a different combination of the two tensor components of the dimer (see Eqs. (21) and (19)):

$$\beta_{\text{HRS}} = \sqrt{\frac{6}{35} \beta_{ZZZ}^2 + \frac{16}{105} \beta_{ZZZ} \beta_{ZXX} + \frac{38}{105} \beta_{ZXX}^2} \quad (27)$$

$$\beta_{Z, \text{EFISHG}} = \beta_{ZZZ} + \beta_{ZXX} \quad (28)$$

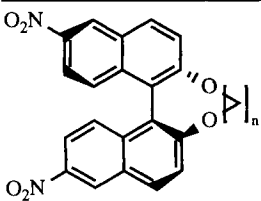
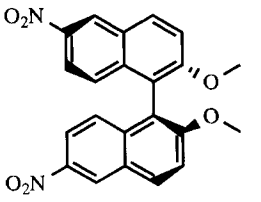
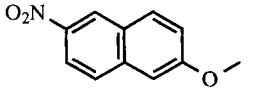
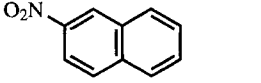
The dihedral angle was determined using AM1 semi-empirical calculations and X-ray diffraction. β_{mono} was then calculated independently of both β_{HRS} and β_{EFISHG} . The results are summarized in Table 4.

The close agreement between the β_{mono} as calculated from HRS and EFISHG again demonstrates the validity of the additive approach for the dimer hyperpolarizability. If the molecule is forced into a more planar conformation, a blue shift of the charge transfer absorption band occurs and β_{mono} is reduced substantially. This effect is attributed to the increased ring strain that reduces the overlap of the oxygen donor electron pairs with the conjugated system. Thus, for $n = 1$, the oxygen donor pairs are virtually noninteracting with the conjugated system, and the β_{mono} is almost equal to that of 2-nitronaphthalene. As n increases, the ring strain is reduced, and β_{mono} evolves to that of 6-nitro-2-methoxynaphthalene. Simultaneously, β_{ZXX} increases in magnitude relative to β_{ZZZ} , from $\beta_{ZXX}/\beta_{ZZZ} = 3/19$ for $n = 1$ to $\beta_{ZXX} = \beta_{ZZZ} = 19$ for $n = 4$.

The crystallization of binaphthol derivatives yielded crystals of low quality, probably because of the large dimer dipole moment and the nonplanar molecular shape [75]. X-ray diffraction was done on the chiral (*S*)-2,2'-diethoxy-1,1'-binaphthyl-6,6'-dicarbaldehyde. The crystallographic spacegroup was $P4_32_12$. Analysis of the unit cell showed that all the dipole moments along the dimer twofold axis cancel symmetrically, even though the space group of the optically pure enantiomer is non-centrosymmetric. For this space group all the nonlinear susceptibility tensor components disappear, and no frequency doubling was observed in a Kurtz-Perry powder test.

A significant enhancement of the off-diagonal tensor components, β_{ZXX} and β_{XZX} , was reported for C_{2v} -symmetric benzene [76] and carbazole derivatives [77]. For the carbazole derivatives, the amino donor is shared by the two acceptor groups, and quantum chemical calculations confirmed the existence of a two-dimensional charge transfer transition. A combination of (depolarized) HRS and EFISHG measurements showed that $\beta_{ZXX} = \beta_{XXZ} = \beta_{XZX}$ and $\beta_{ZZZ} = 0.28\beta_{ZXX}$

Table 4. Molecular structure, dihedral angle θ between the plane of the naphthalene subunits, wavelength of maximum absorption λ_{\max} and the first molecular hyperpolarizability of the naphthalene subunit calculated from HRS or EFISHG measurements (1064 nm, CHCl_3).

Molecular structure		θ [deg]	λ_{max} [nm]	β_{mono} [10^{-30} esu] ^a	
				HRS	EFISHG
	$n = 1$	44	306	12	10
	$n = 2$	72	308	18	18
	$n = 3$	56	326	24	16
	$n = 4$	90	332	–	27
		92	336	–	26
		–	336	27	26
		–	305	10	8

^afor some derivatives, HRS could not be used to measure β due to multi-photon induced fluorescence and only the EFISHG values are given.

[24]. Due to these large off-diagonal components, a poled film of a 3,6-substituted carbazole derivative has $d_{31} = d_{33}$ [78]. A similar enhancement of the off-diagonal tensor components was also verified for C_{2v} -symmetric benzene derivatives with EFISHG and HRS experiments.

It has been shown that poled films of molecules with large off-diagonal tensor components show a slower relaxation than poled films of dipolar molecules having only a β_{zzz} tensor component [79]. Frequency doubling through the off-diagonal components possibly offers the advantage of better phase-matching because of the almost equal refractive indices for the ω and 2ω waves, and a reduced absorption of the frequency-doubled wave in a poled film [80]. More success in obtaining non-centrosymmetric crystals was reported for the dimers of 4-nitroaniline bonded together via a methylene bridge in a Λ -shaped conformation [81]. Similarly, a dimer with a roof-shaped conformation crystallized in a crystal with large $\chi^{(2)}$ [82]. A re-

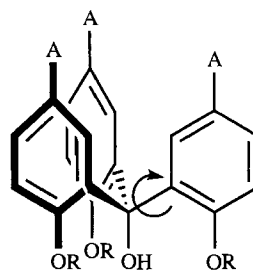


Figure 5. General structure of a triphenylcarbinol derivative.

view of these molecules and polysiliciated multi-dipolar compounds is given in Ref. [83]. A detailed determination of the crystal structure of the dimer 2,6-bis(4-hydroxybenzylidene)cyclohexanone and its implications for the nonlinear optical coefficients has been reported [84]. The Λ -shaped molecules of Heppke and co-workers form liquid crystals, of which an initial nonpolar mesophase could be converted into a polar state by applying an electric field of a few volts per micrometer, and nonlinear coefficients d_{31} as large as 16 pm V^{-1} have been reported [85]. The first hyperpolarizabilities of these Λ -shaped molecules were determined by hyper-Rayleigh scattering [86].

Trimers: triphenylcarbinol derivatives

The triphenylcarbinol derivatives have the general structure shown in Figure 5 [87]. It should be noted, however, that these molecules are not conformationally rigid at room temperature since a rapid rotation around the α -bond occurs. This conformational flexibility complicates the data analysis. The time-averaged dipole moment from capacitance measurements was not significantly larger for the trimer than for the monomeric reference compounds. The hyperpolarizability calculated from HRS measurements only showed a significant increase for the triphenylcarbinol derivative of methoxynitrostilbene compared with that of monomeric methoxynitrostilbene. These results indicate that triphenylcarbinol exists in various conformations, and that the average structure possibly has significant octopolar character. Other examples of correlated molecules with octopolar symmetry will be discussed in Section 8.3.3.

Polymers

The attachment of several chromophores to a rigid polymeric backbone can also lead to a significant enhancement of the overall hyperpolarizability and dipole moment of the polymer. The three polymeric conformations that have been shown to affect the overall nonlinear response are schematically depicted in Figure 6. They include I) polymers with a helical backbone and pendant groups that have a fixed orientation relative to the axis of the central helix, II) dendrimers with pendant chromophores attached in the outer shell, and III) main-chain polymers with a rigid backbone.

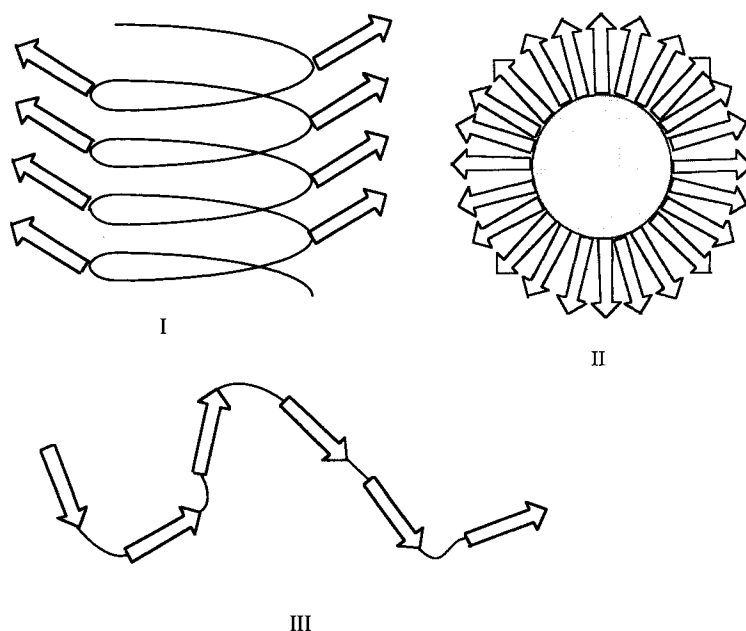


Figure 6. Polymeric geometries that lead to a microscopic orientation of the attached nonlinear optical chromophores and affect the nonlinear optical response.

Examples of helix-forming polymers are poly(isocyanides) and poly(glutamates). The repeat units of these polymers are shown in Figure 7. For poly(isocyanides), each carbon atom of the polymer backbone was functionalized with a nonlinear optical chromophore (Figure 7, I). Because of large steric interactions between the

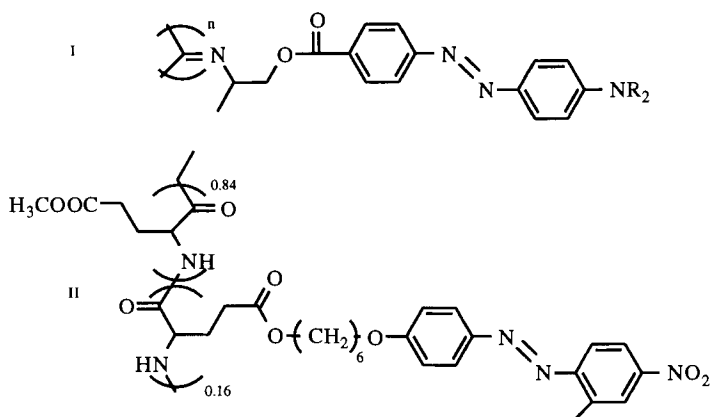


Figure 7. Structural formula of the repeat units of the functionalized I) poly(isocyanide) and II) poly(γ -benzyl-L-glutamate) polymers that adopt a helical conformation in solution.

bulky chromophores, a planar conformation or conformations combining *R* and *S* helices is unfavorable, and the most probable conformation is a full *R* or *S* helix with 3.8 pendant chromophores per turn at an angle of 60° with the central helix [88]. The investigated samples had a total of 100 chromophores per polymer. The actual increase in the polymer hyperpolarizability was smaller than calculated on the basis of the proposed conformation and the monomer hyperpolarizability, but was still a substantial factor of 5–10. More important, the off-resonant $\mu\beta$ product extrapolated from EFISHG measurements for the polymer was found to be a factor of 1.5 larger than would be found for an uncorrelated assembly of the same proportion of chromophores.

The first report of an enhanced nonlinearity due to the formation of an organic superstructure was for an α -helix forming poly(γ -benzyl-L-glutamate) of molar mass 550 000 g mol⁻¹, where the total dipole moment was 6000 D and a polymer nonlinear polarizability of 500×10^{-30} esu was found [89]. A poly(γ -benzyl-L-glutamate) copolymer with 16 % functionalized groups and an average degree of polymerization of 77 was later synthesized (Figure 7, II) and studied with a combination of EFISHG and dipole moment measurements [90]. For the superstructure, a dipole moment of 460 D and a static $\mu\beta$ of $119\,000 \times 10^{-30}$ esu were found, which represent an enhancement in $\mu\beta$ by a factor of 35 over a system of uncorrelated chromophores.

Poly(propylene imine) dendrimers of generations 4, 8, 16, 32, and 64 were functionalized with the dipolar chromophore 4-dimethylaminophenylcarboxamide end groups [23]. Even though the packing of the chromophores around the dendritic core results in a reduction of the nonlinearity (Figure 6, II), valuable information about the dynamics and rigidity of the dendrimers was obtained. The nonlinear optical response was studied by HRS. For the lower generations of dendrimers (4, 8, and 16) the hyperpolarizability calculated for the whole dendritic structure increases linearly with the number of chromophores. At higher concentrations, this increase becomes smaller and eventually disappears. This evolution shows that, at low generations, the pendant chromophores behave essentially independently, whereas at higher generations the conformational freedom is restricted and a rigid, sphere-like structure is formed. From the concentration dependence of the chemical shift of the amide protons it was concluded that intradendritic hydrogen bonding assists in the formation of a more rigid structure for the higher generations.

Enhancement of $\mu\beta$ in rigid multi-chromophore systems was also reported for main-chain polymers [91]. In these polymers, a head-to-tail alignment of the dipolar chromophores will result in an overall larger nonlinearity (Figure 6, III). A series of small oligomers with head-to-tail dipolar chromophores exhibited significant dipole moment additivity in both solution and polymer film [92]. An enhancement by 1.6-fold was reported for the electro-optic coefficient of a film of the tetramer compared with a film of analogous monomer. A large fraction of the homopolymers with dipolar repeat units had low solubility, which prevented further characterization. For an AB copolymer of α -cyano-*m*-methoxy-*p*-(ω -oxypropoxy)-cinnamate with ω -hydroxydodecanoate, an enhancement of $\mu\beta$ by a factor of 20 was found in EFISHG experiments, but this enhancement was not observed in thin films [93]. Recently, a strong cooperative enhancement effect by a factor of 40 was reported for a liquid crystalline head-to-tail 50/50 copolymer

of 2-nitro-4-carboxy-4'-[N-(11-hydroxyundecyl)-N-methylamino]azobenzene and 4-carboxy-4'-[N-(11-hydroxyundecyl)-N-methylamino]azobenzene [94].

A complex multi-chromophoric system comprises the purple membrane patches from *Halobacterium salinarium*. These patches are composed of about 3000 bacteriorhodopsin proteins. The hyperpolarizability of solubilized monomeric bacteriorhodopsin was measured by HRS and found to be 2100×10^{-30} esu at 1064 nm. This high value is due to the presence of a chromophore in the protein, the protonated Schiff base of retinal. A purple membrane patch can be treated as a two-dimensional crystal of bacteriorhodopsin proteins, and its structure is known in considerable detail. The analysis of the purple membrane tensor was performed by adding the hyperpolarizabilities of the individual proteins in the purple membrane. From (depolarized) HRS measurements on purple membrane suspensions, the structure of the purple membrane patches, and an average membrane size measured by atomic force microscopy, a β value of 2200×10^{-30} esu was calculated for bacteriorhodopsin [22]. The organization of the dipolar protonated Schiff base chromophores in the membranes was found to be predominantly octopolar.

8.3.3 Octopolar Molecules

In the early 1990s, octopolar molecules were introduced in the field of second-order nonlinear optics [95]. In contrast to dipolar molecules where it is favorable to have a large change in dipole moment upon excitation in order to maximize β , octopolar molecules are nonpolar molecules that combine second-order nonlinear optical properties with a strict cancelation of all vector-like observables, including the ground- and excited-state dipole moment. Consequently, the hyperpolarizability of such molecules cannot be described by the classical two-level model, since the difference between excited- and ground-state dipole moments $\Delta\mu_{ge}$ cancels. Zyss and co-workers used a three-level system containing the ground state and a double-degenerate excited state to describe the hyperpolarizability of octopoles [96, 97]. The expression for β within this model is:

$$\beta = \frac{3}{2} \frac{M_{eg}^2 M_{ee}}{(\hbar\omega_{eg})^2} \frac{\omega_{eg}^4}{(\omega_{eg}^2 - 4\omega^2)(\omega_{eg}^2 - \omega^2)} \quad (29)$$

with M_{ee} the transition dipole moment connecting the degenerate states. Note that the dispersion behavior of β is similar to that of the two-level description (Eq. (23)).

Furthermore, Lee et al. used a four-state model to describe the NLO properties of an octopolar molecule such as crystal violet [98]. In addition, they showed that one can use the concept of bond order alternation (BOA) to analyze the NLO structure–property relationship in octopolar molecules.

Prior to discussing the properties of octopolar molecules, it is instructive to consider first some of the basic properties of tensors. In general, any tensor of rank n can be decomposed in a sum of so-called irreducible tensors $T_{(n)}^{(\gamma, J)}$ that are invariant under three-dimensional rotation [99]:

$$T(n) = \sum_{\oplus \gamma, J} T_{(n)}^{(\gamma, J)} \quad (30)$$

Equation (30) is called the reduction spectrum of the tensor $T(n)$. Each irreducible tensor $T_{(n)}^{(\gamma, J)}$ of rank n and weight J has 3^n components labeled by n indices, and its 3^n components form the basis of an irreducible representation of the three-dimensional rotation group of degree $2J + 1$. Hence, each irreducible tensor with weight J has $2J + 1$ independent components. The superscript γ distinguishes between different components of identical weight. For example, the reduction spectrum of the hyperpolarizability tensor β (rank three) is:

$$\beta(3) = \beta_{(3)}^{(0)} + \beta_{(3)}^{('1)} + \beta_{(3)}^{('',1)} + \beta_{(3)}^{('',1)} + \beta_{(3)}^{('2)} + \beta_{(3)}^{('',2)} + \beta_{(3)}^{(3)} \quad (31)$$

In addition, it can be shown that each irreducible tensor of rank n and weight J can be expressed as an irreducible tensor of rank J (the natural form of the tensor). Natural tensors of rank (and weight) 0, 1, 2, 3 are called scalars, vectors, deviators, and septors, respectively. The corresponding physical properties are said to have a scalar ($J = 0$), dipolar ($J = 1$), quadrupolar ($J = 2$), and octopolar ($J = 3$) character.

For the hyperpolarizability of purely octopolar molecules, all irreducible tensorial components of weight strictly lower than three cancel due to symmetry requirements and $\beta = \beta_{(3)}^{(3)}$ [99]. For other molecules, the hyperpolarizability can contain contributions of all irreducible tensor components, depending on the symmetry of the molecule.

Let us clarify this by considering the two hypothetical molecules shown in Figure 8. Molecule **a** is a typical dipolar donor–acceptor molecule with C_{2v} symmetry and

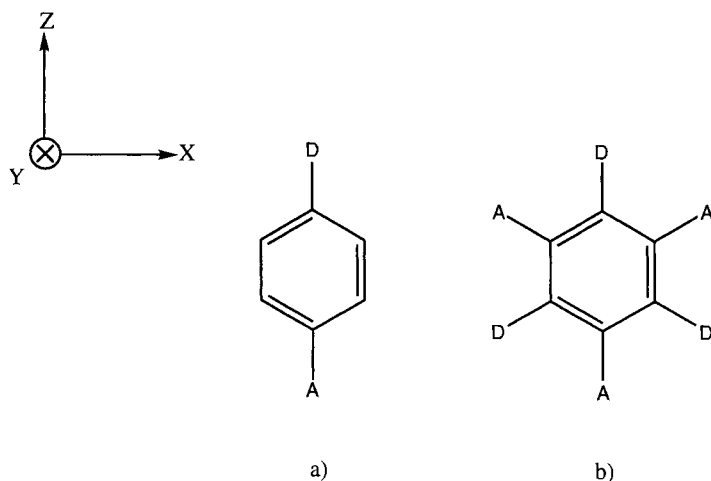


Figure 8. Schematic representation of a) a typical dipolar donor–acceptor molecule with C_{2v} symmetry and b) a purely octopolar molecule with D_{3h} symmetry.

molecule **b** is a purely octopolar molecule with D_{3h} symmetry. Molecular symmetry considerations reduce the number of independent β coefficients which can be further reduced by Kleinman index permutation symmetry. Under this condition, the non-vanishing hyperpolarizability components for the C_{2v} symmetry group are zzz , $zxx = xzx = xxz$, $zyy = yzy = yyz$ (the hyperpolarizability components are represented by their Cartesian coordinates) [3]. In addition, for two-dimensional molecules like **a** all y -containing β coefficients can be assumed negligible. The hyperpolarizability can be represented in a simplified form as a 3×6 matrix [3],

$$\beta = \begin{bmatrix} 0 & 0 & 0 & 0 & zxx & 0 \\ 0 & 0 & 0 & 0 & 0 & 0 \\ zxx & 0 & zzz & 0 & 0 & 0 \end{bmatrix} \quad (32)$$

Under the assumption of Kleinman symmetry, the hyperpolarizability tensor is fully symmetric and the reduction spectrum simplifies to

$$\beta(3) = \beta_{(3)}^{(1)} + \beta_{(3)}^{(3)} \quad (33)$$

Following standard procedure [99], the vector part of the hyperpolarizability of molecule **a** is

$$\beta_1^1 = \begin{bmatrix} 0 \\ 0 \\ zzz + zxx \end{bmatrix} \quad (34)$$

which can be embedded into a third-rank tensor

$$\beta_3^1 = \frac{1}{5} \begin{bmatrix} 0 & 0 & 0 & 0 & zzz + zxx & 0 \\ 0 & 0 & 0 & zzz + zxx & 0 & 0 \\ zzz + zxx & zzz + zxx & 3(zzz + zxx) & 0 & 0 & 0 \end{bmatrix} \quad (35)$$

The septor part is given by

$$\beta_3^3 = \frac{1}{5} \begin{bmatrix} 0 & 0 & 0 & 0 & 4zxx - zzz & 0 \\ 0 & 0 & 0 & -zxx - zzz & 0 & 0 \\ 4zxx - zzz & -zxx - zzz & 2zzz - 3zxx & 0 & 0 & 0 \end{bmatrix} \quad (36)$$

In Figure 9 we plotted the ratio of the magnitude (square root of the sum of the squares of all components) of the vector part and the septor part $|\beta_3^1|/|\beta_3^3|$ vs. β_{zxx}/β_{zzz} for molecules with only two independent hyperpolarizability components

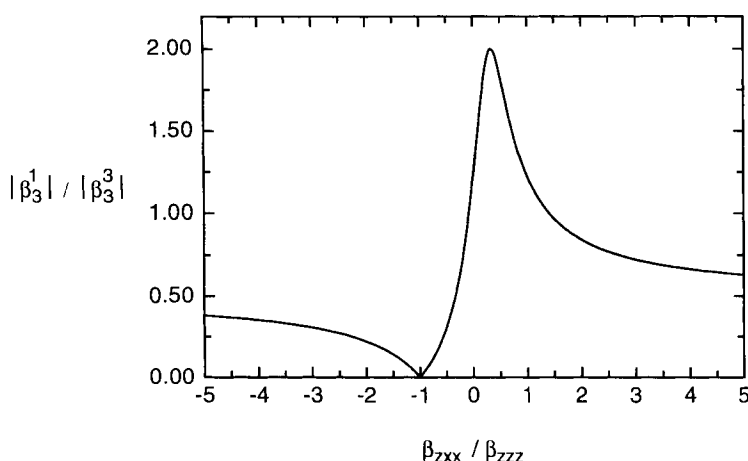


Figure 9. $|\beta_3^1|/|\beta_3^3|$ vs. β_{zxx}/β_{zzz} for a hypothetical molecule with only two independent β tensor components.

(such as molecule **a**). $|\beta_3^1|/|\beta_3^3|$ peaks when $\beta_{zxx}/\beta_{zzz} = 0.3$, showing a dominant dipolar contribution.

However, for most other ratios of β_{zxx}/β_{zzz} the octopolar contribution to the nonlinearity is dominant. The dipolar contribution to the hyperpolarizability completely vanishes when $\beta_{zxx}/\beta_{zzz} = -1$ and the molecule is purely octopolar. This situation occurs for molecule **b** with purely octopolar D_{3h} symmetry and non-vanishing hyperpolarizability components $zzz = -zxx = -xxz = -xzx$. The hyperpolarizability tensor then reduces to

$$\beta = \beta_3^3 = \begin{bmatrix} 0 & 0 & 0 & 0 & -zzz & 0 \\ 0 & 0 & 0 & 0 & 0 & 0 \\ -zzz & 0 & zzz & 0 & 0 & 0 \end{bmatrix} \quad (37)$$

One property that makes octopoles interesting is the lack of dipole moment in the ground state. This should increase the probability of non-centrosymmetric crystallization and prevent detrimental dipolar (aggregate) interaction. In addition, the ratio of off-diagonal versus diagonal β tensor components is higher than that for traditional dipolar systems, which opens up the possibility of less stringent polarization schemes for parametric and electro-optic processes [95]. Furthermore, it has been shown that the efficiency–transparency trade-off favors octopolar molecules over traditional dipolar molecules [96].

Since octopolar molecules lack a dipole moment, the hyperpolarizability of purely octopolar molecules cannot be determined with the EFISHG technique. Therefore, the experimental determination of these nonpolar molecules remained a problem until the development of the hyper-Rayleigh scattering technique (HRS). As explained in Section 8.2.2, HRS provides a sensitive tool for the determination of the hyperpolarizability of nonpolar molecules in solution.

One of the first octopoles that was shown to have a considerable second-order nonlinearity is the highly polarizable cyanoform anion, which belongs to the purely octopolar symmetry group D_{3h} [100]. The β_{zzz} of the cyanoform anion as measured by HRS was found to be on the order of 7×10^{-30} esu. Other octopoles that have been investigated include tetraorganotin compounds, symmetrically substituted benzenes and triazines, and tertiary amines [101–105]. Recently, a number of very efficient octopolar structures have been identified. For example, the octopolar crystal violet cation was shown to be considerably nonlinear, with a hyperpolarizability at least five times higher than the traditional dipolar benchmark molecule dimethylaminonitrostilbene (DANS) [106].

8.3.4 Metallo-organic Compounds

Although the search for organic materials displaying high NLO properties has been a continuously expanding domain for many years, the field of metallo-organic nonlinear optics is rather young and unexplored. In the last decade, researchers only sporadically investigated the NLO properties of metallo-organic compounds, and just recently have they begun a more systematic investigation of the molecular properties that determine the NLO response of these metallo-organic complexes. Today, this new class of materials is recognized to have potential for NLO purposes, particularly because they show strong absorption bands (metal-to-ligand charge transfer, MLCT and ligand-to-metal charge transfer, LMCT) in the UV–Vis region. As these are associated with low transition energies and high transition dipole moments the two-level model predicts large hyperpolarizabilities for metallo-organic molecules [36]. Further, numerous types of geometry are available, as a palet of coordination patterns is at hand for metals. Multipolar species become accessible and/or the molecular hyperpolarizability can be manipulated by small changes in ligands, even in the NLO-inactive ones. In addition, the possibility of chirality, which may induce a non-centrosymmetrical crystallization, can lead to a useful macroscopic arrangement. Good summaries of the NLO work performed on metallo-organic compounds can be found in several recent review articles [7, 106–109]. In this section we will focus on those metallo-organic compounds that have been proven successful in recent years (see Figure 10).

In 1987, Green et al. had already drawn attention to metallo-organic species for NLO when they revealed a SHG efficiency as high as 62 times that of urea for *cis*-[1-ferrocenyl-2-(4-nitrophenyl)ethylene] [110]. Nevertheless, it took three years before a profound EFISHG study of the molecular properties governing the hyperpolarizability of metallocenes was performed [111, 112]. Analogously to organic systems, the prolongation of the conjugated bridge, as well as the addition of electron-donating substituents (e.g., methyl groups) to the metallocene donor, was shown to enhance the hyperpolarizability. Further, the donor strength of ferrocene resembled that of the organic methoxyphenyl donor. Yet ferrocenes were expected to be stronger donors, on the basis of their binding energies and redox potentials. The discrepancy between the expected and the observed electron donor efficacy was ascribed to the poor coupling of the metal and the organic π -system which may

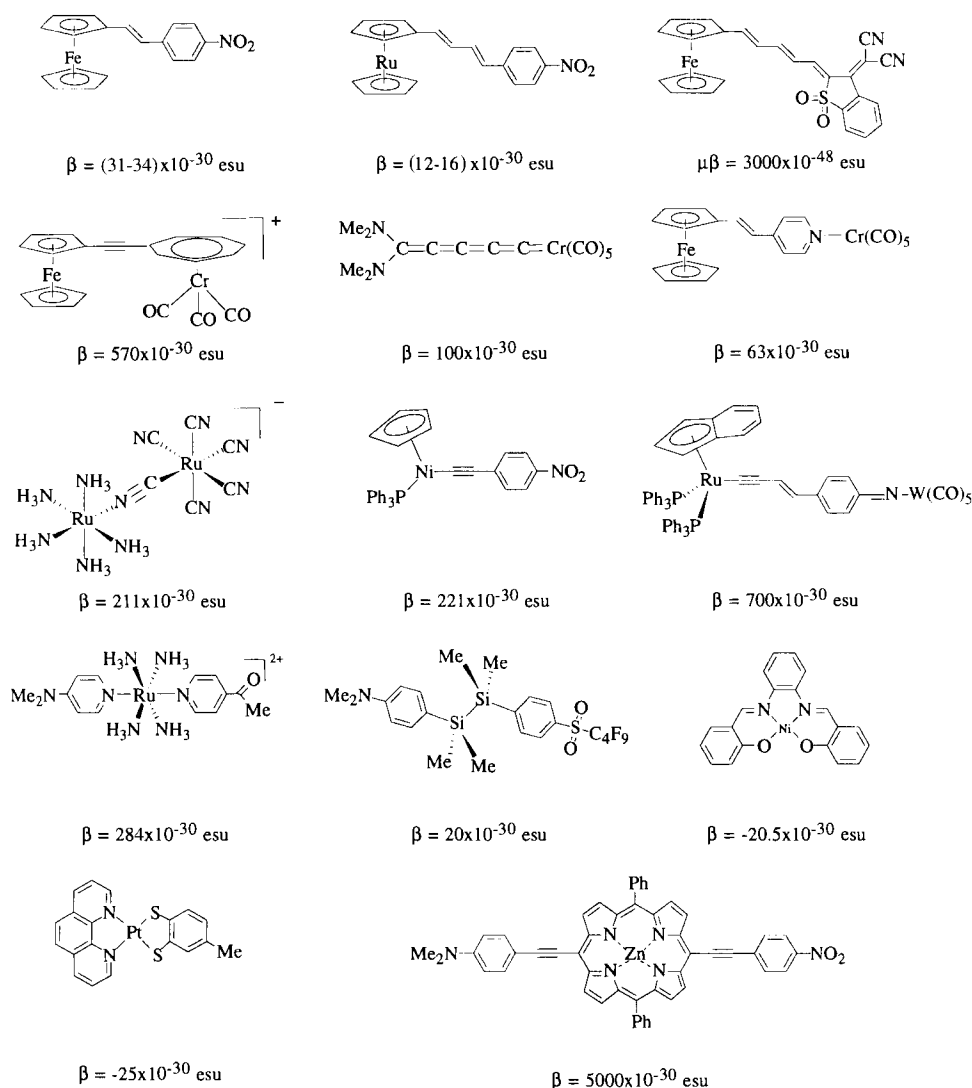


Figure 10. Metallo-organic complexes for nonlinear optics.

reduce the donor properties of the metal center in these *out-of-plane* structures. Calabrese et al. suggested the use of *in-plane* metallo-organic complexes, i.e., complexes with the MLCT in the plane of the organic π -system, to obtain large NLO efficiencies (Figure 11) [112].

Notwithstanding the drawbacks associated with the *out-of-plane* geometry, a series of conjugated ferrocene compounds with heterocyclic acceptors have recently been shown to exhibit large resonantly enhanced $\mu\beta$ values up to 3000×10^{-48} esu. Again, the increase in conjugation length or acceptor strength clearly led to en-

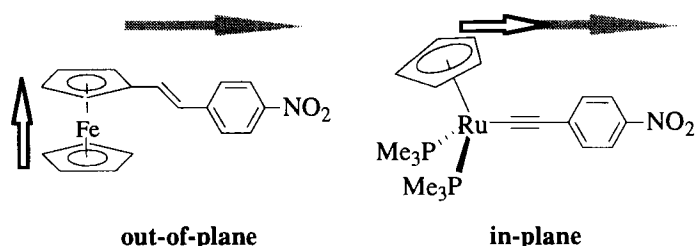


Figure 11. Examples of *out-of-plane* and *in-plane* complexes.

hanced hyperpolarizabilities [113]. On the other hand, substitution of Fe(II) with Ru(II) results in a blue shift and a clear reduction of the NLO efficiency, in accordance with the higher reduction potential of ruthenium [112, 113]. Nevertheless, the ruthenium complexes display a better nonlinearity-transparency trade-off.

In contrast to most organic compounds, two optical transitions contribute significantly to the optical nonlinearity of metallocene complexes [112, 114, 115]. In this regard, several hypotheses have been made on the nature of these transitions (Figure 12). Earlier models attribute the low-energy transition to either a ligand-field d-d excitation (**a**) or an MLCT transition to a bridge-localized LUMO+1 molecular orbital (**b**), while the high-energy transition is proposed to originate from a transition between either the metal (**a**) or a bridge-localized HOMO-3 orbital (**b**) and the acceptor-based LUMO. However, a more recent model by Barlow et al. (**c**) assumes the metal to the acceptor-centered LUMO and the bridge-localized HOMO-3 to the LUMO to be the low- and high-energy transitions respectively [115]. The latter hypothesis perfectly predicts the photoelectron, electrochemical and NLO properties of ferrocenes and ruthenocenes. An important consequence for the discussion of NLO properties of metallocenes is that the two-level model no longer holds for this class of materials.

Recently, the quadratic hyperpolarizabilities of heterobimetallic metallocenes have also been studied using the HRS technique [116–118]. The addition of a metal-pentacarbonyl function to a pyridyl acceptor group appeared to substantially increase the NLO efficiencies of the ferrocene-pyridyl compound [117, 118]. Notwith-

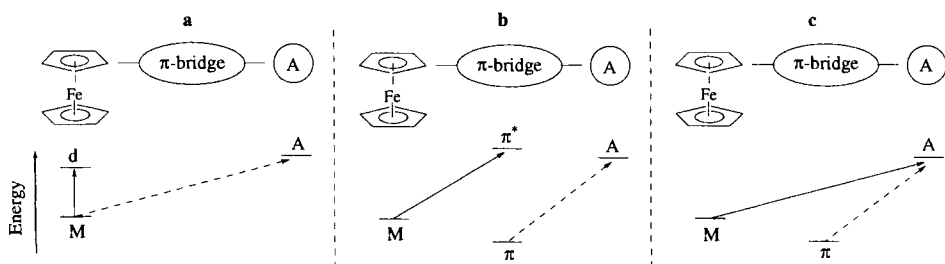


Figure 12. Schematic representation of the different hypotheses on the CT contributions to the molecular hyperpolarizability.

standing some inconsistencies between the studies of Lee et al. and Mata et al. concerning the magnitude of the hyperpolarizabilities, they both demonstrate the role of the metacarbonyl group in these complexes to be that of an inductive acceptor, lowering the energy of the pyridyl-centered LUMO [119]. Therefore the hyperpolarizability follows the series $\text{Cr}(\text{CO})_5 < \text{Mo}(\text{CO})_5 < \text{W}(\text{CO})_5 < \text{Mn}(\text{CO})_5^+ < \text{Re}(\text{CO})_5^+$. The improvement of the acceptor strength in this series is confirmed by a positive shift of the reduction potential of the Fe(II)/Fe(III) couple. Recently, the group 6 metal pentacarbonyl function was also proven successful as an acceptor in Fischer-type carbene complexes and amino-substituted cumulenylidenes [120, 121]. For these compounds, the differences in acceptor strength between Cr(0) and W(0) are less pronounced.

In another approach, transition metals have been used to stabilize the chemically reactive sesquifulvalene [116, 122]. In an early report, the bimetallic (Fe–Cr) complex was reported to exhibit hyperpolarizabilities up to 570×10^{-30} esu. However, for some other ferrocene derivatives of the sesquifulvalene complexes multi-photon luminescence has been observed which prohibits the determination of the hyperpolarizability by HRS. However, replacement of Fe(II) by Ru(II) results in luminescence-free derivatives [122, 123]. Monometallic manganese(I) sesquifulvalene complexes, on the other hand, are reported to exhibit only modest hyperpolarizabilities [124].

Aside from metallocene derivatives, *in-plane* metallo-organic complexes have been the subject of a number of NLO investigations. Formerly, large hyperpolarizabilities had been found for several mixed-valence bimetallic ruthenium complexes [125–127]. Moreover, for this class of molecules an intervalence charge transfer (IVCT) transition was suggested to account for the augmented hyperpolarizability. Confirmation was found in Stark (or electroabsorption) spectroscopy, which revealed large differences in dipole moment to accompany this low-energy IVCT transition [128].

During the last few years, a systematical study of gold(I), nickel(II), and ruthenium(II) σ -arylacetylide complexes has been performed by Whittall and co-workers. The hyperpolarizabilities were found to increase from the 14-electron gold complexes to the 18-electron nickel complexes and further to the 18-electron, more oxidizable, ruthenium compounds. Moreover, the influences of different types of π -systems, chain lengthening, acceptor, and ligand have been investigated [129–134]. As expected, the molecular hyperpolarizability relates to the chain length and acceptor strength. Changes in the metal periphery, though, only have a limited influence for these compounds. Similar results are obtained by other groups for analogous η^5 -monocyclopentadienyl- or indenyl-metal complexes [135, 136]. For aryl nitrile complexes, the hyperpolarizability was demonstrated to increase in the series $\text{Co(III)} < \text{Ni(II)} < \text{Ru(II)} < \text{Fe(II)}$, with about a three-fold increase from Ru(II) to Fe(II) [136]. Yet the Fe(II)–arylnitrile complexes were still less NLO efficient than their ruthenium–arylacetylide counterparts, indicating the superiority of the acetylide bridge [129, 136]. In addition, heterobimetallic complexes with a ruthenium bis(triphenylphosphine) (indenyl)acetylide donor were reported that exhibit the largest hyperpolarizabilities recorded to date for bimetallic systems [7, 135, 137]. The combination of the ruthenium–acetylide donor with the pyridyl-metal-

pentacarbonyl acceptor delivered larger NLO properties than their metallocene derivatives (vide supra). This is in agreement with the better electron donor properties experienced for the metal–acetylide group [7]. Recently, octopolar alkynylruthenium complexes were synthesized to reduce the nonlinearity–transparency trade-off [138]. The octopolar symmetry was shown to enhance the molecular hyperpolarizability without any loss in transparency.

Another dipolar *in-plane* route toward NLO chromophores involves donor/acceptor-substituted *trans*-tetraamineruthenium(II) complexes $\text{trans}[\text{Ru}(\text{NH}_3)_4(\text{L}^{\text{A}})(\text{L}^{\text{D}})]^{n+}$ (L^{A} = an acceptor-substituted pyridine ligand; L^{D} = an N-donor ligand) that show coplanarity of the axial ligands which can allow π – π coupling through the polarizable ruthenium center. The π – π coupling was suggested to induce large hyperpolarizabilities that can easily be modified by an appropriate choice of substituents. Indeed, the studies of Coe et al. revealed large, tunable hyperpolarizabilities $((10\text{--}410) \times 10^{-30}$ esu) [139–143]. However, no coupling between L^{A} and L^{D} was observed. Moreover, the electrochemical and NLO properties strongly suggest that the role of the donor ligand is restricted to the fine-tuning of the electronic properties of the metal, which remains the effective donor. Furthermore, the effect of the oxidation state of the metal upon the molecular optical nonlinearity was addressed. Chemical oxidation of the metal was proven to be an excellent tool to reversibly switch the molecular first hyperpolarizabilities of the *trans*-substituted ruthenium complexes [142]. Modulation “after synthesis” of the molecular hyperpolarizability was also performed for octopolar ruthenium(II) trisbipyridine. Both electrochemical and optical switching ($\text{Ru(II)} \rightarrow \text{Ru(III)}$) led to an apparent decrease in the SHG signal as a result of the reduced electron donor strength of Ru(III) [144–146].

Functionalization of the bipyridine ligand (enlarging the conjugation) proved an excellent tool for working toward ruthenium(II)trisbipyridine complexes with substantially enhanced nonlinearities [147]. Although the initially reported hyperpolarizabilities, obtained by HRS, were overestimated due to luminescence contributions, the fluorescence-free hyperpolarizabilities $((800\text{--}1000) \times 10^{-30}$ esu) are still impressive [127, 148].

Furthermore, the second-order NLO properties of metal–Schiff base complexes have been investigated [149–152]. For (*N,N'*-disalicylidene-1,2-phenylenediaminato)- M(II) ($\text{M} = \text{Co}, \text{Ni}, \text{Cu}$) the hyperpolarizability as measured with EFISHG, as well as the calculated values, increased on going from the closed shell d^8 Ni(II) to the open-shell d^9 Cu(II) and d^7 Co(II) analogs [149]. Improved accessibility of lower-lying excited states in the case of the open-shell complex was suggested to account for the larger hyperpolarizability. As for metallocenes, the two-level model does not hold for open-shell complexes, in contrast to the closed-shell ones. However, results on a similar metal–Schiff base complex present a similar hyperpolarizability for both the open-shell Cu(II) and the closed-shell Ni(II) complex, and thus undermine the previous findings [151].

For a series of square planar metal(diimine)(dithiolate) complexes, the relationship between the optical CT properties and the molecular hyperpolarizability has been studied. Compared with the Pd(II) and Ni(II) derivatives, the Pt(II) metal ion provides the largest NLO response, resulting from its low transition energy and

greater oscillator strength [153]. Furthermore, the HOMO (LUMO) is shown to be centered on the dithiolate (diimine) ligand.

The largest hyperpolarizability reported to date for a metallo-organic compound is that of the push–pull 5-{{4'-(dimethylamino)phenyl}ethynyl}-15-[(4''-nitrophenyl)-ethynyl]-10,20-diphenylporphinato]Zn(II) complex [154, 155]. Note, however, that compared with acetylenyl-bridged D–porphyrin–A systems, phenyl-bridged metalloporphyrins exhibit rather small hyperpolarizabilities [155, 156]. In the absence of the acetylenyl bridge, the electronic communication between donor and acceptor through the porphyrin bridge is strongly reduced as a consequence of the dihedral angle between the phenyl rings and the porphyrin base. In fact, it is this electronic communication that plays an important role, as evidenced by transient spectroscopy as well as by Stark spectroscopy [157, 158]. The latter reveals that the large dipole moment difference between ground and excited states, required by the two-level model for good hyperpolarizabilities, does originate from the communication between donor and acceptor through the porphyrin bridge.

Silicon can be incorporated as a donor, bridge, or even as an acceptor into an organic system [159–161]. Studies report rather moderate quadratic hyperpolarizabilities, the largest efficiency being found for the silicon donor. The main advantage of these systems compared with other metallic complexes is their transparency in the visible region.

In general, the addition of the metal leads to an increased hyperpolarizability compared with that of the free ligand. However, like organic compounds, metallo-organic complexes suffer from the nonlinearity–transparency trade-off. As mentioned, the MLCT/LMCT transitions that are responsible for the hyperpolarizabilities are very strong and lie in the visible region, especially in the case of the most promising metallo-organic complexes such as rutheniumtris(bipyridine), ruthenium- σ -arylacetylide or zincarylacetylporphyrins.

8.4 Macroscopic Nonlinearities

A strict requirement for induction of second-order nonlinear optical effects in a macroscopic material is the absence of centrosymmetry. Macroscopic non-centrosymmetry has proven to be much more difficult to achieve than molecular non-centrosymmetry. It can be achieved by, for example, non-centrosymmetric crystallization, electric-field or optical poling, self-assembly or Langmuir–Blodgett film formation [5, 6, 162]. One important requirement for these materials, in order to be useful for applications, is high nonlinearity. For example, it has been shown that for frequency-doubling applications a material should have a second-order susceptibility on the order of 60 pm V^{-1} ($1 \text{ pm V}^{-1} = 3.387 \times 10^{-9} \text{ esu}$). For electro-optic applications, an electro-optic coefficient of at least 10 pm V^{-1} is required [91]. Other issues that are important from an applications point of view are thermal, (photo)chemical, and mechanical stability, and a high transparency at the operating wavelength of the device.

For electro-optic applications, the most promising method to achieve non-centrosymmetry is probably electric-field poling of polymers containing nonlinear optical chromophores (NLO polymers) [91]. Such materials are inexpensive, easy to fabricate, have good film-forming properties for making waveguide structures, and are compatible with existing semiconductor technologies. It has already been demonstrated that high-performance electro-optic devices based on poled polymers can be made. For example, 113 GHz electro-optic modulation with low drive voltages has been demonstrated from a polymer-based phase modulator [163]. On the other hand, the development of polymeric materials for frequency conversion processes has been less successful, in particular because of low nonlinearities, absorption losses, and phase-matching problems.

To produce a non-centrosymmetric polymer film, an NLO polymer is spin-coated onto an ITO (indium tin oxide)-coated substrate. The films are carefully dried under vacuum at elevated temperatures, yielding thin films (micrometer thickness) of excellent optical quality. Subsequently, the films are heated to their glass transition temperature (T_g) where they become rubbery. A strong applied static electric field (by corona discharge or contact poling) can then orient the chromophores in the matrix to impose a non-centrosymmetric $C_{\infty v}$ symmetry on the polymer film. The chromophores in the films are oriented by coupling of their static dipole moment with the poling field. Then the film is cooled to room temperature in the presence of the electric field to freeze in the alignment of the NLO molecules. Now the field can be safely removed since the orientation of the chromophores is strongly hindered below T_g . The symmetry of the poled film is $C_{\infty v}$ and its second-order nonlinearity can be described by two independent (under the assumption of Kleinman permutation symmetry) susceptibility components zzz and zxx (z -axis perpendicular to the film plane and x -axis in the plane of the film) [91]. However, note that in order to design electro-optic (EO) devices, thin film preparation and poling are not the only issues that need to be considered. A careful electrode design, the identification of suitable buffer or cladding layers and channel waveguide patterning are equally crucial in the design strategy of a practical modulator [162].

NLO polymers are designed by incorporating nonlinear chromophores into a polymer matrix. The simplest approach is the use of polymer solutions, so-called guest–host systems, in which the nonlinear chromophore is dissolved in a compatible polymer matrix. Unfortunately, the solubility of guest molecules in a polymer matrix is usually low, which limits the magnitude of the NLO response. This problem is solved by attaching the chromophores covalently to the polymer backbone (side chain polymers) or by incorporating them into the backbone of the polymer (main chain polymers).

One of the major problems associated with poled polymer films is their inherent thermodynamic instability: the chromophores in the polymer matrix tend to relax with time, eventually leading to a centrosymmetric system. Methods to circumvent this problem include crosslinking and the use of polymers with very high glass transition temperatures.

Unfortunately, electric-field poling is not applicable to octopolar systems, because of the absence of a dipole moment. However, the recently developed all-optical poling might be useful in obtaining the required non-centrosymmetry. All-optical

poling is based on the fact that combinations of certain light fields exhibit polarity. For example, the coherent superposition of a field at frequency $\omega[E(\omega)]$ and one at frequency $2\omega[E(2\omega)]$ leads to a time-averaged cubic interference term $\langle E^3 \rangle$ where $E = E(\omega) + E(2\omega)$. Furthermore, its irreducible tensor decomposition has a component with octopolar symmetry. Therefore coupling of this field with a molecule is permitted even in the absence of a dipole moment [162]. Recently, the octopolar molecule ethyl violet was oriented in a sol-gel matrix by all-optical poling. The sample had a second-order susceptibility with octopolar symmetry of 0.6 pm V^{-1} (measured at 1064 nm) [164].

A second approach to achieve macroscopic non-centrosymmetry is the formation of crystals [6]. In principle, single crystals are very attractive NLO materials (both for frequency conversion and the electro-optic effect) because of their superior long-term stability and very high density of active components. However, the fabrication of single crystals of good quality is often a very tedious and time-consuming procedure and the fabrication of waveguide structures might be difficult. In addition, only a few highly nonlinear chromophores have been incorporated into a useful crystalline material over the past few years. The reason is that most of the highly nonlinear organic molecules crystallize centrosymmetrically. In addition, the orientation of the chromophores in the crystal lattice needs to be optimized in order to obtain a useful material. Several strategies have been used to induce non-centrosymmetric crystallization. For example, the use of chiral molecules automatically introduces non-centrosymmetry into the crystal but does not necessarily lead to an optimum arrangement of the nonlinear optical chromophores in the crystal lattice [165]. A new strategy for crystal engineering in which different materials are mixed takes advantage of specific intermolecular interactions (such as hydrogen bonds) to favor non-centrosymmetric packing. For example, co-crystals of a merocyanine dye and methyl 2,4-dihydroxybenzoate, in which the merocyanine and the dihydroxybenzoate are linked by a short hydrogen bond, were shown to be highly efficient materials for electro-optic applications (electro-optic coefficient 30 pm V^{-1} at 1535 nm) [166]. Recently, Hulliger et al. introduced NLO chromophores in the channels of perhydrotriphenylene crystals, leading to highly efficient SHG inclusion materials [167].

Another approach to organizing molecules non-centrosymmetrically has been to incorporate NLO chromophores into Langmuir-Blodgett films [6]. The advantage of this approach is the much better chromophore alignment and chromophore density. A major drawback is the often poor optical quality due to microdomain formation and the poor temporal stability and fragility. A related approach that is based on covalent self-assembly techniques to make artificial superlattices solves the problem of stability and fragility by covalently linking different layers of the superlattice [168]. On the other hand, since each layer of the superlattice involves a chemical reaction, the question remains of whether sufficiently thick layers (of micrometer thickness) with good optical quality can be obtained. Both approaches have shown some encouraging results, leading to relatively stable films with useful nonlinearities [168–172].

Chiral materials are also potentially interesting for applications in second-order nonlinear optics. For example, chirality has been extensively used to prevent cen-

trosymmetric crystallization [165]. In addition, since chiral materials are inherently non-centrosymmetric, even highly symmetric media (such as isotropic solutions of chiral molecules) are non-centrosymmetric and therefore possess a non-vanishing second-order susceptibility. For example, sum-frequency generation from a sugar solution was already observed in the early days of nonlinear optics [173]. Although this particular process cannot be phase-matched, the result is significant because the thermodynamic stability of the material was not sacrificed. However, second-harmonic generation from isotropic chiral solutions is forbidden.

Recently, it was theoretically shown, on the basis of standard density-matrix formalism of nonlinear optics, that chiral isotropic media can possess an electro-optic response [174]. Such materials would be inherently stable and could therefore be extremely useful for the development of electro-optic devices. Contrary to usual electro-optic materials, index (absorption) modulation in such media is due to the imaginary (real) part of the electro-optic susceptibility. The response relies on the damping of the material response.

Acknowledgments

We acknowledge the support of this work by the Belgian Government (IUAP P4/11), the Fund for Scientific Research—Flanders (G.0308.96) and the University of Leuven (GOA 95/1). SH, EH and TV are postdoctoral researchers, and KC is a senior research associate, of the Fund for Scientific Research—Flanders.

References

1. T. H. Maiman, *Nature* **1960**, 187, 493.
2. P. A. Franken, A. E. Hill, C. W. Peters, G. Weinreich, *Phys. Rev. Lett.* **1961**, 7, 118.
3. R. W. Boyd, *Nonlinear Optics*, Academic Press, San Diego **1992**.
4. B. E. A. Saleh, M. C. Teich, *Fundamentals of Photonics*, John Wiley & Sons, New York **1991**.
5. P. N. Prasad, D. J. Williams, *Introduction to Nonlinear Optical Effects in Molecules and Polymers*, Wiley-Interscience, New York **1991**.
6. C. Bosshard, K. Sutter, P. Prêtre, J. Hulliger, M. Flörsheimer, P. Kaatz, P. Günter, *Organic Nonlinear Optical Materials, Vol. 1*, Gordon & Breach, Amsterdam **1995**.
7. I. R. Whittall, A. M. McDonagh, M. G. Humphrey, M. Samoc, *Adv. Organomet. Chem.* **1998**, 42, 291.
8. I. R. Whittall, A. M. McDonagh, M. G. Humphrey, M. Samoc, *Adv. Organomet. Chem.* **1998**, 43, 349.
9. R. R. Tykwinski, U. Gubler, R. E. Martin, F. Diederich, C. Bosshard, P. Günter, *J. Phys. Chem. B* **1998**, 102, 4451.
10. B. F. Levine, C. G. Bethea, *J. Chem. Phys.* **1975**, 63, 2666.
11. K. D. Singer, A. F. Garito, *J. Chem. Phys.* **1981**, 75, 3572.
12. G. R. Meredith, *Rev. Sci. Instr.* **1982**, 53, 48.
13. J. Jerphagnon, *Phys. Rev. B* **1970**, 2, 1091.
14. D. A. Kleinman, *Phys. Rev.* **1962**, 126, 1977.
15. K. Clays, A. Persoons, *Phys. Rev. Lett.* **1991**, 66, 2980.
16. K. Clays, A. Persoons, *Rev. Sci. Instr.* **1992**, 63, 3285.
17. K. Clays, A. Persoons, L. De Maeyer in *Modern Nonlinear Optics, Part 3, Vol. 85* (Eds.: M. Evans, S. Kielich), John Wiley & Sons, New York **1994**, p. 455.

18. S. J. Cyvin, J. E. Rauch, J. C. Decius, *J. Chem. Phys.* **1965**, *43*, 4083.
19. R. Bersohn, Y.-H. Pao, H. L. Frisch, *J. Chem. Phys.* **1966**, *45*, 3184.
20. M. Kauranen, A. Persoons, *J. Chem. Phys.* **1996**, *104*, 3445.
21. G. J. T. Heesink, A. G. T. Ruiter, N. F. v. Hulst, B. Bölger, *Phys. Rev. Lett.* **1993**, *71*, 999.
22. E. Hendrickx, A. Vinckier, K. Clays, A. Persoons, *J. Phys. Chem.* **1996**, *100*, 19672.
23. E. J. H. Put, K. Clays, A. Persoons, H. A. M. Biemans, C. P. M. Luijckx, E. W. Meijer, *Chem. Phys. Lett.* **1996**, *260*, 136.
24. C. Boutton, K. Clays, A. Persoons, T. Wada, H. Sasabe, *Chem. Phys. Lett.* **1998**, *286*, 101.
25. E. Hendrickx, C. Boutton, K. Clays, A. Persoons, S. v. Es, T. Biemans, B. Meijer, *Chem. Phys. Lett.* **1997**, *270*, 241.
26. E. Hendrickx, C. Dehu, K. Clays, J.-L. Brédas, A. Persoons in *American Chemical Society Symposium Series 601: Polymers for Second-order Nonlinear Optics* (Eds.: G. A. Lindsay, K. D. Singer), American Chemical Society, Washington DC **1995**, p. 82.
27. M. C. Flipse, R. de Jonge, R. H. Woudenberg, A. W. Marsman, C. A. van Walree, L. W. Jenneskens, *Chem. Phys. Lett.* **1995**, *245*, 297.
28. N. W. Song, T.-I. Kang, S. C. Jeoung, S.-J. Jeon, B. R. Cho, D. Kim, *Chem. Phys. Lett.* **1996**, *261*, 307.
29. O. F. J. Noordman, N. F. v. Hulst, *Chem. Phys. Lett.* **1996**, *253*, 145.
30. G. Olbrechts, R. Strobbe, K. Clays, A. Persoons, *Rev. Sci. Instr.* **1998**, *69*, 2233.
31. G. Olbrechts, K. Wostyn, K. Clays, A. Persoons, *Opt. Lett.* **1999**, *24*, 403.
32. G. Olbrechts, K. Wostyn, K. Clays, A. Persoons, S. H. Kang, K. Kim, *Chem. Phys. Lett.* **1999**, *308*, 173.
33. K. Clays, K. Wostyn, G. Olbrechts, A. Persoons, A. Watanabe, K. Nogi, X.-M. Duan, S. Okada, H. Oikawa, H. Nakanishi, D. Beljonne, H. Vogel, J.-L. Brédas, *J. Opt. Soc. Am. B* **1999**, in press.
34. K. Clays, G. Olbrechts, T. Munters, A. Persoons, O.-K. Kim, L.-S. Choi, *Chem. Phys. Lett.* **1998**, *293*, 337.
35. L. R. Dalton, W. H. Steier, B. H. Robinson, C. Zhang, A. Ren, S. Garner, A. Chen, T. Londergan, L. Irwin, B. Carlson, L. Fifield, G. Phelan, C. Kincaid, J. Amend, Jen, A., *J. Mater. Chem.* **1999**, *9*, 1905.
36. N. Bloembergen, Y. R. Shen, *Phys. Rev. A* **1964**, *133*, 37.
37. J. L. Oudar, D. S. Chemla, *J. Chem. Phys.* **1977**, *66*, 2664.
38. S. J. Lalama, A. F. Garito, *Phys. Rev. A* **1979**, *20*, 1179.
39. S. R. Marder, D. N. Beratan, L.-T. Cheng, *Science* **1991**, *252*, 103.
40. S. R. Marder, C. B. Gorman, F. Meyers, J. Perry, G. Bourhill, J.-L. Bredas, B. M. Pierce, *Science* **1994**, *265*, 632.
41. F. Meyers, S. R. Marder, B. M. Pierce, J.-L. Bredas, *J. Am. Chem. Soc.* **1994**, *116*, 10703.
42. C. Dehu, F. Meyers, E. Hendrickx, K. Clays, A. Persoons, S. R. Marder, J.-L. Bredas, *J. Am. Chem. Soc.* **1995**, *117*, 10127.
43. G. Bourhill, J.-L. Bredas, L.-T. Cheng, S. R. Marder, F. Meyers, J. W. Perry, B. G. Tiemann, *J. Am. Chem. Soc.* **1994**, *116*, 2619.
44. S. R. Marder, C. B. Gorman, B. G. Tiemann, L.-T. Cheng, *J. Am. Chem. Soc.* **1993**, *115*, 3006.
45. M. Blanchard-Desce, V. Alain, P. V. Bedworth, S. R. Marder, A. Fort, C. Runser, M. Barzoukas, S. Lebus, R. Wortmann, *Chem. Eur. J.* **1997**, *3*, 1091.
46. S. M. Risser, D. N. Beratan, S. R. Marder, *J. Am. Chem. Soc.* **1993**, *115*, 7719.
47. G. U. Bublitz, R. Ortiz, S. R. Marder, S. G. Boxer, *J. Am. Chem. Soc.* **1997**, *119*, 3365.
48. M. Blanchard-Desce, M. Barzoukas, *J. Opt. Soc. Am. B* **1998**, *15*, 302.
49. R. Wortmann, C. Poga, R. J. Twieg, C. Geletneky, C. R. Moylan, P. M. Lundquist, R. G. Devoe, P. M. Cotts, H. Horn, J. E. Rice, D. M. Burland, *J. Chem. Phys.* **1996**, *105*, 10637.
50. B. Kippelen, F. Meyers, N. Peyghambarian, S. R. Marder, *J. Am. Chem. Soc.* **1997**, *119*, 4559.
51. S. R. Marder, L.-T. Cheng, B. G. Tiemann, A. C. Friedli, M. Blanchard-Desce, J. Perry, J. Skindhoj, *Science* **1994**, *263*, 511.
52. M. Ahlheim, M. Barzoukas, P. V. Bedwordt, M. Blanchard-Desce, A. Fort, Z.-Y. Hu, S. R. Marder, J. W. Perry, C. Runser, M. Staehelin, B. Zysset, *Science* **1996**, *271*, 335.

53. A. W. Harper, S. Sun, L. R. Dalton, S. M. Garner, A. Chen, S. Kalluri, W. H. Steier, B. H. Robinson, *J. Am. Chem. Soc.* **1998**, *120*, 329.
54. B. H. Robinson, L. R. Dalton, A. W. Harper, A. Ren, F. Wang, C. Zhang, G. Todorova, M. Lee, R. Aniszfeld, S. Garner, A. Chen, W. H. Steier, S. Houbrechts, A. Persoons, J. Zyss, *Chem. Phys.* **1999**, *245*, 35.
55. D. M. Bishop, E. K. Dalskov, *J. Chem. Phys.* **1996**, *104*, 1004.
56. B. Kirtman, B. Champagne, J. M. Andre, *J. Chem. Phys.* **1995**, *103*, 4157.
57. D. P. Shelton, J. J. Palubinskas, *J. Chem. Phys.* **1996**, *104*, 2482.
58. P. Zuliani, M. Del Zoppo, C. Castiglioni, G. Zerbi, T. Andruad, T. Brotin, A. Collet, *J. Phys. Chem.* **1995**, *99*, 16242.
59. D. M. Bishop, *Adv. Chem. Phys.* **1998**, *104*, 1.
60. B. Kirtman, B. Champagne, *Int. Rev. Phys. Chem.* **1997**, *16*, 389.
61. D. M. Bishop, B. Champagne, B. Kirtman, *J. Chem. Phys.* **1998**, *109*, 9987.
62. E. Kelderman, L. Derhaeg, W. Verboom, J. F. Engbersen, S. Harkema, A. Persoons, D. N. Reinhoudt, *Supramol. Chem.* **1992**, *2*, 183.
63. E. Kelderman, L. Derhaeg, G. J. Heesink, W. Verboom, J. F. Engbersen, N. F. van Hulst, A. Persoons, D. N. Reinhoudt, *Angew. Chem. Int. Ed. Engl.* **1992**, *31*, 1075.
64. L. C. Groenen, J.-D. van Loon, W. Verboom, S. Harkema, A. Casnati, R. Ungaro, A. Pochini, F. Ugozzoli, D. N. Reinhoudt, *J. Am. Chem. Soc.* **1991**, *113*, 2385.
65. E. Kelderman, G. J. T. Heesink, L. Derhaeg, T. Verbiest, P. T. A. Klaase, W. Verboom, J. F. J. Engbersen, N. F. van Hulst, K. Clays, A. Persoons, D. Reinhoudt, *Adv. Mater.* **1993**, *5*, 925.
66. P. J. A. Kenis, O. F. J. Noordman, S. Houbrechts, G. J. van Hummel, S. Harkema, F. C. J. M. van Veggel, K. Clays, J. F. J. Engbersen, A. Persoons, N. F. van Hulst, D. N. Reinhoudt, *J. Am. Chem. Soc.* **1998**, *120*, 7875.
67. K. Clays, E. Hendrickx, T. Verbiest, A. Persoons, *Adv. Mater.* **1998**, *10*, 643.
68. J. O. Morley, M. Naji, *J. Phys. Chem.* **1997**, *101*, 2681.
69. E. Brouyere, A. Persoons, J.-L. Bredas, *J. Phys. Chem.* **1997**, *101*, 4142.
70. M. S. Wong, J. F. Nicoud, *J. Chem. Soc. Chem. Commun.* **1994**, 249.
71. M. S. Wong, J. F. Nicoud, *Nonlinear Optics* **1995**, *9*, 181.
72. C. Andraud, T. Brotin, C. Garcia, F. Pelle, P. Golman, B. Bigot, A. Collet, *J. Am. Chem. Soc.* **1994**, *116*, 2094.
73. I. Baraldi, G. Ponterini, J. Momicchioli, *J. Chem. Soc. Faraday Trans.* **1987**, *283*, 2139.
74. H.-J. Deussen, E. Hendrickx, C. Boutton, D. Krog, K. Clays, K. Bechgaard, A. Persoons, T. Bjornholm, *J. Am. Chem. Soc.* **1996**, *118*, 6841.
75. H.-J. Deussen, T. Bjornholm, C. Boutton, E. Hendrickx, A. Persoons, T. Geisler, N. Thorup, K. Bechgaard, *Chem. Eur. J.* **1998**, *4*, 240.
76. J. J. Wolff, D. Langle, D. Hillenbrand, R. Wortmann, R. Matschiner, C. Glania, P. Kramer, *Adv. Mater.* **1997**, *9*, 138.
77. T. Isoshima, T. Wada, Y.-D. Zhang, E. Brouyere, J.-L. Bredas, H. Sasabe, *J. Chem. Phys.* **1996**, *104*, 2467.
78. T. Wada, Y. Zhang, M. Yamakado, H. Sasabe, *Mol. Cryst. Liq. Cryst.* **1993**, *85*, 227.
79. H. S. Nalwa, T. Watanabe, S. Miyata, *Adv. Mater.* **1995**, *7*, 754.
80. R. Wortmann, P. Kramer, C. Glania, S. Lebus, N. Detzer, *Chem. Phys.* **1993**, *173*, 99.
81. R. A. Huijts, G. L. Hesselink, *Chem. Phys. Lett.* **1989**, *156*, 209.
82. T. Tsunekawa, T. Gotho, H. Mataka, M. Iwamoto, *SPIE Proc.* **1990**, *1337*, 285.
83. J. Zyss, I. Ledoux in *Molecular Nonlinear Optics*, Vol. (Ed.: J. Zyss), Academic Press, Inc., New York **1994**, p. 166.
84. I. G. Voigt-Martin, L. Gao, U. Kolb, H. Kothe, A. V. Yakimanski, A. V. Tenkovtsev, C. Gilmore, *Phys. Rev. B* **1999**, *59*, 6722.
85. R. Macdonald, F. Kentischer, P. Warnick, G. Heppke, *Phys. Rev. Lett.* **1998**, *81*, 4408.
86. F. Araoka, B. Park, Y. Kinoshita, K. Ishikawa, H. Takezoe, J. Thisayukta, J. Watanabe, *Jap. J. Appl. Phys.* **1999**, *38*, 3526.
87. E. Kelderman, W. A. Starmans, J. P. M. van Duynhoven, W. Verboom, J. F. J. Engbersen, D. N. Reinhoudt, L. Derhaeg, T. Verbiest, K. Clays, A. Persoons, *Chem. Mater.* **1994**, *6*, 412.

88. M. Kauranen, T. Verbiest, C. Boutton, M. N. Teerenstra, K. Clays, A. J. Schouten, R. J. M. Nolte, A. Persoons, *Science* **1995**, 270, 966.
89. B. F. Levine, C. G. Bethea, *J. Chem. Phys.* **1976**, 65, 1989.
90. T. Verbiest, C. Samyn, C. Boutton, S. Houbrechts, M. Kauranen, A. Persoons, *Adv. Mater.* **1996**, 8, 756.
91. D. M. Burland, R. D. Miller, C. A. Walsh, *Chem. Rev.* **1994**, 94, 31.
92. H. E. Katz, M. L. Schilling, T. Fang, W. R. Holland, L. King, H. Gordon, *Macromolecules* **1994**, 24, 1201.
93. M. Mitchell, J. Mulvaney, H. J. Hall, C. Willand, H. Hampsch, D. Williams, *Polym. Bull.* **1992**, 28, 381.
94. C. Heldmann, M. Warner, *Macromolecules* **1998**, 31, 3519.
95. J. Zyss, I. Ledoux, *Chem. Rev.* **1994**, 94, 77.
96. M. Joffre, D. Yaron, R. J. Silbey, J. Zyss, *J. Chem. Phys.* **1992**, 97, 5607.
97. J. Zyss, I. Ledoux, *Chem. Rev.* **1994**, 94, 77.
98. Y.-K. Lee, S.-J. Jeon, M. Cho, *J. Am. Chem. Soc.* **1998**, 120, 10921.
99. J. A. R. Coope, R. F. Snider, F. R. McCourt, *J. Chem. Phys.* **1965**, 43, 2269.
100. T. Verbiest, K. Clays, A. Persoons, F. Meyers, J. L. Brédas, *Opt. Lett.* **1993**, 18, 525.
101. T. Verbiest, K. Clays, C. Samyn, J. Wolff, D. Reinhoudt, A. Persoons, *J. Am. Chem. Soc.* **1994**, 116, 9320.
102. M. Lequan, C. Branger, J. Simon, T. Thami, E. Chauchard, A. Persoons, *Adv. Mater.* **1994**, 6, 851.
103. S. Stadler, F. Feiner, C. Braüchle, S. Brandl, R. Gompper, *Chem. Phys. Lett.* **1995**, 245, 292.
104. S. Stadler, C. Braüchle, S. Brandl, R. Gompper, *Chem. Mater.* **1996**, 8, 414.
105. R. Wortmann, C. Glania, P. Krämer, R. Matschiner, J. Wolff, S. Kraft, B. Treptow, E. Barbu, D. Längle, G. Görlitz, *Chem. Eur. J.* **1997**, 3, 1765.
106. T. Verbiest, S. Houbrechts, M. Kauranen, K. Clays, A. Persoons, *J. Mater. Chem.* **1997**, 7, 2175.
107. H. S. Nalwa, *Appl. Organomet. Chem* **1991**, 5, 349.
108. S. R. Marder in *Inorganic Materials* (Eds.: D. W. Bruce, D. O'Hare), Wiley Interscience, Chichester **1992**, p. 115.
109. N. J. Long, *Angew. Chem. Int. Ed. Engl.* **1995**, 34, 21.
110. M. L. H. Green, S. R. Marder, M. E. Thompson, J. A. Bandy, D. Bloor, P. V. Kolinsky, R. J. Jones, *Nature* **1987**, 330, 360.
111. L.-T. Cheng, W. Tam, G. R. Meredith, S. R. Marder, *Mol. Cryst. Liq. Cryst.* **1990**, 189, 137.
112. J. C. Calabrese, L.-T. Cheng, J. C. Green, S. R. Marder, W. Tam, *J. Am. Chem. Soc.* **1991**, 113, 7227.
113. V. Alain, M. Blanchard-Desce, C.-T. Chen, S. R. Marder, A. Fort, M. Barzoukas, *Synth. Metals* **1996**, 81, 133.
114. D. R. Kanis, M. A. Ratner, T. J. Marks, *J. Am. Chem. Soc.* **1992**, 114, 10338.
115. S. Barlow, H. E. Bunting, C. Ringham, J. C. Green, G. U. Bublitz, S. G. Boxer, J. W. Perry, S. R. Marder, *J. Am. Chem. Soc.* **1999**, 121, 3715.
116. U. Behrens, H. Brussaard, U. Hagenau, J. Heck, E. Hendrickx, J. Koernich, J. G. M. van der Linden, A. Persoons, A. L. Spek, N. Veldman, B. Voss, H. Wong, *Chem. Eur. J.* **1996**, 2, 98.
117. I.-S. Lee, S. S. Lee, Y. K. Chung, D. Kim, N. W. Song, *Inorg. Chim. Acta* **1998**, 279, 243.
118. J. Mata, S. Uriel, E. Peris, R. Llusa, S. Houbrechts, A. Persoons, *J. Organomet. Chem.* **1998**, 562, 195.
119. D. R. Kanis, P. G. Lacroix, M. A. Ratner, T. J. Marks, *J. Am. Chem. Soc.* **1994**, 116, 10089.
120. E. Licandro, S. Maiorana, A. Papagni, P. Hellier, L. Capella, A. Persoons, S. Houbrechts, *J. Organomet. Chem.* **1999**, 583, 111.
121. G. Roth, H. Fischer, T. Meyer-Friedrichsen, J. Heck, S. Houbrechts, A. Persoons, *Organometallics* **1998**, 17, 1511.
122. J. Heck, S. Dabek, T. Meyer-Friedrichsen, H. Wong, *Coord. Chem. Rev.* **1999**, 192, 1217.
123. J. Heck, S. Dabek, T. Meyer-Friedrichsen, H. Wong, *Proc. SPIE-Int. Soc. Opt. Eng.* **1999**, 3796, 267.
124. M. Tamm, A. Grzegorzewski, T. Steiner, J. T., W. Werncke, *Organometallics* **1996**, 15, 4984.

125. W. M. Laidlaw, R. G. Denning, T. Verbiest, E. Chauchard, A. Persoons, *Nature* **1993**, 363, 58.
126. W. M. Laidlaw, R. G. Denning, T. Verbiest, E. Chauchard, A. Persoons, *Proc. SPIE-Int. Soc. Opt. Eng.* **1994**, 2143, 14.
127. I. D. Morrison, R. G. Denning, W. M. Laidlaw, M. A. Stammers, *Rev. Sci. Instrum.* **1996**, 67, 1445.
128. F. Vance, L. Karki, J. K. Reigle, J. T. Hupp, M. A. Ratner, *J. Phys. Chem. A* **1998**, 102, 8320.
129. I. R. Whittall, M. G. Humphrey, A. Persoons, S. Houbrechts, *Organometallics* **1996**, 15, 1935.
130. I. R. Whittall, M. G. Humphrey, A. Persoons, S. Houbrechts, *Organometallics* **1996**, 15, 5738.
131. I. R. Whittall, M. P. Cifuentes, M. G. Humphrey, B. Luther-Davies, M. Samoc, S. Houbrechts, A. Persoons, G. A. Heath, D. Bogsanyi, *Organometallics* **1997**, 16, 2631.
132. I. R. Whittall, M. P. Cifuentes, M. G. Humphrey, B. Luther-Davies, M. Samoc, S. Houbrechts, A. Persoons, G. A. Heath, D. C. R. Hockless, *J. Organomet. Chem.* **1997**, 549, 127.
133. R. H. Naulty, M. P. Cifuentes, M. G. Humphrey, S. Houbrechts, C. Boutton, A. Persoons, G. A. Heath, D. C. R. Hockless, B. Luther-Davies, M. Samoc, *J. Chem. Soc., Dalton Trans.* **1997**, 4167.
134. R. H. Naulty, M. C. McDonagh, I. R. Whittall, M. P. Cifuentes, M. G. Humphrey, S. Houbrechts, J. Maes, A. Persoons, G. A. Heath, D. C. R. Hockless, *J. Organomet. Chem.* **1998**, 563, 137.
135. V. Cadierno, S. Conojero, M. P. Gamasa, J. Gimeno, I. Asselberghs, S. Houbrechts, K. Clays, A. Persoons, J. Borge, S. García-Granda, *Organometallics* **1999**, 18, 582.
136. W. Wenseleers, A. W. Gerbrandij, E. Goovaerts, M. H. Garcia, M. P. Robalo, P. J. Mendes, J. C. Rodrigues, A. R. Dias, *J. Mater. Chem.* **1998**, 8, 925.
137. S. Houbrechts, K. Clays, A. Persoons, V. Cadierno, M. Pilar Gamasa, J. Gimeno, *Organometallics* **1996**, 15, 5266.
138. A. M. McDonagh, M. G. Humphrey, M. Samoc, B. Luther-Davies, S. Houbrechts, T. Wada, H. Sasabe, A. Persoons, *J. Am. Chem. Soc.* **1999**, 121, 1405.
139. B. J. Coe, M. C. Chamberlain, J. P. Essex-Lopresti, S. Gaines, J. C. Jeffery, S. Houbrechts, A. Persoons, *Inorg. Chem.* **1997**, 36, 3284.
140. B. J. Coe, J. P. Essex-Lopresti, S. Houbrechts, A. Persoons, *Chem. Commun.* **1997**, 1645.
141. B. J. Coe, J. A. Harris, L. J. Harrington, J. C. Jeffery, L. H. Rees, S. Houbrechts, A. Persoons, *Inorg. Chem.* **1998**, 37, 3391.
142. B. J. Coe, S. Houbrechts, I. Asselberghs, A. Persoons, *Angew. Chem., Int. Ed. Engl.* **1999**, 38, 366.
143. B. J. Coe, J. A. Harris, I. Asselberghs, A. Persoons, J. C. Jeffery, L. H. Rees, T. Gelbricht, M. B. Hursthouse, *J. Chem. Soc., Dalton Trans.* **1999**, 20, 3617.
144. A. Persoons, K. Clays, M. Kauranen, E. Hendrickx, E. Put, W. Bijmens, *Synth. Metals* **1994**, 67, 31.
145. H. Sakaguchi, T. Nagamura, T. Matsuo, *Jpn. J. Appl. Phys.* **1991**, 30, L377.
146. H. Sakaguchi, T. Nagamura, T. L. Penner, D. G. Whitten, *Thin Solid Films* **1994**, 244, 947.
147. C. Dhenaut, I. Ledoux, I. D. W. Samuel, J. Zyss, M. Bourgault, H. Le Bozec, *Nature* **1995**, 374, 339.
148. T. Renouard, H. Le Bozec, S. Brasselet, I. Ledoux, J. Zyss, *Chem. Commun.* **1999**, 871.
149. S. Di Bella, I. Fragalà, I. Ledoux, T. J. Marks, *J. Am. Chem. Soc.* **1995**, 117, 9481.
150. S. Di Bella, I. Fragalà, T. Marks, M. A. Ratner, *J. Am. Chem. Soc.* **1996**, 118, 12747.
151. P. G. Lacroix, S. Di Bella, I. Ledoux, *Chem. Mater.* **1996**, 8, 541.
152. S. Di Bella, I. Fragalà, I. Ledoux, M. A. Diaz-Garcia, P. G. Lacroix, T. J. Marks, *Chem. Mater.* **1994**, 6, 881.
153. S. D. Cummings, L.-T. Cheng, R. Eisenberg, *Chem. Mater.* **1997**, 9, 440.
154. S. M. Lecours, H.-W. Guan, S. G. Dimagno, C. H. Wang, M. J. Therien, *J. Am. Chem. Soc.* **1996**, 118, 1497.
155. S. Priyadarshy, M. J. Therien, D. N. Beratan, *J. Am. Chem. Soc.* **1996**, 118, 1504.
156. A. Sen, P. C. Ray, P. K. Das, V. Krishnan, *J. Phys. Chem.* **1996**, 100, 19611.
157. L. Karki, F. W. Vance, J. T. Hupp, S. M. LeCours, M. J. Therien, *J. Am. Chem. Soc.* **1998**, 120, 2606.

158. S. M. LeCours, C. M. Philips, J. C. de Paula, M. J. Therien, *J. Am. Chem. Soc.* **1997**, *119*, 12578.
159. G. Mignani, A. Kraemer, G. Puccetti, I. Ledoux, G. Soula, J. Zyss, R. Meyrueix, *Organometallics* **1990**, *9*, 2640.
160. G. Mignani, M. Barzoukas, J. Zyss, G. Soula, F. Balegroune, D. Grandjean, D. Josse, *Organometallics* **1991**, *10*, 3660.
161. P. F. van Hutten, G. Hadziioannou, R. Bursi, D. Feil, *J. Phys. Chem.* **1996**, *100*, 85.
162. *Poled Polymers and Their Applications to SHG and EO Devices*, Vol. 4, Gordon & Breach, Amsterdam **1997**.
163. H. Fetterman, D. Chen, A. Udupa, D. Bhattachaya, B. Tsap, S. Lee, A. Chen, W. Steier, J. Dalton, *IEEE/LEOS Summer Topical Meeting, Organic Optics and Optoelectronics* **1998**, p. 9.
164. C. Fiorini, F. Charra, J. M. Nunzi, I. D. W. Samuel, J. Zyss, *Opt. Lett.* **1995**, *20*, 2469.
165. J. Zyss, D. S. Chemla, *Nonlinear Optical Properties of Organic Molecules and Crystals*, Vol. 1, Academic Press, Orlando, FL **1987**.
166. M. S. Wong, F. Pan, M. Bösch, R. Spreiter, C. Bosshard, P. Günter, V. Gramlich, *J. Opt. Soc. Am. B* **1998**, *15*, 426.
167. J. Hulliger, O. König, R. Hoss, *Adv. Mater.* **1995**, *7*, 719.
168. T. J. Marks, M. A. Ratner, *Angew. Chem., Int. Ed. Engl.* **1995**, *34*, 155.
169. K. Clays, N. J. Armstrong, M. C. Ezenyilimba, T. L. Penner, *Chem. Mater.* **1993**, *5*, 1032.
170. W. M. K. P. Wijekoon, S. K. Wijaya, J. D. Bhawalkar, P. N. Prasad, T. L. Penner, N. J. Armstrong, M. C. Ezenyilimba, D. J. Williams, *J. Am. Chem. Soc.* **1996**, *118*, 4480.
171. T. L. Penner, H. R. Motschmann, N. J. Armstrong, M. C. Ezenyilimba, D. J. Williams, *Nature* **1994**, *367*, 49.
172. G. J. Ashwell, P. D. Jackson, W. A. Crossland, *Nature* **1994**, *368*, 438.
173. P. M. Rentzepis, J. A. Giordmaine, K. W. Wecht, *Phys. Rev. Lett.* **1966**, *16*, 792.
174. M. Kauranen, A. Persoons, *Nonlinear Optics* **1999**, *19*, 309.

Volume V

Part 2

Imaging and Information

1 Electron Transfer Processes in Silver Halide Photography

John R. Fyson, Peter J. Twist, and Ian R. Gould

1.1 Introduction

Silver halide color photography represents one of the most technologically complex applications of electron transfer chemistry in use today. The photosensitive component of a typical color negative film consists of 10–15 layers with a total thickness of only ca. 20 μm , each with different optical properties and chemical functions. Modern films typically contain over 100 different organic compounds and several million silver halide microcrystals per square millimeter. The light-induced image capture events, and the subsequent image development processes involve a variety of homogeneous and heterogeneous photochemical and thermal electron transfer reactions. In the image capture step, light which is absorbed by sensitizing dyes adsorbed onto the surface of silver halide microcrystals results in transfer of electrons to silver halide. Transfer of only a small number of electrons results in the formation of a small, stable speck of metallic silver. Otherwise undetectable by conventional analytical techniques, this silver speck serves as a latent image which catalyzes the formation of a visible dye image in the development step. The dye-forming processes involve oxidative coupling reactions with transfer of four electrons to the silver halide for each dye molecule formed. Importantly, a single latent image of a few silver atoms in a crystal can catalyze the formation of millions of dye molecules. It is this huge amplification factor that makes silver halide materials unique in imaging applications. Subsequent to development, the metallic silver formed in the development process is removed in a bleaching step by electron transfer to an oxidizing agent to reform silver ions, which are then dissolved out of the film in the fixing step. Thus, electron transfer reactions are involved in the entire image forming process.

A description of the entire photographic process is clearly beyond the scope of this article, which concentrates on the chemical and physical aspects of the significant electron transfer reactions involved the three fundamental steps described above, i.e., image capture, development, and bleaching. Other aspects of photo-

graphic chemistry and physics, i.e., fixing and washing, are included here only when necessary to provide the proper context. The important electron transfer chemistry involved in image development and the bleaching process is described first, followed by the more physical aspects of the spectral sensitization processes involved in the primary image capture events.

1.2 Developers

1.2.1 Introduction

It is estimated that the amount of silver required in the latent image needed to produce all the amateur photographic images captured in 1998 only amounted to less than 10 g. The energy used in creating this silver from silver halide is perhaps as little as 10 kJ. This is spread over perhaps 10^{12} images. This small amount of silver which constitutes the latent image has to be amplified to render it visible, to be seen by the eye, by a scanner, or by a piece of photographic paper in a printer or enlarger. The property of the developer is to detect this latent image and to amplify it, ideally in a fashion that is related directly to the exposure.

The presence of the latent image in exposed silver halide was first observed by Daguerre [1], who discovered that hidden images on exposed photographic plates were rendered visible when kept inadvertently in a cupboard with bottles of mercury. He attributed this effect to the mercury revealing this hidden image by amalgamating with it. This process was improved and became popular as Daguerreotypes. At the same time Fox Talbot was experimenting with silver salts adsorbed to paper. He heard that Reade had observed that a mixture of gallic acid, 3,4,5-trihydroxybenzoic acid, and silver nitrate turned black in sunlight [2]. Talbot found that if he included the reducing agent gallic acid in the paper he no longer required the image to become visible before processing it [3]. It could be rendered visible by further treatment with a solution of gallic acid and silver nitrate. This mixture was probably the first photographic developer in the sense that we know it today, with properties of a physical developer. He also discovered that the image would appear spontaneously if left in the dark for a few minutes. Thus he had been able to make the first incorporated developer material. Images produced in this way were known as Calotypes. Other reducing agents that were tried include pyrogallol (1,2,3-trihydroxybenzene) and transition metal complexes, especially those of iron(II) [4]. The first observations that development might involve electrical activity appear to have been made by Terry [5]. He described development as being the result of galvanic action. One might dispute the logic of his hypothesis but it fits with more modern thinking. He also described the use of a developer of mixed iron(II) and iron(III) complexes [4] to get the best image, or discrimination as we would now call it. It was necessary to have a developing agent of reducing power that was sufficient to develop silver at the latent image site, but not too powerful so as to render all the image black. Cramp and Hillson [6] used a similar technique to examine the excess energy of the latent image some 130 years later! In 1880 Abney

[7] reported a new developer, hydroquinone, that had been used to develop collodion silver bromide plate. This was originally a very expensive natural product [8], but a synthetic process reduced its cost and it became a popular developing agent used with sulfite [9]. It was also discovered that *p*-aminophenols [10] and naphthols [11] would act as developers. These had different characteristics from the hydroquinone developers. The image would appear immediately but did not reach such a high density as with hydroquinone. When the two types of developer were mixed, the image appeared rapidly and good image tones were formed [12]. This was the first “superadditive” developer.

p-Phenylenediamines could also be used as developers. Fischer [13] discovered that the oxidation product of the development reaction would react readily with color formers, now known as couplers, to form various colored images. He also suggested a three-color process by incorporating different couplers to form different colors in separated layers containing silver sensitized to different wavelengths of light. This reaction was the basis of the chromogenic color process. The technology of retaining the couplers in the emulsion was not available and it was the Kodachrome process, invented by Mannes and Godowsky [14], that became the first color film process to rely on different couplers, but these were added in three separate developers. Color-forming couplers were found that could be coated and did not diffuse out of the photographic layer, and a practical reversal system was launched in 1936. This was quickly followed by negative working films and papers.

A typical color process in use today (see Table 1), using this chromogenic method of forming color, consists of a number of steps. The developer forms the color and simultaneously generates unwanted silver. This is removed in the bleach. Silver halide retained in the film is then removed in the fixer. The washes remove unwanted residual chemicals in the film and prevent contamination of one bath by another.

1.2.2 Chemical Development

Changes in silver halide caused by development

The exposure of a light-sensitive photographic material based on silver halide causes microscopic changes to occur in the silver halide crystal. These changes result in

Table 1. A typical color process [15].

Step	Time [s]	Temperature [°C]
Develop	195	37.8
Bleach	260	35–41
Wash	65	24–41
Fix	260	35–41
Wash	195	24–41
Stabilise	65	24–41
Dry	as required	as required

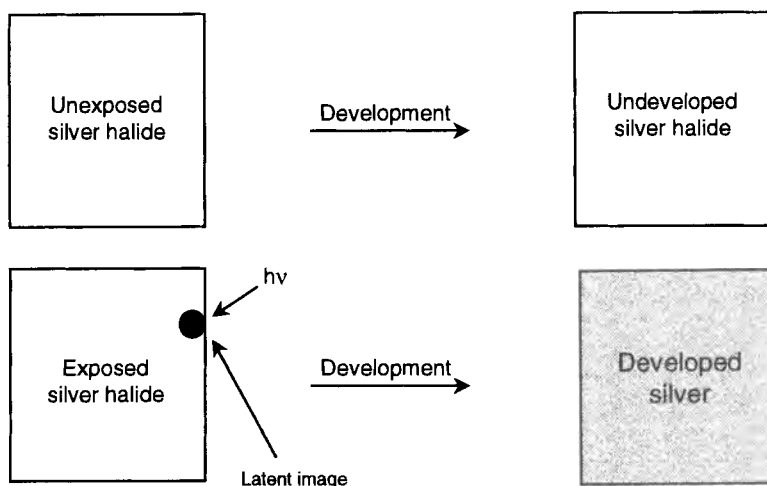


Figure 1. Idealized development of exposed and unexposed silver halide. In practice a small amount of development occurs, even in the unexposed silver halide.

what is called a latent image (Figure 1). The latent image consists of a few to several hundred atoms of silver metal. The latent image is too small to be visible and chemical development is the term used to describe the process of rendering an exposed image visible. The minimum size of the latent image that is able to initiate development is four atoms of silver and two atoms of gold [16]. Gold can be incorporated into the latent image because it is used to chemically sensitize silver halide in order to improve its light sensitivity. Development reduces solid silver halide to silver metal with the release of halide ions and the amplification factor involved in this process is large, at about 10^7 – 10^9 . A modern ISO 400 speed silver halide emulsion has an average grain volume of about $0.5 \mu\text{m}^3$ (A. Codling, private communication), and silver bromide has a density of 6.473 [17] and a molecular weight of 187.78; from this the average number of molecules of silver bromide per grain can be calculated at 10.24×10^9 . If the latent image contained four atoms the amplification factor for complete development of the average grain to metallic silver is therefore about 2.5×10^9 . This number is higher than that for most normal exposures when the latent image will contain many more silver atoms. In addition, silver halide grains are only partially developed in high-speed color negative films.

Developed silver is usually filamentary in nature and often occupies about the same volume as the original silver halide grain but as a complex tangle of silver filaments (Figure 2).

Chemical development follows two stages [18], the first being the relatively slow initiation period during which visible silver is not formed but in which the latent image grows spherically before gross reduction of the silver halide commences. This stage has also been called the induction period, although another definition of in-

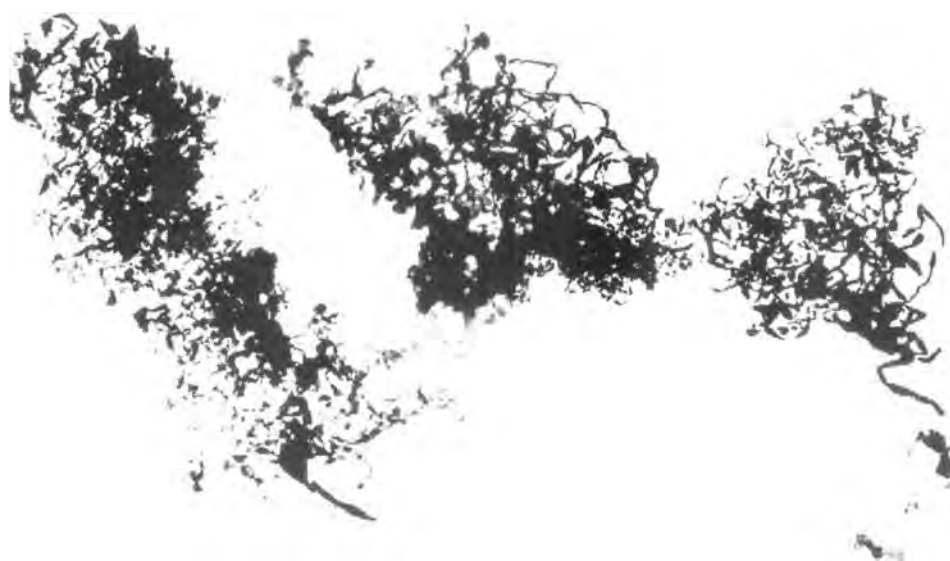


Figure 2. Photomicrograph of silver halide grains and developed silver.

duction period refers to it as the period, over which the rate of growth of image density increases. The second stage of chemical development, the continuation stage, involves the reduction of the entire silver halide grain to silver. It is during this stage that filamentary silver is formed. Increase in exposure mainly causes an increase in the number of developed silver grains with a relatively small change in the degree of development per grain, although the number and size of latent image sites can also increase. Some silver halide emulsions are designed to be partially developed: in this case only part of a given silver halide grain is reduced to silver. This process is encouraged in color negative films by the use of special compounds, called development inhibitor releasers, incorporated into photographic layers which inhibit the development process in order to improve the graininess of the image.

The response of a photographic material to exposure and development is represented by means of a density vs. relative log exposure (D vs. $\log E$), or H and D curve after Hurter and Driffield [19]. A typical curve for black-and-white development is shown in Figure 3.

The rate of development can be represented by a development-time plot; the shape of this curve can vary depending on the type of developer used, as shown in Figure 4. In this plot the main developing ion has a charge of 0, 1-, 2-, or 3-; in order to explain the curve shape for different developing agents James [20] proposed the charge-barrier theory, according to which a negative charge barrier caused by the adsorption of halide ions is formed at the silver halide surface and represents an obstacle through which developing agent ions must pass to cause development. Uncharged developing agents are not affected and develop from the start, whereas

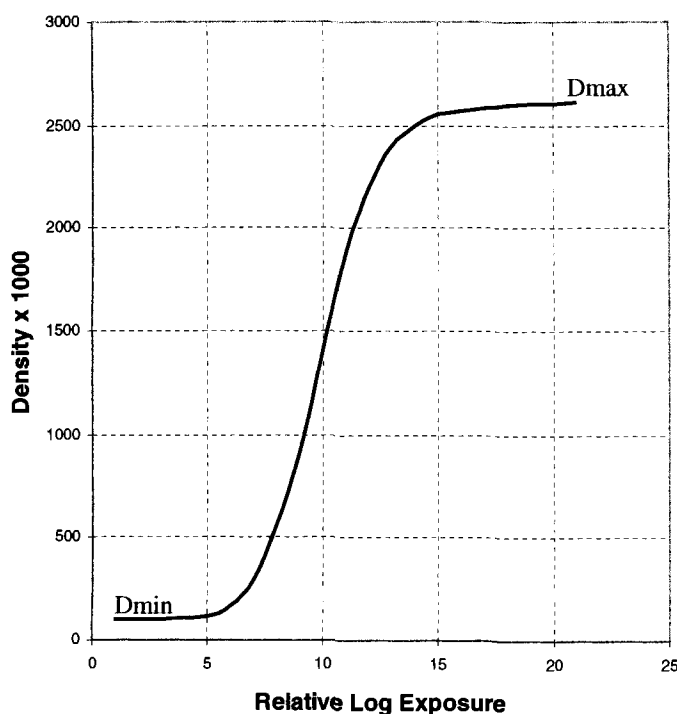


Figure 3. A typical development vs. relative log exposure curve or D vs. $\log E$ curve.

with increasing charge on the developing agent ion there is an increasing induction period. This is due to the lower concentration of negative developing agent ions close to the negatively charged silver halide surface, which lowers the development rate in the early stages. As development proceeds, silver halide is replaced by developed silver and the charge barrier is reduced, enabling the development to accelerate. In general the curve for zero-charged agents, when treated in terms of developed silver rather than silver density, shows the expected behavior for autocatalytic development based on the increasing surface area of the developed silver. Hillson [21] has treated this concept from an electrochemical point of view and concludes that a decrease in the charge barrier is not necessary in order to explain the kinetics.

The rate of development is related to the concentration of developing agent in solution and the rate equation takes the form

$$d[\text{Ag}]/dt = k[C]^n \quad (1)$$

where n is often fractional but usually between 1 and 0.5. The rate can also depend on the amount of silver reduced, as found by Fyson and Levenson [22], who observed two types of relationship involving silver, depending on which developing agent was

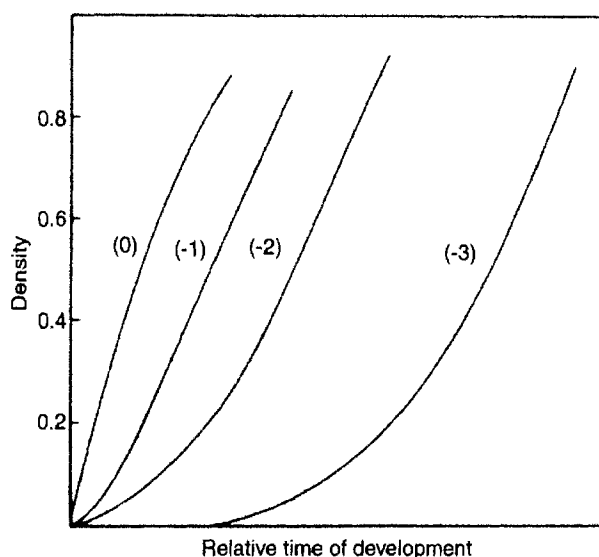


Figure 4. Density vs. relative time of development for differently charged developing agents [20]. The charges are shown on the curves.

used. In Eq. (2),

$$d[\text{Ag}]/dt \propto [\text{Ag}]^{2/3}(1 - [\text{Ag}]) \quad (2)$$

where $[\text{Ag}]$ is the amount of silver reduced, the first term indicates dependence on the surface area of the growing silver image and the second term indicates dependence on the remaining unreduced silver halide. The second type of relationship was Eq. (3),

$$d[\text{Ag}]/dt \propto (1 - [\text{Ag}]) \quad (3)$$

in which the rate depends on the remaining silver halide.

If the development rate by negatively charged developing agent ions is monitored until all the silver halide is reduced, it follows a typical S-shaped curve that has been interpreted as a consequence of autocatalysis caused by the increasing surface area of the developed silver. An alternative interpretation by Gavrik [23] holds that this autocatalysis is a consequence of simpler kinetics and that development is better represented by simple relations where developed silver mass is proportional to development time with an initial induction period and a final exhaustion period when all the silver halide has been reduced. Levenson [24], however, has reaffirmed the autocatalytic view.

Physical development is another type of development, in which soluble and usually complexed silver ion is reduced from solution onto nuclei, which can be latent image nuclei, other suitable nuclei, or silver produced by chemical development. "Chemical development" and "physical development" are traditional terms derived

from early in the understanding of photographic processes, yet both are processes of chemical reduction or electron transfer.

Developing solutions

The essential ingredient in a photographic developer solution is the developing agent, which is a special type of reducing agent capable of reducing only those silver halide crystals that bear a latent image and not those which do not have a latent image (see Figure 1). This is the ideal case and even the most carefully chosen developing agents will cause the reduction of some crystals of unexposed silver halide, giving what is colloquially referred to as fog. Fog is kept to a minimum by very closely controlled precipitation of the silver halide crystals to give a photographic emulsion which is actually a dispersion of silver halide, usually in gelatin solution. The term "photographic emulsion" is a misnomer since strictly speaking it is a dispersion, but the term emulsion is universally used to describe it. In addition the developer solution is carefully designed to minimize fog and often contains restrainers and antifoggants which help in this regard. A black-and-white film developer composition is given in Table 2 and a color film developer composition in Table 3.

Table 2. Example of a black-and-white developer.

Function	Component	Concentration
pH buffer	Na ₂ CO ₃	37.5 g
Restrainer	KBr	2.0 g L ⁻¹
Antifoggant	BTAZ ^a	0.15 g L ⁻¹
Antioxidant	Na ₂ SO ₃	75 g L ⁻¹
Primary developing agent	phenidone ^b	0.25 g L ⁻¹
Secondary developing agent	hydroquinone	8 g L ⁻¹
pH		9.5

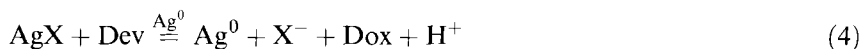
^a 5-methylbenzotriazole, ^b 1-phenyl-3-pyrazolidinone.

Table 3. Example of a color developer.

Function	Component	Concentration
Anti-calcium agent	DTPA · Na ₅ (40 %) ^a	6.5 mL L ⁻¹
pH buffer	K ₂ CO ₃	37.5 g L ⁻¹
Restrainer	NaBr	1.3 g L ⁻¹
Antioxidant	HAS ^b	2.0 g L ⁻¹
Antioxidant	Na ₂ SO ₃	4.25 g L ⁻¹
Color developing agent	CD4 ^c	4.5 g L ⁻¹
pH	KOH	to pH 10.0

^a diethylenetriaminepentaacetic acid sodium salt, ^b hydroxylamine sulfate, ^c 4-amino-3-methyl-*N*-ethyl-*N*-(hydroxyethyl)aniline sulfate.

Thermodynamically, developing agents are capable of reducing all the silver halide crystals in a photographic emulsion to silver metal, and the primary function of the silver latent image is to act as a catalyst to accelerate the development of those crystals bearing the latent image relative to those which do not. Electron transfer from the developing agent to silver halide is slow whereas electron transfer from the developing agent to the latent image is fast. Thus photographic development of the latent image is a kinetically controlled reaction and discrimination of the photographic image depends on this reaction being faster than the development of unexposed silver halide. The main reaction involved in development by a one-electron developing agent is generally described by Eq. (4)



where Dev is the reduced form of the developing agent and Dox is the oxidized form. Hydrogen ions are one of the products of the reaction when organic developing agents are used. Organic developing agents are thus involved in both electron transfer and proton transfer reactions and the development reaction is therefore a pH-dependent redox process.

This overall reaction can be considered as two electrochemical half-cell reactions each involving the transfer of one electron (Eqs. (5) and (6)).



Each of these half-cell reactions has a redox potential, E_{Ag} for reaction (5) and E_{Dev} for reaction (6), which can be measured experimentally at an electrode in an electrochemical cell relative to a reference such as the hydrogen or calomel electrode. In order for reduction of silver ion to proceed, the difference $E_{\text{Ag}} - E_{\text{Dev}}$ must be positive, whereas if it is negative silver dissolution or bleaching reaction occurs. In addition it has been found that the magnitude of the difference $E_{\text{Ag}} - E_{\text{Dev}}$ needs to be above a value referred to as the critical potential, for significant development to be observed. Reinders found that the critical potential was about 90 mV, below which no development was observed [25]. A range of critical potential values from about 50 to 160 mV has been found, depending on developer composition [26]. In contrast to these values for the development of silver halide, no critical potential was observed by Pontius et al. [27] for physical development on colloidal or latent image nuclei. It was observed, however, that as $E_{\text{Ag}} - E_{\text{Dev}}$ increased, so did the rate of physical development. This is discussed further in the next section. The electrochemical thermodynamics of the half-cell reactions is described by the Nernst equation; for the silver half-cell it is Eq. (7),

$$E_{\text{Ag}} = E_{\text{Ag}}^\circ + \frac{RT}{F} \ln \frac{[\text{Ag}^+]}{[\text{Ag}]} \quad (7)$$

where E_{Ag}° is the standard silver potential measured at 25°C and unit activity, $[\text{Ag}^+] = 1.0 \text{ M}$, the activity of solid silver $[\text{Ag}]$ is defined as 1.0 and E_{Ag} is the potential at other Ag^+ ion concentrations and other temperatures. The silver ion concentration depends on the type of silver halide that is being reduced and is affected by the free halide concentration at the development site. The solubility product of the silver halide K_{sp} is given by Eq. (8), which when substituted in Eq. (7) gives Eq. (9).

$$K_{\text{sp}} = [\text{Ag}^+][\text{Br}^-] \quad (8)$$

$$E_{\text{Ag}} = E_{\text{Ag}}^\circ + \frac{RT}{F} \ln \left(\frac{K_{\text{sp}}}{[\text{Br}^-]} \right) \quad (9)$$

At 25°C this becomes Eq. (10).

$$E_{\text{Ag}} = E_{\text{Ag}}^\circ + 0.0591 \log_{10} \left(\frac{K_{\text{sp}}}{[\text{Br}^-]} \right) \quad (10)$$

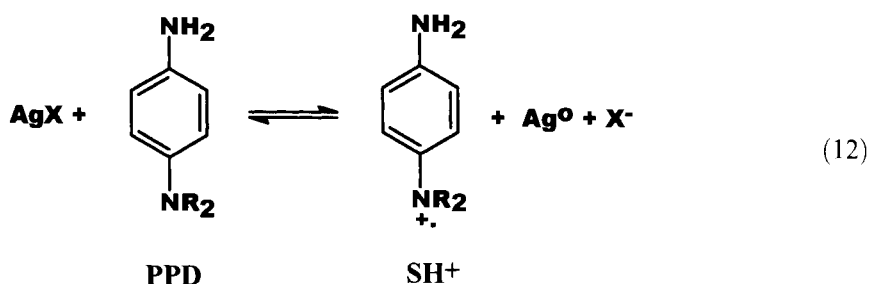
The solubility products K_{sp} are $\text{AgCl} = 1.56 \times 10^{-10}$, $\text{AgBr} = 7.7 \times 10^{-13}$, and AgI , 1.5×10^{-16} [17], and $E_{\text{Ag}}^\circ = 799 \text{ mV}$ (NHE). In color developer solutions a common level of sodium chloride or bromide is about $1\text{--}2 \text{ g L}^{-1}$ or about 10^{-2} M . Under these conditions the silver potentials (NHE) for the different halides are $\text{AgCl} = 338 \text{ mV}$, $\text{AgBr} = 202 \text{ mV}$, and $\text{AgI} = -17 \text{ mV}$. The silver ion concentration can also be influenced by the presence of silver ion ligands. A silver ion complexing agent will lower the silver ion concentration and so lower the silver potential.

The developer half-cell potential is given by Eq. (11).

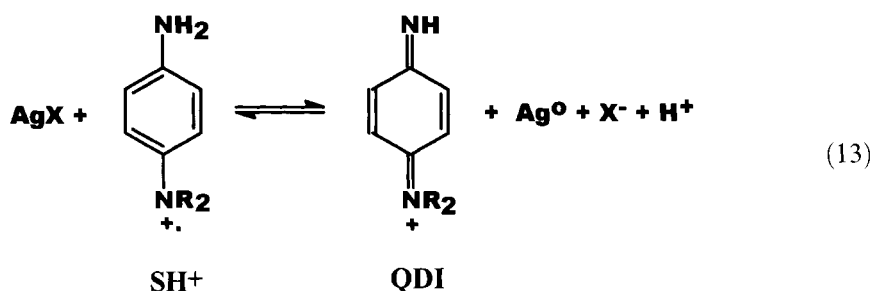
$$E_{\text{Dev}} = E_{\text{Dev}}^\circ + \frac{RT}{F} \ln \frac{[\text{H}^+][\text{Dox}]}{[\text{Dev}]} \quad (11)$$

The driving force $E_{\text{Ag}} - E_{\text{Dev}}$ for the development reaction with a given developing agent becomes less on going from silver chloride to silver bromide to silver iodide, and so development is more difficult and the development rate tends to be lower down this series. A more formal discussion of the dependence of development rate on overpotential is given in the section entitled "Development mechanism", below.

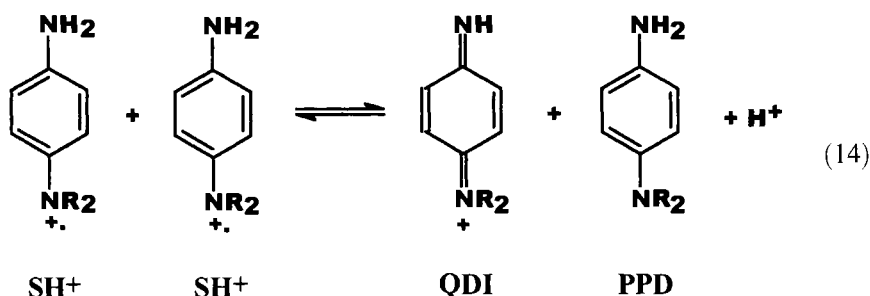
In practice many developing agents, such as *p*-phenylenediamines, *p*-aminophenols and hydroquinones, are two-electron reducing agents. In general *p*-phenylenediamine developing agents have one nitrogen substituted with alkyl or alkoxy groups and the like, in order to influence properties such as solubility, reactivity, and stability of dyes formed by coupling (see Section 1.2.3). The reaction of a typical *p*-phenylenediamine (PPD) with silver halide is shown in Eq. (12).



The semiquinone (SH^+) is unstable and can lose another electron to form the quinonediimine QDI (Eq. (13)) [28].



In addition the semiquinone (SH^+) can undergo a reversible dismutation [29], to generate PPD and QDI (Eq. (14)).



This equilibrium is very rapidly established and, for example, in the case of *N,N*-diethyl-*p*-phenylenediamine (CD1) the rate constant for the forward reaction is $k_f = 2.0 \times 10^6 \text{ L mol}^{-1} \text{ s}^{-1}$ and the rate constant for the backward reaction is $k_b = 6.3 \times 10^{11} \text{ L}^2 \text{ mol}^{-2} \text{ s}^{-1}$ [29c].

The oxidation potentials E_1 and E_2 for transfer of the first and second electrons in the development of silver halide have been estimated [28] for several developing agents: the rate of development correlates better with E_1 than with E_2 , suggesting that the oxidation to the semiquinone is the rate-determining step in development.

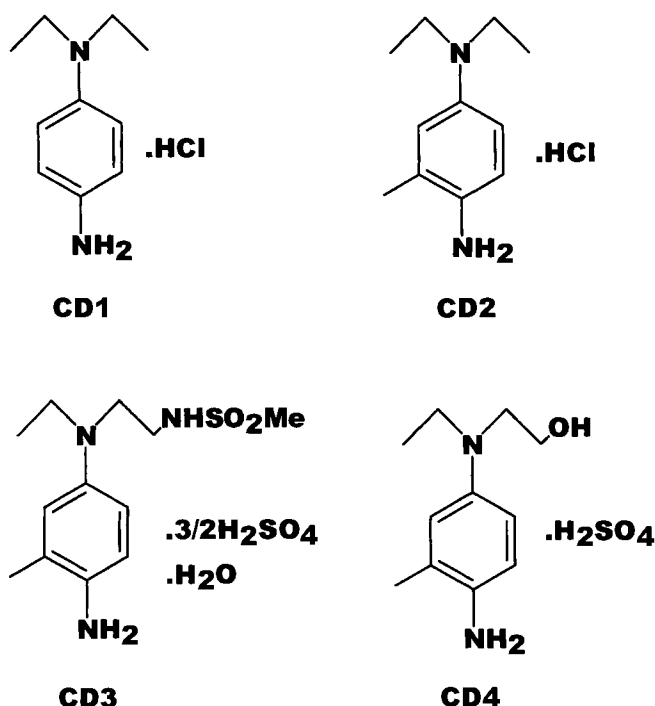
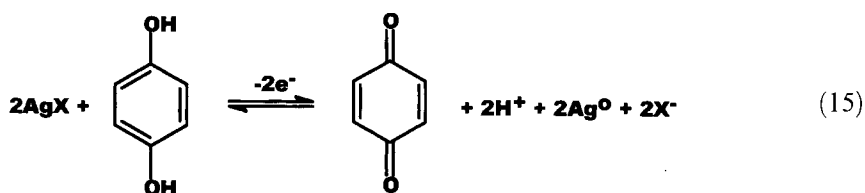


Figure 5. Typical *p*-phenylenediamine color developing agents, known as CD1–CD4 in the photographic industry.

The quinonediimine (QDI) is an important species in color development since it is this that forms dye on reaction with a coupler molecule and transforms a black-and-white image into color (see Section 1.2.3).

Typical *p*-phenylenediamine color developing agents are shown in Figure 5.

Hydroquinone (H₂Q) is another developing agent and is commonly used in black-and-white processes, usually in conjunction with an auxiliary developing agent such as Metol (*N*-methyl-*p*-aminophenol), which is also called Elon, or Phenidone (1-phenylpyrazolidin-3-one) (see Figure 6), a heterocyclic agent (see Section 8.2.5). The overall reaction of hydroquinone with silver halide is shown in Eq. (15). In fact hydroquinone undergoes two sequential one-electron transfer steps, with an intermediate semiquinone (S[•]) and with *p*-benzoquinone (Q) as the final product.



The half-cell reaction for hydroquinone is given in Eq. (16),



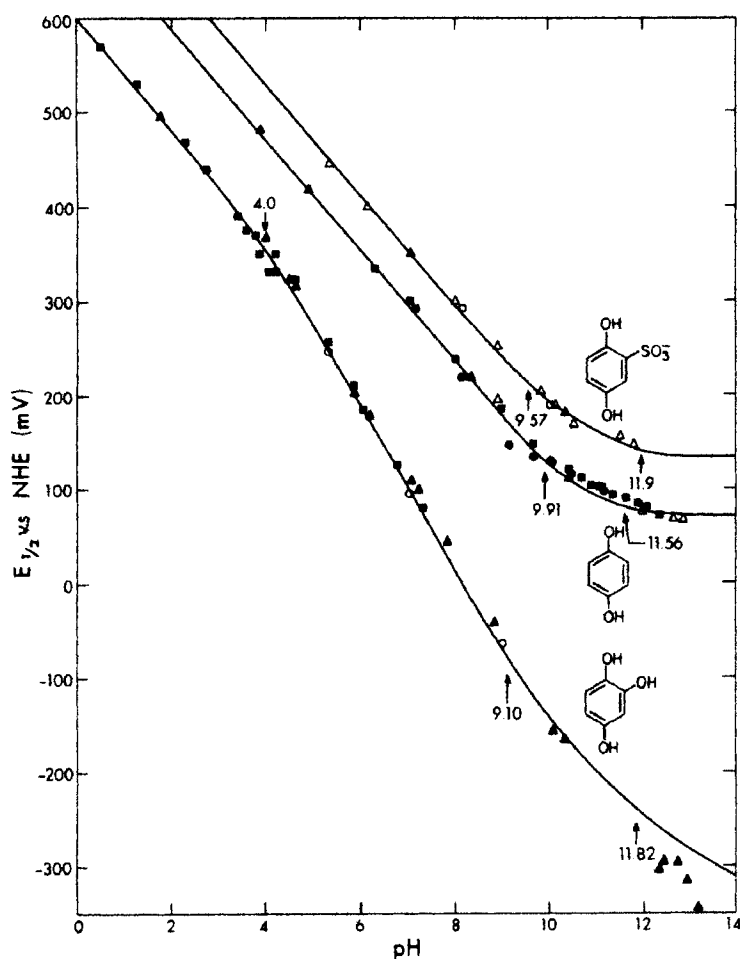


Figure 6. Half-wave potentials for the oxidation of three hydroquinones as a function of pH [28–30].

where Q is *p*-benzoquinone and H₂Q is hydroquinone. In this half-cell reaction two electrons and two protons are transferred. The Nernst equation is Eq. (17).

$$E_{\text{HQ}} = E_{\text{HQ}}^{\circ} + \frac{RT}{2F} \ln \frac{[\text{H}^+]^2[\text{Q}]}{[\text{H}_2\text{Q}]} \quad (17)$$

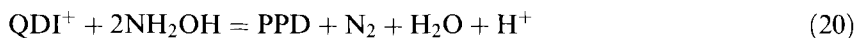
The potential for equal amounts of oxidized and reduced forms of the developing agent is closely related to the polarographic half-wave potential and differs only by a term containing the ratio of the diffusion coefficients for the oxidized (D_{Ox}) and reduced forms (D_{R}) [30].

$$E_{1/2} = E_m + \frac{RT}{nF} \ln \left(\frac{D_r}{D_{ox}} \right) \quad (18)$$

where $E_{1/2}$ is the polarographic half-wave potential and E_m is the median potential of the redox system when the oxidized and reduced forms are at equal concentration, which would be obtained from a potentiometric titration. pH vs. potential diagrams are a convenient way to examine the redox properties of developing agents, as shown in Figure 6 for some hydroquinones and Figure 7 for some *p*-phenylenediamines.

Although the equilibrium potentials for many developing agents can be calculated from the Nernst equation for a given pH, the potential values that apply in practical developer solutions are less well defined. In practice the reactions occurring in development are not at equilibrium, the reaction is almost all in one direction to form silver metal and oxidized developing agent, which is removed quickly from the reaction site before a significant amount of the reverse reaction can occur. This means that there is usually a large excess of the reduced form of the developing agent and a fleeting and indeterminate amount of the oxidized form. It is clear from some of the potential pH diagrams and from the silver ion potentials for the different silver halides that development would not occur over most of the pH range unless the reduced form of the developing agent was in considerable excess. The ratio of oxidized to unoxidized forms has been estimated to be about 10^{-4} , which is equivalent to a potential that is lower by about 120–240 mV than the half-wave potential. This is because the removal of the oxidized form of the developing agent by diffusion out of coated layers is assisted by good agitation and by several reactions which the oxidized developing agent can undergo, as outlined below for color developing agents such as *p*-phenylenediamines.

In all practical color developer solutions an antioxidant is present to help preserve the color developing agent against aerial oxidation. Aerial oxidation is slow, of the order of hours to days, compared with the development reaction, which is of the order of seconds to minutes. The antioxidant converts oxidized developing agent back to its reduced form, thus regenerating it. This reaction is again relatively slow compared with the development reaction and subsequent coupling to form dye (see Section 1.2.3), so there is only a small amount of unwanted loss of oxidized developing agent. The most common antioxidants for color developer solutions are based on hydroxylamine and its derivatives. The reactions involved are represented by Eqs. (19) and (20) [31],



where PPD is a *p*-phenylene diamine and QDI is a quinonediimine. This is one suggested stoichiometry and the reaction is probably more complicated since oxidation of hydroxylamine can give several other products such as nitrous oxide and hyponitrite. Thus the level of oxidized developer present in a practical developer is

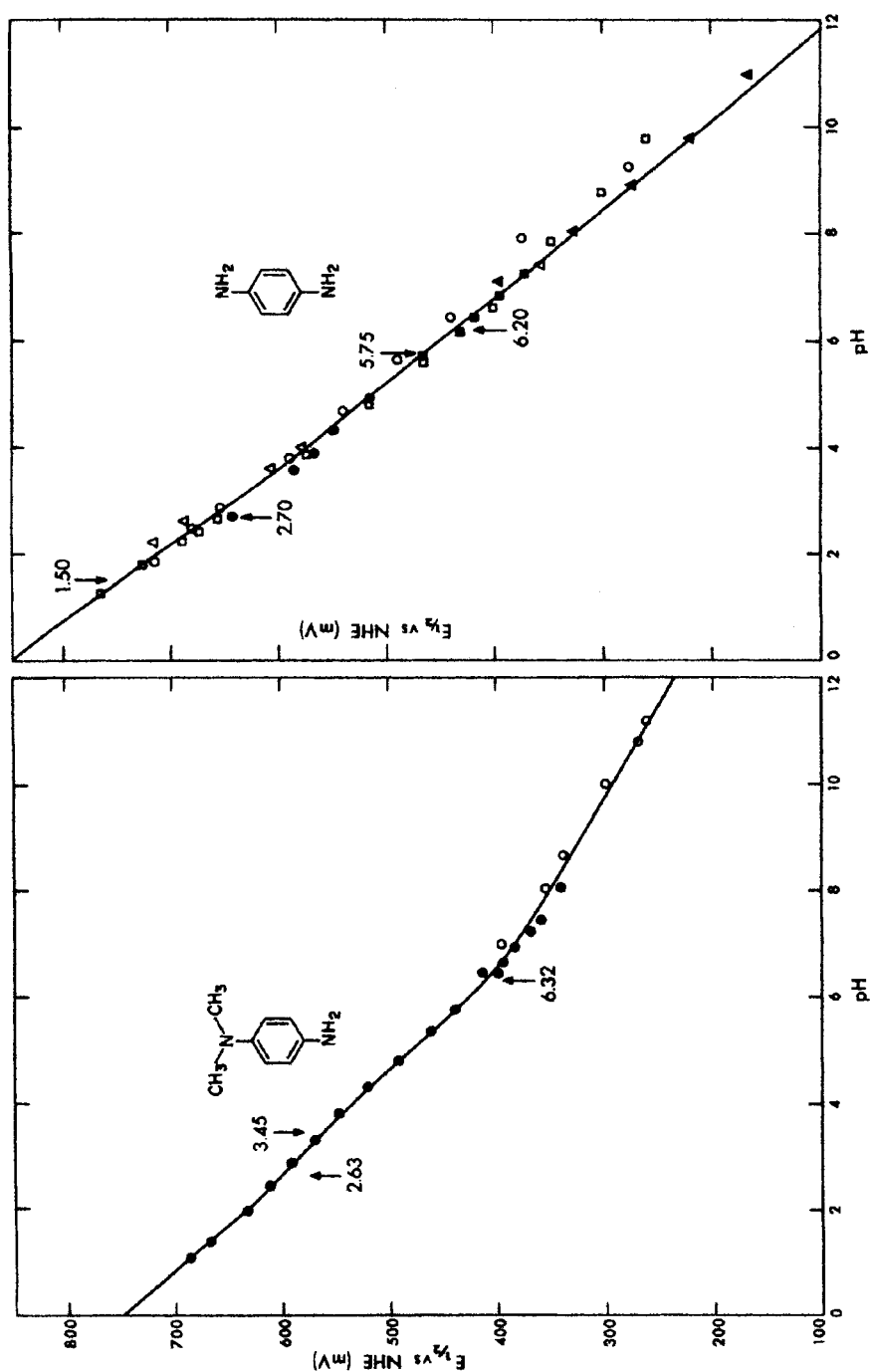
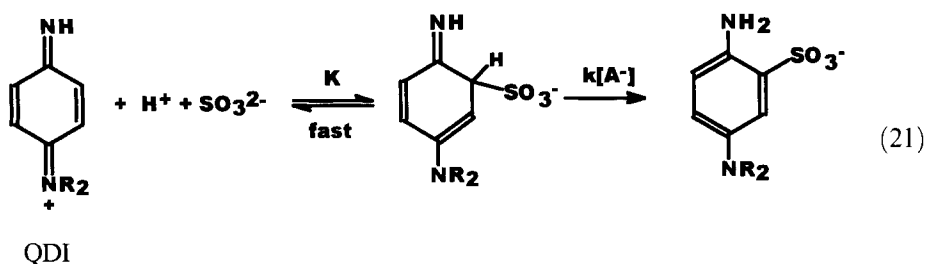


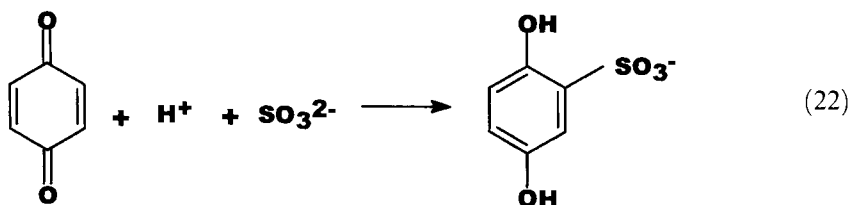
Figure 7. Left-hand curve: Half-wave potential for oxidation of *N,N*-dimethyl-*p*-phenylenediamine as a function of pH Right-hand curve: Half-wave potential for oxidation of *p*-phenylenediamine as a function of pH [30].

low, and not much above zero. The rate of development is not affected by moderate exposure to the air, indicating little buildup of oxidized developing agent.

Sulfite ion has been used as a preservative in photographic developer solutions since 1882 [31]. It is present at a relatively low level in many modern color developers and can act as a preservative by removing oxygen from solution and also by removing developer oxidation products as shown in Eq. (21).

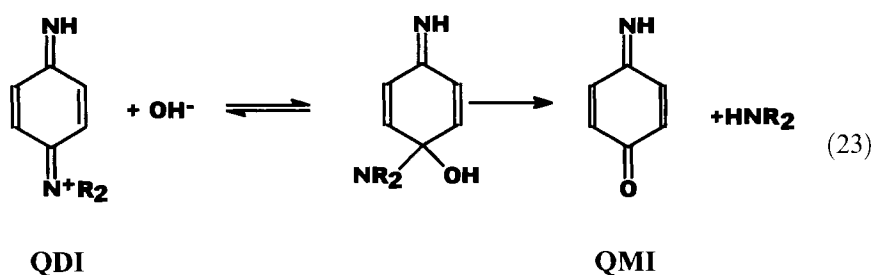


These reactions involve proton and electron transfer and kinetic data suggest that the mechanism involves a protonated intermediate followed by base-catalyzed deprotonation of the ring [32]. In black-and-white developers the amount of sulfite present is usually very high at about 60 g L⁻¹ of sodium sulfite (0.5 M), and almost all the oxidized developer formed is immediately removed from the reaction site. (At low sulfite levels the effects of accumulated oxidation products can have a significant effect on the development rate, particularly for hydroquinone developers; see the section on "Lith development"). In the case of hydroquinone the reaction with sulfite is similar to that of *p*-phenylenediamine (Eq. (22)).



This reaction involves both proton and electron transfer and rapidly removes the oxidation product of hydroquinone development and generates the sulfonated form of the developing agent. The sulfonated hydroquinone is also a developing agent but has a potential about 70 mV higher at pH 10 and is therefore less active than hydroquinone. In addition to removing oxidized developing agent, sulfonation also raises the pH of the solution, which can be of practical importance.

The reactions of quinonediimine are reviewed by Brown [33]. The quinonediimine (QDI) is susceptible to hydroxide ion attack and forms the quinonemonoimine (QMI) according to the mechanism shown in Eq. (23) [34].

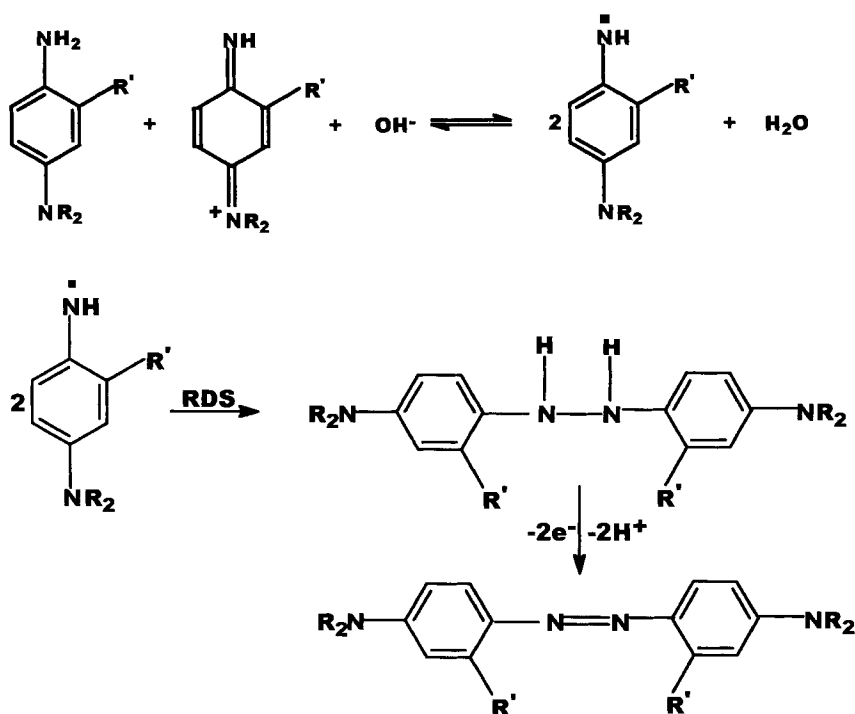


Azo dyes can be formed by the self-condensation of a quinonediimine and a *p*-phenylenediamine [35]. The rate dependence has been found to be given by Eq. (24),

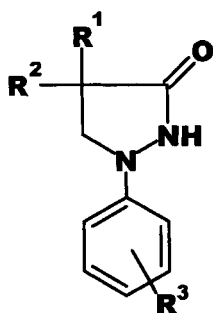
$$\frac{d[\text{Azo}]}{dt} = k_1[\text{PPD}][\text{QDI}^+][\text{OH}^-] \quad (24)$$

which can be interpreted by the mechanism shown in Scheme 1.

Coupling of oxidized developing agent with couplers incorporated in the sensitized material lowers the level of oxidized developer (see Section 1.2.3).



Scheme 1. Suggested mechanism for formation of azo dye from a quinonediimine and a *p*-phenylenediamine. RDS, rate determining step.



Phenidone: $R^1 = R^2 = R^3 = H$
 Dimezone: $R^1 = R^2 = CH_3$; $R^3 = H$
 MOP: $R^1 = CH_3$; $R^2 = OCH_3$; $R^3 = H$

Figure 8. Pyrazolidone developing agents.

Coated photographic layers are immersed in developer solutions and rely on the diffusion of active components into and out of the layer. Since chemical development occurs at local sites within the layer, agitation helps to remove oxidized developing agent into the effectively infinite sink of the bulk developer solution, and to replace it with the reduced form. In addition agitation removes development by-products which can influence the course and rate of development.

Another complicating factor is that the oxidized form of the developing agent can in some cases accelerate rather than retard development, as in the case of Lith development.

In addition to the three main types of organic developing agents mentioned above, there are many other types, including heterocyclic compounds and also inorganic ones. Phenidone, or 1-phenyl-3-pyrazolidin-3-one, and related compounds are an important class of heterocyclic developing agents (Figure 8).

Physical development

Physical development involves the reduction of silver ions from solution onto latent image or other nuclei. Solution physical development occurs when silver halide is chemically developed in the presence of a silver halide solvent or silver ion complexing agent. Some silver halide dissolves as a mobile complex and is deposited as silver on the latent image or on silver that has been or is being developed by chemical development. This can be observed as a thickening of the silver filaments often produced in chemical development. Some physical development probably occurs in most developers, even though it may be to a small degree and unintended, because of the presence of some silver ion complexing ability by components present for other purposes, e.g., sulfite ion, and even by *p*-phenylenediamine developing agents themselves.

Direct physical development occurs by design, for example to form an image by transfer of dissolved silver ion from a donor sheet to a nucleated receiver sheet, as in diffusion transfer processing. Model systems to study the chemistry of development conveniently consist of "physical developers" containing developing agent and soluble complexed silver ion from which silver is deposited onto colloidal nuclei suspended in the developer or coated in gelatin on a separate substrate (Figure 9). Silver reduction onto colloidal metal nuclei such as gold, silver, or metal sulfides

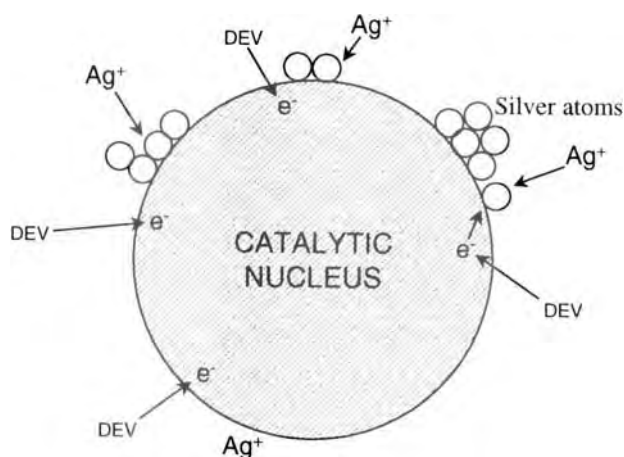


Figure 9. Physical development of silver on a spherical catalytic nucleus. DEV, developer.

involves the same electron transfer and proton transfer reactions as in chemical development. The nuclei act in a similar way to the latent image, facilitating electron transfer between the developing agent and silver ion. The nuclei grow as silver is deposited, again in a similar way to the growth of the latent image in the early stages of chemical development.

Various scenarios for the deposition of silver onto colloidal nuclei can be considered. The process could be diffusion-controlled as suggested by Matejec and by Turkevich et al. [36]. In this case the rate was found to be proportional to the radius of the growing spherical nucleus so that:

$$dm/dt = k_d m^{1/3} \quad (25)$$

where m = mass of silver and k_d is a rate constant. On integration the diffusion-controlled growth of a spherical nucleus would be given by Eq. (28),

$$m_t^{2/3} - m_0^{2/3} = k_d t \quad (26)$$

where m_t = mass of silver at time t and m_0 = mass of silver at $t = 0$. In general, however, the deposition of silver from a hydroquinone physical developer onto colloidal suspensions of catalytic nuclei appears to follow a rate law in which the rate of growth is proportional to the surface area of the growing nucleus [37], as described in Eqs. (27) and (28),

$$dm/dt = k_s m^{2/3} \quad (27)$$

$$m_t^{1/3} - m_0^{1/3} = k_s t \quad (28)$$

where k_s is the specific rate constant, see Figure 10 as an example.

Activation energies for the deposition of silver onto gold nuclei are about 12.1 kcal mol⁻¹. The overall rate equation for silver deposition onto gold nuclei is shown

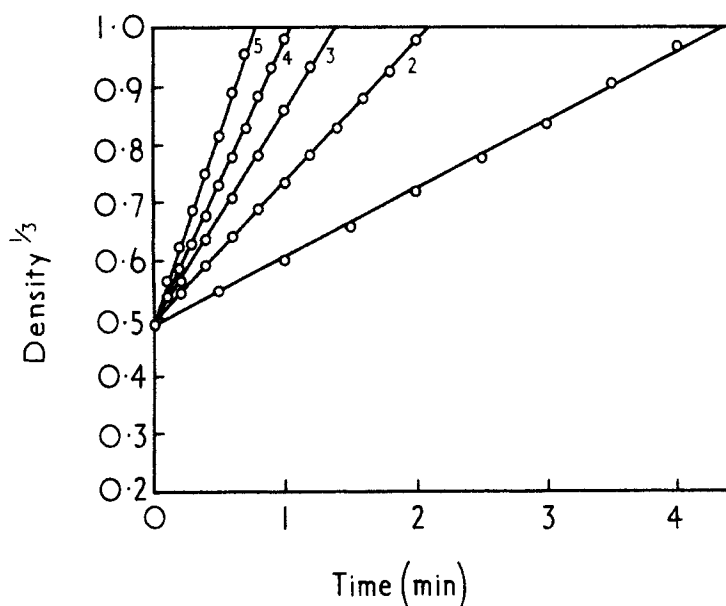


Figure 10. Density^{1/3} vs development time for silver physical development onto gold nuclei (5.52×10^{-6} M), at different concentrations of hydroquinone ($M \times 10^3$) 1 = 0.42, 2 = 0.84, 3 = 1.26, 4 = 1.68, 5 = 2.10. [41a]

in Eq. (29),

$$\text{Rate} = \frac{kK_1[\text{H}_2\text{Q}_\text{T}][\text{Ag}^+]^{0.5}}{[\text{H}^+] + K_1} \quad (29)$$

where k is the rate constant, K_1 is the equilibrium constant for the first dissociation of hydroquinone, and $[\text{H}_2\text{Q}_\text{T}]$ is the total concentration of hydroquinone [38].

The nucleus or development center in physical development can be described as a dual electrode on which the reduction of silver ion to silver and the oxidation of developing agent take place simultaneously. Electrochemical measurements of silver physical development in a hydroquinone/Phenidone physical developer with silver ion complexed with thiocyanate proceed as a catalytic electrode process [39].

The rate of the cathodic reduction of silver ion from silver complexes is rapid compared with the anodic oxidation rate of the developing agent, Phenidone. Thus the physical development rate is governed by the anodic reaction [40]. Charge barrier effects have been seen in physical development as well as in chemical development [41].

Diffusion transfer development

Diffusion transfer development is a photographic processing system which involves both chemical development and solution physical development. Diffusion transfer

refers to the transfer of image chemistry either as dissolved and complexed silver ion or as a dye image. A black-and-white diffusion transfer system has been used in the document copying process called Instafax. In this system two sheets consisting of a donor and receiver are laminated together after passing through a developer containing a silver halide solvent, sodium thiosulfate. The sequence of events is as follows: development of the exposed image in the donor sheet, dissolution of the undeveloped silver halide in the donor sheet, diffusion of the dissolved silver ion to the receiver sheet, physical development onto nuclei in the receiver sheet followed by peel-apart of the two sheets to reveal a positive image in the receiver sheet and a negative image in the donor sheet. The nuclei coated in the receiver sheet can be silver, gold, or metal sulfides such as silver sulfide, nickel sulfide, cadmium sulfide, and zinc sulfide.

In another version of the system described above the physical development nuclei can be coated in the same sheet below the silver halide layer, which is designed to “wash off” during processing, leaving the positive image behind.

Color systems based on diffusion transfer can be made by means of dye developers (Polaroid) which are coated with a negative silver halide emulsion. Upon development the dye developer becomes immobilized, whereas in the unexposed non-developing areas the dye diffuses to a mordanted receiving layer either in a separate peel-apart sheet or in the same sheet.

Reversal processing

In reversal processing a direct positive image is obtained by using either a reversal emulsion or a normal negative emulsion in which the process has two development steps. In color reversal processing used for transparency production, the first step is a black-and-white development using a hydroquinone–Phenidone mixture which brings up a negative silver image. The unexposed silver halide is then either light-exposed or chemically fogged using strong reducing agents such as borohydride, aminoboranes, or stannous chloride. Unlike the development reaction, the chemical fogging action of borohydride is indiscriminate and electron injection will occur for all silver halide grains, forming developable centers. If the film contains incorporated color-forming couplers and the second development step uses a color developer, then a direct positive color image is formed. The silver image is then oxidized and removed to reveal the color image.

Superadditivity

Superadditivity is a synergistic phenomenon in which a primary developing agent and a secondary developing agent are used together to provide a more active developer than either can provide singly. Levenson [42] has identified “superadditivity of densities” and “superadditivity of rates”. Superadditivity of densities arises as indicated in Figure 11, in which the broken curve for the arithmetic sum ($A + B$) is computed by adding the rates for A and B . Superadditivity is shown only if the curve for “ A with B ” lies above the broken curve. By considering only the densities reached in time T , curves lying between A and $A + B$ would give an erroneous impression of superadditivity [38].

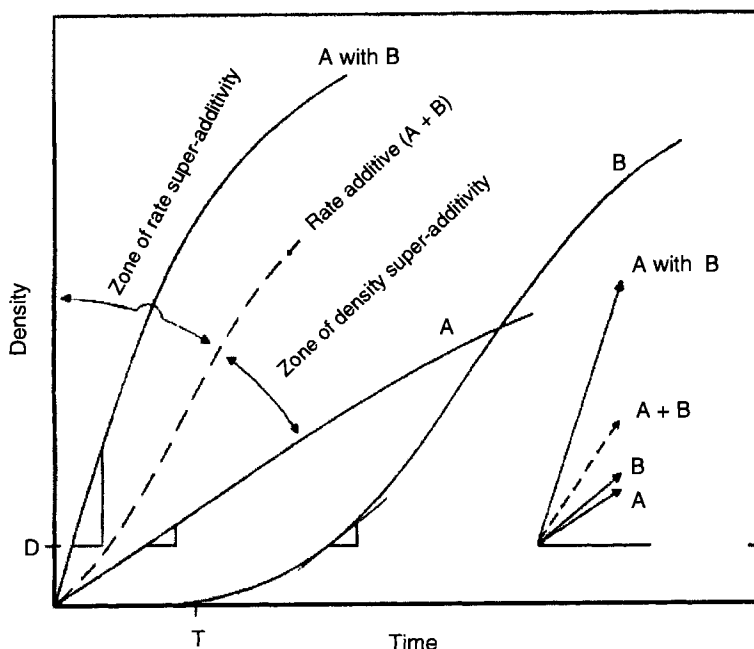


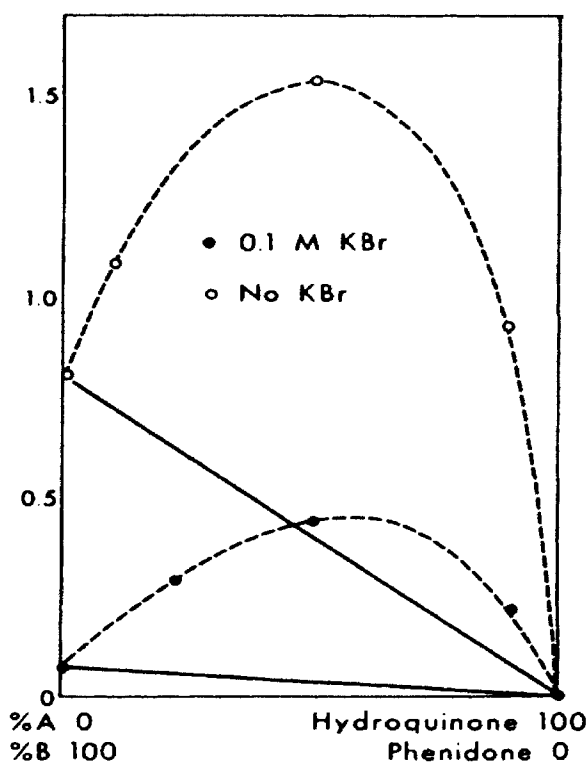
Figure 11. Diagrammatic time vs. density curves for two developers with agents A and B and for the combined developer ("A with B"). Slope rates at a finite density D are shown inset.

Thus "density superadditivity" is only an apparent superadditivity even though the sum of the silver densities for the separate developers A and B appears to be less than that for the A + B curve. This is because developer B would not have an induction period in the presence of developer A and so would contribute to the overall development almost immediately, giving the broken curve A + B which is merely additive. In kinetic terms, true superadditivity occurs when the rate of growth of density or silver for the combined "A with B" developer is greater than the sum of the rates of growth of density or silver for the A developer and the B developer separately.

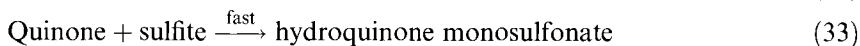
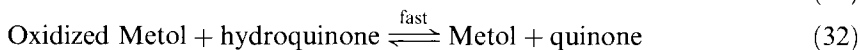
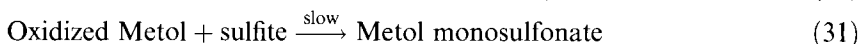
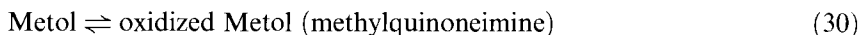
This is shown clearly in the data of Lee and James [43] in Figure 12, in which the sum of the separate rates of development increases to a maximum for a given ratio of the two developing agents, hydroquinone and Phenidone.

Hydroquinone and *N*-methyl-*p*-aminophenol (Metol) form superadditive mixtures and a complex, "Metoquinone", consisting of one hydroquinone and two Metol molecules, was proposed by Lumière, Lumière and Seyewitz [44] to be the species with higher activity than the separate agents. A similar complex between hydroquinone and 1-phenyl-3-pyrazolidinone (Phenidone) consisting of one molecule of hydroquinone and one molecule of Phenidone has been observed in the solid state by Kurosaki [45] and Mutter and Schneider [46]. Although these complexes can be crystallized from concentrated solutions of hydroquinone and Metol, and hydroquinone and Phenidone, there is no evidence of their existence in solution.

Figure 12. Relation between the rate of chemical development and the ratio of developing agents present (0.01 M = 100 %); solid lines, theoretical curves obtained if the rates were additive; dashed lines, experimental curve [43].



Hydroquinone and *N*-methyl-*p*-aminophenol (Metol) form a superadditive mixture which was shown by Tausch and Levenson [47] to involve the consumption primarily of hydroquinone with the preservation of Metol. This led to the regeneration theory proposed by Levenson, that Metol was acting as the developing agent at the silver halide surface and that oxidized Metol was reduced back to Metol by hydroquinone as outlined in Eqs. (30)–(33).



In order for hydroquinone to be effective in regenerating Metol by the mechanism proposed, it is necessary that the quinone reacts with sulfite more rapidly than does methylquinoneimine.

Thus superadditivity can be viewed as a sequence of two types of electron transfer reaction, one which is heterogeneous between Metol and the latent image, resulting in silver development, and one which is homogeneous between hydroquinone and

oxidized Metol, resulting in the regeneration of Metol. It is also possible that the second electron transfer is also heterogeneous in which the adsorbed oxidation product of Metol is regenerated on the surface.

Effective superadditive mixtures result from combinations of 1-phenyl-3-pyrazolidinone (Phenidone) [48] and its derivatives with hydroquinone, ascorbic acid, *p*-hydroxyphenylaminoacetic acid, hydroxylamines, pyrogallol, and other agents. In general, superadditivity is a phenomenon primarily used in black-and-white developers but it has also been observed in color development [49].

A similar regeneration scheme to that proposed by Levenson also applies to Phenidone/hydroquinone developers. Phenidone (P) undergoes a heterogeneous one-electron transfer with exposed silver halide to form a relatively stable radical R^{\bullet} (Eq. (34)), which can then undergo an irreversible dismutation ($k = 170$ to $570 \text{ M}^{-1} \text{ s}^{-1}$) [50], to give P and the fully oxidized 1-phenylpyrazolidinone Py (Eq. (35)). The radical R^{\bullet} can undergo a homogeneous one-electron transfer with hydroquinone to give P and oxidized hydroquinone. Ionized Phenidone (P^-) exists at pH 10.0, which is a common developer pH. HQ^- is the half-ionized form of hydroquinone which also exists at pH 10. $S^{\bullet-}$ is the semiquinone of hydroquinone, and Q is benzoquinone.



The semiquinone, which is a relatively stable species, can undergo an irreversible dismutation (Eq. (37)) or react with another R^{\bullet} (Eq. (38)), although the latter reaction is unlikely at low levels of $S^{\bullet-}$.



Regeneration of one developing agent by another is not in itself necessarily an explanation of a superadditive rate of development, even though it clearly occurs. In its simplest form regeneration would merely maintain the concentration of the primary developing agent and prevent loss of development rate by exhaustion. It appears necessary to suppose that regeneration has some additional effect, such as:

- 1) the removal of an inhibiting oxidation product; or
- 2) generation of a more active species, such as a semiquinone; or
- 3) a lowering of the limiting effect of diffusion control by regenerating the active(primary) developer with the inactive(secondary) developer, thereby increasing the apparent concentration of the primary developer; or
- 4) combination of regeneration with action according to the charge-barrier theory of development. The charge-barrier theory of James [51] was proposed to explain the kinetic behavior of differently charged developing agents (see the section on

- “Change in silver halide caused by development”) and could also be used as a mechanism of superadditivity. In this case the induction period of negatively charged agents such as hydroquinone, which occur according to the charge-barrier theory because of a negative charge barrier at the silver halide surface, is removed by an uncharged or positively charged auxiliary developing agent, or
- 5) acting as an “activator” for the secondary developer which is relatively inactive by itself, as in the electrochemical theory of catalytic currents outlined below.

Superadditivity has been observed in both chemical and physical development [52]; thus the presence of silver halide is not a necessary condition for its occurrence but is likely to modify its detailed course. This would appear to rule out the charge-barrier theory in its original form, although charge effects might also occur at silver as well as at silver halide surfaces.

The removal of an inhibiting oxidation product was demonstrated by Levenson and Twist [52c] in studies of physical development onto colloidal nuclei. In this case the very early stages of silver ion reduction were followed and it was found that silver ion reduction by Phenidone was initially high but fell after less than 1 min to a much lower rate (of about $1/25$ of the initial rate; see Figure 13) even though only 30 % of the Phenidone had been consumed. It is suspected that this inhibition is due to the Phenidone radical. The addition of hydroquinone, which did not develop by itself under these conditions, restored the initial rate of development by Phenidone.

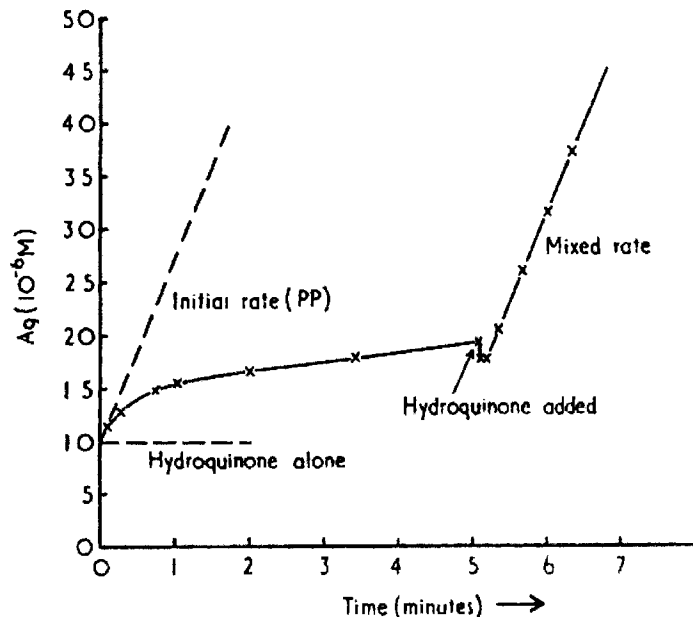
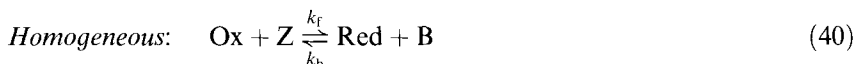


Figure 13. Physical development with Phenidone, showing the high initial rate followed by a slower rate ($1/25 \times$ the initial rate). Hydroquinone addition (1.38×10^{-4} M) after the slow rate is established restores the initial rate [52c].

This indicates that superadditivity arises by the removal of an inhibiting species in Phenidone oxidation, probably the Phenidone radical as in case 1 above. Lee and Miller [53] showed that development of silver halide by the Phenidone radical generated in a flow system was much slower than that by Phenidone itself by a factor of about 24, which agreed very closely with the results of Levenson and Twist [52c], and Shiao and Dedio [54] also found that superadditivity of ascorbic acid and a Phenidone derivative (MHP) was explained by scavenging the MHP radical, thus eliminating any inhibition. A similar inhibition by oxidation products of development was proposed to explain the behavior of ascorbic acid physical developers [55].

Electrochemical measurements by Jaenicke and co-workers [56] indicate two possible mechanisms by which superadditivity could arise. In the first, a developer showing irreversible oxidation becomes reversible in the presence of a second developing agent. In the second, when the mixed potential is in the limiting current region of the anodic reaction, superadditivity occurs if the limiting current rises because the number of electrons delivered per molecule of a first developer, for example hydroquinone, is increased by the addition of a second developer, such as Phenidone. This could happen with hydroquinone development in the presence of sulfite because the reaction product, hydroquinone monosulfonate, is a poor developer by itself but in the presence of Phenidone it is activated.

Regeneration of the second developing agent could be envisaged to take place either homogeneously or heterogeneously. The theory of catalytic currents in electrochemical kinetics is equivalent to homogeneous regeneration and some studies by Jaenicke and Kobayashi [57] indicate that the catalytic processes could be:



where Z and B are essentially electroinactive under the conditions used and the catalyst is the system Red/Ox. In the hydroquinone/Phenidone system Red is Phenidone and Ox is the Phenidone radical, Z is oxidized hydroquinone and B is hydroquinone. The limiting catalytic current at a rotating disk electrode for a process as indicated by Eqs. (39) and (40) has been derived [58] according to Eq. (41), where

$$i_c = nFC_{\text{red}}(Dk_f C_z)^{1/2} \quad (41)$$

D = the diffusion coefficient of Red, and C_{red} and C_z = bulk concentrations of Red and Z.

Anodic catalytic waves for hydroquinone were observed at a rotating gold electrode, confirming the regeneration mechanism with a rate constant for Phenidone regeneration of $1.3 \times 10^6 \text{ L mol}^{-1} \text{ s}^{-1}$ [57].

Physical development can occur on nuclei with the simultaneous reduction of silver ion and oxidation of the developing agent. The two partial processes can also be separated in a model cell so that the effect of solution composition on the separate anodic and cathodic parts can be seen (Figure 14). Kawashima et al. [59]

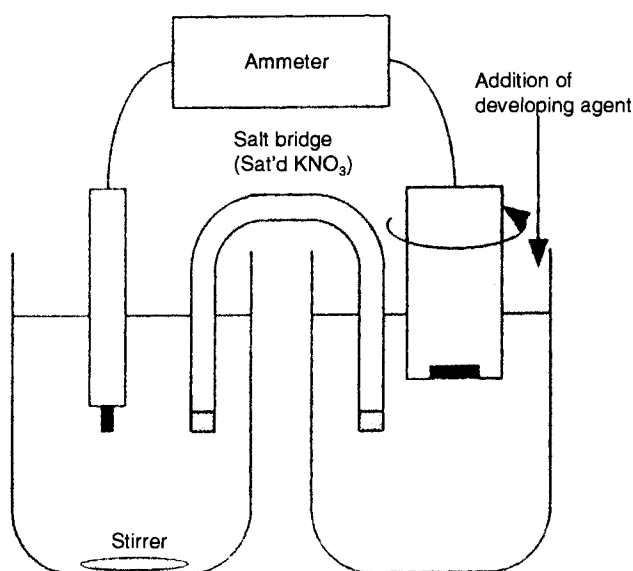


Figure 14. Model physical development cell in which the anodic and cathodic partial processes are separated.

Cathode:
Stationary Ag electrode
with strong stirring.

Anode:
Rotating Ag electrode
Rotating speed = 209 rad s^{-1}

Electrolyte:
Physical developer without developing agent

showed that the development rate of a thiocyanate developer with Phenidone/hydroquinone and Phenidone/ascorbic acid agreed with that calculated from the theoretical equation for the catalytic current, and indicated no effect of thiocyanate on the anodic process. Superadditive mixtures based on the silver thiosulfate complex showed inhibition of the anodic process by adsorbed thiosulfate.

Lith development

In Lith development, very high-contrast silver images are produced and used to form half-tone dot images in the process called lithography. Lith development occurs with high-chloride silver halide monodisperse emulsions [60] and is characterized by a long induction period which is exposure-dependent, followed by sudden rapid development in regions of higher exposure.

A comparison of conventional, Lith and nucleated development is shown in Figure 15.

Lith developers are based on hydroquinone and have a low level of sulfite ion which is critical for the high contrast to be obtained. In conventional developers based on hydroquinone, a relatively large amount of sulfite ion is present which removes the oxidation products by sulfonation. In Lith developers the low sulfite ion concentration allows the buildup of oxidation products which can accelerate

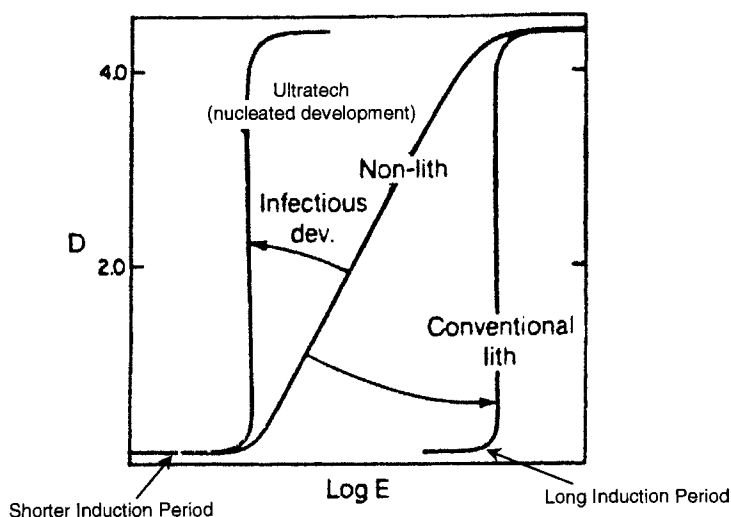
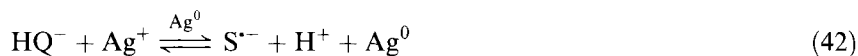


Figure 15. A diagrammatic comparison of non-Lith development, conventional Lith development, and nucleated development.

development. One mechanism proposed by Yule [61] suggests that the oxidation products of development, benzoquinone and hydroquinone semiquinone, are responsible for the rapid phase of Lith development. Eggers [62] has shown that in the absence of hydroquinone, *p*-benzoquinone itself acts as a Lith developer, but only after prolonged times of about 16 min. He also showed by ESR measurements that hydroquinone semiquinone is formed at pH 10 in solutions of *p*-benzoquinone by the action of OH^- ions. This suggests that *p*-benzoquinone is not directly responsible for the Lith effect but that the hydroquinone semiquinone is. In addition to any hydroquinone semiquinone generated by the action of OH^- on *p*-benzoquinone, hydroquinone semiquinone is generated in a rapid equilibrium between hydroquinone and unsulfonated *p*-benzoquinone. This view is supported by more recent investigations of Hefter [63] in which the buildup of semiquinone was demonstrated by ESR spectroscopy in hydroquinone development. Work by Umberger and Herbert [64] supports the view of Lith development being based on development acceleration by the accumulation of hydroquinone semiquinone. The slow stage of Lith development can be outlined as in Eqs. (42)–(44).



Lith developers operate at about pH = 10.0 and as a consequence the main developing species is the mono-anion (HQ^-) of hydroquinone ($\text{p}K_a = 9.91$), which

is a relatively weak developing species, unlike the di-anion of hydroquinone ($pK_a = 11.56$), which is much stronger. During the induction period or slow stage in Lith development the low level of sulfite is sufficient to remove *p*-benzoquinone to give the sulfonated product, which is a weaker developer than hydroquinone, and development proceeds at a relatively slow pace. As the latent image size increases and the sulfite is used up, a second phase of development can start.

The semiquinone $S^{\cdot-}$ can also undergo the reversible dismutation reaction mentioned above, but in Eq. (45) we write it the opposite way round for clarity. This reaction is very rapid ($k = 10^8 \text{ M}^{-1} \text{ s}^{-1}$) [67] and controls the semiquinone concentration.



It is proposed that the semiquinone is an active developing agent, estimated by Umberger [64] to be 10 times as active as the hydroquinone dianion. The low sulfite level in Lith developers allows the *p*-benzoquinone (Q) to build up, which boosts the semiquinone concentration via the dismutation reaction. The increased semiquinone level accelerates development which produces more *p*-benzoquinone and semiquinone according to Eqs. (46), (47),



and so on, giving an exponential form of development.

The acceleration of development occurs in exposed grains adjacent to already-developing grains and although Lith development is sometimes referred to as “infectious development” there appears not to be any gross migratory development acceleration. This implies that the accelerating species are not fogging agents as in some materials described in the section on “Nucleated development”. James [65] has shown, however, that a motion picture positive film that has been partially developed in a hydroquinone developer containing quinone retains its increased rate of development even after thorough washing followed by development in a quinone-free hydroquinone developer. This clearly indicates an additional factor in which the film has been permanently altered by hydroquinone oxidation products, which is not apparent in the Yule mechanism. This can be resolved if it is possible that hydroquinone oxidation products can chemically latensify latent sub-images, rendering grains developable which would otherwise not be developable.

Hydroxyhydroquinone has also been suggested as one of the reaction products of *p*-benzoquinone with hydroxyl ions which might cause the Lith effect [66]. Another mechanism suggested by James [67] involves the reaction of the oxidation products of hydroquinone with the amino groups of gelatin to form amino-substituted species which might act in a superadditive manner with hydroquinone to accelerate development and cause the Lith effect. Another alternative mechanism proposed by Zwicky [68] involves a “silver ion hypothesis” in which silver ion is solubilized by liberated halide ions in the vicinity of rapidly developing grains. The mobile silver

ions are then physically developed on filaments and on developing centers in adjacent grains to give the Lith effect. This latter mechanism appears to conflict with the known effect of sulfite ion on Lith development, which is to suppress it entirely. Sulfite ion is a strong solubilizing agent for silver chloride but not silver bromide. Increasing levels of sulfite ion should therefore enhance the concentration of mobile silver ion, enhance any physical development effects, and on the basis of the silver ion hypothesis enhance the Lith effect.

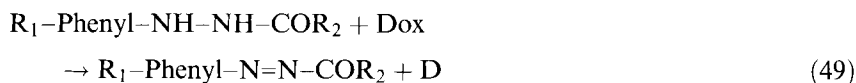
Although the mechanisms described above are reasonable it should be emphasized that the main effect of oxidation products of development is a retarding one, as indicated in the section on "Changes in silver halide caused by development", above. This basic property is still present even though other reactions of the development oxidation products can have dramatic effects. In this regard it has also been suggested [67] that some of the restraint in weakly exposed areas in Lith development is due to the retarding action of quinone.

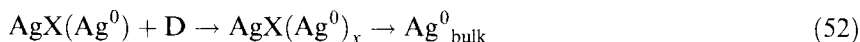
Suga [69] has further outlined the "redox-Lith effect" in which quinone can oxidize latent image centers. Smaller latent image centers are oxidized, thus retarding image formation at lower exposures, whereas larger latent image centers are unaffected, allowing development to occur. The overall effect is to promote high-contrast development as observed in the Lith process.

Another possibility that could explain Lith development is the apparently contradictory phenomenon of "bleach enhanced fog" or BEF [70]. In this case compounds known as silver bleaches can cause fog in grains with sub-developable silver centers. Two-atom silver centers cannot initiate development and would be bleached by oxidants, for example, benzoquinone, to a one-atom silver center. A single silver atom is thermally unstable and can dissociate, without the need for an oxidant, into a silver ion and a mobile conduction-band electron. If several two-atom centers are present on a grain, a developable center can arise from the accumulation of these mobile electrons at a suitable site.

Infectious or nucleated development

High-contrast halftone dot images can now be produced by development of a special film, such as Kodak Ultratec Film [71], which contains incorporated nucleator precursors. The end result is similar to that of Lith development but the images are of higher contrast and higher photographic speed, less sensitive to processing conditions, and can be developed in a superadditive developer and so be formed more rapidly. The usual nucleator precursor is a phenyl formyl hydrazide which reacts with oxidized developing agent to generate a strong nucleating species. The nucleating species is capable of direct electron injection into sub-developable and unexposed silver halide grains close to an exposed developing grain to generate a developable grain. The mechanism can be described by Eqs. (48)–(53).





Thus exposed grains develop, and oxidized developing agent reacts with the nucleator precursor to generate the nucleator ($\text{R}_1\text{-Phenyl-N=NH, N}$) which is capable of direct electron injection into silver halide to create developable grains adjacent to an already developing grain. These nucleated grains develop, producing more nucleator, and so the effect is a cascade; all grains above a toe exposure will develop giving a high-contrast image. Recent work [72] has confirmed the mechanism outlined above and that the nucleator species (N) is capable of direct electron injection into silver halide.

Proximity development

This type of development has been reported by several workers and occurs at high coverages of silver halide, i.e., about 2 g m^{-1} [73]. As the amount of silver halide coated is increased, more silver is developed than expected and in addition anomalous granularity measurements are obtained. If a silver halide emulsion is coated and developed, a normal development is observed. If the same silver halide emulsion is pre-exposed before coating, then coated and developed, most of the silver develops regardless of further exposure after coating. If now a proportion of pre-exposed silver halide is coated with unexposed silver halide, then it is found that more silver is developed than the sum of the exposed and unexposed coated separately. This effect is only significant as the total amount of silver halide coated is increased to high levels, and the effect increases with coating level. This indicates some interaction between exposed and unexposed grains and is likely to be due to physical contact of developed and developing silver with adjacent unexposed grains. Electron transfer from the silver of a developing grain then initiates development in an unexposed grain, which once started will proceed.

Redox amplification

Another oxidant in addition to silver halide has been employed for a variety of photographic systems, one of which is the dye bleach system of Schinzel [74] (see Section 1.3.6) in which direct positive images are formed by bleaching dyes catalyzed by a silver image. A system for the catalytic reduction of dyes to produce color images was described by Gaspar [75]. Matejec [76] formed dye images from palladium, gold, and silver nuclei and from photographically produced silver by the catalytic oxidation of *N,N*-diethyl-*p*-phenylenediamine with sodium perborate and hydrogen peroxide. This method of dye formation has been called RX or RedoX amplification. Bissonette [77] has used other oxidants such as cobalt(III) complexes, e.g., $\text{Co}(\text{NH}_3)_6\text{Cl}_3$ (COHEx). Peroxy compounds such as perborate and hydrogen

Table 4. An RX developer composition.

Component	Concentration
AC5 ^a	0.6 g L ⁻¹
AC8 ^b	2.0 mL L ⁻¹
K ₂ HPO ₄ · 3H ₂ O	40 g L ⁻¹
KBr	1 mg L ⁻¹
KCl	0.5 g L ⁻¹
HAS ^c	2.0 g L ⁻¹
CDS ^d	0.3 g L ⁻¹
CD3 ^e	4.5 g L ⁻¹
H ₂ O ₂ (30 %)	4.0 mL L ⁻¹
pH	11.5
Temperature	32 °C

^a60 % solution of 1-hydroxyethylidene-1,1-diphosphonic acid, ^b40 % solution of the pentasodium salt of diethylenetriamine pentaacetic acid, ^cHAS is hydroxylamine sulfate, ^dCDS is catechol 3,5-disulfonate, ^eCD3 is *N*-[2-(4-amino-*N*-ethyl-*m*-toluidino)ethyl]methanesulfonamide sesquisulfate hydrate.

peroxide have been commonly used, particularly with photographic layers where the main light-sensitive material is silver chloride, whereas COHEX materials work better than peroxide with silver bromide light-sensitive materials.

An RX developer based on hydrogen peroxide is shown in Table 4.

In RedoX or RX development the mechanism involves an additional stage or reaction in the process leading to dye formation. If the color developer solution contains a special type of oxidant, a silver metal catalyzed oxidation of color developing agent occurs which then results in dye formation independent of normal silver development and dye formation. This reaction is imagewise since it is catalyzed by the silver image formed by conventional development and as a result there is a further amplification factor (about 10×) in addition to that of normal silver halide development. The overall reactions involved where hydrogen peroxide is the oxidant are given in Eqs. (54)–(56).



The third reaction of the sequence is the silver-catalyzed oxidation of color developing agent which leads to dye formation by coupling as in normal color development. This process allows a lowering of the coated silver level but still produces a full-density color image (Figure 16). Typically the coated silver level is 10 % of that required for normal color development, which means that 90 % of the dye image is formed by the RX amplification reaction.

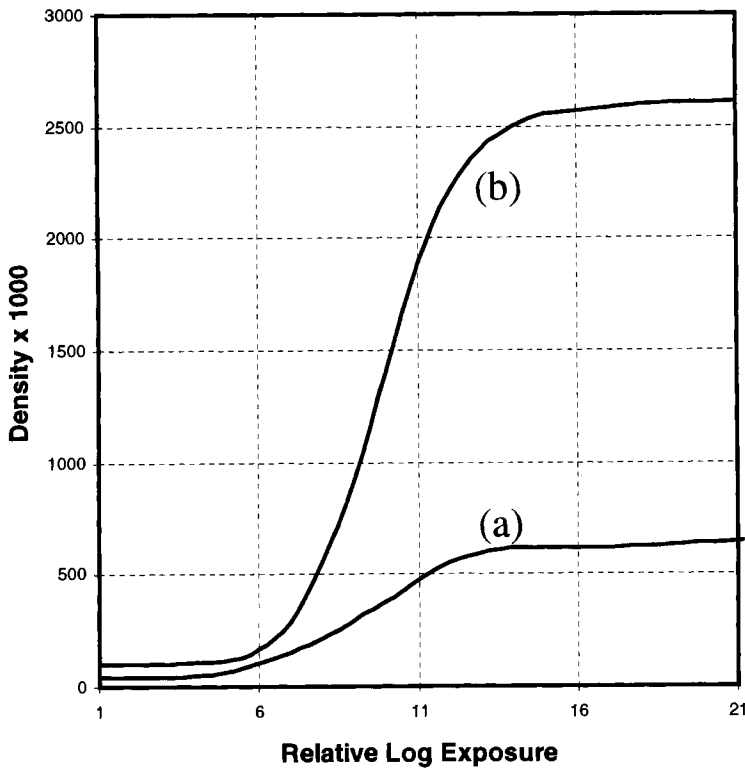


Figure 16. Dye density versus relative log exposure for a low-silver coating (a) developed normally and (b) developed in an RX amplifying developer.

In the same way that the latent image and image silver catalyzes the electron transfer reaction between color developing agent and silver halide, the silver image catalyzes the electron transfer reaction between the developing agent and hydrogen peroxide. In this case the hydrogen peroxide takes the place of silver halide as the oxidant. The drawback of this is that the lower silver halide level results in a smaller number of silver halide grains per unit area and thus a higher granularity.

One particular practical difficulty with RX photographic developers is their instability. The combination of a developing agent and an oxidant in the same solution leads inevitably to decomposition of the developing agent and the solution becomes unusable. The stability of RX developers like that in Table 3 have been examined by Wildman et al. [78], who identified several factors that show an improvement which allows RX developers to be used in a normal processing machine.

Nickel and Liu [79] have studied the silver-catalyzed oxidation of *N,N*-dimethyl-*p*-phenylenediamine by $\text{Co}(\text{NH}_3)_5\text{Cl}_3$ by means of a silver colloid and a rotating silver electrode. They conclude that the reaction can be quantitatively explained by means of the theory of mixture potential and mixture current of Wagner and Traud

[80]. The electrocatalytic reaction starts with electron transfer from *p*-phenylenediamine to the cobalt(III) complex via the silver at a high reaction rate. A competitive reaction involving the oxidative formation of silver halide then begins. This silver halide may be reduced by *p*-phenylenediamine, which is thus oxidized directly by the cobalt(III) complex and also by the silver halide formed by the oxidation of silver.

Latent image bleaching

This is a phenomenon which has been referred to in Lith development but it has also been observed in conventional color development. A strongly developing grain produces development by-products which are capable of influencing the course of development of other grains nearby. If the developing grain has a neighbor which is slow to start developing, then the oxidized developer formed by the strongly developing grain can theoretically diffuse in the layer and bleach the latent image on the neighbor [81]. The release of halide ions during development of the strongly developing grain will enhance this effect by lowering the silver ion potential. The effect is shown in Figure 17.

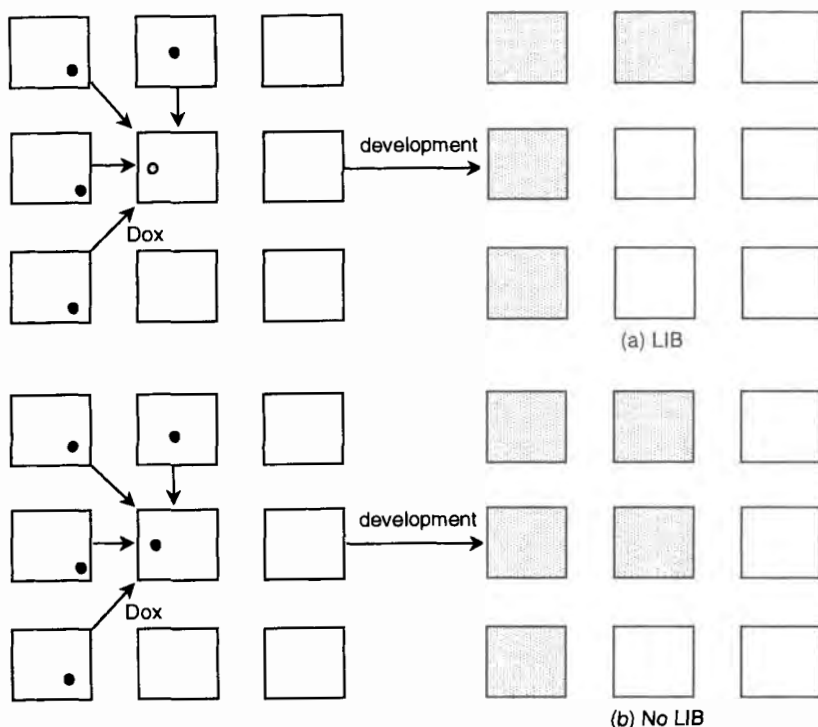


Figure 17. (a) Latent image bleaching by development products generated by adjacent developing grains; (b) development without latent image bleaching (LIB).

A method of demonstrating that this effect can occur in color development was described by Jarvis and Twist [81e]. This involves a two-stage development procedure:

<u>Process P1</u>	<u>Process P2</u>
Develop C-41	Develop C-41 + sodium ascorbate
Wash	Wash
Develop C-41 + sodium ascorbate	Develop C-41
Fix	Fix
Wash	Wash

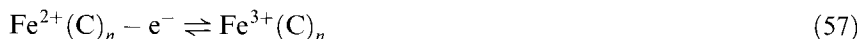
Kodak C-41 developer is the standard developer for color negative films and it is in this developer that the occurrence of latent image bleaching (LIB) is being tested. Sodium ascorbate is a strong developing species which does not have a sufficiently stable oxidation product to cause LIB; it also removes the oxidation products of the color development that are formed in C-41 developer. The two types of development, P1 and P2, give the same total development but with the two development steps reversed. If LIB does not occur, then P1 and P2 will give the same result. If LIB occurs, then at some exposures P1 will show less development and a smaller number of developed grains, because in P1 the stage at which LIB could occur, with C-41 developer, comes first. In P2 C-41 developer comes second, after most of the development has already occurred, and so LIB is not possible.

The result is shown in Figure 18, a LIB diagram [82], which shows that latent image bleaching has occurred in P1 and that the lower density in the image is associated with a smaller number of developed grains. Most of the LIB occurs in the mid to upper scale and not in the regions of lower exposure. Another phenomenon was observed which has been called developer-induced fog (DIF), which occurs in the toe and unexposed regions. The latter was attributed to electron injection into unexposed grains by the color developer semiquinone, rendering them developable.

Redox buffers and the critical size of latent image centers

In practical developers there is usually an excess of the reduced form of the developing agent with a small and variable amount of the oxidized form. Except for certain cases, such as in Lith development, the oxidation products are not allowed to accumulate. This means that the redox potentials are uncertain because the system is not in equilibrium. Redox buffers are solutions which are in equilibrium and contain definite amounts of oxidized and reduced forms. Many organic developing agents have oxidized forms which undergo side reactions, particularly in alkaline solution, which prevent them from being used as redox buffers; for that reason, metal ion couples are used instead.

The reversible redox reaction of iron(II)/iron(III), usually complexed with a suitable ligand, is ideal for this purpose. The redox reaction



where C is a complexing agent, has redox potentials which depend on the ratio of

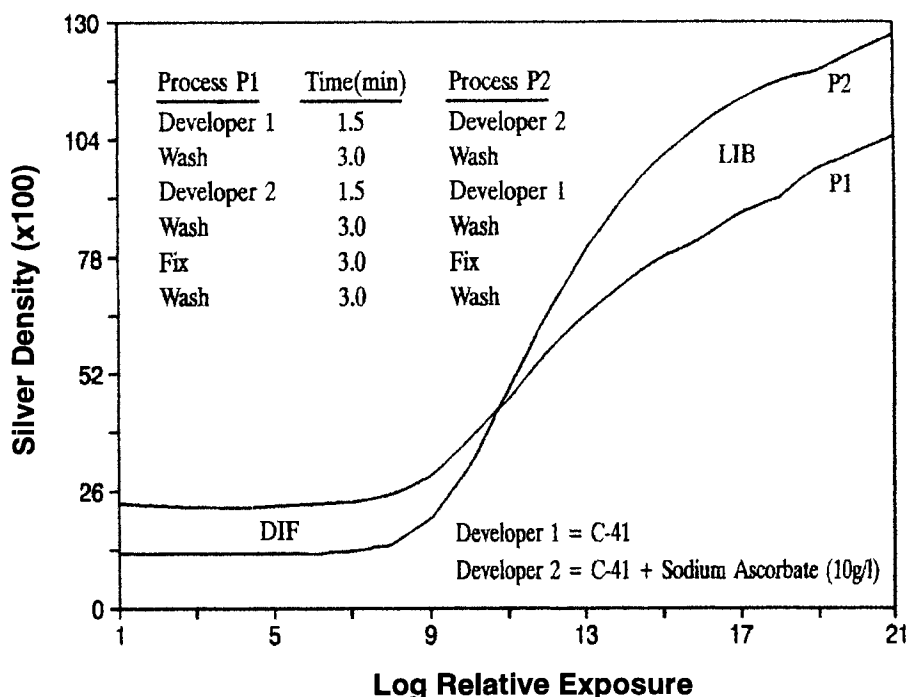


Figure 18. Two-stage development method to reveal latent image bleaching during development [86].

$\text{Fe}^{2+}/\text{Fe}^{3+}$, so if air is excluded from the system a range of redox buffers can be made with definite potentials by adjusting this ratio. The complexing agent C can be oxalate [83], citrate, tartrate, ethylenediamine tetraacetate (EDTA), DTPA, or other amino carboxylic acids.

Early in Section 1.2.2 it was shown that if the potential of a developing agent is more negative than the silver ion potential, then development or silver ion reduction is thermodynamically possible. The difference between the equilibrium silver potential E_{Ag} and the developer or redox buffer potential E_{dev} is:

$$\Delta E = E_{\text{Ag}} - E_{\text{dev}} \quad (58)$$

Thus redox buffers with potentials more negative than the silver ion potential (ΔE positive) would be expected to grow latent images and those with potentials more positive (ΔE negative) than the silver ion potential would be expected to bleach latent images. Several workers [84] have shown that development starts only when the potential is some 50–160 mV more negative than the equilibrium potential of bulk silver. It was also shown by Hillson [84b] that redox buffers with a potential more positive than the silver potential eventually destroyed all the surface latent image, as expected, whereas redox buffers with a potential more negative than the

Table 5. Typical redox buffer solution [86].

Ion	Concentration (M)	Substance
Fe ²⁺	0.2	(NH ₄) ₂ Fe(SO ₄) ₂ · 6H ₂ O
Fe ³⁺	0.01–0.2	Fe(NO ₃) ₃ · 9H ₂ O
Citric acid	0.15	(CH ₂ COOH) ₂ C(OH)CO ₂ H
Ag ⁺	0.001	AgNO ₃

silver potential proceeded to a limiting value which was ascribed to the destruction of all latent image centers smaller than a critical size. Larger centers were not destroyed but were enlarged by the redox buffer. Thus, by using a series of buffers with different redox potentials, it is possible to grade surface latent images into size classes and to determine the redox potentials of these size classes. The cause of the shift in redox potential has been ascribed to the higher free energy of small silver particles compared with that of bulk silver, although Matejec and Moisar [85] believe that latent images have a similar potential to bulk silver. Some of the differences between interpretations might be due to the presence of gelatin and its effect on the stability of small silver particles and on the redox potential that actually pertains in the layer [84c]. In order to resolve this Galashin and Senchenkov, and later Konstantinov et al. [86], looked at the effect of redox buffers on the stability of evaporated silver particles. The composition of a typical redox buffer solution is shown in Table 5. The redox potential is changed by varying the ferric nitrate concentration and then measured using a platinum electrode and calomel electrode.

The Gibbs–Thomson equation describes the effect of the size of a small particle on the potential relative to that of the bulk material. For silver particles:

$$\eta_r = E_{\text{Ag}} - E_r = \frac{2\sigma V_m}{rF} \quad (59)$$

where E_{Ag} is the equilibrium potential for the bulk silver electrode, E_r is the potential of a microscopic silver electrode of radius r , V_m is the molar volume of silver metal, and σ is the specific free surface energy of the metal/solution interface. From Eq. (58),

$$\Delta E_r = \Delta E - \frac{2\sigma \cdot V_m}{rF} \quad (60)$$

which is the potential acting on small silver particles. In a given redox buffer there will be a critical size r_0 for which

$$\Delta E_{r_0} = \Delta E - \frac{2\sigma \cdot V_m}{r_0 F} = 0 \quad (61)$$

so that the potential difference η_{r_0} at which a silver particle is just in equilibrium in a redox buffer is given by

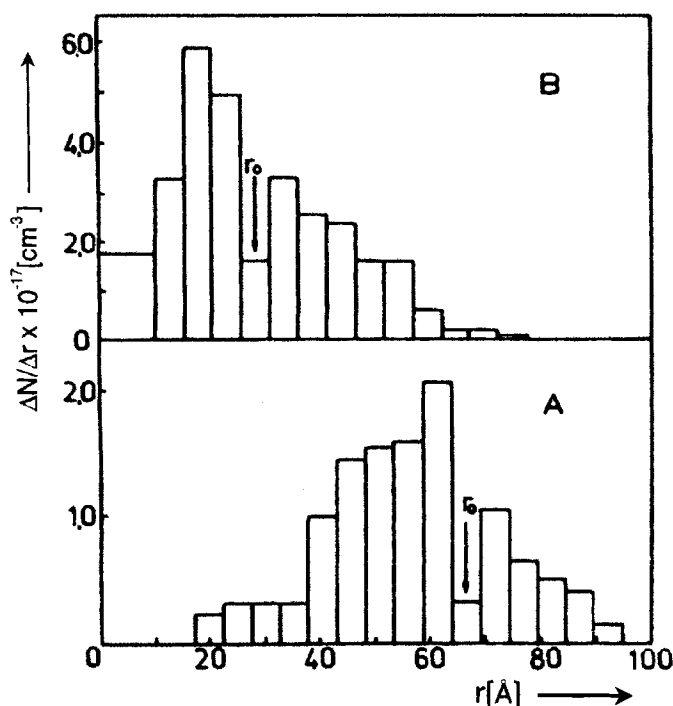


Figure 19. Histograms of samples treated in a chemical developer having $\Delta E = 19.3$ mV. The arrows indicate the stable critical size class r_0 . (A) uncoated with gelatin, development 120 min; (B) overcoated with gelatin, development 180 min. In the presence of gelatin the size of the stable specks is considerably smaller [86].

$$\eta_{r_0} = \Delta E = \frac{2\sigma \cdot V_m}{r_0 F} \quad (62)$$

Konstantinov [86] observed a minimum in the size distribution curve at the size class corresponding to r_0 after short treatment times in a redox buffer (Figure 19). The minimum occurs because particles at the extremes of size class r_0 dissolve or grow, and thus the size class is depleted from two directions; it disappears after prolonged treatment and the distribution moves to larger sizes. The critical size r_0 is inversely related to ΔE of the redox buffer as required by the Gibbs–Thomson equation. This is illustrated in Table 6.

Further work [86] showed that the specific surface free energy of silver particles was the same whether they were evaporated on carbon or silver bromide, but was lowered by coating with gelatin. The latter is given as the reason for the stabilizing effect of gelatin on latent image specks.

Cramp and Hillson [87] have shown that the Gibbs–Thomson equation, which from a thermodynamic viewpoint should be valid only for large assemblies of atoms, appears to be valid down to latent images with only 12 atoms (Figure 20).

Table 6. Critical particle size versus redox potential.

r_0 [Å]	ΔE [mV]
30 ± 3	66.8
39 ± 3	50.7
43 ± 3	43.8
70 ± 4.5	26.5
192 ± 17	10.0

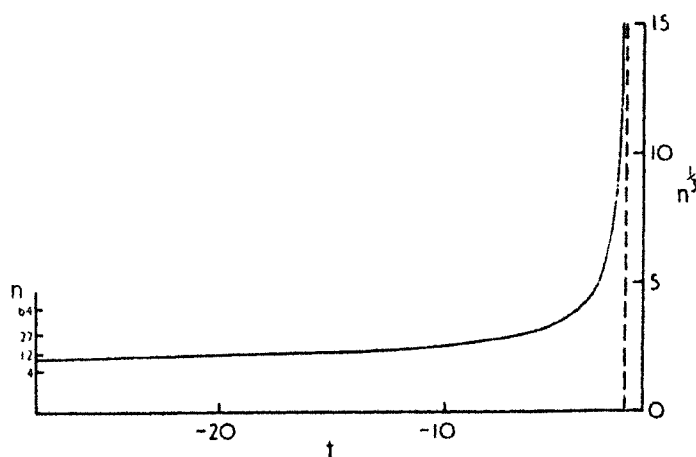


Figure 20. Pre-filamentary growth of development centers: t is development time and n is the number of silver atoms in the developing center. Note the sharp change in activity when n is about 12 atoms [87].

They have estimated that due to the excess energy of very small particles the induction period for development increases sharply for clusters of less than 12 atoms. This effect has been cited to explain discrimination in chemical development of silver halide, on which practical photographic systems depend. The excess energy of small particles slows down the early stages of development to provide this discrimination between exposed and unexposed grains.

The effect of gold sensitization of emulsions is to alter the shape of the curve shown in Figure 20 because of the incorporation of gold into the latent image. Gold is more active than silver as a catalyst for silver deposition [88] and also has been shown to be able to catalyze development with a two-atom center, compared with the minimum of four atoms for silver. The curve will now come down more steeply and not turn over to long induction periods until n is very small.

Hada et al. [89] compared experimental characteristic curves with theoretical curves based on a model of exposure and development. A marked difference in the ability of specks to initiate development was found between silver specks smaller than Ag_4 and those larger than Ag_4 .

Tani [90] has examined the properties of silver clusters by means of redox buffer solutions, and showed that the oxidation potential of latent images formed by sulfur-plus-gold sensitization was much more positive than for those formed in unsensitized, sulfur-sensitized, reduction-sensitized, and iridium-sensitized emulsions. The oxidation potential of fog centers with excessive sulfur sensitization was much more positive than that of fog centers with excessive reduction sensitization. In general this reflects the relative ease of bleaching of silver centers compared with silver sulfide centers.

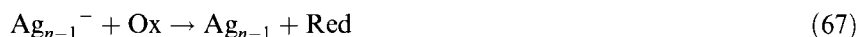
Kawasaki et al. [91] looked at the oxidation kinetics of large photolytic silver clusters in redox buffer solutions. The process was analyzed in terms of a series of stepwise reactions involving electron transfer and silver ion elimination. It was shown that the single-step oxidation:



proceeds via the steps:



and not via:



The ionization potential of Ag_n and the dissociation energy of Ag_n^+ are the dominant factors influencing oxidation. It was concluded that with increase in cluster size the ionization potential decreases and the dissociation energy increases.

Mostafavi et al. [92] generate very small silver aggregates by a pulse radiolysis method and follow their aggregation and growth in the presence of an electron donor, the radical anion of sulfonatopropyl viologen (SPV) generated in the same pulse. They use this method to study the size dependence of the electrochemical potential of small silver clusters and conclude that a critical silver aggregate is $\text{Ag}_5^+/\text{Ag}_5$, which has $E^\circ = -410 \text{ mV (NHE)}$.

Ohzeki [93] has examined the rate of development and size of latent image centers in chemically sensitized emulsions. He concludes that there are fast and slow components in development and that the fast component corresponds to latent images of five atoms or more and the slow component to latent images of less than five atoms. The fast component can be explained by electrode reaction theory whereas the slow component can be explained by the stepwise one-by-one growth of the latent image center, which results in a long induction period for development of grains with less than five atoms.

Federov and Zakarov [94] studied the thermodynamics of silver particle growth. Silver particles have a critical size which can initiate development, whereas particles of smaller size can grow only by coalescence.

Tani [95] has reviewed the properties and formation of silver clusters on silver halide grains. It is demonstrated that latent image centers composed of four atoms are formed with high efficiency and bring about large-scale amplification during development.

Development mechanism

In the classical theory of Ostwald, Abegg, and Schaum [96] the homogeneous reduction of silver ion is assumed to be rapid and is followed by the physical deposition of silver on a latent image nucleus from a supersaturated solution of silver. The term “physical development” arises from this description and developers used at this time often deliberately contained soluble silver ion. It is now considered that physical and chemical development are both chemical, or electrochemical, processes in which silver ion reduction occurs at the latent image surface.

The latent image catalyzes the reduction of silver ion either from the solid silver halide phase, as in chemical development, or from a soluble source of silver ion, as in physical development (Figure 21). One view of chemical development is that interstitial silver ions move through the silver halide crystal and are reduced on the underside of the latent image speck. In purely physical development complexed silver ion moves through the solution and is reduced on the nucleus. In this sense physical development and the early stages of chemical development are similar.

The main difference between the two types of development depicted in Figure 21 is that the silver ion source is from a limited direction (anisotropic) underneath the latent image in chemical development but is from every direction (isotropic) in purely physical development. This difference has been used to explain the filamentary nature of the silver formed in the rapid or continuation stage of chemical development. It appears that in the early stages of chemical development the latent image grows but subsequently silver filaments are “extruded” from the silver halide grain. In the Gurney and Mott [97] theory of development silver filaments are “extruded” due to

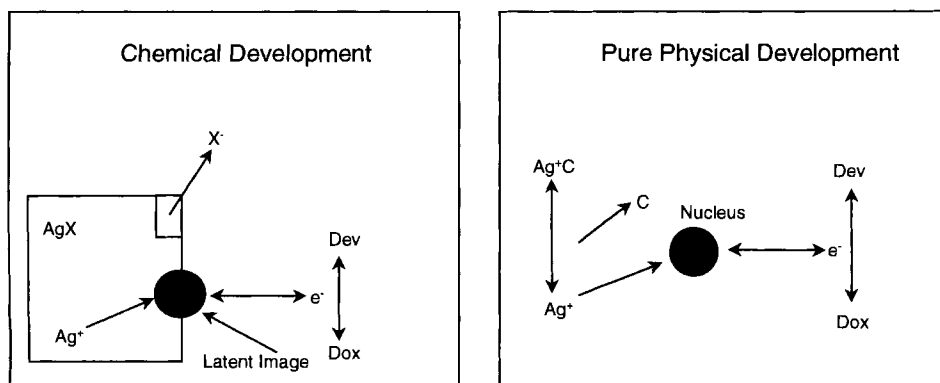


Figure 21. Chemical and physical development. In chemical development the silver ion source is solid silver halide. In physical development the silver ion source is a soluble silver ion complex.

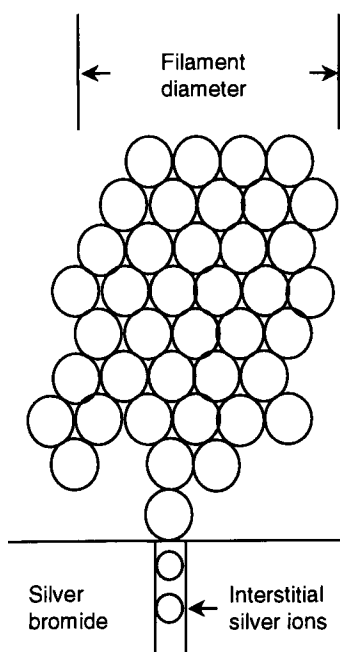


Figure 22. Metallic silver growing at an AgBr surface. The spherical particle becomes elongated when the diameter of the sphere grows too large for the silver to diffuse over the whole sphere in the time available. Typical 200 Å filaments are 70 atoms wide [98].

the pressure of silver atoms accumulating on the underside of the latent image speck.

The spherical growth of the latent image will accelerate because of the increase in surface area and Berry [98] suggested that once the rate reaches a value such that the rate of diffusion of silver atoms on the surface of the growing speck is unable to maintain a spherical shape, silver filaments move out from the grain surface.

It has been shown by Metz and confirmed by Miura and Sakaguchi [99] that the far end of a filament is the part originally on the surface, thus indicating that the primary filament grows out rather than being formed by deposition of silver from outside the silver halide grain (Figure 22).

Filaments can be single strands or loops and it is likely that the base of the filament can split to form a branch and rejoin to form a loop (Figure 23).

It is known, however, that in the development of silver halide in the presence of silver halide solvents, thickening of filaments formed originally by chemical development occurs by solution physical development on the surface of the filament. It has also been suggested that the silver halide grain can dissolve on the underside of the latent image speck, thus providing soluble silver ions which can then be reduced by physical development on the base of a growing filament (Figure 24). In this sense chemical development then becomes a version of solution physical development and the distinction between chemical and physical development is blurred.

Matejec and Meyer [101] suggest that the concentration of interstitial silver ions is insufficient to account for the rates of development observed in practice. Calcu-

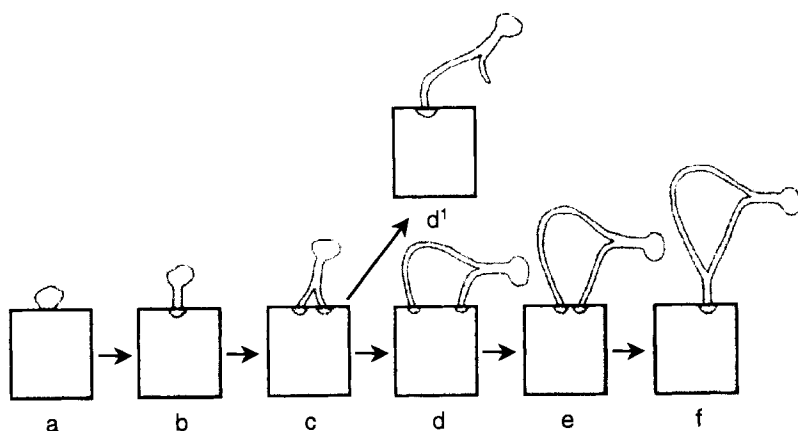


Figure 23. The sequence, a to f, schematically shows the generation of the filament loop. A transition of the kind c–d¹, i.e., the tearing-off of a filament from the AgBr surface, is a rare occurrence [99].

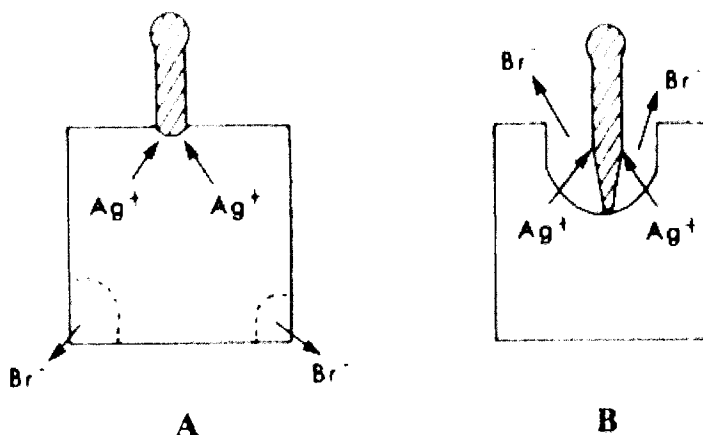


Figure 24. Schematic representation of filament growth (A) by silver ion transport through the crystal and extrusion, and (B) by dissolution of the AgBr followed by reduction of silver ions in the vicinity of the growing filament [100].

lations by Milchev and Malinowski [102], however, support the view that there is no limitation caused by insufficient silver ion flux through the silver halide crystal.

Absolute reaction rate theory considers the formation of an activated complex intermediate between reactants and products (Figure 25). The activated complex can decay to products or back to reactants. Heterogeneous catalysis considers the adsorption of reactants as a means of lowering the activation energy of reaction which occurs on the surface followed by desorption of the products. The mechanism of development can be considered as a combination of these ideas.

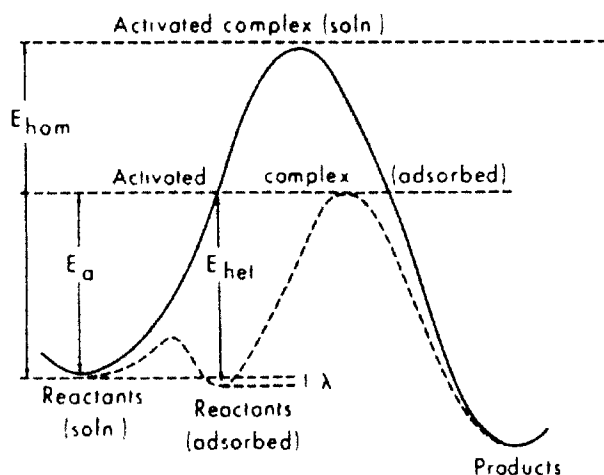


Figure 25. Schematic representation of the activation energies involved in the homogeneous and heterogeneous reduction of silver ions.

Here the activated complex that is formed between the developing agent and silver ion does not decompose significantly to products in the homogeneous phase. If the activated complex forms in the adsorbed state on the latent image surface, then the activation energy for reaction is lowered and products are formed. Thus the latent image acts as a heterogeneous catalyst. The rate of the reaction will depend on the activation energy by means of the Arrhenius relation (Eq. (68)) where E_a is the activation energy of the reaction. The pre-exponential factor A (Eq. (69)) contains reactant concentrations, a rate constant, k , and the catalyst surface area, S .

$$\text{Rate} = A \exp(E_a/RT) \quad (68)$$

$$A = k[\text{Dev}]^\alpha [\text{Ag}^\oplus]^\beta S \quad (69)$$

The fractional order can be explained by means of the surface coverage of adsorbed components which becomes more difficult as it approaches a complete monolayer. The heat of adsorption decreases with the extent of adsorption because of the increasing closeness and interaction of adsorbed species. This can be interpreted by means of an adsorption isotherm such as the Freundlich isotherm which relates the solution concentration to the surface concentration according to Eq. (70),

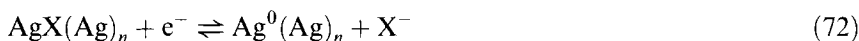
$$C_a = aC^{1/x} \quad (70)$$

where C_a is the surface concentration and C is the bulk solution concentration of active developer components. Thus if the rate of development is proportional to the concentration of adsorbed species it will deviate from simple integral reaction order and become fractional order as surface coverage increases. Other adsorption isotherms such as that of Langmuir might also be applied.

Electrochemical mechanisms of development have received considerable attention and support in the last 40 years and are generally regarded as the best means of

describing a complex phenomenon. There have been many models proposed and although none of them is complete in its description, considerable progress has been made in understanding both chemical and physical development.

The Gurney–Mott theory [97] of chemical development is based on a short-circuited local cell where the latent image acts as an anode for the developer half-cell and as a cathode for the silver ion half-cell reactions. The developer reacts at the solution/latent image interface (Eq. (71)) and silver ion reacts at the latent image/silver halide interface (Eq. (72)):



where the silver ion source is solid silver halide AgX, and $(\text{Ag})_n$ represents the latent image. This mechanism has been treated quantitatively [100]. Berg [103] suggested an electrochemical mechanism similar to that of Gurney and Mott. Bagdasaryan [104] proposed an electrochemical mechanism assuming that the anodic process is rate-limiting and that the silver has the potential of the silver/silver ion couple.

Pontius, Willis, and co-workers [105] measured the induction times for several developer types and found a correlation between them and the half-wave potential of the developer

$$\log k_i = 1.94 + 6.9E_{1/2} \quad (73)$$

for development by *p*-phenylenediamines and *p*-aminophenols, according to Eq. (73), where k_i is the rate constant for the induction period.

Hoffman and Friedman [106] proposed a mechanism for the induction time in development based on heterogeneous electrochemical theories of corrosion. The model explains the empirical relation derived by Pontius and Willis. In this case the two half-cell reactions of silver and developer give rise to a mixed or corrosion potential, E_{corr} , which if electron transfer is rate-limiting can be described by Eq. (74),

$$E_{\text{corr}} = \frac{1}{2}[E_{\text{D}}^{\circ} + E_{\text{Ag}}^{\circ}] + \frac{1}{2}\beta \ln \frac{k_{\text{Ag}}^0 A_{\text{Ag}} [\text{Ag}^+]}{k_{\text{D}}^0 [\text{D}] A_{\text{D}}} \quad (74)$$

where k_{Ag}^0 = the heterogeneous rate constant for the cathodic process, k_{D}^0 = the heterogeneous rate constant for the anodic process, $[\text{Ag}^+]$ = concentration of silver ion, $[\text{D}]$ = concentration of developer, A_{Ag} = cathodic surface area, A_{D} = anodic surface area, E_{D}° = the formal potential of the developer couple, and E_{Ag}° = the formal potential of the silver couple.

On the basis of further assumptions they arrived at Eq. (75),

$$E_{\text{D}}^{\circ} \equiv E_{1/2} = E' + \beta \ln \frac{k_{\text{D}}^0}{k_{\text{Ag}}^0} \quad (75)$$

which is formally similar to the empirical relation of Pontius and Willis, where:

$$E' = 2E_{\text{corr}} - E_{\text{Ag}}^{\circ} - \beta \ln \frac{A_{\text{Ag}}[\text{Ag}^+]}{A_{\text{D}}[\text{D}]} \quad (76)$$

Pontius and Willis [107] formulated a rate equation (Eq. (77)) for the early stages of chemical development of a single grain, which describes the growth of the latent image during the induction period and the subsequent filamentary growth:

$$\frac{d\text{Ag}}{dt} = k_f^0[\text{R}]S \exp\left(\alpha nF \frac{\Delta E}{RT}\right) - k_b^0[\text{O}]S \exp\left((1 - \alpha)nF \frac{\Delta E}{RT}\right) \quad (77)$$

where k_f^0 is a rate constant for the forward reaction, k_b^0 is a rate constant for the backward reaction, $[\text{R}]$ is the concentration of the reduced form of the developing agent, $[\text{O}]$ is the concentration of the oxidized form of the developing agent, S is the surface area of the silver in contact with the solution, α is the symmetry factor (this is the portion of the potential between the solution and the silver which favors the forward reaction), n is the number of electrons transferred per molecule of R or O and ΔE is the overpotential between the silver surface and the solution. Since the concentration of R far exceeds that of O , the reverse reaction can be neglected so that the rate is described by the first term in Eq. (77). The assumptions made are:

- 1) that electron transfer from the developing agent in solution to the silver surface is the rate-determining step, and
- 2) that there is always an adequate supply of silver ions in the grain to accommodate every electron transfer.

This implies that the latent image has the potential of the silver half-cell and so the overpotential ΔE is the difference between the potentials of the silver and developer half-cells (Eq. (78)).

$$\Delta E = E_{\text{Ag}^0/\text{Ag}^+} + \frac{RT}{nF} \ln[\text{Ag}^+] - E_{\text{R/O}} - \frac{RT}{nF} \ln \frac{[\text{O}]}{[\text{R}]} \quad (78)$$

If this is substituted in Eq. (77) the silver ion concentration has its influence by changing the overpotential via the exponential term. The silver ion concentration is that at the silver/solution interface, not that inside the grain.

The overall rate equation predicts that:

- 1) the rate of growth of the development center is proportional to its surface area;
- 2) it is first order in developer concentration;
- 3) $\log k$ should be proportional to $\log(1/[\text{Br}])$.

These predictions are confirmed for development by ascorbic acid (Figures 26 and 27).

In Figure 28 a summary of the general observations on the exposure, nucleation, detection, growth, and amplification of the latent image is shown.

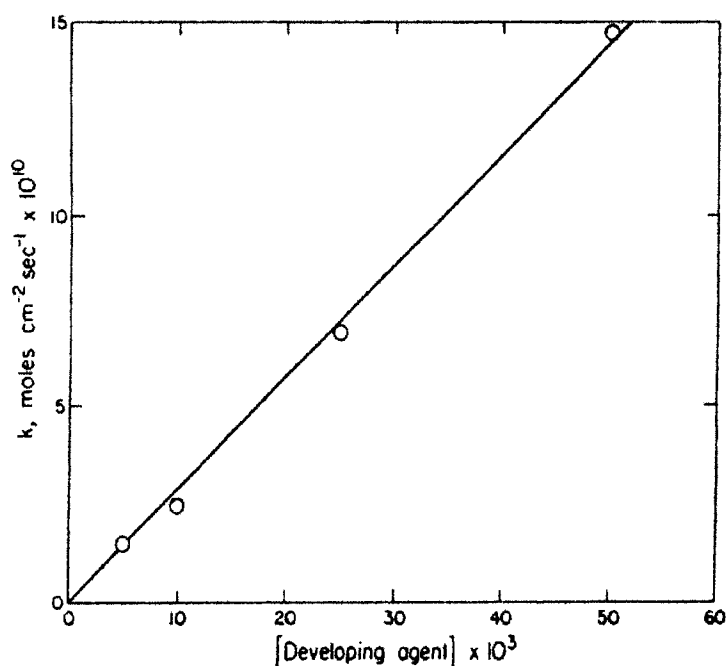


Figure 26. Dependence of the specific rate constant upon developing agent (ascorbic acid) concentration [107].

Brown and Tong [108] proposed an electrochemical model for the development of a single silver halide grain in which it is assumed that:

- 1) equilibrium exists at the surface of the development site and mass transport to and from that surface is the rate-controlling step;
- 2) silver ion supply through the grain is not rate-limiting;
- 3) the latent image speck does not change in surface area.

The developing silver speck can be regarded as a dual electrode which acts for the developer as an anode and for silver ions as a cathode. A mixed potential E_m is produced by a net flow of electrons from the anode site, where developer is oxidized, to the cathode site, where interstitial silver ion is reduced. The anode potential becomes more positive as oxidized developer is formed and the cathode potential becomes more negative as halide ions are produced at the electrode. It is assumed that the mixed potential of the nucleus E_m is governed by the equilibrium potentials of the two half-cell reactions. This means that the heterogeneous half-cell reactions are fast enough to maintain equilibrium or Nernstian behavior. The supply of silver ions diffusing through the silver halide is considered to be adequate at all times. The model is chosen to represent the point in time when the developing nucleus is still spherical, i.e., before filamentary growth. The assumption made is

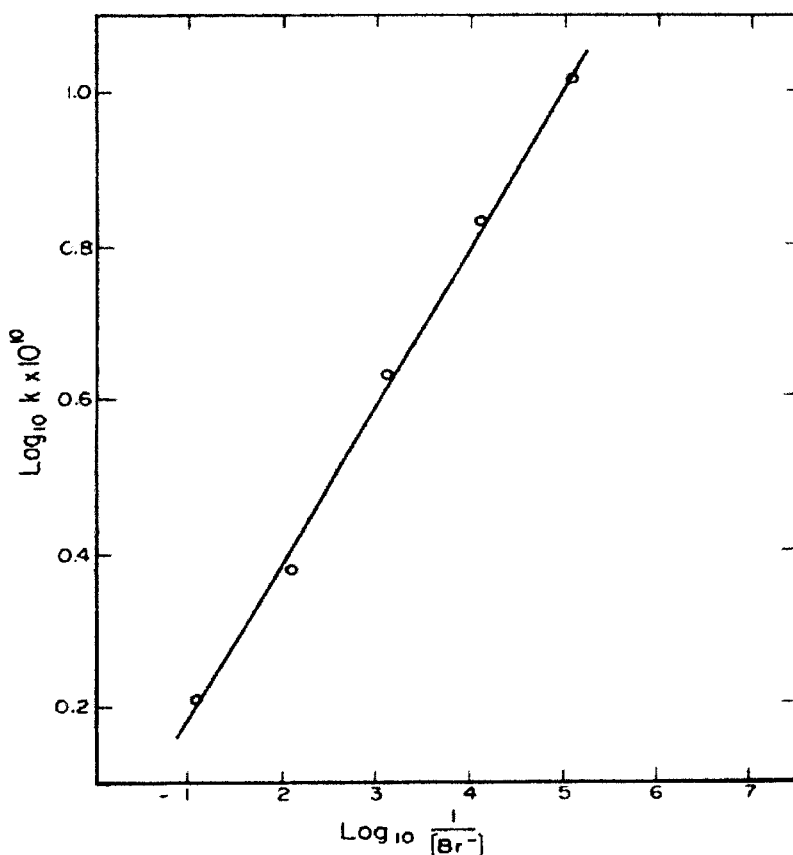


Figure 27. Dependence of specific rate constant for pre-filamentary center growth upon bromide ion concentration, showing conformity with the Butler–Volmer law of electrode kinetics. Developing agent, 10^{-2} M ascorbic acid [107].

that the area of the nucleus is constant and so the model is time-independent and does not describe the autocatalytic nature of the development process.

Mass transport of developer to, and oxidized developer and halide ions from, the silver speck is calculated by the method of spherical diffusion. The surface concentrations of the active species are then used in the Nernst equation to calculate E_m , the surface potential of the developing nucleus. The rate equation (79) obtained is:

$$1000W = \frac{4\pi aR^*D_R(1 + \lambda a)}{(1 + \lambda a) + \frac{D_R}{D_Q} \exp \left[\frac{-nF}{RT} (E_{\text{AgX}}^\circ + E_\eta - E_{1/2}^{\text{Dev}}) \right]} \left[X^* + \frac{1000nW}{4\pi bD_X} \right]^n \quad (79)$$

where R^* = is the initial concentration of reduced species, X^* = initial bulk halide

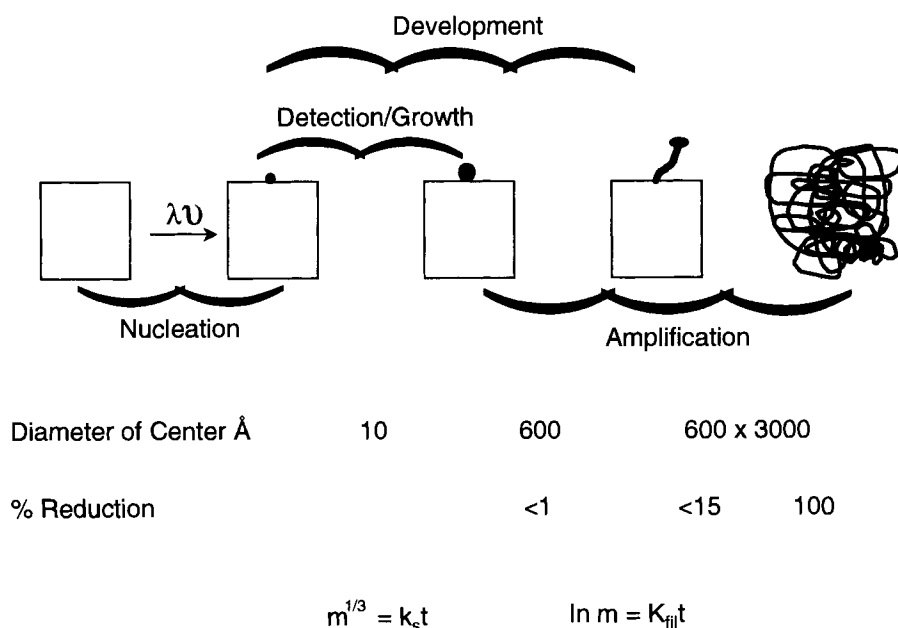


Figure 28. Kinetic aspects of development.

concentration, W = is the development rate in mol s^{-1} (1000 converts mol cm^{-3} to mol L^{-1}), D_R = diffusion coefficient for the reduced developer [$\text{cm}^2 \text{s}^{-1}$], D_Q = diffusion coefficient for the oxidized developer [$\text{cm}^2 \text{s}^{-1}$], D_X = diffusion coefficient of halide [$\text{cm}^2 \text{s}^{-1}$], a = radius of developing nucleus [cm], b = radius of the silver halide grain [cm], $\lambda = (k/D_Q)^{1/2}$, k = summation of all pseudo first-order decompositions of oxidized developer [s^{-1}], E_{AgX}° = the standard potential for a silver electrode in unit activity of halide ion, $E_{1/2}^{\text{Dev}}$ = the half-wave potential for the developing agent, E_η = an overpotential term to correct for the different silver potential of small particles compared with bulk silver.

There are some limiting cases of the complete equation.

- 1) When the rate is determined solely by the diffusion of reduced developer, it becomes:

$$1000W = 4\pi a D_R R^* \quad (80)$$

Here the rate is linear in developer concentration but independent of developer potential, halide ion concentration and rate of scavenging of oxidized developer. Such cases have not been seen experimentally.

- 2) When the second denominator is much larger than the first and the overall halide concentration is nearly equal to the bulk level (this occurs at very low developer concentrations), Eq. (79) becomes:

$$1000W = \frac{4\pi aR^*D_Q(1 + \lambda a)}{\exp \frac{-nF}{RT} \left\{ E_{AgX}^\circ + E_\eta - E_{1/2}^{Dev} - \frac{RT}{F} \ln(X^*) \right\}} \quad (81)$$

Here the rate is first-order in developer concentration and has the expected potential dependence.

- 3) This occurs when the second term in the denominator is larger than the first term and the rate is also large:

$$1000W = \frac{4\pi aD_Q(1 + \lambda a)R^*}{(1000n/4\pi bD_X)^n \exp \frac{-nF}{RT} (E_{AgX}^\circ + E_\eta - E_{1/2}^{Dev})} \quad (82)$$

When this applies the rate is proportional to the developer concentration to the $1/(n+1)$ th power. Such dependencies have been observed in practice for several developing agents.

A review of electrochemical models of development has been given by Sahyun [109] in which selectivity is treated in terms of the Marcus and Gerischer [110] theories of electron transfer.

Shiao and Dedio [111] formulated an electrochemical model of development which used the same diffusion calculations of Brown and Tong but included a term for the increasing surface area of the growing speck. Numerical methods were used to provide solutions to the equations and the rates of development of ascorbic acid and 4-methyl-4-hydroxymethyl-1-phenyl-3-pyrazolidone (MHP) were modeled in fair agreement with experiment. The important features treated by the model include the redox potential of the developing agent, the overpotential, diffusion and adsorption of developing agents, halide ions, and oxidized developing agents, and the inhibition of development by oxidized developing agent and halide ions.

Many of the electrode theories have assumed that the anodic reaction is rate-limiting and that the cathodic reduction of silver ions from silver halide is not rate-limiting and might not present any limitations to the process of development. Hamano et al. [112] contend that there are instances where the cathodic process does influence development. They use the Butler-Volmer equation as the basis for their development rate model and derive Eq. (83),

$$\frac{dm_i}{dt} = 2\pi r_i^2 M \frac{J}{F} \left\{ \exp \left[\frac{\alpha nF}{RT} \left(E_{AgBr} - E_{redox} - \delta E - \frac{0.85 \times 10^{-8}}{r_i} \right) \right] - \exp \left[\frac{-(1-\alpha)nF}{RT} \left(E_{AgBr} - E_{redox} - \delta E - \frac{0.85 \times 10^{-8}}{r_i} \right) \right] \right\} \quad (83)$$

where J = development current density, m_i = mass of the development center, M = atomic weight of silver, S = surface area of the development center in contact with the developer, E_{AgBr} = potential of silver in contact with a large silver particle, E_{redox} = potential of the developer, r_i = the reduced radius of the spherical center

starting from a latent image of i atoms, δE = reduction in overpotential used to calculate the development current from the observed development current–potential curve, $0.85 \times 10^{-8}/r_i$ = correction of the silver potential for small particles.

These workers demonstrate that the cathodic process is important in the effect of benzotriazole antifoggants on the development rate. These materials retard the development rate by ascorbic acid but do not adsorb to metallic silver, whereas they do adsorb to silver halide. In this sense benzotriazoles should not influence the anodic process, but might influence the cathodic process.

Hamano et al. [112a] extended their electrode model to include superadditivity and the effects of halide ions and quaternary salts on development.

Friedrich and Eilers [113] have proposed a corrosion model of development and derived electron transfer equations based on the Butler–Volmer expression which can be simplified into three cases. Case 1 is when both the forward and reverse processes of developer oxidation are important. Case 2 is when the net rate is limited by the forward rate of developer oxidation. Case 3 corresponds to a rate which is limited by the kinetics of both developer oxidation and silver halide reduction.

Boyack [114] has used an electrode theory of development to derive characteristic curves of photographic development and its temperature dependence. The conclusions indicate that:

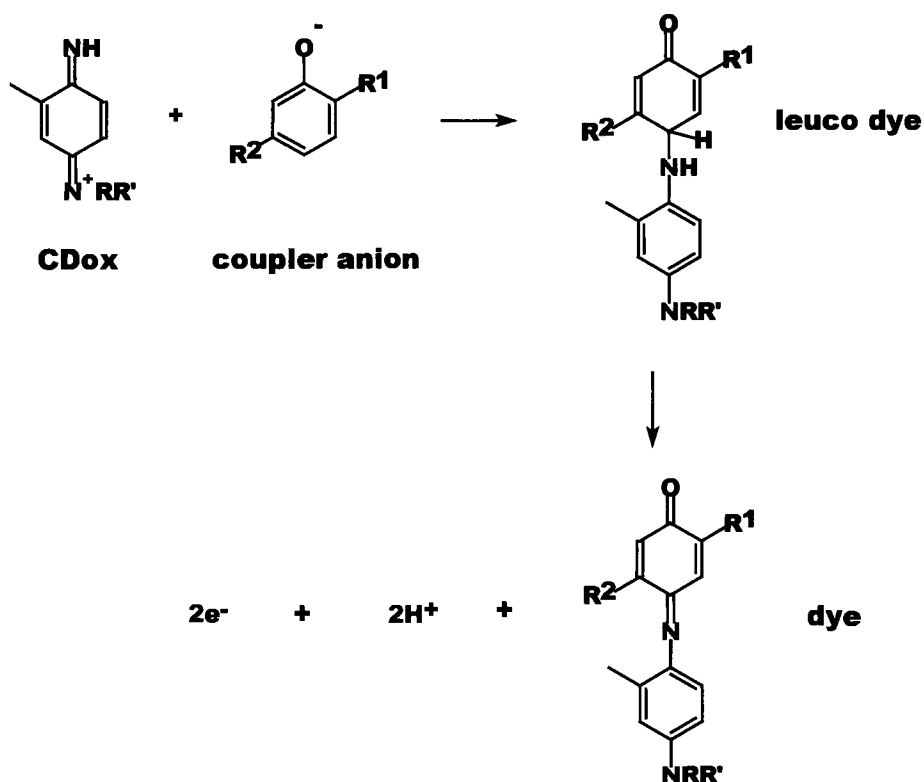
- 1) at constant temperature changes in development conditions should only cause an expansion or contraction of the time scale;
- 2) the apparent activation energy depends on the potential difference between the developer and silver/silver halide potentials;
- 3) the activation energy varies with latent image size.

The single-grain model was extended by use of grain size distributions to give the mass fraction developed as a function of exposure.

Shiao and Bistrovich [115] added the ability to model physical development to the original chemical development model of Shiao and Dedio, and included inhibition by iodide released during development. Also, unlike the model of Pontius and Willis, certain cases where the cathodic process can be the rate-limiting step are identified. The model is able to describe the silver development kinetics of liquid emulsions and in coated layers using E-6 first developer.

1.2.3 Coupling

The useful reaction of oxidized *p*-phenylenediamines is to generate dye. They can react with an electron-rich species, a coupler anion, to form a leuco dye which either oxidizes or loses a fragment to form the dye. As an example, oxidized *p*-phenylenediamine can react with a phenol to form a cyan dye as shown in Scheme 2. The leuco dye oxidation usually takes place with the consumption of another molecule of CDox, which is reduced back to the color developer. Thus production of a molecule of dye by this route uses two molecules of CDox or four silver ions and is known as a four-equivalent reaction. Dye formation can proceed by a two-equivalent route if there is a good leaving group such as a chlorine atom at the reaction site on the coupler anion.



Scheme 2. Cyan dye formation from *p*-phenylenediamines.

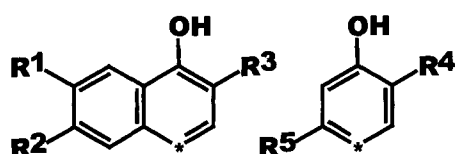
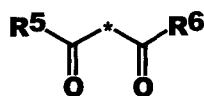
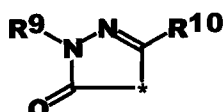
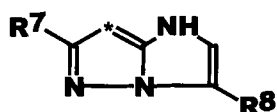
The color of the dye produced is determined by the structure of the coupler. In general the dye produced in a particular photographic layer is complementary to the sensitization of the emulsion in that layer, i.e., cyan dye is produced in layers containing red-light-sensitive emulsions, magenta dye is produced in layers containing green-light-sensitive emulsions and yellow dye is produced in layers containing blue-light-sensitive emulsions. A good, detailed description of this process can be found elsewhere [116].

Examples of some coupler structures are shown in Figure 29.

1.3 Bleaching/Bleach-Fixing

1.3.1 Introduction—General Mechanisms

In color chromogenic photographic systems, silver is generated along with the dye. This silver desaturates the color and generally has to be removed. The removal

**cyan dye forming****yellow dye forming****magenta dye forming****Figure 29.** Some coupler structures: *, position at which coupling with CD-ox occurs.

process must take out the silver but retain the dyes unharmed. A typical process is Kodak Process C-41, shown earlier in Table 1.

There is also a requirement for the removal of silver in some black-and-white processes. In the case of black-and-white reversal processing the initially imagewise exposed silver is removed before the second development stage. An example of a process might be as shown in Table 7 [117].

Table 7. A typical black-and-white reversal process.

Process step	Time [s]
Develop	120
Rinse	30
Bleach	50
Rinse	30
Clear	30
Rinse	30
Re-expose	
Re-develop	50
Rinse	30
Fix	50
Wash	120
Dry	

Bleaches are sometimes used to reduce the density of black-and-white images by removing silver, in solutions that are confusingly known as “reducers”. These bleaches can be solvent bleaches, where the oxidized silver dissolves in the bleach, essentially without complexation. Alternatively they can contain a silver complexing agent and act as a bleach–fix.

In this section we shall discuss bleaches in detail. The first part will deal with general kinetics related to bleaches and the later parts will deal with specific types of bleaches that are currently in use and will discuss their deviation from the expected behavior.

The process of bleaching is the reversal of development, i.e., it is the conversion of silver metal back to silver ions (Eq. (84)).



The bleaching reaction is controlled thermodynamically and kinetically. For the reaction to take place it must be thermodynamically favorable and also kinetically possible. We shall see that there are some bleaching agents for which the bleaching reaction is strongly favorable but the reaction is hindered and catalysts are necessary for them to be useful. The kinetics are also dependent on the movement of the bleaching agents and other solution components to and from the reaction site through swollen gelatin.

The thermodynamics of the reaction can be considered from the point of view of the silver grain being an electrode in the same way as it might be considered for developers. The potential of the redox couple of the bleaching agent can be written as Eq. (85),

$$E_{\text{Red/Ox}} = E_{\text{Red/Ox}}^\circ + (RT/zF) \ln([\text{Ox}]/[\text{Red}]) \quad (85)$$

where z is the number of electrons transferred by the bleaching agent, and that of the silver grain as Eq. (86).

$$E_{\text{Ag/Ag}^+} = E_{\text{Ag/Ag}^+}^\circ + (RT/F) \ln[\text{Ag}^+] \quad (86)$$

The reaction will proceed to bleach the silver if the redox couple potential is more positive than that of the silver. If it is not, the reaction may reverse and we have development.

1.3.2 Solvent Bleaches

The silver electrode potential is influenced by the constitution of the bleach solution. The high value of the standard redox potential of silver ($E_{\text{Ag/Ag}^+}^\circ = 0.799$ V vs. NHE) demands strong oxidants for an irreversible oxidation of silver. The types of bleach working in this way are known as solvent bleaches. The silver is oxidized and then dissolves in the bleach. This type of bleach is almost exclusively reserved

Table 8. Electrode potentials of some bleaching agents.

Bleaching agent	System	E° (vs. NHE) at 25°C [mV]
Persulfate	$\text{S}_2\text{O}_8^{2-} + 2\text{e}^- \leftrightarrow 2\text{SO}_4^{2-}$	~2.00
Permanganate	$\text{MnO}_4^- + 4\text{H}^+ + 3\text{e}^- \leftrightarrow \text{MnO}_2 + 2\text{H}_2\text{O}$	1.65 – 0.079 pH
Hydrogen peroxide	$\text{H}_2\text{O}_2 + 2\text{H}^+ + 2\text{e}^- \leftrightarrow 2\text{H}_2\text{O}$	1.36 (1.0 M at pH 7.0)
Dichromate	$\text{Cr}_2\text{O}_7^{2-} + 14\text{H}^+ + 6\text{e}^- \leftrightarrow 2\text{Cr}^{3+} + 7\text{H}_2\text{O}$	1.33 – 0.138 pH
Iron	$\text{Fe}^{3+} + \text{e}^- \leftrightarrow \text{Fe}^{2+}$	0.77
Hexacyanoferrate	$\text{Fe}(\text{CN})_6^{3-} + \text{e}^- \leftrightarrow \text{Fe}(\text{CN})_6^{4-}$	0.46
Iron EDTA	$\text{FeEDTA}^- + \text{e}^- \leftrightarrow \text{FeEDTA}^{2-}$	0.117

for the reversal black-and-white process, where the developed silver has to be removed from the film before the second development; see Table 7.

There is a range of oxidants that are currently used as bleaching agents. They have a wide range of oxidising potential (Table 8).

As can be seen by inspection, there are only a few oxidising agents that are likely to be suitable for making a solvent bleach: dichromate, permanganate, persulfate and hydrogen peroxide. The last two in the list are very poor bleaching agents as their oxidation appears to be kinetically hindered. They can only be used in the presence of a suitable catalyst, which will be described later.

The bleaching agent is chosen for use depending on the process, ease of use, environmental considerations, and cost. Some of these points will become more apparent in the sections dealing with particular types of bleach.

The bleaching reaction is dynamic and the electrode potentials are dependent on the concentration of ions at the silver grain surface. As the reaction proceeds, silver ions build up at the surface and the silver electrode potential rises. The silver electrons diffuse away, through gelatin to the bulk bleach solution. Similarly, the bleaching agent has to diffuse to the silver surface where it is reduced. The reduced species lowers the oxidant's potential and it must diffuse away for the reaction to proceed. The solvent bleaching reaction is thus controlled by the potentials and the diffusion of species through the photographic layers. For a diagrammatic representation of the bleaching of one grain in a photographic layer, see Figure 30.

However, if the silver ion concentration is kept low in another way, the silver potential is low and less powerful oxidants can be used for bleaching. The silver ion concentration can be reduced by precipitation with halide ions (Eq. (87)).



This gives a rehalogenating bleach. Rehalogenating bleaches usually contain oxidants with lower electrode potentials.

The silver halide formed can then be dissolved and removed in a later fixing step. Alternatively the silver ion can be complexed, usually to form a water-soluble species, which washes out of the gelatin. This gives the process step known as a bleach-fix as it combines both steps. The potential of the silver electrode in a

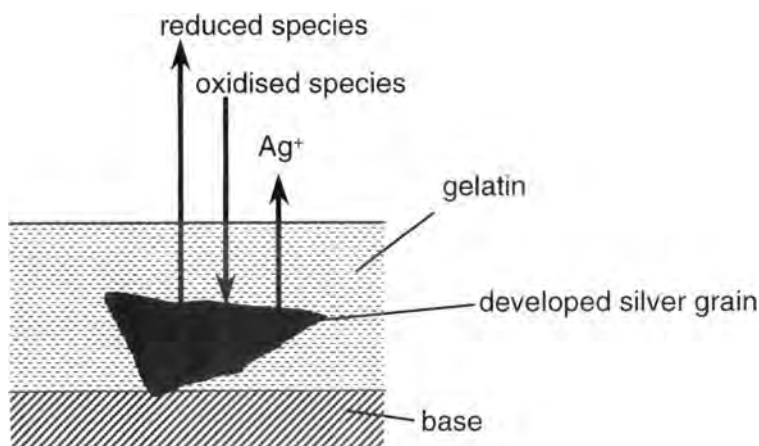


Figure 30. The bleaching process.

halide solution can be written as Eq. (88),

$$E_{\text{Ag}/\text{Ag}^+} = E_{\text{Ag}/\text{Ag}^+}^{\circ} + (RT/F) \ln(\text{SP}/[\text{X}^-]) \quad (88)$$

where SP is the solubility product of the silver halide, or using the silver halide electrode potential:

$$E_{\text{Ag}/\text{Ag}^+} = E_{\text{Ag}/\text{AgX}}^{\circ} - (RT/F) \ln[\text{X}^-] \quad (89)$$

The solubility products of the halides are shown in Table 9. By inspection we see that iodide reduces the silver potential to the lowest point at the same concentration. In practice bromide is usually used, as the silver bromide formed is more readily dissolved in the subsequent fixing step. The concentration of halide at the bleaching site is also influenced by the reaction and the diffusion of halide to the surface of the bleaching grain. Nickel et al. [118] have investigated the bleaching reaction electrochemically, removing the electrons from the silver in a cell by applying a potential to a rotating silver disk electrode electrically. They determined the influence of the halide ions and point out that in this case only halide ions have to pass through the solution/solid boundary. They measured both the rate of formation of silver halide and the rate of reduction of bleaching agents at this electrode.

Table 9. Solubilities of silver halides.

Halide	Solubility product, SP, in water at 25°C
Silver chloride	1.6×10^{-10}
Silver bromide	7.7×10^{-13}
Silver iodide	1.5×10^{-16}

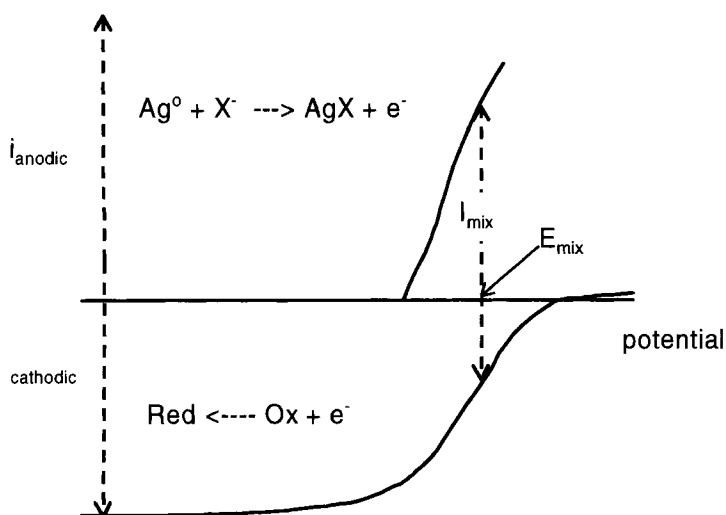


Figure 31. Redox potential diagram showing mixed potentials for bleaching.

They measured the zero potential point of the system, which depends on the halide concentration and type as described by the equations above. They were able to measure the effect of diffusion of species to the electrode and were able to determine a mixed potential of the electrode where the forward transfer of electrons from the silver was equal to the rate of reduction of the oxidant. This is shown diagrammatically in Figure 31. Nickel et al. found that the adsorption of halide to the silver surface did not influence the potential if the halide layer was less than 5 μm thick, but they did note that at a clean silver surface the silver halide formation began at a higher potential than expected, which they attributed to the high solubility of microscopic silver on the surface.

However, Matsuo et al. [119] found that the halide on the surface of a silver plate reduced the rate of bleaching. The amount of bleaching with time was determined at different temperatures for a number of different bleaches. All the bleaches showed the same characteristic curve shape, which was largely independent of the halide concentration. By way of example, Figure 32 shows data for an iron(III) EDTA/bromide bleach. Plotted also on the graphs are the expected gradients if the rate of bleaching is proportional to the inverse of the depth of silver halide ($\gamma = 1/2$) or if the rate is proportional to the inverse square of the halide thickness ($\gamma = 1/3$). From the log-log plots of these curves it was deduced that the rate was determined by the rate of migration of species through the silver halide. Matsuo et al. suggested that it was the silver ions or electrons that migrated through the silver lattice. The results also showed that the potential of the oxidant had only a small effect on the rate of bleaching of a silver sheet.

Similarly Fyson and Levenson [120] showed that the rate of bleaching of silver was hindered by the silver halide on the surface in much the same way. However, they found that the rate of bleaching in a hexacyanoferrate(III) bleach was depen-

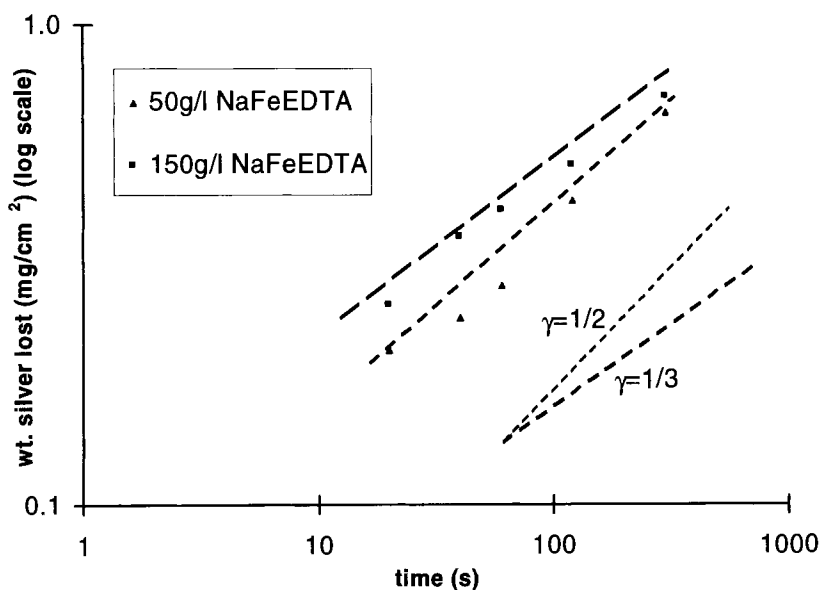


Figure 32. Rate kinetics of rehalogenating bleaching.

dent on the halide concentration, where there was an optimum halide concentration for the extent of bleaching; see Figure 33. It appears that this maximum rate corresponds to the minimum solubility of silver bromide [121] in bromide solutions. However, this does not correspond to the minimum concentration of silver ion because at high bromide concentrations the silver ions are further complexed with halide ions to form complex species, further reducing the silver ion concentration. Electron micrographs of the bleached surface showed that the bleaching had not taken place evenly (Figure 34).

Observations of silver halide crystals formed by bleaching [122] in different halide concentrations, as shown in Figure 35, suggested that the silver halide was mobile during bleaching and that recrystallization could occur. This process could be likened to the Ostwald ripening [123] that takes place during the precipitation of silver halide to make the original photographic emulsion. At high bromide the silver becomes more soluble due to the formation of complex species AgBr_2^- , AgBr_3^{2-} , and can diffuse to make thermodynamically more stable large crystals. It is possible that silver halide at high bromide concentrations might cause a more continuous layer of silver halide to form over the bleaching crystal but this has yet to be demonstrated.

Matsuo did point out that because silver normally develops to give filamentary silver [119, 124], this is much more easily bleached than a mass of silver. He demonstrated the difference in the rate of bleaching a developed silver grain as compared with a silver surface. This implies that the means by which the silver is developed determines the bleaching rate. Silver that has been developed in a developer

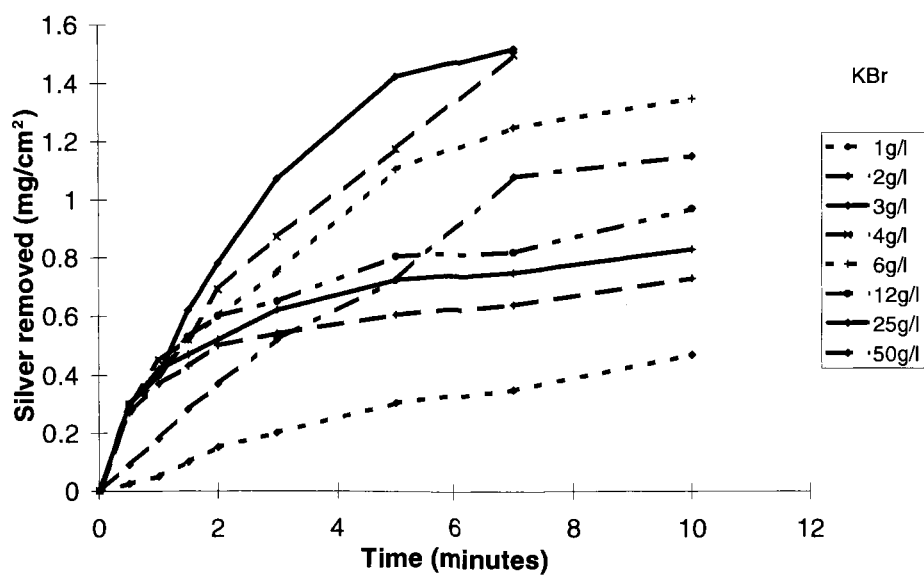


Figure 33. Effect of halide concentration on rate of bleaching with hexacyanoferrate(III).

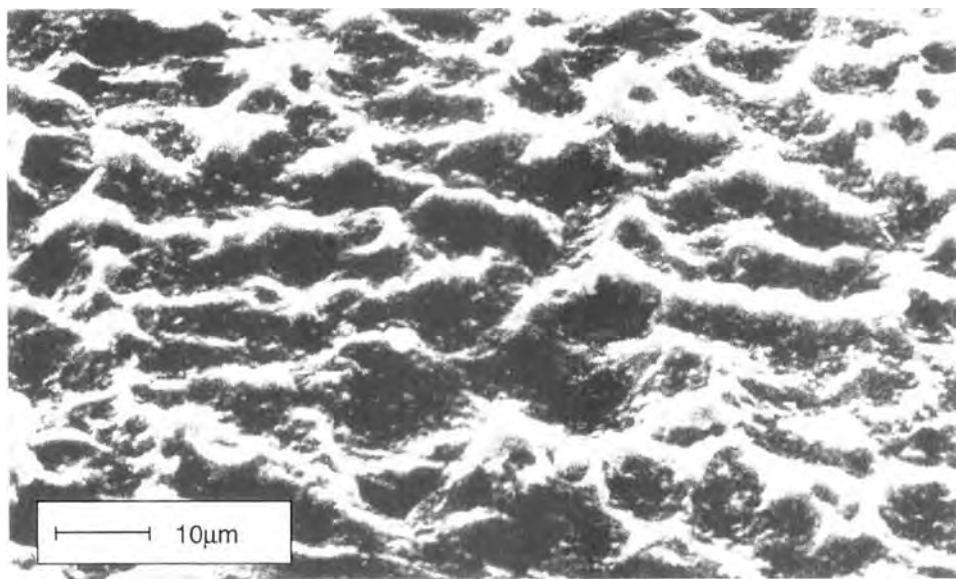


Figure 34. Electron micrograph of bleached silver sheet.

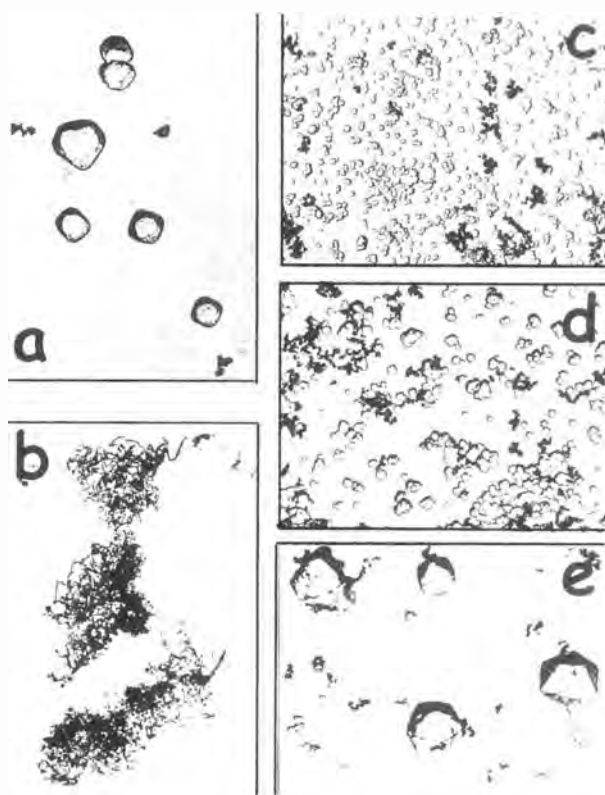


Figure 35. Effect of bleach halide concentration [M] on structure of bleached grains: (a) Original grains; (b) Developed and Final grains; (c) 10g/l KBr; (d) 50 g/l KBr; (e) 100 g/l KBr.

with a large amount of physical development, and therefore more massive silver speck, might be expected to bleach more slowly than a totally chemically developed filamentary speck.

Fyson [125] showed that the potential of the oxidant did affect the extent of bleaching of large, developed silver grains in a photographic layer (Figure 36). The greater the bleach potential, the more silver was bleached and the smaller was the effect of the halide coating of the grain surface.

1.3.3 Bleach-Fixes

There are other ways to decrease the silver ion activity in the bleaching system to allow the oxidation of silver to proceed. The silver ions can be complexed. An expression relating silver complexation to potential can be written. If the silver forms a complex with n ligand molecules, it has form of Eq. (90):

$$E_{\text{Ag}/\text{Ag}^+} = E_{\text{Ag}/\text{Ag}^+}^{\circ} - n(RT/F) \ln \beta[\text{L}^-] \quad (90)$$

where β is the cumulative stability constant of the complex of ligand L and where

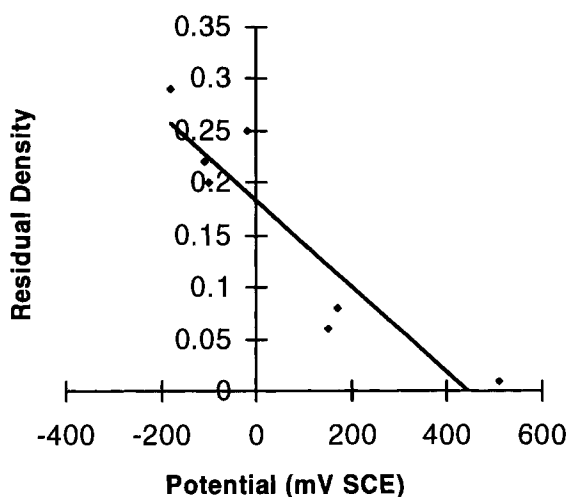


Figure 36. Effect of bleach potential on bleaching efficacy. The lower the residual density the more efficacious the bleach.

there is little mono-ligand complexation. A bleach containing a complexing agent is usually known as a bleach-fix, or blix. Matsuo et al. showed [119] that the rate of bleach-fixing was almost constant after an initial, more rapid reaction (Figure 37). The results are shown for a number of different silver complexing agents. It is believed that in the initial phase, the reaction is reaching a constant rate while the silver ion concentration equilibrates. The rate of formation of silver oxidation products equilibrates with diffusion away from the reaction site of the silver complexes. This steady state is quickly set up. The results also indicate that, at least at high concentration levels, the type of the complexing agent is not very significant.

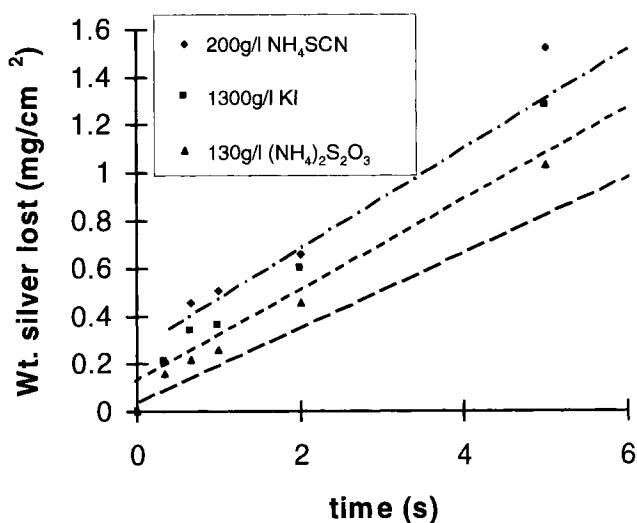


Figure 37. Effect of silver complexing agent on bleaching rate [119].

Matsuo et al. also found that at concentrations exceeding 0.8 M thiosulfate, the rate of bleach–fixing was almost independent of thiosulfate concentration.

Care has to be taken with the choice of bleaching agent and complexing agent in bleach–fixes. The fixing agent is usually thiosulfate, which itself is a reducing agent. The bleaching agent has to be chosen so that it will not oxidize the fixing agent but has sufficient oxidation potential to oxidize silver. Thiosulfate has a very high stability constant with silver ions, and so the silver ion concentration at the bleaching site is reduced, lowering the silver/silver ion potential and thus reducing the constraint on the bleaching agent. Most long-lasting practical bleach–fixes use iron(III) complexes as oxidizing agents. Choice of the ligand and solution pH allows fine tuning of the oxidizing potential so that bleaching is rapid and decomposition of the thiosulfate is slow [126].

1.3.4 Diffusion

The potential of the redox couple is governed by the concentration of oxidizing and reducing species at the reaction site. With a rotating disk electrode, Nickel et al. [118] found that the redox couple was quickly established at the surface of the silver for iron complex systems and that the rate of reaction was almost entirely dependent on the diffusion rate of the oxidized and reduced species to and from the surface. In a photographic system, developed silver grains that are to be bleached are suspended in swollen gelatin in the photographic layer. In order to maintain the electrode potential at the bleaching silver grain, oxidized species must diffuse to it and reduced species diffuse away from it through the gelatin. The rate of diffusion of these species through gelatin is therefore important. Matsuo [127] and Fyson [125] have investigated the diffusion of some bleaching agents through gelatin. In the manufacturing process coated gelatin is usually hardened so that it is more robust, can be processed at higher temperature [128], and is more scratch-resistant. The hardening, which involves crosslinking the long gelatin chains, reduces the ability of the gelatin to swell when it is put into water. This “swellability” influences the diffusion rate of species through the gelatin as the diffusing molecules have to avoid the gelatin chains. It also restricts the distances that species have to travel through the gelatin. There is an optimum swell of the photographic layer which gives the fastest process in diffusion-controlled systems [129].

Both Fyson [125] and Matsuo [127] measured the diffusion coefficients in gelatins that had been treated with different amounts of hardener and therefore had different swellability. Fyson found that the diffusion coefficient in gelatin, D_{gel} , could be related to the diffusion coefficient in water, D_{water} , and the swelled to dry thickness ratio, Z , of the hardened gelatin. The empirical relationship was found to be Eq. (91).

$$D_{\text{gel}} = D_{\text{water}} \exp[-7/(Z + 0.7)] \quad (91)$$

This could be rationalized in terms of reactive species having to “squeeze” their way through the gelatin polymer strains, and could be related to Cohen and Turnball’s

Table 10. Diffusion coefficients of some bleaching agents.

Bleaching agent	Diffusion coefficient in water at 21 °C [$\text{cm}^2 \text{s}^{-1} \times 10^6$]
Potassium hexacyanoferrate(III)	7.5
Copper(II) sulfate	11.0
Sodium iron(III) ethylenediamine tetraacetic acid complex	4.2
Sodium iron(III) iminodiacetic acid complex	3.2
Sodium iron(III) nitrilotriacetic acid complex	3.5
Sodium iron(III) methyliminodiacetic acid complex	4.8
Iron(III) chloride	5.2
Potassium dichromate	5.0

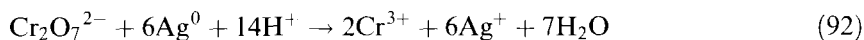
relationship [130] for the movement of hard spherical particles through holes in the polymer matrix. From the experimental results the diffusion coefficients in water were determined (Table 10).

1.3.5 Specific Bleaching Agents

Dichromate

Bleaching based on dichromate as the oxidant has been used extensively in the past and is useful for providing solvent bleaches as the dichromate has sufficient potential (see Table 10) without the need to add halide or a silver complexing agent. Solvent bleaches are especially useful for black-and-white reversal systems where they are still used extensively.

Dichromate bleaches have the property of hardening the gelatin [131] due to the formation of chromium(III) ions that form strong complexes with the gelatin strands similarly to aluminum. It is for this reason that dichromate bleaches have found use in making phase holograms [132], which rely on the different refractive indices of hard and soft gelatin. The hologram is exposed and developed. It is then bleached in a dichromate bleach, which leaves an image of hard and soft gelatin. The soft gelatin may be washed off in warm water.



As can be seen from Eq. (92), the system is very sensitive to hydrogen ions, and dichromate bleaches are always acid, usually having sulfuric acid as the buffer. The sulfate ion does not bind with the silver ion; therefore the silver ion retains its solubility and can diffuse away from the reaction site.

The use of dichromate bleaches in general has declined. Chromium(VI) is considered to be very toxic and its discharge to sewers is severely restricted in many countries [133]. The use of a dichromate bleach would have to be accompanied by

measures at the processing plant to prevent the discharge of chromium(VI), and this is not considered economic.

Iron(III) complexes

The most widely used bleach until the 1970s was hexacyanoferrate(III): ferricyanides, as such compounds were more commonly known, were inexpensive and readily available. They gave bleaches that were pH-insensitive but required a halide to be present so as to reduce the silver potential below that of the bleaching agent (see Table 8). They also gave bleaches that were strong enough to oxidize any leuco dye that might have been formed in the developer (see Section 1.2.3). The potential of the hexacyanoferrate(III) ion is sufficient to oxidize color developer that might be carried into the bleach from a previous step in the process. If this were to happen, the color developer would be oxidized and couple indiscriminately with any ionized coupler that was available, giving an overall undesirable coloration, or "stain", to the film. For this reason there is always at least one bath or wash between a color developer and hexacyanoferrate(III) bleach. There are regulations in some countries on the discharge to sewer of hexacyanoferrate(III), most for fear of the material coming into contact with a strong acid and liberating toxic hydrogen cyanide. This problem is somewhat alleviated by oxidizing the waste hexacyanoferrate(II) (ferricyanide) at the processing site with either ozone or persulfate, and recovering the ferricyanide for reuse.

Iron(III) chloride is used as a bleaching agent in some commercial processes as it is a powerful oxidant. It has to be used in acid solution to ensure that there is no precipitation of hydroxy species or reaction of the hexaaquo iron(III) ion with the gelatin to form a highly colored species that stains the gelatin. This stain is difficult to remove and relies on there being powerful iron complexing agents, such as citrate, in subsequent baths.

By far the most commonly used bleaching agents are aminocarboxylate complexes of iron(III). The potential of a simple iron complex redox system can be written as Eq. (93),

$$E_{\text{Fe(III)/Fe(II)}} = E_{\text{Fe(III)/Fe(II)}}^{\circ} + (RT/F) \ln \frac{[\text{Fe(III)}]}{[\text{Fe(II)}]} - \frac{n_{\text{Fe(III)}}}{n_{\text{Fe(II)}}} (RT/F) \ln \frac{\beta_{\text{Fe(III)}}}{\beta_{\text{Fe(II)}}} [\text{L}^-] \quad (93)$$

where $n_{\text{Fe(III)}}$ and $n_{\text{Fe(II)}}$ are the numbers of complexing agent molecules per iron(III) and iron(II) respectively and $\beta_{\text{Fe(III)}}$ and $\beta_{\text{Fe(II)}}$ are the cumulative complexing coefficients of the complexing agent with the respective iron species. By inspection of the formula it can be seen that by choosing complexing agents of different complexing coefficients, the iron redox potential can be modified to suit an application.

This equation is very much simplified, as there are other reactions of the complex or the ligands that affect the potential. For instance, ethylenediaminetetraacetic acid

(EDTA) is a favorite ligand as it is relatively inexpensive, it is nontoxic, and it readily forms stable iron complexes with a useful redox potential. The concentration of the fully ionized ligand is determined by the four ionization constants of the EDTA free acid. The iron complex also has a vacant ligand site that can pick up a hydroxyl ion and therefore has a further complexing constant for the hydroxy species. It has also been observed that this hydroxy species can react with another to form a dimer, altogether making a complex system. The potential for this system with excess EDTA can be described by Eq. (94), a modified version Eq. (93), taking into account the other equilibrium constants:

$$E_{\text{Fe(III)/Fe(II)}} = E_{\text{Fe(III)/Fe(II)}}^{\circ} + (RT/F) \ln \frac{[\text{Fe(III)}]}{[\text{Fe(II)}]} - (RT/F) \ln \frac{\beta_{\text{Fe(III)}}}{\beta_{\text{Fe(II)}}} \alpha [\text{L}]$$

$$\times \frac{[\text{H}^+]^2 + K_1^{\text{Fe(III)}} [\text{H}^+] + K_1^{\text{Fe(III)}} K_2^{\text{Fe(III)}} + 2K_D K_1^{\text{Fe(III)2}} [\text{Fe(III)}]}{[\text{H}^+]^2 + K_1^{\text{Fe(II)}} [\text{H}^+] + K_1^{\text{Fe(II)}} K_2^{\text{Fe(II)}}} \quad (94)$$

where $K_1^{\text{Fe}(n)}$, $K_2^{\text{Fe}(n)}$ are the ionization constants of the respective iron complexes, K_D is the dimerization constant of the iron(III) hydroxy-EDTA complex, and α is the relative concentration of the fully ionized ligand of EDTA and can be described by Eq. (95),

$$\alpha = \frac{K_1 K_2 K_3 K_4}{[\text{H}^+]^4 + K_1 [\text{H}^+]^3 + K_1 K_2 [\text{H}^+]^2 + K_1 K_2 K_3 [\text{H}^+] + K_1 K_2 K_3 K_4} \quad (95)$$

where K_1 , K_2 , K_3 , K_4 are the ionization constants of EDTA.

If the various constants are known, the potential can be determined. Brown [134] has made this determination and the results are shown for two iron concentrations in Figure 38. The redox potential between pH 4 and 6 is 117 mV (NHE) and is such that a bleach made with this oxidizing agent can immediately follow a developer with little risk of the developer being oxidized and subsequently forming unwanted dye. For example, CD3 has a half-wave potential of 0.399 V (NHE) at pH 5. Assuming Nernstian behavior, it can be shown that the proportion of developer oxidized in the bleach is governed by Eq. (96).

$$RT \ln \frac{[\text{CDox}]}{[\text{CD}]} = -0.282 + RT \ln \frac{[\text{Fe(III)}]}{[\text{Fe(II)}]} \quad (96)$$

If a bleach is about 90 % iron(III) in operation, we would only expect about 0.02 % of the developer to be oxidized and usually this is insufficient to form unwanted dye, especially as at pH 5 most of the coupler in film would not be ionized and therefore would not couple.

With a potential of 117 mV (NHE), iron(II) species are readily oxidized by air, which is usually passed through a bleach solution in a processor to regenerate

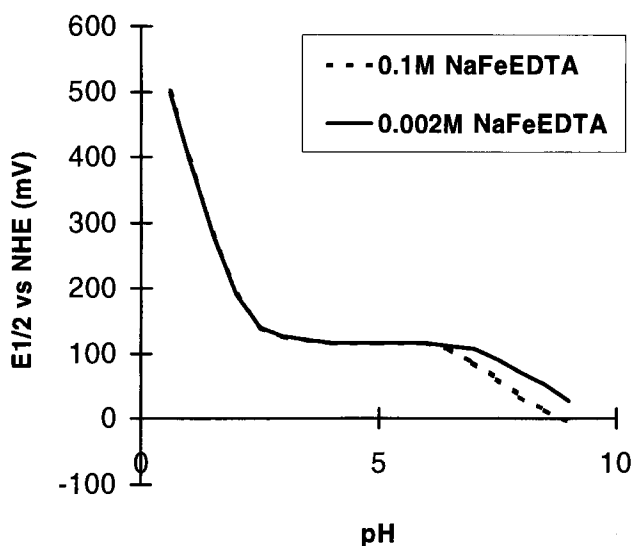


Figure 38. The effect of iron(III) EDTA dimerization on electrode potential.

iron(III). This oxidation has been extensively studied by Brown and Mazzarella [135].

Other iron complexes with slightly different properties can be used. Iron(III) 1,3-propylenediaminetetracetic acid (PDTA) has largely replaced the EDTA complex in film processes as it has a higher potential (230 mV NHE at pH 5) and bleaches more rapidly. It is used in more acid solution than iron(III) EDTA bleaches and this prevents formation of unwanted oxidized developer. Iron(III) EDTA is still the oxidizing agent of choice in bleach-fixes where the oxidant is mixed with a silver solvent. The potential of iron(III) EDTA is low enough not to oxidize thiosulfate used as the fixing agent. If iron(III) PDTA is used, the solution rapidly decomposes.

With such a low working electrode potential, these bleaches are susceptible to being inhibited by material adsorbed to the silver metal or silver halide surface. After development, sensitizing dye remains on the surface of the metal or unreduced silver halide and this can inhibit bleaching. Matsuo [136] carried out experiments with a number of sensitizing dyes adsorbed onto silver surfaces and found that bleaching by iron(III) EDTA was inhibited by sensitizing dyes with a high heat of adsorption, suggesting that they prevented the passage of electrons from the silver surface. He also discovered that the charge on the dye was important, the negatively charged dyes inhibiting bleaching. He postulated that these were repelling the negatively charged bleaching agent. He also found that with more powerful oxidants such as iron(III) chloride the effect of dyes was not seen.

Persulfate

The rate of attack on silver by powerful oxidizing agents such as persulfate is impeded. Levenson [137] suggested that this is caused by the formation of a skin of silver oxide on the surface of the metal. He produced a simplified diagram from the

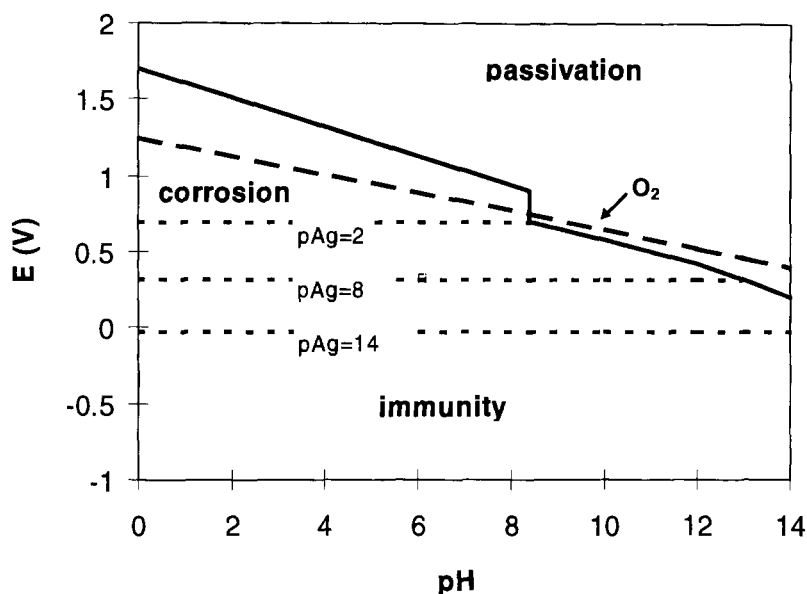


Figure 39. Corrosion diagram for silver [138].

data of Vanleughenaghe et al. [138], showing the domains of immunity, corrosion, and passivation for a silver system (Figure 39).

It can be seen that at low pH the oxidation is most likely to occur but the potential of persulfate is always in the passivation region. It was observed by Lumières and Seyewetz [139] that “reduction” of the image density with persulfate had a notable induction period and the reaction appeared to be autocatalytic. It was suggested that silver ions themselves catalyze the reaction. It is possible that the buildup of silver ions lowered the silver potential sufficiently for corrosion to occur; alternatively the production of silver(III) compounds might be responsible for the acceleration.

Persulfate bleaches can be used efficiently, provided a catalyst is present. The catalyst might either be expected to disrupt any layer formation on the surface of the silver or be an electron transfer agent that can act as intermediary for electrons between the silver and persulfate ions.

Willems [140] showed that positively charged onium compounds I–IV (Figure 40) would catalyze persulfate bleaching (Figure 41). He suggested that they worked by reducing the negative charge barrier on the silver or silver halide surface. These compounds were generally positively charged and Willems suggested that for electron transfer to take place, they must be adsorbed to the silver or growing silver halide surface. However, he also found that they tended to slow down bleaching by hexacyanoferrate(III). He suggested that these compounds repelled the positively charged center of the hexacyanoferrate(III) ion. However, this seems unlikely with such a tightly formed species as hexacyanoferrate(III). An alternative explanation

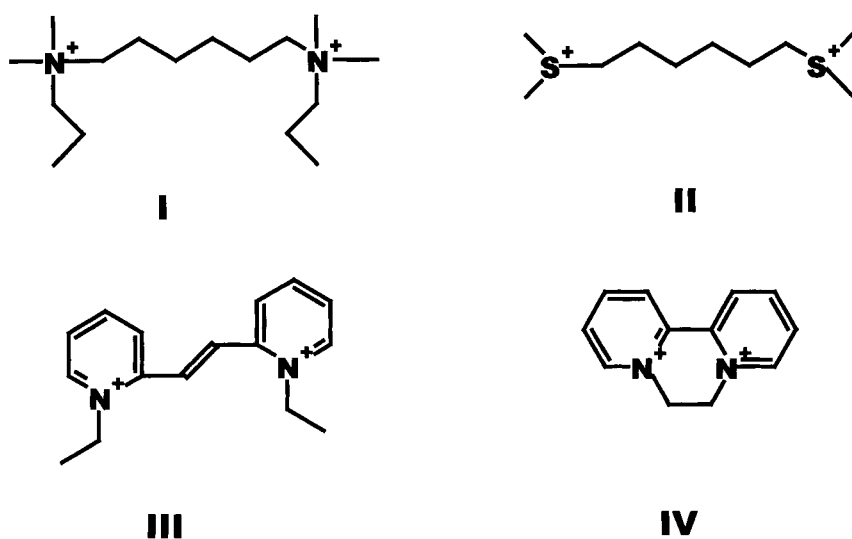


Figure 40. Onium catalysts for persulfate bleaching [140].

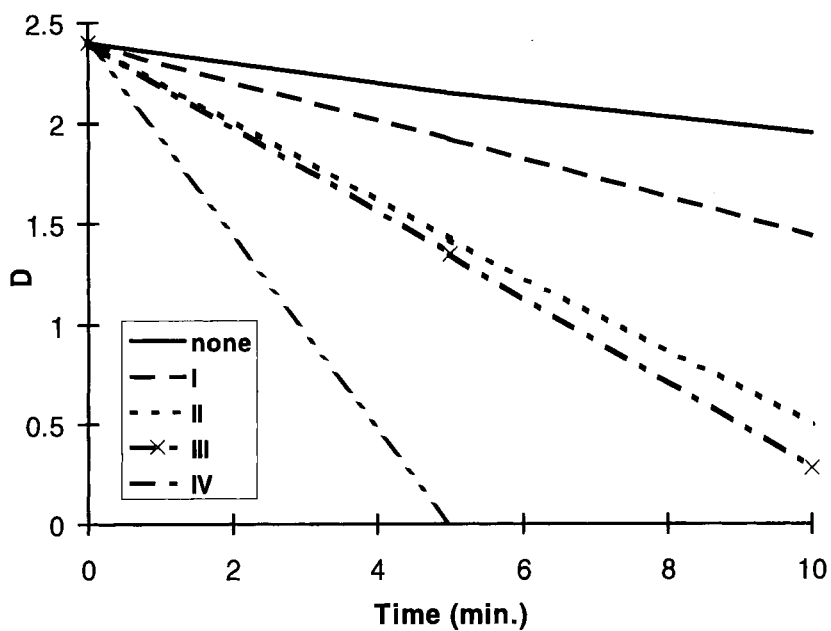


Figure 41. Effect of onium catalysts I-IV on bleaching rate in persulfate.

might just be that the onium compound alters the silver electrode potential so that it falls in a region where persulfate or one of its derived radical species can react without passifying the surface.

Willems also showed, in the same article, that some compounds that formed stable radicals would also catalyze silver bleaching by persulfate. He suggested that these compounds acted as electron transfer agents, performing as a shuttle for electrons from the silver to the persulfate; thus a superadditive mechanism, similar to that seen in development, could operate. Kobayashi et al. [141] observed a similar effect with *N,N,N',N'*-tetramethyl-*p*-phenylenediamine but also showed that this compound was destroyed by the action of persulfate, and benzoquinone was formed. It was this quinone that acted as the electron transfer agent in aged solutions.

Hydrogen peroxide

Hydrogen peroxide bleaches are rare, even though they might be expected to be “environmentally friendly” as the by-product of the reaction is water. Figure 42, a diagram of the electrode potential of hydrogen peroxide using the data of Vanleuvenhaghe et al. [138], includes the domains of bleaching or corrosion and decomposition. In order for bleaching to occur, the potential of the silver must be controlled so that it falls in this region. If it falls in the decomposition region oxygen is evolved in the gelatin, destroying its structure, and vesiculation occurs. Even when the electrode potential is controlled so that it falls in the bleaching region, the reaction is quite slow. It appears that the described reaction is kinetically inhibited.

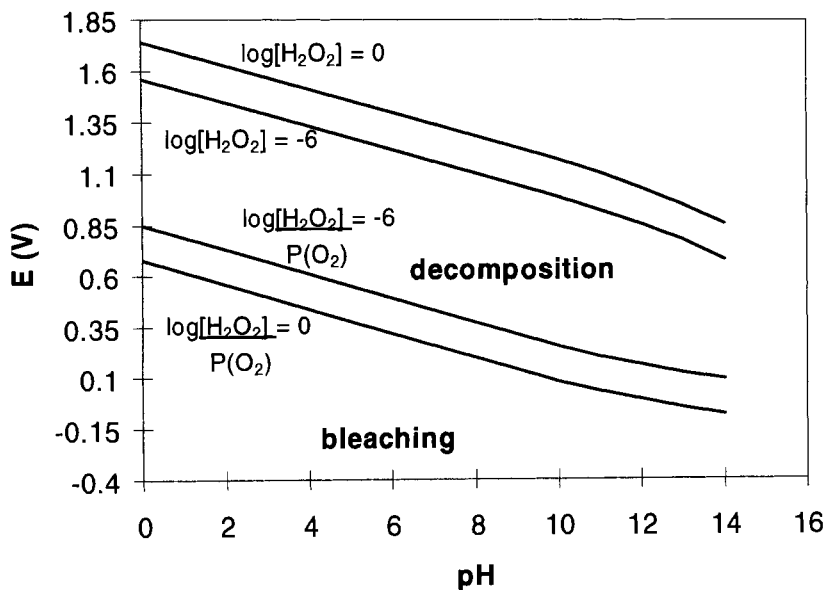
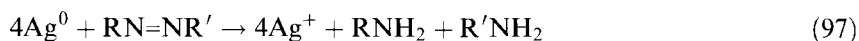


Figure 42. Electrode potential diagram for hydrogen peroxide system.

There have been a number of patents recently that have given reasonable bleaches but none has been employed commercially. The useful peroxide bleaches control the silver electrode potential by complexing the silver [142] or by careful control of the halide concentration [143].

1.3.6 Dye-Bleaches

Bleaching can be carried out by a colored oxidant which is reduced by the silver metal to colorless compounds. This is the basis of the dye-bleach process. The overall reaction may be written as Eq. (97).

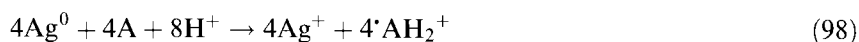


The dye-bleach material has at least three layers, one for each color record. Associated with each record is a color-sensitized emulsion and a diazo dye of the complementary color. The material is exposed and then processed as follows:

Black-and-white develop
Dye-bleach
Bleach
Fix
Wash

The imagewise silver negative is formed during the development step. In the dye-bleach the dye coats in the film are bleached where silver is present, and remain in the area where there is no silver. In this way a positive image is built up. Thirtle gives a detailed description of the process [116a].

The process as described above is much simplified. The dyes are usually immobile and therefore cannot reach the developed silver surface. It is therefore necessary to include a water-soluble electron transfer agent, or ETA, in the system. It is also necessary to tie up the silver ion formed to prevent the reverse reaction. This is done by including a halide or a silver-complexing agent such as thiourea in the system. The electron transfer agents are usually quinoxalines, phenazines, or naphthazines [144]. The mechanism for reaction has been extensively studied by Deuschel, Schellenberg, and Gunter and Matejec [145]. It is postulated that the initial reaction is the reduction of the ETA, A, to a dihydro radical, $\bullet\text{AH}_2^+$, that disproportionates to a reactive dihydro derivative, AH_2 . This reactive reduced dihydro derivative reacts with a diazo dye to form colorless products that can be washed from the layer. The reactions can be written as Eqs. (98)–(100).



After the dye-bleach process, any remaining silver is bleached in a conventional bleach, which is followed by a fix to remove silver halide and a wash to remove any residual processing components and dye fragments.

1.3.7 Fixing and Washing

Although fixing and washing are not usually considered as electron transfer reactions, they are important parts of photographic processing as they confer stability to the processed material and will be discussed briefly.

Fixing is the process whereby any remaining light-sensitive silver halide compounds are removed from the developed and possibly bleached material. There are many silver complexing agents that might be used; Pouradier et al. give an extensive list [121]. Thiosulfate is almost always the substance of choice as it is inexpensive and easy to handle. The fixing reaction is:



where n is usually 2 or 3 depending on the conditions and the concentrations of the solution components. The kinetics of reaction are complex, depending on the diffusion of the fixing agent to the silver halide grain, the solution of the silver halide, and the diffusion of the resulting silver complex away from the grain. Examples of fixing reactions being controlled by any one of these steps can be found in Ref. [146].

Washing is required to remove all the processing chemicals remaining in the film after processing that might have a deleterious effect on the stability of the image. It is also used as an intermediate step in some processes to prevent contamination of one bath from a preceding one or from unwanted reaction taking place in the gelatin layer.

1.4 Spectral Sensitization

1.4.1 Introduction

For color photography, a silver halide system must be sensitive to wavelengths throughout the visible region of the spectrum. As detailed below, the intrinsic absorptions of silver halides only occur in the blue and ultraviolet regions. Suitable dyes, called sensitizing dyes, are used to induce longer-wavelength sensitivity. The process, called spectral sensitization [147], was discovered in 1873 by Vogel [148]. Vogel's discovery was serendipitous. He observed that photographic plates to which a dye had been added to reduce scattered light were made sensitive to the wavelengths that the dye absorbed [149]. He and other chemists tried many other dyeing materials, mainly from natural sources, including even bullock's blood! [149]. The chemical technology of spectral sensitization is now highly advanced, and several

aspects are discussed in the following sections. Spectral sensitizers are usually synthetic dye molecules, of which several examples are given below. Much early work was devoted to discussions of the mechanism of the sensitization process, and particularly whether energy or electron transfer was responsible [147]. It is now well accepted that sensitization takes place via electron transfer from the excited state of the sensitizing dye to the silver halide [147, 150], consistently with the Gurney–Mott mechanism for latent image formation [97].

In addition to inducing sensitivity beyond the intrinsic region of the silver halide crystal, the sensitizing dyes are used to separate the sensitivity of the silver halide emulsion into the red, green, and blue regions of the visible spectrum, as required for full color reproduction [151]. An ideal sensitizing dye should be strongly adsorbed to the surface of the silver halide microcrystal, have strong electronic absorptions, and have narrow absorption bands so that the different parts of the spectrum can be selected [152]. Most importantly, the energy properties of the dye's excited states should be such that electron transfer from the excited state of the dye to the conduction band of the silver halide is exothermic.

1.4.2 Electronic Properties of Silver Halides

Silver halide microcrystals used in photographic applications consist of silver bromide, silver chloride, or silver bromide with added silver iodide and/or silver chloride [153]. Intrinsic (band-gap) light absorption of these materials occurs in the blue and near-UV regions of the spectrum [154]. Absorption in this region results in promotion of an electron from the valence band of the semiconductor silver halide, and formation of either a “free” conduction band electron (and a corresponding valence band hole), or a weakly bound exciton, in which the electron and hole are coupled [154]. The band-gap absorption consists of higher-energy allowed “direct” or “vertical” transitions, and lower-energy “indirect” or “nonvertical” transitions, which are observed as a long-wavelength tail. The exact absorption spectra of the crystals depend upon their composition, crystal structure, and preparation method. Representative spectra are shown in Figure 43 [155, 156]. In the language of solid-state physics, the indirect transitions involve a change in wavenumber vector, k , which means that the electronic transition involves a change in the linear momentum of the electron, and are thus partially forbidden [155, 156]. To conserve momentum, such transitions must take place via a mechanism involving vibrations of the crystal lattice, i.e., phonons, and are thus also somewhat temperature-dependent [154]. In the higher-energy region, exciton absorptions may also occur. The extent to which the band-gap and exciton transitions overlap is a function of silver halide composition and crystal structure. The excitons may dissociate into free electrons and holes, and in fact the energies required to do so are rather small, ca. 0.002 eV for AgBr and ca. 0.04 eV for AgCl [157].

Thus, absorption of light with any energy larger than the indirect band-gap energy (3.29 and 2.70 eV for AgCl and AgBr, respectively [158], which correspond to wavelengths of around 410 nm for AgCl and around 490 nm for AgBr) results in the efficient formation of conduction band electrons. As discussed above, it is the

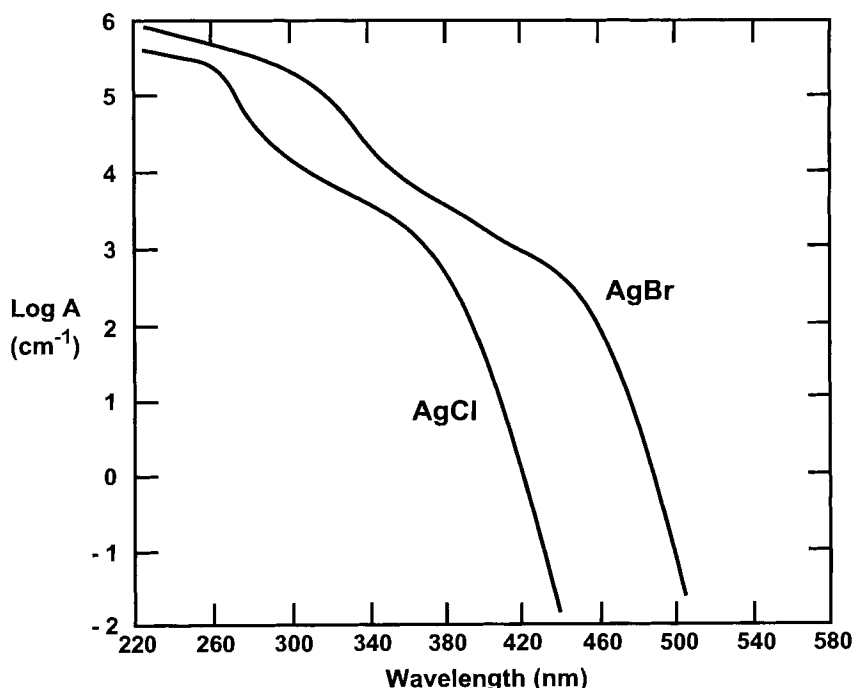


Figure 43. Optical absorption spectra of silver chloride and silver bromide crystals at room temperature. A is the absorption coefficient, which is defined as the fractional decrease in transmitted light intensity due to absorption, per unit thickness [154]. Figure adapted from [154].

accumulation of such conduction band electrons in suitable trap sites that results in the formation of the latent image [159]. Latent image formation occurs with variable quantum efficiency, depending upon the number and nature of the electron trap sites. Modern photographic emulsions are chemically doped to optimize electron trapping [160], and a stable cluster of four silver atoms can be formed with absorption of only a small number of photons, usually around 15–20 [161].

1.4.3 Sensitizing Dyes

The most useful dyes for photographic applications belong to the cyanine class [152, 162]. Typical examples are given in Table 11, together with relevant electrochemical data and excitation energies. The structures consist of two heterocycles joined by a methine chain of variable length (Figure 44).

Historically, the terms simple cyanine, carbocyanine and dicarbocyanine have been used to designate generic cyanine structures containing one, three, and five methine carbons in the chain joining the two heterocycles (Figure 44). Dyes that differ only in the number of methines in the chain are called a vinylogous series. The

Table 11. Excited-state energy and electrochemical data for representative cyanine spectral sensitizing dyes.

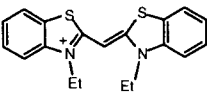
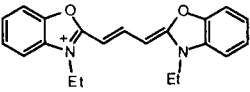
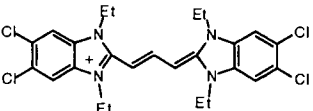
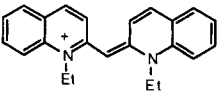
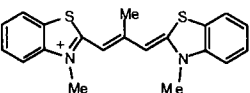
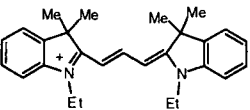
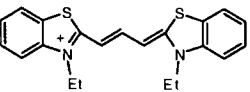
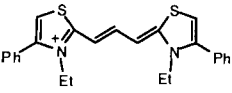
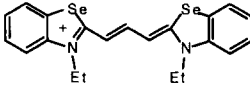
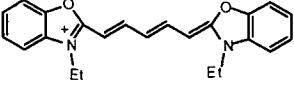
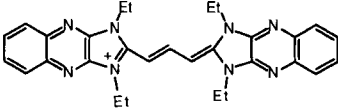
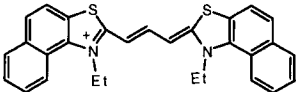
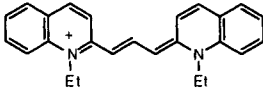
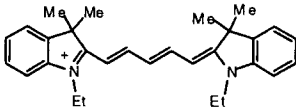
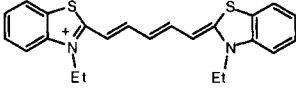
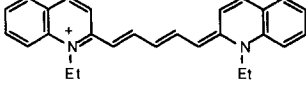
	λ_{\max}^a [nm]	E_{ex}^b [eV]	E_{red}^c [V]	E_{ox}^d [V]
	422	2.94	-1.445	0.662
	485	2.56	-1.310	1.020
	514	2.41	-1.506	0.662
	522	2.34	-1.128	1.113
	540	2.30	-1.125	0.897
	545	2.27	-1.000	1.088
	557	2.23	-1.060	0.902
	559	2.22	-1.280	0.634
	570	2.18	-1.014	0.898
	580	2.14	-1.045	0.697

Table 11 (continued)

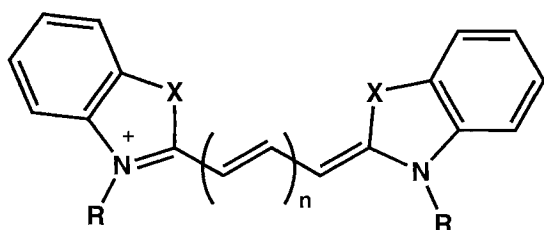
	$\lambda_{\text{max}}^{\text{a}}$ [nm]	E_{ex}^{b} [eV]	$E_{\text{red}}^{\text{c}}$ [V]	E_{ox}^{d} [V]
	581	2.13	-0.780	1.096
	597	2.08	-1.068	0.77 ^e
	605	2.05	-1.035	0.757
	636	1.95	-0.820	0.775
	650	1.91	-0.885	0.630
	708	1.75	-0.884	0.513

^adye absorption maximum [152], ^bdye excited-state energy [152], ^cdye reduction potential versus Ag/AgCl reference electrode [177], ^ddye oxidation potential versus Ag/AgCl reference electrode [177], ^eapproximate value [177].

absorption maxima for a representative of such a series are given in Figure 45. The maximum shifts by approximately 100 nm to the red per unit increase in the number of vinyl groups.

Adsorption isotherms of cyanine dyes on silver halide crystals are consistent with Langmuir behavior, and indicate a close-packed monolayer of dye on the surface of the silver halide crystal [163]. This is supported by the observation of large shifts in the absorption spectra of the adsorbed dyes compared with the absorption spectra of the dyes in dilute organic solution. An example is shown in Figure 46.

The spectral shifts are assigned to the formation of dye aggregates. Two kinds of aggregates are commonly observed for dye structures such as these, the so-called J- and H-aggregates [152, 164, 165]. The differences between these two are best under-



$n = 0$, simple cyanine
 $n = 1$, carbocyanine
 $n = 2$, dicarbocyanine
 $n = 3$, tricarbocyanine

$R = \text{CH}_2\text{CH}_3, (\text{CH}_2)_3\text{CH}_2\text{SO}_3^-, \text{etc.}$

$X = \text{S}, \text{O}, \text{Se}, \text{CH}_2=\text{CH}_2, \text{etc.}$

Figure 44. Schematic representation of the chemical structures of some typical cyanine-type spectral sensitizing dyes.

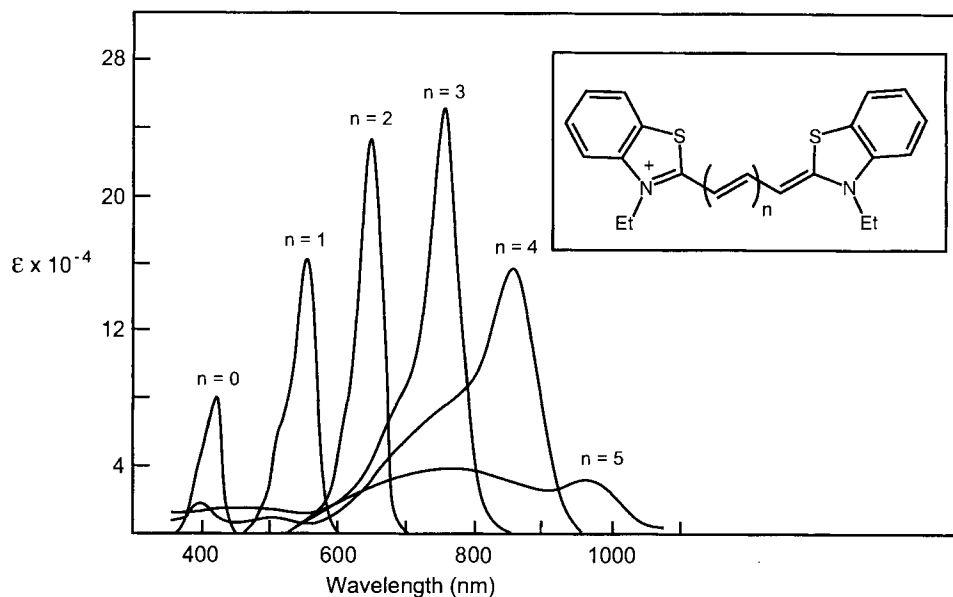


Figure 45. Absorption spectra of a vinylogous series of symmetrical cyanine dyes. The absorption maximum increases with increasing chain length. The extinction coefficient maximizes for seven methine carbons in the chain. Figure adapted from [152].

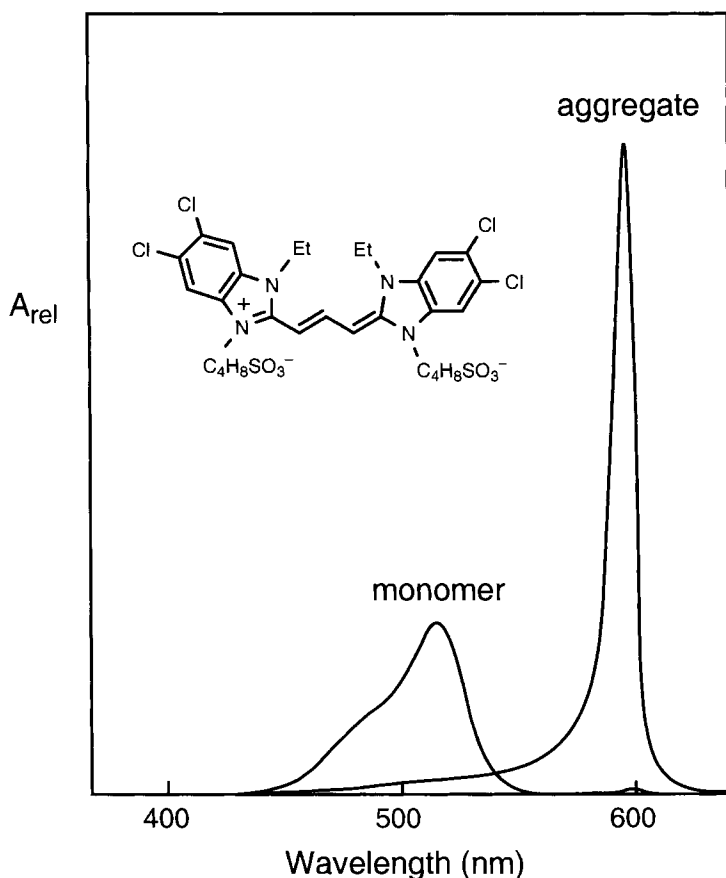


Figure 46. Absorption spectra of the monomeric and J-aggregated form of a cyanine dye in solution. A_{rel} is the relative absorbance of the two species. Data from [157].

stood in terms of the simplified pictorial representation given in Figure 47, which shows the influence of dimerization on the absorption spectrum of an idealized molecule with a long-axis polarized electronic transition. Exciton theory predicts that the absorption band of the monomer will be split into two new bands in a corresponding dimer as a result of dipole–dipole interactions [165, 166]. The two transitions correspond to the two possible relative directions for the change in dipole moment in the two molecules upon excitation, as indicated in the Figure. The structures in Figure 47 represent extreme situations. In aggregated dyes, a range of relative orientations between the dyes are possible, defined by the angle between the transition dipole moment and a line joining the molecules, α , as shown in Figure 48. As α tends towards zero, the electronic properties of the aggregate resemble those of the end-to-end dimer of Figure 47, and the lower-energy transition becomes allowed. As α increases towards 90° , the electronic properties resemble

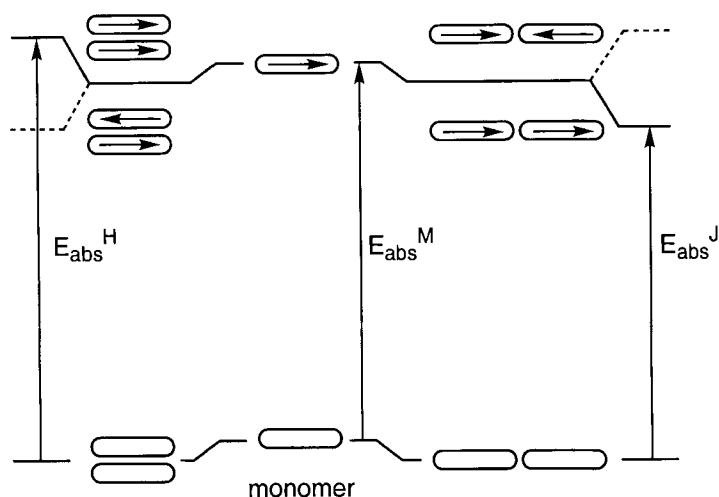


Figure 47. Idealized energy levels and most probable electronic absorptions, E_{abs} , of one monomeric and two dimeric dye structures. The arrows represent the directions of the localized transition dipole moments. The transition in the “face-to-face” aggregate is representative of that in an H-aggregate and the transition in the “end-to-end” structure is representative of that in a J-aggregate.

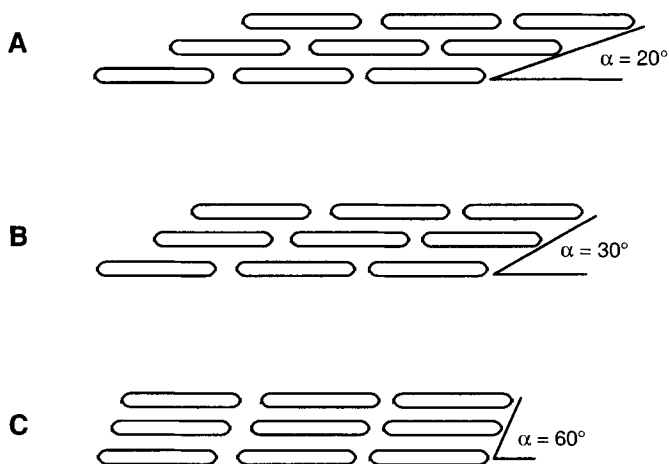


Figure 48. Some representative arrangements for aggregated dye molecules. A and B have values for α which are less than 45° and are examples of J-aggregates. C, with a value for α of greater than 45° , is an example of an H-aggregate [157].

the face-to-face dimer more, and the higher-energy transition becomes allowed. The J-aggregates are those with small values of α , in which the low-energy transition is observed to be stronger in absorption than the higher-energy transition. The H-aggregates have larger values of α and the higher-energy transition is observed to be stronger of the two. It is the longer-wavelength absorbing J-aggregates which are found to be the most photographically useful. Recent scanning tunneling microscopy (STM) work on J-aggregated cyanine dyes on silver halide crystals has confirmed that the schematic ideas of their structure derived from the theory considerations given above and extrapolations from crystal structures of the dyes are basically correct [167].

The formation of a J-aggregate has a significant influence on the excited-state dynamics of the sensitizing dyes [168–170]. On silver halide crystals, the excitation is found to be very mobile within the aggregate and is found to sample many molecules during the excited-state lifetime [171]. As a consequence of this high mobility, the excited state is extremely sensitive to quenching [158]. As a consequence, the J-aggregate dynamics are found to be sensitive to the details of the surface and the method of adsorption. Experiments have been performed in which the aggregate size was varied by dilution of a sensitizing dye by another geometrically similar dye with a much higher excited-state energy. It was found that the total rates of non-radiative decay increased with increasing aggregate size [172, 173]. This was assumed to be a consequence of the fact that with increasing aggregate size, the excitation is delocalized over a larger area and is thus more susceptible to quenching (see below). There is the possibility of coherent delocalization of the excitation over a number of molecules in the aggregate which is predicted to give rise to an enhanced (superradiant) radiative decay for the aggregate [174, 175]. Although such an effect has been observed in a low-temperature glass [168], no significant superradiance has yet been observed for J-aggregates adsorbed on silver halide [172, 173].

1.4.4 Sensitization Mechanisms

As discussed in Section 1.4.1, the relative importance of electron injection and energy transfer was debated in the earlier literature on spectral sensitization [147]. Support for the former mechanism accumulated, however, from extensive correlations of the effectiveness of sensitization with the electrochemical redox properties of the dyes [147, 157, 176, 177], to the extent that energy transfer mechanisms are no longer considered. The usual electron injection spectral sensitization mechanism for silver halide is illustrated in the schematic energy diagram shown in Figure 49(a). The energy of the lowest unoccupied molecular orbital (LUMO) of the dye (E_{LUMO}) is higher than that of the conduction band (CB) of the silver halide, so that electron transfer from the LUMO to the CB is exothermic. The energy of the highest occupied molecular orbital (HOMO) of the dye (E_{HOMO}) is higher than that of the valence band (VB) of the silver halide. The HOMO–LUMO energy gap is smaller than the VB–CB energy gap, so that light absorption by the dye occurs at lower energy and longer wavelength than that of the silver halide. Thus, light absorption by the dye results in promotion of an electron from the HOMO to the

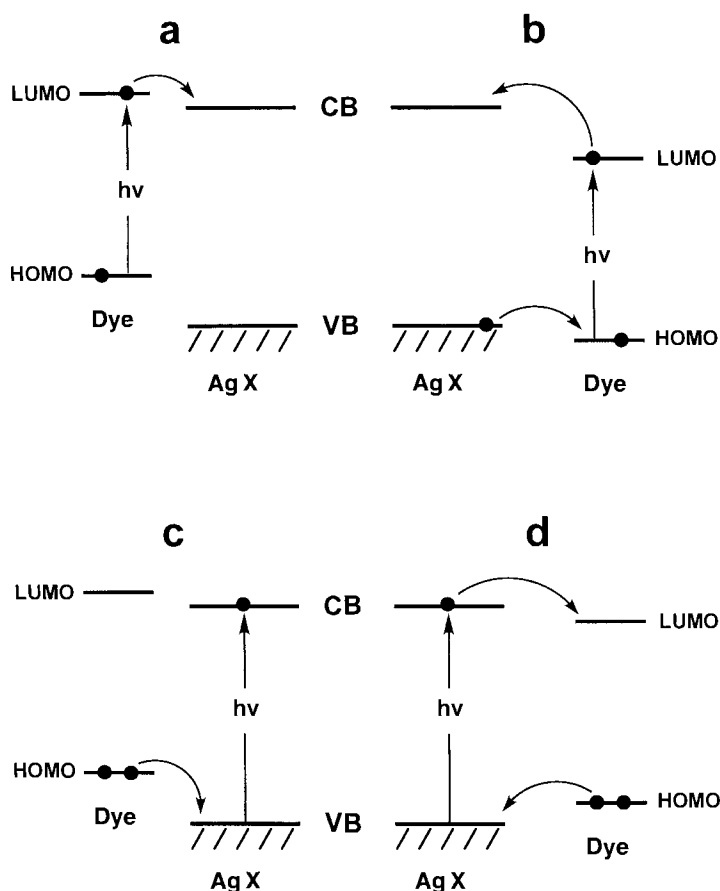


Figure 49. Some possible photoinduced electron transfer processes involving dyes adsorbed to the surface of crystalline silver halide. CB and VB refer to the conduction and valence bands of the silver halide, AgX, and HOMO and LUMO refer to the highest occupied and lowest unoccupied molecular orbitals of the sensitizing dye. a) Electron injection from the excited state of the dye; b) hole injection from the excited state of the dye; c) electron transfer to the valence band after excitation of the silver halide; d) desensitization by an adsorbed dye.

LUMO, which is subsequently injected into the CB of the silver halide. This sensitization mechanism is known as the electron-injection mechanism, for obvious reasons. Another practical mechanism is indicated in Figure 49(b). Here, the energy gap ($E_{\text{LUMO}} - E_{\text{HOMO}}$) is still smaller than the band-gap energy of the silver halide, but in this case E_{HOMO} is slightly lower than the energy of the VB, and E_{LUMO} is thus necessarily lower than the energy of the CB. Excitation of the dye in this case does not result initially in transfer of an electron from the LUMO to the CB, but in electron transfer from the VB to the now singly occupied HOMO. The product is the radical anion of the dye, which can then transfer an electron to the CB of the

silver halide in a slower second step. Note that this second electron transfer is endothermic. However, unlike the excited state of the dye, the radical anion has a comparatively long lifetime which may allow this endothermic reaction to occur. Once the electron is transferred to the CB it is delocalized and susceptible to trapping, and thus the electron transfer from the dye is essentially irreversible. This sensitization mechanism is called hole-transfer sensitization. The products of these two processes are initially different, an oxidized dye in the case of electron injection, and a neutral dye in the case of hole injection. On longer timescales, however, the "holes" in the valence band and/or the dye may be "filled" by electrons from one or more components of the gelatin matrix.

Figures 49(c) and 49(d) show two other important processes which can occur when the silver halide is excited directly in the presence of adsorbed dyes. In these cases an electron is transferred from the VB to the CB upon excitation, and the holes in the VB may be filled by electron transfer from the HOMO of the adsorbed dye. The product of this process in Figure 49(c) is the same as that from the electron-injection dye sensitization in Figure 49(a), i.e., a dye radical cation and a conduction band electron which may be trapped and contribute to latent image formation. Illustrated in Figure 49(d) is the consequence of excitation of silver halide in the presence of a dye in which the energy of the LUMO is lower than that of the CB. In this case, direct excitation of the silver halide results in a conduction band electron which can be transferred to the LUMO of the dye. Subsequent electron transfer of an electron from the HOMO of what would then be a dye radical anion results in effective deactivation of the band-gap excitation, and overall reduced photographic sensitivity of the silver halide toward direct excitation due to the presence of the dye. This process is known as dye desensitization.

A quantitative understanding of these mechanisms clearly relies upon accurate determinations of the energy levels of the CB and VB of the silver halide, and the dye HOMO (E_{HOMO}) and LUMO (E_{LUMO}). These energies are often related to the appropriate ionization potentials (IP) and electron affinities (EA) measured in the gas phase. Measurements of IP and EA for several dyes have also been made in the solid state and on silver halide using UV photoelectron spectroscopy, although satisfactory quantitative relationships with photographic measurements were not easily obtained [178]. Because of difficulties such as these, most workers have resorted to electrochemical measurements of electron-donating and -accepting ability. Studies using phase-selective second-harmonic AC voltammetry have been shown to be particularly useful, since accurate thermodynamically meaningful redox data for many sensitizing dyes have been obtained in this way [177, 179]. In principle, the energies of the CB and VB by ionization potential and electron affinity measurements can be related to electrochemical data such as these [176]. However, difficulties in determining an appropriate vacuum level, among others, mean that useful values for the CB and VB are not available in this way. Indeed, photographic spectral sensitivity experiments are usually used to determine the effective energies of the CB and the VB on the electrochemical scale [176].

As indicated above, phase-selective second-harmonic AC voltammetry has provided accurate and thermodynamically meaningful redox data for a number of dyes. One interesting consequence of obtaining such accurate electrochemical data

is that the relationship between excitation energy and redox parameters could be explored. The difference between the electrochemical oxidation potential (E_{ox}) and reduction potential (E_{red}) should be approximately equal to the singlet electronic excitation energy for the dye, E_{ex} [180] (Eq. (102)). These two quantities differ by a factor, C , which is a

$$E_{\text{ex}} = (E_{\text{ox}} - E_{\text{red}}) + C \quad (102)$$

measure of the difference in the solvation effects for the redox and excitation processes [177]. C also contains a contribution which arises from the fact that the electronic configurations in the initial and final states for the two processes are not the same [181, 182]. These effects should presumably be fairly constant for small differences in molecular structures, i.e., for a particular class of dyes. For example, a plot of E_{ex} versus $(E_{\text{ox}} - E_{\text{red}})$ for a series of carbocyanine dyes is linear with a slope of essentially unity and an intercept of -0.298 eV [177].

The efficiencies of spectral sensitization are usually measured in terms of a relative quantum yield, Φ_{rel} , which is defined in Eq. (103). Φ_{rel} is the ratio of the number of photons which are required to produce a specific developed optical density in a photographic film to the

$$\Phi_{\text{rel}} = (400E_{400}A_{400})/(\lambda E_{\lambda}A_{\lambda}) \quad (103)$$

number required to produce the same optical density for excitation at a wavelength which is absorbed by the sensitizing dye. Often an optical density of ca. 0.6 above the unexposed level is chosen for the optical density determination, and a wavelength of 400 nm is chosen for the direct excitation of the silver halide, since the sensitizing dyes usually do not absorb at that wavelength. Thus, in Eq. (103), E_{400} [erg cm $^{-2}$] is the incident radiant energy at 400 nm and A_{400} is the fraction of this energy which is absorbed by the film. E_{λ} and A_{λ} are the corresponding quantities at the wavelength of excitation of the dye, λ . The absolute efficiency of electron injection from the excited state of the dye, Φ_s , is given by Eq. (104). Here, k_s is the rate constant for injection of the electron by the dye, k_f is the dye's radiative rate constant, and k_{nr} represents the sum of the rate constants for all of the other processes which deactivate the dye when adsorbed to the surface of the silver halide. Φ_s is equal

$$\Phi_s = k_s/(k_s + k_f + k_{\text{nr}}) \quad (104)$$

to Φ_{rel} when the efficiency of latent image formation is the same for the electrons formed by silver halide and dye irradiation. The difference between the two processes is illustrated in Figures 49(a) and 49(c). Φ_s is equal to Φ_{rel} when all of the holes formed by direct excitation are filled by the sensitizing dyes. That this usually occurs has been clearly demonstrated in many cases.

According to Figure 49(a), electron injection occurs from the LUMO of the dye, the energy of which is related to E_{red} as indicated above. Thus Φ_s should be optimum when the energy of the LUMO is at least equal to the energy of the CB, and

probably higher to accommodate any activation energy associated with the electron transfer process. This means that, on an electrochemical scale, E_{red} should be more negative than the energy of the CB on the same scale. When E_{red} is sufficiently more negative than the energy of the CB, the electron injection efficiency is expected to be constant at the optimum value and should not increase with increasingly negative E_{red} . This is because of the continuum of acceptor states in the conduction band of the silver halide. At every energy level of the LUMO of the dye, there is a corresponding acceptor level in the silver halide, and thus the rate of electron injection is expected to be constant. For dyes with increasingly less negative E_{red} , Φ_s should decrease rapidly as the energy of the LUMO becomes lower than the energy of the CB. In addition to reducing Φ_s , dyes with LUMO energies below that of the CB should also cause desensitization, as indicated in Figure 49(d). All of these effects have been observed experimentally (see, for example, Refs. [147, 150, 152, 183–187]), which is taken as strong support for the electron transfer mechanism of spectral sensitization, rather than an energy transfer mechanism.

More recent work has concentrated on quantitative evaluations of the dependence of Φ_s on E_{red} . Two studies in particular have examined the dependence of spectral sensitization efficiency on the redox potentials of the sensitizers using classical Marcus theory (Eqs. (105), (106)) [188].

$$k_s = k_s^0 \exp(\Delta G^\ddagger/kT) \quad (105)$$

$$\Delta G^\ddagger = (\Delta G^0 + \lambda)^2/4\lambda \quad (106)$$

Here, k_s is the rate constant for electron transfer from the dye to the silver halide as defined above, ΔG^\ddagger is the activation free energy for the reaction, λ is the reorganization energy which is a measure of the extent of nuclear reorganization of the dye molecule and the medium associated with the reaction, and k_s^0 is the maximum attainable rate constant. In the classical Marcus theory, k_s^0 is the rate constant for the barrierless reaction ($\Delta G^\ddagger = 0$), which occurs when $-\Delta G^0$ is equal to λ , i.e., when the reaction exothermicity is equal to the reorganization energy. For bimolecular reactions, the rate constant decreases with increasing exothermicity for values of $-\Delta G^0$ greater λ , the so-called Marcus inverted region [188]. This occurs because of an increasing mismatch between the available energy and that required for optimum reaction. For the case of electron transfer to the semiconductor silver halide, however, the almost continuous range of accessible electronic energy levels above the conduction band means that this energy mismatch does not occur. Thus, for sufficiently exothermic reactions, the reaction rate is expected to be close to the maximum attainable rate, and to be independent of ΔG^0 .

Tani et al. measured Φ_{rel} for various cyanine dyes with differing values of E_{red} , ranging from ca. -1.3 V to ca. -1.6 V vs. SCE [187]. Φ_{rel} was equated to Φ_s (Eqs. (103), (104)), and a value of 10^{10} s^{-1} was assumed for $(k_f + k_{\text{nr}})$. The dependence of Φ_{rel} on E_{red} was then calculated using Eqs. (105) and (106) for k_s , with ΔG^0 assumed to be equal to the difference between E_{red} and the potential for thermoneutral electron transfer from the dye to the CB, E_{red}^* (Eq. (107)). E_{red}^* is thus equivalent to the potential

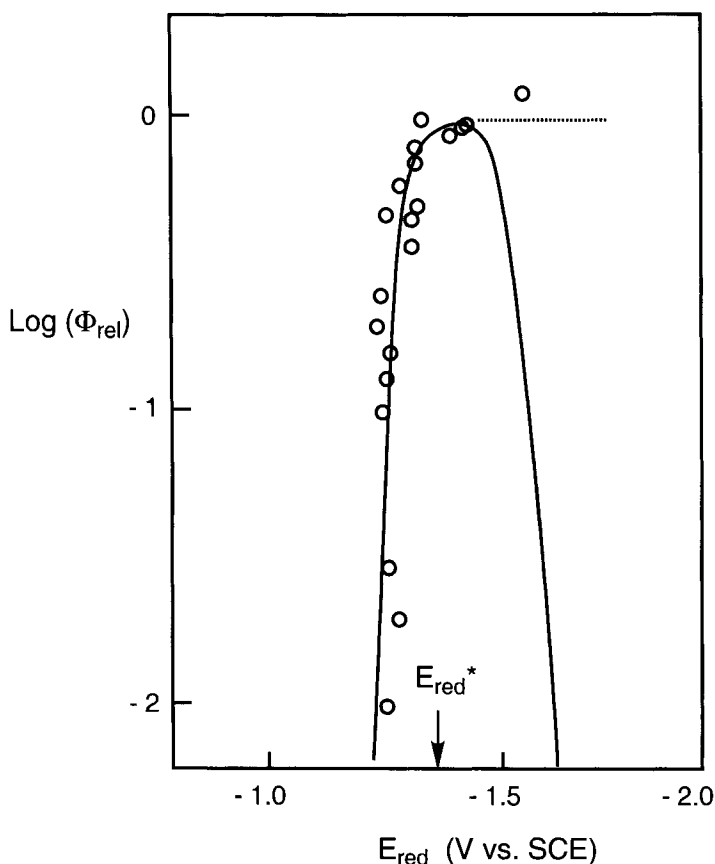


Figure 50. Dependence of Φ_{rel} on sensitizer reduction potential [187]. The solid curve represents the expected dependence based on Marcus theory using a value for λ of 0.05 eV. The energy obtained for the CB of the cubic silver bromide crystals used in this experiment, E_{red}^* , is -1.37 V, vs. SCE. Figure adapted from [187].

$$\Delta G^\circ = -(E_{\text{red}} - E_{\text{red}}^*) \quad (107)$$

of the CB vs. SCE. With these assumptions, E_{red}^* and λ are the variable parameters. The experimental data and the calculated dependence of Φ_{rel} on E_{red} are shown in Figure 50. The values of the parameters used for the calculated fits were -1.37 V for E_{red}^* and 0.05 eV for λ , respectively. Note the independence of Φ_{rel} of E_{red} when the reaction becomes sufficiently exothermic, as expected for electron transfer to the continuum of states in the CB.

A related series of experiments were described by Hailstone in 1984 [189]. A re-interpretation of his experimental data was given by Muentert et al. in 1985 [190] and in 1999 [158], using more accurate redox parameters, and recognizing that his

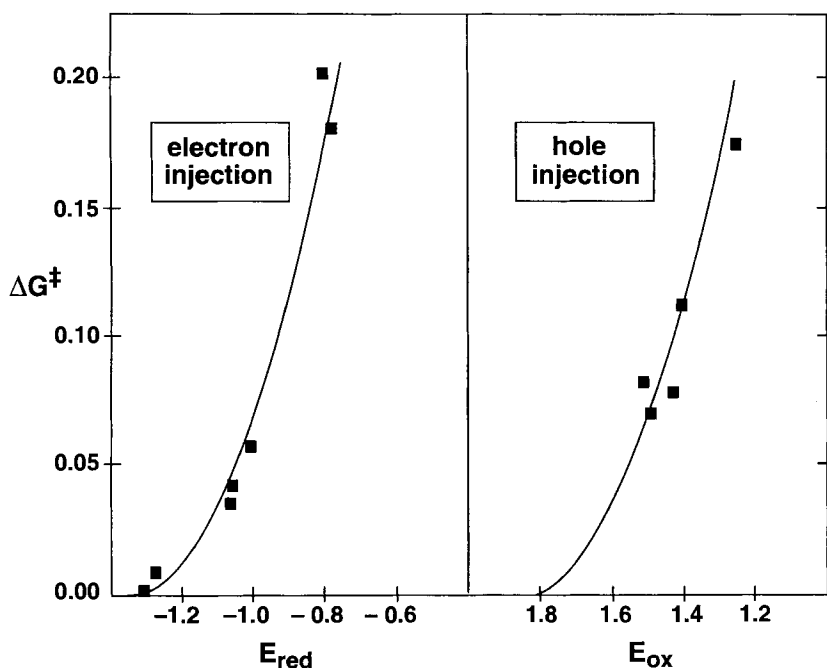


Figure 51. Plots of apparent activation energies for (left) electron injection and (right) hole injection into cubic AgBrI microcrystals versus reduction and oxidation potentials of the sensitizing dyes, and the expected dependencies for ΔG^\ddagger based on Marcus theory, using 0.42 eV for λ , -0.92 V versus Ag/AgCl for E_{red}^* and 1.41 V versus Ag/AgCl for E_{ox}^* . Figure adapted from [158].

experiments included both electron-injection sensitization (Figure 49a) by some dyes, and hole-injection sensitization (Figure 49b) by others. Values for ΔG^\ddagger were assumed to be equal to the apparent activation energies for the sensitization efficiencies [189]. The data were analyzed using the classical Marcus equation for k_s , and the variable parameters were λ and E_{red}^* for the electron-injecting dyes, and E_{ox}^* for the hole-injecting dyes, where E_{ox}^* is the potential for thermoneutral hole-transfer. E_{ox}^* is thus equivalent to the potential of the VB on the electrochemical scale. The experimental data and the calculated dependencies on E_{red} are shown in Figure 51. The values of the parameters used for the calculated fits were -0.92 V for E_{red}^* , 1.41 V for E_{ox}^* , and 0.42 eV for λ , respectively.

Both experiments clearly provide strong support for the electron transfer mechanism, and valuable data related to the energies of the CB and VB, and also the reorganization energies which characterize the reactions. However, the quantitative agreement between the experiments is not particularly good. The differences in the energies of the CB may be due to a large extent to a difference in the values of E_{red} , by ca. 0.2 V, used in the two experiments, presumably as a consequence of differences in the working electrode used in the electrochemical experiments [158]. The difference in the λ values may be due to the fact that only monomeric dyes were

used in the Hailstone experiment, whereas in the Tani experiment the dyes were aggregated, at least to some extent. The differences may also simply reflect the difficulty in obtaining accurate and quantitative experimental data from photographic experiments [191]. Another complication is that the reorganization energy associated with the medium in the photographic systems is probably not the same as the classical solvent reorganization energy assumed in Marcus theory. In the gelatin matrix the medium almost certainly can not completely reorganize on the timescale of the electron transfer process, because of the rigidity of the protein structure. Under these conditions, the energy differences due to different solvation environments may appear as a distribution in energies for the reaction, and not as a reorganization energy. Exactly this situation has been observed recently for electron transfer reactions in polymer glasses [192]. The overall consequence is a smaller apparent medium reorganization energy and more complex kinetics [192].

1.4.5 Kinetic Measurements of Electron Injection

Direct measurements of k_s can, in principle, be made from time-resolved experiments. The problem with such experiments on photographic systems is their extreme sensitivity to light. Indeed, it is virtually impossible to perform many time-resolved experiments with the photon intensities typically used to take actual photographs. Much higher intensities are usually required, with the consequence that much higher concentrations of transient species are produced than in practical applications, and the systems are susceptible to deterioration due to the irreversible nature of the chemistry. Nevertheless, several experiments have been described from which useful data have been obtained.

Early work showed that low light intensity excitation sources had to be used to avoid excited-state annihilation processes [193, 194]. Using a low-intensity mode-locked laser source and single photon counting, Muentert measured the rates of fluorescence decay, k_d , for some typical monomeric cyanine dyes on silver chloride and silver bromide cubic crystals [195]; k_s was obtained from Eq. (108) for k_d , and assuming that $(k_f + k_{nr})$ could be determined from measurements of dye lifetimes in

$$k_d = k_s + k_f + k_{nr} \quad (108)$$

dilute solutions in gelatin. Estimates for k_s of $(1-3) \times 10^9 \text{ s}^{-1}$ and $(3-8) \times 10^9 \text{ s}^{-1}$ were obtained for dyes absorbed on silver chloride and silver bromide respectively. However, at surface coverages greater than 1 %, energy migration was observed and nonexponential decays were observed, even down to 0.2 % coverage [158]. This was attributed to local environment effects due to surface heterogeneity. However, it should be noted that a contribution to the nonexponential decay may arise as a consequence of the medium not being able to reorganize on the timescale of the reaction, as discussed above.

Spittler and Willig and co-workers measured the temperature dependence of k_s for a cyanine dye adsorbed onto silver bromide octahedral crystals [196]. Non-exponential experimental decays were observed and a curve subtraction technique

was used to estimate exponential rates of reaction. From an Arrhenius-type plot of the data, values for ΔG^\ddagger and k_s^0 of 0.09 eV and $3 \times 10^{11} \text{ s}^{-1}$ were obtained. Work on similar systems by Muentert et al., who performed fluorescence lifetime and photographic response measurements as a function of temperature, gave a similar value for ΔG^\ddagger , but a considerably smaller k_s^0 [197]. It was suggested that differences in data analysis techniques were perhaps responsible for the different k_s^0 values. The significance of k_s^0 is that it is related to the magnitude of the electronic coupling between the excited state of the dye and the states that comprise the CB of the silver halide. In the nonadiabatic limit, k_s^0 is given by Eq. (109), where H is the electronic

$$k_s^0 = (4\pi^2/h)H^2(4\pi\lambda kT)^{-1/2} \quad (109)$$

coupling matrix element and the other symbols have their usual meaning [198]. For the range of k_s^0 values which have been reported, H would be ca. $5\text{--}30 \text{ cm}^{-1}$. This is considerably lower than the magnitude of the coupling found in related work on dye sensitization of other semiconductors such as SnS_2 and TiO_2 , where maximum electron transfer rates in the 10^{13} s^{-1} range have been observed [199–201]. The smaller values on silver halide may reflect the fact that, in the experiments performed so far, the energy of the dye LUMO was toward the bottom of the CB where the density of electronic levels may not be as high. Alternatively, the presence of the gelatin medium and/or adsorbed water on the crystal surface may prevent intimate dye contact with the surface [158].

Other time-resolved experiments have attempted to define the effect of aggregation on the rate of electron injection. Muentert and co-workers combined Φ_s and k_d data to determine k_s as a function of the size of the dye aggregate [202, 203]. The aggregate size was varied by diluting with a geometrically similar dye with a much higher electronic optical transition. In experiments on silver bromide octahedra, and silver bromide and silver chloride cubic crystals, an increase in k_s with aggregate size was observed. This was attributed to the fact that as the excitation becomes more delocalized with increasing aggregate size, the probability increases of “finding” a site on the surface of the crystal where electron injection is particularly facile. It was also found that the rate of radiationless decay, k_{nr} , also increases with increasing aggregate size. This was also attributed to the fact that the excitation will have a higher probability of encountering a trap site with increasing delocalization. Tani et al. also studied the effect of aggregate size on the rates of electron injection for AgBr octahedral crystals [204]. The aggregate size was varied from ca. 6 to ca. 14 molecules by varying the agitation temperature used to prepare the emulsion. In contrast to the results of Muentert et al., the data were interpreted as indicating a decrease in both k_s and k_{nr} with increasing aggregate size. The reasons for the differences in the behavior seen in the two sets of experiments are not clear. Willig, Spitler, and co-workers made measurements of the temperature dependence of the fluorescence lifetime of a J-aggregated dye on AgBr octahedral crystals from room temperature down to 6 K [205]. A weak temperature dependence was observed for the rate of electron injection, which was explained as a consequence of a near-coincidence between the energies of the dye LUMO and the conduction band. An estimate for the electron transfer matrix element of ca. $5\text{--}30 \text{ cm}^{-1}$ was obtained,

which is in the same range as that estimated for monomeric dyes on silver halide, discussed above. Significantly, the reorganization energy for electron transfer was estimated to be considerably smaller for the J-aggregated system, ca. 0.03 eV, compared with a related dye monomer system studied previously, ca. 0.3 eV. This was also the conclusion from experiments in which the temperature dependence of fluorescence lifetimes and photographic sensitivity were measured for dyes N and M [206]. In each case a smaller temperature dependence for the aggregate was observed compared with the corresponding monomer, consistent with a smaller reorganization energy for the former. For N, a value for λ of 0.14 eV was estimated for the aggregate, and ca. 0.46 eV for the monomer. The appropriate redox potentials for the aggregates are generally not known, however, and in their absence, interpretation of such experimental data for aggregates will always be uncertain [206].

1.4.6 Supersensitization

Addition of a second dye to a spectrally sensitized silver halide system, where the second dye does not sensitize in the spectral region of the sensitizer, may lead to either a decreased activity (desensitization), or in some cases an increased sensitivity. This latter effect is called supersensitization, and is of great importance in practical photographic applications [207]. The effect has been observed with molar ratios of sensitizer to supersensitizer as high as $10^4:1$, but usually this is closer to ca. 10:1 [207]. More than one mechanism has been suggested for supersensitization; however, an extensive series of studies has provided considerable evidence for the hole-trapping mechanism shown in Figure 52 [208–211]. The clearest evidence in favor of the hole-transfer mechanism is that supersensitization is only observed when the HOMO of the supersensitizer is higher than that of the dye [210]. In later work it was observed that ESR signals attributed to the radical cation of the supersensitizer were observed upon irradiation of the sensitizer [211]. In Gilman's original proposal, the supersensitizer donates an electron to the excited state of the dye,

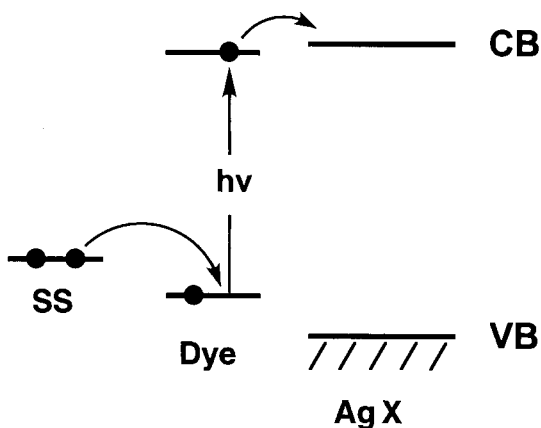


Figure 52. Hole-trapping mechanism for supersensitization. The supersensitizer, SS, transfers an electron to the excited state of the dye to form the radical anion of the dye, before electron transfer occurs to the silver halide. The radical anion subsequently injects the electron to the CB [207].

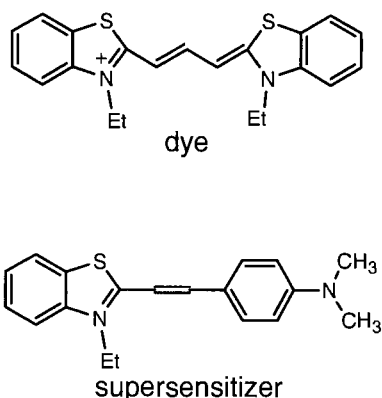


Figure 53. Typical sensitizer/supersensitizer combination.

so that the radical anion of the dye transfers an electron to the silver halide. In this way the supersensitizer prevents recombination both from the LUMO of the dye before transfer and also from the CB of the silver halide after transfer. Alternatively, the supersensitizer could donate an electron to the dye after transfer to the silver halide. It is clearly difficult to distinguish between these two mechanisms. In principle, a supersensitizer can be any molecule which is capable of donating an electron to the excited state of the dye (or its radical cation). However, most of the compounds which have been shown to be effective as supersensitizers are cyanine-type dyes or their analogs. A typical supersensitizer/sensitizer combination is shown in Figure 53. Compounds such as these may co-aggregate with the sensitizers, and thus be physically located close to the excited and oxidized sensitizers.

References

1. E. Stenger, *The History of Photography*, Mack Printing Company, Easton, PA, **1939**, p. 6.
2. H. Gernsheim, *The Origins of Photography*, Thames and Hudson, London, **1982**, p. 60.
3. C. E. K. Mees, *Photography*, Macmillan, New York, **1942**.
4. W. A. Terry, *Br. J. Phot.* **1867**, *14*, 174.
5. W. A. Terry, *Br. J. Phot.* **1867**, *14*, 452.
6. J. H. W. Cramp, P. J. Hillson, *J. Photogr. Sci.* **1976**, *24*, 25.
7. W. Abney, *Photogr. News* **1880**, *24*, 345.
8. G. I. P. Levenson, *J. Photogr. Sci.* **1982**, *30*, 153.
9. H. Pocklington, *Br. J. Photogr.* **1883**, *32*, 542.
10. R. Meldola, *Photogr. News*, **1890**, *34*, 69.
11. J. M. Eder, *Photogr. Corres.* **1889**, *26*, 519.
12. Anon., *Anthony's Photographic Bulletin* **1899**, *20*, 699.
13. R. Fischer, British Patent 15055, **1912**.
14. J. H. Coote, *The Illustrated History of Colour Photography*, Fountain Press, London, **1993**.
15. Kodak Publication Z-131, *Using Kodak Flexicolour Chemicals*.
16. J. F. Hamilton, P. C. Logel, *Photogr. Sci. Eng.* **1974**, *18*, 5057.
17. R.C. Weast, *Chemical Handbook*, 52nd edition, The Chemical Rubber Company, Cleveland, OH, **1971**.
18. T.H. James, *The Theory of the Photographic Process*, 4th edition (Ed. T. H. James), Macmillan, New York, **1977**.

19. F. Hurter, V.C. Driffield, *J. Soc. Chem. Ind.* **1890**, 9, 455.
20. T. H. James, *J. Phys. Chem.* **1939**, 43, 701.
21. P. J. Hillson, *J. Photogr. Sci.* **1975**, 23, 15.
22. J. R. Fyson, G. I. P. Levenson, *J. Photogr. Sci.* **1977**, 25, 147, 164.
23. V.V. Gavrik, *J. Imaging Sci.* **1998**, 46, 32, 43.
24. G.I.P. Levenson, *J. Imaging Sci.* **1998**, 46, 40.
25. W. Reinders, *J. Phys. Chem.* **1934**, 38, 783.
26. a) N. Kameyama, S. Kikuchi, *J. Soc. Chem. Ind. Japan* **1936**, 39, 147B; b) R.M. Evans, W.T. Hanson, Jr., *J. Phys. Chem.* **1937**, 41, 509; c) H. Socher, *Z. Wiss. Phot.* **1938**, 37, 51; d) A. Vassy, *Sci. Inds. Photogr. (2)* **1947**, 18, 65; e) M. Abribat, J. Pouradier and J. David, *Sci. Inds. Photogr. (2)* **1949**, 20, 121; f) P. J. Hillson, *J. Photogr. Sci.* **1958**, 6, 97; g) M. Abribat, *Photogr. J.* **1952**, 92B, 25.
27. R. B. Pontius, C. R. VanDerVoorn, R. M. Cole, *Photogr. Sci. Eng.* **1968**, 12, 102.
28. L. K. J. Tong, M. C. Glesman, C.A. Bishop, *Photogr. Sci. Eng.* **1964**, 8, 326.
29. a) L. K. J. Tong, M. C. Glesman, *J. Am. Chem. Soc.* **1957**, 79, 583; b) L. K. J. Tong, M. C. Glesman, *Photogr. Sci. Eng.* **1964**, 8, 319; c) R.C. Baetzold and L. K. J. Tong, *J. Am. Chem. Soc.* **1971**, 93, 1347.
30. E. R. Brown, In *The Theory of the Photographic Process*, 4th edition (Ed. T. H. James), Macmillan, New York, **1977**, p. 293.
31. H.B. Berkely, *Photogr. News*, **1882**, 26, 41.
32. L.K.J. Tong, In *The Theory of the Photographic Process*, 4th edition (Ed. T. H. James), Macmillan, New York, **1977**, p. 344.
33. E.R. Brown, In *The Chemistry of the Quinoid Compounds*, Vol. 2 (Ed. S. Patai, Z. Rappaport), **1988**, Wiley, New York, Chapter 21.
34. a) L.K.J. Tong, *J. Phys. Chem.* **1954**, 58, 1090; b) L. K. J. Tong, M. C. Glesmann, R. L. Bent, *J. Am. Chem. Soc.* **1960**, 82, 1988; c) L. K. J. Tong, M. C. Glesmann, *J. Am. Chem. Soc.* **1956**, 78, 5827.
35. C.A. Bishop, L. K. J. Tong, *Photogr. Sci. Eng.* **1967**, 11, 30.
36. a) R. Matejec, *Photogr. Korr.* **1968**, 104, 153; b) J. Turkevich, P.C. Stevenson, J. Hillier, *Discuss. Faraday Soc.* **1951**, 11, 55.
37. a) G.I.P. Levenson, P.J. Twist, *J. Photogr. Sci.* **1973**, 21, 211; b) G.P. Faerman, E.D. Voikova, *Uspekhi nauch. Fotogr.* **1955**, 3, 714; c) *J. Phot. Sci.* **1955**, 4, 150; d) D.C. Shuman, T.H. James, *Photogr. Sci. Eng.* **1971**, 15, 42; e) R. Matejec and R. Meyer, *Photogr. Sci. Eng.* **1963**, 7, 265.
38. a) G.I.P. Levenson P.J. Twist, *J. Photogr. Sci.* **1973**, 21, 211; b) T. H. James, *J. Am. Chem. Soc.* **1939**, 61, 648, 2379; c) T.H. James, *J. Phys. Chem.* **1941**, 45, 623.
39. a) H. Kobayashi, T. Ohno, S. Mizusawa, *Denki Kagaku* **1982**, 50, 382; b) H. Kobayashi, S. Kawashima, T. Ohno, S. Mizusawa, *J. Imaging Sci.* **1986**, 30, 121.
40. W. Jaenicke, H. Kobayashi, *Photogr. Sci. Eng.* **1981**, 25, 152.
41. G.I.P. Levenson, P.J. Twist, *J. Photogr. Sci.* **1977**, 25, 1.
42. G.I.P. Levenson, *Photogr. Sci. Eng.* **1969**, 13, 299.
43. W. E. Lee, T. H. James, *Photogr. Sci. Eng.* **1962**, 6, 32.
44. A. Lumière, L. Lumière, A. Seyewetz, *Br. J. Photogr.* **1903**, 50, 646.
45. K. Kurosaki, *Nippon Kagaku Zasshi* **1961**, 82, 1694.
46. E. Mutter, W. Schneider, *Photogr. Korr.* **1969**, 105, 83.
47. a) E. Tausch, *Zur Chemie der Photographischen Entwickler*, Thesis Tech. Hochs. Berlin, Triltsch and Huthner, Berlin, **1934**; b) G.I.P. Levenson, *Phot. J.* **1948**, 88B, 102; c) G.I.P. Levenson, *Photogr. J.* **1949**, 89B, 2; d) G.I.P. Levenson, *Photogr. J.* **1952**, 92B, 109; e) G.I.P. Levenson, Thesis, University of London, **1947**.
48. a) J.D. Kendall, British Patent 542502, **1940**; b) J.D. Kendall, *Br. J. Photogr.* **1953**, 100, 56.
49. G.F. Van Veelen, *J. Photogr. Sci.* **1972**, 20, 94.
50. a) W. Jaenicke, H. Hoffman, *Z. Elektrochem.* **1962**, 66, 814; b) W.E. Lee, D.W. Miller, *Phot. Sci. Eng.* **1966**, 10, 192; c) C.J. Battaglia, W.E. Lee, D.W. Miller, E.S. Allen, W.J. Glover, *Photogr. Sci. Eng.* **1970**, 14, 39; d) A. Castellan, F. Maseti, U. Mazzucato, E. Vianello, *J. Photogr. Sci.* **1966**, 14, 164.
51. T.H. James, *PSA J.* **1953**, 19B, 156.

52. a) G.F. Van Veelen, R. Berendsen, M. DeMeyer, *Photogr. Korr.* **1965**, 7, Sonderheft 71; b) W.E. Lee, T.H. James, *Photogr. Sci. Eng.* **1962**, 6, 32; c) G.I.P. Levenson, P.J. Twist, *J. Photogr. Sci.* **1978**, 26, 44.
53. W. E. Lee, D. W. Miller, *Photogr. Sci. Eng.* **1966**, 10, 192.
54. D. D. F. Shiao, E. L. Dedio, *Photogr. Sci. Eng.* **1981**, 25, 145.
55. H. Kobayashi, T. Ohno, S. Mizusawa, *J. Photogr. Sci.* **1983**, 31, 181.
56. a) W. Jaenicke, H. Raithel, M. Brezina, *Photogr. Sci. Eng.* **1971**, 15, 230; b) M. Brezina, W. Jaenicke, H. Raithel, *Photogr. Sci. Eng.* **1969**, 13, 320.
57. W. Jaenicke, H. Kobayashi, *J. Photogr. Sci.* **1983**, 31, 69.
58. J. Koutecky, V.G. Levich, *Zh. Fiz. Khim.* **1958**, 32, 1565.
59. S. Kawashima, T. Ohno, H. Kobayashi, *J. Photogr. Sci.* **1996**, 44, 130.
60. D.A. Pullen, M.C. Lloyd, *Print Technol.* **1970**, 14, 69.
61. J.A.C. Yule, *J. Franklin Inst.* **1945**, 239, 221.
62. J. Eggers, *Photogr. Sci. Eng.* **1971**, 15, 128.
63. H.J. Hefter, *Photogr. Sci. Eng.* **1975**, 19, 179.
64. a) J.Q. Umberger, *Photogr. Sci. Eng.* **1966**, 10, 8; b) J.Q. Umberger, *Photogr. Sci. Eng.* **1970**, 14, 131; c) G. Herbert, *Photogr. Sci. Eng.* **1976**, 20, 82.
65. T.H. James, *J. Phys. Chem.* **1940**, 44, 42.
66. a) J.E. LuValle, *Photogr. Sci. Eng.* **1954**, 5, 273; b) J.E. LuValle, G.M. Goldberg, *J. Photogr. Sci.* **1968**, 6, 176.
67. a) T.H. James, *Photogr. Sci. Eng.* **1968**, 12, 67; b) T. Suga, *J. Soc. Sci. Photogr. Japan* **1969**, 32, 87, 138, 216.
68. H. Zwicky *J. Photogr. Sci.* **1985**, 33, 36.
69. a) T. Suga, *International Congress of Photographic Science, Dresden* **1974**, 3; b) T. Suga, *Proceedings of the International Congress of Photographic Science, Cologne* **1968**, 386.
70. R.P. Clifford, G.W.W. Stevens, *J. Photogr. Sci.* **1975**, 23, 22.
71. a) D. Beaumont, P.J. Coldrick, *25th SPSE Meeting on Imaging*, November **1985**; b) J. M. Simson *25th SPSE Meeting on Imaging*, November, **1985**.
72. a) H. Kobayashi, L. Shen, T. Nakamura, Y. Okawa, T. Ohno, *J. Photogr. Sci.* **1995**, 43, 186; b) P. Chen, R. Sun, X. Li, D. Zheng, *J. Imaging Sci. Technol.* **1993**, 37, 281.
73. a) P.J. Twist, unpublished results; b) R. Beels, F.H. Claes, *J. Photogr. Sci.* **1975**, 23, 23.
74. K. Schinzel, *Br. J. Photogr.* **1905**, 52, 608.
75. B. Gaspar, US Patents 2020775 and 2004625; British Patents 397159 and 419810.
76. R. Matejec, US Patent 3674490.
77. V. L. Bissonette, US Patent 3748138.
78. N.R. Wildman, P.J. Twist, J.R. Fyson, *Proceedings of the International Congress of Photographic Science, Antwerp*, **1998**, 153.
79. a) U. Nickel, C.-Y. Liu, *J. Photogr. Sci.* **1987**, 35, 191; b) U. Nickel, C.-Y. Liu, *J. Imaging Sci.* **1990**, 35, 8.
80. C. Wagner, W. Traud, *Z. Elektrochem. Ber. Bunsenges. Phys. Chem.* **1938**, 44, 39.
81. a) S. Couprie *J. Photogr. Sci.* **1972**, 20, 89; b) R.G. Willis, D.E. Turk, *Photogr. Sci. Eng.* **1973**, 17, 142; c) A. Miyamoto, K. Omodera, K. Komorita, K. Ohbayashi, M. Kajiware, *Nippon Shashin Gakkaish* **1982**, 44, 342; d) H. Kobayashi, *Proceedings from the 16th symposium of Nippon Shashin Kokkat*, May **1986**; e) J.R. Jarvis, P.J. Twist, *J. Imaging Sci.* **1989**, 33, 230.
82. T.R. Clayton, P.J. Twist, *J. Photogr. Sci.* **1993**, 41, 68.
83. a) M. Carey Lea, *Br. J. Photogr.* **1977**, 24, 292; b) M. Carey Lea, *Br. J. Photogr.* **1880**, 27, 27; c) T.G. Ovechkina, D. M. Shub, D. V. Pakhomov, V. I. Sheberstov, *Zh. Nauch. Prikl. Fotogr. Kinematogr.* **1972**, 17, 267.
84. W. Reinders, *J. Phys. Chem.* **1934**, 38, 783; b) P. J. Hillson, *J. Photogr. Sci.* **1958**, 6, 97; c) W. F. Berg, E. A. Frei, *Photogr. Sci. Eng.* **1969**, 13, 81.
85. R. Matejec and E. Moisar, *Photogr. Korr.* **1964**, 100, 39.
86. a) E. A. Galashin, E. P. Senchenkov, *Zh. Nauch. Prikl. Fotogr. Kinem.* **1971**, 16, 5; b) I. Konstantinov, A. Panov and J. Malinowski, *J. Photogr. Sci.* **1973**, 21, 250; c) I. Konstantinov and J. Malinowski, *J. Photogr. Sci.* **1975**, 23, 1.
87. J. H. W. Cramp, P. J. Hillson, *J. Photogr. Sci.* **1976**, 24, 25.
88. P. J. Hillson, H. H. Adam, *J. Photogr. Sci.* **1975**, 23, 104.

89. H. Hada, M. Kawasaki, H. Fujimoto, *Photogr. Sci. Eng.* **1980**, 24, 232.
90. T. Tani, *Photogr. Sci. Eng.* **1983**, 27, 75.
91. M. Kawasaki, H. Hada, S. Otani, *J. Photogr. Sci.* **1985**, 33, 29.
92. M. Mostafavi, J. Marignier, J. Amblard, J. Belloni, *Radiat. Phys. Chem.* **1989**, 34, 605.
93. K. Ohzeki, *J. Imaging Sci. Technol.* **1996**, 40, 591.
94. Y. V. Federov, V. N. Zakarov, *IS&T's 50th Annu. Conf.* **1997**, 152.
95. T. Tani, *Kikan Kagaku Sosetsu* **1998**, 38, 139.
96. a) W. Ostwald, *Lehrbuch der Allgemeinen Chemie*, 2nd revised edition, Vol. 2, Englemann, Leipzig, **1910**, p. 1078; b) R. Abegg, *Ann. Physik. Chem.* **1897**, 62, 425; c) R. Abegg, *Arch. Wiss. Photogr.* **1899**, 1, 15, 109; d) K. Schaum, *Arch. Wiss. Photogr.* **1899**, 1, 139.
97. a) R. W. Gurney, N. F. Mott, *Proc. Roy. Soc. London, Ser. A* **1938**, 164, 151; b) N. F. Mott, *Photogr. J.* **1948**, 88B, 119.
98. C. R. Berry, *Phot. Sci. Eng.* **1969**, 13, 65.
99. a) H. J. Metz, *J. Photogr. Sci.* **1972**, 20, 111; b) T. Miura, T. Sakaguchi, *Nippon Shashin Gakkaishi* **1983**, 46, 18.
100. W. Jaenicke, F. Sutter, *Z. Elektrochem.* **1959**, 63, 722.
101. R. Matejec, R. Meyer, *Z. Wiss. Photogr.* **1963**, 57, 45; *Phot. Sci. Eng.* **1963**, 7, 267.
102. A. Milchev, J. Malinowski, *J. Photogr. Sci.* **1975**, 22, 12.
103. W. F. Berg, *Trans. Faraday Soc.* **1943**, 39, 115.
104. a) Kh. S. Bagdasaryan, *Zh. Fiz. Khim.* **1943**, 17, 336; b) Kh. S. Bagdasaryan, *Acta Physicochim. URSS* **1944**, 19, 421.
105. a) R. G. Willis, F. E. Ford, R. B. Pontius, *Photogr. Sci. Eng.* **1970**, 14, 141; b) R. G. Willis, R. B. Pontius, *Photogr. Sci. Eng.* **1970**, 14, 149.
106. A. Hoffman, F. Friedman, *Photogr. Sci. Eng.* **1972**, 16, 201.
107. R. B. Pontius, R. G. Willis, *Photogr. Sci. Eng.* **1973**, 17, 326.
108. E. R. Brown, L. K. J. Tong, *Photogr. Sci. Eng.* **1975**, 19, 314.
109. M. R. V. Sahyun, *Electrochim. Acta.* **1978**, 23, 1145.
110. R. A. Marcus, *Electrochim. Acta.* **1968**, 13, 995; b) H. Gerischer, *Electrocatalysis on Non-metallic Surfaces*, National Bureau of Standards Special Publication No. 455, **1975**, p. 1.
111. D. D. F. Shiao, E. L. Dedio, *Photogr. Sci. Eng.* **1981**, 25, 145.
112. a) H. Hamano, H. Tabe and S. Kichuchi, *International Congress of Photographic Science, Royal Photographic Society, Cambridge*, **1982**, p. 319; b) H. Hamano, G. Arai, *J. Photogr. Sci.* **1979**, 27, 203, 17.
113. L. E. Friedrich, J. E. Eilers, *International Congress of Photographic Science, Cologne*, **1986**.
114. J. R. Boyack, *International Congress of Photographic Science, Cologne*, **1986**, p. 391.
115. D. D. F. Shiao, T. Bistrovich, *J. Imaging Sci.* **1991**, 35, 279.
116. a) J. R. Thirtle, *In The Theory of the Photographic Process*, 4th edition (Ed. T. H. James), Macmillan, New York, **1977**, p. 335; b) R. G. W. Hunt, *The Reproduction of Colour*, 4th edition, Fountain Press, London, **1987**.
117. Anon., *Kodak Data Book*, PR-4, pp. 1-4.
118. U. Nickel, G. Brehm, C.-Y. Liu, *J. Imaging Sci. Technol.* **1993**, 37, 286.
119. S. Matsuo, F. Suzuki, S. Sato, *Nippon Shashin Gakkaishi* **1975**, 38, 446.
120. J. R. Fyson, G. I. P. Levenson, *J. Photogr. Sci.* **1980**, 28, 231.
121. a) A. M. Comey, D. A. Hahm, *A Dictionary of Chemical Solubilities, Inorganic*, Macmillan, New York, **1921**, p. 1.
122. J. Pouradier, J. Pailliotet, C. R. Berry, *In The Theory of the Photographic Process*, 4th edition (Ed. T. H. James), Macmillan, New York, **1977**, pp. 194-195.
123. C. R. Berry, *In The Theory of the Photographic Process*, 4th edition (Ed. T. H. James), Macmillan, New York, **1977**, p. 88.
124. S. Matsuo, *Nippon Shashin Gakkaishi* **1976**, 41, 14-20.
125. J. R. Fyson, *J. Photogr. Sci.* **1984**, 32, 234.
126. W. Schneider, W. Brodersen, German Patent 866605.
127. S. Matsuo, *Nippon Shashin Gakkaishi* **1976**, 39, 81.
128. a) D. M. Burness, J. Pouradier, *In The Theory of the Photographic Process*, 4th edition (Ed. T. H. James), Macmillan, New York, **1977**, p. 77; b) M. D. Serman, M. A. Faust, D. J. Genova, *J. Photogr. Sci.* **1971**, 18, 183; c) J. R. Fyson, *J. Photogr. Sci.* **1993**, 41, 110.

129. A. Green, G. I. P. Levenson, *J. Photogr. Sci.* **1976**, *24*, 193.
130. M. H. Cohen, D. J. Turnbull, *J. Chem. Phys.* **1959**, *31*, 1164.
131. E. Weyde, German Patent 973769, **1940**.
132. B. A. Gorin, P. Ho, US Patent 4510227.
133. For example, in the US, NTIS PB89-141584, EPA 440588026.
134. E. R. Brown, In *The Theory of the Photographic Process*, 4th edition (Ed. T. H. James), Macmillan, New York, **1977**, p. 295.
135. E.R. Brown, J.D. Mazzarella, *J. Electroanal.* **1987**, *222*, 173.
136. S. Matsuo, *Nippon Shashin Gakkaishi* **1978**, *41*, 14.
137. G.I.P. Levenson, In *The Theory of the Photographic Process*, 4th edition (Ed. T. H. James), Macmillan, New York, **1977**, p. 437.
138. C. Vanleughenaghe, M. Pourbaix, P. van Rysselberge, *Atlas of Electrochemical Equilibria in Aqueous Solution*, Pergamon Press, London, **1966**.
139. A. Lumière, L. Lumière, L. Seyewetz, *Bull. Chem. Soc. Fr.* **1910**, *1*, 392.
140. J. F. Willems, *Photographic Processing*, Academic Press, New York, **1973**, p. 223.
141. H. Kobayashi, S. Sakai, T. Ohno, S. Mizusawa, *J. Photogr. Sci.* **1986**, *34*, 53.
142. J. L. Hall, J. J. Hastreiter, US Patent 4737450.
143. a) S. E. Haye, C. A. Wilson-Bonner, K. R. Ballou, US Patent 5763147; b) S. E. Haye, US Patent 5773202.
144. A. Meyer, *J. Photogr. Sci.* **1965**, *13*, 90.
145. a) W. Deuschel, *Chimia* **1969**, *23*, 381; b) M. Schellenberg, H. Mollet, *Helv. Chim. Acta* **1971**, *54*, 2431; c) E. Gunter, R. Matjec, *J. Photogr. Sci.* **1971**, *19*, 106.
146. a) M. Kulaneck, R. Landsberg, *Wiss. Z. Tech. Hochsch. Chem.* **1961**, *6*, 301; b) V. Sahyun, *Photogr. Sci. Eng.* **1973**, *17*, 171.
147. W. West, P. B. Gilman, In *The Theory of the Photographic Process*, 4th edition (Ed. T. H. James), Macmillan, New York, **1977**, p. 251.
148. H. W. Vogel, *Berichte* **1873**, *6*, 1302.
149. J. R. Thirtle, D. M. Zwick In *Kirk-Othmer: Encyclopedia of Chemical Technology*, Vol. 6, 3rd edition, **1979**, p. 617.
150. T. Tani *Photographic Sensitivity*, Oxford University Press, New York, **1995**, Chapter 5.
151. J. R. Thirtle, In *The Theory of the Photographic Process*, 4th edition (Ed. T. H. James), MacMillan, New York, **1977**, p. 335.
152. D. M. Sturmer, D. W. Heseltine, In *The Theory of the Photographic Process*, 4th edition (Ed. T. H. James), Macmillan, New York, **1977**, p. 194.
153. T. H. James, In *Advances in Photochemistry*, Vol. 13 (Ed. D. H. Volman, G.S. Hammond, K. Gollnick), Wiley, New York, **1986**, p. 1.
154. F. Moser, R. K. Ahrenkiel, In *The Theory of the Photographic Process*, 4th edition (Ed. T. H. James), Macmillan, New York, **1977**, p. 37.
155. J. F. Hamilton, *Adv. Phys.* **1988**, *23*, 359.
156. A. P. Marchetti, R. S. Eachus, In *Advances in Photochemistry*, Vol. 17 (Ed. D. H. Volman, G. S. Hammond, D. C. Neckers), Wiley, New York, **1992**, p. 145.
157. T. Tani, *Photographic Sensitivity*, Oxford University Press, New York, **1995**, p. 60.
158. R. S. Eachus, A. P. Marchetti, A. A. Muentner, *Annu. Rev. Phys. Chem.* **1999**, *50*, 117.
159. J. Hamilton, In *The Theory of the Photographic Process*, 4th edition (Ed. T. H. James), Macmillan, New York, **1977**, p. 105.
160. J. M. Harbison, H. E. Spencer, In *The Theory of the Photographic Process*, 4th edition (Ed. T. H. James), Macmillan, New York, **1977**, p. 149.
161. R. K. Hailstone, N. B. Liebert, M. Levy, J. F. Hamilton, *J. Imaging Sci.* **1987**, *31*, 185.
162. S. Daehne, *Science* **1978**, *199*, 1163.
163. A. H. Herz, R. Danner, G. Janusonis, *Adv. Colloid Interface Sci.* **1977**, *8*, 237.
164. G. Scheibe, *Angew. Chem.* **1936**, *49*, 563.
165. E. G. McRae, M. Kasha, *J. Chem. Phys.* **1958**, *28*, 721.
166. M. Kasha, H. R. Rawls, M. A. Elbayoumi, *Pure Appl. Chem.* **1965**, *11*, 371.
167. M. Kawasaki, H. Ishii, *J. Imaging Sci. Technol.* **1995**, *39*, 210.
168. S. DeBoer, D. A. Wiersma, *Chem. Phys. Lett.* **1990**, *165*, 45.
169. M. van Burgel, D. A. Wiersma K. Duppen, *J. Chem. Phys.* **1995**, *102*, 20.

170. D. V. Brumbaugh, A. A. Muentner, W. Knox, G. Mourou, B. Wittmershaus, *J. Lumin.* **1984**, 31/32, 783.
171. A. A. Muentner, W. Cooper, *Photogr. Sci. Eng.* **1996**, 20, 79.
172. A. A. Muentner, D. V. Brumbaugh, J. Apolito, L. A. Horn, F. C. Spano, S. Mukamel, *J. Phys. Chem.* **1992**, 96, 2783.
173. J. M. Lanzafame, A. A. Muentner, D. V. Brumbaugh, *Chem. Phys.* **1996**, 210, 79.
174. F. C. Spano, S. Mukamel, *J. Chem. Phys.* **1989**, 91, 683.
175. F. C. Spano, J. R. Kuklinski, S. Mukamel, *J. Chem. Phys.* **1991**, 94, 7534.
176. a) R. W. Berriman, P. B. Gilman, *Photogr. Sci. Eng.* **1973**, 17, 235; b) P. B. Gilman, *Photogr. Sci. Eng.* **1974**, 18, 475.
177. J. Lenhard, *J. Imaging Sci.* **1986**, 30, 27.
178. T. Tani, *Photographic Sensitivity*, Oxford University Press, New York, **1995**, pp. 126–132.
179. T. Tani, K. Ohzeki, K. Seki, *J. Electrochem. Soc.* **1991**, 138, 1411.
180. M. Peover In *Electroanalytical Chemistry*, Vol. 2 (Ed. A. Bard), Marcel Dekker, New York, **1972**, p. 1.
181. R. O. Loutfy, J. H. Sharp, *Photogr. Sci. Eng.* **1976**, 20, 165.
182. R. O. Loutfy, R. O. Loutfy *Can. J. Chem.* **1976**, 55, 1454.
183. I. H. Leubner, *Photogr. Sci. Eng.* **1976**, 20, 61.
184. D. M. Sturmer, W. S. Gaugh, B. J. Bruschi, *Photogr. Sci. Eng.* **1974**, 18, 49.
185. D. M. Sturmer, W. S. Gaugh, B. J. Bruschi, *Photogr. Sci. Eng.* **1974**, 18, 56.
186. a) I. H. Leubner, *Photogr. Sci. Eng.* **1978**, 22, 270; b) I. H. Leubner, *Photogr. Sci. Eng.* **1980**, 24, 138.
187. T. Tani, T. Suzumoto, K. Ohzeki, *J. Phys. Chem.* **1990**, 94, 1298.
188. R. A. Marcus, *Annu. Rev. Phys. Chem.* **1964**, 15, 155.
189. R. K. Hailstone, *J. Photogr. Sci.* **1984**, 32, 25–36.
190. A. A. Muentner, P. B. Gilman, J. R. Lenhard, T. L. Penner, presented at *Fall Conf. Soc. Photogr. Sci. Technol. Jpn., Kyoto*, **1985**.
191. M. Spitler, A. Ehret, R. Kietzmann, F. Willig, *J. Phys. Chem.* **1997**, 101, 2552–2557.
192. T. A. Rhodes, S. Farid, J. L. Goodman, I. R. Gould, R. H. Young, *J. Am. Chem. Soc.* **1999**, 121, 5340.
193. D. V. Brumbaugh, A. A. Muentner, W. Knox, G. Moreau, *J. Lumin.* **1984**, 31&32, 2178.
194. K. Takahashi, K. Obi, I. Tanaka, T. Tani, *Chem. Phys. Lett.* **1989**, 154, 233.
195. A. A. Muentner, *J. Phys. Chem.* **1976**, 80, 2178.
196. R. Kietzmann, A. Ehret, M. Spitler, F. Willig, *J. Am. Chem. Soc.* **1993**, 115, 1930.
197. R. S. Eachus, A. P. Marchetti, A. A. Muentner, *Annu. Rev. Phys. Chem.* **1999**, 50, 130.
198. J. Jortner, *J. Chem. Phys.* **1976**, 64, 4860.
199. J. M. Lanzafame, R. J. D. Miller, A. A. Muentner, B. A. Parkinson, *J. Phys. Chem.* **1992**, 96, 2820.
200. T. Hannappel, B. Burfeindt, W. Storck, F. Willig, *J. Phys. Chem. B* **1997**, 101, 6799.
201. Y. Tachibana, J. E. Moser, M. Grätzel, D. R. Klug, J. R. Durrant, *J. Phys. Chem.* **1996**, 100, 20056.
202. A. A. Muentner, D. V. Brumbaugh, J. Apolito, L. A. Horn, F. C. Spano, S. Mukamel, *J. Phys. Chem.* **1992**, 96, 2783.
203. J. M. Lanzafame, A. A. Muentner, D. V. Brumbaugh, *Chem. Phys.* **1996**, 210, 79.
204. T. Tani, T. Suzumoto, K. Kemnitz, K. Yoshihara, *J. Phys. Chem.* **1992**, 96, 2778.
205. B. Trösken, F. Willig, K. Schwarzburg, A. Ehert, M. Spitler, *J. Phys. Chem.* **1995**, 99, 5152.
206. R. S. Eachus, A. P. Marchetti, A. A. Muentner, *Annu. Rev. Phys. Chem.* **1999**, 50, 133.
207. W. West, P. B. Gilman, In *The Theory of the Photographic Process*, 4th edition (Ed. T. H. James), Macmillan, New York, **1977**, p. 259.
208. P. B. Gilman, *Photogr. Sci. Eng.* **1967**, 11, 222.
209. P. B. Gilman, *Photogr. Sci. Eng.* **1968**, 12, 230.
210. P. B. Gilman, *Photogr. Sci. Eng.* **1974**, 18, 418.
211. T. Tani, Y. Sano, M. Saito, *Photogr. Sci. Eng.* **1979**, 23, 240.

2 Electrophotography

David S. Weiss, J. Robin Cowdery, and Ralph H. Young

2.1 Introduction

The electrophotographic copying and printing industry is based on the inventions of Chester F. Carlson [1]. The fascinating story of Carlson and the development of xerography has been told in books and biographical articles [2]. Carlson received a BS in Physics from the California Institute of Technology in 1930. Following a brief time as an engineer at the Bell Telephone Laboratories he joined the patent department at the P. R. Mallory Company. There he became a registered patent attorney and obtained a law degree from the New York University. Based on personal experience and intuition he saw the need for a method of making copies of documents that would supplant the labor-intensive, time-consuming, and low-quality methods available at the time. In his makeshift kitchen laboratory Carlson discovered that a thin film of an insulating photoconductor on a metal plate could be tribocharged by rubbing with an appropriate material such as cotton. This surface charge could be dissipated in an image-wise manner by exposure through a mask with light of a wavelength where the material was photoconductive. The earliest photoconductive materials used were sulfur and anthracene coated on a zinc plate. The invisible electrostatic image could then be visualized, or developed, by contacting it with a powder comprising particles having a charge opposite to that of the surface. In the earliest embodiment of his invention, Carlson used lycopodium powder. The first image was “10.-22.-38 Astoria”. The image was then transferred to wax paper and fixed by heating. Carlson later dubbed this process “xerography” from the Greek meaning “dry writing”. In 1939 Carlson filed a patent on the electrophotographic process and sought in vain for a company willing to invest in this technology. US Patent 2297691 was issued on October 6, 1942. Finally, in 1944 the Battelle Development Corp., a subsidiary of the Battelle Memorial Institute in Columbus, Ohio, accepted the project. This activity attracted the attention of Joseph Wilson, president of the Haloid Company in Rochester, New York. Haloid manufactured and sold sensitized photographic paper and wet-chemical based

photocopying machines. Wilson, and his research director John Dessauer, saw a promise in this new technology that all the business analysts of the top corporations in the United States had overlooked and Haloid agreed to provide financial support beginning in 1947, through Battelle, for its development. It took many years to bring the technology to commercial fruition. The first commercial application, the XeroX Copier Model A, appeared in 1949. This machine achieved limited success because it required 14 complex manual operations in the making of a copy. In 1955 the XeroX Copyflo printer was introduced. This machine automatically made prints from microfilm. As the commercial emphasis of Haloid shifted to xerography, the company changed its name to Haloid–Xerox. In 1959 Haloid–Xerox introduced the Xerox 914 fully automatic copying machine and this marked the beginning of a true revolution. In the decade after the introduction of the 914, operating revenues grew from \$33 million to \$1.4 billion and in 1969 Haloid–Xerox became the Xerox Corporation. Today xerography and related technologies represent a multibillion-dollar business with many corporations with thousands of employees vying for business.

A schematic of the electrophotographic printing and copying process is shown in Figure 1. At the “heart” of the process is the photoreceptor element. This is a photoconductive drum or a belt as shown, around which all the other process elements are situated. The photoreceptor acquires a surface charge by means of a charging device involving an air corona or a charged roller. The surface charge is then dissipated in an image-wise manner by a light exposure. In a copier the exposure comes from light reflected from a document. In a printer the exposure comes from a computer-driven laser scanner or light-emitting diode (LED) array. The

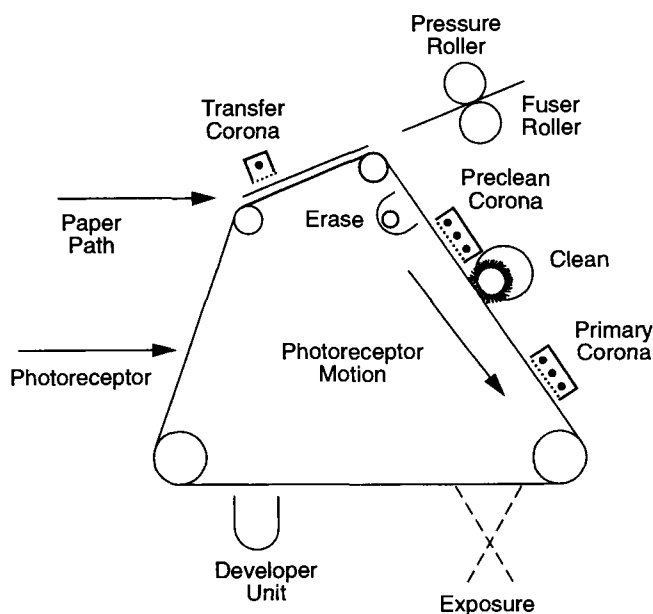


Figure 1. An electro-photographic process with web-based photoreceptor. (Reprinted with permission from Ref. [3q].)

wavelength of the exposing light must match the photoreceptor sensitivity. Contacting the photoreceptor surface with charged toner particles develops the electrostatic “latent image”. In a copier the exposure is carried out so that in dark areas, such as letters in textual material, the surface charge is retained. In a printer it is the background which retains the surface charge. In most copiers and some printers the charged areas of the latent image are developed with toner particles having a charge of opposite polarity to that of the photoreceptor. In other printers the discharged areas are developed with toner particles having a charge of the same polarity as the photoreceptor. Toner particles (typically 8–15 μm in diameter) comprise colorant, charge control agents, polymeric binder, and additives such as wax and silica. The toner may be in a dry form or dispersed in an insulating liquid. Dry development systems may contain “carrier” particles. These are usually magnetic materials with a coating to control the triboelectric characteristics when mixed with toner. The toned image is then transferred to the desired receiver, typically paper or transparency media, and the image is rendered stable by a combination of pressure and heat. The photoreceptor is then cleaned with a brush or blade to refresh the surface by removal of residual toner and receiver debris. In many cases, at the end of the cycle the photoreceptor is “erased” by a blanket light exposure to ensure that the surface potential has the desired uniformity with subsequent corona charging. In a high-volume printer or copier the photoreceptor undergoes more than 10^5 imaging cycles before replacement. Its composition and architecture and its interactions with the electrophotographic process subsystems primarily determine the life of the photoreceptor. Each photoreceptor must be optimized for the specific process in which it will function. There are many books and review articles on electrophotographic technologies [3].

Photoreceptors are generally divided into two classes, inorganic (such as amorphous Si, amorphous Se, or other chalcogenide glasses) and organic (dyes, pigments and other organic molecules in polymeric binders). We will focus on organic photoreceptors in our discussions. There are many aspects of the electrophotographic process that involve electron transfer. Surface charging of the toner occurs by tribocharging against polymer surfaces and surface charging of the photoreceptor occurs by exposure to ions (generated in an air corona, for example). The mechanistic aspects of these processes will be only briefly discussed. The bulk of the chapter will be concerned with the processes that occur within a photoreceptor during the creation of the electrostatic latent image. Charge generation is initiated with the absorption of light and charge transport occurs within the photoreceptor driven by the internal electric field. Each of these latter subjects will be discussed in greater detail.

2.2 Electrophotographic Developers

There are primarily two types of developer. Single-component developers, typically used in desktop printers, are made up of toner particles only. Two-component de-

velopers, commonly used in high-throughput devices, comprise a mixture of toner and carrier particles. Toner particles generally comprise pigment suspended in a polymeric matrix. The choice of pigment depends on its hue and dispersibility in the binder polymer [4a]. The choice of an appropriate binder polymer is based on its having desirable characteristics for toner manufacturing as well as providing good adhesion to paper and giving the desired surface finish to the toned image. Charge control agents are also commonly used in toner formulations. These are added to control the polarity and magnitude of charge on the toner particles. The charging capability of the toner depends on the chemical composition and concentration of the charge control agent in the toner composite. The ratio of toner to carrier charging sites controls the overall toner charging capability and is altered by changing the relative surface content of each, either by relative concentrations and/or particle sizes [4a]. Toner particles (8–15 μm in diameter) are generally smaller than carrier particles (30–200 μm in diameter), but in some systems the carrier is of comparable size to the toner [4b]. Increasing print quality standards have led to the use of smaller toner particles.

The carrier in a two-component developer is generally ferromagnetic metal or oxide particles coated with a polymeric toner charge control agent. The carrier is used to transport the toner from the development station to the surface of the photoreceptor by forming a “magnetic brush” around a magnetic development roller, with the toner particles electrostatically held to the carrier particles [4a]. Tribocharging occurs during the mixing of toner with carrier. A major challenge in the formulation of developers is to provide a toner with the desired charge that is stable with time and with changes in ambient conditions such as relative humidity (RH) and temperature.

At present, two models are used to describe toner–carrier tribocharging. One invokes electron transfer in which electrons in the occupied orbitals of the material with the smaller work function (higher chemical potential) move to the vacant orbitals in the material with the larger work function (lower chemical potential) [5]. This model is derived from the contact charging mechanism for metals and semiconductors where the driving force for electron transfer is the difference between work functions of the contacting materials [4a, 6a]. Electron transfer proceeds until the Fermi levels of the toner and carrier surfaces become equal, at which point the transfer of electrons ceases. The ratio of toner mass to toner charge has been mathematically modeled as a linear function of toner mass to carrier mass, with the slope and intercept depending on particle sizes, mass densities, and surface state densities [4b].

Another model that describes the charge transfer process between toner and carrier particles invokes “ion transfer”. In this model the tribocharging process involves the transfer of ionic species, not just electrons [5b, 6]. The transferred ions are derived from charge control additives which are present as either ionomers or molecular salts in the polymer binder. For ion transfer to occur, dissociated and mobile ions must be present on the particle surface. Initially, each surface contains ions of both polarities, but after repeated contacts the two surfaces become equally but oppositely charged [6a]. The polarity and magnitude of charge transfer can be predicted for certain systems, based on the structure and composition of the ionic

components. The ion transfer model differs from the electron transfer model in that it takes into account the chemical nature of the ionic components. The ion transfer process has been modeled mathematically to correlate the equilibrium charge between the two surfaces with the chemical structure of the contact ions [6a].

2.3 Organic Photoreceptor Fabrication and Characterization

Figure 2 schematically shows a microscopic cross-section of a typical “dual-layer” organic photoreceptor. Photoreceptors can be fabricated on either a flexible polymeric belt substrate or a rigid drum, depending on the electrophotographic process requirements for a given copier/printer. There are advantages and disadvantages for either type of support, depending on the details of the electrophotographic process [3].

In the photoreceptor represented in Figure 2, the first layer is the substrate belt or drum. Belt substrates are typically organic polymers such as poly(ethylene terephthalate). Drum substrates are typically aluminum. The next layer is the conductive electrode used to make a connection to electrical ground. For metallic drums the electrode is the metal substrate. For nonconductive substrates the grounding layer can be a thin metal layer such as Al, Ni, or Ti, or any material that forms a continuous layer with sufficient conductivity. Next is a layer or layers designed to promote adhesion to the electrode and/or to act as an electrical blocking layer to prevent unwanted dark charge injection. A smoothing layer is often used on aluminum drum photoreceptors. If insulating, these layers will prevent complete photodischarge of the photoreceptor which may be undesirable, depending on the magnitude of the residual potential and the electrophotographic process. For this reason these layers are made as thin as possible. The photoactive layer(s) of most practical photoreceptors include a charge generation material (CGM) and a charge transport material (CTM) in a polymeric binder. The format can be a monolayer,

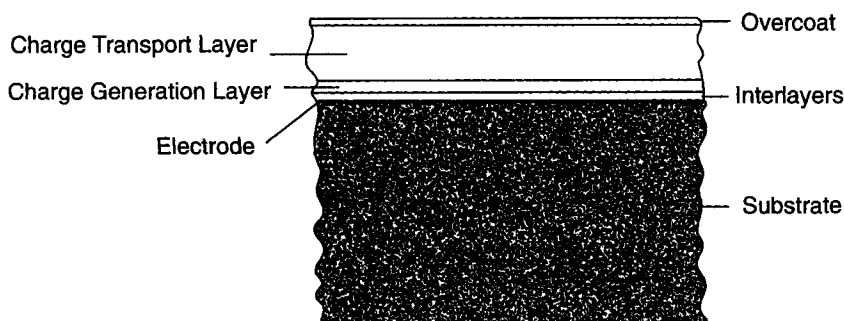


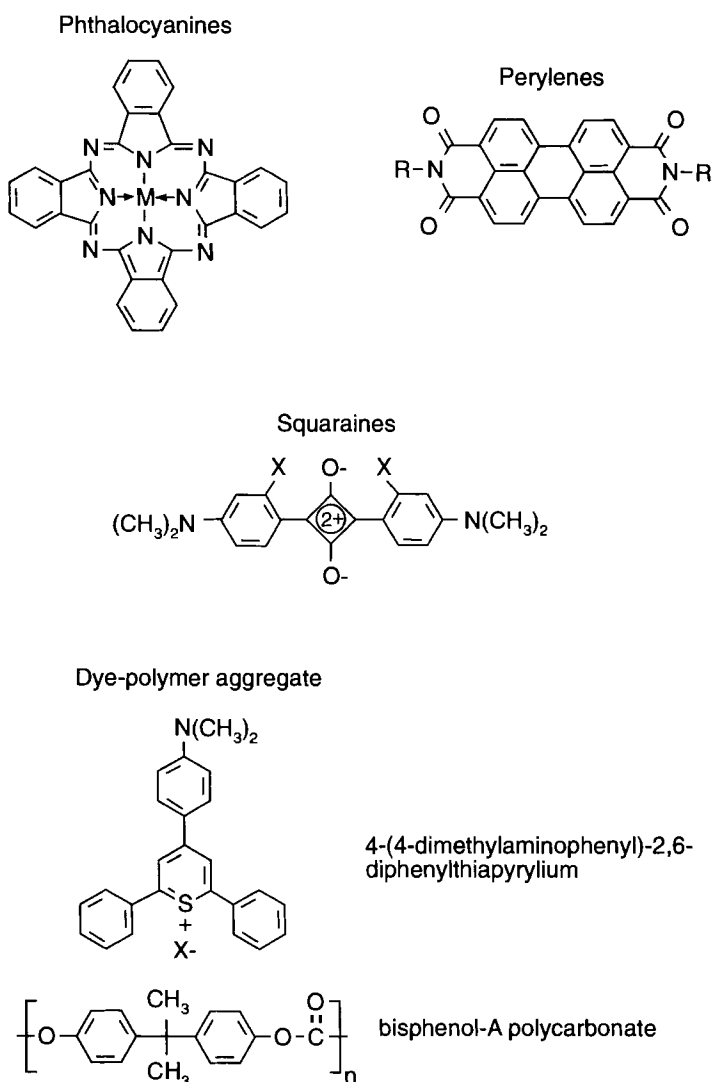
Figure 2. A schematic microscopic cross-section of a dual-layer photoreceptor. (Reprinted with permission from Ref. [30].)

dual-layer or multilayer structure. In a dual-layer photoreceptor, the charge generation and transport functions are separated into a relatively thin charge generation layer (CGL), typically 0.5–2.0 μm , and a thick charge transport layer (CTL), typically 10–30 μm . The latter controls the device capacitance and therefore the surface charge density at a given surface potential. All commercial photoreceptors utilize hole-dominated transport. Thus, in the configuration shown in Figure 2, the photoreceptor receives a negative surface charge. If a positive surface charge is desired, either a single-layer photoreceptor or an inverted dual-layer photoreceptor (with the CGL on “top”) can be used. Finally, an overcoat layer may be added for physical protection from abrasion and scratches, as well as protection from the corrosive chemicals generated in an air corona. Other than the electrode, all layers are typically coated consecutively from solution with appropriate coating aids, using solvents and coating conditions such that previously deposited layers are not adversely affected by the subsequent coating procedures.

Charge generation materials generally comprise pigment dispersions in a polymer binder. The materials must be manufacturable at the desired cost and amenable to the milling, dispersion, and coating procedures required in CGL preparation. The resulting CGL must have good absorption of light of the wavelength used in the electrophotographic process and have charge generation efficiency consistent with the sensitivity required for the process. There are many types of charge generation materials. Typical examples are phthalocyanines, diimides of perylene-3,4,9,10-tetracarboxylic acid, squaraines, azo pigments, the charge transfer complex between poly(*N*-vinylcarbazole) and 2,4,7-trinitro-9-fluorenone (TNF), and an aggregate of a pyrylium-type dye with bisphenol-A polycarbonate (Scheme 1). These materials and the current understanding of carrier generation will be discussed later.

Charge transport layers comprise high concentrations (40–50 wt.%) of charge transport materials dissolved in a polymer binder. The CTMs must be manufacturable in large scale and soluble in the binder and solvent of choice, yielding a formulation that coats readily to form a uniform CTL. CTMs must exhibit adequate charge mobility in the polymeric binder of choice. Useful hole transport materials have a low oxidation potential and a stable cation radical. Most useful CTMs utilize oxidation of the lone pair of electrons on a nitrogen atom. Typical examples, with the chemical functionality in parentheses, are: arylamines (N-Ar), hydrazones ($-\text{C}=\text{N}-\text{N}-$), enamines ($-\text{C}=\text{C}-\text{N}-$), oxadiazoles (heterocyclic $-\text{C}=\text{N}-\text{N}=\text{C}-\text{O}-$), oxazoles (heterocyclic $-\text{C}=\text{C}-\text{N}=\text{C}-\text{O}-$), and pyrazolines (heterocyclic $-\text{N}-\text{C}-\text{C}=\text{C}=\text{N}-$) (Scheme 2). To date, there has been far less work done on electron transport materials than on hole transport materials. Useful electron transport materials must have a reduction potential below that of oxygen, a common electron trap, and a stable anion radical (Scheme 3). Electron-withdrawing groups, such as nitro or dicyanomethylene, are often used to lower the reduction potential of a parent compound. However, these substituents also tend to decrease solubility and electron mobility. In addition, electron mobility is generally much lower than hole mobility in doped polymer films.

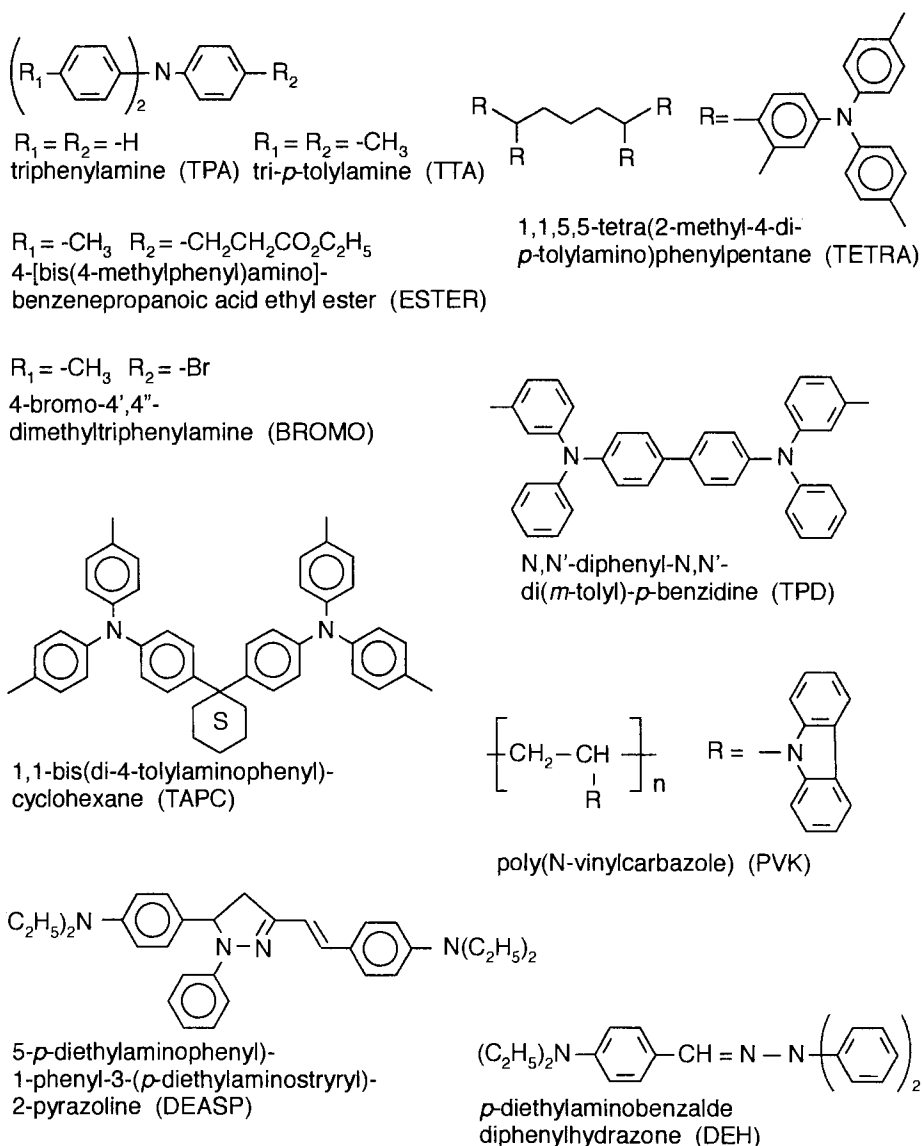
Overcoat layers are used to protect the photoreceptor surface from scratching and abrasion, and chemical degradation due to corona by-products [7]. Overcoats may be relatively thick polymeric layers (microns) or thin (submicron) refractory



Scheme 1. Chemical structures of some typical charge generation materials. See Schemes 4 and 5 for examples of azo pigments.

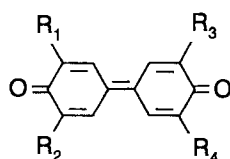
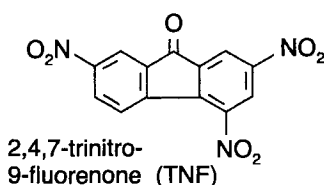
materials. These must be applied without damaging the underlying photoreceptor. The sol-gel process has recently been used in the preparation of silsesquioxane coatings that are excellent for abrasion resistance [7a-c]. Diamond-like carbon and other overcoats have been prepared with plasma-enhanced chemical vapor deposition [7d-f].

Evaluation of photoreceptor performance includes tests of dark conductivity and photoconductivity. Dark conductivity is determined by charging the surface to the

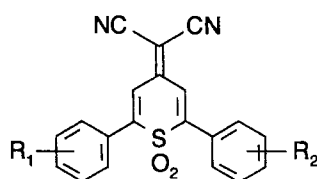


Scheme 2. Chemical structures of some typical hole-transporting materials.

desired potential, then recording the decrease in surface potential with time. Photosensitivity is determined by charging to the desired potential in the dark and then determining the decrease in surface potential on exposure to light of the desired wavelength. Exposing with a light source identical to that in the intended electrophotographic process is the most useful, but both continuous and flash exposures

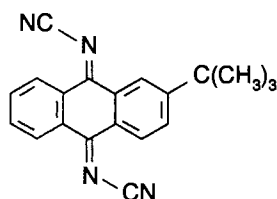


3,5-dimethyl-3',5'-di-*t*-butyl-4,4'-diphenylquinone (DPQ)

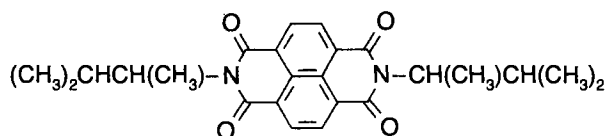


1,1-dioxo-2-(4-methylphenyl)-6-phenyl-4-(dicyanomethylidene)thiopyran (PTS)

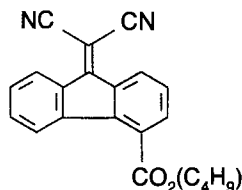
$R_1 = R_2 = -m-CF_3$ (M)
 $R_1 = R_2 = -p-CF_3$ (P)



2-*t*-butyl-9,10-*N,N'*-dicyanoanthraquinonediimine (DCAQ)



N,N'-bis(1,2-dimethylpropyl)-1,4,5,8-naphthalenetetracarboxylic diimide (NTDI)



n-butyl 9-dicyanomethylenefluorene-4-carboxylate (BCMF)

Scheme 3. Chemical structures of some typical electron-transporting materials.

are commonly used for convenience. Charge/expose cycling, over a range of temperature and relative humidity, is used to determine the dark and photoconductive stability of a photoreceptor. This testing is often configured to mirror the electrophotographic process for which the photoreceptor is intended.

Photoreceptors may be characterized by optical microscopy for layer structure and architecture. Surface defects may be characterized by atomic force microscopy. Scratch resistance can be characterized by scratching the photoreceptor surface with a stylus of known dimensions under specified loads. Brittleness measurements are

accomplished on films by pulling a loop through a wedge having a specific size of orifice.

2.4 Corona Charging

In the electrophotographic process, the first step in the making of an electrostatic image is to produce a uniform surface charge density on the thin photoconductive layer in the dark. The surface charge, along with the countercharge on the underlying grounded electrode, produces a high field within the photoconductor that facilitates charge generation and transport. The photoreceptor structure approximates a parallel plate capacitor and the surface potential is determined by the surface charges per unit area and the effective capacitance. In Carlson's original implementation the surface charge was obtained by vigorously rubbing a handkerchief on a sulfur-coated zinc plate. The seminal 1942 US Patent mentions rubbing with a silk or cotton handkerchief or a soft fur brush [1a]. Carlson's 1944 US Patent describes an "electrophotographic apparatus" with a charging system consisting of a brush or a roller with a surface of "plush, fur, wool, woven or knit cotton, silk or rayon fabric, felt, hair, velvet or other suitable charging material" [1b]. A major advance in making the electrophotographic process practical was the development of a method for using the ions produced by electrical breakdown in air. Applying a very high potential (several thousand volts) to a conductive wire in air produces a corona discharge [8]. Ions from the corona drift to the surface of the photoconductor under the influence of the electric field between the wire and the grounded electrode underneath the photoconductor film. Key inventions were described in patents issued to Carlson (1952) [9a] and Walkup (1957) [9b] and aspects of the science and technology of corona charging are discussed by Schaffert [3f] and Williams [3i]. In a "corotron" device the corona wire is partially enclosed in a shield with the opening facing the photoconductor. In a "scorotron" the opening is covered with a wire screen. The screen is held at the surface potential desired and acts to control the flow of ions from the corona to the photoconductor surface. When the surface potential reaches that of the control grid, ion flow from the corona wire to the photoreceptor ceases. A third, commonly used, charging device is a charging roller. In this device a conductive roller at a high potential contacts the photoconductor surface. Air ionization occurs across a narrow air gap near the nips, where the roller makes and breaks contact with the photoreceptor, and ions are deposited on the photoconductor surface. All these methods have their advantages and disadvantages, depending on the details of the process and marketing requirements for the copier or printer. The electron transfer chemistry that occurs in the formation of a corona in air will not be discussed here [8].

Using mass spectroscopy, the chemical composition of air coronas has been determined by Shahin. In a corona produced at a positively charged wire, in the presence of even trace amounts of water, the predominant ions are hydrated proton clusters, $(\text{H}_2\text{O})_n\text{H}^+$ [10a]. At 20 % RH, $n = 6$ predominates and at 1 % $n = 4$ pre-

dominates. At $RH < 1\%$, other hydrated ionic species are observed: $(H_2O)_nO_2^+$, $(H_2O)_nNO^+$, and $(H_2O)_nNO_2^+$. In a negative corona the dominant ion is CO_3^- [10b]. Even at a relative humidity of 20–50 %, hydrated ions $(H_2O)CO_3^-$, $(H_2O)O^-$, and $(H_2O)O_3^-$ make up less than 10 % of the total ion population. At 50 % RH the average ion mobility is $1.7 \text{ cm}^2 \text{ V}^{-1} \text{ s}^{-1}$ for both positive and negative ions, and their kinetic energy is negligible. Photoconductor charging was suggested to involve either charge exchange or ion adsorption at the surface [10c]. The charging of selenium was described in terms of electron (negative charging) or proton (positive charging) transfer with the appropriate “surface states”, with trapping of the charged species near the free surface.

Subsequent studies of the corona charging and dark decay characteristics of semiconductor materials have taken into account the effects of mobile charges in the photoreceptor. Such charges might arise from interfacial charge injection (at either the free or the electroded surfaces) as well as depletion of charge carriers trapped in the bulk. Bulk charge depletion results from the thermal generation and subsequent drift of mobile carriers with the countercharge being trapped [10d]. These processes are obviously important in the charging of a photoconductor surface and underscore the observation that corona charging is a dynamic process with the production of both trapped and mobile charge, the latter giving rise to dark decay. Charge mobility in semiconductor bands is beyond the scope of this review. However, charge mobility in doped polymer systems will be covered later.

There have been extensive studies on the corona charging and dark discharging mechanisms in semiconductors such as selenium [10e–g], selenium–tellurium [10h], and selenium–arsenic alloys [10i], and amorphous silicon [10j]. The models for charging of organic photoconductors have followed similar lines [10k]. Thus the dark discharge characteristics of a photoreceptor using the photoconductive charge transfer complex of poly(*N*-vinylcarbazole) and 2,4,7-trinitrofluorenone (PVK-TNF) [10l], and *p*-diethylaminobenzaldehyde diphenylhydrazone (DEH) in a polycarbonate binder [10m], are understood in terms of interfacial charge injection and depletion of thermally generated bulk charge. Ing and Neyhart discuss positive corona charging of arsenic triselenide in terms of bulk hole generation and surface hole injection [10i]. The surface contribution was found to decrease with exposure to air or with the application of a thin surface-insulating layer. The authors speculate that the effect of air is to produce either an oxide layer and/or a selenium-rich surface. Similar effects are observed with a-Si and a thin surface layer is necessary to retard the surface injection of holes [11]. Thus, the charging of photoconductor surfaces is believed to involve either corona ion absorption and/or electron exchange from corona ions to “surface states”. The details of this process and chemical nature of the “surface states” remain open questions.

In addition to the ionic species, air coronas produce ozone, various oxides of nitrogen, and light from the emission of excited molecular nitrogen [12a]. Corona discharge treatment of polymer films is common in the coating industry. This treatment results in surface oxidation and increased surface energy, for improved adhesion of subsequently coated layers [12b,c]. Goldman and Sigmond, in a study of aluminum corrosion, found that exposure to a corona gave rise to mixtures of aluminum nitrates, hydroxides, and oxides [12d]. The corrosion was greatest with a

negative corona at high RH. They conclude that the corona environment behaves as a unipolar gaseous electrolyte that reacts with aluminum in a manner akin to aqueous oxidation. Nashimoto has shown that the emission of ozone and NO_x depends on the corona polarity, wire composition, and wire diameter [12e].

It has not been fully appreciated that during corona charging of photoconductors the surface of the material being charged is exposed to reactive chemical species, as well as light, and chemical modification of the exposed surface during charging is very likely. There is little doubt that many of the anomalies observed in mechanistic studies of corona charging are due to surface chemistry. Nevertheless, there are few reports on the chemical changes resulting from such exposures and how they impact the electrical characteristics of importance in electrophotographic applications.

Lichtensteiger and Webb reported that negative corona charging of cadmium sulfide and zinc selenide results in surface oxidation [13a], and ozone exposure of amorphous selenium in electrophotographic copiers and printers has been shown to cause surface oxidation to selenium dioxide [13b]. Styrenic charge transport molecules, doped at high loading into a binder polymer to form the hole transport layer of an organic photoconductor, undergo ozonolysis during corona charging in the electrophotographic process [13c]. The chemical breakdown of the hole transport material renders the charged photoreceptor incapable of undergoing complete photo-discharge. This results in a residual potential that increases as the photoreceptor is cycled in the electrophotographic process. Weiss has shown that tri(*p*-tolyl)amine, a typical low-oxidation-potential charge transport material, undergoes a one-electron oxidation to the radical cation when exposed to the neutral gases produced in an air corona [13d]. Because the arylamine radical cations are the charge carriers in hole-transport-based organic photoconductors, increased dark conductivity is observed. Following the corona gas exposure the concentration of the radical cation of tri(*p*-tolyl)amine decreases and there is concomitant formation of nitrated transport material. This chemistry is explained in terms of the electron transfer mechanism of electrophilic aromatic substitution with a nitrogeous species (NO_x , HNO_3 , etc.) serving as the oxidizing agent. Similar effects were observed when the photoconductors were exposed to the gases over concentrated nitric acid. Although there are few literature reports on the effects of corona-generated oxidizing agents, the patent literature has many examples of the use of antioxidants doped into photoconductors to eliminate such effects.

2.5 Charge Carrier Generation

2.5.1 Background and Methodologies

In the xerographic process the charged photoreceptor is image-wise exposed with a light source having an emission at wavelengths that are absorbed by the charge generating material. As a result of this exposure, charges are generated and drift through the photoreceptor, reducing the internal field and neutralizing the surface

charge. This produces an image-wise pattern of surface charge, and surface potential, on the photoreceptor. In this section we will discuss the electron transfer aspects of the chemistry and physics of charge generation in organic photoreceptors. A subsequent section will cover the process of charge transport.

Photoinduced charge generation in organic crystals has been of interest for many years [14], and in recent work the assembly of controlled architectures holds the promise of many potential applications [15]. Inorganic semiconductors have also been extensively studied for photoconductive characteristics. Amorphous selenium and arsenic triselenide [16], as well as hydrogenated amorphous silicon [17], are all currently used in electrophotographic photoreceptors. Discussion of these materials is beyond the scope of this review and we will concentrate on charge generation mechanisms relevant to organic photoreceptors. Many reviews of organic photoreceptors are available [3f,l,o,q, 18]. In organic photoreceptors the bulk of the material making up the photoconductive element is polymeric binder. The active materials are categorized according to their major function in the photoreceptor device, as charge generation or charge transport. Several classes of charge generation materials have seen use in xerography: charge transfer complexes, molecular aggregates, and organic pigments. Transport materials are generally molecular species of low oxidation potential or reduction potential, depending on whether hole or electron transport will be the dominant mode. Transport materials may be homogeneously dissolved, "molecularly doped" in an inert polymeric matrix, or chemically bonded into a polymer. Transport materials and charge transport in xerographic photoreceptors will be discussed separately. In an organic photoreceptor the chemical materials with charge generation and transport functions may be co-dispersed/dissolved in a single layer or separated into charge generation and charge transport layers. Studies of such elements are difficult because of their heterogeneous nature, and interfacial physical and chemical effects, such as mixing and charge transfer, can make unambiguous experimentation difficult to achieve. This section will be divided into discussions of experimental techniques for probing charge generation, current models of charge generation, and application of experimental techniques and models to an understanding of charge generation in organic photoreceptors for xerographic applications. The latter will be discussed largely according to the type of charge generation material.

The quantity of fundamental interest for the characterization and study of electrophotographic photoreceptors is the quantum efficiency of carrier generation. This is the ratio of the number of carriers collected to the number of photons absorbed. The sensitivity of the quantum efficiency to excitation wavelength and to environmental conditions such as temperature, applied field, and photoreceptor composition has been investigated in the elucidation of charge generation mechanisms. In a typical heterogeneous and multilayer structure the overall quantum efficiency is determined by the quantum yield for carrier generation and the efficiencies of charge separation and subsequent transport. In practice these quantities are difficult to separate. Experimental techniques include measurements of transient photocurrent, photoinduced discharge, fluorescence quenching, photoacoustics, and thermally stimulated current.

The transient photocurrent method requires that the dielectric relaxation time be

longer than the carrier transit time. The sample is sandwiched between two electrodes, a field is applied, and the sample is exposed to a short light pulse. Carriers are generated and some fraction is free to drift under the influence of the field to the appropriate electrode. Either the magnitude or time integral of the current may be used to estimate the generation efficiency. There are several limitations with this method. It requires the deposition of an electrode onto an electrophotographic photoreceptor that may influence the dark and/or photoelectric characteristics, and deep trapping may occur at low fields. A technique utilizing delayed-field collection has been developed for application to low-field measurements. In this technique the exposure is carried out at low field and after a short delay (typically a few milliseconds) a high collection field is applied. Since charge transport occurs at high field, low-field transport limitations are avoided. Difficulties with this technique are the possibility that carriers generated at low field may undergo diffusion and/or recombination, which might change the probability of charge separation when the high field is applied [19].

The most common method for determining quantum efficiencies is with a photoinduced xerographic discharge. In this method the photoreceptor is charged with a corona and the sample is photodischarged with a low-intensity exposure. If the charge produced is small with respect to the surface charge the discharge is "emission-limited" and space charge effects are minimized. In practice either the initial photodischarge rate or the voltage decrease produced with a small exposure is determined. Both measurements can be related to generation efficiency by calculating the change in surface charge density (σ) assuming a parallel-plate capacitor geometry with $\sigma = CV$, where V is the measured surface potential and C is the geometrical capacitance per unit area. For organic materials a dielectric constant of 3 is commonly assumed. Quantum efficiencies determined with this technique are influenced by contributions from recombination and carrier transport limitations. With this measurement one must be careful to avoid chemical changes in the photoreceptor caused by exposure to the corona. Because of the difficulty of accurately determining optical densities in thin multilayer film structures, the "xerographic gain" (G_x), defined as charge pairs produced per incident photon, is often determined. Since xerographic discharge involves both charge transport and generation, these measurements are influenced by transport limitations of one or both carriers. Photoreceptors with xerographic gain action spectra which mirror their absorption spectra are described as "sympatric", and those where they are opposed are "antipatric". The latter behavior is generally an indication of charge trapping, surface, or interfacial effects.

Field-enhanced fluorescence quenching has emerged as a valuable tool in the study of carrier generation. An electrode is applied to the free surface of the photoreceptor and the fluorescence emission from the charge generation material is monitored as a function of the applied field. It is assumed that carrier generation is the only field-dependent photophysical process, so field-induced fluorescence quenching can be directly related to carrier generation. This technique is unaffected by transport limitations but depends on the assumption of a simple partitioning mechanism where carrier generation is the only process influenced by the applied field.

Photoacoustics have been used in a few instances to determine carrier generation efficiencies [20]. In this technique one determines the heat produced in a photoreceptor sample upon exposure. The energy provided by photon absorption is partitioned between processes that give off heat, such as radiationless decay and geminate charge recombination; and those which do not, such as radiative decay, charge generation, and photochemistry. The photoacoustic signal is determined as a function of field applied to the sample. To simplify the analysis, the sample is chosen such that radiative decay and photochemistry may be neglected and the excitation wavelength is positioned near the low-energy absorption edge. Thus, assuming that heat production and charge generation are competing processes, the generation efficiency is determined from the change in the photoacoustic signal as a function of applied field. An advantage of this method is that it is unaffected by charge transport limitations. Disadvantages are experimental complexity and the necessity to assume a simple energy-partitioning mechanism.

Thermally stimulated currents have been used in a few cases to study carrier generation mechanisms in organic photoreceptors [21]. In this method the sample, with a field applied, is cooled to a low temperature and irradiated. The sample is then slowly warmed and the current measured as a function of temperature. Since geminate pair recombination is retarded at low temperatures, the charges are released only upon warming. By this technique charge generation, recombination, and separation can be studied as a function of applied field and temperature. Experimental complexity is the main disadvantage of this method and the results obtained do not directly address room-temperature phenomena.

2.5.2 Models

Photoinduced charge transfer has been the subject of intense research and summaries can be found in texts [18b, 22] and many reviews. Electron transfer in polymer matrices has been reviewed [22b].

The mechanism(s) of charge generation in organic photoreceptors utilized in electrophotographic applications are complex because most photoreceptors comprise a combination of a pigment (or molecular complex) and a host—a polymer medium doped with an electron donor or acceptor—in one or more often two thin layers. The physics of such devices has been extensively studied but only recently has the chemistry been similarly scrutinized. For example, only recently has it been discovered that the chemical structure of the light-absorbing pigment in some photoreceptors that have been studied for decades was not as had been supposed. This will be discussed later. Also, the importance of the chemical makeup of the polymeric binder is still largely unknown. These are complex systems of immense commercial importance and the details of how they function have been the subject of many penetrating investigations. Recent reviews of charge generation in organic photoreceptors are available [3q, 18d,e].

In organic photoreceptors photoinduced charge generation occurs through an excited state to produce a geminate electron–hole pair bound by their coulombic attraction. These separate into free carriers by a combination of diffusion and drift

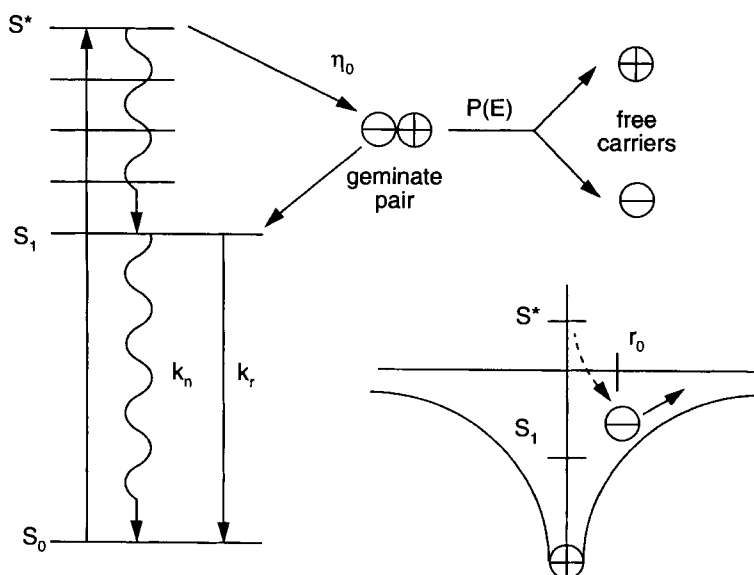


Figure 3. The Onsager model with an insert showing an electron in the coulomb well of a hole. (Reprinted with permission from Ref. [18d].)

in the applied electric field. Free carrier generation is described as “intrinsic” when it involves only one molecular species. When charge generation involves interactions of the excited state with a donor or acceptor it is described as “extrinsic” or “sensitized”. The dependence of the carrier generation efficiency in organic photo-receptors on field, temperature, and excitation wavelength has been described within the framework of models that will be described below.

An extensively used model is based on a 1938 theory from Onsager describing geminate ion pair recombination (Figure 3) [23a]. In this model it is assumed that a hot excited state (S^*) partitions between geminate pair formation and radiationless decay to S_0 . Onsager’s 1938 theory derives from the solution of the diffusion equation for a charge pair under the influence of both their coulombic attraction and an applied field. The model has two parameters, the quantum yield for geminate pair formation, η_0 , and the initial separation distance of the charges, r_0 . The only electric-field-dependent process is assumed to be separation of the geminate pair. In much of the early work a spherically symmetric δ -function was assumed for the distribution of geminate pair separations. Thus the generation efficiency is determined by the probability for geminate pair formation and the subsequent branching ratio of the geminate pair in the field-dependent formation of free carriers versus recombination. With this form of the model it is predicted that at very low fields the generation efficiency becomes a linear function of the applied electric field where the dependence (slope/intercept ratio) is determined solely by the dielectric constant and temperature. Agreement with this prediction is considered to validate the use of the model. Applying this model to systems with charge transfer excited states

resulted in unreasonable initial separation distances of 2–3 nm. The 1938 Onsager theory assumes a boundary condition of total geminate recombination at zero charge pair separation, and Braun has proposed that this assumption is inconsistent with a metastable charge transfer state [23b]. He proposed a more appropriate model based on a 1934 Onsager theory describing the effect of an applied electric field on ion pair dissociation in a weak electrolyte. Recently, Smirnov and Braun proposed the use of a nonspherical distribution for the initial ion pair distribution in charge generation from charge transfer or exciplex states [23c]. This modification of the Onsager model provided intuitively reasonable initial ion pair separation distances. The Onsager-based models predict a photoconductivity threshold at higher energies than the absorption threshold, and wavelength-dependent quantum yields for carrier generation. Fluorescence from S_1 will be field-dependent to the extent that geminate pair recombination to S_1 occurs in competition with field-dependent carrier separation. Applications of this model to charge generation in amorphous materials have been reviewed [23d]. Noolandi has reviewed theories relating to the time dependence of geminate recombination with respect to the Onsager models [23e]. Ries and Bässler have applied Monte Carlo techniques to the study of geminate recombination [19b]. From the simulations it was concluded that recombination within an amorphous solid with a Gaussian energy disorder could be explained by carrier diffusion into trapping sites which are a consequence of the disorder plus traps of unknown origin. For the latter, incipient dimers were suggested.

In many organic photoreceptor systems the absorption and photoconductivity thresholds coincide and the quantum efficiency of free carrier generation is independent of excitation wavelength. The internal conversion model has been proposed for these systems. This model is a special case of a more general theory of geminate recombination from Noolandi and Hong [24]. In this model internal conversion results in S_1 , which produces a geminate charge pair in competition with fluorescence and radiationless decay (Figure 4). This model predicts coincidence of the photoconductivity and absorption thresholds, wavelength-independent quantum yield for carrier generation, and fluorescence quenching with increasing applied electric field.

Sensitized carrier generation occurs when the thermalized excited state (S_1) undergoes electron transfer with an electron donor or acceptor followed by diffusion and field-assisted drift of the free carriers (Figure 5). This mechanism was proposed by Needler to explain the photoconductivity and fluorescence quenching observations in polymers containing dissolved dyes and arylamine donors [25a]. In most organic photoreceptors the excitation occurs within a pigment particle and the singlet exciton diffuses to the surface, where it may undergo electron transfer with either a donor or acceptor which is also typically the charge transport molecule used in the photoreceptor. Characteristics of this mechanism are fluorescence quenching and enhanced carrier generation efficiency in the presence of the small molecule donor or acceptor. The charge transfer mechanism of carrier generation has generally been analyzed in terms similar to solution-photoinduced charge transfer reactions. Key factors are thought to include the extent of charge transfer interaction, the free energy of the electron transfer, and the reorganization energy of the surrounding medium.

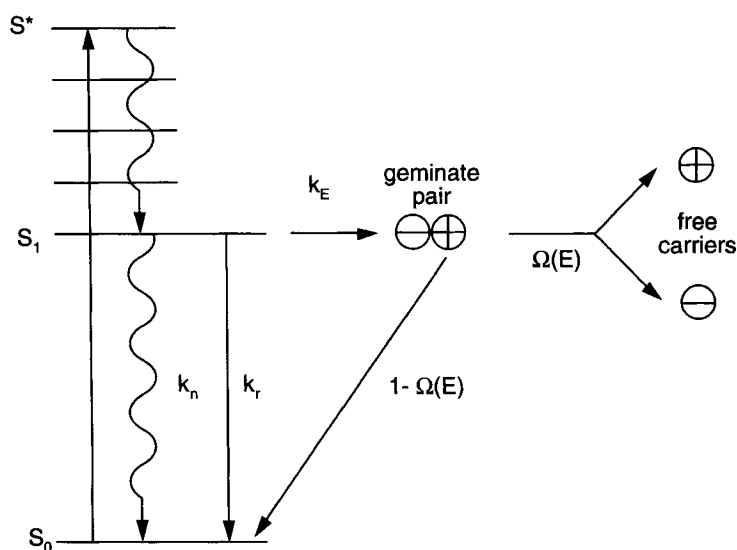


Figure 4. The internal conversion model. k_n , k_r and k_E are rate constants for radiationless relaxation, radiative relaxation, and geminate pair production, respectively. (Reprinted with permission from Ref. [18d].)

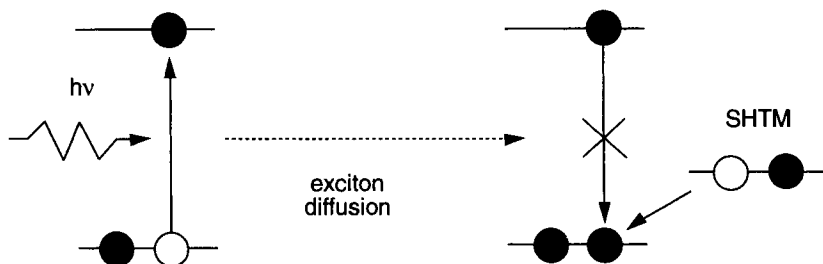


Figure 5. The sensitized photogeneration model with electron transfer from photoexcited dye to hole transport molecule. (Reprinted with permission from Ref. [18d].)

A triplet exciton annihilation mechanism has been proposed for charge generation in molecularly doped polymers initiated with very fast, high-intensity, excitation [25b,c]. In this mechanism it is proposed that both charge separation, associated with the Onsager model, and the fusion process are very strongly field-dependent. This model has not been invoked in recent years.

The above models describe the events giving rise to free carrier generation in a photoconductor. In the photodischarge of an electrophotographic photoreceptor there are other processes which may reduce the overall quantum efficiency of the photodischarge. One such process is deep trapping of either or both carriers due to impurities, at interfaces, etc. Thus, the determination of charge generation quantum

efficiencies in organic photoreceptors is complicated by carrier transport limitations. Much of the development of commercially viable photoreceptors for electrophotography has involved the technology for ensuring that such trapping does not occur. Xerographic discharge is exquisitely sensitive to the effects of carrier trapping with the telltale signature of an increasing residual potential (incomplete photo-discharge) with cycling. Photoreceptors for high-volume copiers and printers have intended lifetimes of $>10^6$ imaging cycles.

Another charge-depleting process is the recombination of free carriers as they drift in opposite directions through the bulk of the photoreceptor layer(s). Diffusion-controlled bimolecular recombination depends upon the carrier concentrations and has been described by a theory due to Langevin [26a]. The effects of bimolecular (Langevin) recombination on photocurrent and photoinduced discharge have been modeled by Chen [26b], Kerr and Rokos [26c], and Young [26d]. If the observed photodischarge depends on the total exposure and not the exposure duration, the photoreceptor is said to exhibit reciprocity. High-intensity reciprocity failure describes the situation where the photodischarge efficiency is decreased with high-intensity, short-duration exposures due to bimolecular recombination. Such a situation has been described in a single-layer photoreceptor based on a dye-polymer aggregate charge generation material (discussed in more detail later) [26e]. Figure 6 shows the effects of exposure intensity (6 ns laser pulse) in the photodischarge of this photoreceptor with strongly absorbed light with electron-transport-dominated discharge. The emission-limited discharge data were obtained using sequential low-intensity, 6 ns, laser flashes. The high-intensity exposure data were obtained with individual charge-expose photodischarges with different intensities. Similar results

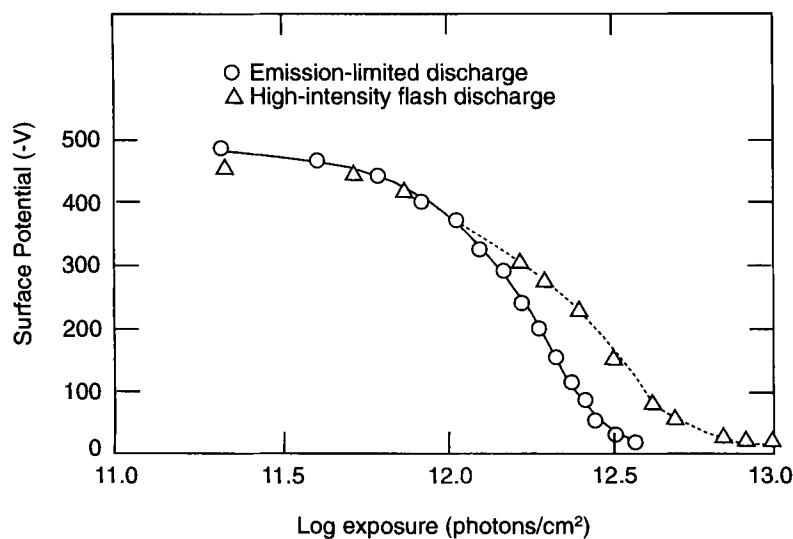


Figure 6. Surface potential vs. exposure characteristics for a single-layer photoreceptor with a dye-polymer aggregate CGM. The exposure (680 nm) is strongly absorbed and the initial surface potential is -500 V. (Reprinted with permission from Ref. [26d].)

were obtained for hole-dominated photodischarge. These results were explained by a combination of Langevin recombination and carrier trapping. Buettner and Mey both predict and demonstrate that high-intensity reciprocity failure does not occur in photoreceptors with a linear field dependence for carrier generation [26f].

2.5.3 Organic Photoreceptors

In an electrophotographic process the sensitivity of the charged photoreceptor to the exposing light is of paramount importance. The exposure must produce a surface potential discharge sufficient for the success of the subsequent development process. As has been discussed, this sensitivity is related to the carrier generation efficiency of the photoreceptor. Although high photosensitivity is generally desired it is more important that the photosensitivity be mated to the exposing light source wavelength and intensity, and that the desired photodischarge characteristics are maintained over thousands or even hundreds of thousands of imaging cycles. Thus, although high-field carrier generation efficiencies of >0.8 are readily achieved using today's technology, this alone does not ensure commercial viability. It is in this mating of materials with technology that successful photoreceptors have been realized.

The simplest possible embodiment of an electrophotographic photoreceptor would be a single layer of a polymer molecularly doped with a charge transport material or a polymer with a transport-active pendant group. In the absence of a specific charge generation material such a device would generally only be sensitive to ultraviolet exposure and would have no practical utility. Nevertheless, many fundamental studies were carried out on such devices and the results obtained are of interest, especially in terms of the changes in mechanism observed with the addition of a charge generation material.

Poly(*N*-vinylcarbazole) and molecularly doped polymers

Poly(*N*-vinylcarbazole) (PVK) is the prototypical photoreceptor hole transport material. It was among the first to be investigated and it still finds application in organic photoreceptors. Many reviews of charge generation in PVK are available [3o,q, 18a, 27a–e]. In 1965 Hoegl reported photoinduced discharge of PVK films [28a]. The xerographic gain was found by Regensburger to closely follow the absorption spectrum (Figure 7) [28b]. The sample comprised a 7.6 μm PVK layer solvent-coated on an aluminum substrate. The illuminated surface was corona-charged positively to 630 V. Also shown on this plot is the fluorescence emission spectrum obtained with 253.7 nm excitation. The two emission bands are believed to be due to two excimers differing slightly in the extent of face-to-face carbazole overlap. As we will see later, these excimers figure prominently in the charge generation mechanism of PVK. The field and wavelength dependencies of the photogeneration efficiency were determined by Borsenberger and Ateya (Figure 8) using the photoinduced discharge method [28c]. In these experiments the PVK was solvent-coated onto a nickelized poly(ethylene terephthalate) (PET) substrate. The

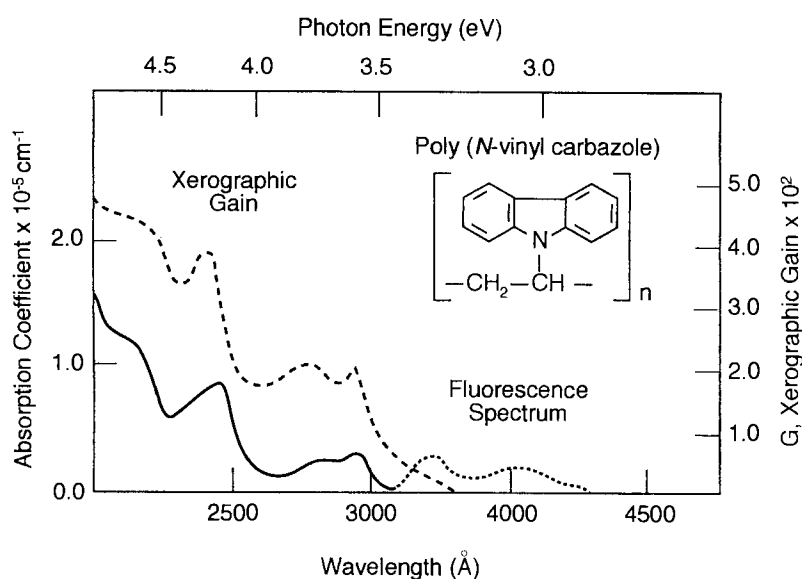


Figure 7. Absorption and fluorescence spectra, and the xerographic gain of poly(*N*-vinylcarbazole). The initial surface potential was 630 V. (Reprinted with permission from Ref. [28b].)

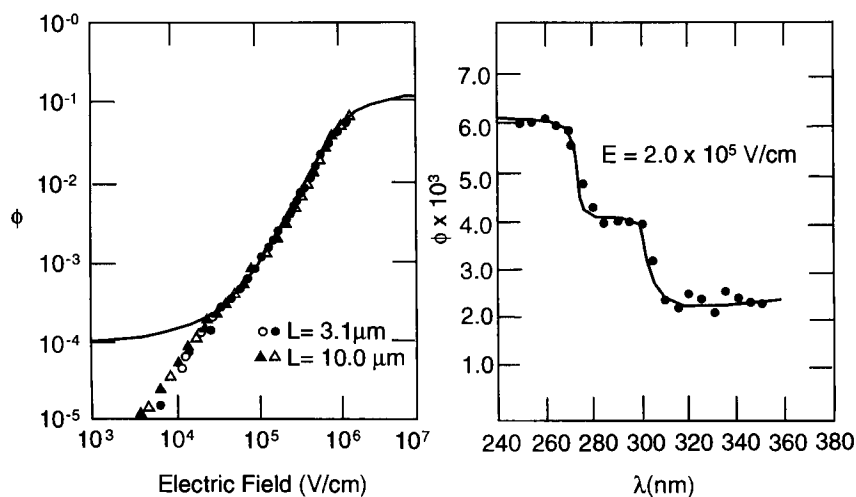


Figure 8. Wavelength dependence of the photogeneration efficiency in poly(*N*-vinylcarbazole). (Reprinted with permission from Ref. [28c].)

exposure was incident on the positively charged surface. Exposure of a negatively charged surface produced no photodischarge, showing that holes are the only mobile species produced in PVK. The quantum efficiency was independent of film thickness and of which surface was irradiated. The field dependence data (345 nm excitation, 23 °C) were fitted to the 1938 Onsager model with $r_0 = 2.6$ nm and $\eta_0 = 0.11$. With increasing temperature r_0 remained constant but η_0 increased to 0.15 at 51 °C. There is substantial deviation of the experimental data from the theory at low applied fields. The authors attribute this to surface recombination or trapping. The observed wavelength dependence is similar to that of Regensburger (Figure 7). In this case the quantum efficiency increased in steps with decreasing wavelength. The transition wavelengths were identified with transitions to higher excited states of PVK. From the field dependencies in each region it was determined that η_0 remained constant but the thermalization distances, r_0 , increased with decreasing wavelength from 2.6 to 2.8 to 3.0 nm. These results were interpreted in terms of ionization occurring from three distinct, vibrationally relaxed, excited states.

More recently Cimrová and Nešpůrek carried out similar investigations of the field dependence of charge generation in PVK films produced by solvent coating on a nickel substrate [28d]. For excitation into the first and third excited states they determined r_0 values of 2.6 and 2.9 nm and η_0 values of 0.17 and 0.14, in reasonable agreement with the Borsenberger and Ateya results. However, the 1938 Onsager model was inadequate at very high electric fields, the temperature dependence of the photogeneration efficiency could not be explained, and the r_0 suggested an unreasonably high charge transfer state energy. Based on their experiments they proposed a new model that was refined in subsequent publications (Figure 9) [28e,f]. The

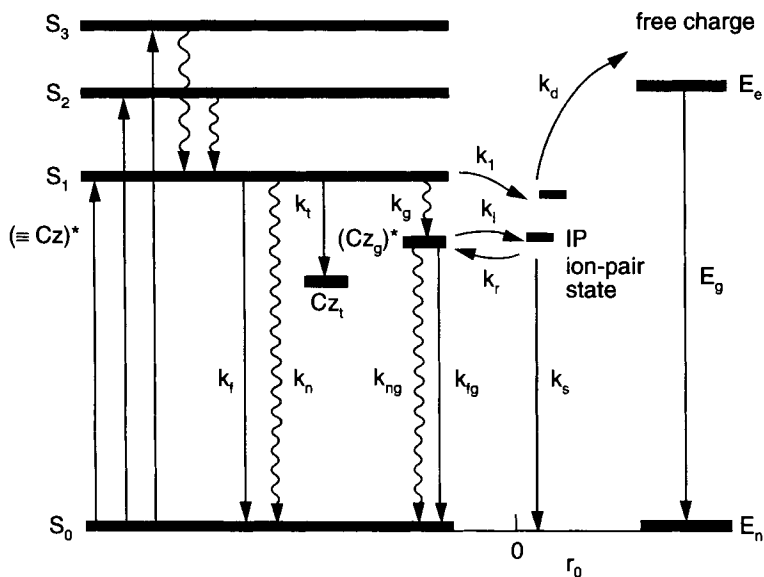


Figure 9. Schematic of the photophysics and photogeneration mechanism in poly(*N*-vinylcarbazole). (Reprinted with permission from Ref. [28f].)

charge generation mechanism in PVK was studied by emission-limited photo-discharge [28d]. The field and temperature dependencies of the generation efficiency could not be satisfactorily fitted with any of the Onsager models, irrespective of the form chosen to describe the distribution of geminate pair separations. The proposed model incorporated the two excimer states of PVK. In this model the excited carbazole moiety (Cz) in PVK undergoes rapid radiationless conversion to S_1 . S_1 partitions among radiative or nonradiative relaxation to the ground state (k_f and k_n), trapping at either of two excimer sites Cz_g and Cz_t (k_g and k_t), or formation of an electron-hole pair (k_i). Only the higher-energy Cz_g excimer trapping center is presumed to be active for charge carrier generation (k_i). The electron-hole pairs can recombine (k_r) or undergo field-assisted diffusion (k_d) with formation of free carriers.

Since excimer emission predominates in PVK it was assumed that ion pair formation from Cz directly (k_i) could be neglected. Using this kinetic scheme, and the Onsager theory to express k_d , the best data fit was obtained with a Gaussian distribution to describe the geminate pair separation distances. For absorption into S_1 (355 nm) the quantum efficiency for generation was 0.87 and the Gaussian distribution parameter was 0.6 nm. Absorption into S_3 (254 nm) gave a lower efficiency, 0.44, and a larger separation, 0.8 nm. These differences were explained in terms of the penetration depths for the two wavelengths. With 254 nm excitation the light is absorbed near the surface, where with ESCA (electron spectroscopy for chemical analysis) it was determined that the oxygen concentration was approximately double its concentration in the bulk. Oxygen quenching of the excited state was proposed to account for the decreased generation efficiency with 254 nm excitation. Thus, in this model, charge pair formation occurs at excimer sites. The hole (radical cation) is localized at the excimer site and the counterion (electron) at an adjacent carbazole or an acceptor (such as oxygen). Such stabilization could account for the very long lifetimes observed with delayed-field collection [28g].

Many molecularly doped polymers have been studied for photogeneration. Most are single-layer photoreceptors comprising a dopant dissolved in a polymeric binder. The dopant is typically a molecule that will transport holes or electrons. As an example Borsenberger, Contois, and Hoesterey reported on triphenylamine (TPA) dissolved in bisphenol-A polycarbonate (PC) [28h]. The generation quantum efficiency and ion pair separation were determined from the field dependence of generation analyzed according to the Onsager theory of geminate recombination. At a TPA concentration of 45 wt.% the system was described with an η_0 of 0.03 and an r_0 of 2.7 nm. This system was also examined in different polymer binders with 40 wt.% TTA. The field dependence of carrier generation was unchanged but the carrier generation efficiency (η_0) was strongly dependent on the polymer going from 0.027 in PC, to 0.009 in polystyrene, to 0.001 in poly(vinyl butyral) [28i]. Other than this, there have been very few studies of the effects of the polymer binder on carrier generation in molecularly doped polymer systems.

Donor-acceptor charge transfer complexes

It was recognized early in the study of PVK that doping with donors or acceptors dramatically increased the photoconductivity through donor-acceptor charge

transfer complexes [28a, 29a]. The dopant that has received the most attention, and eventually led to the first commercial organic photoreceptor, is 2,4,7-trinitro-9-fluorenone (TNF). Meltz evaluated the field dependence of the quantum efficiency with 550 nm excitation using the 1938 Onsager model and determined an η_0 of ~ 0.23 and r_0 of 2.5 nm for films with a TNF/PVK molar ratio of 0.06 [29b]. At a molar ratio of 1.0, η_0 was unchanged but the ion pair separation distance, r_0 , was increased to 3.5 nm. Hughes determined that bulk carrier recombination in PVK-TNF films was in agreement with the Langevin model for bimolecular recombination [29c,d]. Pfister and Williams studied sensitization by trichloroacetic acid [29e]. A great deal of mechanistic work has been carried out by Yokoyama and Mikawa and co-workers using a variety of electron acceptors [29f,g]. In the PVK/dimethyl terephthalate system, field-induced quenching of exciplex fluorescence was interpreted in terms of a charge generation mechanism involving field-assisted thermal dissociation from a “nonrelaxed” higher excited exciplex state to produce an ion pair with 2.2 nm separation [29h–j]. The ion pair separation increased with increasing electron affinity of the acceptor dopant. Similar fluorescence quenching results were obtained with PVK doped with the electron acceptor 1,2,4,5-tetracyanobenzene and a similar charge generation mechanism was proposed [29k–m]. With these results the authors proposed a general mechanism for extrinsic carrier generation in a donor–acceptor system which involves both exciplex and charge transfer complex states (Figure 10) [29m,n]. The unique mechanistic feature in this scheme is ion pair generation from an excited exciplex state and not from the relaxed exciplex, which fluoresces. The energy diagram for this process is shown in Figure 11. The authors

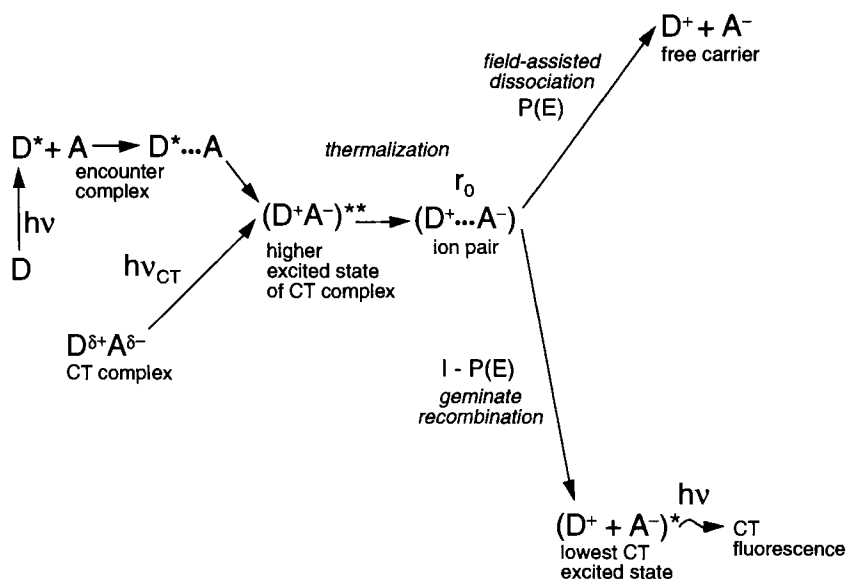


Figure 10. Schematic of a general mechanism for extrinsic carrier generation in a donor–acceptor charge transfer system. (Reprinted with permission from Ref. [29n].)

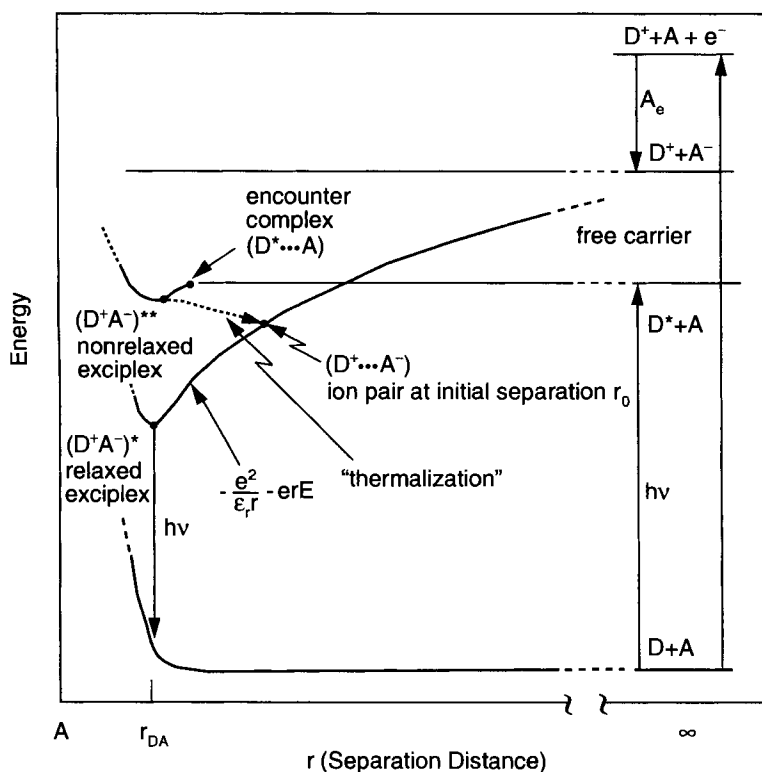


Figure 11. Schematic energy diagram for extrinsic carrier generation in a donor–acceptor charge transfer system. (Reprinted with permission from Ref. [29n].)

argue that in the relaxed exciplex, with an ion pair separation of $\sim 0.3\text{--}0.4$ nm, field-assisted thermal dissociation would be energetically unlikely. Furthermore, the measured ion pair separation of ~ 3 nm is consistent with a more loosely bound excited exciplex precursor.

In 1969 IBM commercialized a xerographic photoreceptor using the charge transfer complex formed between poly(*N*-vinylcarbazole) and 2,4,7-trinitrofluorenone (PVK–TNF). This was the first commercialization of an organic photoreceptor for electrophotography. The photoconductor is composed a single layer of a 1:1 molar ratio of PVK–TNF coated from tetrahydrofuran solution onto a metallized flexible support at a thickness of ~ 20 μm [30a]. As a photoreceptor, PVK–TNF has low dark conductivity and adequate photosensitivity to visible light due to the absorption of the charge transfer complex (maximum ~ 500 nm). A unique characteristic of this material is that both holes (carbazole radical cations) and electrons (TNF radical anions) exhibit field-driven charge mobility. Thus, PVK–TNF photoreceptors can be corona-charged either positively (hole-dominated transport) or negatively (electron-dominated transport). Because of the bipolar nature of the

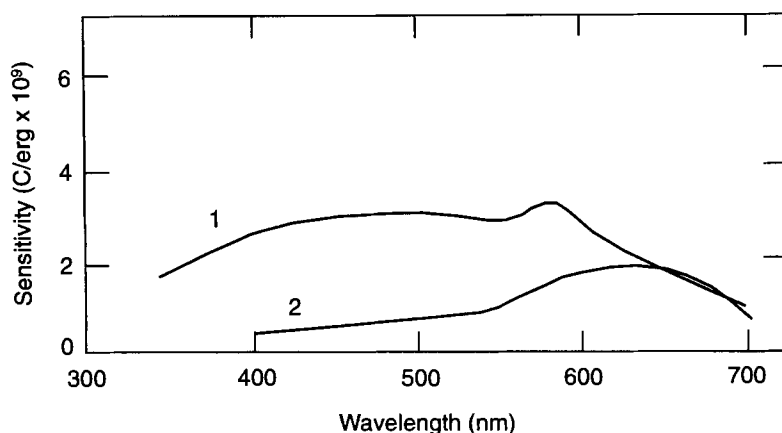


Figure 12. Spectral sensitivity of PVK–TNF (1:1) charge transfer complex. The sensitivity units (per unit area) are coulombs of surface charge dissipated per erg of incident light. The initial surface charge density is 3.5×10^{-8} C. Curve 1 is for negative surface charge (electron-dominated photo-discharge) and Curve 2 is for positive surface charge (hole-dominated photodischarge). (Reprinted with permission from Ref. [30a].)

PVK–TNF photoreceptor there is very little carrier trapping and it can undergo many thousands of charge/discharge cycles with little performance degradation. The spectral sensitivity with positive and negative surface charging is shown in Figure 12. In the IBM 3800 printing system the web-based photoconductor was wrapped around a drum with a supply roll and take-up roll inside. When the photoreceptor became unusable the web was advanced to place fresh photoreceptor around the drum. The photoreceptor was corona-charged to about -750 V and discharged to about -200 V with exposure ($\sim 5.5 \mu\text{J cm}^{-2}$) from a helium–neon laser (632.8 nm) [30b]. Because of potential toxicity questions with TNF this photoreceptor is no longer used.

Donor–acceptor charge transfer complex based photoreceptors continue to be described in the literature and studied using modern spectroscopic techniques but none has been commercialized. For example, the photoconducting charge transfer complex between poly(*N*-epoxypropylcarbazole) and TNF has been studied with transient absorption and time-resolved fluorescence. On the basis of Monte Carlo simulations, the results were interpreted in terms of a heterogeneity of charge transfer complexes with different radiative probabilities and a distribution of initial charge pair separation distances [30c].

Aggregate materials

Developed in 1971 at the Eastman Kodak Company, aggregate photoconductors comprise an aggregate phase of dye–polymer dispersed in an amorphous polymeric matrix [31a]. With the addition of a donor molecule to enhance the photosensitivity and improve the hole mobility, this material was commercialized in both single- and

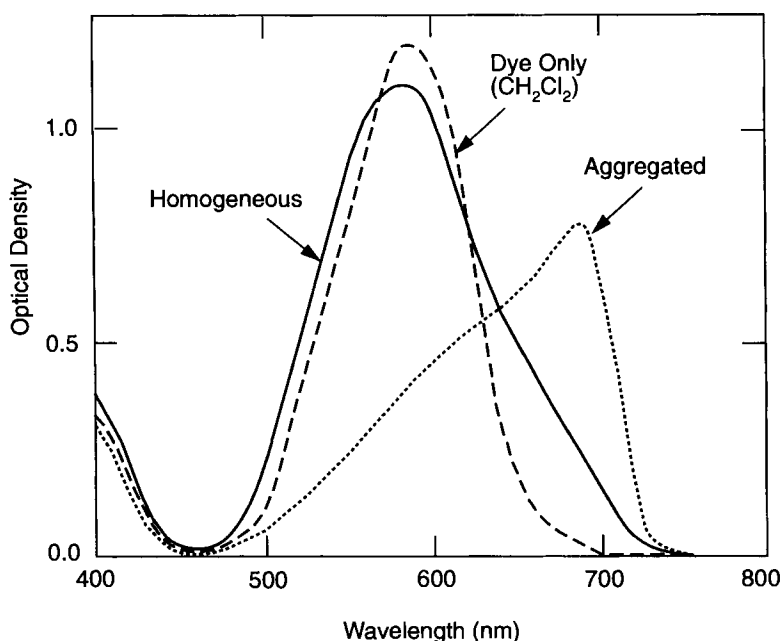


Figure 13. Absorption spectra of the dye-polymer aggregate CGM. Also shown are the solution spectra of the dye and the nonaggregated dye-polymer film (homogeneous). (Reprinted with permission from Ref. [31b].)

later dual-layer (aggregate generation layer and molecularly doped polymer hole transport layer) architectures. Two-layer aggregate-based photoreceptors are still successfully utilized in copiers and printers manufactured by Heidelberg Digital. The aggregate is a complex between a thiapyrylium dye (4-(4-dimethylaminophenyl)-2,6-diphenylthiapyrylium perchlorate or other suitable anion) (~ 10 wt.%) and bisphenol-A polycarbonate. It forms when a homogeneous film of dye dissolved in the polymer is exposed to dichloromethane vapors [31b]. In the homogeneous film the dye has an absorption maximum at 580 nm. Upon aggregation a dense filamentary fractal-like phase appears and the absorption maximum shifts to 680 nm (Figure 13). Doping with about 40 wt.% of an electron donor such as bis(2-methyl-4-diethylaminophenyl)phenylmethane results in a dramatic increase in the sensitivity as determined from xerographic discharge. Figure 14 shows the aggregate photosensitivity action spectra for the homogeneous film, and the aggregated film with and without donor. In the donor-sensitized aggregate photoreceptor, holes are mobile in the continuous phase and electrons are mobile in the aggregate phase. Electron-transport-dominated photodischarge exhibits a threshold due to high-field trapping in the dead ends of the aggregate filaments and subsequent release of the trapped electrons when the field strength drops [31c]. Figure 15 shows the spectral dependence of the xerographic gain for a single-layer aggregate photoreceptor with

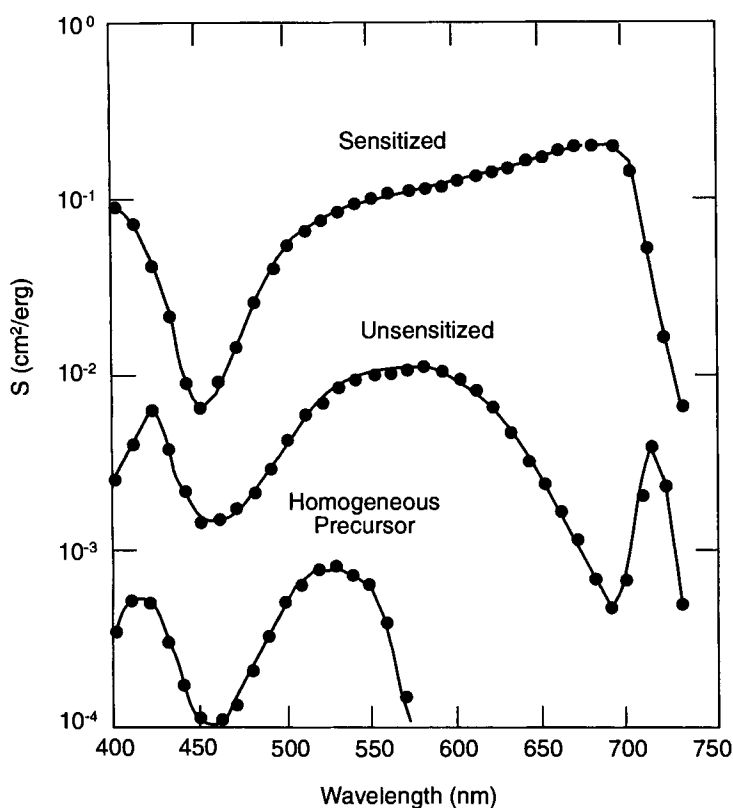


Figure 14. The spectral dependence of the xerographic sensitivity of the nonaggregated homogeneous dye-polymer film, the aggregated film, and the aggregated and sensitized film. The sensitivity is the reciprocal of the energy required for a photodischarge from 500 to 250 V. (Reprinted with permission from Ref. [31].)

positive charging (hole-dominated photodischarge) and negative charging (electron-dominated photodischarge). Analysis of the field dependence of photogeneration for hole-dominated photodischarge with the 1938 Onsager theory gave a primary quantum yield, η_0 , of 0.58 and a thermalization distance, r_0 , of 4.4 nm independent of the exposing wavelength [31d]. Charge generation was explained in terms of a surface-enhanced exciton dissociation mechanism. Thermalized excitons in the aggregate phase diffuse to the homogeneous phase, where exciton dissociation occurs by electron transfer with the donor dopant. Holes are then transported through the continuous phase. Hole photogeneration in dual-layer aggregate photoreceptors follows the same mechanism [31e]. In this case the aggregate charge generation layer containing tri-*p*-tolylamine (TTA) as the sensitizer was in contact with a polyester-based charge transport layer with 40 wt.% TTA as the hole transport material. Since only holes are transported through the transport layer, this photoreceptor was negatively charged in use. From measurements of the field dependence

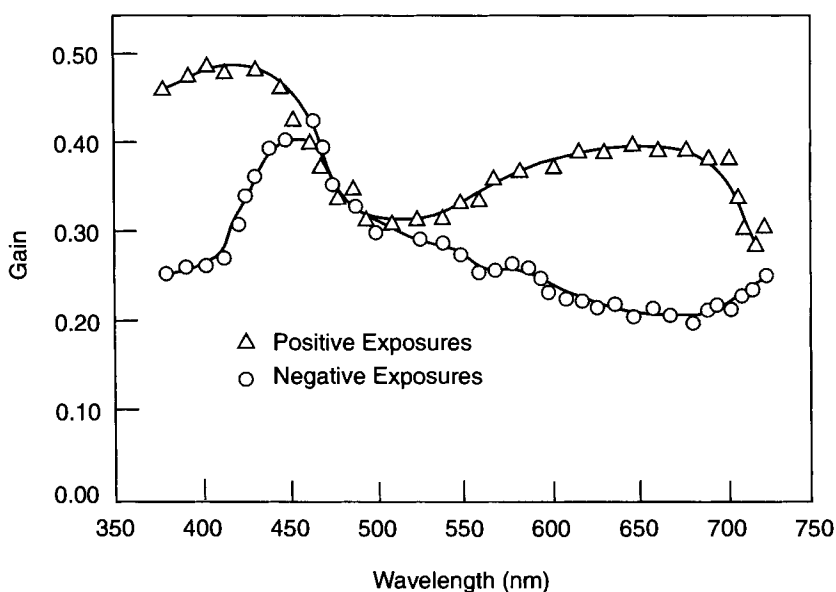
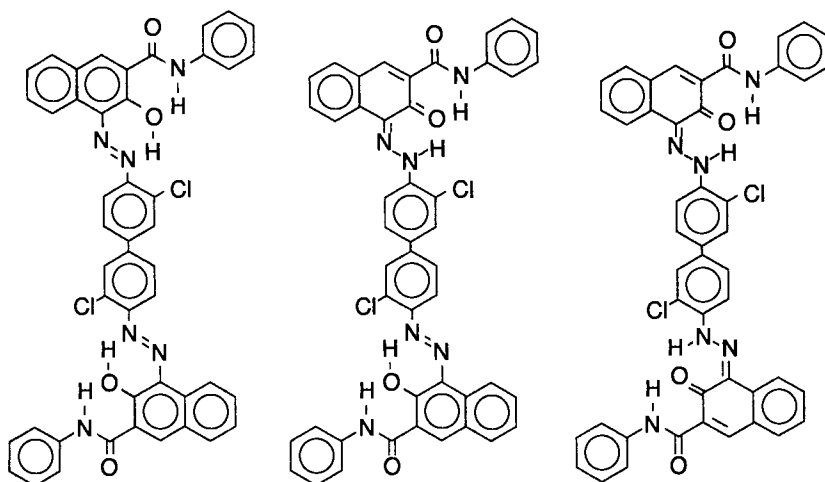


Figure 15. The spectral dependence of the xerographic gain for positive and negative surface potentials. (Reprinted with permission from Ref. [31c].)

of the photogeneration efficiency with 680 nm exposure, a quantum yield, η_0 , of 0.60 was determined. The thermalization distance, r_0 , depended on the concentration of TTA in the transport layer from 2.0 nm (5 wt.% TTA) to 6.0 nm (40 wt.% TTA). Detailed discussions of charge generation in the aggregate photoreceptor can be found in 1982 reviews by Perlstein [31f] and Perlstein and Borsenberger [31g].

Azo pigments

Azo pigments have been used in electrophotographic photoreceptors for many years. In 1984 McMurtry et al. reported that the IBM 3800 high-speed printer used a two-layer photoreceptor with the bisazo pigment chlorodiane blue (CDB), 3,3'-dichloro-4,4'-biphenylbis(1''-azo-2''-hydroxy-3''-naphthanilide) (Scheme 4), as the charge generation material in a 0.1 μm thick layer and *p*-diethylaminobenzaldehyde diphenylhydrazone (DEH) as the hole transport material in a 16 μm thick layer [32a]. Melz and co-workers (1977) studied the field dependence of the "injection" efficiency determined with the xerographic photodischarge technique [32b]. This is the same as the "xerographic gain" as defined above. The photoinjection efficiency changed by over two orders of magnitude as the CTL was varied from PVK through CTLs composed of an unnamed polymer doped at ~ 50 wt.% with pyrazoline CTMs. The efficiencies decreased with increasing oxidation potential of the CTM. They concluded that for efficient hole injection a CTM with a low ionization potential is required. Kakuta et al. examined photoreceptors with CDB CGLs and CTL comprising polycarbonate or polyester doped at 33 wt.% with a wide variety



Scheme 4. Molecular structures of bisazo pigments demonstrating the three tautomeric forms. (Reprinted with permission from Ref. [33d].)

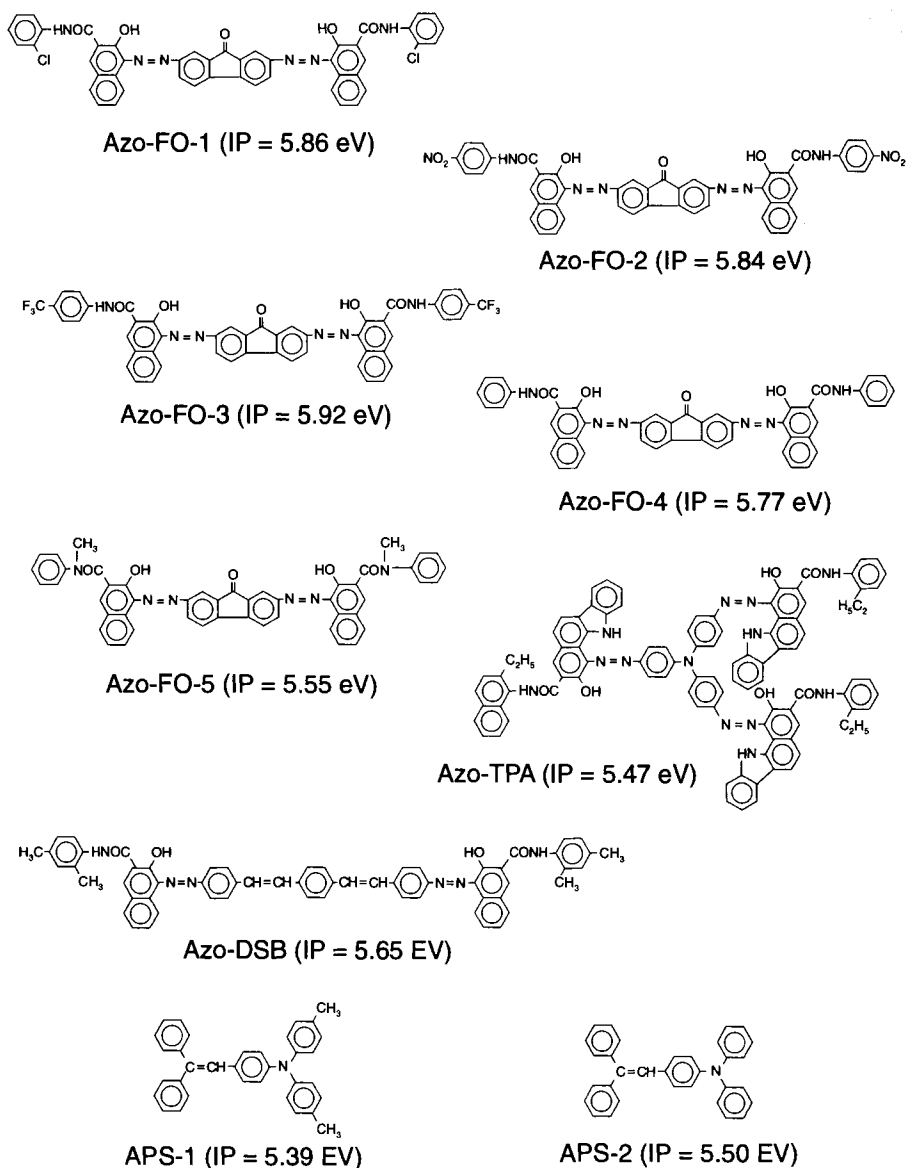
of hole transport materials [32c]. They found that the energy for half-discharge of the photoreceptor exhibited a linear correlation with the CTM ionization potential. The material with the lowest ionization potential, 2-(*p*-dipropylaminophenyl)-4-(*p*-dimethylaminophenyl)-5-(*o*-chlorophenyl)-1,3-oxazole, had the highest xerographic gain of over 0.2 at the peak sensitivity of 650 nm. Khe and co-workers (1984) prepared and examined a single-layer photoreceptor for positive charging applications [32d]. It was composed of a bisazo pigment, similar to CDB, and a hydrazone hole transport material, in a polyester binder. Charge generation was proposed to occur at the pigment CTM interface. The photoreceptor could be discharged with either hole- or electron-dominated transport (positive or negative surface charge respectively) but the former was more efficient. The xerographic gain reached a maximum of 0.7 at 660 nm and a field of 10^6 V cm^{-1} . Thus the carrier generation efficiency under these conditions is ≥ 0.7 , depending on the various charge loss mechanisms previously discussed.

Perinone bisazo pigments have been studied as generation materials by Murayama and co-workers at Mitsubishi Kasei Corporation for use in dual-layer photoreceptors with CTLs based on hydrazone transport material [33a,b]. The photoreceptors had high sensitivity throughout the visible region and exhibited significantly higher injection efficiencies than a comparable CDB-based photoreceptor. From solid-state ^{13}C -NMR data on bisazo pigment based generation layers, Ono et al. concluded that some pigments were in the hydroxy-azo and some in the keto-hydrazone tautomeric forms [33c]. Their results indicated that hydroxy-azo-based pigments were preferred for increased stability to visible light exposure. Pacansky and Waltman (1992) studied CDB and concluded that the keto-hydrazone tautomer gave greater xerographic gain [33d]. Scheme 4 shows the three tautomeric forms of CDB. From absorption spectra they concluded that CDB is in the azo form in the as-coated

CGL but exposure to tetrahydrofuran, as would happen when it is overcoated with the CTL solution, results in significant conversion to the red-shifted absorption of the hydrazone tautomer. Based on published absorption spectra of CDB-based photoreceptors they propose that the keto-hydrazone tautomer gives the highest xerographic gain. Using a variety of spectroscopic techniques Law et al. proposed that bisazo pigments synthesized using 2-hydroxy-3-naphthanilide derivatives (Naphthol AS and related derivatives) exist as the keto-hydrazone tautomer in the solid state [33e]. They suggest that this is due to a combination of intra- and intermolecular hydrogen bonding. Thus, interpreting quantum efficiency data in photoreceptors with azo-pigment-based CGLs is problematic because the same pigment may actually comprise a different mixture of tautomers, depending on the details of photoreceptor preparation. A great deal of work has gone into the synthesis and examination of various bisazo pigments, in a wide variety of photoreceptor formulations, in the search for those with superior electrophotographic characteristics [33f-j].

Attempts have been made to find relationships between the $E_{0.5}$ xerographic sensitivity (energy for photodischarge to half the original surface potential) and the *p*-phenyl substituents in bisazo pigments prepared from 2-hydroxy-3-naphthanilide. Law and co-workers found that the sensitivity increased up to a point with electron-withdrawing substituents but that very electronegative substituents, such as trifluoromethyl and nitro, actually reduced the sensitivity [33k,l]. Based on X-ray powder diffraction they propose that this effect does not relate to any energetic considerations but is due to the crystallinity, or more specifically the surface area, of the pigment. Pigments with the lowest crystallinity and greatest surface area exhibit the highest sensitivity.

Extensive mechanistic studies have been reported by Umeda and co-workers at Ricoh Co., Ltd. Their work has involved studies of several bisazo and a trisazo pigment (Scheme 5). The latter has commercial interest because of its photosensitivity in the near-infrared. Much of this work has been summarized in recent reviews [34a-c]. Studies on a dual-layer photoreceptor with a fluorenone-based bisazo pigment CGL and a triarylamine CTM-based CTL were interpreted in terms of: 1) absorption in the bulk of the CGL with exciton diffusion to the CGL/CTL interface, 2) competition between exciton deactivation and electron transfer to produce a geminate pair at the interface, and 3) competition between geminate pair recombination and dissociation into free carriers [34d,e]. Figure 16 shows the proposed reaction mechanism. In one study the CGL comprised the pigment Azo-FO-1 dispersed in poly(vinyl butyral) in a 4:10 weight ratio with a thickness of 0.09–0.49 μm . The CTL comprised the CTM APS-1 and a polycarbonate in a 9:10 weight ratio with a thickness of $\sim 22 \mu\text{m}$. Single-layer photoreceptors were prepared which had the same composition as the dual-layer CGL, with thicknesses of 0.15 and 0.27 μm . Luminescence quenching in the dual-layer structure was determined on samples with 0.15 μm CGL and 1.9 μm CTL. Figure 17 is a plot of the xerographic discharge quantum efficiency and photoluminescence intensity as a function of field for the various photoreceptors with excitation at the pigment absorption maximum of 580 nm. The large increase in efficiency from the single- to the dual-layer structure, along with wavelength-independent quenching of pigment lumines-



Scheme 5. Molecular structures and ionization potentials of the bisazo pigments and hole transport materials used in [34b]. (Reprinted with permission from Ref. [34b].)

cence, argues for an extrinsic mechanism [34f]. Thus, the intrinsic mechanism is inefficient because of its large activation energy and geminate pair formation occurs via electron transfer from the CTM to the relaxed pigment exciton. From electro-absorption studies the pigment excited singlet state for Azo-FO-1 was identified as a

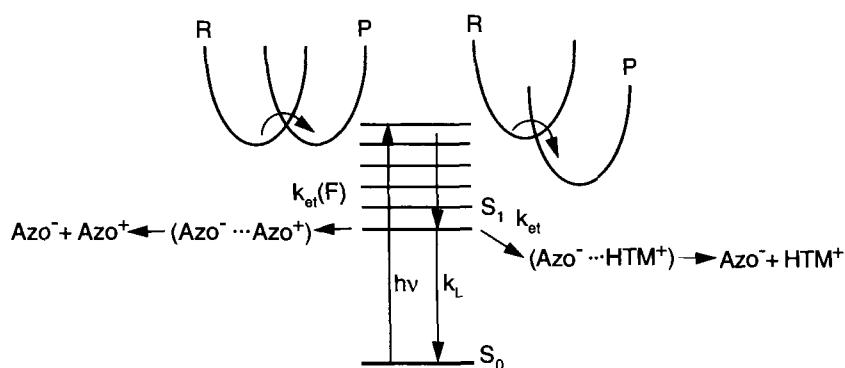


Figure 16. Schematic energy diagram for intrinsic photogeneration in an azo pigment and extrinsic photogeneration in the presence of a donor hole transport molecule. (Reprinted with permission from Ref. [34b].)

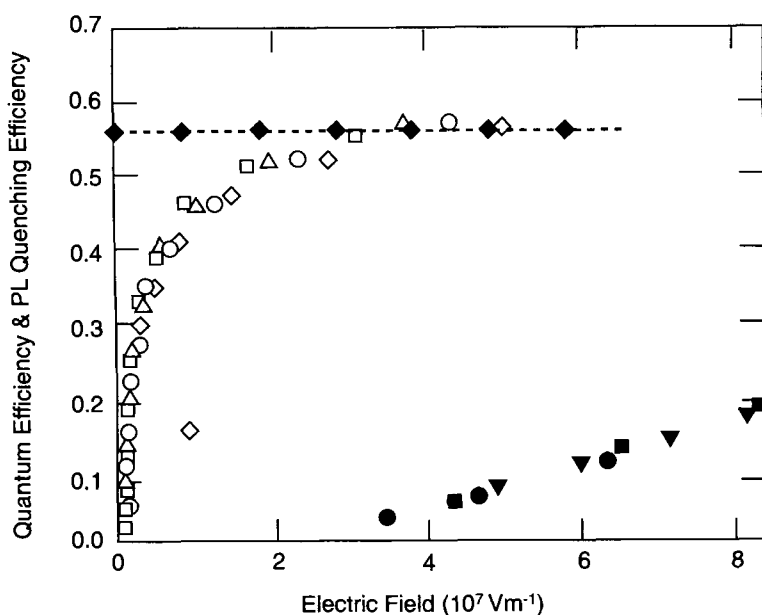


Figure 17. The electric field dependence of the photogeneration quantum efficiency (580 nm excitation) for photoreceptors with bisazo-based CGMs. Dual-layer photoreceptors (open symbols) with CGL (0.09–0.49 μm) and CTL (22 μm) had a negative surface charge. Single-layer photoreceptors (filled symbols) (0.15 and 0.27 μm) were given negative, and for the thicker sample positive, surface charging. The photoluminescence quenching efficiency (filled diamonds—broken line) was determined on a dual-layer sample CGL (0.15 μm) and CTL (1.9 μm). (Reprinted with permission from Ref. [34c].)

Frenkel exciton. Because the CTL materials penetrate into the CGL during the solvent coating operation, pigment particles are surrounded by CTM and the electron transfer efficiency is not limited by the exciton diffusion length [34f–h]. With the dual-layer photoreceptor, luminescence quenching is independent of field and the xerographic quantum efficiency approaches the luminescence quenching efficiency at high fields [34i]. This is interpreted as electric-field-assisted dissociation of the geminate pair such that at fields $> 3 \times 10^7 \text{ V m}^{-1}$ dissociation is 100 % efficient. At a field of $4 \times 10^7 \text{ V m}^{-1}$ the quantum efficiency is independent of excitation wavelength. Back electron transfer from the geminate pair to re-form the singlet exciton is neglected because of the large energy gap (0.47 eV). In the photoreceptor with a CGL thickness of 0.16 μm and a CTL thickness of 20.3 μm the rate of surface charge neutralization was found to be a linear function of light intensity, indicating that bimolecular recombination is negligible.

The effect of the energy gap on the xerographic quantum efficiency was determined using 26 photoreceptors formulated with three azo pigments and 26 CTMs (Figure 18) [34b,j]. The interfacial electron transfer rates were analyzed in terms of the Marcus theory [34k]. At the high field used in the experiment ($3 \times 10^7 \text{ V m}^{-1}$) the geminate pair dissociation efficiency is unity and is given by the xerographic efficiency. The electron transfer rate constant (k_{et}) was calculated from the xerographic efficiency using the measured photoluminescence lifetime (k_{L}) determined with a single-layer photoreceptor. The electron transfer rate increases with increasing energy gap but does not decrease at very large values as predicted by the Marcus theory. It is clear that the inverted region is not observed in this system. Excited-state polarizabilities of the azo pigments were obtained from electroabsorption studies. Pigment polarizability had no effect on the efficiency of electron transfer but there was an excellent correlation of polarizability with increased probability for geminate pair dissociation into free carriers.

Electroabsorption of Azo-TPA (Scheme 5) is interpreted in terms of a charge transfer exciton rather than a Frenkel exciton as formed by Azo-FO [34l]. From this and other studies it is suggested that carrier generation from charge transfer excitons is more efficient than from Frenkel excitons [34m].

Thermally stimulated currents (TSC) have been used to probe the carrier generation mechanism in a dual-layer photoreceptor with an azo-pigment-based CGL and hydrazone-based CTL. It appears that this technique may be a useful tool in understanding the carrier generation process in organic photoreceptors [21].

In a recent study, exciton diffusion and charge carrier generation were studied in a dual-layer photoreceptor with an azo pigment (4,4'-[(2,5-diphenyl-1,3,4-oxadiazole)-bisazo]bis(3-hydro-2*H*-benzimidazo[2,1-*a*]benz[*d,e*]isoquinolin-7-one))-based CGL and a triarylamine hole transport material (1,3,5-tris[4-(diphenylamino)phenyl]-benzene) in the CTL [34n]. The study utilized steady-state photoconductivity and time-of-flight experiments. The results were interpreted in terms of charge generation via diffusion of strongly bound excitons to the interface region, where the azo pigment and CTM intermix, and electron transfer occurs. This result underscores the importance of CGM/CTM intermixing during the coating process in azo-pigment-based systems where the pigment excited state is a Frenkel exciton.

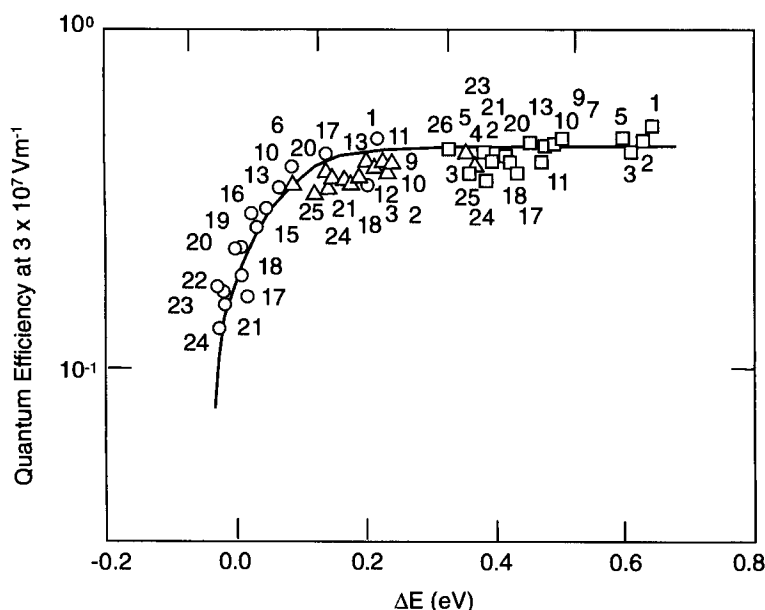


Figure 18. The energy gap dependence of the carrier generation quantum efficiency for combinations of bisazo pigments (symbols) and hole transport molecules (numbers). (Reprinted with permission from Ref. [34b].)

Phthalocyanine pigments

Discovered in 1927, phthalocyanine (Pc) pigments have been used as colorants in paints and inks for many years. Phthalocyanines have excellent thermal and photostability. The colorant characteristics depend not only on the molecular structure but also on physical factors such as crystal structure, crystal morphology, and particle size and shape. Because of their polymorphism and chemical intractability, their development for use in photoreceptors has taken considerable effort. Nevertheless, this class of pigment is utilized in most commercial copiers and printers that use near-infrared LED or laser exposure sources. Phthalocyanine may be metal-free (H_2Pc), or coordinated with a central metal atom. Metal phthalocyanines which have been studied as generation-layer pigments in photoreceptors include: $AlXPc$, $CoPc$, $CuPc$, $CrXPc$, $FePc$, $GaXPc$, $InXPc$, $MgPc$, $NiPc$, $SnPc$, $TiOPc$, $VOPc$, and $ZnPc$, where X is typically a halogen. Reviews of the xerographic characteristics of these photoreceptors are available [3l,o,q, 18d,e]. However, only metal-free H_2Pc , and more recently $TiOPc$, have been studied extensively with respect to the mechanism of carrier generation.

Phthalocyanines are extremely difficult to purify and characterize because most are only sparingly soluble in common solvents. The typical purification procedure, acid pasting, entails dissolving the pigment in concentrated sulfuric acid followed by precipitation into ice water. It has been found that both the synthetic route and the

purification method have an effect on purity [35a]. In fact, acid pasting may lead to an increase in trace metal impurities in the phthalocyanine. Transition metal impurities were found to introduce energetic states that would be expected to influence both the dark and photoelectrical characteristics [35b]. Train sublimation has been used for phthalocyanine purification. In this technique the material is placed in the hot end of a heated tube which is under vacuum. An inert carrier gas, such as argon or nitrogen, is passed through the tube and the sublimed material condenses in the colder sections of the tube [35c]. Phthalocyanines purified in this manner have altered characteristics when used as generation materials in organic photoreceptors [35d]. A great deal of effort has gone into characterizing the different polymorphs of a particular phthalocyanine and into methodologies for controlling and obtaining the desired polymorph in the charge generation layer of a photoreceptor. Pigment polymorphs have been characterized by electrochemistry, X-ray powder diffraction patterns, optical absorption, and infrared, fluorescence, and ^{13}C -NMR spectroscopy. The various polymorphs of a given phthalocyanine exhibit different photo-generation characteristics and in most cases there is a polymorph with enhanced absorption in the near-infrared which imparts superior characteristics to an electrophotographic photoreceptor. It should be noted that in some cases different groups have used different nomenclature for apparently the same pigment form.

Recently, the chemical structure of some of the polymorphs has come into question. Thus, ClAlPc has been found to form a dihydrate with identical absorption and X-ray powder diffraction characteristics to those that had previously been assigned to a near-infrared absorbing polymorph produced by ball milling [35e]. Also, the X-ray powder diffraction data and infrared spectral analysis of the X-form of H_2Pc have shown it to be the β -form in fact [35f]. In this same work it was suggested that α -MgPc is actually a mixture of O_2 and N_2 complexes. Thus, the chemical structures of the pigments that are formulated into the generation layers of organic photoreceptors are not fully understood. It is clear that the confusion around the chemical structure, polymorph, crystal type, etc., for phthalocyanines used in photoreceptors will be reflected in generation mechanism studies.

Metal-free phthalocyanine (H_2Pc) exists in the α , β , τ , and X polymorphic forms. The α , β , and X forms have been characterized by electrochemistry [36a], fluorescence spectroscopy [36b], and optical absorption [36c]; and α , β , and τ forms by ^{13}C -NMR spectroscopy [36d], optical absorption, and X-ray powder diffraction [36e]. Figure 19 shows the optical absorption spectra of the four forms. The τ form has been further characterized as to particle shape (Types I and II) [36f]. The as-synthesized β - H_2Pc is converted to α - H_2Pc by acid pasting and this can be converted to the X or τ forms with mechanical milling under specific conditions. The X and τ forms convert to the β with thermal, solvent, or extended mechanical treatment.

A dual-layer τ - H_2Pc -based photoreceptor used in Hitachi laser printers has been reported [36e.g]. For optimum photoreceptor performance the milling procedure used to convert α - to τ - H_2Pc had to be tuned to produce needle-like crystals with dimensions of $0.1\ \mu\text{m} \times 1.0\ \mu\text{m}$. The CGL and CTL thickness was 0.5 and 20 μm respectively. The peak sensitivity, $\sim 800\ \text{nm}$, was $5\ \text{erg cm}^{-2}$ for half-discharge from $-600\ \text{V}$ and the photoreceptor exhibited good stability in printing $> 50\,000$ pages. In contrast, another report indicates that extended milling, to convert τ - H_2Pc needle

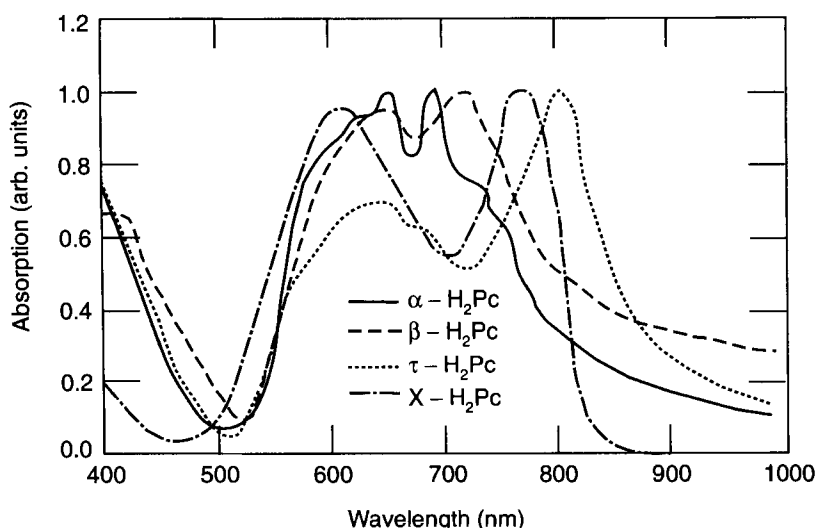


Figure 19. Absorption spectra of several forms of H_2Pc . Data for α -, β -, and τ - H_2Pc were obtained from [36e] and X - H_2Pc from [36c].

crystals (Type I) to $<0.5 \mu m$ “granular” (Type II) crystals, produced the best photoreceptor [36f]. With CGL and CTL thickness of 0.1 and 20 μm respectively the peak photosensitivity (780 nm) was 2.5 erg cm^{-2} for half-discharge from -600 V . It is also reported that photoreceptors prepared with τ - H_2Pc exhibit higher generation efficiency with increasing dielectric constant of the binder polymers: poly(methyl methacrylate) $>$ silicone $>$ poly(vinyl butyral) $>$ polysulfone $>$ polycarbonate $>$ polystyrene [36h]. The quantum efficiency was also increased in the presence of fine γ -alumina particles. This was ascribed to an increased concentration of oxygen near the pigment surface.

Single crystals of β - H_2Pc were grown from the vapor phase in a tube furnace [36i]. Measured under high vacuum, both holes and electrons had the same mobility ($\sim 1 \text{ cm}^2 \text{ V}^{-1} \text{ s}^{-1}$); the quantum efficiency for carrier generation was found to be 10^{-8} at 400 K and had an exponential temperature dependence with an activation energy of 0.21 eV. A mechanism involving phonon-induced exciton ionization was proposed. Pulsed photoconductivity was used to obtain transient action spectra of vacuum-sublimed layers of β - H_2Pc in air [36j]. These were obtained by thermal treatment (320 $^\circ\text{C}$ for 2 h) of the as-deposited layers of α - H_2Pc . An increase in the initial quantum efficiency (2.5×10^{-4}) with time was ascribed to increased absorbed oxygen. Particle dispersions of 5 % β - H_2Pc dispersed in bisphenol-A polycarbonate were studied with delayed-collection photoconductivity, and field-induced fluorescence quenching [36k]. The quantum efficiency was independent of wavelength at low fields; fluorescence quenching was a quadratic function of the applied field. At higher fields there was a linear correlation between carrier generation and fluorescence quenching, indicating 100 % efficiency in geminate pair separation (Figure

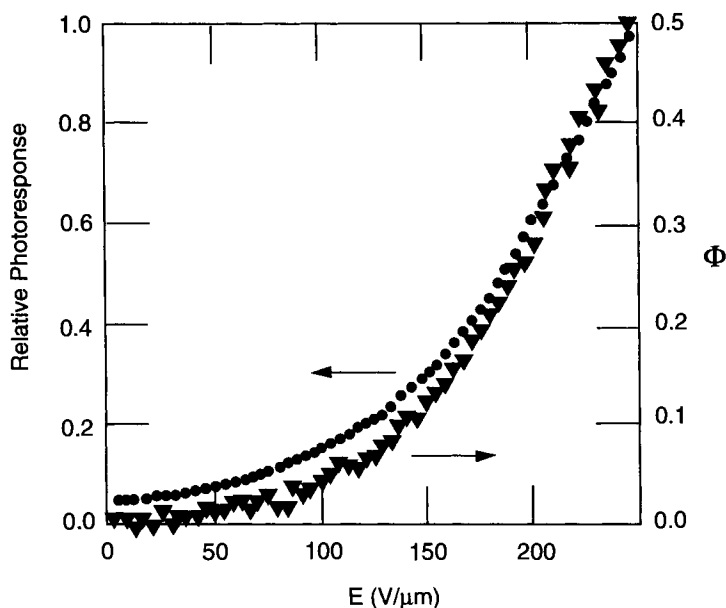


Figure 20. Fluorescence quenching and relative photoresponse for β -H₂Pc as a function of applied field with the collection field at $30 \text{ V } \mu\text{m}^{-1}$. (Reprinted with permission from Ref. [36k].)

20). These results were interpreted in terms of the internal conversion model (Figure 4), in which the relaxed singlet state produces a geminate pair (charge transfer state) which dissociates into free carriers under the influence of the applied field. Delayed-collection field experiments indicated that the geminate pair lifetime was tens of milliseconds. In a subsequent study the low-field slope/intercept ratio of the field dependence of the quantum yield approached the Onsager theory prediction only after significant delay times [36l]. This was interpreted in terms of carrier trapping.

X-H₂Pc is prepared by dry ball milling the α -form [36m]. Xerographic quantum efficiencies have been determined in both single- (PVK dispersion) and double-layer (PVK as CTL) architectures as a function of applied field and temperature [36n]. The quantum efficiency saturated at ~ 0.4 (300 K) and increased with temperature. Efficient photoresponse at $>1000 \text{ nm}$ was interpreted in terms of the lowest triplet state as precursor to charge generation. Charge generation studies have been carried out on X-H₂Pc dispersions in a polymer matrix using the photoinduced discharge method [36o], field-induced fluorescence quenching [36p,q], and recombination luminescence [36r]. At low fields fluorescence quenching is a quadratic function of field. At higher fields there is a linear correlation between carrier generation and fluorescence, indicating that at these fields the probability of geminate pair separation into free carriers is unity. The limiting generation efficiency at high fields was ~ 0.8 . The results were interpreted in terms of the internal conversion mechanism for carrier generation, involving dissociation of the first excited singlet state into electron-hole pairs. The effects of doping were determined with fluorescence

quenching studies on X-H₂Pc dispersed in poly(vinyl acetate) [36s]. Metal impurities were doped into H₂Pc at 5000 ppm during acid pasting. The pigment was then purified, converted to the X form, milled with the binder polymer, and coated. Mg, Cd, Mn, Fe, and Pb dopants all produced modest increases in the carrier generation efficiency and all resulted in fluorescence quenching. At higher Fe doping levels the generation efficiency enhancement was less. Generation mechanisms were extended to include doping with electron donors and acceptors, including *N,N'*-diphenyl-*N,N'*-di(*m*-tolyl)-*p*-benzidine (TPD) and 2,4,7-trinitrofluorenone (TNF) [36t]. In all cases there was an increase in the carrier generation efficiency and fluorescence quenching. At approximately monolayer coverage of dopant the generation efficiency in the presence of TNF increased from 27 to 61 %, with the fluorescence quenched 86 %. With TPD the generation efficiency increased to 32 % while the fluorescence was 48 % quenched. There was no evidence for ground-state charge transfer complex formation. These results were interpreted in terms of migration of the singlet exciplex to the pigment surface and charge transfer exciplex formation. The exciplex subsequently relaxes by recombination or undergoes field-assisted dissociation into free carriers. The suggestion is made that perhaps all charge generation in phthalocyanines is extrinsic, involving exciplexes with electron acceptors such as oxygen. Transient photoconductivity studies of metallophthalocyanines are consistent with oxygen charge transfer giving rise to the observed localized-state distribution [36u].

α -, β -, τ -, and X-H₂Pc have been characterized in CGLs, 0.2 μ m dispersed in a polyester, and overcoated with a 10 μ m CTL of 50 wt.% *p*-diethylaminobenzaldehyde diphenylhydrazone (DEH) in polycarbonate [36v]. Quantum yields from the xerographic photodischarge technique depended on the crystal structure, with τ - > X- > β - > α -H₂Pc (Figure 21). The time dependence of the decrease in collected charge with delay in the application of the collection field was also dependent on the crystal form, with α - > X- = τ - > β -H₂Pc. The β -H₂Pc exhibited no decrease in collected charge out to 100 ms (the longest delay investigated). These features were interpreted in terms of the stacking habit of the various forms, with the X and τ forms having a dimer structure.

The effects of interfacial charge trapping were studied in photoreceptors with a vacuum-deposited H₂Pc CGL, or X-H₂Pc dispersed in a polymer binder, overcoated with a CTL of DEH in polyester [36w]. Xerographic charge/expose cycling was used to probe charge trapping. The results indicate that there is significant hole trapping at the CGL/CTL interface and electron trapping in the CTL. Doping the CGL with the electron acceptor and transport material TNF both increases the generation efficiency and reduces CGL electron trapping. The effects of charge trapping at the CGL/CTL interface was studied by comparing the generation efficiencies obtained with photoacoustic and xerographic discharge methods. The photoacoustic generation efficiency is interpreted in terms of geminate and non-geminate recombination in the CGL. The xerographic discharge generation efficiency is interpreted as carrier generation in the CGL, hole injection from the CGL into the CTL, and transport of holes through the CTL [36x]. The injection efficiency at a given field is the ratio of the generation efficiencies determined by the two methods. The photoreceptor was composed of vacuum-deposited H₂Pc overcoated

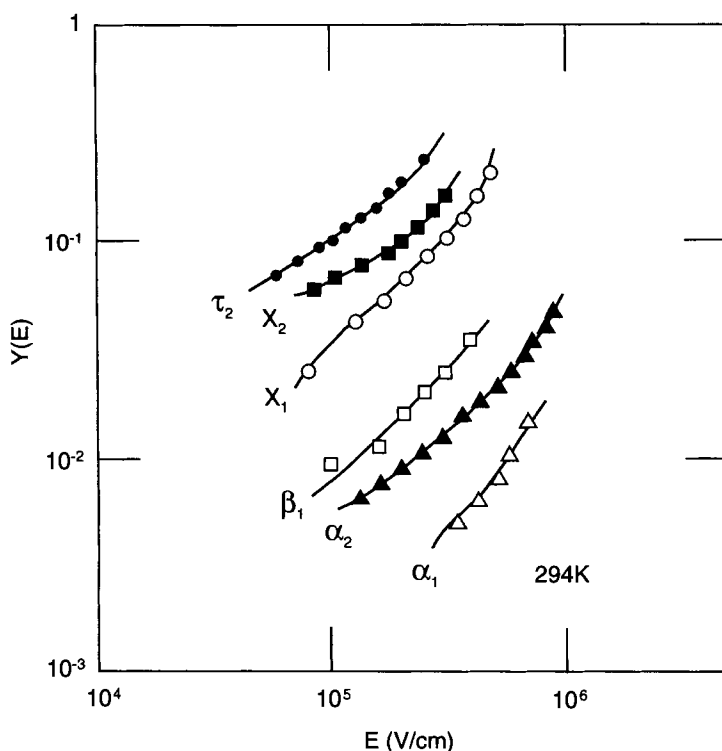


Figure 21. Photogeneration quantum yield for the various forms of H_2Pc as a function of field. Subscripts indicate single- or dual-layer photoreceptor architectures. (Reprinted with permission from Ref. [36v].)

with DEH in a polyester binder. The injection efficiency was found to be highly field-dependent. The study was extended by varying the DEH concentration in the CTL to show that the injection efficiency was determined by competition between interfacial hole trapping and interfacial transport (Figures 22 and 23) [36y]. Increasing photoacoustic generation efficiency with increasing DEH concentration in the CTL was interpreted in terms of both generation and interfacial hole transport. In addition, photoacoustic generation efficiencies were independent of several transport materials, all of which had mobility of $\sim 7 \times 10^{-7} \text{ cm}^2 \text{ V}^{-1} \text{ s}^{-1}$.

Titanyl phthalocyanine (TiOPc) is probably the phthalocyanine most often utilized in commercial electrophotographic photoreceptors. In a study of the wavelength dependence of photoconductivity in single- and dual-layer photoreceptors it was concluded that the pigment was p-type and that generation occurred in the pigment bulk and was unaffected by the presence of a hole-transport molecule electron donor [34n]. The pigment form was not identified in this study.

There are many published reports on photoreceptor fabrication and carrier generation mechanisms using TiOPc. However, this pigment exhibits a wealth of crys-

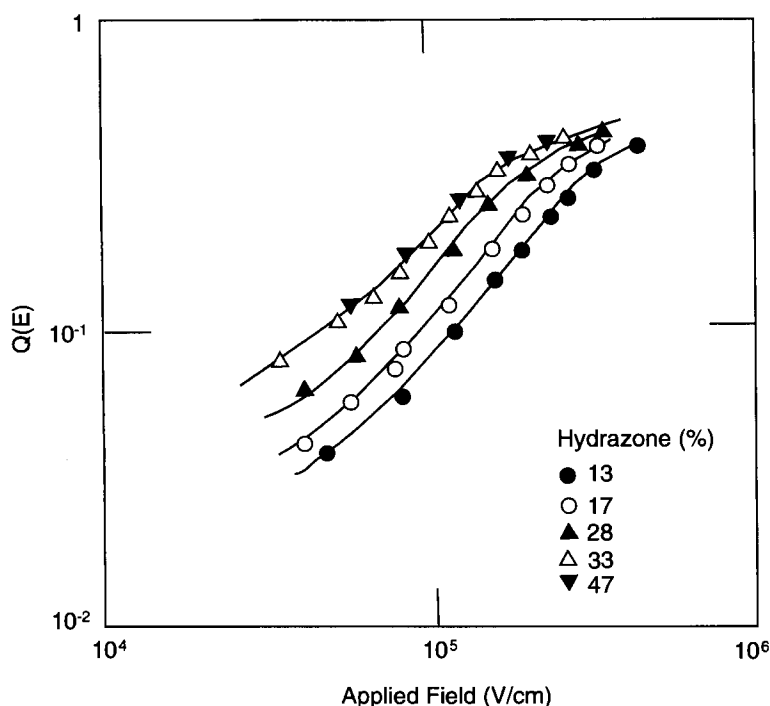


Figure 22. Photogeneration quantum yield for H_2Pc -based photoreceptors with varying percentages [wt. %] of hydrazone (DEH), as a function of applied field. (Reprinted with permission from Ref. [36y].)

tal morphologies, forms, phases, types, etc., depending on the details of synthesis, purification, treatments, and photoreceptor preparation. Different groups of workers have coined their own terminology to identify the various forms. Thus, Type I and the A form are apparently the same material as are Type IV and the Y form.

Enokida and co-workers report the preparation of several forms: α (acid pasting and acetone treatment), β (wet milling of the as-synthesized pigment in quinoline at 200°C), γ (milling of acid-pasted pigment in *n*-butanol), *m* (acid pasting of the crude pigment in the presence of octachloro- TiOPc), and amorphous (dry ball milling of the crude pigment) [37a]. The forms were characterized by ^{13}C -NMR and X-ray powder diffraction, as well as infrared, ESR, and absorption spectroscopy. The various forms were used in the preparation of dual-layer photoreceptors. Those prepared with the γ form and amorphous TiOPc exhibited high photosensitivity from 600 to 800 nm [37b]. In all cases the photosensitivity increased with decreasing CTM ionization potential.

Researchers from Canon Inc. have reported that the as-synthesized α - TiOPc was converted to the amorphous form by extended ball milling. Stirring in methanol resulted in conversion to a metastable $\text{M-}\alpha$ form [37c]. Milling of the metastable

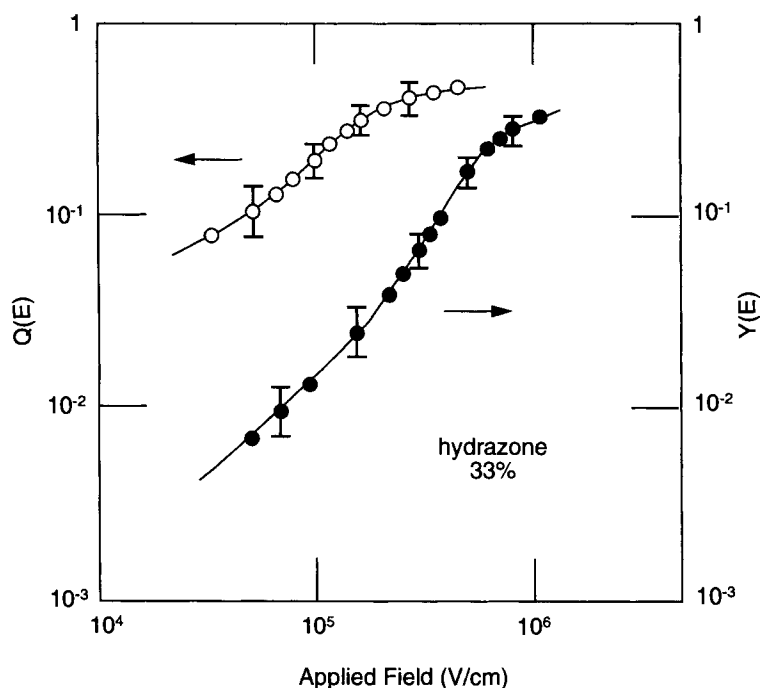


Figure 23. Photogeneration quantum yield for H_2Pc -based photoreceptors with 33 wt.% hydrazone (DEH) CTM, as a function of applied field. Open-circle data were obtained by xerographic discharge and filled-circle data from photoacoustic measurements. (Reprinted with permission from Ref. [36y].)

form in alcohol solvents gave rise to new M, E, G, and H forms; milling in non-polar solvents produced a novel I form. Photoreceptors with the I form as the CGL pigment exhibited high photosensitivity in the near-infrared. They also reported that acid pasting with sulfuric acid resulted in demetallization to metal-free phthalocyanine and that the use of 1-chloronaphthalene as solvent in the synthesis resulted in $TiOPc$ with some ring chlorination.

Several forms have been described in reports from the Xerox Research Center of Canada. Experiments were designed to find an optimum acid pasting procedure for $TiOPc$ purification [37d]. Acid pasting the as-synthesized pigment using sulfuric acid with precipitation into water gives Type II pigment. However, acid pasting with 20 vol.% trifluoroacetic acid in dichloromethane followed by precipitation into a variety of solvent mixtures produces the following forms: Type I (diethyl ether), Type II (isopropanol), Type III (95:5 methanol/water or 1:1 acetone/water), Type IV (water or 1:1 toluene/water or 1:1 chlorobenzene/water or 1:1 isopropanol/water), Type Z-1 (methanol), Type Z-2 (1:1 ethylene glycol/water), Type X (1:1 methanol/water or 1:1 ethanol/water). Type IV is reconverted to Type I on exposure to dichloromethane. The Type I and V pigments produced high-sensitivity photoreceptors. Type I pigment prepared via different methods had different X-ray

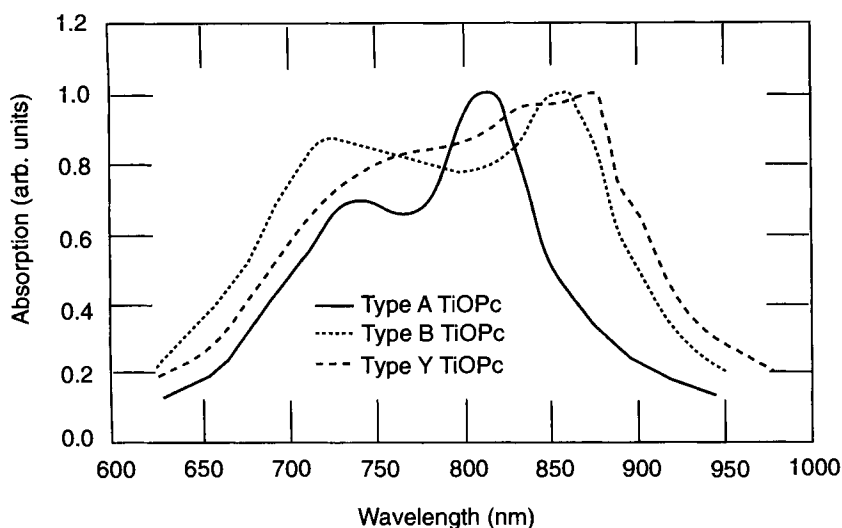


Figure 24. Absorption spectra of Types A, B, and Y TiOPc. (Data obtained from Ref. [37h].)

diffraction, absorption characteristics, and electrophotographic characteristics. Dual-layer photoreceptors were prepared from the various TiOPc forms [37e]. Those with generation layers based on Type I exhibited sensitivity and dark decay characteristics which depended on the method of preparation. The electrophotographic characteristics of the high-sensitivity Type IV were improved by using trifluoroacetic acid in dichloromethane as opposed to sulfuric acid pasting.

Reports from Konica Corp. describe the conversion of amorphous TiOPc (from acid pasting) with solvent treatment [37f]. Treatment with *o*-dichlorobenzene/water (2:1 by weight) produced the Y form, refluxing *o*-dichlorobenzene gave the A form, refluxing tetrahydrofuran gave the B form, and refluxing dimethyl sulfoxide gave the C form. Absorption spectra of the A, B, and Y forms are shown in Figure 24. Calorimetry on the Y form indicated water desorption at 90°C and conversion to the A form at 255°C. These were tested in dual-layer photoreceptors with the CGL composed of 50 wt.% pigment in a mixture of silicone resin and *t*-butyl acetate. The photoreceptor with CGL containing the Y form was the most sensitive. This form had enhanced absorption in the near-infrared that was interpreted in terms of molecular stacking being important for efficient charge generation. The "typical" method of synthesis, using TiCl_4 , resulted in the production of some chlorinated phthalocyanine that had a deleterious effect on carrier generation. TiOPc was found to form adducts with 1,2-diols but these did not exhibit enhanced near-infrared absorption and photoreceptors prepared from them had low sensitivity. Photoreceptors prepared with Y form pigment, synthesized using a chlorine-free synthetic method, exhibited superior photosensitivity and stability over 100,000 printing cycles [37g]. The xerographic action spectra of photoreceptors with CGLs based on the Y and A forms of TiOPc and $\tau\text{-H}_2\text{Pc}$ are compared in Figure 25. The Y form

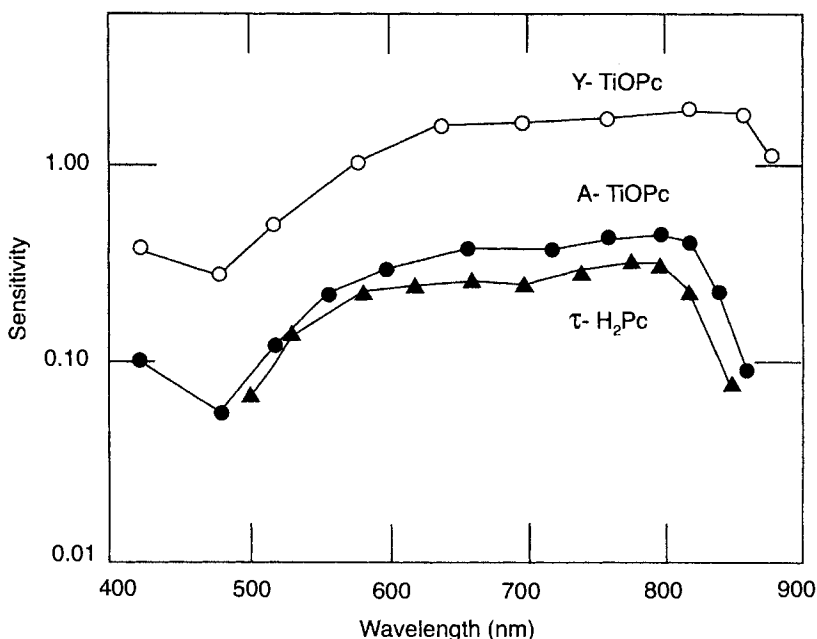


Figure 25. Spectral sensitivity of Types A and Y TiOPc compared with τ -H₂Pc. The sensitivity is the reciprocal of the energy for photodischarge from -600 to -300 V. (Reprinted with permission from Ref. [37h].)

photoreceptor had peak sensitivity at 850 nm and required 0.75 erg cm^{-2} for a -600 to -300 V photodischarge. This sensitivity corresponds to a xerographic quantum efficiency of 0.9.

Takano and co-workers from NEC Corporation report the preparation and characterization of the Phase I, II, and III forms of TiOPc by solvent treatment [37h]. The pigments were characterized by X-ray powder diffraction and IR spectroscopy, and as dual-layer photoreceptors. Phase III (treatment with tetrahydrofuran) gave the highest-sensitivity photoreceptor.

From studies of xerographic photoreceptor sensitivities it is apparent that carrier generation is influenced by pigment "form". From the chemical and physical characterizations of forms it is clear that differences include crystal structure, pigment morphology, and particle size, as well as adsorbed species such as water or alcohol. Mechanistic studies of charge generation should include a physical and chemical definition of the material under investigation. It has been proposed that differences in photosensitivity among the various forms are related to the molecular overlapping pattern [37i]. Molecular modeling of the Type I and Type IV (near-infrared sensitive) polymorphs indicates that they differ only in a slight rotation of the phthalocyanines about the O-Ti axis and that some of the claimed polymorphic forms are most probably actually due to particle size differences [37j]. The effects of temperature on the absorption spectra of various forms has been interpreted in

terms of intermolecular π - π interactions [37k]. In this study, evaporated films of TiOPc were thermally converted to the Phase I form, then converted to the Phase II form by exposure to acetone vapor or to the Y form by exposure to the vapors of chlorobenzene/water.

The Y form of TiOPc, which has characteristic X-ray diffraction peaks at $2\theta = 9.5^\circ$ and 27.3° , has received considerable mechanistic attention because of its high photosensitivity. The X-ray data correspond to an interplanar separation distance of 93 nm and an interplanar separation along the stacking axis of 33 nm [37g]. Several forms have been independently characterized which have similar X-ray powder patterns and high photosensitivity: the I Form [37c], Type IV [37d,e], Phase 3 [37h], and the γ form [37b]. Water adsorbed on the Y form crystal surface was found to be connected with its high photosensitivity and it was suggested that it was acting as an electron acceptor in carrier generation [37l]. Molecular dynamics calculations were used to model the thermal loss of water with heating in the conversion of the Y to the A form [37m]. Photocurrent and electroabsorption studies of the Y form (and Phase II) indicated charge transfer excitons, whereas only the Frenkel exciton was observed in amorphous TiOPc [37n].

Popovic and co-workers have found a linear correlation between field-induced fluorescence quenching and carrier generation, indicating photogeneration from the first excited singlet state [37o]. In this study the photoreceptor had a dual-layer architecture, having a $0.5\ \mu\text{m}$ CGL (1:1 by weight pigment dispersed in poly(vinyl butyral)) and a CTL of 35 wt.% TPD in bisphenol-A polycarbonate. At 50 % RH the generation efficiency was high and weakly field-dependent (zero-field efficiency of ~ 0.4). The fluorescence intensity decreased and carrier generation efficiency increased with increasing relative humidity but the field dependencies were unchanged. The fluorescence intensity was independent of the presence of TPD or a dry nitrogen atmosphere, ruling out oxygen involvement in carrier generation. These results were interpreted in terms of exciton migration to the pigment surface, where interaction with water leads to carrier generation with concomitant fluorescence quenching. It was suggested that the weak field dependence of generation is due to excitation dissociation in the pigment bulk. Time-resolved fluorescence spectroscopy indicated carrier generation from both relaxed and nonrelaxed intrinsic excited singlet states, but that generation does not occur from trapped excitons [37p]. A carrier precursor state with charge transfer character was suggested from the field dependence of fluorescence quenching. Recently, electric-field-modulated picosecond time-resolved fluorescence spectroscopy has been used to study the carrier generation mechanism [37q]. From the fluorescence decays two singlet excitons were identified. The shorter-lifetime exciton had charge transfer character and was identified as the primary intermediate in carrier generation. Although differing in details, these studies provide a consistent mechanism for carrier generation in Y-TiOPc. The temporal characteristics of fluorescence and charge generation have been studied by nonlinear exciton-exciton annihilation [36r]. This study was carried out in a thin dispersion of Y-TiOPc dispersed in poly(vinyl butyral) binder. Carrier generation was found to occur shortly after creation of the exciton, in an interval (~ 1 ps) which was much shorter than the fluorescence lifetime. Thus, under these conditions of excitation, fluorescence (first excited state) and carrier generation

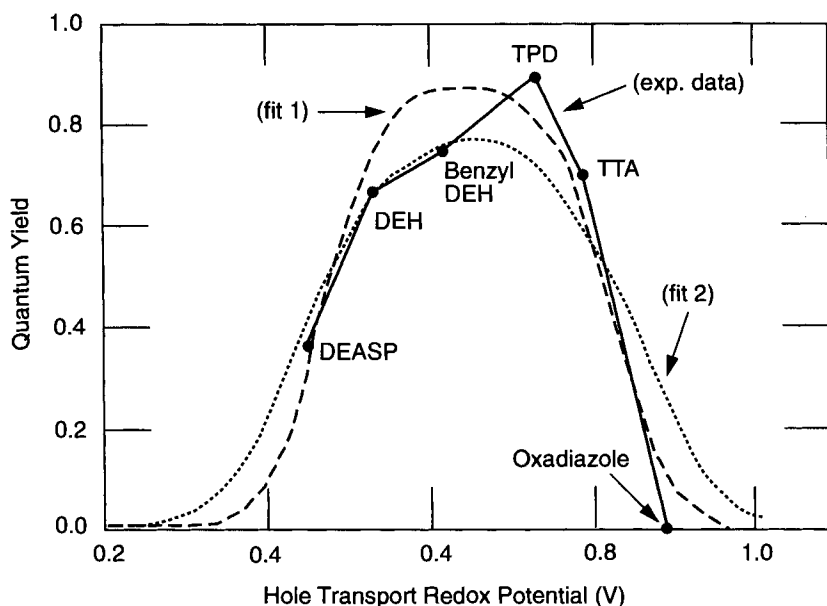


Figure 26. Quantum yield for charge injection as a function of the redox potential of the hole transport molecule for a TiOPc-based photoreceptor. (Reprinted with permission from Ref. [37t].)

originate from different excited states. It was argued that this result is consistent with many current charge generation models if generation occurs from the non-relaxed lowest excited state or before exciton trapping occurs.

In a study of photoconductivity in single- and dual-layer photoreceptors, with a CGL based on an undefined form of TiOPc pigment, it was concluded that the pigment was p-type and that generation occurred in the pigment bulk and was unaffected by the presence of a hole-transport molecule electron donor [34n].

The influence of CTM oxidation potential on charge injection efficiencies in dual-layer xerographic photoreceptors with TiOPc-based CGL has been investigated [37s]. In interpreting the data it was assumed that the injection efficiency is dominated by electron transfer from the generation site on the pigment particle into the CTM. The data (Figure 26) exhibit a "Marcus inverted region" such that the efficiency decreases with CTMs of very low oxidation potential. A CGM/CTM energy difference of 0.3 V was found to be optimum for electron transfer and the solvent reorganization energy λ was found to be 0.14 or 0.25 eV, depending on the assumptions made for the oxidation potential of TiOPc.

Hydroxygallium phthalocyanine (HOGaPc) has only recently been exploited as a charge generation material. This pigment exists in several forms and structural modifications that are interconverted with various thermal and milling treatments [38a]. Thus, acid pasting produces Phase I that is converted to the high-sensitivity near-infrared absorbing Phase V (absorption maximum 849 nm) by milling with dimethylformamide [38b,c]. Humidity had no effect on the photodischarge charac-

teristics of photoreceptors prepared with the Phase V pigment. Milling with xylene produces the XI form of HOGaPc (absorption maximum ~ 900 nm) and milling with methanol produces CH_3OGaPc . All of these are converted to $(\text{GaPc})_2\text{O}$ with heat (400°C). Electroabsorption studies show that the absorptions have charge transfer character. Crystal structure analysis using the Rietveld technique showed that HOGaPc Phases V and XI involve stacked dimers with staggered overlap. Furthermore, the xerographic gain increased linearly with the magnitude of the electromodulation, indicating that the charge transfer character of the excited state is related to the generation efficiency [38d]. Photogeneration in Phase V HOGaPc has been studied with delayed-collection photoconductivity and fluorescence quenching [38e]. Dual-layer devices were studied. The CGL comprised $0.4\ \mu\text{m}$ of 40 % pigment in poly(vinyl butyral). The CTL was $10\ \mu\text{m}$ of 40 wt.% TPD hole transport material in polycarbonate. At high fields the geminate pair dissociation probability is unity so from fluorescence quenching the zero-field quantum efficiency for geminate pair formation is 0.64, independent of RH. The linear correlation between fluorescence quenching and generation efficiency implicates photogeneration by dissociation of the first excited singlet state. The effects of pigment preparation, the acid pasting process in particular, on xerographic performance has been reported [38f].

Vanadyl phthalocyanine (VOPc) has three crystal forms. Phase I has the major absorption at 725 nm and Phase II at 840 nm [39a]. Figure 27 shows the absorption spectra of Phases II, V, and XI. A dual-layer xerographic photoreceptor with VOPc as the charge generation material had a high-field photogeneration efficiency of ~ 0.2 from 400 to 900 nm [39b]. The effects of molecular structure on aggregation have been studied with *t*-butyl-substituted VOPcs [39c]. Such substitution increases

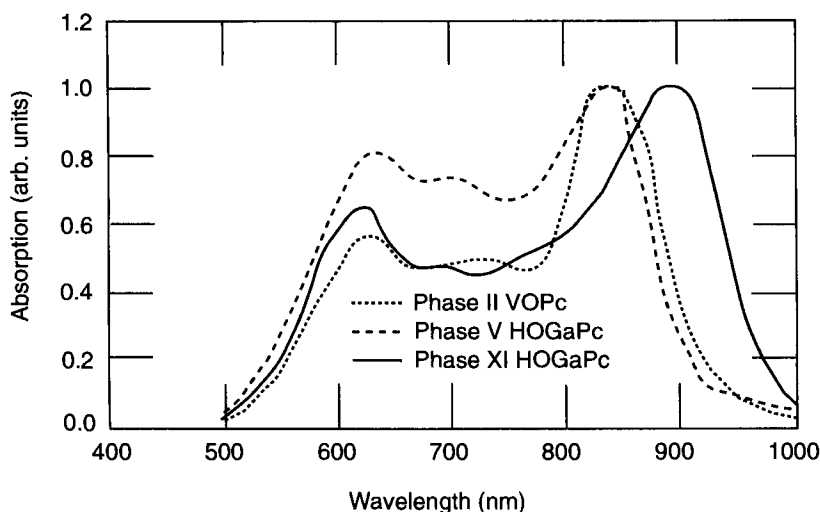


Figure 27. Absorption spectra of Phase II VOPc (data from [39a]) and Phase V and Phase XI HOGaPc (data obtained from [38b].)

solubility, permitting the use of standard purification techniques. However, the steric bulk prevents formation of the near-infrared absorbing Phase II form. These materials were studied with xerographic discharge [39d]. The Phase II crystalline phase is >300 times more sensitive than Phase I.

Squaraine (squarylium) pigments

In 1982 Wingard at IBM reported a dual-layer photoreceptor using a CGL based on a squaraine pigment (2,4-bis(4-dimethylamino-2-methylphenyl)cyclobutenediylum-1,3-diolate) for use in a printer having a GaAs laser (830 nm) exposing system [40a]. The CTM was the pyrazoline, 5-(*p*-diethylaminophenyl)-1-phenyl-3-(*p*-diethylaminostyryl)-2-pyrazoline (DEASP). This photoreceptor had high photosensitivity from 500 to 900 nm. With a -850 V initial surface potential an exposure of 5 erg cm^{-2} at 830 nm produced a photodischarge to -150 V within 0.25 s. Melz and co-workers had previously reported on photoinjection efficiencies with pyrazoline-based CTLs as a function of applied field [32b]. The initial photodischarge rate was the method used in this study. The pyrazoline CTM with the lowest ionization potential (DEASP) exhibited the weakest field dependence and highest efficiency. At a field of $4 \times 10^5 \text{ V cm}^{-1}$ and 550 nm exposure the injection efficiency of this photoreceptor was 0.4. Another report described, in great detail, a similar squaraine-based dual-layer photoreceptor for use in an IBM printer [40b]. Xerographic characteristics of squaraine-based photoreceptors have been surveyed [40c–e]. Law and co-workers at Xerox have published several accounts of the effects of various squaraine features on xerographic performance. Included are a new squaraine synthesis method for reduced impurities and smaller particle size [40f], CGM binder effects [40g], and squaraine molecular structure [40h]. Law reports that a novel unsymmetrical fluorinated squaraine (3,4-dimethoxyphenyl-2'-fluoro-4'-(dimethylamino)phenylsquaraine) was used to fabricate a photoreceptor with high sensitivity from the visible to the near-infrared [40i]. The CGL comprised squaraine (80 wt.%) in poly(vinyl formal) binder ($\sim 0.4 \mu\text{m}$) and the CTL a solution of 40 wt.% TPD in bisphenol-A polycarbonate ($\sim 26 \mu\text{m}$). The $E_{1/2}$ photodischarge exposure from ~ 1000 V at the peak sensitivity (790 nm) was 1.9 erg cm^{-2} .

Like other pigment generation materials, squaraines that form crystalline aggregates have high photosensitivity. Aggregation results in a broadening of the absorption spectrum into the near-infrared [39d]. Furthermore, in the fabrication of CGLs with bis(4-dimethylaminophenyl)squaraine using poly(vinyl butyral) binder there was a pronounced solvent effect on the xerographic characteristics [40j]. Fluorescence spectroscopy was used to infer that these effects were due to complex formation between the pigment surface and the hydroxyl moieties in the binder polymer. Using a series of squaraines with differing oxidation potentials, it was found that efficient hole injection into the hole-transport material (TPD) occurred when the electron transfer was exergonic [40k]. On the basis of a photoelectrochemical study of a squaraine monolayer, Law and co-workers proposed that carrier generation in squaraine photoreceptors involves electron transfer from excited squaraine to O_2 followed by interfacial electron transfer from the charge transport material to the holes in the squaraine [40l]. Tam used an optoacoustic method to

study photogeneration in a dual-layered photoreceptor with a squaraine-based CGL [20]. At 799 nm ($2.5 \times 10^5 \text{ V cm}^{-1}$) the generation efficiency is 0.039.

Perylene pigments

Perylene-3,4,9,10-tetracarboxylic diimides and related materials have been utilized as charge generation materials in organic photoreceptors for many years. In 1978 Schlosser reported on a dual-layer photoreceptor using the *N,N'*-di(3,5-dimethylphenyl) derivative as CGM [41a]. Using the xerographic technique the limiting quantum efficiency was determined to be ~ 0.3 . This was the same in the presence or absence of a hole-transport electron donor material. The photosensitivity of this photoreceptor decreases rapidly beyond 600 nm, limiting its commercial utility. A single-layer photoreceptor using the same perylene has been studied [41b]. When it was charged positively the quantum efficiency was found to be enhanced by the presence of an electron acceptor (2,5-dichloro-*p*-benzoquinone) and it was suggested that this might be due to electron trapping with a reduction in recombination losses. Increased photosensitivity in the near-infrared has been a major goal of research on perylenes as generation materials in xerographic photoreceptors [41c]. Loutfy and co-workers evaluated several photoreceptors prepared using vacuum-deposited perylene pigments (0.1 μm) as CGMs overcoated with 35 wt.% TPD in bisphenol-A polycarbonate as CTL (15 μm) [41d]. A photoreceptor with bisbenzimidazole substitution had particularly good electrophotographic characteristics with high photosensitivity at 500–700 nm. Calculations and molecular modeling have been extensively utilized in an effort to understand the factors responsible for the molecular overlap leading to enhanced absorption in the near-infrared [41e–g]. These principles have then been applied to the synthesis of new perylene pigments [41h,i]. Popovic has studied the generation mechanism using the delayed-collection field and field-induced fluorescence quenching techniques on electroded samples of pigment dispersed in bisphenol-A polycarbonate [41j]. The quantum yield for carrier generation with a bisbenzimidazole perylene pigment was determined to be 0.36 (100 $\text{V } \mu\text{m}^{-1}$ applied field). A follow-up study was carried out on a dual-layer photoreceptor with a TPD-based CTL. In the presence of TPD the pigment fluorescence was quenched and the carrier generation efficiency was substantially increased, exceeding 0.6 at fields above $\sim 40 \text{ V } \mu\text{m}^{-1}$. This was interpreted as strong evidence for surface sensitization of carrier generation. The field dependencies of carrier generation with and without TPD are very different as well. The charge generation mechanism was suggested to involve exciton diffusion to the pigment/CTL interface where a hole was transferred to surface-adsorbed TPD. An exciton diffusion length of 0.27 μm was determined from the front and rear exposure action spectra [41k]. Another perylene bisimide, the *N,N*-bis(2-phenethyl) derivative, has found utility as a carrier generation material [41l]. Vacuum deposition onto a cooled substrate produces amorphous material whereas deposition at room temperature or above provides polycrystalline material. The latter has enhanced absorption in the red, and higher photogeneration efficiency. Only electrons are transported in the vacuum-deposited pigment layer. The field dependencies of photogeneration, determined by the xerographic method, were analyzed according to

the Onsager formalism to give primary quantum yields of 0.4 (amorphous) and 0.9 (polycrystalline) and thermalization distances of ~ 3 nm for both. Sensitization with tri-*p*-tolylamine (TTA) has recently been reported [41m]. Pigment was vacuum-deposited onto substrates of bisphenol-A polycarbonate doped with TTA. The samples were then exposed to dichloromethane vapors to convert the pigment to the active form and to allow diffusion and intermixing at the CGL/CTL interface. At high fields fluorescence quenching correlated linearly with carrier generation. However, the results indicated a significant component of carrier generation not associated with TTA sensitization but originating from direct dissociation of the fluorescent first excited singlet state into free carriers.

Mixed pigments

Photoreceptors with mixed pigment CGLs have enhanced photogeneration efficiencies as measured by the xerographic technique [42a]. Single- and dual-layer photoreceptors prepared with mixed perylene/metal-free phthalocyanine pigments exhibited enhanced photogeneration efficiencies. Thus, a dual-layer photoreceptor with the mixed pigment (5 wt.% perylene/0.4 wt.% phthalocyanine in poly(vinyl butyral)) exhibited approximately a four-fold increase in generation efficiency at 750 nm over a photoreceptor where the CGL contained only the phthalocyanine at the same concentration. It was found that the perylene, an n-type pigment, had negative surface charge when ball-milled in tetrahydrofuran whereas the phthalocyanine, a p-type pigment, had a positive charge under the same conditions. When mixed in the milling process, the pigments agglomerated and it was suggested that this produces micro p-n heterojunctions that act as sites for efficient carrier generation. Hiramoto and co-workers studied carrier generation in a perylene pigment, 3,4,9,10-perylenetetracarboxylic-3,4:9,10-bis(methylimide), mixed with a small amount of metal-free phthalocyanine [42b]. The mixed pigments were ball-milled in tetrahydrofuran and then dispersed in a polycarbonate binder polymer dissolved in dichloromethane. The addition of 1 wt.% phthalocyanine resulted in >50 % quenching of the perylene fluorescence. This is believed due to either formation of a nonradiative exciplex or energy transfer to the phthalocyanine. At 5 wt.% phthalocyanine, and a field of 10^8 V m $^{-1}$, the generation yield doubled. The fluorescence of both pigments was strongly quenched with increasing applied field. However, for the mixed system the fluorescence quenching decreased with applied field. This unexpected result was interpreted by assuming a dual-path mechanism for carrier generation. Thus a new charge transfer state, with field-independent carrier generation, is formed at the perylene/phthalocyanine interface. This extrinsic mechanism competes with the intrinsic generation from perylene charge transfer states.

2.5.4 Summary of Carrier Generation Mechanisms

From this brief review one can appreciate the complexity of the task of unraveling the mechanism of carrier generation in organic photoreceptors used in electrophotography and the large number of experimental techniques which have been utilized. In most cases the carrier generation mechanism is adequately explained by

variants of the Onsager model, the “internal conversion model” or the “sensitized model” as described. In all pigment systems there appears to be a preferred crystal “form” or “Phase” which has enhanced absorption in the red or near-infrared and in which carrier generation is most efficient. In the simplest cases, a single layer of a pure material, intrinsic generation appears to involve excited states with charge transfer character. Thus, it seems that the excited-state interactions which lead to new low-energy states, and enhanced red absorption, are those which are involved in carrier generation. The presence of donors or acceptors with appropriate energy levels brings in extrinsic, or sensitized, carrier generation. Finally, there is some evidence that in mixed pigment systems an interfacial interaction can enhance carrier generation. Recent studies have probed the energetics of the electron transfer as it effects the rate in the context of Marcus theory. Rates are found to increase to a limiting value with increasing energy gap with no evidence for a so-called “inverted region”. Since many of the photoreceptors studied have multiple components, are heterogeneous, and are contained in an amorphous polymer binder, it is no wonder that the mechanisms are complex and difficult to unravel. Nevertheless, great progress has been made in our understanding of the photogeneration of charges. One measure of this success can be seen in the many commercial applications of organic photoreceptors in electrophotographic copiers and printers.

2.6 Charge Transport

2.6.1 Typical Materials

In an organic photoreceptor photodischarge occurs with the field-driven transport of generated charge through the bulk of the structure. Photodischarge is typically dominated by the transport of one sign of charge even when the charge generation and transport materials are combined in a single-layer architecture. Studies of the mechanisms of charge transport are typically carried out on devices that are designed so that the majority of charge transport occurs in a charge transport layer (CTL). The materials in a CTL must satisfy many requirements.

- 1) Except where charge is injected from the charge-generation layer, the CTL must be very good insulator, so that unexposed areas do not discharge substantially. A 1 cm^2 area of a typical CTL must have a resistance of ca. $10^{12} \Omega$ or more, corresponding to a bulk resistivity of ca. $10^{15} \Omega^{-1} \text{ cm}^{-1}$. Conductivity along the surface of the CTL, which tends to blur an image, must also be very low.
- 2) Nevertheless, where charge is injected from the charge generation layer (CGL), it must be transported rapidly enough for the discharge to be substantially complete before the development step begins (typically a fraction of a second after exposure and charge generation).
- 3) “Deep” charge trapping must be negligible. A gradual accumulation of trapped charge can cause the electrical properties of the photoreceptor to change with

repeated cycling. A rapid accumulation can cause “ghosts” of previous images to be superimposed on subsequent images.

- 4) Injection of charge from the CGL into the CTL must also be rapid and not subject to significant trapping.
- 5) The CTL must be transparent to the image-forming light.
- 6) The CTL must be mechanically rugged, to withstand abrasion by the developer. In machines using a photoreceptor belt (rather than a drum), the entire photoreceptor must also be flexible enough to withstand frequent bending without developing cracks.
- 7) These properties must be stable for long periods at elevated operating temperatures (typically $\sim 40^\circ\text{C}$ inside a high-speed copier). They must not be impaired by reactive species produced in the corona discharge (see above), by contamination from the developer, or by accidental exposure to room light.
- 8) In the course of coating the CTL over the CGL, some intermixing is inevitable. Such “contamination” of the CGL is often important to making the CGL efficient (see above), and in any case it must not impair the performance of the CGL.

Most commercial CTL materials are “molecularly doped polymers” (MDP). In this context, an MDP is a homogeneous solid solution of an electrically active compound (“dopant”, or “charge transport material”, CTM) in a polymeric host. The solution need not be thermodynamically stable, as long as it does not phase-segregate during the anticipated lifetime of the photoreceptor. Typical CTMs are shown in Schemes 2 and 3. The CTM is an easily oxidized electron donor (for a CTL that transports positive charge) or easily reduced electron acceptor (for a CTL that transports negative charge). The polymer is typically a polycarbonate or polyester. It supplies the necessary mechanical properties (toughness, etc.) as well as being an electrical insulator. It does not participate in transport per se, although it can dramatically influence the transport properties of a CTM dissolved in it. For practical purposes, the mechanical properties are paramount, and the transport properties are optimized by using high concentrations of CTM (as high as 1:1 CTM/polymer by weight). The CTM may also act as a plasticizer for the polymer, making it more pliable but also reducing the glass transition temperature. The polymer must satisfy the mechanical requirements described above when it is in a highly plasticized state. CTMs which impart abrasion resistance by virtue of CTL antiplasticization have been reported [43].

Most, if not all, commercial photoreceptors are based the transport of positive charge. The CTM is an electron donor, the charge carrier is a “hole” resulting from donation of an electron from the highest occupied molecular orbital (HOMO), and the charge transport process is formally a self-exchange reaction (Eq. (1)),



repeated thousands of times. The donors are usually triarylamines, tetraarylbendines, or mixed arylamine/hydrazone compounds (Scheme 2). These, and almost all CTMs, feature nitrogen atoms with (formal) lone pairs. Their oxidation potentials

(E_{ox}) are low (cathodic), typically between 0.6 and 1.0 V vs. SCE in acetonitrile or dichloromethane [44].

At least in some cases, a low E_{ox} facilitates the generation and/or injection of a positive charge carrier from the CGL (see above). A low E_{ox} also makes it unlikely that an impurity might have a much lower value and act as a trap for holes [44h]. For obvious reasons, the cation radicals of these compounds must be stable in the CTL environment, and some of the better donors indeed form remarkably stable radical-ion salts, even in fluid solution [44a]. The CTM must be highly soluble in the polymeric host and the solvent used to fabricate the CTM. It must provide a high concentration of electrically active moieties without plasticizing the host polymer excessively. Compounds that meet these requirements are typically rather large and flexible, and they may contain more than one electrically independent moiety per molecule, e.g., 1,1-bis(di-4-tolylaminophenyl)cyclohexane (TAPC) in Scheme 2.

For some applications, a photoreceptor that transports negative charge would be preferable. In fact, the first commercial organic photoreceptor, poly(*N*-vinylcarbazole) doped with 2,4,7-trinitrofluorenone, PVK-TNF, was capable of electron (as well as hole) transport [30a, 45]. Electron-transporting materials have received considerable study though none has performed well enough for current practical applications [3q]. Now the CTM is an electron acceptor, the charge carrier is an electron in the lowest unoccupied molecular orbital (LUMO), and the charge transport process is again a self-exchange reaction (Eq. (2)).



Materials that transport electrons passably tend to have rather low (anodic) reduction potentials (ca. -0.1 to -0.6 V vs. SCE) [46]. This is presumably to prevent electron trapping by O_2 , although this explanation has not actually been proven. The requirements on solubility, etc., are the same as for hole-transporting materials.

Instead of dissolving a CTM in a polymer, one can incorporate it in the polymer chain or as a pendant group. The archetypal example is poly(*N*-vinylcarbazole) [27]. A more recent example is poly(tetraphenylbenzidine) [47]. Many other examples can be found in the literature [48]. While the mechanical properties and thermal stability of such polymeric transport materials can be superior to those of the corresponding doped polymers, the charge transport properties are often inferior [48d,e,h]. Polymers of a quite different kind, the polysilylenes and polygermylenes (or “polysilanes” and “polygermanes”) exhibit excellent charge transport [48h,49]. These polymers transport holes through the silicon or germanium backbone.

2.6.2 Charge Carrier Mobility

Experimental method and typical results

Charge transport in a practical charge transport layer (CTL) must satisfy two basic requirements. First, charge carriers must be mobile enough to cross the CTL in the time available. We will focus on this aspect. Second, deep trapping (such that the

carriers are detained by several seconds or longer) must be rare. Although this latter aspect is equally critical, relatively little mechanistic information has been published.

Almost all commercial organic photoreceptors employ hole-transporting molecularly doped polymers as CTLs, and only a few kinds of hole-transporting CTMs and host polymers are widely used [3q]. Nevertheless, a fairly wide range of materials has been investigated, to elucidate the physics and chemistry governing the charge transport process and/or search for useful new materials. These include both hole- and electron-transporting CTM and a considerable variety of host polymers. In addition, many of the CTM can be prepared as thermally stable monocomponent glasses, and the transport properties of these glasses have also been examined extensively. The underlying physics appears to be the same, and we shall include both molecularly doped polymers and amorphous molecular glasses under the general rubric of "amorphous molecular solids". Some of the same hole-transporting glasses are used in organic light-emitting diodes; however, the electron-transporting glasses discussed below generally have too anodic a reduction potential, or too large an electron affinity, for that purpose. On the other hand, we will not discuss transport in molecular *crystals*. There have been only a few, cursory, studies of crystals chemically analogous to our CTM [50]. However, transport in most organic molecular crystals is qualitatively different from that in the amorphous systems in that it is generally slower by orders of magnitude, and depends much more strongly on electric field strength and temperature in amorphous media [14a].

In a given material, at a given temperature (T) and electric field strength (E), charge carriers move with some average velocity $v(E, T)$. In a crystalline material, usually $v \propto E$, and one can characterize transport succinctly in terms of the proportionality constant, the mobility $\mu(T) = v/E$. In amorphous materials, v usually increases superlinearly with increasing E , but it is still customary to describe transport in terms of the mobility, which now depends on E as well as T , namely as $\mu(E, T)$. Most studies have concentrated on these dependences and the influence of chemical composition upon them.

Mobility is most commonly measured using a time-of-flight experiment (Figure 28a). A film of the material of interest is sandwiched between two electrodes. Blocking layers may be utilized to prevent dark charge injection. At least one electrode is semitransparent. A short pulse of charge carriers is injected briefly from one side, an electric field drives them across the film, and the time required to reach the other side (the transit time, t_t) indicates their velocity, $v = d/t_t$, where d is the thickness of the film. Most commonly, the carriers are launched by a relatively thin charge generation layer (CGL) that is "turned on" briefly by a flash of visible light. It is sometimes possible to omit the CGL and generate the carriers in the transport material itself, using a flash of shallowly penetrating ultraviolet light. It is also possible to use an electron beam [51], or an injecting contact activated by a voltage pulse [47b, 52]. The electric field is supplied by a voltage V applied between the electrodes. The film is usually between 1 and 30 μm thick, the applied voltage is usually several tens or hundreds of volts, and the resulting field strength ($E = V/d$) is usually between 10^4 and 10^6 V cm^{-1} . As the carriers cross the film, the external circuit must supply charge to the electrodes in order to hold V constant. The corresponding current is proportional to the number of carriers and their average

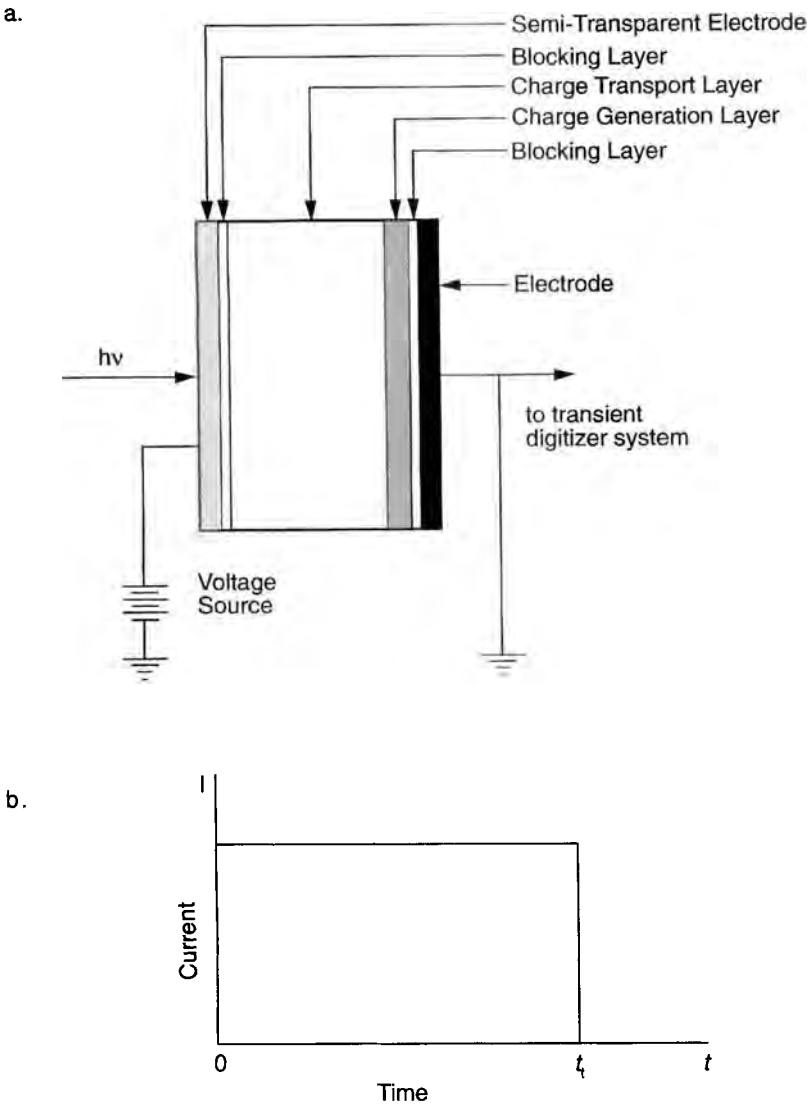


Figure 28. a) A schematic of a time-of-flight experiment. A multilayer sandwich is constructed by depositing the CTL, and other layers (CGL for example) as desired, on a suitable substrate. One electrode is connected to a power supply and the other is connected to ground via a load resistor. The voltage applied by the power supply produces a uniform electric field in the sample. A pulsed exposure generates charge carriers which cross the sample under the influence of the applied field. As they move, current flows through the load resistor to ground and a voltage signal, generated across the resistor, is recorded. The signal is proportional to the number and average velocity of the charge carriers. b) Idealized current (I) signal vs. time (t) from a time-of-flight experiment. The current rises from zero when holes are generated ($t = 0$), remains constant as they drift across the CTL at a constant velocity, and drops back to zero when they reach the collecting electrode (t_i , the transit time or time of flight).

velocity. Recording of this current monitors the progress of the charge carriers as they cross the film. The current begins when they are launched and it ceases when all have reached the collecting electrode. This experiment is repeated over a range of field strengths and temperatures. The field strength usually ranges from the highest value that does not risk catastrophic electrical breakdown of the sample, down to the lowest value at which an adequate signal can be obtained. The temperature usually ranges from a high value near the glass transition temperature, where the sample begins to soften, down to the lowest value at which data can be obtained over a significant range of field strengths.

An ideal time-of-flight signal is shown in Figure 28(b), and real signals are shown in Figure 29. The signal in Figure 29(a) approaches the ideal. However, there is an initial narrow spike of undetermined origin, a brief period of rising current before the steady-state plateau, and a final "tail" of significant duration. The initial spike and the final tail are general phenomena; the rise to the plateau may be an experimental artifact. The end of the plateau marks the time at which holes begin to reach the collecting electrode. The falling tail represents the arrival of additional holes, and the baseline is reached eventually, when all holes have been collected. Thus, there is some spread in the times that holes require to cross the sample. The end of the plateau (t_i in Figure 29a) marks the transit time of the fastest holes, whereas the point at which the current has fallen to half of its plateau value ($t_{1/2}$) represents, loosely speaking, the transit time of an "average" hole. Most of the data discussed below use t_i as the transit time, even though $t_{1/2}$ is a more realistic indication of how rapidly charge is transported by the sample [53]. Other operational definitions of the transit time have been proposed [54]. Figure 29(b) shows a more typical signal. The spike and the tail are broader, and the plateau (in this case) is not entirely flat. The end of the plateau is not abrupt, and the transit time is defined operationally by the crossing of tangents drawn to the plateau (where it is closest to level) and the tail (where it is steepest). In cases where the spike and the tail are much wider and the "plateau" slopes much more steeply, it may be difficult or impossible to discern a "transit time" from linear I - t plots such as Figures 29(a) and 29(b). In such cases, it is frequently possible to discern such a time on a plot of $\ln I$ vs. $\ln t$. As illustrated in Figure 29(c), such a plot often exhibits two approximately linear portions, and the break point between them can be taken as an operationally defined transit time. Generally, this point is identified by a crossing-of-tangents construction like that in Figure 29(b).

In most amorphous molecular solids, the dependence of mobility on electric field strength and temperature has the form illustrated in Figures 30 and 31. Typical field-strength data at various temperatures are shown in Figure 30. At a given temperature, the mobility increases with increasing field strength. With increasing temperature, the mobility increases and the field dependence weakens. The non-linear scales of E and μ are chosen to illustrate that $\ln \mu$ (or $\log \mu$) is usually a linear function of $E^{1/2}$ (Eq. (3)), or μ is an exponential function of $E^{1/2}$ (Eq. (4)), over a wide range of field strengths.

$$\ln \mu(E, T) = \ln \mu(0, T) + S(T)E^{1/2} \quad (3)$$

$$\mu(E, T) = \mu(0, T) \exp(S(T)E^{1/2}) \quad (4)$$

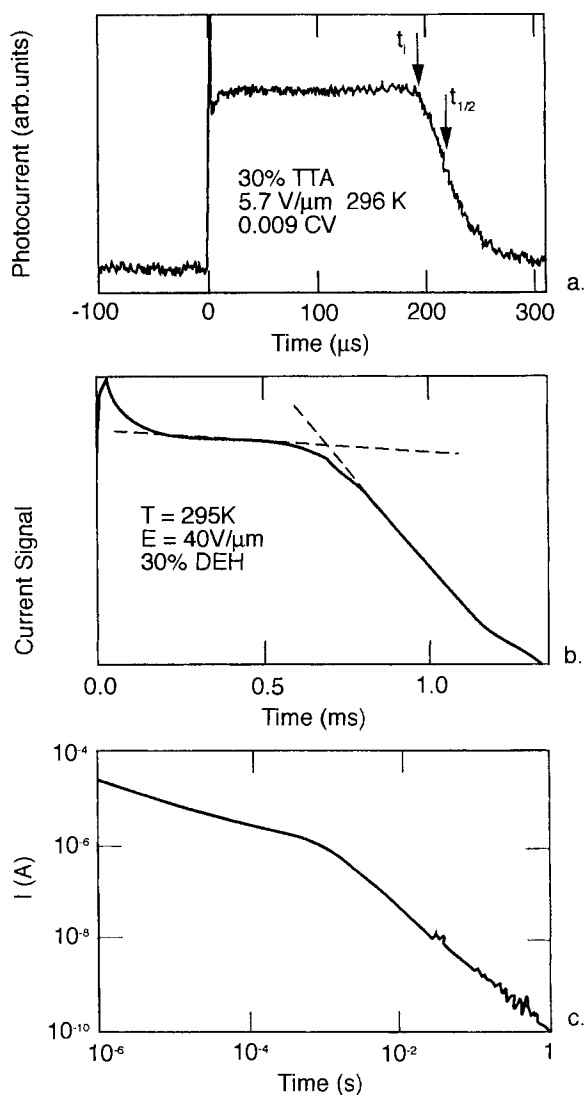


Figure 29. Representative time-of-flight signals for hole transport. a) tri-*p*-tolylamine (TTA) (30 wt.%) in polystyrene. (Reprinted with permission from Ref. [60b].) Two operational definitions of the transit time are indicated by t_i and $t_{1/2}$. b) *p*-Diethylamino-benzaldehyde diphenylhydrazone (DEH) (30 wt.%) in bisphenol-A polycarbonate. (Reprinted with permission from Ref. [60i].) c) A polysiloxane with *N*-alkylcarbazole pendant groups. (Reprinted with permission from Ref. [72g].)

The entire data set, $\mu(E, T)$, can be summarized by the intercept, $\mu(0, T)$, and slope, $S(T)$, as functions of temperature. A typical temperature dependence of $\mu(0, T)$ is illustrated in Figure 31. While the data may be described qualitatively as “activated”, μ exponential in T^{-1} , the dependence is actually somewhat stronger, μ exponential in T^{-2} , as if there were a temperature-dependent activation energy. Whenever the data permit one to judge between T^{-1} and T^{-2} , an exponential dependence on T^{-2} is usually the better description. This dependence can be characterized by its $T \rightarrow \infty$ limit, μ_0 (a hypothetical mobility at infinite temperature), and a slope T_0^{-2} (where T_0 may be viewed as a characteristic temperature) (Eq. (5)).

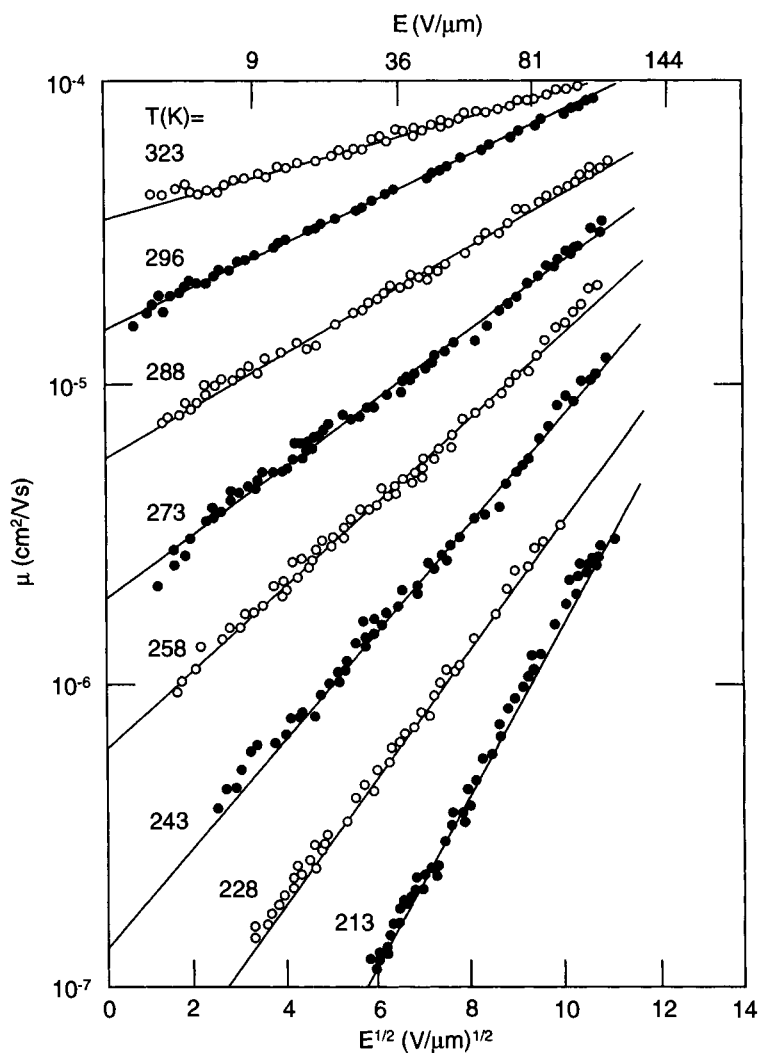


Figure 30. Mobility, μ , plotted linearly in $\ln \mu$, as a function of electric field strength (E), plotted as $E^{1/2}$, for holes in tri-*p*-tolylamine (TTA) (40 wt.%) in bisphenol-A polycarbonate. The range of field strengths is approximately 10^4 – 10^6 V cm $^{-1}$ (1–100 V μ m $^{-1}$). The mobility depends exponentially on $E^{1/2}$. With increasing temperature, the overall magnitude of μ increases while the dependence on E weakens. These dependences are observed in nearly all amorphous molecular solids. (Reprinted with permission from Ref. [73r].)

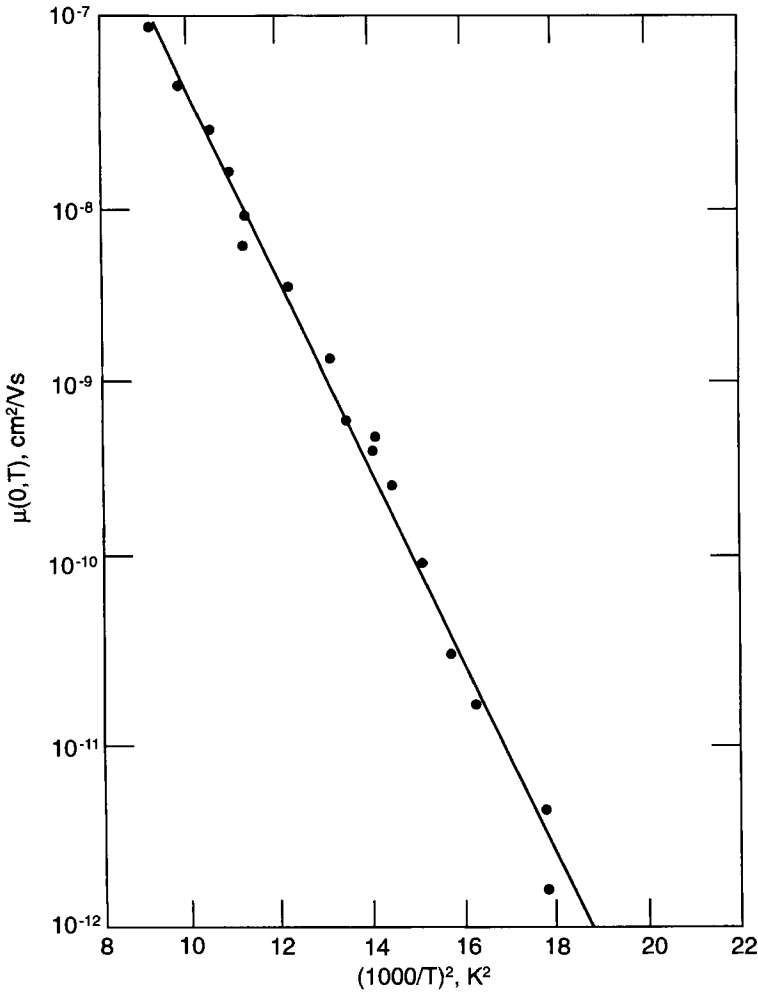


Figure 31. Temperature (T) dependence of the “zero-field mobility”, $\mu(0, T)$, for electron transport in 4-*n*-butoxycarbonyl-9-fluorenylidene malononitrile (BCMF) (30 wt.%) in a polyester. The data are plotted as $\ln \mu$ vs. T^{-2} . (Reprinted with permission from Ref. [60j].)

$$\mu(0, T) = \mu_0 \exp(-(T_0/T)^2) \quad (5)$$

The temperature dependence of the slope parameter, $S(T)$, is illustrated in Figure 32. With increasing temperature, $S(T)$ decreases in a manner that is usually a linear function of T^{-2} .

The mobility depends strongly on the concentration of the charge transport material (CTM). Figure 33 illustrates this dependence at room temperature for hole transport in *N*-isopropylcarbazole (NIPC)-doped bisphenol-A polycarbonate from

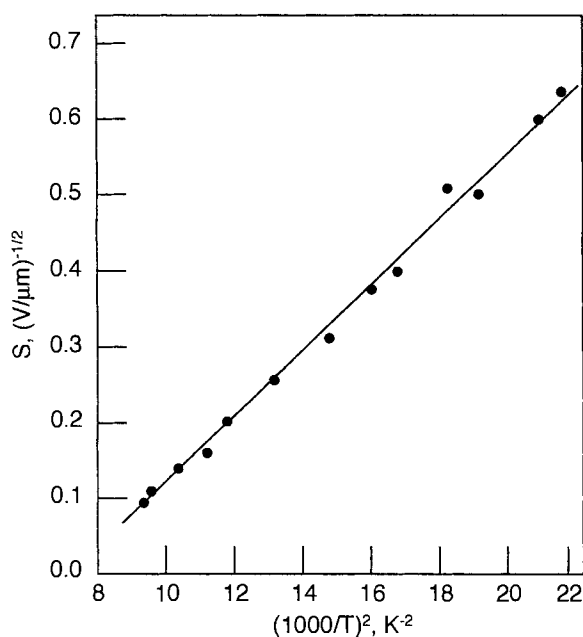


Figure 32. Field-dependence parameter S vs. temperature (T), plotted linearly in T^{-2} for hole transport in tri-*p*-tolylamine (TTA) (40 wt.%) -doped bisphenol-A polycarbonate. (Adapted from Ref. [73r].)

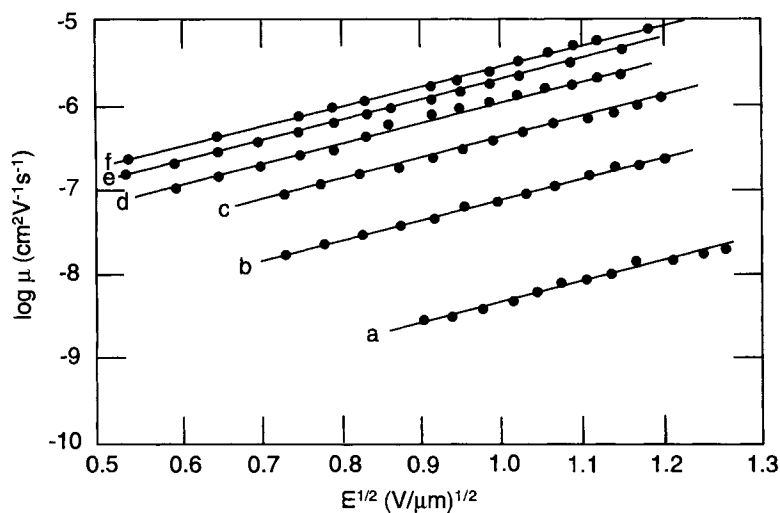


Figure 33. Dependence of the mobility on CTM concentration: mobility of holes (μ) in *N*-isopropylcarbazole (NIPC)-doped bisphenol-A polycarbonate as a function of field-strength (E), plotted as $E^{1/2}$, for a) 9 %, b) 17 %, c) 23 %, d) 29 %, e) 33 %, and f) 38 % NIPC by weight. (Reprinted with permission from Ref. [51].)

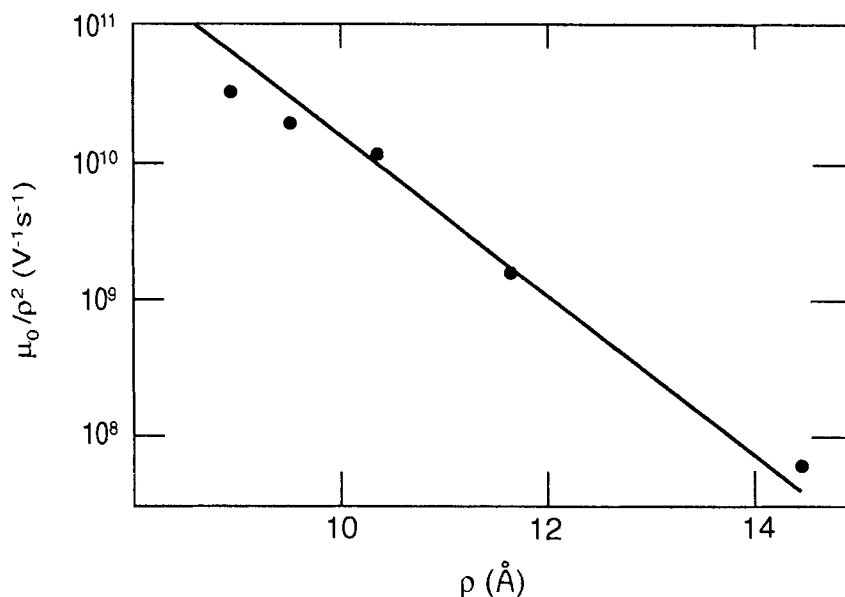


Figure 34. Dependence of the overall-magnitude parameter μ_0 on separation between NIPC molecules (ρ) in NIPC-doped bisphenol-A polycarbonate. The slowly varying factor ρ^{-2} compensates for variation of the average hopping distance. Data taken from Ref. [51].

9 wt.% CTM (below the “practical” concentration range) up to 38 wt.% (approximately the solubility limit) [51]. The functional form of the field and temperature dependences does not change over this range of concentration, and the only quantitative parameter that varies strongly is the overall magnitude of the mobility μ_0 . To illustrate this dependence, in Figure 34, μ_0 is plotted vs. an “average” separation between CTM molecules, ρ . The distance ρ is defined such that the concentration of CTM is one molecule per volume ρ^3 .

One other compositional effect is exceedingly significant. Given a doped polymer in which the CTM and the polymer host are relatively nonpolar, and a similar material in which a highly polar species is present, the mobility in the polar system is usually much smaller and more strongly dependent on field strength and temperature. Figure 35 illustrates this trend with the zero-field mobilities, $\mu(0, T)$, plotted as functions of temperature, for tri-*p*-tolylamine (TTA) in two polymers [55a]. The dipole moment of TTA is small, ~ 0.9 D [55b]. The dipole moment of polystyrene, 0.4 D per repeat unit [55c], is much smaller than that of poly(4-chlorostyrene), ~ 1.9 D per repeat unit, approximated by the dipole moment of *p*-chlorotoluene [55d]. The mobility in the polar host is much smaller and depends much more strongly on temperature. There are many literature examples of the polymer host effect on mobility [55e–k]. Figure 36 provides another illustration, in which TTA/polystyrene is co-doped with equimolar, small amounts (~ 2 wt.%) of highly polar additives [56a].

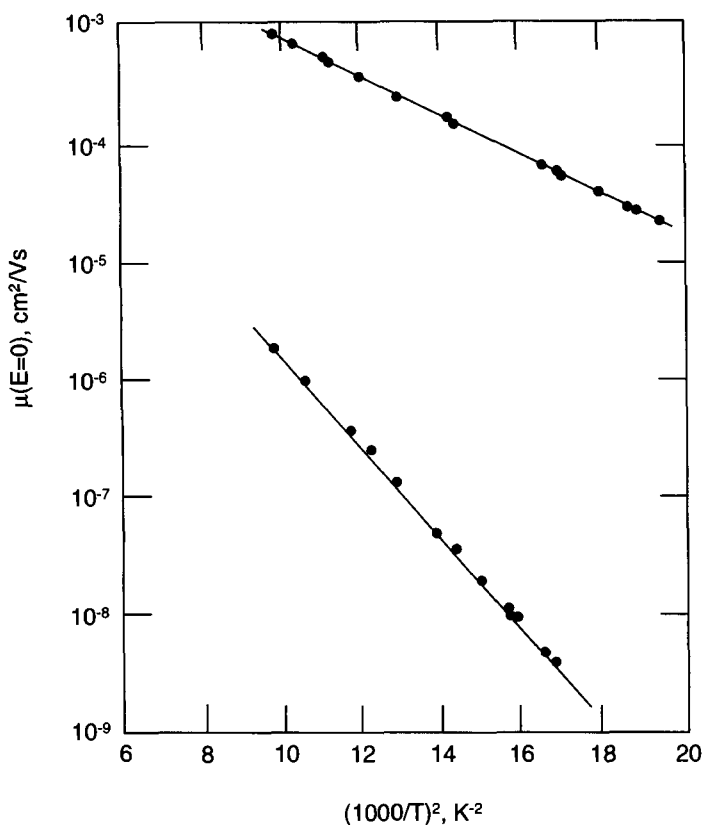


Figure 35. Zero-field mobility (μ) for hole transport in TTA (40 wt.%) -doped polystyrene (above) and poly(*p*-chlorostyrene) (below), shown as functions of temperature (T , plotted as T^{-2}). (Reprinted with permission from Ref. [55a].)

The larger the dipole moment of the additive, the lower the mobility and the steeper its field dependence becomes. The literature has many examples of the effect of polar third components [55g, 56a–f]. If the dominant polar component is a hole-transporting CTM itself, the mobility largely correlates with its dipole moment, even across various chemical families (Figure 37) [56g–m].

Qualitative explanations

Before presenting some additional experimental observations, we pause to discuss, qualitatively, how the foregoing trends and dependences may be understood. (A quantitative theory of charge transport in amorphous molecular solids will be discussed later.) In any charge transport process, whether the carriers are electronic or ionic, and whether the medium is crystalline, amorphous, or fluid, each individual carrier undergoes a random walk in which there is a preference (large or small, de-

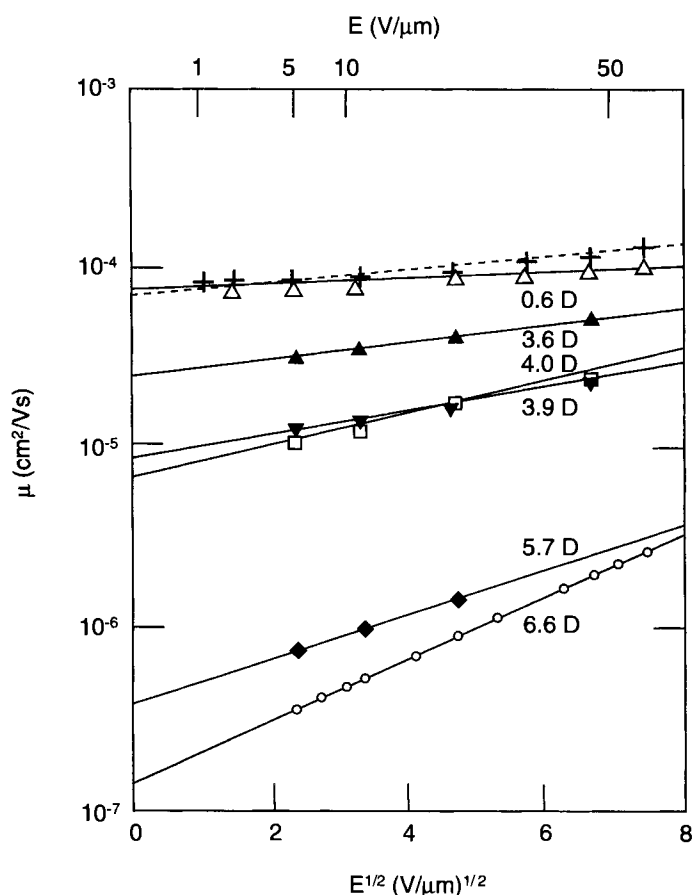


Figure 36. Mobility (μ) and its dependence on field strength (E) for TTA (30 wt.%) -doped polystyrene (broken line) and TTA-doped polystyrene containing small amounts of polar additives. Their dipole moments are indicated beside the corresponding lines. The concentration of each additive was 1.3×10^{20} molecules cm^{-3} , corresponding to 2–4 wt. %: *p*-dinitrobenzene (0.6 D), *m*-dicyanobenzene (3.6 D), 1-cyanonaphthalene (3.9 D), 3-nitrobiphenyl (4.0 D), *o*-dicyanobenzene (5.7 D), and 4-*t*-amylphthalonitrile (6.6 D). (Reprinted with permission from Ref. [56a].)

pending on the field strength) for steps in the forward direction (Figure 38). In an amorphous molecular solid, the random walk may be viewed as a sequence of hops (electron transfer reactions, Eq. (1) or (2)) between nearby sites (CTMs). At each site, the carrier has a “site energy” equivalent to the energetic cost of producing the cation or anion of the corresponding CTM (i.e., its solid-state ionization potential or electron affinity). With this definition, thermodynamics favors occupancy of low-energy sites for hole, as well as electron, transport. For electrons, a low-energy site has a low-energy LUMO; for holes, it has a high-energy HOMO. The site energy varies randomly from site to site, because an amorphous molecular solid is (by

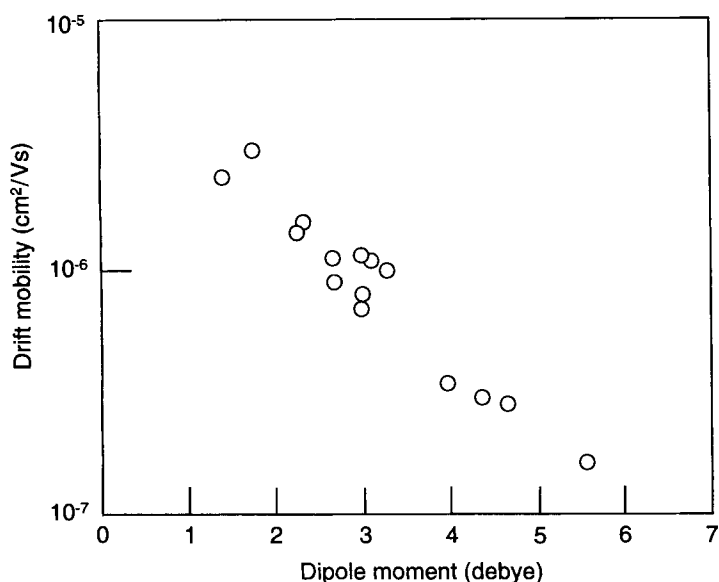


Figure 37. Hole mobility (μ) vs. dipole moment of the charge transport material (CTM) (50 wt.%) in a polycarbonate host. The CTMs belong to various chemical classes. The field strength was $2.5 \times 10^5 \text{ V cm}^{-1}$. (Reprinted with permission from Ref. [56g].)

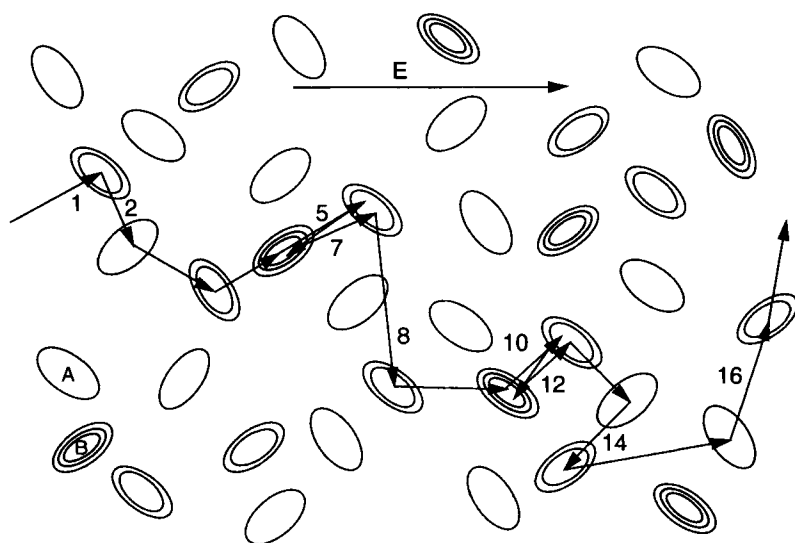


Figure 38. Schematic of an amorphous molecular solid with both energetic and geometrical disorder. Each randomly oriented hopping site (CTM) is represented by a disk with the number of concentric rulings representing the energy of a charge carrier. (Site A is relatively shallow; site B is very deep.) Electric field direction is E. See the text for a detailed explanation.

definition) disordered, and different CTMs are in different environments. This factor is known as energetic, or diagonal, disorder. Therefore, each hop generally involves an energy increment, and the hopping rate constant depends on that increment. Since most hops involve sites of different energy, they are only formally self-exchange reactions. Moreover, a charge carrier tends to spend most of its time at relatively low-energy sites. In addition to energetic factors, there are geometrical factors as well. Even if there were no disorder, steps from one site to its nearest neighbors would have different rate constants because of the asymmetric shapes of typical CTMs and their HOMOs or LUMOs. In a disordered material, the relative orientations and separations of near neighbors also vary randomly, a factor known as geometrical, or off-diagonal, disorder.

The distribution of site energies (DOS, for “density of states”) is generally assumed to be Gaussian, with an r.m.s. (root mean square) width several times larger than $k_B T$ (the thermal energy). For qualitative purposes, some important consequences of such a DOS are the following.

- 1) If there were no electric field, the thermal average energy would be deep in the low-energy “tail” of the DOS. In the presence of a field, the steady-state distribution of energies is no longer that of thermal equilibrium. Nevertheless, as it crosses the sample, a carrier spends most of its time in such low-energy sites.
- 2) Those sites are sufficiently rare, and hence sufficiently far apart, that a carrier cannot simply hop from one to another. Rather, it must first hop to a nearby site of higher energy (in the central portion of the DOS) and undergo further hops among other sites of similar energy, before eventually finding another low-energy site.
- 3) As the temperature decreases, the average energy decreases, i.e., carriers sink deeper and deeper into the tail of the DOS.
- 4) Hops from deep sites to nearby, higher-energy sites contribute to the activation energy for transport. At lower and lower temperature, that contribution increases because a carrier spends most of its time in deeper and deeper sites. The apparent temperature-dependent activation energy mentioned in conjunction with Eq. (5) is easily understood on this basis. (Of course, any reorganization energy for the electron transfer process may also contribute to the temperature dependence.)
- 5) The energy differences among nearby sites are altered by the presence of an electric field, and, therefore, so are the hopping rate constants. It is plausible, if not entirely obvious, that energetic disorder should generally make the mobility more strongly field-dependent.
- 6) Suppose that, at the start of a time-of-flight experiment, carriers are injected into states in the center of the DOS. They would then take many rapid steps among sites of similar energy before coming to (temporary) rest at a rare, low-energy site. This initial, rapid motion is one possible explanation of the initial spike in the photocurrent signal (Figure 29). The plateau represents a subsequent steady state.
- 7) The time that an individual carrier requires to cross the sample is the sum of the times (residence times) that it spends at each site along the way, which is

approximately equal to the sum of times spent at a few very deep sites. Different carriers encounter different numbers of such sites, and since these numbers are small, the *relative* variation among them is large. The extended tail of the time-of-flight signal (Figure 29) is a consequence.

The concentration dependence of the mobility is also easily understood. The CTMs are not in close contact, so electron transfer between them is presumably nonadiabatic [34k], and the rate constant(s) should have roughly an exponential dependence on the distance between molecules. (Adiabatic transport is reported in some systems [57a–c]. However, the interpretation in terms of adiabatic transport requires problematic values for an electron transfer integral and phonon frequency [57b].) The mobility ought to exhibit a similar exponential dependence on the average separation. Indeed, the trendline in Figure 34 has a slope of 1.35 \AA^{-1} , comparable with the rate at which electron transfer rate constants typically vary with intermolecular separation [57d–f]. (The mobility must depend on not only the rate constant(s), but also the average distance ($\sim \rho$) over which a charge carrier moves in an individual electron transfer event. To compensate for this factor, in plots like Figure 34, the abscissa is usually μ or μ_0 divided by a factor such as ρ^2 . Additional divisors are sometimes included, to remove the influence of other presumed theoretical factors (see the section on geometrical disorder, below).)

The influence of polar components can also be understood in terms of energetic disorder. Near any site, there are polar molecules (or moieties) oriented at random, and the electrostatic interactions between their dipole moments and a charge carrier make random contributions to the site energy. Thus, the presence of polar components increases the total energetic disorder (viz. the width of the DOS) and, thereby, the strength of the dependence on temperature and field strength. Most probably, the dipoles reorient somewhat in response to the presence of a charge at that site, and the corresponding reorganization energy should also contribute to the temperature dependence. This contribution is probably minor, because the materials are rigid in the temperature range of interest. The dielectric constants of the host polymers are governed by the same ability of the dipoles to reorient, and they are typically small (3.0 for polycarbonate [58a], 2.6 for poly(*p*-chlorostyrene) [58b], 2.6 for poly(methyl methacrylate) [58c]. In cases where they have been evaluated, the dielectric constants of the doped polymers are also low [56d,1]. (An early assertion that a small amount of a highly polar additive dramatically increases the dielectric constant [56b] could not be reproduced [56d].)

The Gaussian Disorder Model

A simple model, the Gaussian Disorder Model of Bässler and co-workers, has been very useful in rationalizing charge transport data on many amorphous molecular solids [59]. Its present version consists of the following assumptions.

- 1) Transport sites are arrayed on the points of a simple cubic lattice. The lattice parameter is denoted a .

- 2) The site energies ε_i^0 (before application of an electric field) belong to a Gaussian distribution characterized by its r.m.s. width (standard deviation, σ), (the term “variance”, often used synonymously, more properly refers to σ^2) with no correlation between the energies of different sites.
- 3) A wavefunction-overlap parameter, Γ_{ij} , is assigned to each pair of sites. It is assumed to be a sum of individual-site contributions Γ_i and Γ_j , each belonging to a Gaussian distribution. The values at neighboring sites are uncorrelated. The resulting average value and standard deviation of the Γ_{ij} are denoted $\bar{\Gamma}$ and Σ . This assumption is intended to model geometrical disorder.
- 4) The rate constant for hopping from site i (located at \mathbf{r}_i) to site j (at \mathbf{r}_j) depends on the site energies $\varepsilon_i^0, \varepsilon_j^0$ and the overlap parameter Γ_{ij} according to Eq. (6),

$$v_{ij} = v_0 \exp(-\Gamma_{ij}\mathbf{r}_{ij}/a) \exp(-\beta(\varepsilon_{ij}^0 - q\mathbf{E} \cdot \mathbf{r}_{ij})) \quad (6)$$

where v_0 is an additional constant determining the overall rates, $\beta = (k_B T)^{-1}$, q is the charge of the carrier, $\varepsilon_{ij}^0 = \varepsilon_j^0 - \varepsilon_i^0$, and $\mathbf{r}_{ij} = \mathbf{r}_j - \mathbf{r}_i$.

The consequences of this model have been explored by Monte Carlo simulation [59b]. A model sample is constructed, using a Gaussian random-number generator to assign an ε_i^0 and a Γ_i to each lattice site. A carrier is placed on an arbitrary initial site, and its random walk through the lattice is generated. A random-number generator is used to decide how long the carrier resides at each site and which site it visits next, taking into account the rate constants for various possible hops from this site to nearby sites. This process is repeated for several carriers on a given lattice, then a new sample is constructed and more random walks are generated. The average velocity and other statistics are collected. The results have been summarized by formulas for the zero-field (limiting) mobility (Eq. (7)) and the slope of the field strength (Eq. (8)) as functions of temperature (cf. Eqs. (3)–(5)):

$$\mu(0, T) = \mu_0 \exp(-(\frac{2}{3}\hat{\sigma})^2) \quad (7)$$

$$S(T) = C(\hat{\sigma}^2 - \hat{\Sigma}^2) \quad (8)$$

Here, μ_0 is a constant (proportional to v_0); $\hat{\sigma} = \sigma/k_B T$; $\hat{\Sigma} = \Sigma$ or 1.5, whichever is greater; and $C = 2.9 \times 10^{-4} \text{ cm}^{1/2} \text{ V}^{-1/2}$.

Equations (7) and (8) have been used to fit the data on many amorphous molecular solids. They reproduce the T^{-2} temperature dependence of the mobility that is often observed, both at zero [Eq. (5)] and nonzero field strength [60a]. The slope of a plot of $\mu(0, T)$ vs. T^{-2} (see Figures 31, 35) can be used to evaluate σ . Equation (8) also predicts a T^{-2} dependence for the slope parameter, viz. $S(T) = [C(\sigma/k_B)^2]T^{-2} + \text{constant}$ (see Eq. (4)), and this dependence is consistent with the experimental data. For the example shown in Figure 32, the slope of a plot of $S(T)$ vs. T^{-2} can be combined with the value of σ evaluated from the temperature dependence of $\mu(0, T)$ to evaluate the proportionality constant C . The result in that case is $2.6 \times 10^{-4} \text{ cm}^{1/2} \text{ V}^{-1/2}$, in remarkable agreement with the predicted value of

$C = 2.9 \times 10^{-4} \text{ cm}^{1/2} \text{ V}^{-1/2}$. This level of agreement is typical although C values as low as 1.6×10^{-4} and as high as $4.4 \times 10^{-4} \text{ cm}^{1/2} \text{ V}^{-1/2}$ have been reported [60b,c].

Another prediction of the model is the following. Imagine two doped polymers in which the identity, concentration, and packing of the CTM are the same (i.e., the geometrical disorder is the same) but the degree of energetic disorder is different. The mobility in the two materials should be described by the same values of μ_0 and Σ . Data shown in Figure 35 illustrate approximately the anticipated behavior. Over the experimental temperature range, the zero-field mobilities differ by orders of magnitude. Nevertheless, when the data are analyzed according to Eq. (7), the resulting values of μ_0 differ by only a factor of approximately 3! (The values of μ_0 are 0.042 in polystyrene and 0.013 in poly(*p*-chlorostyrene) [55a].) Numerous similar cases are known [55i, 56l, 60]. This comparison is based on the assumption that the arrangement of the CTM is the same in the two materials (or that it does not matter much). Molecular packing in amorphous solids is neither controlled nor well understood; so, it is not surprising that some counterexamples are also known, particularly in comparisons between structurally very different host polymers [55j, 60h].

As described above, the effect of polar components has been ascribed to a contribution of random charge–dipole interactions to the overall disorder. When data on polar and nonpolar systems are compared using the Gaussian Disorder Model, the polar systems generally have larger values of σ . In fact, the difference between well-matched polar and nonpolar systems, such as those illustrated in Figure 35, can be reproduced at least semiquantitatively on the following basis. In the polar system, assume that the charge–dipole contributions to the site energies are uncorrelated with the remaining (“nondipolar”) contributions, and assume that the nondipolar contributions are the same in the two systems. Further, to model the charge–dipole interactions, consider a point charge surrounded by a simple cubic lattice, with randomly oriented point dipoles occupying random lattice points [61]. Then the predicted relationship between σ values [eV] for the polar and nonpolar materials, σ_p and σ_n , is given by Eqs. (9) and (10),

$$\sigma_p^2 - \sigma_n^2 = \sigma_d^2 \quad (9)$$

$$\sigma_d[\text{eV}] = 0.173 p \kappa^{-1} M^{1/2} (a')^{-1/2} \quad (10)$$

where p and M are the dipole moment [Debyes] and concentration [mol L^{-1}] of the polar component, κ is the relative dielectric constant of the doped polymer, and a' is the lattice constant [\AA] for the model lattice [61d]. If the polar component is the CTM, $a = a'$. If it is an additional dopant or part of the polymer, the best choice of a' is generally not equal to a . The result is model-dependent, but weakly so, provided that a' is chosen to be of molecular dimensions. For example, the temperature dependences shown in Figure 35 imply σ values of 0.082 and 0.122 eV for TTA in polystyrene and poly(*p*-chlorostyrene), respectively, whence $\sigma_d = 0.086$ eV. Using Eq. (10) with $p = 1.9$ D [55d] and $M = 4.3 \text{ mol L}^{-1}$ for chlorophenyl moieties, neglecting the contribution of less polar components, and taking $\kappa = 3$ (a reasonable value for the low-frequency dielectric constant, but the actual value unknown), and $a' = 7 \text{ \AA}$ (the sum of estimated radii of a TTA molecule and a chlorostyrene unit)

gives a remarkably similar value, 0.091 eV. This degree of agreement is surely fortuitous; only rough agreement should be expected from so simple a model. In addition to the use of point charges and dipoles and a uniform, cubic lattice, the dielectric constant is introduced in an ad hoc manner. Moreover, the most appropriate value of κ may not be that of the rigid amorphous solid, which is in any case unknown. Nevertheless, even rough agreement offers some confirmation of the Gaussian Disorder Model as a whole, as well as its explanation of the effect of polar components. The literature offers numerous examples, although some comparisons of different materials using an equivalent of Eq. (10) need to be adjusted to account for differences in molecular weight [55a,i, 56l,m, 60a,e,g, 62a-c].

Despite the considerable success of Eq. (7) in consistently rationalizing mobility data in many systems, the Gaussian Disorder Model misses the mark in one major way. The field-strength (E) dependence predicted for a realistic value of $\hat{\sigma}$ (3.0, approximately the smallest $\hat{\sigma}$ ever encountered in practice) and various values of Σ is shown in Figure 39 [63a,b]. Only for strong fields (sometimes only above 10^6 V cm^{-1}) are the results adequately described as linear functions of $E^{1/2}$, whereas experimentally this linearity usually extends to the lowest values of E accessible (sometimes as low as 10^4 V cm^{-1}) [60b, 63c,d]. It was initially proposed that the

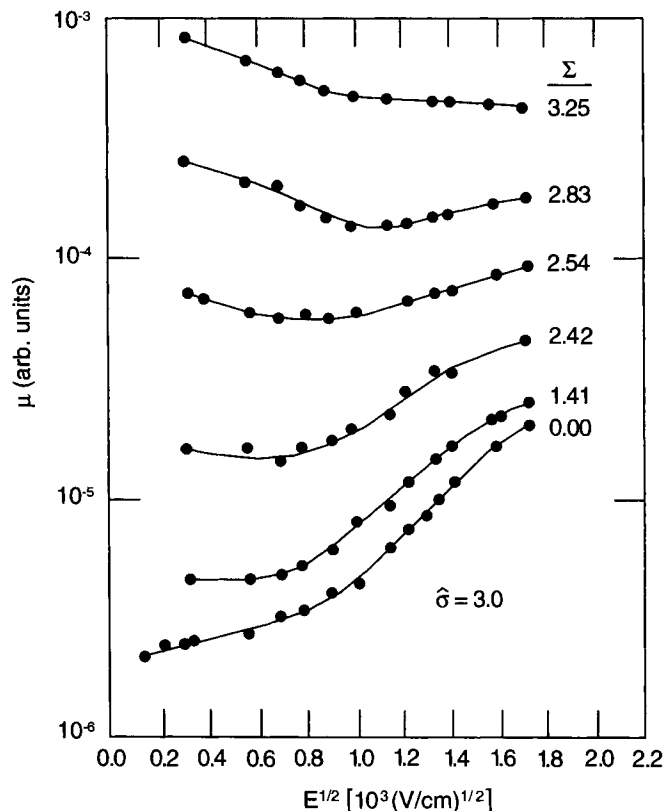


Figure 39. Field-strength (E) dependence of the mobility (μ) predicted by the Gaussian Disorder Model. (Reprinted with permission from Ref. [63b].)

discrepancy at low E was due to different operational definitions of mobility in the simulations and experiments [63b]; however, further experimental observations make this rationalization unlikely [60b]. The Slope values in Eq. (8) are taken from a fit to just the high-field linear portion [63b]. Given that the field dependence is not reproduced properly over the typical experimental range, it may well be fortuitous that the experimental slope parameter C agrees so well with the value predicted from this fit [$2.9 \times 10^{-4} \text{ cm}^{1/2} \text{ V}^{-1/2}$]. The observed value of C is $\sim (e\rho/k_{\text{B}}T)^{1/2}$, a rather natural scaling factor for $E^{1/2}$ [63e]. In fact, the quality of the agreement deteriorates somewhat when the experimental data are reanalyzed with a more exact theory (Eq. (12), below). Moreover, the model of geometrical disorder that gives rise to this prediction is quite arbitrary, other simple models give different field dependences [63e], and a different field dependence also arises if an alternative, equally plausible dependence on site energies is assumed for the hopping rate constant [63f]. There is no particular reason to favor one model over another. The assumption of a Gaussian distribution of Γ_{ij} values is, in fact, not very plausible. It is equivalent to the assumption that the orbitals involved in electron transfer are a) spherically symmetric and b) characterized exclusively by variation of their “orbital radii” via the site parameters Γ_i . Neither assumption is particularly realistic, and assumption b) entails an unphysical correlation among the prefactors ν_{ij} for hops originating at the same site (i) [63e]. Geometrical disorder represents the distribution of intermolecular electron transfer matrix elements (V) among nearby pairs of CTMs, and V has a complicated dependence on intermolecular separation and mutual orientation [63g]. The resulting distribution of V has not been evaluated. A promising alternative explanation of the specific form of the field dependence will be sketched in the next section.

Although the general outlines of the Gaussian Disorder Model are probably correct, it is important to note some additional concerns.

- 1) A Gaussian distribution of site energies is expected when each site energy is the sum of many independent contributions of comparable size. The model of dipolar effects underlying Eq. (10) indeed predicts such a distribution, essentially because the charge–dipole interaction is relatively long-ranged and, indeed, many dipoles affect the energy of a given site [61d]. The energetic disorder in a rigid medium is roughly a frozen-in version of the energy level fluctuation that occurs rapidly in a fluid medium. The Gaussian distribution that is assumed to describe static disorder is analogous to the parabolic distribution of (free) energies ascribed to fluctuations in a fluid solution [64a,b]. However, in materials lacking large dipole moments, the relevant interactions of a charge carrier with nearby molecules (charge–polarizability, charge–quadrupole, etc.) are relatively short-ranged, and there may not be enough independent contributions to yield a Gaussian distribution of site energies, especially in the low-energy tail where charge carriers spend most of the time.
- 2) An independent estimate (i.e., spectroscopic) of the magnitude of the energetic disorder in these materials is needed. To date, σ has been largely a fitting parameter. The fact that a theoretical estimate of the dipolar contribution (σ_{d}) agrees reasonably well with experiment is encouraging, but not definitive.

- 3) The specific energy dependence of the microscopic rate constant, Eq. (6), is not of the form usually encountered in electron-transfer theory [64c,d], nor is it consistent with the current understanding of charge transport in molecular crystals [64e]. Equation (6) was originally derived to represent trap-to-trap hopping in crystalline semiconductors at cryogenic temperatures [64f], and it is not obviously applicable to molecular solids around room temperature [64g,h]. The literature has examples of calculations employing other functional forms for the microscopic rate constants [63f, 64e,i–n].
- 4) The simulations themselves were done using fixed values of the parameters, $a = 6 \text{ \AA}$ and $\Gamma = 10$. The values that would be appropriate to model a given system depend on the concentration of CTM (6 \AA is invariably too small), and the results, e.g., the value the factor of $2/3$ in Eq. (7), depend on these parameters [64o].
- 5) The simulation results are more accurately represented by a formula that differs somewhat from Eqs. (7) and (8), i.e., Eqs. (11) and (12),

$$\mu(0, T) = \frac{T_r}{T} \mu_0 \exp(-(\frac{2}{3}\hat{\sigma})^2) \quad (11)$$

$$S(T) = C(\hat{\sigma}^2 - \hat{\Sigma}^2) \left(\frac{T_r}{T} \right)^{1/2} \quad (12)$$

where T_r is a reference temperature (e.g., the temperature for which the simulations were actually done, 295 K) [64H]. Use of these formulas, instead of Eqs. (7) and (8), gives very similar values of μ_0 , σ , and Σ , but significantly different values of C [56l, 60b, 64H, 64p].

The Correlated Disorder Model

The ubiquitous dependence of the mobility on field strength, exponential in $E^{1/2}$ (Figure 30) has puzzled researchers for decades [45, 63c,d]. Such a dependence can arise if the material contains charged traps (the Poole–Frenkel effect) [3q], but this explanation seems implausible for the following reason. In most amorphous molecular solids, such traps would have to be accidental impurities; their concentration would most likely vary from batch to batch or from laboratory to laboratory, and so should the observed mobility values. While there are variations in measured values from one laboratory to another, they are usually not severe enough to support this explanation. As indicated above, the Gaussian Disorder Model fails to reproduce the E dependence at low field strengths, and the reason may be obvious in hindsight. The observed $E^{1/2}$ dependence sometimes extends below 10^4 V cm^{-1} [60b, 63c,d]. The relative energies of two sites $\sim 10 \text{ \AA}$ apart (a typical near-neighbor separation) are shifted by no more than 5 meV by a field of even, say, $5 \times 10^4 \text{ V cm}^{-1}$, and it is hard to see how a shift that is so small relative to $k_B T$ can have a nonlinear influence on charge-carrier dynamics. What is needed is an influence that somehow introduces a greater length scale, and such an influence has recently been proposed.

In the original Gaussian Disorder Model, it was assumed that the energy of any site was uncorrelated with the energy of any other site. A correlation among the energies of sites over distances longer than the average intersite separation can profoundly alter the field dependence of the mobility [65a,b]. Charge–dipole interactions necessarily lead to such a correlation. The interaction of a charge and a dipole, itself, has a rather long range. The energy of interaction of a point charge and a point dipole at a distance R is proportional to R^{-2} . Although this quantity decreases fairly rapidly with increasing distance, the number of dipoles at distances between R and $R + \delta$ increases as R^2 . It is important to note that the correlation of interest is not between the orientations of neighboring dipoles (which may also occur), but between the contributions of distant dipoles to the energies of sites that are not very far apart. The energy at a given site includes significant contributions from dipoles that are far away (relative to the average intersite spacing), and the same dipoles make approximately equal contributions to the energies at other sites near the first one. Consequently, the energies at different sites are correlated, and the length scale of the correlation is greater than the intersite spacing [65a,c,d].

The Correlated Disorder Model of Novikov et al. is like the Gaussian Disorder Model except that each lattice point bears a randomly oriented point dipole as well as a transport site, and the site energy is evaluated by explicitly calculating the energy of a point charge in the presence of the lattice of dipoles [63f]. Thus, the correlations between energies at different sites are built into the model. Simulations of charge-carrier motion on this lattice are able to reproduce the observed $E^{1/2}$ dependence over most of the accessible range of field strengths [63f, 64i, 65c,e,m]. An example is shown in Figure 40. An explanation of how this correlation among the energies of neighboring sites leads specifically to an $E^{1/2}$ dependence of the mobility has been proposed [65b,f]. Based on such simulations, a new formula has been proposed to replace Eqs. (7) and (8) for fitting experimental data [63f, 65g].

Although this model offers a satisfying explanation of the $E^{1/2}$ dependence, it applies only to materials in which interactions between a charge carrier and static dipoles are important. In relatively nonpolar materials, the dominant sources of disorder are probably the interactions of a charge carrier with dipole moments that it induces in its environment [59a], interactions with static higher-order multipoles [65g], and perhaps variations of the ionization potential or electron affinity associated with variations in conformation of the charge-transporting molecule [60c, 65h]. These contributions are all of shorter range than the charge–static dipole interaction and can be expected to give different field-strength dependences. It remains to be seen whether the differences are large enough to be tested, or small enough that the “ \sqrt{E} ” problem has finally been solved [65g,i]. Recent literature has other proposals about the origin of the $E^{1/2}$ field dependence [64j,k, 65j–l].

Recent literature has many examples of theoretical and experimental estimates of the nondipolar (“van der Waals”) component [56m, 59a, 60a,e, 62b,c, 63f, 66a–l]. These estimates may need revision in light of the new understanding of how charge–dipole interactions affect the mobility.

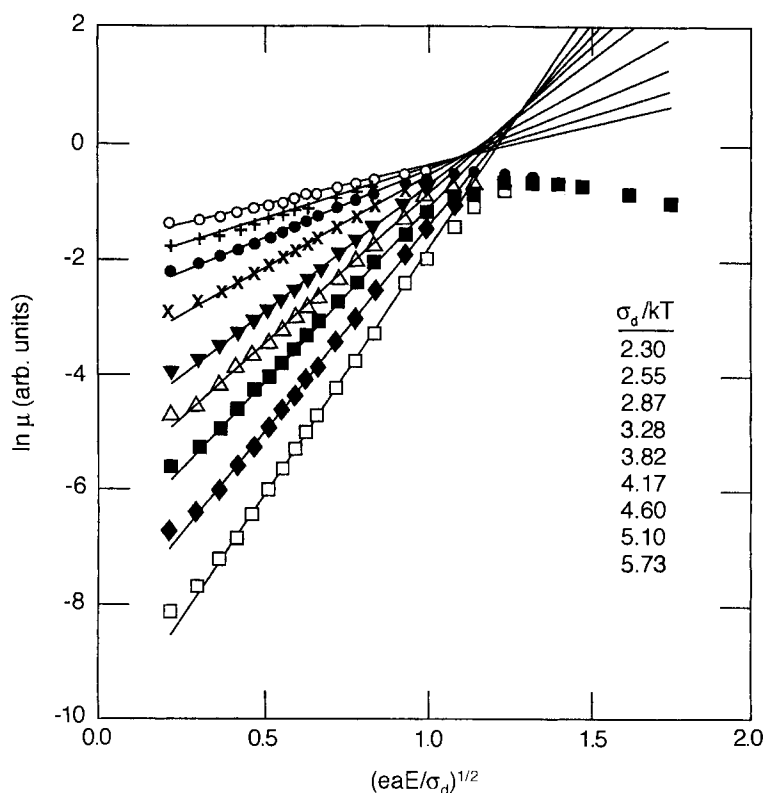


Figure 40. Mobility (μ , plotted as $\ln \mu$) vs. field strength (E , plotted on a scale proportional to $E^{1/2}$) as predicted by the Correlated Disorder Model for DOS of various r.m.s. widths σ_d . The disorder is assumed to arise purely from random charge-dipole interactions. The lattice parameter is a . For $a = 10 \text{ \AA}$ and $\sigma_d = 0.1 \text{ eV}$, $eaE/\sigma_d = 1$ corresponds to a field strength of 10^6 V cm^{-1} . (Reprinted with permission from Ref. [63f].)

The influence of polar components or dipolar disorder

Since dipolar disorder (or, empirically, the presence of polar components) is a major factor governing the mobility, it is worthwhile to make several additional comments on the subject.

To a remarkable degree, it has been possible to correlate the mobility in a given hole-transporting CTM with its net dipole moment, as illustrated in Figure 37. (When molecules with different chemical structures and molecular weights are compared at “equal concentrations”, however, there is some question concerning what measure of concentration to hold constant—weight fraction, molar concentration, etc. [55b].) There are exceptions, CTMs with small dipole moments that, nevertheless, exhibit low mobility for reasons that have not been identified [55b]. It is frequently not possible to determine whether the correlation is with net dipole moment or the overall content of polar groups [55b], and there are cases where the

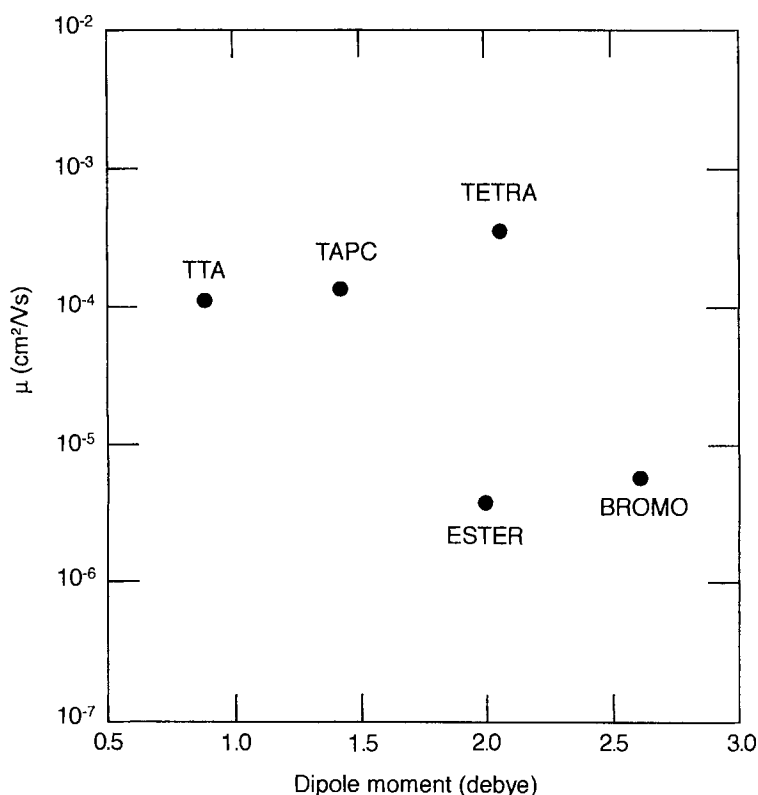


Figure 41. Correlation of mobilities (μ), in the limit of zero-field strength, with the net dipole moment of hole-transporting molecules doped into polystyrene. The hole-transporting unit is essentially the same in each case, a substituted triphenylamine, and it is present at the same molar concentration. The mobility is much reduced for the molecules whose dipole moments are larger because they contain polar substituents (ESTER, BROMO). It is essentially independent of dipole moment for the molecules whose dipole moments are larger just because several triarylamine groups with small dipole moments are chemically linked (TTA, TAPC, TETRA). (Reprinted with permission from Ref. [55b].)

correlation fails for rather obvious reasons. For example, Figure 41 presents a series of five triarylmines at equal molar concentrations of the charge-transporting moiety in a nonpolar host. Two, 4-[bis-(4-methylphenyl)amino]benzenepropanoic acid ethyl ester (ESTER), and 4-bromo-4',4''-dimethyltriphenylamine (BROMO), contain fairly polar groups and exhibit lower mobilities. The remaining three are a monomer (TTA), a dimer (TAPC), and a tetramer (TETRA) of essentially the same triarylamine moiety (Scheme 2). For these three, the concentrations of (weakly) polar moieties are the same, and the main reason that the larger molecules have larger dipole moments is probably just the random addition of several triarylamine group moments [55b].

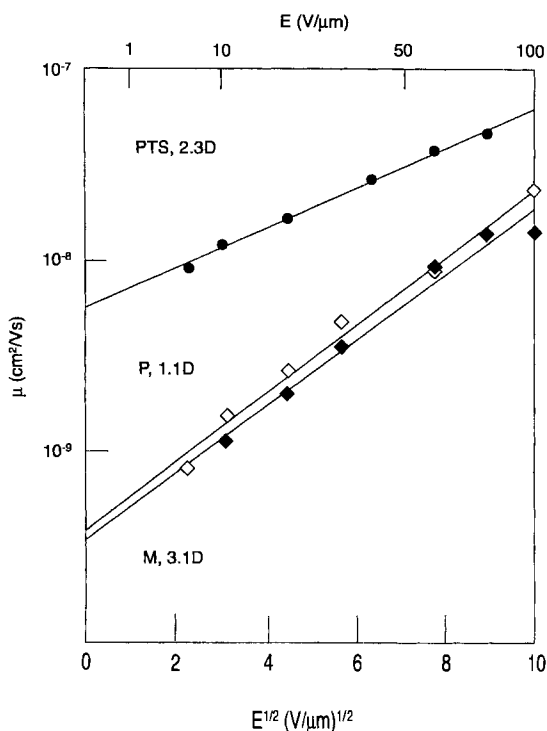


Figure 42. The mobility of electrons in this family of compounds is affected by the presence of additional polar substituents ($-\text{CF}_3$ substitution for $-\text{H}$ on a phenyl sidegroup), rather than the net dipole moment. In contrast to the order of the dipole moments, the mobilities (μ) in **M** and **P** are nearly equal, and they are much lower, and more strongly dependent on electric field strength (E), than the mobility in **PTS**. (Reprinted with permission from Ref. [64p].)

Electron-transporting molecules generally contain multiple highly-polar, electron-withdrawing substituents in order to adjust their electron affinities. The mobilities in such materials are usually relatively low, and the presence of such polar groups is likely to be a contributing factor, even when they are arranged in such a way that the net dipole moment is zero, e.g., *N,N'*-bis(1,2-dimethylpropyl)-1,4,5,8-naphthalenetetracarboxylic diimide (NTDI) (Scheme 3) or 3,5-dimethyl-3',5'-diisopropyl-4,4'-diphenylquinone (DPQ) (Scheme 3) [67]. One case where the presence of polar groups is demonstrably important, regardless of whether their contributions to the net dipole moment partially cancel or reinforce each other, is illustrated in Figure 42 [64p]. Studies were carried out on materials related to 1,1-dioxo-2-(4-methylphenyl)-6-phenyl-4-(dicyanomethylidene)thiopyran (**PTS**) (Scheme 3). Compounds **M** [1,1-dioxo-2,6-bis(3-trifluoromethylphenyl)-4-(dicyanomethylidene)thiopyran] and **P** [1,1-dioxo-2,6-bis(4-trifluoromethylphenyl)-4-(dicyanomethylidene)thiopyran] contain CF_3 groups (~ 2.6 D), located so that the net dipole moments are in the order **M** > **PTS** > **P**. Yet, the mobilities are in the order **PTS** \gg **P** \approx **M**, and the energetic disorder parameters σ are in the corresponding (reverse) order (**PTS** < **P** \approx **M**).

There is presently no theoretical estimate of the effect of *group* dipole moments when they are linked in such a way that their orientations are partially correlated. There has been a preliminary treatment of the case in which they are rigidly linked to form a net quadrupole [65g].

The clearest examples of the influence of polar constituents usually involve materials in which no more than one component has a large dipole moment, such as a relatively nonpolar CTM doped into nonpolar and polar polymers, a nonpolar polymer doped with relatively nonpolar and polar CTMs, or a relatively nonpolar CTM and nonpolar polymer additionally doped with a highly polar additive. Similar effects are sometimes seen when a polar polymer is doped with CTMs having various dipole moments [56g–j, 64p]. Often, however, the mobility in a highly polar CTM is independent of, or only weakly affected by, the nonpolar or polar character of the host polymer [68a–c]. Often, too, for a highly polar CTM, σ is independent of CTM concentration, contrary to what one would expect on the basis of Eq. (10). A possible explanation is the tendency of neighboring dipoles to have antiferroelectrically correlated orientations [61a].

The nonpolar polymer that has received the most attention is polystyrene. A few studies have included alkyl-substituted polystyrenes, and the majority support the assumption that polystyrene is representative of nonpolar aromatic polymers in general [60b,d, 68d]. There are, in addition, a few data on not-very-polar polymers with quite different chemical structures where, at least, the mobilities at room temperature are similar to those in polystyrene [55k].

Geometrical disorder, molecular packing, excimer-forming sites

We have concentrated on the influence of polar components because, to date, it has received the most thorough study and because it appears to be the most important factor determining charge carrier mobility. Certainly the electronic structure and degree of delocalization of the charge-bearing orbital and the packing of the CTM bearing this orbital must have an influence. We turn briefly to these connected subjects.

A priori, even if the total concentration of CTM is held constant, the manner in which a particular species of CTM packs in the polymer host ought to influence the matrix elements (V) governing electron transfer between neighboring molecules (or the distribution of V), and the mobility should be affected. One would expect some change in the overall magnitude of the mobility, represented by μ_0 in Eq. (5), and perhaps in the slope of the field dependence, S in Eq. (4). It is impossible to control the packing, but it should be possible to influence it by use of bulky substituents or by linking CTMs together so that their mutual orientations are constrained. An example of the latter kind is a comparison of tri-*p*-tolylamine (TTA) and TAPC, which is essentially a dimer of TTA (Scheme 2), both in a polystyrene host. In general, in such comparisons one may have to account for differences in energetic disorder that result from differences in the packing of molecular dipoles. This is a particularly favorable case in that none of the materials is very polar and dipolar disorder should be relatively unimportant. Remarkably, at “normal” concentrations (~ 30 and ~ 50 wt.% CTM), the mobilities in the two CTMs are nearly identical (Figure 43). The difficulty with such “potluck” approaches is that there is no

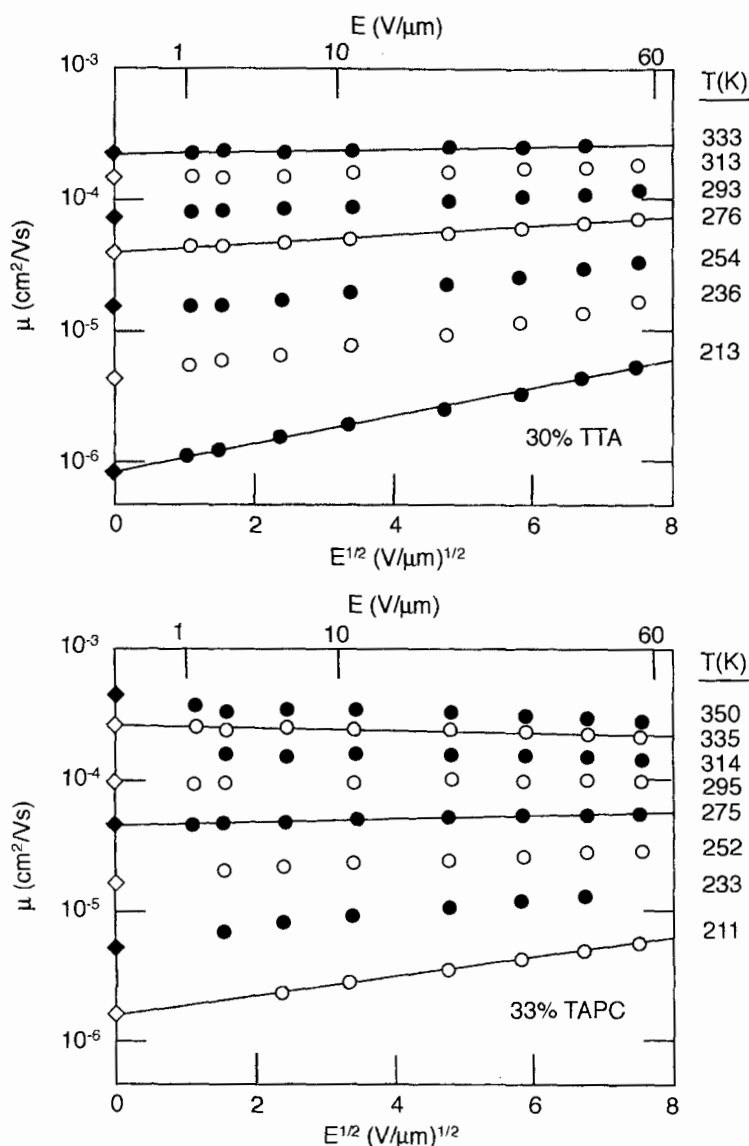


Figure 43. Comparison of the mobilities of holes in polystyrene doped with equivalent molar concentrations of TTA (above, 30 wt.%) and TAPC (below, 33 wt.%) at various field strengths and temperatures. Because the two triarylamine moieties in TAPC are linked, their arrangement should be somewhat different from that in TTA, yet the mobility behavior is nearly identical. At least in this example, differences in molecular packing do not lead to major differences in the mobility. Zero field values are extrapolations. (Reprinted with permission from Ref. [60b].)

way to know how much the chemical differences actually affect the way that the CTM pack. Nevertheless, the data on TTA and TAPC suggest that variations in molecular packing, per se, need not have much effect on the mobility.

At high concentrations, a large part of the geometrical disorder must be associated with the relative orientations of neighboring CTMs. At lower concentrations, a second factor grows in importance: the fact that TTA may be homogeneously dispersed, whereas TAPC (at an equivalent concentration of triarylamine moieties) must consist of pairs of triarylamine moieties, close together, with a greater distance between neighboring *pairs*. Indeed, at lower concentrations, there are substantial differences in the transport behavior of TTA, TAPC, and a tetrameric analog, TETRA, 1,1,5,5-tetrakis(2-methyl-4-di-*p*-tolylamino)phenylpentane (Figure 44) [69a]. At low concentrations of the dimeric and tetrameric species, $\ln \mu$ is no longer a linear function of $E^{1/2}$, nor even a monotonically increasing function. In TETRA at high field strength, not only the mobility but even the *velocity* of the holes decreases with increasing field strength. Other examples where drift velocity decreases with increasing field strength can be found in the literature [60b, 69b]. The stronger the field, the more slowly the carriers progress! Such low-concentration effects are outside the scope of this article but explanations have been proposed [60b, 69a,b], and the effect simulated [64].

There is, at present, no realistic theoretical model of the effect of geometrical disorder. A proper model must take into account the complicated orientation dependence of the matrix element (V) [63g], as well as the distribution of positions and orientations of the CTM. The simple treatment adopted by the Gaussian Disorder Model predicts a dependence of the prefactor mobility (μ_0) on the geometrical disorder parameter Σ , namely $\mu_0 \propto \exp(\frac{1}{2}\Sigma^2)$ [63a], and this relationship has been used often to analyze experimental data. The comparison of TTA and TAPC at low concentrations disagrees with this prediction, and it appears to be untenable a priori anyway [60b, 63c]. A worthy challenge for future work will be to construct a model with enough realism to have predictive value. Recent reports indicate progress in this direction [64l,o].

A “packing effect” that does appear to matter in certain materials is the presence of dimer or excimer-forming sites. These are sites, relatively rare, where two CTM adopt a close, cofacial (sandwich) configuration. The presence of such sites is inferred from the presence, in the fluorescence spectrum of the material, of an “excimer” component attributable to excited states that are trapped at such sites [27e, 70a–c]. The low mobility of holes in poly(*N*-vinylcarbazole) is believed to result from temporary trapping of holes at these sites [44h, 70d]. In fact, among polymers and doped polymers containing an *N*-alkylcarbazole as the hole-transporting moiety, a higher mobility correlates with a lower propensity for excimer emission [70e–g]. There are many recent studies of excimer-forming sites and hole trapping at such sites [71a–h].

Photocurrent tails, dispersive transport, and trapping

In this section, we touch briefly on several additional aspects of charge transport in amorphous molecular solids.

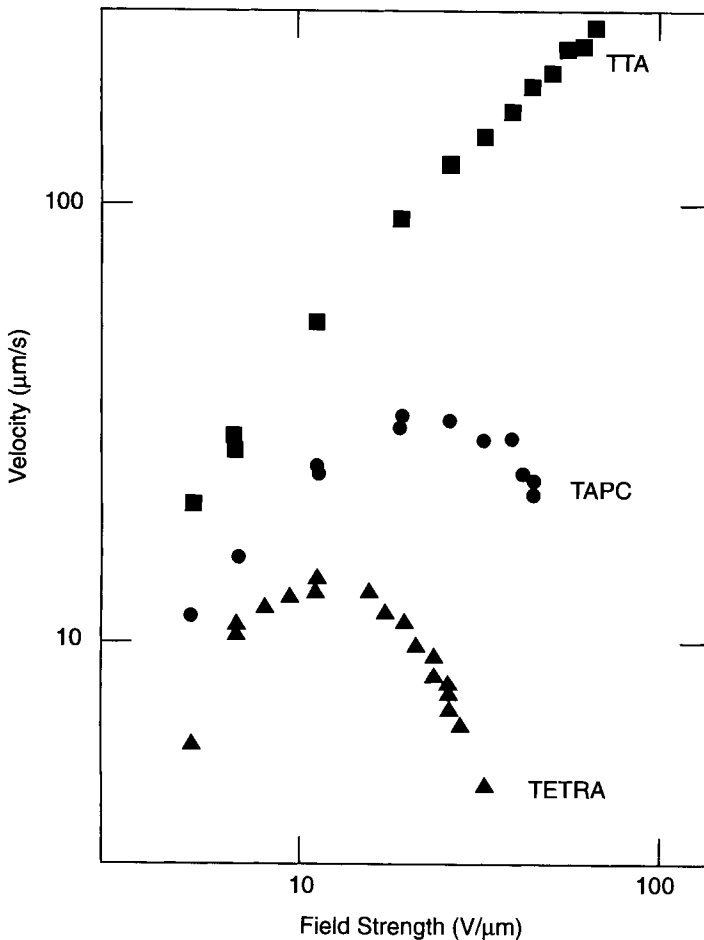


Figure 44. Velocity (v , not mobility) of holes in polystyrene doped with equivalent, low molar concentrations of TTA (6.8 wt.%), TAPC (7.5 wt.%), and TETRA (7.3 wt.%), all at ~ 335 K. Unlike the situation at high concentrations (Figure 43), linking the triarylamine groups in clusters of two (TAPC) or four (TETRA) dramatically affects the transport behavior. In TETRA, at high field strengths (E), the mobility (v/E) drops so rapidly that even the velocity itself decreases with increasing E . (Reprinted with permission from Ref. [69a].)

We have focused on the mobility as the main parameter characterizing charge transport. The photocurrent transients, however, typically extend well past the nominal transit time (t_t), so that the nominal mobility extracted from t_t underestimates the time required for charge to be transported across a photoreceptor film. A proper characterization of a material, therefore, requires some quantity indicating the width of the tail relative to t_t [72a]. As discussed previously, the tail is believed to arise because individual carriers sample various numbers of “slow sites”,

so it offers another window on the microscopic physics underlying the transport process. The literature has many reports of studies of this subject [64j, 72a–f].

We have tacitly assumed that the measured mobility is a well-defined, steady-state, bulk property of a material. This assumption is tenable whenever the photocurrent signal exhibits a broad, flat plateau and a narrow tail, as in Figure 29(a). In this context, the significance of a narrow tail is that most carriers may be described individually by approximately the same time-averaged drift velocity and mobility. Even for the rather well-behaved material represented by Figure 29(b), however, the “plateau” region slopes somewhat, indicating that transport does not reach a steady state during the time of flight. In extreme cases, the “plateau” slopes so steeply that it cannot be distinguished from a “tail”, and one cannot see a break-point to identify as a nominal transit time. In such cases, it is often possible to extract a nominal transit time from a log–log plot, as in Figure 29(c). The significance of this time is limited, however. Roughly speaking, a monotonically decreasing photocurrent implies that (on average) the velocity of the carriers decreases during their passage through the sample. If so, the time required to cross a thicker sample should be more than proportionately longer. That is, this “transit time” should not be proportional to the thickness of the sample, and the corresponding “effective mobility” should decrease with increasing sample thickness. An example is shown in Figure 45 [72g].

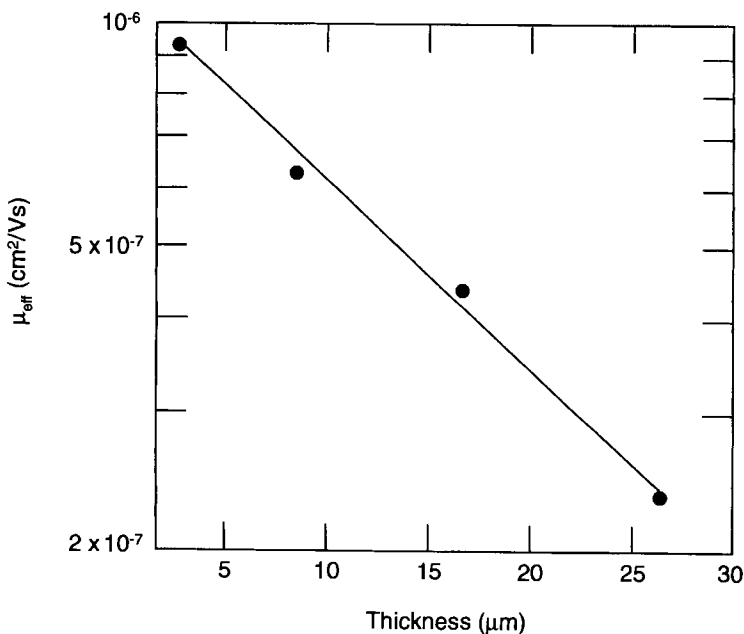


Figure 45. Thickness dependence of the effective mobility (μ_{eff}) for hole transport in a material exhibiting dispersive transport. The line represents a power-law dependence. The material is a polysiloxane with a carbazole pendant group. The field strength was $2 \times 10^5 \text{ V cm}^{-1}$, and the temperature 293 K. (Reprinted with permission from Ref. [72g].)

When charge transport fails to reach a steady state during the time available, the most likely reason is that the transit time is dominated by the time required to escape from the slowest site(s) that a carrier encounters as it crosses the sample. Furthermore, the distribution of release times is such that the carrier continues to encounter slower and slower sites as it crosses a sample. Transport under such conditions is called dispersive, and has been the subject of much study since a seminal paper by Scher and Montroll [73a–e]. The term “dispersive” alludes to the wide dispersion in release times and/or the fact that carriers that are injected simultaneously spread out, disperse, to an anomalous extent as they cross the sample. The literature has several examples of studies of this subject in amorphous molecular solids [66b, 73f–h]. Some materials undergo a transition from essentially dispersive transport at low temperatures to essentially nondispersive transport at higher temperatures, and this dispersive-to-nondispersive transition has been the subject of significant attention [73i–p].

It is easy to tell when transport is essentially nondispersive—the current transients approach the ideal, rectangular shape. It is more difficult to tell whether apparently dispersive transport is an intrinsic property of a material. For example, an early study of triphenylamine (TPA)-doped polycarbonate found that the transport was highly dispersive [73q], but later studies of tri-*p*-tolylamine (TTA)-doped polymers revealed relatively nondispersive transport [57b, 73r]. Commercial triphenylamine is typically contaminated with *N,N,N',N'*-tetraphenylbenzidine, which contributes very deep sites for hole transport (hole traps) [73s], whereas as-received TTA is apparently free of such impurities. This is probably the reason why the two, very similar materials appear to have very different transport properties. In fact, when TPA is purified adequately, the transport properties approximate those of TTA [73t].

As illustrated by this example, an impurity can drastically affect charge transport if its solid-state ionization potential is much smaller than that of a hole transport material or its electron affinity is much larger than that of an electron transport material [44b,f, 74a–i,q,r]. An extraordinary species involving the CTM itself can have the same effect, as illustrated by the (presumed) charge-trapping effect of excimer-forming sites in poly(*N*-vinylcarbazole). The effect of relatively small amounts of a hole-trapping “impurity” on the photocurrent transients in a hole-transporting doped polymer is illustrated in Figure 46 [74i]. The hole-transporting material is TTA (40 wt.%) in a polycarbonate host. The “impurity”, 1,1-bis(*p*-diethylaminophenyl)-4,4-diphenyl-1,3-butadiene (BD), has a much smaller solid-state ionization potential (5.11 eV) than does TTA (5.7 eV). With increasing impurity concentration, the duration of the photocurrent transient increases; i.e., holes take longer and longer to cross the sample. Simultaneously, the photocurrent transient that was fairly nondispersive in the absence of the impurity becomes highly dispersive. In this regime, holes encounter traps as they cross the sample, and more traps at higher concentrations, but apparently they do not sample enough traps to establish a steady state between trapping and release. At 1100 ppm, the transient again becomes fairly nondispersive, suggesting that an approximately steady-state condition has been reached. With a further increase in trap concentration, the transient becomes yet less dispersive, while the timescale continues to increase. Between

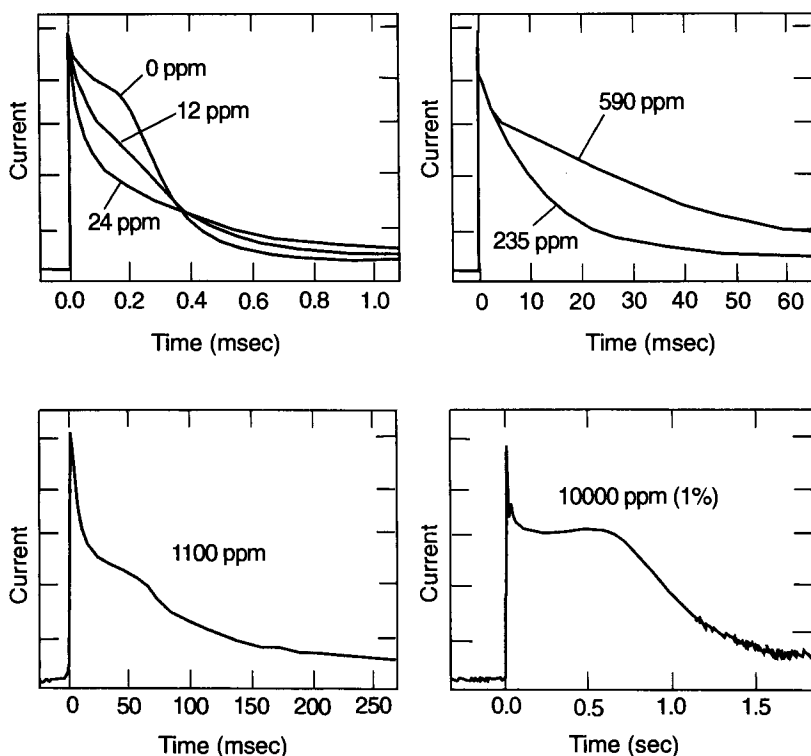


Figure 46. Photocurrent transients for hole transport in TTA (40 wt.%) doped polycarbonate containing as an added impurity 1,1-bis(*p*-diethylaminophenyl)-4,4-diphenyl-1,3-butadiene (BD) at various concentrations. The current (vertical) scale is arbitrary. The samples were $\sim 16 \mu\text{m}$ thick, the temperature 298 K, and the field strength $3.75 \times 10^5 \text{ V cm}^{-1}$. (Reprinted with permission from Ref. [74j].)

BD concentrations of 0 and 1 %, the transit time increases by a factor of ca. 3000. The corresponding mobility, referred to as the trap-limited mobility, decreases by the same factor, roughly in inverse proportion to the impurity concentration. The decrease is actually somewhat faster, proportional to $(\text{concentration})^{-1.3}$, probably indicating that true steady state has not yet been achieved [53a]. While the outlines of the effect of a charge-trapping impurity seem simple, the details are not [74i]. The literature has several examples of recent work on this subject [44c, 46d, 53a, 65g,i, 74j–o].

2.6.3 Chemical Desiderata for Charge-transporting Materials

As mentioned before, a low ionization potential (cathodic oxidation potential) or a high electron affinity (anodic reduction potential) makes a potential CTM less susceptible to trapping by adventitious impurities. Whether or not charge-trapping

impurities are actually present, however, depends on details of synthesis and ease of purification of the CTM. Furthermore, the CTM must be thermally and photochemically stable to conditions experienced during its lifetime in an electrophotographic printer or copier [3q]. The cation or anion radical of the CTM must be chemically stable, at least in the host polymer. If a compound has a very low ionization potential or a very high electron affinity, and if the radical ion is stable, the compound may be susceptible to contamination by ion-radical salts that increase the dark conductivity of a photoreceptor. In addition, a CTM must be very soluble in a suitable polymer host, but compounds with very low ionization potential or very high electron affinity tend to be quite insoluble. There are conflicting reports as to whether the ionization potential (or electron affinity), per se, matters, at least within the relatively narrow range usually investigated [3q].

Charge-transporting molecules with relatively high carrier mobilities generally lack large net dipole moments or highly polar groups. For electron transport, however, highly polar groups ($-\text{CN}$, $-\text{NO}_2$, $-\text{SO}_2$, etc.) are generally required in order to bring the electron affinity into an acceptable range. One conceivable escape from this dilemma is the use of stable hydrocarbon free radicals such as BDPA (α,γ -bis(diphenylene- β -phenylallyl)), which achieve a relatively high electron affinity (and low ionization potential) by virtue of a half-filled molecular orbital [75].

The degree to which an added electron or hole is delocalized over a CTM must affect the electron transfer matrix elements (and perhaps their dependence on intermolecular separation) and, presumably, the mobility. All other things being equal, in a given host polymer, it is also possible that the distribution of site energies is narrower for a CTM with a more highly delocalized charge distribution. The host environment presumably varies on the molecular distance [\AA] scale, and the site energy is determined by some sort of average over contributions of the various environments to which the charge distribution is exposed. The more extended the charge distribution, the more averaging may occur, and the narrower the resulting distribution of (averaged) site energies. This factor may be responsible for apparent differences in the nondipolar (van der Waals) contribution to disorder between CTMs of different chemical classes. Attempts at correlating mobility with the molecular orbital structure or degree of delocalization of the charge carrier within a CTM can be found in the literature [46b,e, 76].

Solubility in a host polymer (and a suitable coating solvent) is an important practical parameter for CTMs in general, and especially for electron-transporting materials with planar structures and highly polar substituents (features that tend to make a compound insoluble). In addition, electron mobilities tend to be relatively low, so that acceptable values can be achieved only with high concentrations of CTMs. Solubility can be enhanced by mixing CTMs with nearly identical ionization potentials or electron affinities [55j], by reducing the molecular symmetry using asymmetric substituents, by use of bulky solubilizing groups, or by connecting two or more charge-transporting moieties in a noncoplanar or flexible manner. This is the reason for asymmetric aryl groups in PTS [77a], the branched alkyl groups in NTDI [77b], the *t*-butyl group in DCAQ (2-*t*-butyl-9,10-*N,N'*-dicyanoanthraquinonedimine), and the "dimeric" structure of TAPC (Scheme 2). An additional advantage of bulky CTMs is that they tend to have relatively high glass transition temperatures

(T_g) by themselves, and, therefore, the necessary high concentrations in the host polymer may be achieved without reducing the composite T_g unacceptably. A disadvantage of bulky substituents is that they do not contribute to charge transport but do add to the molecular mass, thereby increasing the solubility requirements (on a weight basis) for given level of performance. These tradeoffs illustrate the “practical” considerations that influence the development of new charge-transporting materials at least as much as the “theoretical” considerations that we have discussed.

References are provided for additional extensive reviews featuring various viewpoints [3q, 14a, 59b, 77c].

2.7 Concluding Remarks

Organic photoreceptor technology is a major component of the multibillion dollar international business based on electrophotographic copiers and printers. From the original Xerox black-and-white copier, the business now encompasses products from desktop copiers and printers to high-speed commercial machines for on-demand printing applications. Today, color electrophotography is the area of greatest growth, from large and expensive high-speed color printers to relatively low-cost desktop devices for home and small office use. Most of these machines utilize organic photoreceptors as their photosensitive element. For these many applications, photoreceptors come in a variety of formulations coated on drum or polymer substrates. Each photoreceptor must have a manufacturing cost structure, and must provide the image quality required of the product, as determined by business analysis. Thus, the sensitometric and the physical characteristics of the photoreceptor must not degrade to the point that image quality suffers, over the product lifetime. Of course, the requirements for a small home or office printer are very different from those of a commercial printer. In a low-volume home or office machine the photoreceptor lifetime is often coupled with the toner capacity of a replaceable cartridge. When toner is depleted the entire assembly is replaced. Typically, the photoreceptor drum actually has remaining life, and the refinishing of used photoreceptor drums for resale has become a significant business. The situation is different in higher-volume electrophotographic devices. In these machines, replacement of the photoreceptor drum or belt is typically carried out by a highly trained service person. Degraded image quality results in a service call that requires diagnosis and repair. In newer models machines may be linked via computer to a service center for remote diagnosis. Because the photoreceptor element is central to the electrophotographic process it may become damaged in many different ways. Surface scratches, buildup of toner/paper deposits, and surface wear are common reasons for photoreceptor replacement. In these machines there is usually an advantage in having the photoreceptor last as long as possible. This means machine designs that prevent the accidental introduction of paper clips and staples, and component design for efficient photoreceptor cleaning without damage or excessive wear. In today's high-speed machines the organic photoreceptor elements typically last for

hundreds of thousands of imaging cycles. Thus, the electron transfer chemistry involved in each imaging cycle—corona charging, photoinduced charge generation, and field-driven charge transport—are repeated hundreds of thousands of times during the photoreceptor lifetime without substantial changes in their efficiency. This triumph of chemistry and physics is the product of many years of scientific study and technological development. Those fundamentals, which are the basis of organic photoreceptors, are now being applied to new areas such as organic light-emitting diodes, and organic photorefractive materials. Thus, the science and technology are moving together into new areas that will be the basis of the technologies of tomorrow.

References

1. a) C. F. Carlson, **1942**, US Patent 2297691; b) C. F. Carlson, **1944**, US Patent 2357809.
2. a) A. Dinsdale, *Photographic Sci. Eng.* **1963**, 7, 1; b) J. H. Dessauer, *My Years With Xerox—The Billions Nobody Wanted*, Manor Books, New York, **1971**; c) J. Mort, *The Anatomy of Xerography*, McFarland, Jefferson, **1989**; d) D. J. Golembeski, *Invention and Technology*, **1989**, Winter, 8; e) J. Mort, *Physics Today* **1994**, April, 32.
3. a) N. Langer, *Electrophotography* **1944**, Radio News, Eng. Dept. 32, 22; b) R. M. Schaffert, C. D. Oughton, *J. Opt. Soc. America* **1948**, 38, 991; c) J. H. Dessauer, G. R. Mott, H. Bogdonoff, *Photogr. Eng.* **1955**, 6, 250; d) J. H. Dessauer, H. E. Clark, *Xerography and Related Processes*, Focal Press, London, **1965**; e) V. M. Fridkin, *Physics of the Electrophotographic Process*, Focal Press, London, **1972**; f) R. M. Schaffert, *Electrophotography*, Focal Press, London, **1975**; g) M. E. Scharfe, F. W. Schmidlin, *Advances in Electronics and Electron Physics* **1975**, 38, 83; h) P. K. Watson, *Inst. Phys. Conf. Ser.* **1979**, No. 48, 1; i) E. M. Williams, *The Physics and Technology of Xerographic Processes*, Wiley, New York, **1984**; j) M. Scharfe, *Electrophotography Principles and Optimization*, Research Studies Press, Letchworth, **1984**; k) D. M. Burland, L. B. Schein, *Physics Today* **1986**, May, 46; l) P. M. Borsenberger, D. S. Weiss, in *Handbook of Imaging Materials* (Ed.: A. Diamond), Marcel Dekker, New York, **1991**, p. 379; m) L. B. Schein, *Electrophotography and Development Physics*, Second Edition, Springer-Verlag, Berlin, **1992**; n) D. M. Pai, B. E. Springett, *Reviews of Modern Physics* **1993**, 65, 163; o) P. M. Borsenberger, D. S. Weiss, *Organic Photoreceptors for Imaging Systems*, Marcel Dekker, New York, **1993**; p) J. W. Weigl, *Angew. Chem. Int. Ed. Engl.* **1977**, 16, 374; q) P. M. Borsenberger, D. S. Weiss, *Organic Photoreceptors for Xerography*, Marcel Dekker, New York, **1998**.
4. a) J. H. Anderson, D. E. Bugner, L. P. DeMejo, R. A. Guistina, N. Zumbulyadis, *J. Imaging Sci.* **1993**, 37, 431; b) J. H. Anderson, *J. Imaging Sci.* **1994**, 38, 378.
5. a) L.-H. Lee, *Photogr. Sci. Eng.* **1978**, 22, 228; b) A. F. Diaz, J. Guay, *IBM J. Res. Dev.* **1993**, 37, 249; c) J. H. Anderson, E. Fox, *J. Adhesion* **1995**, 51, 27; d) L. B. Schein, *J. Imaging Sci. Technol.* **1993**, 37, 1; e) L. B. Schein, M. LaHa, D. Novotny, *Phys. Lett.* **1992**, A176, 79; f) E. J. Gutman, G. C. Hartmann, *J. Imaging Sci. Technol.* **1992**, 4, 335; g) H. W. Gibson, *J. Am. Chem. Soc.* **1975**, 97, 3832; h) H. W. Gibson, J. M. Pochan, F. C. Bailey, *Anal. Chem.* **1979**, 51, 483.
6. a) A. F. Diaz in *Fundamentals of Adhesion at Interface*, Gordon and Breach, **1999**, p. 111; b) A. F. Diaz, D. Fenzel-Alexander, *Langmuir* **1993**, 9, 1009; c) M. Kamiyama, M. Maeda, H. Okutani, K. Koyama, H. Matsuda, Y. Sano, *J. Appl. Polymer Sci.* **1994**, 51, 1667; d) Y. Takahashi, W.-S. Lee, *Proceedings IS&T's 12th International Congress on Advances in Non-impact Printing Technologies* **1996**, p. 526; e) K. Y. Law, I. W. Tarnawskyj, D. Salamida, T. Debies, *Polymer Preprints* **1996**, 37, 105; f) D. Fenzel-Alexander, P. Brock, A. Diaz, *Langmuir* **1994**, 10, 3323; g) A. F. Diaz, D. Fenzel-Alexander, D. C. Miller, D. Wollman, A. Eisenberg, *J. Polymer Sci. Polymer Lett.* **1990**, 28, 75; h) H. A. Mizes, E. M. Conwell, C. P. Salamida, *Appl. Phys. Lett.* **1990**, 56, 1597.

7. a) W. T. Ferrar, D. S. Weiss, J. R. Cowdery-Corvan, *Proceedings IS&T's NIP15: 1999 International Conference on Digital Printing Technologies*, **1999**, p. 672; b) W. T. Ferrar, D. S. Weiss, J. R. Cowdery-Corvan, *J. Imaging Sci. Technol.* **1999**, *43*, 280; c) W. T. Ferrar, D. S. Weiss, J. R. Cowdery-Corvan, *Proceedings IS&T's NIP14: 1998 International Conference on Digital Printing Technologies*, **1998**, p. 520; d) H. Nakaue, T. Mitani, H. Kurokawa, *Diamond Films Technol.* **1993**, *3*, 45; e) X. S. Miao, Y. C. Chan, E. Y. B. Pun, *Appl. Phys. Lett.* **71**, *2*, 184; f) X. M. He, S. T. Lee, Y. C. Chan, L. Shu, X. S. Miao, *J. Phys.: Condens. Matter* **1998**, *10*, 7835.
8. a) R. S. Sigmond, M. Goldman in *Electrical Breakdown and Discharges in Gases, Part B* (Eds.: E. E. Kunhardt, L. H. Luessen), Plenum, New York, **1981**, p. 1; b) A. Goldman, J. Amouroux in *Electrical Breakdown and Discharges in Gases, Part B* (Eds.: E. E. Kunhardt, L. H. Luessen), Plenum, New York, **1981**, p. 293.
9. a) C. F. Carlson, **1952**, US Patent 2588699; b) L. E. Walkup, **1957**, US Patent 2777957.
10. a) M. M. Shahin, *J. Chem. Phys.* **1966**, *45*, 2600; b) M. M. Shahin, *Appl. Opt. Suppl.* **3** **1969**, 106; c) M. M. Shahin, *Photogr. Sci. Eng.* **1971**, *15*, 322; d) S. Jeyadev, D. M. Pai, *Proceedings IS&T's Eleventh International Congress on Advances in Non-impact Printing Technologies*, **1995**, p. 141; e) L. B. Schein, *Phys. Rev. B* **1974**, *10*, 3451; f) M. Abkowitz, F. Jansen, A. R. Melnyk, *Phil. Mag. B* **1985**, *51*, 405; g) A. Kubilius, Br. Petretis, V. I. Archipov, A. I. Rudenko, *J. Phys. D: Appl. Phys.* **1985**, *18*, 901; h) M. Abkowitz, *SPIE* **1987**, *763*, 88; i) S. W. Ing, Jr., J. H. Neyhart, *J. Appl. Phys.* **1972**, *43*, 2670; j) H. Kakinuma, T. Watanabe, *J. Appl. Phys.* **1987**, *62*, 1837; k) S. Mishra, D. M. Pai, *Proceedings IS&T's NIP 12: International Conference on Digital Printing Technologies*, **1996**, 464; l) J.-Y. Moisan, B. Andre, R. Lever, *Chem. Phys.* **1991**, *153*, 305; m) J. C. Scott, G. S. Lo, *Proceedings IS&T's Sixth International Congress on Advances in Non-impact Printing Technologies* **1990**, p. 403.
11. a) A. Ikeda, T. Kawakami, K. Ejima, B. Itoh, T. Sasaki, Y. Shimono, K. Wakita, *Proceedings IS&T's Eighth International Congress on Advances in Non-impact Printing Technologies*, **1992**, p. 227; b) E. Inoue, I. Shimizu, *Photogr. Sci. Eng.* **1982**, *26*, 148.
12. a) C. F. Gallo, A. G. Leiga, J. A. McNally, *Photogr. Sci. Eng.* **1967**, *11*, 11; b) *Polymer Surface Modification: Relevance to Adhesion; Part 1. Plasma Surface Modification Techniques* (Ed.: K. L. Mittal), VSP, Utrecht, **1996**; c) F. D. Egitto, L. J. Matienzo, *IBM J. Res. Dev.* **1994**, *38*, 423; d) M. Goldman, R. S. Sigmond, *J. Electrochem. Soc.* **1985**, *132*, 2842; e) K. Nashimoto, *J. Imaging Sci.* **1988**, *32*, 205.
13. a) M. Lichtensteiger, C. Webb, *Appl. Phys. Lett.* **1981**, *38*, 323; b) M. D. Erickson, G. M. Trischan, C. W. Frank, *Oxidation of Metals* **1975**, *9*, 153; c) S. Takenouchi, A. Hirano, H. Yoshioka, Y. Fujimaki, H. Moriguchi, *Advance Printing of Paper Summaries SPSE's 4th International Congress on Advances in Non-impact Printing Technologies*, **1988**, p. 44; d) D. S. Weiss, *J. Imaging Sci.* **1990**, *34*, 132.
14. a) M. Pope, C. E. Swenberg, *Electronic Processes in Organic Crystals and Polymers*, 2nd ed., Oxford University Press, New York, **1999**. b) E. A. Silinsh, V. Čápek, *Organic Molecular Crystals, Interaction, Localization, and Transport Phenomena*, AIP, New York, **1994**.
15. a) S. R. Forrest, *Chem. Rev.* **1997**, *97*, 1793; b) *Electrical and Related Properties of Organic Solids* (Eds.: R. W. Munn, A. Miniewicz, B. Kuchta), NATO ASI Series, Kluwer Academic, Dordrecht, **1997**.
16. a) D. M. Pai, *Adv. Mater. Conf. Proc.* **1987**, *107*, 331; b) *Electronic and Structural Properties of Amorphous Semiconductors* (Eds.: P. G. Le Comber, J. Mort), Academic Press, London, **1973**; c) *Photoconductivity and Related Phenomena* (Eds.: J. Mort, D. M. Pai), Elsevier Scientific, Amsterdam, **1976**; d) S. O. Kasap, in *Handbook of Imaging Materials* (Ed.: A. S. Diamond), Marcel Dekker, New York, **1991**, p. 329.
17. a) J. Mort in *Handbook of Imaging Materials* (Ed.: A. S. Diamond), Marcel Dekker, New York, **1991**, p. 447; b) I. Shimizu, *Semiconductors and Semimetals Part D* **1984**, *21*, 55.
18. a) J. Mort, G. Pfister, *Polym.-Plast. Technol. Eng.* **1979**, *12*, 89; b) M. Grätzel, *Heterogeneous Photochemical Electron Transfer*, CRC, Boca Raton, **1989**; c) N. V. Joshi, *Photoconductivity: Art, Science, and Technology*, **1990**, Dekker, New York; d) Z. D. Popovic, *Proceedings IS&T's 9th International Congress on Advances in Non-impact Printing Technologies/Japan Hardcopy '93*, **1993**, 591; e) K. Y. Law, *Chem. Rev.* **1993**, *93*, 449; f) P. Di Marco, G. Giro, *Appl. Phys.* **1994**, *4*, 791.

19. a) F. Stolzenburg, B. Ries, H. Bässler, *Chem. Phys. Lett.* **1985**, 116, 73; b) B. Ries, H. Bässler, *J. Mol. Electronics* **1987**, 3, 15.
20. A.C. Tam, *Appl. Phys. Lett.* **1980**, 37, 978.
21. a) S. Aramaki, T. Murayama, *Proceedings IS&T's Eleventh International Congress on Advances in Non-impact Printing Technologies*, **1995**, p. 26; b) T. Shoda, S. Aramaki, T. Murayama, *Proceedings IS&Ts NIP 14: 1998 International Conference on Digital Printing Technologies*, **1998**, p. 508.
22. a) G. J. Kavarnos, *Fundamentals of Photoinduced Electron Transfer*, VCH, New York, **1993**; b) A. V. Vannikov, A. D. Grishina, *Russian Chem. Rev.* **1989**, 58, 1169.
23. a) L. Onsager, *Phys. Rev.* **1938**, 54, 554; b) C. L. Braun, *J. Chem. Phys.* **1984**, 80, 4157; c) S. N. Smirnov, C. L. Braun, *J. Imaging Sci. Technol.* **1999**, 43, 425; d) D. M. Pai in *Physics of Disordered Materials* (Eds.: D. Adler, H. Fritzsche, S. R. Ovshinsky), Plenum, New York, **1985**, p. 579; e) J. Noolandi, *J. Electrostatics* **1985**, 12, 13.
24. J. Noolandi, K.M. Hong, *J. Chem. Phys.* **1979**, 70, 3230.
25. a) W. C. Needler, *J. Chem. Phys.* **1965**, 42, 2972; b) T. E. Orlowski, H. Scher, *Phys. Rev. B* **1983**, 27, 7691; c) H. Scher, T. E. Orlowski, *Phys. Rev. Lett.* **1983**, 50, 775.
26. a) P. Langevin, *Ann. Chim. Phys.* **1903**, 28, 289; b) I. Chen, *J. Appl. Phys.* **1978**, 49, 1162; c) J. W. Kerr, G. H. S. Rokos, *J. Phys. D: Appl. Phys.* **1977**, 10, 1151; d) R. H. Young, *J. Appl. Phys.* **1986**, 60, 272; e) W. Mey, E. I. P. Walker, D. C. Hoestery, *J. Appl. Phys.* **1979**, 50, 8090; f) A. V. Buettner, W. Mey, *Photogr. Sci. Eng.* **1982**, 26, 80.
27. a) V. S. Mylnikov, *Advances in Polymer Science*, **1994**, 115, 1; b) W. D. Gill in *Photoconductivity and Related Phenomena* (Eds.: J. Mort, D. M. Pai), Elsevier, Amsterdam, **1976**, p. 303; c) J. M. Pearson, *Pure Appl. Chem.* **1977**, 49, 463; d) S. Nešpůrek, V. Cimrová, J. Pflieger, *Colloid Polym. Sci.* **1991**, 269, 556; e) R. C. Penwell, B. N. Ganguly, T. W. Smith, *J. Polymer Sci.: Macromol. Revs.* **1978**, 13, 63.
28. a) H. Hoegl, *J. Phys. Chem.* **1965**, 69, 755; b) P. J. Regensburger, *Photochem. Photobiol.* **1968**, 8, 429; c) P. M. Borsenberger, A. I. Ateya, *J. Appl. Phys.* **1978**, 49, 4035; d) V. Cimrová, S. Nešpůrek, *Chem. Phys.* **1994**, 184, 283; e) S. Nešpůrek, M. Menšík in *Electrical and Related Properties of Organic Solids* (Eds.: R. W. Munn, A. Miniewicz, B. Kuchta), NATO ASI Series, Kluwer Academic, Dordrecht, **1997**, p. 39; f) M. Menšík, *Polym. Adv. Technol.* **1998**, 9, 635; g) J. Mort, M. Morgan, S. Grammatica, J. Noolandi, K. M. Hong, *Phys. Rev. Lett.* **1982**, 48, 1411; h) P. M. Borsenberger, L. E. Contois, D. C. Hoestery, *J. Chem. Phys.* **1978**, 68, 637; i) P. M. Borsenberger, L. E. Contois, D. C. Hoestery, *Chem. Phys. Lett.* **1978**, 56, 574.
29. a) H. Hoegl, G. Barchietto, D. Tar, *Photochem. Photobiol.* **1972**, 16, 335; b) P. J. Meltz, *J. Chem. Phys.* **1972**, 57, 1694; c) R. C. Hughes, *Appl. Phys. Lett.* **1972**, 21, 196; d) R. C. Hughes, *J. Chem. Phys.* **1973**, 58, 2212; e) G. Pfister, D. J. Williams, *J. Chem. Phys.*, **1974**, 61, 2416; f) K. Okamoto, S. Kusabayashi, H. Mikawa, *Bull. Chem. Soc. Jpn.* **1973**, 46, 2613; g) M. Yokoyama, Y. Endo, H. Mikawa, *Bull. Chem. Soc. Jpn.* **1976**, 49, 1538; h) M. Yokoyama, Y. Endo, H. Mikawa, *Chem. Phys. Lett.* **1975**, 34, 597; i) M. Yokoyama, Y. Endo, H. Mikawa, *J. Luminescence* **1976**, 12/13, 865; j) M. Yokoyama, Y. Endo, A. Matsubara, H. Mikawa, *J. Chem. Phys.* **1981**, 75, 3006; k) M. Yokoyama, A. Matsubara, S. Shimokihara, H. Mikawa, *Polymer J.* **1982**, 14, 73; l) M. Yokoyama, A. Matsubara, S. Shimokihara, H. Mikawa, *Polymer J.* **1982**, 14, 77; m) M. Yokoyama, S. Shimokihara, A. Matsubara, H. Mikawa, *J. Chem. Phys.* **1982**, 76, 724; n) M. Yokoyama, H. Mikawa, *Photogr. Sci. Eng.* **1982**, 26, 143.
30. a) R. M. Schaffert, *IBM J. Res. Dev.* **1971**, 15, 75; b) U. Vahtra, R. F. Wolter, *IBM J. Res. Dev.* **1978**, 22, 34; c) D. Abramavicius, V. Gulbinas, A. Ruseckas, A., Undzenas, L. Valkunas, *Chem. Phys.* **1999**, 111, 5611.
31. a) W. A. Light, **1971**, US Patent 3615414; b) W. J. Dulmage, W. A. Light, S. J. Marino, C. D. Salzberg, D. L. Smith, W. J. Staudenmayer, *J. Appl. Phys.* **1978**, 49, 5543; c) P. M. Borsenberger, A. Chowdry, D. C. Hoestery, W. Mey, *J. Appl. Phys.* **1978**, 49, 5555; d) P. M. Borsenberger, D. C. Hoestery, *J. Appl. Phys.* **1980**, 51, 4248; e) M. B. O'Regan, P. M. Borsenberger, E. H. Magin, T. Zubil, *J. Imaging Sci. Technol.* **1996**, 40, 1; f) J. H. Perlstein in *Electrical Properties of Polymers* (Ed.: D. A. Seanor), Academic Press, New York, **1982**, p. 59; g) J. H. Perlstein, P. M. Borsenberger in *Extended Linear Chain Compounds*, Vol. 2 (Ed.: J. S. Miller), Plenum, New York, **1982**, p. 339.

32. a) D. McMurtry, M. Tinghitella, R. Svendsen, *IBM J. Res. Dev.* **1984**, 28, 257; b) P. J. Melz, R. B. Champ, L. S. Chang, C. Chiou, G. S. Keller, L. C. Licican, R. R. Nelman, M. D. Shattuck, W. J. Welche, *Photogr. Sci. Eng.* **1977**, 21, 73; c) A. Kakuta, Y. Mori, H. Morishita, *IEEE Transactions on Industry Applications* **1981**, 1A-17, 382; d) N. C. Khe, O. Takenouchi, T. Kawara, H. Tanaka, S. Yokota, *Photogr. Sci. Eng.* **1984**, 28, 195.
33. a) S. Otsuka, T. Murayama, H. Nagasaka, *SPSE Proceedings 3rd International Congress on Advances in Non-impact Printing Technologies*, **1986**, p. 16; b) H. Ono, I. Takagishi, E. Matuda, T. Murayama, *Proceedings IS&T's Sixth International Congress on Advances in Non-impact Printing Technologies*, **1991**, p. 318; c) H. Ono, I. Takagishi, E. Matsuda, T. Murayama, *Proceedings IS&T's Sixth International Congress on Advances in Non-impact Printing Technologies*, **1990**, p. 312; d) J. Pacansky, R. J. Waltman, *J. Am. Chem. Soc.* **1992**, 114, 5813; e) K.-Y. Law, S. Kaplan, R. Crandall, and I. W. Tarnawskyj, *Chem. Mater.* **1993**, 5, 557; f) G. DiPaola-Baranyi, C. K. Hsiao, A. M. Hor., *J. Imaging Sci.* **1990**, 34, 224; g) K.-Y. Law, I. W. Tarnawskyj, *Dyes and Pigments* **1994**, 25, 281; h) K.-Y. Law, I. W. Tarnawskyj, *J. Imaging Sci. Technol.* **1995**, 39, 1; i) K.-Y. Law, I. W. Tarnawskyj, *J. Imaging Sci. Technol.* **1995**, 39, 126; j) O. Murakami, T. Uenaka, S. Otsuka, S. Aramaki, T. Murayama, *Proceedings IS&T's Seventh International Congress on Advances in Non-impact Printing Technologies*, **1991**, p. 318; k) K.-Y. Law, I. W. Tarnawskyj, *J. Imaging Sci. Technol.* **1993**, 37, 22; l) K.-Y. Law, I. W. Tarnawskyj, Z. D. Popovic, *J. Imaging Sci. Technol.* **1995**, 38, 118.
34. a) M. Umeda, *IS&T's Tenth International Congress on Advances in Non-impact Printing Technologies*, **1994**, p. 239; b) M. Umeda, *SPIE* **1998**, 3471, 212; c) M. Umeda, *J. Imaging Sci. Technol.* **1999**, 43, 254; d) M. Umeda, T. Niimi, M. Hashimoto, *Jpn. J. Appl. Phys.* **1990**, 29, 2746; e) M. Umeda, M. Hashimoto, *J. Appl. Phys.* **1992**, 72, 117; f) M. Umeda, T. Niimi, *Jpn. J. Appl. Phys.* **1994**, 33, L1789; g) M. Umeda, T. Niimi, *J. Imaging Sci. Technol.* **1994**, 38, 281; h) T. Niimi, M. Umeda, *J. Appl. Phys.* **1994**, 76, 1269; i) T. Niimi and M. Umeda, *J. Appl. Phys.* **1993**, 74, 465; j) M. Umeda, T. Shimada, T. Aruga, T. Niimi, M. Sasaki, *J. Phys. Chem.* **1993**, 97, 8531; k) R. A. Marcus, *Annu. Rev. Phys. Chem.* **1964**, 15, 155; l) M. Umeda, M. Yokoyama, *Jpn. J. Appl. Phys.* **1995**, 34, L44; m) M. Umeda, M. Yokoyama, *J. Appl. Phys.* **1997**, 81, 6179; n) A. Schreiber, R. Bilke, J. Pan, I. Bleyl, J. Bondkowski, D. Adam, D. Haarer, *SPIE* **1998**, 3471, 224.
35. a) R. O. Loutfy, C.-K. Hsiao, *Can. J. Chem.* **1979**, 57, 2546; b) R. O. Loutfy, Y. C. Cheng, *J. Chem. Phys.* **1980**, 73, 2902; c) H. J. Wagner, R. O. Loutfy, *J. Mater. Sci.* **1982**, 17, 2781; d) T. Kitamura, S. Imamura, M. Kawamata, *J. Imaging Technol.* **1988**, 14, 136; e) J. B. Whitlock, G. R. Bird, M. D. Cox, P. Panayotatos, *Thin Solid Films* **1992**, 215, 84; f) R. Kubiak, J. Janczak, K. Ejsmont, *Chem. Phys. Lett.* **1995**, 245, 249.
36. a) R. O. Loutfy, J. H. Sharp, *J. Appl. Electrochem.* **1977**, 7, 315; b) E. R. Menzel, K. J. Jordan, *Chem. Phys.* **1978**, 32, 223; c) R. O. Loutfy, *Can. J. Chem.* **1981**, 59, 549; d) T. Enokida, R. Hirohashi, N. Morohashi, *Bull. Chem. Soc. Jpn.* **1991**, 64, 279; e) A. Kakuta, Y. Mori, S. Takano, M. Sawada, and I. Shibuya, *J. Imaging Technol.* **1985**, 11, 7; f) T. Enokida, R. Hirohashi, S. Mizukami, *J. Imaging Sci.* **1991**, 35, 235; g) A. Shimada, M. Anzai, A. Kakuta, T. Kawanishi, *IEEE Trans. Ind. Appl.* **1987**, 1A-23, 804; h) T. Saito, T. Kawanishi, A. Kakuta, *Jpn. J. Appl. Phys.* **1991**, 30, L1182; i) G. A. Cox, P. C. Knight, *J. Phys. C: Solid State Phys.* **1974**, 7, 146; j) Z. D. Popovic, J. H. Sharp, *J. Chem. Phys.* **1977**, 66, 5076; k) Z. D. Popovic, *Chem. Phys.* **1984**, 86, 311; l) Z. D. Popovic, S. Mesbah, *Chem. Phys. Lett.* **1993**, 215, 636; m) J. F. Byrne, P. F. Kurz, **1967**, US Patent 3357989; n) C. F. Hackett, *J. Chem. Phys.* **1971**, 55, 3178; o) Z. D. Popovic, *J. Appl. Phys.* **1981**, 52, 6197; p) E. R. Menzel, Z. D. Popovic, *Chem. Phys. Lett.* **1978**, 55, 177; q) Z. D. Popovic, *J. Chem. Phys.* **1982**, 76, 2714; r) R. F. Code, Z. D. Popovic, *Appl. Phys. Lett.* **1981**, 39, 662; s) E. R. Menzel, R. O. Loutfy, *Chem. Phys. Lett.* **1980**, 72, 522; t) R. O. Loutfy, E. R. Menzel, *J. Am. Chem. Soc.* **1980**, 102, 4967; u) H. Naito, K. Kishimoto, T. Nagase, *Thin Solid Films* **1998**, 331, 82; v) Y. Kanemitsu, A. Yamamoto, H. Funada, Y. Masumoto, *J. Appl. Phys.* **1991**, 69, 7333; w) Y. Kanemitsu, H. Funada, S. Imamura, *J. Appl. Phys.* **1990**, 67, 4152; x) Y. Kanemitsu, S. Imamura, *Appl. Phys. Lett.* **1989**, 54, 872; y) Y. Kanemitsu, S. Imamura, *J. Appl. Phys.* **1990**, 67, 3728.
37. a) T. Enokida, *Jpn. J. Appl. Phys.* **1992**, 31 Pt. 2, L1135; b) T. Enokida, R. Hirohashi, T. Nakamura, *J. Imaging Sci.* **1990**, 34, 234; c) H. Miyazaki, K. Iuchi, I. Yamazaki, H. Takai, M. Matsumoto, *Proceedings IS&T's Sixth International Congress on Advances in Non-impact*

- Printing Technologies*, **1990**, p. 327; d) J. D. Mayo, *Proceedings IS&T's Ninth International Congress on Advances in Non-impact Printing Technologies/Japan Hardcopy '93*, **1993**, p. 652; e) T. I. Martin, J. D. Mayo, C. A. Jennings, S. Gardner, C. K. Hsiao, *Proceedings IS&T's Eleventh International Congress on Advances in Non-impact Printing Technologies*, **1995**, p. 30; f) K. Watanabe, A. Itami, A. Kinoshita, Y. Fujimaki, *Proceedings IS&T's Ninth International Congress on Advances in Non-impact Printing Technologies/Japan Hardcopy '93*, **1993**, p. 659; g) Y. Fujimaki, H. Tadokoro, Y. Oda, H. Yoshioka, T. Homma, H. Moriguchi, K. Watanabe, A. Konishita, N. Hirose, A. Itami, S. Ikeuchi, *J. Imaging Technol.* **1991**, *17*, 202; h) S. Takano, Y. Mimura, N. Matsui, K. Utsugi, T. Gotoh, C. Tani, K. Tateishi, N. Ohde, *J. Imaging Technol.* **1991**, *17*, 46; i) K. Oka, O. Okada, *J. Imaging Sci. Technol.* **1993**, *37*, 607; j) G. D. Hinch, G. W. Haggquist, *Proceedings IS&T's NIP 13: 1997 International Conference on Digital Printing Technologies*, **1997**, p. 202; k) J. Mizuguchi, G. Rihs, H. Karfunkel, *J. Phys. Chem.* **1995**, *99*, 16217; l) Y. Fujimaki, *Proceedings IS&T's Seventh International Congress on Advances in Non-impact Printing Technologies*, **1991**, p. 269; m) O. Okada, M. L. Klein, *Proceedings IS&T's Fourteenth International Conference on Digital Printing Technologies*, **1998**, p. 512; n) T. Saito, W. Sisk, T. Kobayashi, S. Suzuki, T. Iwayanagi, *J. Phys. Chem.* **1993**, *97*, 8026; o) Z. D. Popovic, A.-M. Hor, *Mol. Cryst. Liq. Cryst.* **1993**, *228*, 75; p) Z. D. Popovic, M. I. Khan, S. J. Atherton, A.-M. Hor, J. L. Goodman, *J. Phys. Chem. B* **1998**, *102*, 657; q) S. Yamaguchi, Y. Sasaki, *J. Phys. Chem. B* **1999**, *103*, 6835; r) V. Gulbinas, R. Jakubenas, S. Pakalnis, A. Undzenas, *J. Chem. Phys.* **1997**, *107*, 4927; s) C. Randolph, J. Neely, *Proceedings IS&T's Thirteenth International Conference on Digital Printing Technologies*, **1997**, p. 274.
38. a) K. Yamasaki, O. Okada, K. Inami, K. Oka, M. Kotani, H. Yamada, *J. Phys. Chem. B* **1997**, *101*, 13; b) K. Daimon, K. Nukada, Y. Sakaguchi, R. Igarashi, *Proceedings IS&T's Tenth International Congress on Advances in Non-impact Printing Technologies*, **1994**, p. 215; c) K. Daimon, K. Nukada, Y. Sakaguchi, R. Igarashi, *J. Imaging Sci. Technol.* **1996**, *40*, 249; d) K. Yamasaki, M. Kotani in *Electrical and Related Properties of Organic Solids* (Eds.: R. W. Munn, A. Miniewicz, B. Kuchta), NATO ASI Series, Kluwer Academic, Dordrecht, **1997**, p. 219; e) A.-M. Hor, Z. D. Popovic, *Proceedings IS&T's Tenth International Congress on Advances in Non-impact Printing Technologies*, **1994**, 236; f) J. D. Mayo, B. Keoshkerian, C.-K. Hsiao, R. E. Gaynor, S. J. Gardner, *Proceedings IS&T's Tenth International Congress on Advances in Non-impact Printing Technologies*, **1994**, 223.
39. a) T.-H. Huang, J. H. Sharp, *Chem. Phys.* **1982**, *65*, 205; b) S. Grammatica, J. Mort, *Appl. Phys. Lett.* **1981**, *38*, 445; c) K.-Y. Law, *Inorg. Chem.* **1985**, *24*, 1778; d) K.-Y. Law, *J. Phys. Chem.* **1988**, *92*, 4226.
40. a) R. E. Wingard, *IEEE Ind. Appl.* **1982**, 1251; b) R. B. Champ, *SPIE* **1987**, *759*, 40; c) R. O. Loutfy, A.-M. Hor, C.-K. Hsiao, G. Baranyi, P. Kazmaier, *Pure App. Chem.* **1988**, *60*, 1047; d) P. M. Kazmaier, R. Burt, G. DiPaola-Baranyi, C.-K. Hsiao, R. O. Loutfy, T. I. Martin, G. K. Hamer, T. L. Bluhm, M. G. Taylor, *J. Imaging Sci.* **1988**, *32*, 1; e) G. DiPaola-Baranyi, C. K. Hsiao, P. M. Kazmaier, R. Burt, R. O. Loutfy, T. I. Martin, *J. Imaging Sci.* **1988**, *32*, 60; f) K.-Y. Law, F. C. Bailey, *J. Imaging Sci.* **1987**, *31*, 172; g) K.-Y. Law, *J. Imaging Sci.* **1987**, *31*, 83; h) K.-Y. Law, *J. Imaging. Sci.*, **1992**, *36*, 567; i) K.-Y. Law, *Chem. Mater.* **1992**, *4*, 605; j) K.-Y. Law, *J. Imaging Sci.* **1990**, *34*, 38; k) K.-Y. Law, J. S. Facci, F. C. Bailey, J. F. Yanus, *J. Imaging Sci.* **1990**, *34*, 31; l) Y.-S. Kim, K. Liang, K.-Y. Law, D. G. Whitten, *J. Phys. Chem.* **1994**, *98*, 984.
41. a) E.-G. Schlosser, *J. Appl. Photogr. Eng.* **1978**, *4*, 118; b) N. C. Khe, S. Yokota, K. Takahashi, *Photogr. Sci. Eng.* **1984**, *28*, 191; c) J. M. Duff, A. M. Hor, C. G. Allen, A. Melnyk, D. Teney, *Proceedings IS&T's Seventh International Congress on Advances in Non-impact Printing Technologies*, **1991**, p. 284; d) R. O. Loutfy, A. M. Hor, P. Kazmaier, M. Tam, *J. Imaging Sci.* **1989**, *33*, 151; e) P. M. Kazmaier, A. J. McKerrow, E. Buncel, *J. Imaging Sci. Technol.* **1992**, *36*, 373; f) A. J. McKerrow, E. Buncel, P. M. Kazmaier, *Can. J. Chem.* **1993**, *71*, 390; g) P. M. Kazmaier, R. Hoffmann, *J. Am. Chem. Soc.* **1994**, *116*, 9684; h) P. M. Kazmaier, *Proceedings IS&T's Twelfth International Conference on Digital Printing Technologies*, **1996**, p. 456; i) J. M. Duff, G. K. Hamer, A. M. Hor, *Proceedings IS&T's Ninth International Congress on Advances in Non-impact Printing Technologies*, **1993**, p. 644; j) Z. D. Popovic, R. O. Loutfy, A.-M. Hor, *Can. J. Chem.* **1985**, *63*, 134; k) Z. D. Popovic, A.-M. Hor, R. O. Loutfy, *Chem. Phys.* **1988**, *127*, 451; l) E. H. Magin, P. M. Borsenberger, *Proceedings IS&T's Eighth International Con-*

- gress on *Advances in Non-impact Printing Technologies*, **1992**, p. 243; m) Z. D. Popovic, R. Cowdery, I. M. Khan, A.-M. Hor, J. Goodman, *J. Imaging Sci. Technol.* **1999**, 43, 266.
42. a) T. Nakazawa, A. Kawahara, Y. Watanabe, Y. Mizuta, *J. Imaging Sci. Technol.* **1994**, 38, 421; b) M. Hiramoto, Y. Sakaue, M. Yokoyama, *Bull. Chem. Soc. Jpn.* **1994**, 67, 2011.
 43. R. E. Cais, M. Nozomi, M. Kawai, A. Miyake, *Macromolecules* **1992**, 25, 4588.
 44. a) E. T. Seo, R. F. Nelson, J. M. Fritsch, L. S. Marcoux, D. W. Leedy, R. N. Adams, *J. Am. Chem. Soc.* **1966**, 88, 3498; b) H.-J. Yuh, D. Abramsohn, M. Stolka, *Phil. Mag. Lett.* **1987**, 55, 277; c) P. M. Borsenberger, W. T. Gruenbaum, U. Wolf, H. Bässler, *Chem. Phys.* **1998**, 234, 277; d) L.-B. Lin, R. H. Young, M. G. Mason, S. A. Jenekhe, P. M. Borsenberger, *Appl. Phys. Lett.* **1998**, 72, 864; e) L.-B. Lin, M. G. Mason, R. H. Young, D. E. Schildkraut, P. M. Borsenberger, S. A. Jenekhe, *Mater. Res. Soc. Symp. Proc.* **1998**, 488, 689; f) M. Stolka, M. A. Abkowitz, K. M. McGrane, F. E. Knier, R. J. Weagley, H.-J. Yuh, *Proceedings IS&T's Fourth International Congress on Advances in Non-impact Printing Technologies*, **1988**, p. 31; g) P. M. Borsenberger, W. T. Gruenbaum, E. H. Magin, S. A. Visser, D. E. Schildkraut, *J. Polymer Sci. B: Polymer Physics* **1999**, 37, 349; h) H. Bässler, *Phil. Mag. B*, **1984**, 50, 347.
 45. W. D. Gill, *J. Appl. Phys.* **1972**, 43, 5033.
 46. a) C. H. Chen, G. A. Reynolds, H. R. Luss, J. H. Perlstein, *J. Org. Chem.* **1986**, 51, 3282; b) M. R. Detty, R. S. Eachus, J. A. Sinicropi, J. R. Lenhard, M. McMillan, A. M. Lanzafame, H. R. Luss, R. Young, J. E. Eilers, *J. Org. Chem.* **1995**, 60, 1674; c) Y. Yamaguchi, H. Tanaka, M. Yokoyama, *J. Chem. Soc., Chem. Commun.* **1990**, 222; d) P. M. Borsenberger, W. T. Gruenbaum, E. H. Magin, S. A. Visser, *Phys. Stat. Solidi (A)* **1998**, 166, 835; e) H. Tanaka, Y. Yamaguchi, M. Yokoyama, *Denshi Shashin Gakkai-shi* **1990**, 29(4), 366.
 47. a) M. A. Abkowitz, J. S. Facci, W. W. Limburg, *Mol. Cryst. Liq. Cryst.* **1993**, 230, 83; b) M. Abkowitz, J. S. Facci, M. Stolka, *Chem. Phys.* **1993**, 177, 783.
 48. a) H. Bässler, G. Schönherr, M. Abkowitz, D. M. Pai, *Phys. Rev. B* **1982**, 26, 3105; b) M. Abkowitz, M. Stolka, M. Morgan, *J. Appl. Phys.* **1981**, 52, 3453; c) V. Gaedelis, V. Kriščiūnas, E. Montrimas, *Thin Solid Films* **1976**, 38, 9; d) R. Oshima, T. Uryu, M. Senō, *Macromolecules* **1985**, 18, 1043; e) M. Stolka, D. M. Pai, D. S. Renfer, J. F. Yanus, *J. Polymer Sci.: Polymer Chem. Ed.* **1983**, 21, 969; f) S. R. Turner, *Macromolecules* **1980**, 13, 782; g) H. Ohkawa, T. Furuichi, R. Oshima, T. Uryu, *Macromolecules* **1989**, 22, 2266; h) M. A. Abkowitz, *Phil. Mag.* **1992**, 65, 817.
 49. a) M. A. Abkowitz, H. Bässler, M. Stolka, *Phil. Mag. B* **1991**, 63, 201; b) T. Dohmaru, K. Oka, T. Yajima, M. Miyamoto, Y. Nakayama, T. Kawamura, and R. West, *Phil. Mag. B* **1995**, 71, 1069.
 50. a) W. D. Gill, *Proc. 5th Internat. Conf. on Amorphous and Liquid Semiconductors*, **1973**, p. 910; b) J. H. Sharp, *J. Phys. Chem.* **1967**, 71, 2587; c) D. C. Hoesterey, G. M. Letson, *J. Chem. Phys.* **1964**, 41, 675; d) H. Kitayama, M. Yokoyama, H. Mikawa, *Mol. Cryst. Liq. Cryst.* **1981**, 69, 257; e) H. Kitayama, M. Yokoyama, H. Mikawa, *Mol. Cryst. Liq. Cryst.* **1981**, 76, 19.
 51. S. J. Santos Lemus, J. Hirsch, *Phil. Mag. B* **1986**, 53, 25.
 52. M. Abkowitz, D. M. Pai, *Phil. Mag. B* **1986**, 53, 193.
 53. a) S. V. Novikov, *J. Imaging Sci. Technol.* **1999**, 43, 444; b) R. H. Young, *J. Appl. Phys.* **1992**, 72, 2993.
 54. a) J. C. Scott, L. Th. Pautmeier, L. B. Schein, *Phys. Rev. B* **1992**, 46, 8603; b) A. Hirao, H. Nishizawa, M. Sugiuchi, *Phys. Rev. Lett.* **1995**, 75, 1787; c) A. Hirao, H. Nishizawa, *Phys. Rev. B* **1996**, 54, 4755.
 55. a) P. M. Borsenberger, E. H. Magin, M. B. O'Regan, J. A. Sinicropi, *J. Polymer Sci. B: Polymer Physics* **1996**, 34, 317; b) R. H. Young, J. J. Fitzgerald, *J. Phys. Chem.* **1995**, 99, 4230; c) P. Hedwig, *Dielectric Spectroscopy of Polymers*, Hilger, Bristol, **1972**, p. 24; d) A. L. McClellan, *Tables of Experimental Dipole Moments*, Freeman, San Francisco, **1963**; e) H.-J. Yuh, D. M. Pai, *Phil. Mag. Lett.* **1990**, 62, 61; f) S. Aratani, T. Saito, T. Kawanishi, N. Kinjo, *Jpn. J. Appl. Phys.* **1990**, 29, L1682; g) H.-J. Yuh, D. M. Pai, *J. Imaging Sci. Technol.* **1992**, 36, 477; h) P. M. Borsenberger, H. Bässler, *J. Chem. Phys.* **1991**, 95, 5327; i) P. M. Borsenberger, J. J. Fitzgerald, E. H. Magin, *J. Phys. Chem.* **1993**, 97, 11314; j) P. M. Borsenberger, L. J. Rossi, *J. Chem. Phys.* **1992**, 96, 2390; k) J. A. Pavlisko, L. J. Sorriero, R. H. Young, **1993**, US Patent 5232800.

56. a) R. H. Young, J. J. Fitzgerald, *J. Chem. Phys.* **1995**, *102*, 2209; b) A. V. Vannikov, A. Yu. Kryukov, A. G. Tyurin, T. S. Zhuravleva, *Phys. Stat. Solidi (A)* **1989**, *115*, K47; c) P. M. Borsenberger, H. Bässler, *Phys. Stat. Solidi (B)* **1992**, *170*, 291; d) R. H. Young, J. J. Fitzgerald, *J. Chem. Phys.* **1995**, *102*, 6290; e) R. H. Young, J. J. Fitzgerald, *J. Chem. Phys.* **1995**, *102*, 9380; f) H. Valerián, E. Brynda, S. Nešpůrek, W. Schnabel, *J. Appl. Phys.* **1995**, *78*, 6071; g) M. Sugiuchi, H. Nishizawa, *J. Imag. Sci. Technol.* **1993**, *37*, 245; h) A. Hirao, H. Nishizawa, *Phys. Rev. B* **1997**, *56*, R2904; i) Y. Kanemitsu, Y. Sugimoto, *Phys. Rev. B* **1992**, *46*, 14182; j) P. M. Borsenberger, J. J. Fitzgerald, *J. Phys. Chem.* **1993**, *97*, 4815; k) P. M. Borsenberger, *Mol. Cryst. Liq. Cryst.* **1993**, *228*, 167; l) R. H. Young, J. A. Sinicropi, J. J. Fitzgerald, *J. Phys. Chem.* **1995**, *99*, 9497. m) P. M. Borsenberger, E. H. Magin, and J. Shi, *Physica B* **1996**, *217*, 212.
57. a) L. B. Schein, J. X. Mack, *Chem. Phys. Lett.* **1988**, *149*, 109; b) L. B. Schein, D. Glatz, J. C. Scott, *Phys. Rev. Lett.* **1990**, *65*, 472; c) T. Kitamura, M. Yokoyama, *Jpn. J. Appl. Phys.* **1991**, *30*, 1015; d) M. D. Newton, N. Sutin, *Annu. Rev. Phys. Chem.* **1984**, *35*, 437; e) J. R. Miller, J. V. Beitz, R. K. Huddleston, *J. Am. Chem. Soc.* **1984**, *106*, 5057; f) R. C. Dorfman, Y. Lin, M. D. Fayer, *J. Phys. Chem.* **1989**, *93*, 6388.
58. a) G. J. Pratt, M. J. A. Smith, *Br. Polymer J.* **1986**, *18*, 105; b) R. D. McCammon, R. G. Saba, R. N. Work, *J. Polymer Sci., Part A-2*, **1969**, *7*, 1721; c) W. Wunderlich, in *Polymer Handbook*, Third Edition (Eds.: J. Brandrup, E. H. Immergut), Wiley, New York, **1989**, p. V/77.
59. a) H. Bässler, *Phys. Status Sol. (B)* **1981**, *107*, 9; b) H. Bässler, *Phys. Stat. Sol. (B)* **1993**, *175*, 15.
60. a) J. A. Sinicropi, L.-B. Lin, P. M. Borsenberger, E. H. Magin, *Jpn. J. Appl. Phys.* **1997**, *36*, 7259; b) R. H. Young, *J. Chem. Phys.* **1995**, *103*, 6749; c) H. Kageyama, K. Ohnishi, S. Nomura, Y. Shirota, *Chem. Phys. Lett.* **1997**, *277*, 137; d) P. M. Borsenberger, E. H. Magin, J. J. Fitzgerald, *J. Phys. Chem.* **1993**, *97*, 8250; e) P. M. Borsenberger, W. T. Gruenbaum, E. H. Magin, *Jpn. J. Appl. Phys.* **1996**, *35*, 2698; f) J. A. Sinicropi, J. R. Cowdery-Corvan, E. H. Magin, P. M. Borsenberger, *SPIE* **1996**, *2850*, 202; g) S. A. Visser, W. T. Gruenbaum, E. H. Magin, P. M. Borsenberger, *Chem. Phys.* **1999**, *240*, 197; h) P. M. Borsenberger, *J. Appl. Phys.* **1990**, *68*, 5188; i) J. X. Mack, L. B. Schein, A. Peled, *Phys. Rev. B* **1989**, *39*, 7500; j) P. M. Borsenberger and H. Bässler, *J. Imaging Sci.* **1991**, *35*, 79.
61. a) A. Dieckmann, H. Bässler, P. M. Borsenberger, *J. Chem. Phys.* **1993**, *99*, 8136; b) S. V. Novikov, A. V. Vannikov, *Sov. Phys. JETP* **1994**, *79*, 482 [*Zhurnal Eksp. Teor. Fiz.* **1994**, *106*, 877]; c) S. V. Novikov, A. V. Vannikov, *J. Imaging Sci. Technol.* **1994**, *38*, 355; d) R. H. Young, *Phil. Mag. B* **1995**, *72*, 435.
62. a) P. M. Borsenberger, J. R. Cowdery-Corvan, E. H. Magin, J. A. Sinicropi, *Thin Solid Films* **1997**, *307*, 215; b) W. T. Gruenbaum, E. H. Magin, P. M. Borsenberger, *Jpn. J. Appl. Phys.* **1996**, *35*, 2704; c) P. M. Borsenberger, J. Shi, *Phys. Status Solidi (B)* **1995**, *191*, 461.
63. a) L. Pautmeier, R. Richert, H. Bässler, *Syn. Metals* **1990**, *37*, 271; b) P. M. Borsenberger, L. Pautmeier, H. Bässler *J. Chem. Phys.* **1991**, *94*, 5447; c) L. B. Schein, *Phil. Mag. B* **1992**, *65*, 795; d) L. B. Schein, A. Peled, and D. Glatz, *J. Appl. Phys.* **1989**, *66*, 686; e) Yu. N. Gartstein, E. M. Conwell, *J. Chem. Phys.* **1994**, *100*, 9175; f) S. V. Novikov, D. H. Dunlap, V. M. Kenkre, P. E. Parris, A. V. Vannikov, *Phys. Rev. Lett.* **1998**, *81*, 4472; g) J. H. Slowik, I. Chen, *J. Appl. Phys.* **1983**, *54*, 4467.
64. a) R. Richert, R. F. Loring, *J. Phys. Chem.* **1995**, *99*, 17265; b) R. A. Marcus, *J. Phys. Chem.* **1989**, *93*, 3078; c) J. Ulstrup, J. Jortner, *J. Chem. Phys.* **1975**, *63*, 4358; d) R. A. Marcus, *J. Chem. Phys.* **1984**, *81*, 4494; e) D. H. Dunlap, V. M. Kenkre, *Chem. Phys.* **1993**, *178*, 67; f) A. Miller, E. Abrahams, *Phys. Rev.* **1960**, *120*, 745; g) D. Emin, *Proc. SPIE* **1996**, *2850*, 159; h) R. H. Young, *Phil. Mag. B* **1994**, *69*, 577; i) D. H. Dunlap, P. E. Parris, V. M. Kenkre, *Proc. SPIE* **1999**, *3799*, 88; j) Z. G. Soos, S. J. Schmidt, D. Mukhopadhyay, *Proc. SPIE* **1996**, *2850*, 147; k) Z. G. Soos, S. J. Schmidt, *Chem. Phys. Lett.* **1997**, *265*, 427; l) Z. G. Soos, S. Bao, G. W. Hayden, *Proc. SPIE* **1999**, *3799*, 102; m) Z. G. Soos, S. Bao, J. M. Sin, G. W. Hayden, *Chem. Phys. Lett.* **2000**, *319*, 631; n) M. van der Auweraer, F. C. De Schryver, P. Borsenberger, *Chem. Phys.* **1994**, *186*, 409; o) P. E. Parris, *Proc. SPIE* **1998**, *3471*, 202; p) R. H. Young, T.-M. Kung, J. A. Sinicropi, N. G. Rule, J. J. Fitzgerald, J. E. Eilers, C. H. Chen, N. W. Boaz, *J. Phys. Chem.* **100**, 17923 (1996).

65. a) Yu. N. Gartstein, E. M. Conwell, *Chem. Phys. Lett.* **1995**, 245, 351; b) D. H. Dunlap, V. M. Kenkre, P. E. Parris, *J. Imaging Sci. Technol.* **1999**, 43, 437; c) D. H. Dunlap, P. E. Parris, V. M. Kenkre, *Phys. Rev. Lett.* **1996**, 77, 542; d) S. V. Novikov, A. V. Vannikov, *J. Phys. Chem.* **1995**, 99, 14573; e) S. V. Novikov, A. V. Vannikov, *Proc. SPIE* **1997**, 3144, 100; f) P. E. Parris, D. H. Dunlap, V. M. Kenkre, *Phys. Status Solidi (B)* **2000**, 218, 47; g) S. V. Novikov, D. H. Dunlap, V. M. Kenkre, *Proc. SPIE* **1988**, 3471, 181; h) Y. Shiota, *J. Mater. Chem.* **2000**, 10, 7; i) S. V. Novikov, *Phys. Status Solidi (B)* **2000**, 218, 43; j) D. H. Dunlap, *Phys. Rev. B* **1995**, 52, 939; k) D. H. Dunlap, *J. Imaging Sci. Technol.* **1996**, 40, 291; l) S. Rackovsky, H. Scher, *J. Chem. Phys.* **1999**, 111, 3668; m) S. V. Novikov, A. V. Vannikov, *Synthetic Metals* **1997**, 85, 1167.
66. a) W. T. Gruenbaum, L.-B. Lin, E. H. Magin, P. M. Borsenberger, *Phys. Stat. Sol. (B)* **1997**, 204, 729; b) P. M. Borsenberger, W. T. Gruenbaum, J. E. Kaeding, E. H. Magin, *Phys. Stat. Sol. (B)* **1995**, 191, 171; c) P. M. Borsenberger, E. H. Magin, *Macromolecular Symp.* **1997**, 116, 51; d) P. M. Borsenberger, in *Electrical and Related Properties of Organic Solids* (Eds.: R. W. Munn, A. Miniewicz, B. Kuchta), NATO ASI Series, Kluwer Academic, Dordrecht, **1997**, p. 25; e) P. M. Borsenberger, D. S. Weiss, *J. Imaging Sci. Technol.* **1997**, 41, 185; f) P. M. Borsenberger, W. T. Gruenbaum, E. H. Magin, *Proc. SPIE* **1995**, 2526, 63; g) P. M. Borsenberger, M. B. O'Regan, *Chem. Phys.* **1995**, 200, 257; h) P. M. Borsenberger, W. T. Gruenbaum, E. H. Magin, *Physica B* **1996**, 228, 226; i) P. M. Borsenberger, W. T. Gruenbaum, E. H. Magin, *Physica B* **1996**, 228, 233; j) P. M. Borsenberger, W. T. Gruenbaum, *J. Polymer Sci. B: Polymer Physics* **1996**, 34, 575; k) J. A. Sinicropi, J. R. Cowdery-Corvan, E. H. Magin, P. M. Borsenberger, *Chem. Phys.* **1997**, 218, 331; l) P. M. Borsenberger, E. H. Magin, J. A. Sinicropi, L.-B. Lin, *Jpn. J. Appl. Phys.* **1998**, 37, 166.
67. a) P. M. Borsenberger, W. T. Gruenbaum, M. B. O'Regan, L. J. Rossi, *J. Polymer Sci. B: Polymer Physics* **1995**, 33, 2143; b) P. M. Borsenberger, W. T. Gruenbaum, E. H. Magin, *Phys. Stat. Solidi (B)* **1995**, 190, 555; c) M. B. O'Regan, P. M. Borsenberger, W. T. Gruenbaum, *Phys. Stat. Solidi (A)* **1995**, 148, 259.
68. a) P. M. Borsenberger, H.-C. Kan, E. H. Magin, W. B. Vreeland, *J. Imaging Sci. Technol.* **1995**, 39, 6; b) P. M. Borsenberger, L. B. Schein, *J. Phys. Chem.* **1994**, 98, 233; c) P. M. Borsenberger, L. B. Schein, *Chem. Phys.* **1993**, 177, 773; d) P. M. Borsenberger, W. T. Gruenbaum, E. H. Magin, L. J. Sorriero, *Chem. Phys.* **1995**, 195, 435.
69. a) R. H. Young, N. G. Rule, *Phys. Rev. Lett.* **1994**, 72, 388; b) M. Van der Auweraer, F. C. De Schryver, P. M. Borsenberger, H. Bässler, *Adv. Mater.* **1994**, 6, 199.
70. a) W. Klöpffer, *Kunststoffe* **1971**, 61, 533; b) P. C. Johnson, H. W. Offen, *J. Chem. Phys.* **1971**, 55, 2945; c) G. E. Johnson, *J. Chem. Phys.* **1975**, 62, 4697; d) M. Fujino, Y. Kanazawa, H. Mikawa, S. Kusabayashi, M. Yokoyama, *Solid State Commun.* **1984**, 49, 575; e) T. Sasakawa, T. Ikeda, S. Tazuke, *Macromolecules* **1989**, 22, 4253; f) M. Yokoyama, K. Akiyama, N. Yamamori, H. Mikawa, S. Kusabayashi, *Polymer J.* **1985**, 17, 545; g) N. Tsutsumi, M. Yamamoto, Y. Nishijima, *J. Polymer Sci. B: Polymer Physics* **1987**, 25, 2139.
71. a) G. Giro, P. G. DiMarco, *Chem. Phys. Lett.* **1989**, 162, 221; b) Y. Tsujii, A. Tsuchida, M. Yamamoto, N. Nishijima, *Macromolecules* **1988**, 21, 665; c) M. Yamamoto, Y. Tsujii, A. Tsuchida, *Chem. Phys. Lett.* **1989**, 154, 559; d) X. Guo, G. D. Mendenhall, *Chem. Phys. Lett.* **1988**, 152, 146; e) J. Masnovi, R. B. Krafcik, R. J. Baker, R. L. R. Towns, *J. Phys. Chem.* **1990**, 94, 2010; f) Y. Tsujii, A. Tsuchida, M. Yamamoto, T. Momose, T. Shida, *J. Phys. Chem.* **1991**, 95, 8635; g) R. J. Baker, Z. Chen, R. B. Krafcik, J. Masnovi, *Acta Cryst.* **1991**, C47, 2167; h) A. Tsuchida, A. Nagata, M. Yamamoto, H. Fukui, M. Sawamoto, T. Higashimura, *Macromolecules* **1995**, 28, 1285; i) U. Rauscher, H. Bässler, *Macromolecules* **1990**, 23, 398.
72. a) H.-J. Yuh, M. Stolka, *Phil. Mag. B* **1988**, 58, 539; b) L. B. Schein, J. C. Scott, L. Th. Pautmeier, R. H. Young, *Mol. Cryst. Liq. Cryst.* **1993**, 228, 175; c) P. M. Borsenberger, L. T. Pautmeier, H. Bässler, *Phys. Rev. B* **1993**, 48, 3066; d) P. M. Borsenberger, H. Bässler, *J. Appl. Phys.* **1994**, 75, 967; e) L. Pautmeier, R. Richert, H. Bässler, *Phil. Mag. B* **1991**, 63, 587; f) P. E. Parris, D. H. Dunlap, V. M. Kenkre, *J. Polymer Science B: Polymer Physics* **1997**, 35, 2803; g) H. Schnorer, H. Domes, A. Bumen, D. Haarer, *Phil. Mag. Lett.* **1988**, 58, 101.
73. a) H. Scher, E. W. Montroll, *Phys. Rev. B* **1975**, 12, 2455; b) H. Scher in *Photoconductivity and Related Phenomena* (Eds.: J. Mort, D. M. Pai), Elsevier Scientific, Amsterdam, **1976**, Ch. 3; c) G. Pfister, H. Scher, *Adv. Phys.* **1978**, 27, 747; d) H. Scher, M. F. Schlesinger, J. T. Bendler,

- Physics Today* **1991**, 44, 26; e) D. Haarer, A. Blumen, *Angew. Chem., Int. Ed. Engl.* **1988**, 27, 1210; f) N. Crisa, *Phys. Stat. Solidi (B)* **1983**, 116, 269; g) J. Mort, G. Pfister, S. Grammatica, *Solid State Commun.* **1976**, 18, 693; h) M. Grasruck, A. Schreiber, U. Hofmann, S. J. Zilker, A. Leopold, S. Schlöter, C. Hohle, P. Strohmriegel, D. Haarer, *Phys. Rev. B* **1999**, 60, 16543; i) G. Pfister, C. H. Griffiths, *Phys. Rev. Lett.* **1978**, 40, 659; j) E. Müller-Horsche, D. Haarer, H. Scher, *Phys. Rev. B* **1987**, 35, 1273; k) L. Pautmeier, R. Richert, H. Bässler, *Phil. Mag. Lett.* **1989**, 59, 325; l) H. Bässler, P. M. Borsenberger, *Chem. Phys.* **1993**, 177, 763; m) P. M. Borsenberger, R. Richert, H. Bässler, *Phys. Rev. B* **1993**, 47, 4289; n) P. M. Borsenberger, H.-C. Kan, W. B. Vreeland, *Phys. Stat. Solidi (A)* **1994**, 142, 489; o) P. M. Borsenberger, L. T. Pautmeier, H. Bässler, *Phys. Rev. B* **1992**, 46, 12145; p) J. M. Casado, J. J. Mejías, *Phil. Mag. B* **1994**, 69, 39; q) G. Pfister, *Phys. Rev. B* **1977**, 16, 3676; r) P. M. Borsenberger, *J. Appl. Phys.* **1990**, 68, 6263; s) N. G. Rule, private communication; t) N. G. Rule, R. H. Young, unpublished results.
74. a) G. Pfister, J. Mort, S. Grammatica, *Phys. Rev. Lett.* **1976**, 37, 1360; b) D. M. Pai, J. F. Yanus, M. Stolka, *J. Phys. Chem.* **1984**, 88, 4714; c) A. V. Vannikov, A. Yu. Kryukov, *J. Inf. Rec. Mater.* **1990**, 18, 341; d) K. Yokoyama, M. Yokoyama, *J. Appl. Phys.* **1990**, 67, 2974; e) K. Yokoyama, M. Yokoyama, *Solid State Commun.* **1990**, 73, 199; f) M. A. Abkowitz, M. Stolka, *Polymer Preprints* **1990**, 31, 254; g) Y. Kanemitsu, H. Funada, Y. Masumoto, *Appl. Phys. Lett.* **1991**, 59, 697; h) L. Pautmeier, J. C. Scott, L. B. Schein, *Chem. Phys. Lett.* **1992**, 197, 568; i) J. Veres, C. Juhasz, *Phil. Mag. B* **1997**, 75, 377; j) P. M. Borsenberger, E. H. Magin, S. A. Visser, *Jpn. J. Appl. Phys.* **1998**, 37, 1945; k) L.-B. Lin, P. M. Borsenberger, E. H. Magin, S. A. Visser, W. T. Gruenbaum, *Proc. SPIE* **1998**, 3471, 174; l) P. M. Borsenberger, W. T. Gruenbaum, E. H. Magin, S. A. Visser, D. E. Schildkraut, *J. Polymer Science B: Polymer Physics* **1999**, 37, 349; m) K. Watanabe, T. Asahi, H. Masuhara, *J. Phys. Chem.* **1996**, 100, 18436; n) U. Wolf, H. Bässler, P. M. Borsenberger, W. T. Gruenbaum, *Chem. Phys.* **1997**, 222, 259; o) S. Nomura, K. Nishimura, Y. Shiota, *Thin Solid Films* **1996**, 273, 27; p) S. V. Novikov, D. H. Dunlap, V. M. Kenkre, A. V. Vannikov, *Proc. SPIE* **1999**, 3799, 94; q) S. Heun, Dissertation (Philipps Universität Marburg, 1995); r) S. Nomura, K. Nishimura, Y. Shiota, *Mol. Cryst. Liq. Cryst.* **1994**, 253, 79.
75. D. E. Bugner, T.-M. Kung, R. H. Young, **1994**, US Patent 5324604.
76. a) T. Kitamura, M. Yokoyama, *J. Appl. Phys.* **1991**, 69, 821; b) S.-I. Okada, *Proceedings IS&T's Eighth International Congress on Advances in Non-impact Printing Technologies*, **1992**, p. 261; c) S. Aratani, T. Kawanishi, A. Kakuta, *Jpn. J. Appl. Phys.* **1996**, 35, Part 1, 2184; d) H. Sugimura, Y. Kojima, S. Nishigaki, K. Emoto, *Proceedings IS&T's Ninth International Congress on Advances in Non-impact Printing Technologies* **1993**, p. 627; e) A. Hirano, E. Tsuruoka, Y. Takeda, *Proceedings IS&T's Eleventh International Congress on Advances in Non-impact Printing Technologies*, **1995**, p. 60; f) N. Hirose, H. Hayata, Y. Fujimaki, *Proceedings IS&T's Eighth International Congress on Advances in Non-impact Printing Technologies* **1992**, p. 26; g) R. Q. Zhang, C. S. Lee, S. T. Lee, *Appl. Phys. Lett.* **1999**, 75, 2418.
77. a) N. G. Rule, T.-M. Kung, **1991**, US Patent 5039585; b) W. T. Gruenbaum, T.-M. Kung, R. H. Young, **1995**, US Patent 5468583; c) P. M. Borsenberger, E. H. Magin, M. van der Auweraer, F. C. de Schryver, *Phys. Stat. Solidi (A)* **1993**, 140, 9.

3 Photorefractive Materials

David P. West and Mark D. Rahn

3.1 The Photorefractive Effect in Crystals and Amorphous Organic Media

3.1.1 Scenarios of Potential Applications

This chapter describes materials in which optical generation of mobile charges, followed by charge movement, leads to a change in refraction within a material. Photorefraction is an unusual optical phenomenon in some respects. Photorefractive materials react to the total fluence (the product of the exposure time and the intensity) of light incident upon them, not just the intensity, with the result that even very weak light may be used to control an optical system. The altered refraction is not local, it is shifted slightly in space away from the optical pattern that causes it with the result that the material can transfer energy from one light wave to another. The optical control of the material is completely reversible optically, so that the materials may be re-used as new. It is useful to consider the use of photorefractive materials in holography in order to describe the phenomenon. Many, but not all, of the applications that have been proposed for such materials depend on holography within the bulk of the material.

Many people are familiar with the idea of the hologram. The most common form of hologram is now mass-produced, creating a three-dimensional image that changes in appearance as the viewing angle is changed, and features on a credit card as an impediment to fraud. The ability for holograms to appear dramatically different at different viewing angles is an indication that much more information can be contained in this form than in a simple, two-dimensional image such as a photograph. Holograms are used commonly to provide a three-dimensional representation of an object; however, the images viewed from different angles need not be connected in any way (Figure 1). The hologram must be rotated or the viewing angle must be changed in order to see the different perspectives that are possible. It is this angle selectivity, this ability to isolate a particular image by the angle at which the light is observed, that leads to the proposal to store information with an ultrahigh density

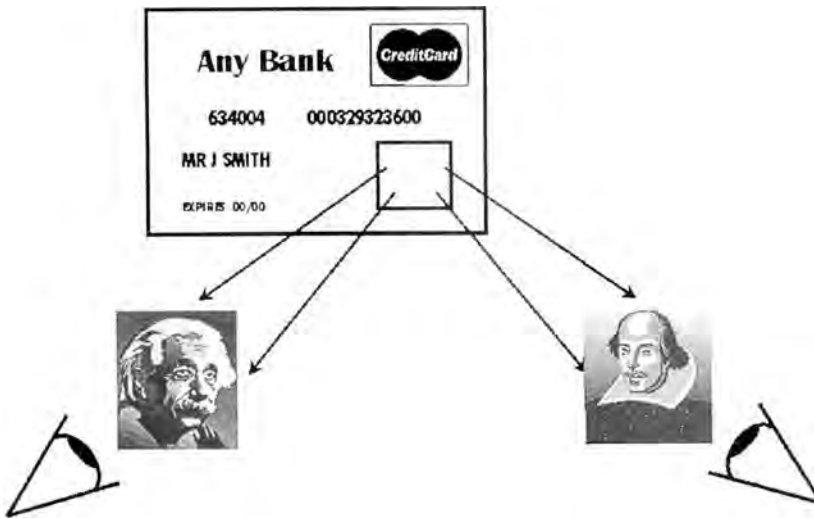


Figure 1. A credit card is protected against fraud, using a simple hologram. Different images may be seen in the hologram from different viewing angles, illustrating the high information capacity of the hologram.

by writing many different holograms at different angles within the same volume of material. The hologram on a credit card is a permanent recording. An information storage system would be most useful if the information within it could be erased after use and then the storage medium could be re-used, in the same way as computer memory is re-used. Photorefractive materials offer this possibility.

The electronic signal amplifier is a common device, used to increase the power in electronic audio signals in a radio or a CD player, for example. An optical amplifier may be constructed using a population inversion within a laser gain medium. But can we amplify a beam that contains an image, to make the image brighter (Figure 2)? Using a photorefractive material we can construct a hologram by overlapping the image beam with an intense, uniform beam. The hologram that is created within a photorefractive material is shifted in phase relative to the optical interference pattern that creates it and allows coupling of light energy from one beam into the other, making such an image beam amplifier possible.

There are other applications of photorefractive materials that have been investigated, including associative optical memories that identify a clear image from a corrupted input [1], novelty filters to detect only changing features in an image [2], and neural networking in analogy with the human brain [3].

3.1.2 An Overview of the Sequence of Processes Leading to Photorefractivity

The trigger for photorefractive response is the exposure of the medium to an optical irradiation with a nonuniform intensity pattern. In practice, this usually means that two or more optical beams from the same source must overlap within the medium.

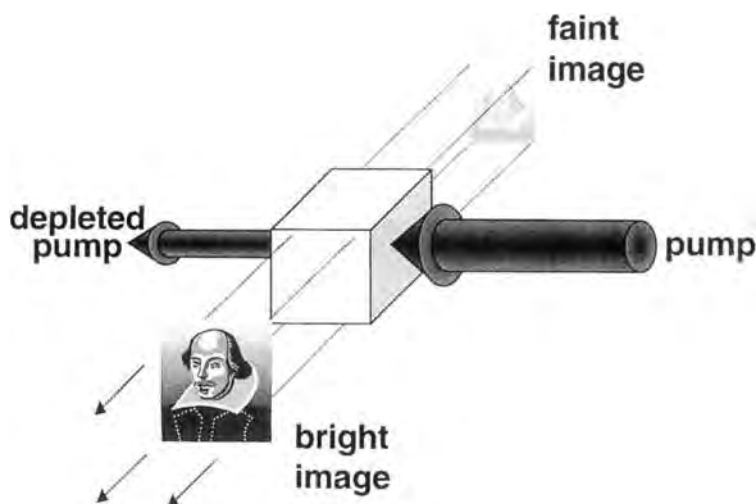


Figure 2. Amplifying a beam containing an image. Using a photorefractive material, the energy from a poor-quality, uniform pump beam can be coupled into the high-quality, weak beam containing an image. The beam is amplified and the image is retained.

If the two beams have a well-defined phase relationship, they will interfere to produce regions of darkness as well as regions of bright illumination. It is this coherent interference that has been used for over half a century to produce holograms in thick photographic emulsions such as silver halides.

In a photorefractive material the presence of light will lead to photoinduced electron transfer, which creates a charged ion together with a free charge carrier of opposite polarity. In the majority of amorphous organic photorefractive materials, a mobile hole is generated together with an immobile anion. The process of mobile charge generation after the absorption of a photon is generally assumed to be very fast ($\tau < 10^{-9}$ s) in comparison with the subsequent phenomena involved in photorefractive response. Typically the free hole population becomes saturated quickly because the lifetime of holes is short (although an estimate for amorphous organic media could be as long as $\tau_h \sim 10^{-4}$ s). During subsequent processes the rate of optical generation of carriers will be equaled by the rate at which they recombine with the immobile anion distribution.

In most cases an external electric field is applied across the material with the result that the mobile carrier distribution will experience drift in the field toward a new position. Even in the absence of an applied field, the nonuniform distribution of the mobile charge carriers created will lead to their relocation due to diffusion. Although the free carriers are generated where the optical intensity is high, their recombination with counterions (in the case of hole transport these are anions) may occur anywhere in the medium. This includes recombination where the intensity is low, resulting in the separation of the charge distributions. Subsequent optical excitation is unlikely in these darker regions. We know that the counterions exist in

dark regions because without them, holes would recombine only at sites of anions generated optically. The final state would then be indistinguishable from the initial state and no photorefraction would be observed.

Then, how is it that anions can exist in the darker regions, able to capture the mobile holes? Each mobile hole that is generated leaves behind an acceptor molecule that becomes charged negatively. The population of mobile holes saturates quickly in response to optical excitation, in a time equal to the mobile hole recombination lifetime. In order that charge redistribution may take place, the anion distribution must have a number density greater than that of the saturated mobile hole population. In these circumstances the immobile anion sites have a lifetime considerably longer than that for the mobile holes. The anion number density must have been large prior to optical irradiation. To preserve the electrical neutrality of the bulk material it is necessary that a similarly large and stable, immobile, cationic site density also exists. It is the presence of these immobile and passive charged sites of the same polarity as the mobile holes which makes it possible to have a large and steady population of immobile anions without a physically improbable high electric potential in the bulk of the material. For this reason, the immobile cations are sometimes referred to as compensators. The standard model of photorefraction assumes that the saturated population of mobile carriers is at least an order of magnitude lower in number density than the compensator density. The immobile cations and anions are distributed throughout the material, even in the dark regions, and electrical near-neutrality is preserved (Figure 3). In most cases of organic, glassy, photorefractive materials such as polymers, the matrix is a donor (hole) transport material. The anions are formed by the addition of sensitizer molecules, which have a higher oxidation potential and thus act as electron acceptors.

Recombination of the mobile charges in dark regions is not necessary for the photorefractive effect to be observed, but it is beneficial. If the mobile charges were to be removed completely, or redistributed uniformly with no dependence on the intensity pattern applied, then an immobile pattern of counterions would still be

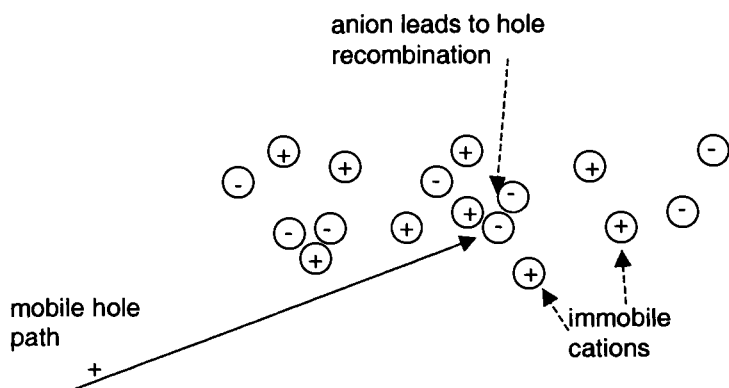


Figure 3. Random distributions of ionized sensitizer anions and immobile cations coexist, trapped so that the recombination time is long. The smaller population density of mobile holes can be trapped by the anions anywhere within the medium.

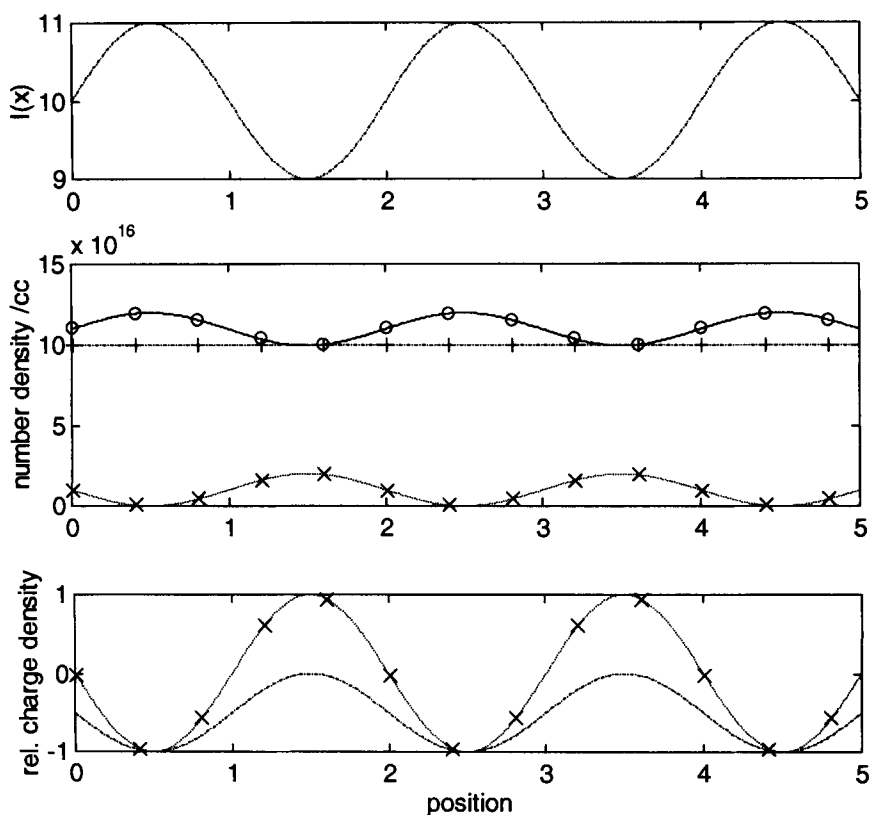


Figure 4. The photorefractive effect with and without trapping. Top: the intensity pattern on the material. Middle: \circ , anion density; $+$, cation density; \times , ideal distribution of trapping of mobile holes. Bottom: comparison of the net charge distribution in the ideal case (no. of cations – no. of anions + no. of trapped holes, \times) with the corresponding space charge field in the absence of any trapping or recombination (no. of trapped holes = 0), (—).

created (Figure 4). The photorefractive effect is stronger when the mobile charges are subject to recombination. The term *trapping* is often used in photorefractive materials literature, and in most cases this refers to carrier recombination.

The initial sensitizer anion presence makes recombination of mobile holes possible in the dark regions. Which are the compensator sites? Here, there exist different explanations. One possibility is that some of the electro-optic dye molecules present in photorefractive composites to provide refractive index change may become charged positively. An alternative theory in the case of amorphous materials is that the amorphous disorder leads to defect sites forming local potential minima at which positive charge may be immobilized (Figure 5).

The mobile charge distribution becomes displaced relative to the static counterion distribution. This leads to localized regions with a nonzero net charge density, whilst the material remains close to neutral as a whole. Gauss' law of electrostatics

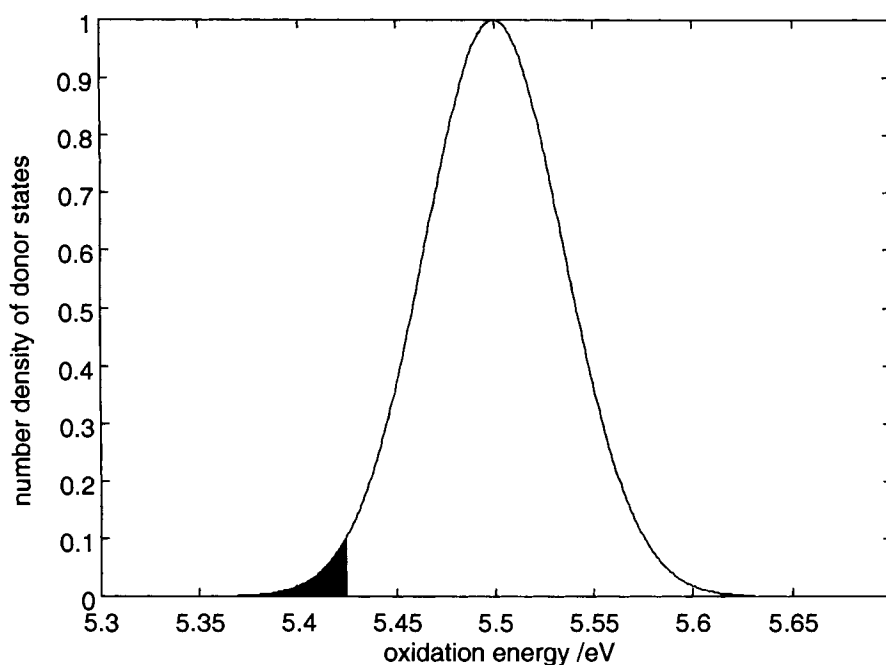


Figure 5. The amorphous structure of an organic matrix leads to a Gaussian density of states for the HOMO of the donor transport matrix. Some of the donors will have a relatively small oxidation potential (in the shaded region) and these sites are likely to experience a potential barrier inhibiting charge hopping to adjacent sites of higher oxidation potential. A hole may in this way become an immobilized cation.

dictates that the electric field must diverge from regions where there is a net charge density. Taking a simple example, if holes are created in a bright region and captured in a dark region, then the equilibrium anion densities will be highest in bright regions (net negative charge) and lowest in dark regions (net positive charge). The electric field is thus maximal where the intensity pattern is changing most rapidly, between the bright and dark regions (Figure 6), and is directed from dark region to bright region. In the simple case of a sinusoidal intensity pattern, the phase of the electric field profile is shifted relative to the intensity pattern by up to $\pi/2$ radians.

The difference between the locations of the mobile carrier generation and carrier recombination processes will build up a pattern of anions. A steady state of equilibrium will be reached in which the net distribution of charge no longer changes with time. At this point the electric field due to the relocation of mobile charge (the space charge field) has become strong enough to counteract the applied field in most cases of amorphous photorefractives (Figure 7). More generally the space charge field reaches a steady state for one of two possible reasons. Either the effect of the space charge field on the hole distribution becomes equal and opposite to the combined effects of diffusion and drift in the applied field, or all the available anion sites become filled.

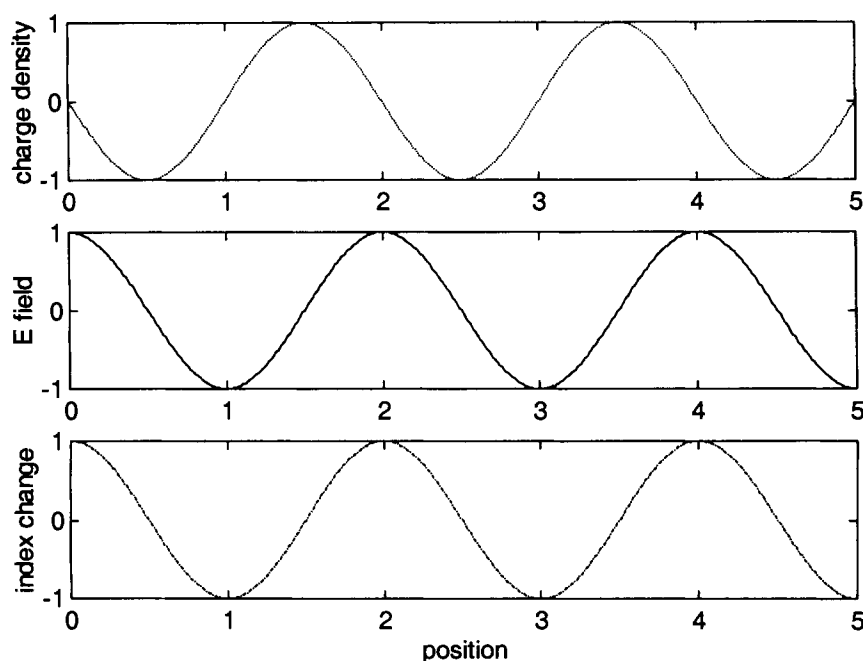


Figure 6. The photorefractive effect. Top: in an idealized hole transport material, the net charge density is π radians out of phase with the intensity pattern. Middle: the electric field, E , due to this net charge density, ρ , is given by Gauss' law, $\partial E / \partial x = \rho / \epsilon$, and is shifted in phase by $\pi/2$ radians relative to the charge density distribution. Bottom: the refractive index will then follow the phase of the electric field. In real materials the charge distribution is not always π radians out of phase relative to the intensity pattern, as competition between drift and diffusion currents leads to a reduced phase shift. The refractive index contrast might therefore be shifted by only $\pi/10$ radians relative to the intensity pattern in some polymers.

An important aspect of the photorefractive effect is that the optical response of the material is nonlocal. In Figure 7, the position of the space charge field is displaced to the right of the initial excitation, in the direction of the applied electric field. In the case of a sinusoidal intensity pattern the phase shift between the optical excitation of charges and the electric field their movement produces is a parameter characteristic of a photorefractive material. It depends on the balance between the processes of drift and diffusion of mobile charges and on the number density of sites able to capture the mobile charges.

The electro-optic effect leads to the modification of the refractive index of a suitable material when an electric field is applied (Figure 8). The electro-optic effect must be present in a photorefractive material, so that the space charge electric field pattern due the relocated charges will lead to a patterned refractive index in the material: this is a hologram.

Just as a nonuniform intensity distribution was the trigger for the creation of a

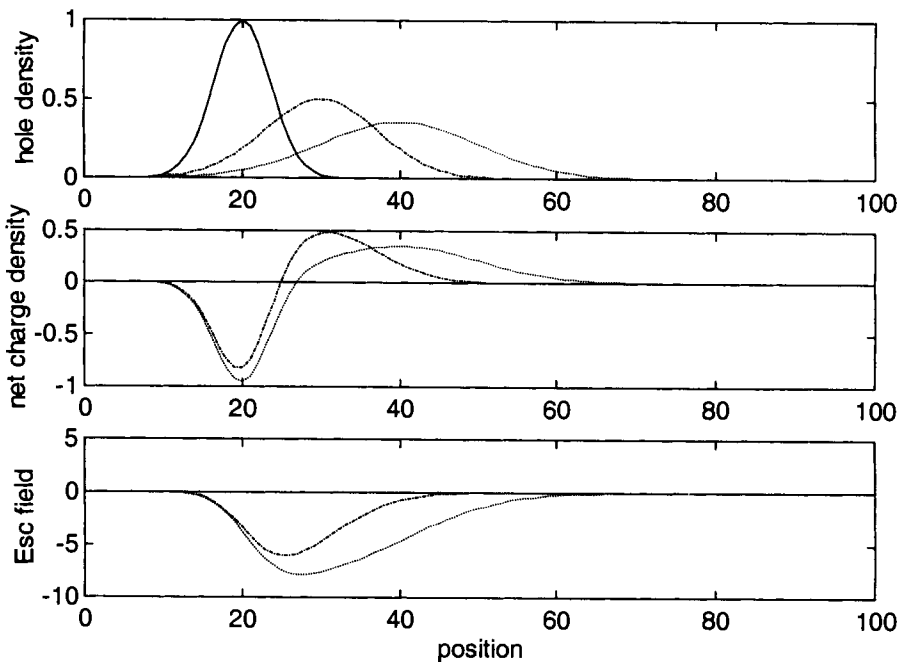


Figure 7. Diffusion and drift of mobile holes. Top: the three curves show three instants in the process of drift and diffusion, equally spaced in time. —, A Gaussian distribution of mobile holes is created (with a corresponding distribution of photogenerated immobile anions). - - -, An applied field leads to drift of the holes to the right whilst the anions remain static, and as the holes drift, diffusion spreads out the hole distribution to twice its original width. · · ·, Later, the distribution has moved twice as far to the right and the diffusion has broadened the distribution to $2\sqrt{2}$ times the original width. (Hole recombination and space charge field effects have been ignored.) Middle: net charge distribution in space (no. of holes – no. of photogenerated anions) corresponding to each of the three instants. Bottom: electric field due to the space charge distribution corresponding to each of the three instants. The space charge field is acting to the left, opposite to the applied field. Eventually a steady state may be reached where the space charge field negates the effect of the applied field on the mobile holes.

hologram, so a uniform intensity distribution (such as from a single beam) can be used to distribute the mobile charge carriers uniformly. This is how a hologram in a photorefractive material can be erased.

3.1.3 A Historical Perspective

Earlier work on photorefractive materials was centered on the discovery of the properties of the phenomenon in optical crystals, most notably lithium niobate, strontium barium niobate, and barium tantalate. Both the mathematics of the theory of photorefractive materials outlined above and its application to these materials and

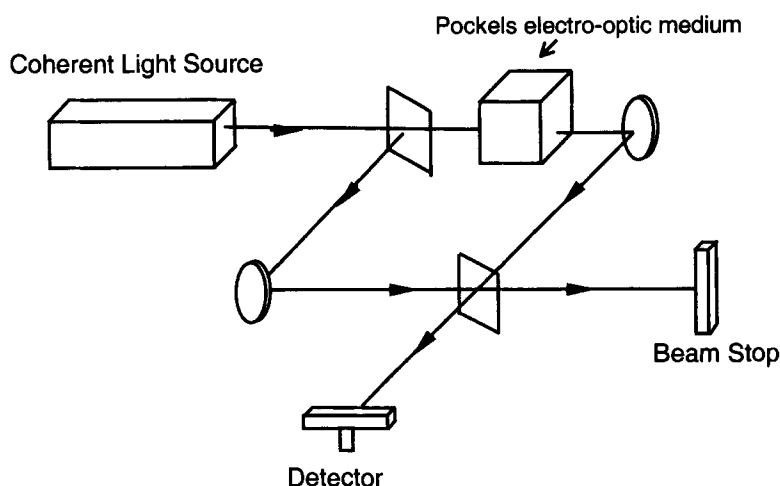


Figure 8. The Pockels effect leads to a change in the refractive index of an electro-optic material due to the application of a static electric field. This can be used to build a Mach-Zehnder intensity modulator, for example, which will have an optical transmission dependent on the electric field applied to the Pockels material.

other crystals are reviewed thoroughly in [4]. Photoexcitation produces mobile electrons in these crystals and these are trapped and re-excited in the optical field until they have moved away from the light. The electrons originate at defect and impurity points in the crystal such as Fe atoms. They may be trapped at other Fe atoms (Figure 9). The motion of the electrons is determined by a parameter called the mobility, which is well defined. (It is possible for a wave of electron density to travel through a crystal and remain largely intact.) The electric field that is produced by the modified electron density distribution will lead to a change in the refractive index because these crystals are electro-optic. The Pockels electro-optic effect is an instantaneous material response to an electric field, which leads to a change in refractive index that is proportional to the static electric field strength. The main issue for photorefractive crystal research from a materials perspective has been the difficulty in controlling the impurity concentrations within the crystal boules to an adequate degree such that the properties of crystals from different sources may be comparable.

More recently the promising range of applications for photorefractive materials has motivated the rapid development of amorphous, organic materials with a strong photorefractive response [5]. Here the chemical composition of the materials may be varied with relative ease and the opportunity to compare materials from different sources should exist. The various processes necessary for photorefraction may be obtained by a single material, or many different molecular species may be mixed in a composite to provide the range of properties needed. These amorphous materials do not have a well-defined mobility for the photogenerated holes that

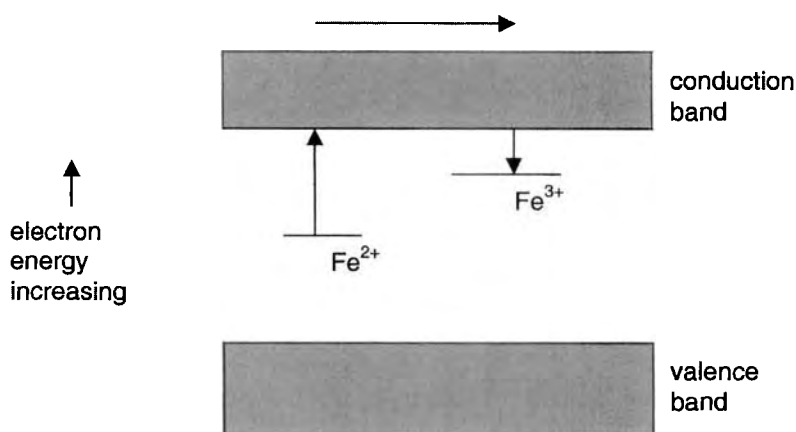


Figure 9. Conventional model of photorefraction in crystals; iron impurity forms defect states of variable valence within the forbidden band gap of a lithium niobate crystal. Optical excitation of the divalent state leads to creation of a mobile electron in the conduction band. This is able to move and recombines with a trivalent iron impurity at another location which becomes divalent. The displacement of charge leads to an electric field and the Pockels electro-optic effect leads to local modification of the refractive index.

move through the medium. A wave of charge density will spread out as it travels through them, as the dwell time between hops depends on the varying microscopic environment. The electric field produces a change in the refractive index, often by rotating individual dye molecules which are anisotropic. There are many possibilities for new composites that are as yet untried. A photorefractive polymer composite was only first reported in 1991 [6]. The field is, as yet, immature, with much left to learn of the distinct physics and materials engineering of these new materials.

3.2 Electron Transfer in Amorphous Organic Photorefractive Media

The field of photorefractivity in organic polymers and glasses has been in existence for less than a decade. The understanding of charge generation in these materials (which are often composites) is not yet mature, and the behavior of some of the more common constituents is understood better. Much of the literature on photorefractivity describes free carrier generation quantum efficiency measurements only briefly, before a more detailed discussion of other factors such as mobility and electro-optic response. Some of the relevant information pertinent to free carrier generation in these materials is presented here, to be followed by a review of this aspect of the amorphous photorefractives literature.

3.2.1 Optical Generation of Bound Pairs

Free charge is generated indirectly in response to light within a typical photosensitive organic material. The initial optical excitation of the material will lead firstly to electron density transfer. The electric potential that binds together the two regions of opposite charge must then be overcome in order to create free charge. For many free charges to be created within the bulk of a material, both optically induced electron transfer and the subsequent dissociation of the charges must be efficient processes.

When a photon is absorbed, an excited state may be created in which a hot electron is created, along with a localized hole. The electron thermalizes at some distance away from the hole, leading to a charge transfer state. The electron and hole of the charge transfer state are not free charge carriers. The opposite charges associated with the two sites will lead to an electric attraction between them and a significant degree of geminate recombination will occur. For free charge carriers to be generated a proportion of the electron-hole pairs will have to dissociate so that the distance between them is sufficient to overcome the electric attraction.

In the conventional analysis after Onsager [7], the probability of forming such a bound charge pair and the distance between the two charges generated are material parameters independent of temperature or electric field, but inversely proportional to the photon energy of the excitation wave. An efficient pair generation process will be associated with longer excitation wavelengths and greater separations between the hole and the electron that are generated. In the case of molecular doped materials an increase in the concentration of the dopant will increase the thermalization distance and the primary yield of charge transfer states.

The Onsager formalism has its shortcomings: it assumes that direct thermalization of the hot electron takes place and this implies that there should be an excitation wavelength dependence for the primary yield of charge transfer states. In real organic materials any such wavelength dependence is weak and it is possible that there is some form of internal conversion process or intermediate that removes the expected spectral dependency [8]. This point is rarely made in the interpretation of experimental results, as it requires additional, unknown parameters to be fixed during the analysis of data.

The oscillator strength of the charge transfer absorption will depend on the overlap integral for the transition involved. Both the spatial arrangement and energetic relationship between the donor site and the acceptor site will influence this. A charge transfer absorption band in an absorption spectrum is usually a broad peak across the visible or near-infrared. In contrast to this, stronger and more defined peaks are observed at shorter visible and near-ultraviolet wavelengths which correspond to more localized excitations associated with a specific donor or acceptor moiety within a molecule. Highly localized molecular excitons able to transfer between molecules may be created at these shorter wavelengths (Frenkel excitons).

The electric attraction between the photogenerated electron-and-hole pair must be overcome for free charge to be generated. The distance between the two charges must be increased until each charge is free from the electric field of the other. Within a

uniform homogeneous material, this may be achieved efficiently under the influence of an electric field drawing the opposite charges in opposite directions. For example, in pure TiO-phthalocyanine (TiOPc), carrier generation is observed to take place within the bulk of the TiOPc material. A molecule in an excited state will accept an electron from a neighboring molecule in an interaction which is dependent on an applied electric field, and a bound pair is created.

The mobility of holes is greater typically than the mobility of electrons in organic media [9]. Organic donor molecules will often form an efficient hole transport medium and a suitable photosensitizer for this must act ultimately as an electron acceptor after illumination. When a sensitizer such as TiOPc is used either in particle form or in layers within a hole-transporting material, then a reaction may occur between a photogenerated bound pair in the TiOPc and the surrounding donor matrix at the surface of the TiOPc. The hole of the bound pair may be filled by an exothermic electron transfer from the adjacent donors. The result is a bound electron-hole pair in which the positive charge is within a hole transport medium whilst the negative charge is still within the photosensitizer. According to the (classical) Marcus theory [10] this forward reaction will be associated with the release of a characteristic reorganization energy typically of 0.05–0.2 eV. The process is efficient if the difference in the ionization potentials of the photosensitizer and the hole transport molecule is approximately equal to this reorganization energy.

In practical organic devices for the photogeneration of charge, a heterostructure is often used in which there is a second material with a different energy level structure. There may be a catalytic effect at an interface between a photosensitive dopant layer and a hole transport layer. In this, the difference between the ionization potentials on either side of the interface creates an energy gradient, lowering the activation energy required for the generation of an electron-hole pair. The donor cation and the acceptor anion have a lower collective energy than their neutral ancestors and this helps to stabilize the charge transfer. In sensitizers based on azo dyes, an exciton-driven reaction creates two charged ions from neutral molecules by the movement of a charge. The products are bound together more tightly than the reagents and the process is efficient if it is sufficiently exothermic (relative to the reorganization energy) [11]. Laminar devices in which hole-transporting layers are alternated with photosensitive layers have formed highly efficient photoreceptor systems. The primary yield of bound pairs from the extrinsic (interface) mechanism is found experimentally (by photoluminescence quenching measurements [12]) to be independent of applied electric field. Without the laminar heterostructure and the consequent surface enhancement, a single-layer device exhibits strong electric field dependence for the yield of bound electron-hole pairs [9].

Experiments using a two-layer heterostructure in which the photocurrent action spectra are observed both for front and rear (sympatric and antipatric) illumination of the interface between a photosensitizer and a hole transport layer have shown that the surface enhancement of bound pair generation is due to a layer typically 300–500 nm thick [13]. Within this distance of the interface, excitons generated by the optical absorption may diffuse toward the interface and initiate bound pair generation. The importance of these excitons for a specific photoreceptor can be iden-

tified from electroabsorption measurements. Frenkel exciton excitation is identified where the electroabsorption spectrum matches the derivative of the linear absorption spectrum with respect to the photon energy [14].

3.2.2 Dissociation of Bound Pairs into Free Charges

The process of bound pair generation is independent of electric field in laminated azo dye-sensitized devices. In contrast to this, the dissociation of the bound pairs depends strongly on an applied electric field. Consequently, in low electric fields the free charge generation process is limited by dissociation whilst under the influence of strong electric fields the process of generation of bound pairs is the factor limiting the efficiency of free charge photogeneration.

The efficiency of generation of free charge can be measured experimentally using xerographic discharge or time-of-flight techniques, discussed later. It is conventional to regard the charge photogeneration efficiency as the product of the efficiency of electron transfer to create bound pairs and the efficiency of dissociation to create free charges. The dissociation efficiency must be deduced from the ratio of the quantum efficiency of charge generation to the efficiency of electron transfer (from photoluminescence quenching).

In azo-dye-based laminar photoreceptor systems, neither the dissociation efficiency nor the primary yield of bound pairs is dependent on excitation wavelength [11–13]. There is a strong positive linear correlation between the dissociation efficiency and the peak value of the dipole moment associated with the transition between the ground and first excited states in the azo photosensitizer (obtained from electroabsorption data) [14]. It is likely that in these systems the efficiency of dissociation is constrained by the electron transport process away from the interface into the bulk of the sensitizer material, because transport of holes through the donor matrix is much more rapid.

3.2.3 Choice of Photosensitizer

The photosensitizer within a molecular doped material exhibiting hole transport must act as an acceptor. Common hole transport materials are based on triphenylamines, aromatic amines such as carbazoles, fluorenones, and benzenes. Common acceptors include dyes (such as malachite green), trinitrofluorenone, and the fullerenes C_{60} and C_{70} . Of these, the fullerenes are unique in their properties [15]. The thermalization distance for hot electrons generated by fullerene sensitization (0.65 nm) is smaller than the size of the fullerene itself (0.7 nm) in experiments using polyimides as electron acceptors with pendant triphenylamine donors. For very low concentrations of doping (0.07 mol% C_{60}) under high applied fields the absorption cross-section for fullerene is 300 times greater than that for intrinsic or dye-sensitized photogeneration. The dipole strength of the fullerene-sensitized photogeneration transition appears to be as great as 26 D, greater by a factor 17 than the dipole for the intrinsic or dye-sensitized processes. It is not possible, however, to project this

high performance of C₆₀ to higher concentrations within photorefractive composites. Fullerene performance falls at higher concentrations. At concentrations of C₆₀ above 1 wt.% in a typical photorefractive composite black carbon deposits are found to separate out within the composite during the sample fabrication process.

Within inorganic photorefractive crystals the optical generation of carriers is associated usually with the oxidation of defect and impurity states within the optical band gap of the crystal, such as iron impurity within lithium niobate crystals, as in Figure 9.

Much of the initial work on photorefractive polymers and organic glasses was based on this prior understanding of the analogous crystal process. Host matrices have been adopted which, when pure, are transparent to visible light because there is a wide optical band gap between the HOMO and LUMO levels which corresponds typically to excitation in the near-ultraviolet region of the spectrum. The absence of a crystal field makes the addition of an electro-optic material necessary for photorefraction to be observed. The optical nonlinearity is obtained normally from a significant concentration of chromophores, so-called because they exhibit a charge transfer resonance at blue or green optical wavelengths which gives them a distinct color. These chromophores have an optical band gap that is smaller than that of the host matrix. Sensitizer material is added at a low concentration, to perform a role which is analogous to the defect density in crystals. The reduction of the sensitizer dopant leads to photogeneration of mobile holes within the oxidized donor transport matrix. A charge photogeneration resonance is required that is further spectrally toward the red than the long-wavelength tail of the chromophore resonance, as in Figure 10. This is normally obtained by using a sensitizer which forms a charge transfer complex with the donor transport matrix.

The host matrix itself is a charge transport system in many of the high-performance, glassy photorefractive materials: the most common matrix for photorefractive composites is poly(*N*-vinylcarbazole), PVK. In some early materials, a dielectric host matrix was used into which a transparent donor charge transport agent such as *p*-diethylaminobenzaldehyde diphenylhydrazone, DEH, was doped [16, 17]. In the latter case, transparency at visible wavelengths is maintained if the HOMO level of the dopant is sufficiently close to the HOMO of the host dielectric matrix, so that a large electron energy band gap is preserved.

The intrinsic optical absorption of the host matrix and the nonlinear chromophores should be minimized at the operating wavelength. Such absorption may lead to undesired, photochromic, refractive index modulation that is in phase with the optical intensity pattern within the material. (Photochromism is a photoinduced change of molecular state which could lead to changes in refractive index and absorption coefficient.) The photochromic response will have a distorting effect on hologram formation and reduce the phase shift of the refractive index profile relative to the intensity pattern. The additional absorption acts parasitically to reduce the amplitude of the photorefractive response. The performance of photorefractive materials is optimized by selecting an optical wavelength for recording and readout for which there is sufficient absorption due to the presence of the charge generation sensitizer within the donor matrix. At the same wavelength the absorption due to the host matrix or the nonlinear chromophore alone should be low.

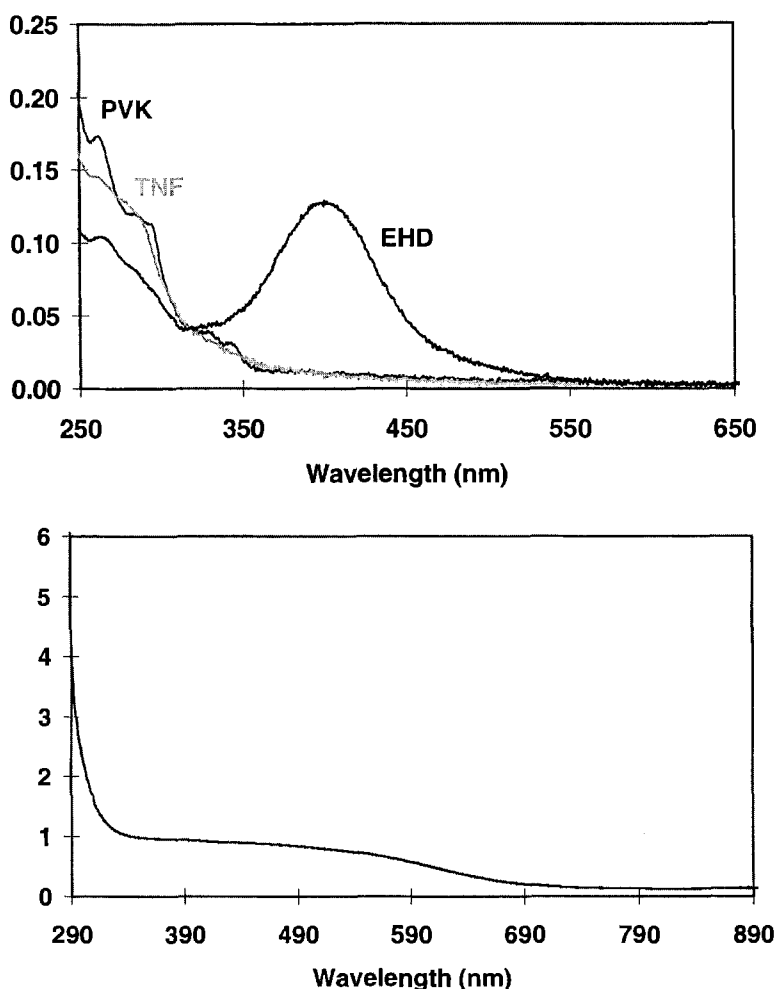


Figure 10. Top: liquid-phase absorbance spectrum of each component of a typical photorefractive polymer composite. Each component, *N*-vinylcarbazole (PVK), 2,4,7-trinitro-9-fluorenone (TNF), and typical chromophore (EHDNPB), is diluted in dichloromethane separately. (Absorption due to the solvent has been subtracted.) Bottom: the absorbance of light in a solid sample due to the charge transfer complexation between PVK and TNF. The sample was prepared from a 9:1 ratio of PVK/TNF. The extension of absorption to longer wavelengths is clear.

The energetic positions of the HOMOs of the nonlinear chromophores (and the charge transport agents, if used) are obtained approximately (relative to the host matrix) using cyclic voltammetry in solution. The solvation energy and polarization energy may lead to discrepancies between the solution-based experimental results and the actual energy levels within a solid solution or polymeric material. As an acceptor, the sensitizer will have an oxidation energy greater than the charge-

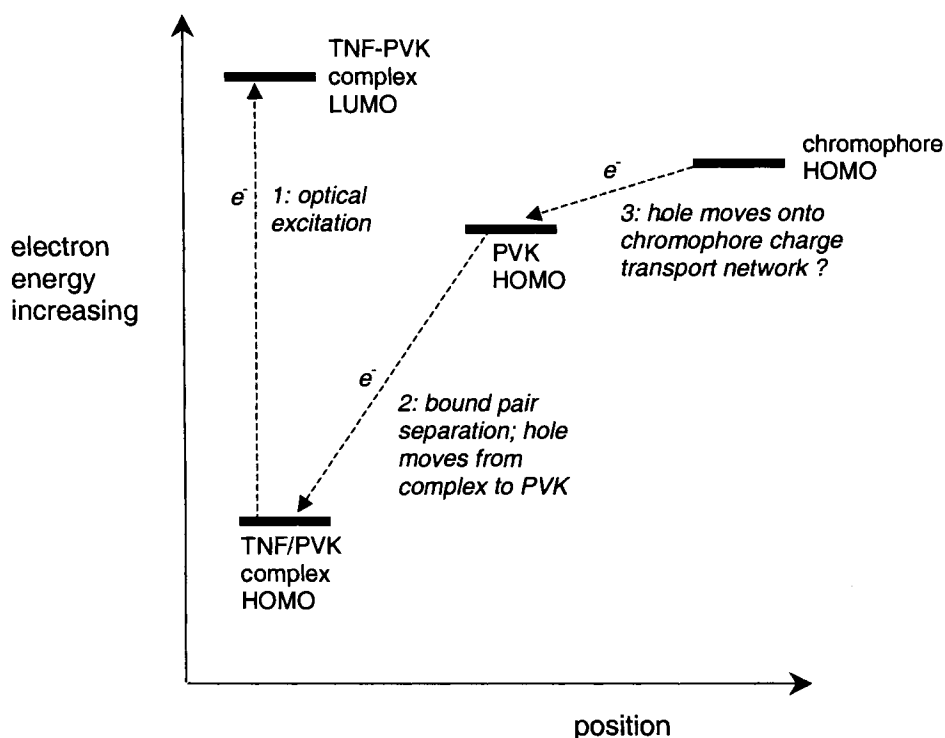


Figure 11. Possible relative positions of the energy levels in a typical guest–host photorefractive polymer composite containing PVK, TNF, and an azo-chromophore. A possible sequence of events leading to mobile charge generation is also included.

transporting donor network. The oxidation energy of the nonlinear chromophores is likely to be lower than that of the sensitizer and it is possible that the chromophores may be oxidized more readily than the donor network. The chromophores are present at a significant concentration and thus they may affect either the charge generation or the charge transport process, as in Figure 11.

Most of the potential applications for photorefractive materials are based on the creation of holograms within the bulk of the material. The material is intended generally to be homogeneous under uniform illumination, and of high optical quality, and the optical scatter of light should be minimized. For this reason, molecular doping of sensitizer is used typically at a low (~ 1 wt.%) concentration to produce weak photoabsorption at the operating wavelength, which is typically in the region 650–750 nm. The primary quantum yield of bound pairs in organic, glassy, photorefractive materials is as high as 40 %, although relatively few reports have been made [17, 18]. The dissociation of photogenerated bound pairs is expected to be strongly field-dependent because heterostructures that introduce an interface between a bulk photosensitizer layer and a hole-transporting layer are not

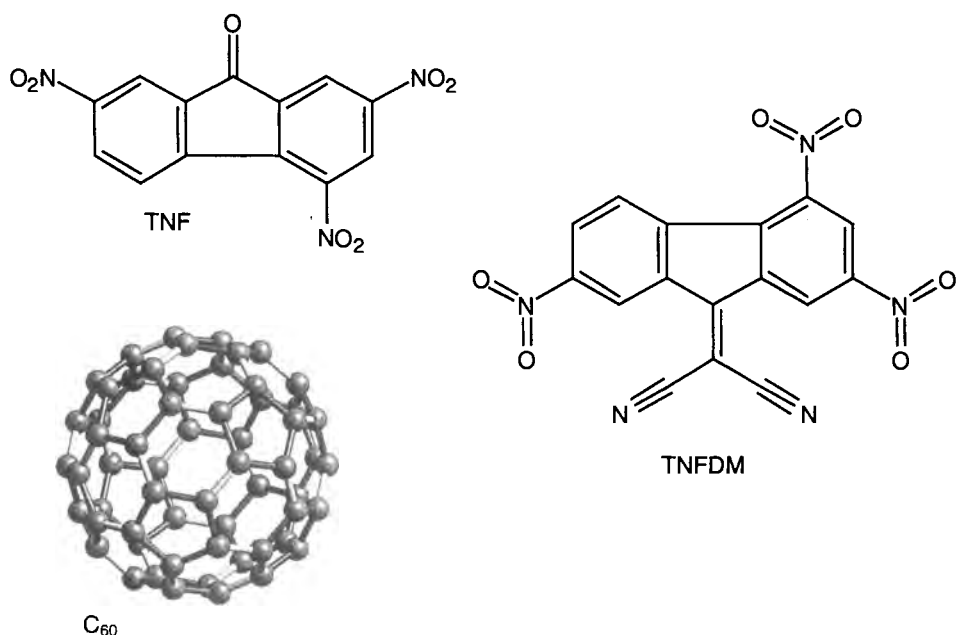


Figure 12. Charge sensitizers used in organic photorefractive materials.

used. An electric field of up to $100 \text{ V } \mu\text{m}^{-1}$ will lead to a quantum efficiency of mobile carrier photogeneration that is only a few percent.

3.2.4 Specific Material Systems

The most common format for a glassy organic photorefractive material is to use a charge-transporting polymer or glass such as PVK, polysilanes (PS), polysiloxanes (PSX), triphenylamine (TPA), or the starburst molecule and its derivatives. Earlier work also included the passive matrices poly(methyl methacrylate) (PMMA) and polycarbonate, into which a charge transport agent, such as DEH, was added. To complement the hole transport material, a specific charge sensitizer is also added; Figure 12 shows the chemical structures of some of the charge sensitizers that have been studied.

In the case of PVK, a charge transfer complex may be formed by the addition of a small amount of 2,4,7-trinitro-9-fluorenone (TNF). The PVK–TNF system has been studied widely in xerography and as a two-component material it is well understood [19]. It also has the additional advantage of a particularly low photoconductivity in the absence of light. Photoconduction due to the complex is efficient across the visible region of the spectrum, with the excited state exhibiting 80 % electron transfer from a carbazole unit of the PVK to an adjacent TNF unit. The dissociation of holes occurs in the two-component system by hole transfer to

neighboring carbazole units, away from the immobile TNF anion. It is unclear at present to what extent the presence of the nonlinear chromophores at up to 55 wt.% concentration affects this process. Charge transfer complexation between the sensitizer and the chromophores is possible and this may reduce the free charge photogeneration efficiency. Trinitrofluorenone dimalenitrile (TNFDM) is a derivative of TNF with an increased electronegativity that leads to a charge transfer complex with carbazole units of PVK. The complex between PVK and TNFDM has a spectrum of sensitivity for charge photogeneration which extends further into the infrared than the corresponding complex between PVK and TNF. At the longer wavelengths, chromophore absorption and optical loss are reduced.

As might have been anticipated, C_{60} has been found to be very effective as an acceptor-sensitizer for homogeneous photorefractive polymers. The absorption associated with the C_{60} molecule in isolation is unusually low, which minimizes parasitic optical losses and inhibits photochromic grating formation. The efficiency of photogeneration of free carriers is relatively high, despite the absence of bulk photosensitizer layers; this may be linked to the small thermalization radius associated in the Onsager picture with C_{60} and the correspondingly high efficiency of dissociation. Under strong electric fields of up to $100 \text{ V } \mu\text{m}^{-1}$ the quantum efficiency of photogeneration of free carriers from photons absorbed has been found to remain nearly constant in a photorefractive composite as the intensity of illumination is increased by three orders of magnitude, up to 1 W cm^{-2} . The photoconduction of the composites is near-linear with intensity ($\sigma \propto I^{0.85}$ to $I^{0.9}$) [20].

The efficiency of charge generation within the photorefractive material is one of the key parameters governing the rate of response of the material. A simple model based on instantaneous charge transport and trapping may be used to calculate an upper limit to the rate at which a photorefractive grating is recorded optically, due to the limited rate of free charge photogeneration. The rate of growth of the electric space charge field, E_{sc} , is constrained due to the need for charge generation according to Eq. (1),

$$\frac{\partial E_{sc}}{\partial t} \leq \frac{\phi \alpha I}{\hbar \omega} \frac{e \Lambda}{2 \pi \epsilon_s} \quad (1)$$

where ϕ is the product of the primary yield of bound pairs and their dissociation efficiency, α is the absorption coefficient, I is the intensity contrast, e is the electronic charge, Λ is the period of the intensity pattern, $\hbar \omega$ is the photon energy, and ϵ_s is the static dielectric constant. This model idealizes the mobility of charge and the characteristic transport length of the free charge carriers. It is obtained from the standard model of photorefractive under the assumptions of a long hole lifetime and a high mobility.

The effect of a limited mobility of holes in the material may be accounted for in Eq. (1) by using a parameter called the mobility field, E_m , which is the electric field necessary for a hole to drift 1 radian across a sinusoidal intensity pattern in one hole recombination lifetime. The assumptions of long lifetime and high mobility make the mobility field small in comparison with the projection of the poling field along

the diffraction grating vector, $E_0 = E_{\text{pol}} \sin \theta_{\text{int}}$: the correction factor to the rate limit in Eq. (1) for a mobility field which is not negligible is $|E_0(E_m + jE_0)^{-1}|$.

We can estimate the highest rate of growth of the space charge field in various composites, from data published for the growth of grating diffraction efficiency. In the literature, time constants are most often quoted for the growth of the refractive index contrast, Δn , of a grating. Most of the efficient photorefractive materials are close to the glass transition temperature at room temperature. The chromophores typically have a significant electric dipole moment in their ground state and they change orientation slightly in an electric field. In one time constant of field formation, the field reaches 63 % of its maximum value, which is limited by the poling field projection, E_0 . The gradient of the rising exponential has a peak value around 50 % greater than the linear approximation from the origin to 63 % of saturation in one lifetime (Figure 13). Accordingly we estimate a peak value of observed field growth rate to be given by Eq. (2),

$$\left. \frac{\partial E_{\text{sc}}}{\partial t} \right|_{\text{max}} \approx 0.63(1.5) \frac{E_0}{\tau_{\text{fast}}} \quad (2)$$

where τ_{fast} is the fast time constant of index contrast growth quoted. Many of the amorphous photorefractive materials come close to the charge generation limit in their rate of holographic response, as shown in Table 1. The difference between the charge generation limit of Eq. (1) and the observed peak field growth rate calculated using Eq. (2) may indicate that in the experiments referred to in Table 1, the magnitude of the mobility field was close to that of the projection of the poling field. One caution in this analysis is that data for the quantum efficiency, ϕ , of generation of mobile holes due to incident photons of light are not reported in many papers describing photorefractive materials. Accordingly, the quantum efficiency must

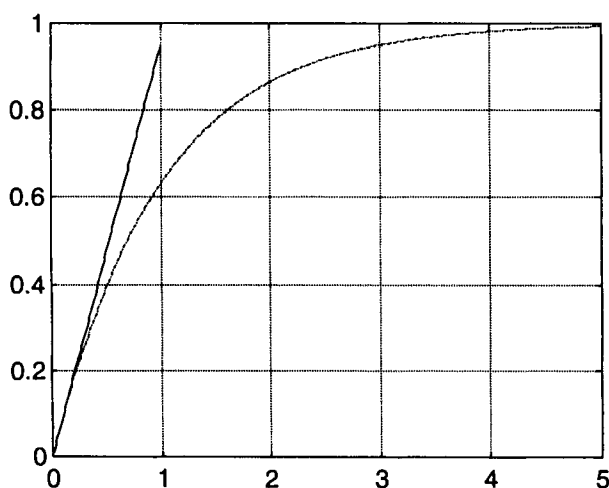


Figure 13. A comparison of the single rising exponential function and a linear fit with a gradient 50 % higher than the linear approximation over one lifetime. The linear fit has been used as an estimate of the maximum gradient in the exponential function.

Table 1. Rate of response of selected photorefractive polymer composites: a comparison of the experimental fast time constant of growth of contrast in refractive index in response to a nonuniform intensity pattern and the theoretical rate limit based on charge photogeneration rate.

Materials ^a ([wt.%])	Poling field, E_{pol} [V μm^{-1}]	Estimated quantum efficiency, ϕ^b	Intensity contrast, I [W cm^{-2}]	Fast time constant observed, τ_{fast} [s]	Charge generation limit obtained ^d [%]	Reference
PMMA (39.8) DTNBI (60) C ₆₀ (0.2)	40	0.005	2	0.43	94	[21]
ODNPB (47.5) PVK (51.5) TNF (1)	50	0.01	0.8	0.22	98	[22]
DBOP-PPV (52) DMNPAA (20) MNPA (20) DPP (5) PCBM (3)	62	<0.0001 ^c	0.3	0.60	>14400	[23]
PSX (66) FDEANST (33) TNF (1)	80	0.01	2	0.50	42	[24]
EPNA (39) PVK (60.9) TNF (0.1)	85	0.02	1.2	0.60	122	[25]
NPP (5.74) PVK (56.5) TCP (37.5) CdS (0.1)	107	0.01	0.43	7.3	100	[26]

^aPMMA, poly(methyl methacrylate); DTNBI, 1,3-dimethyl-2,2-tetramethylone-5-nitrobenzimidazole; MNPA, 5-methyl-4-(p-nitrophenylazo)benzene; PCBM, (6,6)-Phc61-butyracide methylester; EPNA, 4-(diethylamino)nitrobenzene; NPP, N-(4-nitrophenyl)-(L)-proline; other abbreviations are defined in the text and Figures, ^bquantum efficiency of mobile charge photogeneration has been estimated where necessary, ^conly an upper limit to the quantum efficiency was quoted in this case; the explanation of this result is unclear, ^da relative static dielectric constant of 20 has been assumed.

be estimated in many cases; the efficiencies used in this comparison in Table 1 are stated.

A number of recent reports have described hologram recording on time scales of 1–10 ms, using a high optical intensity and uniform preillumination (see Table 2). There is not yet a clear consensus in the literature as to how the fast responses have been possible: several factors may be involved.

Table 2. Rate of response of “fast” amorphous photorefractive materials: a comparison of the experimental fast time constant of growth of contrast in refractive index in response to a nonuniform intensity pattern and the theoretical rate limit based on charge photogeneration rate.

Materials ^a ([wt. %])	Poling field, E_{pol} [V μm^{-1}]	Estimated quantum efficiency, ϕ^b	Intensity contrast, I [W/cm ⁻²]	Fast time constant observed, τ_{fast} [ms]	Charge generation limit obtained ^c [%]	Reference
PVK (50) ECZ (25) Dye C9 (25) C ₆₀ (1)	40	0.0011	0.25	60	60	[27]
PVK (49.5) BBP (15) C ₆₀ (0.5) AODCST (35)	50	0.01	0.2	96	200	[28]
PTPDac-BA2 (84.9) DEANST (14.9) C ₆₀ (0.2)	70	0.05	0.5	7.5	360	[29]
TFB (59) DMNPAA (30) DOP (10) C ₆₀ (1)	76.5	0.05	1.44	1.25	350	[30]
DR1-DCTA (71) DOP (28) C ₆₀ (1)	80	0.06	2.4	30	12.5	[31]
FTCN (15.2) PVK (56) TNFDM (0.8) ECZ (28)	95	0.03	0.5	4	80	[32]
PVK (49.5) BBP (15) C ₆₀ (0.5) AODCST (35)	100	0.07	1	5	230	[28]

^aAODCST, 2-[4-bis(2-methoxyethyl)amino]benzylidene malononitrile; PTPDac-BA2, copolymer, 65% wt N-(4-acryloyloxymethylphenyl)-N'-phenyl-N,N'-bis(4-methylphenyl)-[1,1'-biphenyl]-4,4'-diamine, 35% wt A-butylacetate; DOP, dioctyl phthalate; DR1-DCTA, 4,4'-di(carbazol-yl)-4''-(2-{N-ethyl-N-[4-(4-nitrophenyl)azo]phenyl}amine)ethoxy)-triphenylamine; other abbreviations are defined in the text and Figures, ^bquantum efficiency of mobile charge photogeneration has been estimated where necessary, ^ca relative static dielectric constant of 3 and a linear electro-optic response have been assumed.

In Table 2, the analysis of these fast results for hologram recording time has been adapted to take account of the fact that reorientation of the chromophores may not be possible on a time scale of milliseconds. This has two consequences. Firstly, the space charge field formation process depends on the static dielectric constant. In materials with significant chromophore reorientation at room temperature, the static dielectric constant is in the region of $20\epsilon_0$ (this is the value of dielectric constant that has been used in the preparation of Table 1). If the process of space charge field growth becomes faster than the reorientation process, the dielectric constant will drop close to the value at optical frequencies, in the region of $3\epsilon_0$. For a time less than the reorientation time for the chromophores in the photorefractive composites, the rate of space charge field formation in the charge generation limit is almost an order of magnitude enhanced.

Table 2 compares the holographic growth time constants reported for several fast materials with the "fast" charge generation limit to space charge field formation, valid when the reorientation of chromophores is slower than the initial rate of space charge field formation. The response rate calculated for many fast materials appears to have exceeded even the adapted charge photogeneration limit, which is not possible. This contradiction may be due to uncertainty in the quantum efficiency estimations used (which may not have been confirmed experimentally). A more systematic explanation may be that the space charge field is not reaching its *poling field limit* in these cases within the time scales described: the analysis used in Table 2 still assumes the space charge field reaches 63 % of its poling field limit within one time constant. In this case the amplitudes of the fast signals diffracted are likely to be small. It is not possible to confirm the amplitudes of diffraction from the papers published to date.

Uniform preillumination is discussed in the literature in two different time regimes. Fast diffraction response is obtained from materials which are illuminated uniformly and intensely for a few seconds before a second writing beam is used to pattern the intensity in the material and begin hologram formation. This maximizes the mobile hole density in the material at the time of hologram formation and helps to reach the charge generation limit of Eq. (1).

According to the literature, uniform and intense preillumination in an electric field for a period of hours has been introduced as a means of material modification. The extended preillumination has been demonstrated to increase the rate of response in transient photocurrent measurements, but to decrease the magnitude of the photoconductivity [27]. This is because the hole recombination lifetime is reduced due to an increased population of sensitizer anions. In the case of C_{60} as a sensitizer, the population density of the anion has been confirmed spectroscopically to rise as expected after extended preillumination. What is the effect of this on the rate of the hologram formation process? In typical materials the correlation between photoconductivity and hologram recording rate exists only under conditions of constant mobility \times lifetime product for the mobile holes. The exception to this is when the mobility is unusually low. Under the normal operating conditions of a typical amorphous photorefractive material, hole diffusion may be neglected relative to drift in the poling field and the space charge field is not normally limited by

the saturation of recombination sites. The preillumination over a period of hours will increase the anion density, increase the saturated electric field when all available recombination sites are filled, and consequently slow down the hologram recording process.

3.2.5 Fully Functional and Permanently Poled Materials

The requirement for high optical quality has encouraged the development of multipurpose molecules for photorefractive composites and also the synthesis of single-polymer, fully functional materials. In fully functional materials charge photogeneration, transport, and electro-optic response have been combined through the use of distinct monomer units or side-chain substitutions. These materials are less common in the literature, due primarily to the great synthetic effort that is needed for each modification to the materials. Two examples are presented in Figure 14. Of these, an interesting and contrasting case is of a fully functional polymer containing a ruthenium–ligand charge transfer complex for photogeneration of electrons [33]. The polymer backbone is a π -conjugated electron transport material and an electron is promoted to a mobile state when the Ru^{2+} ion is oxidized to the trivalent state. This material is in some respects very different from the majority of photorefractive polymers and glasses. The most notable difference is that electron transport occurs leading to recombination at cationic sites such as Ru^{3+} . The high phase shift of the photorefractive response suggests that there may be a low electron trap density. The quantum efficiency of 0.2 % for 690 nm wavelength illumination in a poling field of $95 \text{ V } \mu\text{m}^{-1}$ is not particularly high, however. The authors noted that an internal field of about $20 \text{ V } \mu\text{m}^{-1}$ was observed in the absence of an applied field in this material, due to permanent corona poling of the polymer above the glass transition at 130°C . Such a permanently poled polymer exhibits a photorefractive response without a poling field applied, but the response is slow—on the order of 700 s—and the refractive index contrast is not enhanced by the room-temperature reorientation of chromophores.

3.3 Charge Transport Processes in Amorphous Organic Media

Charge transport processes are essential to the operation of organic photorefractive materials. Positive and negative charge must move and separate to enable a space charge field to be established. There are several reports indicating that holes dominate charge transport in organic photorefractive materials [5]. Thus holes produced upon the excitation of a charge-generating molecule or charge transfer complex must be able to migrate from their point of origin and become separated from their corresponding sensitizer anions.

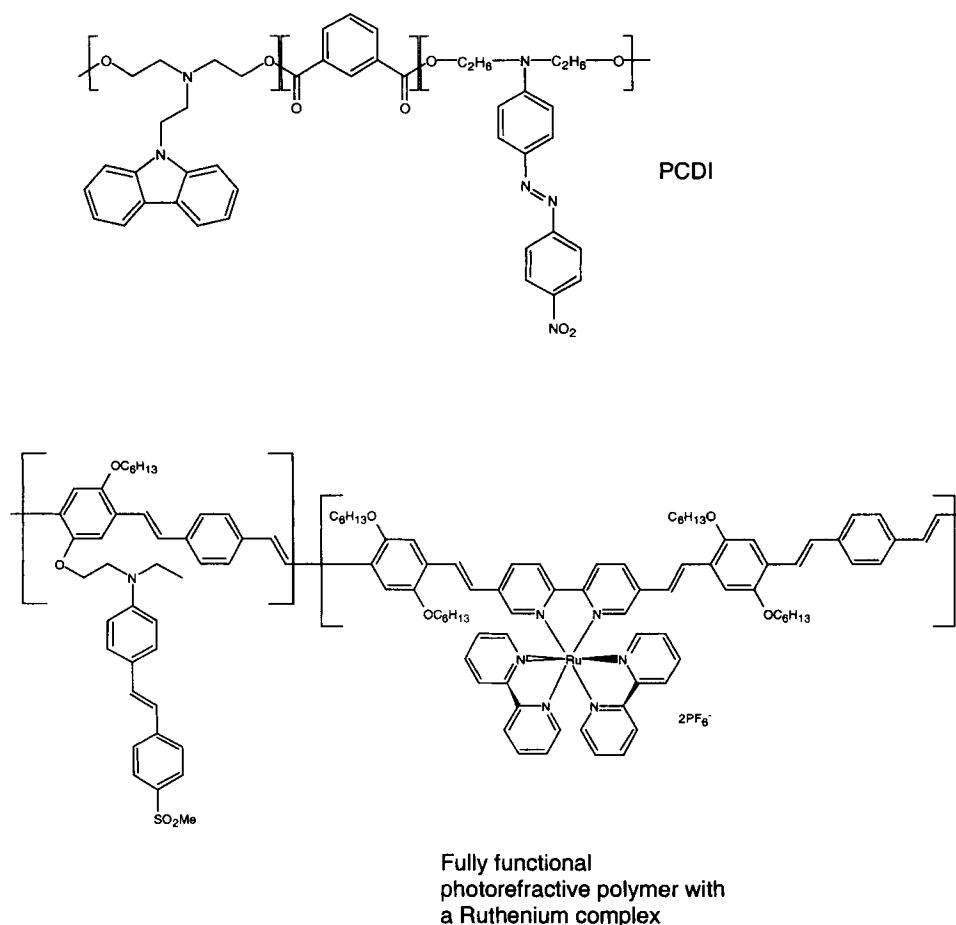


Figure 14. Examples of fully functional photorefractive polymers.

3.3.1 Transport in Disordered Media

Hole mobilities in glassy organic materials are often studied using the time-of-flight (TOF) technique (Figure 15). In this technique mobile charge generation is induced optically on one surface of a thin film of the material under study. Optical absorption must occur principally near one electrode. If the absorption is insufficient for this, then an extra charge generation layer with a high absorption is used. A short (usually nanoseconds) optical pulse is applied to photogenerate mobile charge and the time evolution of the photocurrent is measured. A typical signal is shown in Figure 16, where the position of the shoulder indicates the time taken for the charge packet to cross the device, after which the current decays. The transit time, t_{tr} , is

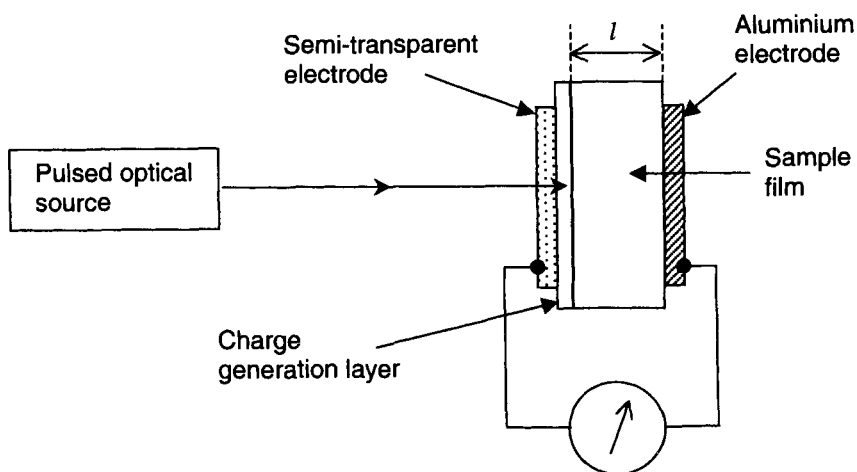


Figure 15. Experimental arrangement for time-of-flight measurements. One edge of a thin film ($\approx 1 \mu\text{m}$ total thickness) is optically excited and charge carriers are produced near the surface of the film. If the optical density of the film is insufficient to absorb the bulk of the irradiation in the first 10 % or so of the film, then a separate charge generation layer is used. A current is detected as the charges migrate across the film until all the photogenerated charge reaches the other electrode.

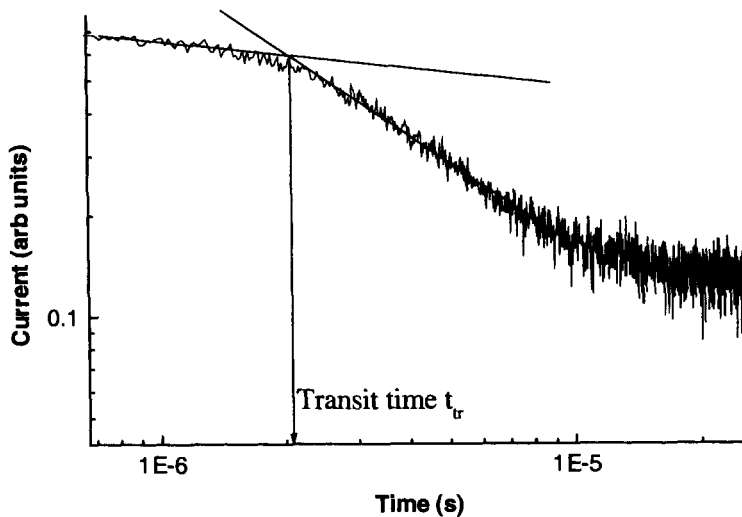


Figure 16. Transient photocurrent signal from a time-of-flight measurement of a photorefractive polymer composite containing 47.5 % electro-optic dye (EHDNPB), 1 % TNF with PVK polymer making up the remainder; 21 V was applied across the 100 nm polymer film and a 10 nm thick rhodamine 6G charge generation layer was used. The hole mobility in this material is thus $2.5 \times 10^{-6} \text{ cm}^2 \text{ V}^{-1} \text{ s}^{-1}$.

related to the hole mobility by Eq. (3),

$$t_{\text{tr}} = \frac{l^2}{\mu V} \quad (3)$$

where l is the thickness of the film, V is the voltage applied across the sample and μ is the mobility of the primary charge carriers, usually holes in amorphous organic photorefractives.

All experimental data collected to date indicate that hole transport in most organic photorefractive materials is dispersive in nature, which is a characteristic of most glassy organic materials. In the regime of dispersive transport, charge carriers do not have a clearly defined mobility and the sheet of charge generated in the TOF experiment broadens as it drifts across the device (recall Figure 7). This is a consequence of holes dwelling for different periods of time at different individual sites within the material before hopping to their next dwell site. The dwell time distribution arises from many sources, including positional disorder (a distribution of the distances between individual hopping sites). The dwell time distribution can be described using the empirical distribution first reported by Scher and Montroll [34] (Eq. (4)),

$$\psi(t) \approx \text{constant} \times t^{-(1-\alpha)} \quad (4)$$

where α is the disorder parameter ($0 < \alpha < 1$) which governs the width of the dwell time distribution. This distribution implies a mobility dependence on the disorder parameter: $\mu \propto (l^2/V)^{1-1/\alpha}$. The analysis of Scher and Montroll is, however, incomplete, as it cannot explain the mobility dependence on temperature or applied electric field adequately.

The treatment by Bässler is more complete [9, 35]. This includes two mechanisms for a distribution of dwell times in glassy organic materials arising from positional and energetic disorder. For a hole to hop between hopping sites, the wavefunctions corresponding to each site must overlap. Figure 17 is an illustration of the theory using the example of hole hopping sites represented by square potential wells. It can be seen that a distribution in the distance between two wells will affect the dwell time. The difference between the depths of two wells will also affect the dwell time. In a unidirectional hole drift process, the dwell time will be longer if the next available site has a higher energy. Energetic disorder arises from fluctuations of the molecular energy levels in amorphous materials. This energetic disorder is brought about by variations in the van der Waals, ion-induced dipole, or ion-permanent dipole interactions between molecules at neighboring dwell sites and results in Eq. (5) for the hole mobility,

$$\mu(T, E) = \mu_0 \exp - \left(\frac{T_0}{T} \right)^2 \exp \left(\frac{E}{E_0} \right) \quad (5)$$

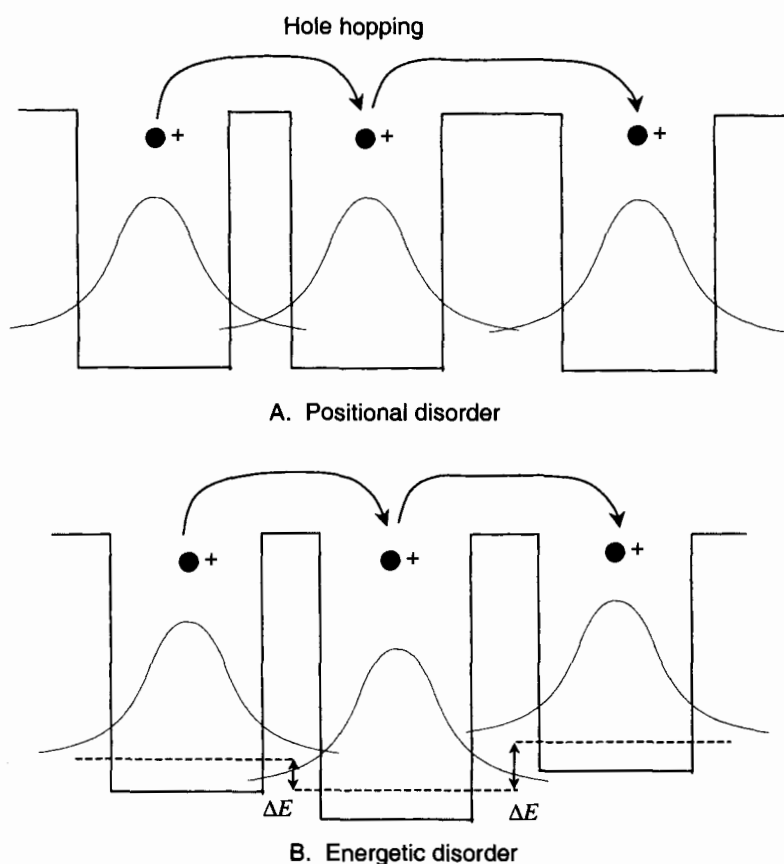


Figure 17. The effects of A) positional and B) energetic disorder on hole hopping. The separation between hopping sites affects the overlap between the wavefunctions of adjacent sites, and therefore the rate of tunneling between sites. The distribution of energies is assumed to have no effect when hopping to a site of lower energy, but the hopping rate to a site of increased energy is impeded by a Boltzmann factor $\exp[-\Delta E/kT]$.

where μ_0 is the mobility in a similar system lacking disorder, and T_0 and E_0 are material parameters which increase and decrease respectively with increasing width of the energy level distribution. The general conclusion of this theory is that increased energetic disorder effectively increases the width of the energy level distribution and reduces the apparent hole mobility. Experimentally it has been confirmed that an increase in the size of dipole moments within the polymer can increase ion-permanent dipole interactions and thus increase the width of the energy level distribution and yield significant reductions in mobility [36]. Increases in the average distance between hopping sites (by dilution with a nontransporting material, for

example) yield more modest mobility changes, typically by less than an order of magnitude.

3.3.2 Specific Examples of Hole Transport Materials for Organic Photorefractives

Figure 18 shows a selection of the hole-transporting organic materials that have been used to date as components in photorefractive composite materials. The hole transport process in these materials occurs via hopping between the aromatic moieties. Mobility data are given in Table 3. Most, but not all, of these materials are polymers. The polymer chains can be regarded as existing in a disordered, glassy state; thus hole hopping occurs simply between adjacent moieties, wherever they lie and not necessarily along discrete polymer chains. More recently fully functional glasses have been developed using low molecular weight molecules incorporating both electro-optic chromophore and hole transport moieties. These materials are not polymeric, but form glassy matrices that are likely to have similar hole-transporting properties.

Table 3 illustrates how the hole mobilities of a selection of relevant materials vary significantly from $10^{-3} \text{ cm}^2 \text{ V}^{-1} \text{ s}^{-1}$ in poly-(9,9'-dioctylfluorene-*co*-*N*-(4-butylphenyl)-diphenylamine) (TFB) through $1.5 \times 10^{-5} \text{ cm}^2 \text{ V}^{-1} \text{ s}^{-1}$ for a polysilane-based polymer to $2 \times 10^{-6} \text{ cm}^2 \text{ V}^{-1} \text{ s}^{-1}$ in a PVK-TNF complex. TFB is an interesting polymer as it combines hole-transporting fluorene groups with a conjugated polymer. This combination technique produces high-mobility polymers. Other polymers similar to TFB show no dispersion for hole transport because of a subtle canceling-out of positional and energetic disorder.

The addition of large quantities of TNF to PVK reduces the hole mobility by two orders of magnitude [19]. Table 3 indicates mobilities in pure hole-transporting materials rather than doped materials. The hole mobility obtained when these pure materials are incorporated into photorefractive composites also containing the associated nonlinear and charge generation components is almost always lower by anything between a small factor and many orders of magnitude, as shown in Table 4. Only in one material given here, consisting of the polysilane polymer and the dye Coumarin 153, was the hole mobility higher in the composite than in the pure hole transport material. This indicates the possibility of significant hole transport in the dye; thus it is misleading to assert that hole transport necessarily occurs in the recognized hole transport material within a composite (recall Figure 11).

Also shown in Table 4 is the hole transit time, calculated from the hole mobility for each photorefractive material, across a typical grating spacing that would occur in a photorefractive hologram. This time would be the response time for grating growth if all the other processes were fast, including charge generation and chromophore reorientation (see Sections 3.2 and 3.4). It can be seen that the mobility-limited response time is always much faster than the actual response time of the material. In fact, even if the lowest mobility is taken, the response time would not be much slower than that of the fastest material yet reported. It can be concluded, therefore, that the mobility is not a critical parameter for the optimization of organic photorefractives.

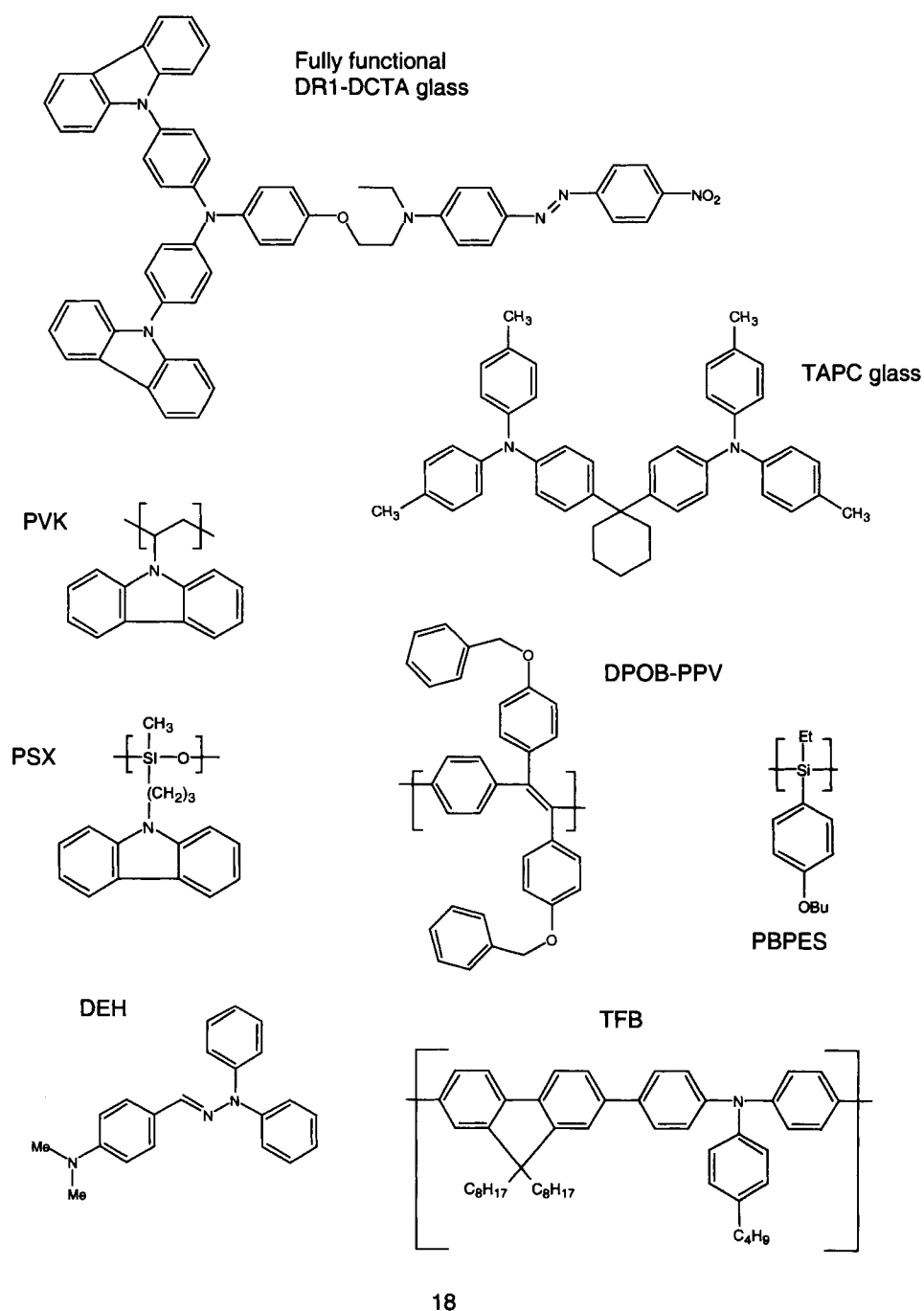


Figure 18. A selection of organic hole-transporting polymers or glasses for photorefractives.

Table 3. Selection of charge transport parameters from some pure charge-transporting components of organic photorefractive materials.

Material ^a	Ref.	Experimental parameters		Hole mobility [cm ² V ⁻¹ s ⁻¹]
		Temperature [K]	Field [V μm ⁻¹]	
90 % PVK ^b	[16]	297	50	2.0×10^{-6}
10 % TNF				
50 % PVK ^b	[16]	297	50	2.0×10^{-8}
50 % TNF				
50 % MPS ^b	[37]	298	50	1.0×10^{-4}
50 % PC				
50 % DEH ^b	[37]	298	50	1.0×10^{-5}
50 % PC				
50 % OXD ^b	[37]	298	50	1.0×10^{-6}
50 % PC				
75 % TAPC ^b	[38]	301	50	1.5×10^{-5}
25 % PC				
TFB	[39]	300	6.25	$>10^{-3}$
PBPES	[40]	300	50	1.5×10^{-5}

^a MPS, 4-N,N-bis(4-methylphenyl)amino- α -phenylstilbene; OXD, 2,5-bis(4'-diethylaminophenyl)-1,3,4-oxdiazole; PBPES, poly[(4-n-butoxyphenyl)-ethylsilane]; other abbreviations are defined in the text and Figures, ^b hole-transporting component.

3.3.3 Pulsed Excitation and Charge Trapping

An alternative and seldom used technique for measuring hole mobility is the holographic time-of-flight technique [40]. Like time of flight, holographic time of flight (HTOF) measures the transit time of charge carriers across a known distance, but this time across a grating period ($\approx 3 \mu\text{m}$) within a hologram in the bulk of a thick film. This experiment utilizes a degenerate four-wave mixing experimental arrangement. Two coherent pulsed laser beams interfere within a sample to produce a sinusoidal intensity distribution in the bulk of the material. Assuming that excitation and charge separation processes occur quickly compared with charge transport across the intensity modulation period, overlapping sinusoidal distributions of mobile holes and corresponding stationary sensitizer anions are formed. As the mobile holes drift under the influence of an external poling field, they become separated from their sensitizer anions and a space charge field is generated. Traversing half a period of the intensity pattern, charge separation reaches a maximum along with the space charge field. After traversing one full period, holes again spatially coincide with their sensitizer anions and the space charge field reaches a minimum. In the absence of significant dispersion or recombination, the space charge field amplitude would oscillate as waves of hole density drift through the bulk of the material. If the material were electro-optic, the space charge field would produce a refractive index grating and the diffraction efficiency of a continuous probe beam would oscillate with the space charge field. A time of flight could be established from the oscillation period, yielding the transit time across a period of the hologram.

Table 4. Selection of charge transport parameters from some organic photorefractive materials.

Material type	Ref.	Material ^a	Experimental parameters		Hole mobility [cm ² V ⁻¹ s ⁻¹]	Transit time over 3 μ m grating spacing [ms]	Actual response time [ms]
			Temp. [K]	Field [V μ m ⁻¹]			
Reorientational guest/host polymer composite	[22]	47.5 % EHDNPB 51.5 % PVK 1 % TNF	300	25	2.5×10^{-6} (1×10^{-6} estimated at 50 V μ m ⁻¹)	0.6 (estimated at 50 V μ m ⁻¹)	400
Reorientational glass	[40, 41]	75 % stilbene3-DCTA 24 % DOP 1 % C ₆₀	300	75	2.0×10^{-6}	0.2	30
Hole transport agent doped nonlinear optical polymer	[17]	70 % bisA-NAS 30 % DEH	298	75	2.5×10^{-8}	16	— ^b
Photorefractive guest/host polymer	[42]	59.9 % PVK 0.1 % TNF 40 % HONB	300	55	1.5×10^{-7}	4	— ^b
Photorefractive guest/host polymer	[43]	59 % TFB 30 % DMNPAA 10 % DOP 1 % C ₆₀	300	50	2×10^{-6}	0.4 (4 μ m grating spacing cited)	1.25
Photorefractive guest/host polymer	[40]	80 % PBPEs 20 % coumarin 153 C ₆₀	300	50	7×10^{-4}	0.0008	86

^a EHDNPB, 1-(2'-ethylhexyloxy)-2,5-dimethyl-4-(4"-nitrophenylazo)benzene; stilbene 3-DCTA, N,N-bis[4-(9H-carbazol-9-yl)phenyl]-4-[3-(4-[2-(4-nitrophenyl)ethenyl]phenoxy]propoxy]benzenamine; DOP, dioctyl phthalate; bisA-NAS, poly[4,4'-isopropylidenediphenol-co-4-nitro-4'-bis(2,3-epoxypropyl)aminostilbene; HONB, 4-(hexyloxy)nitrobenzene; PBPEs, poly[(4-n-butoxyphenyl)-ethyltolilane]; other abbreviations are defined in the text and Figures, ^b —, data not available.

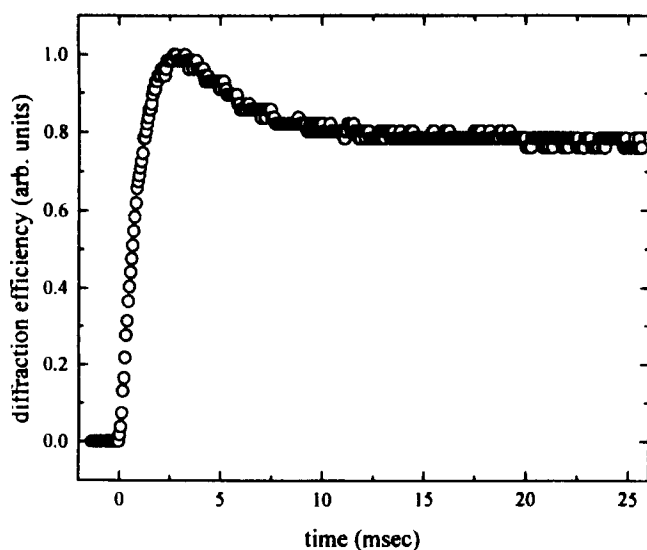


Figure 19. A typical HTOF signal from the photorefractive polymer composite PVK/0.1 wt.% TNF and 40 wt.% 4-(hexyloxy)nitrobenzene electro-optic chromophore, reproduced with permission from [42]. A clear peak is observed which represents the transit time of holes across half a grating period. Eventually a steady state is reached due to the spatial hole distribution being smeared out by dispersive transport and hole recombination.

Figure 19 shows the diffraction efficiency obtained from a photorefractive polymer in an HTOF experiment. A maximum diffraction is followed by a decay to a steady state, due to dispersive transport and charge recombination. In reorientational materials, the time constant for orientation must be either considerably longer or shorter than the transit time for an interpretable signal to be obtained. Even in the absence of reorientational effects, dispersive transport smears out the sinusoidal hole distribution into a uniform one during the drift process. Under these circumstances, no oscillation is observed and the space charge field is formed primarily via the stationary, sinusoidal distribution of sensitizer anions. The space charge field is therefore semipermanent, erased by uniform illumination under an applied electric field. Hole recombination occurs almost uniformly. The initial concentration of sensitizer anions is approximately equal to the photorefractive trap density.

3.4 An Overview of Amorphous Organic Photorefractives and Their Applications

3.4.1 The Electro-optic Response

In order for the space charge field to produce a refractive index modulation and hence a grating or a hologram within the organic photorefractive material, the

material has to show an electro-optic response. Like inorganic materials, organic photorefractives can yield a refractive index modulation via the Pockels effect. If the material is fully functional it will have a known nonlinear moiety attached covalently to provide an appreciable Pockels response. Alternatively, the material may be doped with a relatively high concentration of a nonlinear optical chromophore. Examples of chromophores used are shown in Figure 20. Additionally the material must be anisotropic, which generally means that the material must be electric-field-poled to provide some degree of alignment. Many organic photorefractive materials also possess an enhanced nonlinear response via reorientational birefringence. Reorientational birefringence occurs if the glass transition temperature of the material is below ambient and the dipolar chromophores can reorientate themselves in response to an applied electric field or a space charge field modulation. The low glass transition temperature is achieved by the addition of a suitable

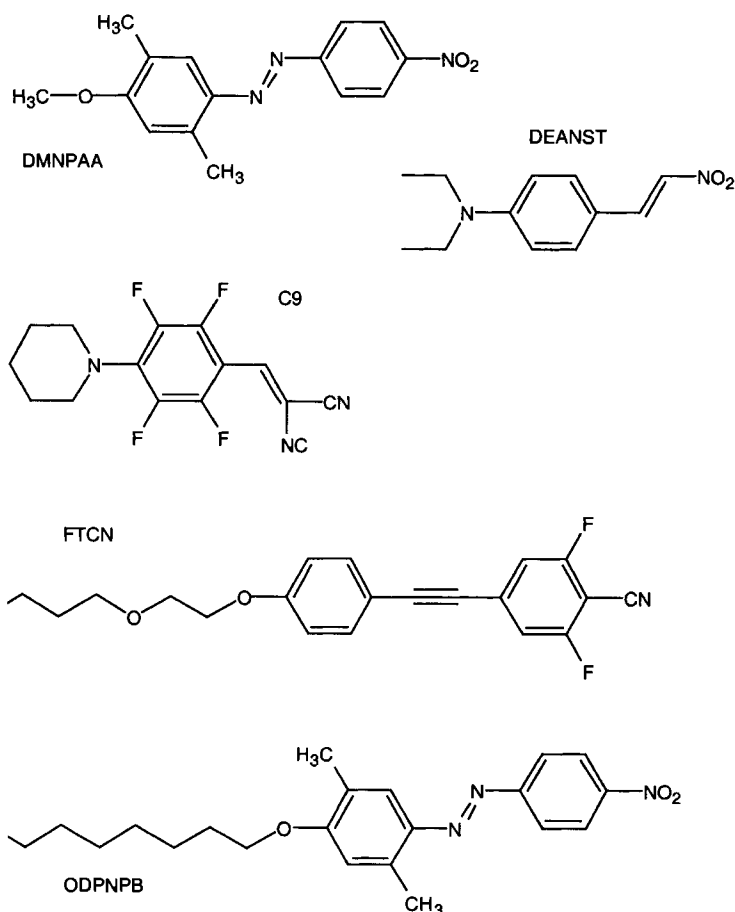


Figure 20. A selection of chromophores used in guest-host organic photorefractive materials.

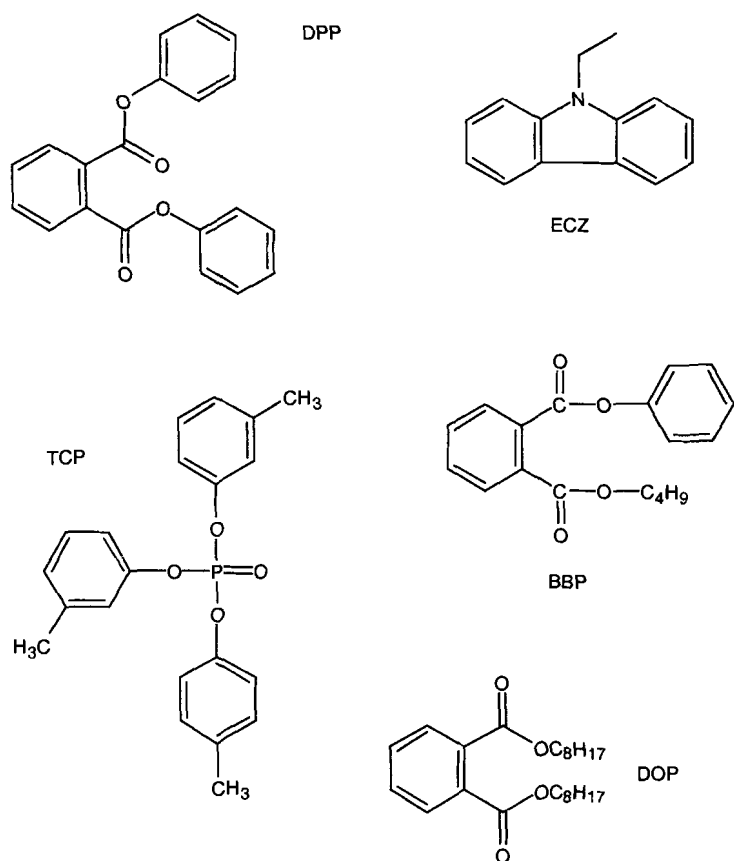


Figure 21. A selection of plasticizers used in organic photorefractive materials

plasticizer to the composite [44] (Figure 21), although in some cases simply adding a high concentration of a suitable electro-optic chromophore provides sufficient plasticization [45].

Molecular alignment distorts the index ellipsoid and rotates it to align along an electric field. An applied electric field thus causes the refractive index for an optical beam to change. An optical beam with an associated electric field E_{opt} directed along, or perpendicular to, the applied electric field E_{appl} will experience a refractive index change due to molecular alignment (neglecting the Pockels effect) according to Eqs. (6),

$$\begin{aligned}\Delta n(E_{\text{opt}} \parallel E_{\text{appl}})_B &\propto \frac{2}{3} A_2 \\ \Delta n(E_{\text{opt}} \perp E_{\text{appl}})_B &\propto -\frac{1}{3} A_2\end{aligned}\quad (6)$$

where the second-order coefficient, A_2 , is related to the average angle, θ , between

the optical axis of the chromophore and the electric field such that Eq. (7) holds.

$$A_2 = \frac{1 + \cos^2 \theta}{2} = 1 - \frac{3}{u} \left(\frac{u \cosh u - \sinh u}{u \sinh u} \right) \quad (7)$$

Here $u = \mu E/kT$ and μ is the dipole moment of the chromophore. For low applied fields, when $u < 1$, the approximation that $A_2 \approx u^2/(15 + u^2)$ may be used and the change in refractive index is nearly proportional to the square of the applied field. When a sinusoidal space charge field, E_{sc} , is superposed onto a uniform applied field, E_{appl} , the degree and direction of the molecular alignment, A_2 , follow the sum of both fields ($E_{total} = E_{sc} + E_{appl}$).

The amplitude of the space charge field is equal to the projection of the applied field in the direction of the grating vector and thus, for moderate fields, is proportional to the poling field E_{pol} according to Eq. (8),

$$|E_{sc}| = \frac{\sigma_p}{(\sigma_p + \sigma_d)} m |E_{pol}| \left[1 + \left(\frac{|E_{pol}|}{E_q} \right)^2 \right]^{-1/2} \quad (8)$$

where m is a parameter describing the intensity contrast, σ_p and σ_d are the photoconductivity and dark conductivity respectively, and E_q is the saturation field, which is the maximum space charge field attainable in the material [46]. The space charge field exists via an immobile charge distribution and is thus limited by the maximum density of immobile charge possible, termed the trap density. In most photorefractive organic materials under a poling field of less than $50 \text{ V } \mu\text{m}^{-1}$, the trap density does not limit the space charge field, which thus increases linearly with the applied field. The holographic refractive index contrast obtained, Δn_h , is proportional to the product of the space charge field and the applied field according to Eq. (9),

$$\Delta n_h \propto E_{sc} E_{appl} \propto E_{appl}^2 \quad (9)$$

and thus is proportional to the applied field squared.

With reference to Eq. (7), in most situations the holographic index contrast increases quadratically with the dipole moment of the chromophore. The dipole moment thus provides a parameter for material optimization, albeit at the expense of increased disorder slowing down charge transport. Transport rate appears not to be critical, however.

For a purely reorientational electro-optic response, a characteristic angle of propagation through the material will result in the optical beam experiencing a minimum holographic refractive index modulation, as illustrated in Figure 22(A). This is because the index changes for parallel and perpendicular optical polarizations are opposite in sense. Unlike the reorientational birefringence refractive index change, the refractive index change arising from the reorientationally enhanced Pockels effect is always positive in sense, such that

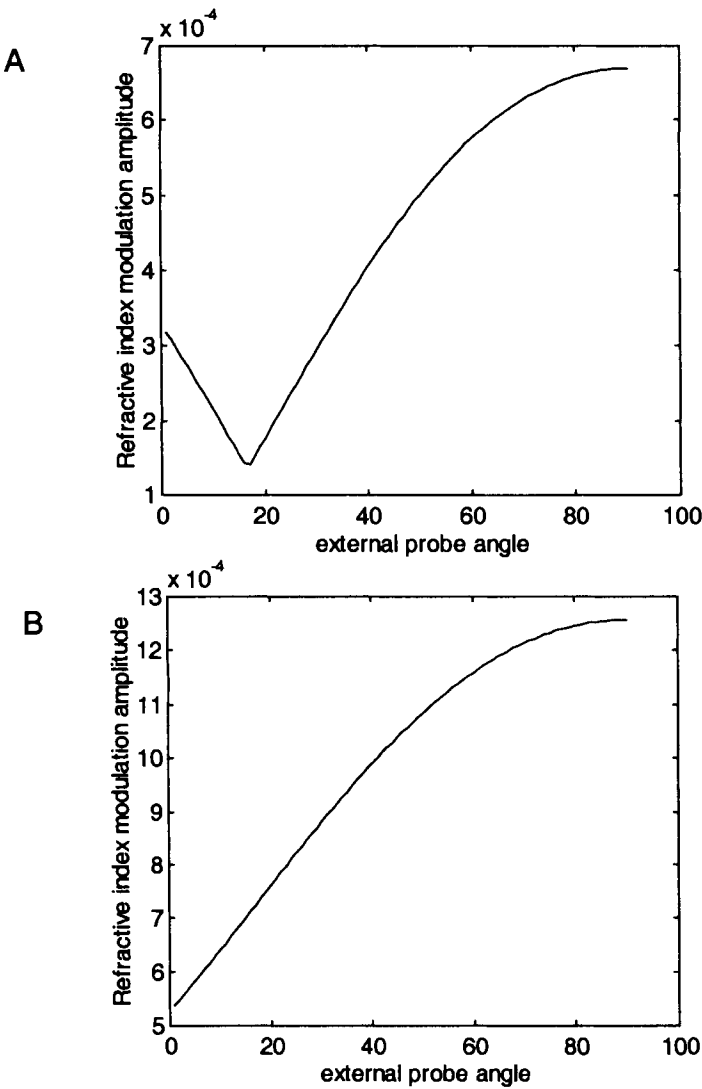


Figure 22. Refractive index modulation as a function of the external angle of the probe beam with respect to the sample normal for the material given in [20], when the writing beams are arranged at a constant 55° and 75° to the sample normal. A) angular variation if reorientational birefringence is dominant; B) angular variation if Pockels response were the primary source of index contrast.

$$\begin{aligned}\Delta n(E_{\text{opt}} \parallel E_{\text{appl}})_{\text{Pockels}} &\propto \frac{3}{2} A_2 \\ \Delta n(E_{\text{opt}} \perp E_{\text{appl}})_{\text{Pockels}} &\propto \frac{1}{2} A_2\end{aligned}\tag{10}$$

As illustrated in Figure 22(B), this does not provide a minimum in refractive index modulation. Thus, increasing the Pockels contribution to the overall birefringence also provides a route for materials development.

Not all organic photorefractive materials are reorientational. Some materials have a glass transition temperature above ambient, resulting in a fixed orientation of dipoles within the material. In these materials there are various possible procedures for recording holograms. First, a device may be heated to above the glass transition temperature before and during the recording of an index grating, and allowed to cool. The glass transition temperature is then above ambient and the chromophore alignment pattern is frozen, meaning the hologram can be read even after the applied field is removed. The main disadvantage with this method is the requirement to reheat the sample to above the glass transition temperature for subsequent hologram erasure or re-recording; furthermore any contraction upon cooling will alter the grating spacing. Alternatively, the device is heated and poled once only in a uniform poling field. A space charge field is then recorded with or without an external field. When no external poling field is used, a space charge field can be formed via charge diffusion instead of charge drift. The performance is superior when a poling field is used however, as the diffusion field is generally small in organic photorefractive materials. In this class of materials lacking reorientational enhancement, statistically uniform chromophore alignment occurs without local variations and refractive index contrast is obtained entirely from the Pockels effect. A comparison of the photorefractive performance parameters from a range of contrasting materials is presented in Table 5.

In Table 5 the difference between the photorefractive performance of a range of different reorientational materials and one permanently poled material is modest. A typical index contrast is 10^{-3} under an applied poling field of $50 \text{ V } \mu\text{m}^{-1}$ for reorientational materials. Higher index contrasts have been achieved using reorientational liquid crystals with 2×10^{-3} at the low field of $22 \text{ V } \mu\text{m}^{-1}$ but at the expense of response speed and optical quality. As discussed previously, the speed of space charge field formation in almost all cases of organic photorefractive materials depends upon the charge generation rate. For most sensitive materials, the charge generation limited rate can only be seen practically when reorientation is either fast, by the use of large concentrations of plasticizer, or slow so that the material is essentially permanently poled over the time scale of space charge field formation.

3.4.2 Holographic Optical Data Storage and Other Applications

A major application of photorefractive polymers as holographic data storage media is a real possibility. In this application two interfering laser beams write a hologram

Table 5. A comparison of the photorefractive performance parameters from a range of materials exhibiting different alignment properties and/or different mechanisms for generating a refractive index contrast.

Type	Ref.	Example material ^a	Poling field [V μm^{-1}]	Required poling field intensity [mW cm^{-1}]	Index contrast, Δn (DFWM or 2BC) ^a	Grating growth speed [s]	Optical quality	Device lifetime [months]
Reorientational guest/host polymer	[47]	49.5 % PVK 35 % PDCST 15 % BBP 0.5 % C ₆₀	100	1000	2.5×10^{-3}	0.05	Good	>5
Reorientational guest/host polymer	[45]	55 % EHDNPB 44 % PVK 1 % TNF	55	10	1.2×10^{-3}	<1	Good	>24
Permanently poled	[48]	99 % PCDI 1 % TNF	90 ^b 50 ^c	1200	9×10^{-4}	1.5	Good	>6
Reorientational glass	[40]	71 % DRDCTA 28 % DOP 1 % C ₆₀	50	1200	1×10^{-3}	0.035	Good	>12
Guest/host polymer	[43]	59 % TF'B 30 % DMNPAA 10 % DOP 1 % C ₆₀	50	1440	1.6×10^{-4}	0.00125	— ^d	— ^d
Reorientational liquid crystal	[49]	45 % PMMA 33 % E49 liquid crystal 21 ECZ 1 % TNF	22	51 000	2×10^{-3}	≈ 200	— ^d	— ^d

^aDFWM, degenerate four wave mixing; 2BC, two beam coupling; PDCST, (4-piperidinobenzylidene)-malononitrile; DRDCTA, 4,4'-di(N-carbazolyl)-4''-(2-N-ethyl-4-[2-(4-nitrophenyl)-1-azo] anilinoethoxy)-triphenylamine; DOP, dioctyl phthalate; PMMA, poly(methyl methacrylate); other abbreviations are defined in the text and Figures, ^belectric field applied during grating growth; required for charge generation, drift and the buildup of a space charge field, ^cpoling field applied before grating growth, in conjunction with a temperature rise to 40 °C, to provide molecular alignment, ^d—, data not available.

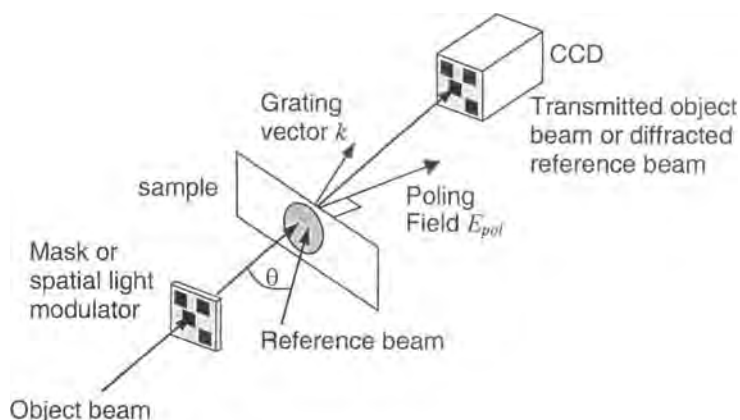


Figure 23. A typical holographic data storage arrangement using a photorefractive polymer device. For space charge field production, k must not be collinear with E_{pol} . During hologram recording, the object and reference beams interfere within the polymer, forming a hologram. During readout, the reference beam diffracts off the hologram and the binary image is recorded via a CCD array. The diffracted reference beam always coincides spatially with the transmitted object beam, which facilitates alignment and testing via comparison of the transmitted and diffracted beams. By utilizing an arrangement similar to that used for X-ray scattering off crystals, angle multiplexing of different holograms may be performed by rotating the reference beam by varying θ .

in the bulk of the material via the photorefractive effect. One beam, sometimes termed the object beam, is passed through a spatial light modulator to encode binary information before being focused into the material, as in Figure 23. The other beam, sometimes termed the reference beam, is a plane wave. After hologram recording, the reference beam diffracts off the hologram onto a charge-coupled device (CCD) array for information retrieval. The angle of incidence of the reference beam may be changed for multiple hologram recording in the same volume.

The material property that is most important for hologram recording is optical quality. Without good optical quality a high error rate of data retrieval occurs. The biggest issue surrounding optical quality is phase separation [45, 50], which arises as a result of large concentrations of polar molecules crystallizing out of the less polar glassy matrix. Phase separation results in severe optical scattering and can occur almost instantly after device fabrication or after a few days, weeks, or months. It can, however, be circumvented by several techniques, including the use of aliphatic groups substituted on the chromophore which are well known to prevent crystallization. Although the holographic index contrast of many organic materials is large, much larger than in inorganic photorefractive materials, field-dependent photo-generation and molecular alignment both contribute to the requirement for an applied electric field of $\sim 50 \text{ V } \mu\text{m}^{-1}$. This precludes the use of films much thicker than $200 \text{ } \mu\text{m}$. The number of holograms that it is possible to store is a function of

both the device thickness and the holographic index contrast, and currently only a few holograms can be stored in a single film. This problem can be addressed, however, by lamination of several layers to produce thicker samples for the same operating voltage, although maintaining high optical quality from laminated substrates has proved problematic [23, 51].

Consideration of electron transfer processes in holographic data storage becomes relevant when addressing the speed of hologram recording and erasure, because in many organic photorefractive systems the response speed is proportional to the photoconductivity. Thus the exact nature of mobile charge generation and transport mechanisms needs to be considered when designing fast materials.

Photorefractive polymers may facilitate other optical applications. One example is optical image correlation. Optical image correlation allows an image to be compared with a bank of images, stored holographically in the material. The images could be fingerprints of known criminals, for example, and the correlator would be able to find a match. In this technique, Fourier transforms of the two images are combined interferometrically before recovering the image. If the two input images are not correlated, there will be no output image [52]. A single image may also be split up into two parts, with one part recording a hologram in a photorefractive material. The image may be reproduced from the hologram and correlated with its original. If the original changes, then no correlation will be observed until the hologram has had sufficient time to update itself, which is dependent upon space charge field reformation as discussed above. This technique, often referred to as “novelty” filtering, provides a way of detecting changes to an image [46].

As with all fast rewritable holographic storage media, optical phase conjugation is possible. In a four-wave mixing geometry, two waves record a hologram and a third wave (the probe beam), which is collinear with one of the writing beams, is diffracted off the resulting hologram. The fourth wave is the diffracted probe beam, is collinear with the second writing beam, and has the useful property of being a phase conjugate of it. The process of phase conjugation can be used to eliminate optical distortions (Figure 24).

Another application for photorefractive polymers is optical limiting. Optical limiting prevents high light fluences from passing through the optical limiter, whilst allowing low light levels to pass unperturbed. This serves as protection against optical damage to a system or, more importantly, a user. A suitable organic photorefractive can be processed as a coating to a wide variety of devices for protection. An intense incoming beam scatters in the bulk or off the surface of the optical limiting layer. The incoming beam then forms a hologram with its scatter, which produces yet more scatter, eventually making the material opaque—which is referred to as beam fanning. Naturally, to provide any real protection against a laser, the diffraction efficiency needs to approach 100 % and the response speed needs to be fast. Low-level protection may be used to combat glare when driving.

Other interesting applications for organic photorefractives result from the phase shift between the original optical interference pattern and the holographic refractive index modulation. The phase shift is unique to photorefractive materials and allows

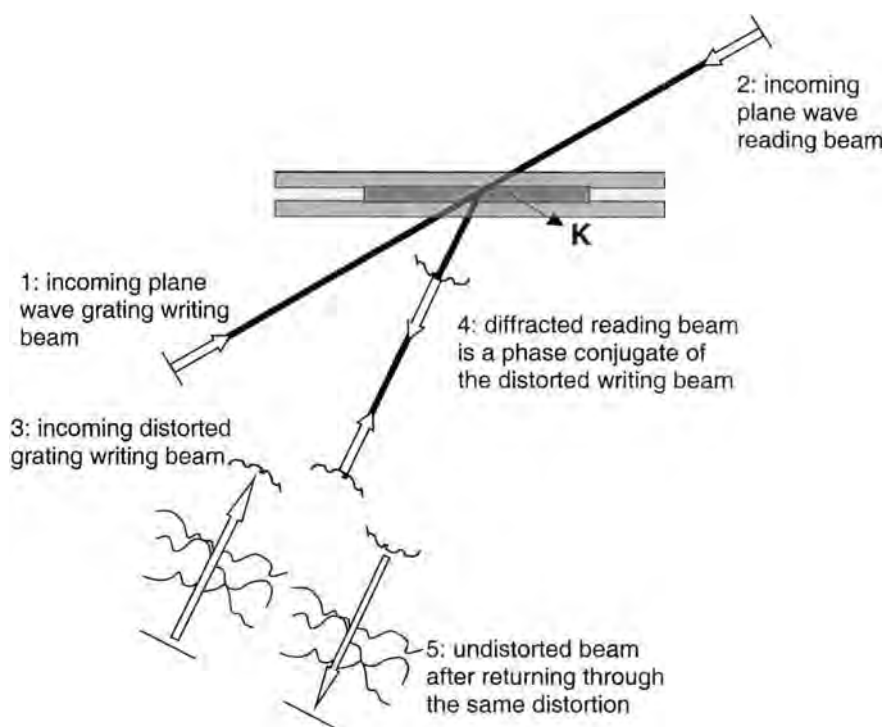


Figure 24. Degenerate four-wave mixing experimental arrangement and optical phase conjugation with photorefractive polymers

asymmetric two-beam coupling in which the energy from one beam couples into the other (recall Figure 2). One beam thus experiences optical loss (the pump beam) and the other experiences gain (the probe beam). If the intensity of the pump beam is much greater than that of the probe beam, then the regime of negligible depletion is applicable and small signal amplifications as high as $500\times$ are possible with a moving grating technique [53]. Such a system can be regarded as similar to a transistor and may form the basis of switching or routing in optical computing or telecommunications applications (Figure 25).

Their potential applications make organic photorefractive materials an important new class of materials. Versatile and inexpensive organic processing procedures are available to form bulk materials, thin films, or coatings. Synthesis of more optimized materials should be relatively straightforward. These factors distinguish amorphous organics as promising photorefractive materials that provide the possibility of a wide range of inexpensive devices. The rate of progress, both in understanding and in material development, is fast.

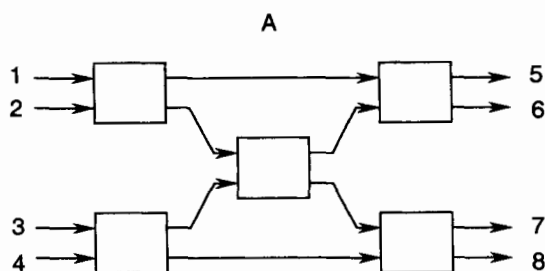
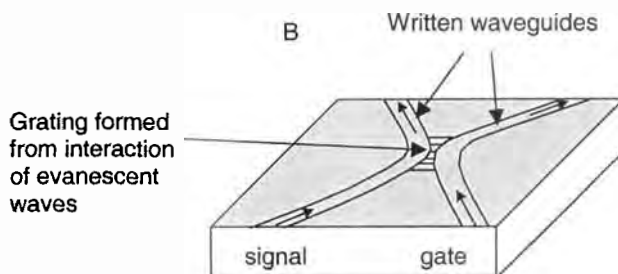


Figure 25. A) Optical switching directing telephone calls from callers 1–4 to possible receivers 5–8. B) The five individual switches utilize the two-beam coupling effect in photorefractive polymers, possibly in a waveguide geometry. By applying a gating input the signal can be redirected to an alternative output route.



Acknowledgements

The authors thank Professor Dr. Heinz Bässler, Professor G. G. Malliaras, Dr. D. Binks, K. Khand, and H. Thatcher for their help with the preparation of this chapter, and the Engineering and Physical Sciences Research Council of the UK for financial support.

References

1. A. Yariv, S. K. Hong, K. Kyuma, *Appl. Phys. Lett.* **1986**, 48, 1114–1116.
2. D. Z. Anderson, J. Feinberg, *IEEE J. Quant. Electron.* **1989**, 25, 635–647.
3. D. Psaltis, D. Brady, K. Wagner, *Appl. Opt.* **1988**, 27, 1752–1759.
4. L. Solymar, D. Webb, A. Grunnet-Jepson, *The physics and applications of photorefractive materials*, OUP, Oxford, **1996**, Chap. 4.
5. a) W. E. Moerner, A. Grunnet-Jepson, C. L. Thompson, *Annu. Rev. Mater. Sci.* **1997**, 27, 585–623; b) Y. Zhang, R. Burzynski, S. Ghosal, M. K. Casstevens, *Adv. Mater.* **1996**, 8(2), 111–125; c) W. E. Moerner, S. M. Silence, *Chem. Rev.* **1994**, 94, 127–155.
6. S. Ducharme, J. C. Scott, R. J. Twieg, W. E. Moerner, *Phys. Rev. Lett.* **1991**, 66, 1846–1848.
7. L. Onsager, *Phys. Rev.* **1938**, 54, 554.
8. J. Noolandi, K. M. Hong, *J. Chem. Phys.* **1978**, 70, 3230.
9. P. M. Borsenberger, D. S. Weiss, *Organic photoreceptors for imaging systems*, Dekker, New York, **1993**.
10. a) R. A. Marcus, *J. Chem. Phys.* **1956**, 24, 966; b) R. A. Marcus, *Annu. Rev. Phys. Chem.* **1964**, 15, 155.

11. M. Umeda in *Xerographic photoreceptors and organic photorefractive materials IV* (Eds.: S. Ducharme, J. W. Stasiak), Proc. SPIE 3471, **1998**, pp. 212–223.
12. T. Niimi, M. Umeda, *J. Appl. Phys.* **1993**, 74(1), 465–468.
13. A. Schreiber, R. Bilke, J. Pan, I. Bleyl, J. Bondkowski, D. Adam, D. Haarer in *Xerographic photoreceptors and organic photorefractive materials IV* (Eds.: S. Ducharme, J. W. Stasiak), Proc. SPIE 3471, **1998**, pp. 224–234.
14. M. Pope, C.E. Swenberg, *Electronic processes in organic crystals*, OUP, New York, **1982**, Chap. 4.
15. a) Y. Wang, A. Suna, *J. Phys. Chem. B* **1997**, 101, 5627–5638; b) Y. A. Cherkasov, N. V. Kamanina, E. L. Alexandrova, V. I. Berendyaev, N. A. Vasilenko, B. V. Kotov in *Xerographic photoreceptors and organic photorefractive materials IV* (Eds.: S. Ducharme, J. W. Stasiak), Proc. SPIE 3471, **1998**, p. 254.
16. W. D. Gill, *J. Appl. Phys.* **1972**, 43(12), 5033–5040.
17. S. Schlöter, A. Schreiber, M. Grasruck, A. Leopold, M. Kol'chenko, J. Pan, C. Hohle, P. Strohmriegel, S. J. Zilker, D. Haarer, *Appl. Phys. B* **1999**, 68, 899–906.
18. C. A. Walsh, D. M. Burland, *Chem. Phys. Lett.* **1992**, 195(4), 309–315.
19. G. Weiser, *Phys. Stat. Sol. A* **1973**, 18, 347–359.
20. a) D. Wright, M. A. Diaz-Garcia, J. D. Casperson, M. DeClue, W. E. Moerner, R. J. Twieg, *Appl. Phys. Lett.* **1998**, 73(11), 1490–1492; b) G. Bauml, S. Schlöter, U. Hofmann, D. Haarer, *Opt. Comm.*, **1998**, 154(1–3), 75–78.
21. a) S. M. Silence, G. C. Bjorklund, W. E. Moerner, *Opt. Lett.* **1994**, 19(22), 1822–1804; b) S. M. Silence, J. C. Scott, J. J. Stankus, W. E. Moerner, C. R. Moylan, G. C. Bjorklund, R. J. Twieg, *J. Phys. Chem.* **1995**, 99(12), 4096–4105.
22. K. S. West, D. P. West, M. D. Rahn, J. D. Shakos, F. A. Wade, K. Khand, T. A. King, *J. Appl. Phys.* **1998**, 84(11), 5893–5899.
23. E. H. Mecher, C. Brauchle, H. H. Horhold, J. C. Hummelen, K. Meerholz, *Phys. Chem. Chem. Phys.* **1999**, 1(8), 1749–1756.
24. P. M. Lundquist, C. Poga, R. G. DeVoe, Y. Jia, W. E. Moerner, M. P. Bernal, H. Coufal, R. K. Grygier, J. A. Hoffnagle, C. M. Jefferson, R. M. Macfarlane, R. M. Shelby, G. T. Sincerbox, *Opt. Lett.* **1996**, 21(12), 890–892.
25. G. G. Malliaras, V. V. Krasnikov, H. J. Bolink, G. Hadzioannou, *Appl. Phys. Lett.* **1994**, 65(3), 262–264.
26. J. G. Winiarz, L. M. Zhang, M. Lal, C. S. Friend, P. N. Prasad, *J. Am. Chem. Soc.* **1999**, 121(22), 5287–5295.
27. E. Hendrickx, Y. D. Zhang, K. B. Ferrio, J. A. Herlocker, J. Anderson, N. R. Armstrong, E. A. Mach, A. P. Persoons, N. Peyghambarian, B. Kippelen, *J. Mater. Chem.* **1999**, 9, 2251–2258.
28. M. A. Diaz-Garcia, D. Wright, J. D. Casperson, B. Smith, E. Glazer, W. E. Moerner, L. I. Sukhomlinova, R. J. Twieg, *Chem. Mater.* **1999**, 11(7), 1784–1791.
29. K. Ogino, T. Nomura, T. Shichi, S. Park, H. Sato, T. Aoyama, T. Wada, *Chem. Mater.* **1997**, 9, 2768–2775.
30. U. Hofmann, A. Schreiber, D. Haarer, S. J. Zilker, A. Bacher, D. D. C. Bradley, M. Redecker, M. Inbasekaran, W. W. Wu, E. P. Woo, *Chem. Phys. Lett.* **1999**, 311(1–2), 41–46.
31. C. Hohle, U. Hofmann, S. Schlöter, M. Thelakkat, P. Strohmriegel, D. Haarer, S. J. Zilker, *J. Mater. Chem.* **1999**, 9, 2205–2210.
32. J. A. Herlocker, K. B. Ferrio, E. Hendrickx, B. D. Guenther, S. Mery, B. Kippelen, N. Peyghambarian, *Appl. Phys. Lett.* **1999**, 74(16), 2253–2255.
33. Z. H. Peng, A.R. Gharavi, L. P. Yu, *Appl. Phys. Lett.* **1996**, 69(26), 4002–4005.
34. H. Scher, E. W. Montroll, *Phys. Rev. B* **1975**, 12, 2455.
35. H. Bässler, *Phys. Stat. Sol. B—Basic Research* **1993**, 175(1), 15–56.
36. A. Dieckmann, H. Bässler, P. M. Borsenberger, *J. Chem. Phys.* **1993**, 99(10), 8136–8141.
37. Y. Kanemitsu, H. Funada, Y. Masumoto, *J. Appl. Phys.* **1992**, 71(1), 300–303.
38. M. Van der Auweraer, F. C. De Schryver, P. M. Borsenberger, H. Bässler, *Adv. Mater.* **1994**, 6(3), 199–213.
39. M. Redecker, D. D. C. Bradley, M. Inbasekaran, W. W. Wu, E. P. Woo, *Adv. Mater.* **1999**, 11(3), 241–248.

40. S. M. Silence, J. C. Scott, F. Hache, E. J. Ginsburg, P. K. Jenkner, R. D. Miller, R. J. Twieg, W. E. Moerner, *J. Opt. Soc. Am. B* **1993**, *10*(12), 2306–2312.
41. S. J. Zilker, M. Grasruck, J. Wolff, S. Schlöter, A. Leopold, M. A. Kol'chenko, U. Hofmann, A. Schreiber, C. Hohle, D. Haarer, *Chem. Phys. Lett.* **1999**, *306*, 285–290.
42. G. G. Malliaras, V. V. Kransikov, H. J. Bolink, G. Hadziioannou, *Phys. Rev. B* **1995**, *52*(20), R14324–14327.
43. A. Goonesekera, S. Ducharme, J. M. Takacs and L. Zhang, *J. Chem. Phys.* **1997**, *107*(20), 8709–8712.
44. H. J. Bolink, V. V. Krasnikov, G. G. Malliaras, G. Hadziioannou, *J. Phys. Chem.* **1996**, *100*(40), 16356–16360.
45. A. M. Cox, R. D. Blackburn, D. P. West, T. A. King, F. A. Wade, D. A. Leigh, *Appl. Phys. Lett.* **1996**, *68*(20), 2801–2803.
46. D. D. Nolte in *Photorefractive effects and materials* (Ed.: D. D. Nolte), Kluwer Academic, Dordrecht, **1995**, Chap. 1, pp. 12–17.
47. A. Grunnet-Jepsen, C. L. Thompson, R. J. Twieg, W. E. Moerner, *Appl. Phys. Lett.* **1997**, *70*(12), 1515–1517.
48. S. Schlöter, U. Hofmann, K. Hoechstetter, G. Bäuml, D. Haarer, K. Ewert, C.-D. Eisenbach, *J. Opt. Soc. Am. B* **1998**, *15*(10), 2560–2565.
49. A. Golemme, B. L. Volodin, B. Kippelen, N. Peyghambarian, *Opt. Lett.* **1997**, *22*(16), 1226–1228.
50. K. Meerholz, B. L. Volodin, Sandalphon, B. Kippelen, N. Peyghambarian, *Nature* **1994**, *371*(6497), 497–500.
51. a) C. Poga, P. M. Lundquist, V. Lee, R. M. Shelby, R. J. Twieg, D. M. Burland, *Appl. Phys. Lett.* **1996**, *69*(8), 1047–1049; b) P. M. Lundquist, C. Poga, R. G. DeVoc, Y. Jia, W. E. Moerner, M. P. Bernal, H. Coufal, R. K. Grygier, J. A. Hoffnagle, C. M. Jefferson, R. M. Macfarlane, R. M. Shelby, G. T. Sincerbox, *Opt. Lett.* **1996**, *21*(12), 890–892.
52. a) N. Nagayama, M. Yokoyama, *Mol. Cryst. Liq. Cryst. Sci. Tech. A: Mol. Cryst. Liq. Cryst.* **1999**, *327*, 19–22; b) D. Vacar, A. J. Heeger, B. Volodin, B. Kippelen, N. Peyghambarian, *Rev. Sci. Instr.* **1997**, *68*(2), 1119–1121.
53. A. Grunnet-Jepson, C. L. Thompson, W. E. Moerner, *Opt. Comm.* **1998**, *145*(1–6), 145–149.

4 Photoinduced Electron Transfer Initiating Systems for Free-radical Polymerization

Jerzy Pączkowski and Douglas C. Neckers

4.1 Introduction

Photoinitiated polymerization uses the energy of light for the rapid conversion of monomeric liquids to solid polymeric products. The term *photopolymerization* implies that the initiation step of a radical, cationic, or anionic chain reaction producing a macromolecule requires the absorption of a photon. Since the absorption of one photon may start the reaction of up to 10^5 monomeric units, photoinitiated polymerization is, in practice, one of the most powerful chemical amplification techniques.

In this review we will consider only photoinitiated polymerization reactions in which the chain processes involve free-radical intermediates. The process may be initiated by direct photolysis of a precursor providing free radicals by bond dissociation, or the radicals may be formed by electron transfer reactions. Panchromatic sensitization of polymerization often requires the presence of a suitable dye as the primary light absorber. This can then either transfer energy, or undergo electron transfer. Energy transfer is less common than the literature about the subject would suggest while photoinduced intermolecular electron transfer (PET) is likely more so. PET uses light to initiate electron transfer from a donor to an acceptor molecule. The process is possible because electronically excited states are both better oxidants and better reductants than their ground-state counterparts. The concept involved in PET reaction is simple: promotion of an electron from the highest occupied molecular orbital (HOMO) in the ground state to the lowest unoccupied molecular orbital (LUMO); an unpaired electron with high reduction potential in the LUMO orbital and high oxidizing potential in the residual HOMO orbital characterizes the new electronic configuration.

Translating these to the initiation of free-radical polymerization, one can anticipate that two types of reaction, oxidation and reduction, will occur with the excited state.

- 1) Dye *photoreduction* leading to subsequent polymerization was first reported in 1954 [1] when Oster identified several groups of dyes that are photoreduced in the presence of suitable reductants such as ascorbic acid and triethanolamine. The dyes included the acridines, xanthenes, and thiazines.
- 2) Dye *photooxidation* leading to subsequent polymerization requires molecules that are strong electron acceptors in the ground state. Systems composed of onium salts, reducing agents, and sensitizer/electron transfer donors are examples of such systems. They are excellent photoinitiators for the polymerization of acrylates [2–4].

There are many review articles on various aspects of photoinitiated polymerization [5–11], covering both applications of dye-sensitized polymerization and basic research studies. However, there are essentially no reviews describing, in detail, the mechanistic aspects of photoinduced electron transfer processes as applied in photocuring technologies, the PET process applied to photopolymerization processes, or the latest photoredox pairs to be used as photoinitiators.

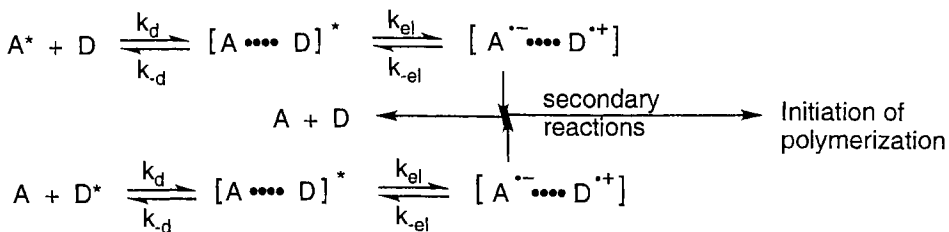
In the present chapter we consider the inter- or intramolecular photoinduced electron transfer phenomenon. We mainly focus on photoinduced electron transfer processes that lead to the photoinitiation of polymerization, and on processes initiated by photoreduced or photooxidized excited states. We concentrate especially on a description of the kinetic schemes, a description of the reactions that follow the primary process of electron transfer, and the characteristics of intermediates formed after electron transfer. Understanding the complexity of the processes of photo-initiated polymerization requires a thorough analysis of the examples illustrating the mechanistic aspects of the formation of free radicals with the ability to start polymerization.

4.2 General Scheme

Scheme 1 is a good starting point: k_d is the rate constant representing the rate of diffusive encounters between reactants, k_{-d} denotes the rate of separation of the reactants after collision, and k_{el} is the first-order rate constant of electron transfer. The reverse step is designated by the rate constant k_{-el} , while k_r denotes the rate of return electron transfer. The key steps of the mechanism are the quenching of the chromophore excited state, either the excited singlet or triplet state, by electron transfer, and the various steps following the primary process.

Marcus [12–14] provided a simple approach allowing the prediction of the kinetics of the process, using thermodynamic parameters and spectroscopic measurements. Marcus theory assumes that bimolecular electron transfer, as shown in Scheme 1, occurs in three stages:

- 1) the formation of the precursor complex,
- 2) electron transfer, and



Scheme 1.

- 3) the change in organization of solvent cage in which electron transfer primary products exist.

It is commonly assumed that solvent reorganization will dominate electron transfer kinetically. Depending on the thermodynamics of the electron exchange, it is possible to quantitatively predict a relationship between the free energy of activation for electron transfer and the free energy associated with solvent reorganization based on Marcus theory.

Considering these principles and the interaction between the dye (chromophore) and an electron donor in the ground state and after an electron transfer process, dye photoinitiators can be classified in three different groups:

- 1) Donor–acceptor pairs with electrostatic interaction in the ground state (ground-state ion pair) but neutral after the photoinduced electron transfer process.
- 2) Donor–acceptor pairs without electrostatic interaction in the ground state and, after an electron transfer, at least one component that is neutral in the ground state.
- 3) Donor–acceptor pairs that are neutral in the ground state and charged after electron transfer. In this case the resulting product is a radical ion pair.

Since photoinitiation occurs in specific monomeric mixtures, as Marcus theory predicts, the properties of the to-be-photopolymerized mixture (polarity, viscosity, electron-donating or electron-accepting properties) may play an important role in the overall efficiency of the process. Considering this, the monomer can participate in the photoinduced electron transfer process, either as a light-absorbing chromophore, as a hydrogen atom source, or as an electron donor/electron acceptor.

The main question arising during the analysis of the photoinduced polymerization is how one can know that the dye-coinitiator system, after excitation, forms a species that is able to start polymerization chain reaction. The main factors are:

- 1) Direct observation of radical ions formed subsequent to exposure to laser flash photolysis.
- 2) Experimental evidence that the rate of photopolymerization is a function of the properties of the photo-redox pair. (Note: one should take into account only the rates that are directly affected by the PET processes.) The PET process affects

the rate up to the limit proscribed by microviscosity of the medium, which can be measured using spectroscopic probes [15–21]. Various studies of the degree of polymerization at maximum conversion indicate that for monofunctionalized monomers, at least up to 70–75 % of conversion, the overall rate of polymerization follows steady-state kinetic theory. Up to this degree of conversion there is no limitation of rate that is related to the diffusion of small molecules. For multifunctional monomers the processes that regulate the overall rate of polymerization are more complex. Therefore the relationship between PET and the rate of polymerization is limited to the initial time of polymerization (3–5 % of monomer conversion) only [22].

- 3) Fulfillment of the Marcus equation requirements for the primary process, e.g., for the process of the quenching of the dye excited state.
- 4) The presence of species able to initiate polymerization as observed by other spectroscopic tools such as electron spin resonance spectroscopy (ESR), emission spectroscopy, transient absorption spectroscopy or chemically induced dynamic nuclear polarization (CIDNP).

4.3 Dye Photoinitiators—mechanisms

4.3.1 Photoinitiating Donor–Acceptor Pairs with Electrostatic Interaction in the Ground State (Ground-state Ion Pair) and Neutral after Photoinduced Electron Transfer Process

Cyanine borate salts

Schuster and co-workers discovered that 1,4-dicyanonaphthalene solutions containing an alkyltriphenylborate salt, when irradiated, yield one-electron oxidation of the alkyltriphenylborate leading to carbon–boron bond cleavage and formation of free alkyl radicals [23]. In Gottschalk's hands [24, 25], it was shown that ionic salt pairs formed from cyanine dyes and alkyltriphenylborates (Figure 1) could be used as photoinitiators [26] that were active in the visible region of the spectrum.

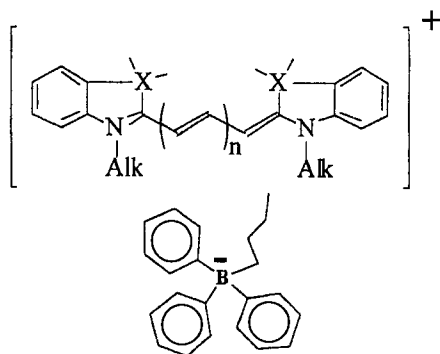


Figure 1. Ionic salt pairs active as photoinitiators in the visible region.

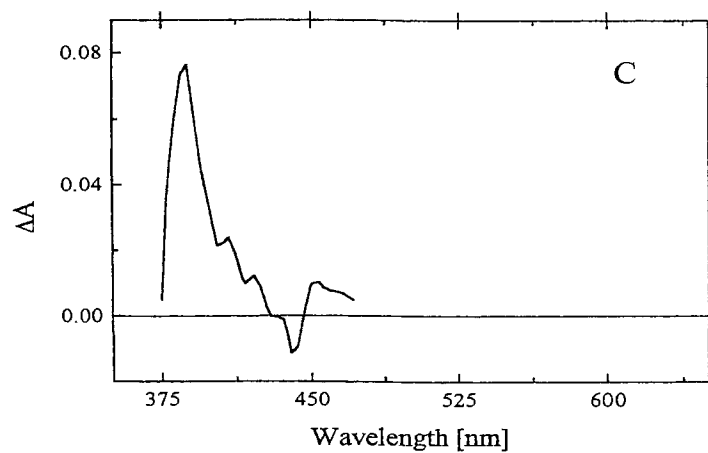
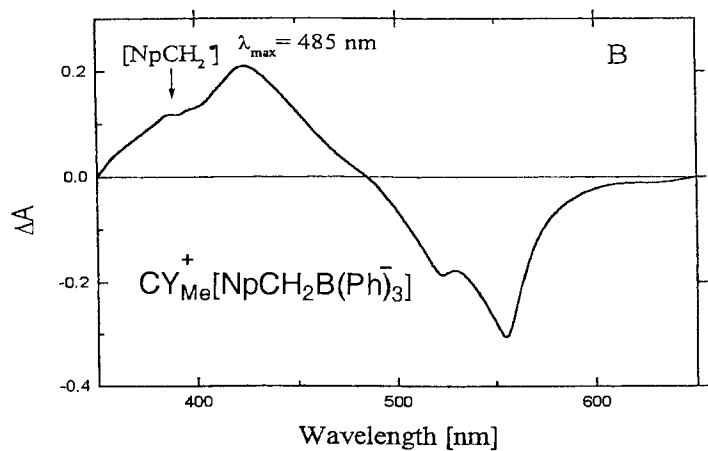
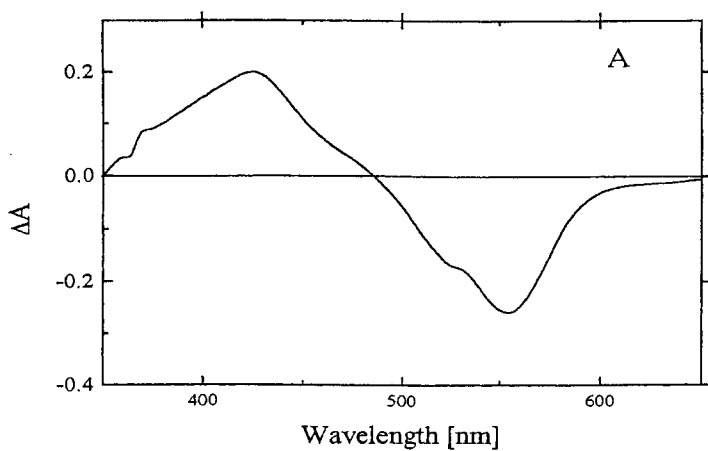
Cyanine borates exist as tight ion pairs; certain of the salts have even been shown to form ion pairs in which the center-to-center distance between the ions is less than the sum of the individual radii [27–29]. Since the lifetime of the excited singlet state of cyanine dye is quite short, too short to allow an efficient encounter at an achievable concentration of borate in a situation in which diffusion is necessary, the self-association of the cyanine cation and borate anion is a prerequisite for efficient photoinduced reaction.

The evidence for radical formation from the cyanine borates is the following:

- 1) Irradiation of an oxygen-free benzene solution of a cyanine *n*-butyltriphenylborate at 532 nm gives *n*-octane among other products. Since octane can only form from the coupling of *n*-butyl radicals, one can conclude that irradiation of cyanine *n*-butyltriphenylborate generates free butyl radicals.
- 2) Irradiation of a benzene solution of ethylindocarbocyanine benzyltriphenylborate with an 18 ps light pulse at 532 nm gives the transient spectrum shown in Figure 2(A). Analysis of the spectrum indicates the negative absorption is due to the bleaching of the dye and a new absorption band with a maximum at 430 nm. This maximum was assigned to the cyanine dye radical. For di-*n*-butyltetramethylindocarbocyanine borates containing leaving groups that absorb in the mid-UV, e.g., di-*n*-butyltetramethylindocarbocyanine (α -methylnaphthyl)triphenylborate, laser photolysis gives a new feature. In this case, an absorption at 385 nm (see Figure 2B) that can be attributed to the 2-methylnaphthyl radical is observed. The transient absorption spectrum of this radical can be obtained by subtracting A from B (Figure 2C) [25]. Note that Scaiano et al. [32], using laser flash photolysis, in the same region observed the presence of annular type of free radicals.

Laser flash photolysis of the benzyltriphenylborate salt shows rapid bleaching of the cyanine absorption and formation of the cyanine dye radical (Figure 3). Similar experiments were carried out using vinyltriphenylborate and show that the processes occur with an efficiency significantly less than was observed for the benzyltriphenylborate. The conclusion is that the radical elimination step impacts the kinetics of the overall electron transfer process. With the tetraphenylborate salt one finds little formation of cyanine radical and the excited singlet state of the dye is nearly completely returned to the cyanine ion ground state by the end of the pulse. (Note, however, that tetraphenylborate salts with light-absorbing counterions are also good photoinitiators [30, 31].)

Figure 2. a) Transient absorption spectra recorded after excitation of di-*n*-butyltetramethylindocarbocyanine benzyltriphenylborate in benzene solution with a 18 ps laser pulse. Negative absorbance related to the bleaching of the dye absorption. The band at $\lambda_{\max} = 430$ nm is attributed to the presence of the cyanine dye radical; b) transient absorption spectra recorded after excitation of naphthyltriphenyl borate in benzene solution with a 18 ps laser pulse. The new feature is attributed to the presence of the (2-naphthyl)methyl radical; c) the difference spectrum obtained by subtracting spectrum A from spectrum B: the maximum at 385 nm is characteristic for the 2-methylnaphthyl radical. Data are taken from [25].



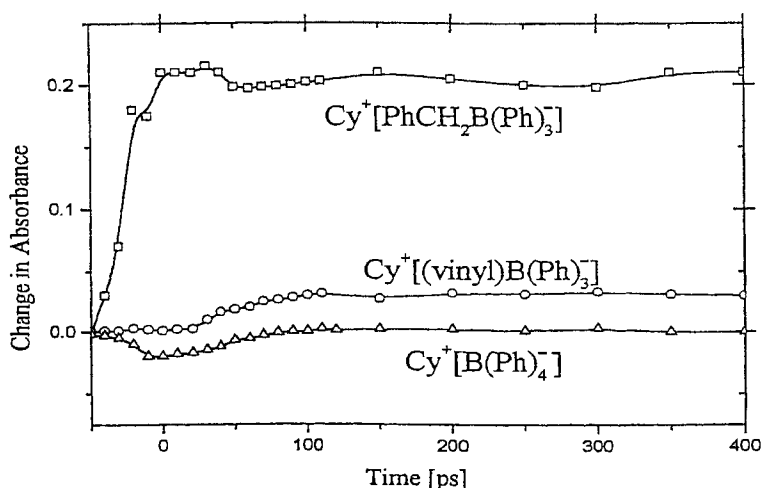


Figure 3. The absorption of cyanine dye (Cy) radicals monitored at 430 nm following excitation of a benzene solution with an 18 ps laser pulse. The time dependence of the absorption changes of cyanine radical for the benzyltriphenylborate case is faster than its decay. For the vinyltriphenylborate, back electron transfer and the reaction that follows electron transfer have competitive rates. For the tetraphenylborate salt, the back electron transfer process dominates after electron transfer, therefore the boron–carbon bond cleavage does not occur and almost no cyanine dye radical formation is observed (data adapted from [25]).

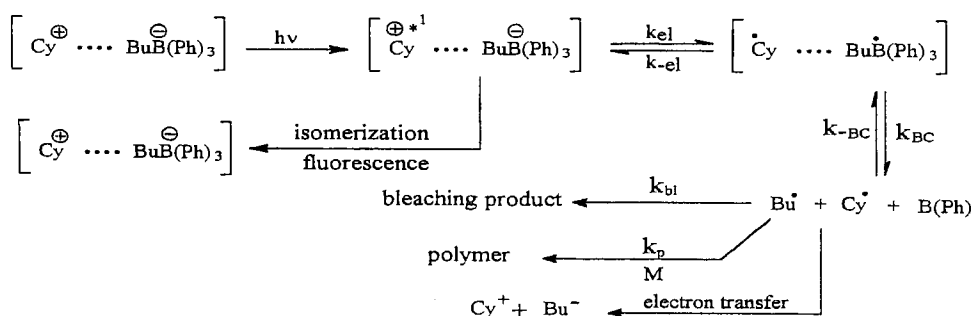
These data, by analogy, suggest the mechanism of the polymerization initiation process. Photoinduced electron transfer from the borate anion to the singlet excited state of the cyanine dye is followed by rapid cleavage of the alkyl–boron bond of the boranyl radical forming the alkyl radical (see Scheme 2), which serves as the radical chain initiator. Here k_{BC} denotes the rate of the carbon–boron bond cleavage. The reverse step is designated as k_{-BC} and k_{bl} is the rate constant of the cross-coupling step yielding bleached dye.

It is well known that a principle prerequisite for PET reactions to be allowed processes can be calculated from the Rehm–Weller [33, 34] equation (Eq. (1)). The basic Rehm–Weller requirement states that the free energy of activation for the PET (ΔG_{et}) process should have a negative value.

$$\Delta G_{et} = E_{ox}(D/D^{+}) - E_{red}(A^{-}/A) - Ze^2/\epsilon a - E_{0,0} \quad (1)$$

In Eq. (1) $E_{ox}(D/D^{+})$ is the oxidation potential of the electron donor, $E_{red}(A^{-}/A)$ is the reduction potential of the electron acceptor, $E_{0,0}$ the energy of the excited state undergoing reaction and $Ze^2/\epsilon a$ is the coulombic energy associated with the process.

Such electrochemical potentials are generally measured in a polar solvent such as acetonitrile. The electrochemical reduction of the cyanine cation (Figures 4B, 4C) in acetonitrile solution is reversible. Borate anions behave similarly (Figure 4A);



Scheme 2.

therefore the values obtained may have thermodynamic meaning. The procedure that allows calculation of the ΔG_{et} value of the process must also consider the effect of the solvent polarity on both ground and excited states. Incorporating these values gives, according to Schuster [25], the estimated values for cyanine borate ion pairs as listed in Table 1.

The absorption maximum of the cyanine dye can be changed by altering the number of conjugated alkene units linking the cyanine chromophores. This makes the cyanine borate photo-redox pair a so-called “tunable” photoinitiator, in that compounds which absorb throughout the visible and infrared spectrum can be obtained. Recently, Kabatc et al. [35] described the important features of cyanine borate photo-redox pairs (Table 2). The structures of dyes tested are shown in Figure 5.

The quantum efficiency of these cyanine borates when they are used as photoinitiators depends strongly on structure (Figure 6). However, in general, cyanine borates are not particularly efficient photoinitiators. For example the RBAX-*N*-phenylglycine photo-redox pair [36] is much more efficient. The main value of the cyanine borates is that they give substantial wavelength flexibility so they can be used in cases where polychromaticity is required (Figure 7).

Irradiation of the cyanine borates often causes bleaching, indicating that coupling of the alkyl radical with the cyanine radical [37] competes with the free-radical cage-escape process (Scheme 2). Since the bleaching process occurs with maximum quantum yields in the range $\Phi_{bl} = 0.001\text{--}0.02$, bleaching is at least one order of magnitude less efficient than is alkyl radical formation. Comparison of the quantum yields of free-radical formation (Table 1) and of the bleaching process reveals that the effect of the radical coupling reaction on the efficiency of polymerization can be neglected.

The data summarized in Table 2 indicate that the series of cyanine borates with the *n*-butyltriphenylborate counterion possess a negative ΔG_{et} value, i.e., they fulfill the basic Rehm–Weller requirements for effective photoinduced electron transfer processes. Extending this to a practical application of the Marcus equation (see

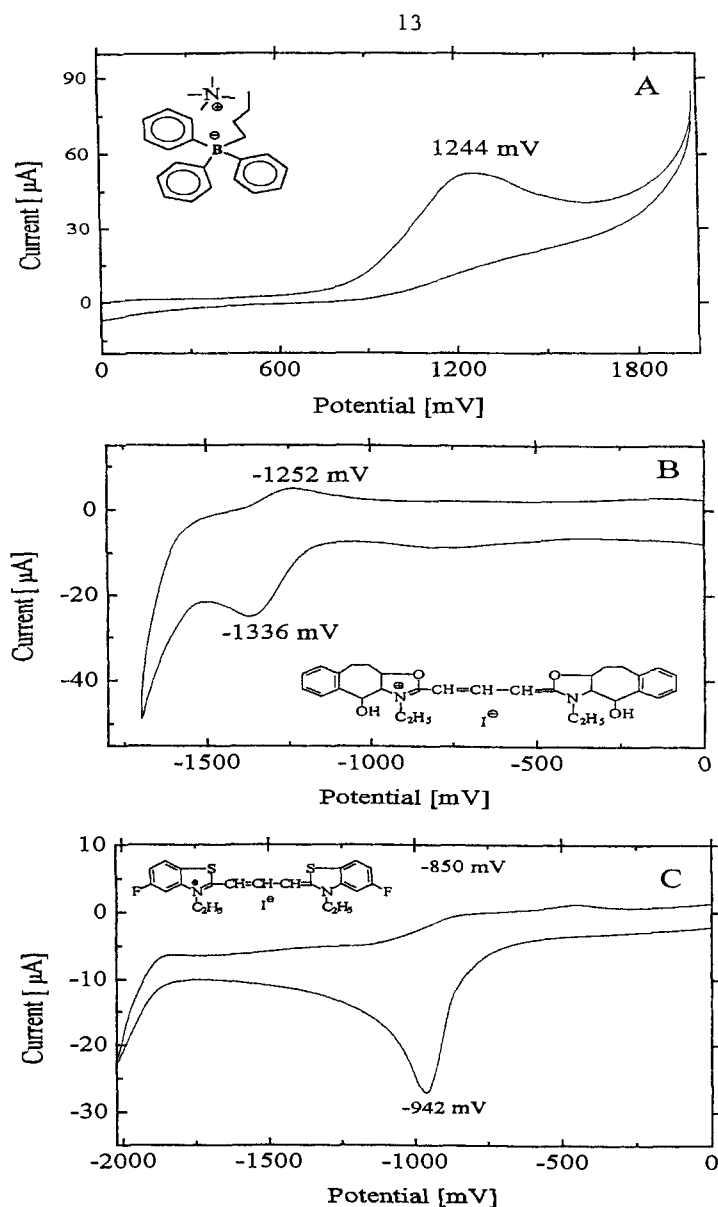


Figure 4. Cyclic voltammograms of selected compounds. The types of molecule tested are shown in insets. For measurements an electroanalytical Cypress System Model CS-1090 was used. A platinum 1 mm disk electrode was used as the working electrode and an Ag–AgCl electrode served as the reference electrode. The supporting electrolyte was 0.5 M tetrabutylammonium perchlorate in dry acetonitrile.

Table 1. Oxidation and reduction potential data, rate constants for electron transfer for cyanine borates in acetonitrile and benzene solution, and efficiency of cyanine radical formation.^{a,b}

Borate ion	$(E_{\text{ox}} - E_{\text{red}})_{\text{MeCN}}$	$(E_{\text{ox}} - E_{\text{red}})$	ΔG_{et} [eV]	k_{et} [s ⁻¹]	Φ_{cy}
[PhC≡CB(Ph) ₃] ⁻	2.51	1.41	0.30	$\sim (5 \times 10^9)$	
[Ph ₄ B] ⁻	2.45	1.35	0.24	4×10^{10}	0.067
[H ₂ C=CHB(Ph) ₃] ⁻	2.45	1.35	0.24	4.8×10^{10}	0.18
[cyclo-C ₃ H ₅ -B(Ph) ₃] ⁻	2.43	1.33	0.22	8.9×10^{10}	0.21
[CH ₃ B(Ph) ₃] ⁻	2.39	1.29	0.18	1.1×10^{11}	0.50
[<i>n</i> -BuB(Ph) ₃] ⁻	2.21	1.11	-0.01	2.4×10^{11}	0.73
[PhCH=CHB(Ph) ₃] ⁻	2.16	1.06	-0.05	1.2×10^{11}	0.14
[PhCH ₂ B(Ph) ₃] ⁻	2.09	0.99	-0.13	3.3×10^{11}	1.00
[<i>m</i> -tolCH ₂ B(Ph) ₃] ⁻	2.10	1.00	-0.11		
[NpCH ₂ B(Ph) ₃] ⁻	2.07	0.97	-0.14	3.9×10^{11}	0.95
[<i>n</i> -BuB(Ar) ₃] ⁻	2.11	1.01	-0.10	3.0×10^{11}	0.87

^a $\Delta G_{\text{bet}} = -\Delta E^* - \Delta G_{\text{et}} = -(E_{\text{ox}} - E_{\text{red}})_{\text{MeCN}}$, ^b data taken from Refs. [24] and [25].

Table 2. Characteristics of the cyanine borates tested (see [35]).

Compd.	Z	R ¹	R ²	R ³	R	λ_{max}^A * [nm]	E_{red}^a [V]	ΔG_{et}^b [eV]
1	O	Cl	H	H	C ₂ H ₅	484	-1.16	-0.736
2	O	CH ₃	H	H	C ₂ H ₅	488	-1.31	-0.576
3	O	H	H	H	C ₆ H ₁₃	486	-1.27	-0.561
4	O	C ₆ H ₅	H	C ₂ H ₅	C ₂ H ₅	502	-1.13	-0.55
5	O	H	H	H	C ₂ H ₅	482	-1.30	-0.544
6	O	H	H	H	C ₃ H ₇	484	-1.24	-0.542
7	O	H	H	H	CH ₃	482	-1.28	-0.526
8	O	C ₆ H ₅	H	H	C ₂ H ₅	494	-1.12	-0.502
9	O	C ₆ H ₅	H	C ₂ H ₅	C ₂ H ₅	502	-1.29	-0.454
10	O	CH ₃ O	H	C ₂ H ₅	C ₂ H ₅	504	-1.37	-0.377
11	O	CH ₃ O	H	H	C ₂ H ₅	498	-1.31	-0.540
12	S	F	H	H	C ₂ H ₅	562	-0.94	-0.491
13	S	H	H	H	C ₃ H ₇	558	-1.04	-0.460
14	S	CH ₃	H	H	C ₂ H ₅	564	-0.99	-0.449
15	S	H	CH ₃	CH ₃	C ₂ H ₅	542	-1.44	-0.440
16	S	H	H	H	C ₂ H ₅	572	-1.10	-0.376
17	S	CH ₃ O	H	C ₂ H ₅	CH ₂ CH ₂ OH	564	-1.026	-0.366
18	S	H	C ₂ H ₅	H	C ₂ H ₅	572	-1.014	-0.408
19	S	NO ₂	H	H	C ₂ H ₅	556	-1.086	-0.405

^a measured in 0.5 M tetrabutylammonium perchlorate in dry CH₃CN, ^b calculated using Rehm–Weller equation.

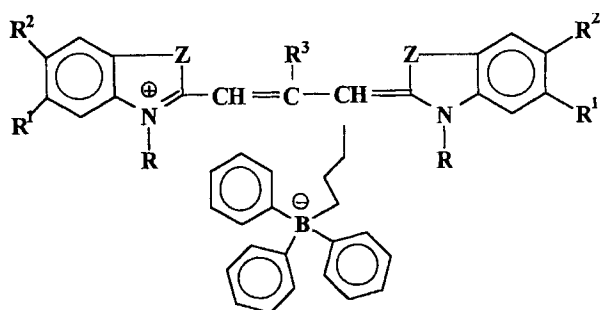


Figure 5. General formula of the cyanine borates tested by Kabatc et al. [35]. For Z, R¹, R², and R³ see Table 2.

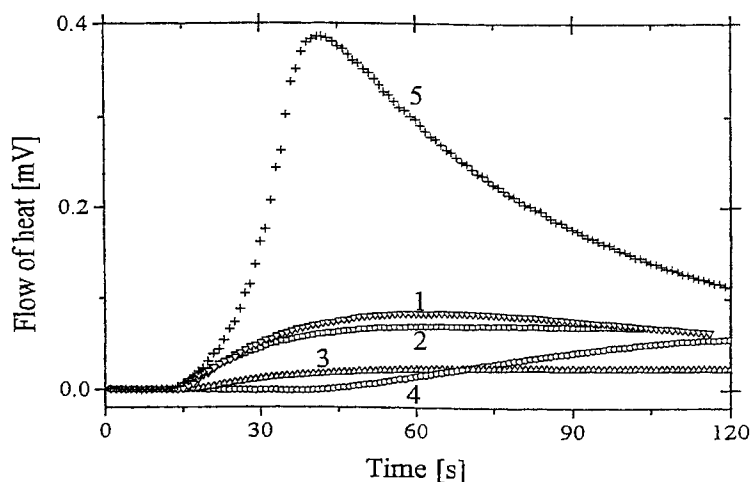


Figure 6. Rate of heat evolution during argon-ion laser-photoinitiated polymerization of 1-methyl-2-pyrrolidinone (MP), 9 ML of 2-ethyl-2-(hydroxymethyl)-1,3-propanediol triacrylate (TMPTA), and the dyes at a concentration of 10^{-3} M. Initiators: 1) **19**, 2) **18**, 3) **10**, 4) **16**, 5) RBAX (rose bengal derivative; prepared from rose bengal, which is first decarboxylated and then acetylated [36]).

Section 4.4) on the photoinitiation process, one can anticipate that under certain conditions (identical free radicals formed), the rules regulating the primary processes can also be applied for the secondary processes. The results presented in Figure 8 confirm this expectation. It is clear from the data (Figure 8) that the rate of polymerization as initiated by the series of cyanine borates in Table 2 increases as the driving force of the electron transfer increases. This behavior is predicted by the classical theory of photoinduced electron transfer.

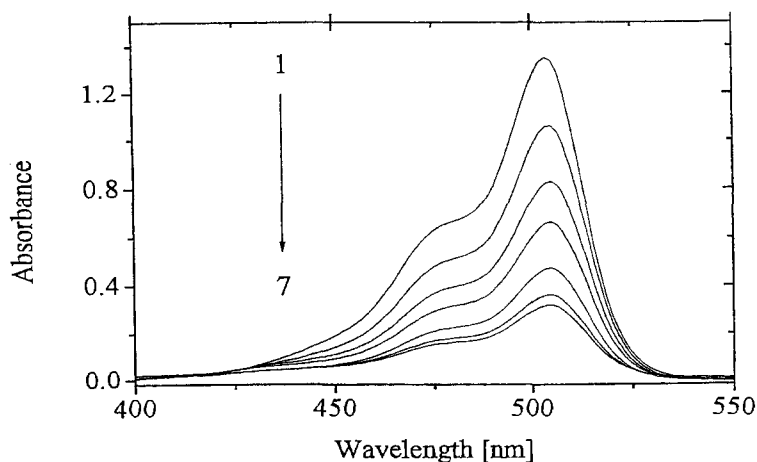


Figure 7. Changes in the electronic absorption spectra of **10** (Table 2) during argon-ion laser irradiation. $I_a = 20$ mW in EtAC solution ($v = 4.0$ ML, $C = 1 \times 10^{-5}$ M, time of irradiation [s]: 1) 0.0, 2) 20.0, 3) 40, 4) 60, 5) 80, 6) 150, 7) 180 (adapted from [35]).

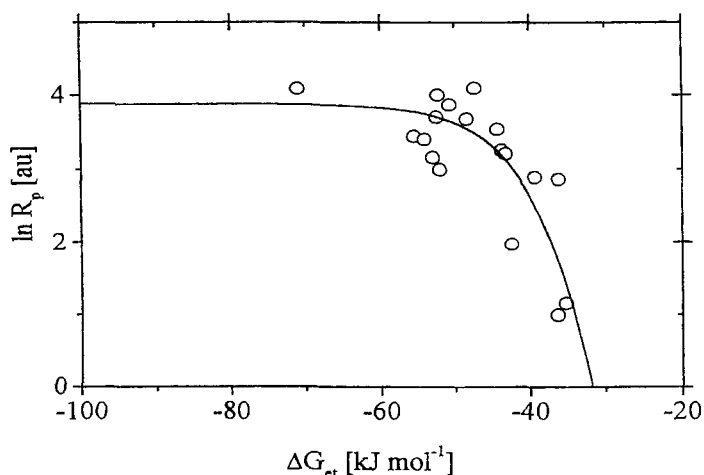


Figure 8. Dependence of the rate of photoinitiated polymerization on the free energy for photo-induced electron transfer from borate to the excited state of cyanine dyes, listed in Table 2.

Schuster's original measurements were performed in benzene, where the cyanine borates are known to exist as tight ion pairs. In practice, the monomers used in most photopolymerization systems possess higher dielectric constants than benzene. Therefore the degree of dissociation of the cyanine borate in monomer or mixtures of monomers is expected to be higher than it is in benzene. As an example, the data

Table 3. Degree of dissociation and ion pair stabilization energy for cyanine hexafluorophosphate in solvents of various dielectric constants.

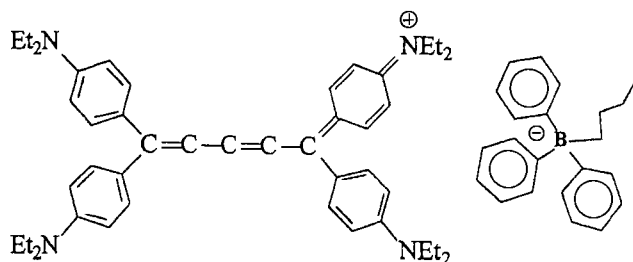
Solvent	Dielectric constant, ϵ	Degree of dissociation [%]		Ion pair stabilization energy [kJ/mol]
		1×10^{-3} M cyanine dye	0.1 M cyanine dye	
CH ₃ CN	36	32	1.22	4.82
CH ₂ Cl ₂	9.0	3.4	0.039	25.1
THF	7.6	0.73	0.013	30.9
CH ₃ COOC ₂ H ₅	6.0	0.016	0.0018	37.6
C ₆ H ₅ Cl	5.6	0.0094	0.0017	40.5
CHCl ₃	4.8	0.0044	0.00082	44.4
C ₆ H ₆	2.3	$\approx 3 \times 10^{-7}$	$\approx 5 \times 10^{-8}$	92.6
Dioxane	2.1	$\approx 0.7 \times 10^{-7}$	$\approx 1.3 \times 10^{-8}$	96.5

^acalculated from the data presented in [25].

measured and calculated for cyanine hexafluorophosphate in solvents of various polarities are presented in Table 3. These data clearly show that for monomers such as methacrylates or acrylates that have dielectric constants similar to those for ethyl acetate, at concentrations used in practice (from 10^{-3} M for thick layer technology, to 0.1 M for thin layer technology), the degree of dye dissociation is quite low. Thus the cyanine dyes exist under such circumstances exclusively as ion pairs. They are organized in a molecular array that *accelerates* the rate of the photochemical primary process. Therefore, the cyanine–borate ion pair is literally a *supramolecular* photoinitiating system.

Numerous classes of cationic dyes, many of which were cyanines, have been prepared for photographic applications. Therefore a complete spectrum of such dyes is available to be considered for such purposes.

Since the initial report, photoinitiators containing other cationic dyes have appeared. These include indolenine dyes [38, 39], azulene dyes [40], pyrylium dyes, and

**Figure 9.** A cyanine borate absorbing in the infrared region [37].

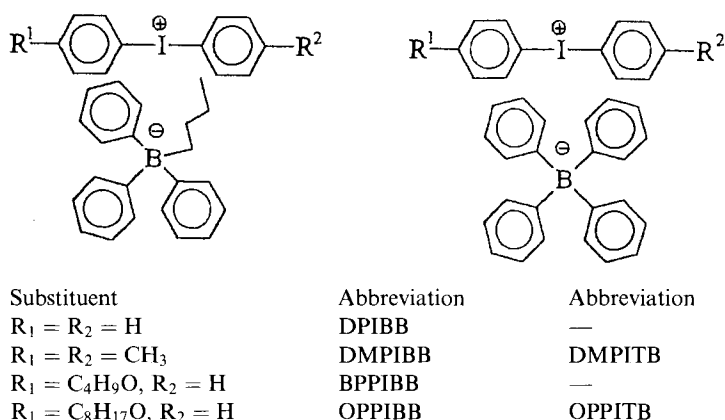


Figure 10. Iodonium borate salts used as photoinitiators.

thiopyrylium dyes [41]. Research in this area is continuing, with additional patents and papers published often.

Onium borate salts

Positive ion onium salts such as diaryliodonium [42–46], triarylsulfonium [44–48], and dialkylphenacysulfonium [48] are typical electron-accepting initiators. Each can be reduced by an electron-donating light absorber such as a xanthene dye [50–52]. The photochemical reaction occurring between onium salts and light-absorbing dyes is a pure electron transfer process. Photoinitiating systems containing an onium cation and a borate anion have recently been described [53, 54] (Figure 10). The compounds were described first by DeRaaff et al. [53a] and later by Feng et al. [54], as isolable onium borate complexes with their own unique spectral characteristics. These compounds can be used to initiate the polymerization of a standard acrylate resin (Figure 11), and the decomposition can be sensitized with visible-light-absorbing sensitizers such as 2,4-diiodo-6-butoxy-3-fluorone, DIBF [53a,b].

The absorption spectra of the iodonium borates depend on the solvent [53, 54]. In acetonitrile, the absorption spectra are equal to the additive spectra obtained from the components (up to 300 nm) [55, 56]. In less polar solvents onium borates exhibit a weak, extended absorption tail in the 320–450 nm region that is attributed to an intra-ion-pair ground-state charge transfer transition from the borate anion to the iodonium cation. Photopolymerization using the iodonium borates can be effectively initiated only by UV irradiation and by violet light of the visible region.

Diaryliodonium salts [53c, 57–59] form iodobenzene, biphenyl, benzene, iodobiphenyl, and several other products during irradiation. The photolysis of butyltriphenylborate salts in the presence of electron acceptors generates biphenyl and the butyl radical [24, 54a, 60, 61], while the photolysis of the analogous tetraphenylborates also produces biphenyl as the major product.

Iodonium borates exist as tight ion pairs, so in nonpolar solvents or in solvents of moderate polarity photoinduced electron transfer should occur directly from anion

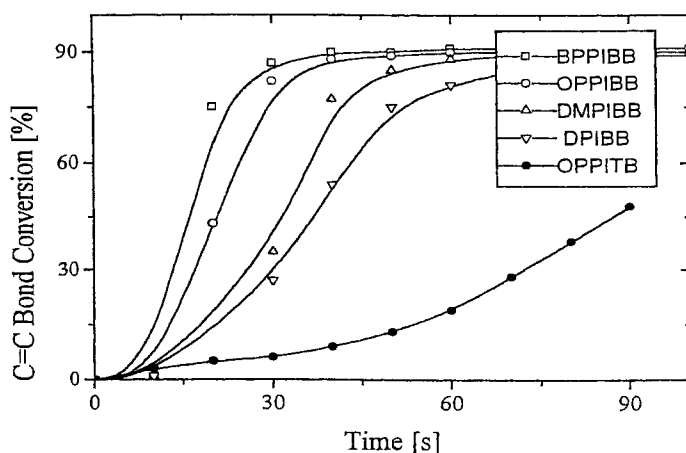


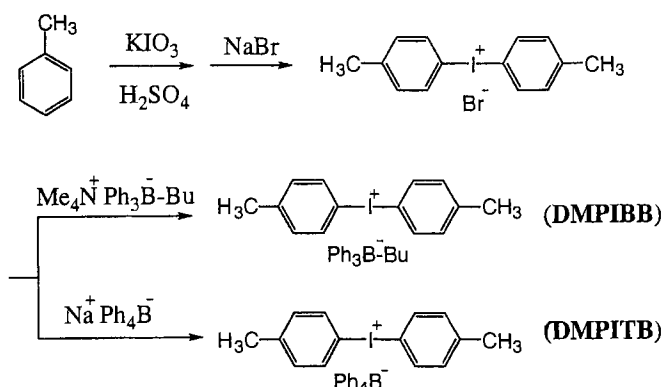
Figure 11. Photopolymerization of SLG-1 resin (70 % Ebecryl 8800-20R, 20 % tripropyleneglycol diacrylate, 10 % ethoxyethoxyethyl acrylate) irradiated by UV light (2×400 W medium-pressure Hg lamp). The photoinitiators used (see key) are listed in Figure 10.

to cation within the solvent cage. Photolysis carried out after purging with oxygen shows that decomposition is slower than that of an identical system purged with argon. Analysis of the products indicates that aryl iodide and biphenyl are the major products. Thus iodonium butyltriphenylborate salts simultaneously produce a butyl radical from the borate anion and an aryl radical from the iodonium cation. Iodonium tetraphenylborate was found to produce an aryl radical, but this radical arose only from the iodonium cation. Both radicals initiate polymerization of acrylic monomers (see below).

Sensitized photoinitiators

The first report of a charge transfer complex photoinitiating system involving onium borates was by De Raaff et al. [53a]. These workers showed the structure of the proposed charge transfer complex between a diphenyliodonium salt and a borate, indicated that a patent application had been filed [53b], and suggested that the iodonium salt–borate anion complex system would serve as a photoinitiator in the UV region of the spectrum. The UV spectrum of the complex was shown in Figure 10 of Ref. [53a]. Since the addition of iodonium salts to to-be-polymerized mixtures containing visible initiators such as DIBF and an ammonium borate greatly accelerated the rate of polymerization, a major emphasis in the work was on visible-light sensitization of the decomposition of various borate salts, including triphenylbutylborate and others, that were more soluble in monomer. Stable onium-borate complexes were readily isolated and subsequent papers by Sarker et al. [54b] and Feng et al. [54a] provided details of their use in reactions with acrylates.

The method of iodonium salt synthesis using iodonium bromide was similar to that published by Crivello and co-workers [57–59]. Symmetrical iodonium salts

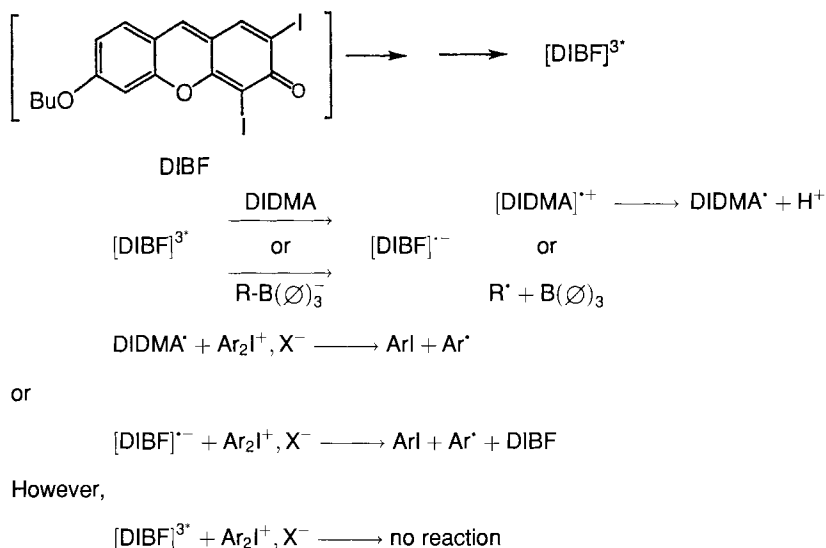


Scheme 3. Syntheses of DMPIBB and DMPITB.

such as di-(*p*-methylphenyl)iodonium bromide were prepared from the reaction of toluene with potassium iodate and sulfuric acid, and followed by the addition of a solution of sodium bromide. Asymmetric iodonium bromides were prepared by direct coupling of an aromatic compound with iodobenzene diacetate in the presence of sulfuric acid, followed by mixing with a solution of sodium bromide. The iodonium bromide obtained was treated with tetramethylammonium butyltriphenylborate or sodium tetraphenylborate to produce isolable iodonium butyltriphenylborate salts or iodonium tetraphenylborate salts in high yield. The syntheses of *p,p'*-dimethylphenyliodonium triphenylborate (DMPIBB) and *p,p'*-dimethylphenyliodonium tetraphenylborate (DMPITB) are shown in Scheme 3.

The importance of this work cannot be overestimated. It led to subsequent studies of the addition of the radicals formed from these compounds to acrylates, and subsequent isolation of a number of such products. Sensitized reactions of borates using DIBF (2,4-diiodo-6-butoxy-3-fluorone) in the absence of, and presence of, iodonium salts were also part of this investigation. The rate coefficients for triplet quenching both by tertiary aromatic amines such as diisopropylidimethylaniline (DIDMA) had been measured previously by Hassoon [54c], as had the rate constants of triplet quenching by borate, by oxygen, and by iodonium salts. The deductions from this work were that DIBF triplet was quenched most rapidly by oxygen, that the rate of quenching by DIDMA and several different borates was almost identical, and that iodonium salt quenching of the triplet of DIBF did not occur. The conclusion was that in the presence of iodonium salt, DIBF triplet reduction was followed by a ground-state oxidation reaction involving the iodonium salt. In this process the radical formed following reduction either from the amine or from the borate was, depending on its lifetime, oxidized. In the absence of such a secondary reaction, the DIBF radical anion furnished the reducing electron. Both reactions caused reductive decomposition of the iodonium salt with chain reactions following that were initiated by the thereby formed phenyl radical. This is shown in Scheme 4.

Stable iodonium borate complexes show minor, but real, absorptions that differ from the sum of absorptions of compounds containing the individual ions when the



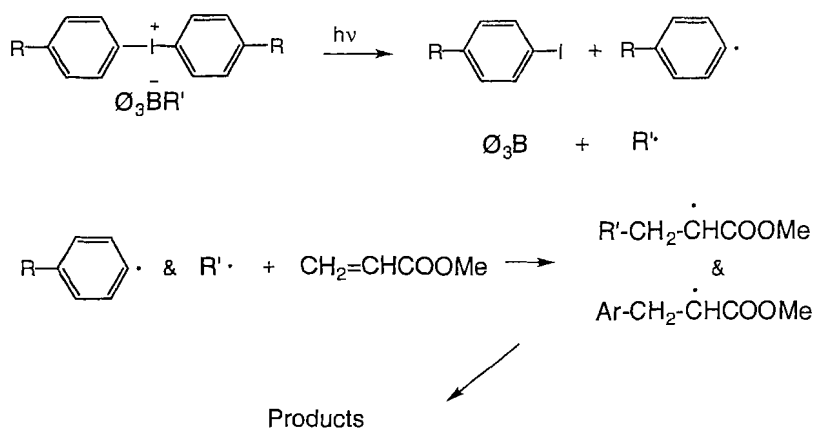
Scheme 4.

spectra are taken separately in identical solvents. The absorptions are red-shifted relative to the components, thus allowing for excited-state access using light in the near-ultraviolet region of the spectrum.

Feng isolated photoproducts from the reactions of several of the isolated iodonium borate salts when irradiated in the presence of simple acrylates. The conclusion was that aryl radicals in iodonium borates, regardless of whether or not there are aryl groups in the borate, owe their formation to the iodonium salt. To prove this point the classical physical organic method, study of a mixed system, was used. This work is important in that it confirms that products such as biphenyl find their origin only in the borate (Scheme 5). These products do not arise from free phenyl radicals such as might be formed from such borates.

Subsequently to the work on DIBF above, two other aromatic ketones, 2-chlorothioxanthone (CTX) and Michler's ketone (MK) were studied as photosensitizers for the decomposition of onium borates [55, 56]. Each absorbs light at 365 nm and their photochemistry and photophysics are well known. The time dependence of the photopolymerization of tetrahydrofurfuryl acrylate (THFA) in MeCN solution in the presence of CTX with selected onium borates (Figure 12) is shown in Figure 13. The rate of polymerization is dependent on the solvent with the fastest polymerizations observed when the onium borates are used in solvents where they form tight ion pairs. Thus higher rates are observed in the less polar CH_2Cl_2 . It is obvious that the rate of photopolymerization without sensitizer is much slower (two orders of magnitude) than that observed for sensitized photoinitiated polymerization.

As in the case of DIBF, both CTX and MK are triplet sensitizers. However, CTX appears to undergo triplet oxidation, in that a new band attributed to the



Scheme 5. Photoreaction of iodonium borate in the presence of methyl acrylate. There are no products formed via a phenyl radical (\bigcirc) path. The biphenyl that forms occurs via an intramolecular reaction and originates in the borate.

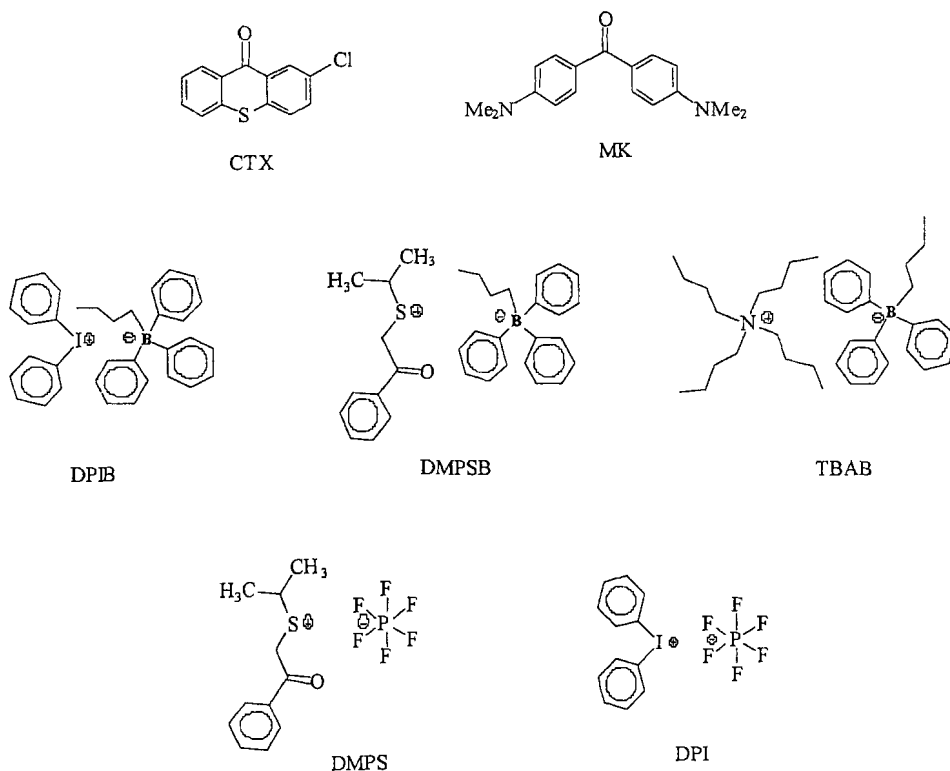


Figure 12. Onium borates used in sensitized photopolymerization of THFA (Figure 13).

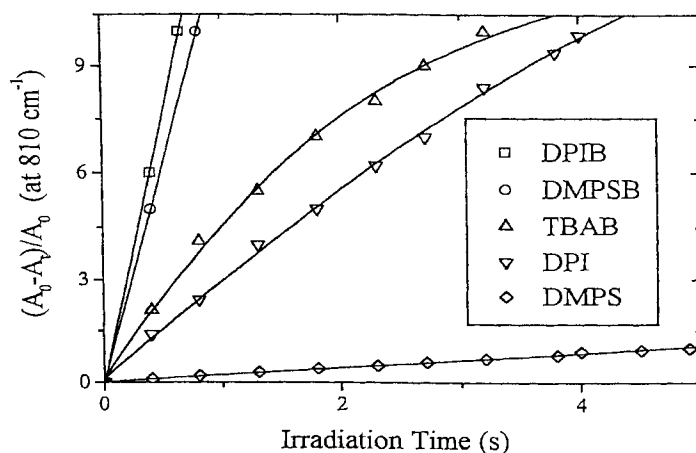


Figure 13. Influence of type of ion pair (1.4×10^{-3} M) on the CTX (5.8×10^{-3} M)-sensitized photopolymerization of THFA (9.2×10^{-1} M) in MeCN solution. Rate of polymerization measured using IR spectroscopy. The light intensity (365 nm) was 1.6 mW cm^{-2} . Data from Ref. [55]

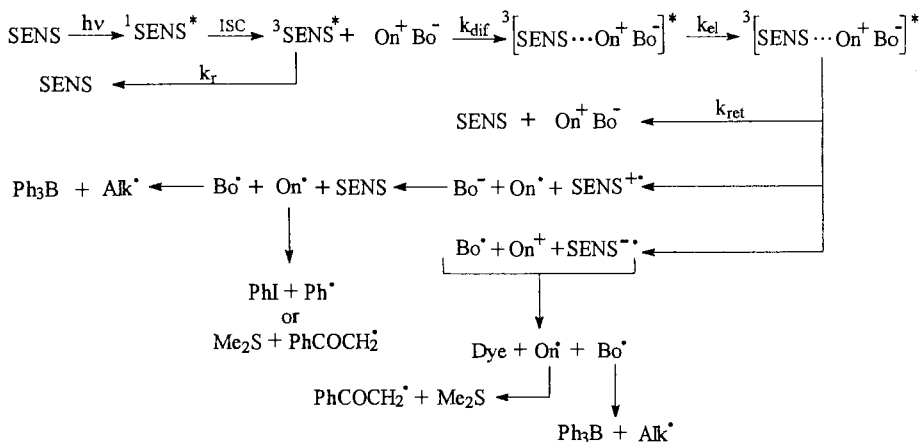
cation radical at 420 nm appears at the sacrifice of the triplet. CTX also is not bleached. The absorption spectra of CTX in an argon-saturated solution containing DPIB or DMPSB show no change with irradiation whereas solutions containing DPI or TBAB bleach. Iodobenzene and biphenyl were detected in the irradiated solution of CTX–DPIB. In the case of CTX–DMPSB, dimethyl sulfide was detected instead of iodobenzene. In the laser flash photolysis of a CTX solution containing TBAB, a new, very weak, transient absorption band at 700 nm, attributed to the presence of the CTX anion radical, was observed.

In contrast to the situation with DIBF, the free energy changes (ΔG_{et}) for the photoinduced electron transfer reactions (see Table 4) calculated using the Rehm–Weller equation [33, 34] suggest that CTX and MK may serve also as electron acceptors. It is expected that in the case of DPIB and DMPSB, a photoinduced

Table 4. Free energy of activation (ΔG_{et}) for electron transfer reactions between triplet sensitizers (CTX and MK) and anions and cations tested.

	Sensitizer	
	CTX	MK
E^{T} [kJ mol^{-1}]	252	260
E_{ox} [V vs. SCE $^{-1}$]	1.52	0.87
E_{red} [V vs. SCE $^{-1}$]	−1.62	−2.48
$\Delta G^{\text{T}} (^3\text{Sens} \rightarrow \text{DPI}^+)$ [kJ mol^{-1}]	−43.4	114
$\Delta G^{\text{T}} (^3\text{Sens} \rightarrow \text{DMPS}^+)$ [kJ mol^{-1}]	−7.7	−78
$\Delta G^{\text{T}} (\text{Bo}^- \rightarrow ^3\text{Sens})$ [kJ mol^{-1}] ^a	−14.5	61

^a Bo^- , borate anion.



Scheme 6.

electron transfer reaction occurs between the sensitizer and either the onium cation or the borate anion of the salts.

The mechanism shown in Scheme 6 is proposed. The posulate in the case of the CTX–DPIB system is that the CTX radical cation is formed by electron transfer from the CTX triplet state to the diphenyliodonium salt, and then CTX^{•+} immediately reduces the butyltriphenylborate anion of DPIB, re-forming CTX. These processes are presumed to form the diphenyliodonium and butyltriphenylboranyl radicals, both of which are unstable. As shown by Feng's work [54a], the iodonium salt is the source of the aryl radicals, while the alkyl radical derives from the borate. CTX is recovered virtually unchanged after this process. The reaction pathway can be predicted from the values of the free energy change ΔG_{et} of radical cation formation, which is more negative ($\Delta G_{\text{et}} = -43.4 \text{ kJ mol}^{-1}$) than that calculated for the formation of the radical anion ($\Delta G_{\text{et}} = -14.5 \text{ kJ mol}^{-1}$). The opposite situation pertains in the case of CTX–DMPSB. The free energy change for the formation of the radical cation is -7.7 kJ mol^{-1} , while ΔG_{et} for CTX radical anion formation is more negative ($\Delta G_{\text{et}} = -14.5 \text{ kJ mol}^{-1}$). This result suggests that in the case of the CTX–DMPSB system, CTX^{•-} is formed by electron transfer from the butyltriphenylborate anion of DMPSB to the triplet of CTX, and CTX^{•-} is immediately oxidized by the dimethylphenacylsulfonium cation, re-forming CTX. In the case of the MK–onium borate system, a process similar to that observed with CTX–DPIB results. The above systems are effective photoinitiators because during the process one electron generates two active radicals, and because there is no consumption of the primary absorber.

Supramolecular photoinitiators of the chromophore–linker–electron donor type

Cyanine borates belong to a specific group of photoinitiating systems. Both components exist as ions, so in nonpolar solvents they exist predominantly as ion pairs. After electron transfer the [Cy[•]] [R[•]] pair of radicals diffuses from the initial solvent cage giving free radicals because it is no longer solvent-stabilized. We have shown

[61] that when one irradiates a mixture of tetramethylammonium phenyltriethylborate (TPTB) in the presence of benzophenone, one-electron oxidation of TPTB by the excited state of benzophenone leads to the formation of an alkyl radical and that such alkyl radicals, when formed, add to alkenes. In view of our previous interest in intramolecular energy transfer from benzophenone triplets within an easily dissociated perester [62–64], we studied the photochemistry of benzophenone and other chromophores, covalently linked with tertiary ammonium or triphenyl-*n*-butylgallate salts, where complexation of an electron donor occurs in close proximity to the electron-accepting chromophore. Such a supramolecular structure might permit intra-ion-pair electron transfer and this would produce a butyl radical from the borate counterion. This would efficiently initiate the free-radical polymerization [30, 31, 65–69] (see Figure 14 and Table 5).

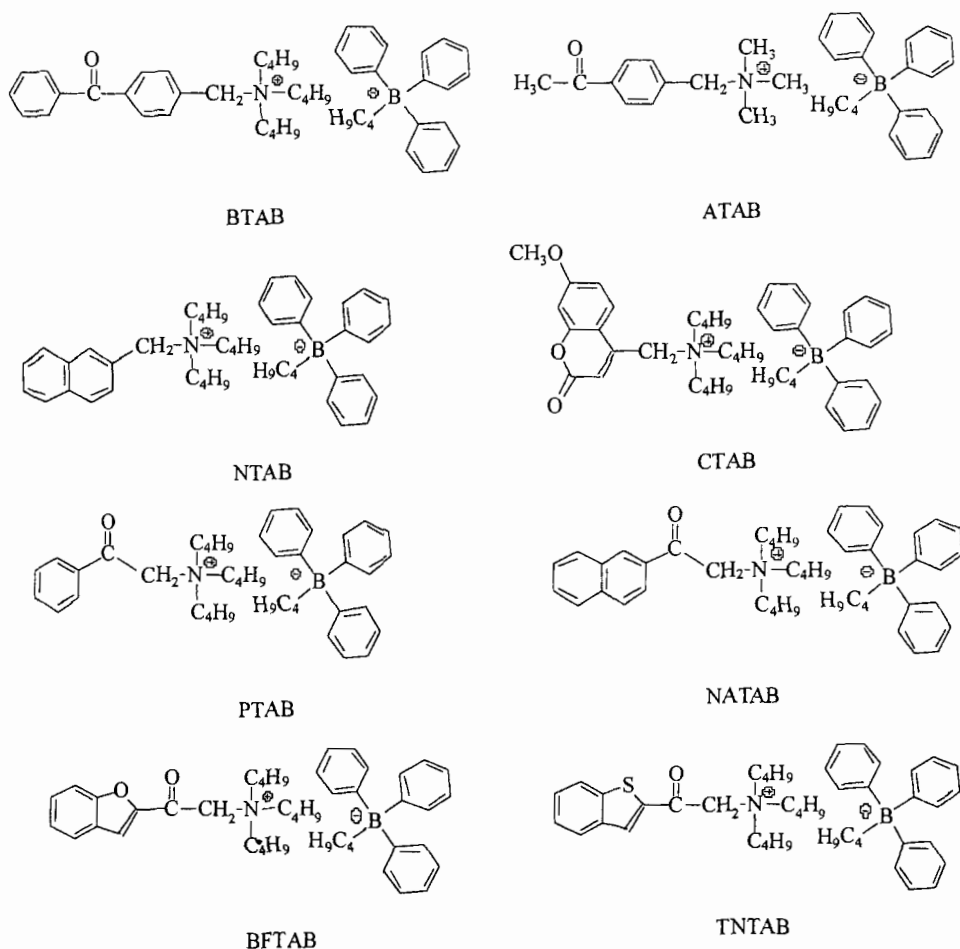


Figure 14. Chromophore-linker-electron donor systems used as initiators of free-radical polymerization. For all the compounds shown, tetraphenylborate salts were also prepared and tested.

Table 5. Reduction potentials (E_{red}), excited triplet (singlet for NTAB and CTAB) energies, free energy changes (ΔG_{et}) and quenching rate constants (k_{q} , measured for *n*-butyltriphenylborate anion) of the light absorbing molecules used as initiators of free-radical polymerization.

	BTAB	ATAB	NTAB	CTAB	PTAB	NATAB	BFTAB	TNTAB
E_{red} [V vs SCE]	−1.49	−1.62	−2.10	−1.30	−1.62	−1.27	−1.32	−1.15
$E_{\text{T,S}}$ [kJ mol ^{−1}]	290 ^a	305 ^b	374 ^c	350 ^d	304	245	243	225
k_{q} [M ^{−1} s ^{−1}]	—	—	—	—	—	1.28×10^8	1.23×10^9	2.53×10^9
ΔG_{et} [kJ mol ^{−1}]	−79	−81	−104	−157	−81	−55	−49	−46

^a Ref. [70], ^b Ref. [71], ^c Ref. [72], ^d Ref. [73].

A detailed study was carried out on (benzophenonylmethyl)-tri-*n*-butylammonium triphenylbutylborate (BTAB). Nano- and picosecond laser photolysis demonstrated electron transfer from the borate counteranion to the excited triplet state of the benzophenone moiety. This leads to formation of a benzophenone moiety and a boranyl radical that dissociates rapidly to form butyl radicals. In the nonpolar solvent benzene the short lifetime of the triplet state (300 ps) suggests an intra-ion-pair process. The addition of 1 % MeCN caused an increase in the triplet lifetime to 1.2 ns, suggesting formation of a solvent-separated ion pair. For a 10^{-3} M solution in neat MeCN triplet decay is a function of tetrabutylammonium triphenyl-*n*-butylborate concentration.

The results clearly indicate that quenching of benzophenone triplets in polar solvents is a bimolecular process. This means that the ions exist mostly as separated ions and that the electron transfer process occurs mainly as an inter-ion-pair reaction [66, 67]. Analysis of the products after irradiation of *N*-(*p*-benzoylbenzyl)-*N,N,N*-tri-*n*-butylammonium triphenyl-*n*-butylborate (BTAB, Figure 14) indicates formation of *p,p'*-(benzoyl)dibenzyl, *p*-pentylbenzophenone and tributylamine. This indicates that electron transfer from the borate anion to the acceptor excited state leads to homolytic C–N bond scission and formation of the tertiary amine.

More recently, several other benzophenonyl and naphthyl ammonium triphenylbutyl- and tetraphenylborate salts differing only in the structure of the ammonium moiety have been tested as photoinitiators (Figure 15).

This kinetic study has shown that the borate must produce an α -aminoalkyl radical in order to be an effective initiator. All tetraphenylborates forming such radicals resemble, in efficiency, triphenylbutylborates of similar structure. Triphenylbutylborates not capable of producing α -amino radicals are inefficient radical initiators.

A representative mechanism proposed for processes occurring via either singlet or triplet states for the *n*-butyltriphenylborate compounds and involving inter- and intra-ion-pairs is given in Scheme 7.

A pre-organized donor–acceptor system is possible if one prepares a polymeric system bearing a benzophenone borate salt (Figure 16) [75]. In comparison with the low molecular weight compound at lower concentrations of the requisite benzophenone moiety, the highest activity was observed for the model compound. At

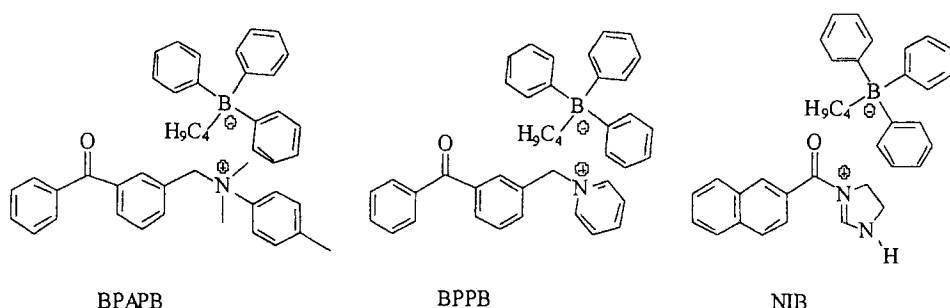
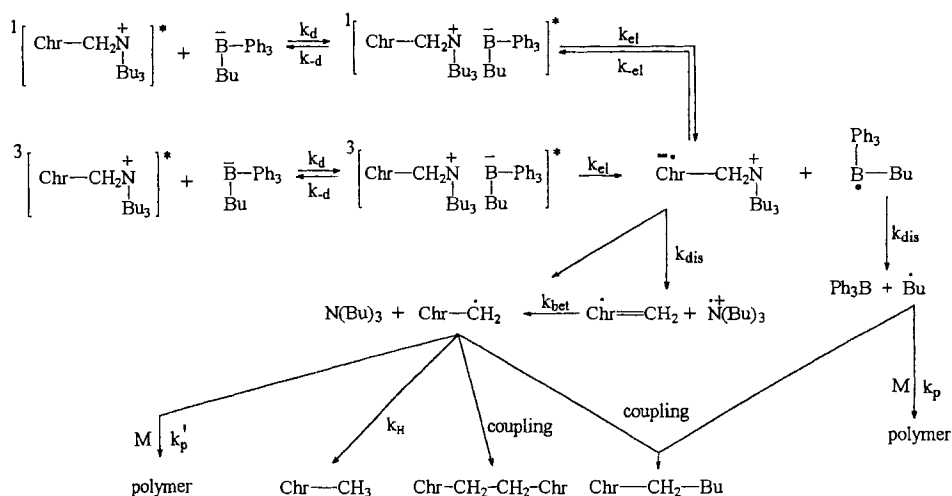


Figure 15. Chromophores that have been tested as photoinitiators. For all those shown, tetraphenylborate (denoted BPAPBa, BPPBa, and NIBa respectively) and bromide (denoted BPAPBb, BPPBb, and NIBb respectively) salts were also prepared and tested.



Scheme 7.

higher concentrations the homopolymer bearing the benzophenone borate salt gave superior performance. Polymeric systems are exceptionally stable compared with conventional, small-molecule photoinitiators. When crystalline, such polymers are insensitive to air and moisture.

4.3.2 Photoinitiating Donor–Acceptor Pair without Electrostatic Interaction in Ground State and after an Electron Transfer

We next discuss photoinitiating systems that contain a photo-redox pair but which consist of one neutral (dye) and a second charged (electron donor) component. After electron transfer a charged and a second neutral product are formed. There is

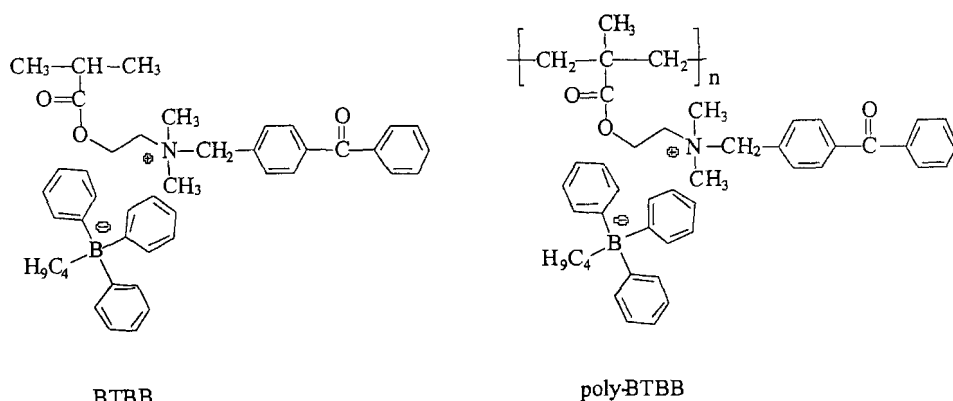


Figure 16. BTBB monomer and polymer.

no electrostatic interaction between the donor–acceptor pair in the ground state and no electrostatic interaction between the primary products formed after the electron transfer process.

In the initial description of the cationic dye–borate system [24, 76], it was postulated that electron transfer was possible because, in nonpolar solvents, dye/borate salts exist predominantly as ion pairs. Since the lifetime of the cyanine singlet excited state is quite short [24, 25], this prerequisite is crucial for effective photo-induced electron transfer. Recently initiator systems in which neutral dyes are paired with triarylalkylborate anions have appeared in the literature [77]. In the latter case, the borate ion acts as the electron donor while neutral merocyanine, coumarin, xanthene, and thioxanthene dyes act as the electron acceptors. It is obvious that these initiating systems are not organized for effective electron transfer processes. The formation of an encounter complex (EC) between excited dye and electron donor is required.

The first such system employed a neutral electron acceptor RBAX (Figure 17) (a derivative of rose bengal, prepared first by decarboxylation, and then acetylation)

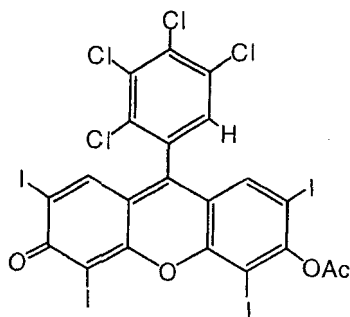


Figure 17. RBAX, $E_{\text{red}}(A^{\cdot-}/A) = -0.80$ V, $E_{0,0}^T = 164$ kJ mol⁻¹.

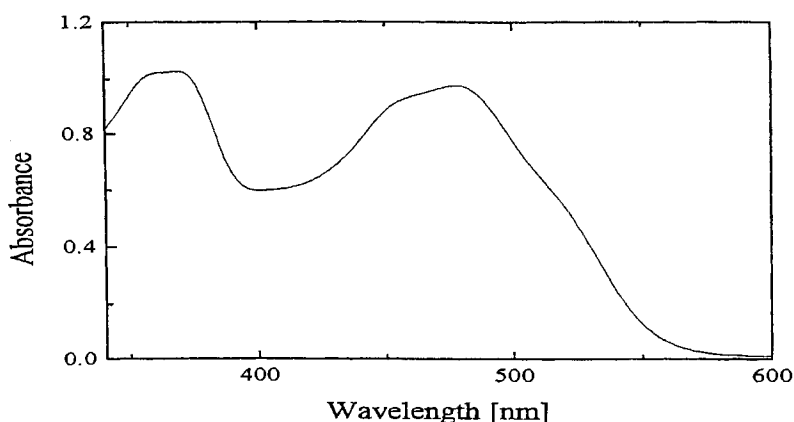


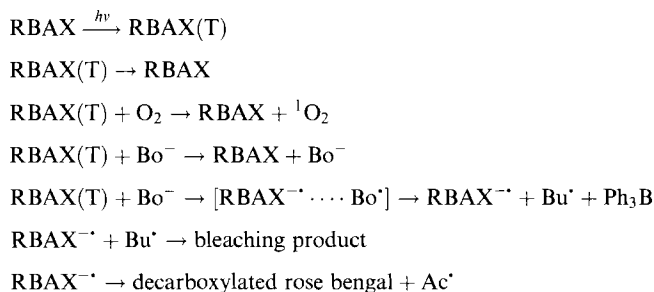
Figure 18. Electronic absorption spectra of RBAX (0.6×10^{-4} M) in CH_2Cl_2 .

and triphenyl-*n*-butylborate as the electron donor [36]. Irradiation of this system also led to the formation of a free alkyl radical, as evidenced by the system's ability to initiate the polymerization of acrylate monomers.

Figure 18 shows that the spectral shape and the molar absorptivity are similar to those for nonpolar derivatives of rose bengal [78, 79].

The photochemical reaction between RBAX and a butyltriphenylborate salt is similar to that of eosin with the same electron donor [80–82]. This dye produces three transients in the microsecond, or longer, time regime after absorbing a pulse of light. These are the radical cation that absorbs at 454 nm, the radical anion with λ_{max} at 405 nm, and the triplet which absorbs at 560 nm [36]. Irradiation of RBAX in the presence of butyltriphenylborate results in bleaching and the appearance of an absorption band, suggesting formation of the ionic form of rose bengal. Based on the known products of the bleaching of rose bengal under reductive conditions [83] and the fact that oxidation of the butyltriphenylborate ion generates the butyl radical, formation of the coupling products between RBAX and the butyl group is to be expected. A mechanism consistent with these observations and consistent with the similarity between eosin and RBAX is presented in Scheme 8.

The photophysics of this and similar systems was clarified using new dyes based on the 3-hydroxy-6-fluorone skeleton [84–89]. Figure 19 shows absorption spectra,



Scheme 8.

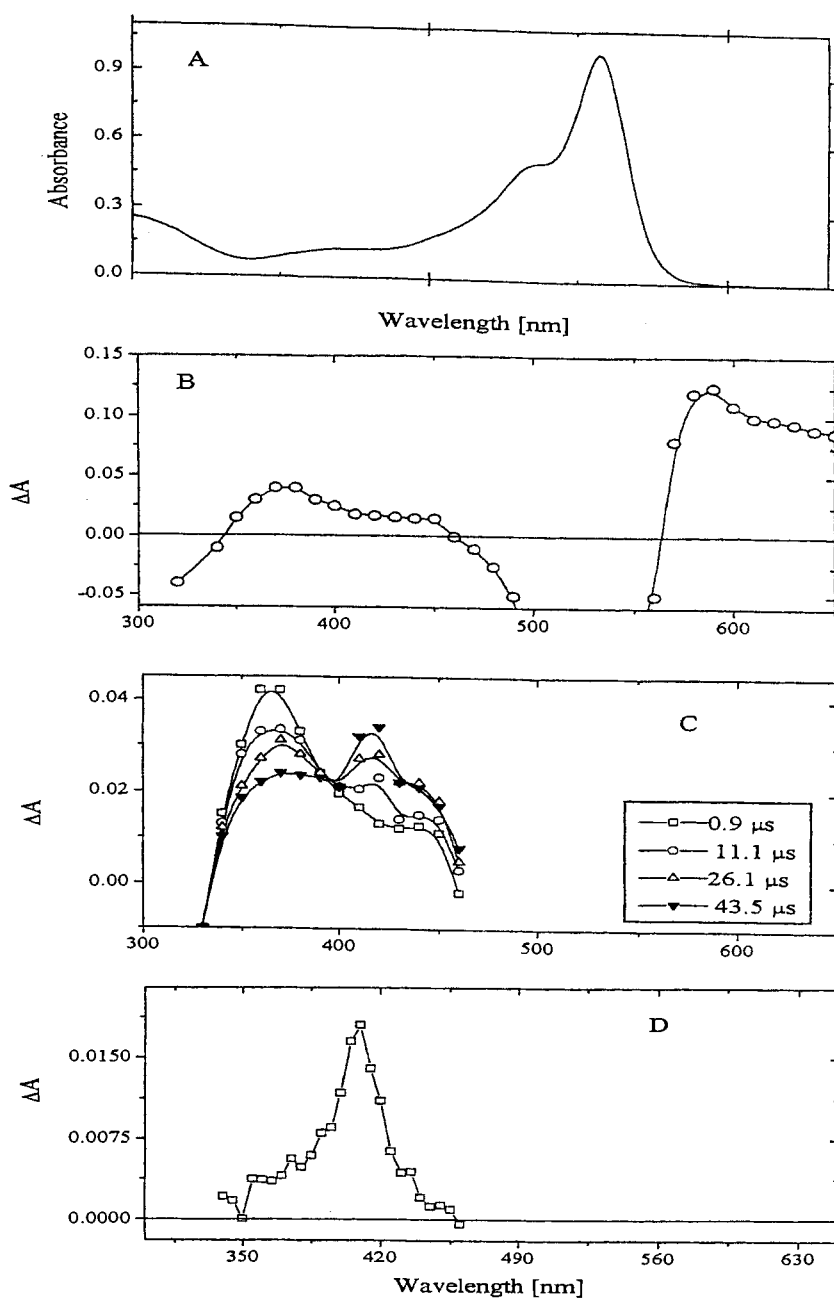
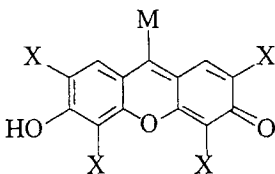


Figure 19. A) Electronic absorption spectra of THIF in MeOH, B) triplet-triplet transient absorption of THIF in EtOH taken 1 μ s after laser excitation, C) transient absorption spectra recorded from 10^{-5} M THIF in EtOH (delays are shown in the Key), D) absorption spectrum obtained from 10^{-5} M THIF in EtOH in the presence of 10^{-3} M triethanolamine. Recorded 12 μ s after laser excitation. Data from Ref. 86.

Table 6. Basic spectroscopic, photochemical, and photophysical properties of xanthene dyes based on the 3-hydroxy-6-fluorone skeleton.


	TBHF	TIHF	TBHCF	TIHCF
M	H	H	CN	CN
X	Br	I	Br	I
λ_{\max} (EtOH) [nm], (ϵ_{\max})	530 (39 300)	536 (91 200)	626 (51 400)	638 (80 000)
λ_{\max} (EtOH) [nm], (τ_{Fl} [ns])	539 (2.33)	548 (0.65)	638 (1.45)	654 (0.69)
λ_{ph} at 77 K (EtOH) [nm]	660	676	755	777
Φ_{fl}	0.52	0.13	0.20	0.02
Φ_{ph}	0.25	0.87	0.53	0.99
ϵ_{TT} [$\text{M}^{-1} \text{cm}^{-1}$]	2.4×10^3 (580 nm)	9.0×10^3 (580 nm)	4.4×10^3 (340 nm)	6.3×10^3 (340 nm)
ϵ_{R} [$\text{M}^{-1} \text{cm}^{-1}$]	1.22×10^4 (410 nm)	1.45×10^4 (410 nm)	9.65×10^3 (410 nm)	1.70×10^4 (410 nm)
k_{TT} [$\text{M}^{-1} \text{s}^{-1}$]	1.7×10^9	1.2×10^{10}	—	—
k_{sq} [$\text{M}^{-1} \text{s}^{-1}$]	3.7×10^8	1.4×10^9	2.0×10^8	1.0×10^9
E_{red} [V, vs. SCE]	−0.95	−0.28	−0.64	−0.46
ΔG_{et} [kJ mol $^{-1}$] ^a	−34.7	−27.0	−52.0	−44.4
k_{q} [$\text{M}^{-1} \text{s}^{-1}$] ^b	1.5×10^7	2.4×10^7	1.5×10^9	8.9×10^8

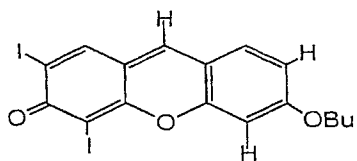
^acalculated for *N,N*-diethylaniline, ($E_{\text{ox}} = 0.7 \text{ V}$ [30]), ^bquencher *N,N*-diethylaniline.

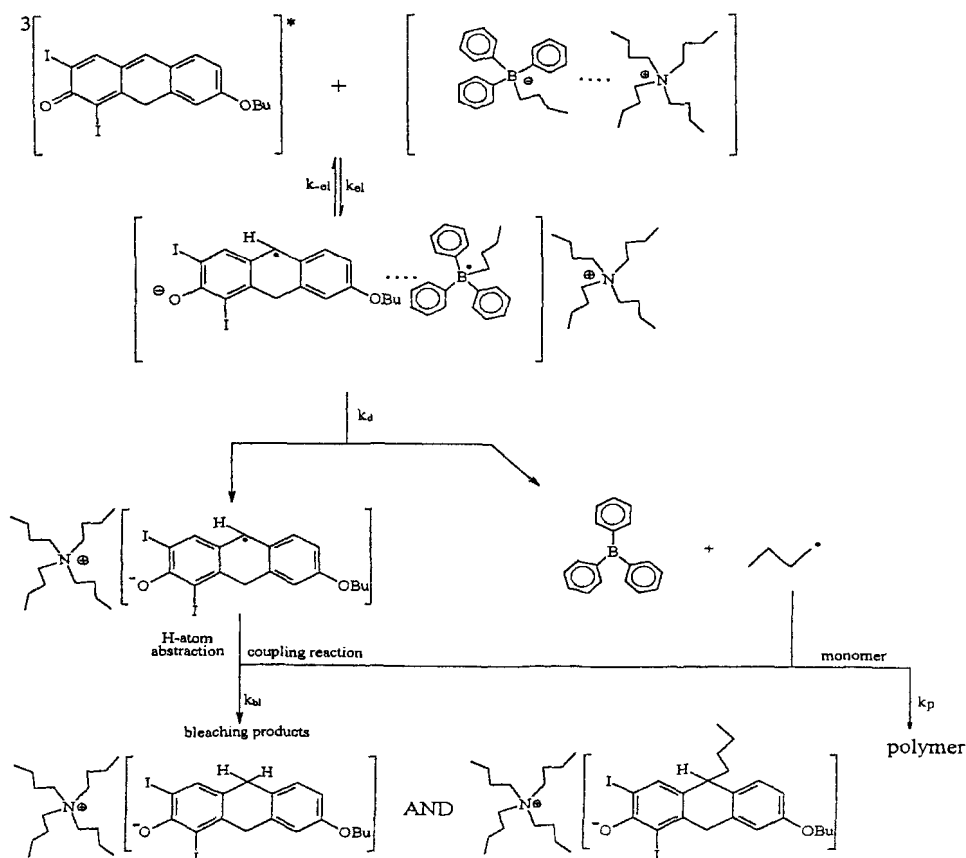
as well as the spectra of transients, recorded for tetraiododihydrofluorescein (TIHF).

On the basis of the laser flash photolysis, photophysical properties of this class of dyes were established. The data are summarized in Table 6.

A working mechanistic hypothesis for photoreduction of such dyes by borate salts is shown for the photoreduction of 2,4-diiodo-6-butoxy-3-fluorone (DIBF), shown in Figure 20 [88].

When tetrabutylammonium triphenylalkylborate was used as the electron donor, the dye radical anion ($\text{DIBF}^{\cdot-}$) was observed as the only transient formed by quenching the dye triplet. The electron transfer rate calculated for the electron transfer process is $7.6 \times 10^7 \text{ s}^{-1}$, i.e., three orders of magnitude below the diffusion-controlled limit. The photobleached products and the transient phenomena observed

**Figure 20.** DIBF, $E_{\text{red}}(\text{A}^{\cdot-}/\text{A}) = -0.90 \text{ V}$, $E_{0,0}^{\text{T}} = 222 \text{ kJ mol}^{-1}$.



Scheme 9.

(nanosecond laser flash photolysis) confirm that the photoreduction of DIBF in the presence of borate salt is a one-electron transfer process. A proposed mechanism is shown in Scheme 9.

The rate of photoinitiated polymerization depends on the borate anion that is used as the coinitiator [89]. For tetraorganoborates the radical anion is formed at the same rate as the triplet state of the DIBF decays. This indicates that electron transfer is the only quenching process of the triplet. Using the Rehm–Weller equation [33, 34] and knowing the oxidation potentials of borates, the reduction potential of DIBF ($E_{\text{red}} = -0.9 \text{ V}$) and knowing its triplet energy ($E_{\text{T}} = 2.3 \text{ eV}$, 222 kJ mol^{-1}), one can calculate the free energy change (ΔG_{et}) for this electron transfer process. Negative values of ΔG_{et} indicate that reaction is thermodynamically allowed and, on the basis of the theory of the electron transfer process [12–14], one can predict the tested system should fulfill the Marcus equation. This is shown in Figure 21 for a DIBF–tetraorganoborate system.

The same trend is observed for the rate of photoinitiated polymerization (Figure 22). This suggests that:

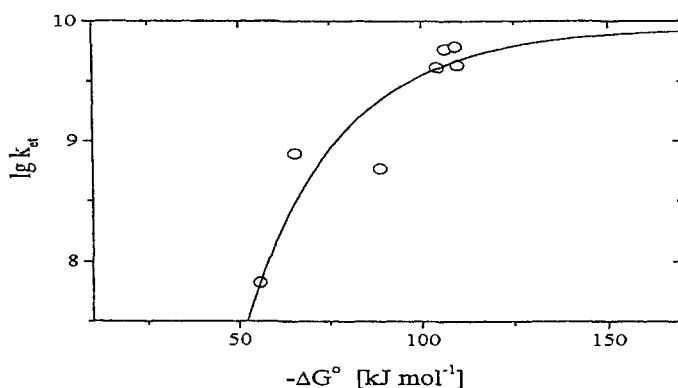


Figure 21. Dependence of rate constant for electron transfer on the free energy change for transfer of an electron from the borate anion to the triplet state of DIBF. Data for calculation of free energy change from Ref. [89].

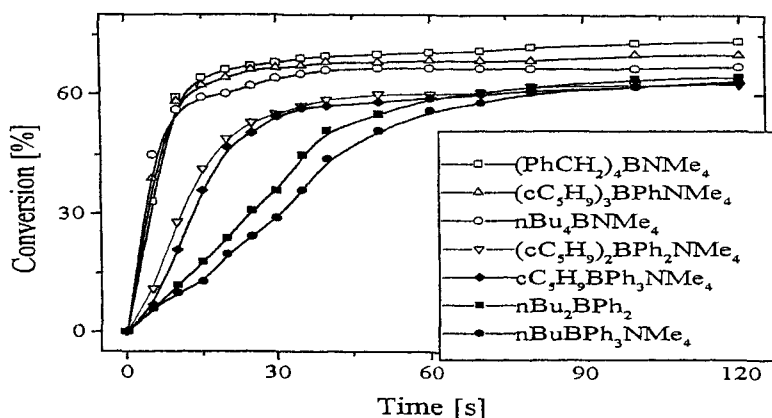


Figure 22. Visible-light polymerization of acrylic formulation with DBIF and tetramethylammonium tetraorganoborates as electron donors. Data from Ref. [89].

- 1) there is direct relationship between the rate of electron transfer and the rate of polymerization, e.g., the rate of the primary process is the limiting step of the photoinitiation reaction, or
- 2) the ease of oxidation of the borates is related to the stability and reactivity of the radicals formed.

A comparative analysis of the borate salts as electron donors with DIBF shows that the number of alkyl groups per boron atom determines reactivity. Dialkyldi-phenylborates initiate polymerization much more rapidly than do alkyltriarylborates and are more stable in formulations. Therefore dialkyldiarylborates are likely to be preferred over the slower, less stable alkyltriarylborates.

4.3.3 Photoinitiating Donor–Acceptor Pair Neutral in a Ground State and Charged after an Electron Transfer (Radical-ion Pair).

Each of the terms in Eq. (1) must be known in order to calculate the free energy change for a photoinitiated electron transfer process (Eq. (2)).

$$\Delta G_{\text{et}} = E_{\text{ox}} - E_{\text{red}} - E_{00} - (W_{\text{p}} - W_{\text{r}}) \quad (2)$$

E_{ox} and E_{red} are the oxidation and reduction potentials of the electron donor and acceptor, E_{00} is the energy of the excited state, W_{r} is the energy needed for bringing the reactants from infinity to the encounter distance, and W_{p} is a term associated with separating the products from the encounter to infinity [91–96].

One can find the energy needed for separating the products from encounter to infinity (W_{p}) by analyzing the equation describing the free energy change for a photoinduced electron transfer process. For a system that, after photoinduced electron transfer, forms one neutral component, this term can be set as $W_{\text{p}} \approx 0$. However, for a system that after electron transfer forms two radical ions, the term $W_{\text{p}} \neq 0$. The value of W_{p} varies with the polarity of the solvent in which the photoinduced electron transfer process is carried out. In polar solvents, one can set $W_{\text{p}} \approx 0$, and under this condition radical ions formed separated radical ions easily. For nonpolar solvents such as benzene this term can reach up to 90 kJ mol^{-1} [25]. Such a high energy will force the radical ions to remain in the solvent cage, in which different reactions may occur, than those observed for separated radical ions. This may have a critical influence on the route of processes following electron transfer.

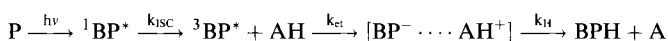
Electron–proton transfer systems

Amines

Benzophenone–amine systems

In 1972 Sandner et al. [97] observed that the addition of a small amount of triethylamine (0.02 M) greatly increased the rate of photoinduced polymerization of methyl acrylate in *t*-butanol in the presence of benzophenone (BP). This photopolymerization was not affected by triethylamine alone, nor by BP–triphenylamine, BP–isopropanol, or BP–benzhydrol. The quantum yield of benzophenone disappearance suggests that the triplet state of BP was *quenched* by methyl acrylate. Though monomer quenching decreases the efficiency of hydrogen atom abstraction from *t*-butanol or benzhydrol, it has only a marginal effect on the efficiency of interaction between excited benzophenone and triethylamine, suggesting that something other than direct hydrogen atom abstraction from amine was involved. Mechanistic studies on the process resulted from a fundamental contribution by Cohen et al. [98] (Scheme 10).

The primary intermediates formed from the benzophenone triplet state in the presence of tertiary amines such as dimethylaniline have been observed by picosecond transient absorption spectroscopy [99]. The initial step of the process involves one-electron transfer from amine (dimethylaniline, DMA) to the triplet state



Scheme 10.

of benzophenone. The process initially generates a solvent-separated ion-radical pair (SSIRP, transient at 715 nm) consisting of the BP radical ion and the DMA radical cation. The SSIRP collapses to the contact ion-radical pair (CIRP, transient at 690 nm), during a period of 200 ps. This is manifested by a blue shift in the absorption maximum. Similar behavior was observed during the photoreduction of BP with diethylaniline or DABCO (1,4-diazobicyclo[2.2.2]octane). A rapid protonation of the ketyl radical ($\lambda_{\max} = 545$ nm) follows and this is kinetically coupled to the 690 nm transient. The rate constant for proton transfer was determined to be $2.0 \times 10^9 \text{ s}^{-1}$ for a solution of 1.0 M DMA. This is approximately three orders of magnitude faster than the corresponding rate constant for hydrogen atom transfer, even with very good hydrogen donors.

Photoinduced oxidation of amines leads to the formation of amine radical cations. These intermediates display both radical and cationic character with the N–H protons of the primary and secondary amine cation radicals being acidic. As a result, an efficient deprotonation occurs at the carbon α to the nitrogen radical cation giving aminyl radicals (Eq. (3)) [100].



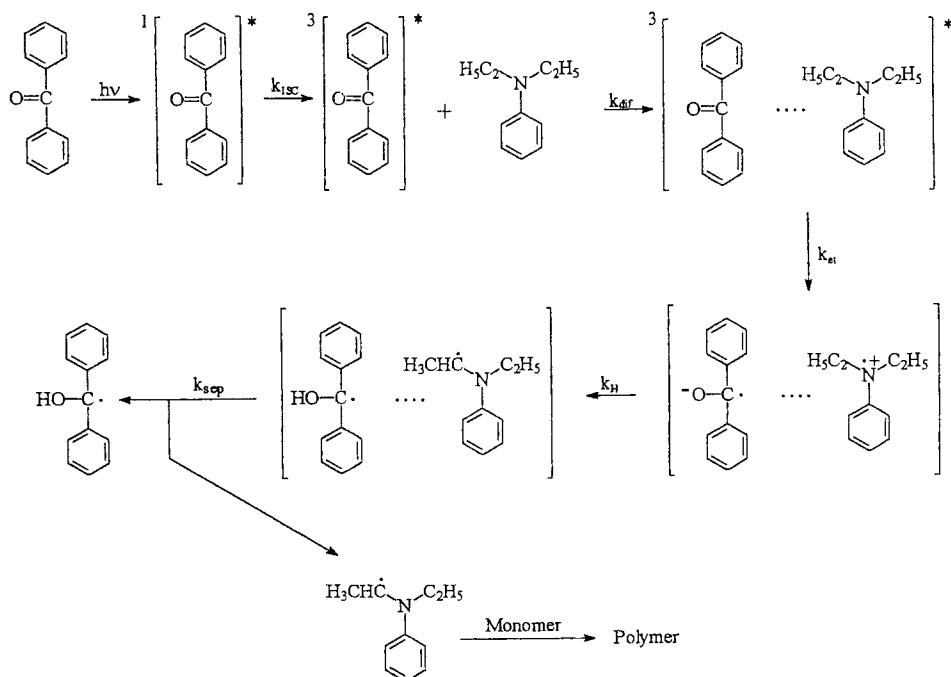
Tertiary ammonium radicals are also acidic so, if α -CH protons are present in the amine, deprotonation of these intermediate products stabilizes the α -amino radicals (Eq (4)).



The formation of radicals by the deprotonation of α -amino radical cations is an important method of initiating free-radical polymerization. A mechanism of polymerization photoinitiated by the BP–amine couple (Scheme 11) involves such a process [101–104].

Gosh and Gosh [105] studied photoinitiated polymerization of methyl methacrylate initiated by the BP–*N,N*-dimethylaniline couple, and Clarke and Shanks [106] tested the influence of a variety of amines on benzophenone-initiated polymerization. That amino radicals resulted during the initiation the polymerization by benzophenone–tertiary aromatic amines was shown by Li through the use of ESR and spin-trapping methods [107]. It was shown that the rate of photoinitiated polymerization depends on the structure of the amine. More recently [108] benzophenone–tertiary aromatic amines were studied as initiators of the free-radical polymerization of polyol acrylates. Illustrative kinetic curves recorded during photoinitiated polymerization of TMPTA are shown in Figure 23.

The structures and properties of the benzophenones evaluated are summarized in Table 7. The electrochemical properties of the tertiary aromatic amines (TAA) tested are summarized in Table 8, below.



Scheme 11.

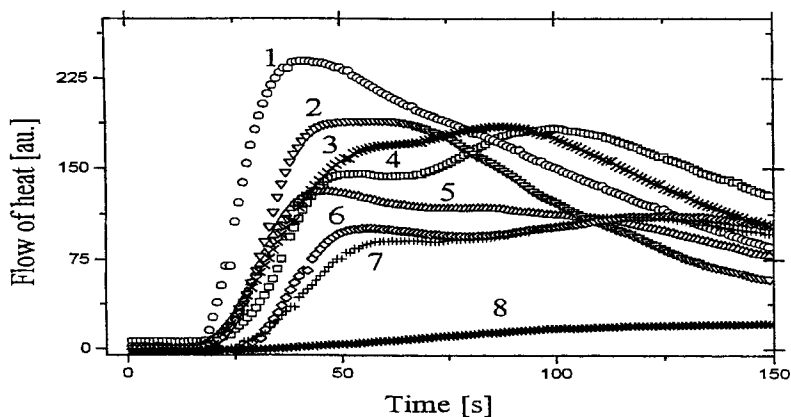
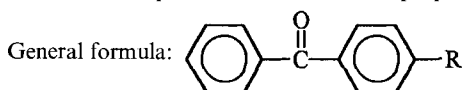


Figure 23. The family of curves recorded during measurements of the flow of heat during photo-initiated polymerization of TMPTA initiated by benzophenone-4-bromo-*N,N*-dimethylaniline initiating photo-redox pairs. The benzophenones were: 1) 4-Ph, 2) 4-C(O)OEt, 3) 4-Me, 4) 4-H, 5) 4-Cl, 6) 4-F, 7) 4-OMe, 8) 4-NO₂.

Table 7. Benzophenones and their basic properties

R	$E_{\text{red}} (\text{A}^{\cdot-}/\text{A}) [\text{V}]^{\text{a}}$	$E_{00}^{\text{T}} [\text{kJ mol}^{-1}]$	Hammett constant (σ) of R ^b
H	−1.550	289	0
OH	−1.784	286	−0.37
OMe	−1.676	287	−0.27
Me	−1.702	287	−0.17
F	−1.572	292	0.06
NO ₂	−1.204	287	0.78
Cl	−1.628	288	0.23
Ph	−1.540	254	−0.01
C(O)OEt	−1.630	279	0.45
COOH	−1.690	279	0.45

^afrom Ref. [108], ^bfrom Ref. [109].

Table 8. The electrochemical properties of tertiary aromatic amines [122] (TAA) used as electron-donating molecules for xanthene dye–TAA initiating pairs.

Electron-donating compound	$E_{\text{ox}} [\text{V}]$	Electron-donating compound	$E_{\text{ox}} [\text{V}]$
<i>N,N</i> -Dimethylaniline	0.71	<i>N,N</i> ,3,5-Tetramethylaniline	0.731
Jolidine	0.59	Butyl 4-(<i>N</i> -piperidino)benzoate	0.854
Ethyl 4-dimethylaminobenzoate	1.103	Butyl 4-(<i>N</i> -morpholino)benzoate	1.173
1-Phenylpiperidine	1.095	4-Nitro- <i>N,N</i> -dimethylaniline	1.353
4-(Dimethylamino)benzophenone	0.975	<i>N</i> -Methylindoline	0.61
<i>N</i> -Phenylmorpholine	0.947	4-(<i>N,N</i> -Dimethyl)toluidine	0.58
4-Bromo- <i>N,N</i> -dimethylaniline	0.965	4-(Dimethylamino)benzonitril	1.222
<i>N,N,N',N'</i> -(Tetramethyl)- <i>p</i> -phenylenediamine, monoperchlorate	1.21	1-Methyl-4-(4-nitrophenyl)piperazine	0.590
<i>N,N,N',N'</i> -(Tetramethyl)- <i>p</i> -phenylenediamine	0.196	Diethyl 4-(<i>N,N</i> -dimethylamino)benzal-malonate	0.975
<i>trans</i> -4-(Dimethylamino)cinnamionitrile	0.747	Ethyl 4-(<i>N,N</i> -dimethylamino)cinnamate	0.84

For all the BP–amine couples, measured relative rates of polymerization were plotted as a function of free energy change $f(\Delta G_{\text{et}})$ (Figure 24).

The data in Figures 23 and 24 clearly show that the efficiency of the BP–TAA as a polymerization initiator couple depends on both the benzophenone structure and the structure of the tertiary amine. Since the trend observed in Figure 24 is characteristic for kinetic phenomena in what is known as the *inverted Marcus region* [12–14, 110, 111], and since benzophenone triplet quenching cannot display this specific kinetic phenomena, one concludes that the rate of polymerization photoinitiated by

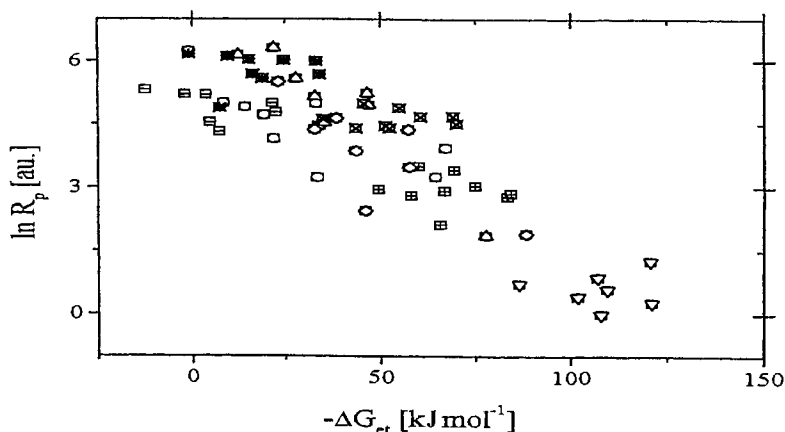
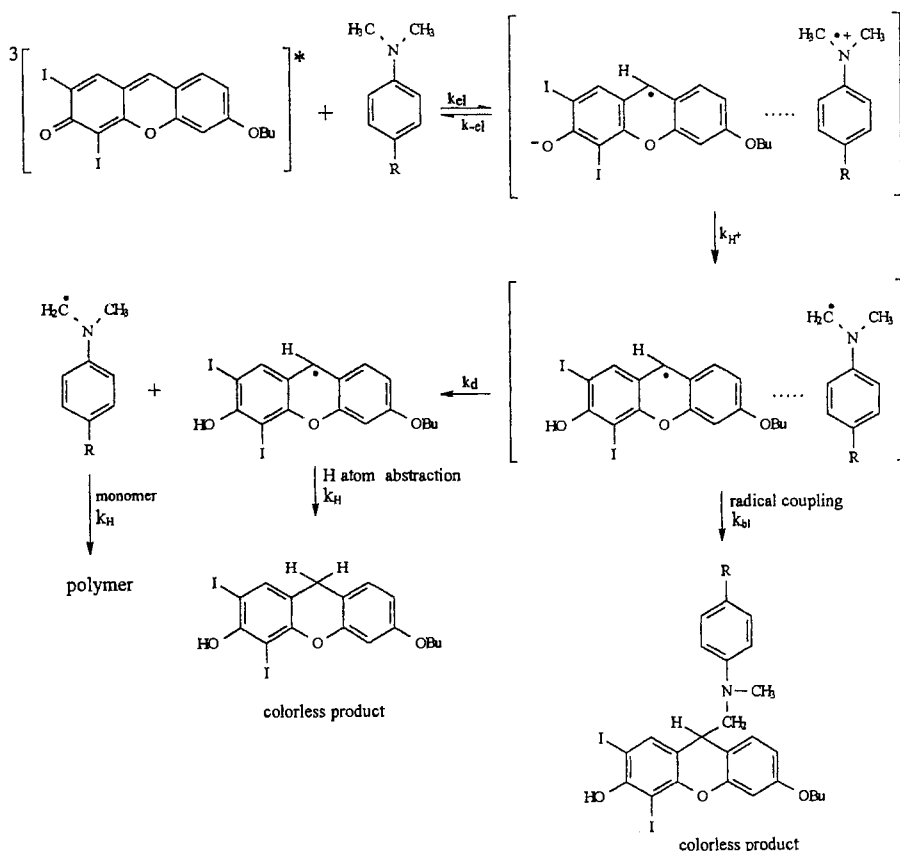


Figure 24. Relationship between the rate of polymerization (TMPTA) and the free energy change for photo-redox reaction for benzophenone–TAA initiating systems. Irradiation of the polymerization mixture was carried out using part of the UV emission (300–400 nm) of a xenon lamp (Philips CSX 150 W/1) with intensity of irradiation $I = 120 \text{ mW cm}^{-2}$.

a series of BP–TAAs is not limited by the rate of the primary process, e.g., the rate of photoinduced electron transfer.

Xanthene dye–amine systems

The photoreduction of 2,4-diiodo-6-butoxy-3-fluorone (DIBF) in the presence of *N,N*-dimethyl-2,6-diisopropylaniline is also a well documented example [88, 89]. The triplet state of the dyes, based on the 3-hydroxy-6-fluorone skeleton [87], is quenched by several electron donors, mainly aromatic amines or tertiary aliphatic amines. The process is described by a bimolecular rate constant and is accompanied by the growth of the peak at 410 nm. The position of this peak can be assigned to the dye anion radical ($D^{\bullet-}$) [112–115], indicating that the reaction between dye triplet and amines is an electron transfer process. In DIBF the dye radical anion cannot be detected on the nanosecond time scale. Instead, the neutral dye radical (DIBF $^{\bullet}$) is observed [88]. This observation permits one to conclude that, after initial electron transfer from the amine to the dye triplet, DIBF $^{\bullet-}$ and the amine cation radical are generated. The dye radical anion promotes rapid proton transfer from the carbon α to the nitrogen of the amino cation radical, giving the neutral dye radical and the amine radical [116]. In other words, the proton transfer process is too fast (large k_{H^+}) to be measured on the nanosecond time scale. The estimated electron transfer rate is equal to the rate of triplet quenching, $1.21 \times 10^8 \text{ s}^{-1}$. Flash photolysis results confirm that the photoreduction of DIBF in the presence of tertiary amine is a one-electron transfer process. Based on this, one can propose a mechanism illustrating the photoreduction of xanthene dyes in the presence of tertiary amine yielding free radicals able to initiate polymerization (Scheme 12).



Scheme 12.

This type of photoinitiating system has been studied carefully using a series of 6-alkoxy-2,4-diiodo-3-fluorones and 2-acyl- or 7-alkyl-2,4,5-triiodo-3-fluorones [117–120] as the primary light absorbers. The systems have been further evaluated as initiators for photopolymerization in the presence of a tertiary aromatic amine. Photoinitiated polymerization was triggered with an argon-ion (514.5 nm line) or He–Ne (632 nm line) laser.

A variety of amines (Table 8) and various xanthene dyes (Figure 25) were tested as visible-light photoinitiators of free-radical polymerization [108, 121]. The rate of photoinitiated polymerization depends on the type of amine used as the electron donor (Figure 26) [122, 123].

Camphorquinone–amine system

In the 1960s, the photopolymerization of polyol acrylates found a variety of applications in dentistry, including dental composite resins, adhesives, dentures, and

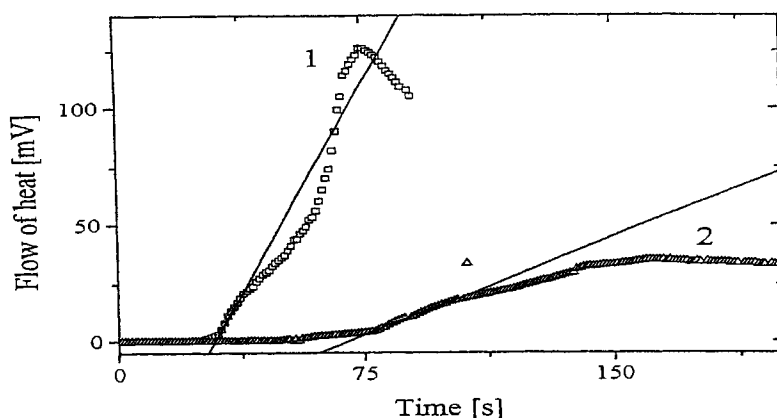


Figure 26. Rate of heat evolution during an argon-ion laser-initiated polymerization of 2-ethyl-2-(hydroxymethyl)-1,3-propanediol triacrylate (TMPTA) and 1-methyl-2-pyrrolidinone (MP) mixture (9:1) photosensitized by RBAX (10^{-3} M) in the presence of: 1) 4-(dimethylamino)benzophenone (0.1 M) and 2) *N,N*,3,5-tetramethylaniline (0.1 M).

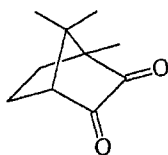


Figure 27. Camphorquinone (CQ), $\Phi \approx 1.0$, $E_{\text{red}}(\text{CQ}^{\cdot-}/\text{CQ}) = -1.25$ V, $E_T = 210$ kJ mol $^{-1}$.

tiary aromatic amines. Previous correlations of the ionization potentials (IP) of quenching agents and the rate of quenching of the ketone triplet state [127] suggested that the reaction of an amine with an excited ketone involves electron transfer followed by proton transfer [128]. As a matter of fact, there is some support for this thesis in the report by Depew and Wan [129], who showed that the one-electron reduction of camphorquinone in 2-propanol produced camphorquinone radical anions [130]. Time-resolved chemically induced electron paramagnetic resonance (CIDEP) experiments suggested a dual mechanism for formation of the radical ion and evidence of both singlet and triplet precursors for the electron transfer. Partial evidence was provided by energy transfer to CQ from the benzophenone triplet which clearly showed that the CQ triplet led to $\text{CQ}^{\cdot-}$. Quenching of the CQ singlet by tertiary amine was observed using both CIDEP and fluorescence quenching ($\lambda_{\text{max}} = 505$ nm) with a bimolecular rate constant of about 2×10^8 M $^{-1}$ s $^{-1}$. Cook, observing a lack of this type of correlation for CQ–amine systems, suggested that the initiating radicals originate from a hydrogen atom abstraction reaction of the triplet state of CQ with α -dicarbonyl compounds such as α -keto esters. We find this quite unlikely. It is necessary to emphasize that photoinduced electron transfer reactions in which amines serve as ground-state electron donors are initiated by redox processes. In view of the general requirement for the

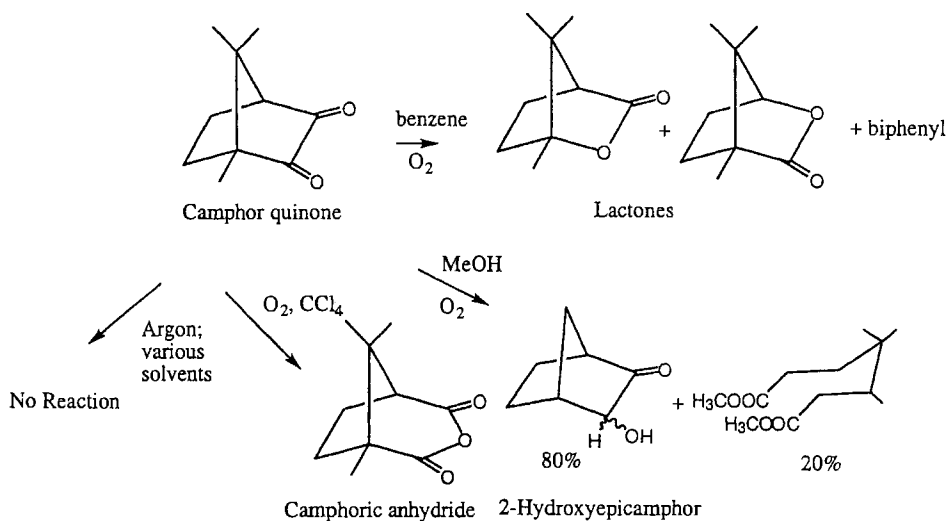
photoinduced electron transfer process that the thermodynamics of the process ($\Delta G_{\text{et}} = E_{\text{ox}} - E_{\text{red}} - E_{00}$) is governed by the amine oxidation potential (E_{ox}) and the acceptor excited-state reduction potential ($E_{00} - E_{\text{red}}$), where E_{00} is the excited-state energy and E_{red} is the reduction potential of the acceptor [100], considering a property of only one component (the ionization potentials of amines) may lead to misinterpretation and to improper conclusions. As an illustration, one can compare properties of CQ–amine and benzophenone (BP)–amine couples (see the data in Table 8 and the equation mentioned above). The free energy change (ΔG_{et}) for CQ–4,4′-bis(dimethylamino)benzophenone (MK) is 6.4 kJ mol^{-1} , while for BP–4,4′-bis(dimethylamino)benzophenone it is $-76.6 \text{ kJ mol}^{-1}$. These data suggest that electron transfer for the CQ–MK couple is thermodynamically forbidden (positive ΔG_{et}) and if free radicals are formed from amine, a process other than PET is involved during the reaction. For the BP–MK couple, since ΔG_{et} is negative, photo-reduction of BP will proceed via an electron transfer mechanism. On the other hand for the CQ–*N,N*-dimethylaniline photo-redox pair the free energy change is $-12.9 \text{ kJ mol}^{-1}$ and for BP–*N,N*-dimethylaniline it is $-96.0 \text{ kJ mol}^{-1}$. The above data indicate that for both photo-redox pairs analyzed, PET is thermodynamically allowed and the formation of free radicals for the CQ–*N,N*-dimethylaniline photo-redox pair will also be more likely occur via a photoinduced electron transfer process. This simple comparison of two different electron donors evidently shows that the prediction of the reaction mechanism on the basis of only one selected specific property might lead to uncertain conclusions. Recently CQ–amine systems were extensively studied, but research on these systems is mostly focused on their application in dentistry [131].

We find all of this mechanistic speculation quite irrelevant and suggest CQ behaves as do other α -diketones and undergoes, predominantly, α -cleavage. Our evidence for this comes from the work of Meinwold and Klingele [132], who isolated the products from the photoreactions of CQ in a number of solvents (Scheme 13). A principle observation was the CQ is totally inert in the absence of oxygen in all solvents. In the presence of oxygen, however, the products depend on the solvent and suggest formation of the peroxide. The pertinent products are the two isomeric lactones formed in benzene, and the anhydride that is produced in carbon tetrachloride as the predominant product. There is also some evidence of the photo-reduction products, *exo* and *endo*-2-hydroxyepicamphor, but these are formed mainly in methanol, and also require the presence of oxygen.

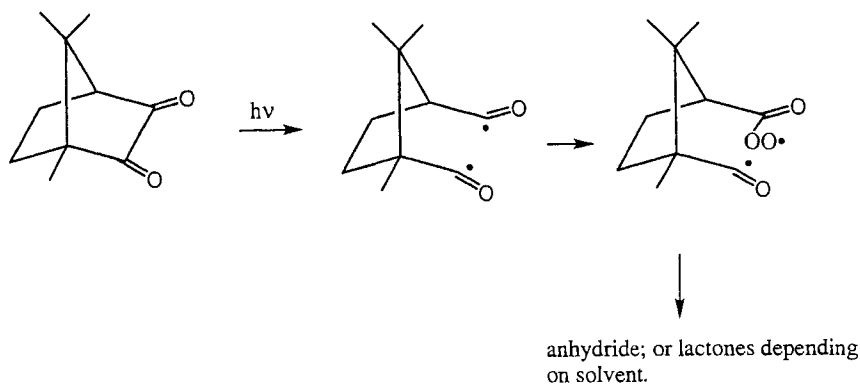
Accordingly, we suggest the principle mechanism for the catalysis of polymerization by camphorquinone, which is always used in the presence of tertiary amines, is first formation of the peroxide and then ground-state electron transfer which leads to radicals (Scheme 14). Thus the initiation of polymerization is caused by the same intermediates as it might be, were it to occur by initial electron transfer from the amine to CQ, followed by generation of an initiating radical. But oxygen quenching of the α -diketone diradical is first required (Scheme 15).

Anthraquinone–amines

Anthraquinone (AQ)–triethylamine (TEA), a photoinitiating system for the polymerization of methyl methacrylate (MMA) [133], clearly functions by electron

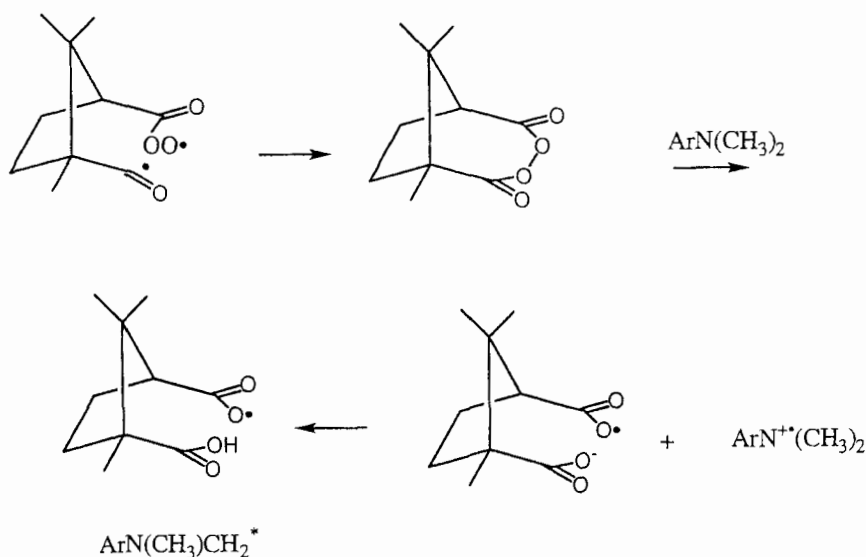


Scheme 13.



Scheme 14.

transfer. In the absence of TEA and in a solvent that is a poor hydrogen donor, AQ is a poor photoinitiator. Addition of amine significantly increases the photo-initiation rate in nonpolar solvents. Free-radical formation occurs from quenching of AQ triplets by TEA, leading to AQ photoreduction at a rate that is nearly diffusion-controlled [134–136]. This quenching produces radical ions which deactivate by pathways typical for such intermediates. After proton transfer, one produces the anthrasemiquinone (AQH \cdot) radical and the triethylamine radical. Such semiquinone radicals disproportionate to yield AQH $_2$ and AQ. The rate of AQ disappearance in the mixture of AQ–TEA decreases considerably in the presence of methyl methacrylate (Figures 28A, 28B). The decrease in photoreduction of AQ in



Scheme 15.

the presence of MMA can be attributed either to trapping of the AQ triplet, the contact radical-ion pair, separated radical ions and/or the AQH[•] radical. Encinas and his colleagues explained these specific behaviors as an effect of the quenching of the radical-ion pair by MMA. A simplified photopolymerization mechanism of MMA in benzene, is shown in Scheme 16 [137].

Thioxanthone–amine system

Thioxanthones (TX) absorb strongly in the near-ultraviolet region of the spectrum, and their reaction with amines comprises a bimolecular initiator system competitive with photodissociative initiators [138–150]. The photochemistry and photophysics of TX in the presence of amines are similar to that observed for other aromatic ketones, and can be summarized by the scheme proposed by Davidson [148] (Scheme 17).

Other chromophore–amine systems

Other compounds containing light-scavenging chromophores, with tertiary amines, also form couples able to initiate polymerization via photoinduced electron transfer. Safranin T (Figure 29) [151] forms radicals by the quenching of the dye singlet excited state. The rate constant of quenching is near the diffusional limit. Flash photolysis studies of safranin T in the presence of amines show the reaction involves an electron transfer process ($k_q(T)$ oscillates between 0.13×10^8 and $9.4 \times 10^8 \text{ M}^{-1} \text{ s}^{-1}$) followed by fast proton transfer to yield amine free radical.

Encinas et al. [152–154] were the first to report that the polymerization of vinyl

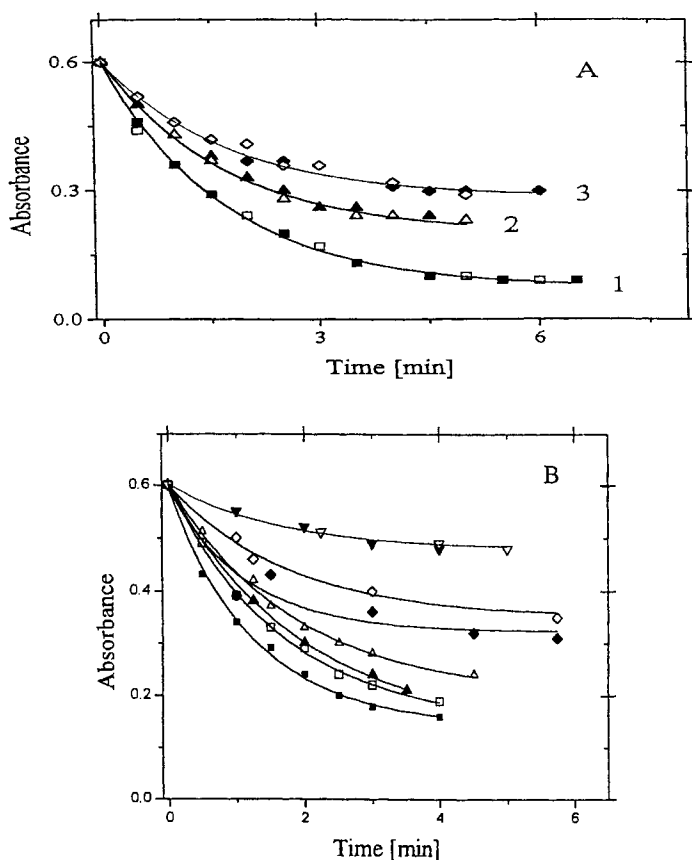
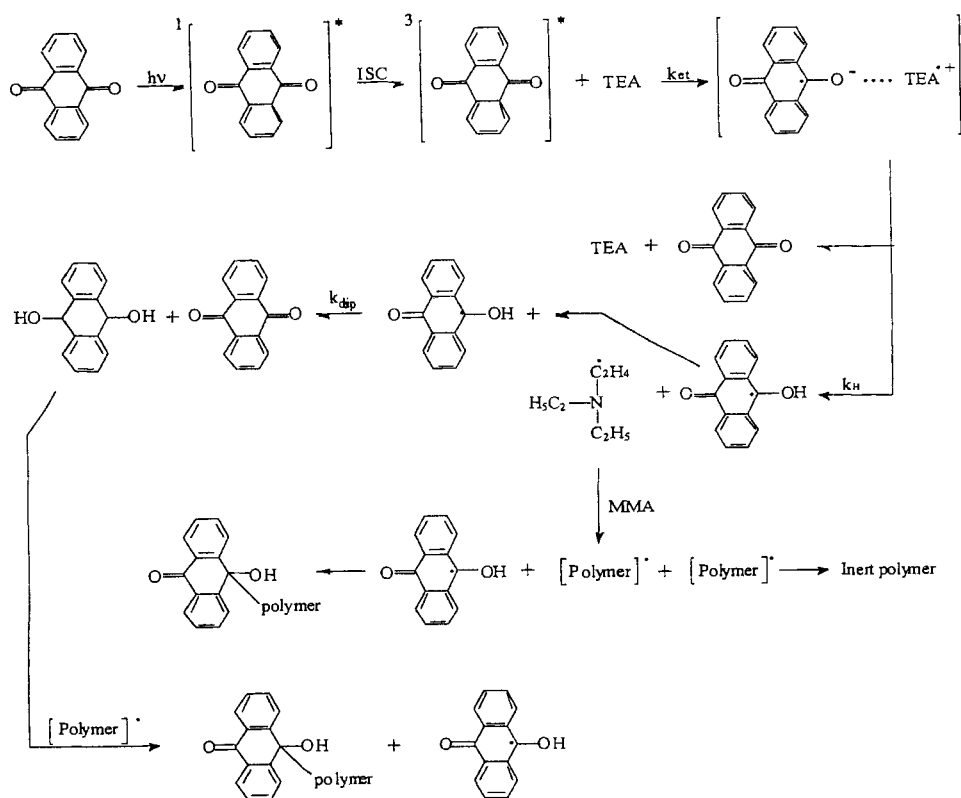


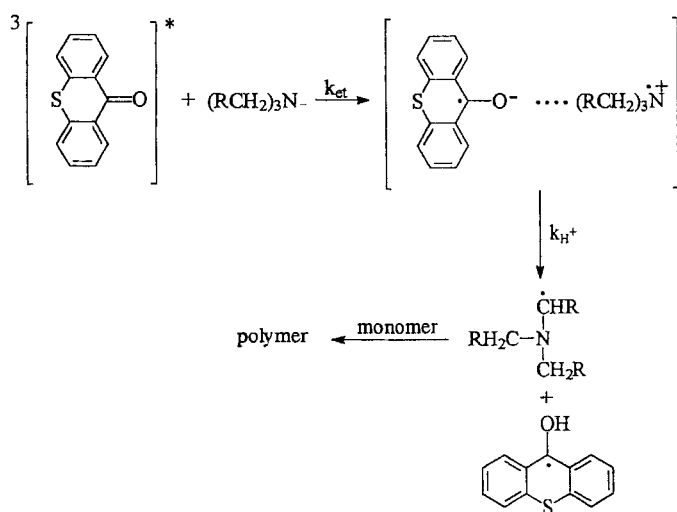
Figure 28. Absorption of the AQ-TEA mixture as a function of irradiation time at various TEA and methyl methacrylate (MMA) concentrations. Closed symbols, $[\text{TEA}] = 0.036 \text{ M}$; open symbols, $[\text{TEA}] = 0.2 \text{ M}$. A) Solvent benzene; 1) $[\text{MMA}] = 0.0 \text{ M}$; 2) $[\text{MMA}] = 0.79 \text{ M}$; 3) $[\text{MMA}] = 3.15 \text{ M}$ (data from Figure 3 of Ref. [133]). B) Solvent, ethanol; \square , \blacksquare , $[\text{MMA}] = 0.00 \text{ M}$; \triangle , \blacktriangle , $[\text{MMA}] = 0.22 \text{ M}$; \diamond , \blacklozenge , $[\text{MMA}] = 0.79 \text{ M}$; ∇ , \blacktriangledown , $[\text{MMA}] = 1.58 \text{ M}$ (data from Figure 4 of Ref. [133]).

monomers was photoinitiated by pyrene-amine combinations. This is one of the rare systems in which radical intermediates are formed via a singlet excited state that is not initially organized (compare cyanine borates [24, 25]). The efficiency of the system is due to the relatively long lifetime of the pyrene singlet excited state (Figure 30) [154].

The absorption band (λ_{max} 488 nm) in the transient spectrum corresponds to the pyrene radical ion ($\text{Py}^{\bullet-}$) [155, 156], while the band at $\lambda_{\text{max}} \approx 400 \text{ nm}$ is assigned to the absorption of the 1-hydro-1-pyrenyl radical (Py^{\bullet}) [157, 158]. Steady-state photolysis of pyrene in the presence of TEA leads to its disappearance, and addition of vinyl monomers decreases the rate of pyrene photoreduction. The photobleaching process follows first-order kinetics. Encinas et al. [154] suggest that the photoinitiation of polymerization by pyrene-TEA is catalyzed by the pyrene radical ion,



Scheme 16.



Scheme 17.

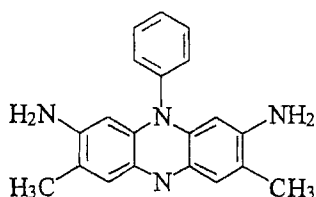


Figure 29. Safranin T.

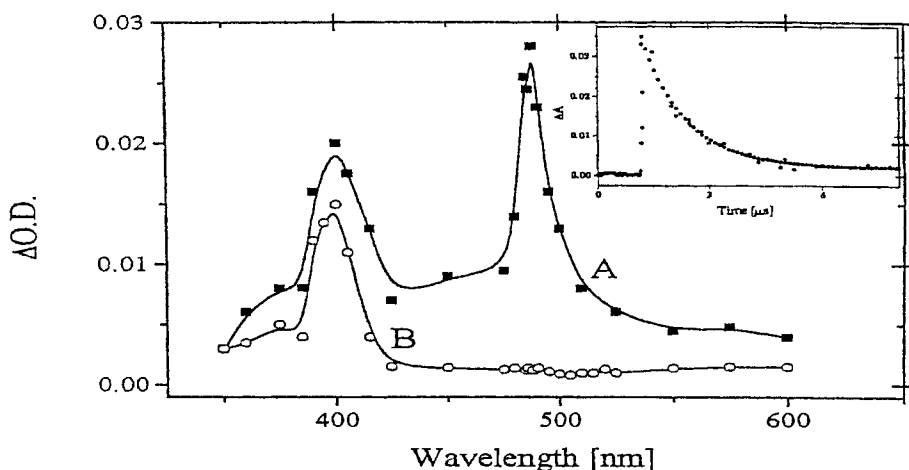
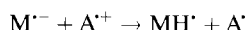
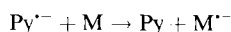


Figure 30. Transient absorption spectrum of pyrene-TEA in an acetonitrile-ethyl acetate solution. Delay time after the laser pulse: A) 500 ns, B) 6 μ s. Inset: typical first-order decay trace monitored at 488 nm (data from Figure 1, Ref. [154]).

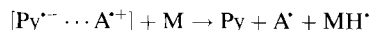
on the basis of the observation that the 488 nm $\text{Py}^{\bullet-}$ transient absorption is efficiently quenched by monomers, as well as because the monomer decreases the lifetime of $\text{Py}^{\bullet-}$ without changing its initial intensity. The mechanism (Scheme 18) involves the interaction of the pyrene radical ion, either free or formed first in the solvent cage, with a monomer, followed by the initiation of the chain reaction by the amine-derived free radical.

2,2',4,3',5,5'-Hexaarylbisimidazoles (HABIs) (Figure 31) are among the most widely used photoinitiators [11]. HABIs are both thermochromic and photochromic, and cleave either thermally or photochemically (when irradiated in the 255–275 nm or 300–375 nm regions respectively) to a pair of tetraarylimidazolyl radicals (lophyl radicals \equiv L). These radicals recombine in the dark. The L radical generated in the photodecomposition can interact with a chain transfer agent either by direct hydrogen atom abstraction or by electron transfer to produce an initiating species capable of addition to the monomer.

Photoinitiated polymerization with HABI systems can be achieved with visible light in the presence of absorbing dyes that are good electron donors [159]. Reaction



or



Scheme 18. A, amine; A[•], the amine-derived radical on the α-carbon; M, monomer molecule. According to Encinas et al. [155], both radicals A[•] and MH[•] are able to initiate polymerization of vinyl monomers.

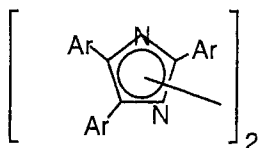


Figure 31. 2,2',4,3',5,5'-Hexaarylbisimidazole (HABI).

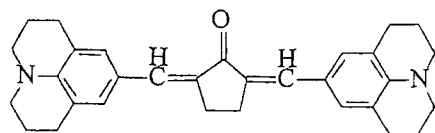
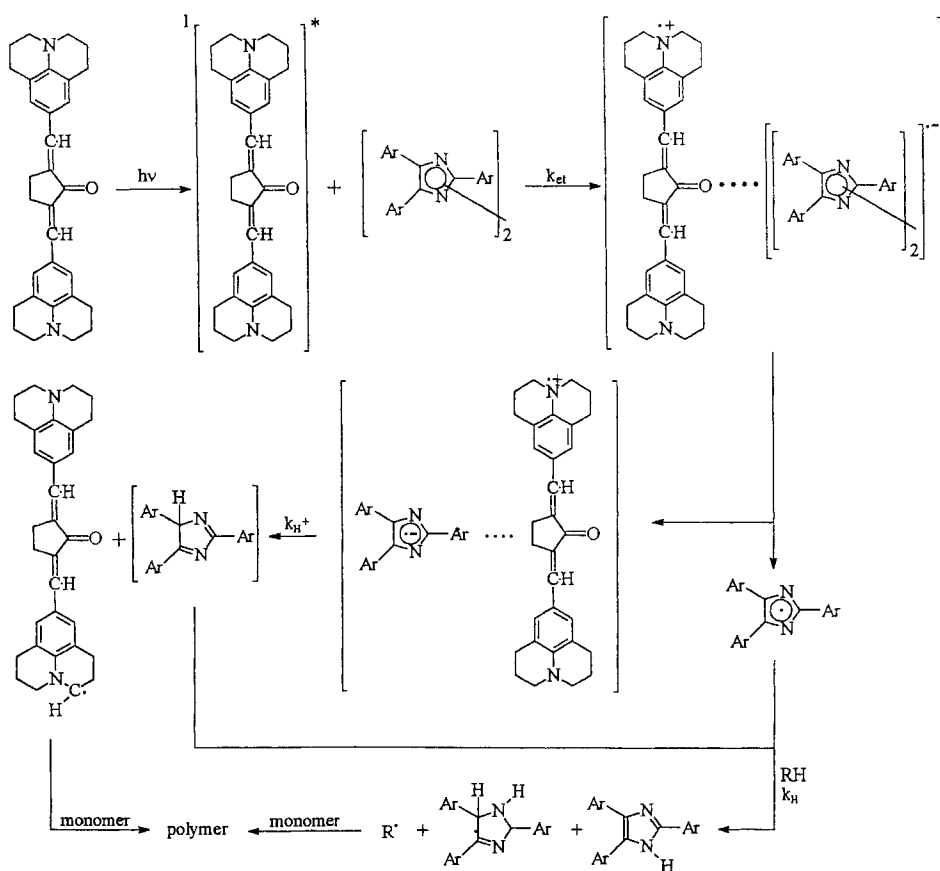


Figure 32. JAW.

between the HABI and sensitizer involves the singlet excited state, and the products, lophyl radicals, are formed mostly through singlet dissociation [160, 161]. A combination of ESR [162] and laser flash photolysis [162, 163] has established an electron transfer mechanism for the reaction between a HABI and sensitizer, 2,5-bis[(1*H*,5*H*-benzo [*i,j*]quinolizin-1-yl)methylene]cyclopentanone (JAW, Figure 32). (Energy transfer from JAW to the HABI on the singlet manifold is not energetically feasible because HABI absorbs at higher energy than the subject of JAW.)

It was mentioned earlier that the lophyl radical is a poor initiator of free-radical polymerization; however, it is an excellent hydrogen atom abstractor. The design of HABI compounds for photopolymerization has been optimized to exploit this difference [164].

The mechanism proposed for the photoinitiation of acrylates with HABIs takes into account that, after electron transfer, HABI dimer dissociates yielding free radical and HABI–JAW radical-ion pairs. The lophyl radicals then leave the solvent cage and react with good hydrogen donors, producing the initiating radicals. The components that remain in the solvent cage produce a radical-ion pair (stabilized by electrostatic interaction) that subsequently undergoes a proton transfer to form two radicals, one from JAW and the second from the HABI. The lophyl radical behaves as mentioned earlier, and the radical resulting from JAW is likely to react with



Scheme 19.

monomer to start polymerization. Analysis of Scheme 19 indicates one more important feature of the system, i.e., that one quantum of light generates three free radicals that are able to start free-radical polymerization.

One other important difference should be emphasized. For traditional dye-amine systems electron transfer occurs from the ground state of the amine donor to the excited state of the dye. For the HABI-JAW system the *electron transfer occurs from the excited state of amine (JAW) to the ground state of the HABI*. This specific behavior significantly differentiates this system from other dye-amine systems.

Electron-proton transfer or other secondary reaction systems

N-phenylglycines (NPGs)

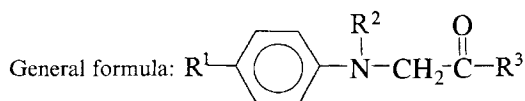
Benzophenone-sensitized decarboxylation of acids of the type $RXCH_2COOH$ (where $X = O, S, \text{ and } NH$) [165-167] appears to go by electron transfer from the

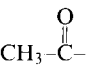
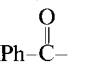
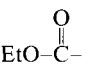
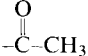
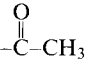
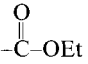
- 1) diffusion of the radical-ion pair and
- 2) intramolecular proton transfer of the radical-ion pair that is retained in the solvent cage.

A large series of *N*-phenylglycine derivatives (Table 9) was studied as electron donors in photoinduced free-radical polymerization [108]. *N*-Phenylglycine deriva-



Scheme 20.

Table 9. Structures, oxidation potentials of *N*-phenylglycine derivatives tested as electron donors.

N-substituent, R ²	<i>p</i> - (<i>o</i> -, <i>m</i> -) substituent, R ¹	R ³	<i>E</i> _{ox} [mV]
H	H	OH	426
H	NC	OH	707
H	NO ₂	OH	781
H		OH	635
H		OH	661
H		OH	639
H	Cl	OH	479
H	CH ₃	OH	437
H	<i>t</i> -But.	OH	436
H	PhO	OH	479
H	MeO	OH	343
Me	H	OH	—
	H	OH	2000
H	H	OE _t	1080
H	CN	OE _t	1642
H	NO ₂	OE _t	1598
H		OE _t	1352
H		OE _t	1340
H	Me	OE _t	1010
H	<i>p</i> -Cl	OE _t	1132
H	<i>o</i> -Cl	OE _t	1266
H	<i>m</i> -Cl	OE _t	1244
H	OMe	OE _t	862
H	H	NH ₂	984
Ph	H	OE _t	1064

tives were used with xanthene dyes (Figures 25, 33, and 34), as well as with camphorquinone [175].

The data in Figures 33 and 34 show typical thermodynamic properties (normal Marcus region) for the electron transfer reaction. In these examples, the rate of the process increases as the driving force of the reaction ($-\Delta G_{\text{et}}$) increases. The properties observed in Figures 33 and 34 also predict the type of radical formed after electron transfer. From studies of sulfur-containing amino acids and sulfur-containing carboxylic acids [170–175] it is known that decarboxylation occurs only if the carbox-

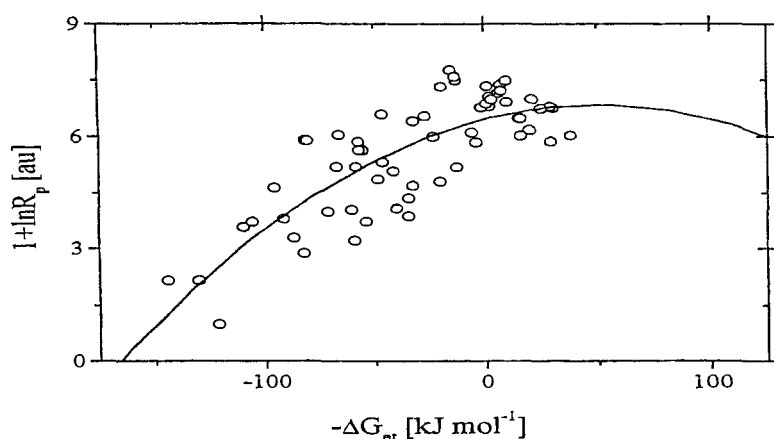


Figure 33. Relationship between the rate of polymerization (TMPTA/MP, 9:1) and the free energy change for photo-redox reactions for series of four different initiating systems: TDEF–NPG, ETDEF–NPG, TDPF–NPG, and BTDBF–NPG (for abbreviations see Figure 25). Data from Ref. [108].

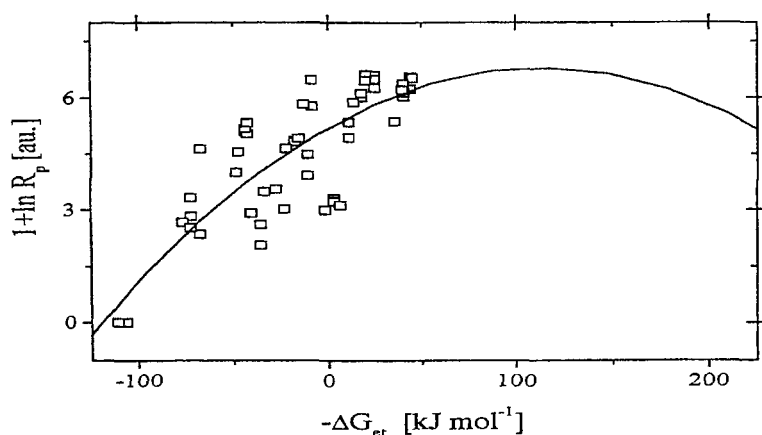


Figure 34. Relationship between the rate of polymerization (TMPTA/MP, 9:1) and the free energy change for photo-redox reactions for series of two different initiating systems: ATIHF–NPG, and EDIHF–NPG (for abbreviations see Figure 25). Data from Ref. [108].

ylic acid group is dissociated. The facts that the esters of *N*-phenylglycine derivatives and other *N*-phenylglycines behave similarly (located on the same curve in the $1 + \ln R_p = f(-\Delta G_{et})$ relationship; R_p = rate of polymerization), and that esters do not decarboxylate, suggest that under conditions of photoinitiated polymerization (medium-polarity and viscous monomer mixture), there is no separation of the radical ions. The proton transfer process yields a free radical centered on α -carbon with respect to the carboxylic group. This conclusion is supported by the quantum

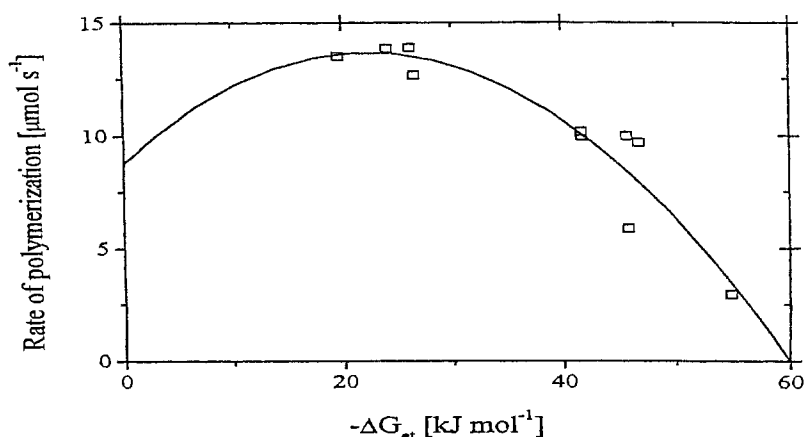


Figure 35. Rate of polymerization as a function of free energy change ($-\Delta G_{et}$) for photoinitiated CQ-NPG systems. Polymerizing monomer mixture: 2-ethyl-2-(hydroxymethyl)-1,3-propanediol triacrylate (TMPTA) and ethylated bisphenol-A dimethacrylate (bis-EMA) (1:1). Polymerization was initiated by an argon-ion laser beam. Data from Ref. [175].

yield of decarboxylation, measured for *N*-phenylglycine by Nishimoto [168], which varies with the dielectric constant, ϵ , of the nonviscous solvent. When applied to a formulation of monomers (TMPTA/MP, 9:1) which possesses a dielectric constant of 13, the quantum yield of *N*-phenylglycine decarboxylation varies in the range of 7–8 %.

A similar study performed for CQ-NPG initiator systems [175] showed a rather different kinetic behavior (Figure 35). The rate of polymerization is reduced when the thermodynamic driving force ($-\Delta G_{et}$) of the process is increased, and this demonstrates “inverted-region-like” kinetic behavior. The authors explained this variation in reactivity as due to the reactivity of the free radicals formed as a result of processes occurring after electron transfer [123].

N-Phenylglycine was used as the electron donor in photopolymerizations initiated by azomethine dyes [176]. The primary light absorber, ChAD (Figure 36 and Table 10), is based on the quinoxalin-2-one residue [177, 178]. Kinetic traces recorded for

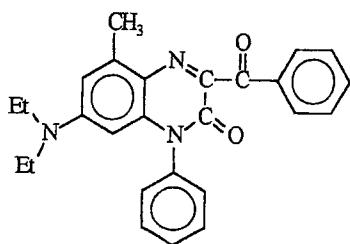
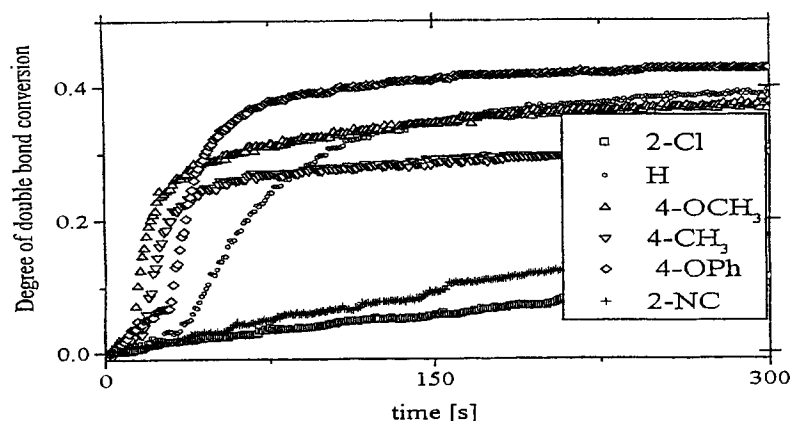


Figure 36. 3-Benzoyl-7-diethylamino-5-methyl-1-phenyl-1*H*-quinoxalin-2-one (ChAD).

Table 10. Photophysical properties of 3-benzoyl-7-diethylamino-5-methyl-1-phenyl-1*H*-quinoxalin-2-one (ChAD).

Absorption, λ_{\max} [nm]	$\varepsilon_{\lambda_{\max}}$ [L cm ⁻¹ mol ⁻¹]	E_{red} [V]	E_{T} [kcal/mol]	$\Phi_{\text{T}}^{\text{a}}$	τ_{T} [μs]	k_{q}^{T} [M ⁻¹ s ⁻¹] ^b	$\Delta G_{\text{ET}}^{\circ}$ [kJ mol ⁻¹] ^c
643	6000	-1.208	44	0.078	25	1.2×10^7	-26.4

^aevaluated based on the efficiency of singlet oxygen formation, ^b*N*-phenylglycine used as the triplet state quencher, ^ccalculated for *N*-phenylglycine as electron donor.

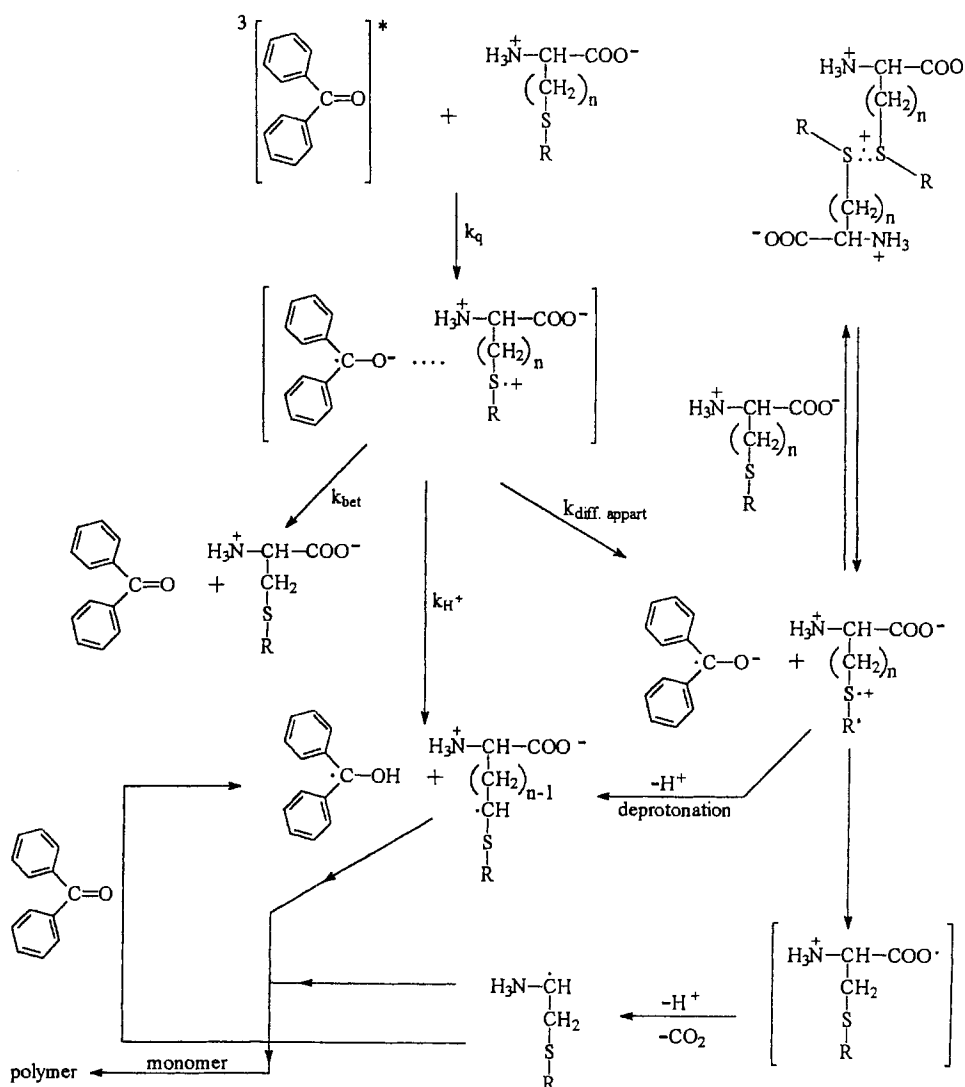
**Figure 37.** Rate of vinyl double bond conversion of TMPTA-MP, measured using RTIR methodology [179–181]. Initiator: ChAD; electron donor: *N*-phenylglycine substituted as indicated in the key.

this polymerization (Figure 37) show a strong effect of electron donor structure on the rate of photoinitiation by ChAD polymerization.

Sulfur-containing amino acids (SCAA) and sulfur-containing carboxylic acids (SCCA)

To our knowledge, there is only one paper in the literature describing polymerization photoinitiated by a redox system of 4-carboxybenzophenone and sulfur-containing amino acids [182]. However, considering the potential application of these photoinitiating systems for polymerization in aqueous media and the interesting mechanism of free-radical generation, it is worth describing this system in more detail (Scheme 21).

Sensitized photooxidation of sulfur-containing amino acids in neutral aqueous solution occurs via electron transfer from the sulfur to the triplet state of the sensitizer (the mechanism can be adapted to other dye-sensitized photoinitiated polymerization). Electron transfer quenching in the system is followed mainly by diffusion of the sulfur-centered radical cation and benzophenone radical anion. Laser



Scheme 21.

flash photolysis [183] indicates two pathways of ketyl radical formation. The fast formation of ketyl radicals is ascribed mainly to the protonation of the initially produced ketyl radical anion and results from proton transfer in the radical-ion pair in the solvent cage. Slow formation of the ketyl radicals is assigned to the one-electron reduction of the benzophenone ground state by the α -aminoalkyl radical formed as a result of decarboxylation of the sulfur-centered radical cation. The formation of the ketyl radical through the reaction of the benzophenone ground state and the α -aminoalkyl radical competes with addition of the α -aminoalkyl

radical to monomer. An intermediate resulting during the process is an intermolecular three-electron-bonded radical cation formed from the sulfur-centered radical cation and neutral sulfur-containing amino acid. This intermediate is formed during a reversible process and therefore its formation does not compete with initiation of polymerization.

A series of sulfur-containing carboxylic acids demonstrate similar photophysical and photochemical features as electron donors. This is demonstrated in Table 11 [184].

Laser flash photolysis experiments allow one to establish the mechanism (see Scheme 22) of the major processes occurring during irradiation of CB-SCCA photo-redox pairs.

Photopolymerization experiments were carried out to compare the efficiency of the photoinitiated polymerization as a function of the SCCA structures. The rates of polymerization determined from the efficiencies of the photopolymerization after 6 min of irradiation are also presented in Table 11. A reference sample containing CB and other components, but without any co-initiator, did not show any polymerization. The results in Table 11 show that the rate of photoinitiated polymerization depends on the SCCA used.





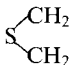
Aliphatic and aromatic sulfides

Aliphatic sulfides can be efficient co-initiators for the photoinduced polymerization induced by benzophenone [185, 186]. An exceptionally strong effect was observed for 2,4,6-trimethyl-1,3,5-trithiane (TMT). A model reaction for free-radical formation during photoreduction of an initiator triplet state by a sulfide is the photoreduction of benzophenone by dimethyl sulfide [171, 187–189]. In this process it was established that electron transfer from the sulfur atom to the triplet state of the benzophenone is a primary photochemical step. In this step, radical ions are formed. The overall quantum yields of photoproducts (ketyl radicals and radical anions) are low ($\Sigma\Phi \approx 0.26$) in aqueous solution, in the range 0.16–0.20 in mixed water–acetonitrile solution and less than 0.01 in pure acetonitrile. These results suggest that, in organic solvents, back electron transfer within the radical-ion pair to regenerate the reactants is the dominant process.

Polymerization of butane-1,4-diol dimethacrylate, sensitized by benzophenone in the presence of three different sulfides, has been described by Andrzejewska et al. [190]. The measurements show that in the absence and in the presence of propyl sulfide and 2,2'-thiobisethanol no polymer was formed. This can be explained by the effective back electron transfer process that occurs in the radical-ion pair in organic solvents. Effective polymerization was observed only in the presence of TMT. Laser flash photolysis studies performed for the benzophenone–TMT pair allow one to construct a scheme (Scheme 23) explaining characteristic features of the mechanism of polymerization initiated by the system. The results prompted the authors to study other symmetrically substituted 1,3,5-trithianes as electron donors for benzophenone-sensitized free-radical polymerization (Figure 38; Table 12) [191].

Most 1,3,5-trithianes are active co-initiators in benzophenone-induced polymerization. The most efficient is β -TMT, whose reactivity significantly exceeds that of the α -isomer. Consideration of the order of the quantum yields (Table 12) suggests

Table 11. Photophysical and photochemical properties of sulfur-containing carboxylic acids tested as electron donors in 4-carboxybenzophenone-sensitized polymerization.

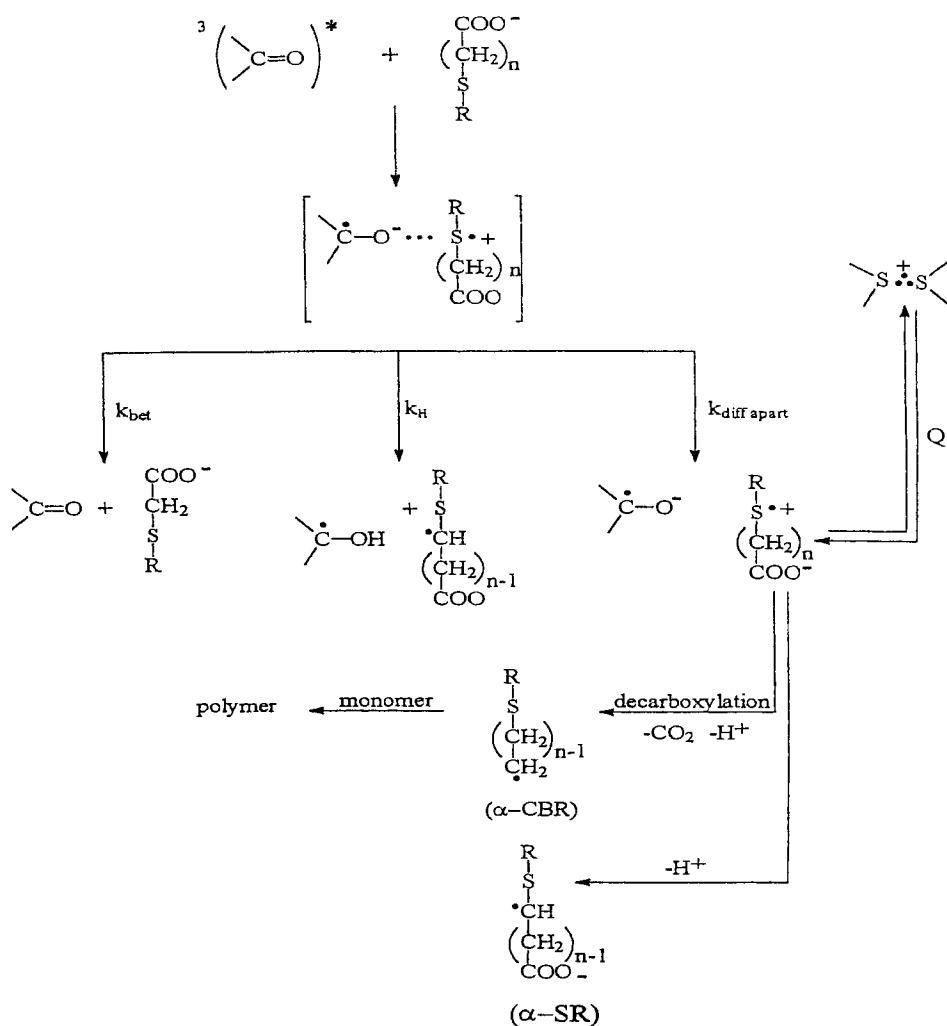
No.	Co-initiator structure	$k_q \times 10^{-9}$ ($M^{-1} s^{-1}$)	$\Phi_{CO_2}^a$	$\Phi_{CB\cdot}^b$	$\Phi_{CBH\cdot}^b$	R_p [%] (6 min)
1	 -S-CH ₂ COOH Phenylthioacetic acid	1.85	0.92 (± 0.09)	0.97	0	70
2	 -CH ₂ -S-CH ₂ COOH S-Benzylthioglycolic acid	1.54	0.57	0.84	0.16	48
3	CH ₃ -S-  -CH ₂ COOH 4-(Methylthio)phenylacetic acid	1.9	0.29			43
4	CH ₃ -S-CH ₂ COOH 2-(Methylthio)ethanoic acid	2.1	0.86	0.87	0.12	42
5	CH ₃ -S-  -COOH 4-(Methylthio)benzoic acid	1.9	<0.05			6
6	HOOC-CH ₂ -S-CH ₂ -COOH 2,2'-Thiodiethanoic acid	0.95	0.80	0.84	0.16	7
7	 -CH ₂ -CH ₂ -COOH 3,3'-Thiodipropionic acid	1.0	<0.03	0.90	0.09	no
8	CH ₃ S-CH ₃ Dimethyl sulfide	4.9	—	0.16	0.10	8

^a from steady-state measurements, extrapolated to zero percent of carboxyphenone (CB) conversion,^b from laser flash photolysis extrapolated to the end of the flash.

that the most active co-initiator should be β -TPT. In general, it was found that the polymerization efficiency of the co-initiators did not follow the efficiency of photo-induced free-radical formation.

4.4 Kinetics

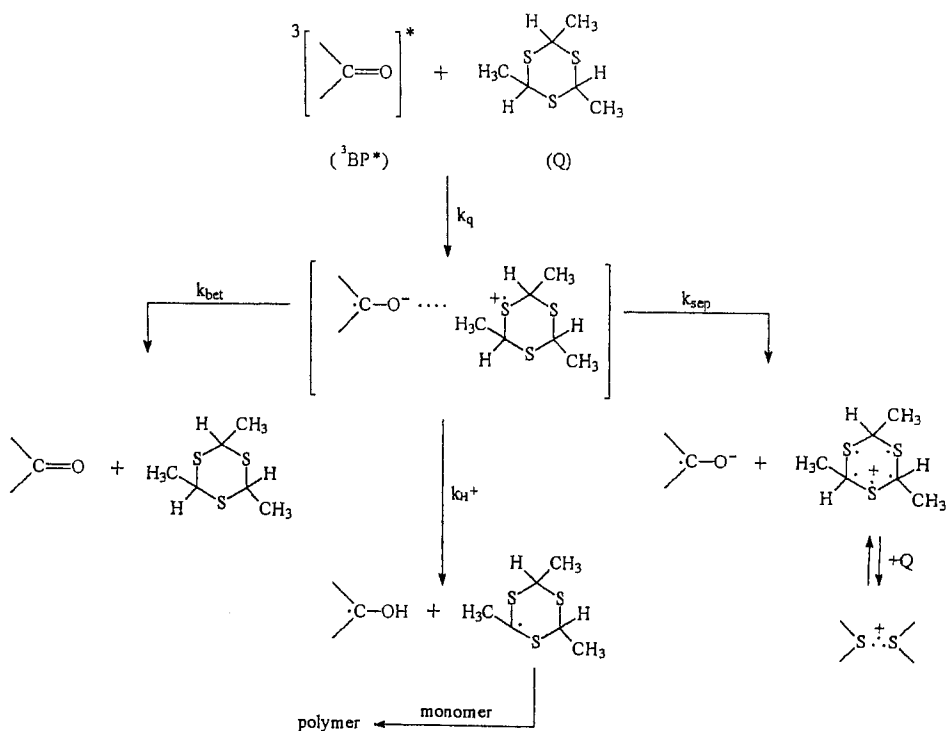
Free-radical-initiated polymerization via an intermolecular transfer process involves many steps, including electron transfer between an excited acceptor (A) and an electron donor (D). For aromatic amines the electron transfer is followed by a



Scheme 22.

proton transfer from the donor radical cation to the dye radical anion, which yields a neutral radical initiating polymerization and the reduced radical of the dye. The radicals are formed from the electron donor and a dye. Cross-coupling between radical pairs terminates photoreaction [192]. Cross-coupling competes with the initiation of polymerization. Additionally, if the reaction takes place within the solvent cage, the products that are formed might revert to starting reactants or leave the solvent cage by ion dissociation.

Scheme 24 summarizes the possible processes that can occur during a free-radical polymerization induced via an intermolecular electron transfer process (PET) in the presence of aromatic amines; k_{dif} is the rate constant of diffusive encounters be-



Scheme 23.

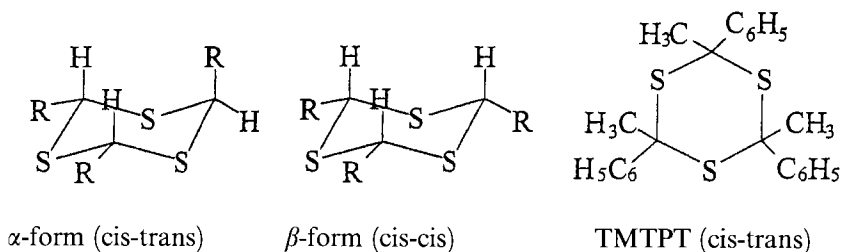
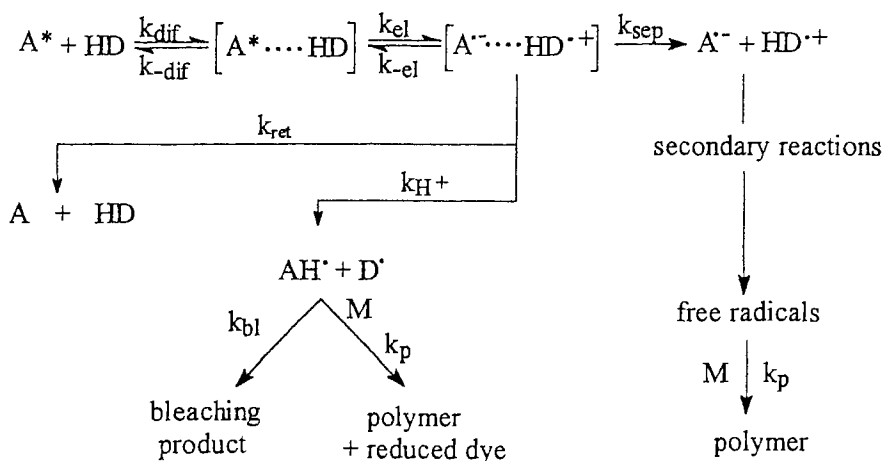


Figure 38. Symmetrically substituted 1,3,5-trithianes.

Table 12. Trithianes studied and their basic photochemical properties.

Substituent R	Trithiane	Abbreviation	k_q ($\text{M}^{-1} \text{s}^{-1}$)	Φ_{BPH^+}
H	1,3,5-trithiane	TT	2.5×10^8	0.28
CH ₃	α -2,4,6-trimethyl-1,3,5-trithiane	α -TMT	4.2×10^8	0.62
CH ₃	β -2,4,6-trimethyl-1,3,5-trithiane	β -TMT	3.4×10^8	0.53
C ₆ H ₅	α -2,4,6-triphenyl-1,3,5-trithiane	α -TPT	2.1×10^8	0.81
C ₆ H ₅	β -2,4,6-triphenyl-1,3,5-trithiane	β -TPT	1.6×10^8	0.32
	2,4,6-trimethyl-2,4,6-triphenyl-1,3,5-trithiane	TMTPT	$\leq 5 \times 10^6$	



Scheme 24.

tween reactants (these can dissociate with a rate constant k_{-dif}), k_{el} is the first-order rate constant of electron transfer with the reverse step denoted by the rate constant k_{-el} , and k_H is the rate constant of proton transfer between ion radicals. The cross-coupling step is designated by the rate constant k_{bl} . The polymerization step is designated by k_p and k_{ret} denotes the rate constants for the process of electron return. Scheme 24 can also be used for kinetic analysis of the photoinitiated polymerization sensitized by dye-NPGs. Generalizing, the above scheme can be applied to any system which is not stabilized in the ground state by an electrostatic interaction but that is electrostatically stabilized after electron transfer. For cyanine borates, for example, the formation of the ion pair in the ground state, and one noncharged intermediate after electron transfer, would lead to a quite different kinetic scheme (see Scheme 2).

In this section an illustrative discussion on kinetics of photopolymerization initiated via an intermolecular photoinduced electron transfer for a dye-tertiary aromatic amine initiating photo-redox couple [193] and for 4-carboxybenzophenone-sulfur-containing carboxylic acids initiating systems will be presented.

On the bases of Scheme 24, one can assume the following. Applying the steady-state approximation to the donor neutral free radical $[D^{\cdot}]$, one obtains Eq. (5),

$$\frac{d[D^{\cdot}]}{dt} = k_H[HD^{\cdot+} \cdots A^{\cdot-}] - k_{bl}[D^{\cdot} \cdots A^{\cdot}H] - k_t[D^{\cdot}M]^2 = 0 \quad (5)$$

where k_t is the constant rate of the macroradical termination process and $[D^{\cdot}M]$ is the concentration of polymeric macroradical formed from an initiating radical D^{\cdot} and monomer. For $[HD^{\cdot+}]$ the steady-state approximation yields Eq. (6), and

$$\frac{d[HD^{\cdot+}]}{dt} = k_{obs} - k_{ret}[HD^{\cdot+} \cdots A^{\cdot-}] - k_H[HD^{\cdot+} \cdots A^{\cdot-}] = 0 \quad (6)$$

thus we obtain Eq. (7),

$$k_{\text{obs}} - k_{\text{ret}}[\text{HD}^{\bullet+} \cdots \text{A}^{\bullet-}] - k_t[\text{D}^{\bullet}\text{M}]^2 - k_{\text{bl}}[\text{D}^{\bullet} \cdots \text{A}^{\bullet}\text{H}] = 0 \quad (7)$$

where k_{obs} denotes the rate constant of the simplified photochemical process represented by Eq. (8).



The traditional [7] kinetic scheme used for the description of light-induced polymerization processes is given by Eqs. (9)–(12).



The rate of reaction (9) is I_a for singlet-state or $\Phi_T I_a$ for triplet-state, reaction; the rates of processes (11) and (12) are $k_p[\text{R}^{\bullet}][\text{M}]$ and $k_t[\text{RM}^{\bullet}]^2$, respectively (I_a is the intensity of light).

In the steady state:

$$\frac{d[\text{R}^{\bullet}]}{dt} - \frac{d[\text{RM}^{\bullet}]}{dt} = 0 \quad (13)$$

and

$$\frac{d[\text{R}^{\bullet}]}{dt} = \frac{d[\text{RM}^{\bullet}]}{dt} = k_t[\text{RM}^{\bullet}]^2 \quad (14)$$

Thus

$$[\text{R}^{\bullet}] = \sqrt{\frac{2I_a}{k_t}} \quad \text{or} \quad [\text{R}^{\bullet}] = \sqrt{\frac{2I_a\Phi_T}{k_t}} \quad (15)$$

The rate of polymerization is then

$$-\frac{d[\text{M}]}{dt} = k_p\sqrt{\frac{2I_a}{k_t}}[\text{M}] \quad \text{or} \quad -\frac{d[\text{M}]}{dt} = k_p\sqrt{\frac{2I_a\Phi_T}{k_t}}[\text{M}] \quad (16)$$

This scheme does not take into consideration the rate constant for the intermolecular electron transfer process. This is possible to include by entering into Eq. (6) the relationship from Eq. (14). It should be noted that the dye radical usually

terminates the macroradical or forms the bleaching product. This is the dihydro-dye (e.g., the electron transfer is followed by a proton transfer and then the radical anion abstracts a hydrogen atom either from solvent or from other electron donor molecule.) Under these conditions $k_{bl}[\mathbf{D}^{\bullet} \cdots \mathbf{A}^{\bullet}\mathbf{H}] \ll k_t[\mathbf{RM}^{\bullet}]^2$; thus for the concentration of free radicals one obtains Eq. (17), and

$$[\mathbf{D}^{\bullet}] = \sqrt{\frac{k_{\text{obs}} - k_{\text{ret}}[\mathbf{HD}^{\bullet+} \cdots \mathbf{A}^{\bullet-}]}{k_t}} \quad (17)$$

then the rate of polymerization is given by Eq. (18).

$$R_p = -\frac{d[\mathbf{M}]}{dt} = k_p[\mathbf{M}] \sqrt{\frac{k_{\text{obs}} - k_{\text{ret}}[\mathbf{HD}^{\bullet+} \cdots \mathbf{A}^{\bullet-}]}{k_t}} \quad (18)$$

Since the process of electron return for triplet dyes requires intersystem crossing in the radical-ion pair, the rate constant of this process is negligible in comparison with the rate constants for other processes. Thus, the rate of polymerization becomes

$$R_p = -\frac{d[\mathbf{M}]}{dt} = k_p[\mathbf{M}] \sqrt{\frac{k_{\text{obs}}}{k_t}} \quad (19)$$

For further consideration it is necessary to express the rate of radical-ion pair formation as a function of light intensity, e.g., to describe the step of radical-ion pair formation starting from the acceptor molecule in its ground state (Eq. (20)).



The rate is then $k'_{\text{obs}}I_a[\mathbf{D}]$. For very high donor concentration k'_{obs} becomes practically a first-order rate constant and the rate of the process can be expressed in a simpler form as $k_{\text{obs}}I_a$.

One should take into account that back electron transfer in the successor complex might compete with a slow electron transfer step. This can be described by one composite unimolecular rate constant k_3 ($k_3 = k_{\text{ret}} + k_{\text{H}^+} + k_{\text{sep}}$). A steady-state treatment of the concentrations of the precursor and successor complexes leads to the conclusion that k_{obs} should be related to the microscopic rate constants of Scheme 1 as in Eq. (21):

$$k_{\text{obs}} = \frac{k_{\text{dif}}}{1 + (k_{-\text{dif}}/k_{\text{el}})[1 + k_{-\text{el}}/k_3]} \quad (21)$$

and in the inverted form as

$$\frac{1}{k_{\text{obs}}} = \frac{1}{k_{\text{dif}}} + \frac{1}{K_d k_{\text{el}}} + \frac{1}{K_d k_{\text{el}}} \left(1 + \frac{k_{-\text{el}}}{k_3} \right) \quad (22)$$

There are several possibilities by means of which to simplify Eq. (22). The easiest for verification is that for a reaction in the solid state or in very viscous media (diffusionless electron transfer). Under this condition Eq. (23) holds:

$$k_{\text{obs}} \cong k_{\text{el}} \quad (23)$$

If $k_{\text{obs}}I_a$ is known, one can enter Eq. (23) into Eq. (19). This gives a final equation describing the rate of initial polymerization for viscous media such as mixtures of polyol(meth)acrylates

$$R_p = -\frac{d[M]}{dt} = k_p[M] \sqrt{\frac{I_a k_{\text{el}}}{k_t}} \quad (24)$$

The limiting step, k_{el} , of the electron transfer reaction can be expressed by Eq. (25),

$$k_{\text{el}} = \chi Z \exp(-\Delta G^\# / RT) \quad (25)$$

where Z is a universal frequency factor, ca. $6 \times 10^{12} \text{ s}^{-1}$ at 25°C , χ is the transmission coefficient, k_{el} is the unimolecular rate constant describing the rate of electron transfer, and $\Delta G^\#$ is the total free energy of activation given by the Marcus equation [12–14] for neutral reactants by Eq. (26).

$$\Delta G^\# = (\lambda + \Delta G_{\text{et}})^2 / 4\lambda \quad (26)$$

Here $\Delta G^\#$ is the sum of the individual free energies:

$$\Delta G^\# = \Delta G_v^\# + \Delta G_s^\# \quad (27)$$

where the subscripts refer to the energy involving bond distortions of interacting molecules (v) and solvent changes in the ionic sphere surrounding the reactants (s = solvent); λ is defined as the total reorganization energy. Thus, $\lambda = \lambda_v + \lambda_s$, where λ_v is the inner-sphere reorganization energy referring to the energy changes of the molecule geometry during the electron transfer step, and λ_s is the outer-sphere reorganization energy which is caused by the energy change as the solvent shell surrounding the reactants rearranges. Finally ΔG_{et} is expressed by the Rehm–Weller [33, 34] equation (Eq. (1)).

Combination of Eqs. (23) and (24) gives Eq. (28),

$$R_p = -\frac{d[M]}{dt} = k_p[M] \sqrt{\frac{I_a \chi Z \exp(-\Delta G^\# / RT)}{k_t}} \quad (28)$$

and after introducing the Marcus equation (26), Eq. (29) holds:

$$R_p = -\frac{d[M]}{dt} = k_p[M] \sqrt{\frac{I_a \chi Z \exp[-(\lambda + \Delta G_{\text{et}})^2 / 4\lambda RT]}{k_t}} \quad (29)$$

Considering that the initial time of polymerization for pure monomers where $[M] \cong \text{constant}$, $[D] \cong \text{const}$, $k_p \cong \text{const}$, and $I_a \chi Z / k_t \cong \text{constant}$, one obtains Eq. (30), in logarithmic form:

$$\ln R_p = A - (\lambda + \Delta G_{\text{et}})^2 / 4\lambda RT \quad (30)$$

Equation 30 shows that if an intermolecular electron transfer process between the excited dye and an electron donor is a limiting step for photoinitiated polymerization, one should observe a parabolic relationship between the logarithm of the rate of polymerization and the thermodynamic parameter ΔG_{et} . ΔG_{et} is a measurable quantity and is accessible by experimental determination. In order to reduce the effect of diffusion-controlled termination [194–198], the effect of network formation and the Norrish–Tromsdorf effect, the initial rates of polymerization should be taken into account for further consideration. The experimental results (Figures 33 and 34) suggest that the intermolecular electron transfer process might be the limiting step in the photoinitiated polymerization. The data show that the rate of polymerization is increased when the thermodynamic driving force ($-\Delta G_{\text{et}}$) is increased. This demonstrates *normal-region* kinetic behavior.

There are, however initiating systems, which demonstrate the *inverted-region-like* kinetic behavior (Figure 39), e.g., they show that the rate of polymerization is reduced when the thermodynamic driving force ($-\Delta G_{\text{et}}$) is increased. This specific behavior is a clear indication that the rate of intermolecular electron transfer is not the limiting step for the entire process.

As observed in Figure 39, the relationship is roughly linear. Linear relationships (Figure 30) are also observed between the Hammett constant- and the phororedox properties of photoinitiating systems.

Assuming

$$\ln R_p = \rho \sigma_p \quad (31)$$

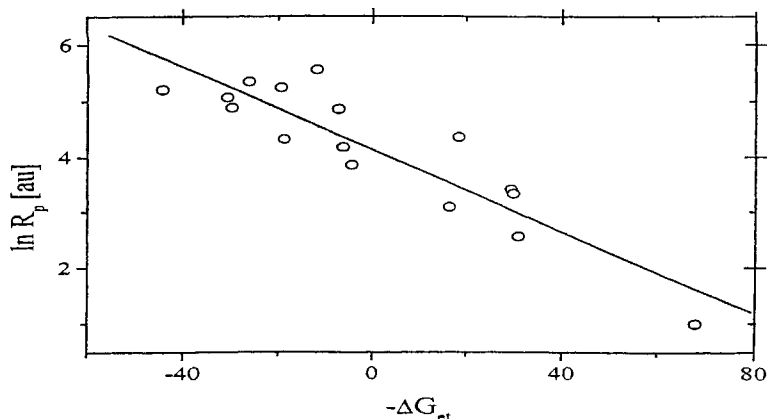


Figure 39. Inverted-region-like behavior. Relationship between the rate of polymerization (TMPTA-MP, 8:1) and the free energy change for RBAX-TAA's initiating system.

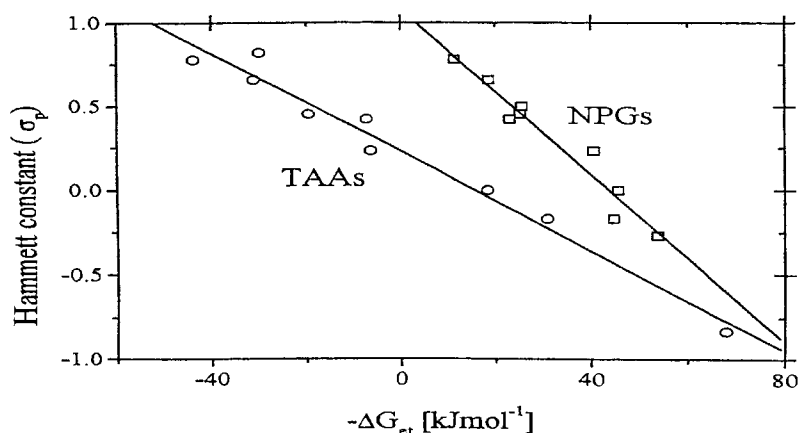


Figure 40. Relationship between Hammett constant and ΔG_{et} for RBAX-TAAs and RBAX-NPGs photoinitiating systems.

and

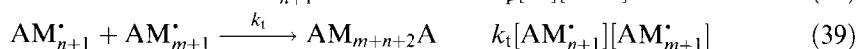
$$-\Delta G^\circ = \rho' \sigma_p \quad (32)$$

where ρ and ρ' are respectively, and combining Eqs. (31) and (32), gives Eq. (33)

$$\ln R_p = \frac{\rho}{\rho'} (-\Delta G^\circ) \quad (33)$$

Equation (33) clearly shows the linear relationship between the rate of polymerization and the Hammett constant, which is illustrated in Figure 39.

For processes in which the rate of polymerization is not limited by the rate of electron transfer, the equation describing the rate of polymerization, one can obtain during the analysis of simple kinetics a scheme of photoinitiated polymerization. A mechanism describing a photoinitiated polymerization via PET (not considering the kinetics of free-radical formation, because this process does not affect the rates of polymerization), that contains all the major reaction steps, can be represented by Eqs. (34)–(39).



The reactivity of free radicals depends on their structure; therefore, in the initiation of the chain Eq. (36) only some of the free radicals participate efficiently. For aromatic radicals, one can apply the Hammett equation of the description of initiation rate constant, k_i :

$$k_i = k_i^\circ e^{\rho\sigma} \quad (40)$$

where k_i is the rate constant for the initiation process for a given free radical and k_i° is the rate constant of initiation for a reference radical. Under steady-state conditions,

$$k_i^\circ [M][I_a \Phi_{A^\bullet}] = k_t [AM_{n+1}^\bullet][AM_{m+1}^\bullet] = k_t [A^\bullet]^2 \quad (41)$$

Thus the free-radical concentration is described by Eq. (42):

$$[A^\bullet] = ([\Phi_{A^\bullet}])^{0.5} (I_a)^{0.5} [M]^{0.5} (k_i^\circ e^{\rho\sigma})^{0.5} (k_t)^{-0.5} \quad (42)$$

Under this condition the rate of polymerization is

$$R_p = k_p [M]^{1.5} ([\Phi_{A^\bullet}])^{0.5} (I_a)^{0.5} (k_i^\circ e^{\rho\sigma})^{0.5} (k_t)^{-0.5} \quad (43)$$

or in logarithmic form,

$$\ln R_p = \ln A + 0.5\rho\sigma \quad (44)$$

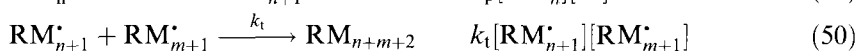
where A for the initial time of polymerization is the sum: $\ln k_p - 0.5 \ln k_t + 1.5 \ln [M] + 0.5 \ln \Phi_{A^\bullet} + 0.5 \ln k_i^\circ + 0.5 \ln I_a$. Equation (44) clearly shows that the rate of polymerization depends on the reactivity of the free radicals yielded after the photoinduced electron transfer process.

Kinetic analysis gives additional information related to the reactivity of the free radicals obtained during the processes following a photoinduced electron transfer process. A variation in radical reactivity could be caused, for example, by their stability or their reactivity with monomer, as in the case of photoinitiation by 4-carboxybenzophenone–sulfur-containing carboxylic acid of free-radical polymerization [184].

The rate of photoinitiated polymerization can be controlled by any of the processes that limit the formation of free radicals. These processes could include the primary process, e.g., the photochemical electron transfer (PET) process, but also consequences related to this phenomenon. A good example is the photopolymerization initiated by 4-carboxybenzophenone–sulfur-containing carboxylic acid pairs. Analyzing the rate of the CB triplet-state quenching (see Table 11), one can conclude, that for these CB/SCCA systems, rates of quenching are very similar and vary only slightly in the range of $(1.0\text{--}2.0) \times 10^9 \text{ M}^{-1} \text{ s}^{-1}$. This leads to the conclusion that, under the experimental conditions used, more than 95 % of the CB triplets are quenched by the co-initiators. The results in Table 11 show that the main photochemical channel is the diffusion apart of the radical-ion pairs, leading to the

formation of $\text{CB}^{\bullet-}$ and $\text{S}^{\bullet+}$ radical ions. This strongly suggests that the primary process should not limit the observed rate of the photoinitiated polymerization. Therefore, the differences in the measured rates of the polymerizations are likely to be affected by the yield of the secondary processes that follow PET, e.g., decarboxylation or deprotonation, and/or by the reactivity of the free radicals.

From the kinetic point of view, a mechanism describing photoinitiated polymerization via a PET process can be represented by Eqs. (45)–(51),



where ED is the electron donor (co-initiator), M is the monomer, I_A is the intensity of absorbed light, and $\Phi_{\text{R}^{\bullet}}$ is the quantum yield of free radical formation.

Assuming the rate of reaction (46) is slow relative to reactions (47) and (48), making the steady-state assumption for the total radical concentration, and taking $k_r = k_t = k'_t$, one can obtain the Eq. (52) describing the rate of polymerization [199].

$$R_p = k_p[\text{M}] \sqrt{\frac{\Phi_{\text{R}^{\bullet}} \phi_{\text{RM}^{\bullet}} I_A}{k_t}} \quad (52)$$

where $\phi_{\text{RM}^{\bullet}}$ is a branching ratio defined by Eq. (53):

$$\phi_{\text{RM}^{\bullet}} = \frac{k_i[\text{M}]}{k_i[\text{M}] + k_d} \quad (53)$$

Analyzing Eqs. (52) and (53) one can consider two specific conditions:

1) for $k_d \ll k_i[\text{M}]$, one obtains for the rate of polymerization

$$R_p = k_p[\text{M}] \sqrt{\frac{\Phi_{\text{R}^{\bullet}} I_A}{k_t}} \quad (54)$$

2) for $k_d \gg k_i[\text{M}]$, the rate of polymerization is described by Eq. (55),

$$R_p = k_p[\text{M}]^{1.5} \sqrt{\frac{k_i \Phi_{\text{R}^{\bullet}} I_A}{k_t k_d}} \quad (55)$$

Equations (54) and (55) clearly show that the rate of polymerization depends on the monomer concentration, the quantum yield of free-radical formation, and the reactivity of the free radicals produced after the photoinduced electron transfer process.

There is another interesting feature of Eqs. (54) and (55). They also show that the rate of photoinitiated polymerization is proportional to the square root of the quantum yield of free-radical formation ($\Phi_{R^{\bullet}}$). It is evident from Scheme 21 that there are two types of processes that could initiate polymerization. The quantum yield of α -CBR radical production can be taken to be equal to the quantum yield of CO_2 . The quantum yield of α -SR radical could be estimated by

$$\Phi_{\alpha\text{-SR}} = \Phi_{\text{CBH}^{\bullet}} + (\Phi_{\text{CB}^{\bullet-}} - \Phi_{\text{CO}_2}) \quad (56)$$

The co-initiators in Table 11 appear to fall neatly into two separate groups with respect to their polymerization rates; the first four have significantly larger R_p values than do the last four. In addition, the first four also have rather large quantum yields of decarboxylation compared with three of the last four co-initiators. When these observations are considered in conjunction with Eqs. (54) and (55), a tentative hypothesis is that $\Phi_{R^{\bullet}}$ can be replaced in Eqs. (54) and (55) by Φ_{CO_2} . This is equivalent to assuming that the α -CBR radicals (Scheme 21) are primarily responsible for initiating the polymerization. As a first approximation, it is also assumed that the other parameters associated with the polymerization remain the same for the different co-initiators. With these assumptions, there should be a linear relationship between R_p and $(\Phi_{\text{CO}_2})^{1/2}$. A plot of R_p vs. $(\Phi_{\text{CO}_2})^{1/2}$ is shown in Figure 41 for all the co-initiators used.

From Figure 23, it is evident that phenylthioacetic acid (point 1) has the highest rate of polymerization and the largest CO_2 yields. This is consistent with Eqs. (54) and (55) and the assumption that $\Phi_{R^{\bullet}} = \Phi_{\text{CO}_2}$. Based on the analysis above, there is only one radical, α -CBR, capable of initiating polymerization when phenylthio-

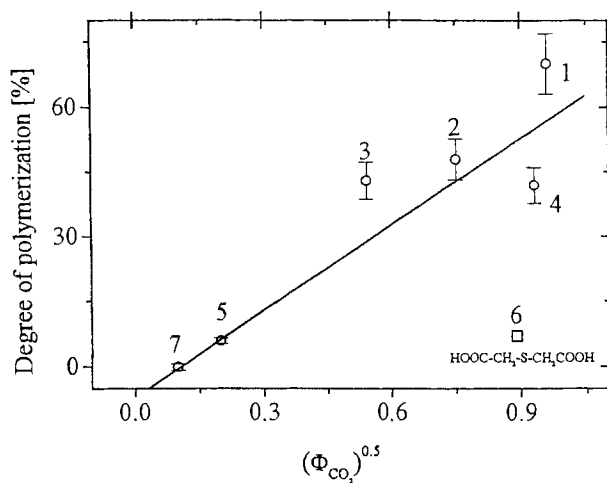


Figure 41. Relationship between the rate of polymerization of acrylamide and quantum yield of free radicals formation for 4-carboxybenzophenone (CB)-sulfur-containing carboxylic acids (SCCA) initiating system. SCCA listed in Table 11.

acetic acid is used as the co-initiator with CB. Thus the highest initiating ability is observed for the system in which there is no in-cage proton transfer process, e.g., there is no formation of radicals localized on carbons adjacent to the carboxylate ion. Several additional conclusions follow from the experimental data:

- 1) The rates of polymerization of the CB/SCCA/acrylamide systems are affected by the yields of secondary processes that follow photoinduced electron transfer, e.g., decarboxylation or deprotonation. This is in addition to the reactivity of the free radicals themselves.
- 2) The highest initiation yield is observed for the system where there is efficient diffusion of the radical-ion pairs, followed by efficient decarboxylation. The resulting radicals are localized on carbons adjacent to the sulfur atom.
- 3) Free radicals with aromatic moieties are better initiators than are the analogous aliphatic radicals.
- 4) Radicals that retain the carboxylate moiety are inefficient initiators.
- 5) Photopolymerization of these systems appears to proceed by the conventional mechanism where termination is bimolecular.

Acknowledgments

The contribution from Faculty of Chemical Technology and Engineering, University of Technology and Agriculture, to this area were made possible by the support of the State Committee for Scientific Research (KBN), Warsaw, grant no. 3 TO9B 087 15. Discussion with Professor Bromislaw Marciniak is gratefully acknowledged.

References

1. G. Oster, *Nature* **1954**, 173, 300.
2. J.P. Fouassier, E. Chesneau *Macromol. Chem.* **1981**, 192, 1307.
3. J.P. Fouassier, S.K. Wu, *J. Appl. Polym. Sci.* **1992**, 44, 1779.
4. M. Kawabata, Y. Takimoto, *J. Photopolym. Sci.* **1990**, 2, 147.
5. J. G. Kloosterboer, *Advances in Polymer Science* **1988**, 84, 4–61.
6. D.F. Eaton, *Pure Appl. Chem.* **1984**, 56, 1191.
7. D.F. Eaton, In: *Topics in Current Chemistry*, Mattay, J., Ed., Springer-Verlag, Berlin, **1990**, Vol. 156, p. 199.
8. H.-J. Timpe, In: *Topics in Current Chemistry*, Mattay, J., Ed., Springer-Verlag, Berlin, **1990**, Vol. 156, p. 167.
9. J.P. Fouassier, *Photoinitiators, Photopolymerization and Photocuring*, VCH, Weinheim, **1995**.
10. J.F. Rabek, *Mechanisms of Photophysical and Photochemical Reactions in Polymers*, Wiley, Chichester, **1987**.
11. B.M. Monroe, G.C. Weed, *Chem. Rev.* **1993**, 93, 435.
12. R.A. Marcus, *J. Chem. Phys.* **1956**, 24, 966.
13. R.A. Marcus, *J. Chem. Phys.* **1963**, 67, 853.
14. R.A. Marcus, *J. Chem. Phys.* **1965**, 43, 679.
15. R.O. Loutfy, *Macromolecules* **1981**, 14, 270.
16. R.O. Loutfy, *J. Polym. Sci. Phys. Ed.* **1982**, 20, 825.
17. R.O. Loutfy, *Pure Appl. Chem.*, **1986**, 58, 1239.

18. H. Morawetz, *J. Luminescence* **1989**, *43*, 59.
19. J. Pączkowski, D.C. Neckers, *Chemtracs—Macromol. Chem.*, **1992**, *3*, 75.
20. D.A. Holden, J.E. Guillet, *Developments in Polymer Photochemistry*, Applied Science, London, **1980**, Vol. 1, Chapter 2, pp. 27–68.
21. J.E. Guillet, *Polymer Photophysics and Photochemistry*, Cambridge University Press, Cambridge, **1985**.
22. J.G. Kloosterboer, *Advances in Polymer Science*, **1988**, *84*, 1.
23. L.Y. Lan, G.B. Schuster, *Tetrahedron Lett.* **1986**, *27*, 4261.
24. S. Chatterjee, P. Gottschalk, P.D. Davis, G.B. Schuster, *J. Am. Chem. Soc.* **1988**, *110*, 2326.
25. S. Chatterjee, P.D. Davis, P. Gottschalk, B. Kurz, X. Yang, G.B. Schuster, *J. Am. Chem. Soc.* **1990**, *112*, 6329.
26. For examples of cyanine dyes, see: P. Gottschalk, D.C. Neckers, G.B. Schuster, U.S. Patent 4772530, **1980**; *Chem. Abstr.* **1987**, *107*, 187434n; U.S. Patent 4842980, **1988**; *Chem. Abstr.* **1987**, *107*, 187434n; (b) P. Gottschalk, U.S. Patent 4874450, **1989**; (c) G.C. Weed, B.M. Monroe, U.S. Patent 5143818, **1992**.
27. X. Yang, A. Zaitsev, B. Sauerwein, S. Marphy, G.B. Schuster, *J. Am. Chem. Soc.* **1992**, *114*, 793.
28. S. Murphy, X. Yang, G.B. Schuster, *J. Org. Chem.* **1995**, *60*, 2411.
29. D.J. Owen, G.B. Schuster, *J. Am. Chem. Soc.* **1996**, *118*, 259.
30. A.M. Sarker, A. Mejiritski, B.R. Wheaton, D.C. Neckers, *Macromolecules* **1997**, *30*, 2268.
31. A.M. Sarker, A. Lungu, A. Mejiritski, Y. Kaneko, D.C. Neckers, *J. Chem. Soc., Perkin Trans. 2* **1998**, 2315.
32. D. Griller, K.U. Ingold, L.K. Patterson, J.C. Scaiano, R.D. Small Jr., *J. Am. Chem. Soc.* **1979**, *101*, 3780.
33. D. Rehm, A. Weller, *Ber. Bunsen-Ges. Phys. Chem.* **1969**, *73*, 834.
34. D. Rehm, A. Weller, *Isr. J. Chem.* **1970**, *8*, 259.
35. N. Kabate, M. Pietrzak, J. Pączkowski, *Macromolecules* **1998**, *31*, 4651.
36. O. Valdes-Aguilera, C.P. Pathak, J. Shi, D. Watson, D.C. Neckers, *Macromolecules* **1992**, *25*, 541.
37. M. Matsuoka, T. Hikida, K. Murobushi, Y. Hosoda, *J. Chem. Soc., Chem. Commun.* **1993**, 299.
38. J. Yamaguchi, F. Shinizaki, M. Okazaki, K. Adachi, U.S. Patent 4952480, **1990**; *Chem. Abstr.* **1989**, *111*, 222119v.
39. J. Yamaguchi, M. Okazaki, Y. Inagaki, U.S. Patent 5011760, **1991**; *Chem. Abstr.* **1989**, *111*, 205472n.
40. J. Yamaguchi, M. Okazaki, T. Hioki, U.S. Patent 4902604, **1990**; *Chem. Abstr.* **1989**, *111*, 244332m.
41. K. Kawamura, Y. Okamoto, U.S. Patent 4971891, **1990**; *Chem. Abstr.* **1989**, *111*, 222173h.
42. J.L. Dektar, N.P. Hacker, *J. Org. Chem.*, **1990**, *55*, 639.
43. S.P. Pappas, L.R. Gatechair, J.H. Jilek, *J. Polym. Sci., A: Polym. Chem.* **1984**, *22*, 77.
44. S.P. Pappas, B.C. Pappas, L.R. Gatechair, J.H. Jilek, *Polym. Photochem.*, **1984**, *5*, 1.
45. R.J. DeVoe, M.R.V. Sahyun, E. Schmidt, N. Serpone, D.K. Sharma, *Can. J. Chem.* **1988**, *66*, 319.
46. M. Tilley, B. Pappas, S.P. Pappas, Y. Yagci, W. Schnabel, J.K. Thomas, *J. Imaging Sci.* **1989**, *33*, 62.
47. J.L. Dektar, N.P. Hacker, *J. Am. Chem. Soc.* **1990**, *112*, 6004.
48. K. Iu, J. Kuczynski, S.J. Fuerniss, J.K. Thomas, *J. Am. Chem. Soc.* **1992**, *114*, 4871.
49. J.V. Crivello, J.L. Lee, *Macromolecules* **1981**, *14*, 1141.
50. S.M. Linden, D.C. Neckers, *J. Photochem. Photobiol. A: Chem.* **1988**, *47*, 543.
51. S.M. Linden, D.C. Neckers, *J. Am. Chem. Soc.* **1988**, *110*, 1257.
52. Y. Bi, D.C. Neckers, *J. Photochem. Photobiol. A: Chem.* **1993**, *74*, 1993.
53. a) A.M. DeRaaff, T.L. Marino, D.C. Neckers, *RadTech Report*, May, **1996**, pp. 7–16; b) D.C. Neckers, A.M. Sarker, S.A. Hassoon, A.Y. Polykarpov, A.M. DeRaaff, T.L. Marino, "Photoinitiator Composition Containing a Borate Salt and a Hypervalent Heteroatom-containing Salt and Anaerobic Photohardenable Composition Employing the Same", PCT/US 9619806; WO 97/21/211737; June 19, **1997**.

54. a) K. Feng, H. Zang, D. Martin, T.L. Marino, D.C. Neckers, *J. Polym. Sci.: Part A: Polym. Chem.* **1998**, *36*, 1667; b) A.M. Sarker, A.Y. Polykarpov, A.M. DeRaaff, T.L. Marino, D.C. Neckers, *J. Polym. Sci., Part A: Polym. Chem.* **1996**, *34*, 2817; c) S.A. Hassoon, D.C. Neckers, *J. Phys. Chem.* **1995**, *99*, 9416.
55. Y. Toba, Y. Usui, M.M. Alam, O. Ito, *Macromolecules* **1998**, *31*, 6022.
56. Y. Toba, M. Yasuike, Y. Usui, *Chem. Commun.* **1997**, 675.
57. J.V. Crivello, J.H.W. Lam, *Macromolecules* **1977**, *10*, 1307.
58. J.V. Crivello, J.L. Lee, *J. Polym. Sci., Part A: Polym. Chem.* **1989**, *27*, 3951.
59. F. Castellanos, J.P. Fouassier, C. Priou, J. Cavezzan, *J. Appl. Polym. Sci.* **1996**, *60*, 705.
60. T. Tanabe, A. Torres-Filho, D.C. Neckers, *J. Polym. Sci., Part A: Polym. Chem.* **1995**, *33*, 1691.
61. A. Y. Polykarpov, D.C. Neckers, *Tetrahedron Lett.* **1995**, *36*, 5483.
62. S. Gupta, N. Gupta, D.C. Neckers, *J. Polym. Sci.: Polym. Chem. Ed.* **1981**, *19*, 103.
63. S. Gupta, N. Gupta, D.C. Neckers, *J. Polym. Sci.: Polym. Chem. Ed.* **1982**, *20*, 147.
64. E. Morlino, M. Bohorques, D.C. Neckers, M.A.J. Rodgers, *J. Am. Chem. Soc.* **1991**, *113*, 2599.
65. S. Hasson, A. Sarker, M.A.J. Rodgers, D.C. Neckers, *J. Am. Chem. Soc.* **1995**, *117*, 11369.
66. S. Hasson, A. Sarker, A.Y. Polykarpov, M.A.J. Rodgers, D.C. Neckers, *J. Phys. Chem.* **1996**, *100*, 12386.
67. A.M. Sarker, Y. Kaneko, A.V. Nikolatichik, D.C. Neckers, *J. Phys. Chem.* **1998**, *102*, 375.
68. R. Popielarz, A.M. Sarker, D.C. Neckers, *Macromolecules* **1998**, *31*, 951.
69. S. Hu, A.M. Sarker, Y. Kaneko, D.C. Neckers, *Macromolecules* **1998**, *31*, 6476.
70. W.J. Leigh, D.R. Arnold, *J. Chem. Soc., Chem. Commun.* **1980**, 406.
71. J.B. Gallivan, *Can. J. Chem.* **1972**, *50*, 3601.
72. B.L. Selinger, *Aust. J. Chem.* **1966**, *19*, 825.
73. W.W. Mantulin, P.S. Song, *J. Am. Chem. Soc.* **1973**, *95*, 5122.
74. O. Grinevich, P. Serguevski, A.M. Sarker, W. Zhang, A. Mejiritski, D.C. Neckers, *Macromolecules* **1999**, *32*, 328.
75. A.M. Sarker, A. Lungu, D.C. Neckers, *Macromolecules* **1996**, *29*, 8047.
76. G.B. Schuster, X. Yuang, C. Zou, B. Sauerwien, *J. Photochem. Photobiol. A: Chem.* **1992**, *65*, 191.
77. N. Kita, M. Koike, U.S. Patent 4937 161, 1990; *Chem. Abstr.* **1989**, *110*, 183029y.
78. J.J.M. Lamberts, D.R. Schumacher, D.C. Neckers, *J. Am. Chem. Soc.* **1984**, *106*, 5879.
79. J. Pączkowski, J.J.M. Lamberts, B. Pączkowska, D.C. Neckers, *J. Free Radicals Biol. Med.* **1985**, *1*, 341.
80. V. Kasche, L. Lindquist, *Photochem. Photobiol.* **1965**, *4*, 923.
81. V. Winttges, J.C. Scaiano, S.M. Linden, D.C. Neckers, *J. Org. Chem.* **1989**, *54*, 5242.
82. D.C. Neckers, K.S. Raghuveer, O. Valdes-Aguilera, *Polymeric Mater. Sci. Eng.* **1989**, *60*, 15.
83. A. Zakrzewski, D.C. Neckers, *Tetrahedron* **1987**, *43*, 4507.
84. J. Shi, X. Zhang, D.C. Neckers, *J. Org. Chem.* **1992**, *57*, 4418.
85. J. Shi, X. Zhang, D.C. Neckers, *Tetrahedron Lett.* **1993**, *34*, 6013.
86. E. Klimtchuk, M.A.J. Rodgers, D.C. Neckers, *J. Phys. Chem.* **1992**, *96*, 9817.
87. S. Hassoon, D.C. Neckers, *J. Phys. Chem.* **1995**, *99*, 9416.
88. D.C. Neckers, S. Hassoon, E. Klimtchuk, *J. Photochem. Photobiol. A: Chem.* **1996**, *95*, 33.
89. A.Y. Polykarpov, S. Hassoon, D.C. Neckers, *Macromolecules* **1996**, *29*, 8274.
90. E.T. Seo, R.F. Nelson, J.M. Fritsch, L.S. Marcoux, O.W. Leedy, R.N. Adams, *J. Am. Chem. Soc.* **1966**, *88*, 3498.
91. A.K. Chibisov, *Russ. Chem. Rev.* **1981**, *50*, 615.
92. A. Weller, *Z. Physik. Chem. Neue Folge* **1982**, *133*, 93.
93. M. Kuzmin, I.V. Soboleva, *Prog. React. Kinet.* **1986**, *14*, 157.
94. E.M. Kosower, *Annu. Rev. Phys. Chem.* **1986**, *37*, 127.
95. G.J. Kavarnos, N.J. Turro, *Chem. Rev.* **1986**, *86*, 401.
96. P. Suppan *Chimia* **1988**, *42*, 320.
97. M.R. Sandner, R.M. Osborn, D.J. Trecker, *J. Polym. Sci. A-1* **1972**, *10*, 3173.
98. S.G. Cohen, J.B. Parola, G.H. Parsons, *Chem. Rev.* **1973**, *73*, 141.
99. J.D. Simon, K.S. Peters, *J. Am. Chem. Soc.* **1981**, *103*, 6403.

100. U.G. Yoon, P.S. Marino, R.S. Givens, B.W. Atwater III, "Photoinduced Electron Transfer Chemistry of Amines and Related Electron Donors", In *Advances in Electron Transfer Chemistry*, JAI Press, **1994**, Vol. 4, pp. 117–205.
101. L.E. Manring, K.S. Peters, *J. Am. Chem. Soc.* **1985**, *107*, 6452.
102. C. Gevadoss, R.W. Fessenden, *J. Phys. Chem.* **1990**, *94*, 4540.
103. C. Gevadoss, R.W. Fessenden, *J. Phys. Chem.* **1991**, *95*, 7253.
104. H. Miyasaka, K. Morita, K. Kamada, N. Mataga, *Chem. Phys. Lett.* **1991**, *178*, 504.
105. P. Gosh, R. Gosh, *Eur. Polym. J.* **1981**, *17*, 817.
106. S.R. Clarke, R.A. Shanks, *J. Macromol. Sci.* **1982**, *A17*, 77.
107. T. Li, *Polymer Bull.* **1990**, *24*, 397.
108. J. Kabatc, Z. Kucybała, M. Pietrzak, F. Ścigalski, J. Pączkowski, *Polymer* **1999**, *40*, 735.
109. S.L. Murov, I. Carmichael, G.L. Hug, *Handbook of Photochemistry*, 2nd ed., Marcel Dekker, New York, **1993**.
110. L. Ebersson *Electron Transfer Reactions in Organic Chemistry*, Springer-Verlag, Berlin, **1987**.
111. P. Suppan, "The Marcus Inverted Region", In *Topics in Current Chemistry*, Springer-Verlag, Berlin, **1992**, Vol., pp. 95–130.
112. S. Kato, T. Watanabe, S. Nagak, M. Koizumi, *Bull. Chem. Soc. Jpn.* **1980**, *33*, 262.
113. V. Kasche, L. Lindquist, *J. Phys. Chem.* **1967**, *68*, 817.
114. A. Mills, C. Lawrence, P. Douglas, *J. Chem. Soc., Faraday Trans. 2* **1986**, *82*, 2291.
115. S.G. Cohen, A. Pavola, A. Parsons, Jr., *Chem. Rev.* **1973**, *73*, 141.
116. S.G. Cohen, *J. Am. Chem. Soc.* **1980**, *102*, 1419.
117. A. Torres-Filho, D.C. Neckers, *J. Polym. Sci.: Part A: Polymer Chem.* **1994**, *51*, 931.
118. T. Tanabe, A. Torres-Filho, D.C. Neckers, *J. Polym. Sci.: Part A: Polymer Chem.* **1995**, *33*, 1691.
119. Y. Bi, D.C. Neckers, *Macromolecules* **1994**, *27*, 8683.
120. T. Marino, O.L. Long, D.C. Neckers, *I&EC Research* **1995**, *34*, 4549.
121. J. Pączkowski, *RadTech Europe 97, Academic Days Lyon, France*, **1997**, pp. 77–84.
122. J. Pączkowski, Z. Kucybała, *Macromolecules* **1995**, *28*, 269.
123. H. Mateo, P. Bosh, A.E. Lozano, *Macromolecules* **1994**, *27*, 7794.
124. J. Hutchison, A. Ledwith, *Adv. Polym. Sci.* **1974**, *14*, 49.
125. A. Ledwith, In: *Developments in Polymerization*, Haward, R.N., Ed., Applied Science, London, **1982**, Chapter 2.
126. W.D. Cook, *Polymer* **1992**, *33*, 600.
127. a) R.W. Yip, R.O. Loutfy, Y.L. Chow, L.K. Magdzinski, *Can. J. Chem.* **1972**, *50*, 3426; b) J.B. Guttentplan, S.G. Cohen, *J. Am. Chem. Soc.* **1972**, *94*, 4040.
128. H. Rau, *Chem. Rev.* **1983**, *83*, 535.
129. M.C. Depew, J.K.S. Wan, *J. Phys. Chem.* **1986**, *90*, 6597.
130. G.A. Russell, K.Y. Chang, *J. Am. Chem. Soc.* **1965**, *87*, 4192.
131. a) A. Wrzyszczyński, E. Adamczak, L.-Å. Lindén, S. Morgen, J.F. Rabek, *Proceedings RadTech, Europe 95*, Maastricht, Netherlands, **1995**, p. 107; b) E. Adamczak, L.-Å. Lindén, J.F. Rabek, A. Wrzyszczyński, *Proceedings RadTech Asia'95*, Guilin, China, **1995**, p. 196; c) J. Nie, L.-Å. Lindén, J.F. Rabek, J.P. Fouassier, F. Morlet-Savary, F. Scigalski, A. Wrzyszczyński, E. Andrzejewska, *Acta Polym.* **1998**, *49*, 145; d) J. Nie, L.-Å. Lindén, J.F. Rabek, J. Ekstrand, *Angew. Makromol. Chem.* **1998**, *45*.
132. J. Meinwald, H.I. Klingele, *J. Am. Chem. Soc.* **1966**, *88*, 2071.
133. M.V. Encinas, C. Majmund, E.A. Lissi, *J. Polym. Sci.: Part A: Polym. Chem.* **1990**, *28*, 2465.
134. K. Hamanoue, K. Yokoyama, Y. Yamamoto, K. Sawada, Y. Yuhara, H. Teranishi, *Bull. Chem. Soc. Jpn.* **1988**, *61*, 1121.
135. K. Hamanoue, K. Yokoyama, Y. Kajiwara, M. Kimoto, T. Nakayama, H. Teranishi, *Chem. Phys. Lett.* **1985**, *113*, 207.
136. K. Hamanoue, K. Yokoyama, Y. Kajiwara, K. Nakajima, H. Teranishi, *Chem. Phys. Lett.* **1984**, *110*, 25.
137. T. Kausche, J. Säuberlich, Trobitzsch, D. Beckert, K.P. Dinse, *Chem. Phys.* **1996**, *208*, 375.
138. N.S. Allen, F. Catalina, P.N. Green, W.A. Green, *Eur. Polym. J.* **1986**, *22*, 49.
139. N.S. Allen, F. Catalina, P.N. Green, W.A. Green, *Eur. Polym. J.* **1986**, *22*, 347.

140. N.S. Allen, F. Catalina, B. Moghaddam, P.N. Green, W.A. Green, *Eur. Polym. J.* **1986**, 22, 691.
141. N.S. Allen, F. Catalina, P.N. Green, W.A. Green, *Eur. Polym. J.* **1986**, 22, 793.
142. N.S. Allen, F. Catalina, P.N. Green, W.A. Green, *Eur. Polym. J.* **1986**, 22, 871.
143. F. Catalina, C. Peinado, J.L. Mateo, P. Bosch, N.S. Allen, *Eur. Polym. J.* **1992**, 28, 1533.
144. N.S. Allen, F. Catalina, P.N. Green, W.A. Green, *J. Photochem. Photobiol.* **1987**, 36, 99.
145. F. Catalina, T. Corrales, C. Peinado, N.S. Allen, W.A. Green, A. Timms, *Eur. Polym. J.* **1993**, 29, 125.
146. F. Catalina, C. Peinado, J.L. Mateo, P. Bosch, N.S. Allen, *Eur. Polym. J.* **1992**, 28, 1533.
147. R.S. Davidson, P.F. Lambeth, *J. Chem. Soc., Chem. Commun.* **1967**, 1265.
148. R.S. Davidson, In: *Advances in Physical Organic Chemistry*, Bethell, D., Gold, V. (Eds.), Academic Press, London, **1983**, Vol. 16, p. 1.
149. R.S. Davidson, P.F. Lambeth, J.F. McKellar, P.H. Turner, R. Wilson, *J. Chem. Soc., Chem. Commun.* **1969**, 732.
150. D.G. Anderson, R.S. Davidson, J.J. Elvery, *Polymer* **1996**, 37, 2477.
151. C.M. Previtali, S.G. Bertolotti, M.G. Neumann, I.A. Pastre, A.M. Rufs, M.V. Encinas, *Macromolecules* **1994**, 27, 7454.
152. M.V. Encinas, C. Majmund, J. Garrido, E.A. Lissi, *Macromolecules* **1989**, 22, 563.
153. M.V. Encinas, C. Majmund, E.A. Lissi, J.C. Scaiano, *Macromolecules* **1991**, 24, 2111.
154. M.V. Encinas, E.E. Lissi, C. Majmund, J.J. Cosa, *Macromolecules* **1993**, 26, 6284.
155. T. Okada, I. Karaki, N. Mataga, *J. Am. Chem. Soc.* **1982**, 104, 7191.
156. N. Mataga, T. Okada, Y. Kanda, H. Shioyama, *Tetrahedron* **1986**, 42, 6143.
157. Y. Hirata, T. Saito, N. Mataga, *J. Phys. Chem.* **1987**, 91, 3119.
158. Y. Hirata, N. Mataga, *J. Phys. Chem.* **1985**, 89, 2439.
159. G.A. Delzene, *Adv. Photochem.* **1979**, 11, 1.
160. A.L. Prokhoda, V.A. Krongauz, *Khim. Vys. Energ.* **1970**, 4, 176; **1970**, 5, 262.
161. X.Z. Qin, A. Liu, A.D. Trifunac, *J. Phys. Chem.* **1991**, 95, 5822.
162. A. Liu, A.D. Trifunac, V.V. Krongauz, *J. Phys. Chem.* **1992**, 96, 207.
163. Y. Lin, A. Liu, A.D. Trifunac, V.V. Krongauz, *Chem. Phys. Lett.* **1992**, 198, 200.
164. M.D. Zammit, T.P. Davis, G.D. Willett, *Macromolecules* **1997**, 30, 5655.
165. R.S. Davidson, P.R. Steiner, *J. Chem. Soc., Chem. Commun.* **1971**, 1682.
166. R.S. Davidson, P.R. Harrison, P.R. Steiner, *J. Chem. Soc., Chem. Commun.* **1971**, 3480.
167. D.R. Barthomolew, D.R.G. Brimage, R.S. Davidson, *J. Chem. Soc., Chem. Commun.* **1971**, 3482.
168. S.-i. Nishimoto, H. Tada, T. Kagiya, *J. Chem. Soc., Perkin Trans. II* **1983**, 873.
169. B. Marciniak, K. Bobrowski, G.L. Hug, *J. Phys. Chem.* **1993**, 97, 11937.
170. K. Bobrowski, M. Marciniak, G.L. Hug, *J. Photochem. Photobiol.* **1994**, 81, 159.
171. B. Marciniak, K. Bobrowski, G.L. Hug, J. Rozwadowski, *J. Phys. Chem.* **1994**, 98, 4854.
172. K. Bobrowski, G.L. Hug, M. Marciniak, H. Kozubek, *J. Phys. Chem.* **1994**, 98, 537.
173. B. Marciniak, G.L. Hug, K. Bobrowski, H. Kozubek, *J. Phys. Chem.* **1995**, 99, 13560.
174. B. Marciniak, G.L. Hug, J. Rozwadowski, K. Bobrowski, *J. Am. Chem. Soc.* **1995**, 117, 127.
175. Z. Kucybała, M. Pietrzak, J. Pączkowski, L.-Å. Lindén, J.F. Rabek, *Polymer* **1996**, 37, 4585.
176. Z. Kucybała, J. Pączkowski, *Polymer* **1993**, 34, 1558.
177. Z. Kucybała, M. Pietrzak, J. Pączkowski, *Chem. Mater.* **1998**, 10, 2555.
178. Z. Kucybała, J. Pączkowski, *J. Photochem. Photobiol., A: Chem.* **1999**.
179. C. Decker, K. Moussa, *Makromol. Chem.* **1988**, 189, 2381.
180. C. Decker, K. Moussa, *Macromolecules* **1989**, 22, 4455.
181. C. Decker, K. Moussa, *ACS Symp. Ser.* **1990**, 417, 439 and references therein.
182. A. Wrzyszczyński, *Polymer*, **1999**, 40, 3247.
183. K. Bobrowski, B. Marciniak, G.L. Hug, *J. Am. Chem. Soc.* **1992**, 114, 102279.
184. A. Wrzyszczyński, P. Filipiak, G.L. Hug, B. Marciniak, J. Pączkowski, *Macromolecules* **2000**, 33, 1577.
185. E. Andrzejewska, *J. Polym. Sci. A: Polym. Chem.* **1992**, 30, 485.
186. E. Andrzejewska, M. Andrzejewski, *Polimery (Warsaw)* **1994**, 39, 22.
187. J.B. Gutterman, S.G. Cohen, *J. Org. Chem.* **1973**, 38, 2001.
188. S. Inbar, H. Linschitz, S.G. Cohen, *J. Am. Chem. Soc.* **1982**, 104, 1679.

189. J.C. Ronfard-Haret, R.V. Bensasson, J.C. Gramain *Chem. Phys. Lett.* **1983**, 96, 31.
190. B. Marciniak, E. Andrzejewska, G.L. Hug *J. Photochem. Photobiol., A: Chem.* **1998**, 112, 21.
191. E. Andrzejewska, G.L. Hug, M. Andrzejewski, B. Marciniak, *Macromolecules* **1999**, 32, 2173.
192. G. Pandey, *Topics in Current Chemistry* **1993**, 168, 175.
193. J. Pączkowski, M. Pietrzak, Z. Kucybała, *Macromolecules* **1996**, 29, 5057.
194. K.S. Anseth, C.M. Wang, C.N. Bowmann, *Macromolecules* **1994**, 27, 650.
195. B. Pączkowska, J. Pączkowski, D.C. Neckers, *Polimery* **1994**, 39, 527.
196. K.S. Anseth, C.M. Wang, C.N. Bowman, *Polymer* **1994**, 35, 3243.
197. D.L. Kurdikar, N.A. Peppas, *Macromolecules* **1994**, 27, 4084.
198. E. Andrzejewska, M.B. Bogacki, *Macromol. Chem. Phys.* **1997**, 198, 1649.
199. M.P. Stevens, *Polymer Chemistry*, Oxford University Press, New York, **1999**, p. 178.

Volume V

Part 3

Energy and the Environment

1 Solar Energy Conversion

Michael Grätzel and Jacques-E. Moser

1.1 Introduction and Scope

There can be no question that the quality of human life is intimately associated with the ready availability of energy resources. At present, the world's energy consumption rate already exceeds the stunning figure of 6000 GW. This is expected to grow rapidly in the next decades due to the increase in demand from the developing countries. The overwhelming part of our energy supply arises from the chemical energy stored in the fossil fuels. These reserves are being rapidly depleted and their combustion has led to unacceptable levels of pollution of our environment. Further acceleration of this process would lead to disastrous climatic consequences. It is evident that the wellbeing of mankind is threatened unless renewable energy resources can be developed in the near future. Photochemistry is expected to make decisive contributions to identifying environmentally friendly solutions to the energy problem. One attractive strategy discussed below is the development of systems that mimic natural photosynthesis in the conversion and storage of solar energy. Electron transfer reactions play a vital role in the light-induced charge separation that forms the basis of this process. Our review will treat such redox processes that lead to the conversion of light to electric power and the storage of solar energy in the form of chemical fuels such as hydrogen. We shall focus our discussion on heterogeneous electron transfer reactions that occur on solid–liquid interfaces that are of particular interest in this connection. To start with, we shall briefly analyze the thermodynamic limitations of light energy conversion processes.

1.2 Efficiency Restrictions in Photochemical Conversion

The primary concern of photochemists and chemists when they run a reaction is the mass yield of product. In chemical reactions whose aim is to convert chemicals into

fuels, in electrochemical reactions which convert electricity to chemical potential or vice versa, and in photochemical reactions which convert light into chemical potential or work, the free energy yield is of equal importance. The laws of thermodynamics impose limitations on the efficiency of the conversion of light energy into chemical potential. Free energy losses in the sequence of steps during a photochemical process have several origins, which will be considered in the following order [1]: 1) nonequilibrium conditions at maximum power, 2) the entropy of the radiation source, 3) the entropy increase on scattering or absorption of the original radiation, 4) the inefficiency of energy conversion under polychromatic radiation. Further limitations associated to the storage of the chemical potential will not be discussed here.

1.2.1 Maximum Power Extraction

General to all reactions, whether photochemical or not, is the loss of free energy caused by nonequilibrium conditions due to finite power extraction. Consider a chemical reaction in which a reactant A at chemical potential μ_A is converted into a product B at chemical potential μ_B .



The rate of storage of chemical potential in the product B per unit of volume is $J \cdot \mu_B$, where the flux $J = -d[A]/dt = d[B]/dt$. If A and B are in equilibrium, the rates of the forward and back reactions are equal and the net flux to the product $J = j_f - j_b = 0$. Under nonequilibrium conditions where the forward reaction takes place with $J > 0$, there is a net overall entropy increase and $\mu_B < \mu_A$. If K is the equilibrium constant for reaction $\text{A} \rightleftharpoons \text{B}$ in ideal conditions, the change in chemical potential is given by the van't Hoff isotherm:

$$\Delta\mu = \mu_B - \mu_A = -RT \ln K + RT \ln([B]/[A]) \quad (2)$$

By putting $K = k_f/k_b$, where k_f and k_b are the rate constants of reactions $\text{A} \rightarrow \text{B}$ and $\text{B} \rightarrow \text{A}$, respectively, and by substituting the fluxes defined by $j_f = k_f [A]$ and $j_b = k_b [B]$, one obtains the expression for the free energy loss in a spontaneous reaction:

$$\Delta\mu = RT \ln(1 - \varphi) \quad (3)$$

where $\varphi = J/j_f$. The conversion power P of the reaction is given by the rate of production of chemical potential in the form of the product B at the potential μ_B : $P = J\mu_B = J(\mu_A + \Delta\mu)$. At maximum power, the reaction flux J is given by:

$$\frac{\varphi}{1 - \varphi} - \ln(1 - \varphi) = \frac{\mu_A}{RT} \quad (4)$$

and the free energy transfer efficiency η_p is:

$$\eta_p = \frac{\mu_A + \Delta\mu}{\mu_A} \quad (5)$$

The amount of chemical potential converted in a photochemical reaction is typically of the order of 1–2 eV. If $\mu_A = 1$ eV, one calculates from the latter equations $\varphi = 0.972$, $\Delta\mu = -0.093$ eV, and $\eta_p = 0.91$.

If the product B is involved in a leakage reaction to yield an undesired product C with a rate constant k_l , Eq. (4) can be rewritten:

$$\frac{\varphi - \kappa}{1 - \varphi} - \ln(1 - \varphi) = \frac{\mu_A}{RT} \quad (6)$$

with $\kappa = k_l/(k_b + k_l)$, and the free energy conversion efficiency at maximum power is:

$$\eta_p = \left[1 - \frac{k_l(\varphi - 1)}{k_b} \right] \cdot \frac{\mu_A + \Delta\mu}{\mu_A} \quad (7)$$

Assuming a leakage reaction with $k_l = k_b$, and $\mu_A = 1$ eV, one obtains $\kappa = 0.5$, $\varphi = 0.986$, $\Delta\mu = -0.110$ eV, and $\eta_p = 0.89$. If k_l is increased by a factor of ten, the efficiency decreases slightly to $\eta_p = 0.85$.

1.2.2 Limitations due to the Entropy of Light

The fact that radiation possesses entropy imposes additional constraints on the possible changes in a material system interacting with light. These constraints determine, in particular, the efficiency of processes involving the utilization of radiant energy.

Let consider a photochemical reaction without leakage, where the only fates of the product A^* are reaction to give the final product (with flux i) and reverse reaction (with flux j_b). The potential of the reactants is composed of the chemical potential μ_A of A and the potential μ_R of the radiation or, by analogy with chemical potentials, the partial molar free energy of the absorbed light quanta.



The change in potential during the light absorption process is given by:

$$\Delta\mu = \mu_{A^*} - \mu_A - \mu_R = RT \ln(1 - \varphi) \quad (9)$$

If the radiation is monochromatic at wavelength λ , its total energy is Q_R [J Einstein⁻¹] = $\mathcal{N}_A \cdot hc/\lambda$, where \mathcal{N}_A is Avogadro's number, and the entropy associated with it $\Delta S_R = \Delta Q_R/T_R$. The effective temperature T_R of the monochromatic radiation of wavelength λ and of a given spectral irradiance I_λ is expressed by Eq. (10),

$$T_R = \frac{hc}{k_B \lambda} \cdot \frac{1}{\ln \left(1 + \frac{2hc^2 \Omega}{\lambda^5 I_\lambda} \right)} \quad (10)$$

where Ω is the solid angle subtended by the source at the receiver (including any optical concentrator). The spectral irradiance I_λ is the energy of the radiation incident on a unit area per unit time and unit wavelength interval at a given wavelength λ . Thus, we may write the dimensions of I_λ as, for example, $[I_\lambda] = W \, m^{-2} \, nm^{-1}$. Equation (10) for T_R is the same as the Planck formula for a black body giving the same spectral irradiance I_λ at the same wavelength λ for unit wavelength interval and unit solid angle. Thus rays of light propagating in a specified direction and delivering at the receiver a spectral irradiance I_λ possess a temperature equal to that of a black body emitting radiation and giving rise to the same irradiance.

The entropy of the radiation ΔS_R is lost when the light disappears in the absorption process. An equivalent amount of entropy must then be created in the absorber at ambient temperature T_A . Therefore, the maximum energy available to do work at temperature T_A is given by:

$$\mu_R = \frac{Q_R(T_R - T_A)}{T_R} \quad (11)$$

The maximum possible conversion efficiency is then expressed by what appears to be simply the Carnot formula applied to radiation:

$$\eta_r = \frac{\mu_R}{Q_R} = \frac{T_R - T_A}{T_R} \quad (12)$$

The Sun delivers a spectral irradiance at the Earth's surface at AM 1.0 (air mass), without concentrator, of $1.16 \, W \, m^{-2} \, nm^{-1}$ at $\lambda = 700 \, nm$ [2]. The solid angle represented by the Sun seen from the Earth is $\Omega = 6.8 \times 10^{-5}$ steradian. From Eq. (10), one calculates in this case $T_R = 5500 \, K$, and from Eq. (12) with $T_A = 298 \, K$ one obtains $\eta_r = 0.946$. If the solar spectrum were that of a black body, all wavelengths would lead to the same values of T_R and η_r . Figure 1 shows that this condition is fulfilled only if the receiver is outside the atmosphere. At the Earth's surface, absorption by atmospheric oxygen, ozone, water, and carbon dioxide makes the structured solar irradiance spectrum deviate significantly from the ideal black-body spectrum and requires $T_R(\lambda)$ to be calculated for each wavelength.

1.2.3 Further Increase of Entropy on Absorption or Scattering

Apart from the entropy of the original radiation, a second source of entropy must be taken into account that causes losses of free energy in the course of the photochemical reaction. Upon absorption, the directionality of the radiation beam is indeed completely lost. The entropy thus increases, while the radiation temperature

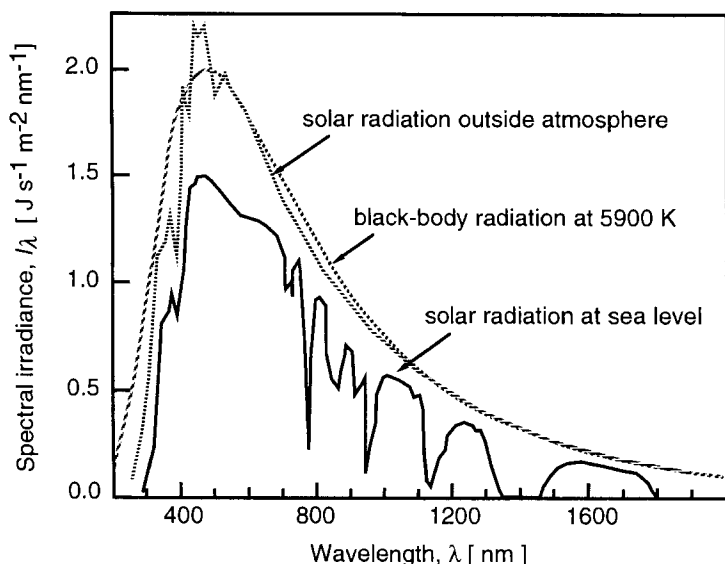


Figure 1. Spectral irradiance of the Sun at mean Earth–Sun separation.

decreases. An equivalent effect is obtained when the original directional radiation concentrated in a small solid angle is scattered in all directions. The temperature of the scattered light is obtained by replacing the solid angle Ω in Eq. (10) by the value 4π corresponding to isotropic radiation at the receiver:

$$T_{Rs} = \frac{hc}{k_B \lambda} \cdot \frac{1}{\ln \left(1 + \frac{8\pi hc^2}{\lambda^5 I_\lambda} \right)} \quad (13)$$

With the same numerical values as above for the irradiance of the Sun at 700 nm, the scattering of the radiation over 4π , or (which is strictly equivalent) its absorption in a photochemical reaction, cause its effective temperature to decrease from $T_R = 5500$ K to $T_{Rs} = 1297$ K. The maximum efficiency calculated from Eqs. (11) and (12) then drops from $\eta_r = 0.95$ to $\eta_{rs} = 0.77$. The solid angle does no longer appears in Eq. (13). It should be borne in mind, however, that if the solid angle of collection is increased at the absorber by use of an optical concentrator, the measured irradiance, and hence the temperature, potential, and efficiency increase in proportion. In the same conditions as in the example above, concentration of the incident radiation by a factor of 10, for instance, translates into a rise of the radiation temperature from 1297 to 1517 K and an augmentation of the maximum conversion efficiency from 0.77 to 0.80.

Under optimum conditions of maximum power, the extraction flux $J = J_{\max}$ is given by Eq. (4), or more generally, if there are leakage processes, by Eq. (6). The global efficiency η_g of conversion of light into chemical potential at maximum

power can be expressed by:

$$\eta_g = \frac{\lambda(\mu_{A^*} - \mu_A)}{\mathcal{N}_A hc} = 1 - \frac{T_A}{T_R} - \frac{RT_A \lambda}{\mathcal{N}_A hc} \cdot \ln(4\pi/\Omega) + \frac{RT_A \lambda}{\mathcal{N}_A hc} \cdot \ln(1 - \varphi) \quad (14)$$

The last three terms represent the fractional losses due to 1) the entropy of the original radiation, 2) the entropy increase due to absorption or scattering of light, and 3) the minimum loss caused by nonequilibrium conditions at power extraction. For $\lambda = 700$ nm and AM 1.0 solar radiation, $\mu_{R_s} = 1.36$ eV. By substitution of $\mu/RT = 52.9$ in Eq. (4), one obtains $\varphi = 0.97$, the maximum global efficiency being finally estimated as $\eta_g = 1 - 0.055 - 0.180 - 0.058 = 0.71$.

If there are leakages from the excited state due to radiationless deactivation processes, Eq. (6) must be used with $\kappa = 1 - \Phi_f$, where Φ_f is the fluorescence quantum yield of A in the absence of reaction. These leakages will increase the last term of the summation in Eq. (14) and hence lower the global conversion efficiency. In the above example, if $\Phi_f = 0.5$ ($\kappa = 0.5$), the flux ratio φ is increased from 0.98 to 0.99 and the global conversion efficiency at maximum power is slightly reduced from 0.71 to 0.70.

1.2.4 Efficiency of Energy Conversion under Polychromatic Radiation

So far, calculations have assumed that the energy of the excited state is equal to that of the absorbed photon. This is not the case for polychromatic radiation when a single absorber is used. Losses due to nonabsorption or the degradation of energy in excess of the excitation energy of A^* are generally not avoidable. The simplest and most important case with which we are concerned is that of an absorber with a threshold excitation wavelength λ_t . In a somewhat idealized form, the properties of a threshold converter are:

- 1) the absorbance of the system is 0 for light with wavelength λ superior to the threshold wavelength λ_t ;
- 2) all absorbed quanta produce the same excited state with an excitation energy hc/λ_t ;
- 3) the excess energy $hc/\lambda - hc/\lambda_t$ is transferred to the medium as radiation or heat (Figure 2).

Assuming that no reaction can take place from hot excited-state levels, all absorbed photons, after degradation of excess energy, give rise to the same excitation energy hc/λ_t . The fraction θ of the energy absorbed from a polychromatic source which is available in the photochemical conversion process is given by Eq. (15),

$$\theta = \frac{\int_0^{\lambda_t} F_\lambda \frac{\lambda}{\lambda_t} d\lambda}{\int_0^\infty F_\lambda d\lambda} \quad (15)$$

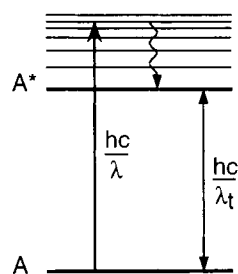


Figure 2. Schematic of threshold conversion.

where F_λ is the spectral radiation flux incident on the converter from an external source. For a threshold wavelength of 700 nm and AM 1.0 solar radiation (Figure 1), the fraction $\theta = 0.38$ [3].

Obviously, the value of θ , and thus that of η_0 , depends on the value of the threshold wavelength λ_t . For a given spectral distribution of the incident radiation energy, an optimal threshold wavelength exists which yields a maximum θ . The optimal threshold wavelength for a given spectrum of the incident radiation may be determined from Eq. (15). The calculation shows, for example, that for Planckian radiation (whose spectral distribution matches that of a black body at the same temperature) with a temperature $T_R = 5200$ K (direct solar light at AM 1.5), the optimal wavelength is $\lambda_t^{\text{opt}} = 1273$ nm, and accordingly $\theta^{\text{opt}} = 0.44$. This wavelength is near the absorption threshold of silicon solar cells. Therefore, at $\lambda = 700$ nm, $T_A = 25^\circ\text{C}$, and for AM 1.5 radiation, the maximum thermodynamic overall energy conversion efficiency of these photovoltaic cells is $\eta_o = \eta_g \times \theta = 0.70 \times 0.44 = 0.31$. For green plants, the threshold wavelength determined by the optical properties of chlorophyll is 700 nm. In this case, for AM 1.5 irradiation $\theta = 0.34$, giving an overall conversion efficiency $\eta_o = 0.24$. Molecular photovoltaic devices that will be discussed in Section 1.4 are based on dye-sensitizers whose absorption threshold, for the most efficient ones, is typically $\lambda_t = 800\text{--}900$ nm. The thermodynamic limiting energy conversion efficiency for these photoconverters is thus somewhat lower than that of silicon cells and does not exceed 0.27 at any wavelength under AM 1.5 solar irradiation.

1.3 Status of Photochemical Energy Conversion Systems

Photovoltaic devices are based on the concept of charge separation at an interface of two materials having different conduction mechanisms, normally between solid-state materials, either n- and p-type regions with electron and hole majority carriers in a single semiconductor material, heterojunctions between different semiconductors, or semiconductor–metal (Schottky) junctions. In photoelectrochemical cells, the junctions are semiconductor–electrolyte interfaces. In recent years, despite prolonged effort, disillusion has grown about the prospects of electrochemical photo-

effects at these interfaces giving rise to competitive photovoltaic devices, since those semiconductors with bandgaps sufficiently narrow for efficient optical absorption of visible-light photons are necessarily insufficiently stable against photocorrosion. The width of the bandgap is a measure of the chemical bond strength. The semiconductors stable under illumination, typically the ceramic oxides of reactive metals such as titanium, therefore have a wide bandgap, an absorption edge toward the ultraviolet and a consequent insensitivity to the visible spectrum. Hence the breakthrough represented by the separation of the optical absorption and the charge separation processes in photoelectrochemistry, realized by the association of a redox dye as light-absorbing material with the wide-bandgap semiconductor. These sensitized semiconductor systems will be discussed further below.

The main thrust of the research in photoelectrochemistry during the 1970s and 1980s has been to develop systems for the splitting of water into hydrogen and oxygen. The main obstacles to direct photoelectrolysis of water are the lack of efficient light absorption (for reasonable solar efficiencies, the bandgap must be less than 2.0 eV), corrosion of the semiconductor (thermodynamically, most useful semiconductors are photochemically unstable in water), and energetics (i.e., the difficulty of matching the semiconductor band-edge energies with the H_2 and O_2 evolution reactions). The most photochemically stable semiconductors in aqueous solution are oxides, but either their bandgaps are too large for efficient light absorption or their semiconductor characteristics are poor. Semiconductors with better solid-state characteristics are typically thermodynamically unstable with respect to oxidation. However, p-type semiconductors generally offer some protection against photocorrosion, because under illumination the surface is cathodically protected. p-Type indium phosphide is stable in strong acid under illumination and H_2 evolution, but requires an external bias for water splitting. This earlier work on the photoelectrolysis of water has been reviewed [4].

1.4 Molecular Photovoltaics

In a conventional p-n junction photovoltaic cell made, for example, of silicon, the semiconductor assumes two roles simultaneously: it harvests the incident sunlight and conducts the charge carriers produced under light excitation. In order to function with a good efficiency, the photons have to be absorbed in the vicinity of the p-n interface. Electron-hole pairs produced away from the junction must diffuse to the p-n contact, where the local electrical field separates the charges. To avoid charge carrier recombination during the diffusion, the concentration of defects in the solid must be small. This imposes severe requirements on the purity of the semiconductor material, rendering solid-state devices of the conventional type quite expensive. Molecular photovoltaic systems separate the functions of light absorption and carrier transport. Light harvesting is carried out by a dye-sensitizer which initiates electron transfer events leading to charge separation. This renders unnec-

essary the use of expensive solid-state components in the system. Although they are simple from the conceptual point of view, the practical implementation of such devices must overcome several serious obstacles if the aim is to develop molecular systems which convert sunlight to electricity at an efficiency comparable with that of silicon cells, and meet the stability criteria for practical applications.

1.4.1 Mimicking Natural Photosynthesis

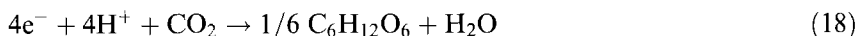
Natural photosynthesis is the most important of the many interesting photochemical processes known in biology. Not only was the evolution of the Earth's atmosphere dependent on it, but it is also the main route by which the free energy of the environment is made available to the living world. Green plants, algae and cyanobacteria make use of sunlight to drive a thermodynamically uphill reaction, the reduction of carbon dioxide to carbohydrates by water:



The input chemicals are carbon dioxide and water, while the output is oxygen and carbohydrates. The latter serve as a feedstock for other organic products such as wood, coal, oil, and gas constituting the World's fossil fuel reserves. It is estimated that about 10^{11} tons of carbon dioxide are assimilated annually by plants on Earth, whereby the amount of solar energy harvested by natural photosynthesis is 3×10^{18} kJ, corresponding to the continuous generation of 90 000 GW of electrical power.

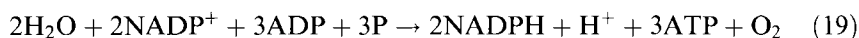
Most of the key features of the manner in which photosynthetic energy conversion operates are known by now. Light-induced charge separation is achieved through judicious spatial arrangement of the pigments and elements of the electron transport chain in the tylakoid membrane. Cooperative interaction between these components allows the electron transfer to proceed in a vectorial fashion. Although strategies to design artificial photoconversion devices should not attempt to blindly imitate all the intricacies of natural photosynthesis, it is inconceivable to accomplish the challenging task of converting visible light into electrical work or chemical potential without suitable engineering on the molecular level. Efficient molecular photovoltaic devices described below and tandem systems for water cleavage by visible light presented in Section 1.5 use similar concepts to those involved in harvesting and conversion of solar energy by green plants. It is therefore useful to review the salient features of their natural analogs.

The essence of natural photosynthesis is the use of photochemical energy to split water and reduce CO_2 . Molecular oxygen is evolved in the reaction, although it appears at an earlier stage in the sequence of reactions than the reduction of carbon dioxide. Photochemical processes produce compounds of high chemical potential, which can drive a multistep synthetic sequence from CO_2 to carbohydrate in a cyclic way. Reaction (16) is quite endoergic and thus thermodynamically very improbable in the dark ($\Delta G^0 = 522$ kJ per mole of CO_2 converted). Production of one molecule of oxygen and concomitant conversion of one molecule of carbon dioxide require the transfer of four electrons:



Reaction (16) is the sum of reactions (17) and (18). Clearly, if each photon harvested by the system can lead to the transfer of one electron, then a minimum of four photons are required for the conversion of each CO_2 molecule. Experimental measurements of the quantum yield indicate that eight photons are actually needed, suggesting that two photons are used for each electron transfer and that a two-step process is taking place with long-lived intermediates coupling the steps.

Photosynthesis comprises a light-induced and a dark reaction. The first, called photophosphorylation, involves the two-electron reduction of nicotinamide adenine dinucleotide phosphate (NADP^+) by water, to produce NADPH and oxygen. The redox reaction is coupled to the generation of adenosine triphosphate (ATP) from adenosine diphosphate (ADP):



where P stands for the phosphate PO_4^{3-} anion. This light-driven reaction takes place in the tylakoid membranes located in the interior of the chloroplasts of plant cells. The photosynthetic unit assembled in these membranes is composed of antenna pigments for light energy harvesting, i.e., chlorophyll and carotenoids, as well as a reaction center consisting of two photosystems. The photons absorbed by the antenna pigments are first transferred to a chlorophyll dimer that is part of the reaction center. The electronic excitation causes electrons to be ejected from the chlorophyll dimer and then passed on to various electron-transferring mediators. The judicious spatial arrangement of these components allows the electrons to be transferred in a vectorial fashion from the inner to the outer part of the membrane (Figure 3). The positive charges left behind produce oxygen and protons from water while the electrons reduce NADP^+ to NADPH. The latter is nothing else but a hydride, i.e., a stored form of hydrogen. The pH gradient generated across the membrane is used to store additional energy via the phosphorylation of ADP to ATP. There are two light-absorbing photosystems, PS I and PS II, each containing chlorophyll, that operate in series. Photoexcitation of PS II initiates a series of redox steps resulting in the transfer of electrons from water to plastoquinone (pQ). This product is the electron donor for PS I, which under illumination performs the reduction of NADP^+ to NADPH (Figure 4).

The dark reaction, known as the Calvin cycle, uses the reducing power of NADPH as well as the free energy stored in the ATP to assimilate carbon dioxide in the form of carbohydrates. The way by which Nature achieves carbon fixation is via the reaction of CO_2 with ribulosebiphosphate (RuBP) to give two molecules of 3-phosphoglycerate, a process which is catalyzed by the enzyme RuBP-carboxylase. The phosphoglycerate is converted further to fructose 6-phosphate, the final product of the Calvin cycle. The overall reaction, despite its complex mechanism, corresponds to the simple Eq. (16) above.

Most green plants operate with photosynthesis efficiencies of a few percent. Eucalyptus trees are particularly efficient in this respect and reach as high as 5 %,

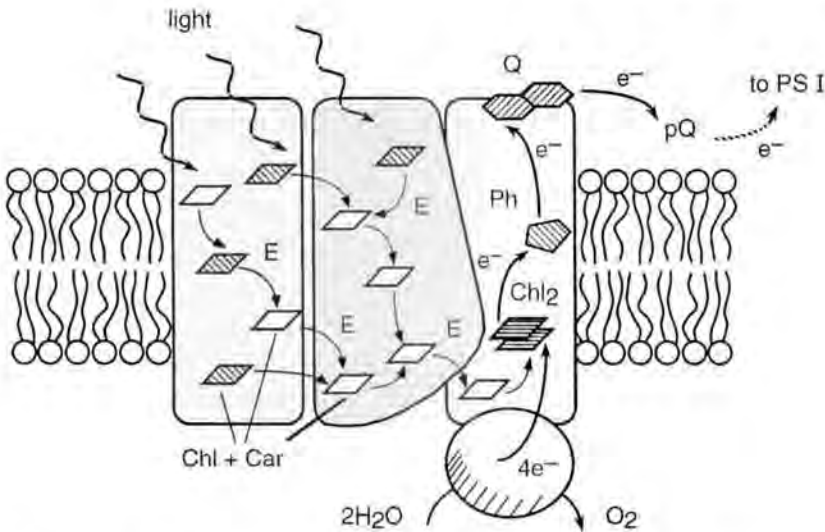


Figure 3. Functional organization of photosystem II in protein complexes contained in the thylakoid membrane. Excitation energy is harvested by chlorophyll (Chl) and carotenoids (Car) molecules and transferred to the special pair (Chl_2). Vectorial electron transfer across the membrane takes place from excited Chl_2^* to plastoquinone (pQ) via pheophytin (Ph) and quinone (Q) electron mediators.

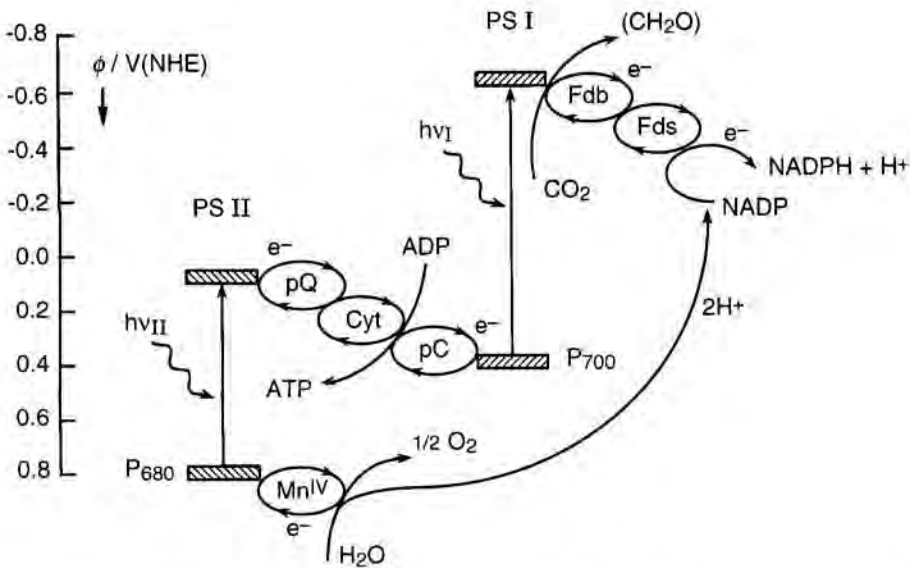


Figure 4. The Z-scheme of green plant photosynthesis: coupling of the two pigment systems, I and II. P_{680} and P_{700} = chlorophyll; pQ = plastoquinone; Cyt = cytochrome; pC = plastocyanine; Fdb, Fds = ferredoxin.

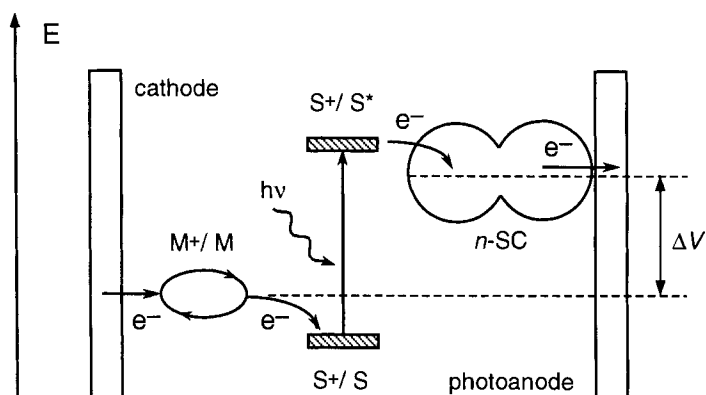


Figure 5. Schematic representation of the principle of the nanocrystalline injection photovoltaic cell showing the electron energy level in the different phases. The cell voltage ΔV obtained under illumination corresponds to the difference in the Fermi level of the semiconductor and the electrochemical potential of the redox couple (M^+/M) used to mediate charge transfer between the electrodes.

one-fifth of the thermodynamic maximum energy conversion efficiency discussed in Section 1.2. In plant leaves, sunlight is only weakly absorbed by chlorophyll and carotenoid molecules. These dyes, however, are contained in the membrane of stacked pancake-shaped vesicles, the thylakoids, that are grouped in the chloroplast cells. Efficient harvesting of sunlight is eventually achieved by absorption through numerous pigment layers. Furthermore, light harvesting and charge separation functions are carried out separately in the natural photosynthetic system, and end up in the transport of opposite charges on both sides of the thylakoid membrane.

In molecular photovoltaic devices discussed hereafter, the incident photons excite a dye-sensitizer that injects an electron into the conduction band of a wide-bandgap semiconductor. Positive holes left in the dye are then carried away by an electrolyte mediator or conducted through a hole-transporting medium (Figure 5). Mimicking the key features of natural photosynthesis, these devices rely on a mesoporous film structure to ensure efficient harvesting of sunlight using a molecular absorber. As well, light absorption and electron collection functions are separated in such systems. Electron injection into semiconducting nanoparticles which achieves charge separation across the solid/electrolyte interface is analogous to charge separation in the photosynthetic membrane.

1.4.2 Mesoscopic Oxide Semiconductor Films

Light harvesting by monomolecular dye layers

Absorption of incident radiation by a molecular sensitizer adsorbed as a monolayer to the surface of a solid come up against the fundamental problem of a limited

light-capture cross-section of the dye molecules. The absorption cross-section σ [cm^2] is related to the decadic molar extinction coefficient ε [$\text{L mol}^{-1} \text{cm}^{-1}$] by Eq. (20):

$$\sigma = \varepsilon \times 1000 \times \ln(10) / \mathcal{N}_A \quad (20)$$

where \mathcal{N}_A is Avogadro's number. Since ε characterizes molecules in solution whose spatial orientation is random, favorable orientation of the chromophores upon adsorption on a surface can lead to an increase of the effective cross-section by at most a factor of two. Typical ε values for dyes lie between 10^4 and $2 \times 10^5 \text{ L mol}^{-1} \text{cm}^{-1}$, yielding for the light-capture cross-section values between 0.0038 and 0.15 nm^2 . The area the sensitizer molecules occupies on the surface of the supporting solid is much larger, e.g., about $1\text{--}2 \text{ nm}^2$. Hence, at most a few percent of the incident light can be absorbed. Deposition of a multilayer of dye on the surface in order to increase its light absorption is generally a mistaken tactic, since energy transfer between sensitizer molecules rarely gives rise to efficient antenna effects and outer dye layers act only as a light filter, with no contribution to photocatalysis.

A successful strategy to solve the problem of light absorption through such molecular layers is found in the application of films of high internal surface area, consisting of nanocrystalline oxide particles with a diameter of $10\text{--}20 \text{ nm}$. The mesoporous morphology of the layer plays a crucial role in the harvesting of sunlight. Depending on film thickness, their real exposed surface area can easily be made 1000 times larger than the apparent geometric one. When light penetrates the dye-covered solid "sponge", it travels through hundreds of adsorbed dye monolayers and is efficiently captured. Consider the case of a $3 \mu\text{m}$ thick mesoporous film whose effective surface area is 300 times larger than that of a compact solid and that the film is covered by a monolayer of dye molecules each of which occupies an area of 1 nm^2 . On the geometric projection of such a rough surface a dye coverage of $\Gamma = 3 \times 10^{16} \text{ cm}^{-2}$ is reached. Its absorbance A [—] is given by Eq. (21):

$$A = \Gamma \times \sigma \quad (21)$$

where Γ is the chromophore surface concentration and σ its absorption cross-section. Suppose that the dye molecule at the wavelength of its absorption maximum has a light-capture cross-section of $5 \times 10^{-17} \text{ cm}^2$ ($\varepsilon = 1.3 \times 10^4 \text{ L mol}^{-1} \text{cm}^{-1}$). As a result the absorbance of the film would be $A = 1.5$. Neglecting light scattering by the film, its light-harvesting efficiency (*LHE*), namely the absorptance, is given by Eq. (22), implying that 97% of the incident photons are absorbed.

$$LHE = 1 - 10^{-A} \quad (22)$$

Preparation and morphology of mesoscopic oxide semiconductor films

Over recent years, nanocrystalline materials have attracted increasing attention from the scientific community because of their extraordinary physical and chemical

properties. These result from the ultrafine structure (i.e., grain size < 50 nm) of the materials. Nanocrystalline electronic junctions are constituted by a network of mesoscopic oxide or chalcogenide particles, such as TiO_2 , ZnO , Fe_2O_3 , Nb_2O_5 , WO_3 and Ta_2O_5 , or CdS and CdSe , which are sintered together to constitute transparent mesoporous films, typically a few microns thick. As electrons can rapidly percolate between interconnected particles through the film, the entire surface-adsorbed molecular layer can be electronically addressed. Charge transfer events involving adsorbed molecule can thus be induced through the nanocrystalline support and recorded as electrical current. Optical monitoring is also facile as the signals arising from the grafted molecules are greatly enhanced due to the huge internal surface area of the junction. For 15 years titanium dioxide has been the semiconductor of choice. The material has many advantages for sensitized photo-electrochemistry: like most wide-bandgap oxides, it is stable and does not tend to corrode in liquid electrolytes. The Lewis acidity of its surface affords a convenient handle for attachment of dye molecules by way of electron-rich anchoring groups. Moreover, TiO_2 is a low-cost, widely available, nontoxic, and even biocompatible, substance that is widely used in domestic applications.

Mesoporous oxide films are commonly produced via a sol-gel type of process involving a hydrothermal step. The procedure is illustrated for TiO_2 in Figure 6. The initial precipitation of the oxide involves controlled hydrolysis of a Ti(IV) compound, usually an alkoxide such as titanium tetraisopropoxide or TiCl_4 , followed by peptization. Autoclaving of the sols obtained (heating at $200\text{--}250^\circ\text{C}$ for 12 h) allows for controlled growth of the primary particles and improves their crystallinity. During this hydrothermal growth, smaller particles dissolve and fuse to large particles by a process known as "Ostwald ripening". After partial removal of solvent and addition of a binder, the sol is ready for deposition on the substrate. For the latter, a conducting glass (sheet resistance = $8\text{--}10\ \Omega/\text{square}$) is often used. The sol is deposited by doctor blading or screen printing and briefly fired in air. During the firing, the binder and possible organic contaminants are burned out, thus producing a clean, mostly dehydroxylated, oxide surface. The film thickness is typically $5\text{--}10\ \mu\text{m}$ and the film mass about $1\text{--}2\ \text{mg cm}^{-2}$. The electronic contact between particles is produced by sintering during the firing treatment at about 450°C . A mesoporous structure with a very high effective surface area is thereby formed. Analysis of the layers shows their porosity to be about 60 % and the average pore size 12 nm. Figure 7 displays the morphology of such a nanocrystalline TiO_2 (anatase) layer deposited on a transparent conducting oxide (TCO) glass. A large fraction of the particles has a bipyramidal shape, which is typical of anatase crystalline form. The exposed surface faces are mostly oriented in the (101) direction [5]. The mean particle diameter is 20 nm in this case. Their size and morphology can be adjusted by varying the conditions of the sol-gel process used for film preparation. Films of self-assembled rodlike particles have been obtained when the hydrothermal treatment of the TiO_2 colloid is done in the presence of tetramethylammonium hydroxide at $190\text{--}230^\circ\text{C}$. The rodlike particles were observed to have (100) faces terminated from the (001) side. The pores diameter of the film in this case is 4 nm with a very narrow size distribution [6].

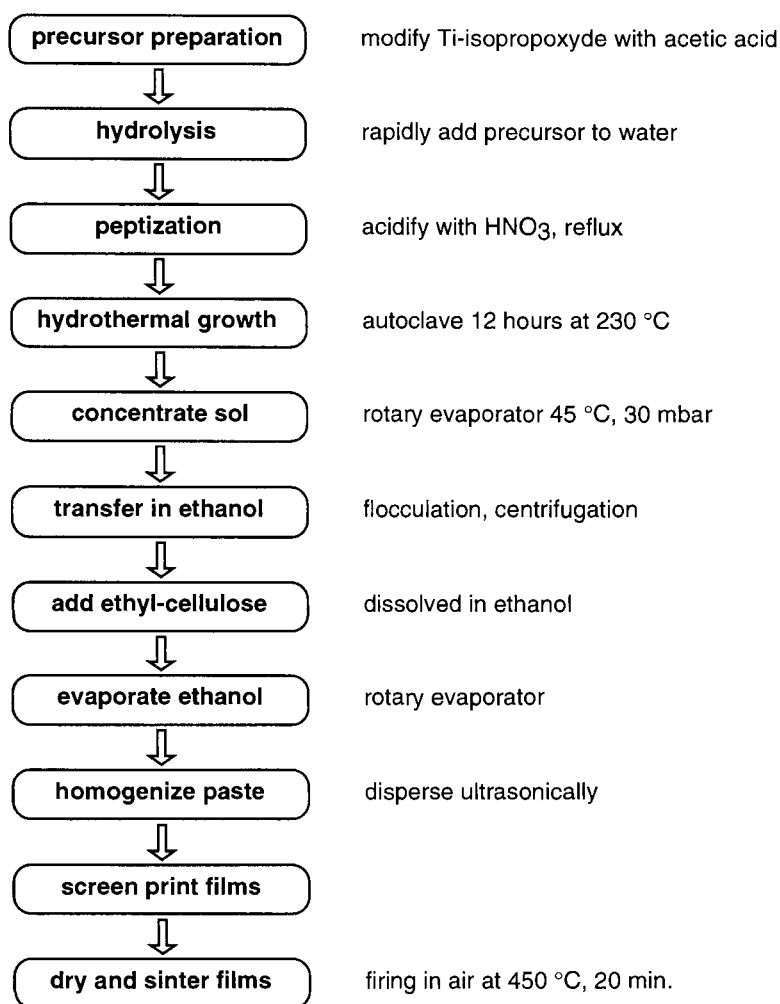


Figure 6. Outline of the steps involved in the preparation of mesoporous TiO₂ film electrodes.

1.4.3 Photoinduced Charge Separation at the Solid/Electrolyte Interface

The use of mesoporous oxide films as a substrate to anchor the dye molecules allows sunlight to be harvested over a broad spectral range in the visible region. Similarly to chlorophyll in the green leaf, the dye acts as an electron transfer sensitizer. Upon excitation by light, it injects an electron into the conduction band of the oxide, resulting in the separation of positive and negative charges. Charge transfer from photoexcited dyes into semiconductors was discovered more than a century

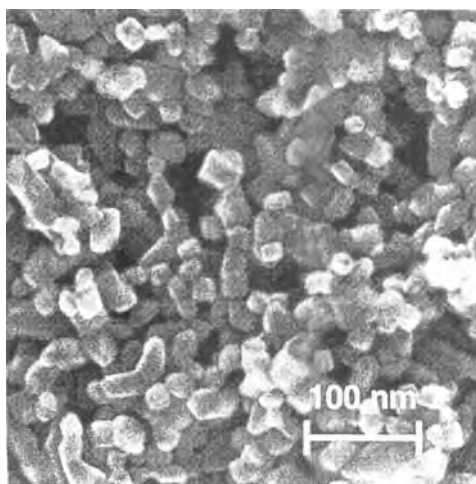


Figure 7. Scanning electron micrograph of a mesoporous TiO_2 film supported on conducting glass. The predominant facets of the anatase crystals have the (101) orientation.

ago in a famous experiment by Moser [7]. He observed that the photoelectric effect reported earlier by Becquerel on silver plates [8] was enhanced in the presence of erythrosin dye. The one-page publication describing his observations is shown in Figure 8. A few years before, Vogel in Berlin had associated dyes with the halide semiconductor grains to make them sensitive to visible light [9]. This led to the first panchromatic film, able to render the image of a scene realistically in black and white [10]. However, the clear recognition of the parallelism between the two procedures, a realization that the same dyes in principle can function in both systems [11], and a verification that their operating mechanism is by injection of electrons from photoexcited dye molecules into the conduction band of the n-type semiconductor substrates [12] date to the 1960s. In subsequent years the idea developed that the dye could function most efficiently if chemisorbed on the surface of the semiconductor [13, 14]. The concept emerged of using dispersed particles to provide a sufficient interface [15], then photo-electrodes were employed [16, 17]. Finally, the use of nanocrystalline TiO_2 films sensitized by a suitable molecular dye provided an important technological breakthrough [18]. These mesoporous membranes have allowed in effect for the first time the development of a regenerative photoelectrochemical cell based on a simple molecular light absorber, which attains a conversion efficiency commensurate with that of silicon-based photovoltaic devices, but at a much lower cost.

Molecular engineering of dye sensitizers

Many studies based on the observed bulk photoelectrochemical effects and on direct probing of the processes occurring at the solid surface have provided firm evidence that the sensitizing mechanism involves as a primary step electron or hole injection by the electronically excited sensitizer molecule (S^*) into the semiconductor (SC).

Notiz über Verstärkung photoelektrischer Ströme durch optische Sensibilisierung.¹

Von Dr. James Moser.

Aus dem physikalisch-chemischen Laboratorium der Wiener Universität.

(Vorgelegt in der Sitzung am 23. Juni 1887.)

Ich erlaube mir mitzutheilen, dass ich die von Herrn E. Becquerel entdeckten photoelektrischen Ströme erheblich dadurch verstärken konnte, dass ich die beiden chlorirten, jodirten oder bromirten Silberplatten in einer Farbstofflösung, z. B. Erythrosin, badete.

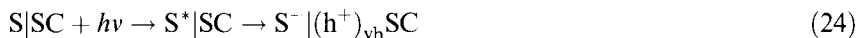
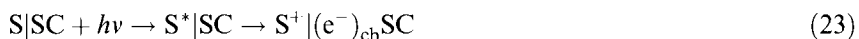
Beispielsweise war zwischen zwei chlorirten Silberplatten die elektromotorische Kraft im Sonnenlicht 0·02, zwischen zwei anderen in gleicher Weise behandelten, aber gebadeten Platten 0·04 Volt.

Bisher sind nur an jodirten Platten von Herrn Egoroff elektromotorische Kräfte beobachtet, und zwar bis $\frac{1}{15}$ Volt. Ich konnte bei jodirten und bromirten Platten durch Baden in Erythrosin $\frac{1}{4}$ Volt erreichen.

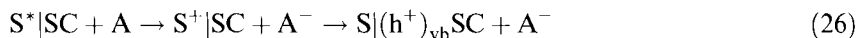
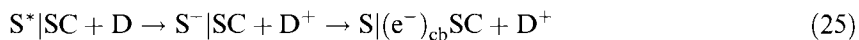
Ich halte es für meine Pflicht, schon an dieser Stelle Herrn Max Reiner, der mir bei diesen Versuchen assistirt, meinen verbindlichsten Dank auszusprechen.

¹ Akadem. Anzeiger Nr. XVI.

Figure 8. A copy of the 1887 publication by J. Moser on the amplification of photoelectric currents by optical sensitization of silver halides by erythrosin [7]. The system described in this paper was indeed the first dye-sensitized photovoltaic solar cell.



Alternatively, charge injection into the semiconductor can involve the reductive or oxidative quenching of the dye excited state by a redox-active species (a *super-sensitizer*) followed by thermal interfacial electron transfer [19].



In the case of the injection of an electron from the excited state of a molecular sensitizer into the conduction band of a semiconductor (Eq. (23)), the thermodynamics of the photo-redox reaction requires the oxidation potential of the dye excited state $\phi^\circ(S^+/S^*)$ to be more negative than the conduction band flatband potential of the semiconductor, and thus:

$$\phi^\circ(S^+/S) < \phi_C + \Delta E_{0,0}/\mathcal{F} \quad (27)$$

where $\phi^\circ(S^+/S)$ is the oxidation standard potential of the dye, $\Delta E_{0,0}$ its excitation energy, ϕ_C (SC) the conduction band flatband potential, and \mathcal{F} the Faraday constant.

The redox potential for the dye can shift upon adsorption from solution due to coulombic or stronger covalent interactions with the solid substrate. This potential change can amount to several hundreds of millivolts. While n-type semiconductors cannot be used generally to measure oxidation potentials of adsorbed dye sensitizers by conventional cyclic voltammetry, reduction potential $\phi^\circ(S/S^-)$ is often more accessible. Assuming oxidation and reduction potentials of the dye ground state on the surface are linked by a constant relation:

$$\phi^\circ(S/S^-) = \phi^\circ(S^+/S) - \Delta E_{0,0}/\mathcal{F} + x \quad (28)$$

the energetic threshold for charge injection from the dye excited state into the conduction band of the solid would require the reduction potential of the adsorbed dye to be $\phi^\circ(S/S^-) < \phi_{CB} + x$, where the last term has been found for a large number of various organic sensitizer molecules to be $x = 0.35$ V [20].

The ideal sensitizer for a single-junction photovoltaic cell should absorb all light below a threshold wavelength of at least 900 nm. In addition, it should be anchored to the semiconductor oxide surface and inject electrons to the conduction band with a quantum yield of unity. Its redox potential should also be sufficiently high for it to be regenerated rapidly via electron donation from an electrolyte or a hole conductor. Finally, it should be stable enough to sustain at least 10^8 redox turnovers under illumination, corresponding to approximately 20 years of functioning under natural light in day–night cycles. The best photovoltaic performance in terms of both conversion yield and long-term stability has so far been achieved with polypyridyl complexes of ruthenium and osmium [21–24]. Sensitizers having the general struc-

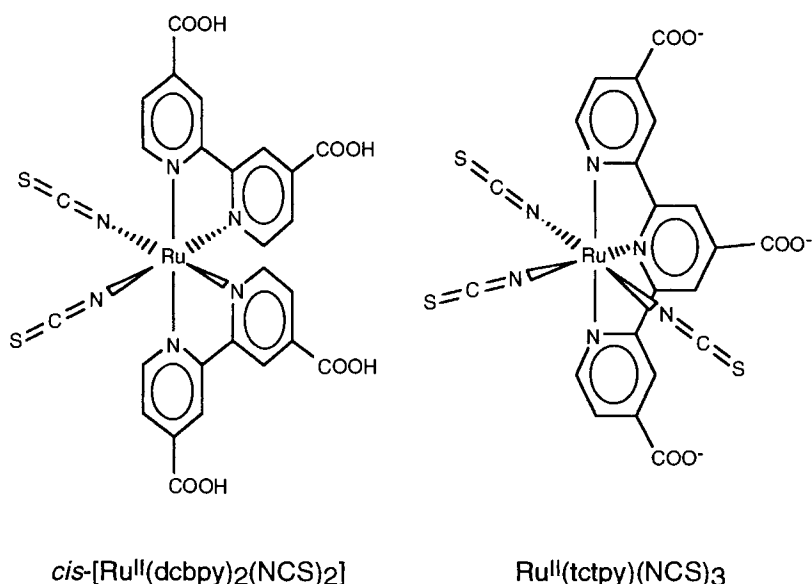


Figure 9. Heterogeneous charge transfer sensitizer for molecular photovoltaic cells.

ture ML_2X_2 , where L stands for 2,2'-bipyridyl-4,4'-dicarboxylic acid (dcbpy), M for Ru(II) or Os(II), and X for halide, cyanide, thiocyanate, or water [21–24], are particularly promising. In recent years, the ruthenium complex dye *cis*- $[\text{Ru}^{\text{II}}(\text{dcbpy})_2(\text{NCS})_2]$ (Figure 9) has emerged as the model of a heterogeneous charge transfer sensitizer for molecular photovoltaic cells. Reported for the first time in 1993 [21], its performance has been unmatched since then. Only recently, a credible challenger has been found with the black dye tri(thiocyanato)-(2,2':6',2''-terpyridyl-4,4',4''-tricarboxylate)ruthenium(II) [$\equiv \text{Ru}^{\text{II}}(\text{tctpy})(\text{NCS})_3$] (Figure 9), which exhibits a better near-IR photoresponse [24].

The efficiency of *cis*- $[\text{Ru}^{\text{II}}(\text{dcbpy})_2(\text{NCS})_2]$ complex as a redox sensitizer of titanium dioxide is conferred by several important features of the molecule. Carboxylic groups carried by the ligands provide a good anchoring of the dye on the acidic surface of TiO_2 . Surface derivatization of the mesoporous oxide film is normally performed by dipping it into a solution of the dye in a 50:50 (v/v) solvent mixture of acetonitrile and *t*-butanol. A monolayer of the sensitizer is formed spontaneously. The adsorption follows a Langmuir isotherm with a binding constant $K = 5 \times 10^4 \text{ L mol}^{-1}$. The area occupied by one molecule at the anatase surface at full monolayer coverage is 1.65 nm^2 . The interaction between the carboxylic group and the oxide is of fundamental importance in determining the geometrical structure of the adsorbed dye state and influencing the electronic coupling with the Ti(3d) conduction band orbital manifold. The most likely configuration supported by IR analysis [25] involves the attachment of the dye via two of its four carboxylate groups. The carboxylate either bridges two adjacent rows of titanium ions through bidentate coordination or interacts with surface hydroxyl groups through hydrogen bonds.

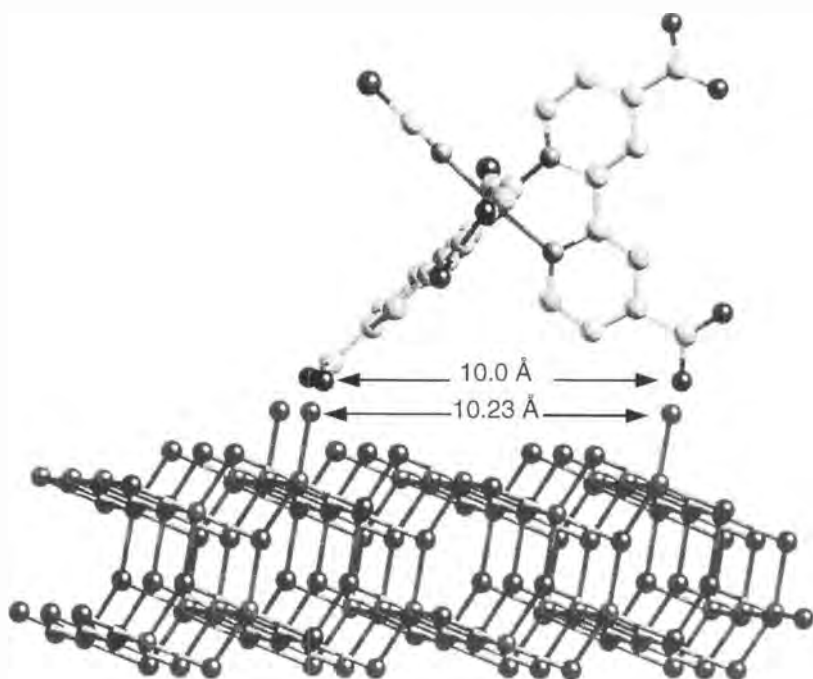


Figure 10. Structural representation of a $\text{Ru}^{\text{II}}(\text{dcbpy})_2(\text{NCS})_2$ molecule adsorbed through two carboxylate groups to the (101) surface of TiO_2 .

Of the two remaining carboxylate groups, one is ionized while the other remains in the protonated form. Model studies, using the dcbpy ligand adsorbed onto single-crystal $\text{TiO}_2(110)$ rutile, investigated by means of X-ray photoelectron spectroscopy, X-ray absorption spectroscopy, and quantum chemical calculations [26], are in favor of the bridging bidentate configuration illustrated in Figure 10. The ligand is oriented at an angle of about 40° with respect to the (001) crystallographic direction. In addition to this linkage mode, calculations suggest the monodentate ester bond is also thermodynamically stable. The bidentate bonding, however, is stronger and thus would be the preferred anchoring configuration for the *cis*- $[\text{Ru}^{\text{II}}(\text{dcbpy})_2(\text{NCS})_2]$ dye on titanium dioxide.

The interfacial electron transfer events will be strongly affected by the electronic structure of the dye in the adsorbed state and the matching of the energy level between its excited state and the conduction band of the semiconductor. Generally, the optical transition of Ru complexes has metal-to-ligand charge transfer (MLCT) character. Excitation of the dye involves transfer of an electron from a metal ion d-orbital to the π^* orbital of the ligand. *cis*- $[\text{Ru}^{\text{II}}(\text{dcbpy})_2(\text{NCS})_2]$ exhibits two such transitions in the visible domain. The absorption maxima in ethanolic solution are located at 518 and 380 nm, the extinction coefficients being 1.33×10^4 and $1.3 \times 10^4 \text{ L mol}^{-1} \text{ cm}^{-1}$, respectively. The complex emits at 750 nm, the excited state lifetime being 60 ns [21].

Results from ab-initio calculation [27] of a decarboxylated *cis*-[Ru^{II}(dcbpy)₂(NCS)₂] complex show that the highest occupied molecular orbital (HOMO) level is shared by both the Ru(II) metal ion and the –N=C=S ligands. Application of photoelectron spectroscopy has confirmed that both Ru 4d and atomic orbitals centered on the –NCS groups, in particular S 3p, contribute to the HOMO of the complex [28]. In a photovoltaic cell, the oxidized dye, after electron injection to the conduction band of the oxide, should quickly be reduced by a redox species in the surrounding electrolyte. The observation that the frontier molecular orbital contains a substantial amount of 3p character from the sulfur atom of the –NCS ligand may play an important role in this process. The thiocyanate groups point in the direction of the electrolyte, which may facilitate reduction by mediators, making it particularly suitable for highly efficient solar cells.

Ab-initio calculations also show that the lowest unoccupied molecular orbital (LUMO) of the *cis*-[Ru^{II}(dcbpy)₂(NCS)₂] complex is concentrated on the π^* structure of the dcbpy ligands. Hence, absorption of visible light by the compound can be assigned to a RuNCS–bpy(π^*) charge transfer transition. Preliminary calculations also indicate that the dcbpy rings share their LUMO with the carboxylate groups, thus enhancing electronic coupling between the dye excited state and the acceptor levels manifold of the solid.

The oxidation potential and excitation energy of the fully protonated form of the dye in solution being $\phi^\circ(\text{S}^+/\text{S}) = +1.10$ V/NHE and $\Delta E_{0,0} = 1.65$ eV, respectively, the oxidation potential of the MLCT excited state of the sensitizer is established at $\phi^\circ(\text{S}^+/\text{S}^*) = -0.55$ V/NHE [21]. The flatband potential of TiO₂ in dry aprotic solvents can be as negative as $\phi_C = -1.25$ V/NHE [29, 30]. In such conditions, the conduction band of the solid would in principle be out of reach of the dye excited state and only deep localized sub-bandgap states could potentially act as acceptor levels in the injection process. Surface protonation via adsorption of the carboxylic groups results, however, in a positive shift of the flatband potential that can amount to several hundred millivolts. Moreover, complete deprotonation of the four carboxylic groups of *cis*-[Ru^{II}(dcbpy)₂(NCS)₂] was demonstrated recently to cause its oxidation potential to shift negatively by ca. 300 mV [31]. Both effects combined together with the presence of traces of H₂O render the interfacial electron transfer from the dye excited state to the conduction band of titanium dioxide thermodynamically favorable.

Dynamics of charge injection in wide-bandgap semiconductors

Photoinduced charge injection from an electronically excited molecular state into a wide continuum of acceptor levels, including the conduction band of a semiconductor, is one of the simplest photochemical surface reactions (Eq. (23)). This process is, however, rather special, in the sense that there are many channels available for the electron transfer. The reaction can choose its energetic path to yield an electron within the band of the solid, which is characterized by a variable amount of kinetic energy. The energy excess should also be carried by the dye cation S⁺, produced concomitantly, in the form of vibrational excitation. As a consequence, provided the driving force is sufficiently large compared with the nuclear reorgani-

$$k_i = \frac{4\pi^2}{h} |H|^2 \frac{1}{h\omega} n_a \quad (30)$$

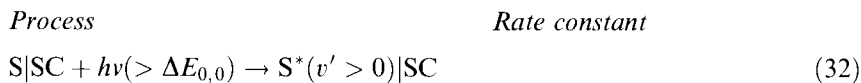
In Eq. (30), the actual density of final states is approximated by the reciprocal energy level spacing $1/h\omega$ of the dye cation oscillator, multiplied by a factor $0 \leq n_a \leq 1$ accounting for the density of empty electronic states available in the solid. Above the flatband energy level, the density of acceptor states in the conduction band of a semiconductor is usually very large and the density of final states is solely determined by the density of energy levels of the dye cation ($n_a \cong 1$). Below the band edge, empty trap states are present, whose density decreases gradually at lower energies ($n_a \rightarrow 0$).

The density of accepting states $N_C(E)$ in the conduction band of a semiconductor is given by Eq. (31) [33]:

$$N_C(E) = 4\pi \left(\frac{2m_{de}^*}{h^2} \right)^{3/2} (E - E_C)^{1/2} \quad (31)$$

where E_C is the energy of the conduction band edge, and m_{de}^* the density-of-state effective mass for electrons. The latter parameter depends strongly on the material. In TiO_2 , for instance, assuming $m_{de}^* \cong m_e^* \geq 6m_e$, the calculated density of states would be at least two orders of magnitude larger than that in ZnO , for example, where $m_{de}^* \cong 0.24m_e$ [35, 36]. The density of states is also expected to be dependent upon the size of the semiconductor nanocrystallites. Strong quantum confinement indeed results in widely spaced electronic levels and therefore in a very low density of states. Although this size quantization effect would be negligible for TiO_2 where the exciton binding energy is very small, it is expected, for example, to play a significant role for ZnO particles whose diameter is smaller than ~ 10 nm.

Equation (30) can only be used when the electron transfer process takes place from a single prepared excited state of the sensitizer. In the general case, absorption of photons, whose energy $h\nu$ is larger than the electronic excitation energy $\Delta E_{0,0}$ of the dye, leads to the population of higher vibronic levels of the molecule (Eq. (32)). Relaxation of these vibrationally excited intramolecular states (Eq. (33)) and of the whole system along the classical reaction coordinate is expected to compete with the electron transfer process (Eq. (34)) [37]. In these conditions, the electronic coupling $|H|$ between the donor and the acceptor states becomes a time- and excitation wavelength-dependent function and can no longer be readily accessed [33].



Two limiting cases could be considered that would, however, let us treat in a simple way the interfacial electron transfer process as involving a single prepared excited state of the sensitizer:

- 1) Charge injection is slow enough compared with the vibrational relaxation of the dye excited state ($k_i' \ll k_r$). In this event, electron transfer would be able to take place only from the lowest excited state ($v' = 0$) (Eq. (35)), and the injection quantum yield Φ_i would be simply controlled by the kinetic competition between the electron injection (Eq. (35)) and the decay of the excited state (Eq. (36)):

$$\Phi_i = k_i / (k_i + \Sigma k_d) = k_i / (k_i + 1/\tau_f) \quad (37)$$

where τ_f is the excited-state lifetime of the sensitizer.

- 2) Charge injection is fast compared with nuclear relaxation of the excited state ($k_i' \gg k_r$). In this case, interfacial charge transfer would take place from the prepared hot vibronic level (Eq. (34)) and the quantum yield for the primary injection process would be close to unity ($\Phi_i \cong 1$). For both limiting cases, $k_i' \ll k_r$ and $k_i' \gg k_r$, relation (30) would be relevant, provided electron transfer is nonadiabatic.

When the electronic coupling of the donor and acceptor becomes sufficiently large (typically $|H| > 150 \text{ cm}^{-1} \cong 0.7kT$), the electron transfer will be increasingly adiabatic and, in the absence of solvent dynamics control, the rate constant will eventually be proportional to a nuclear vibration frequency factor ν_n . In this case the electronic coupling element is not contained in the rate expression. For other cases, where $|H|$ is small enough, the value of the coupling element is needed for a quantitative description of the electron transfer rate. There is obviously a considerable interest in the role of the electronic coupling factor, as the separation distance and anchoring geometry of the sensitizer on the surface will determine its magnitude. The Gamov expression (38) is frequently used to estimate the changes in $|H|$ with separation distance in photoinduced electron transfer where the electron donor and acceptor are fixed relative to one another:

$$|H| = |H|^0 \exp[-\beta(r - r_0)] \quad (38)$$

where the damping factor β has values ranging from 0.85 to 2.5 \AA^{-1} . Provided that other factors besides distance do not influence the electron transfer rate, Eq. (39) can be used to estimate the rate at a known separation distance r :

$$k_{et} = k_{et}^0 \exp[-\beta(r - r_0)] \quad (39)$$

where $k_{et}^0 \cong 10^{13} \text{ s}^{-1}$. Other parameters, such as spin changes, symmetry factors, and the relative orientation of both reactants, may influence the magnitude of the electronic coupling element [38].

In favorable thermodynamic conditions, where the lowest electronic excited-state energy level of the sensitizer lies above the bottom edge of the conduction band, charge injection competes kinetically with the decay of the sensitizer's excited state (Eq. (36)). Hence, for dyes that are characterized by emission lifetimes τ_f of the

order of 1 ns, interfacial electron transfer rate constants of the order of $k_i = 10^{11} \text{ s}^{-1}$ suffice to ensure high injection quantum yields. Most of the previous knowledge on bulk semiconductor–electrolyte interfacial charge transfer is derived from steady-state photocurrent measurements achieved in photoelectrochemical cells. Obtaining electron transfer rate constants from such an indirect method, however, is difficult because the photocurrent depends on many other interfacial and bulk processes.

The rapid dynamics of electron injection can be investigated by application of transient laser spectroscopy to colloidal dispersions or nanocrystalline semiconductor films. Such materials are particularly amenable to time-resolved optical studies, as they display a good transparency throughout all the visible and near-infrared (NIR) spectral domains. Moreover, they are characterized by a high solid surface area exposed to the solution, yielding high sensitizer absorbance for only monolayer dye coverage. Most of the oxide semiconductor systems that are being studied at present, namely TiO_2 , SnO_2 , and ZnO , are also of particular interest for the development of artificial photosynthetic and photovoltaic devices [39].

Earlier studies on dye-sensitized TiO_2 reported nanosecond time constants for the injection kinetics [16, 40–42]. These results were obtained indirectly from the measurement of the injection quantum yield and implicitly assumed that the interfacial electron transfer reaction was competing only with the decay of the dye excited state. Other studies were based on the same assumption but used measurements of the dye fluorescence lifetime, which provided picosecond–femtosecond time resolution [43–45]. Direct time-resolved observation of the buildup of the optical absorption due to the oxidized dye species S^+ has been employed in more recent studies [46–51]. This appears to be a more reliable way of monitoring the charge injection process as it does not require any initial assumption on the sensitizing mechanism.

Figure 12(a) shows the transient difference spectra obtained upon nanosecond laser excitation of *cis*- $[\text{Ru}^{\text{II}}(\text{dcbpy})_2(\text{NCS})_2]$ in ethanolic solution and of nanocrystalline titanium dioxide transparent films onto which the sensitizer was adsorbed. The dye is excited with 605 nm output of a laser system and the absorbance change observed immediately after the laser excitation is plotted as a function of the detection wavelength [52]. Luminescence quenching and photocurrent experiments have confirmed that 600 nm excitation of the sensitizer resulted in the formation of the charge-separated state $\text{S}^+|(\text{e}^-)\text{SC}$. The spectrum obtained upon irradiation of dye-sensitized TiO_2 displays a broad absorption feature peaking around 800 nm whose half lifetime exceeds 0.5 μs . Such a lifetime is more than one order of magnitude longer than that of the isolated dye excited state in solution. The recorded spectrum is comparable to that of the one-electron oxidation product $[\text{Ru}^{\text{III}}(\text{dcbpy})_2(\text{NCS})_2]^+$ of the complex produced by oxidative quenching of the excited state in an alcoholic solution containing methylviologen as an acceptor [47], or generated by pulse radiolysis [53]. It can be readily distinguished from the spectrum of the dye excited state obtained in solution, whose band maximum is located at 710 nm [52]. These observations demonstrate unambiguously that the transient spectral feature observed upon excitation of the sensitized semiconductor cannot be assigned to an excited state of the dye but must be attributed to the charge-separated state $\text{S}^+|(\text{e}^-)_{\text{cb}}$ resulting from interfacial charge injection, where both an LMCT transition of the $-\text{NCS}$ ligands to the $\text{Ru}(\text{III})$ metal ion center in S^+ and absorption by conduction band and/or trapped electrons contribute to the spectrum.

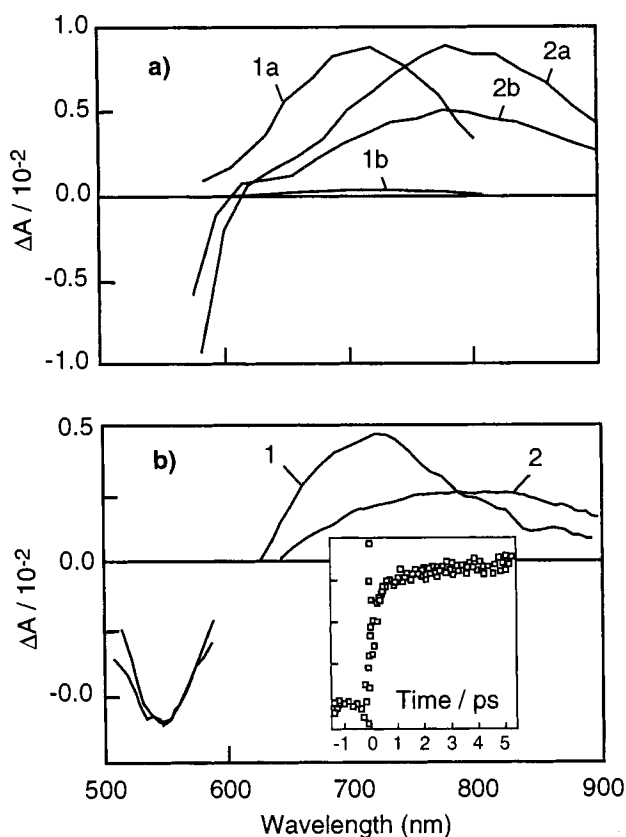


Figure 12. a) Transient absorption spectra obtained upon nanosecond pulsed laser excitation of 1) *cis*-[Ru^{II}(dcbpy)₂(NCS)₂] dye in ethanolic solution, and 2) a sensitized TiO₂ transparent film. Spectra were recorded 50 ns (1a, 2a) and 0.5 μ s (1b, 2b) after the laser excitation pulse ($\lambda = 605$ nm, 5 ns pulse duration). b) Transient absorption spectra recorded 6 ps after ultrafast laser excitation ($\lambda = 605$ nm, 150 fs pulse duration) of 1) *cis*-[Ru^{II}(dcbpy)₂(NCS)₂] dye in ethanol, and 2) a fresh sensitized titanium dioxide film. Insert, the temporal behavior of the absorbance of the latter system, measured at $\lambda = 750$ nm with sub-picosecond time resolution.

Further sub-picosecond data were collected [47]. Transient data measured for dye-sensitized TiO₂ films were compared with those obtained for control dye-coated ZrO₂ films, as the high conduction band edge of the latter material should prevent electron injection. Figure 12(b) shows the absorption difference spectra obtained at a time delay of 5 ps after 605 nm pulsed laser excitation. The spectrum obtained for the dye-sensitized zirconia films exhibits a maximum at 710 nm as observed for the *cis*-[Ru^{II}(dcbpy)₂(NCS)₂] dye in ethanolic solution and is therefore assigned to the dye MLCT excited state. On the other hand, the transient spectrum recorded for sensitized TiO₂ displays a maximum at 800 nm that is characteristic of the dye cation S⁺. In contrast to the data obtained for dye-coated ZrO₂ films, the difference spectra measured with sensitized TiO₂ exhibited some temporal evolution for time delays less than 5 ps. Typical transient absorption data at a probe wavelength of

750 nm are shown in the insert of Figure 12(b). The data show a fast ~ 100 fs instrument response limited signal growth followed by a slower kinetic phase extending to several picoseconds. A detailed multiexponential analysis of the traces obtained revealed at least three kinetic components with lifetimes of <100 fs (35 %), 1.3 ps (22 %), and 13 ps (43 %) [29, 54].

In a recent experiment [36], mid-IR spectroscopy was used to probe directly the buildup of electron concentration inside the semiconductor. Careful examination at different wavelengths and time scales yielded a complex kinetics which could be described by two exponentials with rise times of 50 ± 25 fs (>84 %) and 1.7 ± 0.5 ps (<16 %), the slower component being very sensitive to the sample condition.

The origin of such complex electron transfer kinetics is not clear yet. The participation of various electronic excited states of the Ru(II) dye sensitizer to the reaction was ruled out as no effect of the excitation wavelength could be observed. Nor was a significant difference observed in the results obtained for dyed TiO₂ films exposed to air and in propylene carbonate, thus excluding possible effects due to the solvation dynamics [54]. Direct interfacial electron transfer to various localized defect states could be associated with different electronic coupling elements and could therefore result in a wide distribution of rate constants. The occupancy of these trap states can be modulated by sweeping the Fermi level below the flatband energy upon applying an external electrical bias. Modulation of the applied potential does not appear, however, to result in any noticeable change in the injection yield and kinetics [30]. On the other hand, adsorption of potential-determining cations, such as Li⁺, that causes the flatband potential of the semiconductor to shift positively, apparently also affects the electron injection rate [55]. An acceleration factor of 8-fold was observed in particular for *cis*-[Ru^{II}(dcbpy)₂(NCS)₂]-sensitized nanocrystalline titanium dioxide in pure propylene carbonate upon addition of 0.1 M Li⁺ [30]. These observations suggest that the multiple time constants result from heterogeneities in the energetics of the nanocrystalline TiO₂ films. In addition, adsorption of dye molecules on different surface sites and with various anchoring geometries could also cause an intricate kinetic outcome [56].

The fastest kinetic phase of electron injection in *cis*-[Ru^{II}(dcbpy)₂(NCS)₂]-sensitized nanocrystalline titanium dioxide films apparently takes place in the femtosecond regime. Besides, the vibrational relaxation of the dye excited state is expected to occur typically within 0.4–1 ps ($k_r \cong 10^{12}$ s⁻¹) [57, 58]. Observed injection rate constants of the order of 10^{13} s⁻¹ certainly preclude complete thermalization of the dye excited state S* to the $v' = 0$ level prior to the reaction, and suggest that charge transfer can occur directly from hot ($v' > 0$) excited sensitizer molecules. In systems where the $v' = 0$ energy level of the electronically excited state of the dye lies below the bottom of the conduction band of the semiconductor ($n_a \rightarrow 0$), charge injection from vibrationally relaxed excited molecules of the sensitizer is either slow or unfeasible. However, if electron injection from a hot vibronic state of the dye is able to compete successfully with its nuclear relaxation ($k_i' > k_r$), charge injection should become possible for higher excitation photon energy, and an excitation wavelength dependence of the quantum yield $\Phi_i = k_i'/(k_i' + k_r)$ would be expected.

Figure 13 schematizes the energetics of the *cis*-[Ru^{II}(dcbpy)₂(NCS)₂] dye sensitizer adsorbed on various oxide semiconductors. This dye was chosen because of its

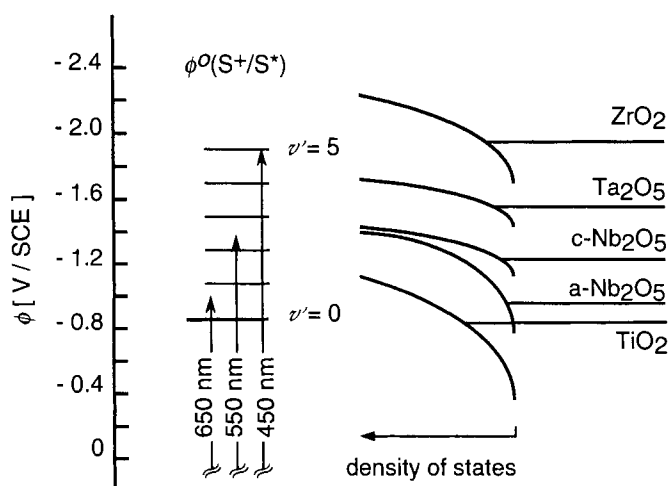


Figure 13. Energy scheme for *cis*-[Ru^{II}(dcbpy)₂(NCS)₂] dye sensitizer adsorbed on various oxide semiconductors. Molecular levels are based on the values of the oxidation potential of the complex: $\phi^0(S^+/S) = +0.86$ V/SCE and excitation energy $\Delta E_{0,0} = 1.85$ eV [21]. The flatband potentials $\phi_{fb}(SC)$ of the different solid oxides were estimated by monitoring the optical absorption at 750 nm of transparent nanocrystalline electrodes in propylene carbonate as a function of applied potential [61].

broad spectrum that should allow the excitation of hot vibronic states upon excitation by photons of energy $h\nu > \Delta E_{0,0}$. Ultrafast studies have indicated that vibrational relaxation of the analogous Ru(bpy)₃²⁺ complex dye is complete within ca. 300 fs [58, 60]. The presence of $-N=C=S$ ligands, which are characterized by a high-frequency stretching mode ($\bar{\omega} \cong 2139$ cm⁻¹) [52] is expected, however, to reduce this relaxation time to even more.

In dry propylene carbonate, the flatband energy of amorphous (a-Nb₂O₅) and crystalline niobia (c-Nb₂O₅), tantalum pentoxide (Ta₂O₅), and zirconia (ZrO₂) was found to be 0.2, 0.4, 0.7, and 1.1 eV respectively higher than that of TiO₂ [61]. As a consequence, the $v' = 0$ level of the MLCT excited state of the adsorbed dye lies below the bottom edge of the conduction band of these materials. Monitoring of the sensitizer's ground-state bleaching signal upon nanosecond laser flash photolysis of the Ru(II) complex clearly exhibited a biphasic kinetic behavior. Excited dye molecules that do not inject into the solid produce a recovery of the ground-state absorption within 15 ns. On the other hand, the dye cation S⁺, generated by the photoinduced electron transfer process, recaptures the injected electron much more slowly in the microsecond time domain [52]. Both kinetic steps, whose rate constants are two orders of magnitude apart from each other, can be easily separated. Quantitative evaluation of their respective amplitudes then allows the evaluation of the absolute injection quantum yield Φ_i at any excitation wavelength, independently of the absorption spectrum of the dye [61]. Results obtained for various

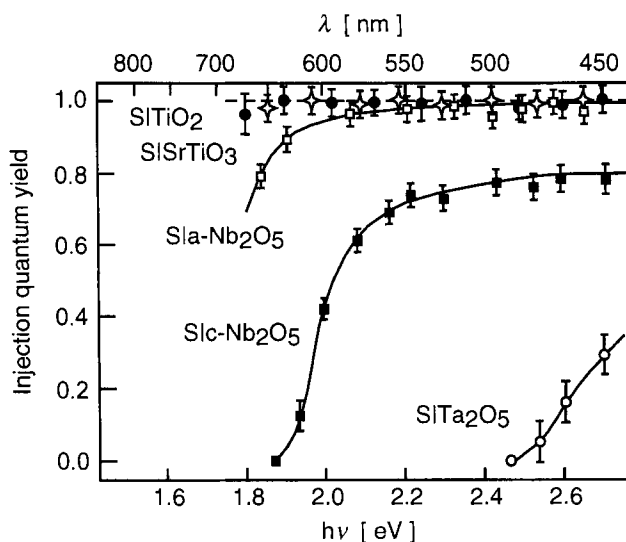


Figure 14. Dependence upon excitation photon energy $h\nu$ of electron injection quantum yield Φ_i obtained for various oxide semiconductors sensitized by $\text{cis-}[\text{Ru}^{\text{II}}(\text{dcbpy})_2(\text{NCS})_2]$.

$\text{Ru}^{\text{II}}(\text{dcbpy})_2(\text{NCS})_2$ -sensitized semiconductors show a strong excitation energy dependence of Φ_i . For $\text{c-Nb}_2\text{O}_5$ a clear wavelength dependence of the injection efficiency is observed between $\lambda = 650$ nm, the onset of injection, and $\lambda = 500$ nm, where the charge transfer quantum yield reaches a plateau value at ~ 0.75 (Figure 14). Measurements carried out in identical conditions with dye-sensitized TiO_2 gave an injection quantum yield close to unity that was independent of the excitation wavelength. On amorphous niobia, whose flatband potential is intermediate between those of TiO_2 and $\text{c-Nb}_2\text{O}_5$, the injection onset is shifted to the red by approximately 0.2 eV compared with the crystalline material. On tantalum pentoxide, the injection onset is found in the blue at $\lambda = 480$ nm. The shift of the electron injection threshold by +0.6 eV for Ta_2O_5 compared with $\text{c-Nb}_2\text{O}_5$ is larger than the energy difference measured between the positions of the respective conduction band edges of each material (0.3 eV) and should probably be related to a lower density of trap states in tantalum oxide. Finally, in accordance with the energy scheme, no charge injection was observed for $\text{cis-}[\text{Ru}^{\text{II}}(\text{dcbpy})_2(\text{NCS})_2]$ adsorbed on ZrO_2 up to an excitation energy of 2.7 eV.

The dependence of the photosensitization efficiency upon the excitation wavelength has also been observed in a photoelectrochemical cell based on TiO_2 sensitized by $\text{Fe}^{\text{II}}(\text{dcbpy})_2(\text{CN})_2$ complex [62]. The absorption band selective photon-to-current conversion efficiency measured in this case suggested that charge injection into the semiconductor is occurring via an ultra-shortlived upper excited state of the dye.

These observations of an excitation wavelength dependence of the charge injection process show that photoinduced interfacial electron transfer from a molecular excited state to a continuum of acceptor levels can take place in competition with the relaxation from upper excited levels. The rather slow growth of the injection

quantum yield above the energy onset suggests that it actually reflects the density of acceptor states in the solid that are present below the conduction band edge. In conditions where the injection quantum yield is unity ($k_i' \gg k_r$) and electron transfer takes place to the conduction band of the semiconductor ($n_a \cong 1$), the occurrence of the electron transfer process from a single prepared state $S^*(v' > 0)$ validates the simple model of Eq. (30) and makes it possible to estimate the electronic coupling matrix element $|H|$. Assuming a frequency of the dye cation oscillator $\bar{\omega}$ of 1500 cm^{-1} , a value of $|H|$ of 113 cm^{-1} ($\cong \frac{1}{2}kT$) would be calculated from the rate constant $k_i = 10^{13} \text{ s}^{-1}$ measured typically for $[\text{Ru}^{\text{II}}(\text{dcbpy})_2(\text{NCS})_2]$ -sensitized nanocrystalline TiO_2 . Although the value used for the cation vibration wavenumber $\bar{\omega}$, and therefore that determined for $|H|$, are here probably overestimated, this figure corresponds to a rather strong electronic coupling and suggests the electron injection rate could have reached the adiabatic limit.

Modulation of the injection efficiency between excited $\text{Ru}(\text{II})$ complexes and nanocrystalline TiO_2 and SnO_2 transparent films was observed upon biasing the Fermi level of the oxide electrodes [63, 64]. Applying a negative bias voltage to the film impaired the photosensitized charge injection, turning on the photoluminescence of the adsorbed dye. On the basis of these results it has been suggested that the rate of heterogeneous electron transfer depends directly upon the driving force of the reaction [64], and follows a normal Marcus-type of behavior. Alternatively, such an effect could also be rationalized by the reduction of the density of acceptor states, which are gradually populated upon raising the Fermi level of the solid. The Franck–Condon factor, which comprises parameters such as the reaction free energy ΔG^0 , the nuclear reorganization energy Λ and the temperature T , is expected to play only a negligible role in systems that are kinetically near-optimum in terms of the Marcus theory and that are characterized by a large number of acceptor states. According to Eq. (30), the rate of interfacial electron transfer for a given sensitizer is controlled only by the electronic coupling matrix element $|H|$ and the acceptor states density. The activationless nature of the charge transfer process has been experimentally confirmed by the observation of temperature-independent injection kinetics [48]. Other reported data show that, in energetically favorable conditions, the rate of electron injection is not controlled by the energetics of the sensitizer's excited state, nor by the medium reorganization, but rather by the density and occupancy of electronic states in the solid [30].

On titanium dioxide, the photoinduced charge injection process was reported to take place on time scales ranging from less than 100 fs to several microseconds, depending on the sensitizer used (Table 1). Such a variation of eight orders of magnitude can be accounted for only by very different values of the electronic coupling between the dye excited state and the acceptor orbitals at the surface of the semiconductor. Using Eq. (30), and assuming that for all systems $n_a = 1$ and a collective vibrational mode frequency of the dye oxidized state $\bar{\omega} = 1500 \text{ cm}^{-1}$, the electronic coupling matrix element can be calculated for each sensitizer. Obtained values of $|H|$ vary from 0.02 to $>160 \text{ cm}^{-1}$. Considering Eq. (38), and assuming a damping factor $\beta = 1.2 \text{ \AA}^{-1}$, this range of figures implies a difference in the electron transfer reaction distance of the order of 8 Å between the slowest and the fastest system. Various types of association of the sensitizer with the oxide surface could

Table 1. Electron injection rate constants k_i , reported for various dye sensitizers adsorbed on nanocrystalline TiO_2 .

Dye sensitizer	Medium	k_i [s^{-1}] ^a	$ H $ [cm^{-1}] ^d	References
$\text{Ru}^{\text{II}}(\text{bpy})_3$ ^b	H_2O , pH 10	2×10^5	2×10^{-2}	[16]
$\text{Ru}^{\text{II}}(\text{dcbpy})_3$	H_2O , pH 3	3×10^7	2×10^{-1}	[16]
$\text{Ru}^{\text{II}}(\text{bpy})_2(\text{dcbpy})$	air	2×10^8	4×10^{-1}	[42]
Eosin-Y	H_2O , pH 3	9×10^8	1	[39, 46]
$[\text{Ru}^{\text{II}}(\text{dcbpy})_2(\text{CN})_2]_3$	EtOH	6×10^9	3	[65]
Fluorescein 27	H_2O , pH 3	$3 \times 10^{12\text{a}}$	6×10^1	[50]
$\text{Ru}^{\text{II}}(\text{dcbpy})_3$	EtOH	4×10^{12}	7×10^1	[43]
Coumarin-343	CH_3OH	$5 \times 10^{12\text{a}}$	8×10^1	[44, 51, 66]
Perylene	vacuum	5×10^{12}	8×10^1	[48]
$\text{Ru}^{\text{II}}(\text{dcbpy})_2(\text{NCS})_2$	EtOH	$10^{13\text{a}}$	10^2	[47]
H_2TCPP	PC	$10^{13\text{a}}$	10^2	[30]
ZnTCPP	PC	$10^{13\text{a}}$	10^2	[30]
$\text{Fe}^{\text{II}}(\text{CN})_6^{4-\text{c}}$	D_2O , pH 2	$> 2 \times 10^{13}$	$> 1.6 \times 10^2$	[67]
Alizarin ^c	EtOH	$> 2 \times 10^{13}$	$> 1.6 \times 10^2$	[68]

^aonly the fastest kinetic component has been taken into account when multiexponential kinetics were reported, ^blinkage of most of the dye molecules onto the surface is ensured by a carboxylic or phosphonic anchoring group; in cases where such a group is lacking, adsorption occurs through purely electrostatic interactions, ^c $\text{Fe}(\text{CN})_6^{4-}$ and alizarin form charge transfer (CT) surface complexes on TiO_2 that are the relevant chromophores in the photosensitization process, ^delectronic matrix elements $|H|$ coupling dye excited states with the acceptor states of the semiconductor were calculated with Eq. (30), assuming for all systems $n_a = 1$ and $\bar{\omega} = 1500 \text{ cm}^{-1}$.

explain such a difference. Adsorption through electrostatic interaction is clearly insufficient. In aqueous medium, water molecules adsorbed on TiO_2 can act as spacers and force the dye sensitizer to stay several ångströms apart from the solid. Moreover, in the case of the symmetric $\text{Ru}(\text{bpy})_3^{2+}$ complex, the LUMO of the dye is delocalized over all three ligands, thus considerably increasing the average separation distance for interfacial electron transfer. Strong electronic coupling between the π^* molecular orbital of the dye excited state and the empty $\text{Ti}(\text{IV})$ 3d orbital manifold of the semiconductor is achieved by directly linking the sensitizer's moiety that carries the lowest-energy π^* orbital to the surface. Carboxylic and phosphonic anchoring groups are quite good at coupling dye-sensitizers onto the surface of TiO_2 . Charge injection rate constants obtained with such systems appear hardly to be dependent on the type of chromophore used, as they all establish at ca. $k_i = 10^{13} \text{ s}^{-1}$, a value which is probably close to the adiabatic limit.

Recapture of the injected electron

Figure 15 schematizes the energetics and dynamics of processes that take place after charge injection from a molecular excited state to the acceptor levels of a semiconductor. Thermalization and trapping of hot injected carriers is known to occur typically with a rate constant $k_{\text{th}} \cong 10^{13} \text{ s}^{-1}$ [69–71]. Reverse transfer of a hot

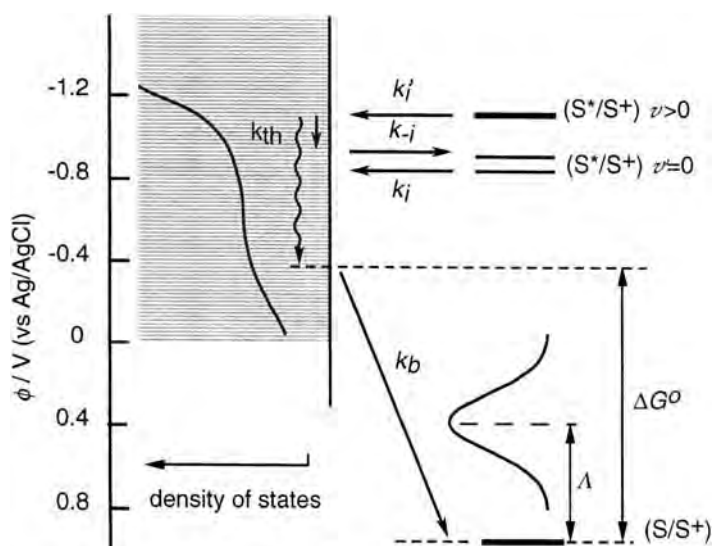


Figure 15. Energetics of the charge recombination following electron injection (k_i) from a dye excited state S^* into the conduction band of a semiconductor. Thermalization and/or trapping of injected electrons (k_{th}) takes place prior to the interfacial electron back transfer to the dye oxidized state S^+ (k_b). The reaction free energy associated to the latter process depends upon the population of the electronic states in the solid and can be distributed over a broad range of values. Numerical potential data shown are those of the *cis*-[Ru^{II}(dcbpy)₂(NCS)₂]/TiO₂ system.

electron (k_{-i}) is therefore generally prevented. The kinetics of back electron transfer from the conduction band to the oxidized dye follow a multiexponential time law, occurring on a microsecond-to-millisecond time scale. Two reasons are suggested for the relatively slow rate of the recapture of the injected electron:

- 1) While electron injection is kinetically near optimum, the high exoergicity of the back electron transfer can make the system lie deep in the inverted Marcus region, where the rate of the charge transfer process is expected to decrease with increasing driving force.
- 2) Alternatively, the dynamics of trapping and detrapping of electrons localized in intra-bandgap states can control the overall reaction kinetics, which would not depend upon the sole interfacial electron transfer rate.

Efficient dye sensitizers of oxide semiconductors are generally characterized by an oxidation potential of their excited state $\phi^\circ(S^+/S^*)$ that is close to the conduction band flatband potential ϕ_b of the solid. As a consequence, the free energy ΔG_b^0 of the back electron transfer can be as negative as -1 to -2 eV, depending on the potential assumed for free and/or trapped electrons involved in the reaction. The total reorganization energy associated with the heterogeneous charge transfer process is typically of the order of 0.5 eV, and is therefore smaller than the reaction

driving force $\Lambda < -\Delta G_b^0$. In terms of current electron transfer theory, this situation, depicted in Figure 15, corresponds to an inverted kinetic region.

For a nonadiabatic process the ET rate constant is generally expressed by Eq. (29). Within the classical limit where the energy of the vibrational modes associated with the activated complex formation is small ($h\nu \ll kT$):

$$FC = \sqrt{2\pi\Lambda kT} \exp(-\Delta G^\ddagger/kT) \quad (40)$$

and

$$\Delta G^\ddagger = (\Delta G^0 + \Lambda)^2/4\Lambda \quad (41)$$

where ΔG^\ddagger is the reaction activation energy. However, this classical expression is not generally adequate to describe the kinetics of electron transfer within the inverted region. Introducing a quantum modification of the Franck–Condon factor by assuming a single collective high-frequency vibrational mode ($h\nu > kT$) yields:

$$FC = \sqrt{2\pi\Lambda_o kT} \exp\left(-\frac{\Lambda_i}{h\nu}\right) \sum_{w=0}^{\infty} \frac{1}{w!} \left(\frac{\Lambda_i}{h\nu}\right)^w \exp\left(-\frac{(\Delta G^0 + w h\nu + \Lambda_o)^2}{4\Lambda_o kT}\right) \quad (42)$$

where Λ_i and Λ_o are the high-frequency mode (inner sphere) and low-frequency mode (inner- and outer-sphere) terms of the reorganization energy, respectively. The quantum treatment of high-frequency vibrational modes has a marked effect in the inverted Marcus region. The large Franck–Condon coupling that generally characterizes the inverted region renders nuclear tunneling a dominant process. The first consequence of this effect is a drastic decrease in the dependence of the electron transfer rate upon its energetics. Nuclear tunneling underneath the nuclear reorganization barrier also means that the electron transfer process in these conditions becomes activationless. As a second consequence, it is therefore expected that the temperature dependence of the electron transfer kinetics vanishes.

In accord with the experimental findings that the charge recombination process exhibits inverted-region kinetic behavior [72–75] and the predictions of the semi-classical model above, pseudo-activationless kinetics were indeed observed. The dynamics of the electron back transfer from the conduction band of TiO₂ nanoparticles to the cations of various organic sensitizers was shown to be essentially insensitive to temperature [75]. The temperature and medium dependence of the kinetics of the back electron transfer process taking place from the conduction band of mesoporous TiO₂ to the oxidized form of the adsorbed *cis*-[Ru^{II}(dcbpy)₂(NCS)₂] dye-sensitizer was also investigated [76, 77]. As expected from the thermodynamics of the process ($\Delta G^\circ \cong -1.75$ eV in ethanol), which should make the reaction lie deep in the inverted region, the effect of the temperature on the reaction rate was very weak. A decrease in the rate constant by a factor of less than 2 was observed when the temperature was varied from 300 K down to 100 K. This and the fact that hardly any medium dependence of the electron transfer rate could be observed

suggested that the Franck–Condon barrier to electron transfer is dominated by high-frequency modes which lead to its rate of crossing being mainly controlled by nuclear tunneling.

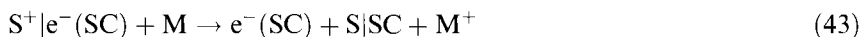
The insignificant role played by the Franck–Condon factor implies the electronic coupling dictates to a large extent the kinetics of the charge transfer process. Fitting of experimental temperature dependence data by Eqs. (29) and (42) yielded values of the electronic coupling matrix element $|H|$ of the order of only a few cm^{-1} [75]. This electronic coupling is fairly weak compared with that of the charge injection, where $|H|$ was found for the same sensitizer to be one or two orders of magnitude larger. This difference could be explained by the configuration of the sensitizer molecules in the adsorbed state. In efficient systems, forward electron transfer is favored by directly anchoring the sensitizer's moiety that carries the LUMO of the dye to the surface. In molecules that possess a large transient dipole moment, charge recombination requires that the electron must be transferred from the semiconductor to the oxidized center over a longer distance. This effect is particularly evident for Ru(II) complexes such as *cis*-[Ru^{II}(dcbpy)₂(NCS)₂]. Electron injection into TiO₂ takes place from the carboxylated bipyridyl ligands that are linked to the oxide surface and carry the lowest π^* orbital. The distance separating the center of the π^* system in the sensitizer's excited state and the first layer of Ti(IV) ions in the solid is approximately 5.5 Å. The reverse reaction, however, involves an electron transfer from the semiconductor to the Ru(III) center of the oxidized state, about 8 Å apart. According to the Gamov expression (Eq. (38)), and assuming $\beta = 1.2 \text{ Å}^{-1}$, a difference of 2.5 Å in the ET distance would imply a variation of the value of the electronic coupling by a factor of 20, in good agreement with experimental data. For systems that do not apparently benefit from this favorable effect, charge recombination was reported to occur in the sub-nanosecond time scale [49, 50, 78]. Logically, the value of the electronic coupling in these cases was estimated to be of the same order of magnitude ($|H| \cong 50\text{--}100 \text{ cm}^{-1}$) as that of the electron injection process [50, 79].

Whether charge transfer occurring through the solid/liquid interface proceeds directly from free electrons in the conduction band or is mediated by surface states is an important clue in the understanding of the mechanism and kinetics of the back electron transfer reaction. In principle, a distribution of energetically different traps for electrons could be responsible for a non-single-exponential recombination rate. Multiexponential kinetics of back electron transfer processes was indeed reported in several recent publications. Durrant and co-workers have presented some new data on this issue, showing the reaction to be strongly dependent on applied potential and electrolyte composition [80]. In agreement with the conclusions reached by Lian and co-workers [66, 81], these observations show that kinetics of charge recombination between electrons injected into nanocrystalline TiO₂ films and adsorbed dye cations are strongly dependent upon occupancy and energetics of the electronic states in the solid. They also suggest that the back electron transfer dynamics is controlled by electron transport between energetically distributed trap sites within the oxide nanoparticles [82]. This may be of relevance for the performance of the cell and should be considered in the modeling of the electrical performance together

with the reaction between the electrolyte mediator and conduction band electrons [83].

1.4.4 Charge Separation in Molecular Photovoltaic Devices

Upon irradiation, redox dye photosensitizers adsorbed on the surface of wide-bandgap metal oxide semiconductors readily inject an electron in the conduction band of the solid. While charge injection has been found for numerous efficient systems to occur in the femtosecond time frame, the electron back transfer takes place much more slowly, typically in the microsecond–millisecond domain. This charge recombination process can be intercepted by reaction of a reducing mediator *M* with the oxidized dye (Eq. (43)). The overall efficiency of the light-induced charge separation then depends upon the kinetic competition between back electron transfer and dye regeneration processes.



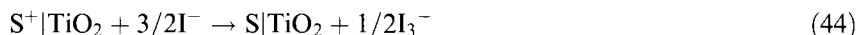
Photovoltaic cells based on the sensitization of mesoporous titanium dioxide by Ru(II) complex dyes in conjunction with the I_3^-/I^- redox couple as a mediator have proved very efficient at exploiting this principle. In such systems, the ionic mediator travels back and forth by diffusion from the working electrode to the counterelectrode, to shuttle to the sensitizer the electrons that have gone through the electrical circuit [18, 21, 84]. Recently, solid-state devices have been described where the liquid electrolyte present in the pores of the nanocrystalline oxide film is replaced by a large-bandgap p-type semiconductor acting as a hole-transport medium [85–88].

Interception of dye cations by a redox mediator

The interception of the oxidized dye by the electron donor in the electrolyte, i.e., iodide, is crucial for obtaining good conversion yields and high cycle lifetime of the sensitizer. For *cis*-[Ru^{II}(dcbpy)₂(NCS)₂] dye, time-resolved laser experiments have shown the interception to take place within about 10 ns under the conditions applied in the solar cell. The S^+/S couple shows reversible behavior in different organic solvents, the standard redox potential in acetonitrile being $\phi^o = 0.83$ V/SCE. The lower limit of 1 s can be derived for the lifetime of the oxidized dye from cyclic voltammetry. This means that interception is 10^8 times faster than intrinsic degradation of the oxidized sensitizer, explaining the fact that *cis*-[Ru^{II}(dcbpy)₂(NCS)₂] can sustain 100 million turnovers in continuous solar cell operation without loss of performance. Lack of adequate conditions for rapid regeneration of the dye leads to dye degradation.

The I_3^-/I^- redox couple has been found to be particularly suited for dye-sensitized photoelectrochemical solar cells based on nanocrystalline TiO₂, as it rapidly regenerates the sensitizer (Eq. (44)) and ferries charges between the two electrodes.

In these devices no other known redox couple works nearly as well. Although in solution I^- is capable of quenching reductively the excited state of many dyes (Eq. (25)), on a semiconductor surface such as SnO_2 and TiO_2 , the iodide quenching is not able to compete kinetically with the ultrafast charge injection [89].



The detailed mechanism of the two-electron transfer dye regeneration reaction (Eq. (44)) has not been fully elucidated and many factors appear to influence its rate [23, 84]. The following one-electron transfer reactions can in principle take place on the surface of the oxide and account globally for the oxidation of iodide to triiodide [23, 90]:



Oxidation of iodide to the $I_2^{\bullet -}$ radical is thermodynamically more favorable than the reaction leading to the iodine atom [91]. Thus, reaction (47) is favored over reaction (45), provided that (I^\bullet, I^-) or (S^+, I^-) ion pairs are present in a significant amount [23, 90].

The kinetics of the oxidation of iodide by the oxidized state of *cis*-[$Ru^{II}(dcbpy)_2 \cdot (NCS)_2$] sensitizer adsorbed on nanocrystalline TiO_2 films was measured by transient laser spectroscopy [92]. Figure 16 shows the transient absorption kinetics recorded in propylene carbonate with various electrolytes added. In all cases, the recovery of the ground-state absorption of the dye, after the fast electron injection into the solid, does not follow a simple kinetic law. In the absence of any electrolyte (trace a), the time needed to reach half of the initial absorbance ($t_{1/2}$) through back electron transfer is 2 μs . Total recovery of the initial absorption, however, requires several hundreds of microseconds to milliseconds. Traces b, c, and d were recorded after addition of a common concentration of 0.1 M of iodide in the form of tetrabutylammonium (TBA^+), Li^+ , and Mg^{2+} salts, respectively. Addition of the electrolyte in all three cases led to a considerable acceleration of the dye regeneration with $t_{1/2} < 200$ ns and complete suppression of the slow kinetic tail.

The rate of the reaction leading to the regeneration of the dye ground state was found to depend strongly on the nature and concentration of cations present in the solution. Small cations able to specifically adsorb onto the oxide surface, such as Li^+ and Mg^{2+} , were found to favor the fast oxidation of iodide by the oxidized state of the sensitizer. A sudden acceleration of the electron transfer process was observed at a critical cation concentration (see insert of Figure 16). Electrophoretic measurements showed that this concentration corresponds to the reversal of the titanium dioxide particle surface charge from negative to positive upon adsorption of ζ -potential-determining species. This observation was interpreted in terms of a

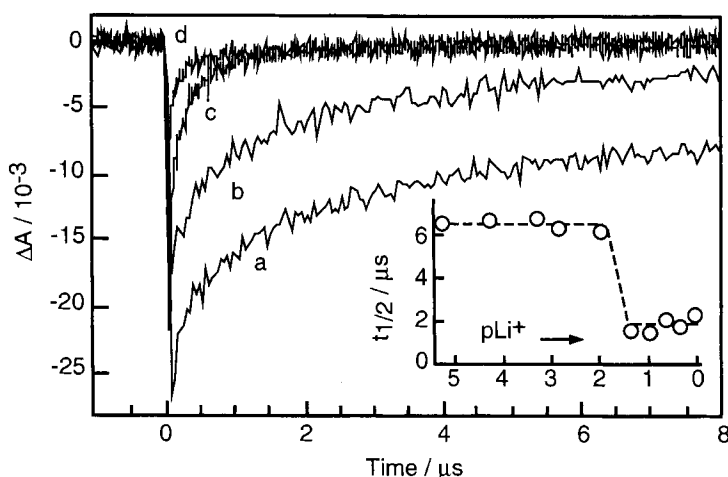


Figure 16. Time course of the transient absorbance changes measured upon laser excitation of *cis*-[Ru^{II}(dcbpy)₂(NCS)₂] dye adsorbed on nanocrystalline TiO₂ films. Bleaching signals were measured at $\lambda = 520$ nm in anhydrous propylene carbonate, a) without electrolyte, and in the presence of b) 0.1 M TBAI, c) 0.1 M LiI, and d) 0.05 M MgI₂. Insert, dependence of the half-lifetime $t_{1/2}$ of the dye ground-state absorbance recovery upon the concentration of Li⁺ cations. Iodide concentration of [I⁻] = 0.1 M was kept constant while $pLi^+ \equiv -\log[Li^+]$ was varied.

change in the reaction mechanism characterized by different rate constants. The slower reaction path, which does not require the iodide anions to be adsorbed onto the surface, was attributed to the thermodynamically unfavorable oxidation of I⁻ to an iodine atom (Eq. (45)). Alternatively, the encounter of an (S⁺, I⁻) complex with a second iodide anion could yield I₂^{-•} radicals directly as a product of the electron transfer process (Eq. (49)).



These reactions should be prevalent as long as the solid surface is negatively charged. When the surface charge is reversed to positive upon adsorption of the cations, a faster mechanism becomes predominant. Because it requires a high local concentration of I⁻ on the surface of TiO₂, the latter was suggested to be due to the thermodynamically more favorable oxidation of I⁻ to I₂^{-•}, which involves prior formation of (I⁻, I⁻) ion pairs on the surface (Eq. (50)).



Apart from recapture of the injected electrons by the oxidized dye, there is an additional loss channel in the nanocrystalline dye-sensitized cell which involves reduction of triiodide ions in the electrolyte present within the mesoporous network:



The back electron transfer reaction between conduction-band electrons and I_3^- (Eq. (51)) is the ultimate fate of photoinjected carriers. This reaction can be directly followed by measuring the dark current of the photovoltaic cell. The latter should be kept at a minimal level as it determines the photovoltage and, hence, the overall conversion efficiency of the device [93–95]. On mesoporous TiO_2 electrodes sensitized by $\text{cis-Ru}^{\text{II}}(\text{dcbpy})_2(\text{NCS})_2$, the rate of the back reaction of injected electrons with I_3^- was measured from intensity-modulated experiments and was observed to be second order in the electron density, with $k = 8.4 \times 10^3 \text{ M}^{-1} \text{ s}^{-1}$ [95]. As for the direct recombination processes discussed above that also imply the reaction of conduction-band and trapped electrons with acceptor molecules at the surface, the rate of charge transfer is expected to depend strongly upon the distribution and occupancy of intra-bandgap states in the semiconductor, and therefore upon the light intensity, the applied potential bias, and the nature and concentration of adsorbates.

Charge carrier percolation through mesoporous solid films

The migration of electrons within the TiO_2 conduction band to the current collector involves charge carrier percolation over the mesoscopic particle network. This important process which leads to nearly quantitative collection of injected electrons is at present attracting a great deal of attention [82, 96–99]. The mesoporous electrode is very different from a compact semiconducting layer because

- 1) the nanocrystalline film possesses only a very low inherent conductivity,
- 2) a space-charge layer is unable to establish within minute individual particles that are smaller than the Debye length, and
- 3) the oxide particles and the pores filled by the electrolyte form interpenetrating networks whose phase boundaries produce a junction of huge contact area.

In an approach to rationalizing the transport phenomena, mesoporous films may be viewed as an ensemble of individual nanoparticles through which electrons can percolate by hopping from one crystallite to the next, rather than regarding them as perforated compact electrodes [39].

A first attempt to model carrier transport in nanocrystalline TiO_2 films suggested diffusion to be the operative mechanism [96]. It turned out, however, to be erroneous to describe the electron motion by a single value of the diffusion coefficient. The transport phenomenon is complex as it involves trapping and detrapping of charges. The traps have various depths, leading to a distribution of trapping and detrapping times. Which type of trap the electron experiences during its random walk through the oxide film depends on its quasi-Fermi level under illumination, i.e., on the light intensity [97]. At low light levels, deep traps participate in the electron motion with a correspondingly low diffusion coefficient D_{e-} , and slow motion is expected. Increasing light intensity ends up in the filling of deeper trap states under steady-state conditions. The transport in this case is faster since it involves only shallow traps, resulting in a higher value for D_{e-} . The central importance of trap states in these systems has recently been discussed by Nelson [82], who applied a dispersive transport model based on the continuous-time random-walk theory of Scher and Montroll [100].

Another currently debated issue concerns space charge control of the photocurrent. It is generally assumed that the negative charge of the moving electron is efficiently screened by cations in the electrical double layer surrounding the semiconductor nanoparticles, making it move with its image charge as an essentially neutral species. There is evidence, however, that the charge compensation on the electrolyte side of the junction can lag behind the electron movement in the solid network. This effect is particularly important in ion-paired organic electrolytes when high photocurrents are drawn. Therefore, it was observed in photocurrent transient measurements that the photocurrent response times became longer with decreasing electrolyte concentration [101]. As well, the calculated value of the effective diffusion coefficient of carriers in the oxide semiconductor $D_{e^-} = 1.5 \times 10^{-5} \text{ cm}^2 \text{ s}^{-1}$, is several orders of magnitude smaller than that in the bulk crystalline material and strikingly similar to the diffusion coefficient of ions in the solution. A description of the coupled electron-ion motion [83] and a quantitative model of the mass transport by the electrolyte in mesoporous systems [102] have been proposed, albeit employing a constant value for the electron diffusion coefficient.

Simple calculation shows that the steady-state carrier concentration in full sunlight corresponds to approximately one electron per TiO_2 particle [103]. However, using this value together with $D_{e^-} = 1.5 \times 10^{-5} \text{ cm}^2 \text{ s}^{-1}$ ends up in a resistance for the illuminated nanocrystalline film which is at least a thousand times higher than the experimentally measured value. This discrepancy may be explained by a Mott transition occurring during the photodoping in the anatase particles that results in a large increase in their conductivity [104]. Clearly, a central question remains, which is how, in the dye-sensitized liquid-junction solar cell, an initially very poorly conducting network of TiO_2 nanoparticles can attain the excellent photocurrent-voltage characteristics presented below in Section 1.4.6.

Charge separation across a solid-state heterojunction

In dye-sensitized photovoltaic cells, practical advantages may be gained by the replacement of the liquid electrolyte with a solid charge transport medium. Inorganic p-type semiconductors, such as CuI [86] and CuSCN [88], and organic hole conductors [85, 105, 106] have been proposed in this regard. Recently, the use of 2,2',7,7'-tetrakis(*N,N*-di-*p*-methoxyphenylamine)-9,9'-spirobifluorene (spiro-MeOTAD) to constitute an amorphous hole-transmitting material, in conjunction with a mesoporous TiO_2 film sensitized by *cis*- $[\text{Ru}^{\text{II}}(\text{dcbpy})_2(\text{NCS})_2]$, made it possible to build a solid-state dye-sensitized solar cell with high photon-to-electron conversion efficiencies [85].

Figure 17 shows an energetic scheme for the electron transfer processes taking place at the dye-sensitized heterojunction of such a device. Electron injection from the sensitizer's excited state into the conduction band of TiO_2 is followed by regeneration of the dye by hole injection into the hole transport material (HTM). Conduction-band electrons in the metal oxide, as well as holes in the organic medium, are then transported by electronic conduction to the anode and the cathode, respectively. Pulsed picosecond laser photolysis has shown that the hole injection from the oxidized dye sensitizer $[\text{Ru}^{\text{III}}(\text{dcbpy})_2(\text{NCS})_2]^+$ into the spiro-MeOTAD

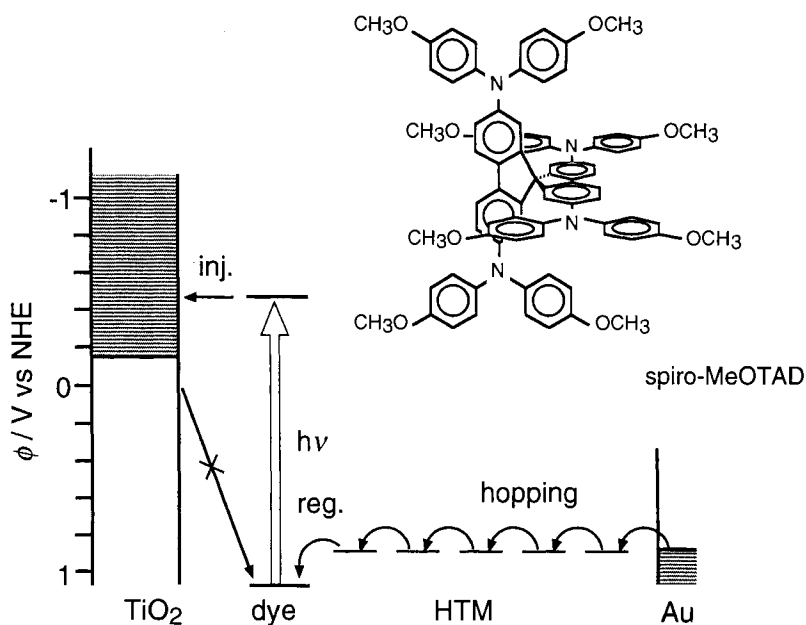


Figure 17. Energetic scheme of electron transfer processes taking place in a dye-sensitized heterojunction photovoltaic cell. Also shown is the structure of the spiro-MeOTAD molecule that constitutes an efficient organic hole transport material (HTM).

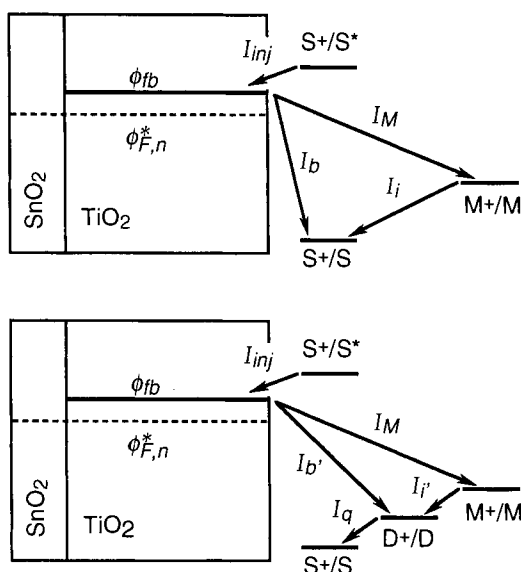
hole conductor proceeds over a broad time ranging from <3 ps to >1 ns [107]. This wide time scale was attributed to a statistical distribution of the dye–hole conductor distances, and suggested that the dye was not perfectly and uniformly contacted by spiro-MeOTAD molecules.

1.4.5 Charge Separation in Nanocrystalline Heterotriads

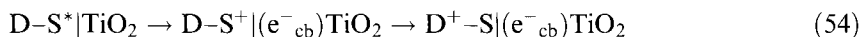
Charge separation resulting from light absorption by molecular chromophores has been extensively studied along two parallel routes. On the one hand, numerous molecular assemblies of donors (D), chromophores (S), and acceptors (A) in many variations have been synthesized, forming dyads, triads, tetrads, or even pentads, to achieve charge separation in solution or in monolayers. On the other hand, charge separation at chromophore–semiconductor interfaces (heterodyad S–A) exploited on films of nanocrystalline metal oxides has allowed the development of dye-sensitized nanocrystalline solar cells. Combining the intramolecular with the interfacial light-induced charge separation strategies is expected to increase the light-to-electricity conversion yield of the photovoltaic systems.

The maximum voltage delivered by the dye-sensitized solar cell corresponds to the difference between the potential corresponding to the quasi-Fermi energy

Figure 18. Electron fluxes for charge separation and recombination processes in a heterodyad (top) and heterotriad (bottom), in the presence of a redox mediator in solution, under open-circuit conditions. In the heterodyad, the injected electrons can either recombine with the oxidized sensitizer S^+ (I_b) or reduce the oxidized mediator M^+ (I_M). S^+ is reduced either by the conduction-band electrons or by the redox mediator M (I_i). In the heterotriad, the electron transfer from the linked donor D to S^+ is much faster than the recombination. The new recombination process occurs at $k'_b < k_b$ due to the larger distance.



level of the electrons in the semiconductor $\phi_F = E_{F,n}^*/\mathcal{F}$ and the redox potential $\phi(M^+/M)$ of the mediator in solution. A higher cell voltage can hence be obtained by lowering the quasi-Fermi potential which depends on the electron concentration in the conduction band of the illuminated sensitized semiconductor. This concentration relaxes to a steady state where the electron injection I_{inj} flux equals the electron escape flux (Figure 18). The escape flux is composed of two contributions: the electron-sensitizer recombination flux I_b (Eq. (52)) and the electron leak to the mediator in the contacting electrolyte I_M (Eq. (53)).



Lowering the quasi-Fermi potential by reducing the former flux requires a lengthening of the lifetime of the charge-separated state $S^+|(e^-_{cb})TiO_2$, a goal which can be reached by removing the hole on S^+ away from the semiconductor surface. This was achieved by replacing the simple chromophoric sensitizer S by a dyad sensitizer $S-D$ in which D is an electron donor possessing a redox potential lower than that of the sensitizer but higher than that of the redox mediator. Consequently, after electron injection, the hole will be transferred from S^+ to D (reaction (54)). The recombination according to Eq. (55) is expected to be slower than the direct recombination (Eq. (52)), because of the exponential decay of the electron transfer rate $k_{et}(r)$ with the distance r , according to Gamov's expression (39). The whole system

D-S[TiO₂] constituted by the dyad adsorbed on the semiconductor, considered as an acceptor, will be referred to as a *heterotriad*.

The quantitative influence of the different rates of electron transfers on the photopotential ϕ_F of the illuminated electrode was established according to the following model. In a heterodyad S[TiO₂] in open circuit (Figure 18, top), the electrons injected into the TiO₂ conduction band at the flux I_{inj} can either recombine with the oxidized sensitizer with the pseudo first-order rate constant k_b or reduce the oxidized redox mediator M^+ in solution with the second-order rate constant k_M . The steady-state electron density n in the semiconductor is thus given by Eq. (56). The quasi-Fermi level $E_{F,n}^*$ of the semiconductor is varying with the electron density according to Eq. (57), where E_C is the conduction band level and N_c is the effective density of states in the conduction band, a constant value for a given material at a given temperature [108]. The corresponding photopotential ϕ_F of the electrode is obtained by division by the Faraday constant \mathcal{F} (Eq. (58)). Combining Eqs. (57) and (58) affords the photopotential as a function of the kinetic parameters (Eq. (59)). In a heterotriad D-S[TiO₂] (Figure 18, bottom), the quenching of the oxidized dye by the linked donor is by far the fastest process ($k_q \gg k'_b$; see examples below). I_b is therefore negligible and the relevant fluxes for the determination of $\Delta\phi_F'$ are I_M which is independent of the sensitizer, I'_{inj} , and the recombination flux I'_b with the oxidized donor. The open-circuit photopotential difference $\Delta\phi_F$ between the two systems is then expressed by Eq. (60), which can be further simplified if $I'_{inj} = I_{inj}$; this can be considered true if the chromophore is the same in the heterodyad and in the heterotriad.

$$n = I_{inj} / (k_b + k_M[M^+]) \quad (56)$$

$$E_{F,n}^* = E_C - kT \ln(N_c/n) \quad (57)$$

$$\phi_F = \phi_c - (kT/\mathcal{F}) \ln(N_c/n) \quad (58)$$

$$\phi_F = \phi_c - (kT/\mathcal{F}) \ln(N_c - (k_b + k_M[M^+])/I_{inj}) \quad (59)$$

$$\Delta\phi_F = (kT/\mathcal{F}) \ln(k_b I'_{inj} / k'_b I_{inj}) \quad (60)$$

An improved solar cell voltage can also be achieved by raising the redox potential of the mediator. The substitution of the heterotriad for the heterodyad is in that case an advantage, too. In fact, the higher redox potential of the (M^+/M) couple results in a reduced driving force for the regeneration of the dye ($S^+ + M \rightarrow S + M^+$) which will be accompanied, in the normal Marcus region, by a reduced rate. If this rate decreases, the competitive recombination flux increases, unless, again, the lifetime of the charge-separated state is prolonged by fast transfer of the hole to a linked donor.

Argazzi et al. followed that strategy to elaborate a nanocrystalline solar cell which incorporates a molecular dyad (**H1**) based on ruthenium bipyridine as a sensitizer and phenothiazine as a donor (Figure 19) [109].

In compound **H1**, the respective redox potentials of the S ($Ru^{III/II}$) and D ($PTZ^{+/0}$) moieties are 1.33 and 0.97 V/NHE, giving a 0.36 V driving force for the charge transfer. In the model compound where the donor is absent, charge recombination

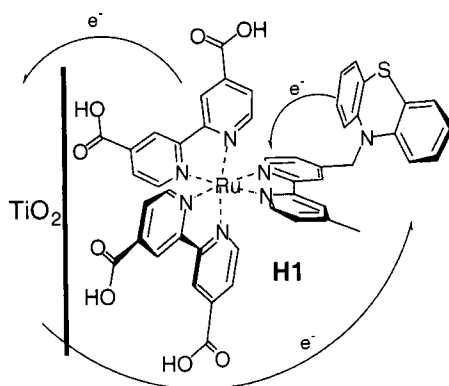


Figure 19. Molecular dyad based on ruthenium bipyridine and phenothiazine [109].

was determined by transient laser spectroscopy to follow a biexponential process, with the kinetic components $k_{b1} = 8.5 \times 10^6 \text{ s}^{-1}$ (77 %) and $k_{b2} = 5.1 \times 10^5 \text{ s}^{-1}$ (23 %). In heterotriad **H1**|TiO₂, electron transfer from the phenothiazine moiety to the oxidized sensitizer took place within the laser pulse (<30 ns) while the charge recombination occurred at the rate $k'_b = 3.6 \times 10^3 \text{ s}^{-1}$, which means a decrease by a factor of 2000 compared with the heterodyad, and a half-lifetime of the charge-separated state of 300 μs . According to Eq. (60), the photopotential of the heterotriad should be 200 mV higher than for the heterodyad. A difference of 175 mV was measured in the absence of redox mediator. The former system still afforded a 100 mV-higher open-circuit voltage than the latter in a cell where the I_3^-/I^- couple was present.

Bonhôte et al. investigated three systems based on ruthenium–terpyridine–phosphonate as sensitizer and triarylamine as donors [110]. The excited form of the considered sensitizer was reported to inject electrons efficiently into TiO₂ [111, 112], while triarylamine are known to form very stable cation radicals [113]. In the two heterotriads **H2**|TiO₂ and **H3**|TiO₂ (Figure 20), the donor and the sensitizer are covalently linked at different distances while the co-adsorbed phosphonated triarylamine **A1** and ruthenium terpyridine sensitizer **H4**, or **H5** constitute *bimolecular* heterotriads. The redox potentials of the different constituents of the heterotriads are given in Figure 20. The driving forces for the $\text{D} \rightarrow \text{S}^+$ charge transfer were 0.55 V for **H2**, 0.65 V for **H3**, and 0.56 V for **A1** + **H5**.

Resonance Raman spectroscopy indicated that in the excited assemblies **H3***|TiO₂ and (**A1** + **H5***)|TiO₂, one electron is promoted from the metal center to the terpyridine ligand linked to the semiconductor, whereas in the system **H2***|TiO₂ the excited electron is located on the ligand linked to the donor. The quantum yield of the charge separation reaction (54) was found to be close to unity for the two former assemblies, but only 60 % for the latter one. In all three cases, the electron injection was very fast (<1 ns) and the hole transfer to the donor was fast (10–20 ns). The half-lifetime of the charge-separated state was 3 μs for (**A1**⁺ + **H5**)|(e[−]_{cb})TiO₂, as in the model system **H5**⁺|(e[−]_{cb})TiO₂; it was 30 μs in **H2**⁺|(e[−]_{cb})TiO₂ and 300 μs in **H3**⁺|(e[−]_{cb})TiO₂, as with **H1**⁺|(e[−]_{cb})TiO₂.

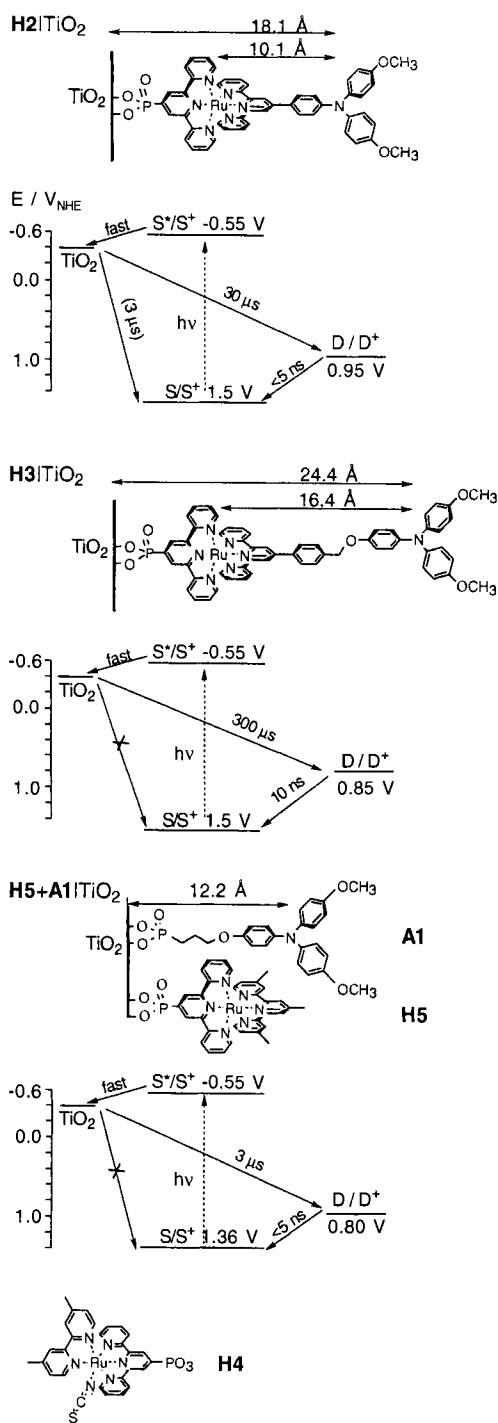


Figure 20. Distances, energy levels and electron transfer half-lives in the heterotriads **H2/TiO₂**, **H3/TiO₂** and **H5+A1/TiO₂**. The distances were calculated by molecular mechanics using CAChe software, assuming a perpendicular arrangement of the molecules on the surface. The energy levels are those obtained and calculated by electrochemistry as well as by absorption and emission spectroscopy. The half-lifetimes reported for the electron transfer processes were obtained by laser flash photolysis. The value of 3 μs for the S⁺[(e⁻_{cb})/TiO₂ → S/TiO₂ recombination was obtained with the heterodiyad **H5/TiO₂**.

The differences in the recombination rates of the different heterotriads can be correlated with the mean distance separating the amine from the surface of the oxide. Perpendicular attachment of the molecules on the surface would imply D–TiO₂ distances of 12, 18, and 24 Å for the heterotriads (**A1**⁺ + **H5**)/TiO₂, **H2**/TiO₂, and **H3**/TiO₂, respectively (Figure 20). Assuming a typical damping factor $\beta = 1.2 \text{ Å}^{-1}$ for “through-space” electronic coupling between conduction band electrons and D⁺, a decrease of the recombination rate by one order of magnitude is expected to correspond to an increase in the mean electron transfer distance by 1.9 Å. The discrepancy between that value and the 6 Å distance difference expected from perpendicular anchoring can be explained by the fact that it is very likely that a large portion of adsorbed molecules adopt a tilted conformation on the surface, leading to a broad distribution of distances for the charge recombination, and hence to a complex kinetic behavior. In fact, attempts to fit the observed temporal curves demonstrated that they are multiphasic, certainly because the adsorption geometry of the molecules is not fixed. This geometry is likely to be dependent on the surface coverage. In a compact monolayer, perpendicular anchoring should be favored, whereas molecules widely dispersed on the surface should be freer to lean over. It was indeed observed for all three heterotriads that the rate of the recombination depends drastically on the surface concentration. At 50 % surface coverage, upon irradiation by a laser pulse of fixed energy, a 50 % reduction of the number of charge-separated pairs is expected. Considering a second-order kinetic law, the rate of recombination is expected to decrease accordingly. It was observed on the contrary that the slowest kinetic components measured for **H3**/TiO₂ at surface saturation disappeared under partial coverage conditions, while the half-lifetime of the charge-separated state $\tau_{1/2}$ was reduced by more than one order of magnitude. An effect of the same amplitude was observed with heterotriads **H2**/TiO₂ and (**A1** + **H5**)/TiO₂. Heterotriad **H3**/TiO₂ represents clearly the most promising system of the series for long-lived charge separation. In an attempt to increase further the lifetime of **H3**⁺|(e[−]_{cb})TiO₂ state, the photodynamics was studied in the ambient-temperature liquid salt 1-ethyl-3-methylimidazolium bis(trifluoromethylsulfonyl)imide [114], which was shown to behave at the molecular scale like a solvent of low dielectric constant ($\epsilon \approx 10$), where the medium reorganization energy should be minimized. The charge recombination was indeed slowed down significantly, with a twice as long $\tau_{1/2}$ as in propylene carbonate. A very long tail in the kinetic curve, accounting for a few percent of the initial absorbance, was even found to extend up to several hundreds of milliseconds ($\tau_{1/4} = 5 \text{ ms}$, $\tau_{1/8} = 120 \text{ ms}$). Careful degassing of the molten salt did not affect this long-time kinetic phase, indicating that removal of the conduction band electrons by molecular oxygen was not competing with the charge recombination.

Under full sun illumination (AM 1.5) in propylene carbonate, heterotriad **H2**/TiO₂ gave a 82 mV higher photopotential than **H5**/TiO₂ of which only 58 mV can be accounted for by the 10-fold reduced recombination rate. Another contribution of 10 mV is expected from the 50 % higher injection flux I_{inj} of the former system, due to the wider absorption spectrum. In spite of a 100-fold lower recombination rate compared with **H5**/TiO₂, expected to yield a 116 mV gain, the heterotriad **H3**/TiO₂ gave the lowest photopotential of the series. This observation must

be related to a supplementary contribution to I_b represented by the short-circuiting pathway constituted by the lateral charge percolation from triarylamine to triarylamine and finally to the SnO_2 , as shown by the electrochromism of H3|TiO_2 . This was confirmed by the observation that the quantum yield of the whole charge separation process increased when **H3** was diluted on the surface by non-electroactive molecules.

In a regenerative solar cell, with the I_3^-/I^- redox couple, the open-circuit photovoltage of H2|TiO_2 was now 139 mV higher than that of H5|TiO_2 . This increased difference can be attributed to a reduced electron–triiodide reaction rate (k_M), shown by the measurement of I_M in the dark under 550 mV reverse bias, probably as a result of a restricted access of the triiodide ions to the semiconductor caused by the presence of the bulky triarylamine groups. Heterotriad H3|TiO_2 , whose photopotential was 31 mV lower than H5|TiO_2 , affords in the regenerative cell a 59 mV higher photovoltage, very probably because, in addition to a lower I_M , the reduction of $\text{H3}^+|\text{TiO}_2$ by iodide competes with the lateral electron transfer. Despite of the limitations caused by lateral charge percolation, the development of heterotriads as efficient charge-separation systems appears promising.

1.4.6 Photovoltaic Performances of Dye-sensitized Nanocrystalline Solar Cells

A scheme for the photovoltaic device used in the generation of electric power from light is shown in Figure 5. The mesoporous semiconductor oxide film is sandwiched between two conducting glass plates, its pore space being filled with a redox electrolyte or a hole conductor. We have shown above how the molecular properties of the sensitizer are chemically engineered to ascertain efficient electron injection from the dye excited state (S^*) into the conduction band of titanium dioxide. We also discussed how the recapture of the electrons by the oxidized dye (S^+) is intercepted by transferring the positive charge to a redox mediator M^+/M , i.e., the triiodide/iodide couple, present in the electrolyte and hence to the counterelectrode. Via this last charge transfer, in which the mediator is returned to its reduced state, the circuit is closed. The system converts light into electricity in a catalytic fashion, i.e., without permanent chemical transformation. The maximum voltage ΔV that such a device could deliver corresponds to the difference between the Fermi potentials in the two conducting electrodes, and thus to the difference between the redox potential of the M^+/M mediator couple and the conduction band edge potential of the semiconductor. Figure 21 compares the spectral dependence of the conversion efficiency of incident monochromatic light in electric current (*IPCE*) for *cis*- $[\text{Ru}^\text{II}(\text{dcbpy})_2(\text{NCS})_2]$ (\equiv “N3”) and $\text{Ru}^\text{II}(\text{tctpy})(\text{NCS})_3$ (\equiv “black dye”) sensitizers. Very high efficiencies of current generation approaching 0.8 were obtained. When corrected for the inevitable reflection and absorption losses in the conducting glass serving to support the nanocrystalline film, the yields are practically quantitative in the plateau region of the curves. However, the response of the “black dye” extends 100 nm further into the near-infrared than that of “N3”. The photocurrent onset is close to 920 nm, i.e., near the optimal threshold for single-junction converters. The overall conversion efficiency η of the photovoltaic cell can easily be calculated from

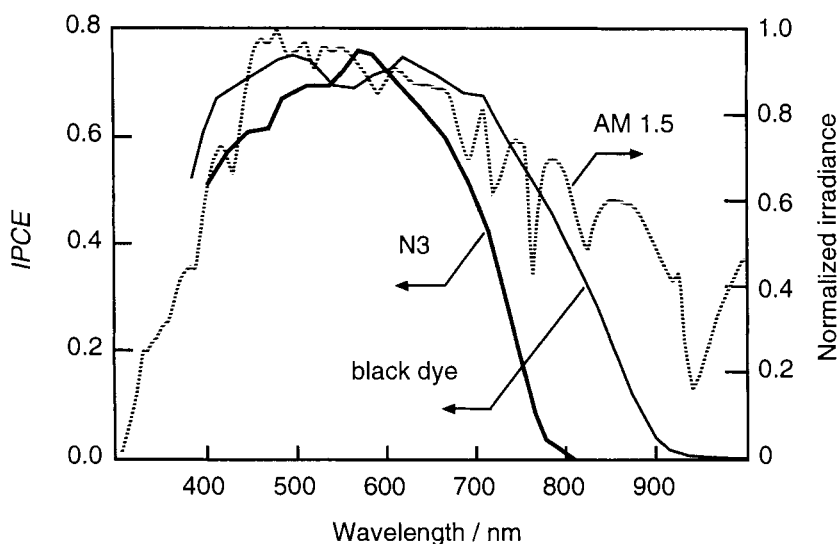


Figure 21. Typical spectral response curve of the incident photon-to-current conversion efficiency (IPCE) for a mesoporous TiO_2 electrode sensitized by “N3” and the “black dye”. A normalized solar irradiance spectrum under AM 1.5 conditions is superimposed for direct comparison.

the integral photocurrent density measured at short-circuit i_{sc} , the open-circuit photovoltage V_{oc} , the fill-factor of the cell f , and the intensity of the incident light I_{R} :

$$\eta = i_{\text{sc}} \times V_{\text{oc}} \times f / I_{\text{R}} \quad (61)$$

Figure 22 gives an example of the current–voltage characteristics of a nanocrystalline injection solar cell based on the *cis*- $[\text{Ru}^{\text{II}}(\text{dcbpy})_2(\text{NCS})_2]$ dye. The overall solar-to-electric conversion efficiency under standard AM 1.5 sunlight conditions, i.e., 1000 W m^{-2} incident intensity, is $\eta = 0.10$, which is commensurate with the performance of silicon-based conventional photovoltaic devices. Nanocrystalline injection solar cells based on the $\text{Ru}^{\text{II}}(\text{tctpy})(\text{NCS})_3$ sensitizer displayed similar results with a confirmed overall energy conversion efficiency as high as 10.4 %. Comparison of the latter value with the maximum thermodynamic conversion efficiency $\eta_0 = 0.27$, earlier discussed in Section 1.2.4, shows that theoretically avoidable losses amount to ca. 63 % of the available free energy. As inferred from the very high current yields obtained in such molecular photovoltaic devices, losses are essentially due to the waste of potential in electron transfer processes and to the dark current of the cell. The driving force of the charge injection process is minimal in the case of N3-sensitized TiO_2 in dry nitrile solvents. While partial degradation of the injected electron energy through trapping in the solid network cannot be neglected, it is apparent that the potential mismatch between the redox couples of the sensitizer S^+/S and the complex mediator I_3^-/I^- is responsible for a major part of the losses.

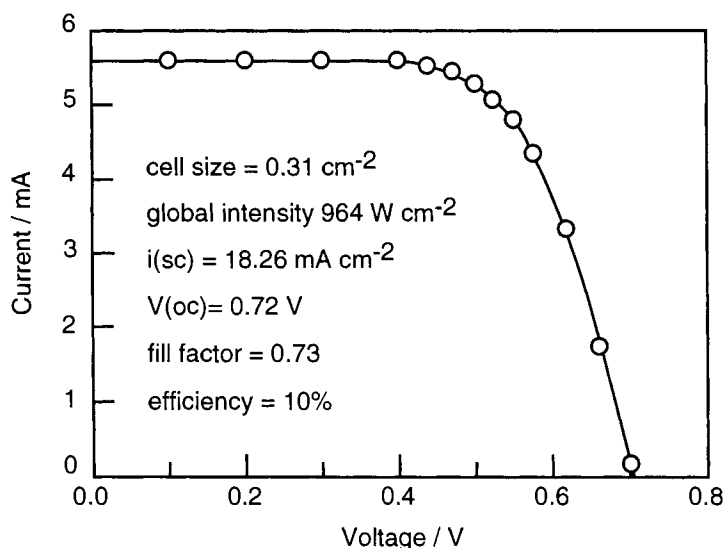
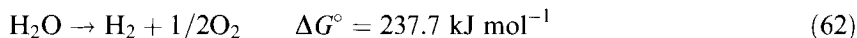


Figure 22. Photocurrent–voltage characteristic of a nanocrystalline photoelectrochemical cell sensitized with *cis*-[Ru^{II}(dcbpy)₂(NCS)₂]: $i(\text{sc})$ is the maximum (short-circuit) current density, and $V(\text{oc})$ the maximum (open-circuit) voltage delivered by the cell. The conversion efficiency is calculated by use of Eq. (61).

1.5 Water Cleavage by Visible Light

As pointed out by Allen Bard and Marye Anne Fox in a recent review [115], the photo-driven conversion of liquid water to gaseous hydrogen and oxygen (Eq. (62)),



is the “Holy Grail” of all photocatalytic reactions. It has been a long standing challenge of practical artificial photosynthetic systems. The hydrogen produced from sunlight and water can be subsequently employed in the catalytic reduction of carbon dioxide to produce fuels such as methane or methanol. The latter could also be used as feedstock for the production of organic chemicals. Alternatively, hydrogen could serve directly as a fuel for transportation purposes or for the production of electricity in fuel cells, without producing pollutants and greenhouse gases upon combustion. For a practical system, a conversion efficiency of at least 10 % is required, implying that the hydrogen and oxygen produced have a fuel value of at least 10 % of the solar energy incident on the system. As the peak solar power incident on Earth is about 1 kW m^{-2} a panel of 1 m^2 collector surface should produce hydrogen at a rate of about 36 L h^{-1} (at standard temperature and pressure) when exposed to direct sunlight.

As water is transparent to sunlight, a molecular sensitizer or semiconductor is required in order to absorb the solar photons and transform their radiant energy to generate the chemical potential required to split the H_2O molecules. The optimal absorption threshold for a single photoconverter has been calculated to be at an energy of 1.6 eV [116], implying that all solar photons below 770 nm should be absorbed. Such a system could split water with an efficiency of up to 30 %. Higher efficiencies of up to 42 % can be obtained by using a tandem device where two photosystems operate in series.

The “brute force” approach to achieve this goal is to employ a solid-state photovoltaic cell to generate electricity that is subsequently passed into a commercial-type water electrolyzer. Although efficiencies obtained are relatively high, i.e., close to 8 %, these devices are very expensive. Hence the price of hydrogen produced this way cannot compete with conventional sources. The long-term outlook is better for systems that borrow their principles from natural photosynthesis (see Section 1.4.1 above).

1.5.1 Analogs of Photosystem II of Green Plants

Researchers have long attempted to prepare catalysts capable of oxidizing water to oxygen (Eq. (17)), as the reaction constitutes the most difficult part in a complete water cleavage system. However, despite considerable efforts there are few man-made catalysts of any kind available, and none has made an impact on industrial chemistry [117, 118]. The difficulty of promoting this seemingly simple reaction has both thermodynamic and mechanistic origins. The catalyst must break the strong OH bonds on two water molecules (enthalpy 500 kJ mol^{-1}) in a concerted fashion. This has to be coupled to the removal of four protons and four electrons. The chemical intermediates formed during the process are so reactive that self-destruction of the catalyst often occurs. Nature solved this problem through evolution of a unique metalloenzyme required for oxygenic photosynthesis in all plants and cyanobacteria. This enzyme is called the Photosystem II water-oxidizing complex, or WOC. Its active site comprises an oxo-bridged tetramanganese cluster, one Ca^{2+} ion, and one or more Cl^- ions. In association with tyrosyl this core catalyzes reaction (17) using a chlorophyll cation radical as terminal electron acceptor.

The most intensively studied molecular systems mimicking the action of the WOC are based on the μ -oxo-bridged ruthenium dimer [*cis*-(bpy) $_2\text{Ru}(\text{OH}_2)]_2\text{O}^{4+}$, where each ruthenium is associated with two bipyridyl ligands and one water molecule. The catalytic water oxidation cycle involves abstraction of two electrons from each of the Ru(II) centers forming two dioxoruthenium(IV) moieties which convert back to the starting state under oxygen release and subsequent re-aquation of the ruthenium metal centers [119].

1.5.2 Colloidal Semiconductor Systems

Photocatalytic water-cleavage systems based on aqueous dispersions of semiconductor particles were extensively studied in the 1980s and this work has been

reviewed [120]. They have the advantage of being cheap but their efficiency is generally below 1 %. The additional drawback is that hydrogen and oxygen are generated simultaneously. Apart from the problem of gas separation, this produces a slowdown of the photoreaction as the two gases accumulate and back-react with each other. A way to avoid the latter problem is to separate the hydrogen and oxygen, generating half-reactions as reported recently by Arakawa and co-workers [121]. However, the efficiency of the process remains low.

1.5.3 Tandem Systems for Water Cleavage by Visible Light

The most promising approach to reach the goal of water cleavage by visible light is by way of a tandem system. The main reason for this is that the constraints imposed by thermodynamics are relaxed when eight photons of light are used instead of four to accomplish the production of two molecules of hydrogen and one molecule of oxygen from water. A tandem system is particularly favorable when complementary parts of the solar spectrum are exploited by the two photosystems operating in series. The maximum thermodynamic efficiency of such device is 42 %.

Khaselev and Turner [122] reported on a direct water-electrolysis system based on a novel, integrated, monolithic photoelectrochemical cell. This was patterned after the GaInP₂/GaAs p/n, p/n tandem cell device grown at the National Renewable Energy Laboratory in Golden, Colorado. The solid-state tandem cell consists of a GaAs bottom cell connected to a GaInP₂ top cell through a tunnel diode interconnect. The top p/n GaInP₂ junction, with a bandgap of 1.83 eV, is designed to absorb the visible portion of the solar spectrum; and the bottom p/n GaAs junction, with a bandgap of 1.42 eV, absorbs the near-infrared portion of the spectrum transmitted through the top junction. The conversion efficiency achieved was 12 %.

A tandem device that achieves the direct cleavage of water into hydrogen and oxygen by visible light was developed in collaboration with two partner groups from the Universities of Geneva and Bern [123]. This is based on the in-series connection of two photosystems. A thin transparent film of nanocrystalline tungsten trioxide or ferric oxide absorbs the blue part of the solar spectrum (Eq. (63)).



The valence band holes (h^+) created by bandgap excitation of the WO₃ or Fe₂O₃ serve to oxidize water to oxygen:



while the conduction-band electrons are fed into the second photosystem. The latter consists of the dye-sensitized nanocrystalline TiO₂ film. It is placed directly behind the WO₃ film, capturing the green and red part of the solar spectrum that is transmitted through the top electrode. The photovoltage generated by the second photosystem enables the generation of hydrogen by the conduction-band electrons:

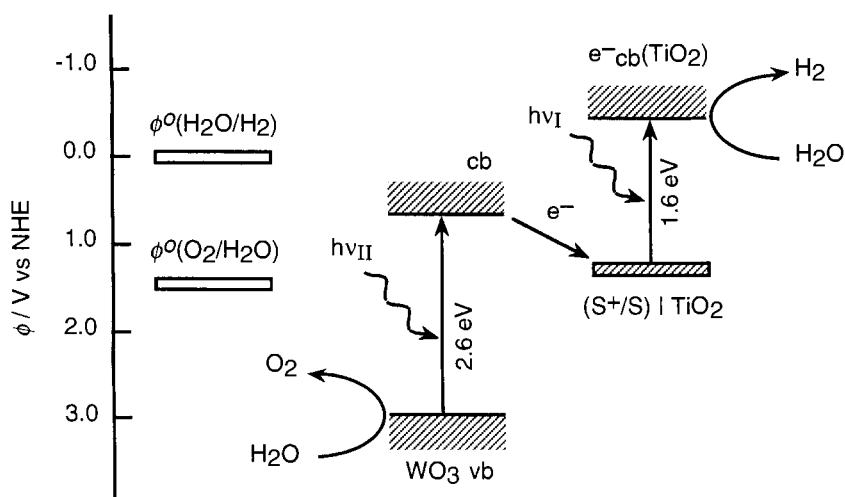


Figure 23. The Z-scheme of biphotonic water photolysis.



The overall reaction corresponds to the splitting of water by visible light.

There is close analogy to the Z-scheme operative in the light reaction of photosynthesis in green plants (Figure 3). This is illustrated by the electron flow diagram shown in Figure 23. In green plants, there are also two photosystems connected in series, one affording water oxidation to oxygen and the other generating the NADPH used in carbon dioxide fixation. As discussed above, the advantage of the tandem approach is that higher efficiencies than with single junction cells can be reached if the two photosystems absorb complementary parts of the solar spectrum. At present, the overall AM 1.5 solar light to chemical conversion efficiency achieved with this device stands at 4.5 %. Figure 24 shows such a cell producing hydrogen and oxygen bubbles vigorously under visible-light illumination. Present endeavors aim at further improving the efficiency of the device.

1.6 Future Outlook and Concluding Remarks

Intensive research is being carried out around the world, focusing on the following issues:

- 1) the molecular design and synthesis of new sensitizers having an enhanced near-infrared light response, examples being phthalocyanines or the black dye discussed above;

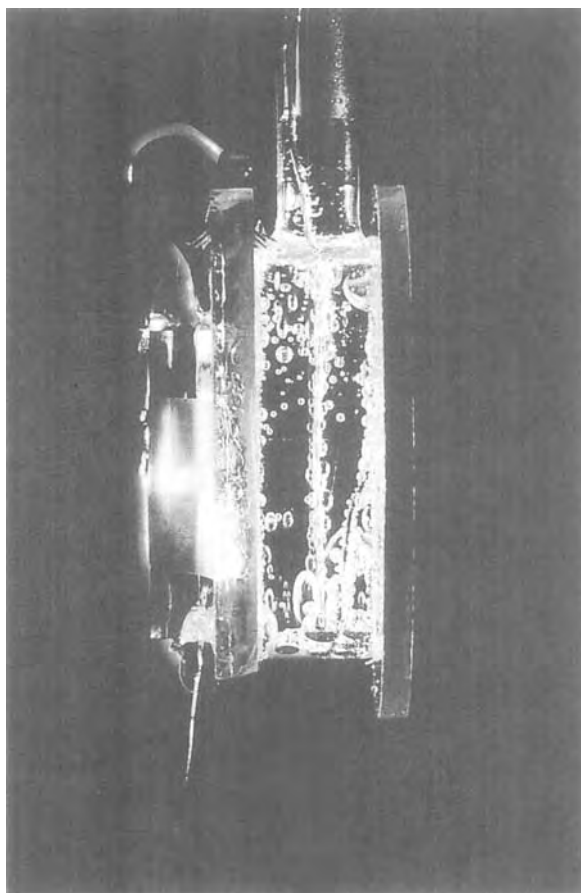


Figure 24. Decomposition of water by visible light in a tandem cell consisting of a mesoporous WO_3 film and a mesoporous dye-sensitized TiO_2 film which is superimposed.

- 2) achievement of a better understanding of the interface, including experimental and theoretical investigation of dye adsorption processes;
- 3) the analysis of the dynamics of interfacial electron transfer processes down to the femtosecond time domain;
- 4) the unraveling of the factors that control electron transport in nanocrystalline oxide semiconductor films; and
- 5) the replacement of the liquid electrolyte by solid materials that serve as a hole conductor.

A great advantage of dye-sensitized cells is that they can be used to produce directly high-energy chemicals from sunlight. Such “photosynthetic” devices solve the principle problem of conventional photovoltaic cells, i.e., the lack of capacity for energy storage. The “Holy Grail” of all photoconversion processes is the splitting of water into hydrogen and oxygen by sunlight, and the improvement of the tandem devices described above will be one of the primary targets of future research. Rapid prog-

ress is expected in these areas as an impressive number of competent teams around the world are actively pursuing this research. These systems will undoubtedly promote the acceptance of renewable energy technologies, not least by setting new standards of convenience and economy.

Acknowledgments

Recognition is due to the members of the Laboratory of Photonics Interfaces of the Swiss Federal Institute of Technology (EPFL), some of whose work is referenced below; to those industrial organizations whose interest in the molecular photovoltaic system has induced them to license the concept and thereby support our research; to EPFL and FNRS (Swiss National Science Foundation) for financial support; and to OFEN (Swiss Federal Office of Energy) for past encouragement and support. Thanks are also due to Dr. Pierre Bonhôte for valuable help in the writing of Section 1.4.5.

References

1. G. Porter, *J. Chem. Soc., Farad. Trans. 2* **1983**, 79, 473–482.
2. *Electro-Optics Handbook*, Radio Corporation of America, Lancaster, PA, **1974**.
3. J. R. Bolton, A. F. Haught, R. T. Ross, in *Photochemical Conversion and Storage of Solar Energy* (Ed.: J. S. Conolly), Academic Press, New York, **1981**, pp. 297–339.
4. *Symposium on Photoelectrochemistry* (Pennington, NJ) (Eds.: K. Rajeshwar et al.), The Electrochemical Society, Pennington, **1997**.
5. C. J. Barbé, F. Arendse, P. Comte, M. Jirousek, F. Lenzmann, V. Shklover, M. Grätzel, *J. Am. Ceram. Soc.* **1997**, 80, 3157.
6. S. D. Burnside, V. Shklover, C. J. Barbé, P. Comte, F. Arendse, K. Brooks, M. Grätzel, *Chem. Mater.* **1998**, 10, 2419.
7. J. Moser, *Monatsh. Chem.* **1887**, 8, 373.
8. E. Becquerel, *Comptes Rendus* **1839**, 9, 561.
9. H. W. Vogel, *Ber. Dtsch. Chem. Ges.* **1873**, 6, 1730.
10. W. West, *Photogr. Sci. Eng.* **1974**, 18, 35.
11. S. Namba, Y. Hishiki, *J. Phys. Chem.* **1965**, 6, 774.
12. H. Gerischer, H. Tributsch, *Ber. Bunsenges Phys. Chem.* **1968**, 72, 437.
13. M. P. Dare-Edwards, J. B. Goodenough, A. Hamnet, K. R. Seddon, R. D. Wright, *Faraday Disc. Chem. Soc.* **1980**, 70, 285.
14. H. Tsubomura, M. Matsumura, Y. Noyamaura, T. Amamiya, *Nature* **1976**, 261, 402.
15. D. Duonghong, N. Serpone, M. Grätzel, *Helv. Chim. Acta* **1984**, 67, 1012.
16. J. Desilvestro, M. Grätzel, L. Kavan, J. Moser, J. Augustynski, *J. Am. Chem. Soc.* **1985**, 107, 2988–2990.
17. M. K. Nazeeruddin, P. Liska, J. Moser, N. Vlachopoulos, M. Grätzel, *Helv. Chim. Acta* **1990**, 73, 1788.
18. B. O'Regan, M. Grätzel, *Nature* **1991**, 355, 737.
19. D. W. Thompson, C. A. Kelly, F. Farzad, G. J. Meyer, *Langmuir* **1999**, 15, 650–653.
20. R. O. Loutfy, J. H. Sharp, *Photogr. Sci. Eng.* **1976**, 20, 165–174.
21. M. K. Nazeeruddin, A. Kay, I. Rodicio, R. Humphry-Baker, E. Muller, P. Liska, N. Vlachopoulos, M. Grätzel, *J. Am. Chem. Soc.* **1993**, 115, 6382.
22. R. Amadelli, R. Argazzi, C. A. Bignozzi, F. Scandola, *J. Am. Chem. Soc.* **1990**, 112, 7029.
23. M. Alebbi, C. A. Bignozzi, T. A. Heimer, G. M. Hasselmann, G. J. Meyer, *J. Phys. Chem. B* **1998**, 102, 7577–7581.

24. M. K. Nazeeruddin, P. Péchy, M. Grätzel, *J. Chem. Soc., Chem. Commun.* **1997**, 1705.
25. K. S. Finnie, J. R. Bartlett, J. L. Woolfrey, *Langmuir* **1998**, *14*, 2744.
26. L. Patthey, H. Rensmo, P. Persson, K. Westermark, L. Vayssieres, A. Stashans, P. Petersson, P. A. Brohwiler, H. Siegbahn, S. Lunell, N. Martensson, *J. Chem. Phys.* **1999**, *110*, 5913.
27. H. Rensmo, S. Lunell, H. Siegbahn, *J. Photochem. Photobiol. A: Chem.* **1998**, *114*, 117–124.
28. H. Rensmo, S. Södergren, L. Patthey, K. Westermark, L. Vayssieres, O. Kohle, P. A. Brohwiler, A. Hagfeldt, H. Siegbahn, *Chem. Phys. Lett.* **1997**, *27*, 51–57.
29. S. A. Haque, Y. Tachibana, R. L. Willis, J. E. Moser, M. Grätzel, D. R. Klug, J. R. Durrant, *J. Phys. Chem. B* **2000**, *104*, 538–547.
30. Y. Tachibana, S. A. Haque, I. P. Mercer, D. R. Klug, J. R. Durrant, *J. Phys. Chem. B* **2000**, *10*, in press.
31. M. K. Nazeeruddin, S. M. Zakeeruddin, R. Humphry-Baker, M. Jirousek, P. Liska, N. Vlachopoulos, V. Shklover, C.-H. Fischer, M. Grätzel, *Inorg. Chem.* **2000**, in press.
32. J. M. Lanzafame, S. Palese, D. Wang, R. J. D. Miller, A. A. Muentert, *J. Phys. Chem.* **1994**, *98*, 11020.
33. R. J. D. Miller, G. L. McLendon, A. J. Nozik, W. Schmickler, F. Willig, *Surface Electron Transfer Processes*, VCH, New York, **1995**.
34. R. A. Smith, *Semiconductors*, Cambridge University Press, Cambridge, **1978**.
35. B. Enright, D. Fitzmaurice, *J. Phys. Chem.* **1996**, *100*, 1027–1035.
36. J. B. Asbury, R. J. Ellingson, H. N. Ghosh, S. Ferrere, A. J. Nozik, T. Lian, *J. Phys. Chem. B* **1999**, *10*, 3110–3119.
37. Y. H. Meyer, P. Plaza, *Chem. Phys.* **1995**, *200*, 235.
38. P. Siders, R. J. Cave, R. A. Marcus, *J. Chem. Phys.* **1984**, *81*, 5613.
39. A. Hagfeldt, M. Grätzel, *Chem. Rev.* **1995**, *95*, 49–68.
40. J. Moser, M. Grätzel, *J. Am. Chem. Soc.* **1984**, *106*, 6557–6564.
41. K. Hashimoto, M. Hiramoto, A. B. P. Lever, T. Sakata, *J. Phys. Chem.* **1988**, *92*, 1016–1018.
42. R. W. Fessenden, P. V. Kamat, *J. Phys. Chem.* **1995**, *99*, 12902.
43. R. Eichberger, F. Willig, *Chem. Phys.* **1990**, *141*, 159.
44. J. M. Rehm, G. L. McLendon, Y. Nagasawa, K. Yoshihara, J. Moser, M. Grätzel, *J. Phys. Chem.* **1996**, *100*, 9577–9578.
45. M. T. Spitler, A. Ehret, R. Kietzmann, F. Willig, *J. Phys. Chem. B* **1997**, *101*, 2552–2557.
46. J. Moser, M. Grätzel, D. K. Sharma, N. Serpone, *Helv. Chim. Acta* **1985**, *68*, 1686–1690.
47. Y. Tachibana, J. E. Moser, M. Grätzel, D. R. Klug, J. R. Durrant, *J. Phys. Chem.* **1996**, *100*, 20056–20062.
48. B. Burfeindt, T. Hannappel, W. Störck, F. Willig, *J. Phys. Chem.* **1996**, *100*, 16463–16465.
49. N. J. Cherepy, G. P. Smestad, M. Grätzel, J. Z. Zhang, *J. Phys. Chem. B* **1997**, *101*, 9342–9351.
50. M. Hilgendorff, V. Sundström, *J. Phys. Chem. B* **1998**, *102*, 10505–10514.
51. J. Wachtveitl, R. Huber, S. Spörlein, J. E. Moser, M. Grätzel, *Int. J. Photoenergy* **1999**, *1*, 131–134.
52. J. E. Moser, D. Noulakis, U. Bach, Y. Tachibana, D. R. Klug, J. R. Durrant, R. Humphry-Baker, M. Grätzel, *J. Chem. Phys. B* **1998**, *102*, 3649–3650.
53. S. Das, P. V. Kamat, *J. Phys. Chem. B* **1998**, *102*, 8954–8957.
54. J. R. Durrant, Y. Tachibana, I. Mercer, J. E. Moser, M. Grätzel, D. R. Klug, *Zeit. Phys. Chem.* **1999**, *212*, 93–98.
55. C. A. Kelly, F. Farzad, D. W. Thompson, J. M. Stipkala, G. J. Meyer, *Langmuir* **1999**, *15*, 7047–7054.
56. B. T. Langdon, V. J. MacKenzie, D. J. Asunsis, D. F. Kelley, *J. Phys. Chem. B* **1999**, *103*, 11176–11180.
57. A. Seilmeier, W. Kaiser, in *Ultrashort Laser Pulses, Vol. 60* (Ed.: W. Kaiser), Springer-Verlag, Berlin, **1993**, pp. 279–317.
58. N. H. Damrauer, G. Cerullo, A. Yeh, T. R. Boussie, C. Shank, J. K. McKusker, *Science* **1997**, *275*, 54.
59. P. J. Carroll, L. E. Brus, *J. Am. Chem. Soc.* **1987**, *109*, 7613.
60. M. K. DeArmond, M. L. Myrick, *Acc. Chem. Res.* **1989**, *22*, 364.
61. J. E. Moser, M. Wolf, F. Lenzmann, M. Grätzel, *Zeit. Phys. Chem.* **1999**, *212*, 85–92.

62. S. Ferrere, B. A. Gregg, *J. Am. Chem. Soc.* **1998**, *120*, 843–844.
63. B. O'Regan, J. Moser, M. Anderson, M. Grätzel, *J. Phys. Chem.* **1990**, *94*, 8720–8726.
64. P. V. Kamat, I. Bedja, S. Hotchandani, L. K. Patterson, *J. Phys. Chem.* **1996**, *100*, 4900–4908.
65. F. Willig, R. Keitzmann, K. Schwarzburg, in *Photochemical and Photoelectrochemical Conversion and Storage of Solar Energy* (Eds.: Z. W. Tian, Y. Cao), International Academic Publishers, Beijing, **1993**, p. 129.
66. H. N. Ghosh, J. B. Asbury, Y. Weng, T. Lian, *J. Phys. Chem. B* **1998**, *102*, 10208–10215.
67. H. N. Ghosh, J. B. Asbury, Y. Weng, T. Lian, *J. Phys. Chem. B* **1998**, *102*, 10208–10215.
68. R. Huber, S. Spörlein, J. E. Moser, M. Grätzel, J. Wachtveitl, *J. Phys. Chem. B* **2000**, *104*, 8995–9003.
69. D. E. Skinner, D. P. Colombo, J. J. Cavaleri, R. M. Bowman, *J. Phys. Chem.* **1995**, *99*, 7853–7856.
70. D. P. Colombo, R. M. Bowman, *J. Phys. Chem.* **1995**, *99*, 11752–11756.
71. D. P. Colombo, R. M. Bowman, *J. Phys. Chem.* **1996**, *100*, 18445.
72. I. Martini, J. H. Hodak, G. V. Hartland, *J. Phys. Chem. B* **1998**, *102*, 607–614.
73. H. Lu, J. N. Prieskorn, J. T. Hupp, *J. Am. Chem. Soc.* **1993**, *115*, 4927–4928.
74. X. Dang, J. T. Hupp, *J. Phys. Chem. B* **1999**, *121*, 8399–8400.
75. J. E. Moser, M. Grätzel, *Chem. Phys.* **1993**, *17*, 493–500.
76. J. E. Moser, S. Widmer, M. Grätzel, *Tenth International Conference on Photochemical Conversion and Storage of Solar Energy (IPS-10)* (Interlaken), *Book of abstracts* (Ed.: G. Calzaferri), **1994**, pp. 195–196.
77. J. E. Moser, *Solar Energy Mater. Solar Cells* **1995**, *38*, 343–345.
78. H. N. Ghosh, *J. Phys. Chem. B* **1999**, *103*, 10382–10387.
79. I. Martini, J. H. Hodak, G. V. Hartland, *J. Phys. Chem. B* **1998**, *102*, 9508–9517.
80. S. A. Haque, Y. Tachibana, D. R. Klug, J. R. Durrant, *J. Phys. Chem. B* **1998**, *102*, 1745–1749.
81. Y. X. Weng, Y. Q. Wang, J. B. Asbury, H. N. Ghosh, T. Lian, *J. Phys. Chem. B* **2000**, *104*, 93–104.
82. J. Nelson, *Phys. Rev. B* **1999**, *59*, 15374–15380.
83. J. Ferber, R. Sangl, J. Luther, *Solar Energy Mater. Solar Cells* **1998**, *53*, 29.
84. R. Argazzi, C. A. Bignozzi, G. M. Hasselmann, G. J. Meyer, *Inorg. Chem.* **1998**, *3*, 4533–4537.
85. U. Bach, D. Lupo, P. Comte, J. E. Moser, F. Weissörtel, J. Salbeck, H. Spreitzer, M. Grätzel, *Nature* **1998**, *395*, 583–585.
86. K. Tennakone, G. R. R. A. Kumara, A. R. Kumarasinghe, K. G. U. Wijayantha, P. M. Sirimanne, *Semicond. Sci. Technol.* **1995**, *10*, 1689–1693.
87. K. Murakoshi, R. Kogure, S. Yanagida, *Chem. Lett.* **1997**, 471–472.
88. B. O'Regan, D. T. Schwartz, *Chem. Mater.* **1998**, *10*, 1501–1509.
89. C. Nasr, S. Hotchandani, P. V. Kamat, *J. Phys. Chem. B* **1998**, *102*, 4944–4951.
90. G. Nord, *Comm. Inorg. Chem.* **1992**, *13*, 221.
91. J. Moser, M. Grätzel, *Helv. Chim. Acta* **1981**, *65*, 1436–1444.
92. S. Pelet, J. E. Moser, M. Grätzel, *J. Phys. Chem. B* **2000**, *104*, 1791–1795.
93. S. Y. Huang, G. Schlichthörl, A. J. Nozik, M. Grätzel, A. J. Frank, *J. Phys. Chem. B* **1997**, *101*, 2576–2582.
94. Y. Liu, A. Hagfeldt, X.-R. Xiao, S.-E. Lindquist, *Solar Energy Mater. Solar Cells* **1998**, *55*, 267–281.
95. A. C. Fischer, L. M. Peter, E. A. Ponomarev, A. B. Walker, K. G. U. Wijayantha, *J. Phys. Chem. B* **2000**, *104*, 949–958. N. W. Duffy, L. M. Peter, R. M. G. Rajapakse, K. G. U. Wijayantha, *J. Phys. Chem. B* **2000**, *104*, 8916–8919.
96. S. Södergren, A. Hagfeldt, J. Olsson, S.-E. Lindquist, *J. Phys. Chem.* **1994**, *98*, 5552–5556.
97. F. Cao, G. Oskam, G. J. Meyer, P. S. Searson, *J. Phys. Chem.* **1996**, *100*, 17021–17027.
98. L. Dłoczik, O. Ieperuma, I. Lauermaann, L. M. Peter, E. A. Ponomarev, G. Redmond, N. J. Shaw, I. Uhlendorf, *J. Phys. Chem. B* **1997**, *101*, 10281–10289.
99. D. Vanmaekelberg, P. E. de Jong, *J. Phys. Chem. B* **1999**, *103*, 747–750.
100. H. Scher, E. W. Montroll, *Phys. Rev. B* **1975**, *12*, 2455.

101. A. Solbrand, S. Södergren, H. Lindström, H. Rensmo, A. Hagfeldt, S.-E. Lindquist, *J. Phys. Chem. B* **1997**, *101*, 2514.
102. N. Papageorgiou, M. Grätzel, P. P. Infelta, *Solar Energy Mater. Solar Cells* **1996**, *44*, 405–438.
103. G. Schlichthörl, S. Y. Huang, J. Sprague, A. Frank, *J. Phys. Chem. B* **1997**, *101*, 8141–8155.
104. A. Wahl, J. Augustynski, *J. Phys. Chem. B* **1998**, *102*, 7820–7828.
105. J. Hagen, *Synth. Met.* **1997**, *89*, 209–215.
106. W. C. Sinke, M. M. Wienk, *Nature* **1998**, *395*, 544–545.
107. U. Bach, Y. Tachibana, J. E. Moser, S. A. Haque, J. R. Durrant, M. Grätzel, D. R. Klug, *J. Am. Chem. Soc.* **1999**, *121*, 7445–7446.
108. Y. V. Pleskov, *Solar Energy Conversion*, Springer Verlag, Berlin, **1990**.
109. R. Argazzi, C. A. Bignozzi, T. A. Heimer, G. J. Meyer, *Inorg. Chem.* **1997**, *36*, 2–3.
110. P. Bonhôte, J. E. Moser, R. Humphry-Baker, N. Vlachopoulos, S. M. Zakeeruddin, L. Walder, M. Grätzel, *J. Am. Chem. Soc.* **1999**, *121*, 1324–1336.
111. P. Péchy, F. P. Rotzinger, M. K. Nazeeruddin, O. Kohle, S. M. Zakeeruddin, R. Humphry-Baker, M. Grätzel, *J. Chem. Soc., Chem. Commun.* **1995**, 65.
112. S. M. Zakeeruddin, M. K. Nazeeruddin, P. Péchy, F. P. Rotzinger, R. Humphry-Baker, K. Kalyanasundaram, M. Grätzel, V. Shklover, T. Haibach, *Inorg. Chem.* **1997**, *36*, 5937.
113. E. Steckhan, *Top. Curr. Chem.* **1987**, *142*, 3.
114. P. Bonhôte, A. P. Dias, N. Papageorgiou, K. Kalyanasundaram, M. Grätzel, *Inorg. Chem.* **1996**, *35*, 1168.
115. A. J. Bard, M. A. Fox, *Acc. Chem. Res.* **1995**, *28*, 141.
116. M. D. Archer, J. R. Bolton, *J. Phys. Chem.* **1990**, *94*, 8028.
117. W. Ruttiger, G. C. Dismukes, *Chem. Rev.* **1997**, *97*, 1–24.
118. M. Freemantle, *Chem. Eng. News* **1998**, October 26, 37–46.
119. C. W. Chronister, R. A. Binstead, J. Ni, T. J. Meyer, *Inorg. Chem.* **1997**, *36*, 3814, and references cited therein.
120. K. Kalyanasundaram, M. Grätzel, E. Pelizzeti, *Coord. Chem. Rev.* **1986**, *69*, 57.
121. G. R. Bamwenda, K. Sayama, H. Arakawa, *J. Photochem. Photobiol. A* **1999**, *122*, 175–183.
122. O. Khaslev, J. Turner, *Science* **1998**, *280*, 455.
123. M. Grätzel, *Cattech* **1999**, *3*, 4–17.

2 Batteries

Catia Arbizzani, Marina Mastragostino, and Francesca Soavi

2.1 Introduction

Volta's discovery of the pile 200 years ago (1799) ushered in the age of electrochemistry. Today, while the battery remains the most widespread practical application of electrochemistry, it is perhaps just as true that the battery is also the most widespread application of electron transfer, the phenomenon at the basis of its operation.

Unlike the past, the term "battery" is now commonly used to indicate either one or more electrochemical cells in series or in parallel. The terms "primary" and "secondary" cell were introduced to distinguish the device's characteristics, i.e., the ability to work until the reactants are exhausted or to sustain both the forward and the reverse processes, reactants \rightarrow products and products \rightarrow reactants. Today secondary cells are also called rechargeable batteries.

Batteries accomplish two functions:

- 1) to convert chemical into electric energy, i.e., to act as a source of electric energy, which is true for both nonrechargeable and rechargeable systems;
- 2) to store the electric energy supplied by an external source, i.e., to act also as energy storage systems, which is true only for rechargeable batteries.

The latter batteries are used for such different applications as in consumer electronics, in vehicles for starting, lighting, and ignition (SLI) and for traction, as emergency power supplies, in load-leveling systems of electric power stations to supply peak demand, and as systems to couple with alternative energy sources.

The battery's energy, which is the amount of electric energy that can be delivered (generally expressed in watt-hours, Wh) is directly related to its size: Table 1 gives a classification of the various battery types associated with their uses. The energy range extends over many orders of magnitude, from 0.1 mWh (single cell) for microelectronic applications to 100 MWh (several cells with in-series or parallel arrays) for load-leveling in electric power stations.

Table 1. Battery types according to size [1] (by permission of Arnold: C.A. Vincent and B. Scrosati, *Modern Batteries. An Introduction to Electrochemical Power Sources*, 2nd edition, 1997).

Type	Energy	Applications
Miniature batteries	0.1 mWh–2 Wh	electric watches, calculators, implanted medical devices
Batteries for portable equipment	2 Wh–100 Wh	cellular phones, laptop computers, flashlights, toys, portable radios, televisions
SLI batteries (starting, lighting and ignition)	100–600 Wh	cars, trucks, buses, tractors
Vehicle traction batteries	20–630 kWh	forklift trucks, locomotives
Stationary batteries	250 Wh–5 MWh	emergency power supplies, local energy storage, remote relay stations
Load-leveling batteries	5–100 MWh	spinning reserve, peak shaving, load leveling

From an historical point of view, it is the introduction of telegraph systems, in the late 1830s, that demonstrated the signal importance of Volta's discovery. Following Volta, Planté developed in 1859 the first lead–acid rechargeable battery and Leclanché in 1866 the primary zinc–manganese dioxide cell bearing his name. In 1890 the invention of the nickel–iron rechargeable cell by Edison opened the door to the development of the nickel–cadmium cell, first proposed in 1899 by Jungner. The advent of the rechargeable systems was greatly stimulated by the demand from the incipient motor car industry, the growing public interest in which was also being fed by the unforgettable exploit like that of the Belgian race driver Jenatzy who, in 1899, established the land speed record of 66 miles per hour in his streamlined electric *Jamais Contente*. However, the initial spurt of enthusiasm for electric vehicles petered out in the next two decades as they became less and less competitive with the petroleum-powered car.

The great discoveries ameliorating the standard of living by the end of the 19th century stimulated the demand—and of course the research—for new, improved batteries. This holds as much for the present as it did for the past. Indeed, a notable impulse to battery research and development was the invention of the transistor in 1950, broadening the range of battery applications from electronics to medical science and the conquest of outer space. With the launch in 1957 of the *Sputnik*, the Soviet satellite whose communications and operating systems were powered by silver–zinc primary cells, the space race was on. In 1960 the first successful pacemaker, containing ten zinc–mercuric oxide primary cells and two transistors, was implanted into a human being. The “oil crisis” in the 1970s was the driving force behind the search for renewable energy sources, while the last two decades of the 20th century saw great advances in circuit miniaturization, an exponential proliferation of portable products requiring primary cells, and a spectacular growth of cellular phones and laptop computers demanding greater performance than ever before from rechargeable systems.

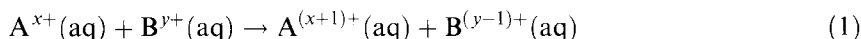
All of this has shifted the focus of research in rechargeable batteries from nickel–cadmium to nickel–metal hydride and lithium-ion systems, with additional impetus from the heightened environmental consciousness in the 1990s extending the range of focus to the development of nonpolluting forms of transport. Although recent advances in automobile engines have made new cars less polluting than older ones, the increase in vehicle numbers offsets the benefits of cleaner engines. Several legislative measures and actions, such as the establishment in 1991 of the US Advanced Battery Consortium (USABC), have also helped to accelerate the development of advanced batteries, such as the lithium-based ones for use in electric vehicles.

Apart from its historical interest, this brief survey over the centuries from 1800 to 2000 helps underscore the fact that key developments in battery research and technology have always come in response to specific sector demands that have in turn followed signal scientific advances. Nowadays, the three main rechargeable systems are the lead-, nickel-, and lithium-based batteries. While the first two, with their roots in the last century, are undergoing continual refinement to improve their performance in today's applications, the last is the result of the most recent research into new materials and the one that offers greater expectations.

The basic thermodynamic and electrochemical kinetic concepts involved in batteries and the parameters used to evaluate their performance are summarized in Section 2.2. The most widespread primary and rechargeable systems are described by highlighting the most recent advances in Section 2.3. Supercapacitors and fuel cells, whose importance in the field of energy conversion is growing, are also briefly treated in this section. The lithium-based rechargeable systems, the most advanced batteries with the highest performance, are discussed in detail in Section 2.4, with particular emphasis on the new materials on which these batteries are based.

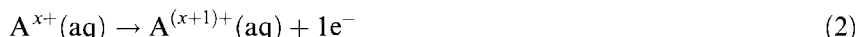
2.2 Basic Aspects

A spontaneous electron transfer process from one ionic species A^{x+} to another B^{y+} , wherein A^{x+} donates electrons that are accepted by B^{y+} , as in the redox reaction (1),



can take place by chemical reaction in homogeneous solution or by heterogeneous electrochemical reaction in an electrochemical cell. The condition for the occurrence of such a spontaneous electron transfer process is a decrease in the reaction's free energy. The electrochemical cell for such redox reactions as (1) is based on two chemically inert metal electrodes—which act as electron sink and source—immersed in solutions containing the A^{x+} and $A^{(x+1)+}$ and the B^{y+} and $B^{(y-1)+}$ ions, respectively; a separator between the two solutions prevents their mixing but permits their electric contact. The A^{x+} ions donate electrons to one metal electrode

by changing their oxidation state, as in



and the B^{y+} ions accept electrons from the other electrode by changing their oxidation state, as in



via the connection by external resistance load of the two metal conductors. This enables the charge to flow round the circuit, which is closed by the ion movement in the solution; hence, the reaction (1) can progress spontaneously and continuously as the sum of the two half-reactions (2) and (3), which involve charge transfer at the metal–solution interfaces. The amount of the $A^{(x+1)+}$ and $B^{(y-1)+}$ ions produced is related by Faraday's laws to the total charge transferred across the metal–solution interfaces. The most important feature is that in an electrochemical cell the spontaneous progress of the reaction (1), driven by its free energy decrease, includes the spontaneous electron flow through the external resistance load and, hence, a direct conversion of the reaction's chemical energy into electric energy takes place; this is basically how a battery works under the discharge process. Batteries, by converting the chemical energy of their electroactive materials directly into electric energy, are portable sources of electric energy and, hence, a widespread application of the electron transfer process.

More generally, a battery consists of two electrodes separated by at least one electrolyte phase. A convenient notational representation of a battery is to write the chemical composition of the phases composing it in the order in which the phases are connected, and to indicate each phase boundary by a vertical line. A double vertical line indicates the contact zone of two electrolyte phases.

During battery discharge, as shown in Figure 1 with the Daniell cell as an example, the electrode (a zinc rod immersed in a zinc sulfate solution) at which the oxidation reaction takes place is called the anode, and is the negative electrode. The other electrode (a copper rod immersed in a copper sulfate solution) at which the reduction reaction takes place is called the cathode and is the positive electrode. The electron flow in the external circuit is from anode to cathode (the current, i , conventionally flows in the opposite direction to that of the electrons), and in the electrolyte phase the ionic flow closes the circuit. The net result of the charge flow round the circuit is the cell reaction, which is made up of the two half-reactions of charge transfer that describe the chemical changes at the two electrodes.

There are also batteries in which the sum of the two electrode half-reactions produces not a chemical reaction but the transfer of a species from one electrode to the other. Such cells are called concentration cells to distinguish them from those in which a chemical reaction takes place.

A battery in which the cell reaction is reversed when the current is made to flow through the cell in the opposite direction by an external electric energy source is a rechargeable battery. During battery recharge the electric energy is converted into chemical energy; hence a rechargeable battery is a storage and energy conversion

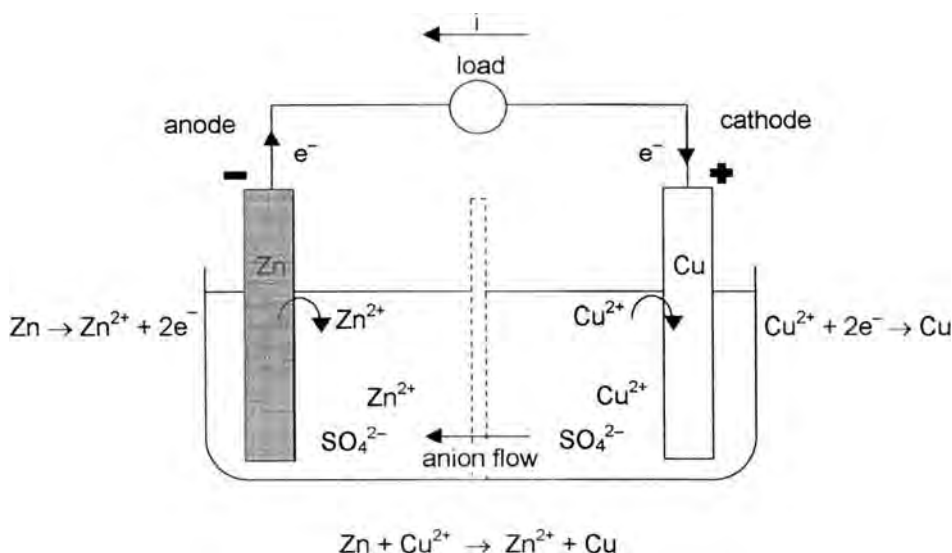


Figure 1. Daniell cell under discharge.

device. In a battery under charge the electrode at which the reduction reaction takes place, i.e., the cathode, is the negative electrode, and that at which the oxidation reaction takes place, i.e., the anode, is the positive electrode. It is worthwhile pointing out that in a battery under discharge the negative electrode is the anode whereas under charge it is the cathode.

When the current does not flow through battery the measurable difference in electric potential between the terminals of the two electrodes is the result of all the equilibrium potential differences at the interphase between the conducting phases in contact. In the example of the Daniell cell, with both electrodes having copper terminals, there are three interfacial potential differences (apart from the small liquid junction potential difference at the contact between the two electrolyte phases): one potential difference at the contact between the zinc rod and the copper terminal (Zn/Cu) and two potential differences at the metal–solution interphases (Zn/Zn²⁺ and Cu/Cu²⁺), which are mainly due to the charge transfer processes.

Let us now look in greater detail at how the potential difference at the metal–solution interphase is built up. When a metal M, such as zinc or copper, enters into contact with a solution containing one of its salts, e.g., zinc sulfate or copper sulfate, at the interface there will be an exchange of M^{x+} metal ions between the two phases. At the beginning, under conditions such that there are more M^{x+} ions leaving the metal crystal lattice than M^{x+} ions entering it, the metal and the solution phases become progressively charged: an excess of electrons builds up on the metal side and an excess of M^{x+} ions builds up on the solution side so that an electrical potential difference develops at the interphase. This potential difference in turn affects the charge transfer rates by depressing the rate at which the M^{x+} ions

leave the metal, i.e., the rate of the oxidation reaction, and by increasing that at which the M^{x+} ions enter the metal, i.e., the rate of the reduction reaction, until the rates of the two processes become equal. At this point a dynamic equilibrium is established—a very small quantity of charge has been transferred—and the difference in the electric potential at the interphase is the “interphase equilibrium potential difference”. A similar description can be given for the buildup of the equilibrium potential difference at the metal–solution interphase of a chemically inert metal M in a solution with the oxidized $A^{(x+1)+}$ and reduced A^{x+} ions. The inert metal acts as the source and sink of electrons: some electrons from the conduction band of the metal are accepted by the $A^{(x+1)+}$ oxidized species in solution and some electrons are donated to the metal by the A^{x+} reduced species in solution. At the beginning the reduction and oxidation rates are unequal, and the metal and solution become progressively charged until the equilibrium is established, resulting in the attainment of the interphase equilibrium potential difference.

When the current flows through the battery—a net reduction reaction takes place at one electrode and a net oxidation reaction takes place at the other—the potential difference at each metal–solution interphase is different from that at equilibrium.

Since it is impossible to measure the individual electric potential differences at the phase boundaries, we shall hereinafter speak only in terms of the difference in electric potential across the two terminals connected to the electrodes of the battery. When in a battery the current is not flowing or tends to zero, the measurable potential difference across the two terminals is called the open-circuit voltage (OCV), V_{oc} , and it represents the battery’s equilibrium potential (or voltage). Since it is related to the free energy of the cell reaction, the OCV is a measure of the tendency of the cell reaction to take place. Indeed, while the conversion of chemical into electric energy is regulated by thermodynamics, the behavior of a battery under current flow (the current is a measure of the electrochemical reaction rate) comes under electrochemical kinetics.

2.2.1 Thermodynamics and Electrochemical Kinetics

At constant temperature (T), pressure (P) and composition, the free energy of cell reaction ΔG , where $\Delta G = \sum v_i \mu_i$ (v_i stoichiometric coefficients and μ_i chemical potentials), is a measure of the maximum electric work (W_{el}) the battery can deliver in association with n moles of transferred electrons; the relevant thermodynamic equation is

$$-\Delta G \geq W_{el} \quad (4)$$

The “equals” sign is valid for a reversible ($i \rightarrow 0$) conversion; the “greater than” sign is valid for an irreversible conversion (finite i). Hence, an electrochemical cell delivers electric work equal to the free energy change only at infinitesimal current flow: under these conditions the cell potential is the OCV and the electric work delivered is the maximum $W_{el,max} = nFV_{oc} = -\Delta G$ (n is the number of moles of transferred electrons and F the Faraday constant).

During the reversible conversion of chemical energy into electric work, heat exchange with the surroundings also takes place, and it is equal to $T\Delta S$, ΔS being the cell reaction entropy change. At constant T , the enthalpy change is $\Delta H = \Delta G + T\Delta S$, and hence a positive ΔS value implies that the electrochemical cell delivers electric work greater than the amount of heat that the reaction produces when it takes place chemically at constant P , i.e., greater than ΔH .

The flow of a finite amount of electric current always determines a certain degree of irreversibility: part of the chemical energy thermodynamically available as electric energy is dissipated as heat because of various “resistances” in the electrolyte and in the electrodes to the transfer of charge through the cell. The potential difference across the two electrode terminals under the flow of a finite current, V_i , is always less than V_{oc} during spontaneous discharge, and it is lower the higher the current flowing, so that only a part of the chemical energy is used to supply electric work. The other part, dissipated as heat, is $Q = T\Delta S - nF(V_{oc} - V_i)$. In the limiting case of short-circuit current, there being no electric work produced, all the chemical energy is dissipated as heat, and the heat emitted to the surroundings is equal to ΔH .

The measurements of OCV, which are taken by high-resistance ($>10^7 \Omega$) electronic voltmeters to satisfy the requirements of $i \rightarrow 0$, make it possible to determine the free energy, the entropy and the enthalpy of cell reactions, in addition to activity coefficients, equilibrium constants, and solubility products.

Given that the cell reaction is composed of the two half-reactions at the electrodes, the battery's V_{oc} can also be estimated as the difference in the equilibrium potentials of the positive and negative electrode (Eq. (5)).

$$V_{oc} = V_{eq+} - V_{eq-} \quad (5)$$

The electrode equilibrium potential, $V_{eq,e}$, as related to the half-reaction $Ox + ne^- \rightarrow Red$, is given by the the Nernst equation:

$$V_{eq,e} = V_{eq}^\circ - (RT/nF) \ln a_{Red}/a_{Ox} \quad (6)$$

where V_{eq}° is the standard potential, and a_{Red} and a_{Ox} are the activities of the reduced and oxidized species. The equilibrium potential of each electrode is not a potential difference at the metal–solution interphase, but it is a physically measurable quantity in that it is defined as the potential difference between the terminals of a cell based on the electrode (half-cell) in question and the standard hydrogen electrode (SHE); to the SHE is arbitrarily assigned a potential of zero volts.

At the electrode equilibrium potential $V_{eq,e}$ the cathodic current, i_c , and the anodic one, i_a , which represent the reduction and oxidation reaction rates at the electrode–solution interphase, respectively, are equal and the net current $i = |i_c| - i_a$ is zero; the $|i_c| = i_a$ value is called the exchange current, i_0 . The passage of net current ($i \neq 0$) through the cell causes some changes with respect to equilibrium, and these are generically indicated by the term “polarizations”. The difference between the value of the electrode potential under flowing current, $V_{i,e}$, and that of the equilib-

rium potential, $V_{\text{eq,e}}$, is called the electrode overvoltage, η_e :

$$\eta_e = V_{i,e} - V_{\text{eq,e}} \quad (7)$$

During the discharge and charge processes of a battery, various forms of charge transfer are involved:

- 1) electron flows in electronic conductors (electrode materials, terminals, load resistance);
- 2) ion flows in the electrolyte;
- 3) charge transfer (ions and electrons) at the electrode–electrolyte interphases.

The charge flow through each part of the circuit is the same, so as to maintain the electroneutrality condition in each part, and the charge transfer process which takes place at the lowest rate becomes the current-limiting step.

As noted above, the passage of a finite current through an electrochemical cell causes a certain shift from the equilibrium potentials. During discharge the battery's potential is less than its equilibrium value V_{oc} , i.e., the cathode's potential is less positive and the anode's is less negative with respect to their equilibrium potentials. By contrast, during the charge process the applied potential has to be higher than V_{oc} , i.e., the cathode's potential has to be more negative and the anode's more positive with respect to their equilibrium potentials. Thus it is important to know how far the cell potential is from V_{oc} , i.e., it is important to determine the cell overvoltage, $\eta = V_i - V_{\text{oc}}$, which is responsible for the energy dissipation, in order to estimate the battery performance.

The main causes of overvoltage are:

- 1) the ohmic drop (iR , ohmic overvoltage) in the electrolyte, separators, electrodes, and terminals;
- 2) the electrode losses (η_e , electrode overvoltages), which include the activation overvoltage (η_{act}) related to the charge transfer rate at the electrode–electrolyte interphase and the concentration overvoltage (η_{conc}) related to the depletion or accumulation of electroactive materials generally near the electrode surface.

Therefore, during the charge process of an electrochemical cell, a potential V_i , which is the sum of the cell equilibrium potential V_{oc} , the cathodic overvoltage ($\eta_{e,c}$), the anodic overvoltage ($\eta_{e,a}$) and the ohmic drop (Eq. (8)),

$$V_i = V_{\text{oc}} + |\eta_{e,c}| + \eta_{e,a} + iR \quad (8)$$

must be applied by an external source; whereas during a discharge process the overvoltages and the ohmic drop have to be subtracted from V_{oc} in order to obtain the potential V_i supplied to the external system (Eq. (9)).

$$V_i = V_{\text{oc}} - |\eta_{e,c}| - \eta_{e,a} - iR \quad (9)$$

A representation of the two situations is shown in Figures 2a and 2b; some details on the ohmic, activation and concentration overvoltages are reported below.

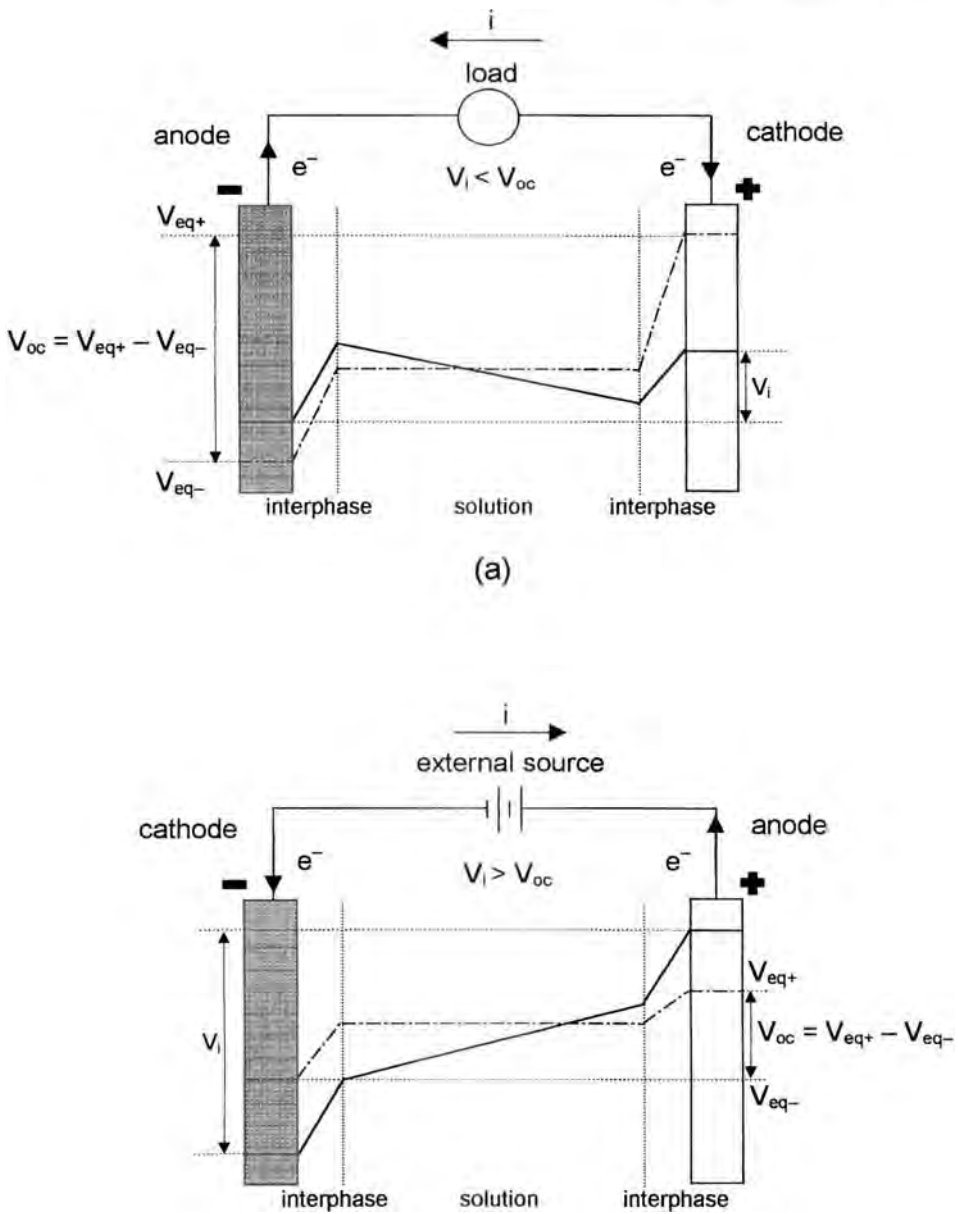


Figure 2. Battery a) under discharge and b) under charge.

The ohmic potential drop, iR , is due to the sum of the internal resistances of the bulk phases within the cell, $R = \sum x_i / (A_i \sigma_i)$, where for each i -phase x is the thickness, A the geometric area and σ the conductivity. While it is generally simple to evaluate the ohmic potential drop due to the electrolyte bulk, in some cases it is difficult to distinguish between the ohmic and electrode polarization taking place in the electrode bulk, especially when porous or composite electrodes are involved. As the main polarization losses in batteries at moderately high current densities are due to the ohmic potential drop, efforts in battery design have to focus on increasing the conductivity of the electrolyte phase, reducing the resistance of electrode materials, choosing suitable current collectors, and minimizing the distance between the electrodes while maintaining a uniform current distribution.

In the case of sufficiently high mass transport, i.e., the absence of concentration polarization phenomena, and when the electrochemical process is controlled by the charge transfer rate at one electrode, the dependency of the current on the electrode potential, $V_{i,e}$, is given by the Butler-Volmer equation (Eq. (10)),

$$i = nFAk_0 \{ C_{Ox,e} \exp[-\alpha nF(V_{i,e} - V_{eq}^\circ)/RT] - C_{Red,e} \exp[(1 - \alpha)nF(V_{i,e} - V_{eq}^\circ)/RT] \} \quad (10)$$

where $C_{Ox,e}$ and $C_{Red,e}$ are the concentrations of the species Ox and Red on the electrode surface, which are equal to those in the solution bulk C_{Ox} and C_{Red} , k_0 is the exchange constant, i.e., the charge transfer rate constant at the standard equilibrium potential V_{eq}° , α the transmission coefficient, and A the electrode area.

Equation (10) expressed in terms of overvoltage ($\eta_e = V_{i,e} - V_{eq,e}$) becomes

$$i = i_0 \{ \exp(-\alpha nF\eta_e/RT) - \exp[(1 - \alpha)nF\eta_e/RT] \} \quad (11)$$

where $i_0 = nFAk_0 C_{Ox}^{(1-\alpha)} C_{Red}^\alpha$, which demonstrates the i - η_e curve's dependence on the α and k_0 parameters.

At high overvoltage, $|\eta_e| > 100$ mV, only the cathodic or anodic current contributes significantly to the net current; e.g., for cathodic overvoltages, Eq. (11) becomes

$$i = i_0 \{ \exp(-\alpha nF\eta_e/RT) \} \quad (12)$$

and the activation overvoltage can be calculated from Eq. (13):

$$\eta_{act} = (RT/\alpha nF) \ln i_0 - (RT/\alpha F) \ln i \quad (13)$$

When the mass transport rate (to simplify, here due only to diffusion) is not high enough, particularly at high current values, a concentration gradient of the electroactive species arises in the region near the electrode: in the case of cathodic current, the concentration of the oxidized species diminishes at the electrode surface, whereas that of the reduced species increases. The current, under linear diffusion control and at constant concentration gradient, is given by

$$i = nFAD_{Ox}(C_{Ox} - C_{Ox,e})/\delta \quad (14)$$

where D_{Ox} is the diffusion coefficient and δ is the diffusion layer thickness. The diffusion current reaches the maximum value (limit current, i_{lim}) when the concentration at the electrode surface is zero ($C_{\text{Ox},e} = 0$):

$$i_{\text{lim}} = nFAD_{\text{Ox}}C_{\text{Ox}}/\delta \quad (15)$$

The concentration changes at the electrode surface due to mass transport limitations are responsible for the concentration overvoltages. When a reduction process takes place (e.g. $\text{Zn}^{2+} + 2\text{e}^- \rightarrow \text{Zn}$), a concentration of the oxidized species at the electrode surface ($C_{\text{Ox},e}$) lower than that in the bulk makes the current, at a given potential, lower than that in the absence of an ion diffusion limitation, and to achieve the same current value an overvoltage (concentration overvoltage) must be imposed. This concentration (or diffusion) overvoltage can be calculated from Eq. (16):

$$\eta_{\text{conc}} = (RT/nF) \ln(C_{\text{Ox},e}/C_{\text{Ox}}) \quad (16)$$

By expressing $C_{\text{Ox},e}/C_{\text{Ox}}$ in terms of diffusion current, the η_{conc} can be estimated from Eq. (17).

$$\eta_{\text{conc}} = (RT/nF) \ln(1 - i/i_{\text{lim}}) \quad (17)$$

Having thus examined how the various polarizations affect the behavior of an electrochemical cell, we can state that a low solution resistance, electrode processes characterized by a high exchange constant, and a high concentration of electroactive species are fundamental requisites for batteries with high efficiency in converting chemical into electric energy.

Let us to conclude this section by stressing that direct conversion of chemical into electric energy by electrochemical systems is a significantly more efficient method of energy conversion than the indirect one based on chemical reactions, in which chemical energy is released as heat that in turn is converted into work (W) by a thermal engine. Limitations intrinsic (Carnot limitations) to the indirect method enable “an ideal engine” to reach a maximum conversion efficiency value, $\varepsilon = -W/\Delta H$, in the 30–50 % range; values drop to 20–30 % in real systems in practice.

The direct electrochemical method makes it possible to produce maximum electric work equal to $-\Delta G$. The values for ΔG at room temperature are usually close to those for ΔH ($T\Delta S$ is small compared with ΔH and it may be positive or negative) and the maximum efficiency value for direct conversion, $\varepsilon_{\text{max}} = -nFV_{\text{oc}}/\Delta H$, may be slightly lower or higher than 100 % depending on the sign of ΔS . The practical conversion efficiency is lower: a part of the energy, as reported above, is spent in propagating the reaction, and the drop is related to the current flow. The practical conversion efficiency of the electrochemical system can be estimated from Eq. (18), and the fuel cells operate in regimes with practical conversion efficiency values in the 60–70 % range, significantly higher than that of the indirect energy conversion methods.

$$\varepsilon = -(nFV_i/\Delta H) = -(nF/\Delta H)(V_{\text{oc}} - \eta_{\text{e,a}} - |\eta_{\text{e,c}}| - iR) \quad (18)$$

2.2.2 Battery Performance

Battery performance is rated on the basis of the charge capacity, available energy, delivered power, and charge retention during OCV conditions; for rechargeable systems, the coulombic efficiency and stability to repeated charge–discharge cycles are also important parameters.

The *theoretical capacity* [Ah] is the charge that a battery delivers when the utilization of its electroactive materials is 100 %, i.e., when the cell is completely discharged (100 % depth of discharge, DOD); when the battery is partially discharged (DOD < 100 %), the corresponding delivered charge is the *practical capacity*. To compare the performance of batteries, the key parameter is the *specific capacity* which includes both gravimetric [Ah kg⁻¹] and volumetric [Ah L⁻¹] capacity. These are obtained by dividing the battery capacity by the mass and the volume, respectively, of its electroactive materials.

The *theoretical energy* E_T [J or Wh] is the available energy for n moles of transferred electrons and is given by the related change in free energy $E_T = -\Delta G = nFV_{oc}$. The *practical energy* depends on the discharge conditions and is given by Eq. (19):

$$E_p = \int_0^{nF} V_i dq = \int_0^t V_i i dt \quad (19)$$

where the cell voltage V_i is farther from the OCV, the higher the discharge current. To compare different systems, important parameters are the *specific energy* [Wh kg⁻¹] and *energy density* [Wh L⁻¹], which can be obtained by dividing theoretical energy by the mass and volume of the electroactive materials, respectively.

The *power* delivered by a battery is given by the product of the current flow and the related cell voltage, $P = iV_i$. The *maximum power* of a battery can be estimated by measuring V_i as a function of current; *specific power* [W kg⁻¹] and *power density* [W L⁻¹] are the parameters used to compare the performance of batteries.

Electroactive materials of a battery, in order to reach the goals of high specific energy and energy density, must meet two important requirements:

- 1) high specific capacity (gravimetric and volumetric, i.e., a high number of available charge carriers per mass and volume unit) and
- 2) a high standard potential of the redox reaction for the positive electrode and a low standard potential of the redox reaction for the negative electrode.

A rechargeable battery also requires highly reversible half-reactions at the two electrodes to maintain its capacity performance for hundreds of charge–discharge cycles. *Coulombic efficiency* values (η) of the charge–discharge cycles (Eq. (20))

$$\eta = \int_0^t i_{\text{disch}} dt / \int_0^t i_{\text{ch}} dt \quad (20)$$

close to 1 are required for a long cycle life; this is true only if the electroactive materials of both electrodes have a near-unity coulombic efficiency of their charge–

discharge processes. The *cycle life* indicates the number of charge–discharge cycles a battery can withstand before its performance drops to a fixed limit, and depends on the DOD. Another important feature of rechargeable batteries (vital for primary batteries) is a low self-discharge for a long shelf life. The *self-discharge* is expressed as the percentage of charge no longer available, with respect to the theoretical capacity, after a storage period in open-circuit voltage conditions.

Both the polarization and discharge curves are used to represent the battery operating conditions. The former is the plot of cell voltage V_i vs. current and shows polarization phenomena; the latter is the plot of the cell voltage V_i at constant current or with an applied constant external load. The abscissa may be calibrated in terms of capacity, percentage of theoretical capacity, or time. A useful method to characterize and compare the discharge curves is to express the discharge currents in terms of theoretical capacity (C-rate). An *C-rate* of x indicates that the theoretical capacity of the cell [Ah] is delivered in a time $t = 1/x$ [h]. For example, 2C, C/2 and C/5 signify discharge times of 0.5, 2, and 5 h, respectively: for a 1-Ah cell, discharge at 2C, C/2 and C/5 means a discharge current of 2 A, 0.5 A, and 0.2 A, respectively.

For a detailed treatment of Section 2, see Refs. [1–4].

2.3 Energy Conversion Systems

The demand for both primary and secondary cells, the former being “non-reusable” products because they are unrechargeable, and the latter “renewable” because they are rechargeable, has been expanding in recent years. The total volume of the worldwide battery market in 1997 was about \$34 billion, with the primary-cell segment accounting for about 30 % and the lead–acid system for over half of the remaining rechargeable battery share [5]. For example, Japanese sales trends from 1985 to 1997 for secondary batteries are depicted in Figure 3 [6]. It is worth highlighting that since 1997 there has been a surge in Japanese turnover of rechargeable batteries due to the growing demand in the cellular phone market (by late April 1998 registered cellular phones in Japan exceeded 33 million), almost every one of these units being equipped with a lithium-ion system [6].

2.3.1 Primary Cells

Figure 4 shows a comparison of practical energy density and specific energy of primary batteries. Two groups can be distinguished: the zinc-based and lithium-based systems.

Zn-based systems

The term zinc–carbon usually indicates both the Leclanché cell, consisting of Zn, manganese dioxide, and an aqueous solution of NH_4Cl and ZnCl_2 , and the zinc

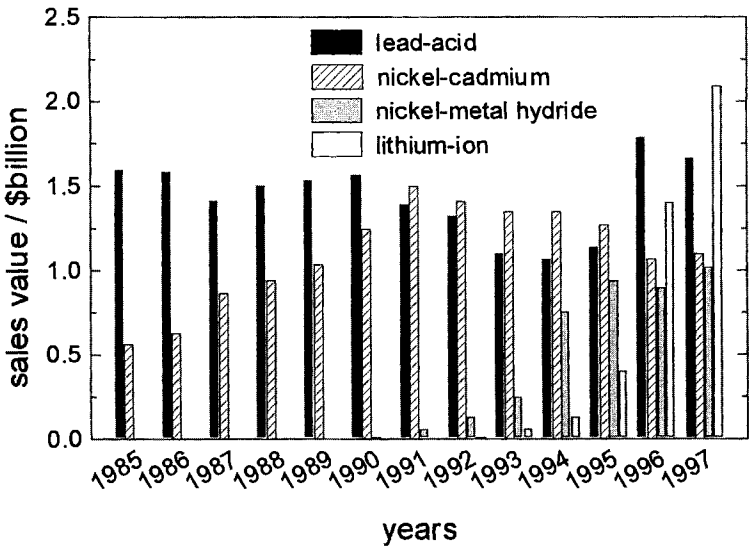


Figure 3. Secondary battery sales in Japan by type.

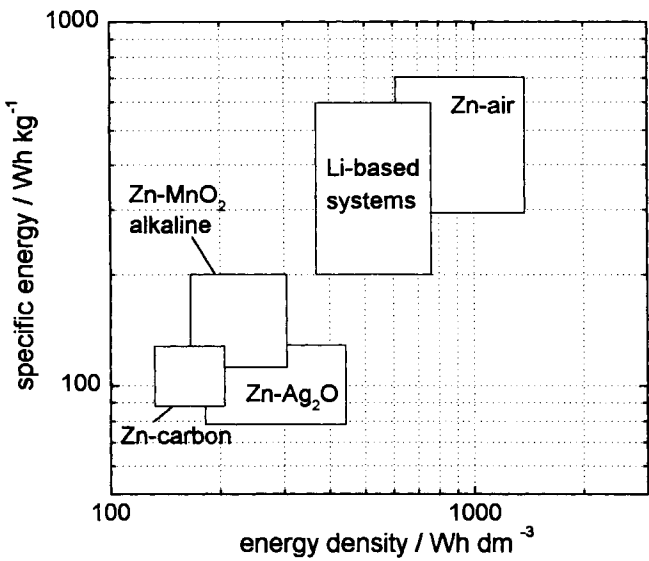
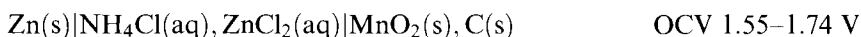


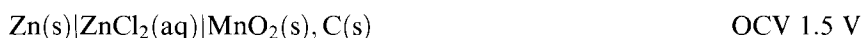
Figure 4. Practical energy density and specific energy of primary systems.

chloride cell, in which ZnCl_2 completely replaces the NH_4Cl . The Leclanché cell and the electrode reactions may be written as:



The reaction products at both electrodes give rise to further reactions so that it is not possible to represent only one cell reaction.

The zinc chloride system and cell reaction can be written as:



The advantage of the latter system with respect to the Leclanché battery is closely related to the electrolyte: insoluble reaction products are less involved and this results in an operating temperature that ranges further down the scale, and higher current densities.

Another variant of the Leclanché cell is the so-called alkaline manganese cell, which with its cell reaction may be written:



The advantages of this cell with respect to the Leclanché are higher practical capacity (up to ten times the Ah capacity of zinc–carbon cells at high discharge currents), longer shelf life and superior low-temperature performance. Figure 5 compares the performance of a D-size alkaline cell, under 2.25Ω continuous test, with the other zinc–manganese dioxide primary systems of the same size. Although the alkaline battery is more expensive than the Leclanché or the ZnCl_2 batteries, it has rapidly become the choice in the ever-widening field of consumer electronics, especially in the USA, where the production of the traditional zinc–carbon systems has been discontinued (Leclanché and ZnCl_2 are now imported there). The alkaline system is also of interest in that it is the basis of a secondary system (Section 2.2.3, under “Zn-based systems”).

Continuous demands from various sectors of the market for improved performance capabilities in the alkaline cells has spurred major research efforts in materials science, leading to a key redesign of their internal structure. For example, mercury, initially used to amalgamate zinc, has been replaced with other zinc-alloying agents; organic corrosion inhibitors have been added; critical impurities of the manganese dioxide cathode have been notably reduced; and the composition of the KOH gelling agents holding the zinc powder in the anode compartment has been modified. As a result, service life has increased by over 30 % compared with 10 years ago and the high current pulse capability has been upgraded [5].

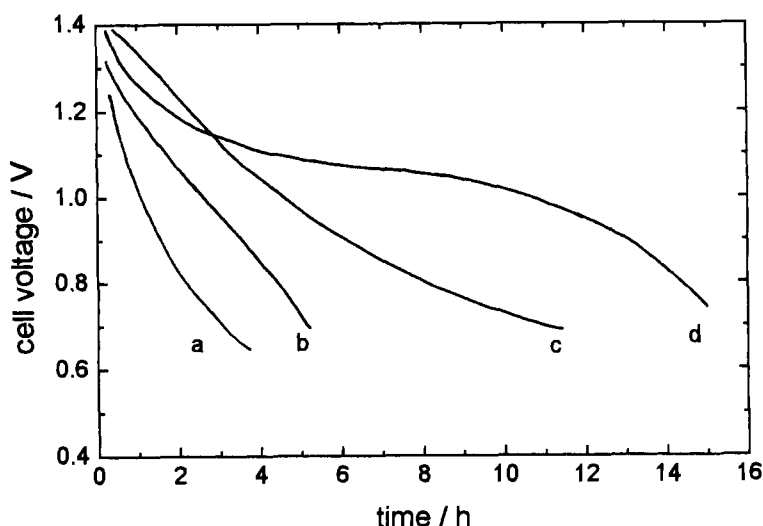
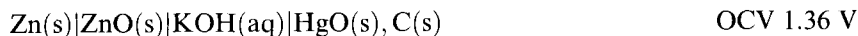
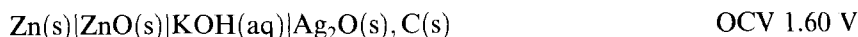


Figure 5. Performance of D-size zinc-manganese dioxide primary systems under $2.25\ \Omega$ continuous test: a) standard Leclanché cell (natural ore), b) high-power Leclanché cell (electrolytic MnO_2), c) zinc chloride cell, d) alkaline manganese cell [1] (by permission of Arnold: C.A. Vincent, B. Scrosati, *Modern Batteries. An Introduction to Electrochemical Power Sources*, 2nd edition, Edward Arnold, London, 1997).

The zinc–mercuric oxide or Ruben–Mallory cell



which was introduced in 1940 and used in the first pacemakers, has been phased out from consumer applications and replaced by the zinc–silver oxide battery (first marketed by Union Carbide in 1961) for miniature portable electronics, as in watches and photographic equipment. This cell and its reaction may be written:



The zinc–silver oxide has a high energy density that can be delivered at relatively high current, and it has an extremely stable discharge voltage, a good shelf life and ability to operate over a wide temperature range. Large zinc–silver oxide cells are used in military and aerospace applications.

The zinc–air battery,

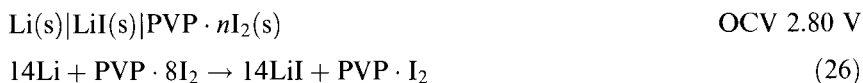


is a hybrid cell, i.e., one of the reagents is in the gas phase. This battery falls between the zinc systems above and fuel cells in which the reactants for both electrode reactions are continuously provided from external sources.

The zinc–air primary button cell has the highest specific energy of all consumer cells (Figure 4, above) due to the oxygen cathode's low weight and infinite capacity. Thus, the button-type zinc–air cell accounts for almost 95 % of the hearing-aid market, although it is also of interest because its chemistry, like that of the alkaline manganese system, is the basis for the rechargeable cell described in Section 2.2.3 under “Zn-based systems”.

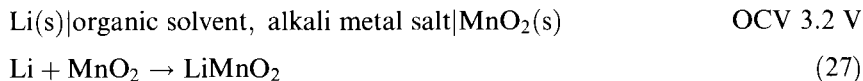
Lithium-based systems

Its high specific capacity (3862 Ah kg^{-1}) and markedly negative redox potential make lithium very attractive as a negative electrode, although its high reactivity can be a drawback. There are three types of lithium primary cells, depending on the type of cathode. For the latter are employed materials that are insoluble in the electrolyte, such as polycarbon fluorides, sulfides, and metal oxides; those that completely dissolve in the electrolyte, such as SO_2 ; or liquids, such as SOCl_2 . The lithium-based systems are lightweight, high-performance power sources for applications in miniaturized apparatus. For example, primary lithium batteries substituted for zinc–mercuric oxide cells in powering pacemakers: the first lithium/iodine-poly(2-vinylpyridine) (PVP) battery was implanted in Italy in 1972 [7] and since then over five million lithium/iodine PVP batteries have been implanted. This is a solid-state battery in which the anode is lithium metal and the cathode is an iodine charge transfer complex formed by combining a poly(2-vinylpyridine) donor and iodine acceptor. By making direct contact between anode and cathode, a thin layer of lithium iodide, which acts as a solid electrolyte, is formed. The cell and reaction are:



Cell discharge is accompanied by the migration of lithium ions from the anode to the cathode. As the discharge progresses, further LiI forms at the cathodic side of the electrolyte and the internal resistance of the cell rises; this is the main disadvantage of this system [8].

Lithium batteries with a manganese dioxide cathode are also used when reduction in size and weight is important, such as for powering 35 mm flash cameras. The lithium–manganese dioxide cell and reaction may be written as:



2.3.2 Secondary Cells

Figure 6 shows a comparison of practical energy density and specific energy of rechargeable batteries. It is worth noting that there is an increasing energy storage

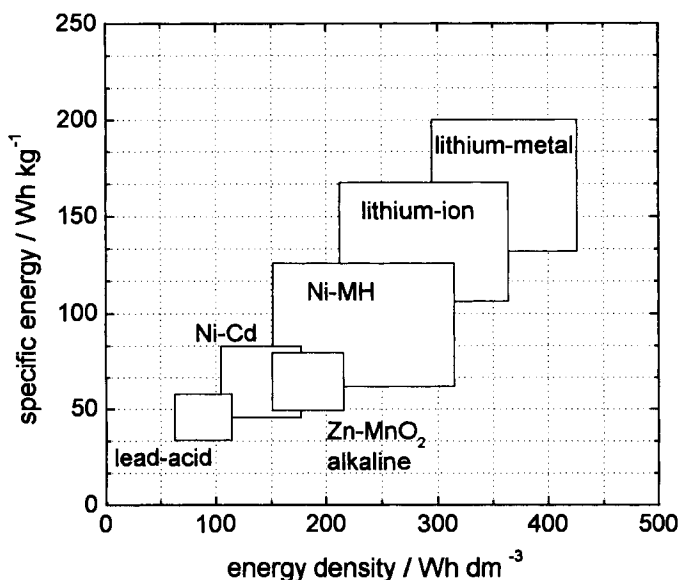
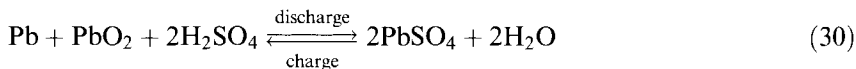
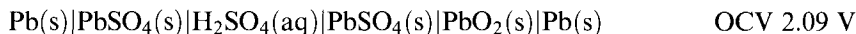


Figure 6. Practical energy density and specific energy of various rechargeable batteries.

capability per mass or volume unit when going from the lead–acid to the lithium–metal systems due to the lithium’s high specific capacity and negative redox potential.

Lead-acid system

The characteristic of the lead–acid battery is that both electrodes are based on the chemistry of lead. The discharge–charge process is known as the double sulfate reaction, with the positive and negative electrodes being the seats of a dissolving–precipitating (and not some kind of solid-state ion transport or film formation) mechanism of the lead sulfate. The cell, the electrode reactions and the cell reaction are:



During discharge sulfuric acid is consumed and water is formed: this strongly affects the OCV, which depends on the electrolyte activity in solution and, consequently, on the state of charge (Figure 7). During discharge the formation of lead sulfate passivates both electrodes and reduces the practical capacity, and during charge lead sulfate is reconverted to Pb and PbO₂. The energy efficiency of charge–discharge is

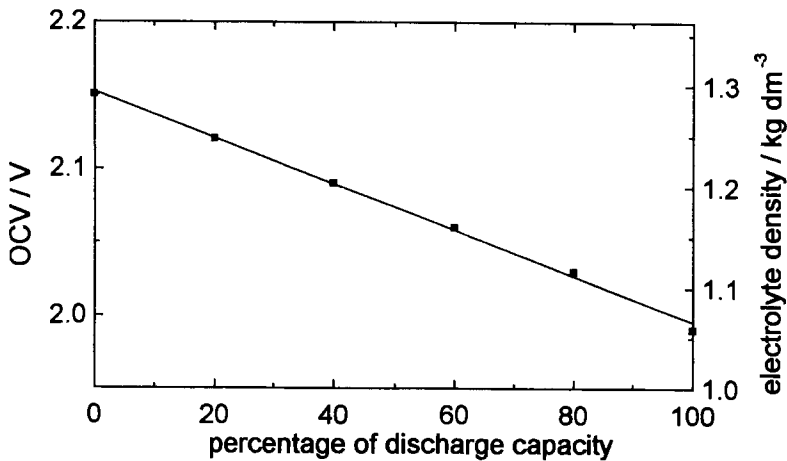


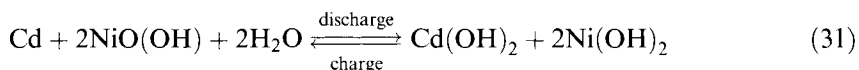
Figure 7. OCV and electrolyte density as a function of the percentage of discharge capacity for the lead-acid cell [1] (by permission of Arnold: C.A. Vincent, B. Scrosati, *Modern Batteries. An Introduction to Electrochemical Power Sources*, 2nd edition, Edward Arnold, London, 1997).

affected by such side reactions as the evolution of oxygen at the positive electrode during charging, when the cell approaches 85–90 % full charge, and the evolution of hydrogen at the negative electrode during overcharge, causing water loss [9].

Today the main use of lead-acid batteries is in vehicle SLI applications. Most vehicles use a 12 V battery with a capacity in the range 40–60 Ah. The lead-acid battery is also in industrial service for traction and stationary purposes, and it has also been tested in electric vehicles. Lead-acid battery technology was developed at the end of the 19th century: the basic chemistry and operating principles have remained unchanged, but continuous improvements have rendered the battery more suited to market demands. The rate of progress in the last 40 years has increased and automotive batteries are now of either low-maintenance or maintenance-free design. It is also worth noting that valve-regulated lead-acid batteries (VRLA) were introduced to minimize water loss by promoting the chemical recombination of the oxygen at the negative electrode. In the early 1990s the VRLA batteries were considered for electric vehicle applications because of their favorable cost and specific power characteristics [10]. Some of the most recent advances in lead-acid battery design are thinner electrodes, based on woven Pb-coated fiberglass grids, which are cut into bipolar plates horizontally stacked, and new separator/acid-retention systems. Whilst all of these are materials and manufacturing improvements, the engineering of the charging systems has also increased cycle life fourfold and improved active-material utilization [10, 11].

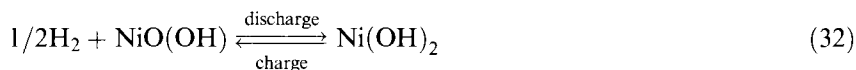
Ni-based systems

The nickel-cadmium battery is the most popular alkaline secondary battery. The cell and its reaction are:



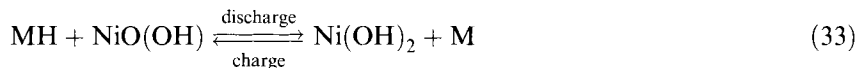
The negative electrode active material is cadmium, the positive one is nickel oxyhydroxide, and their preparation involves different components and methods [9]. During discharge, the cadmium is oxidized to form cadmium hydroxide and trivalent nickel hydroxide is reduced to divalent nickel hydroxide, with water consumption. This type of battery is available in several cell designs and a wide range of sizes. The sealed cells are important in the consumer electronics market in portable cordless appliances, as well as in defense and aerospace applications (in 1964 the first prismatic nickel–cadmium cell flew on *Explorer 23*). Nickel–cadmium cells are characterized by a long cycle life, relatively high rates of charge and discharge, an almost constant discharge voltage and the ability to operate at low temperatures. However, the cost of nickel–cadmium cell construction, higher than that of lead–acid, and the health risks associated with the manipulation of cadmium have spurred the search for alternative systems.

Another interesting nickel-based system is the nickel–hydrogen cell, a hybrid system similar to the zinc–air primary cell described in Section 2.3.1, under “Zn-based systems”. The cell and its reaction are:



Developed in the 1960s, it makes use of different technologies for its electrodes: NiO(OH) is from nickel–cadmium and H₂ from fuel-cell systems. Because of its longer cycle life the main use of the nickel–hydrogen battery is in aerospace applications to replace the nickel–cadmium cells. For example, the Hubble Space Telescope launched in 1990 was equipped with nickel–hydrogen cells [12].

Combining the nickel–cadmium and nickel–hydrogen systems technologies has given rise to the nickel–metal hydride rechargeable battery, one of the most advanced rechargeable systems commercially available and an environmentally friendlier alternative to nickel–cadmium batteries. The cell and its reaction may be written:



New, high-density nickel oxide electrode materials, coupled with nonwoven nickel-fiber current collectors, have significantly improved the performance of the nickel electrode even in the nickel–cadmium cells [5]. The alloys used to form hydride, which capture and release hydrogen in volumes up to nearly a thousand times their own, include rare-earth/nickel alloys (generally based on LaNi₅ and called AB₅)

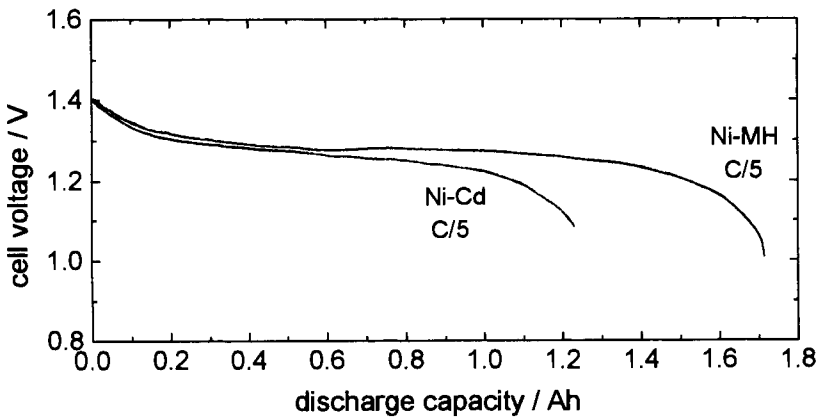


Figure 8. Discharge curves at C/5 of same-size nickel–cadmium and nickel–metal hydride cells at 20 °C (by permission of National/Panasonic).

and titanium or zirconium/manganese alloys (TiMn_2 , ZrMn_2 generally called AB_2). Metal hydride electrodes are made by mixing the alloy powder with a binder and by applying the mixture to a metal foil or a nickel foam substrate [13]. The optimization of this battery is continuously in progress and, as a consequence of the similarity between the nickel–metal hydride and the nickel–cadmium cells, the achievements in the former may be a benefit also for the latter: examples are the development of lightweight $\text{NiO}(\text{OH})$ electrodes (foams), the use of thinner separators, and increasing the packing efficiency of the active material for both the cadmium and metal hydride electrodes by decreasing the pore volume of the respective electrodes. Figure 8 shows a comparison of the performance of nickel–cadmium and of nickel–metal hydride cells. In the case of the nickel–metal hydride system extensive research is also under way to develop new multicomponent, multiphase alloys, to meet such demands as high hydrogen storage capacity, strength of the metal–hydrogen bond, oxidation and corrosion resistance, fast gas recombination kinetics, and reliability at low cost [14]. The nickel-based systems have also benefited from the advent of the power management concept developed for lithium-ion batteries. The circuitry (sometimes incorporated into the battery package) and software developed to allow the exchange of information between the battery and the charging device has greatly enhanced safety and improved cycle life.

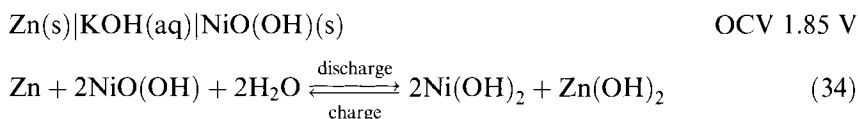
The major issues to be solved for nickel–metal hydride batteries are the temperature control during charge (damage occurs if the cell operates at $T > 65^\circ\text{C}$), the high self-discharge (15 % in two days at 38°C), and cell cost. Nevertheless, efforts to develop nickel–metal hydride batteries for use in electric vehicles have even led several automotive companies to offer models powered by this type of battery [14].

Zn-based systems

Although the rechargeable alkaline Zn-MnO_2 batteries are not performance-competitive with the nickel–cadmium batteries [15], they are midway between a

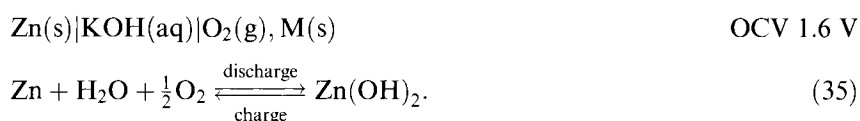
low-cost alternative to rechargeable systems and a cheaper option to the continuous replacement of primary cells. The modification of the internal design of the primary alkaline cell produces a lowering of the capacity of the rechargeable version; nevertheless, the rechargeable alkaline Zn–MnO₂ batteries may be used instead of the primary alkaline cells in applications requiring frequent battery replacement because they can be recharged at least 25 times before being discarded.

Another zinc-based system is the zinc–nickel one, whose key advantages include high voltage, high energy density, good high-rate discharge characteristics, and low cost. The cell and its reaction may be written:



although the main oxidation product of zinc is probably the Zn(OH)₄^{2−} ion. One drawback is poor cycle life, which is mainly due to the morphology of the electrodeposited zinc: dendritic deposits may provoke a short circuit by penetrating through the separator and spongy, loosely adherent deposits reduce capacity. Moreover, electrode shape changes may occur on cycling, as dissolution and re-deposition of the zinc do not take place at the same location and to the same extent and morphology. Alternative zinc electrode designs have been proposed to better the performance of this system, including the use of metallic foam collectors and special conductive additives, coupled with improved NiO(OH) electrodes, to make it competitive with the nickel–cadmium system [16–18].

The zinc–air system has become rechargeable during the last 20 years [19]. The cell and its reaction are:



Several methods have been examined to upgrade the quality of the zinc deposit, such as electrolyte circulation, electrode vibration, and air bubbling to disturb the diffusion layer. New and special porous, highly hydrophobic and electrically conductive modified carbon catalysts are under study to improve the lifetime of the air electrode. The behavior of the electrocatalyst during recharge, when it is necessary to apply high anodic voltages, remains indeed one of the major drawbacks. Nevertheless, since 1997 a zinc–air battery has been manufactured and tested in vehicles as “mechanically rechargeable” cells: at special charging stations, the oxidized zinc electrode will be removed from the cell and a fresh one put in, more or less in the same time it takes to fill up a conventional car. The exhausted zinc electrodes are then put in a separate electrochemical cell and recharged against an inert electrode [20].

Table 2. EV battery performance goals set by USABC.

Parameter	Mid-term target	Long-term target
Life [cycles]	600	1000
Life [years]	5	10
Piece cost [\$ kWh ⁻¹]	150	100
Mass [kg]	500	200
Volume [L]	296	133
Recharge time [hours from 80 % DOD]	6	3
Self-discharge [%]	15 ^a	15 ^b
Specific peak power [W kg ⁻¹]	150	400
Power density [W L ⁻¹]	135	600
Energy density [Wh L ⁻¹]	135	300
Specific energy [Wh kg ⁻¹]	80	200

^a in 48h, ^b in 1 month.

Applications in electric vehicle technology

To conclude this section and as a prolog to Section 2.4 on advanced lithium rechargeable batteries, a few additional words on the applications of rechargeable batteries in electric vehicle (EV) technology are in order. The pressing need to come up with solutions to the problem of urban pollution has increased research efforts in battery systems for zero-emission vehicles, especially in regard to achieving the technological breakthrough enabling such vehicles to attain the performance characteristics of acceleration and range that are comparable with those of today's conventionally powered cars.

As mentioned in Section 2.1, the USABC, which involves the US Department of Energy (DOE), the Electric Power Research Institute (EPRI), and the three car manufacturers Daimler–Chrysler, Ford, and General Motors, set the targets for battery application in EV in terms of practical specific energy, specific power, and cycle life (Table 2). The goals of the USABC are to develop electrical energy systems for EV having performance competitive to gasoline-powered vehicles: meeting the mid-term goals would allow the expansion of the market, while achieving the long-term ones would allow EV to be competitive with internal-combustion vehicles.

In a typical electric car a specific power of 400 W kg⁻¹ and a specific energy of 200 Wh kg⁻¹ would mean that it is possible to achieve 0–60 mph (0–96 km h⁻¹) acceleration in 9 s with a range of 200 miles (320 km) in standard driving conditions. A lifetime of 10 years at a cost of \$100 per kWh would mean that a \$4000 battery could be amortized over 10 years.

Many projects have taken off in the USA, Japan, and Europe involving governmental agencies, universities, and battery and car companies [21]. The projects are focused on achieving both the mid-term and long-term goals mainly by developing nickel–metal hydride systems and lithium-based technologies. Energy and power targets, which determine range and acceleration, appear to be within reach, although challenges remain in cycle life, battery cost, and manufacturing. To cut costs, proj-

ects are focusing on three key areas: raw materials (by lowering material costs or using materials more effectively), battery design (small and lighter batteries lead to enhanced vehicle performance), and mass manufacturing (most of these batteries never have been made in quantity and new production techniques will have to be adopted).

2.3.3 Supercapacitors

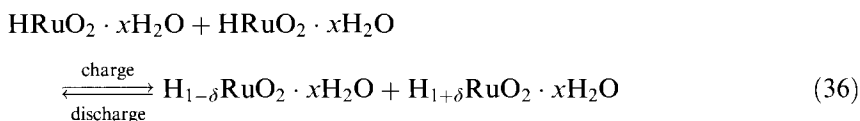
Supercapacitors are devices for high-power applications: they provide a higher power density than batteries and, despite their lower operating voltage, a higher energy density than conventional dielectric capacitors because of the high capacitance of their electrode materials. By the 1970s, a mere decade after industrial research into these devices began in earnest, high-performance supercapacitors were developed both for military systems, which largely demand short and intense bursts of power, and computer memory backup systems, which demand a power supply that is less intense but more steadily extended over time. The increasing interest in these devices has also been stimulated by their potential application as power systems operating in parallel with battery system in electric vehicles [22, 23]: the supercapacitor will deliver peak pulses of power for acceleration and be recharged by the battery during deceleration and braking.

Two types of supercapacitors are currently being investigated: the double-layer and the redox. The former is not based on an electron transfer process: its capacitance, electrostatic in origin, arises from the separation of electronic and ionic charges at the interface between high-specific-area (up to $2500 \text{ m}^2 \text{ g}^{-1}$) carbon electrodes and the electrolyte solution. In the latter, faradaic charge transfer processes take place at the electrode materials, as in a battery, and produce what is called pseudocapacitance [24, 25]. Nevertheless, the research objectives are the same for double-layer and redox supercapacitors: to develop electrode materials with both high specific capacitance (gravimetric [F g^{-1}] and volumetric [F cm^{-3}]) to maximize energy storage and with low electrical resistance to maximize power. Electrode materials must be stable to assure long life of the device and have a high performance-to-cost ratio. The electrolyte in supercapacitors should ideally have a high breakdown voltage for greater energy storage and low electrical resistance for greater power. Low-resistance aqueous electrolytes lead to devices with good power but whose energy storage is limited by a decomposition voltage of about 1 V. Since organic electrolytes break down over 3 V, energy increases up to about one order of magnitude, given its dependence on the square of the voltage. Yet, at the same time, these electrolytes limit power because of their higher resistance. Two classes of electrode materials for redox supercapacitors are under study: metal oxides and conducting polymers [26].

Among the metal oxide pseudocapacitive materials the most representative are the crystalline ruthenium oxide RuO_2 [24] and the amorphous hydrous ruthenium oxide $\text{RuO}_2 \cdot x\text{H}_2\text{O}$ [27, 28], although other materials are under study, for example cobalt oxide [29] and vanadium oxide [30] xerogels, molybdenum-based materials [31, 32], and Ti–V–W–O oxides [33].

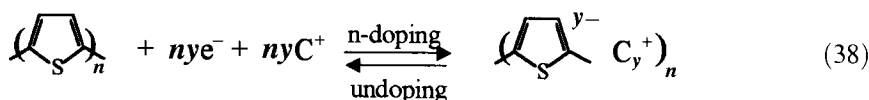
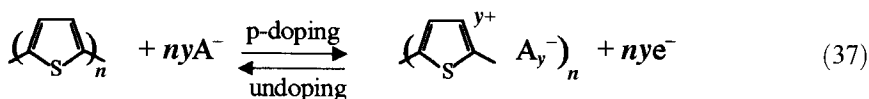
RuO_2 films are yielded in situ by thermal (300–500 °C) decomposition and oxidation of a $\text{RuCl}_3 \cdot x\text{H}_2\text{O}$, whose solution in water or alcohol is previously dipped in or sprayed onto the Ti substrate. The properties of the oxide depend significantly on the preparation temperature. A $\text{RuO}_2 \cdot x\text{H}_2\text{O}$ electrode can be prepared by pressing on Pt mesh a mixture of $\text{RuO}_2 \cdot x\text{H}_2\text{O}$ powder, produced by aqueous sol-gel, and a binder. This sol-gel preparation method yields a material with a capacitance value (760 F g⁻¹) higher than the highest value reported for RuO_2 (380 F g⁻¹) [34–36].

It has been demonstrated that by starting from hydrogenated hydrous ruthenium oxide $\text{HRuO}_2 \cdot x\text{H}_2\text{O}$ (obtained using either an electrochemical or a chemical method from $\text{RuO}_2 \cdot x\text{H}_2\text{O}$ powder) the charge-discharge efficiency is improved ($\eta > 0.9$) from the first cycle, with power and energy density maintained through the cycles. Starting from $\text{RuO}_2 \cdot x\text{H}_2\text{O}$, indeed, results in O_2 evolution and water loss in the first few cycles which damage the cell by reducing the cell performance [34]. The electrochemical reaction for an $\text{HRuO}_2 \cdot x\text{H}_2\text{O}$ -based supercapacitor, when a faradaic current flows through the electrode materials, may be written:

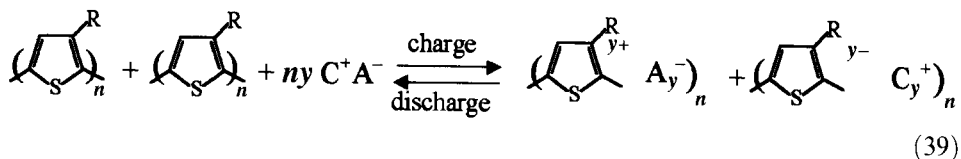


where $0 < \delta < 1$. The positive and negative electrodes are $\text{HRuO}_2 \cdot x\text{H}_2\text{O}$ in the discharged state, and $\text{RuO}_2 \cdot x\text{H}_2\text{O}$ and $\text{H}_2\text{RuO}_2 \cdot x\text{H}_2\text{O}$, respectively, in the fully charged state.

The other materials being investigated for redox supercapacitors are the conducting polymers. In the early 1980s there was much enthusiasm for flexible lithium-polymer cells that use conducting polymers as positive electrodes [37–39]. After a charge transfer process named the doping process, such organic polymers as polypyrrole, polythiophene, and polyaniline, characterized by an extended π -electron delocalization, become conductive. The reactions (37) and (38) show the polythiophene p- and n-doping processes respectively, i.e., the process in which the polymer is oxidized and becomes positively charged, and that in which the polymer is reduced and becomes negatively charged. The doping-undoping, i.e., the charging-discharging process, of the conducting polymers is associated with the insertion-release of the counterions (A^- and C^+) coming from the electrolyte to balance the injected charge; thus the conducting polymers may also be depicted as ion insertion materials [40].



Conducting polymers are used in both aqueous and organic electrolytes in different combinations to yield different types of supercapacitors [41–44] whose storage–charge capacity and operating potential range increase depending on type. The three types are: I) a symmetric supercapacitor in which a p-dopable polymer is the active material on both electrodes; II) an unsymmetric supercapacitor based on two p-dopable polymers selected by virtue of the difference in potential ranges over which they become p-doped; and III) a symmetric or unsymmetric supercapacitor based on p- and n-dopable polymers. In the completely charged state Type I has one polymer electrode in the fully p-doped form and the other one in the undoped form; the cell voltage is typically 1 V. Since in the completely discharged supercapacitor both polymer electrodes are at a half p-doped state, only half of the polymer's total p-doping charge can be delivered by the operating supercapacitor. In the completely charged state Type II has the polymer of the positive electrode in the fully p-doped state and that of the negative electrode in the undoped state and, when this device is discharged, the polymers of both electrodes are partially p-doped. The charge involved in this type of supercapacitor is greater than that of Type I and the operating potential can reach 1.5 V because it is related to the difference between the p-doping potential domains of the two polymers. In the fully discharged state Type III has both electrodes in the undoped states, whereas in the charged state one electrode is p-doped and the other n-doped, according to reaction (39) for a symmetric device, i.e., when the same p- and n-dopable polymer is used for both electrodes.



The advantage of the Type III configuration is that all the doping charge is delivered by the supercapacitor at high potential, up to 3 V, because of the separation between p- and n-doping potential domains, a separation which is related to the polymer energy gap between conduction and valence bands, when the supercapacitor is symmetric. Type III is thus the most promising in terms of energy density; it has a further advantage over Types I and II in that the charged supercapacitor has both electrodes in the doped state, i.e., in the conducting state, and the instantaneous power density is greater [45, 46]. Operating potentials such as 3 V are attainable only in organic electrolytes, and electrolyte optimization, even in terms of salt concentration, is an important target since in Type III supercapacitors, as in double-layer ones, salt consumption occurs during device charge (see reaction (39)).

Figure 9 shows the discharge curves of a Type I polypyrrole-based, a Type II polypyrrole/poly(3-methylthiophene)-based and a Type III poly(dithieno[3,4-*b*;3',4'-*d*]thiophene)-based supercapacitor at 4 mA cm⁻² discharge current. Types I and II can be assembled using such conventional heterocyclic polymers as polypyrrole, polyaniline and polythiophene, which are efficiently p-dopable polymers and can easily be chemically or electrochemically synthesized from inexpensive

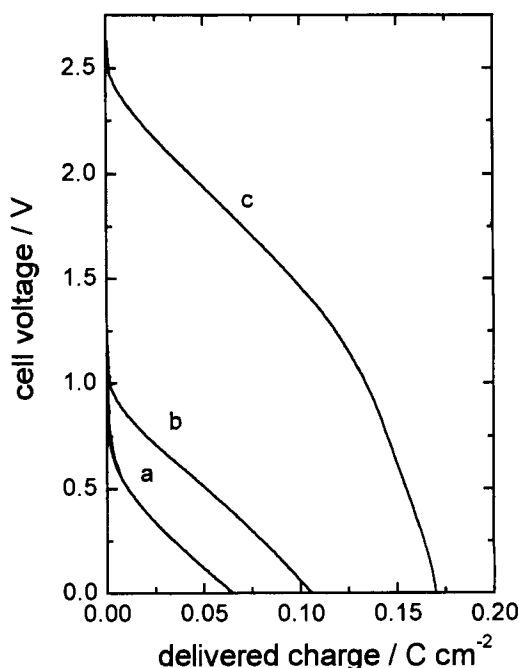


Figure 9. Discharge curves at 4 mA cm^{-2} of the three types of supercapacitors: a) polypyrrole/ LiClO_4 -propylene carbonate (PC)/polypyrrole; b) polypyrrole/ LiClO_4 -PC/poly(3-methylthiophene); c) poly(dithieno[3,4-*b*:3',4'-*d*]thiophene)/ $(\text{C}_2\text{H}_5)_4\text{NBF}_4$ -PC/poly(dithieno[3,4-*b*:3',4'-*d*]thiophene), potentiostatically charged at 1.1 V, 1.15 V, and 3.0 V, respectively.

commercially available monomers. By contrast, the very negative potentials required for n-doping of conventional conjugated polymers, such as polythiophene, make the n-doping a process that requires high-quality electrolytes with very negative breakdown cathodic voltages and a controlled working atmosphere. New materials featuring n-doping at less negative potentials than that of polythiophene have been developed, although the molecular weight of their monomer units is usually significantly higher than that of polythiophene [47, 48]; thus higher doping level values are required for these new materials to reach a high specific capacitance. However, achieving such high doping values involves significant mechanical stress, resulting from the large quantity of ions moving into and out of the polymer structure [49].

Recently, Type III supercapacitors based on conventional polymers have been investigated: symmetric and unsymmetric devices based on a poly(3-methylthiophene) negative electrode and a poly(3-methylthiophene) or polythiophene positive electrode show good cyclability performance to repeated charge-discharge cycles [50]. For a symmetric supercapacitor with composite electrodes prepared by mixing poly(3-methylthiophene), carbon, and binder, Figure 10(a) displays the delivered charge and the coulombic efficiency for 2000–5000 cycles at 5 mA cm^{-2} between 0 and 3.1 V; Figure 10(b) shows the supercapacitor and electrode potential profiles of the 2000th cycle.

Conducting polymers are promising electrode materials because the kinetics of the charge-discharge process, i.e., the doping-undoping, is generally fast; because

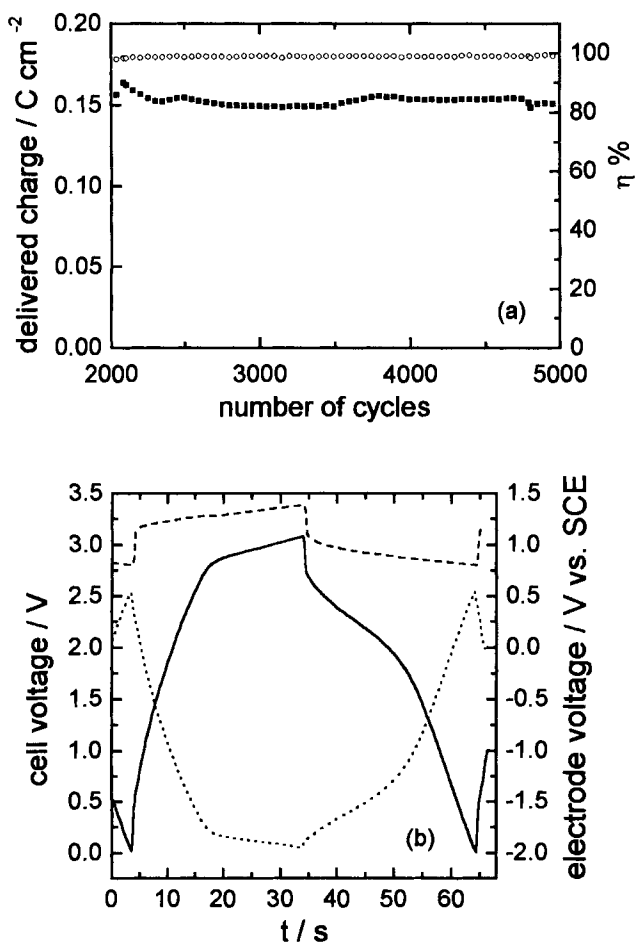


Figure 10. Symmetric supercapacitor with composite poly(3-methylthiophene)–carbon–binder electrodes. a) Delivered charge (■) and coulombic efficiency (○) of galvanostatic cycles (from 2000th to 5000th) at 5 mA cm⁻² between 0 and 3.1 V; b) potential profiles of supercapacitor (solid line), and of positive (broken line) and negative (dotted line) electrodes during the 2000th galvanostatic cycle.

the charge is stored through the volume of the material; and because they can usually be manufactured at a cost that is significantly lower than that of metal oxides such as ruthenium oxides and comparable with that of activated carbons, which at present are the only ones on the market [51].

The distinction between a polymer-based supercapacitor and a polymer-based battery is not very sharp. In the early 1980s Kaneto et al. [52] proposed a polythiophene-based battery in which the electrodes become p- and n-doped upon charge, and undoped upon discharge. A criterion that can be used to distinguish batteries and supercapacitors might be the function they are expected to fulfill in terms of specific energy and power, as the Ragone plot of Figure 11 shows. A supercapacitor is required to deliver a high specific power for a short period (10–30 s), whereas the energy is significantly lower than that of conventional and advanced batteries and fuel cells.

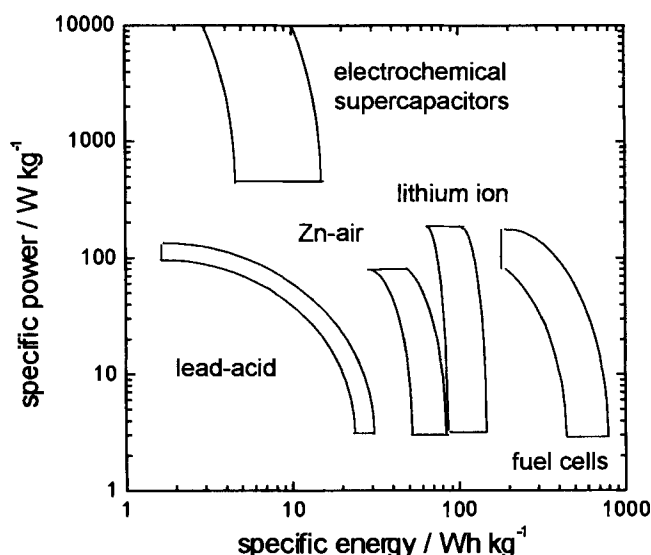


Figure 11. Ragone plot of some electrochemical energy conversion systems.

2.3.4 Fuel Cells

Although a fuel cell operates like a battery, it does not run down or require re-charging from an external electric source, since electric energy is produced so long as fuel is supplied. The hydrogen (or other fuel) continuously flows into the anode and the oxygen (or air) into the cathode: the chemical energy of the cell reaction, which is the sum of the charge transfer reactions at the two electrodes, is converted into electrical energy with the production of water, as Figure 12 shows [53].

The idea of producing electric energy from hydrogen and oxygen, without Carnot limitations and with water as by-product, has been pursued since the 19th century. The first hydrogen–oxygen fuel cells were developed in the 1840s by Grove, who already recognized the need for proper contact of the gas, electrolyte, and solid electrode phases. This so-called three-phase interface is still an issue today, and its improvement is an important goal. In the early 1890s coal was envisioned as fuel, and in 1899, after the discovery of solid oxide electrolytes, the ceramic fuel cell was conceived. A century after Grove, Bacon began work on hydrogen–oxygen forerunners of the modern fuel cells and, by controlling the porosity of the electrodes, optimized the three-phase interface area, greatly increasing the performance of alkaline cells.

Advances in fuel cells were later accelerated by space and defense programs. Fuel cells found initial practical application with the Gemini (1962–1966) and the Apollo (1968–1972) spacecraft missions, and are still used to provide water and electricity for the Space Shuttle. The upgrade in fuel cell performance over the last four decades has been based on the development of new proton-conducting polymers, like Nafion™ and Gore-tex™, ceramics and catalysts, as well as on greater insights into

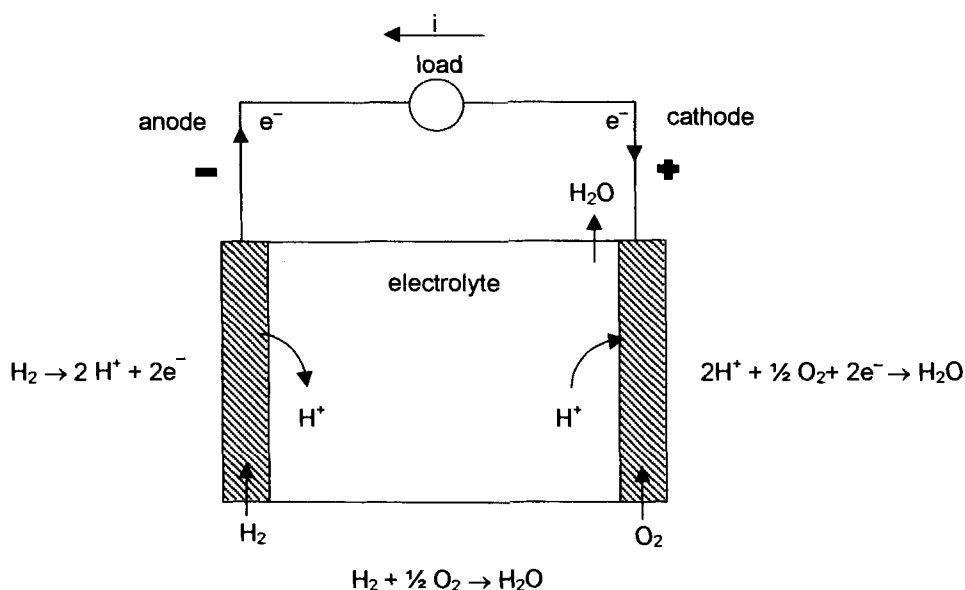


Figure 12. Phosphoric acid fuel cell (PAFC).

the electrochemistry of surface reactions and transport processes within porous systems [54, 55].

The fuel cell electrode reactions are catalyzed by different materials in different temperature ranges. A classification of the fuel cells can be made on the basis of the electrolyte, which in turn determines the operating temperature and, with it, the catalysts to be applied in the electrodes. The electrode reactions that take place in the different types of fuel cells are summarized in Table 3, which also lists the electrolytes and operating temperatures [56].

The solid oxide fuel cells (SOFCs) use porous electrodes and hard ceramic electrolyte, the latter generally being yttria-stabilized zirconia (YSZ) to enable oxygen ions to move from cathode to anode, and they operate at 1000 °C [57, 58]. The molten carbonate fuel cells (MCFCs) work with mixed lithium and potassium carbonate as electrolyte at 650 °C [59, 60]. Both MCFCs and SOFCs can be fed with natural gas: the heat required to sustain the endothermic reforming of low-molecular-weight hydrocarbons can be provided by the electrochemical process, which has led to various internal reforming concepts [61]. The high-temperature fuel cells are very promising, especially for large-scale (0.1–1 MW) power generation [62–64], although small tubular SOFCs fed with biogas are under study [65].

The electrolyte in the phosphoric acid fuel cells (PAFCs), which operate at 200 °C, is phosphoric acid and the electrodes are carbon black or graphite plates in which Pt particles are dispersed. The PAFCs are generally fed by natural gas, and CO has to be removed (only a 1 % concentration is accepted) to avoid Pt poisoning. PAFCs are mainly used for combined heat and power generation (up to 200 kW) in

Table 3. Different types of fuel cells, electrode reactions and operating temperatures.

Type	Electrolyte	Anodic reaction	Cathodic reaction	$T [^{\circ}\text{C}]$
SOFC	solid oxide	$\text{H}_2 + \text{O}^{2-} \rightarrow \text{H}_2\text{O} + 2\text{e}^-$	$1/2\text{O}_2 + 2\text{e}^- \rightarrow \text{O}^{2-}$	1000
MCFC	molten carbonate	$\text{H}_2 + \text{CO}_3^{2-} \rightarrow \text{H}_2\text{O} + \text{CO}_2 + 2\text{e}^-$	$1/2\text{O}_2 + \text{CO}_2 + 2\text{e}^- \rightarrow \text{CO}_3^{2-}$	650
PAFC	phosphoric acid	$\text{H}_2 \rightarrow 2\text{H}^+ + 2\text{e}^-$	$1/2\text{O}_2 + 2\text{H}^+ + 2\text{e}^- \rightarrow \text{H}_2\text{O}$	200
AFC	alkaline	$\text{H}_2 + 2\text{OH}^- \rightarrow 2\text{H}_2\text{O} + 2\text{e}^-$	$1/2\text{O}_2 + \text{H}_2\text{O} + 2\text{e}^- \rightarrow 2\text{OH}^-$	80–100
PEFC	polymer electrolyte	$\text{H}_2 \rightarrow 2\text{H}^+ + 2\text{e}^-$	$1/2\text{O}_2 + 2\text{H}^+ + 2\text{e}^- \rightarrow \text{H}_2\text{O}$	80–100
DMFC	polymer electrolyte	$\text{CH}_3\text{OH} + \text{H}_2\text{O} \rightarrow \text{CO}_2 + 6\text{H}^+ + 6\text{e}^-$	$1/2\text{O}_2 + 2\text{H}^+ + 2\text{e}^- \rightarrow \text{H}_2\text{O}$	80

industry and hospitals [66]; a 200 kW natural gas, fuel cell, stationary power plant is a commercial product (PC25™) from IFC/ONSI [67]. Alkaline fuel cells (AFCs) use alkaline potassium hydroxide as the electrolyte and operate at a lower temperature (80–100 °C) than PAFCs. Long used by NASA on space missions, the AFCs are based on a mature technology, but their high cost and their sensitivity to CO₂ (such that hydrogen and CO₂-free air are required) limit their applications for civilian uses [68].

Polymer electrolyte fuel cells (PEFCs), also called polymer electrolyte membrane fuel cells (PEMFCs) [69], are used at low temperature (they heat themselves to a working temperature of 80–100 °C). The electrolyte is a 100 μm membrane such as Nafion™, able to exchange protons. Porous electrodes are made by depositing electrocatalytic materials (Pt or Pt compounds) on carbon-based substrate. To avoid catalyst poisoning by CO, the fuel has to be pure hydrogen, which is further treated to reduce the CO content to less than 100 ppm. The use of Pt increases the cost of PEFCs, and the CO poisoning and water management represent key problems [70]. According to the US Department of Energy, PEFCs are candidates for light-duty applications both in stationary systems [71, 72] and in vehicles: several car manufacturers have started developing cars powered by fuel cells (the first, NeCar I, was developed in 1994 by Daimler-Benz, which is already aiming at large-scale production of fuel-cell-powered vehicles) [73–75]. Another feature of PEFCs is that they can be directly fed by methanol: direct methanol fuel cells (DMFCs) eliminate the need for reforming the fuel because the methanol is oxidized directly at the anode. This type of fuel cell typically operates in the 60–90 °C temperature range [76].

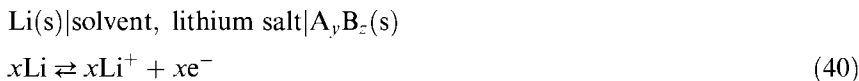
In future, closed-loop power generation looms on the horizon, and studies on regenerative fuel cells have already begun [77]. The water could be electrolyzed into hydrogen and oxygen by a solar-powered system, the hydrogen and oxygen would generate electricity and water, the latter would be recycled back to the solar electrolyzer and the process would then restart.

2.4 Lithium Rechargeable Batteries

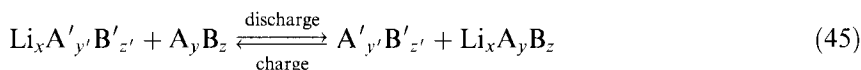
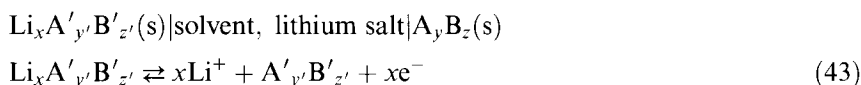
The most promising battery for electric vehicle applications is the lithium battery. Lithium is a promising negative electrode material because it is the lightest of all metals and has the lowest standard redox potential. Batteries based on lithium chemistry have the highest specific energy and energy density of all chemical types (Figure 6), so it is not surprising that the first studies on lithium rechargeable batteries were devoted to electric vehicle applications. Recently, the field of application of this battery has moved toward the growing consumer market and lithium battery technology is fast being developed to provide power to portable devices under the most demanding conditions. These applications require batteries of small dimensions and long life, high cell voltage, design versatility, and good performance-to-cost ratio, and that can operate in a wide temperature range.

There are two main kinds of rechargeable battery based on lithium chemistry: the lithium-metal and the lithium-ion battery. In both the positive electrode is a lithium insertion material; the negative in the former is lithium metal and in the latter it is a lithium insertion host. The reason for the application in lithium batteries of insertion electrode materials, which are electronic and ionic conductive solid matrixes (inorganic and carbon-based), is that electrochemical insertion reactions are intrinsically simple and highly reversible.

The cell, and the electrode and cell reactions, for the lithium-metal battery are:



and for the lithium-ion battery:



Figures 13 and 14 display the discharge processes for the two kinds of lithium battery. During discharge at the anode the lithium ions are formed from the lithium metal or are released from an $\text{Li}_x\text{A}'_{y'}\text{B}'_{z'}$ host material; at the cathode the lithium ions are inserted into the void spaces of the structure of the A_yB_z insertion material. The lithium-ion battery behaves almost like a concentration cell: lithium ions move from a lithium-rich source toward the cathode, which acts as sink, while electrons flow through the external circuit from anode to the cathode.

This section will provide a general description of the lithium-metal battery, especially with regard to the problems arising from the use of lithium metal, and introduce the lithium-polymer batteries as a reliable solution to problems deriving from the use of the lithium-metal electrode. The lithium-ion battery will then be taken up and particular emphasis will be given to the insertion electrode materials used in both the lithium-metal and the lithium-ion batteries.

2.4.1 Lithium-Metal Batteries

The high theoretical specific capacity (3862 Ah kg^{-1}) and capacity density (2047 Ah L^{-1}) of the lithium-metal electrode, together with its promising redox potential, give the battery unique advantages in terms of specific energy and energy density.

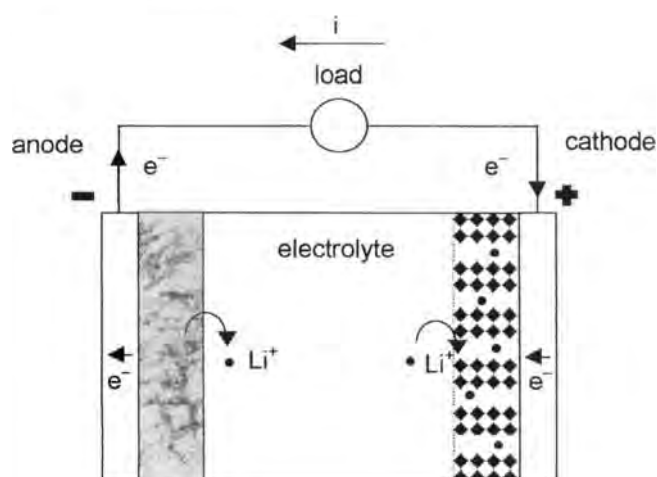


Figure 13. Lithium-metal battery under discharge.

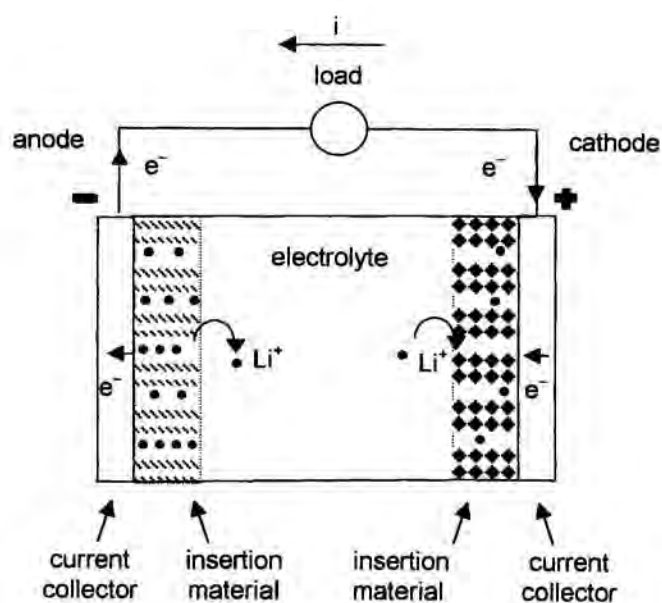


Figure 14. Lithium-ion battery under discharge.

On the other hand the high reactivity of lithium metal gives some problems for its application as the negative electrode in rechargeable configurations.

The strong reducing power of lithium metal makes it highly unstable in most known battery electrolytes. In some media, spontaneous chemical reactions yield passivating films of electrolyte decomposition products that cover the lithium surface and protect it from further corrosion. This surface layer is made up of various organic and inorganic compounds deriving from the reaction of lithium with the solvent, the salt, and impurities, and acts as an electronic insulator and ionic conductor, i.e., as a sieve that is permeable only to the lithium ion [78]. The composition and morphology of lithium passivating film depend on the kind of electrolyte used, and it is possible to obtain a composite or a stratified film structure [79].

The surface layer formation is a crucial phenomenon as it affects the electrode charge transfer rate. Low-conductivity films determine high electrode overvoltages and lower battery performance. The charge transfer resistance can be monitored by impedance spectroscopy measurements, which represent a useful tool for the in-situ characterization of resistive and capacitive processes occurring in different time scales (1 mHz–100 kHz) [80].

Charge–discharge of the lithium electrode means lithium deposition–dissolution, and repeated charge–discharge cycles can result in dendrite formation—a buildup of surface irregularities on the lithium electrode—promoted by surface nonhomogeneity resulting from the lithium–electrolyte interaction. Dendrites can grow to such an extent that they penetrate the separator between positive and negative electrodes and create an internal short circuit. At best, this phenomenon shortens the useful life of a rechargeable lithium-metal battery to 400 cycles or less. At worst, an internal short circuit could cause the battery's internal temperature to rise above the melting point of lithium (181 °C), which could cause severe flaming. Several publications on lithium-metal battery safety tests are available in literature, and the Tadiran Battery Division (Israel) proposed an intrinsically safe device, based on an electrolyte which is stable at low-to-medium temperatures and which polymerizes at temperatures over 125 °C, thereby protecting the cell from short circuit, overcharge and thermal runaway; this electrolyte also showed good compatibility with lithium metal in terms of interface resistance [81].

Many kinds of electrolytes [82, 83] and electrolyte additives, e.g., CO₂ [84], have been investigated in the pursuit of compact and uniform passivation layers for a stable lithium interface resistance, and a smooth lithium surface so as to control dendritic deposition. The high reactivity of lithium to the electrolyte, the related corrosion phenomena, and dendrite formation all contribute to lowering the coulombic efficiency of the charge–discharge process and are detrimental to the battery's cycle life. Hence, to ensure a sufficiently high number of charge–discharge cycles, an amount of lithium in excess of the stoichiometric quantity is needed (Figure 15), although this lowers the specific energy of the battery.

As mentioned above, several strategies have been pursued to improve the rechargeability and reliability of the lithium-metal electrode. One of the most promising, and different, approaches in this connection consists of replacing the liquid electrolyte with a polymer electrolyte. First introduced by Armand in the early

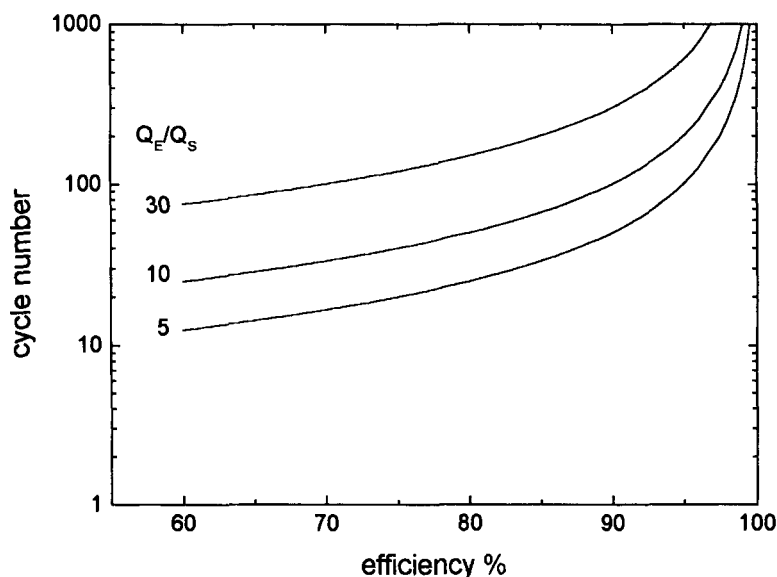


Figure 15. Number of cycles the battery can sustain at different values of lithium excess with respect to the stoichiometric one (Q_E/Q_S) as a function of the efficiency of the lithium deposition–stripping process.

1970s [85], polymer electrolytes typically involve a lithium salt Li^+X^- dissolved in a high-molecular-weight dry polymer such as poly(ethylene oxide) (PEO) [86–88].

Lithium–Polymer Batteries

The substitution of the liquid electrolyte with the less reactive polymer electrolyte has led to lithium–polymer batteries, among the most likely to be commercialized for electric vehicles [89]. It must be stressed that the lithium–polymer battery is still a lithium–metal battery and not a lithium-ion one. Lithium–polymer batteries are solid-state, in that their electrolyte is a solid. A great safety advantage of this type of battery is that the electrolyte will not leak out if there is a rupture in the battery case. Furthermore, it can be assembled in any size and shape, allowing manufacturers considerable flexibility in cell design for electric vehicle or electronic equipment.

Because the conductivity of polymer electrolytes is generally low, thin batteries are assembled (50–200 μm) with electrolyte thickness ranging from 20 to 50 μm . Conventional polymer electrolytes based on PEO and lithium salts, owing to their high crystallinity, reach useful conductivity values only at temperatures above 60°C, i.e., above the melting temperature of the crystalline phase. If the low conductivity at room temperature prevents their application for consumer electronics, this does not represent an obstacle for electric vehicles, for which an operating temperature higher than that of the transition in the amorphous phase is expected.

This is not to say that considerable effort has not been devoted to the development of polymer electrolytes with high conductivity at room temperature. Two different approaches have been pursued:

- 1) polymer modification to reduce their crystallinity by crosslinking [90, 91], by adding pendent short PEO chains [92], by copolymerization [93], or by realization of interpenetrating networks [94]; and
- 2) design and synthesis of new lithium salts with bulky and polarizable anions like $\text{Li}[(\text{CF}_3\text{SO}_2)_2\text{N}]$ [95], which improve polymer conductivity at all temperatures and slow down the crystallization rate.

However, it seems likely that a conductivity value of $10^{-3} \text{ S cm}^{-1}$ at room temperature is a goal that can only be achieved with polymer networks including organic solvents as plasticizers [96] or with polymer matrixes like polyacrylonitrile [97] or poly(methyl methacrylate) [98] entrapping a large amount of organic electrolytic solution, i.e., with “hybrid” and/or gel electrolytes. These electrolytes combine the advantage of the polymer’s mechanical properties with the electrochemical properties of the liquid electrolytes.

The strategy of hybrid and gel electrolytes is very promising for lithium-ion batteries, but it seems less viable for lithium-metal batteries due to the reactivity of lithium metal with the encapsulated solvent. In fact, high conductivity is not the only parameter in selecting a successful polymer electrolyte for the development of lithium batteries: a low interface resistance and a high interface stability over time are also required to assure good cyclability and long life.

Polymer electrolytes have been shown to stabilize the lithium/electrolyte interface, yielding stable and low interface resistance, especially when ceramic additives such as $\gamma\text{-LiAlO}_2$ are used. Furthermore, the $\gamma\text{-LiAlO}_2$ ceramic additive has been shown to stabilize the polymer amorphous phase and to slow down the recrystallization process [99–103]. Thus, the unique electrochemical performance of lithium metal can be applied in practical devices by substitution of the liquid electrolyte with a solid one whose conductivity and stability can be enhanced with ceramic additives.

2.4.2 Lithium-ion Batteries

To avoid the problems associated with lithium metal, lithium insertion materials (e.g., graphitic carbons) are being investigated as negative electrodes. With respect to lithium metal, the use of negative insertion materials improves the cycle life and safety of the battery but lowers the cell voltage, the theoretical specific capacity, and the charge transfer rate [104].

As Figure 14 shows, the combination of two lithium insertion materials (characterized by two different potentials of the lithium insertion process) yields a cell—the so-called “rocking chair battery”, after Armand [105] and Scrosati et al. [106]—in which during discharge lithium ions are released from the anode and travel through the electrolyte toward the cathode without variation in the composition of the

electrolyte. Here electrolyte volume can be minimized to reduce electrolyte ohmic drop and battery weight. When the lithium ions reach the cathode, they are incorporated into the insertion cathode material and the process is highly reversible.

Rechargeable lithium-ion batteries have OCV values up to 4.2 V, i.e., more than twice those of Ni–Cd and Ni–MH batteries, and the specific energies are more than 40 % higher. Lithium-ion batteries can also charge and discharge faster than lead–acid and Ni–MH batteries, and show long cycle life under normal operation because structural changes in the negative and positive electrodes caused by the insertion and removal of lithium ions are quite limited. It is thus not unexpected that with designers demanding smaller, lighter, and more powerful energy sources, lithium-ion batteries are rapidly replacing Ni–Cd and Ni–MH ones (Figure 3).

As with lead–acid and Ni–MH batteries, overcharging of lithium-ion batteries must be carefully controlled to prevent detrimental electrode or electrolyte decomposition. This is one of the problems that advanced battery management systems can obviate, thereby ensuring the safety of lithium-ion batteries even in extreme conditions [107].

The first lithium-ion batteries were based on liquid electrolyte and in 1990 Sony commercially introduced for the consumer electronics market the first rechargeable lithium-ion battery based on a lithium cobalt oxide as the positive electrode and carbon as the negative one [108]. The development of lithium-ion batteries has rapidly increased since then and today much research is focused on plastic lithium-ion batteries in which the separator is a polymer membrane capable of adsorbing a large amount of liquid electrolyte, i.e., a gel electrolyte. The high mechanical stability and flexibility of these membranes enable simple manufacture of thin electrolyte films so that plastic lithium-ion batteries are at the cutting edge of rechargeable battery technology for cell size, easy packaging format, safety, and low cost. Bellcore Laboratories in the USA developed a successful technology to produce cells by laminating the electrode material on a membrane separator formed by a copolymer of vinylidene fluoride and hexafluoropropylene [109]. Replacing the cobalt-oxide-based positive electrode with cheaper insertion materials lowers lithium-ion battery costs. Ultralife Batteries Inc. is a company which has pursued this strategy and has developed a plastic lithium-ion battery with a manganese-oxide-based positive electrode. This battery has specific energy and energy density at the 1 C rate exceeding 120 Wh kg^{−1} and 200 Wh L^{−1}, respectively, and retains 90 % of initial capacity for 500 cycles at room temperature [110].

2.4.3 Insertion Electrode Materials

As reported above, lithium–metal and lithium-ion batteries are based on reversible lithium insertion, which takes place during charge–discharge processes of the positive electrode (and of the negative one for the rocking chair batteries) [111]. According to McKinnon and Haering [112], the reversible insertion of guest atoms into host solids, provided the host structure is not significantly altered during the process, is called intercalation, a special case of the insertion process.

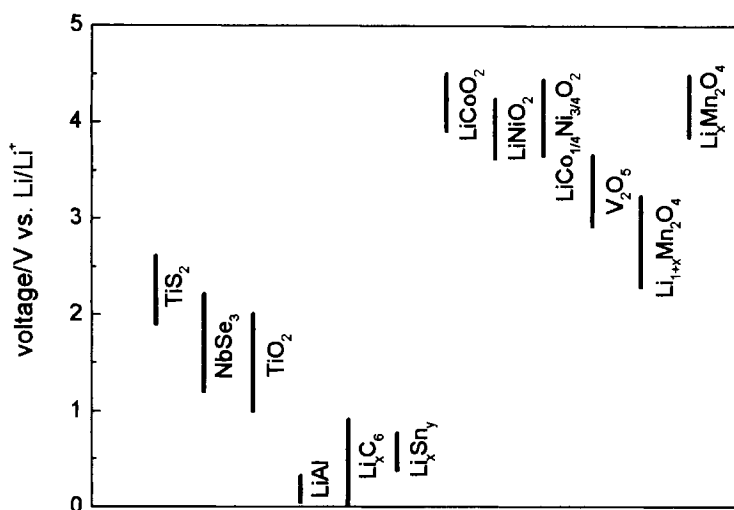


Figure 16. Typical potential regions for the insertion of lithium ions into various hosts.

From the position of two given host structures on a redox potential scale such as that in Figure 16 [1, 113, 114], it is possible to determine which material will act as positive electrode and which as negative. For cell design optimization, it has to be taken into account how the basic properties of insertion materials vary as to composition and temperature. For instance, it is useful to determine how the cell voltage depends on the kind of host matrix and the amount of inserted Li^+ .

The basic requirements for the application of insertion materials in batteries are as follows [115].

- 1) Large free energy of cell reaction to provide high cell voltage for high energy density. Since lithium batteries can have a cell voltage >4 V, a wide electrochemical window of the electrolyte for the cycle life of the device is important [116].
- 2) Wide compositional range, x , for high cell capacity.
- 3) High diffusivity of lithium into the host matrix to enable high current density and high power density. Lithium diffusion into/from the host matrix is accompanied by a lithium concentration gradient across the insertion electrode, resulting in an electrode diffusion overvoltage [117]. The lithium ion transport into the electrode material depends on the type of void spaces available for lithium insertion, which can be one- (tunnel), two- (layer), or three-dimensional, such as those in Figure 17.
- 4) Minimal structural change as a function of composition to ensure good reversibility of the insertion process. The lithium insertion–deinsertion can determine volume changes in the host matrix, resulting in mechanical stress during charge–discharge cycles that in some cases can lead to irreversible cracks in the electrode

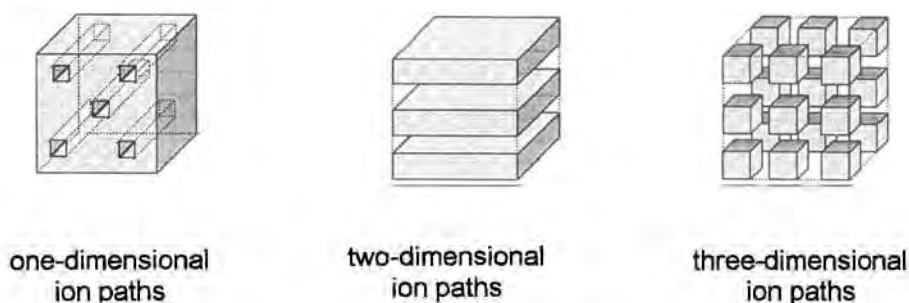


Figure 17. Schematic representation of lithium ion paths in insertion materials.

material (as with lithium alloys). In some cases insertion compounds can be thermodynamically unstable; for instance, the Jahn–Teller distortion of the LiMn_2O_4 spinel lowers the cyclability of this oxide [118]. There is no dearth of literature on the synthesis methods for controlling the structure, impurity, and phase impurity of the insertion materials. Such properties, which influence the electrochemical performance of the materials, were investigated via thermal analysis and by EXAFS, AFM, ASTM, SEM, and RX measurements [119–123].

- 5) Suitable electrode material morphology for enhanced electrochemical properties. Many laboratories are involved in the characterization of lithium insertion nanomaterials. Small particle size increases the lithium ion diffusion and can at times enhance insertion material capacity. For example, hard carbons with nanopores are high-capacity negative-electrode materials. Furthermore, as in the case of lithium alloys, nanoparticles lead to minor mechanical stress due to the volume variation during the insertion–deinsertion processes [124]. However, they also result in high surface area; hence the degradation due to the interactions with the solvent becomes more evident.
- 6) High electronic conductivity to obviate the need for additional conductive materials in the electrode. Additives are often used in composite electrodes to enhance conductivity, to act as binders, or as electrochemically inactive matrixes that attenuate the mechanical stress resulting from the volume variation of the insertion material during the insertion–deinsertion processes.
- 7) Insolubility in the electrolyte medium to eliminate self-discharge. Interactions with the electrolyte may cause irreversible capacity loss and coulombic efficiency values far from 100 %.

Positive Insertion Materials

Positive insertion materials can be based on transition metal oxides or chalcogenides; Table 4 lists the most investigated compounds [111, 120, 125].

The layered lithium insertion cobalt and nickel oxides are materials of industrial importance [126]. The layered structure provides two-dimensional paths for lithium insertion, during which a charge transfer occurs involving the reduction of M^{4+} to

Table 4. The most investigated positive insertion electrode materials.

Positive electrode material	Average electrode voltage [V vs. Li/Li ⁺]	Reversible range ^a [Δx]	Theoretical specific capacity ^a [Ah kg ⁻¹]
Li _x CoO ₂	3.9	0.5	137
Li _x NiO ₂	3.8	0.7	192
MnO ₂ (spinel)	4.0	0.5	154
LiMn ₂ O ₄ (spinel)	3.0	1	148
TiS ₂	2.1	1	239
MoS ₂	1.8	0.8	134
V ₂ O ₅	2.5	1	147

^athe theoretical specific capacity is based on a reversible range Δx of lithium content during the charge–discharge process: $\Delta x\text{Li}^+ + \Delta x\text{e}^- + \text{Li}_x\text{A}_y\text{B}_z \rightleftharpoons \text{Li}_{x+\Delta x}\text{A}_y\text{B}_z$

M³⁺ ions (M = Co, Ni). Diffusion of Li⁺ can result in the expansion of the host structure along the crystallographic *c*-direction.

The Li/Li_xCoO₂ cells exhibit a very high OCV in the 3.9–4.7 V range and a specific energy of ca. 1070 Wh kg⁻¹, based on an average discharge voltage of 3.9 V. At room temperature the lithium diffusion coefficient in LiCoO₂ ranges approximately from 10⁻¹¹ to 10⁻¹² m² s⁻¹, providing evidence for good lithium ion mobility. Reversible lithium insertion in Li_xCoO₂ takes place in a limited range of compositions because the highly oxidizing power of the almost delithiated Li_xCoO₂ causes oxidative decomposition of the electrolyte, with formation of detrimental films on the electrode surface [127].

LiNiO₂ is isostructural with LiCoO₂ and, having a redox potential slightly less positive than that of LiCoO₂, is less prone to electrolyte oxidation problems. Despite its excellent specific capacity (Table 4) and economic advantage over LiCoO₂, the nickel oxide has certain problems that have limited its wide application in practical cells. LiNiO₂ is quite difficult to prepare because of its tendency to form a nickel-rich nonstoichiometric phase which exhibits a lower electrochemical performance [128]. Furthermore, it has lower thermal and cycling stabilities with respect to cobalt oxide, although these can be improved with certain synthesis methods [129]. LiNiO₂ shows an irreversible loss of capacity during the first cycle, and a material with the composition Li_{0.85}NiO₂ is formed at the end of the first discharge. Lithium deinsertion from this material is highly reversible during subsequent charge–discharge cycles in the potential range from 2.5 to 4.1 V vs. Li/Li⁺. To enhance electrode performance, partial substitution of nickel in LiNiO₂ with elements such as Co, Mn, Mg, Fe, and Al has been carried out. Such doping has been founded to limit the various phase transitions which occur while deinserting lithium ions, and to stabilize the layered structure of LiNiO₂ [130].

Much effort has been devoted to the study of manganese oxides as positive electrode materials. Manganese oxides are very promising materials due to their abundance, environmental compatibility, low cost, favorable charge density, relatively high electronic conductivity, and suitable electrode potentials. Different structures of manganese oxides have been investigated and the best known, and the first to be

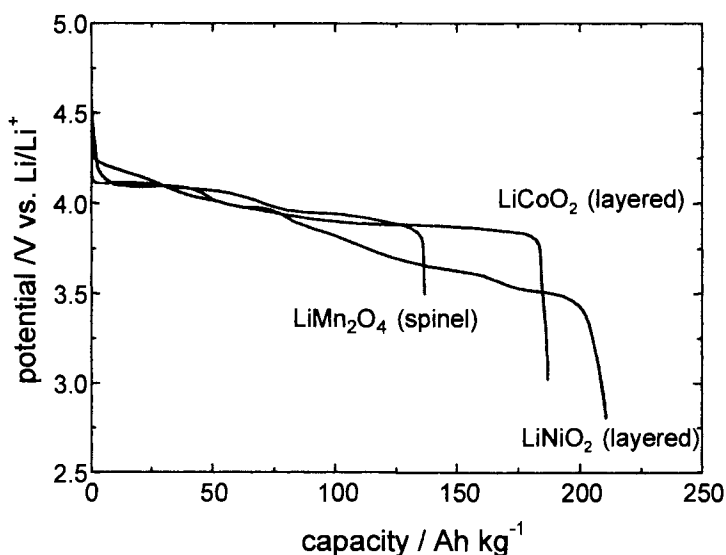


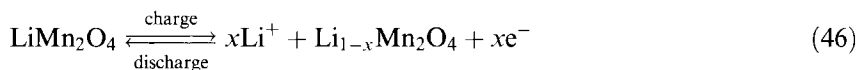
Figure 18. Galvanostatic discharge curves at room temperature and at 0.1 mA cm^{-2} for layered cobalt and nickel oxides, and spinel manganese oxide in ethylene carbonate–diethyl carbonate– $\text{LiN}(\text{CF}_3\text{SO}_2)_2$ [134] (by permission of Elsevier Science S.A.: S. Megahed, B. Scrosati, *J. Power Sources* **1994**, *51*, 79–104).

studied, is the cubic spinel LiMn_2O_4 , which is characterized by a three-dimensional array of interconnected voids for the lithium insertion [131]. Layered manganese oxides [132] and tunnel structures [133], with two- and one-dimensional paths for lithium insertion, respectively, have also been investigated.

Manganese oxides with three-dimensional ion paths have two main advantages over the layered structures: the co-insertion of solvent molecules can be avoided for steric reasons and volume expansion–contraction upon lithium insertion–deinsertion is minor in extent. Besides LiNiO_2 and LiCoO_2 , the lithiated spinel LiMn_2O_4 is at present a very popular positive electrode material; Figure 18 compares galvanostatic discharge curves of the three metal oxides [134].

The LiMn_2O_4 spinel structure, shown in Figure 19, can be described as a cubic close-packed oxygen array with the manganese cations occupying one-half of the octahedral interstitial sites and the lithium cations one-eighth of the tetrahedral sites. The interstitial tetrahedral and octahedral spaces in the $[\text{Mn}_2]\text{O}_4$ framework are interconnected to form three-dimensional pathways for Li^+ ion diffusion (10^{-12} – $10^{-14} \text{ m}^2 \text{ s}^{-1}$).

The electrochemical Li^+ deinsertion from LiMn_2O_4 (Eq. (46))



is reversible and proceeds at about 4 V vs. Li/Li^+ via a two-step process involving a phase transition at $\text{Li}_{0.5}\text{Mn}_2\text{O}_4$. In Figure 20 A and B indicate the corresponding

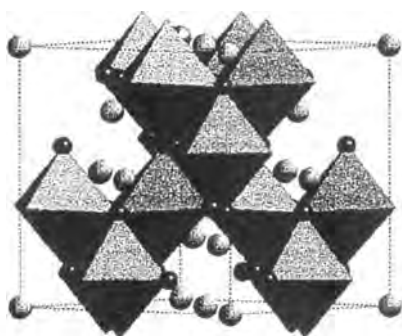


Figure 19. LiMn_2O_4 spinel structure, in which the light gray spheres represent lithium, the dark gray ones the oxygen and the solid areas the manganese.

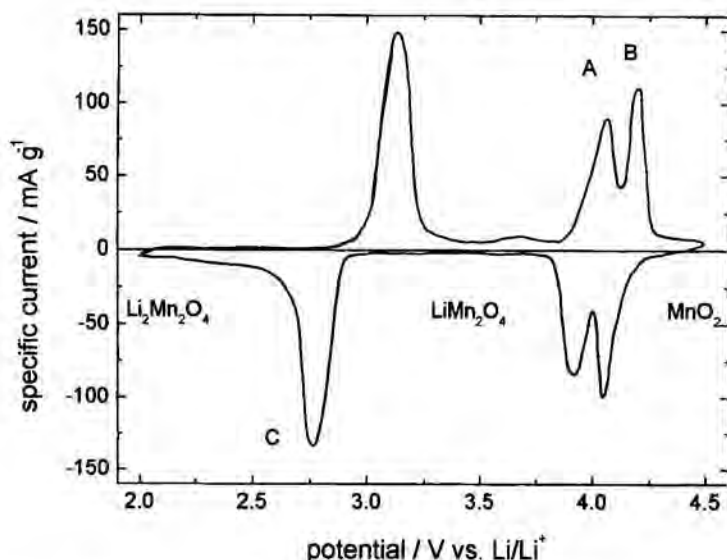


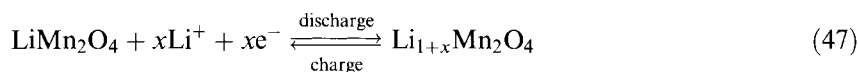
Figure 20. Typical $\text{Li}_x\text{Mn}_2\text{O}_4$ cyclic voltammetry [111] (by permission of Wiley-VCH Verlag GmbH: M. Winter, J.O. Besenhard, M.E. Spahr, P. Novák, *Adv. Mater.* **1998**, *10*, 725–763).

voltammetric peaks. During charging and discharging in the 4 V potential domain, the unit cell exhibits a minimal contraction over a wide composition range, and this results in the satisfactory rechargeability and cycling stability of LiMn_2O_4 . However, at practical potentials (4.5 V vs. Li/Li^+) it is not possible to extract all the lithium electrochemically to yield $\lambda\text{-MnO}_2$.

The empty sites of LiMn_2O_4 can also insert additional Li^+ at about 3 V vs. Li/Li^+ (peak C in Figure 20).

Table 5. Observed specific capacity delivered over 3 V vs. Li/Li⁺ for different mixed oxides.

Composition	Potential range [V]	Observed specific capacity [Ah kg ⁻¹]
Li ₂ CrMn ₃ O ₈	3.4–5.4	125
Li ₂ FeMn ₃ O ₈	3.0–5.3	125
Li ₂ CoMn ₃ O ₈	3.0–5.3	130
Li ₂ NiMn ₃ O ₈	3.9–4.9	111



Cells based on this process (Eq. (47)) show lower cycling performance with respect to those based on the 4 V process because charge–discharge reactions are accompanied by an asymmetric lattice contraction–expansion of the Li_{1+x}Mn₂O₄ electrode. This lattice distortion mainly results from the Jahn–Teller effect of the Mn³⁺ ion which transforms the crystal symmetry of the spinel oxide [118].

Doped spinel manganese oxides in which Mn³⁺ is substituted by other trivalent cations, e.g., Al³⁺, Fe³⁺, Ni³⁺, Co³⁺, or Cr³⁺, have been also investigated; they display enhanced structural stability but decreased specific capacity as compared with the undoped LiMn₂O₄. These compounds are also classified as high-voltage positive electrode materials because they can operate above 4.5 V vs. Li/Li⁺ (Table 5) [135].

With the intent of realizing electrode material with an electrochemical performance as high as that of Ni and Co oxides but less toxic and expensive, layered manganese oxides have also been investigated [132]. The main problem with these materials is that in the final step of the deinsertion process the layered LiMnO₂ irreversibly transforms into the similar spinel structure, thereby reducing cyclability. Recently, a new synthetic method has been proposed that yields a layered manganese oxide featuring a specific capacity of 150 Ah kg⁻¹ and an O2 structure that is stable during repeated charge and discharge cycles [136].

Among the transition metal oxides, mention should also be made of the vanadium oxides, the most studied as positive electrode materials being V₂O₅, V₆O₁₃, and LiV₃O₈, which insert lithium in the potential domain of 3 V vs. Li/Li⁺. For the vanadium oxides, too, doping and suitable structure have been shown to improve their electrochemical performance, and recently a sol–gel process has yielded high-capacity (500–600 Ah kg⁻¹) materials delivering 500 Wh kg⁻¹ at 4 mA cm⁻² [137].

Negative Insertion Materials

Research has also focused on the study of highly reversible negative lithium insertion materials. Transition metal oxides and chalcogenides, such as MoO₂, WO₂, and TiS₂, if combined with a metal oxide positive electrode material yield cells with low OCV values (ca. 1.5–2 V) [111].

Higher OCV values can be attained with lithium alloys (Figure 16), which are under study as negative insertion electrode materials for their high specific capacity

(1700–2000 Ah L⁻¹) and acceptable Li⁺ mobility at room temperature (5.9×10^{-11} – 5.2×10^{-14} m² s⁻¹). Their major drawback is that the corresponding lithium insertion reaction is associated with large volume changes (typically 100 % for Li_xAl alloys) because the reduction of Li_xM alloys yields M⁻ ions which are considerably larger than neutral M atoms. Furthermore, lithium alloys, having a highly ionic character, are fairly brittle and mechanical stresses related to the volume changes can, as an extreme result, lead to “pulverization” of the electrode, thereby limiting the cycle life [113].

Using alloys with micro-, nano-, or subnanoparticle sizes makes it possible to enhance lithium alloy cyclability. With such morphology, relatively large dimensional changes of the crystallites do not cause particle cracking since the absolute changes in the particle dimensions are small [138].

At present, the most widely used insertion negative electrode materials are carbon-based: they exhibit higher specific capacity and more negative redox potentials than most metal oxides and chalcogenides, and, due to their dimensional stability, they show better cycling performance than lithium alloys [139]. The insertion properties of carbonaceous materials depend on their crystallinity, microstructure, and micromorphology and hundreds of types and qualities of carbons have been investigated, including fullerenes [140] and nanotube carbons [141].

Carbonaceous materials can be classified roughly as graphitic and nongraphitic. Graphitic carbons have a layered structure, although with a number of structural defects differentiating them from the ideal graphite structure of Figure 21(a). They are more commonly an aggregate of graphite crystallites of different dimensions. For instance, the highly oriented pyrolytic graphite consists of large aggregates that are relatively free of defects. Under ambient conditions, graphite inserts a maximum of one lithium atom per six carbon atoms; the specific capacity is 372 Ah kg⁻¹ [126].

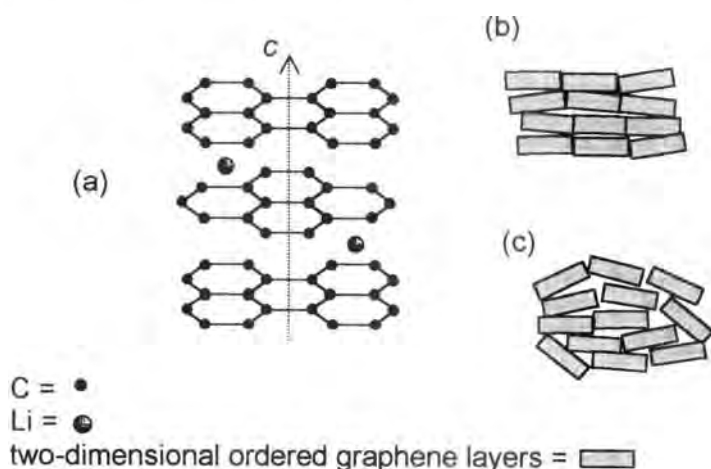


Figure 21. a) Schematic drawing of lithiated hexagonal graphite Li_xC₆, and stacking arrangement by Franklin models for b) soft and c) hard carbons [R.E. Franklin, *Proc. Roy. Soc.* **1951**, A209, 196].

Nongraphitic carbonaceous materials do not show a crystallographic order in the *c*-direction. The structure of these carbons is characterized by both amorphous and graphitic areas and consists of two-dimensional ordered graphene sheets which are randomly stacked. It is common to divide the nongraphitic carbons into “soft” (Figure 21b) and “hard” carbons (Figure 21c), as the former (e.g., cokes and carbon black), unlike the latter, can be graphitized by heat treatment. Hard carbons seem to be the better performing with respect to soft and graphitic ones [142].

In practice, Li^+ insertion into carbon is not fully reversible: during the first cycle there is an irreversible capacity loss, while in the subsequent cycles the coulombic efficiency is close to 100 %. The excess charge (irreversible capacity) consumed in the first cycle is generally ascribed to the formation of a passivating film and to corrosion-like reactions of Li_xC_6 . The magnitude of this irreversible capacity depends on the kind of carbonaceous material and on the electrolyte composition [143, 144].

Often, insertion of Li^+ from organic electrolytes into graphitic carbons leads to the insertion of the solvent, which is associated with extreme expansion of the graphite matrix (ca. 150 %) and the deterioration and exfoliation of the graphite. The resulting decrease in charge storage capability can be limited by using ethylene carbonate-based electrolytes. The decomposition compounds, resulting from the reaction of graphite with these electrolytes, form in the early stages of the first reduction a protective film on the electrode surface which limits the extent of solvent co-insertion [145].

Recently, Fujifilm Celtec has proposed new negative electrode materials with excellent electrochemical properties: tin-based amorphous oxides containing elements of groups III, IV, and V, such as boron and phosphorus. These materials show high specific capacity, up to 600 Ah kg^{-1} and 2200 Ah L^{-1} [146].

2.5 Present Status and Future Prospects

At the moment the plastic lithium-ion batteries are at the cutting edge of battery technology and several companies (Panasonic, Sony, Japan Storage, Hitachi Maxell, and Shubila) have marketed them since 1999 in a range of varying sizes, with graphite and LiCoO_2 as negative and positive electrode materials, respectively.

In future magnesium-based rechargeable batteries might prove to be a viable alternative to lithium-based batteries [147]. Despite the fact that the magnesium redox potential is less negative than that of lithium and the Mg equivalent weight is slightly higher than that of lithium, the natural abundance of magnesium, its low cost, and its safety characteristics make it a promising negative electrode material. However, magnesium electrochemistry near or at room temperature is not fully understood and there are few data on Mg-based electrodes (e.g., Mg^{2+} insertion materials): considerable effort is thus needed before a competitive magnesium-based rechargeable battery can be brought to market.

This chapter is not intended as an exhaustive treatment of batteries as such. Rather, it seeks to bring to the fore the wide-ranging importance of one application of electron transfer: batteries. Of no less importance in this connection is the enormous effort of interdisciplinary research needed to develop batteries responsive to scientific advances and technological innovations—research that is strengthened under the pressure of market demand.

References

1. C.A. Vincent, B. Scrosati, *Modern Batteries. An Introduction to Electrochemical Power Sources*, 2nd edition, Edward Arnold, London, **1997**
2. J. Bard, R. Faulkner, *Electrochemical Methods. Fundamentals and Applications*, John Wiley, New York, **1980**
3. J.O'M. Bockris, A.K.N. Reddy, *Modern Electrochemistry*, (3rd Printing), Plenum Press, New York, **1977**
4. J.O'M. Bockris, D.M. Drazic, *Electro-chemical Science*, Taylor & Francis, London, **1972**
5. R.J. Brodd, *Interface* **1999**, 8, 20–23
6. T. Kodama, H. Sakaebe, *J. Power Sources* **1999**, 81–82, 144–149
7. G. Antonioli, F. Baggioni, F. Consiglio, G. Grassi, R. Lebrun, F. Zanardi, *Minerva Med.* **1973**, 64, 2298–2304
8. C.F. Holmes, *J. Power Sources* **1997**, 65, xv–xx
9. P.D. Bennet, K.R. Bullock, M.E. Fiorino, *Interface* **1995**, 4, 26–30
10. P.T. Moseley, A. Cooper, *J. Power Sources* **1999**, 78, 244–250
11. R.D. Prengaman, *J. Power Sources* **1999**, 78, 123–129
12. G. Halpert, H. Frank, S. Surampudi, *Interface* **1999**, 8, 25–30
13. S.R. Ovshinsky, M.A. Fetcenko, J. Ross, *Science* **1993**, 260, 176–181
14. S.K. Dhar, S.R. Ovshinsky, P.R. Gifford, D.A. Corrigan, M.A. Fetcenko, S. Venkatesan, *J. Power Sources* **1997**, 65, 1–7
15. M.D. Farrington, *J. Power Sources* **1997**, 65, 87–92
16. T.C. Adler, F.R. McLarnon, E.J. Cairns, *J. Electrochem. Soc.* **1993**, 140, 289–294
17. D. Coates, E. Ferreira, A. Charkey, *J. Power Sources* **1997**, 65, 109–115
18. B. Bugnet, M. Costa, R. Rouget, *50th ISE Meeting*, Pavia 5–10 September **1999**, Abstr. 989
19. F.R. McLarnon, E.J. Cairns, *J. Electrochem. Soc.* **1991**, 138, 645–664
20. A. Kaisheva, I. Iliev, *50th ISE Meeting*, Pavia 5–10 September **1999**, Abstr. 1109
21. The USABC has awarded several contracts to battery companies, e.g., Ovonic, SAFT, Varta–Duracell, and others. In Japan the Lithium Battery Energy Storage Technology Research Association (LIBES) has been charged by the New Energy and Industrial Technology Development Organization (NEDO) with research, development, and evaluation of batteries. In almost every European country research and development projects have taken off: for example the authors of this chapter have been involved in developing a lithium metal–polymer battery in the framework of the Italian ALPE project which included the Universities of Bologna and Rome, the national energy agency ENEA and Arcotronics Italia S.p.A.
22. *8th Int. Seminar on Double Layer Capacitors and Similar Energy Storage Devices* (Florida Educational Seminars, Inc.), Deerfield Beach, 7–9 December **1998**
23. *Electrochemical Capacitors II*, F.M. Delnick, D. Ingersoll, X. Andrieu, K. Naoi Eds., *PV96–25*, The Electrochemical Society Proceeding Series, Pennington, **1997**, pp. 1–337
24. I. D. Raistrick in *Electrochemistry of Semiconductors and Electronics—Processes and Devices*, J. McHardy, F. Ludwig Eds., Noyes, New Jersey, **1992**, pp. 297–356
25. B. E. Conway, *3rd Int. Seminar on Double Layer Capacitors and Similar Energy Storage Devices* (Florida Educational Seminars, Inc.), Deerfield Beach, 6–8 December **1993**
26. B. E. Conway in *Electrochemical Capacitors*, F.M. Delnick, M. Tomkiewicz Eds., *PV95–29*, The Electrochemical Society Proceeding Series, Pennington, **1996**, pp. 15–49

27. J.P. Zheng, J. Huang, T.R. Jow, *J. Electrochem. Soc.* **1997**, *144*, 2026–2031
28. T.R. Jow, J.P. Zheng, *J. Electrochem. Soc.* **1998**, *145*, 49–52
29. C. Lin, J.A. Ritter, B.N. Popov, *J. Electrochem. Soc.* **1998**, *145*, 4097–4102
30. S. Passerini, J.J. Ressler, D.B. Le, B.B. Owens, W.H. Smyrl in *Electrochemical Capacitors*, F.M. Delnick, M. Tomkiewicz Eds., *PV95–29*, The Electrochemical Society Proceeding Series, Pennington, **1996**, pp. 86–104
31. A. Yamada, J.B. Goodenough, *J. Electrochem. Soc.* **1998**, *145*, 737–743
32. T.-C. Liu, G. Pell, B.E. Conway, S.L. Robertson, *J. Electrochem. Soc.* **1998**, *145*, 1882–1888
33. Y. Takasu, S. Mizutani, M. Kumagai, S. Sawaguchi, Y. Murakami, *Electrochem. Solid State Letters* **1999**, *2*, 1–2
34. T.R. Jow, J.P. Zheng, *Electrochemical Capacitors II*, F.M. Delnick, D. Ingersoll, X. Andrieu, K. Naoi Eds., *PV96–25*, The Electrochemical Society Proceeding Series, Pennington, **1997**, pp. 26–34
35. J.P. Zheng, T.R. Jow, *J. Electrochem. Soc.* **1995**, *142*, L6–L8
36. J.P. Zheng, P.G. Cygan, T.R. Jow, *J. Electrochem. Soc.* **1995**, *142*, 2699–2703
37. P. Novak, K. Müller, K.S.V. Santhanam, O. Haas, *Chem. Rev.* **1997**, *97*, 207–281
38. C. Arbizzani, M. Mastragostino, S. Panero, P. Prosperi, B. Scrosati, *Synth. Metals* **1989**, *28*, C663–C668
39. C. Arbizzani, M. Mastragostino, T. Hamaide, A. Guyot, *Electrochim. Acta* **1990**, *35*, 1781–1785
40. *Handbook of Organic Conductive Molecules and Polymers*, H. S. Nalwa Ed., John Wiley, Chichester, **1997**
41. A. Rudge, J. Davey, I. Raistrick, S. Gottesfeld, J.P. Ferraris, *J. Power Sources* **1994**, *47*, 89–107
42. C. Arbizzani, M. Mastragostino, L. Meneghello, *Electrochim. Acta* **1996**, *41*, 21–26
43. X. Ren, S. Gottesfeld, J. P. Ferraris in *Electrochemical Capacitors*, F. M. Delnick, M. Tomkiewicz Eds., *PV95–29*, The Electrochemical Proceedings Series, Pennington, **1995**, pp. 138–161
44. A. du Pasquier, J. Gonzales, C. Sarrazin, J. F. Fauvarque in *Electrochemical Capacitors II*, F. M. Delnick, D. Ingersoll, X. Andrieu, K. Naoi Eds., *PV96–25*, The Electrochemical Proceedings Series, Pennington, **1997**, pp. 127–137
45. C. Arbizzani, M. Mastragostino, L. Meneghello, R. Paraventi, *Adv. Mater.* **1996**, *8*, 331–334
46. J.P. Ferraris, M.M. Eissa, I.D. Brotherston, D.C. Loveday, *Chem. Mater.* **1998**, *10*, 3528–3535
47. C. Arbizzani, M. Mastragostino in *Current Trends in Polymer Science*, vol. 2, Research Trends, Trivandrum, **1997**, pp. 217–239
48. J. Roncali, *Chem. Rev.* **1997**, *97*, 173–205
49. M. Mastragostino, C. Arbizzani, R. Paraventi, A. Zanelli, *J. Electrochem. Soc.* **2000**, *147*, 407–412
50. M. Mastragostino, R. Paraventi, A. Zanelli, *J. Electrochem. Soc.* **2000**, *147*, 3167–3170
51. A.F. Burke, M. Miller, *8th Int. Seminar on Double Layer Capacitors and Similar Energy Storage Devices* (Florida Educational Seminars, Inc.), Deerfield Beach, 7–9 December **1998**
52. K. Kaneto, K. Yoshino, Y. Inuishi, *Jap. J. Appl. Phys.* **1983**, *22*, L567–L568
53. T.F. Fuller, *Interface* **1997**, *6*, 26–33
54. R. F. Service, *Science* **1999**, *285*, 682–685
55. K. Joon, *J. Power Sources* **1998**, *71*, 12–18
56. a) *J. Power Sources* **1998**, *71* (1–2, special issue), 1–379; b) *J. Power Sources* **2000**, *86* (1–2, special issue), 1–577
57. D. Hart, *Chem. & Ind.* **1998**, *5*, 344–347
58. J.P.P. Huijsmans, F.P.F. van Berkel, G.M. Christie, *J. Power Sources* **1998**, *71*, 107–110
59. J.B.J. Veldhuis, F.C. Eckes, L. Plomp, *J. Electrochem. Soc.* **1992**, *139*, L6–L8
60. G.J. Kraij, G. Rietveld, R.C. Makkus, J.P.P. Huijsmans, *J. Power Sources* **1998**, *71*, 215–217
61. A. L. Dicks, *J. Power Sources* **1998**, *71*, 111–122
62. A. Casanova, *J. Power Sources* **1998**, *71*, 65–70
63. H. Yasue, H. Kato, K. Takasu, *J. Power Sources* **1998**, *71*, 89–94
64. P.J. Kortbeek, R. Ottervanger, *J. Power Sources* **1998**, *71*, 223–225

65. J. Staniforth, K. Kendall, *J. Power Sources* **1998**, *71*, 275–277
66. T. A. Damberger, *J. Power Sources* **1998**, *71*, 45–50
67. R. Whitaker, *J. Power Sources* **1998**, *71*, 71–74
68. E. Gulzow, *J. Power Sources* **1996**, *61*, 99–104
69. PEM is sometimes referred to as “proton exchange membrane”, but this use is warmly discouraged see D.G. Lovering, *J. Power Sources* **1998**, *71*, 1
70. a) *Electrochim. Acta* **1998**, *43*(24, special issue), 3629–3846; b) M. Uchida, Y. Fukuoka, Y. Sugawara, H. Ohara, A. Ohta, *J. Electrochem. Soc.* **1998**, *145*, 3708–3713
71. S. A. Weiner, *J. Power Sources* **1998**, *71*, 61–64
72. T.R. Ralph, G.A. Hards, *Chem. & Ind.* **1998**, *5*, 337–342
73. F. Panik, *J. Power Sources* **1998**, *71*, 36–38
74. S. Kawatsu, *J. Power Sources* **1998**, *71*, 150–155
75. S.G. Chalk, J. Milliken, J. F. Miller, S.R. Venkateswaran, *J. Power Sources* **1998**, *71*, 26–35
76. S. Wasmus, A. Küwer, *J. Electroanal. Chem.* **1999**, *461*, 14–31
77. F. Mitlitsky, B. Myers, A. H. Weisberg, T. M. Molter, W. F. Smith (LLNL, Livermore, California) UCRL-JC-125220, *Portable Fuel Cell Conference*, Lucerne, Switzerland, 21–24 June **1999**
78. D. Aurbach, I. Weissman, A. Zaban, O. Chusid, *Electrochim. Acta* **1994**, *39*, 51–71
79. J.G. Thevenin, R.H. Muller, *J. Electrochem. Soc.* **1987**, *134*, 273–280
80. J. Ross Macdonald, *Impedance Spectroscopy*, Wiley–Interscience, New York, **1987**
81. E. Mengeritsky, P. Dan, I. Weissman, A. Zaban, and D. Aurbach, *J. Electrochem. Soc.* **1996**, *143*, 2110–2116
82. D. Aurbach, H. Gottlieb, *Electrochim. Acta* **1989**, *34*, 141–156
83. E. Peled, D. Golodnitsky, C. Menachem, D. Bartow, *J. Electrochem. Soc.* **1998**, *145*, 3482–3486
84. T. Osaka, T. Momma, Y. Matsumoto, Y. Uchida, *J. Electrochem. Soc.* **1997**, *144*, 1709–1713
85. M.B. Armand in *Fast Ion Transport in Solids*, W. Van Gool Ed., North-Holland, Amsterdam, **1973**, p. 665
86. P.G. Bruce, C.A. Vincent, *J. Chem. Soc. Faraday Trans.* **1993**, *89*, 3187–3203
87. M. Armand, *Solid State Ionics* **1994**, *69*, 309–319
88. D.F. Shriver, P.G. Bruce in *Solid State Electrochemistry*, P.G. Bruce Ed., Cambridge University Press, Cambridge, **1995**, pp. 95–118
89. C. Létourneau, D. Geoffroy, P. St-Germain, A. Belanger, R. Atanasoski, *15th Electric vehicle Symposium and Exhibition*, Brussels, 30 September–3 October **1998**, Abstr. 160
90. H. Cheradame, J.F. LeNest in *Polymer Electrolyte Reviews 1*, J.R. MacCallum, C.A. Vincent Ed., Elsevier, London, **1987**, pp. 103–138
91. X. Andrieu, J.P. Boeue, T. Vicédo, *J. Power Sources* **1993**, *43–44*, 445–451
92. J.M.G. Cowie, K. Sadaghianizadeh, *Solid State Ionics* **1990**, *42*, 243–249
93. C.V. Nicholas, D.J. Wilson, C. Booth, J.R.M. Giles, *Brit. Polymer J.* **1988**, *20*, 289
94. A. LeMehaute, G. Crepy, G. Marcellin, T. Hamaide, A. Guyot, *Polym. Bull.* **1985**, *14*, 233–237
95. D. Benrabah, D. Baril, J.-Y. Sanchez, M. Armand, G.G. Gard, *J. Chem. Soc. Faraday Trans.* **1993**, *89*, 355–359
96. R. Koksang, I.I. Olsen, D. Shackle, *Solid State Ionics* **1994**, *69*, 320–335
97. K.M. Abraham, H.S. Choe, D.M. Pasquariello, *Electrochim. Acta* **1998**, *43*, 2399–2412
98. G.B. Appetecchi, F. Croce, B. Scrosati, *Electrochim. Acta* **1995**, *40*, 991–997
99. M. C. Borghini, M. Mastragostino, S. Passerini, B. Scrosati *J. Electrochem. Soc.* **1995**, *142*, 2118–2121
100. G. B. Appetecchi, F. Croce, G. Dautzenberg, M. Mastragostino, F. Ronci, B. Scrosati, F. Soavi, A. Zanelli, F. Alessandrini, P.P. Prosini, *J. Electrochem. Soc.* **1998**, *145*, 4126–4132
101. G. B. Appetecchi, F. Croce, M. Mastragostino, B. Scrosati, F. Soavi, A. Zanelli, *J. Electrochem. Soc.* **1998**, *145*, 4133–4135
102. F. Croce, G.B. Appetecchi, L. Persi, B. Scrosati, *Nature* **1998**, *394*, 456–458
103. M. Mastragostino, F. Soavi, A. Zanelli, *J. Power Sources* **1999**, *82*, 729–733
104. G. Nagasubramanian, R.G. Jungst, D.H. Doughty, *J. Power Sources* **1999**, *83*, 193–203

105. M.B. Armand, *Materials for Advanced Batteries*, D.W. Murphy, J. Broadhead, B.C.H. Steel Eds., Plenum, New York, **1980**, p. 145
106. B. Di Pietro, M. Patriarca, B. Scrosati, *J. Power Sources* **1982**, 8, 289
107. P. Biensan, B. Simon, J.P. Pèrès, A. de Guibert, M. Broussely, J.M. Bodet, F. Pertont, *J. Power Sources* **1999**, 82, 906–912
108. T. Nagaura, K. Tozawa, *Prog. Batt. Solar Cells* **1990**, 9, 209
109. J.M. Tarascon, A.S. Gozdz, C. Schmutz, F. Shokoohi, P.C. Warren, *Solid State Ionics* **1996**, 86, 49–54
110. J.S. Xue, R.D. Wise, X.L. Zhang, M.E. Manna, Y.X. Lu, G. DuCharme, E.A. Cuellar, *J. Power Sources* **1999**, 80, 119–127
111. M. Winter, J. O. Besenhard, M.E. Spahr, P. Novák, *Adv. Mater.* **1998**, 10, 725–763
112. W.R. McKinnon, R.R. Haering in *Modern Aspects of Electrochemistry*, R.E. White, J.O'M. Bockris, B.E. Conway Eds., vol. 15, Plenum, New York, **1983**, pp. 235–304
113. M. Winter, J.O. Besenhard, *Electrochim. Acta* **1999**, 45, 31–50
114. T. Ohzuku, K. Nakura, T. Aoki, *Electrochim. Acta* **1999**, 45, 151–160
115. C. Julien, G.A. Nazri, *Solid State Batteries: Materials Design and Optimization*, Kluwer Academic Publishers, Boston, **1994**, pp. 1–96
116. M. Ue, K. Ida, S. Mori, *J. Electrochem. Soc.* **1994**, 141, 2989–2995
117. J.M. McGraw, C.S. Bahn, P.A. Parilla, J.D. Perkins, D.W. Readey, D.S. Ginley, *Electrochim. Acta* **1999**, 45, 187–196
118. A. Yamada, M. Tanaka, K. Sekai, *J. Power Sources* **1999**, 82, 73–78
119. Z. Jiang, K.M. Abraham, *J. Electrochem. Soc.* **1996**, 143, 1591–1598
120. R. Koksang, J. Barker, H. Shi, M.Y. Saidi, *Solid State Ionics* **1996**, 84, 1–21
121. D. Aurbach, M.D. Levi, K. Gamulski, B. Markovsky, G. Salitra, E. Levi, U. Heider, L. Heider, R. Oesten, *J. Power Sources* **1999**, 82, 472–479
122. T. Takada, H. Hayakawa, H. Enoki, E. Akiba, H. Sleg, I. Davidson, J. Murray, *J. Power Sources* **1999**, 82, 505–509
123. I.M. Kötschau, J.R. Dahn, *J. Electrochem. Soc.* **1998**, 145, 2672–2677
124. O. Mao, R.L. Turner, I.A. Courtney, B.D. Fredericksen, M.I. Buckett, L.J. Krause, J.R. Dahn, *Electrochemical and Solid State Letters* **1999**, 2, 3–5
125. K. Brandt, *Solid State Ionics* **1994**, 69, 173–183
126. M. Broussely, P. Biensan, B. Simon, *Electrochim. Acta* **1999**, 45, 3–22
127. J. Barker, R. Pynenburg, R. Koksang, M.Y. Saidi, *Electrochim. Acta* **1996**, 41, 2481–2488
128. A. Rougier, P. Graveau, C. Delmas, *J. Electrochem. Soc.* **1996**, 143, 1168–1175
129. M. Broussely, J.P. Planchat, G. Rigobert, D. Virey, G. Sarre, *J. Power Sources* **1997**, 68, 8–12
130. C. Delmas, M. Ménétrier, L. Croguennec, I. Saadoun, A. Rougier, C. Pouillier, G. Prado, M. Grüne, L. Fournès, *Electrochim. Acta* **1999**, 45, 243–253
131. J.M. Tarascon, D. Guyomard, *Electrochim. Acta* **1993**, 38, 1221–1231
132. A.R. Armstrong, P.G. Bruce, *Nature* **1996**, 381, 499–500
133. M.J. Duncan, F. Leroux, J.M. Corbett, L.F. Nazar, *J. Electrochem. Soc.* **1998**, 145, 3746–3757
134. S. Megahed, B. Scrosati, *J. Power Sources* **1994**, 51, 79–104
135. H. Kawai, M. Tukamoto, A.R. West, *J. Power Sources* **1999**, 82, 67–72
136. J.M. Paulsen, C.L. Thomas, J.R. Dahn, *J. Electrochem. Soc.* **1999**, 146, 3560–3565
137. B.B. Owens, S. Passerini, W.H. Smyrl, *Electrochim. Acta* **1999**, 45, 215–224
138. J. Yang, M. Winter, J.O. Besenhard, *Solid State Ionics* **1996**, 90, 281–287
139. J.R. Dahn, T. Zheng, Y. Liu, J. S. Xue, *Science* **1995**, 270, 590–593
140. L. Firlej, A. Zahab, F. Brocard, P. Bernier, *Synth. Metals* **1995**, 70, 1373–1374
141. G.T. Wu, C.S. Wang, X.B. Zhang, H.S. Yang, Z.F. Qi, P.M. He, W.Z. Li, *J. Electrochem. Soc.* **1999**, 146, 1696–1701
142. H. Azuma, H. Imoto, S. Yamada, K. Sekai, *J. Power Sources* **1999**, 82, 1–7
143. D. Aurbach, B. Markovsky, I. Weissman, E. Levi, Y. Ein-Eli, *Electrochim. Acta* **1999**, 45, 67–86
144. R. Yazami, *Electrochim. Acta* **1999**, 45, 87–97
145. R. Fong, U. von Sacken, J.R. Dahn, *J. Electrochem. Soc.* **1990**, 137, 2009–2013
146. Y. Idota, T. Kubota, A. Matsufuji, Y. Maekawa, T. Miyasaka, *Science* **1997**, 276, 1395–1397
147. P. Novák, R. Imhof, O. Haas, *Electrochim. Acta* **1999**, 45, 351–367

3 Principles of Semiconductor-assisted Photocatalysis for Waste Remediation

Marion C. Thurnauer, Tijana Rajh, and Nada M. Dimitrijevic

3.1 Introduction

Semiconductor photocatalysis has proven to be a promising technology for use in the cleanup of water contaminated with hazardous industrial by-products. Particulate semiconductors have proven to be light-harvesting materials and mediators in the photochemical degradation of several environmental contaminants [1–12]. Due to the large oxidation potential of photogenerated holes, oxidative degradation of the most resistant pollutants by photocatalysis can be achieved. Numerous reports of organic pollutant degradation, with mineralization to inorganic products in several cases, have been published [13–16]. Titanium dioxide, in particular, could be the catalyst of choice for a large variety of applications because it is cheap, non-toxic, and has redox properties which are favorable both for oxidation of many organic pollutants and for the reduction of a number of metal ions or organics in aqueous solution.

To date, the primary focus of TiO_2 -assisted photocatalysis studies has been on the destruction of organic pollutants in solutions, using photocatalytic oxidation. Anatase TiO_2 particulates are proven photooxidizers of a variety of organic compounds (phenols, chlorinated phenols, polychlorinated biphenyls (PCBs), dioxins, DDT, surfactants, saturated aliphatic hydrocarbons, *s*-triazine, etc) [17]. Photo-oxidation leads ultimately to complete degradation of these “pollutants”. However, the detailed mechanism of pollutant degradation differs from one pollutant to another. On the other hand, the common feature of the photocatalytic process always involves reactions via surface-trapped electrons and holes. The process occurs under ambient conditions, minimizes or avoids formation of intermediate products, and leads to complete oxidation of the substrates to CO_2 , thus offering a great potential as an industrial technology to detoxify wastewaters [18]. TiO_2 -assisted photocatalysis may also be useful in the removal of certain heavy metals, including mercury, silver, platinum, palladium, rhodium, and gold, via their reduction followed by deposition at the catalyst surface [17, 19, 20, 21].

Although TiO_2 is very effective from an energetic point of view, it is relatively inefficient. The main energy loss in all investigated systems is due to the recombination of charges generated in the illumination of semiconductor particles, which is manifested as relatively low efficiency of pollutant decomposition. Therefore, the main focus of research for application of semiconductor-assisted photocatalysis is to improve separation of charges and at the same time preserve or improve their redox properties. Additionally, large-bandgap semiconductors such as TiO_2 absorb only a fraction of the white light (5 %), and another issue of concern for the optimization of photocatalysts is to sensitize large-bandgap semiconductors in the visible region by dye or ligand adsorption onto large-surface-area metal oxides [22]. Other novel approaches focus on increasing the energy of the photons used for excitation of metal oxides (in the region of γ -, X- or far-UV-radiation) [23].

3.2 Colloidal Semiconductors

Semiconductors are generally crystalline materials which are assembled into arrays of repeating atomic (molecular) units. When similar atoms are brought together to form a crystal the wavefunctions of their electrons begin to overlap. In order to satisfy Pauli's Exclusion Principle, two electrons cannot have the same quantum numbers and therefore more than two electrons cannot occupy a single orbital. As a consequence, if N atoms are packed within the range of interaction, electrons of the same orbital have to occupy $2N$ different states, forming a band of states instead of discrete levels. Overlap of the energy levels occupied by existing electrons results in the formation of the valence band, while the overlap of the unoccupied excited states results in the formation of the empty conduction band. Between these two bands an energy gap is formed in which no electron states are allowed. It is the extent of the energy gap that determines whether a crystalline solid is a metal, a semiconductor, or an insulator. The energy distribution of the state depends strongly on the interatomic distance. The average amount by which the potential energy has dropped is related to the cohesive energy of the crystal. Since the interatomic distance in a crystal is not isotropic but rather varies with crystallographic direction, it can be expected that the banding of the energy states will vary with crystal planes. Allowed energy states have a parabolic dependence in the wave space for wave vector $\mathbf{k} \sim 0$ ([000]); however, additional minima can occur in a specific crystallographic direction (such as [111] or [110]).

3.2.1 Optical Properties of Semiconductors

The fundamental absorption refers to promotion of electrons from the valence to the conduction band. Due to the continuous nature of the energy bands, semiconductors absorb all the light below the threshold wavelength, which is the direct measure of the bandgap (E_g) energy (Eq. (1)).

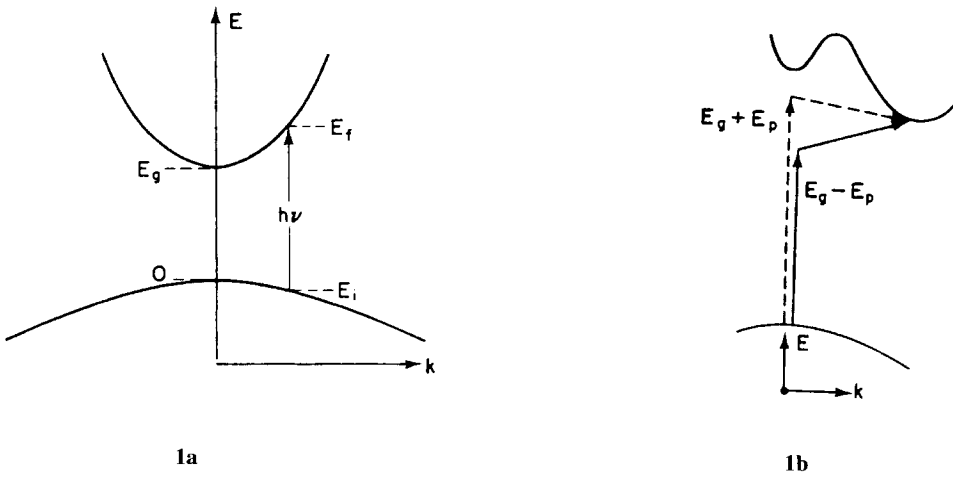


Figure 1. Schematic presentation of a) direct and b) indirect transitions in semiconductors [24].

$$\lambda_g[\text{nm}] = 1238.9/E_g[\text{eV}] \quad (1)$$

For exact determination of the bandgap energy one has to take into account the dependence of the absorption coefficient on the energy of absorbed photons, which differs for various semiconductors. In the case when the energy minimum of the conduction band and the energy maximum of the valence band occur at the same wave vector k value, typically $k = 0$, the transition is considered allowed and direct (Figure 1a). The transition probability, then, is independent of photon energy. Absorption, expressed in terms of a coefficient $\alpha(h\nu)$, defined as the relative rate of decrease in light intensity $L(h\nu)$ along its propagation path in this case is given by Eq. (2),

$$\alpha[h\nu] \propto (h\nu - E_g)^{1/2} [\text{cm}^{-1}] \quad (2)$$

$h\nu$ and E_g being expressed in electronvolts [24]. The graphical presentation of the square of absorption coefficient vs. photon energy is a straight line whose slope and intercept define the bandgap of the semiconductor.

In some materials, quantum selection rules forbid direct transitions at $k = 0$ but allow direct transition at $k \neq 0$. In this case the transition probability increases with k^2 , and the absorption coefficient has spectral dependence according to Eq. (3).

$$\alpha[h\nu] \propto (h\nu - E_g)^{3/2} [\text{cm}^{-1}] \quad (3)$$

In this case the plot of $\alpha^{2/3}$ vs. photon energy reveals the characteristic parameters of a semiconductor.

When the transition requires a change of momentum, as in anatase TiO_2 , an indirect transition between indirect valleys occurs. As a photon cannot produce a

change in momentum, conservation of momentum occurs via a phonon interaction. Among the broad spectrum of phonons, only those with the required momentum change are usable (longitudinal and transverse acoustic phonons). Each of these phonons has the characteristic energy E_p and can be either emitted or absorbed (Figure 1b). The absorption coefficient is then the sum of absorption coefficients associated with emitted and absorbed phonons (Eq. (4)).

$$\alpha(h\nu) = \alpha_a(h\nu) + \alpha_e(h\nu) \quad (4)$$

The α of each of these processes is proportional to the probability of interacting with phonons (i.e., proportional to a function of the number of phonons $f(T, E_p)$) and density of states:

$$\alpha(h\nu)_{a/e} \propto f(T, E_p)(h\nu - E_g \pm E_p)^2 \quad (5)$$

At very low temperatures, the phonon density is very small and therefore the probability of phonon absorption is also low. In this case one finds that the plot of the square root of α has a linear dependence on $h\nu$. At higher temperatures, however, the linear dependence breaks into two linear parts with different slopes corresponding to the emissive and absorptive processes.

3.2.2 Quantization Effect

When the particle size of the semiconductor crystallites is less than the de Broglie wavelength, depending upon the specific electronic properties of the semiconductor such as the effective masses of electrons and holes, very interesting and important effects become apparent. These effects arise because of the physical confinement of electrons and holes in potential wells defined by the crystallite boundaries. As a consequence, only those orbitals that fulfill the condition of having a node at the crystallite boundaries are allowed, i.e., only those orbitals that have $k = \pm n\pi/R$, where R is the radius of a particle, are allowed. The most general consequence of these boundary conditions is that the energy levels available for electrons and holes in the conduction and valence bands become discrete. They are quantized, rather than continuous [25]. However, the most obvious consequence of the boundaries is that the transition at $k = 0$ becomes forbidden, and this is manifest by an apparent increase in the bandgap of a semiconductor, which is inversely proportional to the values of the effective masses of electrons and holes; the magnitude of this increase is significant only for semiconductors with effective masses $\leq 0.5m_e$. These giant molecules (collective entities of 10^3 – 10^6 atoms) exhibit atom-like, size-dependent properties that are different from the properties of their constituents. Because of the relatively broad distribution of particle sizes in the earlier preparations of colloids, the spectral structure resulting from size-dependent properties was washed out. Various size-selective methods have been developed recently [26] that lead to extremely narrow particle distributions and pronounced structure of the absorption spectra. The optical spectra of spherical quantum dots were previously investigated using size-selective physical methods in order to avoid inhomogeneous line broadening

[27]. The quantization effects that result in a size-selective increase in the bandgap of CdTe are illustrated in Figure 2 [28]. The blue shift of the fundamental absorption edge, i.e., the increase in the effective bandgap with a decrease in particle size, is a direct consequence of the size quantization effect. Also, Figure 2 demonstrates that the oscillator strength of the first excitonic state in strong confinement regions (when $R < \text{Bohr radius}$) follows an inverse cube dependence on the particle diameter (increasing with $1/R^3$) due to the overlap of the electron and hole wavefunctions.

Quantization effects also greatly influence the charge transfer processes. The decrease in particle size results in a shift of the conduction band to the more negative values, and of the valence band to more positive ones. Hence, such ultrafine particles exhibit enhanced photoredox properties compared with the bulk material: the redox processes that cannot occur in a bulk semiconductor particle can be facilitated in quantized particles. On the other hand, an increase in the effective bandgap might lead to decreased stability of such particles, because the position of the cathodic and anodic corrosion potentials might fall between the band edges. It was shown that a shift in the reduction potential of about 1.2 V occurs for quantized CdTe particles, a material with extremely low effective masses of electrons and holes. The enhanced photoredox properties of quantized semiconductor particles was undoubtedly proven when the reduction of water to H_2 was achieved with photogenerated electrons from quantized HgSe [29]. The use of bulk HgSe under the same conditions did not result in hydrogen production.

3.2.3 Space Charge Layer and Band Bending

When a semiconductor is brought into contact with an electrolyte, a migration of charge carriers occurs until the Fermi level of the semiconductor is equilibrated with the chemical potential of the electrolyte [30]. This results in the formation of a space charge layer in the surface region of a semiconductor and a Helmholtz double layer in the electrolyte adjacent to the semiconductor surface. The electrons are transferred in and out of a semiconductor surface depending on the relative position of the initial Fermi level of the dry semiconductor and the electrochemical potential of the electrolyte. In the case when the Fermi level of a dry semiconductor is more negative than the electrochemical potential of the electrolyte (n-type semiconductor; electrons are the majority carriers), the electrons leave the semiconductor, resulting in a shift of the Fermi level toward more positive potentials (Figure 3) [30]. The depletion of the surface region creates a barrier for further transfer of electrons to the electrolyte which is manifest by band bending in the space charge layer. In the opposite case (p-type semiconductors) the Fermi level has a negative shift, causing accumulation of electrons in the space charge region. Photons absorbed in the depletion layer produce electron–hole pairs that separate under the influence of the electric field. This separation of the carriers causes the Fermi level in the semiconductor to return toward its original position, i.e., the energy position before a semiconductor/electrolyte junction was established. The space charge region in the solid is fairly large, approximately 1000 Å, while the Helmholtz double region together with the diffuse Helmholtz layer is 100 Å [31]. However, when the size of a semiconductor approaches the size of the space charge layer, the small particle is

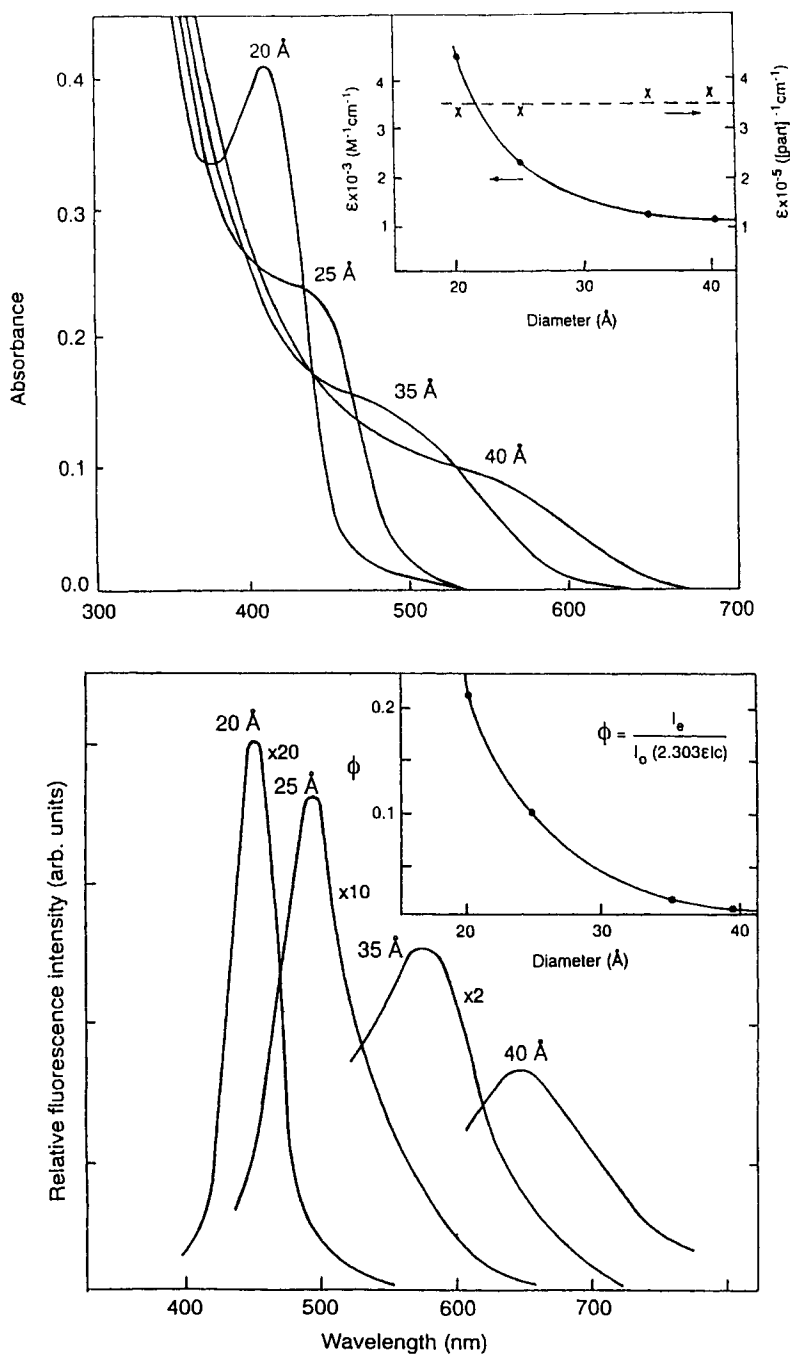


Figure 2. Absorption (top) and emission (bottom) spectra of CdTe with different particle sizes [28]. (Reprinted with permission from T. Rajh, O. I. Micic, A. J. Nozik, *J. Phys. Chem.*, **1993**, 97, 11999. Copyright (2000) American Chemical Society.)

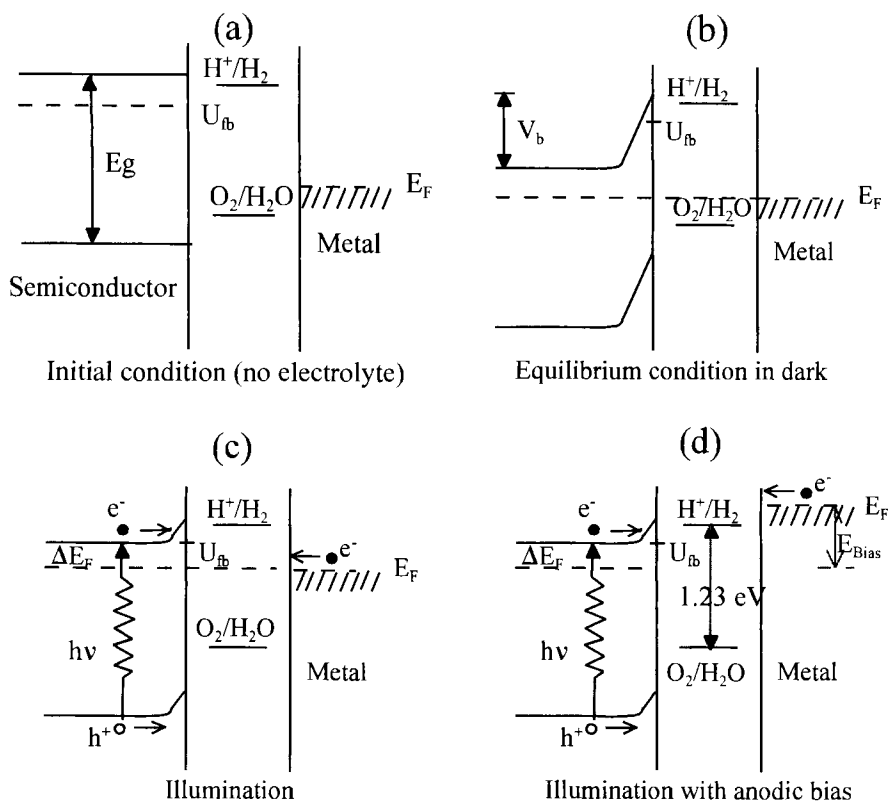


Figure 3. Sequence of energy level diagrams for semiconductor/metal photoelectrolysis cell [30].

depleted almost completely of charge carriers and band bending is negligible. The particles are too small to develop a space charge layer and, in this case, the potential difference resulting from transfer of a charge from a semiconductor to the electrolyte has to drop within the Helmholtz layer (neglecting diffuse layer contributions). As a consequence the position of the band edges of semiconductor particles will shift with the shift in the Fermi level [32]. This has an important consequence because, upon illumination, it allows the negative shift of a conduction band edge of n-type colloidal semiconductors.

3.2.4 Energy Band Structure of TiO_2

Titania particles in the small-particle regime have a tetragonally distorted octahedral anatase structure in which every titanium cation is surrounded by six oxygen atoms in an elongated octahedron geometry (D_{2d}). Due to the resultant crystal field, the 3d levels of Ti^{4+} , which form the conduction band of TiO_2 , are split into $3t_{2g}$ and $3e_g$ sublevels. The unequal length of the six cationic ligand bonds to titanium produces a splitting of the t_{2g} and e_g orbitals into two subsets (Figure 4). Symmetry

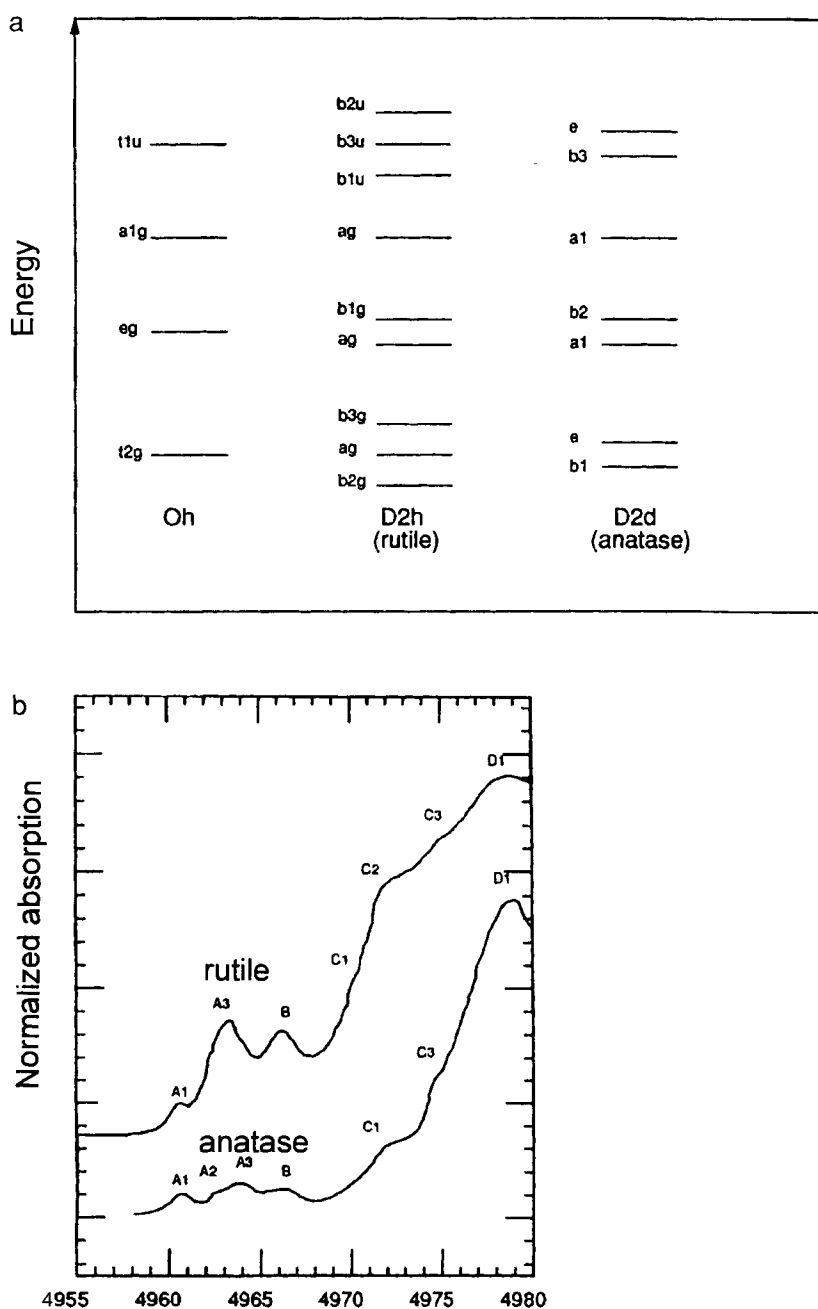


Figure 4. Energy level diagram of the LUMO of a $[\text{TiO}_6]^{8-}$ cluster, a) with O_h , D_{2h} (rutile), and D_{2d} (anatase) symmetry, in conjunction with b) experimental Ti K-edge XANES spectra [33]. (Reprinted with permission from Z. Y. Wu, G. Ouvrard, P. Gressier, C. R. Natoli, *Phys. Rev. B*, **1997**, 55, 10382. Copyright (2000) American Physical Society).

considerations show that the p orbitals of the central Ti atom mix with d orbitals of neighboring Ti atoms and 3d–4p-hybridized sub-bands form the conduction bands of anatase TiO₂. This is exhibited in the X-ray absorption of near-edge structure (XANES) spectrum of TiO₂ [33].

The lowest band of TiO₂ is formed by the b₁ and e sub-bands, which have mainly π character and can overlap in p-type fashion with oxygen p_⊥ orbitals having anionic character. The result is a series of bands in reciprocal space with the maximum of the valence band and minimum of the conduction band in the center of the Brillouin zone (BZ). However, this direct transition $\Gamma_3 \rightarrow \Gamma_1$ is dipole-forbidden (because the HOMO is formed as a mixture of the oxygen p_x and p_y orbitals which correspond to b₁ in *D*_{2d} symmetry, and the LUMO is formed from the lowest of the 3t_g orbitals which correspond to b₁ in *D*_{2d} symmetry). The first allowed transitions are the indirect transitions from the X point at the edge of the BZ to the Γ point in the center of the BZ. The two lowest transitions are X₁ \rightarrow Γ_1 observed with absorption of light with energy 3.026 eV and perpendicular to the crystalline *c* axes, and X₂ \rightarrow Γ_1 observed with absorption of light with energy 3.06 eV and parallel to the crystalline *c* axes. However, the transition $\Gamma_3 \rightarrow X_1$ of 3.19 eV is allowed both with parallel and perpendicular light, accounting for the increase in the transition probability at this energy corresponding to the bandgap energy of anatase TiO₂. The curvature of the bands at these extremes is very small, indicating large effective masses that are determined by different authors to range from 5*m*_e to 30*m*_e [34, 35]. The precise value of the electron effective mass in anatase remains elusive, primarily because of the difficulty of preparation of anatase single crystals. The anatase crystal structure is dominant in the nanocrystalline particle regime, but the rutile structure is the more stable form for bulk crystals. Because of the large effective masses, however, the quantization effect in titania particles is negligible for particle sizes >15 Å, and therefore unimportant. The other significant feature of TiO₂ particles is that the curvature of the wavefunctions on the top of the valence band is larger than the curvature of the bands in the conduction band. This is different from the situation for most semiconductors and indicates that the effective mass of the hole is smaller than the effective mass of the electrons. In the formation of the exciton pairs, a dominant process in small semiconductor particles, the photogenerated holes orbit around the heavier photogenerated electrons. This also suggests that in small titania particles, photogenerated holes would be more likely trapped at the surface of the particle, while electrons would first find trapping sites in the particle interior.

3.3 Basic Mechanisms of Semiconductor-assisted Photocatalysis

3.3.1 Photogeneration of Charge Pairs and Intrinsic Properties of Semiconductors

Semiconductor particles behave as microelectrochemical cells. Absorption of light of energy greater than the bandgap of semiconductor materials generates conduction-

band electrons and valence-band holes. Semiconductor particles are light-harvesting units offering the following distinct advantages in heterogeneous photocatalyzed processes:

- 1) high absorption cross-section of the incident photons;
- 2) fast carrier diffusion; and
- 3) suitable redox levels of the valence and conduction band edges that can yield high efficiencies in converting light energy to useful redox events.

Metal oxides have band structures that are characterized by the existence of an energy gap that separates the highest occupied energy levels (valence band) from the lowest unoccupied energy levels (conduction band). Excitation of, for example, TiO_2 with UV light with energy greater than the bandgap (>3.2 eV) promotes electrons from the valence into the conduction band and generates electron-hole pairs that can be exploited in various processes at the particle interface (Eq. (6)),



where e_{cb}^- is a conduction band (CB) electron and h_{vb}^+ is a valence band (VB) hole. Photogenerated carriers migrate to the particle surface and participate in reduction and oxidation processes at the surface. The thermodynamic limit for the reaction that can be carried out with the photogenerated charge carriers is given by the position of the band edges (i.e., flat band potential). For example, if a reduction of a particular species (A) in the solution is to occur, the conduction band of the semiconductor must be more negative than the relevant redox level, while the oxidation of a particular species (D) by valence band holes requires that the valence band be more positive than the relevant redox potential (Figure 5). Thus, the rela-

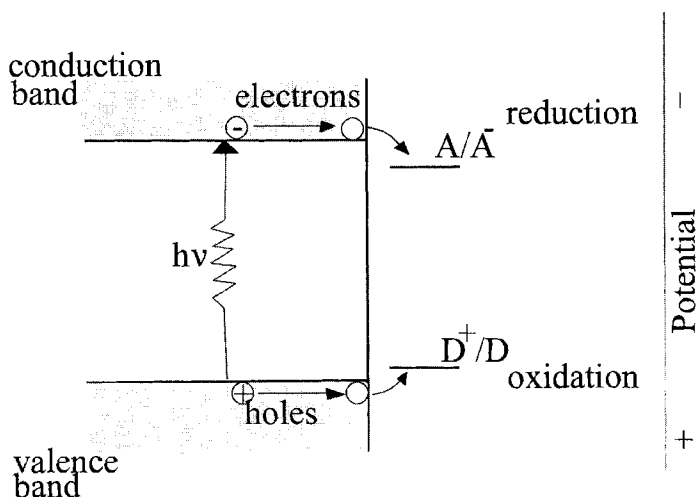


Figure 5. Salient features of the electronic structure of semiconductors.

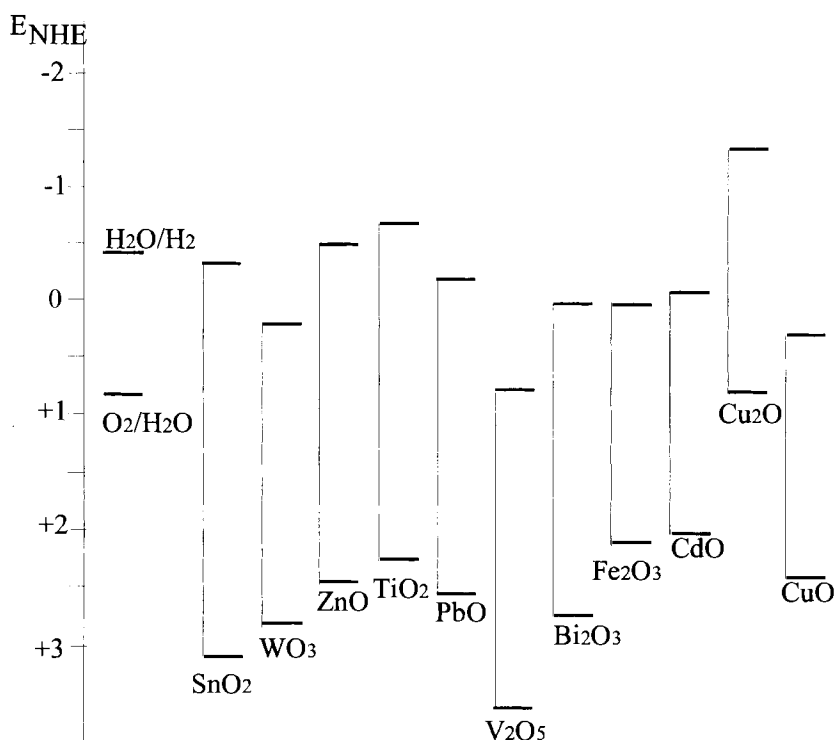


Figure 6. Position of band edges for various semiconductors in electrolytes at pH 7.

tive positions of the band edges in a given semiconductor determine their redox functioning. The threshold energy needed for absorption of light (i.e., the bandgap energy) and the relative positions of the band edges (i.e., the flat band potential) are intrinsic material properties of each semiconductor.

The positions of the valence (VB) and conduction bands (CB) vs. vacuum of the various metal oxides which can be used for removal of pollutants are shown in Figure 6. For example, at pH 7, the potential of conduction band electrons of TiO₂ is -0.54 V (vs. NHE) and that of valence band holes is $+2.7$ V. All redox couples with the standard redox potential more positive than that of the CB electrons and more negative than that of the VB holes can, in principle, be reduced and oxidized respectively on the colloid surface.

In single-crystal electrodes the electric field in the depletion layer of the semiconductor separates the charges and decreases the probability of charge-pair recombination [30]. However, in small-particle colloids such a depletion layer does not exist due to the nanometer particle size, and there is no electrical field to separate the charges [36]. Due to the large recombination rate in small-particle colloids, the lifetime of charged pairs is very short, and only very fast reactions with adsorbed species can lead to efficient charge separation. In order to facilitate chemical pro-

cesses, rapid recombination of the charges must be prevented by removal of one or both of the charge carriers from the regions where they are formed.

3.3.2 Charge Pair Separation and Charge Carrier Trapping

Semiconductor particles have small sizes and their photoelectrochemical properties may not be the same as those of large bulk material. The particle diameter can be smaller than the thickness of the space charge layer and in that case the details of charge separation may not be the same as in a compact semiconductor electrode. The particles also have a large surface-to-bulk ratio and surface states are therefore especially important in the interpretation of the photoelectrochemical behavior of particulate semiconductors. Therefore, once the electron-hole pairs are generated in the conduction/valence bands, the loss of excess energy through their localization on the trapping sites is more favorable than the radiative, band-to-band, recombination process [37].

Electrons and holes that are generated in particulate semiconductors are localized at different defect sites on the surface and in the lattice of the particles. Electron paramagnetic resonance (EPR) results have shown that electrons are trapped as two reduced metal centers—Ti(III) sites—coordinated either [38, 39] 1) with anatase lattice oxygen atoms only, or 2) with OH or H₂O; the holes are trapped as oxygen-centered radicals covalently linked to surface titanium atoms [40] (Figure 7). This is summarized by Eqs. (7)–(9).

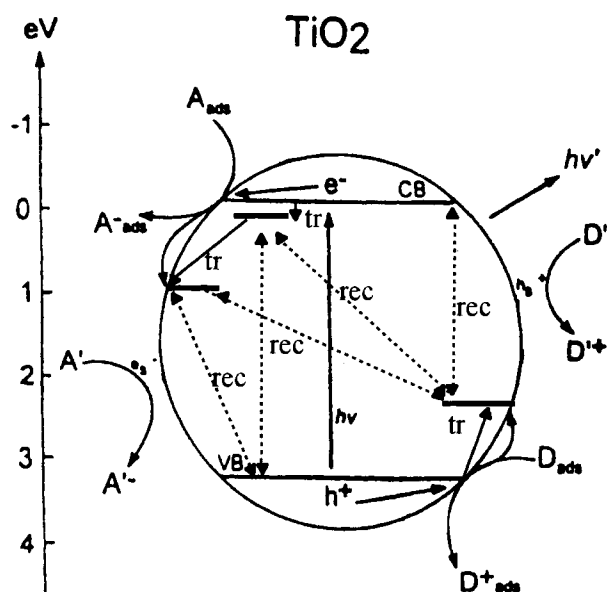
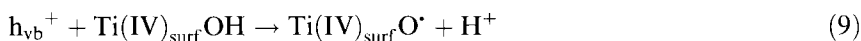
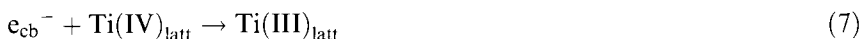


Figure 7. Salient features of the electronic structure of trapping sites in nanocrystalline anatase particles.



The trapping sites are deep and the photogenerated carriers lose a significant amount of energy in the trapping process, but do not attain a large charge separation distance. The position of the Fermi level in small-particle colloids (50 Å) was determined by pulse radiolysis to be slightly more negative (100 mV, shown in Figure 8a) than the flat band potential of single-crystal electrodes [41]. The difference is the consequence of the presence of negative charges on the large surface of small-particle colloids. Using EPR, the relative positions of the levels for electron-trapping sites was found to be the following: $-e_{cb}^- > -\text{Ti(III)}_{\text{latt}} > -\text{Ti(III)}_{\text{surf}}\text{OH}$. The surface trapping sites $-\text{Ti(III)}_{\text{surf}}\text{OH}$ were shown to have optical absorptions peaking at $\lambda_{\text{max}} = 600$ nm [41]. The position of the absorption maximum indicates that the surface electron-trapping sites are deep traps. Therefore, the photogenerated electrons lose significant reducing power in the surface localization process and could not be used effectively for the reduction of species present in the electrolyte.

Similarly, the position of the hole-trapping site was determined to be deep into the mid-gap region, ranging from 2.0 V at pH 3 to 1.5 V at pH 10 vs. NHE (Figure 8b) [42]. Compared with the oxidative power of valence band holes of 2.9 V at pH 3 and 2.5 V at pH 10, one can see an energy loss of almost 1 eV upon trapping. Nevertheless, the oxidative power of trapped holes is still extremely high and can decompose the majority of organic compounds in wastewaters. The only disadvantage is that oxidation is nonselective.

3.3.3 Charge Carrier Recombination and Interfacial Electron Transfer

After they are trapped, charge carriers can either undergo interfacial charge transfer in which they react with redox couples in the surrounding medium, or they can experience electrostatic attraction and recombine. Because the particle diameter is typically smaller than the thickness of the space charge layer, there is no band bending in small particle colloids. Thus, there is no electrostatic field that would drive charge pair separation, and charge pairs are mainly consumed in radiative and nonradiative recombination processes. Different recombination pathways are shown schematically in Figure 7. Most of the recombination processes are nonradiative in TiO_2 , and mainly involve trapped electrons and holes:



Unlike the single-crystal electrodes in which band bending allows efficient charge

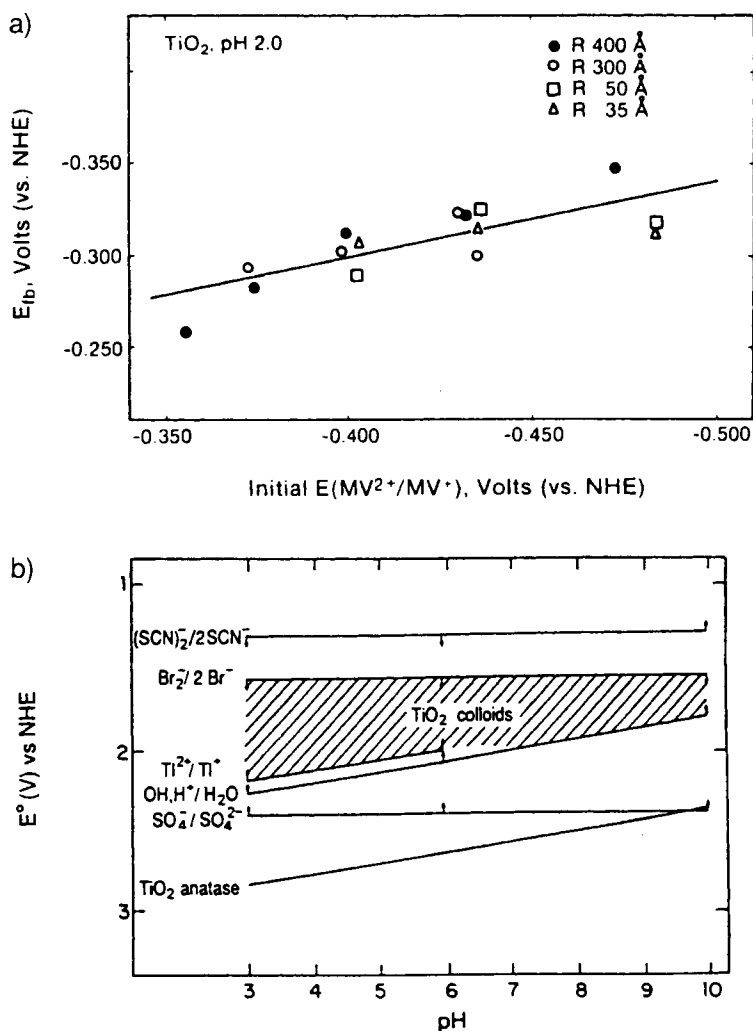


Figure 8. a) Energy level position in nanocrystalline TiO_2 particles of flat band [41]. (Reprinted with permission from N. M. Dimitrijevic, D. Savic, O. I. Micic, A. J. Nozik, *J. Phys. Chem.*, **1984**, 88, 4278. Copyright (2000) American Chemical Society). b) Energy level position of surface-trapped holes [42]. (From O. I. Micic, T. Rajh, M. V. Comor, in *Electrochemistry in Colloids and Dispersions*. (Eds.: R. A. Mackay, J. Texter), VCH, New York, **1992**, p. 457. Reprinted by permission of John Wiley & Sons, Inc.).

separation beyond their correlation distance, in small-particle colloids electron transfer is efficient only if electron donor or acceptor molecules are strongly associated with the particle surface. The overall quantum efficiency for interfacial charge transfer is determined by two critical processes. They are the competition between the free carrier recombination and trapping (time scale of picoseconds) [43]

followed by the competition between trapped carrier recombination and interfacial charge transfer (time scale of microseconds) [44]. Due to the short lifetime of charge carriers, one or both of those formed during illumination have to be removed from the particle before their recombination. This situation can be achieved only by fast reaction with adsorbed species.

3.3.4 Nature of Trapping Sites

In order to be able to block the surface trapping sites and convert them into coupling agents for interfacial electron transfer, one has to determine the nature of trapping sites at the molecular level. It was suggested that interfacial electron transfer in TiO_2 colloids occurs via surface Ti atoms which are coordinated with solvent molecules [45]. Meanwhile, the hole transfer occurs via surface oxygen atoms covalently linked to surface titanium atoms [40]. Both trapping sites have been investigated by several spectroscopic techniques, such as flash photolysis [43, 46], pulse radiolysis [41, 42, 47], and EPR techniques [38, 39, 40].

The coordination environment of surface Ti atoms of particles of different sizes was studied using XANES [48]. Reduction of the particle size was found to result in changes in the relative intensities and peak positions in the pre-edge features of the Ti K-edge spectrum (Figure 9). The XANES results suggest that coordination of Ti surface atoms changes from six-coordinate (octahedral) in 500 Å to pentacoordinate (square pyramidal) in small-particle colloids. The changes in the coordination environment are observed for particle sizes below 200 Å and this distortion of the bond length accounts for the large curvature of small particles and converts surface sites into more reactive “corner defects”.

Detailed investigation of excess holes in TiO_2 colloids reveals the nature of the hole-trapping sites. While pulse radiolysis enables investigation of the kinetics of both hole trapping and reactions of trapped holes, EPR spectroscopy provides a probe of the molecular environment of paramagnetic intermediates on oxidized surfaces. Analysis shows that $\text{O}^{\bullet-}$ radicals that are covalently bound to surface Ti atoms are the primary traps of photogenerated holes. This analysis gives direct evidence that photoinduced holes are located at the colloid surface (nonaxial symmetry) and are not ejected as free hydroxyl radicals (Figure 10). However, Sunada and Heller [49] have reported that upon surface modification with strongly coupled alkane silane modifiers, these deep trapping sites are removed and the formation of highly reactive hydroxyl radicals was observed.

3.3.5 Adsorption

The strong correlation between degradation rates and concentrations of organic pollutants adsorbed on the surface [11, 50] implies that photomineralization requires adsorption. In general, the kinetics of photodegradation of organic substrates sensitized by TiO_2 on steady-state illumination fits a Langmuir–Hinshelwood adsorption kinetic scheme, i.e. Eq. (13),

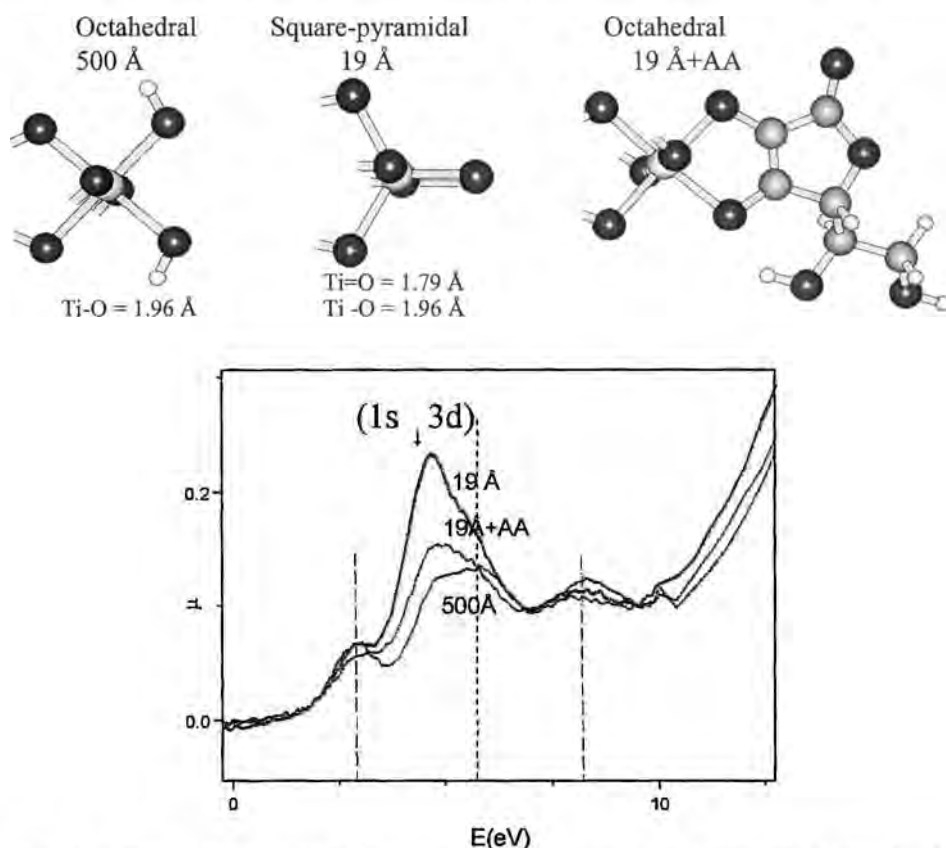


Figure 9. Schematic presentation of the coordination environment of different particle sizes of TiO₂ derived from investigation of XANES studies of the pre-edge Ti K-edge structure [63]. (Reprinted with permission from T. Rajh, J. Nedelkovic, L. X. Chen, O. Poluektov, M. C. Thurnauer, *J. Phys. Chem. B*, **1999**, *103*, 3515–3519. Copyright (2000) American Chemical Society.)

$$R_i = -\frac{d[S]_i}{dt} = \frac{k_s K_s [S]_i}{1 + K_s [S]_i} \quad (13)$$

where R_i is the initial rate of substrate removal, $[S]_i$ is the initial concentration of the organic substrate, K_s is the Langmuir adsorption constant of species S on the surface of TiO₂, and k_s is a proportionality constant which provides a measure of the intrinsic reactivity of the photoactivated surface with S. It was found that the value of K_s is not exactly equivalent to the Langmuir adsorption isotherm for the semiconductor in the dark; additionally, it was found to be dependent on the rate of light absorption (I) as well as the concentration of electron acceptor (commonly O₂). Detailed analysis of the adsorption kinetics on TiO₂ was presented by Mills and Le Hunte [51]. The overall quantum efficiency of photodegradation is defined

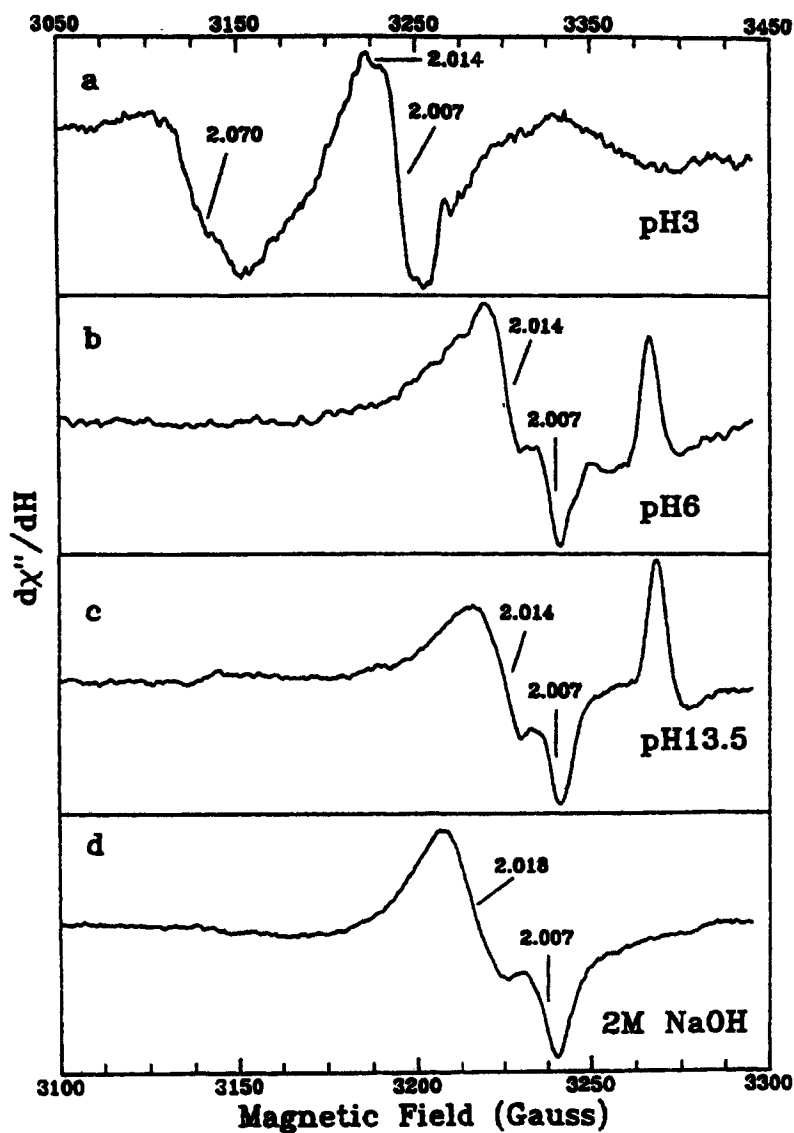


Figure 10. EPR spectra of TiO_2 colloids under illumination with a 308 nm excimer laser [40]. (Reprinted with permission from O. I. Micic, Y. Zhang, K. R. Cromack, A. D. Trifunac, M. C. Thurnauer, *J. Phys. Chem.*, **1993**, 97, 7277. Copyright (2000) American Chemical Society.)

by Eq. (14)

$$\Phi = \frac{\text{rate of reaction}(R_i)}{\text{rate of photon absorption}(I)} \quad (14)$$

and is therefore directly proportional to the adsorption.

The main conclusion from the above measurements is that a critical step in photodegradation is adsorption of the organic substrate on the surface. Therefore the parameters that control photodegradation are directly related to the parameters that govern adsorption processes, and include van der Waals forces, dipole–dipole interaction, ion-exchange, hydrogen bonding, hydrophobic interactions, π – π interactions, and donor–acceptor interactions.

3.4 Enhanced Charge Separation: Route for Efficient Photodegradation

3.4.1 Metallization of Semiconductor Particles

The addition of metal particles to semiconductor photocatalysts increases the photocatalytic activity of these systems because metals efficiently scavenge photo-generated electrons [52]. In fact, metallized semiconductors have been utilized as solar-absorbing coatings and as photocatalysts in the remediation of groundwater contaminants [52, 53]. There have been several photocatalytic studies of platinized titanium dioxide. In solution, Pt/TiO₂ is found to increase the photodecomposition rate of several organic compounds compared with that in the presence of neat TiO₂ [54–58].

Anpo et al. [59] studied Pt-loaded TiO₂ encapsulated in Y-zeolites, and found that TiO₂ photoluminescence is efficiently quenched in the presence of Pt. They have also found efficient electron transfer from the electrons trapped on TiO₂ particles (Ti³⁺) to platinum metal islands, thus promoting charge separation. Enhanced charge separation prevents the reaction between carbon radicals and OH radicals formed on different sites, this promotes the reaction between the carbon radicals and H atoms formed on the Pt metal resulting in formation of CH₄.

Illumination of metal-coated semiconductor particles leads to the accumulation of trapped electrons. Islands of noble metals (Pt, Rh, and Pd) on the surface of particles have higher electron affinity and therefore upon charge pair formation electrons are transferred from the semiconductor particle onto the metal islands. Due to the decreased recombination rate and high electron affinity of noble metals, more than one electron can be stored on metallized particles. Therefore, metal-coated particles can be used for subsequent simultaneous injection of multiple charges, and the reduction of compounds that cannot proceed via a one-electron reduction process. In these processes the crucial parameter that governs charge separation processes is the coupling between semiconductor particles and the metal

islands. Thus a good quality interface, which results in the overlapping of Fermi levels between semiconductor and metal, has to be obtained using photodeposition processes [60].

3.4.2 Surface Modification

The approach that constructively uses surface defect sites and converts them into selective coupling agents tailored for specific bindings of photodegradable substrates is based on surface modification. Photogenerated electrons lose significant energy in the trapping processes at the surface and could not be used effectively for redox chemistry. By blocking the defect sites with appropriate surface modifiers one can enhance the redox properties of photogenerated charges, and at the same time enhance the rate of photodegradation by enhancing the adsorption, i.e., local concentration, of pollutants on the particle surface. The latter will also affect the Fermi level of the metal oxide colloids [61].

Metal oxide colloids have been effectively coupled with multifunctional ligands containing carboxyl groups that bind to the surface of nanoparticles [39]. One can rationally design optimal photocatalysts by tailoring other functional groups for selective adsorption of specific pollutants. For example, extensive work on surface modification for removal of heavy metal ions has recently been performed [62]. The surface of colloidal TiO_2 was modified with a series of bidentate and tridentate organic compounds that have mercapto, carboxyl and amino groups in different relative positions, along with attached hydrocarbon chains of varying lengths.

Analysis of the structural and redox properties of surface-modified TiO_2 colloidal particles together with the dynamics of their photochemistry has indicated principles for the design of an optimal surface modifier for the reduction of heavy metal ions such as lead or cadmium. It was found that the surface modifier must contain a carboxyl group to bind to the colloid surface and at the same time to bind Pb^{2+} and Cd^{2+} ions. A mercapto group that is in an α position relative to a carboxyl group enhances adsorption of both surface modifier and heavy metals to small-particle TiO_2 colloids. The surface modifier must have a hole trap that enhances photo-generated charge-pair separation distances. In these systems, side hydrocarbon groups such as the $-\text{CH}_3$ group in thiolactic acid provide a trapping site for holes. In principle, the aliphatic group can be extended for enhanced charge separation and for the design of the system in which the hydrophobic aliphatic or aromatic part of a surface modifier is to be used selectively for the oxidation of organic compounds.

It was found that surface derivatives modify the redox properties of TiO_2 particles if a surface modifier is an electron-donating species, and that the crucial parameter for effective removal of heavy metal ions is the trade-off between enhanced redox properties of TiO_2 by surface modification and the enhanced redox potential of chelated metal ions. Surface modification can lead to the appearance of a charge transfer complex with small-particle TiO_2 colloids that have an optical absorption threshold at ~ 730 nm. The red shift of the optical absorption provides improved optical properties for use of visible light, i.e., for solar energy conversion [63].

3.4.3 Dye Sensitization

Another aspect of surface modification of semiconductor particles is the extension of their photoresponse toward the visible region. The photocatalytic activity of TiO_2 is limited only to the UV region, and hence solar energy cannot be effectively harvested. Dye sensitization of TiO_2 extends the light absorption and conversion capacity of TiO_2 to the visible spectral region. This is often achieved by attaching sensitizing molecules by direct adsorption or covalent linkage to the particle surface. Several dyes, exhibiting high absorptivity in the visible region, such as porphyrins, ruthenium(II) trisbipyridine, rhodamine, cyanines, and metal phthalocyanines, have been used as sensitizers for TiO_2 [64–68]. The sensitization is achieved by excitation of the dye followed by charge injection from the dye into the conduction band of the semiconductor (Eqs. (15) and (16)).



Because the singlet excited state of a dye is short-lived, it is essential to adsorb these dyes on the particle surface with strong chemical coupling so that electron transfer can occur within the lifetime of the singlet excited state. Coupling of dyes to the TiO_2 surface plays a critical role in achieving fast forward electron transfer and slow back reaction. For example, enhanced degradation of organic pollutants was found for TiO_2 modified with iron(III) phthalocyanines as compared with unmodified TiO_2 . The mechanism is attributed to the cooperative functions of the two components of the photocatalyst (dye and TiO_2). One of the suggested mechanisms of mineralization of organic compounds in the presence of phthalocyanines involves metal–oxene and metal–peroxo types of intermediates that act as the reactive species. Another possibility is that ligation enables enhanced concentration of organic pollutants on the semiconductor surface, which in turn enhances the rate of pollutant destruction.

3.5 Radiation-induced Catalysis on Semiconductor Surfaces

Metal oxides such as SiO_2 and Al_2O_3 have large bandgaps (9.0 and 7.0 eV, respectively) and require high-energy excitation to produce charge separation. Interaction of ionizing radiation with metal oxide semiconductors and dielectrics has been the subject of a number of studies [69, 70] and was found to result in electron excitation from the highest occupied level (valence band) to the lowest unoccupied level (conduction band). Primarily, interaction of ionizing radiation with solids gives rise to energy transfer to the solid medium through inelastic collisions that result in generation of secondary electrons which lose their energy in further collisions with atoms of the solid medium and create a chain formation of radical pairs (Figure

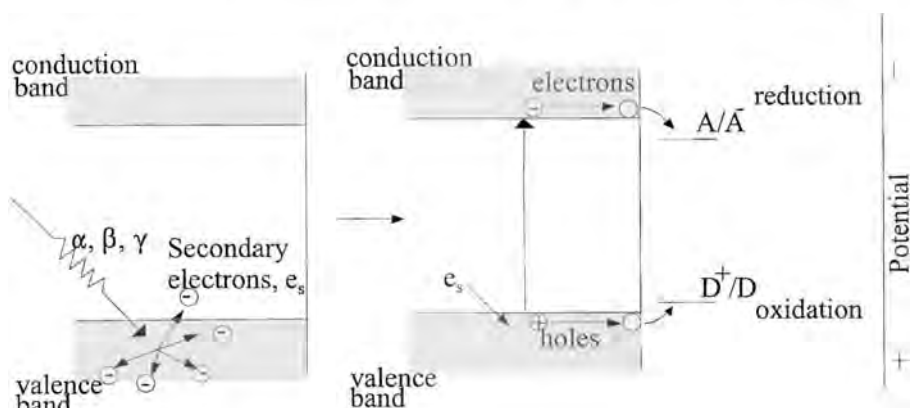


Figure 11. Salient features of the electronic structure of semiconductors under ionizing radiation.

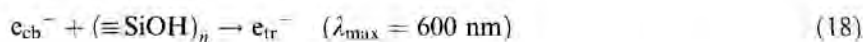
11). These radicals have extremely high potential energy and are able to react non-selectively with adsorbed species. Large radiation doses (>10 kGy) produce atom displacements in the crystal lattice, whereas at lower doses (<100 Gy) adsorbed species are degraded by transfer of the energy initially absorbed by the solid to the adsorbate.

Excitation of TiO_2 particles with ionizing radiation is equivalent to their photo-excitation [69] and generates electron-hole (e^-/h^+) pairs that can be exploited in various processes at the particle interface (Eq. (17)):



The generated carriers migrate to the semiconductor/solution interface where they can oxidize/reduce molecules in solution (Figure 11). The process is analogous to photocatalysis and all the parameters that determine efficient degradation of adsorbed organic pollutants in photocatalysis are present in radiation-induced catalysis. As the relative position of the band edges in a given semiconductor determines their redox functioning, the advantage of radiation-induced catalysis is in the use of large-bandgap semiconductors with thermodynamically very powerful conduction band electrons and valence band holes.

Alumina and silica with high surface areas are among the most examined catalysts [23]. Trapping of free charge carriers has led to the observation of surface-trapped electrons and holes in hydroxylated and in dehydroxylated SiO_2 . Trapping of conduction band electrons results in different trapping sites, depending on the conditions of the surface. Pre-existing defects such as peroxy radicals result in long-lived radicals. However, hydroxylation of the surface introduces short-lived color centers (Eq. (18)).



It has been shown that these visible color centers catalyze chemical reactions [71]. It was recently demonstrated that absorption of ionizing radiation by 22 nm SiO_2 particles suspended in aqueous solutions results in the appearance of hydrated electrons [72], but the holes generated in the particles do not cross the particle/water interface to generate OH radicals [73]. The radiation-induced reductive catalytic degradation of hexachlorobenzene (HCB) adsorbed on alumina colloids was also recently demonstrated [74]. These studies suggest that charge separation and accumulation necessary for the occurrence of multielectron transfer reactions is achievable using high-energy radiation (such as γ -rays or MeV-energy electrons) in the presence of large-bandgap semiconductors.

3.6 Summary

Photoinduced degradation of pollutants is based on the unique properties of anatase TiO_2 and the semiconductor/electrolyte junction. The energetics and kinetics of photoinduced charge transfer reactions across the semiconductor/electrolyte interface are parameters that define the efficiency of photochemical degradation of environmental contaminants. The major advantage of semiconductor-assisted photocatalytic degradation is the great ease with which the semiconductor/electrolyte junction is formed. The semiconductor is simply immersed in the electrolyte, and therefore very small, nanocrystalline particles with extremely large surface areas can be used. This is of significant importance because all previous studies indicate that the parameters that control photodegradation are directly related to the parameters that govern the adsorption processes. However, the main energy loss in all the systems investigated is due to the recombination of charges generated in the illumination of semiconductor particles, which is manifest as a relatively low efficiency of pollutant decomposition. Therefore, the main focus of this review was to understand and discuss the parameters that control charge separation efficiency, and to discuss strategies for improving the overall quantum efficiency of photoassisted degradation of pollutants.

Acknowledgment

The authors acknowledge the insights gained from discussions with Dr. B. Ruscic on molecular orbital transitions in different crystalline structures of TiO_2 . This work was supported by the US Department of Energy, Office of Basic Energy Sciences, Division of Chemical Sciences, under contract W-31-109-Eng-38.

References

1. H. Al-Ekabi, N. Serpone, E. Pelizzetti, C. Minero, M. A. Fox, R. B. Draper, *Langmuir*, **1989**, 5, 250.
2. H. Gerisher, A. Heller, *J. Electrochem. Soc.*, **1992**, 139, 113.
3. *Photocatalysis—Fundamentals and Applications* (Eds.: N. Serpone, E. Pelizzetti), John Wiley and Sons, New York, **1989**.

4. M. A. Fox, *Top. Curr. Chem.*, **1987**, 72, 142.
5. D. F. Ollis, *Environ. Sci. Technol.*, **1985**, 19, 480.
6. *Photocatalytic Purification and Treatment of Water and Air* (Eds.: D. F. Ollis, H. Al-Ekabi), Elsevier Science Publishers, Amsterdam, **1993**.
7. M. Abdullah, G. K. C. Low, R. W. Matthews, *Environ. Sci. Technol.*, **1990**, 24, 6820.
8. G. K. C. Low, S. R. McEnvoy, R. W. Matthews, *Environ. Sci. Technol.*, **1991**, 25, 460.
9. R. W. Matthews, *J. Phys. Chem.*, **1987**, 91, 3328.
10. M. R. Prairie, L. R. Evans, B. M. Stange, S. L. Martienz, *Environ. Sci. Technol.*, **1993**, 27, 1776.
11. C. Kormann, D. W. Bahnemann, M. R. Hoffmann, *Environ. Sci. Technol.*, **1991**, 25, 494.
12. a) N. S. Foster, R. D. Noble, C. A. Koval, *Environ. Sci. Technol.*, **1993**, 27, 350; b) M. Barbeni, E. Pramauro, E. Pelizzetti, E. Borgarello, N. Serpone, *Chemosphere*, **1985**, 14, 195.
13. E. Pelizzetti, M. Borgarello, C. Minero, E. Pramauro, E. Borgarello, N. Serpone, *Chemosphere*, **1988**, 17, 499.
14. R. W. Matthews, *Water Res.*, **1991**, 25, 1169.
15. J. H. Carey, J. Lawrence, H. M. Tosine, *Bull. Environ. Contam. Toxicol.*, **1976**, 16, 697.
16. A. Sclafani, L. Palmisano, M. Schiavello, *J. Phys. Chem.*, **1990**, 94, 829.
17. N. Serpone, *Res. Chem. Intermed.*, **1994**, 20, 953, and references therein.
18. D. F. Ollis, E. Pelizzetti, N. Serpone, *Environ. Sci. Technol.*, **1991**, 25, 1523.
19. J. Doménech, M. Andrés, *Gazzetta Chimica Italiana*, **1987**, 117, 495.
20. N. Serpone, Y. K. Ah-You, R. Harris, H. Hidaka, E. Pelizzetti, T. P. Tran, *Solar Energy*, **1987**, 39, 49.
21. M. R. Prairie, J. Pacheco, L. R. Evans, ASME International Solar Energy Conference, April, SAND91-1285C, Sandia National Laboratory, Albuquerque, NM, **1992**.
22. B. O'Regan, M. Gratzel, *Nature*, **1991**, 353, 737.
23. J. K. Thomas, *Chem. Rev.*, **1993**, 93, 301.
24. J. I. Pankove, *Optical Properties in Semiconductors*, Prentice-Hall, New Jersey, **1971**, p. 34.
25. A. J. Nozik, F. Williams, M. T. Nenadovic, T. Rajh, O. I. Micic, *J. Phys. Chem.*, **1985**, 89, 397.
26. a) C. B. Murray, D. J. Norris, M. G. Bawendi, *J. Am. Chem. Soc.*, **1993**, 115, 8706; b) T. Vossmyer, L. Katsikas, M. Giersig, I. G. Popovic, K. Diesner, A. Chemseddine, A. Eychmuller, H. Weller, *J. Phys. Chem.*, **1994**, 98, 7665.
27. a) T. Rajh, M. W. Peterson, J. A. Turner, A. J. Nozik, *J. Electroanal. Chem.*, **1987**, 228, 55; b) O. I. Micic, C. J. Curtis, J. R. Sprague, K. M. Jones, A. J. Nozik, *J. Phys. Chem.*, **1994**, 98, 4966; c) O. I. Micic, J. R. Sprague, A. J. Nozik, *J. Appl. Phys. Lett.*, **1996**, 68, 3150; d) A. J. Nozik, O. I. Micic, *J. Luminescence*, **1996**, 70, 95; e) S. A. Empedocles, D. J. Norris, M. G. Bawendi, *Am. Phys. Soc.*, **1996**, 77, 3873; f) A. P. Alivasatos, *Science*, **1996**, 271, 933; g) *Semiconductor Nanoclusters: Physical, Chemical and Catalytic Aspects*, vol. 103, (Eds.: P. V. Kamat, D. Meisel), Elsevier, Amsterdam, **1997**; h) *MRS Bulletin*, **1998**, 23, and references therein; i) M. Nirmal, D. J. Norris, M. Kuno, M. G. Bawendi, A. L. Efros, M. Rosen, *Phys. Rev. Lett.*, **1995**, 75, 3728; j) A. L. Efros, M. Rosen, M. Kuno, M. Nirmal, *Phys. Rev. B*, **1996**, 54, 4842.
28. T. Rajh, O. I. Micic, A. J. Nozik, *J. Phys. Chem.*, **1993**, 97, 11999.
29. J. M. Nedeljkovic, M. T. Nenadovic, O. I. Micic, A. J. Nozik, *J. Phys. Chem.*, **1986**, 90, 12.
30. A. J. Nozik, *Annu. Rev. Phys. Chem.*, **1978**, 29, 189.
31. S. R. Morrison, *Electrochemistry at Semiconductor and Oxidized Metal Electrodes*, Plenum Press, New York, **1980**, p. 56.
32. A. Hagfeldt, M. Gratzel, *Chem. Rev.*, **1995**, 95, 49.
33. Z. Y. Wu, G. Ouvrard, P. Gressier, C. R. Natoli, *Phys. Rev. B*, **1997**, 55, 10382.
34. J. Pascual, J. Camassel, H. Mathieu, *Phys. Rev. B*, **1978**, 18, 5606.
35. D. S. Boudreaux, F. Williams, A. J. Nozik, *J. Appl. Phys.*, **1980**, 51, 2158.
36. M. Gratzel, A. J. Frank, *J. Phys. Chem.*, **1982**, 86, 2964.
37. N. Serpone, D. Lawless, R. Khairutdinov, E. Pelizzetti, *J. Phys. Chem.*, **1995**, 99, 16655.
38. a) P. Meriaudeau, M. Che, C. K. Jorgensen, *Chem. Phys. Lett.*, **1970**, 5, 131; b) R. F. Howe, M. Gratzel, *J. Phys. Chem.*, **1985**, 89, 4495; c) M. Anpo, T. Shima, T. Fujii, S. Suzuki, M. Che, *Chem. Lett.*, **1987**, 1997.
39. T. Rajh, A. E. Ostafin, O. I. Micic, D. M. Tiede, M. C. Thurnauer, *J. Phys. Chem.*, **1996**, 100, 4538.

40. a) O. I. Micic, Y. Zhang, K. R. Cromack, A. D. Trifunac, M. C. Thurnauer, *J. Phys. Chem.*, **1993**, 97, 7277; b) O. I. Micic, Y. Zhang, K. R. Cromack, A. D. Trifunac, M. C. Thurnauer, *J. Phys. Chem.*, **1993**, 97, 13284.
41. N. M. Dimitrijevic, D. Savic, O. I. Micic, A. J. Nozik, *J. Phys. Chem.*, **1984**, 88, 4278.
42. O. I. Micic, T. Rajh, M. V. Comor, in *Electrochemistry in Colloids and Dispersions* (Eds.: R. A. Mackay, J. Texter), VCH, New York, **1992**, p. 457.
43. G. Rothenberger, J. Moser, M. Gratzel, N. Serpone, D. K. Sharma, *J. Am. Chem. Soc.*, **1985**, 107, 8054.
44. D. Duonghong, J. Ramsden, M. Gratzel, *J. Am. Chem. Soc.*, **1982**, 104, 2977.
45. U. Kolbe, J. Moser, M. Gratzel, *Inorg. Chem.*, **1985**, 24, 2253.
46. D. Bahnemann, A. Henglein, J. Lilie, L. Spanhel, *J. Phys. Chem.*, **1984**, 88, 709.
47. D. Lawless, N. Serpone, D. Meisel, *J. Phys. Chem.*, **1991**, 95, 5166.
48. a) L. X. Chen, T. Rajh, Z. Wang, M. C. Thurnauer, *J. Phys. Chem.*, **1998**, 101, 10688; b) L. X. Chen, T. Rajh, W. Jager, J. Nedeljkovic, M. C. Thurnauer, *J. Synchrotron Radiation*, **1999**, 6, 445.
49. F. Sunada, A. Heller, *Environ. Sci. Technol.*, **1998**, 32, 282.
50. a) J. Moser, S. Punchicewa, P. P. Infelta, M. Gratzel, *Langmuir*, **1991**, 7, 3012; b) S. Tunesi, M. A. Anderson, *Langmuir*, **1992**, 8, 487.
51. A. Mills, S. Le Hunte, *J. Photochem. Photobiol. A: Chem.*, **1997**, 108, 1.
52. G. A. Nicklasson, *Sol. Energy Mater.*, **1988**, 17, 217.
53. D. M. Blake, *Bibliography of Work on the Heterogeneous Photocatalytic Removal of Hazardous Compounds from Water and Air, Update Number 3 to June 1999*, NREL/TP-570-26797, National Renewable Energy Laboratory, Golden, CO, **1999**.
54. M. D. Driessen, V. H. Grassian, *J. Phys. Chem. B*, **1998**, 102, 1418.
55. I. Izumi, F.-R. F. Fan, A. J. Bard, *J. Phys. Chem.* **1981**, 85, 218.
56. M. R. St. John, A. J. Furgala, A. F. Sammells, *J. Phys. Chem.*, **1983**, 87, 801.
57. M. A. Fox, M. T. Dulay, *Chem. Rev.*, **1993**, 93, 341.
58. A. L. Linsebigler, G. Lu, J. T. Yates, Jr., *Chem. Rev.*, **1995**, 95, 735.
59. M. Anpo, H. Yamashita, Y. Ichisashi, Y. Fujii, M. Honda, *J. Phys. Chem. B*, **1997**, 101, 2632.
60. D. E. Aspnes, A. Heller, *J. Phys. Chem.*, **1983**, 87, 4919.
61. a) A. B. Ellis, S. W. Kaiser, J. M. Bolts, M. S. Wrighton, *J. Am. Chem. Soc.*, **1977**, 99, 2839; b) M. J. Natan, J. W. Thackeray, M. S. Wrighton, *J. Phys. Chem.*, **1986**, 90, 4089.
62. a) T. Rajh, D. M. Tiede, M. C. Thurnauer, *J. Non-crystalline Solids*, **1996**, 207, 815; b) M. C. Thurnauer, T. Rajh, D. M. Tiede, *Acta Chem. Scand.*, **1997**, 51, 610; c) L. X. Chen, T. Rajh, O. Micic, Z. Wang, D. M. Tiede, M. C. Thurnauer, *Nucl. Instr. Meth. Phys. Res. B*, **1997**, 133, 8.
63. T. Rajh, J. Nedeljkovic, L. X. Chen, O. Poluektov, M. C. Thurnauer, *J. Phys. Chem. B*, **1999**, 103, 3515–3519.
64. K. Kalyanasundaram, N. Vlachopoulos, V. Krishnan, A. Monnier, M. Gratzel, *J. Phys. Chem.*, **1987**, 91, 2342.
65. R. Dabestani, A. J. Bard, A. Campion, M. A. Fox, T. E. Mallouk, S. E. Webber, J. M. White, *J. Phys. Chem.*, **1988**, 92, 1872.
66. M. A. Ryan, E. C. Fitzgerald, M. T. Spitler, *J. Phys. Chem.*, **1989**, 93, 6150.
67. K. Hashimoto, M. Hiramoto, T. Sakata, *Chem. Phys. Lett.*, **1988**, 148, 215.
68. I. Bedja, S. Hotchandani, P. V. Kamat, *J. Phys. Chem.*, **1994**, 98, 4133.
69. a) J. Cattery, A. Allen, *J. Phys. Chem.*, **1958**, 62, 33; b) J. Sutherland, D. Stihi, R. Goodrich, *J. Phys. Chem.*, **1967**, 71, 4422; c) G. M. Zhabarova, V. I. Vladimirova, *Russ. Chem. Rev.*, **1969**, 38, 711; d) S. H. Willow, F. O. Findley, *Can. J. Chem.*, **1967**, 45, 2087; e) C. Morterra, M. J. D. Low, *Ann. N.Y. Acad. Sci.*, **1973**, 220, 135; f) V. A. Radtsig, *Khimicheskay Fizika*, **1991**, 10, 1262.
70. E. I. Grigoriev, L. I. Trakhtenberg, *Radiation-chemical Processes in Solid Phase: Theory and Application*, CRC Press, Boca Raton, **1996**, and references therein.
71. G. Zhang, Y. Mao, J. K. Thomas, *J. Phys. Chem. B*, **1997**, 101, 7100.
72. T. Schatz, A. R. Cook, D. Meisel, *J. Phys. Chem.*, **1998**, 102, 7225.
73. N. M. Dimitrijevic, A. Henglein, D. Meisel, *J. Phys. Chem. B*, **1999**, 103, 7073.
74. A. G. Zacheis, K. A. Gray, P. V. Kamat, *J. Phys. Chem. B*, **1999**, 103, 2142.

Index

Roman figures attached to the page numbers refer to the volumes I to V: eg. II/478 refers to page 478 in volume II.

- A.C. method I/542
- conductometric detection I/542
- A/V ratio I/431, I/470ff
- ab initio II/207
- ab initio calculations II/94, II/99, II/101, II/107, II/113, II/909, V/609
- ABN – p-aminobenzonitrile IV/699, IV/711ff, IV/717ff
- absence of dual fluorescence IV/721
- clusters with acetonitrile, methanol, tetrahydrofuran, cyclohexane, water, ammonia IV/727ff
- – dual fluorescence IV/727ff
- – LIF spectrum IV/727ff
- fluorescence emission in a supersonic jet IV/720
- – clusters IV/720
- – monomer IV/720
- lack of CT fluorescence IV/711
- LIF spectra IV/719
- – origin of first electronic transition in a supersonic jet IV/719
- LIF spectra of clusters IV/717
- LIF spectra of complexes with acetonitrile, methanol, water IV/719
- – origin of first electronic transition in a supersonic jet IV/719
- structure of dimers IV/721
- absorbed species V/715ff
- ionizing radiation V/715
- absorptance IV/366
- absorption III/413, III/415, V/592
- transient III/413, III/415
- absorption coefficient IV/306, V/397
- absorption cross-section V/601
- absorption edge IV/512
- perovskite-related layered oxides IV/512
- absorption spectra I/527, III/282ff, III/386, III/502, III/562, III/591, III/605, III/625f, III/645, III/648, V/357
- cadmium catenate III/594
- catenanes III/547ff, III/562
- cobalt catenate III/593, III/596
- copper catenates III/591
- hydrated electron I/527
- metal complexes III/562, III/593ff
- nickel catenate III/593, III/596
- palladium catenate III/595
- pseudorotaxanes III/502ff
- rotaxanes III/547ff, III/645, III/648
- Ru(II)-Rh(III) complexes III/386
- silver catenate III/594, III/596
- silver bromide V/357
- silver chloride V/357
- transient III/282ff, III/605, III/625f
- zinc catenate III/594, III/596
- absorptivities II/602f, II/605f
- abstraction I/510
- reaction with organic molecules I/510
- π acceptors IV/6
- 4-acylated thymidine III/152
- α -cleavage III/152
- π -acid II/907
- AC impedance IV/294ff
- AC impedance spectroscopy IV/555ff
- electron transfer kinetics IV/555ff
- accelerators I/531
- pulse radiolysis I/531
- acceptors II/625, V/516
- cationic II/625
- neutral II/625
- organometallic II/625
- type classification II/15
- accumulation IV/329f, IV/385
- electron IV/330
- layer IV/392

- acenaphthene II/213
 acetaldehyde IV/37
 acetamide II/953
 acetaminophen IV/161
 acetonitrile I/518, II/289, IV/11
 – cyclic voltammetry in II/682ff
 – radiation chemistry I/518
 acetophenone IV/11ff
 – *p*-methoxy IV/13
 – radical anions IV/12
 acetylcholine esterase IV/133, IV/150
 acetylene II/225, II/249
 acid II/463, II/754, II/905, II/920, IV/7
 – catalysis IV/8
 – dissociation constants IV/9
 – pasting V/414
 acid-base neutralization V/166
 acid-catalyzed electron transfer IV/9
 acid-gated photochromic reaction V/234
 acidity II/908
 – dihydrogen complex II/686ff
 – metal hydride II/680ff
 – metal hydride cation radical II/696ff
 acridine II/363, II/367
 – alkylation II/367
 – reductive dimerization II/363
 acridinium salt (AC⁺) III/149
 – quenching by guanine III/149
 – singlet-state reduction potential III/149
 acridizinium II/363
 – reductive dimerization II/363
 acrylonitrile I/461
 action spectrum IV/245
 activated complex I/170, I/181, II/583, II/593
 activation by H-abstraction II/495, II/501ff
 – β -acetato radicals II/504
 – β -chloroalkyl radicals II/504
 – α,β -dihydroxyalkyl radicals II/501ff
 – glycol mono-alkyl ether radicals II/503
 – α -hydroxyalkyl-type radicals from β -amino alcohols II/503
 – α -hydroxy- β -phosphatoalkyl radicals II/503
 – hydroxyl radical II/501
 – α -monoalkoxy- β -chloroalkyl radicals II/506
 activation energy I/180, I/440, II/595, IV/239, IV/558
 – electron transfer kinetics IV/558
 activation free energy (*see also* free activation energy) II/592, II/933
 activation volume IV/262f
 activation-controlled rate constants I/528
 activationless electron transfer V/621
 active aldehyde IV/54
 active site II/910, II/923, IV/127
 2-acylaziridines II/468
 acyl carbanion IV/54
 acyl complex
 – C-H bond dissociation energy II/693
 acyloins II/465
 2-acyl- or 7-alkyl-2,4,5-triiodo-3-fluorones V/550
 acylsilane II/486
 addition I/510
 – reaction with organic molecules I/510
 1,4;1,2-addition II/287
 1,4;1,4-addition II/287
 adduct anions II/289
 adducts, [3+2] I/359
 1,2 adduct II/283, II/303
 1,4 adduct II/283
 adenine III/427ff
 adenine analogues III/151
 – fluorescence quenching III/151
 adenosine triphosphate synthesis III/75
 adhesion promoters III/708
 adiabatic I/10ff, I/64ff, I/69, I/78ff, I/200, I/208, II/587ff, II/608, II/831, III/4, IV/6, IV/56, V/444, V/618
 – approximation I/64ff
 – eigenfunction I/66ff
 – electron transfer IV/69
 – energy II/588
 – energy curve II/587, II/591
 – free energy II/589, II/591
 – limit I/69, I/78ff, III/4, V/618
 – mixing I/208
 – outer-sphere electron transfer IV/56
 – potential I/64ff
 – process IV/6
 – reaction II/593
 – states I/10ff, II/588
 – transport V/444
 – wavefunction II/608
 adiabaticity II/832
 – parameter I/83ff, I/97
 adiponitrile I/461, II/195
 – synthesis II/195
 ADP V/598
 adsorbed species V/709
 adsorption IV/235, IV/250, IV/258f, IV/265f, IV/304, V/709
 adsorption equilibrium I/286ff
 adsorption isotherm V/607
 aerosol IV/328
 affinity complexes IV/155
 affinity interactions IV/151, IV/156
 aggregate V/425f
 – size V/371
 aggregation II/279
 aging process II/739
 agostic interaction II/941
 Al₂O₃ V/714
 AlCl₃ II/752
 alcohol dehydrogenase IV/150, IV/156, IV/162,

- IV/172, IV/175ff
- alcohol oxidase IV/129f
- alcohol radicals I/513
 - selected properties I/513
- aldehydes II/473, II/736, IV/22, IV/38
 - aliphatic II/473, IV/38
- aldimines II/462, II/476, IV/265
- aldose dehydrogenase IV/150
- alignment IV/130, IV/151ff
 - Cyt *c* IV/164
- aliphatic amines II/381
- alkali metal II/462, II/717
- alkali metal atoms IV/776ff
 - clusters of IV/776
 - preparation of, using heated oven IV/777
 - preparation of, using laser-vaporization source IV/777
 - with ammonia IV/776ff
 - with water IV/776
 - solvated IV/776
 - energy level diagram of IV/776
- alkali-metal cation II/209, II/836
- alkali-metal carbides II/726
- alkali-metal dimers IV/649
 - reaction with halogen molecules IV/649
- alkaline earth metal atoms electron transfer reactions
 - chemiluminescent reactions IV/643
 - double harpoon mechanism IV/643
 - leading to products with a double bond IV/644
 - classification of IV/644
- alkaloid II/28
- alkane radical cations
- alkanethiol monolayers IV/545, IV/552, IV/564
- alkenes II/188, II/248, IV/42, IV/566
 - electron transfer bridge IV/566
 - isomerization II/188
 - radical cation II/496f
- alkoxides II/282
- alkoxide complex
 - C-H bond dissociation energy II/694
- alkoxide ions IV/52
- 6-alkoxy-2,4-diiodo-3-fluorenes V/550
- alkyl electron transfer bridges IV/555ff, IV/563ff
- alkylaromatic radical cations II/520ff, II/526ff
 - benzyloxy radical II/533
 - C-C bond cleavage II/537ff
 - C-C bond fragmentation II/536
 - cleavage of side-chain C-H and C-C bonds II/520
 - C-H bond cleavage II/520f
 - comparison of C-H and C-C bond cleavage II/534
 - competition between C-H and C-C bond cleavage II/521
 - deprotonation II/529, II/530
 - HAT mechanisms II/531
 - heterolytic C-H bond cleavage II/532
 - homolytic fragmentation II/532
 - hydrogen-atom transfer II/530
 - intramolecular selectivity in the deprotonation II/526
 - intrinsic barriers II/523
 - kinetic acidity II/522f
 - nucleophilically assisted II/536
 - nucleophilic attack of water on the aromatic ring II/522
 - pK_a values II/522
 - radical zwitterion II/533
 - side-chain reactions II/520
 - stereoelectronic effects II/521, II/526ff, II/535
 - structure of the transition state for C-H deprotonation II/525
 - unactivated alkanes II/531
- 1-alkylaromatic radical cations II/526ff
 - comparison of oxygen and carbon acidity II/532
- alkyl halides I/464, I/475, I/479, I/491ff, I/494ff, II/284, II/325, IV/48
- 4-alkylidenepyrazolines II/231
- 2-alkylthiophenes II/234
- alkyl radicals V/519
- alkyl transfer II/658f
- alkylation II/286, II/299, II/657
 - 4-alkylated NADH analogs II/299
- alkyl-benzenes IV/42
- alkylborates V/216
- alkylidyne complex, dinuclear
 - C-H bond cleavage II/709
- alkylmetallates II/624
- alkylmetals II/621, II/664
- alkylsilanes IV/39
- alkynes II/193, II/736, II/779, IV/566ff
 - Birch reduction II/193
 - electron transfer bridge IV/562ff
- alkyne units III/324
- alkyneone II/460
- all-optical poling V/274
- all-optical switches V/73
- all-optical write-read-erase switches V/55
- allosteric regulation III/455
- alloys II/720
- all-*trans* rule III/204f
- allyl/enol ethers IV/266
- allylhalides II/273
- allylic radical IV/264
- allylsilanes II/476, IV/46
- allylstannanes II/477
- aluminia V/715
- amalgams II/720
- ambient temperature molten salt electrolyte IV/291
- amicyanin IV/35
- amide bond III/285

- amide-linked arrays V/196
- amides II/423
- amidine III/446
- amidinium functionalities III/450
- amidocobalticinium II/788
- amidometallocene II/788
- amines II/379ff, II/402, II/408, II/417, II/422, II/432, II/478, II/732, II/930, IV/35, V/545f, V/553
 - amine radical cations V/546
 - biochemical systems II/402
 - α -cyanation of II/422
 - chemical oxidation II/380
 - electrochemical oxidation II/381
 - electron-transfer reactions II/402
 - enzyme-catalyzed reactions of II/417
 - metal oxide catalyzed reaction II/380
 - oxidation IV/35
 - oxidation catalyzed by cytochrome P-450 II/408
 - oxidation catalyzed by monoamine oxidase II/402
 - oxidation potentials V/553
 - palladium catalysed reactions II/380
 - radiation chemical studies II/383
 - radical cations II/380
 - reaction of metal salts II/380
 - sensitized photoreactions II/432
 - thermal oxidation II/380
- amine (peptide) IV/566
 - electron transfer bridge IV/566
- aminium deprotonation I/370ff
- aminium radical II/380ff, II/935
- amino acids II/302, II/943, IV/161
 - hydroxylase III/80
 - oxidase IV/129f, IV/161
- 9-(aminoalkyl)phenanthrenes II/437
- aminoalkyl radical II/380ff
- α -aminoalkyl radical II/386ff, V/566
- p*-aminoazobenzene II/232
- amino pterin IV/40
- aminocumarin III/132
 - intramolecular quenching III/132
- aminomethylcubane II/406
- Trans*-1-aminomethyl-2-phenylcyclopropane II/405
 - α -amino radical II/474, II/931
- ammonia I/522f, IV/776
 - negatively charged clusters IV/776
 - – electron detachment energy of IV/776
 - solvated electron I/522f
 - – reduction of metal ions I/523
- amorphous IV/285
- amorphous molecular solid V/432, V/442
- amorphous organic matrix V/477
- amorphous Se V/381
- amorphous Si V/381
- amperometric redox biosensor II/786
- amphiphiles V/147
- amphiphilic micellar assemblies II/278
- amphiphilic structure II/280
- amplifiers IV/164
- amplifying a beam V/474
- anatase IV/378, V/602, V/695
- ancillary ligands II/908
- AND gate III/314
- AND logic V/160
- angle multiplexing V/510
- angular distribution of products IV/638
 - reaction of alkali metal atom with a halogen atom donor IV/638ff
- anharmonicity I/56
- 3,4'-anhydrovinblastine II/415
- aniline II/292, II/382
 - oxidation II/382
 - dyad II/307
- anion radical II/189ff, II/983
 - coupling II/195
 - disproportionation II/190
 - pericyclic reactions II/199
 - SOMO II/189
 - spin densities II/189
- anion radical scavenger III/155
 - oxygen III/155
- anion radical/cation radical pair II/202
- anion sensing III/483ff, III/494, III/667
- anionic flavin semiquinone IV/206
- anionic micelles V/168
- anionic water clusters IV/786
- anisotropic photoetching IV/327
- anodic dissolution I/169
- anodic oxidation II/35, II/948, IV/49
- anodization IV/329
- anomalous photoeffect IV/313
- Antenna II/312, II/320, II/322, III/272ff, V/73, V/194, V/186ff, V/598
 - artificial V/187, V/190f
 - effect V/187, V/194
 - molecule II/320
 - natural V/187
 - pigments V/598
 - systems II/322
- antenna-reaction center systems III/324, V/199
- anthracene I/456, II/212f, II/237, II/304, II/323, III/431, III/466, III/475, III/483ff, IV/27, IV/52, V/31, V/37, V/37, V/41, V/43f, V/130
 - derivatives III/431, III/466, III/475, III/483ff
 - 9,10-dimethyl IV/27
 - 9-benzyl IV/52
 - 9-methyl IV/27
 - radical cation IV/52
- anthracene-ammonia adduct IV/764
 - exciplex emission IV/764
- anthracene-aniline adducts IV/747

- conformers IV/747
- exciplex formation IV/747
- anthracenedimethylaniline adduct IV/746ff
- deuteration IV/756
- electron donor acceptor (EDA) IV/795
- onset of exciplex emission IV/756
- anthracenedimethyl-*o*-toluidine adducts IV/751
- hole burning spectra IV/751
- anthracyl receptor IV/75
- anthraquinone II/390, II/437, III/698
- -amines V/553
- 2-sulfonate II/292
- anthrasemiquinone radical V/554
- 9-anthrylaniline IV/799
- CT state IV/799
- LE state IV/799
- torsional potential surface IV/799
- 4-(9-anthryl)aniline (AA) IV/708, IV/711
- 4-(9-anthryl)-N,N-dimethylaniline (ADMA) IV/708, IV/798
- intramolecular charge transfer (ICT) in IV/798
- 9-anthrylmethyl II/243
- anti- π -complex II/99
- antiaging mechanism IV/24
- antibody IV/191
- anticancer IV/24
- antiferromagnetic coupling II/810
- antigen IV/191
- antigen-antibody IV/133
- anti*-Markovnikov II/34
- antimony pentahalide II/751
- antioxidant V/298
- antisymmetrization I/224
- apoenzyme IV/69
- apoenzyme-cofactor interactions IV/68
- aporphine II/364
- synthesis of II/364
- apparent activation energies V/369
- apparent driving force IV/403
- application in dentistry V/553
- APX III/84, III/87, III/93
- cation binding site III/93
- aqueous saturated calomel electrode II/715
- (arena) metal sandwich complexes II/622
- arene complex
- C-H acidity, benzylic II/705 ff
- C-H bond dissociation energy, benzylic II/694, II/705ff
- arene radical cations II/274
- arenediazonium salts II/753
- argon-ion-laser V/527
- aromatic amines II/381
- aromatic bridges V/121
- aromatic carbonyl compounds IV/46
- aromatic ketone IV/16
- aromatic nitro compounds II/805
- aromatic radical anions I/464, I/474ff, I/479ff, I/494ff, II/723ff
- aromatic radical zwitterions II/550ff
- derived from arylalkanoic acids II/554
- derived from benzoic acids II/552
- aromatic stabilization energies V/223
- aromatic stacking IV/73
- aromatic substitution II/253
- arrested precipitation I/289
- Arrhenius relation V/328
- arsenic pentahalide II/751
- arsenic triselenide V/389
- artificial antennas V/187, V/597
- artificial photosynthesis II/271, V/186, V/187, V/597
- aryl II/560
- intramolecular electron transfer II/560
- σ -arylacetylide complexes V/271
- aryl acylamidase IV/161
- arylamines V/384
- ascorbate II/292, II/862
- oxidase IV/130, IV/222
- ascorbic acid II/731, V/310
- aspartase IV/176
- aspartic acid IV/24
- association constants III/414ff
- atom tunneling I/72ff
- atomic collision of the second kind I/84ff
- atomic force microscopy V/387
- atom-transfer-chain (ATC) II/761
- ATP (adenosine triphosphate) II/950, III/39, V/598
- synthase III/311
- atropisomerization III/419
- attempt frequency I/79ff
- attenuation factor V/102, V/110, V/112, V/119
- autocatalysis V/291
- avoided crossing I/66ff, III/181, III/195
- axial ligand II/812, II/927
- aza-cages III/471ff
- aza-crowns III/462ff, III/469ff
- azacyanocarbanions II/252
- azide III/486
- azirine II/39
- PET opening II/39
- azo dyes V/301, V/483
- azo pigments V/384
- azoalkanes II/230f, II/252
- azobenzene II/241, II/252, IV/257, IV/259, IV/261, IV/264, IV/266, V/52
- radical anions IV/17
- azo-FO-1 V/409
- azomethine dyes V/564
- azomethine ylide II/306
- azurin II/860, III/6, III/9, III/13, III/20, IV/130
- B3LYP-DFT IV/69
- Ba + CH₃OH reaction IV/647

- Ba + Cl₂ reaction IV/643ff
- π back donation II/827
- Ba + H₂O reaction IV/647, IV/657
- Ba + N₂O reactions IV/636, IV/645, IV/651, IV/682, IV/683
- Ba + O₃ reaction IV/646
- Ba \cdots (FCH₃) complex IV/675
- Ba₃ + SF₆ reaction IV/683
- σ -basicity II/827
- back donation II/809
- back electron transfer I/274, II/300, II/307f, II/310, II/314f, II/320, II/322, II/324f, II/619, II/637, II/650, II/654, II/937, IV/3, IV/50, IV/368, IV/743, V/522, V/567, V/573, V/620
- back reaction II/854
- bacteria II/909
- bacterial reaction centers III/24ff
- bacteriochlorophyll III/278, III/619, III/629, IV/171, V/188
- dimer III/31ff
- bacteriopheophytin III/36, III/619, IV/171
- bacteriorhodopsin V/264
- band bending I/159ff, I/274, IV/292, V/699, V/707ff
- band edge I/159, V/705, V/715ff
- movement IV/322
- position I/279, IV/236, IV/391
- band gap I/184, IV/4, IV/490, IV/492, IV/487, IV/509, IV/512, IV/514ff, V/356, V/696
- A_{2-x}La₂Ti_{3-x}Nb_xO₁₀ IV/518
- excitation I/271
- Fe₂O₃-clay IV/522
- K₂La₂Ti₃O₁₀ IV/517ff
- K₄Nb₆O₁₇ IV/490
- KTiNbO₅-type oxides IV/509
- perovskite-related layered oxides IV/512
- RbPb₂Nb₃O₁₀ IV/514
- TiO₂-clay IV/522ff
- band shape I/245, I/247, I/265
- band structure V/701
- TiO₂ V/701
- bandwidth I/246, I/261
- Barbier reactions II/466, II/469
- barbituric acid III/440
- barium tantalate V/479
- barrier (energy) for isomer interconversion IV/751
- barrier height I/162
- base II/289, IV/7
- catalysis IV/47
- pairs III/107, III/115
- – proton transfer III/115
- – Watson-Crick III/107
- batteries V/645ff, V/690
- basic aspects V/647ff
- – anode V/648f, V/653
- – cathode V/648f, V/653
- – concentration cells V/648
- – electrical potential V/649f
- – electrodes V/648
- – electrolyte V/648
- – free energy V/647f
- – interfacial potential differences V/649
- – interphase equilibrium potential difference V/650
- – metal-solution interfaces V/648
- – open-circuit voltage V/650
- – oxidation reaction V/650
- – potential differences V/649
- – reduction reaction V/650
- – standard equilibrium potential V/654
- – electrochemical kinetics V/650ff
- – anodic current V/651, V/654
- – anodic overvoltage V/652
- – Butler-Volmer equation V/654
- – cathodic current V/651, V/654
- – cathodic overvoltage V/652
- – concentration gradient V/654
- – concentration overvoltage V/652, V/655
- – conductivity V/654
- – diffusion V/654
- – diffusion coefficient V/655
- – electrical work V/650f
- – electrode overvoltage V/652
- – equilibrium potentials V/651
- – exchange constant V/654
- – exchange current V/651
- – free energy V/650
- – limit current V/655
- – mass transport rate V/654
- – metal-solution interphase V/651
- – Nernst equation V/651
- – ohmic drop V/652, V/654
- – ohmic overvoltage V/652
- – polarizations V/651, V/655
- – potential difference V/651
- – standard hydrogen electrode (SHE) V/651
- – standard potential V/651
- energy V/645
- lead-acid V/646
- load-leveling V/646
- miniature V/646
- nickel-cadmium V/646
- nickel-iron V/646
- performance V/656ff
- – coulombic efficiency V/656
- – C-rate V/657
- – cycle life V/657
- – depth of discharge, DOD V/656
- – energy density V/656, V/667
- – life V/667
- – maximum power V/656
- – power density V/656, V/667
- – practical capacity V/656

- recharge time V/667
- self-discharge V/657, V/667
- shelf life V/657
- specific capacity V/656
- specific energy V/656, V/667
- specific power V/656
- specific peak power V/667
- theoretical capacity V/656
- theoretical energy V/656
- USABC V/667
- portable equipment V/646
- rechargeable battery V/648
- secondary cell V/690
- magnesium-based V/690
- SLI V/646
- stationary V/646
- USABC V/647
- vehicle traction V/646
- zinc-manganese dioxide V/646
- zinc-mercuric oxide V/646
- BCMF V/437
- BDE *see* bond dissociation energy
- bead-on-a-string V/166
- beam amplifying V/474
- Beer-Lambert law I/574
- BEF V/314
- Benesi-Hildebrand equation III/450
- benzaldehyde IV/41
- benzene II/224f
- benzene-iodine complex IV/675
- back electron transfer IV/676
- electronic configuration IV/676
- kinetic energy distribution of product iodine atoms IV/675ff
- ultrafast pump-probe technique IV/675
- benzene-tetracarboxamide III/436
- benzidine II/292
- benzo[a]pyrene II/212
- benzobicyclo[4.1.0]hepta-2,4-diene radical cation II/90
- benzofuran II/352ff
- fluorination II/352
- radical cation II/354
- reaction with tetranitromethane II/353
- benzonorcaradiene II/90
- benzophenone II/244, II/462, II/473, IV/17, IV/46, V/536, V/548
- basic properties V/548
- radical anion II/462, II/724
- benzophenone-amine II/398
- systems V/545
- (Benzophenonylmethyl)-tri-*n*-butylammonium triphenylbutylborate (BTAB) V/537
- benzoquinone II/289, II/961, III/491, IV/9, IV/17, IV/27, IV/150
- 2,6- or 2,5-dichloro-*p*- IV/9
- 2,5-dimethyl-*p*- IV/17
- p*-benzoquinone II/273, IV/8, IV/10, IV/36
- chloro IV/10
- 2,6-dimethyl IV/10
- methyl IV/10
- benzothiazine II/351
- halogenation II/351
- benzothiazolium II/363
- reductive dimerization II/363
- benzotriselenol II/342
- radical cation II/342
- benzotrithiol II/342
- radical cation II/342
- 3-benzoyl-7-diethylamino-5-methyl-1-phenyl 1*H*-quinoxalin-2-one (ChAD) V/564f
- photophysical properties V/565
- 1,4-benzoquinone II/239, IV/132
- benzvalene II/105
- benzyl alcohol II/932, IV/43
- benzyl bromide II/283
- benzyl chloride I/435
- 1-benzyl-1,4-dihydronicotinamide IV/22
- 1-benzyl-1,4-dihydronicotinamide II/293
- 1-benzyl-1,4-dihydronicotinamide (BNAH) IV/29
- benzyl halide II/560
- intramolecular electron transfer II/560
- benzyl radical IV/40, IV/42
- benzylamine IV/36
- benzylhydroperoxyde IV/40f
- benzylic ligand hydroxylation IV/26
- benzylperoxyl radical IV/40
- benzylsilanes IV/46
- Bessel function I/71
- BHA III/86
- 9,9'-bianthryl (BA) IV/701, IV/796
- bias (overpotential) I/165
- bias voltage V/618
- bichromophores I/220, I/220
- bicumene II/639f
- bicyclic linkage III/292ff
- bicyclo[2.1.0]pentane II/107, II/231
- bicyclo[3.1.0]hex-2-ene II/111
- bicyclobutane radical cation II/101
- bicyclic lactams II/439
- bicyclooctyl groups III/288
- bidentate ligands II/808
- biferrocenylene II/754
- bifunctional reagents IV/132
- bilirubin IV/161
- oxidase IV/132, IV/161
- bimetallic catalysis IV/23
- bimetallic zwitterions II/764
- bimolecular electron-transfer reactions II/850
- bimolecular photochemical electron transfer II/845
- bimolecular reaction II/598
- bimolecular recombination V/397

- binaphthol derivatives V/258
- binaphthyl ether V/258
 - chirality V/258
 - conjugation V/259
 - crystal structure V/259
 - hyperpolarizability V/258
- binder polymer V/382, V/414
- bioaffinity interactions IV/133
- biocatalyzed transformations IV/193
- bioenergetic conversion III/409
- bioenergetics III/24ff
- biofuel cell IV/162, IV/164, IV/191
- biological electron transfer IV/202
- biological nitrogen fixation II/886ff
 - alternative nitrogenases II/887
 - ATP hydrolysis II/887
 - electron transfer II/886
 - nitrogenase II/886
 - P-clusters II/887
 - X-ray analysis II/887
- biological redox reactions IV/11
- biological transformations IV/172
- bioluminescence I/318
- biosynthesis of nitric oxide III/79
- biotin-avidin IV/133
- biphenyl (BP) II/224, II/324, II/725
- biphenylene II/213
- biphotonic process II/324
- bipolar photoelectrochemical behaviour IV/342
- 2,2'-bipyridine II/804, II/934
- bipyridinium III/698, IV/132
- biquinoline II/829
- biradicals II/991, III/309ff
 - spin-polarized III/309ff
- Birch reduction II/29, III/189
- bis(4-methoxyphenyl)-methane II/229
- bis(arene)chromium II/733
- bis(arene)iron(II) II/645
- 2,5-bis[(1*H*,5*H*-benzo[*i,j*]quinolizin-1-yl)methylene]cyclopentanone (JAW) V/559
- Trans*-1,2-bis(1-benzyl-4-pyridinium)ethylene III/531
- 4,4'-bis(dimethylamino)benzophenone V/553
- bis(durene)iron(II) II/630, II/633
- bis(hexamethylbenzene)iron(II) II/633
- bis(hydrazines) I/383ff
- [1:2,9:10]bismethanol[2.2]paracyclophane II/92
- 8,9-bis(methylsulfanyl)-acenaphthol[1,2-*b*][1,4]dithiine II/250
- bis(oligonucleotide) conjugates III/135
 - naphthalenedicarboxamide linkers III/135
 - stilbenedicarboxamide linkers III/135
- bis- μ -oxodicopper(III) complex IV/26
- bis(*p*-phenylene)-34-crown-10 III/544, III/552, III/558, III/565ff
 - catenanes III/544, III/565ff
 - rotaxanes III/552, III/558
- 9,10-bis(trifluoroacetoxy)anthracene II/212
- bisazo pigments V/410
- bis-carbene II/761
- bis-functionalized fullerenes II/281f
 - derivatives II/281
- bisphenol-A polycarbonate V/385
- bissilylated adduct II/302
- bistable systems V/55, V/158
- 4,4'-bitoluene II/211
- bixin III/301
- black body V/592
- black dye V/607, V/634
- black-and-white reversal V/337
- bleach enhanced fog V/314
- bleach-fixing V/336, V/344
- bleaching V/336ff, V/573
 - process V/340
 - thermodynamics of V/337
 - agents V/339, V/347ff
 - dye-bleaches V/354
 - electrode potentials V/339
 - hydrogen peroxide V/353
 - iron(III) complexes V/348
 - onium catalyst V/352
 - persulfate V/350
 - rehalogenating V/339, V/342
 - toxicity V/347
- blix *see also* bleach-fix V/345
- block copolymers V/196
- blocking layer V/433
- blue copper proteins III/13, IV/130, IV/218
- Bohr radius V/699
- Boltzmann factor V/498
- Boltzmann function IV/282
- Boltzmann statistics IV/283
- bond activation
 - oxidatively induced II/700, II/702, II/705ff, II/708
 - reductively induced II/704, II/705ff
- bond cleavage I/347ff, I/354ff, II/8, II/14ff, II/17ff, II/23ff, II/299
 - heterolytic vs homolytic I/352ff
 - oxidative II/23ff
 - C-C II/24ff
 - C-Ge II/23
 - C-H II/24ff
 - C-N II/24, II/27
 - C-Si II/25f
 - C-Sn II/23ff, II/28
 - C-S II/25, II/27
 - C-Si II/23, II/28
 - C-X II/27
 - Ge-Ge II/24
 - Ge-O II/28
 - kinetics of II/24, II/27
 - O-C II/28
 - O-P II/28

- O-H II/25
- O(N)-H II/27
- O-Si II/28
- O-Sn II/28
- O-Ti II/28
- O-Zr II/28
- S-C II/28
- Si-Si II/23ff, II/28
- Sn-Ge II/24
- Sn-Si II/24
- Sn-Sn II/24
- thermodynamics of II/24, II/27
- rearrangement of products I/354ff
- reductive II/14, II/17ff
- C-C II/19, II/21f
- C-Cl II/14
- C-Hal II/18ff
- C-N II/14, II/19, II/22
- C-O II/18ff
- C-S II/18ff
- C-Se II/18f
- C-X II/20ff
- kinetics of II/18, II/20, II/22ff
- N-S II/22
- O-O II/18
- O-Si II/19
- Se-S II/19
- Se-Se II/19
- Si-O II/22
- Si(Ge)-Hal II/18
- S-P II/22
- thermodynamics of II/18, II/22
- bond dissociation II/12
- energy of II/12, II/678
- C-H bond in coordinated ligand II/693ff, II/705ff
- dihydrogen complex II/686ff
- ligand effect II/684, II/686ff, II/690
- metal effect II/684, II/686ff
- metal-halide II/701
- metal hydride II/680ff
- metal hydride cation radical II/698ff
- metal-metal bond II/695
- bond energy II/677ff
- bond formation II/8, II/29, II/33ff
- oxidative II/33, II/35f
- C-C II/35
- C-S II/36
- kinetics of II/33
- S-S II/36
- Se-Se II/36
- thermodynamics of II/33
- reductive II/29
- kinetics of II/29ff
- thermodynamics of II/29ff
- bonding II/907
- bond order alternation (BOA) V/254
- borate V/544
- Born energy II/596
- Born-Oppenheimer approximation (BOA) I/10, I/21, I/64, I/86, I/190, I/235, II/598f, IV/83
- boron-dipyrrole pigment V/199
- bound pairs V/482, V/484
- BP 1 III/84
- $\text{Br}^- \cdot (\text{H}_2\text{O})_n$ clusters IV/778
- bra vector I/67
- Bragg reflection I/138
- branched alkane radical cations
 - elimination of methane II/71
 - fragmentation II/71
- branched alkanes II/68
- branched arrays V/66
- branching ratio V/578
- bridges I/9, III/139, III/148, III/201, III/209f, III/212, III/215, III/231ff, III/235, III/243, III/254, III/256, III/266, III/295, III/308, III/412, III/439, V/3, V/6, V/18, V/20, V/24, V/32, V/37ff, V/103
- aromatic III/235
- conjugated III/231ff, III/266
- dithiaspiroalkane III/439
- flexible III/308
- hydrogen-bonded III/412
- mediated electron transfer III/139, III/148
- superexchange mechanism III/148
- norbornylogous III/201, III/209, III/205, III/243, III/256ff
- oligo-spirocyclobutane III/212
- reorganization energy III/210
- rigid III/295
- saturated hydrocarbon III/201, III/215
- steroid III/254
- dynamics I/9
- bridged norcaradiene II/122
- bridged systems IV/697
- anthracene-dimethylaniline IV/746, IV/795
- charge transfer in IV/757ff
- clusters in a supersonic jet IV/716
- coupling of LE and exciplex states IV/760
- cyanonaphthalene-dimethylbutene IV/752
- cyanonaphthalene-*p*-methylaniline IV/759
- 9,10-dicyanoanthracene-naphthalene IV/748
- dimethoxy-naphthalene -- dicarbomethoxy ethylene IV/760
- dual fluorescence IV/698
- effect of bridge rigidity IV/759f
- electronic energy transfer in the gas phase IV/761
- exciplex fluorescence IV/754ff
- hole burning IV/754ff
- LE fluorescence IV/754ff
- $\pi\pi$ interactions in IV/697
- isotopic substitution IV/755
- Jablonski diagram IV/699

- pyrene-dimethylaniline IV/747
- solvation in a supersonic jet IV/716
- bridging ligands III/353ff, V/3, V/7, V/13, V/18, V/25, V/29, V/33, V/37f, V/97, V/99, V/101, V/128, V/130
- photoresponsive V/128
- pyridyltriazole ligands V/100
- redox-responsive V/130
- bromine II/753
- bromodeoxyuridine III/117
- bromonaphthalene phosphor V/167
- p*-bromonitrobenzene II/240
- Bronsted acid IV/8, IV/36
- catalyzed electron transfer IV/36
- Bu₂Sn(OTf)₂ IV/43
- buckminsterfullerene (C₆₀) II/960
- building blocks II/806, V/8, V/10, V/12, V/16, V/99
- metal-containing V/99
- η-Bu₄NOH II/948
- Burnstein-Moss shift IV/386
- buta-1,3-diene II/210
- butadiene II/190, II/228
- anion radical II/190
- – ESR spectroscopy II/190
- 1,3-butadiene cation radical II/137
- *s-cis* and *s-trans* forms II/137
- 2,3-butadienone (biacetyl) III/497
- encapsulated III/497
- butane-1,4-diol dimethacrylate V/567
- Butler-Volmer equation I/171, I/425, V/334
- N*-*tert*-butoxy-4-phenylpyridinium ion II/931
- tert*-butoxyl radical II/931
- 4-*tert*-butylanisole II/213
- tert*-butylbenzene II/211
- butyl radical V/529ff, V/540
- butyltriphenylborate V/540

- CO₂ adduct IV/93ff, IV/115
- CO₂ binding IV/94f, IV/102f, IV/121
- CO₂ fixation IV/88
- CO₂ reduction IV/89ff, IV/97ff, IV/104, IV/116ff
 - electrochemical IV/97, IV/116ff
 - mechanistic and kinetic studies IV/100ff
 - by metal macrocycle IV/89ff
 - photochemical IV/98ff, IV/118ff
 - by rhenium complex IV/104, IV/116ff
 - quantum yield IV/99f, IV/118
- C₁₆H₃₃O₃CNQ V/143
- C₆₀ II/718, II/738, II/836, IV/48, IV/52, IV/133
 - stoppers II/856
- C₇₀ II/276, II/278
- C₇₆ II/274, II/276, II/278
- C₇₈ II/274, II/276, II/278
- C₈₄ II/276
- Ca + HBr reaction IV/668
- Ca···HBr complex IV/668, IV/670, IV/672
- Ca + HCl reaction IV/670ff
- Ca···HF complex IV/668
- Ca···HI complex IV/668
- Ca + HX (X=F, Cl, Br, I) reaction IV/665f
- Cadiot-Chodkiewicz reaction V/16
- cadmium sulfide IV/174
- cage II/753, III/462ff, III/605, V/569
 - reaction II/753
 - solvent V/569
- calcium ion IV/35
- calculations II/91, II/94, II/99, II/101, II/107, II/113ff, II/121
- calf-thymus DANN III/142
- β for electron transfer III/142
- calixarene II/788, II/836f, III/421ff, III/490, V/256f
 - conformation V/256
 - hyperporarizability V/257
- calmodulin III/74
- calorimetry II/682, II/685
- calotypes V/286
- Calvin cycle IV/171, V/598
- CAM III/58
- camphorquinone V/550, V/552
 - amine system V/550
 - radical anions V/552
- capacitative current; *see* double-layer charging current
- capacitor V/388
- capture I/97, II/103
 - cross-section I/97
- carbamates II/423
- carbanionic nucleophile II/758
- carbanions II/246, II/282
- carbazole II/349, V/398, V/484
 - oxidative dimerization II/349
- carbenes II/282
- carbocations II/757
- carbocyanine V/357
- carbodiimide coupling IV/137
- carbon II/915
- carbon acids II/534
 - intrinsic barriers for proton transfer II/534
- carbon black IV/130
- carbon dioxide II/736, IV/162, IV/175ff, IV/190, IV/193, V/597
 - fixation IV/162, IV/175f, IV/179, IV/190, IV/193
- carbon electrode II/786
- carbon monoxide II/919
- carbon particles IV/130
- carbon paste IV/130f, IV/148ff
- carbon powder IV/148
- carbonyl compounds IV/13
- carbonyl ligands II/918, II/921, II/986
- carbonyl metallates II/634, II/654
- carbonyl substitution II/769

- carbonylmetal II/983
- carbonylmetallate II/647
- carboxycytochrome oxidase III/42
 - flash photolysis III/42
- carboxyl radical I/513
 - selected properties I/513
- carboxylate anions II/253
- carboxylate radical V/561
- carboxylate switch III/70
- 4-carboxybenzophenone—sulfur-containing
 - carboxylic acid V/577
- carcerands III/495
- carcinogen III/58
- carcinogenic activity II/19
- Carnot formula V/592
- β -carotene II/292, III/300
- carotenoid polyenes III/306, III/300, III/312
 - radical cation III/306
 - triplet state III/312
- carotenoids V/598f
- carotenoporphyrin III/300
- carriers IV/306, IV/316, IV/389, V/382, V/392, V/397, V/428, V/461, V/476
 - collection IV/306
 - generation IV/306, IV/316
 - – mechanisms V/428
 - mobilities V/461
 - particles V/382
 - recombination V/476
 - transit time V/392
 - carrier transport IV/389
 - – limitations V/397
- cascade cyclization II/34
- cast films III/166
 - electric conductivity III/166
- catalase II/948, III/56
- catalysis II/761, IV/3, IV/23, V/553
 - bimetallic IV/23
 - electron transfer IV/3, IV/83
- catalyst II/300, II/818
- catalytic currents V/310
- catalytic cycle I/281, II/922, IV/39
- catalytic mimics III/94f
 - COX mimic III/95
 - MnP mimic III/94
 - P450 models III/94
- catalytic nucleus V/303
- catechol oxidase IV/129
- catecholate II/982
- catenands III/606ff
- catenanes III/539ff, III/544ff, III/561ff, III/566, III/570, III/573, III/582ff, III/617, III/617, III/629ff
 - absorption spectra III/547, III/562
 - amide-based III/545
 - asymmetry III/630
 - calixarene III/566
 - cyclobis(paraquat-p-phenylene) III/544ff
 - cyclophane ligands III/563
 - diazapyrenium III/573
 - electrochemical properties III/548ff
 - functional III/561
 - hetero III/576
 - isomers III/630
 - luminescence III/562
 - metal complexes III/562
 - poly III/544
 - porphyrins III/566
 - ring motions III/566ff, III/629ff
 - roto III/544
 - sensitized singlet oxygen luminescence III/617
 - switchable III/630
 - synthesis III/539, III/562
 - tetrathiafulvalene (TTF) III/570, III/573
 - triad III/565
- catenates II/809, II/835, III/583ff, III/603ff, III/607, III/612ff, III/631ff, III/636, III/638f
 - absorption spectra III/635f
 - AgAg III/596
 - cadmium III/594
 - cobalt III/593
 - CoCo III/596
 - coordination geometries III/639
 - copper III/587
 - copper-ruthenium III/587
 - electrochemical properties III/583ff, III/595, III/604
 - energy transfer III/612
 - EPR spectra III/634
 - fluorescence III/607, III/613
 - homodinuclear III/596ff
 - lithium III/591
 - luminescence III/605, III/613
 - nickel III/593
 - NiNi III/596
 - nonsymmetrical III/632
 - palladium III/595
 - phosphorescence III/607, III/613
 - photophysical properties III/605
 - polypyridine complexes III/585ff
 - quenching rate constants III/612ff
 - redox potential III/592, III/639
 - resonance Raman III/605
 - ring motions III/633, III/635, III/638
 - ruthenium III/603
 - silver III/594
 - symmetrical III/636
 - synthesis III/596
 - tetrahedral III/584
 - topography III/584
 - topology III/584
 - zinc III/594
 - ZnZn III/596
- [3]catenates III/598ff, III/608ff

- CuAg III/599
- CuCo III/599
- energy transfer III/609
- heterodinuclear III/599
- luminescence III/608, III/610
- multicomponent III/608
- photophysical properties III/608ff
- protonation III/610ff
- redox potentials III/598
- catharanthine II/415
- cathodic photocurrents IV/373
- cathodic reduction II/784
- cation II/27, II/135
 - coupling reactions II/186
 - radicals II/134ff, II/186, III/156, V/384
 - - chain mechanism II/133
 - - cyclizations II/185
 - - cycloadditions II/157, II/166, II/169f
 - - cyclobutanations II/147
 - - Diels-Alder reaction II/170, II/171
 - - discovery II/134
 - - formation II/135, II/166
 - - geometric structures II/136
 - - pi II/137
 - - polymer II/140
 - - radical probes II/167
 - - spin distribution II/135
- cation- π IV/77
- cationic amino acid radical IV/220
- cationic organometallic complex II/732
- catphen II/814, II/817
- cavity volume I/527
 - hydrated electron I/527
- C-C bond formation IV/43
- C-C homocoupling IV/256
- CCD V/510
- CCP III/84ff
 - cavity mutant III/95f
- CD spectra V/237
- $\text{Cd}_{0.8}\text{Zn}_{0.2}\text{S}$ IV/491
 - $\text{K}_{4-x}\text{H}_x\text{Nb}_6\text{O}_{17}$ IV/491
- CDB V/408
- CDMA - *p*-cyano-*N,N'* dimethylaniline IV/698, IV/700ff, IV/708, IV/711ff
 - clusters with acetonitrile, methanol, tetrahydrofuran, cyclohexane, water, ammonia IV/720, IV/723, I, V/727
 - dimer IV/717
 - dual luminescence IV/701
 - existence of two excited states IV/715
 - fluorescence emission in a supersonic jet IV/720
 - geometry of the fluorescent state IV/715ff
 - ground state geometry (by x-rays) IV/708
 - high resolution emission spectra IV/715
 - LIF excitation spectrum IV/714
 - LIF spectra IV/711, IV/719
 - LIF spectra of complexes with acetonitrile, methanol, water IV/719
 - moments of inertia IV/746
 - rotational contour analysis IV/715f
 - solvation in a supersonic state IV/724
 - solvent-solute exciplex IV/700
- CdS IV/174, IV/236, IV/491, V/602
 - $\text{K}_{4-x}\text{H}_x\text{Nb}_6\text{O}_{17}$ IV/491
- CdSe V/602
- CdTe V/699
- cell time constant I/453ff
- cellobiose oxidase IV/145
- carboxylic acid dimers III/414
- cerium (IV) ammonium nitrate (CAN) II/749
- cesium II/717
- cetyltrimethylammonium II/278
- CGM V/397
- C-H heterocoupling IV/256
- CH_3CN^- IV/788
 - electron binding energy (EBE) of IV/788
 - photoelectron spectra IV/788
- $\text{CH}_3\text{I} + \text{Ag}$ surface reaction IV/650
- $\text{CH}_3\text{I} + \text{K}$ reaction IV/638, IV/652
- ChAD V/564
- chain-to-chain electron transfer IV/570
- chalcone V/85
- chalcogenides IV/285
- chemically modified films IV/315
- characteristic frequency of vibration III/30ff
- charge I/470
 - charge accumulation I/293
 - charge barrier theory V/289, V/308
 - charge carriers V/431, V/474, V/596, V/626
 - dynamics V/449
 - mobility V/431
 - motion V/450
 - percolation V/626
 - recombination
- charge combination III/206
- charge density II/136
- charge dipole interaction V/446, V/450
- charge generation V/381, V/383f, V/385, V/390, V/393f, V/396, V/402, V/410, V/433, V/474, V/481, V/489f
 - efficiency V/489
 - extrinsic V/402, V/410
 - intrinsic V/394, V/410
 - layer (CGL) V/383, V/433, V/384
 - limit V/490
 - material (CGM) V/383, V/385, V/390
 - quantum efficiency V/391
 - models V/393
 - sensitized V/394, V/396
- charge hopping V/477
- charge injection I/274ff, IV/393, V/609
 - dynamics V/609
- charge migration IV/375

- DNA III/119
- charge pairs V/703
- charge recombination (charge annihilation)
 - I/312ff, III/148, III/263, II/306, II/313, II/315, II/319, II/121, III/123, III/228, III/282ff, III/310, III/396, IV/378, IV/393, IV/402, V/393, V/620
- distance-dependent III/148
- doublet state, in I/313
- free energy of I/319, III/121
- kinetics of I/319ff
- laser action from I/338
- proton-coupled electron transfer IV/393
- radiative I/312ff, I/321
- singlet state I/313
- triplet state I/313
- charge resonance II/627
- charge separated radical pair II/307
- charge separated state II/309, II/316, II/319f, III/180, III/261, III/278ff, III/396, III/437
- giant III/261
- charge separation II/292, II/308, II/313, II/316, III/121, III/148, IV/170ff, IV/189, IV/280, V/189, V/596ff, V/600, V/603, V/623, V/627f
- distance-dependent III/148
- singlet excited state II/316
- free energy III/121
- charge-shifted state III/180, III/207, III/283
- charge shift reactions III/192
- charge transfer (CT) II/601, II/607, II/637, II/662f, II/943, V/394
- absorption IV/702
- of donor-acceptor π systems IV/702
- spectroscopy I/241, I/245ff, I/257, I/252
- bands II/630ff
- – hypsochromic shift II/631
- – solvatochromism II/630
- coefficient I/169, I/174, I/182
- complex II/292, II/304, II/625, II/663, IV/678, V/401, V/485, V/488, V/494
- crystals II/632f
- emission spectroscopy I/247ff, I/265
- excitation II/637
- fluorescence IV/702
- interaction II/662, III/417, III/501ff, III/546ff
- – catenanes III/546ff
- – pseudorotaxanes III/501
- – rotaxanes III/546ff
- ion pairs II/628, II/634
- – dissociation constants of II/628
- – inner sphere II/634
- material V/429
- salts II/633, II/645, II/654, II/658
- to solvent (CTTS) IV/629, IV/786ff
- of halide anions IV/786
- of OH^- IV/786
- of NO_3^- IV/786
- transition I/238ff, I/248, IV/708
- energy level diagram IV/708
- charge transport III/106, V/440f, V/494, V/498
- device III/266
- HOMO V/441
- hopping sites V/498
- layer (CTL) V/383, V/429, V/433
- requirements V/429
- LUMO V/441
- material (CTM) V/383, V/391, V/430f, V/460
- oxidation potentials V/430
- reduction potential V/431
- requirements V/460
- parameters V/502
- random walk V/440
- site energy V/441
- charge trapping V/429, V/501
- chelate ring II/808, II/833
- chelation II/777
- chemical bath deposition IV/329
- chemical development V/287, V/291, V/325, V/330
- rate equation V/330
- chemical equilibrium I/72
- chemical ionization II/148
- chemical modification IV/337
- chemical oxidation of amines II/380ff
- chemical potential V/590ff
- chemical potential μ I/128ff
- chemically induced dynamic electron polarization (CIDEP) I/545f, II/58, II/78, II/82f, II/88f
- EPR I/545
- NMR I/546
- chemiluminescence I/468, II/857
- chemiluminescent reactions IV/636, IV/647
- alignment dependence IV/660
- long live complex IV/647
- of Ca, Sr, Ba with strong oxidizers IV/647
- statistical distribution of products IV/647
- chemioselectivity II/769
- chemiosmotic model III/24ff
- chemoselectivity I/290, IV/239
- chiral discrimination IV/133f
- chiral materials V/275
- p*-chloranil radical anion IV/23
- chlorinated hydrocarbons I/519
- radiation chemistry I/519
- chlorine II/753, III/281ff, III/438
- exchange II/761
- 3-chloroacetophenone I/450
- chloroaniline (CIA) II/323
- chloronitrobenzenes II/239f
- chloroperoxidase IV/129
- chlorophyll III/300, IV/170f, IV/179, V/598f
- dimer V/598
- chloroplast IV/220
- 2-chlorothioxanthone (CTX) V/532

- cholesterol oxidase IV/129, IV/132
- choline IV/130
- oxidase IV/130, IV/133, IV/143, IV/150
- Chromatium vinosum III/26ff
- chrome *c* peroxidase IV/205
- chromium II/810, II/909
- chromium(III) II/846
- chromophores II/843, II/846, II/853, IV/366, V/504
- quencher systems III/372, III/393
- chronoamperometry I/431ff, IV/164, IV/555ff, IV/558ff
- electron transfer kinetics IV/555ff
- chrysene II/725
- CIA II/323
- CIDEP II/980, V/552
- CIDNP (Chemically Induced Dynamic Nuclear Polarization) I/354ff, I/365, II/103, II/105f, II/111ff, V/519
- effects II/90, II/92
- results II/97
- cinnamylamine-2,3-oxide II/406
- CIP III/84, III/92
- circular dichroism III/111, V/54, V/236
- DNA III/111
- cis*-[R₂Co(bpy)₂]⁺ IV/40
- cis*-dialkylcobalt(III) complexes IV/9
- cis-trans* isomerization II/32
- 1-citrulline III/74, III/78
- Cl[–](H₂O)_n clusters IV/778
- class I system II/590, II/592
- class II system (mixed valence) II/590ff, II/599, II/601, V/20f, V/30, V/32f, V/40
- class III system (mixed valence) II/590f, II/600, V/20, V/30, V/32f, V/40
- classical limit I/73ff
- clays IV/519, IV/525
- MV²⁺ IV/525
- Ru(bpy)₃²⁺ IV/525
- Zn(bpy)₃²⁺ IV/525
- cleavage of duplex DNA III/156
- at the 5'G of a GG step III/156
- isolated guanines III/156
- photochemical oxidants III/156
- singlet oxygen mechanism III/156
- α-cleavage V/553
- clock cycle V/62
- cluster II/275, II/308, II/760, II/761, II/923
- bridge between gas and condensed phases IV/680
- isolated chemical reactions (CICR) IV/630, IV/681ff
- supersonic jet IV/731
- C-N heterocoupling IV/262, IV/265
- CNDO/S I/115
- CNOS III/74
- ¹³CO II/912
- CO binding IV/227
- CO dissociation II/810
- CO stretching frequency
- Re(α-diimine)(CO)₃L IV/107ff
- Co(cyclam) IV/103
- CO₂ II/745
- CO₂ carbon dioxide fixation IV/171
- cobalamins II/979
- cobalt II/816
- complexes III/357ff
- cobalt (II) II/956
- cobalt(I)
- tetraphenylporphyrin II/285
- – anion IV/48
- cobalt-carbon bonds IV/9
- cobaltocene II/732, III/488, III/516
- cobaltocenium II/732
- Co-CO₂ complex IV/93ff
- coenzyme IV/11
- coenzyme Q₁₀ III/418
- cofacial V/456
- cofactor IV/147f, IV/169
- NAD IV/171
- silicon alkoxide IV/148
- coherent control IV/660
- coherent energy transfer I/222
- coherent superpositions of states V/89
- COHEX V/315
- COHMD²⁺ IV/90
- coinitiator V/518, V/543, V/567f, V/580
- cold trapped ions V/179
- collision complex II/397
- Collman reagent I/478, I/487
- colloidal semiconductors V/696
- colloid nanoparticles IV/178
- colloidal II/852
- semiconductor V/637
- – electrodes IV/377, IV/392, IV/405
- colloids IV/173, V/698
- color centers V/715
- color developing agents V/296
- command surfaces IV/169
- compact disk-recordable V/215
- comparative actinometry IV/401
- compensated insulating layer IV/314
- compensators V/475ff
- complementary pairs III/440
- π-complex II/88
- complex function IV/320
- complex I III/26
- complex III III/26
- complex plane (Nyquist) IV/303
- composite carbon-silicate electrode *see* sol-gel material IV/476
- compound III/63
- compound 0 III/88
- compound I II/934, III/66ff, III/75, III/80, III/82,

- III/87ff
- compound II III/67, III/89, III/92
- comproportionation V/21, V/25
 - comproportionation equilibrium V/22
- computational methods II/207
- computational techniques I/45, I/54
- concentration gradient I/424, I/427, I/429
- concentration polarization IV/305
- concentration profiles I/428, I/432, I/474
- concerted reactions IV/7
- condensation V/13f
- Condon approximation I/18, I/45ff, I/70ff, I/235
- conductance V/43f
- conducting properties II/759
- conduction band I/95, I/140ff, II/292, II/851,
 - IV/385, V/356, V/481, V/600, V/696, V/701, V/705ff, V/714ff
- continuum IV/385
- density of states I/96
- direct transitions V/703
- effective masses V/703
- indirect transitions V/703
- localized redox active $\text{Ti}^{\text{IV/III}}$ states IV/385
- rutile V/703
- valence band V/703
- conductive polymer IV/140
- conductivity I/133ff
- conductometric detection I/542
- pulse radiolysis I/542
- configurational mixing (configuration interaction) I/241ff
- confocal microscope V/240
- conformational control IV/221
- conformational disorder III/140
 - dynamic disorder III/140
 - static disorder III/140
- conformational dynamics III/455
- conformational gating I/103, IV/223
- conformational switching IV/75
- $[\text{Co}(\text{NH}_3)_3\text{Cl}]^{2+}$ II/946
- conical intersections IV/631, IV/675, IV/766ff
- conjugated bridges V/122, V/124
- conjugated dienes II/160, II/194
 - Birch reduction II/194
 - dioxygenation II/160
- conjugated ferrocene compounds V/269
- conjugated molecules V/109
- polyalkenes V/109
- polyalkynes V/109
- poly(*p*-phenylene) (PPP) V/109
- poly(phenylene-vinylene) (PPV) V/109
- poly(phenylene-ethylene) (PPE) V/109
- conjugated spacers V/109
- conjugated systems V/104, V/119
- connector V/191
- constant velocity drift V/433
- constructive interference III/223
- contact charging mechanism V/382
- contact ion pair II/397, II/628
- contact radial ion pairs III/138
- continuous flow I/397ff
 - CFMIO I/397
 - flow rate I/397
 - flow velocity I/398
- continuity equation IV/389
 - carrier generation rate IV/389
 - current density in the film IV/389
 - recombination rate IV/389
- continuum states I/95, V/367
- controlled-NOT operation V/178
- convection I/427, I/469
- conversion efficiency V/591ff, V/635f
- conversion factors V/246
 - CGS-SI V/246
- cooperative binding III/145
- coordinated free radical I/528f
 - transition metal complexes I/528
- coordination mode II/993ff
- Cope reaction II/180
 - cation radical II/180
- Cope rearrangement (3,3-sigmatropic shift) I/369
- copper II/820, II/993
 - catenates II/995, III/587ff, III/631ff
 - – absorption spectra III/591
 - – electrochemistry III/588
 - – redox potentials III/587, III/590
 - complexes III/477ff
 - enzymes IV/156
 - -ruthenium catenates III/589
 - – electrochemistry III/589
 - -zinc superoxide dismutase (Cu,Zn-SOD) IV/24
- copper(I) II/849
- copper(II) II/956
 - salts II/748
- corannulene II/323
- ^{60}Co γ -ray I/504
 - ionizing radiation I/504
- core ion I/137
- corner defects V/709
- corona V/380, V/384, V/388
 - charging V/388
 - chemical composition V/388
 - poling V/494
- coronene II/725
- corotron V/388
- correlated disorder model V/449
- corrosion V/329, V/351, V/699
- cosensitizer II/324
- Cottrell equation I/431, I/452
- Coulomb coupling, relayed I/221
- Coulomb force IV/742
- Coulomb integral I/219, I/224
- coulombic efficiency II/763

- coulombic energy V/522
- coulombic interaction II/298, II/607
- coulombic mechanism V/203, V/205
- coulombic stabilization III/276
- coumarin II/931, V/86, V/153, V/205, V/343, V/499
 - derivatives III/124
 - – static and dynamic quenching III/124
- coumarin 2 V/205
- counter electrode I/168ff
- counter-ion exchange I/381
- coupled chemical reactions I/446
- coupled quantum dots V/179
- coupler V/287, V/301, V/337
 - anion V/335
 - structures V/337
- coupling II/34f, V/335
 - radical cation-radical cation II/35
 - radical-nucleophile II/34
 - radical-radical II/34
 - scheme I/67
 - – adiabatic I/67
- covalent attachment IV/140
- covalent self-assembly techniques V/275
- covalently linked systems III/272ff, III/337, III/351ff, III/374
 - bimetallic III/351ff
 - dyads III/374
 - metal complexes III/337
 - porphyrins III/272ff
 - polymetallic III/351ff
- CPO III/90
- p*-cresol methyl hydroxylase IV/129
- Creutz-Taube complex I/380ff
- critical potential V/293
- cross reaction rate I/373
- cross-coupling V/13ff
- cross-linking IV/146, IV/155f, IV/159, V/346
- cross-over IV/313
- cross-reactions II/831
- cross-talk interactions III/219, III/222
- crown ethers II/788, II/836f, III/502ff, III/543f
 - catenanes III/544ff
 - pseudorotaxanes III/502ff
 - rotaxanes III/543ff
- crown-ether-like complex III/299
- cryptands II/720, II/837
- crystal field V/485
- crystal structure II/915, III/109
 - B-form DNA III/109
- crystal violet V/264
- crystalline DNA III/165
 - hopping between shallow traps III/165
 - migration of electrons and holes III/165
- crystallographic orientation IV/299
- Cs + H₂ reaction IV/653
- Cs + O₂ reaction IV/652
- Cs atoms IV/776
 - clusters of IV/776
- Cs-(H₂O)_n clusters IV/781
- Cs₂La₂Oti₃O₁₀ IV/512
- Cs₂La₂Ti₃O₁₀ IV/518
- Cs₂La₂Ti₃O₁₀ IV/519
- CsCa₂Nb₃O₁₀ IV/512
- CsCa₂Nb₃O₁₀ IV/513
- CsLa₂Ti₂NbO₁₀ IV/512
- CsLa₂Ti₂NbO₁₀ IV/519
- CsLaNb₂O₇ IV/512
- CsLaNb₂O₇ IV/513
- CsTi₂NbO₅ IV/509ff
- CsTi₂NbO₇ IV/507ff
- CTL V/429
 - requirements V/429
- CTM V/407, V/461
 - oxidation potential V/407
 - photochemical stability V/461
 - thermal stability V/461
- c*-type cytochromes IV/204
- Cu + F₂ reaction IV/659, IV/660
- Cu⁺-(H₂O)_n clusters IV/778, IV/783
- Cu(II) center IV/22
- Cu_A III/40f, III/44ff
- Cu_B III/40
- cubic (or second) hyperpolarizability V/244
- cularine II/364
 - synthesis of II/364
- cumene IV/43
- cumulene II/234
 - bridges V/123
- Curie temperature V/71
- current I/424, I/470
 - control I/291
 - density IV/389
 - double-layer charging I/431, I/453
 - doubling I/290, IV/267, IV/324
 - efficiency I/470
 - faradaic I/456
 - – overpotential equation I/425, I/492
 - plateau I/461, I/463, I/473ff
 - – potential equation I/424
 - steady-state I/463, I/496
- cyan dye V/336
- cyanate III/487
- cyanide II/912, II/915, II/916, II/920, II/921, III/87, V/18f, V/27, V/29, V/357, V/519ff, V/528
 - borate salts V/519
 - – alkyltriphenylborate V/519
 - hexafluorophosphate V/528
 - ligands II/921, II/923
- cyanine V/520, V/523, V/714
 - benzyltriphenylborate V/520
 - bleaching V/520, V/522
 - borate V/520, V/523ff

- characteristics V/525
- cyclic voltammograms V/524
- degree of dissociation V/527
- efficiency V/525
- general formula V/526
- oxidation and reduction potential data V/525
- quantum efficiency V/523
- radical formation V/520, V/525
- efficiency V/525
- self-association V/520
- *n*-butyltriphenylborate V/520, V/522
- chromophores V/523
- dyes V/216, V/360
- extinction coefficient V/360
- radical V/520
- tetraphenylborate salt V/520
- cyanobacteria V/597
- cyanobacterium *Anabaena* IV/211
- cyanobenzophenone, electron acceptor III/161
- cyanocarbon II/760
- p*-cyano-*N,N'* dimethylaniline (CDMA) IV/698ff, IV/708, IV/711ff
- p*-cyano-*N,N*-dimethylaniline *N*-oxide II/930
- cyanoforn anion V/268
- cyanonaphthalene-trimethylamine complex IV/746
- p*-(cyanophenyl)pentamethyldisilane IV/709
- p*-cyano-2,6,*N,N'* tetramethylaniline (CTMA) IV/699
- p*-cyano-2,*N,N'* trimethylaniline IV/699, IV/709, IV/711ff
- dimer IV/717
- LIF spectra in a supersonic jet IV/714
- LIF spectra of complexes with acetonitrile, methanol, water IV/719
- p*-cyanonitrobenzene II/240
- p*-cyano-2,*N,N'* trimethylaniline IV/715
- cyclam III/462
- cyclic voltammetry (*see also* voltammetry) II/677ff, II/699, II/956, IV/392, IV/555ff, IV/558, V/28f
- electron transfer kinetics IV/555ff, IV/558
- cyclic voltammogram II/270
- differential pulse voltammogram II/270
- cyclization reactions II/184, II/460, II/467ff, II/478
- II/5-*endo-trig* II/472
- II/8-*endo-dig* II/469
- II/8-*endo-trig* II/469
- II/5-*exo-dig* II/467, II/471f
- II/5-*exo-trig* II/460, II/467f, II/472
- II/6-*exo-trig* II/467f, II/471, II/478
- cation radical II/184
- cycloaddition reactions I/364ff II/98, II/147, II/154, II/158, II/165, II/228, II/479, II/644, IV/27
- [2+2] I/364
- [3 + 2] II/154
- [4 + 1] II/154
- [4+2] I/364
- cation radical Diels-Alder II/147
- 1,3-cyclohexadiene II/147
- Diels-Alder I/364ff
- mechanistic diagnosis II/165
- O₂ I/366ff
- ¹O₂ I/367ff - pericyclic II/154
- periselectivity II/158
- cycloalkanes II/99, II/471
- cyclobis(paraquat-*p*-phenylene) III/502, III/542ff, III/544ff
- pseudorotaxanes III/502ff
- rotaxanes III/542ff
- catenanes III/544ff
- cyclobutadimerization II/143, II/145
- *trans*-anethole II/143
- kinetics II/145
- phenyl vinyl ether II/143
- cyclobutanation II/141, II/145f, II/156
- alkynes II/146
- allenes II/146
- cation radical chain II/141
- [2 + 1] cycloaddition II/156
- ketenes II/146
- kinetic driving force II/146
- rates II/145
- stereochemistry II/141
- theoretical considerations II/146
- cyclobutane II/97, II/138
- cation radical II/138
- radical cation II/98f
- cyclobutene cation radical II/182f
- nonelectrocyclic path II/183
- retroelectrocyclic cleavage II/182
- cyclodextrins (CDs) II/277f, II/280, III/301, III/487ff, III/503ff, III/516, V/196
- α- III/503
- β- III/516
- antennas V/197
- -appended chromophores V/211
- β-cyclodextrin III/421, III/664
- dendrimers III/664
- γ-cyclodextrin II/296
- cyclodimerization II/187, II/144f
- acid-catalyzed II/187
- diastereoselectivity II/144
- regioselectivity II/145
- reversible II/144
- 1,3-cyclohexadiene II/323
- cyclohexadiene complex II/758
- cyclohexadienyl complexes II/728
- cyclohexane I/521, II/226, II/942
- radiation chemistry I/521
- cyclohexanediyl radical cations II/125
- cyclohexanone II/459

- cyclometallated V/13, V/30, V/35, V/39, V/41, V/42
- cyclometallating ligand V/31
- cyclometallating units V/115
- cyclooctatetraene II/191, II/237
 - anion radical II/191
 - dianion II/191, II/724
- cyclooctene II/948
- 1,3-cyclopentadiene II/323
- cyclopentane radical cation II/75
- cyclophanes II/211, III/421, III/294ff, III/502, III/541
 - catenanes III/541
 - porphyrins III/294ff
 - pseudorotaxanes III/502ff
 - rotaxanes III/541
- cyclopropanation II/177
 - cation radical II/177
- cyclopropane II/219
- cyclopropane
 - radical cation II/95
 - ring opening II/78
 - Jahn-Teller distortion II/73
 - Type A (trimethylene) structure II/78, II/81, II/88
 - Type B (pi-complex) structure II/84ff
 - stabilization by conjugation II/87f
- cycloreversion quantum yield V/229
- cylindrical column I/504
 - ionizing radiation I/504
- cysteine II/915, II/919ff
- Cyt *c* (see also cytochrome *c*) IV/130f, IV/133, IV/166, IV/168, IV/185, IV/190
- cytochrome II/860, III/24ff, III/56, V/599
 - *a* III/44, III/39f
 - *a*₃ III/39f
 - *b* IV/159
 - *b*₅ IV/135
 - *b*₅₆₂ III/16, III/20, IV/189
 - *b*_{6f} IV/218
 - *c* (see also Cyt *c*) II/943, III/6f, III/15f, III/20, III/40f, III/45, III/87, III/89, IV/135, IV/156, IV/166, IV/209
 - horse IV/209
 - oxidase II/949, II/928, III/39, III/446, III/455, IV/222
 - peroxidase (ccp) III/67, IV/128, IV/204, IV/220
 - *c*₅₅₅ IV/209
 - *c*-cytochrome *c* peroxylase IV/205
 - *c*-peroxidase II/943
 - *f* IV/214, IV/218
 - plastocyanin IV/205
 - oxidase III/40ff, III/44ff, IV/130, IV/156, IV/164, IV/166
 - catalytic cycle III/49
 - compound A III/48
 - electron injection III/42
 - ferrous-oxy III/48
 - F intermediate III/49
 - internal electron transfer III/45
 - internal ET III/45
 - P intermediate III/48
 - structure III/40f
 - electron transfer III/44
 - initial electron acceptor III/44
 - P450 III/58, III/60, III/62, III/64ff, IV/225
 - BM-3 IV/225
 - class I III/60, III/64
 - class II III/60, III/64
 - class IV III/60, III/64
 - crystallographic study III/65
 - molecular structure III/64
 - proton shuttle III/69f
 - proximal cysteine ligand III/68
 - reaction cycle III/60, III/62
 - substrate access channel III/65
 - P450BM-3 IV/205
 - 450s III/56
 - reductase IV/130
- cytosine III/427ff
- D* vs. log *E* curve V/290
- DABCO (1,4-diazobicyclo[2.2.2]octane) V/546
- Daguerreotypes V/286
- d*-amino acid oxidase IV/151
- damping factor V/612, V/622, V/633
 - β III/187, III/193, III/196, III/203ff, III/426
- Daniell cell V/649
- Danishefsky's dienes II/304
- danphen II/817
- dansyl derivative III/465
- dansyl-functionalized receptor III/440
- dark conductivity V/385
- dark decay V/389
- data capture and analysis I/541
 - pulse radiolysis I/541
- DBU (1,8-diazabicyclo[5.4.0]undec-7-ene) IV/54
- DCA II/324
- DCAQ V/387
- DDOP-C-TCNQ V/150
- de Broglie wavelength V/698
- de novo protein IV/159, IV/164, IV/166, IV/192
- dealkylation II/930
- DEASP V/386, V/424, V/426
- deazaflavins IV/206
- deazariboflavin IV/211, IV/223
- 5-deazariboflavin semiquinone IV/206
- Debye length IV/308, V/626
- Debye-Waller factor I/72
- decalin II/225
- decamethylcobaltocene II/33, II/715
- decamethylferrocene II/715, II/733, IV/17
- decarboxylation II/393, II/479, IV/50, V/560,

- V/561, V/578, V/579
- quantum yields V/579
- decay coefficient V/35, V/43
- decay law V/5, V/26, V/30, V/32, V/36, V/38, V/41f
- decay length I/152
- decay slope V/27, V/29, V/31, V/39, V/42f
- deceleration IV/14
- defect sites V/706, V/713ff
- degree of charge transfer II/627, II/632, II/635, II/668
- De-Gussa P-25 TiO₂ IV/379
- DEH V/386, V/389, V/407, V/417, V/435, V/485
- time-of-flight V/435
- dehalogenation II/17
- dehydrodimers IV/249
- dehydrodimerization IV/248
- deligation II/645
- delocalization I/345, II/286, II/597ff, II/602
- π, σ -delocalization II/59, II/87, II/101
- σ -delocalization II/59, II/72
- radical cation II/64
- demodulation curve V/252
- dendrimers II/733, II/835, III/655ff, III/659ff, III/664, III/666ff, III/673, III/678ff, III/682, III/686ff, III/692ff, III/698, III/701ff, III/706ff, V/200, V/203, V/211
- anion sensing III/667
- antenna V/77
- cluster assembly II/769
- anthraquinone III/698
- applications III/709
- bipyridinium III/698
- *p*-dimethoxybenzene III/701
- diphenylacetylene III/701
- electroactive III/656ff
- electrochemical properties III/658ff
- electron transfer theory III/703
- energy transfer V/77
- ferrocene III/657ff
- fullerene III/681f, III/688
- ion recognition III/666ff
- iron-sulphur cluster III/698
- LED III/703
- light emitting diodes (LEDs) III/696
- mixed-metal III/661, III/664, III/673
- multielectron redox process III/692ff, III/697
- nanoparticles III/707
- naphthalene III/701
- naphthalene diimide III/692
- nitroxyl radical III/698
- palladium complexes III/697
- phenylenevinylene III/703
- photoinduced process III/658, III/678, III/682ff, III/691, III/698, III/702, III/706ff, III/709
- phthalocyanines III/682
- polypyridine complexes III/656, III/659, III/706
- porphyrins III/659, III/679, III/688
- pyrene III/701
- ruthenium complexes III/659, III/706
- sensors III/666ff
- stereoisomers III/678
- *o*-terphenyl III/698
- tetrathiafulvalene III/686
- tetrathienylenevinylene III/698
- triaryl amines III/695
- with pendant chromophores V/261
- dendritic antenna complexes V/77
- dendritic effects II/788
- density functional theory (DFT) II/921
- calculations II/75, II/99
- density matrix I/71ff
- phonon I/71
- density of states I/16ff, I/136ff, V/443, V/611, V/618, V/698
- density vs. relative log exposure V/317
- deoxygenating reagent II/732
- deoxyribonucleotides III/455
- deoxyribose-derived radical reactions II/507ff
- chain breaks in DANN II/507
- dependence of rate constant on $-\Delta G^0$ I/521
- electron-transfer I/521
- depletion IV/384
- layer I/159ff, IV/287, V/699, V/705ff
- width IV/288
- spectroscopy (*see also* vibrational depletion spectroscopy) IV/672
- depolarization measurement V/250
- deprotonation II/27, II/66, II/70, II/71, II/81, II/241, II/303, II/325, IV/48, V/300, V/546, V/546, V/578
- derivative spectrum II/986, II/993
- derivatized electrode II/786
- desilylation II/393
- destructive interference III/217, III/220
- detection injection V/603
- detection of disorder of defects IV/555
- monolayer characterization IV/555
- detection of non-luminescent products IV/672
- dethreading/rethreading processes III/512, III/516, III/522
- electrochemically induced III/516, III/522
- photochemically induced III/512
- deuterium I/539, II/919
- isotope effect III/416
- lamps I/539
- developed silver V/289
- developer V/286f, V/292, V/294, V/308, V/333, V/346
- black-and-white V/292
- color V/292
- developing agents V/294

- diffusion V/346
- induced fog (DIF) V/319
- kinetic aspects V/333
- rate of V/295
- regeneration V/308
- solutions V/292
- superadditive V/287
- developing V/292
- development mechanism V/325
- development vs. relative log exposure curve V/290
- development-time plot V/289
- Dewar benzene II/216
- Dexter V/35, V/42, V/73, V/115, V/191, V/211
- energy transfer V/26, V/211
- mechanism V/5, V/102, V/109, V/112, V/123
- theory I/219, I/223
- diffusion-controlled growth V/303
- D-fructose dehydrogenase IV/131
- DFT II/207ff
 - calculations II/816, II/823
 - MO calculation II/734
 - B3LYP IV/81
- di- μ -oxodimanganese complex II/949
- di-(*p*-methylphenyl)iodonium bromide V/531
- diabatic II/584ff, II/598, II/602, II/607
 - configurations III/185
 - free-energy II/584f, II/589f
 - potential I/66ff, I/76ff
 - states I/10ff, II/584, II/598, II/602
 - wavefunction II/607
- diacyldiaminopyridine IV/72
- 2,6-diacylaminopyridine III/436
- diagonal disorder V/443
- dialkyldiphenylborates V/544
- diamine oxidase II/417
- diaminodicarboxylic acid IV/246
- dianion radicals II/191f
 - dibenzolymethide II/192
 - fluorenone II/192
 - tropenone II/192
- dianthracene II/639f
- diarylethenes V/220
- diaryloxycyclobutane II/97
- diastereoselectivity II/220
- 1,8-diazabicyclo[5.4.0]undec-7-ene (DBU) II/272
- 2,3-diazabicyclo[2.2.1]hept-2-ene II/252, II/250
- 2,3-diazabicyclo[2.2.2]oct-2-ene II/230
- 1,4-diazabutadienes II/808
- diazapyrenium derivatives III/524
 - pseudorotaxanes III/524
- diazapyrenium dication III/138
- diazapyrenium salts III/127
 - quenching by nucleotides III/127
- diazenes IV/260
- 1,2-diazenes IV/257
- diazepine II/362
 - ring cleavage II/362
- diazine II/341, II/362
 - electroreduction II/362
 - radical cations II/341
 - ring contraction II/362
- dibenzo[24]crown-8 III/502
 - pseudorotaxanes III/502ff
- dibenzo-1,4-dioxin II/353
 - nitration II/353
 - radical cation II/353
- dibenzo-24-crown-8 III/543, III/562
 - rotaxanes III/543, III/562
- dibenzodioxin II/213, II/345
 - radical cation II/345
- dibenzofuran II/216f, II/353
 - reaction with tetranitromethane II/353
- dibenzoheptafulvene II/238
- dibenzothiophene II/349, II/353
 - oxidative dimerization II/349
 - reaction with tetranitromethane II/353
- dibenzyl adduct II/283
- N,N*-dibenzylammonium III/502
- 1,1'-dibenzyl-4,4'-bipyridinium III/502
- DIBF V/531
- 2,3-dibromonaphthoquinone II/309
- 4,4'-di-*tert*-butyl biphenyl II/211
- 2,6-di-*t*-butylsemiquinone IV/17
- dicarbocyanine V/357
- 2,3-dichloro-5,6-dicyano-*p*-benzoquinone (DDQ) IV/29
- dichloroethane I/520
 - radiation chemistry I/520
- dichloroethane (DCE) II/277, II/314
 - acidity in II/684ff
- dichloromethane I/520
 - radiation chemistry I/520
- dicyanamid V/38, V/40
- dicyanamido V/30
- dicyanamidobenzene V/28
- dicyanoanthracene II/390
- 9,10-dicyanoanthracene II/324, II/476
- dicyanobenzene II/392
- p*-dicyanobenzene II/745
- dicyanonaphthalene II/234, II/432
- 1,4-dicyanonaphthalene II/476
- dielectric constant III/276ff, IV/262, IV/264, V/444
- dielectric continuum III/275
 - theory I/190ff, I/209
- dielectric relaxation time V/391
- Diels-Alder II/228
 - additions II/152
 - PET conditions, under II/152
 - cycloadditions II/154, II/173, II/201
 - allenes II/154
 - anion radical II/201

- indirect II/173
- ketenes II/154
- reaction II/148, II/150ff, II/164, II/303, IV/27
- aminium salt catalyzed II/148
- *endo/exo* diastereoselectivity II/151
- electron rich dienophiles II/152
- ionizable substrates II/152
- kinetic studies II/164
- *cis*-propenyl effect II/150
- regiochemistry II/150
- role-selectivity II/154
- stereochemistry II/150
- steric effects II/152
- stilbene II/153
- dienes IV/27
- dienophiles IV/27
- 4-(diethylamino)-5-methylpyridin IV/699
- clusters with methanol and with water IV/725
- dimer IV/717
- LIF spectra IV/717, IV/719
- LIF spectra in a supersonic jet IV/715, IV/718
- LIF spectra of complexes with acetonitrile IV/718
- LIF spectra of complexes with acetonitrile, methanol, water IV/719
- 4-(diethylamino)pyrimidine IV/699
- clusters with methanol and with water IV/725, IV/726
- dimer IV/717
- LIF spectra IV/717, IV/719
- LIF spectra in a supersonic jet IV/714
- LIF spectra of complexes with acetonitrile, methanol, water IV/719
- rotational contour analysis IV/715
- diethylaniline (DEA) IV/714, V/546
- LIF spectra in a supersonic jet IV/715
- diethyl sulfide - iodine complex IV/677
- differential capacitance I/154
- diffraction limit of light V/239
- diffraction limited spot V/48
- diffusion I/427, IV/262, V/333, V/478
- coefficient I/427, I/435ff, IV/303, V/297, V/346
- constants II/246
- controlled I/528
- rate constants I/528
- layer I/428, I/485
- thickness of I/428, I/469, I/473
- limit III/411
- process V/84
- rate constant II/299
- reaction equation I/100
- recombination IV/305
- transfer development V/304
- diffusional electrochemistry IV/137
- diffusional electron mediators IV/168
- diffusional mediators IV/131
- digermirane II/302
- digital versatile disk-recordable V/215
- α,ω -dihaloalkanes II/282
- 9,10-dihydro-9-alkyl-10-methylacridine (AcrHR) IV/50
- 9,10-dihydroanthracene II/237
- 1,5-dihydroflavin IV/33
- 2',3',4',5'-tetraacetate anion IV/33
- 5,10-dihydroflavin adenine dinucleotide (FADH₂) II/929
- 1,5-dihydroflavin anion IV/33
- dihydrofolate reductase III/446
- dihydrogen II/905, II/908, II/920, II/922, II/924
- activation II/924
- complex II/907
- acidity II/686ff
- M-H bond cleavage II/686ff, II/689
- H-H bond cleavage II/686ff, II/689
- evolution II/924
- heterocyclic splitting II/922
- production III/476
- evolution II/915
- uptake II/915
- 9,10-dihydro-10-methylacridine (AcrH₂) IV/14
- 2,3-dihydro-3-oxo-2,2-diphenyl-1*H*-indol-1-ylloxyl radical IV/21
- diimide anion III/437
- diimide-based assemblies III/433
- diimine IV/104ff
- α -diimine II/808, II/980, II/988, II/992, II/996
- 2,4-diiodo-6-butoxy-3-fluorone (DIBF) V/529, V/531, V/542
- diisopropylidimethylaniline (DIDMA) V/531
- α -diketones V/553
- dimeric 1-benzyl-1,4-dihydronicotinamide [(BNA)₂] IV/20
- dimeric 1-benzyl-1,4-dihydronicotinamide [(BNA)₂] II/952
- dimeric metalloporphyrins II/952
- dimerization II/32, II/650
- aldehyde II/32
- arene II/32
- heteroarene II/32
- ketone II/32
- p*-dimethoxybenzene III/701
- 10,10'-dimethoxy-9,9'-bianthryl II/237
- N*⁶,*N*⁶-dimethyladenosine IV/700
- N,N*-dimethylallylamine II/432
- p*-(dimethylamino)acetophenone IV/699
- p*-(dimethylamino)benzaldehyde IV/699
- 4-(dimethylamino)-5-methylpyrimidine IV/699, IV/706
- dimer IV/717
- 4-(dimethylamino)pyrimidine IV/699
- dimer IV/717
- LIF spectra in a supersonic jet IV/714
- LIF spectra of complexes with acetonitrile,

- methanol, water IV/719
- rotational contour analysis IV/715
- N,N*-dimethylaniline (DMA) II/307, II/930, V/546
- 4-(dimethylanilino)pyrimidine (4-DAAP) IV/706
- CT fluorescence IV/707
- planarity of the excited state IV/707
- resonance structures IV/707
- 2,5-dimethyl-*p*-benzoquinone IV/17
- 1,2-dimethylcyclobutane II/138
- cation radical II/138
- N,N*-dimethyl-2,6-diisopropylaniline (*see also* diisopropylidimethylaniline) V/549
- 1,1-dimethylferrocene IV/132
- N,N*-dimethyl-1-naphthalene IV/46
- dimethyl sulfide V/567
- dimethyl sulfoxide I/522
- radiation chemistry I/522
- dimethylaniline (DMA) II/387ff, III/308, III/433, IV/714
- derivatives III/374, III/450
- LIF spectra in a supersonic jet IV/715
- NMe₂ group torsional motion IV/714
- N-methyl group torsional motion IV/714
- dimethylaurate(I) II/623, II/660
- dimethylbicyclopropenyl radical cation II/106
- dimethylmercury(II) II/623
- 10,10'-dimethyl-9,9',10,10'-tetrahydro-9,9'-biacridine [AcrH]₂ IV/21
- dimethyl-*o*-toluidine (DMOT) IV/750ff
- dimethylviologen IV/132
- 1,5-dinaphtho-38-crown III/563f
- 1,5-dinaphtho-38-crown-10 II/502, III/550
- pseudorotaxanes III/502ff
- 2,3-dinaphtho-30-crown-10 III/527
- dinitrobenzene III/431, III/446f, IV/85
- 1,3-dinitrobenzene II/241, II/245
- 1,4-dinitrobenzene II/245
- 4,4'-dinitrobenzophenone II/239
- dinitrogen II/879ff
- catalytic reduction II/885, II/897ff
- complexes with transition metals II/882
- consecutive cleavage of the triple bonds II/880
- consecutive cleavage transfer II/880
- electronic configuration II/880
- FeMoco as catalyst for the reduction at amalgam surfaces II/901
- linear dinuclear complexes M–N≡N–N II/883
- mononuclear complexes M–N≡N II/883
- N₂ reduction in aprotic media II/891
- physical constants and characteristics II/879
- polynuclear dinitrogen complexes II/884
- protonation by acids II/883
- redox potentials II/881
- reduction in protic media II/892
- reduction by amalgams II/899
- 2,7-dinitronaphthalene II/241
- 2,4-dinitrophenol II/241
- trans-N,N'*-di(1-norbornyl)diazene II/230
- dinuclear complexes V/97, V/107, V/110
- dinuclear compounds V/100, V/109
- dinucleoside monophosphates III/130
- fluorescence quenching III/130
- diode V/157
- array I/396
- equation IV/312
- junction I/186
- Dion-Jacobson series IV/511ff
- 1,2-dioxetanes II/147
- formation II/147
- dioxocyclam III/467
- 1,3-dioxole IV/49
- 2,6-dioxanthracene III/555
- dioxygen II/752
- dioxygenation II/160
- conjugated dienes II/160
- dioxygenyl II/752
- diphenylacetylene III/701
- 1,2-diphenylbenzocyclobutene II/182
- cation radical II/182
- 1,2-diphenylcyclopropane II/247
- radical cations II/124, II/137f
- – long bond II/137
- diphenyldisulfide I/497
- 1,1-diphenylethene II/149
- cyclodimerization II/149
- diphenyliodonium salt II/760
- diphenylmethane IV/43
- diphenylmethyl II/243
- 1,1-diphenyl-2-picryldrazyl (DPPH) IV/22
- 1,3-diphenyltriazenes II/232
- diphosphaalene II/235, II/252
- 1,3-dipolar cycloaddition II/306
- dipolar donor-acceptor-substituted molecules V/253
- dipolar interactions IV/68
- dipolar molecular structures V/252
- dipole bound state IV/786ff
- dipole moment II/602, II/832
- change II/607
- dipole-dipole interaction I/154, I/218ff, V/360
- dip probe, *see* fiber-optic probe
- DIPR-DIP model (DIP – distributed as in photodissociation) IV/640, IV/656, IV/661f, IV/670
- dipyridinium II/363
- reductive dimerization II/363
- diquinane II/470, II/474
- diquinone ensemble III/308
- Dirac or δ -function IV/317
- diradical I/381, II/208
- singlet I/381
- triplet I/381
- direct charge transfer IV/370

- direct interaction with product repulsion (DIPR)
 - model IV/640ff
- direct transitions V/397
- disilane II/302
- disiliranes II/300
- dismutation V/295
- disorder V/497f
 - energetic V/498
 - positional V/498
- dispersion V/292
- dispersity IV/560ff
 - electron transfer kinetics IV/560ff
- dispersive transport V/456, V/459, V/497
- displays II/837
- disproportionation II/764, IV/17, IV/20, IV/52
- disrotatory thermal cycloreversion V/231
- dissociation II/812, V/482, V/484, V/487
- dissociative electron transfer I/347ff
 - in alkyl halides I/347ff
 - in aryl halides I/347ff
 - in DNA I/353
 - in ethers I/352
 - in strained rings I/351
 - in thioethers I/352
- distal/proximal cleavage ratio III/157
- distance dependence IV/550ff, IV/556, IV/564
 - electron transfer IV/550ff, IV/555ff
 - EET I/219
 - ET rates III/11
 - Miller-Abrahams model III/164
 - quantum mechanical charge migration model III/164
 - strand cleavage III/164
 - TET I/225
 - theoretical model III/164
- distance-decay constant III/5, III/10f
- distance decay factor III/18
- distonic cation radical II/136, II/162
 - butanediyl cation radical II/136
 - heterolysis II/162
 - homolysis II/162
- distonic radical cation III/209
- distorted square-pyramidal geometry IV/24
- distorted tetrahedral structure IV/24
- distribution function IV/355
 - absolute temperature T IV/355
 - Boltzmann's constant IV/355
 - occupation probability IV/355
- 1,5-dithiacyclooctane (DTCO) II/941
- dithienylethylene V/128
- dithiin II/347
 - oxidative dimerization II/347
- dithiocarbamate II/250f, II/819
 - complex II/777
- dithiolate II/819
- dithiole II/348
 - oxidative dimerization II/348
- dithiolene II/638
 - complex II/750
- dithionite II/888
- DMA I/588, II/307, II/935
- (DMAEB) ethyl-4-(dimethylamino)benzoate
 - IV/699, IV/721ff
 - fluorescence emission in a supersonic jet IV/720
 - clusters IV/720
 - excimer formation IV/720
 - exciton interaction IV/723
 - monomer IV/720
 - of monomer and of clusters IV/722
 - TOF mass spectra in a supersonic jet IV/722
 - of monomer and of clusters IV/722
- DMAMB (methyl-4-(dimethylamino)benzoate)
 - IV/699, IV/719, IV/721, IV/724
 - fluorescence emission in a supersonic jet IV/720
 - LIF spectra IV/717, IV/719
 - LIF spectra of complexes with acetonitrile, methanol, water IV/719
- DMPSB V/534
- DMSO, cyclic voltammetry in II/682
- DNA II/837, II/860, III/105ff, III/164, III/238, III/266
 - assays I/333ff
 - base stacking III/108
 - B-form III/108
 - charge migration III/105
 - computers V/176
 - conductivity III/164f
 - fibers III/164
 - single crystals III/164
 - crystalline III/165
 - hopping between shallow traps III/165
 - migration of electrons and holes III/165
 - duplex III/105
 - fibers III/165
 - aligned versus nonaligned III/165
 - conductivity III/165
 - hairpins III/147
 - stilbeneamide linker III/147
 - mediated electron transfer III/147, III/153
 - distance-dependent kinetic data III/153
 - values of β III/153
 - tethered metal complexes III/147
 - nucleobases III/107
 - oxidative cleavage III/105
 - quadruplex III/109
 - ropes III/165
 - single-strand III/105
 - strand cleavage III/154
 - photoinitiated III/154
 - radiolysis III/154
 - structure III/106
 - surface-attached III/166

- cyclic voltametry III/166
- triplex III/109
- docked crystal structures III/455
- dodecahedrane II/223
- dodecaphenylporphyrins IV/55
- π -donation II/827
- donors II/621, V/516, V/569
 - organometallic II/621
 - radical cation V/569
- σ -donor II/808
- Donor/acceptor-substituted *trans*-tetraamineruthenium(II) complexes V/272
- donor-acceptor systems III/144, III/149, III/246, III/288ff, III/409ff, III/611, III/618, IV/703ff, V/103
 - π bridged IV/704
 - clusters with polar molecules in a supersonic jet IV/730
 - coupling between CT and LE states IV/705
 - CT fluorescence IV/704
 - energy level diagram for excimer and LE states IV/724, IV/729
 - exciton interaction in dimers IV/723
 - Franck-Condon excited state IV/704, IV/745
 - intramolecular charge transfer in the excited state IV/729
 - LE state IV/705
 - Mulliken two state model IV/704
 - N bonded systems IV/706
 - phenoxazine derivatives as donors IV/706
 - solvent-equilibrated excited state IV/704
 - coupling I/206
 - decreased mobility III/144
 - geometry III/131
 - interaction II/625, III/289, III/611, III/618
 - hydrogen bonded III/409ff
 - linkage III/288ff
 - local concentrations III/144
 - molecule V/169
 - orientation effects III/246ff
 - pairs IV/127, IV/172, IV/187, V/519, V/545
 - separation III/288ff
 - substituted aromatic conjugated systems V/253
 - substituted polyenes V/253
 - π systems IV/703ff
 - Born Oppenheimer approximation IV/703
 - charge transfer (CT) absorption IV/703
 - charge transfer (CT) fluorescence IV/703
 - electron-vibration coupling IV/703
 - Fermi's golden rule IV/703
 - Franck-Condon principle IV/703
 - Gibbs free energy in IV/703
 - potential energy surface IV/771
 - rate constant for charge transfer IV/703, IV/761
 - solvent reorganization energy IV/703
 - weak coupling III/149
- donor atom- π interaction IV/77
- dopant IV/284, V/237
- doping I/141ff, IV/284
- doppler spectroscopy IV/636
- double layer I/429
 - capacitance I/453ff
 - charging current I/431, I/453
 - electrochemical I/155ff
- double-potential-step chronoamperometry I/437ff, I/455ff, I/458
- DPG V/387
- DPIB V/534
- DPQ V/453
- drift velocity V/456
- driving force II/767, III/3
 - dependence, TET I/229ff, I/232
- dual fluorescence (*see also* dual luminescence) II/402, IV/697ff
- dual layer photoreceptor V/383ff, V/411
- dual luminescence IV/700
 - pseudo Jahn-Teller model IV/700
 - RICT model IV/700
 - role of solute-solvent interactions IV/732
 - TICT model IV/700
 - theoretical calculations IV/700
 - vibronic coupling model IV/700
- dual mode ESR cavity II/991
- dual mode switching systems V/229
- duplex interior III/137
 - effective polarity III/137
- durene II/633
- duroquinone radical anion IV/81
- dyads II/305f, II/313, II/319, II/854, III/238, III/250, III/276ff, III/353ff, III/374ff, III/383f, III/392f, IV/187ff, V/98
 - clip-shaped III/238
 - inorganic-organic III/376
 - oligopeptide III/250
 - phenothiazine containing III/375
 - porphyrins III/276
 - Rh(III)-diquat III/393
 - Ru(bpy)₃²⁺-aryl III/392
 - Ru(bpy)₃²⁺-fullerene III/374
 - Ru(II)-Os(II) III/377ff, III/383
 - Ru(II)-Os(III) III/384
 - Ru(II)-phenothiazine III/394
 - Ru(II)-Rh(III) III/383ff
- dye IV/353, V/285, V/519, V/528ff, V/539, V/542, V/549, V/569, V/606
 - adsorbed I/281ff
 - anion radical V/549
 - azulene V/528
 - cation V/614
 - coumarin V/539
 - cyanine V/519
 - desensitization V/365

- desorption IV/330
- indolenine V/528
- inorganic coordination compounds IV/353
- layers V/600
- merocyanine V/539
- neutral V/549
- organic chromophores IV/353
- pyrylium V/528
- radical V/549
- – anion V/542, V/569
- redox potential V/606
- reduced radical V/569
- sensitization IV/280, IV/353, V/714
- sensitizers V/596, V/600, V/604, V/609, V/623,
- – regeneration V/623ff
- – thermodynamics V/609
- thiopyrylium V/529
- thioxanthene V/539
- triplet V/549
- xanthene V/539
- dynamic quenching III/122

ECE mechanism II/761

EDA complexes II/626, II/634, II/640

- formation II/626
- – constants II/626
- molecular II/626
- outer-sphere II/626, II/634
- second-sphere II/626

EDC IV/136

EDTA II/961, IV/173, IV/181ff, IV/206, V/349

effective density I/140ff

- of states I/185

effective mass of electron m_e^* I/139ff

effective masses of electrons and holes V/698

effective surface area IV/377

effective temperature I/79, I/85, I/91

effects of ion pairing IV/556, IV/560ff

- electron transfer kinetics IV/560ff

- electron transfer rate IV/556

efficiency of energy conversion V/594

efficiency of GG cleavage III/161

- effect of base sequence III/161

EHDNPB V/496

EIN (1-ethyl-2,3-dihydro-indole-5-carbonitrile)

- IV/699, IV/711ff, IV/717, IV/720ff

- absence of dual fluorescence IV/721

- clusters with acetonitrile, methanol, tetrahydrofuran, cyclohexane, water, ammonia IV/727

- electrons, solvated IV/776

- fluorescence emission in a supersonic jet IV/720

- lack of CT fluorescence IV/711

- LIF spectra of clusters IV/717

- structure of dimers IV/721

Einstein coefficient II/603

E-isomers (*see also* exciplex) IV/743, IV/750, IV/752

elaecarpidine II/412

electrical conduction III/230

electrical work I/131

electric field V/71f

- -induced second-harmonic generation (EFISHG) V/247ff

- ion pair V/72

- local V/71

- -poled V/504

- poling of polymers V/274

electric vehicle V/667

electroabsorption V/410ff, V/425, V/484

electro acceptors III/277

- porphyrin system III/277ff

electrocatalysis II/836

electrocatalysts II/816

electrochemical IV/354

- activation IV/128

- activity V/229

- cell V/645, V/647

- communication II/786

- data II/809

- electron transfer I/169

- encoding of data V/64

- flow cells I/477ff, I/487

- impedance IV/302

- – AC impedance IV/302

- – diffusion impedance IV/306

- oxidation II/140, II/808

- parameters II/823

- potential I/427, V/699

- – μ_e I/127ff, I/143ff

- properties III/286, III/297, III/501ff, III/548ff, III/565, III/583ff, III/598, III/658ff

- – catenanes III/548ff

- – catenates III/583ff

- – [3]catenates III/598ff

- – dendrimers III/658ff

- – knots III/583ff

- – metal complexes III/565

- – porphyrin-fullerene dyad III/297

- – porphyrin-quinone dyad III/286

- – pseudorotaxanes III/501

- – rotaxanes III/548ff

- rate constants I/171ff, II/832

- reactions I/167ff, II/782

- – kinetics of I/167ff

- recognition II/837

- reduction II/805

- techniques I/422

- wave splitting V/24

electrochemistry I/323ff, II/857, IV/381, IV/459, V/413

- cyclic voltammetry IV/381

- redox chemistry IV/381
- electrochromism V/230
- active units V/229
- applications III/519
- glasses II/837
- electrocyclic reactions II/182, II/200
- anion radical II/200
- cation radical II/182
- electrodes IV/353ff, IV/366
- cathode IV/353
- deposition V/148
- metal electrodes IV/355
- photoanode IV/353
- planar electrodes IV/366
- position IV/329
- potential I/422, I/482ff
- reactions
 - irreversible I/426, I/432, I/441ff, I/449ff
 - quasi-reversible I/426, I/432, I/441ff, I/449ff
 - reversible I/426, I/432, I/441ff, I/449ff
- surface II/816
- electrogenenerated chemiluminescence (ECL) I/313ff
 - DNA, assays for I/333ff
 - sensor applications of I/331ff
 - immunoassays I/333ff
- electrohydrodimerization II/31
- electroluminescence (EL) I/312ff, IV/300
- electrolysis II/283
- electrolyte II/459, V/311
- electrolytic oxidation I/363
- electron I/505, III/27, V/97
 - acceptor I/518, II/270, II/276, II/282, II/318, II/324, III/542, III/544
 - catenanes III/544ff
 - cyanobenzophenone III/161
 - rotaxanes III/542ff
 - adiabatic detachment energy (ADE) IV/791
 - of $\text{I}^{\cdot-}(\text{H}_2\text{O})_n$ clusters IV/791
 - affinity II/6ff, II/55, II/620, II/678, III/193, IV/742, V/453, V/460
 - of alkanes II/55f
 - attachment II/56
 - binding energy (EBE) IV/780
 - CH_3CN^- IV/788
 - $\text{I}^{\cdot-}(\text{acetone})_n$ clusters IV/787
 - $\text{I}^{\cdot-}(\text{CH}_3\text{CN})_n$ clusters IV/788
 - $\text{I}^{\cdot-}(\text{CH}_3\text{I})_n$ clusters IV/787
 - of $\text{I}^{\cdot-}(\text{H}_2\text{O})_n$ clusters IV/790
 - $\text{I}^{\cdot-}(\text{Xe})_n$ clusters IV/794
 - $\text{Li}^{\cdot-}(\text{NH}_3)_n$ clusters IV/780
 - $\text{Na}^{\cdot-}(\text{H}_2\text{O})_n$ clusters IV/782
 - capture agents IV/332
 - carrier II/958
 - cascade V/203
 - chemically induced polarization II/58
 - conductivity and transport III/454
 - coupling II/308
 - delocalization V/112
 - diffusion IV/331, IV/334
 - donors II/282, II/324, II/487, III/60, III/277, III/542, III/544, IV/90, IV/92, IV/119ff
 - catenanes III/544ff
 - porphyrin systems III/277ff
 - rotaxanes III/542ff
 - effective mass V/611
 - energy levels I/177ff
 - exchange II/273, V/203
 - gas I/133ff
 - hole generation IV/280
 - pair I/274, IV/234, IV/253, V/596
 - recombination I/272
 - hopping II/832, II/843, II/992f, V/125
 - frequency II/593, II/598f
 - rate IV/381
 - impact II/56
 - ionization II/57
 - injection II/853, II/859, IV/377, V/364, V/366, V/370, V/600, V/604, V/609ff, V/615ff
 - dynamics V/609f
 - efficiency V/366
 - energetics V/610
 - kinetic V/370
 - mechanism V/364
 - quantum yield V/612
 - dynamics V/615
 - quantum yield V/616ff
 - rate constant V/618ff
 - sensitization V/369
 - limit III/4
 - localization IV/334
 - mediator V/599f, V/623
 - migration III/118
 - time scale III/118
 - mobility I/132
 - paramagnetic resonance (EPR) II/910, III/289, III/431, V/68
 - time-resolved III/431
 - relay IV/135
 - reservoir II/834, II/997
 - complexes II/715, II/734, II/763, II/790
 - rich V/100
 - scavengers III/118
 - intercalating dyes III/118
 - self-exchange II/239, II/936, II/946
 - source IV/14
 - spin resonance II/57ff
 - spin transfer III/188
 - transfer (ET) (*see also* optical charge transfer, rate constant electron transfer) I/64ff, I/109ff, I/161ff, I/239, I/526, I/517, I/521, I/543, I/547, I/558ff, I/569f, I/582f, I/588, II/13, II/18f, II/161, II/165, II/379ff, II/494f, II/618ff, III/3, III/313, II/583ff, II/593, II/598, II/609, II/611f,

- II/637, II/645, II/652ff, II/662f, II/663, II/665, II/668, II/670, II/951, III/32f, III/37, III/24ff, III/106, III/124, III/140ff, III/179, III/188ff, III/194, III/197, III/201ff, III/207f, III/230ff, III/238ff, III/243ff, III/246ff, III/258ff, III/273ff, III/281ff, III/316, III/322ff, III/341ff, III/383, III/387, III/409ff, III/416, III/433, III/446ff, III/448, III/452, III/454, III/475, III/479, III/556, III/618ff, III/658, IV/129, IV/232, IV/353, IV/358f, IV/429, IV/437, IV/487ff, IV/541ff, IV/555ff, IV/69, V/3ff, V/20ff, V/33f, V/59, V/84, V/285, V/356, V/481, V/484, V/516ff, V/535, V/574, V/596ff, V/606, V/612f, V/645, V/707, III/272ff
- AC impedance spectroscopy IV/555ff
- activated adiabatic mechanism III/141
- activation II/495
- activation energy III/143, IV/558
- addition-elimination II/496
- adiabatic I/64ff, I/78ff, I/86ff, I/113, I/194, IV/359, V/612
- vs. nonadiabatic I/21ff, I/345ff
- alkene IV/566
- alkyl IV/555ff, IV/563ff
- alkyne IV/566ff
- amide (peptide) IV/568ff
- amine (peptide) IV/566
- at electrodes I/126ff, I/176ff
- at interfaces I/126ff
- attenuation parameter III/342
- back III/208
- between two metals I/163ff
- bimolecular V/517
- bond-coupled II/165
- bridge IV/555ff, IV/562ff
- effect III/387
- catalysis II/997
- catalyzed reduction II/816
- chain III/33ff
- chain-to-chain IV/570
- -chain catalysis II/761
- characterization IV/546
- charge-hopping mechanism III/232
- charge shift III/188, III/191, III/210
- chronoamperometry IV/555ff
- coherent I/116
- concerted two-electron I/121ff
- CT-activated II/619
- cyclic voltammetry IV/555ff
- density of occupied and unoccupied electronic states IV/359
- dependence of rate constant on $-\Delta G^0$ I/521
- dependence on driving force IV/552
- determination of reaction cross-sections IV/635
- determination of scalar and vector quantities IV/635
- diffusionless V/574
- dispersity IV/560ff
- dissociative II/18
- distance IV/132
- distance dependence III/141, IV/550ff, IV/556, IV/564
- distance effect III/201, III/387
- DNA III/154
- hole-hopping mechanism III/154
- driving force III/281ff, III/341, III/411
- effects of ion pairing IV/560ff
- efficiency V/484
- dynamics III/141
- electrochemical I/169ff
- electron acceptor IV/359
- electron donor IV/359
- electronic coupling III/181, III/194, III/208, III/260, III/275, III/416, III/453, IV/550ff
- electronic coupling
- electronic factor III/342
- electron static field effect III/249ff
- electrostatic field effect III/448
- endergonic III/33
- endothermic I/72
- energy level diagram IV/633
- energy requirement I/561
- ether IV/566ff
- exchange (Förster) mechanism III/442
- excited state III/273ff, III/341
- exothermic I/72
- free energy dependence of I/114, I/118
- free energy of activation V/518
- heterogeneous systems IV/541ff
- hole-hopping mechanism III/141
- homogeneous I/168
- homogeneous systems IV/546
- Hush formalism III/438
- hydrogen-bonded III/452, IV/566, IV/569
- incoherent hopping I/116
- influence of chemical environment IV/560, IV/563
- influence of disorder IV/543
- influence of defects IV/543, IV/546
- in gating III/140
- integrated overall energies IV/359
- inner sphere I/343ff, II/161, II/620, II/654, II/662, II/668
- inner sphere vs. outer sphere I/345ff
- intercalated compounds IV/487ff
- interfacial I/161ff, I/271ff, IV/353, V/606
- intermediates II/636, II/645
- intermolecular I/373ff, III/410ff, V/516
- intervalence compounds I/379ff
- intramolecular II/13
- inverted region III/140
- jet-cooled molecules I/379

- kinetics I/373ff, I/564, II/830, IV/549, IV/555ff
- electrochemical IV/549
- Langmuir-Blodgett (LB) film IV/550ff
- layered oxides IV/487
- ligand transfer I/343ff
- long-range III/316
- magnetic field effects III/313
- Marcus theory I/517, I/521
- material dependence IV/550ff, IV/556, IV/565
- matrix elements V/448, V/461
- mechanism II/644, II/855
- mediated by redox centers IV/571
- mediators II/804
- medium dynamics controlled I/97ff
- mesoporous material IV/412
- microporous material IV/412, IV/429
- mixed (adiabatic/no-adiabatic) I/86ff
- molecular assembly IV/541
- molecular beam studies IV/635
- monolayer assembly IV/541
- multilayer assembly IV/541
- multistep I/118
- $\text{NH}_3 \cdots \text{HCl}$ cluster IV/680
- non-adiabatic I/64ff, I/69ff, I/86ff, I/104, I/114ff, I/194, IV/359
- non-dissociative II/18
- normal region III/140
- nuclear factor III/345
- optical II/583, I/179, III/207, III/210, III/556
- optical vs. thermal I/11ff, I/30ff, I/41ff
- organic chemistry, in I/342ff
- orientation effects III/246ff
- outer sphere I/168, I/343ff, II/20, II/161, II/495, II/620, II/652, II/654, II/662, II/665, II/668, II/670
- oxidative III/475
- parallel multistep III/322ff
- partial electron transfer IV/678f
- path IV/543
- pathway II/728, II/757, III/32
- phenyl IV/566
- phenylene-ethynylene IV/566
- photoactivated II/619
- photochemical IV/549ff
- photoinduced I/558, II/645, III/179, III/197ff, III/272ff, III/341ff, III/383, III/618ff, III/658
- photosensitized II/619
- polar mechanism II/161
- polynorbornyl IV/562ff
- probes II/860
- processes V/98
- product of the transfer frequency IV/359
- properties II/820
- protein III/24ff, III/141
- proton-coupled (PCET) III/124, III/412, III/433, III/446ff, III/448, III/454
- quenching III/123f
- by nucleosides and nucleotides III/124
- dynamic and static III/123
- rate II/583, II/593, IV/556
- effects of ion pairing IV/556
- metal metal macrocycle IV/93
- rate constant I/561, I/563f, IV/127, V/613
- reaction I/342ff, I/463, I/467, I/491ff, II/583f, IV/633ff
- indirect electron transfer IV/680
- self-exchange I/477ff
- solvent as a transport medium IV/680f
- reaction rates I/563
- reactivity II/842
- redox chemistry IV/429
- relation to van der Waals bond force constant IV/679
- relay system II/319
- reorganization energy III/143
- robust III/33, III/37
- salt bridge IV/566, IV/569
- self assembled systems IV/552ff
- self-exchange, I/373ff, IV/381
- semiclassical model III/3
- semiclassical treatment II/587
- sequential multistep III/322ff
- sequential vs. direct I/9ff, I/51ff
- single collision regime IV/635
- sol-gel material IV/412
- solvation IV/571
- solvent dynamics IV/561
- solvent effects III/273, IV/560ff
- solvent induced IV/680
- in clusters IV/680
- solvent-mediated III/258ff
- square scheme III/479
- π -stack mediated III/238ff
- staffane IV/563
- steady state I/7ff
- steric effects IV/561
- stepwise vs. superexchange I/118
- stoichiometry I/564
- superexchange mechanism III/141, III/183ff, III/230ff, III/343ff
- temperature dependence IV/558
- tethered redox probe IV/552ff, IV/557
- theory III/181, III/192, III/222, III/224, III/232, III/273ff, III/438, III/341ff, III/453, IV/127
- thermal II/583, II/618, III/179
- thermodynamic barrier I/561
- three-mode expression II/609, II/611f
- three-stage I/526
- through-bond IV/560, IV/570ff
- through-bond coupling III/183ff, III/189, III/192ff, III/222, III/342

- through-chain IV/555, IV/560
- through hydrogen bonds III/243ff, III/409ff
- through-space III/284, IV/560, IV/570ff
- through-space coupling III/189, III/224, III/342
- "through space" vs. "through bond" I/378
- two-photon absorption V/60
- two-state model II/583
- vectorial V/597
- wire-like behavior III/141
- zeolite IV/412, IV/429
- photoredox chemistry IV/437
- transmission spectroscopy III/192
- electron transport III/231, V/387, V/453
- material V/387
- trapping V/620
- transporting materials V/431
- tunneling I/73, I/161ff, III/27, III/30, III/34, IV/83
- between two metals I/163ff
- dependence III/27
- edge-to-edge distance III/34
- interfacial I/161ff
- probability of I/161ff
- temperature III/27
- temperature dependence III/27ff
- relay III/475
- 19-electron complexes II/735, II/745, II/763, II/790
- bond energy, 2-electron donor II/703
- 20-electron complexes II/741
- 15-electron species II/761
- electronic (*see also* H_{ab})
- communication II/806, V/24f, V/43
- coupling I/26ff, I/64ff, I/109ff, I/215, I/220, I/223, I/345ff, II/670, II/831, II/853, III/10, IV/550ff, IV/564, IV/565, V/109, V/21, V/23, V/27, V/30, V/32, V/33, V/66, V/371, V/607, V/610, V/612, V/611, V/619, V/622
- adiabatic I/66
- adiabatic vs static I/64ff
- conformational dependence I/45ff
- direct "through-space" I/216, I/218, I/221
- distance dependence I/35, I/46ff, I/225
- effective donor-acceptor separation I/31ff, I/39, I/43ff
- electron transfer IV/550ff
- in singlet energy transfer I/219
- in triplet energy transfer I/223ff
- many-electron effects I/27ff, I/40ff
- matrix I/110ff, V/110
- matrix element I/241, I/252ff, III/3, IV/202, V/112, V/371, V/618f, V/622
- mediated "through-bond" I/216, I/221
- medium effects I/28, I/30, I/53
- non-orthogonality effects I/29ff
- notation for matrix elements I/37ff
- pathway analysis I/26, I/27, I/34, I/36ff, I/40ff, I/48
- parity rule I/35ff, I/45
- spin dependence I/28ff
- static I/67
- superexchange I/34, I/38ff
- tunneling model I/36
- energy transfer (EET) I/40, I/215ff
- singlet energy transfer (SET) I/217ff, I/221
- equilibrium I/127ff
- excitation of reactants IV/652, IV/661
- direct excitation of an electron-transfer complex IV/675
- effect on the reaction dynamics IV/654
- effect on the reaction path IV/652, IV/656
- in Hg atom reactions IV/662
- interaction II/248, V/5, V/7, V/22, V/101, V/123, V/126f
- modulation V/123, V/126
- nucleobase III/111
- spectra III/111
- electronically excited polypyridine complex II/837
- electro-optic effect V/478
- electro-optic response V/503
- electrophile II/282, II/300, IV/3
- nucleophile II/928
- electrophilic addition II/757
- electrophore II/6ff, II/15
- electrophotographic developers V/381
- electrophotographic printing V/380
- electrophotography V/379ff
- electropolymerization IV/143
- electroreduction II/784
- electrospray ionization mass spectrometry (ESI) III/443
- electrostatic forces IV/204
- electrostatic image V/379
- electrostatic interaction IV/146, IV/208, IV/77
- electrostatic potential maps IV/71
- electrostatic potentials IV/69
- electrosynthesis I/271ff
- elementary reaction I/563
- elementary step IV/3
- Eley-Rideal mechanism I/289, IV/650
- elimination of H₂ II/71
- elimination reaction II/71
- elon V/296
- emission IV/110, IV/251, IV/253
- lifetime IV/110
- spectrum IV/243
- emissive ³MLCT state II/858
- emulsion V/292
- ENABLED OR logic V/168
- enamines V/384
- encapsulation II/834
- encounter complex II/619, II/668, V/402

- endergonic II/762, IV/176, IV/178
- endergonic cross electron transfer II/775
- endergonic process IV/172
- end-on coordination IV/21
- endoperoxide V/130
- ENDOR II/103, II/114, II/206, II/989
- spectroscopy II/911
- endoreceptors II/788
- energetic disorder V/443ff, V/453
- energy V/187, V/645
- bands I/137ff
- bond dissociation II/9ff
- cascade V/190
- chemical V/645
- electric V/645
- consumption V/589
- conversion III/272
- conversion efficiency V/594
- conversion systems V/657
- primary cells V/657ff
- alkaline manganese cell V/659
- Leclanché cell V/657, V/659
- Li-based system V/658
- lithium-based systems V/657, V/661
- lithium/iodine PVP V/661
- lithium-manganese dioxide V/661
- practical energy density V/657f
- Ruben-Mallory cell V/660
- specific energy V/657f
- tinc-air V/660
- zinc-based systems V/657
- zinc-carbon V/657
- zinc chloride system V/659
- zinc-mercuric oxide V/660
- Zn-Ag₂O V/658
- Zn-air V/658
- Zn-carbon V/658
- Zn-MnO₂ alkaline V/658
- secondary cells V/657f, V/661ff
- alkaline Zn-MnO₂ V/665
- lead-acid V/658, V/662, V/673
- lead-acid system V/662
- lithium-ion V/658, V/662, V/673
- lithium-metal V/662
- Ni-based systems V/663
- Ni-Cd V/662
- nickel-based system V/664
- nickel-cadmium V/663ff
- nickel-hydrogen cell V/664
- nickel-metal hydride V/664f
- Ni-MH V/662
- nickel-cadmium V/658
- nickel-metal hydride V/658
- practical energy density V/662
- SLI V/663
- specific energy V/662
- valve-regulated lead-acid batteries (VRLA) V/663
- zinc-air V/666
- zinc-nickel V/666
- Zn-air V/673
- Zn-based systems V/665
- Zn-MnO₂ alkaline V/662
- supercapacitors V/668ff
- conducting polymers V/668ff
- double-layer V/668
- electrochemical V/673
- metal oxides V/668
- pseudocapacitance V/668
- pseudocapacitive materials V/668
- redox V/668
- donor/acceptor V/97
- electron transfer V/100
- gap I/13ff, I/35ff, I/45, I/53, I/139, III/153, V/363, V/696
- initial and bridge states III/153
- gradients V/202
- hopping V/196, V/206
- level diagrams V/701
- migration V/187, V/205, V/210f
- sink V/200
- storage IV/279
- surface II/583f, II/587
- first order II/587
- zero order II/584
- transfer II/321, II/854, III/254ff, III/339, III/377ff, III/390, III/427ff, III/525, III/609, III/612, IV/361, V/5, V/7, V/23, V/35, V/36, V/38, V/42, V/73, V/80, V/84, V/102, V/115, V/190, V/356
- aromatic units III/390
- catenates III/609, III/612
- coulombic (Dexter) mechanism III/255ff, III/348, III/378
- dendrons V/77
- Dexter V/73
- exchange (Förster) mechanism III/255ff, III/348, III/378, V/73
- Förster formula III/349, III/378
- intramolecular V/112
- pseudorotaxanes III/525
- rate constant III/347, V/102, V/115
- reversible III/390
- Ru(II)-Os(II) dyads III/377ff
- theory III/255ff, III/347ff, III/378
- through-bond-mediated III/254ff
- energy trap V/192, V/206
- energy-gap law II/845
- enol radical cations II/485
- enol silanes IV/44
- enol/allyl ethers and olefins IV/248
- eNOS III/72, III/75, III/77
- enthalpy of activation I/55ff
- enthalpy of solvation IV/776

- entrapment IV/140, IV/143
- entropy I/129ff, V/590ff
 - activation I/55ff
 - light V/591
- envelope II/75
- environmental remediation IV/279
- enzymes II/786, II/905, II/923, IV/127
 - catalysis III/454
 - pathways IV/170
- eosin IV/183f
- epilupine II/433
- epoxy cements IV/145
- EPR I/412, I/545f, II/206, II/209, II/307, II/910, II/913, II/917, V/68, IV/75, V/706, V/709ff
 - chemically induced dynamic electron polarization (CIDEP) I/545
 - fluorescence-detected magnetic resonance (FDMR) I/545
 - free induction decay (FID) I/412, I/546
 - line-broadening II/832
 - oxygen-centered radicals V/706
 - spectra II/912
 - spectroscopy II/815
 - Ti(III) sites V/706
 - trapping sites V/706
- equations I/412, V/522ff, V/534, V/543, V/574, V/577
 - Butler-Volmer I/425
 - Cottrell I/431, I/452
 - current-overpotential I/425, I/492
 - current-potential I/424
 - Eyring I/412
 - Fick's first law I/428, I/431, I/442, I/473
 - Fick's second law I/428, I/431, I/442
 - Hammett V/577
 - Levich I/474
 - Marcus V/523, V/543, V/574
 - Nernst I/422ff, I/443, I/489
 - Nernst-Planck I/427ff, I/473
 - Rehm-Weller V/522ff, V/534, V/543, V/574
 - Tafel I/426
 - thickness of diffusion layer I/428
- equilibrium constant I/423, I/435, II/32
- equilibrium potential I/425
- equilibrium solvation energy II/596
- equipartition law I/75
- equivalent circuit IV/287ff
- erasable holographic data storage V/52
- ergodicity I/82, I/89
- ergonicity II/762
- ESCA V/401
- ESI MS (electrospray ionization mass spectroscopy) II/948, II/953
- ESR I/354ff, I/381, II/103, II/114, II/272, II/299, II/385ff, II/935, II/949, IV/11, IV/20, IV/35, IV/54, IV/496f, V/312, V/419, V/559
 - ENDOR II/101, II/105
 - line broadening in I/374ff
 - spectrum II/98
 - structure of Ni-loaded $K_4Nb_6O_{17}$ IV/496
- esters II/463
- ETC II/761
- Et_3SiClO_4 IV/43
- etching IV/326
 - anisotropic photo IV/326
 - electroless IV/326
 - photo IV/326
 - wet IV/326
- ethane II/943
 - radical cation II/62
- ethanoadenine III/130
 - fluorescence quenching III/130
- ethanol fermentation IV/38
- ethene anion radical II/188
 - three-electron bond II/188
- ethene cation radical II/136f
 - hyperconjugation II/137
- ether IV/566ff
 - electron transfer bridge IV/566ff
- ethidium III/129, III/151
 - bromide III/138
 - – intercalation III/138
 - – proton transfer quenching III/138
 - – upper singlet state reaction III/138
 - dynamics of singlet-state decay III/151
 - electron transfer from nucleotides III/129
 - fluorescence III/142
 - – quenching by diazpyrenium dichloride III/142
- 1-ethyl-2,3-dihydro-indole-5-carbonitrile (EIN) IV/699, IV/711ff, IV/717, IV/720ff
- ethyl-4-(dimethylamino)benzoate (DMAEB) IV/699
- ethylene II/228f
- ethyne II/147
 - cation radical II/147
- etioporphyrin III/307
- europium cryptate V/194
- EXAFS II/914, IV/96, IV/496ff
 - Ni-loaded IV/498
 - structure of Ni-loaded $K_4Nb_6O_{17}$ IV/496
- excess negative charge I/152
- excess positive charge I/152
- exchange coupling II/991
- exchange current I/425, IV/298
 - density I/130, I/174, IV/251
- exchange integral I/219, I/223
- exchange interaction II/210, IV/746
- exchange phenomena II/992
- excimer II/144, V/398, V/454, V/456
 - *trans*-anethole II/144
- exciplex (*see also* E-isomers) II/292, II/306, II/318, II/324, II/397, II/961, III/606, III/618, V/395, V/402, IV/743

- Cu(I)-phenanthrolines III/605, III/618
- formation IV/759, V/196
- - barrier for IV/759
- potential energy surface IV/771
- structure, of gas phase exciplexes IV/769
- - modeling IV/769
- excitation hopping V/196
- excitation sources I/571, I/583
- hydrogen-flashlamp I/583
- excited doublet state V/64
- excited sensitizers II/859
- excited state I/528, I/562, III/276ff, IV/395, V/8, V/21, V/36, V/517ff
- annihilation IV/383
- complex II/292
- electron transfer II/806, II/837, II/853, III/276, V/22, V/33, V/36
- energy II/291, IV/110ff
- interfacial electron transfer IV/397
- - electronic tunneling barrier IV/397
- - escape of the initially prepared wave packet IV/397
- - gradient V/192
- lifetime II/806, II/845
- oxidants II/844
- photoinduced charge separation III/276ff
- photooxidized V/517
- photoreduced V/517
- quenching
- - Re(α -diimine)(CO)₃L IV/111f
- reductants II/844
- reduction potentials IV/371
- Re(α -diimine)(CO)₃L IV/106, IV/109ff
- relaxation I/239, I/249ff, I/265
- singlet IV/395, V/517
- transition metal complexes I/528
- triplet IV/395
- exciton V/356, V/396, V/406, V/423
- annihilation V/423
- delocalization V/189
- excitonic energy transfer IV/375
- exoreceptors II/788
- exposure curve V/290
- extended atom II/992
- extended Hückel I/115
- extension systems III/526
- pseudorotaxanes III/525
- external bias IV/403
- external electric field V/474
- extinction coefficient I/482, I/485, V/601
- extrusion II/761
- E-Z* isomerization V/231
- quantum yield V/231
- FA III/87
- fac-Re(α -diimine)(CO)₂XX IV/104
- fac-Re(α -diimine)(CO)₃X IV/104
- factors affecting stereo- and regiochemistry II/119
- FAD (*see also* flavin adenine dinucleotide) IV/138, IV/151ff, IV/168, IV/225
- -FADH enzyme II/786
- faradaic charge transfer IV/302
- faradaic current I/456
- faradaic process IV/302, IV/324
- faradaic resistance IV/324
- Faraday constant IV/9
- fast electrochemical techniques II/777
- fast electron I/504
- ionizing radiation I/504
- fatigue resistance V/225f, V/231, V/233
- properties V/224
- fatty acid IV/226
- Fc II/950
- Fd IV/210
- ⁵⁷Fe II/911
- Fe(II) II/922
- [Fe^I(η^5 -C₅Me₅)(η^6 -C₆Me₆)] II/793
- [Fe^ICp(η^6 -arene)] II/763
- [Fe^ICp(η^6 -C₆Me₆)] II/792
- [Fe^ICp(arene)] II/735
- [Fe^{II}(η^6 -C₆Me₆)] [PF₆] II/792
- [Fe^{II}(CN)₆]⁴⁻ II/761
- [Fe^{III}(η^5 -C₅Me₅)(η^6 -C₆Me₆)] [SbCl₆]₂ II/793
- [Fe^{III}(CN)₆]³⁻ II/761
- Fe₂O₃ IV/491
- K_{4-x}H_xNb₆O₁₇ IV/491
- Fe₂O₃ V/602
- Fe₂O₃-clay IV/522, IV/524ff
- absorption spectra IV/524
- Fe₄S₄ cluster IV/54
- febtron I/531
- pulse radiolysis I/531
- Fe^I catalyst II/786
- Fe^I complex II/742
- femtochemistry IV/637
- femtosecond mid-IR IV/397
- rise time IV/397
- Fermi-Dirac statistics I/159
- Fermi "golden rule" I/71, I/16ff, I/113, I/195, I/205, I/215, II/606, III/27, III/182, IV/631, IV/703, V/610
- Fermi level I/135, I/274, IV/281ff, IV/293, IV/301, IV/355, V/615, V/699, V/713ff, V/382
- conduction band I/275
- defects I/277
- metal oxide I/281
- photosensitization of I/281
- pinning IV/293, IV/385
- quantization effects I/279
- quasi-Fermi level concept IV/301
- space charge I/277
- Fermi statistics IV/281
- ferredoxin IV/170, V/599

- NADP⁺ reductase (FNR) IV/173, IV/204, IV/210
- oxidoreductase IV/54
- reductase IV/175
- ferric porphyrin π radical cations II/944, II/947
- ferricenium II/272
- ferricyanide IV/132
- ferritin IV/130
- ferrocene II/272, II/292, II/305, II/630, II/633, II/733, II/950, II/962, II/983f, III/372f, III/496, III/516, III/657, III/659ff, III/682, IV/13, IV/17, IV/73, IV/132, IV/135, IV/138, IV/140, IV/148, IV/150, IV/168, V/7, V/18, V/23f, V/33f, V/36, V/40f
- chromophore-ferrocene dyads III/373
- carboxylate IV/144
- carboxylic acid IV/132
- covalently linked systems III/372
- decamethyl IV/17
- dendrimers II/786, III/657, III/659ff, III/682
- derivative III/487
- donor group complexes V/268
- encapsulated III/496
- pseudorotaxanes III/516
- ferrocenium II/733, II/746, II/780
- ferrocenophane II/788
- ferrocenyl V/14, V/18, V/32, V/36, V/38f, V/41
- dendrimers II/733
- ferrocenylmethanol IV/132
- ferrocyanide II/936, IV/143
- ferromagnets II/244
- ferryl III/48f
- fiber-optic probe I/482, I/491, I/492
- Fick's first law I/428, I/431, I/442, I/473
- Fick's second law I/428, I/431, I/442
- field-assisted diffusion IV/334
- field-assisted dissociation V/402
- field-assisted transport IV/335
- FIH⁺ IV/40
- filament V/326
- filamentary growth V/331
- filamentary silver V/289
- first ionization energy II/735
- first-order rate constant IV/310
- five-coordinate complex IV/56
- five-coordinated species II/813
- fixing V/355
- flame experiment IV/637
- reaction of alkali metal atom with a halogen molecule IV/637
- flashlamps I/571
- flash photolysis II/817, V/709ff
- flash-quench technique II/860
- flat-band condition IV/404
- flat-band potential I/290, IV/290, IV/391, V/615, V/617, V/704
- flavin (FAD) IV/11, IV/33, IV/43, IV/68ff, IV/211
- flavin adenine dinucleotide (*see also* FAD) IV/54, IV/129
- 4a-hydroperoxide IV/33
- radical anion II/402
- reductase IV/143f
- -photoexcitation IV/205
- flavocytochrome IV/129, IV/204
- flavocytochrome *b*₂ IV/205
- flavocytochrome *b*₂ (Fcyt *b*) IV/222
- flavodoxin IV/74
- flavoproteins IV/33
- flow cell I/477ff, I/487
- flow-flash III/43
- apparatus III/43
- technique III/43
- fluctuating energy level model I/144ff
- fluctuations I/130, V/497
- fluorenone II/244, IV/16, V/484
- ketyl IV/16
- radical anion IV/17
- fluorescein V/86
- fluorescence I/559, I/569, I/582, I/586, II/305, II/958, III/206, III/273ff, III/279, III/292, III/425, V/49, V/237, V/239, V/395, V/402
- anisotropy V/196
- decay III/279, III/292
- delayed III/206
- detected magnetic resonance (FDMR) I/545, II/98
- - EPR I/545
- emission spectrum IV/743
- ethidium (ET⁺) III/150
- excitation sources I/568
- excitation spectrum IV/743, IV/745
- lifetime IV/746, V/613
- quenching by deazaguanine (Z) III/150
- instrumentation I/582
- intrinsic lifetimes I/582
- lifetime II/958, III/279ff
- quantum yield V/594
- - data III/151
- - distance dependence III/151
- quenching III/145, IV/551, V/392, V/395, V/402
- - distance-dependent III/145
- sensitivity I/582
- spectroscopy II/957
- steady-state III/279
- time resolved III/279ff, III/425
- upconversion I/569, I/586
- fluorescent exciplexes II/390
- fluorescent reagents V/159
- fluoroquinolone II/367
- defluorination II/367
- FMN semiquinone IV/222, IV/225
- fog V/292
- formal potential I/489

- formaldehyde IV/35
- formate dehydrogenase IV/162, IV/179, IV/191
- formation of gated holes V/60
- formato-rhenium complex IV/115
- formulation of monomers V/564
- Förster V/73, V/190f
 - energy transfer V/190
 - mechanism V/102
 - – through-space V/102
 - model I/218ff
 - singlet-singlet mechanism V/190
- Förster and Dexter mechanisms IV/360
- forward-bias IV/298
- fossil fuel V/597
- four-electron reduction II/928, I/949
- four-state valence bond (VB) model I/190, I/198ff
- four-wave mixing V/511
- four-way mixing V/501
- fractal V/405
- fraction of electrolysis I/470
- fragmentation II/640, II/658, I/664
 - radical anions II/559
 - reaction II/71
- Franck-Condon III/27
 - control I/11, I/17
 - excitation IV/704, IV/745
 - excited state I/239, I/249, II/838
 - factor I/72ff, I/109ff, I/218, I/222, I/228, I/232, I/235, I/319, II/607, II/609, III/212, III/215, III/274, III/345, III/449ff, III/453, V/610, V/618, V/621,
 - – electronic I/28
 - – Marcus-Jortner expression for I/228
 - – nuclear I/17ff
 - – Siebrand's expression for I/235
 - – spectral overlap I/218, I/222, I/228
 - principle I/76, I/92, IV/6, IV/628, IV/633, IV/663, IV/700, IV/703, V/7
 - state II/838, II/853, IV/355, IV/401
 - terms IV/202
- free activation energy V/101
- free carrier V/402
- free energy I/13ff, I/19ff, V/590ff
 - activation (*see also* activation free energy) I/14, I/17, I/19ff, I/24ff, I/55ff, II/586, II/590, II/599, II/601
 - change V/534, V/545, V/553
 - curve II/585, II/591
 - diabatic (*see also* diabatic free-energy) II/584f
 - functional I/112ff
 - inverted regimes (*see also* inverted regime, normal regime, barrierless regime) II/586
 - reaction I/70ff, I/94
 - surface I/194, I/203, I/206, I/210ff, II/603
- free induction decay (FID) I/546
- EPR I/545f
- free radical formation quantum yield V/579
- free solvated radical ions II/397
- free-base porphyrin V/199
- free-electron model I/133ff
- free-energy correlation II/663
- free-energy dependence II/665, II/670
- free-energy gradient IV/331
- free-radical intermediates V/516
- Frenkel exciton V/412, V/482
- frequency doubling I/568
- frequency-resolved IV/296
- Freundlich isotherm V/328
- frontier orbitals III/274, III/341
 - model (*see also* HOMO, LUMO) IV/637, IV/647ff, IV/661, IV/705
 - – of LE-CT states coupling IV/705
 - – reaction of alkali metal atom with a halogen molecule IV/637, IV/661
 - – transition metal reactions IV/647
- fructose dehydrogenase IV/129, IV/150
- fuel cells V/673ff
 - AFC V/675
 - alkaline fuel cells (AFCs) V/676
 - direct methanol fuel cells (DMFCs) V/676
 - DMFC V/675
 - MCFC V/675
 - molten carbonate fuel cells (MCFCs) V/674
 - PAFC V/675
 - PEFC V/675
 - phosphoric acid fuel cells (PAFCs) V/674
 - polymer electrolyte fuel cells (PEFCs) V/676
 - polymer electrolyte membrane fuel cells (PEMFCs) V/676
 - SOFC V/675
 - solid oxide fuel cells (SOFCs) V/674
- fulgides V/58
- Fullerenes I/517, I/520, I/523, II/254, III/225ff, III/278ff, III/295, III/299, III/373, III/681, III/688, V/70, V/199
 - C₆₀ V/484
 - C₇₀ V/484
 - C₇₆ II/756
 - carboxylate II/279
 - chromophores III/225ff
 - dendrimers III/681f
 - electron-donor systems II/305
 - excited state III/373
 - pyrrolidine functionalized III/295
 - radical anion I/517, II/291
 - radical cation I/520
 - radical ion III/299
 - π -radical anion II/276, II/280, II/291, II/309
 - π -radical cation II/291
 - reduction potential III/373
 - –surfactant assembly II/278
- fulvalene II/764
- fumarase IV/176

- fumaronitrile II/656
 functional modeling II/918
 functionalised electrodes III/668, III/707
 functionalization II/277, II/305
 functionalized electrodes III/576
 – catenanes III/576
 furan II/339, II/346, II/352, II/356f, II/359
 furan II/370
 – arylation II/370
 – fluorination II/352
 – photochemical reaction with alkenes II/356
 – photochemical reaction with haloquinones II/358f
 – perfluoroalkylation II/357
 – radical cation II/339, II/346
 furyl fulgide V/229
- g* anisotropy II/984, II/988
g factor II/981ff
g value I/518, II/911, IV/18, IV/20
 GaAs V/426, V/638
 GaInP₂ V/638
 galactose oxidase (GAO) IV/22, IV/143
 galvanic cell I/143ff
 galvanostat I/470
 gamma radiolysis II/140
 Gamov expression V/612, V/622, V/629
 gap law I/73
 Gärtner model IV/308
 gas-phase II/323
 gated electron transfer III/146
 gated photochromic reactivity V/227
 gates III/324
 gauche conformations II/64
 gauche conformer II/64ff
 – deprotonation II/66, II/70, II/71
 – pentasil zeolite II/66
 Gauss' law of electrostatic V/476
 gaussian (or cgs) system V/246
 gaussian disorder model V/444ff
 – dependence V/447
 – field-strength V/447
 gaussian distribution IV/289, V/401, V/443, V/445
 – function IV/359
 – Boltzmann constant IV/359
 – reorganization energy IV/359
 gelatin V/292
 geminate ion pairs III/128
 – charge recombination III/128
 – charge separation III/128
 geminate pair V/393ff, V/412
 geminate recombination V/395, V/402, V/482
 – time dependence V/395
 generalized Mulliken-Hush model (GMH) I/32ff, II/608
 generating functions I/73
- geometric isomerization II/97
 geometrical disorder V/443, V/446, V/448, V/454, V/456
 geometry fluctuations I/116ff
 Gerischer theory I/180ff
 Gerischer's distributions IV/399
 Gerischer-like diagram IV/405
 Gerischer-type diagram IV/377
 GG steps III/149
 – cleavage of DNA III/149
 – hole delocalization III/149
 – shallow hole traps III/149
 GGG hole trap III/152
 – electron transfer III/152
 giant dipole I/377
 Gibbs-Thomson equation V/321
 Glaser reaction V/13, V/16
 glass transition temperature V/490
 glassed solvent III/18
 global efficiency V/593ff
 glucose dehydrogenase IV/132, IV/150, IV/155, IV/161
 glucose oxidase (*see also* Gox) II/786, IV/129ff, IV/137f, IV/140, IV/143f, IV/146, IV/148, IV/151, IV/161f, IV/168
 glutaric dialdehyde IV/146, IV/156, IV/159
 glutathione IV/138
 – reductase IV/138, IV/168, IV/179, IV/181, IV/182
 glycerol-3-phosphate oxidase IV/145
 gold nuclei V/304
 gold sensitization V/323
 Gouy layer IV/288
 Gox (*see also* glucose oxidase) IV/149, IV/153ff, IV/164
 graphite II/726
 graphite paste IV/147
 graph-set analysis III/412
 grating V/499
 green plants V/597
 Green's function I/110, I/115
 Grignard II/470
 – reaction I/348, II/727ff
 ground-state complexation III/122
 group dipole moments V/454
 guanidine IV/216
 guanine II/837, III/115, III/427ff
 – oxidation III/116
 – Ru(bpy)₃³⁺ III/116
 – selective oxidation III/115
 guanosine cation radical III/117
 – absorption spectroscopy III/117
 guanylate cyclase III/74
 guest molecule IV/8
 guest-host systems V/274
 guests III/462ff, III/523
 – interchange III/523

- H_2 II/942
 H_2 evolution IV/178
 $H_{2.4}K_{1.6}Nb_6O_{17}$ IV/502
 H_2Pc V/413
 H_2Pc V/418
 – photogeneration quantum yield V/418
 $H_2Ti_3O_7$ IV/507
 $H_2Ti_4O_9$ IV/506ff
 – Fe_2O_3 IV/506
 – TiO_2 IV/506
 H_{ab} II/587, II/589ff, II/598f, II/604f, II/608
 HABI V/559
 – dimer V/559
 hydrated electron II/281
 H-aggregate V/359
 Hagihara-Sonogashira reaction V/18
 hairpin structure III/109, III/136
 – charge recombination III/136
 – charge separation III/136
 – thermodynamic stability III/136
 half-cell V/293
 half chair II/75
 half collision IV/662
 half-field region II/991
 half-peak width I/444ff, I/450
 halftone dot images V/314
 halide complex II/812
 halides II/788
 halogen II/753
 α -halo ketones IV/13
 Hamilton path problem V/175
 Hammett plot I/283
 Hammett constant V/575
 Hammett equation V/577
 Hammett parameters II/829
 hardener V/346
 harmonic generator I/578
 harpoon mechanism III/198, III/264, IV/627,
 IV/633ff, IV/642ff, IV/649ff, IV/659, IV/759
 – alkaline earth metal atoms IV/642
 – clusters in IV/634
 – double harpoon mechanism IV/642, IV/657
 – – reaction with oxidizing agents IV/642
 – electron donor-acceptor system IV/638
 – impulsive regime in IV/638
 – long-lived complex in IV/638
 – Magee's equation IV/638
 – multicenter harpoon reactions IV/649
 – reaction of alkali metal atom with a halogen
 molecule IV/638
 $HBFe_4$ II/755
 $HCa_2Nb_3O_{10}$ IV/512
 $HCa_2Nb_3O_{10}$ IV/513ff
 – silica-pillared IV/513
 $HCa_2Nb_3O_{10}$ IV/514
 – SiO_2 IV/514
 $HClO_4$ IV/12
 He_α impact II/56
 heat of protonation II/685
 heating I/405
 – Joule I/405
 – laser I/405
 – microwave I/405
 – optical I/405
 heat-mode optical recording V/220
 heavy atom effect III/607
 heavy metal ions V/713
 – improved optical properties V/713
 hectorite IV/526
 Heisenberg uncertainty principle V/89
 helicates III/605
 heliotridone II/440
 α -helix II/311, III/12f, III/16f, III/424
 Helmholtz IV/329
 – double layer IV/329
 – layer I/187, IV/288, IV/329, IV/386, V/699
 – region IV/287, IV/329
 heme III/27, III/31ff
 – *b* III/56
 – group II/941
 – peroxidase III/83ff
 – proteins III/15
 – – calcium-binding sites III/87
 – – catalytic mechanism III/88
 – – divalent cations III/92
 – – glycosylation sites III/86
 – – molecular structure III/84
 – oxywater complex III/88
 hemicaged ligands II/834
 hemiacerands III/495
 hemoglobin III/56, IV/133, IV/135, IV/156,
 IV/184
 hemoproteins IV/133, IV/187
 heptane II/943
 hetero cross-coupling V/16
 heterobimetallic metallocenes V/270
 heterocoupling IV/260, IV/270
 heterocycles II/339ff, II/341ff, II/345ff, II/350,
 II/352, II/354, II/356, II/360ff, II/362ff, II/367,
 II/369, II/371
 – alkylation II/364
 – coupling II/346ff
 – cycloaddition II/360, II/371
 – dimerization II/346ff
 – halogenation II/350
 – halogen substitution II/369
 – oxygenation II/360
 – polymerization II/346ff
 – pyridine II/372
 – radical anions II/341f, II/361ff, II/364, II/371
 – – alkylation II/364
 – – dimerization II/363
 – – polymerization II/362f

- rearrangement II/362
- ring opening II/362
- structure II/341ff
- radical cations II/339ff, II/342ff, II/346ff, II/354, II/360
- coupling II/346ff
- cycloaddition II/360
- dimerization II/346ff
- polymerization II/346ff
- structure II/339
- radical ions II/342
- stable II/342
- reaction II/342ff, II/361ff
- with nucleophiles II/354
- rearrangement II/345
- radical cations II/342ff, II/345
- reactions II/342ff
- rearrangement II/345
- ring opening II/345
- reductive cleavage II/367
- ring opening II/345
- ring reduction II/372
- $S_{RN}1$ reaction II/369
- SET alkylation II/356
- SET arylation II/356
- SET dehalogenation II/367
- SET halogenation II/350
- SET nitration II/352
- stable II/342
- structure II/341ff
- heterodinuclear complex IV/24
- heterodyad V/629f
- heterogeneous catalysis V/327
- heterogeneous electron transfer II/831, V/589
- heterogeneous kinetics I/425
- heterolytic bond cleavage II/679
- heterolytic cleavage II/952
- heterometallic complexes V/111
- heteronuclear complexes V/115
- heteronuclear radical anions II/250
- heterostructure V/483
- heterosupramolecular systems III/531, III/576
- heterotriads V/628ff
- 2,2',4,3',5,5'-hexaarylhisimidazoles (HABIs) V/558
- hexacarbonyl complexes I/521
- transition metal complexes I/521
- hexacarbonylchromium II/624
- hexacarbonylvandate II/624, II/647
- hexachlorobenzene V/716
- hexachloroiridate(IV) II/665
- hexad III/318ff, II/322
- hexafluoride II/750
- 1,1,1,3,3,3-hexafluoropropan-2-ol (HFP) II/214
- hexahydropyrene II/213, II/216
- hexamethylphosphoric triamide (HMPA) IV/16
- hexylamine III/524
- Hg + Cl₂ reaction IV/663ff
- HgSe V/699
- high-density data storage systems V/51
- highest occupied molecular orbital (HOMO) IV/79
- high-field ESR II/985
- high-frequency I/228
- demodulation of the multi-photon fluorescence V/251
- high-pressure techniques I/412
- high-spin II/244, II/929, IV/226
- high-valent iron-oxo porphyrin π radical cation II/929
- high-valent metalloporphyrin II/928
- hindered amine base II/165
- HiPIP III/17, III/20
- histidine II/786, II/860, II/950, III/485
- HLaNb₂O₇ IV/511
- HlaNb₂O₇ IV/512
- HNb₃O₈ IV/506ff
- HO₃SCF₃ II/755
- Hofmann-Löffler-Fraytag reaction II/36
- HOGaPC V/425
- hole I/140
- -burning spectroscopy IV/629, IV/732, IV/745, IV/749, IV/751, IV/755
- conductors V/627
- density II/136
- diffusion length IV/305
- generation in zeolites II/70
- hopping III/155, III/163, V/499
- mechanism III/241
- rate constant III/155
- superexchange process III/155
- injection IV/299, IV/377, V/627
- dynamics V/627
- sensitization V/369
- lifetime IV/308
- migration III/119
- mobility IV/308
- rate constant III/163
- recombination V/479
- stilbene-linked hairpins III/163
- transfer II/141, III/117, III/192, III/194, III/211, III/240, III/242, V/3, V/23, V/42
- adenine to guanine III/117
- mechanism III/186
- transfer sensitization V/365
- transport V/386, V/430, V/497, V/628
- dispersive V/497
- glasses V/500
- material V/483, V/499
- medium V/600, V/627
- polymers V/500
- trap III/155
- GG or GGG step III/155
- trapping V/459

- mechanism V/372
- velocity V/457
- holograms V/347, V/472ff, V/487, V/493, V/508
- growth time constants V/493
- erasure V/508
- holographic data storage V/508
- holographic response V/490
- holographic time of flight (HTOF) V/501
- holography V/170, V/472
- HOMO II/5ff, II/12, II/15, II/270, III/199, III/230, III/273ff, III/381, III/628, IV/79, V/363, V/430, V/485, V/516, V/609
- energy of II/12
- LUMO orbitals I/224, I/226ff, I/230, IV/648
- homoconjugation II/91
- homodinuclear complexes IV/25, V/115
- homogeneous absorption bands V/170
- homogeneous catalysis II/779
- homogeneous kinetics I/429
- homogeneous transfer coefficient I/498
- homolysis II/980
- homolytic bond cleavage II/679
- homolytic cleavage II/653
- homometallic dinuclear complex II/835
- homonaphthaquinone II/447
- Hoogsteen associations III/431
- hopping V/125, V/443, V/449
- dynamics III/232
- site V/442
- horse radish peroxidase (*see also* HRP) IV/128f, IV/143, IV/148
- host molecule IV/8
- host-guest complexes III/423, IV/74
- host-guest interactions II/834
- hosts III/462ff, III/519
- interchange III/519
- hot carrier transfer IV/320
- hot electron cooling IV/320
- hot electron injection IV/396
- housanes II/231
- HPb₂Nb₃O₁₀ IV/512
- HPb₂Nb₃O₁₀ IV/515ff
- HPF₆ II/755
- HRP (*see also* horse radish peroxidase) III/84ff, IV/128, IV/130f
- 1,3-H-shift II/99
- HSr₂Nb₃O₁₀ IV/512
- HSr₂Nb₆O₁₀ IV/512
- SiO₂ IV/512
- HTi₂NbO₇ IV/506ff
- HTiNbO₅ IV/535
- HTOF V/501
- Huang-Rhys factor I/71ff, I/91, I/104
- Hubbard Hamiltonian II/826
- humidity V/382
- Hush II/601, II/608, V/21, V/29, V/41
- equation V/26, V/28, V/30, V/40
- formula V/31, V/39
- model I/384ff
- hydrated electron I/507f, I/524, II/275, III/117, V/716
- absorption spectrum I/524, I/527
- cavity volume I/527
- rate constants for some reactions I/508
- reactivity I/507
- selected properties I/507
- hydration shell I/168
- hydrazil radical IV/260
- Hydrazine I/381ff, II/245, II/732,
- hydrazobenzene IV/261
- hydrazone V/384, V/408
- cyclization IV/247
- hydricity II/906
- hydride II/727ff, II/905, II/908, II/911
- abstraction II/757
- donor II/294
- shift II/96
- transfer II/728, IV/29, IV/33, IV/36, IV/174, IV/184
- hydroalkylation of olefins IV/247
- hydrocarbon oxidations II/837
- hydrodimer IV/269
- hydrodimerization I/461
- hydrodimers IV/268
- hydrodynamic electrochemical techniques I/468ff
- preparative electrolysis I/470, I/475
- rotating disc electrode I/463, I/472ff, I/474ff, I/496
- hydrodynamic voltammetry IV/305
- hydrogels IV/146
- hydrogen II/104, II/107, II/905
- abstraction II/36
- atom I/508f, I/525, I/546
- abstraction III/454
- hydride formation I/509
- selected properties I/507
- transfer IV/205
- binding IV/46
- bond III/41ff, III/502, IV/224, IV/566, IV/569ff
- electron transfer bridge IV/566, IV/569ff
- interdomain IV/224
- bonded III/310
- networks III/266
- supramolecules III/409ff
- bonding II/311, IV/7, IV/68, IV/71, V/227
- bounded supramolecules III/453
- donor V/554
- evolution IV/178, IV/180, IV/182f
- isocyanide II/919
- peroxide III/57, III/64, III/83, III/88, IV/34
- production V/635
- shift II/94, II/110

- transfer II/930
- hydrogenase II/905, IV/132, IV/174, IV/179f
- enzymes II/909
- hydrogenation II/655, II/657
- charge-transfer II/657
- hydrogen-atom abstraction II/403
- hydrogen-atom transfer II/410
- hydrogen-bond III/14
- hydrogen-bond couplings III/13
- hydrogen-bonded donor-acceptor pairs IV/84
- hydrometallation II/655, II/657
- charge-transfer II/657
- hydroperoxide II/930, II/83, III/88
- hydrophobic environment IV/37
- hydrophobic interactions IV/204
- 1-hydro-1-pyrenyl radical V/556
- hydroquinone IV/48, V/296, /312
- 2,3-dimethyl IV/48
- half-cell reaction V/296
- quinone pairing III/420
- trimethyl IV/48
- hydroxamate II/834
- hydroxyhydroquinone V/313
- β -hydroxylamines II/408
- hydroxyl radical I/280, I/509f, I/512, I/525, I/545
- oxidation of metal ions I/509
- reaction with inorganic anions I/509
- reaction with organic molecules I/510
- abstraction I/510
- addition I/510
- reaction with metal ions I/509
- selected properties I/507
- reaction with alcohols I/512
- α -hydroxyl radicals II/275, II/278, II/280
- hydroxylamine V/298
- hydroxylation II/942, IV/227
- 2-hydroxy-5-phenyltetrahydrofuran II/405
- hydroxysilyl radicals II/233
- hyperconjugative effects II/272
- hyperfine II/289
- coupling II/59, II/985ff, IV/80
- constant II/307, IV/678f
- mechanisms II/59
- interaction II/977
- splitting IV/678
- hyperpolarizability V/245f, V/247, V/252ff, V/265ff
- bond order alternation V/254
- dipolar molecules V/252
- measurement techniques V/247
- metallo-organic compounds V/268
- mix parameter V/254
- rigid multichromophoric molecules V/255
- septor part V/266
- symmetry restrictions V/245
- tensorial character V/245
- tensor reduction spectrum V/265
- units V/246
- vector part V/266
- vibrational V/254
- hyper-rayleigh scattering (HRS) V/250
- fluorescence-free hyperpolarizability V/252
- hypochlorite salts II/930
- hypochromism III/111
- DNA III/111
- hypothesis for a molecular switch V/62
- Γ -(acetone)_n clusters IV/787
- Γ anion IV/793
- aqueous solution IV/793
- Γ -(CH₃CN)_n clusters IV/788
- Γ -(CH₃I)_n clusters IV/787
- ICT V/168
- Γ -(Xe)_n clusters IV/793ff
- Γ (D₂O)_n clusters IV/681
- Γ (H₂O)_n clusters IV/681, IV/778, IV/790ff
- dipole bound state IV/681
- electron adiabatic detachment energy (ADE) IV/791
- electron binding energy (EBE) of IV/790
- electron solvation dynamics on photoexcitation IV/681
- isomers of IV/681, IV/793
- photoelectron spectra IV/783, IV/790ff
- photofragmentation action spectra IV/790
- structure of IV/793
- ultrafast dynamics of IV/791ff
- vertical detachment energy (VDE) IV/790ff
- vibrational predissociation spectroscopy IV/791
- image V/285
- beam amplifier V/473
- imidazolate IV/24
- imidazole II/950, II/812, III/484, IV/82, IV/130
- I₃[–] redox couple V/623
- imide II/313, II/478, III/278ff, III/316
- 4,5-dinitro-1,8-naphthalenedicarboximide III/316
- imine IV/264
- iminium ion II/931
- iminium salts II/476
- immobile anion V/475
- immunity V/351
- immunoassays I/333ff
- impermeability tensor V/246
- inclusion complex III/507
- independent electron approximation I/133ff
- indilizidone II/440
- indirect band-gap V/356
- indirect electrolysis I/491ff
- indirect electrosynthesis II/486
- indirect transition IV/306, V/397
- indium tin oxidase IV/130
- indol II/349, II/357, II/360, II/357ff, II/359,

- II/359f
 - oxidative dimerization II/349
 - perfluoroalkylation II/357
 - photochemical reaction with haloquinones II/358
 - photocycloaddition with dienes II/360
- indole-O₂ adduct IV/767ff
- indolyl fulgide V/234
- indoxyl II/349
 - oxidative dimerization II/349
- induced dipole moment V/244
- induced polarization V/244
- induction period V/288, V/313, V/323
- industrial conditions I/458ff
- infectious development V/313
- infectious or nucleated development V/314
- influence of chemical environment IV/560, IV/563
 - electron transfer kinetics IV/560, IV/563
- trans*-influence II/906
- information processing III/525, III/575, III/637
- infrared II/908, II/955
 - absorption V/237
 - spectra II/912, II/917, II/922, III/425
- INHIBIT logic V/167
- inhibition IV/251
- inhomogeneous absorption band V/170
- inhomogeneous line broadening V/698
- initiator II/763
- injection/recombination IV/300, IV/303ff
- injects an electron V/603
- inner-shell reorganization II/597
- inner-sphere II/495, II/951
 - electron transfer II/141, II/784
 - reductant II/731
 - reorganization II/831
- inorganic matrices IV/146
- iNOS III/72ff
- in-plane metallo-organic complexes V/269
- instafax V/305
- instrumentation (*see also* measurement techniques) I/564f, I/572, I/575ff
 - CRO I/576
 - excitation sources I/564f, I/580
 - flashlamps I/564f
 - pulsed I/564
 - pump-probe I/580
 - flash-photolysis I/564f
 - fluorescence I/582
 - frequency domain measurements I/586f
 - Debye-Sears cell I/587
 - frequency domain fluorometry I/587
 - modulation ratio I/587
 - kinetic spectrometer I/577, I/572, I/579
 - suprananosecond I/572
 - ultrafast I/572, I/577, I/579
 - CDD spectrograph I/579
 - dynamic surface I/579
 - mid infrared I/579
 - oscilloscope I/576
 - streak cameras I/579
 - suprananosecond I/577
 - IR spectrometry I/577
 - time-correlated single-photon counting I/583ff
 - autocorrelation functions I/585
 - coffee creamer I/585
 - colloidal silica I/585
 - instrument-response profile (IRF) I/584
 - multichannel analyzer (MCA) I/584
 - residuals I/585
 - time-to-amplitude converter (TAC) I/583
 - transient digitizer I/576
- insulators I/140ff
- integration of two logic operations V/165
- intensity I/245, I/265, IV/238,
- interaction II/943, III/446
 - condensed matter I/504
 - ionizing radiation I/504
 - mode I/78
- intercalated compounds IV/487ff, IV/523
 - electron transfer IV/487ff
 - photoactive species IV/523
- intercalated ethidium III/141f
 - electron transfer mechanism III/142
 - fluorescence quenching III/141
 - nearest neighbour binding III/142
- intercalation III/109, IV/387
 - anthraquinone III/109
- interfacial electron transfer I/271ff, II/852, IV/232, IV/392, IV/405, IV/542, V/607
- interfacial exchange flux I/130
- interfacial structure I/149ff
- interferants IV/155
- interference effects III/217
- interference pattern V/473
- interligand interaction II/825
- intermediates II/978ff
- intermolecular k_H/k_D II/933
- internal charge transfer V/168
- internal conversion II/608, III/280ff, V/482
 - model V/395ff, V/416
- internal energy distribution of products
 - reaction of alkali metal atom with a halogen atom donor IV/638
- internal energy of reactants IV/651
 - early barrier IV/651
 - effect on the reaction path IV/651
 - late barrier IV/651
 - Polanyi's rules for IV/651
- internal energy U I/129ff
- internal hydrophobic surface IV/216
- internal reference II/716
- internal reorganization energy II/832
- interprotein IV/202

- interstellar II/55
- interstitial silver V/326
- intersystem crossing II/271, II/291, II/291,
II/293, II/608, II/838, III/280ff, IV/46, IV/382,
V/573
- intervalence V/41
 - band V/7f, V/21f, V/28, V/31, V/39
 - compounds I/379ff
 - – Class II I/379ff
 - – Class III I/380ff
 - organic I/379ff
 - electron transfer V/26, V/30, V/42
 - transition V/21, V/26ff, V/29, V/32f
- intraligand transitions II/809
- intraligand vibrations II/822
- intramolecular cyclizations II/196
 - anion radicals II/196
- intramolecular electron exchange II/241, II/990
- intramolecular electron transfer I/529, II/305,
II/307, II/313, II/315, II/318f, II/321f, II/494,
II/519, II/854, IV/57, IV/708
 - bond formation II/517
 - DANN II/494
 - energy level diagram IV/708
 - photosynthesis II/494
 - proteins II/494
 - reaction of $\cdot\text{OH}$ with II/4-nitrobenzaldehyde
II/517
 - transition metal complexes I/529
- intramolecular energy transfer II/856
- intramolecular isotope effects II/930
- intramolecular nucleophilic capture II/111
- intramolecular photoinduced electron transfer
II/305
- intramolecular vibrations III/294ff
- intramolecular charge separation IV/708
 - energy level diagram IV/708
- intraprotein electron transfer IV/202
 - reactions IV/207f
- intrastrand energy migration V/196
- inverted effect III/8
- inverted region I/75, I/79ff, I/182, I/320, I/377,
III/8, III/45, III/275ff, V/620ff
 - in SET I/222
 - in TET, I/229ff
- iodide IV/130, V/624
- iodine II/753
- iodonium borates V/529
- iodonium salt V/531f
 - asymmetric V/531
 - symmetrical V/530
 - synthesis V/530
- iodosobenzene II/760, III/63
- iodosylbenzene II/930
- ion molecule reactions II/71
- ion pairs I/384, II/141, II/206, II/209ff, II/237,
II/718, II/767, II/831, V/402, V/537
 - annihilation II/647, II/659
 - charge transfer (IPCT) III/412
 - – adduc III/474
 - contact I/321, II/141
 - solvent separated I/321, V/537, II/141
- ion-radical pairs II/619, II/636f, II/638, II/644,
II/664
- ion source II/323
- ion transfer I/169ff, V/382
 - electrochemical I/169ff
- ion transport II/789
- ionic reactions IV/7
- ionic strength II/943, IV/208
 - dependence IV/209
- ionization II/162
 - action spectra IV/745
 - energy II/6ff, II/23, IV/742
 - – $\text{Li}\cdot(\text{H}_2\text{O})_n$ clusters IV/778, IV/781ff
 - – lithium, sodium, cesium atoms IV/742
 - – metal atoms clusters with ammonia IV/777
 - – $\text{Na}\cdot(\text{H}_2\text{O})_n$ clusters IV/781ff
 - mechanistic criteria II/162
 - potential II/55, II/100, II/274, II/678, III/113,
III/193f, V/460
 - – aliphatic hydrocarbons II/55f
 - – bicycloalkanes II/100
 - – effects of base pairing III/113
 - – π -stacking
- ionizing radiations I/504f, III/116, V/714
 - ^{60}Co γ -ray I/504
 - cylindrical column I/504
 - fast electron I/504
 - interaction with condensed matter I/504
 - LET I/504
 - spur I/504
 - stopping power I/504
 - stopping power of water I/505
 - track I/504
- i*- Pr_3TACN IV/26
- IR stretching frequencies
 - $\text{Re}(\alpha\text{-diimine})(\text{CO})_3\text{L}$ IV/107f, IV/119
- iridium II/818, V/324
 - complexes II/849, III/357ff
 - sensitization V/324
- iridoids II/474
- iron II/814, II/847, II/907, II/921, II/924, II/930,
II/956
- iron *meso*-tetrakis(2,3,4,5,6-pentafluorophenyl)
porphyrin chloride [(TPFPP)FeCl] II/930
- iron *meso*-tetraphenylporphyrin chloride II/930
- iron(II) hydride II/919
- iron(III) chloride II/749
- iron-nickel II/909, II/920
- iron-sulfur clusters II/909, II/913, III/698
- irradiation II/978ff
 - charge-transfer II/637
- irreducible tensors V/264

- irreversible electrode reaction I/426, I/432, I/441ff, I/449ff
- isobutene II/224
- isocitrate dehydrogenase IV/175
- isocyclam III/462
- trans* to *cis* isomerization II/761
- isomerization of azobenzene V/52
- isoquinoline II/364, II/367, II/370
 - alkylation II/364, II/367
 - derivatives II/437
 - halo $S_{RN}1$ reaction II/370
 - halo II/370
 - $S_{RN}1$ reaction II/370
- isoretronecanol II/433
- isotope effect I/189, I/212, I/440, II/930f, II/936, II/951, III/433, IV/37
 - kinetic II/931, II/936, II/951
 - intramolecular II/936
- isotopes II/977, II/986ff
- isotopic substitution IV/755
- IVR – intramolecular vibrational redistribution IV/754ff, IV/765
- Jablonski-type diagram IV/382
- J-aggregate II/957, V/359ff
- Jahn-Teller II/117
 - distortion II/60ff, II/97, II/116, II/224
 - active II/97
 - cycloalkane radical cations II/72, II/78
 - cyclohexane radical cations II/77
 - cyclooctane radical cations II/77
 - cyclopropane radical cation II/73
 - ethane radical cation II/62
 - methane radical cation II/60, II/61
 - dynamic II/61, II/73, II/74
 - second-order II/74, II/86
 - static II/60f, II/73, II/74
- jellium model I/151ff
- jellium plane I/169
- jet cooled exciplexes IV/742ff
- jet cooling IV/709, IV/743
 - 4-(9-anthryl)aniline (AA) IV/709
 - 9,9' biantryl IV/709
 - 9-(N-carbazolyl)anthracene IV/709
 - 4-(carbazol-9-yl)benzonitrile IV/709
 - CDMA IV/709
 - dialkylaminobenzoic acid esters IV/709
 - 4-(dialkylamino)pyrimidines IV/709
 - exciplex IV/709
 - excimer IV/709
- Job's plot III/423ff, III/437
- julolidine derivates II/422
- K + CH_3CN reaction IV/661
 - effect of molecular orientation IV/661
 - CN^- product IV/661
 - frontier orbital model for IV/661
- K + CH_3I reaction IV/655
 - bond stretch model IV/655
 - concerted mechanism IV/655
- K + Cl_2 surface reaction IV/650
 - formation of Cl^- anion IV/650
- K + H_2 reaction IV/653, IV/656
 - K^+H^- intermediate IV/653
 - state selectivity in IV/656
 - state specific reaction IV/653
- K + HCl reaction
 - effect of vibrational and translational energy IV/651
 - late barrier in IV/678
 - Polanyi rule IV/678
- $\text{K}_2 + \text{Br}_2$ reaction IV/649f
 - chemiluminescent channels IV/650
 - electron jump distance IV/650
 - ground state products IV/650
 - structure of intermediate complex IV/650
- $\text{K}_2\text{H}_2\text{Nb}_6\text{O}_{17}$ IV/490
- $\text{K}_2\text{La}_2\text{Ti}_3\text{O}_{10}$ IV/511f, IV/517ff, IV/519
- $\text{K}_2\text{Ti}_2\text{O}_5$ IV/509
- $\text{K}_2\text{Ti}_4\text{O}_9$ IV/506ff
- $\text{K}_4\text{Nb}_6\text{O}_{17}$ IV/489ff, IV/517, IV/517ff
 - absorption IV/490ff
 - band-gap IV/490
 - CdS IV/499f
 - hydrates IV/490ff
 - layered structure IV/490
 - Ni-loaded $\text{K}_4\text{Nb}_6\text{O}_{17}$ IV/498
 - Ni-loading IV/495
 - physico-chemical properties IV/489
 - photocatalytic activity IV/491
 - photoconductivity IV/492, IV/494
 - photoluminescence IV/492
 - promoters IV/495
 - quantum efficiency IV/495ff
 - structure of Ni-loaded $\text{K}_4\text{Nb}_6\text{O}_{17}$ IV/496
 - transmittance IV/490ff
- $\text{K}_{4-x}\text{H}_x\text{Nb}_6\text{O}_{17}$ IV/491ff, IV/502, IV/504ff
 - CdS IV/491
 - $\text{Cd}_{0.8}\text{Zn}_{0.2}\text{S}$ IV/491
 - $\text{Cd}_{1-x}\text{Zn}_x\text{S}$ IV/504
 - Fe_2O IV/504
 - Fe_2O_3 IV/491
 - photolysis of HI IV/502
 - Pillarea IV/504
 - potential energy diagram IV/505
 - $\text{Ru}(\text{bpy})_3^{2+}$ IV/502
 - TiO_2 IV/491, IV/504
- Kallmann-London model I/216ff
- Katz mechanism II/779
- $\text{KCa}_2\text{NaNb}_4\text{O}_{12}$ IV/512
- $\text{KCa}_2\text{Nb}_3\text{O}_{10}$ IV/511ff, IV/518
- Kerr effect V/244
- ket vector I/67
- ketene silyl acetals II/296, IV/32f, IV/43

- β , β -dimethyl-substituted IV/32
- ketimines IV/265
- ketones II/457ff, II/460, II/463, II/467, II/473f, II/736, IV/38
 - aliphatic II/457, II/473
 - aromatic II/458, IV/38
 - epoxy II/467
 - unsaturated II/459
 - ε -unsaturated II/474
- ketyl radical II/462, II/724, V/546, V/566
 - anion V/566
- kinetic I/64, I/403ff, I/414ff, II/909, IV/37
 - acidity II/27
 - acidolysis I/416
 - behavior V/575
 - – inverted-region-like V/575
 - – normal-region V/575
 - competition I/414
 - control I/180
 - first-order I/64
 - homolysis I/416
 - isotope effects III/453, IV/29, IV/83
 - opposing first-order I/404
 - order IV/10
 - probe I/414
 - relaxation I/403ff
- K₁LaNb₂O₇ IV/512f
- Kleinman symmetry V/248
- KNb₃O₈ IV/508f
- knots III/582ff, III/601, III/605, III/614, III/617
 - electrochemical properties III/583ff
 - electronic communication III/617
 - demetalation III/603
 - luminescence III/605, III/617
 - quenching by doxygen III/617
 - photophysical properties III/614ff
 - redox potentials III/601
 - sensitized singlet oxygen luminescence III/617
- Kolbe reaction IV/49, II/246,
- Koopman's theorem III/193
- Kramers model I/99ff
- KSr₂Nb₃O₁₀ IV/512f
- K₁TiNbO₅-type oxides IV/505ff, IV/506ff
 - absorption edge IV/506ff
 - catalysis study IV/506ff
 - conduction band edge IV/506ff
 - sensitized IV/509
- labeling experiment II/948
- labile ligands II/909
- laccase IV/129f
- lactate IV/161, IV/222
 - dehydrogenase IV/132, IV/143, IV/156, IV/161, IV/166, IV/172, IV/175f, IV/185
 - oxidase IV/129, IV/145, IV/161, IV/164
- lactoperoxidase IV/129
- laminated substrates V/511
- lamine II/292
- lamps I/539
 - deuterium I/539
 - xenon I/539
- Landau-Zener II/593
 - equation I/84ff
 - theory I/21ff
- Langmuir V/328, V/359, V/607
 - adsorption isotherm IV/381
 - -Blodgett (LB) film II/954, IV/543ff, IV/569ff, V/275
 - – electron transfer IV/550ff
 - – stability IV/545
 - -Blodgett monolayer III/304, IV/369, IV/543ff, IV/551
 - -Blodgett technique V/147
 - -Hinshelwood V/709
 - kinetics I/288
 - – mechanism IV/651
- lanthanide complexes V/194
- lanthanide ion IV/17
- Laplace transform IV/317
- L-Arg III/72, III/75, III/78
- L-arginine-assisted NOS oxygen activation III/81
- laser I/571, I/565ff, V/550
 - argon-ion V/550
- assisted reactions in van der Waals complexes IV/662
 - cavity-dumped I/567
 - cavity I/565f
 - – oscillating bandwidth I/566
 - He-Ne V/550
 - colliding-pulse I/567f
 - Cu vapor I/567
 - diode-pumped solid-state I/568
 - dye I/567f, I/580
 - – amplification I/568
 - – synchronously pumped I/567
 - dye-excimer I/568
 - excimer I/565f
 - femtosecond I/568
 - flash I/403ff, II/860
 - – photolysis I/402ff, II/295, II/300, II/644, II/944, IV/203, IV/211, V/518, V/520, II/304
 - focus world I/563
 - induced fluorescence (LIF) IV/636, IV/671, IV/707ff
 - ion I/568
 - kinetic spectrometer I/576, I/580
 - – dynamic surface I/580
 - – ultrafast I/580
 - optical multichannel analyzer I/576
 - – polychromator I/576
 - – suprananosecond I/576
 - medium I/565
 - mode-locked I/566ff
 - monitoring light source I/574

- quartz-halogen lamp I/574ff
- suprananosecond I/574
- kinetic spectrometer I/574
- tungsten I/574ff
- xenon arc lamp I/574
- Nd:glass I/579
- Nd:(phosphate)glass I/567
- Nd:YAG I/565ff, I/573, I/578f
- Nd:YLF I/569, I/578
- nitrogen I/565
- OPO I/573
- excitation sources I/573
- optronics I/563
- photoassociation IV/662
- photodetector I/575
- photomultiplier tubes I/575ff
- protection V/511
- pulsed I/564
- Q-switched I/565ff, I/573
- pockels cell I/565
- regenerative amplifiers I/567, I/578
- scanner V/380
- solid-state I/566f
- stored energy I/565
- subpicosecond I/567f
- Ti-S I/580
- titanium-sapphire I/566, I/568f, I/577
- oscillator I/568f, I/577
- regenerative amplifier I/569
- ultrafast I/586
- latent image V/285, V/288, V/319, V/321, V/324, V/330, V/381
- bleaching V/318ff
- potential V/330
- redox potential V/321
- size V/319, V/324
- size of the latent image V/288
- lattice I/137ff
- layer-by-layer deposition IV/140
- layered assemblies IV/138
- layered oxides IV/487ff, IV/511
- perovskite-related IV/511
- photocatalysis IV/487
- layered structure V/86
- LDHs IV/527ff
- CdS IV/527ff
- CdS/ZnS IV/527ff
- MV^{2+} IV/528
- polyoxometallates IV/527
- $Ru(BPS)_3^{4+}$ IV/528
- Zn-porphyrin IV/527
- leakage reaction V/591
- lecithin II/279
- LED III/703, V/380, V/413
- Lennard-Jones potential IV/768ff
- LET I/504
- ionizing radiation I/504
- leuco dye V/335
- Levich IV/306
- equation I/474
- plots IV/306
- Lewis acids IV/16
- catalysis IV/43
- catalyzed electron transfer IV/29
- LF excited states II/842
- $Li \cdot (H_2O)_n$ clusters IV/781ff
- VDE, size dependence of IV/781
- structure of IV/781
- ionization potential of IV/781
- photoelectron spectra IV/783
- $Li \cdot NH_3$ clusters IV/778
- ab-initio calculations IV/780
- delocalization of the valence electron IV/780
- electron binding energy (EBE) of IV/780
- photoelectron spectrum of IV/778
- solvation energy IV/780
- solvent shell of IV/780
- $LiAlH_4$ II/727
- LIB V/318ff
- lifetime II/314, III/645
- $Re(\alpha\text{-diimine})(CO)_3L$ IV/106
- ligand III/401
- based reductions II/810
- centered (LC) transitions V/98
- centered electron transfer II/927
- centered oxidation II/946
- dissociation II/833
- gated ET IV/224
- exchange reaction II/761
- field splitting II/842
- field (LF) states IV/382
- localized reductions II/821
- metal interface II/996
- substitution II/650
- to-metal-charge-transfer (LMCT) transitions I/257ff
- light absorber II/853
- light absorption IV/280, IV/306
- sensitizer (LAS) II/840
- light emitting diodes (LEDs) III/696
- dendrimers III/696
- light harvesting V/600
- light harvesting efficiency IV/366
- light-emitting diode V/380
- diodes, organic (LED, OLED) I/337
- light-energy conversion II/806, II/859
- light-fueled motor III/513
- light-harvesting antennae IV/338
- light-harvesting arrays V/197, V/199
- light-harvesting bilayer membrane V/210
- light-harvesting complexes V/188
- light-harvesting dendrimers V/202
- light-harvesting efficiency V/601
- light-harvesting metal-based dendrimers V/203

- light-modulated microwave conductivity IV/319
- linac I/531
- pulse radiolysis I/531
- line broadening I/407ff
- Bloch equations I/409
- coalescence I/408
- contact shift I/409
- ESR I/410
- fast exchange I/408
- line-shape equations I/409
- NMR I/407ff
- slow exchange I/407ff
- linear polarizability V/244
- linear response theory I/98
- linear sweep voltammetry: *see* voltammetry
- line-broadening II/981
- line-width II/980, II/986
- linked donor-acceptor V/536
- LIP III/84ff
- lipid II/292
- bilayer III/418
- – membranes II/954
- lipoamide IV/54
- dehydrogenase IV/173, IV/175
- liquid crystalline porphyrins IV/377
- liquid crystals V/237
- liquid junction potential I/460
- liquid/gas interface I/467
- liquid/liquid interface I/467
- liquids I/515
- free ion yields I/515
- Onsager radii I/515
- Lith development V/300, V/311ff
- lithium II/717
- atoms IV/776
- – clusters of IV/776
- niobate V/479
- perchlorate IV/29
- rechargeable batteries V/676ff
- – insertion electrode materials V/682ff
- – – carbonaceous materials V/689
- – – chalcogenides V/684ff
- – – insertion process V/682ff
- – – intercalation V/682ff
- – – manganese oxides V/685
- – – negative insertion materials V/688
- – – positive electrode materials V/685
- – – positive insertion materials V/684f
- – – specific capacity V/688
- – – theoretical specific capacity V/685
- – – transition metal oxides V/684ff
- ion battery V/677f, V/681f
- insertion material V/678
- rocking chair battery V/681
- metal V/677ff
- – battery V/678, V/681
- – battery safety V/679
- – electrode V/677f
- gel electrolytes V/681
- hybrid V/681
- /electrolyte interface V/681
- polymer batteries V/680
- polymer electrolyte V/679f
- lithography V/311
- local electric field V/71
- localized levels I/141
- localized orbitals III/216
- locally excited (LE) state IV/633, IV/743, IV/748, IV/750
- locking radius IV/661
- logic III/508, III/519ff, III/527, III/553, III/570, III/575
- binary III/527, III/553, III/570, III/575
- families V/157
- fuzzy III/508
- gates III/519ff, V/156
- London interactions I/154
- long-lived excited state II/805
- lophil radicals V/558
- low-energy cut off II/604f
- lowest unoccupied molecular orbital (LUMO) IV/79
- low-spin II/929, IV/226
- LSV slopes I/446ff, I/450, I/457
- lumazine IV/40
- luminescence I/416, III/502ff, III/562, III/607, III/645, IV/11, V/99
- catenanes III/562, III/607
- decay IV/319
- metal complexes III/562
- pseudorotaxanes III/502ff
- quenching V/409
- rotaxanes III/645
- sensors II/861
- LUMO II/5ff, II/10, II/15, II/21ff, II/270, III/199, III/273ff, III/381, III/628, IV/79, V/100, V/363, V/431, V/485, V/516
- energy of II/10
- /HOMO orbitals V/101
- lysine II/786
- M41S / MCM41 *see* mesoporous material
- Mach-Zehnder intensity modulator V/480
- macrocycles II/720, III/281, III/540, III/632
- catenanes III/540ff
- rotaxanes III/540ff
- macrocyclization reactions II/481, II/484
- macroelectrode I/453ff
- macroradical V/571
- macroscopic noncentrosymmetry V/273
- macroscopic nonlinearities V/273
- made-to-order energy migration V/203
- Magee's equation IV/638, IV/655
- magenta dye V/336

- Magic Blue II/756
- magnesium II/472
- magnetic coupling V/23f, V/37f
- magnetic exchange I/40
- magnetic field V/70
- magnetochemical data II/811
- magneto-optic effect V/215
- main chain polymers V/274
- main-chain polymers with a rigid backbone V/261
- majority carriers IV/283
- malachite green V/484
- maleic anhydride II/656
- malic enzyme IV/175
- manganese II/811, II/956, II/990
 - cluster II/947
 - porphyrin dimers II/948
 - dodecaphenylporphyrin II/273
- manual mixing I/395
- Marcus IV/632f, V/20
 - cycle II/596
 - electron transfer I/521, IV/631ff, IV/759
 - activated complex IV/632ff
 - charge transfer quasi-continuum IV/633
 - doorway state IV/633
 - electron jump step IV/632
 - Franck-Condon limitation IV/633
 - locally excited (LE) state IV/633
 - quantum mechanical model IV/633
 - equation II/473, II/933, II/950, IV/69, V/101, V/523, V/543, V/574
 - ET theory IV/202
 - Hush I/418
 - theory I/346ff, I/373ff
 - inverted region II/273, II/315, II/318, II/845, III/122, III/30ff, IV/69, IV/203, IV/393, IV/403, V/61, V/367, V/424, V/548
 - flexible-linked dyads II/318
 - Jortner theory I/228, I/319
 - Levich framework III/453
 - Levich-Jortner equation III/121, III/139
 - theory I/113, I/181ff, I/190, I/319ff, I/517, I/521, II/239, II/663, II/665, II/763, II/831, II/850, II/935, II/946, III/121f, III/182, III/205, III/229, III/253ff, III/276ff, III/29ff, III/346, IV/56, IV/222, V/100, V/367, V/412, V/429, V/483, V/517, V/618, II/270
- Markovnikov addition II/227
- mass transport I/427, IV/304
 - convection I/427, I/469
 - diffusion I/427
 - migration I/427, I/460
- material dependence IV/550ff, IV/556, IV/565
 - electron transfer IV/550ff, IV/555ff, IV/565
- material-dependent attenuation coefficient β
 - IV/551ff, IV/559ff, IV/563ff, IV/568ff, IV/571ff
- matrix II/979
 - dependence II/118
 - dependent ESR spectra II/76
 - effects II/62f
 - cyclopentane radical cation II/76
 - element (T_{DA} , H_{DA} , V_{DA} , etc.) I/109ff
 - distance dependence I/111
 - hydrogen bonding, role of I/111
 - interference effects I/112
 - pathway analysis I/111ff
 - “through-bond” I/112
 - “through-space” I/112
 - two-electron matrix element I/121
 - isolation II/56
 - specific conversion II/94
 - methane radical cation II/60f
 - Jahn-Teller distortion II/60, II/61
 - in interstellar space II/55, II/60
 - matrix isolation II/56, II/57, II/60
- McConnell expression I/221
- McConnell model III/186, III/189, III/196, III/215
- m-chloroperoxybenzoic acid II/936
- (TMP)Fe^{III}(OH) II/936
- M-CO₂ complex IV/93ff
- MDP V/430
- measurement techniques (*see also* instrumentation) I/569ff, I/578ff
 - kinetic spectrometry I/582
 - suprananosecond I/582
 - photomultiplier tubes I/582
 - mid-infrared I/581
 - optically heterodyned absorption anisotropy I/580
 - oscilloscope I/570
 - photodetector I/570ff
 - photoelectric method I/570
 - photodiode I/570
 - photomultiplier tube I/570
 - pump-probe I/582
 - method I/571, I/578
 - continuum I/578
 - continuum generation I/579
 - self-phase modulation I/579
 - spectrometry I/581
 - light-scattering I/581
 - Raman I/581ff
 - time-resolved resonance Raman I/581
 - TR³ I/581ff
 - white-light continuum I/571
- mechanical equilibrium I/129
- mechanical movements III/512, III/516, III/521, III/552ff, III/561, III/566ff, III/573, III/629ff, III/640ff,
 - catenanes III/566ff, III/629ff
 - chemically induced III/561, III/573, III/630ff
 - electrochemically induced III/516, III/521,

- III/553, III/570, III/630ff, III/641,
 - photochemically induced III/512, III/556, III/573, III/630ff, III/644
 - pseudorotaxanes III/504ff
 - rotaxanes III/552ff
 - rotaxanes III/640ff
- mechanically damaged surface IV/314
- mechanism V/112
 - C_rE_i I/430
 - DIM1 I/430, I/448ff, I/457, I/458, I/461
 - DIM2 I/430, I/457
 - DIM3 I/457
 - DISP I/430
 - ECE_h I/430
 - EC_2 I/430
 - E_qC_2 I/449ff
 - E_qC_i I/456
 - E_rC_i I/429, I/433ff, I/438ff, I/446ff
 - E_rC' I/430
 - $E_rC_iE_r$ I/430, I/433
 - nomenclature I/429
- mechanistic criteria II/162
 - σ/σ^+ criterion II/162
- mediated by redox centers IV/571
- electron transfer IV/571
- mediated electron transfer IV/131
- mediator I/492ff, II/461, II/473, II/726, II/782
- medium fluctuations I/113ff
- Meldola blue IV/150
- membrane II/292, IV/338
- memories II/862
- memory devices V/49
- mercaptopyridine IV/130
- mercuration II/640
- mercury II/720
 - electrode I/155
- mercury(II) bis(trifluoroacetate) II/212
- mercury(II) trifluoroacetate II/625
- merocyanine IV/166, IV/168, V/197
- meso*-aryl group III/281
- mesolytic cleavage II/477, II/487
- mesoporous films V/601, V/603, V/626
 - preparation V/601, V/603
- mesoporous material IV/423ff, IV/465ff
 - active redox framework IV/465f
 - CO_2 photoreduction IV/466
 - definition IV/424
 - discovery IV/423
 - electrochemistry IV/468
 - encapsulated complex IV/466f
 - – advantage IV/468
 - – covalently bound transition metal complex IV/466
 - – electrochemistry IV/468f
 - – ion exchange IV/466
 - – Mn-Schiff base complex IV/467
 - – Ru-porphyrin complex IV/467
 - – enzyme entrapment IV/468
 - – insertion of metal atom IV/426
 - M41S / MCM41 IV/424f
 - – cubic IV/425
 - – FSM IV/425
 - – hexagonal IV/425
 - – lamellar IV/425
 - metal leaching IV/466
 - metal oxide IV/427
 - – containing IV/466
 - organic oxidation catalyst IV/465
 - redox chemistry IV/465
 - synthesis IV/424f
 - thin film IV/427
- mesoporous nanocrystalline TiO_2 thin films IV/396
- mesoscopic oxide V/600
- Meso*-tetrakis(2,3,4,5,6-pentafluorophenyl) porphyrin chloride II/932
- meso*-tetramesitylporphyrin chloride [(TMP)FeCl] II/930
- metal I/133ff
 - alkyl II/727ff
 - – C-H bond cleavage II/707
 - aryl II/727ff
 - atom-solvent clusters IV/776
 - – energy level diagram of IV/776
 - – ion pair states IV/776
 - carbon bind II/927
 - carbon bond cleavage II/622, II/660, IV/57
 - carbonyl II/623, II/731
 - – complex II/625, II/764
 - – anionic II/625
 - – neutral II/625
 - cluster II/775
 - centered II/927
 - – oxidation II/934, II/946
 - – redox couples II/827
 - – reduction II/936
 - – states V/99
- cofactor interactions IV/77
 - complexes III/337, III/353ff, III/364, III/370, III/432, III/438, III/446, III/462, III/467, III/471ff, III/477ff, III/482ff, III/489, III/562ff, III/601ff, III/668ff, III/697
 - – absorption spectra III/562
 - – bimetallic III/353ff
 - – building block V/7
 - – catenanes III/562
 - – cobalt III/357ff, III/471ff
 - – copper III/467, III/477, III/565, III/601ff
 - – dinuclear III/564
 - – iridium III/357
 - – iron III/353ff, III/668
 - – manganese III/353ff
 - – mixed-valence III/438ff
 - – mononuclear III/563

- nickel III/364, III/370, III/462
- osmium III/353ff, III/432
- palladium III/355ff III/697
- platinum III/355
- polymetallic III/353ff
- rhenium III/353ff, III/489, III/565
- rhodium III/353ff
- ruthenium III/353ff, III/446, III/489, III/565, III/603, III/669
- silver III/565
- zinc III/482ff
- (dimine)(dithiolate) complexes V/272
- electrode, I/143ff
- halide
- π bonding, $X(p\pi)$ to $M(d\pi)$ II/702ff
- M-X bond cleavage II/701ff
- hexahalide II/750
- hydrides II/623, II/655
- acidity II/680ff
- cation radical
- acidity II/696ff
- bond dissociation energy II/698ff
- M-H bond cleavage II/679
- oxidation II/689
- ions I/513, I/523, I/525, III/109, IV/15
- hyper-reduced states I/513
- redox potentials I/525
- inner and outer sphere complex III/109
- (to) ligand charge transfer excited states (MLCT) II/840
- ligand π delocalization II/825
- macrocycle IV/91
- oxide V/704
- bandgap V/704
- catalyzed reaction of amines II/380
- particles IV/148
- phthalocyanines V/714
- surfaces I/150ff
- transition complexes V/98
- metallation reactions I/347ff
- metallization I/276, V/712
- metallocarboxylate IV/93, IV/97, IV/115
- metallocarboxylic acid IV/115
- metallocene II/622, II/734
- metalloenzymes IV/23
- non-heme IV/23
- metallofullerenes II/302
- metallo-organic chemical vapor deposition IV/336
- metallo-organic complexes V/268
- metallo-organic compounds V/268, V/270
- optical transitions V/270
- metallophthalocyanine I/576
- metalloporphyrin I/520, II/276, II/310, II/313, II/927
- one-electron oxidation I/520
- π -radical anion II/277
- metalloproteins II/860, IV/23
- metallotetraphenylporphyrins I/520
- one-electron oxidation I/520
- metal-oxo complex II/732
- metal-polypyridine units II/834
- metal-Schiff base complexes V/272
- metal-solution interface I/155ff
- metal-to-ligand charge transfer (MLCT) I/261ff
- transitions I/261ff, II/310, II/809, IV/382, IV/393, V/99
- spin-forbidden V/99
- methane II/943
- methanofullerenes II/282
- methanol I/517, IV/35
- dehydrogenase (MDH) IV/35, IV/162
- oxidase IV/164
- oxidation I/517
- methanorolidinofullerenes II/305
- methods I/403ff
- relaxation I/403ff
- methoxide ion II/290
- methoxy adduct II/290
- 1-methoxynaphthalene II/212
- 10-methylacridinium ion (AcrH^+) II/298, II/951
- 10-methylacridinyl radical IV/42
- 10-methylacridone II/297
- methyl acrylate V/545
- 3-methyl-4-chromanone II/447
- 10-methyl-9,10-dihydroacridine (AcrH_2) II/951, II/294, IV/36
- 3-methylumiflavin (3MLF) II/408
- methyl methacrylate V/553f
- methyl-4-(dimethylamino)benzoate (DMAMB) IV/699
- methylamine dehydrogenase IV/129
- methylcubane II/942
- methylene blue IV/176, IV/246
- cation III/138f
- intercalated in poly[dAdT] III/139
- in poly[dGdC] III/139
- methylene green IV/150
- β -methylstyrene-diethylaniline IV/764
- exciplex emission IV/764
- methyltetrahydrofuran and 2,2,4-trimethylpentane I/520
- radiation chemistry I/514ff
- methylviologen II/851, II/855, II/958, IV/500ff, IV/503, IV/510
- $\text{CdS-Ni-K}_4\text{Nb}_6\text{O}_{17}$ mixture IV/499
- $\text{H}^+/\text{CdS-Ni-K}_4\text{Nb}_6\text{O}_{17}$ IV/501
- $\text{H}^+/\text{K}_4\text{Nb}_6\text{O}_{17}$ IV/503
- HNb_3O_8 IV/510
- HTiNbO_5 IV/510
- KTiNbO_5 IV/510
- $\text{K}_2\text{Ti}_4\text{O}_9$ IV/510
- metol V/296, V/306

- complexes III/426
- – cobalt III/426
- – ruthenium III/426
- metoquinone V/306
- M-form DNA III/147
- wire-like behavior III/147
- Mg²⁺ IV/45f
- M-H bond II/906
- M-H complex IV/93
- MHP V/334
- micellar assemblies II/278
- micelle kinetics
 - effects of micelle shape IV/601
 - electron tunneling IV/599ff
 - internal IV/597f
 - Monte-Carlo simulations IV/598f
 - surface IV/598ff
- micelles II/954
 - dopant partitioning in IV/580ff
 - dynamics IV/580ff
 - electron transfer in
 - – electron exchange IV/594
 - – radical chain reactions IV/594
 - – vectorial IV/595f
 - – photoionization yields IV/593
 - – proximity effects IV/593ff
 - interfacial potentials IV/579, IV/589
 - local polarities IV/589f
 - structure IV/579
- Michler's ketone (MK) V/532
- microcrystals V/356
- microelectrode I/453ff
- microelectronics IV/279
- micro-emulsion I/467
- microheterogeneous photocatalysis V/195
- microperoxidase (*see also* MP-II) IV/135
- microperoxidase-11 IV/131, IV/133, IV/156, IV/162
- microperoxidase-8 (MP8) II/944
- microporous material IV/413
 - general description IV/413
- microscopic equilibrium I/95, I/104
- microviscosity IV/579, IV/586f, V/519
- microwave detection I/544
 - pulse radiolysis I/544
- microwave spectroscopy IV/678
- migration I/427, I/460, II/104, II/107, III/117
 - holes and electrons III/117
 - of the electronic energy V/187
- migratory insertion II/761
- mineralization V/695
- minority carrier IV/283
- mitochondria II/950, III/40
- mitochondrial membrane III/39
- mixed metalloporphyrins V/73
- mixed valence V/21ff, V/24f, V/29ff, V/33, V/36ff, V/42ff
- complexes V/3, V/5, V/26
- species I/122, II/990
- state III/42
- systems II/988
- mixing coefficient II/588
- mixing methods I/395
- MLCT II/310f, II/944, V/99, V/608
 - absorption
 - – Re(α -diimine)(CO)₃L IV/106, IV/109
 - excited state I/582, II/858
- Mn + Cl₂ reaction IV/648
- Mn + O₃ reaction IV/648
- HOMO, LUMO orbitals in IV/648
- MnP III/87, III/92
- mobile hole V/474, V/479
 - diffusion V/479
- mobility IV/305, V/432ff, V/448ff, V/458
 - concentration dependence V/444
 - dipolar disorder V/451
 - dipole moment V/439, V/442, V/451f
 - electric field dependence V/434
 - mobility field V/489
 - field dependence V/448, V/450
 - polar components V/451
 - simulation V/450
 - temperature dependence V/434, V/443
 - thickness dependence V/458
 - zero-field V/452
- modified electrode II/958
- modular approach V/190
- modulation frequency IV/325
- molecular assembly IV/543ff, IV/546
- molecular-based information processors V/156
- molecular batteries II/786
- molecular beam epitaxy IV/336
- molecular conduction V/138
- molecular devices IV/75
- molecular dyads II/857
- molecular dynamics (MD) I/115ff, I/168
 - simulation of I/213
- molecular-electronic devices II/837
- molecular electronics V/157
- molecular ferromagnet II/760
- molecular logic systems V/156
- molecular machines III/501ff, III/552ff, III/566ff, III/629ff, III/640
 - catenanes III/566ff, III/629ff
 - pseudorotaxanes III/501
 - rotaxanes III/552ff, III/640
- molecular mechanics II/922
- molecular orbital II/982ff, V/609
 - calculations II/105
 - diagram II/762
 - geometries IV/79
 - – recognition-mediated control IV/79
- molecular oxygen I/224, I/231
- molecular photovoltaic V/596

- devices III/179
- molecular recognition II/837, III/417, III/501, IV/8, IV/68
- hydrogen bond III/417
- pseudorotaxanes III/501
- molecular rectifier V/139
- molecular shift register V/63, V/65, V/80
- energy transfer V/80
- molecular shuttle V/54
- molecular switch V/5, V/14, V/48
- molecular wire III/141, III/230ff, III/344, V/5f, V/12, V/23, V/26, V/103f, V/125
- molecularly doped polymers (MDP) V/398, V/430
- molybdenum II/810, II/909
- molybdopterin IV/224
- monoacetylferrocenium II/747
- mono-alkyl adduct II/272
- monochromatic radiation V/591
- monochromators I/575ff
- mono-directional rotor V/54
- monoelectrochemical oxidation IV/155
- monofunctionalized fullerene derivatives II/279, II/305
- monolayer IV/250, IV/259, IV/265, V/180
- assembly IV/543ff, IV/572
- characterization IV/554
- – chronoamperometry IV/554ff
- – cyclic voltammetry IV/554ff
- – detection of disorder of defects IV/555
- – double-layer capacitance IV/554
- – electrochemical blocking effect IV/554
- – electrochemical methods IV/554
- membranes III/301
- structural characterization IV/547ff
- – atomic force microscopy (AFM) IV/547ff
- – contact angle goniometry IV/548
- – cyclic voltammetry IV/549
- – detection of disorder or defects IV/548ff
- – double-layer capacitance IV/548ff
- – electrochemical blocking effect IV/548
- – electrochemical methods IV/548, IV/552
- – ellipsometry IV/547
- – Fourier transform infrared external reflective spectroscopy (FTIR-ERS) IV/547ff
- – grazing incidence X-ray diffraction IV/547
- – helium diffraction IV/547
- – low-energy electron diffraction IV/547
- – scanning tunneling microscopy (STM) IV/547ff
- – X-ray photoelectron spectroscopy (XPS) IV/547
- thin film IV/541ff
- monomers V/518f
- formulation V/564
- monofunctionalized V/519
- polarity V/518
- viscosity V/518
- mononuclear wires V/3f
- monooxygenase III/57f
- monooxygenation II/928, II/930
- monoxide II/915
- Monte Carlo simulation V/395, V/404, V/445
- montmorillonite IV/522ff
- clay IV/520, IV/523
- – CdS + ZnS IV/520
- – Fe₂O₃ IV/520
- – TiO₂ IV/520
- Fe₂O₃ IV/522ff
- ZnS + CdS IV/522
- 2-morpholino-1,2-diphenylethanol II/395
- Mott-Schottky IV/289ff
- approximation IV/357
- – ϵ is the dielectric constant of the semiconductor IV/357
- – ϵ_0 is the permittivity of free space IV/357
- – amount of band bending IV/357
- – electronic charge IV/357
- relationship IV/357
- – capacitance IV/357
- – electrode area IV/357
- MP-II *see* microperoxidase
- m*-terphenyl II/274
- Mukaiyama-aldol reaction IV/44
- Mukaiyama-Michael reaction IV/43
- Mulliken, R. S. II/601, II/608, IV/675, IV/702
- correlation II/628
- – Hush theory (MH) I/6, I/30ff
- theory II/644, II/662, II/666
- multi-center electron transfer I/109
- multichromophoric array V/193
- multicomponent systems III/322, V/97
- multielectron I/208
- oxidation and reduction I/327
- redox process III/658, III/669ff, III/686ff, III/692ff, III/697, III/709, IV/322
- – dendrimers III/658, III/669, III/682, III/692, III/697, III/709
- reduction II/270
- transfer I/120ff
- multiexponential kinetics V/619, V/622
- multifunctional ligands V/713
- multilayer IV/140
- assembly IV/551, IV/572
- systems IV/528ff
- – anchor layer IV/529ff
- – coumarin IV/533
- – deposition process IV/530
- – energy transfer efficiencies IV/531f
- – fluorescence emission IV/531
- – fluorescein IV/531ff
- – HTiNbO₅ IV/534
- – MDESA IV/531
- – MV²⁺ IV/529ff

- Pd-porphyrin IV/533
- photoinduced charge separation IV/529
- porphyrins IV/531
- rhodamine B IV/531
- Ru(bpy)₃²⁺ IV/532
- sequential adsorption scheme IV/531
- substrates IV/529ff
- α -ZrP IV/534
- thin film IV/541ff
- multimode model I/77ff, I/105
- multiphoton fluorescence V/251
- multipole expansion I/219ff
- multiporphyrin V/211
- multiporphyrin arrays V/197
- multi-proton I/208
- multipurpose molecules V/494
- multistate valence bond model (multistate VB) I/190ff
- multistep electron transfer I/109, I/118, II/960
- multistep tunneling III/19
- multi-wavelength recording V/239
- mutagenesis IV/77
- mutant II/940
- myoglobin II/860, II/940, III/16, III/20, III/56, IV/133, IV/135, IV/155, IV/156, IV/159, IV/182ff,
- ¹⁴N II/911
- 1,8-naphthoquinodimethane II/222
- [NH₄][PF₆] II/755
- ⁶¹Ni II/911
- 4-nitrobenzophenone II/239
- 4-nitrobenzyl chloride I/456
- 4-nitrobenzyl chloride radical anion II/520
- 2-nitropropane IV/49
- anion IV/49
- N₂O + Li atoms on a Rh surface reaction IV/650
- Na + N₂ system IV/653
- back electron transfer IV/653
- bond stretch model IV/653
- Na⁺N₂⁻ intermediate IV/653
- quenching of the Na atom fluorescence IV/653
- Na + CH₃Br reaction IV/654
- steric factor IV/654
- acceptance angle IV/654
- effect of electronic excitation of Na IV/654
- Na + Cl₂ reaction IV/655
- effect of electronic excitation of Na IV/655
- HOMO - LUMO overlap IV/655
- Na⁺Cl₂⁻ intermediate IV/655
- Na + HCl reaction IV/661
- effect of electronic excitation of Na IV/661
- polarization effect IV/661
- Na + O₂ reaction IV/656
- state selectivity in IV/656
- effect of electronic excitation IV/656
- Na⁺O₂⁻ intermediate IV/656
- Na atoms IV/776
- clusters of IV/776
- Na... (FCH₃)_n complex IV/673
- photoinduced charge-transfer dissociation spectrum IV/673
- Na...HF complex IV/673ff
- ab-initio calculation of ground and excited states IV/675
- conical intersection IV/675
- H/D isotope effect IV/674
- photodepletion spectrum IV/674
- photoinduced charge-transfer dissociation spectrum IV/674
- Na... (H₂O)_n clusters IV/778, IV/782ff
- electron binding energy (EBE) of IV/782
- photoelectron spectra IV/782
- vertical detachment energies (VDEs) IV/778
- Na... (H₂O)_n clusters IV/781
- ionization potential of IV/781
- structure of IV/781
- VDE, size dependence of IV/781
- Na... (NH₃)_n clusters IV/778
- binding energy of IV/778
- isomers of IV/778
- photoelectron spectroscopy IV/778ff
- solvation energy IV/780
- Na... (NH₃)_n clusters IV/681, IV/778
- cluster size dependence IV/681
- structures of, by ab-initio calculations IV/778
- ionization potential IV/681
- solvation energy IV/780
- Na⁺-NH₃ clusters IV/681
- structures of, by ab-initio calculations IV/778
- Na₂ + O₂ reaction IV/657
- Na₂... (ClCH₃)₂ complex IV/673
- Na₂... ClCH₃ complex IV/673
- Na₂Gd₂Ti₃O₁₀ IV/511
- Na₂Ti₃O₇ IV/507ff
- NaBH₄ II/727
- NaClO₄ IV/23
- NAD IV/150, IV/155f, IV/161, IV/168, IV/173ff, IV/176, IV/178f
- NADH (dihydronicotinamide adenine dinucleotide) II/293, II/931, III/39, IV/14, IV/29, IV/36
- dehydrogenase IV/132
- NADP V/598
- NADP⁺ IV/210
- NADPH IV/226, V/598, V/639
- Na-H₂O clusters IV/681
- cluster size dependence IV/681
- ionization potential IV/681
- Na-Hg amalgam II/720
- NaI (sodium iodide) IV/751
- electron photodetachment IV/751
- NaLaTiO₄ IV/511

- NAND gate V/168
- NAND logic V/163
- nanocrystalline V/602
 - materials V/601
 - morphology V/602
 - oxide V/601, V/625
 - – surface charge V/625
- nanode I/467
- nanoelectrode I/453ff
- nanojunction V/5f, V/23, V/38, V/43f
- nanoparticles III/576, III/707, IV/130, IV/131, IV/149
- nanophase IV/327
- nanoporous IV/327
- nanoscaled IV/244
- nanostuctured IV/327
- naphthaldehyde IV/46
- naphthalene II/224, II/292, II/725, III/701
 - derivative III/465
 - diimide III/692
 - – dendrimers III/692
 - -1,8:4,5-diimide V/64
 - imide III/139
 - – triplet III/125
 - – – quenching by nucleotides III/125
 - radical anion II/721, II/723
 - tetracarboxamide III/436
- naphthalenedicarboxamide III/125
- quenching by nucleosides III/125
- naphthalenophane II/223
- naphthalimide IV/75
- naphthoquinone III/285ff
- naphthylsodium II/777
- natural antennas V/187
- natural bond orbitals III/196, III/216ff
- natural photosynthesis V/597, V/637
- natural selection III/33, III/37
- Nb₂O₅ V/602
- n*-Bu₄NcIO₄ IV/23
- near-field memory V/239
- near-field optical techniques V/48
- negative activation enthalpy IV/29
- negative bias IV/404
- nematic liquid crystals III/431
- neon matrices II/57
- Nernst equation I/144ff, I/422ff, I/443, I/489, II/907, V/293, V/297
- Nernst expression IV/298
- Nernst method I/488ff
- Nernst-Planck equation I/427ff, I/473
- net flux I/131ff, I/164ff
- neural network V/473
- neutral flavin semiquinone IV/205
- NHA III/74f, III/78
- Ni(cyclam)²⁺ IV/90
- Ni(III) II/922
- nickel II/818, II/907, II/924
 - complexes III/364, III/370, III/462ff
- nickel(II) II/919, II/956
- nicotinamide IV/68
- coenzymes IV/29
- niobates IV/487f
 - layered oxides IV/487
- NIPC V/437
- nitrate II/736, II/784
- reductase IV/135, IV/143, IV/145, IV/156, IV/159, IV/179, IV/181
- – viologen IV/145
- nitrenium ions II/381
- nitric oxide, *see* NO III/71
- synthase *see* NOS III/56, III/71
- nitride II/460, II/463, II/471, II/474
- nitrite II/736, II/784
 - reductase IV/179
- nitroalkenes II/463
- nitroaromatics III/446
- nitrobenzene IV/12
- nitrogen centered radicals IV/21
- nitrogen fixation IV/190, IV/193
- nitrogen pyramidalization I/371, I/381
- nitrosobenzene IV/13
- nitrosonium II/635
- salts II/750
- nitroxide II/979, IV/21
- radicals II/292
- nitroxyl radical III/698
- N*-methyl-9-*t*-butylacridane II/410
- N*-methylacridinium III/127
- quenching by nucleotides III/127
- NMR I/410, I/413f
 - ¹³C I/414
 - high-pressure I/413
 - pulsed I/410
- NMR I/546, II/906, II/981
 - chemically induced dynamic nuclear polarization (CIDNP) I/546
 - computer V/178
- nNOS III/72, III/74, III/77
- NO III/71, III/74f, III/78
- NO⁺ II/223
- NO₂ IV/13
- noble metals V/712
- nonadiabatic I/201, II/593, II/606, V/22
 - electron transfer IV/69, IV/403
 - ET III/10
 - limit I/67ff, III/4, V/371
 - operator I/66
- nonaqueous solvents I/515, I/551
 - one-electron reduction and oxidation I/515
 - purification of materials I/551
- noncentrosymmetric crystallization V/275
- noncovalent interactions IV/68
- nondestructive readout V/227, V/237, V/240
- nondipolar disorder V/450, V/461

- nonequilibrium I/131ff
 - conditions V/590
 - decays V/370
 - solvation I/170, I/181
 - steady state I/131
- nonexponential kinetics V/370
- nonlinear chromophores V/487
- nonlinear optics V/243ff, V/504
- nonmediated electron transfer IV/128
- nonplanar conformation IV/55
- nonpolar solvent I/460
- nonradiative deactivation II/842, II/845
- nonradiative recombination IV/319
- nonradiative transition I/66
- nonsilver photographic system V/216
- nonstoichiometry IV/285
- nonvertical excitation transfer I/235
- NOR logic V/164
- norbornane II/942, III/443
- norcaradiene II/122
 - radical cation II/89, II/120
- norcarene II/111
- normal hydrogen electrode II/716
- normal regime (*see also* free energy regimes) II/586
- normal region I/75, I/79ff
- normalized Gauss function I/149
- Norrish-Tromsdorf effect V/575
- NOS III/71f, III/75ff, III/83
 - domain swapping III/72
 - electron transfer III/83
 - heme active site III/76
 - isoforms III/72
 - mechanism III/78
 - molecular structure III/75
 - pterin cofactor III/72, III/76
 - zinc ion III/77
- NOT logic V/159
- not vibronic states V/616
- novelty filter V/473, V/511
- NTDI V/387, V/453, V/461
- nuclear II/583, II/589, II/602
 - configuration II/583, II/589, II/602
 - magnetic moments II/986ff
 - motion II/583
 - quantum effects I/18ff, I/56
 - reorganization parameter III/3
 - reorganization V/610
 - nuclear reorganization energy III/137
 - spin II/986, IV/20
 - polarization (CIDNP) II/78
- nuclear tunneling V/621
- nucleated development V/313
- nucleator V/315
- nucleobase III/111f, III/427ff
 - analogues III/111, III/152
 - strand-selective quenching III/152
- electron affinities III/112
- fluorescence III/111
- ionization potentials III/111
- redox potentials III/132
 - effect of solvent III/132
- singlet energies III/111
- singlet lifetimes III/111
- nucleophiles II/33, II/282, IV/3
- nucleophilic II/103
 - addition II/96, II/652f, IV/32
 - aliphatic substitution II/241, II/245f
 - attack II/121f
 - capture II/96, II/118f, II/120, II/122
 - intramolecular II/96
 - substitution II/761
- nucleoside III/115
 - redox potentials III/115
 - aqueous solution III/115
 - base pairing III/115
 - nonaqueous solution III/115
 - π -stacking III/115
- number of electrons I/425, I/433ff
- O₂ IV/13
- O₂-sensitivity of organic triplets V/167
- occlusion electrosynthesis IV/339
- octaethylporphyrin (OEP) II/934
- octopolar alkynylruthenium complexes V/272
- octopolar molecules V/264
- [O₂][EF₆] II/752
- OETPP = the dianion of
 - 2,3,7,8,12,13,17,18-octaethyl-5,10,15,20-tetra-phenylporphyrin IV/56
- off-diagonal disorder V/443
- off-diagonal tensor components V/259
- off-on-off V/162
- OH radicals V/716
- OHAPy-C-DNB V/152
- ohmic drop I/446, I/458ff
- olefins IV/267
- oligene bridging ligands V/110f
- oligene oligomers V/109
- oligo(9,10-anthrylene) II/237
- oligonucleotides II/837
- oligonucleotides 2-aminopurine III/132f
 - fluorescence III/132
 - multiple conformations III/133
- oligophenylene rods V/114
- oligoyne bridges V/113, V/121
- olympiadane III/546
- one-electron oxidation I/520, II/379ff, II/931
 - metallotetraphenylporphyrins I/520
 - potential II/270, II/933, IV/42
- one-electron redox equilibria I/526
- one-electron reductants IV/13
- one-electron reduction I/516, I/519, II/929
 - transition metal complexes I/516, I/519

- potential II/273, II/933, IV/9, IV/45
 - one-electron steps II/806
 - one-electron transfer II/380
 - o*-neophyl rearrangement II/245
 - onium V/529
 - borate (*see also* salts) V/530, V/535
 - – free energy change V/535
 - catalysts I-IV V/352
 - cation V/529
 - open electron system I/127ff
 - open-circuit photovoltage IV/293, IV/390
 - open-closed ring system V/55
 - optical excitation IV/306
 - oporphyrin IV/183
 - optical (*see also* electron transfer optical) II/600, II/602ff
 - amplifier V/473
 - band gap V/485
 - band shape II/602, II/604f
 - beams V/473
 - computing V/512
 - concentrator V/593
 - control of chirality V/49
 - damage V/511
 - detection I/533, I/539ff
 - – pulse radiolysis I/533, I/539ff
 - excitation II/838, II/860
 - generation V/482
 - image correlation V/511
 - Kerr effect V/244
 - limiting V/511
 - memories V/473
 - parametric amplifier I/569, I/572, I/578
 - – optical delay I/572
 - – – pump-probe method I/572
 - – – pump-probe method I/572
 - – – continuum I/572
 - – – transition II/603
 - – – charge transfer II/600
 - phase conjugation V/512
 - properties V/696
 - quality V/510
 - rectification V/244
 - rotation dispersion V/236
 - switches II/862
 - vs. thermal ET I/385
 - optically controlled molecular switching V/50
 - optically transparent electrode (OTE) I/483
 - optically transparent thin-layer cell (OTTLE) I/483, I/485ff
 - optoacoustic method V/426
 - optoelectronic gate V/82
 - OR logic V/163
 - orbital overlap II/663
 - orbital symmetry allowedness/forbiddenness II/155
 - orbital symmetry and ET dynamics III/243ff
 - ORD spectra V/237
 - organic conductor II/760
 - organic crystals V/391
 - organic liquids I/514ff
 - radiation chemistry I/514ff
 - – acetone I/518
 - – acetonitrile I/518
 - – chlorinated hydrocarbons I/519
 - – cyclohexane I/521
 - – dichloromethane I/520
 - – dimethyl sulfoxide I/522
 - – methanol I/515
 - – methyltetrahydrofuran and 2,2,4-trimethylpentane I/520
 - – 2-propanol I/517
 - – tetrachloromethane I/519
- organic oxidant II/760
- organic photoreceptors V/381, V/391, V/398, V/462
- organic pollutant V/695
- organic polymers V/481
- organic semiconductors IV/375
- organic-inorganic hybrid solid-state devices V/87
- organized media II/954
- organoborates II/657
- organochromium I/403ff
- organofullerenes II/283
- organometallic catalysis II/779
- organometallic chemistry II/976ff
- organometallic complexes II/623
 - anionic II/623
- organometallic porphyrins II/927
- organometallic radicals II/748
- organosilanes II/296
- orientation dependence, EET I/220
- orientational polarization II/599
- orientation-vibrational polarization II/596
- ortho*-xylylene complex II/741
- oscillator strength I/245, I/261
- oscillator strength II/602
- osmium II/814, II/920, V/202, V/606
 - complexes III/353ff, II/848, IV/136, V/97, V/195, V/202
- osmium(VI) cycloadduct II/642
- osmium(VIII) tetroxide II/641
- osmylation II/641, II/644
 - charge-transfer II/644
 - thermal II/644
- Ostwald ripening V/342, V/602
- outer antenna V/189
- outer-sphere II/935
- outer-sphere electron transfer II/141, II/782, II/950
- outer-sphere reorganization energy II/831
- out-of-plane metallo-organic complexes V/269
- overcoat layer V/384
- overlap integral I/225

- overpotential I/165, I/180, I/425ff, I/492ff, II/461, II/736
- oxadiazole V/384, V/424
- oxazoles V/384
- oxetane formation II/148
 - cation radical chain mechanism II/148
- oxetane radical cation II/98
- oxidant II/745ff, IV/3
- oxidase III/56f, III/409
- oxidation II/621, V/536, V/704
 - catalyst (*see* redox molecular sieves) IV/431
 - fullerenes II/323
 - metal ions I/509
 - – hydroxyl radical I/509
 - one-electron V/536
 - oxidation and reduction potentials III/114
 - – electrochemical III/114
 - – measurements III/114
 - – pulse radiolysis III/114
 - potential II/291, II/485, III/129, V/460, V/522
 - – electron donor V/522
 - – branched alkanes II/68
 - – GMP and AMP III/129
 - state II/912, II/9182
- oxidative chlorination II/751
- oxidative cleavage III/157, III/160
 - distal/proximal cleavage ratios III/160
 - GGG III/160
 - nontethered triplet anthraquinone III/157
 - nontethered triplet naphthalimide III/157
- oxidative coupling IV/40
- oxidative damage IV/24
- oxidative degradation V/695
- oxidative quenching IV/15, IV/173ff, IV/178f, IV/187
- oxidizing agents V/339
- oxidizing conditions I/510
 - water I/510
- oxidoreductase III/418
- oxo complex II/752, II/816
- β -oxoesters II/483
- oxo group transfer IV/224
- 8-oxoguanine III/114
 - ionization potential III/114
 - IP III/114
- 8-oxoguanine hole trap III/159
- oxo ligands II/837
- oxyferrous complex III/66
- oxyferryl intermediate IV/227
- oxyferryl ion IV/220
- oxygen II/35ff, II/386, III/39, III/57
 - acids II/534
 - activation III/66, III/453
 - electrode I/536
 - rebound II/938
 - transfer II/938f
- oxygenase III/56, III/58
 - dioxygenases III/56
 - monooxygenases III/56
- oxygenation II/36
- oxygen-evolving complex (OEC) II/947
- oxyhemocyanin IV/25
- o*-xylene II/211
- ozonolysis V/390
- P450 II/928
 - -catalyzed reactions III/59
- P450BM-3 III/60, III/64f
- P450CAM III/58, III/60, III/62f, III/64ff
 - ferrous oxy III/62
 - ferrous state III/62
 - ferric hydroperoxide III/63
 - ferric peroxide III/63
 - ferric superoxide III/62
 - high-spin complex III/60
 - oxy-ferryl III/63
 - oxyferrous complex III/66
 - reaction cycle III/60
 - resting state III/60
- P450 2C5 III/64
- P450csa III/64
- P450eryF III/64, III/71
- P450nor III/60, III/64
- P450TERP III/64
- packing density III/31
- pagodane II/223
- pair V/518, V/520, V/527, V/529, V/538, V/545ff, V/567, V/573
 - contact radical-ion V/546
 - donor-acceptor V/518
 - ion V/518
 - tight ion V/520, V/527
 - photo-redox V/518, V/538, V/553, V/567
 - radical ion V/518, V/545, V/559, V/567, V/573
 - solvent-separated V/546
 - tight ion V/529
- pair wise interactions IV/769ff
- palladium V/17
 - catalysed reactions II/380
 - complexes I/435, I/464, III/355ff, III/697
 - – dendrimers III/697
- panchromatic film V/604
- paracyclophane II/222f
- [2.2]paracyclophane II/238f
- parallel plate capacitor I/160
- parallel plate model IV/209
- parity rule III/220
- Parkinson's disease II/402
- particle size IV/239
 - control I/290
- particulate semiconductors V/706
- passivation V/351
- Paternò-Büchi reactions II/480f
- pathogenic bacteria IV/161

- pathways model IV/222
 Pauli exclusion principle I/135
 Pauli forces IV/742
 PCR V/176
 peak current I/444
 – ratio I/444
 peak potential I/444, I/450
 – difference I/444ff, I/456
 Pekar Factor II/596
 penta-1,3-diene II/219
 pentacarbonyl metallate II/653
 pentacarbonyliron II/624
 pentacarbonylmanganate II/624, II/647
 pentacene V/50
 1,4,8,11-pentacenetetrone II/238
 pentacoordinate geometry IV/24
 pentacoordinated complex II/813
 pentads III/318ff, III/323
 – carotenodporphyrin-diquinone III/323
 pentafluorophenyl groups III/278ff
 pentasil zeolite II/66
 peptide-based „pathways“ III/424
 peptide-containing conjugates III/424
 peptides IV/161
 peracids III/63
 percarboxylic II/930
 percolation effects IV/334
 pericyclic reaction II/37
 perinone V/408
 periodic excitation IV/319
 peripheral ligands V/97, V/99
 periselectivity II/159
 – conformational effects on II/159
 – cyclobutane II/159
 permethylated transition-metal sandwich II/715
 perovskite-related layered oxides IV/489,
 IV/511f
 – – catalysis study IV/512
 peroxidase I/370, II/934, III/56, III/67, IV/132
 – – horseradish peroxidase (HRP) II/934
 – reaction cycle III/90
 peroxide II/244
 – shunt III/63
 – -bridged complex II/752
 peroxo complex II/752, II/952
 μ - μ^2 : μ^2 -peroxodicopper complex IV/25
 peroxygenase III/57
 persistent photochemical spectral hole-burning
 (PSHB) V/170
 perturbation theory I/118
 perylene II/725, V/50, V/72, V/384f, V/427
 pesticides IV/161
 PET (*see also* photoinduced electron transfer)
 V/159, V/168, V/398
 – thermodynamics V/160
 Ph₃C[•] II/757
 pharaoh ant trail pheromone II/423
 phase boundary I/127
 phase change V/215
 phase relationship V/474
 phase separation V/510
 phase shift V/478
 phase-shift *see* frequency domain measurements
 α -phellandrene II/219
 β -phellandrene II/219
 phenanthrene II/725
 phenanthridine II/364
 – alkylation II/364
 phenanthroline II/352, II/364, II/809, II/817,
 II/931
 – fluorination II/352
 – alkylation II/364
 – spacer III/284
 phenanthrotrithiol II/342
 – radical cation II/342
 – – stable II/342
 phenazine IV/103
 – ethosulfate IV/132
 – methosulfate IV/132
 phenidone V/296
 phenol II/938
 phenolate IV/22
 phenoselenine II/349
 – oxidative dimerization II/349
 phenothiazine II/292, II/312, II/342, II/349,
 II/351f, II/354, II/836, III/374
 – halogenation II/351
 – nitration II/352
 – oxidative dimerization II/349
 – radical cation II/342, II/354
 – – stable II/342
 phenoxathiin II/342, II/349, II/351, II/354
 – anodic oxidation II/354
 – halogenation II/351
 – oxidative dimerization II/349
 – radical cations II/342
 – stable II/342
 phenoxazine II/349, II/351ff
 – halogenation II/351
 – nitration II/352
 – oxidative dimerization II/349
 – formation of sulfinimines II/354
 phenoxy radical II/938, IV/22
 phenoxynaphthacene V/235
 phenoxylthiin II/342
 – radical cation II/342
 phenyl IV/566
 – electron transfer bridge IV/566
 1-phenylcyclopropylamine II/403
 phenyl 4-nitrophenyl sulfone II/240
 phenylacetylene monodendrons V/203
 phenylcyclobutane rearrangement II/175
 – cation radical II/175
 1,4-phenylene bridges II/848

- phenylene-ethynylene IV/566
 - electron transfer bridge IV/566
- phenylenevinylene III/703
- N*-phenylglycines (NPGs) V/523, V/560f
 - derivatives V/561ff
 - – oxidation potentials V/562
 - – structures V/562
- phenylthioacetic acid V/579
- pheophytin IV/170, V/599
- phonon I/71ff, V/356, V/398
 - frequency V/444
 - Hamiltonian I/105
- phosphaalkene II/251
- phosphafulvene II/251
- phosphine II/732
 - dendrimers II/775
- phospholipid bilayer III/310
- phosphonium salt II/655
- phosphorescence I/559, III/273
- phosphorus pentahalide II/751
- photoacoustic V/393, V/417
 - microcalorimetry I/266
- photoaction spectra IV/296, IV/365, IV/387f
 - IPCE IV/387
 - LHE IV/388
- photoactive complex II/845
- photo-active groups II/836
- photoaddition IV/264, II/297
- photoamination II/437
- photoanode I/274, IV/374
 - stabilization IV/337
- photocatalysis I/271ff, II/818, II/836, II/862, IV/4, IV/232ff, IV/495, IV/499f, IV/512f, V/695, V/703
 - CdS and Ni-K₄Nb₆O₁₇ mixture IV/499
 - CdS-Ni-K₄Nb₆O₁₇ IV/500
 - K_{4-x}H_xNb₆O₁₇ IV/502
 - K₄Nb₆O₁₇ IV/495
 - layered perovskite compounds IV/513
 - perovskite-related layered oxides IV/512
- photocatalytic activity IV/491
 - K₄Nb₆O₁₇ IV/491
- photocatalytic cycles II/840, II/850, II/859
- photocatalytic process II/858
- photocatalytic reaction II/844
- photocatalytic splitting of water I/272
- photochemical activation IV/170
- photochemical electron transfer II/840, II/858
- photochemical energy conversion V/211
- photochemical solar energy conversion V/212
- photochemistry II/805, II/838, IV/232ff
 - Re(α -diimine)(CO)₃L IV/109ff, IV/118ff
- photochromic V/225f, V/558
 - by-products V/225f
 - molecules V/220f
 - system V/51V/128
- photochromism V/216, V/230, V/485
- photoconductive IV/329
- photoconductor V/379, V/390, V/404ff, V/426ff
 - aggregate materials V/404, V/406
 - – xerographic sensitivity V/406
 - azo pigments V/407
 - chemical modification V/390
 - mixed pigments V/428
 - perylene pigments V/427
 - – fluorescence quenching V/427
 - – quantum efficiency V/427
 - phthalocyanine pigments V/413
 - polymorphism V/413ff
 - squaraine (squarylium) V/413
 - web-based V/404
- photocontrollable spin dynamics V/68
- photocopy V/379ff
- photocorrosion IV/240ff, IV/326
- photocuring technologies V/517
- photocurrent II/292, II/958, II/963, III/299, IV/244, IV/266, IV/361ff, IV/371, IV/377, V/495
 - action spectrum IV/362
 - anodic IV/361, IV/371, IV/377
 - cathodic II/963, IV/361
 - current onset IV/363
 - density IV/331
 - photoemission currents IV/362
 - losses IV/331
 - multiplication IV/324
 - onset IV/318
 - – voltage behavior IV/365, IV/387
 - – dark current IV/365
 - – surface state-mediated recombination IV/365
 - – voltage measurement IV/363
 - – fill factor IV/364
 - – maximum energy conversion efficiency IV/364
 - – open-circuit voltage IV/364
 - – power point, pp IV/364
 - – short-circuit IV/364
- photocyclodimerization II/144
 - selectivity II/144
- photodealkylation IV/246
- photodecomposition II/859
- photodegradation IV/45, V/712
 - enhanced charge separation V/712
- photodehydrodimerization IV/251, IV/259
- photodetoxification I/272
- photodimerization IV/269
- photodiodes I/539
- photodissolution IV/325
- photoelectric method I/571
 - nanosecond barrier I/571
- photoelectrochemical IV/371
 - activation I/286ff
 - cell II/851, V/604, IV/191, V/595
 - effects V/604

- light energy conversion II/845
- synthesis I/271ff
- photoelectrochemistry I/272ff, II/851, IV/384
- photoelectrochromic IV/339
- photoelectrolysis cell V/701
- photoelectrolytic generation IV/339
- photoelectron spectroscopy (PES) I/380, III/192, III/258, IV/777, IV/779
- magnetic bottle photoelectron spectrometer IV/778
- CH_3CN^- IV/788
- $\text{Cu} \cdot (\text{H}_2\text{O})_n$ clusters IV/782
- $\text{I} \cdot (\text{acetone})_n$ clusters IV/787
- $\text{I} \cdot (\text{CH}_3\text{I})_n$ clusters IV/788
- $\text{I} \cdot (\text{CH}_3\text{CN})_n$ clusters IV/788
- $\text{I} \cdot (\text{Xe})_n$ clusters IV/794
- $\text{I} \cdot (\text{H}_2\text{O})_n$ clusters IV/783, IV/791
- $\text{Li} \cdot (\text{H}_2\text{O})_n$ clusters IV/783
- $\text{Li} \cdot \text{NH}_3$ clusters IV/778ff
- $\text{Na}(\text{NH}_3)_n$ clusters IV/778ff
- $\text{Na}(\text{NH}_3)_n$ clusters IV/779
- solvated metal anions IV/777ff
- $\text{Sr}^+ \cdot (\text{H}_2\text{O})_n$ clusters IV/780
- photoelectrosynthetic cell IV/353, IV/364
- photoexcitation I/559ff, I/563, IV/4
- advantages I/560, I/562
- – control process I/562
- – vast time window I/562
- – wavelength variability I/562
- – energetic considerations I/560
- photokinetics I/563
- photoexcited fullerenes II/271
- singlet II/271
- triplet excited state II/271
- photoexcited states II/927
- singlet excited state II/927
- triplet excited state II/927
- photo-Fenton reaction I/299
- photogalvanic cell IV/361, IV/366, IV/374
- photographic emulsion V/474
- photohydrogenation I/295
- photoinactive mirror symmetry V/227
- photoinduced charge separation III/198, III/202, III/205, III/228, III/397, III/399, III/416
- photoinduced charge transfer IV/84, V/393
- photoinduced electron transfer II/6, II/28, III/31, III/34, II/72, II/79f, II/290, II/292, II/313, II/324, II/389, II/472, II/480, II/957, III/120, III/202, III/272ff, III/338ff, III/393, III/412, III/691, IV/4, IV/12, IV/44, IV/170ff, V/62, V/159, V/187, V/474
- charge-shift III/338, III/393
- dendrimers III/691
- free energy III/120
- oxidative III/338
- reductive III/338
- photoinduced energy transfer V/98, V/116
- photoinduced process V/98, V/100, V/103f, V/109f, V/119
- intercomponent V/100
- intramolecular V/103
- attenuation factors V/109
- photoinduced strand cleavage III/158
- end-stacked anthraquinone III/158
- photoinduced valence isomerization V/55
- photoinitiator IV/207, V/519, V/528, V/530, V/535, V/537f, V/550, V/558
- chromophore-linker-electron donor type V/535, V/537
- – excited triplet V/537
- – energies V/537
- – free energy changes V/537
- – quenching rate constants V/537
- – reduction potentials V/537
- donor-acceptor pair V/538
- supramolecular V/528
- visible light V/550
- photoinjected electrons III/120
- migration distance III/120
- photoionization III/119
- DNA III/119
- hole migration III/119
- photoisomerizable IV/168
- photo-isomerizable command surface IV/166
- photoisomerizations V/52
- photo-Kolbe decarboxylation I/299
- photoluminescence IV/361
- photoluminescence (PL) IV/355, V/483
- photolysis I/417, II/978ff, V/529
- laser flash I/417
- butyltriphenylborate salts V/529
- tetraphenylborates V/529
- photomultipliers I/539
- photonic I/563
- devices II/862, II/928
- sensors II/957
- – mode erasable media V/220
- – mode recording V/220
- wires III/324, V/97
- photo-NOCAS II/31
- photooxidation V/130, V/517
- photophosphorylation V/598
- photophysical properties II/806, IV/382, V/104
- $\text{Re}(\alpha\text{-diimine})(\text{CO})_3\text{L}$ IV/109ff
- photopolymerization V/516
- amplification V/516
- photopolymerization V/529
- photorearrangements V/59
- photoreceptor V/380, V/383
- characterization V/383
- fabrication V/383
- photoredox-active II/846
- photoredox active supramolecular assemblies II/849

- photoredox active supramolecular systems II/855
- photoredox chemistry IV/458, V/699
 - titanium oxide – zeolite composite IV/458
 - UV reduction of CO₂ IV/458
- photoreduction IV/269, V/517, V/542
- photorefractive effect V/472f, V/475f, V/478, V/489
 - electro-optic effect V/478
 - nonlocal V/478
 - rate V/489
 - sequence of process V/473
 - standard model V/475
 - trapping V/476
- photorefractive materials V/472ff, V/479ff
 - amorphous V/480
 - amorphous organic V/481
 - applications V/503
 - crystals V/480
 - fast V/492
 - fully functional V/494
 - hole transport materials V/499
 - organic materials V/480
 - photosensitizer V/484
 - potential applications V/472, V/508
 - rate of response V/491
 - sensitizer V/488
- photosensitivity V/386
- photosensitization IV/232f
- photosensitized electron transfer II/138ff
 - sensitizer II/139
 - co-sensitizer II/140
- photosensitizers II/305, II/840, III/513, IV/89, IV/98f, IV/128, IV/173, IV/176, IV/178, IV/181, IV/187, IV/191
- photoswitchable electrical communication IV/168
- photosynthesis III/24ff, III/179, III/226, III/262, III/272, III/276ff, III/413, III/455, III/618, III/629, IV/170
 - artificial III/272, IV/90, IV/121
 - natural IV/88
 - reaction center III/226, III/262, III/276ff, III/413, III/455, III/618, III/629
- photosynthetic architecture IV/338
- photosynthetic bacteria IV/171
- photosynthetic organisms V/186
- photosynthetic reaction center III/10f, III/40, IV/81, IV/171f, IV/185, V/68
- photosystem I III/24ff, IV/170, IV/211, V/598
- photosystem II II/862, II/947, III/24ff, IV/170, IV/218, V/599, V/637
 - artificial analog V/637
- phototautomeric forms V/171
- photovoltaic cells V/596, V/600, V/605, V/623, V/634
 - conversion efficiency V/634
 - dye-sensitized V/596, V/600, V/605, V/623, V/634
 - p-n junction V/596
 - maximum voltage V/634
 - performance V/634
- photovoltaic device V/595, V/635
- photovoltammetry IV/317
- photovoltammogram IV/333
- photozymes V/195
- pH-sensors II/862
- phthalazine II/363
 - reductive dimerization II/363
- phthalimides II/479, II/481ff
- phthalocyanine III/412, III/682, IV/150, V/199, V/384, V/415ff, V/424
 - calorimetry V/421
 - charge generation V/417
 - charge trapping V/417
 - dendrimers III/682
 - fluorescence quenching V/415
 - geminate pair V/415
 - pigments V/413
 - polymorphism V/413ff, V/419ff, V/424ff
 - quantum efficiency V/415
- physical confinement V/698
- physical development V/291, V/302, V/325
- phytochlorin II/318
- picosecond spectroscopy V/423
- picosecond time domain II/856
- pigment dispersion V/384
- pillars IV/506, IV/512ff, IV/520ff, IV/527ff
 - Fe₂O₃ IV/506
 - HCa₂Nb₃O₁₀ IV/513ff
 - HLaNb₂O₇ IV/511
 - HSr₂Nb₆O₁₀ IV/512
 - K_{4-x}H_xNb₆O₁₇ IV/504
- montmorillonite clay IV/520
- polyoxometallates IV/527
- TiO₂ IV/506
- pinacol II/458
- pinacolate IV/16
- pinacolization II/459, II/466
- piperazine V/85
- pivalaldehyde IV/38
- pK_a (*see also* acidity) II/27, II/243, II/908, II/920
- planar diffusion I/436, I/451
- planar intramolecular charge-transfer state II/402
- planar lipid membranes
 - formation of IV/584
 - lateral diffusion in IV/589
 - electron transport in IV/617
- planar rutile electrodes IV/399
- Planck distribution function I/72
- Planck formula V/592
- planetary atmospheres II/55
 - methane radical cation in II/55, II/60
- plant peroxidase III/84
 - class I III/84
 - class II III/84

- class III III/84
- superfamily III/85, III/92
- – crystal structure III/92
- plantacyanin IV/130
- plasticizers V/505
- plastocyanin III/15, IV/130, IV/209, V/599
- spinach IV/209
- plastoquinone V/598
- plastoquinone V/599
- plateau current I/461, I/463, I/473ff
- platinized titanium dioxide V/712
- platinum II/819, II/988
- black II/751
- complexes II/849, III/355ff, V/126
- plug-socket systems III/525
- pseudorotaxanes III/525
- p*-methylbenzoate II/745
- p*-*n* junction V/596
- PNA/DNA duplexes III/159
- hole migration III/159
- PNP III/84
- Pockels effect V/244, V/480, V/504
- point dipole V/450
- Poisson-Boltzman method I/110
- Poisson equation I/158ff, IV/287
- polar component V/440, V/446
- polar effect II/36
- polar group V/451, V/453
- polar mechanism II/928
- polar substituents V/453
- polarity parameter IV/258
- polarizability I/154, V/448
- π, σ -polarization II/59, II/87
- polaron I/72
- polaron formation III/156
- polaron migration III/156
- poling field V/489
- poling field limit V/493
- pollutants IV/161
- poly(γ -benzyl-*D*-glutamate) V/263
- poly(ethyleneterephthalate) V/383
- poly(glutamates) V/262
- poly(isocyanides) V/262
- poly(*N*-vinylcarbazole) V/384, V/398, V/456
- poly(phenylene-ethynylene) V/80
- poly(*p*-phenylene) IV/140
- poly(propylene imine) dendrimers V/263
- poly(vinyl) butyral V/409
- poly(vinylpyridine) IV/145
- polyacetylene IV/140
- polyacrylamide IV/146
- polyalkylene V/111
- polyaminoacid receptor V/167
- polyaniline IV/140, IV/143, V/670
- poly-aza macrocycles (*see also* aza crowns) III/463
- polyazine II/808, II/828
- polychromatic radiation V/594
- polycrystalline IV/285
- polyelectrolytes IV/145
- polyene V/110
- polyether II/809
- polyferrocene dendrimer II/786
- polygermane II/292
- polyG-polyC duplex III/166
- molecular band III/166
- polyhydride II/906
- polyimides V/484
- polylysine IV/181
- polymer II/816, V/494
- compositers V/491
- film II/836
- matrix IV/181
- polymerase chain reaction (PCR) V/176
- polymer-based antennas V/195
- polymeric matrices IV/140, IV/145f
- polymerization II/172, II/779, V/516f, V/526, V/550, V/563, V/565, V/568f, V/574, V/578f
- 4-carboxybenzophenone V/565
- cation radical chain cyclobutanation II/172
- dental applications V/550
- Diels-Alder II/172
- dye-sensitized V/517, V/565
- general scheme V/517
- initiation V/569
- kinetics V/568
- photoinitiated V/516
- photoinitiated V/563
- rate V/526
- reaction scheme V/569
- initial rate V/574
- mechanism V/578
- rates V/579
- polymers with a helical backbone V/261
- polynorbomane dienes III/192, III/219
- polynorbornyl IV/562ff
- electron transfer bridge IV/562ff
- polynorbornyl IV/562ff
- polyoxomolybdate II/638
- polypeptides II/311, IV/155
- as logic gates V/177
- polyphenol IV/143
- oxidase IV/143
- polypyrindines II/804, II/807, II/819, II/828
- complexes III/350ff, III/426, III/432, III/446, III/563, III/565, III/585ff, III/641, III/656, III/659, III/668ff, V/195
- – catenanes III/565, III/584ff
- – cyclophane ligands III/563
- – dendrimers III/655ff, III/668
- – rotaxanes III/641
- hydrogen bonded III/446
- – dinuclear III/353ff
- – polynuclear III/353ff

- ligands II/564, V/194
- polypyridyl-oxo-Ru complexes IV/49
- polypyrrole IV/130, IV/140, IV/143f, V/670
- polysilane II/292
- polystyrene V/454, V/455
- mobility V/455
- poly-thiamacrocycles (*see also* thia-crowns) III/478
- polythiophene IV/140, V/670
- Poole-Frenkel effect V/449
- porous media IV/413
- general description IV/413
- porphyrazines III/412
- porphyrins II/39, II/314, II/315ff, II/322, II/836, II/930, III/236, III/300ff, III/282ff, III/656, III/272ff, III/278f, III/291, III/293ff, III/295ff, III/300, III/303ff, III/320f, III/324ff, III/413ff, III/431, III/440, III/450, III/452, III/618ff, III/621, III/625f, III/659, III/679ff, III/688, V/73, V/75, V/173, IV/175, IV/178, IV/179, IV/182, IV/184f, IV/187ff, V/714
- arrays III/324ff
- Au(III) tetraarylporphyrin III/284
- -barbiturate conjugate III/440
- *cis*-bisamide III/418
- bisporphyrin III/619
- -centered oxidation II/934
- -carotene dyads III/300
- cobalt III/413
- cofacial bisporphyrin III/440
- cofacial porphyrin-quinone III/417
- cofacial zinc diporphyrin III/320f
- -containing dyads II/960
- -containing triads II/963
- dendrimers III/659ff, III/678ff, III/688
- dicytidine-free base porphyrin III/431
- donor III/236
- electrochemistry III/620
- fluorescence quenching III/300ff
- free base porphyrins III/279
- -fullerene dyad III/295ff
- gold III/284ff, III/619ff
- guanidinium III/301
- guanosine-functionalized zinc porphyrins III/431
- hexagonal V/75
- iron(III) porphyrins III/282
- luminescence III/620
- mono III/431
- octaalkyl-substituted zinc porphyrin III/282ff
- photophysical properties III/278ff, III/621
- porphyrin dyad III/283ff
- porphyrin-imide dyad III/302
- porphyrin-quinone dyad III/286
- Q-bands III/452
- -quinone complex III/414
- radical cation III/293ff, III/625f
- redox potentials III/621
- rigid porphyrin-quinone III/291
- rotaxanes III/618ff
- soret bands III/452
- square V/75
- supramolecules III/450
- triplet excited states III/431
- -viologen III/303ff
- zinc III/278ff, III/450, III/619ff
- – cation radical III/420
- zinc(II) III/414ff
- positive bias IV/404
- positive g-shift II/72
- potassium II/464, II/717
- acenaphthylenide II/726
- graphite II/726
- potential II/621, V/516
- ϕ I/128
- distribution IV/384
- drop I/152ff
- electrochemical I/427
- electrode I/422, I/482ff
- energy I/131
- – surface IV/112
- equilibrium I/425
- formal I/489
- gradient I/427
- over– I/425ff, I/492ff
- peak II/621
- oxidation V/516
- oxidizing V/516
- reduction V/516
- standard I/423, I/448ff, I/482ff, I/489, I/497
- – chemical I/427
- potentiometric titration V/298
- potentiostat I/424, IV/316
- powders IV/173
- power extraction V/590
- p*-phenylene oligomer bridges V/114, V/117, V/119
- p*-phenylenevinylene oligomers III/233
- PQQ (PQQTME) (*see also* pyrroloquinoline quinone) IV/35, IV/153, IV/156, IV/79
- coenzyme IV/35
- trimethyl ester IV/35
- -FAD IV/155, IV/162
- precursor complex II/662, III/410ff, V/517
- precursor state I/558, I/563
- pre-filamentary growth V/323
- preillumination V/491ff
- uniform V/491ff
- prenyltributyltin II/298
- pre-organization III/428
- pre-organized donor-acceptor system V/537
- preparation of solutions I/549
- pulse radiolysis I/549
- preparative electrolysis I/470, I/475

- pressure IV/262, IV/264
- jump I/406
- primary alcohols IV/22
- primary hole transfer III/152
- from deoxyribose to guanine III/152
- primary process V/517
- primary radicals I/507, I/523
- water I/507
- prismane II/115
- probe tip aperture V/239
- product state I/558, I/561, I/563, I/569
- redox-pair I/561
- product well I/68ff
- programmable logic devices V/182
- promoters IV/130
- propagating wave I/135
- 2-propanol I/517
- acetone I/518
- radiation chemistry I/518
- propellane II/223
- propene II/229
- properties II/636
- ferromagnetic II/636
- propionitrile I/461, IV/20
- propyl sulfide V/567
- protection V/511
- protein II/786, III/424, V/370
- protein electron transfer IV/202
- protein matrix IV/68
- protein modification III/5
- protein mutagenesis IV/192
- protein radicals IV/22
- protein-protein complexes III/413, IV/202
- proteins II/860
- protic acids II/754
- protoheme IX III/57
- protonation II/30, II/906, II/913, IV/10, IV/93, V/235
- rate constants II/30, IV/94
- reactions I/523
- proton binding V/84
- proton-coupled back electron transfer IV/400
- proton-coupled electron transfer (PCET) I/189ff, IV/47, IV/82
- Cukier model of I/190, I/206
- rate expression for I/206
- proton/hydrogen atom/hydride transfer III/454
- proton-exit III/51
- proton motive force III/311
- proton pathways III/41, III/50f
- D-pathways III/50f
- K-pathways III/50f
- proton pump III/51, III/311
- direct-coupling mechanisms III/51
- histidine cycle III/51
- indirect-coupling mechanisms III/51
- proton shift III/310
- proton transfer (PT) I/189ff, I/200, I/208, II/931, III/45, III/69, III/310, III/445, IV/29, V/549, V/552, V/559, V/561
- carbon from heterocyclic systems II/518
- – electron addition to 2'-deoxyadenosine II/518
- – electron addition to thymidine II/518
- uncompensated III/445
- vibrationally adiabatic I/196
- vibrationally non-adiabatic I/196
- zeolite matrix II/100
- proton translocation III/50, III/409
- proton tunneling IV/83
- proton uptake III/51
- proton wire III/51
- protoporphyrin IX III/56, IX IV/155, IX IV/159
- proximal cysteine ligand III/64
- proximal ligand III/67
- proximity development V/315
- pseudoazurin IV/130
- pseudoheliotridone II/440
- Pseudomonas putida* III/58
- pseudorotaxanes III/501ff, III/513, III/525
- cyclobis(paraquat-*p*-phenylene) III/502ff
- dendritic III/504
- dethreading/rethreading III/501
- electrochemical properties III/501
- extension systems III/526
- “light-fueled” motor III/513
- plug-socket systems III/525
- poly III/504
- self-assembly III/501
- switches III/527
- PSX V/488
- pteridine IV/45
- pterins IV/68
- p*-terphenyl II/213
- PTS V/387, V/453
- pulse compression I/568
- chirp to I/568
- pulse radiolysis I/226, I/228, I/377, I/523, I/527f, II/817, III/118, III/191, III/210, IV/207, V/324, V/707, V/709ff
- accelerators I/531
- – febetron I/531
- – linac I/531
- – Van de Graaff I/531
- chemical dosimeters I/538
- conductometric detection I/542
- – A.C. method I/542
- – D.C. method I/542
- – dosimetry I/543
- contribution I/528
- data capture and analysis I/541, I/548
- detection methods I/529
- dose monitor I/537
- electron paramagnetic resonance detection

- I/545
 - flat band potential V/707
 - flow system I/531
 - general chemistry I/528
 - high pressure I/527
 - high temperature I/528
 - historical perspective I/523
 - microwave detection I/544
 - mid-gap region V/707
 - nuclear magnetic resonance detection I/546
 - one-button operation I/540
 - optical detection I/533, I/539ff
 - light emission I/540
 - light-scattering measurements I/541
 - preparation of solutions I/549
 - picosecond time resolution I/546
 - polarographic detection I/543
 - purification of materials I/549, I/551f
 - gases I/552
 - nonaqueous solvents I/551
 - water I/551
 - rapid-mixing device I/535
 - sample cell and flow system I/533
 - selected redox indicators I/550
 - stopped-flow method I/536
 - stroboscopic method I/547
 - typical modern facility I/528
- pulsed electrode I/323
- pulsed excitation V/501
- pulsed flow I/398ff
 - pulsed-accelerated-flow I/399
- purification of materials I/549, I/551
 - nonaqueous solvents I/551
- purple membrane V/264
- push-pull
 - 5-[[4'-(dimethylamino)phenyl]ethynyl]-15-[(4''-nitrophenyl)-ethynyl]-10,20-diphenylporphyrinato]Zn(II) complex V/273
- push-pull mechanism III/67f
- putidaredoxin III/60
 - reductase III/60
- PVK V/386, V/398, V/399ff, V/485, V/496, V/499
 - absorption V/399
 - charge generation V/400
 - excimer V/401
 - fluorescence spectra V/399
 - photogeneration efficiency V/399
 - photophysics V/400
 - TNF V/389, V/402, V/404, V/431
 - spectral sensitivity V/404
 - xerographic gain V/399
- p*-xylene II/932
- pyracene II/213
- pyrazolidone V/302
- pyrazolines V/384
- pyrene II/725, III/124, III/701
 - amine V/555
 - complex formation III/124
 - dU conjugates III/132
 - excimer III/133
 - fluorescence III/133
 - oligonucleotide conjugates III/133
 - end-labeled III/133
 - photophysics III/133
 - radical ion V/556
 - static and dynamic quenching III/124
 - triplet III/125
- pyridine II/228, II/341ff, II/352, II/357, II/363, II/367, II/370f, II/836, IV/24
 - alkylation II/367
 - cyano II/371
 - fluorination II/352
 - halo II/370
 - $S_{RN}1$ reaction II/370
 - nucleotide oxidoreductase IV/145
 - perfluoroalkylation II/357
 - photochemical reaction II/371
 - radical anion II/342
 - stable II/342
 - radical cations II/341
 - reductive dimerization II/363
 - SET dehalogenation II/367
 - stable II/342
- 2-pyridine-*N*-carbaldehyde II/808
- 4-pyridinecarboxaldehyde II/760
- pyridinium II/364
 - acceptors II/631, II/651, II/654
 - alkylation II/364
 - cations I/458
 - ions III/375
- pyridium II/363
 - reductive dimerization II/363
 - accepto II/634
- pyridylpyridinium III/303
- pyrimidine II/363
 - reductive dimerization II/363
- pyrolytic graphite IV/130
- pyromellitimide III/302ff
 - acceptor III/302ff
- pyrrole II/339, II/350, II/356ff, II/364, II/370
 - arylation II/370
 - coupling with 2,4,7-trinitrofluoren-9-one II/364
 - oxidative dimerization II/350
 - oxidative polymerization II/350
 - radical cations II/339
 - perfluoroalkylation II/357
 - photochemical reaction with alkenes II/356
 - photochemical reaction with haloquinones II/358f
- pyrrolidine II/302
- pyrrolidinium salt II/280
- pyrrolidinofullerenes II/305
- pyrrolizidone II/440

- pyrroloquinoline quinone (*see also* PQQ) IV/78, IV/45, IV/144, IV/152
 pyruvate IV/222
 – dehydrogenase IV/54
 – oxidase IV/129
 pyrylium V/384
- quadratic (or first) hyperpolarizability V/244
 quadricyclane II/125
 quadricyclane radical cation II/113
 quadron II/196
 – synthesis II/196
 quadrupole V/448
 quantization effect V/698
 quantum computation V/89
 quantum computer V/177
 quantum confinement V/611
 quantum dots V/698
 quantum efficiency (*see also* quantum yield)
 I/292, IV/495ff, IV/534, V/708f
 – adsorption kinetics V/710
 – $\text{K}_4\text{Nb}_6\text{O}_{17}$ IV/495
 – multilayer systems IV/528ff
 quantum mechanical treatment II/606
 quantum particles (or dots) IV/335
 quantum size effects I/279
 quantum wells IV/335
 quantum wires IV/335
 quantum yield (*see also* quantum efficiency)
 II/271, II/293, II/857, II/959, III/279, III/423,
 IV/46, IV/238, IV/254, IV/259f, IV/307,
 V/234, V/564
 – free-radical formation V/579
 quantum-beat effect II/611, II/615
 quantum-chemical techniques II/821
 quartet state II/237
 quartz crystal microbalance IV/135, IV/304
 quasi-bound states IV/672
 quasi-Fermi level V/600
 quasi-reversible electrode reaction I/426, I/432,
 I/441ff, I/449ff
 qubits V/178
 quenching V/115
 – dynamics III/131
 – – conformationally dependent III/131
 – ET^+ by DAP^{2+} III/143
 – – D-A separation increases III/143
 – – reorganization energy III/143
 – – weak coupling III/143
 quinazoline II/363
 – reductive dimerization II/363
 quinydrone III/420
 quinoline II/363f, II/367, II/370
 – alkylation II/364, II/367
 – coupling with indole II/363
 – halo II/370
 – – $\text{S}_{\text{RN}}1$ reaction II/370
 – radical anion II/363
 – reductive dimerization II/363
 quinones I/517, II/313, II/760, III/278ff, III/293ff,
 III/310ff, III/417ff, III/421, III/488, III/494,
 IV/68, IV/132, V/599
 – pK_a III/310ff
 – radical anions III/293, III/421
 o-quinones IV/73
 quinone dianions IV/48
 quinonediimine V/296, V/300
 quintet state II/237
- R group migration IV/57
 Rabi formula II/598
 rack-type complexes III/605
 radial mixer I/398
 radiations V/591
 – chemical yields (*G* values) I/506
 – – water I/506
 – chemistry I/503, I/505, I/514ff, I/537
 – – water I/505
 – – organic liquids I/514ff
 – – dosimetry I/537
 – DNA III/116
 – entropy V/591ff
 – flux V/595
 – induced catalysis V/714
 – induced ionization II/277
 – induced reduction II/275, II/282
 – temperature V/591ff
 radiationless decay V/393
 radiationless transition II/607f
 – theory III/294
 radicals II/27, II/722, II/976ff
 – alkyl radicals, with II/33
 – amine II/27
 – anions I/517f, II/7, II/29ff, II/38, II/235,
 II/341f, II/479, II/560, II/494, II/978, III/188,
 III/191, III/315, V/364, V/535
 – – arene II/31
 – – coupling II/31, II/33
 – – cycloaddition II/38
 – – cyclotrimerization II/38
 – – Diels-Alder II/38
 – – diphenylethane derivatives II/559
 – – C-C bond cleavage II/559
 – – 1,2-diphenylethane derivatives II/567
 – – electrocyclic reaction II/38
 – – fullerene I/517
 – – fumarate II/30
 – – heterocycles II/341f
 – – ketyl II/6, II/29, II/32
 – – metal ion complex IV/16
 – – pericyclic process II/38
 – – phthalimide II/479
 – – pyromellitimide III/315
 – – radical cation I/520

- stable II/342
- cations I/354ff, I/518, II/6, II/28, II/33, II/36, II/38f, II/62, II/97, II/99, II/105, II/107, II/110ff, II/323, II/339ff, II/477, II/494, III/194f, IV/41, IV/253, V/535, V/566f
- additions to σ -bonds of I/357ff
- additions to π -bonds of I/362ff
- alicyclic hydrocarbons
- amine II/6
- branched alkanes II/68ff
- Claisen II/39
- Cope II/39
- cycloadditions II/39
- Diels-Alder II/38
- dimerization II/36
- heterocycles II/339ff
- hole (positive charge) delocalization in I/354ff
- kinetics II/39ff
- maleate II/30
- nucleophilic capture I/362ff, II/119
- olefin II/31
- one-electron σ -bond (1e- σ -bond) I/354ff
- pericyclic process II/38
- phenol II/28
- rearrangement I/354ff, II/39
- spontaneous generation in zeolites II/69
- sulfur-centered V/566
- three-electron bonded V/567
- "vertical" and "non-vertical" I/354
- zeolites II/99
- centers II/107
- chain nucleophilic substitutions IV/49
- clock I/415, II/942
- coupling II/287, II/303, IV/49
- cyclization II/467, II/471
- generation II/978
- homocoupling IV/270
- ions I/342ff, II/5, II/342, II/487, II/519
- heterocycles II/342
- generation of II/5
- reactivity pattern II/5
- pairs II/293, II/316, II/324, III/123, IV/28, IV/3, IV/33
- singlet III/123
- π - π stacked dyad II/316
- triplet III/123
- pairs II/284, II/637, V/561, V/573
- intersystem crossing V/68
- states III/309
- probe II/198
- reaction II/752
- scavenger IV/262
- radiolysis I/523, II/978ff, III/454
- solvent mixtures I/523
- random walk V/440
- random-number generator V/445
- Raney nickel II/463
- rapid mixing I/397
- rapid-scan I/396
- rare-gas compound II/752
- rates V/519, V/530, V/532, V/543, V/546, V/549, V/554
- constants I/528, I/536, II/30, V/517, I/547, V/571
- activation-controlled I/528
- apparent heterogeneous I/443
- cleavage I/451, I/456, I/494ff, I/497
- crosscoupling V/571
- CO₂ as electrophile II/30
- diffusion-controlled I/449, I/457, I/495ff, I/528
- dimensionless I/434, I/439
- heterogeneous I/441, I/445
- dimerization I/448ff, I/458
- electron return V/571
- electron transfer (*see also* electron transfer rates) I/464ff, I/494ff, II/593, V/517, V/571
- homogeneous standard I/498
- oxidation I/424
- polymerization V/571
- protonation II/30
- proton transfer V/571
- reduction I/424
- reductive dimerization II/30
- return electron transfer V/517
- separation V/517
- standard heterogeneous I/423ff, I/444, I/456, I/493
- diffusion-controlled V/549
- photoinitiated polymerization V/543
- photoinitiation V/554
- photopolymerization V/532
- polymerization V/519, V/530
- proton transfer V/546
- triplet quenching V/549
- γ -rays V/716
- Rb₂La₂Ti₃O₁₀ IV/512, IV/518, IV/519
- Rb₄Nb₆O₁₇ IV/490f
- Rb₄Ta₆O₁₇ IV/490f
- RBAX V/539, V/552
- RbCa₂Nb₃O₁₀ IV/512, IV/513
- RbLa₂Ti₂NbO₁₀ IV/512, IV/519
- RbLaNb₂O₇ IV/512f
- RbPb₂Nb₃O₁₀ IV/512, IV/514ff
- absorption edge IV/514
- RC time constant IV/316
- RCOO⁻ IV/49
- RCOOH IV/49
- RDE IV/305
- reactant state I/558f, I/561, I/563, I/582
- spin multiplicity I/561
- reactant well I/66ff
- reactions

- alkali metal atom with a halogen molecule IV/633, IV/638f
- Ba + Cl₂ IV/644
- Ba⁺...Cl₂⁻ intermediate IV/644
- Ba + CH₃OH IV/647
- Ba + H₂O IV/647, IV/657
- Ba + N₂O IV/636, IV/651, IV/683
- Ba + NO₂ IV/646
- Ba + NO₂ IV/644ff
- Ba + O₃ IV/646
- Ba₃ + SF₆ IV/683
- Br₂ + K IV/638, IV/640
- Br₂ + K₂ IV/649
- Ca + HBr IV/668
- Ca + HX (X=F, Cl, Br, I) IV/665ff
- center V/189
- CH₃I + K IV/638, IV/652
- CH₃I + Ag surface reaction IV/650
- Cl₂ + K surface reaction IV/650
- coordinate I/12ff, I/21ff, I/121, I/65ff, II/584, II/586, II/589, II/591f, IV/632
- Cs + H₂ IV/653
- Cs + NO₂ IV/640
- Cs + O₂ IV/652
- Cu + F₂ IV/659, IV/660
- F₂ + Ca IV/642
- reaction free energy I/171
- H + Cl₂ IV/642
- Hg atom IV/663
- Hg + Cl₂ IV/663f
- K₂ + Br₂ IV/649f
- K + CH₃CN IV/661
- K + CH₃I IV/655
- K + Cl₂ surface reaction IV/650
- K + HCl IV/651, IV/678
- K + H₂ IV/653
- Mn + Cl₂ IV/648, IV/659
- Mn₂ + F₂ IV/650
- Mn + O₃ IV/648f
- Na...FH system IV/640
- Na + CH₃Br IV/654f
- Na + Cl₂ IV/655
- Na + HCl IV/655f, IV/661
- Na + O₂ IV/656
- N₂O + Li atoms on a Rh surface reaction IV/650
- order I/440
- rate theory V/327
- SF₆ + Ba surface reaction IV/650
- inorganic anions I/509
- -- hydroxyl radical I/509
- metal ions I/509
- -- hydroxyl radical I/509
- organic molecules I/510
- -- abstraction I/510
- -- addition I/510
- -- hydroxyl radical I/510
- single coordinate approximation IV/633
- reaction stereodynamics IV/635ff
- -- total cross-section IV/635
- Ti + NO IV/648
- Ti + N₂O IV/648
- Ti + O₂ IV/648
- reactive oxygen form III/63
- reactive oxygen intermediate III/80, III/82
- reactivity I/507, II/996
- hydrated electron I/507
- pattern II/487
- re-alkyl complex IV/114
- rearrangement II/107
- receiver sheet V/305
- receptor II/837
- groups II/806
- site II/862
- reciprocity V/397
- Re-CO₂ complex IV/115
- recognition of anions II/788
- recognition of oxoanions II/789
- recombination IV/303, IV/309, V/400, V/475, V/705ff
- capacitance IV/303
- resistance IV/303
- separation V/706
- surface recombination IV/309
- trapping V/706
- reconstitution IV/151f, IV/162, IV/166, IV/168, IV/182, IV/185, IV/187, IV/189, IV/190
- rectification V/48
- rectifiers IV/164
- redox (*see also* reduction and oxidation) II/910
- active bridging ligands V/131
- amplification V/315ff
- buffers V/319f
- catalysis I/494ff, II/782, II/804, II/817, II/834, II/862
- change II/804
- couple II/715
- dimerization V/13
- equilibria I/423
- group V/23
- induced structural changes II/831
- isomerization II/993
- Lith effect V/314
- mediator II/852, V/623
- orbital II/804, II/823
- patterns II/823
- potential I/278ff, I/525, II/6, II/715, II/806, II/936, III/60, III/115, III/278ff, IV/69, IV/260
- -- aqueous solution III/115
- -- metal ions I/525
- -- modulation IV/69
- -- nonaqueous solution III/115
- -- noncovalent interactions IV/69
- -- temperature dependence II/832

- propagation II/763
- property
- rhenium complex IV/104
- proteins IV/128
- reactions I/271,ff
 - at semiconductor surfaces I/273ff
 - oxidations I/294ff
 - reductions I/301ff
 - solvent effects in I/280
- reagent II/714ff
- relay II/21, II/28
- sensors II/804, II/837
- series II/792, II/804, III/677
- site V/8, V/11, V/20, V/25
- steps II/820
- system I/142ff
- titration I/474ff
- reductant II/717, II/731, IV/3,
- reductases II/465, III/409, V/704
- reduction V/712ff
 - Birch II/465
 - metal ions I/523
 - solvated electron I/523
 - potential II/271, II/291, II/305, II/458, II/461, II/478, II/620, IV/354, V/522
 - CO₂ IV/88f
 - electron acceptor V/522
 - metal macrocycle IV/92
 - oxidant IV/354
 - reductant IV/354
 - rhenium complex IV/105
- reductive activation II/241
- reductive dehalogenation of aryl and benzyl halides II/559, II/563f
- comparison of concerted and stepwise cleavage II/564
- effects of the medium II/565
- structural effects II/563
- reductive quenching II/291, II/946, IV/15, IV/174, IV/179
- reductive titrations II/910, II/913
- reductively induced dissociation II/834
- reference electrode I/170ff
- refraction V/472
- refractive index V/481
 - modulation V/506
- regeneration IV/176, IV/179
- regenerative cell IV/353
- regenerative solar cell V/634
- regioselectivity II/766, IV/265
- regiospecific intramolecular capture II/120
- regiospecificity II/107
- Rehm-Weller equation II/80, II/389, II/933, V/522ff, V/534, V/543, V/574
- Rehm-Weller free energy relation II/298
- Rehm-Weller kinetics II/850
- relative effective electron mass IV/305
- relaxation I/278, I/403ff, II/980, II/988f
 - methods I/403ff
 - kinetics I/403ff
 - relaxation time I/409
 - reactions I/407ff
 - exchange I/407ff
- relay II/862
 - catalyst IV/89f, IV/98f
- Re-O₂CH complex IV/115
- reorganization (*see also* inner shell reorganization, reorganization energy) II/584, II/594, II/597ff, IV/6
- nuclear IV/6
- solvent IV/6
- Energy I/14ff, I/19ff, I/25ff, I/55ff, I/110ff, I/120ff, I/199ff, I/206, I/222, I/228ff, I/230, I/242, I/345, I/381ff, I/426, II/273, II/313, II/318, II/597, II/600, II/665, II/678ff, II/692, II/694, II/850, II/933, II/963, III/6, III/8f, III/30ff, III/45, III/47, III/206, III/229, III/274ff, III/345, III/411, III/448, III/627, IV/54, IV/110ff, V/367, V/395, V/412, V/444, V/483, V/574, V/618, V/633
- external (medium) I/230
- inertial I/209
- inner sphere III/345, V/574
- internal (inner sphere) I/195, I/207, I/230ff
- low-frequency I/228
- nuclear I/242
- outer sphere I/110, III/345, V/574
- rotaxanes III/627
- self-exchange I/477ff
- SET I/222
- solvent I/426, I/492, III/8
- TET I/228ff, I/230
- vibrational I/381ff
- inner shell II/598
- parameter λ I/70ff, I/83, I/179ff, II/584, II/594ff, V/559ff, V/569
- inner-sphere λ_i I/91ff, I/100
- outer-sphere λ_o I/91ff, I/100
- total I/102
- theory III/182
- reorientation process V/493
- reorientational birefringence V/504
- repeat unit V/3, V/41, V/43f,
- resistance I/446, I/453ff
- resistive media I/458ff
- resonance enhanced multiphoton ionization (REMPI) IV/629, IV/709, IV/746, IV/750
- resonance enhanced two photon ionization IV/757
- anthracene-dimethyl-*o*-toluidine adducts IV/751
- benzene-argon adducts IV/746
- DMOT-anthracene adducts IV/751
- electron photodetachment IV/751

- resonance integral I/223, I/225
- resonance Raman spectroscopy II/815, III/605, IV/336, V/631
- respiration III/24ff
- retinol II/292
- retro-aldol cleavage reactions of anilinium radicals II/393
- retrocyclobutanation II/200
 - anion radical II/200
- reversal processing V/305
- reverse-bias IV/298
- reversible dimerization II/253
- reversible electrode reaction I/426, I/432, I/441ff, I/449ff
- rhenium complexes II/811, II/847, II/986ff, II/996, III/353ff, III/489, III/515, III/564
 - catenanes III/565
 - cyclophanes III/564
 - pseudorotaxanes III/515
 - sensors III/489
- rhodamine V/714
- rhodamine B IV/246
- rhodium complexes II/849, III/129, III/353ff, IV/174, V/97, V/99
 - luminescence quenching by purine nucleotides III/129
- Rhodobacter sphaeroides III/24ff
- rhodocenium cation II/722
- Rhodospseudomonas viridis III/24ff, III/629
- rhombic EPR spectrum II/911
- ribonucleotide III/455
 - reductase III/75, III/455
- Richardson constant IV/305
- rigid bridge model I/109
- rigid matrix III/291ff
- rigid multichromophoric molecules V/255
- rigidochromic IV/383
- ring-closed II/95, II/97
- ring motions III/566ff, III/570, III/633, III/638
 - catenanes III/566ff, III/631ff
 - catenates III/638
 - electrochemically controlled III/570
- Ring-opened II/78, II/95, II/97, II/103ff
 - cyclopropane radical cation II/93
- ring strain II/79
- R-isomers (*see also* LE states) IV/743, IV/750, IV/752
- Robin and Day's classification V/20
- rod V/109
 - systems V/97
- rose bengal V/539
- rotating disk electrode I/463, I/472ff, I/474ff, I/496
- rotating disk (ring) voltametry I/327
- rotating gold electrode V/310
- rotating silver electrode V/317
- rotational spectroscopy IV/678
 - rotationally resolved spectra IV/745
 - cyanonaphthalene-trimethylamine complex IV/746
 - naphthalene clusters IV/745
 - rotaxanes II/836, III/539ff, III/542ff, III/544, III/547ff, III/552ff, III/576, III/582ff, III/618ff, III/640ff, III/645f, III/648, V/172
 - absorption spectra III/645, III/648
 - branched III/544
 - cyclobis(paraquat-*p*-phenylene) III/542ff
 - electrochemical properties III/643
 - luminescence III/547, III/622, III/645
 - motions III/640ff
 - photochemistry III/622ff
 - photophysical properties III/621
 - poly III/544, III/576
 - polypyridine complexes III/641
 - porphyrins III/618ff
 - quenching constant III/646
 - redox potentials III/621
 - reorganization energy III/627
 - shuttling process III/552ff
 - super-exchange III/627, III/629
 - synthesis III/539
 - through bond electron transfer III/627
 - through space electron transfer III/627
 - transient spectra III/625f
- rough electrode IV/133
- R₄Sn IV/46
- [Ru(bpy)₃]²⁺ III/350ff, III/505, III/558, III/669ff, III/706, IV/11, IV/174, IV/178ff, IV/187, IV/189, IV/417, IV/441, IV/444, IV/446, IV/502, IV/523ff
 - covalently linked systems III/350ff
 - dendrimers III/669, III/706
 - intrazeolitic synthesis IV/417
 - K_{4-x}H_xNb₆O₁₇ IV/502
 - kaolin IV/523
 - montmorillonite IV/523
 - pseudorotaxanes III/505
 - rotaxanes III/558
 - sepiolite clay IV/526ff
- Ru complexes, IV/136, V/97, V/608f
 - luminescence quenching by purine nucleotides III/129
- Ru(II) and Os(II) polypyridine complexes V/202
- Ru(II)-tris-bipyridine IV/185
- Ru(TAP)₂dip²⁺ complex III/134
 - luminescence quenching III/134
- rubidium II/717
- rubredoxin II/919
- Ruddlesden-Popper series IV/516ff, IV/511
- Ru-labeled cytochrome *c* III/42
- Ru-modified cytochrome *c* III/44f
- Ru-modified proteins III/5
- Ru-Os complexes V/115
- ruthenium II/814, II/919f, II/983f, III/5, V/8,

- V/24f, V/27ff, V/31f, V/34, V/38, V/41, V/43, V/202, V/494, V/606
- complexes II/310, II/847, III/353ff, III/426, III/446, III/489, III/505, III/558, III/564f, III/659, III/669, IV/174, IV/178ff, IV/185, IV/187, IV/189, V/195 V/202, V/714
- catenanes III/565
- cyclophanes III/564
- dendrimers III/659ff, III/669
- hydrogen bonded III/446
- rotaxanes III/558
- sensors III/489
- covalently linked systems III/353
- mixed-valence V/35
- modified azurin III/427
- rutile TiO₂ IV/370
- sabinene II/219
- sacrificial electron donor IV/90, IV/92, IV/119ff, IV/173, IV/175, IV/179, IV/181, IV/183f, IV/190
- sacrificial reductant II/732, III/513, III/559
- pseudorotaxanes III/513
- rotaxanes III/559
- saddle point I/78
- safranin T V/555, V/558
- salicylate II/834
- salts V/529
- dialkylphenacylsulfonium V/529
- diaryliodonium V/529
- onium borate V/529
- triarylsulfonium V/529
- bridges I/209, IV/566, III/412, III/443ff, IV/566, IV/569ff
- electron transfer IV/566, IV/569ff
- charge redistribution III/445
- effect II/745
- samarium II/462, II/468
- samarium diiodide II/466
- sample cell and flow system I/533
- pulse radiolysis I/531
- sampled-current voltammetry I/437ff
- sapphyrins III/441
- sarcophagine III/471
- saturable absorber I/568
- saturated rigid bridging ligands V/105
- SbX₅ II/751
- Sc³⁺ IV/46
- scandium ion IV/20
- scandium triflate IV/20
- scanning electrochemical microscopy (SECM) I/318, I/466ff
- scanning electron micrograph IV/379
- scanning probe microscopic methods IV/336
- scanning tunneling microscope V/180
- scattering I/139, V/592
- light V/593
- Scholl reaction II/212
- Schottky barriers IV/292
- Schottky junction IV/385, V/595
- scintillation counting I/418
- scorotron V/388
- SECM, *see* scanning electrochemical microscopy
- secondary electrons V/714
- secondary hole transfer III/152
- from G⁺ to a GGG hole trap III/152
- secondary radicals I/510f
- water I/506ff
- secondary structure III/109
- RNA III/109
- single-strand DNA III/109
- secondary transformations IV/175, IV/187
- second-harmonic AC voltammetry V/365
- second-harmonic generation V/244
- second-order nonlinear optical molecules V/252
- selected properties I/507, I/513
- alcohol radical I/513
- hydrated electron I/507
- selection rules I/224
- selenium V/389
- selenium-arsenic V/389
- selenium-tellurium V/389
- selenocysteine II/916
- self-annihilation I/328
- self-assembled monolayer (SAM) II/954, II/957, III/167, III/224, III/226, III/454, IV/338, IV/368, IV/557ff, V/562, IV/545ff, IV/545ff, IV/553, IV/564
- defects IV/557
- stability IV/562
- electron transport III/167
- self-assembled systems IV/552ff, IV/573,
- electron transfer IV/552ff
- self-assembly V/86, V/145, V/172
- self-association V/520
- self-exchange I/240, II/272, III/472, III/477, III/480
- cobalt complexes III/472
- copper complexes III/477, III/480
- electron transfer I/240, II/831
- reactions II/584, II/586, II/590
- redox reactions II/830
- sufficient monooxygenase III/74
- SEM IV/518
- K₂La₂Ti₃O₁₀ IV/517ff
- semiclassical limit I/73ff, I/91ff
- semiconductors I/273ff, I/140ff, II/140, II/292, II/851, IV/4, IV/173, IV/232ff, IV/353, IV/356, IV/369, IV/378, IV/393, V/606, V/609, V/356, V/596, V/600, V/602, V/620, V/637
- band gap I/273
- colloids V/637
- conduction band (CB) V/609, V/620

- minimum, E_{CB} IV/356
- depletion IV/356
- with Fermi-level pinning IV/356
- doping IV/356
- electrodes II/832, II/851
- electrolyte interface I/274
- electron affinity and work function IV/286
- extrinsic I/141ff, I/158ff
- film V/600
- flat band-condition IV/356
- forbidden energy gap, E_g IV/356
- heavily doped tin oxide semiconductors IV/369
- induced shifts IV/402
- mesoporous film V/600, V/602
- nanoparticles V/600
- *n*-type I/141, I/158ff, I/273, IV/356, V/606
- oxides V/596
- photocatalysis IV/232f
- – type A IV/234f, IV/249
- – type B IV/248, IV/256
- photocorrosion V/596
- photoelectrochemical IV/353
- *p*-type I/141, I/158ff, I/273, IV/356, V/596
- purity V/596
- solution interface I/158ff
- stability V/596
- surfaces I/182ff, II/853
- valence band (VB) maximum, E_{VB} IV/356
- semiquinones II/978, II/982, II/993, III/311, IV/17, V/295, V/312
- radical anions IV/8, IV/52, II/273, IV/17, IV/55
- 2,6-di-*t*-butyl IV/17
- semi-transparent electrode V/433
- sensitive II/914
- sensitization I/281, IV/353
- mechanisms V/363
- sensitized planar electrodes IV/404
- sensitized singlet oxygen luminescence III/617
- catenanes III/617
- knots III/617
- sensitizers II/473, II/476, II/478, II/853, IV/369, IV/393
- sensitizing dyes V/355, V/357
- sensors I/465ff, II/788, II/806, III/374, III/466, III/482f, III/529f, III/666ff, IV/279
- anions III/483
- chemo III/374
- dendrimers III/666ff
- luminescent III/374
- molecular III/466, III/482
- pseudorotaxanes III/529
- signal amplification III/529
- specific base sequences III/166
- sensory device II/789
- sepiolite clay IV/526ff
- sepulchrate III/471
- sequence dependence
 - Miller-Abrahams model III/164
 - quantum mechanical charge migration model III/164
 - theoretical model III/164
 - strand cleavage III/164
 - sequential electron transfer relay II/320
 - sequential electron-proton-electron transfer II/930
 - Ser IV/216
 - sesquifulvalene complexes V/271
 - SET halogenation II/350
 - of heterocycles II/350
 - SET nitration II/352
 - of heterocycles II/352
 - SF_6 + Ba surface reaction IV/650
 - Λ -shaped molecules V/261
 - shape selectivity II/69
 - β -sheet III/12f, III/424
 - Shockley-Reed kinetics IV/390
 - shuttling V/173
 - processes III/552ff, III/556ff, III/561
 - – chemically controlled III/561
 - – electrochemically controlled III/553ff
 - – photochemically controlled III/556ff
 - – rotaxanes III/552ff
 - – solvent-induced III/553
 - SI unit system V/246
 - side chain polymers V/274
 - side-on binding IV/26
 - sigmatropic shifts II/219
 - 3,3-sigmatropic shift (Cope rearrangement) I/369
 - silanes II/475
 - silanone II/233
 - silica II/930, IV/257f, IV/258, V/715
 - silica-alumina II/930
 - silver aggregates I/527
 - reduction potential I/527
 - silver electrode I/56
 - silver filaments V/302
 - silver halide V/340, V/355f,
 - electronic properties V/356
 - photography V/285ff
 - solubilities V/340
 - silver specks V/323
 - silver(I) salts II/747
 - simultaneous electrochemistry and EPR (SEEPR) IV/79
 - single electron transfer (SET) I/109ff, I/279, II/380
 - vs S_N2 competition I/349ff
 - single molecule fluorescence III/134
 - single photon counting V/370
 - single-layer photoreceptor V/384, V/411
 - single-mode model I/69ff, I/80, I/91ff
 - single-photon excitation III/119
 - single-stranded overhangs III/159
 - cleavage III/159

- singlet energy transfer (SET) I/217ff, I/221
- singlet excited state II/291, II/305, II/307f, II/313
- π - π^* singlet excited state IV/46
- singlet radical pair IV/50
- singlet state III/273ff
- n - π^* singlet state IV/46
- singlet-singlet energy transfer V/205
- singlet-triplet splitting IV/110ff
- singly occupied molecular orbital (SOMO) IV/79
- sintering IV/329
- SiO₂ V/714
- siroheme reductase III/446
- site specific mutagenesis IV/203, IV/215
- six-coordinate complex IV/56
- size distribution curve V/322
- size quantization IV/280
 - effect V/611
- slippage III/509
- slow sites V/457
- slow-exchange region NMR I/374ff
- small amplitude modulation I/171ff
- small bandgap semiconductors IV/374
- Smoluchowski equation I/98ff
- Sn₂ II/284
 - reaction I/349ff, IV/48
 - vs single electron competition I/349ff
- SnCl₄ IV/43
 - anion radical IV/43
- SnS₂ V/371
- sodium II/464, II/717
- sodium anthracenide II/726
- sodium dithionite II/731
- sodium naphthalide II/466, II/471
- sodium-potassium alloys II/464
- software I/579
 - LabView I/579
- spiropyran IV/168
- solar cells IV/279
- solar energy IV/232
 - conversion I/271, II/928, II/957, V/187
- sol-gel IV/146ff, V/385, V/602
 - material IV/427ff
 - advantage IV/427f
 - molecular entrapment IV/428
 - photophysical changes of entrapped species IV/428f
 - porosity IV/428
 - synthesis IV/427
- sol-gel material IV/469ff
 - composite carbon-silicate electrode IV/476
 - catalyst modified IV/476
 - enzyme modified IV/476
 - sensor IV/476
 - electrochemistry IV/473ff
 - amperometry IV/475
 - chemical functionalization IV/473
 - electrode development IV/474
 - glucose sensor IV/474
 - gold ceramic composite electrode IV/478
 - ion-selective membranes IV/474
 - molecular encapsulation IV/473
 - peroxide sensor IV/475
 - physical entrapment/doping IV/473
 - ruthenium dispersed electrode IV/477
 - TiO₂/silica gel based sensor IV/476
 - V₂O₅ based sensor IV/475
 - probe mobility IV/473
 - enzyme encapsulation IV/472
 - glucose oxidase IV/472
 - glucose sensor IV/472
 - cytochrome *c* IV/472
 - physical property IV/469
 - molecular encapsulation IV/469
 - physical entrapment IV/469
 - chemical functionalization IV/469
 - photoelectron transfer reaction IV/470f
 - between pyrene and viologen IV/470
 - water reduction IV/471
 - procedures IV/379
 - process V/602
 - technology IV/328
- solid/electrolyte interface V/603
- solid-liquid interface V/589
- solid state II/304
 - heterojunction V/627
 - photovoltaics IV/405
- soliton propagation V/64
- solubility product V/340
- solubilizing groups V/461
- solvated electron I/503, I/505, I/517, I/520, I/522, I/547, II/193, II/275, II/465, II/718, III/116, III/191, IV/776, IV/786ff
- solvated metal anions IV/777
 - photoelectron spectroscopy of IV/777
- solvated proton I/206
- solvation I/144ff, II/289, II/297
 - coordinate I/144ff
 - effects IV/560ff
 - electron transfer kinetics IV/560ff
 - energy IV/11
 - enthalpy I/146
 - term II/825
- solvent V/518, V/530, V/535, V/559, V/564
 - bleaches V/338
 - cage V/518, V/530, V/535, V/559
 - complex II/750
 - coordinate I/193, I/198
 - dynamics I/23ff, II/831, IV/561
 - electron transfer kinetics IV/561
 - effects I/280ff
 - fluctuation I/97ff
 - nonviscous V/564
 - reorganization V/518
 - mixtures I/523

- - radiolysis I/523
- polarity II/632
- polarization I/113
- relaxation II/838, III/127
- - time II/843
- reorganization I/319ff, I/426, I/492, II/596,
- - energy III/137, IV/289
- - contact radical ion pairs III/137
- independent charge separation III/252ff
- separated ion pair II/397
- solute interactions III/413
- SOMO II/11, II/135ff, IV/21, IV/79
- space charge V/627
- field V/476f, V/506
- layer V/699
- region IV/287, V/699
- spacers III/374, III/378ff, III/388, V/3, V/7,
- V/19, V/26, V/32f, V/36f, V/39ff, V/43, V/99,
- V/104, V/109, V/111, V/114f, V/120, V/123
- anthryl III/382
- aryl III/383
- bicyclooctane V/115
- bicyclo[2.2.2]octane III/378
- conjugated V/99, V/109
- cumulene V/123
- length II/957
- naphthalene V/120
- naphthyl III/382
- oligoyne V/111
- - C=C V/111
- phenylene V/114
- phenyl units III/378
- polyene V/109
- polyphenyl III/388
- Pt^{II}bis- σ -acetylide III/379
- rigid V/99
- saturated V/99, V/104, V/109, V/15
- steroid-type III/374
- spatial light modulator V/510
- special pair V/599
- specific surface area IV/239
- spectator stripping model IV/640
- spectral hole-burning V/60, V/170
- spectral irradiance V/592ff, V/635
- spectral overlap I/218, I/222, I/228
- spectral sensitization V/355, V/363, V/366
- efficiencies V/366
- spectroelectrochemistry I/477ff, II/823, II/978
- diffusion-layer imaging I/485
- EPR I/477ff, I/485ff
- internal reflection I/484
- IR I/478ff, I/487
- specular reflectance I/484
- UV I/479ff, I/488
- spectrometry I/569f, I/580
- absorption I/569
- CIDNP I/569
- electronic absorption I/570, I/580
- emission I/569
- ENDOR I/569
- EPR I/569
- light-scattering I/569, I/580
- spectroscopy II/976ff, IV/354
- ESR II/976ff
- models II/917
- probes V/519
- techniques IV/393ff
- fluorescence IV/393
- - up-conversion techniques IV/395
- low-temperature phosphorescence IV/393
- time-resolved
- - anisotropy IV/394
- - electron paramagnetic resonance IV/394
- - IR IV/394
- - photoluminescence IV/394
- transient absorption IV/394f
- spherical diffusion I/436, I/451, I/458, V/332
- spill-over region I/153
- spin I/135
- and charge II/136
- - coupled II/136
- - uncoupled II/136
- control V/71
- conversion II/607
- delocalization II/810, II/990
- density II/136, IV/18, IV/34, IV/80
- - reactivity correlation II/67, II/71
- distribution II/986
- forbidden transitions I/223ff
- multiplicity I/224, I/228
- orbit II/608
- - coupling I/228, I/232, I/235, II/977, II/980ff
- - intersystem crossing V/68
- polarization II/272, IV/80
- relaxation I/407
- state II/838
- transfer δ II/996
- trap II/979
- π, σ spin
- delocalization II/115
- - polarization II/115
- spiral pattern IV/335
- spirofluorene II/91
- spirolactams II/439
- spiropyran IV/166, V/55ff
- spontaneous charge shift V/64
- spontaneous generation of organic radical cations
- II/69
- spray pyrolysis IV/328
- spur I/504
- ionizing radiation I/504
- squalane II/226
- squaraine V/384, V/426
- squarylium V/426

- $\text{Sr}^+(\text{NH}_3)_n$ clusters IV/780
 – photodissociation spectra IV/780
 $\text{S}_{\text{RN}}1$ II/18, II/20, II/22
 stability IV/562
 – self-assembled monolayer IV/562
 π stacking II/314, II/955, III/238ff, III/417, IV/7, IV/68
 staffane IV/563
 – electron transfer bridge IV/563
 standard free energy III/274
 standard potential I/423, I/427, I/448ff, I/482ff, I/489, I/497
 standard rate constant I/423, I/424
 standard redox potentials II/715, V/705
 standing wave I/139
 stannanes II/475
 starburst molecule V/488
 Stark effect V/170
 Stark spectroscopy IV/678
 static dielectric constant IV/288
 static process IV/401
 static quenching III/122, III/143f
 – intercalated ET^+ by methylviologen III/143
 – quenching by Cu^{2+} III/144
 steady-state approximation I/117, V/571
 steady-state current I/463, I/496
 steady-state measurement I/462ff
 steady-state voltammetry *see* voltammetry
 stellacyanin IV/130
 stereochemistry I/226, I/288, II/120, II/305, II/993
 stereodynamics of electron transfer IV/660ff
 stereoselective synthesis IV/191
 steric control II/668
 steric effects IV/561
 – electron transfer kinetics IV/561
 steric hindrance II/286
 steric insulation IV/128
 sterically overcrowded stilbene derivatives V/237
 Stern-Volmer I/417, IV/251
 – constants IV/373
 – plots III/420
 sterpurene II/196
 – synthesis II/196
 stilbene II/241, V/220, V/236
 – amine adduct II/390
 – anion radical III/148
 – formation and decay III/148
 STM V/363
 Stokes shift I/222
 Stokes-Einstein equation II/247
 stopped-flow I/398ff
 – aging loop I/402
 – dead time I/401
 – measurements I/374ff
 – method I/536
 – pulse radiolysis I/536
 – mixing rate I/401
 – mixing ratio I/400
 – sequential flow I/402
 – spectrophotometer IV/17
 – technique II/935
 stopping power I/504
 – ionizing radiation I/504
 – of water I/505
 storage of light II/805
 store information V/472
 strain II/23
 strained ring compounds
 – radical cations of β -strands III/13f, III/17, III/424
 strand breaks in duplex DNA III/119
 – photoionization III/119
 strand cleavage II/861
 strand cleavage III/116, III/120, III/157
 – at the 5'G of a GG step III/156
 – GG sites III/120
 – products III/152
 strand-to-strand hopping III/159
s-trans-1,3-butadiene cation radical II/136
 stretched films III/166
 – electric conductivity III/166
 stroboscopic method I/547
 – pulse radiolysis I/547
 strontium barium niobate V/479
 structural modeling II/920
 structural relaxation I/231
 structural reorganization I/426, I/492
 structure reactivity relationship IV/747
 structures of type B II/87
 styrene IV/764ff
 – adduct with trimethylamine IV/752, IV/764ff
 – electron photodetachment IV/752
 – exciplex emission IV/764
 – fluorescence decay times IV/765
 – MPI spectrum IV/764
 – conical intersection IV/767
 – dissociation energy IV/764
 – E-isomer IV/764
 – energy level diagram IV/766
 – exciplex emission IV/764
 – LE emission IV/764
 – R-isomer IV/764
 – REMPI spectrum IV/764
 – structure of IV/770ff
 styrylamides II/426
 sub-band-gap transitions IV/307
 substituted piperidines II/413
 substitutional lability II/818, II/997
 substrate adsorption IV/250, IV/253
 substrate ionization II/166
 – reversible II/166
 substrate protons III/50
 substrate transport III/455

- successor complex III/410ff
- sugar II/860
 - radical cation III/241
- sulfate IV/224
- sulfenium radical II/938
- sulfide II/731, II/938, V/567
- sulfite IV/224
 - oxidase (SO) IV/205, IV/224
- sulfoxide II/938, IV/13
- sulfur compounds V/565
- sulfur-containing aminoacid V/561ff
- sulfur-containing carboxylic acids V/562, V/568
 - photophysical and photochemical properties V/568
- sulfuric acid II/754
- sulfur-plus-gold sensitization V/324
- Sumi-Marcus model I/101ff
- sun spectral irradiance V/592f
- superacids II/187
 - cation radical II/187
- superadditive V/314, V/353
- superadditivity V/305ff
- superbridges III/223
- supercomplex III/470
- superexchange I/117ff, I/221, III/36, III/164, III/275ff, III/342, III/627, V/73, V/101, V/120, V/125
 - between neighboring guanines III/164
 - coupling III/5
 - models III/10
 - electron transfer III/10
 - hole transfer III/10
 - interaction V/115
 - mechanism III/140, V/120, V/125
 - rotaxanes III/627
 - theory V/101
- superhyperfine coupling IV/20
- supramolecular polyads II/323
- supermolecules II/834
- superoxide I/282ff, II/35ff, IV/25
 - radical anion II/739, II/753
- superoxo complex II/952
- superoxocopper(II) complex IV/26
- superposition principle IV/312
- superpositions of numbers V/177
- supersensitization IV/372, V/606
- supersonic beam apparatus IV/709ff
- supersonic jet (*see also* jet cooling) IV/627f
 - apparatus IV/627f
 - cooling IV/627
 - advantages of IV/628
 - limitations of IV/628
 - donor-acceptor bridged molecules IV/707
 - laser induced fluorescence (LIF) IV/707ff
 - solvation in IV/628
 - spectroscopy IV/707
 - time of flight mass spectroscopy (TOF-MS) IV/707ff
- supported catalysts II/930
- supporting electrolyte I/428, II/715
- suprabiomolecules III/455
- supramolecular assembly II/321, III/236
- supramolecular chemistry II/806, III/512
- supramolecular complexes II/322
- supramolecular effects II/834
- supramolecular photoinitiators V/535
- supramolecular species III/340
- surface IV/266
 - attached DNA III/166
 - cyclic voltametry III/166
 - binding IV/380
 - acetylacetonates IV/380
 - carboxylic acid groups IV/380
 - cyano IV/380
 - ether linkages IV/380
 - groups IV/380
 - phosphonates IV/380
 - charge I/288, V/380
 - density σ I/153
 - coverage II/956, IV/258
 - effects I/287
 - enhanced Raman scattering IV/336
 - ester linkages IV/370
 - hopping model of I/213
 - modification V/709, V/713ff
 - monolayer IV/251
 - plasmon resonance II/959
 - potential I/154
 - sites IV/251
 - state I/160, I/184, IV/311f, IV/293ff, V/706
 - acceptor states IV/312
 - mediation IV/311
 - passivation IV/337
- surfactants II/277f, II/280, IV/132
 - composition IV/578ff
 - structures IV/479
- switchable rotor V/54
- switched energy transfer V/129
- switches III/299, III/463, III/481, III/527, III/552ff, III/566, IV/164, V/126
 - catenanes III/566ff
 - ion selective III/299
 - pseudorotaxanes III/525
 - redox III/465, III/481
 - rotaxanes III/552ff
- switching error V/62
- symmetry II/994
 - effects I/220
 - factor I/423
 - restrictions V/245
- synthetic antenna reaction center V/85
- Ta₂O₅ V/602
- Tafel equation I/426ff, IV/299

- tandem system V/597, V/638
 TAPC V/386, V/455
 TCNE II/323, II/759
 TCNQ II/323, II/759
 TEA IV/100ff, IV/119f
 TEM IV/496ff, IV/515, IV/517
 – $\text{HPb}_2\text{Nb}_3\text{O}_{10}$ IV/515
 – structure of Ni-loaded $\text{K}_4\text{Nb}_6\text{O}_{17}$ IV/496
 – $\text{K}_2\text{La}_2\text{Ti}_3\text{O}_{10}$ IV/517
 temperature dependence IV/558
 – electron transfer kinetics IV/558
 temperature jump I/404ff
 – laser-induced I/406
 – stopped-flow I/406
 temperature-dependent injection IV/402
 template reaction III/549, III/582
 temporary anion states II/72
 tensor coordinate transformation V/245
 tensor notation V/246
 tensor reduction spectrum V/265
 TEOA IV/119ff
 terminal alkyne II/779
 termination V/575
 ternary complex III/424
 terphenyl IV/98ff
o-terphenyl III/698
 Terpyridine II/949, III/18, V/115
 – compounds V/99
 terrylene V/50
 tertiary amine IV/24
 tertiary ammonium radicals V/546
 tertiary aromatic amines V/546, V/548
 – electrochemical properties V/548
 tertiary nitrogen oxidation I/370ff
 tertiary trialkylamine II/932
 tethered chromophore III/145
 – $[\text{Rh}(\text{phen})_2\text{phen}]^{3+}$ III/145
 – $[\text{Ru}(\text{phen})_2\text{dppz}]^{2+}$ III/145
 tethered redox probe IV/557
 – electron transfer IV/557
 tethering IV/135, IV/137, IV/148, IV/168,
 IV/179f, IV/184f
 tetraalkylborates II/657
 tetraazamacrocyclic IV/89
 tetracarbonylcobaltate II/647
 tetracene II/725
 tetrachloromethane I/519
 – radiation chemistry I/519
 tetracyanoanthraquinodimethane (TCAQ) II/309
 tetracyanoethylene (TCNE) II/189, II/323,
 II/627, II/636, II/664
 – anion radical II/189
 tetracyanoquinodimethane (TCNQ) II/323,
 IV/132, IV/150
 7,7,8,8-tetracyano-*p*-quinodimethane (TCNQ)
 IV/30
 tetrads III/311ff, III/318ff, V/71
 3,3',4,4'-tetramethyl biphenyls II/211
 tetraethoxyethene II/292
 tetrahydrofurfuryl acrylate (THFA) V/532
 tetrahydroquinolines II/422
 tetraiododihydrofluorescein (TIHF) V/542
 tetrakis (pentafluorophenyl)porphyrin II/409
 tetrakisadduct II/287
 tetramer V/456
 tetramethylaurate(III) II/660
 tetramethylborate II/623
 tetramethylethylene II/229
 tetramethylnaphthopyran II/213
N,N,N',N'-tetramethyl-*p*-phenylenediamine
 (TMPD) II/247, II/307, II/385
 tetramethylseminone II/285
 tetraphenylborate II/292, II/645, II/659
 tetraphenylporphyrin II/934
 – dianion (TTP) IV/18
 tetraquinanes II/470
 tetrathiafulvalene (TTF) II/233, II/292, II/306,
 III/502ff, III/517, III/570, III/573, III/686,
 IV/73, IV/132, IV/150
 – catenanes III/570, III/573
 – chemically controlled III/573
 – dendrimers III/686
 – pseudorotaxanes III/517
 – ring motions III/573
 tetrathienylenevinylene III/698
 tetrazolium II/362
 – reduction II/362
 TFB V/499
 thallation II/640
 thallium(I) tetracarbonylcobaltate II/634
 thallium(III) trifluoroacetate II/625
 theophylline IV/161
 theophylline oxidase IV/161
 theoretical models II/921, III/164
 – distance and sequence dependence of strand
 cleavage III/164
 – Miller-Abrahams model III/164
 – quantum mechanical charge migration model
 III/164
 theory II/922
 – comparison with experiment I/38ff, I/47ff,
 I/51ff
 thermal activation energy I/148
 thermal electron transfer II/202
 thermal elimination of methane II/71
 thermal equilibrium I/97, I/129
 thermal irreversibility V/231
 thermal oxidation of amines II/380ff
 thermal stability V/232
 thermal velocity IV/305
 thermally stimulated currents (TSC) V/393,
 V/412
 thermionic emission IV/304
 thermochemical cycle II/678, II/680 ff, II/696,

- II/699, II/702, II/704, II/709
 thermochromic photoinitiators V/558
 thermodynamic diving force IV/398, V/564
 thermodynamic equilibrium I/167
 – heterogeneous I/167
 thexi state IV/355, IV/382, IV/393, IV/401
 THF IV/16
 thia-crowns III/477ff
 thiamine diphosphate IV/54
 thianthrene II/342, II/345, II/354f, II/757
 – anodic oxidation II/354
 – electron transfer II/345
 – formation of sulfinimines II/354
 – radical cation II/342, II/345
 – reaction with alkenes II/355
 – reaction with carbazole II/354
 – reaction with phenol II/355
 – reaction with pyridine II/355
 – S-oxidation II/354
 thiapyrylium V/405
 thiazolium salts IV/54
 thin-film II/852
 thin-layer cell I/483
 thioanisole II/234, II/938
 2,2'-thiobisethanol V/567
 thioether II/483
 Thiols II/292, II/955
 – ligand II/922
 thiolate II/921f
 thiophene II/292, II/339, II/347f, II/352, II/357,
 II/359, II/362, II/370, IV/130, V/55
 – arylation II/370
 – desulfurization II/362
 – iodination II/352
 – oxidative dimerization II/347f
 – perfluoroalkylation II/357
 – photochemical reaction with haloquinones
 II/359
 – radical cations II/339
 thioxanthone-amine system V/555
 third harmonic generation V/244
 three-dimensional addressing V/48
 three-dimensional photochromic memory V/240
 three-dimensional recording V/239
 three-electrode electrochemical cell I/170ff
 three-electron σ -bond (3e- σ -bond) I/344
 three-iron clusters II/914
 three-level switching V/55
 three-point hydrogen bonding III/427
 three-sphere model I/118
 three-stage electron-transfer I/526
 three-state model I/120ff, I/378, III/134f
 – dark state in III/134
 – octopolar molecules V/264
 threshold converter V/594
 through-bond IV/560, IV/570ff
 – electron transfer II/305, III/627, IV/560,
 IV/570ff
 – – rotaxanes III/627
 – energy transfer V/86
 – interactions V/138
 – mechanisms IV/203
 through-chain IV/555, IV/560
 – electron transfer IV/555, IV/560
 through-space IV/560, IV/570ff
 – electron transfer III/627, IV/560, IV/570
 – – rotaxanes III/627
 through-space mechanisms IV/203
 through-space tunneling V/138
 α -thujene II/219
 β -thujene II/219
 thylakoid membrane V/599
 Thymine III/427ff
 – dimer III/160
 – – cycloreversion III/160
 – – oxidation potential III/160
 – functionalized terpyridine III/432
 – photodimer III/159
 – – photochemical repair III/159
 – repair II/861
 Ti + NO reaction IV/648
 Ti + N₂O reaction IV/648
 Ti + O₂ reaction IV/648
 TiCl₄ IV/43
 TICT state IV/700
 – acetophenone as an acceptor group IV/706
 – benzonitrile as an acceptor group IV/706
 – dual luminescence IV/700
 – energy level diagram IV/700
 – Franck-Condon principle IV/700
 – methylbenzoate as an acceptor group IV/706
 – pyridine as an acceptor group IV/708
 – solvent equilibrated states IV/700
 tight-binding model V/41ff
 time of flight (TOF) V/484, V/495
 – experiment V/432ff
 – spectrometer IV/787
 time window I/439, I/458
 time-delayed fluorescence V/251
 time-dependent Hamiltonian I/115ff
 time-dependent Schrödinger equation I/115ff,
 I/216
 time-resolved electron paramagnetic resonance
 spectroscopy V/68
 time-resolved microwave conductivity III/203f
 time-resolved spectrophotometry IV/205
 time-resolved spectroscopic techniques II/271
 – laser flash photolysis II/271
 – pulse radiolysis II/271
 time-resolved techniques IV/366
 time-scale II/991
 TiO₂ (*see also* titanium dioxide) II/324, IV/236,
 IV/378, IV/491, V/371, V/600, V/602
 – K_{4-x}H_xNb₆O₁₇ IV/491

- clay IV/514ff, IV/523
- – photocatalytic decomposition of carboxylic acids IV/523
- TiOPc V/413, V/421ff, V/483
 - absorption characteristics V/421
 - carrier generation V/423
 - electroabsorption V/423
 - electrophotographic characteristics V/421
 - fluorescence quenching V/423
 - molecular modeling V/422
 - quantum yield V/424
 - spectral sensitivity V/422
 - X-ray powder diffraction V/422ff
- titanates IV/487ff, IV/505, IV/509
 - catalytic activities IV/509
 - layered oxides IV/487
- titania V/701
 - anatase structure V/701
- titanium II/463, II/476, II/809, II/991
 - dioxide I/284ff, IV/179, IV/328ff, V/602, V/695
 - graphite II/463
 - silicalite IV/431f
 - – application IV/431ff
 - – limitation IV/431f
- titanoniobates IV/488, IV/505
- titanyl phthalocyanine V/418
- TMPD II/307
- TMPTA V/552
- TNF V/387, V/402, V/499
- TNFDm V/488f
- tolane V/16, V/18, V/33
- toluene II/211, II/225, II/932
- toluene radical cation II/520
- toner V/381f
 - charging V/382
 - formulations V/382
 - particles V/382
- topological control V/192, V/201
- topology I/466
- toxicity II/19
- toxins IV/161
- toxoflavine II/368
 - demethylation II/368
- TP model III/12, III/15f
- TPA V/386, V/488
- TPD V/386, V/417, V/424, V/426
- (TPFPP)FeCl II/932
- (TPP)Co IV/18
- Tpphz(tetrapyrido[3,2-*a*:2',3'-*c*:3'',2''-*h*:2'''-3'''-*j*]phenazine V/122
- track I/504
 - ionizing radiation I/504f, I/532
 - – dependence of dose deposition on depth on water I/532
- train sublimation V/413
- transfer III/200
 - charge transfer III/200
 - integral I/65ff, I/78ff, I/97
- transient absorption spectra IV/383, V/520, V/614
- transient laser spectroscopy V/613ff
- transient photocurrent IV/318
- transit IV/316
 - time V/432f, V/457
- transition metals
 - reactivity of IV/647ff
 - frontier orbitals theory IV/647ff
- transitions III/438, III/448, III/605f, III/620, III/635, III/644
 - ligand centered (LC) III/606
 - ligand-to-metal charge-transfer (LMCT) III/606
 - metal centered (MC) III/606
 - metal-to-ligand charge transfer (MLCT) III/448, III/605, III/620, III/635, III/644
 - dipole I/217ff, II/601, II/603
 - – distributed I/233
 - metal cluster II/747
 - metal-carbonyl cluster II/769
 - metal complexes I/516, I/519, I/521, I/528, II/905
 - – coordinated free radical I/528f
 - – hexacarbonyl complexes I/521
 - – intramolecular electron transfer I/529
 - – one-electron reduction I/516, I/519
 - mixed-valence III/438
 - probability II/602
 - state I/64ff, I/79ff, I/89, I/113, I/175, I/563, IV/6
 - – theory (TST) I/8ff, I/16ff, I/23ff, I/79ff, I/97ff
- π to π^* transitions II/607
- translocated protons III/50
- transmission coefficient I/89ff, I/97, I/161ff
- transport V/459
 - pathways III/60
- trap density V/506
- trap-limited mobility V/460
- trapped holes V/476
- trapping V/396, V/400, V/431, V/456, V/459
 - /detrapping IV/334
 - sites V/395, V/706ff, V/715ff
- travelling salesman problem V/175
- TREPR V/68
- triads II/312, II/319f, III/565, II/854, III/279ff, III/304ff, III/312, III/315f, III/375, III/395, III/398, III/443
 - calixarene III/566
 - carotene-diporphyrin III/279ff
 - carotene-porphyrin-fullerene III/312
 - carotene-porphyrin-imide III/316
 - carotene-porphyrin-quinone III/443
 - carotenoid-porphyrin-quinone III/305ff

- catenanes III/566
- chlorin-porphyrin-imide III/316
- inorganic-organic III/398
- phenothiazine containing III/375
- zinc porphyrin-pyromellitimide III/315
- trianion radical II/191f
- spin localized II/192
- triarylamine II/383, III/695, V/452
- dendrimers III/695
- triarylammonium salt II/134, II/140, II/755
- cycloaddition chemistry II/140
- triazolinedione II/371
- cyano II/371
- photochemical reaction II/371
- cycloaddition II/371
- pyridine II/371f
- ring reduction II/372
- tribocharge V/381ff
- tricarboxylic acid cycle III/75
- tricyanomethide II/645
- tricyclanes II/110
- tricyclic *o*-quinones IV/49
- tricyclo[4.3.1.0^{1,6}]deca-2,4-diene radical cation II/90
- tricyclo heptane II/103
- tricyclooctane II/112
- triethylamine II/473, V/545, V/553
- triethylene glycol II/280
- triethylsilane IV/39
- triflic acid II/755
- trifluoroacetic acid II/212
- 9-trifluoroacetoxy II/212
- trifluoromethylated sulfenimines II/426
- trigonal bipyramidal environment IV/24
- trigonal bipyramidal structure IV/16
- triiodide II/753, V/623
- 1,4,7-triisopropyl-1,4,7-triazacyclononane (*i*-Pr₃TACN) IV/26
- trimethyl methane II/229
- trimethylene methane II/222
- trimethylene radical cation II/78
- trimethylene structure II/81
- 2,4,6-trimethyl-1,3,5-trithiane (TMT) V/567
- trinitrofluorenone V/484
- 2,4,7-trinitro-9-fluorenone (TNF) V/384
- triphenylamine V/484
- triphenyl-*n*-butylborate *see also* butyltriphenyl borate V/540
- triphenyl-*n*-butylgallate salts V/536
- triphenylcarbenium ion II/757
- triphenylcarbinol derivatives V/261
- triplet I/223ff, II/991
- acceptors III/125
- anthraquinones III/125
- biradical sublevels III/313
- correlation with electron and hole transfer I/226ff
- energy transfer (TET) I/40ff, I/223ff
- excited state II/293, II/307, IV/45
- lifetimes II/282
- radical ion pair II/305
- recombination II/110
- of radical ion pairs II/124, II/126
- sensitizers V/532
- state II/981, III/273ff
- of flavin IV/205
- triplet annihilation I/314ff, V/167
- triplet energy transfer V/196
- excimer emission I/314ff
- exciplex emission I/314ff
- oxidation I/316ff
- radical ions I/316ff
- reduction I/316ff
- triplex region III/159
- diminished reactivity III/159
- tritycene II/213
- triquinanes II/474
- 1,3,5-trithianes V/567, V/570
- photochemical properties V/570
- Triton X-100 II/278
- trityl salts II/757
- tropenide dianion radical II/192
- equivalent sodium hyperfine splittings II/192
- tropylium cation II/759
- Trp radical IV/221
- Trp-191 II/943
- truth table V/159
- tryptophan tryptophlquinone (TTQ) coenzyme IV/35
- TSC V/412
- TST I/98
- TTA V/386, V/406, V/424, V/435ff, V/455ff, V/460
- concentration dependence V/437ff
- mobility V/436, V/441
- photocurrent V/460
- time-of-flight V/435
- zero-field mobility V/440
- TTF II/234
- tungstacyclobutene II/780
- tungsten II/810, II/909
- tunnel effect V/5
- tunneling I/72ff, II/786, IV/314
- atom I/72ff, I/93
- barrier III/27
- distance I/165
- electron I/72ff
- energy I/110, I/115
- inelastic I/114
- length III/47f
- matrix element V/21
- path length III/12
- pathway (TP) III/11
- phonon I/71ff

- timetable III/14, III/16, III/19f
- β -turn III/425
- turnover rate IV/154
- Tween 20 II/278
- twisted intramolecular charge transfer (TICT)
 - IV/630, IV/697ff, IV/706ff
- state II/401
- two-electron donor II/952, IV/20
- two-electron exchange I/224
- two-electron reduction II/955
- two-electron transfer I/109, I/120ff
 - concerted I/120ff
 - sequential (stepwise) I/121
- two-electron wave II/766
- two-input INHIBIT gate V/167
- two-level system V/49
- two-photon absorption III/321
- two-photon excitation III/119f
 - 2-aminopurine III/120
- two-point hydrogen bonding III/427
- two-stage development V/320
- two-state approximation (TSA) I/4, I/10, I/23, I/28ff
- two-state expression for the first hyperpolarizability V/253
- two-state model I/110ff, I/116ff
 - dynamic I/116
- two-state valence bond (VB) model I/195ff, I/201ff
- tylakoid membrane V/597
- type B structures II/88ff
- tyrosinase IV/161
- tyrosine II/786, IV/22, IV/74
 - hydroxylase III/80
- tyrosyl radical IV/22
- ubiquinone III/24ff, III/418, IV/69, IV/161, IV/171
- ultrafast charge separation III/145
 - cooperative binding model III/145
 - random binding model III/145
- ultra-fast electron injection II/851
- ultrafast electron transfer II/847
- ultrafast energy migration V/189
- ultra-fast hot injection IV/405
- ultra-fast interfacial electron injection studies IV/396
- ultrafast techniques (*see also* femtochemistry) IV/672, IV/675ff, IV/791, IV/793
- ultramicroelectrodes I/436, I/440, I/442, I/445, I/449, I/451ff, I/464ff, II/272, II/832
- Ultratec V/314
- ultraviolet-visible ellipsometry II/957
- umecyanin IV/130
- Umpolung II/485
- uncertainty principle I/83, I/559
- uncoupling III/64, III/69
- unfolding denaturing IV/130, IV/137
- uniform barrier III/11,
 - models III/10
- uniform preillumination V/491ff
- unilamellar vesicles III/301ff
- units V/246
- unrestricted Hartree-Fock (UHF) SCF IV/21
- uracil II/358, IV/73
 - II/5-bromo-1,3-dimethyl II/358
 - photocoupling II/358
- ureas IV/73
- U-shaped systems III/259, III/264
- UV-Vis absorption II/857
- UV-vis spectra
 - $\text{Re}(\alpha\text{-diimine})(\text{CO})_3\text{L}$ IV/106
- vacuum III/20
 - level IV/285
- valence V/705ff
 - band I/140ff, V/356, V/481, V/696, V/714ff
 - – hole I/274
 - bond model (VB) I/190ff
 - tautomerization II/993
- 18+ δ valence electron II/997
- Van de Graaff I/531
 - pulse radiolysis I/531
- van der Waals complexes IV/662, IV/743
 - electron transfer reactions in IV/662
 - – initiation by light IV/662
 - laser assisted reactions IV/662
 - Pauli's principle IV/771
 - polarization IV/771
 - potential energy surface IV/771
- van der Waals distance IV/127
- van der Waals forces IV/742
- van't Hoff isotherm V/590
- vanadium II/462, II/809, II/991
- vanadyl phthalocyanine (VOPc) V/425
- vapor deposition II/57
- carbonyl ligand II/923
- VB V/369
 - potential V/369
- VDE – *see* vertical detachment energy
- vector correlations IV/660
- vectorial electron transfer IV/129, IV/159, IV/164, IV/166, IV/170f, IV/188ff, IV/339
- vertical detachment energy (VDE) IV/776ff
 - electrons from negatively charged anions IV/776ff
 - $\text{Cs}\cdot(\text{H}_2\text{O})_n$ clusters IV/778, IV/781
 - $\text{Cu}\cdot(\text{H}_2\text{O})_n$ clusters IV/783
 - $\text{Li}\cdot(\text{H}_2\text{O})_n$ clusters IV/781
 - $\text{I}\cdot(\text{acetone})_n$ clusters IV/787
 - $\text{I}\cdot(\text{CH}_3\text{CN})_n$ clusters IV/788
 - $\text{I}\cdot(\text{CH}_3\text{I})_n$ clusters IV/787
 - $\text{I}\cdot(\text{H}_2\text{O})_n$ clusters IV/789ff
 - $\text{I}\cdot(\text{Xe})_n$ clusters IV/794

- $\text{Na}^+(\text{H}_2\text{O})_n$ clusters IV/778, IV/781ff
- vertical ionization potential (IP) II/620
- vertical transition II/838
- very strong oxidant II/745
- vesicle II/277, II/280, II/954
 - dopant partitioning IV/583ff
 - dynamics IV/582ff
 - electron transfer in IV/592, IV/607, IV/610ff
 - carrier-mediated IV/613ff
 - electron tunneling IV/610ff
 - photoionization yields IV/602ff
 - proximity effects IV/602ff
 - surface potentials IV/604ff
 - interfacial potentials IV/589
 - kinetics
 - Monte Carlo simulations IV/608
 - surface reactions IV/607
 - transmembrane reactions IV/613, IV/615
 - lateral diffusion in IV/587ff
 - local polarities IV/589ff
 - permeation IV/583f, IV/592, IV/613
 - structure IV/581f
 - transmembrane potentials IV/592, IV/613
 - transverse diffusion in IV/583f
- vesicular systems II/279
 - application to characterization of van der Waals IV/731
 - double resonance IV/731
 - vibrational depletion spectroscopy IV/731
- vibrational excitation I/181
- vibrational modes II/609, II/611
 - high frequency II/609, II/611
 - low frequency II/609, II/611
- vibrational predissociation spectroscopy IV/791
- $\text{I}^+(\text{H}_2\text{O})_n$ clusters IV/791
- vibrational relaxation II/838, V/612, V/616
- vibrationally equilibrated excited state (VeqES) I/239, I/241, I/249ff
- vibrationally hot excited state IV/393
- vibronic coupling I/221, I/384, II/608
- vibronic excitation V/611, V/615
- vicinal dibromides II/282
- vindoline II/415
- N*-vinylcarbazole II/133
 - cation radical chain mechanism II/133
 - cyclodimerization II/133
- vinylcyclobutane rearrangement II/173
 - cation radical II/173
- vinylcyclopropane II/219
 - radical cation II/96, II/111f
 - rearrangement II/176
 - cation radical II/176
- vinylidene II/780
- vinyl monomers V/555
- viologens II/638, III/303ff, III/375f, IV/133, IV/150, IV/162, IV/168, IV/172, IV/179, IV/180, IV/189
 - bipyridinium IV/191
 - quenchers III/376
 - radical monocation III/303
- virtual intermediate I/119ff
- viscosity I/98ff, IV/262f
- visible-light sensitization V/530
- Vis-NIR II/272
- vitamin C II/731
- vitreous carbon electrode II/788
- voltammetry
 - cyclic I/440ff, I/455ff
 - linear sweep I/440ff, I/455ff, I/495ff
 - sampled-current I/437ff
 - steady-state I/436
- volume I/407
 - activation I/412
 - molar I/407
- VOPc V/425
- Walden inversion II/246
- Warburg component IV/303
- washing V/355
- waste remediation V/695
- water I/506ff, III/17ff, IV/776
 - anionic clusters IV/776
 - electron detachment energy of IV/776
 - gas-shift reaction II/818
 - hexamer anion IV/793
 - molecules I/505
 - electronic excitation I/505
 - ionization I/505
 - oxidation (*see also* zeolite) II/947, IV/171, IV/457, V/637
 - catalyst II/862
 - oxidizing conditions I/510
 - primary radicals I/507
 - radiation chemical yields (*G* values) I/506
 - reducing conditions I/512
 - secondary radicals I/510f
 - redox potentials I/511
 - spectral data I/511
 - spur reactions I/506
 - photosplitting II/732
 - splitting V/596f, V/636, V/638
 - purity V/596
 - oxides V/596
 - stability V/596
 - photocorrosion V/596
 - p-type V/596
- Watson-Crick base-pairing III/427
- wave function I/134ff, II/587
 - first order II/587
 - one electron I/134ff
 - zero order II/587
- wave splitting V/25, V/28, V/33, V/36f, V/43
- wave vector I/134ff
- wavelength-dependent electron injection IV/397

- wavenumber vector V/356
- weak electronic coupling II/850
- weak electronic interactions II/277
- weak length dependence V/104
- Weinrub's amide transfer reagent III/450
- Weller equation II/473
- wide-bandgap semiconductors V/609
- Wigner distribution function I/81ff, I/98, I/104ff
- wire V/7, V/10, V/36, V/103
 - behavior V/125
 - like behaviour III/144, III/345
 - systems V/97
- Wittig-Horner reaction V/14
- WO₃ V/602, V/638
- WOC V/637
- work term contributions III/411
- working electrode I/167ff
- write-lock-read-unlock-erase V/162
- write-once optical disks V/218

- X- or Z-type V/148
- XANES IV/96, V/703, V/709ff
- xanthene V/54
- xanthene dye V/542, V/549, V/551, V/562
 - – amine systems V/549
 - – camphorquinone V/562
 - – photoreduction V/549
 - – properties V/551
 - – spectroscopic, photochemical, and photophysical properties V/542
- xanthine oxidase IV/129, IV/132, IV/143
- Xe + halogenated molecules IV/662
 - XeBr product IV/662
 - XeCl product IV/662
 - XeI product IV/662
- xenon I/539
 - lamps I/539
- xerographic discharge V/392, V/397
 - emission-limited V/392
- xerographic gain (G_x) V/392, V/405
- xerographic sensitivity V/409
- xerography V/379, V/412, V/488
 - quantum efficiency V/412
- XeroX V/380
- XNOR gate III/519
- XNOR logic V/166
- XOR gate III/527
- XOR logic V/165
- XPS IV/496ff, IV/515
 - HPb₂Nb₃O₁₀ IV/515
 - structure of Ni-loaded K₄Nb₆O₁₇ IV/496
- X-ray analysis IV/16
- X-ray crystal structures II/632
- X-ray crystallography II/907, II/920
- X-ray diffraction II/916
- X-ray photoelectron II/955
 - spectroscopy V/607
- X-ray structure II/949f, IV/202
- X-type deposition V/147
- xylene II/225, IV/82

- yeast cytochrome *c*-peroxidase II/944
- yellow dye V/336
- YES logic V/158
- yohimbane II/433
- Y-type deposition V/147
- Yule mechanism V/313

- Zeeman interaction III/314
- Zeise's salt II/731
- Zener limit IV/299
- zeolites II/69, II/140, II/224f, II/229, IV/413ff, V/712
 - A IV/414f
 - charge, point of I/157
 - crystallization IV/416
 - electrochemistry IV/459ff
 - – electroactivity mechanism IV/460
 - – electroanalysis IV/463f
 - – electrocatalysis IV/463
 - sensing mechanism IV/463
 - sensor IV/463
 - zeolite-encapsulated complex IV/460
- electron transfer IV/413, IV/429, IV/444
- general description IV/413
- intrazeolitic electrochemistry IV/459, IV/461
- intrazeolitic environment IV/419
 - – electrostatic effect IV/420
 - – micropolarity IV/419
 - – rigidity IV/419
 - – steric effect IV/420
- intrazeolitic molecular assembly IV/416
- ion exchange IV/416
- organometallic complex as template IV/417
- ship-in-a-bottle synthesis IV/416
- ruthenium polypyridyl IV/417
- solvent transport IV/416
- vapor transport IV/416
- L IV/414f
- large pore IV/415
- membrane IV/421, IV/435
- metal cluster photochemistry IV/457
- metal oxide photochemistry IV/457
- – water oxidation with RuO₂-zeolite Y IV/457
- modified electrode IV/459
- mordenite IV/414f
- nanocrystal IV/448
- – Ru(bpy)₃²⁺-bipyridinium system IV/448
- nanocrystalline IV/421
- photochemical hydrocarbon oxidation IV/450f
 - – alkene photo-oxidation IV/453
 - – charge-transfer complex with oxygen IV/451
 - – selective photo-oxidation IV/452
 - – stilbene photo-oxidation IV/453

- photoredox chemistry IV/437ff
- active framework involvement IV/437ff
- intrazeolitic electron transfer process IV/440f
- physical properties IV/415
- redox molecular sieve IV/429ff
- chiral complex IV/436
- enantioselective synthesis IV/436
- framework substitution IV/431
- membrane IV/435
- metal cluster IV/436f
- metal oxide cluster IV/436
- metal phthalocyanine in zeolite X/Y IV/434f
- non-titanium framework IV/433f
- organometallic complex encapsulated IV/434f
- schematic mechanism IV/432
- synthesis IV/430
- titanium framework IV/433
- specific II/95
- structure IV/414
- titanium containing (*see also* titanium silicalite) IV/431
- stabilization of photochemical intermediate via encapsulation IV/454f
- water oxidation by triphenylpyrylium IV/455
- water oxidation by $\text{Ru}(\text{bpy})_3^{2+}$ IV/445
- steady-state photochemistry IV/445
- permanent charge separation IV/445, IV/449
- photosensitized synthesis IV/445
- $\text{Ru}(\text{bpy})_3^{2+}$ -bipyridinium system IV/443
- transient spectroscopy IV/440f
- aromatic hydrocarbon as electron donor IV/440
- $\text{Ru}(\text{bpy})_3^{2+}$ IV/441
- $\text{Ru}(\text{bpy})_3^{2+}$ -bipyridinium model IV/444
- $\text{Ru}(\text{bpy})_3^{2+}$ -bipyridinium system IV/443
- sensitized electron transfer reaction IV/441
- X/Y IV/414f
- ZSM-5 IV/414f
- zero point V/341
- potential V/341
- vibration I/75
- zero-field mobility V/437
- zero-field splitting II/991
- zinc II/465, II/956
- zinc chlorins III/316
- zinc complexes III/482ff
- zinc ion IV/24
- zinc phthalocyanine II/292
- zinc porphyrins V/199
- zinc sulfide IV/249
- zinc tetraphenyl porphyrin II/292
- Zn- cytochrome *c* III/42
- Zn powder II/720
- Zn^{2+} IV/45
- Zn-cytochrome *c* III/44f
- ZnO V/602
- Zn-porphyrin III/7
- ZnS IV/236
- zone diagram I/434, I/439, I/449ff
- Z-scheme IV/170
- Z-scheme V/599, V/639
- Z-type deposition V/147
- zwitterionic II/297